SPRINGER
REFERENCE

H. WILLIAM STRAUSS
GIULIANO MARIANI
DUCCIO VOLTERRANI
STEVEN M. LARSON
EDITORS

Nuclear Oncology

From Pathophysiology to Clinical Applications

Second Edition

Springer

Nuclear Oncology

H. William Strauss
Giuliano Mariani
Duccio Volterrani
Steven M. Larson
Editors

Nuclear Oncology

From Pathophysiology to Clinical Applications

Second Edition

With 992 Figures and 166 Tables

Springer

Editors
H. William Strauss
Molecular Imaging and Therapy Service
Memorial Sloan Kettering Cancer Center
New York, NY, USA

Giuliano Mariani
University of Pisa
Regional Center of Nuclear Medicine
Pisa, Italy

Duccio Volterrani
University of Pisa
Regional Center of Nuclear Medicine
Pisa, Italy

Steven M. Larson
Molecular Imaging and Therapy Service
Memorial Sloan Kettering Cancer Center
New York, NY, USA

ISBN 978-3-319-26234-5 ISBN 978-3-319-26236-9 (eBook)
ISBN 978-3-319-26235-2 (print and electronic bundle)
https://doi.org/10.1007/978-3-319-26236-9

Library of Congress Control Number: 2017949354

1st edition: © Springer Science+Business Media New York 2013
© Springer International Publishing Switzerland 2017
This work is subject to copyright. All rights are reserved by the Publisher, whether the whole or part of the material is concerned, specifically the rights of translation, reprinting, reuse of illustrations, recitation, broadcasting, reproduction on microfilms or in any other physical way, and transmission or information storage and retrieval, electronic adaptation, computer software, or by similar or dissimilar methodology now known or hereafter developed.
The use of general descriptive names, registered names, trademarks, service marks, etc. in this publication does not imply, even in the absence of a specific statement, that such names are exempt from the relevant protective laws and regulations and therefore free for general use.
The publisher, the authors and the editors are safe to assume that the advice and information in this book are believed to be true and accurate at the date of publication. Neither the publisher nor the authors or the editors give a warranty, express or implied, with respect to the material contained herein or for any errors or omissions that may have been made. The publisher remains neutral with regard to jurisdictional claims in published maps and institutional affiliations.

Printed on acid-free paper

This Springer imprint is published by Springer Nature
The registered company is Springer International Publishing AG
The registered company address is: Gewerbestrasse 11, 6330 Cham, Switzerland

This book is dedicated to the scientists and clinicians who have developed the technology and life-saving procedures that we use to diagnose and treat our patients

Preface to the Second Edition

The role of nuclear medicine and molecular imaging in the diagnosis and therapy of cancer patients is growing. The rapid pace of change has been fueled by advances in understanding tumor biology, on the one hand, and the development of specifically targeted medical therapies, diagnostic agents, and radiotherapies, on the other. These advances suggested that an update and expansion of the contents of *Nuclear Oncology* would be timely. The second edition offers specialists in imaging, radiotherapy, cancer surgery, and oncology information that is current to manage patients with cancer.

There are three major changes in this edition: first, the text has been expanded to include more detailed information on performing specific procedures (e.g., radioguided surgery); second, the number of clinical cases has been increased to 170, to provide a broader range of examples, reflecting the clinical range of findings; and third, this edition will be available on Springer's electronic platform, allowing authors to continuously update the content of their chapters.

The second edition is divided into seven parts:

Part 1 consists of 13 chapters of basic science. The first chapter describes our understanding of cancer biology, including mechanisms of initiation of cancer and key tumor pathways that are attacked by specific therapeutic agents. This is followed by a discusion of mechanisms of molecular targeting and approved radiopharmaceuticals for single photon and positron imaging as well as therapy. These chapters are mirrored by three chapters describing agents in development for diagnosis and therapy. Chapters on physics, instrumentation, and radiobiology complete the basic science section.

Part 2 has 26 chapters that address the roles of imaging in the diagnosis and staging in specific types of cancer. Each chapter starts with a review of the epidemiology of the cancer, followed by a description of the typical clinical presentation, criteria for staging, therapeutic alternatives, and monitoring the effectiveness of treatment and suveillance following therapy.

Part 3 has seven chapters that address radionuclide therapy for the treatment of:
- Lymphoma
- Multiple myeloma and leukemias
- Thyroid cancer
- Neuroendocrine tumors, with separate chapters discussing the use of MIBG and peptide therapy
- Skeletal metastases
- Tumors of the liver and biliary tree with radiolabeled particulates

Part 4 has four chapters on specific applications of radioguided surgery. Three chapters describe the instrumentation, radiopharmaceuticals, and clinical goals of radioguided surgery in patients with breast cancer, malignant melanoma, and head and neck cancer. The last chapter of this section covers novel applications of the technology.

Part 5 describes the detection and management of heart disease in the cancer patient.

Part 6 presents adverse effects of cancer therapy.

Part 7 consists of 25 chapters of cases. These chapters of cases supplement the case examples illustrating specific points in each of the clinical chapters.

The text has a detailed index, which will help readers locate the information they seek to care for their patients.

We would like feedback from our readers about the text. Please address your comments to the editors.

New York, NY, USA — H. William Strauss, M.D.
Pisa, Italy — Giuliano Mariani, M.D.
Pisa, Italy — Duccio Volterrani, M.D.
New York, NY, USA — Steven M. Larson, M.D.

Preface to the First Edition

Cancer is a disease that was first described over 3500 years ago. While the designation *cancer* was coined by Hippocrates centuries later, descriptions of individual patients with the disease are found in Egyptian papyri dating from 1600 BCE [1]. Two papyri, the Edwin Smith papyrus (circa 1600 BCE) and the George Ebers papyrus (circa 1500 BCE), contain case descriptions consistent with modern observations of patients with cancer [2]. Hippocrates, in the fifth century BCE, suggested there was no cure for these maladies. Clinical observations and laboratory studies in the intervening 2500 years have led to a better understanding of the pathophysiology of cancer and the realization that the disease can be effectively treated.

There are four phases of most common malignant tumors: (1) Multiple genetic alterations lead to a cell losing control of cell division, apoptosis, and DNA repair, resulting in a malignant change, commonly referred to as transformation. (2) The transformed cells are genetically programmed to grow. (3) The proliferating transformed cells invade surrounding local tissues. (4) Some of the transformed cells depart from the local tumor mass and colonize a distant site, resulting in distant metastases [3].

Our current understanding of the pathophysiology of neoplasia has provided specific information on the numerous genetic changes in the transformed cell and on the impact of these changes on protein production by the transformed genome. Altered protein production may lead to an increase or decrease in the expression of receptors, production of unique epitopes on the cell surface, and changes in substrate utilization by the transformed cells.

Understanding the molecular mechanisms of specific neoplasms has led to the development of novel therapies, addressing specific control points in the life cycle of the transformed cell, and defined the need for detailed staging and characterization of the tumor, to develop a plan of treatment for the patient. This textbook provides the reader with information on the role of nuclear medicine in the diagnosis, staging, and treatment of patients with specific cancers. Each chapter provides material on the incidence, main pathophysiologic and clinical aspects of the disease, staging, and management of specific tumors, with a major focus on the points to be addressed by the nuclear medicine procedures.

The book is composed of seven parts: Basic science is covered in Chaps. 1–6: The first chapter reviews fundamental aspects of the biology of cancer and the tumor mass. The next two chapters describe the chemistry and

radio pharmacy for manufacturing single photon and positron emitting radiopharmaceuticals. The next three chapters deal with the physics of radionuclide decay, principles of instrumentation, followed by radiobiology and dosimetry. Clinical applications are covered in Chaps. 7–25. Radionuclide therapy is covered in Chaps. 26 and 27, and radioguided surgery is discussed in Chap. 28. Heart disease in the cancer patient is covered in Chap. 29, and adverse effects of cancer therapy in Chap. 30. In Part VII, Teaching Cases, the book concludes with a series of cases.

Each clinical chapter discusses the radionuclide procedures within an integrated framework identifying the information required for effective treatment of that specific tumor. The first part of each chapter provides a description of the epidemiology, etiology, histologic and pathophysiologic classification, prognosis, treatment, and the most common outcome for each type of cancer. This information on basic/clinical oncology is essential for the nuclear medicine specialist to understand how radionuclide imaging and therapy should be integrated with other imaging/therapeutic modalities to the benefit of the cancer patient. These discussions also highlight elements that should be contained in the report of the nuclear imaging procedure(s): depending on the type of cancer and the specific goal of imaging (initial staging, evaluation of response to therapy, or surveillance for recurrence), the Impression section of the report should clearly answer the clinical question.

New York, NY, USA H. William Strauss, M.D.
Pisa, Italy Giuliano Mariani, M.D.
Pisa, Italy Duccio Volterrani, M.D.
New York, NY, USA Steven M. Larson, M.D.

References

1. Dib EG, Kidd MR, Saltman DC. Case reports and the fight against cancer. J Med Case Reports. 2008;2:39.
2. Ebers Papyrus. http://www.newworldencyclopedia.org/entry/Ebers_papyrus. Accessed 2 Aug 2011.
3. Kumar V, Abbas AK, Fausto N. editors. Neoplasia. In: Robbins and Cotran pathologic basis of disease. 7th ed. St. Louis: Elsevier Saunders; 2005. p. 269–342.

Acknowledgment

The editors are indebted to our colleagues from different groups who contributed additional teaching cases in the concluding section of the book. Their contributions provide examples of how nuclear oncology plays a practical role in patient management at critical points in the care of patients. The following is a list of the groups and contributors:

- Biomedical Photonic Imaging Group, University of Twente, Enschede, The Netherlands: R.H.J.A. Slart.
- Department of Nuclear Medicine and PET Centre, Aarhus University Hospital, Denmark: K. Bouchelouche, C.M. Hoff, M.R. Jochumsen, M.A. Pedersen.
- Department of Nuclear Medicine and Molecular Imaging, University Medical Center Groningen, The Netherland: E.D. Telenga, A.W.J.M. Glaudemans, R.H.J.A. Slart.
- Division of Nuclear Medicine, Department of Biomedical Sciences, Humanitas University, Milan, Italy: A. Chiti, M. Kirienko, G. Manfrinato, L. Olivari.
- Endocrine Unit, Department of Clinical and Experimental Medicine, University of Pisa, Pisa, Italy: V. Cappagli, R. Elisei, C. Giani, A. Matrone, E. Molinaro, L. Pieruzzi, D. Viola.
- Institute of Nuclear Medicine, UCLH NHS Foundation Trust, London, UK: K. Al-Riyami, S. Al Shammari, J.P. Connelly, F. Fraioli, D. Neriman, S. Wan.
- Nuclear Medicine Department, Hospital Clinic Barcelona, Barcelona, Spain: S. Vidal-Sicart.
- Nuclear Medicine Service, Great Ormond Street Hospital, London, UK: L. Biassoni.
- Nuclear Medicine Unit, "S. Andrea" Hospital, La Spezia, Italy: A. Ciarmiello, V. Duce.
- Nuclear Medicine Unit, "S. Orsola-Malpighi" Hospital, Bologna, Italy: I. Bossert, S. Fanti, C. Nanni, E. Tabacchi.
- Nuclear Medicine Unit, "Santa Maria della Misericordia" Hospital, Rovigo, Italy: A.M. Maffione.
- Nuclear Medicine, University of Pretoria and Steve Biko Academic Hospital, Pretoria, South Africa: T. Boshomane, T. Lengana, F. Reyneke, M. Sathekge.

- Nuclear Medicine/PET-CT, Dana-Farber Cancer Institute, Harvard Medical School, Boston, Massachusetts, USA: H.A. Jacene, C.G. Sakellis, A.D. Van den Abbeele, V. Yerubadi.
- Radiotherapy Unit, "Maggiore della Carità" University Hospital and Department of Translational Medicine, University of "Piemonte Orientale," Novara, Italy: L. Deantonio, M. Krengli.
- Section of Medical Physics, "Maggiore della Carità" University Hospital, Novara, Italy: R. Matheoud.
- Section of Nuclear Medicine, "Maggiore della Carità" University Hospital, Novara, Italy: F. Orsini, G.M. Sacchetti.

Contents

Volume 1

Part I Basic Science 1

1 Cancer Biology of Molecular Imaging 3
Steven M. Larson

2 Principles of Molecular Targeting for Radionuclide Therapy 35
William C. Eckelman, Marie Boyd, and Robert J. Mairs

3 Single-Photon-Emitting Radiopharmaceuticals for Diagnostic Applications 67
Federica Orsini, Erinda Puta, Alice Lorenzoni, Paola Anna Erba, and Giuliano Mariani

4 Positron-Emitting Radiopharmaceuticals for Diagnostic Applications 85
Federica Orsini, Alice Lorenzoni, Erinda Puta, and Giuliano Mariani

5 Radiopharmaceuticals for Therapy 99
Federica Orsini, Sara Mazzarri, Erinda Puta, Federica Guidoccio, Alice Lorenzoni, and Giuliano Mariani

6 Novel Single-Photon-Emitting Radiopharmaceuticals for Diagnostic Applications 115
Federica Orsini, Federica Guidoccio, Erinda Puta, and Giuliano Mariani

7 Novel Positron-Emitting Radiopharmaceuticals 129
Mirkka Sarparanta, Dustin W. Demoin, Brendon E. Cook, Jason S. Lewis, and Brian M. Zeglis

8 Novel Radiopharmaceuticals for Therapy 173
Federica Guidoccio, Sara Mazzarri, Federica Orsini, Paola Anna Erba, and Giuliano Mariani

9 Physics of Nuclear Oncology 199
Dale L. Bailey and John L. Humm

10 Instrumentation for Positron Emission Imaging 217
Pat Zanzonico

11 Instrumentation for Single-Photon Emission Imaging 251
Pat Zanzonico

12 Instrumentation for Intraoperative Detection 275
Pat Zanzonico

13 Radiobiology and Radiation Dosimetry in Nuclear Medicine 305
Massimo Salvatori, Marta Cremonesi, Luca Indovina, Marco Chianelli, Massimiliano Pacilio, Carlo Chiesa, and Pat Zanzonico

Part II Diagnostic Applications of Nuclear Medicine 351

14 Diagnostic Applications of Nuclear Medicine: Lymphomas 353
Heather A. Jacene, Sree Harsha Tirumani, and Richard L. Wahl

15 Diagnostic Applications of Nuclear Medicine: Multiple Myeloma 395
Martina Sollini, Sara Galimberti, Roberto Boni, and Paola Anna Erba

16 Diagnostic Applications of Nuclear Medicine: Leukemias 435
Martina Sollini, Sara Galimberti, Roberto Boni, and Paola Anna Erba

17 Diagnostic Applications of Nuclear Medicine: Brain Tumors 467
Giampiero Giovacchini, Mattia Riondato, Elisabetta Giovannini, and Andrea Ciarmiello

18 Diagnostic Applications of Nuclear Medicine: Head and Neck Cancer 507
Heiko Schöder

19 Diagnostic Applications of Nuclear Medicine: Thyroid Tumors 545
Rossella Elisei, Laura Agate, Sara Mazzarri, Valeria Bottici, Federica Guidoccio, Eleonora Molinaro, Giuseppe Boni, Marco Ferdeghini, and Giuliano Mariani

20 Diagnostic Applications of Nuclear Medicine: Parathyroid Tumors 585
Federica Guidoccio, Sara Mazzarri, Salvatore Mazzeo, and Giuliano Mariani

21 Diagnostic Applications of Nuclear Medicine: Breast Cancer 613
Marsha Camilla Lynch, Jean H. Lee, and David A. Mankoff

22 Diagnostic Applications of Nuclear Medicine: Lung and Mediastinal Tumors 639
Elite Arnon, Thida Win, Ora Israel, Ludmila Guralnik, and Simona Ben-Haim

Volume 2

23 Diagnostic Applications of Nuclear Medicine: Esophageal Cancers 685
Christopher G. Sakellis, Heather A. Jacene, and Annick D. Van den Abbeele

24 Diagnostic Applications of Nuclear Medicine: Gastric Cancers 697
Christopher G. Sakellis, Heather A. Jacene, and Annick D. Van den Abbeele

25 Diagnostic Applications of Nuclear Medicine: Gastrointestinal Stromal Tumors 709
Christopher G. Sakellis, Heather A. Jacene, and Annick D. Van den Abbeele

26 Diagnostic Applications of Nuclear Medicine: Tumors of the Liver and Biliary Tract 725
Mustafa Raoof, Steven M. Larson, and Yuman Fong

27 Diagnostic Applications of Nuclear Medicine: Pancreatic Cancer 749
Elena Tabacchi, Cristina Nanni, Irene Bossert, Anna Margherita Maffione, and Stefano Fanti

28 Diagnostic Applications of Nuclear Medicine: Colorectal Cancer 777
Ettore Pelosi, Désirée Deandreis, Laura Cassalia, and Daniele Penna

29 Diagnostic Applications of Nuclear Medicine: Neuroendocrine Tumors 799
Lisa Bodei, Mark Kidd, Laura Gilardi, Duccio Volterrani, Giovanni Paganelli, Chiara M. Grana, and Irvin M. Modlin

30 Diagnostic Applications of Nuclear Medicine: Kidney and Bladder Cancer 839
Kirsten Bouchelouche

31 Diagnostic Applications of Nuclear Medicine: Prostatic Cancer 883
Emilio Bombardieri, Maria Grazia Sauta, Lucia Setti, Roberta Meroni, Gianluigi Ciocia, and Laura Evangelista

32 Diagnostic Applications of Nuclear Medicine: Testicular Cancer 925
Abedallatif AlSharif, Serena Chiacchio, and Giampiero Giovacchini

33 Diagnostic Applications of Nuclear Medicine: Penile Cancer 943
Serena Chiacchio, Abedallatif AlSharif, Zia Saad, Giampiero Giovacchini, and Jamshed Bomanji

34 Diagnostic Applications of Nuclear Medicine: Vulvar Cancer 959
Sonia Mahajan, Weining Ma, and Neeta Pandit-Taskar

35 Diagnostic Applications of Nuclear Medicine: Uterine Cancers 979
Neeta Pandit-Taskar, Sonia Mahajan, and Weining Ma

36 Diagnostic Applications of Nuclear Medicine: Ovarian Cancer 1021
Neeta Pandit-Taskar, Sonia Mahajan, and Weining Ma

37 Diagnostic Applications of Nuclear Medicine: Sarcomas . . . 1047
Janet F. Eary

38 Diagnostic Applications of Nuclear Medicine: Malignant Melanoma 1065
Andrew M. Scott, Marika Ciprotti, and Sze-Ting Lee

39 Diagnostic Applications of Nuclear Medicine: Pediatric Cancers 1103
Thomas Pfluger, Andrea Ciarmiello, Giampiero Giovacchini, Françoise Montravers, Hubert Ducou Le Pointe, Judith Landman-Parker, Martina Meniconi, and Christiane Franzius

Part III Radionuclide Therapy **1139**

40 Radionuclide Therapy of Lymphomas 1141
Heather A. Jacene, Sree Harsha Tirumani, and Richard L. Wahl

41 Radionuclide Therapy of Leukemias and Multiple Myeloma 1157
Martina Sollini, Sara Galimberti, Roberto Boni, and Paola Anna Erba

42 Radionuclide Therapy of Thyroid Tumors 1197
Rossella Elisei, Laura Agate, Sara Mazzarri, Valeria Bottici, Federica Guidoccio, Eleonora Molinaro, Giuseppe Boni, Marco Ferdeghini, and Giuliano Mariani

43 Neuroendocrine Tumors: Therapy with Radiolabeled Peptides 1243
Lisa Bodei, Laura Gilardi, Duccio Volterrani, Giovanni Paganelli, Chiara M. Grana, Mark Kidd, and Irvin M. Modlin

44 Neuroendocrine Tumors: Therapy with ^{131}I-MIBG 1269
Jorge A. Carrasquillo and Clara C. Chen

45 Targeted Radionuclide Therapy for Bone Metastasis 1307
Neeta Pandit-Taskar and Chaitanya R. Divgi

46 Radionuclide Therapy of Tumors of the Liver and Biliary Tract 1337
Giuseppe Boni, Federica Guidoccio, Duccio Volterrani, and Giuliano Mariani

Volume 3

Part IV Radioguided Surgery **1361**

47 Radioguided Surgery for Breast Cancer 1363
Francesco Giammarile, Federica Orsini, Renato A. Valdés Olmos, Sergi Vidal-Sicart, Armando E. Giuliano, and Giuliano Mariani

48 Radioguided Surgery for Malignant Melanoma 1401
Sergi Vidal-Sicart, Federica Orsini, Francesco Giammarile, Giuliano Mariani, and Renato A. Valdés Olmos

49 Radioguided Surgery for Head and Neck Cancer 1433
Federica Orsini, Erinda Puta, Renato A. Valdés Olmos, Sergi Vidal-Sicart, Francesco Giammarile, and Giuliano Mariani

50 Radioguided Surgery: Novel Applications 1451
Renato A. Valdés Olmos, Federica Orsini, Francesco Giammarile, Sergi Vidal-Sicart, and Giuliano Mariani

Part V Heart Disease in the Cancer Patient **1481**

51 Imaging the Heart in the Cancer Patient 1483
H. William Strauss and Josef J. Fox

Part VI Adverse Effects of Cancer Therapy **1511**

52 Nuclear Medicine in the Assessment of Adverse Effects of Cancer Therapy in the Lung, Kidney, and Gastrointestinal Tract 1513
Diego Alfonso López Mora and Ignasi Carrió

Part VII Teaching Cases in Nuclear Oncology (with Contributions from Various Authors) 1529

53 Teaching Cases in Nuclear Oncology: Lymphomas 1531
Kimiteru Ito, Somali Gavane, and Heiko Schöder

54 Teaching Cases in Nuclear Oncology: Multiple Myeloma . . . 1545
Kimiteru Ito, Somali Gavane, and Heiko Schöder

55 Teaching Cases in Nuclear Oncology: Brain Tumors 1557
Alice Lorenzoni, Alessandra Alessi, and Flavio Crippa

56 Teaching Cases in Nuclear Oncology: Head and Neck Cancer 1569
Kimiteru Ito, Somali Gavane, and Heiko Schöder

57 Teaching Cases in Nuclear Oncology: Thyroid Tumors 1585
Kimiteru Ito, Somali Gavane, and Heiko Schöder

58 Teaching Cases in Nuclear Oncology: Parathyroid Tumors 1607
Kimiteru Ito, Somali Gavane, and Heiko Schöder

59 Teaching Cases in Nuclear Oncology: Breast Cancer 1613
Alice Lorenzoni, Alessandra Alessi, and Flavio Crippa

60 Teaching Cases in Nuclear Oncology: Lung and Mediastinal Tumors 1627
Alice Lorenzoni, Alessandra Alessi, and Flavio Crippa

61 Teaching Cases in Nuclear Oncology: Esophageal Cancers 1643
Duccio Volterrani, Giulia Puccini, Sara Mazzarri, and Federica Guidoccio

62 Teaching Cases in Nuclear Oncology: Gastric Cancers 1655
Duccio Volterrani, Giulia Puccini, Sara Mazzarri, and Federica Guidoccio

63 Teaching Cases in Nuclear Oncology: Small Bowel Cancers 1667
Duccio Volterrani, Giulia Puccini, Sara Mazzarri, and Federica Guidoccio

64 Teaching Cases in Nuclear Oncology: Tumors of the Liver and Biliary Tract 1681
Duccio Volterrani, Giulia Puccini, Sara Mazzarri, and Federica Guidoccio

65 Teaching Cases in Nuclear Oncology: Pancreatic Cancer . . . 1699
Alice Lorenzoni, Alessandra Alessi, and Flavio Crippa

66 Teaching Cases in Nuclear Oncology: Colorectal Cancer . . . 1715
Alice Lorenzoni, Alessandra Alessi, and Flavio Crippa

67 Teaching Cases in Nuclear Oncology: Neuroendocrine Tumors 1729
Alice Lorenzoni, Alessandra Alessi, and Flavio Crippa

68 Teaching Cases in Nuclear Oncology: Kidney and Bladder Cancer 1749
Duccio Volterrani, Giulia Puccini, Sara Mazzarri, and Federica Guidoccio

69 Teaching Cases in Nuclear Oncology: Prostatic Cancer 1771
Duccio Volterrani, Giulia Puccini, Sara Mazzarri, and Federica Guidoccio

70 Teaching Cases in Nuclear Oncology: Testicular Cancer . . . 1799
Kimiteru Ito, Somali Gavane, and Heiko Schöder

71 Teaching Cases in Nuclear Oncology: Penile Cancer 1805
Kimiteru Ito, Somali Gavane, and Heiko Schöder

72 Teaching Cases in Nuclear Oncology: Vulvar Cancer 1813
Alice Lorenzoni, Alessandra Alessi, and Flavio Crippa

73 Teaching Cases in Nuclear Oncology: Uterine Cancers 1823
Alice Lorenzoni, Alessandra Alessi, and Flavio Crippa

74 Teaching Cases in Nuclear Oncology: Ovarian Cancer 1841
Alice Lorenzoni, Alessandra Alessi, and Flavio Crippa

75 Teaching Cases in Nuclear Oncology: Sarcomas 1849
Alice Lorenzoni, Alessandra Alessi, and Flavio Crippa

76 Teaching Cases in Nuclear Oncology: Malignant Melanoma 1865
Alice Lorenzoni, Alessandra Alessi, and Flavio Crippa

77 Teaching Cases in Nuclear Oncology: Pediatric Cancers . . . 1881
Duccio Volterrani, Giulia Puccini, Sara Mazzarri, Federica Guidoccio, and Lorenzo Biassoni

78 Teaching Cases in Nuclear Oncology: Investigating the Heart in Cancer Patients 1917
Josef J. Fox and H. William Strauss

Index 1929

About the Editors

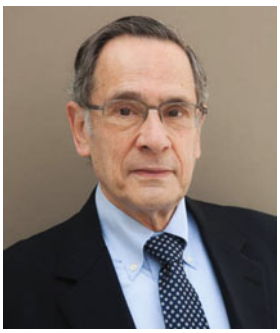

H. William Strauss, M.D., is Professor of Medicine at Icahn School of Medicine, Mount Sinai Hospital, and Attending Physician Emeritus of Molecular Imaging and Therapy Service at Memorial Sloan Kettering Cancer Center. He additionally serves as Professor of Radiology in the Department of Nuclear Medicine at Cornell University, Weill School of Medicine. He is a prolific writer with over 550 original articles, over 70 book chapters, and nine books in his portfolio. He has additionally served on the editorial board of several peer-reviewed journals, including *Journal of Nuclear Medicine*, *European Journal of Nuclear Medicine and Molecular Imaging*, *Journal of Nuclear Cardiology*, *Quarterly Journal of Nuclear Medicine*, and *Annals of Nuclear Medicine*.

Giuliano Mariani From 2001 to 2014, Giuliano Mariani has been Full Professor of Nuclear Medicine, Director of the Regional Center of Nuclear Medicine, and Director of the Specialty School of Nuclear Medicine at the University of Pisa (Pisa, Italy). From 1994 to 2001, he was Associate Professor of Nuclear Medicine, Director of the Nuclear Medicine Service, and Director of the Specialty School of Nuclear Medicine at the University of Genoa (Genoa, Italy).

He obtained his medical degree in 1968 at the Catholic University of Rome (Italy). For the next decade, his postgraduate training prepared him as a specialist in internal medicine, nuclear medicine, medical nephrology, and radiology. He has been a Visiting Scientist at the National Cancer Institute in Bethesda (Maryland, USA) from 1975 to 1977 and a Visiting Professor at the Harvard Medical School in Boston (Massachusetts, USA) from 1986 to 1990.

Initial investigations carried out at the CNR Institute of Clinical Physiology and at the University of Pisa (Pisa, Italy) dealt with the pharmacokinetics of radiolabeled tracers for metabolic studies of endogenous proteins and hormones in various clinical conditions. In the subsequent studies, the interests of Giuliano Mariani have broadened to encompass virtually all fields of Nuclear Medicine for both diagnostic and therapeutic applications. Nevertheless, his main research interests have focused on tumor targeting for diagnosis or therapy with radiopharmaceuticals; he has been the Senior or Principal Investigator on many research projects, several of which were international collaborations. Thanks to his important contributions to the whole field of Nuclear Medicine, in 2014 Giuliano Mariani has been granted honorary membership in the European Association of Nuclear Medicine (EANM), while the Italian Association of Nuclear Medicine (AIMN) bestowed to him the same recognition in 2017. He is a member of the Society of Nuclear Medicine and Molecular Imaging (SNMMI).

Giuliano Mariani serves or has served on the Editorial Board of several journals including, among others devoted to Nuclear Medicine and diagnostic imaging in general, *The Journal of Nuclear Medicine* (currently as an Associate Editor – International), the *European Journal of Nuclear Medicine and Molecular Imaging*, the *American Journal of Roentgenology*, the *Journal of Nuclear Biology and Medicine*, the *Journal of Nuclear Medicine and Allied Sciences*, and the *Quarterly Journal of Nuclear Medicine*. He is also an active referee for many international journals and has been Author/Editor of 16 books and over 80 chapters in books. In addition, he has authored/coauthored over 315 papers in international peer-reviewed journals.

Over the past decade, Giuliano Mariani has served on several occasions as and Expert Consultant for the International Atomic Energy Agency (IAEA, Vienna, Austria), both for in-the-field training missions mostly in low- and middle-income countries to initiate specific Nuclear Medicine applications and for hosting at the Regional Center of Nuclear Medicine in Pisa IAEA Fellows for training in the practice of Nuclear Medicine. These activities have been conducted in collaboration with countries with such diverse levels of development as Albania, Algeria, Chile, Colombia, Cuba, Egypt, Estonia, India, Japan, Lithuania, Lybia, Malaysia, Pakistan, People's Republic of China, South Africa, Sudan, Sultanate of Oman, and Thailand.

Duccio Volterrani is currently Full Professor of Nuclear Medicine, Director of the Regional Center of Nuclear Medicine, and Director of the Post-graduate Specialty School in Nuclear Medicine of the University of Pisa (Pisa, Italy). In 2014, he became Associate Professor of Nuclear Medicine at the University of Pisa, after serving as Assistant Professor at the same University since 1998. Before joining the University of Pisa in 1998, Duccio Volterrani had served as Attending Physician at the Nuclear Medicine Service of the University Hospital of Siena (Siena, Italy) between 1993 and 1998.

After obtaining his medical degree in 1987 at the University of Pisa (Pisa, Italy), Dr. Volterrani was granted Research Fellowships (up until 1993) at the CNR Institute of Clinical Physiology for the analysis of data from the European multicenter study on the diagnostic efficacy of captopril renography in renovascular hypertension and for the investigations on the pathophysiologic changes of systolic and diastolic parameters, assessed by means of radionuclide techniques, in hypertensive cardiomyopathy.

Dr. Volterrani currently holds official courses on diagnostic imaging and nuclear medicine at the University of Pisa, including courses for the Medical School and for the School of Technologists in Diagnostic Imaging and Radiation Oncology, as well as courses for the Post-graduate Specialty Schools in Nuclear Medicine, in Diagnostic Radiology, and in Medical Oncology of the University of Pisa (Pisa, Italy). In 2003, he has been a Visiting Professor at the Nuclear Medicine Service of the Memorial Sloan-Kettering Cancer Center (New York, NY, USA).

Dr. Volterrani's current interests in clinical investigations span virtually the whole spectrum of applications of nuclear medicine (both for diagnosis and for therapy with radionuclides), with a major focus on radionuclide evaluation of dementias and parkinsonisms (through regional blood flow, receptor analysis, and amyloid imaging), PET/CT in oncology, radionuclide therapy of tumors, diagnostic imaging of coronary artery disease, and new tracers for tumor targeting.

Dr. Volterrani is a member of the Italian Association of Nuclear Medicine (AIMN, for which he has served several terms in the Board of Directors and as responsible for quality management for the continuing medical education program), of the European Association of Nuclear Medicine (EANM), and of the Society of Nuclear Medicine and Molecular Imaging (SNMMI). He serves in the Editorial Board of the *Quarterly Journal of Nuclear Medicine* and is also an active referee for many international journals in the field of Nuclear Medicine. He has authored/coauthored over 80 papers in international peer-reviewed journals, and in addition has been Coeditor of 3 books and over 40 chapters in books.

Steven M. Larson M.D., FACNM, FACR is the Donna and Benjamin M. Rosen Chair and Attending in the Molecular Imaging and Therapy Service within the Department of Radiology, as well as the Coleader of the Imaging and Radiation Sciences Program, a component of the Cancer Center Support Grant, at Memorial Sloan Kettering Cancer Center. He serves as Director of the Center for Radioimmunotherapy and Theranostics at the Ludwig Center and member and Lab Head of the Molecular Pharmacology Program at Sloan Kettering Cancer Institute. He is also a Professor of Radiology at Cornell University Medical Center in New York, NY.

Larson's primary expertise is in molecular imaging, targeted radiodiagnosis, and therapy using small molecules and monoclonal antibodies. Dual-boarded in nuclear medicine and internal medicine, Larson has clinical skills in oncology, cancer immunology, and clinical thyroid cancer. He has been responsible for directing and developing successful nuclear medicine and PET programs at several major institutions in the USA, including the Veteran Administration Hospitals in Portland and Vancouver; University of Oregon, Portland; Seattle Veterans Administration Hospital; Clinical Center, National Institutes of Health (NIH); and Memorial Sloan Kettering Cancer Center. He has extensive experience as an Advisor to public and private institutions, having served, among other appointments, as a member of what is now the

MEDI grant review committee of NIH, the Department of Energy Office of Science's Advisory Committee, and the American Board of Nuclear Medicine, and as Chair of the Radiopharmaceutical Advisory Committee of the USFDA, Cochair of the National Research Council of the NAS Committee on Molybdenum-99 production with nonenriched Uranium 235, and Chair of the Molecular Imaging Committee of RSNA. He is now Chair of the Clinical Imaging Steering Committee of the National Cancer Institute and Chair of the Clinical "Impact" Study Section of NIH, as well as a member of the National Academy of Medicine. He has received numerous awards for excellence including the Wylie Prize of the USFDA, the Hevesy Award, and Cassen Prize of the Society of Nuclear Medicine, USA. He is an inventor on seven patents. He has published over 600 peer-reviewed publications in prestigious journals, and his current H-factor is approximately 100. He has trained more than 50 residents in nuclear medicine who are now ABNM-certified.

Contributors

Laura Agate Endocrine Unit, Department of Clinical and Experimental Medicine, University of Pisa, Pisa, Italy

Alessandra Alessi Nuclear Medicine Division, IRCCCS National Cancer Institute, Milan, Italy

Abedallatif AlSharif Department of Radiology and Nuclear Medicine, University of Jordan, Jordan University Hospital, Amman, Jordan

Elite Arnon Department of Nuclear Medicine, Rambam Health Care Campus, Haifa, Israel

Dale L. Bailey Faculty of Health Sciences, The University of Sydney, Camperdown, NSW, Australia

Simona Ben-Haim University College London and UCL Hospitals, NHS Trust, London, UK

Department of Nuclear Medicine, The Chaim Sheba Medical Center, Tel-Hashomer, Israel

Lorenzo Biassoni Nuclear Medicine Service, Great Ormond Street Hospital, London, UK

Lisa Bodei Molecular Imaging and Therapy Service, Department of Radiology, Memorial Sloan Kettering Cancer Center, New York, NY, USA

Jamshed Bomanji Institute of Nuclear Medicine, University College London Hospitals, NHS Foundation Trust, University College Hospital, London, UK

Emilio Bombardieri Department of Nucleare Medicine, Humanitas Gavazzeni Hospital, Bergamo, Italy

Nuclear Medicine Unit, "Humanitas Gavazzeni" Hospital, Bergamo, Italy

Giuseppe Boni Regional Center of Nuclear Medicine, University Hospital of Pisa, Pisa, Italy

Roberto Boni Regional Center of Nuclear Medicine, Department of Translational Research and New Technology in Medicine, University of Pisa, Pisa, Italy

Irene Bossert Nuclear Medicine Unit, "S. Orsola-Malpighi" University Hospital, Bologna, Italy

Nuclear Medicine Service, "Fondazione Salvatore Maugeri" IRCCS, Pavia, Italy

Valeria Bottici Endocrine Unit, Department of Clinical and Experimental Medicine, University of Pisa, Pisa, Italy

Kirsten Bouchelouche Department of Nuclear Medicine and PET Centre, Aarhus University Hospital, Aarhus, Denmark

Marie Boyd Strathclyde Institute of Pharmacy and Biomedical Sciences, Strathclyde University, Glasgow, UK

Jorge A. Carrasquillo Molecular Imaging and Therapy Service, Memorial Sloan-Kettering Cancer Center, New York, NY, USA

Ignasi Carrió Department of Nuclear Medicine, Hospital Sant Pau, Autonomous University of Barcelona, Barcelona, Spain

Laura Cassalia Nuclear Medicine Unit, Department of Biomedical Sciences and of Morphologic and Functional Images, University of Messina, Messina, Italy

Clara C. Chen Division of Nuclear Medicine, Department of Radiology and Imaging Sciences, Clinical Center, National Institutes of Health, Bethesda, MD, USA

Serena Chiacchio Regional Center of Nuclear Medicine, University Hospital of Pisa, Pisa, Italy

Marco Chianelli Department of Endocrinology, Ospedale Regina Apostolorum, Albano, Rome, Italy

Carlo Chiesa Nuclear Medicine Department, National Cancer Institute, Milan, Italy

Andrea Ciarmiello Nuclear Medicine Department, Institute of Nuclear Medicine, S. Andrea Hospital, La Spezia, Italy

Gianluigi Ciocia Nuclear Medicine Unit, "Humanitas Gavazzeni" Hospital, Bergamo, Italy

Radiotherapy Unit, "Humanitas Gavazzeni" Hospital, Bergamo, Italy

Marika Ciprotti Global Clinical Research Oncology, Bristol-Myers Squibb, London, UK

Brendon E. Cook Department of Radiology, Memorial Sloan Kettering Cancer Center, New York, NY, USA

Department of Chemistry, Hunter College of the City University of New York, New York, NY, USA

Ph.D. Program in Chemistry, Graduate Center of the City University of New York, New York, NY, USA

Marta Cremonesi Department of Medical Physics, European Institute of Oncology, Milan, Italy

Flavio Crippa Nuclear Medicine Division, IRCCCS National Cancer Institute, Milan, Italy

Désirée Deandreis Department of Medical Sciences Nuclear Medicine, University of Torino, Torino, Italy

Dustin W. Demoin Department of Radiology, Memorial Sloan Kettering Cancer Center, New York, NY, USA

Chaitanya R. Divgi Jenkintown, PA, USA

Janet F. Eary Cancer Imaging Program, National Cancer Institute, National Institutes of Health, Bethesda, MD, USA

William C. Eckelman Molecular Tracer, Bethesda, MD, USA

Rossella Elisei Endocrine Unit, Department of Clinical and Experimental Medicine, University of Pisa, Pisa, Italy

Paola Anna Erba Regional Center of Nuclear Medicine, Department of Translational Research and Advanced Technologies in Medicine, University of Pisa, Pisa, Italy

Laura Evangelista Nuclear Medicine and Molecular Imaging Unit, Veneto Institute of Oncology IOV - IRCCS, Padua, Italy

Stefano Fanti Nuclear Medicine Unit, "S. Orsola-Malpighi" University Hospital, Bologna, Italy

Marco Ferdeghini Nuclear Medicine Unit, Department of Diagnostics and Public Health, University of Verona, Verona, Italy

Yuman Fong Department of Surgery, City of Hope National Medical Center, Duarte, CA, USA

Josef J. Fox Department of Radiology, Memorial Sloan Kettering Cancer Center, New York, NY, USA

Christiane Franzius Nuclear Medicine and PET/CT Centre Bremen, Bremen, Germany

Centre of Modern Diagnostics (ZEMODI), MRI and MR/PET, Bremen, Germany

Sara Galimberti Hematology Unit, University of Pisa, Pisa, Italy

Somali Gavane Division of Nuclear Medicine, Department of Radiology, Mount Sinai Hospital, New York, NY, USA

Francesco Giammarile Nuclear Medicine and Diagnostic Imaging Section, Division of Human Health, Department of Nuclear Sciences and Applications, International Atomic Energy Agency, Vienna, Austria

Laura Gilardi Division of Nuclear Medicine, European Institute of Oncology, Milan, Italy

Giampiero Giovacchini Nuclear Medicine Department, S. Andrea Hospital, La Spezia, Italy

Elisabetta Giovannini Nuclear Medicine Department, Institute of Nuclear Medicine, S. Andrea Hospital, La Spezia, Italy

Armando E. Giuliano Surgical Oncology, Samuel Oschin Comprehensive Cancer Institute, Cedars-Sinai, Los Angeles, CA, USA

Chiara M. Grana Division of Nuclear Medicine, European Institute of Oncology, Milan, Italy

Federica Guidoccio Regional Center of Nuclear Medicine, Department of Translational Research and Advanced Technologies in Medicine and Surgery, University of Pisa, Pisa, Italy

Ludmila Guralnik The Bruce Rappaport Faculty of Medicine, Technion-Israel Institute of Technology, Haifa, Israel

Department of Radiolody, Rambam Health Care Campus, Haifa, Israel

John L. Humm Department of Medical Physics, Memorial Sloan Kettering Cancer Center, New York, NY, USA

Luca Indovina Department of Medical Physics - Policlinico Universitario A. Gemelli, Rome, Italy

Ora Israel Department of Nuclear Medicine, Rambam Health Care Campus, Haifa, Israel

The Bruce Rappaport Faculty of Medicine, Technion-Israel Institute of Technology, Haifa, Israel

Kimiteru Ito Department of Radiology, Molecular Imaging and Therapy service, Memorial Sloan Kettering Cancer Center, New York, NY, USA

Heather A. Jacene Nuclear Medicine/PET-CT, Department of Imaging, Dana-Farber Cancer Institute and Department of Radiology, Brigham and Women's Hospital, Harvard Medical School, Boston, MA, USA

Mark Kidd Wren Laboratories, Branford, CT, USA

Judith Landman-Parker Department of Pediatric Oncology, Armand-Trousseau Hospital, Assistance Publique Hôpitaux de Paris, Pierre et Marie Curie University, Paris, France

Steven M. Larson Molecular Imaging and Therapy Service, Memorial Sloan Kettering Cancer Center, New York, NY, USA

Hubert Ducou Le Pointe Department of Radiology, Armand-Trousseau Hospital, Assistance Publique Hôpitaux de Paris, Pierre et Marie Curie University, Paris, France

Jean H. Lee Department of Radiology, University of Washington, Seattle, WA, USA

Seattle Cancer Care Alliance, Seattle, WA, USA

Sze-Ting Lee Olivia Newton-John Cancer Research Institute and La Trobe University, Melbourne, VIC, Australia

Department of Molecular Imaging and Therapy, Austin Health, Melbourne, VIC, Australia

Jason S. Lewis Radiochemistry and Imaging Sciences Service, Department of Radiology, Memorial Sloan Kettering Cancer Center, New York, NY, USA

Program in Molecular Pharmacology, Memorial Sloan Kettering Cancer Center, New York, NY, USA

Department of Radiology, Weill Cornell Medical College, New York, NY, USA

Department of Pharmacology, Weill Cornell Medical College, New York, NY, USA

Diego Alfonso López Mora Department of Nuclear Medicine, Hospital Sant Pau, Autonomous University of Barcelona, Barcelona, Spain

Alice Lorenzoni Nuclear Medicine Division, IRCCCS National Cancer Institute, Milan, Italy

Marsha Camilla Lynch Division of Nuclear Medicine, Department of Radiology, University of Pennsylvania, Philadelphia, PA, USA

Division of Nuclear Medicine and Clinical Molecular Imaging, University of Pennsylvania Health System, Philadelphia, PA, USA

Weining Ma Department of Radiology, Memorial Sloan Kettering Cancer Center, New York, NY, USA

Anna Margherita Maffione Nuclear Medicine Unit, Ospedale Santa Maria della Misericordia, Rovigo, Italy

Sonia Mahajan Department of Radiology, Memorial Sloan Kettering Cancer Center, New York, NY, USA

Robert J. Mairs Institute of Cancer Sciences, University of Glasgow, Glasgow, UK

David A. Mankoff Division of Nuclear Medicine, Department of Radiology, University of Pennsylvania, Philadelphia, PA, USA

Division of Nuclear Medicine and Clinical Molecular Imaging, University of Pennsylvania Health System, Philadelphia, PA, USA

Giuliano Mariani Regional Center of Nuclear Medicine, Department of Translational Research and Advanced Technologies in Medicine and Surgery, University of Pisa, Pisa, Italy

Sara Mazzarri Regional Center of Nuclear Medicine, Department of Translational Research and Advanced Technologies in Medicine and Surgery, University of Pisa, Pisa, Italy

Salvatore Mazzeo Department of Diagnostic and Interventional Radiology, University of Pisa, Pisa, Italy

Martina Meniconi Regional Center of Nuclear Medicine, University of Pisa, Pisa, Italy

Roberta Meroni Radiology Unit, "Humanitas Gavazzeni" Hospital, Bergamo, Italy

Irvin M. Modlin Wren Laboratories, Branford, CT, USA

Department of Surgery, Yale School of Medicine, New Haven, CT, USA

Eleonora Molinaro Endocrine Unit, Department of Clinical and Experimental Medicine, University of Pisa, Pisa, Italy

Françoise Montravers Department of Nuclear Medicine, Tenon Hospital, Assistance Publique Hôpitaux de Paris, Pierre et Marie Curie University, Paris, France

Cristina Nanni Nuclear Medicine Unit, "S. Orsola-Malpighi" University Hospital, Bologna, Italy

Federica Orsini Nuclear Medicine Unit, "Maggiore della Carità" University Hospital, Novara, Italy

Massimiliano Pacilio Department of Medical Physics, Azienda Ospedaliera San Camillo Forlanini, Rome, Italy

Giovanni Paganelli Nuclear Medicine and Radiometabolic Units, Istituto Scientifico Romagnolo per lo Studio e la Cura dei Tumori (IRST) IRCCS, Meldola, Italy

Neeta Pandit-Taskar Department of Radiology, Memorial Sloan Kettering Cancer Center, New York, NY, USA

Department of Radiology, Weill Cornell Medical College, New York, NY, USA

Ettore Pelosi PET Center, Affidea IRMET, Torino, Italy

Daniele Penna PET Center, Affidea IRMET, Torino, Italy

Thomas Pfluger Department of Nuclear Medicine, Ludwig-Maximilians-University of Munich, Munich, Germany

Giulia Puccini Regional Center of Nuclear Medicine, University of Pisa, Pisa, Italy

Erinda Puta Nuclear Medicine Unit, "Maggiore della Carità" University Hospital, Novara, Italy

Mustafa Raoof Department of Surgery, City of Hope National Medical Center, Duarte, CA, USA

Mattia Riondato Nuclear Medicine Department, Institute of Nuclear Medicine, S. Andrea Hospital, La Spezia, Italy

Zia Saad Institute of Nuclear Medicine, University College London Hospitals, NHS Foundation Trust, University College Hospital, London, UK

Christopher G. Sakellis Department of Imaging, Dana-Farber Cancer Institute, Boston, MA, USA

Department of Radiology, Brigham and Women's Hospital, Boston, MA, USA

Harvard Medical School, Boston, MA, USA

Center for Biomedical Imaging in Oncology, Dana-Farber Cancer Institute, Boston, MA, USA

Tumor Imaging Metrics Core, Dana-Farber/Harvard Cancer Center, Boston, MA, USA

Massimo Salvatori Nuclear Medicine Institute, Catholic University of the Sacred Heart – Policlinico A. Gemelli, Rome, Italy

Mirkka Sarparanta Department of Radiology, Memorial Sloan Kettering Cancer Center, New York, NY, USA

Laboratory of Radiochemistry, Department of Chemistry, University of Helsinki, Helsinki, Finland

Maria Grazia Sauta Oncology Unit, "Humanitas Gavazzeni" Hospital, Bergamo, Italy

Heiko Schöder Department of Radiology, Molecular Imaging and Therapy Service, Memorial Sloan Kettering Cancer Center, New York, NY, USA

Andrew M. Scott Olivia Newton-John Cancer Research Institute and La Trobe University, Melbourne, VIC, Australia

Department of Molecular Imaging and Therapy, Austin Health, Melbourne, VIC, Australia

Lucia Setti Nuclear Medicine Unit, "Humanitas Gavazzeni" Hospital, Bergamo, Italy

Martina Sollini Department of Biomedical Sciences, Humanitas University, Rozzano, Milan, Italy

H. William Strauss Molecular Imaging and Therapy Service, Memorial Sloan Kettering Cancer Center, New York, NY, USA

Elena Tabacchi Nuclear Medicine Unit, "S. Orsola-Malpighi" University Hospital, Bologna, Italy

Sree Harsha Tirumani Nuclear Medicine/PET-CT, Department of Imaging, Dana-Farber Cancer Institute and Department of Radiology, Brigham and Women's Hospital, Harvard Medical School, Boston, MA, USA

Renato A. Valdés Olmos Nuclear Medicine Section and Interventional Molecular Imaging Laboratory, Department of Radiology, Leiden University Medical Centre, Leiden, The Netherlands

Diagnostic Oncology Division, Nuclear Medicine Department, Netherlands Cancer Institute – Antoni van Leeuwenhoek Hospital, Amsterdam, CX, The Netherlands

Annick D. Van den Abbeele Department of Imaging, Dana-Farber Cancer Institute, Boston, MA, USA

Department of Radiology, Brigham and Women's Hospital, Boston, MA, USA

Harvard Medical School, Boston, MA, USA

Center for Biomedical Imaging in Oncology, Dana-Farber Cancer Institute, Boston, MA, USA

Tumor Imaging Metrics Core, Dana-Farber/Harvard Cancer Center, Boston, MA, USA

Sergi Vidal-Sicart Nuclear Medicine Department, Hospital Clínic Barcelona, Barcelona, Catalonia, Spain

Institut d'Investigació Biomèdica August Pi i Sunyer (IDIBAPS), Barcelona, Spain

Duccio Volterrani Regional Center of Nuclear Medicine, Department of Translational Research and Advanced Technologies in Medicine and Surgery, University of Pisa, Pisa, Italy

Richard L. Wahl Mallinkrodt Institute of Radiology, Washington University School of Medicine, St. Louis, MO, USA

Thida Win University College London, London, UK

University of Buckingham, Buckingham, UK

E&N Heartfordshire NHS Trust, Lister Hospital, Stevenage, UK

Pat Zanzonico Memorial Hospital Research Laboratories, Department of Medical Physics, Memorial Sloan Kettering Cancer Center, New York, NY, USA

Brian M. Zeglis Radiochemistry and Imaging Sciences Service, Department of Radiology, Memorial Sloan Kettering Cancer Center, New York, NY, USA

Department of Chemistry, Hunter College of the City University of New York, New York, NY, USA

Graduate Center of the City University of New York, New York, NY, USA

Department of Radiology, Weill Cornell Medical College, New York, NY, USA

Part I

Basic Science

Cancer Biology of Molecular Imaging

1

Steven M. Larson

Abstract

Cancer is a complex series of stepwise genetic alterations resulting in common biologic changes in the transformed cells. Distinguishing features of cancer include rapid proliferation of cells, immortality, resistance to apoptosis, resistance to suppression of proliferation, metastatic behavior, characteristic changes in metabolism, and resistance to immunologic attack. Cancer cells recruit normal host tissues to support growth of the tumor mass.

Fibrocytes and collagen producing cells provide structure for the tumor cells. Endothelial cells are recruited to form blood vessels. Tumor blood vessels have incomplete endothelium, making the vessels leaky. This allows large molecules to leak into the tumor interstitium.

The middle of the tumor mass has few, if any, lymphatic vessels. The combination of vessel leakiness and few lymphatics results in an increased interstitial pressure in the tumor, making it difficult for chemotherapy to diffuse into the tumor mass.

A common anatomic approach to measure tumor response (RECIST) employs measurements of the size of the mass on CT before and 4 weeks after therapy. Total disappearance of the lesion is required for a complete response, a 30% reduction in the sum of long dimensions defines a partial response, and >20% increase in the sum of long diameters identifies progressive disease. Adding metabolic information recorded with [^{18}F]FDG-PET/CT and the PERCIST criteria may refine these measurements. In addition to [^{18}F]FDG, radiopharmaceuticals are available to measure other attributes of the tumor. Depending on the radiopharmaceutical, images can provide information on tumor hypoxia, expression of integrins, or specific tumor markers that are overexpressed by the lesion, such as carbonic anhydrase, expressed by renal cell cancer, or receptors, such as somatostatin, expressed on neuroendocrine tumors.

Keywords

Biology of cancer • Molecular imaging in cancer • Molecular imaging • Tumor response post-therapy • [^{18}F]FDG and tumor therapy

Glossary

[^{18}F]FDG	2-Deoxy-2-[^{18}F]fluoro-D-glucose
^{18}F-FACBC	*Anti*-1-amino-3-^{18}F-fluorocyclobutane-1-carboxylic acid
^{18}F-FDHT	16β-^{18}F-Fluoro-5-dihydrotestosterone
^{18}F-FGln	^{18}F-Fluoroglutamine
^{18}F-FLT	2-^{18}F-Fluoro-L-thymidine
^{18}F-MISO	^{18}F-Fluoromisonidazole
2-HG	2-Hydroxyglutarate

S.M. Larson (✉)
Molecular Imaging and Therapy Service, Memorial Sloan Kettering Cancer Center, New York, NY, USA

© Springer International Publishing Switzerland 2017
H.W. Strauss et al. (eds.), *Nuclear Oncology*,
https://doi.org/10.1007/978-3-319-26236-9_1

^{68}Ga-PSMA	Glu-urea-Lys-(Ahx)-[^{68}Ga (HBED-CC)]
ABC	ATP-binding cassette, a transport system superfamily
ABL	Abelson murine leukemia
AKT	Protein kinase B
AML	Acute myeloid leukemia
APC	Antigen-presenting cell
AR	Androgen receptor
ASCO	American Society of Clinical Oncology
ATP	Adenosine triphosphate
BRAF	Gene encoding for the B-Raf protein, a serine/threonine-protein kinase; the gene is also known as the proto-oncogene B-Raf and v-Raf murine sarcoma viral oncogene homolog B
BRCA1	Breast cancer type 1 susceptibility protein
BRCA2	Breast cancer type 2 susceptibility protein
BRS	BRAF-RAS score
BSI	Bone scan index
c-Kit	Gene encoding for tyrosine-protein kinase Kit (or CD117), also known as Mast/stem cell growth factor receptor (SCFR)
CA9	Carbonic anhydrase 9 (or carbonic anhydrase IX, CAIX)
CML	Chronic myeloid leukemia
CRPC	Castrate-resistant prostate cancer
CT	X-ray computed tomography
CTL	Cytotoxic T cell
CTLA4	Cytotoxic T-lymphocyte antigen 4, also known as CD152
CTLC	Cutaneous T-cell lymphoma
DHT	Dihydrotestosterone
DOTA	1,4,7,10-Tetraazacyclododecane-1,4,7,10-tetraacetic acid
DOTATATE	DOTA- Tyr^3-octreotate
EGFR	Epidermal growth factor receptor; the mutated form EGFRvIII plays a prominent role in tumorigenesis and pro-angiogenic signaling
EORTC	European Organisation for Research and Treatment of Cancer
EPR	Extravasation and passive retention
ERK	Extracellular signal-regulated kinase
GIST	Gastrointestinal stromal tumor
H&E	Hematoxylin and eosin staining
HER2	Human epidermal growth factor receptor 2, also known as receptor tyrosine-protein
HIF-1	Hypoxia-inducible factor
HK2	Hexokinase 2
hsvTK	Herpes simplex virus-1 thymidine kinase
IDH1	Isocitrate dehydrogenase 1, a cytoplasmic enzyme
IDH1	Isocitrate dehydrogenase enzymes
IDH2	Isocitrate dehydrogenase 2, a mitochondrial enzyme
IL2	Interleukin 2
MEK	Mitogen-activated protein kinase
MI	Molecular imaging
MRI	Magnetic resonance imaging
MSKCC	Memorial Sloan-Kettering Cancer Center
mTOR	Mammalian target of rapamycin
Myc	Regulator gene that encodes for a transcription factor (also known as c-Myc)
NAALADase	N-Acetylated-alpha-linked-acidic dipeptidase, also known as glutamate carboxypeptidase II
NADPH	Nicotinamide adenine dinucleotide phosphate
NIH	United States National Institutes of Health
NSCLC	Non-small cell lung cancer
p53	Tumor protein p53, also known as cellular tumor

	antigen p53, phosphoprotein p53, tumor suppressor p53, antigen NY-CO-13, or transformation-related protein 53 (TRP53)
PARP	Poly adenosine diphosphate ribose polymerase
PARPi	Poly adenosine diphosphate ribose polymerase inhibitor
PD-1	Programmed cell death protein 1, also known as CD279
PERCIST	Positron emission tomography response criteria in solid tumors
PET	Positron emission tomography
PET/CT	Positron emission tomography/Computed tomography
PI13K	Phosphoinositide 3-kinase
PI3K/AKT/mTOR	Intracellular signaling pathway regulating the cell cycle
PR	Partial response
PSMA	Prostate-specific membrane antigen
PTEN	Gene encoding for the phosphatase and tensin homolog protein, a tumor suppressor; PTEN deletions indicate a poor prognosis
Ras	Oncogene regulating signalling cascades
RB	Gene encoding for the retinoblastoma protein
RCHOP	Rituximab, cyclophosphamide, doxorubicin, vincristine, and prednisolone
RECIST	Response evaluation criteria in solid tumors
SCLC	Small cell lung cancer
STEAP	Family of transmembrane epithelial antigens of prostate comprising six members
SUL	Lean body mass corrected standard uptake value
SUL_{peak}	Lean body mass corrected standard uptake value at voxels of maximum
SUV	Standardized uptake value
SUV_{max}	Standardized uptake value at point of maximum
SUV_{peak}	Standardized uptake value at voxels of maximum, based on correction for lean body mass
TCR	T-cell receptor
TDS	Thyroid differentiation score
TIL	Tumor-infiltrating lymphocyte
VEGF	Vascular endothelial growth factor
VEGFR	Vascular endothelial growth factor receptor
VHL	Von Hippel-Lindau

Contents

Author's Introduction 6

The Evolving Context of Molecular Imaging Practice: The Rapid Pace of Discovery in Cancer Genomics 7

Hallmarks of Cancer 7

The Tumor Mass 7

Imaging the Tumor Mass 8

Neovasculature 9

Hypoxia 10

Cellular Constituents and Cell-Cell Synergism of the Tumor Mass 10

Immune Cell Cancer Immunotherapy 11

Imaging the Immune T Cells 14

The Metastatic Process 17

Imaging the Cancer Cell 17

Proliferation Imaging 21

^{18}F-FLT Imaging of Proliferation After Chemotherapy 21

Apoptosis 22

Oncogene and Non-oncogene Addiction 23

Examples of Imaging the Action Driver Mutations in Cancer Cells Indirectly Through Effects on Metabolism 25

BRAF Inhibition in Advanced Melanoma with V600E Mutation 25

Inhibition of MEK, a Downstream Signal Transduction Molecule in the RAS/BRAF/ERK Pathway, Can Reverse ^{131}I Resistance in Patients with Thyroid Cancer 26

Imaging the Driver Oncogene in Castrate-Resistant Prostate Cancer: The Androgen Receptor Axis 27

Androgen Receptor (AR) as Oncogenic Driver in Prostate Cancer 28

Imaging of Carbonic Anhydrase 9 as a Pathognomonic Indication of Clear Cell Renal Cancer 28

Future Applications 29

Radioantibody and Radiopeptide Imaging and Therapy (Theranostics) Will Drive Our Field for the Next Decade and Beyond 30

References 31

Author's Introduction

This is the second edition of this chapter with emphasis on the nexus of cancer biology and molecular radio-imaging and targeted therapy. Those who have read the first edition will find much that is familiar, because the foundations for the cancer biology of molecular radiotargeting have not fundamentally changed, even though enrichments have occurred in relevant knowledge. To this end, I have done my best to include updates. The Cancer Genome Atlas is a huge source of knowledge for molecular radiotargeting and has already impacted thyroid cancer radiotherapy. Also, I have expanded the discussion of metabolomics to include glutamine imaging, provided an example of molecular imaging of an oncogene, and elaborated on androgen receptor (AR) and the integrated biochemical system that it drives (the AR axis in advanced prostate cancer). I added a more complete section on tumor immunology, setting the stage for imaging advances that will undoubtedly come in the years ahead. I have discussed the prospective role of radioantibody imaging, as I truly believe that the future will show astonishing advances based on our ability to perform optimization of immune targeting reagents. Elsewhere in this book, much information about specific applications of radiopeptide imaging and therapy, as well as organ-specific applications, is provided. This chapter does not comprehensively cover all molecular imaging but instead discusses key features of relevant cancer biology, as I see it, from the perspective of someone who has focused on oncologic applications of radiotracers for more than 40 years.

When I was a medical student, I was awarded an NIH fellowship to develop a radiotracer probe, technetium sulfur colloid, which is still in use today. This effort set me on the path of nuclear medicine and targeted probe development. As part of my education, my mentor, Wil B. Nelp of the University of Washington, took me to a conference in Richland, Washington, site of the Hanford National Laboratories. Much testing on the radiobiology of radiation was conducted on this campus, which was also the site of development of bomb-grade weapon materials. At this conference, in 1966, I met Shields Warren, a pathologist who was, at that time, a chairman of the Atomic Bomb Casualty Commission, an effort jointly supported by both the Japanese and US Academy of Sciences and the source of much of the current information on human dosimetry and biologic effects. Dr. Warren wrote an inscription on my program that I will never forget: "Congratulations to a student who can start a career with today's sciences." To all students of molecular imaging and targeted therapy, now 50 years later, these words are more apt than ever!

Molecular imaging offers quantitative detection of the molecules and molecular-based events that are fundamental to the malignant state, in vivo in living subjects. This is nothing new to nuclear medicine and its clinical applications of the tracer principle, but the opportunities have become so vast in the last decade that new excitement extends well beyond nuclear medicine to energize the whole of oncology. This new excitement stems from the recognition that molecular imaging has the potential to expedite laboratory discovery and personalize the care of individual patients with cancer. In this chapter, we will touch on how facets of the biology of cancer can be exploited in the performance of molecular imaging. This chapter is a revision of that presented in the first edition, with key updates and additions regarding cancer immunology, cancer genomics, pharmacology, and theranostics.

The Evolving Context of Molecular Imaging Practice: The Rapid Pace of Discovery in Cancer Genomics

As we have seen, an important hallmark of cancer is genomic instability and mutation that leads to changes in the genome, some of which have a direct consequence on the development of malignant phenotype (driver mutations), but others (passenger mutations) may be alterations that make the cancer different from normal tissues but have no direct effect on tissue phenotype.

In the last 10 years, revolutionary developments in rapid genomic sequencing have led to a sea change in our understanding of the genetic events important to the process of malignant transformation and maintenance of the malignant state. The practical importance of this new understanding of the cancer genome is that it allows a path forward to implement specific therapies that suppress tumor growth. For patients with lung cancer, for example, modern clinical practice includes a rapid genomic profile that may identify an alteration in the patient's own tumor, which will likely make it responsive to treatment with specific drugs. As an example, detection of driver mutations based on substitution of leucine for arginine (L858R mutation) in the gene for epidermal growth factor receptor (EGFR) in some lung cancers allows treatment and likely response with erlotinib-targeted therapy. This kind of precision medicine will undoubtedly lead to expanded opportunities for molecular imaging to monitor these targeted treatments and determine, as is often the case, the point in time when the cancer mutates again and escapes from drug control.

As a high-level first pass, most genes that are directly linked to cancer causation fall into two categories: oncogenes, which are driver mutations for a process that leads to cancer, and suppressor genes, which must be disabled to permit expression of the malignant state. Current estimates are that about 140 such genes have been identified in the genome of tumors to date, of which 80 are tumor suppressor genes and 60 are oncogenes [1]. Oncogenes have received more attention from the molecular imaging community because it is easier to image a molecule or molecular-related event that is additive or increased relative to the tissue of origin. Examples include oncogene mutations that lead to HER2 overexpression seen in breast cancer, c-Kit mutations seen in gastrointestinal stromal tumors, and EGFR mutations seen in brain tumors and lung cancers. Examples of suppressor genes include BRCA 1 and 2 mutations, associated with breast, ovarian, and pancreatic cancer; p53 mutations; breast, sarcoma, and brain tumors; and RB gene in retinoblastoma. See specific examples described in the section entitled "Oncogene and Non-oncogene Addiction" below.

Hallmarks of Cancer

There is growing acceptance of the view that cancer is "a complex collection of distinct genetic diseases, united by common hallmarks." Thus, a general and uniting property of cancer is a common phenotype set of "hallmarks," i.e., the biologic characteristics of malignant tissues that distinguish them from the tissues from which they arise (summarized in Fig. 1).

Distinguishing features of cancer cells include rapid proliferation, immortality, resistance to apoptosis, resistance to suppression of proliferation, metastatic behavior, and a variety of stress responses, which include a characteristic pattern of metabolism such as the Warburg effect and resistance to immunologic attack that allow cancer cells to better survive in hostile environments. The characteristic behaviors that make a cancer cell malignant are now generally believed to occur through a series of stepwise genetic alterations. In principle, the phenotypic alterations of each of these characteristics are associated with underlying key molecules that can be targeted with selective tracers and images.

The Tumor Mass

A general property essential to the long-term growth of cancer cells is the recruitment of a supporting framework to create the mass that

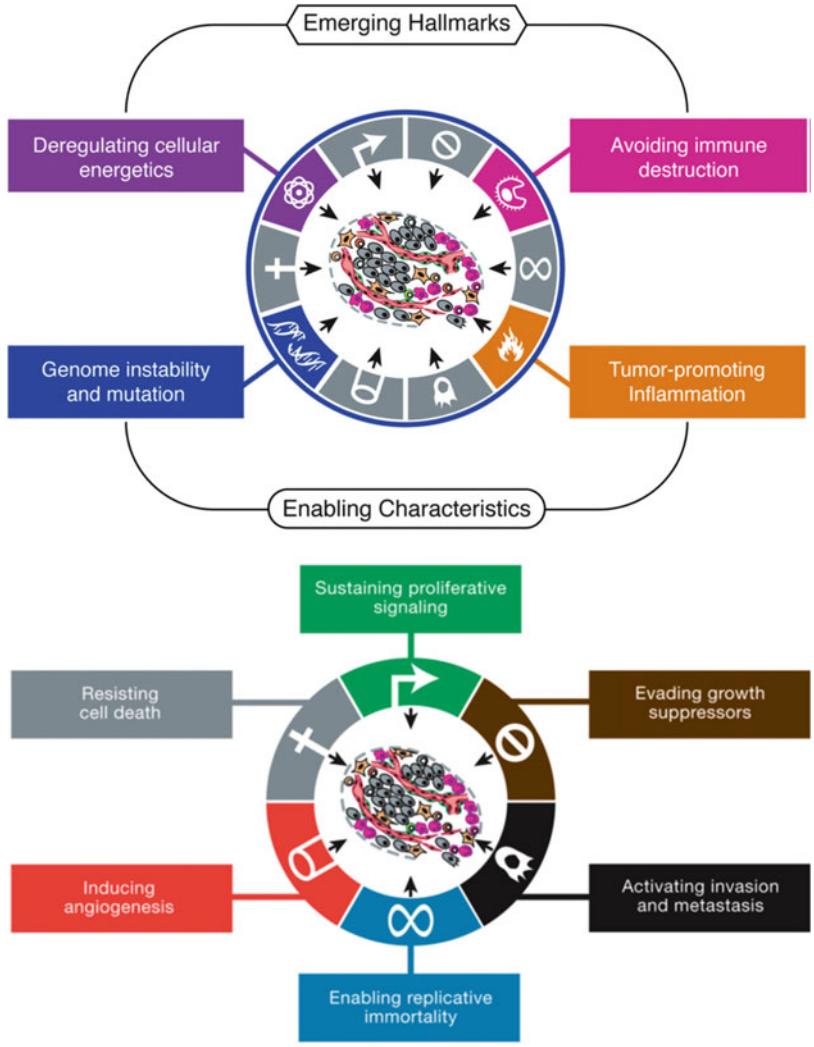

Fig. 1 Emerging hallmarks and enabling characteristics of cancer (*top*) and hallmarks of cancer (*bottom*) (From [2]; permission requested)

characterizes clinical malignancies. Prior to recruitment of blood vessels, the tumor size is limited by the diffusion distance of oxygen in tissues, which is approximately 100–200 microns. Once a blood supply is established, the tumor mass can grow [2].

Imaging the Tumor Mass

For several decades, observing changes in the size of the tumor mass has been the basis for monitoring treatment response. At first, this was done using palpation, but high-resolution cross-sectional CT imaging rapidly became the gold standard for treatment monitoring once it was developed. At present, clinical imaging criteria have serious limitations for detection of masses, and in most situations, 1 gram of tissue or about 10^8 cells is a practical limit. The current criteria depend on the measurement of two perpendicular diameters in up to five soft-tissue masses (RECIST 1.1). For a partial response (PR), >30% change is required in the sum of long dimensions of up to two per organ, and for complete response (CR), disappearance of all lesions is required. Progressive disease is >20% in sum of long diameters, validated at 4 weeks after treatment (Fig. 2).

With the widespread introduction of [^{18}F]FDG-PET imaging, there is recognition that metabolic

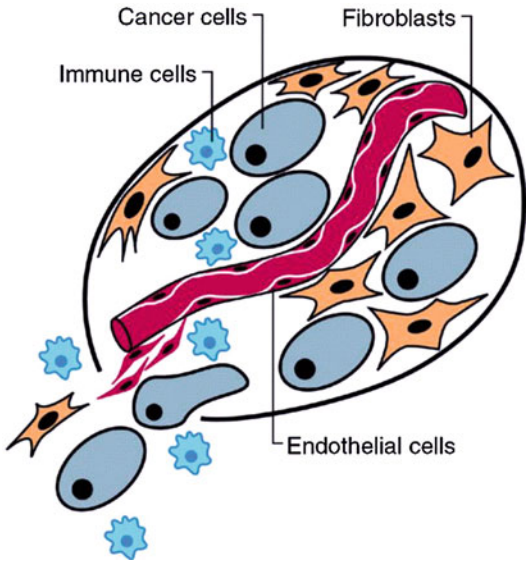

Fig. 2 Fibrocytes, endothelial cells that form vessels which provide nutrients, and immune cells are common constituents of the tumor mass (e.g., which are typically imaged as part of the tumor on CT) (From [2], with permission)

change should also be incorporated into the measurement of tumor treatment response. Initial assessment was based on the EORTC recommendation and employed standardized uptake values for [^{18}F]FDG uptake, normalized to body weight (SUV_{max}) [3]. Expert opinion offers alternative response parameters for making this assessment, such as PERCIST, which incorporates PET SUV measurements into treatment response. PERCIST uses an SUV measure, SUV_{peak}, which is based on lean body mass, and uses a circular region of 1.2 cm in diameter (with an approximate mass of 1 gram) centered around the hottest voxel, over which the standardized uptake value (SUV) is averaged. In order for PERCIST criteria to be applied to measure tumor response to treatment, the SUL_{peak} must be >/SUL average liver, + 2 standard deviation SUL liver. In this way, tumor and liver SUV are compared [4].

Fox and colleagues have recently proposed an alternative that takes advantage of semiautomated lesion-tracking software to look at all the lesions simultaneously in advanced patients; clearly the size and metabolism of the mass in some combination appear likely to be an important measure of treatment response [4]. It is important to keep in mind that when imaging a tumor mass, changes in a particular parameter involve all of the cells in the mass, both malignant and benign; this is true whether imaging gross anatomic measures obtained by CT or a more tumor cell-associated hallmark such as [^{18}F]FDG uptake due to the Warburg effect.

Neovasculature

Once cancer cells are collected into a mass, the cells must recruit blood vessels in order to grow. The blood vessel system in a tumor, called "neovasculature," has some unique characteristics. The vessels are poorly organized, extremely permeable, and often have an incomplete endothelial barrier. Most tumors have minimal lymphatics in the tumor mass, which causes the mass to have a higher pressure than normal tissue, limiting the diffusion of many molecules (especially antibodies) into the tumor mass. The incomplete endothelial barrier of the neovasculature allows tumor cells direct entry to the host vasculature, providing a path for the tumor cells to circulate and metastasize.

Folkman was the first to recognize that inhibition of angiogenesis could inhibit tumor growth and coined the tumor "angiogenic switch," for the moment when a small collection of tumor cells begins the vascularization process [5]. Ferrara discovered that vascular endothelial growth factor (VEGF) played a crucial role in the development of neovasculature [6]. In response to VEGF produced at the site of the tumor cells, stem cells are recruited from the bone marrow and migrate to the tumor mass, where they serve an essential role in the production of neovasculature.

Agents that target VEGF and its receptor include the antibody, bevacizumab, and the peptides sorafenib and sunitinib. Bevacizumab binds to VEGF while the peptides interfere with the receptor. Both show strong antitumor activity against some highly vascular tumors, which exert their antitumor effects by inhibiting the VEGF receptor expressed on tumor cells. Bevacizumab has been radiolabeled with zirconium-89 and

localizes in breast cancer [7]. In patients treated with these agents, serial imaging with [^{18}F]FDG has shown a marked decrease in [^{18}F]FDG uptake, reflecting the effectiveness of anti-VEGF therapy on tumor size and metabolism. The response of tumors to therapy such as single high-dose fraction radiation has been linked by some to endothelial damage, whereby radiation induces catastrophic apoptosis in endothelial cells, which results in irreversible damage to tumors.

In contrast to normal vessels, the leaky neovasculature can be exploited to image the tumor mass. The "leaky" incomplete endothelium allows passage and retention of large molecules and nanoparticles into tumors. This process is called the "extravasation and passive retention (EPR) effect" and is thought to occur because the larger molecules and nanoparticles enter into the perivascular space through relatively large pores, but have difficulty getting back out into the vasculature, much like a lobster has trouble finding its way out of a lobster trap. The continuous expression of angiogenesis factors by the tumor causes a concomitant increased expression of integrin receptors, such as $\alpha_v\beta_3$ integrin or other members of the integrin family, to provide a homing signal for the cells mobilized to create the new blood vessels for the tumor. Agents binding to this integrin have been synthesized and localized in sites of neovascularity, such as tumors [8] and healing infarcts [9, 10]. Other endothelial sites for imaging include the antigens PSMA, which can be imaged with the antibody J591. In fact, in a review by Schliemann and Neri, nine vascular targets were described for which antibodies have been developed [11].

Hypoxia

Solid tumors tend to outgrow their blood supply, causing cancer cells to become hypoxic [12]. The reduced cellular oxygen content that accompanies hypoxia can be imaged using a class of compounds called nitroimidazoles. F-18 misonidazole has been used most often, although numerous alternatives are being developed. The principal localization is passive diffusion into the tumor. Once in the cell, nitroimidazoles undergo a single-electron reduction. In the presence of oxygen, the molecule is immediately reoxidized. As a result, the molecule diffuses back out of normoxic tissue. In the presence of hypoxia, the reoxidation cannot occur, trapping the molecule within the hypoxic but viable tissue. Hypoxia is a key property of tumors that reduces the effectiveness of radiation therapy. Well-oxygenated tissue is about three times more sensitive to radiation damage than hypoxic tissue. Some investigators suggest using ^{18}F-fluoromisonidazole (^{18}F-MISO) to image hypoxic regions within tumors to allow a boost of radiation to the hypoxic region without damaging normal tissues.

Cellular Constituents and Cell-Cell Synergism of the Tumor Mass

The tumor mass contains a mixture of tumor cells and cells recruited from the adjacent normal tissues of the host, such as fibroblasts, collagen fibrils, and vascular endothelium. The amount of stroma is highly tumor dependent, with lesions such as lymphoma having relatively little stroma, and others such as those in the pancreas having relatively few tumor cells and abundant stroma. In addition, tissue macrophages and other immune cells are represented in the mass. Typically, about 3% of cellular mass is represented by endothelial cells. But recent evidence suggests that single-dose fraction radiation's major effect occurs by selectively damaging the vascular endothelium, the most sensitive cell in the tumor [13].

The mass cannot grow without the active synergism of each cellular component. There is also evidence that cells interact with one another in more subtle ways. Small molecules, large molecular complexes, and entire pieces of membrane are exchanged between tumor cells and supporting stroma. For example, P glycoprotein, an ABC transporter protein responsible for multidrug resistance, was shown to transfer from resistant to sensitive cells, as a functional entity, so that sensitive cells could acquire sufficient resistance to resist otherwise lethal levels of anticancer drugs [14].

Immune Cell Cancer Immunotherapy

Cancer cells may be immunogenic enough to be killed by the natural immunity of the body, as described in Fig. 3. The basis for cancer immunity is thought to be immunogenic products formed as a result of the cancer's characteristic of rapid mutation leading to "neoantigens," which are recognized as foreign. Figure 3 depicts the process of immune attack on cancer cells in diagrammatic form, starting with the release of neoantigens by damage to tumor cells, with recognition and process of these antigens by dendritic cells (2), and presentation to T cell in the regional lymph nodes (3). The now immunized T cells migrate through the blood and traverse through the endothelial layer into the tumor mass (5), where they encounter tumor cells (6), recognizing the presence of neoantigens. T cells, most commonly CD8-expressing cells, attack the cancer cell (7). Normally, however, cancer cells escape immune attack based on a system of checks and balances within the tumor cell environment.

The cellular component of the tumor mass includes a variety of tumor immune cells, including T cells, macrophages, and dendritic cells, a group of specialized immune cells that are involved as the first line of defense in alerting the immune system to foreign antigens. In particular, activated T cells, especially CD8 expressing cells within the cancer mass, can play a role in cancer therapy. In the last few years, treatment of cancers with immune therapy has led to significant responses—even complete responses—in advanced cancers, especially advanced melanoma and non-small cell lung cancers. The results are so exciting that in 2013, *Science* magazine selected cancer immunotherapy as the most significant breakthrough of the year [16]. Effective treatments are based on growing knowledge of the role the immune system plays in the delicate balance of immune modulation, a series of checks

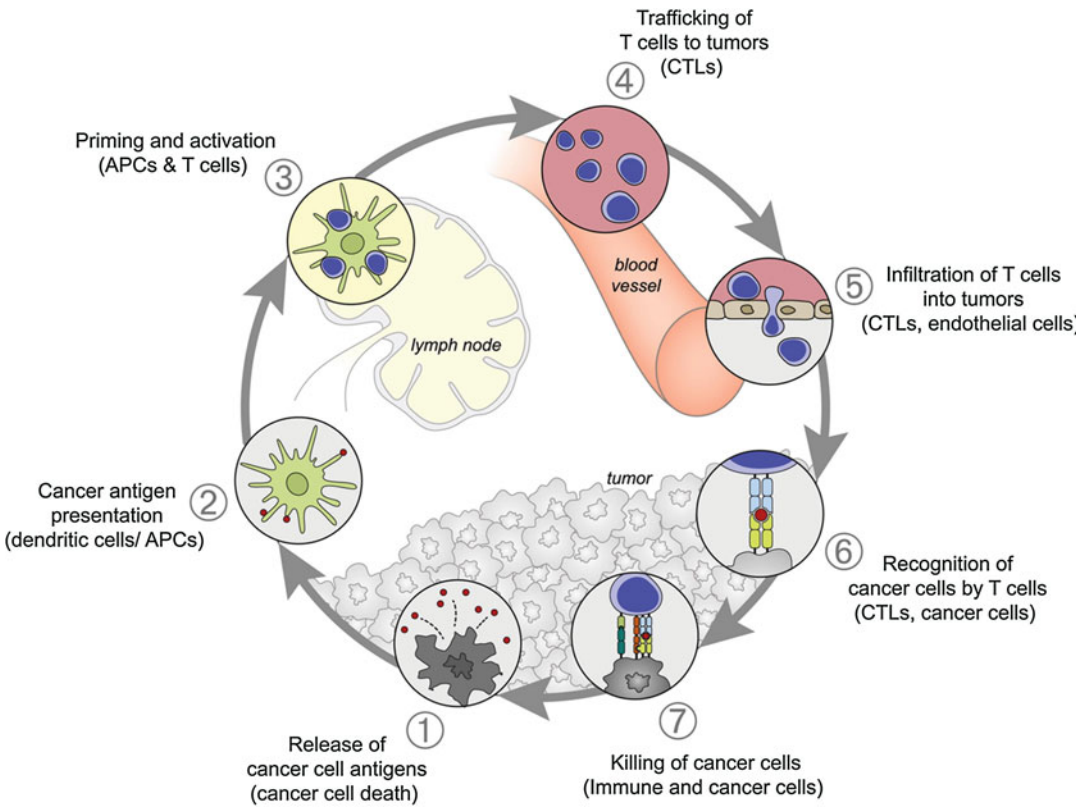

Fig. 3 The cancer immunity cycle (From [14, 47]; permission requested)

and balances on the immune response. One of the newly recognized hallmarks of cancer is the ability of cancer cells to suppress the body's immune response, so much so that the tumor mass is most frequently a sanctuary for proliferation of cancer cells within the tumor mass. Specialized antibody therapies can neutralize key molecules that modulate immune response, and for some tumors, this treatment ("immune checkpoint blockade") can be part of a potent defense against even the most advanced tumors.

Immune checkpoint blockade. Human T cells are a critical component of the activity of the human immune system as part of body's primary defense against invasion by foreign tissue and aberrant normal tissues such as cancer. In general, the native proteins in the body do not provoke an immune response in T cells, but among the millions and millions of T cells in the human body, it is thought that there may be a few that can even be immunized against normal macromolecules of normal tissues. But also, a plethora of antigens can be recognized as foreign, including those that may be only slightly different from the native molecules. These differences could arise due to mutation in the gene from which they arise, or from mistakes in the formation of molecules that lead to a slightly altered structure.

One of the ways the immune system is kept in check so that the body does not destroy itself depends on immune suppressor molecules produced by T cells. CTLA4 is an important suppressor molecule expressed by human T cells that are activated against particular antigens. The role of CTLA4 is to downregulate immune response, and CTLA4 increases on the cell surface whenever a T cell is activated, after recognizing an antigen to which it has been immunized. The mechanism whereby this occurs is illustrated in Fig. 4. CTLA4 checkpoint to suppress inappropriate immunity against normal tissues is obviously of great importance for avoiding immunity against self (often called autoimmunity).

It turns out that cancers, and some cancers in particular (i.e., melanoma, non-small cell lung cancer), have a large number of these slightly altered antigens (often called neoantigens) that can create immunized T cells. These genetic changes may be either driver mutations or passenger mutations, but in any event represent altered features of the tissue, which may be recognized by the immune system. This immunity can be enhanced by therapies that block the action of immune suppressor molecule CTLA4 (such as the antibody Ipilimumab), and the result may be long-term anti-cancer response.

In effect, the anti-CTLA4 treatment "takes the brakes off" the human immune system and may

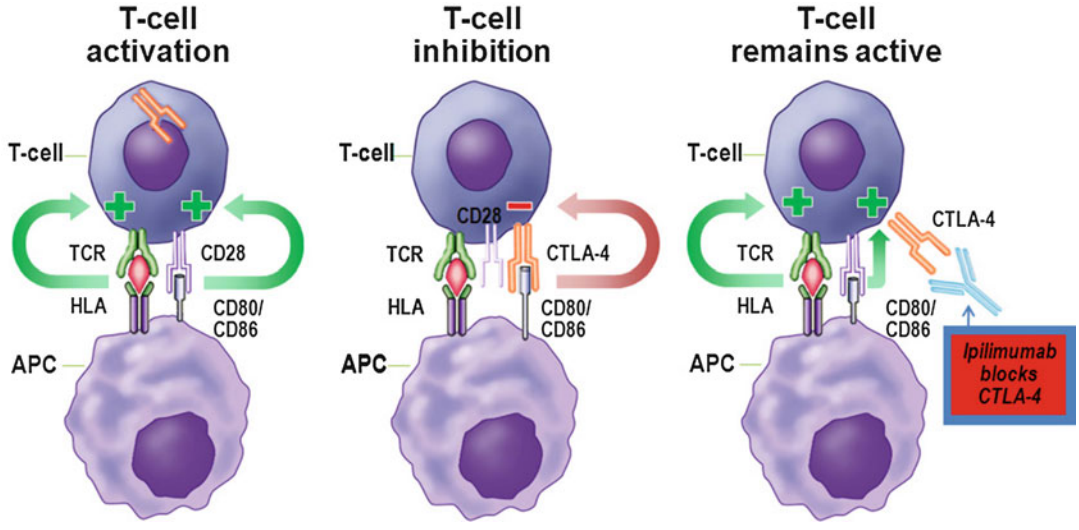

Fig. 4 Ipilimumab augments T-cell activation and proliferation (Adapted from O'Day et al. plenary session presentation, abstract #4, ASCO 2010)

have remarkable effects in killing tumor, even in patients with advanced metastatic disease. An additional immune checkpoint system, shown in Fig. 5, involves PD-1, which is expressed on T cells but may be used in the treatment of solid tumor. Some tumor cells, such as lung cancer, downregulate PD-1 by binding to a high-affinity cognate receptor PD L1, which is expressed on some tumors such as NSCLC. The suppressor action of PD-1 is blocked by the antibody nivolumab, and the antibody PD-L1 may have a similar clinical effect. Immune checkpoint alone, and in combination, offers the possibility of curing major human cancers at the stage of clinical development when patients were previously guaranteed to die of their disease.

It is important to remember that the immune checkpoint inhibitor antibody is not the agent that actually kills the tumor; it is the body's own immune cells which do the killing. An additional fact is that the immune cells must be in direct contact with the tumor in order to kill it, and so the immune cells must be able to enter the tumor, if "immune checkpoint" therapy is to be effective.

The tumor mass is an immunologic sanctuary, in that neo-antigens and oncoproteins manufactured by the malignant cell should be more immunogenic than they are in real life. In an exciting new development with profound clinical implications, so-called immune checkpoint blockade antibodies such as ipilimumab (anti-CTLA4) and nivolumab (anti-PD-1) target molecules on tumor-specific T cells that can suppress this antitumor immunity. Both ipilimumab and nivolumab, either alone or in combination, have been introduced into clinical trials and have induced long-term remissions in a significant portion (20–30%) of very advanced and hitherto intractable solid tumors, such as melanoma and lung cancer [17].

The immunologic invasion that follows immune checkpoint treatment, predominantly T cells, can be intense, enough to cause false positives on cross-sectional volumetric PET-[^{18}F]FDG imaging. Similar findings were observed after ipilimumab and nivolumab therapy and in this case include increase in size of tumor mass because of immune cell infiltration and false positives on PET. For this reason, modified response criteria have been suggested for monitoring the response profile of solid tumors after these powerful immunologic treatments [18].

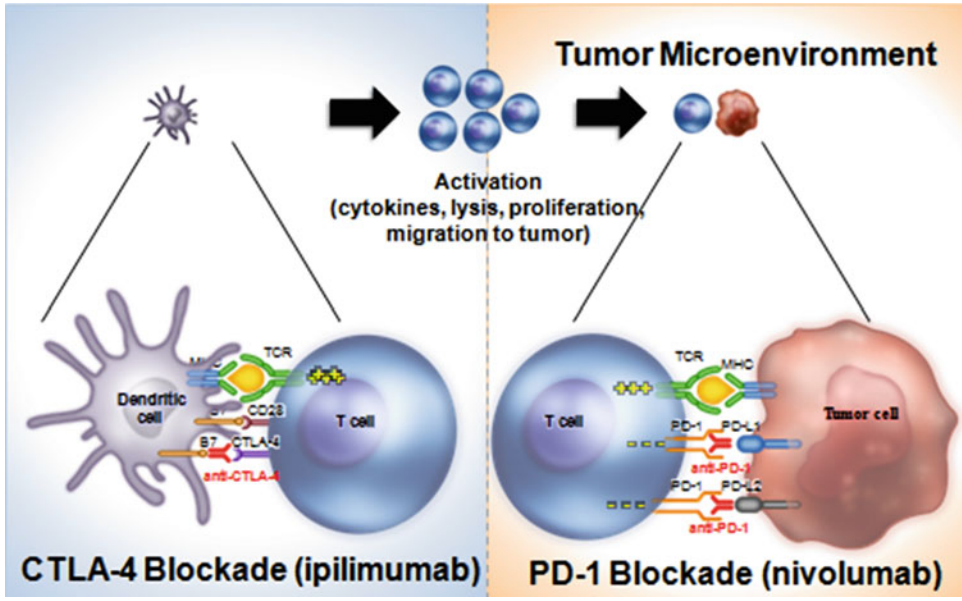

Fig. 5 Blocking CTLA4 and PD-1

Imaging the Immune T Cells

Because of the growing importance of cancer immunotherapy to the treatment of solid tumors, there has been a great deal of interest in imaging the targeting of effector T cells to human tumors. Since the killing of tumor appears to be very dependent on CD8 T cells, this is the group of cells that has been a particular focus. Table 1 summarizes current activity in this area.

Although immune cell imaging in man is limited, the data available is revealing in light of current knowledge about the importance of tumor to tumor. Figures 6 and 7 illustrate data from a patient with malignant melanoma who was injected with ^{111}In-oxine-labeled lymphocytes, which were elutriated from surgically removed tumors after expansion under IL2 stimulation. Six patients with widely metastatic melanoma were studied. An aliquot of approximately 10^{10} cells were labeled with 185–399 microcuries of ^{111}In-oxine, rinsed, and, after resuspension in saline, were infused through a filter into the patient. The amount of labeled activity was 3.9 microcurie per 10^8 cells. Initial distribution as seen in Fig. 8 was observed in the liver, bone marrow, and lung by 2 h, as imaged by planar gamma camera. Sequential studies showed that selective uptake occurred in tumor tissue (see arrows) of up to 40 times the amount in surrounding tissue. Figure 6 shows the time course of uptake, based on regions of interest drawn around six individual tumors in five patients. Localization is seen to increase over time, with a peak at about 72 h. We interpreted this data to indicate that TIL's were capable of trafficking to tumor after injection. These findings were subsequently confirmed in a larger series of 16 patients. It was of interest that the radiolabeled T cells targeted tumor but did not target lymph nodes.

Table 1 Examples of radiolabeling of immune T cells in cancer

Radiotracer	Disease application (reference)
^{111}In-oxine	TIL in melanoma [19]
^{131}I-FAIU /hsvTK	Lymphoma immune cell targeting [20]
^{111}In-anti-CD5 antibody	CTCL in humans [21]
^{89}Zr-anti-CD8 minibody	CD8 imaging [22]

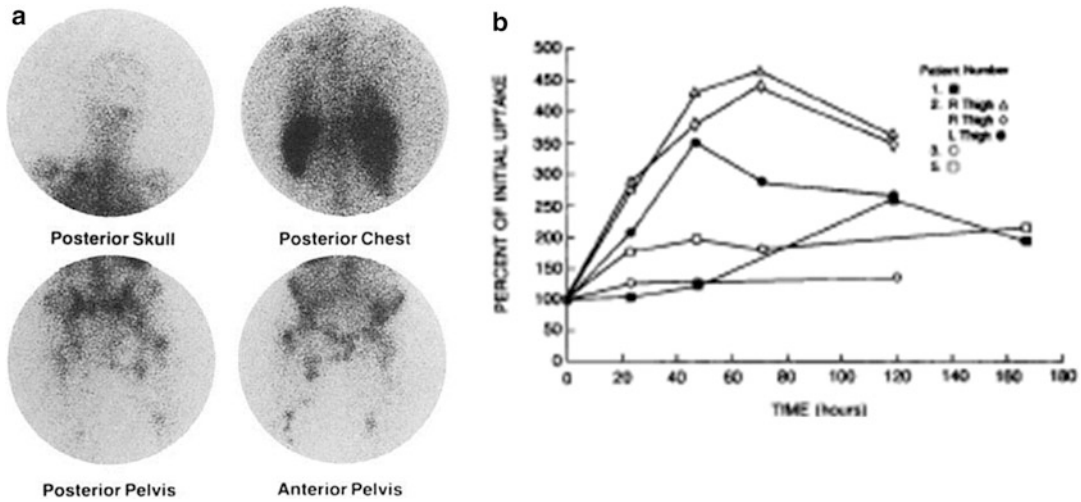

Fig. 6 (**a**) Planar images of head and shoulders, thorax and upper abdomen, and anterior and posterior pelvis (moving clockwise from left upper to left lower) 72 h after injection of ^{111}In-oxine-labeled tumor-infiltrating lymphocytes. Localization in the lungs, liver, bone marrow, and melanoma; tumor in lymph nodes of the pelvis and lesions on upper thighs. (**b**) Time-activity curves over known melanoma tumors, showing migration of radiolabeled TILs into melanoma tumor sites. (For more details, see [18])

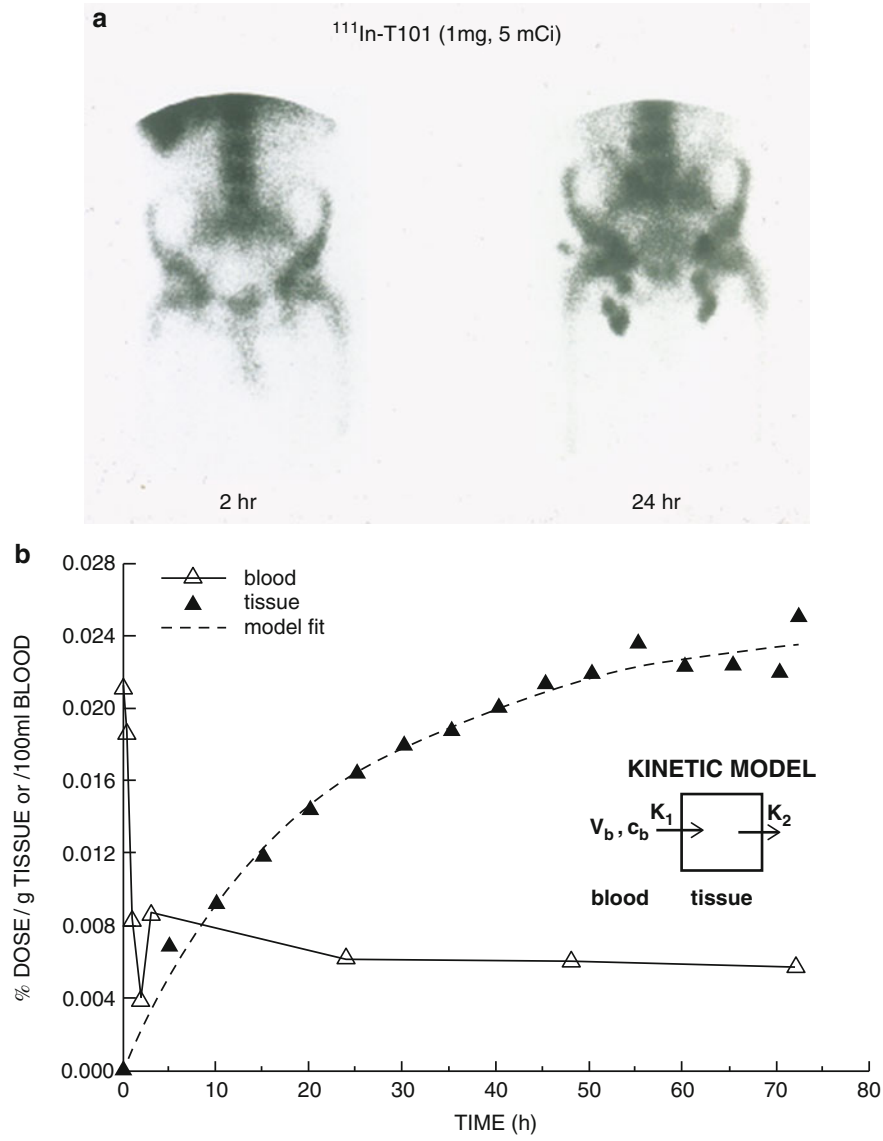

Fig. 7 (**a**) Anterior pelvis images at 2 and 48 h after intravenous injection of ^{111}In-T101 (anti-CD5 antibody) in patients with cutaneous T-cell lymphoma (CTCL). The antibody binds to the cells circulating in the blood and is internalized, migrating eventually to neoplastic lymphadenopathy in the lymph nodes of the groin. (**b**) Kinetics of T101-labeled lymphocyte uptake in lymph nodes. The indicated T-cell activity concentrations in blood (c_b) and the lymph node tissues are averages of data obtained in four patients. The blood data were used in a nonlinear, least squares fit of the indicated compartmental model to the tissue data. The blood volume parameter V_b was fixed at a representative value of 0.05 ml/g, while the best-fit values (mean ± sem) of the parameters K1 and k2 were determined to be 12.6 ± 0.5 ml/g/h and 0.029 ± 0.002 h-1, respectively

An indium-111-labeled anti-CD5 antibody, T101, was used to image malignant T-cell lymphocytes as part of a study in mycosis fungoides (cutaneous T-cell lymphoma). Images of the pelvis are shown, at 2 h and 24 h after injection. More than 95% of the radiolabeled T-101 cleared from the blood within 2 h, binding to T65 antigen on T cells, followed by rapid localization, in liver spleen and bone marrow with subsequent gradual clearing of these tissues and

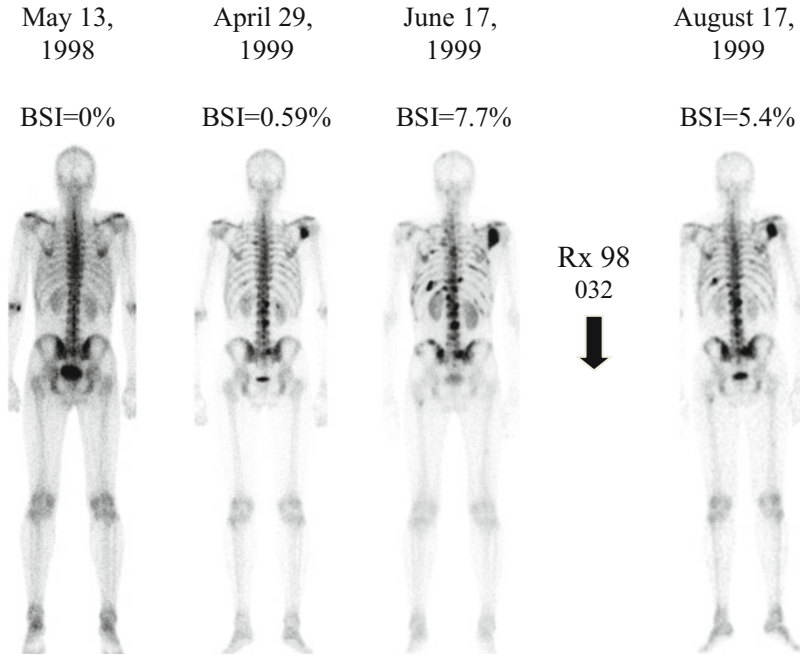

Fig. 8 Progression on bone scan of prostate cancer tumor in bone, measured using the bone scan index (BSI) technique

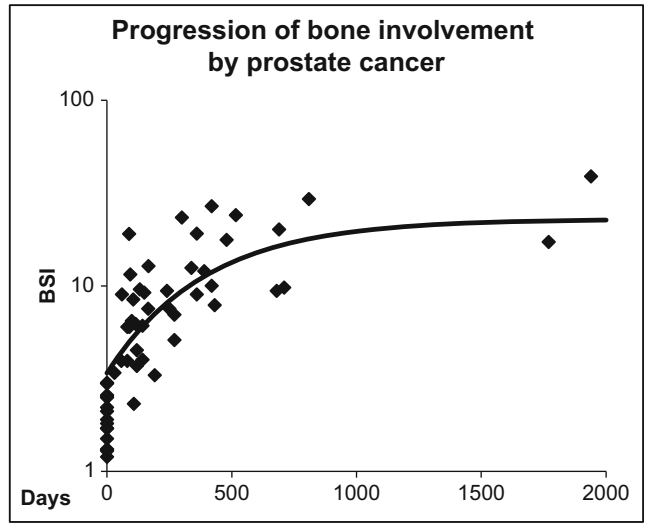

Fig. 9 The rate of progression of tumor in a group of patients followed a Gompertzian group curve, of the form $BSI(t) = BSI_0 \times [\exp^{a/b} \times (1 - \exp^{-bt})]$ with an initial doubling time of 45 days, at 3% BSI involvement. Of note is the characteristic decline in rate of growth until a plateau is reached

concomitant localization to lymph nodes in tumor-involved regions, such as bulky inguinal nodes. Subsequently, using a kinetic model, we estimated the rate of localization of malignant T cells to lymph node in this patient. We calculated that about 3.3×10^7 cells/g/h localized to malignant lymph nodes in this patient and that a plateau occurred at 72 h, when influx was equal to output. At this point, the ratio of cell concentration between lymph node and blood was about 434. Similar studies will likely be performed with improved T-cell labeling methodologies in adoptive tumor cell therapy in man and are likely to give important information about the effectiveness of treatment in individual patients.

The Metastatic Process

Massague and colleagues used a series of passages of human tumors through experimental animals, as a basis for identifying tumor cells with tropism for particular sites of metastases, such as the bone, brain, and adrenals. In breast cancer, individual cells with this tropism were cloned and found to express specific molecules that enabled cells to migrate from the primary site and survive in the new environment [23–25]. Cells in a metastatic site may reseed the primary tumor, and vice versa, in a continuous exchange [26, 27]. These findings have been observed in animal models of breast, colorectal, and lung cancer and melanoma. This process involves circulating tumor cells in blood, including those which appear "differentiated" for tropism to specific tissues. This "tumor reseeding" may help explain why the growth of solid tumors follows Gompertzian kinetics, namely, an exponentially declining exponential growth in which the tumor doubling times are most rapid at the very earliest stage of tumor growth. Another feature of metastatic growth that supports that concept that tumor cells seed organs via circulation in the blood comes from prostate cancer studies that showed that the sites of early bone metastases correlate with regional distribution within the bony skeleton with active red bone marrow, where blood flow is particularly rich. It was also observed in these patients that progression of tumor volume as a proportion of the bony skeleton followed a Gompertzian kinetic form (Fig. 10).

Imaging the Cancer Cell

Imaging the cancer cell phenotype: metabolomics. The altered metabolism of malignancy has been exploited for decades to image human tumors (see Table 2 for a list of commonly used metabolic tracers in malignancies). New knowledge is emerging on the metabolomics of human cancers, and there appears to be a growing role for glutamine.

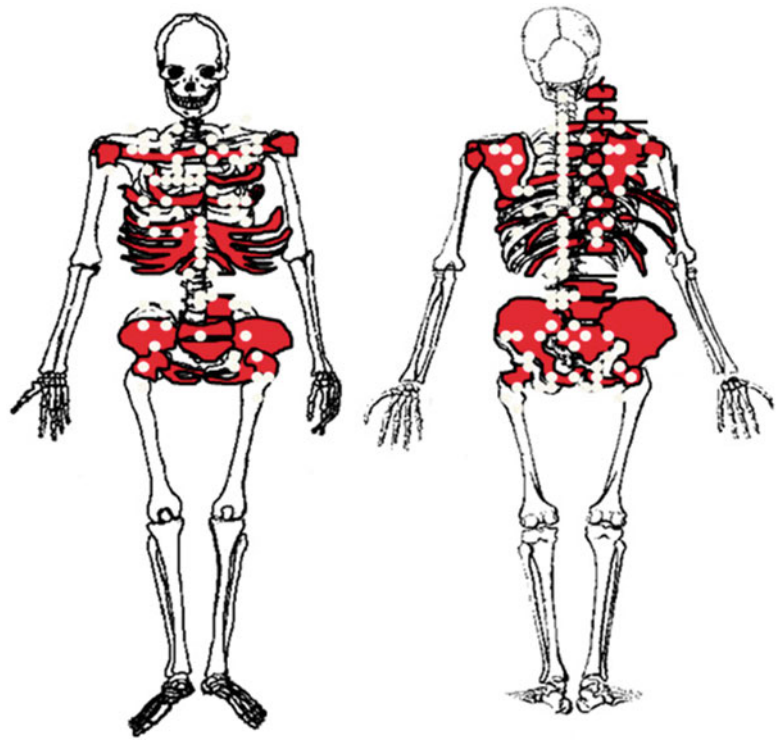

Fig. 10 The initial metastases in these 27 patients occurred exclusively within the pattern of red marrow distribution in the adult male

The Warburg effect. The Warburg effect (Fig. 11) is the term given to a characteristic metabolic pattern of cancer, in which glycolysis is the dominant means of energy production, even in the presence of oxygen, where most of the carbon atoms from metabolism are secreted in the form of lactate [37]. This excessive glucose utilization by many tumors provides the rationale for [^{18}F]FDG PET/CT imaging to identify sites of tumor and evaluate the impact of therapy. More than two million patients per year are imaged with [^{18}F]FDG mostly for the purpose of improved tumor staging, detection of recurrence, and monitoring treatment response.

Table 2 Increasing [^{18}F]FDG uptake and adverse outcome (From [28], with permission)

Tumor type [Ref]	Clinical feature
NSCLC [29]	Survival
SCLC [30]	Survival
Breast cancer [31]	Survival
Thyroid cancer [32]	Survival; ^{131}I uptake
Esophageal cancer [33]	Survival; recurrence
Glioma [34]	Survival
Lymphoma [35]	Survival
Head and neck cancer	Survival; recurrence
Ovarian cancer	Survival
Osteosarcoma	Survival
Prostate cancer [36]	Survival

The initial observation of Warburg was that proliferating tumor cells consume glucose at a higher rate compared to normal cells and that they secrete most of the glucose-derived carbon in the form of lactate rather than oxidizing glucose completely. Warburg's initial hypothesis included the view that mitochondria must be defective in cancer cells as a basis for the shift to aerobic glycolysis. Recent experiments indicate that in most cancer cells at least, there is no problem with oxidative metabolism in mitochondria, and indeed the conversion of pyruvate to lactate based on lactic dehydrogenase enzyme is an important promoter of growth and tumorigenicity [38].

There is growing awareness that the activation of aerobic glycolysis is just one of the metabolic programs that are crucial to the rapidly proliferating

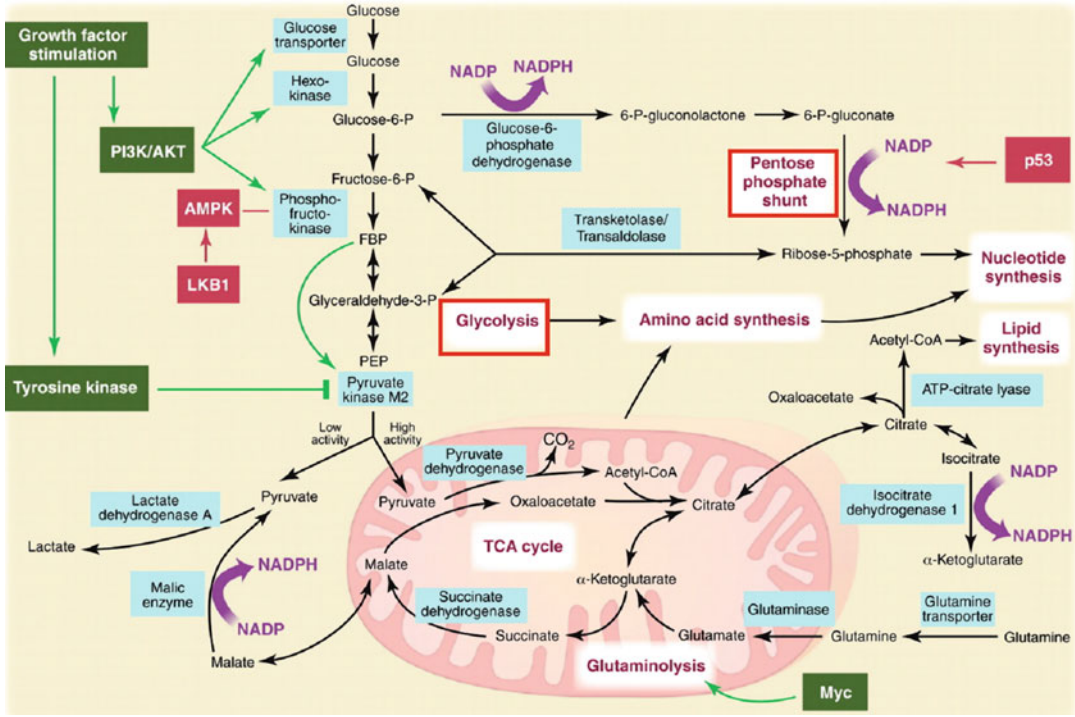

Fig. 11 Emerging view of the Warburg effect

tumor cell. In addition, there is lipid biosynthesis and glutamine-dependent anaplerosis, a term used to describe replacement of intermediates within the Krebs cycle. The purpose of these metabolic flux pathways appears to be threefold: (1) to provide energy for the biochemical processes of growth and metabolism required by proliferating cells; (2) to provide the carbon backbone for key macromolecules such as nucleic acids, lipids, and proteins; and (3) to help control the redox balance within the tumor cell. Signal transduction molecules and gene expression have now been identified that are the natural regulators of these fluxes and include the signal transduction pathways, especially PI3K\AKT\mTor axis, hypoxia-induced growth factor alpha (HIF-1 alpha), and Myc, as some of the more important cellular modulators of metabolism [39].

Thus, a more complete picture is emerging with regard to the altered metabolism of cancer cells. Among the drivers that stimulate the altered metabolism, the tumor microenvironment tends to be hypoxic with increased concentrations of HIF-1 alpha and oncogenic signaling, through a variety of known oncogenes such as Ras or Myc. In addition, suppressor proteins like p53 may play a role. The p53 suppressor protein stimulates the gene encoding synthesis of cytochrome c oxidase protein, so when p53 is disabled by mutation, there is direct interference with the mitochondrial respiratory chain. The altered metabolism confers certain advantages, such as increased biosynthesis of nucleotides, proteins, phospholipids, and fatty acids; increased glycolysis also directly inhibits apoptosis by neutralizing reactive oxygen species through the production of NADPH. In addition, there are liabilities with this approach, because toxic metabolites such as lactate and noncanonical nucleotide species tend to accumulate. Finally, a high energetic demand requires that alternative substrate such as fatty acids may need to be converted to ATP in order to meet the energy requirements of the cell [40].

Recently, glutamine has been recognized as an essential nutrient for cell growth and viability of some cancers, and in fact, tumor cells can become "addicted" to glutamine. In this case, the tumor cells fuel their growth by a combination of glucose and glutamine. Whereas PI3K and AKT are the important signal transduction molecules which control glucose uptake, recent studies suggest that MYC oncogene may be crucial for the control of glutamine uptake. Glutamine plays a key role in maintenance of Krebs cycle intermediates, as well as providing energy in the form of ATP [41]. Thus in the situation of active glutaminolysis, glucose and glutamine are the source of energy, and most of the other substrates which are taken up contribute to macromolecular synthesis.

Figure 12 shows glutamine uptake in brain tumor compared to [^{18}F]FDG imaging. In some cases, ^{18}F-glutamine may be superior to [^{18}F]FDG imaging, because there is negligible uptake of glutamine into cerebral cortex, unlike [^{18}F]FDG uptake driven by glycolysis, and the brain is an obligate user of glucose. From this, it is clear that certain oncogenes, with known functions such as the receptor tyrosine kinases, interact with metabolism through PI3K/AkT/mTor pathway. PTEN, as a natural inhibitor of this pathway, would be expected to have a role in metabolic activation. Other tumor suppressor proteins such as p53 are also thought to have an emerging role in modulating cancer cell metabolism, particularly by favoring oxidative phosphorylation and reducing glycolysis when active. When p53 is deactivated by mutation, glycolysis is favored.

Additional metabolic enzymes that may have oncogenic function include fumarate hydratase (associated with leiomyosarcoma) and succinate dehydrogenase (paraganglioma). When these enzymes are defective, accumulation of fumarate and succinate occurs. The excess of these metabolites causes overexpression of HIF-1 alpha, which promotes the vascularization of tumor as well as increased glycolysis, and may explain the tumor development. Recently, 70% of gliomas have been found to have mutations in isocitrate dehydrogenase enzymes (IDH1 and IDH2), suggesting a role for metabolic enzymes as oncogenes or tumor suppressors [42]. Data recently reported suggests that this mutation in IDH1 is not a loss of function but instead leads to the ability to produce 2-hydroxygutarate, a metabolite whose excess has been associated with human malignancy in patients with inborn errors of 2-HG metabolism [43].

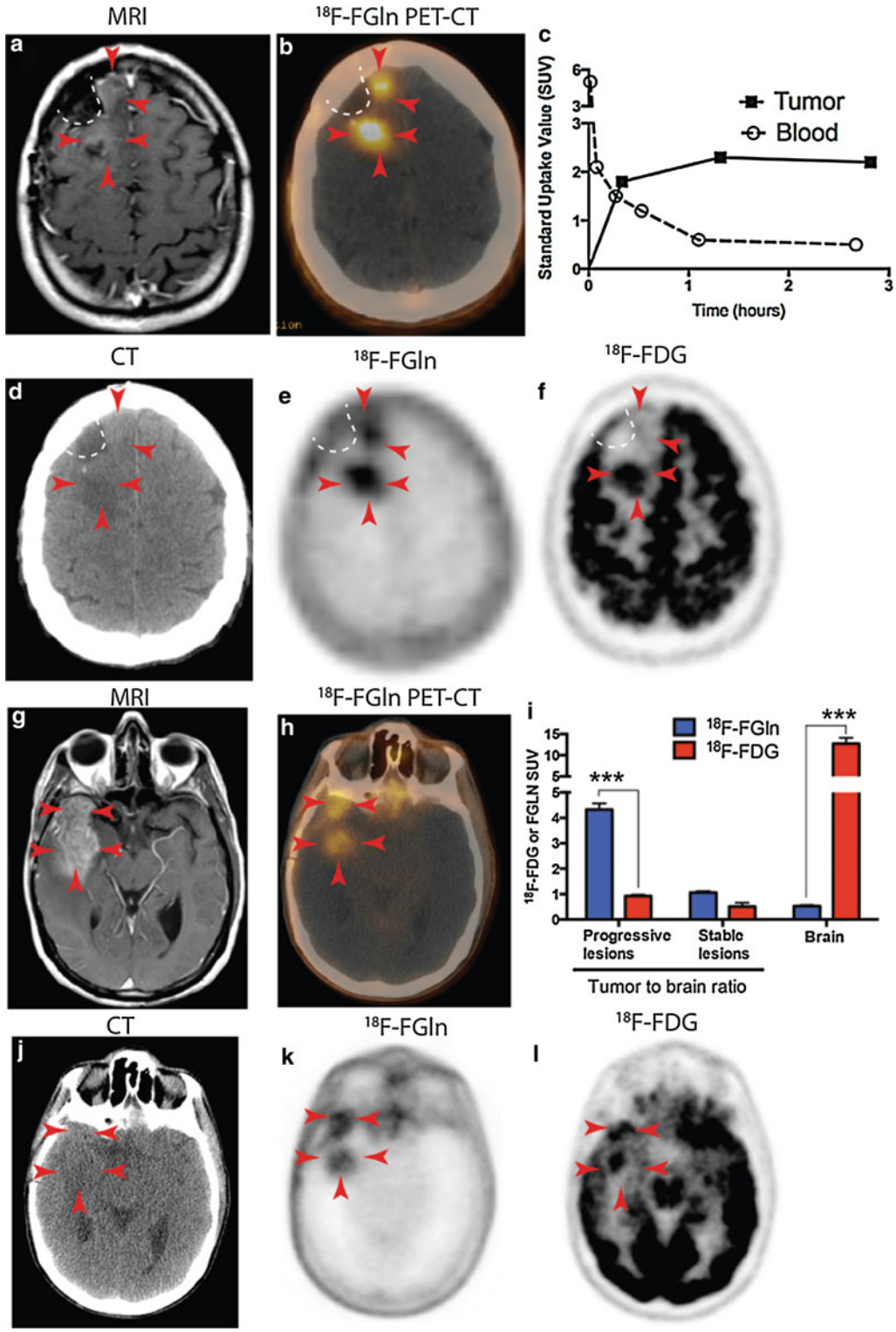

Fig. 12 Uptake in brain tumor: glutamine vs. [^{18}F]FDG (Courtesy of Mark Dunphy, DO of MSKCC)

Correlation of increased [^{18}F]FDG uptake with poor prognosis. Molecular imaging of radiotracers has been greatly enhanced by the introduction of relatively simple quantitative concepts, such as standardized uptake value (SUV). The SUV is a relative uptake in tissue (commonly tumor), corrected for body size and amount of injected activity, and may be expressed as maximum SUV in a region, average SUV, corrected for body weight, lean body mass [44]. (As a mass correction, lean body mass is preferred, since there is the least correlation of this parameter with tumor uptake and blood SUV. Tumor response based on SUV measures has recently been proposed in the "PERCIST" algorithm, and the advantages of PET-[^{18}F]FDG imaging based on SUV measures for monitoring treatment response has been proposed [4]. The SUV in various forms is available as a standard measure on most PET cameras in use over the past 10 years. Therefore it is no surprise that correlations with prognosis and SUV have been estimated for a variety of tumors. Table 2 is a list of tumor types which have shown a strong inverse correlation of SUV with prognosis.

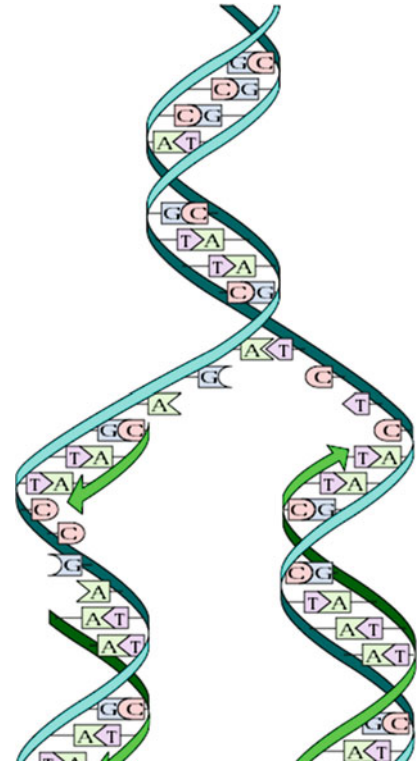

Fig. 13 DNA synthesis. The four component bases found in DNA are adenine (abbreviated *A*), cytosine (*C*), guanidine (*G*), and thymidine (*T*)

Proliferation Imaging

Tumor tissue has an accelerated rate of growth, and this process can be measured by evaluating changes in volume by CT imaging or by molecular imaging of processes that are accelerated during cell division, in particular, the synthesis of DNA and its intermediates. A diagram of the key biochemical form is provided showing the structure of several of these. Several tracers have been proposed to study this phenomenon. DNA may be built up from component bases, as shown in Fig. 13. The bases are added to the pentose sugar ribose to form the nucleoside cytosine, uridine, and thymidine, with subsequent phosphorylation, to the triphosphate, using thymidine kinase. The exchange is quite rapid between tissue and blood during periods of tumor growth, and nucleosides like thymidine are rapidly added to the DNA chain, at the appropriate site (see below). The DNA strand is built up base by base along a backbone formed by the linked sugar molecules, proceeding from the replication fork, thymidine binds to adenine (T-A), cytosine binds to guanine (C-G), and a triplet of bases encode for a single amino acid.

^{18}F-FLT Imaging of Proliferation After Chemotherapy

Several tracers have been proposed to study this phenomenon, and chemical structures of a group of pyrimidine-based tracers are shown in Fig. 14. Of these, ^{18}F-FLT or fluoro-L-thymidine, is the

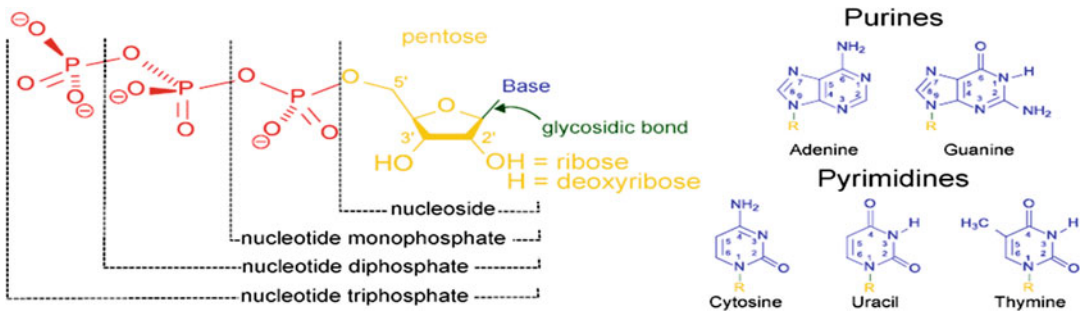

Fig. 14 Chemical structure of key purine and pyrimidine intermediates, along with pattern of phosphorylation prior to incorporation into DNA

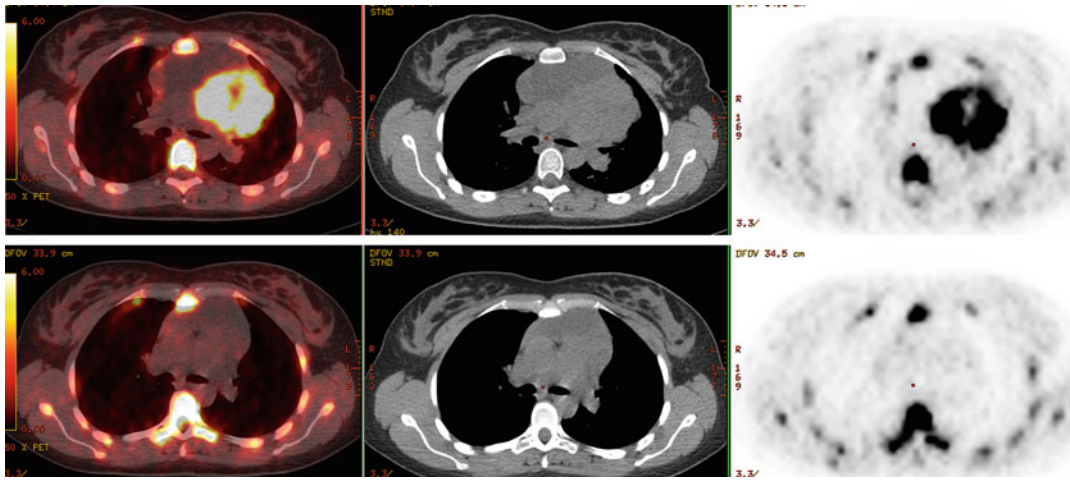

Fig. 15 ^{18}F-FLT imaging after chemotherapy in non--Hodgkin's lymphoma. The patient is imaged after two cycles of RCHOP chemotherapy. The upper row is the baseline study and the *bottom row* is post-therapy. There is rapid proliferation at baseline, which is stopped by effective therapy

most important and has been used extensively in clinical trials. An example is shown of the effect of chemotherapy on the uptake of ^{18}F-FLT in lymphoma is shown in Fig. 15.

The patient in Fig. 15 was imaged after two cycles of RCHOP chemotherapy. The upper row is the baseline study and therapy. Abnormal proliferation is an important component of the malignant state, and a tracer such as ^{18}F-FLT has potential for major benefit in evaluating tumors. ^{18}F-FLT is taken up by nucleoside transporters on the membrane of tumor cells, is phosphorylated by thymidine kinase, and used in the exogenous pathway under the enzymatic control of thymidine kinase, but is not incorporated into DNA. The phosphorylated form is retained in tumor.

Apoptosis

Apoptosis is an important process in the life cycle of normal cells. Programmed cell death allows the cell to undergo an energy-dependent well-orchestrated process of involution. Apoptosis can

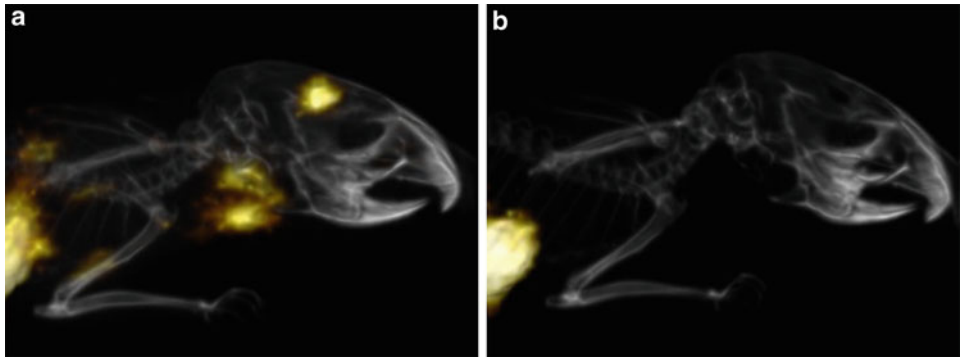

Fig. 16 In vivo whole-body PET/CT imaging of [^{18}F] PARPi in orthotopic brain tumor-bearing mice. (**a**) Fused PET/CT coronal images of a brain orthotopic U251 MG tumor-bearing mouse acquired at 2 h postinjection of [^{18}F] PARPi (*left*) or the blocking agent olaparib (500-fold excess) followed by [^{18}F]PARPi (*right*). (**b**) PET quantification of U251 MG tumors from images acquired at 30 min and 2 h postinjection ($n = 10$) (Courtesy of Drs. Thomas Reiner and Wolfgang Weber, MSKCC; from [46])

be induced by both intrinsic and extrinsic pathways, and one of the hallmarks of cancer is resistance to the apoptotic process [45]. Overcoming this resistance through therapy may contribute to accelerated treatment response in some patients. One of the earliest events in the process of apoptosis is a reversal of the normal cell membrane lipid structure, with exposure of phosphatidylserine on the outer leaflet of the cell membrane. In normal cells, phosphatidylserine is confined to the inner leaflet of the cell membrane. The externalization of this phospholipid allows the involuting cell to bind selectively to clotting factors and proteins. A physiologic protein, annexin V, has an affinity of $>10^{-8}$ for membrane-bound phosphatidylserine. This protein has been labeled with technetium-99 m and was found to localize at sites of apoptosis both in experimental animals and in patients undergoing chemo- or radiotherapy. Apoptosis also occurs in non-neoplastic conditions, such as immune-induced inflammation and acute myocardial infarction. An alternative to annexin as a marker of apoptosis has been developed by comparing many different factors that bind to apoptotic cells.

PARP is an important enzyme in the repair of DNA and is highly overexpressed in cancer. Recently PARP-1 has been recognized as an important therapeutic target in many tumor types. Imaging agents have been developed that successfully image animal models of orthotopic glioblastoma tumors, with uptake that can be blocked by therapeutic PARP-1 inhibitor drugs (Fig. 16).

Oncogene and Non-oncogene Addiction

Cells that are nonmalignant reside within a particular tissue and receive growth and other control signals through a network of signal transduction molecules, which are illustrated diagrammatically as a series of interconnecting lines (Fig. 17). In cancer cells, the process of intracellular communication may be co-opted by specific driver mutations in *otherwise* normal genes, leading to an abnormal gene called the oncogene. The oncogene produces abnormal gene products, oncoproteins, that drive oncogenesis and lead to malignant cell behavior. Driver mutations that are examples of oncogene addiction include overexpression of HER2 in breast cancer, c-Kit mutation in GIST, and ABL kinase mutation in leukemias. Mutations can occur in kinases, which have a signal transmitting function; this

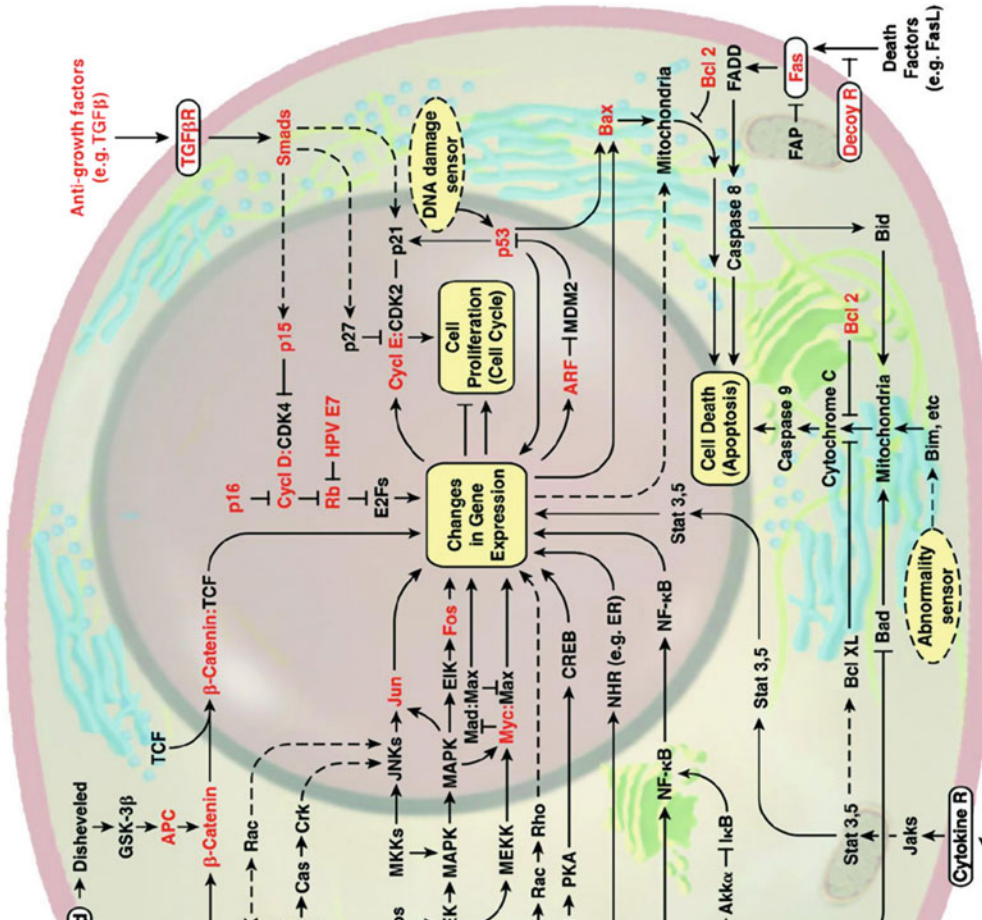

Fig. 17 Diagrammatic illustration of a network of signal transduction molecules as a series of interconnected lines. They transmit growth and other control signals to nonmalignant cells that reside within a particular tissue (From [2, 47], with permission)

can disrupt functioning. Examples include EGFR mutations, c-KiT mutations, and ABL kinase mutations. Other commonly mutated oncogenes include genes controlling Rb, P53, and PTEN, proteins that suppress a tendency toward tumor formation. In fact, cancer occurs when a series of mutations have developed that cooperate to create the complex malignant phenotype.

Examples of Imaging the Action Driver Mutations in Cancer Cells Indirectly Through Effects on Metabolism

The mutations that drive the cancer cell into the malignant state can be thought of in three categories: gain-of-function mutations, translocations, and amplifications. Treatments and imaging are focused on these driver mutations, and in particular, the success of kinase inhibitors has validated this concept.

BRAF Inhibition in Advanced Melanoma with V600E Mutation

The highly specific tyrosine kinase inhibitor PLX 4032 appears effective in patients with metastatic malignant melanoma. About 70% of melanomas have a significant response based on RECIST 1.1 criteria when treated with PLX 4032. Eighteen patients had a CR and one patient had a PR. Patients had a rapid response to the drug, with marked reduction of [^{18}F]FDG uptake. For therapy to be effective, PLX 4032 must be administered at a dose sufficient to inhibit >80% of the BRAF pathway [48] (Fig. 18).

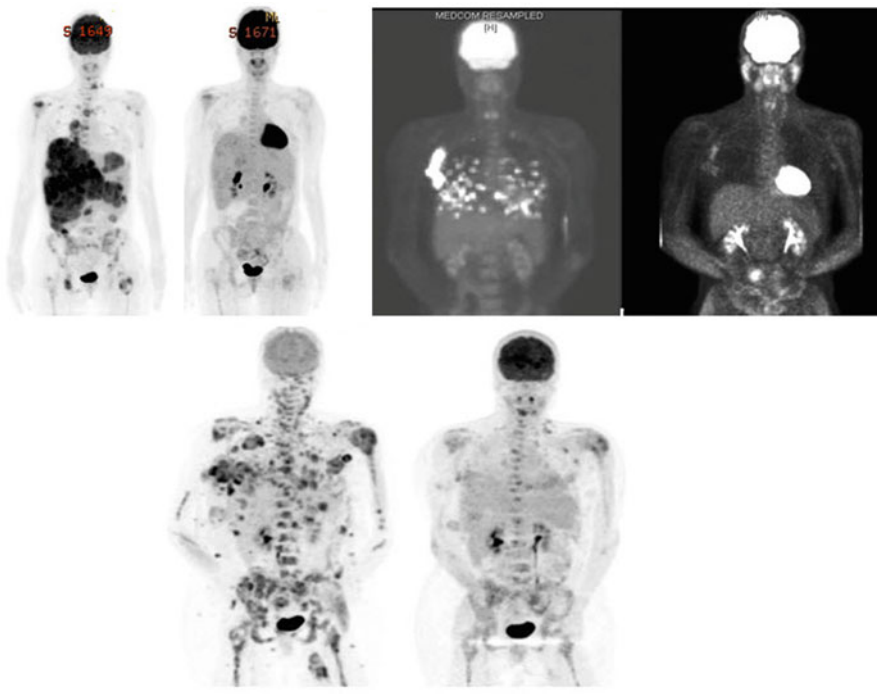

Fig. 18 Of 27 patients, three are shown: baseline study (*left*) and follow-up at 2 weeks posttreatment (*right*) (From [47], with permission)

Inhibition of MEK, a Downstream Signal Transduction Molecule in the RAS/BRAF/ERK Pathway, Can Reverse ^{131}I Resistance in Patients with Thyroid Cancer

Thyroid uptake of iodine in papillary thyroid cancer occurs because of a set of thyroid genes responsible for iodine transport and organification in normal thyroid tissue. These genes are often lost during cancer formation. Recent data mining in the databases for papillary thyroid cancer has led to important correlations between driver mutations responsible for tumor formation, such as the V600E mutation in BRAF, as well as driver mutations in RAS. Agrawal and colleagues have developed a thyroid differentiation score (TDS) consisting of nine genes integral to iodine uptake and differentiation. A heat map of these genes is shown in Fig. 19. In general, the vertical columns, which are mostly red, have higher differentiation scores.

Abnormalities of the BRAF/ERK signaling pathway promote the malignant state in thyroid cancer, and inhibition of MEK leads to redifferentiation of experimental models of human thyroid cancer in animals (James Fagin, personal communication, Sloan Kettering Institute). Patients with ^{131}I refractory thyroid cancer were treated with the MEK inhibitor AZD 6244 for 5 weeks and then restudied with quantitative PET imaging using iodine-124. Approximately two-thirds of the patients had restoration of radioiodine uptake and went on to be treated with ^{131}I-iodide, with excellent clinical response to treatment (Fig. 20) [50].

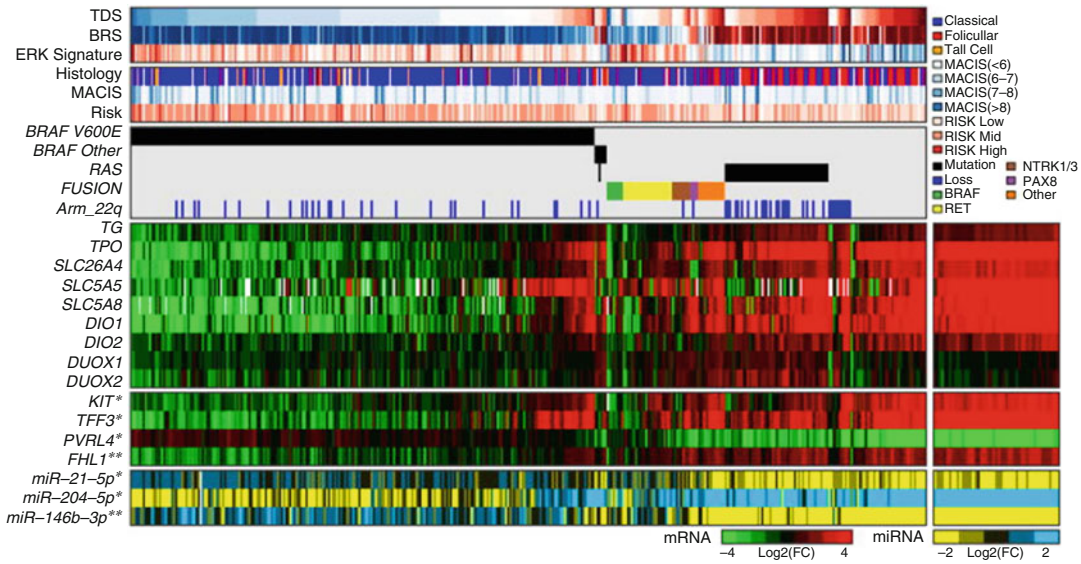

Fig. 19 Thyroid differentiation score (TDS) across the cohort with tumors sorted by driver mutation and TDS. Below TDS are the *BRAF*^{V600E}-*RAS* score (BRS), ERK signature, histological type, MACIS score, risk of recurrence, driver mutations, and gene expression data for nine thyroid genes used to derive the TDS [*TG*, *TPO*, *SLC26A4* (pendrin), *SLC5A5* (Na/I symporter), *SLC5A8* (apical iodide transporter), *DIO1*, *DIO2*, *DUOX1*, and *DUOX2*)], four selected mRNAs correlated to TDS, and three selected miRs correlated to TDS. Featured mRNA (except for 16 thyroid genes) and miRNA genes were selected based on Spearman correlation to TDS in the *BRAF*^{V600E} cohort (*) and the full cohort (**) (From [49], with permission)

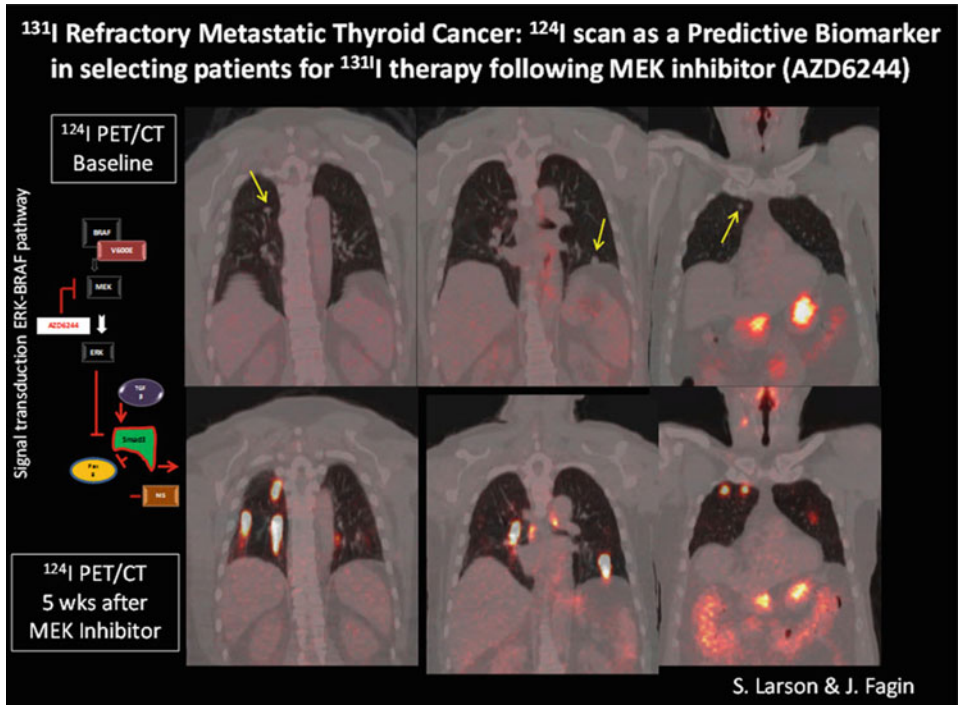

Fig. 20 In baseline scan, *upper image*, coronal projection, *arrows* point out metastatic sites of pulmonary metastases that do not take up radioiodine at 48 h after oral administration. In the *lower image*, taken 5 weeks later after treatment with the MEK inhibitor AZD 6244, all of these lesions have taken up sufficient amounts of radioiodine to predict therapeutic effect. This patient had a reduction in size of pulmonary nodules as well as significant fall in serum thyroglobulin (Data not shown)

Imaging the Driver Oncogene in Castrate-Resistant Prostate Cancer: The Androgen Receptor Axis

Dihydrotestosterone, a metabolite of testosterone, is the most abundant androgen at the tissue level in vivo and binds to AR in vivo. We have extensively studied a radiolabeled analog, ^{18}F-FDHT, to explore AR expression and in vivo binding in patients with the lethal form of prostate cancer, namely, castrate-resistant prostate cancer (CRPC). Toxicity, patient dosimetry, conditions of use, and optimized analysis were assayed, and ^{18}F-FDHT continues to be used in a variety of clinical trials that are ongoing, e.g., 00–095 in metastatic CRPC [51–54].

We have adapted this approach to the study of AR expressing primary and metastatic prostate cancers. We directly image AR under a short-time medical castration to testosterone levels < 50 pg/mL. We have also used glycolysis marker [^{18}F]FDG, a clinical standard tracer, within 24–48 h as a marker of active tumor metabolism, and have demonstrated high patient acceptance of a two-day sequence of imaging, requiring about 1 h of scanning each day. In addition, we have analyzed imaging biopsies to explore the presence of the downstream androgen effector proteins, particularly HK2, PSMA, and STEAP [55–57] for consideration of later AR-axis monitoring using radiolabeled antibody approaches as a possible pharmacodynamic approach of AR-axis inhibition in later drug trials.

The rationale for this approach is summarized in Fig. 21, which is a diagrammatic representation

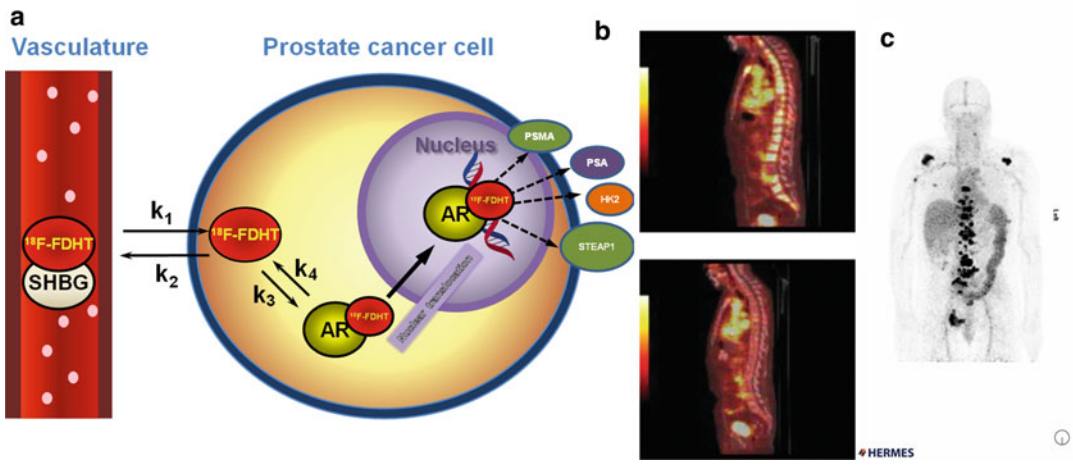

Fig. 21 (**a**) Model of AR axis. (**b**) ^{18}F-FDHT before (*top*) and after (*bottom*) treatment with enzalutamide to suppress AR uptake of ^{18}F-FDHT along the spine. (**c**) ^{89}Zr-anti-STEAP imaging shows uptake in metastases along the spine. The AR axis is driven by androgens that bind to AR in cytoplasm and transport to the nucleus, where the AR complex binds to hormone-responsive elements. Downstream effectors that are activated may be imaged, such as PSMA, PSA, HK2, and STEAP (See [58] for details)

of the binding of the radiolabeled agonist, ^{18}F-FDHT to AR, with the subsequent translocation to the nucleus with binding to hormone-responsive elements on DNA that cause downstream androgen effects.

Androgen Receptor (AR) as Oncogenic Driver in Prostate Cancer

AR is activated in CRPC, the lethal form of the disease. AR inhibitors are an important component of therapy in this disease. Figure 21 shows the application of MI in the form of ^{18}F-FDHT (16β-^{18}F-dihydrotestosterone), an AR-binding ligand. Recently, effective androgen blockade agents have been introduced for therapy of prostate cancer. Figure 22 shows baseline uptake of ^{18}F-FDHT in the metastatic tumor in the vertebrae of a patient with CRPC. All 22 patients treated in this Phase I trial showed displacement of ^{18}F-FDHT tracer by the AR-binding drug MDV3100, indicating that the AR displacement agent was hitting the AR target. The AR axis is responsible for downstream effector molecules that are a part of the androgen effects. For example, common proteins produced by prostatic-like tissues include the four listed in Fig. 21: STEAP, a membrane transport protein; PSMA, a NAALADase enzyme; and PSA and HK2, kallikrein-related peptidases produced to keep semen liquified, thus enhancing sperm motility.

Imaging of Carbonic Anhydrase 9 as a Pathognomonic Indication of Clear Cell Renal Cancer

A driver mutation occurs in renal cancer with mutation of the von Hippel-Lindau (VHL) protein. At normal levels of tissue oxygen, VHL is tightly bound to the transcription factor HIF-1alpha, inactivating it. In renal cell cancer, there is an inactivating mutation of VHL, and HIF-1 alpha is continuously activated, with chronic production of downstream effector proteins, especially VEGFR, and also carbonic anhydrase 9 (CA9), as proteins that are normally

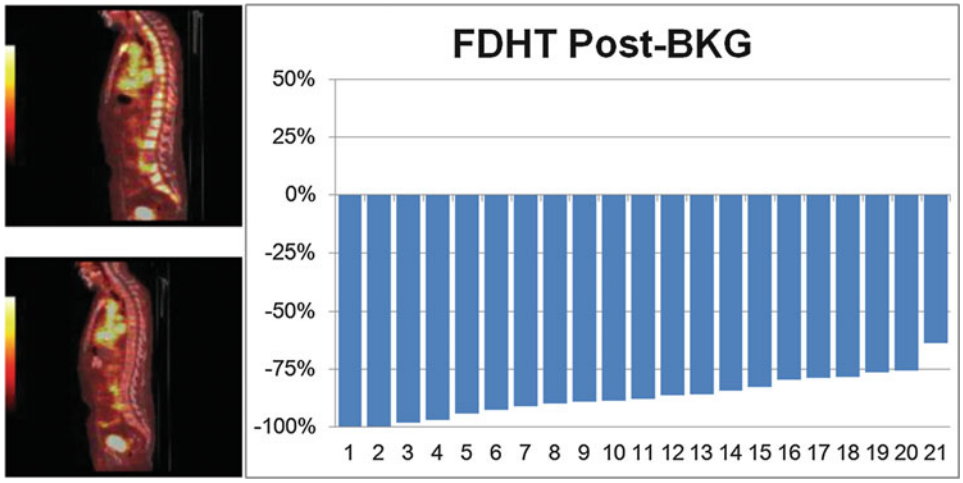

Fig. 22 *Left*, *top*: Baseline sagittal PET imaging obtained with the radiotracer ^{18}F-FDHT (16β-^{18}F-dihydrotestosterone). *Left*, *bottom*: Image obtained 4 weeks after injection of beginning treatment with MDV3100, an AR blocker. The radiotracer is the analog of the dominant androgen at the tissue level in man, namely, dihydrotestosterone (DHT). *Right*: background-corrected changes in average SUV_{max} for all lesions in the treated patients. Therapy of prostate cancer. Fig. 8 shows baseline uptake of ^{18}F-FDHT in the metastatic tumor in the vertebrae of a patient with CRPC. All 22 patients treated in this Phase I trial showed displacement of ^{18}F-FDHT tracer by the AR-binding drug MDV3100, indicating that the AR displacement agent was hitting the AR target

activated in hypoxic tissues. Clear cell renal cancer is produced in this setting. ^{124}I-cG250 is a positron-emitting antibody that targets CA9, which has been introduced to assist in surgical planning of masses of the kidney. As shown in Fig. 23, there is uptake in a mass in the kidney bed with excellent contrast, at 7 days after injection of ^{124}I-cG250 [59]. Targeted therapy with sunitinib and sorafenib is used in this clinical setting to block the action of VEGFR.

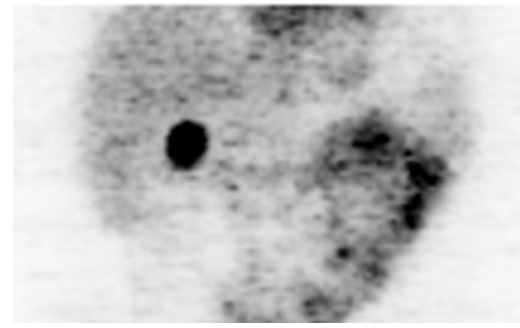

Fig. 23 Uptake in a mass in the kidney bed with excellent contrast, at 7 days after injection of ^{124}I-cG250

Future Applications

Many other molecular imaging approaches are available to characterize one or more aspects of a neoplasm, including ^{18}F-estradiol for breast cancers, amino acid incorporation (FACBC, glutamate), ^{68}Ga-PSMA-ligand for prostate imaging, and ^{68}Ga-DOTATATE for neuroendocrine imaging. Some of these have been approved, and others will likely be available within the next 5 years. However, due to the lengthy process of regulatory approval, the major radiopharmaceutical for evaluation of the tumor patient will remain [^{18}F]FDG. With increased understanding of changes in glucose transporter expression by the tumor cell, it is likely that more sophisticated prognostic indices than SUV_{max} may be developed.

It is also likely that genomic analysis of circulating tumor cells may be used as a gatekeeper, to determine if a more selective MI probe PET/CT study is likely to provide clinically useful information.

The development of radiotracer probes for molecular imaging continues to proceed at a very rapid pace. Moreover, drug companies are beginning to recognize the important role that molecular imaging can play in facilitating drug development through an improved understanding of the biology of the cancer process. It is highly likely that very soon we will see ever more remarkable radiotracers, probably in combination with MRI agents and optical agents, because of the ease with which fusion imaging may be obtained in order to exploit the combined information. The field of nanotechnology offers many opportunities for probe development, including serving as a carrier for highly selective radiotracers such as complementary probes like DNA-binding or RNA-binding proteins, as well as radiolabeled drugs. Theranostic agents combine the potential for diagnosis and therapy, so that agents are not only intended to visualize tumors but in effect guide therapeutic delivery. This is already beginning in the exciting field of image-guided interventional radiology, but will extend to tracers with both diagnostic and therapeutic potential. For example, it is easy to contemplate the radiolabeled drug carried in nanoparticles so that the quantification of the payload delivered will serve as a sensor that provides, through quantitative imaging, the total amount of drug that is both taken up and retained within the tissues. Such theranostic approaches will improve selection of patients for a given type of therapy and may allow for tailoring treatment to the individual patient.

Table 3 Commonly used radioantibodies at MSKCC

Radioantibody	Target
^{68}Ga-Fab'$_2$ herceptin	HER2 receptor (breast, prostate, lung) [60, 61]
^{124}I-A33	A33 antigen (colorectal) (see Fig. 20)
^{124}I-cG250	Carbonic anhydrase 9 (hypoxia, renal cell) [59]
$^{124/131}$I-3F8	GD2 (neuroblastoma, melanoma) [62]
$^{124/131}$I-8H9	B7H3 (melanoma, prostate, pediatric cancers, sarcoma) [63]
^{233}Ac-^{213}Bi-M195	CD33 (AML, CML) [64]
^{89}Zr-J591	PSMA (prostate, tumor vasculature) [65, 66]

Radioantibody and Radiopeptide Imaging and Therapy (Theranostics) Will Drive Our Field for the Next Decade and Beyond

Radiolabeled antibodies and peptides have been used for molecular imaging and in some cases therapy due to the highly selective nature of the antibody-antigen bond. Advances in the molecular biology of antibody production have greatly improved antibodies both as therapeutics and as carriers of radioactive, toxin, or chemotherapy payloads. A table of commonly used antibodies for targeting and therapy applications at MSKCC is shown below (Table 3). Antibodies fall in one of the most rapidly expanding categories of new drugs, and successful drugs include Herceptin (HER2), Avastin (VEGF), rituximab (CD20), ipilimumab (CTLA4), cetuximab (Erbitux), and panitumumab (Vectibix; EGFR). Tumors overexpress antigens that may occur at earlier developmental stages of the cell. Common terms to describe such antigen expression include differentiation antigen (CD33, GD2, PSMA), tumor-testis antigen (A33), oncofetal antigen (GD2, B7H3), and driver mutation-associated antigen (HER2, CA9). There is much more to come, and, in fact, these just represent the tip of the iceberg of biologic agents that will offer new staging and diagnostic benefits in the age of precision medicine. There is great promise, even laboratory evidence [67, 68], that in the decade ahead, we shall be able to achieve therapeutic ratios of radiotargeting to tumor that are curative, even possibly for the most highly resistant solid tumors (Fig. 24)!

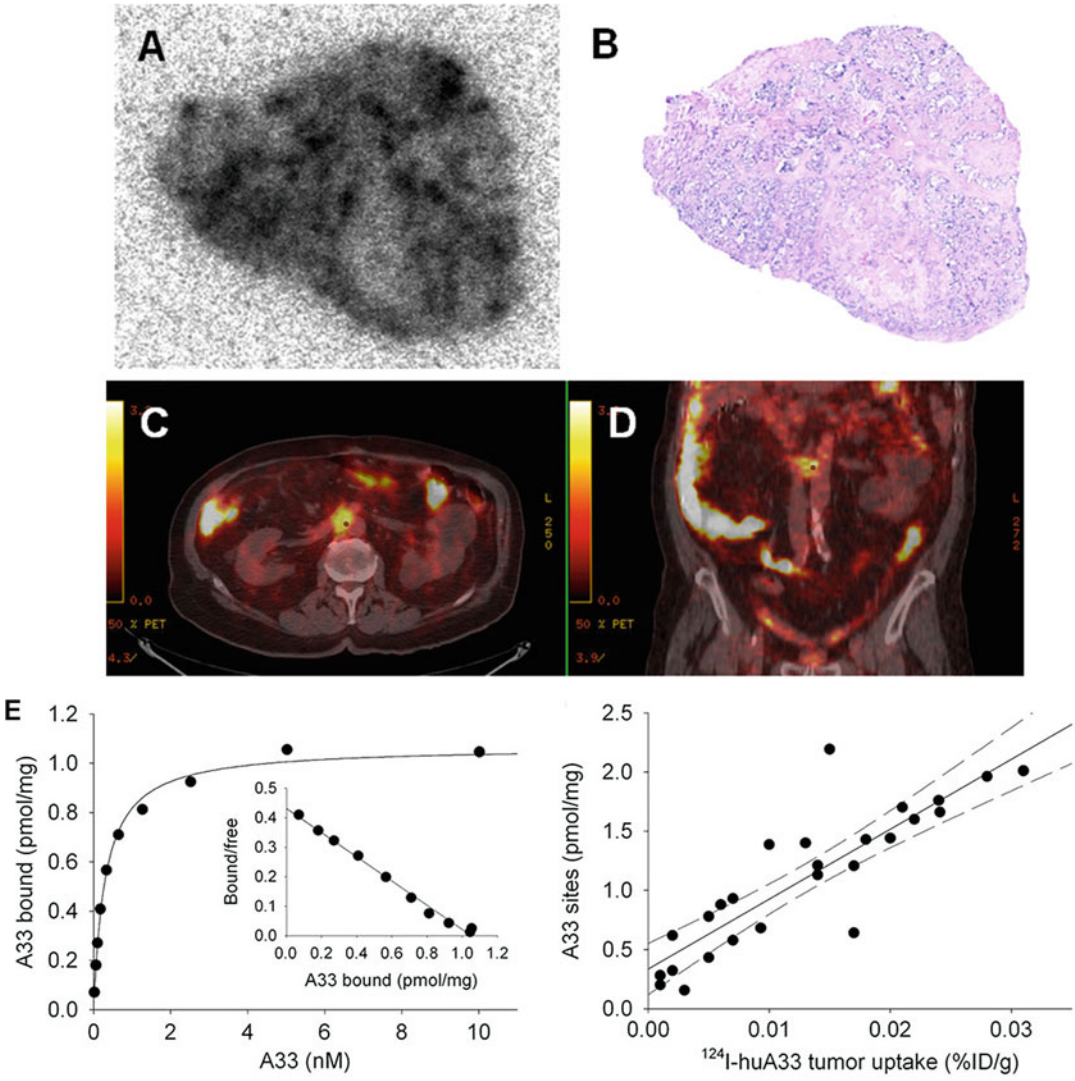

Fig. 24 ^{124}I-A33 images obtained at 5 days postinjection. Protocol involved surgical sampling, which revealed an occult periaortic lymph node containing tumor. Autoradiography (**a**) and H&E histology (**b**) showing that the antibody targets the cellular component of the mass. Fusion images with PET displayed in hot body format, so that the most intense radioactivity is white and the least intense in *red*, overlaid onto the axial (**c**) and coronal (**d**) (Images courtesy of Jorge Carrasquillo, MD). Perhaps the most important concept illustrated by these images is the fact that radioantibody uptake is driven by antigen concentration at the tumor level (**e**). This has important implications, including nonlinear uptake kinetics. Another important fact derived from this study was that occupancy of the tumor receptor (A33, in this case) was in fact at 20–50% occupancy, not at tracer dose levels (From [69])

References

1. Vogelstein B, Papadopoulos N, Velculescu VE, Zhou S, Diaz Jr LA, Kinzler KW. Cancer genome landscapes. Science (New York, NY). 2013;339:1546–58. doi:10.1126/science.1235122.
2. Hanahan D, Weinberg RA. The hallmarks of cancer. Cell. 2000;100:57–70 .S0092-8674(00)81683-9 [pii]
3. Young H, Baum R, Cremerius U, Herholz K, Hoekstra O, Lammertsma AA, et al. Measurement of clinical and subclinical tumour response using [^{18}F]-fAluorodeoxyglucose and positron emission tomography: review and 1999 EORTC recommendations.

European Organization for Research and Treatment of Cancer (EORTC) PET Study Group. Eur J Cancer. 1999;35:1773–82 .S0959804999002294 [pii]
4. Wahl RL, Jacene H, Kasamon Y, Lodge MA. From RECIST to PERCIST: evolving considerations for PET response criteria in solid tumors. J Nucl Med. 2009;50(Suppl 1):122S–50S. doi:10.2967/jnumed.108.057307.
5. Folkman J. Tumor angiogenesis: therapeutic implications. N Engl J Med. 1971;285:1182–6. doi:10.1056/NEJM197111182852108.
6. Ferrara N, Adamis AP. Ten years of anti-vascular endothelial growth factor therapy. Nat Rev Drug Discov. 2016;15:385–403. doi:10.1038/nrd.2015.17.
7. Gaykema SB, Brouwers AH, Lub-de Hooge MN, Pleijhuis RG, Timmer-Bosscha H, Pot L, et al. ^{89}Zr-bevacizumab PET imaging in primary breast cancer. J Nucl Med. 2013;54:1014–8. doi:10.2967/jnumed.112.117218.
8. Zhu Z, Miao W, Li Q, Dai H, Ma Q, Wang F, et al. 99mTc-3PRGD2 for integrin receptor imaging of lung cancer: a multicenter study. J Nucl Med. 2012;53:716–22. doi:10.2967/jnumed.111.098988.
9. Stacy MR, Maxfield MW, Sinusas AJ. Targeted molecular imaging of angiogenesis in PET and SPECT: a review. Yale J Biol Med. 2012;85:75–86.
10. Beer AJ, Grosu AL, Carlsen J, Kolk A, Sarbia M, Stangier I, et al. [^{18}F]galacto-RGD positron emission tomography for imaging of alphavbeta3 expression on the neovasculature in patients with squamous cell carcinoma of the head and neck. Clin Cancer Res. 2007;13:6610–6. doi:10.1158/1078-0432.CCR-07-0528. 13/22/6610 [pii].
11. Schliemann C, Neri D. Antibody-based targeting of the tumor vasculature. Biochim Biophys Acta. 1776;2007:175–92. doi:10.1016/j.bbcan.2007.08.002. S0304-419X(07)00028-5 [pii].
12. Rajendran JG, Wilson DC, Conrad EU, Peterson LM, Bruckner JD, Rasey JS, et al. [^{18}F]FMISO and [^{18}F]FDG PET imaging in soft tissue sarcomas: correlation of hypoxia, metabolism and VEGF expression. Eur J Nucl Med Mol Imaging. 2003;30:695–704. doi:10.1007/s00259-002-1096-7.
13. Garcia-Barros M, Paris F, Cordon-Cardo C, Lyden D, Rafii S, Haimovitz-Friedman A, et al. Tumor response to radiotherapy regulated by endothelial cell apoptosis. Science (New York, NY). 2003;300:1155–9. doi:10.1126/science.1082504. 300/5622/1155 [pii].
14. Levchenko A, Mehta BM, Niu X, Kang G, Villafania L, Way D, et al. Intercellular transfer of P-glycoprotein mediates acquired multidrug resistance in tumor cells. Proc Natl Acad Sci U S A. 2005;102:1933–8. doi:10.1073/pnas.0401851102. 0401851102 [pii].
15. Chen DS, Mellman I. Oncology meets immunology: the cancer-immunity cycle. Immunity. 2013;39:1–10. doi:10.1016/j.immuni.2013.07.012.
16. Couzin-Frankel J. Breakthrough of the year 2013. Cancer immunotherapy. Science (New York, NY). 2013;342:1432–3. doi:10.1126/science.342.6165.1432.
17. Page DB, Postow MA, Callahan MK, Allison JP, Wolchok JD. Immune modulation in cancer with antibodies. Annu Rev Med. 2014;65:185–202. doi:10.1146/annurev-med-092012-112807.
18. Wolchok JD, Weber JS, Hamid O, Lebbe C, Maio M, Schadendorf D, et al. Ipilimumab efficacy and safety in patients with advanced melanoma: a retrospective analysis of HLA subtype from four trials. Cancer Immun. 2010;10:9 .101010 [pii]
19. Fisher B, Packard BS, Read EJ, Carrasquillo JA, Carter CS, Topalian SL, et al. Tumor localization of adoptively transferred indium-111 labeled tumor infiltrating lymphocytes in patients with metastatic melanoma. J Clin Oncol. 1989;7:250–61.
20. Koehne G, Doubrovin M, Doubrovina E, Zanzonico P, Gallardo HF, Ivanova A, et al. Serial in vivo imaging of the targeted migration of human HSV-TK-transduced antigen-specific lymphocytes. Nat Biotechnol. 2003;21:405–13. doi:10.1038/nbt805.
21. Carrasquillo JA, Bunn Jr PA, Keenan AM, Reynolds JC, Schroff RW, Foon KA, et al. Radioimmunodetection of cutaneous T-cell lymphoma with ^{111}In-labeled T101 monoclonal antibody. N Engl J Med. 1986;315:673–80. doi:10.1056/nejm198609113151104.
22. Tavare R, Escuin-Ordinas H, Mok S, McCracken MN, Zettlitz KA, Salazar FB, et al. An effective immuno-PET imaging method to monitor CD8-dependent responses to immunotherapy. Cancer Res. 2016;76:73–82. doi:10.1158/0008-5472.can-15-1707.
23. Kang Y, He W, Tulley S, Gupta GP, Serganova I, Chen CR, et al. Breast cancer bone metastasis mediated by the Smad tumor suppressor pathway. Proc Natl Acad Sci U S A. 2005;102:13909–14. doi:10.1073/pnas.0506517102. 0506517102 [pii].
24. Minn AJ, Kang Y, Serganova I, Gupta GP, Giri DD, Doubrovin M, et al. Distinct organ-specific metastatic potential of individual breast cancer cells and primary tumors. J Clin Invest. 2005;115:44–55. doi:10.1172/JCI22320.
25. Bos PD, Zhang XH, Nadal C, Shu W, Gomis RR, Nguyen DX, et al. Genes that mediate breast cancer metastasis to the brain. Nature. 2009;459:1005–9. doi:10.1038/nature08021. nature08021 [pii].
26. Comen E, Norton L, Massague J. Clinical implications of cancer self-seeding. Nat Rev Clin Oncol. 2011;8:369–77 . doi:10.1038/nrclinonc.2011.64.nrclinonc.2011.64 [pii]
27. Kim MY, Oskarsson T, Acharyya S, Nguyen DX, Zhang XH, Norton L, et al. Tumor self-seeding by circulating cancer cells. Cell. 2009;139:1315–26. doi:10.1016/j.cell.2009.11.025. S0092-8674(09)01437-8 [pii].
28. Lucignani G, Larson SM. Doctor, what does my future hold? The prognostic value of FDG-PET in solid tumours. Eur J Nucl Med Mol Imaging. 2010;37:1032–8. doi:10.1007/s00259-010-1428-y.

29. Downey RJ, Akhurst T, Gonen M, Vincent A, Bains MS, Larson S, et al. Preoperative F-18 fluorodeoxyglucose-positron emission tomography maximal standardized uptake value predicts survival after lung cancer resection. J Clin Oncol. 2004;22:3255–60. doi:10.1200/JCO.2004.11.109. 22/16/3255 [pii].
30. Pandit N, Gonen M, Krug L, Larson SM. Prognostic value of [^{18}F]FDG-PET imaging in small cell lung cancer. Eur J Nucl Med Mol Imaging. 2003;30:78–84. doi:10.1007/s00259-002-0937-8.
31. Cachin F, Prince HM, Hogg A, Ware RE, Hicks RJ. Powerful prognostic stratification by [^{18}F]fluorodeoxyglucose positron emission tomography in patients with metastatic breast cancer treated with high-dose chemotherapy. J Clin Oncol. 2006;24:3026–31. doi:10.1200/JCO.2005.04.6326. JCO.2005.04.6326 [pii].
32. Robbins RJ, Wan Q, Grewal RK, Reibke R, Gonen M, Strauss HW, et al. Real-time prognosis for metastatic thyroid carcinoma based on 2-[^{18}F]fluoro-2-deoxy-D-glucose-positron emission tomography scanning. J Clin Endocrinol Metab. 2006;91:498–505. doi:10.1210/jc.2005-1534. jc.2005-1534 [pii].
33. Pan L, Gu P, Huang G, Xue H, Wu S. Prognostic significance of SUV on PET/CT in patients with esophageal cancer: a systematic review and meta-analysis. Eur J Gastroenterol Hepatol. 2009;21:1008–15. doi:10.1097/MEG.0b013e328323d6fa.
34. Patronas NJ, Di Chiro G, Kufta C, Bairamian D, Kornblith PL, Simon R, et al. Prediction of survival in glioma patients by means of positron emission tomography. J Neurosurg. 1985;62:816–22. doi:10.3171/jns.1985.62.6.0816.
35. Schoder H, Noy A, Gonen M, Weng L, Green D, Erdi YE, et al. Intensity of 18fluorodeoxyglucose uptake in positron emission tomography distinguishes between indolent and aggressive non-Hodgkin's lymphoma. J Clin Oncol. 2005;23:4643–51. doi:10.1200/JCO.2005.12.072.
36. Meirelles GS, Schoder H, Ravizzini GC, Gonen M, Fox JJ, Humm J, et al. Prognostic value of baseline [^{18}F]fluorodeoxyglucose positron emission tomography and ^{99m}Tc-MDP bone scan in progressing metastatic prostate cancer. Clin Cancer Res. 2010;16:6093–9. doi:10.1158/1078-0432.CCR-10-1357.
37. Warburg O. On the origin of cancer cells. Science (New York, NY). 1956;123:309–14.
38. Fantin VR, St-Pierre J, Leder P. Attenuation of LDH-A expression uncovers a link between glycolysis, mitochondrial physiology, and tumor maintenance. Cancer Cell. 2006;9:425–34. doi:10.1016/j.ccr.2006.04.023. S1535-6108(06)00145-0 [pii].
39. Deberardinis RJ, Sayed N, Ditsworth D, Thompson CB. Brick by brick: metabolism and tumor cell growth. Curr Opin Genet Dev. 2008;18:54–61. doi:10.1016/j.gde.2008.02.003. S0959-437X(08)00028-2 [pii].
40. Hsu PP, Sabatini DM. Cancer cell metabolism: Warburg and beyond. Cell. 2008;134:703–7. doi:10.1016/j.cell.2008.08.021. S0092-8674(08)01066-0 [pii].
41. Wise DR, DeBerardinis RJ, Mancuso A, Sayed N, Zhang XY, Pfeiffer HK, et al. Myc regulates a transcriptional program that stimulates mitochondrial glutaminolysis and leads to glutamine addiction. Proc Natl Acad Sci U S A. 2008;105:18782–7. doi:10.1073/pnas.0810199105. 0810199105 [pii].
42. Thompson CB. Metabolic enzymes as oncogenes or tumor suppressors. N Engl J Med. 2009;360:813–5. doi:10.1056/NEJMe0810213. 360/8/813 [pii].
43. Dang L, White DW, Gross S, Bennett BD, Bittinger MA, Driggers EM, et al. Cancer-associated IDH1 mutations produce 2-hydroxyglutarate. Nature. 2009;462:739–44. doi:10.1038/nature08617. nature08617 [pii].
44. Zasadny KR, Wahl RL. Standardized uptake values of normal tissues at PET with 2-[fluorine-18]-fluoro-2-deoxy-D-glucose: variations with body weight and a method for correction. Radiology. 1993;189:847–50.
45. Reshef A, Shirvan A, Akselrod-Ballin A, Wall A, Ziv I. Small-molecule biomarkers for clinical PET imaging of apoptosis. J Nucl Med. 2010;51:837–40. doi:10.2967/jnumed.109.063917.
46. Carney B, Carlucci G, Salinas B, Di Gialleonardo V, Kossatz S, Vansteene A, et al. Non-invasive PET imaging of PARP1 expression in glioblastoma models. Mol Imaging Biol MIB Off Publ Acad Mol Imaging. 2016;18:386–92. doi:10.1007/s11307-015-0904-y.
47. McArthur GA, Puzanov I, Amaravadi R, Ribas A, Chapman P, Kim KB, et al. Marked, homogeneous, and early [^{18}F]fluorodeoxyglucose-positron emission tomography responses to vemurafenib in BRAF-mutant advanced melanoma. J Clin Oncol. 2012;30:1628–34. doi:10.1200/jco.2011.39.1938.
48. Bollag G, Hirth P, Tsai J, Zhang J, Ibrahim PN, Cho H, et al. Clinical efficacy of a RAF inhibitor needs broad target blockade in BRAF-mutant melanoma. Nature. 2010;467:596–9. doi:10.1038/nature09454. nature09454 [pii].
49. Cancer Genome Atlas Research Network. Integrated genomic characterization of papillary thyroid carcinoma. Cell. 2014;159:676–90. doi:10.1016/j.cell.2014.09.050.
50. Ho AL, Grewal RK, Leboeuf R, Sherman EJ, Pfister DG, Deandreis D, et al. Selumetinib-enhanced radioiodine uptake in advanced thyroid cancer. N Engl J Med. 2013;368:623–32. doi:10.1056/NEJMoa1209288.
51. Beattie BJ, Smith-Jones PM, Jhanwar YS, Schoder H, Schmidtlein CR, Morris MJ, et al. Pharmacokinetic assessment of the uptake of 16beta-^{18}F-fluoro-5alpha-dihydrotestosterone (FDHT) in prostate tumors as measured by PET. J Nucl Med. 2010;51:183–92. doi:10.2967/jnumed.109.066159.
52. Scher HI, Beer TM, Higano CS, Anand A, Taplin ME, Efstathiou E, et al. Antitumour activity of MDV3100 in

castration-resistant prostate cancer: a phase 1-2 study. Lancet (London, England). 2010;375:1437–46. doi:10.1016/s0140-6736(10)60172-9.
53. Fox JJ, Morris MJ, Larson SM, Schoder H, Scher HI. Developing imaging strategies for castration resistant prostate cancer. Acta oncologica (Stockholm, Sweden). 2011;50 Suppl 1:39–48. doi:10.3109/0284186x.2011.572914.
54. Fox JJ, Autran-Blanc E, Morris MJ, Gavane S, Nehmeh S, Van Nuffel A, et al. Practical approach for comparative analysis of multilesion molecular imaging using a semiautomated program for PET/CT. J Nucl Med. 2011;52:1727–32. doi:10.2967/jnumed.111.089326.
55. Ulmert D, Evans MJ, Holland JP, Rice SL, Wongvipat J, Pettersson K, et al. Imaging androgen receptor signaling with a radiotracer targeting free prostate-specific antigen. Cancer Discov. 2012;2:320–7. doi:10.1158/2159-8290.cd-11-0316.
56. Evans MJ, Smith-Jones PM, Wongvipat J, Navarro V, Kim S, Bander NH, et al. Noninvasive measurement of androgen receptor signaling with a positron-emitting radiopharmaceutical that targets prostate-specific membrane antigen. Proc Natl Acad Sci U S A. 2011;108:9578–82. doi:10.1073/pnas.1106383108.
57. Pandit-Taskar N, O'Donoghue JA, Ruan S, Lyashchenko S, Carrasquillo JA, Heller G, et al. First-in-human imaging with ^{89}Zr-Df-IAB2M anti-PSMA minibody in patients with metastatic prostate cancer: pharmacokinetics, biodistribution, dosimetry, and lesion uptake. J Nucl Med. 2016;57:1858–64. doi:10.2967/jnumed.116.176206.
58. Pandit-Taskar N, Veach DR, Fox JJ, Scher HI, Morris MJ, Larson SM. Evaluation of castration-resistant prostate cancer with androgen receptor-axis imaging. J Nucl Med. 2016;57:73s–8s. doi:10.2967/jnumed.115.170134.
59. Divgi CR, Pandit-Taskar N, Jungbluth AA, Reuter VE, Gonen M, Ruan S, et al. Preoperative characterisation of traget renal carcinoma using iodine-124-labelled antibody chimeric G250 (^{124}I-cG250) and PET in patients with renal masses: a phase I trial. Lancet Oncol. 2007;8:304–10. doi:10.1016/S1470-2045(07)70044-X.
60. Smith-Jones PM, Solit D, Afroze F, Rosen N, Larson SM. Early tumor response to Hsp90 therapy using HER2 PET: comparison with ^{18}F-FDG PET. J Nucl Med. 2006;47:793–6 .47/5/793 [pii]
61. Smith-Jones PM, Solit DB, Akhurst T, Afroze F, Rosen N, Larson SM. Imaging the pharmacodynamics of HER2 degradation in response to Hsp90 inhibitors. Nat Biotechnol. 2004;22:701–6. doi:10.1038/nbt968.nbt968 [pii].
62. Kramer K, Kushner BH, Modak S, Pandit-Taskar N, Smith-Jones P, Zanzonico P, et al. Compartmental intrathecal radioimmunotherapy: results for treatment for metastatic CNS neuroblastoma. J Neurooncol. 2010;97:409–18. doi:10.1007/s11060-009-0038-7.
63. Modak S, Guo HF, Humm JL, Smith-Jones PM, Larson SM, Cheung NK. Radioimmunotargeting of human rhabdomyosarcoma using monoclonal antibody 8H9. Cancer Biother Radiopharm. 2005;20:534–46. doi:10.1089/cbr.2005.20.534.
64. Jurcic JG, Larson SM, Sgouros G, McDevitt MR, Finn RD, Divgi CR, et al. Targeted alpha particle immunotherapy for myeloid leukemia. Blood. 2002;100:1233–9.
65. Abdelnour AF, Nehmeh SA, Pan T, Humm JL, Vernon P, Schoder H, et al. Phase and amplitude binning for 4D-CT imaging. Phys Med Biol. 2007;52:3515–29. doi:10.1088/0031-9155/52/12/012.S0031-9155(07)37628-8 [pii].
66. Holland JP, Divilov V, Bander NH, Smith-Jones PM, Larson SM, Lewis JS. ^{89}Zr-DFO-J591 for immunoPET of prostate-specific membrane antigen expression in vivo. J Nucl Med. 2010;51:1293–300. doi:10.2967/jnumed.110.076174. jnumed.110.076174 [pii].
67. Cheal SM, Xu H, Guo HF, Lee SG, Punzalan B, Chalasani S, et al. Theranostic pretargeted radioimmunotherapy of colorectal cancer xenografts in mice using picomolar affinity ^{86}Y- or ^{177}Lu-DOTA-Bn binding scFv C825/GPA33 IgG bispecific immunoconjugates. Eur J Nucl Med Mol Imaging. 2016;43:925–37. doi:10.1007/s00259-015-3254-8.
68. Cheal SM, Xu H, Guo HF, Zanzonico PB, Larson SM, Cheung NK. Preclinical evaluation of multistep targeting of diasialoganglioside GD2 using an IgG-scFv bispecific antibody with high affinity for GD2 and DOTA metal complex. Mol Cancer Ther. 2014;13:1803–12. doi:10.1158/1535-7163.mct-13-0933.
69. O'Donoghue JA, Smith-Jones PM, Humm JL, Ruan S, Pryma DA, Jungbluth AA, et al. ^{124}I-huA33 antibody uptake is driven by A33 antigen concentration in tissues from colorectal cancer patients imaged by immuno-PET. J Nucl Med. 2011;52:1878–85. doi:10.2967/jnumed.111.095596.

Principles of Molecular Targeting for Radionuclide Therapy

2

William C. Eckelman, Marie Boyd, and Robert J. Mairs

Abstract

Molecular targeting requires assessing several factors that come into play such as the location of the target, the choice of radionuclide, the inertness of the bifunctional chelate and stability of the covalently bound halogens, matching the residence time in the tumor with the physical half-life of the radionuclide, the scale and scope of the disease, and the absorbed dose sensitivity of the targeted tumor compared to normal tissue. The principles of molecular targeting are well established, but a paradigm shift from designing a medium-affinity radiotracer used to determine target density to designing a high-affinity, high-target density radioligand to maximize the target-to-nontarget ratio should increase the probability of detecting lesions smaller than the instrument resolution.

Developing and validating a therapeutic radiopharmaceutical for a single target is necessary, but often not sufficient to produce a toxic event because of other mechanisms that are only partially understood. These include nontargeted effects due to radiation emitted from neighboring, targeted cells as well as bystander effects produced by the cellular processing of radiation not necessarily impinging on DNA. Both of these indirect consequences of cellular radiation could make a substantial contribution to the efficacy of targeted radionuclide therapy. These mechanisms should be exploited to optimize the efficacy of targeted radiotherapy and overcome the inefficiency of tumor control due to nonuniform distribution of radiation dose. The design approach to take advantage of the indirect consequences of cellular radiation depends heavily on further elucidation of the indirect effect. The successful combination of these two should lead to more effective nuclear radiotherapy.

Keywords

Alpha particles • Beta particles • Auger electrons • Molecular targeting • Therapeutic radionuclides • Theranostics • Double-strand breaks • Bystander effects • Residence time

Glossary

^{18}F-DOPA	2-^{18}F-Fluoro-L-3,4-dihydroxyphenylalanine
^{18}F-FP-TZTP	3-[4-[(3-[^{18}F]fluoropropyl) thio]-1,2,5-thiadiazol-3-yl]-1,2,5,6 tetrahydro-1-methylpyridine

W.C. Eckelman (✉)
Molecular Tracer, Bethesda, MD, USA
e-mail: wceckelman@gmail.com

M. Boyd
Strathclyde Institute of Pharmacy and Biomedical Sciences, Strathclyde University, Glasgow, UK
e-mail: Marie.Boyd@glasgow.ac.uk

R.J. Mairs
Institute of Cancer Sciences, University of Glasgow, Glasgow, UK
e-mail: Robert.Mairs@glasgow.ac.uk

© Springer International Publishing Switzerland 2017
H.W. Strauss et al. (eds.), *Nuclear Oncology*,
https://doi.org/10.1007/978-3-319-26236-9_32

^{125}IUdR	5-[^{125}I]Iodo-2'-deoxyuridine
ADAM	2-[2-(Dimethylamino-methylphenylthio)]-5-[^{125}I] iodophenylamine
ATM	Ataxia telangiectasia mutated
ATR	ATM and RAD3 related
ATSM	Diacetyl-bis(N4-methylthiosemicarbazone
AUC	Area under the time-activity curve
Br-BHPE	Bromo-l,l-bis(4-hydroxyphenyl)phenylethylene
CBF	Cerebral blood flow
CB-TE2A	Cross-bridged macrocyclic chelators
CEA	Carcinoembryonic antigen
CT	X-ray computed tomography
DAT	Dopamine transporter
DFO	Desferrioxamine B
DNA	Deoxyribonucleic acid
DOPA	L-3,4-dihydroxyphenylalanine
DOTA	1,4,7,10-Tetraazacyclo-dodecane-1,4,7,10-tetraacetic acid
EMA	European Medicines Agency
EPR	Enhanced permeability and retention
FACS	Fluorescence-activated cell sorting
FDA	United States Food and Drug Administration
FWHM	Full-width half-maximum
GFP	Green fluorescent protein
GLUT	Glucose transporter
Gy	Gray unit (ionizing radiation dose in the International System of Units, corresponding to the absorption of one joule of radiation energy per kilogram of matter)
HCT116	Cell line of human colon carcinoma
HER	Human epidermal growth factor receptor
IdU	Iododeoxyuridine
INXT	(R)-*N*-methyl-(2-[^{125}I]iodo-phenoxy)-3-phenylpropylamine
IQNB	3-R-Quinuclidinyl 4-S-[^{123}I] iodobenzilate
IUdR	Iododeoxyuridine
IV	Intravenous
IVME2	Iodovinyl-11-beta-methoxyestradiol
LET	Linear energy transfer
LNCaP	Lymph node metastasis from carcinoma of the prostate
LS174T	Colon adenocarcinoma cells line name
MABG	Meta-[^{211}At] astatobenzylguanidine
mAbs	Monoclonal antibodies
mAChR	Muscarinic acetylcholine receptor
MBF	Myocardial blood flow
MCF-7	Michigan Cancer Foundation-7, a breast cancer cell line
MIBG	Meta-iodobenzylguanidine
MIP	Molecular Insight Pharmaceuticals
mRNA	Messenger ribonucleic acid
NET	Norepinephrine transporter
NHL	Non-Hodgkin's lymphoma
NET	Norepinephrine transporter
p-SCN-BN-CB-TE2A	11-bis(carboxymethyl)-1,4,8,11 tetraazabicyclo[6.6.2] hexadecane
p-SCN-BN-DOTA	S-2-(4-Isothiocyanatobenzyl)-1,4,7,10-tetraazacyclododecane tetraacetic acid
PCa	Prostate cancer
PCB-TE2A	Cross-bridged (propyl) TE2A
PET	Positron emission tomography
PMPA	2-Phosphonomethylpentanedioic acid
PSMA	Prostate-specific membrane antigen
RAD3	A 5′ to 3′ DNA helicase involved in nucleotide excision repair and transcription (from "RADiation sensitive")
RIBBE	Radiation-induced biological bystander effects

RNA	Ribonucleic acid
ROS	Reactive oxygen species
SERT	Serotonin transporter
SOD	Superoxide dismutase
SPECT	Single-photon emission computed tomography
SPECT/CT	Single-photon emission computed tomography/computed tomography
SUV	Standardized uptake value
T/B	Target-to-background
T/NT	Target-to-nontarget
TE2A	1,8-*N*,*N*′-bis-(carboxymethyl)-1,4,8,11-tetraazacyclotetradecane
TETA	1,4,8,11-Tetra-azacyclododecane-1,4,8,11-tetraacetic acid
TMS	Transfectant mosaic spheroids
TMX	Transfectant mosaic xenograft
TOC	Therapy operating characteristic
TRODAT	Technetium, 2-[[2-[[[3-(4-chlorophenyl)-8-methyl-8-azabicyclo[3.2.1]oct-2-yl]methyl](2-mercaptoethyl)amino]ethyl]amino]ethanethiolato(3-)-oxo-[1R-(exo-exo)]
Zr-DFO	Zirconium desferrioxamine B

Contents

Introduction 37

The Choice of Radionuclide 43
Nuclear Properties 43
Theranostics 44
Instrument Resolution and Biological Resolution 45

Radiobiological Properties Affecting the Choice of Radionuclide 46
Radiation Microdosimetry and Particle Range 46

The Choice of a Chemical Platform 48
Salts and Covalent Bonds 48
Chelating Agents 48

The Location of the Target: The Challenges of Designing Radiotracers for Intracellular Compartments 50
Critical Subcellular Sites of Interaction with Ionizing Radiation (Direct Effects) 51
Radiation-Induced Biological Bystander Effects (RIBBEs) 52
Critical Subcellular Sites of Interaction with Ionizing Radiation (Indirect Effects) 55
Transfectant Mosaic Spheroid Model 56
Transfectant Mosaic Xenograft Model 57
Media Transfer 58
LET and Dose Rate 58

Conclusion 59

References 59

Introduction

An important criterion for designing a successful targeted molecule is the choice of a particular cancer or a recently defined pathway [1] for which there are relatively few effective therapeutic options [2, 3]. From this information a target can be proposed. The key issue is targeting a saturable site unique to the disease. Most often this is a protein, but lipids are also possibilities (Table 1). Enhanced permeability and retention (EPR) is not considered to be targeted imaging [4].

Once that target unique to a disease is identified, the principles of molecular targeting can be applied to identify and validate therapeutic radiopharmaceuticals. The ligands from these targets are small molecules, often based on endogenous ligands or pharmaceuticals, peptides, sugars, protein, antibody fragments, and antibodies (Table 2, [5]).

Except for radionuclides of iodine, bromine, and astatine, i.e., halogens, therapeutic radionuclides are metals and require a bifunctional chelate conjugated to the targeting molecule. Halogen radionuclides most often are linked via a residualizing group [6]. Based on the cellular location and density of the target, the design of the targeted radiotracer will follow the approach for nuclear diagnostics with certain changes required for therapeutic radiopharmaceuticals [7, 8]. Relevant properties for a diagnostic radiopharmaceutical are an inexpensive radionuclide, high radiochemical yield, high radiochemical purity, and high specific activity including effective specific activity. These are required for therapeutic

Table 1 Potential targets for radioligands

Receptor is defined as a molecule in a cell membrane that responds to a particular neurotransmitter, hormone, antigen, or other substance. To facilitate imaging, radiolabeled antagonists to the receptor rather than lower-affinity, natural ligands are usually employed
Acceptor is defined as a molecule in a cell membrane whose biological activity is not known. The mannose receptor in the liver and the prostate-specific membrane antigen are examples
Enzyme is defined as a substance that acts as a catalyst to bring about a specific biochemical reaction. Inhibitors of the enzyme as often used, for example, radiolabeled fludeoxyglucose at hexokinase, but substrates as well, for example, ^{18}F-DOPA is used to quantify DOPA decarboxylase activity in the brain
Transporter protein is defined as a protein that serves the function of transporting ligands within the cell
Protein antigen is a specific antigen, usually cell surface, that is unique to the tumor. Antibodies and antibody fragments are produced by recombinant and proteolytic methods

Table 2 Potential platforms used in radioligand design

Small molecules are chemical entities that have a molecular weight of <500 Da. They are especially used in neurochemical applications given the requirement to cross the blood-brain barrier
Nanoparticles are usually defined as having a diameter of 100 nanometers or less. They are used in situations where the number of ligands for either diagnostic or therapeutic use can be bound to the surface
Antibodies and fragments: scFv (∼28 kDa), diabody (∼55 kDa), minibody (∼80 kDa), F(ab')$_2$ (100 kDa), and IgG (∼150 kDa). Various proteolytic or recombinant methods result in a combination of the binding region that targets the tumor cell antigen and other fragments present in the IgG
Enhanced permeability and retention (EPR)
This does not involve a single target, but a difference in EPR in target and normal tissue. In the 1980s, Maeda and colleagues found that macromolecules such as polymers and proteins with molecular weights larger than 40–50 kDa showed selective accumulation in tumor tissues, far more than that observed in normal tissues; moreover, they retained in tumor tissues for long periods, i.e., >24 h. They coined this unique phenomenon enhanced permeability and retention (EPR) effect. Accordingly, an EPR-based tumor-targeting strategy (macromolecular therapy) was developed by using polymer modification, nanoparticles, micelles, liposome, etc.

radiopharmaceuticals as well, although a high specific concentration of a therapeutic dose will produce radiolysis unless a radical scavenger is included. High specific activity is still a necessity to avoid saturation of the target and pharmacologic effects given the higher mass dose. For diagnostics, given that external imaging detects photons and not chemical structure, important criteria in vivo are metabolic stability; efficient transfer to the target only, i.e., target specificity; and pharmacokinetics that are more heavily weighted by biochemistry than by delivery although there is an ongoing paradigm shift to favor maximal delivery combined with optimal specific uptake and retention. The same criteria apply for therapeutic radiopharmaceuticals although pharmacokinetics heavily weighted for efficient extraction fraction may have an advantage in delivering a toxic dose to a larger percentage of cancer cells. A higher input area under the curve is also important for therapeutic radiopharmaceuticals. For positron-emitting radionuclides, the distinction between what constitutes diagnostic and therapeutic injected radioactivity is often blurred by the focus on the external emissions of positron annihilation rather than the high LET of the emitted positron.

The major challenge is to deliver the therapeutic radiopharmaceutical to the target whether it is on the cell surface, in the cytosol, or in the nucleus or more generally whether it is a well-characterized target or a phenotypic target obtained by screening [9]. The latter is most often the approach for antibodies obtained by screening antibodies and fragments to the tumor cell surface for specificity and high affinity. Another challenge is to demonstrate binding to the chosen target in the absence of specific and nonspecific binding to other sites

using an array of drugs known to bind to the specific target or to closely related targets including subtypes. Using target-specific knockout mice can also demonstrate specificity [10, 11]. In general, the probability of achieving the therapeutic goal decreases when moving from targets on the cell surface to targets in intracellular compartments.

Another major challenge in radiopharmaceutical design requires a clear approach to the optimal pharmacodynamics, i.e., the ideal combination of flow and permeability, which constitute delivery and kinetics at the target, which is based on the on-rate and the off-rate of radiopharmaceutical binding. The early diagnostic radiopharmaceuticals had very high affinities leading to high target retention to maximize the potential for external imaging, but with this came pharmacokinetics that are heavily delivery related. For example, diagnostic radiotracers such as N-[^{11}C]methylspiperone [12] and 3-quinuclidinyl-4-[^{123}I]iodobenzilate [13] (IQNB) have high affinities and high retention, and therefore their biodistribution is heavily delivery related. For IQNB, given the longer half-life of ^{123}I, the distribution in vivo with time shifted to dependence on muscarinic receptor density [14]. Investigators most often used IQNB to determine if new drugs involve the muscarinic receptor [15]. Experimentally, the ideals of delivery-related radiopharmaceuticals are those that are trapped in capillaries smaller than the particle size. For example, microspheres administered intravascularly, by virtue of efficient trapping in the capillaries, are the gold standard for heavily flow-related agents. In the clinic ^{99m}Tc-labeled microspheres are used to measure lung perfusion in vivo. The therapeutic application that best matches microspheres is intra-arterial radiotherapy, using radiolabeled ^{90}Y microspheres of glass or resin to treat lesions in the liver [16]. Small molecules can approach the extraction efficiency of microspheres if the extraction and retention of the injected radiopharmaceutical in the tumor is >90%, but given the cardiac output to the target after IV injection, only the lung will retain a high percentage of the injected dose.

Most of the diagnostic radiotracers developed subsequently were "more reversible" with slightly lower affinity so although the original distribution might be weighted toward delivery, subsequently (within the time frame of the radionuclide half-life), the distribution would be proportional to the biochemistry involved. Separating flow, permeability, and target binding has been a challenge because rapid and efficient uptake is advantageous for both diagnostic and therapeutic radiopharmaceuticals from a total delivery point of view; therefore, the measure of changes in biochemistry as a function of disease often required a measurable off-rate from the target.

But for diagnostic radiotracers, it is clear that efflux of radioligand not specifically bound to the target in the tissue compartment must be rapid and efficient within the time frame of the radionuclide half-life. In cardiology, radioligands designed to measure changes in biochemical pathways are heavily weighted by distribution and require saturation studies in vivo to determine adrenoceptor density [17]. One example of a reversible ligand from neurochemistry studies is 3-[4-[(3-[^{18}F] fluoropropyl)thio]-1,2,5-thiadiazol-3-yl]-1,2,5,6-tetrahydro-1-methylpyridine (^{18}F-FP-TZTP), whose early distribution correlated with perfusion as measured by [^{15}O]H_2O, i.e., within the range of cerebral blood flow (CBF) values measured, there is excellent agreement between CBF and the K1 of ^{18}F-FP-TZTP [18]. But the later distribution was weighted by a combination of muscarinic receptor density and synaptic acetylcholine concentration [19, 20]. The goal of the "reversible" ligands is to determine the change in target density as a function of disease or treatment. But is this the most valuable use for nuclear diagnostics with the inherent goal of whole-body imaging?

For theranostics and therapeutic radiopharmaceuticals, a high-affinity ligand approach appears to be superior. It seems that detecting the total tumor burden before and after treatment, especially lesions smaller than the twice the instrument resolution, is an important alternative in diagnostic design and is an important approach to developing therapeutic radiopharmaceuticals as well. Not only should the affinity be high, but the target should be present in the highest density possible and not vary to a large extent during treatment, whether during radionuclide therapy alone or combination therapy. The highest affinity (K_i) and the highest density (B_{max}) given

Table 3 Ideal properties of diagnostic and therapeutic targeted radioligands

Target	Bmax fmol/mg protein (nM)	Kd (nM)	Compound	B_{max}/K_d
mAChR	306	0.3	[^{123}I]IQNB	102
DAT (striatum)	2000 (200)	10	[^{99m}Tc]TRODAT	20
SERT (frontal cortex)	194 (19)	0.13	[^{125}I]ADAM	149
NET (frontal cortex)	55 (5)	0.05	2-[^{125}I]INX	110
PSMA (PCa)	292–4254 (29–425)	2.3	[^{68}Ga/^{177}Lu/^{90}Y]PSMA-617	127–185

Assumptions: 10% protein per gram tissue. For detailed assumptions, see Eckelman et al. [22]
Chemical names:
[^{123}I]IQNB: 3-R-quinuclidinyl 4-S-[^{123}I]iodobenzilate
TRODAT: technetium, 2-[[2-[[[3-(4-chlorophenyl)-8-methyl-8-azabicyclo[3.2.1]oct-2-yl]methyl](2-mercaptoethyl) amino]ethyl]amino]ethanethiolato(3-)-oxo-[1R-(exo-exo)]
ADAM: 2-[2-(dimethylaminomethylphenylthio)]-5-[^{125}I]iodophenylamine
INX: (R)-N-methyl-(2-[^{125}I]iodo-phenoxy)-3-phenylpropylamine
Targets:
mAChR: muscarinic acetylcholine receptor
DAT: dopamine transporter
SERT: serotonin transporter
NET: norepinephrine transporter
PCa: prostate cancer

adequate delivery will yield the potential for a high target-to-nontarget ratio based on the equilibrium equations used in in vitro assays (B_{max}/K_i) [21] (Table 3). In addition, total delivery is important to radiotoxicity; therefore, the metabolite-corrected input function should be as extended by design as possible for therapeutic radiopharmaceuticals, whereas clearance and minimizing nontarget binding are important to obtain a diagnostic image with a high target-to-nontarget ratio.

The design criteria (maximum delivery and retention at the target) serve therapeutic radiopharmaceuticals. The target-to-nontarget ratio is important, but relative clearance is also based on dosimetry considerations that maximize absorbed dose to the tumor and minimize absorbed dose to the normal tissue. For example, to detect/treat prostate cancer, two prostate-specific membrane antigen (PSMA) inhibitors, (S)-2-(3-((S)-1-carboxy-5-(4-[^{123}I]iodobenzylamino)pentyl)ureido) pentanedioic acid ([^{123}I]MIP-1072) and (S)-2-(3-((S)-1-carboxy-5-(3-(4-[^{123}I]iodophenyl) ureido) pentyl)ureido)pentanedioic acid ([^{123}I]MIP-1095) (Fig. 1), have similar characteristics with high affinity for PSMA on the cell surface of human prostate cancer LNCaP cells ($K_d = 3.8 \pm 1.3$ nM and 0.81 ± 0.39 nM, respectively). Both [^{123}I] MIP-1072 and [^{123}I]MIP-1095 are internalized in LNCaP cells at 37°C. The association of [^{123}I] MIP-1072 and [^{123}I]MIP-1095 with PSMA is specific for these two glutamate urea analogs since binding was blocked by co-incubation with 2-(phosphonomethyl)pentanedioic acid (PMPA). There was no binding to human prostate cancer PC3 cells, which lack PSMA [24].

The area under the time-activity curve (AUC) for the tumor and the critical organ are key metrics to differentiate between radiotracers with similar physical-chemical properties. The blood AUC is much less for MIP-1072 than for MIP-1095, and the kidney and tumor AUCs are much less also as would be expected based on the input function (Fig. 2). The first study in humans gave similar results to those obtained in rats [23] and led to subsequent clinical studies with the therapeutic radiopharmaceutical analog radiolabeled with ^{131}I [25].

The kidney-to-tumor ratios of AUC are different but given the variability in the two values and the expectation that changes in structure may make only small differences. To reduce the dose to the kidney, the kidney uptake can be blocked using a similar compound if the uptake is receptor based [26] or an FDA-approved positively charged amino acid solution if it is not receptor mediated [27]. A third approach is to bind the targeted radioligand to

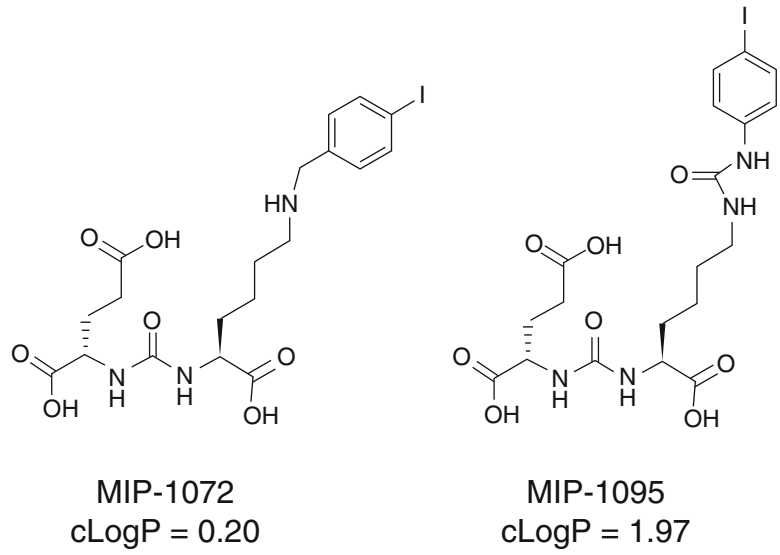

Fig. 1 The structures of (S)-2-(3-((S)-1-carboxy-5-(4-[^{123}I]iodobenzylamino)pentyl)ureido)pentanedioic acid ([^{123}I]MIP-1072) and (S)-2-(3-((S)-1-carboxy-5-(3-(4-[^{123}I]iodophenyl)ureido)pentyl)ureido)pentanedioic acid ([^{123}I]MIP-1095) (Taken from Ref. [23] with permission)

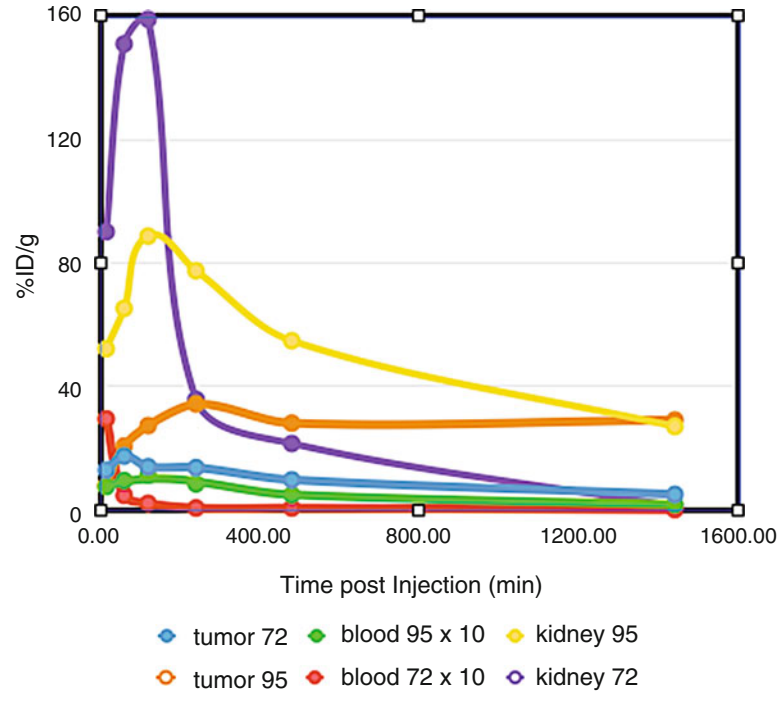

Fig. 2 The time-activity curve for [^{123}I]MIP-1072 and [^{123}I]MIP-1095 for radioactivity in tumor, kidney, and blood (x10) in mice with LNCaP tumors (Plot of data from distribution data from Ref. [24] with permission)

albumin reversibly [28]. This led to a study of therapeutic effectiveness in tumor-bearing mice of a ^{177}Lu-labeled folate analog containing an albumin-binding moiety (Fig. 3) which extended the input function and decreased the kidney uptake versus the bifunctional chelate without the albumin-binding moiety (Fig. 4) [29]. In both situations, design of the molecule to be retained longer in the blood depending on physical-chemical parameters of small molecules and strategies that minimize the biodistribution to normal organs are both key in improving the potential of therapeutic radiopharmaceuticals. The AUC has been the

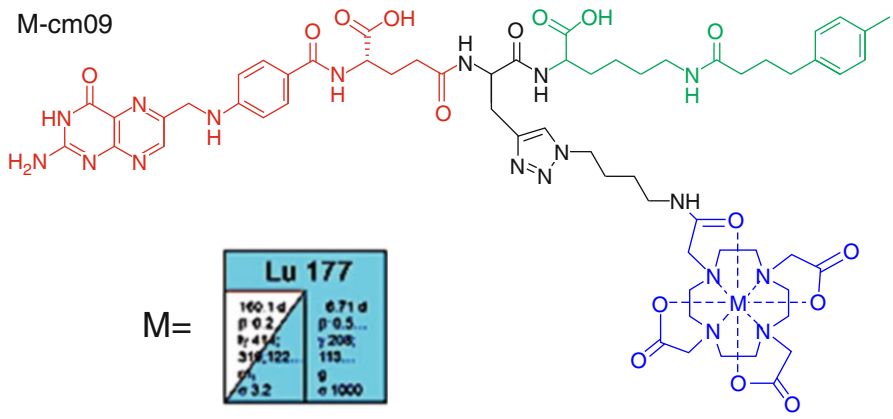

Fig. 3 Structure of ^{177}Lu-DOTA bifunctional chelate (*black*) with folic acid (*red*) and the albumin-binding moiety (*Green*) (Taken from Ref. [28] with permission)

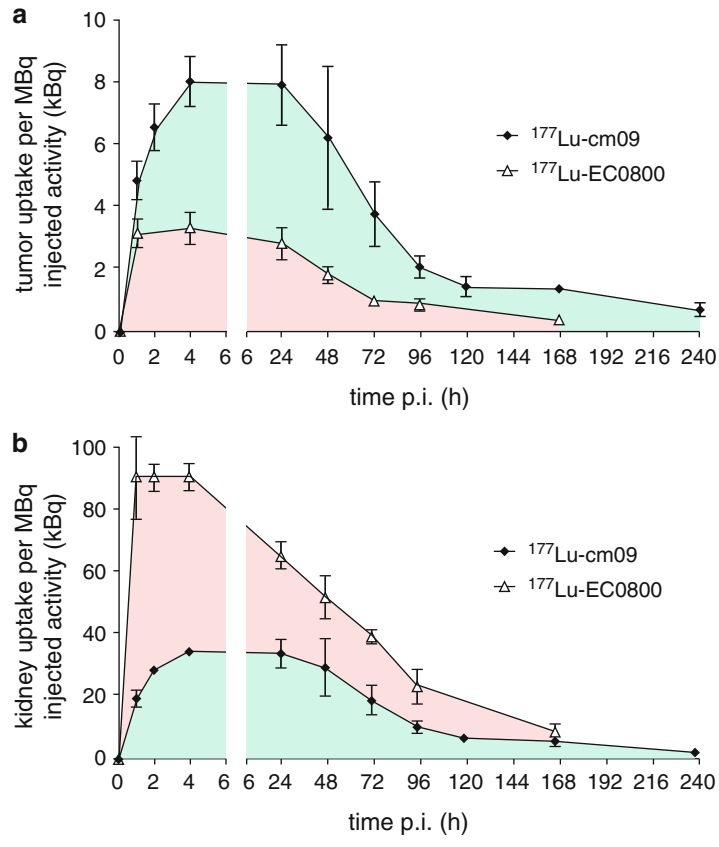

Fig. 4 Time-activity curve showing the relative area under the curve for tumor and kidney. The bifunctional chelate without the albumin-binding moiety (^{177}Lu-EC0800) and the bifunctional chelate with the albumin-binding moiety (^{177}Lu-cm09) at 1 h after injection (Taken from Ref. [29] with permission)

traditional approach to comparing the relative absorbed radiation dose to the target and to normal tissues. However, the AUC analysis does not evaluate the potential of a therapeutic radiopharmaceutical to affect patient outcome. This can only be addressed by outcome studies to determine the therapy operating characteristic (TOC) extracted from a plot of the probability of

tumor control versus the probability of normal tissue complications from clinical data obtained in Phase II/III [30].

Although the location of the target (extra- versus intracellular) is a major design criterion, the development of a therapeutic radiopharmaceutical also depends on the clinical need and the subsequent location of the key target and on a number of other design criteria, which are discussed in the following sections.

The Choice of Radionuclide

Nuclear Properties

Choosing the radionuclide is dependent not only on the location of the target (cell surface, cytosol, nucleus, specifically RNA and DNA) but also on matching the radionuclide physical half-life with the biological half-life of retention at the target. For example, the choice of half-lives for directly labeling antibodies binding to a cell surface target is of the order of days not hours. Matching the emission properties to the scale and scope of the disease being treated is also of critical importance.

There are several possible radionuclides for therapy [31–33] (Table 4). The radionuclides should be listed according to the predominant therapeutic emission (alpha particle, beta particle, Auger electrons) and whether there is a theranostic radioisotope. The alpha emitters most often studied are ^{211}At, ^{212}Pb, ^{212}Bi, ^{213}Bi, and ^{223}Ra. Recent interest has extended the focus to ^{225}Ac and ^{227}Th. Overall, the most frequently proposed beta emitters are those used to treat bone metastases in patients with intractable bone pain The therapeutic radionuclide is administered either as a salt (^{32}P, ^{89}Sr, ^{223}Ra) or a chelate (^{117m}Sn, ^{153}Sm). Metals for other applications, including ^{90}Y, ^{186}Re, ^{166}Ho, ^{131}I, ^{67}Cu, ^{64}Cu, ^{177}Lu, and ^{230}Pa, have half-lives differing from less than 1 day (^{188}Re = 0.71 days) to 50 days (^{89}Sr = 50.5 days) and beta mean energies from 0.13 to 0.93 MeV. The radionuclides recommended for Auger electron therapy are ^{125}I, ^{123}I, ^{111}In, and $^{44m/44}$Sc. In addition, several other therapeutic radionuclides have been proposed given the availability of a 70 MeV cyclotron capable of increased production and purity of ^{211}At, ^{232}Th, and $^{44m/44}$Sc [34].

The approved radionuclide therapies by the FDA and the EMA include iodine-131 iodide for differentiated thyroid cancer, strontium-89 chloride (Metastron) for bone pain, samarium-153 lexidronam (Quadramet) for bone pain, yttrium-90 ibritumomab tiuxetan (Zevalin®) for NHL, iodine-131 tositumomab (Bexxar) for NHL, radium-223 dichloride (Xofigo) for bone metastases, and ^{177}Lu-DOTA-octreotate (Lutathera) for NE tumors. It is interesting that [^{131}I]iodide and [^{223}Ra]radium dichloride are most often used in the clinic. It may be that the unmet need of these two radiotherapeutics at the time of FDA approval was a key metric for their clinical impact.

Generators, as has been the case for the ^{99}Mo/^{99m}Tc generator (67-h half-life of ^{99}Mo and 6-h half-life of ^{99m}Tc), would likely be the most economical if the pharmaceutical requirements, namely, retaining apyrogenicity, sterility, radionuclide yield and purity, and effective specific activity, can be met over the lifetime of the generator. ^{68}Ge/^{68}Ga (271-day half-life of ^{68}Ge and 68-min half-life of ^{68}Ga) is the generator most often used in PET diagnostic procedures and has been registered in Europe. Generators for therapeutic radiopharmaceuticals will most likely be used by central radiopharmacies given

Table 4 Radionuclides of current interest in targeted therapy

Radionuclide	Half-life	Emission	Mean range
^{90}Y	2.7d	β^-	3.8 mm
^{131}I	8 d	β^-	0.4 mm
^{177}Lu	6.7d	β^-	0.2 mm
^{67}Cu	2.6d	β^-	0.2 mm
^{199}Au	3.1d	β^-	0.3 mm
^{211}At	7.2 h	α	0.05 mm
^{212}Bi	1 h	α	0.05 mm
^{125}I	60.5 d	Auger	~1 μm
^{123}I	13.3 h	Auger	~1 μm
^{124}I	4.2 d	β^+	3.8 mm
^{77}Br	0.3 mm	2.4 days	β^+

the pharmaceutical requirements, but the half-lives of the parent nuclide, e.g., ^{225}Ac (with 10-day half-life) for ^{213}Bi (with 46-min half-life) and ^{212}Pb (with 10.6-h half-life) decaying to ^{212}Bi (with 60-min half-life), will limit shipping range.

In most alpha-emitting radionuclides, there is also question of the chemical composition of radioactive daughters in the radiopharmaceutical if there is a delay between the separation of the parent and the injection, for example, the time required for synthesis, quality control, and shipping if produced in a central radiopharmacy (Fig. 5 [35]). Lead-212 is by far the most complicated alpha emitter chain. The alpha emissions come from decay of ^{212}Bi, and so it is important that the Bi is still bound to the targeting molecule. The interesting point is that after 4 h, the ^{212}Pb (61 min) is in secular equilibrium with the daughters. Given that there is no easy method by which to separate the daughters from the radiolabeled antibody or peptide and most likely 4 h has passed since purification, the injection will contain radionuclides in different chemical forms, i.e., not all bound to the chelating agent [36].

Bismuth-213 decays by beta minus emissions (97.9%) to the very short-lived ^{213}Po and 2% by alpha decay to ^{209}Tl. This is interesting because if the ^{213}Bi is purified and chelated, the daughter has such an extremely short half-life that it will remain in the vicinity of the ^{213}Bi [35].

Astatine-211 has been used most often alpha emitter. The challenge is the chemistry of astatine because there is no stable isotope to carry out the necessary analytical studies. Astatine-211 has a half-life of 7.2 h. It decays with 58.3% probability through the electron capture process to ^{211}Po, which has a half-life of 0.52 s, and decays by emitting a 7.45 MeV alpha particle to stable ^{207}Pb. As a consequence of the electron capture process, polonium K X-rays are emitted that permit external imaging, and the two most abundant of these X-rays have energies of 77 and 80 keV with yields of 0.1 and 0.2 per disintegration [35].

Theranostics

Which of the therapeutic radionuclides have gamma-emitting radioisotopes that could be used in a theranostic application? In this situation, it is important to have the same metal (or halogen) for both applications to maintain identical chemistry. For example, it appears that ^{111}In as a gamma-emitting partner for ^{90}Y is not acceptable, whereas

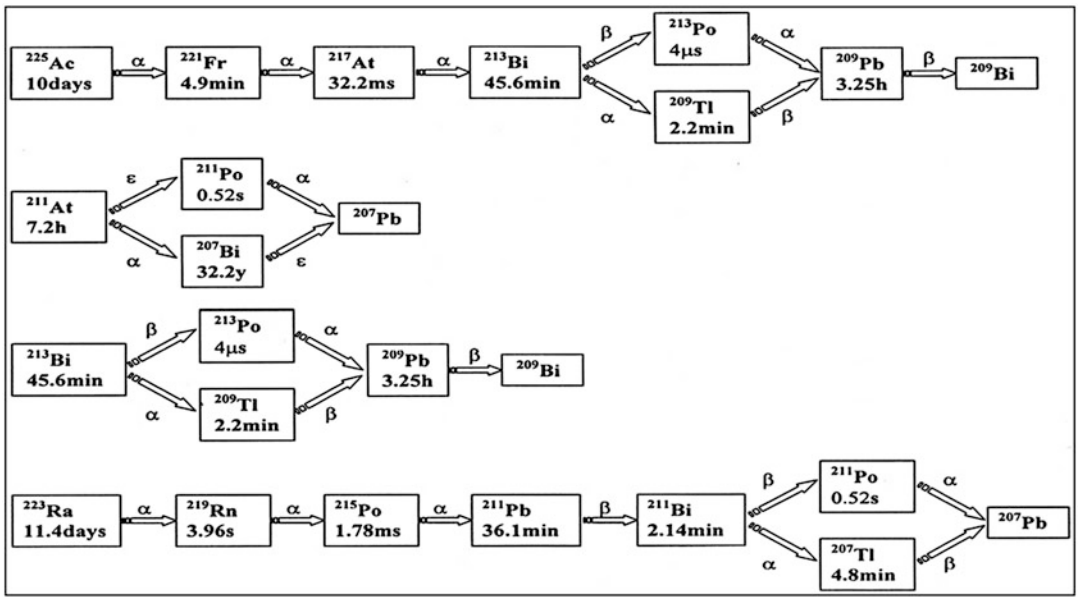

Fig. 5 Decay schemes for ^{225}Ac, ^{211}At, ^{213}Bi, and ^{223}Ra (Taken from Ref. [35] with permission)

^{86}Y is [37]. ^{211}At does not have a high-abundance gamma-emitting radioisotope (nor a stable isotope either), and so surrogates are necessary. The fission product metals generally do not have gamma-emitting radionuclides for imaging although some daughters emit gamma rays. But in decay schemes with multiple radioactive daughters, it is best if the gamma rays are emitted with the decay of the parent and not the decay of the daughters. Suggestions have been made to use bremsstrahlung imaging for ^{90}Y, which only emits high-energy annihilation gamma rays at very low abundance [38, 39].

Instrument Resolution and Biological Resolution

For theranostics, whether the use is in pre-approval studies to choose the optimal therapeutic and to monitor the success of that therapy, the goal of imaging smaller-volume lesions using quantitative emission tomography is crucial. External nuclear imaging is unique in its ability either to identify the target on cancer cells on a whole-body basis or to monitor the number of tumor cells using a radiolabeled biomarker that is targeting a high-density site that is independent of the treatment paradigm. The challenge of monitoring the same site targeted by the therapeutic is in the interpretation of a decrease in targeted radioactivity because a decrease could represent changes in the number of targets per tumor cells or a decrease in the number of tumor cells with the number of targets per cell constant or blocking by the mass dose of the therapeutic. This latter is less of a challenge in high specific activity therapeutic radiopharmaceuticals, but even in that case, achieving the maximal tumor dose may very well represent enough mass to occupy more than 5% of the target.

Monitoring the extent of the disease to include small lesions that are smaller than two to three times the instrument resolution requires a high target-to-nontarget (T/NT) ratio. Counting statistics, spatial resolution blurring, and target-to-background ratios influence the detection of small volumes by external imaging. In one example from 1999, Raylman et al. determined the detectability of small objects using a PET camera of that era with a resolution of ~9 mm [40]. In phantom studies, they found that spheres were detectable when larger than 9 mm in diameter if the target-to-background ratios exceeded 3:1. For smaller-diameter spheres, larger target-to-background ratio was required (18:1) to overcome the resolution blurring and the statistical uncertainty of background radioactivity. However, endogenous ligands radiolabeled with ^{11}C and radiofluorinated analogs of glucose, thymidine, choline, and acetate, along with other radioligands such as ^{18}F-fluoromisonidazole, ^{64}Cu-ATSM, and ^{18}F-florbetapir, have standardized uptake values (SUV) of 3 or lower for the cutoff between normal and abnormal lesions.

The lower resolution of SPECT can be countered with higher target-to-nontarget ratios for diagnostic radiopharmaceuticals. Furthermore, the higher target-to-nontarget ratios favor efficacious monitoring of therapeutic radiopharmaceuticals as described above. Togawa et al. imaged phantoms without scatter and attenuation corrections using a Toshiba three-head rotating SPECT system filled with $^{99m}TcO_4^-$. The FWHM of the SPECT system in this study was 13 mm, and the target-to-nontarget ratio obtained from the image of the phantom with a diameter of 46 mm (3.5 times that of the FWHM) shows a count recovery of 96.7 ± 6.2% of the actual target-to-background (T/B) ratio in the phantom as measured in a gamma counter. In contrast, the count recovery was 81.3 ± 7.2% and 68.1 ± 5.5%, respectively, even when the diameter was 37 mm (2.8 times that of the FWHM) and 29 mm (2.2 times that of the FWHM). For actual target-to-background ratios in the phantom ranged from 2.0 to 8.1 as measured in a gamma counter, the correlation coefficients increased from 0.037 to 0.165, respectively. The authors also reported the target-to-background ratio (T/B) multiplied by the diameter (d) to correct for the partial volume effect. Also, there was a significant linear correlation between T/NT • d obtained from the images and the actual T/B obtained from the gamma counter [41].

Recently, Zeintl et al. demonstrated the ability to obtain accurate data from phantoms in vitro and

in patients after injection of ^{99m}Tc-diphosphonate using SPECT/CT. Although the accuracy in phantom studies and measurements in vivo of radioactivity in the bladder were within 5%, the standard error reflects a need to increase the precision even further [42, 43].

A recent publication using a ^{68}Ga-radioligand for targeting PSMA gave tumor-to-gluteal musculature ratios at 3 h of 28.3 with a wide range between 2.9 and 224.0. These were based on 65 lesions considered typical for metastases or local relapse. The metastases were present in the bone and lymph nodes. Factors such as the radioactivity injected, the mass injected, the PSA value, the size of the lesion, partial volume losses, etc. were not correlated with the ratio by the authors. In a patient study, the ^{68}Ga-ligand uptake was detected in more tumors than were detected with ^{18}F-fluoroethylcholine, which has a lower tumor-to-background ratio [44].

Radiobiological Properties Affecting the Choice of Radionuclide

The most significant limitation of targeted radionuclide therapy is the heterogeneity of binding of radiopharmaceuticals in tumor deposits. Attempts have been made to overcome the nonuniformity of radiopharmaceutical uptake that results in underdosing of some tumor regions by the application of radionuclides that decay to emit long-range particles, so that neighboring nontargeted cells might receive a radiation dose by cross fire. Even with long-range radionuclides such as ^{131}I or ^{177}Lu, because their emissions are of low linear energy transfer (LET), subpopulations of tumor cells might experience less than a sterilizing dose.

An important aspect of targeted radiotherapy is the existence of radiation cross fire between cells, giving rise to a "radiological bystander effect," depending on the range of particles emitted by radionuclide disintegration. In other words, the dose absorbed by a cell depends on the radionuclide delivered to adjacent cells as well as to the cell itself. The principles guiding the selection of radionuclide for the treatment of tumor deposits of various sizes are illustrated in Fig. 6. The treatment of small clusters of malignant cells with a radionuclide whose decay particles are of long range may be energetically unfavorable (Fig. 6a). On the other hand, targeting a heterogeneous mass with a short-range emitter could result in underdosing of some regions (Fig. 6b). Alternatively, the treatment of a heterogeneous clump with a medium-range emitter may overcome the nonuniform deposition of radiation energy and increase the likelihood of delivering a lethal dose of radiation to all cells (Fig. 6c).

Radiation Microdosimetry and Particle Range

The killing of tumor cells by targeted radiotherapy is a consequence mainly of injury to DNA resulting from the traversal of particles (alpha, beta, Auger electrons) ejected from nuclides during radioactive disintegration (Fig. 7a, b, c). The contribution to cell kill by gamma photons is much less significant.

Decay particles have specific energy spectra and capacities for tissue penetration. Some features of therapeutic radionuclides are presented in Table 4. The finite ranges of emitted particles give rise to radiation microdosimetry considerations which are unique to targeted radiotherapy.

Most clinical experience has been acquired with beta emitters whose mean particle range is equivalent to several cell diameters. Therefore, the radiation dose to individual cells is the sum of *cross fire* – radiation emanating from neighboring cells which have accumulated radiolabeled agents – and radiation from radionuclide concentrated within the cell itself. In the case of radionuclides that decay to emit beta particles, cross fire is the most significant constituent of dose received by any cell. Conversely, no cross fire is associated with the uptake by cancer cells of Auger electron emitters. Accordingly, high-LET Auger therapy, while expected to be tumor specific, is anticipated to provide no compensation for heterogeneity of targeting. Then again, emerging evidence suggests that radioactive emission from targeted cells is not the only bystander effect operating in radionuclide

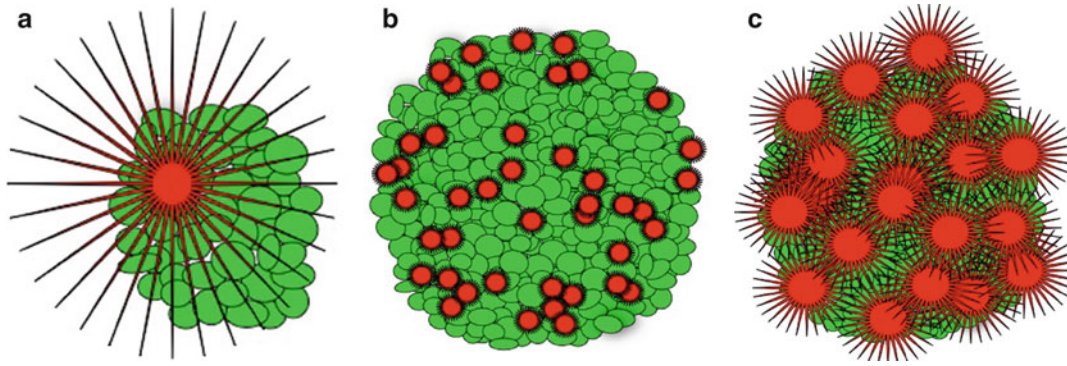

Fig. 6 The effect of target size and the LET of radionuclides. (**a**) Targeting a small heterogeneous clump of tumor cells with a long-range emitter. (**b**) Targeting a heterogeneous clump with a short-range emitter. (**c**) Targeting a heterogeneous clump with a medium-range emitter

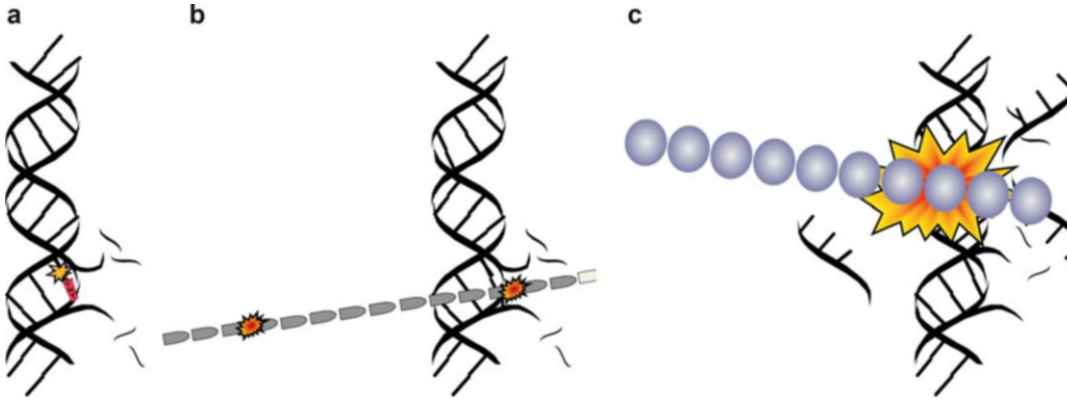

Fig. 7 The killing of tumor cells by targeted radiotherapy. (**a**) Localized damage by incorporation into DNA of an Auger electron emitter conjugated to a DNA building block – e.g., the thymidine analog [^{123}I]IUdR. (**b**) Long-range beta-particle bombardment (e.g., ^{131}I) of DNA. (**c**) Alpha-particle bombardment (e.g., ^{211}At) of DNA

treatment of cancer. It is becoming clear that radiation-induced biological bystander effects (RIBBEs) deriving from the cellular processing of the physical radiation insult, which need not interact directly with DNA, may play an important part in the overall efficacy of radionuclide targeting (see section "Radiation-Induced Biological Bystander Effects (RIBBEs)").

The dimensions of the tumor itself are very important. For micrometastases whose diameter is less than the range of decay particles, absorption of radiation energy is inefficient. Indeed a significant fraction of this energy is deposited outside the tumor [45]. Hence, microtumors will be underdosed and more resistant to sterilization. As tumor size increases, more decay energy is absorbed and the probability of cure is enhanced. However, as tumor size increases beyond particle range, the absorption efficiency reaches a plateau. Furthermore, the presence of a larger number of cells decreases the likelihood of successful treatment.

Such considerations were responsible for the concept of an optimal tumor size for maximal curability by specific radionuclides. Mathematical modeling has demonstrated that the optimal tumor diameter is slightly greater than the mean particle range of the radionuclide. For example, in the case of ^{131}I, homogeneously distributed throughout a tumor, the ideal diameter range for curability is 2.6–5.0 mm [46, 47]. However, with increasing

tumor size, the uptake of radionuclide will be increasingly nonuniform, resulting in greater resistance to radionuclide therapy of macroscopic tumors.

These predictions are supported by experimental evidence of the differential susceptibility to growth inhibition of multicellular tumor spheroids of a range of sizes treated with meta-iodobenzylguanidine (MIBG) labeled with [^{123}I]iodine, [^{125}I]iodine, [^{131}I]iodine, or [^{211}At]astatine [48]. MIBG is selectively accumulated by an active mechanism in cells of neural crest origin [49, 50], and conjugates of ^{123}I and ^{131}I are used for the imaging and therapy, respectively, of neuroendocrine tumors.

The Auger electron-emitting conjugates ([^{123}I]MIBG and [^{125}I]MIBG) and the alpha-emitting conjugate ([^{211}At]MABG) were highly toxic to small spheroids, whereas the beta-emitting conjugate [^{131}I]MIBG was relatively ineffective. Furthermore, the Auger electron emitters were more effective than expected, given the extranuclear localization of MIBG. As dosimetrically predicted, however, [^{211}At]MABG was extremely potent in terms of both concentration of radioactivity and number of atoms per unit volume administered. In contrast, the Auger electron emitters were ineffective in the treatment of larger spheroids, while the beta emitter showed greater efficacy [48]. These findings suggest that short-range emitters would be well suited to the treatment of circulating tumor cells or small clumps, whereas beta emitters would be superior in the treatment of subclinical metastases or macroscopic tumors. Such experimental results provide support for a clinical strategy of combinations ("cocktails") of radioconjugates in targeted radiotherapy.

The Choice of a Chemical Platform

Salts and Covalent Bonds

Some of the diagnostic and therapeutic radionuclides are simple salts: sodium ([^{123}/^{131}I]iodide), [^{67}/^{68}Ga]Ga citrate, ^{201}Tl chloride, ^{223}Ra dichloride, and Na [^{18}F]fluoride. Others are covalently bound to the targeting molecule, for example, *meta* [^{123}/^{131}I]iodobenzylguanidine (MIBG). Likewise, ^{211}At is covalently bound to the targeting molecule. In all cases the stability of the covalent bond is crucial given that in diagnostic agents, the emitted photons do not reveal the chemical structure of the radiotracer and in therapeutic applications it is important that the radionuclide remains with the targeting molecule for maximal therapeutic index [51].

Chelating Agents

To develop a true tracer of a targeting peptide or protein using a bifunctional chelate, the metal must be kinetically inert to hydrolysis and exchange labeling with endogenous proteins in vivo. In addition, metal targets to produce the radioactive metal, solvents, and all containers are potential sources of nonradioactive metals, which can reduce the effective specific activity and lead to possible saturation of a targeted site [52]. The same is true for the residualizing agents labeled with radiohalogens. The effective specific activity of [^{76}Br]bromide can also be lower than the specific activity itself given impurities in the metal target as well as the reagents used in the purification [53].

Brechbiel has pointed out that many chelating agents are misnamed because one of the functional groups has been used to link to the targeted molecule. His recommendation is to link to the targeted molecule using a carbon atom in the backbone to maintain the full functionality of the chelating moiety. He has demonstrated the relative inertness for both acyclic and cyclic (macrocyclic) chelating agents using the latter approach [54].

Endogenous proteins are strong competitors for Ga, Zr, and Cu. Transferrin has a high affinity for Ga. The Ga in Ga-citrate is thought to be transferred to transferrin after injection, and therefore Ga-transferrin is the targeting entity. There may be other proteins that bind Ga as well such as lactoferrin and serum proteins [55].

^{89}Zr-desferrioxamine B (DFO) appears to be stable to metal exchange with serum in vitro, but

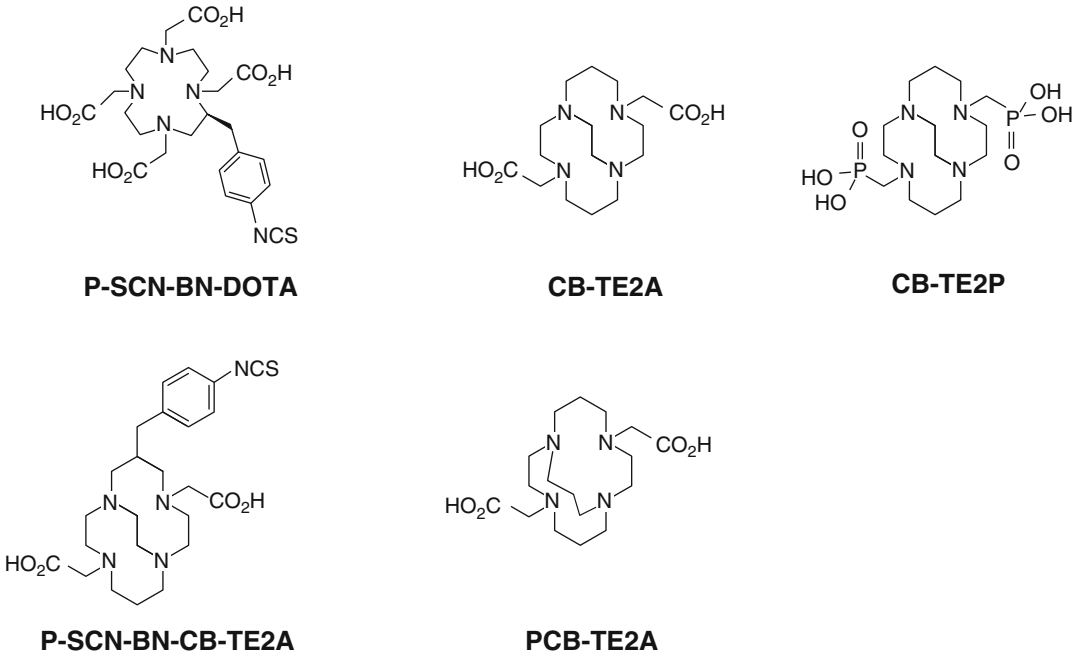

Fig. 8 Structure of ^{64}Cu chelating agents based on 1,4,8,11-tetraazacyclododecane-1,4,8,11-tetraacetic acid (TETA) (Taken from Ref. [61] with permission)

in vivo Zr-DFO shows bone uptake, but significantly less than Zr-citrate [56]. In vivo, transferrin may also be involved in trans-chelation of Zr. Although transferrin receptor upregulation has been demonstrated in specific tumors, enhanced permeability and retention (EPR) effect [57] could also be a factor in the uptake [58]. Earlier studies comparing ^{18}F-albumin and ^{18}F-transferrin in a tumor model containing upregulated transferrin receptor reported higher uptake with albumin rather than transferrin illustrating that the EPR effect could produce higher uptake compared to receptor binding. With the ^{18}F label, the transferrin and albumin were directly assayed by radiolabeling the protein rather than via the chelated metal [59].

Superoxide dismutase (SOD) competes with weaker chelating agents for Cu in vivo and has been identified as one competing protein for Cu that results in higher liver uptake in vivo [60]. Cai and Anderson outlined a more complete listing of Cu-binding proteins in vivo including ceruloplasmin, metallothionein, copper transporters, and chaperones. A cross-bridged macrocyclic chelator, namely, CB-TE2A, was the most inert of the first generation, but the labeling conditions were too harsh for peptides or proteins. One of the first cross-linked macrocyclic chelators that had a propylene bridge in place of the ethylene bridge in CB-TE2A proved to yield milder labeling conditions, followed by the phosphonate-armed chelators which also can be radiolabeled at room temperature (Fig. 8) [61].

The copper transporter has drawn interest because Cu salts appear to localize in cells via the copper transporter. If the Cu can be transferred to the Cu transporter present in hepatocytes and upregulated in tumor cells, this constitutes another pathway to use Cu radionuclides in diagnostic or therapeutic radiopharmaceuticals. The earliest report appears to be from Apelgot et al., who found that 42% of the ^{64}Cu in mouse ascites fluid after i.p. injection of [^{64}Cu]$CuCl_2$ was isolated with the DNA fraction. The electron capture emissions are effective if the metal is associated with DNA. Then the nuclear transformation (transmutation) with the associated changes with decay can produce a lethal event [62]. Others have

followed these early studies with in vivo studies in tumor-bearing mice [63–66].

There is an interesting analogy with the chemotherapeutic, cis-diamminedi-chloroplatinum(II) (cis-Pt), which enters cells via the copper transporter and then binds to the guanine bases in DNA after the two chlorine atoms hydrolyze in the lower pH milieu. Cross-linking DNA through either inter- or intrastrand cross-links seems to be the mechanism of action. Wolf carried out experiments with ^{195m}Pt cis-platinum and reported that the ^{195m}Pt catabolite was bound irreversibly to plasma proteins [67]. The subcellular distribution %ID/g ($\times 10^{-2}$) of ^{195m}Pt 4 h after injection of ^{195m}Pt cis-platinum in tumor-bearing rats was 0.43 in DNA, 4.13 in chromosomal proteins, and 4.2 in cytosolic ligands [68]. However, the DNA binding seems key to the therapeutic action of the drug.

Whether a copper salt will be as effective as a bifunctional chelate containing radiocopper is a question not yet answered. Certainly, the copper salt is taken up in the liver via the receptors in hepatocytes, whereas the biodistribution between the liver and kidney for the bifunctional chelates can be altered, for example, by changes in the linker between the chelate and the targeting molecule.

There is some question of the therapeutic index of fission product radionuclides if through multiple decays the daughter radionuclides do not remain with the chelating agent. Boswell and Brechbiel report a general percentage of released radionuclide to be 30% [33]. The loss of decay product daughters from beta decays is variable. Recently a publication on ^{44m}Sc/^{44}Sc indicates that there is no release during decay [69]. And, of course, catabolism of the linker between the chelating agent and the targeting molecule must be stable to various enzymatic and hydrolytic processes.

Another key consideration for bifunctional chelates is whether the perturbation caused by the linker and metal chelate alters or hinders binding to the target. The tracer principle at least for the biochemistry required for the diagnosis or therapy must be validated. Concern for the perturbation caused by the metal chelate is most often reported, but simple replacement of a hydrogen or hydroxy group with fluorine is not without consequences [70, 71].

In summary, since external imaging for diagnostics and therapeutic index are based on localization of the injected radiopharmaceutical, a kinetically inert covalent bond for the halogens and an inert metal chelate are crucial. It is key for therapeutic radiopharmaceuticals that the radionuclide remains as part of the targeted bifunctional chelate to maximize tumor damage and minimize normal tissue damage. The bystander effect is important. In small animals it could represent a significant effect that won't be characteristic of the human distribution. Furthermore, the lesser effect in Auger electron therapy may necessitate the need for nuclear uptake in a higher percentage of cells.

The Location of the Target: The Challenges of Designing Radiotracers for Intracellular Compartments

Cell surface targets represent a large percentage of the therapeutic targets to date. Internalization of the cell surface target is an advantage if it is a residualizing radiopharmaceutical, that is, it remains within the cell. Metal chelates have been superior to iodinated compounds in that respect because if iodide or iodotyrosine is a catabolic product, the efflux from the cell will be significant. For metal chelates, anion production is less likely, and trans-chelation to an endogenous protein is also a possibility for retaining radioactivity within a cell [6].

DNA and mRNA have been targets, but the small copy number and the challenge to design radiopharmaceuticals that demonstrate efflux of non-bound therapeutic radiopharmaceutical have prevented widespread success. Recently, Lewis et al. have targeted mRNA of bcl-2 using an antisense approach [72]. In this case alpha and beta emitters are preferred depending on the size of the tumor. In general, the targeting of intracellular epitopes is not as developed as targeting a cell surface protein [73].

The emission that is most dependent on location is Auger electron emissions, which must

localize in the nucleus, preferably binding to DNA, to be effective. Radioiodinated estradiol is an interesting example of transfer to the nucleus. DeSombre et al. studied two Auger electron emitters, namely, ^{80m}Br and ^{125}I. 2-[^{80m}Br]Bromo-l,l-bis(4-hydroxyphenyl)phenylethylene (^{80m}Br-BHPE) and the steroidal estrogen 17-alpha-[^{80m}Br]bromovinylestradiol both showed saturable binding to the estrogen receptor, but the decay product of ^{80m}Br, namely, ^{80}Br, emitted beta particles and gamma rays and therefore produced radiation dose, but lower cell killing [74]. ^{80m}Br is also not readily available. Next DeSombre compared [^{125}I]iododeoxyuridine ([^{125}I]IdU) and E-17-alpha ([^{125}I]iodovinyl-11-beta-methoxyestradiol ([^{125}I]IVME2) in vitro in MCF-7 cells expressing estrogen receptors. Both cell kill and double-strand breaks were equivalent for the two radiopharmaceuticals [75]. The analysis of the number of receptors per cell, the achievable specific activity, and the residence time dictated that ovarian cancer metastases in the peritoneal cavity may be a more successful approach [76]. Nevertheless, experiments in animals and theoretical calculations demonstrate the need for a large number of receptors per cell, near-theoretical specific activity of ^{123}I, and hundreds of millicuries of ^{123}I. Given the cost of cyclotron production of very high specific activity of ^{123}I, human studies to affect metastases in the peritoneal cavity have not begun, but rather there is a search for a much higher-affinity constant radioligand to increase the residence time in the cell nucleus.

Antibodies and other high molecular weight proteins or particles have advantages and challenges. Many of the challenges of the size and the consequent lower permeability can be overcome by targeting proteins in the "peritoneum, pleura or intrathecal space or to radiosensitive tumors associated with the hematological system" [77]. The challenges in designing a therapeutic radiopharmaceutical such as radiolabeled estradiol and radiolabeled antibodies are similar. The location plays a part, but the choice of radionuclide, the inertness of the bifunctional chelate, the residence time in the tumor matched with the physical half-life of the radionuclide, the scale and scope of the disease, and the absorbed dose sensitivity of the targeted tumor all come into play.

For small molecules, cell surface targets have been used most often given the access from the blood stream after IV injection. Internalization is a function of the cell as is active transport. To reach a target in the cytosol, the radiopharmaceutical must cross the cell membrane either by passive diffusion or active transport. 2-Fluoro-2-deoxyglucose enters cells via the GLUT transporter and then is metabolically trapped in the cell as the 6-phosphate. [^{11}C]-*meta*-Hydroxyephedrine is taken up in myocytes by the norepinephrine receptor and metabolically trapped. To target DNA or another target in the nucleus requires transfer across another barrier. Estradiol is carried to the nucleus by several active processes.

The major questions in both cytosolic and nuclear localization are whether enough radiopharmaceutical can be delivered to the compartment and whether radiotracer not bound to the target can be removed quickly so that the detected emissions are bound radioactivity and for radionuclide therapy the decay occurs at the target.

Critical Subcellular Sites of Interaction with Ionizing Radiation (Direct Effects)

The Auger electron emitter ^{125}I is highly cytotoxic when concentrated in the cellular nucleus as the thymidine analog 5-[^{125}I]iodo-2′-deoxyuridine (^{125}IUdR) [78]. Moreover, the antitumor efficacy of Auger electron-emitting ^{123}I or ^{125}I conjugated to IUdR has been demonstrated in an ascites tumor model [79, 80]. Therefore, the observation that Auger electron emitters conjugated to benzylguanidine are capable of killing neuroblastoma cells raises questions about the intracellular site of concentration of MIBG and the mechanism of cell kill. Several postulates could account for these findings. MIBG may be taken up by the cell's nucleus. It is also possible that other cellular structures are susceptible to bombardment with Auger electrons – for example, mitochondria. Alternatively, particles other than Auger electrons emitted during the decay of ^{123}I and ^{125}I may have

sufficient range to penetrate the nucleus of a targeted cell. A fourth possibility is that MIBG labeled with Auger electron emitters mediates cell kill through apoptosis triggered by a novel mechanism.

The conventional opinion is that the critical cellular target for ionizing radiation damage is nuclear DNA. Therefore, ultrashort-range radionuclides, such as Auger electron emitters, should be toxic only if delivered to the nucleus of the target cell (Fig. 7a) [81]. This is supported by studies in vitro – using extracellular $Na^{125}I$, cytoplasmic [^{125}I]iododihydrorhodamine, and nuclear ^{125}IUdR, which demonstrated that significant toxicity was associated only with the ^{125}I located in the nucleus [82]. Similar results have also been observed in vivo by Link et al. who compared the therapeutic efficacy of ^{125}I- and ^{211}At-labeled methylene blue to treat mice bearing malignant melanoma [83]. Only ^{211}At-labeled methylene blue produced significant therapeutic effects. As the subcellular fate of this targeting agent is cytoplasmic, it was concluded that ^{125}I-labeled methylene blue was located too far away from the genome to be cytotoxic [83]. Although it has been shown that MIBG concentrates mainly in the cytoplasm of neuroblastoma cells [84, 85], the demonstration that significant cell kill can be achieved with ^{125}I- or ^{123}I-labeled MIBG could represent evidence for a nuclear localization of MIBG. The amount of drug accumulated at this site may be undetectable by conventional means but nevertheless capable of delivering a toxic dose of radiation to the cell nucleus.

Alternatively, MIBG conjugated to Auger electron emitters could be cytotoxic through damage to the mitochondria. Subcellular localization studies have identified mitochondria as sites of MIBG accumulation [84]. Mitochondrial toxicity could result from disruption of inner mitochondrial membrane proteins or by direct effects on the mitochondrial genome. Indeed, mitochondrial DNA is particularly susceptible to radiation damage because of its limited capacity for repair [86].

It is also conceivable that some particles emitted during the decay of ^{123}I and ^{125}I may have sufficient range to reach genomic DNA of a targeted cell despite cytoplasmic or perinuclear localization. Although the entire Auger and Coster-Kronig electron spectra for these radionuclides have not been measured experimentally, calculations using theoretical transition rates and energies indicate that both isotopes emit some electrons with ranges of the order of the radius of a mammalian cell [87, 88]. Assuming a cytoplasmic location for MIBG, it is possible that such emissions would deliver significant doses of radiation to the nucleus. However, this possibility is not supported by the classical experiments of Kassis and colleagues described earlier [82].

A more exotic possibility is that Auger electron irradiation of cytoplasmic targets achieves cell kill by an indirect route, such as the triggering of apoptosis in susceptible cells. Some workers have reported that apoptosis-mediated cell death may result from membrane damage and the consequent generation of ceramide [89, 90] and that this process may be initiated by ionizing radiation damage to cell membranes [91].

Insight into the consequences of nonnuclear targeting of Auger electrons has been provided by Pouget and colleagues (see also section "Critical Subcellular Sites of Interaction with Ionizing Radiation (Indirect Effects)"). Using in vitro and in vivo models, they reported substantial antitumor efficacy of membrane-bound ^{125}I-labeled monoclonal antibodies (^{125}I-mAbs). Moreover, the observed cytotoxicity was greater than that associated with internalizing ^{125}I-mAbs [92, 93].

Previous supporting experimental evidence demonstrating Auger electron-induced cell kill at a distance greater than its path length was provided by Xue et al. following treatment of human colon LS174T adenocarcinoma cells with ^{125}IUdR [94].

Radiation-Induced Biological Bystander Effects (RIBBEs)

The foregoing account of investigations designed to overcome the inefficiency of targeted radiotherapy due to nonuniform uptake of radionuclide in tumors considered only the damage inflicted to neighboring nontargeted cells resulting from cross fire irradiation. According to conventional

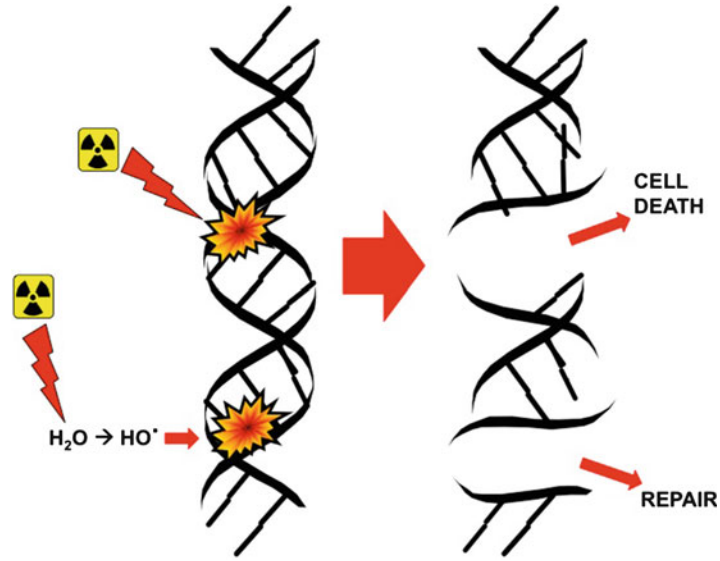

Fig. 9 Traditional concept of the effect of ionizing radiation

opinion, radiation bombardment of DNA (hitherto assumed to be the only significant subcellular structure), either directly or through the intermediacy of oxygen-containing radicals, creates damage which is lethal or repairable (Fig. 9). However, in recent years, numerous studies have demonstrated that factors other than physical aspects of ionizing radiation are responsible for the death of malignant cells that are not directly irradiated during a course of radiotherapy (Fig. 10). It is becoming clear that radiation-induced biological bystander effects (RIBBEs) deriving from the cellular processing of the physical radiation insult, which need not interact directly with DNA, may play an important part in the overall efficacy of targeted radiotherapy (Fig. 11).

After irradiation, cells expel toxins whose consequences to neighboring, unirradiated (bystander) cells include mutation, chromosomal breakage, long-term genomic instability, and death [95–101]. Bystander effects may be induced by radiation dosage as low as 3 mGy. Such exposures are of **safety** concern in diagnostic imaging and intensity-modulated radiotherapy. Accordingly, it is important to understand the mechanisms underlying bystander effects and how these may be manipulated to enhance tumor cell kill.

RIBBEs are most appreciable at low radiation dose and low dose rate [102–106]. These are features of targeted radionuclide treatment of cancer [107]. Therefore, bystander effects induced by radiopharmaceuticals may play a disproportionately large part in their efficacy, and understanding their nature should enable the refinement of this form of radiotherapy. The mechanisms involved are as yet undefined. However, studies using γ-ray and α-particle beams have provided some insight into possible factors. These include oxidative stress [108] (leading to increased radical formation [109, 110]), nitric oxide release [111, 112], cytokine release [113], gap junctional intracellular communication [114], and cellular immunity [115–117]. Agents implicated in bystander signaling have been reviewed [104, 108, 118, 119].

Although substantiation of bystander effects has been gained predominantly through studies involving external beam γ-irradiators and microbeams, some studies have been conducted of RIBBE consequent to the intracellular concentration of radiolabeled drugs. In clusters of unlabeled and [^{3}H]thymidine-labeled cells, death of unlabeled cells was deemed to result from transmission of cytotoxins from cells which had incorporated [^{3}H]thymidine in their DNA rather than

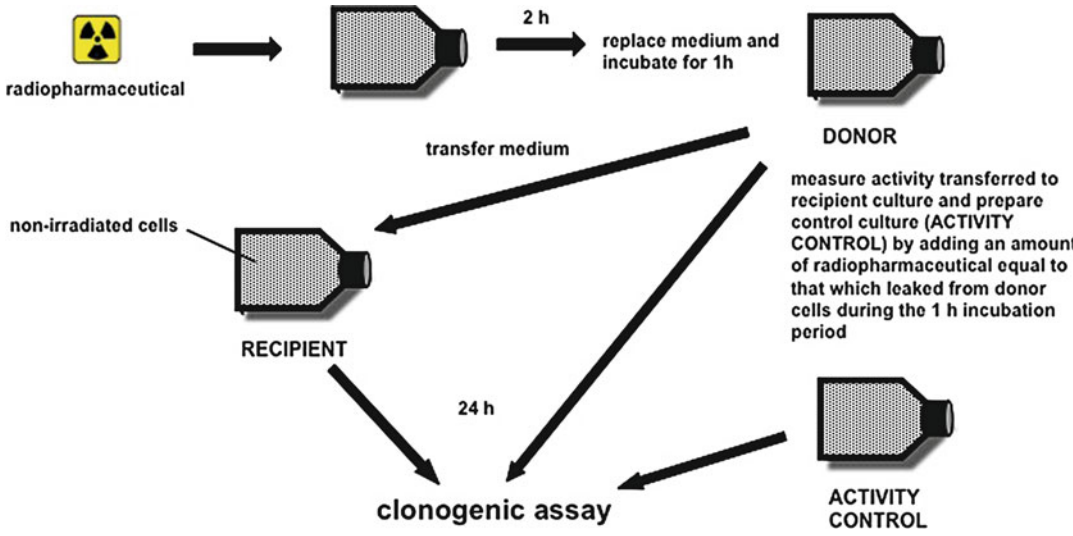

Fig. 10 Manifestation of radiation-induced biological bystander effects (RIBBEs)

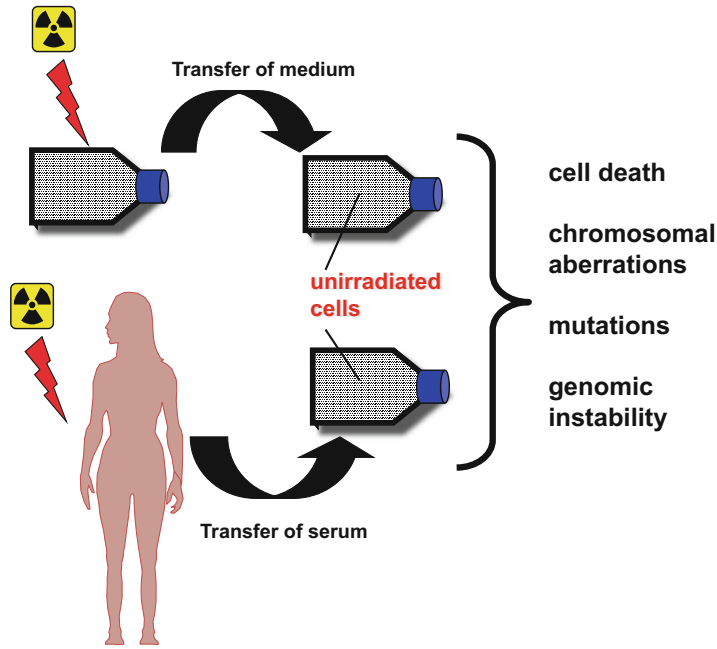

Fig. 11 The radiation-induced biological bystander effect entails the transfer of death signals from irradiated to unirradiated cells

cross fire irradiation because ^{3}H beta-decay particles have insufficient range to impinge upon adjacent cells [120]. Unlabeled cells were protected by dimethyl sulfoxide and lindane, implicating free radicals and gap junctional communication, respectively [121, 122]. Similarly, Xue et al. created tumors in nude mice composed of colon carcinoma cells, unlabeled or containing ^{125}IUdR [94].

Again, inhibition of tumor growth was attributed to RIBBEs because the path length of ^{125}I Auger electrons is too short for direct interaction with neighboring cells. The latter investigation demonstrated that RIBBEs are not simply artifacts

of in vitro manipulations but are significant growth inhibitory factors in vivo [123]. In an analogous study, Mamlouk et al. co-cultured [^{125}I]IUdR-treated lymphocytes with LS174T colon adenocarcinoma cells. This induced a reduction in the rate of proliferation of the malignant cells due to the release of inhibitory factors from the irradiated lymphocytes. The absence of cross fire as a confounding element was confirmed, by the mixture of unlabeled with labeled cells, resulting in loss of bystander response [124]. Akudugu et al. demonstrated that the capacity to succumb to ^{125}I-induced bystander signals is not universal but is dependent on phenotype [125]. The treatment of lymphoid cells with antibodies, labeled with the alpha and beta-particle emitter ^{213}Bi, produced a greater than expected cytotoxicity indicative of RIBBE [126]. This notion was supported by subsequent modeling studies of the outcome of cellular labeling with the alpha emitter ^{210}Po [127].

Significantly, distinct signaling pathways have been observed to participate in the restitution of DNA in directly irradiated compared with untargeted cells. In directly irradiated cells, the kinases ataxia telangiectasia mutated (ATM), ATM and RAD3 related (ATR), and DNA-dependent protein kinase were all required for DNA restitution, whereas the activity of ATR and ATM, but not DNA-dependent protein kinase, resulted in diminished survival of bystander cells [128]. This indicates opportunities for either sensitization or protection specifically of targeted or bystander cells or tissues through alteration of the activity of DNA damage sensors and repair enzymes.

Critical Subcellular Sites of Interaction with Ionizing Radiation (Indirect Effects)

Cell Membrane While DNA has long been regarded as the main target of the harmful consequences of ionizing radiation, it was proposed more than 50 years ago that damage to intracellular sites other than DNA could account for the cytotoxicity of ionizing radiation [129]. Experimental evidence indicates that the cell membrane is an important location for interaction with radiation and free radicals, resulting in the formation of cross-linkage between protein and DNA [130]. Radiation exposure stimulates translocation from lysosomes to the cell membrane of sphingomyelinase [131]. This catalyzes the hydrolysis of membrane-associated sphingomyelin to ceramide which, in turn, activates various kinases and transcription factors resulting in programmed cell death [132]. The plasma membranes of cells contain combinations of glycosphingolipids and protein receptors organized in glycolipoprotein microdomains termed lipid rafts. Notably, ceramide-cholesterol complexes are responsible for the development of lipid rafts which play a significant role in cell signaling [119].

In contrast to the expectation that ultrashort-range, Auger electron emitters must localize in the vicinity of DNA to have cytotoxic effect, it has been demonstrated, in vitro and in vivo, that non-internalizing antibodies, directed against carcinoembryonic antigen (CEA) and labeled with ^{125}I, have significant antitumor effectiveness. Moreover, the potency of these membrane-associated ^{125}I-antibodies was greater than that of internalizing ^{125}I-antibodies with specificity for human epidermal growth factor receptor (HER1). DNA damage-centered signaling pathways are effectively activated during low dose-rate Auger radioimmunotherapy [133]. The antitumor efficacy of ^{125}I-non-internalizing antibodies was not due to a deficiency in DNA damage recognition; nor was it induced by membrane-activated apoptosis; nor was it related to the mean absorbed dose to the nucleus. Instead, it was proposed that bystander factors were involved [106]. These findings imply that nuclear accumulation of ^{125}I is not necessary for its toxicity which is mediated predominantly by bystander effects independent of the subcellular site of localization (nuclear or cell membrane) of ^{125}I.

Mitochondria Mitochondria make up 4–25% of cell volume, rendering them prospective targets for radiation trajectory, and it has been suggested

that cells can be sensitized to radiation as a result of impaired mitochondrial function [134]. Mitochondrial DNA is more susceptible to oxidative damage than nuclear DNA due to its proximity to the main site of generation of reactive oxygen species (ROS), the electron transport chain. Furthermore, mitochondrial DNA is not associated with protective histone proteins and has lower efficiency repair mechanisms [135]. Reports of oncogenic products acting to maintain, in cancer cells, elevated numbers of mitochondria [136] which generate excessive ROS, particularly in response to hypoxia [137], have stimulated the development of agents that enhance mitochondrial ROS production, resulting in the apoptosis selectively of cancer cells [138]. According to the ROS threshold hypothesis [139, 140], low levels of ROS are necessary for the maintenance of cellular metabolism, whereas excessive ROS can be cytotoxic. Therefore, the lethality of ionizing radiation and some chemotherapeutic agents is hypothesized to be due to increasing ROS concentrations to cytocidal levels preferentially in tumors which typically have elevated levels of ROS and impaired antioxidant activity as a consequence of higher rates of proliferation and metabolism [141]. The sensitivity of cancer cells to therapeutic schemes which stimulate cell death through ROS production encourages their application in combination with the specificity afforded by targeted radiotherapy.

Significantly, mitochondria of both directly and indirectly irradiated cells are also involved in the initiation of programmed cell death [142] via the loss of apoptosis-inducing proteins – cytochrome C and apoptosis-inducing factor [143]. Improved understanding of the involvement of mitochondria in the cellular response to ionizing radiation is expected to stimulate innovative targeted therapeutic strategies.

Transfectant Mosaic Spheroid Model

To adequately represent therapeutic effects upon micrometastases (a major aim of targeted radionuclides), a three-dimensional culture system is necessary. Multicellular tumor spheroids were first described by Sutherland et al. [144], and since then, they have been utilized for a variety of experimental applications including tumor response to various treatments [145–148], basic cell biology [149], and investigations of microenvironmental influences on cell growth [150]. Beyond about 300 μm diameter, spheroids from most cell lines have a well-characterized structure, comprised of a necrotic core composed of quiescent or moribund cells surrounded by a viable rim of proliferating cells. This arrangement loosely mimics the initial avascular stages of solid tumor growth in vivo, with highly proliferative activity in proximity to capillaries ranging to necrotic regions at larger distances [151]. As a result, multicellular tumor spheroids have been utilized in a variety of experimental cancer therapy studies relevant to the treatment of micrometastases [152].

Transfectant mosaic spheroids (TMS), composed of different proportions of transfected and non-transfected cells [153], are representative of small tumors in which a range of efficiencies of tumor cellular targeting are achieved (Fig. 12). In order to discriminate between the different cells,

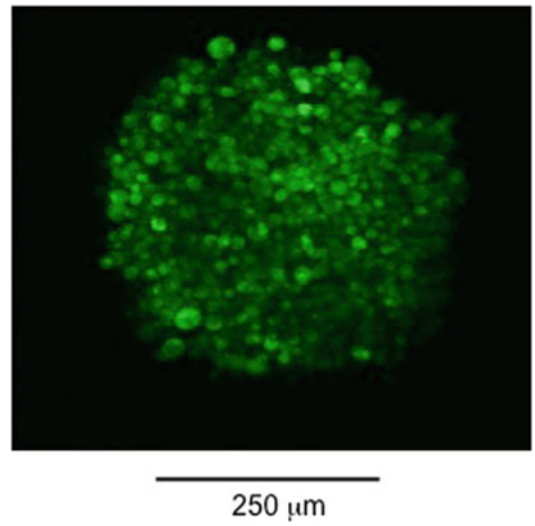

Fig. 12 Expression of jellyfish green fluorescent protein (GFP) in a transfected mosaic spheroid composed of 50% norepinephrine transporter-expressing cells and 50% GFP-expressing cells

the green fluorescent protein (GFP) gene was utilized as a transfection marker for identification, by fluorescence-activated cell sorting analysis and fluorescent confocal microscopy [154], of the cells which had not been transfected with the therapeutic transgene – the norepinephrine transporter gene – enabling MIBG targeting. Fluorescence imaging revealed uniform distribution of GFP-expressing transfectants in TMS. The observed heterogeneous dispersal of the two different transfected cell types was independent of their proportional contribution to the total spheroid mass. FACS analysis of disaggregated TMS confirmed that the ratio of norepinephrine transporter gene transfectants to GFP transfectants in various single-cell mixtures used for the production of TMS was accurately reflected in the percentage of the two types of cell in the spheroids [155]. The TMS model could be used to represent various densities of target expression in metastases. However, it should also be possible to create mosaic spheroids composed of transfected peripheral rims or central regions. Such models could be used to represent heterogeneous uptake of radiopharmaceutical which are dependent upon cellular proliferation or hypoxic promotion of expression, respectively.

TMS were used in the preliminary study of a gene therapy/targeted radiotherapy strategy which conferred the potential for uptake of radiolabeled MIBG by introduction of the norepinephrine transporter gene to cells which previously did not express it [156]. This facilitated the evaluation of the minimum percentage of transfection required to achieve cure of various sizes of metastases. A potentially beneficial substitute for ^{131}I is the heavy halogen astatine-211 (^{211}At) [157]. The α-decay particles of ^{211}At are highly cytotoxic and have a range of 55–70 μm, enhancing the prospect of tumor-selective damage. Moreover, the cytocidal efficiency of α-particles is independent of tumor hypoxia and growth rate [158]. Boyd et al. [153] reported that radioactivity concentrations <20 kBq/ml of [^{211}At]MABG induced the complete sterilization of all clonogens in 250 μm diameter mosaic spheroids composed of only 5% NAT gene transfectants. Because the path length of ^{211}At α-particles is only 55–70 μm, cross fire irradiation from targeted to untargeted cells would be considerably less extensive than that from a β-emitter such as ^{131}I. Therefore, this observation suggests that bystander effects, over and above cross fire irradiation, are operating in α-particle targeted therapy.

These studies indicate the potential for bystander-mediated cell kill and improved clinical efficacy of tumor targeting when only a small proportion of the tumor mass expresses the radiotherapeutic molecular target, in this case, introduced via gene modification. Moreover, RIBBE could compensate for the low levels of gene delivery currently achievable in vivo in cancer gene therapy strategies when married with targeted radionuclide therapy. Rational selection of radiohaloconjugates of MIBG will enable the enhancement of cross fire to maximize neuroblastoma cell kill.

Transfectant Mosaic Xenograft Model

To determine the toxicity of bystander signals in vivo elicited by cells which accumulated Auger electron-emitting radionuclides, Xue et al. incorporated [^{125}I]IUdR into adenocarcinoma cells and mixed these with unlabeled cells before implantation in rodents [94] (see sections "Critical Subcellular Sites of Interaction with Ionizing Radiation (Direct Effects)" and "Radiation-Induced Biological Bystander Effects (RIBBEs)"). They reported inhibition of tumor growth as a consequence of factors released from the labeled cells. The transfectant mosaic xenograft (TMX) model described by Mairs et al. is an alternative means of determining the importance of bystander effects in vivo [159]. TMX were established by subcutaneous injection into athymic mice of tumor cells comprising various proportions of norepinephrine transporter (NET) gene transfected to parental cells – a likely clinical scenario during the development of metastases of neuroendocrine tumors in vivo.

In TMX, following the administration of [^{131}I]MIBG, retardation of tumor growth was observed in tumors comprising only 5% NET

positivity. Moreover, the inhibition of TMX growth by [^{131}I]MIBG treatment was directly related to the proportion of NET-expressing cells. TMX may be suitable for the examination of quantitative aspects of radionuclide treatment and gene therapy. For example, this model will allow, for the first time, the determination of the minimal NET expression necessary for the imaging and sterilization by radiolabeled MIBG of tumors of a range of sizes which are one to two orders of magnitude greater than TMS. The TMX model will also facilitate the determination of optimal therapeutic dosage in relation to normal tissue toxicity and the evaluation of the influence of bystander effects in targeted radiotherapy in vivo.

Media Transfer

For determining radiopharmaceutical-induced biological bystander responses in vitro, Boyd et al. [103] employed an adaptation of the media transfer system developed by Mothersill and Seymour [96]. This allowed their comparison of the induction of bystander effects by external beam γ-radiation with those generated by MIBG labeled with radionuclides emitting ß-particles, α-particles, or Auger electrons [103] (see section "LET and Dose Rate"). The cells used in these experiments were transfected with the norepinephrine transporter (NET) gene to facilitate the active uptake of radiolabeled MIBG. Control cells were untransfected, hence incapable of active accumulation of MIBG. For investigation of RIBBE following γ-irradiation, donor cells were directly irradiated, and their medium was transferred to recipient cells which were not directly irradiated. Twenty-four hours later, cell kill was determined by clonogenic assay. To control for killing of recipient cells due to the transfer of effluxed radiopharmaceutical, a set of cells, designated activity controls, was prepared. Their medium received radiopharmaceutical activity equivalent to that which had leaked from donor cultures (treated with a range of activity concentrations) and would have been transferred to recipient cells (Fig. 13).

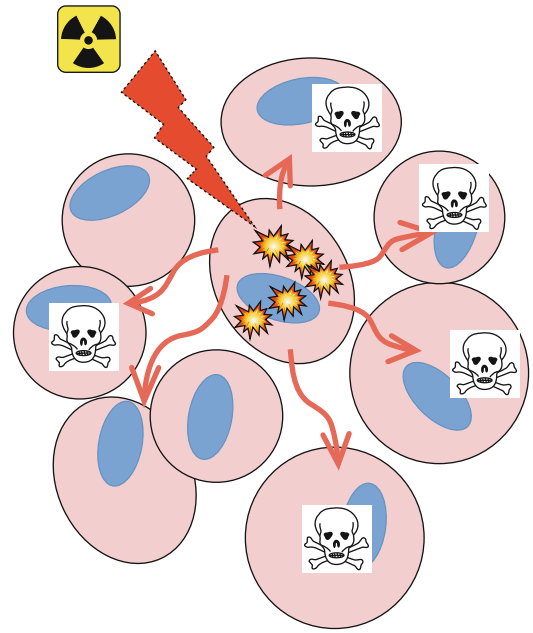

Fig. 13 Procedure for evaluation of cytotoxic bystander effect induced by radiopharmaceutical treatment

LET and Dose Rate

Using the media transfer methodology described in section "Experimental Models," Boyd et al. [103] observed that glioma or bladder carcinoma cell lines exposed to media derived from external beam irradiated cells produced a dose-dependent reduction in survival fraction, at low dosage, followed by a plateau with respect to clonogenic cell kill at levels >2 Gy. In contrast, cells receiving media from cultures treated with [^{211}At]MABG or [^{123}I]MIBG exhibited dose-dependent toxicity at low dose but elimination of cytotoxicity with increasing radiation dose. Cells treated with media from [^{131}I]MIBG demonstrated a dose-response relationship with respect to cell death and no annihilation of this effect at high radiopharmaceutical dosage. These findings suggested that bystander effect mechanisms following radiopharmaceutical administration may be LET dependent and distinct from those elicited by conventional radiotherapy.

To determine the effect of subcellular localization of radiolabeled drugs on direct and indirect

cell kill, Boyd et al. [160] treated NET gene-transfected HCT116 cells (derived from a human colorectal carcinoma) with [^{131}I]MIBG, [^{123}I]MIBG, [^{131}I]IUdR, or [^{123}I]IUdR. [^{131}I]MIBG and [^{131}I]IUdR both caused a dose-related decrease in the survival of cells that had concentrated the radiopharmaceutical and in recipients of the medium from irradiated cells. The concentration of [^{123}I]MIBG and [^{123}I]IUdR by HCT116 cells also induced direct dose-responsive toxicity. However, bystander HCT116 cells succumbed in a dose-responsive manner to the transfer of conditioned medium from donor cultures exposed to low radioactivity concentrations of [^{123}I]MIBG and [^{123}I]IUdR, but the toxic effect diminished with increasing dose of radiopharmaceutical to donors. This biphasic response was similar to the previously reported effect on the survival of clonogens derived from glioma and bladder carcinoma cell lines and treated with medium from cells which had concentrated [^{123}I]MIBG or [^{211}At]MABG [103].These findings not only support previous observations of the toxicity of Auger electron emitters conjugated to compounds which do not covalently bind to DNA [76, 103, 161, 162] but also indicate that the response of bystander cells to internalized Auger electron emitters does not depend on intracellular site of concentration. Further support for this notion has been provided by Pallais et al. [106] who demonstrated significant inhibition of tumor growth by ^{125}I localized to the cell membrane (see section "Critical Subcellular Sites of Interaction with Ionizing Radiation (Indirect Effects)").

Kishikawa et al. observed, in vitro and in vivo, opposing indirect effects induced by the concentration in the DNA of adenocarcinoma cells of ^{123}I or ^{125}I in the form of IUdR. The bystander effect induced by ^{125}I was growth inhibition, whereas that induced by ^{123}I was stimulation of proliferation [163]. These two high-LET, Auger electron emitters have similar emission spectra, but ^{123}I ($t_{1/2}$ = 13.3 h) is characterized by >100-fold greater dose rate than ^{125}I ($t_{1/2}$ = 60.5 days). Therefore, the potency of the RIBBE may be influenced not only by radiation quality but also by dose rate.

Conclusion

Targeting a single protein, whether on the cell membrane or in the nucleus, is necessary, but often not sufficient to produce a toxic event because of other mechanisms that are only partially understood. In targeting a specific protein, the primary factor is the location of the target, but the choice of radionuclide, the inertness of the bifunctional chelate or the stability of the covalently bound halogens, the residence time in the tumor matched with the physical half-life of the radionuclide, the scale and scope of the disease, and the absorbed dose sensitivity of the targeted tumor compared to normal tissue all come into play. But the analysis is complicated from an increasing number of observations that move toxicity from radiation at the target to the total effect. These include untargeted effects due to radiation emitted from neighboring, targeted cells as well as bystander effects produced by the cellular processing of radiation which need not impinge on DNA. Both indirect consequences of cellular radiation could make a substantial contribution to the efficacy of targeted radionuclide therapy. As more knowledge is gained of radiation-induced biological bystander effects in normal and malignant tissue, it is expected that these mechanisms will be exploited to optimize the efficacy of targeted radiotherapy and overcome the inefficiency of tumor control due to nonuniform distribution of radiation dose. The principles of molecular targeting are well established except for the paradigm shift from high-affinity, high-target density approach rather than the medium-affinity approach. Detecting lesions smaller than 2x machine resolution may favor the former approach over the latter. The design approach to take advantage of the indirect consequences of cellular radiation depends heavily on further elucidation of the indirect effect.

References

1. Hopf C, Bantscheff M, Drewes G. Pathway proteomics and chemical proteomics team up in drug discovery. Neurodegener Dis. 2007;4(2–3):270–80.

2. Eckelman WC, Lau CY, Neumann RD. Perspective, the one most responsive to change. Nucl Med Biol. 2014;41(4):297–8.
3. Divgi C. Whither goest thou, radiopharmaceutical therapy? J Nucl Med. 2014;55(1):5–6.
4. Maeda H, Wu J, Sawa T, Matsumura Y, Hori K. Tumor vascular permeability and the EPR effect in macromolecular therapeutics: a review. J Control Release. 2000;65(1–2):271–84.
5. Adams GP. Antibody fragments produced by recombinant and proteolytic methods. In: Stigbrand T, Carlsson J, Adams GP, editors. Targeted radionuclide tumor therapy: biological aspects. Dordrecht: Springer; 2008.
6. Boswell CA, Marik J, Elowson MJ, Reyes NA, Ulufatu S, Bumbaca D, et al. Enhanced tumor retention of a radiohalogen label for site-specific modification of antibodies. J Med Chem. 2013;56(23): 9418–26.
7. Eckelman WC. Choosing a target for targeted radionuclide therapy using biomarkers to personalize treatment. J Diagn Imaging Ther. 2014;1(1):103–9.
8. Eckelman WC, Mankoff DA. Choosing a single target as a biomarker or therapeutic using radioactive probes. Nucl Med Biol. 2015;42(5):421–5.
9. Zheng W, Thorne N, McKew JC. Phenotypic screens as a renewed approach for drug discovery. Drug Discov Today. 2013;18:1067–73.
10. Chopra A, Shan L, Eckelman WC, Leung K, Menkens AE. Important parameters to consider for the characterization of PET and SPECT imaging probes. Nucl Med Biol. 2011;38(8):1079–84.
11. Eckelman WC. The use of gene-manipulated mice in the validation of receptor binding radiotracer. Nucl Med Biol. 2003;30(8):851–60.
12. Wagner Jr HN, Burns HD, Dannals RF, Wong DF, Langstrom B, Duelfer T, et al. Imaging dopamine receptors in the human brain by positron tomography. Science. 1983;221(4617):1264–6.
13. Eckelman WC, Reba RC, Rzeszotarski WJ, Gibson RE, Hill T, Holman BL, et al. External imaging of cerebral muscarinic acetylcholine receptors. Science. 1984;223(4633):291–3.
14. Sawada Y, Hiraga S, Francis B, Patlak C, Pettigrew K, Ito K, et al. Kinetic analysis of 3-quinuclidinyl 4-[^{125}I] iodobenzilate transport and specific binding to muscarinic acetylcholine receptor in rat brain in vivo. J Cereb Blood Flow Metab. 1990;10:781–807.
15. Eckelman WC. Imaging of muscarinic receptors in the central nervous system. Curr Pharm Des. 2006;12 (30):3901–13.
16. Saxena A, Bester L, Shan L, Perera M, Gibbs P, Meteling B, et al. A systematic review on the safety and efficacy of yttrium-90 radioembolization for unresectable, chemorefractory colorectal cancer liver metastases. J Cancer Res Clin Oncol. 2014;140 (4):537–47.
17. Eckelman WC, Dilsizian V. Chemistry and biology of radiotracers that target changes in sympathetic and parasympathetic nervous systems in heart disease. J Nucl Med. 2015;56(Suppl 4):7S–10S.
18. Carson RE, Kiesewetter DO, Jagoda E, Der MG, Herscovitch P, Eckelman WC. Muscarinic cholinergic receptor measurements with [^{18}F]FP-TZTP: control and competition studies. J Cereb Blood Flow Metab. 1998;18(10):1130–42.
19. Podruchny TA, Connolly C, Bokde A, Herscovitch P, Eckelman WC, Kiesewetter DO, et al. In vivo muscarinic 2 receptor imaging in cognitively normal young and older volunteers. Synapse. 2003;48(1):39–44.
20. Cohen RM, Podruchny TA, Bokde AL, Carson RE, Herscovitch P, Kiesewetter DO, et al. Higher in vivo muscarinic-2 receptor distribution volumes in aging subjects with an apolipoprotein E-epsilon4 allele. Synapse. 2003;49(3):150–6.
21. Eckelman WC, Kilbourn MR, Mathis CA. Specific to nonspecific binding in radiopharmaceutical studies: it's not so simple as it seems! Nucl Med Biol. 2009;36(3):235–7.
22. Eckelman WC, Kilbourn MR, Mathis CA. Discussion of targeting proteins in vivo: in vitro guidelines. Nucl Med Biol. 2006;33:449–51.
23. Barrett JA, Coleman RE, Goldsmith SJ, Vallabhajosula S, Petry NA, Cho S, et al. First-in-man evaluation of 2 high-affinity PSMA-avid small molecules for imaging prostate cancer. J Nucl Med. 2013;54(3):380–7.
24. Hillier SM, Maresca KP, Femia FJ, Marquis JC, Foss CA, Nguyen N, et al. Preclinical evaluation of novel glutamate-urea-lysine analogues that target prostate-specific membrane antigen as molecular imaging pharmaceuticals for prostate cancer. Cancer Res. 2009;69(17):6932–40.
25. Zechmann CM, Afshar-Oromieh A, Armor T, Stubbs JB, Mier W, Hadaschik B, et al. Radiation dosimetry and first therapy results with a ^{124}I/^{131}I-labeled small molecule (MIP-1095) targeting PSMA for prostate cancer therapy. Eur J Nucl Med Mol Imaging. 2014;41(7):1280–92.
26. Mathias CJ, Wang S, Waters DJ, Turek JJ, Low PS, Green MA. Indium-111-DTPA-folate as a potential folate-receptor-targeted radiopharmaceutical. J Nucl Med. 1998;39:1579–85.
27. Carrasquillo JA, Lang L, Whatley M, Herscovitch P, Wang QC, Pastan I, Eckelman WC. Aminosyn II effectively blocks renal uptake of ^{18}F-labeled anti-tac disulfide-stabilized Fv. J Nucl Med. 2001;42(10): 1538–44.
28. Muller C, Struthers H, Winiger C, Zhernosekov K, Schibli R. DOTA conjugate with an albumin-binding entity enables the first folic acid-targeted ^{177}Lu-radionuclide tumor therapy in mice. J Nucl Med. 2013;54: 124–31.
29. Haller S, Reber J, Brandt S, Bernhardt P, Groehn V, Schibli R, et al. Folate receptor-targeted radionuclide therapy: preclinical investigation of anti-tumor effects and potential radionephropathy. Nucl Med Biol. 2015;42:770–9.

30. Barrett HH, Alberts DS, Woolfenden JM, Liu Z, Caucci L, Hoppin JW. Quantifying and reducing uncertainties in cancer therapy. Proc SPIE Int Soc Opt Eng. 2015;21:9412.
31. Jackson MR, Falzone N, Vallis KA. Advances in anticancer radiopharmaceuticals. Clin Oncol (R Coll Radiol). 2013;25(10):604–9.
32. Vallabhajosula S. The chemistry of therapeutic radiopharmaceuticals. In: Aktolun C, Goldsmith SJ, editors. Nuclear medicine therapy. New York: Springer; 2013. p. 339–68.
33. Boswell CA, Brechbiel MW. Development of radioimmunotherapeutic and diagnostic antibodies: an inside-out view. Nucl Med Biol. 2007;34(7): 757–78.
34. Huclier S. Preface of the workshop on innovative personalized radioimmunotherapy (WIPR 2013). Nucl Med Biol. 2014;41(Suppl):e1–6.
35. Hamacher KA, Den RB, Den EI, Sgouros G. Cellular dose conversion factors for alpha-particle – emitting radionuclides of interest in radionuclide therapy. J Nucl Med. 2001;42(8):1216–21.
36. Azure MT, Archer RD, Sastry KS, Rao DV, Howell RW. Biological effect of lead-212 localized in the nucleus of mammalian cells: role of recoil energy in the radiotoxicity of internal alpha-particle emitters. Radiat Res. 1994;140(2):276–83.
37. Lövqvist A, Humm JL, Sheikh A, Finn RD, Koziorowski J, Ruan S, et al. Pharmacokinetics and biodistribution of ^{86}Y-Trastuzumab for ^{90}Y dosimetry in an ovarian carcinoma model: correlative MicroPET and MRI. J Nucl Med. 2001;42(8):1281–7.
38. Walrand S, Flux GD, Konijnenberg MW, Valkema R, Krenning EP, Lhommel R, et al. Dosimetry of yttrium-labelled radiopharmaceuticals for internal therapy: ^{86}Y or ^{90}Y imaging? Eur J Nucl Med Mol Imaging. 2011;38(Suppl 1):S57–68.
39. Wright CL, Zhang J, Tweedle MF, Knopp MV, Hall NC. Theranostic imaging of yttrium-90. Biomed Res Int. 2015;2015:481279.
40. Raylman RR, Kison PV, Wahl RL. Capabilities of two- and three-dimensional FDG-PET for detecting small lesions and lymph nodes in the upper torso: a dynamic phantom study. Eur J Nucl Med. 1999;26:39–45.
41. Togawa T, Yui N, Kinoshita F, Yanagisawa M. Quantitative evaluation in tumor SPECT and the effect of tumor size: fundamental study with phantom. Ann Nucl Med. 1997;11:51–4.
42. Zeintl J, Vija AH, Yahil A, Hornegger J, Kuwert T. Quantitative accuracy of clinical ^{99m}Tc SPECT/CT using ordered-subset expectation maximization with 3-dimensional resolution recovery, attenuation, and scatter correction. J Nucl Med. 2010;51(6):921–8.
43. Ritt P, Vija H, Hornegger J, Kuwert T. Absolute quantification in SPECT. Eur J Nucl Med Mol Imaging. 2011;38(Suppl 1):S69–77.
44. Afshar-Oromieh A, Zechmann CM, Malcher A, Eder M, Eisenhut M, Linhart HG, et al. Comparison of PET imaging with a ^{68}Ga-labelled PSMA ligand and ^{18}F-choline-based PET/CT for the diagnosis of recurrent prostate cancer. Eur J Nucl Med Mol Imaging. 2014;41(1):11–20.
45. Humm JL. Dosimetric aspects of radiolabelled antibodies for tumour therapy. J Nucl Med. 1986;27: 1490–7.
46. Wheldon TE, O'Donoghue JA, Barrett A, Michalowski AS. The curability of tumours of differing sizes by targeted radiotherapy using I-131 and Y-90. Radiother Oncol. 1991;21(2):91–9.
47. O'Donoghue JA, Bardies M, Wheldon TE. Relationships between tumour size and curability for targeted radionuclide therapy. J Nucl Med. 1995; 36:1902–9.
48. Cunningham SH, Mairs RJ, Wheldon TE, Welsh PC, Vaidyanathan G, Zalutsky MR. Radiotoxicity to neuroblastoma cells and spheroids of beta-, alpha- and Auger electron-emitting conjugates of benzylguanidine. Br J Cancer. 1998;77:2061–8.
49. Wieland DM, Wu J, Brown LE, Mangner TJ, Swanson DP, Bierwaltes WH. Radiolabelled adrenergic neuron-blocking agents: adrenomedullary imaging with [^{131}I]iodobenzylguanidine. J Nucl Med. 1980;21:349–53.
50. Jacques Jr S, Tobes MC, Sisson JC, Baker JA, Wieland DM. Comparison of the sodium dependence of uptake of meta-iodo-benzylguanidine and norephrine into cultured bovine adrenomedullary cells. Mol Pharmacol. 1984;26:539–46.
51. Adam MJ, Wilbur DS. Radiohalogens for imaging and therapy. Chem Soc Rev. 2005;34:153–63.
52. Cooper MS, Ma MT, Sunassee K, Shaw KP, Williams JD, Paul RL, Donnelly PS, Blower PJ. Comparison of ^{64}Cu-complexing bifunctional chelators for radioimmunoconjugation: labeling efficiency, specific activity, and in vitro/in vivo stability. Bioconjug Chem. 2012;23:1029.
53. Szajek LP, Kao C-H K, Kiesewetter DO, Sassaman MB, Lang L, Plascjak P et al. Semi-remote production of Br-76 and preparation of high specific activity radiobrominated pharmaceuticals for PET studies. Radiochimica Acta: 2004;92, Issue 4–6, pp. 291–295. Stöcklin Memorial Issue.
54. Brechbiel MW. Bifunctional chelates for metal nuclides. Q J Nucl Med Mol Imaging. 2008;52(2): 166–73.
55. Larson SM. Mechanisms of localization of gallium-67 in tumors. Semin Nucl Med. 1978;8:193–203.
56. Deri MA, Zeglis BM, Francesconi LC, Lewis JS. PET imaging with ^{89}Zr: from radiochemistry to the clinic. Nucl Med Biol. 2013;40(1):3–14.
57. Maeda H, Tsukigawa K, Fang J. A retrospective 30 years after discovery of the EPR effect of solid tumors: next-generation chemotherapeutics and photodynamic-therapy-problems, solutions. Prospects Microcirc. 2016;23:173–82.
58. Severin GW, Jørgensen JT, Wiehr S, Rolle AM, Hansen AE, Maurer A, et al. The impact of weakly bound ^{89}Zr on preclinical studies: non-specific

accumulation in solid tumors and aspergillus infection. Nucl Med Biol. 2015;42(4):360–8.
59. Aloj L, Jogoda E, Lang L, Caracò C, Neumann RD, Sung C, et al. Targeting of transferrin receptors in nude mice bearing A431 and LS174T xenografts with [^{18}F]holo-transferrin: permeability and receptor dependence. J Nucl Med. 1999;40(9):1547–55.
60. Bass LA, Wang M, Welch MJ, Anderson CJ. In vivo transchelation of copper-64 from TETA-octreotide to superoxide dismutase in rat liver. Bioconjug Chem. 2000;11(4):527–32.
61. Cai Z, Anderson CJ. Chelators for copper radionuclides in positron emission tomography radiopharmaceuticals. J Label Compd Radiopharm. 2014;57(4): 224–30.
62. Apelgot S, Coppey J, Grisvard J, Guillé E, Sissoeff I. Distribution of copper-64 in control mice and in mice bearing ascitic Krebs tumor cells. Cancer Res. 1981;41:1502–7.
63. Jørgensen JT, Persson M, Madsen J, Kjær A. High tumor uptake of ^{64}Cu: implications for molecular imaging of tumor characteristics with copper-based PET tracers. Nucl Med Biol. 2013;40(3):345–50.
64. Kim KI, Jang SJ, Park JH, Lee YJ, Lee TS, Woo KS, et al. Detection of increased ^{64}Cu uptake by human copper transporter 1 gene overexpression using PET with $^{64}CuCl_2$ in human breast cancer xenograft model. J Nucl Med. 2014;55(10):1692–8.
65. Cai H, Wu JS, Muzik O, Hsieh JT, Lee RJ, Peng F. Reduced ^{64}Cu uptake and tumor growth inhibition by knockdown of human copper transporter 1 in xenograft mouse model of prostate cancer. J Nucl Med. 2014;55 (4):622–8.
66. Qin C, Liu H, Chen K, Hu X, Ma X, Lan X, et al. Theranostics of malignant melanoma with $^{64}CuCl_2$. J Nucl Med. 2014;55(5):812–7.
67. Cole WC, Wolf W. Preparation and metabolism of a cisplatin/serum protein complex. Chem Biol Interact. 1980;30(2):223–35.
68. Parti R, Wolf W. Quantitative subcellular distribution of platinum in rat tissues following i.v. bolus and i.v. infusion of cisplatin. Cancer Chemother Pharmacol. 1990;26(3):188–92.
69. Huclier-Markai S, Kerdjoudj R, Alliot C, Bonraisin AC, Michel N, Haddad F, et al. Optimization of reaction conditions for the radiolabeling of DOTA and DOTA-peptide with $^{44m/44}$Sc and experimental evidence of the feasibility of an in vivo PET generator. Nucl Med Biol. 2014;41:e36–43.
70. Krohn KA, Mankoff DA, Muzi M, Link JM, Spence AM. True tracers: comparing FDG with glucose and FLT with thymidine. Nucl Med Biol. 2005;32(7): 663–71.
71. Duatti A. Nonisotopic substitution: is fluorine a replacement for hydrogen? Nucl Med Biol. 2013;40 (7):871–2.
72. Jia F, Balaji BS, Gallazzi F, Lewis MR. Copper-64-labeled anti-bcl-2 PNA-peptide conjugates selectively localize to bcl-2-positive tumors in mouse models of B-cell lymphoma. Nucl Med Biol. 2015; 42:809.
73. Cornelissen B. Imaging the inside of a tumour: a review of radionuclide imaging and theranostics targeting intracellular epitopes. J Label Compd Radiopharm. 2014;57(4):310–6.
74. DeSombre ER, Mease RC, Hughes A, Harper PV, DeJesus OT, Friedman AM. Bromine-80m-labeled estrogens: Auger electron-emitting, estrogen receptor-directed ligands with potential for therapy of estrogen receptor-positive cancers. Cancer Res. 1988;48(4):899–906.
75. DeSombre ER, Shafii B, Hanson RN, Kuivanen PC, Hughes A. Estrogen receptor-directed radiotoxicity with Auger electrons: specificity and mean lethal dose. Cancer Res. 1992;52(20):5752–8.
76. DeSombre ER, Hughes A, Hanson RN, Kearney T. Therapy of estrogen receptor-positive micrometastases in the peritoneal cavity with Auger electron-emitting estrogens–theoretical and practical considerations. Acta Oncol. 2000;39(6):659–66.
77. Larson SM, Carrasquillo JA, Cheung NK, Press OW. Radioimmunotherapy of human tumours. Nat Rev Cancer. 2015;15(6):347–60.
78. Bloomer WD, Adelstein SJ. 5-^{125}I-Iododeoxyuridine as prototype for radionuclide therapy with Auger emitters. Nature. 1977;265:620–1.
79. Bloomer WD, Adelstein SJ. Therapeutic application of iodine-125 labeled iododeoxyuridine in an early ascites tumor model. Curr Top Radiat Res Q. 1977;12:513–25.
80. Baranowska-Kortylewicz J, Makrigiorgos GM, Van den Abbeele AD, Berman RM, Adelstein SJ, Kassis AI. 5-[^{123}I]iodo-2′-deoxyuridine in the radiotherapy of an early ascites tumor model. Int J Radiat Oncol Biol Phys. 1991;21:1541–51.
81. Charlton DE. The range of high LET effects from ^{125}I decays. Radiat Res. 1986;107:163–71.
82. Kassis A, Fayad F, Kinsey BM, Sastry KSR, Taube RA, Adelstein SJ. Radiotoxicity of ^{125}I in mammalian cells. Radiat Res. 1987;111:305–18.
83. Link EM, Brown I, Carpenter RN, Mitchell JS. Uptake and therapeutic effectiveness of ^{125}I- and ^{211}At-methylene blue for pigmented melanoma in an animal model system. Cancer Res. 1989;49:4332–7.
84. Gaze MN, Huxham IM, Mairs RJ, Barrett A. Intracellular localization of metaiodobenzylguanidine in human neuroblastoma cells by electron spectroscopic imaging. Int J Cancer. 1991;47:875–80.
85. Clerc J, Halpern S, Fourre C, Omri F, Briancon J, Eusset J, et al. SIMS microscopy imaging of the intratumour biodistribution of meta-iodobenzylguanidine in the human SK-N-SH neuroblastoma cell line xenografted into nude mice. J Nucl Med. 1993;34:1565–70.
86. Tritschler H-J, Medori R. Mitochondrial DNA alterations as a source of human disorders. Neurology. 1993;43:280–8.
87. Howell RW. Radiation spectra for Auger electron emitting radionuclides. Report No 2 of AAPM-

Nuclear-Medicine-Task-Group No 6. Med Phys. 1992;19:1371–83.
88. Sastry KSR. Biological effects of the Auger emitter $^{125}I^-$ a review. Report No 1 of AAPM-Nuclear-Medicine-Task-Group No 6. Med Phys. 1992;19:1361–70.
89. Jarvis WD, Kolesnick RN, Fornari FA, Traylor RS, Gewirtz DA, Grant S. Induction of apoptotic DNA damage and cell death by activation of the sphingomyelin pathway. Proc Natl Acad Sci U S A. 1994;91:73–7.
90. Obeid LM, Linardic CM, Karolak LA, Hannun YA. Programmed cell death induced by ceramide. Science. 1994;259:1769–71.
91. Haimovitz-Friedman A, Kan C-C, Ehleiter D, Persaud RS, McLoughlin M, Fuks Z, et al. Ionizing radiation acts on cellular membranes to generate ceramide and initiate apoptosis. J Exp Med. 1994;180:525–35.
92. Pouget JP, Santoro L, Raymond L, Chouin N, Bardiès M, Bascoul-Mollevi C, et al. Cell membrane s a more sensitive target than cytoplasm to dense ionization produced by auger electrons. (Translated from eng). Radiat Res. 2008;170(2):192–200.
93. Santoro L, Boutaleb S, Garambois V, Bascoul-Mollevi C, Boudousq V. Pierre- Kotzki P-O, et al. Noninternalizing monoclonal antibodies are suitable candidates for ^{125}I radioimmunotherapy of small-volume peritoneal carcinomatosis. J Nucl Med. 2009;50(12):2033–41.
94. Xue LY, Butler NJ, Makrigiorgos GM, Adelstein SJ, Kassis AI. Bystander effect produced by radiolabeled tumor cells in vivo. Proc Natl Acad Sci U S A. 2002;99(21):13765–70.
95. Nagasawa H, Little JB. Induction of sister chromatid exchanges by extremely low doses of alpha-particles. Cancer Res. 1992;52:6394–6.
96. Mothersill C, Seymour CB. Radiation induced bystander effects: past history and future directions. Radiat Res. 2001;155:759–67.
97. Mothersill C, Seymour CB. Radiation-induced bystander effects–implications for cancer. Nat Rev Cancer. 2004;4:158–64.
98. Lyng FM, Seymour CB, Mothersill C. Early events in the apoptotic cascade initiated in cells treated with medium from the progeny of irradiated cells. Radiat Prot Dosim. 2002;99:169–72.
99. Lorimore SA, Wright EG. Radiation-induced genomic instability and bystander effects: related inflammatory-type responses to radiation-induced stress and injury? A review. Int J Radiat Biol. 2003;79:15–25.
100. Morgan WF. Is there a common mechanism underlying genomic instability, bystander effects and other nontargeted effects of exposure to ionising radiation? Oncogene. 2003;22:7094–9.
101. Little JB. Genomic instability and bystander effects: a historical perspective. Oncogene. 2003;22:6978–87.
102. Carlsson J, Aronsson EF, Hietala S-O, Stigbrand T, Tennvall J. Tumour therapy with radionuclides: assessment of progress and problems. Radiother Oncol. 2003;66:107–17.
103. Boyd M, Ross SC, Dorrens J, Fullerton NE, Tan KW, Zalutsky MR, et al. Radiation-induced biologic bystander effect elicited in vitro by targeted radiopharmaceuticals labeled with alpha-, beta-, and auger electron-emitting radionuclides. J Nucl Med. 2006;47(6):1007–15.
104. Prise KM, O'Sullivan JM. Radiation-induced bystander signalling in cancer therapy. Nat Rev Cancer. 2009;9(5):351–60.
105. Brady D, O'Sullivan JM, Prise KM. What is the role of the bystander response in radionuclide therapies? Front Oncol. 2013;3:215.
106. Paillas S, Boudousq V, Piron B, Kersual N, Bardiès M, Chouin N, et al. Apoptosis and p53 are not involved in the anti-tumor efficacy of (125)I-labeled monoclonal antibodies targeting the cell membrane. Nucl Med Biol. 2013;40(4):471–80.
107. Prise KM, Schettino G, Folkard M, Held KD. New insights on cell death from radiation exposure. Lancet Oncol. 2005;6(7):520–8.
108. Havaki S, Kotsinas A, Chronopoulos E, Kletsas D, Georgakilas A, Gorgoulis VG. The role of oxidative DNA damage in radiation induced bystander effect. Cancer Lett. 2015;356(1):43–51.
109. Lehnert BE, Goodwin EH. Extracellular factor (s) following exposure to alpha particles can cause sister chromatid exchanges in normal human cells. Cancer Res. 1997;57:2164–71.
110. Narayanan PK, Goodwin EH, Lehnert BE. Alpha particles initiate biological production of superoxide anions and hydrogen peroxide in human cells. Cancer Res. 1997;57:3963–71.
111. Matsumoto H, Hayashi S, Hatashita M, Ohnishi K, Shioura H, Ohtsubo T, et al. Induction of radioresistance by a nitric oxide-mediated bystander effect. Radiat Res. 2001;155:387–96.
112. Shao C, Furusawa Y, Aoki M, Matsumoto H, Ando K. Nitric oxide-mediated bystander effect induced by heavy-ions in human salivary gland tumour cells. Int J Radiat Biol. 2002;78:837–44.
113. Iyer R, Lehnert BE. Factors underlying the cell growth-related bystander responses to alpha particles. Cancer Res. 2000;60:1290–8.
114. Zhou H, Ivanov VN, Lien YC, Davidson M, Hei TK. Mitochondrial function and nuclear factor-kappa B-mediated signaling in radiation-induced bystander effects. Cancer Res. 2008;68(7):2233–40.
115. Demaria S, Ng B, Devitt ML, Babb JS, Kawashima N, Liebes L, et al. Ionizing radiation inhibition of distant untreated tumors (abscopal effect) is immune mediated. Int J Radiat Oncol Biol Phys. 2004;58(3):862–70.
116. De Ridder M, Jiang H, Van Esch G, Law K, Monsaert C, Van den Berge DL, et al. IFN-gamma+ CD8+ T lymphocytes: possible link between immune and radiation responses in tumor-relevant hypoxia. Int J Radiat Oncol Biol Phys. 2008;71(3):647–51.
117. Lee Y, Auh SL, Wang Y, Burnette B, Wang Y, Meng Y, et al. Therapeutic effects of ablative radiation

on local tumor require CD8+ T cells: changing strategies for cancer treatment. Blood. 2009;114(3): 589–95.
118. Brady D, O'Sullivan JM, Prise KM. What is the role of the bystander response in radionuclide therapies? Front Oncol. 2013;3:1–5.
119. Pouget J-P, Lozza C, Deshayes E, Boudousq V, Navarro-Teulon I. Introduction to radiobiology of targeted radionuclide therapy. Front Med. 2015;2:1–11.
120. Bishayee A, Rao DV, Howell RW. Evidence for pronounced bystander effects caused by nonuniform of radioactivity distributions using a novel three-dimensional tissue culture model. Radiat Res. 1999;97152:88–97.
121. Bishayee A, Hill HZ, Stein D, Rao DV, Howell RW. Free radical- initiated and gap junction- mediated Bystander effect due to nonuniform distribution of incorporated radioactivity in a three-dimensional tissue culture model. Radiat Res. 2001;155:335–44.
122. Persaud R, Zhou H, Baker SE, Hei TK, Hall EJ. Assessment of low linear energy transfer radiation- induced bystander mutagenesis in a three-dimensional culture model. Cancer Res. 2005;65: 9876–82.
123. Kassis AI. In vivo validation of the bystander effect. Hum Exp Toxicol. 2004;23:71–3.
124. Mamlouk O, Balagurumoorthy P, Wang K, Adelstein SJ, Kassis AI. Bystander effect in tumor cells produced by Iodine-125 labeled human lymphocytes. Int J Radiat Biol. 2012;88:1019–27.
125. Akudugu JM, Azzam EI, Howell RW. Induction of lethal bystander effects in human breast cancer cell cultures by DNA-incorporated Iodine-125 depends on phenotype. Int J Radiat Biol. 2012;88:1028–38.
126. Chouin N, Bernardeau K. Evidence of extranuclear cell sensitivity to alpha-particle radiation using a microdosimetric model. II. Application of the microdosimetric model to experimental results. Radiat Res. 2009;171(6):664–73.
127. Howell RW, Rajon D, Bolch WE. Monte Carlo simulation of irradiation and killing in three-dimensional cell populations with lognormal cellular uptake of radioactivity. Int J Radiat Biol. 2012;88:115–22.
128. Burdak-Rothkamm S, Rothkamm K, Prise KM. ATM acts downstream of ATR in the DNA damage response signaling of bystander cells. Cancer Res. 2008;68(17):7059–65.
129. Alper T. Effects on irradiated micro-organisms of growth in the presence of acriflavine. Nature. 1963;200:534–6.
130. Hussain SP, Hofseth LJ, Harris CC. Radical causes of cancer. Nat Rev Cancer. 2003;3(4):276–85.
131. Corre I, Niaudet C, Paris F. Plasma membrane signaling induced by ionizing radiation. Mutat Res. 2010;704(1–3):61–7.
132. Kolesnick RN, Haimovitz-Friedman A, Fuks Z. The sphingomyelin signal transduction pathway mediates apoptosis for tumor necrosis factor, Fas, and ionizing radiation. Biochem Cell Biol. 1994;72(11–12):471–4.
133. Piron B, Paillas S, Boudousq V, Pèlegrin A, Bascoul-Mollevi C, Chouin N, et al. DNA damage-centered signaling pathways are effectively activated during low dose-rate Auger radioimmunotherapy. Nucl Med Biol. 2014;41(Suppl):e75–83.
134. Butterworth KT, Coulter JA, Jain S, Forker J, McMahon SJ, Schettino G, et al. Evaluation of cytotoxicity and radiation enhancement using 1.9 nm gold particles: potential application for cancer therapy. Nanotechnology. 2010;21:295101.
135. Kam WW, Banati RB. Effects of ionizing radiation on mitochondria. Free Radic Biol Med. 2013;65:607–19.
136. Samper E, Morgado L, Estrada JC, Bernad A, Hubbard A, Cadenas S, et al. Increase in mitochondrial biogenesis, oxidative stress, and glycolysis in murine lymphomas. Free Radic Biol Med. 2009;46:387–96.
137. Poyton RO, Ball KA, Castello PR. Mitochondrial generation of free radicals and hypoxic signaling. Trends Endocrinol Metab. 2009;20:332–40.
138. Liou G-Y, Storz P. Reactive oxygen species in cancer. Free Radic Res. 2010;44:1–31.
139. Laurent A, Nicco C, Chéreau C, Goulvestre C, Alexandre J, Alves A, et al. Controlling tumor growth by modulating endogenous production of reactive oxygen species. Cancer Res. 2005;65:948–56.
140. Wang J, Yi J. Cancer cell killing via ROS: to increase or decrease, that is the question. Cancer Biol Ther. 2008;7:1875–84.
141. Ralph SJ, Rodríguez-Enríquez S, Neuzil J, Saavedra E, Moreno-Sánchez R. The causes of cancer revisited: "mitochondrial malignancy" and ROS-induced oncogenic transformation – why mitochondria are targets for cancer therapy. Mol Asp Med. 2010;31:145–70.
142. Murphy JE, Nugent S, Seymour C, Mothersill C. Mitochondrial DNA point mutations and a novel deletion induced by direct low-LET radiation and by medium from irradiated cells. Mutat Res. 2005;585 (1–2):127–36.
143. Hei TK, Zhou H, Ivanov VN, Hong M, Lieberman HB, Brenner DJ, et al. Mechanism of radiation-induced bystander effects: a unifying model. J Pharm Pharmacol. 2008;60(8):943–50.
144. Sutherland RM, Inch WR, McCredie JA, Kruuv J. A multi-component radiation survival curve using an in vitro tumour model. Int J Radiat Biol Relat Stud Phys Chem Med. 1970;18:491–5.
145. Mueller-Klieser W. Multicellular spheroids. A review on cellular aggregates in cancer research. J Cancer Res Clin Oncol. 1987;113:101–22.
146. Knuechel R, Sutherland RM. Recent developments in research with human tumour spheroids. Cancer J. 1990;3:234–43.
147. Carlsson J, Nederman T. Tumour spheroids as a model in studies of drug effects. In: Bjerkvig R, editor. Spheroid culture in cancer research. Boca Raton: CRC Press; 1992. p. 245–69.
148. Mikhail AS, Eetezadi S, Allen C. Multicellular tumor spheroids for evaluation of cytotoxicity and

tumor growth inhibitory effects of nanomedicines in vitro: a comparison of docetaxel-loaded block copolymer micelles and Taxotere. PLoS One. 2013;8(4):e62630.
149. Hickman J, Graeser R, de Hoogt R, Vidic S, Brito C, Gutekunst M, Van der Kuip H. Three-dimensional models of cancer for pharmacology and cancer cell biology: capturing tumor complexity in vitro/ex vivo. Biotechnol J. 2014;9:1115–28.
150. Hirschhaeuser F, Menne H, Dittfeld C, West J, Mueller-Klieser W, Kunz-Schughart LA. Multicellular tumor spheroids: an underestimated tool is catching up again. J Biotechnol. 2010;148(1):3–15.
151. Sutherland RM. Cell and environment interactions in tumour microregions: the multicell spheroid model. Science. 1988;240:177–84.
152. Senavirathna LK, Fernando R, Maples D, Zheng Y, Polf JC, Ranjan A. Tumor spheroids as an in vitro model for determining the therapeutic response to proton beam radiotherapy and thermally sensitive nanocarriers. Theranostics. 2013;3(9):687–91.
153. Boyd M, Mairs SC, Stevenson K, Livingstone A, McCluskey AG, Ross SC, Mairs RJ. Transfectant mosaic spheroids: a new model for the evaluation of bystander effects in experimental gene therapy. J Gene Med. 2002;4:567–76.
154. Lybarger L, Dempsey D, Franek KJ, Chervenak R. Rapid generation and flow cytometric analysis of stable GFP-expressing cells. Cytometry. 1996;25: 211–20.
155. Boyd M, Mairs RJ. Tumour spheroids. In: Freshney RI, editor. The culture of animal cells. 5th ed. New York: Alan R. Liss; 2006. p. 281–98.
156. Boyd M, Cunningham SH, Brown MM, Mairs RJ, Wheldon TE. Noradrenaline transporter gene transfer for radiation cell kill by [^{131}I]meta-iodobenzylguanidine. Gene Ther. 1999;6:1147–52.
157. Vaidyanathan G, Affleck DJ, Alston KL, Zhao XG, Hens M, Hunter DH, et al. A kit method for the high level synthesis of [^{211}At]MABG. Bioorg Med Chem. 2007;15:3430–6.
158. Zalutsky MR, Vaidyanathan G. Astatine-211-labeled radiotherapeutics: an emerging approach to targeted alpha particle therapy. Curr Pharm Des. 2000;6: 1433–55.
159. Mairs RJ, Ross SC, McCluskey AG, Boyd M. A transfectant mosaic xenograft model for the evaluation of targeted radiotherapy in combination with gene therapy in vivo. J Nucl Med. 2007;48:1519–26.
160. Boyd M, Mairs SC, Stevenson K, Livingstone A, McCluskey AG. Radiation quality-dependent bystander effects elicited by targeted radionuclides. J Pharm Pharmacol 2008;60:951–958.
161. Sisson JC, Shapiro B, Hutchinson RJ, Zasadny KR, Mallette S, Mudgett EE, Weiland DM. Treatment of neuroblastoma with [^{125}I]metaiodobenzylguanidine. J Nucl Biol Med. 1991;35:255–9.
162. de Jong M, Bakker WH, Breeman WAP. Pre-clinical comparison of [DTPA^{0}] octreotide, [DTPA^{0}, Tyr^{3}] octreotide and [DOTA^{0}, Tyr^{3}] octreotide as carriers for somatostatin receptor-targeted scintigraphy and radionuclide therapy. Int J Cancer. 1998;75:406–11.
163. Kishikawa H, Wang K, Adelstein SJ, Kassis AI. Inhibitory and stimulatory bystander effects are differentially induced by iodine-125 and iodine-123. Radiat Res. 2006;165:688–94.

Single-Photon-Emitting Radiopharmaceuticals for Diagnostic Applications

3

Federica Orsini, Erinda Puta, Alice Lorenzoni, Paola Anna Erba, and Giuliano Mariani

Abstract

Radiopharmaceuticals contain a radionuclide and an agent to direct the radionuclide to a receptor, antigen, ionic pump, or other sites of interest. Some radiopharmaceuticals are simple, such as the ionic form of the radionuclide, while most radiopharmaceuticals have a complex chemical structure where the radionuclide provides a signal, indicating the site of localization of the carrier molecule.

Common single-photon radiopharmaceuticals used for oncological diagnosis include the agents labeled with ^{99m}Tc such as ^{99m}Tc-bisphosphonates (that accumulate at sites of bone mineral deposition), ^{99m}Tc-labeled colloids (that are used for lymphoscintigraphy and for imaging of the liver and spleen), ^{99m}Tc-hexakis-methoxy-isobutyl-isonitrile, and ^{99m}Tc-tetrofosmin (initially employed for myocardial perfusion imaging, and also used for localization of parathyroid adenomas and for identification of other malignant tumors).

The most commonly used radiopharmaceuticals labeled with radioiodine (^{123}I or ^{131}I) include iodide itself (for localization of thyroid tissue) and the catecholamine analog meta-iodobenzylguanidine (MIBG, for localizing pheochromocytoma and neuroblastoma). Thallium-201 chloride (^{201}Tl) is used for myocardial perfusion imaging as well as tumor perfusion imaging, while ^{111}In-pentetreotide detects overexpression of somatostatin receptors, especially in neuroendocrine tumors and in lesions arising from the neural crest, such as carcinoid, paragangliomas, and medullary thyroid carcinomas. ^{111}In-capromab pendetide is a murine monoclonal antibody recognizing a transmembrane glycoprotein expressed by poorly differentiated and metastatic prostate adenocarcinomas. ^{67}Ga-citrate receptors are overexpressed on membranes of both tumor and inflammatory cells.

Keywords

Single-photon emission imaging • Radiopharmaceuticals • Radiotracer

F. Orsini (✉) • E. Puta
Nuclear Medicine Unit, "Maggiore della Carità" University Hospital, Novara, Italy
e-mail: federica.orsini@maggioreosp.novara.it; erinda.puta@maggioreosp.novara.it

A. Lorenzoni
Nuclear Medicine Division, IRCCCS National Cancer Institute, Milan, Italy
e-mail: alice.lorenzoni@istitutotumori.mi.it

P.A. Erba
Regional Center of Nuclear Medicine, Department of Translational Research and Advanced Technologies in Medicine, University of Pisa, Pisa, Italy
e-mail: paola.erba@unipi.it

G. Mariani
Regional Center of Nuclear Medicine, Department of Translational Research and Advanced Technologies in Medicine and Surgery, University of Pisa, Pisa, Italy
e-mail: giuliano.mariani@med.unipi.it

© Springer International Publishing Switzerland 2017
H.W. Strauss et al. (eds.), *Nuclear Oncology*,
https://doi.org/10.1007/978-3-319-26236-9_2

Glossary	
[^{123}I]MIBG	*meta*-[^{123}I] Iodobenzylguanidine
[^{131}I]MIBG	*meta*-[^{131}I] Iodobenzylguanidine
[^{18}F]FDG	2-Deoxy-2-[^{18}F]fluoro-D-glucose
^{99m}Tc-DTPA	^{99m}Tc-Diethylenetriaminepentaacetic acid
^{99m}Tc-HDP	^{99m}Tc-Hydroxyethylenediphosphonate
^{99m}Tc-MAA	^{99m}Tc-Macroaggregated albumin
^{99m}Tc-MDP	^{99m}Tc-Methylene diphosphonate
COMT	Catecholamine-*O*-methyltransferase
COPD	Chronic obstructive pulmonary disease
DIT	Diiodotyrosine
DTPA	Diethylenetriaminepentaacetic acid
EDDA	Ethylenediamine-N,N'-bis(2-hydroxyphenyl)acetic acid
EMA	European Medicines Agency
FDA	United States Food and Drug Administration
HYNIC	6-Hydrazinopyridine-3-carboxylic acid, also known aso hydrazidonicotinic acid/ hydrazinonicotinamide
LDL	Low-density lipoproteins
MAO	Monoamine oxidase
MIBG	*Meta*-iodobenzylguanidine
MIT	Monoiodotyrosine
NIS	Sodium–iodide symporter
PET	Positron emission tomography
PSMA	Prostate-specific membrane antigen
ROLL	Radioguided occult lesion localization
SLN	Sentinel lymph node
SPECT	Single-photon emission tomography
SST	Somatostatin
SSTR	Somatostatin receptor
TSH	Thyroid-stimulating hormone

Contents

Background 68
^{99m}Tc-Labeled Radiopharmaceuticals 69
Lung Ventilation Radiopharmaceuticals 77
Radioiodinated Agents 78
^{201}Tl-Chloride 80
^{111}In-Pentetreotide 81
^{111}In-Capromab Pendetide 82
^{67}Ga-Citrate 82

Suggested Readings 83

Background

A radiopharmaceutical is a sterile, pyrogen free compound containing a radionuclide for the detection, characterization, or treatment of disease usually coupled to a directing agent - such as a peptide, antibody, or small molecule. Fundamental properties commonly associated with radiopharmaceuticals are: (1) they are administered in mass amounts that rarely elicit a pharmacologic response, and (2) interaction of radiopharmaceuticals with physiological systems is not linked to their physical properties (emission of ionizing radiation) but rather to their chemical nature.

The chemistry of some radiopharmaceuticals is very simple (such as the ionic form of the radionuclide itself), whereas most radiopharmaceuticals have a complex chemical structure in which the radionuclide only serves for emission of the physical sign (see below), while interaction with the biological systems is due to the chemical structure of the main carrier molecule.

Radiopharmaceuticals employed for diagnostic purposes produce a physical signal, i.e., emission of γ-rays or β^+-particles (the latter in turn undergoing annihilation when combining with a β^--particle, with ensuing emission of two high-energy photons). Dedicated radiation sensors can detect either the γ-rays and/or the high-energy annihilation photons. The nuclear medicine

equipment employed for imaging (scintigraphy) produces an image that represents the distribution of the radiopharmaceutical in the body.

The diagnostic information provided by scintigraphic imaging (or the desired therapeutic effect) derives from the characteristic distribution within the body of any given radiopharmaceutical. Most radiopharmaceuticals are administered systemically (i.e., intravenously); less frequent modalities of administration include the oral, interstitial, intracavitary, or even the intra-arterial routes. The main parameters that determine the scintigraphic information are the rate of disappearance (or clearance) from blood, accumulation, retention, and washout at a specific tissue/organ of interest. Changes in the distribution reflect pathophysiological changes of function or metabolism. Many of the abnormalities that can be demonstrated using radiopharmaceuticals occur at an early stage of the pathogenetic cascade that characterizes a disease, often before morphological modifications in shape, size, and/or structure of the tissue/organ of interest can be detected using anatomic imaging modalities.

Radiopharmaceuticals consisting of only the radionuclide in its ionic form usually concentrate in specific target tissue/organs either because they are radioisotopes of a naturally occurring element of biological interest (such as ^{123}I, ^{124}I, or ^{131}I undergoing the same physiologic distribution of native ^{127}I) or because they share chemical similarities/analogies with native elements of biological interest (such as ^{201}Tl or ^{82}Rb mirroring the physiologic distribution of native ^{39}K).

For more complex radiopharmaceuticals, the radionuclide is incorporated in the main carrier molecule through a chemical process denominated "radiolabeling" (see also ▶ Chap. 2, "Principles of Molecular Targeting for Radionuclide Therapy" of this book). The radionuclides most widely employed in nuclear medicine for imaging based on single-photon emission and their main physical characteristics are reported in Table 1.

Radiopharmaceuticals can also be classified based on physical characteristics of the radionuclide (type and energy of the characteristic emissions, physical half-life) or else on the physicochemical properties of the molecule (size, hydro- or lipophilicity, positive, negative, or neutral electrical charge) and mechanism of localization (Table 2).

Table 3 schematically summarizes the main radiopharmaceuticals used in conventional nuclear medicine for single-photon imaging.

^{99m}Tc-Labeled Radiopharmaceuticals

Because of its favorable gamma energy (140 keV), lack of particulate radiation, its ready availability and its 6-h half-life, ^{99m}Tc (a transition metal radionuclide) is employed

Table 1 Most widely used radionuclides in conventional nuclear medicine imaging and their main physical and chemical properties

Radionuclide	Chemical nature and charge	$T_{1/2}$	Energy (keV)	Emission
^{123}I[a]	Halogen, 1^-	12.8 h	159	γ
				Auger electrons
^{131}I	Halogen, 1^-	196.8 h	284, 364, 637	γ
			810	β^-
^{99m}Tc	Transition metal, 4^+, 5^+, 6^+, 7^+	6.06 h	140	γ
^{111}In[a]	Post-transition rare metal, 3^+	67.9 h	172, 245	γ
				Auger electrons
^{67}Ga[a]	Rare metal, 3^+	78.3 h	93, 185, 296	γ
^{201}Tl[a]	Post-transition metal, 1^+ (3^+)	72 h	135–167	γ
			69–83	x-ray

[a]Decay also with electron capture and secondary emission of a characteristic x-ray; decay is also associated with 1.4% incidence of 528 keV photon, which requires the use of medium energy collimation

Table 2 Main mechanisms of in vivo distribution/localization of radiopharmaceuticals

Mechanism(s)	Rationale	Example
Mechanical trapping (capillary blockade)	The regional distribution of perfusion in an organ can be assessed by administering in the afferent blood vessel radiolabeled particles that, because of their large size (tens of μm), cause microembolization in the precapillary bed of an organ	^{99m}Tc-MAA for planning radioembolization of liver tumors (intra-arterial injection)
Phagocytosis	Upon interstitial administration, micellar-size radiopharmaceuticals are drained through the lymphatic system and are engulfed by macrophages lining the sinusoidal spaces of lymph nodes	^{99m}Tc-radiocolloid for lymphoscintigraphy and radioguided sentinel lymph node biopsy
Ion exchange (chemisorption)	Exchange of ions between two electrolytes or between an electrolyte solution and a complex (binding to hydroxyapatite crystals or to amorphous calcium phosphate)	^{99m}Tc-labeled bisphosphonates for bone scintigraphy
Membrane transport: simple, facilitated, and active transport	Passive transmembrane diffusion of lipophilic, cationic molecules that bind to cytosolic components or accumulate into mitochondria	^{99m}Tc-tetrofosmin or ^{99m}Tc-sestamibi
	Active, energy-dependent transmembrane transport of molecules against a concentration gradient: sodium–iodide symporter	Radioiodine and ^{99m}Tc-pertechnetate for thyroid scintigraphy
Receptor-mediated probes	The radiopharmaceutical competes with the physiologic ligands for binding with the target receptor	Somatostatin analogs used for neuroendocrine tumors as vehicles to guide radioactivity to tissues expressing somatostatin receptors
Radioaerosols and radioactive gases	Direct inhalation	Radiopharmaceutical for lung ventilation

for about 80% of single-photon imaging procedures performed in nuclear medicine. The main characteristics that make this radionuclide almost ideal for use in diagnostic nuclear medicine based on single-photon emitting radiopharmaceuticals are:

- Emission of a γ-radiation with a monoenergetic emission peak (140 keV) which is optimal for detection using the current gamma camera detector systems and instrumentation for radioguided surgery
- Lack of particulate emission, thus limiting the radiation burden to patients
- High chemical reactivity with a variety of compounds and chemical species, thus making it possible to prepare a wide range of diagnostic agents labeled with the same radionuclide
- A physical decay half-life (6 h) which is relatively short yet is compatible with the time frame within which most of the diagnostic procedures currently performed with conventional gamma cameras are completed
- A physical decay half-life which is sufficiently short for limiting not only the radiation burden to patients linked to γ-emission but also the unwanted radiation to the general population (when the patient leaves the imaging department after completing the scan), as well as handling of radioactive waste

In principle, a short physical decay half-life would constitute a limitation in the distribution logistics of radionuclides/radiopharmaceuticals to remote locations. Despite its short physical half-life, ^{99m}Tc is widely available in any nuclear medicine center – whichever is the distance from the manufacturers – thanks to the possibility of in situ production starting from a parent radionuclide with longer half-life through the use of a molybdenum-99-based generator (^{99}Mo/^{99m}Tc).

Table 3 Common single-photon radiopharmaceuticals used for diagnosis

Radionuclide	Radiopharmaceutical
^{99m}Tc	^{99m}Tc-sodium pertechnetate has similar biological distribution to iodide and concentrates mainly in thyroid tissue
	^{99m}Tc-bisphosphonates accumulate at sites of bone mineral rearrangement
	^{99m}Tc-labeled colloids are used for lymphoscintigraphy and for imaging liver, spleen, bone marrow
	^{99m}Tc-hexakis-methoxy-isobutyl-isonitrile and ^{99m}Tc-tetrofosmin (both cationic compounds) are used for myocardial perfusion imaging, identification of parathyroid adenoma, and identification of some tumors
^{123}I or ^{131}I	Iodide, used for localization of functioning thyroid tissue and follicle-derived tumors
	Metaiodobenzylguanidine (MIBG), a catecholamine analog localizing in pheochromocytoma and neuroblastoma, as well as in other tumors arising from the neural crest
^{201}Tl	Ionic thallium used for myocardial perfusion and tumor imaging
^{111}In	Pentetreotide, a somatostatin analog that detects overexpression of somatostatin receptors, especially in neuroendocrine tumors and lesions arising from the neural crest, such as carcinoid, paragangliomas, and medullary thyroid carcinomas
	Capromab pendetide is a murine monoclonal antibody which recognizes a transmembrane glycoprotein expressed by poorly differentiated and metastatic prostate adenocarcinomas
^{67}Ga	At physiological pH, the Ga ion dissociates from the radiopharmaceutical ^{67}Ga-citrate, and forms a complex with transferrin or lactoferrin. Receptors for this complex are overexpressed on membranes of tumor and inflammatory cells

Molybdenum is a transition metal (with electrical charge 2^-) normally found as a constituent of different minerals. There are numerous isotopes of molybdenum, some of which occurring naturally while others can be produced artificially. In particular, most of the ^{99}Mo utilized for the ^{99}Mo/^{99m}Tc generators is produced through a nuclear fission reaction in highly enriched uranium-235 targets (a process that results in the production of ^{131}I and ^{133}Xe as well), while other sources can be through the use of a linear accelerator or of low enriched uranium targets. ^{99}Mo decays with a physical half-life of 66 h, mainly with the emission of high-energy β^--particles (1.214 MeV) and of γ-rays with a wide energy spectrum; the end product of ^{99}Mo decay is ^{99m}Tc.

In the ^{99}Mo/^{99m}Tc generator, the parent radionuclide (^{99}Mo, which is insoluble in water or in physiological saline) is bound to a chromatography anion exchange resin, which constitutes the stationary phase of the system usually designed as a small glass column (about 40 mm long and less than 10 mm wide) containing the resin with ^{99}Mo firmly bound to it in the form of molybdate. The ^{99m}Tc produced during the continuous decay of ^{99}Mo is periodically removed from the column (every approximately 24 h) by elution with physiological saline. In fact, in this system the daughter radionuclide (^{99m}Tc) is produced in the chemical form of pertechnetate anion ($[^{99m}TcO_4]^-$); the chloride ions present in the saline solution exchange with the $[^{99m}TcO_4]^-$ ions in the column, thus permitting their elution in physiological saline for any subsequent use.

$[^{99m}TcO_4]^-$ is a coordination compound with a very compact structure with tetrahedral geometry and oxidation state +7. Pertechnetate, the highest possible oxidation state for this metal, is also a very stable chemical species in aqueous solution. Thus, to use $[^{99m}TcO_4]^-$ to label a given molecule, it is necessary to remove the oxygen atoms bound to the metal through a reducing agent and to replace them with new ligand-coordinated atoms. During this process, the oxidation state of technetium is reduced to values lower than +7. The stannous ion (Sn^{2+}) is generally used as a reducing agent, being added in aqueous solution as a chloride salt ($SnCl_2$) in such small amounts that it does not alter solubility of the preparation or cause toxicity to the patient. Removal of the oxygen atoms from $[^{99m}TcO_4]^-$ occurs through the formation of $Sn(OH)_4$ and other similar compounds. The atom of technetium is now free to coordinate with a binder (or chelating agent, such

as DTPA) that has been preattached to the molecule to be labeled. The binder must have a high technetium coordinating ability to ensure stability of new ^{99m}Tc-labeled radiopharmaceutical and prevent it from recombining with the oxygen atoms in aqueous solution and thus return back to the anion pertechnetate or form technetium dioxide (TcO_2), a secondary compound of oxygen that tends to form colloidal particles. Other ^{99m}Tc-labeling reactions involve different chemical approaches, such as derivatization with 6-hydrazinopyridine-3-carboxylic acid (HYNIC) for cross-linking.

^{99m}Tc-Sodium Pertechnetate

^{99m}Tc-sodium pertechnetate ($Na^{99m}TcO_4$) is obtained when eluting a ^{99}Mo/^{99m}Tc generator with saline and can be used as a radiopharmaceutical by itself. After i.v. administration, the pertechnetate ions circulate in the blood partly in their free form and partly bound to plasma proteins; free ions leave the vascular compartment and migrate to the interstitial fluids. As their concentration in blood diminishes other $[^{99m}TcO_4]^-$ ions are released from their binding to plasma proteins. Therefore, visualization of the vascular space observed in early scintigraphic acquisitions decreases gradually over time. $Na^{99m}TcO_4$ half-life in plasma is about 3 h and approximately 25% is excreted through the kidneys during the first 24 h.

Pertechnetate ions have similar biological distribution to iodide and perchlorate, as they concentrate in tissues such as the thyroid, stomach, salivary glands, intestine, choroid plexus, and kidney. Sodium pertechnetate is commonly used for thyroid scintigraphy. Accumulation of $[^{99m}TcO_4]^-$ in thyroid follicular cells is mediated by the sodium–iodide symporter (NIS), a transmembrane protein consisting of 643 amino acids arranged in 13 domains with extracellular amino-terminal and intracellular carboxy-terminal (molecular weight ranging between 79 and 90 kDa, depending on the degree of glycosylation). NIS is located on the basolateral membrane of thyroid cells, and it is able to simultaneously transport sodium and iodide (with a stoichiometric ratio of 2:1) from the extracellular space within the thyroid cells. Expression of this protein is regulated, by thyroid-stimulating hormone (TSH, with upregulation) and by the concentration of iodide in extracellular fluids (downregulation), and is encoded by a gene on chromosome 19p12–13.2. The extraction of iodine from plasma and its concentration in thyroid cells is a saturable and active process that takes place against an electrochemical gradient (the intracellular concentration of iodine is 20–40 times higher than in plasma) and requires energy, which is ensured by the Na/K-dependent ATPase system.

The pertechnetate ion is transported by NIS from the extracellular to the intracellular compartment because it mimics the iodide ion, to which $[^{99m}TcO_4]^-$ is similar in terms of mass, size, and charge density; however, once inside the thyroid cell, $[^{99m}TcO_4]^-$ does not undergo subsequent organification as iodide does to participate in the synthesis of thyroid hormones.

In nuclear oncology, $[^{99m}TcO_4]^-$ is used in patients with thyroid nodules to define a nodule as either "hot" (increased uptake of the radiopharmaceutical relative to normal parenchyma) or "cold" (decreased uptake). Hot nodules correspond to hyperfunctioning tissue and are very rarely malignant. Cold nodules correspond to thyroid tissue with reduced function, and they can harbor malignancy. Differential diagnosis of a cold nodule as benign or malignant can only be made with fine-needle aspiration cytology. As mentioned above, the prevalence of thyroid cancer in hot nodules is very low (between 0% and 4% in adults), while up to 20% of the cold nodules are malignant.

Sodium pertechnetate is indicated as well for the salivary gland scintigraphy and the localization of ectopic gastric mucosa (Meckel's diverticulum).

^{99m}Tc-Diphosphonates

Virtually all radiopharmaceuticals employed for bone scintigraphy exhibit a similar pattern of distribution, characterized by accumulation in the bone linked to deposition of the mineral component. Early investigations on bone metabolism employed radionuclides with unfavorable

physical properties. Agents such as ^{32}P (in the chemical form of orthophosphate), radioactive calcium (^{45}Ca, ^{47}Ca, both beta emitters, suitable for turnover studies, but not suitable for imaging) or calcium analogs (^{85}Sr, ^{87m}Sr) in ionic form, and ^{18}F-fluoride (a positron emitting nuclide, (see also ▶ Chap. 4, "Positron-Emitting Radiopharmaceuticals for Diagnostic Applications" of this book) were used for evaluating the rate of bone turnover. Although images were obtained with ^{85}Sr, it was only after the introduction of ^{99m}Tc-labeled phosphate agents (including pyrophosphate, polyphosphates, and phosphonates) that bone scintigraphy actually became one of the most frequently performed diagnostic nuclear medicine procedures.

Present-day radiopharmaceuticals for bone scintigraphy are ^{99m}Tc-bisphosphonates, also called diphosphonates. The P–C–P bond between the two phosphates makes the molecule extremely resistant to hydrolysis by the enzyme phosphatase. Slightly different chemical forms of radiolabeled bisphosphonates are now being used in clinical practice. The most commonly used diphosphonates are ^{99m}Tc-medronate (MDP) and ^{99m}Tc-oxidronate (HDP) with equivalent lesion detectability properties (Fig. 1).

^{99m}Tc-bisphosphonates accumulate at sites of bone mineral rearrangement by chemisorption on the surface of newly formed hydroxyapatite crystals. Tin (involved in the radiolabeling reaction, see above) and ^{99m}Tc are hydrolyzed and bind to the bone, individually or jointly, in the form of tin hydroxide and TcO_2, respectively. ^{99m}Tc-MDP probably also binds to the organic matrix (after interaction with different enzymes), but in a proportion that is not exactly known. Uptake of the radiopharmaceutical in the bone is also directly correlated with local blood flow, although not in a linear relationship; in fact, a three- to fourfold increase in blood flow enhances uptake by only 30–40%.

After i.v. administration, the radiopharmaceutical rapidly diffuses into the extracellular space, and uptake in bone begins immediately. About 10% of the initial activity remains in the circulation 30 min after injection, decreasing to about 1% by 4 h after administration. The mechanism of radiopharmaceutical clearance from the body is through renal excretion, and about 50% of the intact radiopharmaceutical is excreted in the first 6 h after injection.

In bone scintigraphy the intensity of uptake of ^{99m}Tc-diphosphonate reflects the deposition of new hydroxyapatite crystals. This event is an intrinsic component of the osteoblastic reaction, which is associated with both osteolytic and osteoblastic lesions. Such conditions include both benign bone disease, primary bone tumors (benign as osteoid osteoma or malignant such as osteosarcoma), and bone metastases.

^{99m}Tc-Radiocolloids

From the biological point of view, a "colloid" includes all particles ranging from 1 nm to about 4 μm that are found in the body fluids. These particles are generally constituted by debris

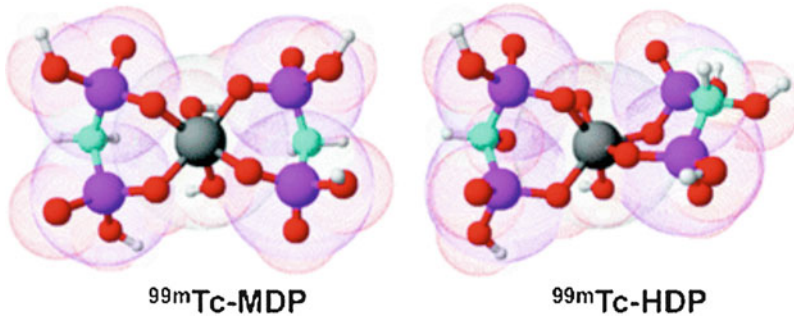

Fig. 1 Tridimensional representation of chemical structure of ^{99m}Tc-labeled bisphosphonates employed for diagnostic bone scintigraphy. The *gray* atom at the center of each 3-D structure represents ^{99m}Tc. Other elements are represented with the following color codes: *red* = O, *white* = H, *fuchsia* = P, *light blue* = C

of microorganisms, fragments of cells produced during the physiologic processes of tissue renewal, or products of intestinal absorption (especially fat). Colloids are generally removed from circulation by phagocytosis (a mechanism by which materials in the extracellular space are internalized into cells, a process that is especially active in macrophages), except for products of intestinal absorption that undergo their physiological metabolism in the liver or at other metabolic sites. Although macrophages are ubiquitous cells, they are concentrated mostly in the reticuloendothelial system, especially in the liver, spleen, bone marrow, and lymph nodes, as well as at sites of infection/inflammation. Phagocytosis is facilitated by several properties of the particles, such as size between 2.5 nm and 1 μm, negative charge, and possible opsonization by a class of macromolecules that include the complement fractions C3, C4B, and C5, as well as some α- and β-globulins.

Radiopharmaceuticals with colloidal properties include ^{99m}Tc-labeled albumin colloids consisting of particles of denatured human albumin ranging in size between 30 and 1,000 nm (i.e., 0.03–1 μm). Albumin colloid is used for lymphoscintigraphy mainly as a preliminary phase to radioguided sentinel lymph node biopsy. The radiocolloid is administered intradermally or interstitially at the site of the tumor. From the site of injection, radiocolloids migrate through the lymphatic system; in fact, their size prevents them from entering the venous blood capillaries (that have tight intercellular junctions), while intercellular junctions of the lymphatic capillaries are quite loose. Along the route of such lymphatic drainage, radiocolloids reach lymph nodes, the first one of which is called the "sentinel lymph node" (SLN); this is the lymphatic station where tumor cells possibly entering lymph vessels and migrating along the route of lymphatic drainage encounter the first lymph node (or nodes) of the lymphatic basin draining that specific tumor region. Once inside such lymph nodes, the radiocolloids are engulfed by macrophages lining the sinusoidal spaces enabling scintigraphic localization of the lymph nodes.

The ideal radiopharmaceutical for sentinel lymph node biopsy should allow a rapid visualization of the first lymph node draining from the tumor/injection site and prolonged retention in the SLN possibly without further migration to higher-echelon nodes. In principle, radiocolloids with relatively large-size particles (between 200 and 300 nm) have efficient retention in the first lymph node encountered along the migration route, with very little progression to higher-echelon nodes. Nevertheless, particles of this size migrate quite slowly from the injection site. Since the speed of migration of radiocolloids injected interstitially is inversely related to particle size, some compromise must be found between the speed of lymphatic migration and the degree of phagocytosis of the colloidal particles in lymph nodes.

In patients with breast cancer, 18–37 MBq given as a single intradermal injection over the cutaneous projection of the tumor or subdivided into two to four aliquots for peritumoral or for periareolar injection (0.2–0.4 mL each aliquot) is usually used. In patients with melanoma, multiple intradermal injections are generally performed around the tumor or the surgical scar, each 0.1–0.2-mL aliquot containing about 7–10 MB; total injected activity should not exceed 74 MBq. Another parameter that affects the activity to be selected for injection is the time between tracer injection and surgery, which can range from 1 to 24 h depending on local logistics and organization. With longer waiting times, the injected activity should be increased to compensate for physical decay of ^{99m}Tc.

There are different sizes of radiopharmaceuticals used in nodal mapping and the choice is based usually on local availability. The most widely used radiocolloids are ^{99m}Tc-albumin (Europe), ^{99m}Tc-sulfur colloid (USA), and ^{99m}Tc-antimony sulfide (Canada and Australia). In addition, ^{99m}Tc-stannous phytate, ^{99m}Tc-tin colloid, ^{99m}Tc-rhenium sulfide nanocolloid, and ^{99m}Tc-sulfide nanocolloid can also be utilized. ^{99m}Tc-tilmanocept is now being used as an alternative to radiocolloids for mapping and localization of SLNs:

^{99m}Tc-sulfur colloid is commonly used in the USA, with a wide range of particle sizes (15–5,000 nm) depending on the preparation method. ^{99m}Tc-sulfur colloid has an average

size from 305 to 340 nm and is used for liver imaging and oral gastric emptying imaging. Often, the filtered colloidal form (particle size ranges from 100 to 220 nm) is used for lymphoscintigraphy.

^{99m}Tc-albumin nanocolloid is most frequently used in Europe and represents a good compromise between speed of migration and lymph node retention. It is made up of particles (maximum size 100 nm, mean 5–80 nm) most of which are smaller than 80 nm in size, which easily migrate through the lymphatic system but are not totally retained in the sentinel node. Lymphoscintigraphy will therefore usually display multiple lymph nodes along a certain lymphatic route, an occurrence that can complicate the intraoperative search for the "true" sentinel lymph node using the gamma probe.

^{99m}Tc-mannosyl-DTPA-dextran (^{99m}Tc-Tilmanocept®) is a receptor-targeted radiotracer approved by the FDA (and more recently also by the EMA) for SLN mapping in breast cancer and melanoma as well for lymphatic mapping in other solid tumors. ^{99m}Tc-Tilmanocept® has a molecular size of 7 nm, but, at variance from the other radiocolloids, its uptake mechanism is not dependent on particle size. In fact, ^{99m}Tc-Tilmanocept® binds avidly to the CD206 receptors for mannose on the surface of macrophages and dendritic cells in lymph nodes. The advantages of Tilmanocept® include rapid clearance from the injection site, high sentinel lymph node extraction, and low accumulation on second-echelon nodes.

^{99m}Tc-Magroaggregated Albumin

Magroaggregated albumin (MAA, particle size range 10–90 μm and no greater than 150 μm) labeled with ^{99m}Tc is mainly used for lung perfusion imaging.

When performing a lung perfusion scan, an important factor is the number of particles injected. The standard activity administered to an adult patient is 40–150 MBq containing approximately 400,000 labeled particles. These particles will obstruct only a very small number of pulmonary vessels, negligible from the hemodynamic point of view since there are over 280 billion pulmonary capillaries and 300 million precapillary lung arterioles. Particles in size >150 μm would occlude arterioles of greater caliber with possible undesirable effect.

In patients with known pulmonary hypertension or right-to-left heart shunt, the number of ^{99m}Tc-MAA particles should be reduced to 100,000–200,000. In infants and children, the number of administered macroaggregated albumin particles should be further reduced as a function of age.

After i.v. administration, over 90% of the ^{99m}Tc-MAA particles are trapped in the pulmonary capillaries and precapillary arterioles because of their dimensions. The particles are removed from the pulmonary bed (effective half-life 1.5–3 h) due to enzymatic degradation into smaller particles that enter the circulation assuming nanocolloid characteristics and thus are phagocytized from the macrophages of the reticuloendothelial system.

^{99m}Tc-MAA is also used for radioguided occult lesion localization (ROLL) prior to radioguided surgery. A small volume of a radiopharmaceutical is injected into the lesion under imaging guidance. Because of their size, the ^{99m}Tc-MAA particles remain in the lesion and do not undergo clearance via lymphatic drainage. The lesion is then located and excised intraoperatively using a gamma-detecting probe, according to the same principles as those of SLN biopsy.

^{99m}Tc-MAA scintigraphy after intrahepatic artery administration of 75–150 MBq of the radiopharmaceutical is very important to assess for possible shunt(s) to the pulmonary and/or gastrointestinal circulation, as well as for treatment planning prior to transarterial radioembolization therapy with ^{90}Y-labeled microspheres in patients with primary or metastatic liver malignancies.

^{99m}Tc-Sestamibi

^{99m}Tc-hexakis-2-methoxy-2-isobutyl-isonitrile (^{99m}Tc-sestamibi) is a positively charged lipophilic radiopharmaceutical originally introduced into clinical routine for myocardial perfusion scintigraphy. Its uptake and retention depend on the regional blood flow, cell viability, cell membrane potential, and mitochondrial density/activity.

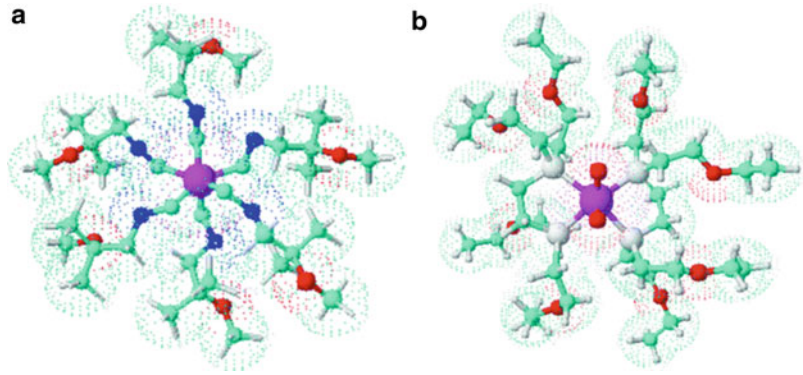

Fig. 2 Tridimensional representation of chemical structure of ^{99m}Tc-sestamibi (**a**) and ^{99m}Tc-tetrofosmin (**b**). The fuchsia atom at the center of each 3-D structure represents ^{99m}Tc. Other elements are represented with the following color codes: *red* = O, *small white* = H, *light blue* = C, *large white* = P, *dark blue* = N

Labeling of ^{99m}Tc-sestamibi occurs through the isonitrile groups with a chemical reaction that requires the presence of stannous ion in reduced state. The structure of ^{99m}Tc-sestamibi consists of a central atom of technetium linked to six octahedral ligands (Fig. 2a).

After i.v. administration, this radiopharmaceutical diffuses rapidly in the extracellular spaces and then crosses cell membranes by passive diffusion (because of its lipophilicity) following a concentration and electrical gradient (as the intracellular space is negatively charged). ^{99m}Tc-sestamibi accumulates in the mitochondria, which are particularly abundant in cells with high energy demand, such as cardiomyocytes and tumor cells. Thus, uptake and retention of ^{99m}Tc-sestamibi depends on local blood flow, cell density, and metabolic activity. ^{99m}Tc-sestamibi is used for myocardial perfusion imaging, for detection of parathyroid adenomas, and for scintimammography.

^{99m}Tc-sestamibi is rapidly cleared from the blood, with only 8% of the administered activity in the circulation 5 min postinjection. The tracer is excreted through the hepatobiliary system (33% at 48 h) and to a lesser extent through the kidneys (27% at 24 h). Its biological half-life in the myocardium is approximately 6 h.

^{99m}Tc-Tetrofosmin

^{99m}Tc-tetrofosmin is a lipophilic cationic diphosphine with localization properties similar as those of ^{99m}Tc-sestamibi. ^{99m}Tc-tetrofosmin is also employed primarily for myocardial perfusion scintigraphy. Myocardial uptake of ^{99m}Tc-tetrofosmin as well as of ^{99m}Tc-sestamibi is proportional to blood flow up to about 2 mL/min per gram, which is twice the resting level, reaching a plateau of extraction at higher flow rates.

Its molecular structure is characterized by a core of four atoms of phosphorus-binding ^{99m}Tc, stabilized by two oxygen atoms (O = Tc = O) and two diphosphines (Fig. 2b). After entering cells with a mechanism similar to that of ^{99m}Tc-sestamibi, ^{99m}Tc-tetrofosmin is retained intracellularly mostly bound to cytosol proteins.

Similarly to ^{99m}Tc-sestamibi, ^{99m}Tc-tetrofosmin undergoes rapid blood clearance following systemic administration, so that less than 5% of the administered activity remains in the circulation 10 min postinjection. About 65% of the administered activity is excreted within 48 h, 40% in the urine and 25% through the hepatobiliary tract. The hepatic clearance of ^{99m}Tc-tetrofosmin is more rapid than that of ^{99m}Tc-sestamibi, thus allowing earlier myocardial imaging.

^{99m}Tc-EDDA/HYNIC-Octreotate

^{99m}Tc-EDDA/HYNIC-octreotate is a ^{99m}Tc-labeled somatostatin (SST) analog with high affinity for SSTR2 used for detecting and staging neuroendocrine neoplasms. It has a similar physiological biodistribution as ^{111}In-pentetreotide (Octreoscan®, see further below). Mainly because of the favorable physical properties and wide availability of ^{99m}Tc, ^{99m}Tc-EDDA/HYNIC-octreotate offers several advantages as compared to Octreoscan®, such as ready availability (because of the possibility to label the lyophilized

kit "on demand" when needed), possibility to administer higher activity amount (because of more favorable dosimetry parameters), faster imaging completed within 4–6 h versus up to 24 h, better image quality and detection capability (with higher target/nontarget ratios because of more favorable counting statistics), and overall better cost-effectiveness.

There are also other ^{99m}Tc-labeled SST analogs, such as ^{99m}Tc-HYNIC-octreotide, ^{99m}Tc-vapreotide, ^{99m}Tc-depreotide, and ^{99m}Tc-demotate. ^{99m}Tc-HYNIC-octreotate differs from ^{99m}Tc-HYNIC-octreotide by the more hydrophilic tyrosine in the third position and the terminal threonine showing a higher receptor affinity and better internalization properties. The administered activity is 370–740 MBq, the higher amounts being preferred when contemplating SPECT acquisition. The highest target/nontarget ratios are usually observed at 4 h postinjection.

Lung Ventilation Radiopharmaceuticals

The multiple radiopharmaceuticals proposed for lung ventilation scintigraphy can be divided into two classes: radioaerosols (^{99m}Tc-DTPA and ^{99m}Tc-technegas) and radioactive gases (^{127}Xe, ^{133}Xe, ^{81m}Kr). An aerosol is a two-phase system consisting of particles that may be liquid, solid, or a combination of two suspended in gas. Ventilation studies using radioactive gases allow dynamic single-breath, equilibrium, or washout phase imaging, while radioaerosol ventilation scintigraphy rather maps the distribution of the aerated lung volume.

^{99m}Tc-DTPA

This is the most commonly used radiolabeled liquid aerosol. ^{99m}Tc-DTPA can be aerosolized by using a nebulizer to produce particles (ideal size 0.1–0.2 μm, diameter <2 μm) capable of being readily inhaled. ^{99m}Tc-DTPA is cleared from the alveolar region by transepithelial diffusion and enters the circulation where it is cleared by the kidneys. The biological half-life in the lung is 55–108 min in healthy people and 15–33 min in healthy smokers.

Even though the activity of ^{99m}Tc-DTPA dispensed in the nebulizer is approximately 900–1,300 MBq, the activity actually reaching the lungs is only 20–40 MBq. This amount is much lower than the activity of ^{99m}Tc-MAA normally injected i.v. for a lung perfusion scan; therefore, when planning a ventilation/perfusion scan in patients with suspected acute pulmonary embolism, the ^{99m}Tc-DTPA ventilation scan (with multi-view planar imaging or with SPECT) should be performed first.

^{99m}Tc-Technegas

The aerosol ^{99m}Tc-technegas, mostly used in Europe, consists of ^{99m}Tc-labeled solid graphite particles (diameter 0.005–0.2 μm) generated at high temperature. The particles tend to grow by aggregation; thus, ^{99m}Tc-technegas should be used within 10 min of generation. The administered activity to the lung is 20–30 MBq. Inhaled ^{99m}Tc-technegas particles adhere to the walls of the alveoli and are slowly cleared by reabsorption. The images obtained with ^{99m}Tc-technegas have superior quality than those obtained with ^{99m}Tc-DPTA or ^{133}Xe; moreover, its use has minimized the problem of particle clumping in patients with chronic obstructive pulmonary disease (COPD) observed when using ^{99m}Tc-DTPA.

Xenon-133

^{133}Xe is a noble, liposoluble radioactive gas, which decays with a physical half-life of 5.3 days through emission of β^-- and γ-radiations. The energy of its γ-emission photopeak (81 keV) is lower than that of ^{99m}Tc (140 Kev); therefore, when performing a ventilation/perfusion scan in patients with suspected acute pulmonary embolism, lung perfusion scintigraphy with ^{99m}Tc-MAA is acquired after the ^{133}Xe ventilation study. After being inhaled in an airtight closed system, ^{133}Xe (370–740 MBq) enters the alveolar wall and the pulmonary venous circulation via the capillaries, returning then to the lungs and being exhaled after a single pass through the peripheral circulation with a short biological half-life (30 s). ^{133}Xe single deep-breath inspiration, equilibrium, and washout

images are acquired allowing high sensitivity for detection of COPD. For radiation safety and in order to avoid dispersion of the radioactive gas in the environment, the room where the scan is performed must be equipped with a special closed system for inhaling ^{133}Xe, and the air conditioning system must include an activated charcoal filter for trapping any radioactive gas before exhaustion of the filtered air in the normal environment.

Xenon-127

The radioactive gas ^{127}Xe has a physical half-life of 36 days, and it decays by electron capture with principal γ-emission with energy photopeaks at 172 keV (25%), 203 keV (63%), and 375 keV (18%). These physical properties make ^{127}Xe preferable to ^{133}Xe for ventilation studies. Furthermore, the radiation burden from ^{127}Xe is lower than that from ^{133}Xe. Due to the higher-energy γ-emission, ^{127}Xe ventilation imaging can be acquired also after performing a lung perfusion scintigraphy with ^{99m}Tc-MAA. Limitations in the use of ^{127}Xe are its high cost and limited availability.

Radioiodinated Agents

Two radioisotopes of this halogen, ^{131}I and ^{123}I, are frequently utilized in the simple form of iodide anion in clinical practice for investigations and/or treatment of patients with thyroid diseases. Furthermore, radioiodine can be introduced into complex molecules through nucleophilic or electrophilic substitution. The most common modality employed to radioiodinate complex molecules is based on the possibility of replacing a hydroxyl radical ($-OH^-$) in the native molecule with the I^- ion. The iodide ion has the same valency and approximately the same spatial volume as the $-OH^-$ radical. Similarities in valency and volume also constitute the basis for substituting a methyl radical ($-CH_3^-$) with radioiodine. Both the $-OH^-$ radical and the $-CH_3^-$ radical are abundant in many molecules of biological interest (due to the presence of amino acids such as tyrosine).

^{131}I (historically one of the first radionuclides available for medical applications) is used both for therapeutic purposes (due to its emission of β^--particles) and for diagnostic purposes (due to its γ-emission). ^{131}I has a relatively high-energy principal photon emission (364 keV) and a long half-life (8 days), both features resulting in a relatively high radiation dose to the patient. On the other hand, ^{123}I offers a reduced radiation burden (because of its short physical half-life of 13.2 h); furthermore, the energy of its γ-emission is optimal for gamma camera imaging (the principal γ-emission photopeak energy is at 159 keV). ^{124}I, which decays with positron emission, offers the advantages of advanced PET imaging quantitation. As a final note, ^{125}I, which has a half-life (60 days) and emits γ-rays unsuitable for gamma camera imaging (35 keV), has been widely used for in vitro investigations (radioimmunological techniques) as well as for biodistribution studies in animal models of disease and for early-stage trials in humans.

Sodium Iodide

Radioiodine (^{123}I) is most commonly administered as sodium–iodide for imaging or (^{131}I) for treating thyroid disorders. The radioactive I^- ions present in the circulation and in interstitial fluid are transported into the thyroid cells by the sodium/iodide symporter. Once inside the thyroid cell, iodine is oxidized by the enzyme peroxidase; this starts the organification process that incorporates iodine into tyrosine, an amino acid contained in the thyroglobulin molecules produced by the endoplasmic reticulum and Golgi apparatus. Molecules of monoiodotyrosine (MIT) and diiodotyrosine (DIT) are thus formed. These two chemical species are then combined to produce the thyroid hormones thyroxine (T4) and triiodothyronine (T3). Thyroid hormones are finally secreted into the circulation by pinocytosis following stimulation by TSH.

In addition to the thyroid, iodine is also concentrated by the salivary glands, sweat glands, stomach, mammary glands, and placenta. These sites of physiologic concentration can produce unwanted side effects when using ^{131}I-iodide for high-dose therapy in patients with differentiated thyroid cancer, possibly causing sialadenitis (sometimes with persistent xerostomia) and gastritis (with nausea and vomiting). ^{131}I uptake in

the placenta and mammary gland would expose the fetus or the baby, respectively, to an unacceptable radiation dose.

^{131}I-iodide has been often used to measure uptake prior to therapy both for hyperthyroidism and for total-body scintigraphy in patients with differentiated thyroid cancer. Administered activities in these two cases are very different: only 0.37–1.85 MBq (or 10–50 μCi) to measure thyroid uptake in hyperthyroid patients and up to 185 MBq (or 5 mCi) for total-body scintigraphy in thyroid cancer patients. In both cases, the radiopharmaceutical is generally administered orally as a capsule, while in pediatric patients or in patients with swallowing problems, a liquid formulation is also available, for either oral or intravenous administration.

^{131}I-iodide, due to its high radiation-absorbed patient dose and high-energy photons, has generally been replaced by ^{99m}Tc-pertechnetate or ^{123}I-iodide for thyroid scintigraphy in patients with benign thyroid disease. ^{123}I-iodide is generally administered orally but an i.v. formulation is also available. The standard activity administered for thyroid scintigraphy in a 70-kg adult patient is 2–111 MBq (2 MBq for uptake studies while up to 111 MBq for thyroid scintigraphy). Higher ^{123}I activities are required for whole-body scans (40–200 MBq) and even higher for SPECT imaging, with images being acquired 24 h after administration.

Radioiodinated Metaiodobenzylguanidine

Metaiodobenzylguanidine (MIBG) is a catecholamine analog in which the benzyl group of bretylium is combined with the guanidine group of guanethidine (Fig. 3). It was developed in 1980 to image tumors of the adrenal medulla. It can be labeled either with ^{123}I (for diagnostic use) or with ^{131}I (for either diagnostic or therapeutic applications).

MIBG is taken up by chromaffin cells through an ATPase-linked energy-dependent process physiologically utilized for the intracellular accumulation of noradrenaline. This accumulation process is abundantly expressed in the sympathetic ganglia, the adrenal medulla, and in all tissues with high adrenergic innervations (myocardium, salivary glands). After being initially stored in the cytoplasmic neurosecretory vesicles, MIBG is then secreted through an exocytosis mechanism following depolarization induced by high transmembrane flux of calcium ions. Neuroendocrine tumors originating from the neural crest typically accumulate this radiopharmaceutical.

MIBG does not bind to postsynaptic adrenergic receptors and is not degraded by the enzymes normally degrading catecholamines, that is, monoamine oxidase (MAO) and catecholamine-O-methyltransferase (COMT). Blood-pool activity early after injection is due to binding of MIBG to circulating platelets. Moderate physiological

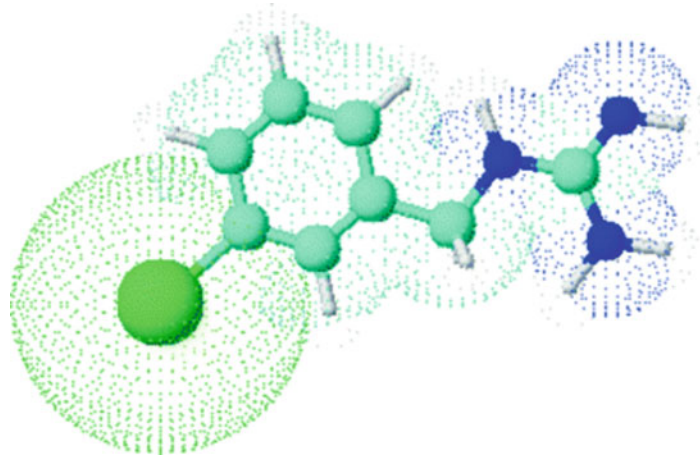

Fig. 3 Tridimensional representation of chemical structure of radioiodinated metaiodobenzylguanidine (*MIBG*). The *green* atom represents radioiodine. Other elements are represented with the following color codes: *white* = H, *light blue* = C, *dark blue* = N

uptake is also observed in the liver (especially the medial portion of the liver), spleen, lungs, salivary glands, myocardium, nasal mucosa, brown fat, colon, musculoskeletal system, and uterus. Visualization of the thyroid is due to free radioactive I^- released during in vivo degradation of the radiopharmaceutical; for this reason, a thyroid-blocking agent (either supersaturated potassium iodide solution or similar) is usually administered prior to injection. Since there is no physiological uptake of MIBG in bones, focal or diffuse bone uptake must be considered expression of skeletal metastases and/or tumor invasion of the bone marrow.

The main clinical applications of MIBG scintigraphy are detection, localization, staging, and follow-up of neuroendocrine tumors and their metastases, especially pheochromocytoma, paraganglioma, neuroblastoma, medullary thyroid carcinoma, and other tumors originating from the neural crest. [^{123}I]MIBG is the radiopharmaceutical of choice for diagnostic applications (especially in children), both because of its more favorable radiation dosimetry and because of the more favorable imaging properties compared to [^{131}I]MIBG.

Following i.v. administration, about 50% of the administered activity is excreted in the urine within the first 24 h, 70–90% of the activity being cumulatively excreted within 48 h. Since more than 95% of radioactivity excretion occurring through the kidneys, the bladder and the excretory urinary tract are seen on the scan; about 3% of MIBG activity is excreted via the gastrointestinal tract. Normal adrenal glands are visualized in 15% of the cases at 48–72 h after injection.

The standard activity administered to adult patients is 40–80 MBq for [^{131}I]MIBG and 370 MBq for [^{123}I]MIBG. Such amounts are reduced in pediatric patients, according to body weight. Due to a certain "mass" effect of radiolabeled MIBG (especially when high doses of [^{131}I]MIBG are given for therapy and/or with low-specificity radiopharmaceuticals), administration may induce the release into circulation of catecholamines previously accumulated in neurosecretory granules, with ensuing possible pharmacologic effect (such as tachycardia and an arterial hypertensive crisis in patients with pheochromocytoma). Some precautions are therefore necessary, such as slow infusion of the radiopharmaceutical (over 1–5 min in the case of a diagnostic procedure, over 1–4 h after dilution in 50 mL of saline in case of therapy), while also monitoring heart rate and blood pressure until about 1 h after administration. Moreover, since many drugs can interfere with MIBG uptake, the patient's medication list should be reviewed and interfering drugs discontinued before MIBG administration.

Non-tumor indications of [^{123}I]MIBG are for functional studies of adrenal medulla, movement disorders, and sympathetic innervation of the myocardium.

^{201}Tl-Chloride

The monovalent cation Tl^+ has biochemical characteristics similar to those of the K^+ ion. Therefore, in excitable cells (typically neurons and muscle cells), it undergoes the continuous transmembrane flux that physiologically occurs during depolarization (a passive process) and repolarization (an energy-dependent process linked to the so-called Na^+/K^+ pump). These sustained transmembrane exchanges explain the high intracellular concentration of Tl^+ ions, mimicking the distribution of the K^+ ions.

Besides typical high accumulation in myocardial cells, $^{201}Tl^+$ ions tend to accumulate in all metabolically active cells, including cancer. ^{201}Tl-chloride is then used for tumor imaging as an indicator of cell viability, particularly for discriminating viable tumor tissue (as due to, e.g., recurrence posttreatment) from fibrous scar tissue after surgery and/or radiation therapy (especially in brain gliomas).

^{201}Tl decays by electron capture with a physical half-life of 73.1 h and emission of X-rays with 68–80-keV energy. Following i.v. administration, $^{201}Tl^+$ ions undergo fast extraction from circulating blood by cardiomyocytes (about 85% at first pass). There is also rapid clearance from the blood so that about 2 min after administration

<5% of the injected activity is still circulating. The tracer has a biological half-life of approximately 10 days.

^{111}In-Pentetreotide

Somatostatin (SST) is a 14-amino acid peptide produced endogenously mainly in the central nervous system. Physiologic functions of SST include inhibition of secretion of various hormones, such as insulin and glucagon, and inhibition of cell growth in neuroendocrine tumors. Five different types of receptors for SST have been identified and cloned, named SSTR1-5 (type 2 being divided into subtypes 2a and 2b). Native SST has a very short biological half-life (3 min), which limits its use both as a therapeutic drug as such and, upon radiolabeling, as a radiopharmaceutical. Several SST analogs have therefore been developed for therapy and for nuclear medicine applications. Octreotide (an eight-amino acid peptide) has longer biological half-life and a biological activity very similar to native SST, with high affinity for SST receptor types 2 and 5.

The presence of a chelating group (DTPA) in DTPA-D-Phe^1-octreotide (pentetreotide) makes radiolabeling with ^{111}In possible (Fig. 4). The cyclotron-produced radiometal ^{111}In has a physical half-life of 2.83 days and emits γ-rays with energy peaks of 172 and 247 keV (in addition to a 23–26-keV X-ray emission). The radiopharmaceutical ^{111}In-pentetreotide (commercial name Octreoscan®) has high binding affinity to type 2 and type 5 SST receptors, which are highly expressed on the cell membrane of many tumors of different origins but especially of neuroendocrine tumors. ^{111}In-pentetreotide scintigraphy is employed primarily in patients with neuroendocrine tumors (especially gastroenteropancreatic and carcinoid tumors) for localization, staging, and follow-up of lesions expressing somatostatin receptors. Increased expression of SST receptors also occurs in tumors originating from the neural crest (paragangliomas, medullary thyroid carcinomas, neuroblastomas, pheochromocytomas) as well as in pituitary tumors and in meningiomas, although in a smaller proportion of patients than observed in patients with other neuroendocrine neoplasms. Varying degrees of SST receptor expression are also observed in non-neuroendocrine tumors, such as breast cancer and some lymphomas (both Hodgkin's and non-Hodgkin's lymphomas). Finally, increased SST receptor expression occurs even in nonneoplastic disorders, especially in subacute and chronic inflammation (mainly of the granulomatous type, as in sarcoidosis).

^{111}In-pentetreotide is mainly excreted by the kidneys, about 90% of injected activity being recovered in the urine 24 h after i.v. administration. A smaller fraction of administered activity (about 2%) is excreted through the hepatobiliary system. Scintigraphic images show physiological uptake in the spleen (about 2.5% of injected activity at 24 h),

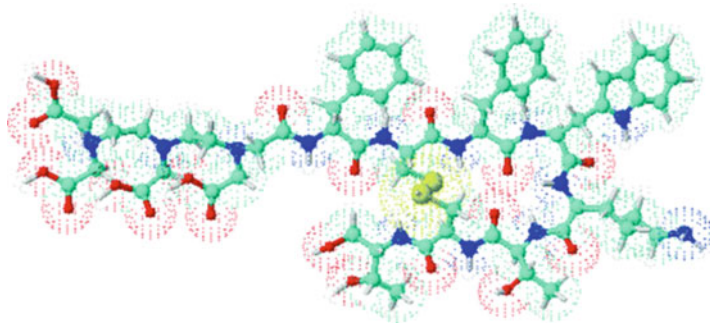

Fig. 4 Tridimensional representation of chemical structure of pentetreotide. The chelating moiety (*DTPA*) is shown on the left end of the molecule (^{111}In atom not represented here), while the receptor-binding moiety is on the right end. Elements are represented with the following color codes: *red* = O, *white* = H, *light blue* = C, *dark blue* = N, *yellow* = S

liver (2%), and kidneys. In most patients, the thyroid, pituitary, and intestine are also visualized during scintigraphy with ^{111}In-pentetreotide.

The standard injected activity into an adult patient is 110–220 MBq. In pediatric patients, the administered activity is reduced according to body weight or body surface area.

Several additional peptide-based radiopharmaceuticals are being evaluated for characterization of neuroendocrine tumors, in particular new SST analogs with more favorable binding characteristics than Octreoscan®. Furthermore, the tumor-targeting properties of new radiopharmaceuticals with high affinity for other receptors overexpressed by neuroendocrine tumors (such as bombesin, bioactive fragments of cholecystokinin, vasoactive intestinal peptide, etc.) are also being tested for possible use in nuclear oncology.

^{111}In-Capromab Pendetide

Capromab pendetide is a murine monoclonal antibody (IgG_k) directed against the prostate-specific membrane antigen (PSMA), a 120-kDa transmembrane glycoprotein expressed by prostate epithelium whose epitope is located on the cytoplasmatic domain. PSMA seems to be maximally expressed in poorly differentiated and metastatic prostate adenocarcinomas. This antibody (7E11-C5.3) is conjugated to the linker-chelator glycyl-tyrosyl-DTPA-lysine hydrochloride for labeling, to form ^{111}In-capromab pendetide.

Immunohistochemistry studies have shown that the antibody reacts with epithelial cells of more than 95% of prostatic adenocarcinomas, in both primary and metastatic lesions. Although expression of PSMA is present in other tissues and in subsets of various types of malignancies, PSMA is still considered to be sensitive and highly specific for prostatic carcinoma.

Use of this radiopharmaceutical is indicated to image newly diagnosed patients who have high risk for pelvic lymph node metastasis as well as post-prostatectomy patients with a rising PSA and a negative or equivocal conventional imaging in whom there is a high clinical suspicion of occult metastatic disease.

Approximately 10% of administered radioactivity is excreted in the urine over 72 h after intravenous infusion of ^{111}In-capromab pendetide. Non-antigen-dependent localization is observed in the liver, spleen, and bone marrow and in some inflammatory sites such as colostomy sites or postoperative bowel adhesions, bowel inflammatory diseases, or degenerative joint disease. Physiologic localization of radioactivity can also be seen in the bowel, blood pool, kidney, and urinary bladder.

The radiopharmaceutical (which is approved by the FDA and available only in the USA) is administered by intravenous infusion in 5 min. The recommended amount of capromab pendetide is 0.5 mg labeled with 185 MBq of ^{111}In. Images should be acquired between 72 and 120 h after administration. In some centers, an early SPECT acquisition is performed 30 min after administration in order to delineate distribution in the blood pool; this procedure helps in differentiating radioactivity localization in the blood pool versus tumor uptake in the late images.

^{67}Ga-Citrate

^{67}Ga is cyclotron produced by the proton irradiation of enriched zinc. It has a physical half-life of 78.3 h and decays by electron capture to stable zinc (^{67}Zn) emitting γ-rays with multiple energy peaks, principally 93 keV, 184 keV, 300 keV, and 394 keV. ^{67}Ga reacts with citric acid to form ^{67}Ga-citrate.

After i.v. administration of ^{67}Ga-citrate, $^{67}Ga^{++}$ ions are formed at physiological pH. Physiological uptake is seen in the liver, spleen, bone marrow, bone, and (less intense) lacrimal, salivary, and mammary glands. The metabolic fate of $^{67}Ga^{++}$ in the body is similar to that of the Fe^{++} ions. About 90% of injected activity binds to plasma proteins, especially transferrin, with ensuing slow blood clearance. During the first 24 h, up to 25% of the injected activity is excreted through the kidneys, while at later time points, the main excretion route becomes the bowel.

The mechanism of ^{67}Ga accumulation in tissues is quite complex and not yet fully clarified, but most of this process is due to intracellular

accumulation mediated by the transferrin receptors. Both human and animal studies have shown that if the number of binding sites is altered by a variety of conditions (such as congenital deficiency of transferrin receptors, iron overload, chemotherapy, or radiotherapy), then physiologic biodistribution is altered.

The main mechanism of accumulation in tumor and inflammation sites appears to be linked to the complex formed by $^{67}Ga^{++}$ with transferrin, for which membrane receptors are present ubiquitously, especially on membranes of tumor and inflammatory cells. In fact, cells undergoing active proliferation and metabolic activation overexpress transferrin receptors to meet the increased metabolic requirements (presence of the Fe^{++} ions is mandatorily required in some enzymatic processes involved in energy production). Therefore, tissues with rapid cell growth and high levels of DNA synthesis (such as cancer or inflammatory cells) express a higher number of transferrin receptors, ensuing an increased uptake of $^{67}Ga^{++}$ ions.

An additional mechanism of ^{67}Ga accumulation is mediated by its binding to lactoferrin. Extracellular inflammatory spaces are rich of lactoferrin, which has slightly greater affinity for ionic compounds than transferrin. Thus, ^{67}Ga reaching inflammation sites bound to transferrin may migrate to lactoferrin, which in turn binds to specific receptors present on macrophage surface. Enhanced expression of lactoferrin receptors has been shown also in lymphoma cells, and this event seems to contribute to ^{67}Ga uptake in this tissue for 10–25% of total uptake.

Following its introduction into clinical practice in the late 1960s, ^{67}Ga-citrate has had a well-defined role both in benign conditions (localization of infection/inflammation, characterization of chronic granulomatous diseases such as sarcoidosis) and in neoplastic conditions (lymphoma, sarcoma), especially for staging, prognosis, and evaluation of residual disease in lymphoma. Many of the traditional applications of scintigraphy with ^{67}Ga-citrate have currently been replaced by [^{18}F]FDG PET imaging. Nevertheless, when [^{18}F]FDG imaging is not available, some specific indications are still of value for nuclear oncology, particularly in patients with Hodgkin's or non-Hodgkin's lymphomas. Regarding availability/access to PET with [^{18}F]FDG, it should be noted that this imaging option – which now constitutes an integral part of the clinical routine in most nuclear medicine centers for the middle- to high-income countries – is not available for most of the low-income countries where the majority of the world population live. In these conditions and assuming that a nuclear medicine center is nevertheless present and accessible, scintigraphy with ^{67}Ga-citrate still remains the only radionuclide imaging option for patients with lymphoma.

The administered activity of ^{67}Ga-citrate to an adult patient for SPECT tumor imaging is approximately 370 MBq. Images should be ideally acquired 48 h after i.v administration due to the optimal tumor to background ratio; sometimes, images are also recorded at 72 and 96 h to determine if subtle regions of activity become more prominent. In this regard, recent reports on the successful use of the positron emitter ^{68}Ga-citrate for PET imaging of infection within about 1 h postinjection question the validity of current knowledge on the mechanisms of $^{67}Ga^{++}$ accumulation in infection. In fact, considering that the chemical species of ^{67}Ga is clearly identical to that of ^{68}Ga, it is unclear why accumulation of the positron emitter at sites of infection is so much faster than that of the single-photon emitter, even taking into account the much more favorable counting statistics of PET versus gamma camera imaging. A possible explanation for this striking difference is represented by the much greater specific activity of ^{68}Ga than ^{67}Ga, probably favoring one type of accumulation versus others – although further investigations are required to elucidate the exact reasons for such discrepancy.

Suggested Readings

1. Ell PJ, Gambhir SS, editors. Nuclear medicine in clinical diagnosis and treatment. 3rd ed. New York: Churchill Livingston; 2004.
2. Herbert JC, Eckelman WC, Neumann RD, editors. Nuclear medicine – diagnosis and therapy. New York: Thieme Medical Publishers; 1996.

3. IAEA. Operational guidance on hospital radiopharmacy. Vienna: International Atomic Energy Agency (IAEA); 2008.
4. IAEA. Technetium-99m radiopharmaceuticals: status and trends. Vienna: International Atomic Energy Agency (IAEA); 2010.
5. IAEA. Radiopharmaceuticals for sentinel lymph node detection: status and trends. Vienna: International Atomic Energy Agency (IAEA); 2015.
6. IAEA. Good practice for introducing radiopharmaceuticals for clinical use. Vienna: International Atomic Energy Agency (IAEA); 2015.
7. Kowalsky RJ, Falen SW, editors. Radiopharmaceuticals in nuclear pharmacy and nuclear medicine. 3rd ed. Washington, DC: American Pharmacists Association; 2011.
8. Owunwanne A, Patel M, Sadek S, editors. The handbook of radiopharmaceuticals. New York: Springer; 1995.
9. Schwochau K, editor. Technetium: chemistry and radiopharmaceuticals. Hoboken: Wiley; 2000.
10. Theobald T, editor. Sampson's textbook of radiopharmacy. 4th ed. London: Pharmaceutical Press; 2010.
11. Vallabhajosula S. Molecular imaging – radiopharmaceuticals for PET and SPECT. New York: Springer; 2009.
12. Welch MJ, Redvanly CS, editors. Handbook of radiopharmaceuticals: radiochemistry and applications. Hoboken: Wiley; 2003.

Positron-Emitting Radiopharmaceuticals for Diagnostic Applications

4

Federica Orsini, Alice Lorenzoni, Erinda Puta, and Giuliano Mariani

Abstract

Positron emission tomography is one of the most important tools in medical imaging with many applications in neurology, oncology, cardiology, neuroscience and infection. Over the past 30 years, technological advances in radiochemistry have led to the development of many radiotracers at the present used in clinical routine.

In this chapter we will discuss the main physical property of PET radionuclide and the main pharmacokinetic characteristics of PET radiotracers commonly used for molecular imaging.

Keywords

Positron Emission Tomography Radiopharmaceuticals • PET tracers • PET Radionuclides

Glossary

[^{11}C]MET	Methyl-[^{11}C]-L-methionine
[^{18}F]FDG	2-Deoxy-2-[^{18}F]fluoro-D-glucose
^{18}F-ETNIM	^{18}F-Fluoroerythronitroimidazole
^{18}F-FCH	^{18}F-Fluoromethylcholine
^{18}F-FDOPA	3,4-Dihydroxy-6-[^{18}F] fluorophenylalanine
^{18}F-FEC	^{18}F-Fluoroethylcholine
^{18}F-FET	*O*-(2-[^{18}F]Fluoroethyl)- L-tyrosine
^{18}F-FETA	^{18}F-Fluoroetanidazole
^{18}F-FMT	L-3-[^{18}F]-Fluoro-α-methyltyrosine
^{18}F-MISO	^{18}F-Misonidazole
APUD	Amine precursor uptake and decarboxylation
DOTA	1,4,7,10-Tetra-azacyclododecane-1,4,7,10-tetraacetic acid
DTPA	Diethylenetriaminepentaacetic acid
FDA	United States Food and Drug Administration
GBq	Gigaelectron volt (10^9 volt)
GLUT	Glucose transporter family
keV	Kiloelectron volt (10^3 volt)

F. Orsini (✉) • E. Puta
Nuclear Medicine Unit, "Maggiore della Carità" University Hospital, Novara, Italy
e-mail: federica.orsini@maggioreosp.novara.it; erinda.puta@maggioreosp.novara.it

A. Lorenzoni
Nuclear Medicine Division, IRCCCS National Cancer Institute, Milan, Italy
e-mail: alice.lorenzoni@istitutotumori.mi.it

G. Mariani
Regional Center of Nuclear Medicine, Department of Translational Research and Advanced Technologies in Medicine and Surgery, University of Pisa, Pisa, Italy
e-mail: giuliano.mariani@med.unipi.it

© Springer International Publishing Switzerland 2017
H.W. Strauss et al. (eds.), *Nuclear Oncology*,
https://doi.org/10.1007/978-3-319-26236-9_33

MeV	Megaelectron volt (10^6 volt)
NET	Neuroendocrine tumor
NOC	1-Nal^3-octreotide
PET	Positron emission tomography
SS	Somatostatin
SSTR	Somatostatin receptor
TATE	Octreotate
TOC	Tyr^3-octreotide

Contents

Introduction 86

Positron-Emitting Radionuclides 86
Carbon-11 (^{11}C) 86
Nitrogen-13 (^{13}N) 87
Oxygen-15 (^{15}O) 87
Fluorine-18 (^{18}F) 88
Gallium-68 (^{68}Ga) 88
Rubidium-82 (^{82}Rb) 88

PET Radiopharmaceuticals 88
2-Deoxy-2-[^{18}F]fluoro-D-glucose 88
Nitrogen-13 Ammonia 90
Oxygen-15 Water 91
Rubidium-82 Chloride 91
[^{11}C]Methionine and Other Tracers for Protein Synthesis 91
Choline-Based Tracers for Phospholipid Synthesis 92
Fluorine-18 Sodium Fluoride 93
Fluorine-18 Misonidazole and Other Hypoxia Tracers 94
Fluorine-18 DOPA and Other Amine Precursors 95
Gallium-68 DOTATOC (Edotreotide) and Other Somatostatin Analogs 96

Suggested Readings 97

Introduction

Positron emission tomography (PET) is based on the coincidence detection of the paired 511 keV γ rays produced in the annihilation process that takes place when a β^- particle (the negative electron, or negatron) in the surrounding matter combines with a β^+ particle (the positive electron, or positron) emitted during nuclear decay of a positron-emitting radionuclide. Neutron-deficient nuclei reduce their proton surplus by emitting positrons; atomic mass of these elements is usually one unit smaller than the most common form of the stable isotope (e.g., positron-emitting ^{15}O, ^{13}N, and ^{11}C versus stable ^{16}O, ^{14}N, and ^{12}C). The annihilation event between a β^+ particle and a β^- particle, which occurs at a certain distance from the decay point (positron range) over which the positron loses part of its energy, creates two 511 keV photons, coincidence detection of the photons constitutes the basis for PET imaging (see ▶ Chap. 10, "Instrumentation for Positron Emission Imaging" of this book).

Some of the positron-emitting radionuclides are low atomic mass elements (e.g., C, N, and O) that are the radioactive counterparts of the fundamental constituents of biological matter; they can therefore be used to directly label molecules of interest without interfering with their biological activity. The maximum energy of positrons emitted by different radionuclides varies considerably, from about 0.635 MeV for ^{18}F to 3.15 MeV for ^{82}Rb (see Table 1 and Fig. 1). Typical specific activities of PET radiopharmaceuticals (radioactivity per unit mass of labeled compound) can be extremely high, so that generally low mass amounts of the radioactive compound are administered, typically in the submicrograms order. The half-life of the radionuclide utilized for a PET investigation should be commensurate with the time scale of the biological process to be explored (see ▶ Chap. 2, "Principles of Molecular Targeting for Radionuclide Therapy" of this book).

Positron-Emitting Radionuclides

Carbon-11 (^{11}C)

Carbon-11 is generally produced by the ^{14}N(p,α)^{11}C nuclear reaction and decays with a 99.8% positron emission and half-life of 20.4 min. ^{11}C-labeled molecules of biological interest in which a native ^{12}C atom has been replaced with an ^{11}C atom behave chemically and biologically exactly as their unlabeled equivalents. ^{11}C is often incorporated into PET radiopharmaceuticals through methylation reactions using [^{11}C]methyl iodide or [^{11}C]triflate. The most common precursors for synthesis are [^{11}C]cyanide, [^{11}C]carbon dioxide, and [^{11}C]carbon monoxide.

Table 1 Main physical characteristics of the β^+ emitting radionuclides most frequently employed for clinical purposes (arranged in increasing order of atomic mass number)

Isotopes	Half-life (min)	Maximum specific activity (GBq/μmol)	Branching β^+ emission (%)	E_{max} β^+ (MeV)	Modality of production	Maximum β^+ range in water (mm)
^{18}F	109.8 min	46.22	96.9	0.634	$^{18}O(p,n)^{18}F$	2.4
^{11}C	20.4 min	249.19	99.7	0.96	$^{14}N(p,\alpha)^{11}C$	4.1
^{15}O	2.03 min	2,479.19	99.9	1.73	$^{14}N(d,n)^{15}O$	8
^{13}N	9.98 min	510.81	99.8	1.199	$^{16}O(p,\alpha)^{13}N$	5.4
^{68}Ga	68.3 min	74.76	87.7	1.899	$^{68}Ge/^{68}Ga$	9
^{82}Rb	1.25 min	4,064.87	95.5	3.36	$^{82}Sr/^{82}Ru$	14.1
^{86}Y	14.7 h	5.76	33	1.25	$^{86}Sr(p,n)^{86}Y$	5.2
^{124}I	4.18 days	0.84	23.3	2.13	$^{124}Te(p,n)^{124}I$	10.2

Data extracted and elaborated from the National Institute of Standards and Technology [http://www.nist.gov/], from the Brookhaven National Laboratory [www.nndc.bnl.gov/nndc/nudat], and from the Laboratoire National Henri Becquerel [http://laraweb.free.fr/]

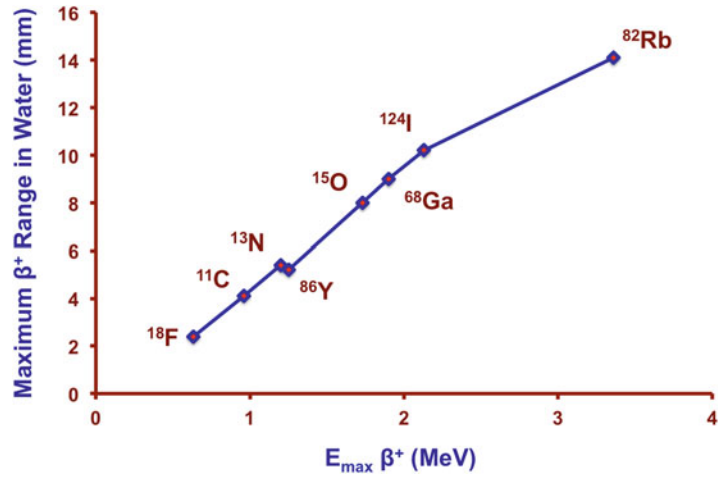

Fig. 1 Correlation between maximum energy (E_{max}, expressed in MeV) and maximum range of β^+ particles emitted during decay of different radionuclides employed for diagnostic PET imaging. Most of the energy deposited by each emission is nevertheless limited within a much shorter range (about 20–25% of the maximum range)

Nitrogen-13 (^{13}N)

Nitrogen-13 can be produced through different nuclear reactions. The $^{16}O(p,\alpha)^{13}N$ reaction is the most commonly used, and it is performed using a solution of ethanol (5 mM) or water; ethanol serves to reduce the amount of [^{13}N] nitrates or nitrites formed in situ. Similarly as for carbon, the stable isotope of nitrogen (^{14}N) is ubiquitous in biologically active organic molecules. Nevertheless, the half-life of ^{13}N (9.96 min) is too short to perform radiochemical synthesis of complex biological molecules. Thus, the most common application of ^{13}N-labeled molecules is in the form of [^{13}N] ammonia, which is routinely employed to assess myocardial blood flow. [^{13}N]Ammonia can also been used to prepare [^{13}N]*cis*platin for investigational purposes.

Oxygen-15 (^{15}O)

Oxygen-15 is produced using either the $^{14}N(d,n)^{15}O$ or the $^{15}N(p,n)^{15}O$ nuclear reactions. The very short half-life (2.04 min) of this radionuclide restricts its use to label simple molecules such as water, gaseous oxygen, and carbon monoxide. [^{15}O]Water is used to investigate cerebral and myocardial perfusion, as well as tumor perfusion, while gaseous $^{15}O_2$ can be

used to investigate oxygen metabolism; [^{15}O]carbon monoxide are employed to image the blood pool.

Fluorine-18 (^{18}F)

Fluorine-18 is the most widely used radionuclide for clinical PET investigations. ^{18}F (which decays to stable ^{18}O with nearly 97% positron emission) can be produced either by the ^{20}Ne(d,a)^{18}F or by the ^{18}O(p,n)^{18}F nuclear reactions. The former reaction leads to the formation of [^{18}F]F_2, while the latter results in the formation of [^{18}F]F^-. The short range in tissues of positrons emitted by ^{18}F (max 2.3 mm in water) contributes to the high-resolution PET images obtained with this radionuclide. The relatively long half-life of this radionuclide (almost 110 min) permits multistep labeling reactions for the synthesis of relatively complex molecules (with radiolabeling yields as high as 20–40%) and also allows for shipment from the production site to peripheral PET centers. Fluorine reacts with many organic and inorganic chemicals, since it is the most electronegative of all the elements; the chemistries most widely employed for incorporating ^{18}F into organic molecules are nucleophilic substitution and electrophilic substitution. Since the electrophilic labeling approach (which uses [^{18}F]F_2) results in molecules with low specific activities, the nucleophilic approach (based on the use of [^{18}F]F^-) is most frequently employed, not only because of the higher specific radioactivity of the compounds so produced but also because of greater selectivity of the radiolabeling reactions.

Gallium-68 (^{68}Ga)

Gallium-68 (half-life 68.3 min, maximum positron energy 1.9 MeV) is eluted from a ^{68}Ge/^{68}Ga radionuclide generator system, similar in concept to that of the ^{99}Mo/^{99m}Tc generator (see ▶ Chap. 3, "Single-Photon-Emitting Radiopharmaceuticals for Diagnostic Applications" of this book). ^{68}Ge decays by electron capture with a physical half-life of 271 days; a single generator allows therefore continuous production of ^{68}Ga for almost 1 year. ^{68}Ga is an excellent positron emitter (88% branching emission of positrons), with a low photon emission (3.22% at 1.077 MeV). This metallic radionuclide is used mostly for labeling peptides, such as somatostatin analogs and a ligand for the prostate specific membrane antigen (PSMA), and yields compounds with high radiochemical purity.

Rubidium-82 (^{82}Rb)

The ultrashort-lived ^{82}Rb (half-life 76 s, with emission of 3.15 MeV positrons) is a potassium analog eluted from a ^{82}Sr/^{82}Rb generator for myocardial perfusion imaging. It decays to stable ^{82}Kr by positron emission (nearly 96%) associated with only about 4% electron capture. Since the parent radionuclide ^{82}Sr has a physical half-life of 25 days, the generator can be used for approximately 1 month.

PET Radiopharmaceuticals

Positron emission tomography is one of the most important tools in medical imaging with many applications in neurology, oncology, cardiology and neuroscience, and infection – just to mention the most frequent clinical applications. Over the past 30 years, advances in radiotracer chemistry have led to the development and evaluation in preclinical and clinical studies of many radiotracers with high specificity and suitable pharmacokinetic characteristics for molecular imaging.

2-Deoxy-2-[^{18}F]fluoro-D-glucose

The glucose analog 2-Deoxy-2-[^{18}F]fluoro-D-glucose ([^{18}F]FDG, Fig. 2) is the most commonly used radiopharmaceutical for clinical PET imaging. 2-Deoxy-D-glucose was initially developed in 1960 as an antitumor chemotherapy agent, with the rationale of inhibiting glucose utilization by cancer cells. In 1976 Dr. Wolf and his colleagues at Brookhaven National Laboratory developed the synthesis of [^{18}F]FDG to explore glucose metabolism in the brain; the first [^{18}F]FDG brain imaging studies were performed in 1977 at the University of Pennsylvania, Philadelphia (Table 2).

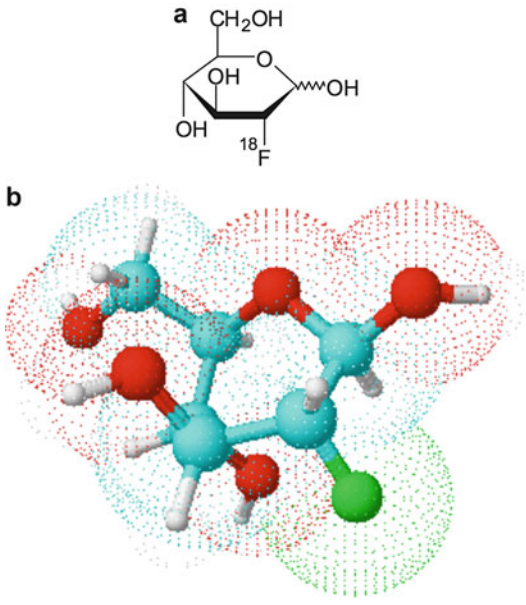

Fig. 2 Chemical formula in extenso (**a**) and tridimensional representation of chemical structure (**b**) of [^{18}F]FDG. Elements are represented with the following color codes: *green* = ^{18}F, *red* = O, *gray* = H, and *light blue* = C (Reproduced with permission from: Volterrani D, Erba PA, Mariani G, eds. Fondamenti di medicina nucleare – Tecniche e applicazioni. Milan: Springer; 2010)

As shown in Fig. 3, [^{18}F]FDG is transported through the cell membrane via glucose transport proteins (GLUTs) and phosphorylated by hexokinase to [^{18}F]FDG-6-PO_4. [^{18}F]FDG-6-PO_4 is not a substrate for the subsequent enzymatic conversion to fructose-6-phosphate by phosphohexose and neither is for other endogenous routes of metabolism; therefore, it does not further participate in the glycolytic pathway and becomes trapped in the cell because of its negative charge. The low activity of the reverse enzyme, glucose-6-phosphatase (which has relevance only in hepatocytes), leads to the tumor cell accumulation of [^{18}F]FDG-6-PO_4. [^{18}F]FDG uptake reflects therefore the magnitude of glucose metabolism, the most intense activity occurring in the brain (9% within 80–100 min), in the sites of inflammation and infection, and in neoplastic cells. Myocardial uptake is variable, and significant [^{18}F]FDG uptake can be seen also in the myocardium even in the fasting state, when the predominant energy source should be fatty acid consumption. Physical activity occurring shortly preceding or during [^{18}F]FDG administration increases tracer accumulation in skeletal muscles. Cancer cells exhibit

Table 2 Main mechanisms of in vivo distribution/localization of PET imaging agents in nuclear oncology

Mechanism(s)	Rationale	Example
Membrane transport: simple, facilitated, and active transport	Facilitated transport mediated by specific transport proteins: glucose transporters (GLUTs 1–5) expressed on the cell membrane as a function of energy demand	[^{18}F]FDG for PET of tumors with enhanced glucose consumption
Enzyme-mediated intracellular trapping	Trapping into cells as the result of a specific interaction of the radiopharmaceutical with an enzyme: phosphorylated [^{18}F]FDG not being the substrate for subsequent metabolic pathways	[^{18}F]FDG for PET of tumors with high glucose demand
Competitive substrates for tumor cell structure	The radiopharmaceutical competes with the endogenous substrate for the same metabolic pathways for the synthesis of proteins or phospholipids	Various imaging agents for tumors: amino acids (protein synthesis) and choline-based tracers (phospholipid synthesis)
Competitive substrates for tumor cell functional processes	The radiopharmaceutical competes with endogenous catecholamine synthesis and storage in neurosecretory vesicles	Imaging agents for neuroendocrine tumors derived from the neural crest: ^{18}F-DOPA
Receptor-mediated probes	The radiopharmaceutical competes with the physiologic ligands for binding with the target receptor	Somatostatin analogs for neuroendocrine tumors expressing somatostatin receptors

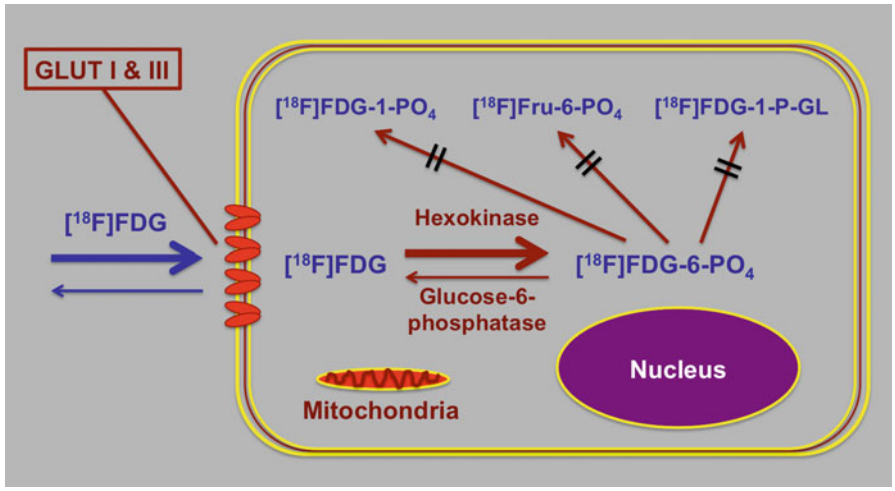

Fig. 3 Diagrammatic representation of the fate of the glucose analog [^{18}F]FDG. The tracer enters cells with the same mechanism as native glucose (GLUT system); intracellular [^{18}F]FDG undergoes enzymatic phosphorylation to [^{18}F]FDG-6-PO_4 through the action of hexokinase, in the same manner as native glucose, whereas the reverse enzyme (glucose-6-phosphatase, which would revert [^{18}F]FDG-6-PO_4 back to [^{18}F]FDG, diffusible outside the cell) normally operates at very low levels and almost exclusively in hepatocytes; [^{18}F]FDG-6-PO_4 cannot be a substrate for any of the metabolic routes that glucose-6-PO_4 normally undergoes and therefore remains trapped inside the cell (Reproduced with permission from: Volterrani D, Erba PA, Mariani G, eds. Fondamenti di medicina nucleare – Tecniche e applicazioni. Milan: Springer; 2010)

high rates of metabolism with increased glucose metabolism (Warburg effect), correlated also to proliferative activity. Gene-mediated regulation of the GLUT system and hexokinase activity contributes to the increased accumulation of [^{18}F]FDG in tumor cells relative to normal tissues; due to this factor, the time-related pattern of [^{18}F]FDG accumulation in malignancy may be different from that of benign lesions and inflammatory processes.

The mechanisms leading to elevated glucose metabolism in cancers are multifactorial and include tumor-related components, biochemical and molecular alterations (e.g., glucose metabolic pathway, hypoxia), and nontumor-related constituents (e.g., inflammation). [^{18}F]FDG is excreted through the kidneys, about 20% of injected activity being excreted in the urine within 2 h after administration. The uptake of [^{18}F]FDG, which competes with endogenous glucose, by tumor tissue depends on plasma glucose levels; in case of high blood glucose levels (as well as low insulin level), the uptake of [^{18}F]FDG is reduced. In the same way, some drugs that modify glucose level (e.g., valproic acid, glucocorticoids, carbamazepine) can alter radiotracer uptake. Many other factors (e.g., chemotherapy, radiation therapy, or recent administration of granulocyte-colony-stimulating factor) interfere with [^{18}F]FDG uptake, thus possibly resulting in false-positive or false-negative imaging data.

[^{11}C]Glucose, the perfect radioactive counterpart of endogenous glucose, has been synthesized, but the short physical half-life of the radionuclide and the production of labeled metabolites with fast washout from tissues and return to circulating blood limit the clinical application of this tracer.

Nitrogen-13 Ammonia

Nitrogen-13 ammonia ([^{13}N]ammonia) is used mostly for quantitative imaging of myocardial blood flow. In physiologic conditions, the majority of [^{13}N]ammonia circulates in the form of the ammonium ion, NH_4^+. Following i.v. injection, [^{13}N]ammonia is rapidly cleared from the bloodstream and diffuses across the cell capillary membrane entering the cells via the ammonium transporter. Once in the cell, it is metabolized to

^{13}N-glutamine by glutamine synthetase and trapped within tissues such as the myocardium, liver, brain, and other organs. Its uptake in the tissues is proportional to blood flow. The main metabolite of [^{13}N]ammonia is [^{13}N]urea, which is excreted through the kidneys.

[^{13}N]ammonia is used clinically for myocardial perfusion studies and quantification of myocardial blood flow and flow reserve. The high net extraction fraction of $^{13}NH_3$ by myocardial cells (80%) and its short positron range (0.4 mm) yield very high-quality PET images.

Oxygen-15 Water

Oxygen-15 water ([^{15}O]H_2O) is excellent to trace blood flow. It is a freely diffusible agent, most frequently used to investigate cerebral and myocardial perfusion, as well as tumor perfusion. Thanks to the short physical half-life, perfusion studies can be repeated every 8–10 min. As a cyclotron product with a very short half-life (2.04 min), its use in the clinical setting is to institutions with an on-site cyclotron.

Rubidium-82 Chloride

Rubidium-82 chloride (^{82}RbCl) is a potassium analog used for PET myocardial perfusion imaging. Once administered intravenously, ^{82}RbCl dissociates rapidly, and the $^{82}Rb^+$ ion is rapidly extracted by the myocardium in a fashion which is proportional to blood flow and enters the myocardial cells through the Na^+/K^+ ATPase pump, similarly to ^{201}Tl. Myocardial activity is noted within the first minute after the i.v. injection. The first-pass extraction fraction is about 50–60% at resting blood flow levels, and several studies have demonstrated that extraction decreases in a nonlinear manner at high blood flow rates. ^{82}Rb decays to stable krypton-82 (^{82}Kr), which is exhaled through the lungs.

Due to the short half-life of ^{82}Rb (76 s) and the rapid replenishment of ^{82}Sr/^{82}Rb generator (making it possible to elute every 10 min), fast sequential resting and pharmacological stress myocardial perfusion studies can be performed, in order to quantitatively assess not only myocardial blood flow but also the coronary artery blood flow reserve.

Despite the ultrashort half-life and the high kinetic energy (3.15 MeV) resulting in a relatively long positron range, ^{82}RbCl still provides very good-quality PET images, and it has been demonstrated that myocardial perfusion studies with ^{82}Rb-PET have superior accuracy than scans based on the use of ^{99m}Tc-labeled agents.

[^{11}C]Methionine and Other Tracers for Protein Synthesis

Tumor cells generally exhibit increased amino acid transport and increased protein synthesis rates. Several processes contribute to enhance amino acid transport per se in addition to overall protein synthesis, including transamination and transmethylation, a specific role of methionine in initiating protein synthesis, and the use of amino acids as glutamine for energy.

Many amino acids and analogs labeled with β^+ emitters have been developed to measure either the rate of protein synthesis or the rate of uptake into the cells; these tracers differ in ease of synthesis, biodistribution, and formation of radiolabeled metabolites in vivo, but only a few have substantial impact in clinical oncology.

The first tracer used for PET imaging to assess protein synthesis was [^{11}C]carboxyl L-leucine (Fig. 4); however, recycling of radiolabeled amino acids deriving from the degradation of radiolabeled proteins greatly limited the feasibility and clinical usefulness of this approach.

Methyl-[^{11}C]-L-methionine ([^{11}C]MET) (Fig. 5) has been used widely in PET imaging. The uptake is increased in brain tumors (even low grade), head-and-neck cancers, lung cancer, and breast cancer. Physiological uptake of this tracer (which is excreted mostly through the kidneys – thus resulting in considerable accumulation in the urinary bladder) is observed in the liver, pancreas, and intestine. Moreover, [^{11}C]MET has been proposed also for localization of parathyroid adenomas (sensitivity 83%, specificity 100%).

Nevertheless, several problems are linked to the use of amino acids labeled with ^{11}C, such as recycling of radiolabeled metabolites, slow incorporation of the amino acid tracers into proteins, and above all the short half-life of ^{11}C. These problems have stimulated ongoing efforts to develop amino acids labeled with β^+ emitters with a longer half-life. In particular, tyrosine analogs such as L-3-[^{18}F]-fluoro-a-methyltyrosine (^{18}F-FMT) and *O*-(2-[^{18}F]fluoroethyl)-L-tyrosine (^{18}F-FET) (Fig. 6) or phenylalanine analogs have been synthesized. ^{18}F-FET enters the cells through amino acid transporters, but does not appear to be directly involved in protein synthesis. Both ^{18}F-FMT and ^{18}F-FET accumulate rapidly (within 30 min postinjection) in brain tumors and then wash out slowly.

Nontumoral uptake of all radiolabeled amino acids (though generally less intense than in tumors) includes ischemic brain areas, scar tissue, sarcoidosis, recently irradiated areas, and hemangiomas. Whereas, their uptake in inflammatory tissue is much lower than [^{18}F]FDG uptake.

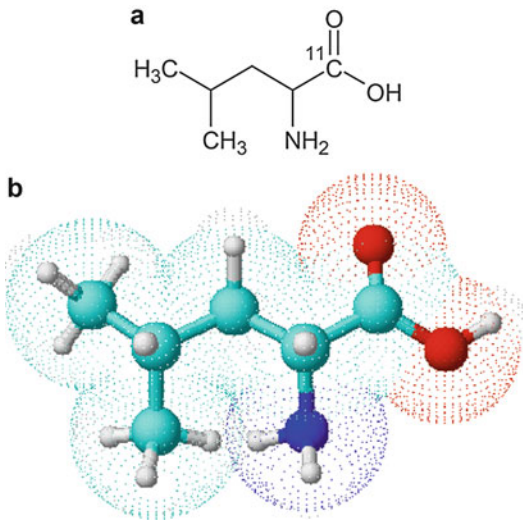

Fig. 4 Chemical formula in extenso (**a**) and tridimensional representation of chemical structure (**b**) of [^{11}C] carboxyl L-leucine. Elements are represented with the following color codes: *red* = O, *gray* = H, *light blue* = C, and *deep blue* = N (Reproduced with permission from: Volterrani D, Erba PA, Mariani G, eds. Fondamenti di medicina nucleare – Tecniche e applicazioni. Milan: Springer; 2010)

Choline-Based Tracers for Phospholipid Synthesis

The synthesis of cell membrane is very rapid in neoplastic tissue, reflecting indirectly the rate of cell proliferation. Choline, an essential element of the phospholipid constituents in the cell membrane, is transported into cells and phosphorylated by choline kinase before being incorporated into

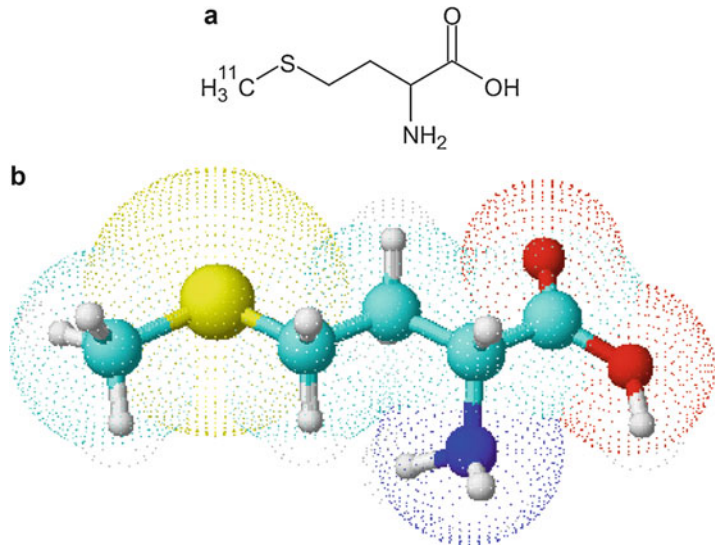

Fig. 5 Chemical formula in extenso (**a**) and tridimensional representation of chemical structure (**b**) of methyl-[^{11}C]-L-methionine ([^{11}C] MET). Elements are represented with the following color codes: *red* = O, *gray* = H, *light blue* = C, *deep blue* = N, and *yellow* = S (Reproduced with permission from: Volterrani D, Erba PA, Mariani G, eds. Fondamenti di medicina nucleare – Tecniche e applicazioni. Milan: Springer; 2010)

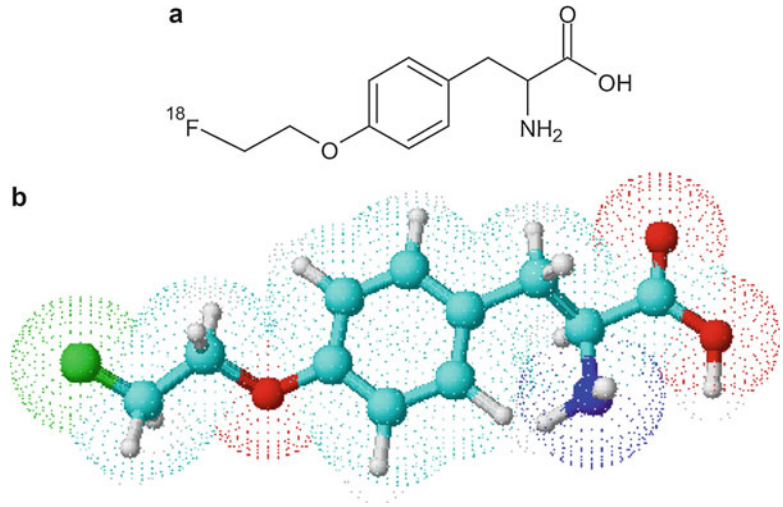

Fig. 6 Chemical formula in extenso (**a**) and tridimensional representation of chemical structure (**b**) of *O*-(2-[^{18}F] fluoroethyl)-L-tyrosine (^{18}F-FET). Elements are represented with the following color codes: *red* = O, *gray* = H, *light blue* = C, *deep blue* = N, and *green* = ^{18}F (Reproduced with permission from: Volterrani D, Erba PA, Mariani G, eds. Fondamenti di medicina nucleare – Tecniche e applicazioni. Milan: Springer; 2010)

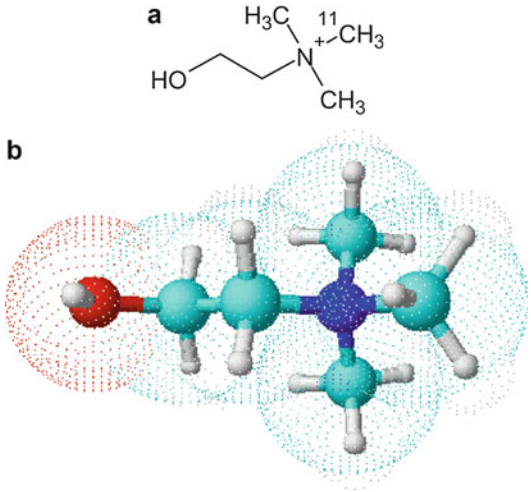

Fig. 7 Chemical formula in extenso (**a**) and tridimensional representation of chemical structure (**b**) of [^{11}C] choline. Elements are represented with the following color codes: *red* = O, *gray* = H, *light blue* = C, and *deep blue* = N (Reproduced with permission from: Volterrani D, Erba PA, Mariani G, eds. Fondamenti di medicina nucleare – Tecniche e applicazioni. Milan: Springer; 2010)

the membrane phospholipids. Besides other molecular signatures of increased energy expenditure and accelerated proliferation, tumor cells have enhanced levels of choline kinase.

[^{11}C]Choline (Fig. 7) has mostly been used for imaging of prostate tumors, non-small cell lung cancer, urinary bladder, and brain neoplasms. The increased incorporation in prostate cancer is linked to enhanced phosphatidylcholine production, phospholipid synthesis, and upregulation of choline kinase and other enzymes. Limitations in the widespread clinical use of [^{11}C]choline are common to other radiopharmaceuticals labeled with ^{11}C, i.e., in situ availability of a cyclotron for the production of this short half-life radionuclide (approximately 20 min).

More usable choline analogs labeled with ^{18}F include ^{18}F-fluoroethylcholine (^{18}F-FEC) (Fig. 8) and ^{18}F-fluoromethylcholine (^{18}F-FCH, the PET agent commercially available) (Fig. 9); they have similar biodistribution patterns, with higher urinary excretion than [^{11}C]choline. Physiologic bowel and liver uptake of radiolabeled cholines limits suitability of these tracers for PET imaging of gastrointestinal and liver cancers.

Fluorine-18 Sodium Fluoride

Fluorine-18 sodium fluoride ([^{18}F]fluoride) was first introduced as a bone-imaging agent for skeletal scintigraphy in the early 1960s and approved by the FDA in 1972. It was then withdrawn from the approval list in 1984 because of technical limitations at that time, that is, the difficulty in imaging the 511 keV annihilation photons with

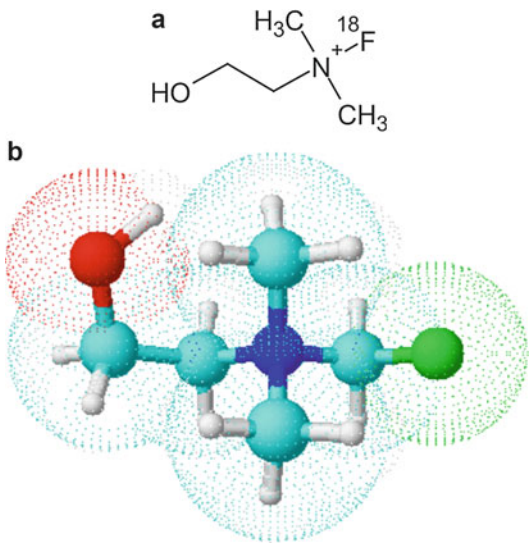

Fig. 8 Chemical formula in extenso (**a**) and tridimensional representation of chemical structure (**b**) of ^{18}F-fluoroethylcholine (^{18}F-FEC). Elements are represented with the following color codes: *red* = O, *gray* = H, *light blue* = C, *deep blue* = N, and *green* = ^{18}F (Reproduced with permission from: Volterrani D, Erba PA, Mariani G, eds. Fondamenti di medicina nucleare – Tecniche e applicazioni. Milan: Springer; 2010)

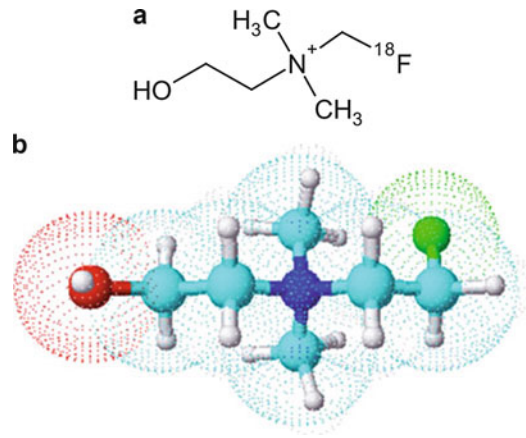

Fig. 9 Chemical formula in extenso (**a**) and tridimensional representation of chemical structure (**b**) of ^{18}F-fluoromethylcholine (^{18}F-FCH). Elements are represented with the following color codes: *red* = O, *gray* = H, *light blue* = C, *deep blue* = N, and *green* = ^{18}F (Reproduced with permission from: Volterrani D, Erba PA, Mariani G, eds. Fondamenti di medicina nucleare – Tecniche e applicazioni. Milan: Springer; 2010)

gamma cameras optimized for 100–200 keV γ rays; the concomitant wide diffusion of ^{99m}Tc-labeled diphosphonates contributed to the declining interest in ^{18}F-fluoride for bone scintigraphy.

Interest in the clinical use of [^{18}F]fluoride as a bone-scanning agent has more recently been revived after the development of modern PET scanners. [^{18}F]Fluoride is administered intravenously (185–370 MBq), and the intensity and extent of its uptake reflects blood flow and bone remodeling. This agent has high and rapid bone uptake combined with a fast, biexponential blood clearance that results in achievement of a high bone-to-background ratio within a short time; in fact, imaging can be performed less than 1 h after administration. ^{18}F-ion exchanges for an OH^- ion on the surface of the hydroxyapatite matrix of the bone and remains then chemisorbed into the crystalline matrix where it is retained until the bone is remodeled. Red blood cell uptake (30% of the injected activity) does not interfere with bone uptake. Within the first 1–2 h upon administration of Na^{18}F, about 20% is excreted through the urinary tract.

The normal biodistribution of Na^{18}F is in general rather uniform, but the axial skeleton has a higher uptake than the appendicular skeleton, and the bone around joints has higher uptake than the shafts of long bones.

Increased fluoride uptake has been reported in both sclerotic and partly lytic metastases. As for ^{99m}Tc-labeled diphosphonates, purely lytic lesions have lower or no uptake at all. ^{18}F-Fluoride is not a tumor-specific tracer, and its clinical usefulness has been demonstrated also for a wide range of benign diseases of the bone.

Fluorine-18 Misonidazole and Other Hypoxia Tracers

The irregular development of tumor-induced neoangiogenesis results in tissue hypoxia, which is associated with the promotion of various metabolic mechanisms; hypoxia is also a prognostic indicator

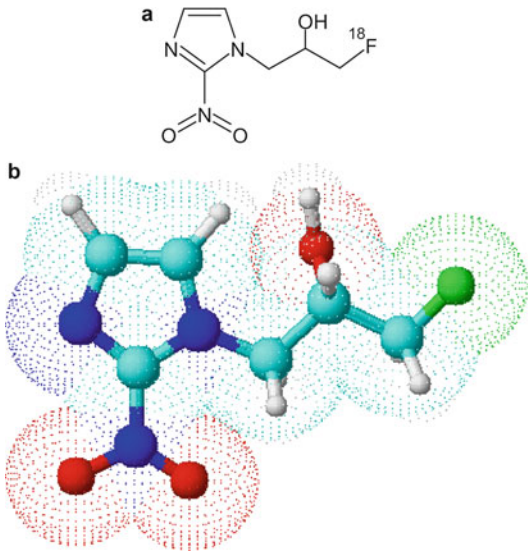

Fig. 10 Chemical formula in extenso (**a**) and tridimensional representation of chemical structure (**b**) of ^{18}F-misonidazole (^{18}F-MISO). Elements are represented with the following color codes: *red* = O, *gray* = H, *light blue* = C, *deep blue* = N, and *green* = ^{18}F (Reproduced with permission from: Volterrani D, Erba PA, Mariani G, eds. Fondamenti di medicina nucleare – Tecniche e applicazioni. Milan: Springer; 2010)

of poor response to radiotherapy and chemotherapy, as it induces resistance to these treatments. Tumors may consist of up to 50–60% hypoxic or anoxic tissue heterogeneously distributed. The first radiotracer, ^{18}F-misonidazole (^{18}F-MISO, Fig. 10) is a nitroimidazole derivative developed in 1984. ^{18}F-MISO is relatively hydrophilic and diffuses slowly across cell membranes; such a passive distribution in normal tissues results in a relatively long waiting time before acquisition of PET imaging, since the lesion-to-background ratio is typically <2:1 at about 90 min after injection. The oxygen-dependent intracellular metabolism of nitroimidazole consists in one-electron reduction and in selective binding to macromolecules within hypoxic cells. The tracer undergoes renal excretion.

PET imaging with ^{18}F-MISO is used to quantitatively assess tumor hypoxia in lung, brain, and head-and-neck cancers (as well as for the evaluation of myocardial ischemia).

Fluorine-18-labeled fluoroetanidazole (^{18}F-FETA), a fluorinated analog of etanidazole, has similar oxygen-dependent binding and tumor retention compared to ^{18}F-MISO, but it releases fewer metabolites in plasma and urine. ^{18}F-Fluoroerythronitroimidazole (^{18}F-ETNIM) is an additional novel promising radiopharmaceutical with faster elimination from well-oxygenated tissues, because it is more hydrophilic.

Fluorine-18 DOPA and Other Amine Precursors

The process of amine precursor uptake and decarboxylation (APUD) is a common feature shared by many endocrine cells producing peptide hormones, including neuroendocrine tumors, and indicates a common embryological origin from the neural crest. Neuroendocrine tumors (NETs) accumulate and decarboxylate the amino acid L-dihydroxyphenylalanine (L-DOPA) due to increased activity of L-DOPA decarboxylase. Following systemic administration, L-3,4-dihydroxy-6-[^{18}F]fluorophenylalanine (^{18}F-DOPA, Fig. 11), an analog of L-DOPA, enters the catecholamine metabolic pathway both in the brain and in peripheral tissues. Based on this property, PET with ^{18}F-DOPA is used in the evaluation of presynaptic striatal dopaminergic function in some neurologic disorders (chiefly movement disorders such as Parkinson's disease and parkinsonisms), as well as for the evaluation of patients with brain tumors, with NETs, with insulinoma (particularly in pediatric patients), with medullary thyroid cancer, with pheochromocytoma, and with extra-adrenal paraganglioma.

After i.v. administration, up to 1% of the injected ^{18}F-DOPA crosses the blood–brain barrier and is transported into presynaptic neurons via the amino acid transport system, where an amino acid decarboxylase converts it to ^{18}F-fluorodopamine, which is stored in intraneuronal vesicles within the striatum.

In peripheral tissues, ^{18}F-DOPA is metabolized to ^{18}F-fluorodopamine or to 3-*O*-methyl-6-fluoro-L-DOPA and excreted mainly through the kidneys. The renal excretion may be reduced by

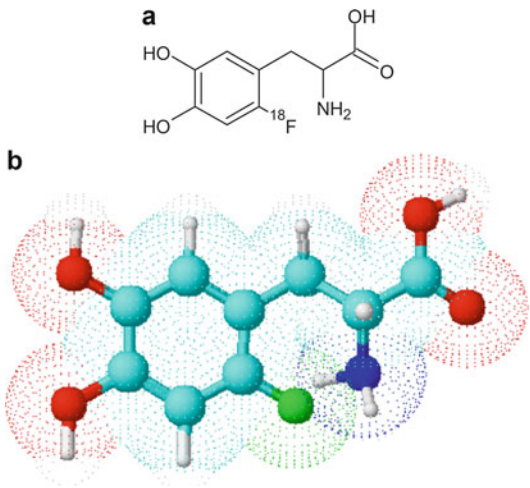

Fig. 11 Chemical formula in extenso (**a**) and tridimensional representation of chemical structure (**b**) of [^{18}F] fluorophenylalanine (^{18}F-DOPA). Elements are represented with the following color codes: *red* = O, *gray* = H, *light blue* = C, *deep blue* = N, and *green* = ^{18}F (Reproduced with permission from: Volterrani D, Erba PA, Mariani G, eds. Fondamenti di medicina nucleare – Tecniche e applicazioni. Milan: Springer; 2010)

premedication with the decarboxylase inhibitor carbidopa, with the goal of improving in general the tumor uptake, except in patients with insulinomas or β-cell hyperplasia.

[^{11}C]hydroxytryptophan is another PET tracer used for the localization of NETs, including insulinomas; this tracer is taken up by tumor cells, decarboxylated, and then stored and irreversibly trapped in vesicles as [^{11}C]serotonin.

Gallium-68 DOTATOC (Edotreotide) and Other Somatostatin Analogs

Neuroendocrine tumors (NETs) are characterized by the presence of peptide receptors on the cell membrane, particularly the somatostatin (SS) receptors. Somatostatin analogs have been radiolabeled with diagnostic radionuclides as well as with emitters of β^- particles for targeted radionuclide therapy. Five specific SS receptor subtypes (SSTR1–SSTR5) with different tissue distribution and affinity for somatostatin analogs have been identified. They are expressed also in peritumoral vessels and in inflammatory and immune cells, and this can account for visualization of those tumors whose cells do not express the receptors. The most commonly used somatostatin analog is octreotide that has high binding affinity to somatostatin receptor subtypes 2 and 5 but binds varyingly to the SSTR3 and SSTR4 subtypes. DOTA-Tyr^3-octreotide (DOTA-TOC, or DOTATOC) can be variously labeled with either γ or β^+ emitters (for imaging), as well as with β^- emitters (such as ^{90}Y or ^{177}Lu, for therapy) (see also ► Chap. 8, "Novel Radiopharmaceuticals for Therapy" of this book). DOTA (1,4,7,10-tetraazacyclododecane-N,N′,N″,N‴-tetraacetic acid) is a macrocyclic chelating agent that forms stable complexes with the metal radionuclide of interest. At variance with DTPA (which is an open structure enabling to label radioconjugates at room temperature), DOTA is a closed structure, and labeling must be performed at high temperature (90 ± 5°C) in order to open the ring circumscribed by the four nitrogen atoms; in turn, the radioconjugates obtained with DOTA derivatives are much more stable in vivo than those obtained with DTPA. The time required to recover ^{68}Ga from the ^{68}Ge/^{68}Ga generator, to synthesize, and to purify the ^{68}Ga-labeled DOTA-conjugated peptides is less than 20 min, resulting in an overall simple and radiochemically efficient processing.

^{68}Ga-DOTATOC (Fig. 12) has a fast pharmacokinetic profile (about 80% of activity being rapidly cleared from circulating blood already at 10 min postinjection) and fast tumor accumulation (maximum after 70 ± 20 min after injection); these features enable effective PET imaging already 1 h after radiotracer administration; excretion occurs predominantly through the kidneys. The accumulation in tissues that do not express somatostatin receptors is generally very low, thus resulting in high tumor/background ratios; nevertheless, particular attention must be paid to imaging interpretation concerning the sites of physiological accumulation such as the spleen, the liver, the

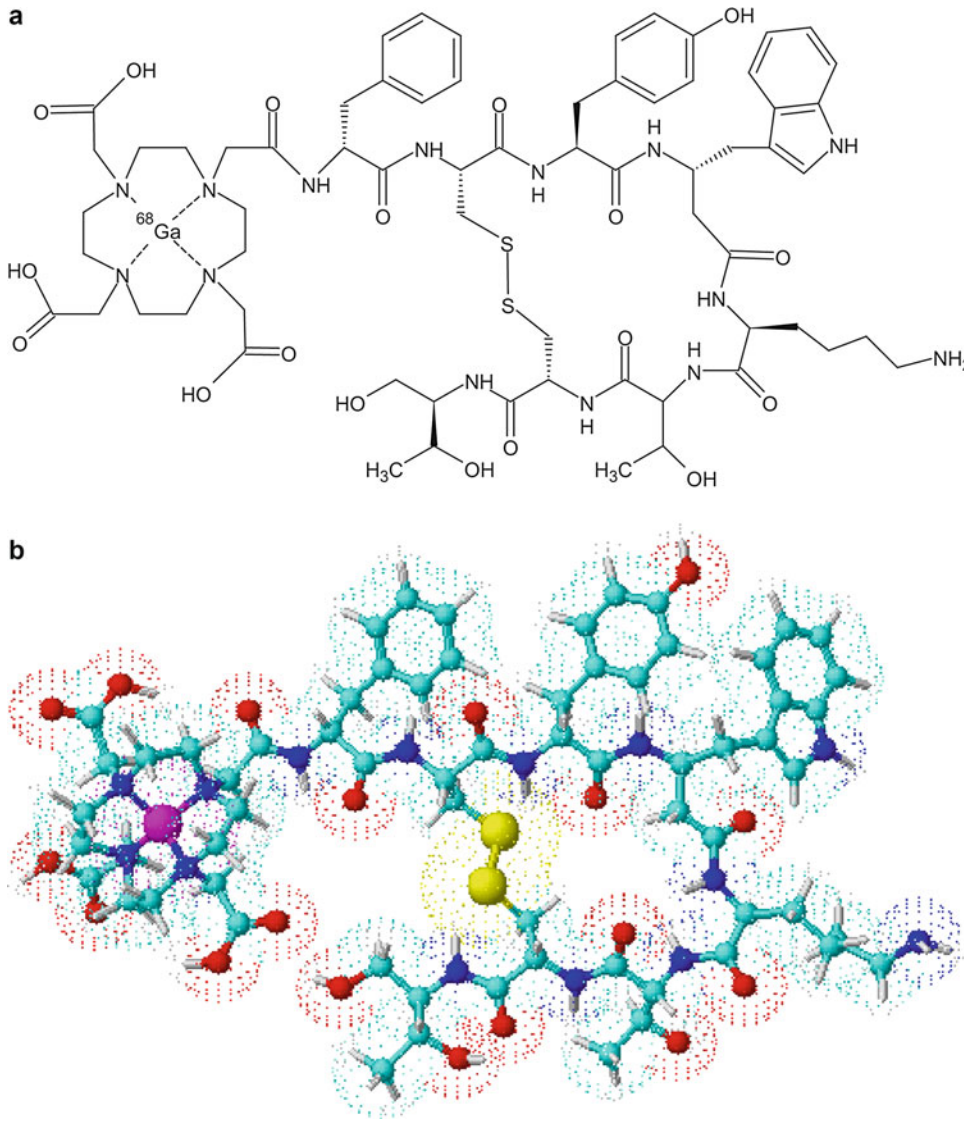

Fig. 12 Chemical formula in extenso (**a**) and tridimensional representation of chemical structure (**b**) of ^{68}Ga-DOTA-Tyr^3-octreotide. Elements are represented with the following color codes: *red* = O, *gray* = H, *light blue* = C, *deep blue* = N, *yellow* = S, and *fuchsia* = ^{68}Ga (Reproduced with permission from: Volterrani D, Erba PA, Mariani G, eds. Fondamenti di medicina nucleare – Tecniche e applicazioni. Milan: Springer; 2010)

adrenal glands, the urinary pathways, and the pituitary gland.

Other radiolabeled somatostatin analogs for PET imaging include ^{68}Ga-DOTA-1-Nal^3-octreotide (^{68}Ga-DOTANOC, with better binding affinities for SSTR2, SSTR3, and SSTR5) and ^{68}Ga-DOTA-Tyr^3,Thr^8-octreotide (^{68}Ga-DOTATATE, with predominant affinity for SSTR2).

Suggested Readings

1. Ell PJ, Gambhir SS, editors. Nuclear medicine in clinical diagnosis and treatment. 3rd ed. New York: Churchill Livingston; 2004.
2. Herbert JC, Eckelman WC, Neumann RD, editors. Nuclear medicine – diagnosis and therapy. New York: Thieme Medical Publishers; 1996.

3. IAEA. Operational guidance on hospital radiopharmacy. Vienna: International Atomic Energy Agency (IAEA); 2008.
4. IAEA. Good practice for introducing radiopharmaceuticals for clinical use. Vienna: International Atomic Energy Agency (IAEA); 2015.
5. Kowalsky RJ, Falen SW, editors. Radiopharmaceuticals in nuclear pharmacy and nuclear medicine. 3rd ed. Washington, DC: American Pharmacists Association; 2011.
6. Owunwanne A, Patel M, Sadek S, editors. The handbook of radiopharmaceuticals. New York: Springer; 1995.
7. Rösch F. Radiochemistry and radiopharmaceuticals chemistry for medicine. In: Choppin GR, Liljenzin J-O-E, Rydberg J, editors. Radiochemistry and nuclear chemistry, 4th edn. Cambridge, Massachusetts: Elsevier Academic Press; 2013.
8. Theobald T, editor. Sampson's textbook of radiopharmacy. 4th ed. London: Pharmaceutical Press; 2010.
9. Vallabhajosula S. Molecular imaging – radiopharmaceuticals for PET and SPECT. New York: Springer; 2009.
10. Welch MJ, Redvanly CS, editors. Handbook of radiopharmaceuticals: radiochemistry and applications. Hoboken: Wiley; 2003.

Radiopharmaceuticals for Therapy

5

Federica Orsini, Sara Mazzarri, Erinda Puta, Federica Guidoccio, Alice Lorenzoni, and Giuliano Mariani

Abstract

Common radionuclides used for radiometabolic therapy include ^{131}I, ^{153}Sm, ^{89}Sr, ^{223}Ra, and ^{90}Y. In this chapter we will focus on therapeutic radiopharmaceuticals are employed for therapy of differentiated follicular thyroid carcinomas,for therapy of pheochromocytoma/paraganglioma/neuroblastomas, for bone pain palliation, for radioimmunotherapy of lymphomas, for peptide radioreceptor therapy of neuroendocrine tumors, and for intra-arterial radioembolization of hypervascularized tumors of the liver.

Keywords

Radiopharmaceuticals • Radionuclides • Nuclear oncology • Radiometabolic therapy • Radioimmunotherapy • Peptide receptor radionuclide therapy • Transarterial radioembolization

Glossary

^{153}Sm-EDTMP	^{153}Sm-ethylenediamine tetramethylene phosphoric acid
^{188}Re-HEDP	^{188}Re-hydro-ethylidene diphosphate
CCK	Cholecystokinin
DIT	Diiodotyrosine
DOTA	1,4,7,10-tetra-azacyclododecane-1,4,7,10-tetraacetic acid (macrocyclic coupling agent to label compounds of biological interest with metal radionuclides)
DOTA-TATE	DOTA-D-Phe^{1}-Tyr^{3}-octreotate
DOTA-TATE	DOTA-Tyr^{3}-Thre^{8}-octreotide
DOTA-TOC	DOTA-D-Phe^{1}-Tyr^{3}-octreotide
GLP-1	Glucagon-like peptide-1
GRP	Gastrin-releasing peptide
Gy	Gray unit (ionizing radiation dose in the International System of Units, corresponding to the absorption of one joule of radiation energy per kilogram of matter)
HACA	Human anti-chimeric antibody
HAHA	Human anti-human antibody

F. Orsini (✉) • E. Puta
Nuclear Medicine Unit, "Maggiore della Carità" University Hospital, Novara, Italy
e-mail: federica.orsini@maggioreosp.novara.it; erinda.puta@maggioreosp.novara.it

S. Mazzarri • F. Guidoccio • G. Mariani
Regional Center of Nuclear Medicine, Department of Translational Research and Advanced Technologies in Medicine and Surgery, University of Pisa, Pisa, Italy
e-mail: saramazzarri@hotmail.it; federica.guidoccio@gmail.com; giuliano.mariani@med.unipi.it

A. Lorenzoni
Nuclear Medicine Division, IRCCCS National Cancer Institute, Milan, Italy
e-mail: alice.lorenzoni@istitutotumori.mi.it

© Springer International Publishing Switzerland 2017
H.W. Strauss et al. (eds.), *Nuclear Oncology*,
https://doi.org/10.1007/978-3-319-26236-9_34

HAMA	Human anti-mouse antibody
KI	Potassium iodide
LET	Linear energy transfer
MIBG	*Meta*-iodobenzylguanidine
MIT	Monoiodotyrosine
NET	Neuroendocrine tumor
NHL	Non-Hodgkin's lymphoma
NIS	Sodium-iodide symporter
PRRT	Peptide receptor radionuclide therapy
RGD	Tripeptide composed of L-arginine, glycine, and L-aspartic acid
RIT	Radioimmunotherapy
SSTR	Somatostatin receptors
T3	3,5,3′-Triiodothyronine
T4	3,5,3′,5′-Tetraiodothyronine
TSH	Thyroid stimulating hormone

Contents

Background 100

Alpha-Particle Emitters 102
Radium-223 (^{223}Ra) 102

Auger Electron Emitters 102

Emitters of β^- Particles 102
Iodine-131 (^{131}I) 103
Yttrium-90 (^{90}Y) 103
Lutetium-177 (^{177}Lu) 104
Samarium-153 (^{153}Sm) 104
Strontium-89 (^{89}Sr) 105
Rhenium-186 (^{186}Re) and Rhenium-188 (^{188}Re) ... 105
Phosphorus-32 (^{32}P) 105

Treatment of Thyroid Disease with ^{131}I-Iodide 106

Treatment of Neuroendocrine Neoplasms Originating from the Neural Crest with [^{131}I] MIBG 107

Peptide Receptor Radionuclide Therapy 108

Bone-Seeking Radiopharmaceuticals 109

Radioimmunotherapy for Hematologic Malignancies 110

Radionuclide Therapy of Primary and Metastatic Liver Tumors 112

Suggested Readings 113

Background

A radiopharmaceutical is a compound containing a radionuclide, which is employed clinically for the detection, characterization, or treatment of disease. While diagnostic radiopharmaceuticals are γ or β^+ emitters, therapeutic radiopharmaceuticals exert their action through the emission of electrically charged particles (β^- or α^{++} particles) that deposit their energy within a relatively limited range in the tissue, thus causing radiation damage to the site of localization, the desired radiobiological effect resulting in cell death. Depending on their energy, the β^- particles emitted by radionuclides utilized for therapeutic radiopharmaceuticals typically travel a few millimeters from their emission point (or even few micrometers, as in the case of the very low-energy Auger electrons); on the other hand, α^{++} particles typically travel few tens of micrometers in tissues. In addition to particle emission causing a cytocidal radiobiological effect, some therapeutic radiopharmaceuticals also emit γ-rays, which can be detected with a conventional gamma camera and thus can provide information on their distribution in the body. This information is useful to confirm that the administered radiopharmaceutical has in fact concentrated in the target tissue of interest (usually tumor lesions) and to allow a posteriori calculation of the radiation dose to the target lesion (s) and to normal tissues/organs.

Therapeutic radiopharmaceuticals can be administered systemically through the i.v. route or orally, intracavitary, or even via the intra-arterial route. Although the focus of this chapter is on radionuclide therapy employed for treatment of various forms of cancer with either curative or palliation purposes, in some instances radionuclide therapy is utilized to reduce an organ's function (e.g., for hyperthyroidism).

Table 1 lists the most widely used radionuclides for labeling currently approved radiopharmaceuticals to be used in nuclear oncology and their main physical properties. Radiopharmaceuticals can be classified based on physical characteristics of the radionuclide (type and energy of the characteristic emissions, physical half-life) or

Table 1 Most widely used radionuclides and their main physical properties for approved therapeutic radiopharmaceuticals in oncology

Radionuclide	$T_{1/2}$	E_{max}/E_{mean} (MeV)	Emissions (main)	Max penetration in water (mm)
^{32}P	14.3 days	1.71/0.694	β^-	7.6
^{89}Sr	50.5 days	1.46/0.58	β^-	6.7
^{90}Y	64.1 h	2.28/0.937	β^-	11–11
^{131}I	8.02 day	0.606/0.18	β^-	2–4
		0.364	γ	
^{153}Sm	45.6 h	0.81/0.71	β^-	3.4
		0.103	γ	
^{177}Lu	6.71 days	0.5/n.a.	β^-	2
		0.113, 0.208	γ	
^{188}Re	16.8 h	2.12/0.76	β^-	11
		0.155	γ	
^{223}Ra	11.4 days	5–7.5	α^{++}	<0.01

Table 2 Main mechanisms of distribution/localization of radiopharmaceuticals used for therapeutic purpose.

Mechanism(s)	Rationale	Example
Mechanical trapping (capillary blockade)	The regional distribution of perfusion in an organ can be assessed by administering in the afferent blood vessel radiolabeled particles that, because of their large size (tens of μm), cause microembolization in the precapillary bed of an organ	^{90}Y-microspheres for treatment of liver tumors (intra-arterial)
Membrane transport: simple, facilitated, and active transport	Active, energy-dependent transmembrane transport of molecules against a concentration gradient: sodium-iodide symporter	^{131}I-ioide for the treatment of malignant or benign thyroid disease
Accumulation in intracellular, neurosecretory vesicles	ATPase-linked energy-dependent process physiologically utilized for the intracellular accumulation of noradrenaline	[^{131}I]MIBG for the treatment of neural-crest-derived neuroendocrine tumors
Non-receptor-mediated binding	Radiolabeled antibodies (whole antibodies or engineered minibodies) targeting specific antigen sites on the surface of tumor cells	^{90}Y-Ibritumomab tiuxetan (anti-CD20) for radioimmunotherapy of non-Hodgkin's lymphoma (NHL)
Receptor-mediated probes	The radiopharmaceutical competes with the physiologic ligands for binding with the target receptor	Somatostatin analogs used for neuroendocrine tumors as vehicles to guide radioactivity to tissues expressing somatostatin receptors
Ion exchange (chemisorption)	Exchange of ions between two electrolytes or between an electrolyte solution and a complex (binding to hydroxyapatite crystals or to amorphous calcium phosphate)	Bone-seeking, bisphosphonate-based radiopharmaceuticals for the treatment of metastatic bone disease

else on their physicochemical properties of the molecule (size, hydro- or lipophilicity, positive, negative, or neutral electrical charge) and mechanism of localization (Table 2).

Selection of the most appropriate radionuclide for any given therapeutic application should take into account the nature of the particulate radiations and their energies, physical half-life, and chemistry in relation to the carrier molecule (see also ▶ Chap. 2, "Principles of Molecular Targeting for Radionuclide Therapy" of this book). The possibility of deriving pretreatment dosimetric

estimates is also very important. The ionizing radiations with therapeutic potential involve β^- particle emitters, α-particle emitters, and emitters of Auger electrons. These radionuclides are linked to carrier molecules capable of (selectively) transporting the radiotracers to the target tissue. The main target for the biologic effects of ionizing radiation is DNA. Biologic response to ionizing radiation depends on many factors: cell radiosensitivity, localization of the radiopharmaceutical, and physical properties such as absorbed dose and linear energy transfer (LET) of the emitted radiation (see also ▶ Chap. 13, "Radiobiology and Radiation Dosimetry in Nuclear Medicine" of this book). The latter parameter, expressed in keV/μm, reflects energy deposition and, therefore, ionization density along the track of a charged particle. Any γ-emission possibly associated to the particle emission does not contribute to the effectiveness of therapy and may even lead to an increase of irradiation to nontarget tissues. Nevertheless, this emission can be exploited to obtain sequential scintigraphic images, therefore to determine the time course of in vivo localization of the radiopharmaceutical, to be used for radiation dosimetry calculations.

Alpha-Particle Emitters

Alpha particles are positive helium nuclei; their emission leads to a daughter nucleus with two fewer protons and two fewer neutrons than in the original radionuclide. These monoenergetic particles are usually emitted with high energy (5–8 MeV) and produce a high density of ionization along their short linear tracks of 40–100 μm, corresponding to about five to ten cell diameters. LET values of α-particles are typically in the 80–100-keV/μm range. Their biologic effect is independent of the oxygenation state or cell cycle phase, as their interaction with the cell nucleus results in single- and/or double-strand DNA breaks that are lethal per se for the cell. The tumoricidal effect is maximal if the α-particles are emitted within the cell nucleus. Despite the existence of over 100 α-emitting radionuclides, investigations on the therapeutic potential of α-particle emitters has focused mainly on five radionuclides (^{223}Ra, ^{211}At, ^{212}Bi, ^{213}Bi, and ^{225}Ac), because either the physical or chemical characteristics of the remainders are not appropriate for therapeutic use.

Radium-223 (^{223}Ra)

^{223}Ra (energy 5.7 MeV, half-life 11.4 days) for medical use is normally produced by a ^{227}Ac generator (half-life 21.8 years), with the intermediate decay step of thorium-227 (half-life 18.7 years); this system guarantees availability of the radionuclide for long periods. ^{223}Ra ultimately provides for the emission of four α-particles per decay. There are also minor associated emissions resulting in the production of β^- (3.6%) and γ (1.1%) radiations with different energies and emission probabilities. Administered as a chloride salt, the $^{223}Ra^{++}$ ion behaves in vivo as a calcium analog and has therefore bone-seeking properties that make this radionuclide useful for treating bone pain from skeletal metastases.

Auger Electron Emitters

Auger electrons are low-energy orbital electrons emitted after electron capture. Electron capture causes a vacancy, which is filled by electrons moving from an outer shell and thus initiating a cascade of electron transitions that shift the vacancy toward the outermost shell. Auger electrons have an extremely short path length in tissues (2–500 nm), with LET ranging from 4 to 26 keV/μm. Localization of the radionuclide within the cell, especially within the cell nucleus, is required to achieve cell killing, as mitochondrial or cell surface localization does not produce significant cytotoxic effects. Auger-electron emitters of radiobiologic interest include ^{67}Ga, ^{75}Se, ^{77}Br, ^{111}In, ^{125}I, ^{123}I, ^{165}Er, ^{197}Hg, ^{117m}Sn and ^{201}Tl.

Emitters of β^- Particles

Radionuclide therapy is presently based almost exclusively on radioisotopes emitting β^- particles. These negatively charged particles have low LET

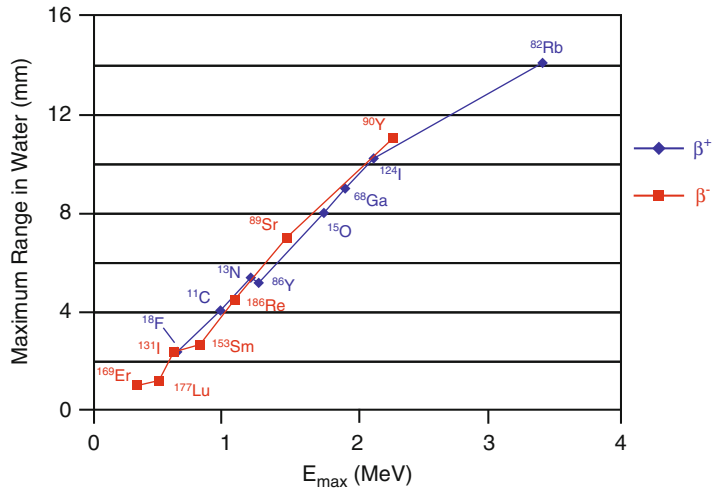

Fig. 1 Correlation between maximum energy (E_{max}, expressed in MeV) and maximum range in water of either β^+ or β^- particles emitted during decay of different radionuclides employed for either diagnostic purposes (β^+) or therapeutic purposes (β^-). Most of the energy deposited by each emission is nevertheless limited within a much shorter range (about 20–25% of the maximum range). The plot demonstrates that electrical charge does not influence the path of β particles, as the only determinant factors are mass and energy

(0.2 keV/μm) and a continuous spectrum of energy. After their emission, the daughter nucleus has one more proton and one less neutron than the original radionuclide. Their maximum path length in tissues ranges from 0.05 to 12 mm (at least for the radionuclides currently employed for therapy), depending on the energy of the particle (see Fig. 1). Therefore, optimal therapeutic activity requires a higher radionuclide concentration within the target tissue compared to α emitters, in order to obtain comparable radiobiologic efficacy. However, the longer path length in tissues results in the so-called crossfire effect, thus irradiating also the cells that have not directly accumulated the radionuclide (Fig. 2). This effect reduces the problems possibly caused by inadequate uptake and heterogeneous distribution of a given radiopharmaceutical within the target tissue.

Iodine-131 (^{131}I)

In addition to γ-rays, the radiohalogen ^{131}I (half-life 8.04 days) emits β^- particles with maximum energy of 0.61 MeV and a maximum path range of 2–4 mm in tissues (mean 0.7 mm). In the chemical form of ^{131}I-iodide, this radionuclide is extensively employed since several decades for treating benign and malignant thyroid diseases. Other therapeutic applications involve radiolabeling with ^{131}I of more complex molecules, such as MIBG or monoclonal antibodies. Incorporation of radioiodine is generally achieved through an oxidation reaction involving, for example, an OH^- radical in a tyrosine residue or a $-CH_3$ group; within certain limits (i.e., number of radioiodine atoms per molecule not to exceed 1), the resulting molecule of biologic interest has a metabolic fate very close to that of the native, unlabeled molecule, since the steric radius of the halogen atom is very similar to that of the hydroxyl or methyl groups.

Yttrium-90 (^{90}Y)

The radiometal ^{90}Y (half-life 64 h) emits high-energy β^- particles (2.2 MeV) with a maximum path length of 11–12 mm. This radionuclide is produced by the generator system ^{90}Sr/^{90}Y and decays to stable ^{90}Zr. Decay is associated with pair production of β^+ particles, although in a minimal proportion (32 β^+ particles per million decays). Radiolabeling of peptides and monoclonal antibodies requires the use of a bifunctional chelate, for example, DOTA or tiuxetan.

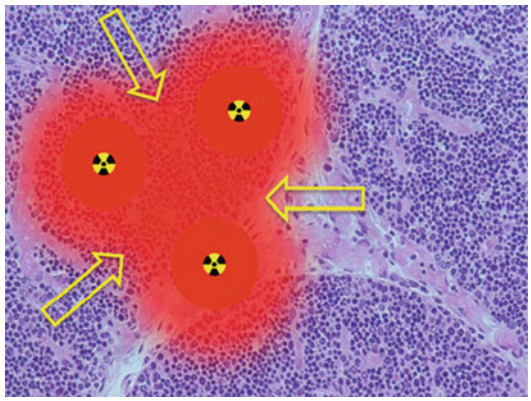

Fig. 2 Schematic representation of the so-called crossfire effect for particle-emitting radionuclides employed for therapy (assumed to be β^- particles for this representation). Because of delivery of energy within a certain range from the point of emission, the radiotoxic effect is not limited to the cells that specifically accumulate the radiopharmaceutical but also involves nearby cells (either they be neoplastic or tumor cells). In this representation, it is assumed that the radiopharmaceutical has accumulated at three specific locations within a tumor lesion (the uptake points are indicated by the radioactivity symbol). The *red* area with decreasing intensity from the center depicts the range in tissue along which the particles travel and deposit their energy, with maximum in the center and decreasing delivery of energy toward the periphery. The *arrows* indicate the tissue zones between the different radionuclide localization points; these are the cells exposed to the crossfire effect (From Volterrani D, Erba PA, Mariani G, eds. Fondamenti di medicina nucleare—tecniche e applicazioni. Milan (Italy): Springer; 2010, with permission)

There are currently three major clinical uses of ^{90}Y: to label a monoclonal antibody for radioimmunotherapy of lymphomas, bound to resin or glass microspheres for transarterial radioembolization of liver tumors, and to label somatostatin analogs for peptide receptor radionuclide therapy of neuroendocrine neoplasms. During radioimmunotherapy with ^{90}Y-tiuxetan-ibritumomab, the radiolabeled antibody binds to lymphocytes expressing the CD20 antigen, resulting in death of these cells. Treatment with ^{90}Y-tiuxetan-ibritumomab is approved for previously untreated follicular NHL that achieve a partial or complete response to first-line chemotherapy and relapsed or refractory, low-grade, or follicular B-cell NHL. Resin or glass microspheres containing ^{90}Y are approved forms of treatment for either primary or metastatic liver tumors, to be administered during selective or super-selective catheterization of the main or the segmental branches of the hepatic artery. Effective forms of peptide receptor radionuclide therapy of neuroendocrine neoplasms expressing somatostatin receptors has initially been based solely on the use of somatostatin analogs labeled with ^{90}Y, although more recently interest is also focusing on peptide analogs labeled with ^{177}Lu (see below). Regarding the use of ^{90}Y for therapy of non-tumoral diseases, ^{90}Y-colloid can be used for radiosynoviorthesis of the large joints.

Lutetium-177 (^{177}Lu)

The radiolanthanide ^{177}Lu (half-life 6.7 days) decays through the emission of β^- and γ-radiations. The β^- particles emitted by ^{177}Lu have a maximum energy of 0.49 keV and a maximum path range of 2 mm in water. The γ-emission has energy photopeaks of 113 keV (6.4%) and 208 keV (11%), which is suitable for imaging with conventional gamma cameras. Lutetium-177 is increasingly being used in patients for receptor-targeted radionuclide therapy with peptides such as DOTA^0-Tyr^3-octreotate. Other possible uses of ^{177}Lu include conjugation with bisphosphonates (e.g., ^{177}Lu-EDTMP), to produce a bone-seeking radiopharmaceutical for treatment of bone pain from skeletal metastases.

Samarium-153 (^{153}Sm)

This radiolanthanide is produced by neutron capture using a samarium target enriched in ^{152}Sm. Its physical decay half-life is 1.9 days, and it emits β^- particles with maximum energy of 0.81 MeV and maximum path range in water of approximately 3 mm. ^{153}Sm also emits γ-rays (103-keV photo peak) suitable for gamma camera imaging. The prevalent use of ^{153}Sm is in the chemical form of a radiolabeled diphosphonate (^{153}Sm-EDTMP; see Fig. 3a), which is employed in the clinical routine for treating osteoblastic bone metastasis.

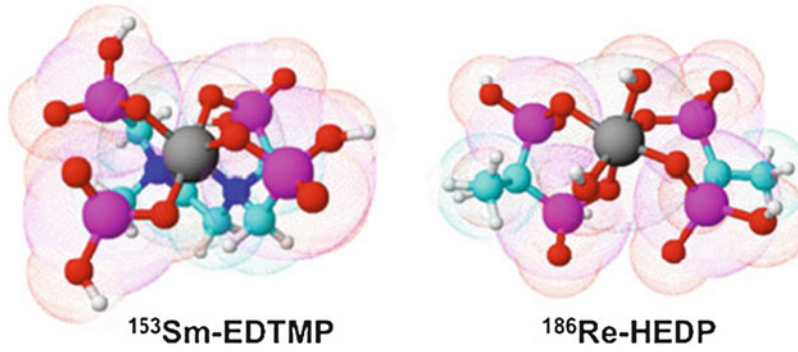

Fig. 3 Chemical structure of the radiolabeled bone-seeking bisphosphonates employed for palliation therapy of bone pain from skeletal metastasis. For simplicity of representation, the *gray* atom at the center of each 3-D structure represents the radionuclide (^{153}Sm for ^{153}Sm-EDTMP, ^{186}Re for ^{186}Re-HEDP). Other elements are represented with the following color codes: *red* = O, *white* = H, *fuchsia* = P, *light blue* = C, *dark blue* = N

Strontium-89 (^{89}Sr)

This alkaline earth metal radionuclide (half-life 50.5 days) is a pure emitter of β^- particles with a maximum energy of 1.46 MeV (average 0.58 MeV). The maximum path length in tissues of these β^- particles is 6–8 mm. Its current clinical use is for treatment of osteoblastic bone metastasis, in the simple chemical form of chloride salt; the $^{89}Sr^{++}$ behaves in vivo as a calcium analog and is therefore rapidly adsorbed on the newly formed bone mineral component, where it is retained with a physical half-life of 50.5 days.

Rhenium-186 (^{186}Re) and Rhenium-188 (^{188}Re)

Rhenium is a group VII metal with labeling chemistry properties similar to those of technetium; for this reason, its radioactive isotopes have attracted attention for the potential of directly translating to rhenium radionuclides the vast radiochemistry experience accumulated with ^{99m}Tc. Rhenium-186 is normally produced by direct neutron activation of metallic rhenium enriched with ^{185}Re via the ^{185}Re(n,γ)^{186}Re nuclear reaction; alternative routes through the ^{186}W(p,n)^{186}Re and the ^{186}W(d,2n)^{186}Re nuclear reactions yield no-carrier-added ^{186}Re. ^{186}Re (half-life 3.7 days) decays with the emission of β^- particles (maximum energy 1.09 MeV and path range 1–2 mm) and a low abundance (9%) of γ-ray (137 keV). Although also ^{188}Re (half-life 16.9 h) can similarly be produced in a thermal reactor through the ^{186}W(n,γ)^{188}Re nuclear reaction, the radionuclide for medical uses is more conveniently produced in the no-carrier-added form using a ^{188}W/^{188}Re generator; ^{188}W has a half-life of 69 days, thus making use of the generator especially convenient for immediate local availability of ^{188}Re on demand with the use of instant-labeling kits also in remote locations. ^{188}Re has maximum energy of 2.12 MeV and decays to stable ^{188}Os, with a γ-ray emission of 155 keV (15%).

These two radionuclides are currently used clinically for treatment of bone pain from skeletal metastases, after conjugation to diphosphonates (see Fig. 3b).

Phosphorus-32 (^{32}P)

Phosphorus-32 is a pure emitter of β^- particles (physical half-life of 14.3 days) with a maximum energy of 1.71 MeV (average 0.659 MeV). The maximum path length in tissues of these β^- particles is 8 mm. Treatment for ^{32}P in the chemical form of orthophosphate is indicated for palliation of bone pain from skeletal metastases, polycythemia vera, and essential thrombocythemia.

Treatment of Thyroid Disease with ^{131}I-Iodide

Iodine-131 is commonly administered as sodium iodide for treating thyroid disorders. The radioactive I^- ions present in the circulation and in interstitial fluid are transported into the thyroid cells by the sodium-iodide symporter (NIS), an active transport mechanism located on the basolateral membrane of thyroid follicular cells that allows entry of iodine into the cell against a concentration gradient, based on energy from the electrochemical gradient of sodium. Similarly as for other parameters of thyroid cell function and growth, the intracellular accumulation of iodine is regulated by serum TSH. Once inside the thyroid cell, iodine is oxidized by the enzyme peroxidase; this starts the organification process that enables to incorporate iodine (either native or radioactive) into tyrosine, an amino acid contained in the thyroglobulin molecules produced by the endoplasmic reticulum and Golgi apparatus. Molecules of monoiodotyrosine (MIT) and diiodotyrosine (DIT) are thus formed. These two chemical species are then combined to produce the thyroid hormones thyroxine (T4) and triiodothyronine (T3). Thyroid hormones are finally secreted into the circulation by pinocytosis, again following stimulation by TSH.

Although with a lower efficiency level, iodine ions are taken up also by other systems, such as the salivary glands, sweat glands, gastric glands, mammary gland, and the placenta. These physiological processes can induce unwanted side effects when using ^{131}I for high-dose therapy in patients with differentiated thyroid cancer, thus possibly causing sialoadenitis (sometimes with persistent xerostomia) and gastritis (with nausea and vomiting). ^{131}I uptake in the placenta and mammary gland would expose the fetus or the baby, respectively, to an unacceptable radiation dose.

^{131}I-iodide is commonly used both in benign thyroid diseases (such as hyperthyroidism in Grave's disease or multinodular goiter or hyperfunctioning Plummer's adenoma) and in malignant disease (differentiated thyroid carcinomas).

Although radiation safety regulations can vary from country to country, radioiodine treatment of hyperthyroidism is generally performed on an outpatient basis, after adequate preparation and dosimetric evaluations. Two methods are commonly used to select the amount of ^{131}I-iodide activities to be administered: (1) administration of a fixed activity based on clinical experience and (2) administration of an activity personalized on the basis of dosimetric calculations according to the target volume and radioiodine uptake of the individual patient. The aim of radioiodine therapy in hyperthyroid patients is to restore euthyroidism or, more commonly, to induce permanent hypothyroidism (which will then be treated with simple thyroid hormone replacement therapy).

The initial step in the treatment of differentiated thyroid carcinoma derived from follicular epithelium (papillary and follicular carcinoma) is thyroidectomy. After surgery, an ablative dose of ^{131}I-iodide is generally administered to patients with intermediate- to high-risk cancer, in order to eliminate any remaining thyroidal cells. Whole-body scintigraphy is then performed 4–7 days after administration of the high-dose amount of ^{131}I-iodide, based on the consistent γ-ray emission of ^{131}I. The images so obtained (often integrated with spot acquisitions – possibly with SPECT/CT) often enable to depict metastatic lesions not recognized at the time of surgery. In addition to ablation of the postsurgical thyroid residue, therapy with ^{131}I-iodide is also used for the treatment of locoregional recurrences and/or distant metastases.

Since the amounts of ^{131}I to administer for radioiodine therapy of patients with thyroid cancer vary from 1.1 to 7.4 GBq (30–200 mCi), in Europe this treatment requires hospitalization in specially equipped rooms for adequate handling of radioactive wastes. In the US, activities up to 200 mCi are usually outpatient procedures. Prior to therapeutic ^{131}I administration, patients are counseled by radiation safety. Patients are discharged when measurements of their radioactivity emissions fall below certain limits, which can vary according to local radiation safety regulations.

Early side effects of treatment with radioiodine are generally mild and usually do not require specific treatments. They consist of pain in the

anterior cervical region (caused by inflammation induced by the cytotoxic action of radioiodine), dysgeusia, anosmia, nausea, and vomiting. In 10–60% of cases, acute or chronic sialadenitis can occur, due to radioiodine accumulation in the salivary glands; it affects mainly the parotid gland, which is particularly rich in ductal cells. In order to prevent this occurrence, some precautions are recommended, such as abundant hydration and frequent stimulation of salivary flow (for instance, with lemon juice). Nausea (rarely vomiting) is the direct effect of some degree of radiation-induced gastritis, since the stomach is the first recipient of a highly concentrated amount of radioiodine; these side effects are prevented by pre-administration of metoclopramide and proton-pump inhibitors. Actinic cystitis (caused by the ionizing radiation due to the presence of urinary excretion of radioiodine in the urinary bladder) is rare and can be prevented by abundant hydration and frequent urination.

About 6 weeks after treatment, a reduction in the circulating levels of platelets and white blood cells can occur; nevertheless, this occurrence is very rare and usually transient if the absorbed dose to the bone marrow is maintained below 200 cGy. As to the long-term side effects of therapy with ^{131}I-iodide in the amounts utilized for patients with differentiated thyroid cancer, the induced risk of a second solid cancer or leukemia is very low, approximately in the same order of magnitude as that determined by other antineoplastic therapeutic approaches, such as chemotherapy.

As for all therapy with radionuclides, absolute contraindications to radioiodine treatment are pregnancy and lactation. Since the specific activity of the radiopharmaceutical used for therapy is very high (typically >200 MBq/μg), the amounts of iodine contained in a therapeutic dose of ^{131}I-iodide is considerably lower than the recommended daily dose in a normal diet. Thus, allergy to iodine is not considered a contraindication.

The administration of ^{131}I-iodide is generally performed orally (capsules or liquid solutions), while the intravenous administration is needed only in uncooperative patients or in case of uncontrolled vomiting; to facilitate and accelerate intestinal absorption, fasting should be observed for at least 6 h prior to and for 3 h after administration.

Treatment of Neuroendocrine Neoplasms Originating from the Neural Crest with [^{131}I]MIBG

Meta-iodobenzylguanidine (MIBG) or iobenguane is a catecholamine analog in which the iodinated benzyl group of bretylium is combined with the guanidine group of guanethidine (see Fig. 4). This molecule was developed in the early 1980s to visualize tumors of the adrenal medulla, and it can be labeled either with ^{123}I (for diagnostic use only) or with ^{131}I (for use either diagnostic or therapeutic applications).

Due to its structural analogy with catecholamines, MIBG is taken up by chromaffin cells through a physiologic active uptake mechanism via the epinephrine transporter used for noradrenaline accumulation in neurosecretory granules. MIBG is then secreted through an exocytosis mechanism following depolarization induced by high transmembrane flux of calcium ions. This accumulation process is abundantly expressed in the sympathetic ganglia, the adrenal medulla, and in all tissues with high adrenergic innervations (myocardium, salivary glands).

Tumors that typically accumulate this radiopharmaceutical are tumors originating from the neural

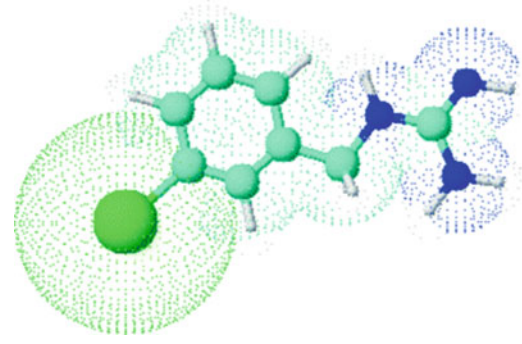

Fig. 4 Tridimensional representation of the chemical structure of radioiodinated *meta*-iodobenzylguanidine (MIBG). The *green* atom represents radioiodine. Other elements are represented with the following color codes: *white* = H, *light blue* = C, *dark blue* = N

crest. The main clinical applications of MIBG scintigraphy are therefore detection, localization, staging, and follow-up and response to treatments of NETs and their metastases, particularly in those of the sympathoadrenal system such as pheochromocytoma, paraganglioma, and neuroblastoma, although other neuroendocrine tumors such as medullary thyroid carcinoma and carcinoids can also be visualized. Diagnostic MIBG scintigraphy is crucial when planning treatment with high activities of [^{131}I]MIBG, to adequately select patients who will most likely benefit from such therapy.

For therapy, the radiopharmaceutical is usually administered through a slow i.v. injection (see further below). About half of the administered activity is excreted in the urine within the first day, 70–90% of the activity being cumulatively excreted within 2 days; therefore, the kidneys, the bladder, and the excretory urinary tract can be intensely visualized even in the late scans. About 3% of MIBG excretion occurs via the gastrointestinal tract.

The most important precaution in the preparation of patients for [^{131}I]MIBG therapy includes discontinuing drugs interfering with MIBG uptake (such as labetalol, tricyclic antidepressants, reserpine, and some sympathomimetic drugs) for an appropriate period before MIBG administration. These drugs can in fact interfere with and reduce MIBG uptake. Free radioiodine produced during in vivo [^{131}I]MIBG degradation can cause accumulation of radioactivity in thyroid and the gastrointestinal tract. Thyroid blocking using potassium iodide (KI) or lugol solution, also in combination with potassium perchlorate, is therefore necessary, generally starting 1 or 2 days prior to treatment and continuing for up to 14 days after treatment.

Administration of [^{131}I]MIBG must be performed very slowly (over 1–4 h after dilution in 50 mL of saline), because therapy dose levels involve injecting a sizable amount of a catecholamine analog that may induce the sudden release into circulation of catecholamines previously accumulated in neurosecretory granules, with possible pharmacologic effect (such as tachycardia, arterial hypertension, nausea, vomiting). For the same reason, the specific activity of [^{131}I]MIBG for therapy should be higher than that for diagnostic purpose (up to 1.8 GBq/mg), with the aim of reducing the incidence of pharmacologic effects.

The role of [^{131}I]MIBG therapy has been best defined in patients with pheochromocytoma and paraganglioma. In these patients symptomatic and biochemical improvements are frequently observed after treatment, while complete response rates are low. In neuroblastoma patients, [^{131}I]MIBG can be used with therapeutic intent, as good responses have been obtained in selected patients with advanced disease where first-line therapy failed. The response rates in these studies using single doses or large cumulative doses of [^{131}I]MIBG were between 25% and 46%. The actual benefit of multiple treatments is still debated. There is currently no consensus on the optimal dosing strategy. In patients treated with median activities of 10 GBq versus 5.5 GBq, higher activities seem to deliver the desired dose faster with a modest increase in toxicity but similar overall response rates.

Peptide Receptor Radionuclide Therapy

The biological basis of peptide receptor radionuclide therapy (PRRT) is the receptor-mediated internalization and intracellular retention of the radiopeptide, linked in turn to the overexpression of somatostatin receptors (SSTR) in most neuroendocrine neoplasms. The rationale for such therapy is to convey radioactivity inside the tumor cells, where the sensitive targets, such as DNA, can be hit as a result of internalization of the somatostatin receptor and radiolabeled analog complex.

The somatostatin analogs (ligands) that are currently in clinical use with the most promising results include DTPA-octreotide, DOTA-D-Phe^{1}-Tyr^{3}-octreotide (DOTA-TOC), DOTA-D-Phe^{1}-Tyr^{3}-octreotate (DOTA-TATE), and DOTA-lanreotide.

The macrocyclic chelator 1,4,7,10-tetraazacyclododecane-N,N′,N″,N‴-tetraacetic acid (DOTA) forms stable complexes with metallic isotopes such as ^{90}Y and ^{177}Lu. The DOTA-coupled somatostatin-based radiopharmaceuticals are ^{90}Y-DOTA-Tyr^{3}-octreotide (^{90}Y-DOTA-TOC), ^{90}Y-

DOTA-lanreotide, and ^{177}Lu-DOTA-Tyr^3-Thre^8-octreotide (^{177}Lu-DOTA-TATE). These compounds differ in their SSTR affinity profile. In particular, the DOTA-TATE derivative exhibits the highest affinity for SSTR2, while DOTA-lanreotide has highest affinity for SSTR5. Tyr^3-octreotide has similar kidney uptake (the dose-limiting organ) as Tyr^3-octreotate but faster renal clearance. Advantages of ^{177}Lu-DOTA-TATE over ^{90}Y-DOTA-TATE include the emission of an associated γ-radiation, which makes it possible to acquire conventional scintigraphic imaging for radiation dosimetry estimates; furthermore, the shorter tissue range of the β^- particles emitted by ^{177}Lu justifies the assumption that use of this radionuclide allows a higher radiation dose be delivered to smaller tumors. On the other hand, the use of ^{90}Y (which emits β^- particles with higher energies and longer tissue ranges) would be more suitable for the treatment of larger tumors, in case of bulky and/or heterogeneous masses.

These radiolabeled peptides are cleared through the kidneys, where they are and reabsorbed and partially retained in the proximal tubules, causing dose-limiting nephrotoxicity. Since residence times of DOTA-TATE in tumor and kidney are longer than those of DOTA-TOC, ^{177}Lu appears more beneficial when using DOTA-TATE for therapy, while ^{90}Y appears more convenient to label DOTA-TOC. The administration of L-lysine and/or L-arginine in order to competitively inhibit the proximal tubular reabsorption of the radiopeptide is now part of the clinical routine, to reduce the renal dose.

Tumor candidates for PRRT are basically all the somatostatin receptor-expressing tumors; scintigraphy with ^{111}In-pentetreotide is currently the most accurate and validated method to assess for the presence of SSTR overexpression. Nevertheless, it is likely that ^{68}Ga-DOTA-TOC and ^{6}8Ga-DOTA-TATE will become the new standard analogs, since they mimic as closely as possible the in vivo pattern of their ^{90}Y- or ^{177}Lu-labeled counterparts used for PRRT.

The radiopeptide that has been most extensively evaluated for PRRT is ^{90}Y-DOTA-TOC, with a recommended activity per cycle of about 5 GBq (cumulative activities: 13–18.5 GBq). Complete and partial remissions have been recorded especially in patients with gastrointestinal neuroendocrine tumors. Promising clinical results of PRRT with the newer radiopeptide ^{177}Lu-DOTA-TATE have been also obtained. More recently, a combination radionuclide therapy using ^{177}Lu- and ^{90}Y-labeled peptides has been proposed in order to improve efficacy in patients with tumors of various sizes and nonhomogeneous receptor distribution.

Other radiopeptide analogs are in less advanced stages of clinical validation. They include cholecystokinin (CCK8) and bombesin for GRP receptors expressed in prostate, breast, lung, and pancreatic cancers (^{188}Re(H_2O)$(CO)_3$-diaminopropionic acid-SSS-bombesin(7-14)NH_2 and ^{177}Lu-DOTA-8-Aoc-BBN[7-14]NH_2), arginine-glycine-aspartate (RGD) peptides to target $\alpha_v\beta_3$ receptors upregulated on tumor cells and neovasculature, glucagon-like peptide-1 (GLP-1), and melanocortin 1 receptor for various tumors.

Bone-Seeking Radiopharmaceuticals

Bone metastases are a frequent and serious complication in advanced stages of neoplastic disease, occurring in about 70% of patients with prostatic cancer or breast cancer and in 30–50% of those with cancers of the lung, bladder, and thyroid. The major complications associated with this condition are pain (initially mild to medium intensity, then increasing), hypercalcemia, radicular compression, and/or spinal cord and pathological fractures. Treatment of patients with pain from skeletal metastases should be based on a multidisciplinary approach, since it can include (in sequence or, sometimes, in association) external beam radiation therapy, surgery, chemotherapy, hormone therapy, pain-killing medications (from simple anti-inflammatory nonsteroidal drugs to opioids), bisphosphonates, and therapy with radiopharmaceuticals.

In patients with metastatic involvement of multiple skeletal segments (therefore not amenable to external radiotherapy and/or surgery), bone-seeking radiopharmaceuticals represent an important strategy for palliation of bone pain (in some cases also with survival benefits). All these agents bind to the mineral component of bone either

because they are calcium analogs or in a similar manner as any typical bisphosphonate agent labeled with ^{99m}Tc for diagnostic purposes, with increased uptake at the sites of active osteogenesis; thus primary bone tumors (osteosarcomas) as well as areas of metastatic involvement predominantly osteoblastic in nature (or of mixed type) can accumulate significantly greater concentrations of the radiopharmaceuticals than the surrounding normal bone. This treatment is therefore indicated in patients with multiple painful osteoblastic skeletal metastases exhibiting high uptake of ^{99m}Tc-labeled bisphosphonates confirmed on a conventional bone scan prior to therapy.

Besides the historical interest *^{32}P-sodium orthophosphate* (which is nevertheless still used in some low-income countries where other agents are not available), the bone-seeking radiopharmaceuticals currently available include strontium-89 chloride ($^{89}SrCl_2$), samarium-153 ethylenediamine tetramethylene phosphoric acid (^{153}Sm-EDTMP), rhenium-186 or rhenium-188 hydro-ethylidene diphosphate (^{186}Re- or ^{188}Re-HEDP), and radium-223 dichloride ($^{223}RaCl_2$). For all these agents, the dose-limiting toxicity is bone marrow suppression, which is generally reversible.

Upon administration of *$^{89}SrCl_2$* (Metastron®), the $^{89}Sr^{++}$ ions follow the same in vivo metabolic fate as calcium, with rapid incorporation into the inorganic matrix of bone. ^{89}Sr is quickly cleared from the blood and selectively localizes in bone mineral, with at least 50% of the injected activity localized in the skeleton within few hours post-administration. The unbound excretion pathways are two-thirds urinary and one-third through the fecal route. Urinary excretion is greatest in the first 2 days following administration. The recommended activity of $^{89}SrCl_2$ is 148 MBq (4 mCi) or alternatively 1.5–2.2 MBq/kg body weight.

^{153}Sm-EDTMP (Quadramet®) also accumulates avidly in the skeleton, where it remains adsorbed on the surface of the newly formed hydroxyapatite crystals. Osteoblastic metastatic lesions accumulate about fivefold more ^{153}Sm-EDTMP than does the healthy skeleton. Following i.v. administration (37 MBq/kg), ^{153}Sm-EDTMP is cleared rapidly from the blood with a half-life of 5.5 min; less than 1% of the administered activity remains in the circulation 5 h postinjection. Up to 55–60% of injected activity remains stably bound to the skeleton and accumulates in metastatic lesions in a 5:1 ratio compared with normal bone uptake. The main excretory route is through the kidneys. The onset of pain relief is generally noted within 2 weeks of radiopharmaceutical administration, with a mean duration of pain relief of 3–4 months; since the critical organ from the radiation dosimetry point of view is the bone marrow, a minimum interval of 8 weeks should be allowed between subsequent administrations in order to allow adequate recovery of bone marrow function.

^{186}Re-HEDP is cleared from the circulation with a relatively long half-life (41 h), since it undergoes some binding with plasma proteins. Its uptake in bone is due to conjugation with the hydroxyapatite crystals through a hydrolysis reaction, and its mean effective biological half-life in bone is about 16 h. About 70% of the administered ^{186}Re-HEDP (usually in a standard activity of 5 GBq) is excreted in the urine within 24 h.

As a calcium analog, *$^{223}RaCl_2$* (Xofigo®) shows a similar pattern of biodistribution as $^{89}SrCl_2$, less than 1% of injected activity remaining in the circulation 24 h after administration. Nevertheless, at variance with other bone-seeking radiopharmaceuticals, a non-negligible fraction of excretion occurs through the gastrointestinal tract and constitutes the basis for the reported gastrointestinal toxicity of this radiopharmaceutical. Each treatment cycle includes four to six administrations at 4-week intervals, and it has been recognized that therapy with $^{223}RaCl_2$ induces not only palliation of bone pain but also a significant benefit in survival. Since this is the latest radiopharmaceutical approved by regulatory agencies for therapy, a much more detailed discussion of the clinical observations that have led to this approval is presented in ▶ Chap. 8, "Novel Radiopharmaceuticals for Therapy" of this book.

Radioimmunotherapy for Hematologic Malignancies

The introduction of immunotherapy in the clinical routine has opened new opportunities for the treatment of some hematologic diseases. In fact,

antigens expressed on the surface of neoplastic cells (usually of the B lineage) are suitable targets for the development of monoclonal antibodies used for immunotherapy. In radioimmunotherapy (RIT), the cytotoxicity caused by an ionizing radiation is conveyed to the neoplastic cells through binding to tumor-specific antigens at the molecular level, a monoclonal antibody acting as carrier of a suitable radionuclide.

Efforts in the past 20 years have focused on the so-called molecular therapy to identify possible tumor antigens against which to address the monoclonal antibody. The selection of the appropriate antigen plays a key role for the efficacy of treatment. The ideal antigen should be densely and uniformly expressed on the surface of malignant cells (but not in normal cells), it should form a stable complex with the antibody, and the antigen/antibody complex should not be internalized (although the latter property is not so crucial).

Another important issue concerns the origin and structure of these antibodies; many monoclonal antibodies were in fact initially developed from murine cells, thus being intrinsically heterologous proteins with immunogenic activity when administered to humans. This immunogenicity is much lower for the chimeric antibodies (made up of components for 60% human and 40% murine) or for those humanized (with 95% of human components, while generally only the binding site for the antigen is murine) developed through genetic engineering techniques. In fact, the formation in the patient receiving these preparations of human anti-mouse antibody (HAMA), anti-chimeric (HACA), or anti-human (HAHA) can alter the pharmacokinetic profiles of the monoclonal antibody or predispose to allergic reactions during repeated administration. The monoclonal products currently used for the preparation of radiopharmaceuticals are characterized by greatly reduced immunogenicity compared to their initial products.

The radiolabeled anti-CD20 antibody ^{90}Y-ibritumomab tiuxetan (Zevalin®) has been approved for the treatment of relapsed or refractory, low-grade, or follicular B-cell non-Hodgkin's lymphoma (NHL) or treatment of previously untreated follicular NHL in patients who achieve a partial or complete response to first-line chemotherapy.

^{90}Y is chelated to tiuxetan, which is covalently linked to the antibody via arginine and lysine. The basis for therapy with ^{90}Y-ibritumomab tiuxetan is that CD20 antigen is expressed on the surface of normal B-lymphocytes (except pre-B cells and secretory B cells) and of more than 90% of B-cell lymphomas. Unlabeled monoclonal antibody (rituximab) is given as part of ^{90}Y-ibritumomab tiuxetan therapy in order to block CD20 antigens on normal B cells and spleen and to facilitate deeper penetration into the tumor. The unlabeled monoclonal antibody itself induces several mechanisms of tumor cell killing.

^{90}Y-ibritumomab tiuxetan is administered as a slow i.v. infusion over 10 min; the pharmacokinetics of ^{90}Y-Ibritumomab tiuxetan is characterized by a plasma half-life of 28 h. The administered activity is generally 15 MBq/kg body weight (0.4 mCi/kg), with a maximum limit of 1.2 GBq (32 mCi). In patients with mild thrombocytopenia (platelet count between 100.000 and 149.0000 per mm^3), the administered activity should be reduced to 11 MBq/kg (0.3 mCi/kg).

Dose-limiting toxicity for ^{90}Y-ibritumomab tiuxetan is bone marrow suppression, which is reversible. However, no statistically significant correlation was noted between the development of hematological toxicity and pharmacokinetic parameters of the compound.

Since ^{90}Y does not emit γ-rays (and on the other hand scintigraphic visualization of the secondary X-rays emitted by the reaction of Bremsstrahlung is not satisfactory), biodistribution can be evaluated by administering a diagnostic-level dose of the surrogate radiopharmaceutical ^{111}In-ibritumomab tiuxetan. The early images (up to about 24 h) typically show activity in the blood pool, with significant uptake in the liver and spleen, while accumulation in the lung and bone is generally low. Dosimetric studies have demonstrated an up to 850-fold greater radiation dose to the tumor lesions than to normal organs, and cumulative urinary excretion is only 7% of administered activity at 7 days post-administration.

Another monoclonal antibody (tositumomab) labeled with ^{131}I has been approved in the United States in 2003, with similar indications as Zevalin® in patients with non-Hodgkin's lymphomas.

^{131}I-tositumomab (Bexxar®) is specifically directed against a different epitope of the same CD20 surface antigen, and the reported response rate is about 70%. However, it has recently withdrawn from the market because of declining sales.

Radionuclide Therapy of Primary and Metastatic Liver Tumors

Liver tumors (both primary and metastatic) have always been considered a major cause of morbidity and mortality in oncologic patients. The treatment options are represented by surgical resection, liver transplantation, systemic chemotherapy, or locoregional treatments. The locoregional treatments consist of percutaneous ablative techniques (radiofrequency ablation, laser coagulation, cryotherapy, percutaneous ethanol injection) and transarterial methods, such as chemoembolization and radioembolization.

Early attempts at radionuclide therapy for primary or metastatic liver cancers began in the 1970s with the use of albumin colloids labeled with ^{32}P, under the rationale that radiocolloids administered systemically accumulate in the reticuloendothelial system, which is particularly abundant in the liver. This approach was soon abandoned due to significant bone marrow toxicity.

Transarterial radioembolization of liver tumors (also defined as "selective internal radiation therapy") can be performed using either ^{131}I-lipiodol or microspheres containing the β^- emitter ^{90}Y. ^{131}I-lipiodol, a mixture of iodized esters of poppy seed oil fatty acid, is still employed for treatment of hepatocellular carcinoma. The rationale for using transarterial ^{131}I-lipiodol is its entrapment and embolization in the microvessels of the tumor as well as endocytosis of this agent by the endothelial cells and the tumor cells themselves.

Nevertheless, this approach is most commonly based on the use of resin or glass microspheres containing ^{90}Y. The advantages of this type of therapy consist in the favorable toxicity profile and in the possibility to combine it with other forms of therapy (such as systemic chemotherapy or hepatic resection) without an increase in toxicity. The rationale for this therapy is radiomicroembolization of the hypervascularized tumor lesions in the liver, which receive their blood supply primarily from the hepatic artery, whereas the normal liver parenchyma receives blood primarily via the portal vein. Thus, microspheres injected into the hepatic artery (most commonly into the right or left hepatic artery – or even more selectively into the proper segmental artery) are trapped within the tumor microvasculature and deliver radiation selectively to the tumor liver lesion. The two types of ^{90}Y–microspheres currently available commercially (resin and glass microspheres) are biocompatible but not biodegradable nor metabolized.

^{90}Y-resin-based microspheres (SIR-Spheres®) are an acrylic polymer in which ^{90}Y is bound to the carboxylic group of the polymer after production of microspheres. They have a diameter size between 20 and 60 μm with a specific activity of 50 MBq per sphere. There are about 40–80 million microspheres per vial, with a total activity of 3 GBq, which can be subdivided to treat two or more patients. Because of their elevated number, resin microspheres used for this treatment may have a moderate embolic effect and must be delivered at a slow rate (no more than 5 mL/min) to avoid reflux down the hepatic artery and into other organs. The shelf-life of the device is 24 h, which restricts clinical flexibility and patient scheduling.

In the ^{90}Y-glass spheres (TheraSphere®), ^{89}Y is embedded in the glass matrix, to be activated to ^{90}Y in a nuclear reactor. Their medium diameter size is 20–30 μm, and the specific activity is 2,500 Bq per sphere. The number of ^{90}Y-glass spheres required for treatment ranges between 1.2 and 8 million, and the preparation is supplied in six sizes of activities: 3, 5, 7, 10, 15, and 20 GBq. The embolic effect linked to treatment with the glass ^{90}Y-microspheres is limited because a lower number of microspheres is injected intraarterially. They can be used also in patients with portal vein thrombosis. The shelf-life of the glass spheres is 15 days from the date of calibration; therefore, no physical manipulation is required to prepare the desired, patient-based activity for administration, which is obtained simply by letting a certain activity to decay to the desired level.

Suggested Readings

1. Baum RP, editor. Therapeutic nuclear medicine. New York: Springer; 2014.
2. Bodei L, Lam M, Chiesa C, Flux G, Brans B, Chiti A, Giammarile F, European Association of Nuclear Medicine (EANM). EANM procedure guideline for treatment of refractory metastatic bone pain. Eur J Nucl Med Mol Imaging. 2008;35:1934–40.
3. Bodei L, Mueller-Brand J, Baum RP, Pavel ME, Hörsch D, O'Dorisio MS, et al. The joint IAEA, EANM, and SNMMI practical guidance on peptide receptor radionuclide therapy (PRRNT) in neuroendocrine tumours. Eur J Nucl Med Mol Imaging. 2013;40:800–16.
4. Ell PJ, Gambhir SS, editors. Nuclear medicine in clinical diagnosis and treatment. 3rd ed. New York: Churchill Livingston; 2004.
5. Giammarile F, Bodei L, Chiesa C, Flux G, Forrer F, Kraeber-Bodere F, et al. EANM procedure guideline for the treatment of liver cancer and liver metastases with intra-arterial radioactive compounds. Eur J Nucl Med Mol Imaging. 2011;38:1393–406.
6. Giammarile F, Chiti A, Lassmann M, Brans B, Flux G, EANM. EANM procedure guidelines for ^{131}I-metaiodobenzylguanidine (^{131}I-mIBG) therapy. Eur J Nucl Med Mol Imaging. 2008;35:1039–47.
7. Haugen BR, Alexander EK, Bible KC, Doherty GM, Mandel SJ, Nikiforov YE, et al. 2015 American Thyroid Association management guidelines for adult patients with thyroid nodules and differentiated thyroid cancer: the American Thyroid Association guidelines task force on thyroid nodules and differentiated thyroid cancer. Thyroid. 2016;26:1–133.
8. Herbert JC, Eckelman WC, Neumann RD, editors. Nuclear medicine – diagnosis and therapy. New York: Thieme Medical Publishers; 1996.
9. IAEA. Good practice for introducing radiopharmaceuticals for clinical use. Vienna: International Atomic Energy Agency (IAEA); 2015.
10. IAEA. Operational guidance on Hospital radiopharmacy. Vienna: International Atomic Energy Agency (IAEA); 2008.
11. Knapp FF, Dash A. Radiopharmaceuticals for therapy. New Delhi: Springer; 2016.
12. Kowalsky RJ, Falen SW, editors. Radiopharmaceuticals in nuclear pharmacy and nuclear medicine. 3rd ed. Washington, DC: American Pharmacists Association; 2011.
13. Luster M, Clarke SE, Dietlein M, Lassmann M, Lind P, Oyen WJ, European Association of Nuclear Medicine (EANM), et al. Guidelines for radioiodine therapy of differentiated thyroid cancer. Eur J Nucl Med Mol Imaging. 2008;35:1941–59.
14. Owunwanne A, Patel M, Sadek S, editors. The handbook of radiopharmaceuticals. New York: Springer; 1995.
15. Schwochau K, editor. Technetium: chemistry and radiopharmaceuticals. Hoboken: Wiley; 2000.
16. Silberstein EB, Alavi A, Balon HR, Clarke SEM, Divgi C, Gelfand M, et al. The SNM practice guideline for therapy of thyroid disease with ^{131}I 3.0*. J Nucl Med. 2012;53:1633–51.
17. Stokkel MP, Handkiewicz Junak D, Lassmann M, Dietlein M, Luster M. EANM procedure guidelines for therapy of benign thyroid disease. Eur J Nucl Med Mol Imaging. 2010;37:2218–28.
18. Tennvall J, Fischer M, Bischof Delaloye A, Bombardieri E, Bodei L, et al. EANM procedure guideline for radioimmunotherapy for B-cell lymphoma with ^{90}Y-radiolabelled ibritumomab tiuxetan (Zevalin). Eur J Nucl Med Mol Imaging. 2007;34:616–22.
19. Theobald T, editor. Sampson's texbook of radiopharmacy. 4th ed. London: Pharmaceutical Press; 2010.
20. Welch MJ, Redvanly CS, editors. Handbook of radiopharmaceuticals: radiochemistry and applications. Hoboken: Wiley; 2003.

Novel Single-Photon-Emitting Radiopharmaceuticals for Diagnostic Applications

6

Federica Orsini, Federica Guidoccio, Erinda Puta, and Giuliano Mariani

Abstract

The armamentarium of approved radiopharmaceuticals for either diagnosis or therapy is at the core of the clinical practice of today's nuclear medicine. Nevertheless, both because the currently approved agents do not meet all the clinical needs for radionuclide targeting and because advancing knowledge in the pathophysiology of tissues/organs open in turn new opportunities, investigations continue at the preclinical and clinical validation level for the development of new radiopharmaceuticals, most of which are not approved yet for commercial use. Concerning in particular the diagnostic applications of nuclear medicine to oncology, ongoing investigations in the search for tumor-targeting agents with better specificity and sensitivity are countless, possibly within the scenario of theranostics – that is, with the dual potential for imaging and for therapy, depending on the specific radionuclide employed for radiolabeling. We will focus this chapter on the most promising imaging agents labeled with single-photon-emitting radionuclides based on some of the mechanisms that are typical for tumor cells/tissues.

Keywords

Cancer biology • Molecular imaging in cancer • Single-photon emission imaging • Radiopharmaceuticals

Glossary

BTAP	Bis(thioacetamido)pentanoyl
DOTA	2-(4-Isothiocyanatobenzyl-1,4,7,10-tetraazacyclododecane-1,4,7,10-tetra-acetic acid (macrocyclic coupling agent to label compounds of biological interest with metal radionuclides)
DTPA	Diethylenetriaminepentaacetic acid
EGF	Epidermal growth factor
EGFR	Epidermal growth factor receptor
FDA	United States Food and Drug Administration
GMP	Good manufacturing practice
HER	Human epidermal growth factor receptor
HPLC	High-performance liquid chromatography (formerly known as high-pressure liquid chromatography)
HYNIC	6-Hydrazinopyridine-3-carboxylic acid, also known as hydrazido-nicotinic acid/hydrazinonico-tinamide (a chelating agent)
MMP	Metalloproteinases, a family of matrix enzymes

F. Orsini (✉) • E. Puta
Nuclear Medicine Unit, "Maggiore della Carità" University Hospital, Novara, Italy
e-mail: federica.orsini@maggioreosp.novara.it; erinda.puta@maggioreosp.novara.it

F. Guidoccio • G. Mariani
Regional Center of Nuclear Medicine, Department of Translational Research and Advanced Technologies in Medicine and Surgery, University of Pisa, Pisa, Italy

© Springer International Publishing Switzerland 2017
H.W. Strauss et al. (eds.), *Nuclear Oncology*,
https://doi.org/10.1007/978-3-319-26236-9_3

MRI	Magnetic resonance imaging
NIRF	Near-infrared fluorescence
PET	Positron emission tomography
RGD	Tripeptide composed of L-arginine, glycine, and L-aspartic acid (a sequence that is a common element in cellular recognition)
SPECT	Single-photon emission tomography
TGF	Transforming growth factor
TKI	Tyrosine kinase inhibitor
TPPTS	3,3,3”-Phosphanetriyltris (benzenesulfonic acid) trisodium salt, a ligand also known as sodium triphenylphosphine trisulfonate
VEGF	Vascular endothelial growth factor

Contents

Introduction and Background 116

Peptide Receptor Targeting 117

Apoptosis 117
^{99m}Tc-Annexin V 117
^{99m}Tc-Duramycin 118

Angiogenesis 119

Integrins 120
^{99m}Tc-αP2 120
^{99m}Tc-NC100692 (or ^{99m}Tc-Maraciclatide) 120
^{99m}Tc-3PRGD$_2$ 120
^{99m}Tc-RGD-BBN 121
Hybrid Radioactive/Fluorescent RGD 121

Extracellular Matrix 121
^{99m}Tc-AP39 121

Matrix Metalloproteinases 122

Epidermal Growth Factor Receptor (EGFR) 122

Folate Receptor Overexpression 123

References 123

Introduction and Background

The armamentarium of approved radiopharmaceuticals for either diagnosis or therapy is at the core of the clinical practice of today’s nuclear medicine. Nevertheless, advancing knowledge in the pathophysiology of tissues/organs opens new opportunities, for the development of new radiopharmaceuticals, most of which are not approved yet for commercial use. There is an ongoing search for tumor-targeting agents with better specificity and sensitivity. There are many new developments of agents with the dual potential for imaging and for therapy, depending on the specific radionuclide employed for radiolabeling [1–3].

Tumor cells and tissues exhibit different characteristics compared to normal cells and due to the altered physiology, tissue composition, and expression of intra- and extracellular molecules [4, 5]. These attributes can be the basis for developing new imaging targets for diagnostic applications as well as for developing new anticancer drugs and for assessing tumor response to treatment [6–9] (see also ▶ Chaps. 1, “Cancer Biology of Molecular Imaging,” and ▶ 2, “Principles of Molecular Targeting for Radionuclide Therapy” of this book).

Single-photon-emitting radiopharmaceuticals can be classified according to different properties, such as their biodistribution and targeting characteristics, their different chemical and physical properties, and their specific interaction with a target. Tumors are known to display an aberrant vascular network and microcirculation, which in turn influence an increase in interstitial pressure, as well as hypoxia and acidosis; all these features contribute to the expression of malignant phenotypes and to resistance to various treatments [10]. Within this environment, tumor cells can also display altered energy metabolism, as reflected, for example, in increased glucose uptake and shifted balances in metabolic products.

Thus, at the preclinical level, a variety of single-photon-emitting tracers are under evaluation for use as markers for (neo)angiogenesis [11–13], hypoxia [14, 15], acidosis [16], metabolic activity [17], and proteolytic activity [18, 19]. Besides metabolic tracers, efforts are being directed also toward the development and validation of single-photon probes specific for tumor target molecules such as cell surface antigens, receptors, or other molecules similarly overexpressed in tumor tissues [20]. The use of peptides interacting with receptors [21], of antibodies or antibody fragments targeting different epitopes of tumor-associated antigens [22], of vitamin-based radiopharmaceuticals [23], and of

nucleoside analogs [24–27] significantly increases the possibilities for tumor detection, localization, and staging. Specific issues of interest in translational preclinical imaging studies include efforts directed at improving specificity for tumor types [28], tumor uptake/retention [29], yet with minimal pharmacological effects of the imaging probes.

The successful choice of a target molecule potentially leads to the development not only of a molecular imaging probe but also of a therapeutic agent capable to inhibit the disease process – according to the approach of theranostics. Receptor targeting with small radiolabeled peptides for receptor-targeted tumor imaging (PET and SPECT) as well as for radionuclide therapy provides good examples of such theranostics potential.

Peptide Receptor Targeting

The best-known examples of this tumor-targeting mechanism are based on the use of somatostatin analogs. For imaging purposes either single-photon-emitting radionuclides (chiefly ^{111}In) or positron-emitting radionuclides (chiefly ^{68}Ga) are used in the clinical routine. For therapeutic purposes, different β^--emitting radionuclides (chiefly ^{90}Y and ^{177}Lu) are currently being used clinically or undergoing extensive validation; although the chief indications for the use of these radiopharmaceuticals regard neuroendocrine neoplasms (see ▶ Chaps. 29, "Diagnostic Applications of Nuclear Medicine: Neuroendocrine Tumors," and ▶ 43, "Neuroendocrine Tumors: Therapy with Radiolabeled Peptides" of this book), the indications for the use of these tracers, with either diagnostic or therapeutic purposes, are expanding to other tumors as well. Thus, the radiolabeled somatostatin analogs are prototypes for a whole spectrum of other peptide receptor systems that are overexpressed in a variety of tumors. The common feature shared by all these systems is that they are members of the so-called G-protein-coupled receptor superfamily and play a major role in the progression and angiogenesis of a number of malignancies.

Briefly, the peptide ligands that have yielded the most promising results so far are the analogs of bombesin, of cholecystokinin, of the vasoactive intestinal peptide, of gastrin, of glucagon, of substance P, of exendin, and of the α-melanocyte-stimulating hormone [30–36]. The use of the so-called RGD-based peptides for targeting the integrin receptor system (another member of the G-coupled family) is discussed further below in this chapter.

Apoptosis

Apoptosis is a process of regulated or programmed cell death, which in its classic form, does not cause inflammation. The mitochondria and ribosomes of the cells undergoing apoptosis remain intact, and surrounding cells internalize them along with the other components of the post-apoptotic cell. Necrotic cells, in contrast, lose membrane integrity, swell, and then release their contents to the surrounding tissue, causing inflammation and possibly initiating an immune response.

Lipid composition of the outer and inner leaflets of the plasma membrane is normally not symmetrical; for instance, some molecules such as phosphatidylserine and phosphatidylethanolamine are normally retained on the intracellular face of the cell membrane. When cells undergo apoptosis, this distribution is altered, so that these molecules are rapidly exposed to the outside of the cell membrane. The most promising single-photon-emitting radiopharmaceuticals targeting phosphatidylserine and phosphatidylethanolamine are represented by radiolabeled annexin and duramycin, respectively.

^{99m}Tc-Annexin V

The discovery of phosphatidylserine externalization as the event initiating apoptosis has opened the way to the search for compounds that have an affinity for phosphatidylserine and could therefore be used to localize in sites of apoptosis. To date, the compound that has received major interest in both the preclinical and clinical arena is annexin V, a non-glycosylated single-chain protein physiologically involved in the inhibition of hemostasis [37]. Annexin V, which is part of a protein family that binds to negatively charged

phospholipids in a Ca^{2+}-dependent manner, is distributed ubiquitously in the human body. Complete functional details of the annexin V pathway have yet to be clarified, but a large body of evidence suggests that annexin acts as a specific ligand for phosphatidylserine, and it is able to prevent activation of the immune response when cells undergo apoptosis [38].

In translational research, annexin V labeled with radionuclides has been used for studying, localizing, visualizing, and measuring apoptosis in vitro as well as in vivo, both in preclinical animal models and in patients [39, 40]. Radiolabeled annexin was first proposed to image blood clots in patients with atrial fibrillation; subsequently this compound gained attention for imaging of apoptosis in tumors [41]. Annexin V used for development of radiolabeled imaging agents is produced by the expression of annexin V complementary DNA in *Escherichia coli*. Several radiolabeled probes and other agents bearing different moieties have been explored preclinically to image annexin V uptake by means of SPECT, PET, MRI, and near-infrared fluorescence (NIRF).

As single-photon imaging probes, numerous methods for labeling annexin with ^{99m}Tc have been identified through the use of chelators such as the bifunctional N_2S_2 chelate to form ^{99m}Tc-4,5-bis(thioacetamido)pentanoyl-annexin V (or ^{99m}Tc-BTAP-annexin V, also known as ^{99m}Tc-Apomate) or hydrazinonicotinamide (HYNIC) to form ^{99m}Tc-HYNIC-annexin V. The former formulation is also available as a good manufacturing practice (GMP) product in a radiolabeling kit [42].

Moreover, animal experiments suggest an improved protocol for annexin labeling via the use of self-chelating annexin V mutants. In this case, the radiotracer exhibits reduced abdominal background and decreased renal radiation dose [43]. At the clinical level, various studies support the notion that ^{99m}Tc-annexin V SPECT allows for noninvasive, reproducible, quantitative apoptosis imaging and for assessing tumor response as early as 24 h after the start of treatment, with the goal of monitoring the effectiveness of therapy in cancer patients. With pioneering work, Belhocine et al. used ^{99m}Tc-BTAP-annexin V to monitor chemosensitivity in a variety of cancer types (e.g., lung cancer, lymphoma, and breast cancer), demonstrating that ^{99m}Tc-BTAP-annexin V uptake after chemotherapy was significantly related to survival and progression-free survival in cancer patients [44].

More recently ^{99m}Tc-annexin V has been probed in clinical studies to assess the efficacy of chemotherapy and radiotherapy [45, 46]. The promising results so far obtained offer the possibility also in this scenario to develop a personalized medicine approach, now primarily explored in genome-based medicine, applicable to all cancer patients.

However, the main problems in a wide clinical application remain the absence of ideal biological properties; experiences with radiolabeled annexin V have indicated that issues such as biodistribution and target-to-background ratio require further improvement [47]. In an attempt to reduce renal uptake, annexin V was also labeled with ^{123}I. ^{123}I-annexin V does indeed show good imaging features for imaging the abdominal region compared to ^{99m}Tc compounds (no liver nor renal radioactivity accumulation 12-h post-injection) but is subject to rapid in vivo dehalogenation and is more expensive, and the labeling procedure is more complex [48].

^{99m}Tc-Duramycin

Duramycin, a 19-amino acid peptide cross-linked by a disulfide bond, has been found to be capable of binding to phosphatidylethanolamine with high affinity and high selectivity; therefore, the radiolabeled ^{99m}Tc-duramycin represents now a novel molecular compound for apoptosis imaging [49].

Similar to phosphatidylserine (the target marker of the earliest apoptosis probe, annexin V), phosphatidylethanolamine is a major component of the inner leaflet of the cell membrane, and its expression on the surface of normal viable cells is extremely low [50–52]. When apoptosis occurs, phosphatidylethanolamine is exposed on the cell surface [53], because of redistribution of phospholipids across the bilayer. Phosphatidylethanolamine becomes accessible to the extracellular milieu during necrosis, because of the

compromised plasma membrane integrity. Thus, phosphatidylethanolamine constitutes a potential target molecule for cell death imaging in general.

Phosphatidylethanolamine expressed on the apoptotic cell surface appears to play a regulatory role in the so-called blebbing and formation of apoptotic bodies. In these constitutive processes of apoptosis, intracellular components are discretely packaged and earmarked for engulfment by scavenger cells without causing inflammation. As one of the morphologic hallmarks of apoptosis, blebbing includes profound membrane structural remodeling. The trans-bilayer movement of phosphatidylethanolamine is especially enhanced on the blebs of apoptotic cells. These morphologic changes are in part attributed to the phosphatidylethanolamine-mediated reorganization of actin filaments [54, 55].

As a novel molecular probe to target apoptosis imaging, duramycin is produced by *Streptoverticillium cinnamoneus* [56, 57]. Biologic activities of duramycin have been well characterized, and their phosphatidylethanolamine binding activity explored with in vitro biologic studies [58–62]. In particular, duramycin binds the head group of phosphatidylethanolamine with high affinity at a molar ratio of 1:1 [63–65]. Duramycin has a compact cyclic configuration, with a single binding pocket that specifically interacts with phosphatidylethanolamine. Stabilized by three internal thioether bonds, duramycin is the smallest known polypeptide that has a defined three-dimensional binding site [56, 57].

In 2008, Zhao et al. originally described the preparation of ^{99m}Tc-labeled duramycin, using a HYNIC ligand with tricine and phosphine as coligands [66]. The low molecular weight of duramycin (~2 kDa) confers favorable pharmacokinetics and biodistribution properties for in vivo imaging of apoptosis. However, in the original formulation, HPLC purification after radiolabeling was a prerequisite for intravenous injection in humans, a cumbersome procedure that limited clinical investigations. The goal to produce high-quality ^{99m}Tc-curamycin in a single-step kit formulation, without additional purification steps, was achieved in 2012 by Zhao and coworkers, with the development of a single-step kit formulation for ^{99m}Tc-labeling of HYNIC-duramycin [67]. An optimal formulation with tricine-to-TPPTS molar ratio of 10:1 was determined, which led to consistent production of high radiochemical purity ^{99m}Tc-duramycin without the need for further purification. The radiopharmaceutical so produced retained phosphatidylethanolamine binding affinity and specificity, while its clearance properties and in vivo biodistribution were consistent with those obtained in prior studies using radio-HPLC-purified preparation.

In a rat model of myocardial ischemia/reperfusion injury, ^{99m}Tc-duramycin showed specific higher uptake in apoptotic cells than in viable control cells, with favorable pharmacokinetic and biodistribution profiles. The tracer was rapidly cleared from the circulation via the renal system with a blood half-life of less than 4 min in rats and a very low liver and gastrointestinal uptake [67, 68]. Similar favorable targeting and biodistribution properties have been observed also in a porcine model of myocardial ischemia/reperfusion, showing high accumulation of ^{99m}Tc-duramycin in tissue sites of injury with high apoptotic activity [69]. In addition, ^{99m}Tc-duramycin has been evaluated for imaging ischemia/reperfusion injury in the brain using the rat model of middle cerebral artery occlusion [70], as well as in a model of oxidative lung injury [71–73], and finally in susceptible tissues after exposure to high-dose radiation [74].

Taken altogether, these investigations suggest the high potential of ^{99m}Tc-duramycin for use in oncology, an assumption that has recently been confirmed by preclinical studies demonstrating high specific uptake of ^{99m}Tc-duramycin in apoptotic cells of colon cancer or breast cancer xenografts responding to chemotherapy [75–77], thus supporting the hypothesis that ^{99m}Tc-duramycin is a potential candidate in cancer patients to assess response to therapy.

Angiogenesis

The formation of the new vessels ("angiogenesis") is an essential process in the growth of solid tumors. Once tumors have reached a size of >1 mm^3, diffusion alone from the capillary bed is no longer sufficient to supply the tumor cells with

adequate amounts of oxygen and nutrients. Further tumor growth is only possible when new blood vessels are formed. Nevertheless, while normal angiogenesis is orderly and highly regulated, tumor angiogenesis is chaotic and irregular. Angiogenesis represents an interesting molecular target not only for imaging but also for targeted forms of therapy. Examples for target anti-angiogenic therapies currently used in the clinical practice are cilengitide (that inhibits integrin receptors $\alpha_v\beta_3$ and $\alpha_v\beta_5$) and bevacizumab, an antibody targeting the vascular endothelial growth factor (VEGF).

Different potential molecular targets to monitor angiogenesis are potentially available for imaging purposes. At the moment the most suitable candidates for tracer development are represented by integrin antagonists, expressed extracellular matrix protein inhibitors or matrix metalloproteinase, as well as by tracers binding to tyrosine kinases or growth factor receptors.

Integrins

Integrins are heterodimeric membrane receptors constituted by α and β subunits that mediate interactions between cells and the extracellular matrix and soluble molecules (such as growth factors). So far 18 different α and 8 different β subunits have been identified, corresponding to 24 different integrin receptors. Integrin $\alpha_v\beta_3$ is one of the most studied in oncology, because it is highly expressed on the cell surface of activated endothelial cells in newly formed blood vessels. In the preclinical setting, a large variety of imaging strategies have been successfully employed for imaging integrin expression.

All the tracers that are used for imaging of integrin expression are based on the tripeptide sequence arginine-glycine-aspartic acid (or RGD in the single letter code) [78]. RGD binds to the integrin containing the α_v subunit, which represents an abundant physiologic integrin-binding ligand in proteins of the extracellular matrix. Accordingly, a variety of radiolabeled RGD-based peptides have been developed for noninvasive imaging of integrin $\alpha_v\beta_3$ expression with either SPECT or, in most of the cases, PET. The ^{99m}Tc-labeled RGD peptides have been the subject of few investigations, and few peptides have been translated into clinical use, such as ^{99m}Tc-NC100692 and ^{99m}Tc-labeled RGD dimeric peptides with PEG_4 and Gly_3.

^{99m}Tc-αP2

This 10-amino acid ^{99m}Tc-peptide first described in 1988 contains two copies of the RGD motif for integrin-specific binding. It has been tested in a clinical study in a patient with malignant melanoma, resulting in a good detection rate of metastases in the neck, axilla, abdomen, and soft tissue 60–120 min after injection; however, sensitivity was somewhat lower for lesions located in the thorax, due to high blood pool activity in the heart and large vessels [79].

^{99m}Tc-NC100692 (or ^{99m}Tc-Maraciclatide)

^{99m}Tc-NC100692 is a new RGD-containing peptide labeled with ^{99m}Tc that binds to integrin $\alpha_v\beta_3$ with high affinity [80]. Clinical studies in patients with breast and lung cancer showed a good detection rate for malignant lesions greater than 1 cm, in the breast, brain, and lung, whereas the detection rate was considerably lower for bone and liver metastases [81–83].

On the other hand, in the scenario of theranostics, some investigators confirm that ^{99m}Tc-NC100692 does target the $\alpha_v\beta_3$ integrin in mice bearing glioma tumors and may, therefore, be useful for identifying patients prior to anti-$\alpha_v\beta_3$ therapy as well as for monitoring tumor response to antiangiogenetic therapy in these patients [84].

^{99m}Tc-3PRGD$_2$

^{99m}Tc-PEG_4-E[PEG_4-c(RGDfK)]$_2$ (or ^{99m}Tc-3PRGD$_2$) is a new single-photon tracer targeting

the integrin $\alpha_v\beta_3$-receptor and has been used preclinically for tumor imaging, for evaluating angiogenesis, and for monitoring antiangiogenic drug efficacy [85, 86].

The new types of RGD peptides show much higher in vitro integrin $\alpha_v\beta_3$-binding affinity than the single RGD tripeptide sequence and exhibit significantly increased tumor uptake and improved in vivo kinetics in animal models. ^{99m}Tc-3PRGD2 is excreted predominantly by the kidneys and has a rapid blood clearance, with less than 1% of the initial radioactivity remaining in the blood circulation at 60 min after injection. No adverse reactions have been observed in animal models or in humans to date. ^{99m}Tc-3PRGD$_2$ can easily be prepared in a kit formulation and has shown excellent in vivo patterns of biodistribution in nonhuman primates [87].

Recently, ^{99m}Tc-3PRGD$_2$ has been used in patients, in particular for characterizing solitary pulmonary nodules [88], as well as palpable and nonpalpable breast lesions [89]. It has also been used with satisfactory results in patients with lung cancer [90], in patients with iodine-refractory thyroid cancer [91], for imaging bone metastases in patients with lung cancer (versus the conventional ^{99m}Tc-MDP bone scan) [92], and for monitoring the response to treatment with antiangiogenetic therapy in a mouse model of glioma [93].

^{99m}Tc-RGD-BBN

A dual receptor-targeted probe, integrin $\alpha_v\beta_3$ and gastrin-releasing peptide receptor (GRPR)-targeted peptide, Glu-c(RGDyK)-bombesin (RGD-BBN) labeled with technetium-99m (^{99m}Tc-RGD-BBN), has been tested with promising results in an animal model [94] and then with pilot studies in humans. In particular, its biodistribution has been evaluated in healthy volunteers (exhibiting a safe profile) and in patients with breast cancer as a novel agent for scintimammography. In this clinical setting, ^{99m}Tc-RCD-BBN has shown excellent properties for tumor detection [95], with the potential of avoiding surgical biopsy in patients with equivocal breast lesions, thanks to its very high negative predictive value for malignancy [96].

Hybrid Radioactive/Fluorescent RGD

^{111}In-labeled RGD has been coupled with a fluorescent dye to produce a hybrid tracer, with the purpose of allowing visualization of tumor margins during surgery as well as the in vivo detection of the tumor and its distant metastases. Only very preliminary preclinical studies have been performed so far with this new hybrid tracer, which appears to exhibit optimal properties for targeted $\alpha_v\beta_3$ integrin detection, with very high tumor-non-tumor ratios [97].

Extracellular Matrix

Fibronectin is a polymorphic matrix protein belonging to the widely distributed family of universal cell-adhesion molecules. Fibronectin can exist in several isoforms implied in a variety of processes such as cell migration, wound healing, and oncogenic transformation. A particular isoform (the splicing variant ED-B) is important in vascular proliferation and is widely expressed in neoplastic tissues while showing a highly restricted distribution in normal tissues [98].

^{99m}Tc-AP39

The ^{99m}Tc-anti-ED-B fibronectin L19-(Gly)$_3$-Cys-Ala scFv antibody fragment (^{99m}Tc-AP39) is a radiolabeled molecular imaging agent developed for single-photon emission imaging of tumor angiogenesis and for guidance during antiangiogenic treatment for tumors.

The single-chain antibody fragment (scFv) derived from the L19 monoclonal antibody (with a high affinity to ED-B fibronectin) was developed by Pini et al. [99] and initially labeled with radioiodine for biodistribution in different animal models, where it exhibited excellent targeting to tumor vessels, without selective accumulation in the vessels of other organs [100].

In order to prepare a stable ^{99m}Tc-labeled L19 fragment, Berndorff et al. [101] inserted the amino

acid sequence $(Gly)_3$-Cys-Ala at the C terminus of L19 to produce the recombinant protein, AP39. These authors demonstrated that the ^{99m}Tc-labeled compound so formed (^{99m}Tc-AP39) has favorable biodistribution and imaging properties in mice bearing a murine embryonal teratocarcinoma. Since high levels of ED-B expression have been found in a variety of cancers including primary and metastatic breast, colorectal, and non-small cell lung cancers [102–104], this anti-fibronectin tracer has the potential of being useful for noninvasive imaging of tumor angiogenesis in all such cancers, virtually as a pancarcinoma-targeting agent.

Besides the potential for tumor targeting with imaging purposes as described above, the very high uptake of the anti-fibronectin ED-B monoclonal constructs in tumor tissues opens promising perspectives for developing new agents for radioimmunotherapy, as described in details in ► Chap. 8, "Novel Radiopharmaceuticals for Therapy" of this book.

Matrix Metalloproteinases

Due to their involvement in tumor metastasis and angiogenesis, the matrix metalloproteinases (MMP) are potential targets for molecular imaging. The MMP family consists of more than 18 different members, with levels in tissues that are controlled by a balance between synthesis of the proenzyme and expression of endogenous MMP inhibitors [105]. Increased proenzyme production causes degradation of the basement membrane and of the extracellular matrix, thus preparing the structural requirements for migration of endothelial cells and formation of vessels [106]. In particular, the MMP-2 and MMP-9 gelatinases are often detected in malignant tissue, and their overexpression correlates with tumor aggressiveness and metastatic potential. Ongoing investigations aim at developing synthetic compounds for targeting MMPs.

Although most studies are in a preliminary phase, some hydroxamate-based tracers with promising binding properties have been identified. In particular, among single-photon-emitting agents, the peptidomimetics [^{111}In]-DTPA-RP782 and [^{99m}Tc]-(HYNIC-RP805)(tricine)(TPPTS) and the picolyl-benzenesulfonamide [^{123}I]I-HO-CGS 27023A appear to specifically target the enzymatic action of MMPs in animal models of various diseases. Nevertheless, preclinical studies in animal models prove that these imaging agents might be more successful for investigating atherosclerosis than for tumor targeting [107].

Epidermal Growth Factor Receptor (EGFR)

The EGFR family consists of four transmembrane receptors, respectively, EGFR properly said (HER1/erbB-1), HER2 (erbB-2/neu), HER3 (erbB-3), and HER4 (erbB-4). EGFR is a glycosylated transmembrane protein composed of an extracellular ligand-binding region, a transmembrane region, and an intracellular tyrosine kinase domain. The extracellular domain binds endogenous growth factors, like epidermal growth factor (EGF) or transforming growth factor alpha (TGF-α). Binding of one of these endogenous ligands triggers erbB receptor aggregation, thus resulting in the formation of receptor homodimers and/or heterodimers, and internalization. Dimer formation leads to activation of the intrinsic receptor tyrosine kinase domain and to a cascade of intracellular signaling pathways.

This mechanism is involved in the regulation of cell growth, as well as in differentiation and survival of cells. These properties have attracted the interest of investigators especially in oncology, and EGFR has been investigated as a major target for the treatment of uncontrolled tumor growth [108]. In fact, EGFR is often overexpressed in human malignancies such as head and neck squamous cell carcinoma, gastrointestinal and abdominal carcinomas, lung carcinomas, carcinomas of the reproductive tract, melanomas, glioblastomas, and thyroid carcinomas [109]. Although data are heterogeneous in this regard, overexpression is often associated with an aggressive tumor phenotype and poor prognosis. To target tumor cell proliferation or growth via EGFR, monoclonal antibodies (mAbs) against this receptor have been developed for therapeutic purpose. One of these agents, cetuximab,

has been approved by the Food and Drug Administration (FDA) in 2004 for treatment of colorectal cancer.

Two predominant classes of EGFR inhibitors have been developed including mAbs that target the extracellular domain of EGFR, such as cetuximab (Erbitux) or trastuzumab (Herceptin), and small molecule tyrosine kinase inhibitors (TKIs) that target the receptor catalytic domain of EGFR, such as gefitinib (Iressa) and erlotinib (Tarceva) [110]. Several SPECT single-photon radiopharmaceuticals have been developed in preclinical trials, such as ^{99m}Tc-Cetuximab as stable complex with ethylenedicysteine [111,112]. Besides an unexpected high kidney uptake observed in rates bearing a human breast tumor, the 6-h physical half-life of ^{99m}Tc was too short for imaging, considering that mAb preparations like cetuximab the highest tracer accumulation in the tumor is expected 2–3 days post-injection. In a pilot clinical study, high uptake of this cetuximab conjugate in tumors was observed, however, without a sufficiently high target-to-background ratio and without a clear correlation with other clinical features in patients with head and neck cancer.

With its relative longer physical half-life (2.8 days), ^{111}In-labeled mAb conjugates obtained using the chelators DOTA or DTPA are in principle more suitable for tumor imaging than the ^{99m}Tc-labeled counterparts. Accordingly, these have been investigated in animal models [113, 114] and in humans [115]. Radiolabeled pertuzumab, a HER2 dimerization inhibitor that binds to an epitope different from that of trastuzumab, was also evaluated to image HER2 downregulation after 3 days of treatment with trastuzumab in human breast cancer xenografts. ^{111}In-diethylenetriaminepentaacetic acid-pertuzumab (^{111}In-DTPA-pertuzumab [116]) demonstrated a reduction in viable, HER2-positive tumor cells after 3 weeks of therapy [117].

Folate Receptor Overexpression

Due to their increased metabolic and structural requirements, tumor cells usually consume high amounts of folate, a compound involved in many biosynthetic processes including DNA synthesis. The folate transporter is usually overexpressed on the surface of tumors such as ovarian cancer and lung cancer, thus representing a possible target for molecular imaging, both for therapeutic [118] and for diagnostic purpose (^{99m}Tc-Etarfolatide or ^{111}In-DOTA-folate) [119]. Interference by important accumulation of this tracer in normal tissues, particularly in the kidneys, makes it difficult to analyze the results of clinical trials with ^{99m}Tc-etarfolatide. To prevent such problem, folic acid or pemetrexed combined with thymidine was administered in patients before tracer injection as an antidote to the potential toxicity [120]. The results of trials with this combination are promising, particularly in patients with ovarian cancer [121–123], and the compound is currently under review by the European Medicines Agency.

References

1. Ravdin P. The use of HER2 testing in the management of breast cancer. Semin Oncol. 2000;27 Suppl 9: 33–42.
2. Roses AD. Pharmacogenetics and the practice of medicine. Nature. 2000;405(6788):857–65.
3. Cornelissen B. Imaging the inside of a tumour: a review of radionuclide imaging and theranostics targeting intracellular epitopes. J Label Compd Radiopharm. 2014;57:310–6.
4. Hanahan D, Weinberg RA. Hallmarks of cancer: the next generation. Cell. 2011;144:646–74.
5. Cavallo F, De Giovanni C, Nanni P, Forni G, Lollini PL. The immune hallmarks of cancer. Cancer Immunol Immunother. 2011;60:319–26.
6. James ML, Gambhir SS. A molecular imaging primer: modalities, imaging agents, and applications. Physiol Rev. 2012;92:897–965.
7. Mariani G, Bruselli L, Duatti A. Is PET always an advantage versus planar and SPECT? Eur J Nucl Med Mol Imaging. 2008;35:1560–5.
8. Pauwels EKJ, Bergstrom K, Mariani G, Kairemo K. Microdosing, imaging biomarkers and SPECT: a multi-sided tripod to accelerate drug development. Curr Pharm Des. 2009;15:928–34.
9. Mariani G, Strauss HW. Positron emission and single-photon emission imaging: synergy rather than competition. Eur J Nucl Med Mol Imaging. 2011;38:1189–90.
10. Vaupel P. Pathophysiology of solid tumors. In: Molls M, Vaupel P, Nieder C, Anscher MS, editors. The impact of tumor biology on cancer treatment and multidisciplinary strategies. Heidelberg: Springer; 2009. p. 51–92.

11. Bredow S, Lewin M, Hofmann B, Marecos E, Weissleder R. Imaging of tumour neovasculature by targeting the TGF-beta binding receptor endoglin. Eur J Cancer. 2000;36:675–81.
12. Zhou Y, Chakraborty S, Liu S. Radiolabeled cyclic RGD peptides as radiotracers for imaging tumors and thrombosis by SPECT. Theranostics. 2011;1:58–82.
13. Tsiapa I, Loudos G, Varvarigou A, Fragogeorgi E, Psimadas D, Tsotakos T, et al. Biological evaluation of an ornithine-modified ^{99m}Tc-labeled RGD peptide as an angiogenesis imaging agent. Nucl Med Biol. 2013;40:262–72.
14. Kimura S, Umeda IO, Moriyama N, Fujii H. Synthesis and evaluation of a novel ^{99m}Tc-labeled bioreductive probe for tumor hypoxia imaging. Bioorg Med Chem Lett. 2011;21:7359–62.
15. Umeda IO, Tani K, Tsuda K, Kobayashi M, Ogata M, Kimura S, et al. High resolution SPECT imaging for visualization of intratumoral heterogeneity using a SPECT/CT scanner dedicated for small animal imaging. Ann Nucl Med. 2012;26:67–76.
16. Weerakkody D, Moshnikova A, Thakur MS, Moshnikova V, Daniels J, Engelman DM, et al. Family of pH (low) insertion peptides for tumor targeting. Proc Natl Acad Sci U S A. 2013;110:5834–9.
17. von Forstner C, Zuhayra M, Ammerpohl O, Zhao Y, Tiwari S, Jansen O, et al. Expression of L amino acid transport system 1 and analysis of iodine-123-methyltyrosine tumor uptake in a pancreatic xenotransplantation model using fused high-resolutionmicro-SPECT-MRI. Hepatobiliary Pancreat Dis Int. 2011;10:30–7.
18. Kondo N, Temma T, Shimizu Y, Watanabe H, Higano K, Takagi Y, et al. Miniaturized antibodies for imaging membrane type-1 matrix metalloproteinase in cancers. Cancer Sci. 2013;104:495–501.
19. LeBeau AM, Duriseti S, Murphy ST, Pepin F, Hann B, Gray JW, et al. Targeting uPAR with antagonistic recombinant human antibodies in aggressive breast cancer. Cancer Res. 2013;73:2070–81.
20. Cai J, Li F. Single-photon emission computed tomography tracers for predicting and monitoring cancer therapy. Curr Pharm Biotechnol. 2013;14:693–707.
21. Schottelius M, Wester HJ. Molecular imaging targeting peptide receptors. Methods. 2009;48:161–77.
22. Heskamp S, van Laarhoven HW, Molkenboer-Kuenen JD, Bouwman WH, van der Graaf WT, Oyen WJ, et al. Optimization of IGF-1R SPECT/CT imaging using ^{111}In-labeled F(ab′)$_2$ and Fab fragments of the monoclonal antibody R1507. Mol Pharm. 2012;9:2314–21.
23. Muller C. Folate based radiopharmaceuticals for imaging and therapy of cancer and inflammation. Curr Pharm Des. 2012;18:1058–83.
24. Kassis AI, Adelstein SJ, Mariani G. Radiolabeled nucleoside analogs in cancer diagnosis and therapy. Q J Nucl Med. 1996;40:301–19.
25. Mariani G, Bodei L, Adelstein SJ, Kassis AI. Emerging roles for radiometabolic therapy of tumors based on Auger electron emission. J Nucl Med. 2000;41:1519–21.
26. Adelstein SJ, Kassis AI, Bodei L, Mariani G. Radiotoxicity of iodine-125 and other Auger-electron emitting radionuclides: background to therapy. Cancer Biother Radio-Pharm. 2003;18:301–16.
27. Bodei L, Kassis AI, Adelstein SJ, Mariani G. Radionuclide therapy with iodine-125 and other Auger-electron-emitting radionuclides: experimental models and clinical applications. Cancer Biother Radiopharm. 2003;18:861–77.
28. Aloj L, Aurilio M, Rinaldi V, D'Ambrosio L, Tesauro D, Peitl PK, et al. Comparison of the binding and internalization properties of 12 DOTA-coupled and ^{111}In-labelled CCK2/gastrin receptor binding peptides: a collaborative project under COST Action BM0607. Eur J Nucl Med Mol Imaging. 2011;38:1417–25.
29. Forrer F, Valkema R, Bernard B, Schramm NU, Hoppin JW, Rolleman E, et al. In vivo radionuclide uptake quantification using a multi-pinhole SPECT system to predict renal function in small animals. Eur J Nucl Med Mol Imaging. 2006;33:1214–7.
30. Behr TM, Béhé M, Becker W. Diagnostic applications of radiolabeled peptides in nuclear endocrinology. Q J Nucl Med. 1999;43:268–80.
31. Behr TM, Béhé MP. Cholecystokinin-B/Gastrin receptor-targeting peptides for staging and therapy of medullary thyroid cancer and other cholecystokinin-B receptor-expressing malignancies. Semin Nucl Med. 2002;32:97–109.
32. Quinn T, Zhang X, Miao Y. Targeted melanoma imaging and therapy with radiolabeled alpha-melanocyte stimulating hormone peptide analogues. G Ital Dermatol Venereol. 2010;145:245–58.
33. Ambrosini V, Fani M, Fanti S, Forrer F, Maecke HR. Radiopeptide imaging and therapy in Europe. J Nucl Med. 2011;52:42S–55.
34. Graham MM, Menda Y. Radiopeptide imaging and therapy in the United States. J Nucl Med. 2011;52:56S–63.
35. Tang B, Yong X, Xie R, Li QW, Yang SM. Vasoactive intestinal peptide receptor-based imaging and treatment of tumors. Int J Oncol. 2014;44:1023–31.
36. Hubalewska-Dydejczyk A, Sowa-Staszczak A, Tomaszuk M, Stefańska A. GLP-1 and exendin-4 for imaging endocrine pancreas. A review. Labelled glucagon-like peptide-1 analogues: past, present and future. Q J Nucl Med Mol Imaging. 2015;59:152–60.
37. Yang MY, Chuang H, Chen RF, Yang KD. Reversible phosphatidylserine expression on blood granulocytes related to membrane perturbation but not DNA strand breaks. J Leukoc Biol. 2002;71:231–7.
38. Bouter A, Carmeille R, Gounou C, Bouvet F, Degrelle SA, Evain-Brion D, et al. Review: annexin-A5 and cell membrane repair. Placenta. 2015;36 Suppl 1:S43–9.
39. Gottlieb RA. Part III: molecular and cellular hematology apoptosis. In: Lichtman MA, Beutler E, Kipps TJ,

editors. Williams' hematology. 7th ed. New York: McGraw-Hill Book; 2007. p. 125–30.
40. Ogawa K, Aoki M. Radiolabeled apoptosis imaging agents for early detection of response to therapy. Sci World J. 2014;2014:732603. doi:10.1155/2014/732603. Epub 2014 Oct 14.
41. Blankenberg FG. In vivo detection of apoptosis. J Nucl Med. 2008;49 Suppl 2:81S–95.
42. Kemerink GJ, Liu X, Kieffer D, Ceyssens S, Mortelmans L, Verbruggen AM, et al. Safety, biodistribution, and dosimetry of ^{99m}Tc-HYNIC-annexin V, a novel human recombinant annexin V for human application. J Nucl Med. 2003;44:947–52.
43. Tait JF, Smith C, Blankenberg FG. Structural requirements for in vivo detection of cell death with ^{99m}Tc-annexin V. J Nucl Med. 2005;46:807–15.
44. Belhocine T, Steinmetz N, Hustinx R, Bartsch P, Jerusalem G, Seidel L, et al. Increased uptake of the apoptosis-imaging agent ^{99m}Tc recombinant human annexin v in human tumors after one course of chemotherapy as a predictor of tumor response and patient prognosis. Clin Cancer Res. 2002;8:2766–74.
45. Schaper FLWVJ, Reutelingsperger CP. ^{99m}Tc-HYNIC-annexin A5 in oncology: evaluating efficacy of anti-cancer therapies. Cancers. 2013;5:550–68.
46. Vangestel C, Peeters M, Mees G, Oltenfreiter R, Boersma HH, Elsinga PH, et al. In vivo imaging of apoptosis in oncology: an update. Mol Imaging. 2011;10:340–58.
47. Vangestel C, Van de Wiele C, Van Damme N, Staelens S, Pauwels P, Reutelingsperger CP, Peeters M. ^{99m}Tc-$(CO)_3$ His-annexin A5 micro-SPECT demonstrates increased cell death by irinotecan during the vascular normalization window caused by bevacizumab. J Nucl Med. 2011;52:1786–94.
48. Lahorte CM, van de Wiele C, Bacher K, van den Bossche B, Thierens H, van Belle S, et al. Biodistribution and dosimetry study of ^{123}I-rh-annexin v in mice and humans. Nucl Med Commun. 2003;24:871–80.
49. Marconescu A, Thorpe PE. Coincident exposure of phosphatidylethanolamine and anionic phospholipids on the surface of irradiated cells. Biochim Biophys Acta. 1778;2008:2217–24.
50. Bevers EM, Comfurius P, Dekkers DWC, Zwaal RFA. Lipid translocation across the plasma membrane of mammalian cells. Biochim Biophys Acta. 1999;439:317–30.
51. Alberts B, Johnson A, Lewis J, et al. Molecular biology of the cell. 4th ed. New York: Garland Science; 2002.
52. Spector AA, Yorek MA. Membrane lipid composition and cellular function. J Lipid Res. 1985;26:1015–35.
53. Emoto K, Toyama-Sorimachi N, Karasuyama H, Inoue K, Umeda M. Exposure of phosphatidylethanolamine on the surface of apoptotic cells. Exp Cell Res. 1997;232:430–4.
54. Umeda M, Emoto K. Membrane phospholipid dynamics during cytokinesis: regulation of actin filament assembly by redistribution of membrane surface phospholipid. Chem Phys Lipids. 1999;101:81–91.
55. Mills JC, Stone NL, Erhardt J, et al. Apoptotic membrane blebbing is regulated by myosin light chain phosphorylation. J Cell Biol. 1998;140:627–36.
56. Hayashi F, Nagashima K, Terui Y, et al. The structure of PA48009: the revised structure of duramycin. J Antibiot (Tokyo). 1990;43:1421–30.
57. Zimmermann N, Freund S, Fredenhagen A, et al. Solution structures of the lantibiotics duramycin B and C. Eur J Biochem. 1993;216:419–28.
58. Aoki Y, Uenaka T, Aoki J, et al. A novel peptide probe for studying the transbilayer movement of phosphatidylethanolamine. J Biochem. 1994;116:291–7.
59. Machaidze G, Ziegler A, Seelig J. Specific binding of Ro 09-0198 (cinnamycin) to phosphatidylethanolamine: a thermodynamic analysis. Biochemistry. 2002;41:1965–71.
60. Guder A, Wiedemann I, Sahl HG. Posttranslationally modified bacteriocins: the lantibiotics. Biopolymers. 2000;55:62–73.
61. Hosoda K, Ohya M, Kohno T, et al. Structure determination of an immunopotentiator peptide, cinnamycin, complexed with lysophosphatidylethanolamine by 1H-NMR1. J Biochem. 1996;119:226–30.
62. Kaletta C, Entian KD, Jung G. Prepeptide sequence of cinnamycin (Ro 09-0198): the first structural gene of a duramycin-type lantibiotic. Eur J Biochem. 1991;199:411–5.
63. Marki F, Hanni E, Fredenhagen A, et al. Mode of action of the lanthioninecontaining peptide antibiotics duramycin, duramycin B and C, and cinnamycin as indirect inhibitors of phospholipase A2. Biochem Pharmacol. 1991;42:2027–35.
64. Iwamoto K, Hayakawa T, Murate M, et al. Curvature-dependent recognition of ethanolamine phospholipids by duramycin and cinnamycin. Biophys J. 2007;93:1608–19.
65. Seelig J. Thermodynamics of lipid-peptide interactions. Biochim Biophys Acta. 1666;2004:40–50.
66. Zhao M, Li Z, Bugenhagen S. ^{99m}Tc-labeled duramycin as a novel phosphatidylethanolamine-binding molecular probe. J Nucl Med. 2008;49:1345–52.
67. Zhao M, Li Z. A single-step kit formulation for the ^{99m}Tc-labeling of HYNIC-Duramycin. Nucl Med Biol. 2012;39:1006–11.
68. Audi S, Li Z, Capacete J, Liu Y, Fang W, Shu LG, Zhao M. Understanding the in vivo uptake kinetics of a phosphatidylethanolamine-binding agent ^{99m}Tc-Duramycin. Nucl Med Biol. 2012;39:821–5.
69. Wang L, Wang F, Fang W, et al. The feasibility of imaging myocardial ischemic/reperfusion injury using ^{99m}Tc-labeled duramycin in a porcine model. Nucl Med Biol. 2015;42:198–204.
70. Zhang Y, Stevenson GD, Barber C, et al. Imaging of rat cerebral ischemia-reperfusion injury using ^{99m}Tc-labeled duramycin. Nucl Med Biol. 2013;40:80–8.

71. Clough AV, Audi SH, Haworth ST, Roerig DL. Differential lung uptake of ^{99m}Tc-hexamethylpropyleneamine oxime and ^{99m}Tc-duramycin in the chronic hyperoxia rat model. J Nucl Med. 2012;53:1984–91.
72. Audi SH, Jacobs ER, Zhao M, Roerig DL, Haworth ST, Clough AV. In vivo detection of hyperoxia-induced pulmonary endothelial cell death using ^{99m}Tc-duramycin. Nucl Med Biol. 2015;42:46–52.
73. Medhora MM, Haworth S, Liu Y, Narayanan J, Gao F, Zhao M, et al. Biomarkers for radiation pneumonitis using non-invasive molecular imaging. J Nucl Med. 2016;57:1296–301.
74. Johnson SE, Li Z, Liu Y, Moulder JE, Zhao M. Whole-body imaging of high-dose ionizing irradiation-induced tissue injuries using ^{99m}Tc-duramycin. J Nucl Med. 2013;54:1397–403.
75. Elvas F, Vangestel C, Rapic S, Verhaeghe J, Gray B, Pak K, et al. Characterization of [^{99m}Tc]duramycin as a SPECT imaging agent for early assessment of tumor apoptosis. Mol Imaging Biol. 2015;17:838–47.
76. Luo R, Niu L, Qiu F, Fang W, Fu T, Zhao M, et al. Monitoring apoptosis of breast cancer xenograft after paclitaxel treatment with ^{99m}Tc-labeled duramycin SPECT/CT. Mol Imaging. 2016;29:15. doi:10.1177/1536012115624918.
77. Elvas F, Boddaert J, Vengestel C, Pak K, Gray B, Kumar-Singh S, et al. ^{99m}Tc-Duramycin SPECT imaging of early tumor response to targeted therapy: a comparison with ^{18}F-FDG PET. J Nucl Med. 2017;58:665–70.
78. Ruoslahti E, Pierschbacher MD. New perspectives in cell adhesion: RGD and integrins. Science. 1987;238:491–7.
79. Sivolapenko GB, Skarlos D, Pectasides D, Stathopoulou E, Milonakis A, Sirmalis G, et al. Imaging of metastatic melanoma utilising a technetium-99m labelled RGD-containing synthetic peptide. Eur J Nucl Med. 1998;25:1383–9.
80. Hua J, Dobrucki LW, Sadeghi MM, Zhang J, Bourke BN, Cavaliere P, et al. Noninvasive imaging of angiogenesis with a ^{99m}Tc-labeled peptide targeted at alpha$_v$beta$_3$ integrin after murine hindlimb ischemia. Circulation. 2005;111:3255–60.
81. Bach-Gansmo T, Danielsson R, Saracco A, Wilczek B, Bogsrud TV, Fangberget A, et al. Integrin receptor imaging of breast cancer: a proof-of-concept study to evaluate ^{99m}Tc-NC100692. J Nucl Med. 2006;47:1434–9.
82. Bach-Gansmo T, Bogsrud TV, Skretting A. Integrin scintimammography using a dedicated breast imaging, solid-state gamma-camera and ^{99m}Tc-labelled NC100692. Clin Physiol Funct Imaging. 2008;28:235–9.
83. Axelsson R, Bach-Gansmo T, Castell-Conesa J, McParland BJ, Study Group. An open-label, multicenter, phase 2a study to assess the feasibility of imaging metastases in late-stage cancer patients with the alpha$_v$ beta$_3$-selective angiogenesis imaging agent ^{99m}Tc-NC100692. Acta Radiol. 2010;51:40–6.
84. Dearling JL, Barnes JW, Panigrahy D, Zimmerman RE, Fahey F, Treves ST, et al. Specific uptake of ^{99m}Tc-NC100692, an $\alpha_v\beta_3$-targeted imaging probe, in subcutaneous and orthotopic tumors. Nucl Med Biol. 2013;40:788–94.
85. Shi J, Wang L, Kim YS, et al. Improving tumor uptake and excretion kinetics of ^{99m}Tc-labeled cyclic arginine-glycine-aspartic (RGD) dimmers with triglycine linkers. J Med Chem. 2008;51:7980–90.
86. Liu Z, Jia B, Shi J, et al. Tumor uptake of the RGD dimeric probe ^{99m}Tc-G3-2P4-RGD$_2$ is correlated with integrin $\alpha_V\beta_3$ expressed on both tumor cells and neovasculature. Bioconjug Chem. 2010;21:548–55.
87. Zhou Y, Kim YS, Chakraborty S, Shi J, Gao H, Liu S. ^{99m}Tc-labeled cyclic RGD peptides for noninvasive monitoring of tumor integrin $\alpha_V\beta_3$ expression. Mol Imaging. 2011;10:386–97.
88. Ma Q, Ji B, Jia B, et al. Differential diagnosis of solitary pulmonary nodules using ^{99m}Tc-3P4-RGD2 scintigraphy. Eur J Nucl Med Mol Imaging. 2011;38:2145–52.
89. Liu L, Song Y, Gao S, Ji T, Zhang H, Ji B, et al. ^{99m}Tc-3PRGD2 scintimammography in palpable and non-palpable breast lesions. Mol Imaging. 2014;13:1–7. doi:10.2310/7290.2014.00010.
90. Zhu Z, Miao W, Li Q, Dai H, Ma Q, Wang F, et al. ^{99m}Tc-3PRGD2 for integrin receptor imaging of lung cancer: a multicenter study. J Nucl Med. 2012;53:716–22.
91. Zhao D, Jin X, Li F, Liang J, Lin Y. Integrin $\alpha_v\beta_3$ imaging of radioactive iodine-refractory thyroid cancer using ^{99m}Tc-3PRGD2. J Nucl Med. 2012;53:1872–7.
92. Miao W, Zheng S, Dai H, Wang F, Jin X, Zhu Z, Jia B. Comparison of ^{99m}Tc-3PRGD2 integrin receptor imaging with ^{99m}Tc-MDP bone scan in diagnosis of bone metastasis in patients with lung cancer: a multicenter study. PLoS One. 2014;9(10):e111221.
93. Ji S, Zhou Y, Voorbach MJ, Shao G, Zhang Y, Fox GB, et al. Monitoring tumor response to linifanib therapy with SPECT/CT using the integrin $\alpha_v\beta_3$-targeted radiotracer ^{99m}Tc-3P-RGD2. J Pharmacol Exp Ther. 2013;346:251–8.
94. Liu Z, Huang J, Dong C, et al. ^{99m}Tc-labeled RGD-BBN peptide for small-animal SPET/CT of lung carcinoma. Mol Pharm. 2012;9:1409–17.
95. Chen Q, Ma Q, Chen M, et al. An exploratory study on ^{99m}Tc-RGDBBN. Peptide scintimammography in the assessment of breast malignant lesions compared to ^{99m}Tc-3P4-RGD$_2$. PLoS One. 2015;10(4):e0123401.
96. Ji T, Sun Y, Chen B, Ji B, Gao S, Ma Q, et al. The diagnostic role of ^{99}mTc-dual receptor targeted probe

and targeted peptide bombesin (RGD-BBN) SPET/CT in the detection of malignant and benign breast tumors and axillary lymph nodes compared to ultrasound. Hell J Nucl Med. 2015;18:108–13.
97. Bunschoten A, van Willigen DM, Buckle T, van den Berg NS, Welling MM, Spa SJ, Wester HJ, et al. Tailoring fluorescent dyes to optimize a hybrid RGD-tracer. Bioconjug Chem. 2016;27:1253–8.
98. Castellani P, Viale G, Dorcaratto A, Nicolò G, Kaczmarek J, Querze G, Zardi L. The fibronectin isoform containing the ED-B oncofetal domain: a marker of angiogenesis. Int J Cancer. 1994;59:612–8.
99. Pini A, Viti F, Santucci A, Carnemolla B, Zardi L, Neri P, Neri D. Design and use of a phage display library. Human antibodies with subnanomolar affinity against a marker of angiogenesis eluted from a two-dimensional gel. J Biol Chem. 1998;273:21769–76.
100. Tarli L, Balza E, Viti F, Borsi L, Castellani P, Berndorff D, Dinkelborg L, Neri D, Zardi L. A high-affinity human antibody that targets tumoral blood vessels. Blood. 1999;94:192–8.
101. Berndorff D, Borkowski S, Moosmayer D, Viti F, Muller-Tiemann B, Sieger S, et al. Imaging of tumor angiogenesis using ^{99m}Tc-labeled human recombinant anti-ED-B fibronectin antibody fragments. J Nucl Med. 2006;47:1707–16.
102. Kaczmarek J, Castellani P, Nicolò G, Spina B, Allemanni G, Zardi L. Distribution of oncofetal fibronectin isoforms in normal, hyperplastic and neoplastic human breast tissues. Int J Cancer. 1994;59:11–6.
103. Pujuguet P, Hammann A, Moutet M, Samuel JL, Martin F, Martin M. Expression of fibronectin ED-A$^+$ and ED-B$^+$ isoforms by human and experimental colorectal cancer. Contribution of cancer cells and tumor-associated myofibroblasts. Am J Pathol. 1996;148:579–92.
104. Santimaria M, Moscatelli G, Viale GL, Giovannoni L, Neri G, Viti F, et al. Immunoscintigraphic detection of the ED-B domain of fibronectin, a marker of angiogenesis, in patients with cancer. Clin Cancer Res. 2003;9:571–9.
105. Gomez DE, Alonso DF, Yoshiji H, Thorgeirsson UP. Tissue inhibitors of metalloproteinases: structure, regulation and biological functions. Eur J Cell Biol. 1997;74:111–22.
106. Foda HD, Zucker S. Matrix metalloproteinases in cancer invasion, metastasis and angiogenesis. Drug Discov Today. 2001;6:478–82.
107. Matusiak N, van Waarde A, Bischoff R, Oltenfreiter R, van de Wiele C, Dierckx RA, et al. Probes for non-invasive matrix metalloproteinase-targeted imaging with PET and SPECT. Curr Pharm Des. 2013;19:4647–72.
108. Sihver W, Pietzsch J, Krause M, Baumann M, Steinbach J, Pietzsch HJ. Radiolabeled cetuximab conjugates for EGFR targeted cancer diagnostics and therapy. Pharmaceuticals (Basel). 2014;7:311–38.
109. Salomon DS, Brandt R, Ciardiello F, Normanno N. Epidermal growth factor-related peptides and their receptors in human malignancies. Crit Rev Oncol Hematol. 1995;19:183–232.
110. Harari PM. Epidermal growth factor receptor inhibition strategies in oncology. Endocr Relat Cancer. 2004;11:689–708.
111. Schechter NR, Yang DJ, Azhdarinia A, Kohanim S, Wendt R, Oh CS, et al. Assessment of epidermal growth factor receptor with ^{99m}Tc-ethylenedicysteine-C225 monoclonal antibody. Anticancer Drugs. 2003;14:49–56.
112. Schechter NR, Wendt RE, Yang DJ, Azhdarinia A, Erwin WD, Stachowiak AM, et al. Radiation dosimetry of ^{99m}Tc-labeled C225 in patients with squamous cell carcinoma of the head and neck. J Nucl Med. 2004;45:1683–7.
113. Price EW, Zeglis BM, Cawthray JF, Ramogida CF, Ramos N, Lewis JS, et al. H_4octapa-trastuzumab: versatile acyclic chelate system for ^{111}In and ^{177}Lu imaging and therapy. J Am Chem Soc. 2013;135:12707–21.
114. Razumienko EJ, Scollard DA, Reilly RM. Small-animal SPECT/CT of HER2 and HER3 expression in tumor xenografts in athymic mice using trastuzumab Fab-heregulin bispecific radioimmunoconjugates. J Nucl Med. 2012;53:1943–50.
115. Divgi CR, Welt S, Kris M, Real FX, Yeh SD, Gralla R, et al. Phase I and imaging trial of indium-111 labeled anti-epidermal growth factor receptor monoclonal antibody 225 in patients with squamous cell lung carcinoma. J Natl Cancer Inst. 1991;83:97–104.
116. Lam K, Scollard DA, Chan C, Levine MN, Reilly RM. Kit for the preparation of ^{111}In-labeled pertuzumab injection for imaging response of HER2-positive breast cancer to trastuzumab (Herceptin). Appl Radiat Isot. 2014;95:135–42.
117. McLarty K, Cornelissen B, Cai Z, Scollard DA, Costantini DL, Done SJ, Reilly RM. Micro-SPECT/CT with ^{111}In-DTPA-pertuzumab sensitively detects trastuzumab-mediated HER2 downregulation and tumor response in athymic mice bearing MDA-MB-361 human breast cancer xenografts. J Nucl Med. 2009;50:1340–8.
118. Müller C, Mindt TL, de Jong M, Schibli R. Evaluation of a novel radiofolate in tumour-bearing mice: promising prospects for folate-based radionuclide therapy. Eur J Nucl Med Mol Imaging. 2009;36:938–46.
119. Müller C, Forrer F, Schibli R, Krenning EP, de Jong M. SPECT study of folate receptor-positive malignant and normal tissues in mice using a novel ^{99m}Tc-radiofolate. J Nucl Med. 2008;49:310–07.
120. Reber J, Struthers H, Betzel T, Hohn A, Schibli R, Müller C. Radioiodinated folic acid conjugates:

evaluation of a valuable concept to improve tumor-to-background contrast. Mol Pharm. 2012;9:1213–21.
121. Maurer AH, Elsinga P, Fanti S, Nguyen B, Oyen WJ, Weber WA. Imaging the folate receptor on cancer cells with ^{99m}Tc-etarfolatide: properties, clinical use, and future potential of folate receptor imaging. J Nucl Med. 2014;55:701–4.
122. Morris RT, Joyrich RN, Naumann RW, Shah NP, Maurer AH, Strauss HW, et al. Phase II study of treatment of advanced ovarian cancer with folate-receptor-targeted therapeutic (vintafolide) and companion SPECT-based imaging agent (^{99m}Tc-etarfolatide). Ann Oncol. 2014;25:852–8.
123. Yamada Y, Nakatani H, Yanaihara H, Omote M. Phase I clinical trial of ^{99m}Tc-etarfolatide, an imaging agent for folate receptor in healthy Japanese adults. Ann Nucl Med. 2015;29:792–8.

Novel Positron-Emitting Radiopharmaceuticals

7

Mirkka Sarparanta, Dustin W. Demoin, Brendon E. Cook, Jason S. Lewis, and Brian M. Zeglis

Abstract

Over the past two decades, nuclear imaging has transformed cancer care. Positron emission tomography (PET) and single photon emission computed tomography (SPECT) can provide clinicians with functional and biochemical information about tumor tissue that complement the anatomical data acquired through magnetic resonance imaging (MRI) and computed tomography (CT). In this chapter, we highlight a number of emerging radiotracers in oncology that are currently employed in clinical trials in the USA and worldwide yet are awaiting regulatory approval in the USA. The radiotracers discussed range from small molecule probes that target cellular transport mechanisms and metabolic pathways to antibody-based agents that target cell-surface receptors. In order to help the reader appreciate the diversity and potential of each of these imaging agents, we present the underlying mechanisms of each agent's targeting and trapping in tumor tissue and provide examples of clinical studies in diverse cancer types as well as descriptions of the utility of each tracer for staging and treatment monitoring.

M. Sarparanta (✉)
Department of Radiology, Memorial Sloan Kettering Cancer Center, New York, NY, USA

Laboratory of Radiochemistry, Department of Chemistry, University of Helsinki, Helsinki, Finland
e-mail: mirkka.sarparanta@helsinki.fi

D.W. Demoin (✉)
Department of Radiology, Memorial Sloan Kettering Cancer Center, New York, NY, USA
e-mail: ddemoin@gmail.com

B.E. Cook (✉)
Department of Radiology, Memorial Sloan Kettering Cancer Center, New York, NY, USA

Department of Chemistry, Hunter College of the City University of New York, New York, NY, USA

Ph.D. Program in Chemistry, Graduate Center of the City University of New York, New York, NY, USA
e-mail: brendoncook.tc99@gmail.com

J.S. Lewis (✉)
Radiochemistry and Imaging Sciences Service, Department of Radiology, Memorial Sloan Kettering Cancer Center, New York, NY, USA

Program in Molecular Pharmacology, Memorial Sloan Kettering Cancer Center, New York, NY, USA

Department of Radiology, Weill Cornell Medical College, New York, NY, USA

Department of Pharmacology, Weill Cornell Medical College, New York, NY, USA
e-mail: lewisj2@mskcc.org

B.M. Zeglis (✉)
Radiochemistry and Imaging Sciences Service, Department of Radiology, Memorial Sloan Kettering Cancer Center, New York, NY, USA

Graduate Center of the City University of New York, New York, NY, USA

Department of Radiology, Weill Cornell Medical College, New York, NY, USA
e-mail: bz102@hunter.cuny.edu

© Springer International Publishing Switzerland 2017
H.W. Strauss et al. (eds.), *Nuclear Oncology*,
https://doi.org/10.1007/978-3-319-26236-9_87

Keywords

Nuclear imaging • Oncology • Positron emission tomography, PET • Single photon emission tomography, SPECT • Radiotracer • Imaging agent • Fluorine-18 • Carbon-11 • Gallium-68 • Zirconium-89 • Technetium-99m • Indium-111 • Amino acid transport • Lipid biosynthesis • Cellular proliferation • Somatostatin receptor • Integrin • Bombesin receptor • Prostate-specific membrane antigen, PSMA • Steroid hormone receptor • Hypoxia

Glossary

[^{123}I]MIBG	[^{123}I]-*meta*-iodobenzylguanidine
[^{18}F]DCFBC	N-[N-[(S)-1,3-dicarboxypropyl]carbamoyl]-4-[^{18}F]fluorobenzyl-L-cysteine
[^{18}F]FACBC	*anti*-1-amino-3-^{18}F-fluorocyclobutane-1-carboxylic acid
[^{18}F]FDG	2-[^{18}F]fluoro-2-deoxyglucose
[^{18}F]FDHT	16ß-[^{18}F]fluoro-5-dihydrotestosterone
[^{18}F]FDOPA	L-3,4-dihydroxy-6-[^{18}F]fluorophenylalanine
[^{18}F]FES	16a-[^{18}F]fluoro-17ß-estradiol
[^{18}F]FET	O-(2-^{18}F-fluoroethyl)-L-tyrosine
[^{18}F]FGln	4-[^{18}F]-(2S,4R) fluoroglutamine
[^{18}F]FLT	3'-deoxy-3'-[^{18}F]fluorothymidine
[^{18}F]FMISO	[^{18}F]-fluoromisonidazole, 1-fluoro-3-(2-nitroimidazol-1-yl)-propan-2-ol
[^{18}F]RGD-K5	[^{18}F]flotegatide-RGD
^{18}F-AH111585	[^{18}F]fluciclatide
^{18}F-alfatide II	[^{18}F]AlF-NOTA-E[PEG$_4$-c(RGDfk)]$_2$
^{64}Cu-ATSM	^{64}Cu-diacetyl-bis(N4-methylsemicarbazone)
^{68}Ga-PSMA-ligand	Glu-urea-Lys-(Ahx)-[^{68}Ga(HBED-CC)]
AACD	Aromatic amino acid decarboxylase
AR	Androgen receptor
ASCT	Alanine-serine-cysteine transporter
BB2	Bombesin receptor subtype-2
BB2r	Bombesin receptor subtype-2
ChoK	Choline kinase
CNS	Central nervous system
COMT	Catechol-*o*-methyl transferase
CT	X-ray computed tomography
DOTA	1,4,7,10-tetra-azacyclododecane-1,4,7,10-tetraacetic acid
DTPA	Diethylenetriaminepentaacetic acid
ER	Estrogen receptor
FAS	Fatty acid synthase
GRPr	Gastrin-releasing peptide receptor
IMRT	Intensity-modulated radiation therapy
LAT1	L-type amino acid transporter 1
MRI	Magnetic resonance imaging
MTC	Medullary thyroid cancer
mTOR	Mammalian target of rapamycin
NET	Neuroendocrine tumor
NSCLC	Non–small cell lung cancer
OC	Octreotide
PEG	Polyethylene glycol
PET	Positron emission tomography
PET/MRI	Positron emission tomography/magnetic resonance imaging
PSA	Prostate-specific antigen
PSMA	Prostate-specific membrane antigen
RGD	Arginine-glycine-aspartic acid
SHBG	Steroid hormone-binding globulin
SPECT	Single photon emission computed tomography

SSR	Somatostatin receptor
SST	Somatostatin
SSTr	Somatostatin receptor
SUV	Standardized uptake value
TATE	Octreotate
TCA	Tricarboxylic acid
TK	Thymidine kinase
TOC	Tyr^3-octreotide
TTP_{min}	Minimum time to peak

Contents

Introduction 131

Targeting Cellular Transport, Metabolism, and Proliferation 133
Overview 133
Imaging Amino Acid Transport and Metabolism ... 133
Imaging Lipid Biosynthesis 141
Imaging Cellular Proliferation with [^{18}F]FLT 145

Targeting Cell Surface Receptors 147
Overview 147
Imaging the Expression of Somatostatin Receptors 147
Imaging the Expression of Integrins 149
Imaging the Expression of Bombesin Receptors 152
Imaging the Expression of Prostate-Specific Membrane Antigen 154
Imaging the Expression of Steroid Hormone Receptors 158

Targeting the Hypoxic Tumor Microenvironment 160
Overview 160
Imaging Tumor Hypoxia with [^{18}F]FMISO 161
Imaging Tumor Hypoxia with ^{64}Cu-ATSM 162

Concluding Remarks 164

References 165

Introduction

Over the past two decades, nuclear imaging has transformed cancer care. Both positron emission tomography (PET) and single photon emission computed tomography (SPECT) have empowered clinicians with imaging tools capable of providing *functional* and *biochemical* information about tissues that complement the *anatomical* maps created by magnetic resonance imaging (MRI) and computed tomography (CT). A remarkable array of radiotracers has been created that enables the visualization of targets ranging from the expression of biomarkers by individual cancer cells to the pH of the tumor microenvironment.

The most widely used radiotracer in oncology – 2-[^{18}F]fluoro-2-deoxyglucose, [^{18}F]FDG – is only one of a few PET radiopharmaceuticals that has been approved by the US Food and Drug Administration. Yet despite its utility, [^{18}F]FDG is limited in many cases and cannot possibly be expected to fulfill all of the imaging needs of clinicians as we enter the era of personalized medicine. As a result, recent years have played witness to ever-increasing efforts toward the development and translation of novel, molecularly targeted imaging agents. *In this chapter, we will focus on radiopharmaceuticals that have reached a particularly critical point in their journey from bench to bedside*: *imaging agents that have been the subject of multiple clinical trials but have yet to be approved by regulatory agencies for routine clinical use*. While a multitude of radiopharmaceuticals have reached the clinic in some capacity, we have chosen to discuss a handful of particularly promising agents as case studies. We truly believe that these radiotracers represent the next generation of clinical nuclear imaging agents. We have organized these imaging agents into three groups according to their target: (I) the machinery of cellular metabolism and biosynthesis, (II) cell surface receptors, and (III) the tumor microenvironment, with a focus on imaging hypoxia. Importantly, the intrinsic technological advantages of PET over SPECT – principally the former's quantitative output and higher resolution – mean that over the past half decade (the time span covered by this chapter), the vast majority of newly translated radiopharmaceuticals have been PET tracers. As a result, this chapter will focus on these agents.

Before we begin, we believe that a brief tutorial on the anatomy of a radiotracer is in order (Fig. 1). Broadly speaking, the vast majority of radiopharmaceuticals are composed of two parts: a targeting vector and a radioisotope. A wide

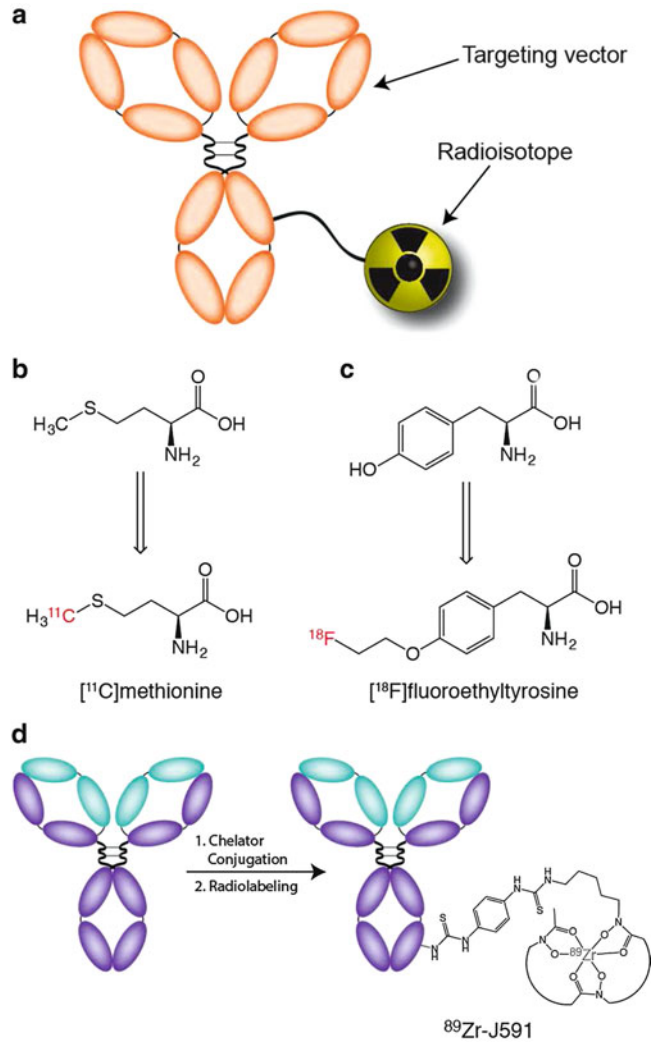

Fig. 1 The basic anatomy of a radiotracer (**a**) as well as three different strategies for the design of radiotracers: the direct replacement of an atom in the parent molecule with a radioactive isotopologue (**b**), the use of a small structural modification to create a "handle" for the incorporation of a radioisotope (**c**), and the use of a chelator along with a radiometal (**d**)

range of molecules has been employed as vectors, including small molecules, peptides, proteins, antibodies, and nanoparticles (and even whole cells!). A similarly varied array of radioisotopes has been used. In this arena, two physical considerations are particularly important: the type of radioactive emission and the half-life of decay. While SPECT radiotracers employ gamma-emitting isotopes such as ^{111}In and ^{99m}Tc, PET agents use positron-emitting nuclides such as ^{18}F, ^{64}Cu, and ^{68}Ga. Radioisotopes with half-lives ranging from 9.97 min (^{13}N) to 4.18 days (^{124}I) have been employed in radiotracers. A key consideration is matching the physical half-life of the radioisotope to the pharmacokinetic half-life of the targeting vector. As a result, short-lived isotopes such as ^{11}C ($t_{1/2} = 20.4$ min) and ^{18}F ($t_{1/2} = 110$ min) are typically used for radiolabeling small molecules, while long-lived nuclides such as ^{89}Zr ($t_{1/2} = 78.4$ h) and ^{111}In ($t_{1/2} = 67.3$ h) are more commonly employed for radiolabeling proteins and antibodies. Finally, the chemistry of radionuclides plays an important role in the design of radiotracers. While nonmetallic radioisotopes such as ^{11}C, ^{15}O, ^{18}F, and ^{124}I can often be incorporated directly into the structure of the radiotracer (e.g., [^{15}O]H_2O or [^{11}C]CO_2), radiometals such as ^{111}In, ^{68}Ga, and ^{89}Zr require that a metal chelator (e.g., DOTA or desferrioxamine) be attached to the vector in order to stably coordinate the radiometal in vivo.

Targeting Cellular Transport, Metabolism, and Proliferation

Overview

The aberrant growth of cancer cells results in numerous metabolic changes that can be targeted for diagnostic imaging. A classic example of a metabolism-targeting radiotracer is 2-[^{18}F]fluoro-2-deoxyglucose ([^{18}F]FDG), a radiolabeled glucose analog that is avidly taken into cancer cells trying to meet their augmented energy requirements by increasing the expression of glucose transporters. Unfortunately, however, because of the ubiquitous role of glucose as an energy source, the increased uptake of [^{18}F]FDG is not a phenomenon specific to cancer cells. Needless to say, this deficiency has spurred significant interest in the development of new, more tumor-selective radiotracers. Over the last decade, several small-molecule radiotracers specific for various metabolic pathways have been developed and clinically evaluated with promising results. Broadly speaking, these tracers can be divided into two groups: (i) radiolabeled amino acids and amino acid analogs that target amino acid transport and metabolism and (ii) acetate, choline, and analogs thereof that target lipid biosynthetic pathways. It is important to note that many of these radiotracers were originally developed for other purposes and only recently have been reevaluated for oncologic imaging. For example, [^{11}C]acetate was initially created for imaging cardiac oxidative metabolism, while *L*-3,4-dihydroxy-6-[^{18}F]fluorophenylalanine ([^{18}F]FDOPA) was developed for imaging dopaminergic neurons in the central nervous system. Lastly, we will highlight the potential for imaging proliferating tumor cells using 3′-deoxy-3′-[^{18}F]fluorothymidine ([^{18}F]FLT), a nucleoside analog that is taken up and retained in proliferating cells without incorporation into DNA.

Imaging Amino Acid Transport and Metabolism

Amino acids are vital sources of carbon and nitrogen and are precursors for the biosynthesis of proteins. Thus, they are an extremely valuable commodity to rapidly proliferating tumor cells. In order to accommodate the increased need for these molecular building blocks, cancer cells often overexpress cell membrane-bound amino acid transporters [1]. Radiolabeled amino acids and their analogs are therefore enticing options for the development of cancer-specific radiotracers. Although radiolabeled amino acids can participate in a variety of metabolic processes, the currently available amino acid radiotracers exclusively visualize the upregulation of transporter expression and the rate of amino acid uptake [2]. More specifically, the amino acid transporter systems known to be upregulated in various cancers are the ASC transporter 2 (ASCT2) and L-type amino acid transporter 1 (LAT1) systems [3, 4]. ASCT2 is responsible for the Na^+-dependent transport of small neutral amino acids – such as alanine, serine, and cysteine (which give the abbreviated name of the transporter) – and is the principal route for the uptake of glutamine. LAT1, in contrast, transports bulky, hydrophobic payloads including leucine, phenylalanine, and tyrosine. The overexpression of amino acid transporters in cancer cells induces nutrient-sensitive mTOR (mammalian target of rapamycin) signaling pathways, resulting in the upregulation of cell growth and proliferation [4]. In addition, unlike in normal cells, the metabolism of cancer cells relies on ASCT2-transported glutamine, which is used as a carbon source for the synthesis of tricarboxylic acid (TCA) cycle intermediates and to maintain pools of nonessential amino acids [5]. The transporter-mediated uptake of amino acid radiotracers and their postulated participation in cellular processes are presented in Fig. 2.

The radiolabeled amino acids currently in clinical use include ^{11}C-labeled L-[^{11}C-methyl]methionine ([^{11}C]methionine), *anti*-1-amino-3-^{18}F-fluorocyclobutane-1-carboxylic acid ([^{18}F]FACBC), 3,4-dihydroxy-6-[^{18}F]fluorophenylalanine ([^{18}F]FDOPA), and O-(2-^{18}F-fluoroethyl)-L-tyrosine ([^{18}F]FET). Moreover, out of the many radiofluorinated analogs of glutamine evaluated to date, 4-[^{18}F]-(2*S*,4*R*)fluoroglutamine ([^{18}F]FGln) looks to be the most promising candidate for clinical

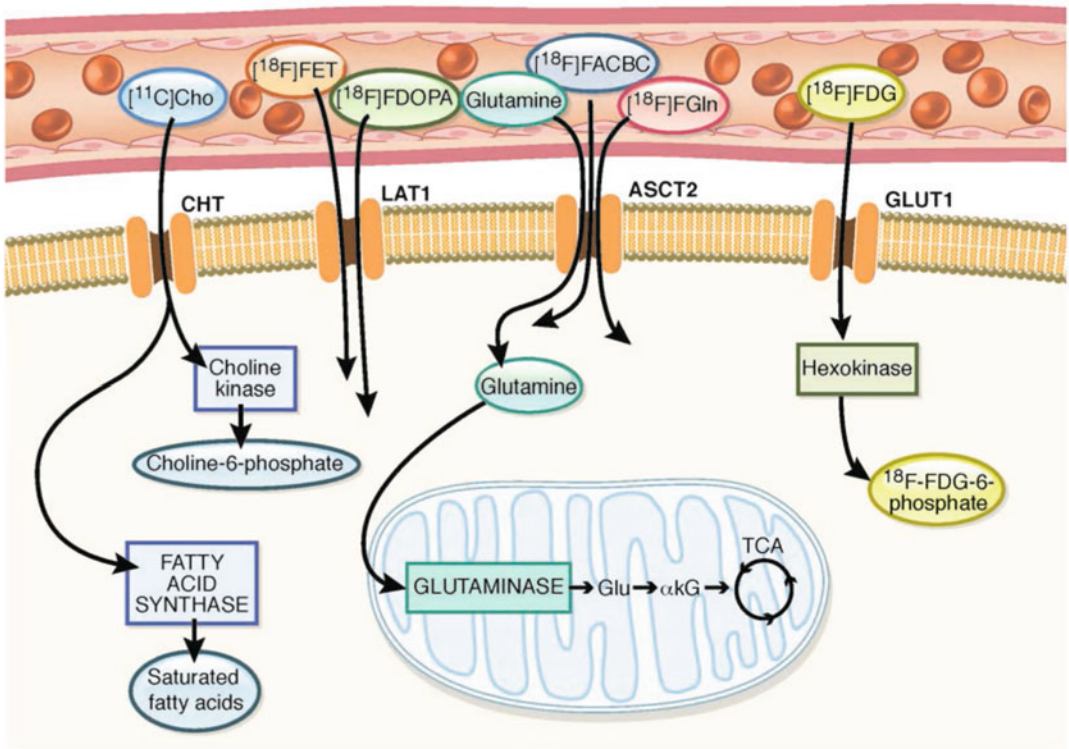

Fig. 2 The transport mechanisms of amino acid radiotracers and the postulated routes of their downstream participation in cellular processes

translation. The structures of these amino acid radiotracers are shown in Fig. 3. As the reader will note, all of these tracers are radiolabeled with the short-lived positron-emitting radioisotopes ^{11}C and ^{18}F. It is important to note that despite their common mode of decay, there are fundamental differences between ^{11}C- and ^{18}F-labeled tracers, and care should be taken to select the appropriately labeled radiotracer for the purpose. Since fluorine is not a common constituent in natural compounds, the introduction of the ^{18}F radiolabel generally yields nonidentical structural analogs in which the label is attached via substitution for another halogen, substitution for a hydroxyl group, or incorporation of an ^{18}F-labeled prosthetic group. In contrast, most radiotracers labeled with ^{11}C are typically chemically *identical* to their non-labeled counterparts, with the only difference being the replacement of a ^{12}C atom with a ^{11}C atom (making the two compounds *isotopologues*). Consequently, the pharmacokinetic and biochemical behavior of the ^{11}C-labeled isotopologue is *identical* to the non-labeled parent compound, and the radiotracer undergoes transport, metabolism, and elimination in the *exact same manner* as the compound it "traces." There are, however, advantages to using ^{18}F-labeled tracers. For example, the longer physical half-life of the isotope allows for multistep syntheses and the transportation of tracers to remote imaging facilities. In addition, in some cases, the chemical differences between the natural molecule and its ^{18}F-labeled counterparts can be useful. For example, the ^{18}F label can block the downstream metabolism of a tracer after it has entered a cell, resulting in intracellular accumulation and higher tumor signal. By far the best example of this phenomenon is the trapping mechanism of [^{18}F]FDG.

One metabolism-targeting radiotracer provides a particularly good example of a case in which a drastic structural modification to the tracer facilitates metabolic trapping. The alicyclic amino

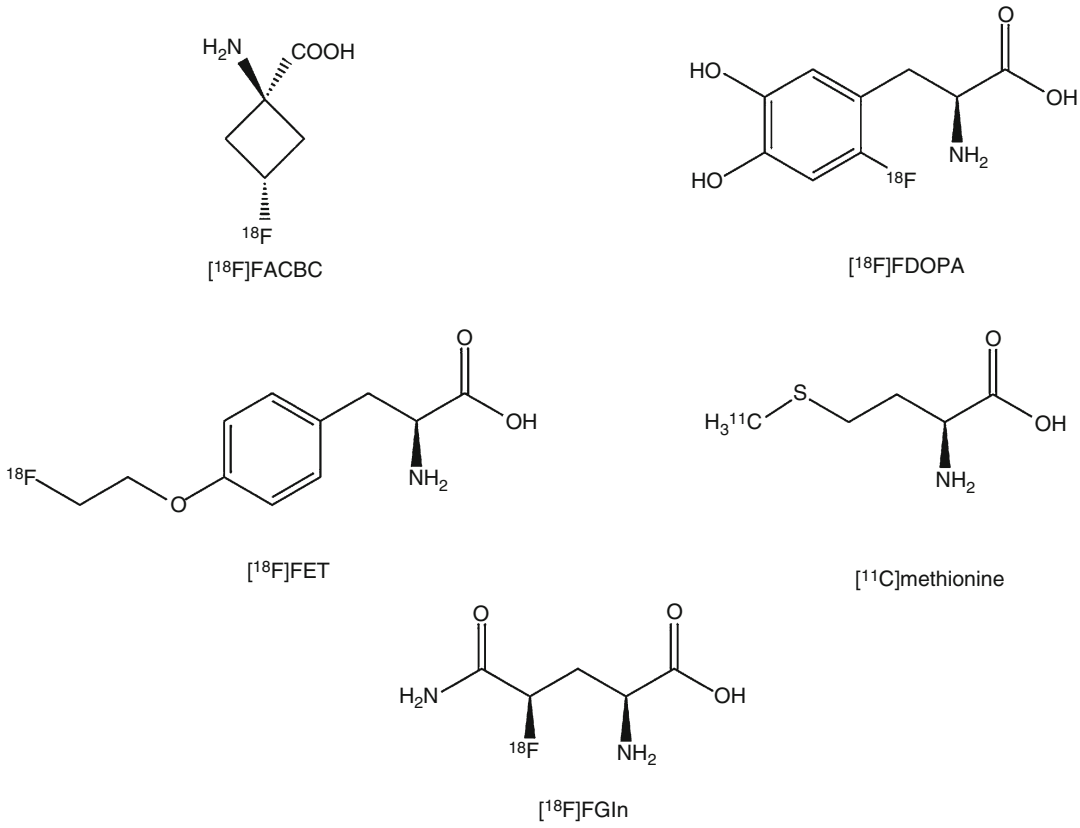

Fig. 3 The structures of selected amino acid radiotracers

acid [^{18}F]FACBC – a compound in which the amino and carboxylic acid termini are joined by a nonnatural ^{18}F-substituted cyclobutane – is still recognized and transported into cells by ASCT2, but the cyclobutane moiety renders the compound immune to subsequent metabolism [6]. To date, [^{18}F]FACBC has been evaluated in clinical studies primarily for the imaging of prostate cancer. Prostate cancer imaging is a particularly promising application of [^{18}F]FACBC, as it takes advantage of the low background accumulation of the tracer in the urinary bladder [7]. In recent clinical trials in patients with primary prostate cancer from Emory University, the National Cancer Institute, and Uppsala University in Sweden, [^{18}F]FACBC uptake was found to correlate well with intraprostatic lesions, while metastases remained largely undetected (Fig. 4) [8–10]. Furthermore, Schuster et al. originally reported a good correlation between [^{18}F]FACBC uptake and histopathology and the Gleason score. However, later reports have challenged this by showing nonspecific uptake of the radiotracer by B and T lymphocytes [11] and, consequently, in inflammatory lesions including prostatitis and benign prostatic hyperplasia as well as benign growths such as osteomata [12]. The sensitivity of [^{18}F]FACBC PET toward malignant lesions was, however, drastically improved when combined with positron-emission tomography/magnetic resonance imaging (PET/MRI). The current consensus on the potential utility of [^{18}F]FACBC PET for clinical applications is that it has potential for the diagnosis of the most aggressive prostate cancer lesions to support radiotherapy planning.

Standing in stark contrast to the unnatural [^{18}F]FACBC, ^{11}C-labeled methionine (L-[^{11}C-methyl]methionine) is a radiotracer in which the radiopharmaceutical is *chemically identical* to the natural amino acid. Developed in the 1970s as part of

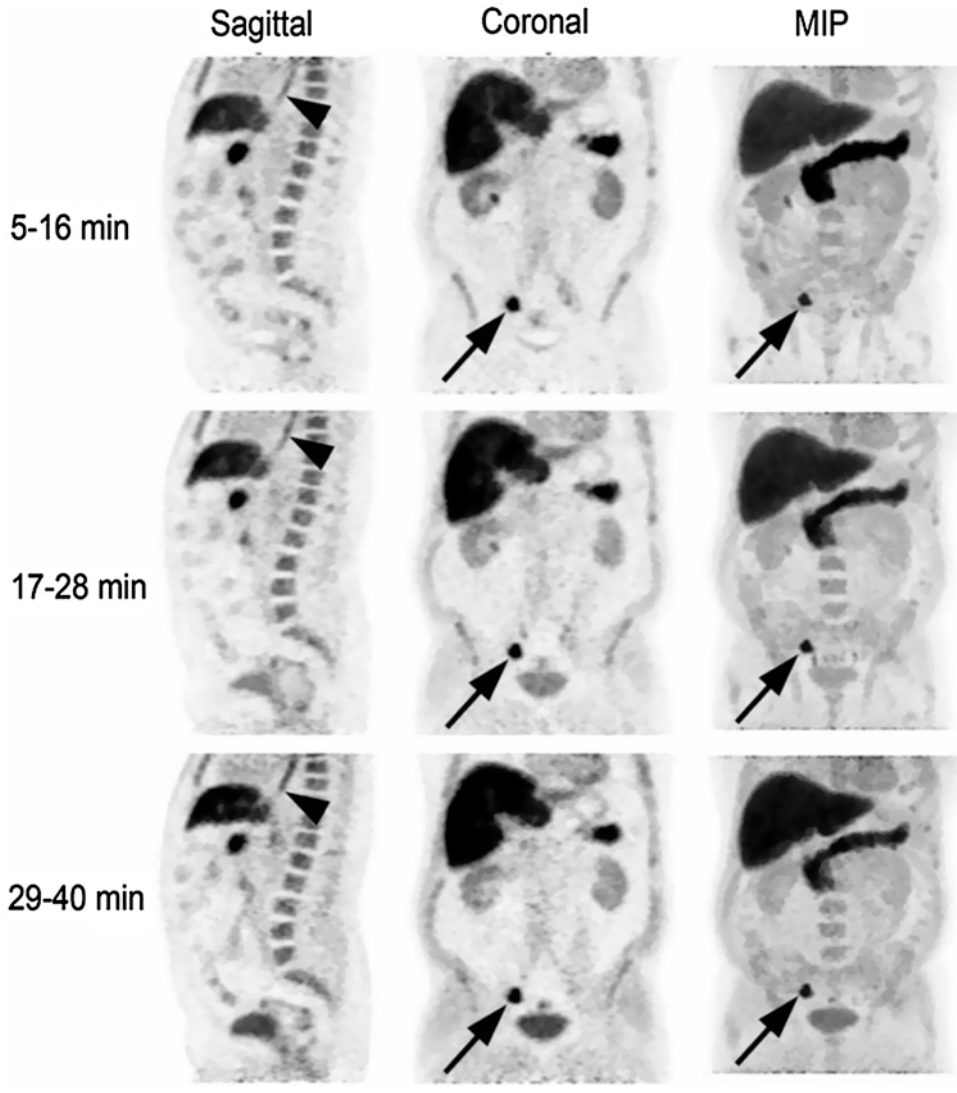

Fig. 4 Sagittal, coronal, and maximum intensity projection (MIP) [^{18}F]FACBC PET images acquired over three time intervals in a patient with recurrent prostate cancer. Uptake can be seen in the right iliac lymph node (*arrows*) at a site of metastatic recurrence. Bladder activity initially is absent but moderately increases with time upon tracer excretion. Also noted is mild to moderate diffuse activity in the esophagus (*arrowheads*) (This research was originally published in *The Journal of Nuclear Medicine*, Schuster et al. [12]. © by the Society of Nuclear Medicine and Molecular Imaging, Inc.)

a series of ^{11}C-labeled amino acid tracers for the assessment of the rate of protein synthesis, [^{11}C] methionine is the only radiotracer from this lot in active clinical use today and can be efficiently radiolabeled in a single-step reaction using [^{11}C] methyl iodide [13]. [^{11}C]methionine is a substrate of the LAT1 transporter and is readily incorporated into proteins during translation. Consequently, [^{11}C]methionine uptake in subjects with glioma and non-small cell lung cancer (NSCLC) has been shown to correlate with both tumor microvessel density (i.e., the upregulation of LAT1) and proliferative capacity (i.e., the rate of tracer incorporation into cells) [14, 15]. Due to their high expression levels of LAT1 and prominent exocrine activity, both healthy liver and pancreas display high uptake of [^{11}C]methionine, limiting the utility of the tracer to visualize

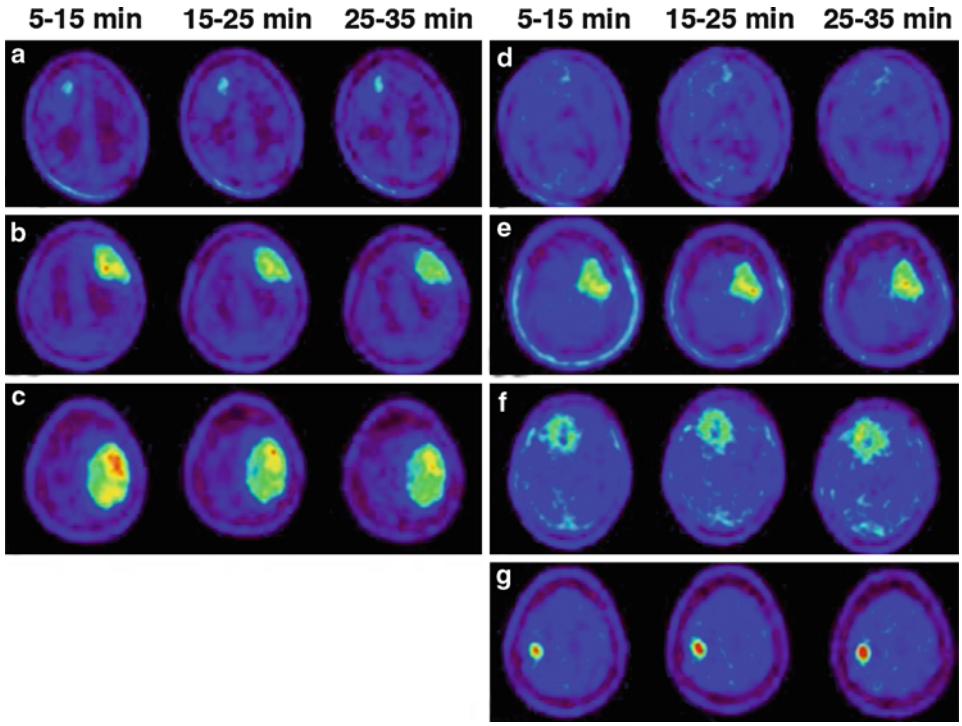

Fig. 5 Dynamic changes in [^{11}C]methionine accumulation in various brain malignancies. (**a**) Oligodendroglioma, (**b**) anaplastic oligodendroglioma, (**c**) meningioma, (**d**) diffuse astrocytoma, (**e**) anaplastic astrocytoma, (**f**) glioblastoma, and (**g**) malignant lymphoma (Reproduced with permission from Springer from Aki et al. [146])

neoplasms in those organs [16, 17]. In contrast, the background accumulation of [^{11}C]methionine in the brain is low. As a result, the tracer's greatest potential lies in the imaging of tumors of the CNS (Fig. 5). Current clinical use of [^{11}C]methionine for the diagnosis and post-treatment follow-up of brain tumors is widespread in both Europe and Japan, where several clinical studies have established the potential of ^{11}C-methionine PET for the sensitive and specific diagnosis of primary gliomas. This allows for the identification of the proliferating tumor margin, which is important for radiotherapy planning [18]. The uptake of [^{11}C]methionine in gliomas may also be used as a survival factor, as initially low tracer uptake correlates with a more favorable prognosis [19]. However, reliable correlation between tracer uptake and the grade of the disease has not been achieved. Additionally, [^{11}C]methionine has been shown to aid in differentiating between tumors and radiation necrosis in conjunction with anatomical imaging modalities MRI and CT (Fig. 6).

^{18}F-labeled *o*-(2-[^{18}F]-fluoroethyl)-L-tyrosine ([^{18}F]FET) is another nonnatural amino acid that localizes into tissues via LAT1-mediated transport [20]. Unlike [^{11}C]methionine, however, [^{18}F]FET cannot be incorporated into proteins and is thus considered non-metabolic. [^{18}F]FET is commonly prepared either using a two-step synthesis based on ^{18}F-labeled fluoroethyltosylate and a protected tyrosine *or* a single-step reaction using an ethyltosylate-substituted tyrosine precursor [21, 22]. As with [^{11}C]methionine, clinical studies with [^{18}F]FET have focused on tumors of the CNS, for which radiolabeled amino acids seem to offer the advantage of low background uptake compared to [^{18}F]FDG [23]. Dynamic [^{18}F]FET imaging has proven to be especially useful in patients with glioma, as differences in the kinetic parameters of [^{18}F]FET uptake allow for the differentiation between low-grade and high-grade gliomas. The time-activity curves for [^{18}F]FET uptake in low-grade and high-grade gliomas from the study of Pöpperl et al. [24] are presented in Fig. 7. More recently,

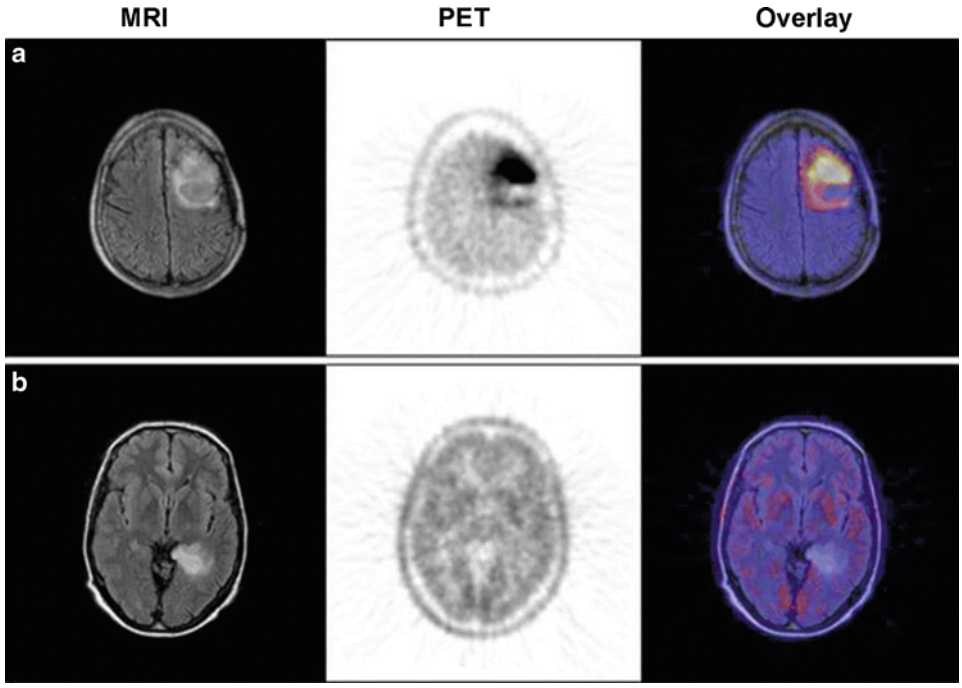

Fig. 6 The MRI, PET, and fused images depicting differences in [^{11}C]methionine uptake in a brain tumor (**a**) and an area of radiation necrosis (**b**) (Reproduced with permission from Springer from Glaudemans et al. [18])

select kinetic parameters – including the minimum time to peak (TTP_{min}) – have been proposed to derive quantitative data from dynamic [^{18}F]FET imaging for the grading and functional characterization of primary brain tumors [25].

A fluorinated analog of the brain-permeable dopamine precursor *L*-dihydroxyphenylalanine (*L*-DOPA) – *L*-3,4-dihydroxy-6-[^{18}F]-fluorophenylalanine ([^{18}F]FDOPA) – was first developed for the study of changes in dopaminergic signaling in the brains of patients with Parkinson's disease [26]. Unlike other fluorinated amino acid analogs, [^{18}F]FDOPA *is* readily metabolized in vivo in the same manner as natural *L*-DOPA by catechol-*o*-methyl transferase (COMT) and aromatic amino acid decarboxylase (AACD) to yield 3-*O*-methyl-6-[^{18}F]-fluoro-L-dopa ([^{18}F]3-OMFDOPA) and [^{18}F]6-fluorodopamine ([^{18}F]FDA), respectively (Fig. 8) [27]. Recently, [^{18}F]FDOPA PET has been explored in oncology for the diagnosis of neuroendocrine tumors (NET). NETs are often challenging imaging targets, as the tumors are small and dispersed and constitute a metabolically and biologically diverse group. The current clinical standards for the diagnostic imaging of NETs are somatostatin receptor (SSR)-targeted PET/CT, [^{18}F]FDG, and SPECT with [^{123}I]-*meta*-iodobenzylguanidine ([^{123}I]MIBG) or ^{111}In-pentetreotide. The preferential uptake of [^{18}F]FDOPA in NETs is a result of the ability of the tumors to synthesize and store biogenic amines and polypeptide hormones [28]. The NET lesions most efficiently delineated with [^{18}F]FDOPA PET are those that originate from the chromaffin cells of the adrenal medulla (pheochromocytomas), paragangliomas of the sympathetic nervous system, and medullary thyroid cancer (MTC) [29]. Figure 9 shows a pancreatic NET lesion that remains completely undetected by [^{18}F]FDG but is clearly visualized with [^{18}F]FDOPA. Comprehensive comparisons between SSR PET/CT and [^{18}F]FDOPA are scarce, but in general, a higher

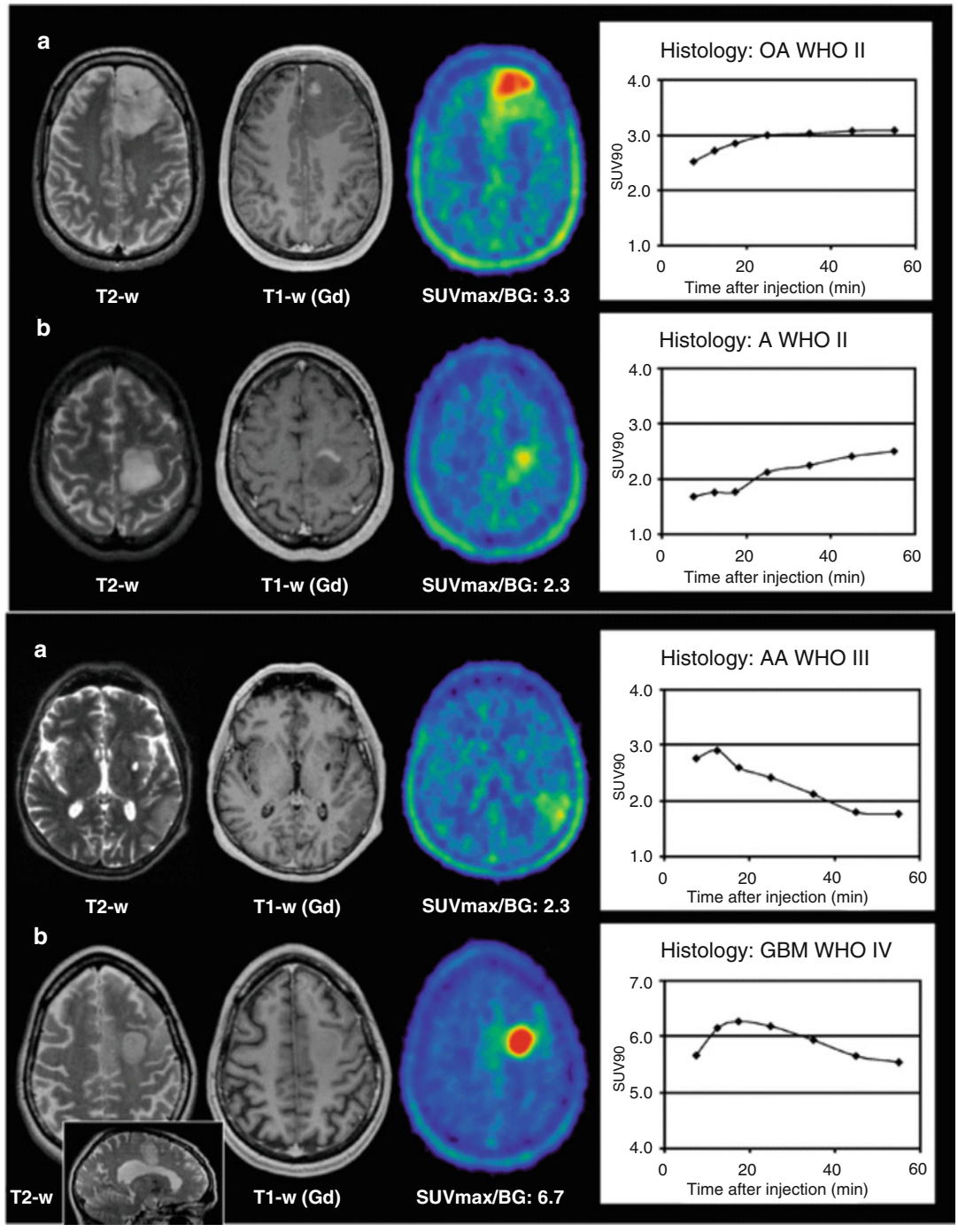

Fig. 7 Differences in the uptake kinetics of [^{18}F]FET in subjects with low-grade (WHO II) and high-grade (WHO III) gliomas. In the latter, a sharp peak in the SUV at early time points after administration can be seen (Reproduced with permission from Springer from Pöpperl et al. [24])

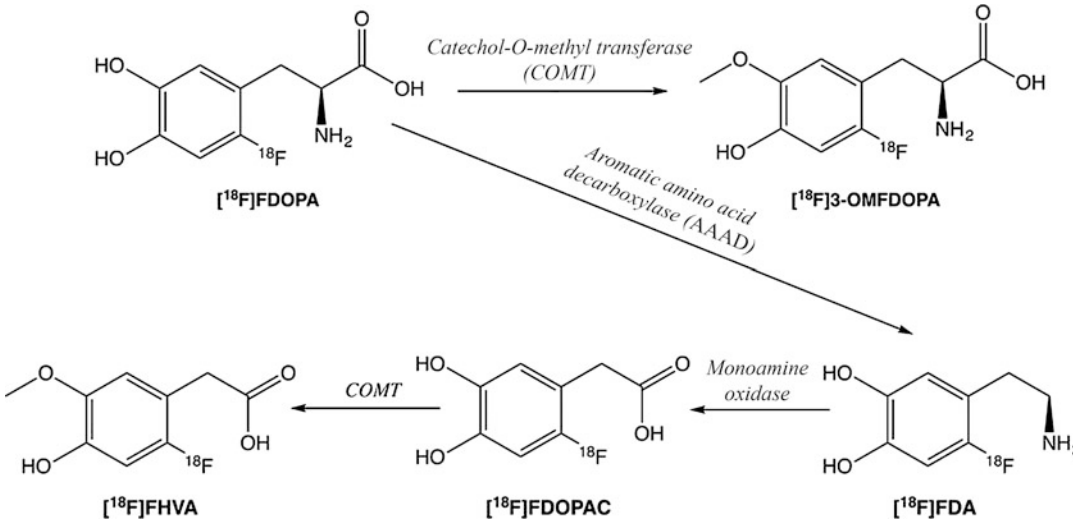

Fig. 8 The metabolic fates of [^{18}F]FDOPA. 3-*O*-Methyl-6-fluoro-L-dopa (3-OMFDOPA), 6-fluorodopamine (FDA), *L*-3,4-dihydroxy-6-fluorophenylacetic acid (FDOPAC), and 6-fluorohomovanillic acid (FHVA) (Figure redrawn from Vallabhajosula [27], with permission from Elsevier)

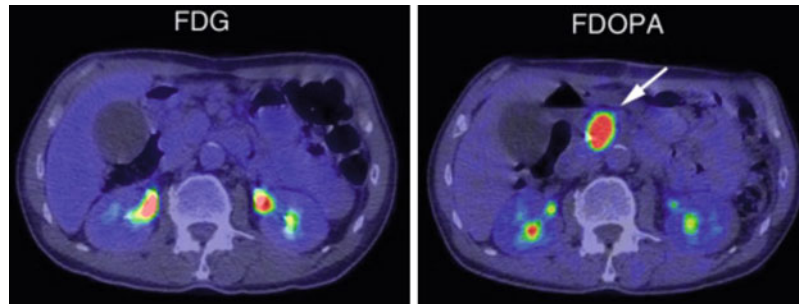

Fig. 9 [^{18}F]FDG and [^{18}F]FDOPA PET images of a patient with a low-grade metastatic pancreatic neuroendocrine tumor showing the lack of [^{18}F]FDG tumor detection and the positive [^{18}F]FDOPA uptake in the lesion (Reprinted from Minn et al. [29], with permission from Elsevier)

tumor burden is detected with SSR PET/CT [30]. Despite these alternative techniques, the utility of [^{18}F]FDOPA PET/CT imaging in NET is highlighted in cases with variable or low SSR expression like medullary thyroid carcinoma or in which a closer metabolic dissection of the tumor is warranted [31]. In CNS tumors, including high-grade glioma, [^{18}F]FDOPA has been shown to yield comparable results to [^{18}F]FET in tumor delineation [32]. However, widespread clinical use of [^{18}F]FDOPA is currently limited by its complex radiosynthesis and the low specific activity of the compound when synthesized via electrophilic radiofluorination. As a result, only a handful of institutes worldwide have access to high specific activity [^{18}F]FDOPA [33]. Thankfully, this is expected to change in the future due to recent developments in the automated enantioselective synthesis of [^{18}F]FDOPA from 2-[^{18}F]fluoro-4,5-dimethoxybenzyl iodide using a phase transfer catalyst [34].

As a source of both carbon and nitrogen, glutamine is a vital feedstock for a number of biosynthetic pathways in cancer cells. This efficient use of glutamine by cancer cells is achieved by the upregulation of glutamine transporters on the cell membrane as well as the increased expression of mitochondrial glutaminase that drives the synthesis of glutamate from glutamine to feed the TCA cycle [35]. The creation of a PET tracer for glutamine-based imaging has required the careful consideration of radiolabeling strategies. The seemingly obvious choices for a radiolabel are ^{11}C and ^{13}N ($t_{1/2}$ = 9.97 min) both of which

could yield chemically identical isotopologues of glutamine. However, in addition to the synthetic challenges posed by the short physical half-lives of the two radioisotopes, ^{11}C- and ^{13}N-labeled glutamine radiotracers undergo rapid degradation and elimination of the radiolabel from the tracer in tumor cells as a result of glutaminolysis.

This has left ^{18}F-radiofluorinated glutamine analogs as the only feasible alternative. The most promising ^{18}F-labeled glutamine analog – 4-[^{18}F]-(2*S*,4*R*)fluoroglutamine ([^{18}F]FGln) – was recently evaluated for the imaging of gliomas in a pilot, open-label human microdosing study [36]. The uptake of [^{18}F]FGln in gliomas was comparable to [^{18}F]FDG, though the uptake of [^{18}F]FGln in healthy brain was markedly lower (Fig. 10). As a result, the use of [^{18}F]FGln was proposed over [^{18}F]FDG due to its improved contrast. However, later studies revealed that [^{18}F]FGln is prone to defluorination in vivo in humans, a problem which could result in the deposition of high concentrations of ^{18}F-fluoride in the bone. Studies investigating new [^{18}F]fluoropropyl-substituted derivatives as alternatives to [^{18}F]FGln with more selective radiosyntheses and improved in vivo stability are underway [37]. The final utility of glutamine-based radiotracers in oncology will remain unknown until these tracers become widely available for clinical studies. Nevertheless, glutamine PET holds great promise as a novel tool for metabolic imaging in oncology.

Imaging Lipid Biosynthesis

In addition to glucose and amino acids, tumor cells also crave nutrients to drive the biosynthesis of the cell membrane lipids needed to sustain rapid cell division. The PET radiotracers suitable for imaging lipid biosynthesis include ^{11}C-labeled acetate, ^{11}C-labeled choline and its ^{18}F-labeled analogs, ^{18}F-fluoromethylcholine, and ^{18}F-fluoroethylcholine (structures are given in Fig. 11).

[^{11}C]Acetate participates in the synthesis of fatty acids and is readily incorporated in phosphatidylcholine in tumor cells [38, 39]. In contrast to normal cells (in which the preferred fate for acetate is oxidative metabolism), cancer cells seem to utilize [^{11}C]acetate almost exclusively as a building block [39, 40]. Fatty acid synthase (FAS, EC 2.3.1.85) catalyzes de novo lipogenesis: the synthesis of saturated fatty acids like myristate, palmitate, and stearate from acetyl-CoA, malonyl-CoA, and NADPH [41, 42]. FAS has been found to be upregulated in many cancers and is considered a potential target for chemotherapy, prompting the use of [^{11}C]acetate in oncologic imaging [43]. To date, the most promising application of [^{11}C]acetate PET lies in prostate cancer, a malignancy in which FAS upregulation is an important part of pathogenesis. Furthermore, the enzyme has been established as a measure of aggressiveness of the disease via correlation with high Gleason scores [44, 45]. Figure 12a shows a typical finding in [^{11}C]acetate PET, in which anatomical (MRI) and histopathological findings correlate well with the uptake of the radiotracer in the primary tumor. In Fig. 12b, a representative whole-body scan of a patient with recurrent prostate carcinoma is shown to illustrate both the avid uptake of the tracer in the pancreas and liver as well as the lack of urinary excretion. These two characteristics combine to make [^{11}C]acetate ideal for the imaging of prostate cancer but of limited value in tumors proximal to the gastrointestinal tract. In addition to the detection of primary tumors, [^{11}C]acetate PET has been shown to be especially effective for the delineation of bone and lymph node metastases and in the diagnosis of recurrent disease with predictive value for treatment response [46, 47]. Recently, Leisser et al. showed that the predictive value of [^{11}C]acetate PET has a positive correlation with serum PSA levels [44].

In addition to FAS, cancer cells upregulate choline kinase (ChoK, EC 2.7.1.32), the first enzyme in the synthetic pathway for another constituent of the cell membrane: phosphatidyl choline. Consequently, ^{11}C-radiolabeled [^{11}C]choline and ^{18}F-labeled choline analogs have been proposed as diagnostic agents in oncology. As with [^{11}C]acetate, the most promising applications of both choline tracers have been found in prostate cancer, in which energy metabolism favors fatty acid oxidation. Like [^{11}C]acetate, [^{11}C]choline behaves in exactly the same way as natural

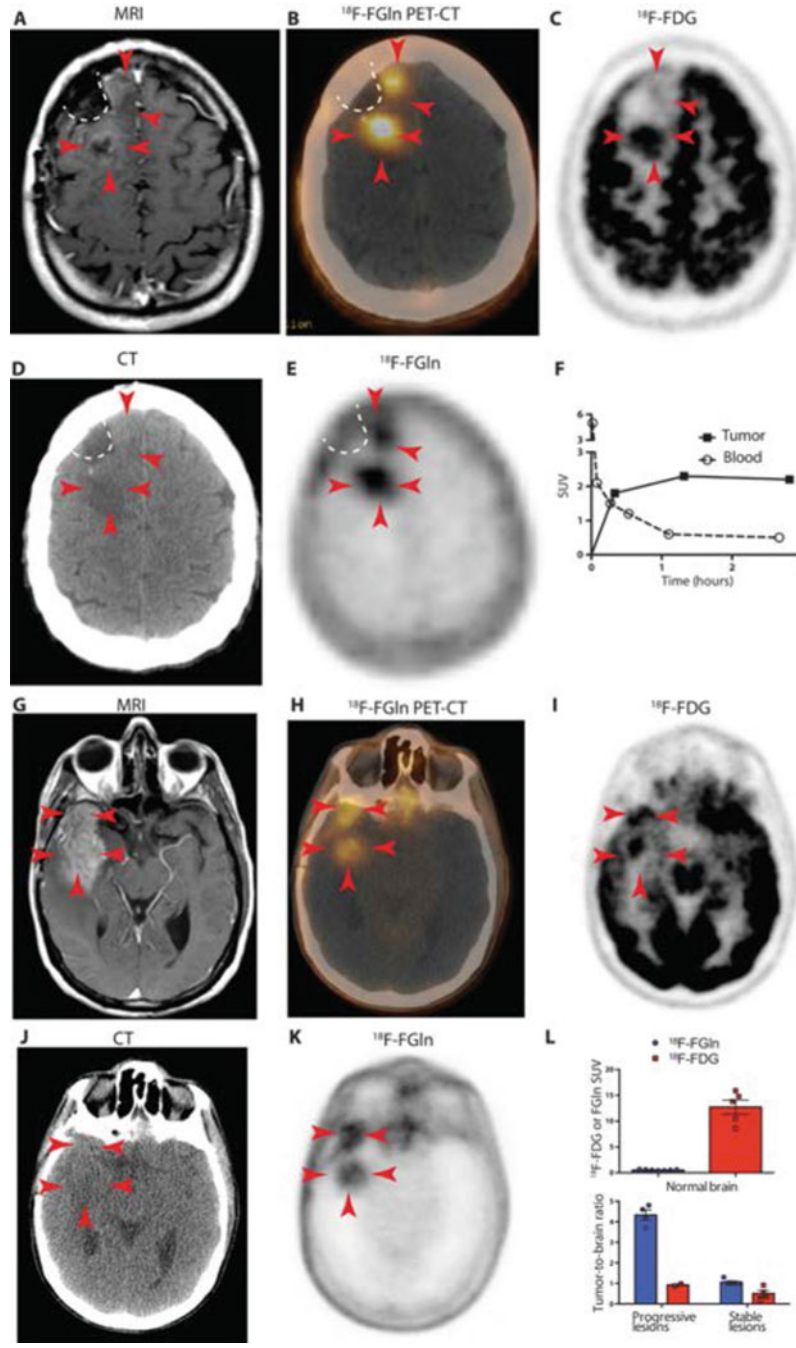

Fig. 10 [^{18}F]FGln PET shows uptake in glioma under progression of the disease in a patient with a IDH1m oligodendroglioma (**a**–**k**) and a patient with a glioblastoma (**g**–**k**). T1-weighted MRI with contrast enhancement (**a** or **g**), fusion image of [18F] FGln PET/CT (**b** or **h**) of CT (**d** or **j**) and [^{18}F]FGln PET (**e** or **k**), and [^{18}F]FDG PET image (**c** or **i**) showing the utility of [^{18}F]FGln PET in delineating tumor (indicated by *red arrows*) from the background brain activity and tumor surgical cavity (*white dotted line*). The standard uptake values (SUV) of [^{18}F]FGln corresponding to tumor uptake (*black squares*) and blood clearance (*clear circles*) plotted over time (**f**). Comparison of [^{18}F] FGln (*blue bars*) and [^{18}F] FDG (*red bars*) illustrates differences in background uptake with both radiotracers in normal brain (*top panel*) and tumor-to-brain ratios from three clinically stable glioma patients and three glioma patients with clinically progressive disease (**l**) (From Venneti et al. [36]. Reprinted with permission from AAAS)

choline: it is metabolized into ^{11}C-labeled phosphatidyl choline and incorporated into cells. Curiously, while two of the methyl groups in choline are necessary for ChoK specificity, longer alkyl chains in the third position *are* well tolerated [48], allowing for the creation of ^{18}F-labeled fluoromethyl and fluoroethyl analogs with favorable imaging properties. The vast majority of recent clinical studies has been carried out using [^{18}F]fluoromethylcholine, which has shown potential for the detection of lymph node and bone metastasis in patients with castration-resistant

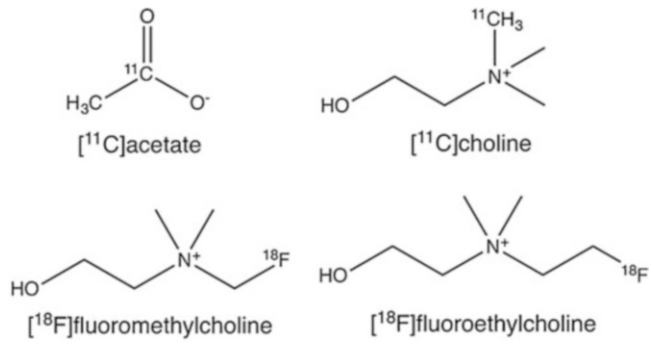

Fig. 11 The structures of [^{11}C]acetate, [^{11}C]choline, [^{18}F]fluoromethylcholine, and [^{18}F]fluoroethylcholine

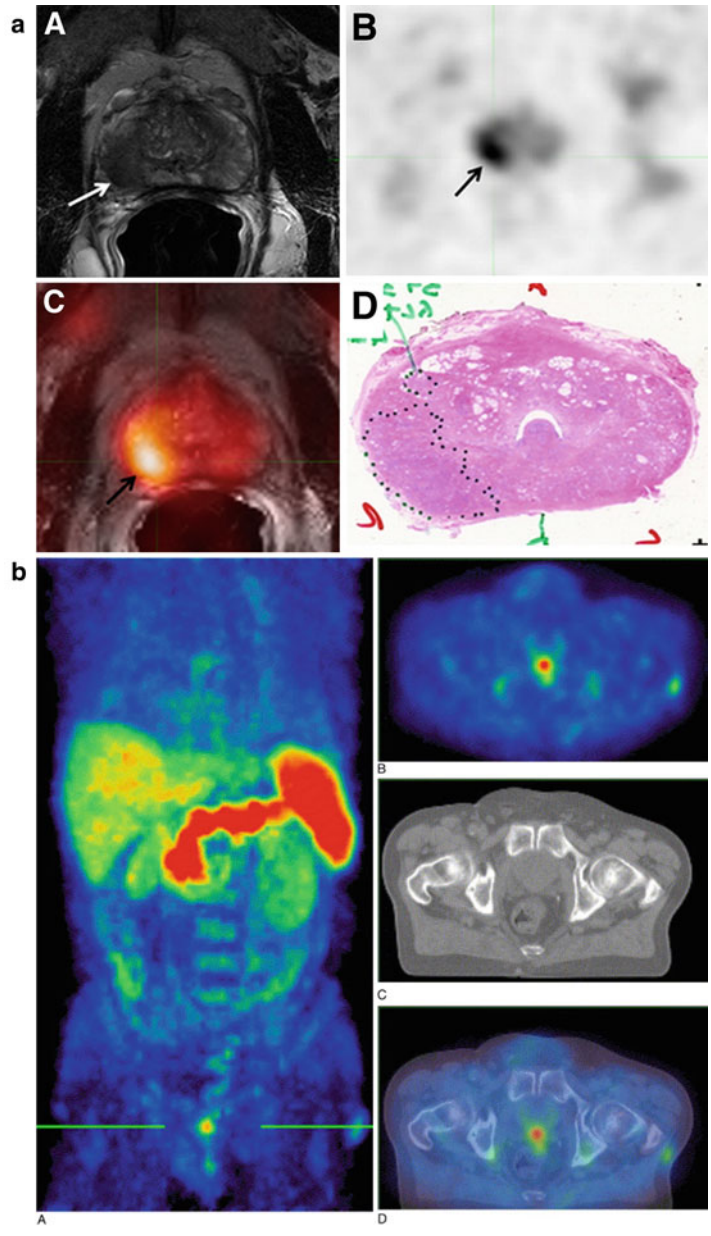

Fig. 12 (**a**) Imaging of a patient with prostate carcinoma – T2-weighed MRI (**a**), [^{11}C]acetate PET image (**b**), and fused [^{11}C] acetate PET/MRI – demonstrates low-intensity focus in right mid-gland peripheral zone (*arrows*). Corresponding pathology (**d**) confirmed tumor with a Gleason score of 3 + 4 (inked in *black*) (This research was originally published in *The Journal of Nuclear Medicine*, Mena et al. [147]. © by the Society of Nuclear Medicine and Molecular Imaging, Inc.). **b** Whole-body [^{11}C]acetate PET (**a**) and transaxial slices through the tumor (*green line* in **a**) of the [^{11}C]acetate PET (**b**), CT (**c**), and fusion PET/CT (**d**) indicating local prostate cancer recurrence in a 74-year-old patient with serum PSA level of 2.5 ng/mL (Reprinted from Sandblom et al. [46], with permission from Elsevier)

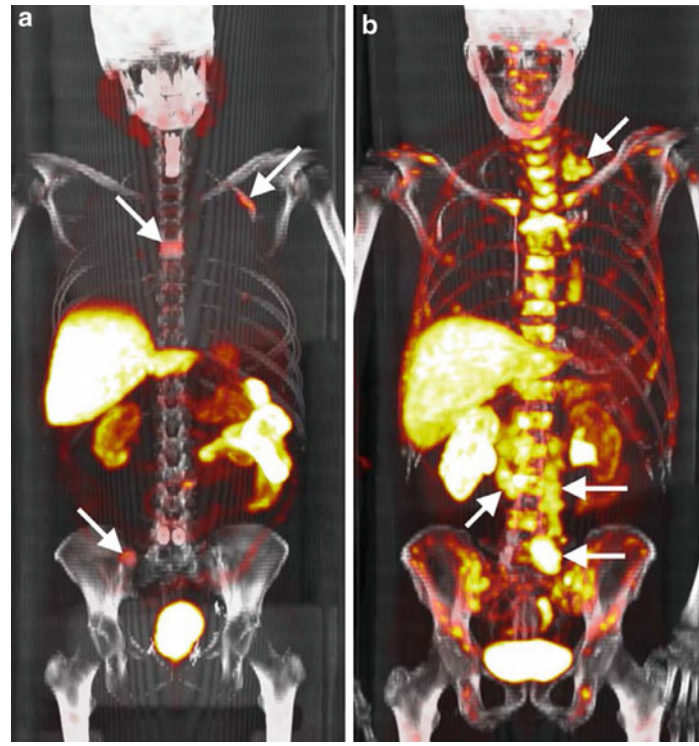

Fig. 13 [^{18}F]fluorocholine PET/CT of a patient with castration-resistant prostate cancer. A patient with relatively low tumor burden and a PSA level of 4.9 ng/mL shows areas of increased [^{18}F]fluorocholine uptake corresponding to lesions in the thoracic spine, ribs, and iliac bone (**a**). In contrast, [^{18}F]fluorocholine PET/CT from a patient with a PSA level of 28.1 ng/mL shows numerous areas of increased [^{18}F]fluorocholine uptake in the skeleton along with the lymph nodes (*arrows*) in the *left* supraclavicular fossa, retroperitoneum, and pelvis (**b**). *Arrows* denote metastatic sites (This research was originally published in *The Journal of Nuclear Medicine*, Kwee et al. [148]. © by the Society of Nuclear Medicine and Molecular Imaging, Inc.)

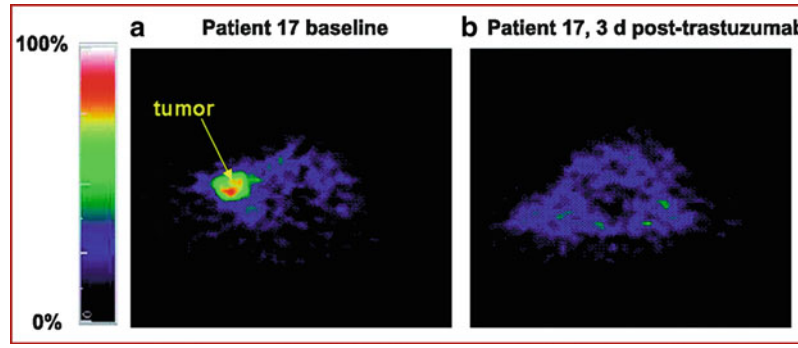

Fig. 14 Representative [^{11}C]choline PET images from a patient with HER+ breast tumor showing response to trastuzumab chemotherapy (Reprinted from Kenny et al. [149]. © by the American Association for Cancer Research)

prostate cancer (Fig. 13). However, contrasting observations have also been reported, warranting further studies before firmly establishing the clinical utility of ^{18}F-fluoromethylcholine PET in the diagnosis and prognosis of prostate cancer [49]. Regardless of the tracer used, the uptake of choline in prostate cancer seems to be dependent on serum PSA levels, allowing for the detection of disease recurrence at a sensitivity exceeding 40% at serum PSA levels of 1 ng/mL [50, 51]. Moving beyond prostate cancer, the upregulation of ChoK and increased intracellular concentrations of phosphocholine have also been observed in breast and epithelial ovarian carcinomas, prompting clinical imaging studies with radiolabeled choline tracers in patients with these malignancies [52, 53]. Figure 14 shows the uptake of [^{11}C]choline in HER2-positive breast cancer at baseline and 3 days after the initiation of trastuzumab chemotherapy, illustrating the potential value of [^{11}C]choline PET for monitoring treatment response. That said, more studies are warranted to establish the utility of [^{11}C]choline PET in malignancies other than prostate cancer.

Imaging Cellular Proliferation with [^{18}F]FLT

Elevated rates of cellular proliferation are one of the hallmarks of cancer [54]. Given that these increased rates of proliferation are often accompanied by the upregulation of free nucleotide scavenging, the latter has attracted a great deal of attention as a target for the imaging of proliferation. Radiolabeled analogs of thymidine have emerged as particularly promising imaging agents for the evaluation of cell proliferation and viability. Chosen for their exclusive incorporation into DNA rather than RNA, thymidine-based radiotracers have yielded varying degrees of success. Easily the most promising variant is 3′-deoxy-3′-[^{18}F]fluorothymidine (FLT), modified from the original nucleoside structure via the substitution of the 3′ hydroxyl group with ^{18}F (Fig. 15). ^{11}C-labeled tracers such as [^{11}C]methionine and [^{11}C]thymidine have been proposed, but the 20-min half-life of ^{11}C has proven to be too short for effective PET imaging [55].

The structure of FLT allows it to interact with enzymes specific to nucleoside uptake, processing, and metabolism. However, the absence of a 3′ hydroxyl group prevents its incorporation into cellular DNA (^{3}H-FLT inclusion <1%) [56]. FLT enters cells either through passive diffusion or facilitated transport via Na^{+}-dependent channels. In a mechanism reminiscent of [^{18}F]FDG, intracellular FLT is phosphorylated by thymidine kinase 1 (TK1) to form [^{18}F]FLT-monophosphate. This traps the radiotracer within the cell where it can undergo further phosphorylation to form FLT-diphosphate and FLT-triphosphate [56]. TK1 activity has been found to be higher in some malignant cell lines, leading to increased retention of FLT and higher uptake within the proliferating tissue [57]. The mechanism of uptake and retention of [^{18}F]FLT is illustrated in Fig. 16.

[^{18}F]FLT PET has been utilized in dozens of clinical trials with a variety of cancers [56, 58]. One of the most common uses of [^{18}F]FLT has been as a noninvasive tool for assessing the viability of tumors. Such scans can be administered following a cycle of chemotherapy or radiation therapy and have been repeatedly confirmed as an

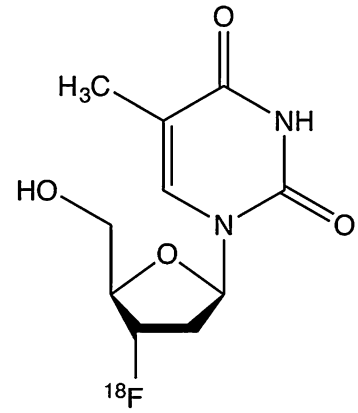

Fig. 15 The structure of [^{18}F]FLT

effective predictive measure of whether a patient will benefit from further treatment. For example, Contractor et al. found that a reduction in [^{18}F]FLT uptake in the weeks following the treatment of breast cancer with docetaxel correlated significantly to lesion size evaluated via ultrasound and CT ($P = 0.004$) [59]. Such results are mirrored in nearly every case: the overall uptake of [^{18}F]FLT decreases significantly in response to therapy, providing an effective method to monitor the progression of treatment [58].

The current clinical standard for monitoring tumor response to treatment is through the use of [^{18}F]FDG. Not surprisingly, there are many studies comparing [^{18}F]FLT and [^{18}F]FDG uptake [60–62]. One potential advantage of FLT over [^{18}F]FDG is that the former does not show increased uptake in inflammatory lesions, a common source of false-positive indications with [^{18}F]FDG [56, 63]. Additionally, due to the low rates of proliferation in healthy brain tissue, excellent tumor-to-background ratios have been achieved in clinical trials with [^{18}F]FLT in gliomas (Fig. 17). Furthermore, [^{18}F]FLT is also able to significantly distinguish high- vs. low-grade tumors, while [^{18}F]FDG was not [64].

Interestingly, in some instances, it has been noted that a "flare effect" can occur immediately following the administration of therapeutic agents, during which there is a marked increase in [^{18}F]FLT uptake at the tumor. This may be due to the inhibition of de novo thymidine synthesis

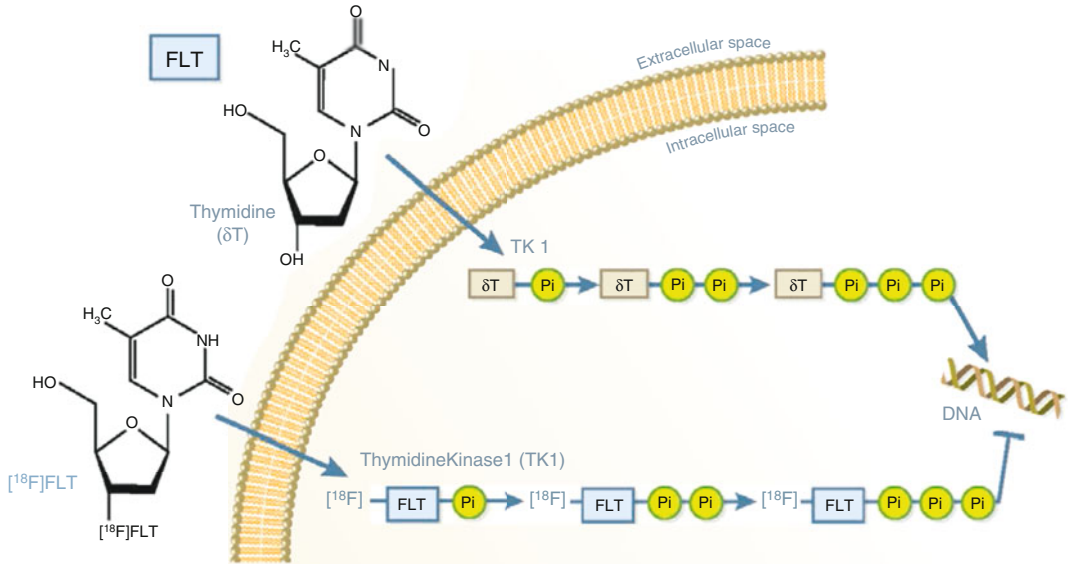

Fig. 16 [^{18}F]FLT enters the cell through identical pathways to thymidine (δT), becoming phosphorylated and trapped in the cell by thymidine kinase 1 (TK1). However, FLT is not incorporated into the DNA due to the absence of a 3′ hydroxyl group

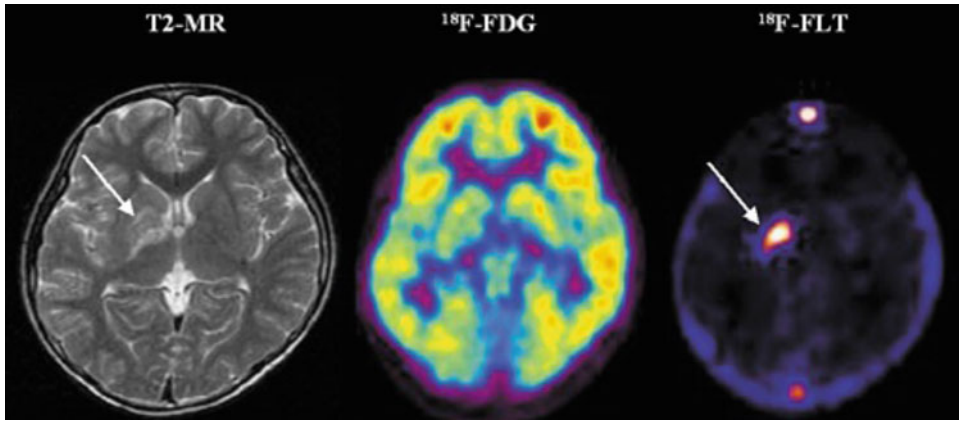

Fig. 17 A germ cell tumor located in the right basal ganglia is obscured by background signal in the [^{18}F]FDG PET scan (*middle*) and shows very slightly decreased uptake. In contrast, the [^{18}F]FLT PET image (*right*) demonstrates significant uptake, revealing a malignant tumor with greater certainty than either MRI (*left*) or [^{18}F]FDG (Reproduced with permission from Springer from Choi et al. [64])

pathways [65]. A greater flare response was found to be associated with poorer patient prognosis and survival rate [66]. Such flares may be useful indicators to evaluate the efficacy of chemotherapy on a patient-by-patient basis.

A significant mechanistic obstacle to the widespread use of [^{18}F]FLT is the ability of some cancers to convert deoxyuridine monophosphate to thymidine monophosphate [67]. Therefore, [^{18}F]FLT uptake does not necessarily correlate to overall cellular proliferation but rather reflects the activity of the thymidine salvage pathway. Going forward, clarifying the relationship between cellular viability, cellular

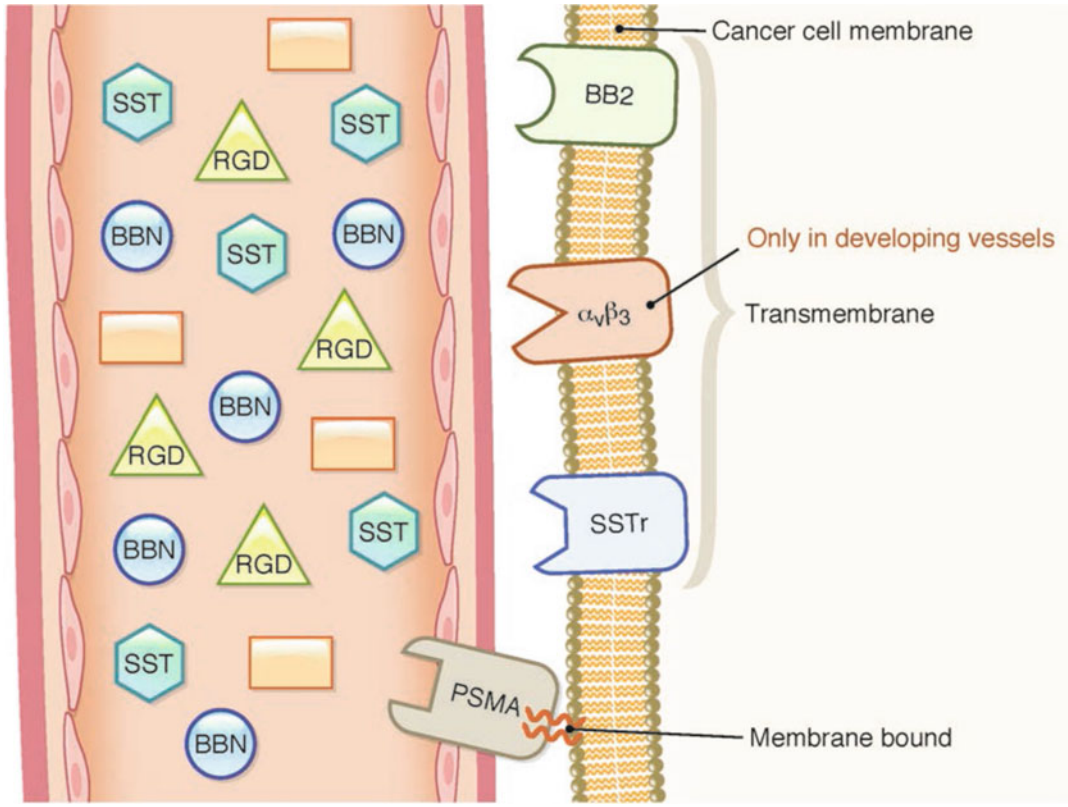

Fig. 18 A schematic illustrating cell surface receptor targeting with molecules designed for molecular imaging

proliferation, and [^{18}F]FLT uptake is crucial to the further clinical implementation of this imaging agent.

Targeting Cell Surface Receptors

Overview

Targeting cancer cells can also be achieved through the use of molecules that interact with cell surface receptors (Fig. 18). In this way, imaging can guide clinicians during the planning and monitoring of receptor-targeted therapies. The caveat to this approach, however, is that many of the cell surface receptors found on cancer cells are *also* expressed on noncancerous cells. Thus, the *specific* targeting of cancer cells requires that the cell surface receptor be expressed in much higher quantities on malignant cells than on healthy cells. Broadly speaking, ligands that target cell surface receptors can be subdivided into two classes: *agonists*, which potentiate the receptor activity, and *antagonists*, which bind to the receptor and render it inactive.

Imaging the Expression of Somatostatin Receptors

Somatostatin receptors (SSTr) are a group of transmembrane G protein-coupled receptors that have been subdivided into five subtypes, numbered 1–5 [68]. Specifically, somatostatin subtype-2 (SST2) receptors are prevalent throughout the body (brain, pituitary gland, pancreatic islets, stomach, and kidney) [69] but are expressed in higher amounts on certain tumor types, including neuroendocrine, pituitary, breast, brain, and small cell lung cancers [70]. Naturally occurring somatostatin (SST) is a cyclic polypeptide that has been used to inspire

Table 1 Naturally occurring SST and a subset of SST2-targeting peptides used to deliver PET radioisotopes to tumor sites. Also shown are two common chelators conjugated to these peptides

Name(s)	**Peptide sequence**[a]
SST-28[b]	SANSNPAMAPRERKAG***C***KNFFWKTFTS***C***
SST-14[b]	AG***C***KNFFWKTFTS***C***
Cortistatin	DRMP***C***RNFFWKTFSS***C***K
Octreotide (OC)	f***C***FwKT***C***-Thr(ol)
Octreotate (TATE)	f***C***YwKT***C***T
Tyr^3-Octreotide (TOC)	f***C***YwKT***C***-Thr(ol)
Lanreotide (NOC)	^{D}βNal-***C***YwKV***C***-Thr(ol)
Vapreotide (VAP)	f***C***FwKV***C***W
JR10	*p*-NO_2-Phe-***c***Y-^{D}Aph(Cbm)-KT***C***y-NH_2
JR11 (OPS202)	Cpa-***c***-Aph(Hor)-^{D}Aph(Cbm)-KT***C***y-NH_2
LM3	*p*-Cl-Phe-***c***Y-^{D}Aph(Cbm)-KT***C***y-NH_2
Abbreviation	**Chelator**
DTPA	Diethylene triamine pentaacetic acid
DOTA	1,4,7,10-Tetraazacyclododecane-1,4,7,10-tetraacetic acid

[a]Standard amino acids are represented by their single-letter abbreviation; nonstandard amino acids are given via common abbreviations [*Thr(ol)* is threoninol, *βNal* is 3(2-naphthyl)alanine, *p-NO₂-Phe* is *p*-nitrophenylalanine, *Aph(Cbm)* is 4-(aminocarbonyl)amino phenylalanine, *Cpa* is cyano-propionic amino acid, *Aph(Hor)* is 4-(4S)-hexahydro-2,6-dioxo-4pyrimidinylcarbonylamino phenylalanine, *p-Cl-Phe* is *p*-chlorophenylalanine]. D amino acids are signified by lowercase letters or superscripted D. Bolded and italicized letters indicate cyclized peptide sequence portions
[b]Naturally occurring peptides that target SSTr

synthetic analogs that have greater receptor affinity while retaining selectivity toward SST2 (Table 1). These compounds consist of a cyclic portion that targets the receptor along with a radiometal chelator moiety coupled to the *N*-terminus of the peptide sequence. In the search for optimal pharmacokinetic properties, a number of different somatostatin analogs have been created; perhaps most notably, altering the *C*-terminal amino acid from Thr(ol) to Thr changes octreotide (OC) to octreotate (TATE) (see Fig. 19). In addition, altering the amino acid sequence has led to some compounds that are agonists [e.g., octreotide (OC), Tyr^3-octreotide (TOC), lanreotide (NOC), and vapreotide] and others that are antagonists [e.g., JR10, JR11(OPS202), and LM3]. Currently, the FDA has approved the use of ^{111}In-DTPATOC – variously known as ^{111}In-DTPA-Tyr^3-octreotide, ^{111}In-DTPA-pentetreotide, Octreoscan™ – for the SPECT imaging of somatostatin receptor-expressing tumors. Additionally, the United States FDA has designated an orphan drug status for ^{68}Ga-DOTATOC in an effort to allow continued investigation of the radiopharmaceutical for the imaging of neuroendocrine tumors and carcinoids.

In the clinic, ^{68}Ga-DOTATOC has been shown to quickly target cranial meningiomas with very good image quality (Fig. 20) [71]. In these studies, there was striking contrast between the meningioma and the pituitary gland, which was further delineated using PET/MRI. Because of the utility of imaging SST-positive tumors with ^{68}Ga-DOTATATE, patients receiving peptide receptor radionuclide therapy (e.g., ^{177}Lu-DOTATATE) have been imaged using PET throughout treatment to assess the efficacy of therapy [72, 73]. In studies in which treatment was monitored by ^{68}Ga-DOTATATE, patients receiving two or more doses of ^{177}Lu-DOTATATE showed no significant progression of disease for longer than those with only one round of therapy [73]. A DOTANOC variant has also been used in the clinic. Lococo et al. showed that pulmonary carcinoids that showed an absence of [^{18}F]FDG uptake were clearly visible in ^{68}Ga-DOTANOC PET scans, while other tumors displayed decreased or similar uptake relative to [^{18}F]FDG [74]. As a result, the authors of this study suggest using both radiopharmaceuticals in concert to identify tumors. Additionally, this multicentered trial showed

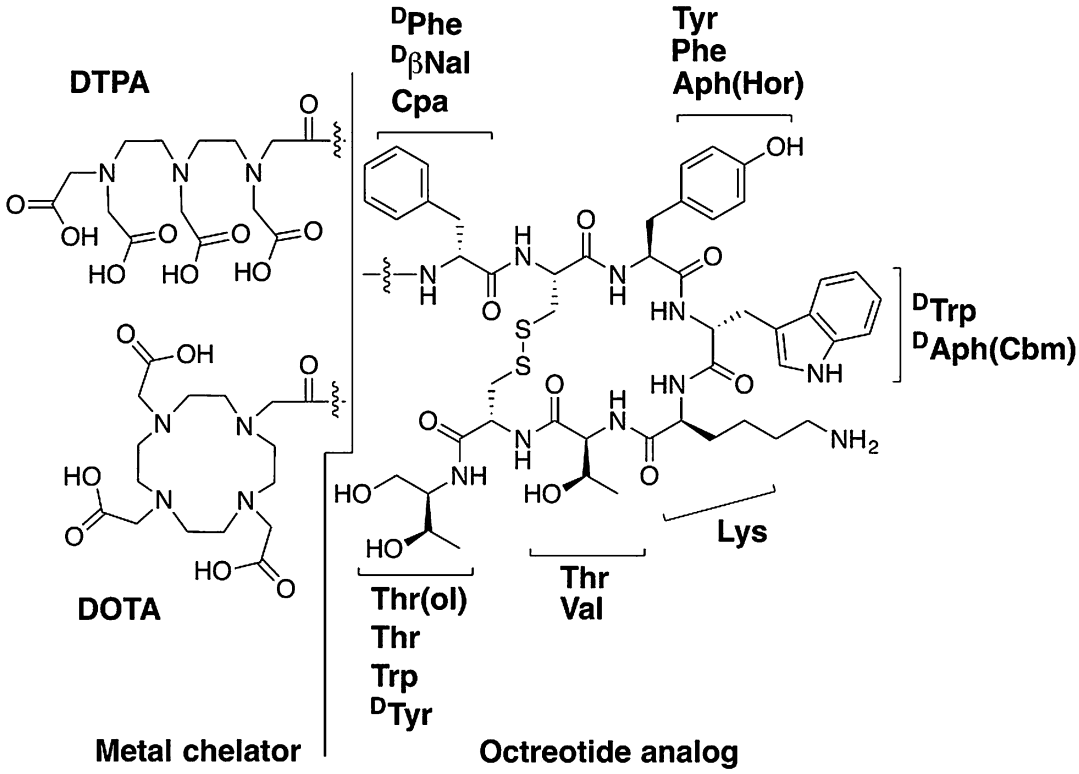

Fig. 19 A schematic depiction of octreotide-like pharmacophores that can be radiolabeled for the PET imaging of SSTr positive tumors. The two most commonly conjugated chelators for octreotide-like radiopharmaceuticals are provided to clarify how they are each attached to the peptide. The amino acid labels indicate variations from octreotide (structure drawn) at each position for the peptides listed in Table 1

that including nonstandard amino acids in the octreotide sequence (i.e., DOTANOC) might not strongly impact the overall targeting ability of the imaging agent. However, other studies have indicated that varying the metal-chelator complex or the peptide sequence *does* impact the radiopharmaceutical's binding affinity for SSTr [75–77]. Specifically, Fani et al. showed that the tumor uptake of antagonist-based radiotracers was greater than that of agonist-based imaging agents [77].

Imaging the Expression of Integrins

Integrin receptors are comprised of two binding regions – α and β – that can be made up of a variety of amino acid sequences, ultimately yielding 24 unique combinations [78]. One of these combinations, the $\alpha_v\beta_3$ integrin receptor, has been associated with cells responsible for angiogenesis in melanoma, neuroblastoma, and glioblastoma as well as ovarian, breast, and lung cancers [70]. Also, it has been shown that the $\alpha_v\beta_3$ integrin receptors are not expressed in most noncancerous tissues [78]. Peptides containing an arginine-glycine-aspartic acid (RGD) sequence mediate cell adhesion and have been shown to target $\alpha_v\beta_3$ integrin receptors [79, 80]. Due to the unique function of RGD peptides, attempts to utilize these peptides to treat or target disease (by tracking angiogenesis or metastatic tumor formation) have been carried out [81, 82]. Notably, three PET imaging agents based on RGD peptides have entered clinical trials: [^{18}F]FPPRGD$_2$, alfatide, and [^{18}F]galacto-RGD. The structures of each of these compounds (as well as a few related structures) are presented in Fig. 21.

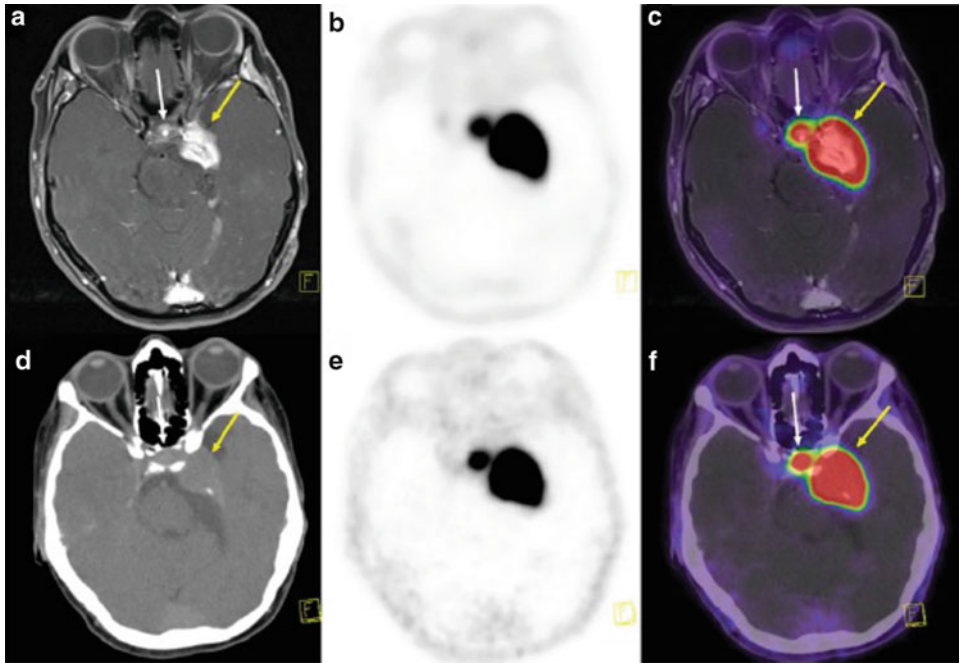

Fig. 20 PET/MRI imaging of a patient injected with ^{68}Ga-DOTATOC at 30 min p.i. (**a**–**c**) and 1 h p.i. (**d**–**f**) indicating tumors (*arrows*) using T1-weighted MRI (**a**, **d**), PET (**b**, **e**), and PET/MRI fusion (**c**, **f**) (Afshar-Oromieh et al. [71], reproduced by permission of the Society for Neuro-Oncology)

Several review articles covering clinical imaging with radiolabeled RGD peptides have cataloged the achievements of these radiopharmaceuticals [83–86]. A variety of modifications to the core RGD structure have been tested to improve the in vivo behavior of the radiotracers. For example, the introduction of a sugar onto a single RGD peptide sequence resulted in improved in vivo stability while maintaining favorable tumor-to-background ratios [87, 88]. Studies with [^{18}F]galacto-RGD showed variation in uptake between patients, indicating differences in tumor vascularization and cancer stage [89]. In a different investigation, in order to decrease the labeling time, a click reaction was used to conjugate an ^{18}F-labeled prosthetic group to galacto-RGD to form [^{18}F]flotegatide-RDG (or [^{18}F]RGD-K5) [90]. In initial human studies, [^{18}F]RGD-K5 uptake did not correlate with that of [^{18}F]FDG, a result similar to that observed with [^{18}F]galacto-RGD. However, [^{18}F]RGD-K5 PET was determined to be an effective tool for the delineation of integrin expression in breast cancers [91]. Thus, the principal utility of [^{18}F]RGD-K5 may be in monitoring response to therapy rather than tumor identification [92]. Yet another RGD-based radiotracer features a polyethylene glycol (PEG) spacer that is radiolabeled with ^{18}F. This compound, [^{18}F]fluciclatide (^{18}F-AH111585), was injected into a small number of patients with metastatic breast cancer and displayed uptake in lesions that were also visible via CT. Unfortunately, in these patients, the liver uptake of the tracer was too high to identify liver metastases. Further [^{18}F]fluciclatide imaging studies in patients with brain tumors, lung cancer, squamous cell carcinoma of the head and neck, differentiated thyroid carcinoma, sarcoma, and melanoma will focus on the ability of the tracer to delineate angiogenesis [92]. In a study utilizing [^{15}O]H_2O as a comparison to [^{18}F]fluciclatide in patients with non-small cell lung cancer and melanoma, Kenny et al. showed that the uptake of [^{18}F]fluciclatide was not merely a function of perfusion and suggested using later imaging time points to determine sites of neovasculature [93].

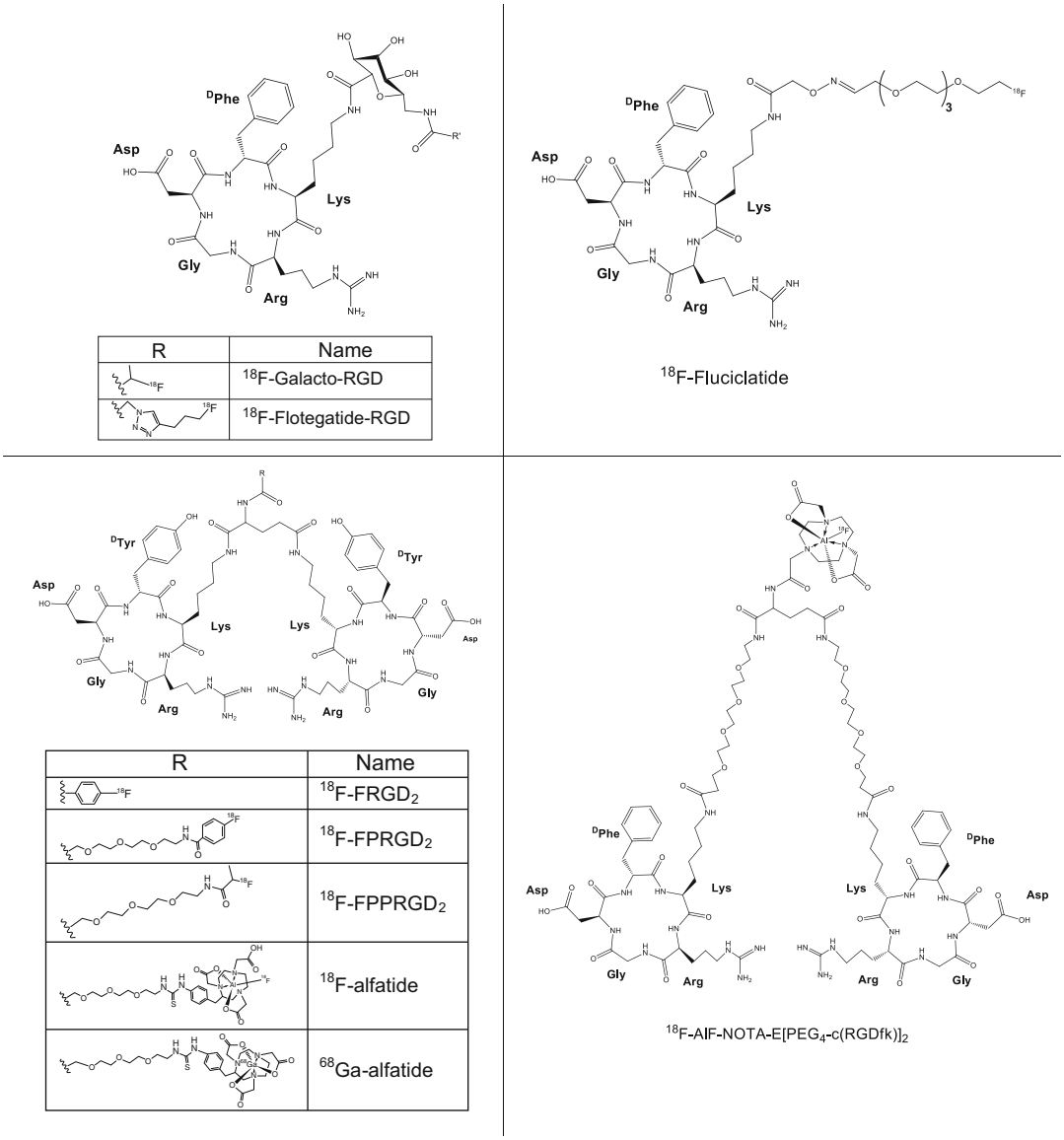

Fig. 21 A schematic of PET tracers used to target $\alpha_v\beta_3$ integrin receptors in clinical studies

Due to their relatively low uptake in tumor lesions (<5%ID/g), suboptimal background contrast, and synthetic complexity, the aforementioned ^{18}F-labeled RGD peptides have shown limited utility in the clinic. This has led to investigations using ^{68}Ga-labeled peptides in hopes of increasing the uptake of the tracer in the tumor or decreasing its uptake in nontarget tissues [94]. For example, ^{68}Ga-NOTA-RGD has been used in patients to identify colorectal cancer metastases prior to therapy [92]. These studies suggest that PET scans using RGD-based peptides could aid in the selection of patients for anti-angiogenic therapy [92].

In another effort to improve the tumor retention of RGD-based peptides, multimeric radiopharmaceuticals have also been investigated. In light of this topic, it is important to diverge – if only briefly – to discuss a concept known as "bivalent targeting." Bivalent targeting strategies are

predicated on the use of two biological targeting moieties that are tethered together (1) to increase the probability of interactions with a single cell surface receptor or (2) to facilitate the binding of two cell surface receptors simultaneously. Homodimers (or homomultimers) utilize the same biological targeting vector to achieve greater cell surface receptor occupancy, whereas heterodimers target different receptors often in an effort to increase the types of cancer targeted by the radiopharmaceutical [95, 96]. The use of two targeting moieties may also increase the chance that the peptide will interact with the cell surface in the correct orientation for receptor binding. Because the distance between any two cell surface receptors is unknown, researchers have attempted to investigate various linking molecules that can accommodate cell surface variations [97]. Additionally, increased linker size may decrease the metabolism rate of the radiopharmaceutical and alter its pharmacokinetic properties, ensuring a longer biological half-life and possibly resulting in greater tumor uptake.

One class of homodimers containing two RGD cyclic peptide sequences (RGD_2) has shown utility across multiple tumor types in a complementary role to [^{18}F]FDG PET imaging. First, Gao et al. noted positive results in identifying lung cancers from hamartomas with the bivalent RGD-based radiotracer ^{18}F-alfatide (Fig. 21) but noted difficulties distinguishing disease from inflammation [98]. Second, Yu et al. used another bivalent agent – [^{18}F]AlF-NOTA-E[PEG_4-c(RGDfk))]$_2$ (^{18}F-alfatide II, Fig. 21) – to visualize 20 brain metastases in nine patients and illustrated that in the same patients, [^{18}F]FDG and CT only identified 10 and 13 metastases, respectively [99]. Third, the analysis of several clinical patient scans with both [^{18}F]FDG and [^{18}F]$FPPRGD_2$ (Fig. 21) has demonstrated differences in maximal uptake in lesions and biodistributions, which may indicate that the information gained from an [^{18}F]$FPPRGD_2$ PET scan may compliment those results from an [^{18}F]FDG scan [100]. Similarly, a preliminary study of [^{18}F]$FPPRGD_2$ uptake in patients with breast cancer demonstrated primary and metastatic imaging utility (Fig. 22) [101]. ^{68}Ga labeling of these agents can also be achieved through the use of NOTA chelators attached to the homodimers; not surprisingly, comparative studies using ^{68}Ga-NOTA-labeled compounds are currently underway.

Imaging the Expression of Bombesin Receptors

Bombesin – a linear, 14-amino acid homolog to the gastrin-releasing peptide – is found in the skin of the European fire-bellied toad (*Bombina bombina*, Fig. 23). Bombesin-based peptides target bombesin receptor subtype-2 (seen in the literature as BB2 and BB2r and originally referred to gastrin-releasing peptide receptor or GRPr), which has been shown to be highly expressed by prostate, breast, pancreatic, small cell lung, and colorectal cancers [70]. BB2 is also highly expressed in the murine pancreas; consequently, preclinical studies with radiolabeled bombesin peptides show increased uptake in the pancreas in non-tumor-bearing mice if the biological targeting portion of the peptide is functioning properly. Importantly, Coy et al. have shown that only the 7th-14th amino acids were necessary for binding to the BB2 [this is commonly abbreviated in the literature as BBN(7-14)] [102]. Further variation in the amino acid sequence has led to a number of bombesin analogs, including RM2, BAY86-7548, and Demobesin 4 (Table 2). Various linkers and chelators have been conjugated to the end of the peptide sequence to alter the pharmacokinetics of the radiopharmaceutical and allow for the use of radiometals with different physical properties and half-lives.

^{68}Ga-labeled BBN analogs have been quickly translated to the clinic. BBN(7-14) conjugated to a radiometallated NOTA chelator via an aminocaproic acid – ^{68}Ga-NOTA-Aca-BBN(7-14) – has been investigated to image primary gliomas. Normal, healthy subjects showed rapid clearance of the ^{68}Ga-NOTA-Aca-BBN(7-14) through the kidneys and had higher accumulation of the radioactivity in the bladder [103]. Twelve patients with high- to low-grade gliomas also showed rapid accumulation of ^{68}Ga-NOTA-Aca-BBN(7-14) in lesions within 30 min with very high tumor-to-background ratios (24 ± 9), and

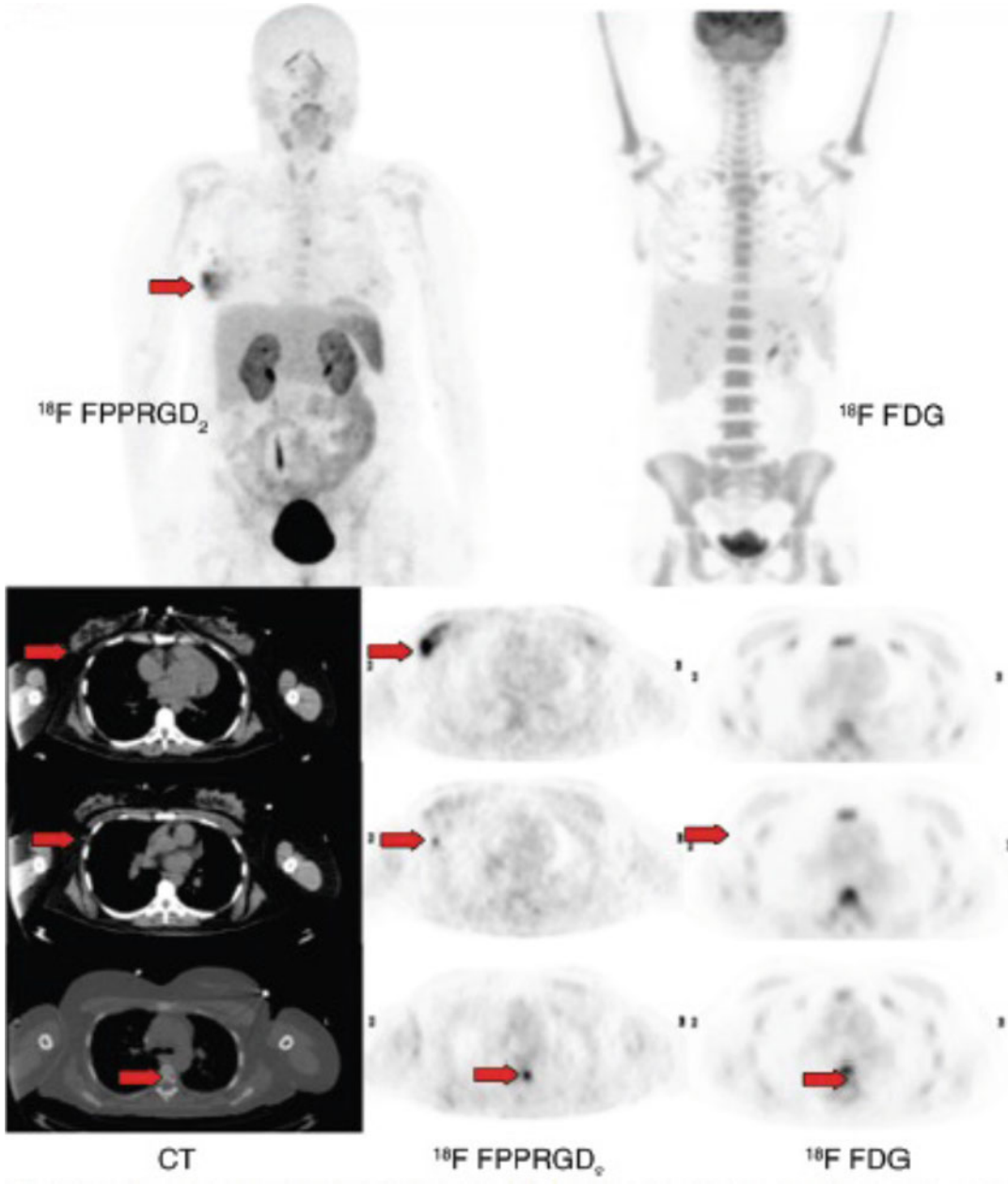

Fig. 22 Comparison of [^{18}F]FPPRGD2 and [^{18}F]FDG in a woman diagnosed with multicentric lobular carcinoma of the right breast. [^{18}F]FDG uptake was not observed at the lesions indicated by the *red arrows* (areas proven to be tumors through biopsy) (From Iagaru et al. [101]. Reprinted with permission from the Radiological Society of North America)

all 14 lesions in the 12 patients were identified [103]. Zhang et al. suggested the possible utility of ^{68}Ga-NOTA-Aca-BBN(7-14) PET not only to identify tumors but also to delineate tumor margins that are difficult to determine clinically using five-aminolevulinic acid (ALA) [103].

Another BB2-targeting radiotracer, ^{68}Ga-BAY86-7548 (^{68}Ga-DOTA-RM2), has been

extensively investigated for imaging prostate cancers. Roivainen et al. reported the clearance and metabolism of ^{68}Ga-BAY86-7548 in normal, healthy patients [104] and indicated that ^{68}Ga-BAY86-7548 was rapidly cleared through the renal-urinary pathway and rapidly metabolized in vivo. Kähkönen et al. demonstrated that ^{68}Ga-BAY86-7548 can be used to visualize primary lesions in the pancreas but is less successful at identifying metastases (Fig. 24) [105]. Borkowski et al. similarly remarked that no off-target binding was observed in prostate cancer patients and that there was high and prolonged uptake in PC-3 tumor xenografts in mice [106].

Utilizing a SPECT radiometal, ^{99m}Tc-Demobesin-4 (Fig. 25) has been investigated for the possible identification of primary and metastatic prostate cancer. Initial studies with ^{99m}Tc-Demobesin-4 indicate that SPECT/CT images of bone metastases in patients with prostate cancer can be visualized as early as 1 h postinjection [107]. However, Mather et al. have also indicated that imaging metastases with ^{99m}Tc-Demobesin-4 in patients who had undergone extensive therapy was not feasible [107]. Thus, ^{99m}Tc-Demobesin-4 may be useful in identifying new patients, but its suitability to visualize response to therapy is limited.

Fig. 23 European fire-bellied toad (*Bombina bombina*)

Imaging the Expression of Prostate-Specific Membrane Antigen

Prostate-specific membrane antigen (PSMA) is a transmembrane glycoprotein with a large extracellular portion and small intracellular segment. PSMA expression has been shown in normal prostate tissue, but the level of expression increases in prostate cancer, making it an enticing target for the imaging and therapy of prostate cancers. Despite the number of studies implicating PSMA expression in the diagnosis of prostate cancer, the normal function of PSMA is still unknown [108]. The elevated levels of shed PSMA in the serum of patients require that PSMA-targeting agents must localize in cancerous tissues in high enough abundance to compensate for high background activity concentrations.

The only commercially available PSMA-targeted imaging agent is ^{111}In-capromab pendetide (ProstaScint®), a murine monoclonal antibody that targets the intracellular portion of the antigen [108]. Unfortunately, ^{111}In-capromab pendetide has two major drawbacks. First, the radiotracer only targets PSMA in apoptotic or necrotic tissues, in which the intracellular portion of PSMA is available due to membrane damage. And second, because of the limited sensitivity and selectivity of the radiolabeled antibody, the clinical use of ^{111}In-capromab requires a relatively long delay between injection and

Table 2 Naturally occurring BBN and a subset of the BB2-targeting peptides used to deliver PET radioisotopes to tumor sites

Name(s)	Peptide sequence[a]
Gastrin	VPLPAGGGTVLTKMYPRGNHWAVGHLM-NH_2
Bombesin (BBN)	pGlu-QRLGNQWAVGHLM-NH_2
Bombesin7-14 [BBN(7-14)]	QWAVGHLM-NH_2
BAY86-7548 [DOTA-RM2]	DOTA-4-amino-1-carboxymethyl-piperidine-fQWAVGHSta-L-NH_2
Demobesin 4 [DB4]	N4-pGlu-QRYGNQWAVGHL-Nle-NH_2

[a]Amino acids are given by the one-letter abbreviation, lowercase indicates D amino acids. Sta is statine and Nle is norleucine, nonstandard amino acids. N_4 refers to a tetraamine ligand used to chelate the dioxotechnetium(V) core

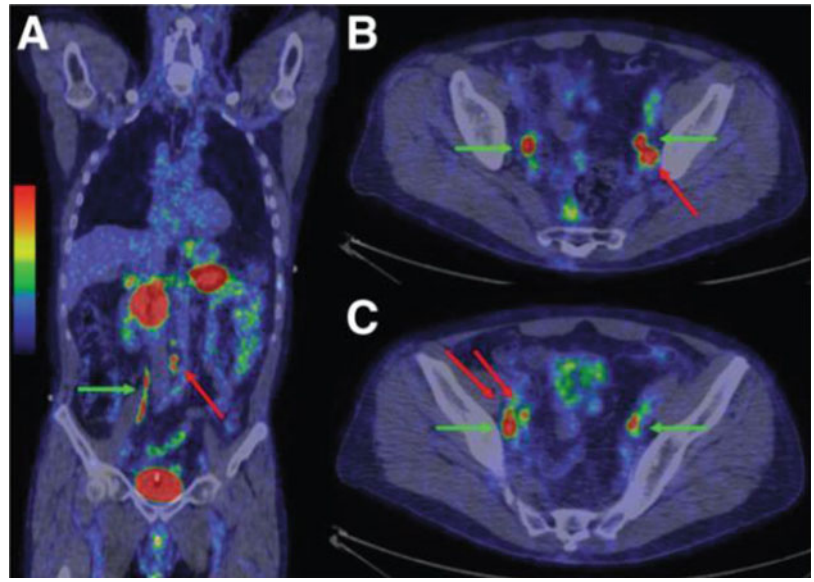

Fig. 24 PET/CT of a patient with prostate cancer metastasis to multiple lymph nodes using ^{68}Ga-BAY86-7548 – coronal (**a**) and axial views (**b**, **c**) – showing increased uptake in metastases (*red arrows*), confirmed through histology. The ureters are indicated with the *green arrows* (Reprinted from Kähkönen et al. [105]. © the American Association for Cancer Research)

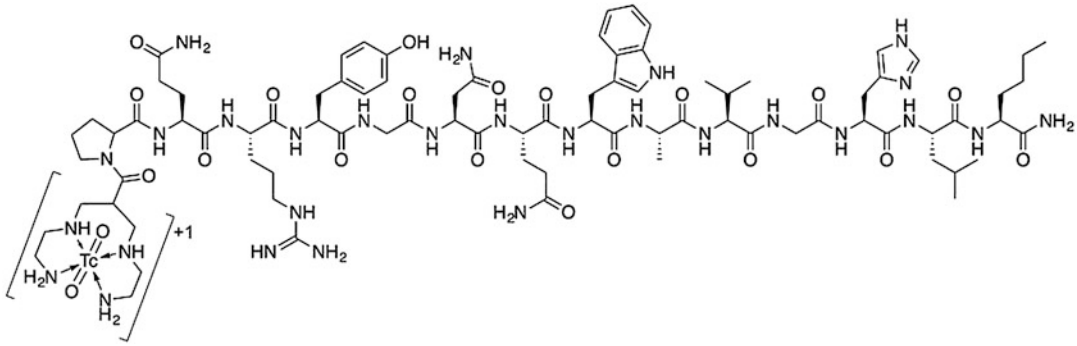

Fig. 25 The structure of ^{99m}Tc-Demobesin 4 (^{99m}Tc-DB4)

imaging in order to increase target-to-background contrast [108, 109].

Due to the higher image resolution and improved quantification in PET and PET/CT, most recent efforts have focused on the creation of tracers for PET rather than SPECT. Specifically, [^{18}F]DCFBC (*N*-[*N*-[(*S*)-1,3-dicarboxypropyl] carbamoyl]-4-fluorobenzyl-L-cysteine, Fig. 26) – a low-molecular-weight urea-based inhibitor of PSMA – shows rapid uptake in PSMA-positive metastases with predominantly renal excretion but with some prolonged liver uptake and blood-pool activity [110]. These limitations in clearance could limit the efficacy of [^{18}F]DCFBC in delineating disease from healthy tissue near major blood vessels [110], but clinical studies have shown the usefulness of [^{18}F]DCFBC in detecting high-grade prostate cancer lesions and differentiating these from nonmalignant tissue (Fig. 27) [111]. The use of [^{18}F]DCFBC in conjunction with MR may also aid in directing clinicians toward which tissues to biopsy [111].

In order to produce a ^{68}Ga-labeled PSMA-targeting small molecule, ^{68}Ga-PSMA – (Glu-urea-Lys-(Ahx)-[^{68}Ga(HBED-CC)]) – was synthesized by conjugating HBED-CC (a chelator for gallium) to a lysine attached via a urea linker to glumatic acid and subsequently radiolabeled with ^{68}Ga (Fig. 26) [112]. In healthy volunteers, high levels of uptake of ^{68}Ga-PSMA-ligand were observed in the salivary

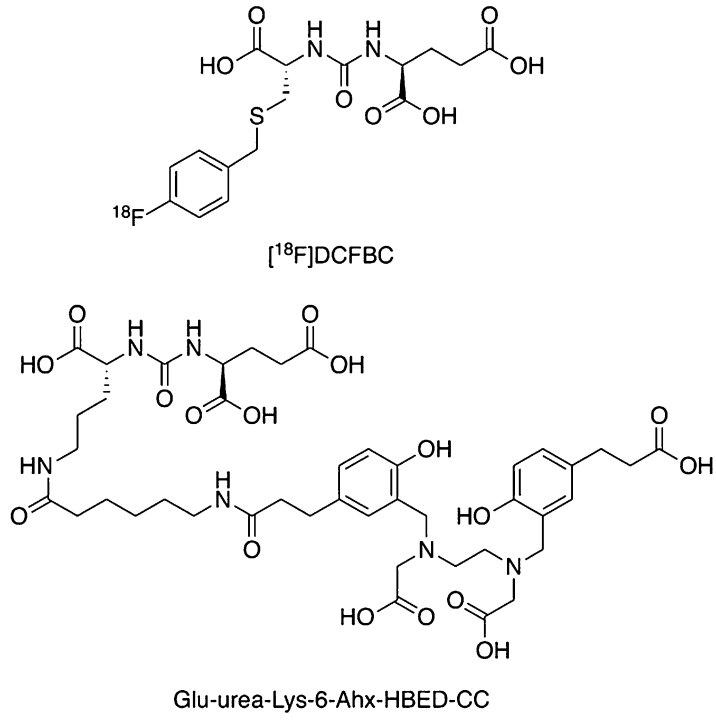

Fig. 26 The chemical structures of [^{18}F]DCFBC and Glu-urea-Lys-6-Ahx-HBED-CC

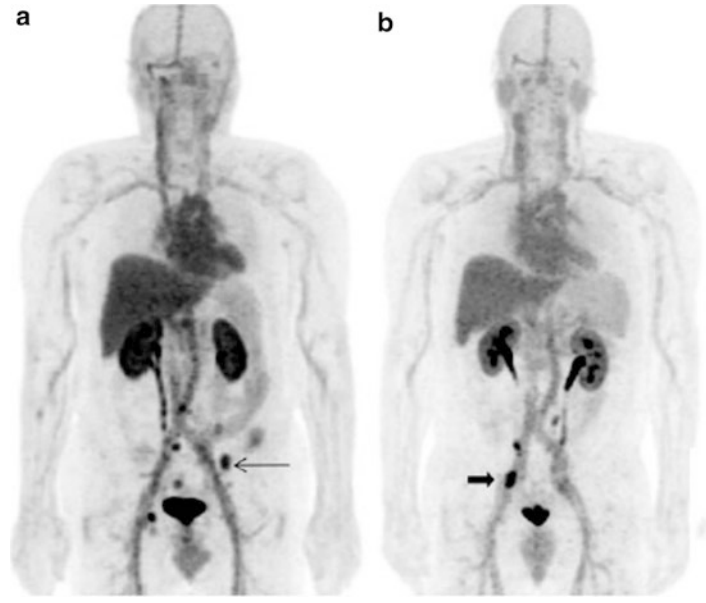

Fig. 27 Anterior MIP at 2 h p.i. of [^{18}F]DCFBC in a patient with bone metastases indicated with an *arrow* (**a**) and a patient with lymph node metastases indicated with an *arrow* (**b**) using PET (This research was published in *The Journal of Nuclear Medicine*, Cho et al. [110]. © by the Society of Nuclear Medicine and Molecular Imaging, Inc.)

glands and the kidneys, while moderate uptake was seen in the lacrimal glands, liver, and gallbladder (Fig. 28) [113]. Afshar-Oromieh et al. noted that 60% of lesions in patients with <2.2 ng/mL PSMA expression in blood and 100% of lesions in patients with >2.2 ng/mL PSMA expression in blood were identified with ^{68}Ga-PSMA-ligand within 1 h of injection, but image contrast may improve with scanning 3 h post-injection (Fig. 28) [113].

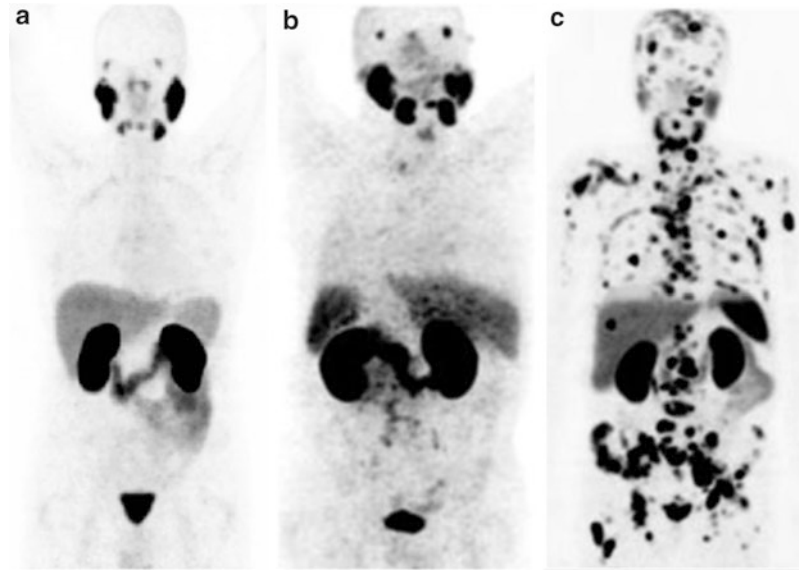

Fig. 28 Maximum intensity projections (MIP) of ^{68}Ga-PSMA-ligand showing in vivo distribution in a healthy patient (**a**, anterior view), a patient with minimal lymph node metastatic prostate cancer (**b**, posterior view), and a patient with extensive lymph node and bone metastatic prostate cancer (**c**, anterior view) (Reproduced with permission from Springer from Afshar-Oromieh et al. [113])

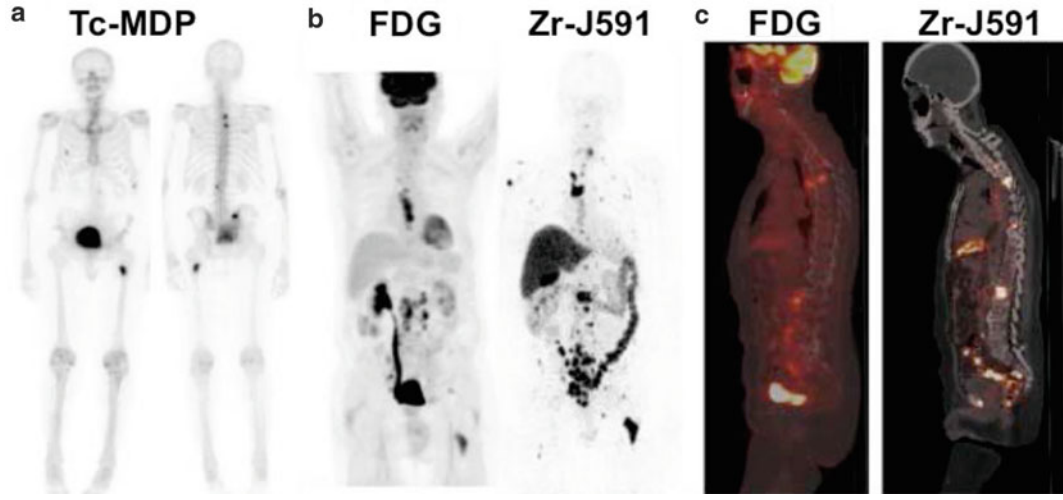

Fig. 29 Comparison of ^{99m}Tc-MDP, [^{18}F]FDG, and ^{89}Zr-J591 uptake in a patient with metastatic prostate cancer using SPECT anterior and posterior images (**a**), PET MIPs (**b**), and planar images of fused PET/CT (**c**) (Reproduced with permission from Springer from Pandit-Taskar et al. [115])

Due to the longer residence times of antibodies in the blood, longer-lived isotopes are necessary for the radiolabeling of antibody-based tracers. Zirconium-89 is a positron-emitting radiometal with a half-life of 3.3 days, which complements the multiday circulation time of antibodies. J591, a humanized monoclonal antibody that targets the extracellular portion of PSMA, has been conjugated to the siderophore-derived chelator desferrioxamine (DFO) to prepare the PET tracer ^{89}Zr-J591 (^{89}Zr-huJ591, ^{89}Zr-DFO-J591). Clinical studies by Pandit-Taskar et al. have indicated that the optimal time to image patients is 7 ± 1 days after the administration of the radiolabeled antibody. Critically, these data reveal significant uptake in tumor tissue with 11 of 12 lesions imaged with ^{89}Zr-J591 and 10 of 12 lesions imaged with [^{18}F]FDG PET/CT [114]. Figure 29 provides an

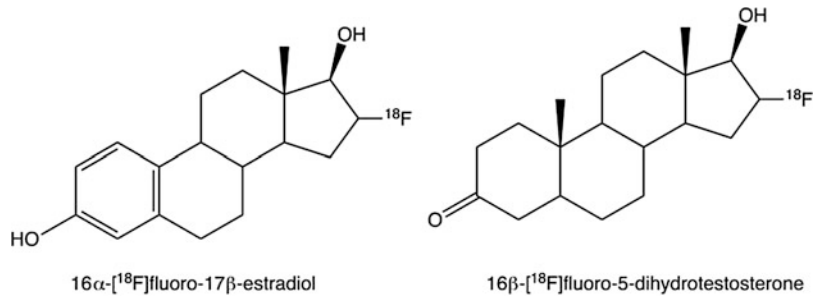

Fig. 30 The structures of [^{18}F]FES and [^{18}F]FDHT

illustration of the potential of ^{89}Zr-J591 compared to [^{18}F]FDG, ^{99m}Tc-MDP, and CT for the imaging of patients with metastatic prostate cancer [114]. Similarly, ^{111}In-labeled J591 has also shown clinical utility for identifying metastases in patients with a variety of PSMA-positive tumor types [115].

Imaging the Expression of Steroid Hormone Receptors

Steroid hormone receptor (SHR) status has been established as an important biomarker in breast and prostate cancer. While the assessment of SHR status in primary tumors is often easily achieved with histological methods, noninvasive molecular imaging could be used to address temporal changes in SHR levels, delineate metastases, and monitor response to treatment [116]. The molecular imaging of steroid hormone receptors relies primarily on the use of ^{18}F-radiolabeled analogs of the endogenous SHR ligands estrogen (17β-estradiol) and testosterone, which target the estrogen (ER) and androgen receptors (AR), respectively. The structures of 16α-[^{18}F]fluoro-17β-estradiol ([^{18}F]FES) and 16β-[^{18}F]fluoro-5-dihydrotestosterone ([^{18}F]FDHT) are presented in Fig. 30. The estrogen and androgen receptors share a common mechanism of action in which the ligand is bound by the intracellular receptor, and the ligand-receptor complex is transported to the nucleus, where it then binds to the respective steroid response elements in DNA and initiates the transcription of hormone-induced genes (Fig. 31) [117, 118]. Additionally, steroid hormones exert nonnuclear actions via a subpopulation of cell surface SHR, but the mechanisms of these nonnuclear effects remain poorly understood. Another notable feature of the biochemistry of sex steroids is their transport in the circulation by the steroid hormone-binding globulin (SHBG). Because of the ^{18}F substitution in the radiotracers, the affinity of [^{18}F]FES and [^{18}F]FDHT for SHBG is lower than that of estradiol and testosterone; consequently, the radiotracers are primarily distributed in the bloodstream nonspecifically bound to serum albumin, which is more abundant than SHBG [119]. Furthermore, both [^{18}F]FES and [^{18}F]FDHT are rapidly metabolized in humans, with only about 20% of the tracer remaining intact 20 min after injection [120, 121].

Estrogen receptor status is an important prognostic indicator of disease-free and overall survival in breast cancer. Figure 32 shows typical PET imaging results in a patient with ER-positive primary breast tumor. In the same study, the authors demonstrated that [^{18}F]FES PET could be used to delineate metastatic sites in the bone and axillary lymph nodes, with the degree of lymph node uptake correlating with disease burden [122]. However, the degree of ER expression in distant sites is variable, and [^{18}F]FES imaging can provide insight on the heterogeneity of metastatic disease, especially when combined with [^{18}F]FDG PET [123]. In a retrospective study of patients undergoing chemotherapy with ER blockade or ligand-depleting agents, Linden et al. have been able to demonstrate that the standard uptake values (SUV) of [^{18}F]FES in tumors is sensitive to changes in circulating estrogen levels as well as ER blockade. In addition, [^{18}F]FES PET imaging was used to distinguish between the pharmacological effects of tamoxifen and fulvestrant, two ER modulators with different

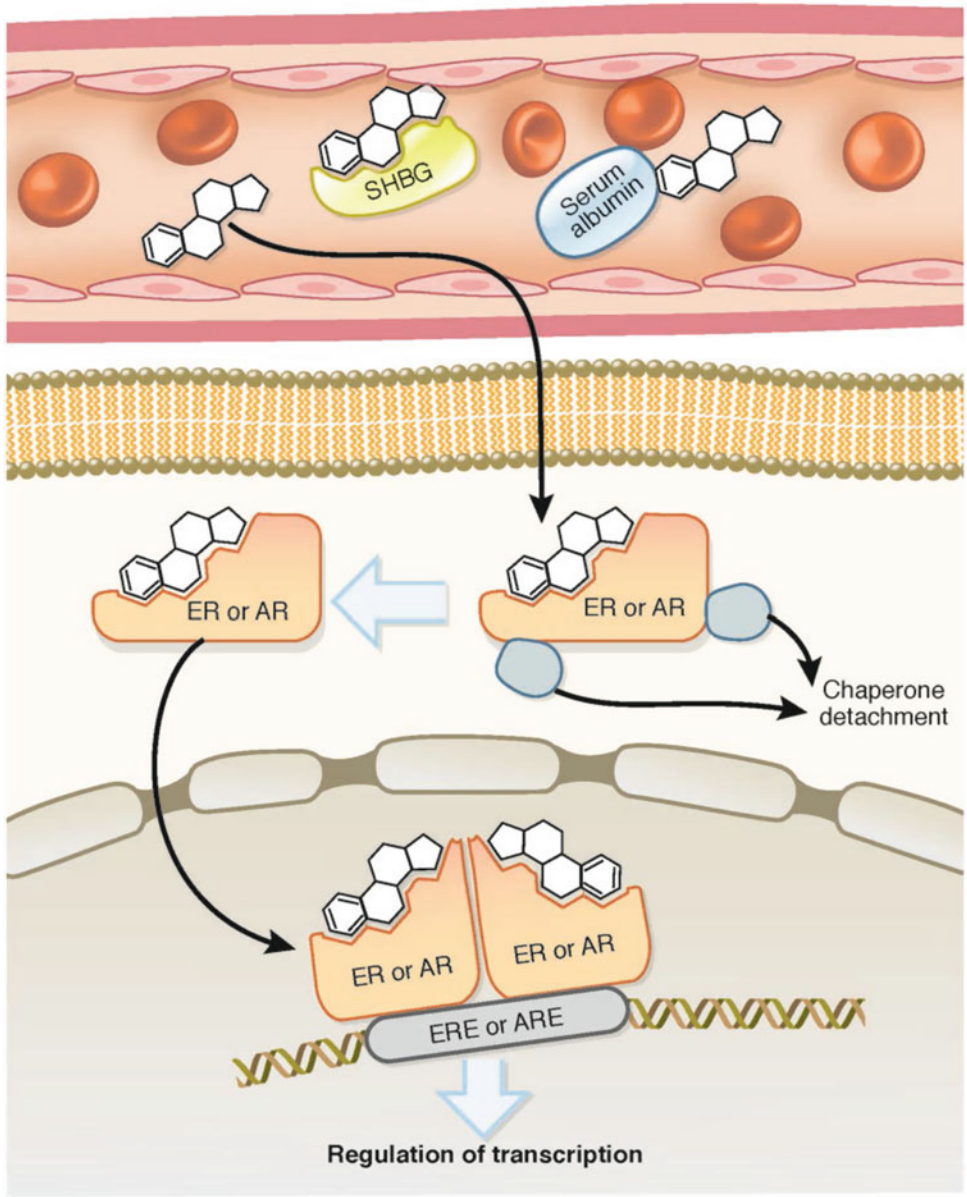

Fig. 31 The uptake mechanisms and interactions of SHR radioligands in cells

mechanisms of action (as illustrated in Fig. 33) [124]. Recently, [^{18}F]FES has been evaluated in small patient populations with various gynecologic cancers including endometrial adenocarcinoma and uterine sarcoma and compared to histopathological findings. These data suggest that [^{18}F]FES PET shows some promise for the evaluation of disease severity and the differentiation of malignant lesions from benign growths like leiomyoma [125].

The use of [^{18}F]FDHT in prostate cancer is, in principle, analogous to that of [^{18}F]FES in breast cancer. Indeed, an estimated 80–90% of newly diagnosed prostate cancers are androgen dependent and thus are likely to benefit from endocrine therapy through AR blockade or androgen depletion [126]. However, [^{18}F]FDHT PET does not exhibit similar predictive value for the success of endocrine therapy because of the relatively high

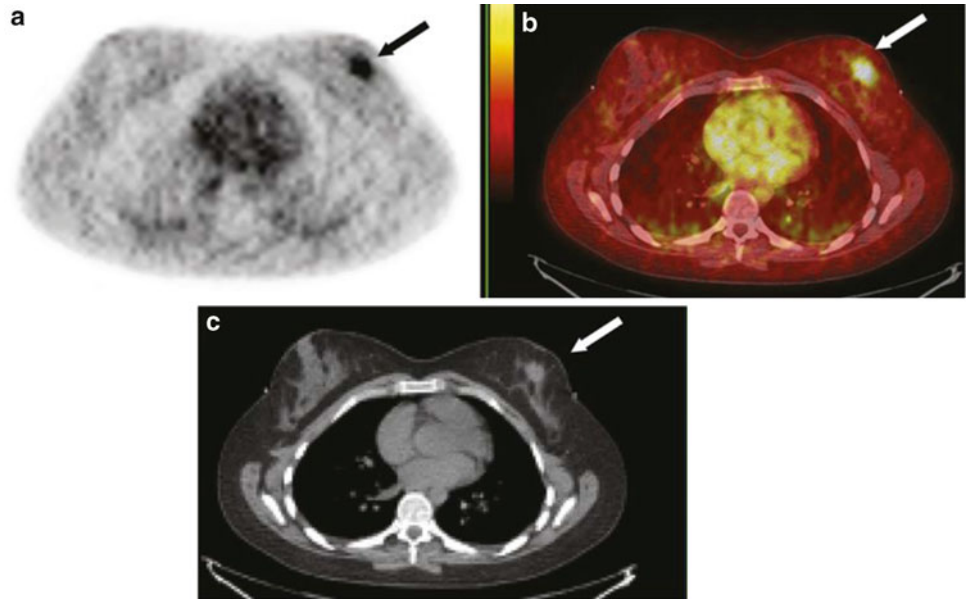

Fig. 32 Axial [^{18}F]FES image in ER-positive breast cancer showing intense uptake (*arrow*) in the left breast lesion (**a**), corresponding to a 2.3-cm lesion seen on CT (**c**) and confirmed by [^{18}F]FES PET/CT overlay (**b**) (This research was published in *The Journal of Nuclear Medicine*, Gemignani et al. [122]. © by the Society of Nuclear Medicine and Molecular Imaging, Inc.)

prevalence of "androgen withdrawal syndrome," whereby clinical improvement is seen after the discontinuation of endocrine therapy as a result of ligand-independent activation of AR [127]. Understandably, the downstream effects of ligand-independent activation and genomic silencing of AR go undetected in molecular imaging studies with [^{18}F]FDHT. Nevertheless, [^{18}F]FDHT has proven to be a powerful tool for imaging AR status in metastatic, progressive, and advanced prostate cancers. The initial patient studies by the groups at Memorial Sloan Kettering Cancer Center [128] and Washington University in St. Louis [129] focused on lesion-by-lesion comparisons of [^{18}F]FDHT and [^{18}F]FDG uptake, as shown in representative images in Fig. 34. In both studies, [^{18}F]FDHT PET allowed for the detection of 79–89% of [^{18}F]FDG-positive lesions, and the tumor uptake of the tracer was established to be AR-mediated. The studies of Vargas et al. [130] established a significant association between the number of bone lesions detected by different imaging modalities including [^{18}F]FDHT PET with overall survival in patients with castration-resistant prostate cancer. Furthermore, the negative correlation of the intensity of [^{18}F]FDHT accumulation in bone metastases with patient survival supports the prognostic value of the tracer in prostate cancer patients undergoing AR blocking therapies.

Targeting the Hypoxic Tumor Microenvironment

Overview

Cancer cells release growth factors such as vascular endothelial growth factor to stimulate angiogenesis from neighboring vasculature. However, these new blood vessels are often poorly formed and inefficient at facilitating the transport of nutrients and oxygen. Within the tumor microenvironment, high rates of cellular proliferation and metabolism combine with this poorly defined vasculature to create local regions of hypoxia [131]. Tumor hypoxia is often indicative of aggressive and metastatic malignant phenotypes and frequent portend

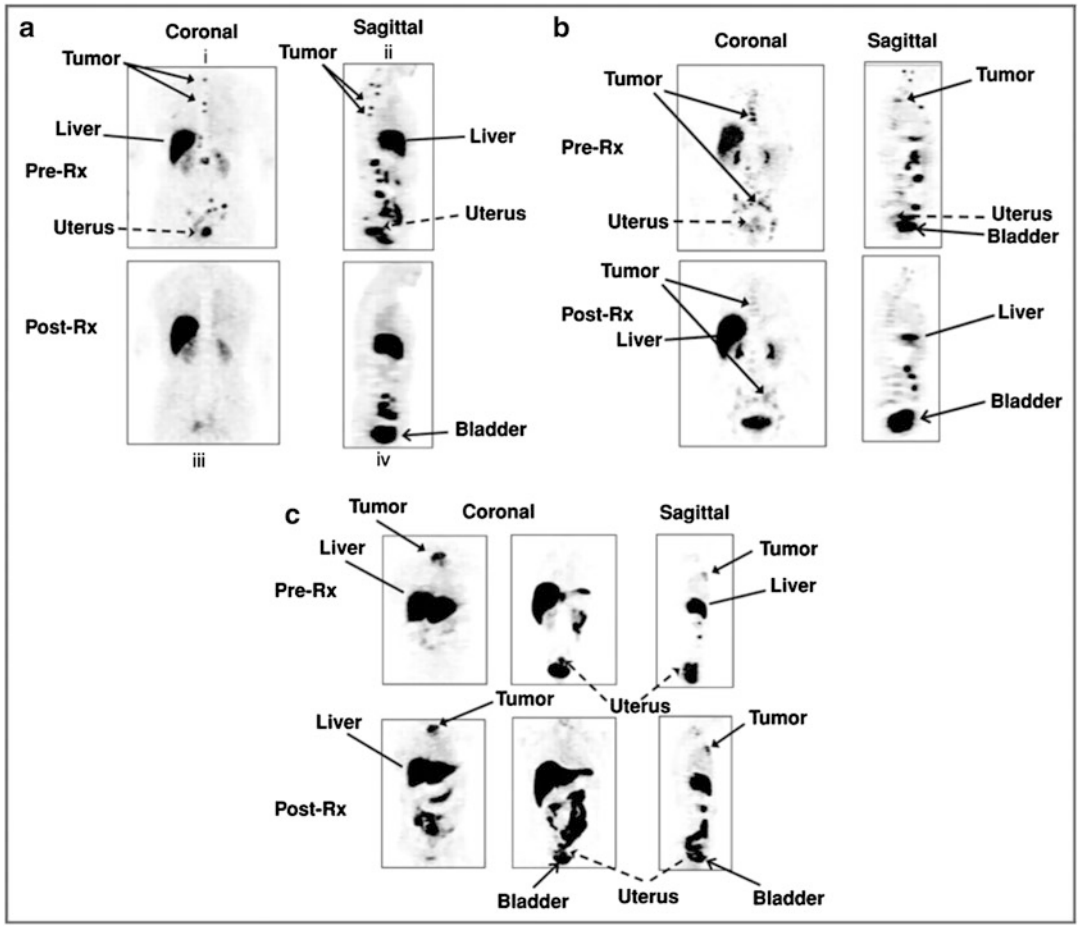

Fig. 33 Pre- and posttreatment [^{18}F]FES PET images in representative patients treated with ER-blocking and estrogen-lowering therapies. Top coronal (i) and sagittal (ii) views pretreatment and bottom panels show the same patient following treatment with coronal (iii) and sagittal (iv) views. Tumor in the upper spine shows baseline uptake and complete ER blockade in the tumor and uterus following 21 days of tamoxifen (**a**). Tumor in mediastinal nodes shows baseline uptake and incomplete ER blockade in tumor and uterus following 68 days of fulvestrant (**b**). Sternal tumor shows ER uptake and no blockade in the tumor and uterus following 29 days of letrozole (**c**) (Reprinted from Linden et al. [124]. © the American Association for Cancer Research)

complications during disease management. As a result, it follows that the ability to noninvasively delineate hypoxic from normoxic tumors could benefit clinicians during staging, prognosis, treatment planning, and treatment monitoring. The presence of tumor hypoxia is often associated with increased resistance to radiation therapy as well, as much of the damage done by radiation is mediated by reactive oxygen species. Therefore, the identification and mapping of hypoxia are also important for planning optimal radiation therapy treatment regimes.

Imaging Tumor Hypoxia with [^{18}F]FMISO

Any imaging agent that is intended to target poorly vascularized tissue must be transported through cellular membranes, thereby allowing it to diffuse through tissue independently of the circulatory system. One of the most widely utilized hypoxia-targeting imaging agents is [^{18}F]FMISO – ([^{18}F]-fluoromisonidazole, 1-fluoro-3-(2-nitroimidazol-1-yl)-propan-2-ol) (Fig. 35) – which was designed to have a partition coefficient

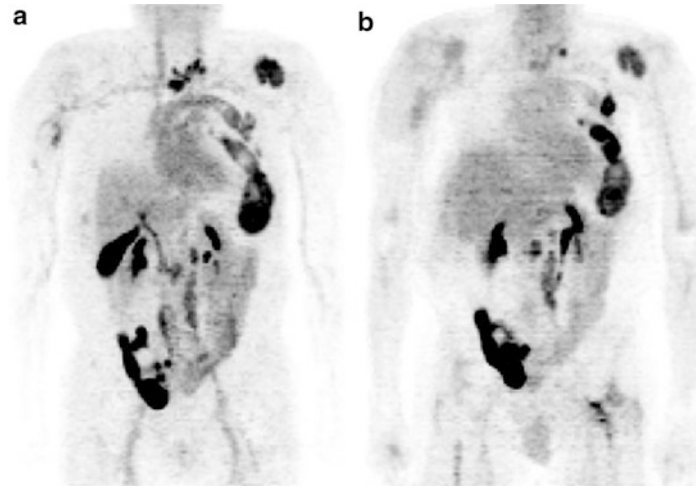

Fig. 34 Maximum intensity projections of [^{18}F]FDHT (**a**) and [^{18}F]FDG (**b**) PET images of a patient with prostate cancer. A greater number of extraprostatic lesions are detected by [^{18}F]FDHT compared to [^{18}F]FDG (This research was published in *The Journal of Nuclear Medicine*, Larson et al. [128]. © by the Society of Nuclear Medicine and Molecular Imaging, Inc.)

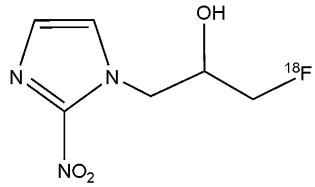

Fig. 35 The structure of [^{18}F]FMISO

of 0.4. This allows the radiotracer to strike a delicate balance: *lipophilic* enough to reach hypoxic tissue but *hydrophilic* enough to be cleared quickly from the blood [132]. The key to [^{18}F]FMISO's selectivity for hypoxic tissue is the redox chemistry of its nitro group. The mechanisms of [^{18}F]FMISO escaping in normoxic and trapping in hypoxic tissues are shown in Fig. 36.

[^{18}F]FMISO accumulation has been shown to be indicative of hypoxia in gliomas, breast, head and neck, lung, and renal tumors [133]. Figure 37 shows a representative [^{18}F]FMISO scan in a patient with a glioma. [^{18}F]FMISO PET has been used to differentiate levels of uptake between grades of glioblastomas, in which low-grade gliomas (grades I and II) were found to have no increased uptake of [^{18}F]FMISO, while all high-grade gliomas studied (grades III and IV) demonstrated increased [^{18}F]FMISO uptake [134] (Fig. 38). Another study showed that images generated through [^{18}F]FMISO PET can help guide the precision targeting of hypoxic regions by intensity-modulated radiation therapy (IMRT), which resulted in an estimated 17% increase in tumor control probability (TCP) [135]. In addition, high uptake of [^{18}F]FMISO in non-small cell lung carcinomas was predictive of increased rates of tumor recurrence following radiation therapy in 90% of patients [136]. Thus, [^{18}F]FMISO has been shown to be useful in determining glioma lesion grades, directing radiation therapy, and predicting subsequent tumor response. Unfortunately, however, [^{18}F]FMISO displays comparatively low contrast between hypoxic tissue and background tissues, which likely results from slow clearance from normoxic tissue. Alternative nitroimidazole-based agents are under investigation to mitigate the limitations of [^{18}F]FMISO.

Imaging Tumor Hypoxia with ^{64}Cu-ATSM

Discussions centered upon the imaging of tumor hypoxia must invariably include ^{64}Cu-ATSM [^{64}Cu-diacetyl-bis(N_4-methylsemicarbazone)] as well (Fig. 39). This tracer – initially developed for the diagnosis of cardiac ischemia – was applied to the imaging of cancer as an alternative to [^{18}F]FMISO. Cu-ATSM is a planar tetradentate metal complex in which a central copper atom is coordinated by two nitrogen and two sulfur atoms. The ATSM ligand has been used to chelate a number of the positron-emitting isotopes of copper, including ^{60}Cu ($t_{1/2}$ = 23.7 min), ^{61}Cu ($t_{1/2}$ = 3.3 h), ^{62}Cu ($t_{1/2}$ = 9.7 min), and ^{64}Cu

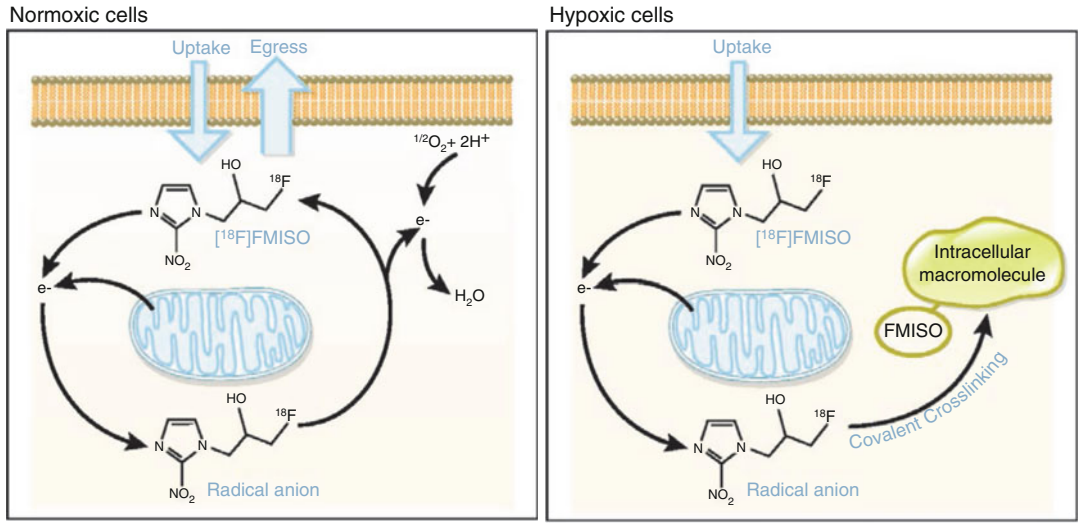

Fig. 36 The mechanism of the uptake and retention of [^{18}F]FMISO. In both hypoxic and normoxic cellular environments, the nitro group of [^{18}F]FMISO picks up electrons released from the electron transport chain, generating a radical anion. Under normoxic conditions, oxygen is able to reduce the nitro group, allowing for the subsequent egress of [^{18}F]FMISO from the cell. Under hypoxic conditions, there is far less O_2 to serve as an oxidizing agent. This permits the radicalized [^{18}F]FMISO to undergo covalent cross-linking with nearby macromolecules, effectively trapping it within the cell

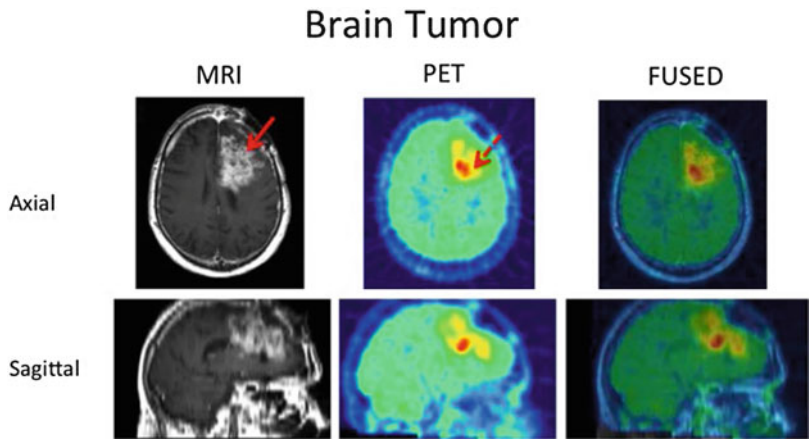

Fig. 37 A glioblastoma in the right superior frontal lobe as imaged by MRI (*left*), [^{18}F]FMISO PET (*middle*), and a PET/MRI overlay (*right*). The fused image shows the areas of highest [^{18}F]FMISO uptake, correlating to localized regions of hypoxia within the tumor mass (Reprinted from Rajendran and Krohn [150], with permission from Elsevier)

($t_{1/2}$ = 12.7 h). Of these, the physical half-life of ^{64}Cu has been shown to best match the biological half-life of the compound and, interestingly, may even produce images with higher tumor-to-background activity concentration ratios than other isotopes of copper [137]. There is some controversy regarding the exact mechanism by which Cu-ATSM is retained in hypoxic cells. Currently, the accepted mechanism of Cu-ATSM retention involves the reduction of Cu(II)-ATSM to Cu(I)-ATSM by reductases present in both hypoxic and normoxic cells (Fig. 40). This reduction causes a conformational shift from Cu(II)-ATSM's initial planar conformation to a less-stable geometry. Under normoxic cellular conditions, molecular oxygen can reoxidize the copper center, thereby restoring the complex to its more stable planar geometry and allowing the compound to diffuse

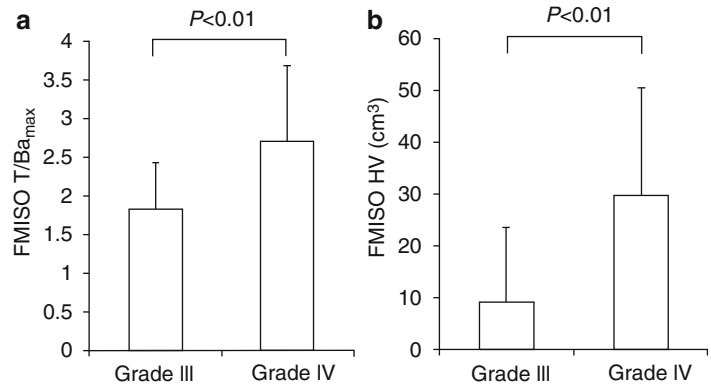

Fig. 38 There is a significant difference ($P < 0.01$) between the T/Bamax of [^{18}F]FMISO (**a**) and the hypoxic volume (HV) of Grade III and Grade IV gliomas (Reproduced with permission from Springer from Kawai et al. [151])

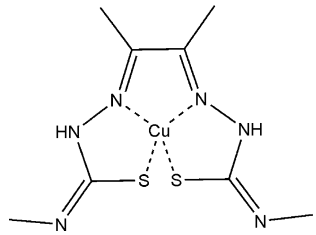

Fig. 39 The structure of ^{64}Cu-ATSM

freely out of the cell. Importantly, however, this reoxidation step does not occur in hypoxic cells. Instead, in these cells, the Cu(I)-ATSM complex is subjected to an acid-catalyzed dissociation reaction, leading to the formation of H_2ATSM and free Cu(I). The Cu(I) can then become irreversibly trapped within the cell by thiol-bearing proteins. This mechanism has been supported by a range of experimental evidence [138–143].

Cu-ATSM has seen clinical applications as a prognostic indicator in head and neck cancer, non-small cell lung cancer, rectal carcinoma, and cervical cancer. As with [^{18}F]FMISO, Cu-ATSM can be utilized to visualize and evaluate the extent of tumor hypoxia (Fig. 41), to direct the application and intensity of IMRT [144], and to determine patient prognosis. ^{64}Cu-ATSM has also shown limited promise as a therapeutic agent in a hamster model of colon cancer, in which ^{64}Cu-ATSM treatment increased survival by six times over control animals [145].

Despite the utility of Cu-ATSM in some cancer models, there is variability in its hypoxia-dependent uptake between different cell lines, which could be due in part to the complexity – and particularly the pH dependence – of its intracellular trapping mechanism. As with [^{18}F]FMISO, a series of Cu-ATSM derivatives have been developed in hopes of improving the hypoxia-selective uptake and tumor retention [143].

Concluding Remarks

In the preceding pages, we have covered a number of extremely promising imaging agents that stand on the cusp of regulatory approval and routine clinical use. The diversity of these radiopharmaceuticals reflects the wide array of information that clinicians seek as they make patient care and treatment decisions. The case studies we have discussed have included small molecules and antibodies, short-lived radiohalogens and long-lived radiometals, and targets ranging from cell surface antigens to tumor hypoxia. Yet despite the potential of these radiopharmaceuticals, the final obstacle (regulatory approval) is often the biggest hurdle of all. In the United States, this has been particularly true – and frustrating – in the case of ^{68}Ga-DOTATOC. In light of this, we are eager to take this opportunity to underscore the paramount importance of the standardization of procedures across clinical trials and institutions, as this is absolutely essential to developing the substantial body of evidence required for regulatory approval. Hopefully, such measures will streamline the path of these imaging agents from the

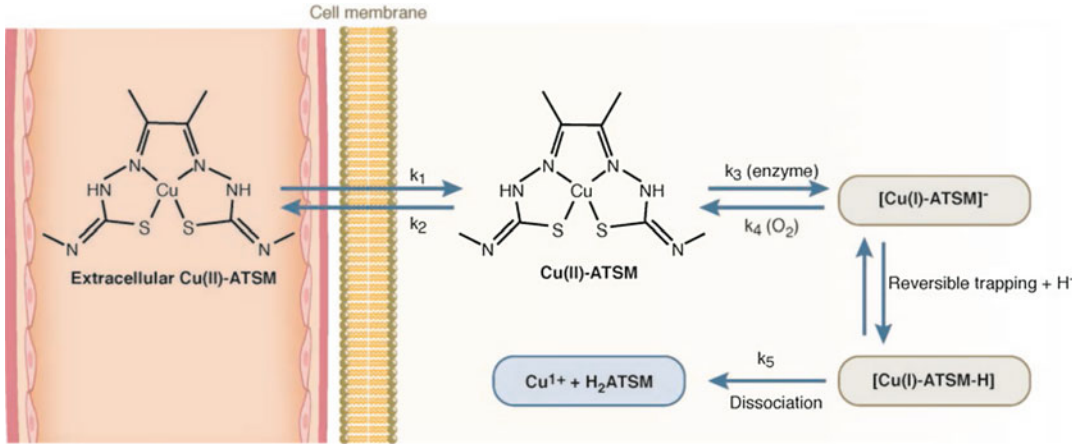

Fig. 40 A schematic depicting the uptake and retention mechanisms of Cu-ATSM. Under anoxic conditions, oxidation by molecular O_2 (k_4) cannot occur, therefore promoting the irreversible trapping of Cu(I) within the cell

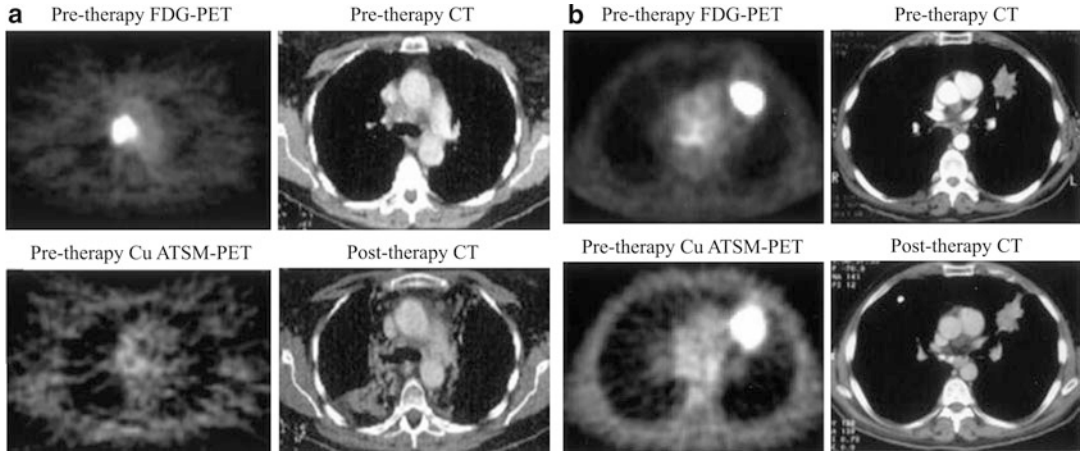

Fig. 41 ^{60}Cu-ATSM uptake can be an indicator of patient response to radiation therapy, as demonstrated here in two lung cancer patients. The responding patient (**a**) exhibited only a minimal increase in uptake of ^{60}Cu-ATSM (T/M = 1.3) and exhibited negligible growth after treatment. In contrast, the non-responding patient (**b**) had a significantly increased uptake (T/M = 3.0), and the tumor size increased over the 3 months following treatment (Reproduced with permission from Springer from Dehdashti et al. [144])

laboratory to the clinic and thus expedite the positive impact that they will undoubtedly have on patient care.

References

1. Ganapathy V, Thangaraju M, Prasad PD. Nutrient transporters in cancer: relevance to Warburg hypothesis and beyond. Pharmacol Ther. 2009;121:29–40.
2. Huang C, McConathy J. Radiolabeled amino acids for oncologic imaging. J Nucl Med. 2013;54:1007–10.
3. Nakanishi T, Tamai I. Solute carrier transporters as targets for drug delivery and pharmacological intervention for chemotherapy. J Pharm Sci. 2011;100:3731–50.
4. Fuchs BC, Bode BP. Amino acid transporters ASCT2 and LAT1 in cancer: partners in crime? Semin Cancer Biol. 2005;15:254–66.
5. DeBerardinis RJ, Mancuso A, Daikhin E, Nissim I, Yudkoff M, Wehrli S, et al. Beyond aerobic glycolysis: transformed cells can engage in glutamine

metabolism that exceeds the requirement for protein and nucleotide synthesis. Proc Natl Acad Sci. 2007;104:19345–50.
6. Shoup TM, Olson J, Hoffman JM, Votaw J, Eshima D, Eshima L, et al. Synthesis and evaluation of [^{18}F]1-Amino-3-fluorocyclobutane-1-carboxylic acid to image brain tumors. J Nucl Med. 1999;40: 331–8.
7. Nye JA, Schuster DM, Yu W, Camp VM, Goodman MM, Votaw JR. Biodistribution and radiation dosimetry of the synthetic nonmetabolized amino acid analogue anti-^{18}F-FACBC in humans. J Nucl Med. 2007;48:1017–20.
8. Turkbey B, Mena E, Shih J, Pinto PA, Merino MJ, Lindenberg ML, et al. Localized prostate cancer detection with ^{18}F FACBC PET/CT: comparison with MR imaging and histopathologic analysis. Radiology. 2014;270:849–56.
9. Sörensen J, Owenius R, Lax M, Johansson S. Regional distribution and kinetics of [^{18}F]fluciclovine (anti-[^{18}F]FACBC), a tracer of amino acid transport, in subjects with primary prostate cancer. Eur J Nucl Med Mol Imaging. 2013;40:394–402.
10. Schuster DM, Taleghani PA, Nieh PT, Master VA, Amzat R, Savir-Baruch B, et al. Characterization of primary prostate carcinoma by anti-1-amino-2-[^{18}F] -fluorocyclobutane-1-carboxylic acid (anti-3-[^{18}F] FACBC) uptake. Am J Nucl Med Mol Imaging. 2013;3:85–96.
11. Oka S, Okudaira H, Ono M, Schuster D, Goodman M, Kawai K, et al. Differences in transport mechanisms of *trans*-1-Amino-3-[^{18}F] Fluorocyclobutanecarboxylic acid in inflammation, prostate cancer, and glioma cells: comparison with L-[Methyl-^{11}C]Methionine and 2-Deoxy-2-[^{18}F] Fluoro-D-Glucose. Mol Imaging Biol. 2014;16: 322–9.
12. Schuster DM, Nanni C, Fanti S, Oka S, Okudaira H, Inoue Y, et al. Anti-1-Amino-3-^{18}F-Fluorocyclobutane-1-Carboxylic acid: physiologic uptake patterns, incidental findings, and variants that may simulate disease. J Nucl Med. 2014;55:1986–92.
13. Långström B, Antoni G, Gullberg P, Halldin C, Malmborg P, Någren K, et al. Synthesis of L- and D-[Methyl-^{11}C]Methionine. J Nucl Med. 1987;28: 1037–40.
14. Okubo S, Zhen H-N, Kawai N, Nishiyama Y, Haba R, Tamiya T. Correlation of L-methyl-^{11}C-methionine (MET) uptake with L-type amino acid transporter 1 in human gliomas. J Neurooncol. 2010;99:217–25.
15. Miyazawa H, Arai T, Iio M, Hara T. PET imaging of non-small-cell lung carcinoma with carbon-11-methionine: relationship between radioactivity uptake and flow-cytometric parameters. J Nucl Med. 1993;34: 1886–91.
16. Harris SM, Davis JC, Snyder SE, Butch ER, Vāvere AL, Kocak M, et al. Evaluation of the biodistribution of ^{11}C-Methionine in children and young adults. J Nucl Med. 2013;54:1902–8.
17. Deloar HM, Fujiwara T, Nakamura T, Itoh M, Imai D, Miyake M, et al. Estimation of internal absorbed dose of *L*-[methyl-^{11}C]methionine using whole-body positron emission tomography. Eur J Nucl Med. 1998;25: 629–33.
18. Glaudemans AWJM, Enting RH, Heesters MAAM, Dierckx RAJO, van Rheenen RWJ, Walenkamp AME, et al. Value of ^{11}C-methionine PET in imaging brain tumours and metastases. Eur J Nucl Med Mol Imaging. 2013;40:615–35.
19. Smits A, Westerberg E, Ribom D. Adding ^{11}C-methionine PET to the EORTC prognostic factors in grade 2 gliomas. Eur J Nucl Med Mol Imaging. 2008; 35:65–71.
20. Heiss P, Mayer S, Herz M, Wester H-J, Schwaiger M, Senekowitsch-Schmidtke R. Investigation of transport mechanism and uptake kinetics of *O*-(2-[^{18}F] Fluoroethyl)-L-tyrosine in vitro and in vivo. J Nucl Med. 1999;40:1367–73.
21. Wester HJ, Herz M, Weber W, Heiss P, Senekowitsch-Schmidtke R, Schwaiger M, et al. Synthesis and radiopharmacology of *O*-(2-[^{18}F] fluoroethyl)-L-tyrosine for tumor imaging. J Nucl Med. 1999;40:205–12.
22. Hamacher K, Coenen HH. Efficient routine production of the ^{18}F-labelled amino acid *O*-(2-[^{18}F]fluoroethyl)-L-tyrosine. Appl Radiat Isot. 2002;57:853–6.
23. Langen K-J, Hamacher K, Weckesser M, Floeth F, Stoffels G, Bauer D, et al. *O*-(2-[^{18}F]fluoroethyl)-L-tyrosine: uptake mechanisms and clinical applications. Nucl Med Biol. 2006;33:287–94.
24. Pöpperl G, Kreth F, Mehrkens J, Herms J, Seelos K, Koch W, et al. FET PET for the evaluation of untreated gliomas: correlation of FET uptake and uptake kinetics with tumour grading. Eur J Nucl Med Mol Imaging. 2007;34:1933–42.
25. Jansen NL, Suchorska B, Wenter V, Schmid-Tannwald C, Todica A, Eigenbrod S, et al. Prognostic significance of dynamic 18F-FET PET in newly diagnosed astrocytic high-grade glioma. J Nucl Med. 2015;56:9–15.
26. Garnett ES, Firnau G, Nahmias C. Dopamine visualized in the basal ganglia of living man. Nature. 1983;305:137–8.
27. Vallabhajosula S. ^{18}F-Labeled positron emission tomographic radiopharmaceuticals in oncology: an overview of radiochemistry and mechanisms of tumor localization. Semin Nucl Med. 2007;37: 400–19.
28. Balogova S, Talbot J-N, Nataf V, Michaud L, Huchet V, Kerrou K, et al. ^{18}F-Fluorodihydroxyphenylalanine vs other radiopharmaceuticals for imaging neuroendocrine tumours according to their type. Eur J Nucl Med Mol Imaging. 2013;40:943–66.
29. Minn H, Kemppainen J, Kauhanen S, Forsback S, Seppänen M. ^{18}F-Fluorodihydroxyphenylalanine in

the diagnosis of neuroendocrine tumors. PET Clin. 2014;9:27–36.
30. Ambrosini V, Tomassetti P, Castellucci P, Campana D, Montini G, Rubello D, et al. Comparison between ^{68}Ga-DOTA-NOC and ^{18}F-DOPA PET for the detection of gastro-entero-pancreatic and lung neuro-endocrine tumours. Eur J Nucl Med Mol Imaging. 2008;35:1431–8.
31. Haug A, Auernhammer C, Wängler B, Tiling R, Schmidt G, Göke B, et al. Intraindividual comparison of ^{68}Ga-DOTA-TATE and ^{18}F-DOPA PET in patients with well-differentiated metastatic neuroendocrine tumours. Eur J Nucl Med Mol Imaging. 2009; 36:765–70.
32. Lapa C, Linsenmann T, Monoranu CM, Samnick S, Buck AK, Bluemel C, et al. Comparison of the amino acid tracers ^{18}F-FET and ^{18}F-DOPA in high-grade glioma patients. J Nucl Med. 2014;55: 1611–6.
33. Pretze M, Wängler C, Wängler B. 6-[^{18}F]Fluoro-L-DOPA: a well-established neurotracer with expanding application spectrum and strongly improved radiosyntheses. BioMed Res Int. 2014;2014:674063.
34. Libert LC, Franci X, Plenevaux AR, Ooi T, Maruoka K, Luxen AJ, et al. Production at the Curie level of no-carrier-added 6-^{18}F-Fluoro-L-dopa. J Nucl Med. 2013;54:1154–61.
35. Rajagopalan KN, DeBerardinis RJ. Role of glutamine in cancer: therapeutic and imaging implications. J Nucl Med. 2011;52:1005–8.
36. Venneti S, Dunphy MP, Zhang H, Pitter KL, Zanzonico P, Campos C, et al. Glutamine-based PET imaging facilitates enhanced metabolic evaluation of gliomas in vivo. Sci Transl Med. 2015;7: 274ra17–ra17.
37. Wu Z, Zha Z, Li G, Lieberman BP, Choi SR, Ploessl K, et al. [^{18}F](2*S*,4*S*)-4-(3-Fluoropropyl)glutamine as a tumor imaging agent. Mol Pharm. 2014;11:3852–66.
38. Yoshimoto M, Waki A, Yonekura Y, Sadato N, Murata T, Omata N, et al. Characterization of acetate metabolism in tumor cells in relation to cell proliferation: acetate metabolism in tumor cells. Nucl Med Biol. 2001;28:117–22.
39. Vāvere AL, Kridel SJ, Wheeler FB, Lewis JS. 1-^{11}C-Acetate as a PET radiopharmaceutical for imaging fatty acid synthase expression in prostate cancer. J Nucl Med. 2008;49:327–34.
40. Armbrecht JJ, Buxton DB, Schelbert HR. Validation of [1-^{11}C]acetate as a tracer for non-invasive assessment of oxidative metabolism with positron emission tomography in normal, ischemic, postischemic, and hyperemic canine myocardium. Circulation. 1990; 81:1594–605.
41. Chirala SS, Wakil SJ. Structure and function of animal fatty acid synthase. Lipids. 2004;39:1045–53.
42. Liu Y. Fatty acid oxidation is a dominant bioenergetic pathway in prostate cancer. Prostate Cancer Prostatic Dis. 2006;9:230–4.
43. Mullen GE, Yet L. Progress in the development of fatty acid synthase inhibitors as anticancer targets. Bioorg Med Chem Lett. 2015;25:4363–9.
44. Leisser A, Pruscha K, Ubl P, Wadsak W, Mayerhöfer M, Mitterhauser M, et al. Evaluation of fatty acid synthase in prostate cancer recurrence: SUV of [^{11}C]acetate PET as a prognostic marker. Prostate. 2015;75:1760–7.
45. Prowatke I, Devens F, Benner A, Grone EF, Mertens D, Grone HJ, et al. Expression analysis of imbalanced genes in prostate carcinoma using tissue microarrays. Br J Cancer. 2006;96:82–8.
46. Sandblom G, Sörensen J, Lundin N, Häggman M, Malmström P-U. Positron emission tomography with ^{11}C-acetate for tumor detection and localization in patients with prostate-specific antigen relapse after radical prostatectomy. Urology. 2006;67:996–1000.
47. Haseebuddin M, Dehdashti F, Siegel BA, Liu J, Roth EB, Nepple KG, et al. [^{11}C]Acetate PET/CT before radical prostatectomy: nodal staging and treatment failure prediction. J Nucl Med. 2013;54:699–706.
48. Clary GL, Tsai C-F, Guynn RW. Substrate specificity of choline kinase. Arch Biochem Biophys. 1987; 254:214–21.
49. Jadvar H. Prostate cancer: PET with ^{18}F-FDG, ^{18}F- or ^{11}C-Acetate, and ^{18}F- or ^{11}C-Choline. J Nucl Med. 2011;52:81–9.
50. Krause BJ, Souvatzoglou M, Tuncel M, Herrmann K, Buck AK, Praus C, et al. The detection rate of [^{11}C]Choline-PET/CT depends on the serum PSA-value in patients with biochemical recurrence of prostate cancer. Eur J Nucl Med Mol Imaging. 2008;35:18–23.
51. Pelosi E, Arena V, Skanjeti A, Pirro V, Douroukas A, Pupi A, et al. Role of whole-body ^{18}F-choline PET/CT in disease detection in patients with biochemical relapse after radical treatment for prostate cancer. Radiol Med. 2008;113:895–904.
52. Contractor KB, Kenny LM, Stebbing J, Al-Nahhas A, Palmieri C, Sinnett D, et al. [^{11}C]Choline positron emission tomography in estrogen receptor–positive breast cancer. Clin Cancer Res. 2009;15:5503–10.
53. Iorio E, Ricci A, Bagnoli M, Pisanu ME, Castellano G, Di Vito M, et al. Activation of phosphatidylcholine cycle enzymes in human epithelial ovarian cancer cells. Cancer Res. 2010;70:2126–35.
54. Hanahan D, Weinberg RA. The hallmarks of cancer. Cell. 2000;100:57–70.
55. Toyota Y, Miyake K, Kawai N, Hatakeyama T, Yamamoto Y, Toyohara J, et al. Comparison of 4′-[methyl-^{11}C]thiothymidine (^{11}C-4DST) and 3′-deoxy-3′-[^{18}F]fluorothymidine (^{18}F-FLT) PET/CT in human brain glioma imaging. EJNMMI Res. 2015;5:7.
56. Been LB, Suurmeijer AJH, Cobben DCP, Jager PL, Hoekstra HJ, Elsinga PH. [^{18}F]FLT-PET in oncology: current status and opportunities. Eur J Nucl Med Mol Imaging. 2004;31:1659–72.

57. Boothman DA, Davis TW, Sahijdak WM. Enhanced expression of thymidine kinase in human cells following ionizing radiation. Int J Radiat Oncol *Biol*Phys. 1994;30:391–8.
58. Soloviev D, Lewis D, Honess D, Aboagye E. [^{18}F] FLT: An imaging biomarker of tumour proliferation for assessment of tumour response to treatment. Eur J Cancer. 2012;48:416–24.
59. Contractor KB, Kenny LM, Stebbing J, Rosso L, Ahmad R, Jacob J, et al. [^{18}F]-3′Deoxy-3′-fluorothymidine positron emission tomography and breast cancer response to docetaxel. Clin Cancer Res. 2011;17:7664–72.
60. Scheffler M, Zander T, Nogova L, Kobe C, Kahraman D, Dietlein M, et al. Prognostic impact of [^{18}F]fluorothymidine and [^{18}F]fluoro-D-glucose baseline uptakes in patients with lung cancer treated first-line with erlotinib. PLoS One. 2013;8:e53081.
61. Hoshikawa H, Mori T, Kishino T, Yamamoto Y, Inamoto R, Akiyama K, et al. Changes in ^{18}F-fluorothymidine and ^{18}F-fluorodeoxyglucose positron emission tomography imaging in patients with head and neck cancer treated with chemoradiotherapy. Ann Nucl Med. 2013;27:363–70.
62. Bhoil A, Singh B, Singh N, Kashyap R, Watts A, Sarika S, et al. Can 3′-deoxy-3′-^{18}F-fluorothymidine or 2′-deoxy-2′-^{18}F-fluoro-D-glucose PET/CT better assess response after 3-weeks treatment by epidermal growth factor receptor kinase inhibitor, in non-small lung cancer patients? Preliminary results. Hell J Nucl Med. 2014;17:90–6.
63. Lee TS, Ahn SH, Moon BS, Chun KS, Kang JH, Cheon GJ, et al. Comparison of ^{18}F-FDG, ^{18}F-FET and ^{18}F-FLT for differentiation between tumor and inflammation in rats. Nucl Med Biol. 2009;36:681–6.
64. Choi SJ, Kim JS, Kim JH, Oh SJ, Lee JG, Kim CJ, et al. [^{18}F]3′-deoxy-3′-fluorothymidine PET for the diagnosis and grading of brain tumors. Eur J Nucl Med Mol Imaging. 2005;32:653–9.
65. Lee SJ, Kim SY, Chung JH, Oh SJ, Ryu JS, Hong YS, et al. Induction of thymidine kinase 1 after 5-fluorouracil as a mechanism for 3′-deoxy-3′-[^{18}F]fluorothymidine flare. Biochem Pharmacol. 2010;80:1528–36.
66. Hong YS, Kim HO, K-p K, Lee J-L, Kim HJ, Lee SJ, et al. 3′-Deoxy-3′-^{18}F-fluorothymidine PET for the early prediction of response to leucovorin, 5-fluorouracil, and oxaliplatin therapy in patients with metastatic colorectal cancer. J Nucl Med. 2013;54:1209–16.
67. McKinley ET, Ayers GD, Smith RA, Saleh SA, Zhao P, Washington MK, et al. Limits of [^{18}F]-FLT PET as a biomarker of proliferation in oncology. PLoS One. 2013;8:e58938.
68. Sun LC, Coy DH. Somatostatin receptor-targeted anti-cancer therapy. Curr Drug Deliv. 2011;8:2–10.
69. Patel YC. Somatostatin and its receptor family. Front Neuroendocrinol. 1999;20:157–98.
70. Carroll V, Demoin DW, Hoffman TJ, Jurisson SS. Inorganic chemistry in nuclear imaging and radiotherapy: current and future directions. Radiochima Acta. 2012;100:653–67.
71. Afshar-Oromieh A, Wolf MB, Kratochwil C, Giesel FL, Combs SE, Dimitrakopoulou-Strauss A, et al. Comparison of ^{68}Ga-DOTATOC-PET/CT and PET/MRI hybrid systems in patients with cranial meningioma: initial results. Neuro Oncol. 2015;17:312–9.
72. Novruzov F, Aliyev JA, Jaunmuktane Z, Bomanji JB, Kayani I. The use of ^{68}Ga-DOTATATE PET/CT for diagnostic assessment and monitoring of ^{177}Lu-DOTATATE therapy in pituitary carcinoma. Clin Nucl Med. 2015;40:47–9.
73. Danthala M, Kallur KG, Prashant GR, Rajkumar K, Raghavendra Rao M. ^{177}Lu-DOTATATE therapy in patients with neuroendocrine tumours: 5 years' experience from a tertiary cancer care centre in India. Eur J Nucl Med Mol Imaging. 2014;41:1319–26.
74. Lococo F, Perotti G, Cardillo G, De Waure C, Filice A, Graziano P, et al. Multicenter comparison of ^{18}F-FDG and ^{68}Ga-DOTA-peptide PET/CT for pulmonary carcinoid. Clin Nucl Med. 2015;40:e183–9.
75. Reubi JC, Schär JC, Waser B, Wenger S, Heppeler A, Schmitt JS, et al. Affinity profiles for human somatostatin receptor subtypes SST1-SST5 of somatostatin radiotracers selected for scintigraphic and radiotherapeutic use. Eur J Nucl Med. 2000;27:273–82.
76. Anderson CJ, Dehdashti F, Cutler PD, Schwarz SW, Laforest R, Bass LA, et al. ^{64}Cu-TETA-Octreotide as a PET imaging agent for patients with neuroendocrine tumors. J Nucl Med. 2001;42:213–21.
77. Fani M, Braun F, Waser B, Beetschen K, Cescato R, Erchegyi J, et al. Unexpected sensitivity of sst_2 antagonists to N-Terminal radiometal modifications. J Nucl Med. 2012;53:1481–9.
78. Rosca EV, Koskimaki JE, Rivera CG, Pandey NB, Tamiz AP, Popel AS. Anti-angiogenic peptides for cancer therapeutics. Curr Pharm Biotechnol. 2011;12:1101–16.
79. Pierschbacher MD, Ruoslahti E. Cell attachment activity of fibronectin can be duplicated by small synthetic fragments of the molecule. Nature. 1984; 309:30–3.
80. Plow EF, Pierschbacher MD, Ruoslahti E, Marguerie GA, Ginsberg MH. The effect of Arg-Gly-Asp-containing peptides on fibrinogen and von Willebrand factor binding to platelets. Proc Natl Acad Sci U S A. 1985;82:8057–61.
81. Ruoslahti E. RGD and other recognition sequences for integrins. Annu Rev Cell Dev Biol. 1996;12:697–715.
82. Liu S. Radiolabeled cyclic RGD peptide bioconjugates as radiotracers targeting multiple integrins. Bioconjug Chem. 2015;26:1413–38.
83. Gaertner FC, Kessler H, Wester HJ, Schwaiger M, Beer AJ. Radiolabelled RGD peptides for imaging and therapy. Eur J Nucl Med Mol Imaging. 2012;39:S126–38.
84. Cai H, Conti PS. RGD-based PET tracers for imaging receptor integrin $\alpha_v\beta_3$ expression. J Label Compd Radiopharm. 2013;56:264–79.

85. Liu Z, Wang F. Development of RGD-based radiotracers for tumor imaging and therapy: translating from bench to bedside. Curr Mol Med. 2013;13: 1487–505.
86. Haubner R, Maschauer S, Prante O. PET radiopharmaceuticals for imaging integrin expression: tracers in clinical studies and recent developments. BioMed Res Int. 2014;2014:871609.
87. Haubner R, Kuhnast B, Mang C, Weber WA, Kessler H, Wester HJ, et al. [^{18}F]Galacto-RGD: synthesis, radiolabeling, metabolic stability, and radiation dose estimates. Bioconjug Chem. 2004;15:61–9.
88. Beer AJ, Haubner R, Goebel M, Luderschmidt S, Spilker ME, Wester HJ, et al. Biodistribution and pharmacokinetics of the $\alpha_v\beta_3$-selective tracer ^{18}F-Galacto-RGD in cancer patients. J Nucl Med. 2005;46:1333–41.
89. Haubner R, Weber WA, Beer AJ, Vabuliene E, Reim D, Sarbia M, et al. Non-invasive visualization of the activated $\alpha_v\beta_3$ integrin in cancer patients by positron emission tomography and [^{18}F]Galacto-RGD. PLoS Med. 2005;2:0244–52.
90. Doss M, Kolb HC, Zhang JJ, Bélanger MJ, Stubbs JB, Stabin MG, et al. Biodistribution and radiation dosimetry of the integrin marker ^{18}F-RGD-K5 determined from whole-body PET/CT in monkeys and humans. J Nucl Med. 2012;53:787–95.
91. Cho HJ, Lee JD, Park JY, Yun M, Kang WJ, Walsh JC, et al. First in human evaluation of a newly developed integrin binding PET tracer, ^{18}F-RGD-K5 in patients with breast cancer: comparison with 18F-FDG uptake pattern and microvessel density. J Nucl Med. 2009;50:1910.
92. Ambrosini V, Fani M, Fanti S, Forrer F, Maecke HR. Radiopeptide imaging and therapy in Europe. J Nucl Med. 2011;52:42S–55.
93. Kenny LM, Tomasi G, Turkheimer F, Larkin J, Gore M, Brock CS, et al. Preliminary clinical assessment of the relationship between tumor alphavbeta3 integrin and perfusion in patients studied with [^{18}F] fluciclatide kinetics and [^{15}O]H_2O PET. EJNMMI Res. 2014;4:1–6.
94. Dumont RA, Deininger F, Haubner R, Maecke HR, Weber WA, Fani M. Novel ^{64}Cu- and ^{68}Ga-labeled RGD conjugates show improved PET imaging of $\alpha\nu\beta3$ integrin expression and facile radiosynthesis. J Nucl Med. 2011;52:1276–84.
95. Eder M, Schäfer M, Bauder-Wüst U, Haberkorn U, Eisenhut M, Kopka K. Preclinical evaluation of a bispecific low-molecular heterodimer targeting both PSMA and GRPR for improved PET imaging and therapy of prostate cancer. Prostate. 2014;74:659–68.
96. Bandari RP, Jiang Z, Reynolds TS, Bernskoetter NE, Szczodroski AF, Bassuner KJ, et al. Synthesis and biological evaluation of copper-64 radiolabeled [DUPA-6-Ahx-(NODAGA)-5-Ava-BBN(7-14)NH2], a novel bivalent targeting vector having affinity for two distinct biomarkers (GRPr/PSMA) of prostate cancer. Nucl Med Biol. 2014;41:355–63.
97. Yan Y, Chen X. Peptide heterodimers for molecular imaging. Amino Acids. 2011;41:1081–92.
98. Gao S, Wu H, Li W, Zhao S, Teng X, Lu H, et al. A pilot study imaging integrin $\alpha_v\beta_3$ with RGD PET/CT in suspected lung cancer patients. Eur J Nucl Med Mol Imaging. 2015;42:2029–37.
99. Yu C, Pan D, Mi B, Xu Y, Lang L, Niu G, et al. ^{18}F-Alfatide II PET/CT in healthy human volunteers and patients with brain metastases. Eur J Nucl Med Mol Imaging. 2015;42:2021–8.
100. Minamimoto R, Jamali M, Barkhodari A, Mosci C, Mittra E, Shen B, et al. Biodistribution of the ^{18}F-$FPPRGD_2$ PET radiopharmaceutical in cancer patients: an atlas of SUV measurements. Eur J Nucl Med Mol Imaging. 2015;42:1850–8.
101. Iagaru A, Mosci C, Shen B, Chin FT, Mittra E, Telli ML, et al. ^{18}F-$FPPRGD_2$ PET/CT: pilot phase evaluation of breast cancer patients. Radiology. 2014;273: 549–59.
102. Coy DH. Short-chain pseudopeptide bombesin receptor antagonists with enhanced binding affinities for pancreatic acinar and Swiss 3T3 cells display strong antimitotic activity. J Biol Chem. 1989;264:14691–7.
103. Zhang J, Li D, Lang L, Zhu Z, Wang L, Wu P, et al. ^{68}Ga-NOTA-Aca-BBN(7-14) PET/CT in healthy volunteers and glioma patients. J Nucl Med. 2016;57: 9–14.
104. Roivainen A, Kähkönen E, Luoto P, Borkowski S, Hofmann B, Jambor I, et al. Plasma pharmacokinetics, whole-body distribution, metabolism, and radiation dosimetry of ^{68}Ga bombesin antagonist BAY 86-7548 in healthy men. J Nucl Med. 2013;54: 867–72.
105. Kähkönen E, Jambor I, Kemppainen J, Lehtiö K, Grönroos TJ, Kuisma A, et al. In vivo imaging of prostate cancer using [^{68}Ga]-labeled bombesin analog BAY86-7548. Clin Cancer Res. 2013;19:5434–43.
106. Borkowski S, Doehr O, Hultsch C, Weinig P, Elger B, Hegele-Hartung C, et al. Preclinical validation of the Ga-68-bombesin antagonist BAY 86-7548 for a phase I study in prostate cancer patients. J Nucl Med Meet Abstr. 2012;53:177.
107. Mather S, Nock B, Maina T, Gibson V, Ellison D, Murray I, et al. GRP receptor imaging of prostate cancer using [^{99m}Tc]Demobesin 4: a first-in-man study. Mol Imaging Biol. 2014;16:888–95.
108. Koo P, Kwak J, Pokharel S, Choyke P. Novel imaging of prostate cancer with MRI, MRI/US, and PET. Curr Oncol Rep. 2015;17:1–10.
109. Franc BL, Lin H. Detection of recurrent non-Hodgkin lymphoma on In-111 capromab pendetide imaging. Clin Nucl Med. 2015;40:585–8.
110. Cho SY, Gage KL, Mease RC, Senthamizhchelvan S, Holt DP, Jeffrey-Kwanisai A, et al. Biodistribution, tumor detection, and radiation dosimetry of ^{18}F-DCFBC, a low-molecular-weight inhibitor of prostate-specific membrane antigen, in patients with metastatic prostate cancer. J Nucl Med. 2012;53: 1883–91.

111. Rowe SP, Gage KL, Faraj SF, Macura KJ, Cornish TC, Gonzalez-Roibon N, et al. ^{18}F-DCFBC PET/CT for PSMA-based detection and characterization of primary prostate cancer. J Nucl Med. 2015;56: 1003–10.
112. Eder M, Schäfer M, Bauder-Wüst U, Hull W-E, Wängler C, Mier W, et al. ^{68}Ga-complex lipophilicity and the targeting property of a urea-based PSMA inhibitor for PET imaging. Bioconjug Chem. 2012;23:688–97.
113. Afshar-Oromieh A, Malcher A, Eder M, Eisenhut M, Linhart HG, Hadaschik BA, et al. PET imaging with a [^{68}Ga]gallium-labelled PSMA ligand for the diagnosis of prostate cancer: biodistribution in humans and first evaluation of tumour lesions. Eur J Nucl Med Mol Imaging. 2013;40:486–95.
114. Pandit-Taskar N, O'Donoghue JA, Beylergil V, Lyashchenko S, Ruan S, Solomon SB, et al. ^{89}Zr-huJ591 immuno-PET imaging in patients with advanced metastatic prostate cancer. Eur J Nucl Med Mol Imaging. 2014;41:2093–105.
115. Pandit-Taskar N, O'Donoghue JA, Divgi CR, Wills EA, Schwartz L, Gönen M, et al. Indium 111-labeled J591 anti-PSMA antibody for vascular targeted imaging in progressive solid tumors. EJNMMI Res. 2015;5:28.
116. Talbot JN, Gligorov J, Nataf V, Montravers F, Huchet V, Michaud L, et al. Current applications of PET imaging of sex hormone receptors with a fluorinated analogue of estradiol or of testosterone. Q J Nucl Med Mol Imaging. 2015;59:4–17.
117. Gruber CJ, Tschugguel W, Schneeberger C, Huber JC. Production and actions of estrogens. N Engl J Med. 2002;346:340–52.
118. Brinkmann AO, Blok LJ, de Ruiter PE, Doesburg P, Steketee K, Berrevoets CA, et al. Mechanisms of androgen receptor activation and function. J Steroid Biochem Mol Biol. 1999;69:307–13.
119. Tewson TJ, Mankoff DA, Peterson LM, Woo I, Petra P. Interactions of 16α-[^{18}F]-fluoroestradiol (FES) with sex steroid binding protein (SBP). Nucl Med Biol. 1999;26:905–13.
120. Peterson LM, Kurland BF, Link JM, Schubert EK, Stekhova S, Linden HM, et al. Factors influencing the uptake of ^{18}F-fluoroestradiol in patients with estrogen receptor positive breast cancer. Nucl Med Biol. 2011;38:969–78.
121. Beattie BJ, Smith-Jones PM, Jhanwar YS, Schöder H, Schmidtlein CR, Morris MJ, et al. Pharmacokinetic assessment of the uptake of 16β-^{18}F-Fluoro-5-α-Dihydrotestosterone (FDHT) in prostate tumors as measured by PET. J Nucl Med. 2010;51:183–92.
122. Gemignani ML, Patil S, Seshan VE, Sampson M, Humm JL, Lewis JS, et al. Feasibility and predictability of perioperative PET and estrogen receptor ligand in patients with invasive breast cancer. J Nucl Med. 2013;54:1697–702.
123. Kumar P, Mercer J, Doerkson C, Tonkin K, McEwan AJ. Clinical production, stability studies and PET imaging with 16-α-[^{18}F]fluoroestradiol ([^{18}F]FES) in ER positive breast cancer patients. J Pharm Pharm Sci. 2007;10:256s–65.
124. Linden HM, Kurland BF, Peterson LM, Schubert EK, Gralow JR, Specht JM, et al. Fluoroestradiol positron emission tomography reveals differences in pharmacodynamics of aromatase inhibitors, tamoxifen, and fulvestrant in patients with metastatic breast cancer. Clin Cancer Res. 2011;17:4799–805.
125. Allott L, Smith G, Aboagye EO, Carroll L. PET imaging of steroid hormone receptor expression. Mol Imaging. 2015;14:11–22.
126. Heinlein CA, Chang C. Androgen receptor in prostate cancer. Endocr Rev. 2004;25:276–308.
127. Miyamoto H, Rahman MM, Chang C. Molecular basis for the antiandrogen withdrawal syndrome. J Cell Biochem. 2004;91:3–12.
128. Larson SM, Morris M, Gunther I, Beattie B, Humm JL, Akhurst TA, et al. Tumor localization of 16β-^{18}F-Fluoro-5α-Dihydrotestosterone versus ^{18}F-FDG in patients with progressive metastatic prostate cancer. J Nucl Med. 2004;45:366–73.
129. Dehdashti F, Picus J, Michalski JM, Dence CS, Siegel BA, Katzenellenbogen JA, et al. Positron tomographic assessment of androgen receptors in prostatic carcinoma. Mol Imaging. 2005;32:344–50.
130. Vargas HA, Wassberg C, Fox JJ, Wibmer A, Goldman DA, Kuk D, et al. Bone metastases in castration-resistant prostate cancer: associations between morphologic CT patterns, glycolytic activity, and androgen receptor expression on PET and overall survival. Radiology. 2014;271:220–9.
131. Koukourakis MI, Giatromanolaki A, Sivridis E, Fezoulidis I. Cancer vascularization: implications in radiotherapy? Int J Radiat Oncol Biol Phys. 2000;48:545–53.
132. Rajendran JG, Wilson DC, Conrad EU, Peterson LM, Bruckner JD, Rasey JS, et al. [^{18}F]FMISO and [^{18}F] FDG PET imaging in soft tissue sarcomas: correlation of hypoxia, metabolism and VEGF expression. Eur J Nucl Med Mol Imaging. 2003;30:695–704.
133. Fleming IN, Manavaki R, Blower PJ, West C, Williams KJ, Harris AL, et al. Imaging tumour hypoxia with positron emission tomography. Br J Cancer. 2015;112:238–50.
134. Yamamoto Y, Maeda Y, Kawai N, Kudomi N, Aga F, Ono Y, et al. Hypoxia assessed by ^{18}F-fluoromisonidazole positron emission tomography in newly diagnosed gliomas. Nucl Med Commun. 2012;33:621–5.
135. Hendrickson K, Phillips M, Smith W, Peterson L, Krohn K, Rajendran J. Hypoxia imaging with [F-18] FMISO-PET in head and neck cancer: potential for guiding intensity modulated radiation therapy in overcoming hypoxia-induced treatment resistance. Radiother Oncol. 2011;101:369–75.
136. Eschmann S-M, Paulsen F, Reimold M, Dittmann H, Welz S, Reischl G, et al. Prognostic impact of hypoxia imaging with ^{18}F-misonidazole PET in non-small cell lung cancer and head and neck cancer before radiotherapy. J Nucl Med. 2005;46:253–60.

137. Lewis JS, Laforest R, Dehdashti F, Grigsby PW, Welch MJ, Siegel BA. An imaging comparison of ^{64}Cu-ATSM and ^{60}Cu-ATSM in cancer of the uterine cervix. J Nucl Med. 2008;49:1177–82.
138. Dearling JL, Lewis JS, Mullen GE, Rae MT, Zweit J, Blower PJ. Design of hypoxia-targeting radiopharmaceuticals: selective uptake of copper-64 complexes in hypoxic cells in vitro. Eur J Nucl Med. 1998;25:788–92.
139. Dearling JL, Lewis JS, Mullen GE, Welch MJ, Blower PJ. Copper bis(thiosemicarbazone) complexes as hypoxia imaging agents: structure-activity relationships. J Biol Inorg Chem. 2002;7:249–59.
140. Lewis JS, McCarthy DW, McCarthy TJ, Fujibayashi Y, Welch MJ. Evaluation of ^{64}Cu-ATSM in vitro and in vivo in a hypoxic tumor model. J Nucl Med. 1999;40:177–83.
141. Maurer RI, Blower PJ, Dilworth JR, Reynolds CA, Zheng Y, Mullen GED. Studies on the mechanism of hypoxic selectivity in Copper bis(Thiosemicarbazone) radiopharmaceuticals. J Med Chem. 2002;45:1420–31.
142. Blower PJ, Dilworth JR, Maurer RI, Mullen GD, Reynolds CA, Zheng Y. Towards new transition metal-based hypoxic selective agents for therapy and imaging. J Inorg Biochem. 2001;85:15–22.
143. Holland JP, Barnard PJ, Collison D, Dilworth JR, Edge R, Green JC, et al. Spectroelectrochemical and computational studies on the mechanism of hypoxia selectivity of Copper radiopharmaceuticals. Chem Eur J. 2008;14:5890–907.
144. Dehdashti F, Mintun MA, Lewis JS, Bradley J, Govindan R, Laforest R, et al. In vivo assessment of tumor hypoxia in lung cancer with ^{60}Cu-ATSM. Eur J Nucl Med Mol Imaging. 2003;30:844–50.
145. Lewis JS, Laforest R, Buettner TL, Song S-K, Fujibayashi Y, Connett JM, et al. Copper-64-diacetyl-bis(N^4-methylthiosemicarbazone): an agent for radiotherapy. Proc Natl Acad Sci U S A. 2001;98:1206–11.
146. Aki T, Nakayama N, Yonezawa S, Takenaka S, Miwa K, Asano Y, et al. Evaluation of brain tumors using dynamic ^{11}C-methionine-PET. J Neuro-Oncol. 2012;109:115–22.
147. Mena E, Turkbey B, Mani H, Adler S, Valera VA, Bernardo M, et al. ^{11}C-Acetate PET/CT in localized prostate cancer: a study with MRI and histopathologic correlation. J Nucl Med. 2012;53:538–45.
148. Kwee SA, Lim J, Watanabe A, Kromer-Baker K, Coel MN. Prognosis related to metastatic burden measured by ^{18}F-fluorocholine PET/CT in castration-resistant prostate cancer. J Nucl Med. 2014;55:905–10.
149. Kenny LM, Contractor KB, Hinz R, Stebbing J, Palmieri C, Jiang J, et al. Reproducibility of [^{11}C] Choline-positron emission tomography and effect of Trastuzumab. Clin Cancer Res. 2010;16:4236–45.
150. Rajendran JG, Krohn KA. F-18 fluoromisonidazole for imaging tumor hypoxia: imaging the microenvironment for personalized cancer therapy. Semin Nucl Med. 2015;45:151–62.
151. Kawai N, Lin W, Cao W-D, Ogawa D, Miyake K, Haba R, et al. Correlation between ^{18}F-fluoromisonidazole PET and expression of HIF-1α and VEGF in newly diagnosed and recurrent malignant gliomas. Eur J Nucl Med Mol Imaging. 2014;41:1870–8.

Novel Radiopharmaceuticals for Therapy

8

Federica Guidoccio, Sara Mazzarri, Federica Orsini, Paola Anna Erba, and Giuliano Mariani

Abstract

In the era of personalized medicine, "target radionuclide therapy" (TRT) is designed to damage only the cancerous cells while sparing unnecessary damage to the adjacent healthy cells/tissues. Unlike conventional external beam radiation therapy, TRT is intended to cause less or no collateral damage to normal tissues, as it aims at achieving targeted drug delivery either to a clinically diagnosed cancer not amenable to surgery or to metastatic tumor cells and tumor cell clusters, thus providing systemic therapy of cancer. Currently there are hundreds of new pathway-targeted anticancer agents undergoing phase II and phase III clinical trials. TRT is just one type within the domain of "targeted therapies." In addition to the effective targeted radiopharmaceuticals already well validated for routine clinical use, newer radiolabeled agents are still in the phase of either preclinical or clinical validation.

This chapter describes the main physical and radiochemical characteristics of radionuclides that have potential or have already been employed to label biologically reactive molecules for the development of novel radiopharmaceuticals for therapy. Some of these agents have entered advanced clinical trials in tumor-bearing patients. Results of these clinical trials cover a wide spectrum of potential clinical usefulness.

The chapter is divided into two main parts depending on the type of particle emission (α- or β-associated or not with the emission of either γ- or β^+-radiation). Within each domain, there is some exchange of experience and shift of focus in the various phases of development, depending on the modalities of ascertaining efficient tumor targeting according to the principles of theranostics. The example of a novel α-emitting radiopharmaceutical that has most recently achieved approval by regulatory agencies for clinical use (^{223}Ra-dichloride) is presented in detail as the paradigm for an agent that is showing a survival advantage besides the original target of pain palliation from bone metastases.

Keywords

Targeted therapies • α-emitters • β-emitters • Auger electron emitters • Antibody • Peptide • Ligand

F. Guidoccio (✉) • S. Mazzarri (✉) • G. Mariani (✉)
Regional Center of Nuclear Medicine, Department of Translational Research and Advanced Technologies in Medicine and Surgery, University of Pisa, Pisa, Italy
e-mail: federica.guidoccio@gmail.com; saramazzarri@hotmail.it; giuliano.mariani@med.unipi.it

F. Orsini (✉)
Nuclear Medicine Unit, "Maggiore della Carità" University Hospital, Novara, Italy
e-mail: federicaors@gmail.com

P.A. Erba (✉)
Regional Center of Nuclear Medicine, Department of Translational Research and Advanced Technologies in Medicine, University of Pisa, Pisa, Italy
e-mail: paola.erba@unipi.it

© Springer International Publishing Switzerland 2017
H.W. Strauss et al. (eds.), *Nuclear Oncology*,
https://doi.org/10.1007/978-3-319-26236-9_36

Glossary	
[^{211}At]SAPC	*N*-succinimidyl 5-[^{211}At] astato-3-pyridinecarboxylate
ALP	Alkaline phosphatase
BBN	Bombesin
BsMAb	Bispecific monoclonal antibody
CAIX	Carbonic anhydrase isoenzyme 9
ccRCC	Clear-cell renal carcinoma
CEA	Carcinoembryonic antigen
CI	Confidence interval
DOTA	2-(4-isothiocyanatobenzyl-1,4,7,10-tetra-azacyclododecane-1,4,7,10-tetraacetic acid (macrocyclic coupling agent to label compounds of biological interest with metal radionuclides)
EBRT	External beam radiation therapy
ECM	Extracellular matrix
EMA	European Medicines Agency
ETDMP	Ethylenediamine tetra(methylene phosphonic acid)
FDA	United States Food and Drug Administration
FN	Fibronectin
GA	Arabic glycoprotein
HA	Hydroxyapatite
HAMA	Human anti-mouse antibody
HER2	Human epidermal growth factor receptor 2, also known as receptor tyrosine-protein kinase erbB-2, or HER2/neu
HSG	Histaminesuccinyl-glutamine hapten
L-19 SIP	Small immunoreactive protein, $(scFv)_2$, derived from monoclonal antibody L19
L-19	Monoclonal antibody recognizing the EDB domain of fibronectin
MAA	Macroaggregated albumin
mAb	Monoclonal antibody
mCRPC	Metastatic castrate-resistant prostate cancer
MIBG	Metaiodobenzyilguanidine
MTA-1	Metastasis-associated protein encoded by the MTA1 gene
MTC	Medullary thyroid cancer
MTD	Maximum tolerated dose
MTRD	Maximum tolerated radiation dose
MX35	A monoclonal antibody recognizing the sodium dependent phosphate transport protein 2b
NaPi2b	Sodium-dependent phosphate transport protein 2b
NCA	No-carrier-added
NHL	Non-Hodgkin's lymphoma
PAI2-uPAR	Proteases, members of the urokinase-type plasminogen activator family
PCa	Prostatic carcinoma
PET	Positron emission tomography
PRRT	Peptide receptor radionuclide therapy
PSA	Prostate-specific antigen
PSMA	Prostate-specific membrane antigen
RE	Radioembolization
RIT	Radioimmunotherapy
SCID	Severe combined immunodeficiency
SPECT	Single-photon emission computed tomography
SRE	Skeletal-related event
TAT	Targeted alpha therapy
TCMC	2-(4-isothiocyanatobenzyl-1,4,7,10-tetraaza-1,4,7,10-tetra-(2-carbamonylmetyl)-cyclododecane (macrocyclic coupling agent to label compounds of biological interest with metal radionuclides)
Theranostic	An agent with both diagnostic and therapeutic capabilities (e.g., ^{131}I-iodide – in low activity it is a diagnostic agent, in high activity it is a therapeutic agent)
TROP-2	Cell-surface glycoprotein overexpressed in adenocarcinomas, correlated with tumor aggressiveness

TRT	Targeted radionuclide therapy
VGEF	Vascular endothelial growth factor
WHO	World Health Organization

Contents

Introduction 175

Alpha-Emitting Agents 175
Phase I Assessment 176
Phase II Assessment 177
Phase III Assessment 178

Beta-Emitting Agents 182

Iodine-131 (^{131}I) 183

Other Radionuclides 190

Concluding Remarks 190

References 192

Introduction

Targeted radionuclide therapy (TRT), is based on the use of high-affinity molecules as carriers of radionuclides to tumor cells (see also ▶ Chap. 2, "Principles of Molecular Targeting for Radionuclide Therapy" of this book). After intravenous administration these radiopharmaceuticals are distributed to tissues, so that they can reach their target molecule on the surface of tumor cells.

In clinical practice, TRT is often administered for the treatment of the most radiosensitive tumors, such as leukemias and lymphomas. Whereas solid tumors are usually more radioresistant, therefore greater ionizing radiation doses are needed for therapy. Because of the combination of a short path length in tissues (50–80 μm) with a high linear energy transfer (100 keV μm^{-1}), targeted α-particle therapy offers the potential for more specific tumor cell killing with less damage to surrounding normal tissue than therapy with β-particle emitters. These favorable physical properties, for which a routine clinical application has already been developed with the novel radiopharmaceutical ^{223}Ra-chloride for therapy of bone metastatic disease, offer the real possibility of targeted (or pre-targeted) α-therapy suitable for clearing minimal residual or micrometastatic disease.

Alpha-Emitting Agents

One of the most intensely explored options for local and/or systemic cancer treatment is TRT based on α-particle emission. Nevertheless, with the noticeable exception mentioned above for ^{223}Ra-chloride, most of the studies have so far not progressed beyond the phases of in vitro experiments with tumor cells or experimental tumor models in animals. Preclinical studies and clinical trials have shown that alpha-emitting radionuclides are able to kill cancer cells while sparing the normal tissues with an ensuing clear reduction of toxicity. The α-emitting radionuclides that are medically relevant and available for potential clinical use at this time are ^{211}At, ^{213}Bi, ^{225}Ac, ^{223}Ra, and ^{212}Pb/^{212}Bi (although a pure β-particle emitter, ^{212}Pb decays to ground state after emission of α-particles through the intermediate daughter radionuclide ^{212}Bi). Table 1 summarizes the main physical characteristic for the radionuclides of interest for targeted alpha therapy in nuclear oncology and their method of production.

The first alpha-emitting radiopharmaceutical that has obtained registration in the USA for treatment of bone metastases from prostate cancer is $^{223}RaCl_2$ (Xofigo®), as described in detail further below in this chapter.

The alpha-emitting radioisotopes ^{211}At, ^{213}Bi, ^{225}Ac, and ^{227}Th are being used to label targeting vectors such as monoclonal antibodies for specific cancer therapy indications. In this review, safety and tolerance issues are considered with respect to microdosimetry, specific energy, Monte Carlo model calculations, biodosimetry, equivalent dose, and mutagenesis. When radiolabeled antibodies against the VEGF receptors are used, the clinical efficacy of targeted alpha therapy (TAT) may be enhanced also by their anti-neoangiogenesis effects, especially in the case of solid tumors. This review emphasizes key aspects of TAT investigations with respect to the PAI2-uPAR complex and the monoclonal antibodies (mAbs) bevacizumab, C595, and J591. Clinical trial outcomes are reviewed for neuroendocrine tumors, leukemia, glioma, melanoma, non-Hodgkin's lymphoma, and bone metastases from prostate cancer.

Table 1 Main characteristics of radionuclides already used or with potential for use in alpha-targeted therapy that are discussed in this chapter (arranged according to rising mass element number)

Radionuclide	$T_{½}$, hr	E_{max}, MeV[a]	Production
^{211}At	7.21	α, 5.9 (42)	Cyclotron
^{213}Bi	0.7	α, 5.8 (97%); β, 1.4 (100%); α/β[b], 0.02	Generator ^{229}T→^{225}Ac→^{213}Bi
^{223}Ra	273.6	α, 5.7 (100%)	Cyclotron
^{225}Ac	240.2	α, 5.7 (100%)	Generator ^{229}T→^{225}Ac
^{227}Th	448.8	α, 6.0 (48%)	Generator ^{227}A→^{227}Th

[a]Percentage of quanta with the indicated energy value in the total amount of quanta of this type emitted by a given radionuclide
[b]Ratio of the amount of quanta of different emission types

Radium-223 (^{223}Ra) is commercially available for therapy of patients with metastatic castration-resistant prostate cancer (mCRPC). Radium-223 has a half-life of 11.4 days and releases 94% of its energy as α-particles with very little γ-emission. It is produced from the ^{227}Ac/^{227}Th system and purified using actinium-resin to immobilize ^{227}Ac and ^{227Th} [1]. α-emission has certain advantages over β-emission, in particular lower bone marrow toxicity due to its narrow range in tissues. Similar to cationic strontium, the radium-223 ion is a calcium analog and therefore constitutes a natural bone seeker as it complexes with hydroxyapatite crystals in osteoblastic bone metastases, inducing non-repairable DNA strand breaks in cells.

The convenient biologic characteristics for alpha-emitters have fueled investigations on the use of radium-223 (administered as the dichloride salt) in preclinical models. In particular, an early study has reported a significant antitumor effect of radium-233 on experimental skeletal metastases [2]. The model used for bone metastases was based on laboratory studies where the human cancer cells were injected intravenously into athymic nude rats. The authors used MTA-1 cells which are an estrogen and progesterone receptor-negative human breast cancer cell line. This model results in bone and bone marrow metastases as well as in the growth of tumor lesions in the spinal cord and in soft tissues. Biodistribution studies in this model identified selective uptake of radium in bone when compared to soft tissue. Over the course of time, the relative content of radium-223 in non-bone metastatic sites (including the liver, spleen, and kidney) increased relative to content in the femur. All tumor-bearing control animals (receiving no therapy) were sacrificed between 20 and 30 days, following the onset of secondary to paralysis caused by spinal infiltration of tumor. In contrast, mice receiving radium-223 developed symptoms significantly later, and many of them (7 out of 19, or 37%) were alive beyond 67 days. Furthermore, examination of sacrificed animals showed no significant changes of the bone marrow after radium-223. In a separate report, Henriksen et al. [3] directly compared the biodistribution of radium-223 with that of strontium-89 in murine xenograft models. Both compounds were found to accumulate in a higher concentration at bony surfaces as compared to soft tissues. Conversely, distribution at soft tissue sites was limited with both compounds. Supporting the notion that beta-emitters may be more myelotoxic than alpha-emitters, radium-223 was found to cause less damage to normal marrow when compared with strontium-89 based on an equal dose-deposition basis.

Phase I Assessment

Results of the first clinical trial with radium-223 dichloride were reported by Nilsson et al. with reference to a phase I study in which 25 patients were enrolled, including 15 with prostate cancer and 10 with breast cancer [4]. Five dose levels of the compound were explored: 46, 93, 163, 213, and 250 kBq kg^{-1}. At each dose level, five patients received a single dose of the agent with evaluation of pain response at weeks 1, 4, and 8. Fifty to sixty percent of patients experienced

improvement in bone pain at each time point. A median overall survival of approximately 20 months was noted, and declines in alkaline phosphatase (ALP) levels were noted in 29% and 52% of breast and prostate cancer patients, respectively. Toxicities were generally mild, even at the highest dose levels explored. The incidence of grade 3 neutropenia was only 12%. In particular, imaging studies (based on the X-ray and gamma emission associated with decay of ^{223}Ra) indicated that the majority of radium-223 accumulated in metastatic bone lesions.

A second phase I study reported by Carrasquillo et al. [5] evaluated a total of ten patients with mCRPC. A different array of dose levels of radium-223 than with the aforementioned experience was explored (50, 100, and 200 kBq kg^{-1}). All patients received a single dose of the agent, while six patients (60%) received a second dose of 50 kBq kg^{-1}. In this small cohort of patients, no dose-limiting toxicities were observed. Radium-223 was rapidly cleared from the circulation, with pharmacokinetic studies suggesting that only 0.5% of the drug remained in the circulating blood 24 h after administration. Most of the excretion occurred through the fecal route, as 52% of administered radium-223 was detected in the gastrointestinal tract at 24 h. As in the previously mentioned phase I experience, most of the observed toxicities were hematologic, with 60%, 70%, and 30% of patients developing any grade anemia, leukopenia, and thrombocytopenia, respectively. Besides grade 3–4 leukopenia observed in three patients (30%), grade 3–4 toxicities were limited.

Phase II Assessment

Three phase II studies have further assessed the activity of radium-223 in the setting of mCRPC. These studies differ slightly regarding eligibility and treatment schedule. The first study followed a randomized placebo controlled design and included 64 patients with mCRPC and either one painful bony lesion or multiple bony metastatic sites [6]. All patients received external beam radiation therapy (EBRT) to a metastatic site and then were randomized to receive four concurrent treatment cycles with radium-223 or saline. Two primary endpoints were evaluated in this study: (1) change in bone ALP levels and (2) time to first skeletal-related event (SRE). The study met the first of these two primary endpoints, with a more significant decline in bone ALP levels with radium-223 (−65.6% vs. +9.3%, $P < 0.0001$). Furthermore, there was a substantial (albeit at borderline of statistical significance) difference in time to first skeletal-related events (SRE, $P = 0.065$). Notably, a follow-up report from this trial suggests a survival advantage with radium-223 (65 vs. 46 weeks, $P = 0.056$), consistent with the subsequently noted phase III experience [7]. A separate phase II study assessed a total of 100 patients with mCRPC and painful bony metastases [8]. In contrast to the previous study design, patients did not receive concomitant external beam radiation therapy (EBRT) and were randomized to receive a single dose of radium-223 at one of four dose levels (5, 25, 50, or 100 kBq kg^{-1}). The primary endpoint of the study was to characterize pain responses using two primary indices: (1) the visual analog scale (VAS) for pain and (2) the use of analgesics for pain control. The study met its primary endpoint, with an increased pain response at higher dose levels of radium-223 observed as early as week 2 ($P = 0.035$). At week 8, the proportions of individuals with a decrease in pain and stable analgesic use (at increasing dose levels) were 40%, 63%, 56%, and 71%, respectively ($P = 0.040$). As with the prior phase II experience, changes in markers of bone turnover were correlated with increasing dose levels, a significant reduction being observed in patients treated with 100 kBq kg^{-1}.

The third and largest randomized phase II trial assessed 122 patients with mCRPC who had failed all available therapeutic modalities [9]. While the previous two studies were designed to evaluate palliative endpoints (time to SRE, pain response, etc.), this study was powered to evaluate the proportion of individuals who achieved a prostate-specific antigen (PSA) decline of $\geq$50%. Patients were randomized in a double-blind fashion to receive a total of three 6-weekly doses of

radium-223 at 25, 50, or 80 kBq kg^{-1}. There was a dose-response relationship, with 0%, 6%, and 13% of the patients achieving ≥50% PSA decline in the respective cohorts ($P = 0.0297$). Greater declines in ALP values were also seen at higher dose levels, with a ≥50% decline in just 16% of patients treated at 25 kBq kg^{-1}, as compared with 66% and 67% of patients treated at 50 and 80 kBq kg^{-1}, respectively.

Phase III Assessment

Radium-223 dichloride is the first radiopharmaceutical to demonstrate a clear survival benefit, as reported by Parker and colleagues in an international phase III randomized trial (ALSYMPCA) [9]. A total of 922 patients with mCRPC received six injections of ^{223}Ra (50 kBq kg^{-1}, every 4 weeks) or placebo. Eligibility criteria included symptomatic patients with progressive mCRPC with two or more bone metastases, no known visceral metastases, and castrate serum testosterone <1.7 nMol/L. In both groups, 57% of patients had received docetaxel, while the remainders did not (either because they were not good candidates for such chemotherapy or because docetaxel was not available).

Planned interim analysis found an improved median survival in the ^{223}Ra group [14.9 vs. 11.3 months, hazard ratio (HR) for survival = 0.7; 95% CI 0.55–0.88, two-sided $P = 0.002$]. This study also demonstrated increased time to SREs (15.6 vs. 9.8 months, HR = 0.66; 95% CI 0.52–0.83, $P < 0.001$) and improved quality of life in the ^{223}Ra-dichloride group [9, 10]. Radium-223 dichloride and placebo shared similar rates of all adverse events (93% vs. 96%, respectively), adverse events of grade 3 or higher (56% vs. 62%) and serious adverse events (47% vs. 60%). Only 16% of the patients enrolled discontinued treatment due to adverse events in the ^{223}Ra arm compared with 21% in the placebo arm. Given the improvement in survival, excellent tolerance and ease of use, ^{223}Ra-dichloride is likely to become the radiopharmaceutical of choice for treating patients with mCRPC and predominant skeletal metastasis. In this regard, it should be noted that other bone-seeking radiopharmaceuticals had been approved by regulatory agencies (FDA in the USA, EMA in Europe) for "palliation of bone pain" from skeletal metastases. Whereas based on the results described above regarding the impact of ^{223}Ra-dichloride on overall survival, this agent has been approved for "therapy" of mCRPC – a notion that has been recognized and embedded in the most recent international guidelines on treatment of mCRPC [11, 12].

Astatine-211 (^{211}At) is a cyclotron-produced α-particle emitter that has a 7.2-h half-life [13]. It offers many potential advantages for α-particle therapy; however, its use for this aim is constrained by its limited availability.

This radionuclide is an attractive option for TAT, such as quantitative α-particle emission with each ^{211}At decay, no long-lived α-particle-emitting daughter products, a half-life well suited for use with a diversity of chemistry applications, and possibility for conjugation with a variety of carrier molecules capable of efficient tumor targeting in vivo. Astatine-211 can be produced in reasonable yield from natural bismuth targets via the ^{209}Bi(α,2n)^{211}At nuclear reaction utilizing straightforward methods. There is some debate as to the best incident α-particle energy for maximizing ^{211}At production while minimizing production of ^{210}At; the latter occurrence is in fact problematic because of its 138.4-day half-life α-particle-emitting daughter, ^{210}Po. The intrinsic cost for producing ^{211}At is reasonably modest and comparable to that of commercially available ^{123}I. The major limitation to ^{211}At availability is the need for a medium energy α-particle beam for its production. On the other hand, there are about 30 cyclotrons in the world that have the beam characteristics required for ^{211}At production [14]. Considering its half-life of only 7.2 h, the current scarcity of ^{211}At production sites limits the ability to ship it to distant sites for therapeutic applications.

Despite this drawback, there are many potential advantages of ^{211}At as a therapeutic α-particle emitter, including cost, satisfactory experience regarding radiochemistry of conjugation, and evidence derived from proof-of-concept clinical

trials. In addition, the decay of ^{211}At also results in the emission of a 77- to 92-keV polonium X-ray, which enables noninvasive imaging of real-time biodistribution with either planar or SPECT scintigraphy [11]. It is conceivable that the current supply bottleneck will be overcome as more clinical evidence provides further proof-of-concept for the use of ^{211}At.

In 1989, labeling of a monoclonal antibody (mAb) with ^{211}At using *N*-succinimidyl 3-(trimethylstannyl) benzoate as a synthon was reported [15]. Studies with an internalizing mAb labeled with ^{211}At using *N*-succinimidyl 5-[^{211}At] astato-3-pyridinecarboxylate ([^{211}At]SAPC) as a synthon showed that astatine-211 was intracellularly retained after internalization [16]. Additional preclinical studies have recently shown that combined treatment with ^{211}At-labeled anti-CD45 combined with bone marrow transplantation prolonged survival in a murine model of disseminated acute myeloid leukemia [17]. Biodistribution studies showed excellent localization of the ^{211}At-anti-murine CD45 mAb 30F11 to the bone marrow and spleen within 24 h. In syngeneic hematopoietic stem cell transplantation studies, radioimmunotherapy (RIT) with a ^{211}At-conjugate improved the median survival of leukemic mice in a dose-dependent fashion, with minimal toxicity.

Feasibility of ^{211}At-RIT was reported in two clinical trials. The first study assessed ^{211}At-RIT with an anti-tenascin mAb followed by chemotherapy in patients with glioblastoma [18]; the radioimmunoconjugate was injected into the resection cavity and the maximal injected activity was 347 MBq (9.4 mCi). Six patients out of 18 had reversible grade 2 neurotoxicity, but no grade 3–4 toxicities were observed. Maximal tolerated activity was not reached and the observed median survival favorably compared with that of historical control groups. In the second phase I study, ^{211}At-MX35-F(ab′)$_2$ was assessed in women in complete response (CR) after a second-line chemotherapy for recurrent ovarian carcinoma; MX35 is a mAb against the sodium-dependent phosphate transport protein 2b (NaPi2b) [19]. The aim was to determine dosimetry and toxicity. MX35-F(ab′)$_2$ was labeled with ^{211}At using *N*-succinimidyl-3-(trimethylstannyl)-benzoate. Nine patients underwent laparoscopy 2–5 days before ^{211}At-RIT. Before intraperitoneal infusion of ^{211}At-MX35-F(ab′)$_2$, the abdominal cavity was inspected to exclude the presence of macroscopic tumor growth or major adhesions. The radioimmunoconjugate was infused at the activity concentration of 22.4–101 MBq/L in the peritoneal dialysis solution via a transcutaneous catheter. The estimated absorbed dose to the peritoneum was 15.6 ± 1.0 mGy per MBq/L, to the red bone marrow 0.14 ± 0.04 mGy per MBq/L, and to the unblocked thyroid 24.7 ± 11.1 mGy per MBq/L (decreasing to 1.4 ± 1.6 mGy per MBq/L when the thyroid was blocked). No adverse effects were reported. This study indicates that intraperitoneal ^{211}At-RIT delivers therapeutic absorbed doses in microscopic tumor clusters, without significant associated toxicity.

Actinium-225 (^{225}Ac) is a particularly attractive radionuclide for therapy, since each decay is associated with the emission of four α-particles; this feature holds high promise for a very potent radiobiological effect – assuming that this radionuclide is conjugated with a selective and efficient tumor-targeting carrier. Actinium-225 has a half-life of 10 days and is produced as a decay product of uranium [20, 21]. In addition to α-particle emission, ^{225}Ac decay also results in the emission of a 440-keV gamma ray that can be used for imaging after administration of a therapeutic agent. The relatively long half-life of ^{225}Ac allows its shipment to potential users from a centralized production or purification site. In the USA, the Oak Ridge National Laboratory currently purifies ^{225}Ac for commercial use from uranium stockpiles. The limiting factor for ^{225}Ac is its cost, which currently exceeds $1,000/mCi. Besides purification from a uranium source, small amounts of high purity ^{225}Ac can also be produced employing a standard proton-beam cyclotron, although using very long irradiation times (7–50 h) [22]. Thanks to the widely available radiochemistry based on macrocyclic bifunctional chelators, ^{225}Ac can be easily conjugated to antibodies and peptides without damaging the in vivo targeting properties of the antibody or peptide

[23, 24]. Nevertheless, in the process of ^{225}Ac conjugation to compounds of biological interest, there is an important radiochemical challenge; in particular, production of radiotoxic daughter products (such as ^{213}Bi) during decay of ^{225}Ac introduces in the system elements that have chemical properties different from those of ^{225}Ac – therefore dissociate from the targeting moiety. A solution to this problem can probably be found in a novel approach based on the so-called ^{225}Ac nanogenerator; in this approach the delivery system is designed to be internalized into the targeted tumor cell, where the toxic daughter elements may dissociate from the targeting molecule but will be trapped inside the cell, thus adding to the therapeutic effect of ^{225}Ac [21, 25]. Moreover, nanotechnology techniques have also been explored to induce intracellular retention of several daughter products during ^{225}Ac-based therapies [26, 27]. In particular, the retention of ^{225}Ac and its radioactive daughters in the targeted tumor cell after internalization, according to the concept of an "in vivo generator," was demonstrated using a mAb derivatized with DOTA [14, 28].

Clinical studies are ongoing in the USA with an ^{225}Ac-labeled anti-CD33 antibody in patients with acute myeloid leukemia. An ongoing phase I trial of alpha-RIT based on the ^{212}Pb/^{212}Bi generator concept uses instead an anti-HER2 mAb infused intraperitoneally in patients with peritoneal carcinomatosis from HER2-expressing tumors [29, 30]. Production of daughter radionuclides during ^{225}Ac decay complicates radiation dosimetry issues to nontarget organs, such as the kidneys, as an excretion route [31].

An interesting approach to the use of an ^{225}Ac-labeled ligand for TAT is based on the high selectivity of the prostate-specific membrane antigen (PSMA) and on the long tumor retention of ligands for PSMA. In particular, a ligand named PSMA-617 has been developed, characterized by optimized tumor cell internalization and reduced kidney excretion versus the PSMA-11 ligand used for PET imaging after labeling with ^{68}Ga. In addition, the PSMA-617 ligand contains DOTA as more universal chelator that makes radiolabeling of this compound with a variety of metal nuclides possible [32, 33]. Besides initial clinical trials with ^{177}Lu-PSMA-617 [34–36], the results of a pilot, proof-of-concept study for the therapeutic use of ^{225}Ac-PSMA-617. This treatment was offered as salvage therapy to two patients with mCRPC who had failed all lines of treatment and had widespread metastatic disease [37]. Therapy consisted in the administration of three cycles of 100 kBq/kg body weight ^{225}Ac-PSMA-617 at bimonthly intervals, followed in one of the two patients by further administration of 6 MBq 2 months later for consolidation. The results achieved following this regimen were impressive both from the imaging point of view (disappearance of virtually all tumor lesions visualized at PET imaging with ^{68}Ga-PSMA-11) and from the biochemical point of view (reduction of serum PSA to $<$0.1 ng/mL from the initial levels $>$3,000 ng/mL in one patient and about 300 ng/mL in the other patient, respectively). Clearly, this pilot experience will need to be confirmed by additional controlled clinical trials, but will most likely open new perspectives in the treatment of advanced mCRPC.

Thorium-227 (**^{227}Th**) is a radionulide that decays to ^{223}Ra, a long-lived radionuclide with proven good tolerance [38]. A recent preclinical study reported the contribution of mAb internalization in the therapeutic efficacy of intraperitoneal ^{212}Pb-RIT for small volume carcinomatosis, compared targeting of HER2 (internalizing) or CEA (non-internalizing) [39, 40]. An advantage was observed using internalizing anti-HER2 compared with non-internalizing anti-CEA ^{212}Pb-labeled antibodies.

Bismuth-213 (**^{213}Bi**) is a short-half-life (46 min) α-particle emitter that is generally supplied through an ^{225}Ac generator. The useful radionuclide production life of such a generator is about 10 days. The main drawbacks in the use of ^{213}Bi as a label for therapy agents are its very short half-life and a somewhat high cost linked to the use of ^{225}Ac, the starting material for the ^{213}Bi generator. Another technical problem with ^{213}Bi is the possible failure of the generator due to radiation damage, causing breakthrough of contaminant radionuclides such as ^{225}Ac [41]. ^{213}Bi is limited by time constraints for radiolabeling and administration into patients of the

tumor-targeting carrier molecule. Nevertheless, despite these limitations, a number of groups that have used ^{213}Bi-labeled agents have been investigated for feasibility studies both in preclinical and in clinical trials [42, 43]. The results of these studies suggest however the superior therapeutic efficacy of the ^{225}Ac-based nanogenerator described above over ^{213}Bi-labeled antibodies, due to its greater α-particle yield per decay; additional roles are played by the longer half-life of ^{225}Ac and its daughter products, which match the longer biologic half-life of large-molecular-weight antibodies [25]. On the other hand, conjugation of ^{213}Bi with biological tumor-targeting peptides might offer advantages because of the faster clearance of these compounds.

An early trial with a ^{213}Bi-labeled anti-CD33 humanized mAb administered to 18 patients with acute myeloid leukemia showed a reduction in circulating blasts in about 80% of the patients, without detectable extramedullary toxicity [44]. In another pilot clinical study, ^{213}Bi-DOTA-substance P was injected intratumorally via an implanted catheter in five patients with WHO grade II–IV gliomas; radiation-induced tumor necrosis was demonstrated after this form of therapy [45]. More recently, an anti-mouse CD138 mAb labeled with ^{213}Bi was employed for ^{213}Bi-RIT in a syngeneic multiple myeloma mouse model [46]; when administered 10 days after engraftment, this treatment significantly prolonged survival and caused only moderate and transient hematologic toxicity.

Lead-212 (^{212}Pb), one of the radionuclides generated during the decay of thorium-232, is currently being investigated to develop new antitumor treatments [47]. There is a definite potential for the clinical use of ^{212}Pb (10.6-h half-life). ^{212}Pb itself is not an α-emitter, but its physical decay results in the emission of two short-lived α-particles with potent therapeutic efficacy to cellular nuclei. ^{212}Pb decays to ^{212}Bi via β-emission. ^{212}Bi, with a 60-min half-life, has a split decay chain and emits an α-particle at 36% frequency with an average energy of 6.1 MeV; ^{212}Bi decays to ^{212}Po for the remaining 64% via β-emission. In turn, ^{212}Po decays to stable ^{208}Pb in microseconds by emission of an 8.8-MeV α-particle. Betas are of low energy and/or frequency such that they are not expected to contribute significantly to toxicity or efficacy. Cumulative energy from the γ-emissions is <12% of those from the α-particles, but the 238.6-keV γ-ray with a 43% yield can provide the basis for imaging with a gamma camera. In preclinical studies, ^{212}Pb has shown significant therapeutic efficacy in both in vitro and in vivo model systems [48, 49]. With the advent of the first clinical trial that employed ^{212}Pb as the therapeutic agent (^{212}Pb-TCMC-trastuzumab), this radionuclide has finally reached a landmark position in the family of α-emitters validated as suitable for such applications [14].

Among the variety of technologies that are available to conjugate radionuclides to a monoclonal antibody (mAb), two chelating systems have been used successfully for labeling with ^{212}Pb, namely, the macrocyclic agents 2-(4-isothiocyanatobenzyl-1,4,7,10-tetraazacyclododecane-1,4,7,10-tetraacetic acid (C-DOTA)) and 2-(4-isothiocyanatobenzyl-1,4,7,10-tetraaza-1,4,7,10-tetra-(2-carbamonylmetyl)-cyclododecane (TCMC)). The TCMC chelate was specifically developed for chelating Pb(II) radionuclides, while C-DOTA is more multipurpose and has been used for chelating other metals including ^{111}In, ^{90}Y, ^{177}Lu, and ^{212}Bi. Although DOTA is known to form strong complexes with both Bi and Pb, a significant portion of ^{212}Bi (~35%) is released from the carrier following the ^{212}Pb/^{212}Bi radioactive decay, thus resulting in the formation of highly ionized daughter atoms. Release of ^{212}Pb after internalization of mAb delivery to cells has been reported as a source of marrow toxicity when using a DOTA conjugate, as the dissociated ^{212}Pb was free to be transported to the bone and subsequently decay to ^{212}Bi [50]. In contrast, the differences in susceptibility to acidic conditions by the Pb(II)-TCMC complex were well demonstrated by Chappell et al. The Pb (II) [4-NCS-Bz-TCMC] complex, which has been very efficiently radiolabeled with Pb(II) radionuclides, was less labile at pH 3.5 than the corresponding DOTA complex, thus conferring enhanced resistance to acid-catalyzed dissociation with the cell. More recently, the structure of the Pb (II)-TCMC complex revealed that Pb(II) is fully

encapsulated by TCMC with the eight-coordinate sphere saturated by the four ring nitrogen and four amide oxygen atoms; this complex is extremely stable and has decreased acid lability for in vivo sequestration of Pb(II) [51–53].

Based on the successful ^{212}Pb preclinical data published from Milenic et al. [54] and from Anderson et al. [55], ^{212}Pb-TCMC-trastuzumab may have potential for an improved therapeutic ratio over β-emitters such as ^{90}Y- and ^{177}Lu-targeted conjugate therapy and thus have beneficial activity against patients with malignancies expressing HER2. Recently, a phase I clinical trial with i.p. ^{212}Pb-TCMC-trastuzumab at the University of Alabama (Birmingham, Alabama, USA) was designed to determine distribution, pharmacokinetics, and safety of i.p. ^{212}Pb-TCMC-trastuzumab in patients with HER2-expressing malignancy [30]. In this study, ^{212}Pb-TCMC-trastuzumab was administered i.p. to three patients with HER2-expressing cancer who had failed standard therapies. After administration of 7.4 MBq/m^2, gamma camera imaging studies showed no distribution of radioactivity out of the peritoneal cavity, nor normal organ uptake. These data were consistent with preclinical studies. Cumulative urinary excretion was <6% in 2.3 half-lives. The maximum external exposure rate immediately post-infusion at skin contact over the abdomen averaged 7.67 mR/h and dropped to 0.67 mR/h by 24 h. The data points correlate closely with ^{212}Pb physical decay. Follow-up for over 6 months showed no evidence of agent-related toxicity, thus indicating good tolerance.

In the second study using ^{212}Pb-TCMC-trastuzumab, Meredith et al. [29] evaluated the safety, pharmacokinetics, immunogenicity, and tumor response of ^{212}Pb-TCMC-trastuzumab administered i.p. in patients with HER2-expressing malignancy [56]. Five dose levels of treatment with i.p. ^{212}Pb-TCMC-trastuzumab resulted in little toxicity in patients with ovarian cancer. Limited redistribution of radioactivity out of peritoneal cavity to circulating blood, which cleared via urinary excretion, and no specific uptake in major organs were observed at 24 h. The highest administered activity concentration at 500 Bq/mL was needed for high therapeutic efficacy without any side effects. Therefore, the phase study I with i.p. ^{212}Pb-TCMC-trastuzumab confirmed its clinical potential and feasibility. The data obtained are consistent with those of prior nonhuman studies showing prolonged retention of ^{212}Pb-TCMC-trastuzumab within the peritoneal cavity, with no evidence for localization to normal organs on planar images. The relatively low radiation dose is also closely comparable to dosimetry data obtained with the use of ^{211}At-MX35-F(ab′)$_2$.

Beta-Emitting Agents

There are currently eight β-emitting agents approved by the FDA for therapy of cancer in humans: ^{131}I-iodide (for differentiated thyroid cancer), ^{131}I-metaiodobenzylguanidine (^{131}I-MIBG, for neural-crest-derived neuroendocrine tumors), ^{131}I-tositumomab and ^{90}Y-ibritumomab tiuxetan (Bexxar® and Zevalin®, respectively, both for CD-20-expressing non-Hodgkin's lymphomas), ^{89}Sr-chloride and ^{153}Sm-EDTMP (Metastron® and Quadramet®, respectively, both for palliation of bone pain from skeletal metastases), and finally ^{90}Y-labeled microspheres (TheraSphere® and SIR-Spheres®, for radioembolization of primary and metastatic liver tumors). Not all these agents meet the criteria to be considered as true "tumor-targeted" therapeutic agents based on specific interaction/binding of the radiopharmaceutical with antigens/receptors on the surface of tumor cells.

On the other hand, numerous preclinical and clinical investigations have addressed a much broader spectrum both of carrier molecules targeting tumor-specific sites and of additional β-emitting radionuclides. A tentative list of the latter includes at least eight radionuclides: lutetium-177 (^{177}Lu), holmium-166 (^{166}Ho), rhenium-186 (^{186}Re), rhenium-188 (^{188}Re), copper-67 (^{67}Cu), promethium-149 (^{149}Pm), gold-198 (^{198}Au), and rhodium-105 (^{105}Rh).

The main physical characteristics are summarized in Table 2.

Table 2 Main characteristics of radionuclides already used or with potential for use in beta-targeted therapy that are discussed in this chapter (arranged according to rising mass element number)

Radionuclide	$T_{½}$, hr	E_{max}, MeV[a]	Production
^{67}Cu	61.9	β, 0.4 (100%)	Cyclotron
^{90}Y	64.8	β, 2.2 (100%)	Generator $^{90}Sr \rightarrow ^{90}Y$
^{177}Lu	160.8	β, 0.5 (100%)	Nuclear reactor
^{188}Re	17.0	β, 2.0 (100%)	Generator $^{188} \rightarrow ^{188}Re$
^{212}Pb	10.6	β, 0.6 (~80%); γ, 0.2 (44%); 0.08 (18%)	Generator $^{228} \rightarrow ^{220}Rn \rightarrow ^{216}Po \rightarrow ^{212}Pb$
^{131}I	8 days	β, 0.6(89%); γ, 0.364 (81%)	Nuclear reactor
^{166}Ho	26.83	β, 1.854 (50%), 1.774 (48.7%); γ, 0.8 (6.7%)	Nuclear reactor
^{175}Y		β, 0.480 (86.5%), 356.2 (3.3%), 0.7 (10.2%)	Nuclear reactor
^{149}Pm	2.21 days	β, 1.07(97%); γ, 0.28 (3%)	Nuclear reactor
$^{198}Gold$	2.7 days	β, 0.96 (100%)	Nuclear reactor
^{105}Rh	36	β, 0.56 (70%); γ, 0.25 (30%)	Nuclear reactor

[a]Percentage of quanta with the indicated energy value in the total amount of quanta of this type emitted by a given radionuclide

Iodine-131 (^{131}I)

Although certainly not the latest emerging β-emitter for therapy, iodine-131 still fulfills an important role in the development of new tumor-seeking radiopharmaceuticals with therapeutic intent. In particular, this radionuclide is being employed in a series of clinical trials based on monoclonal antibody constructs against a family of target antigens that are essential components of the extracellular matrix (ECM). The molecular architecture of the ECM is extremely heterogeneous with wide variation in its constituents in different organs and tissue compartments as well as within the same tissue depending on different developmental and physiologic states [57]. The main components of the ECM are laminins, collagens, fibronectins, and elastins, along with other compounds such as tenascin, thrombospondins, members of the coagulation system, neuronal guidance molecules, and specific growth factor-associated proteins [58, 59]. During oncogenesis, the molecular composition and structure of the ECM is dynamically modified [59].

One of the principal constituents of ECM is fibronectin (FN), a large protein that exists in different isoforms (240–270 kDa) and different molecular forms [57]. FN usually exists as a dimer of two nearly identical ~250 kDa (≈2,500 amino acids) subunits, covalently linked by a pair of disulfide bonds near the C-terminal end of the subunits. Although FNs are the product of a single FN gene, the resulting protein can exist in multiple forms, which – apart from posttranslational modifications – arise from alternative splicing of its primary RNA transcript. This polymorphism leads to the production of as many as 20 different isoforms for human FN. The 3D structure of the alternatively spliced-in EDB domain, a 91-amino acid sequence, is identical in the mouse, rat, rabbit, dog, monkey, and human. EDB has a restricted pattern of expression: undetectable in normal adult tissues and in mature blood vessels, but highly expressed in regenerating tissues and around new blood vessels [60, 61]. The FN isoform containing the ED-B domain is an ideal tumor target since it is widely expressed in the ECM of all solid tumors and is constantly associated with angiogenic processes (i.e., wound healing) [62], but is otherwise undetectable in normal adult tissues [63]. The EDB-FN selective expression pattern has been extensively demonstrated in many different tumor types, in particular on invasive ductal carcinoma [64], brain tumors [63], lymphomas [65], and prostate cancer [66]. High EDB expression is found around the newly forming blood vessels, thus suggesting that EDB is an important target for tumor-associated angiogenesis [67–70].

After the identification of the EDB domain, monoclonal antibodies specific for EDB-FN

were raised. A series of molecular biology experiments finally yielded a high-affinity clone with $K_D = 54$ pM for EDB, termed clone L19 [71, 72]. The enhanced binding affinity of L19 as well as valence (monomeric scFv vs. dimeric scFv) lead also to improved targeting of tumoral angiogenesis, as was shown in biodistribution studies in F9 murine teratocarcinoma-bearing nude mice, where L19 labeled with ^{125}I demonstrated rapid specific localization around tumor blood vessels [73]. Biodistribution experiments in F9 tumor-bearing mice using radioiodinated L19 $(scFv)_2$, L19-SIP ("small immunoreactive protein" format), and L19 IgG_1 showed that L19-SIP offers the best compromise between molecular stability, clearance rate, and tumor accumulation [74–76]. In addition to the established therapeutic benefit, the dosimetric estimates obtained with ^{131}I-L19SIP in murine models of cancer are among the most promising reported so far for radioimmunotherapy (RIT) [77].

The first immunoscintigraphy study in patients with primary tumors and metastatic lesions using ^{123}I-L19 showed selective targeting in aggressive types of lung cancer and colorectal cancer [78]. Following this proof-of-concept study, phase I and phase I/II dose-finding and efficacy studies with ^{131}I-L19SIP in patients with a variety of cancers were initiated. ^{131}I-L19SIP showed an excellent tolerability at radioactive amounts as high as 7,400 MBq (200 mCi) in patients with solid tumors, associated with therapeutic benefit for some patients [65]. During the phase I study, 50 patients received a single dose of 4 mg of ^{131}I-L19SIP radiolabeled with up to 185 MBq (5 mCi) for dosimetric purposes ("dosimetric phase" of the study). Whenever the radiation dose in at least one tumor lesion was found to be at least tenfold higher compared to the dose delivered to the bone marrow (the rate-limiting organ), the patient became eligible for RIT with a single dose of 5 mg ^{131}I-L19SIP radiolabeled with 3,700 MBq (100 mCi) or 5,550 MBq (150 mCi), which constituted the "therapeutic phase" of the study. In an extension of the study, repeated treatments were performed, and patients with hematologic malignancies were included, based on the evidence that EDB is strongly expressed in almost all malignant lymphomas and in certain leukemias. The most impressive therapeutic effect in this study was demonstrated in a young female patient suffering from Hodgkin's lymphoma [79]. In general, uptake of ^{131}I-L19SIP was observed both in primary tumor lesions and in distant metastasis, irrespective of cancer type and location of the lesions. RIT caused G3/G4 hematologic toxicity, but this was not predictable from the dosimetric estimates. Nevertheless, the treatment showed an excellent tolerability profile. Side effects were mostly hematological in nature and all were easily manageable and recovered spontaneously. Concerning in particular patients with hematologic malignancies, 18 patients with either relapsed, progressing lymphoma or multiple myeloma were enrolled as candidates for RIT with ^{131}I-L19SIP. Tumor uptake of sufficient degree to justify RIT was observed in 11/15 patients with lymphoma and in 3/3 myeloma patients. Following a single course of RIT with ^{131}I-L19SIP (standard activity of 3.7 GBq, reduced in some cases to 1.85 GBq because of low body weight), complete response was achieved in two patients with Hodgkin's lymphoma and one patient with large B-cell lymphoma, while partial response was observed in one patient with Hodgkin's lymphoma and patients with multiple myeloma experienced stabilization of disease. The objective response rate was therefore 40%, a highly promising outcome for these patients who had failed all lines of treatment, also considering that RIT with ^{131}I-L19SIP was associated with low toxicity [79].

Labeling of L19SIP with ^{124}I rather than with ^{131}I during the dosimetric phase of the study allows serial PET imaging, with more accurate dosimetric estimates [80]. Further advances in this field include proof of the therapeutic potential in prostate cancer patients [66].

Lutetium-177 (^{177}Lu) is a very promising β-emitter for targeted radiotherapy. Its β-emission, with a maximum energy of 498 keV, is useful in destroying small tumors and metastasis (optimal size 1.2–3.0 mm), while at the same time reducing damage to normal tissues. From this point of view, ^{177}Lu can be seen as a complement to yttrium-90 or to iodine-131 [81]. ^{177}Lu also emits low-energy gamma rays (208 and 113 keV with 10% and 6%

abundance, respectively) [82], which allow direct imaging of the activity distribution in the patients' body for dosimetry calculations following administration of the therapeutic activity.

With its 6.71-day half-life, lutetium-177 lends itself to the use of more sophisticated procedures to synthesize and purify radiopharmaceuticals and to transport them to more distant nuclear medicine departments. As to the potential applications of lutetium-177 for RIT, prostate carcinoma (PCa) seems to be a favorable solid tumor because of its radiosensitivity and the typical metastatic diffusion to sites where there is potentially a high exposure to circulating mAbs (such as bone marrow and lymph nodes). In preclinical and clinical PCa therapy studies, different antibodies or peptides with affinity to mucin, ganglioside (L6), Lewis Y (Ley), adenocarcinoma-associated antigens, the TROP-2 pancarcinoma marker, and prostate-specific membrane antigen (PSMA) have been linked to radionuclides; PSMA appears the most specific of these targets [83, 84].

PSMA is a non-secreted, integral, type II membrane protein with abundant and nearly universal expression on epithelial prostate cells that is strongly upregulated in PCa [85, 86]. PSMA expressed in normal prostatic cells (brush border/luminal location) is not typically exposed to a circulating mAb, and the PMSA's level of expression in non-prostate tissues is 100–1,000-fold less than in prostate tissue. The de-immunized J591 mAb, which links the PSMA's external domain, seems to be the best clinical candidate for clinical RIT in patients with PCa [87].

In a ^{177}Lu-J591 phase I trial, 35 patients were enrolled [88]. The maximum tolerated dose (MTD) was determined to be 2,590 MBq/m^2. In addition, it was shown that repeated dosing (up to three doses of 1,110 MBq/m^2 each) could safely be injected. In all patients, the sites of metastatic disease were successfully imaged with gamma camera scintigraphy after administration of ^{177}Lu-J591. As to the biochemical PSA response, the median duration of posttreatment PSA stabilization was 60 days (range between 28 and 601 days).

A phase II ^{177}Lu-J591 clinical trial has been conducted in mCRPC patients [89]. Patients were enrolled in two cohorts: 2,405 MBq/m^2 in cohort 1 versus 2,590 MBq/m^2 in cohort 2. Fifteen patients were enrolled in cohort 1, while cohort 2 was expanded to enroll 17 patients instead of the 15 patients as originally planned; targeting of 93.6% of the known sites of metastasis was detected by scintigraphy. Hematologic toxicity consisted in reversible thrombocytopenia and neutropenia and observed in 46.8% and 25.5% of the patients, respectively. The cohort 2 patients exhibited a higher PSA responses (46.9% vs. 13.3%, $P = 0.048$) associated with a longer survival (21.8 vs. 11.9 months, $P = 0.03$), but also more frequent hematologic toxicity. This trial shows that radiolabeled de-immunized J591 is well tolerated and non-immunogenic. Radiolabeled J591 effectively targets PCa metastases and induces PSA reduction with a dose-effect relation.

Among several alternative possibilities, pretargeting may be achieved using a first injection of an unlabeled bispecific monoclonal antibody (BsMAb), followed by subsequent injection of a radiolabeled bivalent hapten-peptide [90, 91]. In this approach, the radiolabeled bivalent peptide binds avidly to the BsMAb attached to the antigen at the cell surface, whereas non-targeted hapten-peptide in the circulation clears rapidly through the kidneys. Medullary thyroid cancer (MTC) cells express high amounts of CEA, and encouraging therapeutic results have been obtained using anti-CEA pre-targeted ^{131}I-di-DTPA peptide in two phase I/II and one phase II clinical trials [90, 92].

New-generation BsMAb and bivalent hapten-peptides are currently available. Humanized, recombinant, trivalent BsMAb and the histamine-succinyl-glutamine (HSG) hapten and bivalent HSG hapten-peptides have been created [93, 94]. The use of humanized BsMAb should reduce immunogenicity and the dock-and-lock procedure allows large-scale production. Accordingly, a series of bivalent HSG haptens have been created, offering the possibility of labeling with many radionuclides, including yttrium-90 and lutetium-177 for therapy purposes [95]. The first clinical study evaluating the anti-CEA anti-HSG BsMAb TF2 and the radiolabeled hapten-peptide, ^{177}Lu-IMP288, in patients with mCRPC has been

published recently [93]. Different approaches were explored in four cohorts of five patients each, to identify the optimal molar doses of TF2 and IMP-288 and the optimal holdup between the two infusions: (1) shortening the interval between the BsMAb and peptide administration (1–5 days), (2) escalating the TF2 dose (from 75 to 150 mg), and (3) reducing the peptide dose (from 100 to 25 μg). Rapid and selective cancer uptake was observed within 1 h after the peptide injection, with high tumor-to-tissue ratios at 24 h. The best tumor targeting was obtained with a 1-day pre-targeting interval and with the 25-μg peptide amount. High activities of ^{177}Lu-IMP288 (2.5–7.4 GBq) were well tolerated. Some controllable reactions during the TF2 infusions occurred, and transient grades 3–4 thrombocytopenia was reported in 10% of the patients. Dosimetric analysis showed that red bone marrow and renal uptake of ^{177}Lu-IMP288 were relatively low, although marrow doses increased in subsequent cohorts as the TF2/Lu-IMP288 ratio was improved [95]. The predicted kidney-absorbed doses (<0.50 mGy/MBq) did not restrict the maximum activity that could be injected. None of the patients would exceed the limit of 15 Gy to the kidneys with four cycles of 7.4 GBq ^{177}Lu-IMP288. These data indicate that pre-targeting using dock-and-lock bispecific BsMAb would be most practical to deliver short-half-life radionuclides.

Bound with methylene phosphonic acid (EDTMP), ^{177}Lu can be used as a bone pain palliation radiopharmaceutical. Preclinical studies and initial clinical trials with ^{177}Lu-EDTMP have resulted in encouraging data [96]. Results of clinical studies show that ^{177}Lu-EDTMP is an effective radiopharmaceutical for palliation of metastatic skeletal pain in patients with breast or prostate cancer. An amount of 1,295 MBq (35 mCi) is sufficient for bone pain palliation therapy, but doses as high as 2,590 MBq (70 mCi) have been shown to be safe.

Holmium-166 (^{166}Ho) decays by β-emission to ^{166}Er (stable) with $E\beta_{max}$ of 1.854 MeV (50.0%) and 1.774 MeV (48.7%). It decays with a half-life of 26.83 h. It emits 81-keV gamma photons (6.7%), which are suitable for external imaging to track the in vivo distribution and uptake of the radionuclide. The maximum soft tissue penetration of the β-particles is ~8.5 mm and hence is suitable for certain specific therapeutic applications. Holmium-166 is a very attractive candidate for therapeutic purposes, as this radionuclide emits gamma rays in addition to high-energy beta particles, thus allowing both nuclear imaging and radionuclide therapy, according to the principles of "theranostics." Moreover, holmium can be visualized by computed tomography and magnetic resonance imaging owing to its high attenuation coefficient and paramagnetic properties [97].

Also favorable is its half-life of 26.9 h, which is long enough to overcome logistic problems encountered with the short-lived radionuclides and is sufficient to provide a high radiation dose rate. Its nuclear reaction cross section is comparable with that of rhenium, but ^{165}Ho has a natural abundance of 100%; thus, only one radioisotope, ^{166}Ho, is formed by neutron bombardment. Taking these characteristics into consideration, ^{166}Ho is therefore an attractive candidate for use to tailor the future needs for treatments. The first study with this radionuclide was for the development of radiosynovectomy agents for treatment of rheumatoid arthritis [98, 99]. Development of ^{166}Ho-labeled polylactic acid microspheres was also reported [100, 101]. Hydroxyapatite (HA) particles were selected as they are biodegradable and hence thought to be good as a matrix for radiolabeling with ^{166}Ho and developing a radiosynovectomy agent. An experimental knee joint lesion that closely resembles rheumatoid arthritis was developed in rabbits by injecting ovalbumin. Bioevaluation of the ^{166}Ho-HA particles was carried out by injecting ~2 mCi (74 MBq) of the radiotracer in 200 μL of saline solution which contained ~8 mg of ^{166}Ho-HA particles into the knee joints of New Zealand white rabbits. The ^{166}Ho-HA particles were injected into the arthritis-induced knee joints as well as into knee joints of healthy rabbits. Images of the injected joints of the animals recorded at regular intervals using a gamma camera showed good retention of the radiopharmaceutical. Blood samples were collected from the animals and the blood activity was assayed in a scintillation detector. Experiments

were also carried out under identical conditions in normal rabbits. In both the cases, it was observed that there was no significant extra-articular leakage of the injected activity over the study period of 96 h postinjection and the particles are retained within the synovial joints [99]. About 185 MBq (5 mCi) of the labeled preparation in sterile saline was injected intra-articularly under fluoroscopic guidance to the affected knee joints of the patients. The knee is flexed three to four times after injection and the patients were kept under observation. Gamma camera imaging was recorded to ascertain the localization of the injected dose. More than 100 joints were studied in the clinical trial. Patients suffering from rheumatoid arthritis and hemophilia showed good response from the treatment. Seventy-five percent of the 50 patients treated with the new radiopharmaceutical showed significant reduction in pain.

Although not strictly related to oncological applications, the results of the above study are nevertheless interesting because they constitute the rationale for applying to cancer therapy some of the concepts of using ^{166}Ho-labeled particles and of locoregional administration described above. In this regard, ^{166}Ho-microspheres have recently been introduced as an alternative radiopharmaceutical for intra-arterial therapy in patients with liver tumors. The efficacy of radioembolization for the treatment of liver tumors depends on the selective distribution of radioactive microspheres to tumor tissue. The distribution of ^{166}Ho-poly(L-lactic acid) microspheres can be visualized in vivo both by SPECT and by MRI. In a phase I clinical trial, Smits et al. [102] evaluated the safety and the maximum tolerated radiation dose (MTRD) of ^{166}Ho-radioembolization in patients with liver metastases. Patients were treated with intra-arterial ^{166}Ho-radioembolization in cohorts of three patients, with escalating aimed whole-liver absorbed doses of 20, 40, 60, and 80 Gy. Cohorts were extended to a maximum of six patients if dose-limiting toxicity occurred. Patients were assigned a dose in the order of study entry, with dose escalation until dose-limiting toxicity was encountered in at least two patients of a dose cohort. The most frequently encountered toxicities (including grade 1) were lymphocytopenia, hypoalbuminemia, raised alkaline phosphatase, raised aspartate aminotransferase, and raised gamma-glutamyltransferase, which were all noted in 12 of 15 patients. Stable disease or partial response regarding target lesions was achieved in 14/15 patients (93%, 95% CI 70–99) at 6 weeks and in 9/14 patients (64%, 95% CI 39–84) at 12 weeks after radioembolization. Compared with baseline, the average global health status and quality of life score at 6 weeks after treatment had decreased by 13 points ($P = 0.053$) and by 14 points at 12 weeks ($P = 0.048$). In all patients, ^{99m}Tc-macroaggregated albumin SPECT, ^{166}Ho scout dose SPECT, and ^{166}Ho treatment dose SPECT showed similar patterns of the presence or absence of extrahepatic deposition of activity. The authors concluded by stating that ^{166}Ho-radioembolization is feasible and safe for the treatment of patients with unresectable and chemorefractory liver metastases, and it enables image-guided treatment. Clinical ^{166}Ho-radioembolization should be performed aiming at achieving a whole-liver absorbed dose of 60 Gy [102].

Ytterbium-175 (^{175}Yb) is another low-energy β-emitter, which has been proposed for labeling bone-seeking agents to be employed for bone pain palliation. The low β-energy of ^{175}Yb (480 keV) will induce minimum radiation dose to bone marrow and hence will allow administration of higher levels of radioactivity, to potentially obtain even a therapeutic efficacy similar to that demonstrated for ^{153}Sm and ^{188}Re. Similar to ^{153}Sm, ^{175}Yb can also be chelated to polyamino-poly phosphonate ligands [103].

Thulium-170 (^{170}Tm) conjugated with EDTMP is considered as an alternative to $^{89}SrCl_2$ in palliative therapy of bone metastases. The use of ^{170}Tm would induce low myelosuppression, since it emits lower-energy β-particles ($E\beta_{max} = 968$ keV) than those emitted by ^{89}Sr, and the gamma photons emitted can be used for scintigraphy to detect the accumulated activity and biokinetics at the target sites [104]. The long half-life of 128.6 days could be advantageous in an approach based on mixed radionuclide therapy using ^{170}Tm together with ^{153}Sm, ^{177}Lu, or ^{175}Yb. Such combination could provide both early and sustained long-term pain relief to patients in early stage of disease.

Copper-67 (^{67}Cu) has favorable radiophysical characteristics for RIT, with a half-life of 3.4 days (well suited to pharmacokinetics of whole antibodies) and an emission of β-particles with energy comparable to that of iodine-131 and lutetium-177. Moreover, it emits gamma rays with energy suitable for imaging and a relatively weak abundance, thus reducing irradiation of patients and medical staff as that occurring with iodine-131. The production capacity of copper-67 is limited by a low cross section of the nuclear reaction, which needs high-intensity and high-energy proton beams. Only a limited number of accelerators in the world have such high energy and high intensity. This situation explains the quite limited number of clinical studies performed in the last 30 years.

Two groups of investigators carried out clinical studies in the 1990s in a limited number of patients. De Nardo and coworkers pioneered this field and compared clinical results obtained with the Lym-1 mAb against non-Hodgkin's lymphoma (NHL) labeled with ^{67}Cu, ^{131}I, and ^{90}Y, respectively [105, 106]. The authors concluded that the therapeutic indices (ratio of radiation doses to tumor relative to those to normal tissues) for ^{67}Cu-2IT-BAT-Lym-1 and, to a lesser extent, for ^{90}Y-2IT-BAD-Lym-1 were more favorable than those observed for ^{131}I-Lym-1. The same conclusions were drawn in a clinical study comparing the anti-CEA mAb35 antibody labeled with ^{67}Cu and ^{125}I in patients with colorectal cancer [107]. Copper-67-labeled mAb35 was more favorable than its radioiodine-labeled counterpart due to higher tumor-to-blood ratio; however, the authors observed a potential problem with ^{67}Cu, i.e., non-specific liver and bowel uptake.

In conclusion, copper-67 seems to be more suitable than iodine-131 and possibly than yttrium-90 for labeling mAbs for therapy, but currently lutetium-177 is a radionuclide of choice for RIT. Thus in the future, copper-67 should be compared to lutetium-177 in clinical studies when the production of large activities of copper-67 will be made possible by new high-energy/high-intensity accelerators.

Yttrium-90 (^{90}Y) undergoes ß-decay to zirconium-90 with decay energy of 2.28 MeV (average energy of 0.94 MeV) that allows for high-dose deposition with an average and maximum soft tissue penetration of 2.5 mm and 11 mm, respectively [108–110]. Yttrium-90 has a physical half-life of 64.1 h [111] which makes it amenable for a variety of targeted radiotherapy applications including ^{90}Y-labeled colloid [112, 113], somatostatin receptor-targeting peptides [114, 115], tumor-targeting antibodies [116, 117], and resin/glass microspheres for selective/super-selective embolization of hepatic malignancies and metastases [118–120]. Regardless of the targeted delivery agent used, the selection of ^{90}Y and its use for radiotherapy are complex and necessitate close collaboration among various medical specialties including nuclear medicine, interventional radiology, medical oncology, and radiation oncology [121]. ^{90}Y can be administered via direct injection into a space or cavity (e.g., radiosynovectomy), intravenously for peptide receptor radionuclide therapy (PRRT) and radioimmunotherapy (RIT), and intra-arterially for radioembolization (RE) therapy. Yttrium-90 emits pure β-particles, but lacks gamma photons, and therefore conventional scintigraphic imaging and assessment of the post-therapy distribution cannot be performed. This lack of gamma photons led to the development and use of surrogate gamma-emitting agents such as indium-111-labeled peptides to be used before PRRT and RIT or ^{99m}Tc-labeled macroaggregated albumin (MAA) used as a surrogate radiotracer for planning ^{90}Y-microsphere radioembolization. Yet, using surrogate tracers may still be problematic as to the accuracy of predicting ^{90}Y radiotheraphy effects in vivo and the precise post-therapeutic distribution [122–125]. However, β-particle emission from ^{90}Y produces bremsstrahlung photons which can also be imaged scintigraphically, although with poor-quality images [116]. The ^{90}Y bremsstrahlung photons are generated when the high-energy β-particle is emitted from the ^{90}Y nucleus and then loses its kinetic energy while interacting with adjacent atoms. As the electron slows down, its kinetic energy is converted into the continuous energy spectrum of both primary and scattered photons with no dominant energy photopeak for conventional scintigraphic imaging (i.e., bremsstrahlung radiation).

However, it is important to note that, even if in an extremely small proportion (32 per million), some ^{90}Y decay occurs through internal pair production that generates 511-keV annihilation photons that can be imaged in vivo using positron emission tomography (PET). This emission is in general too small to allow for efficient PET imaging within a reasonable acquisition time when a therapeutic ^{90}Y-radiopharmaceutical is administered systemically and distributes throughout the body (as in the case of RIT or PRRT). Instead, when the therapeutic agent is administered locoregionally and is retained at the site of administration (as in the case of radioembolization of liver tumors with ^{90}Y-microspheres), then even this extremely small fraction of ^{90}Y decay occurring through internal pair production is sufficient to acquire clinically useful PET images that are useful for dosimetric purposes [126].

Gold-198 (^{198}Au) is a β-emitter (β-max = 0.96 MeV) with a relatively short half-life (2.7 days). Thanks to its characteristics, ^{198}Au has been used as a permanent implant either alone or as an adjunct to external beam radiation therapy [127, 128].

Recently, due to the development of nanotechnologies, a paradigm shift in the way diagnostic and therapeutic drugs are designed is occurring. This paradigm is based on achieving target specificity and increasing retention for significant improvement in the treatment of various tumors, including prostatic cancer [129–133]. Nanosized particles have extraordinary capabilities to image or treat cancers at the cellular and molecular levels [134–139]. In this regard, gold nanoparticles (AuNPs) exhibit very high tumor uptake, due to their natural affinity to the leaky tumor vasculature, which is particularly pronounced during tumor's neoangiogenesis [140, 141].

Chanda et al. have reported promising results in a preclinical model of prostatic cancer using gum arabic glycoprotein (GA)-functionalized gold nanoparticles (12–18 nm core diameter, 85 nm hydrodynamic diameter) loaded with 198Au (GA-198AuNPs). This agent exhibited high tumor affinity in severely compromised immunodeficient (SCID) mice bearing human prostate tumor xenografts. In this experiment, a single intratumoral administration of the β-emitting GA-198AuNPs (70 Gy) was performed, to achieve a calculated radiation dose of 70 Gy. This procedure resulted in clinically important cancer regression and successful control in the growth of prostate tumors over 30 days [142]. This observation might constitute the basis for possible clinical translation of this agent in patients with newly diagnosed PCa who are candidate to surgery, in order to reduce tumor size before surgical resection. The study by Chanda et al. revealed no hematologic toxicity, thus confirming that the therapeutic efficacy of this treatment is associated with high in vivo tolerance.

Promethium-149 (^{149}Pm) is a radiolanthanide recently made available characterized by a moderate-energy β-emission (1.07 MeV, 95.9%) and a half-life of 2.21 days. ^{149}Pm also emits a low abundance of an imageable γ-ray (286 keV, 3%) that might permit in vivo imaging after therapy. In a preclinical trial, three ^{149}Pm-complexes with the DO3A-amide chelator with zero and three carbon spacers to the bombesin peptide analog BBN (7–14)NH_2 were synthesized and characterized. The biological properties of the ^{149}Pm-DO3A-amide-βAla-BBN complexes were compared with biodistribution studies in normal mice. Its in vivo behavior as the ^{149}Pm-DO3A-amide-Ala-BBN conjugate is virtually identical to that of the ^{153}Sm- and ^{177}Lu-analogs. This supports the hypothesis that, given the appropriate chelate, the radiolanthanides are similar allowing fine-tuning of the nuclear properties necessary for a particular disease target. No in vivo tumor-targeting trials have as yet been carried out with ^{149}Pm-DO3A-amide-Ala-BBN in patients; however, the fast biological clearance of this conjugate suggests that a longer spacer (five or eight carbon) may be necessary to increase the lipophilicity of the complex and reduce its clearance rate [143].

Rhodium-105 (^{105}Rh) is a reactor-produced radionuclide with properties suitable for radiotherapeutic applications. It is a moderate low-energy β-emitter (0.560 MeV [70%], 0.250 MeV [30%]) with a 36-h half-life, and it is available in "no-carrier-added" (NCA) concentrations. ^{105}Rh also emits a low abundance of imageable γ-rays (306 keV [5%], 319 keV [19%]) that would allow in vivo tracking of the therapeutic dose. ^{105}Rh is

produced by a neutron capture reaction of an enriched ^{104}Ru target to produce ^{105}Ru, which decays to ^{105}Rh with a 4.4-h half-life [144]. The cis-[Rh(III)Cl_2(2,5,8,11-tetrathiadodecane-1,12-dicarboxylic acid)]$^+$ complex shows the most promising in vivo characteristics on which to base the development of a potential therapeutic radiopharmaceutical [145]. For example, ^{105}Rh can be simply conjugated with EDTMP, by heating for 30 min in boiling water, with >99% radiochemical yield. Ando et al. have tested this radiopharmaceutical in animals, and observed that ^{105}Rh-EDTMP has fast blood clearance and selective uptake in the bone, with rapid elimination from irrelevant tissues; thus, it appears to have suitable features for palliative treatment of pain of bone metastases[146].

Other Radionuclides

A few other radionuclides could be of interest for RIT. For example, the use of scandium-47 has been suggested by Pietrelli et al. [147]. This radionuclide can be produced carrier-free by neutron irradiation of titanium-47. It decays into stable titanium by emitting low-energy β^- with a half-life of 3.35 days, with the additional emission of a 159 keV γ-ray (68%) that is suitable for imaging. Very little has been published on scandium-47 because of a poor availability, but interest in scandium-44, a positron emitter, has revived interest in scandium-47 according to the β^+-/β-radionuclide pair concept. Similarly as scandium-44, it may be efficiently complexed by several chelating agent, including DOTA [148].

Terbium-161 has also been proposed recently as a β-emitter of interest in targeted radionuclide therapy [149]. It decays with a half-life of 6.88 days into stable dysprosium-161 by emitting low-energy β-particles. A very interesting feature of the element terbium is the possibility of using other terbium radionuclides, such as terbium-149 (which is an α-particle emitter), terbium-152 (a β^+-emitter), and terbium-155 (a γ-emitter). All these radionuclides possess manageable half-life and decay properties, thus making it possible to perform β- and α-targeted radionuclide therapy, as well as PET and SPECT imaging with isotopes of the same element – according to the principles of theranostics.

Concluding Remarks

It should be emphasized that the development of novel radiopharmaceuticals for therapy often includes several steps that imply the use of different radionuclides before identifying the most suitable ligand-chelator-radionuclide conjugate for clinical use. In general, proof-of-principle studies are based on the demonstration – obtained by imaging studies – that the candidate compound of interest accumulates efficiently and is retained at the tumor site sufficiently so as to predict high radiation dosimetry with a potential therapeutic effect. This demonstration can be achieved using the compound labeled with either a γ-emitter (for single-photon imaging) or a β^+-emitter (for PET imaging). Some of the radionuclides described above decay by emitting both γ-radiation and β-particles (e.g., ^{131}I, ^{153}Sm, ^{177}Lu), a feature that facilitates the studies on tumor targeting. When instead the therapeutic radionuclide is a pure α- or β-emitter, a surrogate γ- or β^+-emitter must be used for imaging in the exploratory phase.

The example described here below will serve to illustrate the multifaceted approach that is being followed for developing a novel therapeutic radiopharmaceutical starting from a monoclonal antibody that has initially been employed primarily for diagnostic purposes in patients with clear-cell renal carcinoma. The murine G250 mAb was raised against the carbonic anhydrase isoenzyme 9 (CAIX), a transmembrane glycoprotein [150–152] that is expressed on the cell surface of the majority (>95%) of these tumors, which constitute approximately 80% of all renal cell carcinomas [153]. The murine mAb G250 labeled with ^{131}I was initially tested to explore its tumor-targeting potential. However, due to the formation of human anti-mouse antibodies (HAMA) [154], a chimeric variant of G250 (cG250) was constructed, with high affinity for the G250 antigen ($Ka = 4 \times 10^9$ L/mol). Immunoreactivity of mAb cG250 with normal human tissues is limited to the upper gastrointestinal mucosa and gastrointestinal-related structures

(bile ducts, pancreas) [155, 156]. Studies on the therapeutic potential of mAb G250 can be divided into studies with the "naked" antibody (administered alone or in combination with cytokines) and radioimmunotherapy (RIT) trials, respectively. In the first dose-escalating RIT study, ^{131}I-G250 was administered to patients with progressing metastatic renal cell carcinoma (mRCC) [154]. Hepatic toxicity occurred, mostly as the result of specific hepatic accumulation of the murine G250 mAb, which declined with increasing doses (thus suggesting saturation of the G250 binding sites). Nevertheless, hepatic toxicity was mild and not dose limiting, whereas dose-limiting toxicity was hematologic. Overall survival of patients treated with ^{131}I-G250 appeared to be improved versus historic control patients (17/33 stable disease and two minor responses). However, high HAMA levels developed in virtually all patients, thus precluding retreatment, a problem that was overcome with the development of cG250.

Following the protein dose-escalation trial with ^{131}I-cG250, which established the most favorable amount of protein for administration, a phase I ^{131}I-cG250 activity escalation study was performed to establish dose-limiting toxicity [157]. A pretherapy imaging phase with ^{131}I-cG250 (administered as a tracer activity of 222 MBq per 5 mg protein) was included with the purpose of selecting CAIX-positive patients for the therapeutic administration of 1.665–2.775 GBq ^{131}I-cG250 (still with 5 mg protein). No hepatic toxicity was observed in this study, probably because the liver compartment was saturated. Dose-limiting toxicity of ^{131}I-cG250 was established at 2.775 GBq/m^2; the maximum tolerated dose was therefore set at 2.220 GBq/m^2. An antitumor response was observed in two out of eight patients: one stable disease for 3–6 months and one partial response >9 months.

A fractionated dose RIT trial was subsequently designed, based on whole-body radiation-absorbed dose [158], under the rationale that in animal models fractionated RIT is more successful than a single administration schedule and is associated with lower toxicity. The primary target of this study was to determine the maximum tolerated whole-body radiation-absorbed dose. Fifteen patients with measurable mRCC were enrolled for this trial, during which it was found that dose-limiting toxicity was hematologic. Moreover, the total dose that could be delivered was relatively low.

In a subsequent study [159], two sequential high doses of ^{131}I-cG250 (2.22 GBq/m^2) were administered after a tracer activity of ^{131}I-cG250 (185 MBq/m^2) to ascertain effective tumor targeting; 29 patients with sufficient cG250 uptake received a first therapeutic dose of ^{131}I-cG250. Patients who did not show a grade 4 hematologic toxicity received a second therapeutic administration 3 months later, with dose escalation from 1.110 to 1.665 GBq/m^2. None of the 16 patients who completed the protocol (out of the 29 enrolled) showed an objective response, but five had stabilization of disease for 3–12 months. The low therapeutic efficacy observed in this trial was probably due to the quite large tumor burden present in these patients. In this regard, dosimetric estimates proved that therapeutic radiation doses (>50 Gy) could be achieved only for lesions smaller than 5 g [160].

Subsequent clinical studies have adopted ^{90}Y or ^{177}Lu to label cG250 for RIT trials. The results of a phase I/II trial with ^{177}Lu-cG250 were recently published [161], a study that was conducted in parallel with a trial based on the use of ^{90}Y-cG250 at Memorial Sloan Kettering Cancer Center (www.clinicaltrials.gov/NCT00199875). In the ^{177}Lu-cG250 trial, 23 patients with progressive mRCC received a diagnostic activity of ^{111}In-cG250 (185 MBq), to ascertain adequate tumor uptake; this was followed by administration of ^{177}Lu-cG250 1 week later. The staring dose of ^{177}Lu-cG250 was 1.110 GB/m^2, with increments of 370 MBq/m^2 (three patients/dose level). In the absence of grade 4 toxicity, patients were suitable for receiving a second (13/23) and a third cycle (4/23), at 75% of the dose level of the previous administration. Hematologic toxicity was dose limiting, and the maximum tolerated dose was 2.405 GBq/m^2 [161]. The majority of patients responded with stabilization of disease, while a partial response that lasted for 9 months was observed in one patient at the 1.850 GBq/m^2 dose level. The tumor-to-red marrow dose ratio was higher for ^{177}Lu-cG250 than for ^{90}Y-cG250, indicating a wider therapeutic window for the

^{177}Lu-conjugate. Stillebroer et al. concluded that RIT with ^{177}Lu-cG250 may stabilize previously progressive metastatic ccRCC [162].

More evidence is needed to prove that cG250 imaging can be used to guide clinical management. As suggested by Divgi et al. [163], the role of cG250 imaging in influencing outcome would perhaps be best assessed in a clinical trial carried out in patients with small renal tumor mass and fewer associated comorbidities. Another issue that needs further investigation is choice of the radionuclide for imaging. ^{111}In-cG250 SPECT may provide the same information as ^{124}I-cG250 PET, with the advantage that it can be made available as an off-the-shelf product to be used on site. Other radionuclides (e.g., ^{89}Zr) might provide a useful alternative for PET imaging. In summary, the cG250 mAb agent has shown significant tumor-targeting capacity; although the main clinical value of the compound seems at present to be its potential as a diagnostic agent, its use as a delivery vehicle for RIT requires further investigations – possibly regarding also choice of the best radionuclide for therapy.

References

1. Bruland OS, Nilsson S, Fisher DR, Larsen RH. High-linear energy transfer irradiation targeted to skeletal metastases by the alpha-emitter ^{223}Ra: adjuvant or alternative to conventional modalities? Clin Cancer Res. 2006;12:6250s–7.
2. Henriksen G, Breistol K, Bruland OS, Fodstad O, Larsen RH. Significant antitumor effect from bone-seeking, alpha-particle-emitting ^{223}Ra demonstrated in an experimental skeletal metastases model. Cancer Res. 2002;62:3120–5.
3. Henriksen G, Fisher DR, Roeske JC, Bruland OS, Larsen RH. Targeting of osseous sites with alpha-emitting ^{223}Ra: comparison with the beta-emitter ^{89}Sr in mice. J Nucl Med. 2003;44:252–9.
4. Nilsson S, Larsen RH, Fossa SD, Balteskard L, Borch KW, et al. First clinical experience with alpha-emitting radium-223 in the treatment of skeletal metastases. Clin Cancer Res. 2005;11:4451–9.
5. Carrasquillo JA, O'Donoghue JA, Pandit-Taskar N, Humm JL, Rathkopf DE, et al. Phase I pharmacokinetic and biodistribution study with escalating doses of ^{223}Ra-dichloride in men with castration-resistant metastatic prostate cancer. Eur J Nucl Med Mol Imaging. 2013;40:1384–93.
6. Nilsson S, Franzén L, Parker C, Tyrrell C, Blom R, Tennvall J, et al. Bone-targeted radium-223 in symptomatic, hormone-refractory prostate cancer: a randomised, multicentre, placebo-controlled phase II study. Lancet Oncol. 2007;8:587–94.
7. Nilsson S, Franzen L, Parker C, Tyrrell C, Blom R, et al. Two-year survival follow-up of the randomized, double-blind, placebo-controlled phase II study of radium-223 chloride in patients with castration-resistant prostate cancer and bone metastases. Clin Genitourin Cancer. 2013;11:20–6.
8. Nilsson S, Strang P, Aksnes AK, Franzen L, Olivier P, Pecking A, et al. A randomized, dose-response, multicenter phase II study of radium-223 chloride for the palliation of painful bone metastases in patients with castration-resistant prostate cancer. Eur J Cancer. 2012;48:678–86.
9. Parker CC, Pascoe S, Chodacki A, O'Sullivan JM, Germá JR, O'Brayn-Tear CG, et al. A randomized, double-blind, dose-finding, multicenter, phase 2 study of radium chloride (Ra 223) in patients with bone metastases and castration-resistant prostate cancer. Eur Urol. 2013;63:189–97.
10. Parker C, Nilsson S, Heinrich D, Helle SI, O'Sullivan JM, Fossa SD, et al. Alpha emitter radium-223 and survival in metastatic prostate cancer. N Engl J Med. 2013;369:213–23.
11. Parker C, Gillessen S, Heidenreich A, Horwich A, on behalf of the ESMO Guidelines Committee. Cancer of the prostate: ESMO Clinical Practice Guidelines for diagnosis, treatment and follow-up. Ann Oncol. 2015;26 Suppl 5:v69–77.
12. NCCN, National Comprehensive Cancer Network. https://www.nccn.org/patients/ guidelines/prostate/files/ assets/common/downloads/files/prostate.pdf. Last accessed 18 Jul 2016.
13. Zalutsky MR, Vaidyanathan G. Astatine-211-labeled radiotherapeutics: an emerging approach to targeted alpha-particle radiotherapy. Curr Pharm Des. 2000;6:1433–55.
14. Miederer M, McDevitt MR, Sgouros G, Kramer K, Cheung NK, Scheinberg DA. Pharmacokinetics, dosimetry, and toxicity of the targetable atomic generator, ^{225}Ac-HuM195, in nonhuman primates. J Nucl Med. 2004;45:129–37.
15. Zalutsky MR, Garg PK, Friedman HS, Bigner DD. Labeling monoclonal antibodies and F(ab′)$_2$ fragments with the alpha-particle-emitting nuclide astatine-211: preservation of immunoreactivity and in vivo localizing capacity. Proc Natl Acad Sci U S A. 1989;86:7149–53.
16. Reist CJ, Foulon CF, Alston K, Bigner DD, Zalutsky MR. Astatine-211 labeling of internalizing anti-EGFRvIII monoclonal antibody using N-succinimidyl 5-[^{211}At]astato-3-pyridinecarboxylate. Nucl Med Biol. 1999;26:405–11.
17. Orozco JJ, Bäck T, Kenoyer A, Balkin ER, Hamlin DK, Wilbur DS, et al. Anti-CD45 radioimmunotherapy using ^{211}At with bone marrow transplantation prolongs survival in a disseminated murine leukemia model. Blood. 2013;121:3759–67.

18. Zalutsky MR, Reardon DA, Akabani G, Coleman RE, Friedman AH, Friedman HS, et al. Clinical experience with alpha-particle emitting ^{211}At: treatment of recurrent brain tumor patients with ^{211}At-labeled chimeric antitenascin monoclonal antibody 81C6. J Nucl Med. 2008;49:30–8.
19. Andersson H, Cederkrantz E, Bäck T, Divgi C, Elgqvist J, Himmelman J, et al. Intraperitoneal alpha-particle radioimmunotherapy of ovarian cancer patients: pharmacokinetics and dosimetry of ^{211}At-MX35 F(ab′)$_2$ – A phase I study. J Nucl Med. 2009; 50:1153–60.
20. Boll RA, Malkemus D, Mirzadeh S. Production of actinium-225 for alpha particle mediated radioimmunotherapy. Appl Radiat Isot. 2005;62:667–79.
21. Apostolidis C, Molinet R, Rasmussen G, Morgenstern A. Production of Ac-225 from Th-229 for targeted alpha therapy. Anal Chem. 2005;77:6288–91.
22. Apostolidis C, Molinet R, McGinley J, Abbas K, Mollenbeck J, Morgenstern A. Cyclotron production of Ac-225 for targeted alpha therapy. Appl Radiat Isot. 2005;62:383–7.
23. Miederer M, Scheinberg DA, McDevitt MR. Realizing the potential of the actinium-225 radionuclide generator in targeted alpha particle therapy applications. Adv Drug Deliv Rev. 2008;60:1371–82.
24. Borchardt PE, Yuan RR, Miederer M, McDevitt MR, Scheinberg DA. Targeted actinium-225 in vivo generators for therapy of ovarian cancer. Cancer Res. 2003;63:5084–90.
25. Song H, Hobbs RF, Vajravelu R, Huso DL, Esaias C, Apostolidis C, et al. Radioimmunotherapy of breast cancer metastases with alpha-particle emitter ^{225}Ac: comparing efficacy with ^{213}Bi and ^{90}Y. Cancer Res. 2009;69:8941–8.
26. Woodward J, Kennel SJ, Stuckey A, Osborne D, Wall J, Rondinone AJ, et al. $LaPO_4$ nanoparticles doped with actinium-225 that partially sequesters daughter radionuclides. Bioconjug Chem. 2011;22:766–76.
27. McLaughlin MF, Robertson D, Pevsner PH, Wall JS, Mirzadeh S, Kennel SJ. $LnPO_4$ nanoparticles doped with Ac-225 and sequestered daughters for targeted alpha therapy. Cancer Biother Radiopharm. 2014;29: 34–41.
28. McDevitt MR, Ma D, Lai LT, Simon J, Borchardt P, Frank RK, et al. Tumor therapy with targeted atomic nanogenerators. Science. 2001;294:1537–40.
29. Meredith R, Torgue J, Shen S, Fisher DR, Banaga E, Bunch P, et al. Dose escalation and dosimetry of first-in-human radioimmunotherapy with ^{212}Pb-TCMC-trastuzumab. J Nucl Med. 2014;55:1636–42.
30. Meredith RF, Torgue J, Azure MT, Shen S, Saddekni S, Banaga E, et al. Pharmacokinetics and imaging of ^{212}Pb-TCMC-trastuzumab after intraperitoneal administration in ovarian cancer patients. Cancer Biother Radiopharm. 2014;29:12–7.
31. Schwartz J, Jaggi JS, O'Donoghue JA, Ruan S, McDevitt M, Larson SM, et al. Renal uptake of bismuth-213 and its contribution to kidney radiation dose following administration of actinium-225-labeled antibody. Phys Med Biol. 2011;56:721–33.
32. Benešová M, Schäfer M, Bauder-Wüst U, Afshar-Oromieh A, Kratochwil C, Mier W, et al. Preclinical evaluation of a tailor-made DOTA-conjugated PSMA inhibitor with optimized linker moiety for imaging and endoradiotherapy of prostate cancer. J Nucl Med. 2015;56:914–20.
33. Benešová M, Bauder-Wüst U, Schäfer M, Klika KD, Mier W, Haberkorn U, et al. Linker modification strategies to control the prostate-specific membrane antigen (PSMA)-targeting and pharmacokinetic properties of DOTA-conjugated PSMA inhibitors. J Med Chem. 2016;59:1761–75.
34. Kratochwil C, Giesel FL, Stefanova M, Benešová M, Bronzel M, Afshar-Oromieh A, et al. PSMA-targeted radionuclide therapy of metastatic castration-resistant prostate cancer with ^{177}Lu-labeled PSMA-617. J Nucl Med. 2016;57:1170–6.
35. Ahmadzadehfar H, Rahbar K, Kürpig S, Bögemann M, Claesener M, Eppard E, et al. Early side effects and first results of radioligand therapy with ^{177}Lu-DKFZ-617 PSMA of castrate-resistant metastatic prostate cancer: a two-centre study. EJNMMI Res. 2015;5(1):114. doi:10.1186/s13550-015-0114-2. Epub 2015 Jun 20.
36. Ahmadzadehfar H, Eppard E, Kürpig S, Fimmers R, Yordanova A, Schlenkhoff CD, et al. Therapeutic response and side effects of repeated radioligand therapy with ^{177}Lu-PSMA-DKFZ-617 of castrate-resistant metastatic prostate cancer. Oncotarget. 2016;7:12477–88.
37. Kratochwil C, Bruchertseifer F, Giesel FL, Weis M, Verburg FA, Mottaghy F, et al. ^{225}Ac-PSMA-617 for PSMA targeting alpha-radiation therapy of patients with metastatic castration-resistant prostate cancer. J Nucl Med. 2016;57:1941–4.
38. Heyerdahl H, Abbas N, Sponheim K, Mollatt C, Bruland Ø, Dahle J. Targeted alpha therapy with ^{227}Th-trastuzumab of intraperitoneal ovarian cancer in nude mice. Curr Radiopharm. 2013;6:106–16.
39. O'Donoghue JA, Bardiès M, Wheldon TE. Relationships between tumor size and curability for uniformly targeted therapy with beta-emitting radionuclides. J Nucl Med. 1995;36:1902–9.
40. Boudousq V, Bobyk L, Busson M, Garambois V, Jarlier M, Charalambatou P, et al. Comparison between internalizing anti-HER2 mAbs and non-internalizing anti-CEA mAbs in alpha-radioimmunotherapy of small volume peritoneal carcinomatosis using ^{212}Pb. PLoS One. 2013;8:e69613.
41. McDevitt MR, Sgouros G, Finn RD, Humm JL, Lurcic JC, Larson S, et al. Radioimmunotherapy with alpha-emitting nuclides. Eur J Nucl Med. 1998; 25:1341–51.
42. Jurcic JG, Pandit-Taskar N, Divgi CR, et al. Alpha particle immunotherapy for acute myeloid leukemia (AML) with bismuth-213 and actinium-225 [abstract]. Cancer Biother Radiopharm. 2006;21:396.
43. McLaughlin MF, Woodward J, Boll RA, Wall JS, Rondine AJ, Kennel SJ, et al. Gold coated lanthanide phosphate nanoparticles for targeted alpha generator radiotherapy. PLoS One. 2013;8:e54531.
44. Jurcic JG, Larson SM, Sgouros G, McDevitt MR, Finn RD, Divgi CR, et al. Targeted alpha particle

immunotherapy for myeloid leukemia. Blood. 2002; 100:1233–9.
45. Supiot S, Faivre-Chauvet A, Couturier O, Heymann MF, Robillard N, Kraeber-Bodéré F, et al. Comparison of the biologic effects of MA5 and B-B4 monoclonal antibody labeled with iodine-131 and bismuth-213 on multiple myeloma. Cancer. 2002;94:1202–9.
46. Chérel M, Gouard S, Gaschet J, Saï-Maurel C, Bruchertseifer F, Morgenstern A, et al. ^{213}Bi Radioimmunotherapy with an anti-mCD138 monoclonal antibody in a murine model of multiple myeloma. J Nucl Med. 2013;54:1597–04.
47. http://www.arevamed.areva.com/EN/home-134/nuclear-medicine.html#tab=tab3
48. Yong KJ, Milenic DE, Baidoo KE, Brechbiel MW. ^{212}Pb-radioimmunotherapy induces G2 cell-cycle arrest and delays DNA damage repair in tumor xenografts in a model for disseminated intraperitoneal disease. Mol Cancer Ther. 2012;11:639–48.
49. Yong KJ, Milenic DE, Baidoo KE, Kim YS, Brechbiel MW, et al. Gene expression profiling upon ^{212}Pb-TCMC-trastuzumab treatment in the LS-174T i.p. xenograft model. Cancer Med. 2013; 2:646–53.
50. Ruegg CL, Anderson-Berg ET, Brechbiel MW, Mirzadeh S, Gansow OA, Strand M, et al. Improved in vivo stability and tumor targeting of bismuth-labeled antibody. Cancer Res. 1990;50:4221–6.
51. Chappell LL, Dadachova E, Milenic DE, Garmestani K, Wu C, Brechbiel MW. Synthesis, characterization, and evaluation of a novel bifunctional chelating agent for the lead isotope ^{203}Pb and ^{212}Pb. Nucl Med Biol. 2000;27:93–100.
52. Ruble G, Wu C, Squire RA, Ganswo OA, Strand M. The use of ^{212}Pb-labeled monoclonal antibody in the treatment of murine erythroleukemia. Int J Radiat Oncol Biol Phys. 1996;34:609–16.
53. McMurry TJ, Brechbiel MW, Kumar K, Gansow OA. Convenient synthesis of bifunctional tetraaza macrocycles. Bioconjugate Chem. 1992;3:108–17.
54. Milenic DE, Garmestani K, Brady ED, Albert PS, Ma D, Abdulla A, et al. Alpha-particle radioimmunotherapy of disseminated peritoneal diseases using a ^{212}Pb-labeled radioimmunoconjugate targeting HER2. Cancer Biother Radiopharm. 2005;20: 557–66.
55. Andersson H, Elgqvist J, Horvath G, Hultborn R, Jacobsson L, Jensen H, et al. Astatine-211-labeled antibodies for treatment of disseminated ovarian cancer: an overview of results in an ovarian tumor model. Clin Cancer Res. 2003;9:S3914–21.
56. Milenic DE, Baidoo KE, Kim YS, Brechbiel MW. Evaluation of cetuximab as a candidate for targeted α-particle radiation therapy of HER1-positive disseminated intraperitoneal disease. MAbs. 2015;7: 255–64.
57. Kostourou V, Papalazarou V. Non-collagenous ECM proteins in blood vessel morphogenesis and cancer. Biochim Biophys Acta. 1840;2014:2403–13.
58. Rosario T, DeSimone DW. The extracellular matrix in development and morphogenesis: a dynamic view. Dev Biol. 2010;341:126–40.
59. Kalluri R. Basement membranes: structure, assembly and role in tumour angiogenesis. Nat Rev Cancer. 2003;3:422–33.
60. Nicolò G, Salvi S, Oliveri G, Borsi L, Castellani P, Zardi L. Expression of tenascin and of the ED-B containing oncofetal fibronectin isoform in human cancer. Cell Differ Dev. 1990;32:401–8.
61. Halin C, Zardi L, Neri D. Antibody-based targeting of angiogenesis. News Physiol Sci. 2001;16:191–4.
62. Castellani P, Viale G, Dorcaratto A, Nicolò G, Kaczmarek J, Querzeé G, Zardi L. The fibronectin isoform containing the ED-B oncofetal domain: a marker of angiogenesis. Int J Cancer. 1994;59:612–8.
63. Carnemolla B, Balza E, Siri A, Zardi L, Nicotra MR, Bigotti A, Natali PG. A tumor-associated fibronectin isoform generated by alternative splicing of messenger RNA precursors. J Cell Biol. 1989;108:1139–48.
64. Kaczmarek J, Castellani P, Nicolò G, Spina B, Allemanni G, Zardi L. Distribution of oncofetal fibronectin isoforms in normal, hyperplastic and neoplastic human breast tissues. Int J Cancer. 1994; 59:11–6.
65. Sauer S, Erba PA, Petrini M, Menrad A, Giovannoni L, Grana C, et al. Expression of the oncofetal ED-B-containing fibronectin isoform in hematologic tumors enables ED-B-targeted ^{131}I-L19SIP radioimmunotherapy in Hodgkin lymphoma patients. Blood. 2009;113:2265–74.
66. Locher R, Erba PA, Hirsch B, Bombardieri E, Giovannoni L, Neri D, et al. Abundant in vitro expression of the oncofetal ED-B-containing fibronectin translates into selective pharmacodelivery of 131I-L19SIP in a prostate cancer patient. J Cancer Res Clin Oncol. 2014;140:35–43.
67. Pujuguet P, Hammann A, Moutet M, Samuel JL, Martin F, Martin M. Expression of fibronectin ED-A$^+$ and ED-B$^+$ isoforms by human and experimental colorectal cancer. Contribution of cancer cells and tumor- associated myofibroblasts. Am J Pathol. 1996;148:579–92.
68. D'Ovidio MC, Mastracchio A, Marzullo A, Ciabatta M, Pini B, Uccini S, et al. Intratumoral microvessel density and expression of ED- A/ED-B sequences of fibronectin in breast carcinoma. Eur J Cancer. 1998;34:1081–5.
69. Karelina TV, Eisen AZ. Interstitial collagenase and the ED-B oncofetal domain of fibronectin are markers of angiogenesis in human skin tumors. Cancer Detect Prev. 1998;22:438–44.
70. Castellani P, Borsi L, Carnemolla B, Biro A, Dorcaratto A, Viale GL, et al. Differentiation between high- and low-grade astrocytoma using a human recombinant antibody to the extra domain-B of fibronectin. Am J Pathol. 2002;161:1695–700.
71. Pini A, Viti F, Santucci A, Carnemolla B, Zardi L, Neri P, et al. Design and use of a phage display library.

Human antibodies with subnanomolar affinity against a marker of angiogenesis eluted from a two-dimensional gel. J Biol Chem. 1998;273:21769–76.
72. Viti F, Tarli L, Giovannoni L, Zardi L, Neri D. Increased binding affinity and valence of recombinant antibody fragments lead to improved targeting of tumoral angiogenesis. Cancer Res. 1999;59:347–52.
73. Demartis S, Tarli L, Borsi L, Zardi L, Neri D. Selective targeting of tumour neovasculature by a radiohalogenated human antibody fragment specific for the ED-B domain of fibronectin. Eur J Nucl Med. 2001; 28:534–9.
74. Borsi L, Balza E, Bestagno M, Castellani P, Carnemolla B, Biro A, et al. Selective targeting of tumoral vasculature: comparison of different formats of an antibody (L19) to the ED-B domain of fibronectin. Int J Cancer. 2002;102:75–85.
75. Berndorff D, Borkowski S, Sieger S, Rother A, Friebe M, Viti F, et al. Radioimmunotherapy of solid tumors by targeting extra domain B fibronectin: identification of the best-suited radioimmunoconjugate. Clin Cancer Res. 2005;11:7053s–63.
76. Tijink BM, Neri D, Leemans CR, Budde M, Dinkelborg LM, Stigter-van Walsum M, et al. Radioimmunotherapy of head and neck cancer xenografts using ^{131}I-labeled antibody L19-SIP for selective targeting of tumor vasculature. J Nucl Med. 2006;47:1127–35.
77. Rybak JN, Trachsel E, Scheuermann J, Neri D. Ligand-based vascular targeting of disease. Chem Med Chem. 2007;2:22–40.
78. Santimaria M, Moscatelli G, Giovannoni L, Leprini A, Neri G, Neri D, et al. Immunoscintigraphic detection of the ED-B domain of fibronectin, a marker of angiogenesis, in patients with cancer. Clin Cancer Res. 2003;9:571–9.
79. Erba PA, Sollini M, Orciuolo E, Traino C, Petrini M, Paganelli G, et al. Radioimmunotherapy with radretumab in patients with relapsed hematologic malignancies. J Nucl Med. 2012;53:922–7.
80. Poli G, Bianchi C, Virotta G, Bettini A, Moretti R, Trachsel E, et al. Radretumab radioimmunotherapy in patients with brain metastasis: a ^{124}I-L19SIP dosimetric PET study. Cancer Immunol Res. 2013;1:134–43.
81. Qaim SM. Therapeutic radionuclides and nuclear data. Radiochim Acta. 2001;89:297–302.
82. Kondev FG. Nuclear data sheets for A ¼ 177. Nucl Data Sheets. 2003;98:801–1095.
83. Tagawa ST, Beltran H, Vallabhajosula S, Goldsmith SJ, Osborne J, Matulich D, et al. Anti-prostate-specific membrane antigen-based radioimmunotherapy for prostate cancer. Cancer. 2010;116:1075–83.
84. O'Donnell RT, DeNardo SJ, Miers LA, Lamborn KR, Kukis DL, DeNardo GL, et al. Combined modality radioimmunotherapy for human prostate cancer xenografts with taxanes and ^{90}yttrium-DOTA-peptide-ChL6. Prostate. 2002;50:27–37.
85. Sokoloff RL, Norton KC, Gasior CL, Marker KM, Grauer LS. A dual-monoclonal sandwich assay for prostate-specific membrane antigen: levels in tissues, seminal fluid and urine. Prostate. 2000;43:150–7.
86. Bostwick DG, Pacellim A, Blute M, Roche P, Murphy GP. Prostate specific membrane antigen expression in prostatic intraepithelial neoplasia and adenocarcinoma: a study of 184 cases. Cancer. 1998;82:2256–61.
87. Liu H, Rajasekaran AK, Moy P, Xia Y, Kim S, Navarro V, et al. Constitutive and antibody-induced internalization of prostate-specific membrane antigen. Cancer Res. 1998;58:4055–60.
88. Bander NH, Milowsky MI, Nanus DM, Kostakoglu L, Vallabhajosula S, Goldsmith SJ. Phase I trial of ^{177}lutetium-labeled J591, a monoclonal antibody to prostate-specific membrane antigen, in patients with androgen-independent prostate cancer. J Clin Oncol. 2005;23:4591–01.
89. Tagawa ST, Milowsky MI, Morris M, Vallabhajosula S, Christos P, Akhtar NH, et al. Phase II study of lutetium-177 labeled anti-prostate-specific membrane antigen monoclonal antibody J591 for metastatic castration-resistant prostate cancer. Clin Cancer Res. 2013;19:5182–91.
90. Barbet J, Peltier P, Bardet S, Vuillez JP, Bachelot I, Denet S, et al. Radioimmunodetection of medullary thyroid carcinoma using indium-111 bivalent hapten and anti-CEA X anti-DTPA-indium bispecific antibody. J Nucl Med. 1998;39:1172–8.
91. Goldenberg DM, Sharkey RM, Paganelli G, Barbet J, Chatal J-F. Antibody pretargeting advances cancer radioimmunodetection and radioimmunotherapy. J Clin Oncol. 2006;24:823–34.
92. Chatal J-F, Campion L, Kraeber-Bodéré F, Bardet S, Vuillez JP, Charbonnel B, et al. Survival improvement in patients with medullary thyroid carcinoma who undergo pretargeted anti-carcinoembryonic-antigen radioimmunotherapy: a collaborative study with the French Endocrine Tumor Group. J Clin Oncol. 2006;24:1705–11.
93. Schoffelen R, Boerman OC, Goldenberg DM, Sharkey RM, van Herpen CML, Franssen GM, et al. Development of an imaging-guided CEA-pretargeted radionuclide treatment of advanced colorectal cancer: first clinical results. Br J Cancer. 2013;109:934–42.
94. Schoffelen R, van der Weg W, Visser EP, Goldenberg DM, Sharkey RM, McBride WJ, et al. Predictive patient-specific dosimetry and individualized dosing of pretargeted radioimmunotherapy in patients with advanced colorectal cancer. Eur J Nucl Med Mol Imaging. 2014;41:1593–02.
95. Schoffelen R, van der Graaf WTA, Franssen G, Sharkey RM, Goldenberg DM, McBride WJ, et al. Pretargeted ^{177}Lu radioimmunotherapy of carcinoembryonic antigen-expressing human colonic tumors in mice. J Nucl Med. 2010;51:1780–7.
96. Liu C, Brasic JR, Liu X, Li H, Xiang X, Luo Z, et al. Timing and optimized acquisition parameters for the whole-body imaging of ^{177}Lu-EDTMP toward performing bone palliation treatment. Nucl Med Commun. 2012;33:90–6.

97. Karagiannis TC. Comparison of different classes of radionuclides for potential use in radioimmunotherapy. Hell J Nucl Med. 2007;10:82–8.
98. Unni PR, Solov SV, Chakraborty S, Chaudhary PR, Venkatesh M, Ramamoorthy N, et al. ^{166}Ho-HA: a new radiopharmaceutical for treatment of arthritis. BARC Newsletter. 2006;208:1–8.
99. Unni PR, Chaudhury PR, Venkatesh M, Ramamoorthy N, Pillai MRA. Preparation and evaluation of ^{166}Ho labeled hydroxyapatite (HA) particles for radiosynovectomy. Nucl Med Biol. 2002;29:199–209.
100. Mumper RJ, Ryo UY, Jay M. Neutron-activated holmium-166-poly(L-lactic acid) microspheres: a potential agent for the internal radiation therapy of hepatic tumors. J Nucl Med. 1991;32:2139–43.
101. Mumper J, Mills BJ, Ryo UY, Jay M. Polymeric microspheres for radionuclide synovectomy containing neutron-activated holmium-166. J Nucl Med. 1992;33:398–402.
102. Smits ML, Nijsen JF, van den Bosch MA, Lam MG, Vente MA, Mali WP, et al. Holmium-166 radioembolisation in patients with unresectable, chemorefractory liver metastases (HEPAR trial): a phase 1, dose-escalation study. Lancet Oncol. 2012; 13:1025–34.
103. Mathew B, Chakraborty S, Das T, Sarma HD, Banerjee S, Samuel G, Venkatesh M, Pillai MRA. ^{175}Yb labeled polyaminophosphonates as potential agents for bone pain palliation. Appl Radiat Isot. 2004;60:635–42.
104. Das T, Chakraborty S, Sarma HD, Tandon P, Banerjee S, Venkatesh M, et al. ^{170}Tm-EDTMP: a potential cost-effective alternative to ^{89}SrCl2 for bone pain palliation. Nucl Med Biol. 2009;36: 561–8.
105. DeNardo SJ, DeNardo GL, Kukis DL, Shen S, Kroger LA, DeNardo DA, et al. ^{67}Cu-2IT-BAT-Lym-1 pharmacokinetics, radiation dosimetry, toxicity and tumor regression in patients with lymphoma. J Nucl Med. 1999;40:302–10.
106. DeNardo GL, DeNardo SJ, O'Donnell RT, Kroger LA, Kukis DL, Meares CF, et al. Are radiometal-labeled antibodies better than iodine-131-labeled antibodies: comparative pharmacokinetics and dosimetry of copper-67-, iodine-131-, and yttrium-90-labeled Lym-1 antibody in patients with non-Hodgkin's lymphoma. Clin Lymphoma. 2000;1:118–26.
107. Delaloye AB, Delaloye B, Buchegger F, Vogel CA, Gillet M, Mach JP, et al. Comparison of copper-67- and iodine-125-labeled anti-CEA monoclonal antibody biodistribution in patients with colorectal tumors. J Nucl Med. 1997;38:847–53.
108. Chu SYF, Ekstrom LP, Firestone B. Table of Isotopes decay data. The Lund/LBNL Nuclear Data Search. February 1999. Last accessed 19 Jul 2016.
109. Minarik D, Sjögreen Gleisner K, Ljungberg M. Evaluation of quantitative ^{90}Y SPECT based on experimental phantom studies. Phys Med Biol. 2008;53: 5689–03.
110. Dancey JE, Shepherd FA, Paul K, Sniderman KW, Houle S, Gabrys J, et al. Treatment of non resectable hepatocellular carcinoma with intrahepatic ^{90}Y-microspheres. J Nucl Med. 2000;41:1673–81.
111. Kossert K, Schrader H. Activity standardization by liquid scintillation counting and half-life measurements of ^{90}Y. Appl Radiat Isot. 2004;60:741–9.
112. Kyle V, Hazleman BL, Wraight PE. Yttrium-90 therapy and ^{99m}Tc Pertechnetate knee uptake measurements in the management of rheumatoid arthritis. Ann Rheum Dis. 1983;42:132–7.
113. Smith T, Crawley JCW, Shawe DJ, Gumpel JM. SPECT using Bremsstrahlung to quantify ^{90}Y uptake in Baker's cysts: its application in radiation synovectomy of the knee. Eur J Nucl Med. 1988;14:498–503.
114. Otte A, Jermann E, Behe M, Goetze M, Bucher HC, Roser HW, et al. DOTATOC: a powerful new tool for receptor-mediated radionuclide therapy. Eur J Nucl Med. 1997;24:792–5.
115. De Jong M, Valkema R, Jamar F, et al. Somatostatin receptor-targeted radionuclide therapy of tumors: preclinical and clinical findings. Semin Nucl Med. 2002;32:133–40.
116. Knox SJ, Goris ML, Trisler K, Negrin, Davis T, Liles TM, et al. Yttrium-90-labeled anti CD20 monoclonal antibody therapy of recurrent B-cell lymphoma. Clin Cancer Res. 1996;2:457–70.
117. Leichner PK, Akabani G, Colcher D, Harisson KA, Eckblade M, Baranowska-Kortylewicz J, et al. Patient-specific dosimetry of indium-111- and yttrium-90-labeled monoclonal antibody CC49. J Nucl Med. 1997;38:512–6.
118. Grady ED. Internal radiation therapy of hepatic cancer. Dis Colon Rectum. 1979;22:371–5.
119. Andrews JC, Walker SC, Ackermann RJ, Cotton LA, Ensminger WD, Shapiro B. Hepatic radioembolization with yttrium-90 containing glass microspheres: preliminary results and clinical follow-up. J Nucl Med. 1994;35:1637–44.
120. Lau WY, Leung WT, Ho S, Leung NW, Chan M, Lin J, et al. Treatment of inoperable hepatocellular carcinoma with intrahepatic arterial yttrium-90 microspheres: a phase I and II study. Br J Cancer. 1994;70:994–9.
121. Kao YH, Steinberg JD, Tay YS, Lim GK, Yan J, Townsend DW, et al. Post-radioembolization yttrium-90 PET/CT – part 1: diagnostic reporting. JNMMI Res. 2013;3:56. doi:10.1186/2191-219X-3-56.
122. Hnatowich DJ, Virzi F, Doherty PW. DTPA-coupled antibodies labeled with Yttrium-90. J Nucl Med. 1985;26:503–9.
123. Wright CL, Werner JD, Tran JM, Gates VL, Rikabi AA, Shah MH, et al. Radiation pneumonitis following yttrium-90 radioembolization: case report and literature review. J Vasc Interv Radiol. 2012;23:669–74.
124. Collins J, Salem R. Hepatic radioembolization complicated by gastrointestinal ulceration. Semin Interv Radiol. 2011;28:240–5.
125. Riaz A, Lewandowski RJ, Kulik LM, Mulcahy MF, Sato KT, Ryu RK, et al. Complications following

radioembolization with yttrium-90 microspheres: a comprehensive literature review. J Vasc Interv Radiol. 2009;20:1121–30.
126. Lhommel R, van Elmbt L, Goffette P, Van den Eynde M, Jamar F, Pauwels S, et al. Feasibility of ^{90}Y TOF PET-based dosimetry in liver metastasis therapy using SIR-Spheres. Eur J Nucl Med Mol Imaging. 2010;37:1654–62.
127. Knight PJ, Dombos JF, Rosen D, Lin JJ, Farha GJ. The use of interstitial radiation therapy in the treatment of persistent, localized, and unresectable cancer in children. Cancer. 1986;57:951–4.
128. Rich TA. Radiation therapy for pancreatic cancer: eleven year experience at the JCRT. Int J Radiat Oncol Biol Phys. 1985;11:759–63.
129. Dhar S, Gu FX, Langer R, Farokhzad OC, Lippard SJ. Targeted delivery of cisplatin to prostate cancer cells by aptamer functionalized Pt(IV) prodrug-PLGA-PEG nanoparticles. Proc Natl Acad Sci U S A. 2008;105: 17356–61.
130. Gommersall L, Shergill IS, Ahmed HU, Arya M, Grange P, Gill IS. Nanotechnology in the management of prostate cancer. Br J Urol Int. 2008;102:1493–5.
131. Shulga OV, Zhou D, Demchenko AV, Stine KJ. Detection of free prostate specific antigen (fPSA) on a nanoporous gold platform. Analyst. 2008;133: 319–22.
132. Thangapazham RL, Puri A, Tele S, Blumenthal R, Maheshwari RK. Evaluation of a nanotechnology-based carrier for delivery of curcumin in prostate cancer cells. Int J Oncol. 2008;32:1119–23.
133. Cheng J, Teply BA, Sherifi I, Sung J, Luther G, Gu FX, et al. Formulation of functionalized PLGA-PEG nanoparticles for in vivo targeted drug delivery. Biomaterials. 2007;28:869–76.
134. Grodzinski P, Silver M, Molnar LK. Nanotechnology for cancer diagnostics: promises and challenges. Expert Rev Mol Diagn. 2006;6:307–18.
135. Nie S, Xing Y, Kim GJ, Simons JW. Nanotechnology applications in cancer. Annu Rev Biomed Eng. 2007;9:257–88.
136. Portney NG, Ozkan M. Nano-oncology: drug delivery, imaging, and sensing. Anal Bioanal Chem. 2006;384:620–30.
137. Sengupta S, Sasisekharan R. Exploiting nanotechnology to target cancer. Br J Cancer. 2007;96:1315–9.
138. Sinha R, Kim GJ, Nie S, Shin DM. Nanotechnology in cancer therapeutics: bioconjugated nanoparticles for drug delivery. Mol Cancer Ther. 2006;5:1909–17.
139. Wang MD, Shin DM, Simons JW, Nie S. Nanotechnology for targeted cancer therapy. Expert Rev Anticancer Ther. 2007;7:833–7.
140. Bhattacharya R, Mukherjee P. Biological properties of "naked" metal nanoparticles. Adv Drug Deliv Rev. 2008;60:1289–306.
141. Mukherjee P, Bhattacharya R, Wang P, Wang L, Basu S, Nagy JA, et al. Antiangiogenic properties of gold nanoparticles. Clin Cancer Res. 2005;11: 3530–4.
142. Chanda N, Kan P, Watkinson LD, Shukla R, Zambre A, Carmack TL, et al. Radioactive gold nanoparticles in cancer therapy: therapeutic efficacy studies of GA-198AuNP nanoconstruct in prostate tumor-bearing mice. Nanomedicine. 2010;6:201–9.
143. Hu F, Cutler CS, Hoffman T, Sieckman G, Volkert WA, Jurisson SS. Pm-149 DOTA bombesin analogs for potential radiotherapy. In vivo comparison with Sm-153 and Lu-177 labeled DO3A-amide-betaAla-BBN(7-14)NH_2. Nucl Med Biol. 2002; 29:423–30.
144. Grazman B, Troutner DE. ^{105}Rh as a potential radiotherapeutic agent. Appl Radiat Isot. 1988;39:257–60.
145. Goswami N, Higginbotham C, Volkert W, Alberto R, Nef W, Jurisson S. Rhodium-105 tetrathioether complexes: radiochemistry and initial biological evaluation. Nucl Med Biol. 1999;26:951–7.
146. Ando A, Ando I, Tonami N, Kinuya S, Okamoto N, Sugimoto M, et al. Production of ^{105}Rh–EDTMP and its bone accumulation. Appl Radiat Isot. 2000;52: 211–5.
147. Pietrelli L, Mausner LF, Kolsky KL. Separation of carrier-free Sc-47 from titanium targets. J Radioanal Nucl Chem. 1992;157:335–45.
148. Müller C, Bunka M, Reber J, Fischer C, Zhernosekov K, Türler A, Schibli R. Promises of cyclotron-produced ^{44}Sc as a diagnostic match for trivalent β-emitters: in vitro and in vivo study of a ^{44}Sc-DOTA-folate conjugate. J Nucl Med. 2013;54: 2168–74.
149. Müller C, Zhernosekov K, Köster U, Johnston K, Dorrer H, Hohn A, et al. A unique matched quadruplet of terbium radioisotopes for PET and SPECT and for α- and β-radionuclide therapy: an in vivo proof-of-concept study with a new receptor-targeted folate derivative. J Nucl Med. 2012;53:1951–9.
150. Pastorek J, Pastorekova S, Callebaut I, Mornon JP, Zelník V, Opavský R, et al. Cloning and characterization of MN, a human tumor-associated protein with a domain homologous to carbonic anhydrase and a putative helix-loop-helix DNA binding segment. Oncogene. 1994;9:2877–88.
151. Opavsky R, Pastorekova S, Zelnik V, Gibadulinová A, Stanbridge EJ, Závada J, et al. Human MN/CA9 gene, a novel member of the carbonic anhydrase family: structure and exon to protein domain relationships. Genomics. 1996;33:480–7.
152. Grabmaier K, Vissers JL, De Weijert MC, Oosterwijk-Wakka JC, Van Bokhoven A, Brakenhoff RH, et al. Molecular cloning and immunogenicity of renal cell carcinoma-associated antigen G250. Int J Cancer. 2000;85:865–70.
153. Uemura H, Nakagawa Y, Yoshida K, Saga S, Yoshikawa K, Hirao Y, et al. MN/CA IX/G250 as a potential target for immunotherapy of renal cell carcinomas. Br J Cancer. 1999;81:741–6.
154. Divgi CR, Bander NH, Scott AM, O'Donoghue JA, Sgouros G, Welt S, et al. Phase I/II radioimmunotherapy trial with iodine-131-labeled

monoclonal antibody G250 in metastatic renal cell carcinoma. Clin Cancer Res. 1998;4:2729–39.
155. Oosterwijk E, Ruiter DJ, Hoedemaeker PJ, Pauwels EK, Jonas U, Zwartendijk J, et al. Monoclonal antibody G250 recognizes a determinant present in renal-cell carcinoma and absent from normal kidney. Int J Cancer. 1986;38:489–94.
156. Pastorekova S, Parkkila S, Parkkila AK, Opavský R, Zelník V, Saarnio J, et al. Carbonic anhydrase IX, MN/CA IX: analysis of stomach complementary DNA sequence and expression in human and rat alimentary tracts. Gastroenterology. 1997;112: 398–408.
157. Steffens MG, Boerman OC, de Mulder PH, Oyen WJ, Buijs WC, Witjes JA, et al. Phase I radioimmunotherapy of metastatic renal cell carcinoma with ^{131}I-labeled chimeric monoclonal antibody G250. Clin Cancer Res. 1999;5(10 Suppl):3268s–74.
158. Divgi CR, O'Donoghue JA, Welt S, O'Neel J, Finn R, Motzer RJ, et al. Phase I clinical trial with fractionated radioimmunotherapy using ^{131}I-labeled chimeric G250 in metastatic renal cancer. J Nucl Med. 2004; 45:1412–21.
159. Brouwers AH, Mulders PF, de Mulder PH, van den Broek WJ, Buijs WC, Mala C, et al. Lack of efficacy of two consecutive treatments of radioimmunotherapy with ^{131}I-cG250 in patients with metastasized clear cell renal cell carcinoma. J Clin Oncol. 2005;23:6540–8.
160. Brouwers AH, Buijs WC, Mulders PF, de Mulder PH, van den Broek WJ, Mala C, et al. Radioimmunotherapy with [^{131}I]cG250 in patients with metastasized renal cell cancer: dosimetric analysis and immunologic response. Clin Cancer Res. 2005;11 (19 Pt 2):7178s–86.
161. Stillebroer AB, Boerman OC, Desar IM, Boers-Sonderen MJ, van Herpen CM, Langenhuijsen JF, et al. Phase 1 radioimmunotherapy study with lutetium 177-labeled anti-carbonic anhydrase IX monoclonal antibody girentuximab in patients with advanced renal cell carcinoma. Eur Urol. 2013;64:478–85.
162. Stillebroer AB, Zegers CM, Boerman OC, Oosterwijk E, Mulders PF, O'Donoghue JA, et al. Dosimetric analysis of ^{177}Lu-cG250 radioimmunotherapy in renal cell carcinoma patients: correlation with myelotoxicity and pretherapeutic absorbed dose predictions based on ^{111}In-cG250 imaging. J Nucl Med. 2012;53:82–9.
163. Divgi CR, Uzzo RG, Gatsonis C, Bartz R, Treutner S, Yu JQ, et al. Positron emission tomography/computed tomography identification of clear cell renal cell carcinoma: results from the REDECT trial. J Clin Oncol. 2013;31:187–9.

Physics of Nuclear Oncology

9

Dale L. Bailey and John L. Humm

Abstract

The study of the basic physics used in nuclear oncology involves understanding the way energy associated with radioactive emissions can be best utilized to image, diagnose, stage, treat, and monitor the patient with cancer. In this chapter we will cover the physics involved in these processes.

Keywords

Physics • Radionuclides • Imaging • Therapy

Glossary

AAPM	American Association of Physicists in Medicine
Bq	Becquerel unit
Bremsstrahlung	Braking radiation
DOTA	1,4,7,10-Tetra-azacyclododecane-1,4,7,10-tetraacetic acid
DOTATE	DOTA-octreotate
e	Electron
E	Energy
EC	Electron capture
eV	Electron volt
Gy	Gray unit (ionizing radiation dose in the International System of Units, corresponding to the absorption of one joule of radiation energy per kilogram of matter)
h	Planck's constant
HCC	Hepatocellular carcinoma
IC	Internal conversion
ICRP	International Commission on Radiological Protection
ICRU	International Commission on Radiation Units and Measurements
IT	Isomeric transition
J	Joule
keV	Kilo-electron volt (10^3 eV)
LET	Linear energy transfer
m	Metastable
MeV	Mega-electron volt (10^6 eV)
MIRD	Medical Internal Radiation Dose Committee
n	Neutron
p	Proton
PET	Positron emission tomography
PSMA	Prostate-specific membrane antigen
SI	International System of Units

D.L. Bailey (✉)
Faculty of Health Sciences, The University of Sydney, Camperdown, NSW, Australia
e-mail: dale.bailey@sydney.edu.au

J.L. Humm (✉)
Department of Medical Physics, Memorial Sloan Kettering Cancer Center, New York, NY, USA
e-mail: hummj@MSKCC.ORG

© Springer International Publishing Switzerland 2017
H.W. Strauss et al. (eds.), *Nuclear Oncology*,
https://doi.org/10.1007/978-3-319-26236-9_4

α	Alpha particle
β	Beta particle
γ	Gamma radiation
λ	Decay constant
λ	Wavelength of a radiation
ν	Neutrino
σ	Atomic cross section
υ	Frequency of a radiation

Contents

Structure of the Atom 200

Energy and Mass 201
Energy and Frequency 201
Energy and Mass 201

Radioactivity and Radiation 201
Electromagnetic Radiation 202
X-Rays 203
Particulate Radiations 204

Interaction of Radiation with Matter 209
Interaction of Particulate Radiation with Matter 209
Interaction of Photons with Matter 210

Attenuation and Scattering of Photons 212
Photon Attenuation 213

Radionuclides Used in Nuclear Oncology 213

References 216

Structure of the Atom

To describe nuclear processes and the energy associated with radioactive decay, we will make use of a simple conceptual model of the atom. At the turn of the twentieth century, soon after the discovery of natural radioactivity and the first production of X-rays, the British physicist Lord Rutherford proposed a model for the atom similar to that used to describe the orbit of the planets of the solar system about the sun (the "planetary" model, see Fig. 1). The Rutherford model had a central positive core, the nucleus, about which a cloud of electrons circulated. It predicted that most of the space in matter was unoccupied (thus allowing particles and electromagnetic radiation to pass through, as had been observed experimentally). The Rutherford model, however, presented a problem because classical physics predicted that the revolving electrons would emit energy continuously, resulting in a spiraling of the electrons into the nucleus. In 1913, Niels Bohr introduced the constraint that electrons could only orbit at certain discrete radii, or energy levels, and that in turn only a small, finite number of electrons could exist in each energy level. Most of what was required to understand the subatomic behavior of particles was now in place. This is referred to as the Bohr (planetary) model of the atom. Later in 1932, the neutron was proposed by James Chadwick as a large particle roughly equivalent to the mass of a proton, but without any charge, that also existed in the nucleus of the atom.

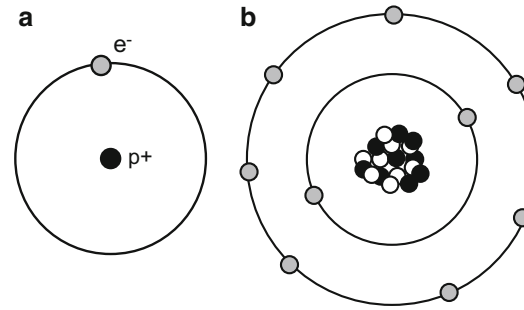

Fig. 1 Examples of the planetary model of the atom are shown for (**a**) hydrogen ($^{1}_{1}H$) and (**b**) fluorine-18 ($^{18}_{9}F$). Protons are indicated by the *solid circles*, neutrons by the hollow *circles*, and circulating electrons by the *gray circles*

We shall continue to use this basic model of the atom for much of our discussion. The model breaks down in the realm of quantum mechanics, where Newtonian physics and the laws of motion no longer apply, and particles approach relativistic speeds (i.e., approaching the speed of light). Also, there are times when we must invoke a nonparticulate model of the atom where the particles need to be viewed as waves (or, more correctly, *wave functions*). Electrons, for example, can be considered at times to be waves. This helps to explain how an electron can pass through a "forbidden" zone between energy levels and appear in the next level without apparently having passed through the forbidden area, defined as a region of space where there is zero probability of the existence of an electron. It can do so if its wave function is zero in this region. For a periodic wave with positive and negative components, this occurs when the wave function takes a value of zero. Likewise, electromagnetic radiation can be viewed

as particulate at times and as a wave function at other times. The planetary model of the atom is composed of nucleons (protons and neutrons in the nucleus of the atom) and circulating electrons. It is now known that these particles are not the fundamental building blocks of matter but are themselves composed of smaller particles called *quarks*.

Energy and Mass

Energy and Frequency

In 1900 Max Planck made the important observation that the energy (E) of electromagnetic radiation was simply related to the frequency of the radiation (υ) by a single constant (Planck's constant, h):

$$E = h\upsilon$$

Planck's constant has a value of 6.626×10^{-34} $J.s$. This provided support to the notion that electromagnetic radiation behaved like a wave. In addition, experiments indicated that the radiation was only released in discrete "bursts." This was a startling result as it departed from the classical assumption of continuous energy to one in which electromagnetic radiation could only exist in integral multiples of the product of $h\upsilon$. The wave-like radiation was said to be quantized, where each quantum contained an amount of energy that was an integer multiple of $h\upsilon$. The unit of energy in the SI system is the Joule (J); however, a derived unit used frequently in discussions of the energy of electromagnetic and particulate radiation is the electron volt (eV). The electron volt is defined as the energy acquired when a unit charge is moved through a potential difference of one volt. Energy in Joules can be converted to energy in electron volts (eV) by dividing by the conversion factor $1.6 \times 10^{-19}\text{J.eV}^{-1}$. Thus the energy in Joules for visible light photons of, for example, 450 nm would be:

$$\begin{aligned} E = h\upsilon = \frac{hc}{\lambda} &= \frac{6.63 \times 10^{-34} J.s \times 3 \times 10^{8} m.s^{-1}}{450 \times 10^{-9} m} \\ &= 4.42 \times 10^{-19} J \end{aligned}$$

which can be expressed in units of eV as:

$$\begin{aligned} E = 4.42 \times 10^{-19}\, J &\equiv \frac{4.42 \times 10^{-19} J}{1.6 \times 10^{-19} J.eV^{-1}} \\ &= 2.76\, eV \end{aligned}$$

X-rays and gamma rays have energies of thousands to millions of electron volts per photon (keV–MeV).

Energy and Mass

Einstein's special theory of relativity published in 1905 predicted, among other things, that the speed of light was constant for all observers independent of their frame of reference (and therefore that time was no longer constant) and, importantly, that mass and energy were *equivalent*. This means that we can talk about the rest-mass equivalent energy of a particle, which is the energy that would be liberated if all of the mass were to be converted to energy. By rest mass we mean that the particle is considered to be at rest, i.e., it has no kinetic energy. Consider the electron, which has a rest mass of 9.11×10^{-31}kg; we can calculate the amount of energy this mass is equivalent to using Einstein's equation:

$$\begin{aligned} E &= mc^2 \\ &= 9.11 \times 10^{-31} kg \times \left(3 \times 10^{8}\right)^2 m.s^{-1} \\ &= 8.2 \times 10^{-14} J \\ &\equiv 8.2 \times 10^{-14} J / 1.6 \times 10^{-19} J.eV^{-1} \\ &= 511\ keV \end{aligned}$$

The reader may recognize this as the energy of the photons emitted in positron–electron annihilation.

Radioactivity and Radiation

Radiation can be classified into electromagnetic or particulate. Ionizing radiation is radiation that has sufficient energy associated with it to remove electrons from atoms, thus causing ionization. This is restricted to high-energy electromagnetic radiation (X- and γ-radiation) and charged particles (α, β^-, β^+). Examples of non-ionizing electromagnetic radiation include light, radio, and microwaves (see Fig. 2). We will concern ourselves specifically with ionizing radiation as this is of

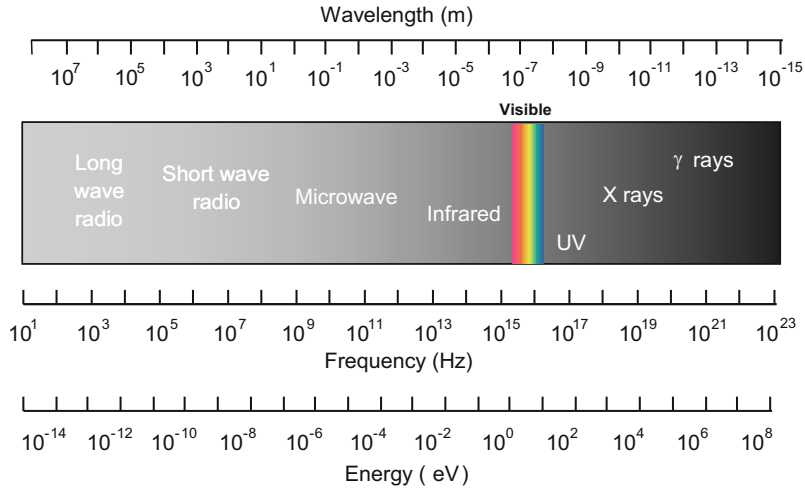

Fig. 2 The electromagnetic spectrum showing energy in units of eV

most interest in nuclear medicine and radiological imaging.

Electromagnetic Radiation

Electromagnetic radiation is pure energy. The amount of energy associated with each "bundle," or quantum, of energy is determined by the frequency or wavelength (λ) of the radiation. Human senses are capable of detecting some forms of electromagnetic radiation, for example, thermal radiation, or heat, ($\lambda \approx 10^{-5}$m), and visible light ($\lambda \approx 10^{-7}$m). The energy of the radiation can be absorbed to differing degrees by different materials: light can be stopped (absorbed) by paper, whereas radiation with longer wavelength (e.g., radio waves) or higher energy (γ-rays) can penetrate the same paper.

It had long been known that light acted like a wave, most notably because it caused interference patterns from which the wavelength of the light could be determined. Radiation was thought to emanate from its point of origin like ripples on the surface of a pond after a stone is dropped into it. This concept was not without its difficulties, most notably, the nature of the medium through which the energy was transmitted. This proposed medium was known as the "ether," and many experiments sought to produce evidence of its existence to no avail. Einstein, however, interpreted some experiments performed at the turn of the twentieth century where light shone on a photocathode could induce an electric current (known as the *photoelectric effect*) as showing that light acted as a particle. Einstein proposed that radiant energy was quantized into discrete packets, called photons. Thus, electromagnetic radiation could be viewed as having wave-like and particle-like properties. This view persists to this day and is known as the wave-particle duality. In 1924 Louis Victor, the duc de Broglie, proposed that if wave-particle duality could apply to electromagnetic radiation, it could also apply to matter. It is now known that this is true: electrons, for example, can exhibit particle-like properties such as when they interact like small billiard balls or wave-like properties as when they undergo diffraction. Electrons can pass from one position in space to another, separated by a "forbidden zone" in which they cannot exist, and one way to interpret this is that the electron is a wave that has zero amplitude within the forbidden zone. The electrons could not pass through these forbidden zones if viewed strictly as particles. An important subsequent postulate proposed by Niels Bohr was that de Broglie's principle of wave-particle duality was complementary. He stated that either the wave or the particle view can be taken to explain physical phenomena, but not both at the same time.

Electromagnetic radiation has different properties depending on the wavelength, or energy, of

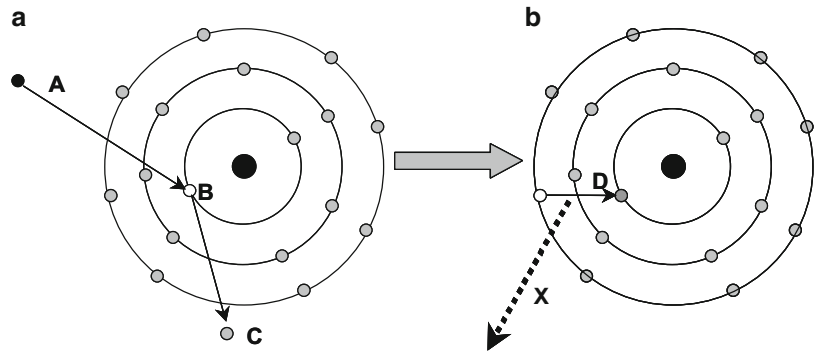

Fig. 3 The production of characteristic X-rays is shown. The electron (*A*) causes a vacancy at *B* with the liberated electron (*C*) leaving the atom. An outer-shell electron (*D*) drops down to fill the vacancy and, in doing so, gives off a discrete amount of radiation as a characteristic X-ray

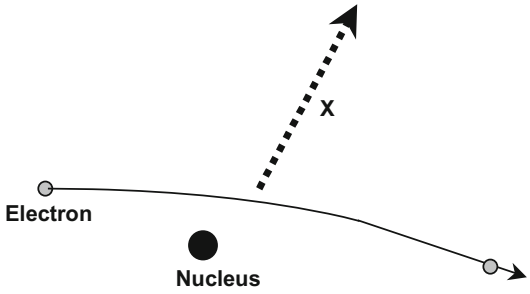

Fig. 4 Continuous radiation emitted by an electron under the influence of the nucleus is known as Bremsstrahlung

the quanta. Only higher-energy radiation has the ability to ionize atoms, due to the energy required to remove electrons from atoms. Electromagnetic radiation which can cause ionization is restricted to X- and γ-rays, which are discussed in the following sections.

X-Rays

X-rays are electromagnetic radiation produced within an atom, but outside of the nucleus. Characteristic X-rays are produced when orbital electrons drop down to fill vacancies in the atom after an inner-shell electron is displaced, usually by firing electrons at a target in a discharge tube. As the outer-shell electron drops down to the vacancy, it gives off energy and this is known as a characteristic X-ray as the energy of the X-ray is determined by the difference in the binding energies between the electron levels (see Fig. 3).

As any orbital electron can fill the vacancy, the quanta emitted in this process can take a number of energies. The spectrum is characteristic, however, for the target metal and this forms the basis of quantitative X-ray spectroscopy for sample analysis. The spectrum of energies emerging in X-ray emission displays a continuous nature, however, and this is due to a second process for X-ray production known as *Bremsstrahlung* (German: "braking radiation"), as shown in Fig. 4.

Bremsstrahlung radiation is produced after a free electron with kinetic energy is decelerated by the influence of a heavy target nucleus. The electron and the nucleus interact via a Coulomb (electrostatic charge) interaction, the nucleus being positively charged and the electron carrying a single negative charge. The process is illustrated in Fig. 6. The electron loses kinetic energy after its deceleration under the influence of the target nucleus, which is given off as electromagnetic radiation. There will be a continuum of quantized energies possible in this process depending on the energy of the electron, the size of the nucleus, and other physical factors, and this gives the continuous component of the X-ray spectrum.

X-rays generally have energies in the range of $\sim 10^3$–10^5 eV and can be used for imaging as well as therapy.

Gamma Radiation (γ)

Gamma rays are electromagnetic radiation emitted from the nucleus after a spontaneous nuclear decay. This is usually associated with the emission of an alpha or beta particle although there are alternative decay schemes. X- and γ-rays are

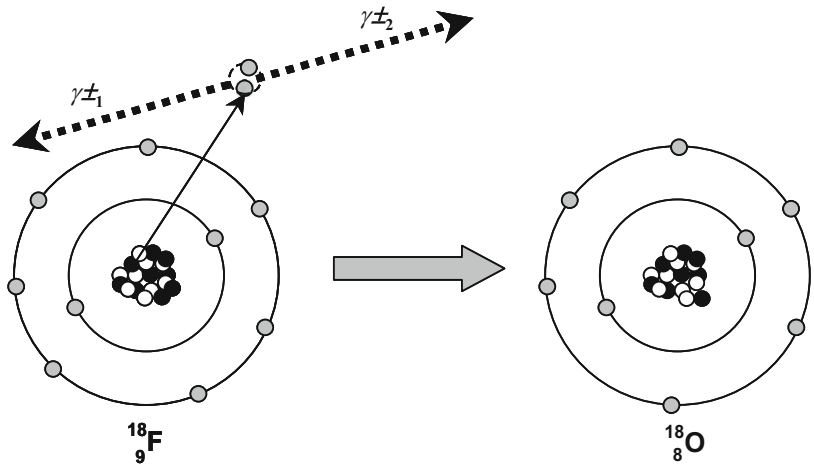

Fig. 5 The radioactive decay of ^{18}F by positron emission is shown. The emitted positron annihilates with an electron in the surrounding environment, and two annihilation photons (γ±) are emitted

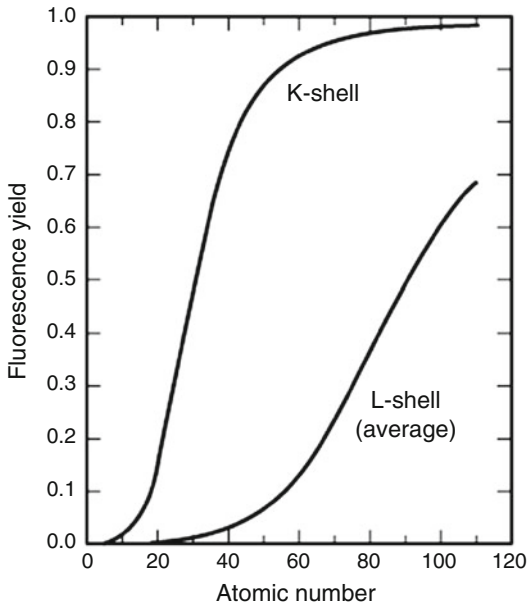

Fig. 6 Fluorescence yield of Auger electrons from the K and L shells is shown as a function of atomic number

indistinguishable after they are emitted from the atom and only differ in their site of origin. After the emission of a particle in a radioactive decay, the nucleus can be left in an excited state and this excess energy is given off as a γ-ray.

Gamma ray emission is characteristic, and it is determined by the difference in energy levels between the initial and final states of the energy level transitions within the nucleus.

Annihilation Radiation (γ±)

Annihilation radiation is the energy produced in the form of photons (usually two) by the positron–electron annihilation process. The energy of the radiation is equivalent to the rest mass of the electron and positron. Annihilation radiation, arising from positron–electron annihilation, is produced outside of the nucleus and often outside of the positron-emitting atom. There are two photons produced by each positron decay and annihilation. Each photon has energy of 0.511 MeV, and the photons are given off at close to 180° opposed directions (see Fig. 5). It is this property of collinearity that we exploit in positron emission tomography (PET), allowing us to define the line of sight of the event without the need for physical collimation. The general equation for β^+ decay is:

$$ {}^{A}_{Z}X \rightarrow {}_{Z-1}{}^{A}Y \quad + \quad \beta^{+} $$

Particulate Radiations

Particle emission from radioactive decay was the first observation of natural radioactivity. Wilhelm Röntgen had produced X-rays in 1896, and a year later, Henri Becquerel showed that naturally occurring uranium produced radiation spontaneously. While the radiation was thought initially to be similar to Röntgen's X-rays, Lord Rutherford showed that some types of radiation were more penetrating than others. He called the less penetrating radiation

alpha (α) rays and the more penetrating ones beta (β) rays. Soon after, it was shown that these radiations could be deflected by a magnetic field, i.e., they carried charge. It was clear that these were not electromagnetic rays and were, in fact, particles.

Alpha Radiation (α)

Alpha particles are emitted from large nuclei, often as part of a radioactive series (e.g., thorium series, radium series). An α-particle consists of two protons and two neutrons and thus is identical to a doubly ionized helium atom. For this reason it is often written as ${}_2^4He^{2+}$. Alpha decay results in a daughter nuclide with an atomic number of 2 less than the parent nuclide and a mass number of 4 less. The equation for α decay is:

$$ {}_Z^AX \rightarrow {}_{Z-2}^{A-4}Y + {}_2^4He^{2+}(\alpha \text{ particle}) + \gamma $$

Over the last several years, researchers have taken an interest in the use of α-particle-emitting radionuclides attached to tumor-specific targeting agents, such as antibodies. The advantage of α-particles for targeted radionuclide therapy is their high energy (5–9 MeV) and short range (50–90 μm) resulting in a high density of local energy deposition close to the decay site. Therefore α-emitters are especially suited to the treatment of disseminated cancers such as leukemias or micrometastatic disease. In addition, the high rate of the energy loss per unit track length, referred to as the linear energy transfer (LET), results in a greater radiobiological effectiveness of cell kill for α-particles relative to β-s and photon (low LET) radiations. Radiation dose estimates to normal tissues for α-particle-emitting radionuclides can be made (if imaging data resulting from concomitant X- or γ-rays emitted have been obtained) using the medical radiation dose committee (MIRD) assumption of total local absorption for non-penetrating radiations. However, the calculated organ and tissue doses need to be accepted with the following caveats: (i) at low doses the stochastic nature of energy deposition must be considered, i.e., an average dose of 0.2 Gy is the consequence of a Poisson distribution of cellular hits in which some cell nuclei receive α-particle hits, while others receive no hits; (ii) the microdistribution of the agent may be non-homogenously distributed with respect to the biological organ or structure, e.g., radium bone-seeking agents may deposit on bone surfaces, leading to high doses at the marrow–bone interface with zero dose to the central marrow regions; and (iii) the selective uptake or accumulation of α-emitters to cells can result in local doses that greatly exceed the average tissue dose.

Although not common, α-particle-emitting radionuclides have begun to be employed in the clinic. Current indications include ^{213}Bi (and ^{225}Ac)-labeled M195 antibody against leukemia, [^{211}At]-anti-tenascin antibody against brain tumors, [^{211}At]-methylene blue for melanoma, and, perhaps most importantly, the recent approval in Europe and the USA of $^{223}RaCl_2$ (Xofigo®) as a therapy for bone metastases in patients with castrate-resistant prostate cancer. Radium, as a calcium analog, localizes in regions of bone remodeling, frequently the sites of metastatic disease. The extremely short range (<80 μm) of the α-emissions mean that the radiation dose is highly locally deposited, killing cancer cells residing at the bone surfaces, yet sparing hematopoietic stem cells, many of which are located deeper within the marrow spaces and beyond the range of the alpha radiation dose.

Beta Radiation (β^-)

Beta decay is any process in which the nuclear charge changes by one. This includes β^-, β^+, and electron capture decays. Beta-minus particles are emitted from nuclei which have an excess of neutrons and are done in an attempt to approach the line of nuclear stability in terms of the relative number of protons and neutrons within the atomic nucleus. A β^- particle consists of an electron ejected from the nucleus after a neutron is converted into a proton. The β^- is ejected so that charge is conserved during this transformation. Beta-minus decay results in a daughter nuclide with an atomic number of 1 greater than the parent nuclide and a mass number which is unchanged. Beta-minus particles have a continuous range of energies up to a maximum. This appeared at first to be a violation of the conservation of energy. To overcome this problem, in 1931 Wolfgang Pauli

proposed that another particle was emitted which he called the neutrino (ν). He suggested that this particle had a very small mass and zero charge. It could carry away the excess momentum to account for the difference between the maximum beta energy and the spectrum of energies that the emitted beta particles displayed. In fact we now refer to the neutrino emitted in beta-minus decay as the antineutrino, indicated by the "¯" over the symbol ν.

The equation for β^- decay is

$$ {}^{A}_{Z}X \rightarrow {}_{Z+1}{}^{A}Y + \beta^- \quad + \overline{\nu} $$

The nucleus of the daughter nuclide is often left in an excited state with excess energy, and therefore this energy is often emitted in the form of a gamma ray after β^- decay.

The following shows an example of a beta-decay scheme for ^{131}I:

$$ {}^{131}_{53}I \rightarrow {}^{131}_{54}Xe + {}^{0}_{-1}\beta^- + \gamma + \overline{\nu} $$

The half-life for ^{131}I decay is 8.02 days. The most abundant β^- particle emitted has a maximum energy of 0.606 MeV, and there are many associated γ-rays, the most abundant (branching ratio = 0.81) having an energy of 0.364 MeV.

β^- Dosimetry

The most commonly used radionuclide for nuclear medicine therapies is ^{131}I, which is used for the treatment of a variety of thyroid disorders, benign and malignant, as well as for a several therapeutic radiolabeled antibody therapies such as ^{131}I-tositumomab (Bexxar®) for the treatment of follicular, non-Hodgkin's lymphoma. The pure β^- emitter ^{90}Y has also become routinely used for radioimmunotherapy applications, e.g., ibritumomab tiuxetan (Zevalin®), for the treatment of B-cell non--Hodgkin's lymphoma. The use of ^{90}Y-resin microspheres (SIR-Spheres®) has also become used as a new intra-arterial therapy for the treatment of hepatocellular carcinoma (HCC) and other diseases metastatic to liver. An advantage of ^{90}Y is the extremely low yield of penetrating photon emissions (only Bremsstrahlung radiation) facilitating the handling of large activities and resulting in lower radiation exposures to personal within proximity of the patients. However, the lack of photons for imaging can be a disadvantage when using ^{90}Y radiopharmaceuticals, and therefore to verify safety of delivery, protocols usually incorporate a pre-scan using the ^{111}In-labeled agent. Another β^--emitting radionuclide in increasing clinical use is ^{188}Re. This radionuclide has the advantage that it is produced from a tungsten-188 generator system, making it more readily available for use in developing nations, without access to radionuclide production facilities. ^{188}Re-lipiodol is an alternative to ^{90}Y-microspheres for the treatment of HCC and has the advantage of allowing imaging (using the 155 keV γ – 15% abundance)-based treatment planning. The average β^--emission energy is high at 795 keV, comparable to the 935 keV of ^{90}Y.

The dose versus distance for a point source of beta particles obeys the relationship first described by Loevinger [1], which consists of an inverse square geometric term and a power term to account for absorption. The dose from a point source therefore falls more sharply than the inverse square law. However, for distributed sources as in most medical applications of radiopharmaceuticals employing β^- sources, the dose is assumed to be uniform within most organ structures. The MIRD methodology classifies all β^- particles as non-penetrating radiations that are deposited locally within the source organ, i.e., cross fire between different organs is considered to be negligible. A detailed discussion of the heterogeneity of β^--emitting radiopharmaceuticals and the dosimetric implications is provided in ICRP Report 67 [2].

Positron Decay (β^+) and Electron Capture (EC)

A proton-rich radionuclide has two options for converting a proton into a neutron in an attempt to reach the line of stability: (i) positron decay and (ii) electron capture. Positron emission from the nucleus is secondary to the conversion of a proton into a neutron as in:

$$ {}^{1}_{1}p^+ \rightarrow {}^{1}_{0}n + {}^{0}_{1}\beta^+ \nu $$

with in this case a neutrino being emitted. The positron is the antimatter conjugate of the electron emitted in beta-minus decay.

The general equation for β^+ decay from an atom is

$$ {}^{A}_{Z}X \rightarrow {}_{Z-1}{}^{A}Y + {}^{0}_{1}\beta^{+} + \nu $$

The atom X is proton rich and achieves stability by converting a proton to a neutron. The positive charge is carried away with the positron. As the daughter nucleus has an atomic number one less than the parent, one of the orbital electrons must be ejected from the atom to balance charge. This is often achieved by a process known as internal conversion, where the nucleus supplies energy to an orbital electron to overcome the binding energy and leave it with residual kinetic energy to leave the atom. As both a positron and an electron are emitted in β^+ decay, the daughter nucleus must be at least two electron masses lighter than the parent.

The β^+ will have an initial energy after emission, which, similar to the case of beta-minus decay, can take a continuum of values up to a maximum. After emission from the nucleus, the β^+ loses kinetic energy by interactions with the surrounding matter.

The competing process, electron capture, occurs when an electron passing in the vicinity of the nucleus is "captured" by the nucleus and combined with a proton to produce a neutron. This has the same effect as positron emission, i.e., that a proton is converted into a neutron. This process, which in many proton-rich radionuclides competes with positron emission, may occur in a significant fraction of nuclear transformations. Many β-emitting tracers involve a competition in which a fraction of the decays occur by each process. For example, ^{18}F decays 96.9% by β^+ emission and 3.1% by electron capture. It is important to note that it is an advantage for β^+ emitters used for PET functional imaging to have shorter half-life to minimize the radiation dose to the patient. However, for applications in which tumor-specific macromolecules such as antibodies that exhibit both slow blood clearance and tumor uptake are employed, long-lived PET radionuclides are mandatory, examples of which are ^{124}I (4.2 days half-life) and ^{89}Zr (3.3 days half-life). These diagnostic PET radionuclides can result in a radiation dose burden to a patient per unit administered activity, which is similar to ^{131}I, the β^- emitter commonly used for therapeutic applications. This places significant restraints on the multiplicative usage of radioimmuno-PET and is a major impetus in the rapid interest in tumor-targeting peptides, whose rapid blood clearance allows the use of short-lived PET radionuclide such as ^{68}Ga; examples include DOTATATE which binds to somatostatin receptors and ^{68}Ga-binding PSMA peptides.

Several of the radionuclides most widely employed in nuclear medicine are those which decay exclusively by electron capture such as ^{67}Ga, ^{123}I, and ^{201}Tl. The equation for electron capture (EC) is

$$ {}^{A}_{Z}X + e^{-} \rightarrow {}_{Z-1}{}^{A}Y + \nu $$

From the dosimetric perspective, such radionuclides have been preferred because instead of high-energy β^- emissions, they emit very low-energy X-ray and particulate emissions called Auger and Coster–Kronig electrons.

Auger Electrons

Auger electrons are emitted as a consequence of atomic relaxation after the electron captured by the nucleus leaving the atom with an inner-shell atomic electron shell vacancy. Most commonly we learn that any inner shall vacancy is rapidly filled by an electron transition from a higher orbital, thereby resulting in a characteristic X-ray of energy equal to the difference between the binding energies of the two electron shells (E_{b1}–Eb_2). However, this same energy can be instantaneously transferred to an additional outer-shell orbiting electron of binding energy E_{b3}, which is ejected with energy equal to (E_{b1}–E_{b2}) – E_{b3}. Electrons emitted from the atom in this way are referred to as either Auger electrons or Coster–Kronig electrons if the ejected electron emanates from the same orbital as the electron involved in the transition to fill the initial

inner-shell vacancy. Electrons are classified by the electron shells involved. For example, an Auger electron could be K–L–M, which would mean that the initial vacancy arose in the K shell was filled by an electron from the L shell resulting in an electron ejected from the M shell (see Fig. 6). Since Auger and Coster–Kronig electrons are the consequence of transitions between electron orbitals, they have discrete energies (unlike β^- particles) which are emitted as an energy spectrum. The energies of Auger and Coster–Kronig electrons range from that just below the characteristic X-ray energies to a few electron volts. The ranges of these electrons are mostly submicron.

The fraction of initial inner-shell vacancies filled by radiative or fluorescent transitions, i.e., with characteristic X-ray emission, relative to the total radiative and non-radiative (Auger) is given by the fluorescent yield. The fluorescent yield decreases with increasing atomic number. This means that radiative transitions for high-Z radionuclides, e.g., ^{201}Tl, the filling of a K-shell vacancy is almost always by radiative transition. However, such transitions are mostly K–L transitions, moving the vacancy to the L shell. Since the fluorescent yield for the L shell is small, these vacancies as well as subsequent to higher shells are mostly non-radiative. A consequence of non-radiative transition is a cascade of inner-shell electron transitions (and Auger electron emission) until all vacancies have reached the outermost atomic shell. Therefore the number of Auger and Coster–Kronig electrons increases with increasing atomic number of the radionuclide.

The total energy emitted during the atomic de-excitation is shared between the Auger and Coster–Kronig electrons and fluorescent X-ray photons emitted. Since the total energy emitted is small, it has often been disregarded in organ and total body dosimetry estimates. In general the dose contribution from Auger and Coster–Kronig electrons is extremely small, hence the appropriate selection of electron capture (and isomeric transition – see later) decaying radionuclides for imaging purposes. However, under specific circumstances, the cascade of soft electrons emitted as a consequence of electron capture decay can produce high-LET-like biological effects. This was first observed in experiments in which the electron capture decaying radionuclide ^{125}I was directly incorporated into the cellular DNA via the thymidine analog [^{125}I]-iododeoxyuridine. However, for decays at other intracellular locations such as in cytosol or membrane bound, the radiation effects were comparable of β^- particles. For a detailed summary of Auger electron dosimetry and their biological effects, the reader is referred to the paper by AAPM Nuclear Medicine task group no. 6 [3].

Auger electron emitters have been used in clinical studies in order to selectively exploit the high-LET effectiveness of these agents when targeted to cancer cells. Such work has included the use of [^{125}I]-thymidine precursors as well as ^{125}I-labeled antibodies. A review of these efforts in Auger targeting therapies can be found by Mariani et al. [4].

Isomeric Transition (IT) and Internal Conversion (IC)

If, subsequent to a nuclear decay, an excited nuclear state exists for a defined period of time (>1 ns), with subsequent release of the excess energy by γ-emission, this is termed an *internal* or *isomeric transition*. We have seen that both α- and β^--emissions are often both associated with spontaneous γ-ray emission. In some cases, however, the nucleus remains in an excited state for an appreciable time, and this is termed an *isomeric* state denoted by the symbol *m* (for "metastable") appended to the mass number (e.g., ^{99m}Tc, ^{113m}In, etc.). As the energy is released via γ-emission, there is no change to the number of nucleons and the only change is the loss of energy. The equation for an isomeric transition is

$$ {}^{Am}_{Z}X \rightarrow {}^{A}_{Z}X + \gamma $$

An alternative to an isomeric transition is a process known as *internal conversion*. In this process, the energy that would have been emitted as a γ-ray is transferred to an orbital electron and the electron is ejected from the atom. The energy of the liberated IC electron is equal to the energy of the corresponding γ-ray minus the binding energy of the electron shell the electron was liberated from.

As with electron capture, internal conversion results in the atom being left in a state with an inner-shell vacancy from which a cascade of inner-shell electron transitions ensues yielding both characteristic X-rays and Auger and Coster– Kronig electrons.

The most common radionuclide used in nuclear medicine is ^{99m}Tc that undergoes this type of decay with a half-life of 6.02 h. De-excitation of the metastable state occurs 88.9% through the emission of a 140.5 keV γ-ray and 11.1% through internal conversion. In addition to radionuclides undergoing isomeric transitions, rapid internal conversion may occur subsequent to any β-decay process. For example, ^{123}I decays by electron capture, but a significant percentage (∼18%) of the 159 keV γ-rays undergoes internal conversion.

Radioactive Decay

The rate at which nuclei spontaneously undergo radioactive decay is characterized by the parameter called the half-life of the radionuclide. The half-life is the time it takes for half of the unstable nuclei present to decay. It takes the form of an exponential function, where the number of atoms decaying at any particular instant in time is determined by the number of unstable nuclei present and the decay constant (λ) of the nuclide. The rate of decay of unstable nuclei at any instant in time is called the activity of the radionuclide. The activity of the nuclide after a time t is given by

$$A_t = A_0 e^{-\lambda_d t}$$

where A_0 is the amount of activity present initially, A_t is the amount present after a time interval t, and λ_d is the decay constant. The decay constant is found from:

$$\lambda_d = \frac{\log_e(2)}{t_{1/2}}$$

where the units for λ_d are time^{-1}. The SI unit for radioactivity is the Becquerel (Bq). One Becquerel (1Bq) equals one disintegration per second.

Interaction of Radiation with Matter

When high-energy radiation interacts with matter, energy can be transferred to the material. A number of effects may follow, but a common outcome is the ionization or excitation of the atoms in the absorbing material. To facilitate the description of these interaction processes, radiations are commonly divided into particulate and non-particulate or photon radiation. Particulate radiations are then further divided into whether they are charged (electrons, protons, α-particles) or uncharged (neutrons) particles.

Interaction of Particulate Radiation with Matter

The particulate emissions encountered in nuclear medicine applications include electrons (β^- particles) and α-particles. β^- particles are light charged particles and therefore continuously undergo electrostatic interactions with the outer-shell atomic electrons of the medium through which they traverse. Each interaction may result in an elastic or nonelastic scattering, changing the direction of the electron. With inelastic scattering events, sufficient energy may be transferred to the orbiting atomic electrons of the medium to either excite or ionize the atom. It is this energy deposition resulting in ionization to tissue that results in the biologically relevant radiation dose. Such energy transfers along the track of the β^- so that the particle slows down until it has no more energy and reaches the end of its range. A small fraction of the electrons pass through the electron clouds and are deflected by the nucleus. The strong positive charge field of the nucleus causes the electron to undergo a massive angular deflection and therefore decelerate. This process of rapid deceleration causes the charged electron to lose energy radiatively by X-ray emission. The X-rays released by this mechanism are referred to as Bremsstrahlung which means "braking radiation." In tissue, the dominant means of energy transfer is through collisional losses from electron– electron interactions. However, the yield of Bremsstrahlung increases with increasing β-particle energy (is important for ^{90}Y or ^{32}P but insignificant for ^{3}H) and

becomes especially important for high-Z materials such as lead (the Bremsstrahlung yield varies with Z^2). It is for this reason that it is better to contain a high-energy β-source, e.g., ^{90}Y, in a plastic vial behind which is lead, rather than place such sources directly into a lead container. β-Sources would produce a significant Bremsstrahlung fluence from a high-Z container, resulting in a greater radiation exposure than from the defined range resulting from the β-particles themselves.

Charged α-particles lose their energy through the same interaction processes as β^- particles. However, α-particles lose their energy much more quickly. Even an 8 MeV α-particle can travel only ~80 μm in the soft tissue. This is because of the much high stopping power associated with the higher (+2) charge and large mass of the He nucleus. As a consequence α-particles are not a significant radiation protection concern unless radionuclides emitting such particles are directly ingested.

Neutrons are uncharged particles that interact with matter through direct collisions with intranuclear nucleons (protons and neutrons). It is through "knock-on" protons that charged particles are set in motion and atomic ionizations occur. Since neutron (or proton) sources are not used in nuclear medicine applications, they are beyond the scope of this book.

Interaction of Photons with Matter

High-energy photons interact with matter by three main mechanisms, depending on the energy of the electromagnetic radiation. These are (i) the photoelectric effect, (ii) the Compton effect, and (iii) pair production. In addition, there are other mechanisms such as coherent (Rayleigh) scattering, an interaction between a photon and a whole atom which predominates at energies less than 50 keV, triplet production, and photonuclear reactions, where high-energy gamma rays induce decay in the nucleus and which require energies of greater than ~10 MeV. We will focus on the three main mechanisms which dominate in the energies of interest in imaging in nuclear medicine.

Photoelectric Effect

The photoelectric effect occupies a special place in the development of the theory of radiation. During the course of experiments which demonstrated that light acted as a wave, Hertz and his student Hallwachs showed that the effect of an electric spark being induced in a circuit due to changes in a nearby circuit could be enhanced if light was shone upon the gap between the two coil ends. They went on to show that a negatively charged sheet of zinc could eject negative charges if light was shone upon the plate. Philipp Lenard demonstrated in 1899 that the light caused the metal to emit electrons. This phenomenon was called the photoelectric effect. These experiments showed that the electric current induced by the ejected electrons was directly proportional to the intensity of the light. The interesting aspect of this phenomenon was that there appeared to be a light intensity threshold below which no current was produced. This was difficult to explain based on a continuous wave theory of light. It was these observations that led Einstein to propose the quantized theory of the electromagnetic radiation in 1905, for which he received the Nobel Prize.

The photoelectric effect is an interaction of photons with orbital electrons in an atom. This is shown in Fig. 7. The photon transfers all of its energy to the electron. Some of the energy is used to overcome the binding energy of the electron,

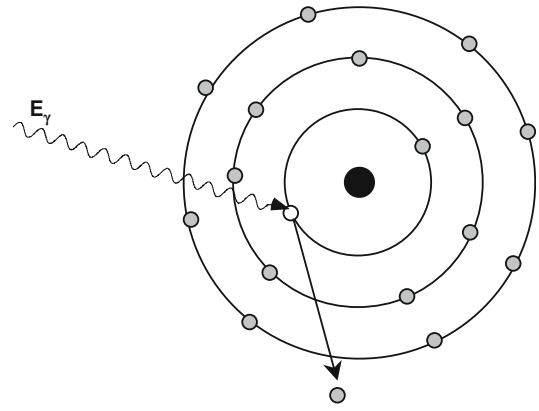

Fig. 7 The photoelectric effect. An incident photon displaces an inner-shell electron, thereby ionizing the atom. X-rays and Auger electrons may be produced after as the vacancy is filled by an outer-shell electron

and the remaining energy is transferred to the electron in the form of kinetic energy. The photoelectric effect usually occurs with an inner-shell electron. As the electron is ejected from the atom (causing ionization of the atom), a more loosely bound outer orbital electron drops down to occupy the vacancy. In doing so it will emit radiation itself due to the differences in the binding energy for the different electron levels. This is a characteristic X-ray. The ejected electron is known as a photoelectron. Alternately, instead of emitting an X-ray, the atom may emit a second electron to remove the energy and this electron is known as an Auger electron. This leaves the atom doubly charged. Characteristic X-rays and Auger electrons are used to identify materials using spectroscopic methods based on the properties of the emitted particles.

The photoelectric effect dominates in human tissue at energies less than approximately 100 keV. It is of particular significance for X-ray imaging and for imaging with low-energy radionuclides. It has little impact at the energy of annihilation radiation (511 keV), but with the development of combined PET/CT systems, where the CT system is used for attenuation direction of the PET data, knowledge of the physics of interaction via the photoelectric effect is extremely important when adjusting the attenuation factors from the X-ray CT to the values appropriate for 511 keV radiation.

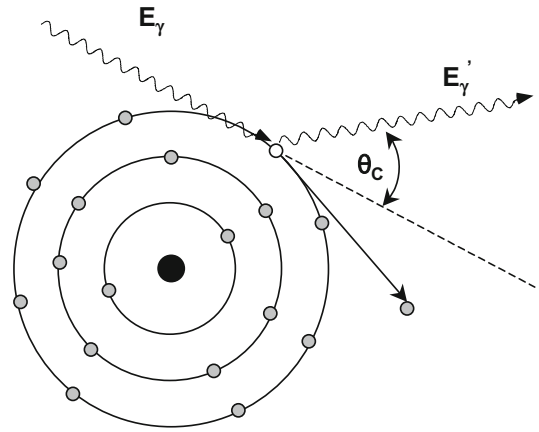

Fig. 8 Compton scattering occurs when a photon interacts with a loosely bound electron in an outer orbital shell. The atom is ionized and the photon undergoes a deflection causing a change in direction through the angle $\boldsymbol{\theta}_C$. This interaction is of most interest as a degrading factor in nuclear medicine imaging and quantification

Compton Scattering

Compton scattering is the interaction between a photon and a loosely bound orbital electron. The electron is so loosely connected to the atom that it can be considered to be essentially free. This effect dominates in the human tissue at energies above approximately 100 keV and less than ~2 MeV. The binding potential of the electron to the atom is extremely small compared with the energy of the photon, such that it can be considered to be negligible in the calculation. After the interaction, the photon undergoes a change in direction and the electron is ejected from the atom. The energy loss by the photon is divided between the small binding energy of the energy level and the kinetic energy imparted to the Compton recoil electron. The energy transferred does not depend on the properties of the material or its electron density.

The energy of the photon after the Compton scattering can be calculated from the Compton equation:

$$E'_\gamma = \frac{E_\gamma}{1 + \frac{E_\gamma}{m_0 c^2}(1 - \cos(\theta c))}$$

where E_γ and E'_γ are the incident and resulting gamma ray energies, respectively, m_0c^2 is the rest-mass equivalent energy of the electron, and θ_C is the scattering angle of the photon (see Fig. 8). From the consideration of the Compton equation, it can be seen that the maximum energy loss occurs when the scattering angle is 180° (cos $\{180°\}) = -1$), i.e., the photon is backscattered.

Pair Production

The final main mechanism for photons to interact with matter is by pair production. When photons with energy greater than 1.022 MeV (twice the energy equivalent to the rest mass of an electron) pass in the vicinity of a nucleus, it is possible that

they will spontaneously convert into two electrons with opposed signs, to conserve charge. This direct electron pair production in the Coulomb field of a nucleus is the dominant interaction mechanism at high energies. Above the threshold of 1.022 MeV, the probability of pair production increases as energy increases. At 10 MeV, this probability is about 60%. Any energy left over after the production of the electron–positron pair is shared between the particles as kinetic energy, with the positron having slightly higher kinetic energy than the electron as the interaction of the particles with the nucleus causes an acceleration of the positron and a deceleration of the electron.

Pair production was first observed by Anderson using cloud chambers in the upper atmosphere, where high-energy cosmic radiation produced tracks of diverging ionization left by the electron–positron pair.

The process of pair production demonstrates a number of conservation laws. Energy is conserved in the process as any residual energy from the photon left over after the electron pair is produced is carried away by the particles as kinetic energy; charge is conserved as the incoming photon has zero charge and the outgoing positive and negative electrons have equal and opposite charge; and momentum is conserved as the relatively massive nucleus absorbs momentum without appreciably changing its energy balance (see Fig. 9).

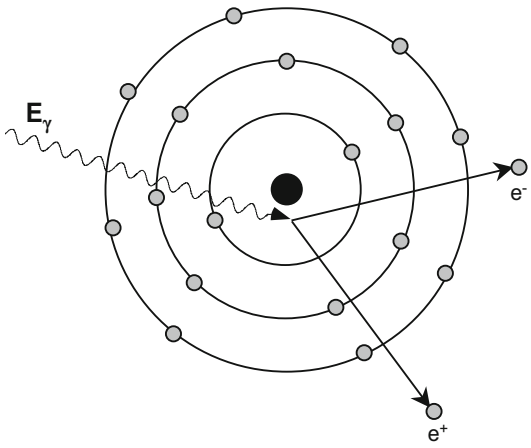

Fig. 9 Pair production occurs when a high-energy photon passes in the vicinity of the strong nuclear force. A positron–electron pair may be spontaneously created

At energies above four rest-mass equivalents of the electron, pair production can take place in the vicinity of an electron. In this case it is referred to as "triplet production" as there is a third member of the interaction, the recoiling electron.

Attenuation and Scattering of Photons

In the previous section, we have seen how radiation interacts with matter at an atomic level. In this section we will examine the bulk "macroscopic" aspects of the interaction of radiation with matter, with particular reference to positron emission and detection.

Calculations of photon interactions are given in terms of atomic cross sections (σ) with units of cm^2/atom. An alternative unit, often employed, is to quote the cross section for interaction in barns/atom (b/atom) where 1 barn = 10^{-24} cm^2. The total atomic cross section is given by the sum of the cross sections for all of the individual processes, i.e.,

$$\sigma_{\text{tot}} = \sigma_{\text{pe}} + \sigma_{\text{incoh}} + \sigma_{\text{coh}} + \sigma_{\text{pair}} + \sigma_{\text{tripl}} + \sigma_{\text{nph}}$$

where the cross sections are for the photoelectric effect (pe), incoherent Compton scattering (incoh), coherent (Rayleigh) scattering (coh), pair production (pair), triplet production (tripl), and nuclear photoabsorption (nph). Values for attenuation coefficient are often given as mass attenuation coefficients (μ/ρ) with units of $cm^2.g^{-1}$. The reason for this is that this value can be converted into a linear attenuation coefficient (μl) for any material simply by multiplying by the density (ρ) of the material:

$$\mu_l\left(\text{cm}^{-1}\right) = \mu/\rho\left(\text{cm}^2 \cdot \text{g}^{-1}\right)\mu/\rho\left(\text{g} \cdot \text{cm}^{-3}\right)$$

The mass attenuation coefficient is related to the total cross section by

$$\mu/\rho\left(\text{cm}^2 \cdot \text{g}^{-1}\right) = \frac{\sigma_{\text{tot}}}{u(g)A}$$

Table 1 Narrow-beam (scatter-free) linear attenuation coefficients for some common materials at 140 keV (the energy of ^{99m}Tc photons) and annihilation radiation (511 keV) (Tabulated from Hubbell [5] and *ICRU Report 44 [6] and [7], [8]). ¶This is the density of non-inflated lung. §Measured experimentally

Material	Density(ρ) [g×cm^{-3}]	μ (140 keV) [cm^{-1}]	μ (511 keV) [cm^{-1}]
Adipose tissue*	0.95	0.142	0.090
Water	1.0	0.150	0.095
Lung*	1.05¶	∼0.04–0.06§	∼0.025–0.04§
Smooth muscle	1.05	0.155	0.101
Perspex (Lucite)	1.19	0.173	0.112
Cortical bone*	1.92	0.284	0.178
Pyrex glass	2.23	0.307	0.194
NaI(Tl)	3.67	2.23	0.34
Bismuth germanate (BGO)	7.13	∼5.5	0.95
Lead	11.35	40.8	1.75

where $u(g) = 1.661 \times 10^{-24}$g is the atomic mass unit ($1/N_A$ where N_A is Avogadro's number) defined as 1/12th of the mass of an atom of ^{12}C and A is the relative atomic mass of the target element.

Photon Attenuation

We have seen that the primary mechanism for photon interaction with matter at energies in the range 0.1–2 MeV is by a Compton interaction. The result of this form of interaction is that the primary photon changes direction (i.e., is "scattered") and loses energy. In addition, the atom where the interaction occurred is ionized.

For a well-collimated source of photons and detector, attenuation takes the form of a mono-exponential function, i.e.,

$$I_x = I_0 e^{-\mu x}$$

where I represents the photon beam intensity; the subscripts "0" and "x" refer, respectively, to the unattenuated beam intensity and the intensity measured through a thickness of material of thickness x; and μ refers to the attenuation coefficient of the material (units: cm^{-1}). Attenuation is a function of the photon energy and the electron density (Z number) of the attenuator. The attenuation coefficient is a measure of the probability that a photon will be attenuated by a unit length of the medium. The situation of a well-collimated source and detector is referred to as narrow-beam condition. The narrow-beam linear attenuation coefficients for some common materials at 140 keV and 511 keV are shown in Table 1.

However, when dealing with in vivo imaging, we do not have a well-collimated source, but rather a source emitting photons in all directions. Under these uncollimated, broad-beam conditions, photons whose original emission direction would have taken them out of the acceptance angle of the detector may be scattered such that they are counted. This is known as a "broad-beam" conditions indicating increased acceptance of scattered photons leading to an overall lower effective attenuation coefficient.

Radionuclides Used in Nuclear Oncology

Nuclear medicine uses radionuclides for both diagnostic studies (including some non-imaging ones) and therapeutic applications. Diagnostic studies include γ-emitting radionuclides produced in nuclear reactors or cyclotrons as well as β^+-emitting radionuclides. Therapeutic radionuclides always emit a particle and may or may not emit a γ-ray which can be used to image the radionuclide distribution and uptake. Table 2 summarizes the main radionuclides of interest in nuclear oncology and their principal emissions and other characteristics. Only the dominant emissions are shown.

Table 2 Radionuclides of interest in nuclear oncology

Radionuclide	Half-life	Principal radiations emitted	Energy of emission (MeV)	Abundance (in same order as emissions)
^{11}C	20.5 min	$\beta^+(\gamma\pm)$	0.39	100%
^{13}N	9.97 min	$\beta^+(\gamma\pm)$	0.49	100%
^{15}O	122.2 s	$\beta^+(\gamma\pm)$	0.74	100%
^{18}F	109.8 min	$\beta^+(\gamma\pm)$	0.24	96.9%
^{32}P	14.2 days	β^-	0.695	100%
^{64}Cu	12.8 h	$\beta^+(\gamma\pm),\beta^-$	0.28 (β^+),0.19 (β^-)	17% (β^+),39% (β^-)
^{67}Cu	61.8 h	β^-,γ	0.116, 0.149, 0.184 (β^-), 0.185 (γ_1), 0.093 (γ_2)	57% (β^+_1), 22% (β^+_2), 20% (β^+_3), 49% (γ_1), 16% (γ_2)
^{67}Ga	78 h	γ	0.093, 0.184, 0.300, 0.394	38%, 24%, 16%, 4%
^{68}Ga	68 min	$\beta^+(\gamma\pm)$	0.74	88%
^{82}Rb	75 s	$\beta^+(\gamma\pm)$	1.4	96%
^{89}Sr	50.5 days	β^-	0.585	100%
^{89}Zr	78.4 h	$\beta^+(\gamma\pm),\gamma$	0.396 (β^+),0.909 (γ_1)	23% (β^+), 99.9% (γ_1)
^{90}Y	64 h	β^-	0.93	100%
^{99m}Tc	361.2 min	γ	0.1405	89%
^{111}In	67.4 h	γ	0.172, 0.247	89%, 94%
^{123}I	13 h	γ	0.159	97%
^{124}I	4.2 day	$\beta^+(\gamma\pm),\gamma$	0.97 (β^+_1), 0.69 (β^+_2) 0.603 (γ_1),1.69 (γ_2)	11% (β^+_1),12% (β^+_2), 62% (γ_1), 10% (γ_2)
^{125}I	60.2 days	γ	0.036	7%
^{131}I	8.04 days	β^-,γ	0.19 (β^-), 0.364 (γ_1), 0.637 (γ_2)	90% (β^-), 83% (γ_1), 7% (γ_2)
^{131}Cs	9.7 days	γ	0.353	100%
^{153}Sm	1.95 days	β^-,γ	0.20 (β^-_1), 0.23 (β^-_2), 0.27 (β^-_3), 0.070 (γ_1), 0.103 (γ_2)	32% (β^-_1), 50% (β^-_2), 18% (β^-_3), 5% (γ_1), 28% (γ_2)
^{166}Ho	26.8 h	β^-	0.70 (β^-_1), 0.65 (β^-_2)	50% (β^-_1), 49% (β^-_2)
^{169}Er	9.4 days	β^-	0.10	100%
^{177}Lu	6.73 days	β^-,γ	0.15 (β^-_1),0.12 (β^-_2)	79% (β^-_1), 9% (β^-_2)

^{186}Re	3.78 days	β^-,γ	1.07 (β^-_1), 0.93 (β^-_2), 0.140 (γ)	74% (β^-_1), 21% (β^-_2), 9% (γ)
^{188}Re	17.0 h	β^-,γ	0.79 (β^-),0.73 (β^-_2)	70% (β^-_1), 26% (β^-_2)
^{198}Au	2.7 days	β^-,γ	0.32 (β^-), 0.40 (γ)	99% (β^-), 96% (γ)
^{201}Tl	73 h	γ,X	0.167 (γ), 0.070 (X_1),0.080 (X_2)	8% (γ), 74% (X_1), 20% (X_2)
^{211}At	7.14 h	α	5.868	42%
^{212}Pb	10.64 h	β^-	0.096 (β^-_1), 0.173 (β^-_2), 0.239 (γ), 0.148 (IC)	82.5% (β^-_1), 12.3% (β^-_2), 43% (γ), 32% (IC)
				^{212}Pb decays to an α-emitting progeny ^{212}Bi
^{212}Bi	1.01 h	α,β^-	6.1 (α), 2.25 (β^-)	34% (α) + 66% (^{212}Po α), 55% (β^-)
				The β^- decay branch to ^{212}Po ($\tau = 0.299$ μs) undergoes further α decay to the ground state ^{208}Pb
^{213}Bi	45.6 min	α	5.5–5.9 (α)	100% (α)
^{223}Ra	11.4 days	α,γ	5.5–5.7 (α), 0.270 (γ)[a]	100% (α), 14% (γ)
				There are four α-emitted from parent to stable daughter
^{225}Ac	10.0 days	α,γ	5.8 (α), 0.218 (γ from ^{221}Fr daughter)	100% (α), 12% (^{221}Fr γ)
			0.440 (γ from ^{213}Bi daughter)	26% (^{213}Bi γ)
				There are four α-emitted from parent to stable daughter

Average energy of β-emission

[a]Radium-223 and its progeny emit numerous γ-rays. Only the most abundant γ-ray emitted by the parent is provided in the table

References

1. Loevinger R. The dosimetry of beta radiations. Radiology. 1954;62:74–82.
2. Adelstein SJ, Green AJ, Howell RW, Humm JL, Leichner PK, O'Donoghue JA, Strand S-E, Wessels BW. ICRU Report 67: "Absorbed-dose specification in nuclear medicine", International Commission on Radiation Units and Measurement, 2002.
3. Humm JL, Howell RW, Rao DV. Dosimetry of Auger-electron-emitting radionuclides: report no. 3 of AAPM Nuclear Medicine Task Group No. 6. Med Phys. 1994; 21:1901–15.
4. Mariani G, Bodei L, Adelstein SJ, Kassis AI. Emerging roles for radiometabolic therapy of tumors based on auger electron emission. J Nucl Med. 2000;41:1519–21.
5. Hubbell JH, Seltzer SM. Tables of X-ray mass attenuation coefficients and mass energy-absorption coefficients 1 keV to 20 MeV for Elements Z = 1 to 92 and 48 additional substances of dosimetric interest. Gaithersberg: US Dept of Commerce, National Ist of Standards and Technology; 1995.
6. ICRU. ICRU report 44: tissue substitutes in radiation dosimetry and measurement. Bethesda: International Commission on Radiation Units and Measurements; 1989. p. 189.
7. Ninkovic MM, Raicevic JJ, Adrovic F. Air kerma rate constants for gamma emitters used most often in practice. Radiat Prot Dosim. 2005;115:247–50.
8. Madsen M, Ponto J. Handbook of nuclear medicine. Madison, WI, USA: Medical Physics Publishing; 1992.

Instrumentation for Positron Emission Imaging

10

Pat Zanzonico

Abstract

This chapter reviews the underlying physical principles of positron emission tomography (PET) and the design and operation of state-of-the-art PET scanners. Although now a mature technology, PET has undergone, and continues to undergo, steady advances in hardware and software and, as a result, ongoing improvements in performance and functionality. Recent noteworthy advances include improvements in detector technology and image reconstruction, implementation of time-of-flight (TOF) technology, and the introduction of PET/MRI (positron emission tomography/magnetic resonance imaging) scanners.

Keywords

PET • PET/CT • PET/MRI • Scintillation detectors • Ionization detectors • Image reconstruction

Glossary

ACD	Annihilation coincidence detection
ACF	Attenuation correction factor
ACR	American College of Radiology
APD	Avalanche photodiode
BGO	Bismuth germinate
CBM	Continuous bed motion
CdZnTe (or CZT)	Cadmium zinc telluride
CF	Calibration factor
CT	X-ray computed tomography
CZT	Cadmium zinc telluride
DCE	Dynamic contrast-enhancement
DICOM	Digital imaging and communications in medicine
DOI	Depth-of-interaction
eV	Electron volt
FBP	Filtered back-projection
FOV	Field of view
FWHM	Full-width half-maximum
GSO	Cerium-doped gadolinium orthooxysilicate
keV	Kiloelectron volt (10^3 eV)
LOR	Line of response
LSO	Cerium-doped lutetium orthooxysilicate
LYSO	Cerium-doped lutetium-yttrium oxyorthosilicate
MeV	Megaelectron volt (10^6 eV)
MFP	Mean free path
MLEM	Maximum likelihood expectation maximization
MRI	Magnetic resonance imaging
MRSI	Magnetic resonance spectroscopic imaging
NaI(Tl)	Thallium-doped sodium iodide

P. Zanzonico (✉)
Memorial Hospital Research Laboratories, Department of Medical Physics, Memorial Sloan Kettering Cancer Center, New York, NY, USA
e-mail: zanzonip@mskcc.org

© Springer International Publishing Switzerland 2017
H.W. Strauss et al. (eds.), *Nuclear Oncology*,
https://doi.org/10.1007/978-3-319-26236-9_37

NECR	Noise-equivalent count rate
NEMA	National Electrical Manufacturers Association
OSEM	Ordered-subset expectation maximization
PEM	Positron emission mammography
PET-MRI	Positron emission tomography/magnetic resonance imaging
PET	Positron emission tomography
PET/CT	Positron emission tomography/computed tomography
PL	Penalized likelihood
PMT	Photomultiplier tube
PSF	Point-spread function
PSPMT	Position-sensitive photomultiplier tube
RAMLA	Row-action maximization-likelihood algorithm
RF	Radiofrequency
SiPM	Silicium-based photomultiplier
SNR	Signal-to-noise ratio
SPECT	Single-photon emission computed tomography
SPECT/CT	Single-photon emission computed tomography/computed tomography
SSRB	Single-slice rebinning
SUV	Standardized uptake value
TOF	Time-of-flight

Contents

Introduction 218
Basic Principles of Radiation Detection 218
PET Scanner Design 222
Data "Corrections" 231
Noise-Equivalent Count Rate (NECR) 235
Image Reconstruction 236
Quantitation 240
Multimodality Devices 241
Commercial Devices 243
Concluding Remarks 247
References 248

Introduction

This chapter reviews the underlying physical principles of positron emission tomography (PET) and the design and operation of state-of-the-art PET scanners. Although now a mature technology, PET has undergone, and continues to undergo, steady advances in hardware and software and, as a result, ongoing improvements in performance and functionality. Recent noteworthy advances include improvements in detector technology and image reconstruction, implementation of time-of-flight (TOF) technology, and the introduction of PET/MRI (positron emission tomography/magnetic resonance imaging scanners.

Basic Principles of Radiation Detection

Radiation detectors are generally characterized as either scintillation or ionization detectors [1–3]. The application of scintillation and ionization detectors in gamma cameras and single-photon emission tomography is discussed in ▶ Chap. 11, "Instrumentation for Single-Photon Emission Imaging". In scintillation detectors, visible light is produced as radiation excites atoms of a crystal and is converted to an electronic signal, or pulse, and amplified by a photomultiplier tube (PMT) or other photodetector. In ionization detectors, free electrons produced when radiation ionizes a stopping material are collected to produce a small electronic signal. Clinical devices based on solid-state ionization detectors are available for single-photon (i.e., non-PET) imaging but remain far less common than scintillation detector-based devices.

Scintillation detectors. In scintillation detectors (Fig. 1) [1, 2], radiation interacts with and deposits energy in a scintillator. The radiation energy thus deposited is converted to visible light, with the amount of light produced being proportional to the radiation energy deposited. Because the light is emitted isotropically, the inner surface of the light-tight crystal housing is coated with a reflective material so that light emitted toward the sides and front of the crystal is

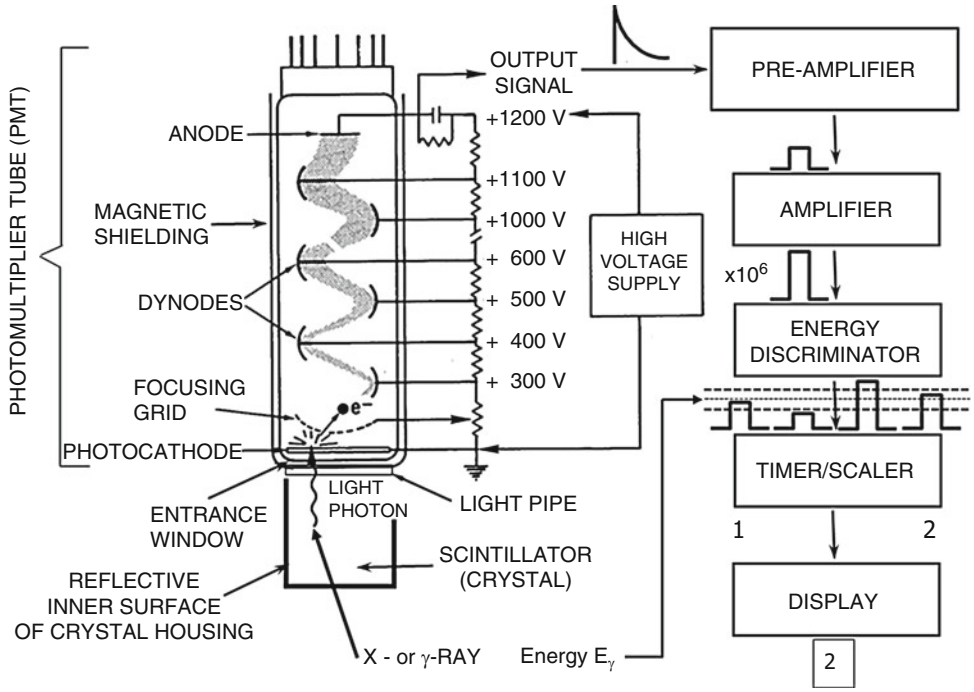

Fig. 1 Basic design and operation of a scintillation detector. Note that only two of the four pulses have heights lying between the preset pulse height ranges (indicated by the *two dash horizontal lines* below the energy discriminator, that is, corresponding to photon energies within the preset photopeak energy window) (see Fig. 1c). Thus, only those two photons are counted (in the case of a radiation counter) or included in the image (in the case of a radiation imager). The other two photons, with pulse heights and therefore energies outside the photopeak energy window, are not counted or included in the image (Adapted from references [1, 2] with permission)

reflected back toward the PMT; this maximizes the amount of light collected and therefore the overall sensitivity of the detector and ensures that the amount of light detected is proportional to the energy of the absorbed photon. Interposed between the back of the crystal and the entrance window of the PMT is the light guide, sometimes simply a thin layer of transparent optical gel. The light guide optically couples the crystal to the PMT and thus maximizes the transmission of the light signal from the crystal into the PMT.

The PMT consists of an evacuated glass enclosure, containing a series of electrodes maintained at different voltages. Coated on the inner surface of the PMT's entrance window is the photocathode. When struck by the light from the crystal, the photocathode ejects electrons. The probability that each visible light photon will eject an electron from the photocathode is 15–25%. Immediately beyond the photocathode is the focusing grid, maintained at a relatively low positive voltage relative to the photocathode. Once the "focused" electrons pass through the focusing grid, they are attracted by a relatively large positive voltage relative to the photocathode, ~300 V, on the first of a series of small metallic elements called dynodes. The resulting high-speed impact of each electron results in the ejection from the dynode surface of an average of three electrons. The electrons thus ejected are then attracted by the even larger positive voltage, ~400 V, on the second dynode. The impact of these electrons on the second dynode surface ejects an additional three electrons on average for each incident electron. Typically, a PMT has 10–12 such dynodes (or stages), each ~100 V more positive than the preceding dynode, resulting in an overall electron amplification factor of 3^{10}–3^{12} for the entire PMT. At the

collection anode, an output signal is generated. The irregularly shaped PMT output signal is shaped into a logic (i.e., square-wave) pulse that can be electronically manipulated. In the past, this was accomplished by a preamplifier; nowadays, pulse shaping, amplification, etc. are performed using solid-state electronics and computer software. The amplitudes (or "heights") of the resulting electrical pulses are proportional to the number of electrons produced at the PMT photocathode and thus the energy of the incident radiation. These pulses can then be sorted according to their respective heights by an energy discriminator (also known as a pulse height analyzer), and those pulses with a pulse height (i.e., energy) within a preset photopeak energy window are counted or included in the image. Importantly, implicit in the foregoing discussion, the amount of light produced in a scintillation detector is proportional to the radiation energy deposited in the scintillator.

In recent years, new PMT configurations have been developed that allow enhanced approaches to position determination in PET scanners. These include the position-sensitive PMT (PSPMT), which provides two-dimensional position information via two sets of wire anodes perpendicular to one another. The electrons from the last dynode stage are read out on each set of anode wires. The position of the incident light on the photocathode can then be estimated from the electron distribution on each wire. Readout of the wire anodes is typically accomplished via separate internal resistors (or functionally equivalent components) for x- and y-position information.

The silicon photodiode is an alternative to the PMT for conversion of scintillation light into electronic signals. Photodiodes typically have a gain of only 1 (compared to the ~10^6-fold gain of PMTs) and thus require low-noise electronics. The so-called avalanche photodiodes (or APDs), in which the number of electrons produced by the visible light is amplified, have considerably higher gains, of the order of 100–1,000, but still require low-noise readout electronics. An alternative to traditional vacuum-tube PMTs, Si photomultipliers (or "SiPMs"), are single-photon-sensitive devices built from a multi-pixel APD array on a Si substrate [4] and achieve essentially one-to-one correspondence between each detector element and the PMT [5]; this so-called digital SiPM design has been implemented in the Philips Vereos™ PET scanner. In the "analog" SiPM design, the signals from multiple pixels in the APD array are summed, effectively minimizing the impact of electronic noise but at the cost of additional circuitry [5]. The dimension of each single APD can vary from 20 to 100 μm and their density can be up to 1,000/mm^2. The supply voltage typically varies between 25 and 70 V, 30- to 50-fold lower than that required for traditional PMTs. Performance parameters of SiPMs are comparable to those of traditional PMTs but with a much more compact form factor.

The scintillation detection materials most widely used in Nuclear Medicine – all inorganic scintillators – are bismuth germanate (BGO, $Bi_4Ge_3O_{12}$), cerium-doped gadolinium oxyorthosilicate (GSO (Ce) or GSO, Gd_2SiO_5:Ce), cerium-doped lutetium oxyorthosilicate (LSO(Ce) or LSO, Lu_2SiO_5:Ce), and cerium-doped lutetium-yttrium oxyorthosilicate (LYSO(Ce) or LYSO, Lu_2YSiO_5:Ce) as well as thallium-doped sodium iodide (NaI(Tl)) (Table 1) [1, 2, 6, 7]. PET scanners primarily use BGO, GSO, LSO, or LYSO. The most important practical features of scintillation detectors include:

high mass density (ρ) and effective atomic number (Z_{eff}) – to maximize the photon stopping power (i.e., intrinsic efficiency ε) of the detector;
high light (scintillation) output – to maximize the signal and thus minimize statistical uncertainty in the energy of the detected signal;
for PET, speed of the output light pulse – to shorten the coincidence timing window (τ) and thus minimize the number of random events (see below) without sacrificing a significant portion of the signal.

As noted, higher-ρ and higher-Z_{eff} atomic materials such as BGO, GSO, LSO, and LYSO have emerged as the detectors of choice for PET because of their greater stopping power for 511-keV annihilation γ-rays. The mean free path (MFP) for 511-keV γ-rays is at least twice as long in NaI(Tl) than in BGO, GSO, or LSO. GSO,

Table 1 Physical properties of scintillation detector (crystal) materials [1, 2, 6, 7]

Material[a]	Composition	Density, ρ (gm/cm^3)	Effective atomic number Z_{eff}	Linear attenuation coefficient, μ, for 511 –keV γ-rays (/cm)	Relative probability of photoelectric interaction (%)	Light output (photons per MeV)	Scintillation decay time (ns)	Scintillation wavelength λ (nm)	Energy resolution at 511 keV (% FWHM)	Hygroscopic?
Bismuth germanate (BGO)	$Bi_4Ge_3O_{12}$	7.1	75	0.95 ε(2 cm) = 0.72[a]	40	9,000	300	480	16	No
Cerium-doped gadolinium oxyorthosilicate (GSO)	Gd_2SiO_5:Ce	6.7	59	0.70 ε(2 cm) = 0.57[a]	25	8,000	60	440	12	No
Cerium-doped lutetium oxyorthosilicate (LSO)	Lu_2SiO_5:Ce	7.4	66	0.88 ε(2 cm) = 0.69[a]	32	30,000	40	420	20	No
Cerium-doped lutetium-yttrium oxyorthosilicate (LYSO)	$LuYSiO_5$:Ce	7.4	66	0.87 ε(2 cm) = 0.68[a]	30	17,000	42	430	20	No
Thallium-doped sodium iodide NaI(T1)	NaI:T1	3.7	51	0.34 ε(2 cm) = 0.24[a]	17	41,000	230	410	8	Yes

Except for NaI(Tl), which is the scintillator used almost exclusively in gamma cameras, the other scintillators are used for PET

[a]The intrinsic efficiency of 2-cm thick coincidence detectors for 511-keV annihilation γ-rays

LSO, and LYSO have almost tenfold faster light output than BGO, with LSO and LYSO having a much greater (two- to threefold greater) light output than either BGO or GSO. The light output of scintillators (expressed as the number of light photons produced per MeV of radiation energy absorbed) is largely determined by quenching (i.e., the combined effect of all radiationless de-excitation processes in which the deposited energy is ultimately degraded to heat). GSO has somewhat better energy resolution, and therefore scatter rejection capability, than either BGO or LSO. A notable disadvantage of LSO and LYSO is the presence of a naturally occurring long-lived radioisotope of lutetium, lutetium-176 (^{176}Lu) [6]. ^{176}Lu has an isotopic abundance of 2.6% and a half-life of ~4×10^{10} years and emits two prompt γ-rays (88% abundance) of 201 and 306 keV in energy; their summed energy of 507 keV falls well within the 511-keV energy windows commonly used in PET scanners. For example, the presence of ^{176}Lu results in a measured background count rate of 240 cps/cm^3 of LSO. For most applications, however, this has a negligible impact on typical PET scans.

Semiconductor-based ionization detectors. Semiconductor radiation detectors represent the main alternative to scintillator detector-based imaging systems. Such detectors are so-called direct-conversion devices, a major advantage of which is that they avoid the random effects associated with scintillation production and propagation and conversion of the optical signal to an electronic signal. When an x- or γ-ray interacts in a semiconductor detector, one or more energetic electrons are created and subsequently lose energy through ionization, among other processes. The ionization creates electron-hole (e-h) pairs, where a hole is the positively charged electron vacancy in the valence band left when the electron has been raised into the conduction (i.e., mobile-electron) band. Application of a bias voltage creates an electric field that causes the two types of charge carriers to migrate in opposite directions. These moving charges induce transient currents in the detector electrodes, thereby allowing measurement of the detector's response to an incident x- or γ-ray.

Semiconductor detectors offer several potential advantages over scintillator detectors [8]. By eliminating the need for bulky PMTs, semiconductor imaging systems can be made much more compact, simplifying their mechanics in comparison to those of a conventional PMT-based imaging system (see below). More importantly, the direct conversion of energy deposited by x- or γ-rays into electron-hole pairs eliminates the light-to-electrical signal transduction step and the associated loss of signal. Further, since the energy required to create an e-h pair in most semiconductors employed as radiation detectors is sufficiently small (typically 3–5 eV), each incident photon generates a large number of charge carriers. In principle, therefore, Poisson noise is considerably less and energy resolution considerably better in semiconductor detectors than in scintillation detectors. Defects (i.e., inherent irregularities in the crystal lattice) can trap electrons produced by radiation and thus reduce the total charge collected. As a result of such incomplete charge collection due to "charge trapping," statistical uncertainty (i.e., noise) is increased and energy spectra broadened, that is, the otherwise excellent energy resolution of semiconductors is degraded. Thin semiconductors have fewer traps overall than thick detectors, but also have a lower intrinsic efficiency. Trapping can be reduced by increasing the bias voltage across the detector, but at the expense of increasing its leakage current. This results in greater electronic noise and therefore poorer overall performance. Practical, reasonably economical crystal-growing techniques have been developed for cadmium telluride (CdTe), mercuric iodide (HgI_2), and cadmium zinc telluride (CdZnTe) (also known as "CZT"), which have been incorporated into commercial intraoperative gamma probes and gamma cameras [8, 9] but not PET scanners.

PET Scanner Design

PET is based on the annihilation coincidence detection (ACD) of the two colinear (approximately 180° apart) 511-keV photons resulting from the mutual annihilation of a positron and an

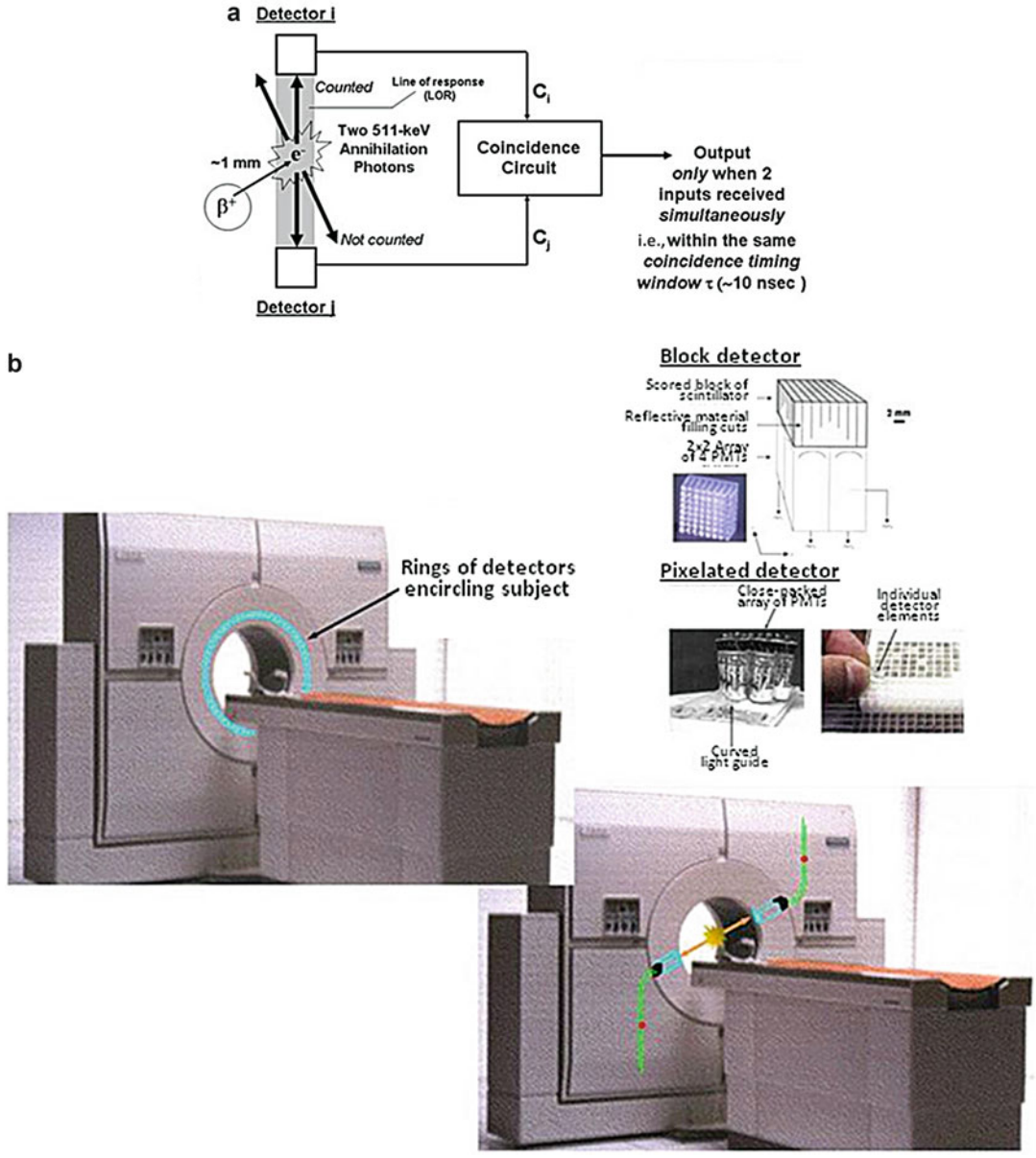

Fig. 2 **a** Annihilation coincidence detection (ACD) of the two opposed 511-keV photons resulting from positron decay and positron-electron annihilation. Note that the true coincidence (or "trues") count rate is much less than C_i and C_j. The short coincidence timing window, τ, is short (<10 ns) which minimizes the number of random coincidence events (see Fig. 8). At the same time, however, most of the annihilation photons therefore do not produce coincidence events. **b** A photograph of a PET scanner, illustrating one of a number of rings of discrete detectors encircling the subject (*left-hand panel*) and ACD of an annihilation photon by a pair of these detectors. In the insert are shown a block detector (*top*) and pixilated detectors (*bottom*) used in PET scanners. The block detector consists of a cubic piece of scintillator scored to variable depths into a two-dimensional array of detector elements, typically backed by a 2 × 2 array of PSPMTs. Pixilated detectors consist of individual scintillator detector elements backed by a continuous light guide and a close-packed array of PMTs. For both the block and pixilated detectors, the individual detector elements are typically ~2 × 2 mm in area (Adapted from reference [7] with permission)

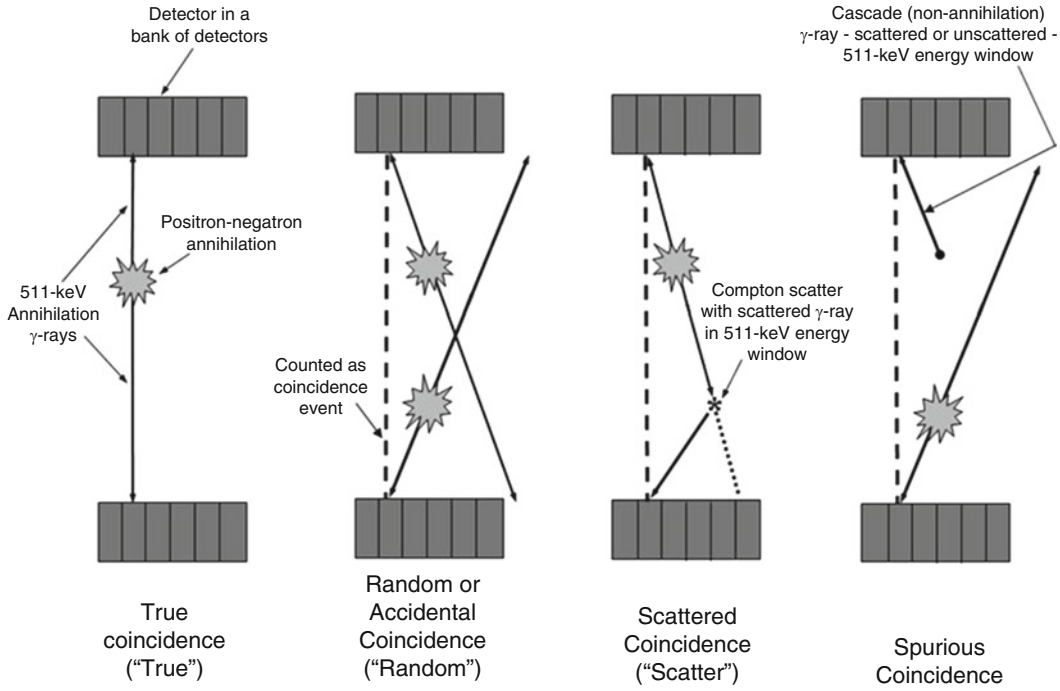

Fig. 3 The various events associated with ACD of positron-emitting radionuclides, illustrated for two opposed banks of coincidence detectors and assuming only one opposed pair of detectors, are in coincidence. A true coincidence ("true") is counted only when each of the two 511-keV annihilation photons for a single positron-electron annihilation are not scattered and are detected within the timing window τ of the two coincidence detectors. A random or accidental coincidence ("random") is an inappropriately detected and positioned coincidence (the *dashed line*) which arises from two separate annihilations, with one γ-ray from each of the two annihilations detected within the timing window τ of the coincidence-detector pair. A scattered coincidence ("scatter") is a mispositioned coincidence (the *dashed line*) resulting from a single annihilation, with one of the γ-rays undergoing a small-angle Compton scatter but retaining sufficient energy to fall within the 511-keV energy window. A spurious coincidence is an inappropriately detected and positioned coincidence (the *dashed line*) which arises from an annihilation and a cascade γ-ray, scattered or unscattered but having sufficient energy to fall within the 511-keV energy window. Spurious coincidences occur only for radionuclides which emit both positrons and high-energy prompt cascade γ-rays, that is, γ-rays with an energies (either scattered or unscattered) lying within the 511-keV energy window (From reference [7] with permission)

electron (Fig. 2a) [1, 2, 7]; a typical PET scanner and the detector configurations used in modern scanners are shown in Fig. 2b. Each individual annihilation photon is referred to as a "single" event, and the total count rate of individual annihilation photons is called the "singles count rate." When both photons from an annihilation are detected simultaneously (in coincidence), this triggers the coincidence circuit, and a "true coincidence event" ("true") is generated. The various events associated with ACD of positron-emitting radionuclides, including trues, randoms, scatter, and spurious coincidences, are illustrated in Fig. 3 [7].

The volume between the opposed coincidence detectors absorbing the two annihilation photons (the shaded area in Fig. 4) is referred to as a "line of response (LOR)" even though it is actually a volume of response. In PET, LORs are defined electronically, and an important advantage of ACD is that absorptive collimation (as is used in gamma cameras) is not required. As a result, the sensitivity of PET is two to three orders of magnitude higher than that of SPECT. Modern PET scanners generally employ a series of rings of discrete, small-area detectors (i.e., scored block detectors or pixilated detectors) encircling the subject (Fig. 2b) and, in clinical PET scanners,

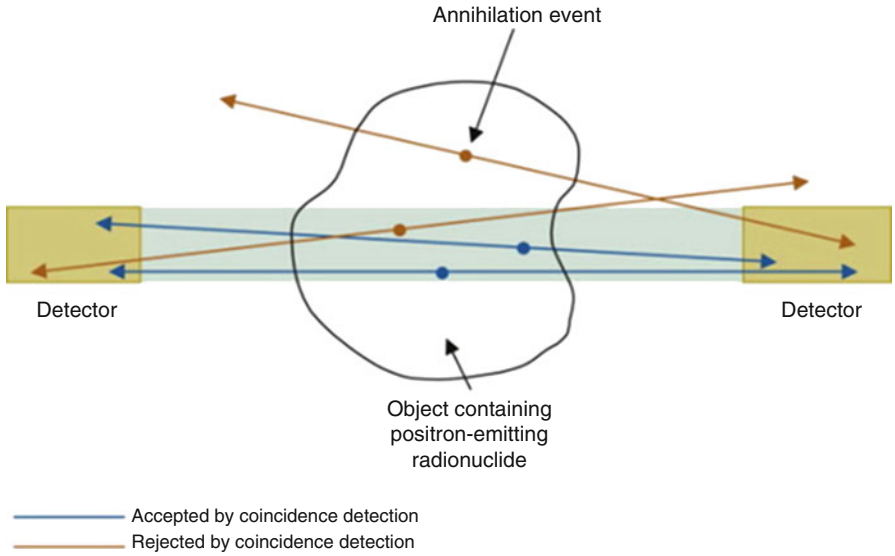

Fig. 4 For PET and annihilation coincidence detection, the 3D "line" (actually, volume) of response corresponds to the elongated cube whose cross-sectional area is defined by that of the opposed detector elements (Adapted from reference [29] with permission)

typically spanning a distance (or axial field of view (FOV)) of 15–20 cm in the patient's longitudinal direction. Recently, however, at least one PET scanner (the General Electric Discovery IQ™ scanner) with an axial FOV up to 26 cm has been marketed. Thus, a whole-body PET scan will typically require data acquisition at six to seven discrete bed positions and subsequently merge, or "knit," the discrete images into a single whole-body image. Of course, scanners with longer axial FOVs require fewer bed positions but require more detectors and front-end electronics. As its name implies, the Siemens continuous bed motion (CBM) feature allows whole-body scanning with continuous motion of the patient bed, analogous to the bed motion in spiral CT.

PET ring scanners originally employed lead or tungsten walls, or septa, positioned between and extending radially inward from the detector blocks [7] (Fig. 5). In this approach, known as two-dimensional (2D) PET, these inter-ring annular septa define plane-by-plane LORs and largely eliminate out-of-plane annihilation photons. By eliminating most of the contribution from out-of-plane randoms and scatter, image quality is improved, especially for large-volume sources (i.e., as in whole-body PET). However, 2D PET also eliminates most of the trues as well and thus reduces sensitivity. Removing the septa altogether and including coincidence events from all of the LORs among all the detectors significantly increase PET detector sensitivity. This is known as three-dimensional (3D) PET and is the prevailing design among state-of-the-art PET scanners [7, 10]. Sensitivity is increased up to ~fivefold in 3D relative to 2D PET – but with a considerable increase in the randoms and scatter count rates. Clinically, the scatter-to-true count rate ratios range from 0.2 (2D) to 0.5 (3D) in the brain and from 0.4 (2D) to 2 (3D) in the whole body [11].

A notable refinement in PET detectors has been the use of adjacent layers of two different materials with significantly different scintillation decay times (such as LSO and GSO, with decay times of approximately 40 and 60 ns, respectively); these are known as phoswich detectors [11]. Based on the pulse shape of the scintillation signal, the depth of the interaction of the annihilation photon in the detector can therefore be localized in the upper or lower layer [12]. As a result, the resolution-degrading depth-of-interaction (DOI) effect (see below) is

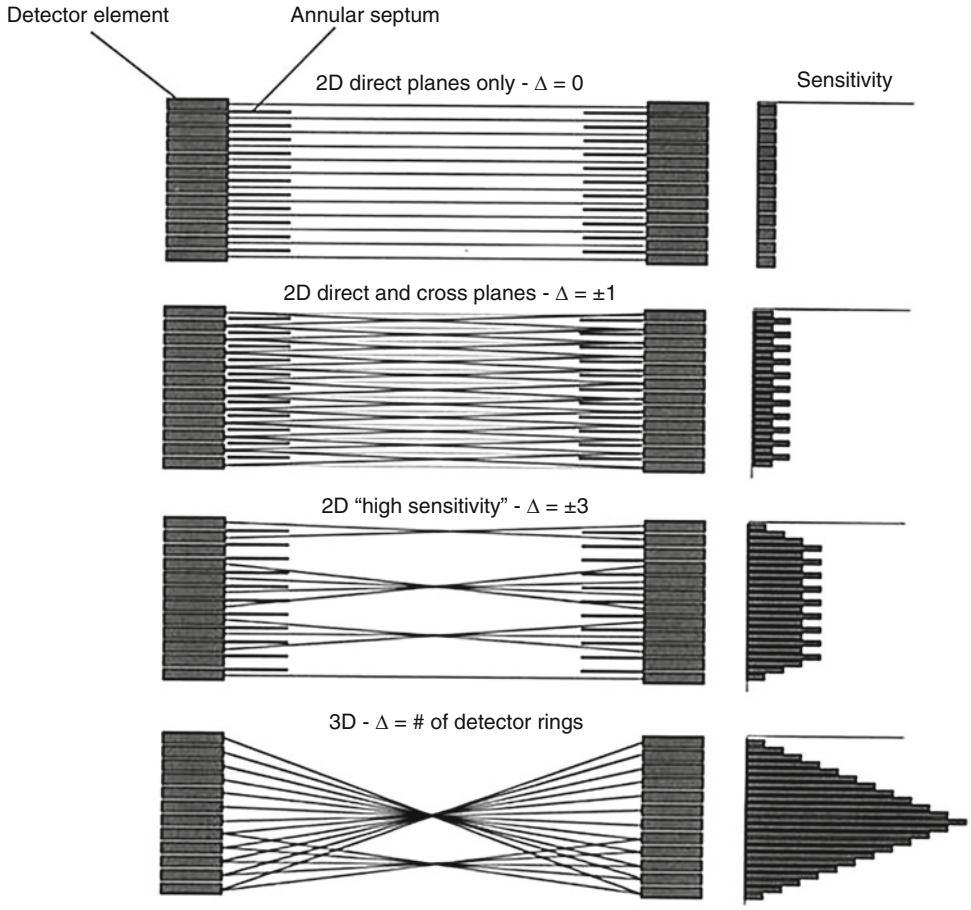

Fig. 5 Two-dimensional (2D) and three-dimensional (3D) PET data acquisition schemes (axial cross-sectional views of a multi-ring scanner) and the corresponding axial sensitivity profiles. **a**–**c** 2D data acquisition with a ring difference Δ of 0, 1, and 3, respectively. The ring difference refers to the number of different detector-element rings between which coincidence events are allowed. A ring difference of Δ of 0, for example, indicates that only intra-detector ring (i.e., direct planes) coincidences are allowed. **d** 3D (septa-less) data acquisition. The sensitivity profiles show the nonuniformity of response as a function of position along the axial FOV (Adapted from reference [11] with permission)

reduced. However, the fabrication of phoswich detectors is more complex than that of single-component detectors, and to date it has seen only limited use in commercial PET scanners, specifically preclinical scanners.

Increasingly important, time-of-flight (TOF) PET scanners utilize the measured difference between the detection times of the two annihilation photons arising from the decay of a positron (Fig. 6). This allows at least approximate spatial localization (to within ~10 cm) of the annihilation event along the LOR with current values, ~500 psec, of coincidence time resolution [13, 14]. This does not improve the spatial resolution of state-of-the-art PET scanners (~5 mm), but reduces the random coincidence rate and thus improves the signal-to-noise ratio (SNR), especially for large subjects [15]. This is important, as conventional (i.e., non-TOF) PET image quality is degraded with increasing patient size due to more pronounced attenuation and scatter and fewer trues. The use of faster digital SiPMs should improve the performance of TOF PET scanners.

The overall spatial resolution of PET scanners results from a combination of physical and instrumentation factors. There are several important

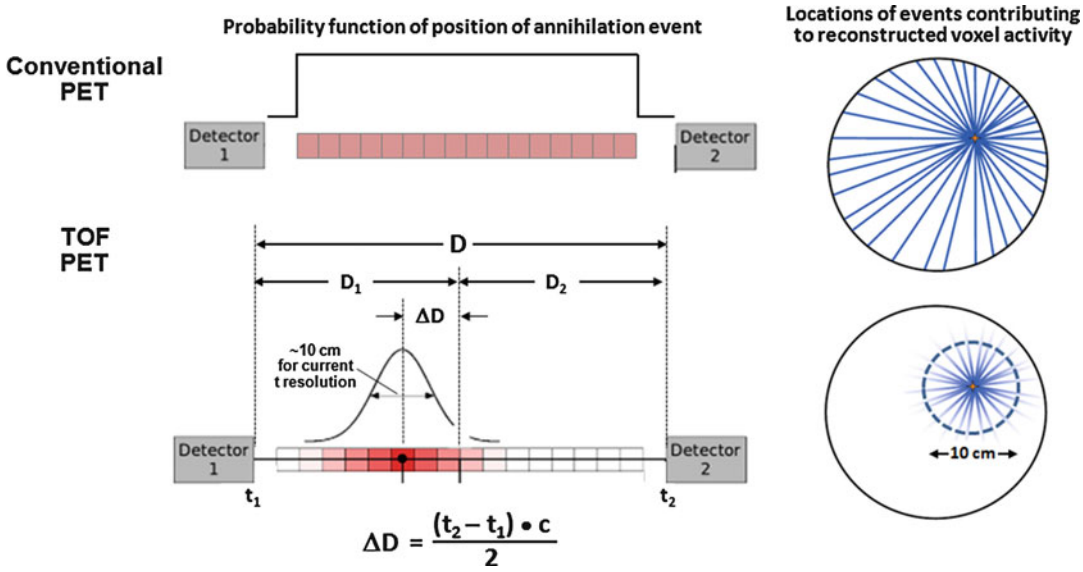

Fig. 6 Time-of-flight (TOF) PET. In conventional (i.e., non-TOF) PET, the position of a detected annihilation event may be anywhere along the LOR between the coincidence detectors. In TOF PET, the most likely position of the coincidence event along the LOR is a distance ΔD from the midpoint of the two coincidence detectors, where ΔD is proportional to the difference, $t_2 - t_1$, in times of arrival of the two annihilation photons at the two detectors (t_2 and t_1, respectively) and the speed of light, (**c**). As shown in the right panel, by localizing the position of the annihilation event, even approximately, the contribution of scatter, randoms, etc. to the reconstructed counts in each image voxel is reduced, and the SNR therefore improves. The shorter the coincidence time resolution, the more precisely the distance ΔD and the position of the coincidence event can be determined and the greater the improvement in the SNR

limitations imposed on resolution by the basic physics of positron-electron annihilation. First, for a given radionuclide, positrons are emitted over a spectrum of initial kinetic energies ranging from 0 to a characteristic maximum, or end point, energy, $E_{\max}$; the associated average positron energy, $\bar{E}$, is approximately one-third of its end point energy, $\bar{E} \approx \frac{1}{3} E_{\max}$. As a result, emitted positrons will travel a finite distance from the decaying nucleus ranging from 0 to a maximum called the extrapolated range, R_e, corresponding to its highest-energy positrons (Fig. 7a) [16]. For positron emitters used to date in PET (Table 2), the maximum energies ($E_{\max}$) vary from 0.58 to 3.7 MeV, the extrapolated ranges (R_e) from 2 to 20 mm, and the root-mean-square (rms) ranges (R_{rms}) from 0.2 to 3.3 mm. Although the finite positron range acts to blur PET images (i.e., degrade spatial resolution), the range-related blurring is mitigated by the spectral distribution of positron energies for a given radioisotope as well as the characteristically tortuous path positrons travel [16, 17]; these effects are reflected by the fact the rms positron ranges are much shorter than the extrapolated positron ranges (Table 2). The radial distance the positron travels is thus considerably shorter than its actual path length. The overall effect of positron range on PET spatial resolution, $FWHM_{\mathrm{range}}$, is illustrated quantitatively in Fig. 7b [16]. The positron range degrades spatial resolution by only ~0.1 mm for ^{18}F (E_{max} = 0.640 MeV) and ~0.5 mm for ^{15}O (E_{max} = 1.72 MeV) [16]; these values are much shorter than the respective extrapolated positron ranges.

The second physics-related limitation on PET performance is the non-colinearity of the two annihilation photons: because a positron typically has some small residual (nonzero) momentum and kinetic energy at the end of its range, the two annihilation photons are not always emitted exactly back to back (i.e., 180° apart) but deviate from colinearity by an average of 0.25° [18]. The non-colinearity-related blurring, $FWHM_{180°}$, varies from

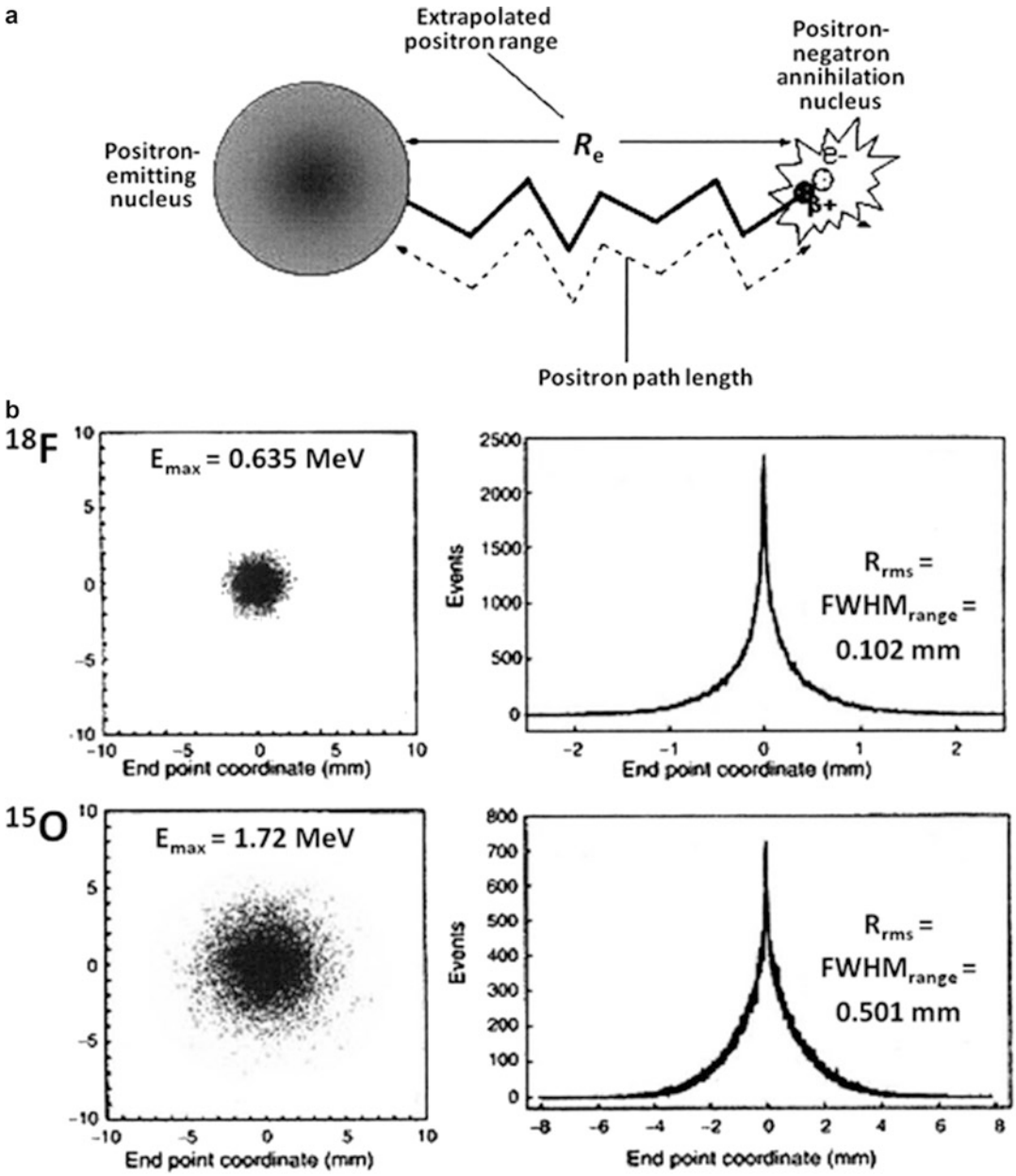

Fig. 7 Effect of positron range on PET spatial resolution. **a** Positrons travel a finite distance before undergoing annihilation, resulting in blurring of PET images. **b** The spatial dispersion of positron-electron annihilations for ^{18}F (E_{max} = 0.640 MeV) and ^{18}O (E_{max} = 1.72 MeV) as determined by Monte Carlo simulation. The annihilations for the higher-energy ^{18}O positrons are clearly more widely dispersed than those for the lower-energy ^{18}F positrons (*left panel*). A graphical representation of the resulting range-related blurring in PET, $FWHM_{range} = R_{rms}$: 1.03 mm and 4.14 mm for ^{18}F and ^{18}O, respectively (Reproduced from reference [16] with permission)

~2 mm for a 90-cm-diameter whole-body PET to ~0.7 mm for a 30-cm-diameter brain PET to ~0.3 mm for a 12-cm-diameter small-animal PET (Fig. 8) [11].

Among instrumentation-related determinants of overall spatial resolution are the intrinsic detector resolution and the depth-of-interaction effect. For discrete detector elements, the intrinsic

Table 2 Physical properties of positron-emitting radionuclides used in PET [1, 7, 70, 71]

						X- and γ-rays >0.25 MeV		
	Physical half-life	**β⁺ Branching** ratio	Maximum **β⁺** energy	**β⁺** Range in water[a] (mm)		Energy	Abundance	
Radionuclide	$T_{1/2}$	(%)	(MeV)	R_e	R_{rms}	(MeV)	(%)	Production
Carbon-11	20.4 min	99	0.96	3.9	0.4	N/A	0	Cyclotron
Nitrogen-13	9.96 min	100	1.2	5.1	0.6	N/A	0	Cyclotron
Oxygen-15	2.05 min	100	1.7	8.0	0.9	N/A	0	Cyclotron
Fluorine-18	1.83 h	97	0.64	2.3	0.2	N/A	0	Cyclotron
Copper-62	9.74 min	98	2.9	15	1.6	0.876-1.17	0.5	Generator (Zinc-62)
Copper-64	12.7 h	19	0.58	2.0	0.2	N/A	0	Cyclotron
Gallium-66	9.49 h	56	3.8	20	3.3	0.834-4.81	73	Cyclotron
Gallium-68	1.14 h	88	1.9	9.0	1.2	1.08 1.88	3.1	Generator (Germanium-68)
Bromine-76	16.1 h	54	3.7	19	3.2	0.473-3.60	146	Cyclotron
Rubidium-82	1.3 min	95%	3.4	18	2.6	0.777	13	Generator (Strontium-82)
Yttrium-86	14.7 h	32	1.4	6.0	0.7	0.440-1,920	240	Cyclotron
Zirconium-89	78.4 h	23	0.90	3.8	0.4	0.909 1.62-1.75	99 10	Cyclotron
Iodine-124	4.18 day	22	1.5	7.0	0.8	0.603-1.69	23	Cyclotron

[a] R_e is the maximum extrapolated range and R_{rms} the root-mean-square (i.e., mean) range of the β^+ particle in water and other soft tissue-equivalent media

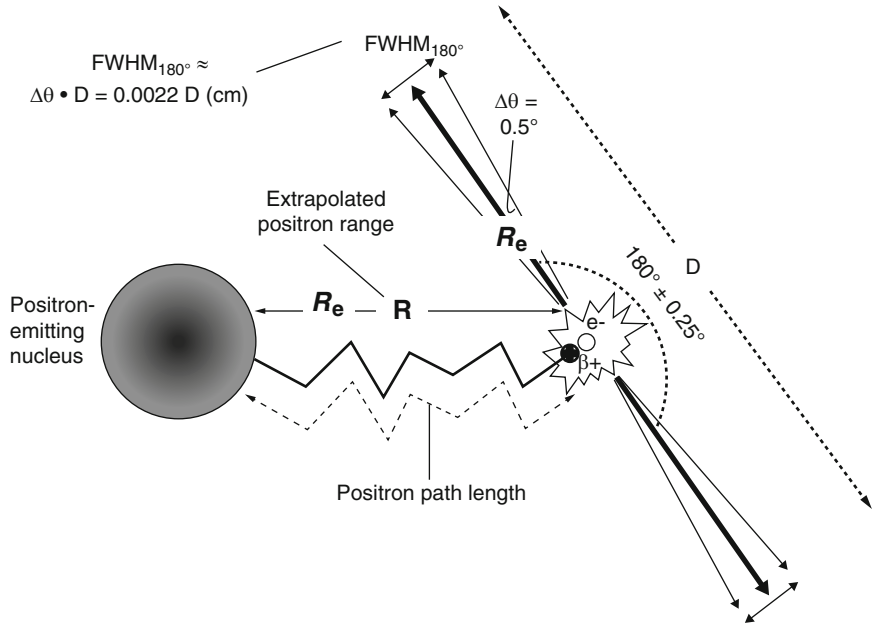

Fig. 8 Effects of the non-colinearity of the annihilation photons on PET spatial resolution. The 511-keV annihilation photons resulting from positron-electron annihilation are not always exactly colinear but may be emitted $180° \pm 0.25°$ apart [18]. The non-colinearity-related blurring, $FWHM_{180°}$, may be calculated geometrically and depends on the separation, D, of the coincidence detectors (Adapted from reference [11] with permission)

resolution, $FWHM_{\text{intrinsic}}$, is determined by the detector element width (d), increasing from $\frac{d}{2}$ midway between opposed coincidence detectors to d at the face of either detector [11].

For PET systems employing rings of discrete, small-area detectors, the depth (x) of the detector elements (2–3 cm) results in a degradation of spatial resolution termed the depth-of-interaction (DOI), or parallax, effect [11]. As illustrated in Fig. 9, with increasing radial offset of a source from the center of a detector ring, the effective detector width (d') and, with it, the intrinsic resolution, $FWHM_{\text{intrinsic}}$, increases [11]:

$$d' = d \cos\theta + x \sin\theta \tag{1}$$

and, along chords of the ring,

$$FWHM_{\text{intrinsic}} = \frac{d'}{2} \tag{2a}$$

$$= \frac{d}{2}\left(\cos\theta + \frac{x}{2}\sin\theta\right) \tag{2b}$$

where θ is the angular position of the coincident detector pair, d is the detector element width, and x is the detector element depth. In whole-body PET scanners, the detector depth (x) is typically 2–3 cm (20–30 mm), the detector width (d) about 4 mm, and the detector ring diameter about 80 cm (800 mm), and the DOI effect thus degrades spatial resolution by up to 50% at 10 cm from the center of the detector ring. Because the DOI effect decreases as the detector ring diameter increases (Fig. 9), clinical PET systems have detector rings substantially larger in diameter than that needed to accommodate patients. A variety of approaches have been developed to correct for the DOI effect in small-diameter, preclinical PET scanners, where the DOI effect is pronounced [11, 12, 19].

The spatial resolution at the center of the FOV (where the DOI effect is negligible) of a PET system, $FWHM_{\text{system}}$, can be obtained by combining the resolution of the respective components of the system:

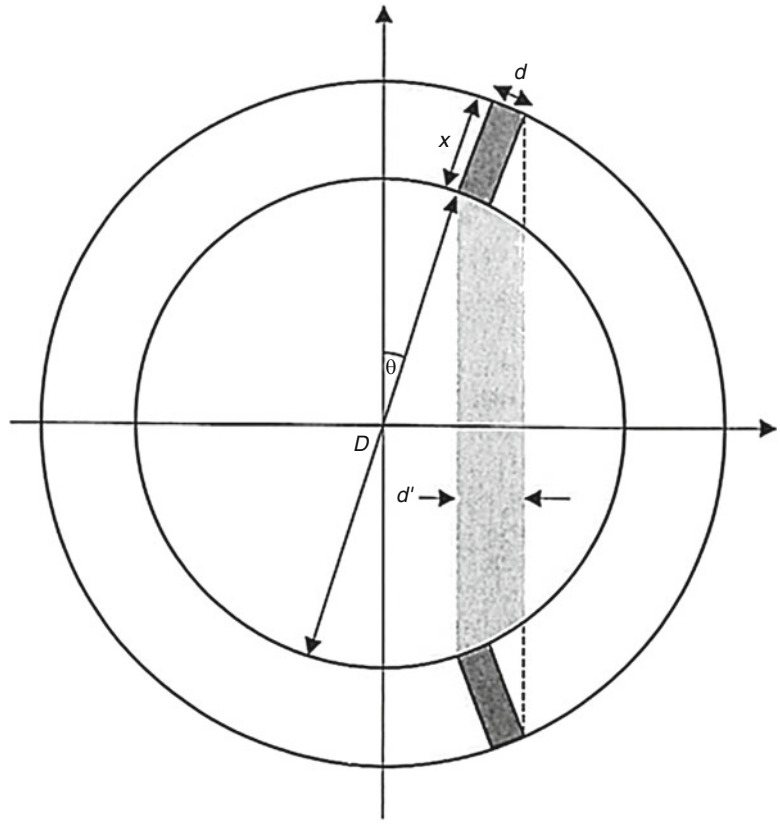

Fig. 9 The depth-of-interaction (DOI) effect. In PET scanners, the apparent width of a detector element, d′, increases with increasing radial offset from the center of the scanner. Because the depths with the detector elements at which the annihilation γ-rays interact are unknown, the apparent detector element width and therefore the effective line of response (i.e., the shaded volume) are wider than those corresponding to the actual detector element width d. The angle θ increases, and therefore the magnitude of this resolution-degrading effect, increases for sources offset further from the center of the rotation and for scanners with a smaller diameter D and a larger detector element depth x. (Reproduced from reference [11] with permission)

$$FWHM_{\text{system}} = \sqrt{FWHM_{\text{intrinsic}}{}^2 + FWHM_{\text{range}}{}^2 + FWHM_{180^\circ}{}^2} \quad (3)$$

Data "Corrections"

Even optimally performing PET scanners exhibit some nonuniformity of response [7, 20, 21]. Among the thousands of detector elements in a PET scanner, slight variations in detector thickness, light emission, optical coupling, electronic performance, etc. result in slightly different measured count rates for the same activity. In principle, such nonuniform response can be corrected by acquiring data from a uniform flux of γ-rays and normalizing to the *mean* count rate from all the LORs. This "normalization" table corrects for the nonuniform count rates among the individual LORs. One example of the effects of nonuniformity of scanner response and of the correction for nonuniform response is illustrated in Fig. 10 [20]. The normalization may be acquired using a positron-emitting rod source (e.g., germanium-68 (^{68}Ge)) spanning the entire axial FOV and rotating around the periphery of the FOV, exposing the detector pairs to a uniform photon flux per revolution. Alternatively, a uniform cylinder of a positron-emitting radionuclide can be scanned and the data thus acquired analytically corrected for attenuation; for a well-defined geometry such as a uniform cylindrical source, this correction is straightforward. However, for 3D PET, the contribution of and correction for scatter with such a large-volume source are nontrivial. Acquisition of the data required for uniformity correction is somewhat problematic in practice because of statistical considerations: typically, hundreds of millions (PET) of counts must be acquired to avoid possible "noise"-related artifacts in the uniformity correction table.

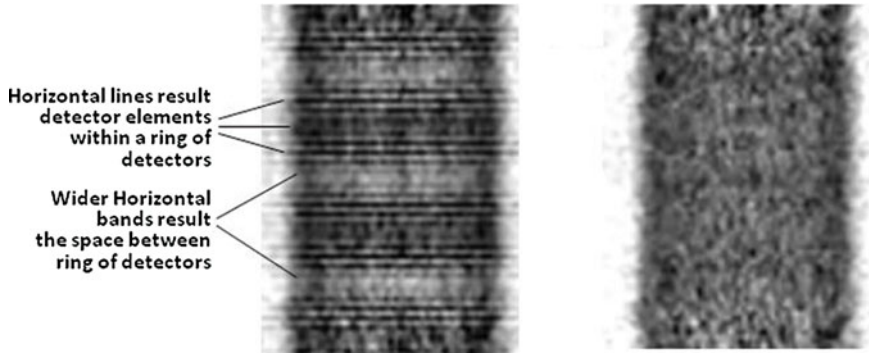

Fig. 10 Normalization (uniformity) corrections and their effects. Reconstructed PET images (coronal view) of a germanium-68 uniform-cylinder phantom without (*left panel*) and with (*right panel*) the normalization applied. The un-normalized (i.e., uncorrected) image has obvious artifacts attributable to the differences in sensitivities between direct and cross planes and the presence of separate rings of detectors. Appropriate normalization virtually eliminates these and other artifacts related to non-uniformity of the scanner response (From reference [20] with permission)

Radiation detectors are characterized by a finite "dead time" and associated count losses [11]. The dead time, typically of the order of 1–10 μsec, is the interval of time required for a counting system to record an event, during which additional events cannot be recorded. As a result, the measured count rate is systematically lower than the actual count rate. Such count losses are significant, however, only at "high" count rates (i.e., greater than ~100,000 counts per second (cps) per detector, which is of the order of the inverse of the dead time in seconds, for modern detectors). Real-time correction for dead time count losses is routinely applied in PET to the measured count rates, most commonly by scaling up the measured count rate based on an empirically derived mathematical relationship between measured and true count rates.

In PET, randoms increase the detected coincidence count rate by introducing mispositioned events and thus reduce image contrast and distort the relationship between image intensity and activity concentration [7]. One approach to random correction is the so-called delayed-window method, based on the fact that the random-coincidence photons are temporally uncorrelated (i.e., not simultaneously emitted) [22]. Briefly, once events in the coincidence timing window (typically ~10 ns or less) are detected, the number of events in a timing window equal in duration to, but much later (>50 ns later) than, the coincidence timing window is determined. More specifically, the coincidence timing window accepts events whose time difference is $\pm \tau$, while the delay window accepts events whose time difference is the delay $\pm \tau$. The number of events in the delayed timing window thus provides an estimate of the number of randoms in the coincidence timing window. Real-time subtraction of the delayed-window counts from the coincidence-window counts for each LOR thus corrects for randoms.

Another random-correction method, the "singles" method, uses the measured singles count rate for each detector and the coincidence timing window τ to calculate the random rate for each pair of coincidence detectors [23]. This approach does not require a separate measurement in a delayed-coincidence window and thus lessens the data-processing requirements on the coincidence electronics. Further, because the singles count rate is typically at least an order of magnitude higher than the coincidence-event count rate, the statistical uncertainty (noise) in the estimate of the number of randoms is much smaller than that in the number of prompt coincidences. The singles method is thus the method of choice for random correction in modern PET scanners.

Scatter results in generally diffuse background counts in reconstructed images, like randoms,

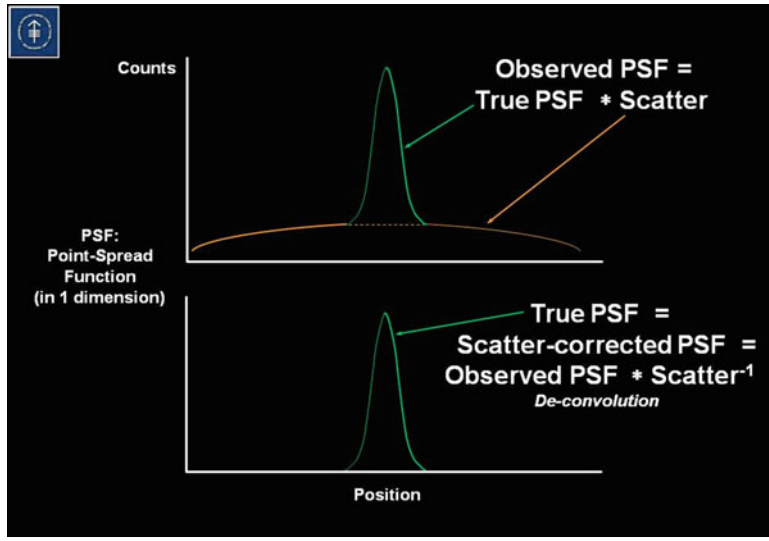

Fig. 11 The "Gaussian-fit" scatter-correction method. In practice, the point-spread function (PSF) of a PET scanner includes both primary (unscattered) and scattered counts, with the former corresponding to the Gaussian, or bell-shaped, curve and the latter corresponding to the peripheral tails extending from the Gaussian curve. The tails can be subtracted (deconvolved) from the total PSF to yield scatter-corrected PSF. In a similar manner, this scatter correction can be applied to projection images prior to reconstruction to yield scatter-corrected reconstructed images

reducing contrast and distorting the relationship between image intensity and activity concentration [24–26]. Scatter as a portion of the total PET events is far more abundant in 3D than in 2D PET (especially for body imaging of larger (i.e., adult) patients), and its correction is more challenging in 3D than in 2D PET. Perhaps the simplest scatter correction method is the "Gaussian-fit" technique [27, 28] (Fig. 11). Once the random correction has been applied, the peripheral "tails" in the projection-image count profiles, presumably due to scatter, are fit to a mathematical function and then subtracted (or deconvolved) from the measured profile to yield scatter-corrected profiles for tomographic image reconstruction. While this approach works reasonably well for 2D PET and small source volumes (e.g., the brain) in 3D PET, it is not adequate for 3D PET generally. Scatter corrections for 3D PET include dual-energy window-based approaches, convolution-/deconvolution-based approaches (analogous to the correction in 2D PET), direct estimation of scatter distribution (by computer modeling of the imaging system), and iterative reconstruction-based scatter compensation approaches (also employing computer modeling) [25, 26].

The correction for the attenuation of the photons as they pass through tissue is generally the largest correction in PET. The correction factors can range up to ~15 for a PET scan of the abdomen (equivalent to a 30-cm diameter water-equivalent cylinder). The magnitude of the correction depends on the energy of the photons (511 keV for PET studies), the thickness of tissue(s) that the photons must travel through, and the attenuation characteristics of the tissue(s). One of the attractive features of PET is the relative ease of applying accurate corrections for attenuation, based on the fact that attenuation depends only on the total thickness of the attenuation medium (at least for a uniformly attenuating medium) (Fig. 12). For a positron-emitting source and a volume of thickness L, the attenuation factor is $e^{-\mu L}$ and the attenuation correction factor $e^{\mu L}$ regardless of the position (i.e., depth) of the source. Accordingly, if a rod source of a positron emitter such as ^{68}Ge is extended along the axial FOV and rotated around the periphery of the FOV first with and then without the subject in the imaging position – the

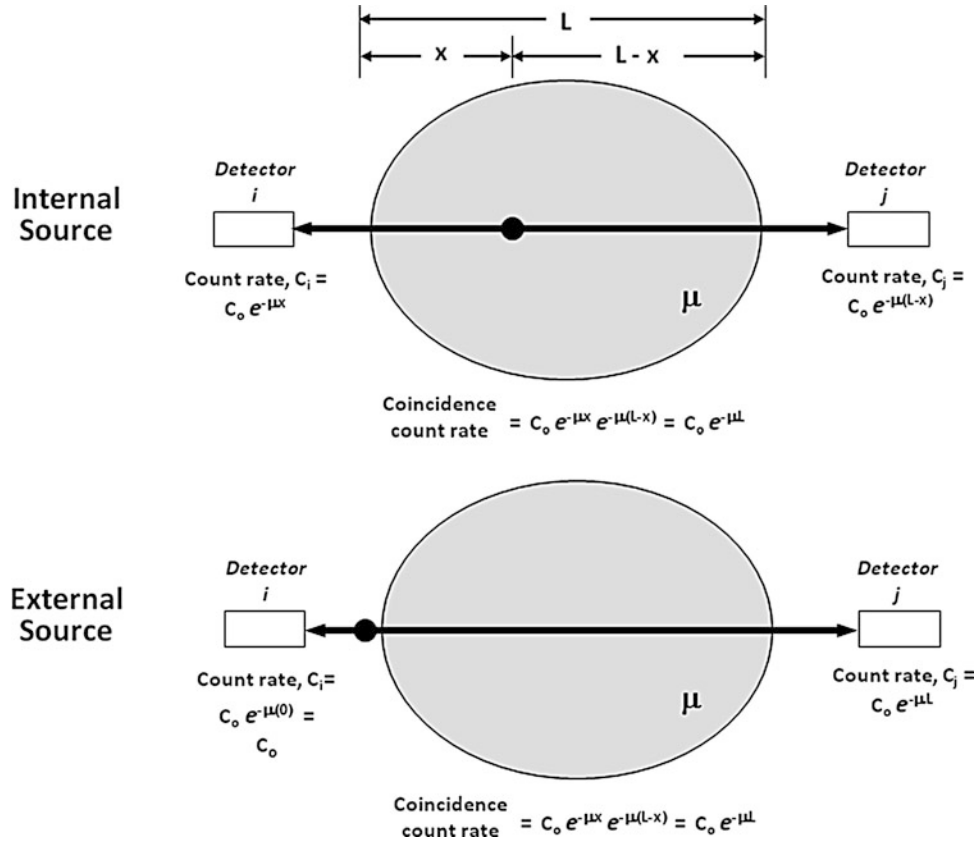

Fig. 12 In PET, attenuation of the annihilation photons for a uniformly attenuating medium depends only on the total thickness (L) of the absorber, that is, it is independent of the position (depth x) of the source in the absorber (*upper panel*). An external positron emitter can therefore be used for attenuation correction (*lower panel*). C_o is the actual source count rate, and C_i and C_j are the count rates measured by detectors i and j, respectively; μ is the linear attenuation coefficient of the absorber for 511-keV photons (Adapted from reference [7] with permission)

transmission and the blank scans, respectively – the attenuation correction factor (*ACF*) can be derived from the ratio of the counts in these respective scans:

$$ACF_{ij} = e^{\mu L}ij \tag{4}$$

$$= \frac{\left[(C)_{Blank}\right]_{ij}}{\left[(C)_{Trans}\right]_{ij}} \tag{5}$$

where ACF_{ij} is the attenuation correction factor between coincident detectors *i* and *j*, L_{ij} is the thickness of the volume between coincident detectors *i* and *j*, and $((C)_{Blank})_{ij}$ and $((C)_{Trans})_{ij}$ are the external-source counts between detectors *i* and *j* in the blank and transmission scans, respectively. In practice, a blank scan is acquired only once a day. The transmission scan can be acquired before the subject has been injected with the radiotracer, after the subject has been injected with the radiotracer but before or after the emission scan, or after the patient has been injected with the radiotracer and at the same time as the emission scan. Preinjection transmission scanning avoids any interference between the emission and transmission data but requires that the subject remain on the imaging table before, during, and after injection of the radiotracer. It is the least efficient operationally and is rarely used in practice. Postinjection transmission scanning minimizes the effects of motion, relying on the much higher external-source count rates for reliable

subtraction of the emission counts from the transmission counts. It was the most commonly used approach in "PET-only" scanners. Simultaneous emission/transmission scanning is obviously the most efficient (fastest) approach but may result in excessively high randoms and scatter counter rates in the emission data.

With the introduction of hybrid PET/CT scanners, attenuation correction is now performed using CT rather than transmission sources. A CT image is basically a two-dimensional map of attenuation coefficients at the CT X-ray energy (~80 keV). For attenuation correction of the PET emission data, however, these must be appropriately scaled to the 511-keV energy of the annihilation photons. The mass-attenuation coefficients (μ_m) for CT X-rays (~80 keV) and for 511-keV annihilation photons are 0.182 and 0.096 cm^2/gm, 0.209 and 0.093 cm^2/gm, and 0.167 and 0.087 cm^2/gm in soft tissue, bone, and lung, respectively. The corresponding μ_m ratios are therefore 1.90, 2.26, and 1.92, respectively. Thus, ACFs derived from CT images cannot be scaled to those for 511-keV annihilation photons simply using a single global factor. Accordingly, CT-based attenuation correction in PET has been implemented using a combination of segmentation (to delineate soft tissue, bone, and lung compartments) and variable scaling (to account for the different μ_m ratios in these respective tissues).

Noise-Equivalent Count Rate (NECR)

A PET scanner actually measures a so-called prompt coincidence count rate (R_{prompt}) that comprises true, scatter, and random coincidence count rates (R_{true}, $R_{scatter}$, and R_{random}, respectively):

$$R_{true} = R_{prompt} - R_{scatter} - R_{random} \qquad (6)$$

The noise-equivalent count rate (NECR) is a commonly cited performance parameter of PET scanners which accounts for the additional statistical noise introduced by the corrections for randoms and scatter (see below) [29]. It is defined as the equivalent count rate that yields the same noise level as the observed count rate after correction for randoms and scatter:

$$\mathrm{NECR} = \frac{{R_{true}}^2}{R_{true} + aR_{scatter} + bR_{random}} \qquad (7)$$

where a is the fraction of each projection that is occupied by the object being imaged and b equals 1 or 2 if the singles method or the delayed-windows method, respectively, is used for random correction. A typical plot of the NECR as function of the activity concentration is shown in Fig. 13. Because the NECR depends on the size of the object being imaged (as indicated by parameter a in Eq. 7), the plot in Fig. 13 is

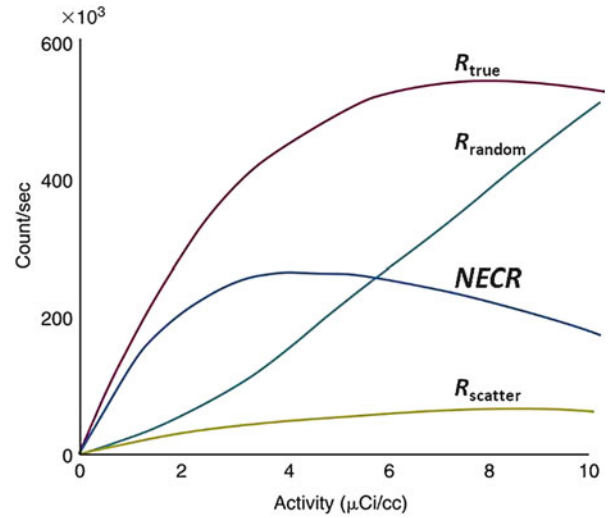

Fig. 13 The NECR and the true, scatter, and random coincidence count rates (R_{true}, $R_{scatter}$, and R_{random}, respectively) as functions of activity concentration in the fields of view for a typical clinical whole-body 3D PET scanner. The NECR indicates that the best signal-to-noise ratio is achieved at an activity concentration of ~4 μCi/cc (Adapted from reference [29] with permission)

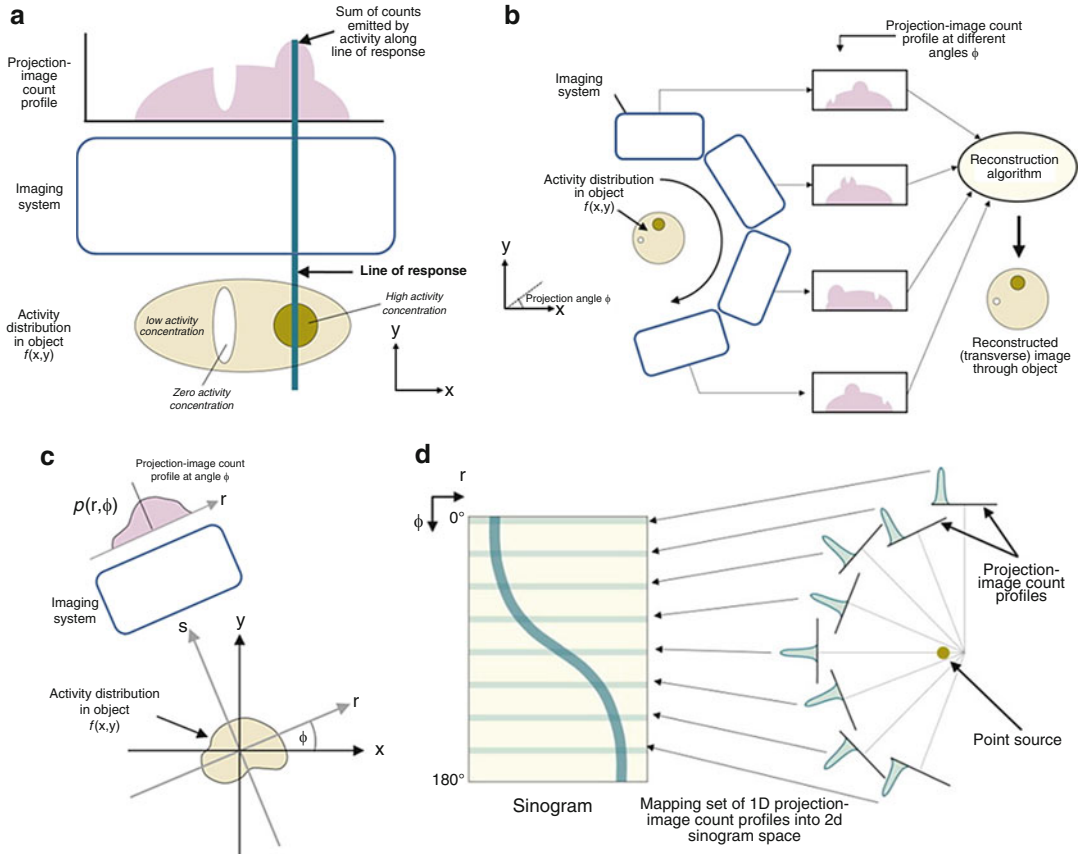

Fig. 14 Emission tomography data acquisition and sinogram display. **a** Projection-image count profile under idealized conditions (such as no attenuation or scatter). **b** Acquisition of multiple projection images and their corresponding count profiles at various projection angles ϕ about the longitudinal axis of the object being imaged. **c** The (*r*, *s*) coordinate system is rotated by projection angle ϕ with respect to the (*x*.*y*) coordinate system of the cross-section of the object being imaged. The (*r*, *s*) coordinate system is fixed with respect to the imaging system and the (*x*.*y*) coordinate system is fixed with respect to the object. **d** Two-dimensional (2D) count display, or sinogram, of a set of projection-image count profiles. Each row in the sinogram corresponds to an individual projection-image count profile, displayed for increasing projection-image angle ϕ from top to bottom. As shown, a point source of radioactivity traces out a sinusoidal path in the sinogram (Adapted from reference [29] with permission)

neither unique nor unambiguous for a particular scanner. Nonetheless, for purposes of comparison of the performance among scanners, a standard phantom can be used for derivation of the activity concentration-dependent NECR.

Image Reconstruction

In emission tomography generally, the emission data which are reconstructed to yield the tomographic images correspond to the projected sum of counts (or parallel-ray integrals) in two dimensions at various angles about the axis of the scanner (Fig. 14). In 3D PET, the projections correspond to a set of two-dimensional (x_r, y_r) integrals with azimuthal angle ϕ *and* oblique, or polar, angle θ (Fig. 15) [30]. (Correction of the emission data after the real-time dead time and random corrections and before image reconstruction – namely, normalization, scatter correction, and then attenuation correction – is typically performed in sinogram space (Fig. 14d).) The first step in deriving the 2D parallel-ray

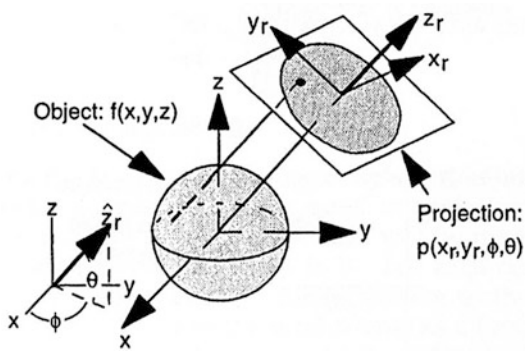

Fig. 15 In 3D PET, the projections are two-dimensional (x_r, y_r) parallel line integrals with azimuthal angle ϕ and oblique angle θ. The 3D projection data are represented as a set of sinograms, with one sinogram per polar angle θ, each row representing the projected intensity across a single polar angle θ and each column the projected intensity at the same position x_r across the projection at successive azimuthal angles ϕ (From reference [30] with permission)

projection-image data is to re-bin the 3D PET data set into a 2D data set such that each oblique (or indirect) projection ray is placed within the data for a particular non-oblique (or direct) transverse slice. The simplest approach to 3D-to-2D re-binning is known as "single-slice re-binning (SSRB)," wherein an oblique projection ray between a detector at axial position a and a detector at axial position b is positioned as if it were a projection from a directly opposed detector pair midway between these detectors (i.e., at axial position $(a + b)/2$) (Fig. 16a) [29, 31]. For projection rays at a large angle with respect to the transverse planes (i.e., corresponding to LORs between detectors located at opposite ends of the gantry), significant repositioning errors and degraded tomographic image quality result. SSRB has been replaced, therefore, with a more sophisticated and more accurate repositioning technique known as Fourier re-binning [32, 33] (Fig. 16b). In contrast to SSRB, however, Fourier re-binning cannot be performed in real-time and thus requires the full 3D data set.

Once the 3D data have thus been re-binned into 2D data, the resulting 2D fanbeam data must then be reformatted into parallel-beam data for the actual image reconstruction. The procedure for creating parallel-beam projections from fanbeam projections is shown in Fig. 17a. The resulting parallel-ray spacing Δx_r is given by:

$$\Delta x_r = \Delta d_t \sqrt{1 - \left(\frac{X_r}{R_D}\right)^2} \tag{8}$$

where $\Delta d_t = \frac{2\pi R_D}{N_D}$ is the center-to-center detector spacing of the detector elements in the transverse plane, R_D is the radius of the transaxial detector ring, and N_D is the number of detector elements in a single transaxial detector ring (Fig. 17b). Thus, as a result of the curvature of the PET gantry, the parallel-ray spacing decreases with increasing distance from the center of the detector ring. Near the center of the detector ring (i.e., for $x_r << R_D$), Δx_r can be equated with Δd_t; toward the periphery of the detector ring, however, interpolation must be performed to yield uniform parallel-ray spacing across detector gantry. This is known as the "arc correction."

The foregoing 2D parallel-beam data derived from the PET emission data (i.e., the 3D fanbeam data) can then be reconstructed into the tomographic images. There are two basic classes of image-reconstruction methods, analytic and iterative. Historically, perhaps the most widely used analytic algorithm for reconstruction of tomographic images from 2D data (or 3D data re-binned into 2D projections) has been filtered back projection (FBP) [21, 30]. In PET, however, FBP has been replaced by iterative reconstruction methods. FBP is still used rather widely in single-photon emission computed tomography (SPECT) and is discussed in ▶ Chap. 11, "Instrumentation for Single-Photon Emission Imaging". Iterative algorithms [33] attempt to progressively refine estimates of the activity distribution, rather than directly calculating the distribution, by maximizing or minimizing some "target function." The solution is said to "converge" when the difference of the target function between successive estimates (iterations) of the activity distribution is less than some prespecified value. Importantly, iterative reconstruction algorithms allow incorporation of realistic modeling of the data acquisition process (including effects of attenuation and of scatter), modeling of statistical noise,

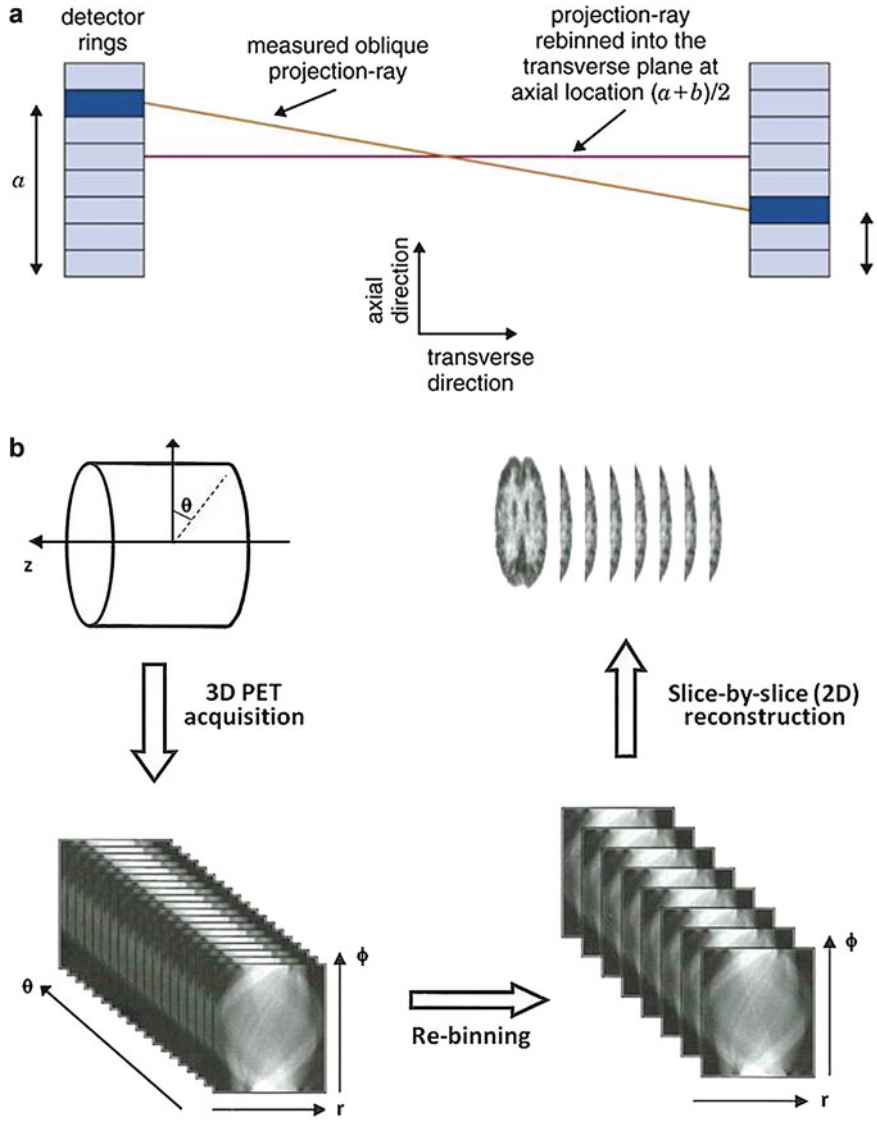

Fig. 16 **a** The single-slice re-binning algorithm in which an oblique (i.e., indirect) projection ray between detector pairs a and b is placed within the projection data for a non-oblique (i.e., direct) slice corresponding to a traverse detector pair at axial location $(a + b)/2$ (from reference [29] with permission). **b** The Fourier re-binning algorithm for re-binning 3D PET data into 2D data. The basic steps of Fourier re-binning are creating a stack of oblique sinograms, calculating the 2D Fourier transform for each oblique sinogram, normalizing the resulting 2D sinogram for the number of oblique slices contributing to the oblique sinogram, and calculating the 2D inverse Fourier transform of the resulting normalized sinograms to yield the 2D re-binned data for image reconstruction (From reference [33] with permission)

and inclusion of pertinent a priori information (e.g., only nonnegative count values). The maximum-likelihood expectation maximization (MLEM) algorithm is based on maximizing the logarithm of a Poisson-likelihood target function [34, 35]. The MLEM algorithm suppresses statistical noise, but large numbers of iterations typically are required for convergence, and therefore processing times are long. To accelerate this slow convergence, the ordered-subset expectation maximization (OSEM)

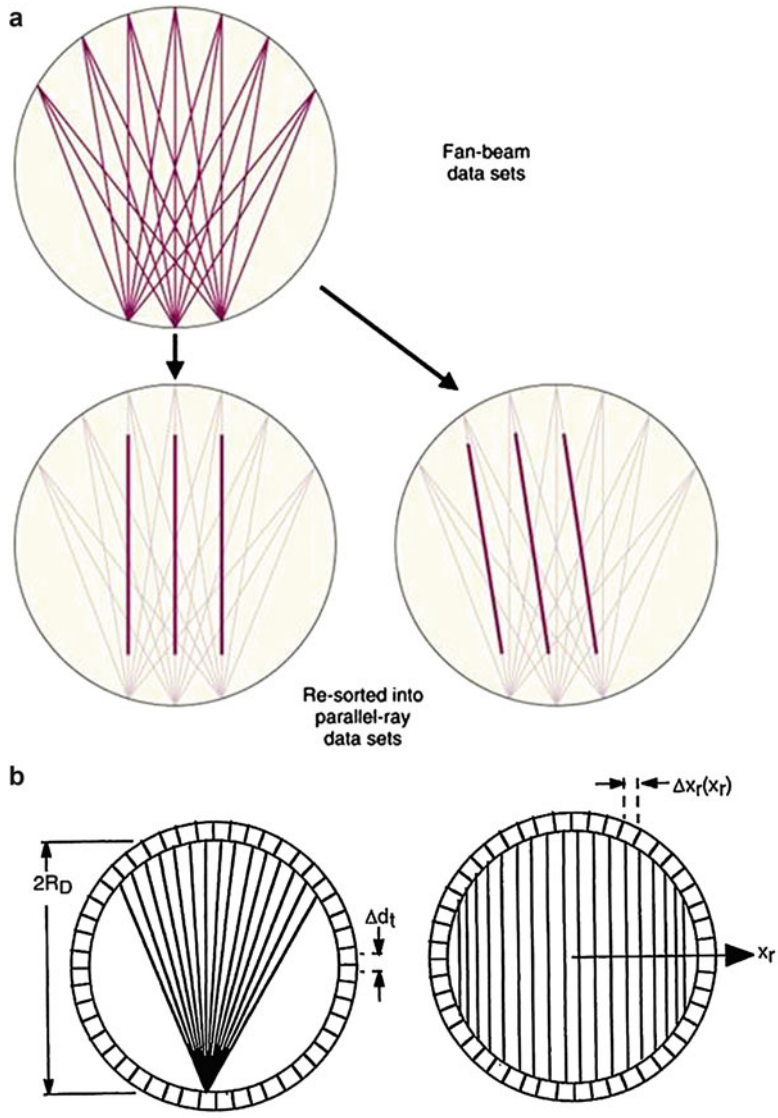

Fig. 17 **a** Procedure for creating parallel-beam projections from fanbeam projections (from reference [29] with permission). **b** Nonuniform parallel-ray spacing when creating parallel-beam projections from fanbeam projections, necessitating the so-called arc correction. (From reference [30] with permission)

algorithm [36] groups the projection data into subsets comprised of projections uniformly distributed around the source volume. The OSEM algorithm, which is a modified version of the MLEM algorithm in that the target is still maximization of the log-likelihood function, converges more rapidly than MLEM and is now the most widely used iterative reconstruction method in PET as well as SPECT [37].

In practice, OSEM is usually stopped after a relatively small number of iterations and post-filtered to dampen image noise and therefore may not achieve optimal quantitation accuracy. As an alternative to OSEM, Ahn et al., among others, have recently implemented a penalized likelihood (PL) image reconstruction algorithm in order to improve quantitation accuracy without compromising visual image quality [38]. Preliminary studies have demonstrated visual image quality including lesion conspicuity in images reconstructed by the PL algorithm is better than or at least as good as that in OSEM-reconstructed images. Despite the benefits, PL methods have not yet been widely adopted in clinical PET. Besides

computational time and complexity, the limited use of such methods in clinical PET may be that it has not been convincingly demonstrated that PL methods can provide improved quantitation accuracy compared to OSEM while maintaining clinically acceptable visual image quality.

The row-action maximization-likelihood algorithm (RAMLA), related to the OSEM algorithm, has been implemented for direct reconstruction of 3D PET data. The so-called 3D-RAMLA, which eliminates 2D re-binning of the 3D data, employs partially overlapping, spherically symmetric volume elements called "blobs" in place of voxels [37, 39, 40]. Reconstruction times are fairly long by clinical standards but the results have been excellent [41].

An important, recently introduced feature of iterative reconstruction is the 3D modeling of the scanner-specific point-spread function (PSF) map. Scanner spatial resolution deteriorates toward the periphery of the FOV but can be modeled in image reconstruction to not only improve the uniformity of spatial resolution across the FOV but also to improve spatial resolution overall. This correction is known as "resolution recovery" and is now available on most modern PET scanners. Effective tomographic image resolution as low as 2 mm has been achieved using resolution recovery.

Quantitation

Once the emission data have been corrected for dead time, randoms, system response (by normalization), scatter, and attenuation, the count rate per voxel in the reconstructed tomographic images is proportional to the local activity concentration. A factor which adversely effects the quantitative accuracy of PET is partial-volume averaging: for a source which is "small" relative to the spatial resolution of the imaging system, the image-derived activity or activity concentration in such a source underestimates the actual value, and the smaller the source, the greater the degree of the underestimation [24, 42]. The dimensions of a source must be at least two times the FWHM spatial resolution of the imaging system to avoid such underestimation of the activity or activity concentration [42]. Since the source-size dependence of the partial-volume effect can be measured (e.g., by phantom studies), the underestimated activity or activity concentration can be corrected if the source dimensions can be independently determined (e.g., by CT) [43]. Another key factor which limits the quantitative accuracy of SPECT and PET is subject motion. As in photography, subject motion blurs PET images, dispersing the counts in a source region over an apparently larger volume than the actual volume of that region. This results not only in an overestimate of the source region volume but also an underestimate of the source region activity concentration. For sources (e.g., tumors) in the lung and the dome of the liver, a particularly important source of such inaccuracies is respiratory motion [44–47]. Practical, reasonably accurate methods for respiratory gating of PET studies have been developed and result in more reliable estimates of the volumes and activity concentrations in pulmonary lesions [44–47].

To make the images absolutely quantitative, the count rate per voxel (cps), $\dot{C}_{ijk}$, in voxel *ijk* must be divided by a measured system calibration factor ((μCi/cc)/(cps/voxel)), CF, to yield the activity concentration [7]:

$$\{A\}_{ijk} = \frac{\dot{C}_{ijk}}{CF} \tag{9}$$

where $\{A\}_{ijk}$ is the activity concentration (e.g., μCi/cc) in voxel *ijk*. The calibration factor (CF) can be derived by scanning a calibrated standard, that is, a water-filled or water (tissue)-equivalent volume source with all linear dimensions at least twice that of the system spatial resolution and with a uniform, well-defined activity concentration at the time of the scan. The requirement for water equivalence is to ensure that effects such as scatter and attenuation are comparable in both the subject and the standard. And the requirement for linear dimensions at least twice that of the system spatial resolution is to ensure that the effect of partial-volume averaging and associated underestimation of local count rates is negligible. Activity concentration

is often expressed in terms of the decay-corrected fraction or percent of the administered activity per cubic centimeter (cc) or, more commonly in clinical PET, in terms of the standard uptake value (*SUV*):

$$SUV = \frac{\mu\text{Ci/cc of tissue}}{\mu\text{Ci injected/gm body mass}} \qquad (10)$$

An advantage of using *SUV* to express activity concentration is that, in first order, it is independent of the body mass of the subject.

The practical quantitative accuracy of PET (expressed, e.g., as the percent difference between the image-derived and actual activity or activity concentration in a source region) is difficult to characterize unambiguously, as it depends on such factors as the count statistics, the size of the source region, the source-to-background activity concentration ratio, the subject motion, and the accuracy of all applicable corrections. Under favorable circumstances (i.e., for a high-count study of a large, stationery source region with a high source-to-background ratio), the accuracy of the PET is of the order of 10% [42].

Multimodality Devices

Image registration and fusion have become increasingly important components of both clinical and laboratory imaging and have led to the development of a variety of pertinent software and hardware tools, including multimodality devices which transparently provide registered and fused 3D image sets [48–52]. In addition to anatomic localization of signal foci, image registration and fusion provide intra- as well as inter-modality corroboration of diverse images and more accurate and more certain diagnostic and treatment-monitoring information. There are two practical approaches to image registration and fusion, "software" and "hardware" approaches. In the software approach, images are acquired on separate devices, imported into a common image-processing computer platform, and registered and fused using the appropriate software. In the hardware approach, images are acquired on a single, multimodality device and transparently registered and fused with the manufacturer's integrated software. Both approaches are dependent on software sufficiently robust to recognize and import diverse image formats. The availability of industry-wide standard formats, such as the ACR-NEMA DICOM standard (i.e., the American College of Radiology (ACR) and National Electrical Manufacturers Association (NEMA) for Digital Imaging and Communications in Medicine (DICOM) standard [53, 54]), is therefore critical.

PET/MRI. All manufacturers of PET and CT scanners market multimodality scanners, combining PET with CT scanners in a single device. These instruments provide near-perfect registration of images of in vivo function (PET) and anatomy (CT) using a measured, and presumably fixed, rigid transformation (i.e., translation and rotation in three dimensions) between the image sets. The rigid transformation matrix can be used to align the PET and the CT image sets. This matrix can be measured using a phantom, that is, an inanimate object with PET- and CT-visible landmarks arranged in a well-defined geometry. The transformation matrix required to align these landmarks can then be stored and used to automatically register *all* subsequent multimodality studies, since the device's geometry and therefore this matrix should be fixed. Although generally encased in a single seamless housing, the PET and CT gantries in such multimodality devices are separate; the respective fields of view are separated by a distance of the order of 1 m, and the PET and CT scans are performed sequentially.

PET/MRI. Despite its unquestioned clinical utility, PET/CT has certain notable shortcomings, including the inability to perform simultaneous data acquisition, the significant radiation dose to the patient contributed by CT, and the inability of non-contrast CT to distinguish different soft tissues [55–57]. Compared to CT, MRI provides not only better contrast among soft tissues but also functional imaging capabilities. The combination of PET/MRI may thus provide advantages which go well beyond simply combining functional

information with structural MRI information. Among multimodality imaging studies, therefore, PET/MRI may ultimately provide the greatest yield of information by combining the quantitative molecular imaging capabilities of PET (including the large number and variety of radiotracers) with the excellent anatomic resolution, marked soft tissue contrast, and functional imaging capabilities provided by MRI (e.g., perfusion by dynamic contrast-enhanced (DCE) imaging) and magnetic resonance spectroscopic imaging (MRSI) (e.g., quantitation of regional concentrations of metabolites such as lactate, citrate, and choline) [55–57].

As noted, an important advantage of PET/MRI is that the image data can be acquired *simultaneously* because the PET and MR imaging signals (i.e., gamma- or X-rays and radiofrequency (RF) waves, respectively) do not interfere with one another. Registration of sequentially acquired functional and structural images is very forgiving of the short time interval (typically only several minutes) between the PET and CT scans, as anatomy does not actually change over such short time intervals (except, perhaps, for filling of the urinary bladder, transit of gas through the bowel, etc.). Registration of sequentially acquired functional images, however, is potentially more problematic, as functional properties, such as blood flow, hypoxia, neuronal activation, etc., may change transiently over time frames of minutes and even seconds. However, many technical challenges, related to possible interference between the modalities' hardware, have to be solved when combining PET and MRI [55, 57–65]. Most notably, conventional PET and SPECT detectors are based on PMTs, which do not operate properly in the presence of a magnetic field, and various approaches have been pursued to overcome this and other challenges in combining nuclear and MR modalities. The most straightforward approach is placement of the PET and MR scanners in series in a manner analogous to current PET/CT devices. However, this would require magnetic shielding of the PET scanner and/or imposition of a relatively large distance between the PET and MR scanners. Further, because data acquisition for PET and MRI individually is time-consuming, sequential imaging may result in prohibitively long overall study times (well over 1 h) in a clinical setting. Space constraints are also a consideration. Most importantly, physical separation of the scanners would eliminate the ability to perform the nuclear and MR scans simultaneously, which, as noted, is perhaps the most compelling feature of such hybrid devices. The preferable approach, therefore, is integration of the PET hardware into the MR gantry.

Due to its various hardware components, the PET subsystem can interfere with the performance of the MRI subsystem by compromising the homogeneity of the MRI's main magnetic field and the RF field and thereby degrade MR image quality. BGO and LSO crystals, for example, produce only minor magnetic-field distortion, while GSO and LYSO have sharply different magnetic susceptibilities than tissue and thus markedly distort MR images. At the same time, the variable MR gradients may induce eddy currents in conductive materials of the nuclear detectors and distort the effective applied gradient field. As noted, the effects of the high magnetic fields of the MR subsystem exclude the use of PMTs employed in conventional PET detectors, as the path of the electrons between the dynodes in the evacuated PMT is deflected from their normal trajectory by the external magnetic field [55, 66]. In addition, the RF fields and also the gradient system pulses of the MR subsystem can degrade the performance of and even damage the PET electronics. One approach to overcoming this limitation is the use of long optical fibers (up to several meters in length) to couple the detector crystal to a PMT positioned outside the MR subsystem's fringe field (i.e., at magnetic fields of no greater than 10 mT). In this way, only the X-ray and γ-ray detection elements lie within the magnetic field, and the scintillations are directed out of the field by the fibers. Despite the challenges presented by such systems, including the large number of optical fibers required (one per detector element) and partial loss of the light signal over the length of the fibers, several prototypes of such PET/MRI scanners (with field strengths up to 3 T) have been fabricated.

An alternative, and ultimately more practical approach, to PET/MRI is elimination of the PMTs

altogether by using solid-state scintillation detectors such as APDs or SiPMs. APDs and SiPMs are relatively insensitive to magnetic fields and thus can be coupled directly to the scintillation detector blocks via conventional (i.e., short) light guides. It is still important, however, to provide RF shielding of the PET subsystem components within the magnetic field, for example, using copper mesh.

MR images do not directly provide attenuation information, and in PET/MR systems, the attenuation correction maps must therefore be estimated indirectly. Software methods have been proposed for MR-based attenuation correction, based on image segmentation or co-registration of templates with preassigned tissue-specific attenuation coefficients. A method proposed by Martinez-Moeller et al. has been utilized in clinical systems, with a two-point Dixon VIBE MR sequence to obtain fat and water compartments for calculating attenuation. Lung tissue in the MR images is identified by image segmentation. Software-constructed attenuation maps obtained from MR may not reflect true photon attenuation, since several classes of tissue can be defined. In addition, the actual attenuation coefficients may be different than standard assumed values.

Commercial Devices

Clinical. All of the major manufacturers of medical imaging equipment, including General Electric, Philips, Siemens, and Toshiba, currently market clinical PET devices (Tables 4 and 5, respectively). Since 2005, PET scanners have been marketed exclusively as multimodality (i.e., PET/CT) scanners; clinical "PET-only" scanners are no longer marketed. The PET subsystems of commercial PET/CT scanners utilize BGO, LSO, or LYSO as the detector material, with most now operating exclusively in 3D mode and all except the BGO-based systems incorporating TOF capability. The dimensions of the detector elements are typically $4 \times 4 \times 20$ mm^3, though slightly larger-area and thicker detector elements are found in some units. The axial fields of view are typically 20 cm in length, and whole-body studies therefore require six or seven bed positions. PET system spatial resolution (FWHM) is of the order 5 mm among clinical systems. The design and performance parameters of the PET subsystem of currently marketed clinical whole-body PET/CT scanners are summarized in Table 3 [5].

Several "special-purpose" clinical scanners have been marketed as well. These include positron emission mammographs (PEMs) [67]. The PEM Flex Solo II (Naviscan PET Systems, Inc.) [68] is a limited-angle, focal-plane tomography system with two opposed 6×16.4-cm^2 LYSO detectors ($2 \times 2 \times 13$-mm^3 detector elements) backed by PSPMTs and mounted inside compression paddles for immobilization and compression of the breast. The detectors, mounted on an articulating arm that rotates to allow imaging from different views, can scan up to 24 cm across the FOV in the direction of their 6-cm dimension, yielding a maximum FOV of 24×16.4 cm^2. The PEM Flex Solo II, with an in-plane spatial resolution of ~2.5 mm, thus differs markedly from conventional PET scanners in that the detectors do not encircle the object (in this case, the breast) being imaged.

At least two PET/MRI systems capable of simultaneously collecting MR and PET image data with almost no degradation of either MR or PET performance are now commercially available from Siemens and General Electric [5]. As previously discussed, simultaneous acquisition of MR and PET data presents significant engineering challenges due to cross interference between PET and MR hardware. To minimize this cross interference in the PET subsystem, PMTs are replaced with APDs and SiPMs in the Siemens and General Electric systems, respectively. The Siemens mMR™ system is based on a Verio™ MR scanner with a modified body radiofrequency (RF) coil, gradient coil, and patient-handling system. In this system, the APD PET detectors are arrayed around a cylinder that is inserted into the bore of the MR scanner, reducing the bore diameter from 70 to 60 cm. LSO scintillator crystals ($4 \times 4 \times 20$ mm^3) are arranged in eight rings of 56 blocks comprised of 8×8 crystals backed by a 3×3 array of APDs per block. The MR

Table 3 Design and performance parameters of the PET subsystem in current commercially available clinical PET/CT scanners [5]

PET/CT model	Ingenuity TF	Discovery 710	Biograph mCT flow (TrueV)	Discovery IQ (5 rings)	Vereos
Patient port (cm)	70 Open view	70	78	70	70
CT (slices)	64, 128	16, 64, 128	20, 40, 64	16	64, 128
Patient scan range (cm)	190	200	195	200	190
Maximum patient weight (kg [lb])	195 (430)	226 (500)	226 (500)	226 (500)	195 (430)
Acquisition modes	3D S&S	3D S&S	3D S&S and continuous	3D S&S	3D S&S
Number of image planes	45 or 90	47	109	79	72
Plane spacing (mm)	2 or 4	3.27	2	3.27	1, 2, or 4
Crystal size (mm^3)	4 × 4 × 22	4.2 × 6.3 × 25	4 × 4 × 20	6.3 × 6.3 × 30	4 × 4 × 22
Number of crystals	28,336	13,824	32,448	19,200	23,040
Number of PMTs	420	256	768	720	SiPM
Physical axial FOV (cm)	18	15.7	21.8	26	16.3
Detector material	LYSO	LYSO	LSO	BGO	LYSO
System sensitivity (%)	0.74	0.75	0.95	2.2	2.2[b]
Transaxial resolution at 1 cm (mm)[a]	4.7	4.9	4.4	4.9	4.0
Transaxial resolution at 10 cm (mm)[a]	5.2	5.5	4.9	5.5	4.5
Axial resolution at 1 cm (mm)[a]	4.7	5.6	4.5	5.1	4.0
Axial resolution at 10 cm (mm)[a]	5.2	6.3	5.9	5.5	4.5
Peak NECR (kcps) at kBq/ml[a]	120 at 19 kBq/ml	130 at 29.5 kBq/ml	175 at 28 kBq/ml	120 at 9 KBq/ml	650 at 50 kBq/ml
Time-of-flight resolution (picoseconds)	550	544	540	n.a.	345
Time-of-flight localization (cm)	8.9	8.2	8.1	n.a.	5.2
Coincidence window (nanoseconds)	4.5	4.9	4.1	9.5	1.5

S&S Step-and-shoot whole-body scanning, *n.a.* Not applicable

[a] Performance measurements of positron emission tomographs. NEMA Standards Publication NU 2-2001 [72]

[b] Vendor-defined "effective sensitivity," which includes TOF positioning gain

Table 4 Design and performance parameters of current commercially available clinical PET-MR scanners [5]

PET/MR model	GE Signa	mMR
Patient port (cm)	60	60
MR model (3 T)	Discovery 750 w (3 T)	Verio
Patient scan range (cm)	188 (PET)/205 (MR)	200
Maximum patient weight (kg [lb])	226 (500)	200 (441)
Acquisition modes	3D and S&S	3D S&S
Number of image planes	89	127
Plane spacing (mm)	2.8	2
Crystal size (mm^3)	4 × 5.3 × 25	4 × 4 × 20
Number of crystals	20,160	28,672
Number of PMTs	SiPM	APD
Physical axial FOV (cm)	25	25.8
Detector material	LYSO	LSO
System sensitivity at 0 cm (%)[a]	2.1	1.5
Transaxial resolution at 1 cm (mm)[a]	4.2	4.1
Transaxial resolution at 10 cm (mm)[a]	5.2	5.2
Axial resolution at 1 cm (mm)[a]	5.8	4.3
Axial resolution at 10 cm (mm)[a]	7.1	6.6
Peak NECR (kcps)[a]	210 at 17.5 kBq/ml	175 at 21.8 kBq/ml
Time-of-flight resolution (picoseconds)	400	n.a.
Time-of-flight localization (cm)	6.0	n.a.
Coincidence window (nanoseconds)	4.6	5.9

S&S Step-and-shoot whole-body scanning, *n.a.* Not applicable

[a] Performance measurements of positron emission tomographs. NEMA Standards Publication NU 2-2001 [72]

gradient system is cooled and the PET detectors are shielded with copper to reduce electromagnetic interference. The APDs do not distort the main magnetic field, and the acquisitions of the MR and PET subsystems are synchronized to reduce possible distortion of the PET signals by the MR RF and gradient pulses. The PET component of the Siemens scanner has a 25.8-cm axial FOV. However, this system does not offer TOF capability, due to relatively low timing resolution of APDs. The GE Signa™ PET-MR uses SiPMs to achieve TOF with a coincidence timing resolution of 400 and 390 ps with RF "on" and "off," respectively. It offers a 25-cm PET axial FOV and a sensitivity of 2.1%. The PET subsystem comprises five rings of 112 detector blocks (each a 4 × 9 array of LYSO crystals, 3.95 × 5.3 × 25 mm^3) backed by a 1 × 3 arrays of SiPMs. The PET detector ring is centered inside the MR gradient set of a GEMR750w™ 3 T scanner on the outer diameter of the RF body coil. Figure 18 shows the digital PET detector modules used in the Siemens mMR™ and the GE Signa™ PET/MR systems [5] and Table 4 [5] the design and performance parameters of these systems.

Preclinical. A number of preclinical PET devices are commercially available, both from major manufacturers and smaller "niche" companies. Preclinical PET scanners, which operate exclusively in 3D mode, are diverse in design, utilizing different scintillation detectors in combination with either PSPMTs or APDs. The superior spatial resolution of preclinical versus clinical PET scanners, 1–2 mm versus 4–6 mm, is due in part to the much smaller gantry diameter and therefore a less pronounced resolution-degrading effect of the non-colinearity of the annihilation γ-rays. Preclinical devices are currently marketed as "PET-only" scanners or as multimodality devices with integrated CT scanners, typically conebeam devices with flat-panel detectors. The Carestream Albira™, Gamma Medica Triumph LabPET Solo™, and Siemens Inveon™ are available as trimodality PET-SPECT/CT systems. The design and performance parameters of currently marketed preclinical PET scanners are summarized in Table 5.

Table 5 Design and performance parameters of current commercially preclinical PET scanners

	Bioscan (Philips) NanoPET	Bioscan BioPET	Carestream Albira	Clairvivo PET	Gamma Medica Triumph LabPET Solo	Oxford quad HIDAC	Ray test ClearPET	Sedecal Argus[a]	Siemens Inveon	Genisys Sofie
Detectors	LYSO + PSPMTs[b]	Phoswich (LYSO + GSO) + APDs[c]	LYSO + PSPMTs[a]	LYSO + PSPMTs[a]	Phoswich (LYSO + GSO) + APDs	Multi-wire proportional gas chambers	Phoswich (LYSO + LuYAP) + PSPMTs	Phoswich (LYSO + GSO)	LSO + PSPMTs[a]	BGO
Transaxial FOV[d] (cm)	Up to 12.5		8.0	10.2	3.7	0	14 – Mice[e] 27 – Rats[e]	6.8	10.0	4.4
Axial FOV[d](cm)	3.0		Up to 14.8	15.1	Up to 10	28	Not available	4.7	12.7	9.5
Detector elements (mm^3)	1.12 × 1.12 × 13	1.45 × 1.45 × 15	n.a.	1.28 × 2.68 × 7	n.a.	n.a.	2.0 × 2.0 × 10	1.45 × 1.45 × 15	1.59 × 1.59 × 10	1.8 × 1.2 × 7
Spatial resolution (FWHM in mm)	1.2		1.4	1.5	1.0–1.4	0.9	1.4	1.1	1.4	1.4
Sensitivity (%)	8.3		Up to 9	8.2	Not available	1.8	Not available	6.5	10	14

Preclinical scanners are all operate exclusively in 3D mode and are currently marketed as "PET-only" scanners or as multimodality devices with integrated CT and/or SPECT scanners. The Carestream Albira, Gamma Medica Triumph LabPET Solo, and Siemens Inveon are available as trimodality PET-SPECT/CT systems

Extracted from the marketing literature of the respective manufacturers and from references [12, 73–75]

[a]Formerly the General Electric eXplore Vista

[b]PSPMTs: Position-sensitive photomultiplier tubes

[c]APDs: Avalanche photodiodes

[d]FOV: Field of view

[e]The Ray Test ClearPET has an adjustable detector ring diameter, and the detector rings rotate at the larger diameter to compensate for the space between detector blocks at the larger diameter

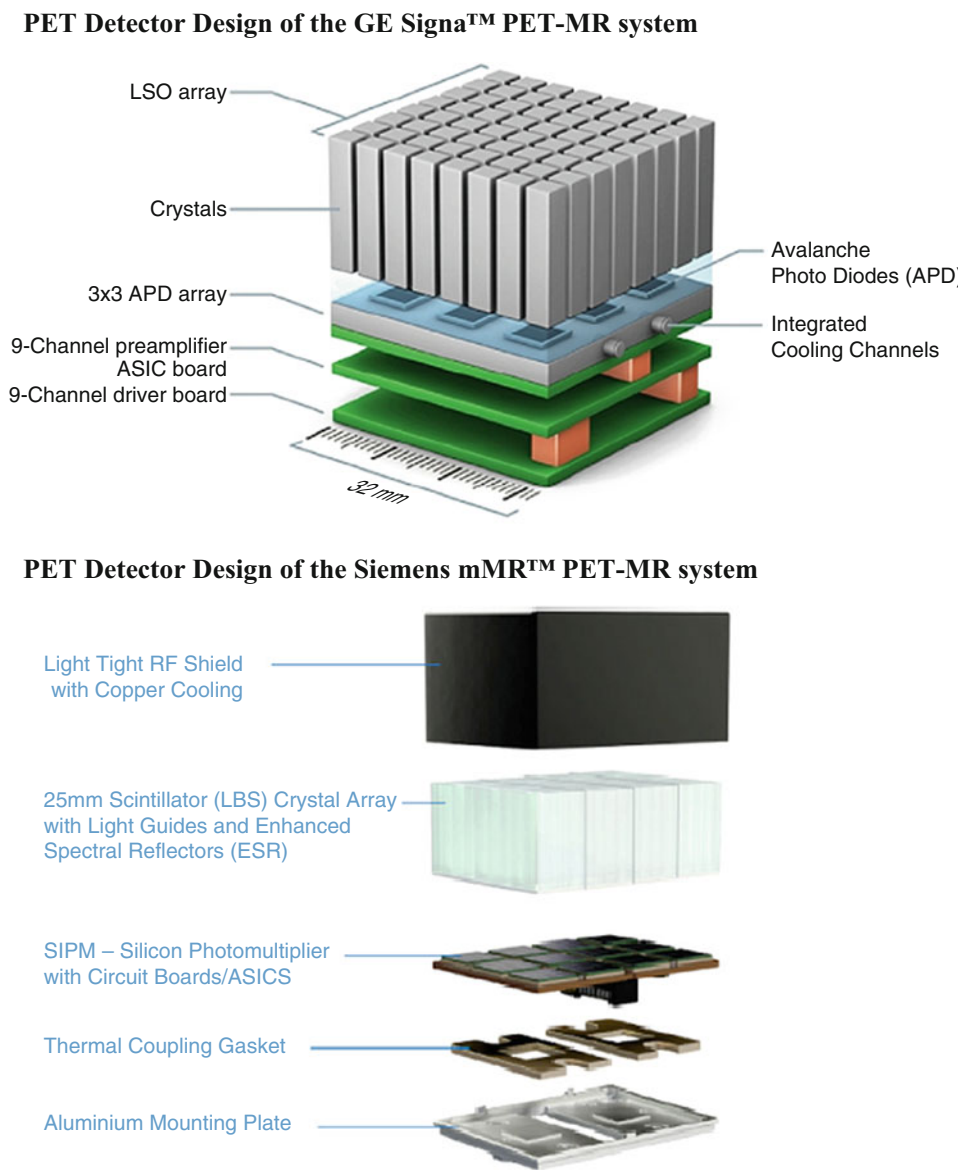

Fig. 18 The digital PET detector modules used in the Siemens mMR™ and the GE Signa™ PET/MR systems (From reference [5] with permission)

Concluding Remarks

The use of PET and of PET/CT has grown dramatically over the last several decades. In contrast to PET/CT, however, where there are temporal and spatial offsets between the PET and the CT studies, PET and MRI studies (including dynamic studies) can be performed simultaneously. The recent introduction of PET/MRI [55–57, 64] multimodality devices will no doubt lead to new and important applications of molecular imaging [69].

References

1. Zanzonico P. Principles of nuclear medicine imaging: planar, SPECT, PET, multi-modality, and autoradiography systems. Radiat Res. 2012;177:349–64.
2. Zanzonico P, Heller S. Physics, instrumentation, and radiation protection. In: Biersack HJ, Freeman LM, editors. Clinical nuclear medicine. Heidelberg: Springer; 2007. p. 1–33.
3. Zanzonico P. Radionuclide imaging. In: Cherry S, Badawy R, Qi J, editors. Essentials of in vivo biomedical imaging. Boca Raton: CRC Press; 2015. p. 1765–224.
4. Otte N. The silicon photomultiplier – a new device for high energy physics, astroparticle physics, industrial and medical applications, in SNIC symposium. Palo Alto: STanford University; 2006.
5. Slomka PJ, Pan T, Germano G. Recent advances and future progress in PET instrumentation. Semin Nucl Med. 2016;46:5–19.
6. Humm JL, Rosenfeld A, Del Guerra A. From PET detectors to PET scanners. Eur J Nucl Med Mol Imaging. 2003;30:1574–97.
7. Zanzonico P. Positron emission tomography: a review of basic principles, scanner design and performance, and current systems. Semin Nucl Med. 2004;34:87–111.
8. Zanzonico P, Heller S. The intraoperative gamma probe: basic principles and choices available. Semin Nucl Med. 2000;30:33–48.
9. Heller S, Zanzonico P. Nuclear probes and intraoperative gamma cameras. Semin Nucl Med. 2011;41:166–81.
10. Townsend DW, Bendriem B. Introduction to 3D PET. In: Bendriem B, Townsend DW, editors. The theory and practice of 3D PET. Dordrecht: Kluwer Academic Publishers; 1998. p. 1–10.
11. Cherry SR, Sorenson JA, Phelps ME. Physics in nuclear medicine. 3rd ed. Philadelphia: Saunders; 2003.
12. Mosset JB, Devroede O, Krieguer M, et al. Development of an optimised LSO/LuYAP phoswich detector head for the ClearPET camera. In: Nuclear science symposium conference record, 2004 IEEE. Lyon: Institute of Electrical and Electronics Engineers; 2004. p. 2439–2443.
13. Lewellen TK. Time-of-flight PET. Semin Nucl Med. 1998;28:268–75.
14. Moses WW. Recent advances and future advances in time-of-flight PET. Nucl Instrum Methods Phys Res A. 2007;580:919–24.
15. Karp JS, Surti S, Daube-Witherspoon ME, et al. Benefit of time-of-flight in PET: experimental and clinical results. J Nucl Med. 2008;49:462–70.
16. Levin CS, Hoffman EJ. Calculation of positron range and its effect on the fundamental limit of positron emission tomography system spatial resolution. Phys Med Biol. 1999;44:781–99.
17. Derenzo SE. Mathematical removal of positron range blurring in high-resolution tomography. IEEE Trans Nucl Sci. 1986;NS-33:565–9.
18. Berko S, Hereford FL. Experimental studies of positron interactions in solids and liquids. Rev Modern Phys. 1956;28:299–307.
19. Yang Y, Wu Y, Qi J, et al. A prototype PET scanner with DOI-encoding detectors. J Nucl Med. 2008;49:1132–40.
20. Zanzonico P. Routine quality control of clinical nuclear medicine instrumentation: a brief review. J Nucl Med. 2008;49:1114–31.
21. Zanzonico PB. Technical requirements for SPECT: equipment and quality control. In: Kramer EL, Sanger JJ, editors. Clinical applications in SPECT. New York: Raven; 1995. p. 7–41.
22. Hoffman EJ, Huang SC, Phelps ME, et al. Quantitation in positron emission computed tomography: 4. Effect of accidental coincidences. J Comput Assist Tomogr. 1981;5:391–400.
23. Rokitta O, Casey M, Wienhard K, Pictrzyk U. Random correction for positron emission tomography using singles count rates. In: Merelli D, Surget J, Ulma M, editors. Nuclear science symposium conference record, 2000 IEEE. Lyon: Institute of Electrical and Electronics Engineers; 2000. p. 1737–1740.
24. Frey EC, Humm JL, Ljungberg M. Accuracy and precision of radioactivity quantification in nuclear medicine images. Semin Nucl Med. 2012;42:208–18.
25. Meikle SR, Badawi RD, et al. Quantitative techniques in PET. In: Bailey DL, editor. Positron emission tomography: basic sciences. London: Springer; 2005. p. 93–126.
26. Bailey DL. Quantitative procedures in 3D PET. In: Bendriem B, Townsend DW, editors. The theory and practice of 3D PET. Dordrecht: Kluwer Academic Publishers; 1998. p. 55–109.
27. Cherry SR, Huang SC. Effects of scatter on model parameter estimates in 3D PET studies of the human brain. IEEE Trans Nucl Sci. 1995;42:1174–9.
28. Stearns CW. Scatter correction method for 3D PET using 2D fitted Gaussian functions. J Nucl Med. 1995;36:105P.
29. Cherry SR, Sorenson JA, Phelps ME. Physics in nuclear medicine. 4th ed. Philadelphia: Saunders; 2012.
30. Defrise M, Kinahan P. Data acquisition and image reconstruction for 3D PET. In: Bendriem B, Townsend DW, editors. The theory and practice of 3D PET. Dordrecht: Kluwer Academic Publishers; 1998. p. 11–53.
31. Daube-Witherspoon ME, Muehllehner G. Treatment of axial data in three-dimensional PET. J Nucl Med. 1987;28:1717–24.
32. Defrise M, Kinahan PE, Townsend DW, et al. Exact and approximate rebinning algorithms for 3-D PET data. IEEE Trans Med Imaging. 1997;16:145–58.
33. Defrise MK, Kinahan PE, Michel CJ. Image reconstruction algorithms in PET. In: Bailey DL, Townsend DW, Valk PE, Maisey MN, editors. Positron emission tomography: basic sciences. London: Springer; 2005. p. 63–91.

34. Miller TR, Wallis JW. Fast maximum-likelihood reconstruction. J Nucl Med. 1992;33:1710–1.
35. Miller TR, Wallis JW. Clinically important characteristics of maximum-likelihood reconstruction. J Nucl Med. 1992;33:1678–84.
36. Hudson HM, Larkin RS. Accelerated image reconstruction using ordered subsets of projection data. IEEE Trans Med Imaging. 1994;13:601–9.
37. Tarantola G, Zito F, Gerundini P. PET instrumentation and reconstruction algorithms in whole-body applications. J Nucl Med. 2003;44:756–69.
38. Ahn S, Ross SG, Asma E, et al. Quantitative comparison of OSEM and penalized likelihood image reconstruction using relative difference penalties for clinical PET. Phys Med Biol. 2015;60:5733–51.
39. Matej S, Lewitt RM. Efficient 3D grids for image reconstruction using spherical-symmetric volume elements. IEEE Trans Nucl Sci. 1996;42:1361–70.
40. Matej S, Lewitt RM. Practical considerations for 3-D image reconstruction using spherically symmetric volume elements. IEEE Trans Med Imaging. 1996;15: 68–78.
41. Daube-Witherspoon ME, Matej S, Karp JS, et al. Application of the 3D row action maximum likelihood algorithm to clinical PET imaging. IEEE Trans Nucl Sci. 2001;48:24–30.
42. Hoffman EJ, Huang SC, Phelps ME. Quantitation in positron emission computed tomography: 1. Effect of object size. J Comput Assist Tomogr. 1979;3:299–308.
43. Erlandsson K, Buvat I, Pretorius PH, Thomas BA, Hutton BF. A review of partial volume correction techniques for emission tomography and their applications in neurology, cardiology and oncology. Phys Med Biol. 2012;57:R119–59.
44. Nehmeh SA, Erdi YE. Respiratory motion in positron emission tomography/computed tomography: a review. Semin Nucl Med. 2008;38:167–76.
45. Nehmeh SA, Erdi YE, Ling CC, et al. Effect of respiratory gating on quantifying PET images of lung cancer. J Nucl Med. 2002;43:876–81.
46. Nehmeh SA, Erdi YE, Ling CC, et al. Effect of respiratory gating on reducing lung motion artifacts in PET imaging of lung cancer. Med Phys. 2002; 29:366–71.
47. Nehmeh SA, Erdi YE, Rosenzweig KE, et al. Reduction of respiratory motion artifacts in PET imaging of lung cancer by respiratory correlated dynamic PET: methodology and comparison with respiratory gated PET. J Nucl Med. 2003;44:1644–8.
48. Israel O, Goldsmith SJ, editors. Hybrid SPECT/CT: imaging in clinical practice. New York: Taylor & Francis; 2006. p. 244.
49. Townsend DW. A combined PET/CT scanner: the choices. J Nucl Med. 2001;42:533–4.
50. Townsend DW, Beyer T. A combined PET/CT scanner: the path to true image fusion. Br J Radiol. 2002;75 (Spec No):S24–30.
51. Townsend DW, Beyer T, Blodgett TM. PET/CT scanners: a hardware approach to image fusion. Semin Nucl Med. 2003;33:193–204.
52. Townsend DW. Positron emission tomography/computed tomography. Semin Nucl Med. 2008;38:152–66.
53. Horii S. ACR-NEMA DICOM support for exchange media: a report on the activity of working group V. Adm Radiol. 1993;12:68–9.
54. Bidgood Jr WD, Horii SC. Introduction to the ACR-NEMA DICOM standard. Radiographics. 1992; 12:345–55.
55. Pichler BJ, Kolb A, Nagele T, et al. PET/MRI: paving the way for the next generation of clinical multimodality imaging applications. J Nucl Med. 2010;51:333–6.
56. Pichler BJ, Wehrl HF, Kolb A, et al. Positron emission tomography/magnetic resonance imaging: the next generation of multimodality imaging? Semin Nucl Med. 2008;38:199–208.
57. Judenhofer MS, Wehrl HF, Newport DF, et al. Simultaneous PET-MRI: a new approach for functional and morphological imaging. Nat Med. 2008; 14:459–65.
58. Judenhofer MS, Cherry SR. Applications for preclinical PET/MRI. Semin Nucl Med. 2013;43:19–29.
59. Ng TS, Bading JR, Park R, et al. Quantitative, simultaneous PET/MRI for intratumoral imaging with an MRI-compatible PET scanner. J Nucl Med. 2012;53: 1102–9.
60. Peng BJ, Walton JH, Cherry SR, et al. Studies of the interactions of an MRI system with the shielding in a combined PET/MRI scanner. Phys Med Biol. 2010; 55:265–80.
61. Pichler BJ, Judenhofer MS, Catana C, et al. Performance test of an LSO-APD detector in a 7-T MRI scanner for simultaneous PET/MRI. J Nucl Med. 2006;47:639–47.
62. Hofmann M, Pichler B, Scholkopf B, et al. Towards quantitative PET/MRI: a review of MR-based attenuation correction techniques. Eur J Nucl Med Mol Imaging. 2009;36 Suppl 1:S93–104.
63. Kolb A, Wehrl HF, Hofmann M, et al. Technical performance evaluation of a human brain PET/MRI system. Eur Radiol. 2012;22:1776–88.
64. Pichler BJ, Judenhofer MS, Wehrl HF. PET/MRI hybrid imaging: devices and initial results. Eur Radiol. 2008;18:1077–86.
65. Sauter AW, Wehrl HF, Kolb A, et al. Combined PET/MRI: one step further in multimodality imaging. Trends Mol Med. 2010;16:508–15.
66. Catana C, Wu Y, Judenhofer MS, et al. Simultaneous acquisition of multislice PET and MR images: initial results with a MR-compatible PET scanner. J Nucl Med. 2006;47:1968–76.
67. Moadel RM. Breast cancer imaging devices. Semin Nucl Med. 2011;41:229–41.
68. MacDonald L, Edwards J, Lewellen T, et al. Clinical imaging characteristics of the positron emission

mammography camera: PEM Flex Solo II. J Nucl Med. 2009;50:1666–75.
69. Beyer T, Freudenberg LS, Czernin J, et al. The future of hybrid imaging-part 3: PET/MR, small-animal imaging and beyond. Insights Imaging. 2011;2:235–46.
70. Firestone RB, Shirley VS, editors. Table of isotopes. 8th ed. New York: Wiley; 1996.
71. Weber D, Eckerman K, Dillman L, et al., editors. MIRD: radionuclide data and decay schemes. New York: Society of Nuclear Medicine; 1989. p. 447.
72. NEMA. Performance measurements of positron emission tomographs. NEMA Standards Publication NU 2-2001. Rosslyn: National Electrical Manufacturers Association (NEMA); 2001.
73. Larobina M, Brunetti A, Salvatore M. Small animal PET: a review of commercially available imaging systems. Curr Med Imaging Rev. 2006;2:187–92.
74. Constantinescu CC, Mukherjee J. Performance evaluation of an Inveon PET preclinical scanner. Phys Med Biol. 2009;54:2885–99.
75. Mizuta T, Kitamura K, Iwata H, et al. Performance evaluation of a high-sensitivity large-aperture small-animal PET scanner: clear PET. Ann Nucl Med. 2008; 22:447–55.

Instrumentation for Single-Photon Emission Imaging

11

Pat Zanzonico

Abstract

This chapter reviews the underlying physical principles of single-photon emission tomography (SPECT) and the design and operation as well as the capabilities and limitations of SPECT scanners used clinically and preclinically. This is the "companion" chapter to the earlier chapter on positron emission tomography (PET) instrumentation; the material in that chapter on the basic principles of radiation detectors, iterative image reconstruction, and multimodality imaging applies as well to SPECT.

Keywords

SPECT • Scintillation detectors • Ionization detectors • Gamma cameras • Filtered back-projection • Cardiac imaging

Glossary

ACF	Attenuation correction factor
APD	Avalanche photodiode
ASIC	Application-specific integrated circuit
COR	Center of rotation
CsI(Tl)	Thallium-doped cesium iodide
CT	X-ray computed tomography
CZT	Cadmium zinc telluride
ESSE	Effective scatter source estimation
eV	Electron volt
FBP	Filtered back-projection
FL	Focal length
FOV	Field of view
FWHM	Full-width half-maximum
GAP	General all-purpose
keV	Kilo-electron volt (10^3 eV)
LEAP	Low-energy all-purpose
LEHR	Low-energy high-resolution
LEHS	low-energy high-sensitivity
LOR	Line of response
MeV	Mega-electron volt (10^6 eV)
MR	Magnetic resonance
MRI	Magnetic resonance imaging
NaI(Tl)	Thallium-doped sodium iodide
PET/MR	Positron emission tomography/magnetic resonance
PET	Positron emission tomography
PET/CT	Positron emission tomography/computed tomography
PMT	Photomultiplier tube
RF	Radiofrequency
ROI	Region of interest
SAD	Source-to-aperture distance
SPECT/MR	Single-photon emission computed tomography/magnetic resonance

P. Zanzonico (✉)
Memorial Hospital Research Laboratories, Department of Medical Physics, Memorial Sloan Kettering Cancer Center, New York, NY, USA
e-mail: zanzonip@mskcc.org

© Springer International Publishing Switzerland 2017
H.W. Strauss et al. (eds.), *Nuclear Oncology*,
https://doi.org/10.1007/978-3-319-26236-9_5

SPECT	Single-photon emission computed tomography
SPECT/CT	Single-photon emission computed tomography/computed tomography
TEW	Triple-energy window

Contents

Introduction 252
Radionuclides for SPECT 252
Gamma Camera Design 253
SPECT Data Acquisition 258
Data "Corrections" 259
Image Reconstruction 263
Quantitation 264
Multimodality Imaging: SPECT/CT and SPECT/MRI 266
Commercial Devices 267
Concluding Remarks 272
References 272

Introduction

This chapter reviews the underlying physical principles of single-photon emission tomography (SPECT) and the design and operation as well as the capabilities and limitations of SPECT scanners used clinically and preclinically [1–4]. This is the "companion" chapter to ▶ Chap. 10, "Instrumentation for Positron Emission Imaging" of this book; the material in that chapter on the basic principles of radiation detectors, iterative image reconstruction, and multimodality imaging applies as well to SPECT.

SPECT, like PET, is now a mature but continually improving technology. Among the most noteworthy refinements in recent years have been the application of solid-state ionization detector (i.e., semiconductor)-based gamma cameras, the introduction of novel, application-specific detector and collimator configurations (most notably in nuclear cardiology), and the improved quantitative accuracy.

Radionuclides for SPECT

Implicit in the suitability of a radionuclide for in vivo imaging is that it emits sufficient abundance radiations penetrating enough to escape from the body and interact with external detectors. These emissions include γ-rays and characteristic x-rays ("single photons") used for SPECT and planar gamma camera imaging generally or the 511-keV annihilation photons associated with positron (β^+) decay and used for PET. In addition, imaging radionuclides ideally should emit few or no non-penetrating radiations, that is, particulate radiations such as β particles and electrons (excluding, of course, positrons necessary for signal generation in the case of PET). Such particulate radiations typically have ranges in tissue of the order of 1 mm or less and thus cannot escape from the body and be detected externally. These contribute to the radiation dose to tissues and organs without providing any imageable signal. High-energy ($\geq$ ~1-MeV) beta particles (e.g., those emitted by the pure beta-particle emitter yttrium-90) produce a small but imageable amount of *bremsstrahlung* ("braking radiation" x-rays) as they slow down in tissue. *Bremsstrahlung* imaging is not widely used, however, and produces rather poor-quality images. Further, an imaging radionuclide ideally should have a physical half-life comparable to the time required for the administered radiotracer to localize in the tissue of interest. This will provide sufficient time for it to localize in that tissue while still retaining a near-maximal imaging signal, followed by elimination of the radioactivity by a combination of physical decay and biological clearance. The radiation dose to patients and individuals around them and the potential problem of radioactive contamination are thereby minimized. The pertinent physical properties of single-photon radionuclides for imaging are summarized in Table 1 [1, 2, 5, 6].

For planar imaging as well as SPECT, a radionuclide emitting x- and γ-rays with energies of 100–200 keV and with an abundance of 100% (i.e., one x- or γ-ray emitted per decay) and with minimal emission of particulate radiations and of higher-energy x- and γ-rays is ideal. The abundance of imageable x- or γ-rays relative to

Table 1 Physical properties of single-photon-emitting radionuclides used in gamma camera imaging and SPECT [1, 2, 5, 6]

Radionuclide	Physical half-life	Decay mode	Energies of imageable x- and γ-rays (MeV)	Abundance imageable x- and γ-rays (%)	x- and γ-ray-to-β particle, conversion electron, and Auger electron energy-per-decay ratio[a]	Production
Gallium-67	3.26 days	Electron capture	0.0933	40	4.5	Cyclotron
			0.185	24		
			0.300	16		
Technetium-99m	6.01 h	Isomeric transition	0.140	89	7.8	Generator (Molybdenum-99)
Indium-111	2.83 days	Electron capture	0.172	90	12	Cyclotron
			0.247	94		
Iodine-123	13.2 h	Electron capture	0.159	84	6.1	
Iodine-131	8.04 days	β^- decay	0.364	82	2.0	Reactor

[a]As discussed, the ratio of the energy emitted per decay in the form of β particles, conversion electrons, and Auger electrons (i.e., non-penetrating particulate radiations) to that emitted in the form of x- and γ-rays should be high for a radionuclide for gamma camera imaging

particulate radiations is expressed by the x- and γ-ray-to-β particle, conversion electron, and Auger electron energy-per-decay ratio in Table 1; the higher the value of this parameter, the better a radionuclide will be for imaging. With a mean free path in soft tissue of the order of 10 cm and in NaI (Tl) of less than 0.5 cm, 100- to 200-keV photons provide adequate penetrability through tissue but are low enough in energy to be efficiently collimated (see below) and stopped in relatively thin scintillation and even ionization detectors, yielding optimum-quality images with reasonably low radiation doses. The absence of higher-energy x- and γ-rays (i.e., with energies in excess of several hundred keV) is important because such radiations cannot be efficiently collimated and detected. Yet, they may undergo scatter in the patient and/or detector hardware and contribute, even with energy discrimination, mispositioned, and otherwise spurious counts to the image. Based on the foregoing criteria (Table 1), ^{99m}Tc is a near-ideal radionuclide for gamma camera imaging, emitting only a 140-keV γ-ray and little particulate radiations. Iodine-131 (^{131}I), on the other hand, emits a relatively high-energy, difficult-to-collimate 364-keV γ-ray and abundant β particles.

Gamma Camera Design

Developed in the late 1950s by Hal Anger, the gamma camera (Fig. 1), also known as the scintillation or Anger camera, has long been the predominant imaging device in nuclear medicine [1, 3]. Its large detector area allows simultaneous and therefore rapid data acquisition over a large area of the body. Gamma camera crystals, almost universally, are composed of a plate of NaI(Tl) and vary in thickness from 6.35 to 25.4 mm. A 9.53-mm-thick crystal thus provides a reasonable balance between sensitivity and resolution and is the most widely used for general gamma camera imaging. About 95% of the 140-keV photons from ^{99m}Tc are absorbed in a 9.54-mm crystal. For clinical applications, gamma camera crystals are most commonly rectangular in shape and ~50 × 60 cm in area for general-purpose imaging.

Once the incident radiation passes through the collimator (see below), it strikes, and may produce a scintillation within, the crystal. The resulting light signal is distributed among a two-dimensional array of photomultiplier tubes (PMTs) backing the crystal, the light intensity varying inversely with the distance between the scintillation and

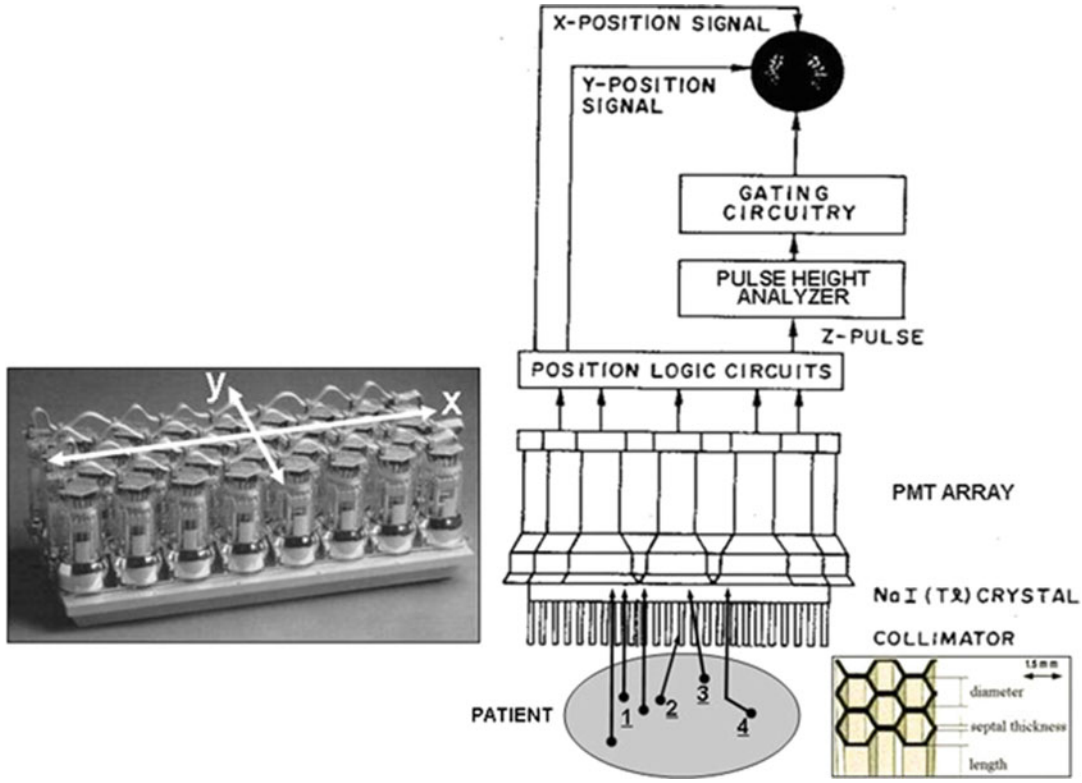

Fig. 1 Basic design of a conventional gamma camera, consisting of a multi-hole collimator, a thin large-area NaI(Tl) crystal, a two-dimensional array of PMTs and associated electronics (high-voltage power supply, preamplifier, and amplifier), position logic circuitry, energy discriminator, and image display. Note that there are actually two position logic circuits – for the determination separately of the x- and y-positions of the scintillation within the crystal. Note further that the output signal from each PMT is actually split into three parts, one (the z pulse) for the determination of the energy of the incident radiation as well as one each for the determination of its x- and y-positions. In current-day gamma cameras, the output signal from each PMT is digitized, and the position of each event is determined with computer software. The *left inset* shows a photograph of the two-dimensional PMT array backing the crystal in a typical *rectangular* field-of-view gamma camera. The *right inset* shows a drawing of a portion of a parallel-hole collimator, identifying the dimensions – aperture diameter, septal thickness, and septal length – of such a collimator. The "desirable" events (*arrows* labeled "1") are unscattered (i.e., photopeak) photons traveling in a direction parallel or nearly parallel to the axes of the apertures and thus yielding correctly positioned counts in the gamma camera image. "Undesirable" events include (1) scattered as well as unscattered photons traveling in a direction oblique to the axes of the apertures (2) and thus eliminated by attenuation by one or more collimator septa; septal penetration (3), that is, unscattered photons traveling in a direction oblique to the axes of the apertures yet passing through the septa and yielding mispositioned counts; scatter (4), that is, photons undergoing Compton scatter within the patient and either eliminated by energy discrimination or not eliminated and yielding mispositioned counts (From Refs. [1, 3] with permission)

the respective PMT: the farther the PMT is from the scintillation, the less light it receives, and the smaller is its output pulse. This inverse relationship is the basis of the Anger position logic circuitry for determining the precise location of a scintillation within the crystal. In the older gamma cameras, the x- and y-coordinates were calculated by analog circuitry, that is, using matrices of resistors. In current models, this is done by digitizing the output signal from each PMT and using digital electronics.

The gamma camera collimator, almost always comprised of lead, "directionalizes" the incoming radiation (Fig. 1). Any radiation traveling at

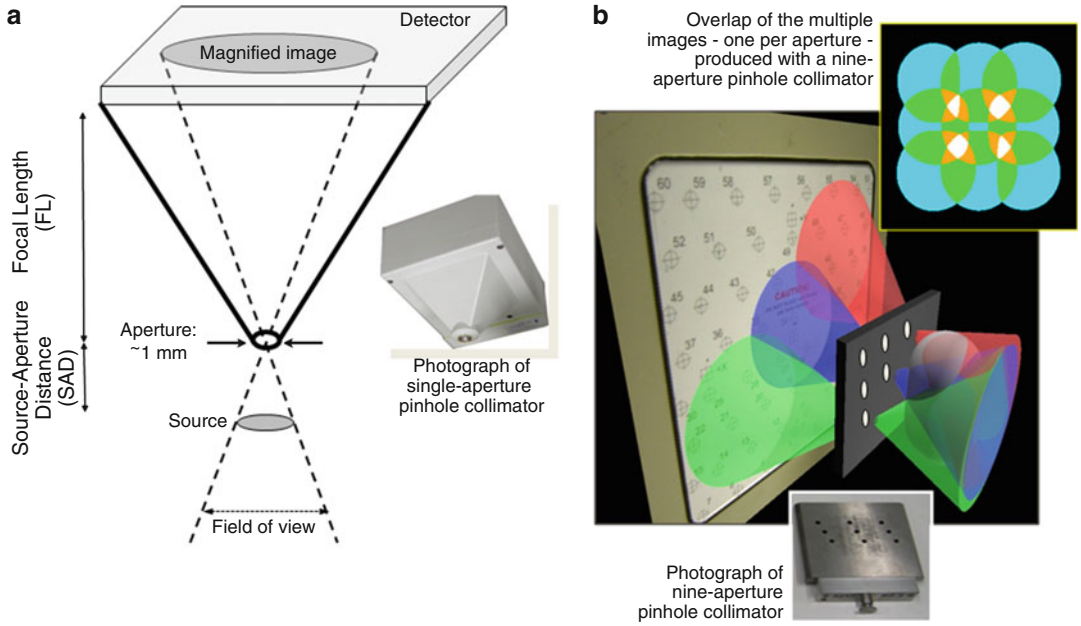

Fig. 2 Pinhole collimation for gamma cameras. (**a**) A single-aperture pinhole collimator. Pinhole collimation provides a magnification effect and thereby improved "effective" resolution. For example, if a source were placed at distance of 3 cm from the aperture (i.e., source-to-aperture distance (*SAD*) = 3 cm) of a pinhole collimator having a focal length of 9 cm (i.e., focal length (FL) = 9 cm) fitted to a detector with an intrinsic spatial resolution of 3 mm (i.e., FWHM = 3 mm), the magnification is FL/SAD = 9/3 cm = 3, and the effective resolution therefore improves to FWHM/(FL/SAD) = 3 mm/(9/3 cm) = 3 mm/3 = 1 mm (Photograph courtesy of Gamma Medica (Northridge, CA)) (**b**) A multi-aperture pinhole collimator, now the standard approach to preclinical (i.e., mouse and rat) SPECT imaging. As shown, however, each of the apertures produces an image, and the resulting multiple images – one per aperture – overlap. The apertures are angled with respect to one another to minimize this overlap. If larger-area detectors are used, this angulation can be increased and therefore the image overlap further minimized and image quality improved (Courtesy of Bioscan (Washington, DC))

an oblique angle to the axes of the holes (apertures) will strike the lead walls (septa) between the holes and not reach the crystal. As a result, only radiations traveling perpendicular to the crystal surface pass through the apertures and contribute counts to the resulting image. A certain fraction of photons striking the septa will nonetheless pass through them and reach the crystal; this phenomenon, which degrades image quality, is known as septal penetration. Most collimators used clinically are parallel-hole collimators, with the apertures and septa parallel to one another. In addition, single-aperture pinhole collimators, most commonly used for thyroid imaging because of their pronounced magnifying effect, are available as well (Fig. 2a). Pinhole collimators, however, suffer from low sensitivity, limited field of view, and geometric distortion, since image magnification varies with both source-aperture distance and lateral position in the field of view, and therefore are rarely used for clinical imaging other than for the thyroid (normally a small, relatively flat organ). For preclinical (i.e., mouse and rat) imaging, multi-aperture pinhole collimation is now the standard approach, since it combines the magnification effect (and improved resolution) of pinhole collimation with the greater sensitivity afforded by multiple apertures (Fig. 2b).

Gamma camera collimators are "rated" with respect to photon energy and resolution/sensitivity. Low-energy, or "technetium," collimators, including "low-energy all-purpose (LEAP)" (or "general all-purpose (GAP)"), "low-energy high-resolution

(LEHR)," and "low-energy high-sensitivity (LEHS)" collimators, are designed to image radionuclides emitting x- and γ-rays less than 200 keV in energy. These include ^{99m}Tc (photopeak energy: 140 keV) as well as thallium-201 (^{201}Tl) (68–80 keV) and iodine-123(^{123}I) (159 keV). Medium-energy, or "gallium," collimators are designed for radionuclides emitting x- and γ-rays 200–300 keV in energy, including gallium-67 (^{67}Ga) (93, 185, and 300 keV) as well as indium-111 (^{111}In) (172 and 247 keV). High-energy, or "iodine," collimators are designed to image radionuclides emitting x- and γ-rays greater than 300 keV in energy, including ^{131}I (364 keV). In progressing from low- to medium- to high-energy collimation, the collimators are made longer and the septa thicker in order to interpose more lead between the subject and the crystal. This is done in order to maintain septal penetration (i.e., expressed as the percent of counts in an image attributable to photons penetrating the septa) at or below an acceptably low level, typically set at 5%. This, in turn, reduces the overall fraction of emitted x- and γ-rays reaching the crystal. To compensate, at least in part, for the resulting lower sensitivity, the apertures are made wider in progressing from low- to medium- to high-energy collimators. This, however, degrades spatial resolution by dispersing the counts passing through each aperture over a large area of the crystal (Figs. 3 and 4). Overall, therefore, gamma camera images are progressively poorer in quality for radionuclides emitting low- versus medium- versus high-energy x- and γ-rays. For each energy rating (and as indicated above for low-energy collimators), collimators may also be further rated as "general purpose" (or "all purpose"), "high resolution," or "high sensitivity." High-resolution collimators have narrower apertures (and therefore lower sensitivity), and high-sensitivity collimators have wider apertures (and therefore coarser resolution), respectively, than general-purpose collimators. In instances where a radionuclide emits multiple photons, it is the highest-energy photon which dictates the collimator to be used. For example, a medium-energy collimator must still be used to image gallium-67 (photon energies: 93, 185, and 300 keV) even if only the two lower-energy (i.e., the 93 and 185 keV) photons are used for imaging.

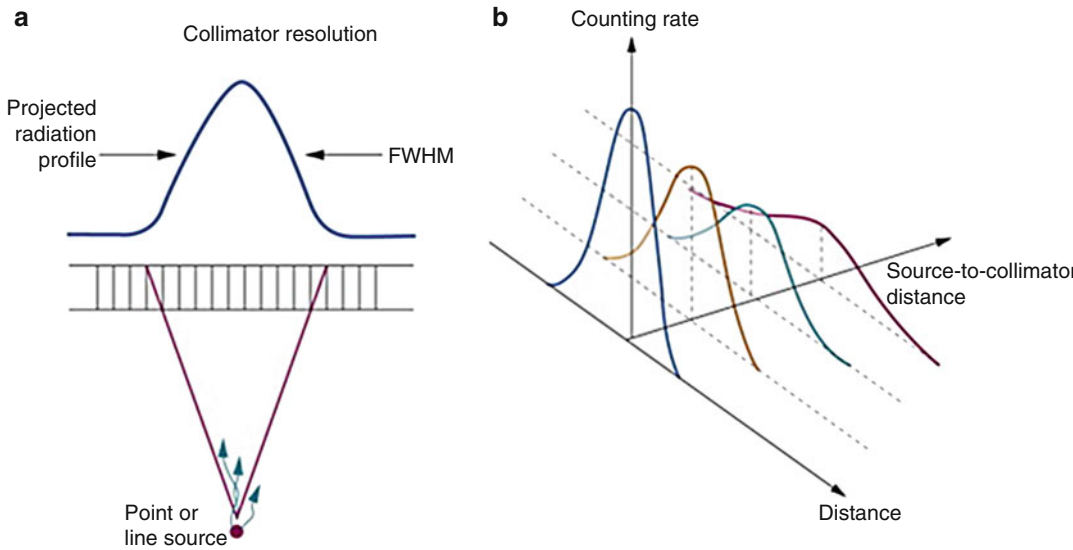

Fig. 3 (**a**, **b**) In gamma camera imaging with parallel-hole collimation, the 3D volume subtended by a point source of radiation is a cone, with the area of the detector over which radiations from the source are dispersed increasing, and therefore the spatial resolution worsens, with increasing source-to-collimator distance (Adapted from Ref. [40] with permission)

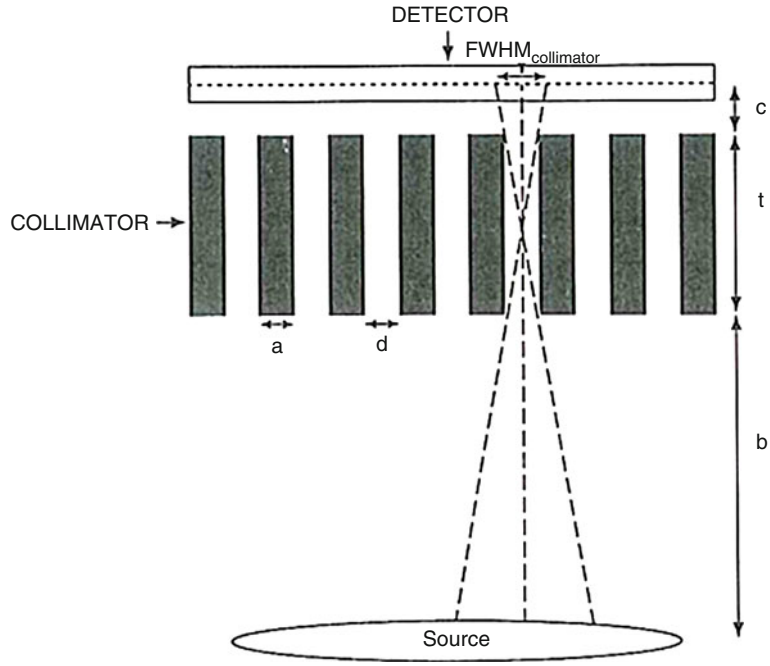

Fig. 4 Collimator spatial resolution, $FWHM_{collimator}$, for a parallel-hole collimator with thickness *t*, aperture diameter *d*, septal thickness *a*, and source-to-collimator face distance *b*. The collimator is fitted to a detector whose midplane is at a distance *c* from the back surface of the collimator (From Ref. [9] with permission)

Solid-state ionization (i.e., semiconductor)-based gamma cameras utilizing cadmium zinc telluride (or CZT) are now commercially available [7, 8]. CZT detectors are more expensive than detectors based on NaI(Tl) crystal coupled with PMTs in the conventional Anger camera but offer several important advantages, including improved energy resolution (typically resulting in a 30% reduction of the scatter counts in the photopeak energy window) and superior intrinsic spatial resolution [7, 8]. The mass density of CZT is higher than that of NaI(Tl) (5.8 vs. 3.7 g/cc), but due to considerations of the higher cost and in order to maintain excellent energy resolution, CZT detectors are thinner (~5 mm) than the typical 3-/8-in. (9.5-mm) NaI(Tl) crystals. The intrinsic sensitivities of CZT and NaI(Tl) are therefore comparable. However, the compact form factor of CZT detectors (Fig. 5) allows for novel detector geometries and, in turn, high-sensitivity collimation.

The full-width half-maximum (FWHM) spatial resolution, $FWHM_{system}$, of gamma cameras is determined by a combination of physical and instrumentation factors. Intrinsic resolution, $FWHM_{intrinsic}$, is the component of spatial resolution contributed by the crystal and associated electronics and is

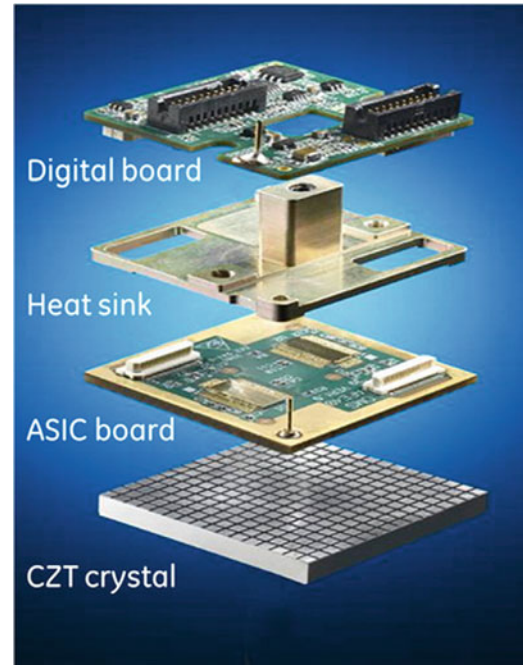

Fig. 5 Typical configuration of a CZT-based semiconductor detector. *ASIC*, application-specific integrated circuit (From Ref. [8] with permission)

related to statistical fluctuations in pulse formation; typical values are of the order of 5 mm. These statistical fluctuations include variations in the production of light photons resulting from x- or γ-ray interactions in the crystal and in the number of electrons emitted by the photocathode and the series of dynodes in the PMTs. Collimator, or geometric, resolution, $FWHM_{collimator}$, represents the major contribution to system resolution and is determined by the collimator design (Figs. 3a and 4). The spatial resolution of a parallel-hole collimator, the most common type, is determined by the geometric radius of acceptance of each aperture, as illustrated in Fig. 4:

$$FWHM_{\text{collimator}} = \frac{d(t_e + b + c)}{t_e} \qquad (1)$$

where d is the diameter of the collimator aperture, b the source-to-collimator face distance, c the collimator back-to-mid-crystal distance, and $t_e = t - 2/\mu$ the effective thickness of the collimator where t is the actual collimator thickness and μ is the radiation energy-dependent linear attenuation coefficient of the collimator material [9]. As indicated by Eq. 1, collimator resolution is improved (i.e., lowered) by reducing the diameter d of the collimator aperture, the source-to-collimator face distance b, and the collimator thickness t. System resolution is further degraded by the contributions of septal penetration resolution, $FWHM_{penetration}$, and by scatter resolution, $FWHM_{scatter}$. The spatial resolution of a gamma camera system, $FWHM_{system}$, can be obtained by combining the resolution of the respective components of the system [9]:

$$FWHM_{\text{system}} = \sqrt{FWHM_{\text{intrinsic}}{}^2 + FWHM_{\text{collimator}}{}^2 + FWHM_{\text{penetration}}{}^2 + FWHM_{\text{scatter}}{}^2} \qquad (2)$$

In clinical practice, the collimator resolution generally dominates the system resolution.

SPECT Data Acquisition

Although there are many possible combinations of detector number, geometry, and motion that can acquire the necessary projection data, rotating gamma camera-based SPECT systems are the most common [4]. Nowadays, two-detector systems predominate clinically and two- to four-detector systems preclinically. The basic SPECT imaging paradigm includes acquisition of planar projection images from multiple angles around the subject, correction of the acquired data for nonuniform scanner response and possibly other signal-degrading effects, and mathematical reconstruction of thin (several-millimeter-thick) transverse tissue section images [4]. The raw data are acquired as a series of discrete planar images at multiple angles about the longitudinal axis of the patient (Fig. 6). The number of counts recorded in each projection-image pixel represents the ray sum, or line integral, of the sampling line perpendicular to and extending from the detector through the subject. The following are typical SPECT acquisition parameters: 20–30 min for data acquisition; ~60 to ~120 projection images at ~6 to ~3° angular increments, respectively; and a 180 or 360° rotation for cardiac or noncardiac studies, respectively. An angular increment in excess of 6° between successive projection images will result in prohibitive undersampling artifacts in the reconstructed images. Because of the length of time (20–30 min) required for an acquisition, dynamic SPECT and whole-body SPECT remain largely impractical at the current time. It should be emphasized that SPECT images can in principle be quantitative in absolute terms, with voxel values representing the local activity concentration [10–12]. However, in contrast to PET, this is often not the case in routine practice because of the confounding effect of scatter and attenuation as well as limited count statistics. Accurate correction for

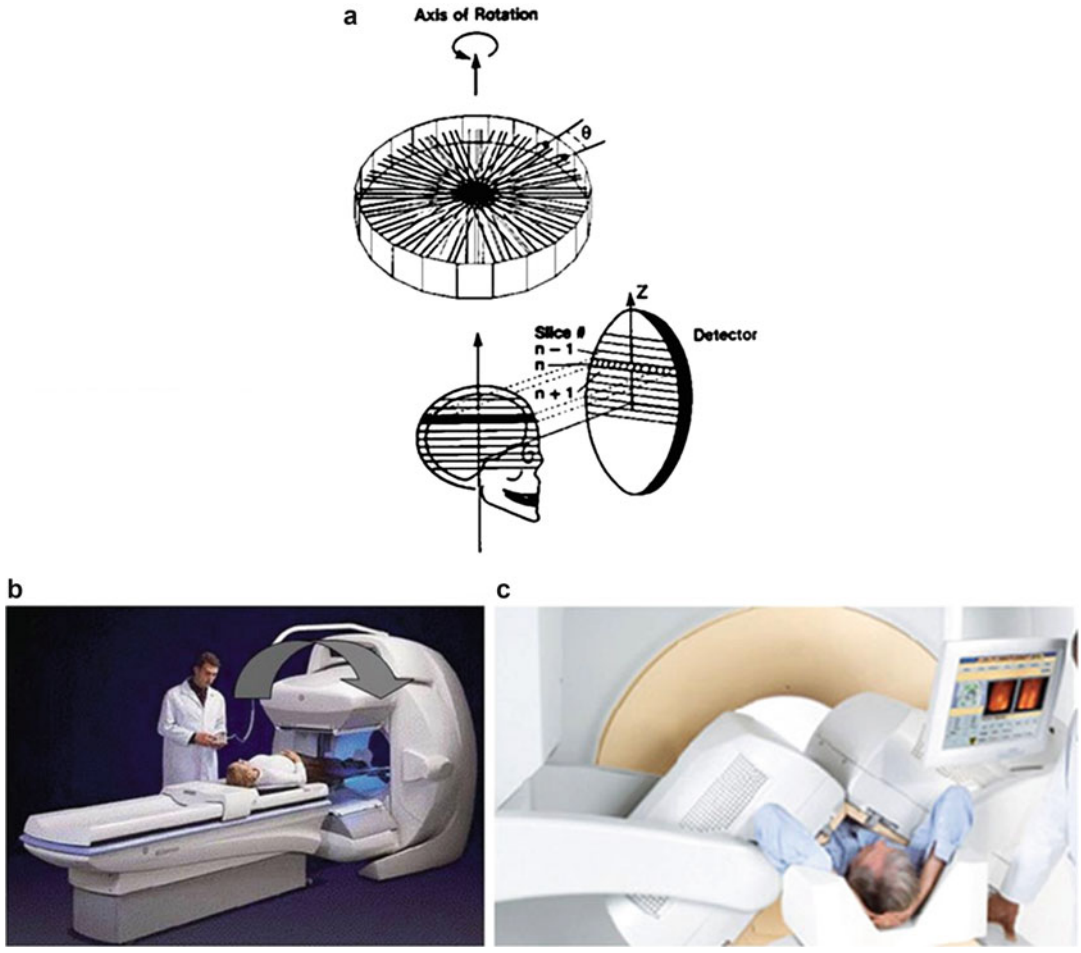

Fig. 6 (**a**) The basic data acquisition paradigm in rotating gamma camera SPECT. Photographs of a dual-detector gamma camera, with (**b**) the two detectors in opposed positions, as routinely used for a 360° rotation and general (noncardiac) SPECT and (**c**) the two detectors perpendicular to each other, as routinely used for a 180° rotation and cardiac SPECT (with projection images acquired from approximately right anterior oblique to left posterior oblique). The advantage of such two-detector systems is that two projection images can be acquired simultaneously and, in first order, either the acquisition time halved or the acquired counts doubled (From Ref. [4] with permission)

these effects remains more challenging in SPECT than in PET [10, 11].

Although PET offers important advantages over SPECT (i.e., generally better spatial resolution, higher sensitivity, and more accurate activity quantitation), SPECT offers the capability of multi-isotope imaging. Because different SPECT radionuclides emit x- and γ-rays of different energies, multiple isotopes and therefore multiple radiotracers can be imaged simultaneously using distinct, isotope-specific photopeak energy windows.

Data "Corrections"

Uniformity correction. Even optimally performing SPECT scanners exhibit some nonuniformity of response [4, 13, 14]. Among the thousands of pixels in a SPECT projection image, slight variations in detector thickness, light emission or coupling properties, electronics performance, etc. result in slightly different measured count rates for the same activity. In principle, such

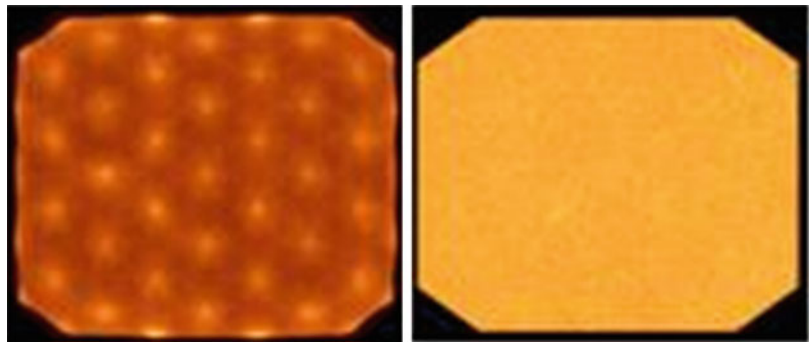

Fig. 7 Uniformity correction and its effects. The *left panel* shows gamma camera image of a uniform source of radioactivity without the uniformity correction applied. The pattern of PMTs is apparent in this grossly nonuniform, uncorrected image. In contrast, the corrected image in the *right panel* is uniform

nonuniform response can be corrected by acquiring data from a uniform flux of γ-rays and normalizing to the *mean* count rate from all the pixels in SPECT. This "uniformity map" corrects for the nonuniform count rate of the individual pixels or lines of response (LORs) to thereby yield a pixel-by-pixel uniformity correction. The effects of nonuniformity of scanner response and of the correction for nonuniform response are illustrated in Fig. 7 [14].

For gamma camera imaging, a correction table may be acquired using either a uniform flood source placed on the detector or a point source placed sufficiently far (typically 1–2 m) from the uncollimated detector to deliver a uniform photon flux. Acquisition of the data required for uniformity correction is somewhat problematic in practice because of statistical considerations: tens of millions must be acquired to avoid possible "noise"-related artifacts in the uniformity correction table.

Deadtime correction. In SPECT, deadtime count losses are generally minimal at diagnostic administered activities. While real-time correction for deadtime count losses is routinely applied in PET, this is generally not the case in SPECT. Count rates encountered in PET are much higher than in SPECT – in part because of the use of electronic rather than absorptive collimation – and therefore accurate deadtime correction is more critical in PET.

Center-of-rotation misalignment correction. In rotating gamma camera SPECT, the location of the projection of the center of rotation (COR) on the projection-image matrix must be constant [14–16]. If the mechanical and electronic CORs are aligned, the pixel location of the projection of the COR onto the projection-image matrix will be the same for all projection images, and, for all such images, the counts in each pixel will then be projected across the appropriate row of pixels in the tomographic image matrix. If, however, the mechanical and electronic CORs are not aligned, the pixel location of the COR will vary among the projection images, and the counts in each projection-image pixel will be projected across different locations in the tomographic image matrix, and blurred images will result (Fig. 8a). In today's SPECT systems, COR misalignment may be easily measured, and corrections are created and automatically applied using the system's software (Fig. 8b). In contrast, PET scanners typically utilize fixed rings of detectors and thus do not suffer from COR misalignment.

Scatter correction. Scatter results in generally diffuse background counts in reconstructed images, reducing contrast and distorting the relationship between image intensity and activity concentration [10, 17, 18]. Several methods, characterized as energy distribution- or spatial distribution-based methods, have been proposed for SPECT scatter correction [12]. However, only the dual-energy window-based or triple-energy window (TEW)-based estimation and the effective scatter source estimation (ESSE) method have been

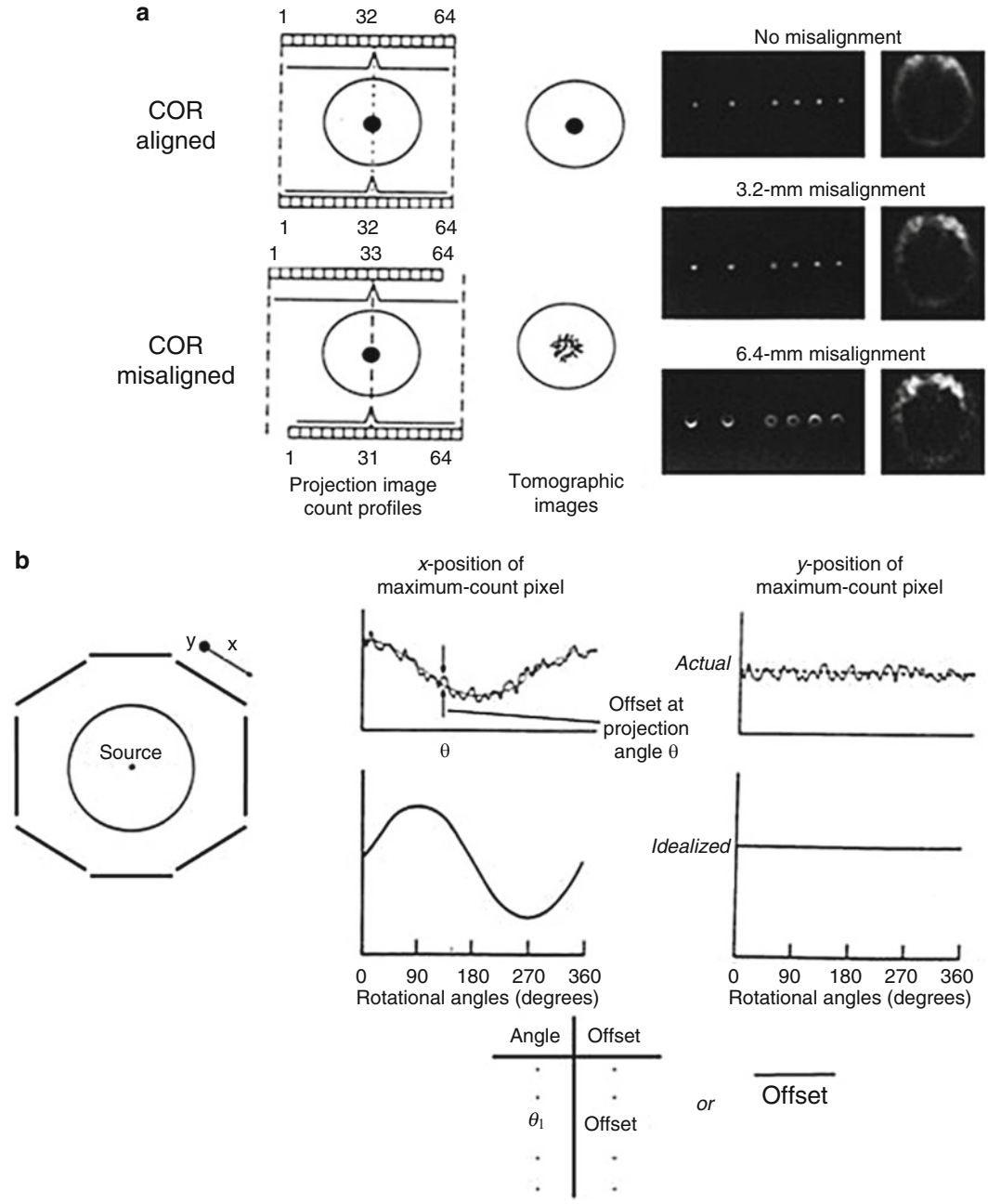

Fig. 8 (**a**) Center-of-rotation (*COR*) misalignment and resulting image-blurring artifacts in rotating gamma camera SPECT. The degree of blurring is related to the magnitude of the spatial misalignment of the mechanical and electronic CORs. A misalignment as small as 3.2 mm (or ½ a pixel for a 64 × 64 image matrix) can produce perceptible blurring in SPECT images, with the blurring substantially worse for a misalignment of 6.4 mm (1 pixel) (Adapted from Ref. [15] with permission). Note that for a cross-sectional image of a line source, COR misalignment blurs the expected point into a full or partial circle depending on the position of the source in the FOV: if it is at or near the center of the FOV, the line source appears as a full circle in cross section; if it is near the periphery of the FOV, it appears as a partial circle. (**b**) COR misalignment can be measured and corrected based on acquiring a 360° circular SPECT study of a ^{99m}Tc point source and constructing graphs of the x- and y-positions (perpendicular

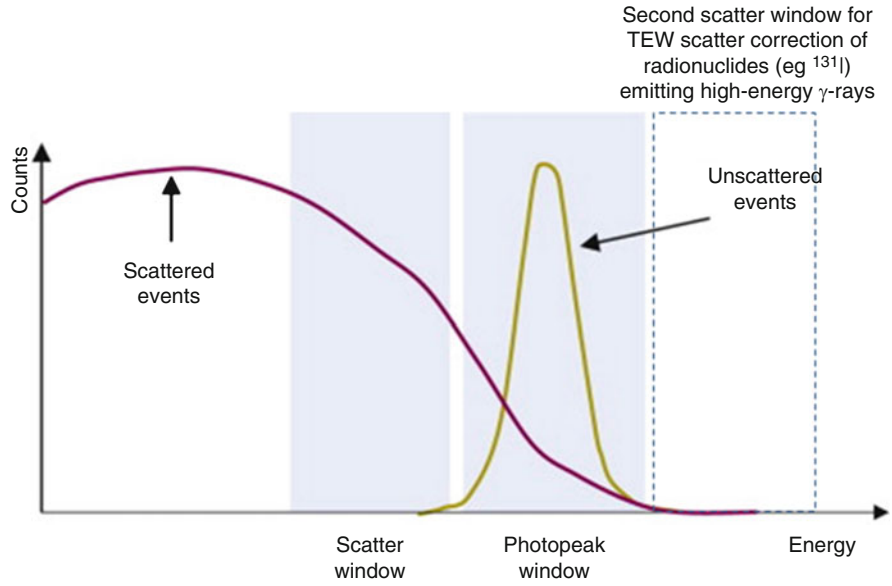

Fig. 9 Dual-energy windows (*shaded boxes*) superimposed on the energy spectrum of unscattered and scattered events for a patient-sized phantom filled with ^{99m}Tc. In contrast to ^{99m}Tc, a radionuclide such as ^{131}I emits a higher-energy γ-ray which will produce scattered events in the photopeak (unscattered-event) energy window in addition to those from scatter of the primary "imaging" γ-ray. For such radionuclides, the dual-energy window method may be generalized to the triple-energy window (*TEW*) method by using a second scatter energy window (indicated by the *dashed-line box*) immediately above the photopeak window (Adapted from Ref. [40] with permission)

implemented clinically. In multi-energy window-based methods [19] (Fig. 9), the number of scattered photons in the photopeak energy window is estimated based on counts in one or more scatter windows. In the TEW method, for example, the scatter is estimated as the area of the trapezoid beneath the line joining the two adjacent narrow scatter windows; for radionuclides emitting a single x- or γ-ray, the upper scatter window can be omitted. For each projection-image pixel *i,j*, the number of scatter counts in the photopeak window, $(C_{i,j})_{\text{scatter}}$, is calculated as:

$$(C_{i,j})_{\text{scatter}} = \left\{ \frac{(C_{i,j})_{\text{lower}}}{W_{\text{lower}}} + \frac{(C_{i,j})_{\text{upper}}}{W_{\text{lower}}} \right\} \frac{W_{\text{photopeak}}}{2} \tag{3}$$

where $(C_{i,j})_{\text{lower}}$ and $(C_{i,j})_{\text{upper}}$ are the counts in the lower and upper scatter energy windows, respectively, for projection pixel *i,j* and $W_{\text{photopeak}}$, W_{lower}, and W_{upper} are the widths (in keV) of the photopeak, lower scatter, and upper scatter windows, respectively. Typically, 20% photopeak and ~5% scatter energy windows are used. Because of the use of such narrow scatter energy windows, the

Fig. 8 (continued) and parallel to the axis of rotation, respectively) of the position of the maximum-count pixel in each projection image versus angular position. The x- and y-position-versus-angle graphs should be a sinusoidal curve and a straight line, respectively. The angle-by-angle deviation between the x-position on the best-fit sine curve and the x-position of the actual maximum-count pixel thus yields a correction table indicating the offset by which each projection image must be shifted at each angular position to align the CORs. Alternatively, the average of the offsets may be used at each angular position (Adapted from Ref. [14, 15] with permission)

TEW estimate of scatter counts tends to be noisy. In the ESSE method [20], a model-derived scatter function is used to calculate and correct for the scatter in the projection data based on the estimate of the activity distribution. An effective scatter source is calculated, and the attenuated projection of that source yields the scatter component of the SPECT projections. Other, more sophisticated and presumably more accurate approaches to scatter modeling include Monte Carlo simulation-based methods [21–23] and analytic methods using the Klein-Nishina formula for Compton scattering [24]. These methods are computationally intensive, however, and have been limited to use in research settings but likely will become clinically practical as computing power continues to increase.

Attenuation correction. As in PET, correction for the attenuation of the γ-rays as they pass through tissue is generally the largest correction in SPECT. The correction factors for a ^{99m}Tc SPECT scan of the brain (roughly equivalent to a 10-cm diameter water-equivalent cylinder) are ~2, for example. The magnitude of the correction depends on the energy of the γ-rays, the thickness of tissue(s) that the γ-rays must travel through, and the attenuation characteristics of the tissue(s).

Like scatter corrections, attenuation corrections in SPECT are not yet as well developed or as reliable as those in PET – because, for single photons, the attenuation correction factor (ACF) also depends on the depth of the source [4]. For many years, if attempted at all, SPECT attenuation correction factors were calculated (as in Chang's first-order correction and the Sorenson method [25, 26]) based on the assumptions – neither of which is generally accurate – that the body is a uniform medium with a single, well-defined value of μ and that the body's contour is known. At one time, manufacturers incorporated long-lived radioactive sources (such as gadolinium-153 (^{153}Gd)) into SPECT scanners to perform attenuation correction. As part of the SPECT procedure, a shutter opens at each projection-image angle to expose a highly collimated line source, and a transmission image is acquired. The transmission images thus acquired are reconstructed into an ACF map for correction of the SPECT study. The introduction of hybrid SPECT/CT scanners (see below) is resulting in more practical and more accurate CT-based attenuation correction in SPECT [27].

Image Reconstruction

In emission tomography, the emission data correspond to the projected sum of counts (or line integrals) at various angles about the axis of the scanner. The full set of 2D projection data is usually represented and stored as a two-dimensional matrix in polar coordinates (distance r, angle ϕ) known as a "sinogram" [28] (see Fig. 14 in the chapter entitled "Instrumentation for Positron Emission Tomography").

There are two basic classes of image reconstruction methods, analytic [4, 28] and iterative [29]. For PET, iterative reconstruction is used almost exclusively nowadays and was reviewed in the earlier chapter on PET instrumentation. For SPECT, on the other hand, analytic image reconstruction (i.e., filtered back projection [4, 28]) is still widely used, though the use of iterative methods is increasing. The basic procedure for image reconstruction by filtered back-projection (FBP) is as follows: each angular projection is Fourier transformed from real to frequency (or "k") space; the projection is filtered in frequency space using a ramp filter (to enhance high and suppress low spatial frequencies and thereby minimize blurring artifacts) (Figs. 10a–c); the filtered projection is inverse Fourier transformed from frequency back to real space; and the filtered projection data in real space are uniformly distributed, or back projected, over the reconstructed image matrix [4, 28]. To compensate for the high noise levels resulting from the relatively low counts in most nuclear imaging studies, low-pass, or apodizing, filters (known as Shepp-Logan, Hann, etc.) are used in place of the ramp filter to eliminate those spatial frequencies above a specified cutoff frequency (Fig. 10d–g). In this way, the high spatial frequencies characteristic of statistical noise are eliminated (or at least minimized) in the reconstructed images.

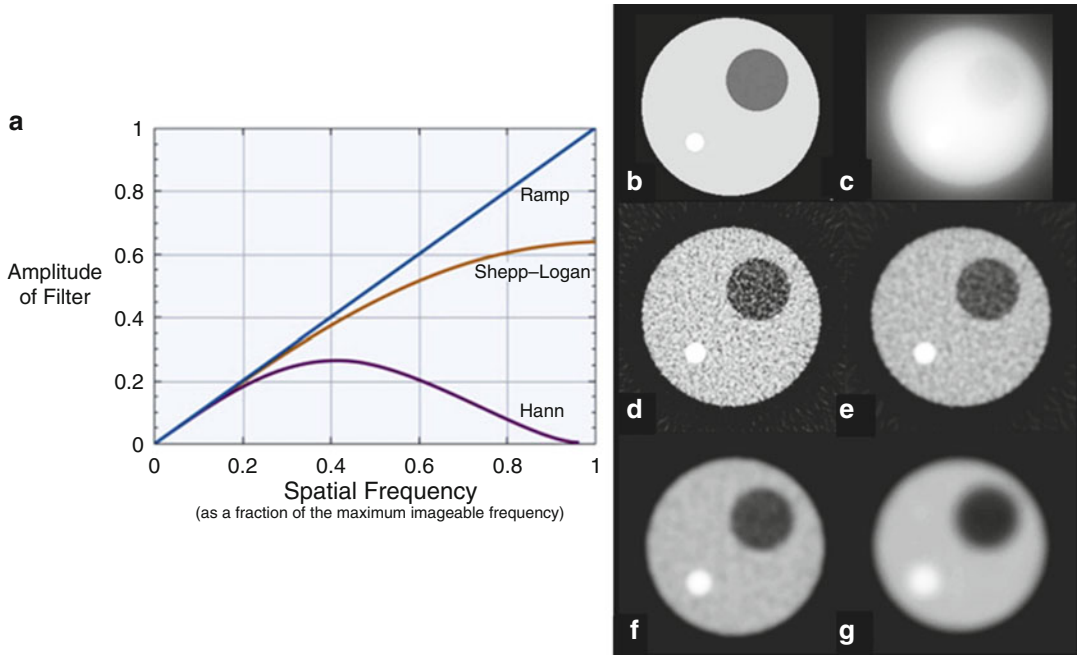

Fig. 10 (**a**) Graphical representation of the ramp and two other mathematical filters used in reconstruction of tomographic images. Note that the cutoff spatial frequencies of all three filters are set to the maximum frequency that can be imaged with the system being used to reduce noise amplification artifacts in the reconstructed images. Note further that the Shepp-Logan and Hann filters "roll off" gradually with increasing spatial frequency to further reduce noise amplification and other artifacts. (**b**) Cross section through a phantom containing high (*white*), intermediate (*light gray*), and low (*dark gray*) activity concentrations. (**c**) Tomographic image of phantom reconstructed by "simple" back-projection, that is, with no mathematical filtering of the projection images. Note the resulting blurring and other artifacts in the reconstructed image. (**d**–**g**) Tomographic images of phantom reconstructed by filtered back-projection using a Shepp-Logan filter with cutoff frequencies equal to 1, 0.8, 0.6, and 0.2 times of the maximum spatial frequency that can be imaged with the system. Note the reduction in noise (i.e., graininess or mottle) but coarser delineation of edges (i.e., poorer resolution) as the cutoff frequency is reduced. For clinical SPECT studies, which generally have limited numbers of counts, cutoff frequencies lower than the maximum imageable frequency are used routinely (Adapted from Ref. [40] with permission)

Quantitation

Once the SPECT emission data have been corrected for dead time, system response (by uniformity correction), scatter, and attenuation, the count rate per voxel in the reconstructed tomographic images is proportional to the local activity concentration [10, 17, 18]. In routine practice, however, scatter and attenuation corrections are generally less accurate for SPECT than for PET (as previously noted) and reconstructed SPECT images less quantitatively accurate than PET images. Further, acquired SPECT data generally include far fewer counts than do PET data because of the use of absorptive collimation for SPECT and electronic collimation for PET, increasing the statistical uncertainties in SPECT.

Another consideration which adversely effects the quantitative accuracy is partial-volume averaging: for a source which is "small" relative to the spatial resolution of the imaging system, the image-derived activity or activity concentration in such a source underestimates the actual value, and the smaller the source the greater the degree of the underestimation [10, 30]. The dimensions of a source must be at least two times the full-width

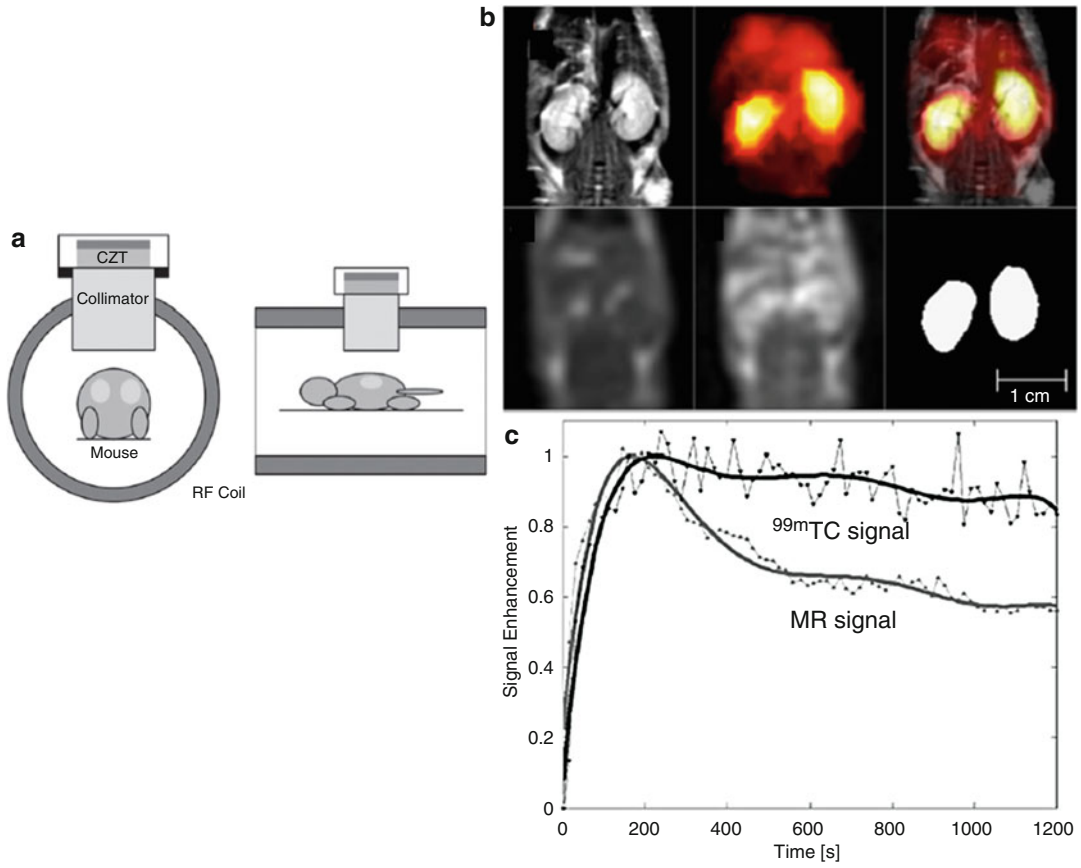

Fig. 11 Proof-of-principle single-photon scintigraphy-MR imaging study in a mouse. (**a**) Diagrammatic representation of the system for simultaneous single-photon scintigraphy using a CZT ionization detector and MR imaging. Note that this is not a SPECT (i.e., tomographic) system but rather a planar imaging system. (**b**) Static non-contrast T1-weighted MR image (*upper left panel*). Frame from dynamic ^{99m}Tc-sestamibi study (*upper middle panel*). "Fusion" of T1-weighted MR and ^{99m}Tc-sestamibi images. Since the ^{99m}Tc-sestamibi image is a planar image (*upper right panel*), the MR and scintigraphic images are not truly fused. (**c**) Frame from a dynamic MR study prior to injection of gadopentetate dimeglumine contrast (*lower left panel*). Frame from a dynamic contrast (gadopentetate dimeglumine)-enhanced MR study (*lower middle panel*). Kidney ROIs extracted from the static non-contrast T1-weighted MR image (*lower right panel*). (**d**) Renal signal-versus-time curves following the ^{99m}Tc-sestamibi and gadopentetate dimeglumine injections (Adapted from Ref. [37] with permission)

half-maximum (FWHM) spatial resolution of the imaging system to avoid such underestimation of the activity or activity concentration [30]. Since the source size dependence of the partial-volume effect can be measured (e.g., by phantom studies), the underestimated activity or activity concentration can be corrected if the source dimensions can be independently determined (e.g., by CT) [31]. Another key factor which limits quantitative accuracy is, of course, subject motion.

As noted in the earlier chapter on PET instrumentation, under favorable circumstances (i.e., for a high-count study of a large, stationery source region with a high source-to-background ratio), the quantitative accuracy of the PET is of the order of 10% [30]. A comparable accuracy, ~10%, is achievable for SPECT with state-of-the-art attenuation and scatter corrections [32]. With routinely available corrections, however, the quantitative accuracy of SPECT generally exceeds 20% [33].

Multimodality Imaging: SPECT/CT and SPECT/MRI

SPECT/CT scanners are, of course, now commercially available [27]. The paradigm for SPECT/CT scanners is similar to that of PET/CT in that the SPECT and CT gantries are separated and the SPECT and CT scans are acquired sequentially, not simultaneously. In such devices, the ~1-m separation of the SPECT and CT scanners is more apparent because the rotational and other motions of the SPECT detectors effectively preclude encasing them in a single housing with the CT scanner. Multimodality imaging devices for small animals (i.e., rodents) – PET/CT, SPECT/CT, and even SPECT-PET/CT devices – are now commercially available as well.

Unlike PET/MR devices, neither clinical nor preclinical SPECT/MR scanners are commercially available at the present time. Investigational preclinical SPECT/MR devices have been developed, however, and proof-of-principle studies have been performed (Fig. 11) [34–37]. As an alternative to scintillation detectors coupled to either PMTs or APDs, prototype SPECT/MR scanners have utilized solid-state (i.e., semiconductor) ionization detectors [34–37]. However, when a semiconductor detector is placed in a magnetic field, electron-hole pairs created by the absorption of x- and γ-rays are subject to the so-called Lorentz force. As a result, when such a detector is placed in any orientation other than parallel or antiparallel to the magnetic field, electrons traveling toward the anode will undergo a shift in their detected position (Fig. 12). For the prototype "MRSPECT" system described by Hamamura et al., for example, a mean "Lorenz shift" of 1.4 mm was measured [34, 35]. In this system, the correction for the Lorentz shift was performed prior to SPECT image reconstruction by shifting the nuclear projection data to their proper locations; this pixel-by-pixel correction was derived by imaging of a uniform flood source, analogous to derivation of gamma camera uniformity corrections generally. The detector elements were coupled to an application-specific integrated circuit (ASIC) readout board, and the detector-ASIC board housing and cables were wrapped with a fine copper mesh for RF shielding.

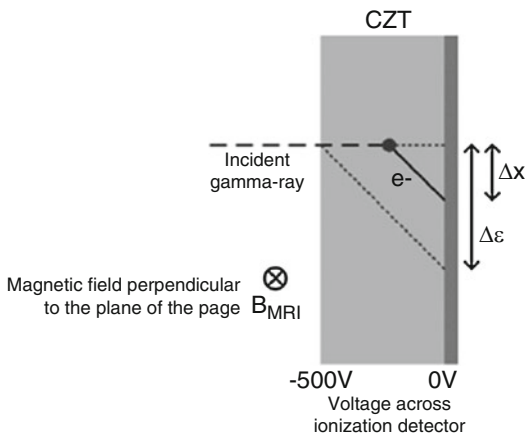

Fig. 12 Diagrammatic illustration of the Lorentz shift. After the interaction of an incident gamma ray with an ionization detector such as CZT, the resulting electron is deflected by a distance Δx due to the Lorentz force. Since the exact depth of the interaction of the gamma ray in the detector is statistical and can occur anywhere along the thickness of the element, there is a range of possible deflected distances Δε (Adapted from Ref. [34] with permission)

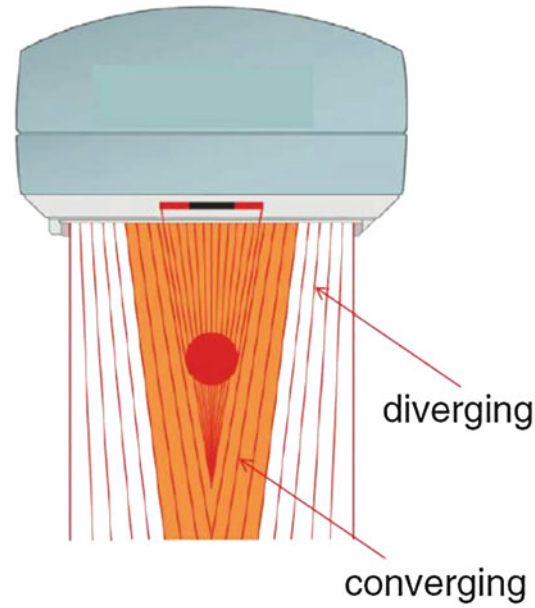

Fig. 13 Data acquisition geometry with the Siemens SmartZoom™ cardio-focal (diverging/converging) collimator. It provides higher sensitivity in the heart region by selective maximal magnification of that region (From Ref. [7] with permission)

Commercial Devices

Clinical. All of the major manufacturers of medical imaging equipment, including General Electric, Philips, Siemens, and Toshiba, currently market clinical SPECT devices. SPECT scanners continue to mainly utilize dual NaI(Tl) detectors (most commonly ~10 mm in thickness) in an opposed configuration; many commercial systems allow rotation of the detectors to an angle of 90° with respect to one another for cardiac studies. SPECT system spatial resolution (FWHM) with low-energy, high-resolution (LEHR) collimation is typically 7–8 mm for ^{99m}Tc at a source-to-collimator distance of 10 cm.

Conventional dedicated cardiac SPECT scanners generally employ two scintillation detectors fixed at a right angle to one another and, in some models, radioactive sources for transmission imaging-based, patient-specific attenuation correction [7, 8]. Cardiac imaging typically involves acquisition of projection data over only a 180° orbit (instead of the 360° orbit used for general SPECT imaging) – from right anterior oblique to left posterior oblique – because of the left, anterior position of the heart within the thorax. By positioning the two detectors at a right angle to one another, both detectors can simultaneously acquire usable data over the 180° orbit; if the two detectors were in the usual opposed position, only one of the two detectors would actually acquire usable data. Dedicated cardiac SPECT scanners with two scintillation detectors fixed at a right angle to one another include the Philips CardioMD™ and the Siemens CCam™.

Siemens has also introduced so-called "cardiofocal" (SmartZoom™) field-upgradeable collimators for high-sensitivity cardiac imaging with conventional dual-head gamma cameras (Fig. 13) [7, 8].

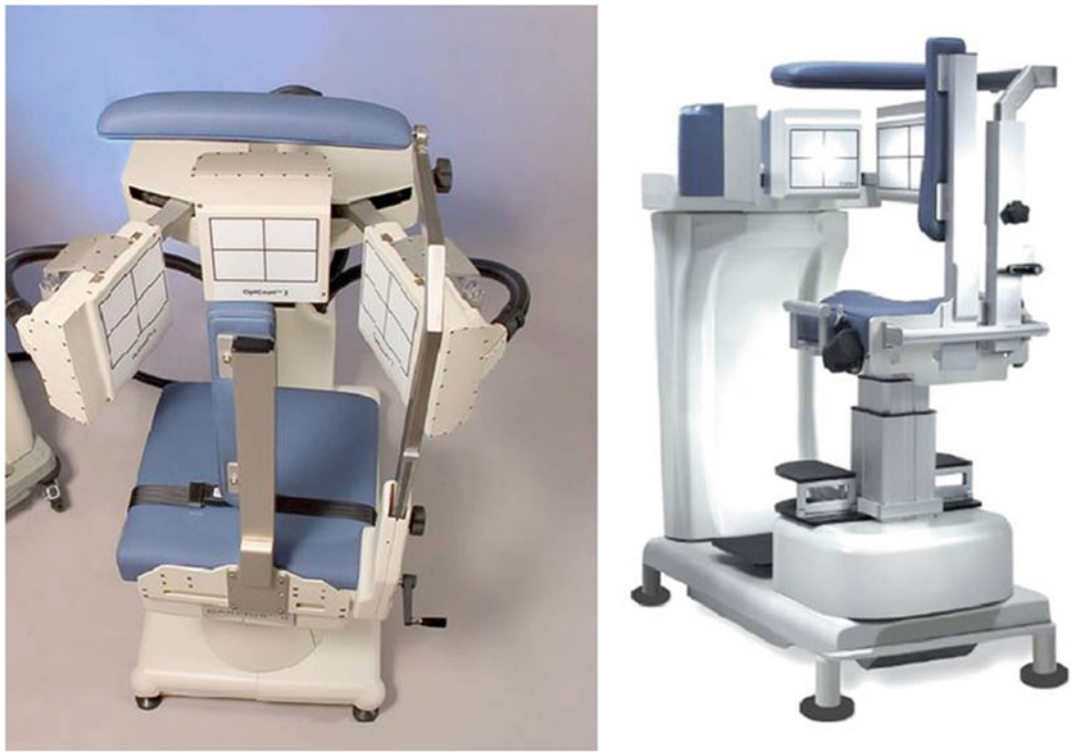

Fig. 14 Photographs of the Digirad Cardius 3 XPO™ system. The patient is seated upright, and the chair rotates to achieve the required angular sampling (From Ref. [7] with permission)

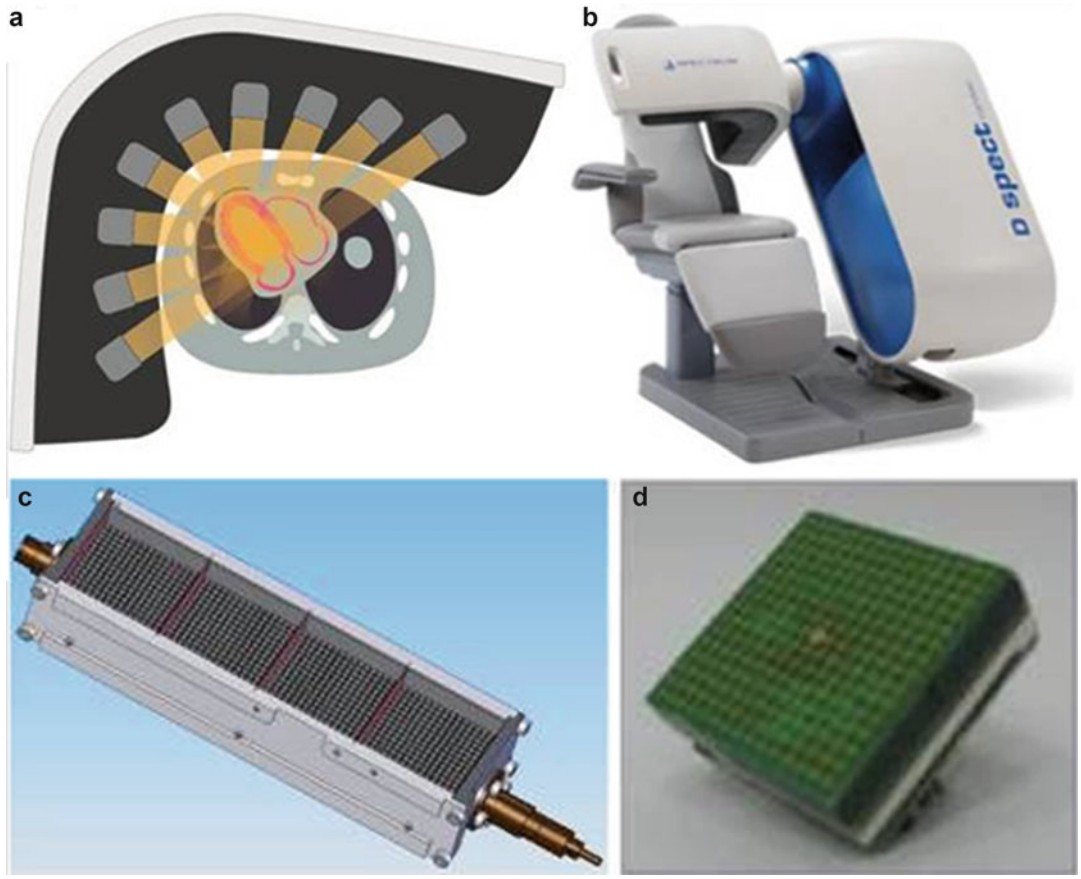

Fig. 15 (**a**) Detector configuration (*top view*) of the Spectrum Dynamics D-SPECT™ system with nine angularly directed detector blocks. (**b**) Photograph of the system. The patient may be seated upright or the chair reclines so that the patient may lie nearly supine. (**c**) One of the nine detector blocks. (**d**) One of the CZT detectors (From Ref. [7] with permission)

Also known as "astigmatic" collimation, with such a converging/diverging collimator, the converging collimation magnifies the center of the field of view (FOV) in both the axial and transaxial directions, while the diverging collimation minifies the periphery of the FOV to provide coverage of the entire body and thereby avoid truncation artifacts commonly seen with fanbeam collimators when imaging the torso. Such cardio-focal collimators can increase sensitivity for cardiac imaging by approximately twofold compared to that with high-resolution parallel-hole collimator.

The Digirad Cardius 3 XPO™ cardiac scanner employs three pixilated CsI(Tl) scintillation detectors and images patients in an upright seated position (Fig. 14) [7, 8]; one- and two-detector Cardius systems are available as well. It uses fanbeam collimators in the three-detector configuration coupled to photodiode detectors. The two outer detectors are positioned at a 67.5° angle relative to the central detector. Data are acquired by rotating the chair (rather than detectors) by 67.5°, yielding an acquisition arc of 202.5°. Its SPECT spatial resolution (FWHM) is 11.0 mm (radius of rotation: 20 cm) and sensitivity 160 cpm/μCi for ^{99m}Tc and LEHR collimation. The Digirad Cardius X-ACT™ system augments the Cardius 3 XPO™ with a fanbeam x-ray source for CT imaging. The CardiaArc HD-SPECT™ [38] also images patients in an upright seated position. It is comprised of three curved stationery NaI (Tl) crystals backed by three rows of 20 PMTs,

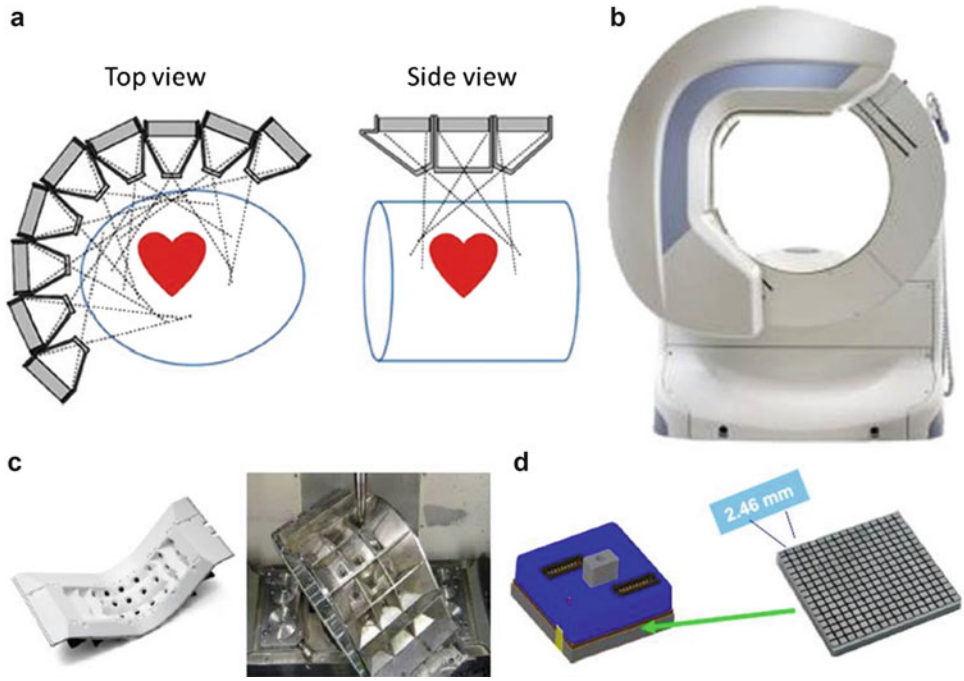

Fig. 16 (**a**) Detector configuration (*top* and *side views*) of the General Electric NM 530c™ system with nine detector block arrays. (**b**) Photograph of the system. The patient lies supine. (**c**) The pinhole collimation. (**d**) One of the CZT detectors (Adapted from Ref. [7] with permission)

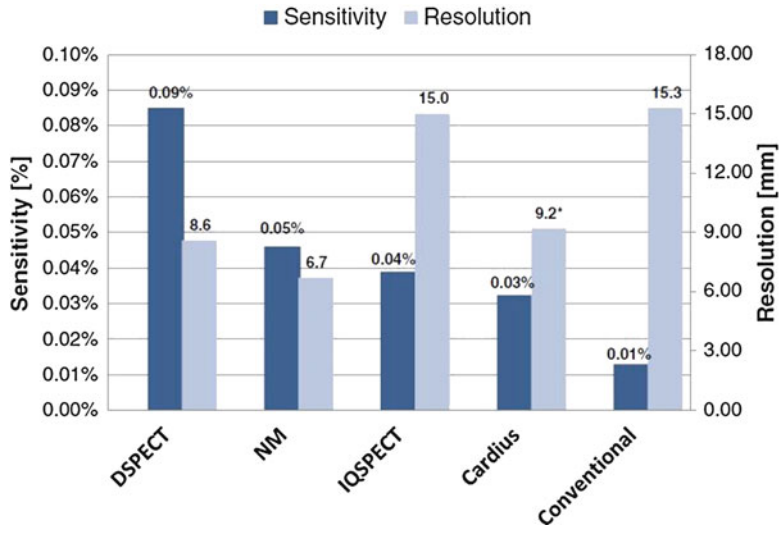

Fig. 17 Sensitivity in % (*left axis*) and reconstructed image resolution in mm (*right axis*) of dedicated cardiac SPECT systems compared to those of a conventional dual-head system. DSPECT: Spectrum Dynamics DSPECT™ system; NM: GE 530c/570c™ system; IQSPECT: Symbia system with dual-head Siemens SmartZoom™ cardiofocal (diverging/converging) collimators; Cardius: Cardius Digirad X·ACT™ system with fanbeam collimators; Conventional: conventional dual-headed SPECT with low-energy high-resolution collimators (From Ref. [7] with permission)

Table 2 Design and performance parameters of commercially available clinical SPECT scanners[a,b]

	General Electric Discovery NM/CT 670c™	General Electric Infinia Hawkeye™	Philips Brightview™	Philips CardioMD™	Siemens Symbia TruePoint™	Siemens CCam™	Toshiba TCam™
Detector material	NaI(Tl)	NaI(Tl)	NaI(Tl)	NaI(Tl)	NaI(Tl)	NaI(Tl)	NaI(Tl)
Number of detectors	2	2	2	2	2	2	2
Angle between detectors[c]	Variable – 90–180°	Variable – 90–180°	Variable – 90–180°	Fixed – 90°	Variable – 90–180°	Fixed – 90°	Variable – 90–180°
Crystal thickness (in)	3/8	3/8	3/8	3/8	3/8	1/3	3/8
Uniformity CFOV IU (%)[d,e]	3.0	3.0	2.5	2.6	2.9	2.5	3.7
Energy resolution (%)	9.8	9.8	9.4	9.4	9.6	9.4	10
Intrinsic spatial resolution[e] (FWHM in mm) – ^{99m}Tc	3.8	3.8	3.7	3.7	3.8	3.7	3.9
System spatial resolution @ 10 cm[e] (FWHM in mm) – ^{99m}Tc with LEHR[f] collimation	7.4	7.4	7.2	7.7	8.7	7.6	7.4
System sensitivity[e] (cps/MBq) – ^{99m}Tc with LEHR[f] collimation	72	72	74	86	91	82	91
SPECT spatial resolution[e] (FWHM in mm) – ^{99m}Tc with LEHR[f] collimation	9.9	9.9	9.8	Not available	11	Not available	Not available

[a]SPECT scanners are currently marketed as "SPECT-only" scanners or as multimodality devices with either "diagnostic-grade" or "nondiagnostic-grade" CT scanners; the latter are used only for attenuation correction and anatomic orientation

[b]Extracted from the marketing literature of the respective manufacturers

[c]Gamma cameras in which the angle between the two detectors may be varied from 90 to 180° are general-purpose (including cardiac) imaging devices; those in which the two detectors are fixed at a 90° angle with respect to one another are dedicated cardiac imaging devices

[d]CFOV IU: central field-of-view integral uniformity, ((maximum counts per pixel – minimum counts per pixel)/(maximum counts per pixel – minimum counts per pixel) 100% for a high-count "flood" image

[e]Gamma camera and SPECT scanner performance parameters and their measurement are described in references [41–43]

[f]*LEHR* low-energy high-resolution

with a thin curved lead collimator (the so-called aperture arc) having six vertical slots for horizontal collimation and rotating slowly back and forth every 10 s. The CardiaArc™ quotes a spatial resolution of 3.6 at an 82-mm source-to-detector distance to 7.8 mm at a 337-mm source-to-detector distance.

Two vendors have introduced CZT-based cardiac SPECT systems [7, 8]. The Spectrum Dynamics D-SPECT™ utilizes pixilated CZT detector arrays mounted in nine vertical columns, with four detectors in each column, placed in a 90° gantry geometry (Fig. 15). Each column consists of an array of 1,024 CZT elements (2.46 × 2.46 × 5-mm thick) arranged in a 16 × 64 element array with a size of 40 × 160 mm, achieving 16 cm of coverage of the thorax. Each detector array is fitted with square aperture, high-sensitivity, parallel-hole collimators such that the dimensions of each hole are matched to the size of a single detector element. Spectrum Dynamics also recently introduced a less expensive six-detector column system. In the other CZT-based camera design found in the General Electric Discovery NM 530c™ and Discovery NM/CT 570c™, a curved array of 19 5-mm-thick CZT-pixilated detector arrays each with a focused pinhole collimator is used (Fig. 16). Each detector array consists of four detectors, each with 246 CZT detector elements (2.46 × 2.46 × 5-mm thick) arranged in a 16 × 16 element array. In these two systems, the detector gantry does not rotate or otherwise move [7, 8]. The remarkably high sensitivity of these systems is not related to the intrinsic sensitivity of the CZT detectors but rather the high-sensitivity geometric arrangement and collimation of the detectors.

The foregoing dedicated cardiac scanners provide better spatial resolution and higher sensitivity than conventional gamma cameras, as illustrated in Fig. 17 [7, 8, 39]. These systems provide up to a sevenfold increase in sensitivity and twofold improvement in reconstructed image resolution compared with those of conventional dual-head systems. Cardiac imaging times with these scanners thus range from 2 to 3 min for systems with solid-state detectors to 4 min on scintillation detector systems with cardio-focal collimation [7, 8, 39]. The design and performance parameters of other commercially available clinical SPECT scanners are summarized in Table 2.

Table 3 Design and performance parameters of commercially available preclinical SPECT scanners[a,b]

	Mediso NanoSPECT™	Carestream Albira™	Gamma Medica Triumph™	MI Labs Vector™[c]	Siemens Inveon™
Detectors	NaI(Tl)	NaI(Tl)	CZT	NaI(Tl)	NaI(Tl)
Number of detectors	4	2	Up to 4	Not available	Up to 4
Parallel-hole collimation?	Yes	No	Yes	No	Yes
Pinhole collimation?	Yes	Yes	Yes	Yes (Tungsten)	Yes
Number of apertures per pinhole collimator	9	Up to 5	"Multiple"	5 rings of 15 apertures each	Up to 5
SPECT spatial resolution (FWHM in mm) – ^{99m}Tc with pinhole collimation	1.2	0.8	0.4	0.35	1.0–1.5
Sensitivity (cps/MBq ^{99m}Tc) – with pinhole collimation	1,640	1,000	Up to 6,500	Up to 1,600	400–600

[a]Preclinical scanners are currently marketed as "SPECT-only" scanners or as multimodality devices with integrated CT and/or PET scanners. As noted, the Carestream Albira, Gamma Medica Triumph LabPET Solo, and Siemens Inveon are available as trimodality PET-SPECT/CT systems

[b]Extracted from the marketing literature of the respective manufacturers

[c]The MI Labs Vector also functions as a PET scanner by collimated single-photon (i.e., noncoincidence) detection of the 511-keV annihilation gamma rays accompanying positron emission

Preclinical. A number of preclinical SPECT devices are commercially available. The various preclinical SPECT scanners are rather similar in design, generally utilizing multiple NaI(Tl) scintillation detectors fitted with multi-aperture pinhole collimators. The superior spatial resolution of preclinical versus clinical SPECT scanners, ~1 versus ~10 mm, is due to the magnification effect afforded by the pinhole collimation (Figure 2b). Of course, this is achieved at the cost of lower sensitivity, though the use of multi-aperture collimators and multiple (up to four) detectors as least partially mitigates the reduction in sensitivity. Preclinical devices are currently marketed as "SPECT-only" scanners, as multimodality devices with integrated CT scanners (typically conebeam devices with flat-panel detectors) or even as trimodality PET-SPECT/CT systems. The design and performance parameters of commercially available preclinical SPECT scanners are summarized in Table 3.

Concluding Remarks

Although the spatial resolution of SPECT (~1 and ~10 mm for preclinical and clinical devices, respectively) is excellent by historical standards for this modality, it remains relatively coarse compared to that of such high-resolution "anatomic" imaging modalities as CT and MRI (0.1–1 mm). Nonetheless, the distinctive and important advantages of radionuclide-based imaging – high detection sensitivity, "image ability" of non-perturbing doses of radiotracers, quantitative accuracy, and a vast array of radiotracers – ensure that SPECT (particularly in combination with CT and, potentially, MRI) will remain an invaluable molecular imaging modality in clinical practice and in clinical and preclinical research.

References

1. Zanzonico P. Principles of nuclear medicine imaging: planar, SPECT, PET, multi-modality, and autoradiography systems. Radiat Res. 2012;177:349–64.
2. Zanzonico P. Radionuclide imaging. In: Cherry S, Badawy R, Qi J, editors. Essentials of in vivo biomedical imaging. Boca Raton: CRC Press; 2015. p. 1765–224.
3. Zanzonico P, Heller S. Physics, instrumentation, and radiation protection. In: Biersack H-JF, Leonard M, editors. Clinical nuclear medicine. Heidelberg: Springer; 2007. p. 1–33.
4. Zanzonico PB. Technical requirements for SPECT: equipment and quality control. In: Kramer EL, Sanger JJ, editors. Clinical applications in SPECT. New York: Raven Press; 1995. p. 7–41.
5. Firestone RB, Shirley VS, editors. Table 11 of isotopes. 8th ed. New York: Wiley; 1996.
6. Weber D, Eckerman K, Dillman L, et al. MIRD: radionuclide data and decay schemes. New York: Society of Nuclear Medicine; 1989. p. 447.
7. Slomka PJ, Berman DS, Germano G. New cardiac cameras: single-photon emission CT and PET. Semin Nucl Med. 2014;44:232–51.
8. Slomka PJ, Pan T, Berman DS, et al. Advances in SPECT and PET hardware. Prog Cardiovasc Dis. 2015;57:566–78.
9. Saha GS. Physics and radiobiology of nuclear medicine. New York: Springer; 1993. p. 107–23.
10. Frey EC, Humm JL, Ljungberg M. Accuracy and precision of radioactivity quantification in nuclear medicine images. Semin Nucl Med. 2012;42:208–18.
11. Tsui BM, Zhao X, Frey EC, et al. Quantitative single-photon emission computed tomography: basics and clinical considerations. Semin Nucl Med. 1994;24:38–65.
12. Dewaraja YK, Frey EC, Sgouros G, et al. MIRD pamphlet no. 23: quantitative SPECT for patient-specific 3D dosimetry in internal radionuclide therapy. J Nucl Med. 2012;53:1310–25, in press.
13. Zanzonico P. Positron emission tomography: a review of basic principles, scanner design and performance, and current systems. Semin Nucl Med. 2004;34:87–111.
14. Zanzonico P. Routine quality control of clinical nuclear medicine instrumentation: a brief review. J Nucl Med. 2008;49:1114–31.
15. Greer K, Jaszczak RJ, Harris C, et al. Quality control in SPECT. J Nucl Med Technol. 1985;13:76–85.
16. Harkness BA, Rogers WL, Clinthorne NH, et al. SPECT: quality control and artifact identification. J Nucl Med Technol. 1983;11:55–60.
17. Meikle SR, Badawi RD. Quantitative techniques in PET. In: Bailey DL et al., editors. Positron emission tomography: basic sciences. London: Springer; 2005. p. 93–126.
18. Bailey DL. Quantitative procedures in 3D PET. In: Bendriem B, Townsend DW, editors. The theory and practice of 3D PET. Dordrecht: Kluwer; 1998. p. 55–109.
19. Ogawa K, Harata Y, Ichihara T, et al. A practical method for position-dependent Compton-scatter correction in single photon-emission CT. IEEE Trans Med Imaging. 1991;10:408–12.

20. Frey EC, Tsui B. A new method for modeling the spatially-variant, object-dependent scatter response function in SPECT. IEEE; 1996.
21. Beekman FJ, de Jong HW, van Geloven S. Efficient fully 3-D iterative SPECT reconstruction with Monte Carlo-based scatter compensation. IEEE Trans Med Imaging. 2002;21:867–77.
22. Dewaraja YK, Ljungberg M, Fessler JA. 3-D Monte Carlo-based scatter compensation in quantitative I-131 SPECT reconstruction. IEEE Trans Nucl Sci. 2006; 53:181–8.
23. Ouyang J, El Fakhri G, Moore SC. Improved activity estimation with MC-JOSEM versus TEW-JOSEM in ^{111}In SPECT. Med Phys. 2008;35:2029–40.
24. Shcherbinin S, Celler A, Belhocine T, et al. Accuracy of quantitative reconstructions in SPECT/CT imaging. Phys Med Biol. 2008;53:4595.
25. Chang LT. A method for attenuation correction in radionuclide computed tomography. IEEE Trans Nucl Sci. 1978;25:638–43.
26. Sorenson JA. Quantitative measurement of radioactivity in whole-body counting. In: Hine GJ, Soresnon JA, editors. Instrumentation of nuclear medicine. Waltham: Academic; 1974. p. 311–48.
27. Israel O, Goldsmith SJ, editors. Hybrid SPECT/CT: imaging in clinical practice. New York: Taylor & Francis; 2006. p. 244.
28. Defrise M, Kinahan P. Data acquisition and image reconstruction for 3D PET. In: Bendriem B, Townsend DW, editors. The theory and practice of 3D PET. Dordrecht: Kluwer; 1998. p. 11–53.
29. Defrise M, Kinahan PE, Michel CJ. Image reconstruction algorithms in PET. In: Bailey DL et al., editors. Positron emission tomography: basic sciences. London: Springer; 2005. p. 63–91.
30. Hoffman EJ, Huang SC, Phelps ME. Quantitation in positron emission computed tomography: 1. Effect of object size. J Comput Assist Tomogr. 1979;3: 299–308.
31. Erlandsson K, Buvat I, Pretorius PH, Thomas BA, Hutton BF. A review of partial volume correction techniques for emission tomography and their applications in neurology, cardiology and oncology. Phys Med Biol. 2012;57:R119–59.
32. Sgouros G, Frey E, Wahl R, et al. Three-dimensional imaging-based radiobiological dosimetry. Semin Nucl Med. 2008;38:321–34.
33. Flux G, Bardies M, Monsieurs M, et al. The impact of PET and SPECT on dosimetry for targeted radionuclide therapy. Z Med Phys. 2006;16:47–59.
34. Hamamura MJ, Ha S, Roeck WW, et al. Development of an MR-compatible SPECT system (MRSPECT) for simultaneous data acquisition. Phys Med Biol. 2010; 55:1563–75.
35. Hamamura MJ, Ha S, Roeck WW, et al. Initial investigation of preclinical integrated SPECT and MR imaging. Technol Cancer Res Treat. 2010;9:21–8.
36. Ha S, Hamamura MJ, Roeck WW, et al. Development of a new RF coil and gamma-ray radiation shielding assembly for improved MR image quality in SPECT/MRI. Phys Med Biol. 2010;55: 2495–504.
37. Hamamura MJ, Roeck WW, Ha S, et al. Simultaneous in vivo dynamic contrast-enhanced magnetic resonance and scintigraphic imaging. Phys Med Biol. 2011;56: N63–9.
38. Travin MI. Cardiac cameras. Semin Nucl Med. 2011;41: 182–201.
39. Imbert L, Poussier S, Franken PR, et al. Compared performance of high-sensitivity cameras dedicated to myocardial perfusion SPECT: a comprehensive analysis of phantom and human images. J Nucl Med. 2012;53:1897–903.
40. Cherry SR, Sorenson JA, Phelps ME. Physics in nuclear medicine. 4th ed. Philadelphia: Saunders; 2012.
41. Hines H, Kayayan R, Colsher J, et al. Recommendations for implementing SPECT instrumentation quality control. Nuclear Medicine Section – National Electrical Manufacturers Association (NEMA). Eur J Nucl Med. 1999;26:527–32.
42. Hines H, Kayayan R, Colsher J, et al. National Electrical Manufacturers Association recommendations for implementing SPECT instrumentation quality control. J Nucl Med. 2000;41:383–9.
43. NEMA. Performance measurements of scintillation counters. NEMA Standards Publication NU1-2001. Rosslyn: National Electrical Manufacturers Association (NEMA); 2001.

Instrumentation for Intraoperative Detection

12

Pat Zanzonico

Abstract

Focusing on nuclear and optical modalities, the current chapter reviews the rapidly advancing technologies in intraoperative detection and imaging. This chapter reviews not only currently routine intraoperative imaging technologies but also investigational technologies potentially adaptable to the intraoperative setting.

Keywords

Intraoperative imaging • Optical imaging • Gamma probes • Beta probes • Cerenkov imaging • Photoacoustic imaging • Raman effect

Glossary

[^{18}F]FDG	2-deoxy-2-[^{18}F]fluoro-D-glucose
ALA	5-aminolevulinic acid
CARS	Coherence anti-Stokes Raman scattering
CCD	Charge-coupled detector
CdTe	Cadmium telluride
CdZnTe (or CZT)	Cadmium zinc telluride
CMOS	Complementary metal oxide semiconductor
CsI(Na)	Sodium-doped cesium iodide
CsI(Tl)	Thallium-doped cesium iodide
CT	X-ray computed tomography
DOT	Diffuse optical tomography
EPR	Enhanced permeability and retention
FITC	Fluorescein isothiocyanate
FLI	Intraoperative fluorescence imaging
FLuc	Gene encoding for firefly luciferase
FOV	Field of view
FWHM	Full-width half-maximum
GFP	Green fluorescent protein
GSO	Cerium-doped gadolinium orthooxysilicate
HgI_2	Mercuric iodide
ICG	Indocyanine green
LED	Light-emitting diode
LEHR	Low-energy high-resolution
LSO	Cerium-doped lutetium orthooxysilicate
MBq	Mega-Becquerel (10^6 Becquerel)
MR	Magnetic resonance
MRI	Magnetic resonance imaging
MSOT	Multispectral optoacoustic tomography
NaI(Tl)	Thallium-doped sodium iodide

P. Zanzonico (✉)
Memorial Hospital Research Laboratories, Department of Medical Physics, Memorial Sloan Kettering Cancer Center, New York, NY, USA
e-mail: zanzonip@mskcc.org

© Springer International Publishing Switzerland 2017
H.W. Strauss et al. (eds.), *Nuclear Oncology*,
https://doi.org/10.1007/978-3-319-26236-9_38

NBI	Narrowband imaging
NIR	Near-infrared
OCT	Optical coherence tomography
PA	Photoacoustic
PET	Positron emission tomography
PMT	Photomultiplier tube
POCI	Peroperative compact imager
PpIX	Protoporphyrin IX
RF	Radiofrequency
RGD	Tripeptide composed of L-arginine, glycine, and L-aspartic acid
SERS	Surface enhanced Raman scattering (or surface enhanced Raman spectroscopy)
SLN	Sentinel lymph node
SPECT	Single-photon emission tomography
SSGC	Small semiconductor gamma camera
US	Ultrasonography

Contents

Introduction 276
Nuclear Counting and Imaging 276
Optical and Near-Infrared (NIR) Imaging 285
Concluding Remarks 300
References 300

Introduction

Focusing on nuclear and optical modalities, the current chapter reviews the rapidly advancing technologies in intraoperative detection and imaging. This chapter reviews not only currently routine intraoperative imaging technologies but also investigational technologies potentially adaptable to the intraoperative setting. The reader is referred to a recently published volume entitled, "Imaging and Visualization in the Modern Operating Room: A Comprehensive Guide for Physicians," which provides a detailed overview of the many logistical as well as technical considerations in modern intraoperative imaging [1].

Nuclear Counting and Imaging

Beginning with the pioneering studies of Sweet [2] 60 years ago, intraoperative probes (i.e., counters) have evolved into an important, well-established technology in the management of cancer [3–6]. Such probes (see Fig. 1) are used in radioguided surgery to more expeditiously identify and localize sentinel lymph nodes and thereby reduce the extent and potential morbidity of surgical procedures and, to a much lesser extent, to identify and localize tumor margins as well as visually occult disease following systemic administration of a tumor-avid radiotracer (e.g., 2-deoxy-2-[^{18}F]fluoro-D-glucose ([^{18}F]FDG)).

Radionuclide-based detection and localization of tumors, especially small tumors, has several well-known limitations [7] which are mitigated through the use of intraoperative probes and, potentially, intraoperative gamma cameras. First, absolute tumor uptake of cancer-targeted radiotracers remains generally quite low, typically ~0.1% or less of the administered activity per gram. Second, overall radiation detection sensitivity in vivo is low as well, ranging from about 0.1% for gamma camera imaging (including SPECT) to ~10% for PET. This is exacerbated, of course, by the signal-degrading effect of attenuation of emitted radiation by overlying tissue. Third, a significant portion of the counts apparently emanating from a tumor or other targeted tissue may actually include counts originating elsewhere (i.e., from background activity in adjacent tissues) because of contrast- and resolution-degrading Compton scatter. However, because of the close proximity of a collimated detector to a tumor or sentinel lymph node which can be achieved at surgery, radionuclide detection of such structures can be enhanced using intraoperative probes or gamma cameras. In a study of simulated tumors in a torso phantom having uniform background activity, for example, Barber et al. demonstrated that a scintillation probe detected tumors with greater sensitivity than a gamma camera over a wide range of conditions provided the probe was placed within 1 cm of the tumor [8]. Alternatively, tumor or sentinel lymph node detection may also

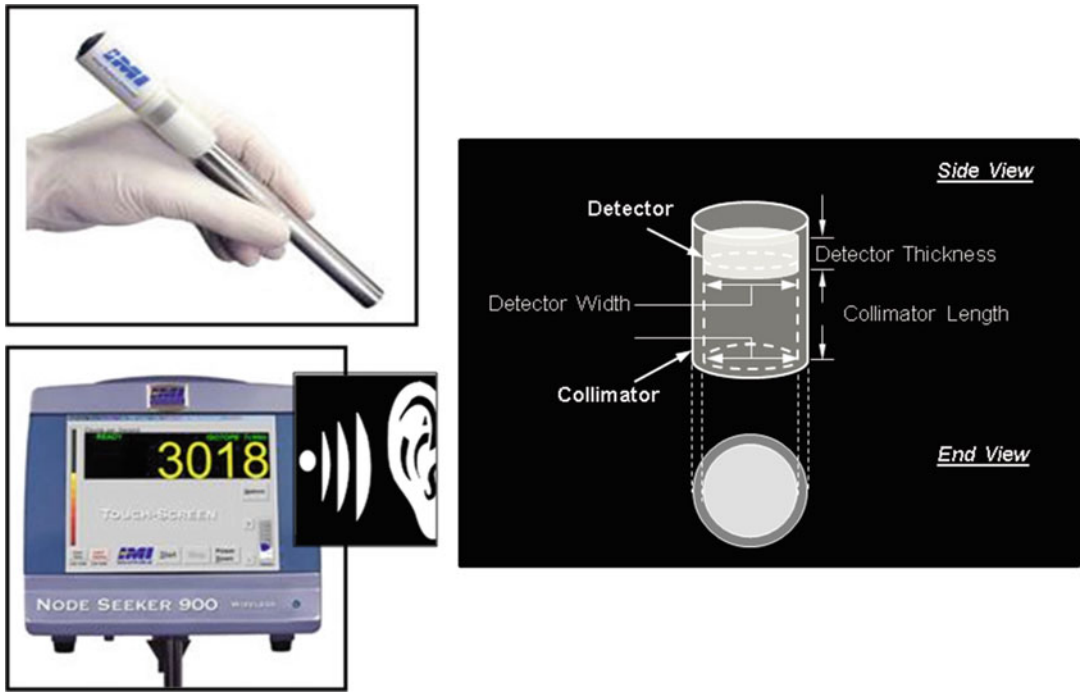

Fig. 1 The general design and operating principles of an intraoperative gamma probe. The handheld probe (*upper left panel*) is comprised of a collimated, small-area (typically ~1 cm in diameter) scintillation or solid-state ionization (i.e., semiconductor) detector (*right panel*). The probe itself is connected to a control unit (*lower left panel*) which typically provides both a visual readout of the count rate and an audible signal related to the count rate, with the frequency of the latter signal increasing or decreasing in relation to the detected count rate [12–14]

be improved under some circumstances using beta (negatron or positron), rather than gamma, detection [9–11] because the very short range (typically ~1 mm or less) of such particulate radiations eliminates the contribution of confounding counts from activity other than in the immediate vicinity of the detector. Of course, the short range of particulate radiations also limits the application of beta probes to intraoperative or endoscopic settings with the lesion near the surface of the exposed tissue.

Gamma probes. The most widely used type of intraoperative probe (e.g., in sentinel node detection) is the general-purpose "gamma" probe (Fig. 1), designed for counting of radionuclides emitting x- and/or γ-rays; such "single-photon" (i.e., non-positron) emitters include technetium-99m (^{99m}Tc), indium-11 (^{111}In), iodine-123 (^{123}I), and iodine-131 (^{131}I) [12–14]. Gamma probes generally use inorganic (i.e., nonplastic) scintillation detectors or solid-state (i.e., semiconductor) ionization detectors and lead or tungsten shielding and collimation. Scintillators used in such probes include thallium-doped sodium iodide (NaI(Tl)), thallium- and sodium-doped cesium iodide (CsI(Tl) and CsI(Na), respectively), and cerium-doped lutetium orthooxysilicate (LSO). Semiconductors used in intraoperative probes include cadmium telluride (CdTe), cadmium zinc telluride (CZT), and mercuric iodide (HgI_2). The former offer high sensitivity while the latter better energy resolution (and therefore better scatter rejection). Clinically, however, scintillation detector- and ionization detector-based probes provide generally comparable performance [12–14]. Positron emitters such as fluorine-18 (^{18}F) may also be counted with such probes by single-photon (i.e., noncoincidence) counting of the 511-keV annihilation γ-rays. As illustrated in Fig. 2, however, this requires thicker collimation and shielding to prevent penetration of significant numbers of such highly energetic γ-rays emitted from

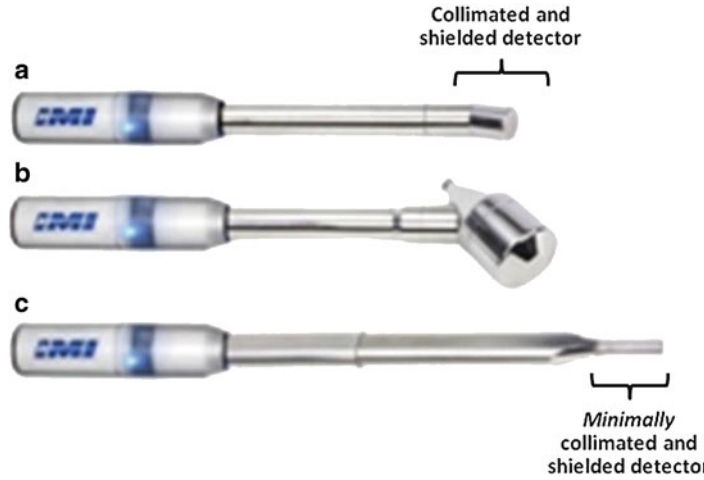

Fig. 2 Comparative thickness of gamma probe collimation and shielding required for low- to medium-energy x- and γ-rays of single-photon emitters (**a**), for high-energy (511-keV) annihilation γ-rays of positron emitters (**b**), and for negatrons and positrons of beta particle emitters (**c**). Note the much thicker collimation and shielding required for counting of the annihilation γ-rays and the minimal collimation and shielding for counting of beta particles [12] (Courtesy of IntraMedical Imaging, Los Angeles, CA)

outside of the field of view (FOV) (as defined by the collimator aperture) from reaching the detector and thereby degrading spatial resolution as well as target-to-background contrast. This has also been demonstrated in preliminary clinical and preclinical studies [15–18]. GF&E Tech GmBH (Seeheim, Germany) has marketed a novel probe for 511-keV annihilation photons using "electronic collimation" based on the time differences in activation among multiple CsI(Tl) crystals [19].

Beta probes. Because x- and γ-rays penetrate relatively long distances (circa 10 cm) of soft tissue, a major limitation of the use of gamma probes to specifically identify the target tissue in radioguided surgery is the presence of variable, generally high levels of background activity in normal tissues. Thus, even with a gamma probe centered over a tumor, the contribution of counts originating from activity in normal tissue underlying the tumor and even outside the field of view (due to penetration of the collimation and shielding) may degrade the tumor-to-normal tissue contrast (e.g., reducing tumor-to-normal tissue count ratios to less than 1.5:1 [15, 20, 21]) and thus tumor detectability to the point where lesions may be missed. A potential solution to this limitation of radioguided surgery is the use of so-called "beta" probes, that is, intraoperative probes which specifically count only charged particle (negatrons or positrons) radiation. Because they have such short ranges in soft tissues (typically of the order of 1 mm or less), beta particles emitted by a tracer source outside the probe's FOV or underlying the surface tissue do not reach the detector and are not counted (by the same token, minimal if any collimation and shielding is required (Fig. 2c). As a result, the discrimination between higher-activity tumor and lower-activity normal tissues is enhanced (i.e., the tumor-to-normal tissue count ratios are increased). Of course, the short path length of beta particle restricts the use of such probes to surface lesions; beta probes could not be used, for example, for (percutaneous) detection of sentinel lymph nodes.

Beta probes generally utilize either semiconductor or plastic scintillator detectors, since such detectors have lower effective atomic numbers and mass densities than inorganic scintillators such as NaI(Tl) and thus lower intrinsic efficiencies for x- and γ-rays, minimizing the potentially confounding count contribution of tracers emitting both beta (or conversion electron) and gamma radiation (e.g., iodine-131) [9–11, 21, 22]. For a

pure beta particle emitter such as phosphorus-32, this would not be a problem [9, 23]. Daghighian et al. [9] have developed and evaluated a plastic scintillator-based positron probe (Fig. 3). The basic design of this dual-detector probe (Fig. 3a) includes two scintillation detectors, a central solid cylinder detector (designated "Detector 1" in Fig. 3a) and a hollow cylinder detector (designated "Detector 2" in Fig. 3a) in 1-mm-thick stainless steel cladding; the outputs of the two detectors are passed by fiber-optic cabling to separate PMTs (PMT 1 and PMT 2, respectively). The Detector 1 counts result from both positrons and the 511-keV annihilation photons associated with positron emission, while the stainless steel cladding of Detector 2 completely attenuates the positrons and allows only the annihilation photons to enter the detector and generate counts from that detector. Because of the differences between Detectors 1 and 2, their sensitivities for the 511-keV photons are different. The Detector 1-to-Detector 2 ratio of the measured sensitivities for 511-keV photons is the weighting factor by which the Detector 2 count rate is multiplied and then subtracted from the Detector 1 count rate to yield the Detector 1 positron-only count rate. This probe was evaluated using the phantom setup shown in Fig. 3b, with a small ^{18}F-containing capsule simulating a tumor and a uniform ^{18}F-filled cylindrical container simulating underlying normal

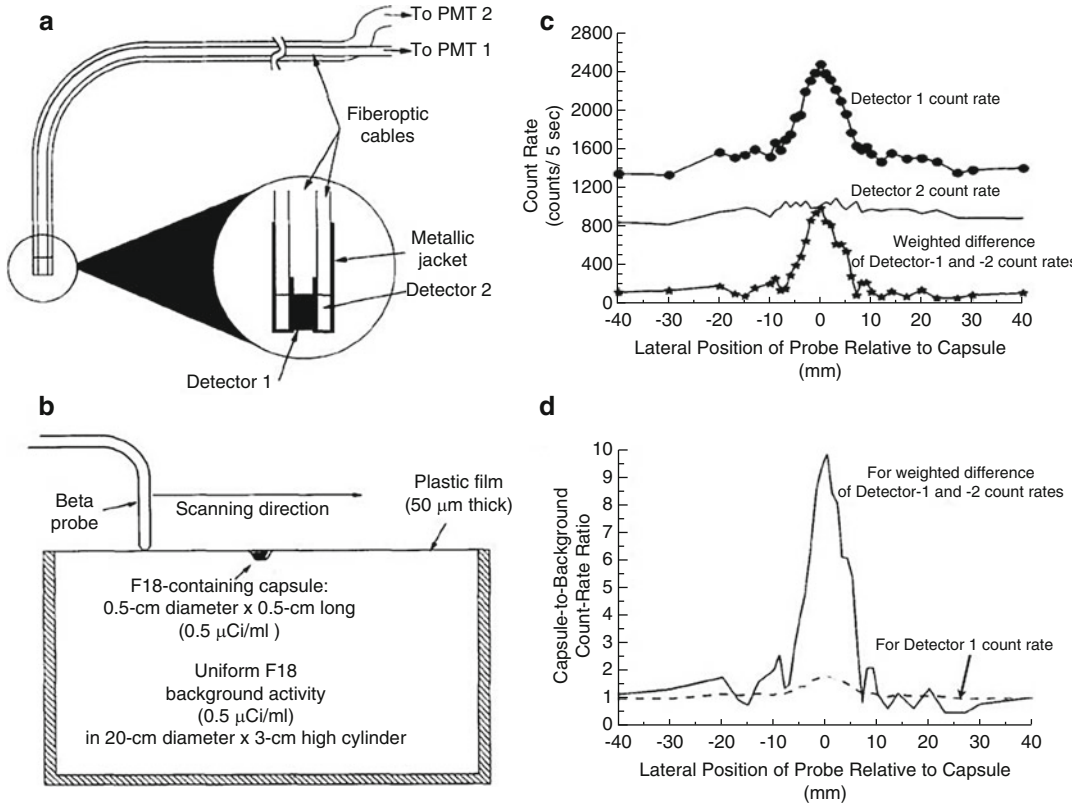

Fig. 3 (**a**) Basic design of a dual-detector beta probe [9]. (**b**) Experimental phantom setup for evaluation of the performance of the probe shown in (**a**). The phantom consisted of a small ^{18}F-containing capsule simulating a tumor and a uniform ^{18}F-filled cylindrical source simulating underlying normal tissue activity. The probe was then scanned across the phantom. Note that the capsule (i.e., tumor)-to-background (i.e., normal tissues) activity concentration ratio was 10:1. (**c**) The measured Detector 1 and 2 count rates and the calculated weighted difference of the Detector 1 and 2 count rates (see text) as a function of the lateral position of the probe relative to the capsule. (**d**) The capsule (i.e., tumor)-to-background count rate ratios for Detector 1 with and without weighted subtraction of the Detector 2 count rates (see text) (From [9] with permission)

tissue activity. The probe was then scanned across the phantom and the Detector 1 and 2 count rates at lateral positions relative to the "tumor" (i.e., capsule) recorded; the results, in terms of the measured count rates and the capsule (i.e., tumor)-to-background ratios, are plotted in Fig. 3c and d, respectively. These results (particularly the dramatic improvement – from ∼2 to ∼10 – in the tumor-to-background ratios (Fig. 3d)) clearly demonstrate the feasibility of this dual-detector design and weighted subtraction algorithm for beta probes in general and positron probes in particular. This has also been demonstrated in preliminary clinical and preclinical studies [17, 18].

Intraoperative gamma cameras. The sensitivity and specificity of detection of sentinel lymph nodes using current approaches such as the preoperative gamma camera imaging, gamma probes, and "blue dye" technique are quite high. Newman [24], for example, performed a meta-analysis of nearly 70 published studies and found an overall sensitivity of over 90% and a false-negative rate of only 8.4% for detection of such nodes in breast cancer. For preoperative gamma camera imaging, detection rates of 72–85% have been reported [25]. Sentinel lymph nodes were successfully detected using intraoperative gamma probes in 98% of patients in whom such nodes were successfully imaged preoperatively, with a false-negative rate of only 7%. And, for sentinel nodes not visualized by preoperative lymphoscintigraphy, there was a 90% detection rate intraoperatively. Importantly, however, negative preoperative lymphoscintigraphy often predicted a negative intraoperative probe result, and the foregoing improvement in the detection rate intraoperatively was primarily due to the use of blue dye [25]. The American Society of Breast Surgeons has recommended a sensitivity of at least 85% and a false-negative rate of less than 5% as acceptable for sentinel node detection in breast cancer [26]. There remains a need, therefore, to develop techniques to improve the sensitivity and the false-negative rates of sentinel lymph node detection. Intraoperative gamma camera imaging may provide the improvement required to satisfy the foregoing requirements. Mathelin et al. [27–29], for example, found that the use of an intraoperative small (5 × 5 cm) FOV gamma camera for detection of sentinel lymph nodes in breast cancer was practical. In a case report [28], intraoperative gamma camera imaging allowed detection of an additional sentinel lymph node (metastatic and with low radiotracer uptake) that was not detected by preoperative imaging or with a gamma probe, suggesting that intraoperative gamma camera imaging may reduce the false-negative rate. In addition to gamma camera and probe technology, the tracer employed (e.g., sulfur colloid versus nanocolloid, versus tilmanocept) and the injection site (e.g., intradermal versus subcutaneous, versus peri-tumoral) may account for the variation in lymph node detection.

Despite such promising preliminary data, it is not clear that the development and deployment of intraoperative gamma camera technology and the incremental improvement in the sentinel lymph node detection rate that such technology may provide will prove to be cost-effective. Certain considerations, however, lend support to the development of this technology. One such consideration is the variable level of proficiency among surgeons in gamma probe-based detection of sentinel lymph nodes [26]: even with considerable training and experience, not all surgeons achieve a detection rate of 90% or better. In addition, certain sentinel lymph nodes are problematic anatomically or otherwise in terms of detectability. These include nodes which are unusually deep, close to (less than 30 mm from) the injection site or high-activity normal tissues, or have a low (less than 1%) radiotracer uptake [25, 29–31]. A gamma camera system having a spatial resolution of 3 mm or better at a distance (depth) of the order of 1 cm would likely visualize such problematic nodes intraoperatively. Such an imaging system would offer other practical advantages over probes: the signal is provided in the familiar format of a scintigraphic image rather than a numerical display or variable-frequency tone; the larger FOV of even small gamma cameras (several centimeters) than that of probes (less than 1 cm) allows more rapid interrogation of large areas and/or longer sampling, with collection of more counts and reduction in statistical uncertainty (noise); more straightforward reexamination of the surgical site post-lymph node excision to verify removal of

foci of activity; and less reliance on potentially obliterated and otherwise ambiguous preoperative skin markings directing where measurements are to be performed intraoperatively [31]. Intraoperative gamma camera systems thus merit development and evaluation.

A number of small FOV intraoperative gamma camera systems have been developed [12, 32, 33]. The earliest systems were handheld devices having FOVs of only 1.5–2.5 cm in diameter and using conventional NaI(Tl) or CsI(Tl) scintillation detectors. Later units used two-dimensional arrays (mosaics) of scintillation crystals connected to a position-sensitive PMT and, more recently, semiconductors such as CdTe or CdZnTe (CZT). The main problems with these early units were their very small fields of view and the resulting large number of images required to interrogate the surgical field and the difficulty in holding the device sufficiently still for the duration (up to 1 min) of the image acquisition. More recently, larger field-of-view devices have developed which are attached to an articulating arm for convenient and stable positioning. These systems are nonetheless fully portable and small enough overall to be accommodated in typical surgical suites.

Abe et al. [34] evaluated a handheld CZT-based semiconductor gamma camera known as the eZ-SCOPE (Anzai Medical, Tokyo, Japan). As illustrated in Fig. 4, the device is light enough (820 g) to hold for a short time (up to ~1 min). The CZT detector has a 3.2 × 3.2-cm FOV and is 5 mm thick, with an efficiency of 87% and energy resolution of 9% for ^{99m}Tc γ-rays. Its collimators are easily exchanged. The CZT crystal is divided into a 16 × 16 array of 2 × 2-mm pixels, with integral and differential uniformities of 1.6% and 1.3%, respectively, with low-energy high-resolution (LEHR) collimation. System spatial resolution with the LEHR collimation was 2.3-, 8.0-, and 15-mm full-width half-maximum (FWHM) at source-to-collimator distances of 1, 5, and 10 cm, respectively. As shown in Fig. 4b, c, this camera is able to clearly image sentinel lymph nodes as well as lymphatic vessels. The small 3.2 × 3.2-cm FOV remains limiting, however; as shown in Fig. 4b, c, for example, a single lymph node occupies nearly half of the FOV and searching the surgical field can thus be time-consuming. A pinhole collimator was therefore subsequently incorporated into a newly designed version of the system, the Sentinella 102 (see below). In order to generate a larger

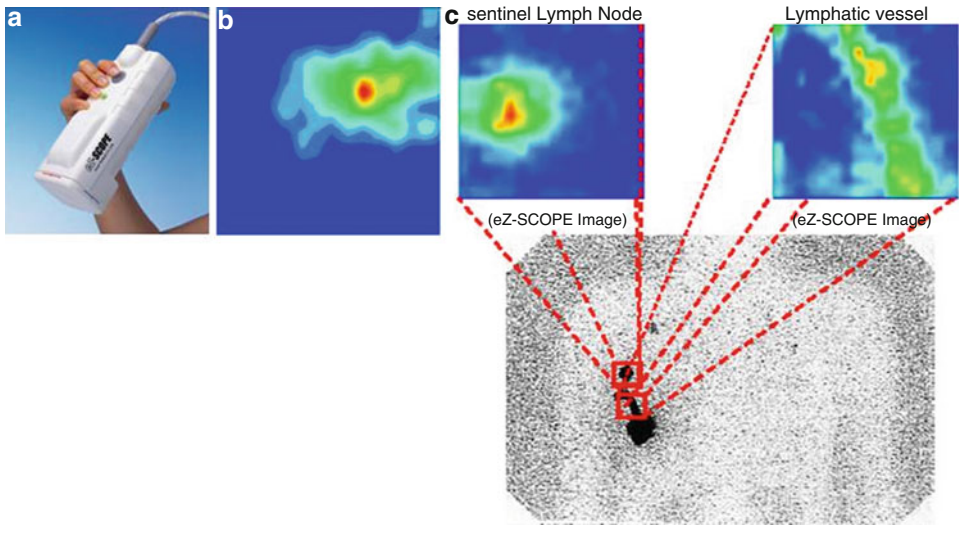

Fig. 4 (**a**) Photograph of the eZ-SCOPE intraoperative gamma camera (Anzai Medical, Tokyo, Japan). (**b**) Sample eZ-SCOPE image of a lymph node in a patient. (**c**) Sample eZ-SCOPE images of a lymph node (*top left*) and lymphatic vessel in a patient (*top right*) and conventional gamma camera image of the same patient obtained preoperatively (*bottom*). See text for additional details

effective FOV (30 × 30 cm), a computer program to integrate multiple adjacent images was developed and tested in mouse studies. The exact spacing of the individual images and the occasional low-count pixels at the periphery of the images were problematic, however. Initial experience with the eZ-SCOPE was nonetheless favorable overall.

A CZT-based semiconductor gamma camera with a larger FOV, 4 × 4 cm, than that of the eZ-SCOPE was developed by General Electric (Haifa, Israel). The 4 × 4-cm pixilated detector consists of a 16 × 16 array of 2.5 × 2.5-mm pixels. Using parallel-hole collimation, the spatial resolution was 5-mm FWHM at a distance of 5 cm with a sensitivity of 100 cps/MBq. Energy resolution for ^{99m}Tc was 8.0%, somewhat better than the ~10% value typically quoted for conventional gamma cameras. In one experiment, this system could clearly resolve ^{99m}Tc-filled spheres 1 cm in diameter in contact with one another at distances of up to 6 cm; a gamma probe could only distinguish the two sources at a 1-cm depth and only when separated by at least 2 cm. A potential advantage of gamma camera imaging is the ability to resolve sources that may overlap one another in one view by acquiring additional views at different angles, as illustrated by the results of the phantom experiment shown in Fig. 5. This may be helpful, especially in breast cancer, in localizing a sentinel lymph node at a different depth from the injection site and obscured by the injected activity.

A handheld camera, known as the POCI ("perioperative compact imager") and utilizing a CsI (Na) scintillation crystal coupled to a focusing image intensifier tube and position-sensitive diode, was developed in France [35] (Fig. 6a). Its field of view is 4.0 cm in diameter. With

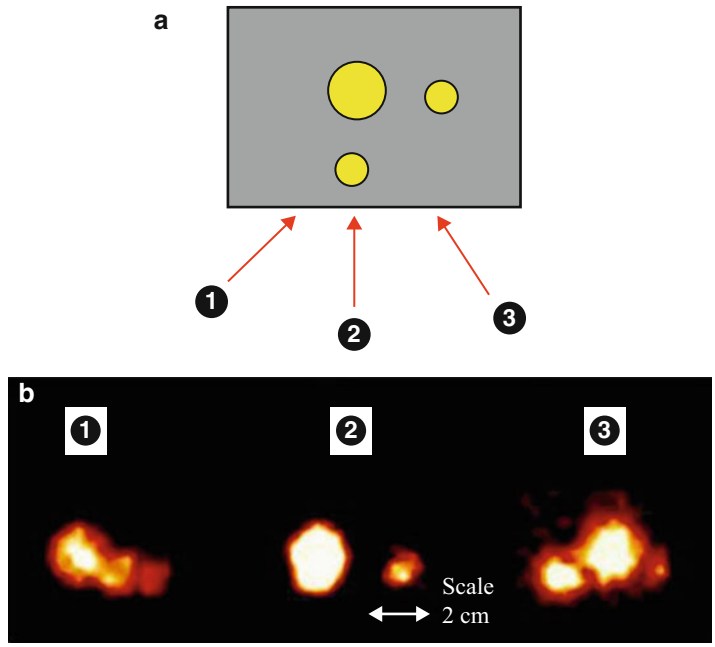

Fig. 5 Setup and results of a ^{99m}Tc phantom imaging experiment with the intraoperative gamma camera developed by General Electric (Haifa, Israel) [88, 89]. (**a**) Schematic diagram (*side view*) of phantom, with two 1-cm spheres at depths of 2 and 4 cm and a third sphere, 1.4 cm in diameter, at a depth of 2 cm and directly over the 2-cm sphere at a depth of 4 cm. The two small spheres and the large sphere had activity concentrations of 1 and 2.5 μCi/ml, respectively. (**b**) Images (identified as "1," "2," and "3," respectively) were acquired at angles of −45°, 0°, and +45° relative to an axis perpendicular to the top of the phantom (i.e., an axis in the plane of the diagram). The resulting gamma camera images demonstrate the ability to resolve overlying foci of activity by acquiring views at multiple angles (From [88, 89] with permission)

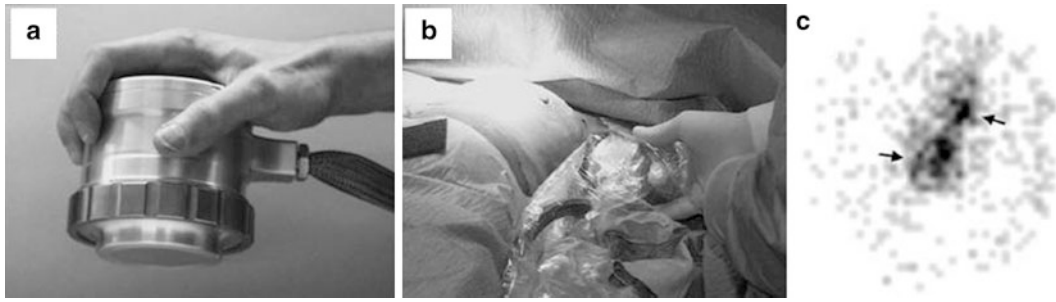

Fig. 6 (**a**) Photograph of the POCI (per-operative compact imager) intraoperative gamma camera. (**b**) Intraoperative lymphoscintigraphy, with the POCI in position for imaging of the patient's left axilla. (**c**) POCI image (10 s acquisition time), showing two foci of activity corresponding to two neighboring lymph nodes (From [35] with permission)

high-resolution parallel-hole collimation, its ^{99m}Tc sensitivity with scatter is 250 cps/MBq at 1 cm and 125 cps/MBq at 5 cm and its spatial resolution 3.9-, 4.8-, and 7.6-mm FWHM at 1, 2, and 5 cm, respectively. Images are acquired in a matrix of 50 × 50 pixels. The energy resolution of the POCI, 28%, is rather poor, however, and the wide energy windows thus required result in inclusion of substantial amounts of scatter in the image, a particular disadvantage when a lymph node is close to the injection site. Figure 6b illustrates the manual positioning of the POCI camera during intraoperative lymphoscintigraphy. Figure 6c presents a representative intraoperative image, with clear visual discrimination of two adjacent lymph nodes. In a preliminary clinical study, lymph nodes in all three patients were identified with the POCI, including one in whom two deep nodes were missed with a gamma probe (most likely due to depth-related loss of sensitivity and proximity of the nodes to the injection site). The total imaging times depended upon the scan area and varied from 15 s to 3 min.

Another semiconductor gamma camera, utilizing CdTe, was developed by Tsuchimochi and colleagues in Japan [36–38]. Their choice of CdTe was based on its superior uniformity (integral uniformity, 4.5%) and energy resolution (7.8%) compared to CZT. The camera, referred to as the "small semiconductor gamma camera (SSGC)," uses an array of 32 × 32 5-mm-thick CdTe elements, with a matrix of 1.2 × 1.2-mm pixels and a 4.5 × 4.5-cm FOV. The collimation, comprised of tungsten, had 1.2 × 1.2-mm square apertures to match the pixel arrangement. Spatial resolution without scatter was 3.9-, 6.3-, and 11.2-mm FWHM at 2.5, 5, and 10 cm, respectively. The ^{99m}Tc sensitivity at the surface without scatter was 300 cps/MBq, comparable to that of the POCI and better than that of a conventional gamma camera with LEHR collimation (∼100 cps/MBq). The results of preliminary phantom and clinical imaging studies with the SSGC were encouraging.

A small FOV gamma camera equipped with pinhole collimation, known as the Sentinella 102, has been developed by General Equipment for Medical Imaging, Spain [39–43]. It uses a single 4 × 4-cm CsI(Na) scintillation crystal and a position-sensitive PMT, with images acquired in a 300 × 300 matrix. Interchangeable pinhole apertures 1.0, 2.5, and 4.0 mm in diameter are available, yielding an effective FOV of 20 × 20 cm at a distance of 18 cm. The detector assembly weighs 1 kg and is mounted on an articulating arm (Fig. 7a). The ^{99m}Tc sensitivity ranged from 200 to 2,000 cps/μCi at 1 cm and 60 to 160 cps/μCi at 10 cm, depending on the pinhole aperture used. The FWHM spatial resolution over the detector face is 5.4–8.2 mm, 7.3–11 mm, and 10–18 mm at 3, 5 and 10 cm, respectively, again depending on the pinhole aperture used. Beyond ∼3 cm, therefore, the spatial resolution is poorer than that of cameras with parallel-hole collimation. However, despite the coarser resolution, the advantage of a pinhole collimation lies in the larger effective FOV at such distances. Such a system can therefore be used at a large distances to rapidly

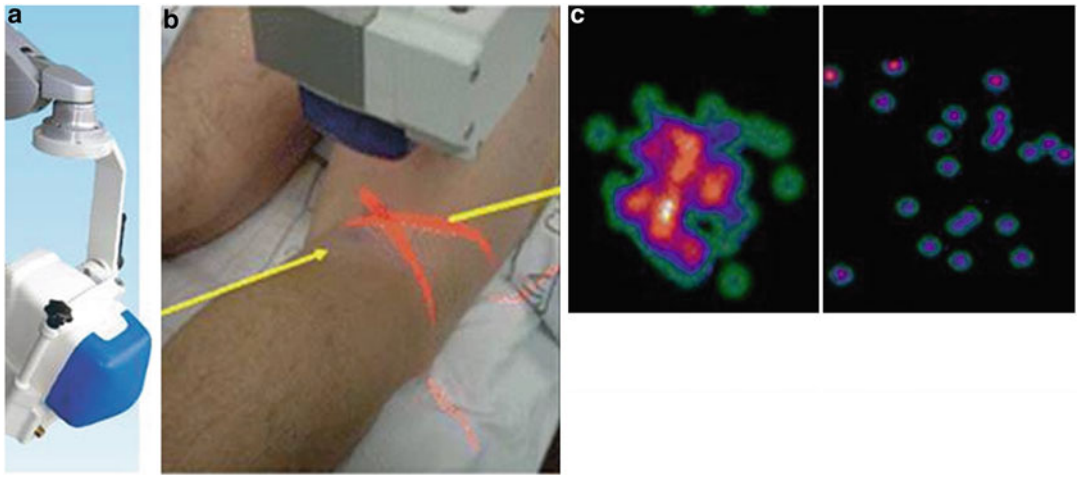

Fig. 7 (**a**) Photograph of the Sentinella 102 small FOV gamma camera (General Equipment for Medical Imaging, Spain). The detector assembly is shown mounted on the system's articulating arm. (**b**) Illustration of the device's laser positioning system, with two intersecting *red lines* projected onto posterior surface of the patient's right knee joint. This patient had malignant melanoma of the right heel, and lymphoscintigraphy was performed to identify the popliteal sentinel lymph node. (**c**) Posterior gamma camera images of the patient's right knee joint before (*left*) and after (*right*) surgical excision of the popliteal node. The pre-excision image (*left*) clearly shows the node centered in the field of view, and the post-excision image (*right*) is notably absent of any such focus of activity, demonstrating complete removal of the node

survey, with coarser resolution, a large area and then examine suspicious areas at smaller distances and finer resolution [39, 40, 44]. In initial clinical studies, acquisition times of 20–60 s per image were required. Because the distortion associated with pinhole collimation varies with position within the FOV (i.e., is worse toward the periphery) as well as distance, the Sentinella 102 camera is equipped with a laser positioning system, with two intersecting lines being projected onto the surface of the region being imaged (Fig. 7b). This allows positioning of suspicious foci of activity at the center of the field of view, where image quality is best (Fig. 7c). The Sentinella 102 camera is also equipped with a long-lived gadolinium-153 (^{153}Gd) pointer for real-time positioning; the image of the ^{153}Gd pointer source is acquired in a separate energy window from the ^{99m}Tc image and is displayed as a small marker superimposed on the ^{99m}Tc image.

The Institut Pluridisciplinaire Hubert Curien (Strasbourg, France) developed an intraoperative gamma camera known as the "CarollReS" [27–29]. This device has a relatively large-area 50 × 50-mm cerium-doped gadolinium orthooxysilicate (GSO) scintillation crystal and parallel-hole collimation with 2-mm-wide apertures. Its ^{99m}Tc spatial resolution was 10-mm FWHM at 5 cm, sensitivity 130 cpm/kBq, and energy resolution 45%. A prototype version of this device with a larger 100 × 100-mm FOV has been fabricated as well. In a preliminary clinical study with the CarollReS camera, Mathelin et al. [29] compared the depth of lymph nodes estimated by imaging to their actual depth measured at surgery and found a generally good correlation, except in instances where only a portion of the sentinel lymph node was in the camera's FOV. For 7 of 11 nodes whose depth could be estimated, the image-derived depth was correct.

Crystal Photonics GmbH (Berlin, Germany) markets a light (800-g) handheld gamma camera with a 5-mm-thick CZT detector having a 40 × 40-mm field of view, a photon energy range of 40–250 keV, and interchangeable tungsten or lead parallel-hole collimators. The spatial resolution at 3.5 cm is 5.4 mm with the high-resolution collimator to 9.2 mm with the high-sensitivity collimator, with the latter providing ~fourfold higher sensitivity than the former.

The SurgicEye GmbH (Munich, Germany) has introduced an intraoperative SPECT imaging technology termed "freehand SPECT" [45, 46]. In contrast to conventional SPECT systems, the Declipse® SPECT does not employ a gantry-mounted gamma camera rotating around the patient, but a handheld gamma probe interfaced to an infrared 3D tracking system. A 1- to 2-min scan is performed at anterior-posterior and lateral directions around the patient. The device can be used with low-energy photon emitters such as ^{99m}Tc and is compatible with different commercially available gamma probes. The Declipse™ SPECT website reports a reconstructed spatial resolution of 5 mm; details of the data acquisition and processing yielding this resolution were not specified, however.

Overall, small FOV gamma cameras have demonstrated detection rates for sentinel lymph nodes equal to or better than those of non-imaging gamma probes, despite having sensitivities (e.g., expressed in cps/MBq) typically about tenfold lower than those of such probes. The ability of such devices to image a surgical field intraoperatively and thus insure complete excision of lesions is a potentially useful enhancement of surgical management of cancer. The acquisition times per image are typically well under 1 min, so the overall duration of the surgical procedure should not be significantly prolonged. In addition, the use of pinhole collimation, despite having lower sensitivity than parallel-hole collimation, permits initial imaging at longer distance to visualize a larger anatomic area of interest followed by imaging at shorter distance to pinpoint and otherwise characterize suspicious foci of activity. Importantly, the scintigraphic image format is familiar to surgeons, likely facilitating clinical acceptance and integration of intraoperative imaging.

Intraoperative PET scanners. Prescient Imaging LLC is currently developing a portable compact whole-body PET scanner adaptable to intraoperative imaging [47]. It incorporates a 360-degree detector with an axial FOV of 22 cm. The detectors are assembled into three sets, one planar and the other two circular arcs of 90° each connected with a hinge. One of the arcs is fixed while the other can be rotated about the hinge and thereby opened and closed. The planar detector is fixed horizontally such that it can fit under a patient table. By placing the moveable arc in the closed position, the 360° of detector coverage about the patient is achieved. Attenuation correction will be performed using a rotating rod transmission source.

Optical and Near-Infrared (NIR) Imaging

Despite the very limited penetrability of optical and near-infrared (NIR) light in tissue, specialized technologies have led to widespread and very productive use of light – both bioluminescence and fluorescence – for in vivo imaging of rodents [48, 49] and, to a much more limited extent to date, of human subjects; in the case of the latter, this has been restricted to fluorescence imaging [50]. In the most common (i.e., preclinical) optical imaging paradigm, animals are placed in a light-tight imaging enclosure, and the emitted optical or NIR signal is imaged by a charge-coupled detector (CCD). In bioluminescence imaging (Fig. 8a), cells (e.g., tumor cells) which are to be localized or tracked in vivo must first be genetically transduced ex vivo to express a so-called reporter gene, most commonly, a luciferase gene (such as the firefly luciferase, or *FLuc*, gene). After the cells have been implanted, infused, or otherwise administered to the experimental animal, the luciferase substrate (e.g., D-luciferin in the case of firefly luciferase) is systemically administered. Wherever the administered substrate encounters the luciferase-expressing cells, the ensuing reaction (such as the D-luciferin-luciferase reaction) emits light, which is detected and localized by the imaging system. The CCD in bioluminescence imaging is maintained at a very low temperature (of the order of −100 °C), thereby ensuring that any electronic output it produces results from light striking the CCD rather than the background "dark current" (which would be prohibitively high at ambient temperatures). In this way, the otherwise undetectably small signal originating in vivo and escaping from the surface

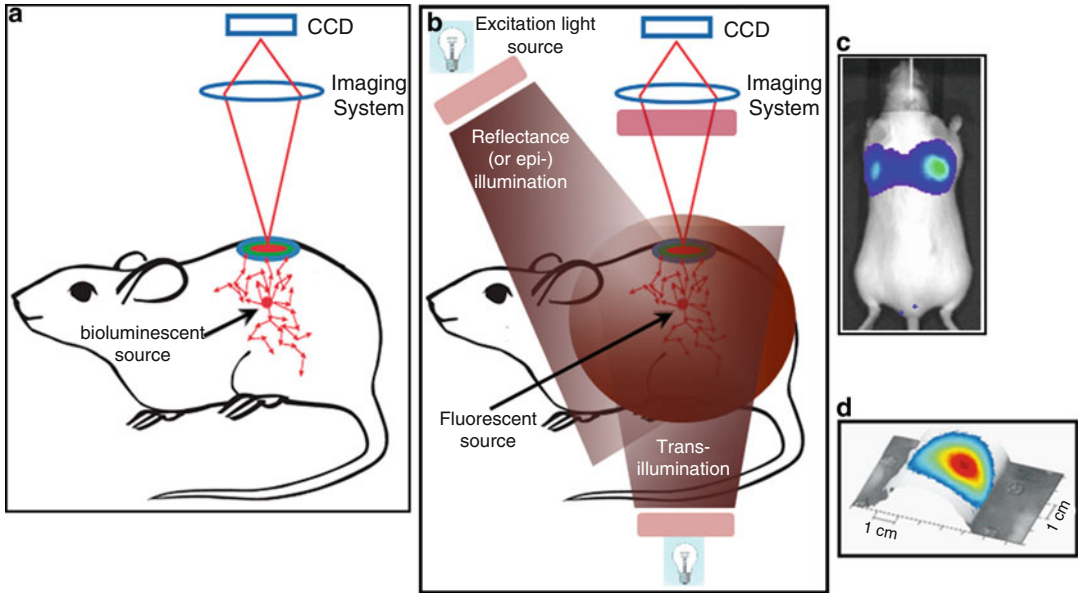

Fig. 8 (**a**) Bioluminescence and (**b**) fluorescence optical or NIR in vivo imaging. For fluorescence imaging, the excitation light source may be a white-light source whose emitted light is passed through conventional glass filters to yield a light over a narrow wavelength range centered about the excitation wavelength of the fluorophore being imaged. Alternatively, it may be a laser light source tuned to the appropriate wavelength. In so-called "multispectral" systems, multiple excitation and emission wavelengths and thus multiple fluorophores may be imaged simultaneously. (**c**, **d**) These sample images show a pseudo-color bioluminescence images superimposed on a *gray*-scale photograph and on a three-dimensional rendering of a mouse, respectively (From [90] with permission)

of the animal can produce an image. In fluorescence imaging (Fig. 8b), cells to be imaged may either be genetically transduced ex vivo to express a fluorescent molecule (or fluorophore) such as green fluorescent protein (GFP) or a fluorophore probe targeting the cells of interest may be systemically administered. In either case, the animal is then illuminated with light at an appropriate excitation wavelength (obtained by filtration or with a laser) to energize the fluorophore in situ, and the resulting emitted light (which has a slightly different wavelength than the excitation light) is itself filtered and detected by the CCD; the difference in wavelengths between the excitation and emitted light is known as the Stokes shift. The excitation light may be provided by reflectance (or epi-illumination) or by transillumination of the animal. Further, by computer processing, the abundant spontaneous fluorescence of the animal's tissues as well as of foodstuffs in the gut must be mathematically separated, or "de-convolved," from the overall fluorescence to yield an image specifically of the fluorophore; this is sometimes known as "spectral unmixing." In practice, the resulting luminescence or fluorescence image is generally superimposed on a conventional (i.e., white-light) photograph of the animal to provide some orientation as to the anatomic location of the signal(s) in vivo (Fig. 8c).

Because light emitted at any depth of tissue is scattered and otherwise dispersed as it passes through overlying tissue before emanating from the surface of the animal, the apparent size of the light source (Fig. 8c, d) is considerably larger than its actual size. Despite the excellent spatial resolution of the CCDs themselves, the effective resolution of optical and NIR imaging is generally rather coarse. Further, for planar optical and NIR imaging, the resulting images are only semiquantitative: absorption and scatter of the emitted light as it passes through overlying tissue makes the measured signal highly depth dependent. Thus, a focus of cells lying deep within tissue may appear less luminescent or fluorescent than an identical focus of cells at a more shallow depth; if excessively deep, such a focus of cells may be

undetectable altogether. NIR radiations, however, have a substantially higher penetrability through tissue than blue to green radiations. Importantly, therefore, by using laser transillumination for excitation of administered NIR molecular probes in situ, tomographic fluorescence images can be mathematically reconstructed [49]. The resulting three-dimensional images – in contrast to planar images – are at least semiquantitative: the signal intensity thus reconstructed is related to the local concentration of the fluorophore.

Bioluminescence imaging, because it requires genetic modification of the cells to be imaged, likely has very limited applicability in patients but has proven invaluable in preclinical research. However, with recent advances in adoptive immunotherapy of cancer, bioluminescence imaging conceivably may have some clinical utility in an intraoperative or endoscopic setting to assess tumor targeting of immune effector cells. To date, however, no such studies have been performed. Intraoperative, endoscopic, and even surface fluorescence imaging of patients has been performed and continues to advance (see below).

Fluorescence imaging. As noted, the clinical application of optical imaging to date has utilized fluorescence imaging in endoscopic and intraoperative settings. Fluorescence cystoscopy, for example, is now widely used to identify and localize urinary bladder cancer [51]. The photosensitizer 5-aminolevulinic acid (ALA) is a precursor of the photoreactive (at 375–440 nm) protoporphyrin IX (PpIX). Although the mechanism is not yet well understood, ALA accumulates selectively in cancerous tissue, yielding tumor-to-non-tumor activity concentration ratios of ∼20:1 within 2 h of topical administration within the bladder. As illustrated in Fig. 9, fluorescence cystoscopy allows more sensitive and specific visualization of bladder cancer in vivo than conventional (i.e., white-light) imaging.

Narrowband imaging (NBI) is a notable refinement of non-fluorescence optical cystoscopy that improves the visualization of blood vessels and bladder mucosa and thereby enhances the contrast between cancerous and normal bladder epithelium (given that urothelial lesions are typically hypervascularized due to elevated microvessel density) [52]. NBI exploits these angiogenic features of bladder cancers by filtering white light into two discrete wavelength bands, one blue (415 nm) and one green (540 nm), both of which are absorbed by hemoglobin. The shorter-wavelength 415-nm light penetrates only the superficial layers of the mucosa and yields brownish images of the superficial capillaries. The longer-wavelength 540-nm light penetrates deeper into the bladder wall and produces greenish images. Bladder tumors are thus

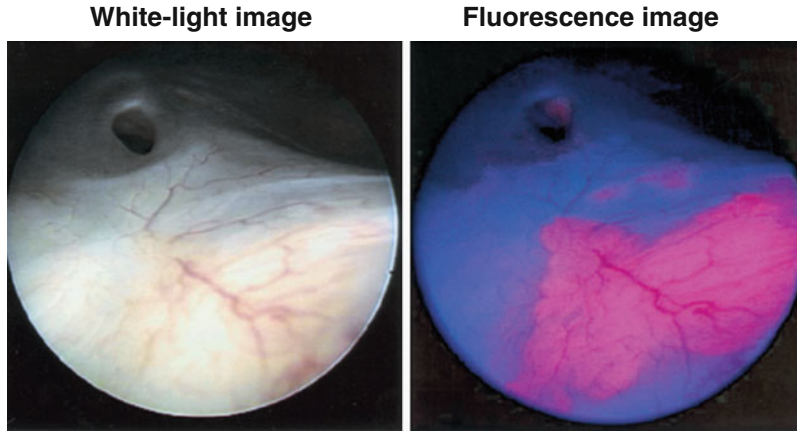

Fig. 9 Cystoscopic imaging of urinary bladder cancer. Conventional (i.e., white-light) image (*left panel*) and fluorescence image (*right panel*) following topical administration of the protoporphyrin IX (PpIX) precursor 5-aminolevulinic acid (*ALA*). The red coloration of the cancerous tissue makes it far more apparent in the fluorescence image than in the white-light image (From [51] with permission)

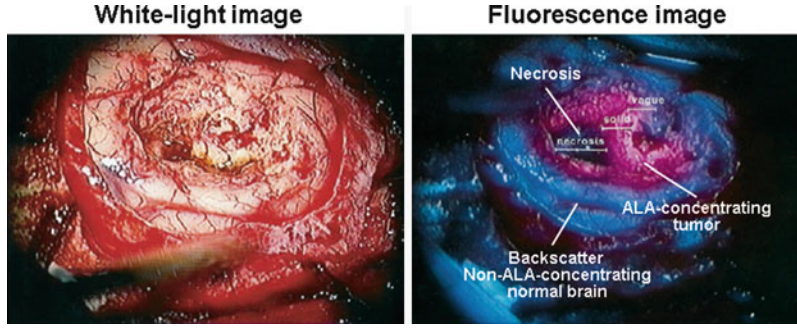

Fig. 10 Intraoperative white-light image (*left panel*) and fluorescence image (*right panel*) following systemic administration of ALA (20 mg/kg 3 h prior to surgery) of the intracranial resection site of a glioblastoma. The *red* coloration of the cancerous tissue, *blue* coloration of normal brain, and lack of color of non-perfused, necrotic tissue allow easier discrimination of these respective tissues than does the white-light image. This in turn should facilitate a more complete resection of the tumor and, presumably, better local control (From [53] with permission)

visually identified by the intensity of brown-green coloration that is characteristic of the elevated vessel density of tumors and distinct from the pink-to-white coloration of the normal mucosa.

In addition to endoscopic fluorescence imaging, large-field, planar optical, and NIR fluorescence imaging potentially may improve human surgery by providing real-time image guidance to surgeons to identify tissue to be resected (such as tumors) and tissue to be avoided (such as blood vessels and nerves). As illustrated in Fig. 10, the use of ALA has been extended to systemic administration and fluorescence imaging-guided resection of glioblastomas [53]. Based on the overexpression of folate receptor-α, intraoperative fluorescence imaging has also been applied to resection of ovarian cancer using folate conjugated via an ethylene diamine spacer to fluorescein isothiocyanate (FITC) (Fig. 11). To further advance the practical implementation of fluorescence imaging-guided surgery, Dr. John Frangione and colleagues have developed the so-called Fluorescence-Assisted Resection and Exploration (FLARE™) system [54–60]. Briefly, the FLARE™ system consists of an imaging head mounted on an articulated arm and a cart containing control equipment, computer, and monitors (Fig. 12). The imaging head includes light-emitting diodes (LEDs) as the excitation light source, heat dissipation technology to maintain stability of the LEDs, and complementary metal oxide semiconductor (CMOS) cameras; it can be positioned anywhere in 3D space with six degrees of freedom. A customized software system enables the real-time display of color video and two NIR fluorescence channels at a rate of up to 15 frames per second. The software is capable of displaying the NIR fluorescence signal as a pseudo-colored overlay on the color video, thereby providing anatomic guidance to the surgeon. Among its many applications to date, the FLARE™ system has been applied to sentinel lymph node resection in breast cancer surgery (Fig. 13) [60] and has demonstrated improved visualization of nodes and of tumors [54–61].

In collaboration with Dr. Michelle Bradbury and colleagues, Quest Medical Imaging has developed an enhanced intraoperative NIR imaging device, the ArteMIS™ (now Spectrum™) handheld fluorescence camera system (Fig. 14a) for either minimally invasive laparoscopic or open surgery configurations [62]. This system is capable of true multiplexing, with simultaneous imaging (at a frame rate of 30 frames per second) and real-time spectral unmixing of the signals in two NIR channels (700 and 800 nm, respectively) and a conventional color channel, as illustrated in Fig. 14b [63].

Cerenkov imaging. Cerenkov imaging is a new approach to optical imaging based on the emission of a continuum of visible light associated with the decay of certain radionuclides (actually, with the particles emitted as result of the radionuclide decay) [64–73]. This phenomenon, now known as the "Cerenkov effect," was first observed in the 1920s and characterized in the 1930s by Pavel

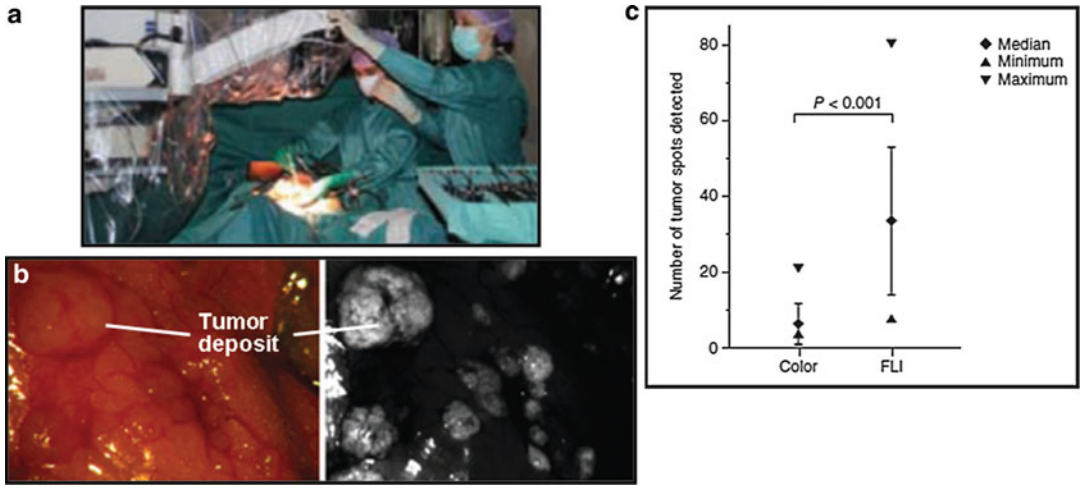

Fig. 11 (**a**) Photograph of intraoperative use of fluorescence imaging system developed by Ntziachristos and colleagues. (**b**) Conventional color image (*left panel*) and fluorescence *gray*-scale image (*right panel*) following systemic administration of FITC-conjugated folate (0.3 mg/kg) of intra-abdominal resection site of ovarian cancer. The tumor deposits are more clearly visualized on the fluorescence image than on the color image. (**c**) Graphical presentation of the results of conventional versus fluorescence imaging-assisted resection of ovarian cancer, demonstrating that intraoperative fluorescence imaging (*FLI*) visualized significantly more ovarian cancer deposits than conventional imaging (Adapted from [91] with permission)

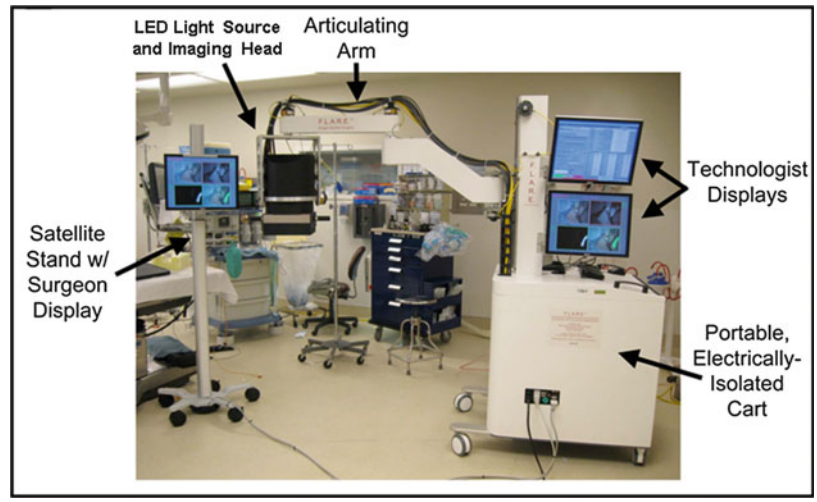

Fig. 12 Photograph of the FLARE™ system developed by Frangione and colleagues for intraoperative fluorescence imaging (Adapted from [60] with permission)

Cherenkov [65]. In 1958, Cerenkov shared the Nobel Prize in Physics with colleagues Ilya Frank and Igor Tamm for the discovery and explanation of the effect which now bears his name. Cerenkov radiation is perhaps familiar to some readers as the bluish "glow" observed in the water pools containing spent, but still radioactive, fuel rods at nuclear reactors. It arises when charged particles such as beta particles travel through an optically transparent, insulating medium at a speed greater than that of light in that medium. The Cerenkov effect, often analogized to the sonic boom that occurs at the instant a supersonic plane exceeds the speed of sound in air, occurs as the charged particles dissipate their kinetic energy by polarizing the electrons in the insulating medium (most commonly, water) as they travel through the medium. As these polarized electrons then relax

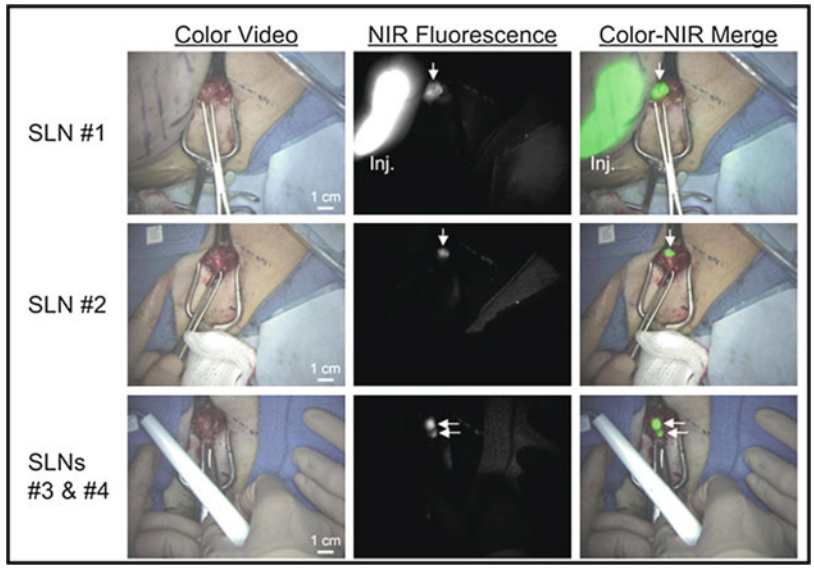

Fig. 13 Use of the FLARE™ system in intraoperative localization and resection of sentinel lymph nodes (*SLNs*) in breast cancer surgery. Four peri-tumoral injections were performed of indocyanine green (*ICG*) conjugated to human serum albumen (10 μg of ICG in 0.2 mL per injection). The conventional color video images in the *left panels* show the surgical field and the incision in the proximity of four SLNs. The NIR fluorescence video images (100 ms per exposure) show the injection site (*top middle panel*) and the four ICG-albumen-concentrating SLNs (*middle panels*). For the images in the lower two *middle panels*, the injection site was covered with an opaque surgical drape. The *left panels* show the overlaid, or merged, color and fluorescence images. The SLNs are clearly far more apparent in the fluorescence than in the color images (Adapted from [60] with permission)

(or re-equilibrate), and if the charged particle is traveling faster than light, constructive interference of the light thus emitted occurs, producing the grossly visible Cerenkov radiation.

The application of Cerenkov radiation to in vivo radionuclide imaging is a recent development [64, 66–73]. Phantom studies by Ruggiero et al. have demonstrated, using a commercial optical imaging system (Ivis 200, Caliper Life Sciences) equipped with a cryo-cooled CCD, measurable emission of Cerenkov radiation associated with a number of clinically relevant radionuclides, including ^{18}F, copper-64 (^{64}Cu), zirconium-89 (^{89}Zr), iodine-124 (^{124}I), iodine-131 (^{131}I), and actinium-225 (^{225}Ac) [72] (Fig. 15a, b). Importantly, the optical Cerenkov signal is linearly related to activity concentrations (Fig. 15c), at least where the effects of attenuation and scatter are minimal. Ruggiero et al. have also produced planar Cerenkov images of the tumor localization of a ^{89}Zr-labeled antibody in prostate tumor xenografts in mice which compare favorably, both qualitatively and quantitatively, with the ^{89}Zr PET images [72] (Fig. 16). Using intradermal tail injections of [^{18}F]FDG, Thorek et al. subsequently performed both PET- and Cerenkov imaging-based lymphography in mice, with both modalities demonstrating excellent visualization of lymph nodes [73] (Fig. 17). Initial clinical trials of Cerenkov imaging are currently underway to delineate its potential clinical utility. As illustrated in Fig. 17, assisting the resection of sentinel lymph nodes appears to be one potential application. In a clinical pilot study, for example, Thorek et al. evaluated the feasibility of Cerenkov imaging of patients ($n = 4$) undergoing standard diagnostic [^{18}F]FDG scans to detect nodal disease [74]. Two 5-min scans were performed for each patient at ~70 min postinjection of [^{18}F]FDG (12 mCi), one over the site of the [^{18}F]FDG-avid axillary lymph node by PET scanning and one over the contralateral side of the patient without detectable nodal disease as a negative control. An intensified CCD camera (Mega10z, Stanford

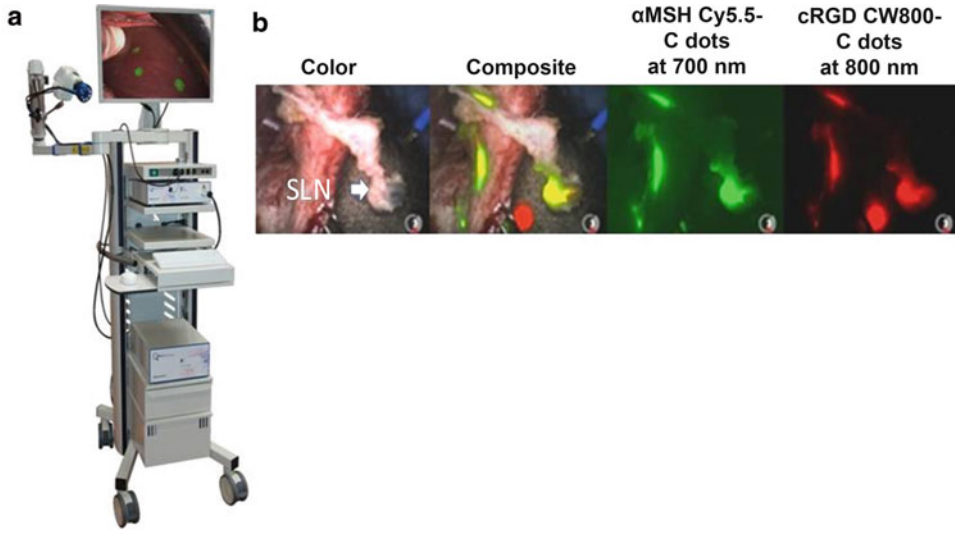

Fig. 14 (**a**) Photograph of the ArteMIS™ (now Spectrum™) handheld NIR fluorescence camera system. The compact form factor of this system makes it particularly suitable for the intraoperative setting (Courtesy of Quest Medical Imaging). (**b**) Preclinical sentinel lymph node study in a spontaneous melanoma miniswine model. The miniswine received percutaneous peri-lesional co-injections of ultrasmall (<10 nm) fluorescent Cornell-dot (C-dot) silica nanoparticles surface-functionalized with alpha-melanin-stimulating hormone (α-MSH) and with cyclic arginine-glycine-aspartic acid-tyrosine (cRGDY) for targeting the MSH receptors and integrin receptors, respectively, overexpressed on the surface of the melanoma cells (as confirmed by immunohistochemical staining of the excised node); the α-MSH- and the cRGDY-functionalized C dots were loaded with the Cy5.5 and the CW800 fluorophores, respectively. The real-time multiplexing capability of the ArteMIS™ (now Spectrum™) system provided clear visual discrimination of the two types of functionalized nanoparticles in the diseased sentinel lymph node. Such molecularly targeted nanoparticle probes thus are not only capable of highly sensitive visual detection of sentinel lymph nodes but also of phenotypic characterization of such nodes (Adapted from [63] with permission)

Photonics) was used. The single-photon-counting camera consisted of a dual-microchannel plate-intensifier system behind a photocathode read off a Peltier-cooled CCD (XX285, Sony Corp). The optics consisted of a quartz high-ultraviolet-transmission 50-mm f/0.8 lens and a long-pass filter with a cutoff at 605 nm (Chroma Technology). High-frame-rate acquisitions (120 frames per second) were integrated in the Piper Control software (Stanford Photonics), a background baseline was subtracted, and the images were processed and analyzed in *Image J* (National Institutes of Health) (13). The camera with lens and filter was mounted on a standard photography tripod, and the subjects imaged at a distance of ~8 cm. The patients were imaged with the room lights on for a white-light photograph and then with the lights off, the light-sealed door to the room closed, and an optical drape used to eliminate any remaining ambient light. A representative patient study is shown in Fig. 18. Despite the low yield of Cerenkov light and the suboptimal Cerenkov light spectrum for in vivo imaging (primarily in the highly attenuated blue-green range), based on this and other studies [74, 75], Cerenkov imaging of patients is feasible, though its ultimate clinical utility remains to be determined.

Photoacoustic imaging. In photoacoustic imaging [76–78], tissues are illuminated with laser light. When radiofrequency (RF) pulses are used, the technology is termed, "thermoacoustic imaging." Some of the delivered energy will be absorbed and converted into heat, leading to transient thermoelastic expansion of the illuminated tissue and thus ultrasonic (i.e., MHz-frequency) emissions. The ultrasonic waves thus emitted are then detected by ultrasonic transducers to form images. Image contrast is provided by the differential absorption among tissues of the incident excitation light. In contrast to fluorescence imaging, in which scattering

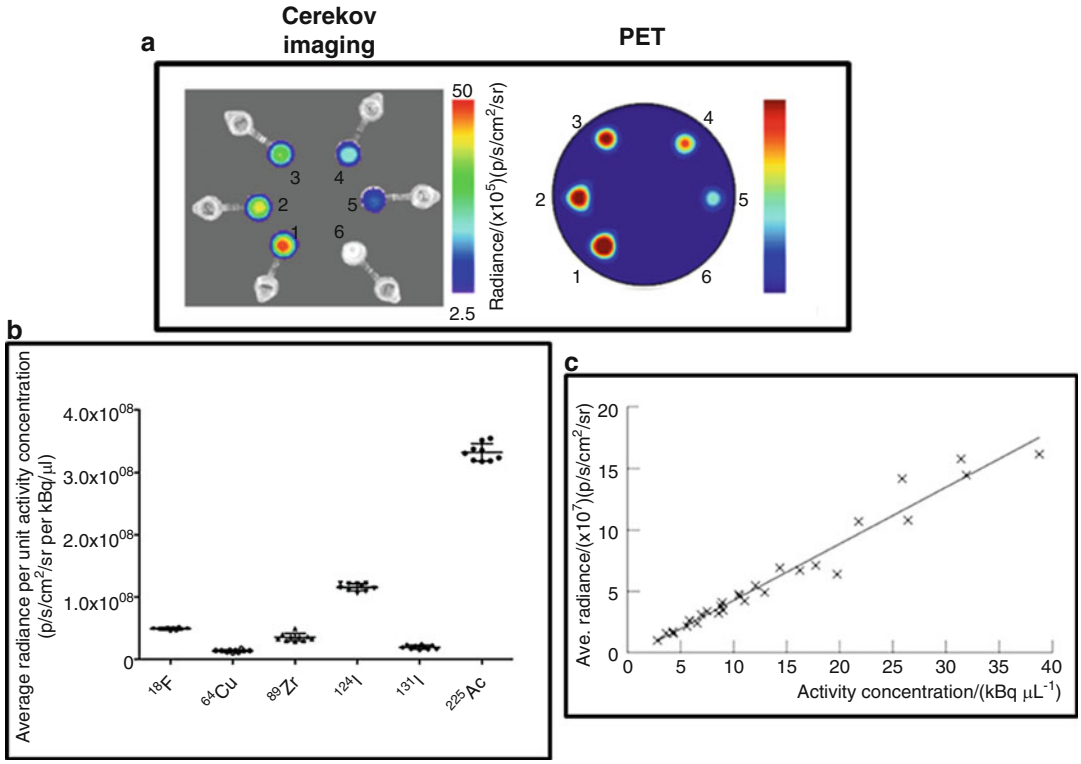

Fig. 15 (**a**) Phantom for evaluation of Cerenkov imaging of positron-emitting radionuclides, comprised of a circular arrangement of six 1-ml Eppendorf tubes filled with increasing activity concentrations. *Left panel*: Cerenkov image superimposed on a photograph of the phantom acquired with an Ivis 200 optical imaging system (Caliper Life Sciences). *Right panel*: PET image of the phantom acquired with a Focus 120 microPET scanner (Concorde Microsystems). (**b**) Average radiance per unit activity concentration (in photons (p)/second (s)/cm^2/steradian (sr) per kBq/μL) for different radionuclides as measured using the phantom arrangement and instrumentation described in (**a**). (**c**) Linear correlation ($r = 0.98$) between average radiance (in p/s/cm^2/sr) and activity concentration (in kBq/μL) for ^{89}Zr evaluated again using the phantom arrangement and instrumentation described in (**a**) (Adapted from [72] with permission)

in tissue degrades spatial resolution with increasing depth, photoacoustic imaging provides better spatial resolution (of the order of 100 μm) and deeper imaging depth (of the order of 1 cm or greater) because there is far less absorption and scattering in tissue of the ultrasonic signal compared to the emitted light signal in fluorescence imaging. When compared with ultrasound imaging, in which the contrast is limited because of the similarity in acoustical properties among tissues, photoacoustic imaging provides better tissue contrast as a result of the wider range of tissue optical properties. The optical absorption in biological tissues can be due to endogenous molecules such as hemoglobin or melanin or exogenously administered contrast agents. Since blood exhibits orders of magnitude higher light absorption than other tissues, there is sufficient endogenous contrast provided by oxygenated hemoglobin (HbO_2) and deoxygenated hemoglobin (Hb) for photoacoustic imaging to visualize blood vessels.

Most commonly, photoacoustic scanners use either a tomographic geometry (with an array of up to several hundred US transducers partially surrounding the subject) [76] or a planar geometry employing a linear transducer array [79, 80]. The tomographic approach offers a large effective aperture for data collection, but suffers from a low frame rate (>10 min per frame), due to the need for hundreds to thousands of laser pulses per

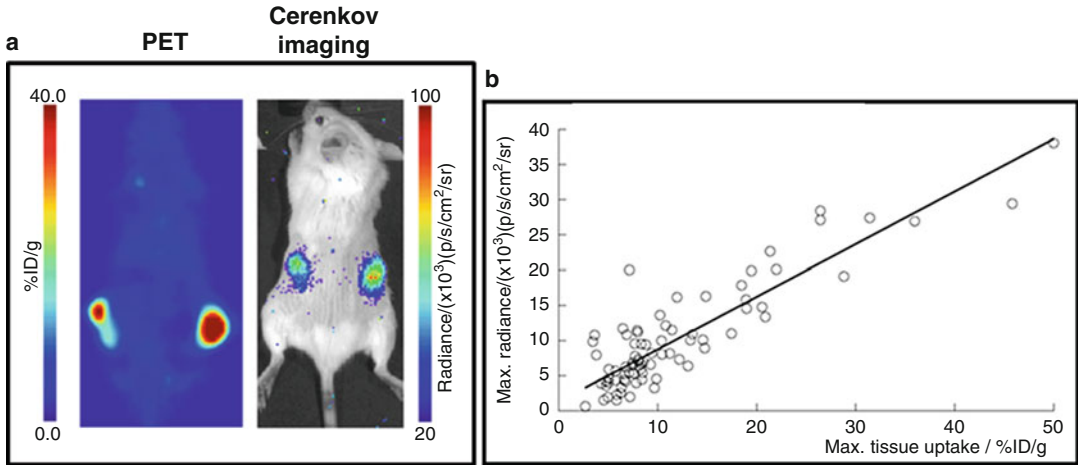

Fig. 16 (**a**) PET image (*left panel*) and Cerenkov image (*right panel*) of a ^{89}Zr-anti-PSMA (prostate-specific membrane antigen) antibody (J591) in a mouse with bilateral flank LNCaP prostate tumor xenografts at 96 h post-injection. The Cerenkov image is superimposed on a photograph of the mouse. The two xenografts are clearly visible in both images. (**b**) Linear correlation ($r = 0.89$) between the Cerenkov image-derived average radiance (in p/s/cm^2/sr) and the PET image-derived maximum tissue uptake (in percent of the injected dose per gram,%ID/g) (Adapted from [72] with permission)

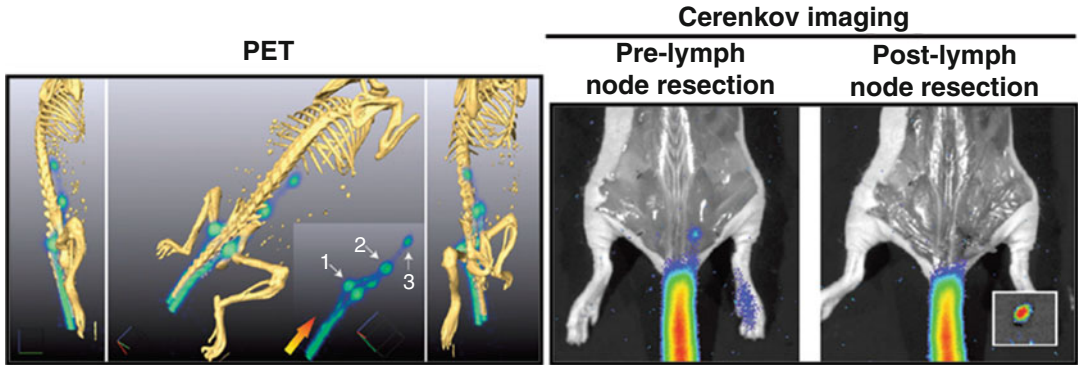

Fig. 17 Cerenkov imaging-guided lymph node resection in a normal mouse following intradermal tail injection of [^{18}F]FDG (30 μCi). *Left panel*: Volume rendering of fused CT image (*yellow* color table) and PET image (*green* color table) showing lymphatics and lymph nodes in relation to the skeleton. *Right panel*: Cerenkov image superimposed on a photograph of the mouse following removal post-sacrifice of the dorsal skin before (*left* image) and after (*right* image) resection of a luminescent inguinal lymph node. The resected node ex vivo is shown in the inset image (Adapted from [73] with permission)

frame. The use of a linear array eliminates the need for scanning, and thus a two-dimensional frame can be acquired with many fewer laser pulses, providing much higher frame rates. In addition, in the tomographic geometry, the surface of the transducers is of the order of 1 cm from the surface of the subject (up to now, rodents) to accommodate an array of transducers encircling the subject. As a result, the mouse or rat must be immersed in water to provide the necessary acoustical coupling to the transducer; in the multispectral optoacoustic tomography (MSOT) system marketed by iThera Medical, the animal is suspended in a very thin membrane and then immersed in the water, thereby keeping the animal completely dry (Fig. 19a). Another preclinical

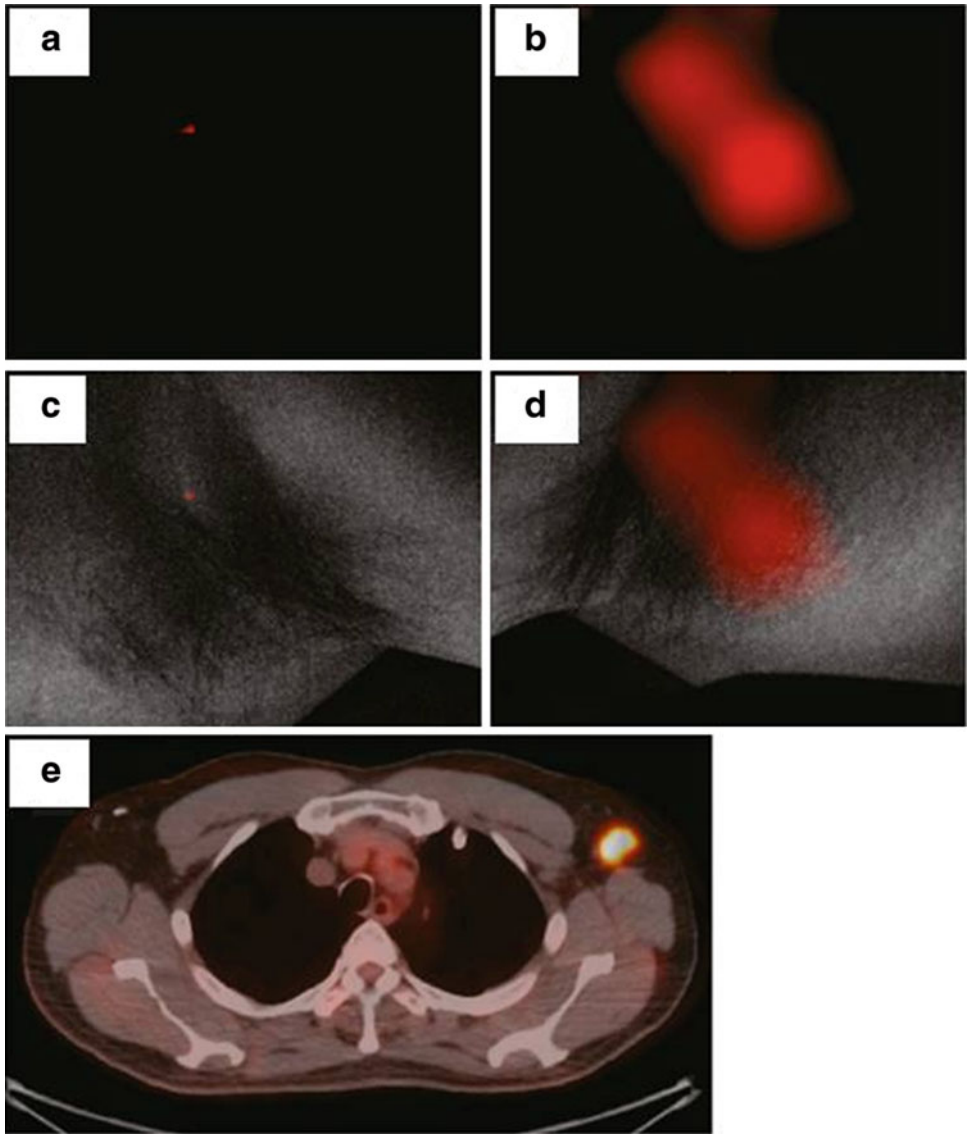

Fig. 18 Representative Cerenkov and PET/CT images of a [^{18}F]FDG-positive axillary lymph node. (**a**, **b**) Cerenkov scans of patient's right (*R*) and left (*L*) axillae, respectively. (**c**) Negative Cerenkov scan in light-protected environment of right axilla without [^{18}F]FDG-positive lymph node overlaid with white-light photograph. No significant Cerenkov emission associated with [^{18}F]FDG is seen. (**d**) White-light photograph from left axilla, overlaid with significant Cerenkov signal (shown in *red*-hue pseudocolor). (**e**) Transverse section of [^{18}F]FDG PET/CT scan through the patient's axillae, demonstrating that the Cerenkov signal co-localized (at least grossly) with the nodal focus of [^{18}F]FDG activity. There was no focus of [^{18}F]FDG activity in the contralateral disease-free axilla, consistent with the corresponding Cerenkov scan (From [74] with permission)

photoacoustic imaging system, employing a linear transducer array, is marketed by VisualSonics.

Photoacoustic imaging has been used successfully in preclinical models for tumor perfusion angiogenesis monitoring (see Fig. 19 [77]), blood oxygenation mapping, functional brain imaging, and melanoma detection, among other applications. The resulting functional images can be superimposed on high-resolution B-mode anatomic images.

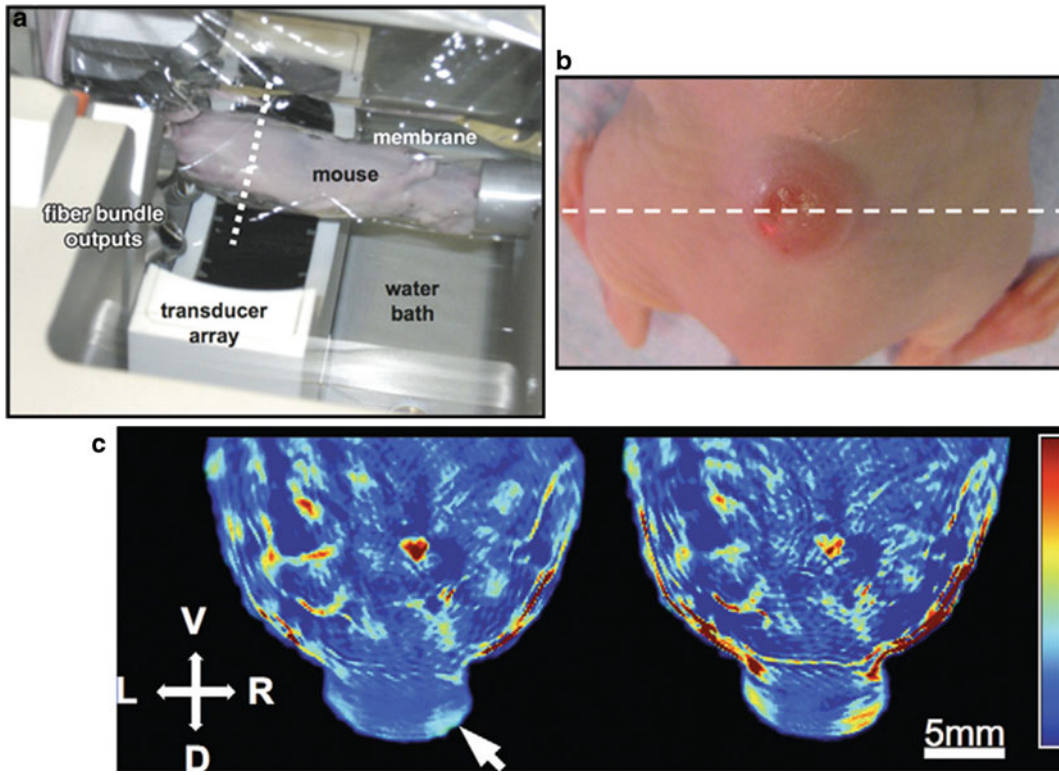

Fig. 19 (**a**) Setup for photoacoustic imaging of regional perfusion in a tumor xenograft on the dorsal surface of a nude mouse. Note that the tumor (on the dorsal surface of the animal and therefore not seen) is "immersed" in water. The animal remains dry, however, because of the presence of a thin membrane between the animal and the water. (**b**) Photograph of the 4T1 xenograft on the dorsal surface of the mouse. In (**a**, **b**), the *dashed line* indicates the approximate position of the transverse tissue section being imaged. (**c**) Images (acquired at 790 nm) before (*left panel*) and 30 s after (*right panel*) intravenous injection of IGC (*V* ventral, *D* dorsal, *L* left, *R* right). Note the increase in image contrast in and around the tumor (*arrow*) after injection, identifying the more highly perfused portions of the tumor (Adapted from [77] with permission)

While the clinical implementation of MSOT is still progressing and its clinical impact remains to be determined, the ability of this technology to visualize in real time the distribution and concentration of intrinsic and exogenous chromophores (including currently approved chromophores such as ICG and methylene blue) is such that it merits clinical evaluation. The Acuity™, marketed by iThera, is one of the very first clinical MSOT systems [81, 82] and appears adaptable to intraoperative imaging (Fig. 20). It is equipped with a fast-tunable 50-Hz laser and 2D or 3D detectors (128–512 elements, 2.5–10 MHz) and provides cross-sectional in-plane spatial resolution of 80–250 μm.

Diffuse optical tomography. Diffuse optical tomography (DOT) utilizes NIR light to generate quantitative functional images of tissue with a spatial resolution of 1–5 mm at depths up to several centimeters [83, 84]. Propagation of NIR light through a medium is dominated by scattering rather than absorption – tissue absorption path lengths are ~10 cm while scattering path lengths are less than 50 μm – and can be modeled as a diffusion process where photons behave stochastically (in a manner analogous to that of particles in random-walk modeling of diffusion). Quantitative measurements can be obtained by separating light absorption from scattering using spatial or temporal modulation techniques. Tissue molecular composition,

Fig. 20 Photograph of the iThera Acuity™ clinical MSOT system (Courtesy of iThera)

including the determination of the concentrations of oxy- and deoxyhemoglobin, water, lipid, and exogenous probes, and tissue structure can be determined from absorption and scattering measurements, respectively. Time modulation systems use picosecond optical pulses and time-gated photon-counting detectors; frequency modulation systems use a RF-modulated light source, PMTs or fast photodiodes, and RF phase detectors. DOT has been applied to breast cancer diagnostics, joint imaging, and blood oximetry (i.e., activation studies) in the human muscle and brain tissue as well as to cerebral ischemia and cancer studies in small animals and is adaptable to intraoperative imaging. Commercial instruments are now available that yield tomographic and volumetric image sets. These devices are compact, portable, and relatively inexpensive (~$150 K).

Optical coherence tomography. Optical coherence tomography (OCT) is an interferometric technique, typically employing low-coherence NIR light, to produce two-dimensional images of tissue surface layers and structure [85]. The principle of OCT is analogous to that of pulse-echo (i.e., B-mode) ultrasound imaging except OCT uses light instead of acoustic waves to delineate tissue structure by measuring reflectance of light rather than sound waves and thus achieves far better spatial resolution but with less depth penetration. The technique has been described as "an optical biopsy," since OCT can produce near-histologic images (spatial resolution, 1–15 μm) without excision. Due to photon absorption and scattering, its sampled depth is limited to within several millimeters of the tissue surface. The two-dimensional images can be assembled to construct a volumetric image set. In OCT, the axial resolution is proportional to the center wavelength and inversely proportional to the bandwidth of the light source and improves with the index of refraction of the sample. Originally developed for and still most commonly applied to ophthalmology (to obtain detailed images of retinal structure), OCT is being applied for cancer diagnosis, evaluation of coronary artery disease and tissue characterization.

Raman spectroscopic imaging. When light interacts with matter, most of the light is elastically scattered, retaining its original energy, frequency, and wavelength; this phenomenon is also known as Rayleigh scattering (Fig. 21a). However, a small fraction of light is inelastically scattered, with the scattered light having a lower energy and frequency and longer wavelength than the incident light. The process leading to this inelastic scatter is termed the Raman effect [86], and the difference in wavelength between the incident and scattered light is called the Raman shift. Because photons with optical energies interact with outer-shell, or valence, atomic electrons, which are responsible for the intramolecular chemical bonds among atoms, materials having different molecular

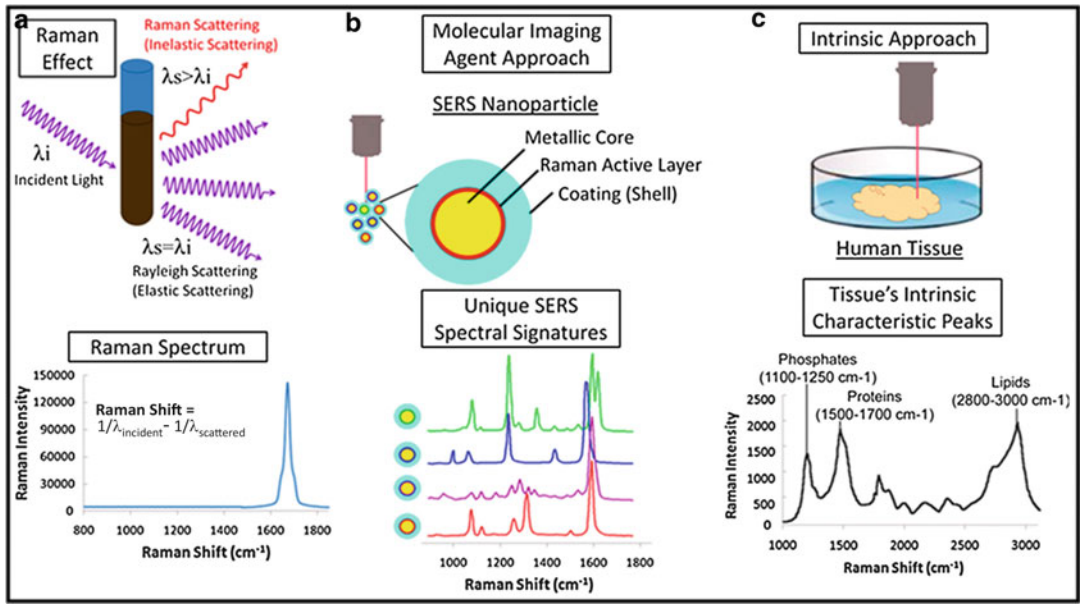

Fig. 21 (**a**) Raman effect, showing sample being illuminated with incident photons of wavelength (λi). Most of the incident photons are scattered elastically (Rayleigh scattering) and resulting scattered photons have same wavelength (λs) as the incident photons (i.e., $\lambda s = \lambda i$). A few photons are inelastically scattered (Raman scattering) at wavelengths longer than incident photons (i.e., $\lambda s > \lambda i$). The relative proportion of inelastically scattered photons is typically depicted using a Raman spectrum, which is a plot of scattered photon intensity versus the Raman shift (i.e., the wave number difference between the incident and scattered photons). Multiple different wavelengths of inelastically scattered light can occur, and a spectrum plot can therefore include multiple peaks, although a single primary peak, as shown, is also possible. (**b**) Molecular imaging agent approach showing SERS nanoparticles, which consist of a metallic core, a Raman-active layer adsorbed onto the metal surface, and a shell coating the entire particle. An array of unique spectral signatures can be obtained by modifying the Raman-active layer of the nanoparticle. These unique Raman nanoparticles can serve as molecular imaging agents for in vitro and in vivo procedures. (**c**) The intrinsic approach, showing a human tissue specimen being illuminated with a laser. The intrinsic Raman spectral signature of tissue can reveal important information about phosphate, protein, and lipid content of cells or tissue of interest (From [86] with permission)

compositions will inelastically scatter light differently. Every molecule therefore has a distinct Raman spectrum (or "signature"), that is, a different Raman shift-dependent intensity of the scattered light; this is the basis of using Raman spectroscopy to identify the molecular constituents of various materials [86]. By illuminating a sample with a highly collimated beam of light and at the same time either translating a scattered light detector or the sample in two dimensions, spatial indexing of the Raman spectrum can be performed and a Raman spectrum image created. Though they may appear similar, the Raman effect is distinct from fluorescence in that the former represents a light-scattering phenomenon and the latter light absorption and reemission. Like fluorescence imaging, Raman spectroscopic imaging has been applied to endogenous (or intrinsic) molecules naturally present in tissue and to exogenously administered materials (as in surface-enhanced Raman scattering (SERS) (see below)).

A drawback of the Raman effect as an analytical tool is that it is a very weak phenomenon, producing only one inelastically scattered photon for every ten million elastically scattered photons. Technical advances, such as the introduction of lasers and of resonance-based enhancements, have greatly expanded the practical applications of the Raman effect. For years now, the Raman effect has been used in a variety of analytical applications and, more recently, in various in vitro cell assays and microscopy. The most

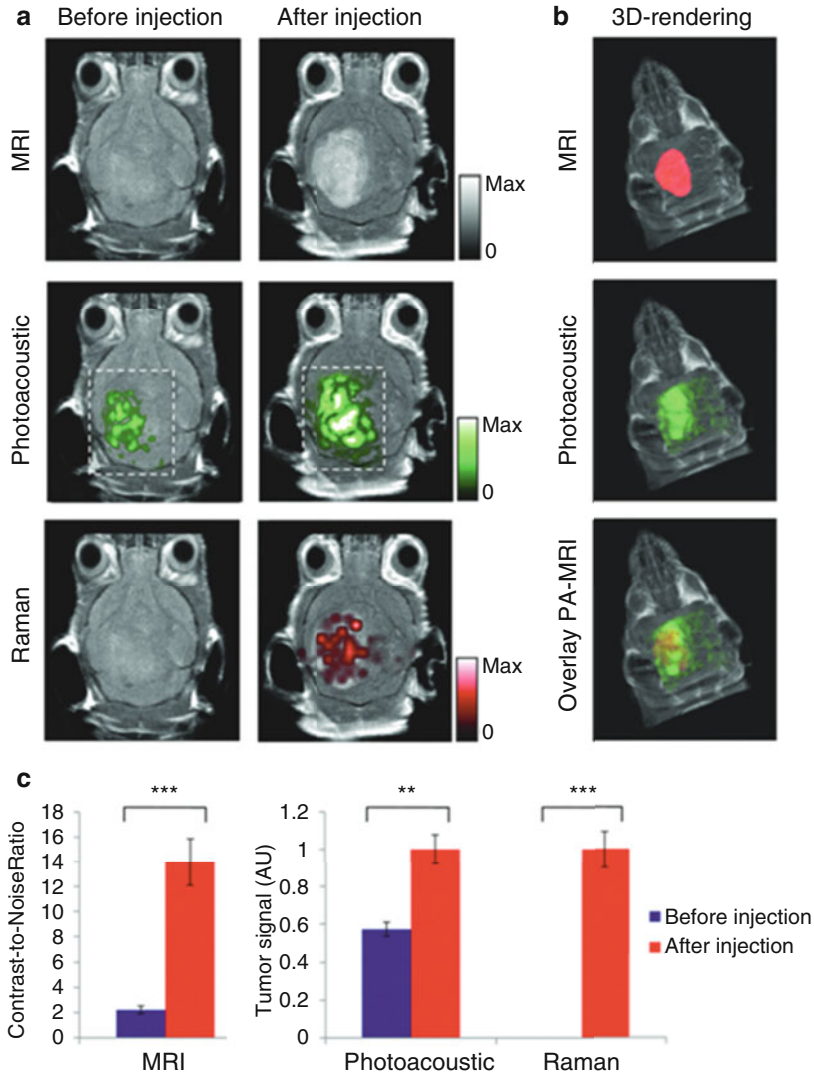

Fig. 22 Triple-modality detection with nanoparticle probes of brain tumors in mice. Three weeks after orthotopic implantation with U87MG glioblastoma cells, the brain tumor-bearing mouse was injected intravenously with the nanoparticles, which localized in the tumor due to the EPR (enhanced permeability and retention) effect. Photoacoustic (*PA*), Raman, and MR images of the brain (skin and skull intact) were acquired before and 2, 3, and 4 h postinjection, respectively. Raman imaging was performed using a commercial Raman microscope (inVia, Renishaw) with a computer-controlled x, y-translation stage. (**a**) Axial MR, PA, and Raman images. The postinjection images of all three modalities demonstrated clear tumor visualization. The PA and Raman images were co-registered with the MR image, demonstrating good concordance within the tumor of the nanoparticle distribution among the three modalities. (**b**) Volumetric rendering of MR images with the tumor segmented (*red*, *top panel*); overlay of the 3D PA image (*green*) over the MR image (*middle panel*); and overlay of the tumor-segmented MR and PA images (*bottom panel*) showing good co-localization of the PA signal within the tumor. (**c**) Quantification of the imaging signals in the tumor shows a significant increase in the MRI, PA, and Raman signals after versus before the nanoparticle injection ("***" indicates $p < 0.001$, "**" indicates $p < 0.01$). Error bars represent the standard error of the mean, AU, arbitrary units (From [87] with permission)

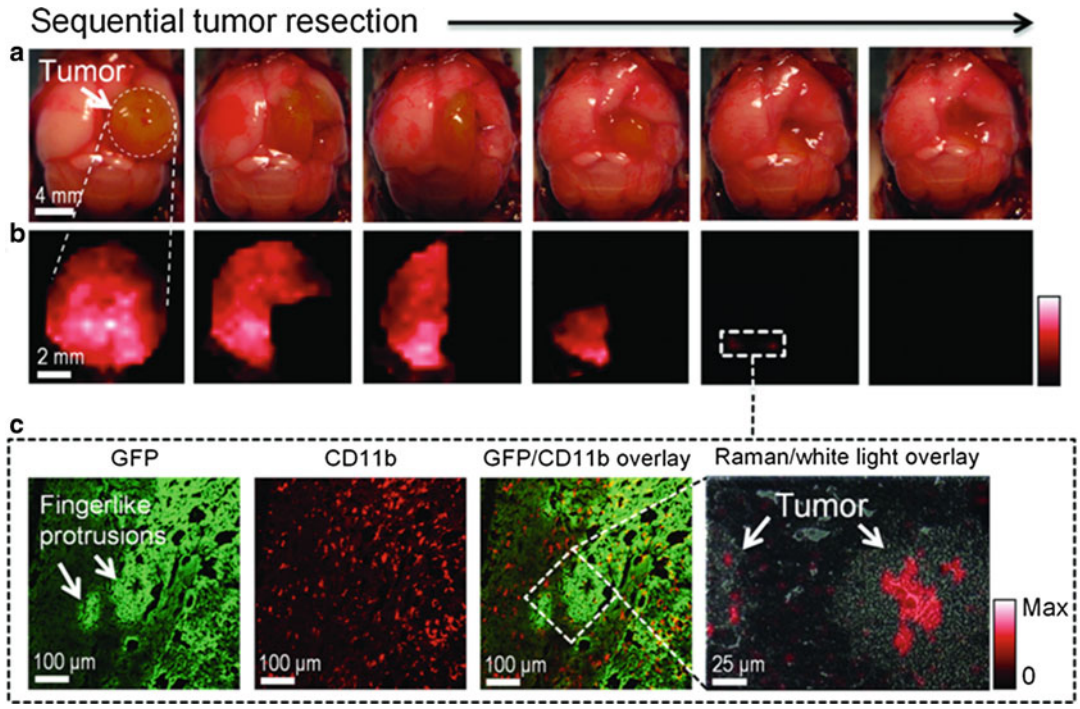

Fig. 23 Preclinical model of Raman-guided surgery. (**a**) Following orthotopic implantation with GFP-transduced U87MG glioblastoma cells, the brain tumor-bearing mouse underwent craniotomy under general anesthesia. Quarters of the tumor were then sequentially removed (as illustrated in the photographs). (**b**) Intraoperative Raman imaging was performed after each resection step, until the entire tumor had been removed by visual inspection. After the gross removal of the tumor, several small foci of Raman signal were found in the resection bed (outlined by the *dashed white square*). (**c**) Subsequent immunohistochemical analysis of sections from these foci demonstrated an infiltrative pattern of the tumor in this location, forming fingerlike protrusions extending into the surrounding brain tissue. CD11b (second panel from *left*) is a widely used microglial immunohistochemical marker. As shown in the Raman microscopy image (*right panel*), the Raman signal was observed within these protrusions, indicating the selective presence of MPRs in these protrusions. The *white dashed box* not drawn to scale. Raman signal in linear *red* color table (From [87] with permission)

commonly used enhancement methods are surface-enhanced Raman scattering (SERS) and coherence anti-Stokes Raman scattering (CARS); both SERS and CARS enhance the Raman signal by orders of magnitude. SERS involves adding metal (e.g., gold) nanoparticles which absorb the optical energy and yield an enhanced Raman signal by virtue of the metal surface transferring energy to nearby molecules (Fig. 21b). The resulting Raman signal provides picomolar sensitivity, which is compatible with tissue tracer concentrations achievable in vivo. Furthermore, labeling SERS nanoparticles with several different molecular ligands can provide simultaneous assay of multiple molecular components. CARS involves illumination with photons of different energies, with one photon energizing a molecule of interest from its ground state to an initial excited state and a second photon energizing the molecule from a "relaxed" state (i.e., at an energy level after releasing energy during the "laser-off" time interval following absorption of the first photon) to a different higher-energy level; this second (or higher) tier of vibrational energy is ~fivefold more intense than the Raman signal after the original pulse (Fig. 21c). The CARS technique is often used for high-

resolution, three-dimensional microscopy. Its advantages are that there is no need for administered probes (as in SERS) and rapid acquisition of images. Several preclinical studies have utilized the SERS or CARS techniques for in vivo molecular imaging of cell receptors (e.g., RGD-carbon nanotubes that bind to $\alpha_5\beta_3$ integrin-expressing tumors), tumor microvessels, enzyme activity, pH, lipid composition, and myelin composition (Fig. 22).

Over the last decade, the biomedical applications of Raman spectroscopic imaging have grown dramatically. Because it is essentially a surface imaging technique (like most optical imaging techniques), Raman spectroscopic imaging has been applied mainly to examination of skin and of pathological specimens as well as to small animals. For example, Raman mapping has enabled accurate identification of malignant from benign lesions and normal tissue in the skin, brain, larynx, parathyroids, breast, and urinary bladder. Raman spectroscopic imaging has also been applied endoscopically in the colon. Recently, Kircher et al. have reported a molecular imaging strategy using a novel triple-modality MRI-photoacoustic-Raman nanoparticle probe [87] clinically translatable to the intraoperative setting (Fig. 23).

Concluding Remarks

The last decade has featured remarkable technical advances in intraoperative imaging and techniques potentially adaptable to intraoperative imaging. While intraoperative nuclear counting using handheld probes is now routine, intraoperative nuclear imaging remains largely investigational. While certain applications of intraoperative and endoscopic optical imaging (such as optical cystoscopy) are also now fairly routine, more exotic forms of optical imaging such as Cerenkov imaging and photoacoustic imaging have only recently been translated to the clinic. Other promising forms of optical imaging such as Raman spectroscopic imaging have not yet been clinically translated to any significant extent. Multimodality intraoperative probes capable of simultaneously detecting both nuclear and optical signals are being developed as well. The ultimate clinical impact of these new imaging modalities in intraoperative and endoscopic settings remains to be determined.

References

1. Fong Y, Giulianotti P, Lewis J, et al. Imaging and visualization in the modern operating room: a comprehensive guide for physicians. New York: Springer; 2015.
2. Sweet WH. The use of nuclear disintegration in diagnosis and treatment of brain tumors. N Engl J Med. 1951;245:875–8.
3. Cody III HS, editor. Sentinel lymph node biopsy. London: Martin Dunitz; 2002.
4. Mariani G, Giuliano AE, Strauss HW, editors. Radioguided surgery: a comprehensive team approach. New York: Springer; 2008.
5. Povoski SP, Neff RL, Mojzisik CM, et al. A comprehensive overview of radioguided surgery using gamma detection probe technology. World J Surg Oncol. 2009; 7:11.
6. Gulec SA, Moffat FL, Carroll RG. The expanding clinical role for intraoperative gamma probes. In: Freeman LM, editor. Nuclear medicine annual 1997. Philadelphia: Lippincott-Raven Publishers; 1997. p. 209–37.
7. Woolfenden JM, Barber HB. Intraoperative probes. In: Wagner HN, Szabo Z, Buchanan JW, editors. Principles of nuclear medicine. 2nd ed. Philadelphia: WB Saunders; 1995. p. 292–7.
8. Barber HB, Barrett HH, Woolfenden JM, et al. Comparison of in vivo scintillation probes and gamma cameras for detection of small, deep tumours. Phys Med Biol. 1989;34:727–39.
9. Daghighian F, Mazziotta JC, Hoffman EJ, et al. Intraoperative beta probe: a device for detecting tissue labeled with positron or electron emitting isotopes during surgery. Med Phys. 1994;21:153–7.
10. Raylman RR, Fisher SJ, Brown RS, et al. Fluorine-18-fluorodeoxyglucose-guided breast cancer surgery with a positron-sensitive probe: validation in preclinical studies. J Nucl Med. 1995;36:1869–74.
11. Raylman RR, Wahl RL. A fiber-optically coupled positron-sensitive surgical probe. J Nucl Med. 1994;35: 909–13.
12. Heller S, Zanzonico P. Nuclear probes and intraoperative gamma cameras. Semin Nucl Med. 2011;41:166–81.
13. Zanzonico P. The intraoperative gamma probe: design, safety, and operation. In: Cody III HS, editor. Sentinel lymph node biopsy. London: Martin Dunitz; 2008. p. 45–68.
14. Zanzonico P, Heller S. The intraoperative gamma probe: basic principles and choices available. Semin Nucl Med. 2000;30:33–48.
15. Essner R, Daghighian F, Giuliano AE. Advances in FDG PET probes in surgical oncology. Cancer J. 2002; 8:100–8.

16. Essner R, Hsueh EC, Haigh PI, et al. Application of an [^{18}F]fluorodeoxyglucose-sensitive probe for the intraoperative detection of malignancy. J Surg Res. 2001;96:120–6.
17. Strong VE, Galanis CJ, Riedl CC, et al. Portable PET probes are a novel tool for intraoperative localization of tumor deposits. Ann Surg Innov Res. 2009;3:2.
18. Strong VE, Humm J, Russo P, et al. A novel method to localize antibody-targeted cancer deposits intraoperatively using handheld PET beta and gamma probes. Surg Endosc. 2008;22:386–91.
19. Meller B, Sommer K, Gerl J, et al. High energy probe for detecting lymph node metastases with ^{18}F-FDG in patients with head and neck cancer. Nuklearmedizin. 2006;45:153–9.
20. Wasselle J, Becker J, Cruse W, et al. Localization of malignant melanoma using monoclonal antibodies. Arch Surg. 1991;126:481–4.
21. Schneebaum S, Essner R, Even-Sapir E. Positron-sensitive probes. In: Mariani G, Giuliano AE, Strauss HW, editors. Radioguided surgery: a comprehensive team approach. New York: Springer; 2008. p. 23–8.
22. Raylman RR. Performance of a dual, solid-state intraoperative probe system with ^{18}F, ^{99m}Tc, and ^{111}In. J Nucl Med. 2001;42:352–60.
23. Reinhardt H, Stula D, Gratzl O. Topographic studies with ^{32}P tumor marker during operations of brain tumors. Eur Surg Res. 1985;17:333–40.
24. Newman LA. Current issues in the surgical management of breast cancer: a review of abstracts from the 2002 San Antonio Breast Cancer Symposium, the 2003 Society of Surgical Oncology annual meeting, and the 2003 American Society of Clinical Oncology meeting. Breast J. 2004;10 Suppl 1:S22–5.
25. Goyal A, Newcombe RG, Mansel RE, et al. Role of routine preoperative lymphoscintigraphy in sentinel node biopsy for breast cancer. Eur J Cancer. 2005;41:238–43.
26. Tafra L, McMasters KM, Whitworth P, et al. Credentialing issues with sentinel lymph node staging for breast cancer. Am J Surg. 2000;180:268–73.
27. Mathelin C, Salvador S, Bekaert V, et al. A new intraoperative gamma camera for the sentinel lymph node procedure in breast cancer. Anticancer Res. 2008;28:2859–64.
28. Mathelin C, Salvador S, Croce S, et al. Optimization of sentinel lymph node biopsy in breast cancer using an operative gamma camera. World J Surg Oncol. 2007;5:132.
29. Mathelin C, Salvador S, Huss D, et al. Precise localization of sentinel lymph nodes and estimation of their depth using a prototype intraoperative mini gamma-camera in patients with breast cancer. J Nucl Med. 2007;48:623–9.
30. Britten AJ. A method to evaluate intra-operative gamma probes for sentinel lymph node localisation. Eur J Nucl Med. 1999;26:76–83.
31. Aarsvold JN, Alazraki NP. Update on detection of sentinel lymph nodes in patients with breast cancer. Semin Nucl Med. 2005;35:116–28.
32. Hoffman EJ, Torni MP, Levin CS. Gamma and beta intra-operative imaging probes. Nucl Instrum Methods Phys Res. 1997;392:324–9.
33. Scopinaro F, Soluri A. Gamma ray imaging probes for radioguided surgery and site-directed biopsy. In: Mariani G, Giuliano AE, Strauss HW, editors. Radioguided surgery: a comprehensive team approach. New York: Springer; 2008. p. 29–36.
34. Abe A, Takahashi N, Lee J, et al. Performance evaluation of a hand-held, semiconductor (CdZnTe)-based gamma camera. Eur J Nucl Med Mol Imaging. 2003;30:805–11.
35. Pitre S, Menard L, Ricard M, et al. A hand-held imaging probe for radio-guided surgery: physical performance and preliminary clinical experience. Eur J Nucl Med Mol Imaging. 2003;30:339–43.
36. Oda T, Hayama K, Tsuchimochi M. Evaluation of small semiconductor gamma camera – simulation of sentinel lymph node biopsy by using a trial product of clinical type gamma camera. Kaku Igaku. 2009;46:1–12.
37. Tsuchimochi M, Hayama K, Oda T, et al. Evaluation of the efficacy of a small CdTe gamma-camera for sentinel lymph node biopsy. J Nucl Med. 2008;49:956–62.
38. Tsuchimochi M, Sakahara H, Hayama K, et al. A prototype small CdTe gamma camera for radioguided surgery and other imaging applications. Eur J Nucl Med Mol Imaging. 2003;30:1605–14.
39. Sanchez F, Benlloch JM, Escat B, et al. Design and tests of a portable mini gamma camera. Med Phys. 2004;31:1384–97.
40. Sanchez F, Fernandez MM, Gimenez M, et al. Performance tests of two portable mini gamma cameras for medical applications. Med Phys. 2006;33:4210–20.
41. Vermeeren L, Meinhardt W, Bex A, et al. Paraaortic sentinel lymph nodes: toward optimal detection and intraoperative localization using SPECT/CT and intraoperative real-time imaging. J Nucl Med. 2010;51:376–82.
42. Vermeeren L, Valdes Olmos RA, Klop WM, et al. A portable gamma-camera for intraoperative detection of sentinel nodes in the head and neck region. J Nucl Med. 2010;51:700–3.
43. Vermeeren L, Valdes Olmos RA, Meinhardt W, et al. Intraoperative imaging for sentinel node identification in prostate carcinoma: its use in combination with other techniques. J Nucl Med. 2011;52:741–4.
44. Ortega J, Ferrer-Rebolleda J, Cassinello N, et al. Potential role of a new hand-held miniature gamma camera in performing minimally invasive parathyroidectomy. Eur J Nucl Med Mol Imaging. 2007;34:165–9.
45. Naji S, Tadros A, Traub J, et al. Case report: improving the speed and accuracy of melanoma sentinel node biopsy with 3D intra-operative imaging. J Plast Reconstr Aesthet Surg. 2011;64:1712–5.
46. Wendler T, Herrmann K, Schnelzer A, et al. First demonstration of 3-D lymphatic mapping in breast cancer using freehand SPECT. Eur J Nucl Med Mol Imaging. 2010;37:1452–61.

47. Daghigian F, Fong Y. Detectors for intraoperative molecular imaging: from probes to scanners. In: Fong Y et al., editors. Imaging and visualization in the modern operating room: a comprehensive guide for physicians. New York: Springer; 2015. p. 55–67.
48. Contag PR, Olomu IN, Stevenson DK, et al. Bioluminescent indicators in living mammals. Nat Med. 1998; 4:245–7.
49. Ntziachristos V, Ripoll J, Wang LV, et al. Looking and listening to light: the evolution of whole-body photonic imaging. Nat Biotechnol. 2005;23:313–20.
50. Taruttis A, Ntziachristos V. Translational optical imaging. AJR Am J Roentgenol. 2012;199:263–71.
51. Witjes JA, Douglass J. The role of hexaminolevulinate fluorescence cystoscopy in bladder cancer. Nat Clin Pract Urol. 2007;4:542–9.
52. Herr H. Narrow band cystoscopy. In: Fong Y et al., editors. Imaging and visualization in the modern operating room: a comprehensive guide for physicians. New York: Springer; 2015. p. 257–69.
53. Stummer W, Novotny A, Stepp H, et al. Fluorescence-guided resection of glioblastoma multiforme by using 5-aminolevulinic acid-induced porphyrins: a prospective study in 52 consecutive patients. J Neurosurg. 2000; 93:1003–13.
54. Ashitate Y, Stockdale A, Choi HS, et al. Real-time simultaneous near-infrared fluorescence imaging of bile duct and arterial anatomy. J Surg Res. 2012;176:7–13.
55. Ashitate Y, Tanaka E, Stockdale A, et al. Near-infrared fluorescence imaging of thoracic duct anatomy and function in open surgery and video-assisted thoracic surgery. J Thorac Cardiovasc Surg. 2011;142:31–8. e1-2.
56. Frangioni JV. In vivo near-infrared fluorescence imaging. Curr Opin Chem Biol. 2003;7:626–34.
57. Frangioni JV. New technologies for human cancer imaging. J Clin Oncol. 2008;26:4012–21.
58. Hutteman M, Choi HS, Mieog JS, et al. Clinical translation of ex vivo sentinel lymph node mapping for colorectal cancer using invisible near-infrared fluorescence light. Ann Surg Oncol. 2011;18:1006–14.
59. Lee BT, Hutteman M, Gioux S, et al. The FLARE intraoperative near-infrared fluorescence imaging system: a first-in-human clinical trial in perforator flap breast reconstruction. Plast Reconstr Surg. 2010;126: 1472–81.
60. Troyan SL, Kianzad V, Gibbs-Strauss SL, et al. The FLARE intraoperative near-infrared fluorescence imaging system: a first-in-human clinical trial in breast cancer sentinel lymph node mapping. Ann Surg Oncol. 2009; 16:2943–52.
61. Kosaka N, Mitsunaga M, Longmire MR, et al. Near infrared fluorescence-guided real-time endoscopic detection of peritoneal ovarian cancer nodules using intravenously injected indocyanine green. Int J Cancer. 2011;129:1671–7.
62. Bradbury M, Pauliah M, Wiesner U. Ultrasmall fluorescent silica nanoparticles as intraoperative imaging tools for cancer diagnosis and treatment. In: Fong Y et al., editors. Imaging and visualization in the modern operating room: a comprehensive guide for physicians. New York: Springer; 2015. p. 167–79.
63. Bradbury MS, Pauliah M, Zanzonico P, et al. Intraoperative mapping of sentinel lymph node metastases using a clinically translated ultrasmall silica nanoparticle. Wiley Interdiscip Rev Nanomed Nanobiotechnol. 2015.
64. Beattie BJ, Thorek DL, Schmidtlein CR, et al. Quantitative modeling of Cerenkov light production efficiency from medical radionuclides. PLoS ONE. 2012; 7, e31402.
65. Cerenkov PA. Visible emission of clean liquids by action of gamma-radiation. C R Dokl Akad Nauk SSSR. 1934;2:451–4.
66. Dothager RS, Goiffon RJ, Jackson E, et al. Cerenkov radiation energy transfer (CRET) imaging: a novel method for optical imaging of PET isotopes in biological systems. PLoS ONE. 2010;5, e13300.
67. Holland JP, Normand G, Ruggiero A, et al. Intraoperative imaging of positron emission tomographic radiotracers using cerenkov luminescence emissions. Mol Imaging. 2011;10:177–86.
68. Li C, Mitchell GS, Cherry SR. Cerenkov luminescence tomography for small-animal imaging. Opt Lett. 2010; 35:1109–11.
69. Liu H, Ren G, Miao Z, et al. Molecular optical imaging with radioactive probes. PLoS ONE. 2010;5, e9470.
70. Lucignani G. Cerenkov radioactive optical imaging: a promising new strategy. Eur J Nucl Med Mol Imaging. 2011;38:592–5.
71. Robertson R, Germanos MS, Li C, et al. Optical imaging of Cerenkov light generation from positron-emitting radiotracers. Phys Med Biol. 2009;54: N355–65.
72. Ruggiero A, Holland JP, Lewis JS, et al. Cerenkov luminescence imaging of medical isotopes. J Nucl Med. 2010;51:1123–30.
73. Thorek DL, Abou DS, Beattie BJ, et al. Positron lymphography: multimodal, high-resolution, dynamic mapping and resection of lymph nodes after intradermal injection of ^{18}F-FDG. J Nucl Med. 2012;53: 1438–45.
74. Thorek DL, Riedl CC, Grimm J. Clinical Cerenkov luminescence imaging of ^{18}F-FDG. J Nucl Med. 2014; 55:95–8.
75. Spinelli AE, Ferdeghini M, Cavedon C, et al. First human cerenkography. J Biomed Opt. 2013;18:20502.
76. Xu MH, Wang LHV. Photoacoustic imaging in biomedicine. Rev Sci Instrum. 2006;77:41–101.
77. Herzog E, Taruttis A, Beziere N, et al. Optical imaging of cancer heterogeneity with multispectral optoacoustic tomography. Radiology. 2012;263:461–8.
78. Ku G, Fornage BD, Jin X, et al. Thermoacoustic and photoacoustic tomography of thick biological tissues toward breast imaging. Technol Cancer Res Treat. 2005;4:559–66.

79. Kruger RA, Kiser WL, Reinecke DR, et al. Thermoacoustic computed tomography using a conventional linear transducer array. Med Phys. 2003; 30:856–60.
80. Zeng Y, Da X, Wang Y, et al. Photoacoustic and ultrasonic coimage with a linear transducer array. Opt Lett. 2004;29:1760–2.
81. McNally LR, Mezera M, Morgan DE, et al. Current and emerging clinical applications of multispectral optoacoustic tomography (MSOT) in oncology. Clin Cancer Res. 2016;22:3432–9.
82. Neuschmelting V, Burton NC, Lockau H, et al. Performance of a multispectral optoacoustic tomography (MSOT) system equipped with 2D vs 3D handheld probes for potential clinical translation. Photoacoustics. 2016;4:1–10.
83. Hielscher AH. Optical tomographic imaging of small animals. Curr Opin Biotechnol. 2005;16:79–88.
84. Jian H. Diffuse optical tomography: principles and applications. Boca Raton: CRC Press; 2010.
85. Huang D, Swanson EA, Lin CP, et al. Optical coherence tomography. Science. 1991;254:1178–81.
86. Zavaleta CL, Kircher MF, Gambhir SS. Raman's "effect" on molecular imaging. J Nucl Med. 2011; 52:1839–44.
87. Kircher MF, de la Zerda A, Jokerst JV, et al. A brain tumor molecular imaging strategy using a new triple-modality MRI-photoacoustic-Raman nanoparticle. Nat Med. 2012;18:829–34.
88. Kopelman D, Blevis I, Iosilevsky G, et al. Sentinel node detection in an animal study: evaluation of a new portable gamma camera. Int Surg. 2007;92:161–6.
89. Kopelman D, Blevis I, Iosilevsky G, et al. A newly developed intra-operative gamma camera: performance characteristics in a laboratory phantom study. Eur J Nucl Med Mol Imaging. 2005;32:1217–24.
90. Zanzonico P. Noninvasive imaging for supporting basic research. In: Kiessling F, Pichler BJ, editors. Small-animal imaging: basics and practical guide. Heidelberg: Springer; 2011. p. 3–16.
91. van Dam GM, Themelis G, Crane LM, et al. Intraoperative tumor-specific fluorescence imaging in ovarian cancer by folate receptor-alpha targeting: first in-human results. Nat Med. 2011;17:1315–9.

Radiobiology and Radiation Dosimetry in Nuclear Medicine

13

Massimo Salvatori, Marta Cremonesi, Luca Indovina, Marco Chianelli, Massimiliano Pacilio, Carlo Chiesa, and Pat Zanzonico

Abstract

Radionuclide therapy (RNT) uses systemically administered radiopharmaceuticals directed to a specific cancer-associated target to provide low-dose-rate (LDR) treatment. The radiation dose is delivered to the tumor cells by continuous, but declining, exposure that is a function of the initial uptake and the variable half-life. The average dose rate for RNT is typically of the order of 2–8 Gy/day, and the maximum absorbed dose may be up to 50 Gy delivered over a period of many days. This is in marked contrast to the situation with external beam radiotherapy (EBRT), where the dose is delivered at a high-dose rate (HDR), typically 1–5 Gy/min, and also in contradistinction to the dose rate at which brachytherapy is delivered, typically 1–5 Gy/h. The mechanisms by which cells respond to LDR exposures are fundamentally different from those occurring at HDR. LDR exposures tend to promote loss of clonogenic potential in some cell types (e.g., lymphomas) by activating apoptotic responses, whereas high doses tend to cause necrosis as their primary mechanism of cytotoxicity. The ability to induce apoptosis varies inversely with dose rate. Many cell types exhibit an initial hypersensitive response at doses below ~25 cGy followed by a region of increasing radioresistance up to ~50 cGy. This phenomenon probably involves an alteration in the cellular processing of DNA damage as a function of dose. Radiation damage to cells is due primarily to indirect effects such as formation of free radicals in water (with their diffusion and subsequent interaction with cellular

M. Salvatori (✉)
Nuclear Medicine Institute, Catholic University of the Sacred Heart – "Policlinico A. Gemelli", Rome, Italy
e-mail: msalvatori@rm.unicatt.it; massimo.salvatori@unicatt.it

M. Cremonesi
Department of Medical Physics, European Institute of Oncology, Milan, Italy
e-mail: marta.cremonesi@ieo.it

L. Indovina
Department of Medical Physics, Catholic University of the Sacred Heart – "Policlinico A. Gemelli", Rome, Italy
e-mail: luca.indovina@policlinicogemelli.it

M. Chianelli
Department of Endocrinology, "Ospedale Regina Apostolorum", Albano, Rome, Italy
e-mail: marcochianelli@libero.it

M. Pacilio
Department of Medical Physics, Azienda Ospedaliera San Camillo Forlanini, Rome, Italy
e-mail: mpacilio@scamilloforlanini.rm.it

C. Chiesa
Nuclear Medicine Department, National Cancer Institute, Milan, Italy
e-mail: carlo.chiesa@istitutotumori.mi.it

P. Zanzonico
Memorial Hospital Research Laboratories, Department of Medical Physics, Memorial Sloan Kettering Cancer Center, New York, NY, USA
e-mail: zanzonip@mskcc.org

© Springer International Publishing Switzerland 2017
H.W. Strauss et al. (eds.), *Nuclear Oncology*,
https://doi.org/10.1007/978-3-319-26236-9_6

components, mostly DNA) and to some degree direct damage to DNA. Different tissues and different individuals have different abilities to respond to and repair this damage. The value of LDR therapy with radionuclides in patients with differentiated thyroid carcinoma, somatostatin receptor-expressing tumors, neuroendocrine tumors, lymphoma, liver tumors, and treatment of metastatic bone pain is discussed.

Keywords

Radionuclide therapy • Radiobiology • Radiation dosimetry • Therapeutic radiopharmaceuticals • DNA damage and radiation dose

Glossary

3D-ID	3D-internal
[^{18}F]FDG	2-deoxy-2-[^{18}F]fluoro-D-glucose
ASCT	Autologous stem cell transplantation
BED	Biologic effective dose
BSA	Body surface area
CRPC	Castration-resistant prostate cancer
CT	X-ray computed tomography
CTDI	CT dose index
DMSA	Dimercaptosuccinic acid
DOTA	1,4,7,10-Tetra-azacyclododecane-1,4,7,10-tetraacetic acid
DOTANOC	DOTA-1-Nal^3-octreotide
DOTATATE	DOTA- Tyr^3-octreotate
DSB	Double-strand breaks
DTC	Differentiated thyroid cancer
DTPA	Diethylenetriaminepentaacetic acid
DVH	Dose–volume histograms
EANM	European Association of Nuclear Medicine
EBRT	External beam radiation therapy
ECD	Ethyl cysteinate dimer
ED	Effective dose
EU	European Union
FDA	United States Food and Drug Administration
FISH	Fluorescence in situ hybridization
FSH	Follicle-stimulating hormone
GBE	*Ginkgo biloba* extract
GI	Gastrointestinal
Gy	Gray unit (ionizing radiation dose in the International System of Units, corresponding to the absorption of one joule of radiation energy per kilogram of matter)
HCC	Hepatocellular carcinoma
HDR	High-dose rate
HMPAO	Hexamethylpropylenamine oxine
ICRU	International Commission on Radiological Units
LDH–IRR	Low-dose hyper-radiosensitivity–increased radioresistance
LDR	Low-dose-rate
LET	Linear energy transfer
LPL	Lethal–potentially lethal
LQ	Linearquadratic
LSF	Lung shunt fraction
LSS	Life span study
MAA	Macroaggregated albumin
MAG3	Mercaptoacetyltriglycine
MDP	Methylene diphosphonate
MIBG	Meta-iodobenzylguanidine
MIRD	Medical internal radiation dose
MRI	Magnetic resonance imaging
MN	Micronuclei
NAT	Noradrenaline transporter
NHL	Non-Hodgkin's lymphoma
NSCLC	Non-small cell lung cancer
NT	Non-tumor tissue
NTCP	Normal tissue complication probability
OLINDA	Organ level internal dose assessment
PET	Positron emission tomography
PET/CT	Positron emission tomography/Computed tomography
PET/MRI	Positron emission tomography/Magnetic resonance imaging

PRRT	Peptide receptor radionuclide therapy
RBE	Relative biological effectiveness
RE	Relative effectiveness per unit dose
RILD	Radio induced liver disease
RIT	Radioimmunotherapy
ROI	Region of interest
ROS	Reactive oxygen species
SF	Surviving fraction
SNM	Society of Nuclear Medicine
SPECT	Single-photon emission computed tomography
SPECT/CT	Single-photon emission computed tomography/Computed tomography
STASIS	Stress or aberrant signaling-induced senescence
SUV	Standardized uptake values
Sv	Unit of radiation absorption in the International System of Units (SI), which takes into account the relative biological effectiveness (RBE) of ionizing radiation
TACE	Transarterial chemoembolization
TARE	Trans-arterial radioembolization
TBA	Total-body absorbed
TCP	Tumor control probability
TNF	Tumor necrosis factor
TRAIL	TNF-related apoptosis-inducing ligand
VOI	Volume of interest
WBD	Whole-body radiation dose
WBS	Whole-body scan
γ-H2AX	Phosphorylated member X of the H2A histone family

Contents

Radiobiology 308
Conventional Radiobiological Models 308
Cell Death Mechanisms 310
Possible Contributing Mechanisms to RNT Tumor Responses 310
Low-Dose/Dose-Rate Apoptosis 310
Low-Dose Hyper-radiosensitivity–Increased Radioresistance 310
G2 Synchronization, Bystander, and Cross-Fire Effects 311
Adaptive Responses 312
Fractionated RNT and Hypoxia 312
Future Directions 312
Dosimetry: Overview on Methods 312
Clinical Experience 315
^{131}I-Iodide Therapy of Differentiated Thyroid Carcinoma 315
Peptide Receptor Radionuclide Therapy 318
Radioimmunotherapy of Lymphoma 322
Radioembolization of Liver Tumors 324
Therapy of Neuroendocrine Malignancy 327
Treatment of Metastatic Bone Pain 330
Biological Dosimetry 331
Assays in Biological Dosimetry 332
Chromosome Painting 333
Comet Assay 333
γ-H2AX 334
Conclusions 334
Diagnosis 335
Medical Radiation Exposures: Societal Concerns 335
Radiation Doses in Diagnostic Nuclear Medicine 335
Multimodality Studies: PET/CT and SPECT/CT ... 337
Dose–Response Relationships in Radiation Carcinogenesis 338
Risk–Benefit Considerations 339
Considerations for Sensitive Populations: Prospective Parents, Pregnant Women, and Nursing Mothers 340
Nursing Mothers 342
References 342

New radiopharmaceuticals have led to increasing success of radionuclide therapy (RNT) [1, 2]. To plan treatment with RNT requires understanding dosimetry to both the target organ and other sites of tracer localization [3, 4]. However, despite the fact that maximizing radiation-absorbed dose to tumor while minimizing damage to normal tissues is the central objective of RNT, up till now RNT dosimetry has not gained wide acceptance as a necessary clinical tool. The need for dosimetry to individually optimize the therapeutic activity to be administered

has been far from self-evident, and efforts in this direction are in an infancy stage [4].

This chapter describes the progress that has been achieved in the fields of dosimetry and radiobiology, including a brief overview of the techniques used in biological dosimetry.

Radiobiology

There are three major approaches to the delivery of radiation therapy to treat patients with cancer: (1) locoregional delivery, such as in external beam radiotherapy (EBRT), (2) sealed-source interstitial/intracavitary radiotherapy (brachytherapy), and (3) RNT which include the use of receptor-directed ligands, metabolic precursors, or monoclonal antibodies (i.e., radioimmunotherapy) [5].

The key clinical and basic characteristics of RNT are the systemic administration of a radiopharmaceutical directed to a specific cancer-associated target and the rate at which the radiation dose is delivered to that target [5].

According to the principle of very low-dose rate (LDR), in RNT the radiation dose is delivered to the tumor cells by continuous, but declining, exposure that is a function of the initial uptake and the variable half-life. The average dose rate for RNT is typically of the order of 2–8 Gy/day, and the maximum absorbed dose may be up to 50 Gy delivered over a period of many days. This is in marked contrast to the situation with EBRT, where the dose is delivered at a constant high dose rate (HDR), typically 1–5 Gy/min, and also at variance with the dose rate brachytherapy is delivered, 1–5 Gy/h [5].

To date, most radiobiological models of RNT have been based on the extrapolation of data obtained following homogeneous exposures to acute single or fractionated doses of EBRT and have assumed that EBRT and RNT administered are substantially equivalent from the biological point of view. However, emerging evidence suggests that the mechanisms of cellular response to LDR exposures are fundamentally different from those occurring at HDR with either EBRT or brachytherapy [3, 6].

The combination of prolonged response, limited toxicity, and the ability to treat on multiple occasions suggests that the mechanism of action of LDR therapies is different from that seen with HDR exposures. Accordingly, treatment plans, clinical trials, and outcome assessment should be designed to consider this difference. Current radiobiological research points to a way in which RNT can be more effectively administered to patients by taking into account the biology of the mechanism of action of therapy as well as the physical characteristics of the radionuclide [5].

Conventional Radiobiological Models

A number of basic principles, emerged from early studies describing the effects of acute single or fractionated doses of EBRT on the clonogenic survival of cells, generally held that a cell must be "hit" by a radiation track in order to be killed, that genomic DNA was the principal "target" for killing, and that double-strand breaks (DSBs)/clustered lesions/multiply damaged sites were the principal DNA lesions leading to cell death [3].

Early models focused largely on the mechanical or metabolic challenges that DSBs might pose to a cell when it attempts to replicate its DNA (in S-phase) or divide (in mitosis). The linear-quadratic (LQ) model of fitting and interpreting clonogenic cell survival curves became a cornerstone of experimental radiation oncology and indeed is still widely used for predicting the clinical impact of changes in dose fractionation or dose rate on biological effect [5].

This model assumes two components of cell killing, one proportional to the dose D (αD) and the other is a quadratic term (βD^2) in which two sublesions are presumed to interact to produce a lethal event. The relationship between cell survival (surviving fraction, SF) and dose is then described by: $-\ln[\mathrm{SF}] = \alpha\mathrm{D} + \beta\mathrm{D}^2$. The two-hit/quadratic (β) term represents the fraction of cell killing caused by damage that can be spared either by dose fractionation or by decreasing the dose rate. In contrast, the one-hit/linear α-type lethal events

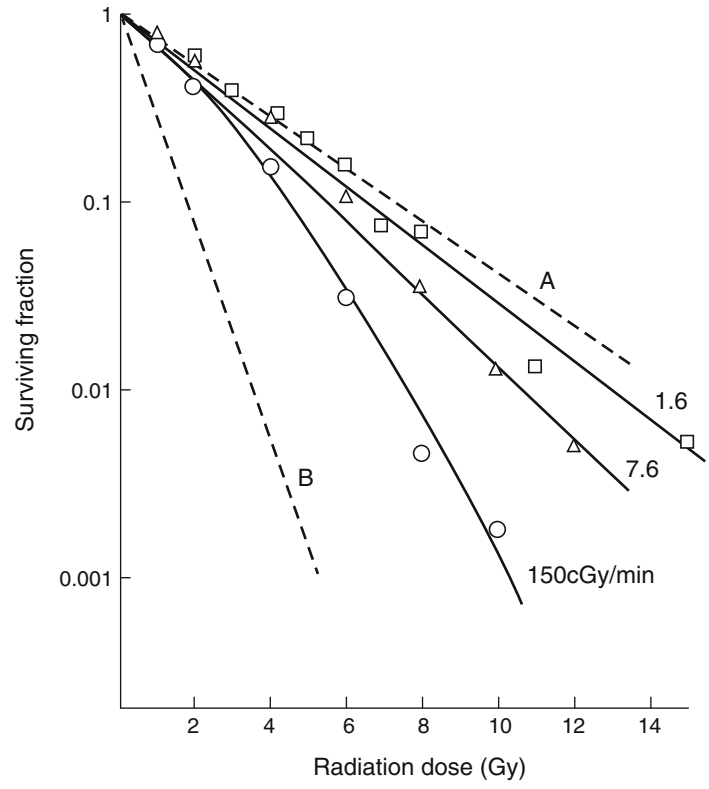

Fig. 1 Conventional dose-rate effect for cell killing as the dose rate is lowered from 150 to 1.6 cGy/min. The *dashed curves* represent the best fit to the data set obtained using the lethal–potentially lethal (LPL) model assuming either full repair (**a**) or no repair (**b**), respectively

are independent of time and thus of fractionation or dose rate [3, 5].

Application of the LQ model to HDR exposures indicates that cell killing generally decreases as the dose is fractionated, and this sparing would reflect the repair that takes place between fractions of the individual "sublethal" lesions that, in combination, would otherwise have contributed to β-type cell killing. Survival curves for large numbers of small fractions ultimately approximate the initial slope (α) of the HDR curve.

The typical dose rates used for both clinical EBRT and radiobiological studies are of the order of minutes (~1–5 Gy/min), exposure times not long enough for DNA repair to occur during the irradiation process. As the dose rate is lowered, the time taken to deliver a given dose increases, and it is then possible for DNA repair to take place during irradiation and for radiosensitivity to gradually decline [3, 5].

Survival curves at decreasing LDR become straighter and ultimately extrapolate the initial slope (α) of the HDR curve, with a sparing effect that would be attributed to the repair of sublethal lesions occurring during the protracted exposure (Fig. 1).

At very LDRs (≤2 cGy/min), cell proliferation can occur during the irradiation, thus leading to repopulation of the pool of clonogenic cells. Clearly, based on this assumption, RNT should be ineffective, although this expectation is not consistent with many clinical observations. Such phenomenon, in which decreasing the dose rate results in increased cell killing, has been defined "inverse dose-rate effect." The effect has been attributed both to the lower-dose rate (permitting the cells to progress through the cell cycle into more radiosensitive phases) and to some hypersensitivity of cells to low-dose/LDR exposures, as will be discussed below [3, 5].

Cell Death Mechanisms

Most cellular responses to ionizing radiation-induced DNA damage are genetically regulated and involve specialized DNA damage-recognition factors that trigger a cascade of signaling events that alter the expression and/or activity of specific genes/proteins involved in cell cycle arrest, DNA repair, accelerated senescence, and apoptosis at the cellular level and in tissue repair at the tissue level [5].

Necrosis, a form of cell death that has been variously described as generalized, nonspecific, accidental, or passive (i.e., it is not a genetically regulated process), generally occurs after high doses in cells that enter mitosis carrying high levels of unrepaired DNA damage [5].

In contrast, apoptosis is an energy-dependent, genetically controlled "suicide" process that involves the activation of degradative proteolytic enzymes called caspases and tends to occur at low doses of radiation. Apoptotic postirradiation cell death is mediated by two pathways, both resulting in activation of the cascade of caspases that function as cell executioners. Firstly, signals from the nucleus or cell membrane can activate the "intrinsic" pathway of apoptosis with a series of sequential events that cause final activation of caspases 3,6,7, and 8. Secondly, the "extrinsic" pathway of apoptosis is mediated by death receptors that are activated by ligands, such as the Fas ligand, tumor necrosis factor-α (TNF-α), and TNF-related apoptosis-inducing ligand (TRAIL). TRAIL induces apoptosis in response to ionizing radiation through the clustering of DR4 and DR5 receptors in the cell membrane [7].

Other modes of cell death are the "accelerated" or "premature" senescence or "STASIS" (stress or aberrant signaling-induced senescence), a genetically programmed response to DNA damage [8], and the mitotic catastrophe, generally defined as the failure of a cell to properly undergo mitosis after DNA damage. It has recently been recognized that mitotic catastrophe is not a mode of cell death per se, but a death that generally occurs secondarily to mitotic catastrophe, apoptosis, or accelerated senescence [9]. Death secondary to mitotic catastrophe has been suggested to account for a significant proportion of the cytotoxicity observed after radiation exposure.

Possible Contributing Mechanisms to RNT Tumor Responses

Low-Dose/Dose-Rate Apoptosis

Different mechanisms of cytotoxicity appear to operate in different dose and dose-rate ranges for a given cell type. Indeed, several experimental studies support the tenet that LDR exposures tend to promote loss of clonogenic potential in some cell types (e.g., lymphomas) by activating apoptotic responses, whereas high doses tend to cause necrosis as their primary mechanism of cytotoxicity [10]. For example, low doses of EBRT induce substantial apoptosis in tumor cells and that the dose–response curve for apoptosis plateaus above ~7.5 Gy [11]. Furthermore, multiple small fractions of EBRT were found to produce a higher level of apoptosis than a large single dose. Clinical effectiveness of lower doses of RNT and other LDR therapies could be related to their ability to optimize such effects, such as apoptosis exhibiting an inverse dose-rate effect [5].

Low-Dose Hyper-radiosensitivity–Increased Radioresistance

Many cell types exhibit an initial hypersensitive response at doses below ~25 cGy, followed by a region of increasing radioresistance up to ~50 cGy, the survival curve above 1 Gy closely following the expected LQ response [12]. This phenomenon, illustrated in Fig. 2, has become known as the "low-dose hyper-radiosensitivity–increased radioresistance" (LDH–IRR) response. The mechanism of LDH–IRR probably involves an alteration in the cellular processing of DNA damage as a function of dose. One possibility is that the transition from LDH to IRR may involve the activation of

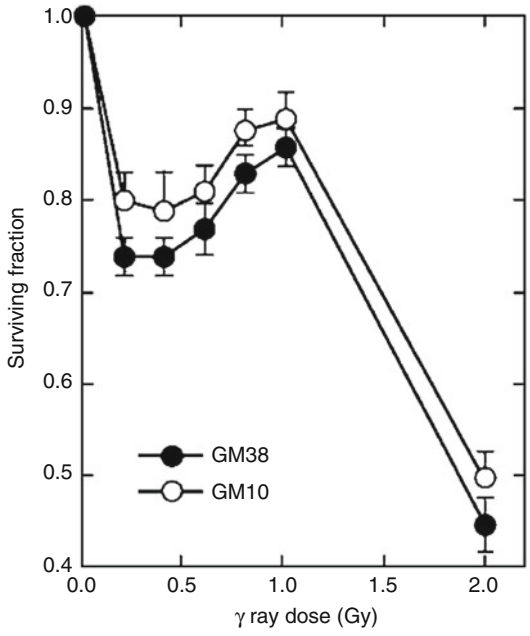

Fig. 2 Cellular survival responses of two normal human fibroblast strains, GM38 and GM10, following exposure to ^{60}Co γ-radiation

radioprotective DNA-repair pathways that are triggered by a certain threshold level of DNA damage. Cells would then be hypersensitive to low doses of radiation that produce insufficient DNA damage to trigger this protective process.

LDH–IRR seems to be preferential and possibly limited to a fraction of cells in the G2 phase of the cell cycle, and an important consequence of the LDH–IRR response is that the conventional LQ model greatly underestimates cellular radiosensitivity after acute low doses. This limitation was addressed by Joiner et al. [12] in a modified LQ model that incorporates the impact of an induced repair threshold.

If the LDH–IRR response occurs also during LDR therapies, the latter could exert much greater cytotoxicity per unit of absorbed dose than would be predicted by the conventional LQ model. The LDH–IRR model leads to the prediction that DNA-repair processes should be less efficient after doses below the IRR threshold (i.e., typically ≤40 cGy) if this response is related to induced DNA repair.

G2 Synchronization, Bystander, and Cross-Fire Effects

In some tumor cell lines, LDR exposures in the range of 10–300 cGy/h have been shown to cause the partial synchronization of cells in the G2/M phase as a result of the prolonged activation of the G2 checkpoint [13]. This effect could have two consequences for LDR therapies. Firstly, it might abrogate the competitive effects of proliferation on the elimination of clonogenic tumor cells. Secondly, it might enhance the relative effectiveness of LDR radiation by holding the cells in G2, which is a relatively radiosensitive phase of the cell cycle, a mechanism that was invoked to explain the inverse dose-rate effect seen in some cell lines at LDR.

The "bystander" effect refers to the phenomenon whereby manifestations of damage (such as cell death) are observed in cells adjacent to those that are traversed by an ionizing particle but that are not themselves "hit" [5]. This means that a cytotoxic response in the presence of the bystander effect will be greater than that predicted on the basis of classical dosimetric estimates. The biological bystander effect appears to reflect the generation of a "damage signal" emanating from irradiated cells that is communicated to the non-irradiated adjacent cells through a variety of signaling mechanisms. These include intercellular cross talk, the release of reactive oxygen species (ROS) or of clastogenic factors, and intracellular signal transduction pathways. The contribution from these mechanisms probably varies among different model systems, leading to some controversy as to their relative importance.

The bystander effect is quite distinct from the *cross-fire effect*, another mechanism of RNT, in which an ionizing particle emanating from a source radionuclide in one cell deposits its energy in a distant target volume represented by a neighboring or distant cell [13]. Cross-fire effects depend predictably on the particle range and play a major role in the effectiveness of RNT using β-emitting isotopes such as those generated by ^{131}I that have a range of millimeters in tissue. Such cross-fire

effects with β-emitters are also important for therapeutic responses, because they should help to overcome the limitations imposed on RNT by heterogeneity in the distribution of the radiopharmaceutical within the tumor mass, which is especially important in solid tumor.

Adaptive Responses

The in vitro *adaptive response* is the phenomenon whereby exposure of cells to a low "priming" dose of radiation induces resistance to a subsequent higher-dose exposure [14]. Like LDH–IRR, the adaptive response has been suggested to involve inducible radioprotective mechanisms, such as DNA-repair pathways, although not all studies are consistent with such a mechanism. A possible explanation for these diverse findings is the broad range of cell types, assays, priming treatments, and times of observation employed in different studies; furthermore, adaptive responses typically occur only within a narrow dose range of ~0.5–20 cGy. With respect to the potential role of adaptive responses in RNT, it has been noted that LDR irradiation can be regarded as a series of priming doses briefly separated in time; the adaptive response could, therefore, have a negative influence on the efficacy of LDR therapies, unless, of course, it is not activated under these conditions.

Fractionated RNT and Hypoxia

Fractionated delivery of RNT is designed mostly to compensate for the anticipated heterogeneity of RNT dose distribution, which determines absent or suboptimal intratumoral radionuclide deposition, an event that is especially important in large, poorly vascularized tumors that contain regions of hypoxia [10]. The development of hypoxia in tumors is believed to represent a major barrier to successful EBRT, in part because hypoxic cells are ~threefold resistant to acute exposures to ionizing radiation with respect to normoxygenated cells [15]. Conventional dose fractionation partially overcomes the negative effect of hypoxia, by allowing for the reoxygenation of hypoxic cells between fractions, and it is reasonable to assume that the same would be true for protracted LDR therapies. Under some conditions, fractionated delivery of radiolabeled antibodies and peptides has shown efficacy, with fractionated delivery causing less toxicity than a single administration. In general, both preclinical models and clinical radioimmunotherapy (RIT) evidence suggest that RNT fractionation results in a beneficial effect and in a more uniform radiation dose distribution. This has certainly proved to be an effective strategy with ^{131}I-metaiodobenzylguanidine (^{131}I-MIBG), with obvious increases in clinical effectiveness, and there are now data to support the use of fractionated treatment with radiopeptides as a way of reducing toxicity.

Future Directions

There is no doubt that a better understanding of the radiobiology and mechanisms of action of RNT will facilitate the development of newer radiopharmaceuticals and the design of prospective phase III and IV clinical trials [5]. Although our understanding of the low-dose-related phenomena has increased dramatically in the last few years, it is important to validate these effects in the clinical setting. In particular, validation of a role for the bystander effect in RNT in vivo will impact the assessment of therapeutic response to RNT, as well as risk estimates for therapeutic and diagnostic radiopharmaceuticals. In addition, application of high-throughput genomic/proteomic screening methods (DNA arrays, single nucleotide polymorphism analysis, and protein arrays) will allow a rapid and accurate prediction of patient response, both in the tumor and in normal tissues [5]. Other issues, such as the role of metabolic markers in selecting therapies and dosage schedules, and the potential interactions between low-dose chemotherapy and RNT, constitute additional important areas for clinical development.

Dosimetry: Overview on Methods

The basic goal of RNT is to deliver enough radiation-absorbed dose to the tumor while

minimizing the risk of toxicity to the bone marrow and to other normal tissues. For RNT, many physicians administer approximately the same activity to all patients, while ideally administered activity should be adjusted using a patient-specific treatment planning strategy based on radiation-absorbed dose. With a patient-specific approach, activity administration is optimized to maximize treatment efficacy while minimizing deleterious side effects to normal organs.

In RNT the absorbed dose is the energy deposited (E) per unit mass of matter (m) (with units of J/kg, 1 J/kg = 1 Gy). In RNT, E is the number of radionuclide disintegrations in a particular volume multiplied by the energy emitted per disintegration of the radionuclide and the fraction of emitted energy that is absorbed by a particular mass (m).

To improve the correlation between dose and the exposure effect, other quantities must be defined, such as relative biological effectiveness (RBE), radiation weighting factors, and tissue weighting factors. This suggests that energy absorbed per unit mass does not predict response at all levels, and some other factors must be considered.

Damage to cells is due primarily to indirect effects of radiation (formation of free radicals in water that diffuse and subsequently interact with cellular components, mostly DNA) and to some degree to direct effects (direct damage to DNA from radiation interaction). Also, different tissues and different individuals have different abilities to respond to and repair this damage. Thus, physical quantities such as the absorbed dose must be linked to radiobiological quantities to completely understand and be able to predict effects in a system.

Internal dose can be calculated by the following simple equation from the medical internal radiation dose (MIRD) Committee of the Society of Nuclear Medicine (SNM) [16, 17]:

$$D_{T-S} = \frac{\vec{A} \times \Delta \times \phi_{T-S}}{M_T} = \vec{A} \times S = A_0 \times \tau \times S \tag{1}$$

where D is the absorbed dose in a target organ (Gy), $\tilde{A}$ is the cumulated activity in source region S, Δ is the energy emitted by the radionuclide per disintegration, $\phi_{T \to S}$ is the fraction of energy emitted by the radionuclide in source region S that is absorbed in the target region, and M_T is the mass of region T. Furthermore, τ is the residence time, which is simply equal to $\tilde{A}$ /A_0, the cumulated activity divided by the patient's administered activity (A_0). S is the absorbed dose per unit cumulated activity and it is given by

$$S = \frac{\Delta \times \phi_{T-S}}{M_T} \tag{2}$$

Equation 1 means that the absorbed dose depends on the half-life of the radionuclide and its spatial and temporal distribution in the target. The latter are typically obtained by images collected at different times after administration of the radiopharmaceutical and used to estimate the amount or concentration of radioactivity in a specific region. The level of activity obtained at different times after injection, plotted against time, gives a time–activity curve for a particular target, such as an organ or tissue. The integral of this curve gives the total number of disintegrations or the cumulated activity ($\tilde{A}$) for the region. Therefore, the main input data needed for evaluation of radiation dose are the biokinetic data that characterize the distribution and retention of the radiopharmaceutical throughout the biological system.

This absorbed dose could be used to estimate the biologic effective dose (BED) [18]:

$$\text{BED} = D \times \text{RE} \,\text{where}\, \text{RE} = \left[1 + \frac{D\lambda}{(\alpha/\beta)(\mu + \lambda)}\right] \tag{3}$$

where D is the absorbed dose, μ is the exponential repair rate constant that quantifies the rate of sublethal damage repair, and λ is the effective clearance rate constant (given by the sum of the physical decay and the biological clearance rate constants). It means that the BED may be defined as the product of the total physical dose D and a modifying factor named the *relative effectiveness per unit dose*, RE, that quantifies dose-rate effects with respect to radiosensitivity and repair of radiation damage.

The BED equation is derived from the linear-quadratic (LQ) model that describes the surviving fraction (S_f) of target cells after a radiation dose (D):

$$S_f = \exp\left(-\alpha D - \beta D^2\right)$$

where the linear component αD describes the DSBs induced by a single ionizing event, and the quadratic component βD^2 describes the same effect induced by two separate ionizing events; α and β are the tissue-specific coefficients for radiation damage, α being proportional to dose (one single event is lethal) and β being proportional to squared dose (two sublethal events required for lethal damage). The α/β ratio is also named "repair capacity" and quantifies the sensitivity of a given tissue to changes in fractionation. Typical values for the α/β ratio are about 5–25 Gy for early-reacting normal tissues and tumors and about 2–5 Gy for late-responding normal tissues.

Also with the biological effective dose, the focus in radionuclide dosimetry study is to calculate the absolute amount of energy delivered per mass unit of tissue, i.e., the absorbed dose D.

In order to plan and design an appropriate dosimetric study, it is necessary to know approximately how the compound will be taken up and cleared from various organs and the whole body, by collecting multiple samples. Most therapeutic agents have a relatively fast phase of organ uptake and initial clearance, followed by more general systemic removal that lasts for many days. Therefore, a typical sampling scheme is to collect several samples in the first hours after administration and then about once or twice a day for a few days to several weeks.

To calculate the cumulated activity, the integral of the time–activity curve for each source organ may be obtained by (1) direct integration of data, for example, with the trapezoidal method, (2) a fit of the data to yield a mathematical expression of the uptake and retention in the target organ, and (3) using compartmental models, if the pharmacokinetics inside the target tissue is available.

Specific quantification techniques have been summarized for 2D and 3D imaging in the MIRD16 and MIRD 17 [19, 20]. Using planar data (2D imaging), the most accepted technique is to obtain images from the posterior and anterior projections and then correct the projected data in each region of interest (ROI) for attenuation and scatter. The most popular technique for attenuation correction involves the use of a Cobalt-57 (or other appropriate radionuclide) projection source imaged with and without the patient in the view, the attenuation coefficient for the system having been characterized in advance. For scatter correction, the two- or three-energy window method is widely accepted and applied when gamma camera software permits simultaneous acquisition in multiple energy windows. One of the best known packages able to offer mean absorbed doses in the organs, based on uniform activity distribution in organs/tissues, was the MIRDOSE3.1 package that implemented the use of whole-body MIRD-stylized mathematical phantoms representing adult males and females, children, and pregnant women [21]. The MIRDOSE3.1 software could be used for calculating internal dose for a large number of radiopharmaceuticals, the rapid comparison of calculations for different cases, examination of dose contributions to different organs, and regional marrow dose calculations.

MIRDOSE3.1 has been updated to a new generation code, Organ Level Internal Dose Assessment (OLINDA), employing the Java programming language and the Java Development Kit environment [22]. The entire code was rewritten, but all of the basic functions of the MIRDOSE code were retained, while others were extended. More individual organ phantoms were included, the number of radionuclides was significantly increased (including alpha emitters), and the ability to perform minor patient-specific adjustments to doses reported for the standard phantoms was made possible.

Quantitative 3D imaging using single-photon emission computed tomography (SPECT) methods is considerably more complex. The essential requirements for 3D imaging-based dosimetry are the availability of 3D anatomic imaging studies, such as CT or MRI, at least one 3D imaging study of the radioactivity distribution (e.g., PET or SPECT), and software that implements a point-kernel or Monte Carlo calculation methodology to

estimate the spatial distribution of absorbed dose. Two fully developed packages are 3D-Internal Dosimetry (3D-ID) and DOSIMG [23, 24].

Clinical Experience

Clinical applications of dosimetry are not widely adopted in RNT, mainly because data from prospective randomized clinical trials that may prove the effectiveness of dosimetry in predicting clinical outcome after treatment are lacking. In order to prove that dosimetry-based RNT is of additional benefit over administration of fixed empirical activities or activities per body weight, prospective randomized phase III trials with appropriate endpoints should be undertaken [25]. So far, the lack of standardized methodology for calculating the absorbed doses and the continued use of approaches based on administrations of fixed empirical activities irrespective of personalized radiation dose estimates has hampered efforts to compare clinical outcomes in different patient populations and has led to significant difficulty in comparing results among different trials [4].

^{131}I-Iodide Therapy of Differentiated Thyroid Carcinoma

Radioiodide therapy has largely been proven to be a safe and effective method in the treatment of patients with DTC after total or near-total thyroidectomy [26]. Nevertheless, although it has been shown to be useful for ablation of thyroid remnants and for treatment of locoregional or distant metastases, at present there is no consensus on the activity of ^{131}I-iodide to administer, because of the lack of prospective, randomized data [27]. Many excellent reviews of empiric fixed prescribed activity have been previously published, and the most frequently used sets of empiric fixed prescribed activities range from 1.1 to 5.5 GBq for ablation to 5.5–11.0 GBq for treatment of metastases [28].

The advantages of using the empiric fixed prescribed activity are convenience, a long history of use, an acceptable rate and severity of complications, and the possibility to avoid the "stunning" phenomenon due to the diagnostic ^{131}I-iodide activity [27].

However, the persistence of disease in a significant proportion of patients and the possibility for multiple small empiric activities to have less therapeutic benefit than the same total activity given at one time have led to attempts to improve such empiric approach to therapy [28].

Efforts to meet this goal have led to two basic dosimetrically determined prescribed activity approaches, each one addressing a different aspect of this problem. Benua et al. developed an approach to define the maximum activity of radioiodide that can be administered without significant bone marrow suppression [29]. Maxon developed a method to evaluate the activity of radioiodide needed to adequately treat metastatic lymph nodes [30].

The limited bone marrow toxicity method (Benua approach) was developed at the Memorial Sloan Kettering Cancer Center, by setting an upper limit for the radiation dose to the patient's blood, which is considered as a surrogate for the critical organ, i.e., the red bone marrow [29].

Since radioiodide concentration is almost identical in blood as in inner organs including the red bone marrow, assessing the blood absorbed dose allows to estimate the radiation-absorbed dose that will be delivered to the hematopoietic system of the individual patient during therapy [30]. A summary of the methodologies used can be found in the review article by van Nostrand [28] and in the guidelines of the Dosimetry Committee of the European Association of Nuclear Medicine (EANM) for pre-therapeutic dosimetry [31].

The method allows estimation of the radiation dose that will be delivered to the hematopoietic system per unit activity administered to a given patient and restricts such dose to no more than 2 Gy to the blood [29, 31]. Therefore, the maximum activity for treatment is calculated as the amount of ^{131}I-iodide that would deliver an absorbed dose of 2 Gy to the blood compartment [32].

This method requires evaluation of the kinetics of activity in the blood and in the whole body, obtained by conjugate views of a whole-body scan (WBS) acquired with a dual-head gamma camera equipped with high-energy collimators [28].

To evaluate the blood kinetics, five blood samples should be obtained over 1 week (e.g., at 2, 6, 24, 96, and 144 h) after administration of ^{131}I-iodide, and the blood activity should be measured in a calibrated well counter from aliquots of blood samples [28].

The first WBS measurement obtained 2 h after tracer administration represents 100% of administered activity, while measurements are repeated at 24, 48, 72, and 96 h (or later if uptake and/or renal clearance is delayed). As an alternative to WBS conjugate-view imaging obtained with a gamma camera, measurements with an external probe can be used [28].

To calculate the whole-body activity as a function of time and circulating activity per mL of blood, the geometric mean of corresponding net counts obtained by conjugate views and all blood activities are normalized to the first data point and to the administered activity, respectively [28, 31].

The curves, $A(t)$, describing the activity in the blood and in the total body as a function of time after the administration are usually multi-exponential, and bi-exponential fitting is usually appropriate to determine the function describing time–activity curves in the blood and in the total body, respectively.

The residence times in the whole body and activity concentration in blood, $\tau_{\mathrm{TotalBody}}[\mathrm{h}]$ and $\tau_{\mathrm{Blood}}[h]$, are calculated by integrating the corresponding retention function $R(t) = A(t)/A_0$.

According to the generally accepted MIRD formalism, the mean absorbed dose to the blood per unit administered activity is determined by the sum of contributions of blood self-irradiation and of penetrating radiation from the whole body.

The mean blood absorbed dose per unit administered tracer activity can therefore be calculated as

$$\frac{\bar{D}_{\mathrm{Blood}}}{A_0}\left[\frac{\mathrm{Gy}}{\mathrm{GB_q}}\right] = 108 \times \tau_{\mathrm{Blood}}[h] + \frac{0.0188}{\mathrm{wt[kg]}} \times \tau_{\mathrm{TotalBody}}[\mathrm{h}]$$

The activity to be administered for a blood absorbed dose of 2 Gy is

Table 1 Problems and difficulties of limited bone marrow dosimetry (Benua approach)

No valid clinical data or outcome rates yet exist on a benefit of the strategy
The approach does not estimate the absorbed dose to the thyroid remnant or metastasis
"Stunning effect" due to diagnostic activity of ^{131}I could alter lesion biokinetics and the absorbed dose in a subsequent ^{131}I therapy
Increased cost and practical inconvenience

$$A_{\mathrm{Adm}}\left[\mathrm{GB_q}\right] = \frac{2 \times A_0[\mathrm{Gy/GBq}]}{D_{\mathrm{Blood}}}$$

Under the conservative assumption that the activity concentrations within the hematopoietic tissue and the blood are identical [33], a red marrow-based approach for the determination of the maximum activity to be administered has been proposed [33]. Although this method seems to be accurate, no systematic clinical validation of the red marrow absorbed dose versus toxic effect has yet been undertaken.

The limited bone marrow dosimetry is easy to perform both pre-therapeutically and peri-therapeutically, thus allowing administration of additional activity for selected patients without risk of severe side effects. However, the original method might not to be applied in the presence of extended metastatic bone involvement, as the blood-based absorbed dose calculation could underestimate the absorbed dose to the red marrow. Similarly, it should be carefully applied also in the case of patients with diffuse lung micrometastases, because the critical organ could be the lung itself instead of the hematopoietic red marrow [34, 35]. The main limitations of this method are reported in Table 1.

The goal of the lesion-based dosimetry (Maxon approach) is to individualize radioiodide activity that delivers the recommended absorbed doses to ablate thyroid remnant or to treat metastatic disease while minimizing the risk to the patient [36]. These absorbed doses are traditionally considered to be $\geq$300 Gy to ablate thyroid remnant and $\geq$80 Gy to successfully treat metastatic disease [36].

In order to determine the activity required to deliver the absorbed doses, it is necessary to measure the uptake, clearance, and concentration of ^{131}I contained in the identifiable thyroid remnants and/or metastases. One way to ascertain these parameters is through an analysis of selected regions of interest (ROIs) on conjugate-view gamma camera images or on SPECT images, obtained at sequential time points after administration of a tracer activity. Typically, these images should be acquired at 24, 48,72, and 96 h after tracer administration, but later time sampling might be necessary if the uptake and clearance are delayed. In addition, transmission images to correct for attenuation in the lesion area, scatter images, as well as calibration procedures are necessary. A curve-fitting procedure is then employed to determine the assumed single-exponential half-life value and to extrapolate the curve to zero time to determine the initial activity in the lesion [28].

Pre-therapeutic dosimetric assessments of the activity required to achieve a certain prescribed absorbed dose to a remnant or lesion are often based on adaptations of the generic MIRD equation for absorbed dose, as previously described:

$$\bar{D} = \vec{A} \times S$$

where $\bar{D}$ denotes the mean absorbed dose to the remnant/lesion, $\tilde{A}$ is the cumulative activity, and S is the "S factor" of the MIRD scheme depending on the lesion/remnant mass.

For dosimetry of metastases, CT, MRI, or US can be used for attenuation correction and to determine the mass, while no thoroughly validated method is yet available for ablative treatments to exactly calculate the thyroid remnant volume after surgery.

If the lesions are small, the "nodule module" of the OLINDA/EXM software might be useful to generate a spherical model of the remnant and/or tumor. Furthermore, if the size of the lesion is smaller than 5.0 mm (assuming that such small size can actually be accurately determined), then the tissue range of the beta particles can no longer be neglected in the dose calculation. This as well as other limitations of the lesion-based method is reported in Table 2.

Table 2 Problems and difficulties of lesion-based dosimetry (Maxon approach)

Non uniform absorbed doses within each lesion
An accurate estimate of the lesion mass is not always possible
Low uptake in lesions and, therefore, low count rates may cause statistical errors in the measurements
The biological effectiveness of dosimetry-guided ^{131}I therapy is not proven yet
"Stunning effect" due to diagnostic activity of ^{131}I could alter lesion biokinetics and the absorbed dose in a subsequent ^{131}I therapy

Conventional radiopharmaceuticals that allow quantitation of radioiodide uptake in thyroid remnants and metastases, such as 123I-iodide or ^{131}I-iodide, have limitations; in fact, there are problems regarding cost and the logistics of supply for ^{123}I-iodide, while ^{131}I-iodide has poor imaging properties (that translate into relatively low sensitivity) and its use can cause the so-called "stunning" phenomenon [27]. In contrast, with the introduction of hybrid positron emission tomography/computed tomography (PET/CT) devices to the clinic, ^{124}I PET/CT is becoming an emerging and attractive methodology for lesion dosimetry in the management of patients with DTC [37]. With its ability to determine the concentration of ^{124}I-iodide at anatomical sites of interest, PET/CT provides quantitative images and provides higher spatial resolution and imaging sensitivity than gamma camera-based devices [37].

Using the PET data as input to a fully three-dimensional dose planning program, Sgouros et al. [38] calculated spatial distributions of absorbed doses, isodose contours, dose–volume histograms, and mean absorbed dose estimates for a total of 56 tumors. The mean tumor-absorbed dose for each patient ranged widely, from 1.2 to 540 Gy, while distribution of values for the absorbed dose in individual tumor voxels was even more dispersed, ranging from 0.3 to 4,000 Gy.

Median per patient tumor radiation-absorbed doses between 1.3 and 368 Gy were reported by de Keizer et al. [39], who performed tumor dosimetry after rhTSH stimulated ^{131}I-iodide treatment. Dosimetric calculations were performed using tumor radioiodide uptake measurements from

posttreatment ^{131}I scans, while tumor volumes were estimated from radiological images.

In general, a ^{124}I-iodide PET/CT dosimetry protocol involves estimating the absorbed dose per administered ^{131}I activity for each radioiodine-positive lesion, allowing the calculation and the choice of the actual recommended ^{131}I activity. However, pre-therapeutic ^{124}I PET/CT dosimetry requires the knowledge of lesion volumes in order to adequately correct for partial volume effects. Such effects can reduce measured activity concentrations in lesions by up to ~three times the spatial system resolution, i.e., up to ~2 cm in diameter.

Often no morphological CT correlates can be assigned to ^{124}I-iodide PET foci. This can be partially attributed to the fact that CT examinations prior to radioiodine therapy need to be performed without contrast media to avoid iodine contamination. If no CT correlates exist, the target volumes must then be assessed from PET images alone by applying various threshold methods. The original ^{124}I PET dosimetry protocol entailed five PET measurements at 4, 24, 48, 72, and 96 h after ^{124}I-iodide administration, although simplified models by using four, three or two points (24 h/96 h) have been proposed [40].

There are only a few published studies that have examined the absorbed dose in thyroid remnants and metastases using ^{124}I PET/CT. Freudenberg et al. [41] determined a median LDpA of 95 Gy/GBq for bone metastases ($n = 73$), 113 Gy/GBq for lymph node metastases ($n = 32$), and 86 Gy/GBq ($n = 14$) for lung metastases in those patients who were eligible for RIT.

At the moment, considering the slow progression disease and long follow-up period, it is difficult both to evaluate the long-term benefits and to design classical blinded and randomized studies in DTC patients submitted to pre-therapy ^{124}I PET/CT dosimetry. However, pre-therapy ^{124}I PET/CT dosimetry seems to be very useful in selected patients with locoregional or distant metastases who may benefit from radioiodine therapy with an individually tailored escalated activity or to abandon the therapy because of insufficient obtainable dose in the lesions.

Besides being a promising method to obtain accurate dosimetry in patients with metastases, ^{124}I PET/CT imaging is a useful diagnostic tool for accurate pre-radioiodine therapy staging, with a diagnostic accuracy similar to the WBS obtained after high therapeutic activities of radioiodine.

Peptide Receptor Radionuclide Therapy

Peptide receptor radionuclide therapy (PRRT) represents a promising option for patients with somatostatin receptor-expressing tumors. Several clinical trials have proven its efficacy, especially for neuroendocrine tumors [42, 43]. However, possible radiation-induced renal damage and large inter-patients' variability in biodistribution and tumor uptake require accurate dosimetry-based therapy planning. Recent improvements in dosimetry methods [44–51] and radiobiological models [18, 52, 53] have resulted in promising results and correlations that constitute challenging perspectives for optimized PRRT and for other radionuclide therapies as well [53–57].

^{90}Y-DOTATOC, ^{90}Y-DOTATATE, and ^{177}Lu-DOTATATE are the most widely employed radiopharmaceuticals for PRRT. Pilot trials also considered ^{111}In-octreotide for therapy, due to the high LET of its Auger-electron emission. However, since tumor response was seldom achieved, ^{111}In-based PRRT protocols have virtually been abandoned [42].

The physical half-life of ^{90}Y is compatible with the peptide kinetics, while the high energy of the β-particles confers high probability of killing all neoplastic cells in a certain volume around the uptake site through the cross-fire effect. Conversely, ^{90}Y is not easily suitable for imaging due to the lack of γ-emission, even if promising results have been shown for planar and SPECT bremsstrahlung ^{90}Y-images corrected for scatter and detector response, either based on Monte Carlo simulations or obtained by new-generation equipments (SPECT/CT) [58–60]. The possibility to obtain ^{90}Y-PET images due to the low incidence of pair production of ^{90}Y (branching ratio of 32×10^{-6}) is also challenging. It has already found application in the radioembolization of

liver lesions using ^{90}Y-microspheres [61, 62] and has been recently studied to be applied in ^{90}Y-PRRT [63].

^{111}In-octreotide, ^{86}Y-octreotide, and ^{68}Ga-peptides have been proposed as alternative options to ^{90}Y-imaging. Due to their similar chemical characteristics, the assumption of comparable behavior in vivo of ^{111}In- and ^{90}Y-derivatives has been widely accepted [64]. Thus, several authors have used the identical molecule labeled with either ^{111}In or ^{90}Y for imaging or for therapy, respectively (e.g., ^{111}In-DOTATOC and ^{90}Y-DOTATOC). Since the physical $T_{1/2}$ of ^{111}In is almost identical to that of ^{90}Y and is compatible with the distribution kinetics of peptides, the diagnostic activities usually administered (~185 MBq) allow one to obtain serial images (planar, SPECT) over 3–4 days, although some difference in the chemical structure of ^{111}In-octreotide cannot offer identical biokinetics of the corresponding ^{90}Y-conjugate. A fortiori, even less recommendable is a dosimetry plan based on the distribution of ^{111}In-octreotide (Octreoscan©), even though some authors claim its use for a "practical" dosimetry [65, 66]. The same compound labeled with ^{86}Y (^{86}Y-DOTATOC) represents a further option, since it totally preserves the chemical nature of ^{90}Y-derivatives and offers PET resolution. However, limitations of this approach are due to the physical $T_{1/2}$ of ^{86}Y (14.7 h, too short to follow the kinetics of uptake peptide and retention), complex image quantification, cost, and poor availability [64]. Similarly, ^{68}Ga-peptides are not suitable for dosimetry purposes, despite the high-quality PET images provided, because of the extremely short $T_{1/2}$ of ^{68}Ga (68 min) as compared to the kinetic pattern of peptide distribution. Furthermore, the chemical properties of ^{68}Ga might slightly alter the biodistribution kinetics of the radiolabeled peptide as compared to the therapeutic agent [64].

In comparison with ^{90}Y, ^{177}Lu induces less damage by cross-fire effect, but releases higher energy in smaller tissues. Moreover, the γ-rays emitted by ^{177}Lu are suitable for imaging and dosimetry, although for proper scintigraphic imaging, diagnostic/dosimetric activities of at least of 370–740 MBq should be administered. Most often dosimetry is evaluated after administering therapeutic activities of ^{177}Lu-DOTATATE (i.e., 3.7–7.4 GBq), as treatment is usually given in multiple cycles. So, the activity to be administered in cycles after dosimetry can, in case, be adjusted based on the dosimetry results.

^{90}Y- and ^{177}Lu-peptides have shown similar biological half-lives for organs and lesions, with varying uptakes depending on the different expressions of somatostatin receptors with respect to the peptide affinity. The same dosimetry methods and time schedules for data recording can be used for ^{90}Y- and ^{177}Lu-PRRT, but dosimetry must be assessed specifically for every used radiopeptide, and for the single patient, due to wide intra-patient variations as well as frequent inter-patient differences on tumor uptake.

The absorbed doses per unit activity for ^{177}Lu-peptides are much lower (two- to fourfold) than for ^{90}Y-peptides [64]. The activities administered in ^{177}Lu- or ^{90}Y-PRRT should vary accordingly, although the therapeutic protocols most commonly employed in clinical studies are not yet uniformly established with respect to activities administered and number of cycles [67–69].

Table 3 reports a summary of the dosimetric results for the most commonly used ^{90}Y- and ^{177}Lu-peptides (^{90}Y-DOTATOC and ^{177}Lu-DOTATATE), which share some properties: (1) the pharmacokinetics are characterized by very fast blood clearance and urinary elimination, leading to low exposure of the whole body (Fig. 3); (2) the spleen, kidneys, and liver receive the highest absorbed doses; (3) the kidneys are the dose-limiting organs; and (4) no significant uptake in bone or red marrow is typically reported.

To reduce renal radiation burden, preclinical and clinical studies showed that the infusion of protective agents (negatively charged amino acids) allows 25–65% reduction of the kidney uptake [70]. Despite such protection, the cumulative dose to the kidneys could still be borderline with the limits considered for nephropathy induction, especially with ^{90}Y-peptides.

Increased application of PRRT has stimulated interest in improving calculation of the radiation burden to organs at risk. There are two remarkable studies by Sandstrom et al. that focus on individualized kidney and bone marrow dosimetry and

on the method dependence, observer variability, and kidney volumes of dosimetry for ^{177}Lu-PRRT [48, 49]. Some papers use SPECT/CT-based renal dosimetry in ^{177}Lu-PRRT [50, 51], while an accurate method for planar image activity quantification and absorbed dose assessment in general is described by the group of Sjögreen et al. The clinical value of the absorbed dose to the kidney is the topic discussed by Swärd et al. [45].

Table 3 Absorbed dose estimates for the principle PRRT trials with ^{90}Y-DOTATOC and ^{177}Lu-DOTATATE

	Absorbed doses per unit activity (Gy/GBq) mean values among patients published by different authors	
	^{90}Y-DOTATOC	^{177}Lu-DOTATATE
Red marrow	0.03; 0.06; 0.09; 0.17	0.02; 0.04; 0.07
Kidneys[a]	1.71; 2.44; 2.73; 3.84	0.62; 0.81; 0.88; 0.97
Liver	0.27; 0.66; 0.75; 0.86; 0.92	0.13; 0.18; 0.21
Spleen	2.19; 4.74; 5.36; 7.20	0.64; 1.2; 2.15
Bladder	1.04; 1.59; 2.61	0.31
Total body	0.10; 0.15; 0.28	0.05
Tumors[b]	(1.4–31); (2.1–30); (2.4–42)	(0.6–56); (3.9–38)

Adapted from Cremonesi et al. [64], with permission
[a]Absorbed dose values reported include renal protection
[b]For tumors, instead of the mean values, the ranges of variability are presented

Two papers compared planar and SPECT images of ^{177}Lu-PRRT, both considering planar images corrected for scatter, background, attenuation, and response of the system, and SPECT images corrected for attenuation and response of the system. The first, by Garkavij [44], observed ~10% difference in the dosimetric results for the kidneys when comparing planar images using two different background corrections, ~20% difference when comparing planar with SPECT images, and ~10% difference when comparing the hybrid method using SPECT combined to planar images with the 3D SPECT method. The second, by Sandström [67], obtained a difference within 14% for the kidneys when comparing SPECT vs. planar images, while a difference within 10% for kidneys up to 23% for the liver when comparing two different 3D methods to draw the volumes of interest.

Other comparisons were made by Larsson et al. who focused on different planar dosimetric methods for the kidneys and studied the influence of the number of time points and the use of standard organ sizes. The authors found a large interindividual variation – which increased in case of the lack of late acquisition on day 7 – and demonstrated the need of personalized dosimetry and treatment planning [47]. Guerriero et al. further increased the accuracy of the biokinetics of kidneys and tumors in both, ^{177}Lu- and ^{90}Y-peptide

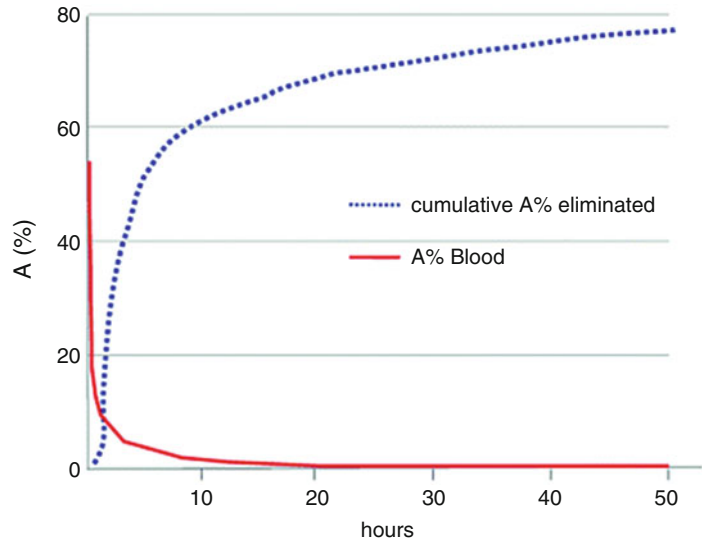

Fig. 3 Radiopeptides blood clearance (*red curve*) and urine excretion (*blue dotted curve*)

therapy. They investigated the most adequate timing for imaging and interpolation of the time–activity curve, the performance of a simplified dosimetry by means of only one to two scans, and the influence of renal risk factors and different peptides (DOTATOC vs. DOTATATE) [71]. The trapezoidal method followed by physical or biological decay after experimental data was compared with mono- and bi-exponential fits, skipping or not the 6 h and the 3-day time points. The authors found that data should be collected at least up to ~100 h for ^{177}Lu therapy and ~70 h for 90Y therapy in order to minimize dose uncertainties.

Another important issue for biokinetics is the possible variation among cycles. The study by Garkavij et al. compared dosimetry to the same patients in different cycles and showed that the first two of the four planned therapy cycles make the major contribution to the tumor-absorbed dose, possibly due to a saturation of the peptide receptors, while the different cycles contribute on average equally, within 10%, to the absorbed dose to the kidneys [44]. These findings apply in general and have been confirmed by other investigations [57], but there is a minority of cases in which the tumor is so avid of radiopeptides that it sequesters a very high percentage of the injected activity, leading to a so-called sink effect that decreases the activity concentration in healthy organs including the kidneys. In such cases, if the tumor is responsive during the course of therapy, the biokinetics in subsequent cycles may vary consistently, and dosimetry at a certain cycle is no more representative of the other cycles and not useful to estimate the cumulative doses to organs at risk and tumor [72].

In the attempt to improve accuracy of renal dosimetry estimates, the standard methods that assume uniform activity distribution in kidneys have been shifted to the multi-region MIRD model for a sub-organ kidney dosimetry and dose-rate effects [22, 55, 73, 74]. Some authors proposed the analysis of SPECT images to assign activity to the cortex or to the medulla for a patient-specific dosimetry [66]. In truth, the resolution of SPECT images is unable to provide a reliable activity distribution within the kidney substructures, being too low as compared to the 1–3 mm thickness of the cortex, for instance. More detailed information on intrarenal distribution has been derived instead from experimental results of renal autoradiograms [75].

The impact of the physical characteristics of the radionuclides with respect to inhomogeneous activity distribution (also within sub-organ regions) is a further issue concerning potential nephrotoxicity [69]. A threshold biologically effective dose (BED) of 33 Gy for kidney radiation damage and a BED50 (defined as the BED value derived from the TD50 value derived from the EBRT) of 44 Gy were found for ^{90}Y-PRRT [55]. Besides the most relevant impact on PRRT, these findings have shown the great potential of sharing information from different radiation release modalities. As a further support for the radiobiological model, clinical experience has shown that multiple-cycle protocols lower the nephrotoxicity, while patients with higher BED values and more serious side effects to the kidneys received the treatment in a few cycles [69, 76, 77]. This observation perfectly matches with the theoretical expectation from the BED concept: for a given cumulative dose, the higher the number of cycles, the lower the total BED, thus the lower the damage [69, 78]. Clinical results on ^{90}Y-PRRT have provided evidence of the safety up to a BED of about 40 Gy to the kidneys, cumulatively, and that risk factors (such as hypertension and diabetes) lower the tolerability to a BED of about 28 Gy [55, 76].

Treatment protocols based on multiple therapy cycles represent a useful modality to lower toxicity for a same cumulative activity, and/or improve the therapeutic outcome for a same fixed BED to the kidneys, owing to the different radiosensitivity of most tumors versus the kidney tissue. Cycles seemed especially effective in ^{90}Y-PRRT, where frequent occurrence of renal impairment has been clinically confirmed [69, 76, 79].

^{90}Y-peptides appear to be less nephrotoxic [43, 80, 81]. Possible reasons for these different outcomes are the different particle ranges in tissues and different peptide localizations. The short-range β-particles of ^{177}Lu-peptides, or the Auger electrons of ^{177}Lu-peptides, might irradiate the tubuli (radioresistant cells) more selectively while the long-range β-particles of ^{90}Y-peptides may increase the irradiation of the more radiosensitive

glomeruli, with consequent higher toxicity [69, 75, 78]. On the other hand, the advantage of cycling PRRT with ^{177}Lu is not as important with ^{90}Y. This is clear when considering that the contribution to the cumulative absorbed dose to the tumor after each therapy cycle gradually decreases [44] and that the absorbed dose to the kidneys with ^{177}Lu-PRRT is much lower at the activities usually administered in clinical trials, leading to a lower risk of nephrotoxicity. Overall, the use of too many cycles is not recommendable for ^{177}Lu-PRRT, while four cycles or possibly less seem to offer a better chance to avoid repair of sublethal cell damage and repopulation without dramatically alter the renal risks.

Despite long-term data analysis of ^{90}Y-trials and ^{177}Lu-trials, the intrinsic toxicity of the two radiopeptides is still to uncertain [64, 77, 82, 83]. Because the ^{177}Lu-based and the ^{90}Y-based clinical protocols use fixed total activities (e.g., ^{177}Lu, four cycles of 7.4 GBq; ^{90}Y, three cycles of 3.7 GBq) that lead to lower kidney absorbed dose and BED values for ^{177}Lu-schemes as compared with ^{90}Y. A reliable comparison of ^{177}Lu- vs. ^{90}Y-peptide therapy would require randomized trials conceived to release the same absorbed dose or BED using different radiopeptides. The choice of the most suitable radiopharmaceutical can be made based on individual differences in tumor mass and location, adjacent tissues, and targeting compound affinity. In principle, the physical characteristics of ^{177}Lu, with lower tissue penetration, make it more suitable for small tumors and micrometastases, while the cross-fire effect ^{90}Y might have the advantage of a higher radiation burden to larger lesions [64]. This hypothesis has been supported by preclinical findings and is the basis for new clinical rationales proposing cocktails of ^{177}Lu- and ^{90}Y-radiopeptides. New interesting approaches propose tandem treatments with ^{90}Y- and ^{177}Lu-peptides, with equal or different administered activities of the two radiopharmaceuticals [84, 85].

For tumor response, a first remarkable correlation has been observed between tumor-absorbed dose and tumor reduction with ^{90}Y-DOTATOC [65]. Responding tumors could be identified as those receiving much higher doses compared to nonresponding (up to sixfold, ~230 vs. ~40 Gy). Moreover, when correlating tumor-absorbed dose versus lesion mass reduction, a trend versus a dose–effect relationship was found, although not statistically significant, with a correlation coefficient of 0.5.

Excellent correlations were obtained between absorbed doses and tumor volume reduction after ^{177}Lu therapy, with a correlation coefficient of 0.6 for tumors bigger than 2.2 cm and a correlation coefficient of 0.9 in tumors bigger than 4 cm. These results were obtained by the improvement of dosimetry methods, namely, by correcting for the partial volume of the lesions identified in SPECT images [57].

Many parameters may influence the response of tumors – such as tumor dimension, vascularization, radiosensitivity, and activity distribution. Larger series of data with specific radiobiological parameters for different tumor characteristics are to be collected and will certainly improve outcome prediction.

Studies have measured circulating NET tumor transcripts (NETest), based on several marker genes to monitor tumor gene activity levels. The results confirmed that this test provides assessment of disease status and treatment effectiveness with significantly higher accuracy and earlier time points as compared with other biomarkers (such as cromogranine A) and morphological/functional imaging [86, 87]. It is quite clear that interdisciplinarity including dosimetry and genetic profile will play a crucial role in radionuclide therapies, allowing identification of patients that are not likely to be responsive and/or patients with a low risk of adverse sequelae, guiding trials, and tailoring therapies.

Radioimmunotherapy of Lymphoma

Radioimmunotherapy (RIT) offers an important option for the treatment of follicular low-grade non-Hodgkin's lymphoma (NHL) refractory or relapsed after treatment with the current best practice [88]. Two radiolabeled antibodies are

commercially available for treatment, tositumomab and ibritumomab, that are the radiolabeled immunoglobulin components of Bexxar and Zevalin, respectively [88, 89].

Bexxar is the ^{131}I-labeled anti-CD20 antibody tositumomab, while Zevalin is the ^{90}Y-labeled anti-CD20 antibody ibritumomab. Although both tositumomab and ibritumomab recognize a partially overlapping epitope on antigen CD20 (one of many epitopes expressed on the mature B cell), they have slightly different binding characteristics [88].

For both radiopharmaceuticals, an unlabeled antibody is infused before administration of the radiolabeled murine anti-CD20 antibody component. In the Bexxar regimen, both the labeled and unlabeled antibody are tositumomab. In the Zevalin regimen, the unlabeled antibody is rituximab (the chimeric antibody used as an immunotherapeutic and marketed as Rituxan), while the labeled antibody is ibritumomab [88, 89].

In Europe only Zevalin is commercially available, while in the USA and Canada, both Zevalin and Bexxar have been approved for clinical use [88].

No direct comparison in a randomized blinded trial has been performed to assess whether the difference in physical characteristics of the two radionuclides, ^{131}I and ^{90}Y, have different therapeutic effects or toxicity.

In principle, the greater energy of the β emitted by ^{90}Y is thought to be advantageous in the therapy of larger tumor masses, whereas the lower energy of the ^{131}I-particle emission is thought to be an advantage for treating patients with small tumor foci and marrow involvement. In the non-myeloablative setting, the use of either agent is contraindicated for patients with lymphomatous infiltration exceeding 25% of the bone marrow [90].

For Bexxar and Zevalin, different protocols and dose determinations have been reported, also due to the different approval requirements by regulatory agencies in the USA and Europe. However, for both radiopharmaceuticals, the red bone marrow is the dose-limiting organ due to its intrinsic radiosensitivity, to the rapid equilibration of the radiolabeled antibodies within its extracellular fluid volume, and to the long retention kinetics in the bone marrow [88].

When using Bexxar, dosimetry is estimated to determine the whole-body radiation-absorbed dose, since hematological toxicity and the dose–clinical response relationship depend on the whole-body radiation-absorbed dose rather than on a MBq/kg dosing schedule [91].

The optimal clinical benefit with acceptable hematological toxicity has been observed at 65–75-cGy whole-body radiation-absorbed dose, considering 65 cGy for patients with platelet counts between 100,000 and 150,000 and 75 cGy for patients with platelet counts greater than 150,000 [88].

The whole-body radiation-absorbed dose is determined from three WBS acquisitions after the administration of 185 MBq of ^{131}I-tositumomab (with prior infusion of 450 mg of unlabeled tositumomab), administered for determining the residence time which is necessary for dosimetric estimates.

The purpose of the scan is simply to evaluate the whole-body total counts rather than to produce a diagnostic image, because the parameters involved in visualizing a tumor (dose administered, tumor size, and location) are different from those involved in radiobiological response evaluations [88].

Whole-body counts are determined from the total counts on the anterior and posterior WBS acquired 1 h postinjection (day 0), then 2 days (day 2) and 5 days (day 5) later, to determine the radiopharmaceutical residence time (τ) and cumulated activity ($\tilde{A}$) in the body.

To calculate the desired therapeutic activity, the following equation can be used:

$$\text{Theraputic dose} = \frac{\vec{A}}{\tau}\frac{\text{Desired TBD(cGy)}}{75\text{cGY}}$$

The calculation simply divides a cumulated activity, $\tilde{A}$ (tabulated for several patient's weight), that would result in the patient receiving a 75-cGy whole-body radiation-absorbed dose, by the patient-specific residence time, τ. This would result in the activity associated to a 75-cGy whole-body absorbed dose that could be also rescaled by an

absorbed dose ratio if a value of total-body absorbed (TBD) dose different from 75 cGy is desired.

Seven to 9 days after the initial "dosimetric" study, the infusion sequence (unlabeled tositumomab followed by ^{131}I-tositumomab) is repeated with the ^{131}I-tositumomab therapeutic activity (1.85–5.5 GBq) that had been determined by dosimetry (Table 4).

In the USA and EU countries, biodistribution studies are not required because of the lack of correlation between red marrow dose and toxicity and considering that red marrow toxicity is reversible. This choice (which seems to be dictated mainly by practical/economical reasons) is arguable, as cases in which only the scintigraphic images were able to predict toxicity of the treatment are not so rare [92]. However, when using larger activities in clinical trials involving myeloablative doses with stem cell transplantation, personalized dosimetry estimates are required to avoid unpredictable toxicity. In fact, with bone marrow rescue, it is not possible to identify a priori a "safe" maximal activity or a unique critical organ for all patients, because of the wide intra-patient variability in doses to the vital organs.

At present, neither ^{90}Y-ibritumomab tiuxetan dosimetry outcomes in favor of its predictivity have been found nor correlation between red marrow dose and hematological toxicity has been demonstrated [91, 93–96]. This consideration has discouraged the practice of red marrow dosimetry for Zevalin. In this regard, toxicity in these patients is most likely linked to involvement of bone marrow by the disease and to reduced bone marrow reserve due to previous aggressive chemotherapy regimens [97].

Table 4 Organ radiation absorbed doses (mGy/MBq) for ^{90}Y-ibritumomab tiuxetan (Zevalin®), based on pre-therapeutic ^{111}In imaging

Organ	Number of patients	Median and range (mGy/MBq)
Spleen	166	7.35 (0.37–29.7)
Liver	179	4.32 (0.85–17.5)
Lungs	179	2.05 (0.59–4.86)
Red marrow (blood derived)	179	0.59 (0.09–1.84)
Red marrow (sacrum derived)	179	0.97
Kidneys	179	0.22 (0–0.95)
Bone surfaces	179	0.53 (0.09–1.31)
Urinary bladder wall	179	0.89 (0.38–2.32)
Other organs	179	0.41 (0.06–0.62)
Total body	179	0.54 (0.27–0.78)

The therapeutic activity of Zevalin for the non-myeloablative therapy of rituximab-refractory or relapsed patients with low-grade follicular non-Hodgkin's lymphoma is prescribed proportionally to the patient's weight, with recommended administered activity of 15 MBq/kg up to a maximum limit of 1,200 MBq [94]. Patients with platelet counts between 100,000 and 150,000 should receive 11 MBq/kg [94]. Much higher activities, ranging from 29 to 55 MBq/kg, have been used under myeloablative regimens, followed by autologous stem cell transplantation (ASCT) [98].

Radioembolization of Liver Tumors

Trans-arterial radioembolization (TARE) is a loco-regional treatment developed in order to release high radiation doses to malignant hepatic lesions by intra-arterial administration of a radiation vehicle. The rationale is the same as for trans-arterial chemoembolization (TACE): liver tumors are mainly fed by arterial blood, while normal tissue by portal blood. TARE consists of the intra-arterial administration of a radioactive agent. This is permanently trapped in the microcapillaries where it delivers its radiation until complete physical decay. In the last decade, significant response rates have been achieved with this approach in patients with unresectable primary hepatocarcinoma (HCC) [99] or secondary hepatic malignancies [100].

Several techniques have been tested in research trials, including the administration of radiolabeled molecules (such as ^{90}Y-,^{131}I-,^{188}Re-,^{166}Ho-Lipiodol) or of microspheres loaded with radionuclides (e.g., ^{90}Y, ^{166}Ho), differing in size, material, and specific radioactivity. However, the impressive increase in the number of treated patients in the last decade follows the registration of only two medical devices, i.e., microspheres loaded with ^{90}Y: (1) SIR-Spheres made in plastic resin (Sirtex Medical, Lane Cove, Australia) and (2) TheraSphere made in

glass (MDS Nordion, Ottawa, Canada). The main difference between the two products is the number of administered particles, which is ten times higher for resin particles. This implies a truly embolic behavior, never observed in glass microspheres. The second difference is the approved indication in the USA versus Europe. The FDA approved the use of resin spheres in patients with colorectal carcinoma metastatic to the liver, while glass spheres in HCC patients with or without portal vein thrombosis. In Europe and in various countries worldwide, both agents have regulatory approval for liver neoplasms in general.

The amount of activity to be administered should generally be established taking into account the clinical and dosimetric factors which affect the outcome: basal liver function (Child-Pugh score, presence of portal vein thrombosis, previous or concomitant treatment), tumor burden, targeted organ fraction, predicted absorbed dose to normal tissue, and absorbed dose to lesions. Actually in Europe, the Council Directive 2013/59 in Article 56 prescribes that any radiation treatment be optimized using dosimetry. In practice, the choice of the injected activity has been based on empirical approaches or on rough dosimetric evaluations, as summarized hereinafter.

For both devices, therapy is generally simulated by intra-arterially administered ^{99m}Tc-albumin macroaggregates (^{99m}Tc-MAA), in order to evaluate possible shunting to the lungs (lung shunt fraction, LSF), which limits the administrable activity, or avoid gastrointestinal (GI) shunt, which is an absolute contraindication to treatment. A planar trunk scintigram and a liver SPECT scan are usually accomplished. A major advantage deriving from the permanent trapping is that, differently from all other radiopharmaceuticals, images can be quantitatively analyzed to perform dosimetric evaluation though taken at only one time point. The adequacy of ^{99m}Tc-MAA for simulation is under discussion. Although similar distribution patterns of ^{99m}Tc-MAA and bremsstrahlung ^{90}Y-microsphere images have been generally reported, some dissimilarities have also been observed, possibly due to the different size and number of MAA versus microspheres or to occasional alterations of the original vascular anatomy produced by angiography [101]. Nevertheless, the acquisition of pre-therapeutic images represents a suitable source of clinical and dosimetric information for risk/benefit evaluation, through a treatment planning session similar to that ordinarily performed in external beam radiotherapy. Post-therapy images can be obtained either as bremsstrahlung SPECT or as ^{90}Y-PET. The latter are by far more accurate from the quantitative point of view. Post-therapy imaging has almost the same level of importance as the ^{99m}Tc-MAA scan, since it demonstrates the real therapeutic biodistribution.

Patient-specific dosimetry requires a detailed slice-by-slice volume of interest (VOI) drawing around tumor (T) and non-tumor tissue (NT). Using the mean dose approach, values of the absorbed doses per unit activity can easily be derived from two simple equations. The first is the way to convert counts in the image in 90Y activity:

$$A_{\mathrm{VOI}}\left({}^{90}Y\right) : A_{\mathrm{total}({}^{90}Y)} = \mathrm{VOI}_{\mathrm{counts}} : \mathrm{total}_{\mathrm{counts}}$$

$$D[\mathrm{Gy}] = 50 \cdot \frac{A_{\mathrm{VOI}}[{}^{90}Y]}{M_{\mathrm{VOI}}[\mathrm{kg}]}$$

A more sophisticated evaluation can be made by the voxel dosimetry approach or by Monte Carlo modeling that provides information on dose distribution and expected radiobiologic effects at the voxel level [102].

Producers indicate different approaches to choose the amount of activity to be injected for the two radiopharmaceuticals [101]. Three main methods are suggested [101] for resin spheres: the empirical method, the body surface area (BSA)-based method, and the partition method.

The empirical method does not personalize the treatment for different liver dimensions or tumor avidity, but it takes into account the tumor involvement and attempts to lower the radiation risks to the lungs and the NT tissues. With this, method activities range from 1.2 to 3.0 GBq, and the doses received by the lungs and by the NT are within 18 and 83 Gy, at most. According to Kennedy et al. [100]. "The Radio Induced Liver Disease (RILD) was diagnosed in 28 of 680 treatments (4%), with 21 of 28 cases (75%) from one center, which used the empiric method."

The BSA method, probably the most widely employed for resin microspheres, has been proposed since in normal patients, liver mass correlates with BSA. The basic equation, empirical, includes the patient body surface area: $[\mathrm{BSA}(\mathrm{m}^2) = 0.20247 \times \mathrm{H}0.725 \times \mathrm{W}\ 0.425, \text{with}\ \mathrm{H} = \text{height}(\mathrm{m})\ \text{and}\ \mathrm{W} = \text{weight}(\mathrm{kg})]$ and provides a maximum activity supposed to be safe for NT and lungs, once applying the same restrictions for lung shunt as above:

$$A = (\mathrm{BSA} - 0.2) + \frac{M_\mathrm{T}}{M_\mathrm{T} + M_\mathrm{L}}$$

where A = activity (GBq), M_T = tumor mass, and M_L (g) = total liver mass. In general, the activities calculated by the BSA method are more conservative than those derived from the empiric method, never exceeding 2.5 GBq. Although including some individual parameters, the reliability of this method in terms of tailored evaluation should not be overemphasized. In fact, direct measurements in patients have provided evidence that the BSA-based estimates do not correlate with liver mass nor with tumor involvement. Comparison between the BSA-based and the dosimetry methods showed discrepancies in activities to be administered ranging from −30% to 35% [103].

In the partition method [104], the activity to be administered is calculated within the MIRD equations, once a limit dose is prescribed for NT; lung safety is also considered. Liver involvement, tumor avidity as compared to the NTL, and the possible occurrence of lung shunt are taken into account by the following equation:

$$A = D_\mathrm{nL} = \frac{A_\mathrm{T} \times M_\mathrm{nL} + A_\mathrm{L} \times M_\mathrm{nL}}{49,670 \times A_L(1 - \mathrm{LSF})}$$

where A = activity, D_nL(Gy) = absorbed dose (Gy) limit for NTL, A = tumor activity (GBq), A = liver activity (GBq), M (g) = NTL mass, and LSF = lung counts/(lung + liver counts).

Although this model was originally designed for single or discrete nodules, appropriate modification by a weighted T/NT ratio makes it easily applicable also to multiple lesions [105]. The review paper by Cremonesi et al. [101] provides the absorbed dose limits applied by several authors, including the most common recommendations [106] and more conservative approaches [105].

The model proposed for RE with glass spheres relies on a simplified dosimetry equation, in which the dose averaged on the injected liver (D_L) is prescribed:

$$A = D_\mathrm{L} \times \frac{V_\mathrm{L} \times 1.03}{50(1 - \mathrm{LSF})}$$

where A = activity, D_L(Gy) = prescribed liver dose, V_L = total liver volume, and LSF = lung shunt fraction.

Absorbed doses to tumor and NT are not separately calculated, so no distinction is made for different tumor involvement or uptake ratios. Several studies [106] have indicated prescribed radiation doses (DL) of at least 100 Gy for a maximal effect on tumors, based on the fact that no dose-limiting organ toxicity has been observed in patients who had received nominal absorbed doses of up to 150 Gy. Mean cumulative doses to the treated liver as high as 200 Gy or even 390 Gy have been described as tolerated in patients affected by HCC with Okuda stage II and stage I who received multiple treatments [107]. Overall, these doses are apparently quite far from the limits recommended in the ^{90}Y-resin approaches and much farther than the tolerance doses set by external beam radiotherapy (30–35 Gy) to avoid excessive risk of radiation hepatitis [105]. This is explained with the nonuniformity of absorbed dose deposition at the microscopic level, which is markedly higher for the less numerous glass microspheres [108]. Another basic point is the usually different administration technique. From the US experience following the split registration, glass spheres against HCC have been injected lobarly, while resin spheres against metastases were administered in the common hepatic artery. These are two completely different situations, since the lobar approach exploits the organ reserve and the regeneration capability of the liver [109].

The possibility of performing a real treatment planning in radioembolization is emphasized by the result of three studies, which applied radiobiological models to analyze response and toxicity after standard administration of microspheres.

Strigari et al. [110] derived the normal tissue complication probability (NTCP) and tumor control probability (TCP) for HCC treated with resin spheres using post-therapy bremsstrahlung SPECT. TCP (50%) was at 150 Gy, while a dose above 200 Gy demonstrated response in all cases. Liver toxicity higher than G2 had a NTCP (50%) value of 52 Gy. Flamen et al. [111] found a good ^{99m}Tc-MAA dose - [^{18}F]FDG response correlation in colorectal metastases treated with resin spheres. Chiesa et al. [112] determined retrospectively with ^{99m}Tc-MAA SPECT the NTCP curve for Child A patients treated lobarly with glass microspheres, with a risk of radioinduced liver decompensation at 70 Gy if averaged over the whole non-tumoral parenchyma, including the non-injected lobe. This mean inclusive on the non-treated tissue is the simplest way to include the well-known liver volume effect (the smaller the irradiated fraction, the higher the tolerance). TCP was dramatically dependent upon the lesion size, being TCP (50%) = 250 Gy for masses less than 10 g and around 1,300 Gy for larger tumors. Garin et al. [113] were able to demonstrate a correlation between lesion absorbed dose and overall survival in HCC patient treated with glass spheres, with a cutoff of 205 Gy. Compared to Chiesa et al.'s results, this means that glass spheres require at least 205 Gy to stabilize the disease, while objective response requires higher dose. Individualized dosimetry-based administrations with increase of administered activity with respect to the producer indication were also safe and successful [114]. The unexplored way toward treatment planning in radionuclide treatment is open, thanks to dosimetry in radioembolization, which is the less demanding and that with higher impact among all kinds of radiopharmaceutical type of dosimetry. As a confirmation, for the first time in the history of nuclear medicine therapy, both ^{90}Y-microsphere producers made investment in multicenter research about dosimetry [62].

Therapy of Neuroendocrine Malignancy

In the late 1980s, ^{131}I-meta-iodobenzylguanidine (^{131}I-MIBG) started to be used as a radiotherapeutic metabolic agent in neuroectodermal tumors, i.e., those tumors derived from the primitive neural crest (which develops to form the sympathetic nervous system). Malignant neuroectodermal tumors include pheochromocytoma, paraganglioma, carcinoid tumors, medullary thyroid cancer, and neuroblastoma.

As an analog of noradrenaline, at low concentrations ^{131}I-MIBG is taken up into cells of neuroectodermal origin by the noradrenaline transporter (NAT). Once internalized, it is stored in intracellular storage granules. Transfer of MIBG from the cytoplasm into neurosecretory granules is mediated by an ATPase-dependent proton pump, and MIBG is not metabolized but excreted unchanged [115].

Treatment with ^{131}I-MIBG is indicated for tumors showing adequate uptake and retention of radiolabeled MIBG on the basis of a pre-therapy diagnostic scan, which is performed using ^{123}I-MIBG in children and either ^{123}I-MIBG or ^{131}I-MIBG in adults [116].

Most treatments regard neuroblastoma, the most common extracranial solid tumor affecting children (approximately 1 per 10,000 live births), most of the cases being diagnosed before the age of 4. Most of these malignancies originate in the nervous system, although about two-thirds of the cases arise in the abdomen near the adrenal glands. Distant metastases at diagnosis are frequent, and treatment of high-risk neuroblastoma includes surgery, chemotherapy, and ^{131}I-MIBG [117].

In high-stage neuroblastoma, treatment with ^{131}I-MIBG may be either palliative therapy, first-line therapy as a single agent or combined with chemotherapy, or consolidation therapy after induction of partial remission. More recently, this treatment has been used as second-line therapy after failed induction chemotherapy, combined with topotecan and stem cell rescue in children with metastatic neuroblastoma or with myeloablative chemotherapy and autologous stem cell transplantation in refractory neuroblastoma [118].

In addition to uptake in the tumor, ^{131}I-MIBG accumulates in the liver, heart, lungs, and adrenal glands, while the bladder is irradiated by the urine-excreted metabolites of ^{131}I-MIBG.

Thyroid uptake of free radioiodide is prevented using oral stable iodine. Since many drugs can interfere with MIBG uptake and storage, these drugs should be withdrawn for adequate periods before treatment, and patients should be stabilized on alternative medication.

High-specific activity (up to 1.48 GBq/mg) is recommended for therapy, and single-administered activities range between 3.7 and 11.2 GBq, according to tumor burden or local legislation. Since several cycles of therapy with ^{131}I-MIBG may be required to achieve objective response, these treatments are often repeated at widely different intervals, depending on blood count recovery; treatment is continued until the maximum clinical response is achieved.

Red bone marrow is the dose-limiting organ for ^{131}I-MIBG therapy, and activity reduction should be considered in patients with myelosuppression or with impaired renal function. In patients with neuroblastoma who had received prior intensive chemotherapy, the dose-limiting toxicity of ^{131}I-MIBG therapy is myelotoxicity at 2-Gy whole-body dose, according to the pre-therapeutic ^{131}I-MIBG scans. This threshold can be circumvented if bone marrow stem cell support is available. A total of 4.0-Gy whole-body dose with stem cell rescue has been given with good tolerance and no other short-term, dose-limiting organ toxicity [119].

The approach to administer fixed activity "fractions" of 3.7–11.1 GBq offers the advantages of simplicity and shorter isolation and hospitalization period required for radioprotection; this feature in non-negligible when treating very sick children with poor prognosis.

Administration of high activities of ^{131}I-MIBG based on body weight (555–777 MBq/kg), with stem cell support if necessary, has also been reported. A maximum tolerated activity of 444 MBq/kg is reported, combined with myeloablative chemotherapy and autologous stem cell transplantation [120].

However, when using fixed activities, no dose–response assessment or optimization on the basis of absorbed radiation dose is possible. Furthermore, the relatively LDR of radiation compared with (ultra)high doses may be viewed as radiobiologically suboptimal.

The results obtained over more than two decades demonstrate that whole-body absorbed doses correlate both with administered ^{131}I-MIBG activity and with the subsequent development of hematological toxicity [121, 122].

An administered activity of 444–666 MBq/kg of ^{131}I-MIBG may deliver 50–700 cGy of whole-body absorbed dose; 80% of patients with advanced chemorefractory stage III/IV neuroblastoma can develop grade 3 or 4 hematotoxicity at a whole-body absorbed dose of 2.5 Gy established from a pre-therapy ^{131}I-MIBG scan.

In relapsed or refractory neuroblastoma, the whole-body absorbed dose calculated according to the standard MIRD schema can be prescribed accurately and allows higher activities of ^{131}I-MIBG to be administered within the safety limits for bone marrow toxicity [123].

The mean absorbed dose, D, is given by the product of the cumulated activity and the MIRD whole-body-to-whole-body S value, that is [124]:

$$\bar{D}_{(\mathrm{WB}\leftarrow\mathrm{WB})} = \vec{A} \times S_{(\mathrm{WB}\leftarrow\mathrm{WB})}$$

Value $S_{(\mathrm{WB}\leftarrow\mathrm{WB})}$ is often obtained using the following equation (correction for body weight):

$$S_{(\mathrm{WB}\leftarrow\mathrm{WB})} = 1.34 \times 10^{-4} m_{\mathrm{p}}^{-0.921}$$

where m_{P} is the patient's mass in kilograms. This equation was generated by interpolating the S(WB ← WB)values from the MIRD phantoms for a newborn as well as for 1-year, 5-year, 10-year, and 15-year-old children, and finally for an adult, each of which has a specific mass. Table 5 reports the absorbed doses to the organs calculated for unit of ^{131}I-MIBG activity administered.

An experimental MIBG protocol has been proposed in which the aim was to deliver a total whole-body absorbed dose of 4.0 Gy in two fractions, in combination with topotecan, after failure of induction chemotherapy [125]. Post-therapy dosimetry is performed after a first fixed fraction

Table 5 Median and range organs absorbed doses values (Gy) for ^{131}I-MIBG, per unit of activity administered (MBq/kg)

	Fielding [74]	Matthay [79]	Gaze [81]	Koral [82]	DuBois [78]
^{131}I-MIBG activities (MBq/kg, range)		555 (93–770)	444	572 (431–683)	666 (599–770)
Organ	Absorbed doses (Gy, range)				
Whole body	1.9 (0.7–2.6)	2.28 (0.57–6.50)	2.19 (1.7–2.9)		2.92 (1.73–4.18)
Red marrow	2.0 (0.9–2.6)	2.20 (0.44–3.29)			3.47 (2.06–5.02)
Blood	0.8 (0.2–1.9)	1.77 (0.79–3.53)			
Liver	5.3 (1.6–11.3)			13.1 (7–19)	

of 444 MBq/kg, with calculation of the activity dose to be administered with the subsequent second fraction in order to achieve the desired total whole-body absorbed dose of 4 Gy [126].

Recent studies analyzed the whole-body radiation dose (WBD) and tumor-absorbed doses from ^{131}I-MIBG therapy in relation to tumor response and toxicities. Trieu et al. [127] retrospectively evaluated a cohort including 213 patients with high-risk neuroblastoma treated with ^{131}I-MIBG between 1996 and 2015 to correlate WBD from ^{131}I-MIBG with tumor response, toxicities, and other clinical factors. The WBD was calculated for every patient using radiation exposure rate measurements obtained by a ceiling-mounted ionization chamber or by a handheld ionization chamber. They found that WBD correlated with ^{131}I-MIBG activity, particularly with ^{131}I-MIBG administered per kilogram suggesting that activity prescriptions for ^{131}I-MIBG therapies should be made based on patient weight as opposed to a predetermined total activity dose in order to achieve a targeted WBD. A recent study by Minguez et al. proposed an equation, which describes whole-body absorbed dose per unit of administered activity as a function of patient mass, as an alternative for prescriptions of activity on first administration when dosimetry data for the individual patient are unknown [128]. However, Trieu et al. [127] found no relationship between WBD and overall response, and they were unable to establish any relationship between hematologic or thyroid toxicity and WBD. This unexpected finding prompts future studies to evaluate tumor dosimetry, rather than just WBD, as a tool for predicting response following therapy with ^{131}I-MIBG.

A study like this has been made by George et al. [129] who evaluated the response, toxicity, and long-term outcome of ^{131}I-MIBG therapy in the treatment of refractory or relapsed neuroblastoma following a dosimetry-based 3D individualized approach performed in 8 of the 25 patients.

To calculate tumor-absorbed doses, image data were obtained by 38 SPECT acquisitions performed on consecutive days following the treatment. Reconstructed SPECT scans for each patient were sequentially coregistered to allow 3D voxelized dosimetry to be performed using an in-house dosimetry software package (Qrius). The image-based 3D dosimetry application provided an absorbed dose map of consecutive therapies from which dose–volume histograms (DVH) were derived.

To date, there is no clearly defined methodology to incorporate DVHs in patient-specific planning or to compare DVHs for individual therapies or to relate to outcome. However, it is clear that dose heterogeneity could affect the outcome of subsequent therapies and may partially explain the variation in responses. In light of this, a 3D dosimetry approach where DVHs are taken together with tumor-absorbed dose as well as dose-limiting criteria provides a reasonable method to help plan patient-specific treatment and should be used as a guideline to inform subsequent therapies.

A dosimetry-based approach on the basis of patient pharmacokinetics may often result in the administration of higher activities with excellent response rates while keeping toxicity within acceptable limits. However, to date, there are currently no published randomized controlled trials of ^{131}I-MIBG therapy for neuroblastoma at any stage of treatment [21]. To maximize the therapeutic potential of ^{131}I-MIBG therapy and to determine its place within the patient pathway, well-designed clinical trials incorporating dosimetry are needed.

Future studies, including more accurate tumor dosimetry such as ^{124}I-MIBG with PET/CT technology, could improve the assessment of the relationship between WBD, tumor-absorbed doses, and overall response [130, 131]. Seo et al. [130] estimated expected radiation dose in tumors from ^{131}I-MIBG therapy using ^{124}I-MIBG micro-PET/CT imaging data in a murine xenograft model of neuroblastoma transduced to express high levels of the human norepinephrine transporter. The three-dimensional tool used for estimating the radiation dose that evaluated a range of activity of 52.8–206 MBq could deliver about 20 Gy to tumors.

Patient-specific dosimetry, using quantitative ^{124}I-MIBG PET/CT with a GEometry ANd Tracking 4 (Geant4)-based Monte Carlo method, was used by Huang et al. [131] in a 10-year-old girl with relapsed neuroblastoma. Organ-absorbed dose for the salivary glands was 98.0 Gy, heart wall 36.5 Gy, and liver 34.3 Gy, while tumor-absorbed dose ranged from 143.9 to 1,641.3 Gy in different sites.

Finally, the use of ^{124}I-MIBG PET/magnetic resonance imaging (MRI), performed with an integrated PET/MRI system, could be a promising technique in dosimetry as it improves tumor delineation because of the high soft tissue contrast in MRI. In a case reported by Hartung-Knemeyer et al. [132], PET/MRI allowed a more accurate volumetry in comparison to PET/CT, resulting in a reduction of the calculated lesion dose in abdominal muscle lesions up to 70%.

Treatment of Metastatic Bone Pain

Bone pain due to osseous metastases constitutes the most frequent type of pain among all cancer patients, with different prevalence among the various types of cancers. In general, oncological practice, breast and prostate cancers are responsible for more than 80% of the cases with bone metastases [133].

The pathophysiology is not well understood, and multiple mechanisms are postulated, including tumor-induced cytokines, stimulating factors released by tumor cells, direct nerve injury, and infiltration of the bone trabeculae and matrix by tumor cells causing osteolysis [134]. The appropriate management of painful skeletal metastasis includes the use of systemic analgesics, hormones, chemotherapeutic agents, steroids, external beam radiation therapy (EBRT), radiofrequency ablation, local surgery, and radiopharmaceuticals.

Curative options for multiple skeletal metastases unfortunately, do not exist, and most of the described treatments are palliative [133]. Systemic RNT has shown its value in the management of painful bone metastasis in clinical practice, although it remains an infrequently used treatment modality for many physicians, even those working in the fields of oncology and nuclear medicine [133, 135].

Phosphorus-32 (^{32}P-ortophosphate) and strontium-89 (^{89}Sr-chloride) were the first bone-seeking radiopharmaceuticals approved for the treatment of painful bone metastases [136], while bisphosphonates labeled with either ^{153}Sm [137], ^{186}Re [138], or ^{188}Re [139] are newer among the traditional bone-seeking radionuclides [140].

Although there are some differences in the physical half-life, beta energy, penetration range, and biochemical characteristics among the various bone-seeking radiopharmaceuticals, no clear advantage in terms of increased response rate has emerged. A uniform response rate of approximately 70% has been reported with all bone-seeking radiopharmaceuticals, and the response appears to be inversely proportional to disease extent and Karnofsky index [133, 135].

Several detailed dosimetric studies have been reported for bone-seeking radioisotopes. All the radiopharmaceuticals have shown an approximate tenfold therapeutic ratio between the metastasis and bone, although there is an order of magnitude difference in absorbed dose calculations (5–50 Gy) between individual metastases [133, 135, 140].

Table 6 Radiation dosimetry of radiopharmaceuticals used for treatment of refractory metastatic bone pain

Organ	^{89}Sr-chloride (mGy/MBq)	^{153}Sm-EDTMP (mGy/MBq)	^{186}Re-HEDP (mGy/MBq)
Bone surface	17.0	6.8	1.4
Bone marrow	11.0	1.5	1.3
Lower bowel wall	4.7	0.01	0.57
Bladder wall	1.3	1.0	0.54
Testes	0.8	0.005	0.008
Ovaries	0.8	0.009	0.019
Kidneys	0.8	0.02	1.5

From Bodei et al. [141], with permission

Radiation dosimetries for ^{89}Sr-chloride, ^{153}Sm-lexidronam (^{153}Sm-EDTMP), and ^{186}Re-etidronate (^{186}Re-HEDP) are reported in Table 6 [141].

Hematological toxicity is the dose-limiting factor, usually presenting as thrombocytopenia. Although there is a clear relationship between metastatic burden and toxicity, the correlation between thrombocytopenia and absorbed dose calculations is difficult to be noticed [133] even though there have been some exceptions [142].

The bone-seeking agent of choice has not yet been determined. Since all the commonly used radiopharmaceuticals have similar efficacy profiles, the agent should be selected in a case-based fashion taking into consideration the availability, toxicity, and goal of therapy.

It is intriguing that all studies that have searched for a dose–response relationship have failed to show a correlation between absorbed dose to metastasis and clinical response. Some of these calculations have shown clinical responses at absorbed doses for which classical radiobiological paradigms would predict no likelihood of response. Furthermore, no correlations have been found with primary endpoints, such as overall survival.

Recently, many clinical trials have shown the safety and efficacy of the ^{223}Ra-dichloride for patients affected by metastatic castration-resistant (hormone-refractory) prostate cancer (CRPC), leading to approve the ^{223}Ra-based drug (Xofigo©) for the treatment of adults with CRPC, symptomatic bone metastases, and no known visceral metastases. For the first time, therapy with a bone-seeking agent showed a life expectancy longer than that of patients in the placebo group, delaying the start of bone fractures and pain [143]. ^{223}Ra is a calcium mimetic (half-life 11.4 days) alpha emitter. The high linear energy transfer (LET) of alpha radiation gives rise to a greater biological effectiveness than beta radiation and to cytotoxicity that is independent of dose rate, cell cycle growth phase, and oxygen concentration [144]. The range of alpha particles (<100 μm) is much shorter than that of beta radiation, causing less hematological toxicity for a given absorbed dose to the bone surface than beta emitters [145]. Actually, several trials are ongoing for dose escalation and combination therapy (e.g., with hormone therapy). ^{223}Ra emits also a small number of photons useful for imaging, so in vivo image-based dosimetry is feasible (even though challenging), allowing investigations on a macrodosimetric scale [146–148], as well as the traditional microdosimetric approach to study the mechanisms of action of the alpha radiation [144].

Biological Dosimetry

Study of the biological effect induced by ionizing radiation on living organisms has systematically relied on the analysis of cytogenetic indicators, requiring the definition of several theoretical approaches to be interpreted [149]. Biological dosimetry, based on the investigation of biophysical and biological endpoints to estimate absorbed dose, is usually employed in cases of actual or suspected radiation overexposure. Although several biological samples can be considered representative of individual exposure, dose assessment is usually performed on peripheral lymphocytes. This cell population represents a suitable biological model to investigate radiation-induced effects, since it circulates in the body and remains quiescent in the G0 stage of the cell cycle for a relatively long time.

Chromosomal aberrations induced by ionizing radiation can be classified as stable or unstable

abnormalities. Stable anomalies, being consistent with cell survival, can persist for many years and involve reciprocal, nonreciprocal, and interstitial translocations. Unstable anomalies, inducing mitotic cell death, decrease with time and include dicentrics, centric rings, and acentric aberrations. Chromosomal aberrations scored in lymphocytes represent a suitable long-term biomarker of whole-body exposure and provide a fairly accurate index of bone marrow dose [149]. The estimate of individual exposure is obtained comparing the dose–effect relationships of aberrations measured by scoring with the dose–response relationships observed in in vitro models.

Biological dosimetry may be particularly useful in the assessment of individual response to radiation, providing an important contribution to the development of personalized therapy planning and radiation protection, as well as to establish radiation-induced risk and drugs effects, meant to decrease the radiation-induced side effects.

Although the efficacy of biological dosimetry is established in many cases, the method has some limitations. Accurate dose assessment in case of RNT can be very complex, because of the inhomogeneities in body irradiation and the LDR of irradiation. Correction for inhomogeneous irradiations can be performed, employing contaminated Poisson distribution method. The distribution of observed aberrations among cells is compared with that expected from a normal Poisson distribution. Nevertheless, a large number of aberrations, not always achievable, are required [150]. In case of LDR of exposure, the comparison with in vitro exposure can be hazardous. Indeed, repair can occur during exposure, reducing the quadratic component with dose rate decreasing as exposure is spread over a longer period of time [150]. No valid solution for this problem has yet been developed.

Furthermore, biological dosimetry assessment is complex when long retrospective dosimetry is needed, because of disappearance of lymphocytes carrying unstable aberrations [150]. Several years after exposure, scoring of stable aberrations might appear more appropriate, although involving more laborious and expensive techniques (G-banding, FISH). The sensitivity of biological dosimetry is reduced when doses are very low (e.g., below 0.1–0.2 Gy), because of the relevant contribution from environmental factors (light, chemicals, oxidative species originated by metabolism, smoking, and aging) to DNA damage. Moreover, individual variability in repair of radiation damage can affect dosimetry outcome. Finally, the biological effects on circulating lymphocytes due to exposure of low radiation doses are sparse and difficult to measure, so cumulative radiation exposure can be slightly underestimated.

Assays in Biological Dosimetry

Dicentrics

One of the most commonly used biology dosimetry assay is the count of dicentric chromosomes, selected as suitable biomarkers because of their rare spontaneous occurrence and their specificity for ionizing radiation [149].

Despite the high specificity observed for acute exposure radiation damage, the method appears cumbersome and unsuitable for dose assessment with prolonged delayed blood sampling. Even if lymphocytes with aberrations continue to circulate in peripheral blood for many years after irradiation, a delay longer than 6 weeks between irradiation and sampling can cause reduction in aberration yield, with a consequent dose underestimation.

Chronic exposures may not be easily determined by dicentric aberration scoring. It would be reasonable to postulate that repair must play a significant role in the effects of LDR. A study by M'Kacher et al. [151] described the use of biological dosimetry in patients receiving repeated treatments with 131I-iodide for differentiated thyroid cancer (DTC), resulting in cumulative doses from 1.0 to 3.5 Gy. A reliable retrospective dosimetry based on chromosomal aberration analysis (number of dicentric and chromosome 4 painting) was achieved only for samples collected following the first two treatment cycles but not from the third treatment and onward. At this stage, estimated doses were considerably lower than those delivered, suggesting that apoptosis occurring in lymphocytes with multiple chromosomal anomalies could affect the dosimetry outcome following repeated irradiations [151].

Micronuclei

Micronuclei (MN) can be the result of small acentric chromosome fragments that are not incorporated into the daughter nuclei during cell division. They are enveloped by a nuclear membrane and appear as small nuclei – micronuclei – in the cytoplasm outside the main daughter nuclei. They arise during exposure to various clastogenic agents and are the result of non- or misrepaired DNA double-strand breaks. Because of its high reliability and reproducibility, the MN assay has become one of the standard cytogenetic techniques for genetic toxicology testing in human and for mammalian cells in general [149].

The baseline, spontaneous frequency of MN is quite variable and can be affected by factors related to diet, age, and gender. Such variability clearly poses limitations on using MN as a biological dosimeter, particularly for low doses where pre-existing individual background frequencies are not known.

The MN assay in peripheral blood lymphocytes is an appropriate biological dosimetry tool to evaluate in vivo radiation exposure and to assess in vitro radiosensitivity and radiation risk. Many studies showed that the number of radiation-induced MN is strongly correlated with radiation dose and radiation quality, but sensitivity of the assay is limited to 0.2 Gy. This is due to the relatively high and variable spontaneous MN yield that is an inherent limitation of the assay for low-dose estimation. The spontaneous MN yield increases systematically with age, and MN disappearance is very similar to that observed for dicentrics. This result is in agreement with the decline in the MN frequency following irradiation (around 60%, 1-year post-treatment), observed in patients undergoing radiotherapy.

In a study by Monsieurs et al. [152], the MN assay was used to estimate the radiation-associated risk in patients receiving ^{131}I-iodide treatment for hyperthyroidism and thyroid remnant ablation after surgery for thyroid carcinoma. Surprisingly, the number of micronuclei induced by the different procedures, although the activity of ^{131}I-iodide was much higher in the thyroid cancer group, was similar. When this was compared to MN induction by EBRT in patients with cervical carcinoma or with Hodgkin's lymphoma, it was seen that EBRT was associated with a much higher degree of radiation toxicity. The author concluded that this might have been a suitable explanation of the different rates of induction of secondary cancer observed in the two therapeutic approaches.

A recent study employed the MN assay to evaluate the radioprotective effect of ginkgo biloba extract (GBE). It was demonstrated that the use of GME significantly reduced the number of MN after ^{131}I-iodide ablation therapy in thyroid cancer patients [153].

Chromosome Painting

Fluorescence in situ hybridization (FISH) allows a rapid and accurate characterization of chromosome or chromatid region by using specific DNA sequences labeled with fluorescent molecular probes. FISH painting is a single rapid method, allowing simultaneous evaluation of many types of aberration (dicentrics and single or complex translocations) [149]. Accuracy in translocation detection can be improved by using multiple color painting. Although dicentrics are less stable than translocations, they have background frequencies that are lower in unexposed people. This makes it easier to detect the effects of lower exposure doses, provided that exposure was recent and acute. In contrast, the relative stability of translocations makes them more suitable for analysis of chronic or temporally displaced exposures. Although translocation frequencies were initially thought by some investigators to be fully persistent, many studies have observed their decline with time following exposure, in some cases reaching a dose-related plateau [153].

Comet Assay

The comet assay (single-cell gel electrophoresis) is a fast, sensitive, and not expensive technique to measure DNA damage in a single cell [154]. At variance with the cytogenic assays previously described, the comet assay can be performed in any phase of the cell cycle, cells do not need to be

cultured, and sterile conditions are not required. It can be applied to all cell types, only a few hundreds are needed, and by this technique it is possible to measure single- or double-strand DNA breaks and the apoptotic index.

In the comet assay, cells are mixed with agarose and layered on microscope slides, where they are lysed and subjected to electrophoresis; staining with fluorescent dyes such as DAPI or ethidium bromide permits microscopic visualization of the "comets." DNA containing breaks unwinds and migrates away from the "head" (the nucleus), forming a "tail"; quantification of the amount of DNA in tails and in heads of comets provides an estimate of the frequency of strand breaks. Chromosomal aberrations measured by comet assay do not last long, since they can either be repaired or lead to cell death [155].

Gutierrez et al. [156] used the comet assay to measure the radiation damage in patients treated with ^{131}I-iodide for hyperthyroidism, reporting only a slight increase in DNA breaks 1 month after treatment. These results, however, were less clear to interpret compared to the MN assay, owing to the high sensitivity of the test, but the poor specificity that may affect the results especially in longitudinal studies.

γ-H2AX

The nucleosomal core histone variant γ-H2AX forms part of the cellular DNA damage response. Exposure to ionizing radiation triggers the large-scale activation of specific DNA damage signaling and repair mechanisms. This includes the phosphorylation of H2AX in the vicinity of a DSB. Foci of phospho-H2AX (γ-H2AX) form over large chromatin domains surrounding DSBs. The formation and loss of γ-H2AX foci have been measured following exposure to radiation doses as low as 1 mGy, and foci yields have been shown to increase linearly with dose [157]. Moreover, the initial number of γ-H2AX foci formed per cell nucleus following ionizing irradiation agrees with the yield of induced DSBs. Foci disappearance over time follows DSB rejoining in repair-competent cells; there is a close one-to-one relationship between initial and residual radiation-induced DSBs and γ-H2AX foci. These include rapid and potentially automatable processing and analysis, sensitivity to doses of a few milligrays, linear dose response across a broad dose range, ability to use unstimulated lymphocytes obtained by minimally invasive procedures, and potential to reveal partial body exposures. A recent article described the use of γ-H2AX in thyroid cancer patients undergoing thyroid remnant ablation therapy. The technique was used to assess double-strand breaks starting 0.5–120 h after treatment, and it was possible to demonstrate the early start of DNA damage by a linear dose-dependent increase and a bi-exponential response function describing a fast and a slow repair component [158].

However, severe limitations associated mainly with the rapid loss of the γ-H2AX signal following irradiation have to be considered. They are likely to restrict the use of the γ-H2AX to very recent radiation exposures – less than 2 days before blood sampling. Since the yield of γ-H2AX per unit dose changes rapidly over time, dose–effect curves for calibration of the assay are required for multiple time points.

Conclusions

Although dosimetry has been of great value in the preclinical phase of radiopharmaceutical development, its clinical use to optimize administered activity on an individual patient basis has been less evident. Similarly, little attention has been paid to radiobiology in therapeutic nuclear medicine, which exhibits significant differences with respect to the biologic effects of EBRT. However, data in the literature which underscore the potential of dosimetry to avoid under- and overdosing and the importance of radiobiology in RNT are increasing.

The recent proliferation of PET/CT and SPECT/CT cameras, the development of patient-specific 3D imaging-based dosimetry, and the availability of faster computers and improved Monte Carlo methods will offer more and more major scientific and clinical opportunities in RNT dosimetry improving the physics of absorbed dose estimation. Furthermore, the increasing scientific interest in the radiobiological features specific to radionuclides

will improve our knowledge in nuclear medicine therapy and will advance our ability to administer this treatment modality optimally.

As stated by Edith Quimby in 1969 "Radionuclide dosimetry is not a finished product, but it has come a long way from the early empiric days. We must be grateful to the patient people who have spent untold hours on these developments" [158].

Diagnosis

By incorporating adequately large activities of appropriate radionuclides into target tissue-avid radiopharmaceuticals, a sufficiently high radiation dose can be delivered to produce a therapeutic response in tumors or other tissues. However, such high administered activities can also ensue some radiation injury in normal tissues. Nevertheless, nuclear medicine remains largely a diagnostic specialty, where relatively low administered activities are administered to yield important clinical information whose benefit far outweighs the small potential risk associated with the attendant low normal tissue radiation doses. The radiation doses associated with diagnostic administration of radiopharmaceuticals are typically of the order of 1 cSv [159], well below the threshold doses associated with the deterministic effects of radiation described in the prior section. Average normal tissue doses are received by the "standard" patient, found in package inserts for approved radiopharmaceuticals and in reports issued by authoritative bodies such as the International Commission on Radiological Units (ICRU), even though the actual doses received by a particular patient may deviate significantly from these average values. For such procedures, the radiation effects of practical concern are stochastic (or statistical) effects, i.e., possible germ-cell mutagenesis and, in particular, carcinogenesis.

Medical Radiation Exposures: Societal Concerns

The clinical applications of diagnostic nuclear medicine, particularly PET and nuclear cardiology, as well as computed tomography (CT), have grown dramatically over the last several decades. In the USA, for example, the annual number of nuclear medicine procedures has increased threefold (from 7 to 20 million) and the annual number of CT procedures 20-fold (from 3 to 60 million) between 1985 and 2005 [160], much of the increase in the latter being related to the use of CT in children (up to $\sim$ 10% of all such procedures). As a result of this increased medical exposure of the population, the average (i.e., per capita) annual background dose in the USA has nearly doubled, from 3.0 to 5.6 mSv [161]. There has been increasing concern in the medical profession and in the popular press over the potential public health impact – namely, an increased risk of cancer – associated with this dramatic growth in exposure from diagnostic radiology and nuclear medicine. Brenner and Hall, for example, have estimated that as much as 2% of all cancers in the USA may be attributable to CT irradiation [162]. While nuclear medicine diagnostic procedures are not performed as frequently as CT scans and the radiation doses are generally not as high, the radiogenic cancer risk per procedure is comparable. For all the diagnostic procedures, the relevant parameters should always be judiciously selected to deliver the minimum radiation dose consistent with yielding the clinical information being sought, according to a commonsense approach as emphasized in the "Image Gently" campaign [163–166] promoted by many agencies and professional organizations.

Nuclear medicine practitioners must be prepared to rationally address the "cancer-risk" concerns of patients, referring physicians, regulators, and other stakeholders.

Radiation Doses in Diagnostic Nuclear Medicine

Radiopharmaceuticals

Table 7 is a compilation of radiation doses for common diagnostic nuclear medicine procedures in terms of the effective dose (ED) for the 70-kg standard adult anatomic model [159, 167, 168]. Effective dose is used in radiation protection to compare the stochastic risk of a nonuniform

Table 7 Radiation doses for diagnostic nuclear medicine procedures for the 70-kg standard man anatomic model

Procedure	Radiopharmaceutical[a]	Administered activity (MBq)	Effective dose cSv/MBq	cSv total
Brain	^{99m}Tc-HMPAO-exametazime	740	0.00093	0.69
Brain	^{99m}Tc-ECD-neurolite	740	0.00077	0.57
Brain	[^{18}F]FDG	740	0.0019	1.41
Thyroid scan	^{123}I Na	25	0.0075[b]	0.19
Thyroid scan	^{99m}Tc-pertechnetate	370	0.0013	0.48
Parathyroid scan	^{99m}Tc-sestamibi	740	0.0009	0.67
Cardiac stress–rest test	^{201}Tl-chloride	185	0.022	4.1
Cardiac rest–stress test	^{99m}Tc-sestamibi 1-day protocol	1,100	0.00085[c]	0.94
Cardiac rest–stress test	^{99m}Tc-sestamibi 2-day protocol	1,500	0.00085[c]	1.3
Cardiac rest–stress test	Tc-tetrofosmin	1,500	0.00076	1.1
Cardiac ventriculography	^{99m}Tc-labeled red blood cells	1,110	0.0007	0.78
Cardiac	[^{18}F]FDG	740	0.0019	1.4
Lung perfusion	^{99m}Tc-MAA	185	0.0011	0.20
Lung ventilation	^{133}Xe	740	0.000074	0.050
Lung ventilation	^{99m}Tc-DTPA	1,300[d]	0.00049	0.020
Liver–spleen	^{99m}Tc-sulfur colloid	222	0.00094	0.21
Biliary tract	^{99m}Tc-disofenin	185	0.0017	0.31
Gastrointestinal bleeding	^{99m}Tc-labeled red blood cells	1,110	0.0007	0.78
Gastrointestinal emptying	^{99m}Tc-labeled solids	14.8	0.0024	0.04
Renal	^{99m}Tc-DTPA	370	0.00049	0.18
Renal	^{99m}Tc-MAG3	370	0.0007	0.26
Renal	^{99m}Tc-DMSA	370	0.00088	0.33
Renal	^{99m}Tc-glucoheptonate	370	0.00054	0.20
Bone	^{99m}Tc-MDP	1,110	0.00057	0.63
Infection/tumor	^{67}Ga-citrate	150	0.0100	1.5
Pentetreotide	^{111}In	222	0.0054	1.2
White blood cells	^{99m}Tc	740	0.0011	0.81
White blood cells	^{111}In	18.5	0.0360	0.67
Tumor	[^{18}F]FDG	740	0.0019	1.4

From Mettler et al. [207], with permission

[a] *DMSA* dimercaptosuccinic acid, *DTPA* diethylenetriaminepentaacetic acid, *ECD* ethyl cysteinate dimmer, *^{18}F* fluorine-18, *FDG* fluoro-deoxyglucose, *HMPAO* hexamethylpropylenamine oxine, *^{111}In* indium-111, *MAA* macroaggregated albumin, *MAG3* mercaptoacetyltriglycine, *MDP* methylene diphosphonate, *^{99m}Tc* technetium-99m, *^{201}Tl* thallium-201

[b] 15% thyroid uptake

[c] 0.00079 cSv stress, 0.00090 cSv rest

[d] 40 MBq actually inhaled

exposure to ionizing radiation with the risk associated with a uniform whole-body exposure. It is a weighted sum of the doses to the individual tissues/organs of the body, where the tissue weighting factor reflects the relative susceptibility of that tissue to stochastic damage (i.e., carcinogenesis or, in the case of germ cells, germ-cell mutagenesis). EDs for such procedures are usually of the order of 1 cSv

for typical administered activities, meaning that the overall risk of carcinogenesis (and germ-cell mutagenesis) is roughly equivalent to that of a uniform whole-body dose of 1 cGy. Anatomic models and relevant dosimetric quantities such as absorbed fractions are now available [168], and radiopharmaceutical doses have thus been estimated for newborns, 1-year-olds, 5-year-olds, 10-year-olds, and 15-year-olds as well as adults [168–170]. There is typically a several-fold or greater difference in doses among organs for a particular radiopharmaceutical and anatomic model [171] for fluorine-18-labeled fluorodeoxyglucose ([^{18}F]FDG) in the Standard Adult anatomic model. Furthermore, as emphasized by several authors [172–174], one should use organ-, age-, and gender-specific doses and risk factors, rather than the ED and the overall risk factor, to estimate the cancer risk(s) associated with a particular procedure.

Multimodality Studies: PET/CT and SPECT/CT

As noted, there has been growing concern regarding the radiation dose associated with CT studies, particularly for the pediatric patient population [162, 172]. When CT is performed as part of a SPECT/CT or a PET/CT study, the axial field of view may be much larger than that of conventional CT studies, routinely extending from the base of the skull to the mid-thigh and thus potentially yielding an ED considerably greater than that of conventional, limited field-of-view CT studies [175]. Accordingly, when the CT component of a PET/CT study is used for attenuation correction and anatomic localization rather than for radiologic diagnosis, the CT scan parameters can, and should, be adjusted to appropriately reduce the CT dose. X-ray beams are characterized by (1) the current (expressed in units of milliampere (mA)) between the anode and cathode and (2) the maximum or peak (p) voltage (expressed in thousands of volts (V), or kilovolts (kV), and represented as "kVp") between the filament and the metallic target, where the electrons accelerated across this potential difference are stopped and the bremsstrahlung X-rays produced. Helical, or spiral, CT scans are also characterized by the pitch, the distance of travel of the patient table per rotation of the X-ray tube, and detector assemblies. The X-ray intensity and therefore the radiation dose are proportional to the mA and approximately proportional to the square of the kVp value. The dose is inversely related to the pitch. To determine the minimum-dose CT acquisition parameters that are compatible with accurate attenuation correction, investigators have systematically evaluated the impact of such parameters and therefore patient dose on both CT and PET image quality. Kamel et al. [176], for example, found no significant effect of tube current (10, 40, 80, and 120 mA) on [^{18}F]FDG standard uptake values (SUVs) and measured lesion sizes, with no significant difference in SUVs and lesion sizes between ^{68}Ge- and CT (80 mA)-attenuation-corrected PET scans. The authors concluded that CT scans using tube currents as low as 10 mA yield adequate attenuation correction for PET. Fahey et al. [175] subsequently evaluated the dose from the CT component of PET/CT studies to determine minimum-dose CT acquisition parameters (10, 20, 40, 80, 160 mA; 80, 100, 120, 140 kVp; 0.5 and 0.8 s per rotation; 1.5 pitch) that provide adequate attenuation correction for a range of patient sizes (i.e., anatomic phantoms) from newborns to adults. The CT dose index (CTDI), a commonly used CT dosimetry parameter indicative of the ED, varied by two orders of magnitude for each phantom over the range of acquisition parameters (e.g., for the 10-year-old-sized phantom, the CTDIs were 0.030 and 2.1 cSv for 80 kVp, 10 mAs, and 0.8 s and for 140 kVp, 160 mAs, and 0.8 s, respectively). The CTDI for the newborn phantom was twice that for the adult phantom for the same CT acquisition parameters. The ^{68}Ge rod source dose was only 0.003 cSv (3-min scan). Although CT statistical uncertainty (i.e., mottle or "noise") varied substantially among acquisition parameters, its contribution to PET noise was minimal ($<\sim$2%). In a pediatric phantom, PET images generated using CT performed with 80 kVp and 10 mA for attenuation correction were qualitatively and quantitatively indistinguishable from

those generated using CT performed with 140 kVp and 160 mA. Importantly, however, with very low-dose CT (80 kVp, 10 mA) for the adult phantom (i.e., for the combination of both low kVp and low mA), systematic undercorrection of the PET data for attenuation resulted. The impact on dose of these different CT acquisition parameters is significant. A diagnostic-quality CT (e.g., with "standard" kVp of 140, mAs of 190, and pitch of 1.25) delivers an ED of 2.2 cSv [175, 177–179] and therefore a total ED of 3.3 rem. However, for attenuation correction of an [^{18}F]FDG PET scan in an adult, a quantitatively accurate but non-diagnostic CT scan (e.g., with a kVp of 120, mAs of 60, and pitch of 1.5) delivers an ED of only 0.60 cSv [175, 177–179] and therefore a total ED of 1.7 cSv. For smaller patients a tube current as low as 60 mA can be used (with a kVp of 120 and a pitch of 1.5); the CT ED is only 0.1 cSv [175, 177–179]. Thus, if the purpose of the CT component of a SPECT/CT or PET/CT study is attenuation correction and anatomic registration and not radiologic diagnosis, appropriately judicious selection of the CT parameters can reduce the total ED by over 50% without compromising the diagnostic information content and quantitative accuracy of the PET study.

Dose–Response Relationships in Radiation Carcinogenesis

The largest and best characterized human cohort exposed to significant amounts of ionizing radiation remains the A-bomb survivors in Hiroshima and Nagasaki. Not surprisingly, A-bomb dosimetry had long been uncertain and plagued by a number of unresolved issues, including the yield of the Hiroshima bomb, the dose contribution of activation products, and the RBE and magnitude of the neutron dose. The latest A-bomb dosimetry system, Dosimetry System 2002 (DS02), improves on the Dosimetry System 1986 (DS86) and earlier A-bomb dosimetry systems in many important details, including the specifics of the radiation released by the bombs, addition of significant numbers of survivors to the so-called Life Span Study (LSS), and the effects of shielding by structures and terrain, and has thus resolved many of the outstanding dosimetric issues [180].

Choice of the correct model (i.e., mathematical relationship) between the excess cancer risk and radiation dose for extrapolation of the A-bomb dose–response data from its historical "high-dose" (>100 cSv) range to the diagnostic or "low-dose" (<10 cSv) range has long been controversial. The basic choices for such a mathematical extrapolation model are the supralinear model, the sublinear (i.e., linear-quadratic) model, and the linear, no-threshold model (Fig. 4). A supralinear model implies that the cancer risk per cSv is actually higher at low doses than at high doses; there are no data or biophysical evidence to support such a model that has never been creditably considered. The sublinear (i.e., linear-quadratic) model has for many years been the generally accepted dose–response model. The available human data are generally consistent with such a model, as are certain biophysical models of radiation action at the molecular level. Importantly, the sublinear model implies that the risk per cSv is lower at lower doses than at the higher doses (at which data are actually available). With the publication of the BEIR V and BEIR VII Reports [181, 182], however, the linear, non-threshold model is now the prevailing model for solid tumors, while the linear-quadratic model is the model of choice for leukemias [181, 182]. The linear, non-threshold model implies that the risk per cSv is constant at all doses, and it further implies that any excess radiation dose (i.e., above background), no matter how small, carries with it a finite (i.e., nonzero) excess risk of cancer and genetic damage. The available A-bomb survivor data for solid tumors – now including significant numbers of survivors receiving doses as low as 5 cSv on the basis of DS02 [180, 183] – are consistent with the linear, non-threshold model as well as with the linear-quadratic model. That is, on the basis of statistical considerations such as goodness-of-fit, one cannot actually distinguish between the sublinear (i.e., linear-quadratic) and the linear, non-threshold models. The linear, non-threshold model is more conservative (i.e., predicts a higher risk

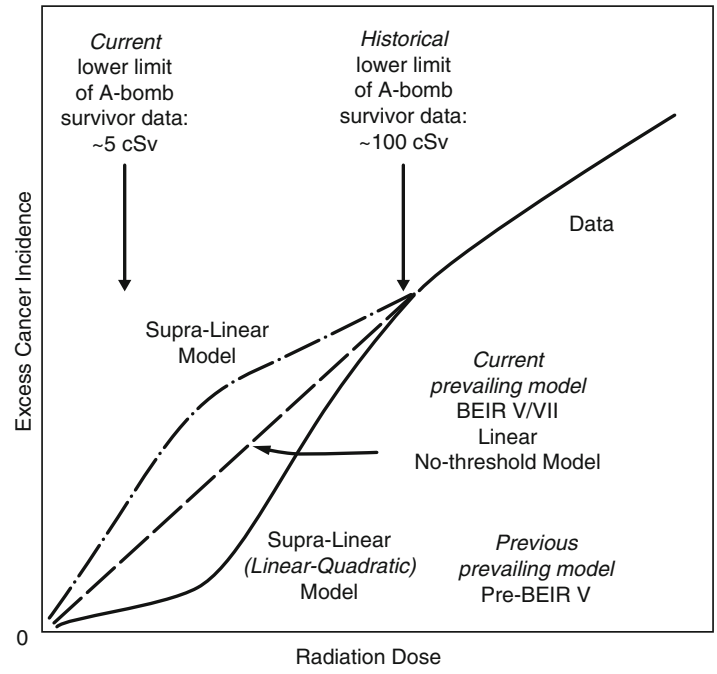

Fig. 4 Schematic representation of the basic choices for mathematical extrapolation of the A-bomb dose–response (i.e., excess cancer risk vs. radiation dose) data from its historical "high-dose" (>100 cSv) range to the diagnostic or "low-dose" (<10 cSv) range

per cSv at low doses) than the sublinear model and is therefore considered "safer" and thus more appropriate by some for radiation protection purposes. As noted, however, this issue remains controversial.

The BEIR VII age at exposure- and gender-specific risk factors for solid tumor and leukemia incidence and mortality shows pronounced differences in radiogenic cancer risk (in terms of both incidence and mortality) depending on age at exposure and gender (especially at younger ages); there are large differences depending on the cancer site, with female breast, lung, colon, and urinary bladder being the most susceptible to radiation-induced cancer [182]. The risk factors incorporate a so-called dose-rate effective factor of 1.5, meaning that HDR ($> \sim 10$ cSv/min or higher) radiation has a 50% higher risk factor than LDR ($<\sim 1$ cSv/min or lower) [182]. It is possible, however, that the dose-rate effectiveness factor may actually be higher than 1.5 and that the risk factors may therefore overestimate somewhat the cancer risk associated with the LDRs typical of diagnostic radiopharmaceuticals. Moreover, although stratified by age and gender, the risk factors within each stratum represent population-averaged values and thus do not account for individual differences in radiation sensitivity related to any preexisting condition, genetic susceptibility to radiogenic damage, etc. [174]. Importantly, as noted by Brenner and colleagues [162, 184], the risk factors they employed to estimate the numbers of radiogenic cancers associated with CT scanning are based on A-bomb incidence data at doses as low as 5 cSv – comparable to cumulative doses actually received by patients undergoing multiple CT procedures (as is often the case clinically) [4] – and not model-based extrapolation from higher (i.e., "supra-clinical")-dose data.

Risk–Benefit Considerations

Our discussion thus far has focused on the risks, most notably, the risk of cancer, associated with low (i.e., diagnostic)-level radiation – to the exclusion of any concrete consideration of its medical benefit. This is rather typical in the scientific literature: other than a perfunctory acknowledgment that the benefits of diagnostic procedures far outweigh any radiogenic risks,

such benefits are rarely, if ever, quantitated in a manner comparable to that of quantitation of risk. An unintended consequence of such "unbalanced" analyses – that is, quantitation of risk without comparable consideration of benefit – may be the mistaken perception that the medical benefit of a diagnostic procedure does not far outweigh radiogenic risk. Alternatively, the lack of quantitation of benefit may result in procedures in which risk outweighs benefit unjustifiably persisting in clinical practice. As illustrated by the case study which follows, risk–benefit analyses should thus quantitatively incorporate both the medical benefit and the radiogenic risk of diagnostic procedures.

Van Tinteren et al. [185] compared the management and clinical of suspected non-small cell lung cancer (NSCLC) with and without preoperative [^{18}F]FDG PET. With the conventional preoperative evaluation of NSCLC, that is, without [^{18}F]FDG PET, 81% of patients underwent thoracotomy, and 41% of those thoracotomies were futile, that is, non-potentially curative, because of the progression of disease disclosed at surgery. In series of Van Tinteren et al. [185], the surgery-related mortality was 6.5%. Adding [^{18}F]FDG PET to the preoperative evaluation reduced the proportion of NSCLC patients undergoing thoracotomy to 65%, with only 21% being futile. Thus, a non-curative operation was avoided in 20% of patients with the addition of [^{18}F]FDG PET. If one extrapolates the foregoing data to the US population, with 174,470 new lungs per year, the conventional preoperative evaluation will result in $174,470 \times 0.81 \times 0.41 \times 0.065 = 3,766$ futile surgical deaths each year; the addition of [^{18}F]FDG PET to the preoperative evaluation reduces the number of futile surgical deaths per year to $174,470 \times 0.65 \times 0.21 \times 0.065 = 1,547$ – a gross benefit of [^{18}F]FDG PET $3,766 - 1,547 = 2,219$ lives saved per year. However, for a 370-MBq administered activity of [^{18}F]FDG, the ED is 1.4 cSv [159] and the number of radiogenic cancer-related deaths therefore $174,470 \times 1.4\ \text{cSv} \times 0.0005/\text{cSv} = 122$, where 0.0005/cSv is the mean cancer risk factor (i.e., the lifetime age- and gender-averaged fractional increase in excess cancer mortality) [182]. Thus, the addition of [^{18}F]FDG PET to the preoperative evaluation of suspected lung cancer results in a net benefit of $2,219 - 122 = 2,097$ lives saved per year. Such a balanced quantitative analysis thus provides some perspective for objective consideration of radiogenic risks and medical benefits.

Considerations for Sensitive Populations: Prospective Parents, Pregnant Women, and Nursing Mothers

Prospective Parents

Experimental studies in a number of nonhuman systems have established that gonadal irradiation at sufficiently high doses can result in demonstrable abnormalities in subsequently (i.e., postirradiation) conceived offspring of the irradiated parent(s). Importantly, however, despite comprehensive studies of well over 10,000 children born to the atomic bomb survivors in Hiroshima and Nagasaki receiving mean gonadal doses of over 30 cGy and individual gonadal doses of up to several hundred cGy, there remains no evidence for heritable radiation effects in man [182, 186]. Specifically, in children born to A-bomb survivors at least several years after the bombings, there was no statistically significant increase in any radiogenic heritable effect. This implies that for diagnostic nuclear medicine procedures, where the gonadal doses are of the order of only 1 cSv (an order of magnitude less the 30-cSv mean gonadal dose received by the A-bomb survivors), there is no significant risk of heritable adverse effects among the offspring of patients who undergo such procedures. The estimation of human genetic risks is thus based largely on data derived from laboratory studies in animals, introducing the considerable uncertainty of extrapolation from nonhuman systems to humans [187]. The estimated absolute and relative risk factors are approximately 50 additional genetic effects/million live births/cSv and approximately 0.01%/cSv, respectively, in the F1 generation [182].

Not surprisingly perhaps, the absence of germ-cell damage in diagnostic nuclear medicine does not extend to therapeutic applications of radionuclides. Although a number of patients are small, demonstrable gonadal damage, such as reduced

sperm counts and impaired fertility, may occur among ^{131}I-iodide therapy patients over the first year posttreatment [182]. However, even among thyroid cancer patients treated with large (GBq) amounts of ^{131}I-iodide and receiving gonadal doses of the order of 100 cSv, such damage is transient [188, 189]. For example, follow-up studies of such patients indicate that among male patients there is a time-dependent recovery of sperm count and serum follicle-stimulating hormone (FSH) to control levels by 2 years posttreatment [190]. Long-term studies (i.e., 10 years or longer posttreatment) among both male and female patients indicate that fertility and the frequencies of miscarriages and congenital abnormalities among their offspring are comparable to control values [190].

Pregnant Women

It is an established radiobiological principle that the conceptus is particularly sensitive to radiation effects. Radiation doses to the conceptus associated with diagnostic procedures – generally of the order of or less than 0.1 cSv per 37 mBq administered to the mother [191–198] – are nonetheless well below the threshold doses for deterministic effects such as radiogenic fetal death or congenital malformations. Although modification of the standard anthropomorphic adult anatomic model [168] has yielded reasonably accurate dosimetric models of the conceptus–pregnant woman [191, 197, 198], radiopharmaceutical kinetic data in utero and therefore fetal dose estimates remain quite limited. For such procedures and at such in utero doses, the practical concern is the increased risk of childhood cancer. Published data, including the seminal Oxford Survey of Childhood Cancers [182, 199], indicate an excess risk of childhood cancer as high as 20% per Sv received in utero, with a linear response down to doses as low as 1 cSv. Signs alerting female patients and containing wording similar to, "If you are pregnant or if it is possible you may be pregnant, please notify the staff before the beginning of any procedure," should therefore be prominently posted throughout a nuclear medicine department, particularly in waiting and/or dressing areas. Once informed that a female patient of childbearing age is pregnant or may be pregnant, the nuclear medicine physician should confer with the referring physician to arrive at a medically informed, documented decision that the planned procedure is or is not justified. In particular, because RNT typically involves the administration of high (typically GBq) activities, such therapy is generally contraindicated in pregnant women, unless there is no viable alternative. A serum pregnancy test should be performed before RNT in any female patient of childbearing age. Assertions by the patient and/or her family regarding the impossibility of a pregnancy because of medical condition, sexual inactivity, use of birth control measures, or recent menstrual history should not preclude performing a serum pregnancy test prior to RNT.

The use of ^{131}I-iodide therapy for thyroid diseases in pregnant or potentially pregnant women is particularly problematic because radiogenic destruction of the iodine-avid fetal thyroid may result from such treatment and may result in hypothyroidism in utero with consequent cretinism [200]. The fetal thyroid begins concentrating iodine at the 12th–15th week of gestation, and fetal absorbed doses can be over 1,000 cSv per 3.7 GBq administered to the mother, depending on gestational age and maternal thyroid uptake. Therapeutic administered activities of 0.37–3.7 GBq of iodine would therefore result in fetal thyroid absorbed doses from 10,000 to 100,000 cSv, respectively. Case reports that include administered activity, gestational age, and follow-up of pregnant women treated with radioiodide for hyperthyroidism or thyroid cancer indicate that the outcome of pregnancy with regard to fetal thyroid function at birth did not appear to be compromised in the cases when radioiodide was given before the tenth week of pregnancy. However, there was essentially a 100% risk for congenital hypothyroidism and/or cretinism when radioiodine was administered thereafter, even in amounts less than 5 GBq [200]. Pregnancy is thus a contraindication to radioiodide therapy, and as stated above, a serum pregnancy test should be performed before administration of such therapy in any female patient of childbearing age.

Nursing Mothers

Virtually any systemically administered material, including a radiopharmaceutical, will appear to some extent in the breast milk of a lactating female, producing high activity concentrations in breast milk and potentially delivering significant radiation doses to nursing infants [201–206]. In one study, for example, the cumulative breast milk activity ranged from 0.03% to 27% of 131I-iodide administered for thyroid uptake studies [206]. Because of an infant's small size and the inverse relationship between absorbed dose and mass, ingestion of even a relatively small amount of activity will result in proportionately large total-body and organ absorbed doses. Furthermore, because of proximity of the infant to the mother when nursing, there is a potentially significant external absorbed dose to the infant. Signs alerting women with language such as, "If you are breast-feeding, please notify the staff before the beginning of any procedure," should therefore be prominently posted throughout a nuclear medicine department. Using a variety of dosimetric criteria (e.g., an effective dose equivalent to the nursing infant of 0.1 cSv), a number of authors have recommended different interruption periods prior to resuming breast-feeding following administration of radiopharmaceuticals [201–206]. The duration of the cessation of nursing will depend on the radionuclide and its effective half-life in vivo, the administered activity, and the extent to which radioactivity is concentrated in breast milk. While there is no absolute consensus, the following are representative of the published recommendations: 24 h following any administration of ^{99m}Tc, 2–4 weeks following administration of ^{67}Ga-citrate, and permanently for the current nursing infant following any administration of ^{131}I-iodide, especially for administration of therapeutic amounts of ^{131}I.

References

1. Brans B, Linden O, Giammarile F, et al. Clinical applications of newer radionuclide therapies. Eur J Cancer. 2006;42:994.
2. Larson SM, Krenning EP. A pragmatic perspective on molecular targeted radionuclide therapy. J Nucl Med. 2005;46(Suppl 1):1S.
3. Kassis AI, Adelstein SJ. Radiobiologic principles in radionuclide therapy. J Nucl Med. 2005;46(Suppl 1):4S.
4. Sgouros G. Dosimetry of internal emitters. J Nucl Med. 2005;46(Suppl 1):18S.
5. Murray D, Mc Ewan AJ. Radiobiology of systemic radiation therapy. Cancer Biother Radiopharm. 2007; 22:1–23.
6. Dale R, Carabe-Fernandez A. The radiobiology of conventional radiotherapy and its application to radionuclide therapy. Cancer Biother Radiopharm. 2005;20:47–51.
7. McBride WH, Chiang CS, Olson JL, et al. A sense of danger from radiation. Radiat Res. 2004;162:1–19.
8. Roninson IB. Tumor senescence as a determinant of drug response in vivo. Drug Resist Updates. 2002; 5:204.
9. Erenpreisa J, Cragg MS. Mitotic death: a mechanism of survival? A review. Cancer Cell Int. 2001;1:1.
10. De Nardo GL, Schlom J, Buchsbaum DJ, et al. Rationales, evidence, and design considerations for fractionated radioimmunotherapy. Cancer. 2002;94 (Suppl 4):1332.
11. Meyn RE. Apoptosis and response to radiation: implications for radiation therapy. Oncology (Huntingt). 1997;11:349.
12. Joiner MC, Marples B, Lambin P, et al. Low-dose hypersensitivity: current status and possible mechanisms. Int J Radiat Oncol Biol Phys. 2001;49:379–89.
13. Dixon KL. The radiation biology of radioimmunotherapy. Nucl Med Commun. 2003;24:951–7.
14. Wolff S. The adaptive response in radiobiology: evolving insights and implications. Environ Health Perspect. 1998;106(Suppl 1):277–83.
15. Hall EJ. Radiobiology for the radiologist. 5th ed. Philadelphia: Lippincott Williams and Wilkins; 2000.
16. Loevinger R, Budinger TF, Watson EE. MIRD primer for absorbed dose calculations. Revisedth ed. - New York: The Society of Nuclear Medicine; 1991.
17. Snyder WS, et al. MIRD pamphlet no. 11 – "S" absorbed dose per unit cumulated activity for selected radionuclides and organs. New York: Society of Nuclear Medicine; 1975.
18. Baechler S, Hobbs RF, Prideaux AR, et al. Extension of the biological effective dose to the MIRD schema and possible implications in radionuclide therapy dosimetry. Med Phys. 2008;35:1123–34.
19. Siegel J. MIRD pamphlet no 16 – techniques for quantitative radiopharmaceutical biodistribution data acquisition and analysis for use in human radiation dose estimates. J Nucl Med. 1999;40:37S–61.
20. Bolch WE, et al. MIRD pamphlet no 17: the dosimetry of nonuniform activity distributions – radionuclide S values at the voxel level. J Nucl Med. 1999;40:11S–36.
21. Stabin MG. MIRDOSE: personal computer software for internal dose assessment in nuclear medicine. J Nucl Med. 1996;37:538–46.

22. Stabin MG, Sparks RB, Crowe E. OLINDA/EXM: the second-generation personal computer software for internal dose assessment in nuclear medicine. J Nucl Med. 2005;46:1023–7.
23. Sgouros G. Treatment planning for internal emitter therapy: methods, applications, and clinical implications. In: Stelson A, Stabin M, Sparks R, editors. Presented at the sixth international radiopharmaceutical dosimetry symposium held May 7–10, 1996 in Gatlinburg: Oak Ridge Associated Unversities; 1999. p. 13–25.
24. Tagesson M, et al. The SIMDOS Monte Carlo code for conversion of activity distributions to absorbed dose and dose-rate distributions. In: Stelson A, Stabin M, Sparks R, editors. Presented at the sixth international radiopharmaceutical dosimetry symposium held May 7–10, 1996 in Gatlinburg: Oak Ridge Associated Universities; 1999. p. 425–40.
25. Brans B, Bodei L, Giammarile F, et al. Clinical radionuclide therapy dosimetry: the quest for the "Holy Gray". Eur J Nucl Med Mol Imaging. 2007;34:772–86.
26. Maxon HR, Smith HS. Radioiodine-131 in the diagnosis and treatment of metastatic well differentiated thyroid cancer. Endocrinol Metab Clin North Am. 1990;19:685–718.
27. Schlumberger M, Pacini F. Thyroid tumors. 5th ed. Paris: Editions Nucléon; 2003.
28. Van Nostrand D, Atkins F, Yeganeh F, et al. Dosimetrically determined doses of radioiodine for the treatment of metastatic thyroid carcinoma. Thyroid. 2002;12:121–34.
29. Benua RS, Cicale NR, Sonenberg M, et al. Relation of radioiodine dosimetry to results and complications in treatment of metastatic thyroid cancer. Am J Roentgenol Radium Ther Nucl Med. 1962;87:171–82.
30. Maxon HR. Quantitative radioiodine therapy in the treatment of differentiated thyroid cancer. Q J Nucl Med. 1999;43:313–23.
31. Lassmann M, Hänscheid H, Chiesa C, et al. EANM Dosimetry Committee series on standard operational procedures for pre-therapeutic dosimetry I: blood and bone marrow dosimetry in differentiated thyroid cancer therapy. Eur J Nucl Med Mol Imaging. 2008;35:1405–12.
32. Tuttle RM, Leboeuf R, Robbins RJ, Qualey R, Pentlow K, Larson SM, et al. Empiric radioactive iodine dosing regimens frequently exceed maximum tolerated activity levels in elderly patients with thyroid cancer. J Nucl Med. 2006;47:1587–91.
33. Traino AC, Ferrari M, Cremonesi M, et al. Influence of total body mass on the scaling of S-factors for patient-specific, blood-based red-marrow dosimetry. Phys Med Biol. 2007;52:5231–48.
34. Sgouros G, Song H, Ladenson PW, et al. Lung toxicity in radioiodine therapy of thyroid carcinoma: development of a doserate method and dosimetric implications of the 80-mCi rule. J Nucl Med. 2006;47:1977–84.
35. Song H, Prideaux A, Du Y, et al. Lung dosimetry for radioiodine treatment planning in the case of diffuse lung metastases. J Nucl Med. 2006;47:1985–94.
36. Luster M, Clarke SE, Dietlein M, et al. Guidelines for radioiodine therapy of differentiated thyroid cancer. Eur J Nucl Med Mol Imaging. 2008;35:1941–59.
37. Freudenberg LS, Jentzen W, Stahl A, Bockisch A, Rosenbaum-Krumme SJ. Clinical applications of ^{124}I-PET/CT in patients with differentiated thyroid cancer. Eur J Nucl Med Mol Imaging. 2011;38 (Suppl 1):S48–56.
38. Sgouros G, Kolbert KS, Sheikh A, et al. Patient-specific dosimetry for I-131 thyroid cancer therapy using I-124 PET and 3-dimensional internal dosimetry (3D-ID) software. J Nucl Med. 2004;45:1366–72.
39. de Keizer B, Brans B, Hoekstra A, et al. Tumour dosimetry and response in patients with metastatic differentiated thyroid cancer using recombinant human thyrotropin before radioiodine therapy. Eur J Nucl Med. 2003;30:367–73.
40. Jentzen W, Bockisch A, Ruhlmann M. Assessment of simplified blood dose protocols for the estimation of the maximum tolerable activity in thyroid cancer patients undergoing radioiodine therapy using 124I. J Nucl Med. 2015;56:832–8.
41. Freudenberg LS, Jentzen W, Görges R, Petrich T, Marlowe RJ, Knust J, et al. ^{124}I-PET dosimetry in advanced differentiated thyroid cancer: therapeutic impact. Nuklearmedizin. 2007;46:121–8.
42. van Essen M, Krenning EP, Kam BL, et al. Peptide-receptor radionuclide therapy for endocrine tumors. Nat Rev Endocrinol. 2009;5:382–93.
43. Bodei L, Cremonesi M, Kidd M, et al. Peptide receptor radionuclide therapy for advanced neuroendocrine tumors. Thorac Surg Clin. 2014;24:24333–49.
44. Garkavij M, Nickel M, Sjögreen-Gleisner K, Ljungberg M, Ohlsson T, Wingårdh K, Strand SE, Tennvall J. ^{177}Lu [DOTA^0, Tyr^3] octreotate therapy in patients with disseminated neuroendocrine tumors: analysis of dosimetry with impact on future therapeutic strategy. Cancer. 2010;116(Suppl 4):1084–92.
45. Swärd C, Bernhardt P, Ahlman H, et al. [^{177}Lu-DOTA^0 Tyr^3]-octreotate treatment in patients with disseminated gastroenteropancreatic neuroendocrine tumors: the value of measuring absorbed dose to the kidney. World J Surg. 2010;34:1368–72.
46. Lassmann M, Chiesa C, Flux G, et al. EANM Dosimetry Committee guidance document: good practice of clinical dosimetry reporting. Eur J Nucl Med Mol Imaging. 2011;38:192–200.
47. Larsson M, Bernhardt P, Svensson JB, et al. Estimation of absorbed dose to the kidneys in patients after treatment with ^{177}Lu-octreotate: comparison between methods based on planar scintigraphy. EJNMMI Res. 2012;2:49.
48. Sandström M, Garske-Román U, Granberg D, et al. Individualized dosimetry of kidney and bone marrow in patients undergoing ^{177}Lu-DOTA-octreotate treatment. J Nucl Med. 2013;54:33–41.
49. Sandström M, Ilan E, Karlberg A, et al. Method dependence, observer variability and kidney volumes in

radiation dosimetry of ^{177}Lu-DOTATATE therapy in patients with neuroendocrine tumours. EJNMMI Phys. 2015;2:24.
50. Gustafsson J, Brolin G, Cox M, et al. Uncertainty propagation for SPECT/CT-based renal dosimetry in ^{177}Lu peptide receptor radionuclide therapy. Phys Med Biol. 2015;60:8329–46.
51. Ljungberg M, Celler A, Konijnenberg MW, Eckerman KF, Dewaraja YK, Sjögreen Gleisner K. MIRD pamphlet no. 26: joint EANM/MIRD guidelines for quantitative ^{177}Lu SPECT applied for dosimetry of radiopharmaceutical therapy. J Nucl Med. 2016;57: 151–62.
52. Dale R. Use of the linear-quadratic radiobiological model for quantifying kidney response in targeted radiotherapy. Cancer Biother Radiopharm. 2004;19: 363–70.
53. Strigari L, Benassi M, Chiesa C, Cremonesi M, Bodei L, D'Andrea M. Dosimetry in nuclear medicine therapy: radiobiology application and results. Q J Nucl Med Mol Imaging. 2011;55:205–21.
54. Barone R, Borson-Chazot F, Valkema R, et al. Patient-specific dosimetry in predicting renal toxicity with ^{90}Y-DOTATOC: relevance of kidney volume and dose rate in finding a dose-effect relationship. J Nucl Med. 2005;46(Suppl 1):99S–106.
55. Wessels BW, Konijnenberg MW, Dale RG, Breitz HB, Cremonesi M, Meredith RF, et al. MIRD pamphlet no. 20: the effect of model assumptions on kidney dosimetry and response-implications for radionuclide therapy. J Nucl Med. 2008;49:1884–99.
56. Strigari L, Konijnenberg M, Chiesa C, et al. The evidence base for the use of internal dosimetry in the clinical practice of molecular radiotherapy. Eur J Nucl Med Mol Imaging. 2014;41:1976–88.
57. Ilan E, Sandström M, Wassberg C, et al. Dose response of pancreatic neuroendocrine tumors treated with peptide receptor radionuclide therapy using ^{177}Lu-DOTATATE. J Nucl Med. 2015;56:177–82.
58. Minarik D, Sjögreen Gleisner K, Ljungberg M. Evaluation of quantitative ^{90}Y SPECT based on experimental phantom studies. Phys Med Biol. 2008;53: 5689–703.
59. Minarik D, Ljungberg M, Segars P, Gleisner KS. Evaluation of quantitative planar ^{90}Y bremsstrahlung whole-body imaging. Phys Med Biol. 2009;54: 5873–83.
60. Fabbri C, Sarti G, Cremonesi M, et al. Quantitative analysis of ^{90}Y Bremsstrahlung SPECT-CT images for application to 3D patient-specific dosimetry. Cancer Biother Radiopharm. 2009;24:145–54.
61. Martí-Climent JM, Prieto E, Elosúa C, et al. PET optimization for improved assessment and accurate quantification of ^{90}Y-microsphere biodistribution after radioembolization. Med Phys. 2014;41: 092503.
62. Willowson KP, Tapner M, QUEST Investigator Team, et al. A multicentre comparison of quantitative ^{90}Y PET/CT for dosimetric purposes after radioembolization with resin microspheres: the QUEST Phantom Study. Eur J Nucl Med Mol Imaging. 2015;42:1202–22.
63. Fabbri C, Bartolomei M, Mattone V, et al. ^{90}Y-PET/CT imaging quantification for dosimetry in peptide receptor radionuclide therapy: analysis and corrections of the impairing factors. Cancer Biother Radiopharm. 2015;30:200–10.
64. Cremonesi M, Botta F, Di Dia A, et al. Dosimetry for treatment with radiolabelled somatostatin analogues. A review. Q J Nucl Med Mol Imaging. 2010;54:37–51.
65. Pauwels S, Barone R, Walrand S. Practical dosimetry of peptide receptor radionuclide therapy with ^{90}Y-labeled somatostatin analogs. J Nucl Med. 2005;46(Suppl 1):92S–8.
66. Baechler S, Hobbs RF, Boubaker A, et al. Three-dimensional radiobiological dosimetry of kidneys for treatment planning in peptide receptor radionuclide therapy. Med Phys. 2012;39:6118–28.
67. Sandström M, Garske U, Granberg D, et al. Individualized dosimetry in patients undergoing therapy with ^{90}Y-DOTA-D-Phe^{1}-Tyr^{3} octreotate. Eur J Nucl Med Mol Imaging. 2010;37:212–25.
68. Bodei L, Mueller-Brand J, Baum RP, et al. The joint IAEA, EANM, and SNMMI practical guidance on peptide receptor radionuclide therapy (PRRNT) in neuroendocrine tumours. Eur J Nucl Med Mol Imaging. 2013;40:800–16.
69. Sarnelli A, Guerriero F, Botta F, et al. Therapeutic schemes in ^{177}Lu and ^{90}Y-PRRT: radiobiological considerations. Q J Nucl Med Mol Imaging. in print.
70. Rolleman EJ, Melis M, Valkema R, Boerman OC, Krenning EP, de Jong M. Kidney protection during peptide receptor radionuclide therapy with somatostatin analogues. Eur J Nucl Med Mol Imaging. 2010;37:1018–31.
71. Guerriero F, Ferrari ME, Botta F, et al. Kidney dosimetry in ^{177}Lu and ^{90}Y peptide receptor radionuclide therapy: influence of image timing, time-activity integration method, and risk factors. Biomed Res Int. 2013;2013:935351.
72. Beauregard JM, Hofman MS, Kong G, et al. The tumour sink effect on the biodistribution of ^{68}Ga-DOTA-octreotate: implications for peptide receptor radionuclide therapy. Eur J Nucl Med Mol Imaging. 2012;39:50–6.
73. Bouchet 2003, Green 2004, Stabin 2005 LG, Bolch WE, Blanco HP, et al. MIRD Pamphlet No 19: absorbed fractions and radionuclide S values for six age-dependent multiregion models of the kidney. J Nucl Med. 2003;44:1113–47.
74. Green A, Flynn A, Pedley RB, Dearling J, Begent R. Nonuniform absorbed dose distribution in the kidney: the influence of organ architecture. Cancer Biother Radiopharm. 2004;19:371–7.
75. Konijnenberg M, Melis M, Valkema R, Krenning E, de Jong M. Radiation dose distribution in human kidneys by octreotides in peptide receptor radionuclide therapy. J Nucl Med. 2007;48:134–42.

76. Bodei L, Cremonesi M, Ferrari M, et al. Long-term evaluation of renal toxicity after peptide receptor radionuclide therapy with ^{90}Y-DOTATOC and ^{177}Lu-DOTATATE: the role of associated risk factors. Eur J Nucl Med Mol Imaging. 2008;35:1847–56.
77. Imhof A, Brunner P, Marincek N, et al. Response, survival, and long-term toxicity after therapy with the radiolabeled somatostatin analogue [^{90}Y-DOTA]-TOC in metastasized neuroendocrine cancers. J Clin Oncol. 2011;29:2416–23.
78. Cremonesi M, Ferrari M, Di Dia A, Botta F, De Cicco C, Bodei L, Paganelli G. Recent issues on dosimetry and radiobiology for peptide receptor radionuclide therapy. Q J Nucl Med Mol Imaging. 2011;55:155–67.
79. Cybulla M, Weiner SM, Otte A. End-stage renal disease after treatment with ^{90}Y-DOTATOC. Eur J Nucl Med. 2001;28:1552–4.
80. Kwekkeboom DJ, Mueller-Brand J, Paganelli G, et al. Overview of results of peptide receptor radionuclide therapy with 3 radiolabeled somatostatin analogs. J Nucl Med. 2005;46(Suppl 1):62S–6.
81. Bodei L, Cremonesi M, Grana CM, et al. Peptide receptor radionuclide therapy with ^{177}Lu-DOTATATE: the IEO phase I–II study. Eur J Nucl Med Mol Imaging. 2011;38:2125–35.
82. Kwekkeboom DJ, de Herder WW, Kam BL, et al. Treatment with the radiolabeled somatostatin analog [^{177}Lu-DOTA^{0}, Tyr^{3}]octreotate: toxicity, efficacy, and survival. J Clin Oncol. 2008;26:2124–30.
83. Bodei L, Kidd M, Paganelli G, et al. Long-term tolerability of PRRT in 807 patients with neuroendocrine tumours: the value and limitations of clinical factors. Eur J Nucl Med Mol Imaging. 2015;42:5–19.
84. Kunikowska J, Królicki L, Hubalewska-Dydejczyk A, et al. Clinical results of radionuclide therapy of neuroendocrine tumours with ^{90}Y-DOTATATE and tandem ^{90}Y/^{177}Lu-DOTATATE: which is a better therapy option? Eur J Nucl Med Mol Imaging. 2011; 38:1788–97.
85. Seregni E, Maccauro M, Chiesa C, et al. Treatment with tandem [^{90}Y]DOTA-TATE and [^{177}Lu]DOTA-TATE of neuroendocrine tumours refractory to conventional therapy. Eur J Nucl Med Mol Imaging. 2014;41:223–30.
86. Bodei L, Kidd M, Modlin IM, et al. Gene transcript analysis blood values correlate with ^{68}Ga-DOTA-somatostatin analog (SSA) PET/CT imaging in neuroendocrine tumors and can define disease status. Eur J Nucl Med Mol Imaging. 2015;42:1341–52.
87. Bodei L, Kidd M, Modlin IM, et al. Measurement of circulating transcripts and gene cluster analysis predicts and defines therapeutic efficacy of peptide receptor radionuclide therapy (PRRT) in neuroendocrine tumors. Eur J Nucl Med Mol Imaging. 2016; 43: 839–51.
88. Goldsmith SJ. Radioimmunotherapy of lymphoma: Bexxar and Zevalin. Semin Nucl Med. 2010;40: 122–35.
89. Kaminski MS, Tuck M, Estes J, et al. ^{131}I-tositumomab therapy as initial treatment for follicular lymphoma. N Engl J Med. 2005;352:441–9.
90. Wahl RL. Tositumomab and ^{131}I therapy in non-Hodgkin's lymphoma. J Nucl Med. 2005;46(Suppl 1):128S–40.
91. Witzig TE, Flinn IW, Gordon LI, et al. Treatment with ibritumomab tiuxetan radioimmunotherapy in patients with rituximab-refractory follicular non-Hodgkin's lymphoma. J Clin Oncol. 2002;20:3262–9.
92. Aricò D, Grana CM, Vanazzi A, et al. The role of dosimetry in the high activity ^{90}Y-ibritumomab tiuxetan regimens: two cases of abnormal biodistribution. Cancer Biother Radiopharm. 2009;24:271–5.
93. Wagner HN, Wiseman GA, Marcus CS, et al. Administration guidelines for radioimmunotherapy of non-Hodgkin's lymphoma with ^{90}Y-labeled anti-CD20 monoclonal antibody. J Nucl Med. 2002;43: 267–72.
94. Tennvall J, Fischer M, Bischof Delaloye A, et al. EANM procedure guideline for radio-immunotherapy for B-cell lymphoma with ^{90}Y-radiolabelled ibritumomab tiuxetan (Zevalin). Eur J Nucl Med Mol Imaging. 2007;34:616–22.
95. Wiseman GA, Kornmehl E, Leigh B, et al. Radiation dosimetry results and safety correlations from ^{90}Y-ibritumomab tiuxetan radioimmunotherapy for relapsed or refractory non-Hodgkin's lymphoma: combined data from 4 clinical trials. J Nucl Med. 2003;44:465–74.
96. Fisher DR, Shen S, Meredith RF. MIRD dose estimate report No. 20: radiation absorbed-dose estimates for ^{111}In- and ^{90}Y-ibritumomab tiuxetan. J Nucl Med. 2009;50:644–52.
97. Bodei L, Cremonesi M, Grana C, et al. Receptor radionuclide therapy with ^{90}Y-[DOTA]^{0}-Tyr^{3}-octreotide (^{90}Y-DOTATOC) in neuroendocrine tumours. Eur J Nucl Med Mol Imaging. 2004;31:1038–46.
98. Cremonesi M, Ferrari M, Grana CM, et al. High-dose radioimmunotherapy with ^{90}Y-ibritumomab Tiuxetan: comparative dosimetric study for tailored treatment. J Nucl Med. 2007;48:1871–9.
99. Lewandowski RJ, Riaz A, Ryu RK, et al. Optimization of radioembolic effect with extended-shelf-life yttrium-90 microspheres: results from a pilot study. J Vasc Interv Radiol. 2009;20:1557–63.
100. Kennedy AS, McNeillie P, Dezarn WA, et al. Treatment parameters and outcome in 680 treatments of internal radiation with resin ^{90}Y-microspheres for unresectable hepatic tumors. Int J Radiat Oncol Biol Phys. 2009;74:1494–500.
101. Cremonesi M, Chiesa C, Strigari L, et al. Radioembolization of hepatic lesions from a radiobiology and dosimetric perspective. Front Oncol. 2014;4: 210.
102. Gulec SA, Sztejnberg ML, Siegel JA, et al. Hepatic structural dosimetry in ^{90}Y microsphere treatment: a Monte Carlo modeling approach based on lobular microanatomy. J Nucl Med. 2010;51:301–10.

103. Ferrari M, Cremonesi M, Bartolomei M, et al. Different evaluations for safe ^{90}Y-microspheres in selective internal radiation therapy (SIRT). Eur J Nucl Med Mol Imaging. 2007;34(Suppl 2):S178.
104. Ho S, Lau WY, Leung TW, et al. Partition model for estimating radiation doses from yttrium-90 microspheres in treating hepatic tumours. Eur J Nucl Med. 1996;23:947–52.
105. Cremonesi M, Ferrari M, Bartolomei M, et al. Radioembolisation with ^{90}Y-microspheres: dosimetric and radiobiological investigation for multi-cycle treatment. Eur J Nucl Med Mol Imaging. 2008;35:2088–96.
106. Salem R, Thurston KG. Radioembolization with ^{90}Yttrium microspheres: a state-of-the-art brachytherapy treatment for primary and secondary liver malignancies. Part 1: technical and methodologic considerations. J Vasc Interv Radiol. 2006;17: 1251–78. Erratum in: J Vasc Interv Radiol. 2006; 17:1594.
107. Riaz A, Lewandowski RJ, Kulik LM, et al. Complications following radioembolization with yttrium-90 microspheres: a comprehensive literature review. J Vasc Interv Radiol. 2009;20:1121–30.
108. Walrand S, Hesse M, Chiesa C, Lhommel R, Jamar F. The low hepatic toxicity per Gray of ^{90}Y glass microspheres is linked to their transport in the arterial tree favoring a nonuniform trapping as observed in post-therapy PET imaging. J Nucl Med. 2014;55: 135–40.
109. Gaba RC, Lewandowsi RJ, Kulik LM, Riaz A, Ibrahim SM, Mulcahy MF. Radiation lobectomy: preliminary findings of hepatic volumetric response to lobar yttrium-90 radioembolization. Ann Surg Oncol. 2009;16:1587–96.
110. Strigari L, Sciuto R, Rea S, Carpanese L, Pizzi G, Soriani A, Iaccarino G, Benassi M, Ettorre GM, Maini CL. Efficacy and toxicity related to treatment of hepatocellular carcinoma with ^{90}Y SIR spheres: radiobiological considerations. J Nucl Med. 2010;51: 1377–85.
111. Flamen P, Vanderlinden B, Delatte P, et al. CORRIGENDUM: multimodality imaging can predict the metabolic response of unresectable colorectel liver metastases to radioembolization therapy with yttrium-90 labeled resin micropheres. Phys Med Biol. 2014;59:2549.
112. Chiesa C, Mira M, Maccauro M, et al. Radioembolization of hepatocarcinoma with 90-Y glass microspheres: development of an individualized treatment planning strategy based on dosimetry and radiobiology. Eur J Nucl Med Mol Imaging. 2015;42:1718–38.
113. Garin E, Lenoir L, Rolland Y, Edeline J, Mesbah H, Laffont S. Dosimetry based on ^{99m}Tc-macroaggregated albumin SPECT/CT accurately predicts tumor response and survival in hepatocellular carcinoma patients treated with ^{90}Y-loaded glass microspheres: preliminary results. J Nucl Med. 2012;53: 255–63.
114. Garin E, Lenoir L, Edeline J, et al. Boosted selective internal radiation therapy with ^{90}Y-loaded glass microspheres (B-SIRT) for hepatocellular carcinoma patients: a new personalized promising concept. Eur J Nucl Med Mol Imaging. 2013;40:1057–68.
115. Giammarile F, Chiti A, Lassmann M, et al. EANM procedure guidelines for ^{131}I-meta-iodobenzylguanidine (^{131}I-mIBG) therapy. Eur J Nucl Med Mol Imaging. 2008;35:1039–47.
116. Monsieurs M, Brans B, Bacher K, et al. Patient dosimetry for neuroendocrine tumours based on ^{123}I-MIBG pretherapy scans and ^{131}I-MIBG post therapy scans. Eur J Nucl Med. 2002;29:1581–7.
117. Fielding SL, Flower MA, Ackery D, et al. Dosimetry of iodine-131metaiodobenzylguanidine in resistant neuroblastoma: results of a UK study. Eur J Nucl Med. 1991;18:308–16.
118. Matthay KK, Quach A, Franc BL, et al. ^{131}I-Metaiodobenzylguanidine (^{131}I-MIBG) double infusion with autologous stem cell rescue for neuroblastoma: a new approaches to neuroblastoma therapy (NANT) phase I study. J Clin Oncol. 2009;27: 1020–5.
119. Buckley SE, Chittenden S, Saran FH, et al. Whole-body dosimetry for individualized treatment planning of ^{131}I-MIBG radionuclide therapy for neuroblastoma. J Nucl Med. 2009;50:1518–24.
120. Matthay KK, Jessica C, Villablanca J, et al. Phase I dose escalation of iodine-131-metaiodobenzylguanidine with myeloablative chemotherapy and autologous stem-cell transplantation in refractory neuroblastoma: a new approaches to neuroblastoma therapy consortium study. J Clin Oncol. 2006;24:500–6.
121. Monsieurs MA, Thierens HM, Vral A, et al. Patient dosimetry after I-131-MIBG therapy for neuroblastoma and carcinoid tumours. Nucl Med Commun. 2001;22:367–74.
122. DuBois SG, Messina J, Maris JM, et al. Haematological toxicity of high-dose iodine-131-metaiodobenzylguanidine therapy for advanced neuroblastoma. J Clin Oncol. 2004;22:2452–60.
123. Matthay KK, Panina C, Huberty J, et al. Correlation of tumour and whole-body dosimetry with tumour response and toxicity in refractory neuroblastoma treated with ^{131}I-MIBG. J Nucl Med. 2001;42: 1713–21.
124. Flower MA, Fielding SL. Radiation dosimetry for ^{131}I-mIBG therapy of neuroblastoma. Phys Med Biol. 1996;41:1933–40.
125. Gaze MN, Chang YC, Flux GD, et al. Feasibility of dosimetry-based high-dose I-131-meta-iodobenzylguanidine with topotecan as a radiosensitizer in children with metastatic neuroblastoma. Cancer Biother Radiopharm. 2005;20:195–9.
126. Koral KF, Huberty JP, Frame B, et al. Hepatic absorbed radiation dosimetry during I-131 metaiodobenzylguanadine (MIBG) therapy for refractory neuroblastoma. Eur J Nucl Med Mol Imaging. 2008;35:2105–12.

127. Trieu M, DuBois SG, Pon E, et al. Impact of whole-body radiation dose on response and toxicity in patients with neuroblastoma after therapy with ^{131}I-metaiodobenzylguanidine (MIBG). Pediatr Blood Cancer. 2016;63:436–42.
128. Minguez P, Flux G, Genolla J, et al. Dosimetric results in treatments of neuroblastoma and neuroendocrine tumors with ^{131}I-metaiodobenzylguanidine with implications for the activity to administer. Med Phys. 2015;42:3969–78.
129. George SL, Falzone N, Chittenden S, et al. Individualized ^{131}I-mIBG therapy in the management of refractory and relapsed neuroblastoma. Nucl Med Commun. 2016; 37: 466–72.
130. Seo Y, Gustafson WC, Dannoon SF, et al. Tumor dosimetry using [^{124}I]m-iodobenzylguanidine micro-PET/CT for [^{131}I]m-iodobenzylguanidine treatment of neuroblastoma in a murine xenograft model. Mol Imaging Biol. 2012;14:735–42.
131. Huang SY, Bolch WE, Lee C, et al. Patient-specific dosimetry using pretherapy [^{124}I]m-iodobenzylguanidine ([^{124}I]mIBG) dynamic PET/CT imaging before [^{131}I]mIBG targeted radionuclide therapy for neuroblastoma. Mol Imaging Biol. 2015;17:284–94 [New].
132. Hartung-Knemeyer V, Rosenbaum-Krumme S, Buchbender C, et al. Malignant pheochromocytoma imaging with [^{124}I]mIBG PET/MR. J Clin Endocrinol Metab. 2012;97:3833–4.
133. Paes FM, Serafini AN. Systemic metabolic radiopharmaceutical therapy in the treatment of metastatic bone pain. Semin Nucl Med. 2010;40:89–104.
134. Krishnamurthy GT, Krishnamurthy S. Radionuclides for metastatic bone pain palliation: a need for rational re-evaluation in the new millennium. J Nucl Med. 2000;41:688–91.
135. Finlay IG, Mason MD, Shelley M. Radioisotopes for the palliation of metastatic bone cancer: a systematic review. Lancet Oncol. 2005;6:392–400.
136. Taylor Jr AJ. Strontium-89 for the palliation of bone pain due to metastatic disease. J Nucl Med. 1994;35: 2054.
137. Eary JF, Collins C, Stabin M, et al. Samarium-153-EDTMP biodistribution and dosimetry estimation. J Nucl Med. 1993;34:1031–6.
138. Graham MC, Scher HI, Liu GB, et al. Rhenium-186-labeled hydroxyethylidene diphosphonate dosimetry and dosing guidelines for the palliation of skeletal metastases from androgen-independent prostate cancer. Clin Cancer Res. 1999;5:1307–18.
139. Liepe K, Kropp J, Runge R, et al. Therapeutic efficiency of rhenium-188-HEDP in human prostate cancer skeletal metastases. Br J Cancer. 2003;89:625–9.
140. Lewington VJ. Bone-seeking radiopharmaceuticals. J Nucl Med. 2005;46:38S–47.
141. Bodei L, Lam M, Chiesa C, et al. EANM procedure guideline for treatment of refractory metastatic bone pain. Eur J Nucl Med Mol Imaging. 2008; 35:1934–40.
142. Pacilio M, Ventroni G, Basile C, et al. Improving the dose–myelotoxicity correlation in radiometabolic therapy of bone metastases with ^{153}Sm-EDTMP. Eur J Nucl Med Mol Imaging. 2014;41:238–52.
143. Parker C, Nilsson S, Heinrich D, McDevitt MR, et al. Alpha emitter radium-223 and survival in metastatic prostate cancer. N Engl J Med. 2013;369:213–23.
144. Sgouros G, Roeske JC, et al. MIRD pamphlet no. 22 (abridged): radiobiology and dosimetry of α-particle emitters for targeted radionuclide therapy. J Nucl Med. 2010;51:311–28.
145. Hobbs RF, Song H, Watchman CJ, et al. A bone marrow toxicity model for Ra-223 α-emitter radiopharmaceutical therapy. Phys Med Biol. 2012;57:3207–22.
146. Chittenden S, Hindorf C, Parker CC, et al. Phase 1, open-label study of the biodistribution, pharmacokinetics and dosimetry of Radium-223 dichloride (^{223}Ra dichloride) in patients with hormone refractory prostate cancer and skeletal metastases. J Nucl Med. 2015;56:1304–9.
147. Pacilio M, Ventroni G, De Vincentis G, et al. Dosimetry of bone metastases in targeted radionuclide therapy with alpha-emitting ^{223}Ra-dichloride. Eur J Nucl Med Mol Imaging. 2016;43:21–33.
148. Pacilio M, Ventroni G, Cassano B, et al. A case report of image-based dosimetry of bone metastases with Alpharadin (^{223}Ra-dichloride) therapy: inter-fraction variability of absorbed dose and follow-up. Ann Nucl Med. 2016;30:163–8.
149. International Atomic Energy Agency. Cytogenetic analysis for radiation dose assessment, Technical report series, vol. 405. Vienna: IAEA; 2001.
150. Léonard A, Rueff J, Gerber GB, et al. Usefulness and limits of biological dosimetry based on cytogenetic methods. Radiat Prot Dosimetry. 2005;115: 448–54.
151. M'Kacher R, Schlumberger M, Lagal JC, et al. Biologic dosimetry in thyroid cancer patients after repeated treatments with iodine-131. J Nucl Med. 1998;39:825–9.
152. Monsieurs MA, Thierens HM, van de Wiele CV, et al. Estimation of risk based on biological dosimetry for patients treated with radioiodine. Nucl Med Commun. 1999;20:911–7.
153. Dardano A, Ballardin M, Caraccio N, et al. The effect of Ginkgo Biloba Extract on genotoxic damage in patients with differentiated thyroid carcinoma receiving thyroid remnant ablation with iodine-131. Thyroid. 2012;22:318–24.
154. Fairbaim DW, Olive PL, O'Neill KL. The Comet assay a comprehensive review. Mutat Res. 1995;339:37–59.
155. Anderson D, Plewa MJ. The international comet assay workshop. Mutagenesis. 1998;13:67–73.
156. Gutierrez S, Carbonell E, Galofre P, et al. Application of the single cell gel electrophoresis (SCGE) assay to the detection of DNA damage induced by 131I treatment in hyperthyroidism patients. Mutagenesis. 1998;13:95–8.

157. Rothkamm K, Horn S. γ-H2AX as protein biomarker for radiation exposure. Ann Ist Super Sanita. 2009;45:265–71.
158. Quimby E. The development of radiation dosimetry in nuclear medicine. In: Medical radionuclides: radiation dose and effects. Washington, DC: U.S. Atomic Energy Commission; 1970. p. 7–15. AEC Symposium Series 20.
159. Eberlein U, Scherthan H, Bluemel C, et al. DNA damage in peripheral blood lymphocytes of thyroid cancer patients after radioiodine therapy. J Nucl Med. 2016;57:2173–9.
160. Amis Jr ES, Butler PF, Applegate KE, et al. American College of Radiology white paper on radiation dose in medicine. J Am Coll Radiol. 2007;4:272–84.
161. Mettler Jr FA, Bhargavan M, Faulkner K, et al. Radiologic and nuclear medicine studies in the United States and worldwide: frequency, radiation dose, and comparison with other radiation sources – 1950–2007. Radiology. 2009;253:520–31.
162. Brenner DJ, Hall EJ. Computed tomography – an increasing source of radiation exposure. N Engl J Med. 2007;357:2277–84.
163. Goske MJ, Applegate KE, Bell C, et al. Image gently: providing practical educational tools and advocacy to accelerate radiation protection for children worldwide. Semin Ultrasound CT MR. 2010;31:57–63.
164. Goske MJ, Applegate KE, Boylan J, et al. Image gently (SM): a national education and communication campaign in radiology using the science of social marketing. J Am Coll Radiol. 2008;5:1200–5.
165. Goske MJ, Applegate KE, Boylan J, et al. The image gently campaign: working together to change practice. AJR Am J Roentgenol. 2008;190:273–4.
166. Goske MJ, Frush DP, Schauer DA. Image gently campaign promotes radiation protection for children. Radiat Prot Dosimetry. 2009;135:276.
167. Harrison JD, Streffer C. The ICRP protection quantities, equivalent and effective dose: their basis and application. Radiat Prot Dosimetry. 2007;127:12–8.
168. Cristy M, Eckerman K. Specific absorbed fractions of energy at various ages from internal photon sources (I–VII), Oak Ridge National Laboratory Report ORNL/TM-8381/V1-7. Springfield: National Technical Information Service, Dept of Commerce; 1987.
169. Stabin MG, Gelfand MJ. Dosimetry of pediatric nuclear medicine procedures. Q J Nucl Med. 1998; 42:93–112.
170. Treves ST, Davis RT, Fahey FH. Administered radiopharmaceutical doses in children: a survey of 13 pediatric hospitals in North America. J Nucl Med. 2008; 49:1024–7.
171. Stabin MG, Stubbs JB, Toohey RE. Radiation dose estimates for radiopharmaceuticals. Washington, DC: US Nuclear Regulatory Commission; 1996 (NRC. Report No.: NUREG/CR-6345).
172. Brenner D, Elliston C, Hall E, Berdon W. Estimated risks of radiation-induced fatal cancer from pediatric CT. AJR Am J Roentgenol. 2001;176:289–96.
173. Einstein AJ, Henzlova MJ, Rajagopalan S. Estimating risk of cancer associated with radiation exposure from 64-slice computed tomography coronary angiography. JAMA. 2007;298:317–23.
174. Martin CJ. Effective dose: how should it be applied to medical exposures? Br J Radiol. 2007;80(956): 639–47.
175. Fahey FH, Palmer MR, Strauss KJ, Zimmerman RE, Badawi RD, Treves ST. Dosimetry and adequacy of CT-based attenuation correction for pediatric PET: phantom study. Radiology. 2007;243:96–104.
176. Kamel E, Hany TF, Burger C, Treyer V, Lonn AH, von Schulthess GK, Buck A. CT vs ^{68}Ge attenuation correction in a combined PET/CT system: evaluation of the effect of lowering the CT tube current. Eur J Nucl Med Mol Imaging. 2002;29:346–50.
177. Brix G, Lechel U, Glatting G, Ziegler SI, Munzing W, Muller SP, Beyer T. Radiation exposure of patients undergoing whole-body dual-modality ^{18}F-FDG PET/CT examinations. J Nucl Med. 2005;46:608–13.
178. Groves AM, Owen KE, et al. 16-detector multislice CT: dosimetry estimation by TLD measurement compared with Monte Carlo simulation. Br J Radiol. 2004;77:662–5.
179. Huda W, Vance A. Patient radiation doses from adult and pediatric CT. AJR Am J Roentgenol. 2007;188:540–6.
180. Preston DL, Pierce DA, Shimizu Y, Cullings HM, Fujita S, Funamoto S, Kodama K. Effect of recent changes in atomic bomb survivor dosimetry on cancer mortality risk estimates. Radiat Res. 2004;162: 377–89.
181. NRC. National Research Council, Committee on the Biological Effects of Ionizing Radiation (BEIR V). Health effects of exposure to low levels of ionizing radiations. Washington, DC: National Academy Press; 1990.
182. NRC. National Research Council, Committee on the Biological Effects of Ionizing Radiation (BEIR VII-phase 2). Health risks from exposure to low levels of ionizing radiation. Washington, DC: National Academy Press; 2006.
183. Preston DL, Ron E, Tokuoka S, Funamoto S, Nishi N, Soda M, Mabuchi K, Kodama K. Solid cancer incidence in atomic bomb survivors: 1958–1998. Radiat Res. 2007;168:1–64.
184. Brenner DJ, Elliston CD, Hall EJ, Berdon WE. Estimates of the cancer risks from pediatric CT radiation are not merely theoretical: comment on "point/counterpoint: in x-ray computed tomography, technique factors should be selected appropriate to patient size against the proposition". Med Phys. 2001;28: 2387–8.
185. van Tinteren H, Hoekstra OS, Smit EF, van den Bergh JH, Schreurs AJ, Stallaert RA, van Velthoven PC, Comans EF, Diepenhorst FW, Verboom P, van Mourik JC, Postmus PE, Boers M, Teule GJ. Effectiveness of positron emission tomography in the preoperative assessment of patients with suspected

non-small-cell lung cancer: the PLUS multicentre randomised trial. Lancet. 2002;359:1388–93.
186. Neel JV, Schull WJ, Awa AA, Satoh C, Kato H, Otake M, Yoshimoto Y. The children of parents exposed to atomic bombs: estimates of the genetic doubling dose of radiation for humans. Am J Hum Genet. 1990;46:1053–72.
187. Neel JV, Lewis SE. The comparative radiation genetics of humans and mice. Annu Rev Genet. 1990;24: 327–62.
188. Edmonds CJ, Smith T. The long-term hazards of the treatment of thyroid cancer with radioiodine. Br J Radiol. 1986;59:45–51.
189. Sarkar SD, Beierwaltes WH, Gill SP, Cowley BJ. Subsequent fertility and birth histories of children and adolescents treated with ^{131}I for thyroid cancer. J Nucl Med. 1976;17:460–4.
190. Handelsman DJ, Turtle JR. Testicular damage after radioactive iodine (I-131) therapy for thyroid cancer. Clin Endocrinol. 1985;18:465–72.
191. Cloutier RJ, Smith SA, Watson EE, Snyder WS, Warner GG. Dose to the fetus from radionuclides in the bladder. Health Phys. 1973;5:147–61.
192. Hedrick WR, DiSimone RN, Wolf BH, Langer A. Absorbed dose to the fetus during bone scintigraphy. Radiology. 1988;168:245–8.
193. Husak V, Wiedermann M. Radiation absorbed dose estimates to the embryo from some nuclear medicine procedures. Eur J Nucl Med. 1980;5:205–7.
194. Marcus CS, Mason GR, Kuperus JH, Mena I. Pulmonary imaging in pregnancy. Maternal risk and fetal dosimetry. Clin Nucl Med. 1985;10:1–4.
195. Ponto JA. Fetal dosimetry from pulmonary imaging in pregnancy. Revised estimates. Clin Nucl Med. 1986;1:108–9.
196. Smith EM, Warner GG. Estimates of radiation dose to the embryo from nuclear medicine procedures. J Nucl Med. 1976;17:836–9.
197. Stabin MG, Watson EE, Marcus CS, Salk RD. Radiation dosimetry for the adult female and fetus from iodine-131 administration in hyperthyroidism. J Nucl Med. 1991;32:808–13.
198. Watson E, Stabin M, Eckerman K, Cristy M, Ryman J, Davis J. Model 2: mathematical models of the pregnant woman at the end of the first and third trimesters. In: Schlafke-Stelson A, Watson E, editors. Proceedings of the fourth international radiopharmaceutical dosimetry symposium (Conf-85113 (DE86010102)). Oak Ridge: US Dept of Energy and Oak Ridge Associated Universities; 89. p. 104–1986.
199. Stewart A. Oxford survey of childhood cancers. Nurs Mirror Midwives J. 1971;133:25–6.
200. Zanzonico PB, Becker DV. Radiation hazards in children born to mothers exposed to ^{131}-iodine. In: Beckers C, Reinwein D, editors. The thyroid and pregnancy. Stuttgart: Schattauer; 1991; p. 189–202.
201. Ahlgren L, Ivarsson S, Johansson L, Mattsson S, Nosslin B. Excretion of radionuclides in human breast milk after the administration of radiopharmaceuticals. J Nucl Med. 1985;26:1085–90.
202. Mountford PJ, Coakley AJ. Guidelines for breast feeding following maternal radiopharmaceutical administration [editorial]. Nucl Med Commun. 1986;7:399–401.
203. Mountford PJ, Coakley AJ. A review of the secretion of radioactivity in human breast milk: data, quantitative analysis and recommendations. Nucl Med Commun. 1989;10:15–27.
204. Romney B, Nickoloff E, Esser P, Alderson P. Radionuclide administration to nursing mothers: mathematically derived guidelines. Radiology. 1986;160:549–54.
205. Rubow S, Klopper J, Wasserman H, Baard B, van Niekerk M. The excretion of radiopharmaceuticals in human breast milk: additional data and dosimetry [see comments]. Eur J Nucl Med. 1994;21:144–53.
206. Weaver J, Kamm M, Dobson R. Excretion of radioiodine in human milk. JAMA. 1960;173:872–5.
207. Mettler Jr FA, Huda W, Yoshizumi TT, Mahesh M. Effective doses in radiology and diagnostic nuclear medicine: a catalog. Radiology. 2008;248:254–63.

Part II

Diagnostic Applications of Nuclear Medicine

Diagnostic Applications of Nuclear Medicine: Lymphomas

14

Heather A. Jacene, Sree Harsha Tirumani, and Richard L. Wahl

Abstract

Hodgkin and non-Hodgkin lymphomas are lymphoid neoplasms arising from B cells, T cells, or NK (natural killer) cells. [^{18}F]FDG PET/CT is more accurate for the primary staging of lymphoma, particularly because it can detect disease in normal-sized lymph nodes, liver, spleen, and bone marrow. A major advantage of [^{18}F]FDG PET in determining the outcome of therapy is distinguishing active lymphoma from fibrosis/necrosis in residual masses. Posttherapy [^{18}F]FDG PET provides important prognostic information and has been incorporated into the currently used criteria for evaluating response to therapy in lymphoma (Lugano/Lyric Classifications). Interim [^{18}F]FDG PET/CT also provides prognostic information and is being evaluated for "risk-adapted therapy" in setting of clinical trials.

Keywords

Lymphoma • [^{18}F]FDG-PET/CT • [^{18}F]FDG • Hodgkin • non-Hodgkin • Staging • Response to therapy

Glossary

[^{18}F]FDG	2-Deoxy-2-[^{18}F]fluoro-D-glucose
^{18}F-FLT	3′-^{18}F-fluoro-3′-deoxythymidine
ABVD	Therapy with adriamycin, bleomycin, vinblastine, and dacarbazine
ASCT	Autologous stem cell transplantation
BEACOPP	Therapy with bleomycin, etoposide, doxorubicin, cyclophosphamide, vincristine, prednisone, and procarbazine
cHL	Classical Hodgkin lymphoma
CHOP	Therapy with cyclophosphamide, doxorubicin, vincristine, and prednisolone
CLL	Chronic lymphocytic leukemia
CT	X-ray computed tomography
DLBCL	Diffuse large B-cell lymphoma
EBV	Epstein-Barr herpesvirus (EBV)
ECOG	Eastern Cooperative Oncology Group
EFS	Event-free survival
EORTC	European Organisation for Research and Treatment of Cancer

H.A. Jacene (✉) • S.H. Tirumani (✉)
Nuclear Medicine/PET-CT, Department of Imaging, Dana-Farber Cancer Institute and Department of Radiology, Brigham and Women's Hospital, Harvard Medical School, Boston, MA, USA
e-mail: hjacene@partners.org; sreeharsha_tirumani@dfci.harvard.edu

R.L. Wahl
Mallinkrodt Institute of Radiology, Washington University School of Medicine, St. Louis, MO, USA

© Springer International Publishing Switzerland 2017
H.W. Strauss et al. (eds.), *Nuclear Oncology*,
https://doi.org/10.1007/978-3-319-26236-9_7

EPOCH-R (or R-EPOCH)	Therapy with rituximab, etoposide, prednisolone, oncovin (vincristine), cyclophosphamide, and hydroxydaunorubicin (doxorubicin)
EPOCH	Therapy with etoposide, prednisolone, oncovin (vincristine), cyclophosphamide, and hydroxydaunorubicin (doxorubicin)
FLIPI	International Prognostic Index for follicular Hodgkin lymphoma
G-CSF	Granulocyte colony-stimulating factor
GEP	Gene expression profiling
HCT	Hematopoietic cell transplantation
HL	Hodgkin lymphoma
ICE	Therapy with ifosfamide, carboplatin, and etoposide
IFRT	Involved-field radiation therapy
IPI	International Prognostic Index
IPS	International Prognostic Score
IWG	International Working Group
LDH	Lactate dehydrogenase
lpHL	Lymphocyte-predominant Hodgkin lymphoma
MALT	Mucosa-associated lymphoid tissue
MOPP	Therapy with mechlorethamine, vincristine, procarbazine, and prednisone
MRU	Minimal residual uptake
NCCN	National Comprehensive Cancer Network
NHL	Non-Hodgkin lymphoma (NHL)
NK cell	Natural killer cells
NPV	Negative predictive value
OS	Overall survival
PCR	Polymerase chain reaction
PET	Positron emission tomography
PET/CT	Positron emission tomography/Computed tomography
PETAL	Positron emission tomography guided therapy of aggressive lymphomas
PFS	Progression-free survival
R-CHOP	Rituximab, cyclophosphamide, doxorubicin, vincristine, and prednisolone
R-EPOCH (or EPOCH-R)	Therapy with rituximab, etoposide, prednisolone, oncovin (vincristine), cyclophosphamide, and hydroxydaunorubicin (doxorubicin)
R-ICE	Therapy with rituximab, ifosfamide, carboplatin, and etoposide
RS cell	Reed-Sternberg cell
RSNA	Radiological Society of North America
SLL	Small lymphocytic lymphoma
SUV	Standardized uptake value
WBC	White blood cell

Contents

Hodgkin Lymphoma 355
Epidemiology and Etiology 355
Pathology and HL Subtypes 355
Genetic Features 356
Clinical Presentation, Evaluation, Staging, and Prognosis 356
Treatment and Follow-Up 358

Non-Hodgkin Lymphoma 359
Epidemiology and Etiology 359
Pathology and NHL Subtypes 360
Genetic Features 360
Clinical Presentation, Evaluation and Staging, and Prognosis 361
Treatment and Follow-Up 362

Nuclear Medicine Imaging for Lymphoma 363

[^{18}F]FDG-PET for Detecting and Histologic Grading of Lymphoma 364

[^{18}F]FDG-PET for Initial Staging of Lymphoma 365

[^{18}F]FDG-PET/CT Versus PET Alone 367

Post-Therapy Response Assessment by [^{18}F]FDG-PET and PET/CT 368

Integration of [^{18}F]FDG-PET and PET/CT into Tumor Response Criteria 368

Interim PET and Risk-Adapted Therapy 371
Theory and Biologic Basis 371
Clinical Trials of Risk-Adapted Therapy for Aggressive NHL 372
Clinical Trials of Risk-Adapted Therapy for Hodgkin Lymphoma 374
Interpretation of Interim Therapy PET Scans 375

Surveillance PET for Lymphoma 376

Tracers Beyond [^{18}F]FDG 377

Additional Challenges and Limitations in the Interpretation of [^{18}F]FDG-PET in Lymphoma 378

Summary 380

References 381

Lymphoma is a hematologic malignancy characterized by abnormal proliferation of lymphoid cells (i.e., lymphocytes, histiocytes), most commonly arising in lymph nodes, but potentially involving any organ or tissue in the body. There are two major classifications of lymphomas that are determined by distinct morphologic features: Hodgkin lymphoma (HL) and non-Hodgkin lymphoma (NHL). Diagnostic nuclear medicine procedures, in particular 2-deoxy-2-[^{18}F]fluoro-D-glucose positron emission tomography/computed tomography ([^{18}F]FDG-PET/CT), have emerged in the past two decades as an integral component in the evaluation of many patients with lymphoma to optimize therapeutic strategies.

Investigators began studying the use of [^{18}F]FDG-PET in patients with lymphoma in the late 1980s [1]. Initial studies showed great benefit and promise from metabolic tumor imaging, but the lack of anatomic information was a limitation. [^{18}F]FDG-PET detected more lesions than CT [2]. In 2001, combined PET/CT scanners were introduced for widespread clinical use, and the power of the hybrid imaging technique was soon realized. Current roles of [^{18}F]FDG-PET and PET/CT for patients with lymphoma include determining if disease is present, staging, restaging, evaluating response to therapy, identifying transformation and guiding biopsy, and offering prognostic information. PET is sometimes used to diagnose infections in patients with lymphoma, as well. PET-based "risk-adapted" therapy is currently the subject of numerous ongoing investigations.

This chapter will provide a brief clinical overview of the lymphoma subtypes as well as a review of the current and possible future roles of nuclear medicine imaging in patients with lymphoma.

Hodgkin Lymphoma

Epidemiology and Etiology

Hodgkin lymphoma represents approximately 10% of all lymphomas. In the United States, there were an estimated 9,050 new cases of HL and 1,150 deaths due to HL in 2015 [3]. The number of deaths due to HL has been decreasing over the past four decades due to better treatments [3].

HL has bimodal age peaks in the third and seventh decades of life and a slight male predominance. The exact etiology of HL is uncertain. Factors associated with higher risk of HL vary depending on geographic location (i.e., the industrial development of a country), socioeconomic status, immune suppression, and even age. Epstein-Barr herpesvirus (EBV) has been implicated in the pathogenesis of EBV-positive HL (about 40% of HL cases [4]), but is less likely to have role in EBV-negative HL [5]. Close family members of patients with HL, particularly identical twins [6, 7], are at higher risk for developing HL. One hypothesis for the etiology of HL based on the socioeconomic and genetic epidemiologic data is delayed exposure to a common (infectious) antigen in genetically susceptible individuals [8].

Pathology and HL Subtypes

There are two major subclasses of HL, classical and lymphocyte-predominant HL (cHL and lpHL). HL tumor is characterized by the presence of

distinctive, large, malignant cells (Reed-Sternberg (RS) cells in cHL and lymphocytic and histiocytic cells in lpHL) which represent only a minority, 1–5%, of the tumor in cHL. Background infiltrates consisting of a mixture of lymphocytes, histiocytes, eosinophils, plasma cells, and fibroblasts comprise the rest of the tumor [9]. There are four variants of cHL: nodular sclerosing, mixed cellularity, lymphocyte–rich, and lymphocyte–depleted. The variants are determined based on the morphology of the malignant cells and the composition and pattern of the background infiltrate [9].

Sufficient tissue is needed to make the diagnosis of HL because of the composition of the tumors, and excisional biopsy is recommended [10]. Immunohistochemistry is a helpful adjunct to morphology for establishing the diagnosis of HL. cHL and lpHL are both monoclonal B-cell disorders arising from germinal centers, although surface antigen expression between the two subclasses is different [11, 12]. Typically, the Reed-Sternberg (RS) cell in cHL expresses CD30 and in about 80–90% of cases also expresses CD15 [13, 14]. The malignant lymphocytic and histiocytic cells in lpHL express the B-cell antigen CD20, but varying frequencies (20–35%) of CD20 expression on malignant RS cells in cHL have been reported [15, 16]. Additional immunohistochemistry stains are also useful for differentiating cHL from lpHL as well as from T-cell-rich B-cell NHL and anaplastic large cell NHL which are often in the differential diagnosis [8]. An excellent review of the biologic classifications of HL is provided by Mani and Jaffe [17].

Genetic Features

Most cHL shows clonal, somatically mutated rearrangement of V, D, and J segments of immunoglobulin heavy-chain locus in RS cells on sensitive polymerase chain reaction (PCR) techniques indicative of mature B lymphocytes [18]. Clonal cytogenetic abnormalities with marked intraclonal variability are common in cHL [19, 20]. Abnormalities of 14q [20] and amplifications of PDL1 and PDL2 genes on chromosome 9 [21] are frequent. EBV is frequently associated with lymphocyte-depleted and mixed cellularity cHL, less common in lymphocyte-rich cHL and infrequent in nodular sclerosis subtypes [22, 23]. Molecular genetics of RS cells have shown an inactivating mutation of TNFAIP3 gene which encodes negative regulator of NF-kappaB [24]. Gene expression profiling (GEP) studies of RS cells have shown distinct expression profiles in cHL [25].

Clinical Presentation, Evaluation, Staging, and Prognosis

HL often presents as painless adenopathy, most commonly supradiaphragmatic in the supraclavicular and low neck lymph nodes. The pattern of nodal involvement varies depending on the histologic subtype. Thirty percent of patients also have systemic "B" symptoms (fevers, night sweats, and/or weight loss) [8] probably due to the production of cytokines by the malignant and background infiltrative cells [26].

History and physical exam, laboratory tests, and imaging are routinely performed at the initial diagnosis of HL for staging and assessing organ function prior to treatment. As will be discussed below, HL is typically [^{18}F]FDG-avid and [^{18}F]FDG-PET/CT is now the preferred noninvasive imaging modality for staging HL [27, 28]. According to the most recent recommendations for staging HL and NCCN guidelines, bone marrow biopsy for staging HL is no longer required if [^{18}F]FDG-PET/CT is performed, but may be warranted for further evaluation of cytopenias if the [^{18}F]FDG-PET/CT is negative [8, 10, 28].

The modified Ann Arbor staging system is used for staging HL (Table 1) [29, 30]. HL typically spreads to contiguous nodal groups. Stage is based on the number of nodal groups involved and is based on involvement in nodes above and/or below the diaphragm, extra-nodal organ involvement, and the presence or absence of "B" symptoms. Accurate staging is critical because along with several prognostic factors, staging guides the initial treatment plan.

Patients with early-stage HL (stage I/II) are subdivided into favorable and unfavorable risk groups for overall management. The grouping definitions differ between Europe and North

Table 1 Revised staging of primary nodal lymphomas: Lugano Classification

Limited Disease	
Stage I	1 LN region or lymphoid structure
Stage II	≥2 LN regions on same side of diaphragm
Advanced Disease	
Stage III	LN regions on both sides of the diaphragm or above diaphragm with splenic involvement
Stage IV	LN regions and noncontiguous extra-nodal sites
All stages (only HL)	A – no symptoms B – Fever (>38°C), night sweats, 10% body weight loss
Stages 1,2	E – involvement of extra-nodal site
Designation E is used for only patients with limited disease and not for advanced disease	
For bulky disease, documenting the diameter is recommended and not the designation X	

Table 2 International Prognostic Score (IPS) and Indices (IPI) for HL and NHL

	Factors[a]	Risk Group
IPS	Male gender Age >45 Stage IV Hemoglobin <10.5 g/L WBC count >15 x 10^9/L Lymphocyte count <0.6 x 10^9/L or <8% WBC Serum albumin <40 g/L	Risk increasing with each increase in number of adverse factors
IPI	Age >60 Elevated serum LDH ECOG performance status ≥2 Ann Arbor clinical stage III or IV >1 involved extra-nodal disease sites	Low: 0–1 Low intermediate: 2 High intermediate: 3 High: 4–5
Revised IPI	same as IPI	Very good: 0 Good: 1–2 Poor: ≥3
FLIPI	Age >60 Elevated serum LDH Ann Arbor clinical stage III or IV >4 involved nodal disease sites Hemoglobin level <12.0 g/dL	Low: 0–1 Intermediate: 2 High: ≥3

WBC – white blood cell; LDH – lactate dehydrogenase; FLIPI – IPI for follicular NHL
[a]One point given for each factor present

America. Generally, unfavorable disease is considered with larger tumor burden (either bulky mediastinal adenopathy, more nodal groups involved), older age, and "B" symptoms [31, 32]. Approximately 65% of patients with early-stage HL have unfavorable disease [10].

Additional prognostic risk factors have been validated for patients with HL and are used to guide therapy and interpret clinical trials. The International Prognostic Score (IPS) is most commonly used (Table 2) [33], predominantly for patients with advanced-stage III/IV disease. Freedom from progression for 5 years decreases from 84% for those with an IPS of 0 to 42% for those with a score of 5–7 [33]. Gallamini et al. showed that the results of interim [^{18}F]FDG-PET after two cycles of chemotherapy were better than IPS alone for predicting progression-free survival (PFS) in those with advanced HL [34]. This is probably because the results of interim [^{18}F]FDG-PET scan reveal patient-specific chemosensitivity of the tumor, an obvious important factor for good outcome.

Treatment and Follow-Up

The advent of multi-agent chemotherapy in the 1960s beginning with mechlorethamine, vincristine, procarbazine, and prednisone (MOPP) has led to excellent overall response rates and cure of disease in many patients [35–38]. Cure rates are >90% for patients with early-stage and favorable disease, but they are in the 65–70% range for advanced disease. A complete discussion of the evolution of therapy for HL is beyond the scope of this chapter, but general management strategies are presented to place the role of imaging into the therapeutic context.

The treatment choice for early-stage HL aims to achieve cure while balancing the risks of recurrence and late toxicity (i.e., cardiac disease and secondary malignancy). For favorable early-stage HL, either combined chemotherapy and involved-field/involved-site radiation or chemotherapy alone may be appropriate [39–42]. Combined modality therapy improves disease control compared to chemotherapy alone, but studies have not shown differences in overall survival [43, 44]. Shorter courses of chemotherapy may be given and smaller radiation fields applied with combined modality therapy [32, 45]. In the population with favorable early-stage HL, individual patient characteristics, such as age and specific tumor location, guide the decision-making process. For example, in young women sparing radiation to breast tissue is an important consideration.

For unfavorable early-stage HL, combined chemotherapy and radiation is favored over chemotherapy alone, especially for bulky disease [10]. While disease-free survival is also better with combined therapy in this population, the effects on overall survival are less clear. The course of chemotherapy is typically longer (six cycles) for unfavorable, early-stage HL vs. favorable disease [10, 46].

For both early-stage favorable and unfavorable HL, adriamycin, bleomycin, vinblastine, and dacarbazine (ABVD) is the most commonly used initial chemotherapy regimen based on efficacy and toxicity profiles [8, 46–50]. Other initial chemotherapy options are Stanford V and bleomycin, etoposide, doxorubicin, cyclophosphamide, vincristine, prednisone, and procarbazine (BEACOPP). BEACOPP has similar efficacy compared to ABVD, but significantly more toxicity, so it has not been recommended for early-stage disease [46, 51, 52].

Radiation field size has been reduced in recent years to avoid toxicity to normal organs. Many patients now receive involved-site or involved-nodal radiation therapy, which targets the sites of originally involved lymph nodes and considers tumor regression after chemotherapy to spare normal organs. Details are provided in the Guidelines from the International Lymphoma Radiation Oncology Group [45]. Imaging (and increasingly [^{18}F]FDG-PET/CT) is used to optimize these radiation fields. Another goal is lower radiation dose and dose is adjusted based on stage and tumor bulk.

For advanced HL, ABVD has been shown to be superior to MOPP and hybrid regimens [48–50] and is typically given for six cycles. More intensive regimens have been compared to ABVD. The German Hodgkin Study Group trials demonstrated better outcomes with escalated BEACOPP than with ABVD [53], but more acute toxicity and secondary leukemias were seen. Escalated BEACOPP is more widely used in Europe, and NCCN guidelines recommend escalated BEACOPP as an option for advanced HL with IPS >4 [10]. It is not recommended for elderly patients with advanced HL due to acute toxicity [54]. Randomized phase III studies comparing BEACOPP and Stanford V have not shown beneficial results. Initial results from European Organisation for Research and Treatment of Cancer (EORTC) trial number 20012 comparing eight cycles of ABVD ($n = 275$) to four escalated + four standard cycles of BEACOPP ($n = 274$) were presented in 2012 [55]. More relapses were found in the ABVD group and more early discontinuations in the BEACOPP group, but no differences in event-free or overall survival were found between the treatment groups. The randomized Eastern Cooperative Oncology Group (ECOG) trial comparing ABVD to the Stanford V did not show a benefit of Stanford V [56]. The role of radiation therapy to areas of bulky disease in advanced HL is also still uncertain and under investigation.

About one-third of patients with HL are refractory to or relapse after initial therapy and often receive high-dose chemotherapy and stem cell transplant [57]. Despite high response rates post-transplant [58–61], a significant number, 26–65%, of these patients relapse [57, 60–64]. Relapse or decreased survival posttransplant has been associated with a number of risk factors including poor performance status at transplant, chemotherapy-resistant disease, increasing number of failed chemotherapy regimens, more than minimal or bulky disease at transplant, B symptoms at relapse, and extra-nodal disease at relapse [57, 60–64]. Post-transplant, therapy options are limited due to patients' decreased bone marrow reserve. Single-agent chemotherapy, local irradiation, or reduced intensity of chemotherapy followed by allogeneic stem cell transplant can be considered, but therapy is most often given with palliative intent.

Several drugs like bendamustine, lenalidomide, and everolimus have shown activity in relapsed/refractory HL and are being evaluated as second- and third-line therapies [65–67]. The antibody-drug conjugate brentuximab vedotin, which targets CD30, has been approved for treatment of refractory/relapsed HL patients who do not respond to or are not candidates for transplant [68]. Other novel agents such as immune checkpoint inhibitors like anti-programmed death receptor-1 (PD-1) (nivolumab and pembrolizumab) monoclonal antibodies [69] are promising and under investigation.

lpHL has a different, more indolent natural history, and late relapses are more likely to occur compared to cHL [70]. Non-bulky, early-stage (I/II) lpHL without B symptoms is typically treated with radiation alone. Other early and advanced stages may be treated with combinations of chemotherapy, radiation, and/or rituximab. There is no standard chemotherapy regimen for lpHL due to a lack of randomized controlled trials comparing different regimens [10]. Because lpHL routinely expresses the CD20 antigen, rituximab used as a single agent has been studied, and very encouraging response rates have been reported [71–73]. Additional follow-up is needed to further assess the durability of the responses.

Data are limited regarding optimal follow-up of patients with HL after therapy. Generally, history, physical exam, and laboratory evaluations are performed at increasingly spaced intervals up to 5 years after completion of initial treatment. The NCCN guidelines recommend very limited imaging – CT once during the first 12 months and then as clinically needed. The use of [^{18}F]FDG-PET/CT in follow-up is discussed further below. Additional careful follow-up is needed to monitor for late effects of treatment.

Very important considerations in treating patients with HL are the long-term side effects of external beam radiation (e.g., hypothyroidism, premature menopause, carotid and coronary artery stenosis, and secondary breast cancer) and chemotherapy (e.g., infertility, cardiomyopathy, secondary leukemia, and osteoporosis) [8]. Increased risk of death persists for more than 25 years in patients with HL due to late-term treatment complications rather than HL itself [74, 75]. Strategies using interim PET for risk-adapted therapy may be advantageous for this purpose and for guiding dose intensification for those patients who are more likely to relapse and dose de-intensification in those responding well. This is discussed in the section on PET and risk-adapted therapy.

Non-Hodgkin Lymphoma

Epidemiology and Etiology

In 2015, the estimated number of new cases of NHL in the United States was 71,850, and NHL is the sixth most common cancer in men and the fifth most common in women [3]. NHL resulted in about 19,790 deaths from the disease in 2015 – ranking as the ninth and sixth most common cause of cancer deaths for men and women, respectively [3]. The incidence of NHL has been rising since the 1970s, most markedly in the elderly population. The overall increase in incidence is out of proportion to that expected due to the aging population alone, and the reasons for this are mostly unclear. Despite this, the death rate from NHL has been decreasing since 1997 due to improvements in therapy [76]. Most cases of NHL occur in individuals greater than 60 years of age.

Alterations of the immune system, certain viruses, and environmental exposures have been implicated in the etiology of NHL, with varying degrees of evidence. For example, both immune suppression (e.g., posttransplant) and immune stimulation (e.g., Sjogren's syndrome, rheumatoid arthritis) have been associated with increased risk of NHL [77–79]. Viral-lymphoma associations have also been suggested. Environmental exposures linked to NHL include organochlorine-based pesticides, organic solvents, and wood products.

Pathology and NHL Subtypes

NHL consists of a heterogeneous group of diseases that arise from malignant transformation of lymphoid tissues. Initial classification schemes were based primarily on morphology. Advancements in immunologic, molecular, and genetic laboratory techniques have led to several updates and revisions of classification systems for NHL [80–82]. The ability to identify cell surface markers, cytogenetic markers, and molecular markers led to the recognition that subtypes of NHL depend on the stage of maturation when malignant transformation of the lymphocyte occurs as well as the location of the "normal lymphocyte counterpart" within the lymph node.

The currently used World Health Organization classification uses morphologic, immunophenotypic, genetic, and clinical features to define distinct NHL subtypes and was revised in 2008 [81, 82]. The revision further defined and refined definitions of early/in situ lesions, the relevant distinctions in subtypes based on age, and borderline diagnoses (hard to classify as one subtype versus another due to atypical or overlapping features). This is nicely reviewed by Jaffe [81]. The NHL subtypes are grouped by lineage (B-cell or T-cell/natural killer (NK) cell) and the maturity of the cell from which the malignancy is derived (Table 3). Most (80–85%) are B-cell neoplasms [9]. NHL may behave in a manner that, if left untreated, is indolent, aggressive, or very aggressive, and the aggressiveness of a tumor within a histologic subtype can be variable between patients so it is not included in the official classification scheme. Diffuse large B-cell lymphoma (DLBCL) and follicular lymphoma are the most common NHL subtypes in the United States.

Genetic Features

Gene expression profiling (GEP) studies are used to diagnose and classify NHL. Based on GEP, DLBCL is classified into germinal center B-cell type and activated B-cell type [83, 84]. The activated B-cell type has been shown to have inferior 5-year survival rates compared to the germinal center B-cell type [85]. DLBCL has chromosomal translocations, the three most common involving

Table 3 World Health Organization Classification of NHL

B-cell lymphomas	T/NK-cell lymphoma
Precursor B lymphoblastic lymphoma/leukemia	Precursor T-cell lymphoblastic lymphoma
Mature B-cell lymphoma	Mature T-cell lymphoma
Chronic lymphocytic leukemia/small cell lymphoma	Adult T-cell lymphoma/leukemia
Lymphoplasmacitic lymphoma	Mycosis fungoides (Sezary syndrome)
Splenic marginal zone lymphoma	Primary cutaneous anaplastic large cell lymphoma
MALT-lymphoma	Anaplastic large cell lymphoma
Normal marginal zone lymphoma	Peripheral T cell lymphoma, unspecified
Follicular lymphoma	Angioimmunoblastic T-cell lymphoma
Mantle cell lymphoma	Extranodal NK/T cell lymphoma, nasal type
Diffuse large B-cell lymphoma	Enteropathy-type T-cell lymphoma
Mediastinal (thymic) large B-cell lymphoma	Hepatosplenic T-cell lymphoma
Intravascular large B-cell lymphoma	Subcutaneous panniulitis-like T cell lymphoma
Primary effusion lymphoma	Blastic NK cell lymphoma
Burkitt's lymphoma/leukemia	

the oncogenes BCL-2, BCL-6, and c-MYC. Double-hit lymphomas refer to DLBCL with translocations of both c-MYC and BCL-2 or BCL-6 and carry a worse prognosis compared to other types of DLBCL [86]. Double-expressor lymphoma refers to amplification of c-MYC and BCL-2 by mechanisms other than translocation [86].

Clinical Presentation, Evaluation and Staging, and Prognosis

NHL most commonly presents as painless adenopathy, similar to HL, but the rapidity of tumor growth and the exact presentation varies with histologic subtype and aggressiveness of the tumor. NHL spreads in a manner less predictable than HL (more hematogenously than by contiguous nodal spread) and is more likely to involve extra-nodal sites than HL. Systemic "B" symptoms are found in 40% of patients, more common in the aggressive than indolent NHL subtypes [87]. Lymphomatous infiltration of the bone marrow may result in cytopenias, and the presentation of infiltration of other organs may be site specific.

A core or excisional biopsy is usually needed for diagnosis in order to provide sufficient tissue. Fine needle aspiration alone and cytology often do not provide enough tissue for morphologic, immunologic, and genetic assessment. After diagnosis, the initial work-up is similar to that of HL. History and physical exam, laboratory tests, and imaging are performed for staging and assessing organ function prior to treatment. Staging is best performed with PET for NHL subtypes that are typically [^{18}F]FDG avid (i.e., DLBCL). Indolent NHL may sometimes have low metabolic activity, and PET for staging may be less helpful in some of these instances. Variability of [^{18}F]FDG uptake and staging with PET in NHL are discussed further below. Bone marrow biopsy is no longer required for all patients with NHL for staging, but is reserved for those with DLBCL and a negative [^{18}F]FDG-PET/CT in the marrow or those with low-[^{18}F]FDG-avidity lymphomas [28]. Laboratory testing is primarily used for prognostic scoring and to test baseline organ function prior to treatment.

Currently, NHL is also staged according to the modified Ann Arbor staging system (Table 1) [28, 88]. In the Lugano classification, four stages remain, but the subscript E is used for only when there is limited extra-nodal disease and it is not relevant for patients with advanced-stage disease. The designation "X" is replaced by largest tumor diameter for describing bulky disease, and the subdivision of patients based on constitutional symptoms is not incorporated for staging NHL (Table 1). The Lugano classification is discussed later with more detail.

The histopathologic subtype primarily determines the prognosis for patients with NHL. Within each subtype of NHL, disease-specific genetic alterations and molecular markers may provide additional information for predicting outcomes and guiding management. The International Prognostic Index (IPI) was developed in patients with aggressive NHL (Table 2) [89]. Four risk groups were identified (low = IPI 0–1, low intermediate = IPI 2, high intermediate = IPI 3, and high = IPI 4–5) with decreasing 5-year overall survival with increasing IPI score (73%, 51%, 43%, 26%, respectively) [89]. The original IPI was developed and validated prior to the routine use of rituximab in regimens to treat NHL. Sehn et al. [90] retrospectively evaluated the use of the IPI in 365 patients with DLBCL treated with rituximab, cyclophosphamide, doxorubicin, vincristine, and prednisolone (R-CHOP). Using the original IPI groupings, only two (not four) risk groups were identified. The revised IPI redistributed the risk groups (very good = IPI 0, good = IPI 1–2, poor IPI 3–5), and this model was felt to better predict outcome. In the rituximab era, the risk group with 4-year survival $<$50% was no longer identified [90].

Additional variations of the IPI have been developed, including age- and stage-adjusted IPIs to account for the variability of prognoses within these groups [89, 91]. The enhanced IPI (NCCN-IPI) was reported recently in a study of 1,650 patients to discriminate low- and high-risk subgroups better than IPI, a finding validated in another independent cohort of 1,138 patients [92]. The usefulness of the IPI also has been shown to provide prognostic information at the time of relapse [93–96].

There are two versions of the IPI for patients with indolent follicular NHL (FLIPI 1 and 2). Using the first FLIPI version, overall survival decreases with increasing FLIPI score based on three risk groups (low, intermediate, and high) and provides prognostic information for this population, even in the setting of rituximab [97, 98]. Validation of FLIPI 2 is ongoing.

Treatment and Follow-Up

As with the natural history and prognosis of NHL, treatment varies and depends on the specific NHL subtype. Recommendations for detailed management strategies are provided by a panel of experts in the NCCN guidelines [99]. Excellent review articles are available for specific questions and agents for the treatment of NHL, including new biologic agents and treatment strategies [100–105]. We will review overall management strategies for the most common NHLs – DLBCL and follicular NHL. These are also probably the most commonly encountered by the nuclear medicine physician or radiologist. Discussion of treatment for the other subtypes is beyond the scope of this chapter and can be found elsewhere [99, 106].

Indolent NHL is generally considered incurable at present. Patients respond to therapy, but may have multiple relapses and long disease-free or progression-free periods. A major question for those with indolent NHL is when to initiate therapy. Several studies have shown that "wait and watch" is a valid strategy even in the rituximab era outside of clinical trials in patients with advanced-stage low-tumor burden follicular lymphoma [107, 108].

General indications for treatment of indolent NHL are symptoms, organ compromise, rapid or steady progression of tumor, bulky disease, cytopenias due to lymphoma, and patient preference or eligibility for a clinical trial [99]. The treatment plan and aggressiveness of the regimen used are usually tailored for the patient's disease and clinical status. Common regimens include purine analogs, alkylators, anthracyclines, and rituximab alone or in combination with chemotherapy. Selected patients with bulky early-stage disease may be treated with radiotherapy alone.

Sousou and Friedberg nicely reviewed the pivotal studies that investigated the role of rituximab in patients with indolent lymphoma [109]. Treatment with rituximab alone [110–112] and with chemotherapy [113–116] has improved overall response rates and PFS for patients with indolent NHL in both the front line and maintenance settings [117]. There is a suggestion toward improved overall survival [118, 119], which has been confirmed in long-term follow-up data [113]. Patients who respond to first-line therapy can be treated with maintenance rituximab up to 2 years [120]. Consolidation with radioimmunoconjugates in patients initially treated with chemotherapy alone has been shown to improve the quality of remission but not better than initial chemoimmunotherapy alone [121–123]. Areas of continued study for rituximab are use with immune stimulators to improve efficacy, optimal schedule for maintenance dosing, and resistance mechanisms. Other monoclonal antibodies to CD20 are also being developed and investigated [124].

In the relapsed setting, indolent NHL may be treated in a similar manner to initially untreated disease. Overall response rates to rituximab in the relapse setting range from 40% to 60% with complete responses in 10–20% and median progression-free survival (PFS) of 8–24 months [112, 125, 126]. Radioimmunotherapy is more active and produces better results than unlabeled antibody alone, and its use in relapsed (as well as the front line) indolent NHL is discussed in a separate chapter [121–123, 127, 128]. Autologous and allogeneic transplants have been performed safely and with antitumor activity prolonging the overall survival and progression-free survival [129, 130]. If there is a role for transplant in indolent lymphoma, the optimal role is still being defined.

For aggressive B-cell NHL, systemic chemotherapy is the mainstay of treatment. Diffuse large B-cell NHL is the most common aggressive NHL and is discussed as an example. The present regimen of choice is R-CHOP [131–133]. For non-bulky early-stage disease, the NCCN

guidelines recommend three cycles of R-CHOP with IFRT or six cycles of R-CHOP with or without IFRT [88]. Higher doses of IFRT (30–40 Gy) are added to six cycles of chemotherapy for early-stage, bulky disease. The preference at major centers is to treat patients with advanced disease on a clinical trial; otherwise, a full course of chemotherapy is recommended [99, 131]. For germinal center B-cell type DLBCL patients treated outside the setting of a clinical trial, the choice of treatment is R-CHOP-21 (R-CHOP given every 21 days). Two randomized phase III trials have shown that dose-dense R-CHOP-14 does not improve the outcome compared to R-CHOP-21 [134, 135]. Clinical trials of R-CHOP with novel agents like lenalidomide, ibrutinib, and bortezomib are available for patients with advanced activated B-cell-type DLBCL [136–138]. For patients with double-hit DLBCL, dose-adjusted EPOCH-R has been shown to be associated with better outcome than R-CHOP [139, 140]. The NCCN recommends several alternate first-line regimens for frail patients [88].

The role of high-dose therapy and transplant for initial therapy of aggressive NHL is controversial and the subject of clinical trials. Currently, autologous hematopoietic cell transplantation (HCT) is not recommended after initial treatment of DLBCL as there is no survival advantage with HCT [141]. FDG-PET/CT is being used as a prognostic indicator in several of these risk-adapted therapy trials, and these studies are discussed in the section on risk-adapted therapy. In the relapsed setting, there are several salvage chemotherapy regimens that may be used with the ultimate goal of transplant in those patients who respond.

T-cell NHL accounts for ~15% of all lymphomas. Most T-cell lymphomas are clinically aggressive, and with a few exceptions (anaplastic large cell, early-stage T-/NK cell, nasal), most are incurable. CHOP and CHOP-based therapy may be used for initial treatment in these settings with or without radiotherapy [142–144]. Certain subtypes of T-cell NHL can be treated with consolidation radiation or HCT [88]. The optimal regimen for treatment of adult T-cell leukemia/lymphoma is yet to be established. Other approaches have been investigated for T-cell NHL subtypes including investigations of biologic agents (bevacizumab [145] and histone deacetylase inhibitors [146]) and agents against other lymphocyte surface antigens (alemtuzumab [147], mogamulizumab [148], brentuximab [149]).

Follow-up for patients with NHL also depends on the subtype of NHL, treatment intent, and the patient's clinical symptoms. For those treated with curative intent, history and physical exam, laboratory testing, and imaging occur with decreasing frequency over the first 5 years and then annually. Patients must be monitored for late complications of therapy, which are similar to those discussed for HL.

Nuclear Medicine Imaging for Lymphoma

Nuclear medicine imaging has had a role in the evaluation of patients with lymphoma since the 1970s [150]. Gallium-67 imaging preceded [^{18}F]FDG-PET/CT as the functional imaging technique for staging, monitoring response to therapy, and providing prognostic information [151–157]. A negative gallium-67 scan favored a better outcome after treatment and as soon as after one cycle of chemotherapy in both HL and NHL [153–157]. Other agents were also evaluated, for example, indium-111 bleomycin, but they were not shown to be more efficacious than gallium-67 [158, 159].

Today, gallium scanning has been replaced with [^{18}F]FDG-PET/CT imaging, which offers higher-resolution images; higher sensitivity for disease detection, particularly for lower-grade lymphomas; lower radiation doses; and a shorter time from injection until imaging is performed [159–164]. Bone scanning has also been used for detection of lymphomatous involvement in bone; however, these typically marrow-based lesions may be falsely negative on bone scan. In the PET era, bone scanning is considered if patients present with bone pain and a PET scan is not available [8]. [^{18}F]FDG-PET/CT is now well integrated into management strategies for lymphoma. The current roles of PET (disease

detection, staging, and posttreatment assessment) are reviewed. Numerous ongoing clinical trials investigating the role of interim PET, obtained after one to four cycles of chemotherapy, for risk-adapted therapy will be discussed.

[^{18}F]FDG-PET for Detecting and Histologic Grading of Lymphoma

Most lymphomas accumulate [^{18}F]FDG [2]. Weiler-Sagie et al. [165] readdressed this issue in a large retrospective study of 766 patients with newly diagnosed lymphoma referred for initial staging with [^{18}F]FDG-PET/CT. [^{18}F]FDG-avid disease was found in all patients with HL, 94% with aggressive NHL and 83% with indolent NHL. The histologic subtypes of lymphoma less likely to be [^{18}F]FDG-avid were small lymphocytic lymphoma (% [^{18}F]FDG avid – 83%), enteropathy-type T-cell lymphoma (67%), extranodal marginal zone lymphoma (67%), MALT marginal zone lymphoma (54%), lymphomatoid papulosis (50%), and primary cutaneous anaplastic large T-cell lymphoma (40%) [165].

To some extent, the location of lymphomatous involvement may also hinder its detection regardless of histopathologic subtype. The cutaneous location accounted for one-third of the 48 non-[^{18}F]FDG-avid cases in Weiler-Sagie et al.'s study [165], including two with DLBCL. The other most common locations of non-[^{18}F]FDG-avid disease were bowel, bone marrow, effusions, and mucosal surfaces [165]. Clearly tumor burden has an effect, and low tumor burden can be falsely negative.

Weiler-Sagie et al. did not address the degree of [^{18}F]FDG uptake in the histologic subtypes of lymphoma, but this has been done previously [165]. Broadly speaking, low-grade lymphomas take up less [^{18}F]FDG than high-grade lymphomas [166–168]. Standardized uptake values (SUVs – a semiquantitative measure of tumor metabolism) of greater than 10 had a high likelihood of being aggressive and excluded low-grade lymphoma with a specificity of 81% in one study of patients with non-Hodgkin lymphoma [168]. Despite this, there is substantial overlap of [^{18}F]FDG uptake between lymphoma grades with some low-grade tumors exhibiting high levels of [^{18}F]FDG uptake. The level of [^{18}F]FDG uptake likely lies along a continuum based on the histologic grade of the lymphoma, but in an individual patient, the level of [^{18}F]FDG uptake is probably not an adequate single surrogate marker for histologic grading of lymphoma.

One exception may be when a disproportionately high accumulation of [^{18}F]FDG is seen in a single lesion compared to the others in a given patient (Fig. 1). This may be indicative of transformation of a low-grade lymphoma to a high-grade lymphoma in the same patient, and [^{18}F]FDG-PET and PET/CT could help guide biopsies of these lesions [168]. Bruzzi et al. [169] retrospectively evaluated 37 patients with chronic lymphocytic leukemia (CLL), with and without signs

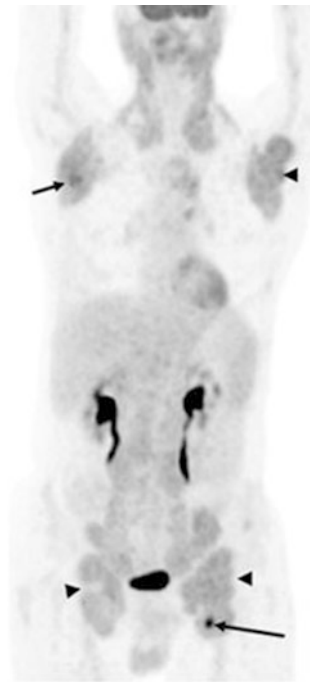

Fig. 1 A 65-year-old man with a history of chronic lymphocytic leukemia/small lymphocytic lymphoma (CLL/SLL). There is mild to moderate [^{18}F]FDG uptake in bilateral cervical, axillary, para-aortic, iliac, and inguinal lymph nodes consistent with indolent NHL (*arrowheads*). Within the left inguinal adenopathy, there is a focus of more intense [^{18}F]FDG uptake (arrow, $SUV_{lbm\text{-}max} = 10.6$). Biopsy of the more intense focus in the inguinal region revealed Richter's transformation. Another area of more moderate uptake suspicious for early transformation can be seen in the right axilla (*arrow*)

and symptoms of transformation, with PET/CT. Using an SUV_{max} cutoff of 5, the negative predictive value of PET for detecting transformation was high (97%); however, the specificity and positive predictive value were low (80% and 53%, respectively) [169].

Bodet-Milin et al. [170] used PET/CT to prospectively guide biopsy in 38 patients with indolent NHL ($n = 23$ follicular, $n = 10$ CLL, $n = 2$ Waldenstrom macroglobulinemia, $n = 3$ marginal zone NHL) and clinical suspicion for transformation. Biopsy was obtained at the most accessible site with the highest SUV_{max}, and 17 patients had histologic transformation on biopsy. The median SUV_{max} and gradient SUV_{max} (highest SUV_{max}-lowest SUV_{max}) were higher for those with histologic transformation. Using receiver operator curve analysis, an SUV_{max} threshold of 14 was optimal for identifying transformation (sensitivity/PPV ~ 94%, specificity/NPV ~95%) [170]. As expected, sensitivity or specificity could be improved one way or the other with higher and lower thresholds. Bodet-Milin's study differed from Bruzzi's in several regards; all patients had a clinical suspicion of transformation, and higher threshold values for transformation likely decreased the false-positive rate. They suggest that a higher threshold may be reasonable for patients with follicular versus chronic lymphocytic leukemia/small lymphocytic lymphoma (CLL/SLL), as CLL/SLL typically has less [^{18}F]FDG uptake at baseline [170]. These data together suggest that PET may be useful for detecting transformation, but tissue confirmation is still required for confirmation at the present time. It should be noted that SUV in all nonfat tissues can be elevated in obese patients; thus, the SUV of 10 is a rough guideline, only.

[^{18}F]FDG-PET for Initial Staging of Lymphoma

It is well established that [^{18}F]FDG-PET is superior to Ga^{67} scintigraphy [160–164] and improves primary staging of lymphoma as compared to CT [171–175]. For nodal status, this is primarily due to the ability of [^{18}F]FDG-PET to detect lymphoma in normal-sized lymph nodes that would be considered benign by CT size criteria. [^{18}F]FDG-PET also detects more extra-nodal lesions, for example, in the liver, spleen, bone, and lung, than CT does (Fig. 2), with less radiation exposure to the patient.

The Lugano classification recommends [^{18}F]FDG-PET/CT as the imaging test of choice for staging all [^{18}F]FDG-avid nodal lymphomas. Contrast-enhanced CT is recommended for the staging of all non-[^{18}F]FDG-avid lymphomas. The modified Ann Arbor staging is still used in the Lugano classification [28] (Table 1). The suffixes A and B for constitutional symptoms are recommended only for HL. The designation E is used for only patients with limited disease and not for advanced disease. For bulky disease, documenting the diameter is recommended and not the designation X (Table 1).

Although biopsy is the gold standard to detect lymphomatous involvement in the bone marrow, bone marrow biopsy and [^{18}F]FDG-PET have been reported to be approximately 80% concordant [173, 176, 177]. The Lugano classification does not recommend bone marrow biopsy in HL if [^{18}F]FDG-PET/CT is performed [28]. This recommendation is based on several studies showing that [^{18}F]FDG-PET/CT is sensitive for detecting involvement of bone marrow in HL [178, 179]. Sampling error on biopsy may result in a "false-positive" PET study, which is actually true positive (Fig. 3). El-Galaly et al. showed that only one-third of 454 HL patients with focal skeletal lesions on [^{18}F]FDG-PET/CT were positive on bone marrow biopsy [178].

In another study, bone marrow involvement could be confirmed in seven of ten patients with negative iliac crest biopsies by [^{18}F]FDG-PET-directed re-biopsy ($N = 4$) or anatomic imaging ($N = 3$) [177]. A meta-analysis investigating the use of [^{18}F]FDG-PET for detecting bone marrow disease revealed sensitivities in the 54–74% range and specificities in the 91–95% range [180]. Only a small number of studies evaluating Hodgkin lymphoma were included. In the case of DLBCL, Lugano classification recommends bone marrow biopsy only in patients without marrow involvement on [^{18}F]FDG-PET/CT. Though [^{18}F]FDG-PET/CT can underdiagnose low-volume disease in DLBCL, several studies have consistently

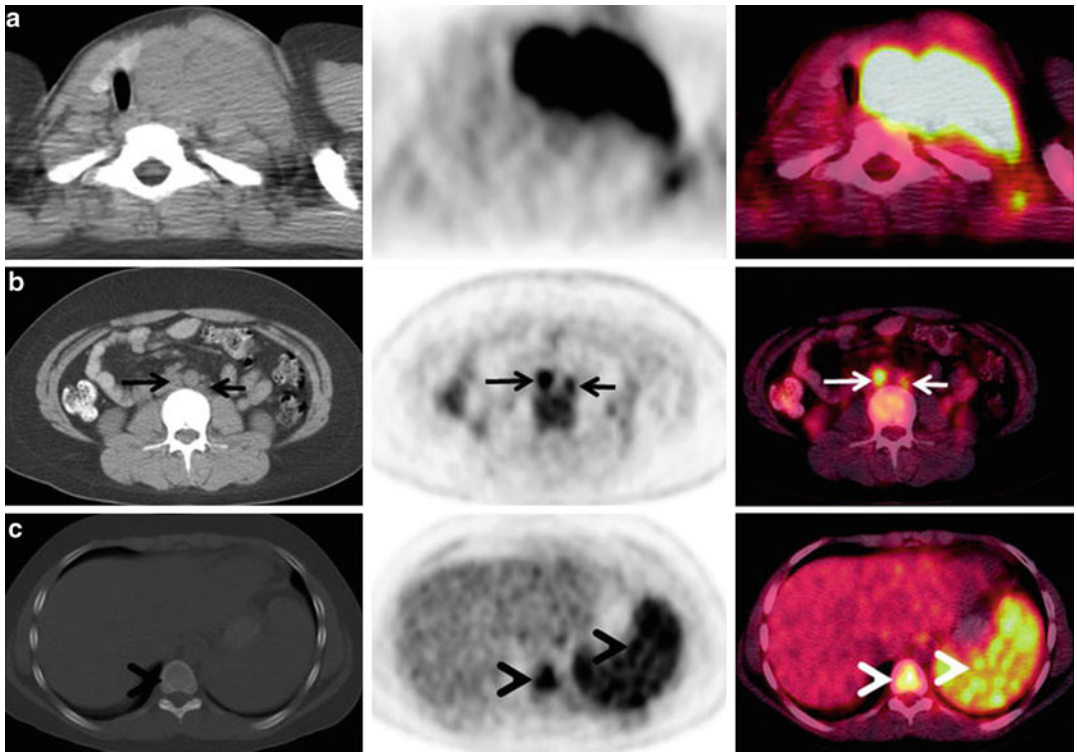

Fig. 2 A 34-year-old woman with Hodgkin lymphoma presented for staging with a PET/CT scan. The diagnostic CT scan with intravenous contrast was done prior to the PET scan and showed enlarged lymph nodes in the mediastinum extending to but not below the aortic arch (not shown). This was consistent with stage II disease. The PET/CT scan shows that the mediastinal mass has intense [^{18}F]FDG uptake (**a**). The PET scan also showed numerous [^{18}F]FDG-avid lymph nodes below the diaphragm (**b**, *arrows*) and in the bone marrow and spleen (**b**, **c**, *arrowheads*). The patient was upstaged to stage IV and received systemic chemotherapy (for **a**, **b**, and **c** – left, CT; center, PET; right, fused PET/CT)

shown that [^{18}F]FDG-PET or PET/CT has better diagnostic performance than bone marrow biopsy for diagnosing marrow involvement [181–183]. In a study of 133 patients with newly diagnosed DLBCL, [^{18}F]FDG-PET/CT was more sensitive (94% vs. 24%) and accurate (98% vs. 81%) than bone marrow biopsy [182]. Bone marrow biopsy is recommended in all other lymphoma histologies [28].

When evaluating an abnormal focus of increased [^{18}F]FDG uptake in the bone, it is important to note that the concurrent CT scan may appear normal up to 50% of the time [184] and the context and entire distribution of uptake must be considered. In the lymphoma population in the study by Nakamoto et al., none of the marrow lesions were seen on CT, but the population was small [184]. [^{18}F]FDG-PET is more likely to detect bone marrow disease when greater than 30% of the marrow is involved. False-negative [^{18}F]FDG-PET scans for bone marrow disease (PET negative, biopsy positive) occur if less bone marrow is involved, in lower-grade histologies, or if the primary nodal disease is not [^{18}F]FDG-avid. Misinterpretation of diffuse [^{18}F]FDG uptake in the marrow due to concurrent systemic illness or recent administration of hematopoietic growth factors can potentially lead to false-positive [^{18}F]FDG-PET scans. This can be avoided by a carefully elicited clinical history.

The addition of [^{18}F]FDG-PET to lymphoma staging procedures correctly alters stage and leads to changes in management in 8–48% of cases [171, 173, 175, 185, 186]. Patients are upstaged more often and consequently receive more

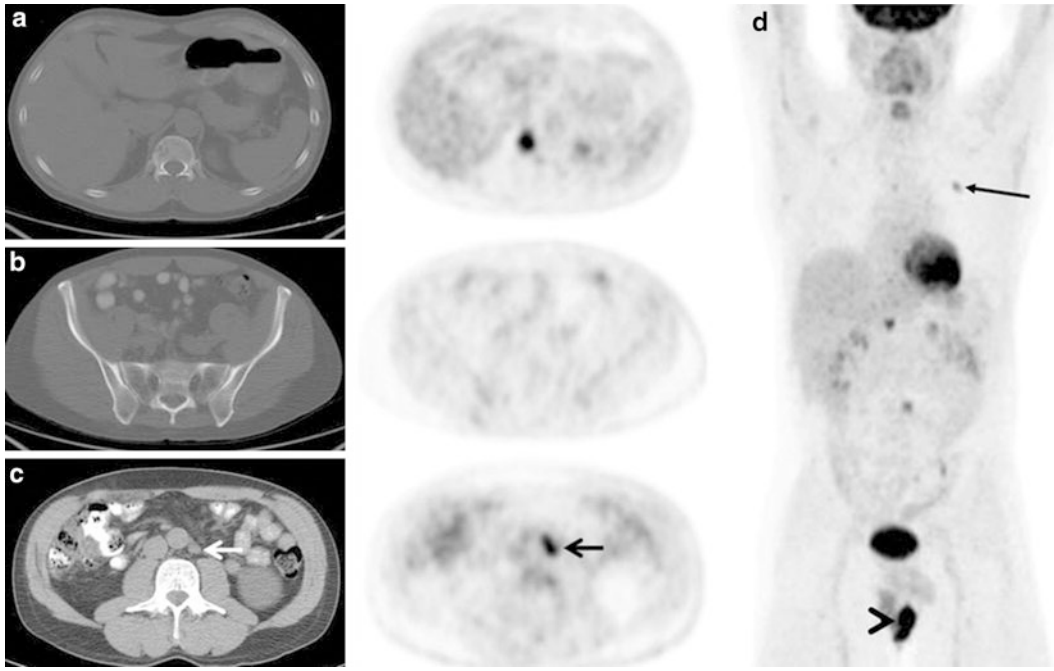

Fig. 3 A 55-year-old man with diffuse large B-cell lymphoma presented for a staging PET/CT scan. A focus of intense [^{18}F]FDG uptake fusing to lytic changes in the right T11 vertebral body is seen (**a**). Biopsy of this lesion confirmed diffuse large B-cell lymphoma. Bone marrow biopsy was negative for lymphomatous involvement. Not surprisingly, the PET scan in the region of standard iliac crest biopsies showed normal marrow uptake. The PET and marrow biopsy were discordant in this case for lymphomatous involvement. Other sites of disease in the marrow were also found in the left rib (**d**, maximum intensity projection image, *arrow*). Additional extra-nodal disease was found in a scrotal mass (**d**, maximum intensity projection image, *arrowhead*), and the only nodal disease was a 1.5 × 1.2 cm left para-aortic lymph node with intense [^{18}F]FDG uptake (**c**, *arrows*). Overall, the findings were consistent with stage IV disease (**a**, *top row*; **b**, *middle row*; **c**, *bottom row*. For **a**, **b**, and **c** – left, CT; right, PET)

aggressive initial therapy; however, downstaging also occurs (Fig. 4). The inclusion of [^{18}F]FDG-PET in the primary staging of lymphoma has substantial impact on patient care. Although this has also been shown to be true for low-grade follicular NHL, the role of [^{18}F]FDG-PET in the staging of other indolent NHLs (i.e., CLL/SLL) may be more limited [187–190].

[^{18}F]FDG-PET/CT Versus PET Alone

A majority of studies investigating the use of metabolic imaging in lymphoma have evaluated [^{18}F]FDG-PET alone. Tatsumi et al. [191] reported that combined [^{18}F]FDG-PET/CT imaging may be better than either modality alone. In 53 patients with lymphoma, 48 of 1,537 findings were discrepant between PET and CT; 40 were correct PET findings, 5 were correct CT findings, and 3 remained uncertain. Nine patients were only staged correctly with PET/CT versus CT alone [191]. Allen-Auerbach et al. [192] found that PET/CT was more accurate than PET alone for the detection of lymphoma (94% versus 84%, respectively). PET/CT improves lesion localization, allows detection of lesions that might be missed by either modality alone, and provides more reliable tumor measurements. Though contrast-enhanced CT with PET can help in improving the sensitivity of detecting nodes and other clinically relevant findings, the impact on patient management is very minimal [193–195]. However, the Lugano classification still recommends contrast-enhanced CT for accurate nodal assessment in the setting of clinical trials, radiotherapy planning, and vascular thrombosis [28].

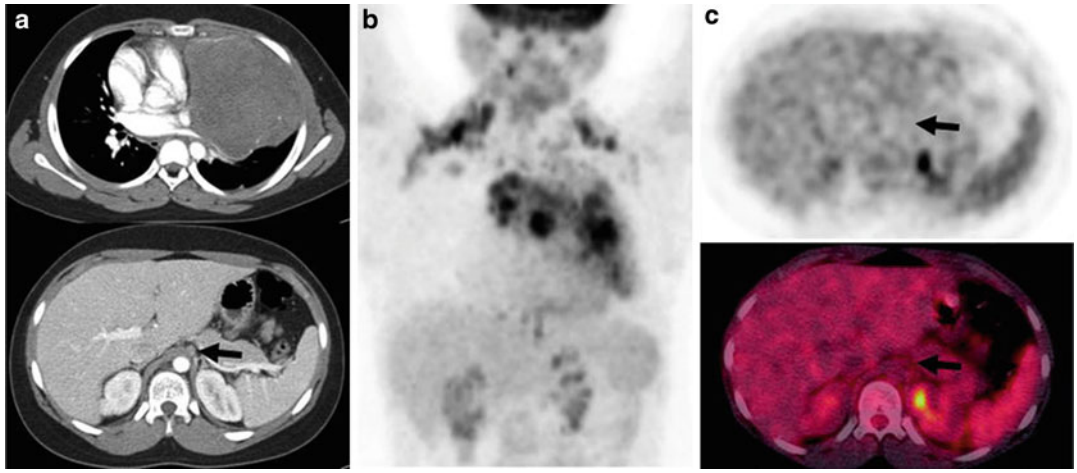

Fig. 4 A 26-year-old man with Hodgkin lymphoma underwent staging procedures. A diagnostic CT scan with intravenous contrast shows the large mediastinal mass (**a** – *right top* and *bottom rows*). There was a borderline abnormal size celiac axis lymph node suspicious for stage III disease (**a** – *bottom row*, *arrow*). The PET/CT scan shows abnormal uptake in the mass and nodes above the diaphragm (**b**), but no abnormal uptake in the celiac axis node below the diaphragm (**c**, *left top* and *bottom rows*, *arrows*). Physiologic renal excretion of [^{18}F]FDG is also seen in the posterior and medial left upper quadrant. The PET downstaged the patient from stage III to stage II, and he received a short course of chemotherapy and radiotherapy (**a**, left column – transaxial IV contrast CT scan slices; **b**, center column – coronal PET image; **c**, right column – transaxial PET (*top*) and fused PET/CT (*bottom*) images)

Post-Therapy Response Assessment by [^{18}F]FDG-PET and PET/CT

Residual masses on anatomic imaging in patients with lymphoma are common post-therapy, but do not always indicate the presence of active malignancy [196]. A major advantage of [^{18}F]FDG-PET is its ability to detect functionally viable tumor cells within the mass, distinguishing active lymphoma from fibrosis/necrosis. The information gained from post-therapy [^{18}F]FDG-PET also provides prognostic information [175, 197–201]. Patients with PET-positive disease post-therapy (Fig. 5) have lower 1- and 2-year progression-free and overall survival rates (0–54%) than those who are PET negative (83–95%) (Fig. 6), regardless of the presence of a residual mass on CT. PET positivity post-therapy predicts subsequent relapse. Therefore, the results of post-therapy [^{18}F]FDG-PET scan have important therapeutic implications.

Despite its improved prognostic implications, a negative post-therapy PET scan does not exclude the presence of residual microscopic disease that falls below the resolution of the PET scanner [175, 197–201]. The resolution of modern PET scanners falls between 0.5 and 1.0 cm [202] which converts to about 10^8–10^9 tumor cells [203]. Patients who are PET negative with a residual mass are more likely to recur than those who are PET negative without residual mass [175, 197–201].

The optimal time to obtain a post-therapy PET is a frequent question of referring oncologists, but the answer is not completely resolved. A minimum of 10 days post-chemotherapy has been recommended to avoid false-negative scans due to the early treatment effect of "stunning" [204]. Longer and more variable times post-external beam radiation have been suggested [205], and optimal interval times post-radioimmunotherapy are beginning to be investigated and discussed in the chapter on radioimmunotherapy [206, 207].

Integration of [^{18}F]FDG-PET and PET/CT into Tumor Response Criteria

[^{18}F]FDG-PET/CT is now an integral component of assessing lymphoma response to therapy. Historically, the first major criteria for assessment of

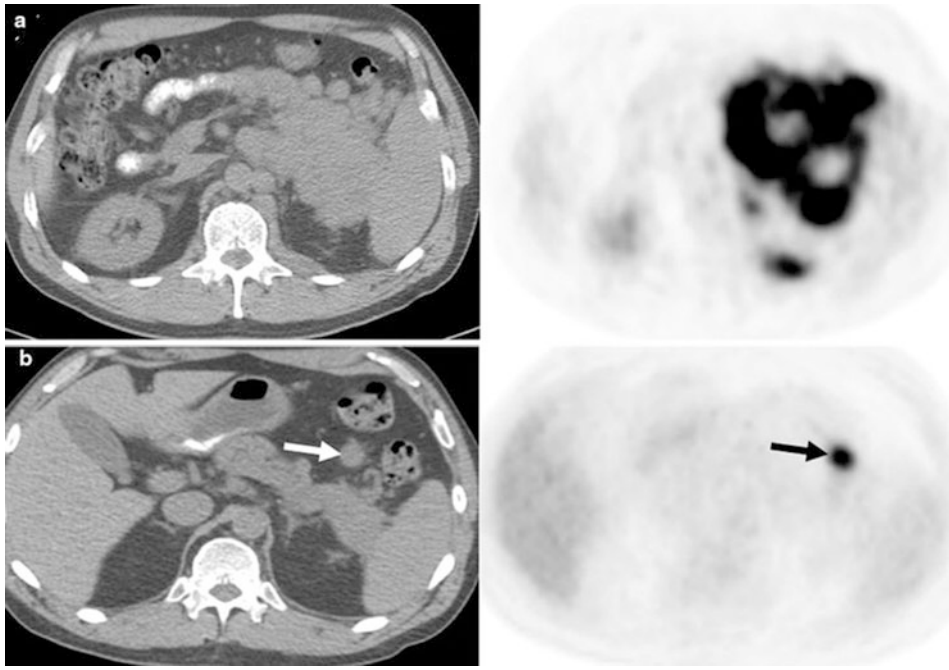

Fig. 5 Pre- and post-therapy PET scans in a patient with diffuse large B-cell lymphoma. The pre-therapy PET scan shows intense [^{18}F]FDG uptake in a left upper quadrant mass, adjacent nodules, and left paravertebral regions (**a**, *top row*). After six cycles of R-CHOP, a 2.3 cm nodule remained in the left upper quadrant with intense [^{18}F]FDG uptake (**b**, *bottom row*, *arrows*) consistent with residual active lymphoma (positive post-therapy PET scan). A positive post-therapy PET scan is associated with a poor prognosis (for **a** and **b** – left, CT; right, PET). In the new Lugano classification and Deauville 5-point scale, this would be rated at score of 5

treatment response in lymphoma were proposed by the International Working Group (IWG) in 1999. Five categories of response were defined based on CT including the category of "complete remission – unconfirmed" for cases with post-therapy residual masses. These IWG criteria [208] were revised in 2007 to include a post-therapy assessment by [^{18}F]FDG-PET [209] based on the numerous studies showing the predictive value of the post-therapy [^{18}F]FDG-PET scan and a retrospective, but pivotal, study in 54 patients with aggressive NHL [210]. In this study, the integrated PET and IWG response criteria more accurately classified lymphoma response by identifying a subset of partial responders by IWG criteria who had a complete metabolic response by [^{18}F]FDG-PET (i.e., PET negative) and a more favorable prognosis [210]. The integrated criteria were subsequently found to be applicable to indolent NHL and HL [211, 212]. At the time of this writing, the most current version of the criteria is the Lugano classification [28].

The Lugano classification was developed to improve both the staging and response criteria for HL and NHL following a workshop held at the 11th International Conference on Malignant Lymphoma in Lugano, Switzerland, in June 2011 and a subsequent workshop at the 12th International Conference on Malignant Lymphoma in 2013 [28].

Although several studies showed the predictive value of interim [^{18}F]FDG-PET/CT (after two to three cycles of chemotherapy) [213–215], it was increasingly realized that the interobserver variability in interpreting the scans and the use of the revised IWG criteria, which were originally designed for end-of-therapy evaluation, resulted in suboptimal evaluation of interim PET/CT. The Deauville criteria were proposed in 2009 for assessment of response on interim [^{18}F]FDG-PET/CT [216, 217]. The Deauville criteria provide a qualitative 5-point scale with uptake in

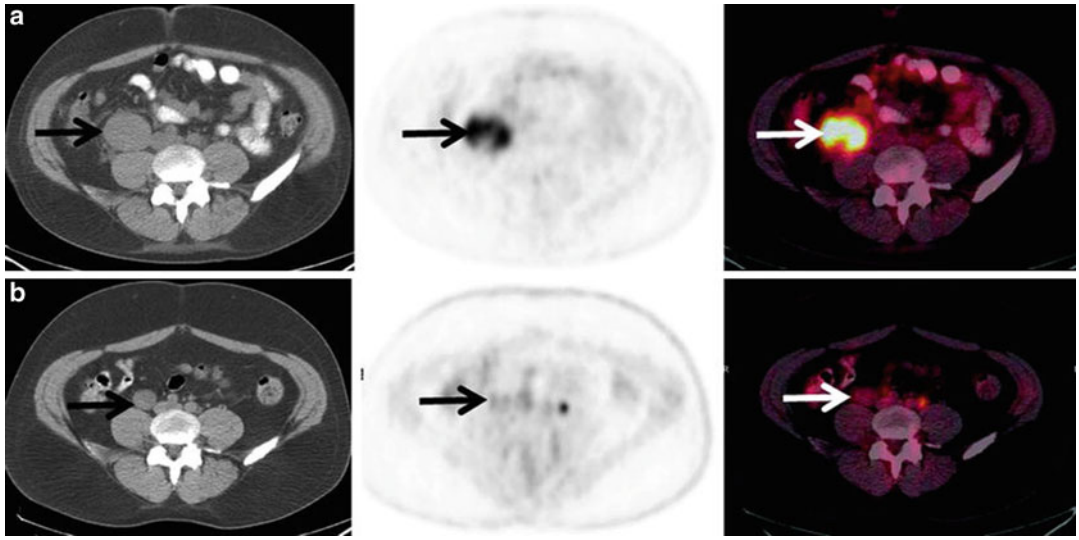

Fig. 6 Pre- and post-therapy PET scans in a patient with diffuse large B-cell lymphoma. The pre-therapy PET scan shows intense [^{18}F]FDG uptake in a right psoas mass (**a**, *top row*). After six cycles of R-CHOP, the PET scan was negative for active lymphoma with tumor uptake equal to background (**b**, *bottom row*). Although residual microscopic disease is not excluded, a negative post-therapy PET scan is associated with a good prognosis even if a residual mass remains on a CT scan. The residual [^{18}F]FDG uptake may be due to post-therapy inflammation (for **a** and **b** – left, CT; center, PET; right, fused PET/CT). In the new Lugano classification and Deauville 5-point scale, this would be rated at score of 2 (Wahl RL, editor. Categorical course in diagnostic radiology: clinical PET and PET/CT imaging, 2007, The Radiological Society of North America [RSNA])

Table 4 Deauville 5-point scale

1	No uptake
2	Uptake $\leq$ mediastinal blood pool
3	Uptake $>$ mediastinal blood pool but $\leq$ liver
4	Uptake moderate $>$ liver
5	Uptake markedly $>$ liver and/or new lesions
X	New areas of uptake unlikely to be related to lymphoma

tumor scored in comparison to mediastinal blood pool and/or liver uptake (Table 4). The prognostic value of Deauville criteria for interim [^{18}F]FDG-PET/CT assessment has been shown in both HL and NHL [218, 219].

In the Lugano classification, the Deauville 5-point scale is the basis for interpretation of both post-therapy and interim [^{18}F]FDG-PET/CT, and there are four categories of response using [^{18}F]FDG-PET/CT for [^{18}F]FDG-avid lymphomas and CT for non-[^{18}F]FDG-avid lymphomas (Table 5). The interpretation of the score depends on the timing of the scan and the clinical scenario. A score of 1 or 2 is interpreted as complete response on both interim and end-of-therapy scans. A score of 4 or 5 is considered a partial response on interim scans if the uptake is less than baseline or as progressive disease if the uptake is greater than baseline. On end-of-therapy PET, a score of 4 or 5 is considered as failure of treatment irrespective of the intensity of uptake compared to baseline. Similarly, a score of 3 is usually considered negative on both interim and end-of-therapy scans, but as an inadequate response in risk-adapted trials evaluating de-escalation strategies. Classification of response based on CT for non-[^{18}F]FDG-avid lymphomas is not significantly different compared to the original IWG criteria in 1999 or the revised IWG criteria in 2007 (Table 5).

Concurrent with the publication of the Lugano classification, the consensus report from the imaging subcommittee of the International Harmonization Project in Lymphoma on the acquisition and interpretation of PET scans that accompanied the revised IWC [220] in 2007 was also updated

Table 5 Lugano Criteria for Response Assessment in Lymphoma

Response	PET/CT[a]	CT
Complete response	Score 1,2,3 with or without residual mass in nodes or extra-nodal sites	Complete disappearance of all sites of disease or decrease in size of nodes to ≤1.5 cm in LDi
Partial response	Score 4 or 5 with decreased uptake compared to baseline and residual masses of any size	≥50% decrease in PPD (single lesion) or SPD of six measurable target nodes and/or extra-nodal sites (multiple lesions); decrease in spleen size >50% in length beyond normal
No response/ stable disease	Score 4 or 5 with no obvious change in [^{18}F]FDG uptake compared to baseline	<50% decrease in PPD (single lesion) or SPD of six measurable target nodes and/or extra-nodal sites (multiple lesions) and no criteria for progressive disease
Progressive disease	Score 4 or 5 with increase in intensity of [^{18}F]FDG uptake compared to baseline or new foci of [^{18}F]FDG uptake compatible with lymphoma	New or increased adenopathy (nodes 1.5 cm > LDi, PPD ≥ 50% from nadir, LDi or SDi increase from nadir by 0.5 cm for lesions ≤2cm and by >1.0 cm for lesions > 2.0 cm), increase in splenic length by >50% of its prior increase from baseline, or by at least 2cm from baseline if no prior splenomegaly, new or recurrent splenomegaly, new nodal or extranodal sites or increase of preexisting nonmeasurable lesions

Notes
[a]Deauville 5-point scale
PET/CT: The interpretation of the score depends on the timing of the scan and the clinical scenario. A score of 1 or 2 is interpreted as complete response on both interim and end of therapy scans. A score of 4 or 5 is considered a partial response on interim scans if the uptake is less than baseline or as progressive disease if the uptake is greater than baseline. On end of therapy PET, a score of 4 or 5 is considered as failure of treatment irrespective of the intensity of uptake compared to baseline. Similarly, a score of 3 is usually considered negative on both interim and end of therapy scans, but as an inadequate response in risk-adapted trials evaluating de-escalation strategies
CT: A measurable node should be 1.5 cm in longest transverse diameter (LDi) and a measurable extranodal site should be 1.0 cm in longest diameter. The longest and shortest (SDi) diameters on the transverse plane of each lesion are multiplied to obtain product of the perpendicular diameters (PPD). Six largest nodes as well as extra-nodal sites which are measurable in two dimensions should be identified from different body regions. The overall disease burden at baseline is quantified by adding the product of the diameters of these six lesions to obtain the sum of the product of the diameter (SPD)

[27]. The general recommendations and major changes from 2007 are summarized in Table 5.

Multiple consensus reports using PET for response assessment (interim and post-therapy) in lymphoma and other tumors stress the importance of obtaining high-quality, standardized PET and CT scans on dedicated PET systems. Detailed discussions on obtaining such scans are found in reports by the National Cancer Institute [221] and the Netherlands multicenter trial group [222] and reviewed in the revised IWC [220] and PET Response Criteria in Solid Tumors (PERCIST) [223].

The use of [^{18}F]FDG-PET for routinely monitoring the response of low-grade follicular and other indolent lymphomas is debatable, but given that the method is more sensitive and specific than CT, it is gaining greater acceptance in clinical practice. Assessments of lower-grade/ indolent lymphomas that are [^{18}F]FDG avid with PET/CT are now included in the new Lugano classification [27, 28].

Interim PET and Risk-Adapted Therapy

Theory and Biologic Basis

Chemotherapy of tumors begins to affect tumor metabolism soon after it is started. In 1993, PET was used sequentially to assess breast cancer response to chemohormonotherapy, and decreases in the amount of [^{18}F]FDG uptake in responding tumors were seen by 8 days into treatment [224]. The clear predictive value of PET in the post-

therapy setting for patients with lymphoma has led investigators to evaluate its usefulness earlier during the course of chemotherapy, and numerous studies have upheld PET's prognostic value in the interim therapy setting [225–231]. Event-free survival (EFS) is consistently lower in patients with positive interim PET scans (0–46%) compared to those with negative interim scans (62–98%), despite variability in the study designs (prospective vs. retrospective, chemotherapy cycles, qualitative vs. quantitative PET assessments), tumor histologies, and treatments employed. This body of work, including a landmark study by Gallamini et al. [34] (discussed below), is the premise for risk-adapted therapy for patients with lymphoma.

Importantly, Gallamini et al. [34] showed that in 190 patients with advanced HL, the results of early interim PET after two cycles of ABVD chemotherapy were more predictive than the widely used and validated IPS. As previously discussed, the IPS for HL and IPI for NHL are both currently used to guide management decisions. Both indices are based solely on pretreatment parameters and do not consider the inherent "chemosensitivity" of the tumor or the rate of tumor kill which are both related to outcome, but PET can assess both of these factors [203].

The conceptual framework for PET providing an early readout on "chemosensitivity" is nicely discussed by Kasamon, Jones, and Wahl, and two underlying points are summarized [203, 232]. First, chemotherapy is expected to kill the same percentage of cells during each cycle (first-order kinetics) [233]. For example, 11 cycles of chemotherapy are needed for cure with 10^{10}–10^{11} cancer cells. Second, due to the lower limit of resolution for current scanners, PET can only detect the initial logs of cell kill. A negative scan after therapy either means cure or residual microscopic disease. A true-negative interim therapy (or soon post-therapy) scan implies that the rate of kill is fast enough to achieve cure by the end of therapy, whereas a positive interim therapy scan does not [203, 232].

The logical question follows, "Can the prognostic information from an interim therapy PET scan be used to improve therapeutic strategies for patients based on their individual risk, hence risk-adapted therapy?" And this can be considered in two ways. First, should therapy be intensified to improve the chance of cure in a patient with a positive interim PET scan as cure is unlikely with the initial therapy? On the other hand, is it safe to omit or decrease therapy in a patient with a negative interim scan? As alluded to in the section above on treatment for early-stage HL, this second option is particularly attractive to reduce the long-term toxicities from therapy in this otherwise curable population.

To date, there are a small number of published trials, but an even larger number of ongoing trials that are investigating these questions. These trials are reviewed and limitations of the use of interim therapy PET for risk-adapted therapy discussed. Until the results of these trials are available and more mature, interim PET scanning and risk-adapted therapy should be performed in the clinical trial setting [209].

Clinical Trials of Risk-Adapted Therapy for Aggressive NHL

A negative interim PET/CT performed after two to three cycles of chemotherapy has been shown to predict a favorable outcome. Kasamon et al. [234] published a phase II study in 59 patients with aggressive NHL, hypothesizing that suboptimal response on interim PET (PET positive) was a sign of chemoresistance and that intensifying therapy in this group of patients would improve their outcome. After two to three cycles, R-CHOP chemotherapy was continued for a negative interim PET (tumor uptake $\leq$ mediastinal blood pool) or intensified to high-dose therapy and autologous stem cell transplant (ASCT) for a positive interim scan (tumor uptake $>$ mediastinal blood pool). On an intent-to-treat basis and at median follow-up time of 34 months, 2-year event-free survival (EFS) was 67% (95% CI 53–86%) in patients with positive interim PET versus 89% (95% confidence interval 77–100%) for negative interim PET. The IPI was not associated with the interim PET result. The outcome of the PET-positive group compared very favorably to historical controls where $<$20% PFS was expected[174]. In another study of 103 patients

with untreated DLBCL who were treated with CHOP with or without rituximab, a negative PET after four cycles of treatment was associated with 5-year EFS of 80% compared to 36% for patient with positive PET [235].

The predictive value of interim PET in DLBCL is, however, less clear as few studies have shown that interim PET can be falsely positive and associated with favorable outcome [236, 237]. Moskowitz et al. [236] performed a phase II study of risk-adapted therapy in advanced DLBCL, but with a slightly different strategy. The treatment scheme was dose-dense R-CHOP followed by PET after four cycles. PET-negative patients received ifosfamide, carboplatin, etoposide (ICE) alone for three more cycles. All PET-positive patients underwent biopsy, contrary to Kasamon's study, and received two cycles of ICE. If the biopsy was negative, an additional cycle of ICE was given, but if positive, therapy was intensified to R-ICE, high-dose therapy, and ASCT. Interim PET scans were positive in 38 of 97 patients. Five of these 38 patients had a positive biopsy for tumor and proceeded to ASCT. The remaining biopsies showed inflammation. At a median of 44 months of follow-up, EFS was not significantly different between interim PET-negative patients and PET-positive/biopsy-negative patients. Three of the five patients who underwent ASCT were alive and progression free at the time of publication.

Possible explanations offered for the high "false-positive" rate on PET were dose-dense initial therapy, increased inflammation due to greater use of rituximab than in prior studies, interim scan occurring relatively soon, a median of 12 days after last therapy (although longer than minimal recommendation of 10 days [220, 221]), the reader threshold for determining "positivity" of a scan, and consolidation to ICE for all patients [236]. The authors concluded and recommended that biopsy be performed to confirm interim-positive PET scan findings prior to treatment intensification to ASCT [236]. It is also possible that false-negative biopsies occurred. It should be noted there is little data on the predictive value of biopsy in this setting. In another study of 88 patients with newly diagnosed DLBCL treated with R-CHOP, there was no significant difference in the 2-year PFS between patients with negative and positive interim PET. The end-of-therapy PET was highly predictive of the 2-year PFS [237].

Clinical trials in aggressive NHL have primarily focused on intensification of therapy if the interim scan is positive and exploring findings of the previous risk-adapted trials. The results of the ECOG 3404 study were recently published [238]. This study evaluated interim PET response-based strategy of switching patients to R-ICE chemotherapy after three cycles of R-CHOP. The interim PET was scored as positive or negative by central review. A 2-year PFS of $\geq$45% was the target response in the interim PET-positive group. The scans were interpreted using customized binary criteria (ECOG criteria). The study enrolled 74 patients and only 16% of patients had a positive interim PET. A rereview of the interim scans by an expert panel was performed due to the low number of the positive scans. Nearly 30% of the interpretations were discrepant among the readers highlighting the need for more accurate scoring system or possibly precise quantitation of the images. The 2-year PFS was 76% in the interim PET-negative group and 42% in the interim PET-positive group treated with R-ICE. The authors concluded that the poor outcome of patients with interim PET positivity despite intensification of therapy indicates innate resistance to treatment and that until further evidence is available, treatment modification in DLBCL patients based on early PET should remain restricted to clinical trials [238].

The current NCCN guidelines also state that treatment modification of DLBCL patients should not be guided by interim PET scan results. Any modifications should be performed only after conforming real positivity on repeat biopsy of residual masses [88]. The demonstration of true benefit of therapy intensification for those with a positive interim PET scan is limited by comparison to historical controls and the lack of randomization to standard versus experimental therapy in the above phase II trials. An ongoing study in Germany, Positron Emission Tomography Guided Therapy for Aggressive Non-Hodgkin's Lymphomas (PETAL), attempts to address this [239]. In this study, patients with positive PET scans are

randomized to either six additional cycles of R-CHOP or a more intense Burkitt's lymphoma regimen. For those randomized to R-CHOP, two additional cycles are given (total eight cycles) compared to those who have a negative interim PET scan (total six cycles). The interim results of this trial have shown relapses more often in patient with positive interim PET than patients with negative interim PET [240]. Recruitment into this trial is ongoing, and the results should provide further insight into the usefulness of PET in the interim setting for aggressive NHL.

Clinical Trials of Risk-Adapted Therapy for Hodgkin Lymphoma

Risk-adapted therapy is also a major focus of research trials for patients with HL. For those with early, unfavorable, or advanced disease, the approach is generally similar to NHL, intensification of therapy based on a positive interim scan. For those with early-stage disease, therapy de-intensification after a negative interim PET is undergoing ongoing evaluation in attempt to reduce the risk of late-term complications from potentially excessive therapy.

There are several trials evaluating risk-adapted strategies in early-stage favorable HL. The interim results of the EORTC/LYSA/FIL H10 trial evaluating the non-inferiority of omitting radiotherapy in early interim PET-negative patients with early HL have been published [42]. A total of 1,137 patients were recruited in the study and assigned to standard and experimental arms. Nine hundred patients (favorable = 381 and unfavorable = 519) had interim PET-negative disease. Interim futility analysis showed that in both favorable and unfavorable groups, the experimental arm (chemotherapy alone) had a greater number of relapses or early progression compared to the standard arm (standard chemotherapy and radiotherapy). Based on these results, the independent data monitoring committee recommended closure of accrual to the PET-negative experimental arm. The UK RAPID trial was a phase III trial which also evaluated the non-inferiority of no further treatment versus involved-field radiotherapy in patients with a negative interim PET [241]. Of the 571 patients who underwent PET scanning in the study, 74.6% patients had negative PET. The 3-year PFS and OS in the no further treatment group ($n = 211$) were 90.8% and 99.0%, respectively, compared to 94.6% and 97.1%, respectively, in the radiotherapy group ($n = 209$). Overall, the study concluded that the strategy of no further treatment was not non-inferior to consolidation radiotherapy although the prognosis was very good in both arms with or without radiotherapy. That said, it appears that the possible benefits of radiotherapy were quite modest relative to the number of patients that needed to receive the treatment.

Dann et al. [242] performed a prospective study of risk-adapted BEACOPP therapy in 108 patients with intermediate- and high-risk HL. Treatment was adapted based on pretreatment risk factors (standard BEACOPP for intermediate-risk disease or escalated BEACOPP for high-risk (IPS $\geq$ 3) disease) and then escalated or de-escalated based on interim functional imaging with gallium-67 or PET after two cycles. With this schema, 5-year EFS and OS were not different between the intermediate- and high-risk groups at a median of 47 months of follow-up. In the high-risk group ($n = 39$), 31 (79%) had therapy de-escalated for negative interim scintigraphy, and the negative predictive value of interim PET was 93%. The authors suggested that it may be feasible to de-escalate therapy in a high-risk group based on negative interim PET. Only 4 of 19 patients (21%) with a positive interim PET scan had progressed at last follow-up (median 47 months). Several additional ongoing trials of risk-adapted therapy for advanced-stage HL, mostly therapy intensification with positive interim PET, are in references [243–245].

The interim data of the response adapted therapy in advanced HL (RATHL) have been recently published [246]. The results of the study indicate good agreement between readers while using the 5-point scale for interim PET assessment. The final results on the role of interim PET in treatment adaptation are awaited.

In the yet-to-be-published GITIL/FIL HD0607 trial, the role of early intensification of therapy in advanced-stage HL patients with positive interim PET has been evaluated [247]. Patients with positive PET after two cycles of ABVD were treated with BEACOPP escalated and BEACOPP baseline (4 + 4) without or with rituximab. On the other hand, patients with negative interim PET received four cycles of ABVD with or without RT. Of the 446 patients with interim PET, 20% had positive scans. Response to treatment was assessed in a cohort of 263 patients (15% with positive interim PET and 84% with negative interim PET). Complete response to treatment was seen in 73% of PET-positive patients and 95.5% of PET-negative patients [247]. The results of many other trials are awaited.

Interpretation of Interim Therapy PET Scans

Most risk-adapted therapy trials have employed qualitative analyses (i.e., visual scales) for interpreting interim PET scans as positive or negative. Several have been used (Juweid et al. [220], ECOG [248] and London criteria [249]), and these scales have evolved over the years. As indicated in the section above, the Deauville criteria are currently used in the interim setting (give Lugano reference).

Cases of [^{18}F]FDG uptake in tumor much less or much greater than background are clear-cut as negative or positive; however, [^{18}F]FDG uptake in tumor occurs along a continuum. Most of the difficulty arises in the concept of "minimal residual uptake" (MRU) and the optimal definition of "background" (and thus the cutoff point for a positive vs. negative scan) in the interim setting. MRU was first defined in 2000 as low-grade uptake on posttreatment PET within an area of previous disease, reported as likely inflammation but where a small volume of malignancy cannot be excluded [250]. The definition of MRU has been adapted slightly over recent years by different investigators, hence the variable criteria and interpretation of interim PET scans for studies of patients with NHL and HL.

In a study of aggressive NHL, Kasamon et al. [234] found that 56% of patients had a positive interim PET scan using mediastinal blood pool as a comparator. In the follow-up ECOG study (E3404), a centralized PET review by a single reader took place, and the rate of positive interim PET scans was lower than expected. As a result, evaluation of the reproducibility of interim PET interpretation took place [248]. Three expert PET readers scored baseline and interim PET scans from 38 patients on E3404 using the ECOG and London criteria without additional training. Only moderate reproducibility among the experts was found for interpreting the interim scans ($k = 0.44$ for ECOG criteria and $k = 0.50$ for London criteria).

The sources of disagreement were lesions in the para-aortic region, bone, and spleen [248]. These sites of disagreement are not completely unexpected as the spleen and bone marrow can have considerably heterogeneous uptake post-therapy due to treatment effects.

On the other hand, Barrington et al. have reported very good agreement among four centers in Europe for interpretation of interim PET using the London criteria (RATHL trial) [249]. The interim PET scans were read independently by the participating centers and then in consensus. The kappa values showed very good agreement for negative (uptake less than or equal to the liver) vs. positive (uptake moderate or markedly increased versus the liver) scans for both the independent ($k = 0.85$, 95% CI 0.74–0.96) and consensus readings ($k = 0.90$, 0.79–1.00) [249]. Agreement was slightly less for independent reads when the category of "uptake greater than mediastinal blood pool but less than liver" was considered separately (from negative or positive). The updated results of the RATHL study made similar conclusions. There was good agreement in the interpretation of the interim PET scans using the Deauville 5-point scale (5-PS) among experts ($k = 0.84$, 0.76–91) and between experts and local readers ($k = 0.77$, 0.68–0.86) [246].

Some uncertainty does remain in the optimal cutoff for altering therapy based on interim PET. Mikhaeel et al. showed that for patients with early-stage NHL, the MRU survival curve lies closer to those who have a negative interim PET, but in late-stage disease, the MRU curve lies closer to the PET-positive curve [230]. The significance may vary based on a combination of factors, including clinical stage, lymphoma subtype, and benefits and risks of the impending therapeutic decision. The use of semiquantitative parameters like the standardized uptake value (SUV) may be helpful in the interim setting to help reduce the variability if PET is performed using standardized methods.

Lin et al. [251] found that in patients with DLBCL, a decline in maximum SUV of >65.7% after two cycles of therapy better predicted outcomes versus visual assessment by reducing the number of false-positive scans. These results did not hold, however, in a subsequent study where PET was performed after four cycles of therapy [252]. Optimal methods for assessing PET may be also be dependent on timing of the scan.

Standardized response criteria for interim PET scanning and the results of the many ongoing trials will hopefully provide the necessary data to determine if risk-adapted therapy is possible and beneficial for individual patients. At the present time, most experts agree that changes in therapy based on interim therapy PET (except for progressive disease) should currently be kept in the context of clinical trials. The current NCCN guidelines recommend interim PET scan assessment with Deauville criteria in both early-stage favorable and advanced-stage disease [10]. In a large retrospective multicenter study published recently, the reproducibility of Deauville 5-PS for interpretation of interim PET was assessed [253]. The study included 260 patients with early-stage unfavorable or advanced-stage HL treated with chemotherapy with or without consolidation radiotherapy. The interim PET scans were positive as per Deauville criteria in 17.3% patients. A three-year PFS was 28% for interim PET-positive patients compared to 95% for PET-negative patients. Interim PET had sensitivity and specificity of 73% and 94% for predicting outcome. There was strong concordance among reviewers while using the Deauville criteria (Cohen's kappa 0.69–0.84) [253].

Full quantitation of images holds the potential to reduce variability among readers, but will require further study.

Surveillance PET for Lymphoma

In HL and aggressive NHL, early detection of relapse is desirable in order to initiate treatment when tumor burden is low. This may increase the chance of successful disease eradication, which ultimately may lead to better outcomes. Several studies have shown that recurrence of lymphoma is often diagnosed by the presence of clinical symptoms before detection or confirmation by imaging [254–256]. PET offers a potential benefit over anatomic imaging for earlier disease detection, but this must be balanced with considerations of radiation exposure to the patient and cost from the increased number of scans obtained during surveillance.

The current literature on the use of [^{18}F]FDG PET for follow-up of patients with lymphoma is limited. However, it does confirm the ability of PET to detect relapse before the patient becomes symptomatic and before anatomic imaging becomes positive, by up to 9 months in one study [257]. PET is also useful for detecting relapse in the setting of a persistent, unchanging residual mass on CT in the follow-up period [258]. For patients who achieve a complete remission after therapy, the negative predictive value of PET for excluding relapse in the follow-up period is high (99–100%) [257–259].

The major limitation of surveillance PET has been a high false-positive rate (low positive predictive value, 11–53%) in several studies [257–259]. This is particularly true in the pediatric population of patients where cure rates are high and the incidence of recurrent disease is low. In the study by Rhodes et al. [258], false-positive results occurred due to reactive neck lymph nodes. Another contributing factor to these high false-positive rates was that PET alone was used, and conditions such as rebound thymic hyperplasia or brown fat were recorded as positive for disease recurrence. This is

much less likely to occur in the current era of PET/CT and as we have gained knowledge in interpretation of post-therapy PET in patients with lymphoma.

Zinzani et al. [260] prospectively performed follow-up PET scans (every 6 months for 2 years and then yearly) in 421 adult patients with lymphoma who achieved a complete response by PET after therapy (160 with HL, 183 with aggressive NHL, 78 with indolent NHL). For HL and aggressive NHL, the number of true-positive scans decreased and true-negative scans increased with time. The incidence of relapse was stable over time for those with indolent NHL, as might be expected. Compared to the prior studies in pediatrics, the false-positive scan rate was low (~1% of 1,789 scans). However, eight percent of patients had inconclusive-positive PET scans, two-thirds with concurrent negative CT scans, and biopsy was important to confirm disease presence in these patients. Most patients with inconclusive negative scans did not relapse [260].

The early studies did show that there may be a subgroup of patients for whom PET might be useful for surveillance. Rhodes et al. [258] suggested that those children with residual masses or unchanging abnormal CT scans might benefit the most from surveillance PET scanning. Zinzani et al. [260] also found that PET positivity was more common in groups with a higher risk of recurrence by prognostic factors for all lymphoma types. These findings are further supported by a more recent study by Petrausch et al. who found that the usefulness of PET for surveillance may be related to risk factors at the time of scanning [261, 262].

Petrausch et al. [262] evaluated 134 patients with HL in remission after first-line therapy that had at least one follow-up PET scan. The predictive value of follow-up PET for detecting recurrence was 98%, all with histologic confirmation. Symptoms at the time of PET, residual mass on CT, and advance stage of disease were risk factors for recurrence. Median recurrence-free survival decreased with the presence of an increasing number of these three risk factors, and importantly, no asymptomatic patient with early-stage disease and no residual mass on CT had evidence of recurrence on PET at a mean follow-up of 38 months. Interestingly, patients with a residual mass were more likely to show recurrence on a PET scan done in the first 24 months of follow-up, whereas after 24 months, the presence of symptoms at the time of PET scanning was more predictive of recurrence. The authors concluded that while PET reliably detects recurrent HL, follow-up with PET/CT may best be based on risk factors. This approach would consider the important concerns of increasing radiation exposure due to medical imaging as well as economic cost.

In summary, the current evidence does not support the routine use of PET for follow-up of patients with lymphoma, and PET is not included as part of routine follow-up in current clinical guidelines [10, 99]. The Lugano criteria accordingly do not recommend routine surveillance imaging especially in patients with HL and DLBCL [28]. In patients with clinical signs and in the setting of clinical trials, a CT scan can be performed for follow-up. For indolent lymphomas, the Lugano criteria recommend judicious use of follow-up scans [28]. Emerging data suggests that PET for surveillance is possibly beneficial for a subset of patients as discussed above. More studies are needed to further define this subset and to evaluate the effects of follow-up PET on patient management, outcomes, and cost-effectiveness. Additionally, since CT surveillance is commonly applied and since PET/CT is more accurate than CT in nearly all studies, logical widespread clinical practice includes using PET/CT for follow-up of patients with NHL, especially those at high risk for recurrence.

Tracers Beyond [^{18}F]FDG

Although [^{18}F]FDG is the only current PET tracer approved and routinely used in the evaluation of patients with lymphoma, several radiolabeled amino acid tracers have also been investigated. Carbon-11 methionine ([^{11}C]methionine), an essential amino acid needed for protein and polyamine synthesis and transsulfuration and transamination reactions, has also been evaluated in a limited number of studies [167, 263–266]. [^{11}C]Methionine is taken

up by all grades of lymphoma (HL and NHL) with a reported sensitivity of 97% for disease detection in a single study of 32 patients [265]. The continuum of uptake between low- and high-grade NHL seen with [^{18}F]FDG is not as apparent with [^{11}C] methionine using semiquantitative measures like SUV, but can be found with more intensive kinetic analysis [265]. [^{11}C]Methionine performed equally well compared to [^{18}F]FDG for staging lymphoma, and uptake in untreated patients was not associated with outcome [265, 266]. Other limitations of [^{11}C] methionine are the need for an on-site cyclotron due to the 20 min half-life of ^{11}C and normal biodistribution in abdominal organs obscuring tumor sites. A current study at St. Jude Children's Research Hospital, Memphis, TN, is investigating methionine PET in a variety of tumor types, including lymphoma [267].

More recently, the thymidine analog 3′-^{18}F-3′-deoxythimidine (^{18}F-FLT) has been investigated [268–270]. ^{18}F-FLT uptake reflects thymidine kinase activity and the fraction of cells in S-phase and is an indirect measure of proliferation [269]. In the first human studies, ^{18}F-FLT uptake was observed in indolent and aggressive NHL which was slightly less than [^{18}F]FDG uptake in lymphoma lesions [268, 269]. ^{18}F-FLT discriminated indolent from aggressive NHL (area under the curve 0.98) better than [^{18}F]FDG (area under the curve 0.78) [269]. There was a high correlation between ^{18}F-FLT SUV and the proliferation index Ki67 [269]. One limitation of ^{18}F-FLT imaging in lymphoma is the high normal accumulation of the tracer in several normal organs (hematopoietic bone marrow, liver, spleen) but particularly the hematopoietic bone marrow (SUV 6–12 range) [268, 269] where disease may be missed [269].

Kasper et al. [271] prospectively evaluated 48 patients with HL ($n = 15$) and NHL ($n = 10$ indolent, $n = 23$ aggressive) at the end of chemotherapy to test the prognostic ability of ^{18}F-FLT PET and [^{18}F]FDG-PET in this setting. The authors reported that both tracers were predictive of outcome (PET positive = worse prognosis) and the combination of tracers did not provide additional information. However, the study is limited in that very heterogeneous treatment regimens were used.

Several preclinical models have shown that ^{18}F-FLT PET may be useful for evaluating early response of lymphoma to therapy [272–276]. Reduced proliferation was shown as soon as 24 h after cytotoxic therapy in one high-grade lymphoma xenograft mouse model [275]. The time course and extent of the anti-proliferation effect may be dependent on the agent employed [272, 273, 275]. For example, a transient rise in ^{18}F-FLT uptake (after a 2-day decline) was observed in a mantle cell mouse model of NHL after mTOR inhibition with rapamycin [272]. The pattern of ^{18}F-FLT uptake partially paralleled cyclin D1 expression. Larger declines in ^{18}F-FLT uptake were seen after cytotoxic therapy than after immunotherapy in animal models and in a single human study [272, 275].

These results are promising, and there are several ongoing clinical trials further evaluating the safety and role of ^{18}F-FLT PET in patients with lymphoma. Some are assessing the overall safety and usefulness of ^{18}F-FLT PET and include patients with lymphoma and other hematologic or solid tumors [277–279]. In a recent prospective study of 65 patients with aggressive lymphoma treated with four cycles of R-CHOP and three cycles of ICE, ^{18}F-FLT PET was performed at baseline and after one to two cycles of chemotherapy and [^{18}F]FDG-PET at baseline, after cycle 4 and at end of therapy. The study found that interim ^{18}F-FLT PET was predictive of PFS and OS. Interim ^{18}F-FLT PET had high negative predictive value for identifying patients with good prognosis. However, the positive predictive value though slightly better than [^{18}F]FDG-PET was still very low. Volumetric parameters were not associated with PFS and OS. The study concluded that ^{18}F-FLT PET could help design risk-adapted therapies due to the high negative predictive value [280].

Additional Challenges and Limitations in the Interpretation of [^{18}F]FDG-PET in Lymphoma

The [^{18}F]FDG-PET and PET/CT techniques have limitations, and confounding factors can make image interpretation challenging. As previously

stated, the system resolution of the scanner limits the ability of both [^{18}F]FDG-PET and PET/CT to detect small lesions. Most modern scanners have resolutions of about 0.5–1 cm [202]. Larger lesions are not only more readily detected, but quantification of tumor metabolism and tumor size is more reliable.

False-positive PET studies can occur due to inflammation or infection [281, 282]. In patients with lymphoma, this is of greatest concern post-therapy (chemotherapy or radiation). New [^{18}F]FDG-avid foci remote from sites of initial disease must be interpreted with caution, particularly if known tumor foci have responded to therapy (Fig. 7, lung infection from RSNA syllabus – copyright requested and pending). Comparison to a baseline study and attention to interval clinical history, for example, recent infections, trauma, and blood counts, are very helpful in the post-therapy evaluation for this purpose.

Adjunctive hematopoietic cytokines reduce the incidence of chemotherapy-induced neutropenia and its associated infectious complications in patients with nonmyeloid malignancies. Granulocyte colony-stimulating factor (G-CSF) administration before [^{18}F]FDG-PET scanning results in altered [^{18}F]FDG biodistribution, such as increased [^{18}F]FDG visualization in the bone marrow and spleen [283, 284]. Consequently, disease in or just adjacent to the bone marrow or spleen may be masked. In these cases, review of images at multiple intensity levels on the computer screen and anatomic images for abnormalities helps the reader to avoid misinterpretation. In addition, G-CSF may decrease the bioavailability of [^{18}F]FDG for (residual) tumor which could result in underestimation of the amount of residual disease post-therapy [283]. The effects of G-CSF are most pronounced closer to the time of administration, but can last up to 28 days [284]. As with chemotherapy, it is probably

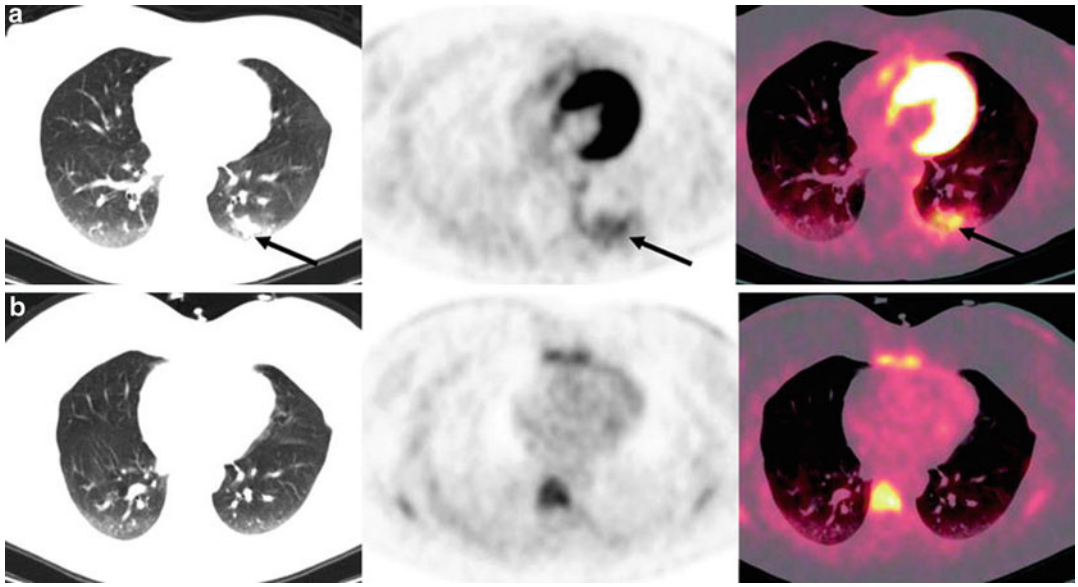

Fig. 7 Reprinted with permission from Jacene [288]. A 54-year-old female with a history of non-Hodgkin lymphoma status post six cycles of rituximab and chemotherapy presented for a post-therapy [^{18}F]FDG-PET/CT scan (**a**). The scan revealed complete resolution of all sites of disease seen on her baseline study; however, a new focus of activity fusing to left lower lobe opacity was identified (*arrow*). Because of the otherwise excellent response to chemotherapy and location of the new finding outside the initial sites of disease, an inflammatory etiology was suspected. The patient returned for a follow-up [^{18}F]FDG-PET/CT scan 3 months later (**b**). The [^{18}F]FDG activity and lung opacity resolved and no new foci of [^{18}F]FDG activity to suggest recurrent lymphoma were visualized, confirming the likely inflammatory etiology (left, CT; center, PET; right, fused PET/CT)

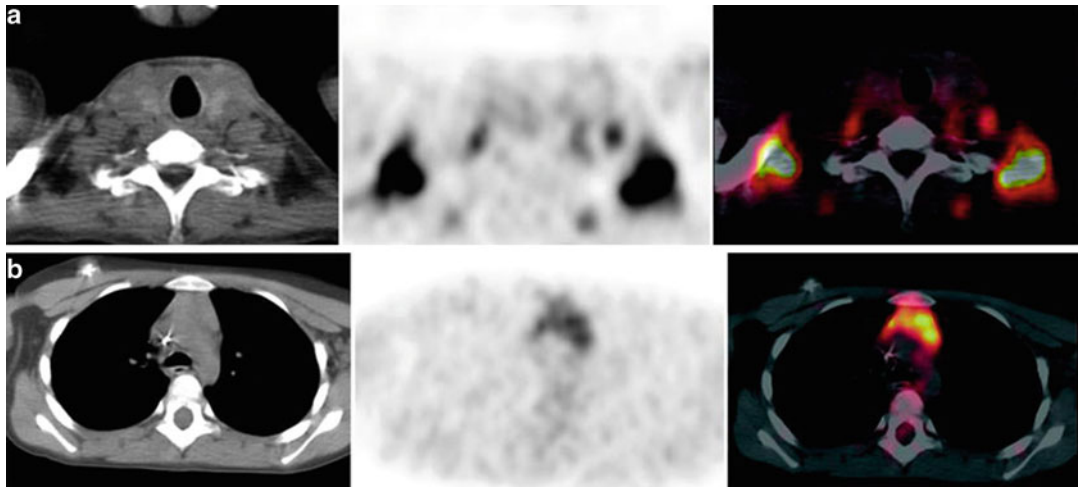

Fig. 8 Reprinted with permission from Jacene [288]. (**a**) Intense [^{18}F]FDG activity fusing to fat on the CT scan is a typical pattern for physiologic hypermetabolism in *brown* fat. (**b**) [^{18}F]FDG uptake in the anterior mediastinum in a triangular shape and fusing to thymic tissue is a typical pattern of thymic hyperplasia (*left*, CT; *center*, PET; *right*, fused PET/CT) (Wahl RL, editor. Categorical course in diagnostic radiology: clinical PET and PET/CT imaging, 2007, The Radiological Society of North America [RSNA])

ideal to wait a minimum of 7–10 days after G-CSF administration before obtaining a post-therapy PET, but the therapeutic schedule should be considered and not delayed. Erythropoietin also increases [^{18}F]FDG uptake in the bone if administered just prior to scanning [285].

Other common causes of false-positive PET scans include physiologic [^{18}F]FDG uptake in thymic hyperplasia [286] and brown adipose tissue (brown fat) [287] (Fig. 8, from RSNA syllabus – copyright requested and pending). Experience, pattern recognition and/or combined PET/CT imaging aids image interpretation in both instances. Typically, thymic uptake is visualized in the anterior mediastinum and has a triangular shape. On combined PET/CT imaging, the [^{18}F]FDG uptake fuses to thymic tissue in the anterior mediastinum. Brown fat was first identified in the head, neck, and supraclavicular regions as foci of intense [^{18}F]FDG uptake that fuse to fat on CT [287]. It has also been visualized in the mediastinum and abdomen. In patients with lymphoma, hypermetabolism in brown fat and involved lymph nodes can coexist, and combined [^{18}F]FDG-PET/CT imaging is essential for proper interpretation.

Summary

[^{18}F]FDG-PET is a useful noninvasive imaging modality for the evaluation of patients with both HL and NHL. A baseline PET/CT scan is more accurate for primary lymphoma staging than anatomic imaging, and obtaining one often facilitates future interpretation of post-therapy scans by defining the initial sites of disease. Post-therapy PET provides valuable functional and prognostic information and is probably most beneficial in patients with initially [^{18}F]FDG-avid tumor. Post-therapy scan results can help define future management decisions as curative or palliative. Knowledge of lymphoma type and clinical history (interval therapy, surgery, concurrent illness, and drug administrations) is critical for accurate image interpretation.

Currently, interim PET scans are best utilized in the clinical trial setting where results can influence decisions along a management tree. Numerous clinical trials are ongoing evaluating interim PET scanning, and the results of these studies should provide further insight into the optimal use of PET/CT for "risk-adapted" therapy. Work on standardization of PET response criteria is ongoing.

References

1. Kuwabara Y, Ichiya Y, Otsuka M, Miyake Y, Gunasekera R, Hasuo K, et al. High [^{18}F]FDG uptake in primary cerebral lymphoma: a PET study. J Comput Assist Tomogr. 1988;12(1):47–8.
2. Newman JS, Francis IR, Kaminski MS, Wahl RL. Imaging of lymphoma with PET with 2-[F-18]-fluoro-2-deoxy-D-glucose: correlation with CT. Radiology. 1994;190(1):111–6.
3. Siegel RL, Miller KD, Jemal A. Cancer statistics. CA Cancer J Clin. 2016;66(1):7–30.
4. Weiss LM, Strickler JG, Warnke RA, Purtilo DT, Sklar J. Epstein-Barr viral DNA in tissues of Hodgkin's disease. Am J Pathol. 1987;129(1):86–91. Pubmed Central PMCID: 1899692.
5. Hjalgrim H, Askling J, Rostgaard K, Hamilton-Dutoit S, Frisch M, Zhang JS, et al. Characteristics of Hodgkin's lymphoma after infectious mononucleosis. N Engl J Med. 2003;349(14):1324–32.
6. Kamper PM, Kjeldsen E, Clausen N, Bendix K, Hamilton-Dutoit S, d'Amore F. Epstein-Barr virus-associated familial Hodgkin lymphoma: paediatric onset in three of five siblings. Br J Haematol. 2005; 129(5):615–7.
7. Mack TM, Cozen W, Shibata DK, Weiss LM, Nathwani BN, Hernandez AM, et al. Concordance for Hodgkin's disease in identical twins suggesting genetic susceptibility to the young-adult form of the disease. N Engl J Med. 1995;332(7):413–8.
8. Horning SJ. Hodgkin's lymphoma. In: Abeloff MAJ, Niederhuber JE, Kastan MB, McKenna WG, editors. Abeloff's clinical oncology. 4th ed. Philadelphia: Churchill Livingstone Elsevier; 2008.
9. Diseases of white cells, lymph nodes, and pleen. In: Cotran RS, Kumar V, Robbins SL, eds, editors. Pathologic basis of sisease. 5th ed. Philadelphia, PA: W.B. Saunders Company; 1994. p. 629–72.
10. NCCN clinical practice guidelines in oncology Hodgkin Lymphoma version 2.2015: NCCN; 2015 [cited 2015 8.21.2015]. Available from: http://www.nccn.org/professionals/physician_gls/f_guidelines.asp#site
11. Foss HD, Reusch R, Demel G, Lenz G, Anagnostopoulos I, Hummel M, et al. Frequent expression of the B-cell-specific activator protein in Reed-Sternberg cells of classical Hodgkin's disease provides further evidence for its B-cell origin. Blood. 1999;94(9):3108–13.
12. Marafioti T, Hummel M, Anagnostopoulos I, Foss HD, Falini B, Delsol G, et al. Origin of nodular lymphocyte-predominant Hodgkin's disease from a clonal expansion of highly mutated germinal-center B cells. N Engl J Med. 1997;337(7): 453–8.
13. Hall PA, D'Ardenne AJ. Value of CD15 immunostaining in diagnosing Hodgkin's disease: a review of published literature. J Clin Pathol. 1987;40(11):1298–304.
14. Pinkus GS, Thomas P, Said JW. Leu-M1 – a marker for Reed-Sternberg cells in Hodgkin's disease. An immunoperoxidase study of paraffin-embedded tissues. Am J Pathol. 1985;119(2):244–52. Pubmed Central PMCID: 1887896.
15. Rassidakis GZ, Medeiros LJ, Viviani S, Bonfante V, Nadali GP, Vassilakopoulos TP, et al. CD20 expression in Hodgkin and Reed-Sternberg cells of classical Hodgkin's disease: associations with presenting features and clinical outcome. J Clin Oncol. 2002; 20(5):1278–87.
16. Watanabe K, Yamashita Y, Nakayama A, Hasegawa Y, Kojima H, Nagasawa T, et al. Varied B-cell immunophenotypes of Hodgkin/Reed-Sternberg cells in classic Hodgkin's disease. Histopathology. 2000;36(4):353–61.
17. Mani H, Jaffe ES. Hodgkin lymphoma: an update on its biology with new insights into classification. Clin Lymphoma Myeloma. 2009;9(3):206–16.
18. Kuppers R, Schwering I, Brauninger A, Rajewsky K, Hansmann ML. Biology of Hodgkin's lymphoma. Ann Oncol. 2002;13 Suppl 1:11–8.
19. M'Kacher R, Bennaceur-Griscelli A, Girinsky T, Koscielny S, Delhommeau F, Dossou J, et al. Telomere shortening and associated chromosomal instability in peripheral blood lymphocytes of patients with Hodgkin's lymphoma prior to any treatment are predictive of second cancers. Int J Radiat Oncol Biol Phys. 2007;68(2):465–71.
20. Poppema S, Kaleta J, Hepperle B. Chromosomal abnormalities in patients with Hodgkin's disease: evidence for frequent involvement of the 14q chromosomal region but infrequent bcl-2 gene rearrangement in Reed-Sternberg cells. J Natl Cancer Inst. 1992; 84(23):1789–93.
21. Green MR, Monti S, Rodig SJ, Juszczynski P, Currie T, O'Donnell E, et al. Integrative analysis reveals selective 9p24.1 amplification, increased PD-1 ligand expression, and further induction via JAK2 in nodular sclerosing Hodgkin lymphoma and primary mediastinal large B-cell lymphoma. Blood. 2010;116(17):3268–77.
22. Herndier BG, Sanchez HC, Chang KL, Chen YY, Weiss LM. High prevalence of Epstein-Barr virus in the Reed-Sternberg cells of HIV-associated Hodgkin's disease. Am J Pathol. 1993;142(4): 1073–9. Pubmed Central PMCID: 1886872.
23. Pelstring RJ, Zellmer RB, Sulak LE, Banks PM, Clare N. Hodgkin's disease in association with human immunodeficiency virus infection. Pathologic and immunologic features. Cancer. 1991;67(7):1865–73.
24. Schmitz R, Hansmann ML, Bohle V, Martin-Subero JI, Hartmann S, Mechtersheimer G, et al. TNFAIP3 (A20) is a tumor suppressor gene in Hodgkin lymphoma and primary mediastinal B cell lymphoma. J Exp Med. 2009;206(5):981–9.
25. Tiacci E, Doring C, Brune V, van Noesel CJ, Klapper W, Mechtersheimer G, et al. Analyzing

primary Hodgkin and Reed-Sternberg cells to capture the molecular and cellular pathogenesis of classical Hodgkin lymphoma. Blood. 2012;120(23): 4609–20.
26. Skinnider BF, Mak TW. The role of cytokines in classical Hodgkin lymphoma. Blood. 2002;99(12): 4283–97.
27. Barrington SF, Mikhaeel NG, Kostakoglu L, Meignan M, Hutchings M, Mueller SP, et al. Role of imaging in the staging and response assessment of lymphoma: consensus of the International Conference on Malignant Lymphomas Imaging Working Group. J Clin Oncol. 2014;32(27):3048–58.
28. Cheson BD, Fisher RI, Barrington SF, Cavalli F, Schwartz LH, Zucca E, et al. Recommendations for initial evaluation, staging, and response assessment of Hodgkin and non-Hodgkin lymphoma: the Lugano classification. J Clin Oncol. 2014;32(27):3059–68.
29. Carbone PP, Kaplan HS, Musshoff K, Smithers DW, Tubiana M. Report of the committee on Hodgkin's disease staging classification. Cancer Res. 1971; 31(11):1860–1.
30. Lister TA, Crowther D, Sutcliffe SB, Glatstein E, Canellos GP, Young RC, et al. Report of a committee convened to discuss the evaluation and staging of patients with Hodgkin's disease: Cotswolds meeting. J Clin Oncol. 1989;7(11):1630–6.
31. Cosset JM, Henry-Amar M, Meerwaldt JH, Carde P, Noordijk EM, Thomas J, et al. The EORTC trials for limited stage Hodgkin's disease. The EORTC Lymphoma Cooperative Group. Eur J Cancer. 1992; 28A(11):1847–50.
32. Engert A, Plutschow A, Eich HT, Lohri A, Dorken B, Borchmann P, et al. Reduced treatment intensity in patients with early-stage Hodgkin's lymphoma. N Engl J Med. 2010;363(7):640–52.
33. Hasenclever D, Diehl V. A prognostic score for advanced Hodgkin's disease. International prognostic factors project on advanced Hodgkin's disease. N Engl J Med. 1998;339(21):1506–14.
34. Gallamini A, Hutchings M, Rigacci L, Specht L, Merli F, Hansen M, et al. Early interim 2-[^{18}F] fluoro-2-deoxy-D-glucose positron emission tomography is prognostically superior to international prognostic score in advanced-stage Hodgkin's lymphoma: a report from a joint Italian-Danish study. J Clin Oncol. 2007;25(24):3746–52.
35. Canellos GP, Anderson JR, Propert KJ, Nissen N, Cooper MR, Henderson ES, et al. Chemotherapy of advanced Hodgkin's disease with MOPP, ABVD, or MOPP alternating with ABVD. N Engl J Med. 1992;327(21):1478–84.
36. Canellos GP, Niedzwiecki D. Long-term follow-up of Hodgkin's disease trial. N Engl J Med.2002; 346(18): 1417–8.
37. DeVita Jr VT, Carbone PP. Treatment of Hodgkin's disease. Med Ann Dist C. 1967;36(4):232–4. passim.
38. Klimo P, Connors JM. MOPP/ABV hybrid program: combination chemotherapy based on early introduction of seven effective drugs for advanced Hodgkin's disease. J Clin Oncol. 1985;3(9):1174–82.
39. Laskar S, Gupta T, Vimal S, Muckaden MA, Saikia TK, Pai SK, et al. Consolidation radiation after complete remission in Hodgkin's disease following six cycles of doxorubicin, bleomycin, vinblastine, and dacarbazine chemotherapy: is there a need? J Clin Oncol. 2004;22(1):62–8.
40. Meyer RM, Gospodarowicz MK, Connors JM, Pearcey RG, Wells WA, Winter JN, et al. ABVD alone versus radiation-based therapy in limited-stage Hodgkin's lymphoma. N Engl J Med. 2012;366 (5):399–408. Pubmed Central PMCID: 3932020.
41. Pavlovsky S, Maschio M, Santarelli MT, Muriel FS, Corrado C, Garcia I, et al. Randomized trial of chemotherapy versus chemotherapy plus radiotherapy for stage I-II Hodgkin's disease. J Natl Cancer Inst. 1988;80(18):1466–73.
42. Raemaekers JM, Andre MP, Federico M, Girinsky T, Oumedaly R, Brusamolino E, et al. Omitting radiotherapy in early positron emission tomography-negative stage I/II Hodgkin lymphoma is associated with an increased risk of early relapse: clinical results of the preplanned interim analysis of the randomized EORTC/LYSA/FIL H10 trial. J Clin Oncol. 2014; 32(12):1188–94.
43. Shore T, Nelson N, Weinerman B. A meta-analysis of stages I and II Hodgkin's disease. Cancer. 1990; 65(5):1155–60.
44. Specht L, Gray RG, Clarke MJ, Peto R. Influence of more extensive radiotherapy and adjuvant chemotherapy on long-term outcome of early-stage Hodgkin's disease: a meta-analysis of 23 randomized trials involving 3,888 patients. International Hodgkin's Disease Collaborative Group. J Clin Oncol. 1998; 16(3):830–43.
45. Specht L, Yahalom J, Illidge T, Berthelsen AK, Constine LS, Eich HT, et al. Modern radiation therapy for Hodgkin lymphoma: field and dose guidelines from the international lymphoma radiation oncology group (ILROG). Int J Radiat Oncol Biol Phys. 2014;89(4):854–62.
46. Klimm B, Diehl V, Pfistner B, Engert A. Current treatment strategies of the German Hodgkin Study Group (GHSG). Eur J Haematol Suppl. 2005;66: 125–34.
47. Carde P, Hagenbeek A, Hayat M, Monconduit M, Thomas J, Burgers MJ, et al. Clinical staging versus laparotomy and combined modality with MOPP versus ABVD in early-stage Hodgkin's disease: the H6 twin randomized trials from the European Organization for Research and Treatment of Cancer Lymphoma Cooperative Group. J Clin Oncol. 1993; 11(11):2258–72.
48. Connors JM, Klimo P, Adams G, Burns BF, Cooper I, Meyer RM, et al. Treatment of advanced Hodgkin's disease with chemotherapy – comparison of MOPP/ABV hybrid regimen with alternating courses of MOPP and ABVD: a report from the National Cancer

Institute of Canada clinical trials group. J Clin Oncol. 1997;15(4):1638–45.
49. Duggan DB, Petroni GR, Johnson JL, Glick JH, Fisher RI, Connors JM, et al. Randomized comparison of ABVD and MOPP/ABV hybrid for the treatment of advanced Hodgkin's disease: report of an intergroup trial. J Clin Oncol. 2003;21(4):607–14.
50. Sieber M, Tesch H, Pfistner B, Rueffer U, Lathan B, Brosteanu O, et al. Rapidly alternating COPP/ABV/IMEP is not superior to conventional alternating COPP/ABVD in combination with extended-field radiotherapy in intermediate-stage Hodgkin's lymphoma: final results of the German Hodgkin's Lymphoma Study Group Trial HD5. J Clin Oncol. 2002; 20(2):476–84.
51. Diehl V, Brilliant C, Engert A, Wolf J, Nogova L, Mueller R, et al. Reduction of combined modality treatment intensity in early stage Hodgkin's lymphoma: interim analysis of the HD10 trial of the GHSG. Eur J Haematol. 2004;73:37.
52. Diehl V, Brilliant C, Engert A, Wolf J, Nogova L, Mueller R, et al. Intensification of chemotherapy and concomitant reduction of radiotherapy dose in intermediate stage Hodgkin's lymphoma: results of the 4th interim analysis of the HD11 trial of the GHSG. Eur J Haematol. 2004;73:37.
53. Diehl V, Franklin J, Pfreundschuh M, Lathan B, Paulus U, Hasenclever D, et al. Standard and increased-dose BEACOPP chemotherapy compared with COPP-ABVD for advanced Hodgkin's disease. N Engl J Med. 2003;348(24):2386–95.
54. Ballova V, Ruffer JU, Haverkamp H, Pfistner B, Muller-Hermelink HK, Duhmke E, et al. A prospectively randomized trial carried out by the German Hodgkin Study Group (GHSG) for elderly patients with advanced Hodgkin's disease comparing BEACOPP baseline and COPP-ABVD (study HD9elderly). Ann Oncol. 2005;16(1):124–31.
55. Carde PP, Karrasch M, Fortpied C, Brice P, Khaled HM, Caillot D, et al. ABVD (8 cycles) versus BEACOPP (4 escalated cycles = > 4 baseline) in stage III–IV high-risk Hodgkin lymphoma (HL): First results of EORTC 20012 Intergroup randomized phase III clinical trial. ASCO Meeting Abstracts. 2012 May 30, 2012;30(15_suppl):8002.
56. Gordon LI, Hong F, Fisher RI, Bartlett NL, Connors JM, Gascoyne RD, et al. Randomized phase III trial of ABVD versus Stanford V with or without radiation therapy in locally extensive and advanced-stage Hodgkin lymphoma: an intergroup study coordinated by the Eastern Cooperative Oncology Group (E2496). J Clin Oncol. 2013;31(6):684–91. Pubmed Central PMCID: 3574266.
57. Akpek G, Ambinder RF, Piantadosi S, Abrams RA, Brodsky RA, Vogelsang GB, et al. Long-term results of blood and marrow transplantation for Hodgkin's lymphoma. J Clin Oncol. 2001;19(23):4314–21.
58. Jagannath S, Armitage JO, Dicke KA, Tucker SL, Velasquez WS, Smith K, et al. Prognostic factors for response and survival after high-dose cyclophosphamide, carmustine, and etoposide with autologous bone marrow transplantation for relapsed Hodgkin's disease. J Clin Oncol. 1989;7(2):179–85.
59. Jones RJ, Piantadosi S, Mann RB, Ambinder RF, Seifter EJ, Vriesendorp HM, et al. High-dose cytotoxic therapy and bone marrow transplantation for relapsed Hodgkin's disease. J Clin Oncol. 1990; 8(3):527–37.
60. Nademanee A, O'Donnell MR, Snyder DS, Schmidt GM, Parker PM, Stein AS, et al. High-dose chemotherapy with or without total body irradiation followed by autologous bone marrow and/or peripheral blood stem cell transplantation for patients with relapsed and refractory Hodgkin's disease: results in 85 patients with analysis of prognostic factors. Blood. 1995;85(5):1381–90.
61. Sureda A, Arranz R, Iriondo A, Carreras E, Lahuerta JJ, Garcia-Conde J, et al. Autologous stem-cell transplantation for Hodgkin's disease: results and prognostic factors in 494 patients from the Grupo Espanol de Linfomas/Transplante Autologo de Medula Osea Spanish Cooperative Group. J Clin Oncol. 2001; 19(5):1395–404.
62. Anderson JE, Litzow MR, Appelbaum FR, Schoch G, Fisher LD, Buckner CD, et al. Allogeneic, syngeneic, and autologous marrow transplantation for Hodgkin's disease: the 21-year Seattle experience. J Clin Oncol. 1993;11(12):2342–50.
63. Gajewski JL, Phillips GL, Sobocinski KA, Armitage JO, Gale RP, Champlin RE, et al. Bone marrow transplants from HLA-identical siblings in advanced Hodgkin's disease. J Clin Oncol. 1996;14(2):572–8.
64. Horning SJ, Chao NJ, Negrin RS, Hoppe RT, Long GD, Hu WW, et al. High-dose therapy and autologous hematopoietic progenitor cell transplantation for recurrent or refractory Hodgkin's disease: analysis of the Stanford University results and prognostic indices. Blood. 1997;89(3):801–13.
65. Fehniger TA, Larson S, Trinkaus K, Siegel MJ, Cashen AF, Blum KA, et al. A phase 2 multicenter study of lenalidomide in relapsed or refractory classical Hodgkin lymphoma. Blood. 2011; 118(19):5119–25. Pubmed Central PMCID: 3217400.
66. Johnston PB, Inwards DJ, Colgan JP, Laplant BR, Kabat BF, Habermann TM, et al. A phase II trial of the oral mTOR inhibitor everolimus in relapsed Hodgkin lymphoma. Am J Hematol. 2010;85(5): 320–4. Pubmed Central PMCID: 4420736.
67. Moskowitz AJ, Hamlin Jr PA, Perales MA, Gerecitano J, Horwitz SM, Matasar MJ, et al. Phase II study of bendamustine in relapsed and refractory Hodgkin lymphoma. J Clin Oncol. 2013; 31(4): 456–60. Pubmed Central PMCID: 3862960.
68. Younes A, Gopal AK, Smith SE, Ansell SM, Rosenblatt JD, Savage KJ, et al. Results of a pivotal phase II study of brentuximab vedotin for patients with relapsed or refractory Hodgkin's lymphoma. J Clin Oncol. 2012;30(18):2183–9.

69. Armand P. Checkpoint blockade in lymphoma. Hematol/Educ Pro Am Soc Hematol Am Soc Hematol Educ Prog. 2015;2015(1):69–73.
70. Jackson C, Sirohi B, Cunningham D, Horwich A, Thomas K, Wotherspoon A. Lymphocyte-predominant Hodgkin lymphoma – clinical features and treatment outcomes from a 30-year experience. Ann Oncol. 2010;21(10):2061–8.
71. Ekstrand BC, Lucas JB, Horwitz SM, Fan Z, Breslin S, Hoppe RT, et al. Rituximab in lymphocyte-predominant Hodgkin disease: results of a phase 2 trial. Blood. 2003;101(11):4285–9.
72. Rehwald U, Schulz H, Reiser M, Sieber M, Staak JO, Morschhauser F, et al. Treatment of relapsed CD20+ Hodgkin lymphoma with the monoclonal antibody rituximab is effective and well tolerated: results of a phase 2 trial of the German Hodgkin Lymphoma Study Group. Blood. 2003;101(2):420–4.
73. Younes A, Romaguera J, Hagemeister F, McLaughlin P, Rodriguez MA, Fiumara P, et al. A pilot study of rituximab in patients with recurrent, classic Hodgkin disease. Cancer. 2003;98 (2):310–4.
74. Dores GM, Metayer C, Curtis RE, Lynch CF, Clarke EA, Glimelius B, et al. Second malignant neoplasms among long-term survivors of Hodgkin's disease: a population-based evaluation over 25 years. J Clin Oncol. 2002;20(16):3484–94.
75. Swerdlow AJ, Higgins CD, Smith P, Cunningham D, Hancock BW, Horwich A, et al. Myocardial infarction mortality risk after treatment for Hodgkin disease: a collaborative British cohort study. J Natl Cancer Inst. 2007;99(3):206–14.
76. Figures. ACSCFa. [updated 4 Jan 2016.]. Available from: http://www.cancer.org/docroot/STT/content/STT_1x_Cancer_Facts__Figures_201.
77. Baecklund E, Iliadou A, Askling J, Ekbom A, Backlin C, Granath F, et al. Association of chronic inflammation, not its treatment, with increased lymphoma risk in rheumatoid arthritis. Arthritis Rheum. 2006;54(3):692–701.
78. Grulich AE, van Leeuwen MT, Falster MO, Vajdic CM. Incidence of cancers in people with HIV/AIDS compared with immunosuppressed transplant recipients: a meta-analysis. Lancet. 2007;370(9581): 59–67.
79. Ramos-Casals M, la Civita L, de Vita S, Solans R, Luppi M, Medina F, et al. Characterization of B cell lymphoma in patients with Sjogren's syndrome and hepatitis C virus infection. Arthritis Rheum. 2007; 57(1):161–70.
80. Harris NL, Jaffe ES, Stein H, Banks PM, Chan JK, Cleary ML, et al. A revised European-American classification of lymphoid neoplasms: a proposal from the International Lymphoma Study Group. Blood. 1994;84(5):1361–92.
81. Jaffe ES. The 2008 WHO classification of lymphomas: implications for clinical practice and translational research. Hematol/Educ Pro Am Soc Hematol Am Soc Hematol Educ Prog. 2009:523–31.
82. Swerdllow S, Campo E, Harris NL. WHO classification of tumours of haematopoietic and lymphoid tissues. France: IARC Press; 2008.
83. Alizadeh AA, Eisen MB, Davis RE, Ma C, Lossos IS, Rosenwald A, et al. Distinct types of diffuse large B-cell lymphoma identified by gene expression profiling. Nature. 2000;403(6769):503–11.
84. Shipp MA, Ross KN, Tamayo P, Weng AP, Kutok JL, Aguiar RC, et al. Diffuse large B-cell lymphoma outcome prediction by gene-expression profiling and supervised machine learning. Nat Med. 2002; 8(1): 68–74.
85. Rosenwald A, Wright G, Chan WC, Connors JM, Campo E, Fisher RI, et al. The use of molecular profiling to predict survival after chemotherapy for diffuse large-B-cell lymphoma. N Engl J Med. 2002;346(25):1937–47.
86. Johnson NA, Slack GW, Savage KJ, Connors JM, Ben-Neriah S, Rogic S, et al. Concurrent expression of MYC and BCL2 in diffuse large B-cell lymphoma treated with rituximab plus cyclophosphamide, doxorubicin, vincristine, and prednisone. J Clin Oncol. 2012;30(28):3452–9.
87. Anderson T, Chabner BA, Young RC, Berard CW, Garvin AJ, Simon RM, et al. Malignant lymphoma. 1. The histology and staging of 473 patients at the national cancer institute. Cancer. 1982; 50(12): 2699–707.
88. NCCN Clinical Practice Guidelines in Oncology Non-Hodgkin's Lymphoma Version 2.2015 NCCN; 2015 [cited 2015 8.21.2015]. Available from: http://www.nccn.org/professionals/physician_gls/f_guidelines.asp#site
89. A predictive model for aggressive non-Hodgkin's lymphoma. The International Non-Hodgkin's Lymphoma Prognostic Factors Project. The New England journal of medicine. 1993 Sep 30;329(14):987–94.
90. Sehn LH, Berry B, Chhanabhai M, Fitzgerald C, Gill K, Hoskins P, et al. The revised International Prognostic Index (R-IPI) is a better predictor of outcome than the standard IPI for patients with diffuse large B-cell lymphoma treated with R-CHOP. Blood. 2007;109(5):1857–61.
91. Miller TP. The limits of limited stage lymphoma. J Clin Oncol. 2004;22(15):2982–4.
92. Zhou Z, Sehn LH, Rademaker AW, Gordon LI, Lacasce AS, Crosby-Thompson A, et al. An enhanced International Prognostic Index (NCCN-IPI) for patients with diffuse large B-cell lymphoma treated in the rituximab era. Blood. 2014;123 (6):837–42.
93. Blay J, Gomez F, Sebban C, Bachelot T, Biron P, Guglielmi C, et al. The International Prognostic Index correlates to survival in patients with aggressive lymphoma in relapse: analysis of the PARMA trial. Parma Group Blood. 1998;92(10):3562–8.

94. Hamlin PA, Zelenetz AD, Kewalramani T, Qin J, Satagopan JM, Verbel D, et al. Age-adjusted International Prognostic Index predicts autologous stem cell transplantation outcome for patients with relapsed or primary refractory diffuse large B-cell lymphoma. Blood. 2003;102(6):1989–96.
95. Lerner RE, Thomas W, Defor TE, Weisdorf DJ, Burns LJ. The International Prognostic Index assessed at relapse predicts outcomes of autologous transplantation for diffuse large-cell non-Hodgkin's lymphoma in second complete or partial remission. Biol Blood Marrow Transplant. 2007;13(4):486–92.
96. Moskowitz CH, Nimer SD, Glassman JR, Portlock CS, Yahalom J, Straus DJ, et al. The International Prognostic Index predicts for outcome following autologous stem cell transplantation in patients with relapsed and primary refractory intermediate-grade lymphoma. Bone Marrow Transplant. 1999; 23(6):561–7.
97. Buske C, Hoster E, Dreyling M, Hasford J, Unterhalt M, Hiddemann W. The Follicular Lymphoma International Prognostic Index (FLIPI) separates high-risk from intermediate- or low-risk patients with advanced-stage follicular lymphoma treated front-line with rituximab and the combination of cyclophosphamide, doxorubicin, vincristine, and prednisone (R-CHOP) with respect to treatment outcome. Blood. 2006;108(5):1504–8.
98. Solal-Celigny P, Roy P, Colombat P, White J, Armitage JO, Arranz-Saez R, et al. Follicular lymphoma international prognostic index. Blood. 2004;104(5):1258–65.
99. Zelenetz AD, Abramson JS, Advani RH, Andreadis CB, Byrd JC, Czuczman MS, et al. NCCN clinical practice guidelines in oncology: non-Hodgkin's lymphomas. J Natl Compr Cancer Netw. 2010; 8(3): 288–334.
100. Cheson BD, Rummel MJ. Bendamustine: rebirth of an old drug. J Clin Oncol. 2009;27(9):1492–501.
101. Coiffier B. Treatment of non-Hodgkin's lymphoma: a look over the past decade. Clin Lymphoma Myeloma. 2006;7 Suppl 1:S7–13.
102. Mihelic R, Kaufman J, Lonial S, Flowers C. Maintenance therapy in lymphoma. Clin Lymphoma Myeloma. 2007;7(8):507–13.
103. Salles GA. Clinical features, prognosis and treatment of follicular lymphoma. Hematol/Educ Pro Am Soc Hematol Am Soc Hematol Educ Prog. 2007:216–25.
104. Tageja N, Padheye S, Dandawate P, Al-Katib A, Mohammad RM. New targets for the treatment of follicular lymphoma. J Hematol Oncol. 2009;2:50. Pubmed Central PMCID: 2805680.
105. Winter JN. Defining the role of immunotherapy and radioimmunotherapy in the treatment of low-grade lymphoma. Curr Opin Hematol. 2007; 14(4):360–8.
106. Wilson W, Armitage J. Non-Hodgkin's lymphoma. Abeloff M, Armitage J, Niederhuber J, Kastan M, McKenna W, editors, editors. Philadelphia: Churchill Livingstone Elsevier; 2008.
107. Ardeshna KM, Smith P, Norton A, Hancock BW, Hoskin PJ, MacLennan KA, et al. Long-term effect of a watch and wait policy versus immediate systemic treatment for asymptomatic advanced-stage non--Hodgkin lymphoma: a randomised controlled trial. Lancet. 2003;362(9383):516–22.
108. Solal-Celigny P, Bellei M, Marcheselli L, Pesce EA, Pileri S, McLaughlin P, et al. Watchful waiting in low-tumor burden follicular lymphoma in the rituximab era: results of an F2-study database. J Clin Oncol. 2012;30(31):3848–53.
109. Sousou T, Friedberg J. Rituximab in indolent lymphomas. Semin Hematol. 2010;47(2):133–42. Pubmed Central PMCID: 2848176.
110. Colombat P, Brousse N, Morschhauser F, Franchi-Rezgui P, Soubeyran P, Delwail V, et al. editors. Single treatment with rituximab monotherapy for low-tumor burden follicular lymphoma (FL): survival analyses with extended follow-up (F/up) of 7 years. ASH Annual Meeting Abstracts; Blood. 2006;108:486
111. Colombat P, Salles G, Brousse N, Eftekhari P, Soubeyran P, Delwail V, et al. Rituximab (anti-CD20 monoclonal antibody) as single first-line therapy for patients with follicular lymphoma with a low tumor burden: clinical and molecular evaluation. Blood. 2001;97(1):101–6.
112. McLaughlin P, Grillo-Lopez AJ, Link BK, Levy R, Czuczman MS, Williams ME, et al. Rituximab chimeric anti-CD20 monoclonal antibody therapy for relapsed indolent lymphoma: half of patients respond to a four-dose treatment program. J Clin Oncol. 1998;16(8):2825–33.
113. Czuczman MS, Weaver R, Alkuzweny B, Berlfein J, Grillo-Lopez AJ. Prolonged clinical and molecular remission in patients with low-grade or follicular non-Hodgkin's lymphoma treated with rituximab plus CHOP chemotherapy: 9-year follow-up. J Clin Oncol. 2004;22(23):4711–6.
114. Forstpointner R, Dreyling M, Repp R, Hermann S, Hanel A, Metzner B, et al. The addition of rituximab to a combination of fludarabine, cyclophosphamide, mitoxantrone (FCM) significantly increases the response rate and prolongs survival as compared with FCM alone in patients with relapsed and refractory follicular and mantle cell lymphomas: results of a prospective randomized study of the German Low-Grade Lymphoma Study Group. Blood. 2004;104(10):3064–71.
115. Marcus R, Imrie K, Belch A, Cunningham D, Flores E, Catalano J, et al. CVP chemotherapy plus rituximab compared with CVP as first-line treatment for advanced follicular lymphoma. Blood. 2005; 105(4):1417–23.
116. Zinzani PL, Pulsoni A, Perrotti A, Soverini S, Zaja F, De Renzo A, et al. Fludarabine plus mitoxantrone with and without rituximab versus CHOP with and

without rituximab as front-line treatment for patients with follicular lymphoma. J Clin Oncol. 2004; 22(13): 2654–61.
117. van Oers MH, Klasa R, Marcus RE, Wolf M, Kimby E, Gascoyne RD, et al. Rituximab maintenance improves clinical outcome of relapsed/resistant follicular non-Hodgkin lymphoma in patients both with and without rituximab during induction: results of a prospective randomized phase 3 intergroup trial. Blood. 2006;108(10):3295–301.
118. Hochster H, Weller E, Gascoyne RD, Habermann TM, Gordon LI, Ryan T, et al. Maintenance rituximab after cyclophosphamide, vincristine, and prednisone prolongs progression-free survival in advanced indolent lymphoma: results of the randomized phase III ECOG1496 Study. J Clin Oncol. 2009; 27(10): 1607–14.
119. Schulz H, Bohlius JF, Trelle S, Skoetz N, Reiser M, Kober T, et al. Immunochemotherapy with rituximab and overall survival in patients with indolent or mantle cell lymphoma: a systematic review and meta-analysis. J Natl Cancer Inst. 2007;99(9): 706–14.
120. Salles G, Seymour JF, Offner F, Lopez-Guillermo A, Belada D, Xerri L, et al. Rituximab maintenance for 2 years in patients with high tumour burden follicular lymphoma responding to rituximab plus chemotherapy (PRIMA): a phase 3, randomised controlled trial. Lancet. 2011;377(9759):42–51.
121. Press OW, Unger JM, Rimsza LM, Friedberg JW, LeBlanc M, Czuczman MS, et al. Phase III randomized intergroup trial of CHOP plus rituximab compared with CHOP chemotherapy plus ^{131}iodine-tositumomab for previously untreated follicular non-Hodgkin lymphoma: SWOG S0016. J Clin Oncol. 2013;31(3):314–20.
122. Samaniego F, Berkova Z, Romaguera JE, Fowler N, Fanale MA, Pro B, et al. 90Y-ibritumomab tiuxetan radiotherapy as first-line therapy for early stage low-grade B-cell lymphomas, including bulky disease. Br J Haematol. 2014;167(2):207–13.
123. Scholz CW, Pinto A, Linkesch W, Linden O, Viardot A, Keller U, et al. (90)Yttrium-ibritumomab-tiuxetan as first-line treatment for follicular lymphoma: 30 months of follow-up data from an international multicenter phase II clinical trial. J Clin Oncol. 2013;31(3):308–13.
124. van Meerten T, Hagenbeek A. CD20-targeted therapy: the next generation of antibodies. Semin Hematol. 2010;47(2):199–210.
125. Davis TA, Grillo-Lopez AJ, White CA, McLaughlin P, Czuczman MS, Link BK, et al. Rituximab anti-CD20 monoclonal antibody therapy in non-Hodgkin's lymphoma: safety and efficacy of re-treatment. J Clin Oncol. 2000; 18(17):3135–43.
126. Davis TA, White CA, Grillo-Lopez AJ, Velasquez WS, Link B, Maloney DG, et al. Single-agent monoclonal antibody efficacy in bulky non-Hodgkin's lymphoma: results of a phase II trial of rituximab. J Clin Oncol. 1999;17(6):1851–7.
127. Davis TA, Kaminski MS, Leonard JP, Hsu FJ, Wilkinson M, Zelenetz A, et al. The radioisotope contributes significantly to the activity of radioimmunotherapy. Clin Cancer Res. 2004;10(23):7792–8.
128. Witzig TE, Gordon LI, Cabanillas F, Czuczman MS, Emmanouilides C, Joyce R, et al. Randomized controlled trial of yttrium-90-labeled ibritumomab tiuxetan radioimmunotherapy versus rituximab immunotherapy for patients with relapsed or refractory low-grade, follicular, or transformed B-cell non-Hodgkin's lymphoma. J Clin Oncol. 2002; 20(10):2453–63.
129. Rohatiner AZ, Nadler L, Davies AJ, Apostolidis J, Neuberg D, Matthews J, et al. Myeloablative therapy with autologous bone marrow transplantation for follicular lymphoma at the time of second or subsequent remission: long-term follow-up. J Clin Oncol. 2007;25(18):2554–9.
130. Sebban C, Brice P, Delarue R, Haioun C, Souleau B, Mounier N, et al. Impact of rituximab and/or high-dose therapy with autotransplant at time of relapse in patients with follicular lymphoma: a GELA study. J Clin Oncol. 2008;26(21):3614–20.
131. Coiffier B, Lepage E, Briere J, Herbrecht R, Tilly H, Bouabdallah R, et al. CHOP chemotherapy plus rituximab compared with CHOP alone in elderly patients with diffuse large-B-cell lymphoma. N Engl J Med. 2002;346(4):235–42.
132. Feugier P, Van Hoof A, Sebban C, Solal-Celigny P, Bouabdallah R, Ferme C, et al. Long-term results of the R-CHOP study in the treatment of elderly patients with diffuse large B-cell lymphoma: a study by the Groupe d'Etude des Lymphomes de l'Adulte. J Clin Oncol. 2005;23(18):4117–26.
133. Habermann TM, Weller EA, Morrison VA, Gascoyne RD, Cassileth PA, Cohn JB, et al. Rituximab-CHOP versus CHOP alone or with maintenance rituximab in older patients with diffuse large B-cell lymphoma. J Clin Oncol. 2006;24(19):3121–7.
134. Cunningham D, Hawkes EA, Jack A, Qian W, Smith P, Mouncey P, et al. Rituximab plus cyclophosphamide, doxorubicin, vincristine, and prednisolone in patients with newly diagnosed diffuse large B-cell non-Hodgkin lymphoma: a phase 3 comparison of dose intensification with 14-day versus 21-day cycles. Lancet. 2013;381(9880):1817–26.
135. Delarue R, Tilly H, Mounier N, Petrella T, Salles G, Thieblemont C, et al. Dose-dense rituximab-CHOP compared with standard rituximab-CHOP in elderly patients with diffuse large B-cell lymphoma (the LNH03-6B study): a randomised phase 3 trial. Lancet Oncol. 2013;14(6):525–33.
136. Ruan J, Martin P, Furman RR, Lee SM, Cheung K, Vose JM, et al. Bortezomib plus CHOP-rituximab for previously untreated diffuse large B-cell lymphoma and mantle cell lymphoma. J Clin Oncol. 2011;29 (6):690–7.

137. Vitolo U, Chiappella A, Franceschetti S, Carella AM, Baldi I, Inghirami G, et al. Lenalidomide plus R-CHOP21 in elderly patients with untreated diffuse large B-cell lymphoma: results of the REAL07 open-label, multicentre, phase 2 trial. Lancet Oncol. 2014; 15(7):730–7.
138. Younes A, Thieblemont C, Morschhauser F, Flinn I, Friedberg JW, Amorim S, et al. Combination of ibrutinib with rituximab, cyclophosphamide, doxorubicin, vincristine, and prednisone (R-CHOP) for treatment-naive patients with CD20-positive B-cell non-Hodgkin lymphoma: a non-randomised, phase 1b study. Lancet Oncol. 2014;15(9):1019–26.
139. Howlett C, Snedecor SJ, Landsburg DJ, Svoboda J, Chong EA, Schuster SJ, et al. Front-line, dose-escalated immunochemotherapy is associated with a significant progression-free survival advantage in patients with double-hit lymphomas: a systematic review and meta-analysis. Br J Haematol. 2015; 170(4):504–14.
140. Petrich AM, Gandhi M, Jovanovic B, Castillo JJ, Rajguru S, Yang DT, et al. Impact of induction regimen and stem cell transplantation on outcomes in double-hit lymphoma: a multicenter retrospective analysis. Blood. 2014;124(15):2354–61.
141. Greb A, Bohlius J, Schiefer D, Schwarzer G, Schulz H, Engert A. High-dose chemotherapy with autologous stem cell transplantation in the first line treatment of aggressive non-Hodgkin lymphoma (NHL) in adults. Cochrane Database Syst Rev. 2008;1:CD004024.
142. Zinzani PL, Bendandi M, Martelli M, Falini B, Sabattini E, Amadori S, et al. Anaplastic large-cell lymphoma: clinical and prognostic evaluation of 90 adult patients. J Clin Oncol. 1996;14(3):955–62.
143. Escalon MP, Liu NS, Yang Y, Hess M, Walker PL, Smith TL, et al. Prognostic factors and treatment of patients with T-cell non-Hodgkin lymphoma: the M. D. Anderson Cancer Center experience. Cancer. 2005;103(10):2091–8.
144. Simon A, Peoch M, Casassus P, Deconinck E, Colombat P, Desablens B, et al. Upfront VIP-reinforced-ABVD (VIP-rABVD) is not superior to CHOP/21 in newly diagnosed peripheral T cell lymphoma. Results of the randomized phase III trial GOELAMS-LTP95. Br J Haematol. 2010;151(2): 159–66.
145. Bruns I, Fox F, Reinecke P, Kobbe G, Kronenwett R, Jung G, et al. Complete remission in a patient with relapsed angioimmunoblastic T-cell lymphoma following treatment with bevacizumab. Leukemia. 2005;19(11):1993–5.
146. Piekarz RL, Robey RW, Zhan Z, Kayastha G, Sayah A, Abdeldaim AH, et al. T-cell lymphoma as a model for the use of histone deacetylase inhibitors in cancer therapy: impact of depsipeptide on molecular markers, therapeutic targets, and mechanisms of resistance. Blood. 2004;103(12):4636–43.
147. Dearden C. Alemtuzumab in peripheral T-cell malignancies. Cancer Biother Radiopharm. 2004; 19(4): 391–8.
148. Ishida T, Joh T, Uike N, Yamamoto K, Utsunomiya A, Yoshida S, et al. Defucosylated anti-CCR4 monoclonal antibody (KW-0761) for relapsed adult T-cell leukemia-lymphoma: a multicenter phase II study. J Clin Oncol. 2012;30(8):837–42.
149. Ansell SM. Brentuximab vedotin. Blood. 2014; 124(22):3197–200.
150. Richman SD, Levenson SM, Jones AE, Johnston GS. Radionuclide studies in Hodgkin's disease and lymphomas. Semin Nucl Med. 1975;5(1):103–8.
151. Adler S, Parthasarathy KL, Bakshi SP, Stutzman L. Gallium-67-citrate scanning for the localization and staging of lymphomas. J Nucl Med. 1975;16(4): 255–60.
152. Even-Sapir E, Bar-Shalom R, Israel O, Frenkel A, Iosilevsky G, Haim N, et al. Single-photon emission computed tomography quantitation of gallium citrate uptake for the differentiation of lymphoma from benign hilar uptake. J Clin Oncol. 1995;13(4):942–6.
153. Front D, Bar-Shalom R, Mor M, Haim N, Epelbaum R, Frenkel A, et al. Hodgkin disease: prediction of outcome with 67Ga scintigraphy after one cycle of chemotherapy. Radiology. 1999;210(2): 487–91.
154. Front D, Bar-Shalom R, Mor M, Haim N, Epelbaum R, Frenkel A, et al. Aggressive non-Hodgkin lymphoma: early prediction of outcome with 67Ga scintigraphy. Radiology. 2000;214(1): 253–7.
155. Israel O, Front D, Lam M, Ben-Haim S, Kleinhaus U, Ben-Shachar M, et al. Gallium 67 imaging in monitoring lymphoma response to treatment. Cancer. 1988;61(12):2439–43.
156. Israel O, Mor M, Epelbaum R, Frenkel A, Haim N, Dann EJ, et al. Clinical pretreatment risk factors and Ga-67 scintigraphy early during treatment for prediction of outcome of patients with aggressive non-Hodgkin lymphoma. Cancer. 2002;94(4): 873–8.
157. Janicek M, Kaplan W, Neuberg D, Canellos GP, Shulman LN, Shipp MA. Early restaging gallium scans predict outcome in poor-prognosis patients with aggressive non-Hodgkin's lymphoma treated with high-dose CHOP chemotherapy. J Clin Oncol. 1997;15(4):1631–7.
158. Bekerman C, Moran EM, Hoffer PB, Hendrix RW, Gottschalk A. Scintigraphic evaluation of lymphoma: a comparative study of ^{67}Ga-citrate and ^{111}In-Bleomycin. Radiology. 1977;123(3):687–94.
159. Jones SE, Lilien DL, O'Mara RE, Durie BG, Salmon SE. Indium-111 bleomycin tumor scanning in lymphoma. Med Pediatr Oncol. 1975;1(1):11–21.
160. Bar-Shalom R, Mor M, Yefremov N, Goldsmith SJ. The value of Ga-67 scintigraphy and F-18 fluorodeoxyglucose positron emission tomography

in staging and monitoring the response of lymphoma to treatment. Semin Nucl Med. 2001;31(3):177–90.
161. Friedberg JW, Fischman A, Neuberg D, Kim H, Takvorian T, Ng AK, et al. FDG-PET is superior to gallium scintigraphy in staging and more sensitive in the follow-up of patients with de novo Hodgkin lymphoma: a blinded comparison. Leuk Lymphoma. 2004;45(1):85–92.
162. Kostakoglu L, Leonard JP, Kuji I, Coleman M, Vallabhajosula S, Goldsmith SJ. Comparison of fluorine-18 fluorodeoxyglucose positron emission tomography and Ga-67 scintigraphy in evaluation of lymphoma. Cancer. 2002;94(4):879–88.
163. Tsukamoto N, Kojima M, Hasegawa M, Oriuchi N, Matsushima T, Yokohama A, et al. The usefulness of ^{18}F-fluorodeoxyglucose positron emission tomography (^{18}F-FDG-PET) and a comparison of ^{18}F-FDG-PET with ^{67}Ga scintigraphy in the evaluation of lymphoma: relation to histologic subtypes based on the World Health Organization classification. Cancer. 2007;110(3):652–9.
164. Yamamoto F, Tsukamoto E, Nakada K, Takei T, Zhao S, Asaka M, et al. ^{18}F-FDG PET is superior to ^{67}Ga SPECT in the staging of non-Hodgkin's lymphoma. Ann Nucl Med. 2004;18(6):519–26.
165. Weiler-Sagie M, Bushelev O, Epelbaum R, Dann EJ, Haim N, Avivi I, et al. ^{18}F-FDG avidity in lymphoma readdressed: a study of 766 patients. J Nucl Med. 2010;51(1):25–30.
166. Lapela M, Leskinen S, Minn HR, Lindholm P, Klemi PJ, Soderstrom KO, et al. Increased glucose metabolism in untreated non-Hodgkin's lymphoma: a study with positron emission tomography and fluorine-18-fluorodeoxyglucose. Blood. 1995;86(9):3522–7.
167. Rodriguez M, Rehn S, Ahlstrom H, Sundstrom C, Glimelius B. Predicting malignancy grade with PET in non-Hodgkin's lymphoma. J Nucl Med. 1995;36 (10):1790–6.
168. Schoder H, Noy A, Gonen M, Weng L, Green D, Erdi YE, et al. Intensity of 18fluorodeoxyglucose uptake in positron emission tomography distinguishes between indolent and aggressive non-Hodgkin's lymphoma. J Clin Oncol. 2005;23(21):4643–51.
169. Bruzzi JF, Macapinlac H, Tsimberidou AM, Truong MT, Keating MJ, Marom EM, et al. Detection of Richter's transformation of chronic lymphocytic leukemia by PET/CT. J Nucl Med. 2006;47(8):1267–73.
170. Bodet-Milin C, Kraeber-Bodere F, Moreau P, Campion L, Dupas B, Le Gouill S. Investigation of FDG-PET/CT imaging to guide biopsies in the detection of histological transformation of indolent lymphoma. Haematologica. 2008;93(3):471–2.
171. Bangerter M, Moog F, Buchmann I, Kotzerke J, Griesshammer M, Hafner M, et al. Whole-body 2-[^{18}F]-fluoro-2-deoxy-D-glucose positron emission tomography (FDG-PET) for accurate staging of Hodgkin's disease. Ann Oncol. 1998;9(10):1117–22.
172. Jerusalem G, Beguin Y, Fassotte MF, Najjar F, Paulus P, Rigo P, et al. Whole-body positron emission tomography using ^{18}F-fluorodeoxyglucose compared to standard procedures for staging patients with Hodgkin's disease. Haematologica. 2001; 86(3):266–73.
173. Moog F, Bangerter M, Diederichs CG, Guhlmann A, Merkle E, Frickhofen N, et al. Extranodal malignant lymphoma: detection with FDG PET versus CT. Radiology. 1998;206(2):475–81.
174. Partridge S, Timothy A, O'Doherty MJ, Hain SF, Rankin S, Mikhaeel G. 2-Fluorine-18-fluoro-2-deoxy-D glucose positron emission tomography in the pretreatment staging of Hodgkin's disease: influence on patient management in a single institution. Ann Oncol. 2000;11(10):1273–9.
175. Weihrauch MR, Re D, Bischoff S, Dietlein M, Scheidhauer K, Krug B, et al. Whole-body positron emission tomography using ^{18}F-fluorodeoxyglucose for initial staging of patients with Hodgkin's disease. Ann Hematol. 2002;81(1):20–5.
176. Carr R, Barrington SF, Madan B, O'Doherty MJ, Saunders CA, van der Walt J, et al. Detection of lymphoma in bone marrow by whole-body positron emission tomography. Blood. 1998;91(9):3340–6.
177. Moog F, Bangerter M, Kotzerke J, Guhlmann A, Frickhofen N, Reske SN. 18-F-fluorodeoxyglucose-positron emission tomography as a new approach to detect lymphomatous bone marrow. J Clin Oncol. 1998;16(2):603–9.
178. El-Galaly TC, d'Amore F, Mylam KJ, de Nully BP, Bogsted M, Bukh A, et al. Routine bone marrow biopsy has little or no therapeutic consequence for positron emission tomography/computed tomography-staged treatment-naive patients with Hodgkin lymphoma. J Clin Oncol. 2012;30(36):4508–14.
179. Moulin-Romsee G, Hindie E, Cuenca X, Brice P, Decaudin D, Benamor M, et al. ^{18}F-FDG PET/CT bone/bone marrow findings in Hodgkin's lymphoma may circumvent the use of bone marrow trephine biopsy at diagnosis staging. Eur J Nucl Med Mol Imaging. 2010;37(6):1095–105.
180. Pakos EE, Fotopoulos AD, Ioannidis JP. ^{18}F-FDG PET for evaluation of bone marrow infiltration in staging of lymphoma: a meta-analysis. J Nucl Med. 2005;46(6):958–63.
181. Adams HJ, Kwee TC, de Keizer B, Fijnheer R, de Klerk JM, Nievelstein RA. FDG PET/CT for the detection of bone marrow involvement in diffuse large B-cell lymphoma: systematic review and meta-analysis. Eur J Nucl Med Mol Imaging. 2014; 41(3):565–74.
182. Berthet L, Cochet A, Kanoun S, Berriolo-Riedinger A, Humbert O, Toubeau M, et al. In newly diagnosed diffuse large B-cell lymphoma, determination of bone marrow involvement with ^{18}F-FDG PET/CT provides better diagnostic performance and prognostic stratification than does biopsy. J Nucl Med. 2013;54 (8):1244–50.
183. Paone G, Itti E, Haioun C, Gaulard P, Dupuis J, Lin C, et al. Bone marrow involvement in diffuse large

B-cell lymphoma: correlation between FDG-PET uptake and type of cellular infiltrate. Eur J Nucl Med Mol Imaging. 2009;36(5):745–50.
184. Nakamoto Y, Cohade C, Tatsumi M, Hammoud D, Wahl RL. CT appearance of bone metastases detected with FDG PET as part of the same PET/CT examination. Radiology. 2005;237(2):627–34.
185. Buchmann I, Reinhardt M, Elsner K, Bunjes D, Altehoefer C, Finke J, et al. 2-[fluorine-18]fluoro-2-deoxy-D-glucose positron emission tomography in the detection and staging of malignant lymphoma. A bicenter trial. Cancer. 2001;91(5): 889–99.
186. Schoder H, Meta J, Yap C, Ariannejad M, Rao J, Phelps ME, et al. Effect of whole-body ^{18}F-FDG PET imaging on clinical staging and management of patients with malignant lymphoma. J Nucl Med. 2001;42(8):1139–43.
187. Blum RH, Seymour JF, Wirth A, MacManus M, Hicks RJ. Frequent impact of [^{18}F]fluorodeoxyglucose positron emission tomography on the staging and management of patients with indolent non-Hodgkin's lymphoma. Clin Lymphoma. 2003; 4(1):43–9.
188. Janikova A, Bolcak K, Pavlik T, Mayer J, Kral Z. Value of [^{18}F]fluorodeoxyglucose positron emission tomography in the management of follicular lymphoma: the end of a dilemma? Clin Lymphoma Myeloma. 2008;8(5):287–93.
189. Jerusalem G, Beguin Y, Najjar F, Hustinx R, Fassotte MF, Rigo P, et al. Positron emission tomography (PET) with ^{18}F-fluorodeoxyglucose (^{18}F-FDG) for the staging of low-grade non-Hodgkin's lymphoma (NHL). Ann Oncol. 2001;12(6):825–30.
190. Karam M, Novak L, Cyriac J, Ali A, Nazeer T, Nugent F. Role of fluorine-18 fluoro-deoxyglucose positron emission tomography scan in the evaluation and follow-up of patients with low-grade lymphomas. Cancer. 2006;107(1):175–83.
191. Tatsumi M, Cohade C, Nakamoto Y, Fishman EK, Wahl RL. Direct comparison of FDG PET and CT findings in patients with lymphoma: initial experience. Radiology. 2005;237(3):1038–45.
192. Allen-Auerbach M, Quon A, Weber WA, Obrzut S, Crawford T, Silverman DH, et al. Comparison between 2-deoxy-2-[^{18}F]fluoro-D-glucose positron emission tomography and positron emission tomography/computed tomography hardware fusion for staging of patients with lymphoma. Mol Imaging Biol. 2004;6(6):411–6.
193. Chalaye J, Luciani A, Enache C, Beaussart P, Lhermite C, Evangelista E, et al. Clinical impact of contrast-enhanced computed tomography combined with low-dose ^{18}F-fluorodeoxyglucose positron emission tomography/computed tomography on routine lymphoma patient management. Leuk Lymphoma. 2014;55(12):2887–92.
194. Pinilla I, Gomez-Leon N, Del Campo-Del Val L, Hernandez-Maraver D, Rodriguez-Vigil B, Jover-Diaz R, et al. Diagnostic value of CT, PET and combined PET/CT performed with low-dose unenhanced CT and full-dose enhanced CT in the initial staging of lymphoma. Q J Nucl Med Mol Imaging. 2011;55(5):567–75.
195. Schaefer NG, Hany TF, Taverna C, Seifert B, Stumpe KD, von Schulthess GK, et al. Non-Hodgkin lymphoma and Hodgkin disease: coregistered FDG PET and CT at staging and restaging – do we need contrast-enhanced CT? Radiology. 2004;232(3):823–9.
196. Jochelson M, Mauch P, Balikian J, Rosenthal D, Canellos G. The significance of the residual mediastinal mass in treated Hodgkin's disease. J Clin Oncol. 1985;3(5):637–40.
197. Jerusalem G, Beguin Y, Fassotte MF, Najjar F, Paulus P, Rigo P, et al. Whole-body positron emission tomography using ^{18}F-fluorodeoxyglucose for post-treatment evaluation in Hodgkin's disease and non-Hodgkin's lymphoma has higher diagnostic and prognostic value than classical computed tomography scan imaging. Blood. 1999;94(2):429–33.
198. Naumann R, Vaic A, Beuthien-Baumann B, Bredow J, Kropp J, Kittner T, et al. Prognostic value of positron emission tomography in the evaluation of post-treatment residual mass in patients with Hodgkin's disease and non-Hodgkin's lymphoma. Br J Haematol. 2001;115(4):793–800.
199. Spaepen K, Stroobants S, Dupont P, Thomas J, Vandenberghe P, Balzarini J, et al. Can positron emission tomography with [^{18}F]-fluorodeoxyglucose after first-line treatment distinguish Hodgkin's disease patients who need additional therapy from others in whom additional therapy would mean avoidable toxicity? Br J Haematol. 2001;115(2):272–8.
200. Spaepen K, Stroobants S, Dupont P, Van Steenweghen S, Thomas J, Vandenberghe P, et al. Prognostic value of positron emission tomography (PET) with fluorine-18 fluorodeoxyglucose ([^{18}F]FDG) after first-line chemotherapy in non-Hodgkin's lymphoma: is [^{18}F]FDG-PET a valid alternative to conventional diagnostic methods? J Clin Oncol. 2001;19(2):414–9.
201. Zinzani PL, Magagnoli M, Chierichetti F, Zompatori M, Garraffa G, Bendandi M, et al. The role of positron emission tomography (PET) in the management of lymphoma patients. Ann Oncol. 1999;10(10):1181–4.
202. Humm JL, Rosenfeld A, Del Guerra A. From PET detectors to PET scanners. Eur J Nucl Med Mol Imaging. 2003;30(11):1574–97.
203. Kasamon YL, Jones RJ, Wahl RL. Integrating PET and PET/CT into the risk-adapted therapy of lymphoma. J Nucl Med. 2007;48 Suppl 1:19S–27.
204. Engles JM, Quarless SA, Mambo E, Ishimori T, Cho SY, Wahl RL. Stunning and its effect on ^{3}H-FDG uptake and key gene expression in breast cancer cells undergoing chemotherapy. J Nucl Med. 2006; 47(4):603–8.
205. Castellucci P, Zinzani P, Nanni C, Farsad M, Moretti A, Alinari L, et al. ^{18}F-FDG PET early after

radiotherapy in lymphoma patients. Cancer Biother Radiopharm. 2004;19(5):606–12.
206. Jacene HA, Filice R, Kasecamp W, Wahl RL. ^{18}F-FDG PET/CT for monitoring the response of lymphoma to radioimmunotherapy. J Nucl Med. 2009;50(1):8–17.
207. Torizuka T, Zasadny KR, Kison PV, Rommelfanger SG, Kaminski MS, Wahl RL. Metabolic response of non-Hodgkin's lymphoma to ^{131}I-anti-B1 radioimmunotherapy: evaluation with FDG PET. J Nucl Med. 2000;41(6):999–1005.
208. Cheson BD, Horning SJ, Coiffier B, Shipp MA, Fisher RI, Connors JM, et al. Report of an international workshop to standardize response criteria for non-Hodgkin's lymphomas. NCI Sponsored International Working Group. J Clin Oncol. 1999; 17(4): 1244.
209. Cheson BD, Pfistner B, Juweid ME, Gascoyne RD, Specht L, Horning SJ, et al. Revised response criteria for malignant lymphoma. J Clin Oncol. 2007; 25(5): 579–86.
210. Juweid ME, Wiseman GA, Vose JM, Ritchie JM, Menda Y, Wooldridge JE, et al. Response assessment of aggressive non-Hodgkin's lymphoma by integrated International Workshop Criteria and fluorine-18-fluorodeoxyglucose positron emission tomography. J Clin Oncol. 2005;23(21):4652–61.
211. Brepoels L, Stroobants S, De Wever W, Spaepen K, Vandenberghe P, Thomas J, et al. Aggressive and indolent non-Hodgkin's lymphoma: response assessment by integrated international workshop criteria. Leuk Lymphoma. 2007;48(8):1522–30.
212. Brepoels L, Stroobants S, De Wever W, Spaepen K, Vandenberghe P, Thomas J, et al. Hodgkin lymphoma: response assessment by revised international workshop criteria. Leuk Lymphoma. 2007; 48(8):1539–47.
213. Markova J, Kahraman D, Kobe C, Skopalova M, Mocikova H, Klaskova K, et al. Role of [^{18}F]-fluoro-2-deoxy-D-glucose positron emission tomography in early and late therapy assessment of patients with advanced Hodgkin lymphoma treated with bleomycin, etoposide, adriamycin, cyclophosphamide, vincristine, procarbazine and prednisone. Leuk Lymphoma. 2012;53(1):64–70.
214. Sher DJ, Mauch PM, Van Den Abbeele A, LaCasce AS, Czerminski J, Ng AK. Prognostic significance of mid- and post-ABVD PET imaging in Hodgkin's lymphoma: the importance of involved-field radiotherapy. Ann Oncol. 2009;20(11):1848–53.
215. Zinzani PL, Rigacci L, Stefoni V, Broccoli A, Puccini B, Castagnoli A, et al. Early interim ^{18}F-FDG PET in Hodgkin's lymphoma: evaluation on 304 patients. Eur J Nucl Med Mol Imaging. 2012;39(1):4–12.
216. Meignan M, Gallamini A, Haioun C, Polliack A. Report on the second international workshop on interim positron emission tomography in lymphoma held in menton, France, 8–9 April 2010. Leuk Lymphoma. 2010;51(12):2171–80.
217. Meignan M, Gallamini A, Itti E, Barrington S, Haioun C, Polliack A. Report on the third international workshop on interim positron emission tomography in lymphoma held in Menton, France, 26–27 September 2011 and Menton 2011 consensus. Leuk Lymphoma. 2012;53(10):1876–81.
218. Biggi A, Gallamini A, Chauvie S, Hutchings M, Kostakoglu L, Gregianin M, et al. International validation study for interim PET in ABVD-treated, advanced-stage hodgkin lymphoma: interpretation criteria and concordance rate among reviewers. J Nucl Med. 2013;54(5):683–90.
219. Itti E, Meignan M, Berriolo-Riedinger A, Biggi A, Cashen AF, Vera P, et al. An international confirmatory study of the prognostic value of early PET/CT in diffuse large B-cell lymphoma: comparison between Deauville criteria and DeltaSUVmax. Eur J Nucl Med Mol Imaging. 2013;40(9):1312–20.
220. Juweid ME, Stroobants S, Hoekstra OS, Mottaghy FM, Dietlein M, Guermazi A, et al. Use of positron emission tomography for response assessment of lymphoma: consensus of the Imaging Subcommittee of International Harmonization Project in Lymphoma. J Clin Oncol. 2007;25(5):571–8.
221. Shankar LK, Hoffman JM, Bacharach S, Graham MM, Karp J, Lammertsma AA, et al. Consensus recommendations for the use of ^{18}F-FDG PET as an indicator of therapeutic response in patients in National Cancer Institute Trials. J Nucl Med. 2006; 47(6):1059–66.
222. Boellaard R, Oyen WJ, Hoekstra CJ, Hoekstra OS, Visser EP, Willemsen AT, et al. The Netherlands protocol for standardisation and quantification of FDG whole body PET studies in multi-centre trials. Eur J Nucl Med Mol Imaging. 2008;35(12):2320–33.
223. Wahl RL, Jacene H, Kasamon Y, Lodge MA. From RECIST to PERCIST: evolving considerations for PET response criteria in solid tumors. J Nucl Med. 2009;50 Suppl 1:122S–50. Pubmed Central PMCID: 2755245.
224. Wahl RL, Zasadny K, Helvie M, Hutchins GD, Weber B, Cody R. Metabolic monitoring of breast cancer chemohormonotherapy using positron emission tomography: initial evaluation. J Clin Oncol. 1993;11(11):2101–11.
225. Haioun C, Itti E, Rahmouni A, Brice P, Rain JD, Belhadj K, et al. [^{18}F]fluoro-2-deoxy-D-glucose positron emission tomography (FDG-PET) in aggressive lymphoma: an early prognostic tool for predicting patient outcome. Blood. 2005;106(4):1376–81.
226. Hutchings M, Loft A, Hansen M, Pedersen LM, Buhl T, Jurlander J, et al. FDG-PET after two cycles of chemotherapy predicts treatment failure and progression-free survival in Hodgkin lymphoma. Blood. 2006;107(1):52–9.
227. Hutchings M, Mikhaeel NG, Fields PA, Nunan T, Timothy AR. Prognostic value of interim FDG-PET after two or three cycles of chemotherapy in Hodgkin lymphoma. Ann Oncol. 2005;16(7):1160–8.

228. Jerusalem G, Beguin Y, Fassotte MF, Najjar F, Paulus P, Rigo P, et al. Persistent tumor ^{18}F-FDG uptake after a few cycles of polychemotherapy is predictive of treatment failure in non-Hodgkin's lymphoma. Haematologica. 2000;85(6):613–8.
229. Kostakoglu L, Coleman M, Leonard JP, Kuji I, Zoe H, Goldsmith SJ. PET predicts prognosis after 1 cycle of chemotherapy in aggressive lymphoma and Hodgkin's disease. J Nucl Med. 2002;43(8):1018–27.
230. Mikhaeel NG, Hutchings M, Fields PA, O'Doherty MJ, Timothy AR. FDG-PET after two to three cycles of chemotherapy predicts progression-free and overall survival in high-grade non-Hodgkin lymphoma. Ann Oncol. 2005;16(9):1514–23.
231. Spaepen K, Stroobants S, Dupont P, Vandenberghe P, Thomas J, de Groot T, et al. Early restaging positron emission tomography with ^{18}F-fluorodeoxyglucose predicts outcome in patients with aggressive non-Hodgkin's lymphoma. Ann Oncol. 2002;13(9):1356–63.
232. Kasamon YL, Wahl RL. FDG PET and risk-adapted therapy in Hodgkin's and non-Hodgkin's lymphoma. Curr Opin Oncol. 2008;20(2):206–19. Pubmed Central PMCID: 3652336.
233. Skipper HE, Schabel Jr FM, Wilcox WS. Experimental evaluation of potential anticancer agents. Xiii. On the criteria and kinetics associated with "Curability" of experimental leukemia. Cancer Chemother Rep. 1964;35:1–111.
234. Kasamon YL, Wahl RL, Ziessman HA, Blackford AL, Goodman SN, Fidyk CA, et al. Phase II study of risk-adapted therapy of newly diagnosed, aggressive non-Hodgkin lymphoma based on midtreatment FDG-PET scanning. Biol Blood Marrow Transplant. 2009;15(2):242–8. Pubmed Central PMCID: 4020440.
235. Dupuis J, Itti E, Rahmouni A, Hemery F, Gisselbrecht C, Lin C, et al. Response assessment after an inductive CHOP or CHOP-like regimen with or without rituximab in 103 patients with diffuse large B-cell lymphoma: integrating 18fluorodeoxyglucose positron emission tomography to the International Workshop Criteria. Ann Oncol. 2009;20(3):503–7.
236. Moskowitz CH, Schoder H, Teruya-Feldstein J, Sima C, Iasonos A, Portlock CS, et al. Risk-adapted dose-dense immunochemotherapy determined by interim FDG-PET in advanced-stage diffuse large B-cell lymphoma. J Clin Oncol. 2010;28(11):1896–903. Pubmed Central PMCID: 3651601.
237. Pregno P, Chiappella A, Bello M, Botto B, Ferrero S, Franceschetti S, et al. Interim 18-FDG-PET/CT failed to predict the outcome in diffuse large B-cell lymphoma patients treated at the diagnosis with rituximab-CHOP. Blood. 2012;119(9):2066–73.
238. Swinnen LJ, Li H, Quon A, Gascoyne R, Hong F, Ranheim EA, et al. Response-adapted therapy for aggressive non-Hodgkin's lymphomas based on early [^{18}F]FDG-PET scanning: ECOG-ACRIN Cancer Research Group study (E3404). Br J Haematol. 2015;170(1):56–65. Pubmed Central PMCID: 4696544.
239. Positron emission tomography guided therapy of aggressive Non-Hodgkin's Lymphomas (PETAL) ClinicalTrials.gov [1.31.2016]. Available from: https://www.clinicaltrials.gov/ct2/show/results/NCT00554164
240. Duhrsen U, Huttmann A, Jockel KH, Muller S. Positron emission tomography guided therapy of aggressive non-Hodgkin lymphomas – the PETAL trial. Leuk Lymphoma. 2009;50(11):1757–60.
241. Radford J, Illidge T, Counsell N, Hancock B, Pettengell R, Johnson P, et al. Results of a trial of PET-directed therapy for early-stage Hodgkin's lymphoma. N Engl J Med. 2015;372(17):1598–607.
242. Dann EJ, Bar-Shalom R, Tamir A, Haim N, Ben-Shachar M, Avivi I, et al. Risk-adapted BEACOPP regimen can reduce the cumulative dose of chemotherapy for standard and high-risk Hodgkin lymphoma with no impairment of outcome. Blood. 2007;109(3):905–9.
243. Positron Emission Tomography (PET)-adapted chemotherapy in advanced Hodgkin Lymphoma (HL) (HD0607) ClinicalTrials.gov [01.31.2016]. Available from: https://www.clinicaltrials.gov/ct2/show/NCT00795613
244. High-dose chemotherapy and stem cell transplantation. In patients PET-2 positive, after 2 courses of ABVD and comparison of RT Versus no RT in PET-2 negative patients (HD0801) ClinicalTrials.gov [01.31.2016]. Available from: https://www.clinicaltrials.gov/ct2/show/NCT00784537
245. HD18 for advanced stages in Hodgkins Lymphoma ClinicalTrials.gov [01.31.2016]. Available from: https://www.clinicaltrials.gov/ct2/show/NCT00515554
246. Barrington SF, Kirkwood AA, Franceschetto A, Fulham MJ, Roberts TH, Almquist H, et al. PET-CT for staging & early response: results from 'Response Adapted Therapy in Advanced Hodgkin Lymphoma' (RATHL) (CRUK/07/033). Blood. 2016;127(12):1531–8
247. Gallamini A, Rossi A, Patti C, Picardi M, Di Raimondo F, Cantonetti M, et al. Early treatment intensification in advanced-stage high-risk Hodgkin lymphoma (HL) patients, with a positive FDG-PET scan after two ABVD courses–first interim analysis of the GITIL/FIL HD0607 clinical trial. Blood. 2012;120:21.
248. Horning SJ, Juweid ME, Schoder H, Wiseman G, McMillan A, Swinnen LJ, et al. Interim positron emission tomography scans in diffuse large B-cell lymphoma: an independent expert nuclear medicine evaluation of the Eastern Cooperative Oncology Group E3404 study. Blood. 2010;115(4):775–7.
249. Barrington SF, Qian W, Somer EJ, Franceschetto A, Bagni B, Brun E, et al. Concordance between four European centres of PET reporting criteria designed for use in multicentre trials in Hodgkin lymphoma. Eur J Nucl Med Mol Imaging. 2010;37(10):1824–33.

250. Mikhaeel NG, Timothy AR, O'Doherty MJ, Hain S, Maisey MN. 18-FDG-PET as a prognostic indicator in the treatment of aggressive Non-Hodgkin's Lymphoma-comparison with CT. Leuk Lymphoma. 2000;39(5–6):543–53.
251. Lin C, Itti E, Haioun C, Petegnief Y, Luciani A, Dupuis J, et al. Early ^{18}F-FDG PET for prediction of prognosis in patients with diffuse large B-cell lymphoma: SUV-based assessment versus visual analysis. J Nucl Med. 2007;48(10):1626–32.
252. Itti E, Lin C, Dupuis J, Paone G, Capacchione D, Rahmouni A, et al. Prognostic value of interim 18F-FDG PET in patients with diffuse large B-Cell lymphoma: SUV-based assessment at 4 cycles of chemotherapy. J Nucl Med. 2009;50(4):527–33.
253. Gallamini A, Barrington SF, Biggi A, Chauvie S, Kostakoglu L, Gregianin M, et al. The predictive role of interim positron emission tomography for Hodgkin lymphoma treatment outcome is confirmed using the interpretation criteria of the Deauville five-point scale. Haematologica. 2014;99(6):1107–13. Pubmed Central PMCID: 4040916.
254. Liedtke M, Hamlin PA, Moskowitz CH, Zelenetz AD. Surveillance imaging during remission identifies a group of patients with more favorable aggressive NHL at time of relapse: a retrospective analysis of a uniformly-treated patient population. Ann Oncol. 2006;17(6):909–13.
255. Oh YK, Ha CS, Samuels BI, Cabanillas F, Hess MA, Cox JD. Stages I–III follicular lymphoma: role of CT of the abdomen and pelvis in follow-up studies. Radiology. 1999;210(2):483–6.
256. Radford JA, Eardley A, Woodman C, Crowther D. Follow up policy after treatment for Hodgkin's disease: too many clinic visits and routine tests? A review of hospital records. BMJ. 1997;314 (7077):343–6. Pubmed Central PMCID: 2125852.
257. Jerusalem G, Beguin Y, Fassotte MF, Belhocine T, Hustinx R, Rigo P, et al. Early detection of relapse by whole-body positron emission tomography in the follow-up of patients with Hodgkin's disease. Ann Oncol. 2003;14(1):123–30.
258. Rhodes MM, Delbeke D, Whitlock JA, Martin W, Kuttesch JF, Frangoul HA, et al. Utility of FDG-PET/CT in follow-up of children treated for Hodgkin and non-Hodgkin lymphoma. J Pediatr Hematol Oncol. 2006;28(5):300–6.
259. Levine JM, Weiner M, Kelly KM. Routine use of PET scans after completion of therapy in pediatric Hodgkin disease results in a high false positive rate. J Pediatr Hematol Oncol. 2006;28(11):711–4.
260. Zinzani PL, Stefoni V, Tani M, Fanti S, Musuraca G, Castellucci P, et al. Role of [^{18}F]fluorodeoxyglucose positron emission tomography scan in the follow-up of lymphoma. J Clin Oncol. 2009;27(11):1781–7.
261. Petrausch U, Samaras P, Haile SR, Veit-Haibach P, Soyka JD, Knuth A, et al. Risk-adapted FDG-PET/CT-based follow-up in patients with diffuse large B-cell lymphoma after first-line therapy. Ann Oncol. 2010;21(8):1694–8.
262. Petrausch U, Samaras P, Veit-Haibach P, Tschopp A, Soyka JD, Knuth A, et al. Hodgkin's lymphoma in remission after first-line therapy: which patients need FDG-PET/CT for follow-up? Ann Oncol. 2010; 21(5):1053–7.
263. Leskinen-Kallio S, Minn H, Joensuu H. PET and [^{11}C] methionine in assessment of response in non-Hodgkin lymphoma. Lancet. 1990;336(8724):1188.
264. Leskinen-Kallio S, Ruotsalainen U, Nagren K, Teras M, Joensuu H. Uptake of carbon-11-methionine and fluorodeoxyglucose in non-Hodgkin's lymphoma: a PET study. J Nucl Med. 1991;32(6):1211–8.
265. Nuutinen J, Leskinen S, Lindholm P, Soderstrom KO, Nagren K, Huhtala S, et al. Use of carbon-11 methionine positron emission tomography to assess malignancy grade and predict survival in patients with lymphomas. Eur J Nucl Med. 1998;25(7):729–35.
266. Sutinen E, Jyrkkio S, Varpula M, Lindholm P, Gronroos T, Lehikoinen P, et al. Nodal staging of lymphoma with whole-body PET: comparison of. J Nucl Med. 2000;41(12):1980–8.
267. Methionine PET/CT studies in patients with cancer ClinicalTrials.gov [01.31.2016]. Available from: https://www.clinicaltrials.gov/ct2/show/NCT00840047
268. Buchmann I, Neumaier B, Schreckenberger M, Reske S. [^{18}F]3′-deoxy-3′-fluorothymidine-PET in NHL patients: whole-body biodistribution and imaging of lymphoma manifestations – a pilot study. Cancer Biother Radiopharm. 2004;19(4):436–42.
269. Buck AK, Bommer M, Stilgenbauer S, Juweid M, Glatting G, Schirrmeister H, et al. Molecular imaging of proliferation in malignant lymphoma. Cancer Res. 2006;66(22):11055–61.
270. Wagner M, Seitz U, Buck A, Neumaier B, Schultheiss S, Bangerter M, et al. 3′-[^{18}F]fluoro-3-′-deoxythymidine ([^{18}F]-FLT) as positron emission tomography tracer for imaging proliferation in a murine B-Cell lymphoma model and in the human disease. Cancer Res. 2003;63(10):2681–7.
271. Kasper B, Egerer G, Gronkowski M, Haufe S, Lehnert T, Eisenhut M, et al. Functional diagnosis of residual lymphomas after radiochemotherapy with positron emission tomography comparing FDG- and FLT-PET. Leuk Lymphoma. 2007;48(4):746–53.
272. Brepoels L, Stroobants S, Verhoef G, De Groot T, Mortelmans L, De Wolf-Peeters C. ^{18}F-FDG and ^{18}F-FLT uptake early after cyclophosphamide and mTOR inhibition in an experimental lymphoma model. J Nucl Med. 2009;50(7):1102–9.
273. Buck AK, Kratochwil C, Glatting G, Juweid M, Bommer M, Tepsic D, et al. Early assessment of therapy response in malignant lymphoma with the thymidine analogue [^{18}F]FLT. Eur J Nucl Med Mol Imaging. 2007;34(11):1775–82.
274. Graf N, Herrmann K, den Hollander J, Fend F, Schuster T, Wester HJ, et al. Imaging proliferation to

monitor early response of lymphoma to cytotoxic treatment. Mol Imaging Biol. 2008;10(6):349–55.
275. Herrmann K, Wieder HA, Buck AK, Schoffel M, Krause BJ, Fend F, et al. Early response assessment using 3′-deoxy-3′-[^{18}F]fluorothymidine-positron emission tomography in high-grade non-Hodgkin's lymphoma. Clin Cancer Res. 2007;13(12):3552–8.
276. Lawrence J, Vanderhoek M, Barbee D, Jeraj R, Tumas DB, Vail DM. Use of 3′-deoxy-3′-[^{18}F]fluorothymidine PET/CT for evaluating response to cytotoxic chemotherapy in dogs with non-Hodgkin's lymphoma. Vet Radiol Ultrasound. 2009; 50(6): 660–8.
277. 3′-Deoxy-3′-[^{18}F] fluorothymidine PET imaging in patients with cancer ClinicalTrials.gov [01.31.2016]. Available from: https://www.clinicaltrials.gov/ct2/show/NCT00935090.
278. A study to demonstrate the safety and preliminary efficacy of ^{18}F-FLT in patients with solid tumours or lymphoma ClinicalTrials.gov [01.31.2016]. Available from: https://www.clinicaltrials.gov/ct2/show/NCT01065805.
279. Therapy for patients with untreated age-adjusted international prognostic index low-intermediate risk, high-intermediate risk, or high risk diffuse large B cell lymphoma ClinicalTrials.gov [01.31.2016]. Available from: https://www.clinicaltrials.gov/ct2/show/NCT00712582.
280. Schoder H, Zelenetz A, Hamlin P, Gavane S, Horwitz S, Matasar M, et al. Prospective study of FLT PET for early interim response assessment in advanced stage B-cell lymphoma. J Nucl Med. 2015;57:728.
281. Sugawara Y, Braun DK, Kison PV, Russo JE, Zasadny KR, Wahl RL. Rapid detection of human infections with fluorine-18 fluorodeoxyglucose and positron emission tomography: preliminary results. Eur J Nucl Med. 1998;25(9):1238–43.
282. Yamada S, Kubota K, Kubota R, Ido T, Tamahashi N. High accumulation of fluorine-18-fluorodeoxyglucose in turpentine-induced inflammatory tissue. J Nucl Med. 1995;36(7):1301–6.
283. Jacene HA, Ishimori T, Engles JM, Leboulleux S, Stearns V, Wahl RL. Effects of pegfilgrastim on normal biodistribution of ^{18}F-FDG: preclinical and clinical studies. J Nucl Med. 2006;47(6):950–6.
284. Sugawara Y, Fisher SJ, Zasadny KR, Kison PV, Baker LH, Wahl RL. Preclinical and clinical studies of bone marrow uptake of fluorine-1-fluorodeoxyglucose with or without granulocyte colony-stimulating factor during chemotherapy. J Clin Oncol. 1998; 16(1):173–80.
285. Blodgett TM, Ames JT, Torok FS, McCook BM, Meltzer CC. Diffuse bone marrow uptake on whole-body F-18 fluorodeoxyglucose positron emission tomography in a patient taking recombinant erythropoietin. Clin Nucl Med. 2004;29(3):161–3.
286. Brink I, Reinhardt MJ, Hoegerle S, Altehoefer C, Moser E, Nitzsche EU. Increased metabolic activity in the thymus gland studied with ^{18}F-FDG PET: age dependency and frequency after chemotherapy. J Nucl Med. 2001;42(4):591–5.
287. Cohade C, Osman M, Pannu HK, Wahl RL. Uptake in supraclavicular area fat ("USA-Fat"): description on ^{18}F-FDG PET/CT. J Nucl Med. 2003;44(2):170–6.
288. Jacene HA. FDG PET, and PET/CT in lymphoma. In: Wahl RL, editor. Categorical course in diagnostic radiology: clinical PET and PET/CT imaging. Oak Brook: Radiological Society of North America; 2007.

Suggested Reading

Barrington SF, Mikhaeel NG, Kostakoglu L, Meignan M, Hutchings M, Mueller SP, et al. Role of imaging in the staging and response assessment of lymphoma: consensus of the International Conference on Malignant Lymphomas Imaging Working Group. J Clin Oncol. 2014;32(27):3048–58.

Cheson BD, Fisher RI, Barrington SF, Cavalli F, Schwartz LH, Zucca E, et al. Recommendations for initial evaluation, staging, and response assessment of Hodgkin and non-Hodgkin lymphoma: the Lugano classification. J Clin Oncol. 2014;32(27):3059–68.

Gisselbrecht C, et al. Radioimmunotherapy for stem cell transplantation in non-Hodgkin's lymphoma: in pursuit of a complete response. Oncologist. 2009;14 suppl 2: 41–51.

Goldsmith SJ. Radioimmunotherapy of Lymphoma: Bexxar and Zevalin. Semin Nucl Med. 2010;40: 122–35.

Hutchings M, Barrington SF. PET/CT for therapy response assessment in lymphoma. J Nucl Med. 2009;50: 21S–30S.

Sharkey RM, Karacay H, Goldenberg DM. Improving treatment of non-Hodgkin's lymphoma with antibody-targeted radionuclides. Cancer. 2010;116(4 suppl): 1134–45.

Diagnostic Applications of Nuclear Medicine: Multiple Myeloma

15

Martina Sollini, Sara Galimberti, Roberto Boni, and Paola Anna Erba

Abstract

Multiple myeloma represents about 1.8% of all cancers and 10% of all hematologic malignancies.

Multiple myeloma (MM) is the most common primary bone cancer. The clonal proliferation of malignant plasma cells in the bone marrow may result both in local growth and in systemic effects due to the overproduction of a monoclonal protein (M-protein). Plasma cell proliferation is linked to a variety of clinical presentations of the disease, ranging from simple monoclonal gammopathy of undetermined significance (MGUS) to smoldering myeloma (SMM) to full-blown "malignant" MM. MM differs from MGUS and SMM by the presence of the end-organ damage associated with a complex syndrome named CRAB. However, in the updated version of the criteria for the diagnosis of plasma cell proliferative disorders established by the International Myeloma Working Group (IMWG), more specific criteria have been established to define MM, MGUS, and SMM. Excess bone marrow plasmacells, M-protein, osteolytic bone lesions, renal disease, and immunodeficiency constitute the pathophysiologic bases of the clinical manifestations of MM. Severe bone pain, pathologic fractures, spinal cord compression, and hypercalcemia are caused by lytic bone lesions. The course of MM is highly variable, and the clinical behavior is remarkably heterogeneous. Many studies have identified prognostic factors capable of predicting this heterogeneity in survival (serum β2-microglobulin, albumin, C-reactive protein, and lactate dehydrogenase). The standard workup of MM is based on a number of laboratory tests that are utilized for risk stratification. The International Staging System (ISS) is a powerful and reproducible three-stage classification in which the ISS3 class is associated with the poorest outcome. Imaging studies demonstrate the extent and severity of bone involvement (intramedullary/extramedullary, site and number of lesions) at baseline, including disease-related complications, such as pathologic fractures; they also serve to assess response to treatment and provide follow-up surveillance. The ISS introduced over 25 years ago is mainly based on serum β_2-microglobulin and albumin levels, without any reference to the presence of bone lesions or to the methodology employed

M. Sollini
Department of Biomedical Sciences, Humanitas University, Rozzano, Milan, Italy

S. Galimberti
Hematology Unit, University of Pisa, Pisa, Italy

R. Boni • P.A. Erba (✉)
Regional Center of Nuclear Medicine, Department of Translational Research and Advanced Technologies in Medicine, University of Pisa, Pisa, Italy
e-mail: paola.erba@unipi.it

© Springer International Publishing Switzerland 2017
H.W. Strauss et al. (eds.), *Nuclear Oncology*,
https://doi.org/10.1007/978-3-319-26236-9_8

for their evaluation. Although the ISS serves as a prognostic indicator rather than as an accurate scoring system, it adequately estimates tumor burden and risk stratification, allowing differentiation of MGUS and SMM from MM. In 1975 Durie and Salmon introduced a clinical staging system based on the presence of bone lesions to grade the severity of the disease. While the original Durie and Salmon system was essentially based on the use of planar x-ray for evaluating bones, a newer version, the PLUS system was released in 2005 to improve the accuracy of staging with advanced imaging modalities such as [^{18}F]FDG-PET/CT, and MRI.

Keywords

Multiple myeloma • Bone tumor • Multimodality imgaging • Hematological malignancy

Glossary

[^{18}F]FDG	2-Deoxy-2-[^{18}F]fluoro-d-glucose
^{68}Ga-DOTATOC	^{68}Ga-DOTA-octreotide
^{99m}Tc-HMPAO	^{99m}Tc-Hexamethylpropyleneamine oxime
^{99m}Tc-MDP	^{99m}Tc-Hydroxymethylene diphosphonate
^{99m}Tc(V)-DMSA	^{99m}Tc-Labeled pentavalent dimercaptosuccinic acid
ABCB 1	Member 1 of the adenosine triphosphate binding cassette superfamily B, also known as multidrug resistance protein 1
ASH	American Society of Hematology
ASCT	Autologous stem-cell bone marrow transplantation
BM	Bone marrow
CR	Complete response
CRAB	Hypercalcemia (C), renal failure (R), anemia (A), and bone lesions (B)
CT	X-ray computed tomography
DCE	Dynamic contrast-enhanced sequences
DEXA	Dual-energy X-ray absorptiometry
DKK1	Dickkopf 1, an inhibitor of osteoblast precursor cells
DMSA	Dimercaptosuccinic acid
DOTA	1,4,7,10-Tetra-azacyclododecane-1,4,7,10-tetraacetic acid
DWI	Diffusion-weighted imaging
ECOG	Eastern Cooperative Oncology Group
FDA	United States Food and Drug Administration
FISH	Fluorescent in situ hybridization
FLC	Free light chain
HDT	High-dose therapy
IMWG	International Myeloma Working Group
Ig	Immunoglobulin
Igh	Immunoglobulin heavy chain
IL	Interleukin
IMPeTUs	Italian Myeloma criteria for PET USe
ISS	International Staging System
LC	Laterocervical
LDCT	low-dose X-ray computed tomography
LDH	Lactate dehydrogenase
MDCT	Multidetector computed tomography
MDEs	Myeloma-defining events
MDR	Multidrug resistance
MGUS	Monoclonal gammopathy of undetermined significance
MIP-1α	Macrophage inflammatory protein 1-alpha
MIP	Maximum intensity projection
MM	Multiple myeloma
MR	Minor response
MRI	Magnetic resonance imaging
n-CR	No complete response
NOPR	National Oncologic PET Registry
OPG	Osteoprogeterin
OS	Overall survival

PAMP	Pathogen-associated myeloma cell proliferation
PCLI	Plasma cell-labeling index
PD	Progressive disease
PET	Positron emission tomography
PET/CT	Positron emission tomography/Computed tomography
PET/MRI	Positron emission tomography/Magnetic resonance imaging
PFS	Progression-free survival
Pgp	P-glycoprotein, also known as multidrug resistance protein 1, or ABCB 1 (member 1 of the adenosine triphosphate binding cassette superfamily B)
POEMS	Syndrome characterized by polyneuropathy, organomegaly, endocrinopathy, monoclonal plasma cell proliferative disorder, and skin changes
PR	Partial response
PTHrP	Parathyroid hormone-related protein
RANK	Receptor activator of nuclear factor kappa B
SAP	Serum amyloid P
sCR	Stringent complete response
SD	Stable disease
SMM	Smoldering myeloma
SPECT	Single-photon emission computed tomography
SSTR	Somatostatin receptor
STIR	Short tau inversion recovery sequence, a modality of magnetic resonance imaging
SUV_{max}	Standardized uptake value at point of maximum
SUV	Standardized uptake value
Sv	Unit of ionizing radiation dose in the International System of Units based on the health effect of ionizing radiation on the human body
SWOG	Southwest Oncology Group
TLRs	Toll-like receptors
TNFalpha	Tumor necrosis factor alpha
TRANCE	Tumor necrosis factor-related activation induced cytokine
TTP	Time to progression
VDT-PACE	Intensive induction chemotherapy based on a combination of bortezomib, dexamethasone, thalidomide, plus a 4-day continuous infusion of cisplatin, adriamycin, cyclophosphamide, and etoposide
VDT	Chemotherapy based on bortezomib, thalidomide, and pegylated liposomal doxorubicin
VEGF	Vascular endothelial growth factor
VGPR	Very good partial response
VRD	Chemotherapy regimen based on the combination of Revlimid®, Velcade®, and dexamethasone
VRD	Bortezoib-lenalidomide-dexamethasone
WBCs	White blood cells
WBLD-CT	Whole-body low-dose computed tomography
WB-MRI	Whole-body magnetic resonance imaging
WB-MDCT	Whole-body multiple detector computed tomography
WBXR	Whole-body X-ray
Wnt	Wingless gene encoding for the proto-oncogene Int-1 homolog, also known as wingless-type MMTV integration site family

Contents

Overview of the Disease 398

Evaluation of Disease Burden with Imaging Modalities 406

Assessing Response to Treatment 421

DEXA Scanning 428

References 428

Overview of the Disease

Multiple myeloma represents about 1.8% of all cancers and about 10% of all hematologic malignancies. Multiple myeloma (MM) is the most common primary bone cancer. The number of new cases estimated in 2016 is more than 30,300 with over 12,650 deaths. Its incidence is higher in men (61%) and in african-americans; some categories of workers (i.e., farmers, workers in wood mills, paper mills, and furniture manufacturing plants) seem to be more prone to develop the disease. The peak of incidence occurs between 45 and 85 years of age, with a median of 69 years, and rarely patients are younger than 40 years (<2%) [1, 2].

Multiple myeloma was first described by Solly [3] in 1844. Solly described an inflammatory process that began with a "morbid action" of the blood vessels in which the "earthy matter of the bone is absorbed and thrown out by the kidneys in the urine." In the early 1900s, Wright recognized plasma cells as the tumor cells present in MM [4].

The clonal proliferation of malignant plasma cells in the bone marrow (Fig. 1) may result both in local growth and in systemic effects due to the overproduction of a monoclonal protein (M protein), first described by Waldenstrom in 1961 as a narrow band of hypergammaglobulinemia on electrophoresis [5]. Most commonly, M protein is IgG (52%) or IgA (21%), rarely IgD or IgE. Biclonal plasma proteins can also be detected, such as IgG and IgA (33%) or IgG and IgM (24%); on the other hand, non-secretive (negative both serum and urine immunofixations) and light chain only subtypes have been described (1%) [6]. Almost all patients evolve from an asymptomatic premalignant stage termed monoclonal gammopathy of undetermined significance (MGUS); through the smoldering myeloma (SMM), to the "malignant" MM [1, 7].

Historically, MM differs from MGUS and SMM by the presence of the end-organ damage associated with a complex syndrome named CRAB [8]: hypercalcemia (C), renal failure (R), anemia (A), and

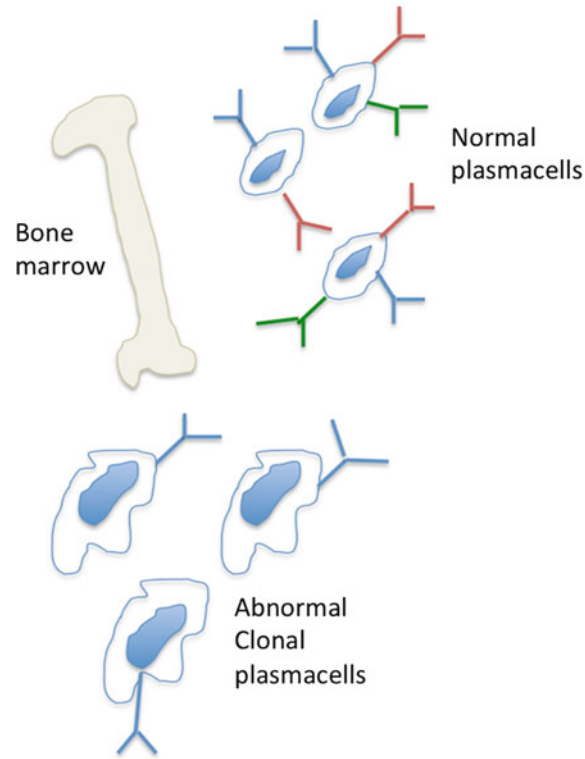

Fig. 1 Plasma cells originate in bone marrow. Normal polyclonal plasma cells secrete different antibodies (*blue*, *red*, *green*). Atypical clonal plasma cells secrete only one type of immunoglobulin, with the same rearrangement of IgH

bone lesions (B). However, in the updated version of the criteria for the diagnosis of plasma cell proliferative disorders established by the International Myeloma Working Group (IMWG), more specific criteria have been established to define MM, MGUS, and SMM [8, 9] (Table 1).

MGUS is distinguished in: (i) non-IgM MGUS (progression rate of 1%/year in MM, solitary plasmacytoma, or immunoglobulin-related amyloidosis), (ii) IgM-MGUS (progression rate of 1.5%/year in Waldenström macroglobulinemia or immunoglobulin-related amyloidosis), and (iii) light-chain MGUS (progression rate of 0.3%/year in light-chain MM or immunoglobulin light-chain amyloidosis).

Smoldering myeloma is defined as serum monoclonal protein (IgG or IgA) $\geq$30 g/L or urinary monoclonal protein $\geq$500 mg per 24 h and/or clonal bone marrow plasma cells 10–60% associated to the absence of myeloma-defining events or amyloidosis. On the other hand, MM is defined as clonal bone marrow plasma cells $\geq$10% or biopsy-proven bony or extramedullary plasmacytoma (clonality should be established by showing k/λ-light-chain restriction on flow cytometry, immunohistochemistry, or immunofluorescence; bone marrow plasma cell percentage should preferably be estimated from a core biopsy specimen) and any one or more of the following myeloma events defined as end-organ damage that can be attributed to the underlying plasma cell proliferative disorder (hypercalcemia, renal insufficiency, anemia, bone lesion).

The same revision stated that the patients with high-risk smoldering myeloma (free light-chain involved/uninvolved ratio >100, more than two focal lesions in the spine or pelvis after MRI evaluation, and more than 60% of clonal atypical plasma cells in the bone marrow, defined as "myeloma-defining events or MDEs) have to receive treatment, because of the very high probability (about 80%) of developing a CRAB sign in a short period [9].

A free light-chain ratio >100 has been described in about 15% of patients with smoldering myeloma; their risk of progression within 2 years was 64–72% [10, 11].

The micro-environment of the bone marrow appears to be crucial for the development, maintenance, and progression of the disease [12]. A proliferative trigger for plasma cells consequent to antigenic stimuli is responsible for plasma cell activation. Toll-like receptors (TLRs), pathogen-associated myeloma cell proliferation (PAMP), and CD126 are important key molecules in the process of plasma cells malignant transformation. Myeloma plasma cells are typically characterized by a very long life (with low thymidine-labeling index, 1–2%), while the other differentiation steps are maintained.

Primary translocations involving the immunoglobulin heavy chain locus on chromosome 14q32 are detectable in about 50% of MGUSs, while in symptomatic MM, several molecular abnormalities are present, such as *Ras* and/or *TP53* and/or *myc* family mutations, p16 methylations, or secondary translocations [13]. High-matrix metalloproteinase-2 levels and enhanced neoangiogenesis are also detectable in MM with increased vascular density typical of active disease, thus suggesting a strong relationship between the progression of myeloma and neovascularisation [14].

Moreover, patients affected by smoldering myeloma but carrying t(4:14), 1q gain, or del(17p) showed a median time to progression (TTP) of 24 months and are considered as "at high risk." Trisomies are associated to a TTP of 34 months, so defining a "intermediate risk" population, whereas other cytogenetic abnormalities and t(11;14) are considered as "at standard risk" (TTP 54 months) [15].

Excess bone marrow plasma cells, M protein, osteolytic bone lesions (present in >90% of patients), renal disease, and immunodeficiency [12] constitute the pathophysiologic bases of the clinical manifestations of MM. Severe bone pain, pathologic fractures (>70%), spinal cord compression (2–3%), and hypercalcemia (15%) are caused by lytic bone lesions (although spinal cord compression is sometimes caused by collapse of a vertebral body due to the disappearance of a lesion in response to therapy) [16].

Although bone lesions in MM can occur in any bone, lesions are found in the spine (49%), skull (35%), pelvis (34%), ribs (33%), and proximal portions of the arms and legs (22% and 13%, respectively) as well as in the mandible (10%). At diagnosis almost 10% of the patients present

Table 1 Criteria for the diagnosis of plasma cell proliferative disorders established by the International Myeloma Working Group [8, 9]

Disease	Diagnostic criteria	
	IMWG	Updated
Monoclonal gammopathy of undetermined significance (MGUS)	All three criteria must be met:	Non-IgM MGUS
	• Serum monoclonal protein <3 g/dL	• Serum monoclonal protein (non-IgM type) <30 g/L
	• Clonal BM plasma cells <10%	• Clonal BM plasma cells <10%*
	• Absence of end-organ damage attributable to the plasma cell proliferative disorder	• Absence of end-organ damage (CRAB) or amyloidosis attributable to the plasma cell proliferative disorder
		IgM MGUS
		• Serum IgM monoclonal protein <30 g/L
		• BM lymphoplasmacytic infiltration <10%
		• No evidence of anemia, constitutional symptoms, hyperviscosity, lymphadenopathy, hepatosplenomegaly, or other end-organ damage attributable to the underlying lymphoproliferative disorder
		Light-chain MGUS
		• Abnormal FLC ratio (<0.26 or >1.65)
		• Increased level of the appropriately involved light chain (increased kFLC in patients with ratio >1.65 and increased λ FLC in patients with ratio <0.26)
		• No immunoglobulin heavy chain expression on immunofixation
		• Absence of end-organ damage (CRAB) or amyloidosis attributable to the plasma cell proliferative disorder clonal BM plasma cells <10%
		Urinary monoclonal protein <500 mg/24 h
Smoldering multiple myeloma (also referred to as asymptomatic multiple myeloma)	Both criteria must be met:	Both criteria must be met:
	• Serum monoclonal protein (IgG or IgA) ≥3 g/dl and/or clonal BM plasma cells ≥10%	• Serum monoclonal protein (IgG or IgA) ≥30 g/L or urinary monoclonal protein ≥ 500 mg per 24 h and/or clonal bone marrow plasma cells 10–60%
	• Absence of end-organ damage attributable to a plasma cell proliferative disorder	• Absence of myeloma-defining events or amyloidosis

(*continued*)

Table 1 (continued)

Disease	Diagnostic criteria	
	IMWG	Updated
Multiple myeloma (MM)	All criteria must be met:	Clonal bone marrow plasma cells ≥10% or biopsy-proven bony or extramedullary plasmacytoma (clonality should be established by showing k/λ-light-chain restriction on flow cytometry, immunohistochemistry, or immunofluorescence) and any one or more of the following myeloma-defining events:
	• Clonal BM plasma cells ≥ 10% or biopsy-proven plasmacytoma	
	• Evidence of end-organ damage that can be attributed to the underlying plasma cell proliferative disorder, specifically	
	Hypercalcemia: serum calcium >11.5 mg/dL	• Evidence of end-organ damage attributable to the underlying plasma cell proliferative disorder, specifically:
	Renal insufficiency: serum creatinine >1.73 μmol/L (or >2 mg/dL) or estimated creatinine clearance <40 mL/min	1. Hypercalcemia: serum calcium >0.25 mmol/L (>1 mg/dL) higher than the upper limit of normal or > 2.75 mmol/L (>11 mg/dL)
	Anemia: normochromic, normocytic with a hemoglobin value of ≥2 g/dL below the lower limit of normal or a hemoglobin value <10 g/dL	2. Renal insufficiency: creatinine clearance <40 mL per min† or serum creatinine >177 μmol/L (>2 mg/dL)
	Bone lesions: lytic lesions, severe osteopenia, or pathologic fractures	3. Anemia: hemoglobin value of >20 g/L below the lower limit of normal or a hemoglobin value <100 g/L
		4. Bone lesions: one or more osteolytic lesions on skeletal radiography, CT, or [^{18}F]FDG PET/CT (if BM has <10% clonal plasma cells, >1 bone lesion is required to distinguish from solitary plasmacytoma with minimal marrow involvement)
		• Any one or more of the following biomarkers of malignancy:
		1. Clonal BM plasma cell percentage ≥60% (clonality should be established by showing k/λ-light-chain restriction on flow cytometry, immunohistochemistry, or immunofluorescence; bone marrow plasma cell percentage should preferably be estimated from a core biopsy specimen)
		2. Involved: uninvolved serum free light-chain ratio ≥100 (values based on the serum Freelite assay; the involved free light chain must be ≥100 mg/L)
		3. >1 focal lesions on MRI studies (size ≥5 mm)

*Bone marrow can be deferred in patients with low-risk monoclonal gammopathy of undetermined significance (IgG type, monoclonal protein <15 g/L, normal free light-chain ratio) in whom there are no clinical features concerning for myeloma.

diffuse osteopenia or osteoporosis. MM bone disease involves more than 50% of a bone surface, and osteoblastic activity is drastically depressed or absent [17].

Transformed malignant plasma cells are responsible, both directly and indirectly, for local bone resorption, through activation of osteoclast activity and inhibition of the osteoblasts. In fact, myeloma cells secrete several osteoclast-activating factors (IL-1, IL-6, TNF-alpha) that stimulate the secretion of the so-called tumor necrosis factor-related activation induced cytokine (TRANCE); this compound interferes with osteoblast differentiation. Furthermore, IL-1, IL-6, and TNF-alpha stimulate the secretion of dickkopf 1 (DKK1), a potent inhibitor of osteoblast precursor cells. The myeloma cells frequently release also the parathyroid hormone-related protein (PTHrP). Figure 2 diagrammatically depicts some of those complex interactions.

The local proliferation of myeloma cells may lead to the appearance of a solid lesion that involves the soft tissue primarily arising outside the bone or extending from a preexistent bone lesion. In the absence of systemic spread (normal BM without evidence of clonal plasma cells, normal skeletal survey, and MRI/CT of spine and pelvis except for the primary solitary lesion), this situation is named solitary plasmacytoma [9, 18].

Excess protein produced by myeloma can increase the viscosity of plasma. Hyperviscosity is associated with impairment of the microcirculation, particularly in the eye and central nervous system causing visual impairment, dizziness, headache, and hearing loss. Rarely there is spontaneous bleeding [19] due to platelet dysfunction. Patients with myeloma are at increased risk of infection due to reduction of normal plasma cell function. Infections are potentially fatal complications that can occur during chemotherapy, at relapse or following bone marrow transplantation, and are most frequently caused by *Streptococcus pneumoniae*, *Haemophilus influenzae*, or *Herpes zoster* virus [20]. Other complications include myocardial ischemia or congestive heart failure due to deposition of light-chain protein (amyloid)

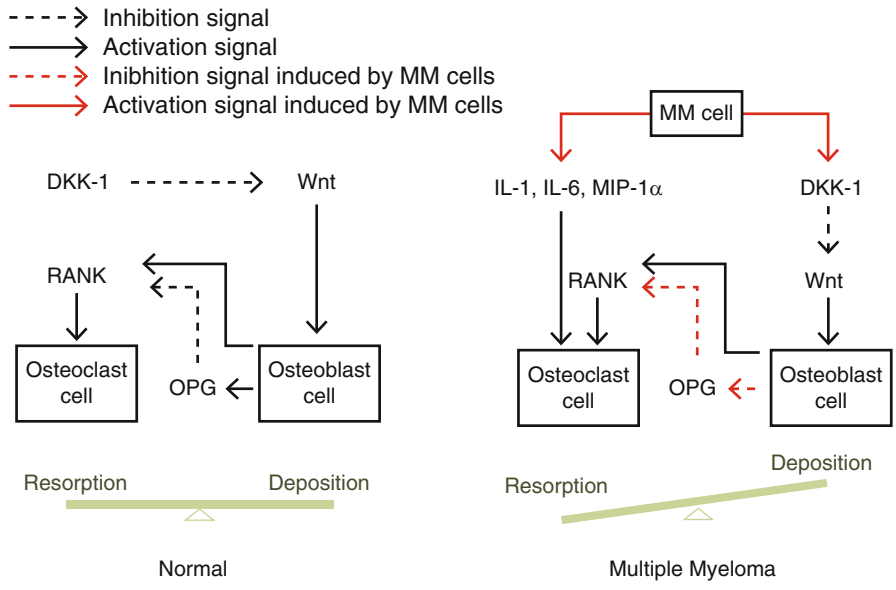

Fig. 2 Schematic representation of interactions between MM cells and bone microenvironment (*left panel*) as compared to the physiological balance (*right panel*). Dickkopf 1, a potent inhibitor of osteoblast precursor cells (DKK1), over-inhibited in normal condition via *wingless* gene (Wnt), is activated by MM cells promoting osteoblasts activity and decreasing osteoprogeterin (OPG) circulating levels. Furthermore, cytokine (IL-1, IL-6, and MIP-1α) and RANK promoting osteoclasts tip the balance toward bone resorption resulting in the typical lytic bone appearance of MM lesions

in the myocardium causing dilated or restrictive cardiomyopathy, as well as a hypersensitivity syndrome and/or anemia [21].

Neuropathy in patients with myeloma is usually symmetric, distal sensory or sensory motor with axonal degeneration, often associated with amyloid deposits, or antibodies against peripheral myelinated fibers [22]. In 1% of the cases, myeloma occurs in a rare syndrome (POEMS syndrome) [12]: this syndrome is characterized by polyneuropathy, monoclonal plasma cell proliferative disorder (almost always λ) associated to one or more major criteria (sclerotic bone lesions, Castleman's disease, or elevated levels of VEGF), and one or more minor criteria (organomegaly, extravascular volume overload, endocrinopathy, skin changes, papilledema thrombocytosis/polycythemia) [9].

Although the presence of lytic bone lesions is highly suggestive for MM, it is not by itself sufficient to establish the diagnosis. The minimum criteria for MM diagnosis are either the detection of at least 10% abnormal plasma cells in the bone marrow (after biopsy) or of M-protein levels >30 g/L in serum or >1 g excreted in the 24-h urine [8].

Initial investigation of a patient with suspected multiple myeloma should include family history (focus on first-degree relatives with the diagnosis of hematologic malignancies, especially lymphoma, chronic lymphocytic leukemia, and plasma cell dyscrasias), past medical history (focus on comorbid conditions, such as coronary artery disease, congestive heart failure, hypertension, renal disorders, liver disorders, and lung diseases), a complete blood count with differential, and a complete biochemistry (including liver function tests, renal function tests, electrolytes, calcium, and albumin) [23].

The clinical course of MM is highly variable, and the clinical behavior is remarkably heterogeneous. Many studies have identified prognostic factors capable of predicting this heterogeneity in survival (serum β2-microglobulin, albumin, C-reactive protein, and lactate dehydrogenase) [1].

The standard workup of MM is based on a number of laboratory tests that are utilized for risk stratification. The international staging system (ISS) is a powerful and reproducible three-stage classification (Table 2), in which ISS3 class is associated with the poorest outcome [8]. Such assessments include complete blood count, routine biochemistry and urine analysis, serum and urine protein electrophoresis (preferably on an aliquot of the 24-h collection), lactate dehydrogenase and β_2-microglobulin levels, immunofixation of serum or urine sample for the detection of M component, nephelometry (for measuring the free light chains employed to monitor also patients with oligo- or nonsecretory myeloma), and cytogenetics or FISH analysis.

Table 2 Mayo risk stratification for high-risk myeloma (From Kyle et al. [8])

High-risk characteristic
Conventional cytogenetics
Deletion of chromosome 13 (monosomy)
Hypodiploidy
Either hypodiploidy or deletion of chromosome 13
Fluorescent in situ hybridization (FISH)
t(4;14)
t(14:16)
17p–
Plasma cell-labeling index (PCLI) studies: PCLI ≥3%

Cytogenetics includes conventional karyotyping and FISH for t(4;14), t(14;16), chromosome 17, and chromosome 1. Indeed, t(4;14), t(4:16), deletion(17p), and (1q) are mostly associated with a poorer outcome. It has recently been demonstrated that combining both t(4;14) and del (17p), along with the ISS stage, could significantly improve the prognostic assessment [24]. Gene-expression profiling may segregate patients with standard or high-risk disease, but this is not yet established in routine practice [1].

The fraction of plasma cells infiltrating the bone marrow is evaluated based on May-Grünwald Giemsa-stained smears. MM plasma cells typically stain positive for CD38, CD56, and CD138 and are usually negative for surface immunoglobulin and CD19. The number of plasma cells in the bone marrow is an important

criterion for distinguishing MM from MGUS and from solitary plasmacytoma. MM is usually characterized by more than 10% plasma cells in the bone marrow, although, due to the heterogeneous distribution of plasma cells in the bone marrow, this fraction may vary substantially depending on the site of sample aspiration; this parameter is therefore not a consistent prognostic factor. Nevertheless, cytology of bone marrow aspirates remains the standard method for quantitating plasma cells infiltration. The bone marrow plasma cell labeling index (PCLI), a parameter of the DNA synthesis rate derived from in vitro incubation with tritiated thymidine, represents an additional predictor of survival [12]. This index is usually low at diagnosis (<1%) in MGUS and SMM, but it increases at relapse since it correlates with neoangiogenesis, therefore with active disease, as well as inversely with survival regardless of the tumor mass. However, 40% of patients with symptomatic MM have normal PCLI [25].

Imaging studies demonstrate the extent and severity of bone involvement (intramedullary/extramedullary, site, and number of lesions) at baseline, including disease-related complications, such as pathologic fractures; they also serve to assess response to treatment and provide follow-up surveillance [7]. The standard skeletal survey reveals punched-out lytic lesions, osteopenia, or fractures in approximately 80% of patients at the time of diagnosis. Due to the lack of the osteoblastic response, the bone scan is insensitive for the detection of many bone lesions in myeloma patients.

The clinical staging system for MM (international staging system, ISS, Table 3), introduced over 25 years ago, is mainly based on serum β_2-microglobulin and albumin levels, without any reference to the presence of bone lesions nor to the methodology employed for their evaluation. Although the ISS serves as prognostic indicator rather than as an accurate scoring system, it has proven to adequately estimate tumor burden and risk stratification, also enabling to distinguish MGUS and SMM from MM [8]. The CRAB criteria are preferred to establish MM-related organ dysfunction [26]. In 1975 Durie and Salmon introduced a clinical staging system

Table 3 International staging system (ISS) for MM (From Kyle et al. [8])

Stage	Criteria
Stage I	Serum $\boldsymbol{\beta_2}$-microglobulin <3.5 mg/L and albumin ≥3.5 g/dL
Stage II	No stage I or III
	There are two categories:
	Serum $\boldsymbol{\beta_2}$-microglobulin < 3.5 mg/L but serum albumin< 3.5 g/dL
	Serum $\boldsymbol{\beta_2}$-microglobulin ranging from 3.5 to <5.5 mg/L irrespective of the serum albumin level
Stage III	Serum $\boldsymbol{\beta_2}$-microglobulin ≥5.5 mg/L

based on the presence of bone lesions to grade the severity of the disease: a normal bone structure or plasmacytoma characterized as stage 1 and advanced lytic bone lesions characterized as stage 3, while stage 2 corresponded to patients who did not fit either stage 1 or stage 3 features (see Table 4a) [27]. While the original Durie and Salmon system was essentially based on the use of planar X-ray for evaluating bones, a newer version, the PLUS system, was released in 2005 (see Table 4b) with the aim of improving the accuracy of staging by the use of advanced imaging modalities such as [^{18}F]FDG-PET, [^{18}F]FDG-PET/CT, and MRI (Table 4b) [28]. These techniques enable to evaluate the total number of bone lesions, to distinguish MGUS or SMM from active myeloma, as well as to better discriminate between stage II and III disease. Nevertheless, the original system based on conventional X-ray only is still employed in areas where access to advanced imaging modalities is limited.

A detailed staging system is crucial, since MM has extremely heterogeneous outcomes, and treatment is strongly dependent on the disease onset. Based on the stage and risk factors, risk-adapted therapeutic strategies can therefore be defined. While MGUS does not require any treatment (except long-term observation), there is no evidence that early treatment of patients with SMM prolongs their survival. The diagnosis of active symptomatic MM requiring therapy is based on end-organ effects of the disease.

Despite all treatment options, MM is still considered an incurable disorder with a median survival of about 2–3 years in high-risk patients

Table 4 Overview of Durie and Salmon staging system (A) and the Durie and Salmon PLUS staging system (B) [26]

	A: Durie/Salmon staging system		B: Durie and Salmon PLUS staging system	
Disease	Criteria	Measured myeloma cell mass in whole body (myeloma cells in billions/m^2)	Classification	MRI and/or [^{18}F] FDG-PET
MGUS	Stage I (low cell mass)	600 billion		All negative
	All of the following:			
	Hemoglobin value >10 g/dL			
	Serum calcium value normal or <10.5 mg/dL			
	Normal bone structure (scale 0) or solitary bone plasmacytoma only at bone X-ray			
	Low M-protein production rates:			
	IgG value <5.0 g/dL			
	IgA value <3.0 g/dL			
	Urine light-chain M protein on electrophoresis <4 g/24 h			
Smoldering or indolent myeloma	Stage II (intermediate cell mass)	600–1200 billion	Stage I A	Can have single plasmacytoma and/or limited disease on imaging
	No Stage I or Stage III			
MM	Stage III (high cell mass)	1200 billion	Stage I B	<5 focal lesions
	One or more of the following:			
	Hemoglobin value <8.5 g/dL			Mild diffuse disease
	Serum calcium value >12 mg/dL			
	Advanced lytic bone lesions at bone X-ray (scale 3)			
	High M-protein production rates			
	IgG value >7.0 g/dL		Stage II A/B	5–20 focal lesions
	IgA value >5.0 g/dL			Moderate diffuse disease
	Urine light-chain M protein on electrophoresis >12 g/24 h		Stage III A/B	20 focal lesions
				Severe diffuse disease
Sub classification (either A or B)				
A: relatively normal renal function (serum creatinine value) <2.0 mg/dL and no extramedullary disease				
B: abnormal renal function (serum creatinine value) ≥ 2.0 mg/dL and extramedullary disease				

compared to 5–7 years with high-dose therapy followed by autologous stem-cell bone marrow transplantation (ASCT) in standard-risk patients. Cytogenetic and FISH studies reveal chromosome abnormalities of prognostic significance in 33% and in 90%, respectively, of the patients with MM [12]. Translocations such as t(4;14), t(14;16), or 17p– are associated with poor prognosis (median survival 25 months), as also is the presence of hypodiploidy 21 or the deletion of chromosome

Table 5 Potential future biomarkers for diagnosis of multiple myeloma (From Rajkumar et al. [9])

	2-year probability of progression
High level of circulating plasma cells	80%
Abnormal plasma cell immunophenotype ≥95% plus immunopairs	50%
Cytogenetics subtypes t(4;14), 1q amp, or del17p	65%
High bone marrow plasma cell proliferative rate (increase in serum monoclonal protein by ≥10% on each of two successive evaluations within a 6-month period)	50%
Unexplained decrease in creatinine clearance by ≥25% accompanied by a rise in urinary monoclonal protein or serum-free light-chain concentration	Unknown

Table 6 5-year survival rate of MM patients accordingly to the stage of disease (Modified from Rajkumar [29])

Stage	5-year survival rate
Stage I	82%
ISS stage I (serum albumin > 3.5 g/dL, serum β_2-microglobulin < 3.5 mg/L)	
No high-risk cytogenetics	
Normal LDH	
Stage II	62%
Neither stage I or III	
Stage III	40%
ISS stage III (serum β_2-microglobulin > 5.5 mg/L)	
High-risk cytogenetics [t(4;14), t(14;16) or del(17p)] or elevated LDH	

13. The concomitant presence of monosomy and/or deletion of chromosome 13 and serum β_2-microglobulin levels greater than 2.5 mg/L are linked to reduced survival. An elevated PCLI also confers a negative prognosis [8]. Potential future biomarkers for diagnosis of multiple myeloma are reported in Table 5 [9]. Table 6 reports the 5-year survival rate of MM patients accordingly to the stage of disease [29].

Evaluation of Disease Burden with Imaging Modalities

In addition to the previous discussion on the incorporation of additional biomarker-defined myeloma-defining events to the standard CRAB features, updates are also needed that take into account the substantial changes to laboratory testing and imaging (e.g., low-dose whole-body CT and [^{18}F]FDG-PET/CT) used in the diagnosis of MM that have happened since the initial publication of the IMWG diagnostic criteria [9, 16, 30, 31]. Appropriate use of imaging techniques is essential both for determining the severity of bone involvement and for identifying and characterizing the skeletal complications. Imaging is also critical for detecting extramedullary foci, for diagnosing infection and other complications, and for evaluating progression of the disease. Recently, the European Myeloma Network provided recommendations for the management of the most common complications of MM [32].

For staging purpose, the detection of osteolytic lesions is generally based on conventional planar X-ray (Fig. 3) which is currently considered to be the standard technique and is recommended for the detection of bone disease in the CRAB criteria that are used for the definition of myeloma-defining events [16, 31, 33]. Lytic lesions on plain X-rays are typically holes, punched-out lesions with absent reactive sclerosis of the surrounding bone, typically localized in the flat bones of the skull and pelvis. In the long bones, lesions may appear as endosteal scalloping, small lytic lesions (<1 cm), mottled areas of multiple small lesions, or large destructive lesions [34]. These lesions are the consequence of nodular replacement of marrow by plasma cells with destruction of the entire bone [35]. Conventional X-ray may also reveal diffuse osteoporosis, which is best recognized in the spine [36]. Radiological and clinical findings (presence of pain) are used in the scoring system (Table 7a) to predict the risk of fracture of long bones and to identify optimal treatment (Table 7b): patients with a high score benefit from internal fixation, whereas patients

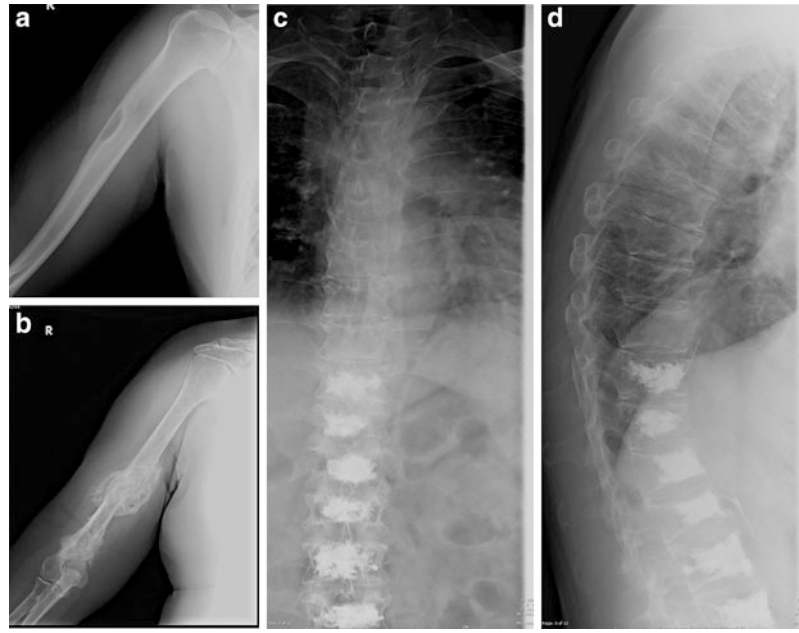

Fig. 3 X-ray appearance of lytic lesions in MM localized at the right humerus and vertebral bodies. Single lytic lesion (**a**) and two lytic lesions with osteoblastic reaction (**b**). Multiple lytic lesions of the dorsal spine (D6–D9) in patient treated with D10-L5 vertebroplasty (**c** anteroposterior view, **d** latero-lateral view)

Table 7 Scoring system for diagnosing impending pathological fractures (Adapted from Winterbottom et al. [20])

A			
	Score		
Variable	1	2	3
Site	Upper limb	Lower limb	Peritrochanteric
Pain	Mild	Moderate	Functional
Lesion	Blastic	Mixed	Lytic
Size	<1/3 diameter	1/3–1/2 diameter	>2/3 diameter
B			
Total score	Risk of impending fracture	Management	
≤7	Low (5%)	Conservative (chemo-/radiotherapy)	
8	Suggestive (15%)	Conservative or surgery (to be evaluated case by case)	
≥9	Diagnostic (33%)	Prophylactic bone fixation	

with a low score can be treated with radiotherapy alone. Asymptomatic patients with X-ray evidence of disease (at least one lytic lesion) have a high risk of progression, with a median time to progression of 8 months.

Whole-body skeletal survey, traditionally used in the Durie and Salmon staging system, is burdened with a relatively high rate of false negatives (30–70%), thus resulting in a significant underestimation of the severity of disease. In fact, conventional X-ray cannot always identify the presence of bone lesions, especially in the early stages of the disease, since lytic lesions become apparent when as much as 30–50% of the bone mineral density is lost. Furthermore, in plain X-rays some areas are not well visualized (i.e., lateral and anteroposterior views of the spine are needed for better visualizing of the vertebral bodies), and it is not possible to distinguish myeloma-related osteoporosis from osteoporosis due to other causes (i.e., steroid-induced or postmenopausal osteoporosis) [37]. Conventional X-ray examinations are also somewhat operator- and technology-dependent, thus increasing the risk of underdiagnosing lytic disease.

A major disadvantage of conventional X-ray is the relatively long imaging time and the necessity of maintaining different positions that not all patients (often elderly and suffering pain for previous pathological fractures) are able to maintain. The potential of low-dose whole-body radiographic

system (Statscan, a radiographic system that records high quality films of the skeleton in a short time) for detecting focal myeloma lesions has been explored; preliminary results are very promising, but clinical experience with this technique (which was originally developed for trauma and emergency patients) is still limited.

However, novel techniques can detect more lytic lesions compared to conventional radiography [32]. Whole-body multidetector computed tomography (WBMD-CT) is more sensitive for the detection of lytic lesions in myeloma compared to conventional radiography (between 70% and 89% for MDCT, depending on stage of the disease), as it can detect more lesions with an extremely high resolution (very small lesions can be detected, even <5 mm) and better performance when evaluating areas that are critical for planar X-ray; it is very quick to perform (2 min or less), it is more accurate for diagnosis and helpful for planning radiotherapy or surgical interventions; furthermore, it can be employed in cases of suspected spinal cord compression when MRI is contraindicated [31, 32, 38–42]. However, specificity of MDCT for assessing certain skeletal changes often associated with myeloma, such as osteopenia, is low. To reduce the radiation burden, whole-body low-dose CT (WBLD-CT) may be used [20, 26]. Also whole-body LDCT was found to be superior to whole-body X-ray for the detection of osteolytic lesions (Table 8) [43].

Since the administration of iodinated contrast agent is not required for evaluating the skeleton with CT, it is useful even in patients with Bence-Jones proteinuria, who are at risk of cast nephropathy and renal failure. However, actual bone destruction must occur for CT imaging to become positive, since focal tumor infiltration confined to the bone marrow remains undetectable. In fact, diffuse interstitial infiltration of the bone marrow is not invariably associated with trabecular/cortical bone destruction, so that the rate of false-negative CT scans is relatively high [44].

Whole-body LDCT advantages over whole-body X-ray include:

1. Superior diagnostic sensitivity for depiction of osteolytic lesions, especially in areas where the whole-body X-ray detection rate is low (i.e., pelvis and spine).
2. Superiority in estimating fracture risk and bone instability.
3. Duration of the examination, which is 5 min or less, an important issue for patients in extreme pain.
4. Production of higher-quality 3D high-resolution images for planning biopsies and therapeutic interventions.

Table 8 Comparison between whole-body LDCT and whole-body X-ray in the detection of osteolytic lesions in MM (Modified from Terpos et al. [43])

References	Study design	Patients, n	Reference test	Key findings
Gleeson et al. [47]	Prospective	39	WBXR, WB-MRI, BM biopsy	WBLD-CT > WBXR, higher detection rate comparable to WB-MRI
Kropil et al. [48]	Prospective	29	WBXR	WBLD-CT > WBXR, detection ratio for lytic lesion WBLD-CT/WBXR = 2.06 (7 for the skull, 2.07 for the thoracic cage, 4.6 for the spine, and 2.54 for the pelvis)
Princewill et al. [46]	Retrospective	51	WBXR	WBLD-CT > WBXR, detection ratio for lytic lesion WBLD-CT/WBXR = 3.9 (1.09 for the skull, 74 for the thoracic cage, 4.92 for the spine, 6.67 for the pelvis and the fat bones, and 2.31 for the long bone); 61% of cases upstaged with WBLD-CT
Wolf et al. [45]	Prospective	52	WBXR	WBLD-CT > WBXR, particularly in the axial skeleton; 63% of cases upstaged with WBLD-CT; 23% of cases negative at WBXR and positive at WBLD-CT

WBXR whole-body X-ray (conventional skeletal survey), *WBLD-CT* whole-body low-dose computed tomography

5. Demonstration of unsuspected manifestations of myeloma or other disease, especially in the lungs and kidneys (33% in the study by Wolf et al. [45]) [38, 45–50].

Major disadvantages of whole-body LDCT include lack of availability in several centers [9, 38], and lack of specificity for the differential diagnosis between malignant and osteoporotic fractures, despite improvements during recent years [51]. Furthermore, although exposure to radiation is much lower compared with standard CT, it continues to be higher than whole-body X-ray: mean dose of whole-body LDCT is approximately 3.6 and 2.8 mSv for females and males, respectively, compared with 1.2 mSv for whole-body X-ray [52]. Nevertheless, the higher diagnostic accuracy of whole-body LDCT and patient comfort, which is particularly important for older patients, renders the dose/quality ratio favorable for whole-body LDCT [43].

Figure 4 represents typical CT examples of lytic lesions of the spine and of a solitary plasmacytoma.

Similarly, positron emission tomography in combination with CT (PET/CT) is superior to conventional radiography in the detection of lytic disease, while whole-body magnetic resonance imaging (WB-MRI) accurately depicts the marrow involvement in MM patients.

MRI identifies bone marrow involvement, based on the loss of the fatty bone marrow component consequent to replacement by plasma cells. MRI has high sensitivity in distinguishing focal or diffuse infiltration of the bone (especially in the spine), as well as detecting destruction of the mineral bone. Myeloma lesions in the marrow appear typically hypointense in T1-weighted sequences and hyperintense in T2-weighted and STIR sequences (Fig. 5).

Five MRI patterns of marrow involvement have been recognized in multiple myeloma:

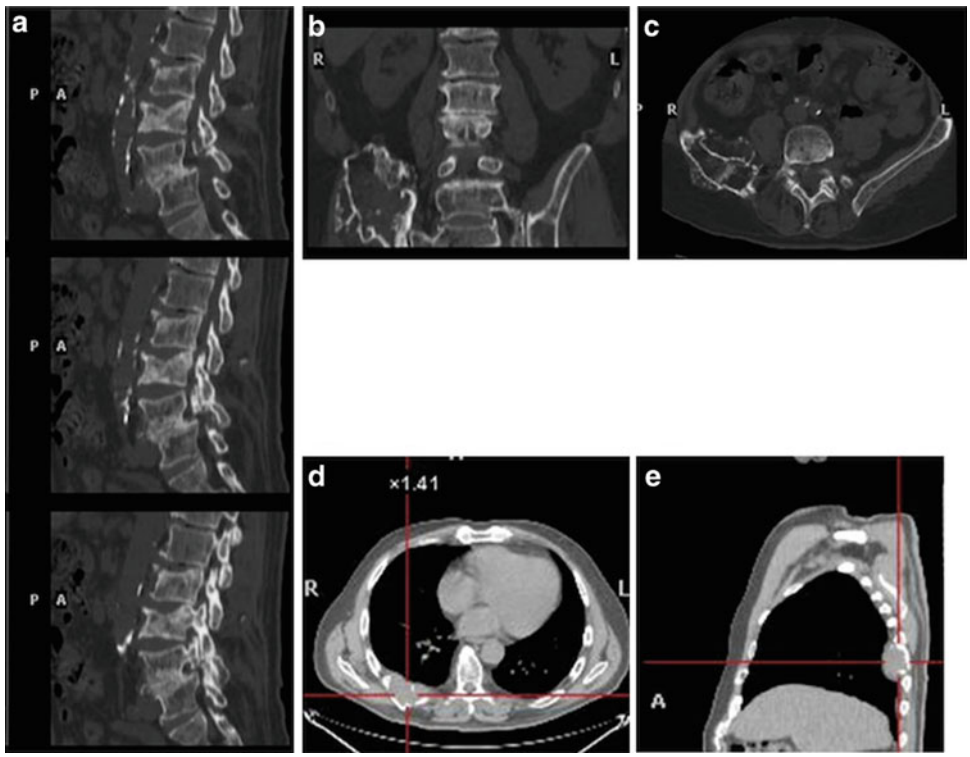

Fig. 4 Typical CT example of lytic lesions of the spine (**a**, sagittal view) and iliac bone (**b** and **c** in coronal and transaxial view, respectively) with the bone window. Panel on the *bottom* shows the transaxial (**d**) and sagittal (**e**) views of a posterior tract of right rib plasmacytoma

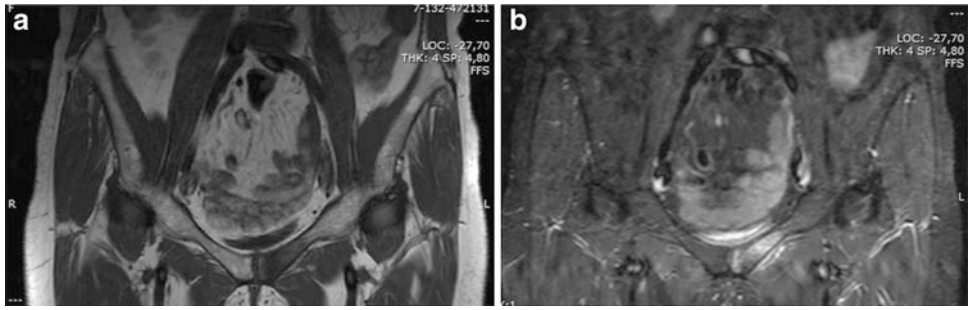

Fig. 5 STIR (**a**) and T2 (**b**) images of a lytic bone lesion of the left pubis. Hyperintense in T2-weighted and STIR sequences

1. A focal pattern that consists of localized areas of myeloma cell infiltration 5 mm or greater in diameter (in 30–50% of patients with advanced MM but also in high-risk smoldering myeloma).
2. A diffuse pattern, characterized by almost complete replacement of normal marrow by myeloma cells (in 25–40% of patients with MM).
3. A combined diffuse and focal pattern (in 10% of patients with MM).
4. A normal bone marrow pattern (in 15–25% of patients with MM).
5. A variegated or "salt and pepper" pattern, with innumerable small bone marrow focal lesions (in 1–5% of patients with MM) [16, 33, 43, 53].

MRI findings reflect pathophysiological processes such as iron overload, amyloid deposition, or reactive marrow hyperplasia. Patients with MM may exhibit normal MRI appearance when the tumor burden is low, while focal or diffuse bone marrow infiltration exhibit variable patterns. At diagnosis, bone marrow infiltration is detected by MRI in 29–50% of the patients with Durie-Salmon stage I disease and negative plain radiographs. Furthermore, MRI offers prognostic information, as the number of lesions detected correlates with response to treatment and with overall survival. Patients with advanced disease and normal MRI respond better to conventional chemotherapy and have better survival than patients with focal/diffuse bone marrow infiltration. Nevertheless, patients with positive MRI do not always require immediate treatment. In fact, in stage I, treatment is not indicated until symptoms appear. The detection of $\geq$10 spine lesions in patients with advanced stage is associated with an increased risk (6–11-fold) of fracture than patients with normal MRI or with less than ten lesions. MRI can distinguish osteoporotic from malignant fractures and is the technique of choice when cord compression is suspected MRI provides accurate information about the epidural space, the level and extension of cord or nerve root compression, and size of the lesion. The main disadvantage of MRI is long scan duration (about 45 min). Moreover, claustrophobic patients or patients with metallic implant/device cannot undergo the exam. The typical MRI protocol for evaluating MM patients does not include some skeletal segments (i.e., the sternum, clavicles, and ribs) and therefore may underestimate the disease burden. Whole-body MRI (WB-MRI, Fig. 6) may overcome those limitations; in fact WB-MRI is more sensitive than WB-MDCT for assessing bone marrow infiltration (both focal and diffuse) and is recommended immediately after the X-ray survey. It allows identifying lesions early in their course (before osteolysis occurs) as well as non-secretory and macrofocal myeloma (especially in the spine and pelvis), which is characterized by lesions with low metabolism and activity.

MRI may also be improved with the use of dynamic contrast-enhanced sequences (DCE-MRI) that evaluate the bone marrow microcirculation caused by myeloma-induced angiogenesis. The DCE-MRI-derived "A" variable describes intensity of the signal (therefore angiogenesis) and is found to be significantly increased in MM patients, in whom it correlates with the presence of osteolytic lesions, with

Fig. 6 A 65-year-old patient with multiple myeloma. WB-MRI demonstrates multifocal osteolysis in the cranial vault, sternum, and ribs (*a* +*b*) and in the lower extremities (*d*). Diffuse infiltration of the lumbar spine and pelvis is shown by the homogeneous signal decrease in bone marrow and demonstrated emanated spinal involvement, particularly in the superior segment

the degree of bone destruction and with the presence of local complications. The amplitude of "A" is a negative prognostic factor for event-free survival and for overall survival in MM [20, 26, 54, 55].

Diffusion-weighted imaging (DWI), which is based on contrast deriving mainly from differences in the diffusivity of water molecules in the tissue environment, is a novel and promising MRI technique. DWI-MRI uses the calculation of apparent diffusion coefficient values to better evaluate myeloma burden and MRI infiltration patterns [56, 57]. Apparent diffusion coefficient values are higher in patients with MM at diagnosis, compared with patients in remission 20 weeks after initiation of treatment [58]. DWI-MRI was found superior to whole-body X-ray for the detection of bone involvement in patients with relapsed/refractory MM in all areas of the skeleton except the skull, where both examinations had equal sensitivity [59]. In a small study, DWI-MRI was found more sensitive than [^{18}F]FDG-PET/CT in detecting myeloma lesions (77% and 47%, respectively) in both newly diagnosed ($n = 15$) and pretreated ($n = 9$) MM patients [60]. In a recent study, 17 patients were evaluated using DWI-MRI, and [^{18}F]FDG-PET/CT and imaging results were compared to bone marrow biopsy. In all studied regions whole-body DWI scores were higher than those produced by [^{18}F]FDG-PET/CT. DWI-MRI was particularly accurate in diagnosing diffuse disease (37% of regions imaged on whole-body DWI scans compared with only 7% on [^{18}F]FDG-PET/CT). Both techniques were equally sensitive in the detection of focal lesions [61].

Bone scintigraphy with ^{99m}Tc-labeled disphosphonate is not useful for diagnosis nor for staging of MM, as the detection of bone lesions is about 35–60% [20, 54] (Fig. 7), with sensitivities

generally lower than that of conventional X-rays. In a comparison of the X-ray skeletal survey versus bone scintigraphy [62], increased uptake of the radiopharmaceutical in radiographically abnormal regions occurred in only 44% of the cases, while normal uptake was seen in 48%, and reduced uptake in 8% of the cases. Lesions that are well defined on the bone scan are the result of complications in MM, mainly osteoblastic response to a compression fracture of a vertebral body or pelvic insufficiency fracture, soft-tissue calcifications within a plasmacytoma [63], or tumor-associated amyloidosis [64]. This pattern is consistent with the prevalent loss of bone mass not associated with osteoblastic activation, which is typical of the myeloma bone lesions. Thus, in MM, bone scintigraphy is generally nearly normal, or it may demonstrate areas with decreased radiopharmaceutical accumulation or the typical osteoporotic pattern (see example in Fig. 8a). On the other hand, bone scintigraphy may be helpful for evaluating some specific skeletal segments such as the sternum and ribs that can hardly be explored with plain X-rays (Fig. 8b).

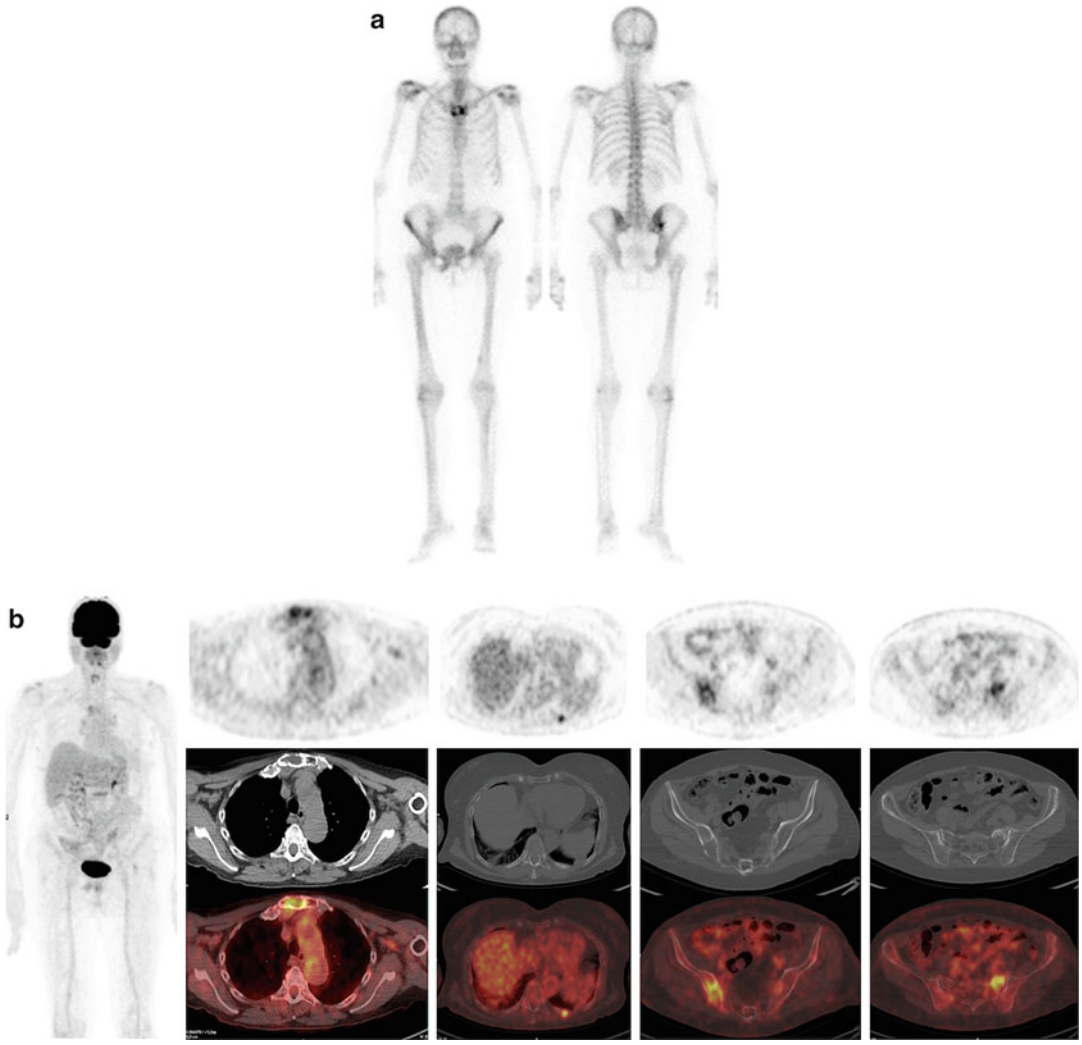

Fig. 7 Bone scintigraphy (**a**) and [^{18}F]FDG-PET/CT (**b**) in a patient with MM IgG. Bone scintigraphy missed lesions in a left rib and in the left sacrum

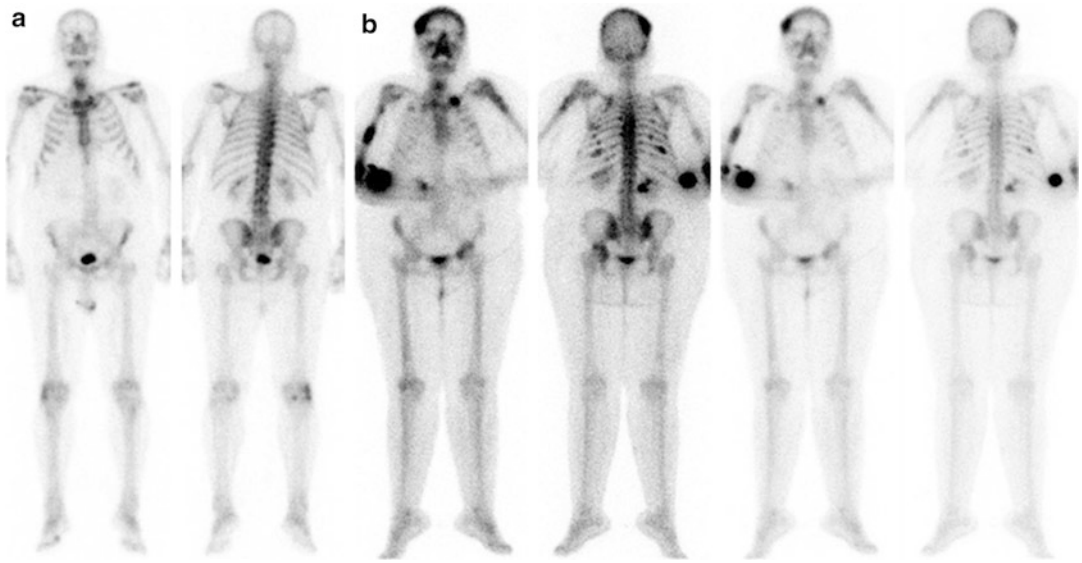

Fig. 8 (**a**) Typical pattern of mild and diffuse ^{99m}Tc-MDP uptake in a patients with MM. (**b**) Atypical appearance of multiple myeloma at bone scan: multiple lesions are evident as in the area of radiopharmaceutical uptake at the skull, left clavicula, humeri, ribs, spine, left iliac bone, and left femur

Nuclear medicine imaging with nonspecific oncotropic radiopharmaceuticals, such as ^{67}Ga-citrate, ^{99m}Tc(V)-DMSA, ^{201}Tl-chloride, ^{99m}Tc-Sestamibi, or [^{18}F]FDG have all met greater success in imaging MM than typical bone-scanning agents. ^{67}Ga-citrate localizes in areas of active tumor either through primary localization within the tumor cells or because of the presence of mononuclear cell and lymphocytic infiltrates observed along with the plasma cells and characterizing the tumor-induced secondary "inflammatory response." Whether these mechanisms act singly or in combination remains unknown [65–67]. ^{67}Ga-citrate is rarely used for tumor detection in MM because increased uptake may be observed in some abnormal soft-tissue sites and in solitary myelomas of bone [62, 68–70], although with variable degrees. Furthermore, the use of ^{67}Ga is hampered by certain disadvantages versus ^{99m}Tc-Sestamibi or [^{18}F]FDG imaging, such as multiday scanning and low resolution. When infection is suspected in MM patients, ^{67}Ga-citrate may be used if ^{99m}Tc-HMPAO/^{111}In-oxine-labeled autologous WBCs are not available. ^{99m}Tc(V)-DMSA has been reported to accumulate in plasmacytoma, irrespective of the presence of amyloidosis [71, 72].

^{201}Tl-chloride has been used for the detection of MM, based on uptake mediated by either increased metabolic demand of the tumor or secondary inflammatory response induced in the marrow [73]. In a study comparing ^{201}Tl-chloride and ^{99m}Tc-labeled bone-seeking agents in patients with MM, ^{201}Tl-chloride was shown to be a promising agent for detecting disease [74]; however, in the clinical routine based on single-photon radiopharmaceuticals for characterizing MM patients, this agent is currently replaced by ^{99m}Tc-Sestamibi, which shows similar localization properties, associated, however, with images of higher quality and lower cost.

^{99m}Tc-Sestamibi accumulates in cells with high metabolic requirements and can therefore be employed to assess in a semiquantitative manner the degree of bone marrow infiltration by plasma cells; this technique is both highly sensitive (92%) and specific (96%). The patterns of ^{99m}Tc-Sestamibi uptake typical of MM can be described as normal (N), focal (F), diffuse (D), and mixed (F+D). Another semiquantitative score (similar to that originally described by Pace et al. [75]) is based on extension (E) and intensity (I) of ^{99m}Tc-Sestamibi uptake, as follows (Fig. 9):

- E0 = no evidence of bone marrow uptake
- E1 = uptake confined to the spine and pelvis
- E2 = uptake in the spine, pelvis and ribs, or in the proximal humeral and femoral epiphyses
- E3 = uptake in the spine, pelvis, ribs, and in distal humeral and femoral epiphyses
- I0 = no evidence of bone marrow uptake
- I1 = bone marrow uptake < uptake in the myocardium
- I2 = bone marrow uptake = uptake in the myocardium
- I3 = bone marrow uptake > uptake in the myocardium

The degree of radiopharmaceutical uptake correlates well with the degree of plasma cell infiltration, with the amount of a monoclonal component, with the clinical status and with stage of the disease. In some studies good correlation was also found between ^{99m}Tc-Sestamibi uptake and other parameters of disease activity, such as the serum levels of lactate dehydrogenase, C-reactive protein, and β_2-microglobulin. Diffuse moderate or intense ^{99m}Tc-Sestamibi uptake, or focal uptake, correlates with poor prognosis. However, ^{99m}Tc-Sestamibi imaging is less sensitive than MRI (50.5% vs. 100%) [76] for evaluating focal lesions localized in the spine (especially in patients with early disease stage), because scintigraphic assessment of such segment is hampered by the high physiologic uptake in the liver and bowel. SPECT imaging has been shown to overcome the relatively poor spatial resolution of planar ^{99m}Tc-Sestamibi scintigraphy. It is important to emphasize that the ^{99m}Tc-Sestamibi scan is always negative in case of MGUS, while false negative results have been described in case of overexpression of P-glycoprotein, associated with multidrug-resistant myeloma [20, 26, 75, 77, 78].

Agool et al. [79] have more recently proposed the use of somatostatin receptor (SSTR) imaging as an alternative method to visualize malignant plasma cells. In fact, in vitro studies have demonstrated that MM cell lines express functional

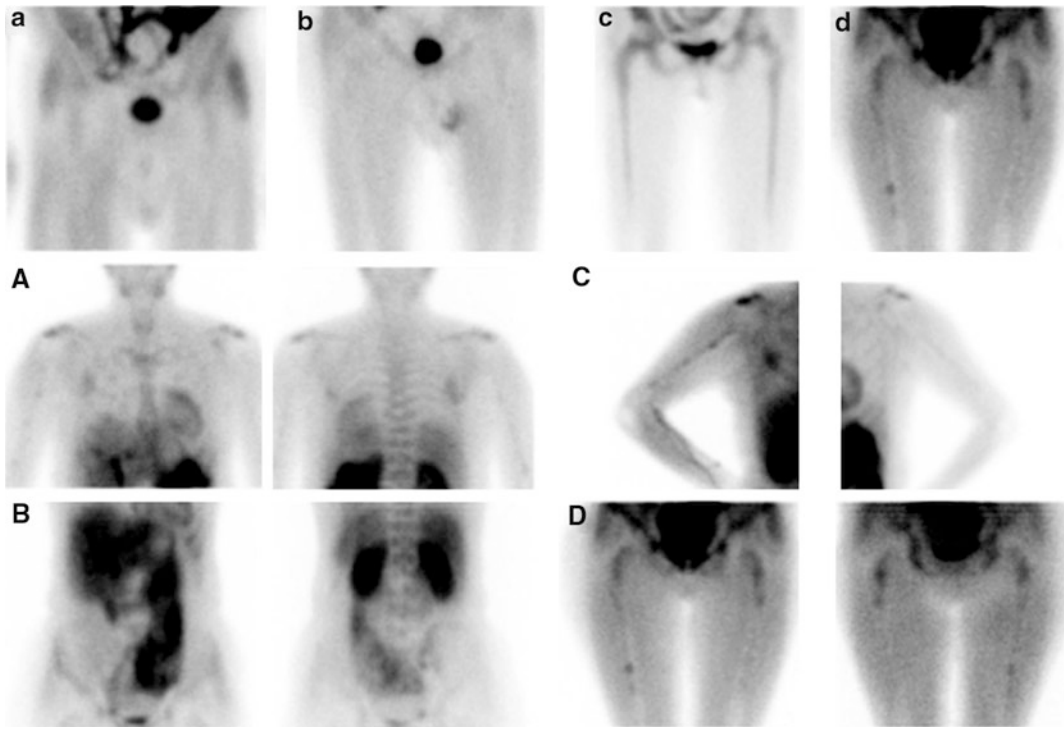

Fig. 9 ^{99m}Tc-Sestamibi scintigraphy demonstrating different degree on bone marrow involvement: focal (**a**, **b**, **d**) and diffuse (**c**) or I3E3 (**a**–**d**)

SSTR2, SSTR3, and SSTR5, the latter being the most represented. Additionally, in vitro growth of myeloma cells can be inhibited by somatostatin and octreotide. Preliminary data in patients with relapsing MM indicate that SSTR imaging is very sensitive, demonstrating abnormal accumulation in 82% of patients compared to a 33% detection rate with whole-body X-ray. Partial or total normalization of the scintigraphic pattern has also been observed in patients responding to treatment. The expression of SSTR could be related to aggressiveness of the disease. However, the limitation represented by poor spatial resolution of planar images (used in this trial) can be overcome either by employing SPECT/CT or by using PET/CT with a positron emitting SSTR analogue (i.e., ^{68}Ga-DOTATOC).

Scintigraphy with the serum amyloid P (SAP) labeled with either ^{99m}Tc or ^{123}I has been proposed to confirm the diagnosis [20, 54, 80] and to quantify the extent of the deposits of light-chain (AL) amyloidosis.

[^{18}F]FDG PET/CT is today the standard for radionuclide imaging in patients with MM, because it identifies early bone marrow infiltration in patients with apparent solitary plasmacytoma and demonstrates the extent of extramedullary involvement. [^{18}F]FDG-PET shows both high sensitivity (86%) and high specificity (92%) [81], with the additional advantage of distinguishing between metabolically active disease ([^{18}F]FDG positive) and clinical conditions characterized by very low burden, such as MGUS or smoldering disease ([^{18}F]FDG negative). Active transformed plasma cells are extremely glucose avid; therefore, [^{18}F]FDG-PET shows focal or diffuse pattern of uptake reflecting the distribution of bone marrow disease. While patients with MGUS generally have a negative [^{18}F]FDG-PET scan (although diffuse low-grade bone marrow uptake can occasionally be observed), the appearance of [^{18}F]FDG focal uptake in a patient with MGUS indicates transformation into an active myeloma. Identification of extramedullary disease on a [^{18}F]FDG-PET scan performed at diagnosis correlates with poor prognosis (see Figs. 10 and 11 for different representative patterns of [^{18}F]FDG uptake in patients with plasmacytoma and MM, respectively). An early clinical investigation on the performance of [^{18}F]FDG-PET in MM (66 patients followed serially) showed the capability of the technique to identify patients with high-risk disease and to monitor patients either in non-secretory myeloma or in complete remission without measurable M component [82]. Such initial observations were subsequently confirmed by other studies, also demonstrating that [^{18}F]FDG-PET could lead to upstaging of the disease in 31–37.5% of patients (depending on the series) and to changes in treatment management in up to 56% of the cases [83]. These results stimulated larger studies with [^{18}F]FDG-PET in patients with myeloma [84, 85]. Data derived from The National Oncologic PET Registry (NOPR), a large prospective program aiming at recording changes of the intended clinical management of cancer patients on the basis of the [^{18}F]FDG-PET/CT findings, have further confirmed this trend. The registry has so far included over 1300 myeloma patients (13.1% scan/incidence in 2007), showing a definite impact on management in about 52% of patients when the scan was requested for staging purpose, 46% in case of restaging, and 51% in presence of suspected recurrence.

In MM the 2.5 threshold for the standardized uptake value (SUV, often considered as the cutoff for other forms of cancer) may not be applicable. In fact, many lesions $<$10 mm (that are obvious on MRI or using dedicated CT) cannot be detected on the [^{18}F]FDG scan using this threshold if one does not take into account the recovery coefficient, whereby SUV decreases along with decreasing lesion size. Figure 12 shows an example of faint pathological [^{18}F]FDG uptake (SUV_{max} under the 2.5 threshold) in a bone lesion and a concomitant larger bone lesion characterized by higher uptake. Therefore, the complementary imaging information provided by the CT component of a [^{18}F]FDG-PET/CT examination is very effective, even if CT is performed in most cases in the low-dose mode (Fig. 13). With all these considerations in mind when interpreting [^{18}F]FDG-PET/CT scans, this imaging modality has reported in this study to be more sensitive than both plain X-ray (89.2% vs. 47.4%) and CT alone (89.2% vs. 70.4%) [86]. In addition to demonstrating persistent or recurrent osseous disease,

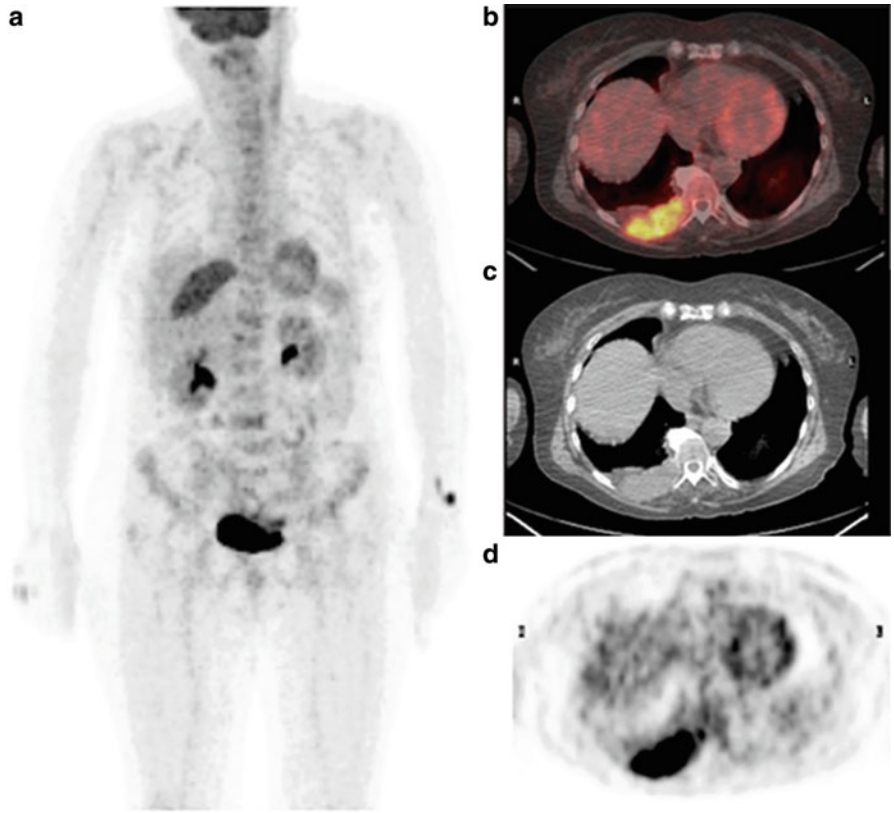

Fig. 10 The typical representative patterns of [^{18}F]FDG uptake in patients with solitary plasmacytoma. MIP images (**a**) and the relative transaxial sections on fused images (**b**), CT (**c**) and PET (**d**), demonstrating an intense area of radiopharmaceutical uptake corresponding to a large lesion developing from the posterior trait of the right rib. No additional lesions are present in any other bone segments

[^{18}F]FDG-PET/CT is more sensitive than other imaging modalities for localizing extramedullary sites of disease, thus revealing additional lesions in almost 30% of the patients who had been diagnosed with solitary plasmacytoma by MRI [87, 88]; this results in upstaging extent of the disease and has therefore a relevant impact on the choice of therapeutic strategies [89–91]. However, sensitivity of [^{18}F]FDG-PET for assessing diffuse disease in the spine and pelvis remains almost half than that of MRI [78].

Thus, while [^{18}F]FDG-PET/CT performs better than either ^{99m}Tc-Sestamibi scintigraphy or MRI in detecting focal bone and bone marrow lesions, MRI remains the method of choice for evaluating diffuse bone marrow infiltration in the spine, considering that diffusely increased non-specific [^{18}F]FDG uptake is frequently observed in the bone marrow of young people or in patients with anemia [78, 83, 92]. [^{18}F]FDG-PET/CT should be preferred for an accurate initial staging of patients with MM (Fig. 14), while MRI is to be preferred when assessing the degree of bone marrow infiltration by plasma cells in the early phase of the disease. By combining MRI of the spine/pelvis and whole-body PET/CT, the ability to detect sites of active MM, both medullary and extramedullary, can be as high as 92%. Although rarely, active disease demonstrated by bone marrow assessment may be missed by both [^{18}F]FDG-PET/CT and MRI (false-negative cases); however, when [^{18}F]FDG-PET/CT and MRI are concordantly positive, no false-positive results are generally observed, thus yielding specificity and positive predictive values close to 100%. This consideration is of value in aiding clinicians to

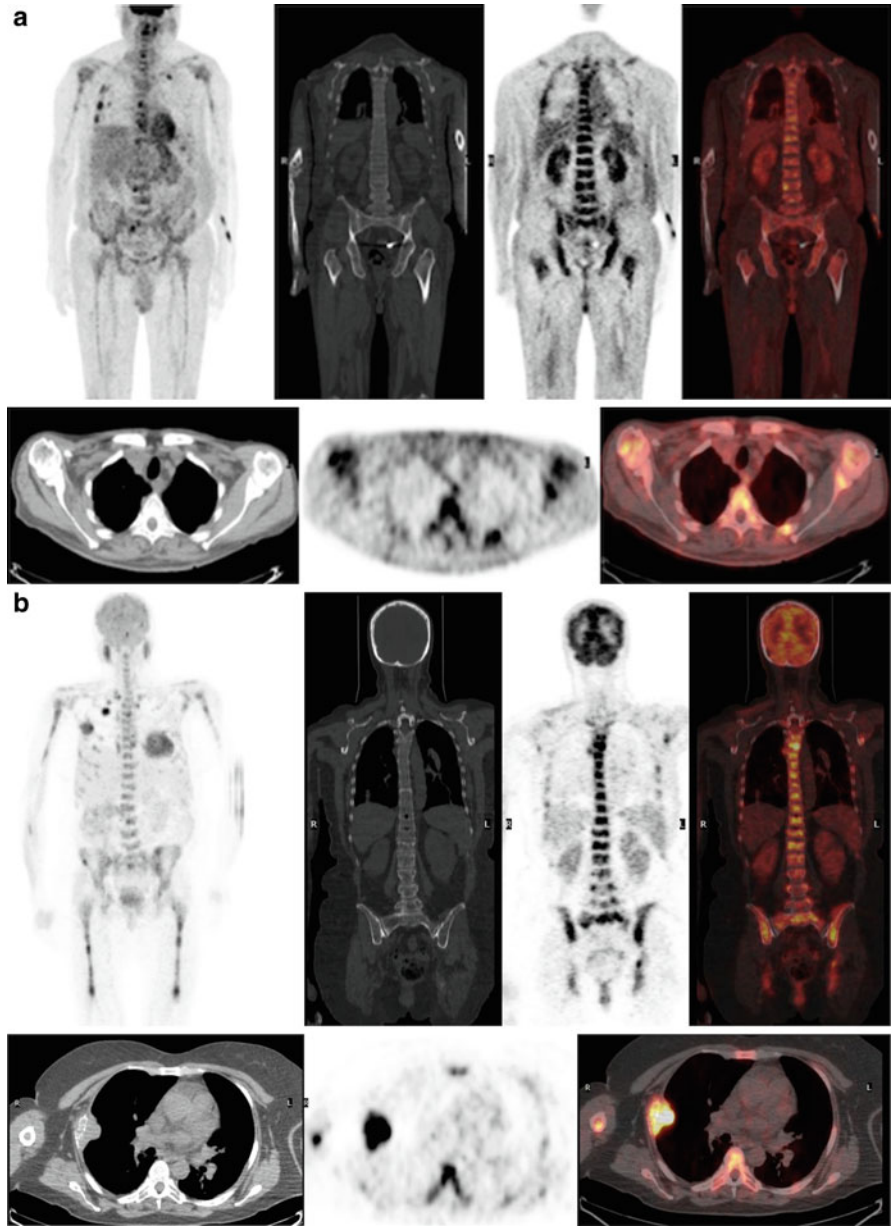

Fig. 11 Different patterns of [^{18}F]FDG uptake in patients with MM. Panel (**a**) diffuse and moderate [^{18}F]FDG uptake in bone (as intense as the liver uptake) with focal area of major accumulation corresponding to multiple bone sites of active myeloma. *Top right* MIP images, coronal view (CT with bone window, PET, and fused images) on *top left*, and transaxial view showing humeral, scapular, spine, and rib involvement on the bottom (CT with mediastinal window, PET, and fused images). Panel (**b**) diffuse and intense [^{18}F]FDG uptake in bone (more intense than the liver) with focal area of major accumulation corresponding to multiple bone and soft-tissue site disease. *Top right* MIP images, coronal view (CT with bone window, PET, and fused images) on *top left*, and transaxial view showing humeral, spine, sternum, and rib involvement with a judge lesion of the lateral right rib involving the chest wall (CT with mediastinal window, PET, and fused images). Of notice, [^{18}F]FDG reproduces the pattern of homogeneous and diffuse uptake along the humeri and femora which is typical of ^{99m}Tc-Sestamibi in advanced myeloma with better spatial resolution

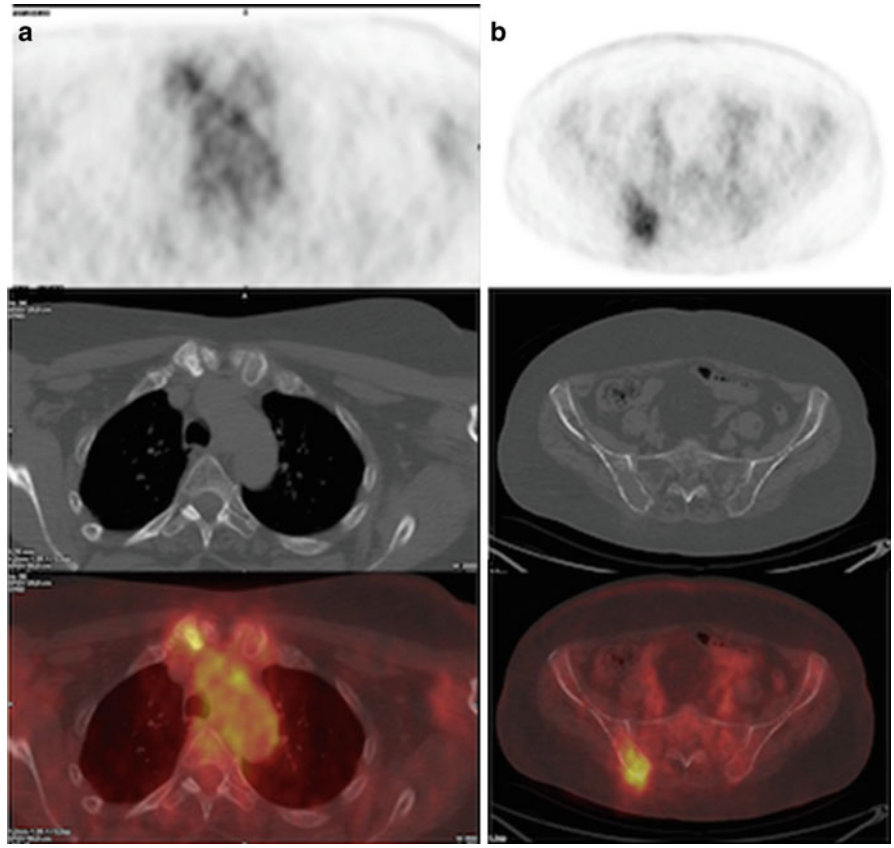

Fig. 12 Example in the same patient of MM lesions characterized by different patterns of [^{18}F]FDG uptake with an SUV_{max} of 2.2 in the right clavicle (**a**) and SUV_{max} of 4 in the right ileum (**b**)

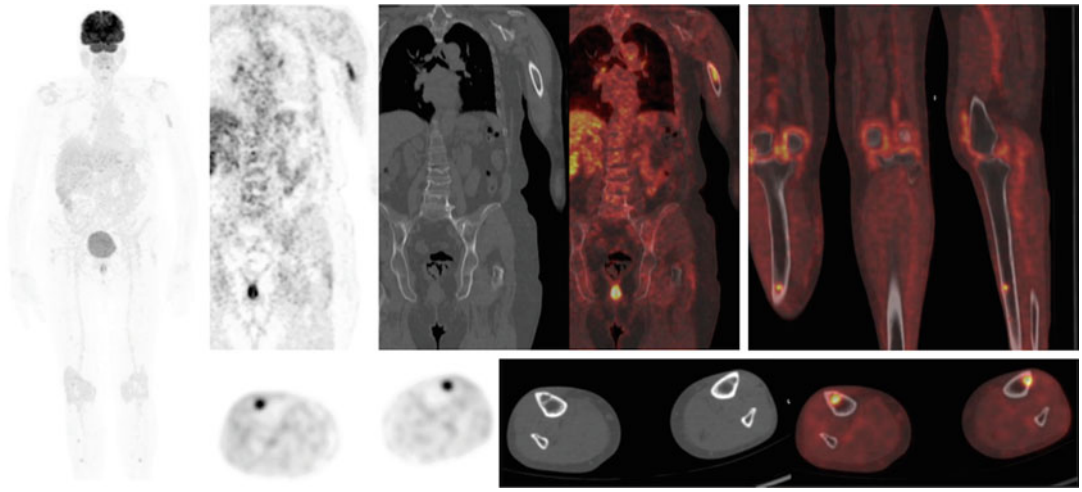

Fig. 13 Example of the complementarity of PET and CT images in a patient with MM

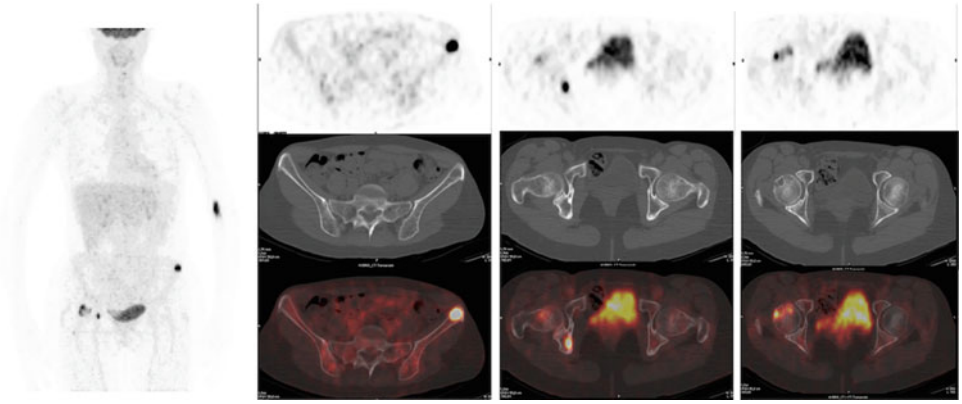

Fig. 14 Staging in a patient with MM IgG k (stage IIIA, ISS1). MIP and axial images show [^{18}F]FDG uptake in the pelvis and right femora

either continue with or change chemotherapy regimens on the basis of persistently positive findings on imaging studies. The low negative predictive values of [^{18}F]FDG-PET/CT (50%) and MRI (59%) and also of the combination of the two (64%) suggest that negative results should always be considered with caution and correlated to other markers of disease activity [93].

The prognostic significance of [^{18}F]FDG-PET/CT is not yet well established. Bartel et al. [94] evaluated the prognostic value of [^{18}F]FDG-PET/CT in patients with newly diagnosed MM. By applying tertile-derived cut-points, several imaging parameters affected overall survival and event-free survival adversely, in particular, the presence of extramedullary disease and the number of lytic lesions detected by metastatic bone survey and the number of focal sites of [^{18}F]FDG uptake. Abnormal MRI findings and high SUV of focal [^{18}F]FDG uptake were associated with shorter event-free survival, while having borderline effects on overall survival. The number of lesions detected by PET/CT was the parameter most closely correlated with other prognostic variables, such as β_2-microglobulin, lactate dehydrogenase, and C-reactive protein and gene expression profiling-derived indices: positive correlation with high risk and two proliferation parameters and inverse correlation with low bone disease subgroup. The PET/CT findings also maintained an independent adverse prognostic value, if combined with positive cytogenetic abnormalities and elevated lactate dehydrogenase levels. [^{18}F]FDG-PET/CT identified 30% of patients who had poorer prognosis despite having low-risk disease as defined by gene expression profiling analysis. Based on logistic regression analysis, the PET findings were independently positively correlated to both MRI and metastatic bone survey. Among the non-imaging parameters, the results of PET correlated positively with C-reactive protein and negatively with gene array-defined low bone disease.

[^{18}F]FDG-PET also offers the advantage of identifying superimposed infection. On the other hand, such high sensitivity can increase the false positive results when the scan is performed within a short interval after radiotherapy or surgery; it is therefore recommended to perform the scan at least 4 weeks after a surgical procedure or 2–3 months after completion of radiotherapy [83, 95].

Limitations of [^{18}F]FDG-PET/CT include the lack of sensitivity for detecting diffuse bone marrow involvement (in this case MRI remains the gold standard) and low-density plasmacyte infiltration. Moreover, physiological [^{18}F]FDG uptake in the brain reduces the sensitivity for small skull lesions [96]. One of the major limitations of [^{18}F]FDG-PET/CT lies in the lack of standardized interpretation criteria and the controversies regarding the use of SUV_{max} to define its positivity. Recently, an Italian panel of experts introduced novel criteria (IMPeTUs) [97] for the

interpretation of PET/CT images in MM. The final version of the criteria (Table 9) includes the description, using 5-point scales, of metabolic state of the bone marrow, number and site of focal PET-positive lesions with or without osteolytic characteristics, presence and site of extramedullary disease, presence of paramedullary disease, and presence of fractures. The visual degree of uptake is defined for bone marrow, the target lesion (i.e., the hottest area), and extramedullary lesions according to the schema proposed in the Deauville criteria for the evaluation of lymphoma patients. The IMPeTUs criteria must be validated in prospective studies to evaluate their clinical value.

The diagnostic potential of non-[^{18}F]FDG positron-emitting radiopharmaceuticals has been investigated in patients with MM. In particular, radiolabled choline (a precursor of phospholipid synthesis whose uptake is increased in proliferating cells) has been compared to [^{18}F]FDG [98, 99]. Authors suggest that the superior sensitivity of radiolabeled choline-PET/CT over [^{18}F]FDG-PET/CT for detecting bone lesions is due to the high phospholipid metabolic rate of myelomatous cells, as these compounds are involved in the modulation of intracellular growth signal transduction pathways. The main clinical disadvantage in the use of radiolabeled choline is its high physiological liver uptake that may prevent the detection of hepatic lesions.

Results of in vitro experiments showing that the radiolabeled amino acid [^{11}C]methionine is incorporated into immunoglobulins produced by the malignant plasma cells have prompted a clinical study performed with [^{11}C]methionine-PET/CT in MM patients by Dankerl et al. [100]. Consistently with the underlying hypothesis, osteolytic lesions exhibited a high uptake of [^{11}C]methionine, similar to that of [^{18}F]FDG. Furthermore, newly diagnosed osteolytic lesions in untreated patients were strongly [^{11}C]methionine positive, while recurring osteolytic lesions were [^{11}C]methionine negative. Although the series evaluated in this study was relatively small, the substantial mismatch between the number of lesions identified by [^{11}C]methionine-PET and those identified by CT represented an important added value of metabolic imaging for

Table 9 The IMPeTUs criteria for the interpretation of PET/CT images in MM (Modified from Nanni et al. [97])

Lesion type	Site	Number of lesion (x)	Grading
Diffuse	Bone marrow[a]		Deauville 5-point scale[b]
Focal	Skull	x = 1 (no lesions)	Deauville 5-point scale[b]
	Spine	x = 2 (1–3 lesions)	
	Extraspinal (all the rest)	x = 3 (4–10 lesions)	
		x = 4 (>10 lesions)	
Lytic		x = 1 (no lesions)	
		x = 2 (1–3 lesions)	
		x = 3 (4–10 lesions)	
		x = 4 (>10 lesions)	
Fracture		At least one at CT	
Paramedullary[c]		At least one	
Extramedullary	Nodal (n = 7)/extranodal (n = 5)[d,]	At least one	Deauville 5-point scale[b]

[a]Appended if increased uptake in limbs and ribs
[b]Deauville 5-point scale
1 = No uptake at all
2 ≤ Mediastinal blood pool uptake (SUV_{max})
3 > Mediastinal blood pool uptake, ≤ liver uptake
4 > Liver uptake more than 10%
5 > Liver uptake (twice)
[c]Bone lesion involving surrounding soft tissues with bone cortical interruption
[d]Nodal disease (*N*) plus site: laterocervical (*LC*), supraclavicular (*SC*), mediastinal (*M*), axillary (*Ax*), retroperitoneal (*Rp*), mesentery (*Mes*), inguinal (*In*); extranodal disease (*EN*) plus site: liver (*Li*), muscle (*Mus*), spleen (*Spl*), skin (*Sk*), other (*Oth*)

early detection of lesions not yet obvious as macroscopic bone changes; these findings would therefore provide an accurate estimate of tumor burden, particularly for clinically silent and unexpected localizations. Very recently, Lapa et al. [101] performed a head-to-head comparison of [^{11}C] methionine and [^{18}F]FDG-PET/CT scans in 43 patients referred for staging or restaging of MM.

PET/CT with 3′-^{18}F-fluoro-3′-deoxy-L-thymidine (^{18}F-FLT, whose uptake mirrors DNA synthesis via thymidine kinase-1) has been proposed to distinguish hematological malignancies from other clinical conditions causing pancytopenia. Although the exact mechanism of ^{18}F-FLT uptake in bone marrow remains unclear, several studies suggest that it is linked to the cycling activity of hematopoietic cells, thus reflecting the state of the entire bone marrow compartment [26]. Bone marrow uptake of ^{18}F-FLT is intense in patients with myelodysplasia and myeloproliferative disorders, while it is lower-to-absent in patients with MM, myelofibrosis, or aplastic anemia. Patients with MM may present variable degrees of ^{18}F-FLT uptake in response to bone marrow expansion into the peripheral bones.

Extensive skeletal involvement has also been incidentally detected during PET with [^{11}C]Acetate [102]. It is not entirely clear why myelomatous lesions would exhibit such high uptake of [^{11}C]Acetate, although this observation is consistent with a much earlier in vitro study with plasma cells obtained from patients with MM, showing enhanced uptake of acetate as a substrate for the Krebs cycle [103]. On the other hand, it is well known that malignant cells (including MM cells) typically have increased glycolysis versus their normal counterparts, as also confirmed by a correspondingly increased [^{18}F]FDG consumption; since the Krebs cycle (whose metabolic substrate is acetate) constitutes a component of overall glycolysis, it is not surprising that uptake of both [^{18}F]FDG and [^{11}C]Acetate occurs in MM.

Although there are some issues that need to be clarified when using sensitive techniques such as WBLD-CT, PET/CT, or MRI (e.g., what the difference is between an MM patient with 4 lytic lesions detected by conventional radiography and another patient with 14 lytic lesions detected by WBLD-CT), data so far support the use of WBLD-CT as standard procedure for the diagnosis of lytic disease in patients with MM (grade 1A) as pointed out by the "European Myeloma Network Guidelines for the Management of Multiple Myeloma-related Complications" [32] (Fig. 15).

Positive lesions in WBLD-CT are considered those with a diameter of 5 mm or more. Conventional radiography can also be used if WBLD-CT is not available. In asymptomatic patients with no lytic disease in WBLD-CT, MRI and [^{18}F]FDG PET/CT are not recommended. In the presence of more than 1 focal lesion, the patients are characterized as having symptomatic disease that needs therapy (grade 1A) [32].

However, in the "Revised International Myeloma Working Group diagnostic criteria for multiple myeloma and smoldering multiple myeloma," the detection of one or more osteolytic lesions on skeletal radiography, CT, or [^{18}F]FDG-PET/CT has been reported. Therefore, the IMWG recommends either [^{18}F]FDG-PET/CT, low-dose whole-body CT, or MRI of the whole-body or spine in all patients with suspected smoldering multiple myeloma. Increased [^{18}F]FDG uptake alone is not adequate for the diagnosis of MM; evidence of underlying osteolytic bone destruction is needed on the CT portion of the examination.

Assessing Response to Treatment

Although there are several studies evaluating the role of imaging at diagnosis, there are limited data for the value of imaging during treatment and follow-up of patients with myeloma [43]. Many criteria can be employed to assess response to therapy in MM patients, including those set by the European Group for Blood and Bone Marrow Transplant/International Bone Marrow Transplant Registry/American Bone Marrow Transplant Registry, by the Chronic Leukemia-Myeloma Task Force, by the Southwest Oncology Group (SWOG), and by the Eastern Cooperative Oncology Group (ECOG). In 2006, the International Myeloma Working

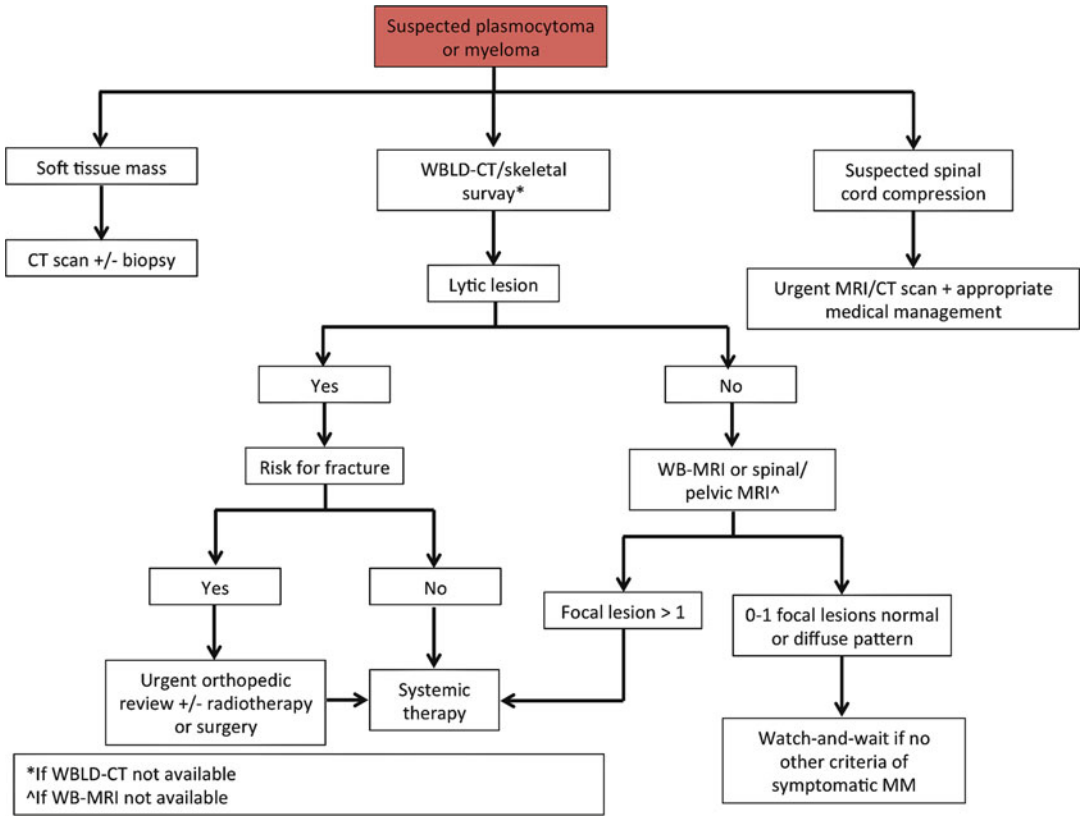

Fig. 15 Algorithm for imaging in multiple myeloma (Modified fromTerpos et al. [32])

group (IMWG) recognized the importance of standardizing such criteria and elaborated the so-called uniform response criteria (Table 10). While adopting the classical categories of Complete Response (CR), Partial Response (PR), Stable Disease (SD) and Progressive Disease (PD), the system introduced the new category of "positive response of additional clinical significance" following treatment. Although the IMWG response criteria deleted the category "minor response" (considered to be somewhat vague and therefore unreliable), more recently this category has been reintroduced by the ASH-FDA in patients with relapsed refractory myeloma, while specific criteria for progression have been defined for SMM (Table 11) [8].

Although changes in BM infiltration are not employed as a guiding criterion for assessing response to treatment, finding <5% plasma cells is one of the requisites for complete remission. Furthermore, in patients without measurable disease, it is possible to monitor the disease by the serum-free, light-chain assay. Irrespective of the specific system employed to classify response to treatment, the main pitfall of these systems is represented by the method used to assess bone marrow and bone lesions. In fact, plain radiography is of limited value for evaluating the response to treatment; in particular, even if the appearance of new bone lesions clearly indicates disease progression, lytic bone lesions rarely show radiologic signs of recovery. Furthermore, new compression vertebral fractures may occur either in case of disease progression or in case of bone loss or in case of reduction of the tumor mass that supports the bone cortex [3, 8, 26, 78]. MDCT is not generally used for assessing response to treatment, since osteolytic lesions rarely recover. In selected cases,

Table 10 International Myeloma Working Group uniform response criteria for MM (From Kyle et al. [8])

Category	Criteria
Complete response (CR)	Negative immunofixation of serum and urine **and** disappearance of any soft-tissue plasmacytomas **and** <5% plasma cells in bone marrow
	Patients with only measurable disease by serum FLC levels: CR is defined as normal FLC ratio (0.26–1.65) in addition to CR criteria listed above
Stringent complete response (sCR)	Negative immunofixation of serum and urine **and** disappearance of any soft-tissue plasmacytomas **and** <5% plasma cells in bone marrow **and** normal FLC ratio **and** absence of clonal cells in bone marrow by immunohistochemistry or immunofluorescence
Very good partial response (VGPR)	Serum and urine M protein detectable by immunofixation but not on electrophoresis or ≥90% or greater reduction in serum M protein plus urine M protein <100 mg/24 h
	Note: Patients with only measurable disease by serum FLC levels, VGPR is defined as a >90% decrease in the difference between involved and uninvolved FLC levels
Partial response (PR)	≥50% reduction of serum M protein **and** reduction in 24 h urinary M protein by ≥90% or to <200 mg/24 h **and** ≥50% reduction in the size of soft-tissue plasmacytomas if present at baseline
	Note: If the serum and urine M protein are unmeasurable, ≥50% decrease in the difference between involved and uninvolved FLC levels
	If serum and urine M protein and serum FLC are unmeasurable, ≥50% reduction in bone marrow plasma cells, provided baseline percentage was ≥30%
Stable disease (SD)	Not meeting criteria for CR, VGPR, PR, or PD
Progressive disease (PD)	>25% from lowest response value in any one or more of the following:
	Serum M protein (absolute increase must be ≥0.5 g/100 mL)[a]
	Urine M protein (absolute increase must be ≥200 mg/24 h)
	Only in patients without measurable serum and urine M-protein levels: the difference between involved and uninvolved
	FLC levels (absolute increase must be >10 mg/L)
	Bone marrow plasma cell percentage (absolute% must be ≥10%)
	Definite development of new bone lesions/soft-tissue plasmacytomas or definite increase in size of existing bone lesions/soft-tissue plasmacytomas
	Development of hypercalcemia (corrected serum calcium >11.5 mg/100 mL) ascribable solely to the plasma cell proliferative disorder

All response categories (CR, sCR, VGPR, and PR) require two consecutive assessments made at any time before the institution of any new therapy; complete PR and SD categories also require no known evidence of progressive or new bone lesions if radiographic studies were performed. Radiographic studies are not required to satisfy these response requirements. Bone marrow assessments need not be confirmed

[a]For PD serum M protein increases of ≥1 gm/100 mL are sufficient to define relapse if starting M protein is ≥5 gm/100 mL

mainly those characterized by significant soft-tissue component (i.e., plasmacytoma), response to therapy can instead be demonstrated by reduction in tumor size as assessed with CT. Moreover, CT may be of value in patients with persistent unexplained symptoms despite therapy or with risk of impending fracture or when no clinico-biochemical response to treatment is observed. The disappearance of any MRI-detectable bone marrow lesion typically represents complete response, while a partial response to therapy is associated with changes of the MRI pattern from diffuse to focal/variegate or with the reduction of the signal on the T2-weighted spin echo images. Nevertheless, MRI has limited value for the early assessment of response to treatment, since complete resolution of bone marrow lesions may take as long as 9–12 months from the completion of the therapy. DCE-MRI is superior to standard MRI for this purpose; in particular, favorable response is indicated by the disappearance of gadolinium enhancement or by the absence of contrast-induced enhancement in a follow-up study as compared to the baseline scan. DCE-MRI derives parameters correlated with microvascular density in the bone marrow both before and after therapy [104, 105]. However, the real added value

Table 11 Additional response criteria for specific disease stages. International Myeloma Working Group uniform response criteria for MM (From Kyle et al. [8])

Category	Criteria
Relapsed MM	At least one prior regimen and not meeting criteria for relapsed and refractory MM
Relapsed and refractory MM	Relapse of disease while on salvage therapy or progression within 60 days of most recent therapy
Minor response (MR) in patients with relapsed refractory MM	≥25% but <49% reduction of serum M protein **and** reduction in 24 h urine M protein by 50–89%, which still exceeds 200 mg/24 h **and** reduction in size (25–49%) of any soft-tissue plasmacytoma **and** no increase in size/number of lytic bone lesions (development of compression fracture does not exclude response)
Progression to active MM in patients with smoldering MM	Evidence of PD based on the IMWG criteria (Table 9) **and** any one or more of the following:
	Development of new lesion (soft-tissue plasmacytoma/bone lesions)
	Hypercalcemia (>11 mg/100 mL)
	Decrease in hemoglobin of ≥2 g/100 mL
	Serum creatinine level ≥2 mg/100 mL

of this technique seems to lie in the possibility to predict which patients might benefit from therapy with anti-angiogenetic drugs, i.e., bevacizumab (a monoclonal antibody that inhibits VEGF). Nevertheless, this approach has not yet gained a definite role in the evaluation of the course of the disease and of activity of the myeloma lesions. Preliminary reports suggest that DWI-MRI may be used for the better definition of response to therapy, but this has to be confirmed in larger studies and in comparison with [^{18}F]FDG-PET/CT results [50, 57]. The combination of DWI and DCE-MRI produced a score with a high agreement (76%) with the IMWG criteria of response in 27 patients with myeloma under treatment [106]; however, more data are needed to evaluate such score in larger studies [43].

Given the heterogeneous nature of the disease and inconsistent response to treatment, along with the relatively small number of published studies in this field, MRI currently has a limited role in response assessment. In general, MRI findings of response to therapy (CR or PR) include resolution or decrease of the extent of focal lesions or diffuse patterns in conventional chemotherapy or novel anti-myeloma agents [107–109]. In a small study with 33 patients who underwent an ASCT, MRI resulted in high specificity and accuracy (86% and 79%, respectively) but only 64% sensitivity for the detection of remission because of false-positive results of nonviable lesions [109]. Thus, for better evaluation of remission, functional imaging techniques (e.g., PET/CT or possibly DWI-MRI) seem to be more appropriate. Nonetheless, in a retrospective study which compared MRI and [^{18}F]FDG-PET/CT in 210 patients with MM, MRI achieved better results than PET/CT for the detection of myeloma at diagnosis and at progression, while PET/CT detected findings of response to anti-myeloma therapy earlier than MRI [110].

Regarding patients with smoldering multiple myeloma with a negative MRI study at diagnosis, the timing of follow-up with MRI and the significance of any findings on these studies have not yet been established. Merz et al. [111] evaluated the role of repeated MRI in 63 patients with smoldering multiple myeloma. The second examination was performed 3–6 months after the first. Approximately one-half of the patients showed progression on MRI, while 40% developed symptomatic disease, according to CRAB criteria.

Other studies [78, 112] have found a close correlation between the results of ^{99m}Tc-Sestamibi scintigraphy (i.e., disappearance of any area of uptake) and the conventional criteria used for defining clinical response to therapy (i.e., measurement of the M-protein component). Overall, these findings support the hypothesis that bone marrow uptake is an indicator of myeloma activity in the bone marrow, even in the absence of focal

areas of increased uptake. This procedure has shown high specificity (86%) in patients in CR, whereas sensitivity was 45% in presence of PR; these findings emphasize the high performance of ^{99m}Tc-Sestamibi scintigraphy for identifying absent disease, whereas its sensitivity is lower for the definition of residual disease when response is not complete. Multivariate analysis also showed that the sensitivity of ^{99m}Tc-Sestamibi scintigraphy was low in the presence of bone marrow infiltration $<30\%$.

The prognostic value of ^{99m}Tc-Sestamibi imaging for predicting recurrence of the disease has been extensively investigated by Pace et al. [75]. In a group of patients evaluated both at baseline and after chemotherapy, they demonstrated a significant association between pretreatment scintigraphic pattern and clinical status at follow-up. In particular, none of the patients responding to therapy had a posttreatment ^{99m}Tc-Sestamibi scan showing focal uptake or diffuse uptake with a summed score higher than 2; by contrast, the nonresponders showed either diffuse bone marrow uptake or areas of focal uptake with summed score higher than 2. A negative baseline ^{99m}Tc-Sestamibi imaging showed high prognostic value for clinicobiochemical remission, and multivariate analysis demonstrated the added value of the ^{99m}Tc-Sestamibi uptake pattern with respect to known prognostic variables, such as C-reactive protein. Furthermore, ^{99m}Tc-Sestamibi imaging patterns at follow-up were significantly associated with the clinical status evaluated after chemotherapy.

In an independent study, a semiquantitative parameter of ^{99m}Tc-Sestamibi washout derived from dual point scintigraphic acquisitions as the counts/pixel at early imaging (10 min) minus counts/pixel at delayed imaging (60 min) divided by counts/pixel at 10 min (corrected for decay) has been also employed to distinguish patients responding to treatment from nonresponders. A fast clearance of ^{99m}Tc-Sestamibi from the bone marrow of patients with MM is associated with poor response to subsequent chemotherapy.

Moreover, ^{99m}Tc-Sestamibi washout reflects the degree of expression of the P-glycoprotein (Pgp), a transmembrane protein encoded by the ABCB1 gene that mediates the outward transport of many cytotoxic compounds including a variety of anticancer agents and confers tumor cells the capability to escape the lethal effect of many cytotoxic compounds, thus causing multidrug resistance (MDR). Overexpression of Pgp in resistant-cultured tumor cells causes a reduced net uptake of ^{99m}Tc-Sestamibi as a consequence of an enhanced Pgp-dependent outward transport of the tracer [113]. Thus, since overexpression of Pgp is one of the primary mechanisms of MDR in MM as well as in other malignancies [114, 115], it can be hypothesized that the ^{99m}Tc-Sestamibi washout rate could serve to predict response to chemotherapy in MM patients.

However, all these studies have included small groups of patients, and none of them evaluated the impact of ^{99m}Tc-Sestamibi scintigraphy on progression-free survival and overall survival.

In case of effective response to therapy, [^{18}F]FDG uptake declines rapidly (within hours). The persistence of a positive [^{18}F]FDG-PET has high prognostic value, as it correlates with early recurrence. Furthermore, [^{18}F]FDG-PET/CT represents the most sensitive imaging technique to evaluate response of the bone lesions to treatment, particularly for distinguishing treated bone marrow lesions from viable neoplastic tissues [8, 26, 92] (Figs. 16 and 17).

[^{18}F]FDG-PET/CT has been employed in patients with newly diagnosed MM as part of the "Total Therapy 3" study, characterized by four distinct phases of induction therapy (two cycles of VDT-PACE with peripheral blood stem cell collection after the first cycle + tandem transplantation with melphalan 200 mg/m^2, consolidation with two cycles of dose-reduced VDT-PACE, and maintenance therapy for 3 years, with monthly cycles of VTD for the first year and thalidomide plus dexamethasone in years 2 and 3) [94]. The exam was performed at baseline (together with metastatic bone survey and MRI) and within 10 days from starting the first induction cycle of VDT-PACE. The follow-up studies included annual metastatic bone survey, while MRI scans were performed before each of two transplantations, before consolidation and maintenance phases, and semiannually thereafter. All imaging studies were also repeated at relapse,

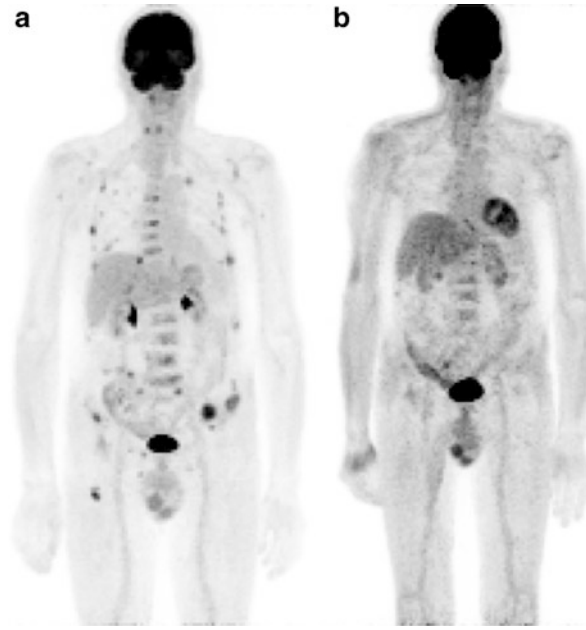

Fig. 16 Treatment response evaluation assessed by [^{18}F]FDG-PET/CT in a patient with MM IgG K (stage IIIb, ISS2). Baseline MIP (**a**) shows many areas of [^{18}F]FDG uptake disappeared (**b**) after chemotherapy (VelDexMyo regimen)

Fig. 17 [^{18}F]FDG-PET/CT of the same patient shown in Fig. 16 after recurrence

defined by M-protein and bone marrow criteria and by any of the imaging procedures. Similarly as in the case of other malignancies such as lymphoma, disappearance of [^{18}F]FDG uptake before transplantation proved to be an independent favorable prognostic factor, thus demonstrating the importance of complete suppression of tumor metabolism in myeloma. Using the [^{18}F]FDG-PET/CT criteria (absence of [^{18}F]FDG focal uptake in bone segments and extramedullary disease), the authors were able to define CR status in 92% at 18 months, which became obvious earlier than the median onset of clinical n-CR (87%) and CR status (56%) by 4 and 12 months, respectively. The cumulative proportion of patients qualifying for MRI-defined CR was 29% at 18 months and reached 59% at 48 months. In patients without focal lesions, MRI-defined CR (hypointensity on STIR images) was reached in 62% at 18 months, similar to 56% of the patients attaining clinical CR status. While very early [^{18}F]FDG-PET/CT changes (at 10 days) did not affect outcome, complete [^{18}F]FDG suppression and extramedullary disease before transplantation conferred

superior overall and event-free survival; in fact, 30 months after the first autotransplantation, 92% and 89% of the patients were alive and event-free compared with 71% and 63% among those with less than 100% disappearance of [^{18}F]FDG uptake. Complete [^{18}F]FDG suppression before the first transplantation correlated with superior outcomes in both low-risk and high-risk gene array-defined risk groups, reaching statistical significance for overall survival in low-risk and for event-free survival in high-risk myeloma. Normalization of the PET findings before transplantation was associated with improved outcomes, whereas gene array-defined high-risk designation conferred poor overall and event-free survival. In the absence of molecular genetic data, the favorable implications of pre-transplantation [^{18}F]FDG suppression were canceled by elevated serum levels of lactate dehydrogenase and β_2-microglobulin. Clinical CR or n-CR status before transplantation did not impact post-transplantation survival outcomes. The prognosis of high-risk patients not achieving complete [^{18}F]FDG suppression was especially poor.

More recently, 700 patients with symptomatic MM eligible for high-dose therapy (HDT) have been randomized to receive either eight cycles of bortezomib-lenalidomide-dexamethasone followed by 1-year maintenance with lenalidomide or three cycles of VRD followed by high-dose therapy and autologous transplantation then VRD consolidation and 1-year lenalidomide maintenance (the IFM-DFCI 2009 study). Spine and pelvis MRI and whole-body PET-CT at diagnosis, after three cycles of VRD, and prior to maintenance were performed. At diagnosis, MRI was positive in 94.7% of patients and PET/CT 91%. Following three cycles, MRI remained positive in 93% and PET/CT in 55% of patients. Normalization of MRI after 3 months of induction therapy was not predictive neither for progression-free survival nor for overall survival, whereas normalization of PET/CT was associated with a significant improvement in PFS but not OS. Prior to maintenance, MRI remained positive in 83%, and PET/CT in 21% of the patients. Normalization of MRI before maintenance was not predictive for survivals, whereas normalization of PET/CT was associated with a prolonged PFS and OS, thus suggesting that PET/CT should be incorporated in the follow-up of MM patients who undergo to high-dose treatment [116].

Quantitative data on kinetics and distribution patterns of [^{18}F]FDG obtained from dynamic PET/CT in 40 patients with MM correlated significantly with percentage of bone marrow infiltration by plasma cells [117]. Furthermore, PET/CT efficiently detected extramedullary disease in patients both at diagnosis and at relapse [118]. PET/CT was tested for better definition of CR in 282 MM patients. The examination was performed at diagnosis and every 12–18 months afterward. At diagnosis, 42% of patients with MM had more than three focal lesions (SUV_{max} >4.2 in 50% of cases). After treatment, PET/CT was negative for 70% of patients, while 53% of patients achieved CR according to IMWG criteria. Approximately 30% of patients at CR had a positive PET/CT. A negative PET/CT was an independent predictor for prolonged PFS and OS in patients with CR. In addition, for patients with CR, median PFS was 50 months for patients with a positive PET/CT and 90 months for patients with negative PET/CT [119].

In smoldering multiple myeloma, 16% of patients with normal whole-body X-ray had positive PET/CT results [120]. The median time to progression (TTP) for patients with positive PET/CT was shorter than patients with negative PET/CT (1.1 years vs. 4.5 year), while the probability of progression at 2 years for patients with positive PET/CT results was 58% [121]. The largest study in the field involved 188 patients with smoldering myeloma: [^{18}F]FDG-PET/CT was positive in 39% of patients. The probability of progression to symptomatic MM within 2 years was 75% for patients with positive PET/CT under observation and 30% for patients with negative PET/CT. This probability was higher if hypermetabolic activity was combined with underlying osteolysis (2-year progression rate of 87%). The median TTP was 21 months compared with 60 months for patients

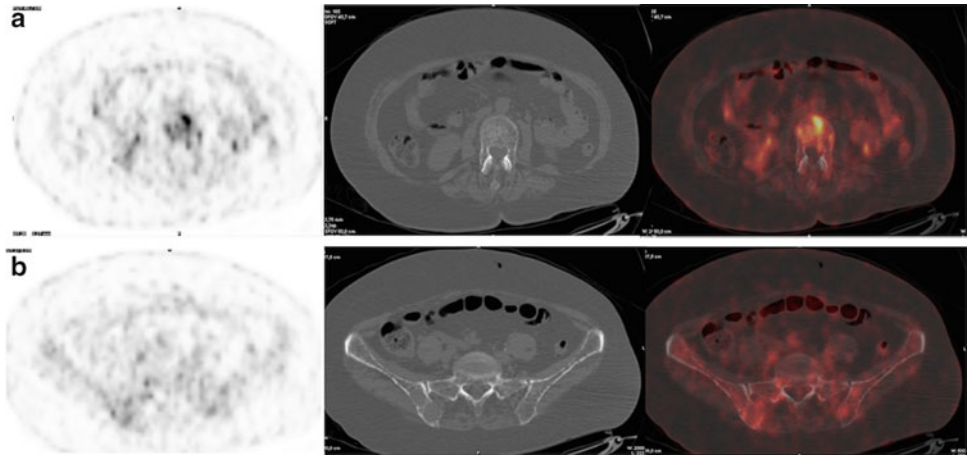

Fig. 18 Different pattern of [18F]FDG-PET/CT in a patient with oligosecretory/nonsecretory MM. Images show an area of focal [^{18}F]FDG uptake in L3 (**a**) while no uptake in the pelvis (**b**)

with positive PET/CT and those with negative PET/CT, respectively [122].

PET/CT has also a role in nonsecretory or oligosecretory myeloma for the detection of active lesions in the body [123] (Fig. 18). In this setting it may be useful also to monitoring treatment response.

PET/MRI represents a novel imaging modality with attractive potential clinical applications. In MM, there is only one prospective study comparing PET/MRI with PET/CT in 30 patients with MM with both techniques performed sequentially. There was high correlation between the two techniques, regarding the number of active lesions and the degree of uptake (SUV) [43, 124].

DEXA Scanning

The World Health Organization has identified dual-energy X-ray absorptiometry (DEXA) as the gold standard for measuring the severity of osteoporosis, for defining the risk of fractures, and for assessing changes in bone mineral density over time. This method is fast, noninvasive, and implies a low radiation burden to patients (between 0.001 and 0.01 mSv). However, bone mineral density can be affected by pathological conditions, such as vertebral collapse and spinal osteophytes that are often concomitant in patients with MM. At present, DEXA scanning cannot distinguish benign osteoporosis from osteoporosis induced by MM. Furthermore, the reduction in bone mineral density in patients with MM usually is not diffuse but is rather confined to the hematopoietically active portions of the skeleton; consequently, bone densitometry studies are not still sufficient to determine the presence of MM bone disease [9].

References

1. Moreau P, San Miguel J, Ludwig H, Schouten H, Mohty M, Dimopoulos M, et al. Multiple myeloma: ESMO clinical practice guidelines for diagnosis, treatment and follow-up. Ann Oncol. 2013;24: vi133–7.
2. Surveillance Research Program, National Cancer Institute. Cancer Stat Fact Sheets [Internet]. Cancer Stat Surveill Res Program Natl Cancer Inst; 2016. Available from: http://seer.cancer.gov/statfacts.
3. Solly S. Remarks on the pathology of mollities ossium; with cases. Med Chir Trans. 1844;27:435–98.
4. Wright JH. A case of multiple myeloma. J Boston Soc Med Sci. 1900;4:195–204.5.
5. Waldenstrom J. Studies on conditions associated with disturbed gamma globulin formation (gammopathies). Harvey Lect. 1961;56:211–31.
6. Pruzanski W, Ogryzlo M. Abnormal proteinuria in malignant diseases. Adv Clin Chem. 1970;13:1970.
7. Mulligan ME, Badros AZ. PET/CT and MR imaging in myeloma. Skeletal Radiol. 2007;36:5–16.
8. Kyle RA, Rajkumar V. Criteria for diagnosis, staging, risk stratification and response assessment of multiple myeloma. Leukemia. 2009;23:3–9.

9. Rajkumar SV, Dimopoulos MA, Palumbo A, Blade J, Merlini G, Mateos MV, et al. International myeloma working group updated criteria for the diagnosis of multiple myeloma. Lancet Oncol. 2014;15:e538–48.
10. Larsen JT, Kumar SK, Dispenzieri A, Kyle RA, Katzmann JA, Rajkumar SV. Serum free light chain ratio as a biomarker for high-risk smoldering multiple myeloma. Leukemia. 2013;27:941–6.
11. Waxman AJ, Mick R, Garfall AL, Cohen A, Vogl DT, Stadtmauer EA, et al. Classifying ultra-high risk smoldering myeloma. Leukemia. 2014;29:751–3.
12. Raab MS, Podar K, Breitkreutz I, Richardson PG, Anderson KC. Multiple myeloma. Lancet. 2009;374: 324–39.
13. Rajkumar SV. Multiple myeloma. Curr Probl Cancer. 2009;33:7–64.
14. Ribatti D, Vacca A, Nico B, Quondamatteo F, Ria R, Minischetti M, et al. Bone marrow angiogenesis and mast cell density increase simultaneously with progression of human multiple myeloma. Br J Cancer. 1999; 79:451–5.
15. Rajkumar S, Gupta V, Fonseca R, Dispenzieri A, Gonsalves W, Larson D, et al. Impact of primary molecular cytogenetic abnormalities and risk of progression in smoldering multiple myeloma. Leukemia. 2013;27:1738–44.
16. Dimopoulos M, Terpos E, Comenzo RL, Tosi P, Beksac M, Sezer O, et al. International myeloma working group consensus statement and guidelines regarding the current role of imaging techniques in the diagnosis and monitoring of multiple myeloma. Leukemia Nat Pub Group. 2009;23:1545–56.
17. Roodman GD. Skeletal imaging and management of bone disease. Hematol Am Soc Hematol Educ Program. 2008;1:313–9.
18. Delorme S, Baur-Melnyk A. Imaging in multiple myeloma. Eur J Radiol. 2009;70:401–8.
19. Lindsley H, Teller D, Noonan B, Peterson M, Mannik M. Hyperviscosity syndrome in multiple myeloma. A reversible, concentration- dependent aggregation of the myeloma protein. Am J Med. 1973;54:682–8.
20. Winterbottom AP, Shaw AS. Imaging patients with myeloma. Clin Radiol. 2009;64:1–11.
21. McBride W, Jackman Jr JD, Gammon RS, Willerson JT. High-output cardiac failure in patients with multiple myeloma. N Engl J Med. 1988;319:1651–3.
22. Latov N, Sherman WH, Nemni R, Galassi G, Shyong JS, Penn AS, et al. Plasma-cell dyscrasia and peripheral neuropathy with a monoclonal antibody to peripheral-nerve myelin. N Engl J Med. 1980;303: 618–21.
23. Dimopoulos M, Kyle R, Fermand JP, Rajkumar SV, San Miguel J, Chanan-Khan A, et al. Consensus recommendations for standard investigative workup: report of the International Myeloma Workshop Consensus Panel 3. Blood. 2011;117:4701–5.
24. Avet-Loiseau H, Durie B, Cavo M, Attal M, Gutierrez N, Haessler J, et al. Combining fluorescent in situ hybridization data with ISS staging improves risk assessment in myeloma: an International Myeloma Working Group collaborative project. Leukemia. 2013;27282:711–7.
25. Greipp PR. Prognosis in myeloma. Mayo Clin Proc. 1994;69:895–902.
26. Lütje S, Rooy JWJ, Croockewit S, Koedam E, Oyen WJG, Raymakers RA. Role of radiography, MRI and FDG-PET/CT in diagnosing, staging and therapeutical evaluation of patients with multiple myeloma. Ann Hematol. 2009;88:1161–8.
27. Durie BG, Salmon SE. A clinical staging system for multiple myeloma. Correlation of measured myeloma cell mass with presenting clinical features, response to treatment, and survival. Cancer. 1975; 36:842–54.
28. Durie BGM. The role of anatomic and functional staging in myeloma: description of Durie/Salmon plus staging system. Eur J Cancer. 2006;42: 1539–43.
29. Rajkumar SV. Updated diagnostic criteria and staging system for multiple. ASCO Educ B. 2016;35: 418–23.
30. Hillengass J, Landgren O. Challenges and opportunities of novel imaging techniques in monoclonal plasma cell disorders: imaging "early myeloma". Leuk Lymphoma. 2013;54:1355–63.
31. Regelink JC, Minnema MC, Terpos E, Kamphuis MH, Raijmakers PG, Pieters-van den Bos IC, et al. Comparison of modern and conventional imaging techniques in establishing multiple myeloma-related bone disease: a systematic review. Br J Haematol. 2013;162:50–61.
32. Terpos E, Kleber M, Engelhardt M, Zweegman S, Gay F, Kastritis E, et al. European myeloma network guidelines for the management of multiple myeloma-related complications. Haematologica. 2015;100: 1254–66.
33. Terpos E, Moulopoulos LA, Dimopoulos MA. Advances in imaging and the management of myeloma bone disease. J Clin Oncol. 2011;29:1907–15.
34. Ågren B, Björkstrand B, Rudberg U, Aspelin PBL. Radiography and bone scintigraphy in bone marrow transplant multiple myeloma patients. Acta Radiol. 1997;38:144–50.
35. Kapadia SB. Multiple myeloma: a clinicopathologic study of 62 consecutively autopsied cases. Medicine (Baltimore). 1980;59:380–92.
36. Chassang M, Grimaud A, Cucchi JM, Novellas S, Amoretti N, Chevallier P, et al. Can low-dose computed tomographic scan of the spine replace conventional radiography? An evaluation based on imaging myelomas, bone metastases, and fractures from osteoporosis. Clin Imaging. 2007;31:225–7.
37. Collins CD. Multiple myeloma. Cancer Imaging. 2004;4:S47–53.
38. Pianko MJ, Terpos E, Roodman GD, Divgi CR, Zweegman S, Hillengass J, et al. Whole-body low-dose computed tomography and advanced

imaging techniques for multiple myeloma bone disease. Clin Cancer Res. 2014;20:5888–97.
39. Mahnken AH, Wildberger JE, Gehbauer G, Schmitz-Rode T, Blaum M, Fabry U, et al. Multidetector CT of the spine in multiple myeloma: comparison with MR imaging and radiography. AJR Am J Roentgenol. 2002;178:1429–36.
40. Huda W, Vance A. Patient radiation doses from adult and pediatric CT. Am J Roentgenol. 2007;188:540–6.
41. Weininger M, Lauterbach B, Knop S, Pabst T, Kenn W, Hahn D, et al. Whole-body MRI of multiple myeloma: comparison of different MRI sequences in assessment of different growth patterns. Eur J Radiol. 2009;69:339–45.
42. Ghanem N, Lohrmann C, Engelhardt M, Pache G, Uhl M, Saueressig U, et al. Whole-body MRI in the detection of bone marrow infiltration in patients with plasma cell neoplasms in comparison to the radiological skeletal survey. Eur Radiol. 2006;16:1005–14.
43. Terpos E, Dimopoulos MA, Moulopoulos LA. The role of imaging in the treatment of patients with multiple myeloma in 2016. Am Soc Clin Oncol Educ Book. 2016;35:e407–17.
44. Baur-Melnyk A, Buhmann S, Becker C, Schoenberg SO, Lang N, Bartl R, et al. Whole-body MRI versus whole-body MDCT for staging of multiple myeloma. AJR Am J Roentgenol. 2008;190:1097–104.
45. Wolf MB, Murray F, Kilk K, Hillengass J, Delorme S, Heiss C, et al. Sensitivity of whole-body CT and MRI versus projection radiography in the detection of osteolyses in patients with monoclonal plasma cell disease. Eur J Radiol. 2014;83:1222–30.
46. Princewill K, Kyere S, Awan O, Mulligan M. Multiple myeloma lesion detection with whole body CT versus radiographic skeletal survey. Cancer Invest. 2013;31:206–11.
47. Gleeson TG, Moriarty J, Shortt CP, Gleeson JP, Fitzpatrick P, Byrne B, et al. Accuracy of whole-body low-dose multidetector CT (WBLDCT) versus skeletal survey in the detection of myelomatous lesions, and correlation of disease distribution with whole-body MRI (WBMRI). Skeletal Radiol. 2009;38:225–36.
48. Kröpil P, Fenk R, Fritz LB, Blondin D, Kobbe G, Mödder U, et al. Comparison of whole-body 64-slice multidetector computed tomography and conventional radiography in staging of multiple myeloma. Eur Radiol. 2008;18:51–8.
49. Ippolito D, Besostri V, Bonaffini PA, Rossini F, Di Lelio A, Sironi S. Diagnostic value of whole-body low-dose computed tomography (WBLDCT) in bone lesions detection in patients with multiple myeloma (MM). Eur J Radiol. 2013;82:2322–7.
50. Horger M, Claussen CD, Bross-Bach U, Vonthein R, Trabold T, Heuschmid M, et al. Whole-body low-dose multidetector row-CT in the diagnosis of multiple myeloma: an alternative to conventional radiography. Eur J Radiol. 2005;54:289–97.
51. Cretti F, Perugini G. Patient dose evaluation for the whole-body low-dose multidetector CT (WBLDMDCT) skeleton study in multiple myeloma (MM). Radiol Medica. 2016;121:93–105.
52. Borggrefe J, Giravent S, Campbell G, Thomsen F, Chang D, Franke M, et al. Association of osteolytic lesions, bone mineral loss and trabecular sclerosis with prevalent vertebral fractures in patients with multiple myeloma. Eur J Radiol. 2015;84:2269–74.
53. Dimopoulos MA, Hillengass J, Usmani S, Zamagni E, Lentzsch S, Davies FE, et al. Role of magnetic resonance imaging in the management of patients with multiple myeloma: a consensus statement. J Clin Oncol. 2015;33:657–64.
54. D'Sa S, Abildgaard N, Tighe J, Shaw P, Hall-Craggs M. Guidelines for the use of imaging in the management of myeloma. Br J Haematol. 2007;137:49–63.
55. Merz M, Moehler TM, Ritsch J, Bäuerle T, Zechmann CM, Wagner B, et al. Prognostic significance of increased bone marrow microcirculation in newly diagnosed multiple myeloma: results of a prospective DCE-MRI study. Eur Radiol. 2016;26:1404–11.
56. Nonomura Y, Yasumoto M, Yoshimura R, Haraguchi K, Ito S, Akashi T, et al. Relationship between bone marrow cellularity and apparent diffusion coefficient. J Magn Reson Imaging. 2001;13:757–60.
57. Terpos E, Koutoulidis V, Fontara S, Zagouri F, Christoulas D, Koureas A, et al. Diffusion-weighted imaging improves accuracy in the diagnosis of MRI patterns of marrow involvement in newly diagnosed myeloma: results of a prospective study in 99 patients. Blood. 2015;126:4178.
58. Messiou C, Giles S, Collins DJ, West S, Davies FE, Morgan GJ, et al. Assessing response of myeloma bone disease with diffusion-weighted MRI. Br J Radiol. 2012;85:2–3.
59. Giles SL, Desouza NM, Collins DJ, Morgan VA, West S, Davies FE, et al. Assessing myeloma bone disease with whole-body diffusion-weighted imaging: comparison with x-ray skeletal survey by region and relationship with laboratory estimates of disease burden. Clin Radiol. 2015;70:614–21.
60. Sachpekidis C, Mosebach J, Freitag MT, Wilhelm T, Mai EK, Haberkorn U, et al. Application of ^{18}F-FDG PET and diffusion weighted imaging (DWI) in multiple myeloma : comparison of functional imaging modalities. Am J Nucl Med Mol Imaging. 2015;5:479–92.
61. Pawlyn C, Fowkes L, Otero S, Jones J, Boyd K, Davies F, et al. Whole-body diffusion-weighted MRI: a new gold standard for assessing disease burden in patients with multiple myeloma? Leukemia. 2016;30:1446–8.
62. Hubner KF, Andrews GA, Hayes RL, Poggenburg Jr JK, Solomon A. The use of rare-earth radionuclides and other bone-seekers in the evaluation of bone lesions in patients with multiple myeloma or solitary plasmacytoma. Radiology. 1977;125:171–6.

63. Shuke N, Okizaki A, Yamamoto W, Usui K, Aburano T. Accumulation of Tc-99m HMDP in extramedullary plasmacytoma of the stomach. Clin Nucl Med. 2001; 26:354–5.
64. VanAntwerp JD, O'Mara RE, Pitt MJ, Walsh S. Technetium-99m-diphosphonate accumulation in amyloid. J Nucl Med. 1975;16:238–40.
65. Kanoh T, Ohno T, Uchino H, Yamamoto I, Torizuka K. Avid uptake of gallium-67 in multiple myeloma. An additional indicator of the aggressive phase. Clin Nucl Med. 1987;12:482–4.
66. Roach PJ, Arthur CK. Comparison of thallium-201 and gallium-67 scintigraphy in soft tissue and bone marrow multiple myeloma: a case report. Australas Radiol. 1997;41:67–9.
67. Lin W, Wang S. Ga-67 scan findings in bone marrow involvement with plasmablastic myeloma and corresponding Tc-99m MIBI images. Clin Nucl Med. 2001;26:963.
68. Posch T, Olson S. Marked soft tissue uptake of bone tracer in a patient with amyloidosis and multiple myeloma. Clin Nucl Med. 1992;17:909.
69. Bekerman C, Hoffer PB, Bitran JD. The role of gallium-67 in the clinical evaluation of cancer. Semin Nucl Med. 1984;14:296–323.
70. Waxman AD, Siemsen JK, Levine AM, Holdorf D, Suzuki R, Singer FR, et al. Radiographic and radionuclide imaging in multiple myeloma: the role of gallium scintigraphy: concise communication. J Nucl Med. 1981;22:232–6.
71. Ohnishi T, Noguchi S, Murakami N, Tajiri J, Morita M, Tamaru M, et al. Pentavalent technetium-99m-DMSA uptake in a patient having multiple myeloma without amyloidosis. J Nucl Med. 1991;32:1785–7.
72. Ohta H, Endo K, Kanoh T, Konishi J, Kotoura H. Technetium-99m (V) DMSA uptake in amyloidosis. J Nucl Med. 1989;30:2049–52.
73. Ishibashi M, Nonoshita M, Uchida M, Kojima K, Tomita N, Matsumoto S, et al. Bone marrow uptake of thallium-201 before and after therapy in multiple. J Nucl Med. 1998;39:473–5.
74. Watanabe N, Shimizu M, Kageyama M, Tanimura K, Kinuya S, Shuke N, et al. Multiple myeloma evaluated with ^{201}Tl scintigraphy compared with bone. J Nucl Med. 1999;40:1138–42.
75. Pace L, Catalano L, Pinto A, De Renzo A, Di Gennaro F, Califano C, et al. Different patterns of technetium-99m sestamibi uptake in multiple myeloma. Eur J Nucl Med. 1998;25:714–20.
76. Mirzaei S, Filipits M, Keck A, Bergmayer W, Knoll P, Koehn H, et al. Comparison of Technetium-99m-MIBI imaging with MRI for detection of spine involvement in patients with multiple myeloma. BMC Nucl Med. 2003;3:2.
77. Kalaga RV, Kudagi V, Heller GV. Role of Tc-99m sestamibi myocardial perfusion imaging in identifying multiple myeloma. J Nucl Cardiol. 2009;16:835–7.
78. Fonti R, Salvatore B, Quarantelli M, Sirignano C, Segreto S, Petruzziello F, et al. ^{18}F-FDG PET/CT, ^{99m}Tc-MIBI, and MRI in evaluation of patients with multiple myeloma. J Nucl Med. 2008;49: 195–200.
79. Agool A, Slart RHJA, Dierckx RAJO, Kluin PM, Visser L, Jager PL, et al. Somatostatin receptor scintigraphy might be useful for detecting skeleton abnormalities in patients with multiple myeloma and plasmacytoma. Eur J Nucl Med Mol Imaging. 2010;37:124–30.
80. Hazenberg BPC, van Rijswijk MH, Piers DA, Lub-de Hooge MN, Vellenga E, Haagsma EB, et al. Diagnostic performance of ^{123}I-labeled serum amyloid P component scintigraphy in patients with amyloidosis. Am J Med. 2006;119(355):e15–24.
81. Bredella MA, Steinbach L, Caputo G, Segall G, Hawkins R. Value of FDG PET in the assessment of patients with multiple myeloma. AJR Am J Roentol. 2005;184:1199–204.
82. Durie BG, Waxman AD, D'agnolo A, Williams C. Whole-body ^{18}F-FDG PET identifies high-risk myeloma. J Nucl Med. 2002;43:1457–63.
83. Breyer RJ, Mulligan ME, Smith SE, Line BR, Badros AZ. Comparison of imaging with FDG PET/CT with other imaging modalities in myeloma. Skeletal Radiol. 2006;35:632–40.
84. Hillner BE, Siegel BA, Liu D, Shields AF, Gareen IF, Hanna L, et al. Impact of positron emission tomography/computed tomography and positron emission tomography (PET) alone on expected management of patients with cancer: initial results from the National Oncologic PET registry. J Clin Oncol. 2008;26: 2155–61.
85. Larson SM. Practice-based evidence of the beneficial impact of positron emission tomography in clinical oncology. J Clin Oncol. 2008;26:2083–4.
86. Chae M, Lee T, Park G, Yu J, Pai M, Kang H, et al. Comparing ^{18}F-FDG-PET/CT with other imaging modalities for detecting involving bone of multiple myeloma. J Nucl Med. 2007;48:351P.
87. Even-Sapir E, Mishani E, Flusser G, Metser U. ^{18}F-Fluoride positron emission tomography and positron emission tomography/computed tomography. Semin Nucl Med. 2007;37:462–9.
88. Schirrmeister H, Buck AK, Bergmann L, Reske SN, Bommer M. Positron emission tomography (PET) for staging of solitary plasmacytoma. Cancer Biother Radiopharm. 2003;18:841–5.
89. Nanni C, Rubello D, Zamagni E, Castellucci P, Ambrosini V, Montini G, et al. ^{18}F-FDG PET/CT in myeloma with presumed solitary plasmocytoma of bone. In Vivo (Brooklyn). 2008;22:513–7.
90. Salaun PY, Gastinne T, Frampas E, Bodet-Milin C, Moreau P, Bodéré-Kraeber F. FDG-positron-emission tomography for staging and therapeutic assessment in patients with plasmacytoma. Haematologica. 2008;93:1269–71.
91. Cook GJR, Wegner EA, Fogelman I. Pitfalls and artifacts in ^{18}FDG PET and PET/CT oncologic imaging. Semin Nucl Med. 2004;34:122–33.

92. Nanni C, Zamagni E, Farsad M, Castellucci P, Tosi P, Cangini D, et al. Role of ^{18}F-FDG PET/CT in the assessment of bone involvement in newly diagnosed multiple myeloma: preliminary results. Eur J Nucl Med Mol Imaging. 2006;33:525–31.
93. Hur J, Yoon C-S, Ryu YH, Yun MJ, Suh J-S. Comparative study of fluorodeoxyglucose positron emission tomography and magnetic resonance imaging for the detection of spinal bone marrow infiltration in untreated patients with multiple myeloma. Acta Radiol. 2008;49:427–35.
94. Bartel TB, Haessler J, Brown TLY, Shaughnessy JD, Van Rhee F, Anaissie E, et al. F18-fluorodeoxyglucose positron emission tomography in the context of other imaging techniques and prognostic factors in multiple myeloma. Blood. 2009;114:2068–76.
95. Gorospe L, Raman S, Echeveste J, Avril N, Herrero Y, Herna NS. Whole-body PET/CT: spectrum of physiological variants, artifacts and interpretative pitfalls in cancer patients. Nucl Med Commun. 2005; 26:671–87.
96. Mesguich C, Fardanesh R, Tanenbaum L, Chari A, Jagannath S, Kostakoglu L. State of the art imaging of multiple myeloma: comparative review of FDG PET/CT imaging in various clinical settings. Eur J Radiol. 2014;83:2203–23.
97. Nanni C, Zamagni E, Versari A, Chauvie S, Bianchi A, Rensi M, et al. Image interpretation criteria for FDG PET/CT in multiple myeloma: a new proposal from an Italian expert panel. IMPeTUs (Italian Myeloma criteria for PET USe). Eur J Nucl Med Mol Imaging. 2016;43:414–21.
98. Nanni C, Zamagni E, Cavo M, Rubello D, Tacchetti P, Pettinato C, et al. ^{11}C-choline vs. ^{18}F-FDG PET/CT in assessing bone involvement in patients with multiple myeloma. World J Surg Oncol. 2007;5:68.
99. Cassou-Mounat T, Balogova S, Nataf V, Calzada M, Huchet V, Kerrou K, et al. ^{18}F-fluorocholine versus ^{18}F-fluorodeoxyglucose for PET/CT imaging in patients with suspected relapsing or progressive multiple myeloma: a pilot study. Eur J Nucl Med Mol Imaging. 2016;43(11):1995–2004.
100. Dankerl A, Liebisch P, Glatting G, Friesen C, Blumstein NM, Kocot D, et al. Multiple myeloma: molecular imaging with ^{11}C-Methionine PET/CT—initial experience ^{1}. Radiology. 2007; 242:498–508.
101. Lapa C, Knop S, Schreder M, Rudelius M, Knott M, Jörg G, et al. ^{11}C-Methionine-PET in multiple myeloma: correlation with clinical parameters and bone marrow involvement. Theranostics. 2016;6:254–61.
102. Lee SM, Kim TS, Lee JW, Kwon HW, Kim YI1, Kang SH, et al. Incidental finding of an ^{11}C-acetate PET-positive multiple myeloma. Ann Nucl Med. 2010;24:41–4.
103. Stjernholm RL. Carbohydrate metabolism in leukocytes. VII. Metabolism of glucose, acetate, and propionate by human plasma cells. J Bacteriol. 1967;93:1657–61.
104. Huang SY, Bin CB, Lu HY, Lin HH, Wei SY, Hsu SC, et al. Correlation among DCE-MRI measurements of bone marrow angiogenesis, microvessel density, and extramedullary disease in patients with multiple myeloma. Am J Hematol. 2012;87:837–9.
105. Merz M, Ritsch J, Kunz C, Wagner B, Sauer S, Hose D, et al. Dynamic contrast-enhanced magnetic resonance imaging for assessment of antiangiogenic treatment effects in multiple myeloma. Clin Cancer Res. 2015;21:106–12.
106. Dutoit JC, Claus E, Offner F, Noens L, Delanghe J, Verstraete KL. Combined evaluation of conventional MRI, dynamic contrast-enhanced MRI and diffusion weighted imaging for response evaluation of patients with multiple myeloma. Eur J Radiol. 2016;85: 373–82.
107. Moulopoulos LA, Dimopoulos MA, Alexanian R, Leeds NE, Libshitz HI. Multiple myeloma: MR patterns of response to treatment. Radiology. 1994;193: 441–6.
108. Hillengass J, Ayyaz S, Kilk K, Weber M-A, Hielscher T, Shah R, et al. Changes in magnetic resonance imaging before and after autologous stem cell transplantation correlate with response and survival in multiple myeloma. Haematologica. 2012;97:1757–60.
109. Bannas P, Hentschel HB, Bley TA, Treszl A, Eulenburg C, Derlin T, et al. Diagnostic performance of whole-body MRI for the detection of persistent or relapsing disease in multiple myeloma after stem cell transplantation. Eur Radiol. 2012;22:2007–12.
110. Spinnato P, Bazzocchi A, Brioli A, Nanni C, Zamagni E, Albisinni U, et al. Contrast enhanced MRI and ^{18}F-FDG PET-CT in the assessment of multiple myeloma: a comparison of results in different phases of the disease. Eur J Radiol. 2012;81:4013–8.
111. Merz M, Hielscher T, Wagner B, Sauer S, Shah S, Ms R, et al. Predictive value of longitudinal whole-body magnetic resonance imaging in patients with smoldering multiple myeloma. Leukemia. 2014;28: 1902–8.
112. Fallahi D, Beiki D, Mousavi SA, Gholamrezanezhad A, Eftekhari M, Fard-Esfahani A, Alimoghaddam K, et al. ^{99m}Tc-MIBI whole body scintigraphy and P-glycoprotein for the prediction of multiple drug resistance in multiple myeloma patients. Hell J Nucl Med. 2009;12:255–9.
113. Piwnica-Worms D, Chiu ML, Budding M, Kronauge JF, Kramer RA, Croop JM. Functional imaging of multidrug-resistant P-glycoprotein with an organotechnetium complex. Cancer Res. 1993;53: 977–84.
114. Mongkonsritragoon W, Kimlinger T, Ahmann G, Greipp P. Is multidrug resistance (P-glycoprotein) an intrinsic characteristic of plasma cells in patients with monoclonal gammopathy of undetermined significance

plasmacytoma, multiple myeloma and amyloidosis? Leuk Lymphoma. 1998;29:577–84.
115. Patriarca F, Melli C, Damiani D, Michieli M, Michelutti A, Cavo M, et al. Plasma cell P170 expression and response to treatment in multiple myeloma. Haematologica. 1996;81:232–7.
116. Moreau P, Attal M, Karlin L, Garderet L, Facon T, Benboubker L, et al. Prospective evaluation of MRI and PET-CT at diagnosis and before maintenance therapy in symptomatic patients with multiple myeloma included in the IFM/DFCI 2009 trial. Blood. 2015;126:92–5599 (abstract 395).
117. Sachpekidis C, Mai EK, Goldschmidt H, Hillengass J, Hose D, Pan L, et al. ^{18}F-FDG dynamic PET/CT in patients with multiple myeloma. Clin Nucl Med. 2015;40:e300–7.
118. Tirumani SH, Sakellis C, Jacene H, Shinagare AB, Munshi NC, Ramaiya NH, et al. Role of FDG-PET/CT in extramedullary multiple myeloma: correlation of FDG-PET/CT findings with clinical outcome. Clin Nucl Med. 2016;41:e7–13.
119. Zamagni E, Nanni C, Mancuso K, Tacchetti P, Pezzi A, Pantani L, et al. PET/CT improves the definition of complete response and allows to detect otherwise unidentifiable skeletal progression in multiple myeloma. Clin Cancer Res. 2015; 21:4384–90.
120. Zamagni E, Nanni C, Patriarca F, Englaro E, Castellucci P, Geatti O, et al. A prospective comparison of ^{18}F-fluorodeoxyglucose positron emission tomography-computed tomography, magnetic resonance imaging and whole-body planar radiographs in the assessment of bone disease in newly diagnosed multiple myeloma. Haematologica. 2007;92:50–5.
121. Zamagni E, Nanni C, Gay F, Pezzi A, Patriarca F, Bellò M, et al. ^{18}F-FDG PET/CT focal, but not osteolytic, lesions predict the progression of smoldering myeloma to active disease. Leukemia. 2016;30: 417–22.
122. Siontis B, Kumar S, Dispenzieri A, Drake MT, Lacy MQ, Buadi F, et al. Positron emission tomography-computed tomography in the diagnostic evaluation of smoldering multiple myeloma: identification of patients needing therapy. Blood Cancer J. 2015;5:e364.
123. Lonial S, Jl K. Non-secretory myeloma : a clinician's guide. Oncology. 2013;27:924–30.
124. Sachpekidis C, Hillengass J, Goldschmidt H, Mosebach J, Pan L, Pet F. Comparison of ^{18}F-FDG PET/CT and PET/MRI in patients with multiple myeloma. Am J Nucl Med Mol Imaging. 2015;5:469–78.

Diagnostic Applications of Nuclear Medicine: Leukemias

16

Martina Sollini, Sara Galimberti, Roberto Boni, and Paola Anna Erba

Abstract

Leukemias are a group of acute and chronic hematological neoplasias characterized by the dissemination of the cancer cells originating in the bone marrow via the bloodstream. In 2016 the estimated number of new leukemia cases was more than 110,000 in all of Europe and 47,000 in the USA. Leukemias, cause of 4% of all cancer deaths and account for 3.6% of all cancers. Historically, leukemias have been divided into four major categories further classified into subtypes based on specific features of cells: acute lymphocytic leukemia (ALL), chronic lymphocytic leukemia (CLL), acute myelogenous leukemia (AML), and chronic myelogenous leukemia (CML). A revised classification of myeloid/lymphoid neoplasms and leukemias has recently been published to better characterize each disease. This updated classification incorporated new scientific and clinical information to refine diagnostic criteria for previously described neoplasms and introduced newly recognized disease entities. In this chapter the main entities of leukemia, with specific regard to imaging for diagnosis, treatment response assessment, and follow-up, will be treated according to what reported in the clinical guidelines.

Keywords

Leukemia • Imaging • Bone cancer • Hematological malignancies

Glossary

[^{18}F]FDG	2-Deoxy-2-[^{18}F]fluoro-D-glucose
^{18}F-FLT	3'-^{18}F-Fluoro-3'-deoxythymidine
aCGH	Array comparative genomic hybridization
aCML	Atypical chronic myeloid leukemia
ALK	Anaplastic large-cell lymphoma
ALL	Acute lymphoblastic leukemia, also defined as "acute lymphocytic leukemia"
AML	Acute myeloid leukemia, also defined as "acute myelogenous leukemia"
B-ALL	B-cell acute lymphoblastic leukemia
BCL2	Gene encoding for the B-cell lymphoma 2 protein

M. Sollini
Department of Biomedical Sciences, Humanitas University, Rozzano, Milan, Italy

S. Galimberti
Hematology Unit, University of Pisa, Pisa, Italy

R. Boni • P.A. Erba (✉)
Regional Center of Nuclear Medicine, Department of Translational Research and Advanced Technologies in Medicine, University of Pisa, Pisa, Italy
e-mail: paola.erba@unipi.it

© Springer International Publishing Switzerland 2017
H.W. Strauss et al. (eds.), *Nuclear Oncology*,
https://doi.org/10.1007/978-3-319-26236-9_39

BCL6	Gene encoding for the B-cell lymphoma 6 protein
BCR-ABL1	Fusion gene formed by a translocation between chromosomes 9 and 22 [t(9;22)]
BM	Bone marrow
CBFB-MYH11	Chimeric transcript created by the inversion (16)(p13;q22)
CEBPA	Gene encoding for the protein CCAAT/enhancer-binding protein alpha
CHOP	Chemotherapy based on cyclophosphamide, vincristine, doxorubicin, and dexamethasone
CLL	Chronic lymphocytic leukemia, also defined as "chronic lymphocytic leukemia"
CML	Chronic myeloid leukemia, also defined as "chronic myelogenous leukemia"
CMML	Chronic myelomonocytic leukemia
CNL	Chronic neutrophilic leukemia
CNS	Central nervous system
CR	Complete response
CRLF2	Cytokine receptor-like factor 2
CT	X-ray computed tomography
DEK-NUP214	Gene fusion created by the t (6;9)(p23;q34) translocation
DLBCL	Diffuse large B-cell lymphoma
EBV	Epstein-Barr virus
ESMO	European Society of Medical Oncology
ET	Essential thrombocythemia
EUTOS	European Treatment and Outcome Study
FGFR	Receptor tyrosine kinase for the fibroblast growth factor family
FISH	Fluorescence in situ hybridization
GATA2	Gene encoding for a protein called GATA binding protein 2, a transcription factor
GEP	Gene expression profiling
HCL	Hairy cell leukemia
HHV8	Human herpesvirus-8
HL	Hodgkin's lymphoma
HLA	Human leukocyte antigen
iAMP21	Intrachromosomal amplification of chromosome 21
IgG	Immunoglobulin G
Igh	Immunoglobulin heavy chain
IGH/IL3	Fusion gene created by the t (5;14)(q31;q32) translocation
IGHV	Immunoglobulin heavy chain
IWCLL	International Working Group on CLL
JAK-STAT	Signaling pathway that transmits information from extracellular chemical signals to the nucleus resulting in DNA transcription and expression of genes involved in immunity, proliferation, differentiation, apoptosis, and oncogenesis
JAK2	Gene encoding for Janus kinase 2, a non-receptor tyrosine kinase
JMML	Juvenile myelomonocytic leukemia
KMT2A	Gene encoding for histone-lysine (K)-specific N-methyltransferase 2A
KMT2C	Gene encoding for lysine (K)-specific methyltransferase 2C
LAIP	Leukemia-associated immunophenotype
MALT	Mucosa-associated lymphoid tissue
MBL	Monoclonal B lymphocytosis
MCL	Mantle cell lymphoma
MDS-RS	Myelodysplastic syndrome with ring sideroblasts
MDS	Myelodysplastic syndrome
MDS/MPN	Myelodysplastic/Myeloproliferative neoplasms
MECOM	Gene econding for the protein MDS1 and EVI1 complex locus protein EVI1, also known as ecotropic virus integration site 1 protein homolog, or positive regulatory domain zinc finger protein 3

MGUS	Monoclonal gammopathy of undetermined significance
MLL-MLLT3	Gene fusion created by the t (9;11)(p22;q23) translocation
MPAL	Mixed phenotype acute leukemia
MR	Molecular response
MRD	Minimal residual disease
MRI	Magnetic resonance imaging
MYC	Avian myelocytomatosis viral oncogene homolog
NGS	Next-generation sequencing
NK	Natural killer
NMP1	Gene encoding for the protein nucleophosmin
NOS	Not otherwise specified
NOTCH1	Notch homolog 1, translocation-associated (Drosophila), a human gene encoding for a single-pass transmembrane receptor
NSCLC	Non-small-cell lung cancer
PB	Peripheral blood
PCM1-JAK2	Gene fusion created by the t (8;9)(p22;p24) translocation which leads to the activation of the Janus kinase 2PCM1 gene encoding for the pericentriolar material 1
PD	Progressive disease
PDGFR	Platelet-derived growth factor receptor
PDGFRA	Gene encoding for the platelet-derived growth factor receptor alpha
PDGFRB	Gene encoding for the platelet-derived growth factor receptor beta
PET	Positron emission tomography
PET/CT	Positron emission tomography/Computed tomography
PI3K/AKT/mTOR	Intracellular signaling pathway important in regulating the cell cycle
PMF	Primary myelofibrosis
PML-RARA	Gene fusion created by the t (15;17)(q22;q12) translocation
PMN	Myeloproliferative neoplasms
PR	Partial response
PTLD	Posttransplant lymphoproliferative disorders
PV	Polycythemia vera
RT-PCR	Reverse transcriptase polymerase chain reaction
RUNX1-RUNX1T1	Gene fusion created by the t (8;21)(q22;q22) translocation
RUNX1	Runt-related transcription factor 1
SBB	Sudan Black B, a non-fluorescent lysochrome (fat-soluble) diazo dye used for tissue staining
SCT	Stem cell transplantation
SEER	Surveillance, Epidemiology, and End Results Program of the National Cancer Institute (National Institutes of Health of the United States)
SLL	Small lymphocytic lymphoma
SNP	Single-nucleotide polymorphism
T-ALL	T-cell acute lymphoblastic leukemia
TAM	Transient abnormal myelopoiesis
TKI	Tyrosine kinase inhibitor
T-ALL	T-cell acute lymphoblastic leukemia
TCF3-PBX1	Chimeric gene created by the t (1;19)(q23;p13) translocation
TFH	T follicular helper
WHO	World Health Organization

Contents

Acute Lymphocytic Leukemia (ALL) in Adult ... 438
Imaging for Diagnosis and Staging of ALL 439
Imaging for the Evaluation of Treatment Response of ALL 445

Chronic Lymphocytic Leukemia (CLL) 445
Imaging for Diagnosis and Staging of CLL 448
Treatment Evaluation of CLL 450
Follow-Up and Long-Term Implications in CLL ... 450

Hairy Cell Leukemia (HCL) 451
Imaging During Follow-Up of HCL 452

Acute Myeloid Leukemia (AML) 452
Imaging for Diagnosis and Staging of AML 455
Response Evaluation and Follow-Up in AML 456

Chronic Myeloid Leukemia (CML) 457
Imaging for Diagnosis and Staging of CML 458
Imaging for Monitoring Treatment of CML 459

References 459

Leukemias are a group of acute and chronic hematological neoplasias characterized by the dissemination in the bloodstream of the cancer cells originating in the bone marrow. The incidence of acute leukemia in adult (either myeloid – AML or lymphoblastic – ALL) is about 4/100,000/year, that of the chronic myeloid leukemia (CML) 1.5/100,000/year, and that of the chronic lymphocytic leukemia (CLL) of 5/100,000/year. Thus, in 2016 the estimated number of new leukemia cases is more than 110,000 in all of Europe and 47,000 in the USA. Leukemias, cause of 4% of all cancer deaths and account for 3.6% of all cancers, with CLL being the most frequent type (60%), followed by AML (25%). Leukemias are most frequently diagnosed among people aged 65–74 years, but all age groups can be affected. ALL are the most common pediatric tumor (about 35% of cancers in children aged 0–14 years), but all age groups can be affected. Approximately 9% were diagnosed before age 20, 9% between 20 and 44, 10% between 45 and 54, 18% between 55 and 64, 22% between 65 and 74, 21% between 75 and 84, and 11% after 85 years of age [1].

A leukemia is considered lymphocytic or lymphoblastic if it occurs in a marrow cell that forms lymphocytes, while it is "myelogenous" or "myeloid" if it occurs in a marrow cell that forms red cells, some kinds of white cells, and platelets (Fig. 1).

Historically, leukemias have been divided into four major categories further classified into subtypes based on specific features of cells [2]:

- Acute lymphocytic leukemia (ALL)
- Chronic lymphocytic leukemia (CLL)
- Acute myelogenous leukemia (AML)
- Chronic myelogenous leukemia (CML)

A revised classification of myeloid/lymphoid neoplasms and leukemias has been recently published in order to better characterize each disease accurately reflecting the specific neoplastic nature. This updated classification incorporated new scientific and clinical information to refine diagnostic criteria for previously described neoplasms and introduced newly recognized disease entities. Table 1 shows the new classification [3, 4].

Acute Lymphocytic Leukemia (ALL) in Adult

In 2016, the estimated number of new cases of ALL was about 6,500, accounting for 0.4% of all new cases of cancer. The number of new cases of ALL was 1.7 per 100,000 per year based on 2009–2013 cases, according to the SEER database. ALL is most frequently diagnosed among people aged <20 (57%); it is most common in children, adolescents, and young adults, with a median age at diagnosis of 15 years. ALL is most common in Hispanics and Whites [1]. ALL occurs both in children and adults. Predisposing risk factors for adult ALL are not known, contrary to childhood ALL [5]. In adults, the age of appearance is one of the most important prognostic determinants. Although the two forms share some common features, fundamental biologic differences may account for the striking variation in outcome. However, although survival in adult patients (>19 years old) remains inferior to that achieved for children with ALL [6], recent advances in molecular testing, the development of new targeted agents, and an improved understanding of the importance of minimal residual disease (MRD) could soon translate into improved prognosis [7]. Recurrent numerical and/or structural cytogenetic abnormalities are found in 70% of adults and 90% of children with ALL and provide important prognostic and certain drug resistance information [8]. Literature data [9, 10] suggest that routine characterization of ALL can aid in the design of more tailored treatment plan.

Furthermore, many chromosomal abnormalities identified in adult ALL have also been found to

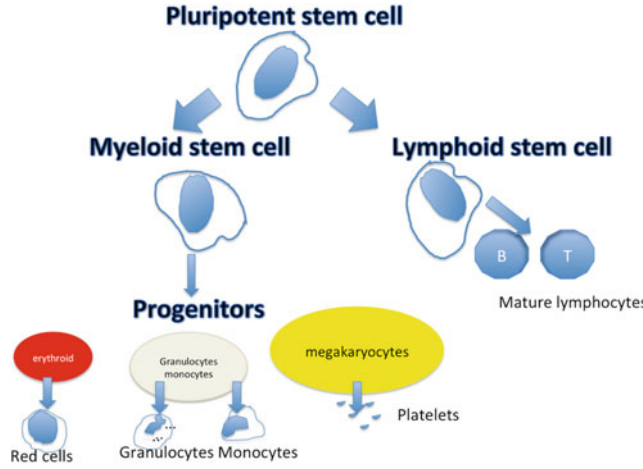

Fig. 1 Schematic representation of leukemias

correlate with prognosis [11–14]. The most important cytogenetic abnormality in adult ALL (found in 15–30%) is the Philadelphia (Ph') chromosome. Ph' chromosome is defined as t(9;22)(q34;q11.2), which results in the BCR-ABL1 fusion gene, with a constitutive and uncontrolled tyrosine kinase activity [15]. A novel subtype of ALL was recently identified by gene expression profiling which clusters with BCR-ABL1 positive ALL. This entity is now referred to as "Ph'-like" disease and represents 15–20% of the adolescent and young adult ALL. These patients have an unfavorable outcome and 5-year disease-free survival of only 25.8% [16]; this subtype has high frequency of kinase-activating alterations providing the lymphoblasts with proliferation advantage. Some of these fusions are sensitive in vitro to tyrosine kinase inhibitors (TKIs), leading to clinical trials assessing their integration into ALL armamentarium [7]. Some advances have been made in the identification of molecular markers of T-cell leukemogenesis. Activating mutations of NOTCH1 (a class I transmembrane heterodimeric glycoprotein that is normally involved in T-cell development and regulation) have been detected in almost 60% of human T-ALL [17]. These activating mutations led to clinical testing of gamma-secretase inhibitors that prevent NOTCH1 activation [18–20].

Epigenetic changes including hypermethylation of tumor suppressor genes or microRNAs and hypomethylation of oncogenes have also been studied in ALL. It represents a novel area of investigation for targeted drugs, such as DNA methyltransferase inhibitors [21–23].

CRLF2 is located in the pseudoautosomal region at Xp22.3/Yp11.3; it is rearranged in 50% of Down syndrome-related ALL and also in Ph'-like ALL [16]. Cells with CRLF2 mutations exhibit activation of the JAK/STAT and of the downstream PI3K/mTOR pathway; thus, in these subtypes, everolimus, temsirolimus, and ruxolitinib could be useful targeted treatments [24]. Other possible targets of interest in ALL include the 22q11.22 deletion and platelet-derived growth factor receptor alpha (PDGFR-alpha) gains that are associated with poor outcome and could predict therapeutic responses to TKIs able to inhibit PDGFR-alpha, such as imatinib [25].

Imaging for Diagnosis and Staging of ALL

A comprehensive diagnostic approach requires the study of cell morphology, immunophenotype, genetics/cytogenetics, and genomics, as detailed in the 2008 World Health Organization (WHO) classification [26] and recently reviewed [4, 27] (Table 1). The initial diagnostic work-up must confirm ALL diagnosis, distinguishing leukemia originating from the B or T lymphocytes, from precursors or more mature cells, and those Ph'

Table 1 Revised classification of myeloid/lymphoid neoplasms and leukemias according to the 2016 WHO classification.

2016 WHO classification	
Myeloid neoplasm and acute leukemia classification	Mature lymphoid, histiocytic, and dendritic neoplasms
Myeloproliferative neoplasms (MPN)	***Mature B-cell neoplasms***
Chronic myeloid leukemia (CML), BCR-ABL1	Chronic lymphocytic leukemia/small lymphocytic lymphoma
Chronic neutrophilic leukemia (CNL)	Monoclonal B-cell lymphocytosis[a]
Polycythemia vera (PV)	B-cell prolymphocytic leukemia
Primary myelofibrosis (PMF)	Splenic marginal zone lymphoma
PMF, prefibrotic/early stage	Hairy cell leukemia
PMF, overt fibrotic stage	Splenic B-cell lymphoma/leukemia, unclassifiable
Essential thrombocythemia (ET)	Splenic diffuse red pulp small B-cell lymphoma
Chronic eosinophilic leukemia, not otherwise specified (NOS)	Hairy cell leukemia variant
MPN, unclassifiable	Lymphoplasmacytic lymphoma
Mastocytosis	Waldenström macroglobulinemia
Myeloid/lymphoid neoplasms with eosinophilia and rearrangement of PDGFRA, PDGFRB, or FGFR1 or with PCM1-JAK2	Monoclonal gammopathy of undetermined significance (MGUS), IgM[a]
Myeloid/lymphoid neoplasms with PDGFRA rearrangement	μ heavy-chain disease
Myeloid/lymphoid neoplasms with PDGFRB rearrangement	γ heavy-chain disease
Myeloid/lymphoid neoplasms with FGFR1 rearrangement	α heavy-chain disease
Provisional entity: myeloid/lymphoid neoplasms with PCM1-JAK2	Monoclonal gammopathy of undetermined significance (MGUS), IgG/A[a] plasma cell myeloma solitary plasmacytoma of bone
Myelodysplastic/myeloproliferative neoplasms (MDS/MPN)	Extraosseous plasmacytoma
Chronic myelomonocytic leukemia (CMML)	Monoclonal immunoglobulin deposition diseases[a]
Atypical chronic myeloid leukemia (aCML), BCR-ABL1	Extranodal marginal zone lymphoma of mucosa-associated lymphoid tissue (MALT lymphoma)
Juvenile myelomonocytic leukemia (JMML)	Nodal marginal zone lymphoma
MDS/MPN with ring sideroblasts and thrombocytosis (MDS/MPN-RS-T)	Pediatric nodal marginal zone lymphoma
MDS/MPN, unclassifiable	Follicular lymphoma
Myelodysplastic syndromes (MDS)	In situ follicular neoplasia[a]
MDS with single-lineage dysplasia	Duodenal-type follicular lymphoma[a]
MDS with ring sideroblasts (MDS-RS)	Pediatric-type follicular lymphoma[a]
MDS-RS and single-lineage dysplasia	Large B-cell lymphoma with IRF4 rearrangement[a]
MDS-RS and multilineage dysplasia	Primary cutaneous follicle center lymphoma
MDS with multilineage dysplasia	Mantle cell lymphoma
MDS with excess blasts	In situ mantle cell neoplasia[a]
MDS with isolated del(5q)	Diffuse large B-cell lymphoma (DLBCL), NOS
MDS, unclassifiable	Germinal center B-cell type[a]
Provisional entity: refractory cytopenia of childhood	Activated B-cell type[a]
Acute myeloid leukemia (AML) and related neoplasms	T-cell/histiocyte-rich large B-cell lymphoma
AML with recurrent genetic abnormalities	Primary DLBCL of the central nervous system (CNS)
AML with t(8;21)(q22;q22.1);RUNX1-RUNX1T1	Primary cutaneous DLBCL, leg type

(*continued*)

Table 1 (continued)

2016 WHO classification	
Myeloid neoplasm and acute leukemia classification	Mature lymphoid, histiocytic, and dendritic neoplasms
AML with inv(16)(p13.1q22) or t(16;16)(p13.1;q22); CBFB-MYH1	EBV^+ DLBCL, NOS[a]
APL with PML-RARA	EBV^+ mucocutaneous ulcer[a]
AML with t(9;11)(p21.3;q23.3);MLLT3-KMT2A	DLBCL associated with chronic inflammation
AML with t(6;9)(p23;q34.1);DEK-NUP214	Lymphomatoid granulomatosis
AML with inv(3)(q21.3q26.2) or t(3;3)(q21.3;q26.2); GATA2, MECOM	Primary mediastinal (thymic) large B-cell lymphoma
AML (megakaryoblastic) with t(1;22)(p13.3;q13.3); RBM15-MKL1	Intravascular large B-cell lymphoma
Provisional entity: AML with BCR-ABL1	ALK^+ large B-cell lymphoma
AML with mutated NPM1	Plasmablastic lymphoma
AML with biallelic mutations of CEBPA	Primary effusion lymphoma
Provisional entity: AML with mutated RUNX1	$HHV8^+$ DLBCL, NOS[a]
AML with myelodysplasia-related changes	Burkitt lymphoma
Therapy-related myeloid neoplasms	Burkitt-like lymphoma with 11q aberration[a]
AML, NOS	High-grade B-cell lymphoma, with MYC and BCL2 and/or BCL6 rearrangements[a]
AML with minimal differentiation	High-grade B-cell lymphoma, NOS[a]
AML without maturation	B-cell lymphoma, unclassifiable, with features intermediate between DLBCL and classical Hodgkin lymphoma mature
AML with maturation	***Mature T and NK neoplasms***
Acute myelomonocytic leukemia	T-cell prolymphocytic leukemia
Acute monoblastic/monocytic leukemia	T-cell large granular lymphocytic leukemia
Pure erythroid leukemia	Chronic lymphoproliferative disorder of NK cells
Acute megakaryoblastic leukemia	Aggressive NK-cell leukemia
Acute basophilic leukemia	Systemic EBV^+ T-cell lymphoma of childhood[a]
Acute panmyelosis with myelofibrosis	Hydroa vacciniforme-like lymphoproliferative disorder[a]
Myeloid sarcoma	Adult T-cell leukemia/lymphoma
Myeloid proliferations related to Down syndrome	Extranodal NK-/T-cell lymphoma, nasal type
Transient abnormal myelopoiesis (TAM)	Enteropathy-associated T-cell lymphoma
Myeloid leukemia associated with Down syndrome	Monomorphic epitheliotropic intestinal T-cell lymphoma[a]
Blastic plasmacytoid dendritic cell neoplasm	Indolent T-cell lymphoproliferative disorder of the GI tract[a]
Acute leukemias of ambiguous lineage	Hepatosplenic T-cell lymphoma
Acute undifferentiated leukemia	Subcutaneous panniculitis-like T-cell lymphoma
Mixed phenotype acute leukemia (MPAL) with t(9;22)(q34.1;q11.2); BCR-ABL1	Mycosis fungoides
MPAL with t(v;11q23.3); KMT2A rearranged	Sézary syndrome
MPAL, B/myeloid, NOS	Primary cutaneous $CD30^+$ T-cell lymphoproliferative disorders
MPAL, T/myeloid, NOS	Lymphomatoid papulosis
B-lymphoblastic leukemia/lymphoma	Primary cutaneous anaplastic large-cell lymphoma
B-lymphoblastic leukemia/lymphoma, NOS	Primary cutaneous γδ T-cell lymphoma
B-lymphoblastic leukemia/lymphoma with recurrent genetic abnormalities	Primary cutaneous $CD8^+$ aggressive epidermotropic cytotoxic T-cell lymphoma
B-lymphoblastic leukemia/lymphoma with t(9;22)(q34.1;q11.2);BCR-ABL1	Primary cutaneous acral $CD8^+$ T-cell lymphoma[a]

(*continued*)

Table 1 (continued)

2016 WHO classification	
Myeloid neoplasm and acute leukemia classification	Mature lymphoid, histiocytic, and dendritic neoplasms
B-lymphoblastic leukemia/lymphoma with t (v;11q23.3);KMT2A rearranged	Primary cutaneous $CD4^+$ small/medium T-cell lymphoproliferative disorder[a] peripheral T-cell lymphoma, NOS
B-lymphoblastic leukemia/lymphoma with t(12;21) (p13.2;q22.1); ETV6-RUNX1	Angioimmunoblastic T-cell lymphoma, follicular T-cell lymphoma[a]
B-lymphoblastic leukemia/lymphoma with hyperdiploidy	Nodal peripheral T-cell lymphoma with TFH phenotype[a]
B-lymphoblastic leukemia/lymphoma with t(5;14) (q31.1;q32.3) IL3-IGH	Anaplastic large-cell lymphoma, ALK^+
B-lymphoblastic leukemia/lymphoma with t(1;19) (q23;p13.3);TCF3-PBX1	Anaplastic large-cell lymphoma, ALK^-[a]
Provisional entity: B-lymphoblastic leukemia/ lymphoma, BCR-ABL1–like	Breast implant-associated anaplastic large-cell lymphoma[a]
T-lymphoblastic leukemia/lymphoma	***Hodgkin lymphoma***
Provisional entity: natural killer (NK) cell lymphoblastic leukemia/lymphoma	Nodular lymphocyte predominant Hodgkin lymphoma
Provisional entity: B-lymphoblastic leukemia/ lymphoma with iAMP21	Classical Hodgkin lymphoma
T-lymphoblastic leukemia/lymphoma	Nodular sclerosis classical Hodgkin lymphoma
Provisional entity: early T-cell precursor lymphoblastic leukemia	Lymphocyte-rich classical Hodgkin lymphoma
Provisional entity: natural killer (NK) cell lymphoblastic leukemia/lymphoma	Mixed cellularity classical Hodgkin lymphoma
	Lymphocyte-depleted classical Hodgkin lymphoma
	Posttransplant lymphoproliferative disorders (PTLD)
	Plasmacytic hyperplasia PTLD
	Infectious mononucleosis PTLD
	Florid follicular hyperplasia PTLD[a]
	Polymorphic PTLD
	Monomorphic PTLD (B- and T-/NK-cell types)
	Classical Hodgkin lymphoma PTLD
	Histiocytic and dendritic cell neoplasms
	Histiocytic sarcoma
	Langerhans cell histiocytosis
	Langerhans cell sarcoma
	Indeterminate dendritic cell tumor
	Interdigitating dendritic cell sarcoma
	Follicular dendritic cell sarcoma
	Fibroblastic reticular cell tumor
	Disseminated juvenile xanthogranuloma
	Erdheim-Chester disease[a]

[a]Changes from the 2008 classification

positive, allowing the most appropriate treatment (anti-CD20, anti-CD19, anti-CD22 antibodies, tyrosine kinase inhibitors) [28].

Aspiration of bone marrow and bone marrow biopsy represent the standard procedure; the bone marrow must contain at least 20% blast cells, as a criterion to differentiate ALL from lymphoblastic lymphoma, but the proportion of circulating blasts is highly variable. ALL blasts are atypical lymphoid or undifferentiated cells. The immunophenotype study plays the key diagnostic role, demonstrating commitment of the blast cell

population to the B- or T-cell lineage. The European Group for the Immunological Characterization of Leukemias recognized distinct BCP/T-ALL subsets, providing a rational immunological classification along with criteria for differential diagnosis [29] subsequently updated and improved [30–32]. The early diagnostic step is completed by a rapid molecular screening by means of reverse transcriptase polymerase chain reaction (RT-PCR) or fluorescence in situ hybridization (FISH) assays, primarily for the detection of BCR-ABL1 rearrangement, sensitive to tyrosine kinase inhibitors (TKIs) [33]. Results from cytogenetics, genetics, and genomics are available at a later stage, allowing the recognition of several ALL syndromes with prognostic and/or therapeutic implications. The more prognostically favorable cytogenetic/genetic subsets are represented by t(12;21)(p13;q22)/TEL-AML1 (rare in adults), the hyperdiploid ALL, and T-ALL with NOTCH-1/FBXW7 mutations. The integration of the conventional studies (karyotype, FISH, qualitative, and quantitative PCR) with the new ones [array comparative genomic hybridization (aCGH), gene expression profiling (GEP), single-nucleotide polymorphism (SNP) array analysis, next-generation sequencing (NGS)] led to the recognition of highly specific poor-risk conditions, whose global incidence is 30%. These assays are not still regularly carried out in clinical practice, but are recommended to improve the risk classification and support targeted therapies [28].

The diagnostic phase is completed by the search for a sensitive molecular marker or an aberrant leukemia-associated immunophenotype (LAIP) for the detection and monitoring of minimal residual disease (MRD) [34]. Human leukocyte antigen (HLA) typing of patients and relatives is recommended at this stage, to facilitate subsequent application of the allogeneic stem cell transplantation (SCT) when necessary [28].

Patients with ALL typically present with constitutional symptoms, bleeding, infections, and/or bone pain, with less than 10% of individuals having symptomatic central nervous system (CNS) involvement at diagnosis. Mature B-ALL can also present as extramedullary (gastrointestinal or testicular) diseases. Mediastinal mass with wheezing and stridor can be a presenting feature of T-cell ALL [35].

Symptomatic CNS involvement is more frequent in patients with mature B-ALL; these patients may present with cranial nerve deficiencies (especially cranial nerves VI, III, IV, and VII), leading to double vision, abnormal ocular movements, facial dysesthesia, and facial droop [36]. Patients with T-ALL frequently present with a mediastinal mass on chest X-ray. If the mass is sufficiently large, it results in stridor, wheezing, pericardial effusions, and superior vena cava syndrome [37]. Involvement of the skin, testicles, kidneys, joints, and bones is uncommon in adults [38, 39]. Approximately 15–25% of ALL patients of all ages have leukemia with a T-cell phenotype, which is associated with higher initial WBC counts, mediastinal mass, male gender, and higher incidence of CNS involvement. In children, the frequency of T-lineage ALL increases with age.

Physical examination may reveal pallor, ecchymoses, or petechiae. Lymphadenopathy and hepatosplenomegaly are infrequent; patients present with signs and symptoms of metabolic hyperactivity, including profound constitutional symptoms, weight loss, and often large abdominal and (especially in children) testicular masses [40]. Involvement of the gastrointestinal tract is also frequent and may cause bleeding or rupture.

Microscopy and cytochemical stains are still essential in the initial work-up: bone marrow is usually hypercellular and replaced with a homogenous population of leukemic blasts [41].

In contrast to lymphoma, leukemia is not staged because it involves the bone marrow, and leukemic cells circulate throughout the bloodstream to all parts of the body.

In patients with atypical presentations or complications, particularly in the presence of bone pain, osteopathy and hypercalcemia, CNS involvement or infectious complications or to detect extramedullary disease, imaging may be helpful [42] (Fig. 2). In the American Cancer Society of Childhood Leukemia Report (2002), several radiological (X-rays, ultrasound, CT, and MRI) and nuclear medicine imaging modalities are useful to assess the disease. However, the recent ESMO guideline does not recommend any radiologic imaging in ALL

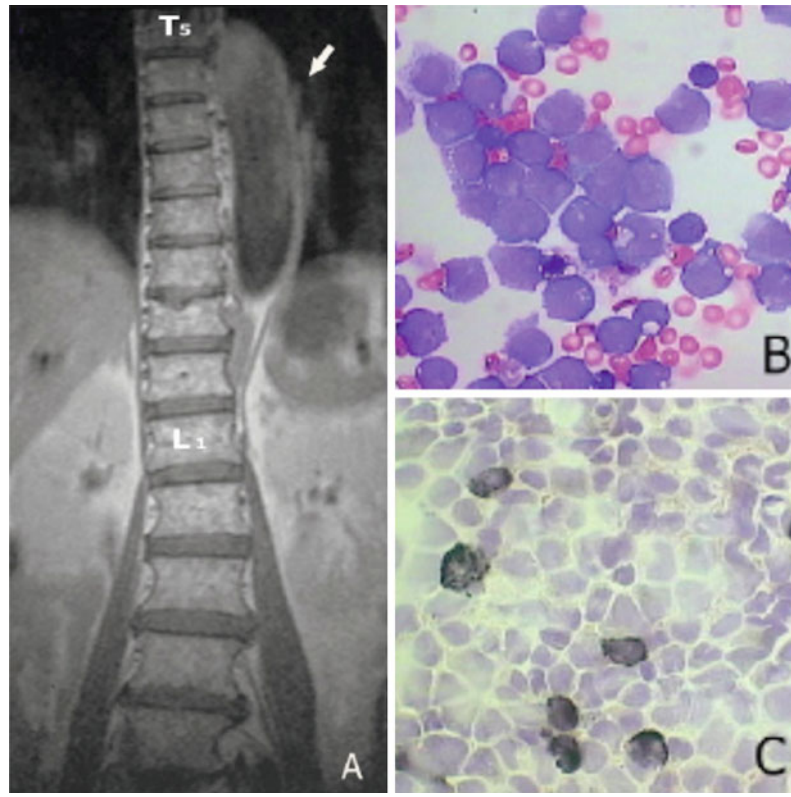

Fig. 2 Sagittal T1-weighted MR image (**a**) showing the spinal cord wrapped by hypointense tissue extending from T5 to T12 (*arrow*). Cerebral spinal fluid smear showing myeloblasts with a high nucleocytoplasmic ratio, monoblasts with more plentiful cytoplasm, and a folded nucleus with a lacy chromatin pattern (May-Grünwald-Giemsa, original magnification 960, (**b**)). Cerebral spinal fluid smear stained with SBB showing few myeloblasts with strong positive granular reaction (*black*) and monoblasts with weaker or absent granular reaction (original magnification 960, (**c**)) (Modified from Potenza et al. [161])

diagnosis or for the initial staging [28]. In clinical practice many patients with ALL present with constitutional symptoms, e.g., fever, and then imaging is part of the diagnostic work-up to identify the cause of fever.

Osteopathy, including bone pain and pathologic fracture, is one of the initial symptoms of ALL, with an incidence of about 20% in childhood ALL [43]. Bone scintigraphy may be helpful to elucidate the etiology of bone pain: in fact, pain localized at joints may be the first presentation of ALL. The knee is the most frequently affected site, followed by the ankle. Bone scintigraphy is able to demonstrate abnormalities in the majority of leukemic patients with bone lesions occurring even in sites without pain. Focal intense uptake in one or several metaphyses as well as in diaphyses represents the typical scintigraphic findings, and the most common affected sites are metaphyses, diaphyses, and epiphyses of long bones, the pelvis, and ribs. Lower limbs are involved more frequently than upper extremities (Fig. 3). Moreover, diffuse uptake in the pelvis and spine may suggest marrow infiltrative disease [44], and bone X-ray may be helpful to detect leukemic changes in bone or joint in the presence of bone pain [45].

Ultrasound and CT scan are generally used to assess extramedullary involvement in the abdomen, and MRI is indicated to assess the CNS for leukemic infiltration, infections or multifocal leukoencephalopathy.

Renal involvement does not necessarily imply a significant organ impairment, because elevated creatinine may occur due to lymphadenopathy compressing renal vessels and/or ureter. Nephromegaly is a common finding in children [46]. Additionally causes of renal parenchymal abnormalities in childhood ALL include infection, lymphoma transformation, nephroblastomatosis, cysts, angiomyolipomas, and metastases. Furthermore, atypical infection with microabscesses in the liver, spleen, and kidneys appear as focal small non-enhancing areas of parenchymal abnormality [47] on CT, especially in children. In patients with

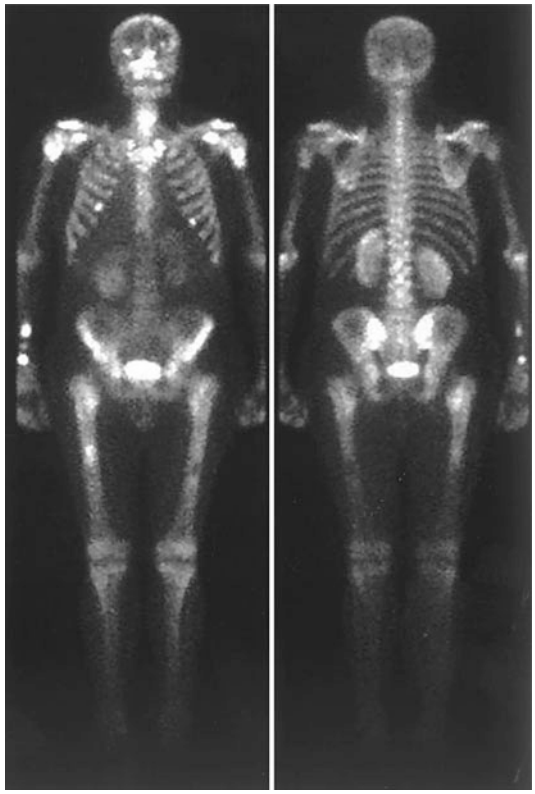

Fig. 3 Bone scintigraphy of a 43-year-old men with a ALL showing increased radiopharmaceutical uptake in all long bone diaphysis, as suggestive of bone marrow expansion (Modified from Benitez et al. [162])

possible CNS infection and negative cultures, MRI may be helpful in revealing the presence of the disease and in the assessment to response to treatment. Early diagnosis of neurologic involvement is essential to insure effective therapy and for detection of treatment-related neurotoxicity, secondary brain tumors, infections, and cerebrovascular disease [48–50]. MRI abnormal enhancement of the meninges and/or nerve roots may result from leptomeningeal or subarachnoid disease/relapse or infection, rarely, both. Other causes of nerve root enhancement on MRI include postsurgical arachnoiditis, mechanical root compression associated with inflammation, cytomegalovirus polyradiculopathy or inflammatory demyelinating polyradiculoneuropathy (Guillain-Barrè syndrome), and rarely spontaneous spinal hematomas [48]. Promising results have been reported in the identification of the extramedullary involvement, specially in recurrent disease, using [^{18}F]FDG-PET/CT [51, 52].

Imaging for the Evaluation of Treatment Response of ALL

The definition of treatment response in ALL does not require any imaging. However, imaging plays an important role for detecting and monitoring treatment.

Treatment-related CNS complications include white matter lesions, small-vessel calcifications, cerebrovascular disorders, treatment-induced tumors, infections, and enlargement of ventricles and/or widening of sulci (sign of cortical atrophy). Leukoencephalopathy is the most common neurotoxicity, usually due to methotrexate in ALL patients. It appears as white matter hyperintensities on T2-weighted MRI, and it may be persistent or transient [53]. Mineralizing microangiopathy is a delayed form of neurotoxicity typically detectable as dystrophic calcifications in the basal ganglia and subcortical white matter.

The detection of iron overload, particularly in myocardium in patients receiving chronic red cell transfusions, is mandatory to prevent ventricular dysfunction. MRI-T2*-weighted images using gradient-echo MRI-T2* allow the determination of myocardial iron amount and may be used both for diagnosis and monitoring myocardial iron overload during and after antileukemic treatment with blood transfusions [54].

Chronic Lymphocytic Leukemia (CLL)

CLL is characterized by a progressive accumulation of monoclonal B lymphocytes and is part of a spectrum of diseases grouped as low-grade lymphoproliferative disorders. CLL is the most common form of all leukemias among adult populations of the Western world and is more common in men. Since this disease is characterized by relatively longer survival rate, its prevalence rate is the highest among all leukemias. In 2016, the estimated number of new cases of CLL is about 19,000,

accounting for 1.2% of all new cases of cancer. CLL is rare in people younger than 50 years, but after this age a fairly rapid rise in incidence takes especially after 55 years. Approximately 9% of cases are diagnosed between 45 and 54 years, 22% between 55 and 64, 28% between 65 and 74, 26% between 75 and 84, and 13% after 85 years of age (about 2% in patients <44 years) [1].

Genetic, rather than environmental, factors are the most likely explanation for the geographic and ethnic differences in incidence. There is an inherited genetic susceptibility for CLL, with a six to ninefold increased risk for family members of CLL patients. There are no clearly identified etiologic factors known in CLL [55].

The diagnosis of CLL is established by the presence in the peripheral blood of $\geq 5 \times 10^9$/L monoclonal B lymphocytes (clonality of the circulating B lymphocytes needs to be confirmed by flow cytometry or assessment of the immunoglobulin heavy chain (IgH) clonal rearrangement by PCR). In the peripheral blood smear, the leukemic cells appear as small, mature lymphocytes with a narrow border of cytoplasm and a dense nucleus lacking discernible nucleoli and with partially aggregated chromatin. Larger, atypical lymphocytes or prolymphocytes may be seen, but they must not exceed 55% [56].

Immunophenotype is useful for distinguishing CLL from other indolent lymphomas, such as the marginal zone, the lymphoplasmacytic, and the mantle cell (MCL) [55]: indeed, in addition to the B markers (CD20, CD19), common to all B lymphomas, the co-expression of CD5 (that occurs also in MCL); the CD79, CD11c, CD103, and FMC7 negativity; and the CD200 and CD23 positivity characterize the B-CLL.

In the WHO classification, small lymphocytic lymphoma (SLL) and CLL are considered as a single entity (Table 1).

The diagnosis of SLL requires the presence of lymphadenopathy and/or splenomegaly with a number of B lymphocytes in the peripheral blood not exceeding 5×10^9/L. SLL cells show the same immunophenotype as CLL. The diagnosis of SLL should be confirmed by histopathological evaluation of a lymph node or tumor mass biopsy, whenever possible. In the absence of lymphadenopathy, organomegaly, cytopenia, and clinical symptoms, the presence of fewer than 5×10^9/L monoclonal B lymphocytes is defined as "monoclonal B lymphocytosis" (MBL) [55–57] which can be detected in 5% of subjects with normal blood count. As described for monoclonal gammopathies and multiple myeloma, progression to CLL occurs in 1–2% of MBL cases per year [57].

CLL cells co-express the CD5 antigen and B-cell surface antigens CD19, CD20, and CD23. The levels of surface immunoglobulin, CD20, and CD79b are characteristically low compared with normal B cells. Each clone of leukemia cells is restricted to expression of either kappa or lambda immunoglobulin light chains [55].

The pathophysiology of CLL involves inhibition of apoptosis [58]. Accumulation of mature B cells that have escaped programmed cell death and undergone cell cycle arrest in the G0/G1 phase is the hallmark of CLL [59]. These cells have a low proliferative activity, and data lend support to the hypothesis that in vivo defective apoptosis accounts for accumulation of B cells.

CLL is generally considered an indolent disease associated with a prolonged chronic course; more than one-third of patients die for other causes and the natural history is very heterogeneous: some patients die within 2–3 years from the diagnosis, mainly because of complications or causes directly related to CLL. Nevertheless, the majority of cases present relatively benign initial course (5–10 years), followed by a terminal phase lasting 1–2 years with considerable morbidity, both from the disease itself and from complications of therapy. The most frequent causes of death are severe systemic infections (especially pneumonia and septicemia), bleeding, and inanition with cachexia. In about 3% of CLL patients, a diffuse large-cell immunoblastic lymphoma supervenes terminally (Richter's transformation), associated with a rapidly progressive course, refractoriness to all chemotherapy, and death within 6 months [60]. Another possible terminal event is the morphologic transformation of blood lymphocytes from the typical small, mature-appearing cell to larger cells with distinct nucleoli and less dense chromatin in the nucleus, called *prolymphocytoid transformation*. Acute leukemia

is rarely observed as a terminal event; it occurs independently by treatment with alkylating agents, and when it does occur, it is myeloid in origin (myelocytic, myelomonocytic, or acute erythroleukemia). There is no widely accepted effective therapy for these terminal transformations of CLL. Patients with CLL are considered to be at a somewhat higher risk than the general population of developing another cancer, usually of lung or gastrointestinal tract. Skin cancers occur with considerably greater frequency among CLL patients than among the general population, but these do not result in higher mortality.

Several systems of clinical staging have been proposed by investigators around the world, but just the Rai system [61] and the Binet system [62] (Table 2a, b) are in wide use in clinical practice as well as in research. In Europe, the Binet staging system is more widely used, whereas in the USA, the Rai system is more commonly applied. Both Binet and Rai staging systems separate three groups of patients with different prognoses [55].

The Rai staging system [61] is based on the concept that in CLL there is a gradual and progressive increase in the burden of leukemic lymphocytes, resulting in sequential clinical manifestations of the disease starting in the blood and bone marrow and then involving the lymph nodes, spleen, and liver or other lymphoid sites. The earliest stage (stage 0) is characterized by no stigmata of disease other than the minimum diagnostic requirements of CLL. About 20–25% of patients at the time of initial diagnosis of CLL are in the earliest clinical stage (stage 0, median survival from the time of diagnosis = 150 months), 25% are in the advanced stages (stages III and IV, median survival = 19 months), and the remaining 50% are in stage I or II (median survival = 101 and 71, respectively). In 1987, however, the system was simplified to consist of only three groups: low (Rai stage 0), intermediate (Rai stages I and II combined), and high (Rai stages III and IV combined) (140). Binet's method [62] classifies all patients with anemia (defined as hemoglobin below 100 g/L) and/or thrombocytopenia (platelets less than 100×10^9/L) as stage C. All of the remaining patients are divided into two groups. This staging takes into consideration five areas: cervical, axillary, and inguinal lymph nodes (whether unilateral or bilateral, each area is counted as one) and the spleen and liver. The International Working Group on CLL (IWCLL) recommended that, in practice, an integrated system using both methods should be used [63]. According to this recommendation, each Binet stage is to be further identified by the appropriate Rai stage (i.e., A-0, A-I, A-II, B-I, B-II, C-III, C-IV). However, this integrated system has not been widely accepted, and most clinicians today use either the Rai's or Binet's method for patient management and therapeutic investigation.

Table 2 Rai (2A) and Binet (2B) staging systems

2A

Rai stage	High levels of lymphocytes	Swollen lymph nodes	Enlarged spleen or liver	Anemia	Low levels of platelets
0	Yes	No	No	No	No
I	Yes	Yes	No	No	No
II	Yes	Yes or no	Yes	No	No
III	Yes	Yes or no	Yes or no	Yes	No
IV	Yes	Yes or no	Yes or no	Yes or no	Yes

2B

Binet stage	Number of lymph node areas	Anemia	Low levels of platelets
A	<3	No	No
B	3 or more	No	No
C	Any number	Yes (or low platelets)	Yes (or anemia)

Both the Rai's or Binet's staging systems rely solely on a physical examination and standard laboratory tests, whereas the role of various imaging procedures (ultrasound, computed tomographic scan, or magnetic resonance imaging [MRI]) has not been validated for staging of CCL. The Binet's method may require some modification in the future, since CT has become a routine part of initial investigations and may reveal enlargement of retroperitoneal or mediastinal nodes that are currently not included among the five sites of palpably enlarged lymphoid areas.

The Rai's or Binet's clinical staging systems alone are not sufficient to estimate the individual prognosis reliably, particularly for patients with early-stage disease. Therefore, additional parameters have been sought to more accurately assess the prognosis of patients with CLL. This search has provided a steadily increasing number of laboratory tests, which predict the response to treatment, progression-free survival, or overall survival of patients with CLL. Several prognostic factors have been tested, including extent of blood lymphocytosis, morphologic features of blood lymphocytes (i.e., the relative proportion of prolymphocytes), presence of normal or abnormal chromosomal karyotype, phenotypic profile of B lymphocytes, age, sex and levels of serum immunoglobulins, molecular genetics makers, beta-2 microglobulin, and adhesion molecules [64]. The mutational status of IgH genes on CLL lymphocytes seems promising: VH gene mutations correlate with significantly longer survival and a relatively more benign disease course than unmutated genes. Testing for gene mutations, however, is not routinely done in hospitals, but perhaps CD38 expression, a readily available test, holds the promise of being useful as a surrogate marker. Patients with mutated VH genes showed a strong correlation with low expression of CD38 and ZAP70 on CLL lymphocytes [65]. These findings were especially strong prognostic indicators for patients in the intermediate-risk category patients, but at the moment these molecular features don't really lead the therapeutic strategy. In fact, CLL cells with unmutated IGVH status have a higher genetic instability with a higher risk of gaining unfavorable genetic mutations. OS and time to treatment intervention are significantly shorter in this patient group. The expression of CD38 and ZAP70 correlates to some extent with the IGHV mutational status, but has no therapeutic impact and is therefore not required.

Imaging for Diagnosis and Staging of CLL

Diagnosis of CLL is essentially based on symptoms, laboratory tests, and physical examination. Before any treatment, history, and physical examination including a careful palpation of all lymph node areas, the spleen, and the liver, a complete blood cell count and differential count, serum chemistry including lactate dehydrogenase, bilirubin, serum immunoglobulins, and direct antiglobulin, should be performed. Particular attention should be paid to the history and status of relevant infections (i.e., hepatitis B and C, cytomegalovirus, human immunodeficiency virus) in order to avoid virus reactivation during chemoimmunotherapy or allogeneic stem cell transplantation (alloSCT) [55]. The diagnostic work-up should include FISH analysis for the detection of deletion of the chromosome 17 [del (17p)] affecting the tumor protein p53 expression and in the absence of del(17p) molecular genetics for the detection of TP53 gene mutation (at least exons 4–10, eventually exons 2–11) [66].

Although a bone marrow biopsy is not really necessary for diagnosis, nevertheless it is recommended for assessing the pattern of bone marrow infiltration and for the diagnostic evaluation of unclear cytopenias. An extended FISH analysis (for chromosome 11, 12, 13, 17) is recommended before the start of therapy because the detection of additional cytogenetic abnormalities [del(11q) or trisomy 12] may have therapeutic consequences. In particular, deletion of chromosome 17 and/or of TP53 is indicative of a worse prognosis or for the possibility of employing the Bruton kinase inhibitor ibrutinib in first line of therapy. CT scans may be helpful to assess the tumor load or to determine the cause of unclear symptoms, but they should not generally be used in asymptomatic patients or for clinical staging. In addition, CT scans may be useful for baseline and final assessment in clinical trials. In elderly

patients, abdominal ultrasound might be considered instead [55, 56].

Abdominal ultrasound and CT may be helpful to detect splenomegaly or bulky disease, findings that may influence therapy planning [56, 67]. Muntanola et al. [68] suggested that the presence of abdominal involvement (splenomegaly or lymphadenopathy) in patients with Rai stage 0 predicts a more aggressive clinical course of the disease with shorter time to progression compared to patients with normal CT findings. Furthermore, abnormal abdominal CT findings correlate with severity of bone marrow infiltration, ZAP-70 expression, and shorter lymphocyte doubling time.

MRI does not provide significant information for CLL management, except in rare cases of central nervous system localization of the disease, as typical for cases of childhood leukemia.

No other nuclear medicine modalities, including [^{18}F]FDG-PET and [^{18}F]FDG-PET/CT, are at the present recommended for patient management. Nevertheless, in case of suspected Richter's transformation (the transformation of CLL cells into aggressive type of lymphoma, most commonly diffuse large B-cell lymphoma, DLBCL), [^{18}F]FDG-PET/CT is considered the method of choice for early assessment. The pattern of [^{18}F]FDG uptake and the PET-derived parameters may help in choosing the site of biopsy [69], and discern Richter's transformation [70]. In fact, in the majority of patients during the indolent course of CLL over many years, cells are characterized by a low metabolic rate and low-grade [^{18}F]FDG uptake into lymphoadenopathies (Fig. 4). The appearance of intense [^{18}F]FDG uptake correlates with increased numbers of large B cells in the bone marrow and/or lymph nodes (CLL acceleration), with the appearance of both localized and/or diffuse pattern of increase [^{18}F]FDG uptake.

The value of [^{18}F]FDG-PET/CT for the detection of Richter's transformation has been reported in 37 CLL patients with very high sensitivity (91%) and negative predictive values (97%) [69]. False-

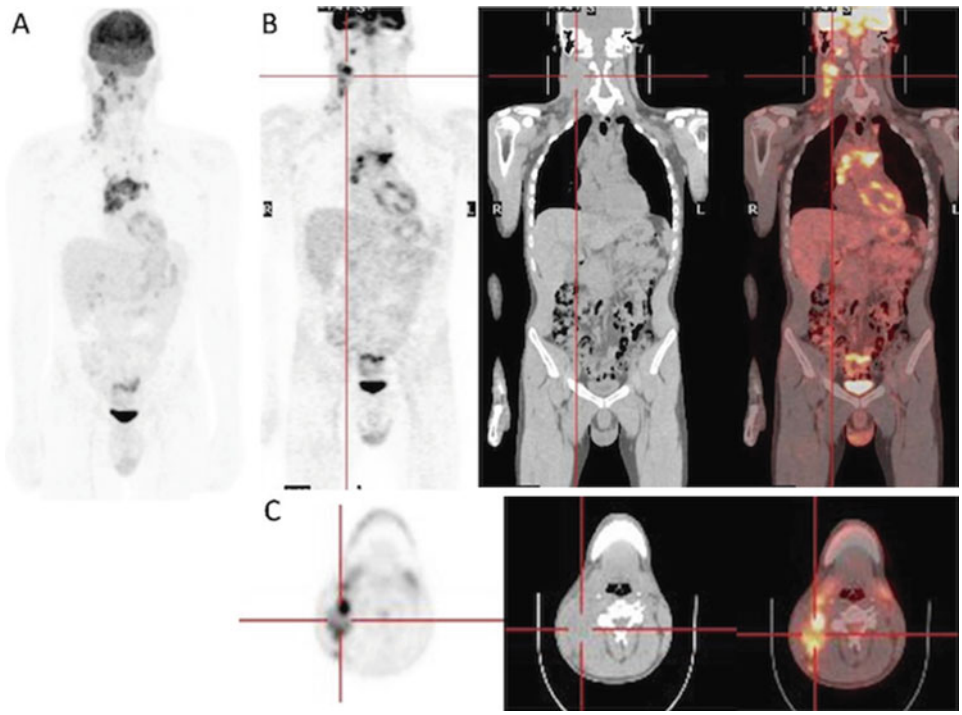

Fig. 4 [^{18}F]FDG PET/CT in patient with CLL and Richter's transformation. Images demonstrate multiple site of lymph node uptake in the neck and mediastinum. (**a**) MIP image. (**b**) Coronal view and (**c**) transaxial view of PET, CT, and PET/CT fused images

positive results in this series were caused by other malignancies (i.e., Hodgkin disease or NSCLC), as frequently observed in CLL patients. The accelerated phase of CLL, an early transition to lymphomatous transformation characterized by increased numbers of more immature cells within the bone marrow and by lymphoid tissue with a higher rate of cell turnover, may represent an additional false-positive [^{18}F]FDG-PET/CT. Finally, infection can also cause false-positive findings on [^{18}F]FDG-PET/CT; the CT component of the PET/CT exam may be employed to improve accuracy in this specific setting. When [^{18}F]FDG-PET/CT is used to guide biopsies, histological analysis remains the gold standard. The prognostic role of [^{18}F]FDG-PET/CT in CLL should be confirmed by histopathology [71].

Treatment Evaluation of CLL

Response evaluation includes a physical examination and complete blood cell count. A bone marrow biopsy may be carried out to define CR. Chest X-ray and an abdominal ultrasound or CT for response evaluation may be carried out, if abnormal before therapy [55]. Table 3 shows CT scan parameters required to assess the treatment response in clinical trials according to Hallek et al. [56]. Detection of minimal residual disease (MRD) by flow cytometry has strong prognostic impact [72, 73]. Patients who are MRD negative after therapy show a longer response duration and survival. Additional clinical consequences of MRD positivity post-therapy remain unclear, except for patients after an allogeneic transplantation, where a positive MRD signal may trigger the reduction of immunosuppressive therapies or the start of antileukemic maintenance therapy. Therefore, MRD assessment is not generally recommended for monitoring post-therapy outside clinical studies [55].

Recently, the next-generation sequencing (NGS) techniques allowed the possibility of recognizing a disease-specific B clone and following it after treatment. The new therapies (rituximab plus bendamustine, ibrutinib, obinutuzumab plus chlorambucil, idelalisib) seem to offer higher rates of molecular remission and correlate with longer disease-free survivals [74–77].

Follow-Up and Long-Term Implications in CLL

CLL is an incurable disease. Therefore, lifelong observation and follow-up is recommended for all patients in order to identify the moment when re-treatment will be necessary. Follow-up of asymptomatic patients should include a blood cell count and clinical evaluation (palpation of the lymph nodes, liver, and spleen) every 3–6 months, depending on the dynamics of the leukemic development. Special attention should be paid to the appearance of autoimmune cytopenias. Moreover, CLL patients have a two

Table 3 CT scan parameters required to assess the treatment response in clinical trials according to Hallek et al. Guidelines for the diagnosis and treatment of chronic lymphocytic leukemia: a report from the International Workshop on Chronic Lymphocytic Leukemia updating the National Cancer Institute–Working Group 1996 guidelines [56]

Complete remission (CR)	Partial remission (PR)	Progressive disease (PD)
Lymph nodes should not be >1.5 cm in diameter and no hepatomegaly or splenomegaly	Reduction in lymphadenopathy defined as: decrease in lymph node size ≥50% either in the sum products of up to 6 lymph nodes or in the largest diameter of the enlarged lymph node(s) detected prior to therapy and no increase in any lymph node and no new enlarged lymph node. In small lymph nodes (<2 cm), an increase <25% is not considered to be significant and a reduction in the noted pretreatment enlargement of the spleen or liver ≥50%	Appearance of any new lesion (such as enlarged lymph nodes >1.5 cm or other organ infiltrates) or increase in the previously noted enlargement of lymph nodes ≥50% or an increase in the previously noted enlargement of the liver or spleen ≥50% or the de novo appearance of hepatomegaly or splenomegaly

to sevenfold increased risk of developing secondary malignancies (mostly solid cancers, but also secondary myelodysplastic syndromes or acute myeloblastic leukemia). The transformation into a diffuse large B-cell lymphoma (DLBCL) or Hodgkin's lymphoma (HL) occurs in 2–15% of CLL during the course of disease [55]. The transformation into DLBCL (Richter's transformation) usually has a very poor prognosis that required therapies used in DLBCL, such as rituximab plus CHOP (cyclophosphamide, vincristine, doxorubicin, and dexamethasone), but response duration is typically short, and an allogeneic HSCT should be recommended in case of available donor and sufficient fitness. The transformation of CLL into Hodgkin's disease represents a separate entity, where conventional chemotherapy against HL often achieves long-lasting remissions [55].

Hairy Cell Leukemia (HCL)

Classical hairy cell leukemia (HCL) is a B-cell chronic lymphoproliferative disorder characterized by splenomegaly, pancytopenia, and bone marrow involvement with fibrosis. HCL represents 2% of all adult leukemias [78]. Approximately 1,600 new cases per year are diagnosed in Europe, with a median age of 52 years at the time of diagnosis [79]. In the USA, a higher frequency of HCL is observed among White Americans than among African-Americans or Asians, as well as in patients following exposure to the herbicide "Agent Orange," used during the Vietnam War [80]. HCL variant (HCL-V) is classified among mature B-cell neoplasias [4]. HCL-V is an uncommon disorder, accounting for approximately 0.4% of chronic lymphoid malignancies and 10% of all HCL cases, without sexual predominance and a median age at diagnosis of 71 years.

The examination of peripheral blood films and immunophenotyping are usually sufficient the diagnosis in the majority of cases. The neoplastic cells are twice the size of small lymphocytes and have a round or kidney-shaped nucleus with excess chromatin and abundant pale cytoplasm with projections. Monocytopenia and macrocytosis are very common; other cytopenias may be present. A diagnosis of HCL based on cytology can be effectively confirmed by flow cytometry studies using anti-B-cell monoclonal antibodies such as CD19, CD20, or CD22, together with a panel of antibodies such as CD11c, CD25, CD103, and CD123, which are more specific to HCL; this combination will allow the differentiation of HCL from other B-cell leukemias and lymphomas with circulating villous cells, such as the marginal lymphoma [78, 81, 82]. In addition, strong expression of CD200 is characteristic of HCL and may be useful as distinctive feature in difficult cases [83]. HCL-V typically presents with high lymphocyte counts, with the cells being nucleolated and lacking monocytopenia. Flow cytometry will indicate the cells to be CD11c+ and often CD103+ but very rarely CD25+ and CD123+. As the bone marrow can rarely be aspirated ("dry tap") in classical HCL, diagnosis is typically performed by a bone marrow trephine biopsy. The degree and pattern of infiltration varies from mild interstitial to diffuse, and the lymphoid cells are surrounded by a clear halo due to the abundant cytoplasm, giving the characteristic "fried egg" pattern. In difficult cases, BRAF V600E mutation of exon 15 may be useful to diagnose classical HCL and MDR [84]. This mutation has been described in 100% of classical HCL, but is absent in HCL-V and in cases with VH4-34 rearrangement [78, 85, 86]. It has also a clinical impact, because the anti-RAF compounds, such as vemurafenib, have been shown to be very effective in relapsed patients [87]. In HCL-V, the infiltration is either intrasinusoidal or interstitial. Immunohistochemistry with the monoclonal antibodies CD20, CD72 (DBA44), CD11c, CD25, CD103, annexin A1, and tartrate-resistant acid phosphatase stain will highlight the lymphoid infiltrates and support the diagnosis of classical HCL [82]. However, annexin A1 is not suitable for detecting residual disease after treatment as it stains myeloid cells. Cyclin D1 may be weakly positive but differential diagnosis with mantle cell lymphoma rarely arises. HCL does not have a distinct chromosomal abnormality. The majority of the cases have mutations of the immunoglobulin heavy chain (IGHV) gene, suggesting that the disease arises on a memory B cell. Unlike other splenomegalic disorders such as

splenic marginal zone lymphoma or HCL-V, there is no evidence of specific IGHV, IGHD, and IGHJ repertoires or stereotypes in HCL [88–90]. Although HCL-V patients lack the BRAF mutation, TP53mutations are present in one-third of cases [91]. There is no worldwide accepted staging system for HCL. In addition to the diagnostic tests on the blood and bone marrow trephine biopsy, a staging work-up should include full blood cell counts with differential and reticulocytes, renal and liver biochemistry, serum immunoglobulins, β2 microglobulin, direct antiglobulin test, Coombs test, and hepatitis virus B and C and human immunodeficiency virus screening. Computed tomography (CT) imaging is desirable at the time of diagnosis (as around 10% of HCL patients have abdominal lymphadenopathy) and should be performed at relapse [78, 92]. MRI is being evaluated as a means for assessing total body burden of disease in the marrow [93].

Imaging During Follow-Up of HCL

A follow-up of asymptomatic patients should include a complete history, physical examination, the blood cell count, and routine chemistry every 3–12 months. CT scan is not necessary outside clinical trials [78]. The frequency of second malignancies is increased in HCL patients, whether treated or untreated. Solid and hematological malignancies develop in 10% of HCL patients, particularly chronic lymphoproliferative diseases (multiple myeloma, Hodgkin's and non-Hodgkin's lymphoma), melanoma, and thyroid cancer [94, 95].

Acute Myeloid Leukemia (AML)

In 2016, the estimated number of new cases of AML is about 20,000, accounting for 1.1% of all new cases of cancer. The number of new cases of AML was 4.1 per 100,000 per year based on 2009–2013 cases according to the SEER database [1]. AML affects adults of all ages, but is especially common among people aged 65–74.

Currently, thanks to advances in transfusion and infectious disease supportive care [96] as well as serial evaluations of different chemotherapeutic approaches, more than 80% of young adults and 60% of all patients can achieve complete remission. Varying with patient age and other factors, from 15% to 50% of these complete responders can be expected to achieve long-term survival with the likelihood that most of these individuals are cured of their disease. Acquired genetic changes in bone marrow stem cells that cause a complete or partial block in normal hematopoietic stem cell maturation are the basis of the development of the disease. The genetic changes may involve mutations that lead to activation of growth-promoting proto-oncogenes, inactivation of tumor suppressor genes, or alterations in transcription factors. Mutations in codons 12, 13, or 61 of the N-*ras* gene encoding a 21 kd guanosine nucleotide-binding protein involved in signal transduction have been noted in a consistent patients with AML. The greatest insight regarding AML pathogenesis has been provided by the identification of genes at cytogenetic breakpoints involved in balanced translocation. The fusion proteins generated by the translocation generally result in disruption of transcription factors believed to be critical in myeloid differentiation [97]. Many of these chromosomal abnormalities [e.g., t(8;21), t(15;17), inv16] are associated with specific AML subtypes and carry prognostic importance. Although the acquired genetic lesions that lead to leukemia are being rapidly defined, DNA damage from a known cause accounts for a small fraction of patients with AML. There have been a number of epidemiologic studies that have attempted to link environmental exposures to leukemia [98]. There may be a small increased risk associated with cigarette smoking [99], whereas exposure to electromagnetic radiation [100] seems an unlikely cause of AML. Occupational exposures, particularly to benzene [101] or petrochemicals [102], have been implicated in the development of AML. Alkylating agents have been associated with deletions of chromosome 5 and 7, whereas etoposide (used in childhood ALL) and high-dose anthracycline/

cyclophosphamide combinations may cause 11q23-associated disease. With these few exceptions, however, there is no clear relationship between environmental exposures and the occurrence of acute leukemia.

AML can present either as a de novo leukemia, without an apparent antecedent illness, or as an evolution from previous marrow disorders, such as myelodysplasia, aplastic anemia, chronic myeloid leukemia (CML), and Fanconi's anemia [103], or after the administration of therapy for other types of cancers or nonmalignant disorders.

The natural history of AML arising de novo in young adults is believed to be a disease of the committed stem cell that is vastly different from the same disease arising from the pluripotent stem cell, as occurs in secondary AML [104].

The diagnosis of AML requires the examination of peripheral blood and bone marrow specimens. The work-up of these specimens should include morphology, cytochemistry, immunophenotyping, cytogenetics, and molecular genetics (PCR, FISH) [105]. In most patients, it is relatively simple to distinguish between AML and ALL on morphologic grounds. In general, the blasts from patients with AML are larger, with more abundant cytoplasm and more prominent, often multiple nucleoli. The definitive diagnosis depends, however, on the presence of Auer rods, on concentrations of myeloid-containing granules (present in 50% of those with AML), or on demonstration of at least 3% granulated precursors [106]. The cells are often reactive with antibodies directed against CD34. Terminal deoxynucleotidyl transferase (TdT) is generally absent, but can sometimes be detected in a minority of blasts. While historically sorted by the largely descriptive French-American-British (FAB) criteria [107], AML are now classified according to the WHO classification [3]. The FAB morphologic classification names the AML according to the normal marrow elements that they most closely resemble [107]. The WHO classification incorporates, in addition to morphological criteria, cytogenetic data, molecular genetics, immunophenotype data, and clinical information into a diagnostic algorithm to delineate clinically significant disease entities. In the WHO classification, the term "myeloid" includes all cells belonging to the granulocytic, monocyte/macrophage, erythroid, megakaryocytic, and mast cell lineage. Despite the dilemma and controversy regarding how to incorporate recently described and clinically important genetic lesions into the revised scheme, the framework of the classification proved flexible enough so that new, well-defined entities could be incorporated as provisional entities, those for which more data need to be collected so that they can be better characterized. One of the major challenges in the revision of the WHO classification is how to incorporate important and/or recently described genetic aberrations into a classification scheme of AML and yet adhere to the WHO principle of defining homogeneous, biologically relevant, and mutually exclusive entities based not only on the prognostic value of a genetic abnormality, but on morphologic, clinical, phenotypic, and/or other unique biologic properties. According to the last version of the WHO classification, different subgroups of AML and related neoplasm may be identified (Table 1): the AML with recurrent genetic abnormalities, the AML with myelodysplasia-related changes, the therapy-related myeloid neoplasms, the AML not otherwise specified, the myeloid sarcoma, the myeloid proliferations related to Down syndrome, and the blastic plasmacytoid dendritic cell neoplasm. A specific section is reserved for acute leukemias of ambiguous lineage.

Recently, a meta-analysis of 9 studies including 4,509 patients affected by AML was performed: the frequency of NPM1 mutations ranged from 7% to 56%. Nevertheless, all data confirmed the positive prognostic value of this mutation, with a double probability of achieving complete remission compared with NPM1 wild type and a significant advantage also on disease-free survival and overall survival [108].

In the subgroup of AML with recurrent genetic abnormalities, variant *RARA* translocations should be diagnosed as AML with the variant partner specifically designated [109]. For all other entities within the category of AML with recurrent genetic abnormalities, 20% or more blasts must be present

in the PB or BM to establish the diagnosis of AML [26, 105]. Although these leukemias are recognized as unique entities, it is important to realize that additional genetic abnormalities may coexist and influence their biologic and clinical behavior, including response to therapy and the overall survival. Studies of AML associated with the chromosomal rearrangements t(6;9)(p23;q34); *DEK*-NUP21, inv(3)(q21q26.2), or t(3; 3)(q21;q26,2); *RPN1-EVI1* and t(1;22)(p13;q13); and *RBM15-MKL1* have provided evidence that these genetic rearrangements, although uncommon, are associated with distinctive morphologic and clinical features that argue for their incorporation in the revised listing of AML with recurrent genetic abnormalities [110–112]. A more controversial issue is whether leukemia initially demonstrating a blastic myeloid proliferation associated with the Ph' chromosome or *BCR-ABL1* is a distinct and easily defined entity. Although *BCR-ABL1*-positive AML has been reported [113–115], criteria for its distinction from CML initially manifesting in a blast phase are not entirely convincing, and for this reason, *BCR-ABL1*-positive AML is not recognized in this classification. Many cases of *BCR-ABL1*-related acute leukemia will meet the criteria for ALL or mixed phenotype acute leukemia, provided that a blast phase of a previously unrecognized CML can be excluded. In addition to the newly listed leukemias associated with cytogenetically detectable rearrangements, AML with mutated *NPM1* or *CEBPA* have been added to the classification as "provisional entities." Mutated *FLT3* frequently accompanies other genetic lesions, and although it is not included as a defining criterion for any distinct entity in the revised WHO classification, the mutational status of *FLT3* should always be ascertained in AML, particularly in cytogenetically normal AML, because of its prognostic importance.

The **AML with myelodysplasia-related changes** is diagnosed when patients have 20% or more blasts in the PB or BM and (1) evolve from previously documented MDS or MDS/MPN, (2) have specific myelodysplasia-related cytogenetic abnormalities, or (3) exhibit dysplasia in 50% or more of the cells in two or more myeloid lineages [26].

The **therapy-related myeloid neoplasms** included t-AML/t-MDS and t-AML/t-MDS/MPN. Most patients who develop therapy-related myeloid neoplasms have received alkylating agents and/or radiation as well as topoisomerase II inhibitors. It has been argued that 90% of patients with therapy-related neoplasms have cytogenetic abnormalities identical to those observed in AML with myelodysplasia-related features or in AML with recurrent cytogenetic abnormalities; therefore, such cases would be more appropriately classified in those categories rather than in a separate, therapy-related category. However, the majority of patients with therapy-related myeloid neoplasms have a worse outcome than do their de novo counterparts with the same genetic abnormalities [3, 26, 116–120].

The group of **AML not otherwise specified** (AML NOS) encompasses those cases that do not fulfill the criteria for any of the other AML categories. The AML NOS will continue to diminish as more genetic subgroups are recognized.

The **myeloid sarcoma** is a pathologic diagnosis for an extramedullary proliferation of blasts of one or more of the myeloid lineages that disrupts the normal architecture of the tissue (any, particularly the skin, gastrointestinal tract, lymph nodes, and bone) in which it is found [121]. Most often, myeloid sarcoma is found concurrently in a patient with previously or recently recognized AML, but it may also precede the appearance of blood or bone marrow disease. In this latter case, the diagnosis of myeloid sarcoma should be considered as synonymous with AML, and the tumor should be evaluated for morphologic, phenotypic, and genetic features that would allow it to be classified further into one of the subgroups of AML. A myeloid sarcoma is evidence of relapse in a patient thought to be in remission of a previously diagnosed AML, is evidence of evolution to AML in a patient with a previously diagnosed MDS or MDS/MPN, and is blast transformation in a patient with MPN [26].

The **myeloid proliferations related to the Down syndrome**, which include transient abnormal myelopoiesis and myeloid leukemia, have unique morphologic, immunophenotypic, clinical, and molecular features, including *GATA1*

mutation, that justify their separation from other myeloid neoplasms [122–125].

The **blastic plasmacytoid dendritic cell neoplasm** recognizes virtually all cases of a tumor that is derived from precursors of a specialized subset of dendritic cells, plasmacytoid dendritic cells, and hence is a myeloid-related neoplasm. This subgroup includes most cases previously designated as "blastic natural killer cell leukemia/lymphoma" [26]. It is a clinically aggressive neoplasm that is usually characterized at its onset by solitary or multiple skin lesions, often with associated regional lymphadenopathy. Many cases will ultimately progress to involve the PB and BM as well. The blasts in such cases do not express myeloperoxidase or cases of AML with minimal differentiation that do not show any lymphoid-associated antigens [126–129].

Imaging for Diagnosis and Staging of AML

AML patients generally present with anemia (median hemoglobin 8 g/dL), thrombocytopenia (median platelet count 40–50 $\times$ 10^9/L), and leukocytosis (median white blood cell count 10–20 $\times$ 10^9/L). Most patients are neutropenic, and morphologic abnormalities (hypogranulation, nuclear hyperlobulation, Pelger-Huët anomaly) are often noted in the remaining neutrophils. Careful examination will detect blasts in most patients, although it can be difficult to distinguish among leukemia subtypes (or occasionally even to be confident of the diagnosis of acute leukemia) in patients with a low number of circulating blasts.

Initial symptoms are typically related to complications of pancytopenia including weakness, easy fatigability, infections of variable severity, or hemorrhagic findings, such as gingival bleeding, ecchymoses, epistaxis, or menorrhagia. Combinations of these symptoms are common. Occasionally patients present because of prominent extramedullary sites of leukemia usually related to either cutaneous or gingival infiltration by leukemia cells. Bone pain is infrequent in adults with AML, although some individuals describe sternal discomfort or tenderness, occasionally with aching in the long bones, particularly of the lower extremities. Most patients have had more subtle evidence of leukemia for weeks, to perhaps months, before diagnosis. The findings on physical examination are variable and generally nonspecific. If fever is present, it is almost always related to infection, and an infectious site must be vigorously sought and generally treated empirically with broad-spectrum antibiotics. Examination of the skin can reveal pallor. Infiltrative skin lesions are suggestive of leukemic involvement. Other coutaneous manifestations may be infection either primary or embolic, or, most commonly, petechiae or ecchymoses related to thrombocytopenia and/or coagulopathy. Examination of the fundus reveals hemorrhages and/or exudates in the majority of patients. Careful examination of the oropharynx and teeth is important because of the occasional occurrence of leukemia involvement and the value of applying effective dental prophylaxis, if time permits, prior to chemotherapy. Palpable adenopathy is uncommon; significant lymph node enlargement is rare as well as hepatomegaly and splenomegaly. None of these findings is diagnostic of acute leukemia, and the final diagnosis and categorization depends on appropriate evaluation of peripheral blood and bone marrow. Routine chemistry including liver and kidney parameters and coagulation profile, as well as blood group and HLA typing of patient and family members, are required as part of the initial work-up of AML. Radiological diagnostic examinations must include dental survey and chest/abdomen CT scan or chest X-ray and abdominal ultrasound [26].

Extramedullary disease in lymph nodes, the CNS, or soft tissue is observed particularly in case of relapse after allogeneic stem cell transplantation or bone marrow transplantation [130].

Due to the increasing value of PET/CT in solid tumors and hematological malignancies, interest has grown in AML. Data on [^{18}F]FDG in AML mainly concern extramedullary involvement, specially in recurrent disease [51, 52], and require further validation before its use in clinical practice. Promising results of [^{18}F]FDG-PET/CT have also been reported in the management of granulocytic sarcomas [131]. In AML another positron emitting radiopharmaceutical, 3′-^{18}F-fluoro-3′-deoxy-L-thymidine

(^{18}F-FLT) has been used to detect extramedullary sites of active disease [132] and for the early assessment of treatment response [133]. The rate of ^{18}F-FLT uptake into lesions is directly proportional to DNA. Published data show that ^{18}F-FLT uptake is significantly increased in patients with myelodysplastic syndromes and myeloproliferative neoplasias [134]. There is intense uptake of ^{18}F-FLT in bone marrow and spleen (Fig. 5), but extramedullary lesions may also be seen.

Response Evaluation and Follow-Up in AML

AML response to treatment is monitored with serial peripheral blood counts and repeated bone marrow examinations. To design the best regimen, the first bone marrow exam is performed at the day +30. Cytogenetic/molecular abnormalities detected at diagnosis and morphological/immunophenotypical response, patients should continue conventional chemotherapy or should be switched to a more intensive treatment, such as autologous or allogeneic transplantation. During intensive chemotherapy, bone marrow should be examined in the aplastic phase to monitor blast clearance, persistence, or early relapse. The usual criteria of response are blast clearance in the bone marrow to <5% of all nucleated cells, a recovered normal hematopoiesis, and return of the peripheral blood cell count to normal levels. Although sensitive PCR methods as well as immunophenotyping are available, permitting molecular follow-up and detection of minimal residual disease in patients with suitable markers (mostly

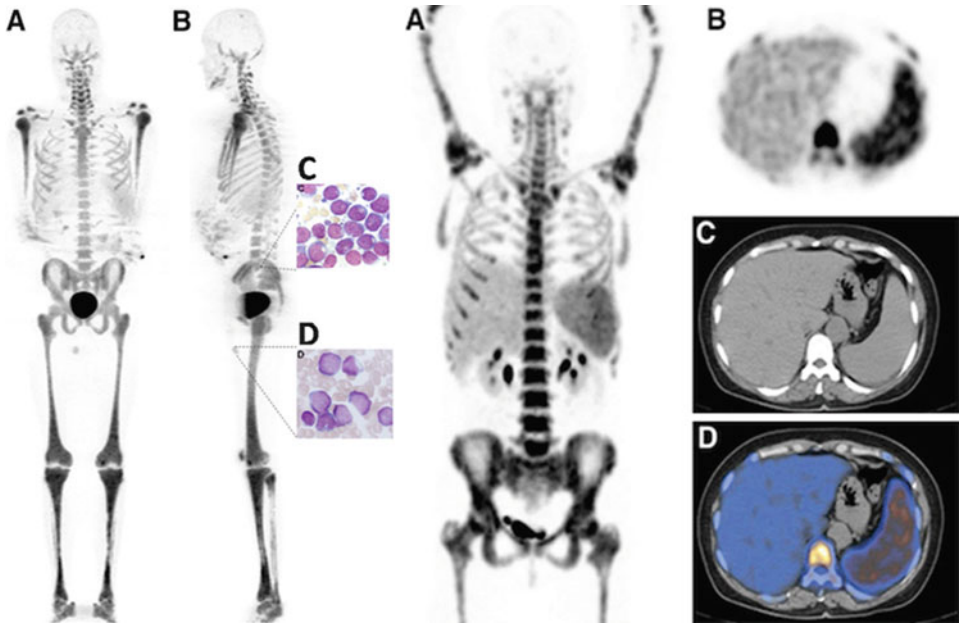

Fig. 5 In vivo biodistribution of ^{18}F-FLT in patient with refractory AML 60 min after injection of radiotracer (whole-body MIP (**a**) and (**b**) *right panel*). Intense uptake of the radiopharmaceutical is evident in hematopoietic bone marrow of central bones and extensive bone marrow expansion with intense tracer uptake. Tracer uptake is absent from bones not containing hematopoietic marrow (forearms and skull). Scans also indicate intense focal extramedullary ^{18}F-FLT uptake in projection of right testicle. Hematoxylin staining of peripheral blood demonstrating 99% leukemic blasts (**c**) and biopsy verification of testicular leukemia manifestation (**d**). ^{18}F-FLT PET demonstrate intense tracer uptake in bone marrow and spleen as typical in patient with initial diagnosis of AML. MIP (**a** *left panel*) and transaxial section of PET (**b**), CT (**c**), and fused images PET/CT (**d**). Other organs are normal, as observed in controls

specific chromosomal translocations or typical antigen expression profiles, respectively), the early detection of molecular relapse in the absence of morphological evidence for recurrent AML is of uncertain therapeutic consequence. Specifically, evidence that early re-induction treatment of such patients still in hematological remission would be of any benefit is lacking [105].

Chronic Myeloid Leukemia (CML)

In 2016, the estimated number of new cases of CML is about 8,200, accounting for 0.5% of all new cases of cancer. The number of new cases of AML was 1.8 per 100,000 per year based on 2009–2013 cases according to the SEER database [1].

CML is a clonal myeloproliferative disorder of a pluripotent stem cell [135] with a specific cytogenetic abnormality, the Philadelphia chromosome that identifies the chromosome (22q-) resulting from the balanced translocation between the long arm of chromosome 9 and 22.

In the great majority of patients, a causative factor cannot be identified. Nevertheless, it is well known that ionizing radiations are leukemogenic, although the most common type of leukemia following radiations is AML [136]. The median age of onset of CML is 64 years; the peak incidence occurs during the ages of 65–74 years [1]. The first phase of the disease, the chronic phase, could terminate, trough an accelerated phase, in acute leukemia (blastic phase), characterized by a short survival [137].

The translocation of the ABL1 gene from chromosome 9–22 t(9;22)(q3.4;q1.1) leads to the formation of a new, hybrid, fusion gene (BCR-ABL1) that codes for an oncoprotein (P210, more rarely P190 or P230) that is located in the cytoplasm and has a strong, constitutively activated tyrosine kinase activity, resulting in the activation of several downstream signals that transform hematopoietic stem cells [138]. Cells carrying the BCR-ABL1 gene show an abnormal interaction with the actin and the stroma, an increased proliferation, and a reduced apoptosis rate due to the activation of the RAS/ERK and PI3K/AKT pathways [139].

Moreover, BCR-ABL-positive cells are genetically unstable and are prone to develop multiple and heterogeneous genomic abnormalities, resulting in the transformation of the leukemic phenotype from chronic to acute, hence leading to the progression from chronic to accelerated and blastic phase [140]. One important event associated with progression is the development of point mutations in the kinase domain (KD) of the ABL1 gene, leading to resistance to the tyrosine kinase inhibitors (TKI), such as imatinib, dasatinib, nilotinib, and bosutinib [141, 142]. Ponatinib is the unique TKI able to bypass the gatekeeper mutation T315I, except in the cases when it is associated with other ABL1 mutations (compound mutations) [143, 144]. BM biopsies taken from untreated patients at diagnosis show increased cellularity due to proliferation of the granulocytic series that turns in different stages of maturation, although myelocytes and segmented forms predominate [26]. No substantial features of dysplasia are found. Eosinophils may be prominent. Blasts must account for $<5\%$ of the whole examined population. Megakaryocytes are smaller than normal with hypolobulated nuclei. Although their number may be normal or slightly decreased, in about 50% of cases there is a moderate to extensive megakaryocytic proliferation. Moderate to marked reticulin fibrosis is encountered in 30% of cases. Pseudo-Gaucher cells and sea-blue histiocytes are usually observed. Notably, the BM picture undergoes important changes (e.g., reduction of the granulocytic cellularity, normalization of megakaryopoiesis, regression of fibrosis, and increase in apoptosis associated with decrease in proliferative activity), particularly following long-term treatment with TKIs [145].

According to the European Leukemia Net guidelines [146], CML patients have to be carefully monitored by cytogenetic and molecular tests: the achievement of a BCR-ABL1/ABL1 ratio lower than 10% at 3 months of therapy (early molecular response), of 1% at 6 months, and of 0.1% at 12 months (MR3) and the achievement of the complete cytogenetic response at 12 months in the absence of additional chromosome abnormalities characterize the optimal responder subject. On the contrary, cases with a BCR-ABL1/ABL1 ratio

higher than 10% at 6 months or 1% at 12 months are categorized as failed patients and so for a different treatment. Nevertheless, TKIs allowed prolong long-term survival up to 90%.

The recognition of disease progression from CP to BP is relevant for prognosis and treatment.

Many studies tempted to characterize the genomic alteration characterizing the transition to the blastic phase: the myeloid one is characterized by the TP53, WT1, RAS, NPM1, IDH1/2, and RB1 mutations, while the lymphoblastic transformation shows acquired mutations of IKZF1, IDH1/2, and CDKN2A [143].

Nevertheless, it is important to remember that the probability of developing a blastic phase is about 6% with imatinib and 2% with nilotinib [147].

Imaging for Diagnosis and Staging of CML

CML symptoms are not specific, including weight loss, asthenia, small fever, sweats, and malaise, and are not frequent, since in more than 40% of cases, the diagnosis is fortuitous, being based on abnormal blood counts. In most cases, diagnosis is based on blood counts (leukocytosis and frequently also thrombocytosis) and differential (immature granulocytes, from the metamyelocytes to the myeloblasts, and basophilia). Splenomegaly is present in half of the cases in the initial chronic phase, but the majority of these patients are asymptomatic [145]. Symptoms and signs usually develop insidiously and include fatigue, anemia, progressive splenomegaly, and leukocytosis. In the chronic phase, the white blood cell count approximates $2{,}000 \times 10^9$/L. The myeloid cells in the peripheral blood show all stages of differentiation, but the myelocytes predominate. More than half of the patients have platelet counts above $1{,}000 \times 10^9$/L, but thrombotic phenomena are unusual. A slight degree of anemia is common. The striking biochemical abnormality in CML is the reduction of leukocyte alkaline phosphatase activity, both in intensity and in the number of neutrophil band forms that stain positively for the enzyme. As the disease evolves, varying degrees of fibrosis occur [148]. Clinically, the most reliable finding is the presence in the peripheral blood, bone marrow, or both of myeloblasts and promyelocytes exceeding 30% of the differential distribution (70% of the cases) [149]. In the absence of frank blast crisis, other criteria include the development of fever of undetermined origin, increasing splenomegaly, a rising white blood cell count, basophilia, an increasing degree of anemia, and thrombocytopenia and refractoriness to previously effective therapy. High blast cell counts may lead to pulmonary and/or cerebral leukostasis and hemorrhage. The median survival after blastic transformation is approximately 3–6 months.

Currently, no imaging modalities are used for CML diagnosis or staging. [^{18}F]FDG-PET in the chronic phase of CML has diffuse increased uptake in the bone marrow [150]. The appearance of [^{18}F]FDG is very similar to the hematopoietic cytokine-mediated [^{18}F]FDG bone marrow uptake [151]. When patients with CML are evaluated under treatment or after cessation of treatment, reduced FDG uptake has been observed in the bone marrow. [^{18}F]FDG-PET/CT may be useful for the diagnosis of granulocytic sarcomas, rare extramedullary manifestations of myeloid (or lymphoblastic leukemia) that may develop anywhere, but most commonly arise in the skull, orbits, and sinuses [152]. Preclinical studies suggested a potential role of [^{18}F]FLT as quantitative and semiquantitative uptake measurement for metabolic imaging [153].

Many prognostic scoring systems have been proposed, including the Sokal [154], the Euro [155], and the EUTOS [156] scores. The first and the second have been developed in the interferon era, based on age and on the percentage of circulating blasts, basophils, and eosinophils and of spleen size weighted as continuous variables. The EUTOS has been proposed after the introduction of imatinib and is based on the spleen dimensions and the basophil count. These risk scores distinguish among three categories the Sokal and Euro and between two categories the EUTOS risk score. The introduction in the clinical practice of the second-generation TKIs reduced the impact of the risk categories on survival. These prognostic classifications are important

because case selection and the results of interferon treatment may influence the presumed therapeutic effect of interferon or other forms of nontransplant treatment.

Imaging for Monitoring Treatment of CML

In CML, responses are classified as hematological (complete if the spleen dimension and blood count is normal), cytogenetic (complete if Ph' metaphases are absent), and molecular. The molecular responses are defined as logarithmic reduction of BCR-ABL1/ABL1 ratio in respect of 100% of diagnosis. MR3 (0.1%) is now considered the goal of treatment at 12 months; nevertheless, today the major attention has been taken to the deep molecular response (4, 4.5, 5 logarithms reduction); indeed, patients treated for more than 5 years with imatinib and with a deep molecular response lasting more than 2 years have a 50% likelihood of remaning in remission after TKI discontinuation [157, 158]. More rapid and deeper molecular responses can be achieved by second-generation TKIs used as first line of treatment [159, 160].

No imaging techniques exist that would be used as surrogate for the molecular response categorization.

Monitoring is essential for treatment optimization and for a cost-effective outcome: at the beginning and during the first 3 months, biochemical and hematological monitoring is recommended every 2 weeks, to ensure the compliance of the patient and exclude relevant toxicities. From the third month on, cytogenetics is recommended every 6 months until the confirmed complete cytogenetic response, and quantitative PCR is recommended every 3–6 months. Screening for ABL1 mutations is recommended only in the case of failure or suboptimal response; ultra-deep sequencing techniques significantly increased the possibility of detecting mutations in cases resulting unmutated after conventional sequencing. This item is clinically relevant because some mutations are TKI specific and induce to change the drug.

As reported at diagnosis, also in the monitoring of responses, no role for imaging modalities is recognized by the current ESMO Clinical Practice Guidelines [145].

References

1. Surveillance Research Program, National Cancer Institute. Cancer stat fact sheets [Internet]. Cancer Stat.Surveill Res Program, Natl Cancer Inst.2016. Available from: http://seer.cancer.gov/statfacts
2. Vardiman JW, Harris NL, Brunning RD. The World Health Organization (WHO) classification of the myeloid neoplasms. Blood. 2002;100(7):2292–302.
3. Arber DA, Orazi A, Hasserjian R, Thiele J, Borowitz MJ, Le Beau MM, et al. The 2016 revision to the World Health Organization (WHO) classification of myeloid neoplasms and acute leukemia. Blood. 2016;127(20):2391–405.
4. Swerdlow SH, Campo E, Pileri SA, Harris NL, Stein H, Siebert R, et al. The 2016 revision of the World Health Organization (WHO) classification of lymphoid neoplasms. Blood. 2016;127(20):2375–90.
5. Inaba H, Greaves M, Mullighan CG. Acute lymphoblastic leukaemia. Lancet. 2013;381(9881):1943–55.
6. Pulte D, Gondos A, Brenner H. Improvement in survival in younger patients with acute lymphoblastic leukemia from the 1980s to the early 21st century. Blood. 2009;113:1408–11.
7. Al Ustwani O, Gupta N, Bakhribah H, Griffiths E, Wang E, Wetzler M. Clinical updates in adult acute lymphoblastic leukemia. Crit Rev Oncol Hematol. 2016;99:189–99.
8. Moorman AV, Harrison CJ, Buck GAN, Richards SM, Lorna M, Martineau M, et al. Karyotype is an independent prognostic factor in adult acute lymphoblastic leukemia (ALL): analysis of cytogenetic data from patients treated on the Medical Research Council (MRC) Karyotype is an independent prognostic factor in adult acute lymphoblast. Blood. 2007;109:3189–97.
9. Belkov VM, Krynetski EY, Schuetz JD, Yanishevski Y, Masson E, Mathew S, et al. Reduced folate carrier expression in acute lymphoblastic leukemia: a mechanism for ploidy but not lineage differences in methotrexate accumulation. Blood. 1999;93:1643–50.
10. Rocha JC, Cheng C, Liu W, Kishi S, Das S, Cook EH, et al. Pharmacogenetics of outcome in children with acute lymphoblastic leukemia. Blood. 2005;105:4752–8.
11. Mohlbacher V, Zenger M, Schnittger S, Weissmann S, Kunze F, Kohlmann A, et al. Acute lymphoblastic leukemia with low hypodiploid/near triploid karyotype is a specific clinical entity and exhibits a very high TP53 mutation frequency of 93%. Genes Chromosom Cancer. 2014;53:524–36.

12. Stock W. Adolescents and young adults with acute lymphoblastic leukemia. Hematology. 2010;2010:21–9.
13. Moorman AV, Chilton L, Wilkinson J, Ensor HM, Bown N, Proctor SJ. A population-based cytogenetic study of adults with acute lymphoblastic leukemia. Cytogenetics. 2010;115:206–14.
14. Gokbuget N, Hoelzer D. Treatment of adult acute lymphoblastic leukemia. Hematology Am Soc Hematol Educ Program. 2006;2006(1):133–41.
15. Lee HJ, Thompson JE, Wang ES, Wetzler M. Philadelphia chromosome-positive acute lymphoblastic leukemia. Cancer. 2011;117:1583–94.
16. Roberts KG, Li Y, Payne-Turner D, Harvey RC, Yang Y-L, Pei D, et al. Targetable kinase-activating lesions in Ph-like acute lymphoblastic leukemia. N Engl J Med. 2014;371:1005–15.
17. Schnapp LM. Another notch on the belt. Blood. 2009;113:1615–6.
18. Dail M, Wong J, Lawrence J, O'Connor D, Nakitandwe J, Chen S-C, et al. Loss of oncogenic Notch1 with resistance to a PI3K inhibitor in T-cell leukaemia. Nature. 2014;513:512–6.
19. Knoechel B, Roderick JE, Williamson KE, Zhu J, Lohr JG, Cotton MJ, et al. An epigenetic mechanism of resistance to targeted therapy in T cell acute lymphoblastic leukemia. Nat Genet. 2014; 46:364–70.
20. Vilimas T, Mascarenhas J, Palomero T, Mandal M, Buonamici S, Meng F, et al. Targeting the NF-kappaB signaling pathway in Notch1-induced T-cell leukemia. Nat Med. 2007;13:70–7.
21. Garcia-Manero G, Yang H, Kuang S-Q, O'Brien S, Thomas D, Kantarjian H. Epigenetics of acute lymphocytic leukemia. Semin Hematol. 2009;46: 24–32.
22. Burke MJ, Lamba JK, Pounds S, Cao X, Ghodke-Puranik Y, Lindgren BR, et al. A therapeutic trial of decitabine and vorinostat in combination with chemotherapy for relapsed/refractory acute lymphoblastic leukemia. Am J Hematol. 2014;89:889–95.
23. Roman-Gomez J, Jimenez-Velasco A, Barrios M, Prosper F, Heiniger A, Torres A, et al. Poor prognosis in acute lymphoblastic leukemia may relate to promoter hypermethylation of cancer-related genes. Leuk Lymphoma. 2007;48:1269–82.
24. Maude S, Tasian S, Vincent T, Hall J, Sheen C, Roberts K, et al. Targeting JAK1 / 2 and mTOR in murine xenograft models of Ph-like acute lymphoblastic leukemia. Blood. 2012;120:3510–8.
25. Rabin K, Mason C, Gurusiddappa S, Eastwood Leung H, Morrison D, Bhojwani D, et al. IKZF1 and 22q11 . 22 deletions and PDGFRA gains are associated with poor outcome in down syndrome acute lymphoblastic leukemia. Blood. 2012;120:289.
26. Vardiman JW, Thiele J, Arber DA, Brunning RD, Borowitz MJ, Porwit A, et al. The 2008 revision of the World Health Organization (WHO) classification of myeloid neoplasms and acute leukemia: rationale and important changes. Blood. 2009;114:937–51.
27. Chiaretti S, Zini G, Bassan R. Diagnosis and subclassification of acute lymphoblastic leukemia. Mediterr J Hematol Infect Dis. 2014;6:6–7.
28. Hoelzer D, Bassan R, Dombret H, Fielding A, Ribera JM, Buske C. Acute lymphoblastic leukaemia in adult patients: ESMO Clinical Practice Guidelines for diagnosis, treatment and follow-up. Ann Oncol. 2016; 00:1–14.
29. Bene MC, Castoldi G, Knapp W, Ludwig WD, Matutes E, Orfao A, et al. Proposals for the immunological classification of acute leukemias. European Group for the Immunological Characterization of Leukemias (EGIL). Leuk Off J Leuk Soc Am Leuk Res Fund UK. 1995;9:1783–6.
30. Béné MC, Nebe T, Bettelheim P, Buldini B, Bumbea H, Kern W, et al. Immunophenotyping of acute leukemia and lymphoproliferative disorders: a consensus proposal of the European LeukemiaNet work package 10. Leukemia. 2011;25:567–74.
31. Matutes E, Pickl WF, Van Veer M, Morilla R, Swansbury J, Strobl H, et al. Mixed-phenotype acute leukemia: clinical and laboratory features and outcome in 100 patients defined according to the WHO 2008 classification. Blood. 2011;117:3163–71.
32. van Dongen JJ, Lhermitte L, Böttcher S, Almeida J, van der Velden VH, Rawstron A. EuroFlow antibody panels for standardized n-dimensional flow cytometric immunophenotyping of normal, reactive and malignant leukocytes. Leukemia. 2012;26:1908–75.
33. Gleißner B, Gökbuget N, Bartram CR, Janssen B, Rieder H, Janssen JWG, et al. Leading prognostic relevance of the BCR-ABL translocation in adult acute B-lineage lymphoblastic leukemia: a prospective study of the German Multicenter Trial Group and confirmed polymerase chain reaction analysis. Blood. 2002;99:1536–43.
34. Brüggemann M, Raff T, Kneba M, Dc W, Bru M, Raff T, et al. Has MRD monitoring superseded other prognostic factors in adult ALL? Blood. 2012;120: 4470–81.
35. Faderl S, O'brien S, Pui C, Stock W, Wetzler M, Hoelzer D, Kantarjian H. Adult acute lymphoblastic leukemia: concepts and strategies. Cancer. 2010;116: 1165–76.
36. Cortes J. Central nervous system involvement in adult acute lymphoblastic leukemia. Hematology. 2008;13: 293–302.
37. Ye CC, Echeverri C, Anderson JE, Smith JL, Glassman A, Gulley ML, et al. T-cell blast crisis of chronic myelogenous leukemia manifesting as a large mediastinal tumor. Hum Pathol. 2002;33:770–3.
38. Jaing TH, Hsueh C, Chiu CH, Shih IH, Chan CK, Hung IJ. Cutaneous lymphocytic vasculitis as the presenting feature of acute lymphoblastic leukemia. J Pediatr Hematol Oncol. 2002;24:555–7.
39. Mayo GL, Carter JE, McKinnon SJ. Bilateral optic disk edema and blindness as initial presentation of acute lymphocytic leukemia. Am J Ophthalmol. 2002;134:141–2.

40. Fenaux P, Bourhis JH. Burkitt's Acute Lymphocytic Leukemia (L3ALL) in adults. Hematol Clin. 2001;15:37–50.
41. Shibata K, Shimamoto Y, Watanabe M, Kikuchi M, Yamaguchi M. Two cases of acute lymphocytic leukaemia associated with bone marrow necrosis–a brief review of recent literature. Eur J Haematol. 1994;52: 115–6.
42. © 2010 MedSolutions Inc. Pediatric and Congenital Imaging Guidelines Oncology and PET. 2010.
43. Soni PN. Hypercalcaemia and multiple osteolytic lesions in childhood acute lymphoblastic leukaemia. Postgrad Med J. 1993;69:483–5.
44. Shalaby-Rana E, Majd M. Scintigraphic findings in children with leukemia : value of early and delayed whole-body imaging. J Nucl Med. 2001;42:878–83.
45. Hann IM, Evans DI, Palmer MK, Morris-Jones PJ, Haworth C. The prognostic significance of morphological features in childhood acute lymphoblastic leukaemia. Clin Lab Haematol. 1979;1:215–26.
46. Araki T. Leukemic involvement of the kidney in children : CT features. J Comput Assist Tomogr. 1982; 6:781–4.
47. Lin P, Chang T, Jang R, Chiou S. Hepatosplenic microabscesses in pediatric leukemia : a report of five cases. Kaohsiung J Med Sci. 2003;19:368–74.
48. Hilmes MA, Dillman JR, Mody RJ, Strouse PJ. Pediatric renal leukemia: spectrum of CT imaging findings. Pediatr Radiol. 2008;38:424–30.
49. Porto L, Kieslich M, Schwabe D, Zanella FE, Lanfermann H. Central nervous system imaging in childhood leukaemia. Eur J Cancer. 2004;40:2082–90.
50. Kayahan Ulu EM, Töre HG, Bayrak A, Güngör D, Coşkun M. MRI of central nervous system abnormalities in childhood leukemia. Diagn Interv Radiol. 2009;15:86–92.
51. Cunningham I, Kohno B. ^{18}FDG-PET/CT: 21st century approach to leukemic tumors in 124 cases. Am J Hematol. 2016;91:379–84.
52. Zhou WL, Wu HB, Wang LJ, Tian Y, Dong Y, Wang QS. Usefulness and pitfalls of F-18-FDG PET/CT for diagnosing extramedullary acute leukemia. Eur J Radiol. 2016;85:205–10.
53. Shuper A, Stark B, Kornreich L, Cohen IJ, Avrahami G, Yaniv I. Methotrexate-related neurotoxicity in the treatment of childhood acute lymphoblastic leukemia. Isr Med Assoc J. 2002;4:1050–3.
54. Lutz K, von Komorowski G, Dürken M, Engelhardt R, Dinter DJ. Myocardial iron overload in transfusion-dependent pediatric patients with acute leukemia. Pediatr Blood Cancer. 2008;51:691–3.
55. Eichhorst B, Robak T, Montserrat E, Ghia P, Hillmen P, Hallek M, et al. Chronic lymphocytic leukaemia: ESMO Clinical Practice Guidelines for diagnosis, treatment and follow-up. Ann Oncol. 2015;26:v78–84.
56. Hallek M, Cheson BD, Catovsky D, Caligaris-Cappio F, Dighiero G, Dohner H, et al. Guidelines for the diagnosis and treatment of chronic lymphocytic leukemia: a report from the International Workshop on Chronic Lymphocytic Leukemia updating the National Cancer Institute-Working Group 1996 guidelines. Blood. 2008; 111:5446–56.
57. Rawstron AC, Bennett FL, O'Connor SJ, Kwok M, Fenton JA, Plummer M, et al. Monoclonal B-cell lymphocytosis and chronic lymphocytic leukemia. N Engl J Med. 2008;359:575–83.
58. Messmer BT, Albesiano E, Efremov DG, Ghiotto F, Allen SL, Kolitz J, et al. Multiple distinct sets of stereotyped antigen receptors indicate a role for antigen in promoting chronic lymphocytic leukemia. J Exp Med. 2004;200:519–25.
59. Caligaris-Cappio F, Hamblin TJ. B-cell chronic lymphocytic leukemia: a bird of a different feather. J Clin Oncol. 1999;17:399–408.
60. Kröber A, Seiler T, Benner A, Bullinger L, Brückle E, Lichter P, et al. V(H) mutation status, CD38 expression level, genomic aberrations, and survival in chronic lymphocytic leukemia. Blood. 2002;100:1410–6.
61. Rai KR, Sawitsky A, Cronkite E, Chanana A, Levy R, Pasternack B. Clinical staging of chronic lymphocytic leukemia. Blood. 1975;46:219–34.
62. Binet J, Auquier A, Dighiero G, Chastang C, Piguet H, Goasguen J, et al. A new prognostic classification of chronic lymphocytic leukemia derived from a multivariate survival analysis. Cancer. 1981;48:198–206.
63. Oppezzo P, Dumas G, Lalanne AI, Payelle-brogard B, Magnac C, Dighiero G, et al. Different isoforms of BSAP regulate expression of AID in normal and chronic lymphocytic leukemia B cells Different isoforms of BSAP regulate expression of AID in normal and chronic lymphocytic leukemia B cells. Blood. 2005;105:2495–503.
64. Fulci V, Chiaretti S, Goldoni M, Azzalin G, Carucci N, Tavolaro S, et al. Quantitative technologies establish a novel microRNA profile. Blood. 2007;109:4944–51.
65. Deaglio S, Vaisitti T, Bergui L, Bonello L, Horenstein AL, Tamagnone L, et al. CD38 and CD100 lead a network of surface receptors relaying positive signals for B-CLL growth and survival. Blood. 2005;105: 3042–50.
66. Baliakas P, Hadzidimitriou A, Sutton L, Rossi D, Minga E, Villamor N, et al. Recurrent mutations refine prognosis in chronic lymphocytic leukemia. Leukemia. 2015;29:329–36.
67. Oscier D, Fegan C, Hillmen P, Illdge T, Johnson S, Maguire P, et al. Guidelines on the diagnosis and management of chronic lymphocytic leukaemia. Br J Haematol. 2004;125:294–317.
68. Muntanola A, Bosch F, Arguis P, Arellano-Rodrigo E, Ayuso C, Giné E, et al. Abdominal computed tomography predicts progression in patients with Rai stage 0 chronic lymphocytic leukemia. J Clin Oncol. 2007; 25:1576–80.
69. Swords R, Bruzzi J, Giles F. Recent advances in the diagnosis and therapy of Richter's syndrome. Med Oncol. 2007;24:17–32.

70. Michallet A-S, Sesques P, Rabe KG, Itti E, Tordot J, Tychyj-Pinel C, et al. An ^{18}F-FDG-PET maximum standardized uptake value >10 represents a novel valid marker for discerning Richter's syndrome. Leuk Lymphoma. 2016;57:1474–7.
71. Mauro FR, Chauvie S, Paoloni F, Biggi A, Cimino G, Rago A, et al. Diagnostic and prognostic role of PET/CT in patients with chronic lymphocytic leukemia and progressive disease. Leukemia. 2015;29: 1360–5.
72. Moreton P, Kennedy B, Lucas G, Leach M, Rassam SMB, Haynes A, et al. Eradication of minimal residual disease in B-cell chronic lymphocytic leukemia after alemtuzumab therapy is associated with prolonged survival. J Clin Oncol. 2005;23:2971–9.
73. Böttcher S, Ritgen M, Fischer K, Stilgenbauer S, Busch RM, Fingerle-Rowson G, et al. Minimal residual disease quantification is an independent predictor of progression-free and overall survival in chronic lymphocytic leukemia: a multivariate analysis from the randomized GCLLSG CLL8 trial. J Clin Oncol. 2012;30:980–8.
74. Vela CM, McBride A, Jaglowski SM, Andritsos LA. Ibrutinib for treatment of chronic lymphocytic leukemia. Am J Health Syst Pharm. 2016;73:367–75.
75. Robak P, Smolewski P, Robak T. Emerging immunological drugs for chronic lymphocytic leukemia. Expert Opin Emerg Drugs. 2015;20(3):423–47.
76. Jain N, O'Brien S. Initial treatment of CLL: integrating biology and functional status. Blood. 2015;126:463–70.
77. Thompson PA, Wierda WG. Eliminating minimal residual disease as a therapeutic end point: working toward cure for patients with CLL. Blood. 2016;127: 279–86.
78. Robak T, Matutes E, Catovsky D, Zinzani PL, Buske C. Hairy cell leukaemia: ESMO clinical practice guidelines for diagnosis, treatment and follow-up. Ann Oncol. 2015;26:v100–7.
79. Ferlay J, Steliarova-Foucher E, Lortet-Tieulent J, Rosso S, Coebergh JWW, Comber H, et al. Cancer incidence and mortality patterns in Europe: estimates for 40 countries in 2012. Eur J Cancer. 2013;49:1374–403.
80. Grever M, Blachly J, Andritsos L. Hairy cell leukemia: update on molecular profiling and therapeutic advances. Blood Rev. 2014;28:197–203.
81. Del Giudice I, Matutes E, Morilla R, Morilla A, Owusu-Ankomah K, Rafiq F, et al. The diagnostic value of CD123 in B-cell disorders with hairy or villous lymphocytes. Haematologica. 2004;89:303–8.
82. Matutes E. Immunophenotyping and differential diagnosis of hairy cell leukaemia. Hematol Oncol Clin North Am. 2006;20:1051–63.
83. Pillai V, Pozdnyakova O, Charest K, Li B, Shahsafaei A, Dorfman DM. CD200 flow cytometric assessment and semiquantitative immunohistochemical staining distinguishes hairy cell leukemia from hairy cell leukemia-variant and other B-cell lymphoproliferative disorders. Am J Clin Pathol. 2013;140:536–43.
84. Andrulis M, Penzel R, Weichert W, Von Deimling A, Capper D. Application of a BRAF V600E mutation-specific antibody for the diagnosis of hairy cell leukemia. Am J Surg Pathol. 2012;36:1796–800.
85. Ahmadzadeh A, Shahrabi S, Jaseb K, Norozi F, Shahjahani M, Vosoughi T, et al. BRAF mutation in hairy cell leukemia. Oncol Rev. 2014;8:22–5.
86. Tiacci E, Trifonov V, Schiavoni G, Holmes A, Kern W, Martelli M, et al. BRAF mutations in hairy-cell leukemia. N Engl J Med. 2011;364:1–2305–15.
87. Dietrich S, Pircher A, Endris V, Peyrade F, Wendtner C-M, Follows GA, et al. BRAF inhibition in hairy cell leukemia with low dose vemurafenib. Blood. 2016; 127(23):2847–55.
88. Hockley SL, Giannouli S, Morilla A, Wotherspoon A, Morgan GJ, Matutes E, et al. Insight into the molecular pathogenesis of hairy cell leukaemia, hairy cell leukaemia variant and splenic marginal zone lymphoma, provided by the analysis of their IGH rearrangements and somatic hypermutation patterns. Br J Haematol. 2010;148:666–9.
89. Forconi F, Sozzi E, Cencini E, Zaja F, Intermesoli T, Stelitano C, et al. Hairy cell leukemias with unmutated IGHV genes define the minor subset refractory to single-agent cladribine and with more aggressive behavior. Blood. 2009;114:4696–702.
90. Arons E, Suntum T, Stetler-stevenson M, Kreitman RJ, Dc W. VH4–34+ hairy cell leukemia, a new variant with poor prognosis despite standard therapy. Blood. 2009;114:4687–95.
91. Hockley SL, Else M, Morilla A, Wotherspoon A, Dearden C, Catovsky D, et al. The prognostic impact of clinical and molecular features in hairy cell leukaemia variant and splenic marginal zone lymphoma. Br J Haematol. 2012;158:347–54.
92. Mercieca J, Puga M, Matutes E, Moskovic E, Salim S, Catovsky D. Incidence and significance of abdominal lymphadenopathy in hairy cell leukaemia. Leuk Lymphoma. 1994;14 Suppl 1:79–83.
93. Janik JE. Tumor markers in hairy cell leukemia. Leuk Lymphoma. 2011;52 Suppl 2:69–71.
94. Hisada M, Chen BE, Jaffe ES, Travis LB. Second cancer incidence and cause-specific mortality among 3104 patients with hairy cell leukemia: a population-based study. J Natl Cancer Inst. 2007;99:215–22.
95. Cornet E, Tomowiak C, Tanguy-Schmidt A, Lepretre S, Dupuis J, Feugier P, et al. Long-term follow-up and second malignancies in 487 patients with hairy cell leukaemia. Br J Haematol. 2014;166:390–400.
96. Steven B, Collins J. The HL-60 promyelocytic leukemia cell line: proliferation, differentiation, and cellular oncogene expression. Blood. 1987;5:3311197.
97. Look AT, Look AT. Oncogenic transcription factors in the human acute leukemias. Science (80-). 1997;278: 1059–64.
98. Crane MM, Keating MJ, Trujillo JM, Labarthe DR, Frankowski RF. Environmental exposures in cytogenetically defined subsets of acute nonlymphocytic leukemia. JAMA. 1989;262:634–9.

99. Stagnaro E, Ramazzotti V, Crosignani P, Fontana A, Masala G, Miligi L, et al. Smoking and hematolymphopoietic malignancies. Cancer Causes Control. 2001;12:325–34.
100. Ahlbom A. A review of the epidemiologic literature about magnetic field and cancer. Scand J Work Environ Heal. 1988;14:337–43.
101. Goldstein BD. Benzene as a cause of lymphoproliferative disorders. Chem Biol Interact. 2010;184: 147–50.
102. Wong O, Raabe GK. Critical review of cancer epidemiology in petroleum industry employees, with a quantitative meta-analysis by cancer site. Am J Ind Med. 1989;15:283–310.
103. Bloom GE, Warner S, Gerald PS, Diamond LK. Chromosome abnormalities in constitutional aplastic anemia. N Engl J Med. 1966;274:8–14.
104. Head DR. Revised classification of acute myeloid leukemia. Leukemia. 1996;10:1826–31.
105. Fey MF, Buske C. Acute myeloblastic leukaemias in adult patients: ESMO clinical practice guidelines for diagnosis, treatment and follow-up. Ann Oncol. 2013;24 Suppl 6:vi138–43.
106. Kibbelaar RE, Mulder JW, Dreef EJ, van Kamp H, Fibbe WE, Wessels JW, et al. Detection of monosomy 7 and trisomy 8 in myeloid neoplasia: a comparison of banding and fluorescence in situ hybridization. Blood. 1993;82:904–13.
107. Bennett JM, Catovsky D, Daniel MT, Flandrin G, Galton DA, Gralnick HR, et al. Proposals for the classification of the acute leukaemias. French-American-British (FAB) co-operative group. Br J Haematol. 1976;33:451–8.
108. Liu Y, He P, Liu F, Shi L, Zhu H, Zhao J, et al. Prognostic significance of NPM1 mutations in acute myeloid leukemia: a meta-analysis. Mol Clin Oncol. 2014;2:275–81.
109. Zelent A, Guidez F, Melnick A, Waxman S, Licht JD. Translocations of the RARalpha gene in acute promyelocytic leukemia. Oncogene. 2001;20: 7186–203.
110. Bitter MA, Neilly ME, Le Beau MM, Pearson MG, Rowley JD. Rearrangements of chromosome 3 involving bands 3q21 and 3q26 are associated with normal or elevated platelet counts in acute nonlymphocytic leukemia. Blood. 1985;66:1362–70.
111. Secker-Walker LM, Mehta A, Bain B. Abnormalities of 3q21 and 3q26 in myeloid malignancy: a United Kingdom Cancer Cytogenetic Group study. Br J Haematol. 1995;91:490–501.
112. Pearson M, Vardiman J, Le Beau M, Rowley J, Schwartz S, Kerman S, et al. Increased numbers of marrow basophils may be associated with a t(6;9) in ANLL. Am J Hematol. 1985;18:393–403.
113. Soupir CP, Vergilio JA, Dal Cin P, Muzikansky A, Kantarjian H, Jones D, et al. Philadelphia chromosome-positive acute myeloid leukemia: a rare aggressive leukemia with clinicopathologic features distinct from chronic myeloid leukemia in myeloid blast crisis. Am J Clin Pathol. 2007;127:642–50.
114. Keung Y, Beaty M, Powell BL, Molnar I, Buss D, Pettenati M. Philadelphia chromosome positive myelodysplastic syndrome and acute myeloid leukemia-retrospective study and review of literature. Leuk Res. 2004;28:579–86.
115. Paietta E, Racevskis J, Bennett JM, Neuberg D, Cassileth PA, Rowe JM, et al. Biologic heterogeneity in Philadelphia chromosome-positive acute leukemia with myeloid morphology: the Eastern Cooperative Oncology Group experience. Leukemia. 1998;12: 1881–5.
116. Smith SM, Le Beau MM, Huo D, Karrison T, Sobecks RM, Anastasi J, et al. Clinical-cytogenetic associations in 306 patients with therapy-related myelodysplasia and myeloid leukemia: the University of Chicago series. Blood. 2003;102:43–52.
117. Andersen M, Larson R, Mauritzson N, Schnittger S, Jhanwar S, Pedersen-Bjergaard J. Balanced chromosome abnormalities inv(16) and t(15;17) in therapy-related myelodysplastic syndromes and acute leukemia: report from an international workshop. Genes Chromosom Cancer. 2002;33: 395–400.
118. Bloomfield CD, Archer KJ, Mrozek K, Lillington DM, Kaneko Y, Head DR, et al. 11Q23 balanced chromosome aberrations in treatment-related myelodysplastic syndromes and acute leukemia: report from an international workshop. Genes Chromosom. 2002;33: 362–78.
119. Rowley J, Olney H. International workshop on the relationship of prior therapy to balanced chromosome aberrations in therapy-related myelodysplastic syndromes and acute leukemia : overview report. Genes Chromosom Cancer. 2002;33:331–45.
120. Slovak ML, Bedell V, Popplewell L, Arber DA, Schoch C, Slater R. 21q22 balanced chromosome aberrations in therapy-related hematopoietic disorders: report from an international workshop. Genes Chromosom Cancer. 2002;33:379–94.
121. Pileri SA, Ascani S, Cox MC, Campidelli C, Bacci F, Piccioli M, et al. Myeloid sarcoma: clinicopathologic, phenotypic and cytogenetic analysis of 92 adult patients. Leukemia. 2007;21:340–50.
122. Gurbuxani S, Vyas P, Crispino JD. Recent insights into the mechanisms of myeloid leukemogenesis in down syndrome. Blood. 2004;103:399–406.
123. Massey GV, Zipursky A, Chang MN, Doyle JJ, Nasim S, Taub JW, et al. A prospective study of the natural history of transient leukemia (TL) in neonates with Down syndrome (DS): Children's Oncology Group (COG) study POG-9481. Blood. 2006;107: 4606–13.
124. Brink DS. Transient leukemia (transient myeloproliferative disorder, transient abnormal myelopoiesis) of down syndrome. Adv Anat Pathol. 2006;13:256–62.
125. Greene ME, Mundschau G, Wechsler J, McDevitt M, Gamis A, Karp J, et al. Mutations in GATA1 in both

transient myeloproliferative disorder and acute megakaryoblastic leukemia of down syndrome. Blood Cells Mol Dis. 2003;31:351–6.
126. Cella M, Jarrossay D, Facchetti F, Alebardi O, Nakajima H, Lanzavecchia A, et al. Plasmacytoid monocytes migrate to inflamed lymph nodes and produce large amounts of type I interferon. Nat Med. 1999;5:919–23.
127. Chaperot L, Bendriss N, Manches O, et al. Identification of a leukemic counterpart of the plasmacytoid dendritic cells. Blood. 2001;97:3210–7.
128. Petrella T, Comeau MR, Maynadie M, Couillault G, De Muret A, Maliszewski CR, et al. "Agranular CD4 + CD56+ hematodermic neoplasm" (blastic NK-cell lymphoma) originates from a population of CD56+ precursor cells related to plasmacytoid monocytes. Am J Surg Pathol. 2002;26:852–62.
129. Pilichowska ME, Fleming MD, Pinkus JL, Pinkus GS. CD4+/CD56+ hematodermic neoplasm ("blastic natural killer cell lymphoma"): neoplastic cells express the immature dendritic cell marker BDCA-2 and produce interferon. Am J Clin Pathol. 2007; 128:445–53.
130. Yildirim I, Uckan D, Cetin M, Tuncer M, Tezcan I. Isolated testicular and bone relapse in children with acute myeloblastic leukemia and chronic graft versus host disease after allogeneic BMT. Turk J Pediatr. 2007;49:206–9.
131. Aschoff P, Hantschel M, Oksuz M, Werner MK, Lichy M, Vogel W, et al. Integrated FDG-PET/CT for detection, therapy monitoring and follow-up of granulocytic sarcoma: initial results. NuklearMedizin. 2009;48:185–91.
132. Buck AK, Bommer M, Juweid ME, Glatting G, Stilgenbauer S, Mottaghy FM, et al. First demonstration of leukemia imaging with the proliferation marker ^{18}F-fluorodeoxythymidine. J Nucl Med. 2008;49:1756–62.
133. Vanderhoek M, Juckett MB, Perlman SB, Nickles RJ, Jeraj R. Early assessment of treatment response in patients with AML using [^{18}F]FLT PET imaging. Leuk Res. 2011;35:310–6.
134. Lee SM, Kim TS, Lee JW, Kwon HW, Kim II Y, Kang SH, et al. Incidental finding of an ^{11}C-acetate PET-positive multiple myeloma. Ann Nucl Med. 2010;24:41–4.
135. Abramson S, Miller RG, Phillips RA. The identification in adult bone marrow of pluripotent and restricted stem cells of the myeloid and lymphoid systems. J Exp Med. 1977;145:1567–79.
136. Bizzozero OJ, Johnson KG, Ciocco A, Kawasaki S, Toyoda S. Radiation-related leukemia in Hiroshima and Nagasaki 1946-1964. I. Distribution, incidence and appearance time. N Engl J Med. 1966;274: 1095–101.
137. Galbraith P, Abu-Zahra H. Granulopoiesis in chronic granulocytic leukaemia. Br J Haematol. 1972;22: 135–43.
138. Quintás-Cardama A, Cortes J. Molecular biology of bcr-abl1-positive chronic myeloid leukemia. Blood. 2009;113:1619–30.
139. Soverini S, De Benedittis C, Machova Polakova K, Linhartova J, Castagnetti F, Gugliotta G, et al. Next-generation sequencing for sensitive detection of BCR-ABL1 mutations relevant to tyrosine kinase inhibitor choice in imatinib-resistant patients. Oncotarget. 2016;7:21982.
140. Hehlmann R, Hochhaus A, Baccarani M. Chronic myeloid leukaemia. Lancet. 2007;370:342–50.
141. Apperley JF. Part I: mechanisms of resistance to imatinib in chronic myeloid leukaemia. Lancet Oncol. 2007;8:1018–29.
142. Apperley JF. Part II: management of resistance to imatinib in chronic myeloid leukaemia. Lancet Oncol. 2007;8:1116–28.
143. Soverini S, De Benedittis C, Mancini M, Martinelli G. Mutations in the BCR-ABL1 Kinase domain and elsewhere in chronic myeloid leukemia. Clin Lymphoma Myeloma Leuk. 2015;15:S120–8.
144. Deininger MW, Hodgson JG, Shah NP, Cortes JE, Kim DW, Nicolini FE, et al. Compound mutations in BCR-ABL1 are not major drivers of primary or secondary resistance to ponatinib in CP-CML patients. Blood. 2016;127:703–12.
145. Baccarani M, Pileri S, Steegmann J, Muller M, Soverini S, Dreyling M, et al. Chronic myeloid leukaemia: ESMO Clinical Practice Guidelines for diagnosis, treatment and follow-up. Ann Oncol. 2012;23: vii72–7.
146. Baccarani M, Deininger MW, Rosti G, Hochhaus A, Soverini S, Apperley JF, et al. European LeukemiaNet recommendations for the management of chronic myeloid leukemia: 2013. Blood. 2013;122:872–84.
147. Eide CA, O'Hare T. Chronic myeloid leukemia: advances in understanding disease biology and mechanisms of resistance to tyrosine kinase inhibitors. Curr Hematol Malig Rep. 2015;10:158–66.
148. Castro-Malaspina H, Moore MA. Pathophysiological mechanisms operating in the development of myelofibrosis: role of megakaryocytes. Nouv Rev Fr Hematol. 1982;24:221–6.
149. Karanas A, Silver R. Characteristics of the terminal phase of chronic granulocytic leukemia. Blood. 1968; 32:445–59.
150. Nakajo M, Jinnouchi S, Inoue H, Otsuka M, Matsumoto T, Kukita T, et al. FDG PET findings of chronic myeloid leukemia in the chronic phase before and after treatment. Clin Nucl Med. 2007;32:775–8.
151. Takalkar A, Yu J, Kumar R, Xiu Y, Alavi A, Zhuang H. Diffuse bone marrow accumulation of FDG in a patient with chronic myeloid leukemia mimics hematopoietic cytokine-mediated FDG uptake on positron emission tomography. Clin Nucl Med. 2004;29: 637–9.
152. Chen C, Zimmerman R, Faro S, Bilaniu L, Chou T, Molloy P. Childhood leukemia: central nervous

system abnormalities during and after treatment. AJNR Am J Neuroradiol. 1996;17:295–310.
153. Lu L, Jiang L, Guan H, Gao Y, Lu H. Imaging proliferation in human leukemia-tumor bearing mice with 18F-FLT: comparison with ^{18}F-FDG PET. Hell J Nucl Med. 2012;15:15–6.
154. Sokal JE, Cox EB, Baccarani M, Tura S, Gomez GA, Robertson JE, et al. Prognostic discrimination in "good-risk" chronic granulocytic leukemia. Blood. 1984;63:789–99.
155. Hasford J, Pfirrmann M, Hehlmann R, Allan NC, Baccarani M, Kluin-Nelemans JC, et al. A new prognostic score for survival of patients with chronic myeloid leukemia treated with interferon alfa. Writing committee for the collaborative CML prognostic factors project group. J Natl Cancer Inst. 1998;90:850–8.
156. Hasford J, Baccarani M, Hoffmann V, Guihot J, Saussele S, Rosti G, et al. Predicting complete cytogenetic response and subsequent progression- free survival in 2060 patients with CML on imatinib treatment : the EUTOS PubMed Commons. Blood. 2011;118:686–92.
157. Mahon FX, Rea D, Guilhot J, Guilhot F, Huguet F, Nicolini F, et al. Discontinuation of imatinib in patients with chronic myeloid leukaemia who have maintained complete molecular remission for at least 2 years: the prospective, multicentre Stop Imatinib (STIM) trial. Lancet Oncol. 2010;11:1029–35.
158. Rousselot P, Charbonnier A, Cony-Makhoul P, Agape P, Nicolini FE, Varet B, et al. Loss of major molecular response as a trigger for restarting tyrosine kinase inhibitor therapy in patients with chronic-phase chronic myelogenous leukemia who have stopped imatinib after durable undetectable disease. J Clin Oncol. 2014;32:424–30.
159. Cortes JE, Saglio G, Kantarjian HM, Baccarani M, Mayer J, Boque C, et al. Final 5-year study results of DASISION: the dasatinib versus imatinib study in treatment-naive chronic myeloid leukemia patients trial. J Clin Oncol. 2016;9–10.
160. Hochhaus A, Saglio G, Hughes TP, Larson RA, Kim D-W, Issaragrisil S, et al. Long-term benefits and risks of frontline nilotinib vs imatinib for chronic myeloid leukemia in chronic phase: 5-year update of the randomized ENESTnd trial. Leukemia. 2016;30(5):1044–54.
161. Potenza L, Luppi M, Riva G, Morselli M, Ferrari A, Imovilli A, et al. Isolated extramedullary relapse after autologous bone marrow transplantation for acute myeloid leukemia: case report and review of the literature. Am J Hematol. 2006;81:45–50.
162. Benitez Velazco A, Gonzalez Garcia FM, Albala Gonzalez MD, Pacheco Capote C, Latre Romero JM. Bone scintigraphy with ^{99m}Tc-MDP in a patient with acute lymphoblastic leukemia initially diagnosed of Still's disease. Rev Esp Med Nucl. 2005;24:319–21.

Diagnostic Applications of Nuclear Medicine: Brain Tumors

17

Giampiero Giovacchini, Mattia Riondato, Elisabetta Giovannini, and Andrea Ciarmiello

Abstract

PET/CT and PET/MR can be used with various radiopharmaceuticals to assess the mechanisms underlying biochemical changes and physiopathology of brain tumors.

Amino acid tracers are frequently used for most clinical questions. These tracers include, among others, [^{11}C]methionine, *L*-3,4-dihydroxy-6[^{18}F]fluorophenylalanine ([^{18}F]FDOPA and O-(2-^{18}F-fluoroethyl)-L-tyrosine (^{18}F-FLT). Amino acid tracers are particularly accurate to distinguish tumor recurrence and radiation necrosis. The role of [^{18}F]FDG, the earliest PET tracer used for diagnosis and monitoring of brain tumors, is being redefined, due to the availability of amino acid tracers. For in vivo prediction of tumor grade, however, [^{18}F]FDG is still more accurate than most amino acid tracers.

Higher baseline values of tracer uptake as well as lower percent changes after therapy in treated patients predict shorter survival – this has been shown for several tracers.

PET/CT and PET/MR can be used after surgery to assess the presence of residual tumor. PET, in combination with MR, is increasingly used for the definition of the tumor volume that has to be irradiated. Identification of the part of the tumor that displays highest metabolic activity can also be used to direct stereotaxic biopsy.

Other tracers have been synthetized to explore different biochemical processes, for example, hypoxia (e.g., [^{18}F]-fluoromisonidazole), DNA synthesis (3-deoxy-3-[^{18}F]-fluorothymidine), and membrane proliferation (radiolabeled choline). However, these tracers have a less established role in clinical practice.

Keywords

Brain tumor • Positron emission tomography/computed tomography (PET/CT) • Positron emission tomography/magnetic resonance (PET/MR)

Glossary

[^{11}C]MET	[^{11}C]methionine
[^{18}F]FDG	2-Deoxy-2-[^{18}F]fluoro-D-glucose
[^{18}F]FDOPA	*L*-3,4-dihydroxy-6-[^{18}F]fluorophenylalanine
^{123}I-IAZA	^{123}I-iodoazomycin arabinoside
^{123}I-IMT	^{123}I-alpha-methyltyrosine, a tyrosine analog transported as L-tyrosine by the neutral amino acid transporter
^{18}F-FAZA	^{18}F-azomycin arabinoside
^{18}F-FES	16α-^{18}F-fluoro-17β-oestradiol

G. Giovacchini • M. Riondato • E. Giovannini • A. Ciarmiello (✉)
Nuclear Medicine Department, S. Andrea Hospital, La Spezia, Italy
e-mail: andrea.ciarmiello@asl5.liguria.it

© Springer International Publishing Switzerland 2017
H.W. Strauss et al. (eds.), *Nuclear Oncology*,
https://doi.org/10.1007/978-3-319-26236-9_9

^{18}F-FET	*O*-(2-^{18}F-Fluoroethyl)-L-Tyrosine, a tyrosine analog
^{18}F-FLT	^{18}F-fluorothymidine
^{18}F-FMAU	^{18}F-2-fluoro-5-methyl-1-beta-d-arabinofuranosyluracil
^{18}F-MISO	^{18}F-fluoromisonidazole
^{64}Cu-ATSM	^{64}Cu-diacetyl-bis(N_4-methylsemicarbazone)
^{99m}Tc-ECD	^{99m}Tc-ethylcisteinate dimer
^{99m}Tc-HMPAO	^{99m}Tc-hexamethylpropyleneamine oxime
ADC	Apparent diffusion coefficient, a parameter of MR imaging
AJCC	American Joint Committee on Cancer
BBB	Blood–brain barrier
BTV	Biological tumor volume (the extent of tumor based on PET imaging); the combination of GTV and BTV provides the planning target volume for radiation therapy
CBF	Cerebral blood flow
CI	Confidence interval
CMR_{glc}	Cerebral metabolic rate for glucose
CNS	Central nervous system
CSF	Cerebrospinal fluid
CT	X-ray computed tomography
DG	2-Deoxyglucose
DOTA	1,4,7,10-Tetraazacyclododecane-1,4,7,10-tetraacetic acid
DOTANOC	DOTA-1-Nal^3-octreotide
DOTATATE	DOTA- Tyr^3-octreotate
DOTATOC	DOTA-octreotate
DTPA	Diethylenetriaminepentaacetic acid
DWI	Diffusion-weighted imaging, an MR imaging technique
EGFR	Epidermal growth factor receptor; the mutated form EGFRvIII plays a prominent role in tumorigenesis and pro-angiogenic signaling
FLAIR	Fluid-attenuated inversion recovery, an MR imaging technique
GBM	Glioblastoma multiforme
GTV	Gross tumor voume (the extent of the tumor on morphologic imaging)
IDH	Isocitrate dehydrogenase; mutations of this enzyme occur more frequently in oligodendroglial and astrocytic tumors
KPS	Karnofsky performance score
LAT1	L-type amino acid transporter 1
M	Metastasis status according to the AJCC/UICC TNM staging system
MDR1	Multidrug resistance gene 1, a characteristic associated with aggressive tumors; this gene encodes for P-glyoprotein
MGMT	Methyl guanine DNA methyl transferase, a DNA repair enzyme; methylation of MGMT promoter is associated with increased overall survival
MIB-1	Marker of cell proliferation used for stratification of grades of brain tumors
MoAb	Monoclonal antibody
MPNST	Malignant peripheral nerve sheath tumor
MR	Magnetic resonance
MRI	Magnetic resonance imaging
N	Lymph node status according to the AJCC/UICC TNM staging system
PET	Positron emission tomography
PET/CT	Positron emission tomography/computed tomography
PET/MR	Positron emission tomography/magnetic resonance
PI3K	Phosphatidylinositol 3-kinase
PNET	Primitive neuroectodermic tumor
pRIT	Pretargeting radioimmunotherapy
PTEN	Phosphatase and tensin homolog is a tumor suppressor; PTEN deletions indicate a poor prognosis
RIT	Radioimmunotherapy

ROC	Receiver operating characteristic, a statistical analysis to assess the performance of a binary classifier
ROI	Region of interest
SPECT	Single photon emission computed tomography
SPECT/CT	Single photon emission computed tomography/computed tomography
SST	Somatostatin
SSTR	Somatostatin receptors
SUV	Standardized uptake value
T	Tumor status according to the AJCC/UICC TNM staging system
T/N	Ratio of tumor uptake to normal brain uptake
TBR	Tumor-to-background ratio
TNM	AJCC/UICC staging system based on parameters "T" (tumor status), "N" (lymph node status), and "M" (distant metastasis status)
TP53	Tumor protein p53, also known as cellular tumor antigen p53, phosphoprotein p53, tumor suppressor p53, antigen NY-CO-13, or transformation-related protein 53 (TRP53)
UICC	Union Internationale Contre le Cancer (International Union Against Cancer)
VEGF	Vascular endothelial growth factor
VOI	Volume of interest
WHO	World Health Organization

Contents

Epidemiology of Brain Tumors 469

Staging and Prognostic Stratification 470

Genetic Predisposition and Underlying Molecular Biology Changes 472

Clinical Presentation 475

Prognosis 475

Clinical Applications 476

Overall Performance of Diagnostic Imaging Other Than Nuclear Medicine 478

Nuclear Imaging for Staging/Prognosis 479

Brain Perfusion Imaging 480

2-Deoxy-2-[^{18}F]fluoro-D-glucose ([^{18}F]FDG) 481

Radiolabeled Amino Acids 484

3-^{123}I-Alpha-Methyltyrosine (^{123}I-IMT) and *O*-(2-^{18}F-Fluoroethyl)-L-Tyrosine (^{18}F-FET) 486

PET/MR 492

Assessing the Efficacy of Treatment 494

Additional Value of SPECT/CT and PET/CT vs Stand-Alone SPECT and PET 495

Common Therapies 497

Meningiomas 498

Conclusion 499

References 500

Primary brain tumors are a heterogeneous group of neoplasms, each with its own biology, prognosis, and treatment. Among primary brain tumors, gliomas constitute the most frequent pathologic finding, being characterized by distinct histologic patterns and grades that are predictive of tumor invasiveness and patient survival. In this chapter we will review the main features of neoplasms of the central nervous system (CNS), and we will focus on the use of positron emission tomography (PET) and single-photon emission computed tomography (SPECT) as well as of hybrid techniques, particularly PET with computed tomography (PET/CT) and PET with magnetic resonance (PET/MR) with various radiopharmaceuticals for the diagnosis, treatment, and follow-up of brain tumors. Even though nowadays all PET tomographs are either PET/CT or PET/MR tomographs, the term PET will be used often either to contrast CT or MR studies or to refer to old studies that were performed with stand-alone PET tomographs.

Epidemiology of Brain Tumors

Many different organizations track the incidence of gliomas. This can be done using data collected through government cancer surveillance

(i.e., statewide or countrywide cancer registries) [1] or through the use of health system records [2]. Incidence rates of glioma vary significantly by histologic type, age at diagnosis, gender, race, and country. Overall age-adjusted incidence rates range from 4.67 to 5.73 per 100,000 persons. Age-adjusted incidence of glioblastoma, the most common and most deadly glioma subtype in adults, ranges from 0.59 to 3.69 per 100,000 persons [3, 4]. Although brain tumors are more frequent in adult subjects, they can occur in pediatric patients and adolescents as well. However, age and gender distribution vary accordingly to histotype. Meningiomas are more common in females than in males with a 3:2 ratio, while gliomas are slightly more common in men. The age-adjusted incidence rates of brain tumors tend to be highest in developed, industrial countries. However, the lower incidence of brain tumors in developing countries may also be attributed to decreased diagnosis [5].

Staging and Prognostic Stratification

The American Joint Committee on Cancer (AJCC) in agreement with the World Health Organization (WHO) classification of tumors of the CNS was updated a few years ago [6]. On the basis of histological origin, the WHO classification identifies six types of CNS neoplasms (Table 1): (1) tumors of the neuroepithelial tissue, (2) tumors of the cranial and paraspinal nerves, (3) tumors of the meninges (meningiomas), (4) lymphomas and hematopoietic neoplasms, (5) germ cell tumors, and (6) tumors of the sellar region. In addition to these primary CNS tumors, metastatic tumors need to be considered as well. Most neuroepithelial tumors are derived from glial cells and therefore are termed gliomas. There are three types of gliomas, namely, astrocytomas, oligodendrogliomas, and ependymomas. The category of astrocytomas is included in the glioblastoma. However, some tumors, such as the medulloblastoma, derive from neurons. In this chapter, we will focus particular attention to the distinction between low-grade and high-grade gliomas and briefly mention meningiomas.

CNS tumors do not currently have TNM designation [6]. Attempts at developing a TNM-based classification and staging system for CNS tumors have been disappointing. There are multiple reasons for this. (1) Tumor size is significantly less relevant than tumor histology and tumor grading (Table 2). Thus, the T classification is less pertinent than the biologic nature of the tumor itself. (2) Because the brain and spinal cord have no lymphatics, the N classification does not apply. (3) An M classification is not pertinent to the majority of CNS tumors, because they have the tendency to recur locally and they virtually never disseminate at distance.

Based on the histological features, CNS tumors are divided into low-grade and high-grade tumors. Grading is based on the degree of nuclear atypia, mitosis, microvascular proliferation, and necrosis. Grading is clinically important because prognosis worsens as tumor grading increases. Tumor grade is determined by multiple histological sampling of tumor tissue. Grading becomes unreliable in treated tumors because blood–brain barrier (BBB) damage and necrosis also can result from the formation of reactive tissue after therapy [7].

Low-grade gliomas are grade I and II, while high-grade gliomas are grade III and IV. Since histological features may vary within different areas of the same tumors, the most malignant region determines the grade of the tumor. Grade III astrocytomas are commonly referred to as anaplastic astrocytomas. Glioblastoma, a grade IV glioma, is the most malignant as well as the most common form of gliomas, accounting for about 50% of all gliomas [8]. All glioblastomas can be divided into two subtypes based on the presence or absence of a precursor lesion of a lower grade. Primary high-grade glioblastomas develop more commonly in subjects younger than 45 years, while secondary glioblastomas that progressed from low-grade gliomas occur more frequently in older subjects (>60 years). Primary glioblastoma is the most common type (>90%) and diagnosed as a de novo lesion without progression from a lower-grade tumor in older patients. Secondary glioblastomas develop through progression from a low-grade diffuse astrocytoma or anaplastic astrocytoma and present in younger patients [9].

Table 1 The 2010 AJCC classification of tumors of the CNS (Adapted from Ref. [6])

(1) *Tumors of neuroepithelial tissue*	
Astrocytic tumors	
Pilocytic astrocytoma	9421/1[a]
Pilomyxoid astrocytoma	*9425/3*[b]
Subependymal giant cell astrocytoma	9384/1
Pleomorphic xanthoastrocytoma	9424/3
Diffuse astrocytoma	9400/3
Fibrillary astrocytoma	9420/3
Gemistocytic astrocytoma	9411/3
Protoplasmic astrocytoma	9410/3
Anaplastic astrocytoma	9401/3
Glioblastoma	9440/3
Giant cell glioblastoma	9441/3
Gliosarcoma	9442/3
Gliomatosis cerebri	9381/3
Oligodendroglial tumors	
Oligodendroglioma	9450/3
Anaplastic oligodendroglioma	9451/3
Oligoastrocytic tumors	
Oligoastrocytoma	9382/3
Anaplastic oligoastrocytoma	9382/3
Ependymal tumors	
Subependymoma	9383/1
Myxopapillary ependymoma	9394/1
Ependymoma	9391/3
Cellular	9391/3
Papillary	9393/3
Clear cell	9391/3
Tanycytic	9391/3
Anaplastic ependymoma	9392/3
Choroid plexus tumors	
Choroid plexus papilloma	9390/0
Atypical choroid plexus papilloma	*9390/1*
Choroid plexus carcinoma	9390/3
Other neuroepithelial tumors	
Astroblastoma	9430/3
Chordoid glioma of the third ventricle	9444/1
Angiocentric glioma	9431/1
Neuronal and mixed neuronal-glial tumors	
Dysplastic gangliocytoma of cerebellum	9493/0
Desmoplastic infantile astrocytoma/ganglioglioma	9412/1
Dysembryoplastic neuroepithelial tumor	9413/0
Gangliocytoma	9492/0
Ganglioglioma	9505/1
Anaplastic ganglioglioma	9505/3
Central neurocytoma	9506/1
Extraventricular neurocytoma	*9506/1*[b]
Cerebellar liponeurocytoma	*9506/1*[b]
Papillary glioneuronal tumor	*9509/1*[b]
Rosette-forming glioneuronal tumor of the fourth ventricle	*9509/1*[b]
Paraganglioma	8680/1
Tumors of the pineal region	
Pineocytoma	9361/1
Pineal parenchymal tumor of intermediate differentiation	9362/3
Pineoblastoma	9362/3
Papillary tumor of the pineal region	*9395/3*[b]
Embryonal tumors	
Medulloblastoma	9470/3
Desmoplastic/nodular medulloblastoma	9471/3
Medulloblastoma with extensive nodularity	*9471/3*[b]
Anaplastic medulloblastoma	*9474/3*[b]
Large cell medulloblastoma	9474/3
CNS primitive neuroectodermal tumor	9473/3
CNS neuroblastoma	9500/3
CNS ganglioneuroblastoma	9490/3
Medulloepithelioma	9501/3
Ependymoblastoma	9392/3
Atypical teratoid/rhabdoid tumor	9508/3
(2) *Tumors of cranial and paraspinal nerves*	
Schwannoma (neurilemoma, neurinoma)	9560/0
Cellular	9560/0
Plexiform	9560/0
Melanotic	9560/0
Neurofibroma	9540/0
Plexiform	9550/0
Perineurioma	
Perineurinoma, NOS	9571/0
Malignant perineurinoma	9571/3
Malignant peripheral nerve sheath tumor (MPNST)	
Epithelioid MPNST	9540/3
MPNST with mesenchymal differentiation	9540/3
Melanotic MPNST	9540/3
(3) *Tumors of the meninges*	
Tumors of meningothelial cells	
Meningioma	9530/0
Meningothelial	9531/0
Fibrous (fibroblastic)	9532/0
Transitional (mixed)	9537/0
Psammomatous	9533/0
Angiomatous	9534/0
Microcystic	9530/0
Secretory	9530/0
Lymphoplasmacyte-rich	9530/0

(*continued*)

Table 1 (continued)

Metaplastic	9530/0
Chordoid	9538/1
Clear cell	9538/1
Atypical	9539/1
Papillary	9538/3
Rhabdoid	9538/3
Anaplastic (malignant)	9530/3
Mesenchymal tumors	
Lipoma	8850/0
Angiolipoma	8861/0
Hibernoma	8880/0
Liposarcoma	8850/3
Solitary fibrous tumor	8815/0
Fibrosarcoma	8810/3
Malignant fibrous histiocytoma	8830/3
Leiomyoma	8890/0
Leiomyosarcoma	8890/3
Rhabdomyoma	8900/0
Rhabdomyosarcoma	8900/3
Chondroma	9220/0
Chondrosarcoma	9220/3
Osteoma	9180/0
Osteosarcoma	9180/3
Osteochondroma	9210/0
Hemangioma	9120/0
Epithelioid hemangioendothelioma	9133/1
Hemangiopericytoma	9150/1
Anaplastic hemangiopericytoma	9150/3
Angiosarcoma	9120/3
Kaposi sarcoma	9140/3
Ewing sarcoma – PNET	9364/3
Primary melanocytic lesions	
Diffuse melanocytosis	8728/0
Melanocytoma	8728/1
Malignant melanoma	8720/3
Meningeal melanomatosis	8728/3
Other neoplasms related to the meninges	
Hemangioblastoma	9161/1
(4) *Lymphomas and hematopoietic neoplasms*	
Malignant lymphomas	9590/3
Plasmacytoma	9731/3
Granulocytic sarcoma	9930/3
(5) *Germ cell tumors*	
Germinoma	9064/3
Embryonal carcinoma	9070/3
Yolk sac tumor	9071/3
Choriocarcinoma	9100/3
Teratoma	9080/1
Mature	9080/0
Immature	9080/3
Teratoma with malignant transformation	9084/3
Mixed germ cell tumor	9085/3
(6) *Tumors of the sellar region*	
Craniopharyngioma	9350/1
Adamantinomatous	9351/1
Papillary	9352/1
Granular cell tumor	9582/0
Pituicytoma	9432/1[b]
Spindle cell oncocytoma of the adenohypophysis	8291/0[b]

(*continued*)

[a]Morphology code of the International Classification of Diseases for Oncology (ICO-O) (614A) and the Systematized Nomenclature of Medicine (http://snomed.org). Behavior is coded /0 for benign tumors, /3 for malignant tumors, and /1 for borderline or uncertain behavior

[b]The italicized numbers are provisional codes proposed for the fourth edition of ICD-O. While they are expected to be incorporated into the next ICD-O edition, they currently remain subject to change

Glioblastomas are highly aggressive tumors that are generally resistant to treatment. Average survival is less than 1 year from diagnosis. Glioblastomas are characterized by hypercellular anaplastic glioma cells with marked mitotic activity as well as necrosis and endothelial proliferation. Neoplastic cells frequently reveal pleomorphism showing different histologic features such as small homogeneous cells with scant cytoplasm, fibrillary-shaped cells, multinucleated giant cells, and cells with pleomorphic nuclei and cytoplasm [10]. Because of such cellular pleomorphism, the tumor is often referred to as glioblastoma multiforme (GBM) [10]. Histologic features in glioblastomas are associated with clinical outcome: greater necrotic component is associated with poor survival, while greater oligodendroglial component is predictive of longer survival [11].

Genetic Predisposition and Underlying Molecular Biology Changes

The traditional classification of brain tumors of the WHO grades II–IV is based on histological features of a heterogeneous population of tumors with varying prognoses and treatments. Histologic visual criteria may be prone to errors, and interpreting

Table 2 WHO grades of CNS tumors

	I	II	III	IV		I	II	III	IV
Astrocytic tumors					Central neurocytoma		●		
Subependymal giant cell astrocytoma	●				Extraventricular neurocytoma		●		
Pilocytic astrocytoma	●				Cerebellar liponeurocytoma		●		
Pilomyxoid astrocytoma		●			Paraganglioma of the spinal cord	●			
Diffuse astrocytoma		●			Papillary glioneuronal tumor	●			
Pleomorphic xanthoastrocytoma		●			Rosette-forming glioneuronal tumor of the fourth ventricle	●			
Anaplastic astrocytoma			●		Pineal tumors				
Glioblastoma				●	Pineocytoma	●			
Giant cell glioblastoma				●	Pineal parenchymal tumor of intermediate differentiation		●	●	
Gliosarcoma				●	Pineoblastoma				●
Oligodendroglial tumors					Papillary tumor of the pineal region		●	●	
Oligodendroglioma		●			Embryonal tumors				
Anaplastic oligodendroglioma			●		Medulloblastoma				●
Oligoastrocytic tumors					CNS primitive neuroectodermal tumor (PNET)				●
Oligoastrocytoma		●			Atypical teratoid/rhabdoid tumor				●
Anaplastic oligoastrocytoma			●		Tumors of the cranial and paraspinal nerves				
Ependymal tumors					Schwannoma	●			
Subependymoma		●			Neurofibroma	●			
Myxopapillary ependymoma		●			Perineurioma	●	●	●	
Ependymoma			●		Malignant peripheral nerve sheath tumor (MPNST)		●	●	●
Anaplastic ependymoma				●	Meningeal tumors				
Choroid plexus tumors					Meningioma	●			
Choroid plexus papilloma		●			Atypical meningioma		●		
Atypical choroid plexus papilloma			●		Anaplastic/malignant meningioma			●	
Choroid plexus carcinoma				●	Hemangiopericytoma		●		
Other neuroepithelial tumors					Anaplastic hemangiopericytoma			●	
Angiocentric glioma		●			Hemangioblastoma	●			
Chordoid glioma of the third ventricle			●		Tumors of the sellar region				
Neuronal and mixed neuronal-glial tumors					Craniopharyngioma	●			
Gangliocytoma		●			Granular cell tumor of the neurohypophysis	●			
Ganglioglioma		●			Pituicytoma	●			
Anaplastic ganglioglioma				●	Spindle cell oncocytoma of the adenohypophysis	●			
Desmoplastic infantile astrocytoma and ganglioglioma		●							
Dysembryoplastic neuroepithelial tumor		●							

Adapted from Ref. [6]

cellularity is not always possible due to the histological heterogeneity of the tumor. Over the last decade, research efforts have resulted in a better understanding of the molecular basis of glioma formation as well as the genetic alterations commonly identified in gliomas [9].

The discovery and characterization of the isocitrate dehydrogenase (IDH) 1 and 2 mutations in brain tumors that occurred in the last 6 years is a major achievement. IDH1 and IDH2 mutations occur more frequently in oligodendroglial and astrocytic tumors and less frequently in GBMs. IDH mutant gliomas have indeed a better prognosis in comparison to IDH wild-type gliomas [12]. Whether mutations in IDH result in a loss of tumor suppressor function or act as an oncogene remains a source of debate. It has been hypothesized that the effects of the IDH mutant enzyme's product, 2-hydroxyglutarate, change a cell's methylation profile and alter cell telomere length and gene expression. The effects of IDH mutations also produce decreased cytoplasmic levels of alpha-ketoglutarate and nicotinamide adenine dinucleotide phosphate oxidase that may in turn stabilize hypoxia-inducible factor 1-α facilitating cellular proliferation [13].

The evolution of a recurrent high-grade glioblastoma is more rapid than a primary high-grade glioblastoma. In the pathway to secondary high-grade glioblastoma, TP53 mutations are the most frequent and earliest detectable genetic alterations, already present in 60% of precursor low-grade astrocytomas [14]. On the contrary, unbalanced translocation of chromosomes 1 and 19 with deletion of the 1p arm and the 19q arm is found in almost 70% of histologically defined oligodendrogliomas. 1p/19q codeletions and TP53 mutations are relatively exclusive of one another, supporting the argument of two separate lineages that can be identified on a molecular basis to supplement histological diagnosis. A 1p/19q codeletion is associated with improved prognosis in low-grade gliomas and it is predictive of improved outcomes with chemotherapy and radiation [15].

The DNA repair enzyme O_6-methyl-guanine-DNA methyltransferase (MGMT) status repairs O^6 alkyl guanine adducts. The repair enzyme mechanism interferes with the overlapping effect of drug, which alkylates at the O_6 position of guanine. Methylation of the promoter of the MGMT gene results in silencing of gene transcription, so that the effect of temozolomide is enhanced. MGMT promoter methylation was identified in 36% of the overall population of glioma series studied, which demonstrated the presence of the mutation improves the effect of temozolomide and ultimately increases overall survival regardless of treatment arm [9, 16]. Numerous trials have shown that MGMT promoter methylation is a prognostic marker associated with improved survival. MGMT promoter methylation can be associated with 1p19q codeletions as well as IDH mutations suggesting it may be an epiphenomenon related to these or other factors that result in improved survival [9, 16].

The epidermal growth factor receptor (EGFR) is a transmembrane receptor in the receptor tyrosine kinase (RTK), phosphatase and tensin homolog, and phosphatidylinositol 3-kinnase (PI3K) cell proliferation pathway. EGFR*vIII*, a mutated form of EGFR, plays a prominent role in tumorigenesis of glioblastoma, but the underlying mechanisms have remained elusive. EGFR*vIII* amplification can lead to increased downstream activity resulting in proangiogenic signaling, increased proliferation, increased tumor cell survival, and migration [17]. EGFR*vIII* amplifications have been reported in approximately 40% of primary glioblastomas. EGFR*vIII* amplification has been reported to be a predictor of poor survival; however, other studies have failed to show this effect. Studies have reported that EGFR*vIII* amplification can predict response to tyrosine kinase inhibitors, especially when PTEN expression is preserved [17, 18].

Phosphatase and tensin homolog (PTEN) is a tumor suppressor gene expressing a protein involved in the same RTK/PTEN/PI3K cell proliferation pathway as EGFR. PTEN mutations are estimated to occur in 15–40% of primary glioblastomas, but up to 80% of glioblastomas have loss of chromosome 10q in the region where PTEN is located (10q23). Chromosome 10q loss, PTEN mutations, and EGFR amplifications are frequently seen together in the small cell phenotype of glioblastoma. PTEN deletions have been

reported to be a poor prognostic factor for pediatric glioblastomas; however, this has not been found true in adult patients [17].

Contrary to other tumors, environmental factors do not play a major role in the development of brain tumors.

Clinical Presentation

Symptoms of brain tumors depend on the location, size, and rate of growth of the tumor. High-grade, fast-growing tumors have early symptom onset, while slow-growing, small-sized tumors may remain asymptomatic for many years, especially if they are located in cerebral mute areas, such as the frontal lobe. In these cases, brain neoplasms can be an incidental finding at CT or MR imaging.

Symptoms can be either focal or generalized and appear in a late phase. Generalized symptoms reflect increased intracranial pressure. The most common symptom is headache. Typically, the headache is diffuse, but it may affect only one side, frequently reflecting the site of the tumor. Generally, headache is more intense on awakening in the morning and responds poorly to analgesics; it wanes spontaneously after few hours. Rarely, headache is throbbing and mimicking migraine. Nausea, vomiting, and sixth-nerve palsy are less common.

Focal symptoms or signs take place when the neoplasm compresses the nearby cerebral parenchyma. They can be motor, sensory, or sensory motor. Aphasia is typical of frontal lobe involvement, ataxia is typical of cerebellar involvement, and diplopia occurs with optic nerve gliomas.

Seizures occur at variable degree in brain tumor patients, being more frequent in low-grade tumors. Typically, the seizures are focal but they may become generalized and cause loss of consciousness.

Prognosis

In addition to the previously mentioned genetic factors, there are other prognostic factors for brain tumors (Table 3).

Table 3 Prognostic factors in CNS tumors

Histology
Pathologic grade
Presence and extent of necrosis
Presence of gemistocytes
Proliferative fraction (Ki-67)
Presence of oligodendroglial component
Presence of cells in mitosis and endothelial proliferation
Age of patient
Functional neurological status
Karnofsky Performance Scale
Extent of resection
Biopsy, subtotal, radical removal
Tumor spread
Presence of local spread
Molecular aspects
Isocitrate dehydrogenase IDH1 and IDH2 mutations (protective factors)
1p/19q codeletion (protective factor)
O_6-methyl-guanine-DNA methyltransferase methylation (protective factor)
TP53 mutations (risk factors)
Epidermal growth factor receptor amplification (risk factor)
Phosphatase and tensin homolog mutations (risk factor)

Tumor histology. Histology is by far the most important variable affecting prognosis, and in many cases it determines the treatment modalities that are employed. Prognosis is worst with highest grade. The latest WHO classification system has combined tumor nomenclature with an associated grading system so that the actual histological diagnosis directly correlates with the histological grade of the tumor. The most common histologies for brain and spinal cord tumors are given in Tables 1 and 2, along with the tumor grade for each different diagnostic category.

Age. Most retrospective outcome studies of brain tumor therapy show that older age at the time of diagnosis is a powerful predictor of poor outcome [5, 19]. This fact holds true for the gliomas, which are the most common primary brain tumors, and for most other tumors that affect the adult population, including most metastatic tumors to the brain. There are, however, some childhood tumors that have a very poor prognosis,

are inherently high grade, and rapidly progress to a fatal outcome. Some metastatic tumors, such as melanoma, occur in younger patients and also violate this general statement with regard to the specific effect of age on prognosis.

Extent of tumor resection. In patients who are treated surgically for tumors of the CNS, the extent of resection is often closely correlated with the outcome. This is a less powerful predictor than tumor histology or age, but most retrospective studies confirm that the extent of removal is positively correlated with survival. For this reason, the documentation of whether a surgical tumor removal is "gross total," "subtotal," or "biopsy only" is useful in determining future therapy and prognosis.

Tumor location. Because of the differential importance of various areas of the brain, the location of a given tumor affecting the brain can have a major impact on the functional outcome, survival, and type of therapy.

Functional neurologic status. Another important prognostic factor in most retrospective studies of CNS tumors is the functional neurologic status of the patient at the time of diagnosis [11]. This has been estimated traditionally using the Karnofsky Performance Scale, which is reproducible, it is well known by most clinicians, and it is in common use for stratification of patients entering clinical trials for the treatment of brain tumors. The outcome and prognosis of patients correlate well with functional neurological status.

Metastatic spread. Tumors affecting the CNS rarely develop extraneural metastases because of inherent biologic characteristics of these tumors and because the brain does not have a well-developed lymphatic drainage system. In addition, many patients with tumors of the CNS have a short life expectancy, which further limits the likelihood of metastatic spread. Certain tumors do spread through cerebrospinal fluid (CSF) pathways, and such spread has a major impact on survival. Dissemination through the CSF pathway is a hallmark of certain childhood tumors, e.g., primitive neuroectodermal tumors, many of which carry a poor prognosis; this event, however, is rarely seen in adult patients with the more common CNS tumors. Primary lymphomas of the CNS may spread along the craniospinal axis and sometimes exhibit intraocular dissemination.

Clinical Applications

Before entering into the issues of PET and SPECT imaging of brain tumors, the clinical situations in which PET/SPECT may be useful are described in Table 4:

1. *Diagnosis*. CNS masses may be incidental findings on MR or CT examinations performed as part of diagnostic staging for non-CNS pathology or following neuroradiological examinations performed for neurological or psychiatric symptoms. In most cases, morphologic assessment by MR imaging is often the first step toward diagnosis of primary brain tumor, allowing the precise assessment of tumor size, margins, mass effect, and the presence or absence of contrast enhancement. However, CT and MR lack specificity and do not allow determination of tumor metabolism and activity. PET may be useful to reinforce the diagnostic hypothesis and to address other issues that are important for presurgical evaluation.
2. In vivo *tumor grading*: Grading is obtained following histological analysis of stereotactic

Table 4 Clinical indications to SPECT or PET imaging in gliomas

Pre-therapy
1. Diagnosis
2. Noninvasive tumor grading
3. Guidance for stereotactic biopsy
4. Surgical planning
5. Identification of metabolically active tumor (or biological target volume, BTV) for radiotherapy planning
6. Evaluation of multidrug resistance
Post-therapy
1. Identification of residual tumor
2. Differential diagnosis between tumor recurrence and radiation necrosis
3. Evaluation of response to therapy
4. Prediction of survival

biopsy or of the surgical specimen, if biopsy is not possible. Thus, it would be desirable to predict tumor grade noninvasively with brain imaging or to use an imaging technique to guide biopsy to the areas that are more likely to be of higher grade.

3. *Guidance for stereotactic biopsy.* A typical feature of gliomas is the variability in histological grade that can occur within the same tumor. This is particularly common in high-grade tumors, which generally evolve from low-grade forms. More than 60% of tumors contain both low-grade and high-grade features. As a consequence, sampling errors on stereotactic biopsy are a matter of particular concern. MR and CT do not provide sufficiently accurate information for distinguishing low-grade from high-grade areas. Whether or not PET can be used for guiding biopsy sampling has been addressed in various studies.
4. *Surgical planning*. MR imaging may underestimate the tumor extent in cerebral gliomas. In fact, margins of the abnormal MR lesion in the autopsy specimens of brains affected by gliomas may have viable tumor cells on histopathological examination. Accurate delineation of tumor extent is critical for a complete resection and for localizing metabolically active areas within the tumor in case of a partial resection.
5. *Radiotherapy planning*. Tumor delineation is also important to define the tumor volume that must be irradiated for therapeutic purposes. Adjuvant radiation therapy improves tumor control and is therefore carried out in all tumor patients. Inaccurate tumor delineation with persistence of viable tumor cells beyond the target area (i.e., geographic misses) is a major cause of treatment failure.

   Radiotherapy planning volume is traditionally based on MR. The target volume defined on the basis of morphological imaging is referred to as gross tumor volume (GTV). One of the most important limitations in the application of image-guided radiotherapy consists in the failure to define the tumor extension precisely, which can be attributed to nonspecific changes of MR after surgery or radiation therapy. Thus, PET has been used to identify the metabolically active brain areas. The metabolically active volume, as identified by PET, is referred to as biological target volume (BTV). The combination of GTV and BTV provides the ultimate planning target volume (PTV).
6. *Differentiation of tumor recurrence* versus *radiation injury.* This is currently the most common indication for a PET study. Radiotherapy is associated with a risk of radiation necrosis, especially in the case of tridimensional, conformal treatments that deliver high local doses to small volumes. The occurrence of necrosis is difficult to predict, and it is necessary to differentiate it from tumor recurrence. Radiotherapy-induced injury of the BBB and brain tissue causes edema, so that contrast enhancement may be evident on both CT and MR. This is a potentially confounding factor, because tumor recurrence is also characterized by contrast enhancement. This typically occurs for high-grade gliomas that invade cerebral vessels, thereby increasing BBB permeability. Thus, the observation of contrast enhancement on CT and MR requires further differential diagnosis.
7. *Assessment of response to therapy.* The majority of non-CNS cancers are responsive to some lines of chemotherapy, and the evaluation of response to therapy is a cornerstone of imaging in oncology. Instead, CNS tumors respond poorly to traditional chemotherapies, and metabolic changes induced by chemotherapy are not routinely evaluated. SPECT and PET studies were performed to assess the biological basis of the poor chemosensitivity of gliomas to most common chemotherapy drugs. Nevertheless, the development of some effective CNS chemotherapy agents, such as temozolomide, and, more recently, of antiangiogenic drugs, such as bevacizumab, has renewed interest in assessing the response to treatment. PET was also used in the past to address the effect on cerebral blood flow and glucose metabolism in response to dexamethasone, which is used to reduce edema and to alleviate neurological symptoms.

8. *Prognostic stratification*. Metabolic pattern as assessed by PET may be useful to predict the behavior of brain tumors. Such prognostic information may be obtained at any time point, i.e., initial staging, response to therapy, and restaging.

This classification of clinical indications for brain tumor imaging is "problem oriented." Not always is a PET scan requested to address all these issues, and some of them are strictly correlated. Using temporal criteria in relation to the main therapeutic events and very similarly to what is done in general oncology, PET scans are indicated in patients with brain tumors:

1. For initial staging
2. After surgery for the evaluation of residual mass
3. For restaging, when suspicious of recurrence or for differential diagnosis from radiation necrosis
4. For the evaluation of response to therapy

Prognostic information can be obtained with appropriate study designs at any time point.

However, tumor recurrence versus radiation necrosis is the typical restaging situation.

Overall Performance of Diagnostic Imaging Other Than Nuclear Medicine

CT is often the first modality employed in a patient presenting with a brain tumor, but MR is the reference imaging modality in brain tumor patients. The role of CT is largely confined to emergent imaging in the detection of hemorrhage, herniation, and hydrocephalus; however, the detection of mass effect from brain tumors and calcification within brain tumors, such as oligodendrogliomas or meningiomas, can have diagnostic relevance [17].

MR sequences exploring morphological features play a major role in the evaluation of and treatment planning of brain tumors. Standard sequences performed utilizing spin-echo techniques include T2 fluid-attenuated inversion recovery (FLAIR), pre-gadolinium T1, and post-gadolinium T1. These sequences are preferably performed in at least two orthogonal planes or obtained with a three-dimensional (3D) sequence that is reformatted into orthogonal planes (i.e., 3D T2 FLAIR). High-resolution isovolumetric sequences such as high-resolution 3D T2 sequences and post-gadolinium T1 spoiled gradient recalled acquisition or similar sequences are generally performed preoperatively with fiducials in place for use with intraoperative navigational software. Similarly, post-gadolinium T1 sequences are performed with a stereotactic head frame in place prior to stereotactic radiosurgery [20]. High-resolution 3D T2* gradient echo sequences, such as susceptibility weighted imaging, are also routinely performed. These susceptibility sensitive sequences are very sensitive to blood degradation products and calcification and may be helpful to depict post-radiotherapy micro-hemorrhages [17].

The primary roles of structural MR in initial brain tumor evaluation include determining the location of the lesion (i.e., intra-axial vs. extra-axial); establishing the specific location within the brain for treatment/biopsy planning; evaluating mass effect on the brain, ventricular system, and vasculature; and suggesting a possible diagnosis. Establishing the diagnosis of a specific tumor type can be challenging, but often the correct diagnosis can be limited to a short list of likely possibilities. Contrast enhancement indicates local breakdown of the blood–brain barrier and is a key feature seen in many brain tumors and other mass lesions. Within gliomas, contrast enhancement is generally considered to be associated with a high-grade tumor although certain low-grade gliomas, such as pilocytic astrocytomas in children, generally show contrast enhancement and certain high-grade gliomas may not enhance. Peritumoral edema is generally T2/FLAIR hyperintense signal abnormality surrounding the main mass lesion. This may in some instances, such as with metastasis, represent predominately vasogenic edema surrounding the lesion. However, with gliomas the peritumoral edema generally also represents infiltrative edema caused by tumor cells infiltrating into the regions of non-enhancing T2/FLAIR signal abnormality. The number of lesions is an important factor to consider

as a large number of lesions may signify certain pathologies, such as metastases. However, metastasis can be solitary, and demyelinating lesions or cerebral abscesses can also mimic tumor. Other potentially discriminating features to note include a cyst and mural nodule morphology (seen with the lower-grade tumor hemangioblastoma, pilocytic astrocytoma, ganglioglioma, and pleomorphic xanthoastrocytoma), calcification (generally seen with oligodendrogliomas), and necrosis and hemorrhage (generally seen in high-grade gliomas and hemorrhage also in certain metastases). Many of the same features are important in the ongoing evaluation of patients with known brain tumors. The updated version of the Response Assessment in Neuro-Oncology working group developed criteria based on MR to define response to treatment [21]. Diffusion-weighted imaging (DWI) offers insight into the diffusion of water molecules in tissues and can be used to calculate the apparent diffusion coefficient (ADC). ADC values derived from DWI have been shown to be reduced in highly cellular tumors, such as high-grade glioma. With regard to gliomas, lower ADC values have been reported in higher-grade gliomas than lower-grade gliomas, and lower ADC values have been reported to have a poorer prognosis independent of tumor grade [22].

Nuclear Imaging for Staging/Prognosis

Historical perspective. Several tracers have been used for imaging brain tumors (Table 5), and there are multiple mechanisms responsible for tracer uptake (Table 6). For several years, nuclear medicine techniques held a primary role for diagnosing brain tumors because CT entered into clinical practice in 1973 and MR a few years later. Pioneering studies with radiopharmaceuticals to detect brain tumors were carried out with ^{131}I-labeled serum albumin and, subsequently, with ^{203}Hg- or ^{197}Hg. Images were recorded with the rectilinear scanner developed by Benedict Cassen in 1950. Subsequently, with the advent of the scintillation camera (1959) [23], ^{99m}Tc-pertechnetate (^{99m}Tc), was primarily used for nuclear brain scanning. The advent of CT scanning, with markedly improved anatomic resolution, resulted in replacement of pertechnetate and ^{99m}Tc-DTPA brain scans. These radiopharmaceuticals display limited transport across the BBB in normal conditions, and the rationale to their use stemmed from altered BBB permeability in CNS pathologies. Dynamic acquisition allowed studying the perfusion of brain vessels, a procedure referred to as nuclear cerebral angiography [24].

Although thallium-201 chloride (^{201}Tl-chloride) and ^{99m}Tc-methoxyisobutylisonitrile (^{99m}Tc-sestamibi) were introduced later, both of them are no longer used today for CNS scintigraphy. ^{201}Tl ionic thallium is a substrate for the Na^+/K^+ ATPase pump, and thus ^{201}Tl uptake

Table 5 Most common current radiotracers for brain tumor imaging

Biological process	Radiotracer
Glucose transport across BBB and metabolism	[^{18}F]fluorodeoxyglucose ([^{18}F]FDG)
Amino acid transport and protein synthesis	[^{11}C]leucine
	[^{11}C]methionine ([^{11}C]MET)
	^{123}I-alpha-methyltyrosine (^{123}I-IMT)
	[^{11}C]tyrosine
	^{18}F-fluoroethyltyrosine (^{18}F-FET)
	alpha-[^{11}C]methyltryptophan
	[^{18}F]proline
Amino acid transport and dopamine metabolism	[^{18}F]fluoro-L-3,4-dihydroxyphenylalanine ([^{18}F]FDOPA)
Cellular proliferation	^{18}F-fluorothymidine (^{18}F-FLT)
	^{18}F-2-fluoro-5-methyl-1-beta-D-arabinofuranosyluracil (^{18}F-FMAU)
Somatostatin receptor imaging	^{111}In-DTPA-octreotide
	^{68}Ga-DOTANOC, ^{68}Ga-DOTATOC
Lipid metabolism	[^{11}C]choline/^{18}F-fluorocholine
Hypoxia	^{18}F-fluoromisonidazole (^{18}F-MISO)
	^{123}I-iodoazomycin arabinoside (^{123}I-IAZA)
	^{18}F-azomycin arabinoside (^{18}F-FAZA)
	^{64}Cu-methylthiosemicarbazone (^{64}Cu-ATSM)

Table 6 Factors affecting uptake of radiopharmaceuticals in gliomas

1. Perfusion and blood–brain barrier integrity
2. Histological grade
3. Glucose metabolic rate
4. DNA proliferation rate
5. Protein synthesis rate
6. Membrane (phospholipid) proliferation rate
7. Expression of membrane transporters
8. Oxygen tissue concentration (hypoxia)
9. Dimension of the lesion (partial volume effect)
10. Necrotic areas
11. Treatment with steroids
12. Radiotherapy treatment
13. Multidrug resistant phenotype
14. Expression of Na^+/K^+ ATPase
15. Expression of catecholamine binding sites
16. Glutathione content and redox potential
17. Intracytoplasmic and transmembrane esterase activity

reflects increased metabolic activity. The detection rate was reported as high as 85% [25–27], but it is important to consider that such figure was obtained with larger tumors than those investigated nowadays. False negatives were typically patients with small tumor size or tumors located in deep structures (basal ganglia and thalamus). Poor spatial resolution was the most important limiting factor for imaging. Investigators often failed to find a correlation between ^{201}Tl uptake and either tumor histology or cellular proliferation rate [28].

^{99m}Tc-sestamibi is a cationic lipophilic compound that accumulates in the cytoplasm and mitochondria as a result of passive diffusion across the negative cellular membranes. Cellular uptake is also dependent on the integrity of the mitochondrial membrane potential. Moreover, ^{99m}Tc-sestamibi kinetics is related to the multidrug resistance system (MDR1) and P-glycoprotein activity, and it may provide prognostic information about disease [29]. Thus, it was of interest to assess whether the tumor's response to chemotherapy can be predicted by ^{99m}Tc-sestamibi SPECT and whether ^{99m}Tc-sestamibi could be used for investigating the poor chemosensitivity of gliomas [30]. ^{99m}Tc-sestamibi findings were compared to the expression of the MDR1 gene and its product P-glycoprotein. SPECT in brain tumor patients showed increased uptake in patients who deteriorated clinically and negligible uptake in patients that did not recur, and MDR1 gene expression was inversely related to grade of malignancy [31]. The recent development of PET tracers for the evaluation of the MDR system drastically reduced the applications of ^{99m}Tc-sestamibi [32].

Brain Perfusion Imaging

^{99m}Tc-hexamethylpropyleneamine oxime (^{99m}Tc-HMPAO) and ^{99m}Tc-ethylcisteinate dimer (^{99m}Tc-ECD) rapidly diffuse across the BBB and distribute in the brain according to cerebral blood flow (CBF). The intracellular trapping mechanisms are different. ^{99m}Tc-HMPAO is reduced by glutathione-enriched molecules to a more hydrophilic compound that is not able to retrodiffuse. However, the redox potential of the cell also plays an important role for intracellular retention of ^{99m}Tc-HMPAO [33]. ^{99m}Tc-ECD enters the neurons and it is hydrolyzed to more hydrophilic forms by an intracellular esterase [34].

The most frequent pattern of the appearance of brain tumors is increased activity compared to the normal parenchyma [35]. Increased vascularity (i.e., blood volume) as well as increased CBF accounts for this finding. Moreover, some metabolic trapping related to glutathione activity and esterase activity has been shown for ^{99m}Tc-HMPAO and ^{99m}Tc-ECD [36]. The mean reported positive detection rate for the detection of brain tumors was around 70% with noteworthy differences among various studies attributed to the tracer (higher for ^{99m}Tc-HMPAO) and size of the lesions [35–37]. Brain tumor perfusion, measured with any of these tracers, did not correlate with tumor histology [36]. Brain tumors may also appear as a hypoactive (cold) area rather than a hot area. Cold tumors on ^{99m}Tc-HMPAO have been related to low glutathione content. Finally, heterogeneous appearance with cold areas mixed to hot areas can be found. This typically occurs in high-grade, large-sized tumors that display necrosis in their core. Similarly to other SPECT tracers, ^{99m}Tc-HMPAO and ^{99m}Tc-ECD dynamic

acquisitions and absolute measurements are not possible, and images have poorer spatial resolution than PET images. Therefore, these tracers should not be considered today of routine clinical use to study brain tumors.

2-Deoxy-2-[^{18}F]fluoro-D-glucose ([^{18}F]FDG)

[^{18}F]FDG allows measurements of tumor glucose metabolism. [^{18}F]FDG was the first PET tracer used for imaging brain tumors and it is still widely used nowadays, after more than 30 years [38]. The rationale for the use of [^{18}F]FDG is that tumor glucose consumption is increased and thus tumor metabolic activity relates to the biological behavior. Warburg first observed that, in contrast to normal differentiated cells, which rely primarily on mitochondrial oxidative phosphorylation to generate the energy needed for cellular processes, most cancer cells rely instead on anaerobic glycolysis, a phenomenon termed "the Warburg effect."

The 2-deoxyglucose (DG) model for quantifying the cerebral metabolic rate for glucose (CMR_{glc}) was defined by Sokoloff following autoradiographic experiments in rats [39]. DG is a glucose analog that differs from glucose by the substitution of fluoride atom for the hydroxyl group on the second carbon atom. It is transported across the BBB by the same transporter as that for glucose. Within the neuron, DG is phosphorylated to DG-6-P by hexokinase. Because of the lack of the hydroxyl group, [^{14}C]DG is not further metabolized and is therefore irreversibly trapped into neurons within the time frame of the experiment [39].

Patients are invited to fast for at least 6 h before tracer injection and hydrated. All modern tomographs are acquired today in 3D mode, which enable increased sensitivity and better signal-to-noise ratio. Between 125 and 250 MBq, [^{18}F]FDG is injected depending on the body weight [40]. A 10-min static acquisition is performed about 45-min postinjection (uptake period). The patient is allowed to rest in a quiet dimly lit room with eyes closed in a condition of minimal audiosensory stimulation during the uptake phase, i.e., from tracer injection to the start of PET scanning. Images are corrected for attenuation, scatter, and random coincidences. Subsequent image reconstruction is performed using filtered back projection or, more frequently, iterative reconstruction [40].

Using arterial input function, dynamic scanning, and kinetic analysis, it is possible to obtain a quantitative measurement of the parameter of interest, e.g., the cerebral metabolic rate of glucose [39, 41]. Using noninvasive approaches and a single static acquisition, it is possible to obtain qualitative or semiquantitative measurements. The standardized uptake value (SUV) and the tumor-to-non-tumor activity ratio are the most common semiquantitative indices.

According to a 2-tissue compartment, irreversible model, cerebral metabolic rate of glucose (CMR_{glc}) can be computed as follows:

$$CMR_{glc} = \frac{C_p}{LC}\frac{K_1 k_3}{k_2 + k_3} \quad (1)$$

where C_p is the mean glucose concentration, LC is the lumped constant (a factor that accounts for kinetic differences between glucose and deoxyglucose), K_1 and k_2 reflect glucose transport from plasma to brain and vice versa, and k_3 reflects glucose phosphorylation by hexokinase. The rate of DG-6-P accumulation is related to neural activity. Physiological consumption of glucose for gray matter is two- to fourfold higher than in white matter. The 2-deoxyglucose model was subsequently adapted to human studies with [^{18}F] labeling for PET.

Diagnosis and grading. Early studies in brain tumor patients stressed the importance of the functional information provided by PET compared to morphologic neuroradiological techniques. Much of this early work is credited to the group headed by Di Chiro at the National Institutes of Health [38, 42, 43]. Di Chiro et al. first used PET with [^{18}F]FDG in 23 patients with cerebral gliomas. All ten high-grade gliomas demonstrated focal tracer uptake that was easily visible (Fig. 1). Cerebral glucose utilization was often depressed in adjacent areas. Mean CMR_{glc} in high-grade gliomas was 7.4 ± 3.5 mg/100 g min. The 13 low-grade

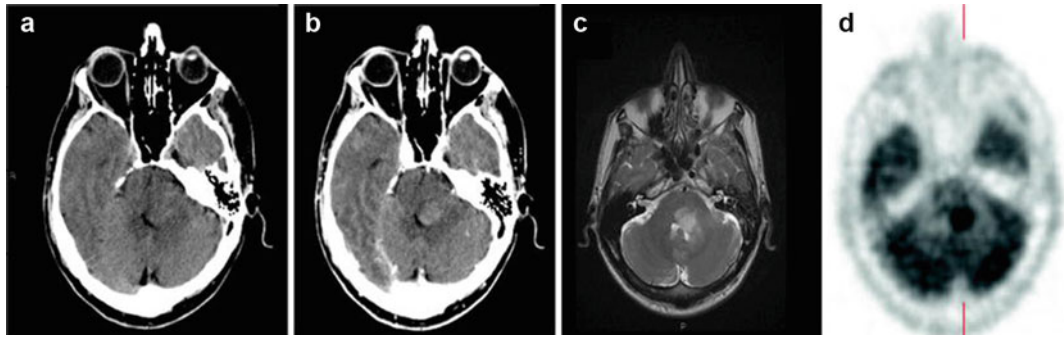

Fig. 1 A 42-year-old patient presented with headache and motor coordination impairment. Unenhanced CT (**a**), contrast enhancement CT (**b**), T2-weighted MR (**c**), and [^{18}F] FDG PET were performed. A focal area of increased glucose consumption in comparison to both *white matter* and *gray matter* is visible in the cerebellum. Visualization of the tumor is sharper on contrast enhancement CT compared to unenhanced CT. Biopsy revealed a high-grade glioma

gliomas had CMR_{glc} of 4.0 ± 1.8 mg/100 g min, with no distinctly visible hot spot. Thus, the rate of glucose metabolism was correlated to tumor malignancy [42]. This finding was considered as a major achievement because in those early times in vivo, noninvasive grading of neoplasms appeared much less intuitive as nowadays. The best cutoffs for the tumor-to-white matter ratio and the tumor-to-gray matter ratio for distinguishing high-grade gliomas and low-grade gliomas were 1.5 and 0.6, respectively. With these cutoffs, sensitivity and specificity were 94% and 77% [42]. Very similar results were obtained in a larger study 13 years later despite significant technological changes that had occurred meantime [44].

Brain tumors may induce suppression of metabolic activity in nearby normal and edematous tissue. Reduced glucose metabolism may occur also in normal brain tissue that is remote, but functionally linked to the site of the tumor (diaschisis) [45]. The cerebellum is a frequent site of metabolic reduction that is typically contralateral to the site of the tumor (crossed cerebellar diaschisis). Cerebellar hypometabolism is ascribed to functional interruption of the contralateral cerebropontine-cerebellar pathway [46].

Qualitative vs. *quantitative*. Which analysis method should be used for interpreting brain tumor images? Each analysis method has advantages and disadvantages (Table 7). PET was originally developed as a quantitative technique, and the first applications used arterial line input function for quantitative measurement of CMR_{glc}. However, for clinical purposes analysis did not always match histopathology results [47]. Moreover, a significant difference in glucose metabolism between high-grade and low-grade gliomas was not always detected [48]. This has noteworthy importance when passing from group analysis of research studies to single subject analysis of the clinical routine. Methodological considerations and technological factors cast into doubt the validity of the [^{18}F]FDG model in brain tumors. Sokoloff first noted that the lumped constant value in tumors was different from that in normal brain. Rate constants could also change as a consequence of altered metabolism [49]. Finally, tissue inhomogeneity, which is thought to introduce an overestimation of CMR_{glc} in normal cerebral tissue, is expected to have a greater effect with old scanners, because of poorer resolution [50]. By partial volume effect, measurements in a certain ROI reflect the spillover of activity into neighbor areas as well spill in of activity from neighbor areas [51]. Partial volume effect would artificially decrease CMR_{glc} in rim-shaped hypermetabolic areas for which ROI analysis would include significant amount of white matter. On the basis of these considerations, visual analysis has been advocated for clinical routine purposes, while PET quantitation with arterial line input function should be limited to restricted research protocols [52].

Table 7 Characteristics of quantitative and semiquantitative brain PET studies with [^{18}F]FDG

	Quantitative studies	Qualitative studies
Arterial input function	Necessary	Not necessary
Acquisition	Dynamic (frames ranging from 30 s to 5 min for a total of 60 min)	Static (10–15-min acquisition 45-min postinjection)
Glycemia	Necessary	Not necessary
Parameters	CMR_{glc} (mg/glc/100-g brain tissue)	SUV
		Tumor-to-non-tumor ratio
		Visual analysis
Data analysis	Time-consuming and technically challenging computer programming	None to simple (ROI analysis)
Diagnostic yield	Greater accuracy than semiquantitative analysis not proven	Sufficient for the vast majority of routine clinical tumor cases
Metabolic specificity	Not specific for tumor	Not specific for tumor
Pitfalls	Lumped constant assumed to be equal to normal brain	Visual analysis subject to subject bias
Application	Preferred for research studies	Preferred for clinical diagnostic routine

Subjectively, [^{18}F]FDG uptake within a tumor region is compared to the contralateral white matter region or, less frequently, to contralateral gray matter region. Accordingly, high-grade tumors have metabolism greater than white matter, and low-grade tumors have metabolism that is similar or lower than white matter. Semiquantitative measurements, such as SUV or tumor-to-white matter ratios, may be useful. Tumor-to-white matter ratios do not have some limits of SUV, because biases due to global factors are being canceled out as the ratio of the two ROIs is computed. Visual analysis is standard today in the clinical activity [48, 53–55].

Glucose loading. It is apparently paradoxical that, while patients are being asked to fast before a PET scan, glucose loading might have been used for increasing the diagnostic possibilities of [^{18}F]FDG PET in patients with brain tumors. Indeed, glucose loading has been used for enhancing detection of gliomas. Hyperglycemia reduces [^{18}F]FDG transport/uptake into the brain due to direct competition with the glucose transporter. This effect is less marked in brain tumors than in normal cortex because [^{18}F]FDG uptake in tumors occurs also through BBB breakdown. Thus, glucose loading resulted in an increased tumor-to-cortex ratio [56, 57]. Although this technique provided promising results and glucose loading is a relatively simple and safe procedure, this approach did not achieve widespread clinical use.

Late acquisition. Delayed or dual time point imaging is a successful approach used in oncological [^{18}F]FDG PET applications with the aim to increase sensitivity. The underlying rationale is that in many tumors, [^{18}F]FDG uptake continues beyond the usual 45-min uptake period, while at this time, the tracer has reached equilibrium between plasma and normal tissues. Because of the slower kinetic of the tracer in neoplasms compared to normal tissue, proportionally greater activity will be detected in tumor tissue compared to normal tissue as the interval from injection to imaging increases. Delayed imaging (90-min postinjection) increased the tumor-to-cortex contrast. This is due to both increased activity in the tumor as well as increased washout of the tracer from normal brain [58].

Tumor recurrence vs. *radiation necrosis*. The gold standard for distinguishing tumor recurrence from radiation necrosis is biopsy. The accuracy and specificity of biopsy can be as high as 95%, although biopsy of an edematous or gliotic site may be nondiagnostic [59]. Early studies showed that CMR_{glc} was increased in patients with tumor recurrence and low in patients with necrosis [60]. Even though these results were confirmed in study groups, false positives often occur on a patient-by-patient basis. Increased [^{18}F]FDG accumulation may occur following radiotherapy because of radiation-induced inflammation. The ratio between glucose metabolism in the tumor and in the contralateral remote white matter increases from 25% to 42% 1 day post-radiotherapy

and then decreases toward baseline values 7 days post-radiotherapy. Therefore, specificity may be as low as 40–60%, while sensitivity is generally high [61].

Stereotactic biopsy guidance. PET has the potential to increase the diagnostic yield of brain biopsy by selecting the areas that display highest tracer uptake and therefore are more likely to contain high-grade histotype. Specifically, stereotactic trajectories in areas of increased uptake are more often diagnostic and yield a higher proportion of high-grade gliomas. Based on these results, and similar findings obtained with other tracers, stereotactic PET-guided biopsy is now recommended [62].

Treatment planning. PET with [^{18}F]FDG showed promise for improving the accuracy of defining the target volume and for radiation dose escalation. An early study indicated that patients with glioblastoma multiforme can be treated with standard conformal fractionated radiotherapy if there is no [^{18}F]FDG uptake, while an additional boost is indicated in patients with increased [^{18}F]FDG uptake. [^{18}F]FDG PET volumes were predictive of survival and time to tumor progression [63]. These results, however, could not be replicated by the same group [64]. The use of [^{18}F]FDG for treatment planning remains a controversial issue considering the current more widespread use of amino acid tracers. [^{18}F]FDG might be of special interest in high-grade gliomas exhibiting marked intratumoral heterogeneity where hot spots could be possible targets for dose escalation [55].

Advantage and disadvantages of [^{18}F]FDG and of most common tracers used for brain tumor imaging are summarized in Tables 8 and 9.

Radiolabeled Amino Acids

Introduction. Neutral L-amino acids are essential amino acids; they cannot be synthesized by the brain, and, therefore, they must be supplied either by breakdown of endogenous proteins or by the diet. Since a single type of transport carrier mediates the transcapillary movement of structurally related amino acids, these compounds compete with each other for entry into the brain. After entering the neurons, amino acids may be used for protein synthesis or for other metabolic pathways.

Amino acids are the building blocks of proteins. The rate of protein synthesis is increased in proliferating brain tumors, which makes its measurement an important target for in vivo imaging. This measurement, however, held several

Table 8 Most important favorable and unfavorable characteristics of common current radiopharmaceuticals for brain tumor imaging

	Advantages	Disadvantages
[^{18}F]FDG	Easily available, overall good accuracy, good-quality images	High physiological uptake in normal brain
	Allows tumor grading	False positive by radiation necrosis and infection
	Correlates with prognosis	
Amino acid tracers	Available for PET as well as for SPECT	Tracer uptake is poorly affected by tumor grade
	Negligible uptake in normal brain	
	Optimal tumor delineation and contrast	
	Correlates with prognosis	
	Very high negative predictive value for distinguishing recurrence from necrosis	
	Useful for definition of radiotherapy plan	
^{18}F-FLT	Negligible uptake in normal brain	Uptake heavily affected by BBB integrity
	Optimal tumor delineation and contrast	Kinetic analysis with metabolite correction is required to distinguish BBB disruption from increased metabolism
	Superior to amino acid tracers for grading	
	Allows differential diagnosis between tumor recurrence and necrosis	

Table 9 Sensitivity and specificity for diagnosis of brain gliomas/gliomas recurrence for most common PET tracers[a]

Tracer	Sensitivity (95% CI)	Specificity (95% CI)	Indication	Reference	Study
[^{18}F]FDG	94%	77%	Diagnosis	[42]	Monocentric
[^{18}F]FDG	75%	81%	Necrosis versus tumor recurrence	[183]	Monocentric
[^{18}F]FDG	0.77 (0.66–0.85)	0.78 (0.54–0.91)	Necrosis versus tumor recurrence	[184]	Meta-analysis
[^{11}C]MET	0.70 (0.50–0.84)	0.93 (0.44–1.0)	Necrosis versus recurrence	[184]	Meta-analysis
[^{11}C]MET	75–95% (range)	87–100% (range)	Diagnosis	[7]	Review
^{18}F-FET	0.82 (0.74–0.88)	0.76 (0.44–0.92)	Diagnosis	[92]	Meta-analysis
^{18}F-FLT	79%	63%	Diagnosis	[185]	Monocentric

[a]Note that these values should be taken cautiously because they depend on several variables, including gold standard, clinical indication, tumor grade and dimension, sample size, analysis method, and type of study (single center, multicenter, or meta-analysis). Multitracer single studies are generally more informative for the comparison between two tracers. For these reasons, only some studies are cited

methodological restrictions. In the deoxyglucose method, intracytoplasmic trapping is the only active metabolic pathway, there are no radioactive metabolites, and computation of glucose metabolism is conceptually easy. For amino acids this is not the case. In addition to protein synthesis, amino acids can either be metabolized by transamination (rapidly followed by decarboxylation for CO_2 production) or enter other metabolic pathways. For some amino acids, typically ^{18}F-FET and ^{123}I-IMT, the intracellular metabolism is negligible and uptake is thought to reflect primarily transport across the BBB [65, 66]. Independently by the targeted biochemical process, amino acid tracers have shown to be useful for imaging brain tumors on several grounds.

[^{11}C]Methionine. Methionine (MET), an essential sulfur amino acid, is necessary for growth and development. At variance with [^{18}F]FDG, labeled amino acid uptake in normal cortex is very low. For this reason their uptake is not sensitive to visual and auditory stimulation enabling a simpler PET procedure. Most importantly, the role of amino acids in mediating an inflammatory tissue response is much less important than for glucose [67]. Thus, high specificity could be predicted. Soon after the publication of rapid high-yield procedures for labeling of methionine with ^{11}C ([^{11}C]MET), experiments were carried out to investigate the clinical role of [^{11}C]MET in various clinical settings.

Diagnostic accuracy. The overall sensitivity of [^{11}C]MET PET for distinguishing gliomas from nonmalignant lesions has been estimated to be around 75–95%, with somewhat lower values sometimes reported in low-grade gliomas, where uptake may occasionally be negligible. More interestingly, specificity of [^{11}C]MET PET ranged between 87% and 100% [68].

Grading. On the other hand, the predictive value of [^{11}C]MET PET for grading is limited. Several studies showed that [^{11}C]MET is taken up by gliomas irrespective of grade and that there is sizeable overlap in uptake values between low-grade and high-grade gliomas. Nevertheless semiquantitative analysis allows differentiating high-grade and low-grade gliomas better than visual analysis [68, 69].

Prognosis. In grades II and III gliomas, higher tumor to contralateral count ratios are associated with reduced survival. No such association was observed within the grade IV glioma group, most likely because of the overall poor prognosis in all these patients [70]. The prognostic value of [^{11}C]MET uptake has been consistently replicated in various studies [71].

Tumor extent determination. The critical factor in determining the edges of the tumors is the

method used for distinguishing significant from negligible tracer uptake. There is currently no consensus on the best method for this purpose. Visual qualitative and several semiquantitative methods have been adopted: fixed percent threshold value of tumor uptake, tumor-to-non-tumor ratios, absolute SUV values, and automatic software-based segmentation algorithm are some examples of such techniques. Irrespective of the method used, [^{11}C]MET PET delineates a larger volume in comparison to MR or [^{18}F]FDG PET. Integrating [^{11}C]MET PET with MR images is useful for planning surgery, with ensuing clinical impact in about 80% of the procedures [72–74]. The integration of [^{11}C]MET PET with morphological imaging was also useful for defining the radiotherapy plan [74, 75] (Fig. 2). PET guidance is considered necessary for defining the amount of tissue to be removed in brain tumors.

Tumor biopsy. Tumor biopsy is necessary before initiating any form of treatment. Although the poorer relation between [^{11}C]MET uptake and grading does not allow predicting the highest tumor grade, [^{11}C]MET PET has been advocated to reduce the number of required biopsy attempts and to reduce the risk of damaging functional areas in patients with brain tumors [72–74].

Therapy assessment and follow-up. Following surgical or radiation therapy, [^{11}C]MET PET can be repeated for assessing response to treatment, as well as for planning potential second-look surgeries. Prolonged survival in grades III and IV glioma patients with no [^{11}C]MET uptake after surgical resection as compared to those with residual [^{11}C]MET uptake has been reported [76].

Tumor recurrence vs. *radiation injury.* Because of limitations of [^{18}F]FDG for discriminating recurrent tumor from radiation injury, several authors investigated the usefulness of [^{11}C]MET PET (Fig. 3). Comparative evaluations show a greater accuracy of [^{11}C]MET PET than [^{18}F]FDG PET for the differential diagnosis. The use of semiquantitative binding provides a more robust tool to the differentiation of tumor recurrence from radiation injury [77].

3-^{123}I-Alpha-Methyltyrosine (^{123}I-IMT) and *O*-(2-^{18}F-Fluoroethyl)-L-Tyrosine (^{18}F-FET)

Several amino acid-derived radiopharmaceuticals can also be labeled with single-photon emitters, allowing a less expensive, more widely accessible

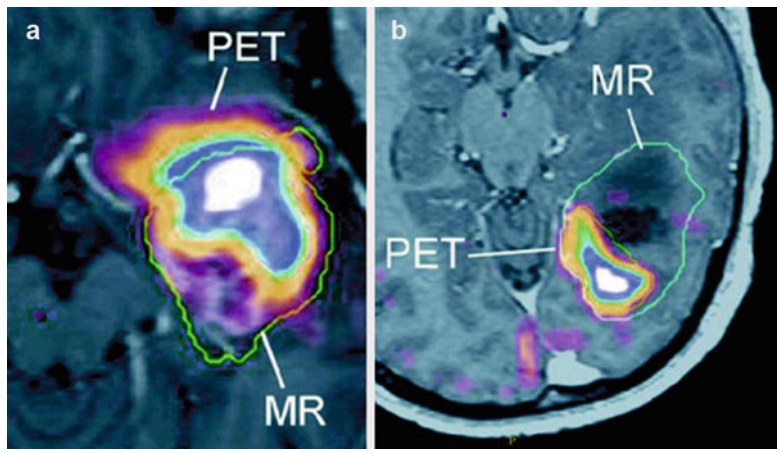

Fig. 2 Two examples of the use of PET in the definition of a radiotherapy plan. Tracer uptake on [^{11}C]MET PET is mapped with different colors according to its intensity. (**a**) Patient with left temporal anaplastic astrocytoma. PET contour projects out of the MR contour and some MR voxel extend out of the PET contour. The integration of both information will define the ultimate radiotherapy treatment plan. (**b**) Patient with left posterior temporal-occipital anaplastic oligoastrocytoma. In this case a greater discrepancy was found between the volume identified by [^{11}C]MET PET and the volume identified by MR (Reprinted with permission from Ref. [74])

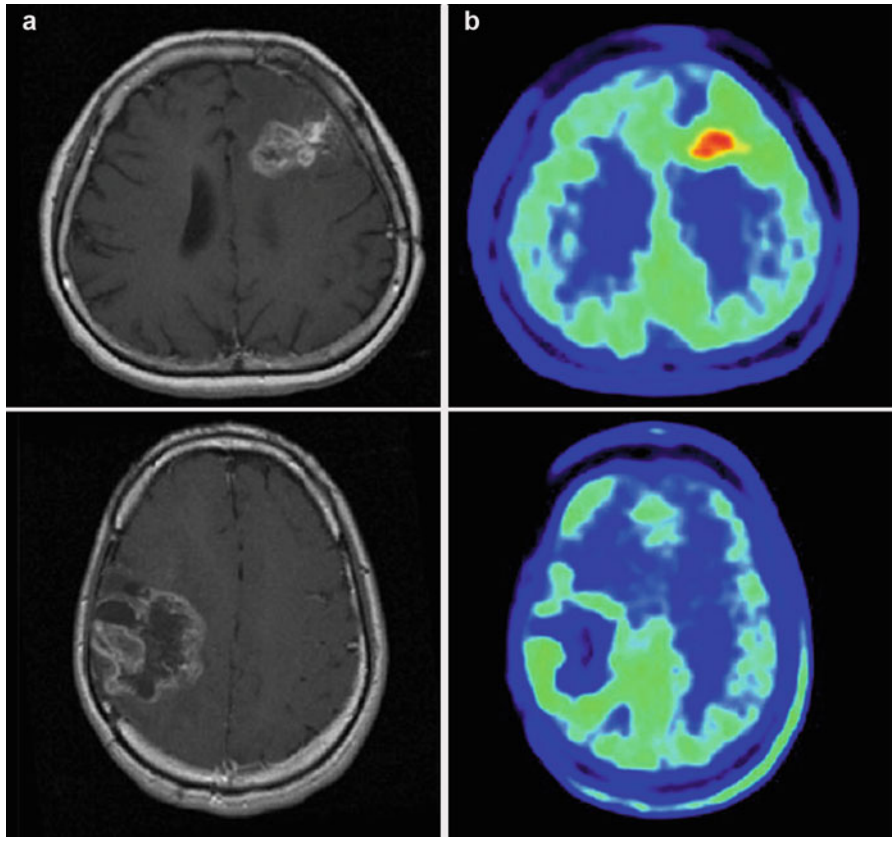

Fig. 3 (*Top*) Images of a 49-year-old woman who had been previously treated for glioblastoma multiforme with tumor resection and conventional radiotherapy at dose of 60 Gy. (**a**) T1-weighted MR image with contrast medium, obtained 13 months after initial surgery, showing contrast-enhanced lesion in the left frontal lobe. (**b**) [^{11}C]MET PET image showing focal accumulation of tracer corresponding to the abnormality on MR image. Recurrent tumor was pathologically confirmed by second surgery. (*Bottom*) Images of a 25-year-old man who had been previously treated for anaplastic astrocytoma with tumor resection and conventional radiotherapy at dose of 60 Gy. (**a**) T1-weighted MR image with contrast medium, obtained 21 months after initial surgery, showing ringlike enhancement of lesion in the right parietal cortex. (**b**) [^{11}C]MET PET image showing slight accumulation of tracer corresponding to abnormality on MR image. Gliosis without tumor was pathologically demonstrated by second surgery. Both images exemplify the primary role exerted by PET with ^{11}C-MET in distinguishing tumor recurrence from radiation necrosis (Reprinted with permission from Ref. [77])

technique for imaging protein synthesis in brain tumors. The interest has been twofold: (1) to develop and validate the clinical use of such tracers and (2) to compare the performance of SPECT tracers to PET tracers.

^{123}I-IMT may be considered the prototype of SPECT amino acid tracers. ^{123}I-IMT has a similar affinity to the neutral amino acid carrier at the BBB as L-tyrosine, but is not further metabolized and not incorporated into proteins [78]. BBB disruption and active transport through the natural amino acid carrier represent the mechanisms of tracer uptake [79]. Uptake in normal brain tissue is negligible, a feature that allows optimal contrast between tumor and surrounding normal cortex [78, 79].

The sensitivity and specificity for discriminating gliomas from nonneoplastic lesions is in about the same range as amino acid PET tracers. The accuracy is generally higher for high-grade gliomas compared to low-grade gliomas [80]. Low-grade gliomas are more difficult to

distinguish from nonneoplastic lesions owing to their lower uptake [81–83].

^{123}I-IMT SPECT has been compared to [^{18}F]FDG PET for studying tumor and non-tumor lesions. Tumor uptake ratios were higher for ^{123}I-IMT than [^{18}F]FDG. Despite the lower resolution and lower sensitivity of SPECT compared with PET, ^{123}I-IMT SPECT was superior to [^{18}F]FDG PET in the detection and delineation of tumor tissue. Better tumor delineation was obtained with PET and either [^{11}C]MET or ^{18}F-FET compared to ^{123}I-IMT SPECT [81, 84].

^{123}I-IMT SPECT may be used in radiotherapy planning. The tumor volume defined by ^{123}I-IMT uptake was compared with the volume of the hyperintensity areas of T2-weighted MR and with the volume of contrast enhancement on T1-weighted MR. ^{123}I-IMT-defined tumor volume increased the radiotherapy target volume based on T2 and T1 images by about 30–40% and led to an increase in boost volume by 20%. Current approaches recommend the use of radiolabeled amino acid SPECT or PET tracers for definition of the target volumes for radiotherapy planning [85].

The wider availability of PET/CT scanners led to an increase of the use of ^{18}F-FET [86]. After i.v. administration ^{18}F-FET is taken up by both tumor and normal brain tissue. ^{18}F-FET uptake increases in normal gray and white matter to reach a plateau 20-min postinjection and the value remains stable until 120-min postinjection [87, 88]. In brain tumors, ^{18}F-FET kinetics depends on histology and grade. ^{18}F-FET is taken up by neoplastic cells, but is not incorporated into proteins, in contrast to natural amino acids such as [^{11}C]MET, which has a 15% incorporation rate [89, 90]. The uptake mechanism of ^{18}F-FET tracer is complex and not fully understood, but it seems to involve multiple pathways, including the specific LAT1 subtype system and the ubiquitous Na-dependent system $B^{0,+}$ and B^0 [91, 92].

As to the imaging protocol, patients should be fasting for about 4 h before trace injection to avoid saturation with unlabeled L-amino acid modifying FET transport into tumor cells. After injection, PET images are dynamically acquired for about 40–60 min (8–12, 5-min frames, or 4–6, 10-min frames) [86, 93].

^{18}F-FET PET image analysis provides both qualitative and quantitative information. The use of last acquired averaged frames (40–50 or 50–60 min) allows the reduction of brain–blood noise and improves the signal-to-noise ratio. Lesion maximum and SUV_{mean} are usually determined by averaging later frames. Moreover, using a manually drawn or an automatic region of interest (ROI), the contralateral normal brain uptake and maximum and mean tumor-to-background ratios (TBR_{max}, TBR_{mean}) may be computed. By locating ROIs on all slices in which the tumor is represented, a volume of interest (VOI) around the tumor is generated, on each frame of the dynamic acquisition to compute time–activity curves [12],

Numerous, but usually small studies assessed ^{18}F-FET PET value in the diagnosis of primary brain tumors. ^{18}F-FET PET was shown to be more accurate than ^{123}I-IMT SPECT [84], [^{18}F]FDG [12, 94], ^{18}F-fluorothymidine PET [95], and ^{18}F-fluorocholine PET [96] to detect brain tumors.

A recent meta-analysis of 13 studies on the use of ^{18}F-FET PET in primary brain tumor including 462 patients showed sensitivity and specificity of 82% (95% confidence interval 74–88%) and 76% (44–92%), respectively [92]. Using ROC analysis TBR_{mean} and TBR_{max} higher than 1.6 and 2.1, respectively, provided the best diagnostic value for differentiating primary brain tumors from non-tumoral lesion. Moreover, TBR_{mean} and TBR_{max} were significantly lower in grade I–II gliomas as compared with grade III–IV gliomas.

Even though on a group basis, SUV and TBR allow identification of differences in ^{18}F-FET uptake and metabolism between gliomas and non-tumoral lesions, on a single subject basis, this discrimination is more difficult because of metabolic overlap found among the different WHO grades [92]. Analysis of time–activity curves allows improving the differentiation between low- and high-grade gliomas. Early (<15 min) maximal uptake followed by a decreasing curve has been related to high-grade glioma, and late (>15 min) maximal uptake followed by a steadily rising curve has been related to low-grade tumor [97–99].

L-3,4-dihydroxyphenylalanine ([^{18}F]fluorodopa, [^{18}F]FDOPA). Among other amino acid

tracers, a growing important role is being played by [^{18}F]FDOPA, which is also sensitive to dopamine metabolism. Other than in the striatum and the substantia nigra, where the uptake of the tracer is physiologically high, [^{18}F]FDOPA displays low uptake in all the remaining brain areas. Contrary to studies performed for the diagnosis of movement disorders, where a dynamic scan or a late scan acquisition at about 70 min are performed, for tumor imaging, an early scan at 20-min post-injection is preferred. With ongoing interval from injection, the specific uptake in the striatum increases, and it may mask either the visualization or tumor in the proximity of the basal ganglia or other tumors that have low [^{18}F]FDOPA uptake. At 20-min p.i., the uptake in tumor is on the contrary similar or higher than in the basal ganglia [100].

[^{18}F]FDOPA PET/CT is highly sensitive and specific for the detection of glioma recurrence, it is superior to [^{18}F]FDG, and it is especially advantageous in patients with low-grade gliomas [101, 102]. Tripathi et al. directly compared the performance of [^{18}F]FDOPA, [^{18}F]FDG, and ^{18}F-FLT in evaluating primary and recurrent low-grade gliomas. SUV_{max} for [^{18}F]FDOPA was two to three times higher than for ^{18}F-FLT, but it was lower than and for [^{18}F]FDG. This shows that ^{18}F-FLT uptake is generally low in gliomas. The authors concluded that [^{18}F]FDOPA is superior to ^{18}F-FLT and [^{18}F]FDG for low-grade gliomas [103].

It was also shown that PET/CT with [^{18}F]FDOPA has greater diagnostic power compared to MR for the differential diagnosis between tumor recurrence and radiation necrosis. Specifically, sensitivity, and accuracy were 92.3%, 44.4%, and 80% for MR and 100%, 88.9%, and 97.1% for [^{18}F]FDOPA [102].

A very interesting study [100] was performed to address the comparative value of [^{18}F]FDOPA versus [^{11}C]MET, which is the most widely used amino acid tracer for detecting tumor recurrence and generally considered as the gold standard. [^{11}C]MET and [^{18}F]FDOPA images matched in all patients and showed all lesions as hot spots with higher uptake than in the contralateral brain. SUVs and tumor/contralateral did not statistically differ between the two tracers. The authors concluded that [^{18}F]FDOPA is accurate as a surrogate for [^{11}C]MET in imaging amino acid transport in malignant cerebral lesions for the purpose of visualization of vital tumor tissue. It combines the good physical properties of ^{18}F with the pharmacological properties of [^{11}C]MET and might therefore be a valuable PET radiopharmaceutical that can be more widely used for brain tumor imaging in centers without a cyclotron [100].

Tumor proliferation. Increased cell proliferation rate is a well-known hallmark of cancer. The key step for cell proliferation is DNA synthesis. Thus, different radiotracers were developed to assess in vivo DNA synthesis. Thymidine is a pyrimidine used for DNA but not for RNA synthesis. This selectivity made this compound the first choice for assessing proliferation. Thymidine is incorporated into DNA through the exogenous (salvage) pathway for pyrimidines, through phosphorylation to thymidine triphosphate. The salvage pathway represents only a minor source for thymidine synthesis because the majority of thymidine is synthesized through the de novo pathway. Nevertheless, as the two pathways are competitive in physiological conditions, both are informative on DNA synthesis, while only the salvage pathway can be measured for the limited number of compartments involved and modeling assumptions. Imaging of DNA proliferation was expected to be superior to imaging of glucose metabolism for assessing response treatment, because cells may maintain their oxidative and glycolytic function in spite of impaired DNA synthesis [104].

Initial PET studies were performed with [^{11}C]thymidine. This tracer is rapidly metabolized producing several labeled compounds, primarily [^{11}C]CO_2, that retrodiffuses into the brain affecting the time–activity curve [105]. The exponentially growing complexity of metabolites correction combined to the low signal-to-noise ratio due to ^{11}C-labeling limited the use of this compound.

More recently, 3-deoxy-3-^{18}F-fluorothymidine (^{18}F-FLT, a thymidine analog) was developed. ^{18}F-FLT offers the advantages of ^{18}F-labeling and a more favorable radiometabolite profile [106]. However, the blood–brain barrier limits cellular uptake of ^{18}F-FLT [107]. ^{18}F-FLT uptake is a function of the plasma input function and the rate of its

transport across the blood–brain barrier; therefore, a complete kinetic model of ^{18}F-FLT uptake, transport, and metabolism is needed to accurately quantify DNA synthesis in brain tumors [108]. Without such a model, ^{18}F-FLT is unlikely to perform better than an inert contrast agent, such as gadolinium chelates, in brain tumor imaging. The assumption that ^{18}F-FLT standardized uptake value reflects primarily the uptake of the tracer into the DNA synthesis pathway is potentially misleading in CNS neoplasms [109].

Patients with brain tumors have increased tracer incorporation (K_i). In high-grade tumors where CBF is also increased, the increased tracer incorporation may partially be related to blood flow [107] (Fig. 4).

Probably owing to the difficult modeling strategy, findings differed among studies. For example, authors reported a significant correlation between ^{18}F-FLT K_i or k_3 and Ki-67 immunostaining, while no significant correlation was found for ^{18}F-FLT uptake ratios [108]. Others reported that uptake ratios have similar power as kinetic analysis to predict long-term survival [110]. ^{18}F-FLT (83%) had slightly lower sensitivity than [^{11}C]MET (88%), and both tracers have 100% specificity. SUV_{max} for [^{11}C]MET was significantly higher in high-grade gliomas compared to low grade, although there was a wide overlap. For ^{18}F-FLT, the difference was more relevant. ^{18}F-FLT was slightly superior to [^{11}C]MET for tumor grading. Although the two tracers explore two different biological processes, there is no substantial additional advantage by their sequential use [111].

Radiolabeled choline. Radiolabeled choline (either [^{11}C]choline or ^{18}F-fluorocholine), a phospholipid precursor, is a tumor-seeking radiopharmaceutical that has emerged because of its alleged potential to image membrane proliferation. While it is known that choline is a precursor of phospholipids (through the synthesis of phosphorylcholine), there are currently insufficient data to support the assumption that [^{11}C]choline labels uniquely membrane phospholipids. The rationale behind the clinical use of this PET tracer derived from in vivo studies with proton magnetic resonance spectroscopy showing elevated signal of choline-containing compounds (i.e., phosphorylcholine and glycerophosphocholine) in brain tumors [69]. Other metabolic pathways include the synthesis of acetylcholine and conversion to

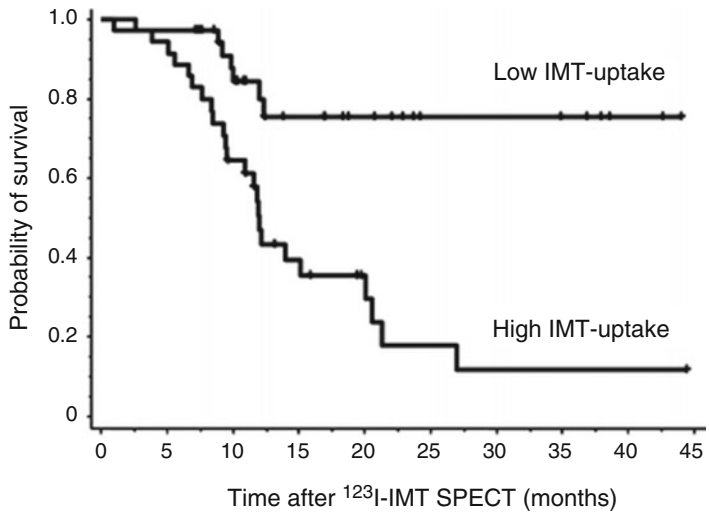

Fig. 4 Kaplan–Meier curves of overall survival among patients with postoperative low ^{123}I-IMT uptake and high ^{123}I-IMT uptake. Survival is significantly shorter in patients with ^{123}I-IMT uptake ratio >1.7 compared to patients with ^{123}I-IMT uptake ratio <1.7. The figure exemplifies the high prognostic power of functional nuclear medicine techniques, even in the case of SPECT (Reprinted with permission from Ref. [83])

betaine, while a significant amount of precursor remains unmetabolized in the cytoplasm [69]. However, regardless of the measured biochemical process, [^{11}C]choline did show to be useful for imaging and for assessing the response to therapy of gliomas and meningiomas.

The tracer displayed an excellent capability to delineate the tumor contours due to the negligible uptake by normal brain. As already noted for PET with amino acid tracers, this feature has been shown to be useful to guide biopsy and for radiotherapy planning [112]. Nevertheless, pitfalls may also occur. False positives are generally of greater concern than false negatives and are due to some accumulation of the tracer in inflammatory lesions [113]. Increased tracer uptake may occur also in brain metastases from other tumors and in meningiomas [114].

Higher [^{11}C]choline uptake has been reported in high-grade gliomas compared to low-grade gliomas [115]. Presently, there are discrepant findings on the issue whether [^{11}C]choline tumor metabolism, as measured by PET/CT, predicts [115–117] or does not predict tumor grade [69]. In a multitracer study, tracer uptake was significantly higher in high-grade gliomas than in low-grade gliomas for [^{11}C]choline, but not for [^{18}F]FDG [116]. However, [^{11}C]choline PET/CT could not differentiate between low-grade gliomas and benign lesions because of the relatively low uptake in low-grade tumors [116]. In a large study enrolling 94 patients with suspected brain tumor, [^{11}C]choline had greater accuracy than [^{18}F]FDG (84% vs. 71%). The authors concluded that, after accounting physiological variants and potential pitfalls of the tracer, [^{11}C]choline might have greater potential than [^{18}F]FDG for brain tumor PET imaging [113]. Another multitracer study compared [^{11}C]MET, [^{11}C]choline, and [^{18}F]FDG. The authors measured the ratio of tumor uptake to normal brain uptake (T/N ratio), using the frontal cortex as reference region, and analyzed the correlations between tracer uptake and tumor grade, type, and proliferation activity. Whereas all three tracers showed a similar correlation between the T/N ratio and tumor grade in astrocytic and oligodendroglial tumors, [^{11}C]MET enabled the most straightforward visual localization of hot lesions [118].

Until now, there have been few applications of [^{11}C]choline PET/CT for radiation therapy planning. [^{11}C]choline PET/CT could better delineate the boundaries between lesions and surrounding normal brain tissues compared with MR, and the standard radiotherapy target volume was changed in 31% of patients [117]. In posttreatment patients with high-grade gliomas, lower [^{11}C]choline uptake predicted longer survival [119]. [^{11}C]choline PET/CT can be used to distinguish brain tumor recurrence from necrosis after radiotherapy with sensitivities and specificity that might be higher than those of MR [120].

Imaging tumor hypoxia. Hypoxia is defined as reduced O_2 tissue concentration. Hypoxia in tumors is associated with progression, as well as resistance to radiotherapy and to some chemotherapy regimens. Several bioreductive radiopharmaceuticals have been evaluated as hypoxia tracers. These tracers include nitroimidazole compounds, e.g., ^{18}F-fluoromisonidazole (^{18}F-MISO), ^{123}I-iodoazomycin arabinoside (^{123}I-IAZA), ^{18}F-azomycin arabinoside (^{18}F-FAZA), and ^{64}Cu-labeled methylthiosemicarbazone (^{64}Cu-ATSM). The common feature of these different tracers is that tissue binding is sensitive to tissue oxygen concentration. Specifically, as the tissue oxygen level decreases, irreversible trapping increases. Different parameters are being used to quantify tissue binding, including tissue-to-plasma ratios, SUV_{max}, a percent threshold of SUV_{max} (hypoxic volume), distribution volume (derived from the plasma input function), and pixel-based maximum-intensity-projection plots obtained using statistical parametric mapping. The correlation of such parameters with tissue oxygen tension measured with fine needle oxygen electrodes (the gold standard for measuring hypoxia) is generally not performed in humans because such procedure is invasive [121].

PET studies of brain tumor hypoxia are relatively scant and mostly limited to the use of ^{18}F-MISO [122]. ^{18}F-MISO freely crosses the blood–brain barrier and rapidly equilibrates within tissues independently of perfusion [123]. Tracer uptake in glioblastomas multiforme is heterogeneous. Increased ^{18}F-MISO tumor uptake is generally found in the periphery but not in the

center of glioblastomas multiforme (Fig. 5). The latter finding is expected, because only viable cells are able to accumulate ^{18}F-MISO, and delivery to necrotic tissue is low. This pattern is also consistent with the spatial distribution of the hypoxia-inducible factor 1 that is more expressed in tumor areas adjacent to necrosis but not in necrosis per se [124].

No correlation was found between delayed ^{18}F-MISO uptake and [^{15}O]water distribution in brain tumors, thus indicating that hypoxia may occur also in cerebral areas with normal CBF. Hypoxic volume measured with ^{18}F-MISO is a significant prognostic factor for survival. ^{18}F-MISO uptake was greater in high-grade gliomas than in low-grade gliomas [125]. In a more recent prospective study of glioma patients who underwent both ^{18}F-MISO and [^{18}F]FDG PET examinations, ^{18}F-MISO PET showed an improved ability to distinguish glioblastoma from lower grades as compared to [^{18}F]FDG [126].

PET/MR

The development of magnetic field-insensitive PET detector technology paved the way from PET/CT to hybrid PET/MR systems, which have been commercially available since 2011. Due to the higher contrast between gray and white matter, MR provides a substantial advantage over CT for diagnosing CNS lesions [127]. For scanning neurological patients, the combination of both PET and MR has often proven to be superior to the single modality approach, with improved workflow and an increase in patient comfort. The ability to characterize different pathophysiological diseases features can be useful especially in research [128]. The acquisition of MR also allows correction for partial volume effect. PET or PET/CT studies vs. MR had shown that, irrespective of the tracer, PET provides more accurate information. PET/MR studies with dedicated PET/MR scanners are now similarly providing evidence of the additional information and synergistic effect of these two techniques.

Studies with PET/MR scanners in brain tumor patients have been so far limited; therefore, we will report about studies that compared PET to MR as well as studies that used dedicated PET/MR hybrid systems.

One study reported a greater accuracy of [^{18}F]FDG PET in comparison to MR for the prediction of survival in patients with high-grade glioma after therapy with temozolomide [129].

Ohtani et al. compared [^{11}C]choline PET, contrast-enhanced MR imaging, and [^{18}F]FDG PET in 22 patients with suspected brain tumors. They found a correlation between [^{11}C]choline and the histological tumor grade, with higher uptake in high-grade gliomas. The authors suggested that the combination of [^{11}C]choline PET and MR imaging could improve the detection of high-grade gliomas. However, [^{11}C]choline PET could not differentiate between low-grade gliomas and benign lesions [116].

Tan et al. used [^{18}F]FDG, [^{11}C]choline PET/CT, and MR to differentiate brain tumor recurrence from necrosis after radiotherapy in 55 patients. Sensitivities of MR, [^{18}F]FDG, and [^{11}C]choline PET/CT in lesion diagnosis were 87%, 77%, and 92%, respectively, and their specificities were 81%, 63%, and 88%, respectively. These results suggested that [^{11}C]choline PET/CT, having higher sensitivity and specificity, may perform better in distinguishing recurrent brain tumor from radionecrosis compared with [^{18}F]FDG PET/CT and MR [120].

Boss et al. reported that the MR and PET data acquired in ten patients was of high diagnostic quality and that there was a high level of concordance between tumor-to-background ratios derived from PET/CT and those derived subsequently from PET/MR [130]. The same group later used MR spectroscopy and [^{11}C]MET PET to classify inconclusive MR findings as either low-grade gliomas or high-grade gliomas and to identify the most malignant parts within tumors before surgery. They found that areas with maximum [^{11}C]MET uptake provided satisfactory tumor grading. The spatial overlap between cerebral areas of high PET uptake and highest metabolite concentrations determined by MR spectroscopy was limited, which suggests that the diagnostic gain provided by MR

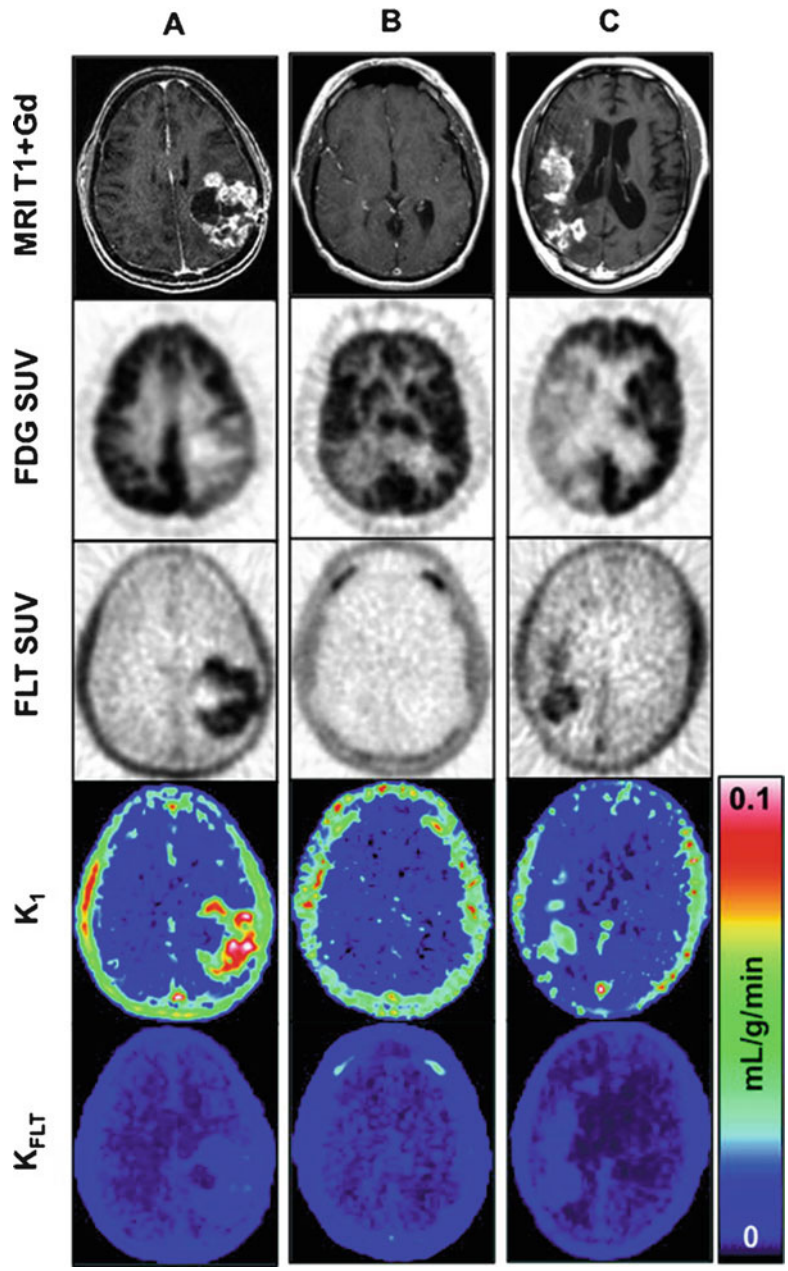

Fig. 5 Three scenarios with different aspects of ^{18}F-FLT and [^{18}F]FDG metabolism are presented. (**a**) A 44-year-old woman with recurrent grade III anaplastic astrocytoma of the left parietal cortex with BBB breakdown treated previously by radiotherapy (59 Gy). (**b**) A 56-year-old man with right parietal grade II oligodendroglioma with intact BBB treated previously by surgical resection followed by chemotherapy. (**c**) A 46-year-old man with recurrent grade II oligodendroglioma of the left temporal and parietal cortex with BBB breakdown treated with radiotherapy (54 Gy) and temozolomide before PET. Surgery and therapy occurred at least 2 years before PET for all three patients. Coregistered images are as follows: MR T1-contrast enhancement; [^{18}F]FDG SUV summed 30–60 min; ^{18}F-FLT SUV summed 30–60 min; parametric map of transport, K_1; and parametric image of metabolic flux, K ^{18}F-FLT. This figure exemplifies two different concepts: (1) the different patterns of various tracers in the same tumor depend on tumor metabolism and BBB integrity; (2) it shows how [^{18}F]FDG uptake is less influenced by BBB breakdown (it is reduced in (**a**) and (**c**) where BBB is disrupted), while ^{18}F-FLT uptake increases notably with BBB disruption (**a** and **c**), but ^{18}F-FLT does not enter the brain if BBB is normal (**b**) (Reprinted with permission from Ref. [107])

spectroscopy is limited [131]. A whole-body hybrid PET/MR system was used in another study by Preuss et al. to obtain [^{11}C]MET PET and MR imaging data necessary for biopsy planning and neuronavigation in a small series of pediatric patients with brain tumor. Representative histopathological specimens were obtained in all patients. Additional anesthesia as well as CT-related radiation exposure could also be avoided [132]. In another small PET/MR series mainly in patients with high-grade gliomas, both modalities provided sufficient diagnostic quality, and the ^{18}F-FET PET findings were in accordance with those of conventional MR [133]. All combined PET/MR imaging studies discussed above agree on the convenience of obtaining all necessary imaging parameters in one session with excellent spatial coregistration of MR and PET data. Moreover, Dunet et al. demonstrated the superiority of the combination of dynamic ^{18}F-FET PET and diffusion-weighted MR over the single modality approach for glioma grading and argued in favor of combined ^{18}F-FET PET/MR in the initial assessment of primary brain tumors [134]. They reported that tumor time–activity curve reached the best accuracy (67%) when considered alone to distinguish between low- and high-grade gliomas, followed closely by ADC histogram analysis (65%). The combination of time–activity curve and apparent diffusion coefficient (ADC) histogram analysis improved the sensitivity to 86% and the specificity to 100% [134].

Assessing the Efficacy of Treatment

The diagnostic value of MR and CT concerning changes in tumor size or contrast enhancement in response to therapy is limited because the known reactive transient BBB alterations with consequent contrast enhancement may mimic tumor progression. This phenomenon, the so-called pseudoprogression, is seen in 20–50% of cases and can lead to unnecessary overtreatment [135]. For this reason, the use of PET appears today as an ideal tool; in fact the efficacy of therapy has been assessed with different radiotracers across times.

Several studies indicate that glucose metabolism, at initial presentation, at recurrence, or in response to therapy, is predictive of survival.

In case of recurrent tumor, the mean survival time of patients with gliomas exhibiting high glucose utilization was shorter than in patients with low glucose utilization (5 vs. 19 months) [136]. Similar results were obtained by Alavi in a study that included mostly treated patients [137]. He reported estimated median survival of 33 months for hypometabolic lesions and 7 months for hypermetabolic lesions. Furthermore, in the subgroup of high-grade gliomas, it was possible to divide patients into a group with low and a group with high metabolic activity with 1-year survival rates of 78% and 29%, respectively [137]. In the setting of recurrence, these results were confirmed by Santra et al. [138]. In a more recent study, Colavolpe et al. retrospectively assessed pretreatment PET scans qualitatively and quantitatively in 41 patients with high-grade gliomas [139, 140]. The authors performed multivariate analysis including traditional prognostic factors (age, KPS, extent of surgery, and histological grade) in addition to either visual metabolic grade or the ratio between the tumor and contralateral SUV_{max}. The semiquantitative evaluation in the pretreatment of [^{18}F]FDG PET/CT provided significant additional prognostic information in newly diagnosed high-grade tumors, it was statistically more robust than the visual evaluation, and it was independent of traditional prognostic factors [139].

PET has been shown to be useful for monitoring the response to chemotherapy. Following treatment with temozolomide, the percentage of decline of CMR_{glc} versus baseline is greater in clinical responders than in nonresponders [141]. In another study, it was shown that early changes in glucose metabolism predicted response to temozolomide, but not temozolomide plus radiotherapy. In the first scenario, a greater metabolic reduction after therapy predicts longer survival [129]. One study reported the greater accuracy of [^{18}F]FDG PET in comparison to MR for predicting survival after therapy [129]. A recent publication based on the National Oncologic PET Registry examined retrospectively data from 479 patients with primary

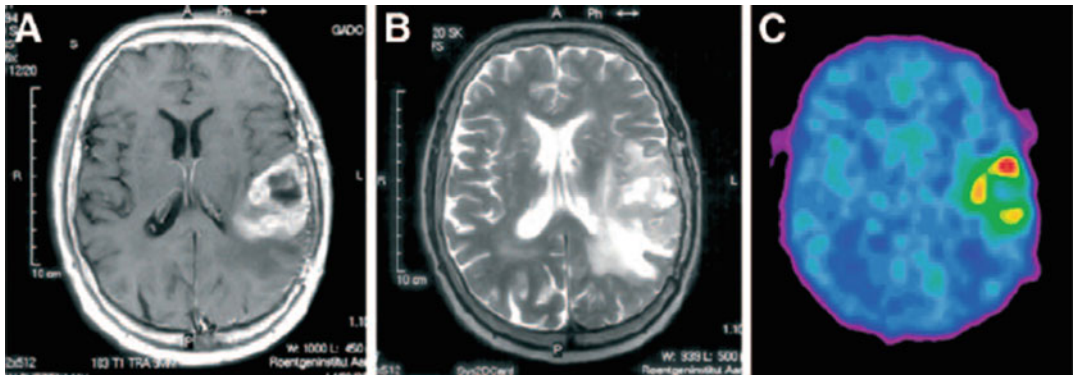

Fig. 6 Gadolinium contrast-enhanced T1- (**a**) and T2-weighted (**b**) MR images in a patient with glioblastoma multiforme in the left temporal lobe. (**c**) Late PET images show ^{18}F-MISO tumor uptake 150–170 min after injection. The figures typically identifies the behavior of a hypoxia tracer that accumulates less in the center of a lesion, where the tissue is hypoxic, and highly accumulates in the periphery of the lesion, where the tumor tissue is well oxygenated (Reprinted with permission from Ref. [124])

brain tumors (72%) or brain metastasis (28%) and found that overall, [^{18}F]FDG PET imaging changed the intended management in 38% of patients with primary brain tumors [142].

^{123}I-IMT uptake has prognostic implications. In patients who had undergone tumor resection 4–6 weeks before SPECT imaging, significant ^{123}I-IMT uptake after tumor resection was associated with shorter survival (Figs. 6 and 7). ^{123}I-IMT uptake ratio remains a significant prognostic factor when age and grading are included in a multivariate model [83].

^{18}F-FET imaging was also shown to have prognostic implications. In low-grade gliomas, baseline low ^{18}F-FET uptake predicted longer time to progression and time to malignant transformation; high uptake predicted conversion into a high-grade glioma [143]. ^{18}F-FET can be used to quantify residual tumor volume after surgery and postsurgical tumor volumes evaluated by PET predict progression-free and overall survivals [144]. Finally, patients with higher decrease in ^{18}F-FET uptake after antiangiogenic therapy with irinotecan–bevacizumab displayed longer survival [145]. Galldiks et al. compared changes in ^{18}F-FET TBR_{max} and TBR_{mean} as well as gadolinium contrast enhancement in 25 glioblastoma patients who underwent radiochemotherapy with temozolomide. Changes in TBR_{max} and TBR_{mean} between therapy and baseline predicted overall survival and progression-free survival, while gadolinium-volume changes did not [146].

Harris et al. created parametric response maps of ^{18}F-FLT and [^{18}F]FDOPA before and at two time points after bevacizumab treatment. They reported that an increase in [^{18}F]FDOPA or ^{18}F-FLT uptake on parametric response maps after bevacizumab treatment predicted shorter progression-free survival and that [^{18}F]FDOPA additionally predicted overall survival in recurrent gliomas [147].

[^{18}F]FDOPA was used at baseline, 2 and 6 weeks after the start of bevacizumab therapy for assessing response to therapy. [^{18}F]FDOPA metabolic tumor volume, but not SUV, predicted overall survival and progression-free survival. Interestingly, absolute metabolic tumor volume at 2 weeks after therapy was the strongest predictor of survival [148].

Additional Value of SPECT/CT and PET/CT vs Stand-Alone SPECT and PET

Radionuclide imaging has per se the capability of identifying disease at early stages, since it visualizes molecular targets that may change before structural tissue changes occur. Adding the CT component may improve correction for photon attenuation, but also allows for easier correlation of areas with

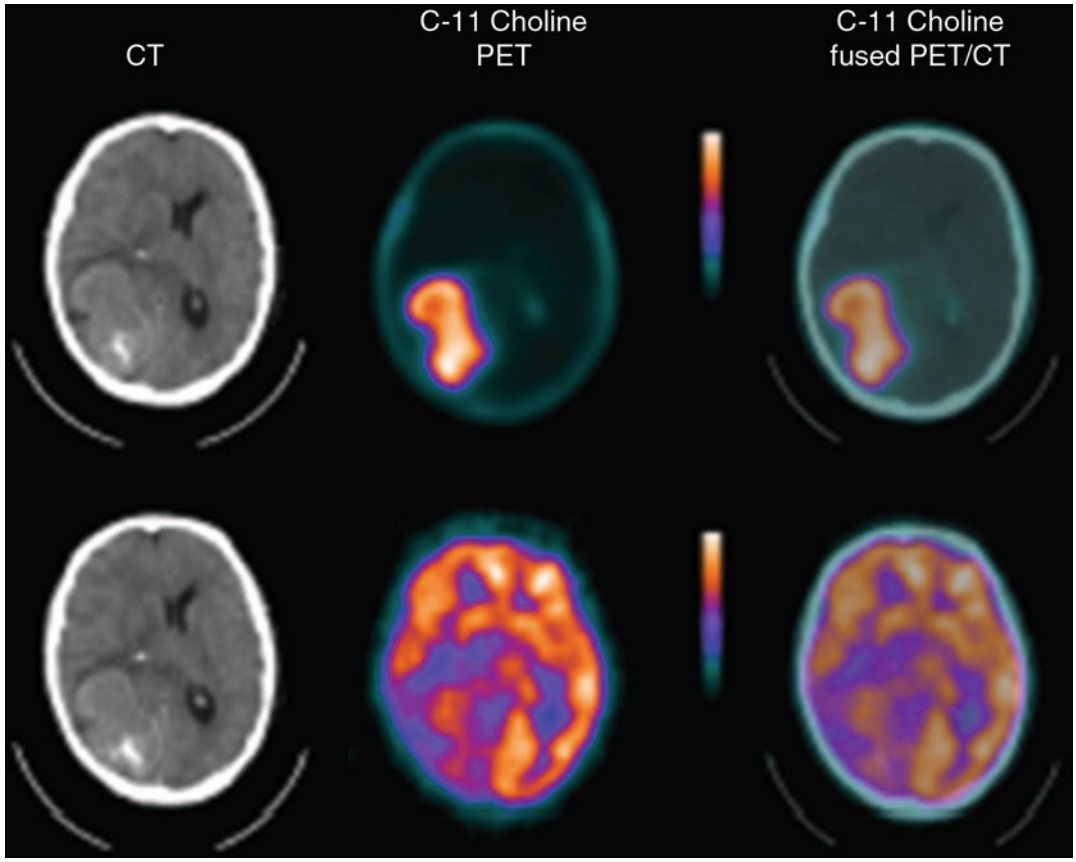

Fig. 7 CT, PET, and fused PET/CT images of a WHO grade II meningioma. CT shows a meningioma in the left temporo-occipital region that reaches medially the ipsilateral thalamus and striatum. There is high [^{11}C]choline uptake in the tumor (*top*), as well as heterogeneous increase in [^{18}F]FDG uptake (*bottom*). Note, however, the different location of the areas of increased [^{11}C]choline uptake (maximal in the posterolateral part of the tumor) and [^{18}F]FDG uptake (maximal in the anteromedial part of the tumor) (Reprinted with permission from Ref. [186])

physiological variants or abnormal tracer accumulation to anatomical landmarks [149].

So far, data on the added value of combined SPECT/CT and PET/CT examinations of the brain remain scanty. In principle, the diagnostic value of various cerebral SPECT examinations, such as cerebral perfusion or receptor studies, might be increased, to some extent, by additional CT examinations. However, considering that the morphological gold standard is represented by MR, the impact of the additional CT component on the diagnosis and clinical management of the patient is actually quite limited.

Low-dose CT is associated with relatively low radiation doses of 1–4 mSv and should be sufficient for anatomic referencing of SPECT lesions and attenuation correction. In clinical practice, if a recent enhanced CT scan is available, then another contrast-enhanced CT scan will not be repeated during SPECT/CT. For this reason, the use of low-dose, nonenhanced spiral CT is generally recommended when SPECT/CT is performed for anatomic referencing or attenuation correction [150]. This holds true also for brain tumor patients since virtually all patients referred to SPECT/CT or PET/CT will have already performed a diagnostic CT or MR. Low-dose CTs are generally acquired with a tube current of 20–40 mA and tube voltage of about 120–140 kV [150].

Usually, CT scan-based attenuation correction of brain SPECT data may lead to improved image quality and more accurate evaluation. In fact, it was shown that attenuation correction based on individual CT scans produces more accurate results than traditional methods based on the uniform linear attenuation coefficient [151].

Some studies have demonstrated the usefulness of SPECT/CT for accurate preoperative detection and localization, for radiotherapy planning, and for treatment monitoring of brain tumors [149]. SPECT/CT achieves precise anatomical localization of viable tumor lesions versus adjacent sites with physiological tracer uptake, such as the ventricles, choroid plexus, and venous sinuses [152, 153], with a proven clinical impact on management in 43% of patients [152].

Common Therapies

Primary brain tumors have a dismal prognosis. Five-year survival rates can be as low as <5% for glioblastoma, 30% for astrocytomas, but up to 100% for benign neoplasms as meningiomas. These rates have remained virtually unchanged over the last years, thus indicating the lack of substantial improvement in prognosis in spite of technological advances in diagnostic and surgical strategies [8].

Therapy is generally a combination of surgery, chemotherapy, and radiotherapy or radioimmunotherapy. Because of the limited efficacy and potentially severe side effects of each treatment, many studies are in progress to enhance the efficacy of this multimodality approach.

Surgery. Surgery remains the primary therapeutic approach for most brain tumors. The goal of surgery is twofold. First, it is necessary for definitive histological diagnosis of the tumor. Second, it allows tumor debulking, which is necessary for preventing or alleviating symptoms. Based on the extent, resections can be classified as either partial or complete. However, except for pilocytic astrocytomas, the necessary extent of surgical resection beyond obtaining a tissue for diagnosis remains controversial. Partial resections are performed for large, deeply infiltrating neoplasms for which only debulking is possible or for neoplasms located near difficult-to-access regions. Complete resection is otherwise preferred. Even normal astrocytes and oligodendrocytes can move preferentially along the preformed fiber paths in the brain, and neoplastic cells often exhibit that capacity even more. Even complete solid tumor removal (or any other local therapy) will not reach these cells, and they will likely cause tumor recurrences. Although a larger resection has greater curative potentials, the surgeon always faces a balanced compromise between the likelihood of increasing the local control and the risk of causing important side effects [4, 109].

Radiation therapy. Radiation therapy has been used extensively in the treatment of malignant and aggressive intracranial tumors, and its use has been associated with prolonged disease-free survival, but not with overall survival [4, 154]. Because of potential side effects, radiation therapy is often deferred until there are signs of progressive recurrence or malignant transformation [4, 154]. In the case of GBM, radiotherapy is complicated by the diffuse infiltrative nature of the disease and by its extreme radioresistance. However, a clear gain of median progression-free survival of GBM patients was also reported [4, 154].

Chemotherapy. The overall efficacy of chemotherapy in brain tumors is limited because the BBB limits access to the brain for molecules with low molecular weight and high lipophilicity, and the multidrug resistance system limits the efficacy of a wide range of drugs. Temozolomide is now the most effective drug and it is approved for refractory anaplastic astrocytoma or GBM [155]. The combination of radiotherapy, lomustine and temozolomide, yielded promising long-term survival data in patients with newly diagnosed glioblastoma, albeit with greater acute toxicity [156, 157].

Antiangiogenic therapy. Neoangiogenesis is another potential target for therapy of gliomas. High-grade gliomas demonstrate high levels of angiogenesis. Antiangiogenic drugs were developed to target vascular endothelial growth factor (VEGF) and VEGF receptor. Emerging literature suggests the efficacy of antiangiogenic therapy,

particularly bevacizumab, for recurrent high-grade gliomas [157, 158].

Radioimmunotherapy. Locoregional radioimmunotherapy (RIT) have been proposed for targeting brain tumors. Monoclonal antibodies (MoAb) conjugated with high-energy β^- emitters (^{131}I, ^{90}Y or ^{177}Lu) are used for this purpose. Tumor cells that do not express the antigen on their surface can be damaged by the "cross-fire effect" [159]. Different strategies have been proposed to improve the tumor-to-non-tumor uptake ratio, such as the three-step pre-targeting radioimmunotherapy (pRIT) ("sandwich" approach) based on the avidin–biotin system, which has been employed with some success [160]. Disease-free survival in the treated patients was significantly longer than in patients undergoing conventional therapy [161]. Patients treated with pRIT and temozolomide have a significantly longer disease-free survival compared to patients treated with pRIT alone [162].

Differently from low aggressive forms of some tumors, such as thyroid cancer and prostate cancer, active surveillance does not represent a valid therapeutic approach for either high-grade or low-grade gliomas.

Meningiomas

Meningiomas are the most common benign intracranial tumors. Their prognosis is excellent, except when they are located in surgically inaccessible anatomical sites. Grade I meningiomas (also commonly referred to as typical meningiomas) have low proliferative rate [163]. Grade II meningiomas (i.e., atypical or anaplastic meningiomas that constitute less than 5% of all meningiomas) have histological features consistent with greater proliferative activity [164]. The recurrence rate after surgery is higher in grade II than in grade I meningiomas. All meningiomas are highly vascularized. Meningiomas express a wide range of receptors, which makes them sensitive to different hormonal controls and potential target for various radioligands. The diagnosis of meningiomas is easily performed on CT. The distinction between typical and atypical meningiomas is not reliable on either CT or MR, and the capacity of PET to predict grading and recurrence of disease has been tested. However, meningiomas located near the base of the skull may be difficult to distinguish from other lesions, such as lymphomas, metastases, or neurinomas [165], and ^{68}Ga-DOTATOC-PET data can complement anatomical data from MR and CT to improve target volume definition, especially in cases with complex infiltration and recurrent disease after surgery [166, 167].

CMR_{glc} is significantly higher in atypical meningiomas than in typical meningiomas and correlates with tumor proliferation rate [168–170]. However, remarkable differences in CMR_{glc} are observed among different types of typical meningiomas [168, 169]. Less frequently [^{18}F]FDG PET did not predict histological or behavioral features [171]. Multivariate analysis showed that, in addition to MIB-1 labeling index, presence of brain invasion, and WHO grade, [^{18}F]FDG uptake in meningiomas predicts tumor recurrence [170].

In addition to [^{18}F]FDG, several other tracers have been shown to accumulate in meningiomas, including [^{11}C]MET, [^{11}C]choline, and ^{18}F-FET. SUV_{max} of [^{11}C]MET but not [^{18}F]FDG was correlated with Ki-67 in meningioma cells [171]. [^{11}C]MET PET/CT can be used for the definition of the GTV delineation in fractionated stereotactic radiotherapy of skull base meningiomas. [^{11}C]MET PET images incorporation into stereotactic radiotherapy plan allowed better definition of the GTV [172] and may lead to changes (both reductions and increases) of the GTV in a significant number of cases [173]. [^{11}C]MET PET was used in the evaluation of the response to therapy with interferon-alpha and be useful for predicting the clinical response, for determining the length of the therapy and for adjusting of drug dosage [174].

Giovacchini et al. described the uptake of [^{11}C]choline in a small group of seven meningioma patients that were also studied with [^{18}F]FDG. The uptake of [^{11}C]choline but not of [^{18}F]FDG was higher in patients with grade II than in grade I meningiomas [114]. Other case reports were subsequently published [175, 176].

SPECT somatostatin receptor scintigraphy, namely, ^{111}In-octreotide, has been used successfully

in the past owing to the frequent overexpression of somatostatin receptors (SSTR) $SSTR_2$ in meningiomas [177]. However, owing to the widespread development of generator-based ^{68}Ga-conjugates, PET has substantially substituted SPECT. The three compounds most commonly used for PET imaging are ^{68}Ga-DOTATOC (^{68}Ga-DOTA-Tyr^3-octreotide), ^{68}Ga-DOTANOC ([^{68}Ga]-DOTA-Nal^3-octreotide), and ^{68}Ga-DOTATATE (^{68}Ga-DOTA-Tyr^3-octreotate). ^{68}Ga-DOTATOC and ^{68}Ga-DOTATATE have high affinity for $SSTR_2$, which is the most common SSTR subtype found in meningiomas. ^{68}Ga-DOTANOC targets a broader range of somatostatin subtype receptors, including $SSTR_2$, $SSTR_3$, and $SSTR_5$ [178]. Initial studies were performed using ^{68}Ga-DOTANOC [179, 180]. Cumbersome kinetic analysis using the plasma input function was adopted [180]. An interesting study performed in an animal model kinetic analysis using the Logan graphical method was used to compute the distribution volume of the three tracers. Although the distribution volume was relatively similar with ^{68}Ga-DOTATATE and ^{68}Ga-DOTATOC, uptake was higher with ^{68}Ga-DOTATATE in the tumor than with ^{68}Ga-DOTANOC and ^{68}Ga-DOTATOC, suggesting a higher diagnostic value of ^{68}Ga-DOTATATE for detecting meningiomas [165]. Later studies have the visibility of qualitative and semiquantitative evaluation for routine clinical questions [181].

16α-^{18}F-fluoro-17β-oestradiol (^{18}F-FES) has been occasionally used to evaluate estrogenic receptors in meningiomas. The identification of meningiomas occurs in about 60% of cases [182].

Conclusion

Several traditional and new tracers have been developed for evaluating brain tumors. This abundance in radiopharmaceuticals together with the technical development of PET/CT tomographs first and then PET/MR has enabled a substantial deepening in the knowledge of morphological and functional properties of brain tumors. PET/MR scanners also have substantial logistic and technical advantages: one single imaging session can be performed for the individual patient ("one-stop-shop") and optimal technical conditions (minimization of movement, accurate coregistration) can be achieved.

Several studies on genetic predisposition and on the corresponding molecular pathology were also performed yielding important information on the pathophysiology and risk factors for brain tumors. Surgery still represents the cornerstone of therapy in gliomas, while the role of radiotherapy is increasing and combinations, with or without escalation, with temozolomide are being tested. Angiogenesis inhibitors, such as the monoclonal antibody bevacizumab, have been tested with promising results.

There are different clinical settings in which PET can be used in the clinical practice. The most frequent is the differential diagnosis between tumor recurrence and radiation injury, where radiological techniques including MR suffer substantially from both sensitivity and specificity. PET, especially in combination with MR, is increasingly more used for the definition of the gross tumor volume to be irradiated. The identification of the metabolically active volume can also be used to direct biopsy, for planning surgery, or can clarify an undetermined finding on MR. A unique capability of PET is to predict in vivo tumor grading better than any other technique. Generally, high metabolic activity is predictive of higher tumor grade, even though there is variable accuracy among tracers in such prediction; for example, [^{18}F]FDG is more accurate than amino acid tracers. Changes in cerebral tracer uptake can be monitored in response to therapy. Changes after therapy as well as baseline values in untreated patients have prognostic value.

Several radiopharmaceuticals have been developed to explore biochemical processes other than glucose metabolism that are associated to tumor growth. Amino acid tracers are sensitive to transport across the BBB and, to some extent, protein synthesis. Contrary to [^{18}F]FDG, amino acids are less involved in inflammation and therefore have higher specificity for differentiating tumor recurrence versus radiation necrosis. Among available tracers, [^{11}C]MET is the one that is nowadays more validated in the clinical setting and more

widely used. Other promising tracers include [^{18}F]FDOPA and ^{18}F-FET. However, the tumor uptake of [^{18}F]FDG has prognostic value. Other tracers, such as hypoxia tracers and radiolabeled choline, presently have a more uncertain role in the clinical routine, even though some interesting results derived from clinical research studies.

References

1. Ostrom QT, et al. CBTRUS statistical report: primary brain and central nervous system tumors diagnosed in the United States in 2006–2010. Neuro Oncol. 2013; 15 Suppl 2:ii1–56.
2. Wohrer A, et al. The Austrian brain tumour registry: a cooperative way to establish a population-based brain tumour registry. J Neurooncol. 2009;95(3):401–11.
3. Ostrom QT, et al. CBTRUS statistical report: primary brain and central nervous system tumors diagnosed in the United States in 2007–2011. Neuro Oncol. 2014; 16 Suppl 4:iv1–63.
4. DeAngelis LM. Brain tumors. N Engl J Med. 2001; 344(2):114–23.
5. Ohgaki H, Kleihues P. Population-based studies on incidence, survival rates, and genetic alterations in astrocytic and oligodendroglial gliomas. J Neuropathol Exp Neurol. 2005;64(6):479–89.
6. Central Nervous System. In: Edge DRBSB, Compton CC, Fritz AG, Greene FL, Trotti A, Moffi HL, editors. AJCC cancer staging manual. New York: Springer; 2010. p. 591–7.
7. Herholz K, et al. Brain tumors. Semin Nucl Med. 2012;42(6):356–70.
8. McLendon RE, Halperin EC. Is the long-term survival of patients with intracranial glioblastoma multiforme overstated? Cancer. 2003;98(8):1745–8.
9. Vigneswaran K, Neill S, Hadjipanayis CG. Beyond the World Health Organization grading of infiltrating gliomas: advances in the molecular genetics of glioma classification. Ann Transl Med. 2015;3(7):95.
10. Kraus JA, et al. Molecular genetic alterations in glioblastomas with oligodendroglial component. Acta Neuropathol. 2001;101(4):311–20.
11. Louis DN, et al. The 2007 WHO classification of tumours of the central nervous system. Acta Neuropathol. 2007;114(2):97–109.
12. Lau EW, et al. Comparative PET study using F-18 FET and F-18 FDG for the evaluation of patients with suspected brain tumour. J Clin Neurosci. 2010;17(1): 43–9.
13. Thompson L, Dong Y, Evans L. Chronic hypoxia increases inducible NOS-derived nitric oxide in fetal guinea pig hearts. Pediatr Res. 2009;65(2):188–92.
14. Barker 2nd FG, et al. Necrosis as a prognostic factor in glioblastoma multiforme. Cancer. 1996;77(6): 1161–6.
15. Weller M, et al. Molecular neuro-oncology in clinical practice: a new horizon. Lancet Oncol. 2013;14(9): e370–9.
16. Hegi ME, et al. MGMT gene silencing and benefit from temozolomide in glioblastoma. N Engl J Med. 2005;352(10):997–1003.
17. Mabray MC, Barajas Jr RF, Cha S. Modern brain tumor imaging. Brain Tumor Res Treat. 2015;3(1):8–23.
18. Mellinghoff IK, et al. Molecular determinants of the response of glioblastomas to EGFR kinase inhibitors. N Engl J Med. 2005;353(19):2012–24.
19. Sneed PK, et al. Large effect of age on the survival of patients with glioblastoma treated with radiotherapy and brachytherapy boost. Neurosurgery. 1995;36 (5):898–903; discussion 903–4.
20. Saconn PA, et al. Use of 3.0-T MRI for stereotactic radiosurgery planning for treatment of brain metastases: a single-institution retrospective review. Int J Radiat Oncol Biol Phys. 2010;78(4):1142–6.
21. Wen PY, et al. Updated response assessment criteria for high-grade gliomas: response assessment in neuro-oncology working group. J Clin Oncol. 2010; 28(11):1963–72.
22. Hilario A, et al. A prognostic model based on preoperative MRI predicts overall survival in patients with diffuse gliomas. AJNR Am J Neuroradiol. 2014; 35(6):1096–102.
23. Anger HO. Medical radioisotope scanning. Vienna: IAEA; 1959.
24. Strauss HW, et al. Nuclear cerebral angiography. Usefulness in the differential diagnosis of cerebrovascular disease and tumor. Arch Intern Med. 1973;131(2): 211–6.
25. Kaplan WD, et al. Thallium-201 brain tumor imaging: a comparative study with pathologic correlation. J Nucl Med. 1987;28(1):47–52.
26. Ancri D, et al. Diagnosis of cerebral lesions by Thallium 201. Radiology. 1978;128(2):417–22.
27. Biersack HJ, Grunwald F, Kropp J. Single photon emission computed tomography imaging of brain tumors. Semin Nucl Med. 1991;21(1):2–10.
28. Ishibashi M, et al. Thallium-201 in brain tumors: relationship between tumor cell activity in astrocytic tumor and proliferating cell nuclear antigen. J Nucl Med. 1995;36(12):2201–6.
29. Ciarmiello A, et al. Tumor clearance of technetium 99m-sestamibi as a predictor of response to neoadjuvant chemotherapy for locally advanced breast cancer. J Clin Oncol. 1998;16(5):1677–83.
30. Benard F, Romsa J, Hustinx R. Imaging gliomas with positron emission tomography and single-photon emission computed tomography. Semin Nucl Med. 2003;33(2):148–62.
31. Yokogami K, et al. Application of SPET using technetium-99m sestamibi in brain tumours and comparison with expression of the MDR-1 gene: is it possible to predict the response to chemotherapy in patients with gliomas by means of 99mTc-sestamibi SPET? Eur J Nucl Med. 1998;25(4):401–9.

32. Vaalburg W, et al. P-glycoprotein activity and biological response. Toxicol Appl Pharmacol. 2005;207 (2 Suppl):257–60.
33. Jacquier-Sarlin MR, Polla BS, Slosman DO. Oxidoreductive state: the major determinant for cellular retention of technetium-99m-HMPAO. J Nucl Med. 1996;37(8):1413–6.
34. Jacquier-Sarlin MR, Polla BS, Slosman DO. Cellular basis of ECD brain retention. J Nucl Med. 1996;37 (10):1694–7.
35. Langen KJ, et al. Tomographic studies of rCBF with [^{99m}Tc]-HM-PAO SPECT in patients with brain tumors: comparison with $C^{15}O_2$ continuous inhalation technique and PET. J Cereb Blood Flow Metab. 1988;8(6):S90–4.
36. Suess E, et al. Technetium-99m-d,l-hexamethylpropyleneamine oxime (HMPAO) uptake and glutathione content in brain tumors. J Nucl Med. 1991;32(9):1675–81.
37. Papazyan JP, et al. Discrepancies between HMPAO and ECD SPECT imaging in brain tumors. J Nucl Med. 1997;38(4):592–6.
38. Di Chiro G. Brain imaging of glucose utilization in cerebral tumors. Res Publ Assoc Res Nerv Ment Dis. 1985;63:185–97.
39. Sokoloff L, et al. The [^{14}C]deoxyglucose method for the measurement of local cerebral glucose utilization: theory, procedure, and normal values in the conscious and anesthetized albino rat. J Neurochem. 1977;28(5):897–916.
40. Varrone A, et al. EANM procedure guidelines for PET brain imaging using [^{18}F]FDG, version 2. Eur J Nucl Med Mol Imaging. 2009;36(12):2103–10.
41. Huang SC, et al. Error sensitivity of fluorodeoxyglucose method for measurement of cerebral metabolic rate of glucose. J Cereb Blood Flow Metab. 1981;1(4):391–401.
42. Di Chiro G, et al. Glucose utilization of cerebral gliomas measured by [^{18}F] fluorodeoxyglucose and positron emission tomography. Neurology. 1982;32(12):1323–9.
43. Patronas NJ, et al. Glycolytic rate (PET) and contrast enhancement (CT) in human cerebral gliomas. AJNR Am J Neuroradiol. 1983;4(3):533–5.
44. Delbeke D, et al. Optimal cutoff levels of F-18 fluorodeoxyglucose uptake in the differentiation of low-grade from high-grade brain tumors with PET. Radiology. 1995;195(1):47–52.
45. DeLaPaz RL, et al. Positron emission tomographic study of suppression of gray-matter glucose utilization by brain tumors. AJNR Am J Neuroradiol. 1983; 4(3):826–9.
46. Patronas NJ, et al. Depressed cerebellar glucose metabolism in supratentorial tumors. Brain Res. 1984;291(1):93–101.
47. Di Chiro G, Brooks RA. PET-FDG of untreated and treated cerebral gliomas. J Nucl Med. 1988; 29(3):421–3.
48. Tyler JL, et al. Metabolic and hemodynamic evaluation of gliomas using positron emission tomography. J Nucl Med. 1987;28(7):1123–33.
49. Piert M, et al. Diminished glucose transport and phosphorylation in Alzheimer's disease determined by dynamic FDG-PET. J Nucl Med. 1996;37(2):201–8.
50. Schmidt K, et al. Errors introduced by tissue heterogeneity in estimation of local cerebral glucose utilization with current kinetic models of the [18F] fluorodeoxyglucose method. J Cereb Blood Flow Metab. 1992;12(5):823–34.
51. Mazziotta JC, et al. Quantitation in positron emission computed tomography: 5 physical – anatomical effects. J Comput Assist Tomogr. 1981;5(5):734–43.
52. Di Chiro G, Brooks RA. PET quantitation: blessing and curse. J Nucl Med. 1988;29(9):1603–4.
53. Padma MV, et al. Prediction of pathology and survival by FDG PET in gliomas. J Neurooncol. 2003;64(3): 227–37.
54. Levivier M, et al. The integration of metabolic imaging in stereotactic procedures including radiosurgery: a review. J Neurosurg. 2002;97(5 Suppl):542–50.
55. Segtnan EA, et al. F-Fluorodeoxyglucose PET/computed tomography for primary brain tumors. PET Clin. 2015;10(1):59–73.
56. Ishizu K, et al. Effects of hyperglycemia on FDG uptake in human brain and glioma. J Nucl Med. 1994;35(7):1104–9.
57. Ishizu K, et al. Enhanced detection of brain tumors by [^{18}F]fluorodeoxyglucose PET with glucose loading. J Comput Assist Tomogr. 1994;18(1):12–5.
58. Spence AM, et al. ^{18}F-FDG PET of gliomas at delayed intervals: improved distinction between tumor and normal gray matter. J Nucl Med. 2004; 45(10):1653–9.
59. Henze M, et al. Detection of tumour progression in the follow-up of irradiated low-grade astrocytomas: comparison of 3-[^{123}I]iodo-alpha-methyl- L-tyrosine and ^{99m}Tc-MIBI SPET. Eur J Nucl Med Mol Imaging. 2002;29(11):1455–61.
60. Patronas NJ, et al. Work in progress: [^{18}F]fluorodeoxyglucose and positron emission tomography in the evaluation of radiation necrosis of the brain. Radiology. 1982;144(4):885–9.
61. Rozental JM, et al. Early changes in tumor metabolism after treatment: the effects of stereotactic radiotherapy. Int J Radiat Oncol Biol Phys. 1991;20(5):1053–60.
62. Pirotte B, et al. PET in stereotactic conditions increases the diagnostic yield of brain biopsy. Stereotact Funct Neurosurg. 1994;63(1–4):144–9.
63. Tralins KS, et al. Volumetric analysis of ^{18}F-FDG PET in glioblastoma multiforme: prognostic information and possible role in definition of target volumes in radiation dose escalation. J Nucl Med. 2002;43(12): 1667–73.
64. Douglas JG, et al. [F-18]-fluorodeoxyglucose positron emission tomography for targeting radiation dose escalation for patients with glioblastoma multiforme: clinical outcomes and patterns of failure. Int J Radiat Oncol Biol Phys. 2006;64(3):886–91.
65. Singhal T, et al. ^{11}C-L-methionine positron emission tomography in the clinical management of cerebral gliomas. Mol Imaging Biol. 2008;10(1):1–18.

66. Herholz K, Coope D, Jackson A. Metabolic and molecular imaging in neuro-oncology. Lancet Neurol. 2007;6(8):711–24.
67. van Waarde A, et al. Comparison of sigma-ligands and metabolic PET tracers for differentiating tumor from inflammation. J Nucl Med. 2006;47(1):150–4.
68. Kubota R, et al. Methionine uptake by tumor tissue: a microautoradiographic comparison with FDG. J Nucl Med. 1995;36(3):484–92.
69. Utriainen M, et al. Evaluation of brain tumor metabolism with [^{11}C]choline PET and 1H-MRS. J Neurooncol. 2003;62(3):329–38.
70. De Witte O, et al. Positron emission tomography with injection of methionine as a prognostic factor in glioma. J Neurosurg. 2001;95(5):746–50.
71. Kim S, et al. ^{11}C-methionine PET as a prognostic marker in patients with glioma: comparison with 18F-FDG PET. Eur J Nucl Med Mol Imaging. 2005;32(1):52–9.
72. Pirotte B, et al. Integration of [^{11}C]methionine-positron emission tomographic and magnetic resonance imaging for image-guided surgical resection of infiltrative low-grade brain tumors in children. Neurosurgery. 2005;57(1 Suppl):128–39.
73. Pirotte B, et al. Positron emission tomography for the early postsurgical evaluation of pediatric brain tumors. Childs Nerv Syst. 2005;21(4):294–300.
74. Pirotte BJ, et al. Positron emission tomography-guided volumetric resection of supratentorial high-grade gliomas: a survival analysis in 66 consecutive patients. Neurosurgery. 2009;64(3):471–81.
75. Grosu AL, et al. Validation of a method for automatic image fusion (BrainLAB System) of CT data and ^{11}C-methionine-PET data for stereotactic radiotherapy using a LINAC: first clinical experience. Int J Radiat Oncol Biol Phys. 2003;56(5):1450–63.
76. Nariai T, et al. Usefulness of L-[methyl-^{11}C] methionine-positron emission tomography as a biological monitoring tool in the treatment of glioma. J Neurosurg. 2005;103(3):498–507.
77. Terakawa Y, et al. Diagnostic accuracy of ^{11}C-methionine PET for differentiation of recurrent brain tumors from radiation necrosis after radiotherapy. J Nucl Med. 2008;49(5):694–9.
78. Biersack HJ, et al. Imaging of brain tumors with L-3-[^{123}I]iodo-alpha-methyl tyrosine and SPECT. J Nucl Med. 1989;30(1):110–2.
79. Langen KJ, et al. SPECT studies of brain tumors with L-3-[^{123}I]iodo-alpha-methyl tyrosine: comparison with PET, ^{124}IMT and first clinical results. J Nucl Med. 1990;31(3):281–6.
80. Kuwert T, et al. Uptake of iodine-123-alpha-methyl tyrosine by gliomas and non-neoplastic brain lesions. Eur J Nucl Med. 1996;23(10):1345–53.
81. Weber W, et al. Fluorine-18-FDG PET and iodine-123-IMT SPECT in the evaluation of brain tumors. J Nucl Med. 1997;38(5):802–8.
82. Schmidt D, et al. 3-[^{123}I]Iodo-alpha-methyl-L-tyrosine uptake in cerebral gliomas: relationship to histological grading and prognosis. Eur J Nucl Med. 2001;28(7):855–61.
83. Weber WA, et al. Correlation between postoperative 3-[^{123}I]iodo-L-alpha-methyltyrosine uptake and survival in patients with gliomas. J Nucl Med. 2001;42(8):1144–50.
84. Pauleit D, et al. Comparison of *O*-(2-^{18}F-fluoroethyl)-L-tyrosine PET and 3-^{123}I-iodo-alpha-methyl-L-tyrosine SPECT in brain tumors. J Nucl Med. 2004;45(3):374–81.
85. Gotz L, et al. PET and SPECT for radiation treatment planning. Q J Nucl Med Mol Imaging. 2012;56(2):163–72.
86. Dunet V, Prior JL. FET PET in neuro-oncology and in evaluation of treatment response. PET Clin. 2013;8:147–62.
87. Pauleit D, et al. Whole-body distribution and dosimetry of *O*-(2-[^{18}F]fluoroethyl)-L-tyrosine. Eur J Nucl Med Mol Imaging. 2003;30(4):519–24.
88. Weber WA, et al. *O*-(2-[^{18}F]fluoroethyl)-L-tyrosine and L-[methyl-^{11}C]methionine uptake in brain tumours: initial results of a comparative study. Eur J Nucl Med. 2000;27(5):542–9.
89. Wester HJ, et al. Synthesis and radiopharmacology of *O*-(2-[^{18}F]fluoroethyl)-L-tyrosine for tumor imaging. J Nucl Med. 1999;40(1):205–12.
90. Heiss P, et al. Investigation of transport mechanism and uptake kinetics of *O*-(2-[^{18}F]fluoroethyl)-L-tyrosine in vitro and in vivo. J Nucl Med. 1999;40(8):1367–73.
91. Langen KJ, et al. Comparison of fluorotyrosines and methionine uptake in F98 rat gliomas. Nucl Med Biol. 2003;30(5):501–8.
92. Dunet V, et al. Performance of ^{18}F-fluoro-ethyl-tyrosine (^{18}F-FET) PET for the differential diagnosis of primary brain tumor: a systematic review and meta analysis. J Nucl Med. 2012;53(2):207–14.
93. Vander Borght T, et al. EANM procedure guidelines for brain tumour imaging using labelled amino acid analogues. Eur J Nucl Med Mol Imaging. 2006;33(11):1374–80.
94. Pauleit D, et al. Comparison of ^{18}F-FET and ^{18}F-FDG PET in brain tumors. Nucl Med Biol. 2009;36(7):779–87.
95. Jeong SY, Lim SM. Comparison of 3′-deoxy-3′-[^{18}F] fluorothymidine PET and *O*-(2-[^{18}F]fluoroethyl)-L-tyrosine PET in patients with newly diagnosed glioma. Nucl Med Biol. 2012;39(7):977–81.
96. Roelcke U, et al. F-18 choline PET does not detect increased metabolism in F-18 fluoroethyltyrosine-negative low-grade gliomas. Clin Nucl Med. 2012;37(1):e1–3.
97. Calcagni ML, et al. Dynamic *O*-(2-[^{18}F]fluoroethyl)-L-tyrosine (F-18 FET) PET for glioma grading: assessment of individual probability of malignancy. Clin Nucl Med. 2011;36(10):841–7.

98. Jansen NL, et al. MRI-suspected low-grade glioma: is there a need to perform dynamic FET PET? Eur J Nucl Med Mol Imaging. 2012;39(6):1021–9.
99. Pyka T, et al. Prediction of glioma recurrence using dynamic ^{18}F-fluoroethyltyrosine PET. AJNR Am J Neuroradiol. 2014;35(10):1924–9.
100. Becherer A, et al. Brain tumour imaging with PET: a comparison between [^{18}F]fluorodopa and [^{11}C]methionine. Eur J Nucl Med Mol Imaging. 2003;30(11):1561–7.
101. Talbot JN, et al. FDOPA PET has clinical utility in brain tumour imaging: a proposal for a revision of the recent EANM guidelines. Eur J Nucl Med Mol Imaging. 2007;34(7):1131–2; author reply 1133–4.
102. Karunanithi S, et al. ^{18}F-FDOPA PET/CT for detection of recurrence in patients with glioma: prospective comparison with ^{18}F-FDG PET/CT. Eur J Nucl Med Mol Imaging. 2013;40(7):1025–35.
103. Tripathi M, et al. Comparative evaluation of F-18 FDOPA, F-18 FDG, and F-18 FLT-PET/CT for metabolic imaging of low grade gliomas. Clin Nucl Med. 2009;34(12):878–83.
104. Shields AF, et al. Cellular sources of thymidine nucleotides: studies for PET. J Nucl Med. 1987;28(9):1435–40.
105. Mankoff DA, et al. Kinetic analysis of 2-[carbon-11] thymidine PET imaging studies: compartmental model and mathematical analysis. J Nucl Med. 1998;39(6):1043–55.
106. Grierson JR, et al. Metabolism of 3′-deoxy-3′-[F-18] fluorothymidine in proliferating A549 cells: validations for positron emission tomography. Nucl Med Biol. 2004;31(7):829–37.
107. Muzi M, et al. Kinetic analysis of 3′-deoxy-3′-^{18}F-fluorothymidine in patients with gliomas. J Nucl Med. 2006;47(10):1612–21.
108. Ullrich R, et al. Glioma proliferation as assessed by 3′-fluoro-3′-deoxy-L-thymidine positron emission tomography in patients with newly diagnosed high-grade glioma. Clin Cancer Res. 2008;14(7):2049–55.
109. Fink J, et al. Multi-modality brain tumor imaging – MRI, PET, and PET/MRI. J Nucl Med. 2015;56:1554–61.
110. Chen W, et al. Predicting treatment response of malignant gliomas to bevacizumab and irinotecan by imaging proliferation with [^{18}F]fluorothymidine positron emission tomography: a pilot study. J Clin Oncol. 2007;25(30):4714–21.
111. Hatakeyama T, et al. 11C-methionine (MET) and ^{18}F-fluorothymidine (FLT) PET in patients with newly diagnosed glioma. Eur J Nucl Med Mol Imaging. 2008;35(11):2009–17.
112. Grosu AL, et al. Positron emission tomography for radiation treatment planning. Strahlenther Onkol. 2005;181(8):483–99.
113. Huang Z, et al. Misdiagnoses of ^{11}C-choline combined with ^{18}F-FDG PET imaging in brain tumours. Nucl Med Commun. 2008;29(4):354–8.
114. Giovacchini G, et al. C-11 choline versus F-18 fluorodeoxyglucose for imaging meningiomas: an initial experience. Clin Nucl Med. 2009;34(1):7–10.
115. Hara T, et al. Use of ^{18}F-choline and ^{11}C-choline as contrast agents in positron emission tomography imaging-guided stereotactic biopsy sampling of gliomas. J Neurosurg. 2003;99(3):474–9.
116. Ohtani T, et al. Brain tumour imaging with carbon-11 choline: comparison with FDG PET and gadolinium-enhanced MR imaging. Eur J Nucl Med. 2001;28(11):1664–70.
117. Li FM, et al. ^{11}C-CHO PET in optimization of target volume delineation and treatment regimens in postoperative radiotherapy for brain gliomas. Nucl Med Biol. 2012;39(3):437–42.
118. Kato T, et al. Metabolic assessment of gliomas using ^{11}C-methionine, [^{18}F]fluorodeoxyglucose, and ^{11}C-choline positron-emission tomography. AJNR Am J Neuroradiol. 2008;29(6):1176–82.
119. Li W, et al. ^{11}C-choline PET/CT tumor recurrence detection and survival prediction in post-treatment patients with high-grade gliomas. Tumour Biol. 2014;35(12):12353–60.
120. Tan H, et al. Comparison of MRI, F-18 FDG, and ^{11}C-choline PET/CT for their potentials in differentiating brain tumor recurrence from brain tumor necrosis following radiotherapy. Clin Nucl Med. 2011;36(11):978–81.
121. Markus R, et al. Statistical parametric mapping of hypoxic tissue identified by [^{18}F]fluoromisonidazole and positron emission tomography following acute ischemic stroke. Neuroimage. 2002;16(2):425–33.
122. Valk PE, et al. Hypoxia in human gliomas: demonstration by PET with fluorine-18-fluoromisonidazole. J Nucl Med. 1992;33(12):2133–7.
123. Grunbaum Z, et al. Synthesis and characterization of congeners of misonidazole for imaging hypoxia. J Nucl Med. 1987;28(1):68–75.
124. Bruehlmeier M, et al. Assessment of hypoxia and perfusion in human brain tumors using PET with ^{18}F-fluoromisonidazole and ^{15}O-H_2O. J Nucl Med. 2004;45(11):1851–9.
125. Swanson KR, et al. Complementary but distinct roles for MRI and ^{18}F-fluoromisonidazole PET in the assessment of human glioblastomas. J Nucl Med. 2009;50(1):36–44.
126. Hirata K, et al. ^{18}F-Fluoromisonidazole positron emission tomography may differentiate glioblastoma multiforme from less malignant gliomas. Eur J Nucl Med Mol Imaging. 2012;39(5):760–70.
127. Werner P, et al. Current status and future role of brain PET/MRI in clinical and research settings. Eur J Nucl Med Mol Imaging. 2015;42(3):512–26.
128. Catana C, et al. PET/MRI for neurologic applications. J Nucl Med. 2012;53(12):1916–25.
129. Charnley N, et al. Early change in glucose metabolic rate measured using FDG-PET in patients with high-grade glioma predicts response to temozolomide but

not temozolomide plus radiotherapy. Int J Radiat Oncol Biol Phys. 2006;66(2):331–8.
130. Boss A, et al. Hybrid PET/MRI of intracranial masses: initial experiences and comparison to PET/CT. J Nucl Med. 2010;51(8):1198–205.
131. Bisdas S, et al. Metabolic mapping of gliomas using hybrid MR-PET imaging: feasibility of the method and spatial distribution of metabolic changes. Invest Radiol. 2013;48(5):295–301.
132. Preuss M, et al. Integrated PET/MRI for planning navigated biopsies in pediatric brain tumors. Childs Nerv Syst. 2014;30(8):1399–403.
133. Garibotto V, et al. Molecular neuroimaging with PET/MRI. Clin Transl Imaging. 2013;1(1):53–63.
134. Dunet V, et al. Combination of MRI and dynamic FET PET for initial glioma grading. Nuklearmedizin. 2014;53(4):155–61.
135. Lustig RA, et al. Imaging response in malignant glioma, RTOG 90–06. Am J Clin Oncol. 2007;30(1): 32–7.
136. Patronas NJ, et al. Prediction of survival in glioma patients by means of positron emission tomography. J Neurosurg. 1985;62(6):816–22.
137. Alavi JB, et al. Positron emission tomography in patients with glioma. A predictor of prognosis. Cancer. 1988;62(6):1074–8.
138. Santra A, et al. F-18 FDG PET-CT for predicting survival in patients with recurrent glioma: a prospective study. Neuroradiology. 2011;53(12):1017–24.
139. Colavolpe C, et al. FDG-PET predicts survival in recurrent high-grade gliomas treated with bevacizumab and irinotecan. Neuro Oncol. 2012; 14(5):649–57.
140. Colavolpe C, et al. Independent prognostic value of pre-treatment 18-FDG-PET in high-grade gliomas. J Neurooncol. 2012;107(3):527–35.
141. Brock CS, et al. Early evaluation of tumour metabolic response using [^{18}F]fluorodeoxyglucose and positron emission tomography: a pilot study following the phase II chemotherapy schedule for temozolomide in recurrent high-grade gliomas. Br J Cancer. 2000;82(3):608–15.
142. Hillner BE, et al. Impact of dedicated brain PET on intended patient management in participants of the national oncologic PET registry. Mol Imaging Biol. 2011;13(1):161–5.
143. Floeth FW, et al. Prognostic value of *O*-(2-^{18}F-fluoroethyl)-L-tyrosine PET and MRI in low-grade glioma. J Nucl Med. 2007;48(4):519–27.
144. Piroth MD, et al. Prognostic impact of postoperative, pre-irradiation ^{18}F-fluoroethyl-l-tyrosine uptake in glioblastoma patients treated with radiochemotherapy. Radiother Oncol. 2011;99(2):218–24.
145. Hutterer M, et al. *O*-(2-^{18}F-fluoroethyl)-L-tyrosine PET predicts failure of antiangiogenic treatment in patients with recurrent high-grade glioma. J Nucl Med. 2011;52(6):856–64.
146. Galldiks N, et al. Assessment of treatment response in patients with glioblastoma using *O*-(2-^{18}F-fluoroethyl)-L-tyrosine PET in comparison to MRI. J Nucl Med. 2012;53(7):1048–57.
147. Harris RJ, et al. ^{18}F-FDOPA and ^{18}F-FLT positron emission tomography parametric response maps predict response in recurrent malignant gliomas treated with bevacizumab. Neuro Oncol. 2012;14(8): 1079–89.
148. Schwarzenberg J, et al. Treatment response evaluation using ^{18}F-FDOPA PET in patients with recurrent malignant glioma on bevacizumab therapy. Clin Cancer Res. 2014;20(13):3550–9.
149. Mariani G, et al. A review on the clinical uses of SPECT/CT. Eur J Nucl Med Mol Imaging. 2010;37 (10):1959–85.
150. Buck AK, et al. SPECT/CT. J Nucl Med. 2008;49(8): 1305–19.
151. Hayashi M, et al. Comparison of methods of attenuation and scatter correction in brain perfusion SPECT. J Nucl Med Technol. 2005;33(4):224–9.
152. Filippi L, et al. Usefulness of SPECT/CT with a hybrid camera for the functional anatomical mapping of primary brain tumors by [Tc99m] tetrofosmin. Cancer Biother Radiopharm. 2006;21(1):41–8.
153. Schillaci O, et al. Single-photon emission computed tomography/computed tomography in brain tumors. Semin Nucl Med. 2007;37(1):34–47.
154. Kortmann RD. Radiotherapy in low-grade gliomas: pros. Semin Oncol. 2003;30(6 Suppl 19):29–33.
155. van den Bent MJ, et al. Phase II study of first-line chemotherapy with temozolomide in recurrent oligodendroglial tumors: the European Organization for Research and Treatment of Cancer Brain Tumor Group Study 26971. J Clin Oncol. 2003;21(13): 2525–8.
156. Glas M, et al. Long-term survival of patients with glioblastoma treated with radiotherapy and lomustine plus temozolomide. J Clin Oncol. 2009;27(8):1257–61.
157. Olson JJ, et al. The role of cytotoxic chemotherapy in the management of progressive glioblastoma: a systematic review and evidence-based clinical practice guideline. J Neurooncol. 2014;118(3):501–55.
158. Chamberlain MC, Raizer J. Antiangiogenic therapy for high-grade gliomas. CNS Neurol Disord Drug Targets. 2009;8(3):184–94.
159. Mariani G, Kassis AI, Adelstein SJ. Antibody internalization by tumor cells: implications for tumor diagnosis and therapy. J Nucl Med Allied Sci. 1990;34(1): 51–4.
160. Paganelli G, et al. Three-step monoclonal antibody tumor targeting in carcinoembryonic antigen-positive patients. Cancer Res. 1991;51(21):5960–6.
161. Grana C, et al. Pretargeted adjuvant radioimmunotherapy with yttrium-90-biotin in malignant glioma patients: a pilot study. Br J Cancer. 2002;86 (2):207–12.
162. Bartolomei M, et al. Combined treatment of glioblastoma patients with locoregional pre-targeted ^{90}Y-biotin radioimmunotherapy and temozolomide. Q J Nucl Med Mol Imaging. 2004;48(3):220–8.

163. Sekhar LN, Levine ZT, Sarma S. Grading of meningiomas. J Clin Neurosci. 2001;8 Suppl 1:1–7.
164. Johnson MD, et al. New prospects for management and treatment of inoperable and recurrent skull base meningiomas. J Neurooncol. 2008;86(1):109–22.
165. Soto-Montenegro ML, et al. Meningiomas: a comparative study of ^{68}Ga-DOTATOC, ^{68}Ga-DOTANOC and ^{68}Ga-DOTATATE for molecular imaging in mice. PLoS One. 2014;9(11):e111624.
166. Milker-Zabel S, et al. Improved target volume definition for fractionated stereotactic radiotherapy in patients with intracranial meningiomas by correlation of CT, MRI, and [^{68}Ga]-DOTATOC-PET. Int J Radiat Oncol Biol Phys. 2006;65(1):222–7.
167. Afshar-Oromieh A, et al. Detection of cranial meningiomas: comparison of ^{68}Ga-DOTATOC PET/CT and contrast-enhanced MRI. Eur J Nucl Med Mol Imaging. 2012;39(9):1409–15.
168. Di Chiro G, et al. Glucose utilization by intracranial meningiomas as an index of tumor aggressivity and probability of recurrence: a PET study. Radiology. 1987;164(2):521–6.
169. Lippitz B, et al. PET-study of intracranial meningiomas: correlation with histopathology, cellularity and proliferation rate. Acta Neurochir Suppl. 1996;65:108–11.
170. Lee JW, et al. ^{18}F-FDG PET in the assessment of tumor grade and prediction of tumor recurrence in intracranial meningioma. Eur J Nucl Med Mol Imaging. 2009;36:1574–82.
171. Iuchi T, et al. Glucose and methionine uptake and proliferative activity in meningiomas. Neurol Res. 1999;21(7):640–4.
172. Grosu AL, et al. ^{11}C-methionine PET improves the target volume delineation of meningiomas treated with stereotactic fractionated radiotherapy. Int J Radiat Oncol Biol Phys. 2006;66(2):339–44.
173. Astner ST, et al. Effect of ^{11}C-methionine-positron emission tomography on gross tumor volume delineation in stereotactic radiotherapy of skull base meningiomas. Int J Radiat Oncol Biol Phys. 2008;72(4):1161–7.
174. Muhr C, et al. Meningioma treated with interferon-alpha, evaluated with [^{11}C]-L-methionine positron emission tomography. Clin Cancer Res. 2001;7(8):2269–76.
175. Bertagna F, et al. Incidental ^{11}C-choline PET/CT brain uptake due to meningioma in a patient studied for prostate cancer: correlation with MRI and imaging fusion. Clin Nucl Med. 2013;38(11):e435–7.
176. Calabria F, et al. A case of intracranial meningioma detected by ^{18}F-choline PET/CT and examined by PET/MRI fusion imaging. Rev Esp Med Nucl Imagen Mol. 2014;33(5):306–7.
177. Schulz S, et al. Immunohistochemical determination of five somatostatin receptors in meningioma reveals frequent overexpression of somatostatin receptor subtype sst2A. Clin Cancer Res. 2000;6(5):1865–74.
178. von Wild KR. New development of functional neurorehabilitation in neurosurgery. Acta Neurochir Suppl. 2003;87:43–7.
179. Henze M, et al. PET imaging of somatostatin receptors using [^{68}GA]DOTA-D-Phe^{1}-Tyr^{3}-octreotide: first results in patients with meningiomas. J Nucl Med. 2001;42(7):1053–6.
180. Henze M, et al. Characterization of ^{68}Ga-DOTA-D-Phe1-Tyr3-octreotide kinetics in patients with meningiomas. J Nucl Med. 2005;46(5):763–9.
181. Afshar-Oromieh A, et al. Comparison of ^{68}Ga-DOTATOC-PET/CT and PET/MRI hybrid systems in patients with cranial meningioma: initial results. Neuro Oncol. 2015;17(2):312–9.
182. Moresco RM, et al. Oestrogen receptors in meningiomas: a correlative PET and immunohistochemical study. Nucl Med Commun. 1997;18(7):606–15.
183. Chao ST, et al. The sensitivity and specificity of FDG PET in distinguishing recurrent brain tumor from radionecrosis in patients treated with stereotactic radiosurgery. Int J Cancer. 2001;96(3):191–7.
184. Nihashi T, Dahabreh IJ, Terasawa T. Diagnostic accuracy of PET for recurrent glioma diagnosis: a meta-analysis. AJNR Am J Neuroradiol. 2013;34(5):944–50, S1–11.
185. Choi SJ, et al. [^{18}F]3′-deoxy-3′-fluorothymidine PET for the diagnosis and grading of brain tumors. Eur J Nucl Med Mol Imaging. 2005;32(6):653–9.
186. Fallanca F, et al. Incidental detection by [^{11}C]choline PET/CT of meningiomas in prostate cancer patients. Q J Nucl Med Mol Imaging. 2009;53(4):417–21.

Diagnostic Applications of Nuclear Medicine: Head and Neck Cancer

18

Heiko Schöder

Abstract

Most head and neck cancers are squamous cell carcinomas (HNSCC) arising in the oral cavity, oropharynx, larynx, and hypopharynx. The incidence of HNSCC is rising in the industrialized world, and there is increasing recognition of the role of human papillomavirus (HPV) infection as an etiologic factor in the development of this disease. In the USA, about 48,330 new cases of head and neck cancer have been diagnosed in 2016, and approximately 9,600 patients died of the disease. CT or MRI is essential to define the extent of the primary tumor, assess lymph node size, and detect bone and bone marrow disease. [^{18}F]FDG PET/CT imaging from the skull base to the floor of the pelvis is essential in patients with locally advanced disease and in all patients who are candidates for definitive chemoradiotherapy to define N and M staging. Interpretation of head and neck PET/CT requires expertise in head and neck anatomy and an understanding of variations of physiologic [^{18}F]FDG uptake in normal tissues. Scan interpretation is primarily based on visual assessment, although SUV measurements may be helpful. However, SUV is related to lesion size and may be underestimated in small primary tumors. Most primary tumors originate in the palatine tonsil, base of tongue, pyriform sinus, nasopharynx, and larynx. HNSCC tends to spread locally with invasion of adjacent structures. T staging is routinely done by either CT or MRI, not PET. However, occasionally [^{18}F]FDG PET may visualize small submucosal primary tumors that are difficult to distinguish from adjacent normal tissues with anatomic imaging studies. The presence of nodal metastases is an independent prognostic factor for survival in patients with head and neck cancer and may affect the choice of surgical or radiation therapy. Early and complete removal of neck node metastases is a prerequisite for cure. PET provides added value in the initial nodal staging. However, false-positive [^{18}F]FDG uptake can occur in inflamed, reactive lymph nodes. False-negative [^{18}F]FDG PET studies may occur when nodes have a small tumor burden, cystic degeneration of metastatic nodes with a small rim of viable tumor tissue, or low tracer uptake in the metastatic node. Nodal metastases in close proximity to the primary tumor may not be detectable as separate hypermetabolic focus when the primary shows very intense tracer uptake. Distant metastases are rare in patients with head and neck cancers, but the frequency increases with higher T stage and size, number of tumor-involved lymph nodes, jugular vein invasion, and in primary tumors in the hypo- and oropharynx. The most common location is

H. Schöder (✉)
Department of Radiology, Molecular Imaging and Therapy Service, Memorial Sloan Kettering Cancer Center, New York, NY, USA
e-mail: schoderh@mskcc.org

© Springer International Publishing Switzerland 2017
H.W. Strauss et al. (eds.), *Nuclear Oncology*,
https://doi.org/10.1007/978-3-319-26236-9_10

the lung, followed by bone and liver. [^{18}F]FDG PET/CT is sensitive for the detection of distant metastases. In patients treated with definitive chemoradiotherapy, [^{18}F]FDG PET/CT should be done approximately 12 weeks after the end of therapy to assess response to treatment.

[^{18}F]FDG PET/CT imaging is particularly useful to detect residual disease in neck lymph nodes. Clinical parameters and structural imaging cannot reliably predict the presence of residual metastatic neck disease; "planned neck dissection" was usually performed in the past after the completion of chemoradiotherapy, especially in patients with initial N2–N3 disease. Recently, in light of the high negative predictive value of posttreatment [^{18}F]FDG PET, this approach seems no longer justified. In patients with suspected recurrence, [^{18}F]FDG PET/CT has the highest sensitivity and specificity regardless of the primary treatment modality. However, posttherapy inflammation remains a potential source for false positive interpretation. Carcinoma of unknown primary accounts for approximately 1–2% of head and neck cancers. Occurrence of nodal metastases in neck levels I–III increases the likelihood for a primary HNSCC. However, in 5–40% of cases a primary malignancy is not identified during diagnostic evaluation, and these patients undergo extensive work-up, including panendoscopy of the upper aerodigestive tract and [^{18}F]FDG PET/CT. The use of [^{18}F]FDG PET/CT may reduce the number of panendoscopies. Other imaging studies are usually not needed, because it is extremely unlikely that they may identify a primary tumor that cannot be detected by [18F]FDG imaging.

In view of its unique epidemiology, tumor biology, and prognosis, nasopharyngeal carcinoma (NPC) should be considered separately. The highest incidence is noted in southern Chinese (20 times more common than in Caucasians). NPC tends to spread submucosally, in parapharyngeal tissues, along the maxillary and the mandibular nerves. Neck lymph node metastases are seen in the vast majority of patients. The lateral retropharyngeal nodes are traditionally considered first echelon nodes. The rate of distant metastases is high, involving bone, lung, and liver. Local disease extent is best defined by MRI, in particular disease involvement of the skull base and intracranial spread. Neck lymph node involvement is probably best characterized by a combination of MRI and [^{18}F]FDG PET/CT. [^{18}F]FDG PET/CT is useful for detection of disease outside the neck. The combination of MRI and [^{18}F]FDG PET/CT also appears most appropriate for chemoradiotherapy response and recurrent disease assessment. Similar to other head and neck cancers, the intensity of [^{18}F]FDG uptake in NPC primary tumors provides prognostic information. The utility of PET for delineating the gross tumor volume (GTV) in radiotherapy has been investigated. Most studies agree that the incorporation of PET in the radiotherapy planning process clearly improves target design over CT-based planning.

Keywords

Head and neck cancer in PET imaging • PET imaging in head and neck cancer • Squamous cell carcinomas of head and neck • Radiotracers in head and neck cancer

Glossary

[^{18}F]FDG	2-Deoxy-2-[^{18}F]fluoro-D-glucose
^{18}F-FAZA	^{18}F-azomycin arabinoside
^{18}F-FET	O-(2-^{18}F-fluoroethyl)-L-tyrosine
^{18}F-FLT	3′-Deoxy-3′-^{18}F-fluorothymidine
^{18}F-FMISO	^{18}F-fluoromisonidazole, 1-fluoro-3-(2-nitroimidazol-1-yl)-propan-2-ol
5-FU	5-Fluorouracil
AJCC	American Joint Committee on Cancer
AKT	Protein kinase B
BOLD	Blood oxygen level-dependent contrast imaging, a magnetic resonance technique
CRT	Chemoradiotherapy
CT	X-ray computed tomogaphy

DCE	Dynamic contrast-enhancement, a magnetic resonance technique
DFS	Disease-free survival
DWI	Diffusion-weighted imaging, a magnetic resonance technique
E2F	Group of genes that encode for a family of transcription factors
EGFR	Epidermal growth factor receptor
GTV	Gross tumor volume
Gy	Gray unit (ionizing radiation dose in the International System of Units, corresponding to the absorption of one joule of radiation energy per kilogram of matter)
HNSCC	Squamous cells carcinomas of the head and neck
HPV	Human papilloma virus
m-TOR	Mammalian target of rapamycin
M	Metastasis status according to the AJCC/UICC TNM staging system
MEK	Mitogen-activated protein kinase
MR	Magnetic resonance
MRI	Magnetic resonance imaging
MTV	Metabolic tumor volume
N	Lymph node status according to the AJCC/UICC TNM staging system
NPC	Nasopharyngeal carcinoma
OPC	Oropharynx cancer
OS	Overall survival
p53	Tumor protein p53, also known as cellular tumor antigen p53, phosphoprotein p53, tumor suppressor p53, antigen NY-CO-13, or transformation-related protein 53 (TRP53)
PET	Positron emission tomography
PET/CT	Positron emission tomography/Computed tomography
PET/MRI	Positron emission tomography/Magnetic resonance imaging
PFS	Progression-free survival
PI3K	Phosphatidylinositol 3-kinase
PTEN	Gene encoding for the phosphatase and tensin homolog protein, a tumor suppressor; PTEN deletions indicate a poor prognosis
RAF	Rapidly accelerated fibrosarcoma, related to retroviral oncogenes
RAS	Oncogene regulating signaling cascades
RB	Retinoblastoma protein
ROC	Receiver operating characteristic, a statistical analysis to assess the performance of a binary classifier
RT	Radiotherapy
RTOG	Radiation Therapy Oncology Group
SUV	Standardized uptake value
T	Tumor status according to the AJCC/UICC TNM staging system
TLG	Total lesion glycolysis
UICC	Union Internationale Contre le Cancer (International Union Against Cancer)
USFNA	Ultrasound-guided fine needle aspiration
VGEF	Vascular endothelial growth factor

Contents

Epidemiology and Biology of HNSCC 510

Treatment Strategies 513

Imaging of Head and Neck Cancer 516

Neck Metastases from an Unknown Primary Tumor 517

Primary Tumor Staging 518

Lymph Node Staging 521

Detection of Distant Metastases and Synchronous Second Primary Malignancies 523

Change in Patient Management 524

Response Assessment After (Chemo-) Radiotherapy 524

Suggested PET Interpretation Criteria for Response Assessment 527

Impact on Patient Management 528

Imaging During Chemoradiotherapy or After Induction Chemotherapy 528
Imaging After Surgery Prior to Adjuvant Therapy 530
Recurrent Disease 531
Prognostic Value of [^{18}F]FDG PET 532
Nasopharyngeal Cancer 533
Radiotracers Other than [^{18}F]FDG for Imaging of HNSCC 535
PET for Radiotherapy Planning 536
Emerging Role for PET/MRI 537
References 537

Epidemiology and Biology of HNSCC

In the Western world, more than 90% of head and neck cancers are squamous cell carcinomas (HNSCC). These tumors arise in the oral cavity, oropharynx, larynx, and hypopharynx (Figs. 1, 2, 3, and 4). In the United States, approximately 48,330 new cases were diagnosed in 2016 [1], and about 9,600 patients died of the disease. Only 40–50% of patients are expected to survive for 5 years. The worst prognosis is seen in patients with un-resectable advanced disease, with a 5-year survival rate of less than 10%, whereas patients presenting with tumors that are confined at the time of diagnosis (T1/2N0M0) have an excellent cure rate. Unfortunately, at the time of initial diagnosis many patients already have regional nodal metastases (~45%) or even distant metastases (Figs. 1, 2, 3, and 4). Also noteworthy is the high rate of second primary malignancies, mostly in the upper aerodigestive tract.

Traditionally, the most important risk factors for HNSCC were tobacco use and alcohol consumption, which seem to have a synergistic effect. In the past decade, a new disease entity has become more common: HNSCC of the oropharynx secondary to infection with human papilloma virus (HPV) [2]. HPV is a known cause of cervical cancer in females. Transmission to the oral cavity occurs through oral sex. In the United States, approximately 60% of patients with oropharynx cancers test positive for HPV-16. The overall incidence of HNSCC is still rising in the industrialized world because the substantial increase in HPV-positive cases (in particular males with carcinoma of the palatine tonsil and base of the tongue) exceeds the decline in HPV-negative cases. Most HPV-positive cases express the viral oncoproteins E6 and E7. E6 oncogene expression induces degradation of p53, and E7 induces inactivation of the retinoblastoma protein (RB). Under normal conditions, p53 induces cell cycle arrest in the G_2 phase to allow for repair of damaged DNA; it also is a master regulator for apoptosis [3]. RB normally binds to, and inactivates, the E2F transcription factors, which control the transition from the G_1 to the S phase of the cell cycle. Only under the influence of mitogen signals is this "brake" of RB on E2F released, thus permitting cell cycle progression. Binding of the viral oncoprotein E7 to RB therefore causes dis-inhibition and un-controlled cell cycle progression [3, 4]. Table 1 summarizes the epidemiologic and biologic features of HPV-positive and HPV-negative HNSCC [3, 5].

Patients with HPV-positive HNSCC have a better prognosis than patients with HPV-negative disease [6, 7]. This was initially shown in a phase II trial that employed induction chemotherapy followed by concurrent chemoradiotherapy in patients with stage III or IV HNSCC of the oropharynx or larynx. Response rates to induction chemotherapy were 82% vs. 55%, 2-year overall survival (OS) was 95% vs. 62%, and the 2-year progression-free survival (PFS) was 86% vs. 53% [7]. Similarly, in a large retrospective analysis [6] the 3-year OS was 82% for the 206 patients with HPV-positive tumors compared with 57% for the 117 patients with HPV-negative tumors. Corresponding rates for PFS were 74% and 38%, respectively. Even after adjusting for age, race, T and N stage, tobacco exposure, and treatment modality (standard fractionation vs. accelerated fractionation radiotherapy), patients with HPV-positive tumors still showed a 58% reduction in the risk of cancer death. Using a risk classification that considered HPV status, T and N stage, and smoking status, patients could be characterized as low, intermediate, or high risk. Whereas the 3-year survival was 93% in the low-risk group (HPV+ tumor and <10 pack years smoking history), it was only 46% in the

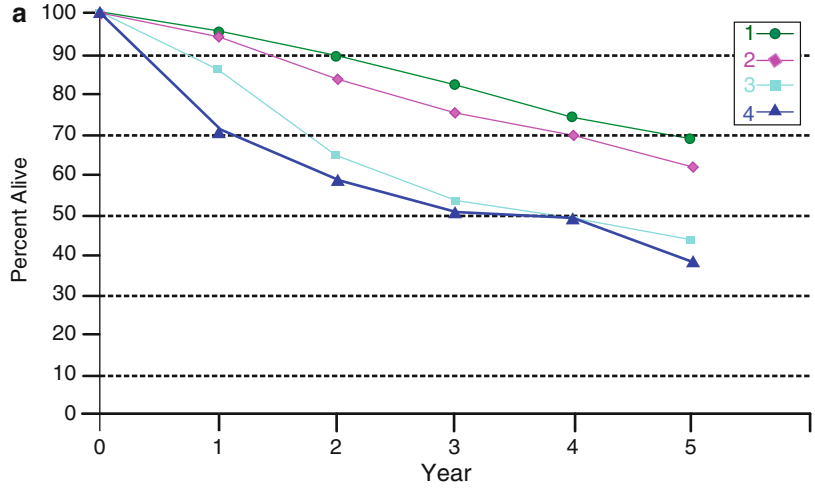

Observed Survival	1	2	3	4	5	95% Cls	Cases
1	95.5	88.8	82.0	74.3	68.7	66.3-71.1	2226
2	93.7	83.7	75.3	69.8	61.8	55.9-67.7	370
3	85.5	64.4	53.1	48.3	43.1	31.0-55.1	82
4	71.2	58.5	50.7	49.3	38.7	28.1-49.4	111

Five-year,observed survival by "combined"AJCC stage squamous cell carcinoma of the lip, 1998-1999

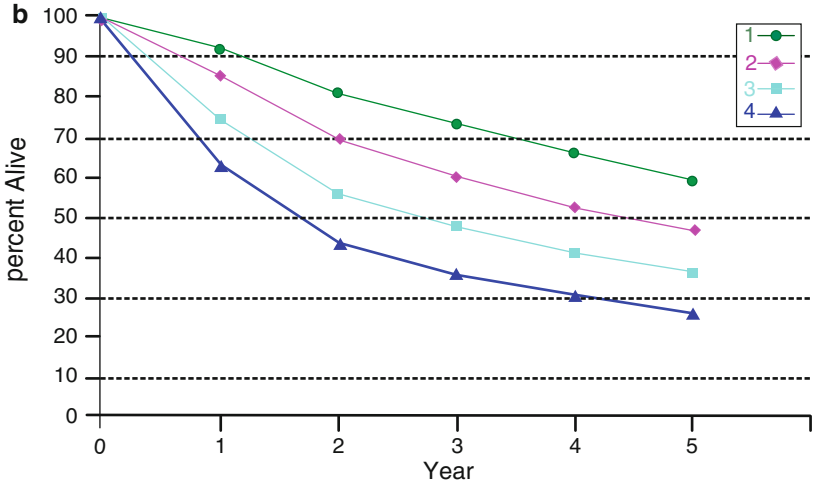

Observed Survival	1	2	3	4	5	95% Cls	Cases
1	92.4	81.3	73.6	66.4	59.2	57.5-60.8	4660
2	85.8	69.8	60.2	52.8	46.9	45.0-48.9	3315
3	74.9	56.4	47.9	41.1	36.3	34.1-38.6	2239
4	63.6	43.7	35.8	30.7	26.5	25.2-27.8	5431

Five-year,observed survival by "combined"AJCC stage squamous cell carcinoma of the oral cavity, 1998-1999

Fig. 1 (**a**) Five-year observed survival by combined AJCC stage squamous cell carcinoma of the lip, 1998–1999. (**b**) Five-year observed survival by "combined" AJCC stage squamous cell carcinoma of the oral cavity, 1998–1999. (From Edge S, et al. editors. AJCC cancer staging manual. 7th ed. New York: Springer; 2010, with permission of Springer Science + Business Media)

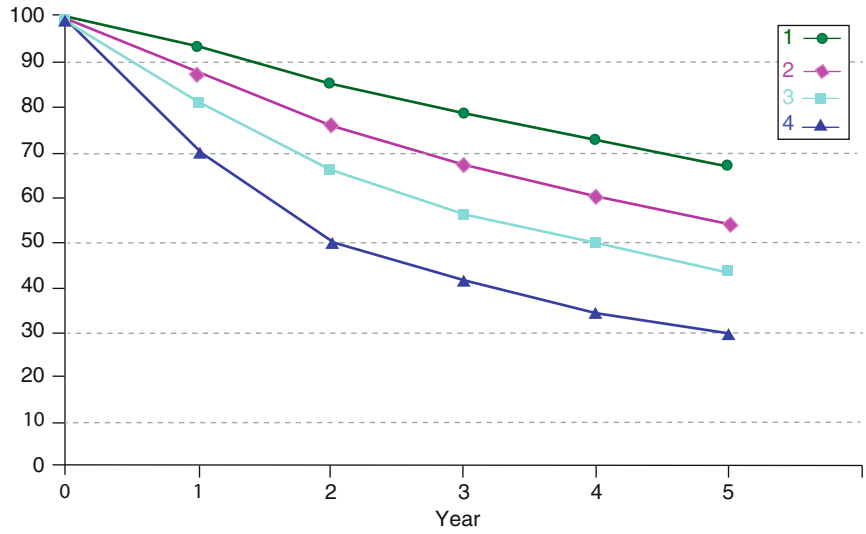

Observed Survival	1	2	3	4	5	95%Cls	Cases
1	94.3	85.8	79.4	73.3	67.2	66.0-68.3	8424
2	88.0	76.7	67.5	60.5	54.0	52.3-55.8	4105
3	81.3	66.3	56.3	49.5	43.3	41.5-45.1	3837
4	70.9	50.5	41.6	34.9	29.9	28.5-31.2	5525

Five-year,observed survival by "combined"AJCC stage squamous cell carcinoma of the larynx,1998-1999

Fig. 2 Five-year observed survival by combined AJCC stage squamous cell carcinoma of the larynx, 1998–1999. (From Edge S, et al. editors. AJCC cancer staging manual. 7th ed. New York: Springer; 2010, with permission of Springer Science + Business Media)

high-risk group (HPV-negative, $\leq$ 10 pack years and T4 or >10 pack years and any TN). Collectively these data, and those reported from other groups, suggest increased sensitivity to chemo- and radiotherapy in HPV-positive tumors. The prognostic value of HPV status was again confirmed in the more recent RTOG 0522 trial [8], in which patients with p16-positive oropharynx cancer (OPC) showed better 3-year PFS and OS than those with p16-negative oropharynx cancer (73% vs. 49%, and 86% vs. 60%, respectively). By contrast, epidermal growth factor receptor (EGFR) expression of thee primary tumor did not predict patient outcome. The mounting evidence on the prognostic value of the p-16 status in oropharynx cancer has led to efforts to perform better risk stratification of patients with HPV-positive tumors. Accordingly, a new staging system has been proposed for patients with HPV-positive disease, in which even patients with the most locally advanced disease (i.e., T4 N3) will be assigned to clinical stage III, and only those with documented distant disease to stage IV, reflecting differences in OS between these groups [9]. In addition, there is growing interest in (a) developing new treatment paradigms for HNSCC that may decrease the amount and duration of standard chemoradiotherapy in low-risk patients (to maintain high cure rates but reduce potential treatment associated long-term side effects, such as dysphagia, xerostomia, feeding tube dependency, or chronic aspiration) and (b) finding more successful therapies for high-risk patients, including early participation in clinical trials [10, 11]. Patients with persistent HPV expression after completion of therapy may require closer surveillance [12]. The potential role of an HPV vaccine for men and the role of an "oral Pap smear" for early detection of oropharynx cancer are under study.

An important consideration in head and neck cancer is the concept of field cancerization. The

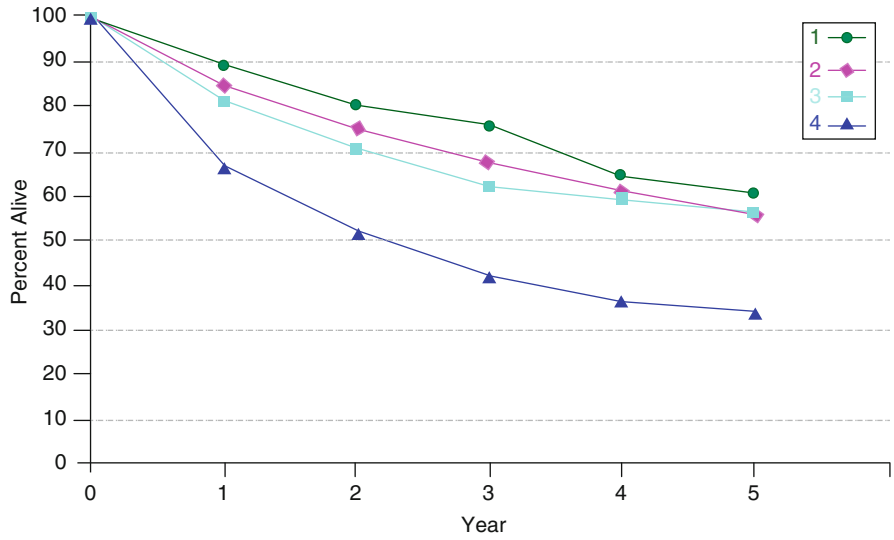

Observed Survival	1	2	3	4	5	95% CIs	Cases
1	89.5	80.8	76.1	65.2	60.6	52.1–69.2	170
2	85.3	75.2	67.8	61.6	56.2	50.1–62.3	322
3	81.8	70.4	61.9	59.2	55.7	50.3–61.0	408
4	66.9	52.1	41.9	37.0	34.1	30.3–37.8	759

Five-year, observed survival by "combined" AJCC stage squamous cell carcinoma of the nasopharynx. 1998-1999

Fig. 3 Five-year observed survival by combined AJCC stage squamous cell carcinoma of the nasopharynx, 1998–1999. (From Edge S, et al. editors. AJCC cancer staging manual. 7th ed. New York: Springer; 2010, with permission of Springer Science + Business Media)

occurrence of multiple synchronous or metachronous primary tumors in the upper aerodigestive tract was first described by Theodor Billroth more than 100 years ago. Over the past few decades knowledge has expanded, and a recent study showed that at least 35% of cases of oral and oropharynx cancers demonstrate genetic abnormalities in the surrounding (histopathologically normal) mucosa [13]. This is often addressed by the clinical term "biologically positive margins," suggesting that local recurrence is likely even though standard histopathology shows no cancer cells at or near the surgical margins of the tumor specimen [14].

As for many other malignancies, genetic alterations and activation or inhibition of cellular signaling pathways are important for the development and progression of many HNSCC. Some signaling factors are of particular interest because they are potential targets for drug therapy, including the EGFR, vascular endothelial growth factor (VEGF), and molecules involved in regulating the PI3K–PTEN/AKT pathway as well as the RAS-RAF-MEK pathway.

Treatment Strategies

The treatment approach varies with the disease stage and site(s) of disease in the head and neck [15]. Approximately one third of patients with HNSCC present with early-stage disease. Depending on tumor location and institutional preferences, they are treated surgically or with radiotherapy, and approximately 80% are cured. Patients with locoregional advanced disease, which is surgically unresectable, and patients in whom definitive treatment is administered with an attempt at organ preservation (e.g., oropharyngeal and laryngeal

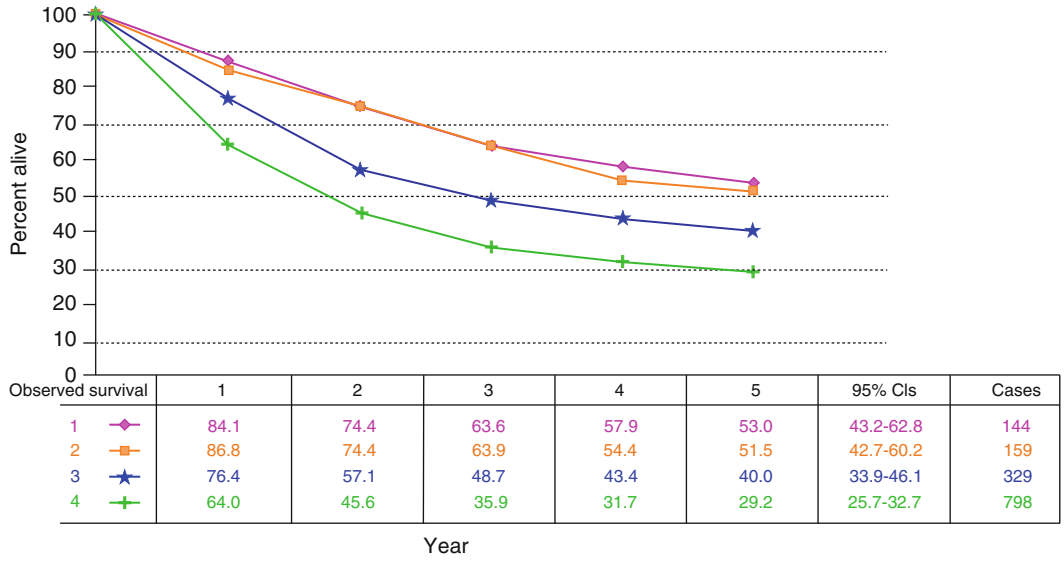

Observed survival	1	2	3	4	5	95% CIs	Cases
1	84.1	74.4	63.6	57.9	53.0	43.2-62.8	144
2	86.8	74.4	63.9	54.4	51.5	42.7-60.2	159
3	76.4	57.1	48.7	43.4	40.0	33.9-46.1	329
4	64.0	45.6	35.9	31.7	29.2	25.7-32.7	798

Five-year.observed survival by combined AJCC stage sinonasal carcinomas (all histologies), 1998-1999.

Fig. 4 Five-year observed survival by combined AJCC stage sinonasal carcinomas (all histologies), 1998–1999. (From Edge S, et al. editors. AJCC cancer staging manual. 7th ed. New York: Springer; 2010, with permission of Springer Science + Business Media)

Table 1 Epidemiology of HNSCC circa 2011

Incidence	HPV-positive HNSCC	HPV-negative HNSCC
	Increasing	Decreasing
Anatomical site	Oropharynx (tonsil, tongue)	All sites
Histology	Non-keratinized	Keratinized
Age	Younger; < 60 years	Older; > 60 years
Sex ratio	3:1 men	3:1 men
T stage	Tx, T1, T2	Any
N stage	Advanced, often cystic-necrotic, multilevel	Any
Risk factors	Sexual behavior	Alcohol, tobacco
Etiology	HPV virus	
Prognosis	Favorable	Unfavorable
New approaches	De-escalation of standard therapy?, vaccination?; oral Pap smear?	Early identification of nonresponders to standard therapy > clinical trials

Adopted from Leemans, Nat Rev. Cancer 2011 [3] and Marur et al., Lancet Oncol 2010 [5]
HPV human papilloma virus, *HNSCC* head and neck squamous cell carcinoma

carcinomas), undergo treatment with concurrent chemoradiotherapy [16, 17]. Cisplatinum is the medication with the most randomized clinical trial data to support its use as a drug enhancing the effects of radiotherapy in this setting. The larynx-preservation paradigm is supported by the results of a study that randomized 547 patients with stage III–IV supraglottic and glottic larynx cancer into three treatment arms: concurrent chemoradiotherapy, induction chemotherapy consisting of cisplatinum and 5-fluorouracil (5-FU) followed by radiotherapy, or radiotherapy alone. After a median follow-up of 3.5 years, the rates of locoregional control were 78%, 61%, and 56% for the three treatment arms, respectively. The fraction of patients who maintained an intact larynx at 2 years (and thus

the ability to speak and swallow after the end of therapy) was also better with the concurrent regimen (88%, 75%, and 70% for the three treatment arms, respectively) [17]. OS rates were similar in all three groups. The utility of concurrent high-dose cisplatinum for other subsites was established in a randomized study of 295 patients with unresectable head and neck cancer [18]. Concurrent chemoradiotherapy is therefore now widely applied as the definitive treatment of choice for locoregional advanced HNSCC. If residual disease is detected after the end of therapy or during follow-up, salvage surgery (e.g., laryngectomy) may be offered.

The management of the neck when using an organ-preservation approach has remained somewhat controversial. Complete response rates in irradiated cervical lymph nodes vary between 59% and 83% and to some degree are related to nodal size, radiotherapy dose, as well as the time point when response is determined: Complete response rates are almost 100% in N1 disease, higher in N2 than in N3 disease, and better when the largest metastatic node is smaller than 3 cm [19]. In N2–N3 disease, residual cancer in neck nodes has been reported in 16–39% of patients achieving a clinical complete response (no overt residual neck mass) [19–21]. Over the past decade, locoregional control rates with concurrent chemoradiotherapy have improved. It is now widely accepted that routine neck dissection is not appropriate in this setting. Instead, fluorodeoxyglucose positron emission tomography/computed tomography ([^{18}F]FDG PET/CT) has emerged as a gatekeeper for the management of the neck in this setting [15] (see next section).

Newer biologic therapies in HNSCC include angiogenesis inhibitors and drugs targeting the EGFR. EGFR is over-expressed and/or activated in the majority of HNSCC relative to normal tissue, and high expression is associated with poor disease control [22, 23]. While these data suggest HNSCC as an ideal malignancy for treatment with EGFR inhibitors, the selection of appropriate patients remains challenging. In studies of anti-EGFR agents in patients with advanced HNSCC, the objective response rates were approximately 10%, depending on the specific agent [24]. Cetuximab, a chimeric IgG_1 antibody against the extracellular domain of EGFR, is the most widely studied agent and has been tested in a number of clinical trials in patients with advanced disease. Cetuximab also enhances the efficacy of radiotherapy. In a randomized study of 420 patients [25], the addition of cetuximab to radiotherapy improved locoregional tumor control and OS without increasing mucositis and dysphagia when compared with radiotherapy alone. The corresponding median PFS was 24 months vs. 15 months, and the median OS was 49 months vs. 29 months. This study showed that concurrent radiotherapy plus cetuximab is a viable treatment option in locoregional advanced HNSCC. Whether this alternate regimen improves outcome vis-à-vis the standard approach with cisplatinum-based chemotherapy and concurrent radiotherapy is under investigation. Other trials investigated the role of adjuvant cetuximab in patients with recurrent or metastatic HNSCC undergoing platinum-based chemotherapy. Preliminary data showed a survival benefit over chemotherapy alone (reviewed in [26]). However, more recently published multicenter studies did not confirm this: In the RTOG trial 0522 [8], which included 981 patients, the addition of cetuximab to concurrent chemoradiotherapy with cisplatin did not improve patient outcome, with 3-year PFS rates of 61% and 59%, and 3-year OS of 73% and 76%, respectively, for those treated without vs. with the addition of cetuximab. The locoregional failure rate and rate of distant metastases were also similar between groups. Recent data have also raised concerns regarding cetuximab-associated side effects leading to lower patient compliance in chemoradiotherapy regimens [27].

Antiangiogenic therapy has mainly been studied using bevacizumab, a recombinant humanized, monoclonal IgG antibody against VEGF-A, usually in combination with chemotherapy or in combination with cetuximab. Preliminary data suggest that partial responses or disease stabilization can be achieved in more than 75% of patients [28]. Other drugs under study include various tyrosine kinase inhibitors. Recent improved understanding of relevant signaling pathways may open up new avenues for targeted drug therapies in HNSCC. For instance, down-regulation of the transforming growth factor beta receptor is frequently found, and the PI3K/PTEN/AKT/m-TOR pathway (important for increased proliferation, evasion of

apoptosis, and increased survival) is frequently up-regulated. A number of drugs interfering with these tumor pathways are under study [26].

Imaging of Head and Neck Cancer

Standard imaging studies for the staging and follow-up of head and neck cancer include contrast-enhanced CT, magnetic resonance imaging (MRI), and [^{18}F]FDG PET/CT. CT or MRI is essential for characterizing the primary tumor and in defining its extent. Bone involvement is better detected with CT, while early bone marrow disease is better detected with MRI. MRI can better define the interface between normal muscle and tumor. It is essential in staging nasopharyngeal carcinoma, and also has particular advantages for detecting intracranial tumor spread and perineural spread and for differentiating entrapped secretions in paranasal sinuses from adjacent tumor.

Lymph node staging is done equally well with either CT or MRI. Traditionally, both imaging tests have relied on the assessment of lymph node size in order to identify metastatic disease. In general, lymph nodes $\geq$1.5 cm in levels I and highest level II, as well as lymph nodes $\geq$1.0 cm in all other locations, are considered abnormal. This approach is suboptimal because metastasis can be present in normal-sized lymph nodes and enlarged nodes may not contain tumor. Depending on the chosen cut-off for lymph node size, one can achieve high sensitivity at the expense of specificity or vice versa [29]. Secondary criteria are the presence of grouped lymph nodes (usually >3 nodes in one location), heterogeneous nodal enhancement, stranding of surrounding fat indicating extracapsular spread, and demonstration of central necrosis (the most reliable criterion for nodal metastasis). Special MRI sequences, such as diffusion-weighted imaging (DWI), or newer MR contrast agents (including ultrasmall superparamagnetic iron oxide particles, or more recently various nanoparticles), may improve the characterization of nodes. However, they are not yet routinely employed and all available data are preliminary.

The vast majority of head and neck cancers show intense [^{18}F]FDG uptake; however, uptake in salivary gland tumors may be variable (high [^{18}F]FDG uptake in some benign tumors, low uptake in some malignant tumors). Combined PET/CT is more accurate than PET alone and has beneficial effects on patient management [30, 31]. We perform [^{18}F]FDG PET/CT imaging from the skull base to the floor of the pelvis for appropriate N and M staging in patients with head and neck cancer. Both distant metastases and potential synchronous primaries in the aerodigestive tract are hypermetabolic and therefore easily detectable. In order to save costs and potentially radiation dose, some investigators have proposed a limited field of view scan (e.g., ending at the level of the diaphragm) for patients with head and neck cancer. We, however, believe that a different approach should be taken: Rather than using [^{18}F]FDG PET in all patients, the test should be used in subsets of patients where imaging findings are most likely to alter management. For instance, it is essential in surgical patients with locally advanced disease. In addition, we use [^{18}F]FDG PET/CT in all patients who are candidates for definitive chemoradiotherapy for the purpose of staging and radiotherapy planning; these scans are performed in the radiotherapy position with a mask. PET/CT is also used for response assessment in patients with advanced disease undergoing chemotherapy, concurrent chemoradiotherapy, or enrolled in experimental protocols.

Interpretation of head and neck PET/CT requires special expertise in head and neck anatomy as well as an understanding of physiologic [^{18}F]FDG uptake in normal tissues and awareness of the many potential normal variants. Scan interpretation is primarily based on visual assessment, although standardized uptake value (SUV) numbers may be helpful in estimating biologic aggressiveness and for response assessment. SUV is related to lesion size and may be underestimated in small primary tumors. Physiologic [^{18}F]FDG uptake is nearly always noted in lymphoid tissues (tonsils) composing "Waldeyer's ring," including the pharyngeal tonsil (upper nasopharynx), symmetrical uptake in the palatine tonsils (unless the patient status is posttonsillectomy or suffers from unilateral tonsillitis or tonsillar carcinoma), and the lingual tonsil at the base of the tongue.

Variable uptake is noted in the tongue and floor of the mouth muscles, and is usually more intense if the patient was moving the tongue or swallowing during the uptake phase. Asymmetrical uptake in a normal tongue can be noted after hemiglossectomy or even resection of smaller unilateral tongue lesions, leading to increased muscle activity and [^{18}F]FDG uptake in the contralateral tongue. This is also noted after unilateral denervation, e.g., after hemimandibulectomy or due to hypoglossal nerve paralysis, where fatty atrophy and lack of [^{18}F]FDG uptake in the denervated hemitongue is associated with relatively intense uptake in the contralateral normal tongue. Asymmetrical uptake, due to spasm, can sometimes be observed in the pterygoid or temporalis muscles. Uptake along the scalene muscles is frequently seen, either symmetrical or asymmetrical, and is easily characterized as a normal variant on fusion images. Retained mucous in paranasal sinuses shows no [^{18}F]FDG uptake unless there is severe inflammation, infection, or tumor. Similar to MRI (but not CT), [^{18}F]FDG PET/CT differentiates well between tumor and entrapped secretions due to sinus outflow obstruction. While mucous retention or small polyps are fairly common in the paranasal sinuses, fluid retention in mastoid air cells should prompt careful assessment of the oropharynx to identify possible reasons for obstruction of the Eustachian tube.

Normally, symmetrical [^{18}F]FDG uptake is seen in the vocal cords and other laryngeal muscles (mild uptake is usually noted even if the patient does not vocalize during the uptake phase). Asymmetrical vocal cord uptake suggests vocal cord paralysis, usually due to damage of the ipsilateral recurrent laryngeal nerve. Secondary CT signs are sometimes helpful in confirming suspected vocal cord paralysis, including a paramedian position of the paralyzed vocal cord, tilting of the thyroid cartilage, displacement of the ipsilateral arytenoid cartilage, dilatation of the ipsilateral piriform sinus, and prominent laryngeal ventricle. Longstanding vocal cord paralysis may lead to atrophy of the posterior cricoarytenoid and thyroarytenoid muscles [32, 33]. In searching for possible reasons for vocal cord paralysis, attention should focus on the upper mediastinum as well as the lower neck to identify possible tumors or metastasis. Other reasons for vocal cord paralysis include nerve damage due to fibrosis (e.g., after radiotherapy) and chemotherapy (vinca alkaloids can cause transient vocal cord paralysis [34]). Asymmetrical or unusual focal [^{18}F]FDG uptake can be observed in patients who received instillation of foreign material (e.g., Radiesse) for attempted medialization of a paralyzed cord. In this case the [^{18}F]FDG uptake occurs on the treated site, likely due to foreign body reaction and inflammation. The instilled dense material is easily identified on the CT images. Large salivary glands usually show symmetrical [^{18}F]FDG uptake (submandibular gland > parotid gland). A common cause for unilateral focal [^{18}F]FDG uptake in parotid glands are pleomorphic adenomas (the most common benign tumor in the parotid gland), or "Warthin's tumors" (which are entrapped normal lymphoid tissue). The submandibular gland is usually removed as part of neck dissections. Asymmetrical uptake in the contralateral remaining normal gland should not be confused with lymph node metastases. Postsurgical muscle flaps can show (physiologic) very intense [^{18}F]FDG uptake, in particular at the flap pedicle, presumably related to hyperemia. This should not be confused with tumor recurrence. Some of the aforementioned normal findings and normal variations are described in detail in several review articles [35, 36].

Neck Metastases from an Unknown Primary Tumor

This condition, also known as carcinoma of unknown primary, accounts for 3–15% of all cancer diagnoses and for approximately 1–2% of head and neck cancers. For practical purposes this entity should be defined as the combination of no history of previous malignancy, no clinical or laboratory evidence of primary neoplasm, and a neck mass that is histologically or cytologically proven to be carcinoma. Occurrence of nodal metastases in neck levels I–III increases the likelihood of a primary HNSCC. However, in 5–40% of cases a primary malignancy is not identified during diagnostic evaluation and long-term follow-up. Provided a primary tumor cannot be

identified, in many institutions these patients are treated with extensive radiotherapy fields that cover the entire pharyngeal mucosa, the larynx, and bilateral necks. This is obviously associated with considerable morbidity. Identification of a primary tumor will direct rational therapy to a single mucosal site and the ipsilateral neck (unless the primary tumor is in, or close to, the midline). Detection of the primary tumor, in general, also allows for less extensive treatment (e.g., smaller radiation fields) and may potentially improve locoregional control. Therefore, these patients undergo extensive work-up. In some cases, the "unknown primary" is already identified in a thorough clinical examination by an experienced head and neck surgeon or oncologist; all other patients should undergo panendoscopy of the upper aerodigestive tract and [^{18}F]FDG PET/CT.

The literature is replete with studies of patients with unknown primary. Unfortunately, most study populations are very heterogeneous, and the definition of unknown primary and methods of verification vary considerably. For this chapter, we have only considered studies in which patients had at least undergone clinical examination, CT or MRI, and office endoscopy prior to PET (Table 2). The percentage of primary tumors detected is quoted as 14–37% [37–48]. When reviewing the literature, it should be noted that the sensitivity of PET is oftentimes stated incorrectly: Since all neck metastases must have an underlying primary tumor, the denominator for calculating sensitivity should be the total number of patients studied (not the much smaller number of patients in whom the primary is eventually detected by imaging and panendoscopy). Therefore, it appears overall less controversial and more meaningful to simply state the rate of primary tumors that were only detected by PET (see Table 2). Depending on the interpretation criteria, some studies report a high number of false-positive findings. It is therefore necessary to strike a reasonable balance between the wish to identify the location of the unknown primary on PET and the danger of calling every little variant suspicious. Potential reasons for false-negative PET studies include a small primary tumor (although lesions as small as 4 mm can be detected as long as there is intense [^{18}F]FDG uptake), low metabolic activity (cystic/necrotic tumor or lymph nodes), or the primary tumor was accidentally removed at the time of neck dissection.

In our institution, patients with unknown primary and negative results from clinical examination and office endoscopy first undergo [^{18}F]FDG PET/CT (Fig. 5), before panendoscopy; panendoscopy is defined as naso-pharyngoscopy, direct laryngoscopy, and upper esophagoscopy (in the absence of specific symptoms or imaging findings, a bronchoscopy is no longer done routinely because the yield is exceedingly low). This approach may reduce the number of necessary panendoscopies and avoid false-positive [^{18}F]FDG uptake after manipulation during endoscopy and biopsy (Fig. 1). Of note, other imaging studies are usually not needed, because it is extremely unlikely that they may identify a primary tumor that cannot be detected by PET. Statistically, most primary tumors originate in the ipsilateral palatine tonsil, base of the tongue, piriform sinus, nasopharynx (more commonly in East Asian populations), and larynx. Particular attention should therefore be focused during PET/CT interpretation to these sites. If the PET study is positive, biopsies should be obtained from the suggested location. If the PET study is negative, panendoscopy with biopsy sampling from suspected locations (based on the location of the lymph node and statistical considerations) should be performed. Depending on the results of these biopsies, the patient may proceed to surgery or radiation therapy.

Primary Tumor Staging

Most HNSCC are diagnosed clinically. The primary goal of imaging studies is therefore not tumor detection, but rather to define the extent of the primary tumor, in particular with regard to structures whose involvement may alter the surgical approach (e.g., depth of soft tissue infiltration, bone invasion, orbital invasion, skull base invasion, tumor "tracking" along nerves and blood vessels).

Head and neck cancers tend to spread locally with invasion of adjacent structures. For instance, many cancers of the oral tongue tend to extend into

Table 2 [^{18}F]FDG PET and PET/CT for the detection of unknown primary tumors in patients with neck lymph node metastases

	N	Prior pan-endoscopy	PET or PET/CT	Total detection rate with all tests	Total PET uptake	PET detection rate for primary	PET false-positive rate %	Distant mets. with PET	Comments
Kole, Cancer 1998 [43]	14	None (was done after PET)	PET	7/14 (50%)	4/14	4/14 (25%)	N/R	N/R	Management change in 21% of pts.
Jungehülsing, ORL 2000 [42]	27	all	PET	7/27 (26%) (5 in HN)	N/R	7/27 (26%)	N/R	N/R	Management change in 29% of pts.
Johansen, Laryngoscope 2002 [41]	42	all	PET	10/42 (24%) (7 in HN)	20/42	10/42 (24%)	10/42 (24%)	N/R	
Fogarty, 2003 [38]	21	N/R	PET	3/21 (14%) (1 path confirmed, 2 probable)	8/21	3/21 (14%)	5/8 (62%)	3/21 (14%)	PET detected more regional neck dz. in 2/21
Wong, Clin Oncol 2003 [47]	17	all	PET	N/R	8/17	5/29 (17%)	3/8 (37%)		Treatment plan changed in 53% of pts.
Bohuslavizki, JNM 2000 [37]	44	all	PET	22/42 (53%)	22/44 (13 in HN)	15/44 (34%) (8 HN = 18%)	5/13 (38%)	N/R	Mixed pt. population
Miller, Head Neck 2008 [44]	31	None (CT/MR, office endoscopy; panendoscopy after PET)	PET	14/31 (45%)	10/31	9/31 (29%)	1 (3%)	N/R	4 addtl. found by panendoscopy, size 0.8–5 mm

(*continued*)

Table 2 (continued)

	N	Prior pan-endoscopy	PET or PET/CT	Total detection rate with all tests	Total PET uptake	PET detection rate for primary	PET false-positive rate %	Distant mets. with PET	Comments
Gutzeit, Radiology 2005 (data shown for pts. with neck metastases only) [39]	18	N/R	PET/CT	6/18 (33%)	7/18	3/18 (33%)	3/16 (19%)	N/R	PET/CT slightly better than CT or PET alone
Wartski, NM Comm 2007 [46]	38	All	PET/CT	14/38 (38%)	26/38	13/38 (34%)	4/17 pts. w/further w/u (23%); addtl. 9 pts. had no further w/u	N/R	Management change in 60% of pts.
Johansen, 2008 [40]	60	41	PET or PET/CT	21/60 (35%)	30/60 (22 in HN)	18/60 (30%) total; (missed 3 HN primaries later found by panendoscopy)	12/30 (40%) total; 10/22 (45%) in HN; 1/8 pre-endoscopy; 11/22 post endoscopy	12/22 (54%) with HN primary	Management change in 25% of pts.
Roh, Oral Oncol 2009 [45]	44	None (was done after PET)	PET/CT	16/44 (36%)	19/44	14/44 (32%)	5/14 (35%)	6/44 (14%)	Subtracting tumors seen on contrast CT, PET detected 7/37 primaries (18%)
Yabuki, Eur Arch Oto 2010 [48]	24	all	PET	9/24 (37%)	12/24	9/24 (37%)	3/12 (25%)	N/R	

PET/CT positron emission tomography/computed tomography, *mets.* metastases, *path* pathologically, *pts*. patients, *dz*. disease, *addtl*. Additional, *w/u* work-up, *HN* head and neck, *N/R*

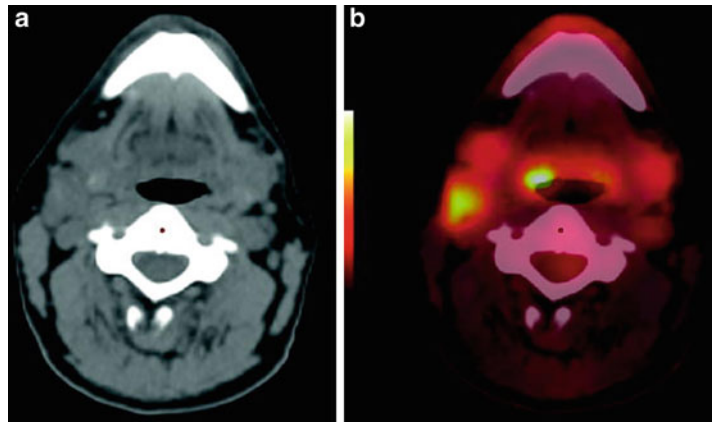

Fig. 5 Carcinoma of unknown primary in a 46-year-old man who presented with a right neck mass from an unknown primary squamous cell carcinoma. Clinical exam and office endoscopy were negative. [^{18}F]FDG PET was performed for localization of primary tumor. Non-contrast CT shows enlarged right neck node (**a**); PET/CT fusion image shows abnormal [^{18}F]FDG uptake in right level two node and at the right base of tongue primary (**b**)

the floor of the mouth. Staging of HNSCC is routinely done using either CT or MRI, not PET. However, occasionally [^{18}F]FDG PET may depict small submucosal primary tumors that are difficult to distinguish from adjacent normal tissues with anatomic imaging studies. In a study of 48 patients with HNSCC (mostly tumors of the oral cavity), [^{18}F]FDG PET detected 35 of 40 primaries known or still present at that time (88%), whereas contrast-enhanced CT of the neck identified a primary tumor only in 18 of the 35 patients (51%) with known or present primary tumors. Of the 17 primaries not detected by CT, 11 were clearly visualized with [^{18}F]FDG PET [49]. PET/CT readers should pay attention to secondary tumor signs. For instance, cancers at the anterior floor of the mouth can cause obstruction of Wharton's duct, through which the submandibular gland empties into the oral cavity. Ductal dilatation and enlargement of the gland, sometimes associated with increased [^{18}F]FDG uptake, may be noted. Perineural spread can occur in various locations in the head and neck, but is particularly common with adenoid cystic carcinoma (submucosal cancers that are common in the hard palate). Therefore, PET/CT readers should also be familiar with the normal branching patterns of cranial nerves relevant for innervation of the head and neck, in particular the facial nerve and trigeminal branches V2 and V3.

Lymph Node Staging

The risk of lymph node metastases is related to the anatomic location of the primary tumor. Tumors originating in sites that are rich in lymphatics, such as the tongue and floor of mouth, metastasize earlier and more often than those in other locations, including the hard palate or upper gum. The presence of nodal metastases is an independent prognostic factor for survival in patients with head and neck cancer; it decreases OS by approximately one half [50]. These historical data were corroborated by a larger retrospective study of 3,800 patients, in which the presence of neck node metastases lowered the 5-year disease-specific survival rate by approximately 30% [51]. The prognosis worsens additionally with the number of lymph nodes involved [52], with extracapsular spread of nodal disease [53], and with metastases located in the lower neck [54, 55]. The presence and extent of nodal metastases may affect the surgical or radiotherapy approach. Early and complete removal of neck node metastases is a prerequisite for cure. Accurate nodal staging of the neck is therefore particularly important.

The clinical neck examination and anatomic imaging studies suffer from a lack of sensitivity and specificity in assessing the extent of nodal

disease [29, 56]. Numerous studies have compared the accuracy of anatomic imaging modalities and [^{18}F]FDG PET for the detection of nodal metastases in the neck [49, 57–62] (Fig. 6). In most studies, PET had a higher sensitivity and/or specificity than CT, MRI, or ultrasound. In 124 patients with oral cavity cancer, the authors compared [^{18}F]FDG PET and neck CT or MRI with surgical histopathology of each dissected neck level; metastatic nodes were found in 95 of 493 dissected neck levels. Overall, and for each neck level, [^{18}F]FDG PET showed a higher accuracy then CT or MRI. The overall sensitivity, specificity, and accuracy for PET vs. CT/MR were 75% vs. 53%, 93% vs. 94%, and 89% vs. 86%, respectively [62]. However, these numbers may be somewhat optimistic, because the same authors later published data from 471 patients with oral cavity cancer, and found a suboptimal sensitivity and specificity of 73% and 58% on a per-patient basis [63]. In a meta-analysis of 35 studies comparing the diagnostic performance of [^{18}F]FDG PET or PET/CT with that of neck CT, MRI, or ultrasound-guided fine needle aspiration (USFNA), [^{18}F]FDG PET had a combined sensitivity and specificity in the range of 73–82% and 86–89%, compared with 74%/76% for CT, and 78%/80% for MRI. For unclear reasons, four studies comparing PET and USFNA showed a surprisingly low sensitivity of ~45% for both modalities (probably due to methodological issues or selection bias); as expected USFNA had a near perfect 96% specificity because it is based on cytology of aspirates [64].

It is important to understand that the sensitivity and specificity of [^{18}F]FDG PET were probably overestimated in earlier studies, when the technique had just been introduced. This is a common phenomenon applicable to any new imaging technique. In addition, CT and MRI techniques have vastly improved over the past 15 years. Readers are encouraged to review the Methods sections of published studies carefully; the most rigorous assessment would require analysis for each neck level (rather than analysis per patient or per neck), comparison with surgical histopathology of neck dissection, and at least 6–12 months of follow-up for non-dissected neck sites. Nevertheless, PET probably provides some (difficult to quantify) added value in the initial nodal staging of HNSCC.

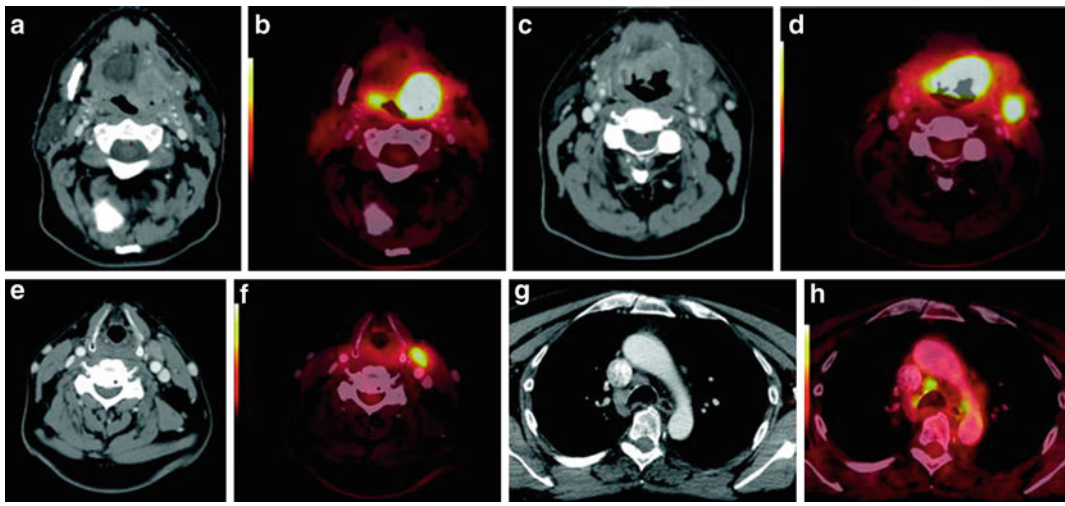

Fig. 6 Staging studies in a 57-year-old man with base of tongue cancer. Contrast-enhanced CT of the neck shows a large enhancing mass at the left base of tongue (**a**), which is intensely hypermetabolic on PET/CT fusion image (**b**). Intense [^{18}F]FDG uptake in lymph node metastases in the left neck level I (**c**, **d**) and level III (**e**, **f**). In addition, the staging scan showed enlarged hypermetabolic nodes in the mediastinum (**g**, **h**). Because of a potential change in management, these mediastinal nodes were biopsied: histopathology showed granulomatous disease (i.e., false-positive [^{18}F]FDG uptake)

False-positive [^{18}F]FDG uptake can occur in inflamed, reactive lymph nodes, a common phenomenon in the "classic" (HPV-negative) patient with HNSCC, secondary to poor oral and dental hygiene. Other reasons for false-positive [^{18}F]FDG uptake include granulomatous disease (Fig. 6) and uptake in the inflamed wall of branchial cleft cysts. The latter may be difficult to distinguish from cystic/necrotic lymph nodes, in particular since these nodal metastases often originate from small, indolent, and clinically occult primary tumors in the oropharynx [65]. Although various SUV cut-offs have been proposed, in clinical reality no single SUV number can reliably distinguish between metastatic and benign lymph nodes. Reasons for false-negative [^{18}F]FDG PET studies may include a small tumor burden in metastatic nodes, cystic degeneration of metastatic nodes only surrounded by a small rim of viable tumor tissue, low tracer uptake in the metastatic node, and imaging artifacts. Nodal metastases in close proximity to the primary tumor may not be detectable as separate hypermetabolic focus when the primary tumor shows very intense tracer uptake.

Detection of Distant Metastases and Synchronous Second Primary Malignancies

Distant metastases are rare in patients with head and neck cancers, but the frequency increases with higher T stage and size and number of tumor-involved lymph nodes and with jugular vein invasion. The risk for distant disease also increases with nodal metastases in the lower neck or supraclavicular region, in primary tumors in the hypo- and oropharynx, and in the setting of locoregional recurrence. The most common location is the lung, followed by bone and liver (with an estimated frequency of 66%, 20%, and 10%, respectively [66]). In contrast to most squamous cell cancers, adenoid cystic and neuroendocrine carcinomas tend to metastasize early and widely, even in the absence of advanced local disease. Although the lung is the most common site of distant disease, a chest CT is insufficient for comprehensive staging if the probability for distant disease is reasonably high, because potential metastases at other sites, including bone and liver, remain undetected [67]. [^{18}F]FDG PET/CT clearly improves the detection rates.

Patients with HNSCC have a higher propensity for synchronous (within 6 months of primary diagnosis) or metachronous (>6 month after primary diagnosis) second primaries compared with many other malignant tumors. This is likely related to synergistic effects from exposure to carcinogens in tobacco and alcohol. In a retrospective study of 1,100 patients, synchronous second primaries were noted in 7% of patients, and metachronous second primaries in another 9% of patients (at a median of 3.5 years after detection of the first head and neck cancer) [68]. However, in other analyses the reported rates for second primary malignancies in patients with HNSCC vary widely, from 7% up to 30%, probably related to selection bias [69–73]. Rather than recording the rate of second primaries, it may be more informative to record a standardized incidence ratio (the ratio between the number of observed to expected primary cancers in patients with prior HNSCC, using a cohort of similar age, sex, and ethnicity as standard of reference) [74]. In a recent analysis of the SEER database [74], the highest standardized incidence ratio was found for primary HNSCC in the hypopharynx, the lowest for primaries in the larynx. Patients with oral cavity or oropharynx index cancer most commonly develop a second primary at other subsites of the head and neck. Interestingly, the rate of second primaries in patients with an index tumor in the oropharynx has declined over the past decade, presumably related to the increasing number of HPV-positive tumors (which carry a better prognosis in general, and apparently also a lower risk for a second primary). Indeed, in a study of 746 patients with oropharynx primary cancer [6], the rate of second primaries at 3 years was 8.9% in total, but it was only 5.9% in patients with HPV-positive tumors compared with 14.6% in patients with HPV-negative tumors. By contrast, the 3-year rate of distant metastases overall was 10%, without significant differences in rates between patients with HPV-negative and those

with HPV-positive tumors (8.7% vs. 14.6%). As discussed earlier, patients with HPV-positive tumors experience higher initial and long-term cure rates for disease in the neck, and for this reason the distribution of any recurrent disease differs in that distant metastases outside the neck are becoming *relatively* more common, and may present later, than in historical controls.

Based on our own experience, a second primary or distant metastases outside the neck will be detected in less than 10% of cases in the staging scan, depending on the location, size, and histology of the primary tumor, as well as presence of bulky lymphadenopathy. Similar data (8–11% prevalence) were reported by other groups [71–73]. The vast majority of second primary tumors are observed in the upper aerodigestive tract and can be identified easily and efficiently with [^{18}F]FDG PET/CT. In a study of 350 patients, second primaries and distant metastases were detected with a sensitivity of 97% and a specificity of 93% [73]. In another study, including 589 patients, [^{18}F]FDG PET/CT identified 56 synchronous primary tumors in 44 patients (as many as three primary tumors in some patients) and missed another nine lesions [72]. Panendoscopy is often performed as part of the initial staging in patients with locoregional advanced HNSCC. A recent study of 311 patients showed, however, that [^{18}F]FDG PET/CT has in fact a higher sensitivity than panendoscopy, although at the expense of slightly lower specificity (100% vs. 74% and 95% vs. 99%, respectively) [71]. However, depending on reader expertise and interpretation criteria, up to 50% of suspected second primaries may be false positive in some studies. Typical sites of false-positive interpretations may include benign lymphoid hyperplasia in the nasopharynx, tonsils, and base of the tongue, as well as granulomatous nodal (Fig. 6) and lung infections. This highlights the need to temper vigilance with reason when interpreting PET scans in patients with HNSCC. Superficial, small-volume lesions in the esophagus and stomach may be missed.

In summary, PET/CT with [^{18}F]FDG is probably the single best test for the evaluation of second primaries and distant metastases; sensitivity in the range of 90–95% has been reported [73, 75]. The specificity, and in particular positive predictive value, may vary depending on reader experience. In patients with elevated risk for distant metastases based on clinical staging parameters (e.g., $\geq$3 lymph node levels involved, level IV and/or bilateral neck involvement, nodal size >5 cm, CT or MR evidence of extracapsular spread, and local recurrence), whole-body PET/CT is cost-effective in the search for distant metastases [76].

Change in Patient Management

Detection of heretofore unknown lymph node metastases or distant disease may change patient management. Patients with distant disease no longer qualify for treatment with curative intent. Additional disease sites in the neck may alter the surgical or radiotherapy approach. This was convincingly demonstrated in a recent study of 71 patients with untreated HNSCC. Referring physicians formulated a management plan prior to PET, which was then adjusted based on PET findings. A change in management occurred in 33% of patients. The referring clinicians rated the impact of PET on patient management as high in 18%, medium in 15%, and low in 66% of the 71 cases. Management changes included a switch from surgery to radiotherapy, changes in the course of radiotherapy or chemotherapy, and adjustments of the radiation field. [77].

Response Assessment After (Chemo-) Radiotherapy

Structural imaging with contrast-enhanced CT or MRI and functional imaging with [^{18}F]FDG PET/CT are now considered standard imaging tests for assessing the response to therapy in HNSCC. To determine the utility of [^{18}F]FDG PET as an indicator of response, we shall focus on studies in which [^{18}F]FDG PET was employed for patients treated with curative intent. Response rates at the site of primary disease are generally very high with concurrent chemoradiotherapy. Therefore, the main focus of posttherapy PET imaging is the detection of residual disease in neck lymph nodes [78–86] (Table 3). Of note, most studies included

Table 3 Response assessment of HNSCC with PET and PET/CT (selected studies)

Author	*N*	Primary site	Stage	Treatment modality	Median Δt wks from end of Rx	Primary		Neck		Comments
						Sen. % (PPV%)	Spec. % (NPV %)	Sen. % (PPV %)	Spec. % (NPV%)	
Porceddu, Head Neck 2005 [78]	39	92% OP, La	3–4	CRT	12	N/A	N/A	83 (*71*)	93 (*97*)	
Andrade, IJROBP 2006 [80][a]	28	85% OC, OP, La	2–4	CRT	8	N/A	N/A	N/A	N/A	Combined analysis for primary and neck; PET: sen./sp./acc. 77/93/86% vs. CT: 92/47/68%; PET more accurate >8 wks after CRT
Tan, Arch Otolaryngol 2007 [81]	48	90% OP, La	4	def CRT	10	N/A	N/A	25 (*15*)	83 (*90*)	
Nayak, Laryngoscope 2007 [82][a]	43	95% OC, OP. La	4		ND (8–26)	N/A	N/A	87 (*70*)	91 (*97*)	
Ong, JNM 2008 [83][a]	65	89% OP, La	3–4	def. CRT	12	N/A	95 (*97*)	71 (*38*)	89 (*97*)	
Yao, IJROBP 2009 [84]	188	85% OC, OP, La	1–4	128 def (96 CRT, 32 RT); 60 postop.	15	86 (*32*)	86 (*99*)	86 (*70*)	97 (*98*)	PET+ pts. have worse 3 years DFS and OS
Moeller, JCO 2009 [85][a]	92	OP, La, HP	1–4	def RT or CRT	8	70 (*58*)	94 (*96*)	75 (*27*)	76 (*96*)	Only post-Rx SUV predicts outcome; PPV better in HPV- tumors
Porceddu, Head Neck 2011 [86][a]	112	OP (74%), NP, La, HP	1–4	Def RT or CRT	12			60 (*33*)	98 (*98*)	Prospective study, PET more accurate than CT; no FN findings;

[a]PET/CT studies

CRT chemoradiotherapy, *DFS* disease-free survival, *HP* hypopharynx, *ND* not defined, *N/A* not available, *NPC* nasopharynx, *NPV* negative predictive value, *Sen*. sensitivity, *OC* oral cavity, *OPC* oropharynx, *OS* overall survival, *PPV* positive predictive value, *pts*. patients, *Spec*. specificity, *RT* radiotherapy, *La* Larynx,*wks* weeks

heterogeneous patient populations, and the treatment strategies varied. Nonsurgical definitive therapy is now usually performed with concurrent chemoradiotherapy; with this approach, a greater extent and degree of inflammation is expected than with radiotherapy alone. Chemotherapy alone is only used for induction therapy or for patients with metastatic disease. In patients undergoing chemoradiotherapy, responses should be assessed with [^{18}F]FDG PET/CT approximately 12 weeks after the end of therapy to avoid false-negative and false-positive findings. The rate of false-positive cases declines with the length of the time interval between end of therapy and PET. A higher rate of false-negative [^{18}F]FDG PET has been observed for scans performed less than 4–6 weeks after the end of therapy [80, 87, 88]. The majority of irradiated cells do not die instantaneously but instead can still undergo several cycles of cell division (only cells irradiated in the mid-to-late S phase show instantaneous cell cycle blockade). The subsequent fate of such cells varies: Some cells may remain dormant for a protracted time and die eventually, but some cells may recover and start dividing again [89, 90]. Indeed, experimental studies in irradiated cell cultures show a rapid decline in [^{18}F]FDG uptake but the tracer uptake is not instantaneously abolished. Dormant cancer cells maintain their capability for glucose uptake and retention as long as their cell membrane is intact and basic metabolic processes continue. Some of these cells eventually die, whereas other cells may recover their full metabolic and proliferative potential. With increasing volume, the residual viable tumor cell nests may eventually become detectable on [^{18}F]FDG PET images.

In three of the larger studies investigating the role of [^{18}F]FDG PET for response assessment after concurrent chemoradiotherapy, [78, 79, 83] the sensitivity and specificity for detection of residual disease in neck lymph nodes were 100% and 94% [79], 83% and 93% [78], and 71% and 89%, respectively [83]. Of note, in all three studies the negative predictive value was 97%–100%. A patient example is shown in Fig. 7. False-positive lymph nodes are secondary to inflammation or granulomatous disease; false-positive uptake at other sites can occur due to inflammation, abscess formation, osteoradionecrosis, etc. Combined PET/CT reduces the fraction of false-positive cases. A prospective study of 121 patients confirmed the aforementioned observations, which largely stemmed from retrospective analyses [86]. Of the 121 patients, 62 achieved a complete response in neck nodes by CT criteria, and 50 did not. In the group of 62 patients, all PET studies were correctly negative (specificity and negative predictive value, 100%). More interestingly, of the 50 patients with residual enlarged nodes on CT, PET was correctly negative in 41 and correctly positive in two cases.

The test performance of PET can probably be refined further when clinical risk parameters are considered. In a study of 92 patients with stage I–IV primary cancer in the oropharynx, larynx, or hypopharynx, who underwent definitive radio- or chemoradiotherapy, both sensitivity and specificity were higher in high-risk patients than in low-risk patients (high risk was defined as stage III–IV, N2b and N3, non-oropharyngeal primary site, smoking history, and HPV-negative status) [85]. This observation re-emphasizes a basic rationale applicable to all imaging tests: The greatest impact on disease detection and patient management is generally observed in patients with intermediate pretest probability.

It needs to be emphasized that the true value of posttherapy [^{18}F]FDG PET in patients treated with current radio- or chemoradiotherapy protocols is the negative predictive value in the range of 95–100% (Fig. 7). This means that many patients who might otherwise proceed to biopsy or “planned neck dissection” can in fact be observed with clinical follow-up and periodic imaging studies. While the positive predictive value of PET after chemoradiotherapy is relatively low, most scans will in fact be negative when interpreted properly. However, true prolonged intense [^{18}F]FDG uptake after definitive therapy indicates a poor treatment outcome or treatment-related complications: A study in patients with larynx cancer treated with intensity-modulated radiation therapy [91] showed an inverse relationship between the intensity of (persistent) [^{18}F]FDG uptake at 12 months after treatment and

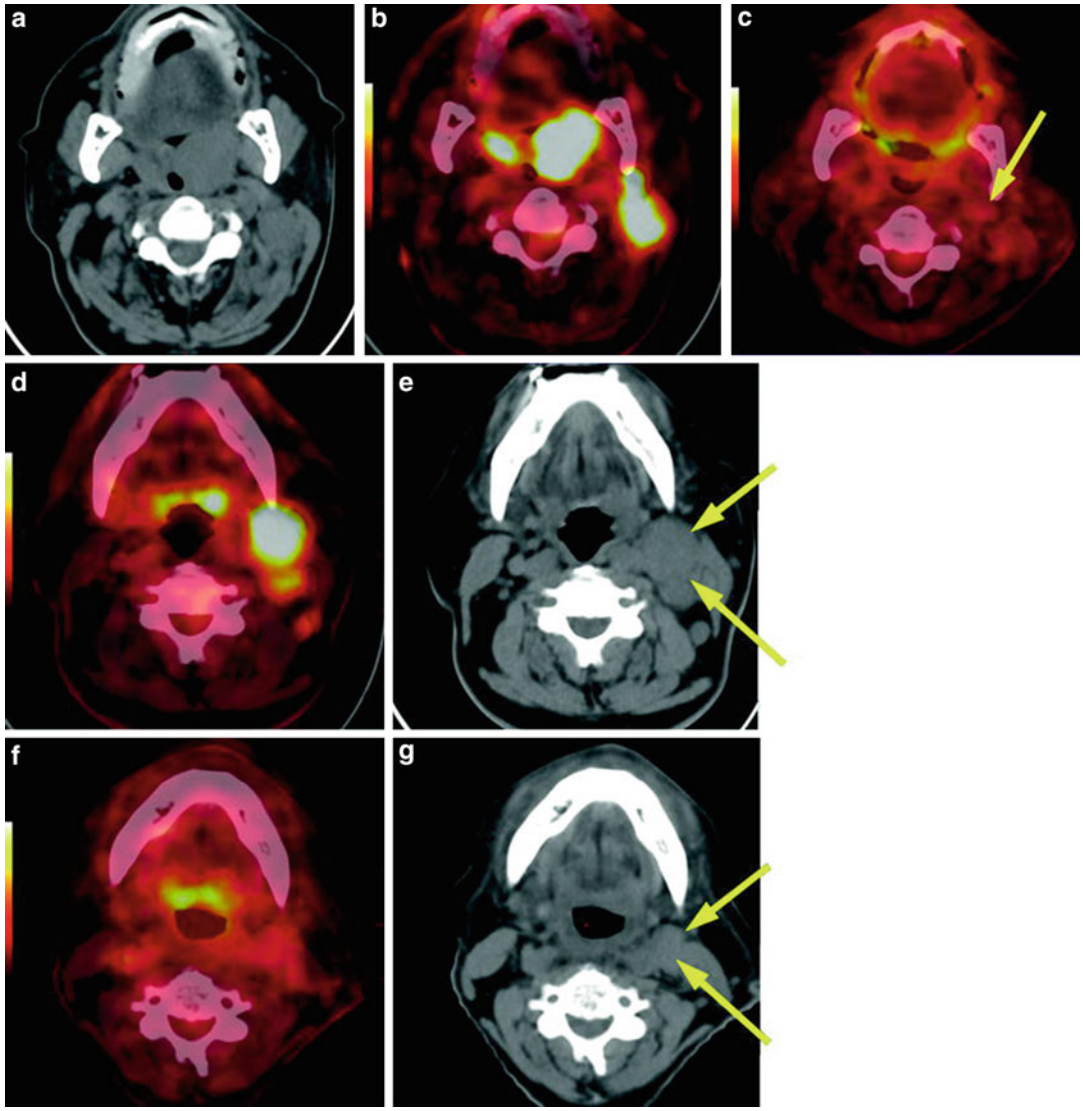

Fig. 7 Response assessment after chemoradiotherapy in a 62-year old male with primary tumor in left tonsillar fossa and left neck node metastases, staged as T3N2B. The patient was treated with concurrent chemoradiotherapy. The baseline staging scan shows the hypermetabolic left tonsillar primary, as well as metastatic neck nodes (**a**, **b**). [^{18}F]FDG PET/CT performed 3 months after the end of treatment shows nonspecific inflammation at the base of tongue and mild nonspecific uptake in a residual level II node (**c**). Another hypermetabolic node in level II measured 2.6 x 2.5 cm on the staging scan (**d**, **e**). After chemoradiotherapy, a residual node measured 1.9 x 1.5 cm (**f**, **g**). Scan findings were interpreted as absence of residual viable tumor in lymph nodes. Nevertheless, because of the large extent of initial nodal metastatic disease this patient underwent left modified neck dissection. The specimen showed only necrotic tumor foci but no viable cells

quality of life, as well as the ability to speak and swallow solid foods. In other words, persistently high [^{18}F]FDG uptake indicates either persistent disease or persistent treatment-induced structural and functional damage to the larynx.

Suggested PET Interpretation Criteria for Response Assessment

In general, focal and asymmetric [^{18}F]FDG with intensity greater than that in surrounding normal

tissues (in particular muscle) and blood vessels should be considered suspicious for residual disease. On PET/CT, such abnormalities should fuse to the site of the primary disease or lymph nodes (rather than blood vessels, fat tissue, skeletal muscle, etc.). By contrast, diffuse (nonfocal) [^{18}F]FDG uptake within the radiation field is usually an indicator of postradiation inflammation. With concurrent chemoradiotherapy, high-grade toxic effects are observed in up to 80% of patients, including grade 3 or 4 mucositis in 41% and laryngeal toxicity in 14% of patients [17]. This has obvious implications for imaging studies: Laryngeal edema and treatment-induced infiltrative changes in perilaryngeal soft tissues are commonly observed on posttreatment CT, along with nonspecific contrast enhancement patterns. Likewise, increased laryngeal or oropharyngeal [^{18}F]FDG uptake may be observed for a prolonged period after chemoradiotherapy. In most cases, this will be of mild-to-moderate intensity and diffuse throughout the larynx or along the oropharynx walls. Again, focal uptake should raise the suspicion of ulceration or persistent disease. In view of the relatively high response rates, persistent disease is uncommon, and this should be considered when interpreting PET scans in this setting. SUV numbers cannot differentiate reliably between residual cancer and inflammation. In clinical practice, scans are usually interpreted as positive or negative, or using a five-point scale (positive, probably positive, equivocal, probably negative, negative), considering focality, intensity, and pattern of residual [^{18}F]FDG uptake in relation to findings on the pretherapy scan.

Impact on Patient Management

Because clinical parameters and structural imaging cannot reliably predict the presence of residual metastatic neck disease, "planned neck dissection" was usually performed in the past after the completion of chemoradiotherapy, especially in patients with initial N2–N3 disease. Historically, the risk for residual cancer in such nodes exceeded 20%. In light of the high negative predictive value of posttreatment [^{18}F]FDG PET, this approach seems no longer justified [92, 93]. In one of the previously cited studies, [83] "planned neck dissection" would have been considered in 51 patients owing to the presence of residual enlarged lymph nodes, but disease was in fact only present in seven of them. Implementing a treatment strategy based on posttherapy PET/CT findings could have reduced the number of planned neck dissections by 75% (from 51 to 13) while missing disease in 2% (two of 84 hemi-necks). Based on our experience over the past decade, we have proposed a clinical algorithm for the management of patients with HNSCC after chemoradiotherapy (Fig. 8). A dedicated neck CT with intravenous contrast and [^{18}F]FDG PET/CT (potentially in one imaging session) should be performed about 10–12 weeks after the end of therapy, unless clinical management requires imaging at an earlier time. This time point strikes a balance between the clinical wish for early yet accurate response assessment and the surgeon's wish not to perform a neck dissection in tissues that have developed extensive fibrosis and scar tissue as the result of chemoradiotherapy. Management of patients with residual enlarged nodes and negative PET findings should be individualized according to the following considerations (Fig 9): Since response rates are high and PET has a high negative predictive value, "planned neck dissection" is unnecessary in the majority of cases. Nevertheless, close follow-up of these patients is required. Only if close clinical follow-up cannot be guaranteed, or if there are extenuating circumstances that indicate a higher likelihood for local recurrence (e.g., extranodal tumor extension), may a neck dissection be indicated. The rationale for this data-driven approach should be discussed with the patient.

Imaging During Chemoradiotherapy or After Induction Chemotherapy

The potential clinical utility of PET for *early response assessment* during chemo- or combined chemoradiotherapy has not been studied systematically in HNSCC. Data from other malignancies [94, 95] suggest that a significant decline in [^{18}F]FDG uptake between baseline and interim PET

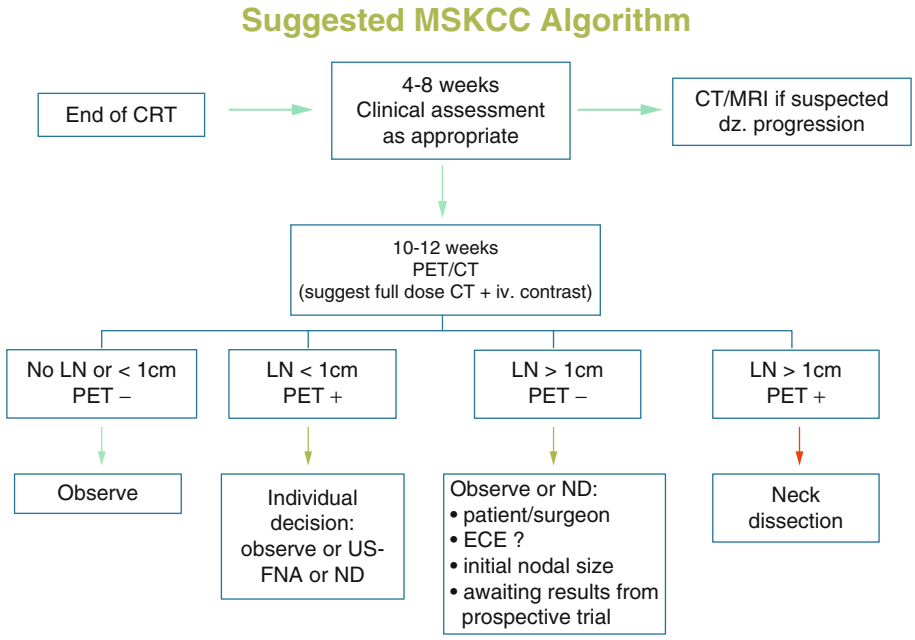

Fig. 8 Suggested algorithm for management of HNSCC patients after chemoradiotherapy. This algorithm is based on our experience at MSKCC; PET/CT is obtained approximately 10–12 weeks after the end of therapy. (Modified from Schoeder et al. J Nucl Med. 2009;50 suppl 1:74S–88S; reprinted by permission of the Society of Nuclear Medicine)

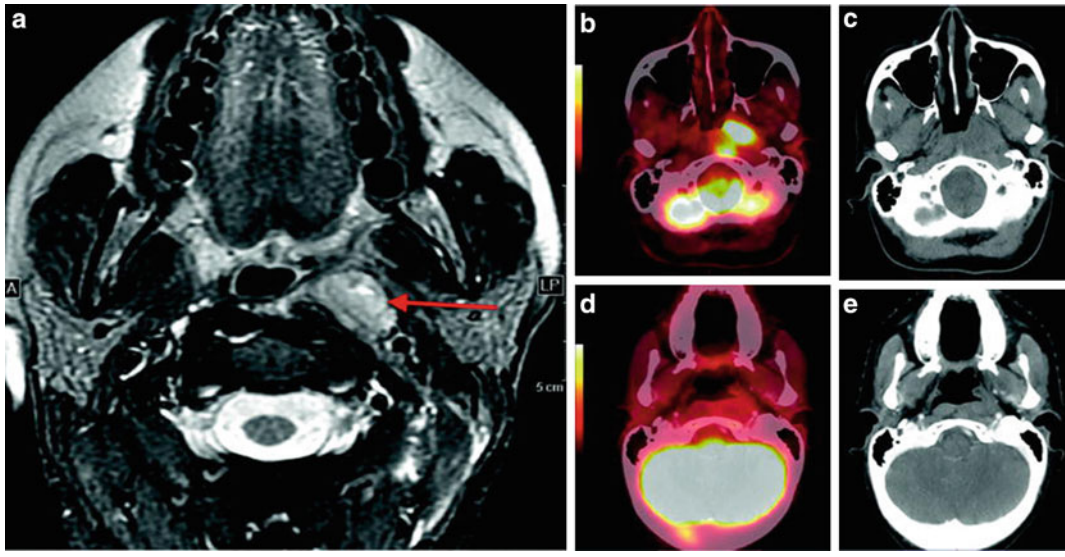

Fig. 9 Nasopharyngeal carcinoma in a 34-year-old female presented with left neck mass. Clinical exam and MRI showed nasopharyngeal mass and left neck nodes. MRI T2-weighted fat suppressed image shows the high signal (white) mass in the left posterolateral nasopharynx (**a**). Staging [^{18}F]FDG PET/CT shows the mass as well as an adjacent retropharyngeal metastatic node (**b**, **c**). After induction chemotherapy, there is mild nonspecific residual [^{18}F]FDG uptake in the nasopharynx (**d**, **e**). The patient subsequently underwent concurrent chemoradiotherapy. (Note the different position of the head for the two scans; the second PET/CT (**d**, **e**) was obtained in the radiotherapy mask and with intravenous contrast)

after a few cycles of chemo- or chemoradiotherapy may indicate a better prognosis and high likelihood of achieving a complete response. Few studies have attempted to address this question in HNSCC [96, 97, 98–100], often including patients with a variety of primary sites (all sites, pharynx only, or focused on oral cavity tumors). One of the earlier studies used coincidence camera imaging and noted an early and significant decline in [^{18}F]FDG uptake in 47 patients with locally advanced disease after one cycle of chemotherapy or 24 Gy of radiotherapy. When dichotomized by the median SUV, individuals with lower ^{18}F-FDG uptake showed a better rate of locoregional control. However, a closer analysis of this study reveals that similar prognostic information could also be derived from the baseline scan alone [96]. Recent studies confirmed that persistent high [^{18}F]FDG uptake on interim PET is associated with worse patient outcome; similarly, a greater and faster decline in SUV or metabolic tumor volume (MTV) may indicate better prognosis after completion of therapy [100]. On the contrary, persistent [^{18}F]FDG uptake and slow decline in SUV or MTV have a low positive predictive value (as low as 30% in one recent study) [101], i.e., even many patients with slow decline in [^{18}F]FDG uptake under therapy may achieve reasonable outcome once the full course of therapy is completed. Currently, the exact role, most meaningful time point, and optimal interpretation criteria for interim PET in patients with HNSCC remain unclear. It is also unclear how interim PET findings might alter patient management (good local control rates with current concurrent chemoradiotherapy, lack of an established alternate therapy). One meaningful approach would be a prospective study investigating the potential utility of treatment de-escalation in low-risk (usually p-16 positive) patients who show rapid response on interim [^{18}F]FDG PET scan.

There are limited data on the role of PET imaging for assessing the response to induction chemotherapy, prior to subsequent concurrent chemoradiotherapy. This is a topic of persistent interest among medical oncologists. Proponents of this approach believe that it may improve clinical outcome (lower rate of distant metastases and better survival) in locoregional advanced HNSCC. However, two recently completed randomized clinical trials (DeCIDE and Paradigm) were not able to prove this hypothesis. Induction chemotherapy did not improve outcome in nonselected patients [102, 103]. If induction chemotherapy is to play a role in the management of head and neck cancer, future studies will need to focus on high-risk patients, using tumor biologic parameters and imaging studies. For instance, if a patient showed very little or no metabolic response after induction chemotherapy, this might indicate a low likelihood for cure with subsequent chemoradiotherapy; perhaps such patients would benefit from immediate salvage surgery after induction therapy, or should be enrolled in more aggressive chemoradiotherapy and posttreatment surveillance protocols. Conversely, patients with good response to induction therapy may perhaps benefit from de-escalation of standard chemoradiotherapy by applying lower radiation doses (e.g., ongoing clinical trial such as NCT01706939).

Imaging After Surgery Prior to Adjuvant Therapy

A few studies [104–106] investigated the role of [^{18}F]FDG PET/CT early after surgical resection and prior to planned adjuvant radiotherapy. Usually these scans are performed relatively early after surgery in order not to delay necessary adjuvant radiotherapy. While early postsurgical imaging is associated with a higher risk for false-positive [^{18}F]FDG findings, these studies nevertheless detected residual [^{18}F]FDG-avid disease in 13–30% of patients, leading to changes in management, such as adjustment of radiation field or dose and abandonment of adjuvant radiotherapy or a switch to palliative chemotherapy, in 15%–30%. Patients with positive surgical margins, perineural spread of disease, or extracapsular extension of nodal disease in the surgical specimen may particularly benefit from pre-radiotherapy PET/CT. Because of the low positive predictive value of [^{18}F]FDG PET in this setting, all suspicious findings should be confirmed by biopsy before changing patient management.

Recurrent Disease

The early detection of recurrent head and neck cancer is important in determining the ability to perform salvage surgery, which can improve the clinical outcome of these patients. For instance, patients with recurrent early-stage HNSCC who undergo salvage surgery have a 70% 2-year relapse-free survival, whereas those with recurrent advanced-stage HNSCC undergoing salvage surgery have a 22% 2-year recurrence-free survival [107]. It is therefore critical to detect potential recurrences early in the course of events. An imaging modality used for this purpose should have a high sensitivity for the detection of disease, but at the same time not yield too many false-positive findings.

CT and MRI, which rely on structural changes, are notoriously unreliable in this setting because of treatment-related alterations of tissue planes, nonspecific contrast enhancement, etc. However, the PET/CT interpretation may also be complicated because postsurgical changes can involve distortions of the normal anatomy related to resection and surgical reconstruction, involving various soft tissue flaps, bone grafts, bone plates, surgical obturators, etc.

It is now clearly established that [^{18}F]FDG PET/CT has a high sensitivity and specificity for the detection of recurrent HNSCC, regardless of the primary treatment modality used [108–115]. In a retrospective study of 143 patients with HNSCC at any site, including 72 patients in whom recurrent disease was ultimately proven, Wong et al. [111] found a sensitivity of 96% for [^{18}F]FDG PET. The specificity varied with the anatomic subsite in the neck that was studied and tended to be lower at sites that showed post-treatment inflammation, whereas it was highest in the nontreated neck or outside the neck (where false-positive uptake would be less likely). This was also confirmed in other studies [109].

As a rule, clinically detectable recurrent disease is extremely unlikely in the setting of an entirely negative PET scan. With adequate patient preparation and combined PET/CT, certain sources of nontumor-related [^{18}F]FDG uptake can be eliminated or at least correctly identified (e.g., laryngeal muscle uptake, radioactive saliva in the throat or vallecula epiglottica, nonspecific [^{18}F]FDG uptake in brown fat tissue of the neck or scalene muscles), but posttherapy inflammation remains a potential source for false-positive interpretation. Accordingly, the sensitivity for the detection of recurrent head and neck cancer is very high, but specificity in the treated (after surgery or radiotherapy) area is lower than elsewhere in the neck or at remote sites, such as lung or bone [109, 111] (Table 4). Since the negative predictive value of [^{18}F]FDG PET/CT is very high, these patients in general do not require any further evaluation. By contrast, the positive predictive value is lower, depending on the location and time interval since treatment, so that sites of [^{18}F]FDG uptake require careful assessment and histologic confirmation before embarking on therapy. If biopsies from the site of [^{18}F]FDG uptake are negative for recurrent disease, close clinical follow-up may be sufficient. Potential reasons for false-positive [^{18}F]FDG uptake include inflammation, infection, and radionecrosis.

SUV numbers or other quantitative and semiquantitative parameters cannot reliably distinguish between recurrence and inflammation or infection. For instance, Lapela et al. [108] reported a wide overlap in SUVs for disease recurrence (range 2.1–36.9) vs. nontumor-related [^{18}F]FDG accumulation (range 1.5–9.3). Using ROC analysis, Wong et al. [111] suggested an SUV of 3.2 to distinguish between recurrent disease and benign conditions, providing a sensitivity of 92% and specificity of 70%. If the SUV decreases in serial scans, malignancy is unlikely and no further intervention is needed. If a high SUV persist or rises further, repeat biopsy may be required, unless there is another obvious explanation, such as infection, fistula, or radionecrosis. However, it should be noted that SUV numbers are affected by [^{18}F]FDG uptake time and technical parameters. Therefore, SUV should be used judiciously: While it may sometimes aid in study interpretation, it is not a surrogate for clinical experience. Indeed, visual interpretation by an experienced reader appears as at least as accurate as SUV-based assessment [111].

Imaging studies should not be ordered "routinely," i.e., in the absence of clinical signs or

Table 4 [^{18}F]FDG PET for detection of recurrent disease

				CT/MR			PET			
				Sen.	Spec.	Acc.	Sen.	Spec.	Acc.	
	N	Sites	RD	%	%	%	%	%	%	Remarks
Lonneux, Laryngoscope 2000 [110]	44	All	26	73	50	64	96	61	81	All pts.; early + late PET
				25	38	33	100	25	50	<12 weeks after all therapy
				90	60	75	96	90	94	>12 weeks after all therapy
Lapela, Eur J Cancer 2000 [108]	56	All	37	59/91	100/78	81/84	84/95	93/84	88/90	Sensitive vs. specific reading
Wong, J Clin Oncol 2002 [111]	143	All	72				96	72		For all findings
							97	79		Local rec. at primary site
							92	95		Regional disease elsewhere in neck
							94	96		Distant disease
Kunkel, Cancer 2003 [109]	97	Oral cavity	49				83	81		For all findings
							87	67		Local recurrence
							87	99		Nodal metastases
							71	93		Distant metastases, 2nd primary
Kubota, EJNM 2004 [112]	36	All	15	75	30	46	87	78	81	PET better than CT/MRI
Salaun, Head Neck 2007 [115]	30	All	9				100	95	97	PET/CT
Abgral, JNM 2009 [113]	91	All	30				100	85	90	PET/CT, summary analysis for primary site, lymph nodes and distant sites

Acc. accuracy, *pts*. patients, *rec*. recurrence, *RD* number of patients with proven locoregional or distant recurrence in each study, *Sen*. sensitivity, *Spec*. specificity

symptoms and without abnormalities on clinical examination. However, there may be a small subgroup of patients at high risk for locoregional recurrence, in whom PET/CT at predefined time intervals may be appropriate, even in the absence of clear abnormalities on the clinical examination: In a prospective study of 44 patients with stage III or IV HNSCC and high risk for recurrence, [^{18}F]FDG PET was performed at 2 and 10 months, thereafter as considered necessary by the treating physician [116]. During the first year of follow-up, PET detected recurrent disease with a sensitivity of 100% and specificity of 93%. Notably, five of the 16 recurrences were only detected with PET. One of the clinically meaningful parameters for risk stratification is the patient's HPV status, since patients with HPV-negative oropharynx tumors are at higher risk for recurrence after completion of chemoradiotherapy, even when reaching a complete clinical and metabolic response [117]. Efforts to study the role of surveillance imaging should therefore be focused on this group of patients.

Prognostic Value of [^{18}F]FDG PET

Several studies have shown that [^{18}F]FDG PET alone can assess the aggressiveness and proliferation rate of HNSCC [118–120]. The intensity of

[^{18}F]FDG uptake at the primary site or neck node metastases correlates with prognosis in patients both with primary and recurrent disease, and regardless of the treatment modality used [63, 77, 109, 111, 121–132], [133–136] (Table 5). In patients with recurrent disease, clinical PET interpretation and SUV are independent prognostic markers for relapse-free survival and OS [109, 111]. More recently, the volume of [^{18}F]FDG-avid disease (MTV) and the combination of SUV and MTV (expressed as total lesion glycolysis) have also been suggested as a prognostic indicator (Table 5). Although high [^{18}F]FDG uptake and a large MTV thus indicate a poor prognosis, no uniform cut-off values have been established. In fact, while most studies confirm that patients with higher SUV, MTV, or total lesion glycolysis have a worse outcome, the cut-off values, methods for separation of prognostic groups (e.g., by median or by lowest p-value), as well as the clinical end points (e.g., 2-year vs. 5-year outcome; local control, disease-free survival or OS) vary remarkably. It also remains to be seen how this important information can be integrated into treatment or follow-up algorithms. For instance, in conjunction with other prognostic markers, a high tumor or nodal SUV or MTV might prompt consideration of induction chemotherapy prior to concurrent chemoradiotherapy or surgery, as well as consideration of postoperative chemoradiotherapy instead of radiotherapy alone, or shorter follow-up intervals.

Nasopharyngeal Cancer

In view of its unique epidemiology, tumor biology, and prognosis, nasopharyngeal carcinoma (NPC) should be considered separately from other head and neck squamous cell carcinomas. This tumor shows a distinct racial and geographical distribution. The highest incidence is noted in southern Chinese, in whom it is more than 20 times more common than among Caucasian people [137]. Of note, the risk for NPC persists in individuals who have emigrated to other parts of the world.

NPC tends to spread submucosally with early infiltration of parapharyngeal tissues. The tumor can spread in all dimensions; intracranial spread can occur along the maxillary nerve, following initial invasion of the pterygopalatine fossa and along the mandibular nerve via the foramen ovale. Neck lymph node metastases, also including level V nodes, are seen in the vast majority of patients. The lateral retropharyngeal nodes are traditionally considered first echelon nodes, but can be bypassed in up to 30% of cases. The rate of distant metastases is higher than for HNSCC, involving bone, lung, and liver.

Standard imaging tests for staging NPC include brain and neck MRI and, at a minimum, [^{18}F]FDG PET/CT. Local disease extent is best defined by MRI, in particular disease involvement of the skull base and intracranial spread. Neck lymph node involvement is probably best characterized by a combination of MRI and [^{18}F]FDG PET/CT (Fig. 9); small retropharyngeal nodes may be detected better with MRI. [^{18}F]FDG PET/CT appears sufficient as the single imaging test for the detection of distant disease outside the neck [138, 139]. A bone scan is no longer part of the staging studies. Although liver involvement can be determined with contrast CT or ultrasound, these additional studies do not appear necessary; instead, it may be advisable to simply perform the CT of the PET/CT at diagnostic dose settings and with intravenous contrast material. With modern treatment techniques, including intensity-modulated radiotherapy, proton beam therapy, and concurrent chemoradiotherapy, the majority of patients can be cured. However, accurate staging and early detection of recurrence are prerequisites to reach this goal. The combination of MRI and [^{18}F]FDG PET/CT also appears most appropriate for response assessment, although it may be possible in many situations to employ PET/CT as the only imaging test for this purpose [140]; outside the nasopharynx (where MR performs better than CT), it may be appropriate to perform the CT component of the PET/CT as a true diagnostic study (rather than low dose CT) with intravenous contrast material. Recurrent disease is best detected by the combination of MRI and [^{18}F]FDG PET/CT [141–143]. In a study of 63 patients with treated NPC, the accuracy for detecting local recurrence was 75% with

Table 5 Prognostic value of [^{18}F]FDG PET in multivariate analysis

Author	*N*	Measured site	Treatment	Outcome	SUV cut-off	MTV or TLG cut-off	Comments
Allal, JCO 2002 [121]	63	All sites	Radical RT	3 years LC and DFS	5.5	–	See their subsequent study in 2004
Halfpenny, Brit J Cancer 2002 [131]	73	All sites	Surgery ± RT or RT alone	2 years OS	10.0	–	
Wong, JCO 2002 [111]	143	All sites	Post surgery or (C)RT	3 years RFS and OS	Best outcome for SUV < 2.0; worst for SUV > 6.0	–	Recurrent disease
Kunkel, Cancer 2003 [109]	97	Oral SCC	Post surgery	3 years OS	Best outcome for SUV < 2.0; worst for SUV > 4.0	–	Recurrent disease
Allal, IJROBP 2004 [122]	120	All sites	47 Surgery, 73 (C)RT	4 years LC and DFS	4.8	–	
Kim, JNM 2007 [126]	52	Oropharynx	Surgery + RT or CRT	3 years DFS	6.0	–	Surg. pts. with high SUV did better than CRT pts. with high CRT; unclear
Scott, JNM 2008 [77]	71	All sites	Surgery or RT	1 years DFS	6.5	–	
Machtay, Head Neck 2009 [129]	60	All sites	RT or CRT	2 years DFS	9.0	–	
Suzuki, Oral Oncol 2009 [130]	24	Oral cavity	Surgery	3 years OS and freedom from distant mets.	12.0	–	
Liao, IJROBP 2009 [128]	109	Oral cavity	Surgery	5 years local control	19.3	–	Tm depth > 12 mm also prognostic
Liao, IJROBP 2009 [132]	120	Neck nodes form oral cavity primary	Surgery and neck dissection	Neck control; freedom from distant mets., DSS and DFS	5.7	–	Extracapsular nodal spread also prognostic
Chung, CCR 2009 [124]	82	77% nasopharynx, 16% oropharynx, rest hypopharynx	CRT (90%), RT alone (10%)	"Short-term DFS" (f/u 12–64 months, mean 34 months)	–	MTV 40 ml	SUV per se not predictive

(*continued*)

Table 5 (continued)

Author	*N*	Measured site	Treatment	Outcome	SUV cut-off	MTV or TLG cut-off	Comments
La, IJROBP 2009 [127]	85	All sites	CRT	2 years LC, DFS, OS	–	Median MTV 11.4 ml; no cut-off provided	Outcome stratified by volume; worst outcome for highest MTV
Farrag, NM Commun 2010 [125]	43	All sites	RT (27) or CRT (16)	2 years OS	8.1	–	Mid treatment SUV also prognostic
Lim, JNM 2012 [135]	176	Oropharynx	CRT	LTFS, DM, OS	–	Median MTV 9.7 ml	MTV and TLG predict OS; doubling of SUV increases hazard for death by 1.8
Chan, NM Comm 2011 [133]	196	Nasopharynx	CRT	DFS, OS	–	Best cut-off for TLG 330	Lower OS when TLG > 330
Chang, JNM 2012 [134]	102	Nasopharynx	RT/CRT	DFS, OS	–	Median TLG 65	Lower DFS when TLG > median; hazard ratio 3.5
Rasmussen, Head Neck 2015 [136]	287	All sites	RT/CRT	DFS, OS	13.0 (median)	–	SUV and GTV (based on PET and CT) > median carry higher risk; SUV and GTV interactive

CRT chemoradiotherapy, *DFS* disease-free survival, *DM* development of distant metastases, *f/u* follow-up, *GTV* gross tumor volume, *LC* local control, *LTFS* local tumor-free survival, *mets*. metastases, *MTV* metabolic tumor volume, *RFS* recurrence-free survival, *OS* overall survival, *RT* radiotherapy, *SUV* standardized uptake value

MRI and 73% with [^{18}F]FDG PET/CT; however, importantly, the combination of both tests increased the accuracy to 95% [141]. Nevertheless, occasionally both imaging tests may have difficulties in differentiating between posttreatment inflammation, early fibrosis, and recurrent disease. Radiotherapy-related treatment complications include temporal lobe necrosis, cranial nerve palsy, and osteoradionecrosis of the skull base (with or without superimposed infection). Of note, the latter may show contrast enhancement on MRI as well as [^{18}F]FDG uptake on PET scan. Similar to other head and neck cancers, the intensity of [^{18}F]FDG uptake, as well as the volume of [^{18}F]FDG-avid disease, in NPC primary tumors provides prognostic information [144]. [134].

Radiotracers Other than [^{18}F]FDG for Imaging of HNSCC

A number of non-[^{18}F]FDG radiotracers have been explored for imaging of head and neck cancers, with potential applications for the study of cancer biology, staging and radiotherapy planning, and response assessment. Imaging with amino acid tracers does not appear to provide any advantage over [^{18}F]FDG. The intense uptake in salivary glands interferes with the detection of metastatic neck nodes [145]. Although initially proposed as more specific than [^{18}F]FDG, false-positive amino acid uptake does occur in inflamed lymph nodes as well. Another amino acid tracer, ^{18}F-fluoroethyl-tyrosine (^{18}F-FET), showed inferior sensitivity

compared with [^{18}F]FDG [146, 147]. Similarly, imaging with [^{11}C]choline was not superior to [^{18}F]FDG PET/CT for response assessment in the head and neck [148]. Several groups are focusing on developing and refining imaging techniques for hypoxia in HNSCC. Hypoxic tumors are resistant to radio- and chemotherapy. It is conceivable that the poor prognosis of patients with hypoxic primary HNSCC or nodal metastases could be improved with modern aggressive treatment strategies. Radiotracers under investigation for hypoxia imaging in the head and neck include ^{18}F-fluoromisonidazole (^{18}F-MISO), ^{18}F-fluoroazomycin (^{18}F-FAZA), and $^{64/60}$Cu-ATSM [149–151]. Ongoing clinical trials are investigating the prognostic value of tumor hypoxia as imaged by PET, and how the hypoxia PET signal can be used for dose escalation in patients with hypoxic tumors (NCT01212354, NCT02352792), or for dose de-escalation in patients with early resolution of hypoxia during chemoradiotherapy (NCT00606294), in an effort at biology-driven modern radiotherapy. Tumor cell proliferation can be imaged with ^{18}F-fluorothymidine (^{18}F-FLT) [152]. ^{18}F-FLT, in general, is not a diagnostic radiotracer; in most disease sites it shows less uptake than [^{18}F]FDG, and false-positive uptake in inflamed lymph nodes can occur [153]. It is conceivable that tumors with high FLT uptake benefit from more intense therapy. However, predominantly ^{18}F-FLT may be a good imaging test for response assessment [154]. Based on limited data from recent studies, ^{18}F-FLT uptake in HNSCC declines earlier and faster than [^{18}F]FDG uptake does and such early decline is associated with better patient outcome [155, 156]. Finally, a number of radiotracers for imaging EGFR and the response to EGFR inhibitors, as well as angiogenesis and the response to angiogenesis inhibitors (both of potential clinical interest in head and neck cancer), are under study and in early clinical investigations.

PET for Radiotherapy Planning

[^{18}F]FDG PET/CT is now an established and essential imaging technique for the staging and planning of patients undergoing definitive (chemo-)radiotherapy (mostly for tumors of the oropharynx, nasopharynx, and larynx) or for post-surgical irradiation. The utility of PET for delineating the gross tumor volume (GTV) has been investigated. Most studies agree that the incorporation of PET in the planning process clearly improves target design over CT-based planning. In the single study of head and neck cancer patients in which data were correlated with histopathology (of laryngectomy specimens), pre-surgical PET was more accurate than CT or MRI in outlining the presumed tumor margins [157]. Nevertheless, in clinical practice, the combination of contrast enhanced CT or MRI and PET is usually applied for treatment planning. Of note, simple physical exam remains necessary and in case of small superficial primary tumors, may be more accurate than any imaging [158]. Several other studies have shown the incorporation of PET in treatment planning improves interobserver agreement. Often the PET-derived GTV is smaller than CT-based volumes, whereas simultaneously tumor extension was shown outside the CT-based GTV. Considerable time and effort have been spent in trying to define a mathematically and biologically correct approach when outlining tumor margins on PET. For instance, [^{18}F]FDG-avid volumes may appear larger or smaller depending on the window setting at the display. To improve objectivity, a number of segmentation algorithms have been proposed; unfortunately all have limitations in daily practice [159]. Therefore, most clinicians rely on visual assessment (and ideally close cooperation between radiation oncologist and nuclear medicine physician) for outlining PET-based tumor volumes. Beyond these clinical applications, there is growing interest in defining a “biologic” target volume. It is hoped that this will help in identifying patients with better or worse prognosis in whom radiotherapy could be escalated (dose, time, fractionation) or de-escalated. Dose escalation to highly metabolically active subvolumes has been proposed by several authors, and was shown to be technically feasible [160, 161]. Modeling studies suggest that hypermetabolic tumors may require 10–30% more dose than tumors with lower [^{18}F]FDG uptake [162]. This concept is supported by studies

showing that a majority of recurrences originate within the site of the original [^{18}F]FDG-avid tumor volumes, and recurrence becomes more likely with increasing tumor avidity [163, 164]. In addition to [^{18}F]FDG, other radiotracers, such as hypoxia imaging agents [149, 165, 166], some amino acids, and proliferation markers are of growing interest in radiation oncology [167].

Emerging Role for PET/MRI

PET/MRI is an emerging imaging technology. It has been applied in head and neck cancer and, depending on the primary tumor site and clinical question, may serve as a surrogate for PET/CT for staging purposes, detection of recurrence, and possibly also response assessment. Various imaging protocols have been proposed and generally attempt to strike a balance between acceptable imaging time and the number and type of MRI sequences that can be acquired in a reasonable time and are clinically necessary. Imaging times are generally longer with PET/MRI than with PET/CT, increasing the likelihood for patient motion [168]. Readers of PET/MRI need to be familiar with a number of technique-specific artifacts, including artifacts in the attenuation map, in order to avoid misinterpretation of imaging findings. There is currently no evidence that PET/MRI is broadly superior to PET/CT for imaging of head and neck cancer. Of course, MRI per se provides better information than does CT for certain clinical questions (e.g., skull base invasion, perineural spread of disease), and in these scenarios combined PET/MRI is likely to offer the most clinical benefit. The role of special MRI techniques, such as dynamic contrast-enhanced (DCE) imaging, diffusion-weighted imaging (DWI) and blood oxygen level-dependent (BOLD) imaging, is under investigation. These techniques may provide valuable (and in some instances prognostic [169, 170]) information as part of an MRI-only protocol, but when obtained as part of an PET/MRI protocol this may be redundant with the information that is already derived from the PET component of the integrated scan, such as pattern, intensity, and volume of radiotracer uptake. In practice, PET/MRI will be applied most appropriately for selected patients with head and neck cancer and for specific clinical questions (Figs. 6, 7, 8, and 9).

References

1. Jemal A, Siegel R, Xu J, Ward E. Cancer statistics, 2010. CA Cancer J Clin. 2010;60:277–300.
2. Gillison ML, Koch WM, Capone RB, et al. Evidence for a causal association between human papillomavirus and a subset of head and neck cancers. J Natl Cancer Inst. 2000;92:709–20.
3. Leemans CR, Braakhuis BJ, Brakenhoff RH. The molecular biology of head and neck cancer. Nat Rev Cancer. 2011;11:9–22.
4. zur Hausen H. Papillomaviruses and cancer: from basic studies to clinical application. Nat Rev Cancer. 2002;2:342–50.
5. Marur S, D'Souza G, Westra WH, Forastiere AA. HPV-associated head and neck cancer: a virus-related cancer epidemic. Lancet Oncol. 2010;11:781–9.
6. Ang KK, Harris J, Wheeler R, et al. Human papillomavirus and survival of patients with oropharyngeal cancer. N Engl J Med. 2010;363:24–35.
7. Fakhry C, Westra WH, Li S, et al. Improved survival of patients with human papillomavirus-positive head and neck squamous cell carcinoma in a prospective clinical trial. J Natl Cancer Inst. 2008;100:261–9.
8. Ang KK, Zhang Q, Rosenthal DI, et al. Randomized phase III trial of concurrent accelerated radiation plus cisplatin with or without cetuximab for stage III to IV head and neck carcinoma: RTOG 0522. J Clin Oncol. 2014;32:2940–50.
9. O'Sullivan B, Huang SH, Su J, et al. Development and validation of a staging system for HPV-related oropharyngeal cancer by the International Collaboration on Oropharyngeal cancer Network for Staging (ICON-S): a multicentre cohort study. Lancet Oncol. 2016;17:440–51.
10. Kumar B, Cordell KG, Lee JS, et al. EGFR, p16, HPV Titer, Bcl-xL and p53, sex, and smoking as indicators of response to therapy and survival in oropharyngeal cancer. J Clin Oncol. 2008;26:3128–37.
11. Worden FP, Kumar B, Lee JS, et al. Chemoselection as a strategy for organ preservation in advanced oropharynx cancer: response and survival positively associated with HPV16 copy number. J Clin Oncol. 2008;26:3138–46.
12. Chuang AY, Chuang TC, Chang S, et al. Presence of HPV DNA in convalescent salivary rinses is an adverse prognostic marker in head and neck squamous cell carcinoma. Oral Oncol. 2008;44:915–9.
13. Tabor MP, Brakenhoff RH, van Houten VM, et al. Persistence of genetically altered fields in head and neck cancer patients: biological and clinical implications. Clin Cancer Res. 2001;7:1523–32.

14. Tabor MP, Brakenhoff RH, Ruijter-Schippers HJ, Kummer JA, Leemans CR, Braakhuis BJ. Genetically altered fields as origin of locally recurrent head and neck cancer: a retrospective study. Clin Cancer Res. 2004;10:3607–13.
15. Schoder H, Fury M, Lee N, Kraus D. PET monitoring of therapy response in head and neck squamous cell carcinoma. J Nucl Med. 2009;50(Suppl 1): 74S–88S.
16. Denis F, Garaud P, Bardet E, et al. Final results of the 94–01 French Head and Neck Oncology and Radiotherapy Group randomized trial comparing radiotherapy alone with concomitant radiochemotherapy in advanced-stage oropharynx carcinoma. J Clin Oncol. 2004;22:69–76.
17. Forastiere AA, Goepfert H, Maor M, et al. Concurrent chemotherapy and radiotherapy for organ preservation in advanced laryngeal cancer. N Engl J Med. 2003;349:2091–8.
18. Adelstein DJ, Li Y, Adams GL, et al. An intergroup phase III comparison of standard radiation therapy and two schedules of concurrent chemoradiotherapy in patients with unresectable squamous cell head and neck cancer. J Clin Oncol. 2003;21:92–8.
19. McHam SA, Adelstein DJ, Rybicki LA, et al. Who merits a neck dissection after definitive chemoradiotherapy for N2-N3 squamous cell head and neck cancer? Head Neck. 2003;25:791–8.
20. Brizel DM, Prosnitz RG, Hunter S, et al. Necessity for adjuvant neck dissection in setting of concurrent chemoradiation for advanced head-and-neck cancer. Int J Radiat Oncol Biol Phys. 2004;58:1418–23.
21. Frank DK, Hu KS, Culliney BE, et al. Planned neck dissection after concomitant radiochemotherapy for advanced head and neck cancer. Laryngoscope. 2005;115:1015–20.
22. Ang KK, Berkey BA, Tu X, et al. Impact of epidermal growth factor receptor expression on survival and pattern of relapse in patients with advanced head and neck carcinoma. Cancer Res. 2002;62:7350–6.
23. Chung CH, Ely K, McGavran L, et al. Increased epidermal growth factor receptor gene copy number is associated with poor prognosis in head and neck squamous cell carcinomas. J Clin Oncol. 2006;24: 4170–6.
24. Cohen EE. Role of epidermal growth factor receptor pathway-targeted therapy in patients with recurrent and/or metastatic squamous cell carcinoma of the head and neck. J Clin Oncol. 2006;24:2659–65.
25. Bonner JA, Harari PM, Giralt J, et al. Radiotherapy plus cetuximab for squamous-cell carcinoma of the head and neck. N Engl J Med. 2006;354:567–78.
26. Papaspyrou G, Werner JA, Dietz A. Pharmacotherapy for squamous-cell carcinoma of the head and neck. Expert Opin Pharmacother. 2011;12:397–409.
27. Magrini SM, Buglione M, Corvo R, et al. Cetuximab and radiotherapy versus cisplatin and radiotherapy for locally advanced head and neck cancer: a randomized phase II trial. J Clin Oncol. 2016;34:427–35.
28. Argiris A, Karamouzis MV, Gooding WE, et al. Phase II trial of pemetrexed and bevacizumab in patients with recurrent or metastatic head and neck cancer. J Clin Oncol. 2011;29:1140–5.
29. Curtin HD, Ishwaran H, Mancuso AA, et al. Comparison of CT and MR imaging in staging of neck metastases. Radiology. 1998;207:123–30.
30. Branstetter BF, Blodgett TM, Zimmer LA, et al. Head and neck malignancy: is PET/CT more accurate than PET or CT alone? Radiology. 2005;235:580–6.
31. Schoder H, Yeung HW, Gonen M, Kraus D, Larson SM. Head and neck cancer: clinical usefulness and accuracy of PET/CT image fusion. Radiology. 2004; 231:65–72.
32. Chin SC, Edelstein S, Chen CY, Som PM. Using CT to localize side and level of vocal cord paralysis. AJR Am J Roentgenol. 2003;180:1165–70.
33. Komissarova M, Wong KK, Piert M, Mukherji SK, Fig LM. Spectrum of ^{18}F-FDG PET/CT findings in oncology-related recurrent laryngeal nerve palsy. AJR Am J Roentgenol. 2009;192:288–94.
34. Annino Jr DJ, MacArthur CJ, Friedman EM. Vincristine-induced recurrent laryngeal nerve paralysis. Laryngoscope. 1992;102:1260–2.
35. Graham MM, Menda Y. Positron emission tomography/computed tomography imaging of head and neck tumors: an atlas. Semin Nucl Med. 2005;35:220–52.
36. Gupta S, Henningsen JA, Wallace MJ, et al. Percutaneous biopsy of head and neck lesions with CT guidance: various approaches and relevant anatomic and technical considerations. Radiographics. 2007;27: 371–90.
37. Bohuslavizki KH, Klutmann S, Kroger S, et al. FDG PET detection of unknown primary tumors. J Nucl Med. 2000;41:816–22.
38. Fogarty GB, Peters LJ, Stewart J, Scott C, Rischin D, Hicks RJ. The usefulness of fluorine 18-labelled deoxyglucose positron emission tomography in the investigation of patients with cervical lymphadenopathy from an unknown primary tumor. Head Neck. 2003;25:138–45.
39. Gutzeit A, Antoch G, Kuhl H, et al. Unknown primary tumors: detection with dual-modality PET/CT – initial experience. Radiology. 2005;234:227–34.
40. Johansen J, Buus S, Loft A, et al. Prospective study of ^{18}FDG-PET in the detection and management of patients with lymph node metastases to the neck from an unknown primary tumor. Results from the DAHANCA-13 study. Head Neck. 2008;30:471–8.
41. Johansen J, Eigtved A, Buchwald C, Theilgaard SA, Hansen HS. Implication of ^{18}F-fluoro-2-deoxy-D-glucose positron emission tomography on management of carcinoma of unknown primary in the head and neck: a Danish cohort study. Laryngoscope. 2002;112:2009–14.
42. Jungehulsing M, Scheidhauer K, Damm M, et al. 2 [F]-fluoro-2-deoxy-D-glucose positron emission tomography is a sensitive tool for the detection of occult primary cancer (carcinoma of unknown

primary syndrome) with head and neck lymph node manifestation. Otolaryngol Head Neck Surg. 2000;123:294–301.
43. Kole AC, Nieweg OE, Pruim J, et al. Detection of unknown occult primary tumors using positron emission tomography. Cancer. 1998;82:1160–6.
44. Miller FR, Karnad AB, Eng T, et al. Management of the unknown primary carcinoma: long-term follow-up on a negative PET scan and negative panendoscopy. Head Neck. 2008;30:28–34.
45. Roh JL, Kim JS, Lee JH, et al. Utility of combined ^{18}F-fluorodeoxyglucose-positron emission tomography and computed tomography in patients with cervical metastases from unknown primary tumors. Oral Oncol. 2009;45:218–24.
46. Wartski M, Le Stanc E, Gontier E, et al. In search of an unknown primary tumour presenting with cervical metastases: performance of hybrid FDG-PET-CT. Nucl Med Commun. 2007;28:365–71.
47. Wong WL, Saunders M. The impact of FDG PET on the management of occult primary head and neck tumours. Clin Oncol (R Coll Radiol). 2003;15:461–6.
48. Yabuki K, Tsukuda M, Horiuchi C, Taguchi T, Nishimura G. Role of ^{18}F-FDG PET in detecting primary site in the patient with primary unknown carcinoma. Eur Arch Otorhinolaryngol. 2010;267: 1785–92.
49. Hannah A, Scott AM, Tochon-Danguy H, et al. Evaluation of ^{18}F-fluorodeoxyglucose positron emission tomography and computed tomography with histopathologic correlation in the initial staging of head and neck cancer. Ann Surg. 2002;236:208–17.
50. O'Brien CJ, Smith JW, Soong SJ, Urist MM, Maddox WA. Neck dissection with and without radiotherapy: prognostic factors, patterns of recurrence, and survival. Am J Surg. 1986;152:456–63.
51. Layland MK, Sessions DG, Lenox J. The influence of lymph node metastasis in the treatment of squamous cell carcinoma of the oral cavity, oropharynx, larynx, and hypopharynx: N0 versus N+. Laryngoscope. 2005;115:629–39.
52. Leemans CR, Tiwari R, Nauta JJ, van der Waal I, Snow GB. Recurrence at the primary site in head and neck cancer and the significance of neck lymph node metastases as a prognostic factor. Cancer. 1994;73:187–90.
53. Johnson JT, Myers EN, Bedetti CD, Barnes EL, Schramm Jr VL, Thearle PB. Cervical lymph node metastases. Incidence and implications of extracapsular carcinoma. Arch Otolaryngol. 1985;111: 534–7.
54. Jones AS, Roland NJ, Field JK, Phillips DE. The level of cervical lymph node metastases: their prognostic relevance and relationship with head and neck squamous carcinoma primary sites. Clin Otolaryngol Allied Sci. 1994;19:63–9.
55. Stell PM, Morton RP, Singh SD. Cervical lymph node metastases: the significance of the level of the lymph node. Clin Oncol. 1983;9:101–7.
56. van den Brekel MW, Stel HV, Castelijns JA, et al. Cervical lymph node metastasis: assessment of radiologic criteria. Radiology. 1990;177:379–84.
57. Adams S, Baum RP, Stuckensen T, Bitter K, Hor G. Prospective comparison of ^{18}F-FDG PET with conventional imaging modalities (CT, MRI, US) in lymph node staging of head and neck cancer. Eur J Nucl Med. 1998;25:1255–60.
58. Kau RJ, Alexiou C, Laubenbacher C, et al. Lymph node detection of head and neck squamous cell carcinomas by positron emission tomography with fluorodeoxyglucose F 18 in a routine clinical setting. Arch Otolaryngol Head Neck Surg. 1999;125:1322–8.
59. Stuckensen T, Kovacs AF, Adams S, Baum RP. Staging of the neck in patients with oral cavity squamous cell carcinomas: a prospective comparison of PET, ultrasound, CT and MRI. J Craniomaxillofac Surg. 2000;28:319–24.
60. Dammann F, Horger M, Mueller-Berg M, et al. Rational diagnosis of squamous cell carcinoma of the head and neck region: comparative evaluation of CT, MRI, and ^{18}FDG PET. AJR Am J Roentgenol. 2005;184: 1326–31.
61. Roh JL, Yeo NK, Kim JS, et al. Utility of 2-[^{18}F] fluoro-2-deoxy-D-glucose positron emission tomography and positron emission tomography/computed tomography imaging in the preoperative staging of head and neck squamous cell carcinoma. Oral Oncol. 2007;43:887–93.
62. Ng SH, Yen TC, Liao CT, et al. ^{18}F-FDG PET and CT/MRI in oral cavity squamous cell carcinoma: a prospective study of 124 patients with histologic correlation. J Nucl Med. 2005;46:1136–43.
63. Liao CT, Wang HM, Huang SF, et al. PET and PET/CT of the neck lymph nodes improves risk prediction in patients with squamous cell carcinoma of the oral cavity. J Nucl Med. 2011;52:180–7.
64. Kyzas PA, Evangelou E, Denaxa-Kyza D, Ioannidis JP. ^{18}F-fluorodeoxyglucose positron emission tomography to evaluate cervical node metastases in patients with head and neck squamous cell carcinoma: a meta-analysis. J Natl Cancer Inst. 2008;100:712–20.
65. Stambuk HE, Karimi S, Lee N, Patel SG. Oral cavity and oropharynx tumors. Radiol Clin North Am. 2007; 45:1–20.
66. Ferlito A, Shaha AR, Silver CE, Rinaldo A, Mondin V. Incidence and sites of distant metastases from head and neck cancer. ORL J Otorhinolaryngol Relat Spec. 2001;63:202–7.
67. Brouwer J, de Bree R, Hoekstra OS, et al. Screening for distant metastases in patients with head and neck cancer: is chest computed tomography sufficient? Laryngoscope. 2005;115:1813–7.
68. Erkal HS, Mendenhall WM, Amdur RJ, Villaret DB, Stringer SP. Synchronous and metachronous squamous cell carcinomas of the head and neck mucosal sites. J Clin Oncol. 2001;19:1358–62.
69. Schwartz DL, Rajendran J, Yueh B, et al. Staging of head and neck squamous cell cancer with extended-

field FDG-PET. Arch Otolaryngol Head Neck Surg. 2003;129:1173–8.
70. Schmid DT, Stoeckli SJ, Bandhauer F, et al. Impact of positron emission tomography on the initial staging and therapy in locoregional advanced squamous cell carcinoma of the head and neck. Laryngoscope. 2003;113:888–91.
71. Haerle SK, Strobel K, Hany TF, Sidler D, Stoeckli SJ. ^{18}F-FDG-PET/CT versus panendoscopy for the detection of synchronous second primary tumors in patients with head and neck squamous cell carcinoma. Head Neck. 2010;32:319–25.
72. Strobel K, Haerle SK, Stoeckli SJ, et al. Head and neck squamous cell carcinoma (HNSCC) – detection of synchronous primaries with ^{18}F-FDG-PET/CT. Eur J Nucl Med Mol Imaging. 2009;36:919–27.
73. Kim SY, Roh JL, Yeo NK, et al. Combined ^{18}F-fluorodeoxyglucose-positron emission tomography and computed tomography as a primary screening method for detecting second primary cancers and distant metastases in patients with head and neck cancer. Ann Oncol. 2007;18:1698–703.
74. Morris LG, Sikora AG, Patel SG, Hayes RB, Ganly I. Second primary cancers after an index head and neck cancer: subsite-specific trends in the era of human papillomavirus-associated oropharyngeal cancer. J Clin Oncol. 2011;29:739–46.
75. Choi JY, Lee KS, Kwon OJ, et al. Improved detection of second primary cancer using integrated [^{18}F] fluorodeoxyglucose positron emission tomography and computed tomography for initial tumor staging. J Clin Oncol. 2005;23:7654–9.
76. Uyl-de Groot CA, Senft A, de Bree R, Leemans CR, Hoekstra OS. Chest CT and whole-body ^{18}F-FDG PET are cost-effective in screening for distant metastases in head and neck cancer patients. J Nucl Med. 2010;51:176–82.
77. Scott AM, Gunawardana DH, Bartholomeusz D, Ramshaw JE, Lin P. PET changes management and improves prognostic stratification in patients with head and neck cancer: results of a multicenter prospective study. J Nucl Med. 2008;49:1593–600.
78. Porceddu SV, Jarmolowski E, Hicks RJ, et al. Utility of positron emission tomography for the detection of disease in residual neck nodes after (chemo)radiotherapy in head and neck cancer. Head Neck. 2005;27: 175–81.
79. Yao M, Smith RB, Graham MM, et al. The role of FDG PET in management of neck metastasis from head-and-neck cancer after definitive radiation treatment. Int J Radiat Oncol Biol Phys. 2005;63:991–9.
80. Andrade RS, Heron DE, Degirmenci B, et al. Post-treatment assessment of response using FDG-PET/CT for patients treated with definitive radiation therapy for head and neck cancers. Int J Radiat Oncol Biol Phys. 2006;65:1315–22.
81. Tan A, Adelstein DJ, Rybicki LA, et al. Ability of positron emission tomography to detect residual neck node disease in patients with head and neck squamous cell carcinoma after definitive chemoradiotherapy. Arch Otolaryngol Head Neck Surg. 2007;133:435–40.
82. Nayak JV, Walvekar RR, Andrade RS, et al. Deferring planned neck dissection following chemoradiation for stage IV head and neck cancer: the utility of PET-CT. Laryngoscope. 2007;117:2129–34.
83. Ong SC, Schoder H, Lee NY, et al. Clinical utility of ^{18}F-FDG PET/CT in assessing the neck after concurrent chemoradiotherapy for Locoregional advanced head and neck cancer. J Nucl Med. 2008;49:532–40.
84. Yao M, Smith RB, Hoffman HT, et al. Clinical significance of postradiotherapy [^{18}F]-fluorodeoxyglucose positron emission tomography imaging in management of head-and-neck cancer-a long-term outcome report. Int J Radiat Oncol Biol Phys. 2009;74:9–14.
85. Moeller BJ, Rana V, Cannon BA, et al. Prospective risk-adjusted [^{18}F]Fluorodeoxyglucose positron emission tomography and computed tomography assessment of radiation response in head and neck cancer. J Clin Oncol. 2009;27:2509–15.
86. Porceddu SV, Pryor DI, Burmeister E, et al. Results of a prospective study of positron emission tomography-directed management of residual nodal abnormalities in node-positive head and neck cancer after definitive radiotherapy with or without systemic therapy. Head Neck. 2011;33:1675–82.
87. Greven KM, Williams 3rd DW, McGuirt Sr WF, et al. Serial positron emission tomography scans following radiation therapy of patients with head and neck cancer. Head Neck. 2001;23:942–6.
88. Ryan WR, Fee Jr WE, Le QT, Pinto HA. Positron-emission tomography for surveillance of head and neck cancer. Laryngoscope. 2005;115:645–50.
89. Forrester HB, Albright N, Ling CC, Dewey WC. Computerized video time-lapse analysis of apoptosis of REC:Myc cells X-irradiated in different phases of the cell cycle. Radiat Res. 2000;154:625–39.
90. Luce A, Courtin A, Levalois C, et al. Death receptor pathways mediate targeted and non-targeted effects of ionizing radiations in breast cancer cells. Carcinogenesis. 2009;30:432–9.
91. Dornfeld K, Hopkins S, Simmons J, et al. Post-treatment FDG-PET uptake in the supraglottic and glottic larynx correlates with decreased quality of life after chemoradiotherapy. Int J Radiat Oncol Biol Phys. 2008;71:386–92.
92. Ferlito A, Corry J, Silver CE, Shaha AR, Thomas Robbins K, Rinaldo A. Planned neck dissection for patients with complete response to chemoradiotherapy: a concept approaching obsolescence. Head Neck. 2010;32:253–61.
93. Wee JT, Anderson BO, Corry J, et al. Management of the neck after chemoradiotherapy for head and neck cancers in Asia: consensus statement from the Asian Oncology Summit 2009. Lancet Oncol. 2009;10: 1086–92.
94. Schoder H, Moskowitz C. PET imaging for response assessment in lymphoma: potential and limitations. Radiol Clin North Am. 2008;46:225–41. viii.

95. Weber WA, Wieder H. Monitoring chemotherapy and radiotherapy of solid tumors. Eur J Nucl Med Mol Imaging. 2006;33(Suppl 1):27–37.
96. Brun E, Kjellen E, Tennvall J, et al. FDG PET studies during treatment: prediction of therapy outcome in head and neck squamous cell carcinoma. Head Neck. 2002;24:127–35.
97. Ceulemans G, Voordeckers M, Farrag A, Verdries D, Storme G, Everaert H. Can 18-FDG-PET during radiotherapy replace post-therapy scanning for detection/demonstration of tumor response in head-and-neck cancer? Int J Radiat Oncol Biol Phys. 2011;81:938–42.
98. Hentschel M, Appold S, Schreiber A, et al. Early FDG PET at 10 or 20 Gy under chemoradiotherapy is prognostic for locoregional control and overall survival in patients with head and neck cancer. Eur J Nucl Med Mol Imaging. 2011;38:1203–11.
99. Chen SW, Hsieh TC, Yen KY, et al. Interim FDG PET/CT for predicting the outcome in patients with head and neck cancer. Laryngoscope. 2014;124:2732–8.
100. Min M, Lin P, Lee MT, et al. Prognostic role of metabolic parameters of ^{18}F-FDG PET-CT scan performed during radiation therapy in locally advanced head and neck squamous cell carcinoma. Eur J Nucl Med Mol Imaging. 2015;42:1984–94.
101. Min M, Lin P, Lee M, et al. Prognostic value of 2-[^{18}F] Fluoro-2-deoxy-D-glucose positron emission tomography-computed tomography scan carried out during and after radiation therapy for head and neck cancer using visual therapy response interpretation criteria. Clin Oncol (R Coll Radiol). 2016;28:393–401.
102. Cohen EE, Karrison TG, Kocherginsky M, et al. Phase III randomized trial of induction chemotherapy in patients with N2 or N3 locally advanced head and neck cancer. J Clin Oncol. 2014;32:2735–43.
103. Haddad R, O'Neill A, Rabinowits G, et al. Induction chemotherapy followed by concurrent chemoradiotherapy (sequential chemoradiotherapy) versus concurrent chemoradiotherapy alone in locally advanced head and neck cancer (PARADIGM): a randomised phase 3 trial. Lancet Oncol. 2013;14:257–64.
104. Dutta PR, Riaz N, McBride S, et al. Postoperative PET/CT and target delineation before adjuvant radiotherapy in patients with oral cavity squamous cell carcinoma. Head Neck. 2015;38 Suppl 1:E1285–93.
105. Liao CT, Fan KH, Lin CY, et al. Impact of a second FDG PET scan before adjuvant therapy for the early detection of residual/relapsing tumours in high-risk patients with oral cavity cancer and pathological extracapsular spread. Eur J Nucl Med Mol Imaging. 2012;39:944–55.
106. Shintani SA, Foote RL, Lowe VJ, Brown PD, Garces YI, Kasperbauer JL. Utility of PET/CT imaging performed early after surgical resection in the adjuvant treatment planning for head and neck cancer. Int J Radiat Oncol Biol Phys. 2008;70:322–9.
107. Goodwin Jr WJ. Salvage surgery for patients with recurrent squamous cell carcinoma of the upper aerodigestive tract: when do the ends justify the means? Laryngoscope. 2000;110:1–18.
108. Lapela M, Eigtved A, Jyrkkio S, et al. Experience in qualitative and quantitative FDG PET in follow-up of patients with suspected recurrence from head and neck cancer. Eur J Cancer. 2000;36:858–67.
109. Kunkel M, Forster GJ, Reichert TE, et al. Detection of recurrent oral squamous cell carcinoma by [^{18}F]-2-fluorodeoxyglucose-positron emission tomography: implications for prognosis and patient management. Cancer. 2003;98:2257–65.
110. Lonneux M, Lawson G, Ide C, Bausart R, Remacle M, Pauwels S. Positron emission tomography with fluorodeoxyglucose for suspected head and neck tumor recurrence in the symptomatic patient. Laryngoscope. 2000;110:1493–7.
111. Wong RJ, Lin DT, Schoder H, et al. Diagnostic and prognostic value of [^{18}F]fluorodeoxyglucose positron emission tomography for recurrent head and neck squamous cell carcinoma. J Clin Oncol. 2002;20:4199–208.
112. Kubota K, Yokoyama J, Yamaguchi K, et al. FDG-PET delayed imaging for the detection of head and neck cancer recurrence after radio-chemotherapy: comparison with MRI/CT. Eur J Nucl Med Mol Imaging. 2004;31:590–5.
113. Abgral R, Querellou S, Potard G, et al. Does ^{18}F-FDG PET/CT improve the detection of posttreatment recurrence of head and neck squamous cell carcinoma in patients negative for disease on clinical follow-up? J Nucl Med. 2009;50:24–9.
114. Goerres GW, Schmid DT, Bandhauer F, et al. Positron emission tomography in the early follow-up of advanced head and neck cancer. Arch Otolaryngol Head Neck Surg. 2004;130:105–9. discussion 20–1.
115. Salaun PY, Abgral R, Querellou S, et al. Does 18fluoro-fluorodeoxyglucose positron emission tomography improve recurrence detection in patients treated for head and neck squamous cell carcinoma with negative clinical follow-up? Head Neck. 2007;29:1115–20.
116. Lowe VJ, Boyd JH, Dunphy FR, et al. Surveillance for recurrent head and neck cancer using positron emission tomography. J Clin Oncol. 2000;18:651–8.
117. Bird T, Barrington S, Thavaraj S, et al. ^{18}F-FDG PET/CT to assess response and guide risk-stratified follow-up after chemoradiotherapy for oropharyngeal squamous cell carcinoma. Eur J Nucl Med Mol Imaging. 2016;43:1239–47.
118. Haberkorn U, Strauss LG, Reisser C, et al. Glucose uptake, perfusion, and cell proliferation in head and neck tumors: relation of positron emission tomography to flow cytometry. J Nucl Med. 1991;32:1548–55.
119. Jacob R, Welkoborsky HJ, Bittinger F, Mann WJ, Amedee R. Histological grading, growth fraction and DNA-ploidy as criteria for the treatment of

pharyngeal and supraglottic squamous cell carcinomas: a preliminary, prospective study. ORL J Otorhinolaryngol Relat Spec. 2001;63:314–20.
120. Minn H, Clavo AC, Grenman R, Wahl RL. In vitro comparison of cell proliferation kinetics and uptake of tritiated fluorodeoxyglucose and L-methionine in squamous-cell carcinoma of the head and neck. J Nucl Med. 1995;36:252–8.
121. Allal AS, Dulguerov P, Allaoua M, et al. Standardized uptake value of 2-[^{18}F]fluoro-2-deoxy-D-glucose in predicting outcome in head and neck carcinomas treated by radiotherapy with or without chemotherapy. J Clin Oncol. 2002;20:1398–404.
122. Allal AS, Slosman DO, Kebdani T, Allaoua M, Lehmann W, Dulguerov P. Prediction of outcome in head-and-neck cancer patients using the standardized uptake value of 2-[^{18}F]fluoro-2-deoxy-D-glucose. Int J Radiat Oncol Biol Phys. 2004;59:1295–300.
123. Kunkel M, Reichert TE, Benz P, et al. Overexpression of Glut-1 and increased glucose metabolism in tumors are associated with a poor prognosis in patients with oral squamous cell carcinoma. Cancer. 2003;97: 1015–24.
124. Chung MK, Jeong HS, Park SG, et al. Metabolic tumor volume of [^{18}F]-fluorodeoxyglucose positron emission tomography/computed tomography predicts short-term outcome to radiotherapy with or without chemotherapy in pharyngeal cancer. Clin Cancer Res. 2009;15:5861–8.
125. Farrag A, Ceulemans G, Voordeckers M, Everaert H, Storme G. Can ^{18}F-FDG-PET response during radiotherapy be used as a predictive factor for the outcome of head and neck cancer patients? Nucl Med Commun. 2010;31:495–501.
126. Kim SY, Roh JL, Kim MR, et al. Use of ^{18}F-FDG PET for primary treatment strategy in patients with squamous cell carcinoma of the oropharynx. J Nucl Med. 2007;48:752–7.
127. La TH, Filion EJ, Turnbull BB, et al. Metabolic tumor volume predicts for recurrence and death in head-and-neck cancer. Int J Radiat Oncol Biol Phys. 2009;74:1335–41.
128. Liao CT, Chang JT, Wang HM, et al. Pretreatment primary tumor SUVmax measured by FDG-PET and pathologic tumor depth predict for poor outcomes in patients with oral cavity squamous cell carcinoma and pathologically positive lymph nodes. Int J Radiat Oncol Biol Phys. 2009;73:764–71.
129. Machtay M, Natwa M, Andrel J, et al. Pretreatment FDG-PET standardized uptake value as a prognostic factor for outcome in head and neck cancer. Head Neck. 2009;31:195–201.
130. Suzuki H, Hasegawa Y, Terada A, et al. FDG-PET predicts survival and distant metastasis in oral squamous cell carcinoma. Oral Oncol. 2009;45:569–73.
131. Halfpenny W, Hain SF, Biassoni L, Maisey MN, Sherman JA, McGurk M. FDG-PET. A possible prognostic factor in head and neck cancer. Br J Cancer. 2002;86:512–6.
132. Liao CT, Chang JT, Wang HM, et al. Preoperative [^{18}F]fluorodeoxyglucose positron emission tomography standardized uptake value of neck lymph nodes predicts neck cancer control and survival rates in patients with oral cavity squamous cell carcinoma and pathologically positive lymph nodes. Int J Radiat Oncol Biol Phys. 2009;74:1054–61.
133. Chan SC, Chang JT, Lin CY, et al. Clinical utility of ^{18}F-FDG PET parameters in patients with advanced nasopharyngeal carcinoma: predictive role for different survival endpoints and impact on prognostic stratification. Nucl Med Commun. 2011;32:989–96.
134. Chang KP, Tsang NM, Liao CT, et al. Prognostic significance of ^{18}F-FDG PET parameters and plasma Epstein-Barr virus DNA load in patients with nasopharyngeal carcinoma. J Nucl Med. 2012;53:21–8.
135. Lim R, Eaton A, Lee NY, et al. ^{18}F-FDG PET/CT metabolic tumor volume and total lesion glycolysis predict outcome in oropharyngeal squamous cell carcinoma. J Nucl Med. 2012;53:1506–13.
136. Rasmussen JH, Vogelius IR, Fischer BM, et al. Prognostic value of ^{18}F-fludeoxyglucose uptake in 287 patients with head and neck squamous cell carcinoma. Head Neck. 2015;37:1274–81.
137. Chong VF, Ong CK. Nasopharyngeal carcinoma. Eur J Radiol. 2008;66:437–47.
138. Liu FY, Lin CY, Chang JT, et al. ^{18}F-FDG PET can replace conventional work-up in primary M staging of nonkeratinizing nasopharyngeal carcinoma. J Nucl Med. 2007;48:1614–9.
139. Ng SH, Chan SC, Yen TC, et al. Staging of untreated nasopharyngeal carcinoma with PET/CT: comparison with conventional imaging work-up. Eur J Nucl Med Mol Imaging. 2009;36:12–22.
140. Chan SC, Yen TC, Ng SH, et al. Differential roles of ^{18}F-FDG PET in patients with locoregional advanced nasopharyngeal carcinoma after primary curative therapy: response evaluation and impact on management. J Nucl Med. 2006;47:1447–54.
141. Comoretto M, Balestreri L, Borsatti E, Cimitan M, Franchin G, Lise M. Detection and restaging of residual and/or recurrent nasopharyngeal carcinoma after chemotherapy and radiation therapy: comparison of MR imaging and FDG PET/CT. Radiology. 2008;249:203–11.
142. Ng SH, Chan SC, Yen TC, et al. Comprehensive imaging of residual/recurrent nasopharyngeal carcinoma using whole-body MRI at 3 T compared with FDG-PET-CT. Eur Radiol. 2010;20:2229–40.
143. Ng SH, Joseph CT, Chan SC, et al. Clinical usefulness of ^{18}F-FDG PET in nasopharyngeal carcinoma patients with questionable MRI findings for recurrence. J Nucl Med. 2004;45:1669–76.
144. Xie P, Yue JB, Fu Z, Feng R, Yu JM. Prognostic value of ^{18}F-FDG PET/CT before and after radiotherapy for locally advanced nasopharyngeal carcinoma. Ann Oncol. 2010;21:1078–82.
145. Krabbe CA, van der Werff-Regelink G, Pruim J, van der Wal JE, Roodenburg JL. Detection of cervical metastases with ^{11}C-tyrosine PET in patients with

squamous cell carcinoma of the oral cavity or oropharynx: A comparison with ^{18}F-FDG PET. Head Neck. 2010;32:368–74.
146. Balogova S, Perie S, Kerrou K, et al. Prospective comparison of FDG and FET PET/CT in patients with head and neck squamous cell carcinoma. Mol Imaging Biol. 2008;10:364–73.
147. Pauleit D, Zimmermann A, Stoffels G, et al. ^{18}F-FET PET compared with ^{18}F-FDG PET and CT in patients with head and neck cancer. J Nucl Med. 2006;47:256–61.
148. Ito K, Yokoyama J, Kubota K, Morooka M, Shiibashi M, Matsuda H. ^{18}F-FDG versus ^{11}C-choline PET/CT for the imaging of advanced head and neck cancer after combined intra-arterial chemotherapy and radiotherapy: the time period during which PET/CT can reliably detect non-recurrence. Eur J Nucl Med Mol Imaging. 2010;37:1318–27.
149. Lee N, Nehmeh S, Schoder H, et al. Prospective trial incorporating pre−/mid-treatment [^{18}F]-misonidazole positron emission tomography for head-and-neck cancer patients undergoing concurrent chemoradiotherapy. Int J Radiat Oncol Biol Phys. 2009;75:101–8.
150. Grosu AL, Souvatzoglou M, Roper B, et al. Hypoxia imaging with FAZA-PET and theoretical considerations with regard to dose painting for individualization of radiotherapy in patients with head and neck cancer. Int J Radiat Oncol Biol Phys. 2007;69:541–51.
151. Minagawa Y, Shizukuishi K, Koike I, et al. Assessment of tumor hypoxia by ^{62}Cu-ATSM PET/CT as a predictor of response in head and neck cancer: a pilot study. Ann Nucl Med. 2011;25:339–45.
152. Menda Y, Boles Ponto LL, Dornfeld KJ, et al. Kinetic analysis of 3′-deoxy-3′-^{18}F-fluorothymidine (^{18}F-FLT) in head and neck cancer patients before and early after initiation of chemoradiation therapy. J Nucl Med. 2009;50:1028–35.
153. Troost EG, Vogel WV, Merkx MA, et al. ^{18}F-FLT PET does not discriminate between reactive and metastatic lymph nodes in primary head and neck cancer patients. J Nucl Med. 2007;48:726–35.
154. Troost EG, Bussink J, Hoffmann AL, Boerman OC, Oyen WJ, Kaanders JH. ^{18}F-FLT PET/CT for early response monitoring and dose escalation in oropharyngeal tumors. J Nucl Med. 2010;51:866–74.
155. Hoeben BA, Troost EG, Span PN, et al. ^{18}F-FLT PET during radiotherapy or chemoradiotherapy in head and neck squamous cell carcinoma is an early predictor of outcome. J Nucl Med. 2013;54:532–40.
156. Hoshikawa H, Mori T, Kishino T, et al. Changes in ^{18}F-fluorothymidine and ^{18}F-fluorodeoxyglucose positron emission tomography imaging in patients with head and neck cancer treated with chemoradiotherapy. Ann Nucl Med. 2013;27:363–70.
157. Daisne JF, Duprez T, Weynand B, et al. Tumor volume in pharyngolaryngeal squamous cell carcinoma: comparison at CT, MR imaging, and FDG PET and validation with surgical specimen. Radiology. 2004;233:93–100.
158. Thiagarajan A, Caria N, Schöder H, et al. Target volume delineation in oropharyngeal cancer: impact of PET, MRI, and physical examination. Int J Radiat Oncol Biol Phys. 2012;83:220–7.
159. Hatt M, Lee JA, Schmidtlein CR, et al. Classification and evaluation strategies of auto-segmentation approaches for PET: report of AAPM task group No. 211. Med Phys. 2017;44:e1–e42.
160. Madani I, Duprez F, Boterberg T, et al. Maximum tolerated dose in a phase I trial on adaptive dose painting by numbers for head and neck cancer. Radiother Oncol. 2011;101:351–5.
161. Wang J, Zheng J, Tang T, et al. A randomized pilot trial comparing Position Emission Tomography (PET)-guided dose escalation radiotherapy to conventional radiotherapy in chemoradiotherapy treatment of locally advanced nasopharyngeal carcinoma. PLoS One. 2015;10:e0124018.
162. Jeong J, Setton JS, Lee NY, Oh JH, Deasy JO. Estimate of the impact of FDG-avidity on the dose required for head and neck radiotherapy local control. Radiother Oncol. 2014;111:340–7.
163. De Felice F, Thomas C, Barrington S, Pathmanathan A, Lei M, Urbano TG. Analysis of loco-regional failures in head and neck cancer after radical radiation therapy. Oral Oncol. 2015;51:1051–5.
164. Due AK, Vogelius IR, Aznar MC, et al. Recurrences after intensity modulated radiotherapy for head and neck squamous cell carcinoma more likely to originate from regions with high baseline [^{18}F]-FDG uptake. Radiother Oncol. 2014;111:360–5.
165. Hoeben BA, Kaanders JH, Franssen GM, et al. PET of hypoxia with ^{89}Zr-labeled cG250-F(ab′)2 in head and neck tumors. J Nucl Med. 2010;51:1076–83.
166. Postema EJ, McEwan AJ, Riauka TA, et al. Initial results of hypoxia imaging using 1-alpha-D: −(5-deoxy-5-[^{18}F]-fluoroarabinofuranosyl)-2-nitroimidazole (^{18}F-FAZA). Eur J Nucl Med Mol Imaging. 2009;36:1565–73.
167. Schoder H, Ong SC. Fundamentals of molecular imaging: rationale and applications with relevance for radiation oncology. Semin Nucl Med. 2008;38:119–28.
168. Kuhn FP, Hullner M, Mader CE, et al. Contrast-enhanced PET/MR imaging versus contrast-enhanced PET/CT in head and neck cancer: how much MR information is needed? J Nucl Med. 2014;55:551–8.
169. Ng SH, Liao CT, Lin CY, et al. Dynamic contrast-enhanced MRI, diffusion-weighted MRI and F-FDG PET/CT for the prediction of survival in oropharyngeal or hypopharyngeal squamous cell carcinoma treated with chemoradiation. Eur Radiol. 2016;26:4162–4172.
170. Preda L, Conte G, Bonello L, et al. Combining standardized uptake value of FDG-PET and apparent diffusion coefficient of DW-MRI improves risk stratification in head and neck squamous cell carcinoma. Eur Radiol. 2016;26:4432–4441.

Diagnostic Applications of Nuclear Medicine: Thyroid Tumors

19

Rossella Elisei, Laura Agate, Sara Mazzarri, Valeria Bottici, Federica Guidoccio, Eleonora Molinaro, Giuseppe Boni, Marco Ferdeghini, and Giuliano Mariani

Abstract

Thyroid cancer (TC) is the most frequent endocrine malignancy. Its incidency has been growing in the last three decades reaching a mean of 12/100,000 women and 4/100,000 men. Since the mortality is low (0.5%), the prevalence is very high especially among women who have a higher rate compared to men (3:1). TCs are distinguished into well-differentiated thyroid cancer (DTC) (i.e., papillary and follicular), poorly differentiated thyroid cancer (PDTC), anaplastic (ATC), and medullary cancer (MTC). Other very rare TC accounts for non-epithelial tumors, lymphoma, and carcinomas characterized by the presence of mucin-producing cells and keratin.

TC usually presents as a thyroid nodule. Thyroid ultrasonography (US) is useful to detect thyroid nodules, but since only 5% of thyroid nodules are malignant, the diagnosis of malignancy is done by fine-needle aspiration cytology (FNAC). Radioiodide or ^{99m}Tc-pertechnetate thyroid scan has a low diagnostic specificity and sensitivity for characterizing thyroid nodules. X-ray of the neck is useful to disclose a deviation of the trachea or lumen restriction, in large nodules and in multinodular goiter. CT and MRI are generally reserved for mediastinal thyroid masses or the identification of regional or distant metastasis.

The most widely used staging system for TC is the TNM classification that has been defined jointly by the Union Internationale Contre le Cancer (UICC) and by the American Joint Committee on Cancer (AJCC). Thyroid remnant ablation with ^{131}I-iodide is indicated in DTC patients with a moderate to high risk of recurrence. Patients are prepared with rhTSH and low iodine diet.

ATC is a rare tumor (<3% of all TCs) derived from follicular cells with a very poor prognosis and almost invariably lethal. The most common clinical presentation of ATC is a new, large, firm thyroid mass, often associated with signs/symptoms of local compression/invasion. Multimodality treatment of ATC includes surgery, EBRT, and combination of chemotherapies. Therapy with ^{131}I-iodide is not useful, since these tumors do not concentrate radioiodide. Preoperative imaging with US, CT, and MRI plays an important role, and [^{18}F]FDG PET is useful to plan the therapeutic strategy.

R. Elisei (✉) • L. Agate • V. Bottici • E. Molinaro
Endocrine Unit, Department of Clinical and Experimental Medicine, University of Pisa, Pisa, Italy
e-mail: rossella.elisei@med.unipi.it

S. Mazzarri • F. Guidoccio • G. Boni • G. Mariani
Regional Center of Nuclear Medicine, Department of Translational Research and Advanced Technologies in Medicine and Surgery, University of Pisa, Pisa, Italy

M. Ferdeghini
Nuclear Medicine Unit, Department of Diagnostics and Public Health, University of Verona, Verona, Italy

© Springer International Publishing Switzerland 2017
H.W. Strauss et al. (eds.), *Nuclear Oncology*,
https://doi.org/10.1007/978-3-319-26236-9_11

MTC is a well-differentiated TC arising from the parafollicular, calcitonin-producing C cells. Its prevalence is 5–10% in all TCs. Sporadic and familial forms are recognized. Elevated baseline serum levels of calcitonin (Ct) are suspicious for MTC. Following surgery, MTC patients are monitored with serum Ct and CEA levels, and serial neck US examinations are performed. Ct doubling time in serum is the most sensitive biomarker for MTC progression. Scintigraphy with ^{123}I-MIBG has very high sensitivity for staging patients with MEN II and familial MTC. However, it has a low sensitivity in patients with increased serum Ct but no clinical site of disease. ^{68}Ga-DOTATATE PET/CT is now the best imaging modality in the detection of metastatic MTC lesions in the presence of high levels of serum Ct. Radionuclide therapy with the radiolabeled somatostatin analogue ^{90}Y-DOTA-Tyr^{3}-octreotide (^{90}Y-DOTA-TOC) has been tested in metastatic MTC. The two TKIs, vandetanib and cabozantinib, represent nowadays the best therapy of metastatic and progressive MTC.

Keywords

^{131}I-Iodide • Calcitonin • Fine needle aspiration • Thyroglobulin • Thyroid cancer

Glossary

[^{18}F]FDG	2-Deoxy-2-[^{18}F]fluoro-D-glucose
^{123}I-MIBG	^{123}I-*meta*-Iodobenzylguanidine
^{18}F-DOPA	2-^{18}F-Fluoro-L-3,4-dihydroxyphenylalanine
AJCC	American Joint Committee on Cancer
ATC	Anaplastic thyroid cancer
BRAF	Gene encoding for the B-Raf protein, a serine/threonine-protein kinase; the gene is also known as the proto-oncogene B-Raf and v-Raf murine sarcoma viral oncogene homolog B
CEA	Carcinoembryonic antigen, a tumor-associated serum marker
CI	Confidence interval
Ct	Calcitonin
CT	X-ray computed tomography
DMSA	Dimercaptosuccinic acid, a metal-chelating agent
DOTA-TOC	DOTA-octreotide
DOTA	1,4,7,10-Tetra-azacyclododecane-1,4,7,10-tetraacetic acid
DOTATATE	DOTA-octreotate
DTC	Well-differentiated thyroid cancer
EBRT	External beam radiation therapy
EFVPTC	Encapsulated follicular variant of papillary thyroid tumor
FNAC	Fine-needle aspiration cytology
FT3	Free circulating form of the thyroid hormone tri-iodothyronine
FT4	Free circulating form of the thyroid hormone tetra-iodothyronine
FTC	Follicular thyroid tumor
FVPTC	Follicular variant of papillary thyroid tumor
GLUT	Glucose transporter family
Gy	Gray unit (ionizing radiation dose in the International System of Units, corresponding to the absorption of one joule of radiation energy per kilogram of matter)
MAP	Mitogen-activated protein
MEN	Multiple endocrine neoplasia
MET	Gene encoding for a protein of the receptor tyrosine kinase family
MIBG	*meta*-Iodobenzylguanidine
MIP	Maximum intensity projection
MRI	Magnetic resonance imaging
MTC	Medullary thyroid cancer

mTOR	Mammalian target of rapamycin
NEFVPTC	Non-encapsulated follicular variant of papillary thyroid tumor
NIFTP	Noninvasive follicular variant of papillary thyroid carcinoma
NIS	Na^+/I^- symporter
p53	Tumor protein p53, also known as cellular tumor antigen p53, phosphoprotein p53, tumor suppressor p53, antigen NY-CO-13, or transformation-related protein 53 (TRP53)
PAX8	A member of the paired box (PAX) family of transcription factors
PDTC	Poorly differentiated thyroid cancer
PET	Positron emission tomography
PET/CT	Positron emission tomography/Computed tomography
PI3K/AKT	Intracellular signalling pathway regulating the cell cycle
PPA Rγ	Gene encoding for the peroxisome proliferator-activated receptor gamma (or PPARG, a nuclear receptor), also known as the glitazone receptor, or NR1C3 (nuclear receptor subfamily 1, group C, member 3)
PTC	Papillary thyroid tumor
RAS	Oncogene regulating signalling intracellular cascades
RET	A proto-oncogene encoding for a receptor tyrosine kinase for extracellular signalling molecules (from "rearranged during transfection")
rhTSH	Recombinant human TSH
SWI/SNF	A nucleosome remodeling complex (from "SWItch/Sucrose Non-Fermentable")
TC	Thyroid cancer
TERT	Gene encoding for telomerase reverse transcriptase, a catalytic subunit of the enzyme telomerase
Tg	Thyroglobulin
TKI	Thymidine kinase inhibitor
TNM	AJCC/UICC staging system based on parameters "T" (tumor status), "N" (lymph node status), and "M" (distant metastasis status)
TRK	Gene encoding for a receptor tyrosine kinase for extracellular signalling molecules
TSH	Thyroid stimulating hormone or thyrotropin
UICC	Union Internationale Contre le Cancer (International Union Against Cancer)
US	Ultrasonography

Contents

Introduction and General Background 548

Differentiated Thyroid Cancer Derived from Follicular Cells 548
Histopathologic Classification and Features 548

Epidemiology 551

Risk Factors 552

Pathogenesis 553

Clinical Presentation 554

Diagnosis 555
Ultrasonography 555
Fine-Needle Aspiration Cytology 555
Thyroid Scintigraphy and Other Diagnostic Imaging Procedures 556

Staging 558

Prognostic Factors 560
Age 561
Gender 561
Histologic Types and Variants 561
Tumor Size 563
Multifocality 563
Extrathyroidal Invasion 563
Lymph Node Metastases 563
Distant Metastases 564
Molecular Prognostic Factors 564

Role of Nuclear Medicine in the Management and Follow-Up of DTC After Surgery 564

Anaplastic Thyroid Cancer 564
Histopathologic Features and Pathogenesis 565
Clinical Presentation and Diagnosis 565
Radionuclide Imaging of ATC 567

Medullary Thyroid Cancer 567
Role of Nuclear Medicine in the Management of MTC 570

Other Thyroid Cancers 571

References 576

Introduction and General Background

Although constituting only about 3.5% of all human cancers, thus being considered a rare tumor, thyroid cancer (TC) is the most common endocrine malignancy. TC comprises different histologic subtypes arising from follicular cell and less frequently from the neural crest-derived parafollicular C cells. Other rare primary TCs include non-epithelial tumors (sarcomas and hemangiosarcomas), thyroid lymphoma, and an extremely rare group of carcinomas characterized by the presence of mucin- and keratin-producing cells.

According to the World Health Organization (WHO) [1], primary thyroid tumors are classified as follows:

1. Papillary thyroid tumors (PTC)
2. Follicular thyroid tumors (FTC)
3. Poorly differentiated thyroid tumors (PDTC)
4. Anaplastic thyroid carcinoma (ATC)
5. Medullary thyroid carcinoma (MTC)
6. Other rare thyroid tumors

The prevalence of thyroid tumors according to histology as observed in a large consecutive series from a single referral center is reported in Fig. 1.

Differentiated Thyroid Cancer Derived from Follicular Cells

Although also MTC is one of the differentiated thyroid cancers, the term "differentiated thyroid carcinoma" (DTC) is routinely employed to define those cancers that originate from thyroid follicular cells. The most frequent type of DTC is PTC, which constitutes about 80% of all cases and is the most prominent malignancy of the endocrine organs.

Histopathologic Classification and Features

PTC and FTC are defined as "differentiated thyroid carcinomas" because they maintain the most important specific features of the follicular normal cells, such as the ability to take up and accumulate iodine, to produce thyroglobulin (Tg), and to respond to the thyroid-stimulating hormone (TSH).

The histologic diagnosis of PTC is based on the typical features of the cell nuclei, which are typically larger than in normal thyroid cells, transparent at the center, and containing hypodense chromatin (so-called ground glass nuclei); furthermore, their shape is irregular and may reveal fissures (thus resembling "coffee beans"). Large, circular, well-delimited intranuclear inclusions, corresponding to cytoplasmic invaginations, may also be present [2]. About 50% of PTCs are also characterized by the presence of calcium deposits named "psammoma bodies" [3]. PTCs are also characterized by the presence of a focal or diffuse pattern of papillae, i.e., fibrovascular structures covered by a single layer of neoplastic cells sometimes associated with follicles filled with colloid; trabecular or lobular patterns, areas of sclerosis, and squamous metaplasia can also be present.

When PTCs show a follicular-like structure, differential diagnosis with FTC is based on the peculiar features of their cell nuclei. In fact, FTCs exhibit frank follicular differentiation, without however the typical nuclei and papillary architecture of PTC [4].

Several variants of PTC have been distinguished (see Fig. 2):

- The "classical" variant of PTC with the papillary architecture
- The "follicular" variant in which the cells are organized in colloid-containing follicles, but are characterized by the typical PTC nuclei [5, 6]

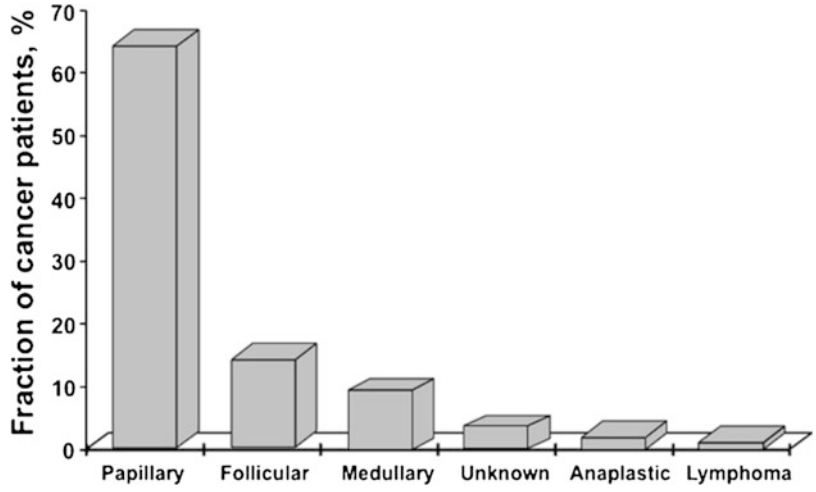

Fig. 1 Prevalence of different histotypes of thyroid cancers in a consecutive series over 8,000 patients followed at the Department of Endocrinology of the University of Pisa Medical School (Pisa, Italy) in the period 1969–2005

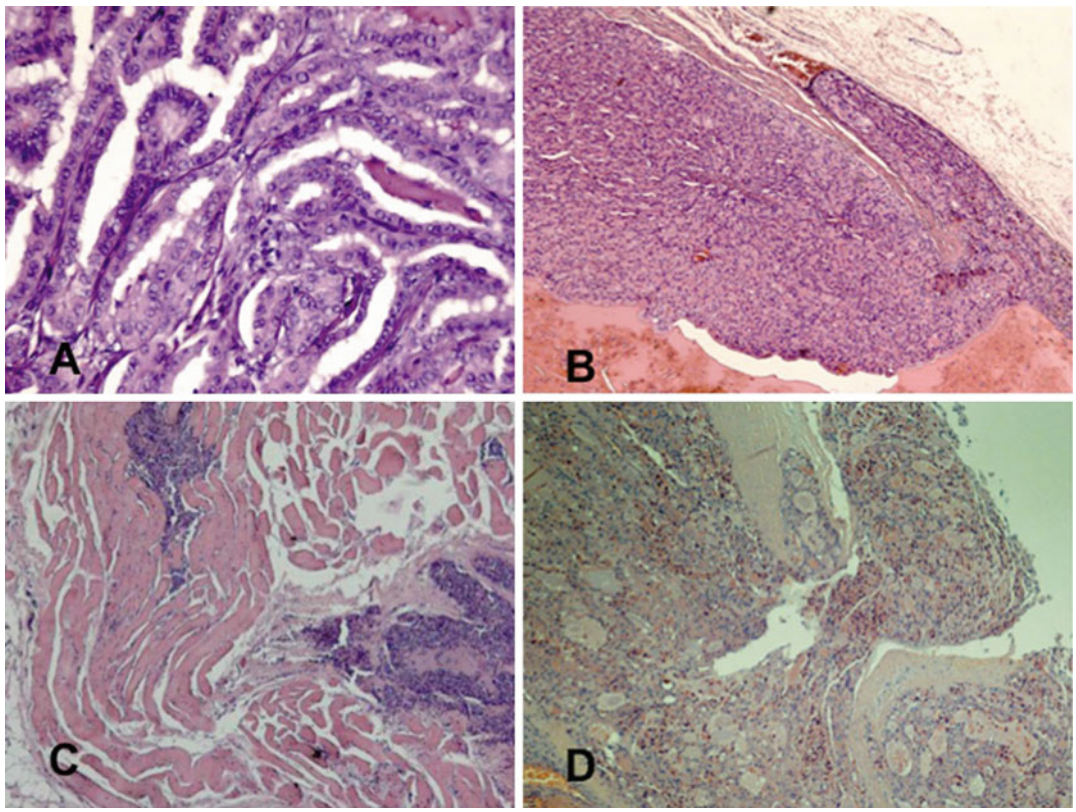

Fig. 2 Examples of different histologic types and variants of DTC. (**a**) Classical variant of papillary thyroid cancer (*PTC*), showing typical papillary pattern. (**b**) Low-magnification image of a follicular thyroid cancer (*FTC*) with minimally invasive pattern; infiltration through the thyroid capsule is shown in the right lower corner of the section. (**c**) Low-magnification image of an FTC showing massive extrathyroidal infiltration; predominant tumor cell population is evident in the *right side of the section*, while the tumor cell nest infiltrating the muscles is evident in the *left side of the section*. (**d**) Low-magnification image of a Hürthle cell PTC, showing the invasion of the thyroid capsule in the *midright side of the section* (Courtesy of Prof. Fulvio Basolo, Division of Pathology, Department of Surgery, University of Pisa, Pisa, Italy)

- The "diffuse sclerosing" variant, characterized by the following morphologic findings: (a) diffuse involvement of one or both lobes, (b) numerous micropapillary formations located within cleft-like spaces consistent with lymph vessels, (c) extensive squamous metaplasia, (d) large number of psammoma bodies, (e) marked lymphocytic infiltration, and (f) prominent fibrosis [7]
- The "tall cell" and the "columnar cell" variants [8, 9], which have a typical papillary pattern but are constituted by elongated cells containing a granular and eosinophilic cytoplasm

The follicular variant of PTC (FVPTC, see example in Fig. 3) was recognized as a new histologic presentation almost 30 years ago [5], and its incidence has increased by 173% in the last decades [10, 11]. FVPTC is actually a heterogeneous disease that includes two distinct subgroups: (1) an infiltrative/diffuse (nonencapsulated) subvariant (NEFVPTC), which resembles classic PTC in its metastatic lymph node pattern and invasive growth, and (2) an encapsulated form (EFVPTC) with a pattern similar as that of follicular adenomas/carcinomas (FTA/FTC).

A different molecular profile has been demonstrated between the "encapsulated" and the "infiltrative" FVPTC; in fact, the former is much more similar to FTA/FTC (high rate of RAS and absence of BRAF mutations), while the latter is much more similar to the classical variant of PTC (concerning especially BRAF mutations). Moreover, the molecular profiles of "encapsulated" and "infiltrative" FVPTCs parallel their different biological patterns of growth [12]. Very recently, a group of pathologists considered as the most expert in the world for the diagnosis of TC published a consensus about the idea that thyroid tumors currently diagnosed as noninvasive encapsulated follicular variant of PTC (EFVPTC), which have a very low risk of adverse outcome, can be now named noninvasive follicular variant of papillary thyroid carcinoma (NIFTP). This reclassification will impact on a large series of patients worldwide and result in a great reduction in psychological and clinical consequences associated with the diagnosis of cancer [13].

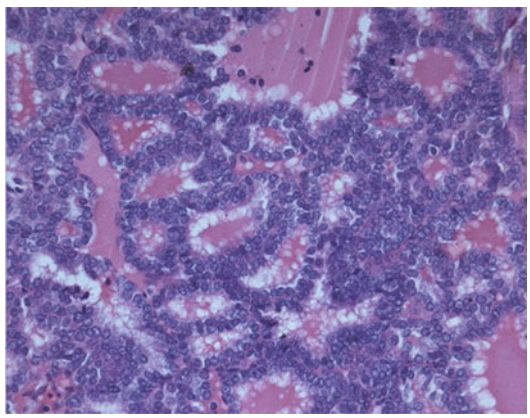

Fig. 3 High-magnification image of a follicular variant of PTC (*FVPTC*): follicular atypical cells with nuclear features typical of PTC lining follicle-like structures (Courtesy of Prof. Fulvio Basolo, Division of Pathology, Department of Surgery, University of Pisa, Pisa, Italy)

While the classical and follicular variants are the most common and the less aggressive PTC variants, both the sclerosing and the tall/columnar variants have a less favorable prognosis. The prognostic value of the different variants has been recently explored in a study in which a very large number of cases were collected and analyzed, thus clearly confirming that the prognosis, especially for recurrence, worsens from follicular to classical to tall cell variant [14].

Tumors with size less than 1 cm in diameter are defined as microcarcinomas [15]. They may exhibit features of a classic, small PTC or may appear as nonencapsulated sclerotic nodules that, although only few mm in size, infiltrate the surrounding thyroid tissue. The large-scale application of high-resolution neck US has led to an increase in the number of microcarcinomas detected more or less incidentally [16]. Since microcarcinomas usually have a good prognosis, their real clinical significance is debated, especially when considering that autopsy studies have found microcarcinomas in up to 35% of subjects who have died for reasons other than TC [17–19]. Nevertheless, when there is extrathyroidal and/or lymph nodal extension, the prognosis of microcarcinomas is the same as for cancers greater than 1 cm in size [20].

About 50% of PTCs exhibit lymphocyte infiltrates resembling those of chronic lymphocytic thyroiditis; such infiltrates can surround the tumor foci or spread in the adjacent normal thyroid tissue [21]. A higher prevalence of thyroid autoantibody positivity has been reported in TC patients than in the general population [22].

Upon accurate histologic analysis, about 50–60% of PTCs are multifocal, affecting both thyroid lobes in more than 30% of the cases. In contrast, FTC is usually unifocal and well encapsulated; invasion of the capsule and vascular invasion distinguish follicular carcinoma from benign follicular adenoma. For this reason, the diagnosis of FTC cannot be made on the basis of cytological findings, as it requires adequate tissue sampling of the capsule for definitive diagnosis; even intraoperative frozen-section histology can be incorrect in this respect. Depending on the degree of invasiveness, FTC is classified as minimally or widely invasive [15], the latter having a worse prognosis. While aggressive PTCs mainly spread through the lymphatics to produce locoregional lymph node metastases, FTCs generally invade the blood vessels and metastasize to the lung or bones and, less frequently, to the brain and liver.

The "oncocytic or oxyphilic" cell type (or Hürthle cell type), belonging to the FTC group, is composed of cells derived from the follicular epithelium, typically large with an abundant granular, eosinophilic cytoplasm, large nuclei, and a prominent nucleolus. The granular appearance of the cytoplasm is conferred by the abundant mitochondria [23]. Macroscopically, the oncocytic variant generally presents as a solitary thyroid nodule with complete or partial encapsulation. It should be noted that Hürthle cells can be found also in a number of benign conditions, including nodular goiter, hyperthyroidism, and Hashimoto's thyroiditis. A nodule can be defined as oncocytic tumor only if >75% of cells exhibit oncocytic features [15]. The same criteria of malignancy as for follicular tumors (i.e., vascular and capsular invasion) also apply to oncocytic cell tumors. Hürthle cell carcinomas with papillary structures but without the specific nuclear features of PTC have been reported in a significant proportion of patients [24]. Furthermore, oncocytic carcinomas are associated with extrathyroid extension and with both distant and lymph node metastases more frequently than are typical FTCs. In several series, the prognosis of Hürthle cell carcinoma is reported to be less favorable than that of the classical FTC [24].

Epidemiology

Despite relevant differences in the rates of incidence among different countries, the incidence of DTC, and particularly PTC, has the highest rate of increase worldwide [16]. However, there are epidemiological evidences that this increasing pattern has reached a plateau, and a trend to a decline is now observed [25]. DTC is more common in women than in men; the annual incidence rates range from 8 to 12 per 100,000 women and between 3 and 6 per 100,000 men. This gender difference declines after menopausal age, but still the majority of cases arise in women.

Although the incidence has increased by about 10% every 5 years in both sexes, mortality has declined by 8% every 5 years for men and by 17% for women. Similar patterns have been observed in a number of developed countries and are well documented in the USA [16]. This discrepancy between the increasing incidence and the declining mortality strongly supports the hypothesis that the rising incidence is most likely due to the increased ability to detect microcarcinomas, which generally have an excellent prognosis [26]. Since the rise in incidence started with the introduction and wide diffusion of neck ultrasound, which is able to detect thyroid nodules even smaller than 0.5 cm, it is conceivable that this diagnostic technique greatly contributed to detection of small DTCs that in the past were found only at autopsy. However, there are also some reports claiming that advanced cases are similarly increasing [27].

DTC is very rare in children and the peak age of incidence is 40–50 years, both in men and in women. The unique big series of childhood DTC was the one reported after the Chernobyl nuclear accident. A few years after the nuclear reactor explosion, an >80-fold of increase in DTC was

observed in children who were living in the regions exposed to the radioactive fallout [28] and in particular in those who were <5 years of age at the time of the accident [29]. When diagnosed in children and adolescents, DTC is usually more aggressive than in adults, but it is still curable if appropriately treated. On the other hand, an older age at diagnosis, especially >60 years, constitutes one of the worst prognostic factors [30].

More than 95% of the patients with DTC survive 30–40 years after diagnosis. Unfavorable prognostic factors for survival include follicular histotype, male gender, advanced age, larger size of the primary tumor, and the presence of local and distant metastases (especially multiorgan distant metastases at the time of diagnosis) [30].

Risk Factors

The most well-established risk factor for DTC, and in particular PTC, is exposure to ionizing radiation. This association has long been known, after observing a significant increase of DTC incidence in subjects who in their childhood/adolescence had been submitted to external beam radiation therapy (EBRT, mostly roentgen therapy) targeted to the neck and/or head or to the upper chest to treat benign diseases such as tonsillitis, tinea capitis, acne, thymic enlargement, and others [31–36]. Several studies have strongly supported the causative role of ionizing radiation exposure in the development of PTC [31, 37–41]. Although a latent period of 5–9 years from exposure is necessary for the tumor to develop (the highest risk being reported between 15 and 29 years), the risk continues to be elevated for 40 or more years after the exposure. Although the risk decreases significantly with increasing age at exposure, still some excess risk exists after age 20. Further confirmation of the relationship between radiation exposure and PTC emerged after the Chernobyl nuclear reactor accident of April 1986, with a huge increase in the incidence of childhood TC in the contaminated areas [42]. The Chernobyl accident also showed that the adult thyroid is less radiosensitive than that of a child. Cardis et al. investigated the role of contamination from radioactive iodine in children with a case-controlled study. An approximately sevenfold excess risk for thyroid cancer was estimated for a dose of 1 Gy, and a linear dose–risk relationship was observed at least up to 2 Gy [43]. Moreover, in vitro studies clearly demonstrated a cause–effect relationship between radiation exposure and in vitro induction of RET/PTC rearrangements [44], which were present at a very high prevalence in post-Chernobyl childhood thyroid cancer [45].

Genetic susceptibility should also be considered among the possible risk factors for DTC. Although the familial cases represent no more than 5–10% of all DTCs, the risk for PTC appears to be from three- to sixfold greater when a TC is diagnosed in a parent or in a sibling, respectively [46]. Furthermore, population studies demonstrated that the risk for DTC is approximately fivefold higher in first-degree relatives of TC patients compared with the general population.

The presence of a benign thyroid disease can influence the development of DTC, goiter, and benign nodules constituting the strongest risk factors with relative risks of approximately 3 and 30, respectively. The role of hypothyroidism and hyperthyroidism is less clear [47]. Considering that DTC occurs approximately three to four times more frequently in women than in men, hormonal factors are hypothesized to play a role in its etiology. A pooled analysis of case–control studies showed that the association between DTC and menstrual or reproductive factors was relatively weak, although stronger among women diagnosed with DTC at a young age [48]. Other studies have demonstrated that therapy-induced menopause is positively associated with DTC, as is the continuous use of oral contraceptives; in this latter regard, the association declines with increasing time since stopping oral contraception [49]. On the other hand, other studies have shown that hormonal and reproductive factors are only weakly associated with DTC [50, 51]. In this regard, the greatest difference in DTC incidence between genders is observed during the reproductive life period, while both in children and in elderly patients, this difference disappears; this observation supports the hypothesis that estrogens possibly favor the

development of DTC, but no clear scientific evidences have been reported so far.

The reduced levels of thyroid hormones due to iodine deficiency cause a rise in TSH secretion. Although the role of TSH in favoring the development of DTC has been known for many years, it is still a matter of ongoing discussion [52]. While endemic iodine deficiency is well established as a risk factor for goiter and FTC [53], other studies suggest that iodine supplementation programs could increase the incidence of PTC, by inducing iodine excess [54]. However, iodine deficiency was associated with a threefold increase of PTC in children exposed to the Chernobyl radioactive fallout, thus representing the most important risk factor in developing radiation-induced childhood thyroid cancer in Belarus [43]. On the other hand, increased surveillance and growing application of improved diagnostic procedures (especially neck US) are most likely responsible for the changing proportion of PTC versus FTC in the iodine-sufficient areas. Concerning other dietary risk factors, no definite relationships between food or drugs and DTC have been reported. A significantly reduced incidence of DTC has been shown with increased consumption of fish/seafood in areas of endemic iodine deficiency, but not in areas where iodine intake is high [54–56]. Seafood is an important natural source of iodine in the diet of different populations; therefore an association between fish intake and TC risk may be mediated by iodine. A panel of experts of the World Cancer Research Fund identified both iodine deficiency and iodine excess as probable and possible risk factors for TC, respectively, whereas vegetables and fruits might have a protective role [57]. On the other hand, even greater body weight and/or height has been found to be significantly associated with increased incidence of TC in both women and men [58]. A possible explanation for this relationship is that body size affects iodine requirement, therefore indirectly associated with TC risk. Alternatively, the association with body oversize might indicate a potential influence of some growth factor or hormone during childhood or adolescence, although the potential role of growth factors on thyroid carcinogenesis is still poorly defined.

Additional environmental factors, such as those associated with volcanic areas, cannot be excluded as risk factors. It is known that the incidence of TC is increased in volcanic islands such as Hawaii and Iceland [59]. A recent study performed in Sicily clearly demonstrated that residents of the Catania province, which includes the Etna volcano, have a higher incidence of PTC than elsewhere in Sicily. It is also interesting to note that the drinking water of the Catania province has much higher levels of vanadium, manganese, boron, and iron than water used in the rest of Sicily. The role of these elements in the pathogenesis of TC remains to be established [60].

Pathogenesis

Several genetic abnormalities, either determining activation of oncogenes or inactivation of tumor suppressor genes, have been described in different types of DTC (Table 1). In particular, H-, N-, and K-RAS gene-activating point mutations have been reported both in follicular adenomas and in FTC, while RET/PTC and TRK rearrangements, BRAF point mutations, and MET overexpression have been detected in PTC. It is of interest that RAS, RET, TRK, MET, and BRAF genes are all involved in the activation of the intracellular MAP kinase cascade whose activation leads to cell proliferation. Abnormal activation of this cascade is one of the best-recognized mechanisms of thyroid tumorigenesis. It is known that RAS gene activation induces cell division and inhibits cell differentiation. RAS oncogenes are activated by point mutations mainly found in three hot spots located in codons 12, 13, and 61. RAS oncogene point

Table 1 Most common genetic alterations in DTC

Gene alteration	FTC (%)	PTC (%)
BRAF^{V600E} point mutation	0	45
H, K, N *Ras* point mutations	40–50	10–20
RET/PTC rearrangements	0	20
PAX8-PPA Rγ rearrangements	35	0
PI3K/Akt mutations	6–13	0

FTC follicular thyroid carcinoma, *PTC* papillary thyroid carcinoma

mutations have been found in nearly 40% of benign and malignant follicular thyroid tumors, while they are much less frequent, although not completely absent, in PTC [61–63]. Interestingly, RAS mutations are more frequent in thyroid tumors of subjects living in countries where iodine intake is inadequate [64].

The RET proto-oncogene, which is located in chromosome 10q11.2, encodes a tyrosine kinase transmembrane receptor involved in the activation of the MAP kinase cascade. This proto-oncogene is normally expressed in a variety of neural cell lineages including thyroid C cells and adrenal medulla, but it is not expressed, or at very low levels, in normal thyroid follicular cells [65]. RET oncogene activation may be determined either by a rearrangement generating the fusion, at the chromosomal level, of the tyrosine kinase domain of RET gene and the 5 domain of different genes [66] or by activating point mutations [67]. RET/PTC rearrangements have been reported almost exclusively in PTC [68] and in few cases of benign follicular adenomas [69]. Recently, few cases of other human tumors have been found to harbor some peculiar RET/PTC rearrangements [70]. RET/PTC rearrangements are related to ionizing radiation exposure, a well-recognized risk factor for PTC. The increased prevalence of RET/PTC rearrangements in childhood post-Chernobyl TC [45] and the possibility of determining RET/PTC rearrangements in vitro in thyroid cells experimentally exposed to ionizing radiation [44] suggest a causative connection between radiation exposure and these chromosomal alterations. Despite this evidence, RET/PTC rearrangements have also been reported in sporadic PTC [69]. The prevalence of RET/PTC rearrangements in thyroid tumors of patients who had no history of neck irradiation ranges from 2.5% to 35% among different series [66, 70–74], while it is much higher (up to 75%) in post-Chernobyl childhood TC [70]. The fact that RET/PTC rearrangements can be found also in micro-PTCs suggests that this is an early event in thyroid carcinogenesis [73, 75]. On the other hand, there is evidence that RET/PTC-positive tumors do not progress to ATC [75], thus suggesting that the presence of RET/PTC rearrangement is a good prognostic factor.

An activating mutation of the B isoform of the Raf kinase gene, which is located in exon 15 and results in a valine to glutamic acid substitution at amino acid 600 (BRAF V600E mutation), is the most common mutation in PTC, with a prevalence ranging from 29% to 83% in different published series [76, 77]. The BRAF V600E mutation, which constitutively activates and promotes tumorigenesis through the MAP kinase pathway, is highly specific for PTC, and it is also present in those ATCs with a PTC component [78]. This mutation has never been described in other malignant thyroid histotypes or in benign tumors [78]. The relationship between the BRAF V600E mutation and the clinical and pathologic features of PTC is still controversial. Some authors demonstrated that BRAF V600E mutations are more frequent in PTCs with an advanced tumor stage at diagnosis [79, 80]. However, in other studies this association has not been or has only partially been confirmed [77]. The BRAF V600E mutation signals a worse prognosis with decreased survival for patients with PTC [81]. Recently, a new oncogene, TERT, has been demonstrated to play a role in thyroid carcinogenesis and in particular in the aggressiveness of TC. The presence of TERT mutation, especially if associated with BRAF V600E mutation, represents a well-established prognostic factor of poor outcome, both in terms of recurrences and survival [82, 83].

A very comprehensive study analyzing more than 400 PTC cases by next-generation sequencing techniques showed that, on the basis of genetic profile and of clinical behavior, PTCs can be distinguished into two different subtypes: the BRAF-like and the RAS-like PTC [84]. On the basis of this evidence, the question of whether PTC should be classified according to the molecular profile more than to the histotype has been raised.

Clinical Presentation

Thyroid tumors usually present as a thyroid nodule, either isolated or within a multinodular goiter. Although thyroid nodules are common, especially in subjects older than 50 years, TC represents only 4–5% of all thyroid nodules. Diagnostic workup

of thyroid nodules to distinguish benign and malignant lesions is therefore necessary. Complete medical history and physical examination of the neck are important steps in this process. A history of familial thyroid cancer and/or of exposure to radiation during childhood increases the risk of malignancy, while accurate palpation yields information on location and size of the nodules, their consistency and motility during swallowing, and on any extra-nodular thyroid tissue. Neck examination can also clarify the presence and extent of lymph node involvement, which is frequently found in PTC [85].

Although not specific for malignancy, the following signs indicate the need for diagnostic workup: nodules that are firm in consistency and irregular or fixed to local tissues, palpable neck lymph nodes, rapid increase in size of the nodules over weeks or months, and dysphagia or hoarseness.

Diagnosis

Although the serum levels of TSH, FT3, and FT4 are routinely measured to assess thyroid function, these parameters are not helpful to distinguish benign from malignant nodules. Also the serum level of thyroglobulin (Tg), which is usually elevated in case of nodular goiter, is not informative as to the nature of the nodule. Only elevated levels of serum Ct can preoperatively suggest the possibility that we are facing with an MTC, and further analysis to confirm this suspicious are required.

Ultrasonography

Thyroid ultrasonography (US) is the most accurate imaging technique for the detection of thyroid nodules, and it is mandatory when a nodule is discovered on palpation. In fact, US is the most accurate means for determining the volume of the gland; for defining the size, number, and structure (cystic, solid, or mixed) of thyroid nodules; for distinguishing thyroidal from extrathyroidal masses; for evaluating lymph node metastasis; and for guiding fine-needle aspiration cytology (FNAC). Furthermore, some US features are more frequent in malignant thyroid nodules [86]. In particular hypoechogenicity, the absence of a peripheral halo, irregular borders, microcalcifications, and hyper-vascularization are strongly suggestive of malignancy, especially when combined [86, 87]. No differences have been observed in the neck US features for PTC, FTC or MTC. Neck US is so relevant in the evaluation of thyroid nodules that in the last international guidelines for the management of thyroid nodules and cancer, it plays a leading role in the choice of the nodules to be submitted to FNAC [88].

Elastosonography is a recently developed dynamic US technique that estimates tissue stiffness by measuring the degree of distortion of the nodule under evaluation when applying an external mechanical force. In fact, under mechanical compression, the softer tissues deform easier than the harder tissues, to define an objective parameter of tissue consistency [89]. Elastosonography has been employed to assess the hardness/elasticity of thyroid nodules as a modality to distinguish malignant from benign lesions [90–92]. More recently, it has been reported that the highest elasticity scores, that indicate greater nodular consistency, are strongly correlated with malignancy, yet with minimal loss of sensitivity, especially in cytologically indeterminate thyroid nodules [93, 94]. On the other hand, conventional US evaluation maintains a pivotal role in identifying those thyroid nodules that are most suitable candidates for elastosonographic characterization. Nodules with a calcified shell and cystic nodules can be excluded from elastosonography evaluation.

Fine-Needle Aspiration Cytology

Fine-needle aspiration cytology is currently the method of choice for presurgical diagnosis of TC, as it can reliably screen the nature of a thyroid nodule, therefore identify those cases requiring thyroid surgery, either because of a diagnosis of PTC or because of findings requiring histologic elucidation (as is the case, e.g., cytology with a microfollicular pattern) [95]. FNAC is best performed using US guidance that improves its

diagnostic accuracy by decreasing the number of inadequate specimens and false-negative results; in fact, the acellular or nondiagnostic aspirate is reduced from 14% to 8% in US-guided FNAC [96], especially if the needle is passed more than once in the nodule under evaluation. This method is a rapid, accurate, and inexpensive means of evaluating thyroid nodules, with sensitivity ranging from 65% to 95%, specificity up to 96%, accuracy 98% [97], and negative predictive value up to 99% [98, 99]. Performing two separate aspirates on separate occasions decreases the false-negative rate to 1.2% [100].

Solid thyroid nodules over 1 cm in size, either solitary or in the context of a multinodular goiter, should be evaluated by FNAC, especially if appearing as "cold" at thyroid scintigraphy and with certain US features (see above). Nodules smaller than 1 cm should be followed with periodic thyroid US but not submitted to FNAC, according to the most recent American Thyroid Association guidelines for the management of thyroid nodules [88]. Cytology of the material obtained by FNA can be classified into five diagnostic categories (see examples in Fig. 4), each one carrying a specific risk of malignancy, therefore different indications for patients' management [101]. These five categories are denominated "Thy 1" to "Thy 5" [102], as follows:

- Thy 1: nondiagnostic aspirate due to inadequate sample or due to the presence of technical artifacts. Aspirates that contain only cyst fluid, histiocytes, and erythrocytes are considered inadequate. A minimum of six clusters of at least ten follicular cells assures the adequacy of cytological sampling [103, 104].
- Thy 2: benign, nonneoplastic lesion consistent with nodular goiter or thyroiditis.
- Thy 3: cytology is not diagnostic (it represents 10–15% of all FNACs) [105, 106]. This category includes all follicular lesions, for which the differential diagnosis between benign follicular lesion and FTC or follicular variant of PTC should be considered. A further subclassification of this category into Thy 3A and Thy 3B has been recognized to identify groups with a lower (10–15%) and higher (40%) risk of malignancy, respectively [107].
- Thy 4: lesion suspicious for malignant carcinoma.
- Thy 5: diagnosis of malignancy.

Immunohistochemical analysis (e.g., HBME-1, galectin-3, and CXCR4) and molecular analysis for genetic biomarkers involved in DTC (such as RET/PTC, PAX-8-PPARγ, and BRAF mutations) could be useful for evaluating indeterminate category cytologies (mostly Thy 3) and also for prognostic purposes in case of malignancy [108]. Very advanced methods of analysis to rule in or rule out the malignancy of these Thy 3 indeterminate nodules [109, 110] have been developed significantly improving the presurgical diagnosis of these nodules. The major concern is the cost of these methods and the fact that they are available only in specific centers and cannot be routinely used.

Thyroid Scintigraphy and Other Diagnostic Imaging Procedures

While thyroid scintigraphy with either radioiodide or ^{99m}Tc-pertechnetate can distinguish nodules as "hot" (i.e., functioning and usually benign) or "cold" (i.e., nonfunctioning), it cannot however distinguish the benign or malignant nature of cold nodules. In fact, the expression of the Na^+/I^- symporter (NIS) gene in DTC is markedly reduced (10- to 1,200-fold) with respect to normal thyroid follicular cells [111], thus resulting in a "cold" appearance on conventional thyroid scintigraphy with either radioiodide or ^{99m}Tc-pertechnetate. However, equally "cold" appears on thyroid scintigraphy as any benign nonfunctioning adenomas, where the expression of the NIS gene is decreased by 2- to 700-fold. Therefore, because of its low specificity, the thyroid scan is employed as an adjunctive rather than as a first-line diagnostic test. In particular, a thyroid scan is helpful when a hyperfunctioning nodule is considered in the differential diagnosis

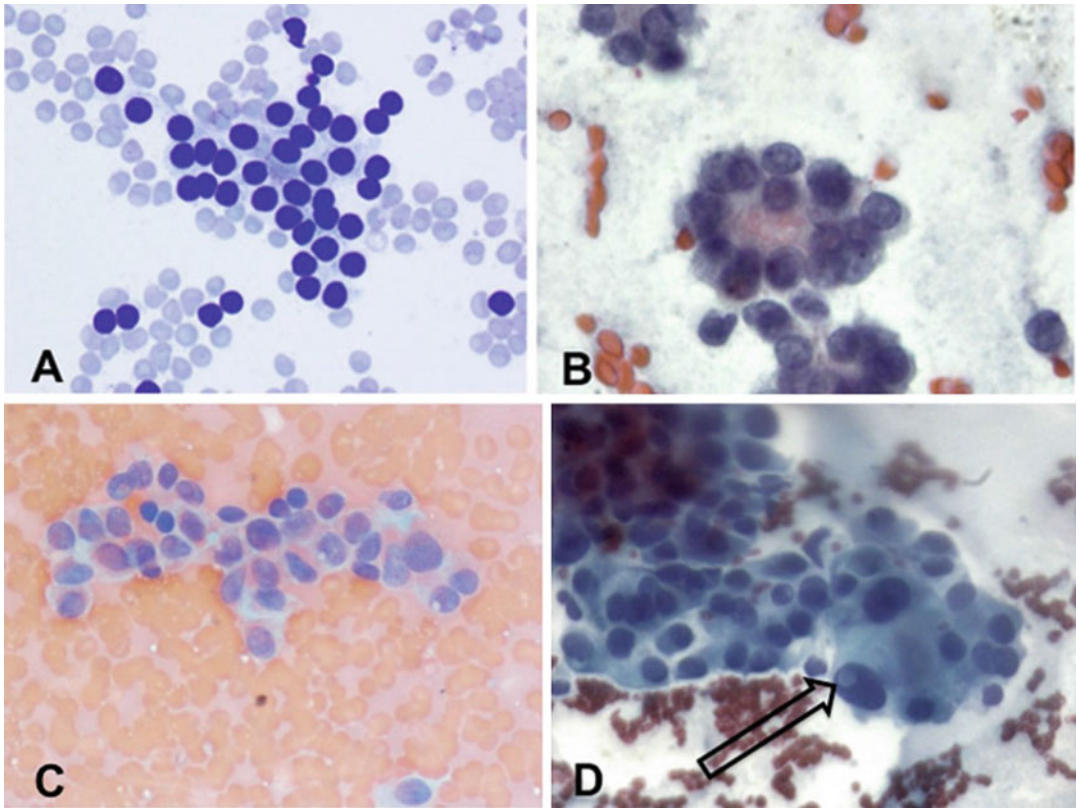

Fig. 4 Examples of different patterns observed in fine-needle aspiration cytology from thyroid nodules. (**a**) Thy 2 (benign lesion): thyroid cells isolated or in clusters, all with regular shape and monomorphous nuclei (erythrocytes in the background serve as a reference for size of thyroid cells and nuclei). (**b**) Thy 3 (indeterminate lesion): clusters of cells in follicle-like structures, with enlarged nuclei and occasional nuclear atypias. (**c**) Thy 4 (suspicious for papillary cancer): cluster of thyroid cells, some of which with enlarged, obviously atypical nuclei. (**d**) Thy 5 (papillary cancer): cluster of thyroid cells with markedly enlarged and polimorphous nuclei; at least one pseudonucleole, typical feature for PTC, is clearly visible (indicated by *black open arrow*) (Courtesy of Prof. Fulvio Basolo, Division of Pathology, Department of Surgery, University of Pisa, Pisa, Italy)

because of a suppressed TSH level [101]. Furthermore, thyroid scintigraphy may be considered as a possible additional diagnostic aid in those cases with indeterminate FNAC (class Thy 3) associated with serum TSH levels seemingly within normal limits or borderline with suppressed levels.

Despite their high sensitivity, all the scintigraphic approaches with tumor-seeking radiopharmaceuticals (such as ^{99m}Tc-sestamibi, see Fig. 5) that have been proposed for diagnosing DTC in patients with nodular goiter have failed because of their very low specificity. In fact, these agents accumulate both in TC and in benign adenomas; considering that DTC only constitutes no more than 5% of all thyroid nodules (very low pre-test probability), this feature translates into an alarmingly low specificity that only triggers further diagnostic testing without appreciably restricting the population of patients with suspected lesions.

The above consideration is also true for the nonspecific tumor-imaging agent [^{18}F]FDG, that has, however, a high negative predictive value for thyroid cancer. Giovanella et al. evaluated [^{18}F]FDG in 88 euthyroid patients with a solitary thyroid nodule and nondiagnostic FNAC (Thy 3 category); in their series, none of the 44 patients with a negative [^{18}F]FDG scan had malignancy, while all 21 patients with DTC had a positive [^{18}F]FDG scan

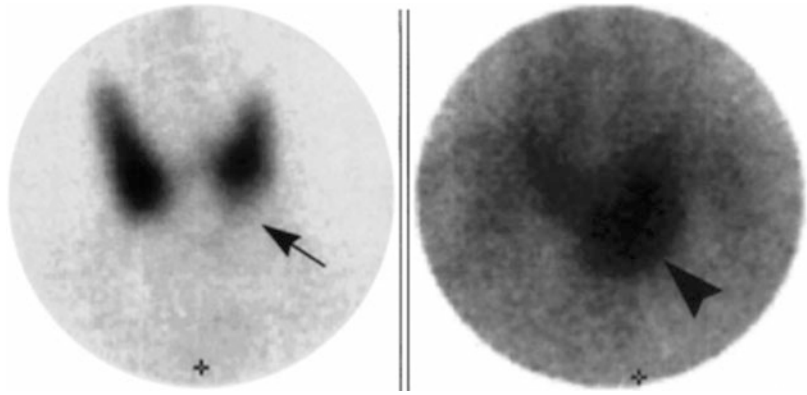

Fig. 5 Thyroid scintigraphy with ^{99m}Tc-pertechnetate (*left*) and with ^{99m}Tc-sestamibi (*right*) in a patient with a solitary nodule at the base of the left lobe, measuring 34 mm on US examination. The nodule appears as "cold" on the ^{99m}Tc-pertechnetate scan (*arrow*), while its uptake of ^{99m}Tc-sestamibi is greater than in the surrounding parenchyma (*arrowhead*). FNAC and definitive histology after thyroidectomy revealed a papillary carcinoma (Reproduced with permission from Földes I, Lévay A, Stotz G. Comparative scanning of thyroid nodules with technetium-99m pertechnetate and technetium-99m methoxy-isobutylisonitrile. Eur J Nucl Med. 1993;20:330–3)

18 out of the 67 patients with a benign thyroid nodule also had a positive scan. These findings result in 100% sensitivity and 100% negative predictive value for [^{18}F]FDG PET/CT, although with lower specificity (69%), overall accuracy (79%), and positive predictive value (62%) [112]. Another prospective study investigated the diagnostic performance of [^{18}F]FDG PET/CT, ^{99m}Tc-sestamibi scintigraphy, and multiparametric neck US in a similar group of 87 patients with Thy 3 FNAC. [^{18}F]FDG PET/CT had significantly greater sensitivity (94%), diagnostic accuracy (66%), and negative predictive value (98%) than either ^{99m}Tc-sestamibi scintigraphy or neck US. The association of PET/CT with US significantly increased specificity, but decreased sensitivity [113].

On the other hand, increased uptake of [^{18}F]FDG in the thyroid gland is detected in a certain fraction (up to 4%) of patients undergoing an [^{18}F]FDG PET/CT scan for thyroid-unrelated reasons, an occurrence defined as "incidentaloma" that can predict thyroid malignancy especially when tracer uptake is focal rather than diffuse (see Figs. 6 and 7) [114, 115]. A meta-analysis of 31 articles reporting the results of 197,296 PET studies and 3,659 focal thyroid incidentalomas concluded that the pooled proportion of malignancy in patients with incidentalomas is 19.8% (95% CI, 15.3%–24.7%) [116]. Based on these results, further diagnostic investigation (e.g., with image-guided FNAC) is recommended in all patients with thyroid incidentaloma detected in the [^{18}F]FDG PET/CT scan performed for any reason, because of the relatively high proportion of thyroid malignancy in these patients – as also confirmed by more recent large cohort studies [117, 118].

X-ray of the neck is only useful to disclose a deviation or lumen restriction of the trachea, as it can be observed in patients with large nodules and multinodular goiter. Computed tomography (CT) or magnetic resonance imaging (MRI) may be useful in identifying the extent and location of advanced thyroid tumors. These imaging studies are generally reserved for characterizing mediastinal thyroid masses and for identifying regional or distant metastases [119].

Staging

The most widely used staging system for TC is the tumor–node–metastasis (TNM) classification system defined jointly by the Union Internationale Contre le Cancer (UICC) and by the American Joint Committee on Cancer (AJCC). It is based on the histopathologic description of the tumor size, local lymph node metastases) and of distant

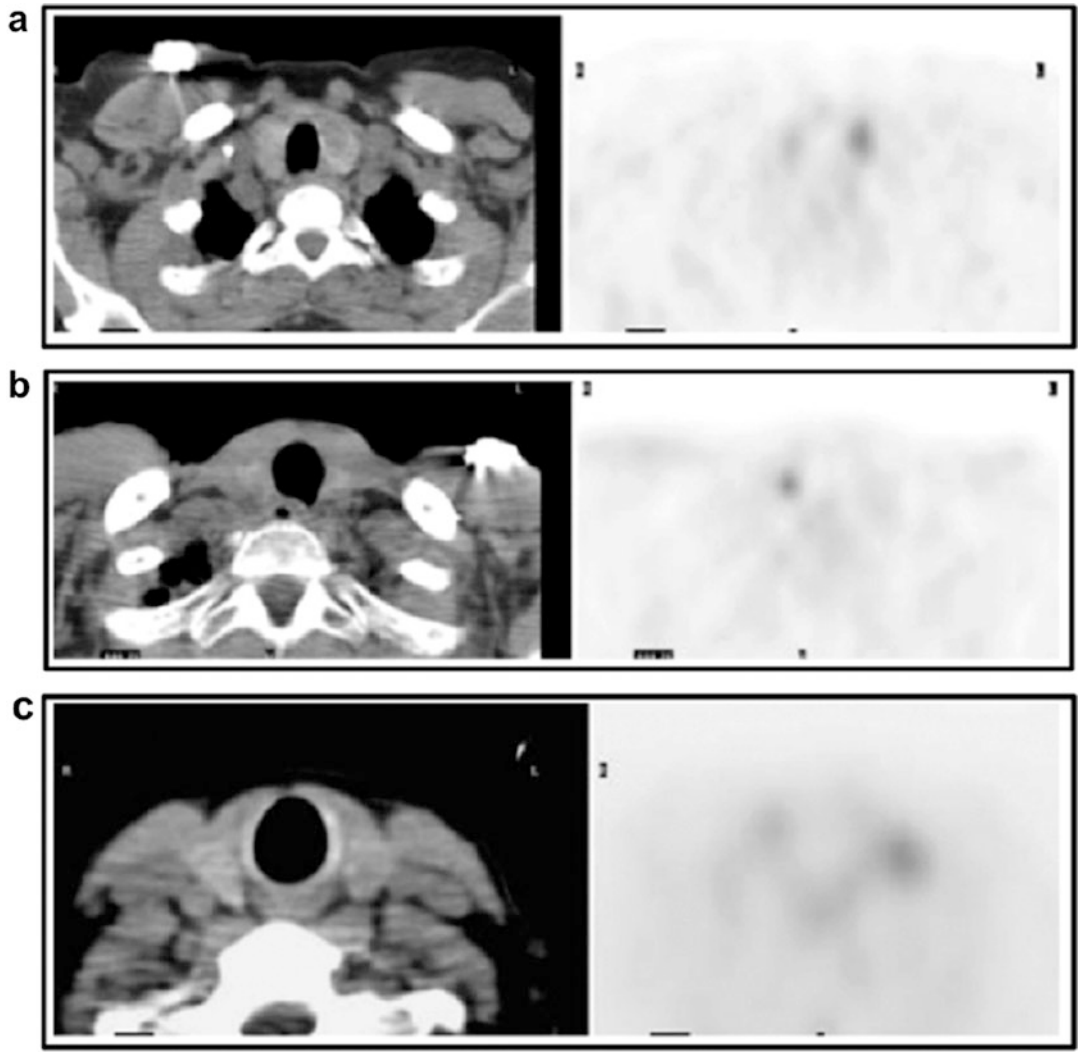

Fig. 6 Examples of thyroid incidentalomas found on whole-body [^{18}F]FDG PET/CT performed for non-thyroid-related indications; although with similar patterns of increased tracer uptake in the thyroid bed, final diagnosis ascertained by FNAC and/or histology can be quite different. For all cases: axial CT image in left panel, corresponding axial [^{18}F]FDG PET image in *right panel*. (**a**) Patient with cervical cancer: mildly increased [^{18}F]FDG uptake in the thyroid with a diffuse pattern, more evident in left lobe. Final diagnosis: chronic thyroiditis. (**b**) Patient with gastric cancer: focal increased [^{18}F]FDG uptake in right thyroid lobe. Final diagnosis: adenomatous goiter. (**c**) Patient with cervical cancer: focal increased [^{18}F]FDG uptake in the left thyroid lobe. Final diagnosis: papillary thyroid cancer (Modified and reproduced with permission from Liu Y. Clinical significance of thyroid uptake on F18-fluorodeoxyglucose positron emission tomography. Ann Nucl Med. 2009;23:17–23)

metastases (M). Age (<45 or >45 years at diagnosis) is also important in this classification. The latest (seventh edition) TNM classification appeared in 2010 and is shown in Table 2. The corresponding prognostic implications in terms of observed 5-year survival for patients with PTC and with FTC are shown in Fig. 8.

If the TNM classification is relevant to indicate the risk of survival, it is not very useful in predicting the risk of recurrence. A new classification based on the risk of recurrence after initial treatment has been proposed, and then widely accepted, by the American Thyroid Association [101]. This risk-based classification distinguishes

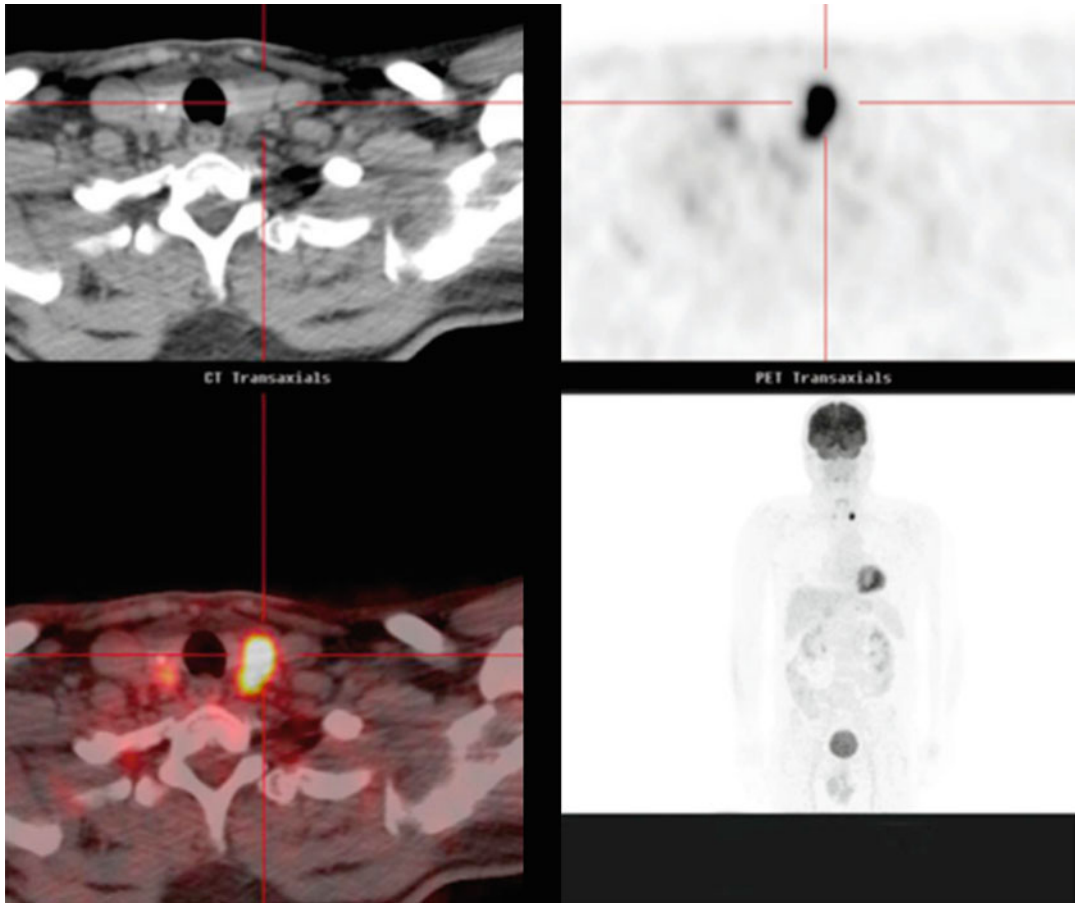

Fig. 7 Incidental detection of PTC in a patient undergoing [^{18}F]FDG PET/CT during follow-up after primary treatment for malignant melanoma. FNAC from the focal lesion in the left thyroid lobe showing markedly increased [^{18}F]FDG uptake (with SUV_{max} >14) showed a Thy 4 pattern. The patient underwent then total thyroidectomy and remnant ablation with ^{131}I-iodide; histology revealed a well-differentiated PTC (>2 cm in maximum diameter). Radioiodide remnant ablation was successful, and subsequent long-term follow-up was characterized by a favorable clinical outcome (From Volterrani D, Erba PA, Mariani G. Fondamenti di Medicina Nucleare - Tecniche e Applicazioni. Milan: Springer, 2010, with permission from Springer Science + Business Media)

three levels of risk (low, intermediate, and high) to develop recurrence during follow-up, and it is very useful from a practical point of view to plan the therapeutic strategy and the follow-up schedule. The possibility to change the level of risk after therapy and during follow-up, the so-called "ongoing" risk re-stratification, has been also demonstrated of clinical usefulness [120].

Most of the information contributing to TNM staging of DTC derives from postsurgical histologic findings regarding either the primary tumor and/or cervical lymph nodes. Radionuclide imaging has little role in the preoperative phase. This consideration includes whole-body PET/CT with [^{18}F]FDG [121], although recent reports highlight the value of contrast-enhanced [^{18}F]FDG PET/CT for preoperatively staging neck lymph nodes in patients with DTC [122].

Prognostic Factors

About 80% of patients with DTC can be cured with initial treatment, and 95–97% of them are still alive after 30 years of follow-up [123]. Despite this good prognosis, some patients are at

Table 2 AJCC/UICC anatomic stage and prognostic group for papillary and follicular (differentiated) carcinoma

Group	T category	N category	M category
Papillary or follicular (differentiated)			
Under 45 years			
Stage I	Any T	Any N	M0
Stage II	Any T	Any N	M1
45 years and older			
Stage I	T1	N0	M0
Stage II	T2	N0	M0
Stage III	T3	N0	M0
	T1	N1a	M0
	T2	N1a	M0
	T3	N1a	M0
Stage IVA	T4a	N0	M0
	T4a	N1a	M0
	T1	N1b	M0
	T2	N1b	M0
	T3	N1b	M0
	T4a	N1b	M0
Stage IVB	T4b	Any N	M0
Stage IVC	Any T	Any N	M1

Used with the permission of the American Joint Committee on Cancer (Chicago)

high risk of developing local recurrence and/or distant metastases, which can end up with death. These patients should be identified at the time of diagnosis to adapt their treatment to their risk, by analyzing the following prognostic factors (especially in combination) [30].

Age

Age at diagnosis is one of the most important independent prognostic factors for both PTC and FTC, as advanced age represents a negative prognostic factor for both recurrence and death. The prognostic significance of age persists when the total death rate is corrected for the overall mortality of a control population of the same sex, age, and year of birth when only cancer-related deaths are considered. The risk of recurrence and death increases linearly with age, particularly after age 40 [30]. Although it is still unclear why they have a worse prognosis, elderly patients tend to have locally invasive tumors at presentation, a higher incidence of distant metastases at diagnosis, and aggressive histological variants; all these factors may signal a worse prognosis.

Thyroid tumors tend to have shorter doubling times in older patients. Furthermore, these tumors are often not well differentiated, so that they are less likely to concentrate radioiodine. On the other hand, children and adolescents, despite frequently displaying locally extensive disease at diagnosis, have an excellent long-term prognosis [124, 125].

Gender

Male gender has been reported to be a risk factor in some series but not in others [126–128]. While it is usually a negative prognostic factor on univariate analysis, it loses its prognostic value on multivariate analysis. The question of whether male sex truly is a negative prognostic factor is therefore still not elucidated.

Histologic Types and Variants

The prognosis of PTC is better than that of FTC. The less favorable prognosis of FTC is more likely related to the patient's older age and to the extent of the tumor at the time of diagnosis than to histology alone. In fact, survival rates for patients with PTC and FTC are similar among patients of comparable age and stage of disease [129–131]. Furthermore, within these two main histological entities, the prognosis may differ among their respective variants [5].

In PTC, the tall cell variant [131], the columnar cell variant [8], the oxyphilic variant [24], and the solid/trabecular variant [132] have a worse prognosis. Prognosis is good when the cancer is well encapsulated [13] and in cases of FVPTC [14], although some tumors are more aggressive [5]. Intermediate prognosis is reported for the diffuse sclerosing variant [7]. While the minimally invasive FTC shows a good prognosis, the widely invasive FTC has a less favorable prognosis; in particular, advanced vascular invasion is a negative prognostic factor

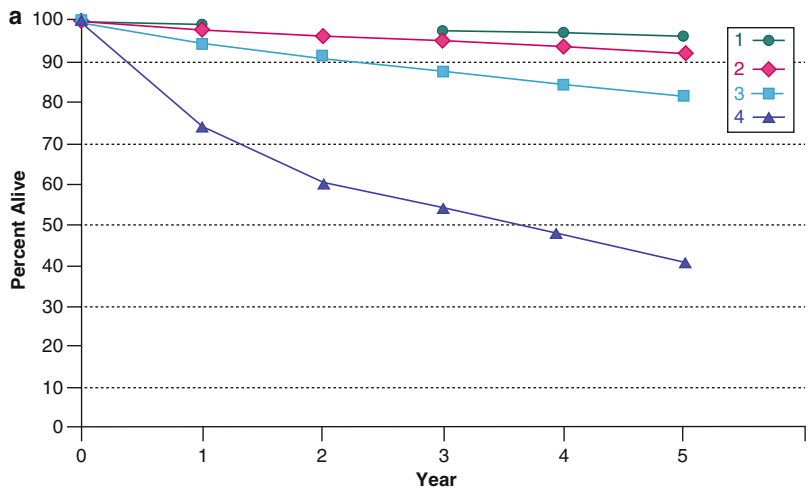

Observed Survival	1	2	3	4	5	95% CIs	Cases
1	99.4	98.8	98.4	97.8	97.1	96.7–97.4	14124
2	98.7	97.3	96.1	94.7	92.8	92.0–93.7	4701
3	95.4	91.3	88.2	85.2	82.0	80.5–83.6	2953
4	74.8	60.6	54.8	47.6	41.4	36.2–46.7	412

Five-year, observed survival by "combined" AJCC stage papillary adenocarcinoma of the thyroid, 1998-1999

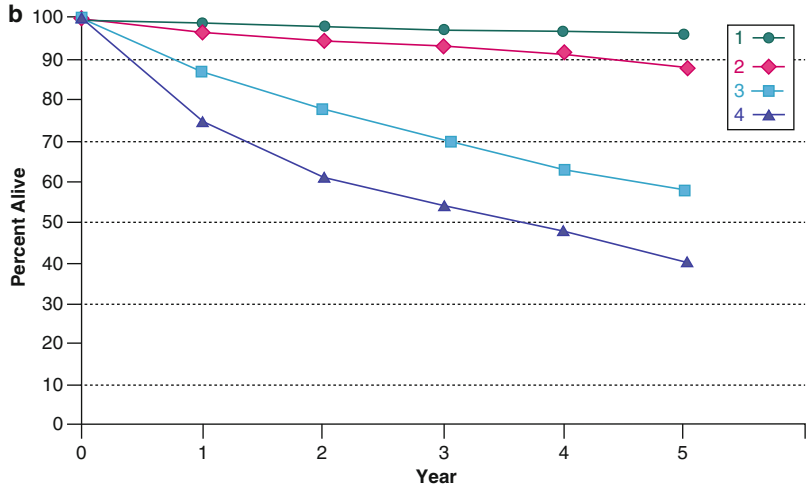

Observed Survival	1	2	3	4	5	95% CIs	Cases
1	99.3	98.6	98.0	97.6	96.7	95.4–97.9	1090
2	97.6	95.3	93.8	91.7	89.1	86.9–91.3	1014
3	87.7	78.3	70.4	63.2	58.2	49.8–66.7	160
4	75.6	61.3	54.9	48.4	40.6	32.7–48.6	191

Five-year, observed survival by "combined" AJCC stage follicular adenocarcinoma of the thyroid, 1998-1999

Fig. 8 Observed 5-year survival rates for patients with either PTC (**a**) or FTC (**b**) according to stage at initial diagnosis (From Edge et al. (eds.), AJCC Cancer Staging Manual, 7th ed., New York, Springer Science+Business Media, 2010, with permission from Springer Science + Business Media)

[133], while the degree of capsular invasion is of limited prognostic relevance [128]. Some FTC variants, such as Hürthle cell carcinoma, poorly differentiated and insular histotypes, have frequently been associated with an unfavorable prognosis [127, 128, 134].

The insular histotype identifies a subtype of PTC, although no consensus has been reached

on this definition. Thus, although it is not listed in the WHO classification as a distinct histological entity by itself [1], it is sometimes considered an independent histological type.

It is of interest that the degree of invasion and the degree of differentiation are not related to each other; therefore, both parameters must be taken into account for overall prognosis. When microscopic foci of undifferentiated cells are found within a DTC, the tumor must be regarded and treated as an ATC, with very poor prognosis; extrathyroidal infiltration and local invasiveness are additional prognostic factors that make the prognosis of thyroid cancer even worse.

Tumor Size

The size of the primary tumor may vary from less than 1 cm in diameter (the most frequent occurrence at present) to a quite large tumor. When they are unifocal and lymph node negative, tumors less than 1 cm (the so-called microcarcinomas) have an excellent prognosis for both overall survival and relapse-free survival [26]. The risk of recurrence and tumor-specific mortality gradually rises as primary tumors increase in size. Nevertheless, this parameter seems to be more predictive for PTCs than for FTCs, in which the prognostic significance of the degree of differentiation and magnitude of invasion prevails over tumor size [30].

Multifocality

Whereas FTC is usually unifocal, PTC is multifocal in about 50% of the cases (from 20% to 80% depending on the number of tissue sections examined) [85]. Multifocal PTCs are more frequently accompanied by lymph node metastases at diagnosis [26] and exhibit more frequently local disease persistence, regional recurrences, and distant metastases. Controversial data have been reported about the relationship between multifocality and mortality [30, 128, 135]. In this regard, it is worthwhile noting that multifocality in one lobe is associated with a higher aggressiveness than when the other lobe is involved as well. This finding can, at least in part, explain why recurrences and cancer-related deaths are less frequent with total thyroidectomy than with less radical surgical procedures.

Extrathyroidal Invasion

Tumor extension beyond the thyroid capsule is an independent predictor of worse prognosis for both PTC and FTC. It is observed in 5–10% of PTCs and in 3–5% of FTCs and is associated with higher rates of local recurrence, distant metastases, and tumor-related death [136, 137]. However, microscopic invasion of the thyroid capsule should be distinguished from macroscopic invasion involving other structures in the neck. The latter occurrence has a bleaker prognosis, especially because of the difficulty of clearing the disease locally from the surgical point of view [138].

Lymph Node Metastases

While lymph node metastases are frequent in PTC (30–60%), they are not so frequent in FTC (15–20%) [139]. They are more common in children, occurring in up to 80% of the cases. Local lymph nodes may be involved even in the event of micro-PTC [26]. While in some series regional lymph node metastases have been found to be associated with higher rates of tumor recurrence and cancer-specific mortality [101, 130, 132, 140], no significant difference in survival was found in other series [141, 142]. Lymph node involvement is associated with a significantly poorer outcome even in patients without extrathyroid invasion.

In the series from the Mayo Clinic, bilateral cervical and mediastinal lymph node metastases were independent prognostic factors predictive of tumor recurrence and cancer-related mortality [128]. Similarly, palpable node metastases represented an independent risk factor for cancer-related death also in the experience at the Institute Gustave-Roussy [129]. We observed a 3.6% cancer-related mortality in patients with lymph node metastases at diagnosis; this value is

extremely high for a disease commonly considered to carry an excellent prognosis [30].

Other than the presence or absence of lymph node metastases, the site, size, number, and extension of metastasis beyond the lymph node capsule probably also impact on prognosis, even though these parameters have not been taken into account in most series.

Distant Metastases

The presence of distant metastases at the time of diagnosis is a negative prognostic factor in patients with either PTC or FTC. Tumor-specific mortality in patients with distant metastases varies from 36% to 47% at 5 years, rising even further to approximately 70% at 15 years [143]. Univariate analysis for distant metastases shows that younger age, well-differentiated histologic type, localization in the lung rather in the bone, the presence of small lesions, and ^{131}I-iodide uptake are associated with better prognosis. Nevertheless, in multivariate analysis extensive metastatic disease has greater prognostic impact than anatomic location (lung or bone). The best outcome is seen in younger patients with micronodular metastases responsive to radioiodine therapy that are not visible on standard x-rays [85].

Molecular Prognostic Factors

Poor outcome is associated with loss of expression of thyroid-specific differentiation genes, such as those for the TSH receptor, the Na^+/I^- symporter, thyroglobulin (Tg), and thyroperoxidase; the expression of these genes is low in poorly differentiated tumors and absent at all in ATCs [144]. Among the oncogenes involved in the pathogenesis of PTC, there are controversial evidences of the negative impact of BRAF V600E on outcome [81, 145], while no prognostic significance has been shown for RET/PTC rearrangements [146]. The copresence of BRAF V600E mutation and the mutation of TERT promoter is now recognized as the most unfavorable prognostic factor for both survival and recurrence in PTC [83]. Somatic mutations of the p53 tumor suppressor gene or overexpression of its encoded protein carry a worse prognosis for ATC, which is a highly lethal tumor [147]. The coexistence of several mutations is an even worse poor prognostic factor [148]. Similarly, overexpression of the p21 protein, which is encoded by the RAS oncogene, has been associated with more aggressive TC [149]. The above findings open new avenues to oncogene products that may constitute novel prognostic factors for thyroid tumors.

Role of Nuclear Medicine in the Management and Follow-Up of DTC After Surgery

While radionuclide imaging has a limited role in the initial diagnostic phase and preoperative staging of DTC, nuclear medicine procedures altogether (both therapy and imaging) take on important roles in the management and follow-up of patients with DTC after surgery, which is the modality of choice for primary treatment of any patient with newly diagnosed DTC. In fact, thyroid remnant ablation with ^{131}I-iodide is indicated in DTC patients with a moderate to high risk of recurrence. The major diagnostic modalities employed to follow patients with DTC treated with remnant ablation are measurement of serum Tg, ^{131}I-WBS, and neck US. In case of cancers with aggressive patterns of tumor growth, PET/CT with [^{18}F]FDG provides information which is important both from the prognostic point of view and for defining the overall burden of disease, as well as for assessing the efficacy of therapies. All these radionuclide-based procedures will be extensively presented in ▶ Chap. 42, "Radionuclide Therapy of Thyroid Tumors" of this book.

Anaplastic Thyroid Cancer

The term "anaplastic thyroid carcinoma" (ATC) includes a small subset of thyroid tumors derived from follicular cells that are however associated with poor prognosis and differ from well-differentiated follicular cell cancers for histopathologic features, biologic behavior, and

treatment. ATC is an uncommon, usually lethal malignancy of older adults that accounts for 2–3% of all TCs [150]. Although in the majority of cases it affects older adults, cases in young adults have been reported with increasing frequency. No major difference is observed in incidence between women and men. Generally, ATC is rapidly fatal with a median overall survival frequently less than 6 months after diagnosis. Long-term survivors are so rare that the diagnosis is questioned in reports that describe the few 5-year survivors [151]. An overall decline in in the incidence of ATC. Several possible explanations have been proposed to justify this decline, such as the fact that several tumors previously diagnosed as ATC have been reclassified as lymphomas or as PDTC. It is also likely that the early diagnosis and treatment of DTC has reduced the incidence of ATC by reducing the risk of dedifferentiation of DTCs into an ATC. Finally, considering that ATC is twice as common in areas with endemic goiter than in areas without, the decline in the incidence of ATC might also be due to a more efficient iodine prophylaxis. Although ATC derives from follicular thyroid cells, the typical cytological and histological features are completely lost and the thyroidal origin of the tumor is recognized only because it grows within the thyroid.

Histopathologic Features and Pathogenesis

The histologic patterns of ATC include giant-cell, spindle-cell, and squamoid-cell tumors (Fig. 9). These subtypes frequently coexist and are not predictive of patients' outcome. Areas of necrosis and hemorrhage are common, and mitotic activity is high. The paucicellular variant (which may be confused with Riedel's struma) and the carcinosarcoma variant (which includes large regions of osteosarcomatous differentiation) are two uncommon variants of ATC [151, 152].

No risk factors are known for the development of ATC, except perhaps a long-standing multinodular goiter [153]. While it is generally accepted that ATC develops from a preexisting DTC that dedifferentiates, it is also possible that it arises de novo; furthermore, it is likely that two types of ATC coexist, as suggested by different molecular features observed between pure ATCs and ATCs including areas of well-differentiated TC. The progression of DTC to ATC is documented by the simultaneous presence of BRAF V600E mutation (that is typical of almost 50% of PTC) or RAS mutation (more frequent in FTC) and the loss of the p53 tumor suppressor gene (which is involved in the control of the cell cycle and apoptosis) [148]. However, p53 mutation is very common (73%) in ATCs, and it is not necessarily associated with BRAF V600E or RAS mutation, thus suggesting that a subgroup of ATCs is likely "pure" and not deriving from DTC through a dedifferentiation process [78]. Another oncogene very frequently mutated in ATC (73%), and to a lower extent (8%) in PDTC is TERT. However, the real genomic hallmark of ATC is that when compared to PDTC and even more to DTC, ATCs show a greater number of multiple mutations, including a higher frequency of mutations in p53, TERT promoter, PI3K/AKT/mTOR pathway effectors, SWI/SNF subunits, and histone methyltransferases [148].

Clinical Presentation and Diagnosis

The clinical presentation of an ATC is usually more impressive than that of a DTC: a big and firm thyroid nodule, recently developed, is the most common presentation often associated with dysphonia or other signs/symptoms of local compression/invasion, such as dysphagia or dyspnea (Fig. 10). The common clinical history reported by patients is the rapidity of growth of a neck lesion either in the thyroid bed or in the lateral part of the neck. The average size of the mass at the time of initial diagnosis is 8 cm (maximum diameter), ranging from 3 to 15 cm [150, 154]. Regional lymph node metastases and vocal cord paralysis are present in 30–40% of the cases [154]. Systemic hematogenous metastases occur in up to 75% of the patients, the lung being the most common site (80%), followed by the bone, skin, and brain [155]. Cardiac and intra-

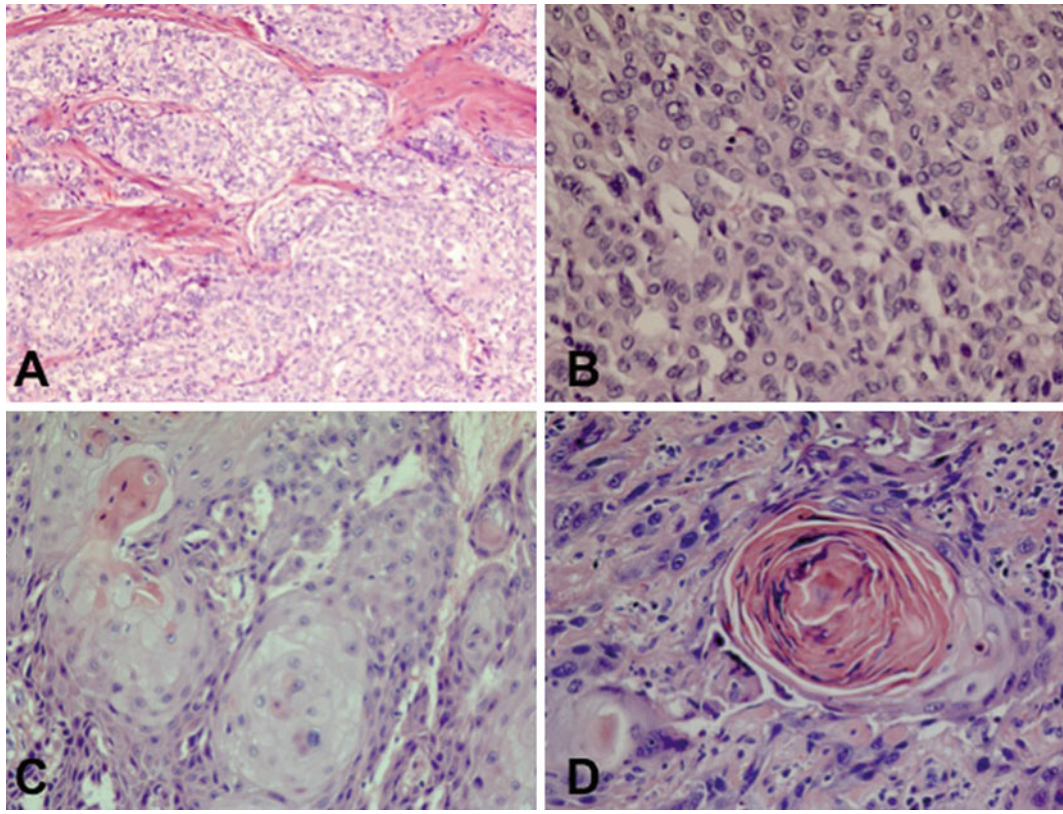

Fig. 9 Histologic patterns of poorly differentiated/anaplastic thyroid cancers. (**a**) Low-magnification field showing obvious fibrous reaction with some necrosis (*upper part of the image*) in abundant undifferentiated neoplastic tissue. (**b**) Higher magnification showing neoplastic cells with highly irregular shape and size, irregular cell nuclei, and frequent mitoses. (**c**, **d**) Squamoid-cell variants (From Chiacchio et al. [150], with permission)

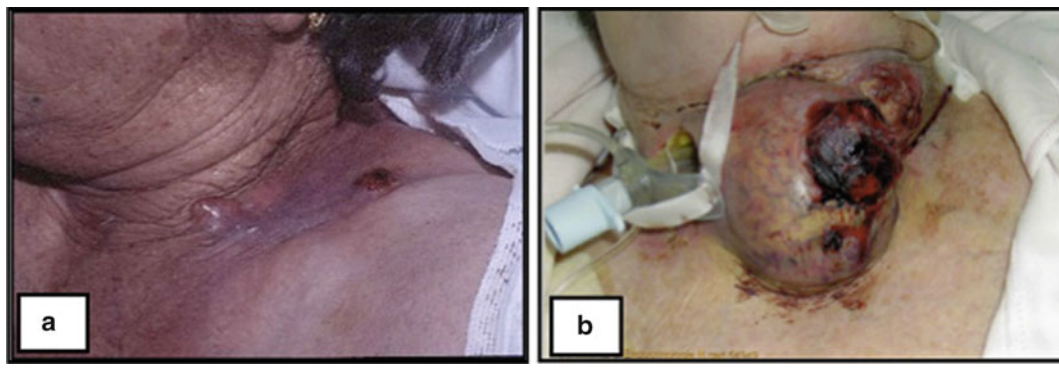

Fig. 10 Patients with very advanced anaplastic thyroid carcinoma. (**a**) Cutaneous metastases in the region of the neck. (**b**) Local infiltration requiring tracheostomy; note the lateral position of tracheostomy due to severe dislocation of the upper airways (From Chiacchio et al. [150], with permission)

abdominal metastases have also been described [155]. Death is usually related to extensive local disease with ultimate airway obstruction rather than to distant metastases. Although ATC can show some typical cytological features [156] (see Fig. 11), histologic confirmation is usually recommended, especially in order to exclude tumors with better prognosis or that require different therapy; such tumors include PDTC, MTC, primary thyroid lymphoma, poorly differentiated metastasis to the thyroid, primary squamous cell carcinoma, and angiomatoid thyroid neoplasms.

Radionuclide Imaging of ATC

ATC cells typically have lost several features of the original thyroid follicular cells, most notably their response to stimulation by TSH and the ability to concentrate iodine. Therefore, the radionuclide techniques employed for staging and monitoring patients with ATC cannot be based on the use of radioiodide. Instead, ATC cells express high levels of glucose transporters and in particular of GLUT1 and GLUT3 [157]. Therefore, PET/CT with [^{18}F]FDG PET constitutes the only radionuclide imaging technique potentially useful in ATC patients, both for initial staging and during follow-up [158–161] (see Fig. 12). On the other hand, morphologic imaging techniques such as US, CT, or MRI also play an important role for defining the local extent of disease in patients with ATC, especially to assess infiltration of the anatomic structures surrounding the thyroid.

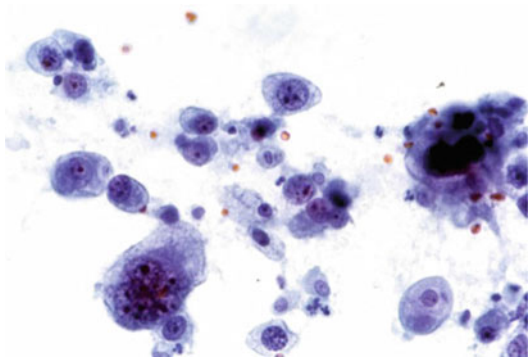

Fig. 11 Cytology from fine-needle aspiration of a thyroid nodule. Obvious abnormal pattern with clearly neoplastic cells varying in shape and size from isolated single-nucleated to giant, multinucleated cells; macronucleoli can also be seen, as well as irregular chromatin. This pattern is typical for anaplastic thyroid cancer (From Chiacchio et al. [150], with permission)

Medullary Thyroid Cancer

MTC is a well-differentiated thyroid tumor maintaining the biochemical and pathological features of the parafollicular, calcitonin-producing C cells from which it derives. Its origin makes it a separate entity from the other DTCs. The parafollicular C cells represent about 1% of all thyroid cells and are located at the basal layer of the follicle. C cells originate from the neural crest and migrate to their final location along with the ultimobranchial body, during embryonic development. There are at least four features that make the C cells a separate entity from follicular cells: (a) the peculiar distribution in the thyroid gland, which is prevalent at the junction of the upper third and the lower two-thirds and along the central vertical axis of each thyroid lobe; (b) the total growth and functional independence from TSH; (c) the inability to concentrate and retain iodide; and (d) the production and secretion of Ct, a biogenic amine which is almost exclusively produced by both normal and malignant C cells.

MTC shows macroscopically as either chalky white or red in color on cross section, with hard and firm consistency. Histologically, MTC is pleomorphic with spindle-shaped or rounded cells characteristically organized in a nested pattern (Fig. 13). Mitoses are not very frequent, nuclei are usually uniform, and the eosinophilic cytoplasm is characterized by the presence of secretory granules. Deposits of amyloid substance are frequently (60–80%) observed between the tumor cells. Sometimes an MTC is difficult to be distinguished from an ATC, or a Hürthle cell or an insular DTC, especially when pseudopapillary elements or giant cells are present. Positive immunohistochemistry for Ct is diagnostic of MTC, although positivity for chromogranin A and

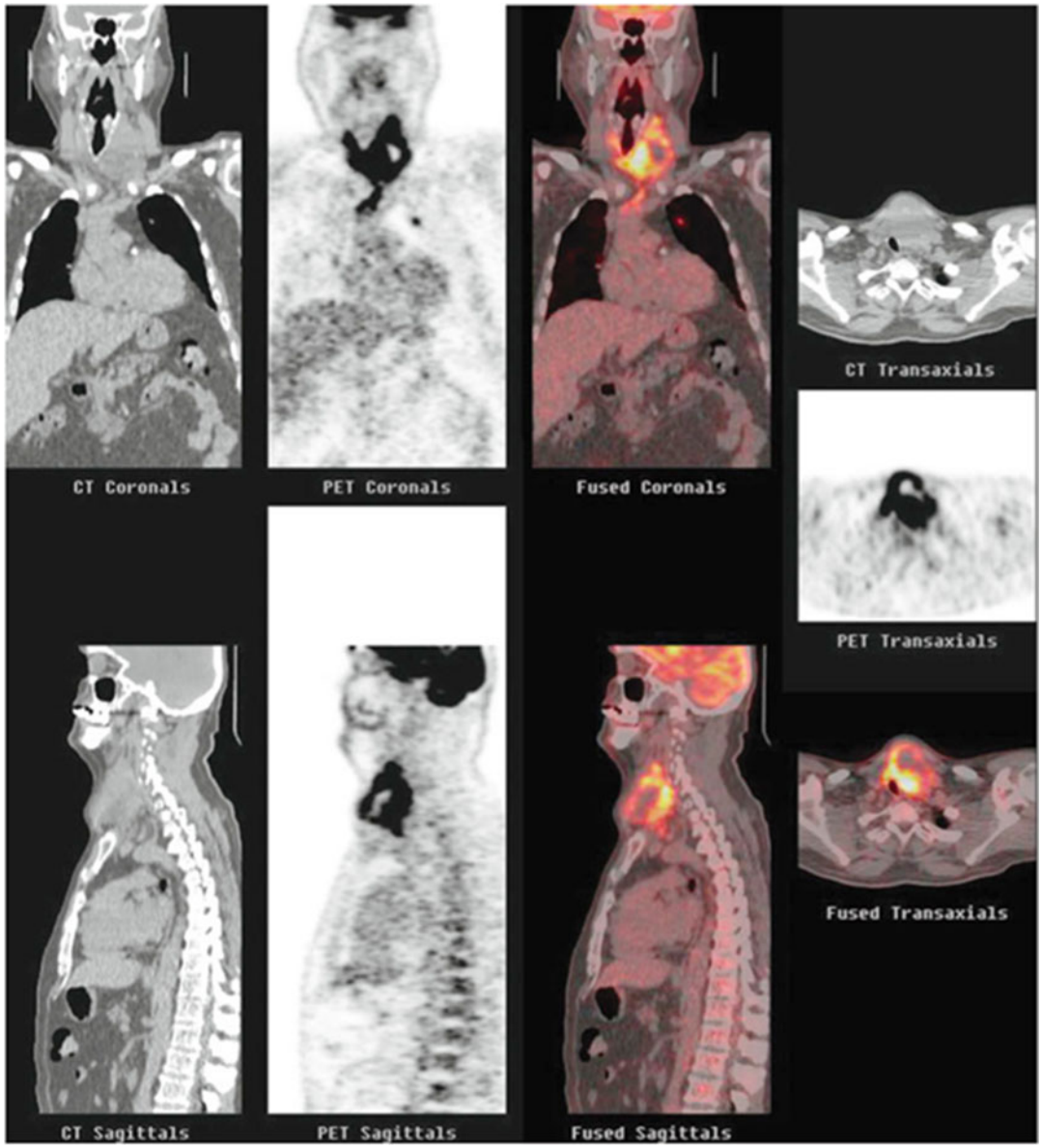

Fig. 12 [^{18}F]FDG PET/CT performed for primary staging in a patient with anaplastic thyroid cancer affecting predominantly the left lobe. Coronal, transaxial, and sagittal sections (CT, PET, and fused PET/CT) define well the local extent of disease, showing a large lesion that dislocates and restricts the trachea. A lung metastasis in the left parahilar region is also detected (Modified from Volterrani D, Erba PA, Mariani G. Fondamenti di Medicina Nucleare — Tecniche e Applicazioni. Milan: Springer, 2010, with permission from Springer Science + Business Media)

carcinoembryonic antigen (CEA) may also be useful [162]. Histopathologic description of MTC must include the number and distribution of tumoral foci as well as the simultaneous presence of C cell hyperplasia. This information is especially important also from the practical point of view, because bilaterality, multicentricity, and C cell hyperplasia are considered the histologic hallmarks of the hereditary forms [163]. No other major differences have been observed in the histologic features between the sporadic and the hereditary forms of MTC.

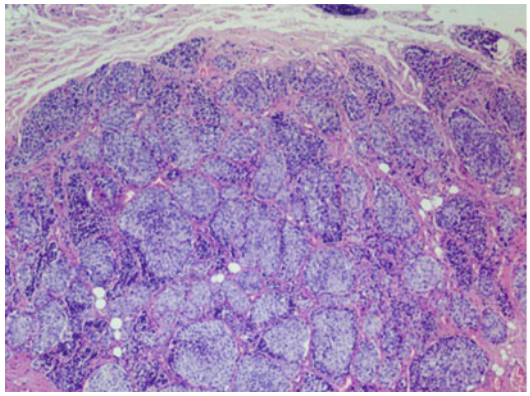

Fig. 13 Histologic pattern of medullary thyroid cancer: nests of neoplastic cells with amyloid stroma in between; immunohistochemical analysis using anti-calcitonin and/or anti-chromogranin antibodies is required to confirm the diagnosis (Courtesy of Prof. Fulvio Basolo, Division of Pathology, Department of Surgery, University of Pisa, Pisa, Italy)

The overall frequency of MTC is not well established, while its prevalence is about 5% in all thyroid malignancies, 0.4–1.4% in all thyroid nodules, and less than 1% in thyroids of subjects submitted to autopsy. Contrary to PTC and FTC, no difference in distribution between women and men is observed. Although occurring mostly in individuals in their fourth and fifth decades of life, a wide range in age at onset is present but children are affected only in the hereditary form.

The biological behavior of MTC is much less favorable when compared with that of the other DTCs, even though it is not as unfavorable as that of ATC. A 10-year survival of about 50% for patients with MTC is reported in several series, both the cure and survival of these patients being positively affected by an early diagnosis [164].

Two different forms of MTC are recognized: the sporadic form, which accounts for about 75% of all the cases, and the hereditary or familial form, which accounts for the remaining 25% and in which MTC is only one component of a hereditary syndrome, since other endocrine glands can also be involved. The three different phenotypes, their prevalence, and the prevalence of involvement of the other glands are reported in Table 3.

No significant environmental factors or ethnical differences associated with the development of sporadic MTC have been identified, so far. Nevertheless, associations with prior thyroid diseases and other disorders such as hypertension, allergies, and gallbladder disease have been reported in a pooled analysis of epidemiological studies [165].

Table 3 Prevalence of different endocrine neoplasms and other clinical manifestations in the type II multiple endocrine neoplasia (MEN) syndromes

Syndrome	Manifestations	Prevalence (%)
MEN IIA	MTC	100
	Pheochromocytoma	40
	Parathyroid adenomas	20
	Cutaneous lichen amyloidosis	<10
MEN IIB	MTC	100
	Mucosal neuromas	100
	Marfanoid habitus	95
	Pheochromocytoma	45
Familial MTC	MTC	100

Activating single nucleotide RET point mutations are typically found in 98% of hereditary MTCs at the germinal level and in about 40% of sporadic MTCs at the somatic level [166]. Germline RET point mutations are mainly localized in exons 10–11 and 13–16, but other rare mutations have been reported also in other exons such as 5 and 8. Somatic RET mutations are mainly concentrated in exon 16, while only few cases have been reported in exons 10 and 11. Moreover, RET somatic mutation prevalence is significantly higher in bigger MTC tumors than in smaller and particularly high in advanced and progressive MTC [167]. A close correlation between genotype and phenotype has been recognized, as well as between certain point mutations and higher or lower aggressiveness of MTC [168]. Four risk levels have been suggested in the recently published "American Thyroid Association guidelines for the diagnosis and treatment of MTC" to classify the different RET mutations and to time surgical treatment of RET gene carriers [169]. Although not yet introduced in the routine clinical practice, it would be worth to know if a patient with sporadic MTC is carrying a RET somatic mutation, since the mutated cases have worse prognosis [170]; thus, a

more aggressive therapeutic strategy or a more stringent follow-up could be reserved to these patients. Moreover, all cases of apparently sporadic MTC should be screened for a germline RET mutation, since about 5–10% of them are misdiagnosed hereditary forms [166].

Role of Nuclear Medicine in the Management of MTC

Derivation of parafollicular C cells from the neural crest makes MTC a member of the so-called neuroendocrine tumors (more recently defined as "neuroendocrine neoplasms"). The molecular targets upon which radionuclide-based imaging and therapy are based are therefore different from those utilized in the diagnostic and therapeutic approach to DTC as defined above. In particular, MTC shares with other neuroendocrine neoplasms the modalities of uptake and intracellular processing of some amines, as well as expression on cell surface of receptors for some regulatory peptides, most notably somatostatin. Besides the production of the hormone Ct (which is specific for the C cells), a somewhat peculiar feature of MTC in the scenario of neuroendocrine neoplasms is that MTC cells express sizable amounts of the tumor-associated carcinoembryonic antigen (CEA) [171].

Despite high diagnostic sensitivity especially in the postoperative workup, at present the use of DMSA labeled with pentavalent technetium-99m (^{99m}Tc(V)-DMSA) as an MTC imaging agent [172, 173] is interesting only from the historical point of view, although this radiopharmaceutical is occasionally still employed as a reference in multiple agent comparative studies [174].

Based on the production of CEA by MTC cells, considerable efforts have been devoted to develop novel approaches to imaging, and possibly therapy, with the use of anti-CEA monoclonal preparations labeled with either indium-111, radioiodine [175–179], technetium-99m [180], or gallium-68 for PET imaging [181].

Furthermore, following promising results in early clinical trials [182], considerable efforts have been devoted to explore the use of monoclonal anti-CEA preparations labeled with iodine-131 for radioimmunotherapy of patients with metastatic MTC; the more recent investigations in this field adopt a pre-targeting approach rather than the direct use of the radiolabeled monoclonal preparation per se [183–186].

Nevertheless, the most intensely investigated nuclear medicine applications for the management of patients with MTC, from both the imaging and the therapeutic viewpoints, are based on two biological features expressed by several types of neuroendocrine neoplasms, namely, the ability to take up and concentrate biological amines and the enhanced expression of membrane-associated receptors for a variety of biological peptides, most notably somatostatin. The first feature is the basis for tumor targeting with radioiodinated MIBG for either imaging purposes and/or therapeutic purposes [187–191] and for PET imaging with ^{18}F-DOPA [192, 193]. The second feature (expression of receptors for regulatory peptides) constitutes the basis for either single-photon [194–196] or PET imaging [193] as well as for possible therapy using properly designed and radiolabeled somatostatin analogues [197, 198].

The issues pertaining to radionuclide imaging and therapy of MTC as a neuroendocrine neoplasm will be discussed more extensively in ▶ Chaps. 29, "Diagnostic Applications of Nuclear Medicine: Neuroendocrine Tumors", and ▶ 43, "Neuroendocrine Tumors: Therapy with Radiolabeled Peptides" of this book. As in the case of other neuroendocrine neoplasms with a somewhat indolent pattern of tumor growth, the diagnostic performance of the most widely used PET tracer in oncology, [^{18}F]FDG, is suboptimal in patients with MTC, unless the disease progresses toward a more aggressive pattern of tumor growth. Therefore, the first-line approach to radionuclide imaging for these tumors is represented by the use of radiopharmaceuticals addressing the specific neuroendocrine features mentioned above rather than by the use of [^{18}F]FDG. Conversely, as neuroendocrine neoplasms take on a biologically aggressive pattern of growth, they tend to lose some of the biological features specific of the tumor of origin; in these cases, PET

with [^{18}F]FDG performs better than imaging with the more neuroendocrine-specific tracers. The examples reported in Figs. 14, 15, 16, and 17 have been chosen to epitomize this variable imaging pattern.

Other Thyroid Cancers

This category comprises a group of extremely rare primary thyroid tumors that include epithelial carcinomas (i.e., mucinous, squamous cell and mucoepidermoid carcinomas, characterized by the presence of keratin- and mucin-producing cells), as well as non-epithelial tumors (e.g., malignant lymphoma) and tumors arising from mesenchymal elements such as sarcomas. On the other hand, the thyroid can be the site of metastasis of cancers originating in other organs, such as the lung, kidney, and breast cancers [199, 200]. Sometimes it can be difficult to distinguish if the thyroid lesion is a primary tumor or a metastasis of another tumor originating in another organ. However, nowadays the molecular profiles of several human tumors are known and their specificity can enable to clearly identify the origin of the tumor [201].

Concerning the primary thyroid tumors, squamous cell thyroid carcinoma should be distinguished both from local involvement caused by a primary squamous cell carcinoma of the neck and from an ATC containing squamous components [202]. Mucinous carcinoma of the thyroid is similar to mucinous carcinomas originating at other sites, and areas of PTC or FTC are not evident. In the case of mucinous adenocarcinoma, the first option to consider is the possibility of secondary thyroid involvement from a tumor originating at another site, since primary thyroid mucinous adenocarcinomas are extremely rare (only six cases reported in literature) [203]. Mucoepidermoid carcinoma most commonly

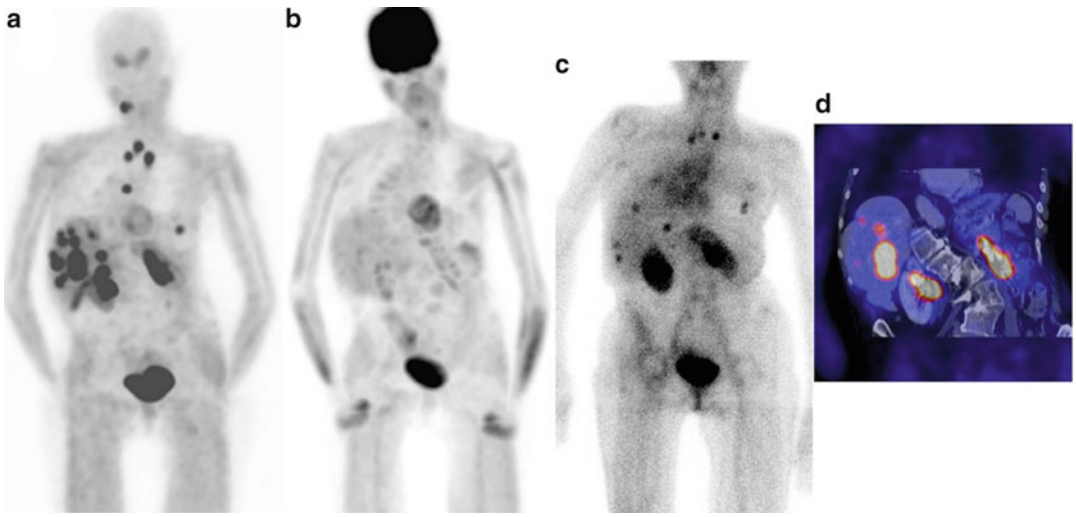

Fig. 14 Imaging with different radiopharmaceuticals in a 68-year-old patient with a MEN 2a-related metastatic MTC; serum calcitonin was 27,190 ng/L and CEA 1,460 μg/L. (**a**) ^{18}F-DOPA PET (anterior MIP) shows lesions located in the neck, upper mediastinum, left thorax, liver, and skeleton. (**b**) [^{18}F]FDG PET (anterior MIP) shows only physiologic uptake but no tumor lesions. (**c**) Whole-body ^{99m}Tc(V)-DMSA (anterior view) shows lesions in upper mediastinum, left thorax, liver, and skeleton, although with much smaller number of lesions than detected by ^{18}F-DOPA PET. (**d**) ^{18}F-DOPA PET/CT coronal fusion slice shows liver lesions (Reproduced from Koopmans KP, de Groot JWB, Plukker JTM, de Vries EGE, Kema IP, Sluiter WJ, et al. ^{18}F-Dihydroxyphenylalanine PET in patients with biochemical evidence of medullary thyroid cancer: relation to tumor differentiation. J Nucl Med. 2008;49:524–31 (permission requested))

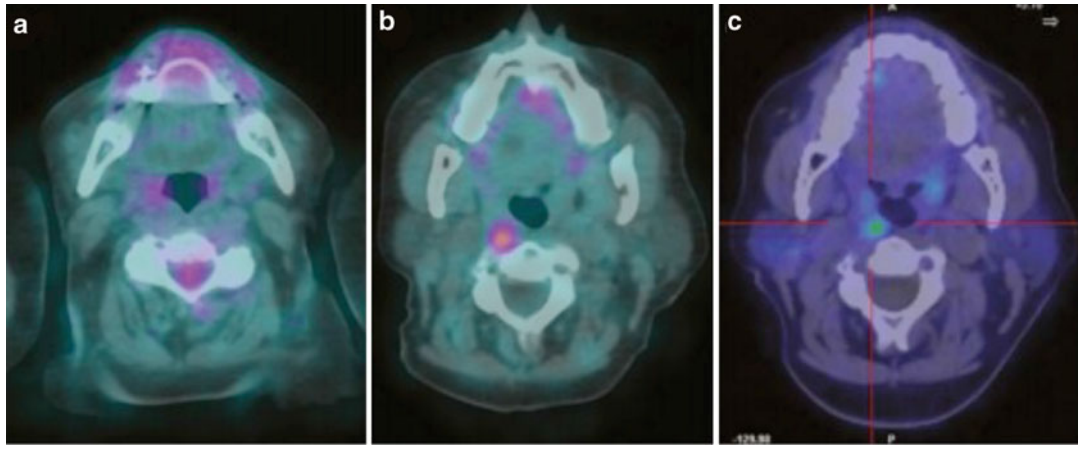

Fig. 15 PET/CT (axial fused images) with [^{18}F]FDG (**a**), ^{18}F-DOPA (**b**), and ^{68}Ga-somatostatin analogue in a 62-year-old patient with rising Ct and CEA levels after surgery for MTC. Increased uptake in a right retropharyngeal lymph node is clearly visible on both the ^{18}F-DOPA and ^{68}Ga-somatostatin analogue scans, but not in the [^{18}F]FDG scan. Recurrent MTC in the lymph node was confirmed by FNAC (Reproduced with permission from Treglia G, Castaldi P, Villani MF, Perotti G, de Waure C, Filice A, et al. Comparison of ^{18}F-DOPA, ^{18}F-FDG and ^{68}Ga-somatostatin analogue PET/CT in patients with recurrent medullary thyroid carcinoma. Eur J Nucl Med Mol Imaging. 2012;39:569–80)

occurs in the salivary glands and shows ductal structures lined with ciliated columnar cells with low-grade malignant potential [204]. Its origin remains unclear, as it can arise from solid cell nests of the ultimobranchial apparatus or from the follicular thyroid epithelium [205]. Malignant mesenchymoma of the thyroid is extremely rare, and it can show chondrosarcomatous, osteosarcomatous, fibrosarcomatous, and rhabdomyosarcomatous patterns. These histologic subtypes are high-grade malignant tumors with poor prognosis [206]. Sarcomas of the thyroid are similar as those arising in other organs, and it is often difficult (if not just impossible) to distinguish a primary thyroid sarcoma from the ATC variant with sarcomatous differentiation.

Malignant lymphomas of the thyroid account for 1–5% of all thyroid malignancies and less than 2% of extranodal lymphomas; they can constitute the only manifestation of the disease or be part of systemic disease [207]. Thyroid lymphomas are almost exclusively derived from B cells of mucosa-associated lymphoid tissue (MALT) [208] and frequently coexist with autoimmune thyroiditis; as for other localizations, optimal imaging of thyroid lymphomas is based on [^{18}F] FDG PET (Fig. 18). Peripheral T-cell lymphoma or primary plasmacytomas of the thyroid are uncommon. Combined chemo-radiation therapy is recommended for all diffuse B-cell or mixed lymphomas. Single-modality therapy with surgery or EBRT alone may be considered for early-stage intrathyroidal MALT lymphomas [209].

Primary paraganglioma of the thyroid is a very rare neuroendocrine tumor the histologic diagnosis of which can be very difficult, as it requires differential diagnosis with the hyalinizing trabecular adenoma and with MTC. The prognosis is favorable with complete surgical excision [210].

Clinically obvious, secondary metastatic carcinomas account for 2–3% of malignant tumors of the thyroid; thyroid involvement does not per se modify overall prognosis of these patients. The occurrence of thyroidal metastases from other primary tumors, mainly from the renal, lung, breast, and colon carcinomas [199–201], is instead much more frequent on autopsy-based surveys, although varying between 1.2% and 24% for different cancers [211]; nevertheless, this condition is usually devoid of any thyroid-specific symptoms. If the thyroid represents the only site of metastasis (as it can be observed especially in patients with clear cell renal carcinoma), total thyroidectomy is recommended.

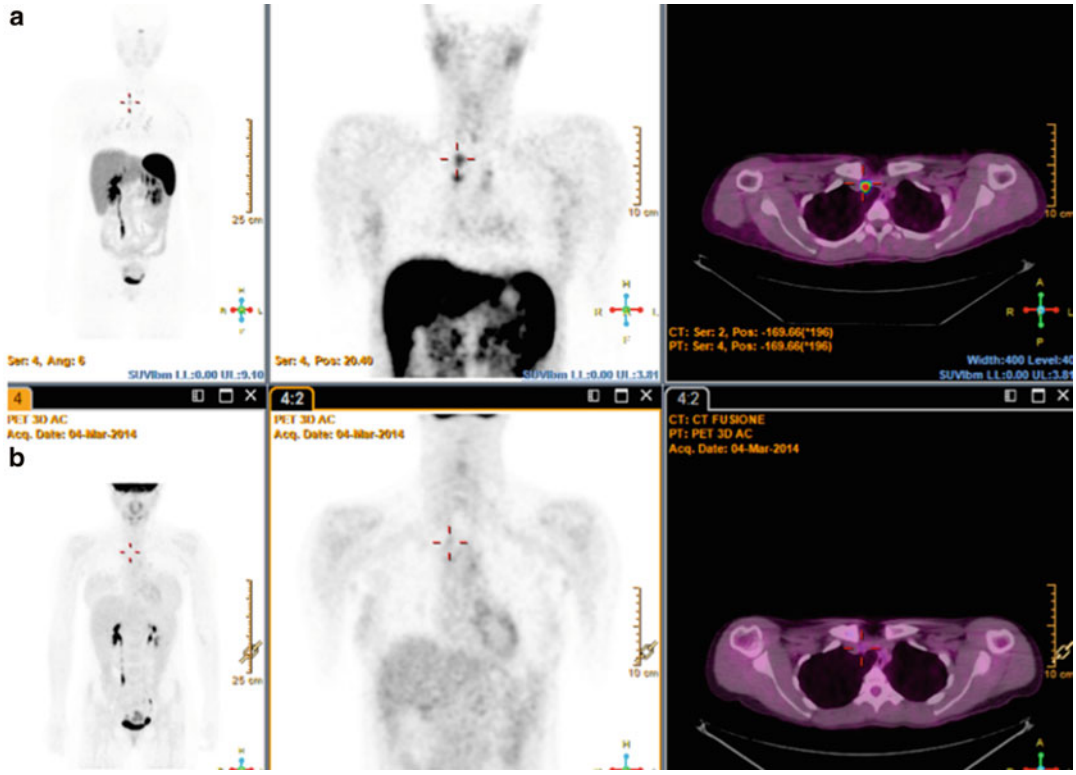

Fig. 16 PET/CT with ^{68}Ga-DOTA-TOC (**a**) and with [^{18}F]FDG (**b**) in a patient previously treated with thyroidectomy because of MTC; MIP image in the *left panel*, coronal PET slice in the *center panel*, axial fused PET/CT slice in the *right panel*. Recurrence of disease was suspected on the basis of slowly rising serum Ct levels. Metastatic disease in mediastinal lymph nodes is clearly depicted by frankly increased uptake of ^{68}Ga-DOTA-TOC, while there is only faint uptake of the glycometabolic tracer [^{18}F]FDG (Supplied by courtesy of Dr. Annibale Versari, Nuclear Medicine Service, "Arcispedale S. Maria Nuova", Reggio Emilia, Italy)

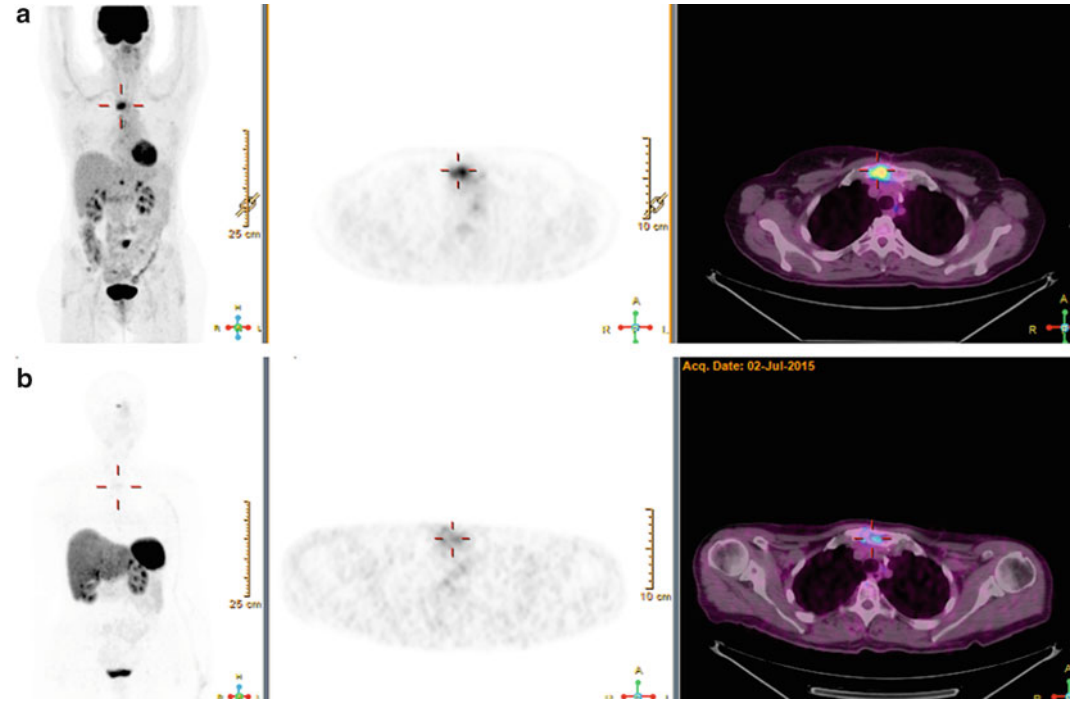

Fig. 17 PET/CT with [^{18}F]FDG (**a**) and with ^{68}Ga-DOTA-TOC (**b**) in a patient previously treated with thyroidectomy because of MTC; MIP image in the *left panel*, coronal PET slice in the *center panel*, axial fused PET/CT slice in the *right panel*. Early after surgery recurrence of disease was suspected on the basis of steeply rising serum Ct levels and painful sternal lesion. Metastatic bone disease in the sternum is clearly depicted by frankly increased uptake of the glycometabolic tracer [^{18}F]FDG, while there is only faint uptake of ^{68}Ga-DOTA-TOC (Supplied by courtesy of Dr. Annibale Versari, Nuclear Medicine Service, "Arcispedale S. Maria Nuova", Reggio Emilia, Italy)

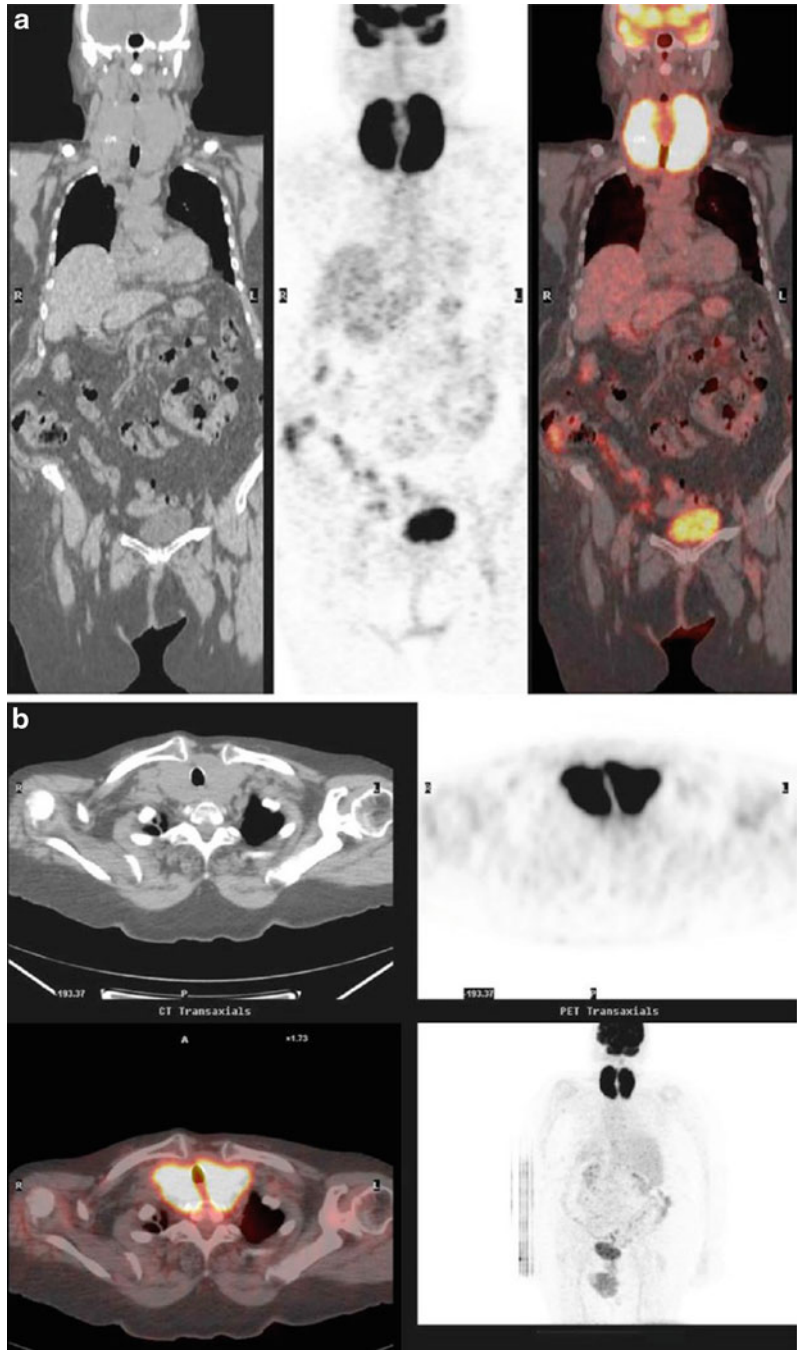

Fig. 18 PET/CT with [^{18}F]FDG in an 87-year-old patient with thyroid B-cell lymphoma as the sole site of disease (primary thyroid lymphoma). (**a**) Coronal CT (*left panel*), PET (*center panel*), and fused imaging sections (*right panel*), showing diffuse involvement and marked enlargement of the entire thyroid gland that extends from the upper cervical region to the upper mediastinum. (**b**) Transaxial CT (*upper left panel*), PET (*upper right panel*), and fused imaging (*lower left panel*), at the level of lower neck (the clavicles are clearly identified); the MIP image is shown in the *lower right panel*. Virtually all the trachea is surrounded by the abnormal tissue, with initial lumen constriction

References

1. Hedinger C, Williams E, Sobin LH, editors. Histological typing of thyroid tumors. Berlin: Springer; 1988.
2. Chan JK, Saw D. The grooved nucleus. A useful diagnostic criterion of papillary carcinoma of the thyroid. Am J Surg Pathol. 1986;10:672–9.
3. Johannessen JV, Sobrinho-Simoes M. The origin and significance of thyroid psammoma bodies. Lab Invest. 1980;43:287–96.
4. LiVolsi VA. Papillary neoplasms of the thyroid. Pathologic and prognostic features. Am J Clin Pathol. 1992;97:426–34.
5. Rosai J, Zampi G, Carcangiu ML. Papillary carcinoma of the thyroid. A discussion of its several morphologic expressions, with particular emphasis on the follicular variant. Am J Surg Pathol. 1983;7:809–17.
6. Tielens ET, Sherman SI, Hruban RH, Ladenson PW. Follicular variant of papillary thyroid carcinoma. A clinicopathologic study. Cancer. 1994;73:424–31.
7. Carcangiu ML, Bianchi S. Diffuse sclerosing variant of papillary thyroid carcinoma. Clinicopathologic study of 15 cases. Am J Surg Pathol. 1989;13:1041–9.
8. Evans HL. Columnar-cell carcinoma of the thyroid. A report of two cases of an aggressive variant of thyroid carcinoma. Am J Clin Pathol. 1986;85:77–80.
9. Mizukami Y, Nonomura A, Michigishi T, Noguchi M, Nakamura S, Hashimoto T. Columnar cell carcinoma of the thyroid gland: a case report and review of the literature. Hum Pathol. 1994;25:1098–101.
10. Gemsenjager E, Heitz PU, Seifert B, Martina B, Schweizer I. Differentiated thyroid carcinoma. Follow-up of 264 patients from one institution for up to 25 years. Swiss Med Wkly. 2001;131:157–63.
11. Albores-Saavedra J, Wu J. The many faces and mimics of papillary thyroid carcinoma. Endocr Pathol. 2006;17:1–18.
12. Ghossein R. Encapsulated malignant follicular cell-derived thyroid tumors. Endocr Pathol. 2010;21:212–8.
13. Nikiforov YE, Seethala RR, Tallini G, et al. Nomenclature revision for encapsulated follicular variant of papillary thyroid carcinoma: a paradigm shift to reduce overtreatment of indolent tumors. JAMA Oncol. 2016;2:1023–9.
14. Shi X, Liu R, Basolo F, et al. Differential clinicopathological risk and prognosis of major papillary thyroid cancer variants. J Clin Endocrinol Metab. 2016;101:264–74.
15. Hedinger C, Williams ED, Sobin LH. The WHO histological classification of thyroid tumors: a commentary on the second edition. Cancer. 1989;63:908–11.
16. Davies L, Welch HG. Increasing incidence of thyroid cancer in the United States, 1973–2002. JAMA. 2006;295:2164–7.
17. Yamamoto Y, Maeda T, Izumi K, Otsuka H. Occult papillary carcinoma of the thyroid. A study of 408 autopsy cases. Cancer. 1990;65:1173–9.
18. Kovacs GL, Gonda G, Vadasz G, et al. Epidemiology of thyroid microcarcinoma found in autopsy series conducted in areas of different iodine intake. Thyroid. 2005;15:152–7.
19. de Matos PS, Ferreira AP, Ward LS. Prevalence of papillary microcarcinoma of the thyroid in Brazilian autopsy and surgical series. Endocr Pathol. 2006;17:165–73.
20. Pellegriti G, Scollo C, Lumera G, Regalbuto C, Vigneri R, Belfiore A. Clinical behavior and outcome of papillary thyroid cancers smaller than 1.5 cm in diameter: study of 299 cases. J Clin Endocrinol Metab. 2004;89:3713–20.
21. Matsubayashi S, Kawai K, Matsumoto Y, et al. The correlation between papillary thyroid carcinoma and lymphocytic infiltration in the thyroid gland. J Clin Endocrinol Metab. 1995;80:3421–4.
22. Pacini F, Mariotti S, Formica N, Elisei R, Anelli S, Capotorti E, Pinchera A. Thyroid autoantibodies in thyroid cancer: incidence and relationship with tumour outcome. Acta Endocrinol (Copenh). 1988;119:373–80.
23. Feldman PS, Horvath E, Kovacs K. Ultrastructure of three Hurthle cell tumors of the thyroid. Cancer. 1972;30:1279–85.
24. Herrera MF, Hay ID, Wu PS, et al. Hurthle cell (oxyphilic) papillary thyroid carcinoma: a variant with more aggressive biologic behavior. World J Surg. 1992;16:669–74.
25. Morris LG, Tuttle RM, Davies L. Changing trends in the incidence of thyroid cancer in the United States. JAMA Otolaryngol Head Neck Surg. 2016;142:709–11.
26. Baudin E, Travagli JP, Ropers J, et al. Microcarcinoma of the thyroid gland: the Gustave-Roussy Institute experience. Cancer. 1998;83:553–9.
27. Morris LG, Myssiorek D. Improved detection does not fully explain the rising incidence of well-differentiated thyroid cancer: a population-based analysis. Am J Surg. 2010;200:454–61.
28. Baverstock K, Egloff B, Pinchera A, Ruchti C, Williams D. Thyroid cancer after Chernobyl. Nature. 1992;359:21–2.
29. Pacini F, Vorontsova T, Demidchik EP, et al. Post-Chernobyl thyroid carcinoma in Belarus children and adolescents: comparison with naturally occurring thyroid carcinoma in Italy and France. J Clin Endocrinol Metab. 1997;82:3563–9.
30. Elisei R, Molinaro E, Agate L, Bottici V, et al. Are the clinical and pathological features of differentiated thyroid carcinoma really changed over the last 35 years? Study on 4187 patients from a single Italian institution to answer this question. J Clin Endocrinol Metab. 2010;95:1516–27.
31. DeGroot LJ. Radiation and thyroid disease. Baillieres Clin Endocrinol Metab. 1988;2:777–91.
32. Dolphin GW, Beach SA. The relationship between radiation dose delivered to the thyroids of children and the subsequent development of malignant tumours. Health Phys. 1963;9:1385–90.

33. Rose RG, Hart field JE, Kelsey MP, McDonald EJ. The association of thyroid cancer and prior irradiation in infancy and childhood. J Nucl Med. 1963;4: 249–58.
34. Toyooka ET, Pifer JW, Crump SL, Dutton AM, Hempelmann LH. Neoplasms in children treated with X rays for thymic enlargement. II. Tumor incidence as a function of radiation factor. J Natl Cancer Inst. 1963;31:1357–77.
35. Pifer JW, Hempelmann LH. Radiation-induced thyroid carcinoma. Ann N Y Acad Sci. 1964;114:838–48.
36. Morris JH, Hardin CA. Thyroid cancer in adult following external irradiation. Arch Intern Med. 1964;113:97–100.
37. Silverman C. Thyroid tumors associated with radiation exposure. Public Health Rep. 1984;99:369–73.
38. Calandra DB, Shah KH, Lawrence AM, Paloyan E. Total thyroidectomy in irradiated patients. A twenty-year experience in 206 patients. Ann Surg. 1985;202: 356–60.
39. Naing S, Collins BJ, Schneider AB. Clinical behavior of radiation-induced thyroid cancer: factors related to recurrence. Thyroid. 2009;19:479–85.
40. Haddy N, Andriamboavonjy T, Paoletti C, et al. Thyroid adenomas and carcinomas following radiotherapy for a hemangioma during infancy. Radiother Oncol. 2009;93:377–82.
41. Sinnott B, Ron E, Schneider AB. Exposing the thyroid to radiation: a review of its current extent, risks, and implications. Endocr Rev. 2010;31:756–73.
42. Moysich KB, Menezes RJ, Michalek AM. Chernobyl-related ionising radiation exposure and cancer risk: an epidemiological review. Lancet Oncol. 2002;3:269–79.
43. Cardis E, Kesminiene A, Ivanov V, et al. Risk of thyroid cancer after exposure to ^{131}I in childhood. J Natl Cancer Inst. 2005;97:724–32.
44. Caudill CM, Zhu Z, Ciampi R, Stringer JR, Nikiforov YE. Dose-dependent generation of RET/PTC in human thyroid cells after in vitro exposure to gamma-radiation: a model of carcinogenic chromosomal rearrangement induced by ionizing radiation. J Clin Endocrinol Metab. 2005;90:2364–9.
45. Nikiforov YE, Rowland JM, Bove KE, Monforte-Munoz H, Fagin JA. Distinct pattern of ret oncogene rearrangements in morphological variants of radiation-induced and sporadic thyroid papillary carcinomas in children. Cancer Res. 1997;57:1690–4.
46. Hemminki K, Eng C, Chen B. Familial risks for nonmedullary thyroid cancer. J Clin Endocrinol Metab. 2005;90:5747–53.
47. Franceschi S, Dal Maso L. Hormonal imbalances and thyroid cancers in humans. IARC Sci Publ. 1999;147:33–43.
48. Negri E, Dal Maso L, Ron E, et al. A pooled analysis of case-control studies of thyroid cancer. II. Menstrual and reproductive factors. Cancer Causes Control. 1999;10:143–55.
49. Thiruvengadam A, Govindarajulu P, Aruldhas MM. Modulatory effect of estradiol and testosterone on the development of N-nitrosodiisopropanolamine induced thyroid tumors in female rats. Endocr Res. 2003;29: 43–51.
50. Mack WJ, Preston-Martin S, Bernstein L, Qian D, Xiang M. Reproductive and hormonal risk factors for thyroid cancer in Los Angeles County females. Cancer Epidemiol Biomarkers Prev. 1999;8:991–7.
51. Rossing MA, Voigt LF, Wicklund KG, Williams M, Daling JR. Use of exogenous hormones and risk of papillary thyroid cancer (Washington, United States). Cancer Causes Control. 1998;9:341–9.
52. Fiore E, Rago T, Provenzale MA, et al. Lower levels of TSH are associated with a lower risk of papillary thyroid cancer in patients with thyroid nodular disease: thyroid autonomy may play a protective role. Endocr Relat Cancer. 2009;16:1251–60.
53. Belfiore A, La Rosa GL, Padova G, Sava L, Ippolito O, Vigneri R. The frequency of cold thyroid nodules and thyroid malignancies in patients from an iodine-deficient area. Cancer. 1987;15:3096–102.
54. Feldt-Rasmussen U. Iodine and cancer. Thyroid. 2001; 11:483–6.
55. Williams ED, Doniach I, Bjamson O, Michie W. Thyroid cancer in an iodide rich area. Cancer. 1997; 39:215–22.
56. Bosetti C, Kolonel L, Negri E, et al. A pooled analysis of case-control studies of thyroid cancer. VI. Fish and shellfish consumption. Cancer Causes Control. 2001; 12:375–82.
57. Dal Maso L, Bosetti C, La Vecchia C, Franceschi S. Risk factors for thyroid cancer: an epidemiological review focused on nutritional factors. Cancer Causes Control. 2009;20:75–86.
58. Kitahara CM, Platz EA, Freeman LE, et al. Obesity and thyroid cancer risk among U.S. men and women: a pooled analysis of five prospective studies. Cancer Epidemiol Biomarkers Prev. 2011;20:464–72.
59. Duntas LH, Doumas C. The 'rings of fire' and thyroid cancer. Hormones (Athens). 2009;8:249–53.
60. Pellegriti G, De Vathaire F, Scollo C, et al. Papillary thyroid cancer incidence in the volcanic area of Sicily. J Natl Cancer Inst. 2009;101:1575–83.
61. Lemoine NR, Mayall ES, Wyllie FS, Williams ED, Goyns M, Stringer B, Wynford-Thomas D. High frequency of ras oncogene activation in all stages of human thyroid tumorigenesis. Oncogene. 1989;4: 159–64.
62. Suarez HG, du Villard JA, Severino M, et al. Presence of mutations in all three ras genes in human thyroid tumors. Oncogene. 1990;5:565–70.
63. Wright PA, Lemoine NR, Mayall ES, Wyllie FS, Hughes D, Williams ED, Wynford-Thomas D. Papillary and follicular thyroid carcinomas show a different pattern of ras oncogene mutation. Br J Cancer. 1989;60:576–7.
64. Shi YF, Zou MJ, Schmidt H, Juhasz F, Stensky V, Robb D, Farid N. High rates of ras codon 61 mutation in thyroid tumors in an iodide-deficient area. Cancer Res. 1991;51:2690–3.

65. Santoro M, Grieco M, Melillo RM, Fusco A, Vecchio G. Molecular defects in thyroid carcinomas: role of the RET oncogene in thyroid neoplastic transformation. Eur J Endocrinol. 1995;133:513–22.
66. Grieco M, Santoro M, Berlingieri MT, et al. PTC is a novel rearranged form of the ret proto-oncogene and is frequently detected in vivo in human thyroid papillary carcinomas. Cell. 1990;60:557–63.
67. Castellone MD, Santoro M. Dysregulated RET signaling in thyroid cancer. Endocrinol Metab Clin North Am. 2008;37:363–74.
68. Fusco A, Grieco M, Santoro M, et al. A new oncogene in human thyroid papillary carcinomas and their lymph-nodal metastases. Nature. 1987;328: 170–2.
69. Elisei R, Romei C, Vorontsova T, et al. RET/PTC rearrangements in thyroid nodules: studies in irradiated and not irradiated, malignant and benign thyroid lesions in children and adults. J Clin Endocrinol Metab. 2001;86:3211–6.
70. Romei C, Ciampi R, Elisei R. A comprehensive overview of the role of the RET proto-oncogene in thyroid carcinoma. Nat Rev Endocrinol. 2016;12:192–202.
71. Bongarzone I, Pierotti MA, Monzini N, et al. High frequency of activation of tyrosine kinase oncogenes in human papillary thyroid carcinoma. Oncogene. 1989;4:1457–62.
72. Bounacer A, Wicker R, Caillou B, Cailleux AF, Sarasin A, Schlumberger M, Suarez H. High prevalence of activating ret proto-oncogene rearrangements, in thyroid tumors from patients who had received external radiation. Oncogene. 1997;15:1263–73.
73. Viglietto G, Chiappetta G, Martinez-Tello FJ, et al. RET/PTC oncogene activation is an early event in thyroid carcinogenesis. Oncogene. 1995;11:1207–10.
74. Zou M, Shi Y, Farid NR. Low rate of ret proto-oncogene activation (PTC/retTPC) in papillary thyroid carcinomas from Saudi Arabia. Cancer. 1994;73: 176–80.
75. Tallini G, Santoro M, Helie M, et al. RET/PTC oncogene activation defines a subset of papillary thyroid carcinomas lacking evidence of progression to poorly differentiated or undifferentiated tumor phenotypes. Clin Cancer Res. 1998;4:287–94.
76. Xing M. BRAF mutation in papillary thyroid cancer: pathogenic role, molecular bases, and clinical implications. Endocr Rev. 2007;28:742–62.
77. Fugazzola L, Puxeddu E, Avenia N, et al. Correlation between B-RAFV600E mutation and clinicopathologic parameters in papillary thyroid carcinoma: data from a multicentric Italian study and review of the literature. Endocr Relat Cancer. 2006;13:455–64.
78. Nikiforova MN, Kimura ET, Gandhi M, et al. BRAF mutations in thyroid tumors are restricted to papillary carcinomas and anaplastic or poorly differentiated carcinomas arising from papillary carcinomas. J Clin Endocrinol Metab. 2003;88:5399–404.
79. Xing M, Westra WH, Tufano RP, et al. BRAF mutation predicts a poorer clinical prognosis for papillary thyroid cancer. J Clin Endocrinol Metab. 2005;90: 6373–9.
80. Puxeddu E, Moretti S, Elisei R, et al. BRAF (V599E) mutation is the leading genetic event in adult sporadic papillary thyroid carcinomas. J Clin Endocrinol Metab. 2004;89:2414–20.
81. Elisei R, Ugolini C, Viola D, et al. BRAF(V600E) mutation and outcome of patients with papillary thyroid carcinoma: a 15-year median follow-up study. J Clin Endocrinol Metab. 2008;93:3943–9.
82. Jin L, Chen E, Dong S, et al. BRAF and TERT promoter mutations in the aggressiveness of papillary thyroid carcinoma: a study of 653 patients. Oncotarget. 2016;7:18346–55.
83. Liu X, Qu S, Liu R, et al. TERT promoter mutations and their association with BRAF V600E mutation and aggressive clinicopathological characteristics of thyroid cancer. J Clin Endocrinol Metab. 2014;99: E1130–6.
84. Cancer Genome Atlas Research Network. Integrated genomic characterization of papillary thyroid carcinoma. Cell. 2014;159:676–90.
85. Schlumberger MJ. Papillary and follicular thyroid carcinoma. N Engl J Med. 1998;338:297–306.
86. Rago T, Vitti P, Chiovato L, et al. Role of conventional ultrasonography and color flow-Doppler sonography in predicting malignancy in 'cold' thyroid nodules. Eur J Endocrinol. 1998;138:41–6.
87. Papini E, Guglielmi R, Bianchini A, et al. Risk of malignancy in nonpalpable thyroid nodules: predictive value of ultrasound and color-Doppler features. J Clin Endocrinol Metab. 2002;87:1941–6.
88. Haugen BR, Alexander EK, Bible KC, et al. 2015 American Thyroid Association management guidelines for adult patients with thyroid nodules and differentiated thyroid cancer: The American Thyroid Association Guidelines Task Force on thyroid nodules and differentiated thyroid cancer. Thyroid. 2016; 26:1–133.
89. Ophir J, Alam SK, Garra B, Kallel F, Konofagou E, Krouskop T, Varghese T. Elastography: ultrasonic estimation and imaging of the elastic properties of tissues. Proc Inst Mech Eng H. 1999;213:203–33.
90. Rago T, Santini F, Scutari M, Pinchera A, Vitti P. Elastography: new developments in ultrasound for predicting malignancy in thyroid nodules. J Clin Endocrinol Metab. 2008;92:2917–22.
91. Rubaltelli L, Corradin S, Dorigo A, Stabilito M, Tregnaghi A, Borsato S, Stramare R. Differential diagnosis of benign and malignant thyroid nodules at elastosonography. Ultraschall Med. 2009;30:175–9.
92. Rago T, Vitti P. Potential value of elastosonography in the diagnosis of malignancy in thyroid nodules. Q J Nucl Med Mol Imaging. 2009;53:455–6.
93. Rago T, Scutari M, Santini F, et al. Real-time elastosonography: useful tool for refining the presurgical diagnosis in thyroid nodules with indeterminate or nondiagnostic cytology. J Clin Endocrinol Metab. 2010;95:5274–80.

94. Cakir B, Aydin C, Korukluoğlu B, et al. Diagnostic value of elastosonographically determined strain index in the differential diagnosis of benign and malignant thyroid nodules. Endocrine. 2011;39:89–98.
95. Baloch ZW, LiVolsi VA. Fine-needle aspiration of the thyroid: today and tomorrow. Best Pract Res Clin Endocrinol Metab. 2008;22:929–39.
96. Layfield LJ, Cibas ES, Gharib H, Mandel SJ. Thyroid aspiration cytology: current status. CA Cancer J Clin. 2009;59:99–110.
97. LiVolsi VA, Gupta PK. Thyroid fine-needle aspiration: intranuclear inclusions, nuclear grooves and psammoma bodies—paraganglioma-like adenoma of the thyroid. Diagn Cytopathol. 1992;8:82–3.
98. Gharib H, Goellner JR, Johnson DA. Fine-needle aspiration cytology of the thyroid. A 12-year experience with 11,000 biopsies. Clin Lab Med. 1993;13:699–709.
99. Poller DN, Stelow EB, Yiangou C. Thyroid FNAC cytology: can we do it better? Cytopathology. 2008;19:4–10.
100. Mehanna HM, Jain A, Morton RP, Watkinson J, Shaha A. Investigating the thyroid nodule. BMJ. 2009;338:705–9.
101. Cooper DS, Doherty GM, Haugen BR, et al. Revised American Thyroid Association management guidelines for patients with thyroid nodules and differentiated thyroid cancer. Thyroid. 2009;19:1167–214.
102. British Thyroid Association, Royal College of Physicians. British Thyroid Association guidelines for the management of thyroid cancer. 2nd ed. London: British Thyroid Association, Royal College of Physicians; 2007.
103. Hegedus L. Clinical practice. The thyroid nodule. N Engl J Med. 2004;351:1764–71.
104. Kelly NP, Lim JC, DeJong S, Harmath C, Dudiak C, Wojcik EM. Specimen adequacy and diagnostic specificity of ultrasound-guided fine needle aspirations of nonpalpable thyroid nodules. Diagn Cytopathol. 2006;34:188–90.
105. Kesmodel SB, Terhune KP, Canter RJ, Mandel SJ, LiVolsi VA, Baloch ZW, Fraker DL. The diagnostic dilemma of follicular variant of papillary thyroid carcinoma. Surgery. 2003;134:1005–12.
106. Yang GC, Liebeskind D, Messina AV. Should cytopathologists stop reporting follicular neoplasms on fine-needle aspiration of the thyroid? Cancer. 2003;99:69–74.
107. Nardi F, Basolo F, Crescenzi A, et al. Italian consensus for the classification and reporting of thyroid cytology. J Endocrinol Invest. 2014;37:593–9.
108. Nikiforov YE. Molecular diagnostics of thyroid tumors. Arch Pathol Lab Med. 2011;135:569–77.
109. Alexander EK, Kennedy GC, Baloch ZW, et al. Preoperative diagnosis of benign thyroid nodules with indeterminate cytology. N Engl J Med. 2012;367:705–15.
110. Nikiforov YE, Carty SE, Chiosea SI, et al. Impact of the multi-gene ThyroSeq next-generation sequencing assay on cancer diagnosis in thyroid nodules with atypia of undetermined significance/follicular lesion of undetermined significance cytology. Thyroid. 2015;25:1217–23.
111. Lazar V, Bidart JM, Caillou B, Mahé C, Lacroix L, Filetti S, Schlumberger M. Expression of the Na+/I− symporter gene in human thyroid tumors: a comparison study with other thyroid-specific genes. J Clin Endocrinol Metab. 1999;84:3228–34.
112. Giovanella S, Suriano S, Maffioli M, Ceriani M. ^{18}FDG-positron emission tomography/computed tomography (PET/CT) scanning in thyroid nodules with nondiagnostic cytology. Clin Endocrinol. 2011;74:644–8.
113. Piccardo A, Puntoni M, Treglia G, Foppiani L, Bertagna F, Paparo F, et al. Thyroid nodules with indeterminate cytology: prospective comparison between ^{18}F-FDG-PET/CT, multiparametric neck ultrasonography, ^{99m}Tc-MIBI scintigraphy and histology. Eur J Endocrinol. 2016;174:693–703.
114. Kim CE, Joyce JM, Patel N, Lichter J. Fortuitous detection of papillary carcinoma of the thyroid with F-18 FDG positron emission tomography in a patient with non-Hodgkin lymphoma. Clin Nucl Med. 2003;28:782–3.
115. Chen W, Li G, Parsons M, Zhuang H, Alavi A. Clinical significance of incidental focal versus diffuse thyroid uptake on FDG-PET imaging. PET Clin. 2007;2:321–9.
116. Nayan S, Ramakrishna J, Gupta MK. The proportion of malignancy in incidental thyroid lesions on 18-FDG PET study: a systematic review and meta-analysis. Otolaryngol Head Neck Surg. 2014;151:190–200.
117. Agrawal K, Weaver J, Ul-Hassan F, Jeannon JP, Simo R, Carroll P, et al. Incidence and significance of incidental focal thyroid uptake on ^{18}F-FDG PET study in a large patient cohort: retrospective single-centre experience in the United Kingdom. Eur Thyroid J. 2015;4:115–22.
118. Demir Ö, Köse N, Özkan E, Ünlütürk U, Aras G, Erdoğan MF. Clinical significance of thyroid incidentalomas identified by ^{18}F-FDG PET/CT: correlation of ultrasonography findings with cytology results. Nucl Med Commun. 2016;37:715–20.
119. Pacini F, Schlumberger M, Dralle H, Elisei R, Smit JW, Wiersinga W. European consensus for the management of patients with differentiated thyroid carcinoma of the follicular epithelium. Eur J Endocrinol. 2006;154:787–803.
120. Tuttle RM, Tala H, Shah J, et al. Estimating risk of recurrence in differentiated thyroid cancer after total thyroidectomy and radioactive iodine remnant ablation: using response to therapy variables to modify the initial risk estimates predicted by the new American Thyroid Association staging system. Thyroid. 2010;20:1341–9.
121. Kim BS, Kim SJ, Kim IJ, Pak K, Kim K. Factors associated with positive F-18 fluorodeoxyglucose positron emission tomography before thyroidectomy

in patients with papillary thyroid carcinoma. Thyroid. 2012;22:725–9.
122. Chong A, Ha JM, Han YH, Kong E, Choi Y, Hong KH, Park JH, Kim SH, Park JM. Preoperative lymph node staging by FDG PET/CT with contrast enhancement for thyroid cancer: a multicenter study and comparison with neck CT. Clin Exp Otorhinolaryngol. 2016. doi:10.21053/ceo.2015.01424. Epub ahead of print.
123. DeGroot LJ, Kaplan EL, McCormick M, Straus FH. Natural history, treatment, and course of papillary thyroid carcinoma. J Clin Endocrinol Metab. 1990; 71:414–24.
124. Ceccarelli C, Pacini F, Lippi F, Elisei R, Arganini M, Miccoli P, Pinchera A. Thyroid cancer in children and adolescents. Surgery. 1988;104:1143–8.
125. Schlumberger M, De Vathaire F, Travagli JP, et al. Differentiated thyroid carcinoma in childhood: long term follow-up of 72 patients. J Clin Endocrinol Metab. 1987;65:1088–94.
126. Akslen LA, Haldorsen T, Thoresen SO, Glattre E. Survival and causes of death in thyroid cancer: a population-based study of 2479 cases from Norway. Cancer Res. 1991;51:1234–41.
127. Mazzaferri EL, Jhiang SM. Long-term impact of initial surgical and medical therapy on papillary and follicular thyroid cancer. Am J Med. 1994;97: 418–28.
128. Brennan MD, Bergstralh EJ, van Heerden JA, McConahey WM. Follicular thyroid cancer treated at the Mayo Clinic, 1946 through 1970: initial manifestations, pathologic findings, therapy, and outcome. Mayo Clin Proc. 1991;66:11–22.
129. Tubiana M, Schlumberger M, Rougier P, et al. Long-term results and prognostic factors in patients with differentiated thyroid carcinoma. Cancer. 1985;55: 794–804.
130. Johnson TL, Lloyd RV, Thompson NW, Beierwaltes WH, Sisson JC. Prognostic implications of the tall cell variant of papillary thyroid carcinoma. Am J Surg Pathol. 1988;12:22–7.
131. Silver CE, Owen RP, Rodrigo JP, Rinaldo A, Devaney KO, Ferlito A. Aggressive variants of papillary thyroid carcinoma. Head Neck. 2010;33:1052–9.
132. Lang W, Choritz H, Hundeshagen H. Risk factors in follicular thyroid carcinomas. A retrospective follow-up study covering a 14-year period with emphasis on morphological findings. Am J Surg Pathol. 1986;10: 246–55.
133. Sakamoto A, Kasai N, Sugano H. Poorly differentiated carcinoma of the thyroid. A clinicopathologic entity for a high-risk group of papillary and follicular carcinomas. Cancer. 1983;52:1849–55.
134. Carcangiu ML, Zampi G, Pupi A, Castagnoli A, Rosai J. Papillary carcinoma of the thyroid. A clinicopathologic study of 241 cases treated at the University of Florence, Italy. Cancer. 1985;55:805–28.
135. Simpson WJ, McKinney SE, Carruthers JS, Gospodarowicz MK, Sutcliffe SB, Panzarella T. Papillary and follicular thyroid cancer. Prognostic factors in 1,578 patients. Am J Med. 1987;83:479–88.
136. Yamashita H, Noguchi S, Murakami N, Kawamoto H, Watanabe S. Extracapsular invasion of lymph node metastasis is an indicator of distant metastasis and poor prognosis in patients with thyroid papillary carcinoma. Cancer. 1997;80:2268–72.
137. Hu A, Clark J, Payne RJ, Eski S, Wal fish PG, Freeman JL. Extrathyroidal extension in well-differentiated thyroid cancer: macroscopic vs microscopic as a predictor of outcome. Arch Otolaryngol Head Neck Surg. 2007;133:644–9.
138. Grebe SK, Hay ID. Follicular cell-derived thyroid carcinomas. Cancer Treat Res. 1997;89:91–140.
139. Akslen LA, Haldorsen T, Thoresen SO, Glattre E. Incidence of thyroid cancer in Norway 1970–1985. Population review on time trend, sex, age, histological type and tumour stage in 2625 cases. APMIS. 1990;98:549–58.
140. Hay ID. Papillary thyroid carcinoma. Endocrinol Metab Clin North Am. 1990;19:545–76.
141. Hay ID, Bergstralh EJ, Goellner JR, Ebersold JR, Grant CS. Predicting outcome in papillary thyroid carcinoma: development of a reliable prognostic scoring system in a cohort of 1779 patients surgically treated at one institution during 1940 through 1989. Surgery. 1993;114:1050–7.
142. Durante C, Haddy N, Baudin E, et al. Long-term outcome of 444 patients with distant metastases from papillary and follicular thyroid carcinoma: benefits and limits of radioiodine therapy. J Clin Endocrinol Metab. 2006;91:2892–9.
143. Hoie J, Stenwig AE, Kullmann G, Lindegaard M. Distant metastases in papillary thyroid cancer. A review of 91 patients. Cancer. 1988;61:1–6.
144. Elisei R, Pinchera A, Romei C, et al. Expression of thyrotropin receptor (TSH-R), thyroglobulin, thyroperoxidase, and calcitonin messenger ribonucleic acids in thyroid carcinomas: evidence of TSH-R gene transcript in medullary histotype. J Clin Endocrinol Metab. 1994;78:867–71.
145. Xing M. BRAF mutation in thyroid cancer. Endocr Relat Cancer. 2005;12:245–62.
146. Basolo F, Molinaro E, Agate L, et al. RET protein expression has no prognostic impact on the long-term outcome of papillary thyroid carcinoma. Eur J Endocrinol. 2001;145:599–604.
147. Basolo F, Pollina L, Fontanini G, Fiore L, Pacini F, Baldanzi A. Apoptosis and proliferation in thyroid carcinoma: correlation with bcl-2 and p53 protein expression. Br J Cancer. 1997;75:537–41.
148. Landa I, Ibrahimpasic T, Boucai L, et al. Genomic and transcriptomic hallmarks of poorly differentiated and anaplastic thyroid cancers. J Clin Invest. 2016;126: 1052–66.
149. Basolo F, Pinchera A, Fugazzola L, Fontanini G, Elisei R, Romei C, Pacini F. Expression of p21 ras protein as a prognostic factor in papillary thyroid cancer. Eur J Cancer. 1994;30:171–4.

150. Chiacchio S, Lorenzoni A, Boni G, Rubello D, Elisei R, Mariani G. Anaplastic thyroid cancer: prevalence, diagnosis and treatment. Minerva Endocrinol. 2008;33:341–57.
151. Ain KB. Anaplastic thyroid carcinoma: behavior, biology, and therapeutic approaches. Thyroid. 1998; 8:715–26.
152. Giuffrida D, Gharib H. Anaplastic thyroid carcinoma: current diagnosis and treatment. Ann Oncol. 2000;11: 1083–9.
153. Are C, Shaha AR. Anaplastic thyroid carcinoma: biology, pathogenesis, prognostic factors, and treatment approaches. Ann Surg Oncol. 2006;13:453–64.
154. Neff RL, Farrar WB, Kloos RT, Burman KD. Anaplastic thyroid cancer. Endocrinol Metab Clin North Am. 2008;37:525–38.
155. Samaan NA, Ordonez NG. Uncommon types of thyroid cancer. Endocrinol Metab Clin North Am. 1990; 19:637–48.
156. Us-Krasovec M, Golouh R, Auersperg M, Besic N, Ruparcic-Oblak L. Anaplastic thyroid carcinoma in fine needle aspirates. Acta Cytol. 1996;40:953–8.
157. Ciampi R, Vivaldi A, Romei C, Del Guerra A, Salvadori P, Cosci B, et al. Expression analysis of facilitative glucose transporters (GLUTs) in human thyroid carcinoma cell lines and primary tumors. Mol Cell Endocrinol. 2008;291:57–62.
158. Conti PS, Durski JM, Bacqai F, Grafton ST, Singer PA. Imaging of locally recurrent and metastatic thyroid cancer with positron emission tomography. Thyroid. 1999;9:797–804.
159. Khan N, Oriuchi N, Higuchi T, Endo K. Review of fluorine-18-2-fluoro-2-deoxy-D-glucose positron emission tomography (FDG-PET) in the follow-up of medullary and anaplastic thyroid carcinomas. Cancer Control. 2005;12:254–60.
160. Palaniswamy SS, Subramanyam P. Diagnostic utility of PETCT in thyroid malignancies: an update. Ann Nucl Med. 2013;27:681–93.
161. Ciarallo A, Marcus C, Taghipour M, Subramaniam RM. Value of fluorodeoxyglucose PET/computed tomography patient management and outcomes in thyroid cancer. PET Clin. 2015;10:265–78.
162. Lloyd RV, Sisson JC, Marangos PJ. Calcitonin, carcinoembryonic antigen and neuron-specific enolase in medullary thyroid carcinoma. Cancer. 1983;51: 2234–9.
163. Rosenberg-Bourgin M, Gardet P, de Sahb R, et al. Comparison of sporadic and hereditary forms of medullary thyroid carcinoma. Henry Ford Hosp Med J. 1989;37:141–3.
164. Elisei R, Bottici V, Luchetti F, et al. Impact of routine measurement of serum calcitonin on the diagnosis and outcome of medullary thyroid cancer: experience in 10,864 patients with nodular thyroid disorders. J Clin Endocrinol Metab. 2004;89:163–8.
165. Negri E, Ron E, Franceschi S, et al. A pooled analysis of case-control studies of thyroid cancer. I. Methods. Cancer Causes Control. 1999;10:131–42.
166. Elisei R, Romei C, Cosci B, et al. RET genetic screening in patients with medullary thyroid cancer and their relatives: experience with 807 individuals at one center. J Clin Endocrinol Metab. 2007;92:4725–9.
167. Romei C, Ugolini C, Cosci B, et al. Low prevalence of the somatic M918T RET mutation in micromedullary thyroid cancer. Thyroid. 2012;22:476–81.
168. Niccoli-Sire P, Murat A, Rohmer V, et al. Familial medullary thyroid carcinoma with noncysteine ret mutations: phenotype-genotype relationship in a large series of patients. J Clin Endocrinol Metab. 2001;86:3746–53.
169. Wells Jr SA, Asa SL, Dralle H, et al. Revised American Thyroid Association guidelines for the management of medullary thyroid carcinoma. Thyroid. 2015; 25:567–610.
170. Elisei R, Cosci B, Romei C, et al. Prognostic significance of somatic RET oncogene mutations in sporadic medullary thyroid cancer: a 10-year follow-up study. J Clin Endocrinol Metab. 2008;93:682–7.
171. Ishikawa N, Hamada S. Association of medullary carcinoma of the thyroid with carcinoembryonic antigen. Br J Cancer. 1976;34:111–5.
172. Ohta H, Yamamoto K, Endo K, et al. A new imaging agent for medullary carcinoma of the thyroid. J Nucl Med. 1984;25:323–32.
173. Rufini V, Salvatori M, Garganese MC, Di Giuda D, Maussier ML, Troncone L. Role of nuclear medicine in the diagnosis and therapy of medullary thyroid carcinoma. Rays. 2000;25:273–82.
174. Ozkan ZG, Kuyumcu S, Uzum AK, Gecer MF, Ozel S, Aral F, Adalet I. Comparison of ^{68}Ga-DOTATATE PET-CT, ^{18}F-FDG PET-CT and ^{99m}Tc-(V)DMSA scintigraphy in the detection of recurrent or metastatic medullary thyroid carcinoma. Nucl Med Commun. 2015;36:242–50.
175. Reiners C, Eilles C, Spiegel W, Becker W, Börner W. Immunoscintigraphy in medullary thyroid cancer using an ^{123}I- or ^{111}In-labelled monoclonal anti-CEA antibody fragment. Nuklearmedizin. 1986;25: 227–31.
176. Zanin DE, van Dongen A, Hoefnagel CA, Bruning PF. Radioimmunoscintigraphy using iodine-131-anti-CEA monoclonal antibodies and thallium-201 scintigraphy in medullary thyroid carcinoma: a case report. J Nucl Med. 1990;31:1854–5.
177. O'Byrne KJ, Hamilton D, Robinson I, Sweeney E, Freyne PJ, Cullen MJ. Imaging of medullary carcinoma of the thyroid using ^{111}In-labelled anti-CEA monoclonal antibody fragments. Nucl Med Commun. 1992;13:142–8.
178. Vuillez JP, Peltier P, Caravel JP, Chetanneau A, Saccavini JC, Chatal JF. Immunoscintigraphy using ^{111}In-labeled F(ab')$_2$ fragments of anti-carcinoembryonic antigen monoclonal antibody for detecting recurrences of medullary thyroid carcinoma. J Clin Endocrinol Metab. 1992;74:157–63.
179. Peltier P, Curtet C, Chatal JF, Le Doussal JM, Daniel G, Aillet G, et al. Radioimmunodetection of

medullary thyroid cancer using a bispecific anti-CEA/anti-indium-DTPA antibody and an indium-111-labeled DTPA dimer. J Nucl Med. 1993;34:1267–73.
180. Baum RP, Hertel A, Lorenz M, Schwarz A, Encke A, Hör G. $^{99}Tc^{m}$-labelled anti-CEA monoclonal antibody for tumour immunoscintigraphy: first clinical results. Nucl Med Commun. 1989;10:345–52. Erratum in: Nucl Med Commun 1989;10:772–3.
181. Bodet-Milin C, Faivre-Chauvet A, Carlier T, Rauscher A, Bourgeois M, Cerato E, et al. Immuno-PET using anti-CEA bispecific antibody and ^{68}Ga-labeled peptide in metastatic medullary thyroid carcinoma: clinical optimization of the pretargeting parameters in a First-in Human trial. J Nucl Med. 2016;57:1505–1511.
182. Juweid M, Sharkey RM, Behr T, Swayne LC, Rubin AD, Hanley D, et al. Targeting and initial radioimmunotherapy of medullary thyroid carcinoma with ^{131}I-labeled monoclonal antibodies to carcinoembryonic antigen. Cancer Res. 1995;55(23 Suppl):5946s–51.
183. Chatal JF, Campion L, Kraeber-Bodéré F, Bardet S, Vuillez JP, Charbonnel B, et al. Survival improvement in patients with medullary thyroid carcinoma who undergo pretargeted anti-carcinoembryonic-antigen radioimmunotherapy: a collaborative study with the French Endocrine Tumor Group. J Clin Oncol. 2006;24:1705–11.
184. Kraeber-Bodéré F, Rousseau C, Bodet-Milin C, Ferrer L, Faivre-Chauvet A, Campion L, et al. Targeting, toxicity, and efficacy of 2-step, pretargeted radioimmunotherapy using a chimeric bispecific antibody and ^{131}I-labeled bivalent hapten in a phase I optimization clinical trial. J Nucl Med. 2006;47:247–55.
185. Kraeber-Bodéré F, Salaun PY, Ansquer C, Drui D, Mirallié E, Faivre-Chauvet A, et al. Pretargeted radioimmunotherapy (pRAIT) in medullary thyroid cancer (MTC). Tumour Biol. 2012;33:601–6.
186. Salaun PY, Campion L, Bournaud C, Faivre-Chauvet-A, Vuillez JP, Taieb D, et al. Phase II trial of anti-carcinoembryonic antigen pretargeted radioimmunotherapy in progressive metastatic medullary thyroid carcinoma: biomarker response and survival improvement. J Nucl Med. 2012;53:1185–92.
187. Endo K, Shiomi K, Kasagi K, Konishi J, Torizuka K, Nakao K, Tanimura H. Imaging of medullary thyroid cancer with ^{131}I-MIBG. Lancet. 1984;2(8396):233.
188. Connell JM, Hilditch TE, Elliott A, Semple PF. ^{131}I-MIBG and medullary carcinoma of the thyroid. Lancet. 1984;2(8414):1273–4.
189. Hoefnagel CA, Delprat CC, Valdés Olmos RA. Role of [^{131}I]metaiodobenzylguanidine therapy in medullary thyroid carcinoma. J Nucl Biol Med. 1991;35:334–6.
190. Divgi C. Targeted systemic radiotherapy of pheochromocytoma and medullary thyroid cancer. Semin Nucl Med. 2011;41:369–73.
191. Sisson JC, Yanik GA. Theranostics: evolution of the radiopharmaceutical meta-iodobenzylguanidine in endocrine tumors. Semin Nucl Med. 2012;42:171–84.
192. Hoegerle S, Altehoefer C, Ghanem N, Brink I, Moser E, Nitzsche E. ^{18}F-DOPA positron emission tomography for tumour detection in patients with medullary thyroid carcinoma and elevated calcitonin levels. Eur J Nucl Med. 2001;28:64–71.
193. Ambrosini V, Morigi JJ, Nanni C, Castellucci P, Fanti S. Current status of PET imaging of neuroendocrine tumours ([^{18}F]FDOPA, [^{68}Ga]tracers, [^{11}C]/[^{18}F]-HTP). Q J Nucl Med Mol Imaging. 2015;59:58–69.
194. Kurtaran A, Scheuba C, Kaserer K, Schima W, Czerny C, Angelberger P, et al. Indium-111-DTPA-D-Phe-^{1}-octreotide and technetium-99m-(V)-dimercaptosuccinic acid scanning in the preoperative staging of medullary thyroid carcinoma. J Nucl Med. 1998;39:1907–9.
195. Parisella M, D'Alessandria C, van de Bossche B, Chianelli M, Ronga G, Papini E, et al. ^{99m}Tc-EDDA/HYNIC-TOC in the management of medullary thyroid carcinoma. Cancer Biother Radiopharm. 2004;19:211–7.
196. Czepczyński R, Parisella MG, Kosowicz J, Mikołajczak R, Ziemnicka K, Gryczyńska M, et al. Somatostatin receptor scintigraphy using ^{99m}Tc-EDDA/HYNIC-TOC in patients with medullary thyroid carcinoma. Eur J Nucl Med Mol Imaging. 2007;34:1635–45.
197. Iten F, Müller B, Schindler C, et al. Response to [^{90}Yttrium-DOTA]-TOC treatment is associated with long-term survival benefit in metastasized medullary thyroid cancer: a phase II clinical trial. Clin Cancer Res. 2007;13:6696–702.
198. Turker O, Dogan I. The clinical role of molecular imaging: positron emission tomography/computed tomography and ^{90}yttrium-DOTATOC in the management of medullary thyroid cancer. Thyroid. 2010;20:233–4.
199. Duggal NM, Horattas MC. Metastatic renal cell carcinoma to the thyroid gland. Endocr Pract. 2008;14:1040–6.
200. Wood K, Vini L, Harmer C. Metastases to the thyroid gland: the Royal Marsden experience. Eur J Surg Oncol. 2004;30:583–8.
201. Bellevicine C, Vigliar E, Malapelle U, et al. Lung adenocarcinoma and its thyroid metastasis characterized on fine-needle aspirates by cytomorphology, immunocytochemistry, and next-generation sequencing. Diagn Cytopathol. 2015;43:585–9.
202. Papi G, Corrado S, LiVolsi VA. Primary spindle cell lesions of the thyroid gland; an overview. Am J Clin Pathol. 2006;125:S95–123.
203. D'Antonio A, Addesso M, De Dominicis G, Boscaino A, Liguori G, Nappi O. Mucinous carcinoma of thyroid gland. Report of a primary and a metastatic mucinous tumour from ovarian adenocarcinoma with immunohistochemical study and

review of literature. Virchows Arch. 2007;451: 847–51.
204. Wenig BM, Adair CF, Heffess CS. Primary mucoepidermoid carcinoma of the thyroid gland: a report of six cases and a review of the literature of a follicular epithelial-derived tumor. Hum Pathol. 1995;26:1099–108.
205. Jung YH, Kang MS. Composite follicular variant of papillary carcinoma and mucoepidermoid carcinoma of thyroid gland: a case report. J Korean Med Sci. 2010;25:1683–7.
206. Shi H, Wang C, Wei L, Lu S, Cao D. Malignant mesenchymoma of the thyroid: case report and literature review. Tumori. 2010;96:345–8.
207. Graff-Baker A, Sosa JA, Roman SA. Primary thyroid lymphoma: a review of recent developments in diagnosis and histology-driven treatment. Curr Opin Oncol. 2010;22:17–22.
208. Graff-Baker A, Roman SA, Thomas DC, Udelsman R, Sosa JA. Prognosis of primary thyroid lymphoma: demographic, clinical, and pathologic predictors of survival in 1,408 cases. Surgery. 2009;146:1105–15.
209. Widder S, Pasieka JL. Primary thyroid lymphomas. Curr Treat Options Oncol. 2004;5:307–13.
210. Ferri E, Manconi R, Armato E, Ianniello F. Primary paraganglioma of thyroid gland: a clinicopathologic and immunohistochemical study with review of the literature. Acta Otorhinolaryngol Ital. 2009;29:97–102.
211. Giuffrida D, Ferra F, Pappalardo A, et al. Metastasis to the thyroid gland: a case report and review of the literature. J Endocrinol Invest. 2003;26:560–3.

Diagnostic Applications of Nuclear Medicine: Parathyroid Tumors

20

Federica Guidoccio, Sara Mazzarri, Salvatore Mazzeo, and Giuliano Mariani

Abstract

The most common causes of hyperparathyroidism (HPTH) are of a benign nature, for either primary or secondary HPTH (as well as the tertiary form). Diagnosis of HPTH is based on clinical and biochemical findings, without any role for diagnostic imaging per se. Imaging is instead important for characterizing the disease, regarding especially number and sites of the hyperfunctioning parathyroid glands, which can be in their classical anatomic location or in ectopic locations. This information is crucial for planning surgery with a minimally invasive approach, associated or not with intraoperative guidance with the help of a handheld gamma-detecting probe – an approach that is common to other applications of radioguided surgery.

In addition to high-resolution ultrasound (US) and Magnetic resonance imaging (MRI) (and ceCT for selected applications), SPECT/CT with ^{99m}Tc-sestamibi has excellent performance for preoperative imaging of hyperfunctioning parathyroid glands. The PET tracer [^{11}C]methionine has also been shown to possess excellent localization properties in patients with HPTH.

Parathyroid carcinoma is a very rare endocrine malignancy that occurs in <1% of primary HPTH. The initial clinical manifestations of parathyroid carcinoma are primarily linked to the effects of markedly elevated serum PTH levels. At initial presentation, very few patients have metastasis at regional lymph nodes or at distant sites. Parathyroid carcinoma tends to infiltrate adjacent structures in the neck. US, CT, and MRI have been used to localize parathyroid carcinomas and to detect mediastinal and thoracic recurrences or distant metastases. ^{99m}Tc-sestamibi scintigraphy can be successful for preoperative localization of the neoplasia and can identify metastases in lymph nodes and at distant sites. PET with [^{18}F]FDG can also detect metastatic parathyroid cancers. Parathyroid carcinoma recurs in more than 50% of the cases and imaging studies should be performed in all patients before reoperation.

Keywords

Parathyroid adenoma • Parathyroid carcinoma • Hyperparathyroidism • Parathyroid scintigraphy • ^{99m}Tc-sestamibi • Single-tracer dual-phase parathyroid scintigraphy • Double-tracer parathyroid scintigraphy • Parathyroid PET/CT • [^{18}F]FDG • [^{11}C]methionine • ^{18}F-DOPA •

F. Guidoccio • S. Mazzarri • G. Mariani (✉)
Regional Center of Nuclear Medicine, Department of Translational Research and Advanced Technologies in Medicine and Surgery, University of Pisa, Pisa, Italy
e-mail: federica.guidoccio@gmail.com; saramazzarri@hotmail.it; giuliano.mariani@med.unipi.it; giuliano.mariani11@gmail.com

S. Mazzeo
Department of Diagnostic and Interventional Radiology, University of Pisa, Pisa, Italy
e-mail: smazzeo@unipi.it

© Springer International Publishing Switzerland 2017
H.W. Strauss et al. (eds.), *Nuclear Oncology*,
https://doi.org/10.1007/978-3-319-26236-9_40

^{18}F-fluorocholine • Ectopic parathyroid • Minimally invasive parathyroidectomy • Radioguided parathyroidectomy

Glossary

[^{18}F]FDG	2-Deoxy-2-[^{18}F]fluoro-D-glucose
^{18}F-DOPA	2-^{18}F-Fluoro-L,3,4-dihydroxyphenyilalanine
$^{99m}TcO_4^-$	^{99m}Tc-pertechnetate
ceCT	Contrast-enhanced computed tomography
CEUS	Contrast-enhanced ultrasound
CT	Computed tomography
DW ratio	Depth/width ratio
EBRT	External beam radiation therapy
ECG	Electrocardiogram
HPT-JT	Hyperparathyroidism-jaw tumor syndrome
HPTH	Hyperparathyroidism
MEN	Multiple endocrine neoplasia
MIRP	Minimally invasive radioguided parathyroidectomy
MRI	Magnetic resonance imaging
mRNA	Messenger RNA
PET	Positron emission tomography
PRAD	Parathyroid adenomatosis oncogene
PTH	Parathyroid hormone
RGS	Radioguided surgery
SPECT	Single photon emission computed tomography
SPECT/CT	Single photon emission computed tomography/computed tomography
US	Ultrasound
VDR	Vitamin D receptor

Contents

Anatomy, Physiology, and Pathophysiology 586
Benign Causes of Hyperparathyroidism 587
Diagnosis and Treatment of Benign Hyperparathyroidism 589
Persistent and Recurrent Hyperparathyroidism 590
Role of Preoperative Imaging 590
Non-radionuclide Imaging Techniques 591
Parathyroid Scintigraphy 594
Minimally Invasive Parathyroidectomy and Radioguided Surgery 596
Parathyroid Carcinoma 600
Pathology 600
Epidemiology 601
Etiology 601
Pathogenesis 601
Clinical Presentation 601
Imaging of Parathyroid Carcinoma 602
Management of Parathyroid Carcinoma 603
Surgery 603
Chemotherapy 604
External Beam Radiation Therapy 604
Management of Hypercalcemia 604
Prognosis 605
Concluding Remarks on Preoperative Parathyroid Imaging When Planning Minimally Invasive Parathyroidectomy 605
References 606

Anatomy, Physiology, and Pathophysiology

There are normally two pairs of parathyroid glands in adult humans, each one measuring approximately 6 × 4 × 2 mm and weighing 30–50 mg (for a total weight of approximately 130–140 mg). Supernumerary parathyroid glands can be found in 2–5% of the general population, while it is very rare to find less than four glands. The parathyroid glands are endodermal in nature and originate embryologically from the third and fourth pharyngeal pouches. From the point of view of their final anatomical location, it is important to notice that their relative position is inverted during their migration in fetal life (Fig. 1). In fact, the two glands that are originally positioned more cranially (in the third pharyngeal pouch) follow in part the descent of the thymus, to reach their final location at the posterolateral surface of the lower lobes of the thyroid; nevertheless, they can also detach from their connection to the thymus and remain located somewhere along their path of descent. The glands that are originally positioned in the fourth pharyngeal pouch (more caudally) are instead closely associated with the embryologic

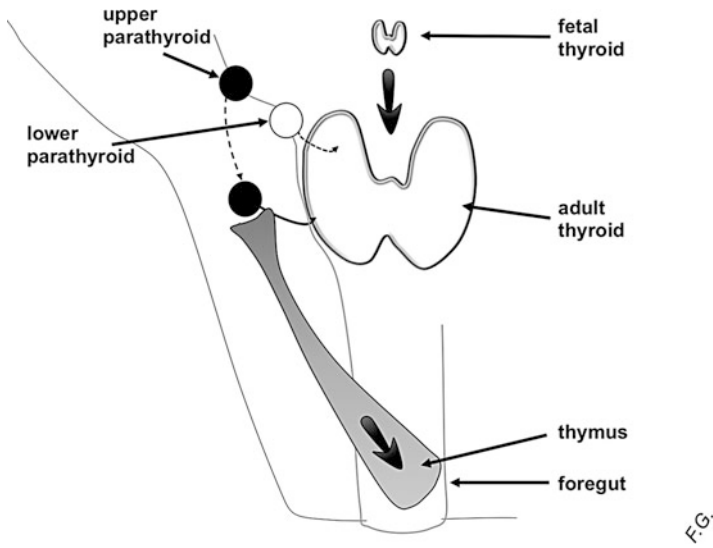

Fig. 1 Embryological origin and routes of descent of the thymus and parathyroid glands during fetal life. The parathyroid glands that originate more cranially (in the third pharyngeal pouch) migrate initially in association with the thymus, to reach their final position more caudally with respect to the parathyroid glands that originate in a lower location (fourth pharyngeal pouch). Therefore, the lower parathyroid glands follow a much longer path of descent, a feature that probably explains the greater frequency of ectopic location in adult life of these glands with respect to the upper parathyroid glands (Modified from: Sadler [171])

structure of the thyroid gland; they maintain a close association with the fetal thyroid until the descent of both structures to their final location in the neck. These parathyroid glands are positioned at the posterolateral surface of the upper poles of the thyroid lobes. The most frequent anatomo-topographic location of the upper glands is posterior to the middle and upper third of the thyroid lobe, cranially to the inferior thyroid artery and posterior to the recurrent laryngeal nerves. The inferior parathyroid glands are located in a more variable position, most likely due to their more complicated pattern of migration from and initial cranial position to a final caudal position [1]. From the surgical point of view, in approximately 50% of the cases, the lower parathyroid glands are located posteriorly or laterally to the lower pole of the thyroid lobe, within a 20 cm radius. Other less frequent locations include within the thyrothymic ligament, within the thymus in the mediastinum, or intrathyroidal [2] (Fig. 2). Enlarged adenomatous or hyperplastic parathyroid glands may change somewhat their location.

The predominant type of cells that constitute adult parathyroid tissue is constituted by the so-called chief cells, followed by the oxyphilic cells (whose histologic appearance is linked to their abundance in mitochondria) and by the intermediate stage of transitional oxyphilic cells [3]. The parathyroid hormone (PTH) acts on different tissues and apparatuses with multifaceted functions, the combined effect of which is to increase calcium concentration in blood. In order to achieve this effect, PTH stimulates bone resorption (thereby mobilizing calcium from bone to circulating fluids) and promotes calcium resorption in the kidneys; at the same time, it decreases tubular resorption of phosphate. Moreover, PTH stimulates the synthesis of the active form of vitamin D, which in turn stimulates calcium absorption in the gastrointestinal tract [4].

Benign Causes of Hyperparathyroidism

Primary hyperparathyroidism (*HPTH*) is characterized by inappropriate PTH production, i.e., not as a response to reduced calcium concentration in circulating blood as it would be the physiologic function of the parathyroid glands; therefore, this inappropriate PTH secretion results in

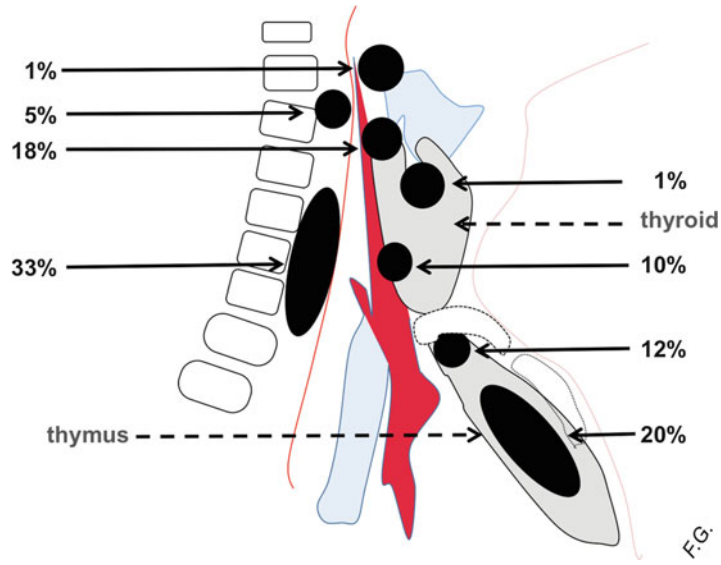

Fig. 2 Diagrammatic representation of the variability in anatomic location of hyperfunctioning parathyroid glands. This data refers to a total of 104 adenomas found at reoperation over a quite long time span (1930–1975) at the Massachusetts General Hospital (Harvard Medical School, Boston, MA); patients underwent second surgery because of recurrent PHPT after prior conventional four-gland exploration surgery. About 65% of all ectopic locations mirror the route of descent of the lower parathyroid glands (longer migration path) (Modified from: Wang [172])

hypercalcemia [5]. The causes of primary HPTH are either a single parathyroid adenoma (80–85% of the cases), hyperplasia or multiple adenomas (10–15% of the cases), or parathyroid carcinoma (0.5–1% of the cases) [6]. Familial forms of primary HPTH include multiple endocrine neoplasia type I (MEN I) and type II (MEN II), the HPTH-jaw tumor syndrome, familial hypocalciuric hypercalcemia, and familial isolated HPTH [7].

The characteristic abnormality in hyperparathyroidism is the downregulated response of parathyroid cells to reduce PTH secretion in response to elevated calcium. In vitro and in vivo studies have focused on the receptor for calcium ions expressed by parathyroid cells (CaR) to explore the role of the calcium sensor in the development of hyperparathyroidism. Abnormalities in CaR expression or function as a consequence of some as yet unidentified genetic mutation(s) may contribute to the failure of PTH secretory regulation [4].

Also genetically linked variations of vitamin D metabolism can be associated with some forms of hyperparathyroidism. In fact, some allelic variants of vitamin D receptors (VDR) are overexpressed in patients with PHPT, combined with a reduced expression of VDR mRNA; as a consequence, the parathyroid cells are less susceptible to inhibition by active vitamin D, a condition that favors hyperplastic or adenomatous changes [4, 8, 9].

Prior irradiation of the neck and upper chest for benign diseases, including treatment of Grave's disease with ^{131}I-iodide, is an additional risk factor for the development of HPTH [10, 11]. Interestingly, this association has not been demonstrated after treatment with radioiodide for thyroid cancer, a condition that is usually treated with much greater amounts of radioactivity than Graves' disease. The genetic alterations found in radiation-associated parathyroid tumors most commonly involve losses in 11q and 1p, similarly as in parathyroid adenomas linked to MEN-1 gene abnormalities; these observations suggest a certain degree of vulnerability of this gene to irradiation.

Secondary HPTH is the result of long-standing hypocalcemia, as a physiologic or pathophysiologic parathyroid response to maintain calcium homeostasis. The most frequent cause of secondary HPTH is chronic renal failure, developing in about 90% of the patients undergoing hemodialysis [12, 13]. Other causes of secondary HPTH include osteomalacia, rickets, and malabsorption.

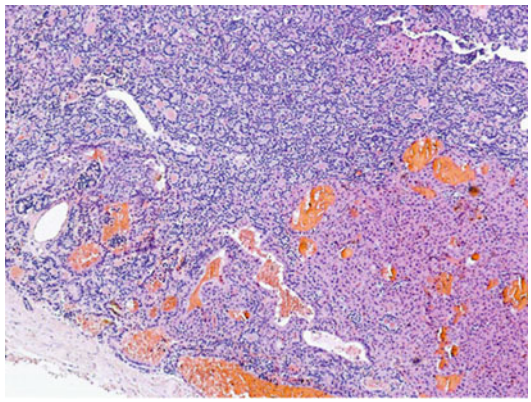

Fig. 3 Histologic pattern of a parathyroid adenoma (low magnification): nests of densely packed cells arranged in follicular and colloid-like structures mimicking the thyroid; scattered lymphocytic infiltrates are also present (Courtesy of Prof. Fulvio Basolo, Division of Pathology, Department of Surgery, University of Pisa, Pisa, Italy)

Tertiary HPTH is referred to the condition of persisting HPTH after successfully treating the cause of a secondary form of HPTH, as it can happen following, e.g., correction of chronic renal failure with kidney transplantation. Tertiary HPTH is usually sustained by hyperplasia of all four glands, but in over 20% of the patients, single or double adenomas are present [12].

Parathyroid adenomas include several histologic patterns, the most frequent of which are the oncocytic variant (constituted of cells with abundant granular eosinophilic cytoplasm) (Fig. 3), the lipoadenoma variant (composed of abundant stromal cells), and the water-clear cell variant. These variants represent clonal expansions, and several molecular abnormalities have been described such as rearrangement of the cyclin-D1/PRAD1 oncogene and mutation of the tumor suppressor MEN1 gene (11q13). Loss of the chromosome 11q locus is the most frequent abnormality found in parathyroid adenomas [14, 15].

Diagnosis and Treatment of Benign Hyperparathyroidism

Besides hypercalcemia, manifestations of symptomatic primary HPTH include overt bone disease, kidney disease, as well as nonspecific gastrointestinal, cardiovascular, and neuromuscular dysfunction. The main renal manifestations include nephrolithiasis (due to hypercalciuria), nephrocalcinosis, and renal dysfunction. Bone disease includes osteopenia (with pathologic fractures) and osteitis fibrosa cystica, while altered neurologic function can manifest with obtundation and delirium [16]. Nevertheless, over 80% of the cases of primary HPTH are today asymptomatic, being only discovered during general check-up evaluations (that now routinely include measurement of the serum calcium levels); there are no clinical factors that predict prognosis of these patients [17, 18]. Diagnosis of primary HPTH is based on persistent hypercalcemia and elevated serum PTH levels. Serum phosphorus is typically low, due to decreased resorption in the kidneys.

Secondary HPTH is characterized by hypocalcemia or normocalcemia (despite increased serum PTH levels) and hyperphosphatemia, associated with decreased vitamin D levels [12]. In tertiary HPTH, there are normal or elevated serum calcium concentrations in combination with moderately elevated PTH levels, decreased vitamin D and phosphate levels, and elevated alkaline phosphatase [12].

Currently, the only promising medical therapy available for primary HPTH is based on the use of the drug "cinacalcet" [19, 20], a novel member of the family of calcimimetics; its mechanism of action is based on direct modulation of the CaR expressed by the chief parathyroid cells, thereby the drug increases the sensitivity of the calcium sensor to extracellular calcium and thus reduces the secretion of PTH [21–23]. Management of patients with secondary HPTH is predominantly medical, and it includes calcitriol, vitamin D, calcimimetics (such as cinacalcet and new phosphate binders) [24, 25]. In tertiary HPTH, medical treatment is generally not indicated, although supplementation with vitamin D can be beneficial.

About 1–2% of patients with secondary HPTH require parathyroidectomy because of calciphylaxis, failure of medical management of hypercalcemia, hypercalciuria, serum PTH >800 pg/mL, hyperphosphatemia (with "calcium × phosphorus" product greater than 70), and associated symptoms [26, 27]. The main

form of treatment for tertiary HPTH is surgery, which is indicated in case of severe or persistent hypercalcemia, severe osteopenia, and clinical symptoms [28].

Complete resection of any hyperfunctioning parathyroid tissue is crucial for surgical treatment with curative intents. Persistent or recurrent HPTH generally results from inadequate initial resection and/or from the presence of an ectopic hyperfunctioning gland that had not been recognized at surgery; this condition requires reoperation. Bilateral neck exploration, based on surgical visualization of all four parathyroid glands, achieves a high success rate with minimal morbidity, if performed by experienced endocrine surgeons [29]. During parathyroid surgery, distinguishing an adenoma from hyperplasia can be problematic, not only on visual analysis but also upon intraoperative frozen section histology.

Preoperative imaging techniques play an important role in the surgical management of patients with HPTH, in order to localize and identify abnormal glands [30]. This approach has been crucial for the development of minimally invasive parathyroidectomy [31, 32], a procedure that can be video-assisted, endoscopic, radioguided, or image-guided unilateral exploration [33–35]. Several imaging techniques are available for preoperative localization of hyperfunctioning parathyroid glands, as detailed further below.

Persistent and Recurrent Hyperparathyroidism

In 5–10% of patients who undergo surgery for primary HPTH, persistent or recurrent HPTH can occur. Hyperparathyroidism presenting after a period of >6 months of normocalcemia following surgery is defined as "recurrent hyperparathyroidism" and is usually linked to regrowth of the remaining parathyroid tissue.

Causes of the immediate failure of surgical treatment failure (inducing persistent HPTH) include inaccurate/incomplete localization of adenoma(s), the insufficient resection of easily recognized multigland disease, and (even though a rare occurrence) the presence of metastatic parathyroid carcinoma. Persistent HPTH is characterized by abnormalities in calcium metabolism in the immediate postoperative period. Surgical failure may be due to either inexperience of the surgeon or interpretation errors during intraoperative frozen section histology. Persistent HPTH is more frequent in patients with familial forms of hyperparathyroidism, especially the MEN-1 syndrome (generally in less than 25% of patients, but up to 40–60% for less-experienced surgeons [36].

Another rare situation of recurrent or persistent hyperparathyroidism is called "parathyromatosis" which is defined as multiple remnants of hyperfunctioning parathyroid tissue scattered throughout the neck or upper mediastinum. This condition may be due either to growth of nests of parathyroid tissue left along the route of descent during embryologic development of the parathyroid glands or to accidental implantation of parathyroid tissue in the surgical bed at the time of parathyroidectomy.

Role of Preoperative Imaging

Preoperative imaging of the parathyroid glands is important to identify the parathyroid glands that are enlarged/hyperfunctioning because of hyperplasia and/or adenoma. Visualization of normal parathyroid glands using conventional imaging is virtually impossible; because of their tissue characteristics and small size and weight (less than 40 mg), they cannot be distinguished from the adjacent thyroid parenchyma. Adequate presurgical imaging not only reduces the surgical time by limiting surgical exploration to the affected side but, above all, allows the detection of parathyroid adenomas in ectopic sites. While approximately 80–85% of parathyroid adenomas are found in their normal location adjacent to the thyroid gland, 15–20% are ectopic [37]; when parathyroid adenomas are located in the mediastinum, into the thyroid gland, in or lateral to the cervical neurovascular bundle, or high in the neck, the term "major ectopy" is employed to describe the condition. Overall ectopic locations include:

- Anterior–superior mediastinum (either within the thymus or in a juxta-thymic position)
- Posterior–superior mediastinum along the esophagus
- Lower thyroid lobe (2–3% of all parathyroid adenomas)
- The middle mediastinum (very rarely)

Other ectopic locations include the carotid sheath (within or even lateral to this anatomic structure), while an undescended lower parathyroid gland is rarely found in the upper neck, anterior to the carotid bifurcation.

Hyperplasia and adenoma(s) of parathyroid glands produce increased cellularity, increased metabolic activity, and increased arterial vascular supply. These features are the basis for visualization using different imaging approaches. Imaging protocol for hyperplastic/adenomatous parathyroid glands usually consists of high-resolution ultrasound, radionuclide imaging, contrast-enhanced computed tomography (CT), and magnetic resonance imaging (MRI) [30, 38–40], used in variable combinations depending on certain patient-specific features as well as on local availability, logistics, cost, and radiation dosimetry considerations. In a recent review [39], the most frequently cited average values of sensitivity for correct localization of the adenoma are 76.1% (95% CI 70.4–81.4%) for ultrasound examination, 78.9% (70.4–90.6%) for scintigraphy with ^{99m}Tc-sestamibi, and 89.4% for CT. The corresponding average positive predictive values are 93.2% (95% CI 90.7–95.3%) for ultrasound, 90.7% (83.5–96%) for scintigraphy, and 93.5% for CT.

Non-radionuclide Imaging Techniques

High-resolution ultrasound (*US*) currently constitutes, in association with nuclear medicine imaging, a reliable first-line modality for preoperative localization of a parathyroid lesion. The main advantages of US are low cost, wide availability, and the noninvasive nature of the technique; furthermore, US has an important role to select patients for other imaging modalities (for instance, in case of negative US studies due to ectopic parathyroid glands located in deep cervical sites or in the mediastinum).

Optimal parameters for best diagnostic performance of US include the use of a high-frequency (7.5–13 MHz) linear array probe. The entire region of the neck including the thyroid gland, the paratracheal groves, and the carotid–jugular axis from the carotid bifurcation superiorly to the sternal notch inferiorly should be carefully explored by transverse and longitudinal scans. In patients with a large thyroid goiter and/or when the thyroid gland is partially plunging in the upper mediastinum, the use of a lower frequency US probe, with deeper penetration, can be helpful to explore the neck. The patient is lying supine and with the neck hyperextended during the US scan; right or left lateral rotation of the head is useful to better visualize the deep sites of the neck, in particular the paraesophageal or paravertebral regions (possible sites of an ectopic parathyroid adenoma/mass) are better visualized with right or left lateral rotation of the head.

A parathyroid mass typically appears on gray-scale US imaging as a rather homogeneous hypoechoic mass adjacent and posterior to the thyroid gland (Fig. 4). Topographically, the mass is usually located anteriorly to the longus colli muscles, medially to the common carotid artery; occasionally the mass is located more inferiorly in the paratracheal and paraesophageal groves. It is not infrequent to detect a clear hyperechoic interface line separating the thyroid gland from the parathyroid lesion (Fig. 5). Structure of an adenomatous/hyperplasic parathyroid gland is mostly frequently constituted by a hypercellular tissue with absent or scarce fluid or stromal components, a feature that explains the hypoechoic pattern of these lesions. Nevertheless, fatty deposition and/or internal calcifications occasionally occur in adenomas, causing the appearance of nontypical inhomogeneous echographic patterns, some of which are characterized by lobulation and/or cystic changes.

On the other hand, it is difficult in most instances to distinguish the US pattern of a hyperplasic parathyroid gland from that of a parathyroid and adenoma. In general, hyperplasic parathyroid glands most frequently have a spherical shape than adenomas and occasionally contain intraparenchymal

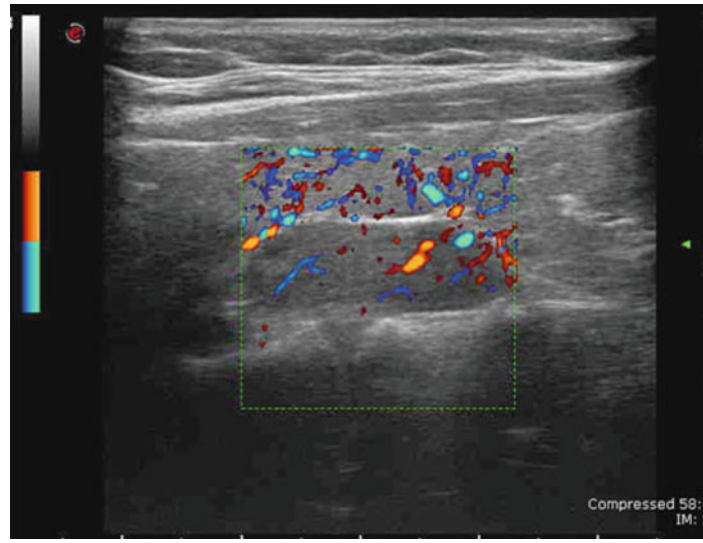

Fig. 4 Ultrasound pattern of a parathyroid adenoma located behind the right thyroid. The thyroid parenchyma is well recognized in the middle part of the image, just below the superficial layers (skin and subcutaneous muscle). The parathyroid adenoma is located just beneath the thyroid tissue, well separated by a hyperechoic capsule and appearing slightly hypoechoic with respect to the thyroid parenchyma; color Doppler evaluation reveals some hypervascularization within the parathyroid adenoma

calcifications. Furthermore, when multiple parathyroid glands are involved in a patient with chronic renal failure, it is easy to diagnose parathyroid hyperplasia. Finally, although the US appearance of a parathyroid carcinoma mimics that of an adenoma, malignancy can be recognized by an irregular shape concomitant with infiltration of the adjacent anatomic structures [41, 42].

The color Doppler pattern is also useful to correctly identify parathyroid lesions that are in general characterized by diffuse intranodular color signals or focal peripheral flow associated with variable degrees of intranodular vascularization. These features are especially useful to distinguish a parathyroid mass from a typical thyroid nodule that generally displays a regular peripheral flow pattern [43–45]. A recent addition to the imaging armamentarium for enlarged parathyroid glands is contrast-enhanced US (CEUS), based on the use of microbubble contrast and contrast-specific imaging software [46]; the underlying rationale is that the blood pool contrast so induced can depict the micro- and macro-circulation of the organ/tissue under evaluation. Both parathyroid adenomas and hyperplastic glands exhibit strong enhancement in the arterial phase, a feature related to the hyperfunctioning nature of these lesions; parathyroid lesions usually display faster washout than lesions pertaining to the thyroid gland. On the other hand, lymph nodes (whose basic US structure can be misinterpreted as a parathyroid mass) display an early central arterial and late parenchymal enhancement without early washout.

The accuracy of parathyroid's localization with US varies as a function of the size and location of the adenoma, being lowest in the evaluation of the substernal, retrotracheal, and retroesophageal spaces [47]. Furthermore, in about 40% of the patients who have undergone prior surgery, US examination does not allow to detect the presence of parathyroid glands because of distorted anatomy and/or the presence of fibrous scar tissue. Notwithstanding these limitations, US still constitutes a reliable first-line imaging approach, in conjunction with radionuclide imaging, for preoperative localization of enlarged parathyroid glands.

CT imaging is less commonly used for preoperative localization and is usually reserved (similarly as for MRI) for detecting suspected ectopic glands in patients in whom prior parathyroidectomy has failed to cure HPTH [48]. CT should also be considered for patients in whom the first-line imaging steps (US and scintigraphy) are negative [39, 49] or for patients in whom the US examination is negative, but scintigraphy suggests an ectopic lesion [50].

CT localizes parathyroid adenomas in the retrotracheal, retroesophageal, and mediastinal spaces better than US. On the other hand,

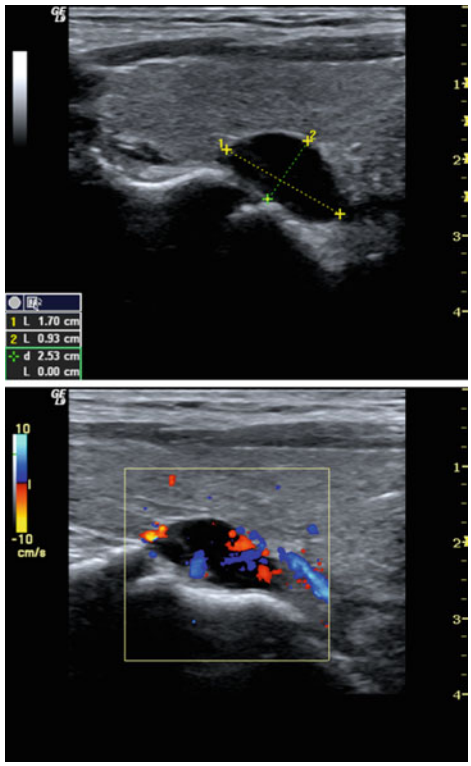

Fig. 5 Ultrasound pattern of a parathyroid adenoma more hypoechoic than the case presented in Fig. 4. Also in this case, the adenoma is located behind the right thyroid lobe of the thyroid, which is well recognized below the skin and subcutaneous muscle and separated from the parathyroid adenoma by a thin hyperechoic capsule (better detected in the *upper panel*). The more hyperechoic structure beneath the thyroid and the parathyroid adenoma is the transverse process of a vertebra in the cervical spine (C4–C5). Color Doppler evaluation (*lower panel*) reveals multiple vessels within the adenoma (Courtesy of Dr. Mario Meola, Department of Clinical and Experimental Medicine, University of Pisa, Pisa, Italy)

parathyroid glands located in the lower neck or close to the thyroid gland are not easily detectable by CT. The overall sensitivity of CT for preoperative identification of hyperplastic parathyroid glands ranges between 46% and 80%. Because of frequent hypervascularization of abnormal parathyroid glands, CT with contrast enhancement results in sensitivity consistently close to 80%. In fact, in patients with multigland disease, CT has high sensitivity and high positive predictive value, especially if performed with the so-called 4D modality [40, 51, 52]. When compared to ^{99m}Tc-sestamibi scintigraphy, CT has the advantage of a shorter examination time, associated with a comparable overall cost; on the other hand, dedicated acquisition protocols should be adopted in order to keep to a minimum the relatively high radiation burden of CT. Although local availability and logistics frequently dictate the sequence of imaging steps for preoperative localization of hyperfunctioning parathyroid lesions, there are some proponents for the use of CT imaging (either alone, combined with US, or combined with ^{99m}Tc-sestamibi scintigraphy) as the first-line approach rather than the combination of US with ^{99m}Tc-sestamibi scintigraphy [53–57].

Obvious disadvantages of CT imaging include a relatively high radiation burden to patients and the need to use an iodinated contrast to be administered i.v.; the latter feature has some associated risks and strict contraindications, for instance, in patients with prior allergic reactions to iodinated contrast agents or in patients with reduced renal function.

MRI is currently less used than CT as a second-line imaging procedure for preoperative localization of parathyroid lesions, mostly due to difficult access to this imaging modality [58]. Nevertheless, MRI is used in patients with negative or discordant localization studies, those with persistent or recurrent disease after prior surgery, or when contrast CT is contraindicated. In general, the sensitivity of MRI for localizing hyperfunctioning parathyroid glands ranges from 43% to 71%, higher when it is employed for detecting ectopic glands (88–96%) [59, 60]. Recent study showed that high-resolution MRI using a 3.0 T magnet could detect adenomas in 57% of patients with PHPT in whom both contrast CT and ^{99m}Tc-sestamibi scintigraphy failed to localize the adenoma [61].

MRI protocols involve the acquisition of multiplanar images of the neck and upper mediastinum. The standard images are obtained from the hyoid bone to the sternal notch; when a mediastinal ectopic parathyroid gland is suspected, additional ECG-gated axial images of the mediastinum are acquired. MRI scans are commonly acquired with standard T1–T2-weighted spin-echo sequences.

On MRI, enlarged parathyroid glands have considerably increased intensity on T2-weighted

and proton density images, but it is not possible to distinguish parathyroid adenomas from either simple hyperplasia or carcinoma.

Parathyroid Scintigraphy

Although there are no radiopharmaceuticals concentrating specifically only in the parathyroid glands, parathyroid scintigraphy plays an important role in the preoperative localization of hyperfunctioning parathyroid glands as a guide to minimally invasive parathyroidectomy. Early radionuclide techniques were based on the subtraction scan using two imaging agents, one accumulating both in the thyroid and parathyroid parenchyma and one exclusively in the thyroid gland, respectively. The two historical approaches to parathyroid imaging with radionuclides are the use of ^{75}Se-methionine (a radiolabeled amino acid accumulating in both tissues) coupled with ^{131}I-iodide (accumulating solely in the thyroid gland) [62–64], and the use of ^{201}Tl-chloride (imaging both parenchymas, similarly as ^{75}Se-methionine) coupled with ^{99m}Tc-pertechnetate (imaging the thyroid only) [65].

However, since its first introduction for parathyroid imaging in 1989 [66], ^{99m}Tc-sestamibi has rapidly become the radiopharmaceutical of choice for parathyroid imaging, with an overall 85–95% accuracy in primary HPTH. Localization of ^{99m}Tc-sestamibi in the parathyroid tissue is a function of metabolic activity, since this agent accumulates preferentially in mitochondria-rich tissues, as typically is a hyperfunctioning parathyroid gland. Although ^{99m}Tc-sestamibi accumulates also in the normal thyroid parenchyma, its washout rate from the parathyroid glands is different from that of the thyroid tissue [67]; in fact, this radiopharmaceutical is released much faster from the thyroid than from the parathyroid tissue. This differential retention kinetics seems to be related to downregulation in the parathyroid tissue of the P-glycoprotein system, which is responsible for the efflux of various compounds (including ^{99m}Tc-sestamibi) from the intracellular to the extracellular space [68]. The so-called single-tracer, double-phase scintigraphy is based on this difference in washout rate; it is performed by acquiring early images of the neck and thorax (about 15 min postinjection) and then imaging again at 2–3 h. A hyperfunctioning parathyroid adenoma appears as an area of early radiopharmaceutical uptake that persists on late imaging [69] (Fig. 6). Thyroid nodules that concentrate ^{99m}Tc-sestamibi avidly can cause difficulties in the interpretation of images [70]. To avoid this drawback, ^{99m}Tc-pertechnetate or ^{123}I-iodide scintigraphy can be performed in patients with thyroid nodular goiter [71]. Furthermore, some

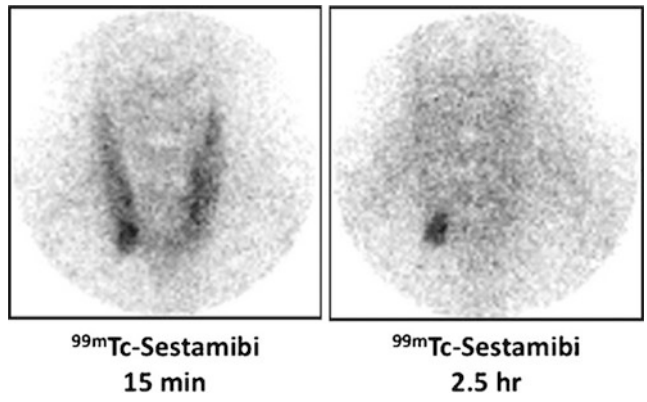

Fig. 6 Planar, single-tracer, dual-phase parathyroid scintigraphy with ^{99m}Tc-sestamibi in a patient with primary hyperparathyroidism, showing early uptake at the base of the right lobe (slightly greater than in the thyroid parenchyma), and selective retention in the delayed imaging. This area corresponded to a parathyroid adenoma that was subsequently removed with radioguided, minimally invasive surgery

parathyroid adenomas exhibit a rapid washout of ^{99m}Tc-sestamibi, thus possibly resulting in false-negative results.

Differently from earlier approaches based on the use of a single tracer, the current version of *dual-tracer subtraction parathyroid scintigraphy* is based on the use of ^{99m}Tc-sestamibi coupled with a second radiopharmaceutical that accumulates specifically in the thyroid gland, either ^{123}I-iodide or ^{99m}Tc-pertechnetate [71]. The thyroid images are subtracted from the ^{99m}Tc-sestamibi image, so that residual focal uptake indicates the presence of hyperfunctioning parathyroid tissue. Due to high cost and limited availability of ^{123}I-iodide (as well as to the relatively long acquisition time with this radionuclide), ^{99m}Tc-pertechnetate is most frequently employed as the pure thyroid imaging agent in the routine clinical practice. The ^{99m}Tc-pertechnetate image (standard activity of 185 MBq) is acquired 20 min after injection; thereafter potassium perchlorate can be administered to induce rapid washout of this agent from the thyroid gland, after which ^{99m}Tc-sestamibi is administered [72]. The $^{99m}TcO_4^-$/^{99m}Tc-sestamibi technique has sensitivity around 90% and specificity close to 100%. Alternatively, administration of ^{99m}Tc-pertechnetate after the delayed ^{99m}Tc-sestamibi acquisition allows to improve the definition of equivocal area of ^{99m}Tc-sestamibi uptake [48] (Fig. 7).

As an alternative to ^{99m}Tc-sestamibi, ^{99m}Tc-tetrofosmin is employed in some centers for parathyroid scintigraphy, although this agent exhibits slower washout from the thyroid gland than washout of ^{99m}Tc-sestamibi [73].

Parathyroid scintigraphy, either with the single-tracer, dual-phase technique or with the dual-tracer subtraction method, shows a sensitivity higher than 90% in primary PHPT, higher than that obtained with the other imaging techniques [31]. Nevertheless, sensitivity to detect hyperplastic glands in secondary HPTH is not higher than 55% [12]. ^{99m}Tc-sestamibi scintigraphy is critical in persistent or recurrent HPTH, with successful identification of the parathyroid remnant in 85% of the patients. SPECT, and especially SPECT/CT imaging, is useful especially in the detection of small or ectopic adenomas and in patients with multinodular goiter or with recurrent HPTH [74, 75] (Fig. 8).

By combining the three-dimensional functional information of SPECT with the anatomic information of CT, hybrid SPECT/CT allows optimal preoperative localization of the enlarged parathyroid glands (Fig. 9), thus complementing and sometimes even clarifying negative/equivocal US findings (Fig. 10). In this regard, it has clearly been demonstrated that SPECT/CT is more accurate than SPECT alone in patients with HPTH and nodular goiter and that the combination of early SPECT/CT with any delayed imaging method (SPECT/CT, SPECT, or planar imaging) is superior to double-phase planar imaging or double-phase SPECT [76–78]. This procedure should therefore be routinely used in the preoperative evaluation of patients with HPTH in whom minimally invasive parathyroidectomy is planned.

Similarly as has been successfully done for planar imaging, attempts have been made to apply subtraction protocols to SPECT acquisitions. In particular, Neumann et al. described a technique based on acquisition of SPECT/CT images with a dual-energy window after administration of ^{123}I-iodide and ^{99m}Tc-sestamibi. Then, the attenuation-corrected SPECT sections were utilized to obtain SPECT subtraction images (^{99m}Tc-sestamibi SPECT subtracted of the ^{123}I-iodide SPECT). In the authors' experience, SPECT/CT was significantly more specific than dual-isotope subtraction SPECT for preoperative localization of parathyroid adenomas [79].

In addition to single-photon imaging with conventional gamma cameras, the use of PET/CT with different tracers has also been proposed for localizing hyperfunctioning parathyroid tissue, particularly in the setting of recurrent HPTH and/or failure of conventional radionuclide imaging. Although the performance of these newer techniques is reported to be highly promising, clinical experience is still limited to a few specialized centers. The PET tracers employed in this scenario include [^{18}F]FDG, [^{11}C]methionine, ^{18}F-fluorocholine, and ^{18}F-DOPA as the most widely employed agents [80–84]. On the basis of recent systematic reviews and meta-analyses, the most promising PET tracers

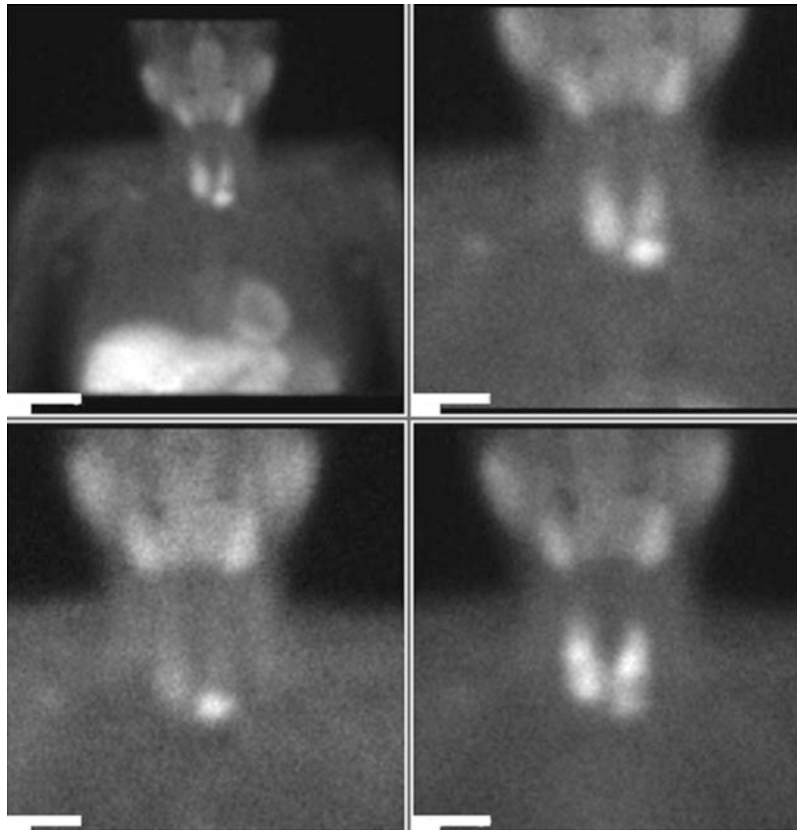

Fig. 7 Dual-tracer parathyroid scintigraphy with ^{99m}Tc-sestamibi and ^{99m}Tc-pertechnetate in a patient with hyperparathyroidism and multinodular goiter. *Upper left panel*: planar image acquired early after injection of ^{99m}Tc-sestamibi (about 10 min), with a field of view including the neck and the whole chest as a preliminary exploration for possible ectopic locations of the adenoma. *Upper right panel*: image acquired about 15 min postinjection, with zoom on the neck and upper chest; there is a suspicious area of abnormal accumulation corresponding to the base of the left thyroid lobe. *Lower left panel*: image acquired about 2.5 h postinjection of ^{99m}Tc-sestamibi, showing partial washout from the thyroid parenchyma and persistent uptake corresponding to the base of the left thyroid lobe. *Lower right panel*: image acquired about 20 min after administering ^{99m}Tc-pertechnetate (digitally subtracted from residual activity in the delayed ^{99m}Tc-sestamibi acquisition), showing selective visualization of the thyroid parenchyma with inhomogeneous uptake throughout the gland due to multinodular goiter. The parathyroid adenoma was located in the area showing slow washout of ^{99m}Tc-sestamibi in the delayed acquisition

appear to be [^{11}C]methionine and ^{18}F-fluorocholine. Although with a high degree of etherogeneity, the currently available clinical evidence for [^{11}C]methionine shows an 81% pooled sensitivity (95% CI 74–86%) with 70% detection rate (95% CI 62–77%) [83]; according to these data, another analysis obtained a pooled 69% sensitivity (95% CI 60–78%) for detecting a lesion in the correct quadrant, with very high specificity (98% pooled estimate for the positive predictive value; 95% CI 96–100%) [84].

Minimally Invasive Parathyroidectomy and Radioguided Surgery

Minimally invasive parathyroidectomy has been facilitated by the introduction of the intraoperative rapid PTH test, which can be performed with the purpose of detecting any remaining abnormal glands. Since the biological half-life of PTH in the circulation is approximately 2 min, serum PTH levels reduced by more than 50% about 15–30 min

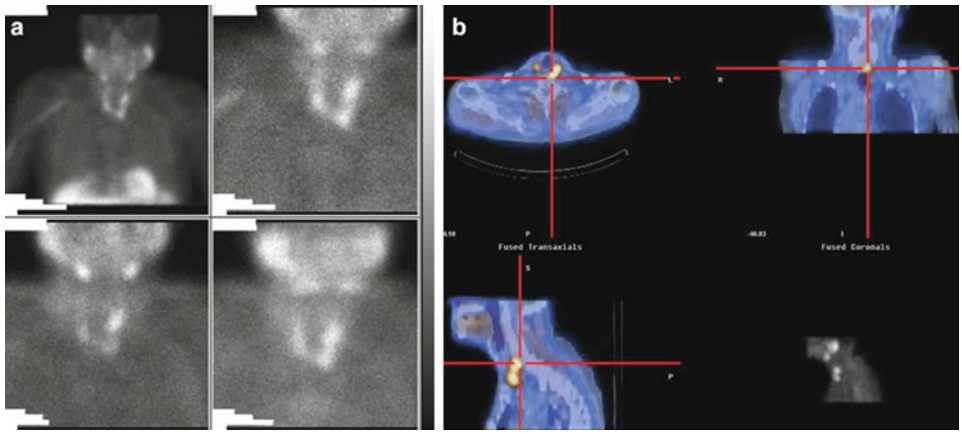

Fig. 8 Dual-tracer parathyroid scintigraphy with ^{99m}Tc-sestamibi and ^{99m}Tc-pertechnetate in a patient with hyperparathyroidism and multinodular goiter. (**a**) *Upper left panel*: planar image acquired early after injection of ^{99m}Tc-sestamibi (about 10 min), with a field of view including the neck and the whole chest as a preliminary exploration for possible ectopic locations of the adenoma. *Upper right panel*: image acquired about 15 min postinjection, with zoom on the neck and upper chest; there is a suspicious area of abnormal accumulation corresponding to the apex of the left thyroid lobe. *Lower left panel*: image acquired about 2.5 h postinjection of ^{99m}Tc-sestamibi, showing partial washout from the thyroid parenchyma and persistent uptake corresponding to the apex of the left thyroid lobe. *Lower right panel*: image acquired about 20 min after administering ^{99m}Tc-pertechnetate (digitally subtracted from residual activity in the delayed ^{99m}Tc-sestamibi acquisition), showing selective visualization of the thyroid parenchyma with inhomogeneous uptake especially at the left thyroid lobe due to multinodular goiter. (**b**) Transaxial, coronal, and sagittal fused SPECT/CT sections defining location of the parathyroid adenoma at the apex of the left thyroid lobe

after removal of a suspected parathyroid adenoma indicate that the source of abnormal production of PTH has actually been removed.

The key to success for focused parathyroidectomy employing minimally invasive approaches relies on preoperative imaging for accurate localization of the adenoma(s) and/or hyperplasia. In addition to preoperative imaging, the surgeon can rely on intraoperative procedures that can help to find the hyperfunctioning parathyroid tissue and/or to assess completeness of surgical resection of the lesion (such as, e.g., the intraoperative serum PTH assay) [85]. One of such procedures is represented by radioguided parathyroid surgery, which is performed with a handheld "gamma probe" for continuous, real-time measurements in the surgical bed after administration of ^{99m}Tc-sestamibi.

The success of radioguided surgery in HPTH patients (especially in case of primary HPTH) is based on the following considerations: (1) in most of the cases (80%) this condition is caused by a single hyperfunctioning adenoma, which is usually located adjacent to the thyroid gland [86–89]; (2) avid uptake of ^{99m}Tc-sestamibi in parathyroid adenomas is the basis for their efficient identification and preoperative localization, thus making it easier to detect intraoperatively the adenoma using the gamma probe [90]. However, there are some well-defined indications for radioguided parathyroid surgery. In particular, this procedure is to be considered only in case of clear identification and localization of a solitary parathyroid adenoma in the ^{99m}Tc-sestamibi scan, as it occurs in 60–70% of the patients with primary HPTH [90]. Indications for a minimally invasive approach can be summarized as follows:

- Both US and scintigraphy have identified only a single adenoma.
- Uptake of ^{99m}Tc-sestamibi in the enlarged parathyroid gland is clear and unequivocal.
- The ^{99m}Tc-sestamibi scan does not show thyroid nodules with persistent tracer uptake.
- A familial form of the disease has been excluded.

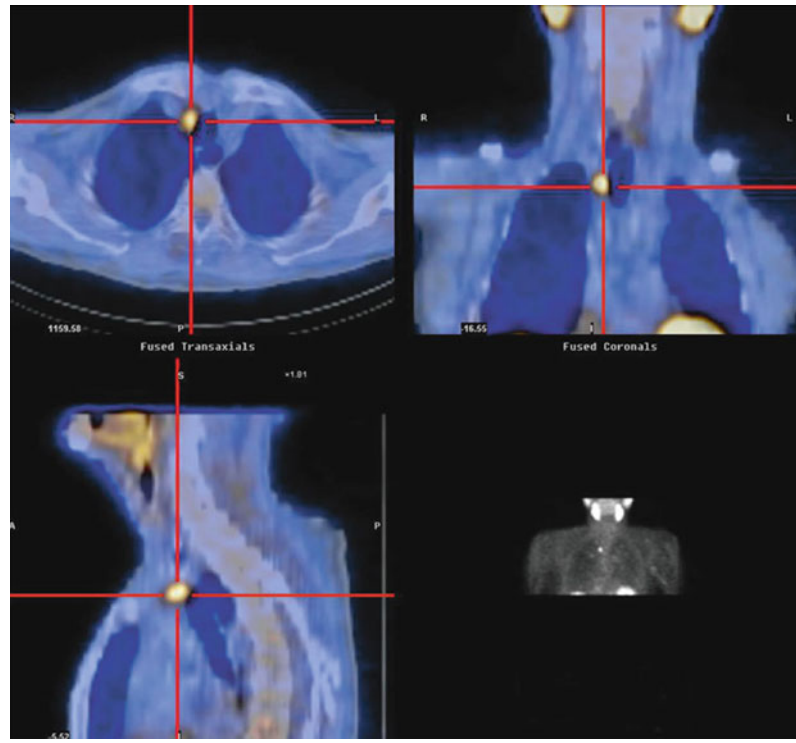

Fig. 9 ^{99m}Tc-sestamibi SPECT/CT (fused transaxial, coronal, and sagittal sections) in patient with persistent HPTH after prior parathyroidectomy (during which thyroidectomy was also performed because of concomitant multinodular goiter). Hybrid imaging defines the exact anatomic coordinates of the ectopic parathyroid adenoma located in the upper mediastinum

- The patient had not been submitted to prior irradiation of the neck.

Whereas, minimally invasive radioguided parathyroidectomy is not contraindicated in patients submitted to prior neck surgery. On the other hand, the open surgery procedure becomes mandatory in case of concomitant presence of a nodular thyroid goiter or of multigland parathyroid disease. Similarly, bilateral neck exploration is recommended when a parathyroid malignancy is suspected [90].

Norman and Chheda described the first protocol for minimally invasive radioguided parathyroidectomy in 1997 [91]. In their "single day" approach, ^{99m}Tc-sestamibi parathyroid scintigraphy was combined with radioguided surgery in the same day. In particular, radioguided surgery is performed 2–3 h after administration of 740–925 MBq of ^{99m}Tc-sestamibi and acquisition of a single-tracer, dual-phase parathyroid scintigraphy. This protocol has two main advantages: (1) the technique is cost-effective in patients with primary or recurrent hyperfunctioning parathyroid adenoma, and (2) the entire procedure (preoperative scintigraphic localization and radioguided surgery) is concentrated in a rather short time window of approximately 3–4 h.

Soon after the first reports by Norman and colleagues, the Padua group proposed a "low-dose" multiple day protocol [92, 93], which consists in performing parathyroid scintigraphy and radioguided surgery in two different days. In particular, the patient is first submitted to a classical dual-tracer parathyroid scintigraphy using full diagnostic activities; surgery is planned based on the findings of this scan. Thereafter, on the day of surgery (which is scheduled according to general logistic and organizational needs), the patient is injected with only 37 MBq of ^{99m}Tc-sestamibi just before starting the radioguided surgery procedure. At variance with the Norman's protocol, the radiation exposure for personnel in the operating room derived from such low radioactivity amount is minimal; furthermore, the surgical approach can be planned and optimized in advance based on the results of the prior full-dose parathyroid scintigraphy [48, 94, 95].

The intraoperative detection rate of parathyroid adenomas is very high with both protocols

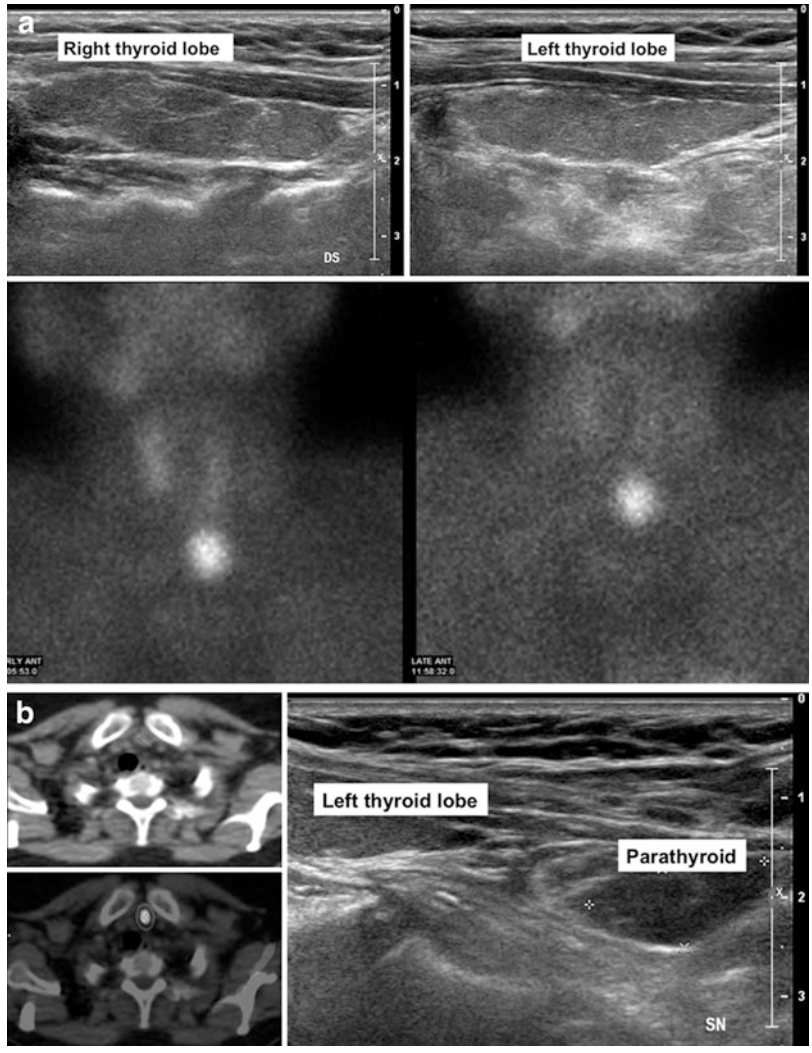

Fig. 10 A 62-year-old woman with clear diagnosis of primary HPTH (serum calcium 11 mg/dL, serum phosphorous 1.9 mg/dL, serum PTH 996 pg/mL). (**a**) An initial US scan of the neck could not reveal abnormal parathyroid lesions in the expected locations (*upper panel*); the *lower panel* shows the early and delayed ^{99m}Tc-sestamibi planar scans, with clear positivity for a hyperfunctioning parathyroid mass located below the left lower thyroid lobe. A SPECT/CT acquisition was additionally performed. (**b**) The *left panels* show the axial sections obtained with hybrid SPECT/CT imaging, confirming prolonged retention of ^{99m}Tc-sestamibi in a mass which was detectable also on the low-definition CT component of the scan (CT image above, fused SPECT/CT image below). A focused US scan was therefore repeated and confirmed the presence of a parathyroid adenoma in an unexpected location, well below the lower end of the left thyroid lobe (Courtesy of Drs. Maria Luisa De Rimini and Pietro Muto, Nuclear Medicine Service, "Monaldi" Hospital, Naples, Italy)

(over 95%); thus, choice of the method depends on local logistic/organizational considerations. However, the "low-dose protocol" is more suited for patient populations in iodine-deficient geographic areas, where there is a high prevalence of nodular goiter. In fact, thyroid nodules can occasionally be ^{99m}Tc-sestamibi avid and with slow tracer washout, an occurrence that could cause false-positive scintigraphic results if relying solely on a single-tracer, dual-phase imaging protocol. In these conditions, dual-tracer parathyroid scintigraphy has better specificity than the dual-

phase scintigraphy adopted in the Norman protocol, therefore allowing better selection of patients meeting for radioguided surgery [96]. More recently, the low-dose protocol has been shown to be highly effective also in patients with secondary HPTH, with clear advantages versus the high-dose protocol [97].

Despite the excellent performance of radioguided surgery reported by several groups around the world, there seems to be a prevailing trend within the USA for parathyroid surgery to shift away from intraoperative radioguidance [98], despite the fact that the fear of exposure to significant levels of radiation for the personnel involved in the procedure has been cleared by recent careful dosimetric measurements demonstrating that the maximum allowed radiation exposure to the surgeon would not be reached until over 5,600 radioguided parathyroidectomies are performed by the same personnel per year [99]. In fact, in most centers surgeons tend to rely on accurate preoperative localization imaging alone, especially if combined with the intraoperative PTH assay. Nevertheless, considerable interest is continuing to focus on radioguided parathyroid surgery [32, 100–102], thanks also to the introduction of newer intraoperative detection/imaging techniques [103, 104], as reported in better details in ▶ Chap. 50, "Radioguided Surgery: Novel Applications" of this book. In addition to primary and secondary HPTH (including primary multigland disease [105]), radioguidance continues to show particular clinical usefulness in diverse additional clinical conditions such as tertiary HPTH [106] and in pediatric patients [107].

Parathyroid Carcinoma

Pathology

Less than 1% of the cases of primary HPTH are sustained by a parathyroid carcinoma [108], a very rare endocrine malignancy (no more than 400 cases had been reported in the literature up to 1997) [109]. Since histology of parathyroid tumors can be equivocal or frankly misleading,

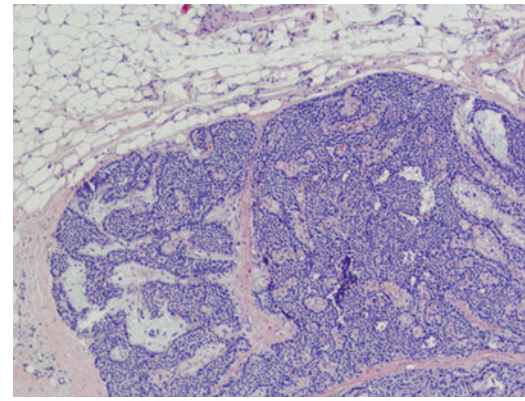

Fig. 11 Histologic pattern of a parathyroid carcinoma (low magnification): nests of densely packed cancer cells with trabecular arrangement (also occasionally arranged in follicular-like structures) separated by fibrous bands incompletely dividing the tumor into lobules. Initial invasion of the tumor capsule is seen at the *upper edge* of the tumor (Courtesy of Prof. Fulvio Basolo, Division of Pathology, Department of Surgery, University of Pisa, Pisa, Italy)

the differential diagnosis between a parathyroid carcinoma and an adenoma is often made only when local recurrence or metastases occur [110, 111]. The histologic features of parathyroid carcinoma are not very specific and difficult to be defined. Generally, neoplastic cells (usually chief cells) are arranged in a lobular pattern partitioned by dense trabeculae (Fig. 11). The more typical features are a high mitotic activity, vascular and capsular invasion, and the presence of thick fibrous bands. Gross infiltration of adjacent structures also strongly suggests the diagnosis of carcinoma; from the clinical point of view, this feature corresponds to a firm mass adherent to surrounding tissues and with very irregular margins. Mean size of the primary tumor at presentation is usually >2–3 cm, and color of the cutting surface is grayish-white [112, 113]. However, many of these features are not specific for malignancy, since they can also be found in parathyroid adenomas. Only the detection of metastatic lesions makes the diagnosis of malignancy certain, but metastasis is rare at presentation [114, 115]. For all these reasons, distinguishing a benign from a malignant parathyroid tumor is very difficult and rarely made at initial histologic evaluation. Immunohistochemistry makes diagnosis of parathyroid

carcinoma easier. Since parathyroid carcinoma usually has an elevated mitotic activity, increased expression of cell cycle-associated antigens, such as Ki-67 and cyclin D1, can make the diagnosis of parathyroid carcinoma more likely than that of adenoma [116, 117]; nevertheless, there is some overlap between benign and malignant forms. Decreased expression of p27, an inhibitor of cyclin-dependent kinase, and abnormal galectine-3 expression have also been demonstrated in parathyroid carcinomas, while evaluation of HRPT2 gene abnormalities constitutes a promising diagnostic tool as well [118]. Finally, loss of heterozygosity and loss (total or focal) of parafibromin expression have been reported in the large majority of parathyroid carcinomas but very rarely in adenomas [119–122].

Epidemiology

In contrast to parathyroid adenomas, where women predominate over men by a ratio of 3–4:1, parathyroid cancer occurs with equal frequency in the two sexes. The mean age at diagnosis is 40 years, which is 10 years earlier than the typical age of onset age for parathyroid adenomas.

Etiology

The etiology of parathyroid carcinoma remains largely unknown. Neck irradiation and a long-standing secondary HPTH might be considered as risk factors for parathyroid carcinoma, but, indeed, this relationship has been demonstrated only for parathyroid adenomas [10, 11]. Most parathyroid carcinomas are sporadic, although a few cases have also been reported in familial isolated HPTH [123] and in the HPTH-jaw tumor syndrome [124], a rare autosomal disorder where a parathyroid malignancy has been reported in as many as 15% of the patients. Parathyroid carcinoma has been reported also in MEN1 syndrome and with somatic MEN1 mutations [125], while only one case of parathyroid carcinoma has been reported in the MEN2A syndrome [126].

Pathogenesis

Several oncogenes and tumor suppressor genes, especially those involved in the control of the cell cycle, such as retinoblastoma (Rb), p53, breast carcinoma susceptibility (BRCA2), and the cyclin Dl/parathyroid adenomatosis gene 1 oncogene (PRAD1) genes [127], have been linked to parathyroid carcinomas. However, none of these genes play a primary role in the pathogenesis of parathyroid carcinoma.

Instead, a strong correlation has been demonstrated between the HPTH-jaw tumor syndrome and mutation of the HRPT2 gene (alias CDC73 and Clorf 28). This gene encodes a 531-amino acid protein called parafibromin which plays a central role in the control of the cell cycle, and subsequently in determining cell fate and promoting tumorigenesis [128]. HRPT2 is frequently mutated both in HPTH-jaw tumor syndromes and in many parathyroid carcinomas [129, 130]. In particular, parathyroid carcinoma occurs with higher frequency in the HPTH-jaw tumor syndrome than in sporadic PHPT (15% versus less than 1%). Similar germline mutations occur in a subset of kindreds with familial isolated HPTH [128, 129]. Most of these mutations are "nonsense" point mutations and result in lack of or reduced protein expression of the encoded parafibromin protein. The prevalence of HRPT2 mutations in sporadic parathyroid carcinomas may be as high as 76.6%. Therefore, HRPT2 mutations are considered one of the most significant molecular events involved in the pathogenesis of most sporadic parathyroid carcinomas. Another mechanism of HRPT2 gene inactivation, methylation of the promoter, has been reported in 2 out of 11 parathyroid carcinomas [131]. Controversial data have instead been reported about the presence of HRPT2 mutations in sporadic benign parathyroid adenomas [108, 130, 132].

Clinical Presentation

The initial clinical manifestations of parathyroid carcinoma are primarily linked to the effects of markedly elevated serum PTH levels

(i.e., hypercalcemia) rather than to local infiltration or distant metastases. From the clinical point of view, parathyroid carcinomas are usually indolent, though progressive. At initial presentation, very few patients have metastasis at regional lymph nodes (<5%) or at distant sites (<2%) [108, 133]. Parathyroid carcinoma tends to recur locally and to infiltrate adjacent structures in the neck. Metastases occur late in the course of the disease, involving cervical lymph nodes (30%) and/or lungs (40%) and/or liver (10%). Distant metastases in the bone, pleura, pericardium, and pancreas are more rare. Severe hypercalcemia with renal involvement (nephrocalcinosis and nephrolithiasis) is present in up to 80% of the patients, while bone involvement (osteitis fibrosa cystica, subperiosteal resorption, "salt and pepper" skull, and diffuse osteopenia) occurs in up to 90% of the patients. In about 80% of the patients with parathyroid carcinoma, a palpable neck mass is present at physical examination. Besides symptoms linked to nephrolithiasis, patients may complain of muscle weakness, fatigue, depression, nausea, polydipsia and polyuria, bone pain, and fractures. Recurrent severe pancreatitis, peptic ulcer disease, and anemia can also occur. However, none of these features are specific for malignancy. A few parathyroid carcinomas do not produce excess PTH [134] and can therefore be confused with thyroid or thymic carcinoma because of locally advanced disease (palpable neck mass, dysphagia, hoarseness due to laryngeal nerve palsy). The correct diagnosis can be defined by immunohistochemistry for PTH (positive staining), while staining for thyroglobulin, thyroid transcription factor 1, and calcitonin is negative. The features that might raise the suspicion of a parathyroid carcinoma in a patient with PHPT include male gender, age <50 years, serum calcium >14–15 mg/dL, markedly elevated serum PTH levels, bone and renal clinical involvement, and tumor size >3 cm.

The identification of HRPT2 gene mutations in patients with apparently sporadic parathyroid cancers as germline events suggests that a subset of these patients might have the HPT-JT syndrome or variant thereof [135]. In these cases, the surveillance for renal and jaw lesions is recommended [130]. Moreover, the relatives of a patient carrying a germline HRPT2 mutation are susceptible to develop a parathyroid cancer or other manifestation of the HPT-JT syndrome. Monitoring of family members with serum calcium determinations and neck US is therefore warranted.

Imaging of Parathyroid Carcinoma

Although not extensively discussed in the literature because of the relative rarity of this tumor, the same imaging techniques as those used for localizing benign parathyroid disease are helpful also for imaging parathyroid cancers. They include US evaluation of the neck, ^{99m}Tc-sestamibi scintigraphy, CT, and MRI, as well as PET [136, 137]. The accuracy of imaging depends on the size and site of the parathyroid carcinoma, while the suspected tissue always requires histologic confirmation [138, 139].

US examination of the neck is useful especially for detecting a space-occupying lesion, while it can also help to distinguish a parathyroid carcinoma from an adenoma, as well as invasion in the surrounding tissue and metastasis in local lymph nodes [140]. Although the US findings are not exquisitely specific for parathyroid cancer, large size, inhomogeneous appearance, and/or irregular borders with a depth/width (DW) ratio >1 are observed in 94% of the cases [141]. During follow-up, US evaluation is useful for detecting local recurrence of parathyroid carcinoma.

CT and MRI have been variously used to localize parathyroid carcinomas and to detect mediastinal and thoracic recurrences or distant metastases [142]. Nevertheless, in the postoperative status artifacts due to surgical clips may make the interpretation of cervical CT scans difficult; in this condition, T1-weighted MRI with gadolinium contrast may be more useful to detect residual locoregional parathyroid carcinoma [143]. Invasive diagnostic procedures, such as selective venous catheterization with measurement of PTH concentration in the effluent blood, may also be used to localize lesions when noninvasive imaging studies have been noncontributory [144]. ^{99m}Tc-sestamibi scintigraphy can be successful for preoperative localization of a parathyroid malignancy (with 80–90% sensitivity). However, it cannot distinguish

a parathyroid adenoma from a carcinoma [145, 146], since ^{99m}Tc-sestamibi localizes in both parathyroid adenomas and parathyroid carcinoma as well as in any other non-tumor hyperfunctioning tissue(s) and in different types of malignancy. The National Cancer Database Report by the American Cancer Society estimates that 15–17% of parathyroid carcinomas, which look identical to parathyroid adenomas on ^{99m}Tc-sestamibi scintigraphy, have concomitant lymph node metastasis at the time of diagnosis [113]. Once parathyroid carcinoma has been diagnosed and resected, ^{99m}Tc-sestamibi scintigraphy can identify recurrences in the surgical bed, as well as metastases in the contralateral neck lymph nodes (Fig. 12) and metastasis at distant sites such as the lung and bone [147]. The evaluation of bone lesions can be challenging from the diagnostic point of view, because skeletal brown tumors (a possible consequence of HPTH) accumulate ^{99m}Tc-sestamibi as well, thus mimicking metastatic parathyroid carcinoma [148]. When performed for surgical planning in patients with recurrent disease, ^{99m}Tc-sestamibi scintigraphy correctly identifies 67% of the recurrences; this compares well with 53% for CT imaging. Although discordant results between the two techniques are reported in 78% of the cases [149], both imaging studies are recommended for optimal preoperative planning [150].

PET with [^{18}F]FDG has also shown to be very helpful for detecting metastatic parathyroid cancers [151], although brown tumors can be [^{18}F]FDG avid as well, thus being possibly incorrectly interpreted as metastatic bone lesion [152]. Overexpression of the P-glycoprotein, a plasma membrane mechanism involved in multidrug resistance through an ATP-dependent drug efflux pump, seems to be involved in the false-negative results at either ^{99m}Tc-sestamibi scintigraphy or [^{18}F]FDG PET [153]. Due to the rarity of parathyroid carcinoma, there is very limited experience with the use of PET agents other than [^{18}F]FDG, occasional reports being usually included in case study populations of HPTH patients in general. Similarly as for benign forms of HPTH, the performance of [^{11}C]methionine PET/CT is expected to be especially promising in patients with parathyroid carcinoma.

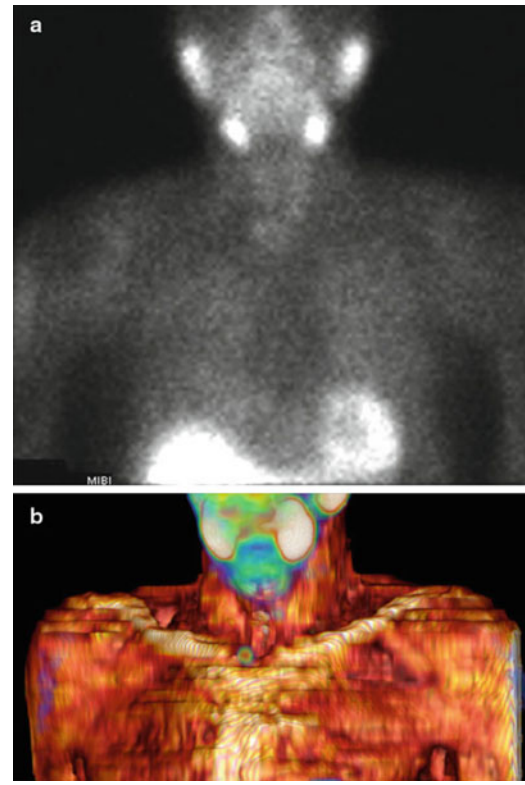

Fig. 12 A 75-year-old patient previously submitted to surgery because of primary HPTH initially thought to be caused by an adenoma of the lower right parathyroid gland. Histology revealed instead parathyroid carcinoma. About 18 months later, local recurrence was treated with a second surgery, after which the PTH levels in blood normalized for several months then started to rise again. (**a**) Planar scan of the neck and chest obtained about 10 min after administration of ^{99m}Tc-sestamibi, suggesting some ill-defined abnormal uptake of the radiopharmaceutical at the base of the neck (*slightly right sided*). (**b**) Tridimensional volume rendering of fused SPECT/CT of the neck and upper chest clearly identifies the site of abnormal ^{99m}Tc-sestamibi uptake in the right paramedian suprasternal space; the lesion corresponds to a previously unrecognized metastasis in a lymph node, as subsequently confirmed histologically

Management of Parathyroid Carcinoma

Surgery

Complete resection of the primary lesion at the time of initial operation is the only curative treatment for parathyroid carcinoma; this is possible

when the cancer is diagnosed at an early stage, when the tumor is small and intraparathyroidal. Patients who present with features suggestive of parathyroid carcinoma warrant thorough exploration of all four parathyroid glands, as parathyroid carcinoma has been reported to coexist along with benign adenomas or hyperplasia.

The most effective surgical approach is en bloc resection with curative intents [154]. Tracheoesophageal, paratracheal, and upper mediastinal lymph nodes should be excised, but extensive lateral neck dissection is indicated only when there is metastasis in the anterior cervical lymph nodes. Despite early diagnosis and a potentially curative resection, parathyroid carcinoma recurs in more than 50% of the cases. Most recurrences occur 2–3 years after the initial operation, although disease-free intervals as long as 20 years have been reported [155].

Imaging studies should be performed in all patients before reoperation. FNA of a suspicious lesion (with measurement of PTH in the needle washing) should be used with caution, if at all, to avoid seeding of malignant cells along the needle track [156]. If noninvasive imaging is negative, arteriography and selective venous sampling for PTH measurement may be useful. The management of recurrent or metastatic lesions is primarily surgical. Recurrences in the neck should be treated with wide resections, including the regional lymph nodes and other involved structures. Accessible distant metastases, particularly in the presence of localized metastatic disease, should also be excised, if possible. Even a small tumor may produce a sufficient amount of PTH to cause hypercalcemia. Although resection of a single metastasis or other foci of malignant tissue is rarely curative, their removal may result in periods of normocalcemia ranging from months to years. Decreasing the tumor burden may also render the patient's hypercalcemia more amenable to medical treatment.

Chemotherapy

Although several chemotherapy regimens have been tried (such as nitrogen mustard, vincristine, cyclophosphamide, actinomycin D, and adriamycin alone or in combination with cyclophosphamide and 5-fluorouracil), none of them has proved to be effective either by themselves or combined [157, 158]. Therefore, chemotherapy has currently no role in the management of patients with parathyroid carcinoma.

External Beam Radiation Therapy

With the exception of a single report of apparent cure (10 years) in a patient with infiltration of the trachea [157], external beam radiation therapy (EBRT) has little, if any, effect in invasive parathyroid cancers [155]. Nevertheless, recent reports suggest the benefit of EBRT as adjuvant therapy. In fact, a median disease-free survival of 60 months has been reported in four patients who received postoperative adjuvant EBRT [159]. Furthermore, a reduced rate of local recurrence has been observed when adjuvant EBRT is given after surgery, irrespective of the type of surgery and stage of the disease [160].

Management of Hypercalcemia

When parathyroid carcinoma has become widely metastatic and no surgical options are available, the control of hypercalcemia becomes the primary medical objective. Hydration with i.v. infusion of saline and loop diuretics is often beneficial in the short term, although drugs that inhibit bone resorption are needed in the longer run. Intravenous bisphosphonates (pamidronate and zoledronate) can be used for transient control of hypercalcemia. Also plicamycin is effective, but the response is transient, and repeated courses may be associated with toxicity. New promising therapies include anti-PTH immunotherapy and dendritic cell immunotherapy [161, 162]. Calcimimetics and allosteric modulators of the calcium receptors reduce PTH secretion by enhancing sensitivity of the parathyroid cells to extracellular calcium [163]. A first generation calciomimetic, R-568, was used for 2 years in a patient with metastatic parathyroid carcinoma, resulting in effective control of

hypercalcemia [164]. Cinacalcet, a more potent second-generation agent with a longer half-life and more predictable hepatic metabolism, has recently replaced R-568. In benign PHPT, cinacalcet normalizes serum calcium and partially reduces PTH levels for up to 3 years [165]. Cinacalcet therefore represents an important new option for managing severe hypercalcemia, especially in patients with inoperable disease. A highly effective approach to the treatment of severe hypercalcemia (that represents the primary cause of mortality in these patients) is based on the use of the monoclonal antibody denosumab against the RANK ligand, with a mechanism involving inhibition of receptor activation of the nuclear factor kB ligand [166–169].

Prognosis

The prognosis of parathyroid carcinoma is quite variable and, although complete cure is unlikely, prolonged survival is common with palliative surgery and medical therapy. The mean time to recurrence is usually 3 years, although periods as long as 20 years have been reported [170]. Once the tumor recurs, 5-year survival rates vary from 40% to 86%. The most favorable prognostic factor is early diagnosis and the complete excision of the tumor at initial surgery.

Concluding Remarks on Preoperative Parathyroid Imaging When Planning Minimally Invasive Parathyroidectomy

There are advantages and limitations in each of the imaging modalities described in this chapter, and various combinations are used to achieve accurate and reliable preoperative localization of the parathyroid lesion(s) for which surgery is planned. Final choice of the patient-specific imaging sequence often depends on local availability and attitudes rather than on strictly designed algorithms.

A practical algorithm has recently been proposed as a guide to imaging in patients with primary HPTH [30] (Fig. 13). The underlying condition is that the diagnosis of primary HPTH has been firmly established on the basis of biochemical parameters, that is, increased serum calcium levels with inappropriately increased PTH levels. High-resolution US examination of the neck is generally the first imaging test in these conditions, since this procedure is widely available, easy to perform and, in experienced hands, frequently enables to identify an orthotopically located parathyroid adenoma (i.e., adjacent to thyroid tissue); furthermore, US-guided FNA cytology can be performed in equivocal/inconclusive cases. On the other hand, the mediastinum and the para-tracheoesophageal space (possible sites of ectopy) cannot be explored with US, and the diagnostic performance is reduced in patients previously submitted to surgery; furthermore, US examination is a highly operator-dependent technique.

Unequivocal identification/localization of a parathyroid adenoma by high-resolution US would in principle be sufficient to guide a minimally invasive surgical approach, possibly associated with intraoperative quick PTH assay for assessing correct resection of the parathyroid lesion (see dotted path in the upper left portion of Fig. 13). Nevertheless, localization of the adenoma is generally confirmed in these patients with ^{99m}Tc-sestamibi scintigraphy, which is useful also to exclude and possible additional, ectopic hyperfunctioning glands (especially if performed with hybrid SPECT/CT imaging). Fused SPECT/CT images yield extremely useful functional and anatomic information for preoperative planning. Furthermore, in case of a positive ^{99m}Tc-sestamibi scan, radioguided surgery can be performed, as indicated by the RGS-MIRP acronym in Fig. 13 (RGS, "radioguided surgery"; MIRP, "minimally invasive radioguided parathyroidectomy").

^{99m}Tc-sestamibi scintigraphy (which entails a much smaller radiation burden than contrast-enhanced CT) is mandatory as a second-line imaging procedure in patients with a negative or inconclusive US examination. Patients with negative US but with positive scintigraphy may undergo a focused surgical approach, especially if radioguided surgery is to be employed. Nevertheless, such discordant findings should be clarified with third-line imaging, such as CT and/or MRI).

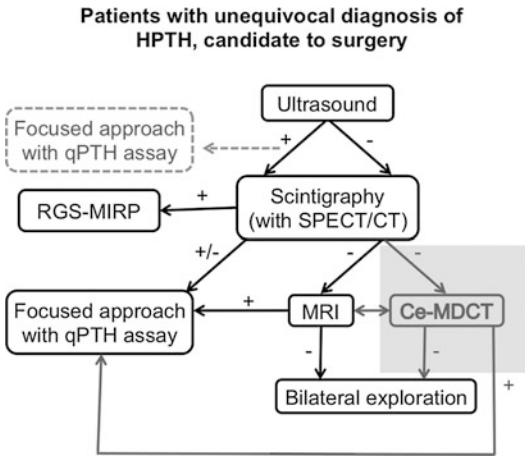

Fig. 13 Flowchart diagram showing an algorithm proposed for noninvasive preoperative imaging of patients with PHPT. The *gray-shaded* path in the *right lower* portion indicates the goal of reducing the use of contrast-enhanced CT in favor of MRI. The *dotted gray* path in the *upper right* portion demonstrates the patient who undergoes focused surgery directly on the basis of unequivocal localization of a parathyroid lesion by US, as in the case of a negative ^{99m}Tc-sestamibi scintigraphy after unequivocal US localization of parathyroid lesion(s). *Ce-MDCT* contrast-enhanced multi-detector computed tomography, *qPTH* intraoperative quick PTH assay, *RGS-MIRP* radioguided surgery minimally invasive radioguided parathyroidectomy

Further investigation with either CT or MRI is recommended for patients in whom both US and ^{99m}Tc-sestamibi scintigraphy are negative. To this purpose, the current practice in most centers is to rely on contrast-enhanced CT, unless there are clear contraindications to administration of the iodinated contrast medium. Since access to MRI is generally more limited than that to CT imaging, MRI is currently reserved for selected cases only, although the use of MRI is to be recommended in the perspective of reducing the radiation burden to patients (especially to the thyroid); this is the reason why the CT path in Fig. 13 is shaded in gray.

In patients with unequivocal localization of parathyroid lesion(s) by either CT or MRI, a minimally invasive procedure (combined with intraoperative PTH assay for) can safely be performed. Finally, a classical bilateral surgical exploration is justified when all the imaging techniques employed have failed to identify the hyperfunctioning parathyroid gland(s) or have provided inconclusive findings.

References

1. Baloch ZW, Livolsi VA. Parathyroids – morphology and pathology. In: Bilezikian JP, Marcu R, Levine MA, Marcocci C, Silverberg SJ, Potts Jr JT, editors. The parathyroids – basic and clinical concepts. 3rd ed. Oxford, UK: Elsevier; 2015. p. 23–36.
2. Rao SD, Bhadada SK, Parfitt AM. Parathyroid growth: normal and abnormal. In: Bilezikian JP, Marcu R, Levine MA, Marcocci C, Silverberg SJ, Potts Jr JT, editors. The parathyroids – basic and clinical concepts. 3rd ed. Oxford, UK: Elsevier; 2015. p. 255–78.
3. Carlson D. Parathyroid pathology: hyperparathyroidism and parathyroid tumors. Arch Pathol Lab Med. 2010;134:1639–44.
4. Brown EM. Control of parathyroid hormone secretion by its key physiological regulators. In: Bilezikian JP, Marcu R, Levine MA, Marcocci C, Silverberg SJ, Potts Jr JT, editors. The parathyroids – basic and clinical concepts. 3rd ed. Oxford, UK: Elsevier; 2015. p. 101–18.
5. Arnold A, Levine MA. Molecular basis of primary hyperparathyroidism. In: Bilezikian JP, Marcu R, Levine MA, Marcocci C, Silverberg SJ, Potts Jr JT, editors. The parathyroids – basic and clinical concepts. 3rd ed. Oxford, UK: Elsevier; 2015. p. 279–96.
6. Madkhali T, Alhefdhi A, Chen H, Elfenbein D. primary hyperparathyroidism. Ulus Cerrahi Derg. 2016;32:58–66.
7. Thakker RV. Familial and hereditary forms of primary hyperparathyroidism. In: Bilezikian JP, Marcu R, Levine MA, Marcocci C, Silverberg SJ, Potts Jr JT, editors. The parathyroids – basic and clinical concepts. 3rd ed. Oxford, UK: Elsevier; 2015. p. 341–64.
8. Bouillon R, Bollersley J, Silverberg SJ. Vitamin D and primary hyperparathyroidism. In: Bilezikian JP, Marcu R, Levine MA, Marcocci C, Silverberg SJ, Potts Jr JT, editors. The parathyroids – basic and clinical concepts. 3rd ed. Oxford, UK: Elsevier; 2015. p. 481–8.
9. Heaney RP. Vitamin D, and parathyroid hormone. In: Bilezikian JP, Marcu R, Levine MA, Marcocci C, Silverberg SJ, Potts Jr JT, editors. The parathyroids – basic and clinical concepts. 3rd ed. Oxford, UK: Elsevier; 2015. p. 633–40.
10. Christmas TJ, Chapple CR, Noble JG, Milroy EJ, Cowie AG. Hyperparathyroidism after neck irradiation. Br J Surg. 1988;75:873–4.
11. Rasmuson T, Damber L, Johansson L, Johansson R, Larsson LG. Increased incidence of parathyroid adenomas following X-ray treatment of benign diseases in the cervical spine in adult patients. Clin Endocrinol (Oxf). 2002;57:731–4.

12. Pitt SC, Sippel RS, Chen H. Secondary and tertiary hyperparathyroidism, state of the art surgical management. Surg Clin North Am. 2009;89:1227–39.
13. Salusky IB, Wesseling-Perry K. The parathyroids in renal disease: pathophysiology and systemic consequences. In: Bilezikian JP, Marcu R, Levine MA, Marcocci C, Silverberg SJ, Potts Jr JT, editors. The parathyroids – basic and clinical concepts. 3rd ed. Oxford, UK: Elsevier; 2015. p. 641–52.
14. Hadar T, Shvero J, Yaniv E, Ram E, Shvili I, Koren R. Expression of p53, Ki-67 and Bcl-2 in parathyroid adenoma and residual normal tissue. Pathol Oncol Res. 2005;11:45–9.
15. Szende B, Farid P, Vegso G, Perner F, Kopper L. Apoptosis and P53, Bcl-2 and Bax gene expression in parathyroid glands of patients with hyperparathyroidism. Pathol Oncol Res. 2004;10:98–103.
16. Bandeira F, Correia A. Clinical presentation of primary hyperparathyroidism: a global perspective. In: Bilezikian JP, Marcu R, Levine MA, Marcocci C, Silverberg SJ, Potts Jr JT, editors. The parathyroids – basic and clinical concepts. 3rd ed. Oxford, UK: Elsevier; 2015. p. 309–16.
17. Bilezikian JP, Potts Jr JT, Fuleihan G-H, Kleerekoper M, Neer R, Peacock M, et al. Summary statement from a workshop on asymptomatic primary hyperparathyroidism: a perspective for the 21st century. J Clin Endocrinol Metab. 2002;87:5353–61.
18. Silverberg SJ, Bilezikian JP. Asymptomatic primary hyperparathyroidism. In: Bilezikian JP, Marcu R, Levine MA, Marcocci C, Silverberg SJ, Potts Jr JT, editors. The parathyroids – basic and clinical concepts. 3rd ed. Oxford, UK: Elsevier; 2015. p. 317–30.
19. Joy MS, Kshirsagar AV, Franceschini N. Calcimimetics and the treatment of primary and secondary hyperparathyroidism. Ann Pharmacother. 2004;38:1871–80.
20. Khan A, Bilezikian J, Bone H, Gurevich A, Lakatos P, Misiorowski W, et al. Cinacalcet normalizes serum calcium in a double-blind randomized, placebo-controlled study in patients with primary hyperparathyroidism with contraindications to surgery. Eur J Endocrinol. 2015;172:527–35.
21. Barman Balfour JA, Scott LJ. Cinacalcet hydrochloride. Drugs. 2005;65:271–81.
22. Mingione A, Verdelli C, Terranegra A, Soldati L, Corbetta S. Molecular and clinical aspects of the target therapy with the calcimimetic cinacalcet in the treatment of parathyroid tumors. Curr Cancer Drug Targets. 2015;15:563–74.
23. Rodríguez M, Goodman WG, Liakopoulos V, Messa P, Wiecek A, Cunningham J. The use of calcimimetics for the treatment of secondary hyperparathyroidism: a 10 year evidence review. Semin Dial. 2015;28:497–507.
24. Martin KJ, Gonzalez EA, Gellens M, Hamm LL, Abboud H, Lindberg J. 19-Nor-1-alpha-25-dihydroxyvitamin D2 (Paricalcitol) safely and effectively reduces the levels of intact parathyroid hormone in patients on hemodialysis. J Am Soc Nephrol. 1998;9:1427–32.
25. Slatopolsky EA, Burke SK, Dillon MA. RenaGel, a nonabsorbed calcium- and aluminum-free phosphate binder, lowers serum phosphorus and parathyroid hormone. RenaGel Study Group. Kidney Int. 1999; 55:299–307.
26. Triponez F, Clark OH, Vanrenthergem Y, Evenepoel P. Surgical treatment of persistent hyperparathyroidism after renal transplantation. Ann Surg. 2008;248:18–30.
27. Girotto JA, Harmon JW, Ratner LE, Nicol TL, Wong L, Chen H. Parathyroidectomy promotes wound healing and prolongs survival in patients with calciphylaxis from secondary hyperparathyroidism. Surgery. 2001;130:645–50.
28. Milas M, Weber CJ. Near-total parathyroidectomy is beneficial for patients with secondary and tertiary hyperparathyroidism. Surgery. 2004;136:1252–60.
29. Irvin 3rd GL, Carneiro DM. Management changes in primary hyperparathyroidism. JAMA. 2000;284: 934–6.
30. Mariani G, Mazzeo S, Rubello D, Bartolozzi C. Preoperative localization of abnormal parathyroid glands. In: Bilezikian JP, Marcu R, Levine MA, Marcocci C, Silverberg SJ, Potts Jr JT, editors. The parathyroids – basic and clinical concepts. 3rd ed. Oxford, UK: Elsevier; 2015. p. 499–518.
31. Johnson NA, Tublin ME, Ogilvie JB. Parathyroid imaging: technique and role in the preoperative evaluation of primary hyperparathyroidism. AJR Am J Roentgenol. 2007;188:1706–15.
32. Desiato V, Melis M, Amato B, Bianco T, Rocca A, Amato M, et al. Minimally invasive radioguided parathyroid surgery: a literature review. Int J Surg. 2016; 28 Suppl 1:S84–93.
33. Harvey A, Bohacek L, Neumann D, Mihaljevic T, Berber E. Robotic thoracoscopic mediastinal parathyroidectomy for persistent hyperparathyroidism: case report and review of the literature. Surg Laparosc Endosc Percutan Tech. 2011;21:e24–7.
34. Garas G, Holsinger FC, Grant DG, Athanasiou T, Arora A, Tolley N. Is robotic parathyroidectomy a feasible and safe alternative to targeted open parathyroidectomy for the treatment of primary hyperparathyroidism? Int J Surg. 2015;15:55–60.
35. Brunaud L, Li Z, Van Den Heede K, Cuny T, Van Slycke S. Endoscopic and robotic parathyroidectomy in patients with primary hyperparathyroidism. Gland Surg. 2016;5:352–60.
36. Metz D, Jensen R, Allen B, et al. Multiple endocrine neoplasia type 1: clinical features and management. In: Bilezikian J, Levine M, Marcus R, editors. The parathyroids. New York: Raven Press; 1994. p. 591–647.
37. Noussios G, Anagnostis P, Natsis K. Ectopic parathyroid glands and their anatomical, clinical and surgical implications. Exp Clin Endocrinol Diabetes. 2012; 120:604–10.
38. Shah S, Win Z, Al-Nahhas A. Multimodality imaging of the parathyroid glands in primary hyperparathyroidism. Minerva Endocrinol. 2008;33:193–202.

39. Kunstman JW, Kirsch JD, Mahjan A, Udelsman R. Parathyroid localization and implications for clinical management. J Clin Endocrinol Metab. 2013;98:902–12.
40. Boury S. New methods for parathyroid imaging: sonography, 4D CT, MRI. Ann Endocrinol (Paris). 2015;76:148–52.
41. Harari A, Waring A, Fernandez-Ranvier G, et al. Parathyroid carcinoma: a 43-year outcome and survival analysis. J Clin Endocrinol Metab. 2011;96: 3679–86.
42. Sidhu PS, Talat N, Patel P, Mulholland NJ, Schulte K-M. Ultrasound features of malignancy in the preoperative diagnosis of parathyroid cancer: a retrospective analysis of parathyroid tumours larger than 15 mm. Eur Radiol. 2011;21:1865–73.
43. Mazzeo S, Caramella D, Lencioni R, Viacava P, De Liperi A, Naccarato AG, et al. Usefulness of echocolor Doppler in differentiating parathyroid lesions from other cervical masses. Eur Radiol. 1997;7:90–5.
44. Mohammadi A, Moloudi F, Ghasemi M. Preoperative localization of parathyroid lesion: diagnostic usefulness of color Doppler ultrasonography. Int J Clin Exp Med. 2012;5:80–6.
45. Devcic Z, Jeffrey RB, Kamaya A, Desser TS. The elusive parathyroid adenoma – techniques for detection. Ultrasound Q. 2013;29:179–87.
46. Agha A, Hornung M, Rennert J, Uller W, Lighvani H, Schlitt HJ, Jung EM. Contrast-enhanced ultrasonography for localization of pathologic glands in patients with primary hyperparathyroidism. Surgery. 2012;151: 580–6.
47. Uden P, Aspelin P, Berglund J, Lilja B, Nyman U, Olsson LE, Zederfeldt B. Preoperative localization in unilateral parathyroid surgery. A cost-benefit study on ultrasound, computed tomography and scintigraphy. Acta Chir Scand. 1990;156:29–35.
48. Mariani G, Gulec SA, Rubello D, Boni G, Puccini M, Pellizzo MR, et al. Preoperative localization and radioguided parathyroid surgery. J Nucl Med. 2003; 44:1443–58.
49. Phillips CD, Shatzkes DR. Imaging of the parathyroid glands. Semin Ultrasound CT MR. 2012;33:123–9.
50. Harari A, Zarnegar R, Lee J, Kazam E, Inabnet III WB, Fahey III TJ. Computed tomography can guide focused exploration in select patients with primary hyperparathyroidism and negative sestamibi scanning. Surgery. 2008;144:970–7.
51. Kelly HR, Hamberg LM, Hunter GJ. 4D-CT for preoperative localization of abnormal parathyroid glands in patients with hyperparathyroidism: accuracy and ability to stratify patients by unilateral vs bilateral disease in surgery-naive and re-exploration patients. AJNR Am J Neuroradiol. 2014;35:176–81.
52. Chazen JL, Gupta A, Dunning A, Phillips CD. Diagnostic accuracy of 4D-CT for parathyroid adenomas and hyperplasia. Am J Neuroradiol. 2012;33:429–33.
53. Lumachi F, Tregnaghi A, Zucchetta P, Marzola MC, Cecchini D, et al. Technetium-99m sestamibi scintigraphy and helical CT together in patients with primary hyperparathyroidism: a prospective clinical study. Br J Radiol. 2004;77:100–3.
54. Rodgers SE, Hunter GJ, Hamberg LM, Schellingerhout D, Doherty DB, Ayers GD, et al. Improved preoperative planning for directed parathyroidectomy with 4D dimensional computed tomography. Surgery. 2006;140:932–41.
55. Starker F, Mahajan A, Björklund P, Sze G, Udelsman R, Carling T. 4D Parathyroid CT as the initial localization study for patient with de novo primary hyperparathyroidism. Ann Surg Oncol. 2011;18: 1723–8.
56. Gafton AR, Glastonbury CM, Eastwood JD, Hogan JK. Parathyroid lesions: characterization with dual-phase arterial and venous enhanced CT of the neck. Am J Neuroradiol. 2012;33:949–52.
57. Madorin CA, Owen R, Coakley B, Lowe H, Nam K, Wewber K, et al. Comparison of radiation exposure and cost between dynamic computed tomography and sestamibi scintigraphy for preoperative localization of parathyroid lesions. JAMA Surg. 2013;148: 500–3.
58. Gotway MB, Reddy GP, Webb WR, Morita ET, Clark OH, Higgins CB. Comparison between MR imaging and ^{99m}Tc MIBI scintigraphy in the evaluation of recurrent of persistent hyperparathyroidism. Radiology. 2001;218:783–90.
59. Wakamatsu H, Noguchi S, Yamashita H, Yamashita H, Tamura S, Jinnouchi S, et al. Parathyroid scintigraphy with ^{99m}Tc-MIBI and ^{123}I subtraction: a comparison with magnetic resonance imaging and ultrasonography. Nucl Med Commun. 2003;24: 755–62.
60. Ruf J, Lopez Hanninen E, Steinmuller T, Rohlfing T, Bertram H, Gutberlet M, et al. Preoperative localization of parathyroid glands. Use of MRI, scintigraphy, and image fusion. Nuklearmedizin. 2004;43:85–90.
61. Grayev AM, Gentry LR, Hartman MJ, Chen H, Perlman SB, Reeder SB. Presurgical localization of parathyroid adenomas with magnetic resonance imaging at 3.0 T: an adjunct method to supplement traditional imaging. Ann Surg Oncol. 2012;19:981–9.
62. Goodwin DA, Crowley LG, Camargo CA. Localization of a mediastinal adenoma by selenomethionine Se 75 scanning. JAMA. 1969;208:2333–5.
63. DiGiulio W, Morales JO. The value of the selenomethionine Se 75 scan in preoperative localization of parathyroid adenomas. JAMA. 1969;209:1873–80.
64. Waldorf JC, van Heerden JA, Gorman CA, Grant CS, Wahner HW. ^{75}Se-Selenomethionine scanning for parathyroid localization should be abandoned. Mayo Clin Proc. 1984;59:534–7.
65. Samanta A, Wilson B, Iqbal J, Burden AC, Walls J, Cosgriff P. A clinical audit of thallium-technetium subtraction parathyroid scans. Postgrad Med J. 1990;66:441–5.
66. Coakley AJ, Kettle AG, Wells CP, O'Doherty MJ, Collins RE. ^{99}Tc^{m} sestamibi – a new agent for parathyroid imaging. Nucl Med Commun. 1989;10:791–4.

67. Hetrakul N, Civelek AC, Stagg CA, Udelsman R. In vitro accumulation of technetium-99m-sestamibi in human parathyroid mitochondria. Surgery. 2001;130:1011–8.
68. Mitchell BK, Cornelius EA, Zoghbi S, Murren JR, Ghoussoub R, Flynn SD, Kinder BK. Mechanism of technetium 99m sestamibi parathyroid imaging and the possible role of p-glycoprotein. Surgery. 1996; 120:1039–45.
69. Rubello D, Gross MD, Mariani G, AL-Nahhas A. Scintigraphic techniques in primary hyperparathyroidism: from pre-operative localisation to intra-operative imaging. Eur J Nucl Med Mol Imaging. 2007;34:926–33.
70. Taillefer R, Boucher Y, Potvin C, Lambert R. Detection and localization of parathyroid adenomas in patients with hyperparathyroidism using a single radionuclide imaging procedure with technetium-99m-sestamibi (double-phase study). J Nucl Med. 1992;33:1801–17.
71. Weber CJ, Vansant J, Alazraki N, Christy J, Watts N, Phillips LS, et al. Value of technetium 99m sestamibi iodine 123 imaging in reoperative parathyroid surgery. Surgery. 1993;114:1011–8.
72. Rubello D, Saladini G, Casara D, Borsato N, Toniato A, Piotto A, et al. Parathyroid imaging with pertechnetate plus perchlorate/MIBI subtraction scintigraphy: a fast and effective technique. Clin Nucl Med. 2000;25:527–31.
73. Okamura T. Imaging the parathyroid glands using ^{99m}Tc-tetrofosmin: current status. Intern Med. 2000; 39:85–6.
74. Spanu A, Schillaci O, Madeddu G. ^{99m}Tc labelled cationic lipophilic complexes in malignant and benign tumors: the role of SPET and pinhole-SPET in breast cancer, differentiated thyroid carcinoma and hyperparathyroidism. Q J Nucl Med Mol Imaging. 2005;49:145–69.
75. Yip L, Pryma DA, Yim JH, Carty SE, Ogilvie JB. Sestamibi SPECT intensity scoring system in sporadic primary hyperparathyroidism. World J Surg. 2009;33:426–33.
76. Lavely WC, Goetze S, Friedman KP, Leal JP, Zhang Z, Garret-Mayer E, et al. Comparison of SPECT/CT, SPECT, and planar imaging with single and dual-phase ^{99m}Tc-sestamibi parathyroid scintigraphy. J Nucl Med. 2007;48:1084–9.
77. Eslamy HK, Ziessman HA. Parathyroid scintigraphy in patients with primary hyperparathyroidism: ^{99m}Tc sestamibi SPECT and SPECT/CT. Radiographics. 2008;28:1461–76.
78. Pata G, Casella C, Besuzio S, Mittempergher F, Salerni B. Clinical appraisal of 99m technetium-sestamibi SPECT/CT compared to conventional SPECT in patients with primary hyperparathyroidism and concomitant nodular goiter. Thyroid. 2010;20:1121–7.
79. Neumann DR, Obuchowski NA, Difilippo FP. Preoperative ^{123}I/^{99m}Tc-sestamibi subtraction SPECT and SPECT/CT in primary hyperparathyroidism. J Nucl Med. 2008;49:2012–7.
80. Rubello D, Fanti S, Nanni C, Farsad M, Castellucci P, Boschi S, et al. ^{11}C-Methionine PET/CT in Technnetium-99m Sestamibi negative hyperparathyroidism in patients with renal failure on chronic hemodialysis. Eur J Nucl Med Mol Imaging. 2006;33:453–9.
81. Michaud L, Burgess A, Huchet V, Lefèvre M, Tassart M, Ohnona J, et al. Is ^{18}F-fluorocholine-positron emission tomography/computerized tomography a new imaging tool for detecting hyperfunctioning parathyroid glands in primary or secondary hyperparathyroidism? J Clin Endocrinol Metab. 2014;99:4531–6.
82. Michaud L, Balogova S, Burgess A, Ohnona J, Huchet V, Kerrou K, et al. A pilot comparison of ^{18}F-fluorocholine PET/CT, ultrasonography and ^{123}I/^{99m}Tc-sestaMIBI dual-phase dual-isotope scintigraphy in the preoperative localization of hyperfunctioning parathyroid glands in primary or secondary hyperparathyroidism: influence of thyroid anomalies. Medicine (Baltimore). 2015;94 (41):e1701. doi:10.1097/MD.0000000000001701.
83. Caldarella C, Treglia G, Isgrò MA, Giordano A. Diagnostic performance of positron emission tomography using ^{11}C-methionine in patients with suspected parathyroid adenoma: a meta-analysis. Endocrine. 2013; 43:78–83.
84. Kluijfhout WP, Pasternak JD, Drake FT, Beninato T, Gosnell JE, Shen WT, et al. Use of PET tracers for parathyroid localization: a systematic review and meta-analysis. Langenbecks Arch Surg. 2016;401:925–35.
85. Harrison BJ, Triponez F. Intraoperative adjuncts in surgery for primary hyperparathyroidism. Langenbeck's Arch Surg. 2009;394:799–809.
86. Greenspan BS, Dillehay G, Intenzo C, Lavely WC, O'Doherty M, Palestro CJ, et al. SNM practice guideline for parathyroid scintigraphy 4.0. J Nucl Med Technol. 2012;40:111–8.
87. Rubello D, Pelizzo MR, Boni G, Schiavo R, Vaggelli L, Villa G, et al. Radioguided surgery of primary hyperparathyroidism using the low ^{99m}Tc-Sestamibi dose protocol: multi-institutional experience from the Italian Study Group on Radioguided Surgery and ImmunoScintigraphy (GISCRIS). J Nucl Med. 2005;46:220–6.
88. Rubello D, Giannini S, De Carlo E, Mariani G, Muzzio PC, Rampin L, Pelizzo MR. Minimally invasive ^{99m}Tc-sestamibi radioguided surgery of parathyroid adenomas. Panminerva Med. 2005;47:99–107.
89. Rubello D, Mariani G, Pelizzo MR, Italian Study Group of Radioguided Surgery and ImmunoScintigraphy. Minimally invasive radio-guided parathyroidectomy on a group of 452 primary hyperparathyroid patients: refinement of preoperative imaging and intraoperative procedure. Nuklearmedizin. 2007;46:85–92.
90. Grassetto G, Rubello D. The increasing role of minimal invasive radioguided parathyroidectomy for treating single parathyroid adenoma. J Postgrad Med. 2013;59:1–3.

91. Norman J, Chheda H. Minimally invasive parathyroidectomy facilitated by intraoperative nuclear mapping. Surgery. 1997;122:998–1003. discussion 1003-4.
92. Casara D, Rubello D, Piotto A, Carretto E, Pelizzo MR. ^{99m}Tc-MIBI radioguided surgery for limited invasive parathyroidectomy. Tumori. 2000;86:370–1.
93. Casara D, Rubello D, Piotto A, Pelizzo MR. ^{99m}Tc-MIBI radio-guided minimally invasive parathyroid surgery planned on the basis of a preoperative combined ^{99m}Tc-pertechnetate/^{99m}Tc-MIBI and ultrasound imaging protocol. Eur J Nucl Med. 2000;27:1300–4.
94. Rubello D, Al-Nahhas A, Mariani G, Grosso MD, Rampin L, Pelizzo MR. Feasibility and long-term results of focused radioguided parathyroidectomy using a "low" 37 MBq (1 mCi) ^{99m}Tc-Sestamibi protocol. Intern Semin Surg Oncol. 2006;3:30.
95. Hindié E, Zanotti-Fregonara P, Tabarin A, Rubello D, Morelec I, Wagner T, et al. The role of radionuclide imaging in the surgical management of primary hyperparathyroidism. J Nucl Med. 2015;56:737–44.
96. Ikeda Y, Takayama J, Takami H. Minimally invasive radioguided parathyroidectomy for hyperparathyroidism. Ann Nucl Med. 2010;24:233–40.
97. Gencoglu EA, Aktas A. The efficacy of low and high dose ^{99m}Tc-MIBI protocols for intraoperative identification of hyperplastic parathyroid glands in secondary hyperparathyroidism. Rev Esp Med Nucl Imagen Mol. 2014;33:210–4.
98. Greene AB, Butler RS, McIntyre S, Barbosa GF, Mitchell J, Berber E, et al. National trends in parathyroid surgery from 1998 to 2008: a decade of change. J Am Coll Surg. 2009;209:332–43.
99. Oltmann SC, Brekke AV, Macatangay JD, Schneider DF, Chen H, Sippel RS. Surgeon and staff radiation exposure during radioguided parathyroidectomy at a high-volume institution. Ann Surg Oncol. 2014;21:3853–8.
100. Denmeade KA, Constable C, Reed WM. Use of ^{99m}Tc 2-methoxyisobutyl isonitrile in minimally invasive radioguided surgery in patients with primary hyperparathyroidism: a narrative review of the current literature. J Med Radiat Sci. 2013;60:58–66.
101. Ilgan S, Ozbas S, Bilezikci B, Sengezer T, Aydin OU, Gursoy A, et al. Radioguided occult lesion localization for minimally invasive parathyroidectomy: technical consideration and feasibility. Nucl Med Commun. 2014;35:1167–74.
102. Livingston CD. Radioguided parathyroidectomy is successful in 98.7% of selected patients. Endocr Pract. 2014;20:305–9.
103. Rahbar K, Colombo-Benkmann M, Haane C, Wenning C, Vrachimis A, Weckesser M, et al. Intraoperative 3-D mapping of parathyroid adenoma using freehand SPECT. EJNMMI Res. 2012;2(1):51. doi:10.1186/2191-219X-2-51.
104. Casella C, Rossini P, Cappelli C, Nessi C, Nascimbeni R, Portolani N. Radioguided parathyroidectomy with portable mini gamma-camera for the treatment of primary hyperparathyroidism. Int J Endocrinol. 2015;2015:134731. doi:10.1155/2015/134731. Epub 2015 Sep 15.
105. Tobin K, Ayers RR, Rajaei M, Sippel RS, Balentine CJ, Elfenbein D, et al. Use of the gamma probe to identify multigland disease in primary hyperparathyroidism. Int J Endocrinol Oncol. 2016;3:13–9.
106. Soimnay YR, Weinlander E, Alfhefdi A, Schneider D, Sippel RS, Chen H. Radioguided parathyroidectomy for tertiary hyperparathyroidism. J Surg Res. 2015;195:406–11.
107. Burke JF, Jacobson K, Gosain A, Sippel RS, Chen H. Radioguided parathyroidectomy effective in pediatric patients. J Surg Res. 2013;184:312–7.
108. Cetani F, Pardi E, Marcocci C. Update on parathyroid carcinoma. J Endocrinol Invest. 2016;39:595–606.
109. Shane E. Parathyroid carcinoma. Curr Ther Endocrinol Metab. 1997;6:565–8.
110. Shane E. Clinical review 122: parathyroid carcinoma. J Clin Endocrinol Metab. 2001;86:485–93.
111. Asare EA, Sturgeon C, Winchester DJ, Liu L, Palis B, Perrier ND, et al. Parathyroid carcinoma: an update on treatment outcomes and prognostic factors from the National Cancer Data Base (NCDB). Ann Surg Oncol. 2015;22:3990–5.
112. Wang CA, Gaz RD. Natural history of parathyroid carcinoma. Diagnosis, treatment, and results. Am J Surg. 1985;149:522–7.
113. Hundahl SA, Fleming ID, Fremgen AM, Menck HR. Two hundred eighty-six cases of parathyroid carcinoma treated in the U.S. between 1985–1995: a National Cancer Data Base Report. The American College of Surgeons Commission on Cancer and the American Cancer Society. Cancer. 1999;86:538–44.
114. Smith JF, Coombs RR. Histological diagnosis of carcinoma of the parathyroid gland. J Clin Pathol. 1984;37:1370–8.
115. Sandelin K, Tullgren O, Farnebo LO. Clinical course of metastatic parathyroid cancer. World J Surg. 1994;18:594–8.
116. Abbona GC, Papotti M, Gasparri G, Bussolati G. Proliferative activity in parathyroid tumors as detected by Ki-67 immunostaining. Hum Pathol. 1995;26:135–8.
117. Vargas MP, Vargas HI, Kleiner DE, Merino MJ. The role of prognostic markers (MiB-1, RB, and bcl-2) in the diagnosis of parathyroid tumors. Mod Pathol. 1997;10:12–7.
118. Rubin MR, Silverberg SJ. Editorial: HRPT2 in parathyroid cancer: a piece of the puzzle. J Clin Endocrinol Metab. 2005;90:5505–7.
119. Cetani F, Ambrogini E, Viacava P, Borsari S, Lemmi M, Cianferotti L, et al. Should parafibromin staining replace HRTP2 gene analysis as an additional tool for histologic diagnosis of parathyroid carcinoma? Eur J Endocrinol. 2007;156:547–54.
120. Rubin MR, Bilezikian JP, Birken S, Silverberg SJ. Human chorionic gonadotropin measurements in

parathyroid carcinoma. Eur J Endocrinol. 2008;159: 469–74.
121. Tan MH, Morrison C, Wang P, et al. Loss of parafibromin immunoreactivity is a distinguishing feature of parathyroid carcinoma. Clin Cancer Res. 2004; 10:6629–37.
122. Cetani F, Marcocci C. Parathyroid carcinoma. In: Bilezikian JP, Marcu R, Levine MA, Marcocci C, Silverberg SJ, Potts Jr JT, editors. The parathyroids – basic and clinical concepts. 3rd ed. Oxford, UK: Elsevier; 2015. p. 409–21.
123. Wassif WS, Moniz CF, Friedman E, Wong S, Weber G, Nordenskjöld M, et al. Familial isolated hyperparathyroidism: a distinct genetic entity with an increased risk of parathyroid cancer. J Clin Endocrinol Metab. 1993;77:1485–9.
124. Chen JD, Morrison C, Zhang C, Kahnoski K, Carpten JD, Teh BT. Hyperparathyroidism-jaw tumour syndrome. J Intern Med. 2003;253:634–42.
125. Agha A, Carpenter R, Bhattacharya S, Edmonson SJ, Carlsen E, Monson JP. Parathyroid carcinoma in multiple endocrine neoplasia type 1 (MEN1) syndrome: two case reports of an unrecognised entity. J Endocrinol Invest. 2007;30:145–9.
126. Jenkins PJ, Satta MA, Simmgen M, Drake WM, Williamson C, Lowe DG, et al. Metastatic parathyroid carcinoma in the MEN2A syndrome. Clin Endocrinol (Oxf). 1997;47:747–51.
127. Arnold A, Shattuck TM, Mallya SM, Krebs LJ, Costa J, Gallagher J, et al. Molecular pathogenesis of primary hyperparathyroidism. J Bone Miner Res. 2002;17 Suppl 2:N30–6.
128. Carpten JD, Robbins CM, Villablanca A, Forsberg L, Presciuttini S, Bailey-Wilson J, et al. HRPT2, encoding parafibromin, is mutated in hyperparathyroidism-jaw tumor syndrome. Nat Genet. 2002;32:676–80.
129. Howell VM, Haven CJ, Kahnoski K, Khoo SK, Petillo D, Chen J, Fleuren GJ, et al. HRPT2 mutations are associated with malignancy in sporadic parathyroid tumours. J Med Genet. 2003;40:657–63.
130. Cetani F, Pardi E, Borsari S, Viacava P, Dipollina G, Cianferotti L, et al. Genetic analyses of the HRPT2 gene in primary hyperparathyroidism: germline and somatic mutations in familial and sporadic parathyroid tumors. J Clin Endocrinol Metab. 2004;89:5583–91.
131. Hewitt KM, Sharma PK, Samowitz W, Hobbs M. Aberrant methylation of the HRPT2 gene in parathyroid carcinoma. Ann Otol Rhinol Laryngol. 2007;116: 928–33.
132. Krebs LJ, Shattuck TM, Arnold A. HRPT2 mutational analysis of typical sporadic parathyroid adenomas. J Clin Endocrinol Metab. 2005;90:5015–7.
133. Dudney WC, Bodenner D, Stack Jr BC. Parathyroid carcinoma. Otolaryngol Clin North Am. 2010;43: 441–53.
134. Fernandez-Ranvier GG, Jensen K, Khanafshar E, Quivey JM, Glastonbury C, Kebebew E, et al. Nonfunctioning parathyroid carcinoma: case report and review of literature. Endocr Pract. 2007;13:750–7.
135. Shattuck TM, Valimaki S, Obara T, Gaz RD, Clark OH, Shoback D, et al. Somatic and germ-line mutations of the HRPT2 gene in sporadic parathyroid carcinoma. N Engl J Med. 2003;349:1722–9.
136. Naji M, Hodolic M, El-Refai S, Khan S, Marzola MC, Rubello D, et al. Endocrine tumors: the evolving role of positron emission tomography in diagnosis and management. J Endocrinol Invest. 2010;33:54–60.
137. Deandreis D, Terroir M, Al Ghuzlan A, Berdelou A, Lacroix L, Bidault F, et al. ^{18}Fluorocholine PET/CT in parathyroid carcinoma: a new tool for disease staging? Eur J Nucl Med Mol Imaging. 2015;42:1941–2.
138. Kebebew E, Clark OH. Parathyroid adenoma, hyperplasia, and carcinoma: localization, technical details of primary neck exploration, and treatment of hypercalcemic crisis. Surg Oncol Clin N Am. 1998;7:721–48.
139. Fang SH, Lal G. Parathyroid cancer. Endocr Pract. 2011;17 Suppl 1:36–43.
140. Daly BD, Coffey SL, Behan M. Ultrasonographic appearances of parathyroid carcinoma. Br J Radiol. 1989;62:1017–9.
141. Hara H, Igarashi A, Yano Y, Yashiro T, Ueno E, Aiyoshi Y, et al. Ultrasonographic features of parathyroid carcinoma. Endocr J. 2001;48:213–7.
142. Mortenson MM, Evans DB, Lee JE, Hunter GJ, Shellingerhout D, Vu T, et al. Parathyroid exploration in the reoperative neck: improved preoperative localization with 4D-computed tomography. J Am Coll Surg. 2008;206:888–95.
143. Kebebew E, Arici C, Duh QY, Clark OH. Localization and reoperation results for persistent and recurrent parathyroid carcinoma. Arch Surg. 2001;136:878–85.
144. Obara T, Fujimoto Y. Diagnosis and treatment of patients with parathyroid carcinoma: an update and review. World J Surg. 1991;15:738–44.
145. Aigner RM, Fueger GF, Lax S. A case of parathyroid carcinoma visualized on Tc-99 m-sestamibi scintigraphy. Nuklearmedizin. 1997;36:256–8.
146. Singhal T, Jacobs M, Mantil JC. Tc-99 m pertechnetate/sestamibi subtraction scan in a case of parathyroid carcinoma. Clin Nucl Med. 2008;33:196–7.
147. Al-Sobhi S, Ashari LH, Ingemansson S. Detection of metastatic parathyroid carcinoma with Tc-99m sestamibi imaging. Clin Nucl Med. 1999;24:21–3.
148. Santiago Chinchilla A, Ramos Font C, Murosde Fuentes MA, Navarro-Pelayo Láinez M, Palacios Gerona H, Moreno Caballero M, Liamas Elvira JM. False negative of the scintigraphy with ^{99m}Tc-sestamibi in parathyroid carcinoma with associated brown tumors. Contributions of the ^{18}F-FDG-PET/CT. Rev Esp Med Nucl. 2011;30:174–9.
149. Clark P, Wooldridge T, Kleinpeter K, Perrier N, Lovato J, Morton K. Providing optimal preoperative localization for recurrent parathyroid carcinoma: a combined parathyroid scintigraphy and computed tomography approach. Clin Nucl Med. 2004;29:681–4.
150. Favia G, Lumachi F, Polistina F, D'Amico DF. Parathyroid carcinoma: sixteen new cases and

suggestions for correct management. World J Surg. 1998;22:1225–30.
151. Arslan N, Rydzewski B. Detection of a recurrent parathyroid carcinoma with FDG positron emission tomography. Clin Nucl Med. 2002;27:221–2.
152. Kemps B, van Ufford HQ, Creyghton W, de Haas M, Baarslag HJ, Rinkes IB, de Klerk J. Brown tumors simulating metastases on FDG PET in a patient with parathyroid carcinoma. Eur J Nucl Med Mol Imaging. 2008;35:850.
153. Sun SS, Shiau YC, Lin CC, Kao A, Lee CC. Correlation between P-glycoprotein (P-gp) expression in parathyroid and Tc-99 m MIBI parathyroid image findings. Nucl Med Biol. 2001;28:929–33.
154. Koea JB, Shaw JH. Parathyroid cancer: biology and management. Surg Oncol. 1999;8:155–65.
155. Sandelin K, Auer G, Bondeson L, Grimelius L, Farnebo LO. Prognostic factors in parathyroid cancer: a review of 95 cases. World J Surg. 1992;16: 724–31.
156. Marcocci C, Mazzeo S, Bruno-Bossio G, Picone A, Vignali E, Ciampi M, et al. Preoperative localization of suspicious parathyroid adenomas by assay of parathyroid hormone in needle aspirates. Eur J Endocrinol. 1998;139:72–7.
157. Wynne AG, van Heerden J, Carney JA, Fitzpatrick LA. Parathyroid carcinoma: clinical and pathologic features in 43 patients. Medicine (Baltimore). 1992; 71:197–205.
158. Rao SR, Shaha AR, Singh B, Rinaldo A, Ferlito A. Management of cancer of the parathyroid. Acta Otolaryngol. 2002;122:448–52.
159. Munson ND, Foote RL, Northcutt RC, et al. Parathyroid carcinoma: is there a role for adjuvant radiation therapy? Cancer. 2003;98:2378–84.
160. Clayman GL, Gonzalez HE, El-Naggar A, Vassilopoulou-Sellin R. Parathyroid carcinoma: evaluation and interdisciplinary management. Cancer. 2004;100:900–5.
161. Bradwell AR, Harvey TC. Control of hypercalcaemia of parathyroid carcinoma by immunisation. Lancet. 1999;353:370–3.
162. Betea D, Bradwell AR, Harvey TC, Mead GP, Schmidt-Gayk H, Ghaye B, et al. Hormonal and biochemical normalization and tumor shrinkage induced by anti-parathyroid hormone immunotherapy in a patient with metastatic parathyroid carcinoma. J Clin Endocrinol Metab. 2004;89:3413–20.
163. Nemeth EF, Steffey ME, Hammerland LG, Hung BC, Van Wagenen BC, DelMar EG, Balandrin MF. Calcimimetics with potent and selective activity on the parathyroid calcium receptor. Proc Natl Acad Sci U S A. 1998;95:4040–5.
164. Collins MT, Skarulis MC, Bilezikian JP, Silverberg SJ, Spiegel AM, Marx SJ. Treatment of hypercalcemia secondary to parathyroid carcinoma with a novel calcimimetic agent. J Clin Endocrinol Metab. 1998; 83:1083–8.
165. Peacock M, Bilezikian JP, Klassen PS, Guo MD, Turner SA, Shoback D. Cinacalcet hydrochloride maintains long-term normo-calcemia in patients with primary hyperparathyroidism. J Clin Endocrinol Metab. 2005;90:135–41.
166. Vellanki P, Lange K, Elaraj D, Kopp PA, El Muayed M. Denosumab for management of parathyroid carcinoma-mediated hypercalcemia. J Clin Endocrinol Metab. 2014;99:387–90.
167. Betea D, Potorac I, Beckers A. Parathyroid carcinoma: challenges in diagnosis and treatment. Ann Endocrinol (Paris). 2015;76:169–77.
168. Fountas A, Andrikoula M, Giotaki Z, Limniati C, Tsakiridou E, Tigas S, et al. The emerging role of denosumab in the long-term management of parathyroid carcinoma-related refractory hypercalcemia. Endocr Pract. 2015;21:468–73.
169. Jumpertz von Schwartzenberg R, Elbelt U, Ventz M, Mai K, Kienitz T, Maurer L, et al. Palliative treatment of uncontrollable hypercalcemia due to parathyrotoxicosis: denosumab as rescue therapy. Endocrinol Diabetes Metab Case Rep. 2015;2015: 150082. doi:10.1530/EDM-15-0082. Epub 2015 Oct 29.
170. Busaidy NL, Jimenez C, Habra MA, Schultz PN, El-Naggar AK, Clayman GL, Asper JA, et al. Parathyroid carcinoma: a 22-year experience. Head Neck. 2004;26:716–26.
171. Sadler TW. Langman's medical embryology (Italian ed. of 8th United States' ed.). Baltimore: Lippincott Williams & Wilkins; 2000. p. 370.6.
172. Wang CA. Parathyroid re-exploration. Ann Surg. 1977;186:140–5.

Diagnostic Applications of Nuclear Medicine: Breast Cancer

21

Marsha Camilla Lynch, Jean H. Lee, and David A. Mankoff

Abstract

This chapter details the use of radiotracer methods in application to breast cancer. We provide a background on breast cancer incidence and clinical features, followed by an overview of current treatment approaches. We then review the use of radionuclide methods applied to major diagnostic tasks for breast cancer that include detection, staging (locoregional and distant), response to therapy, and surveillance.

Keywords

Breast cancer • Diagnosis • Staging • Restaging • Nuclear medicine • [^{18}F]FDG PET/CT • Prognosis

Glossary

[^{18}F]FDG	2-Deoxy-2-[^{18}F]fluoro-D-glucose
^{18}F-FES	16-Alpha-^{18}F-fluoro-17 beta-estradiol
^{18}F-FFNP	21-^{18}F-fluoro-16α,17α-[(R)-(10-α-furylmethylidene)dioxy]-19-norpregn-4-Ene-3,20-dione
^{18}F-FLT	^{18}F-fluorothymidine
^{99m}Tc-HDP or ^{99m}Tc-HMDP	^{99m}Tc-hydroxymethylene diphosphonate
^{99m}Tc-MDP	^{99m}Tc-methylene diphosphonate
ACOG	American College of Obstetricians and Gynecologists
ACR	American College of Radiology
ACS	American Cancer Society
AI	Aromatase inhibitor
AJCC	American Joint Committee on Cancer
BCS	Breast-conserving surgery
BODAICEA	Breast and Ovarian Analysis of Disease Incidence and Carrier Estimation Algorithm
BRCA1	Breast cancer type 1 susceptibility protein
BRCA2	Breast cancer type 2 susceptibility protein

M.C. Lynch • D.A. Mankoff (✉)
Division of Nuclear Medicine, Department of Radiology, University of Pennsylvania, Philadelphia, PA, USA

Division of Nuclear Medicine and Clinical Molecular Imaging, University of Pennsylvania Health System, Philadelphia, PA, USA
e-mail: david.mankoff@uphs.upenn.edu

J.H. Lee
Department of Radiology, University of Washington, Seattle, WA, USA

Seattle Cancer Care Alliance, Seattle, WA, USA

© Springer International Publishing Switzerland 2017
H.W. Strauss et al. (eds.), *Nuclear Oncology*,
https://doi.org/10.1007/978-3-319-26236-9_12

BRCAPRO	BRCA mutation carrier prediction model
BS	Bone scintigraphy
BSGI	Breast-specific gamma imaging, also known as molecular breast imaging
CHEK2	Checkpoint kinase 2
CR	Complete response
CT	X-ray computed tomography
DCIS	Ductal carcinoma in situ
DFS	Disease-free survival
ENE	Extranodal extension
ER	Estrogen receptor
ERBB2	Gene for the HER2 receptor
FISH	Fluorescent in situ hybridization
HER2	Human epidermal growth factor receptor 2, also known as receptor tyrosine-protein kinase erbB-2, or HER2/neu
IM	Internal mammary
LABC	Locally advanced breast cancer
MBC	Metastatic breast cancer
MHT	Menopausal hormone therapy
MRI	Magnetic resonance imaging
mTOR	Mammalian target of rapamycin
$Na^{18}F$	Sodium [^{18}F]fluoride
NAT	Neo-adjuvant therapy
NCCN	National Comprehensive Cancer Network
NPV	Negative predictive value
OS	Overall survival
p53	Tumor protein p53, also known as cellular tumor antigen p53, phosphoprotein p53, tumor suppressor p53, antigen NY-CO-13, or transformation-related protein 53 (TRP53)
PALB2	Partner and localizer of BRCA2, also known as FANCN
pCR	Pathologic complete response
PEM	Positron emission mammography
PET	Positron emission tomography
PET/CT	Positron emission tomography/computed tomography
PR	Progesterone receptor
PTEN	Phosphatase and tensin homolog
RECIST	Response evaluation criteria in solid tumors
SBI	Society of Breast Imaging
SERM	Selective estrogen receptor modulator
SLN	Sentinel lymph node
SNP	Single nucleotide polymorphism
SPECT	Single-photon emission computed tomography
SPECT/CT	Single-photon emission computed tomography/computed tomography
SUV	Standardized uptake value
TNBC	Triple-negative breast cancer
TNM	AJCC staging system based on parameters “T” (tumor status), “N” (lymph node status) and “M” (distant metastasis status)
US	Ultrasonography

Contents

Epidemiology of the Tumor 615
Risk Factors 615
Genetic Predisposition 616
Underlying Breast Cancer Biology Changes 616
Staging Categories and Prognostic Stratification 617

Breast Cancer Detection and Diagnosis, Modalities Other Than Nuclear Medicine for the Tumor 617

Nuclear Imaging for Primary Detection and Diagnosis 619

Nuclear Imaging for Regional Nodal Staging 620

Nuclear Methods for Staging of Distant Metastases 622

Approaches to Breast Cancer Therapy 624

Assessing the Efficacy of Treatment(s) 626

Future Directions 629

References 630

Epidemiology of the Tumor

Breast cancer is the most common non-skin cancer and the second leading cause of cancer mortality in women [1, 2]. Breast cancer is largely a disease of women (one in eight lifetime risk) with an estimated 231,840 new cases expected to be diagnosed in the USA in 2015 [1]. The incidence of breast cancer in men is ~100 times less than in women, with approximately 2,350 new cases expected in 2015. A sharp 7% decline in incidence of breast cancer occurred among white women between 2002 and 2003 attributable to a decline in the use of menopausal hormone therapy (MHT) after a 2002 report linked the use of combined estrogen plus progestin MHT with an increased risk of breast cancer and coronary heart disease [3]. More recently (data from 2007 to 2011), the incidence rates have been stable in white women and increased slightly to 0.3% in black women [2].

There has been a steady decrease in mortality from breast cancer since 1989, attributed to both improvements in early detection, screening programs initiated in the USA in the early 1980s, and treatment [4, 5]. Despite several randomized control trials demonstrating the mortality benefit of screening, there remains controversy on screening guidelines for average-risk women. New 2015 recommendations from the American Cancer Society (ACS) now suggest yearly screening beginning from 45 through 54 and biennial screening from age 55 to age 74 or expected lifetime of less than 10 years [6]. Other organizations including the Society of Breast Imaging (SBI), American College of Obstetricians and Gynecologists (ACOG), and American College of Radiology (ACR) continue to recommend annual screening beginning at age 40. Just over 40,000 women and 400 men are expected to succumb to the disease in 2015. Mortality rates from the most recent data have slightly favored younger more than older women and white more than black women in recent times [2].

Risk Factors

Risk factors for development of breast cancer are due to one or a combination of genetic/familial, reproductive/hormonal, lifestyle, and environmental factors. Further, some of these factors may be classified as modifiable/external or non-modifiable/internal. The most well-established risk factors for female breast cancer include age, family history and genetics, late first pregnancy, and obesity [7]. Besides obesity, other modifiable factors that contribute to breast cancer risk include physical inactivity, use of MHT, long-term heavy smoking, and alcohol consumption [8, 9]. Other well-established non-modifiable risk factors include long menstrual history (early menarche, late menopause), mantle radiation for Hodgkin's lymphoma, and inherited gene mutations (e.g., BRCA1/BRCA 2). Factors shown to decrease the risk of breast cancer include breastfeeding for at least a year, increased physical activity, and, in high-risk women, decreasing endogenous estrogens by either inhibition of the estrogen receptor using selective estrogen receptor modulators (SERMs) or blocking estrogen synthesis using aromatase inhibitors (AIs). It is estimated that in some populations of average-risk women, lifestyle risk reduction measures may contribute to up to a 30% decrease in overall risk and chemopreventive measures using SERMS and AIs may reduce breast cancer risk by up to 50% [9–12].

Age is an important risk factor. The highest risk of developing invasive breast cancer by age group occurs in women 70 and over (1 in 15), while the

risk in women 39 years and younger is only 1 in 208. The majority of women who develop breast cancer are postmenopausal; however, breast cancer is not uncommon in premenopausal women. Breast cancer in younger women tends to be more aggressive than breast cancer diagnosed for older women and is an important cause of mortality in younger patients. Breast cancer is the leading cause of cancer death in women age 20–59, accounting for over 12,000 deaths annually [2].

Genetic Predisposition

Approximately 30% of breast cancer cases are familial and associated with mutations in breast cancer susceptibility genes. Of these, up to 30% are due to high-penetrance mutations in the BRCA1, BRCA2, PTEN, and p53 genes, and these patients face substantially increased lifetime risk of breast cancer, between 40% and 85% over the average-risk women (~12%). Mutations in genes related to DNA repair, such as PALB2 and CHEK2, have also been shown to be associated with moderate risk [13–15]. Several risk assessment models have been developed to estimate the breast cancer risk or probability of carrying a susceptibility genetic mutation, most notably the Gail, Claus, BRCAPRO, Breast and Ovarian Analysis of Disease Incidence and Carrier Estimation Algorithm (BODAICEA), and Tyrer-Cuzick models [16–20]. These models take into account various sets of risk factors to estimate an individual's risk, including genetic mutations, family history, history of chest irradiation and personal history of ductal carcinoma in situ, ovarian cancer, lobular neoplasia, or atypical ductal hyperplasia, which are used to inform provider and patient decision-making regarding an appropriate screening timetable. The ACR/SBI recommends annual screening with mammography and breast MRI for women with a lifetime risk of greater than 20% for developing breast cancer beginning by age 30, for known high-penetrance gene mutations, 10 years earlier than the youngest affected relative or 8 years after chest radiation [21].

There are other common genetic variants, single nucleotide polymorphisms (SNPs), that confer a much smaller increased risk, but may in combination account for a more substantially increased risk of development of breast cancer in the remainder of familial breast cancer patients who do not have an identifiable high-risk or moderate-risk genetic mutation. Currently, there are more than 90 risk loci identified through genome-wide-associated studies, a technique used to identify genetic variations associated with breast cancer, with estimated hundreds more yet to be discovered that might explain significant proportion of familial and sporadic breast cancer risk [22, 23].

Underlying Breast Cancer Biology Changes

Breast cancers arise from the epithelial cells in the breast cancer ducts [24]. The most important histologic feature in the primary tumor is the presence or absence of tumor invasion beyond the ductal architecture. Tumors that have not broken through the outer boundaries of ductal structures are termed noninvasive (ductal carcinoma in situ, DCIS) and rarely metastasize [24]. Invasive cancers are those that have broken through tissue boundaries at the time of diagnosis and have the potential to metastasize both through lymphatic and hematologic spread. Other histologic features of note include the architectural pattern (ductal, lobular, or mixed), nuclear grade (low, intermediate, or high), and the presence or absence of lymphovascular invasion [24]. In addition to morphological analyses, biopsy material is routinely assayed for phenotypic features that include the expression of hormone receptors (estrogen receptor [ER] and progesterone receptor [PR]) and HER2/neu (also known as cerbB2), typically by immunohistochemistry or fluorescent in situ hybridization (FISH).

The use of gene expression profiling methods has yielded further insights into breast cancer phenotype [25] establishing the current understanding of breast cancer, not as a single entity but as a heterogeneous disease with a number of subtypes defined by distinct molecular signatures [26–32]. Perou et al. proposed four breast cancer subtypes: (1) luminal A, typically hormone receptor positive

Table 1 Four major subtypes of invasive breast cancer used clinically (Adapted from [27])

Subtype	Standard immunochemical results and cancer grade	Frequency (%)	Comments
Luminal A	ER^+ PR^+ HER^+, usually low grade	50–55	Best prognosis, low Ki-67 level
Luminal B	ER^+ PR^+ HER^-, usually intermediate to high grade	15	Generally more proliferative (high Ki-67 levels) with less marked hormonal receptor expression than luminal A tumors, approximately 30% are HER2 positive
HER2 enriched	ER^- PR^- HER^+, usually midgrade to high grade	15	Prognosis much improved with directed therapy (e.g., trastuzumab); 30–40% of tumors also express ERs and PRs
Basal-like	ER^- PR^- HER^-, high grade	10–20	Often synonymous with triple negative

and histologically low grade; (2) luminal B, typically hormone receptor positive and histologically medium to high grade; (3) HER2 enriched, which show increased expression of the ERBB2 gene; and (4) basal-like, which express neither the ER/PR receptors nor HER2 ("triple negative") and typically express high levels of genes favoring cellular proliferation. Basal cancers represent the most aggressive tumors (see Table 1).

Measuring levels of certain cellular biomarkers within tumors, e.g., Ki-67, a marker of cellular proliferation, can clarify the molecular portrait of a particular tumor and also aid in prediction of tumor aggressiveness and behavior. Molecules and receptors may also serve as targets for specific therapy, e.g., the HER2 receptor is targeted with the drug trastuzumab [33]. Some predictive expression panels are now approved and used in clinical practice [34]. For example, the 21-gene assay used in the Oncotype DX (Genomic Health Inc.) panel is now routinely used to determine which patients with early-stage ER-positive breast cancer may benefit from adjuvant chemotherapy in addition to endocrine therapy [27, 35, 36].

Staging Categories and Prognostic Stratification

Breast cancer stage at presentation is an important factor in prognosis and treatment. Stages are defined in Table 2. The most widely accepted (AJCC) system uses a TNM approach [37]. There is also a stage classification, which includes groups of TNM categories ranging from early-stage disease (stage I) to late-stage, metastatic disease (stage IV). Improved diagnosis, staging, and especially sentinel lymph node (SLN) biopsy resulted in significant changes in breast cancer staging definitions in the 6th edition of the AJCC staging manual, reviewed in Singletary et al. [37] with no major changes [38] to the breast cancer staging definitions in the currently used 7th edition of the AJCC guidelines [39] published in 2010.

Breast Cancer Detection and Diagnosis, Modalities Other Than Nuclear Medicine for the Tumor

Mammography is the primary imaging modality for breast cancer screening, detection, and diagnosis [40]. The average earlier stage and smaller size of lesions detected by mammographic screening, versus symptomatic and/or palpable lesions, reflects the success of mammographic screening, which has been shown to reduce breast cancer mortality [40]. Full-field digital mammography has largely replaced screen-film mammography. And the recent addition of digital breast tomosynthesis has been shown to reduce false-positive rates and increase cancer detection [41, 42]. Both ultrasound and MRI are important adjuncts to x-ray mammography for detection, diagnosis, characterization, and determination of the extent of breast cancer and are routinely utilized in these roles [43, 44].

MRI has been shown to be useful for screening in high-risk patients, i.e., women with greater than 20% lifetime risk of breast cancer.

Table 2 Summary of the AJCC staging system for breast cancer (Adapted from [37–39])

Tumor (T)
T0 – no primary tumor found
Tis – carcinoma in situ
T1 – invasive cancer <2 cm in greatest dimension
T1mic – microinvasion ≦0.1 cm in greatest dimension
T1a – tumor >0.1 cm but ≦0.5 cm in greatest dimension
T1b – tumor >0.5 cm but ≦1 cm in greatest dimension
T1c – tumor >1 cm but ≦2 cm in greatest dimension
T2 – tumor >2 cm but ≦5 cm in greatest dimension
T3 – tumor >5 cm in greatest dimension
T4 – tumor of any size with direct extension to chest wall or skin
Regional lymph nodes (N) (clinical staging)[a]
N0 – no regional nodal metastases
N1 – metastasis in mobile ipsilateral axillary nodes
N2 – metastasis to fixed ipsilateral axillary nodes (N2a) or ipsilateral internal mammary nodes in the absence of ipsilateral axillary lymph node metastasis (N2b)
N3 – metastases in ipsilateral infraclavicular nodes and axillary nodes (N3a) or ipsilateral internal mammary nodes and axillary nodes (N3b) or metastases to ipsilateral supraclavicular nodes (N3c)
Regional lymph nodes (N) (pathologic staging)[b]
pNX – regional lymph nodes cannot be assessed (e.g., previously removed or not removed for pathologic study)
pN0 – no regional lymph node metastasis histologically, no additional examination for isolated tumor cells
pN0(i−) – no regional lymph node metastasis histologically, negative immunohistochemical staining
pN0(i+) – isolated tumor cells identified histologically or by positive immunohistochemical staining, no cluster >0.2 mm
pN0(mol−) – no regional lymph node metastasis histologically, negative molecular findings
pN0(mol+) – no regional lymph node metastasis histologically, positive molecular findings
pN1 – metastasis in one to three axillary lymph nodes and/or in internal mammary nodes with microscopic disease detected by sentinel lymph node dissection but not clinically apparent[a]
pN1mi – micrometastasis (>0.2 mm, none >2.0 mm)
pN1a – metastasis in one to three axillary lymph nodes
pN1b – metastasis in internal mammary nodes with microscopic disease detected by sentinel lymph node dissection but not clinically apparent[a]
pN1c – metastasis in one to three axillary lymph nodes and in internal mammary lymph nodes[c] with microscopic disease detected by sentinel lymph node dissection but not clinically apparent[a]
pN2 – metastasis in four to nine axillary lymph nodes or in clinically apparent[a] internal mammary lymph nodes in the absence of axillary lymph node metastasis
pN2a – metastasis in four to nine axillary lymph nodes (at least one tumor deposit >2.0 mm)
pN2b – metastasis in clinically apparent[a] internal mammary lymph nodes in the absence of axillary lymph node metastasis
pN3 – metastasis in ten or more axillary lymph nodes or in infraclavicular lymph nodes or in clinically apparent[a] ipsilateral internal mammary lymph nodes in the presence of one or more positive axillary lymph nodes or in more than three axillary lymph nodes with clinically negative microscopic metastasis in internal mammary lymph nodes or in ipsilateral supraclavicular lymph nodes
pN3a – metastasis in ten or more axillary lymph nodes (at least one tumor deposit >2.0 mm) or metastasis to the infraclavicular lymph nodes
pN3b – metastasis in clinically apparent[a] ipsilateral internal mammary lymph nodes in the presence of one or more positive axillary lymph nodes or in more than three axillary lymph nodes and in internal mammary lymph nodes with microscopic disease detected by sentinel lymph node dissection but not clinically apparent[a]
pN3c – metastasis in ipsilateral supraclavicular lymph nodes
Distant metastases (M)
MX – distant metastases cannot be assessed

(*continued*)

Table 2 (continued)

M0 – no distant metastases			
M1 – distant metastases			
Alternate staging system for invasive breast cancer			
Stage I	Stage II	Stage III	Stage IV
T1N0M0	Stage IIA	Stage IIIA	Any T, any N, M1
	T0N1M0	T3N1M0	
	T1N1M0	T1-3N2M0	
	T2N0M0	Stage IIIB	
	Stage IIB	T4N0-2 M0	
	T2N1M0	Stage IIIC	
	T3N0M0	Any T, N3M0	

[a]This system is for clinical staging based upon imaging and physical examination
[b]Pathologic staging for nodal metastases is further classified for sentinel lymph nodes, for detection on the basis of immunohistochemistry assays, and for detection on the basis of molecular assays. Classification is based on axillary lymph node dissection with or without sentinel lymph node dissection. Classification based solely on sentinel lymph node dissection without subsequent axillary lymph node dissection is designated (sn) for "sentinel node," such as pN0(i_)(sn)
[c]If associated with more than three positive axillary lymph nodes, the internal mammary nodes are classified as pN3b to reflect increased tumor burden

In a meta-analysis of 14 studies of high-risk women conducted between 2000 and 2011, MRI was shown to have higher sensitivity for malignancy (84.6%) than mammography (38.6%) or ultrasound (39.6%) [45].

The American Cancer Society recommendations have incorporated MRI for screening in high-risk patients [46]. Mammography, ultrasound, and breast MRI can all be used to direct tissue sampling by needle biopsy for breast cancer diagnosis.

Randomized control trials have shown no survival or quality of life benefit when annual mammography has been compared with intensive imaging or laboratory surveillance in asymptomatic women with early-stage breast cancer [47].

With regard to staging and metastatic workup for asymptomatic women with a history of early-stage breast cancer, stage I, IIA, and IIB, no further imaging is indicated beyond diagnostic mammography (with adjunct use of US and MRI) given the low chance of distant metastases and the higher chance of false-positive findings [48]. For later stage breast cancer patients, stage III and above current guidelines recommend chest CT, abdomen +/− pelvis CT or MR, bone imaging (bone scintigraphy (BS) or $Na^{18}F$ PET/CT), and optional [^{18}F]FDG PET/CT. Bone scan and [^{18}F]FDG PET/CT are the most common nuclear imaging methods used in staging and metastatic workup. These will be discussed later. Again, anatomic imaging modalities are considered the gold standard with chest and abdominopelvic CT, breast MR, and brain MR performed as directed by physical examination and clinical assessment.

Nuclear Imaging for Primary Detection and Diagnosis

Radiotracer methods for primary breast cancer detection and diagnosis have not as yet found widespread use despite some important advantages over anatomic imaging, namely, the potential for more specific targeting of breast cancer tissue, good tumor to background contrast, and uptake independent of breast density [49–53]. ^{99m}Tc-sestamibi is the most common single-photon radiopharmaceutical used in both scintimammography, imaging of the breast using traditional nuclear medicine gamma cameras, and breast-specific gamma imaging (BSGI, also called molecular breast imaging), imaging with dedicated breast small field-of-view gamma cameras. The radiopharmaceutical is taken up and retained differentially in breast tumors from normal breast tissue. The specific mechanism is unknown, but appears to depend on factors relating to regional blood flow, plasma and mitochondrial membrane potential, angiogenesis, and tissue

metabolism [54–56]. Scintimammography, however, has a limited ability to detect lesions less than 1 cm and also has lower sensitivity for non-palpable lesions. BSGI can overcome some of these limitations using dedicated devices that provide high spatial resolution using dedicated breast imaging devices [49, 51, 57]. The disadvantage of both techniques is that they require relatively long imaging times and subject the patient to a substantially increased radiation dose (15–30 times) compared with mammography [57, 58]. At present, they are not indicated for routine screening/primary detection.

PET has also been tested in application to breast cancer detection and diagnosis, spurred by the finding of increased 2-Deoxy-2-[^{18}F]fluoro-D-glucose ([^{18}F]FDG) uptake in cancer compared to normal breast tissue. [^{18}F]FDG uptake in tumors reflects the rate of glucose metabolism and correlates somewhat with histologic type (higher uptake in ductal vs. lobular), tumor histologic grade, and indices of cellular proliferation (higher uptake with higher levels of proliferation) [59, 60]. Overall, the sensitivity of whole-body [^{18}F]FDG PET in the detection of primary breast cancer ranges 64–96%, specificity of 73–100%, positive predictive value of 81–100%, and negative predictive value of 52–89% [61]. Whole-body [^{18}F]FDG PET however has low sensitivity for small, well-differentiated, and in situ cancers [62]. As with ^{99m}Tc-sestamibi scintimammography, this has severely limited its use for primary tumor diagnosis.

Dedicated breast positron emission mammography (PEM) units have been developed [63], and advantages include higher spatial resolution, shorter imaging time, and reduced attenuation compared with whole-body imaging. PEM units allow a co-registration of anatomic and molecular information similar to PET/CT and have biopsy capability [64]. In a large trial of patients with newly diagnosed early breast cancer, PEM showed improvement in specificity over MRI, and the performance of PEM plus conventional imaging is similar to MRI with regard to cancer detection [65].

However, PEM limitations include difficulty in imaging posterior lesions, variable [^{18}F]FDG uptake in small tumors, and false-positive findings from prior biopsy [66, 67]. In addition, similar to single-photon techniques, radiation doses are significantly higher than mammography [57].

Nuclear Imaging for Regional Nodal Staging

Staging is typically divided into regional lymph nodes, especially axillary nodes, and distant or systemic staging of sites beyond regional lymph nodes, especially to visceral organs (lung and liver) and bone. Almost all patients with invasive breast cancer will undergo axillary nodal staging, since the presence or absence of axillary lymph nodes is an important consideration for further treatment after surgery [68].

The traditional approach to axillary nodal staging was the axillary nodal dissection, where axillary contents were removed and examined; however, the morbidity of this process, including a significant incidence of lymphedema, led to the search for a less morbid but equally accurate approach [68]. This consideration motivated sentinel lymph node (SLN) methods, designed to identify and sample the node(s) that are the first draining nodes, i.e., "sentinels" in the axillary drainage basin for the breast lesion. SLN biopsy is a shorter surgical procedure than full axillary nodal dissection with much less morbidity [68]. If sentinel nodes are negative, then the chance of "downstream" nodal metastases is quite small, and the patient can be spared the full dissection. If the sentinel node shows evidence of metastasis, then an axillary dissection may be needed to determine the extent of axillary spread. SLN biopsy has been shown to be highly accurate compared to axillary dissection [69–71] and has emerged as the standard of care for axillary nodal sampling in patients with clinically negative axillae [72]. SLN biopsy has been thoroughly tested in large clinical trials and shown to be safe and accurate, with comparable relapse and survival compared to axillary nodal dissection [73, 74]. Further, a large randomized clinical trial showed that completion axillary dissection is not useful for improved locoregional control or survival in women with smaller (T1/T2) tumors, no palpable adenopathy, and one or two positive nodes positive by SLNB without gross ENE [75].

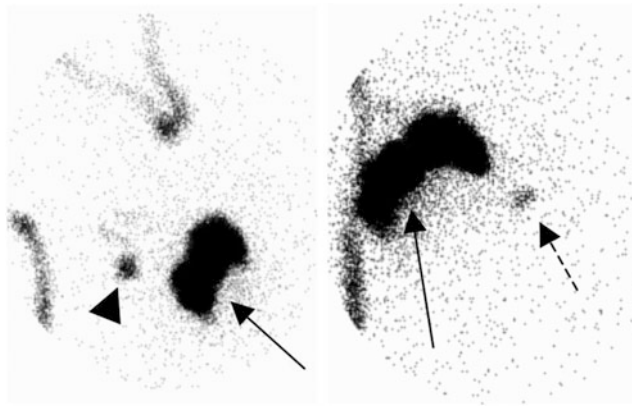

Fig. 1 Lymphoscintigraphy for breast cancer sentinel lymph node mapping. Images (oblique, *left*, and anterior, *right*), with the body contour outline drawn using a radioactive marker, show a peri-lesional injection (*solid arrows*), an axillary sentinel lymph node (*arrowhead*), and drainage to an internal mammary lymph node (*dashed arrow*)

Radionuclide methods play a key role in SLN biopsy (see also ▶ Chap. 47, "Radioguided Surgery for Breast Cancer" of this book). Typically, for SLN mapping, a colloidal radiopharmaceutical (^{99m}Tc-sulfur colloid in the USA, ^{99m}Tc-nanocolloidal albumin or ^{99m}Tc-antimony in Europe) is injected, and sentinel nodes are identified through imaging (lymphoscintigraphy, Fig. 1), gamma probes, or both [76]. Other, more specific agents have been developed and are undergoing testing [77]. Some centers use both radiocolloid and visible blue dye to guide SLN sampling, while some centers use one of the methods without the other [68].

The importance of sampling internal mammary (IM) nodes has been a point of considerable debate [78]. Studies using SLN mapping and lymphoscintigraphy to sample IM lymph have demonstrated the feasibility of this approach [79–81]; however, the overall percentage of positive IM nodes is on the order of 5% or less. And although a significant proportion of breast cancers have primary drainage to the IM nodes, approximately 30% of medial tumors and 15% of lateral tumors, it is rare to have IM lymph node metastasis in the absence of axillary nodal metastases [82]. As a result, most practices in the USA do not routinely sample IM nodes. Yao et al. [83] found that patients with positive axillary nodes and IM nodal drainage, even in the absence of IM nodal sampling, were significantly more likely to relapse and die of breast cancer than those without drainage. Another study found a higher rate of nodal relapse outside the axilla, versus in the axilla, after SLN biopsy [84]. Such studies prompt careful consideration of the approach to SLN mapping in breast cancer and the potential benefit of peri-lesional injection, which have a higher likelihood of drainage demonstrating IM nodal drainage, and lymphoscintigraphy in selected patients to identify extra-axillary drainage [85].

There was considerable interest in [^{18}F]FDG PET as a noninvasive imaging method to detect axillary nodal spread in newly diagnosed breast cancer and avoid the need for invasive biopsy. However, although early studies showed high sensitivity of increased uptake in axillary nodes in breast cancer, multiple subsequent studies including larger multicenter trials have failed to show sufficient sensitivity of PET in the staging of the axilla in patients with early-stage breast cancer [86, 87] to obviate the need for tissue sampling with SLN mapping and biopsy [88–90]. Early-stage breast cancer patients, i.e., those with small tumors less than 2–3 cm with clinically negative axillary nodes, represent the majority of breast cancer patients, many clinically silent and diagnosed by screening mammography. Given the low probability of metastatic disease in this population

and the risk of false positives with whole-body PET/CT, there is no recommended role for [^{18}F]FDG PET in axillary or clinical staging in patients with early-stage disease [21, 91].

Nuclear Methods for Staging of Distant Metastases

Systemic evaluation for metastatic disease is recommended in the initial workup for high-risk and later clinical stage (≥stage III) breast cancer as well as for patients with recurrent breast cancer and known metastatic disease [48]. High-risk disease is commonly defined as locally advanced breast cancer (LABC) [48], including primary tumor larger than 5 cm, skin or chest wall involvement, fixed axillary nodes, positive supraclavicular/infraclavicular/IM nodes, and inflammatory cancer. Patients with LABC have a poor prognosis because of the high incidence of distant metastases during follow-up [92, 93]. In these patients detection of distant metastases is crucial to determine the initial goals of therapy, i.e., curative versus palliative and/or local control, and thus systemic staging is recommended as part of initial evaluation [48]. The bone scan and PET/CT play significant roles in systemic staging in breast cancer patients. Important areas of more distant spread for breast cancer include nodal beds outside the axillary and IM chain, for example, in the mediastinum, the lungs, the liver, and the bones [94].

The skeleton is the most common site for breast cancer metastases, affecting approximately 50–70% of patients, and is the sole site of metastatic disease in almost one half of patients [95–99]. For decades, the bone scan (BS) has been the primary method for staging breast cancer bone metastases despite well-known limitations with respect to sensitivity and specificity (Fig. 2). The most commonly used radiopharmaceuticals are ^{99m}Tc-hydroxymethylene diphosphonate (^{99m}Tc-HMDP or ^{99m}Tc-HDP) and ^{99m}Tc-methylene diphosphonate (^{99m}Tc-MDP) with accumulation within bone metastases related to changes in local blood flow and abnormally increased activity of osteoclasts.

The reported sensitivity ranges from 62% to 100% and specificity ranges from 78% to 100% [100, 101]. False positives can be caused by trauma, degenerative changes, and other benign conditions, while false negatives can occur in the presence of predominantly osteolytic metastases, low bone turnover, or in avascular regions (such as necrosis) [101]. Single-photon emission computed tomography (SPECT) has been shown to improve sensitivity and specificity [102–104], with further improvement in diagnostic confidence shown with SPECT/CT [105–108], likely due to the reduction of false positives through the morphological appearance CT. SPECT is particularly helpful to characterize solitary lesions in the spine and/or to differentiate bone metastases from degenerative lesions. Salvelli et al. reported the sensitivity and specificity of SPECT to be over 90% [102].

Sodium-[^{18}F]fluoride (Na^{18}F) is a bone-seeking positron-emitting agent with a similar mechanism of skeletal uptake as ^{99m}Tc-labeled bone scan agents. Both have uptake related to blood flow and osteoblastic activity; however, Na^{18}F has practical advantages over the single-photon bone scan agents that include faster clearance and higher contrast [109]. The now widespread availability of hybrid PET/CT systems has renewed interest in the relatively higher spatial resolution of Na^{18}F PET/CT for bone imaging, as there has been demonstrated higher diagnostic accuracy over BS (with or without SPECT) and CT for breast cancer and number of other malignancies [110–121] (Fig. 3). Several prospective trials and registries are ongoing which seek to more robustly address issues regarding time needed for interpretation, radiation dose, cost, and clinical impact compared to the BS [115, 122–126].

[^{18}F]FDG PET has also been shown to be complimentary, and in some studies superior to BS in the detection of skeletal metastases in most studies [127–131] (Fig. 4). There is however an important difference compared to bone scans and fluoride imaging. The increased uptake detected on [^{18}F]FDG PET is thought to be within the breast cancer tumor cells thus reflecting tumor activity within the bone rather the osteogenic (blastic) response of the bone architecture to the metastases, as is the case with BS and Na^{18}F uptake. Several studies demonstrated that [^{18}F]FDG PET is superior to bone scanning in the detection of lytic and

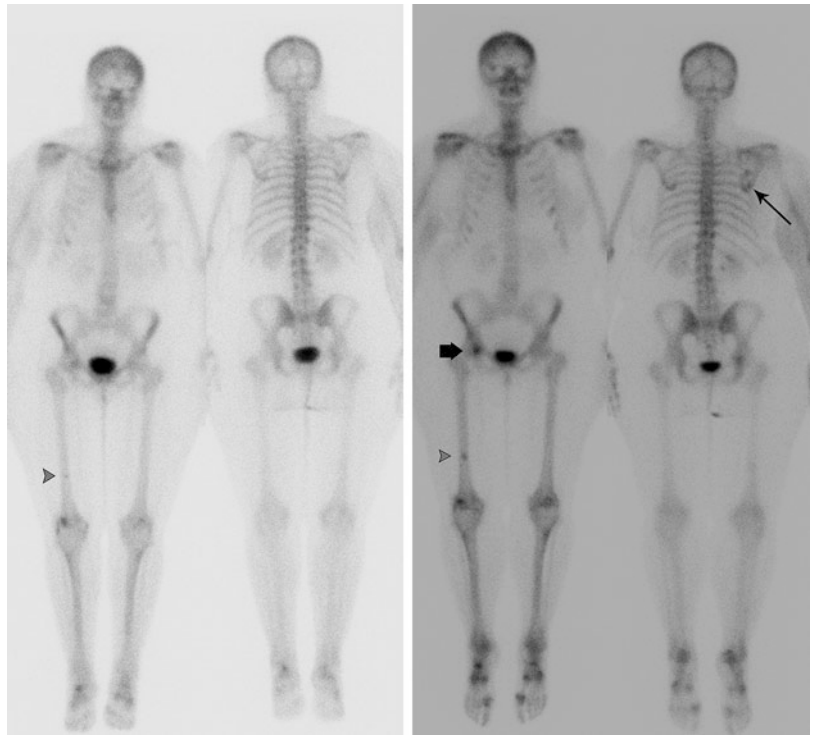

Fig. 2 Bone metastases identified by bone on two subsequent occasions during follow-up. ^{99m}Tc-methylene diphosphonate bone scan shows progression of osseous metastatic disease, for example, radiotracer uptake in the right femoral lesion (*arrowhead*) and new uptake in the right femoral head (*thick arrow*) and right scapula (*thin arrow*)

intramedullary metastases, but inferior for detecting primarily osteoblastic lesions. Cook and colleagues showed that [^{18}F]FDG PET detected the lytic metastases often missed by bone scan, while [^{18}F]FDG PET often missed osteoblastic metastases, for which bone scan is superior [132]. Subsequent studies confirmed these findings (reviewed in Fogelman et al. [63, 109]), showing that [^{18}F]FDG PET is complementary to bone scan and Na^{18}F imaging. Some of the increased sensitivity over BS is likely due to earlier detection of active tumor in bone prior to osteoblastic response [133]. Again, as with hybrid imaging with SPECT/CT and Na^{18}F PET/CT, specificity is gained through reduction of false positives with correlative CT aiding in improved differentiation between benign and malignant lesions. And though [^{18}F]FDG PET has been shown to have lower sensitivity for purely osteoblastic or sclerotic lesions [132, 134, 135], with many demonstrating no uptake, these may be detected by the changes on the accompanying CT [135]. Given reported high concordance between BS and [^{18}F]FDG PET/CT [136], and the known advantages over BS, the question of the necessity of the BS in the era of hybrid PET imaging is being raised. NCCN guidelines still recommend BS for staging in symptomatic patients with early-stage/operable breast cancer, and Na^{18}F PET/CT is now included in current NCCN guidelines as an alternative to BS [48]. In addition, a recent amendment suggests PET/CT may be helpful for problem solving in equivocal cases and that bone scanning/Na^{18}F PET/CT may not be necessary in cases where [^{18}F]FDG PET clearly demonstrate bone metastases [48].

Besides bony metastatic disease, [^{18}F]FDG PET has proven useful in the general detection of distant metastases for initial staging and restaging of breast cancer patients [95, 137–141]. A 48-patient pilot study by van der Hoeven et al. suggested that PET was more sensitive than conventional imaging in detecting distant metastases [138]. Recently, a prospective cohort study by Groheux et al. compared conventional imaging staging (bone scan, chest radiography or dedicated CT, liver ultrasound, enhanced CT abdomen and pelvis) with a single session of

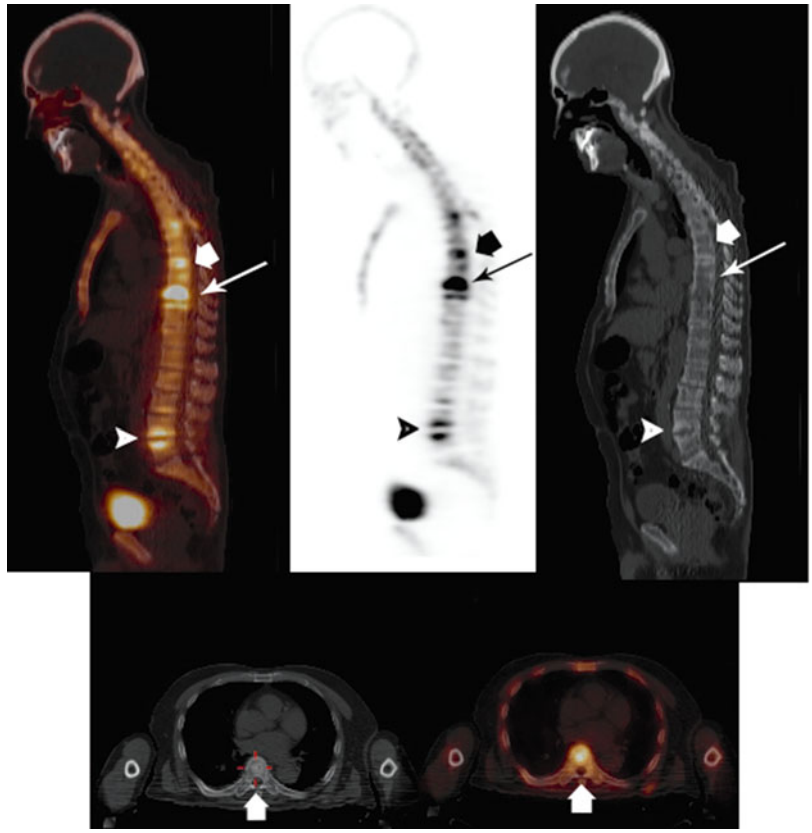

Fig. 3 Bone metastases identified by $Na^{18}F$ PET. Fluoride PET images (sagittal low-dose CT, emission, and fused images (*top*); low-dose CT and fused images (*bottom*)) of a patient with multiple bone metastases demonstrate the increased detail and tomographic information by PET. Sagittal images demonstrate radiotracer uptake in the cervical and thoracic spine compatible with osseous metastases, for example, at the T8 (*fat arrows*) and T10 (*thin arrows*). Axial images at the T8 level demonstrate increased tracer uptake associated with an osseous sclerosis (*fat arrow*). Note linear tracer uptake at the L4/L5 (*arrowhead*) level involving the inferior endplate of L4 and superior endplate of L5 corresponds to degenerate uptake

staging with [^{18}F]FDG PET [95] in 117 patients with LABC. The study found that not only did PET change the clinical stage in 61 patients (52%), PET identified more distant metastases compared to the conventional imaging (43 vs. 28 patients). In addition, PET/CT was found to outperform conventional imaging in detecting bone, distant lymph node, and liver metastases. Diagnostic chest CT outperformed PET/CT, owing to respiratory motion and partial volume effect reducing the sensitivity of PET for sub-centimeter lung nodules, and relatively more difficult visualization of sub-centimeter lung nodules on the lower dose acquisition CT obtained as part of the PET/CT.

There is ongoing study of the utility of PET/CT in staging intermediate risk breast cancer patients, i.e., patients with large breast cancers (T2) or clinical N1 disease [142, 143]. In a recent prospective study of 254 patients with clinical stage IIA through IIIC (as determined by clinical examination, mammography, breast MRI, and locoregional ultrasound), Groheux et al. found that imaging with [^{18}F]FDG PET/CT revealed distant metastatic disease in 2.3% of patients with clinical stage IIA disease (1/44), 10.7% of patients with stage IIB disease (6/56), 17.5% of patients with stage IIIA disease (11/63), 36.5% of patients with stage IIIB disease (27/74), and 47.1% of patients with stage IIIC disease (8/17) [143]. As expected the yield of metastatic disease increases with increasing clinical stage. Further studies are needed to determine clinical impact and cost-effectiveness of staging evaluation with PET/CT of patients in the intermediate risk category.

Approaches to Breast Cancer Therapy

With exception of very early- and late-stage disease, almost all breast cancer care involves a combination of locoregional and systemic treatments.

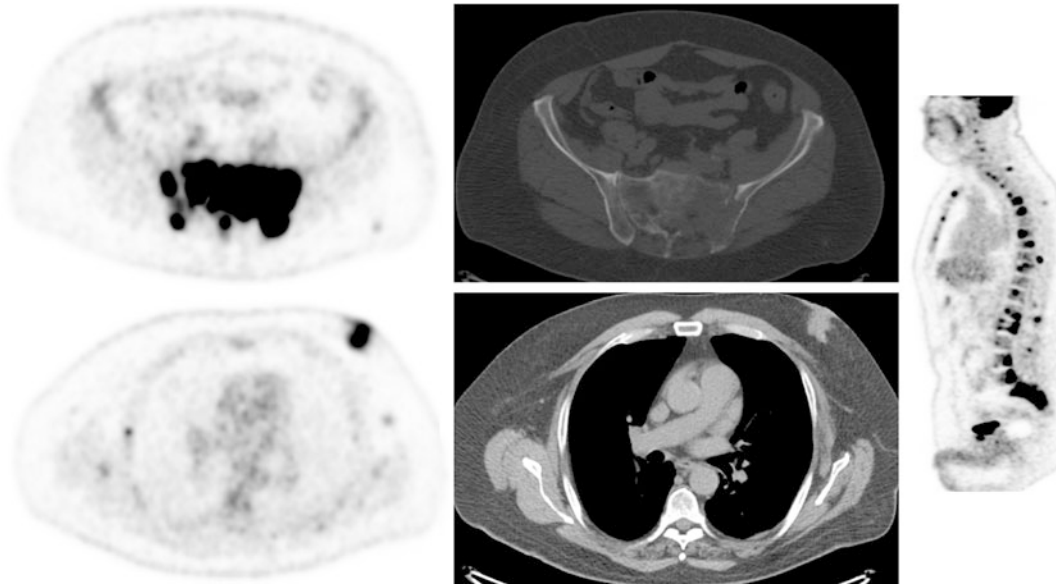

Fig. 4 Breast cancer distant metastases identified by [^{18}F] FDG PET/CT in a male patient presenting with back pain. Axial PET and low-dose CT images (*left* and *middle* columns) demonstrate increased [^{18}F]FDG uptake associated with destructive osseous metastatic lesion involving the sacrum. Sagittal PET (*right*) demonstrates multifocal osseous involvement of the spine and sternum. Axial PET and CT images on the *bottom row* demonstrate intense radiotracer uptake in a left breast nodule, corresponding to the primary invasive ductal carcinoma tumor

Locoregional therapy includes surgery and radiotherapy, and systemic therapy includes chemotherapy (e.g., taxanes), endocrine (hormonal, e.g., aromatase inhibitors) therapy, and/or targeted (biologic, e.g., anti-HER2 drugs) therapy.

Primary tumor excision remains a key component of the treatment of newly diagnosed breast cancer [144]. This includes mastectomy, removal of the entire breast, and breast-conserving surgery (BCS), also known as "lumpectomy" of the cancer [144]. Lumpectomy followed by adjuvant radiotherapy provides low rates of local recurrence and survival similar to mastectomy, but with preservation of the breast [145]. For invasive disease, axillary nodal staging is routinely performed at the time of surgery. The purpose of axillary sampling is largely for diagnosis; the therapeutic value of lymph node removal remains largely unproven [146]. For this purpose, sentinel lymph node has emerged as the preferred method for patients with clinically negative axillae [68], sparing the patient most of the morbidity, principally lymphedema, of full axillary dissection [147].

Breast cancer is one of the solid tumors that is often responsive to systemic therapy. Systemic therapy can be cytotoxic chemotherapy and can also involve more targeted and selective treatments. In all but the earliest cancers, adjuvant systemic therapy is used in addition to locoregional therapy to treat residual microscopic disease [145] and has contributed significantly to reduced breast cancer mortality. Systemic cytotoxic chemotherapy is used in more advanced or aggressive tumors, typically ER- or PR-negative tumors [148], triple-negative tumors, HER2-positive tumors, and large tumors [41, 48].

In ER-expressing tumors, adjuvant endocrine therapy is used, typically an aromatase inhibitor or tamoxifen [149]. In higher-risk ER-expressing tumors, both chemotherapy and endocrine therapy can be used [148]. RNA-based genomic testing can be used to aid in estimating the risk of distant recurrence and identify patients in this group who may benefit from chemotherapy [35]. Both types of treatment are also primary therapy for metastatic disease [150]. For HER2-positive breast cancer, trastuzumab, a HER2-specific monoclonal

antibody has been shown to substantially improve survival [151]. Directed therapy has become a key component of both adjuvant and metastatic systemic therapy for patients with HER2-overexpressing tumors [152, 153]. Pertuzumab, a monoclonal antibody directed against a different epitope than trastuzumab on the HER2 receptor, and lapatinib, a tyrosine kinase inhibitor targeting the HER2 pathway, are both routinely used in therapy regimes for higher-risk HER2-positive disease [48].

New breast cancer targets and therapy combinations continue to be investigated [154, 155]. Improvement in progression-free survival in women with hormone receptor-positive metastatic breast cancer has been demonstrated with the addition of the mTOR inhibitor everolimus [156] and more recently with the addition of the drug palbociclib, an inhibitor of cyclin-dependent kinases 4 and 6 [157].

In ER-negative tumors, chemotherapy is typically an important component of systemic therapy. This is typically combined with HER2-directed therapy in HER2-overexpressing tumors. On the other hand, tumors that are ER/PR/HER2 negative (triple negative, TNBC) are treated primarily using chemotherapy. The ongoing study is particularly important in triple-negative patients where therapies effective in other breast cancer subtypes (endocrine and HER2-targeted therapies) are unlikely to work [158, 159].

For patients with LABC, or those with large tumors who have smaller breasts and/or desire breast conservation, neoadjuvant therapy is considered. The primary purpose of this therapy is to reduce the size to the tumor to better facilitate BCS and local control. However, response to neoadjuvant therapy also provides valuable assessment of the tumor's response to therapy prior to definitive treatment.

Radiotherapy is commonly used as an adjunct to surgery in locoregional breast cancer treatment [160]. Lumpectomy in the absence of breast radiotherapy leads to unacceptably high rates of local recurrence [145]; therefore breast radiotherapy is an integral part of breast conservation treatment. In addition to radiation of the breast in patients undergoing breast conservation, adjuvant irradiation can also be used for the chest wall in mastectomy patients, but it is usually reserved for patients with larger tumors or documented chest wall invasion [160]. Adjuvant radiotherapy is also used in the treatment of involved nodal basins and has been shown to enhance survival in those patients with multiple axillary nodal metastases [161].

Assessing the Efficacy of Treatment(s)

Evaluating the efficacy of systemic treatment is an important diagnostic need for breast cancer. The largest population of patients undergoing systemic therapy for breast cancer receives treatment as adjuvant therapy, after completion of primary surgery. Since there should be no residual macroscopic disease after definitive surgery, imaging is not helpful for response monitoring for adjuvant therapy, except for re-staging upon suspicion of recurrence. Imaging however plays an important role in response evaluation of systemic neoadjuvant therapy (NAT), given prior to definitive surgery primarily in LABC, as well as systemic therapy given as the primary treatment for metastatic, stage IV disease.

In the neoadjuvant setting, studies have demonstrated that the extent of residual breast and axillary disease after treatment is prognostic for both disease-free survival (DFS) and overall survival (OS) [162–164]. Patients demonstrating complete pathologic response (pCR), defined as no residual invasive tumor at post-therapy surgery histopathology, have improved long-term outcome compared to patients without pCR [162, 164]. NAT offers both the opportunity to assess tumor responsiveness while improving surgical options for patients with locally advanced disease by down-staging the primary tumor.

Sized-based approaches such as physical exam and mammography that rely on changes in size for response evaluation (e.g., RECIST criteria [165]) do not reflect early changes at the molecular level that may occur prior to changes in tumor size. Functional imaging therefore may be particularly helpful in determining treatment efficacy earlier in the course, allowing for earlier change of therapeutic strategy, thus avoiding unnecessary toxic systemic side effects of ineffective treatments.

One of the earliest studies showing the use of [^{18}F]FDG PET in the assessment of treatment response was performed by Wahl and colleagues in 1993 [166]. The investigators observed significant quantitative differences in the [^{18}F]FDG uptake measured before and after 2 months of therapy (mid-therapy) for responders versus nonresponders. While nonresponders had no significant change, patients who went on to a good response had declines in [^{18}F]FDG SUV of 50% or more. Most subsequent studies evaluating response at mid-therapy found similar quantitative findings (reviewed in [63, 167, 168]. A meta-analysis of 19 studies including over 900 patients by Wang et al. [169] underscored that imaging earlier in the course of treatment (after the first or second cycle) with cutoffs between 55% and 65% declines from baseline as response criteria offered better correlation with pathologic response of primary tumors.

The knowledge that breast cancer is a molecularly heterogeneous disease has prompted response evaluation studies within the various molecular subsets of breast cancer [170]. Groheux et al. [171] and Humbert et al. [172], in prospective studies including women with HER2-positive breast cancer treated with trastuzumab-containing regimens showed that low residual metabolism post-NAT (SUV $<=3.0$ after two cycles and <2.1 after one cycle, respectively) strongly correlated with pCR. Similar studies in patients with ER-positive/HER2-negative tumors and triple-negative tumors have also been conducted [173–175]. ER-positive/HER2-negative tumor type is somewhat less [^{18}F]FDG avid at baseline and less sensitive to chemotherapy than more aggressive subtypes (e.g., TNBC) [170], and pCR is rarely achieved. Studies have found that for this subtype baseline SUV and changes after one or two cycles of NAT may offer prognostic value in the form of survival rather than pCR [174, 175]. For triple-negative tumors, change in SUV from baseline has been shown to correlate with pCR, which is more closely associated with survival [173]. These studies indicate that assessment of serial PET data to infer breast cancer response to therapy should be considered in light of breast cancer subtype, supported by studies showing that [^{18}F]FDG kinetics may vary by breast cancer subtype [170].

Although some researchers have shown advantages of obtaining specific kinetic parameters of the tumor over the static SUV measurements [176], measuring percentage change in SUV from baseline and measuring absolute SUVs at baseline and follow-up time points are the most commonly used parameters in response assessment studies, likely due to ease of calculation and reproducibility. These studies highlight the need for standardization of the timing of interim [^{18}F]FDG PET evaluation, cutoff points, and criteria used in assessing response to therapy for different subtypes of breast cancer [177, 178]. Further, study outcomes may also be influenced by the specific treatment regimes.

Studies of [^{18}F]FDG PET performed after the completion of chemotherapy have shown reduced sensitivity for residual disease – i.e., that the absence of [^{18}F]FDG uptake is not a reliable indicator of complete pathologic response [167, 179–181]. This is especially true for axillary nodal disease since the sensitivity for residual microscopic disease post-therapy is low. However, recent studies have shown that the presence of [^{18}F]FDG uptake post-therapy is specific and highly predictive of relapse [182]. Therefore, even though [^{18}F]FDG PET may miss small-volume disease post-therapy, the presence or absence of [^{18}F]FDG uptake carries prognostic significance that may be important in directing follow-up.

In the metastatic setting, timely determination of the efficacy of systemic and/or targeted therapy is critical to the overall goal of maximizing survival and minimizing symptoms and side effects. Achieving and correlating with pCR is no longer the aim in this setting, and clinicians rely on clinical evaluation as well as anatomic and functional imaging in their assessment. Again, molecular imaging with [^{18}F]FDG PET can offer more and earlier insight into treatment response, particularly in cases where the regimen may produce an overall cytostatic (reflected in the tumor metabolism) rather than cytotoxic (reflected in tumor size) effect (Figs. 5 and 6). A number of small studies showed, similar to neoadjuvant therapy, that response of metastatic breast cancer (MBC) to

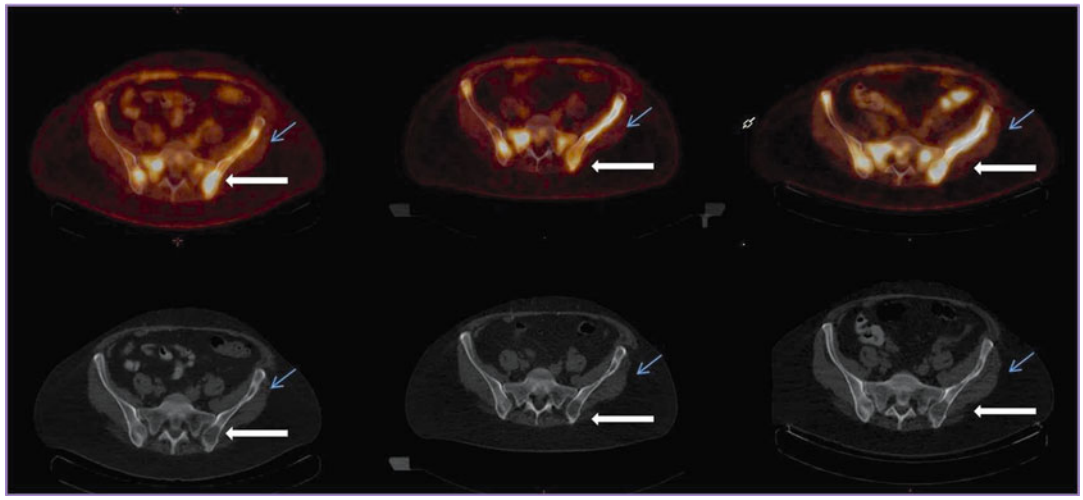

Fig. 5 Evolution of metabolic involvement in the pelvic bones of patient with bone-dominant metastatic at baseline, 4 weeks and 12 weeks post-endocrine therapy. Grossly unchanged lytic osseous change on CT images within the left iliac bone over the interval, however variable metabolic activity, with overall progression. Posterior left iliac bone involvement (*thick arrows*) demonstrates mild decline in metabolic activity at 4 weeks post initiation of therapy (SUV from 7.4 to 4.1) but however increased above baseline (7.9) at 12 weeks. Left iliac wing (*thin arrows*) demonstrates increase in [^{18}F]FDG uptake at 4 weeks, from 5.7 to 8.6, and persistent increase, to 10.8, at 12 weeks, with much more extensive changes. Later clinical follow-up revealed progression of osseous and new visceral metastases, indicating the ability of the serial [^{18}F]FDG PET/CT to indicate early disease progression

therapy is accompanied by substantial drops in [^{18}F]FDG uptake, typically 40–50% or more from the pre-therapy baselines [183–185]. Mortazavi-Jehanno et al. [186] showed that [^{18}F]FDG PET was predictive of progression-free survival in patients with ER-positive MBC tumors undergoing endocrine therapy, and more recently Lin et al. [187] found in a prospective studying including 82 patients with HER2-positive MBC undergoing early-line trastuzumab and lapatinib therapy that [^{18}F]FDG PET was useful for predicting response to therapy by RECIST.

A particularly difficult clinical problem is the evaluation of response for bone metastases [101]. Given that many bone lesions do not demonstrate a measurable soft tissue component, anatomic imaging using RECIST 1.1 is limited particularly with respect to evaluation of osseous metastases. Just as with detection, PET/CT has shown superiority to bone scan in assessment of treatment efficacy with regard to osseous metastases. Though excellent for detection, BS is problematic for response evaluation as changes will significantly lag behind the bone metastasis response and may even transiently worsen or "flare" in response to successful therapy [188, 189]. This flare phenomenon has also been shown with Na^{18}F PET/CT given the similarity in mechanism [190, 191] and thus has implications for the timing of Na^{18}F PET in response evaluations. In addition, given that [^{18}F]FDG PET is not as sensitive for sclerotic lesions and breast cancer bone metastases may be mixed lytic/sclerotic or sclerotic, Na^{18}F PET may provide a complementary role in assessment of response to therapy and has been shown to impact decision-making in treatment monitoring [192].

The observed differences between bone scintigraphy and [^{18}F]FDG PET for visualizing bone metastases [132] led some investigators to hypothesize that [^{18}F]FDG PET might provide a useful and accurate means for assessing bone metastasis response. Stafford and colleagues [193] showed that changes in [^{18}F]FDG uptake correlated with the clinical assessment of response in bone-dominant MBC as well as with changes in breast cancer tumor markers, which are used clinically to assess bone metastasis response. A follow-up

Fig. 6 Breast cancer response to treatment by serial [^{18}F]FDG PET. Sagittal PET and fused images from a patient with ≥30% decline in average lesion SUV_{max} after 4 weeks of endocrine therapy. For example, sternal involvement (*black* and *white arrows*) decreased from SUV_{max} of 16.0 at baseline to 7.2 after 4 weeks. The patient sustained a response with decline in average SUV at 12 weeks and was without progression for 15 months from initiation of this line of endocrine therapy. This was the third-line endocrine therapy for this patient. This case illustrates the ability of serial [^{18}F]FDG PET/CT to predict response of metastatic disease to systemic therapy in disease sites like bone that are challenging to follow by standard imaging such as CT and bone scan

study [194] by Specht et al. showed that changes in [^{18}F]FDG uptake predicted time to progression, and Tateishi et al. [195] showed that both metabolic and structural changes by [^{18}F]FDG PET/CT predicted bone metastasis time to progression.

These studies show the significant role [^{18}F]FDG PET may play in assessing treatment response for bone-dominant MBC.

Future Directions

As breast cancer treatment becomes increasingly targeted and individualized, there are increasing demands upon breast cancer diagnosis to help direct the therapeutic approach. The imaging approaches in current clinical use for diagnosing and staging breast cancer – mammography, ultrasound, contrast-enhanced MRI, CT, bone scan, and [^{18}F]FDG PET/CT – provide important information on disease extent and response to treatment, but are relatively nonspecific. Advances are more specific and quantitative, and molecular imaging methods are poised to help provide the kind of diagnostic data that are needed to help take advantage of new therapeutic options for breast cancer. We highlight some selected examples below. These include imaging tumor receptor expression and imaging tumor proliferation to assess early response to treatment.

The expression of tumor receptors and other proteins involved in cellular signaling is particularly relevant to breast cancer treatment. Targets of interest include the estrogen and progesterone receptors (ER, PR), targets for endocrine therapy, and HER2, the target for HER2-directed therapy. These biomarkers have been traditionally measured by in vitro assay of biopsy material [196]; however, the development of vivo molecular imaging of these targets is setting the stage for more specific guidance on treatment and management of breast cancer. Complementary advantages of imaging to measure receptor expression include its non-invasiveness, the ability to measure receptor expression in the entire disease burden and thus the ability to avoid sampling

error that can occur with heterogeneous receptor expression, and the potential for serial studies of in vivo drug effects on the target [197, 198].

PET imaging of the ER using the radiopharmaceutical 16-alpha-^{18}F-fluoro-17-beta-estradiol (^{18}F-FES) [199] has been validated as a measure of ER expression in breast tumors against ER expression assays of tissue samples by radioligand binding [200] and immunohistochemistry [201]. Higher ^{18}F-FES SUV has been correlated with response to endocrine therapy [197, 202, 203]. A majority of breast cancers express ER (approximately 70%) and ER status is an initial key determinant in therapeutic strategy [204]. Given that there may be substantial heterogeneity of ER expression across tumor sites [205, 206], functional imaging of the ER receptor with PET/CT appears positioned to provide valuable insights into tumor burden characterization and pharmacodynamic response to targeted therapy at different stages of the disease [198]. Interest in imaging of the progesterone receptor (PR) in vivo using 21-^{18}F-fluoro-16α,17α-[(*R*)-(1′-α-furylmethylidene)dioxy]-19-norpregn-4-ene-3,20-dione (^{18}F-FFNP) has been increasing [207] as tumors with ER/PR co-positivity are shown to be more re sponsive to endocrine therapy [208].

HER2 expression in breast cancer has become an important indicator of prognosis and an increasingly important target for therapy, and imaging probes using both single-photon radionuclides (e.g., ^{111}In-labeled-trastuzumab and ^{99m}Tc-ICR12) and positron-emitting radionuclides (e.g., ^{64}Cu-trastuzumab, ^{64}Cu-DOTA-$Z_{HER2:477}$, ^{68}Ga-trastuzumab F(ab′)$_2$ fragments, ^{68}Ga-ABY-002, and ^{89}Zr-trastuzumab) have been developed and validated [209, 210]. ^{89}Zr-trastuzumab PET/CT has emerged as one of the more favorable HER2 imaging methods due to advantageous radionuclide properties, biodistribution characteristics, and straightforward quantification capabilities of PET compared to single-photon techniques [210, 211]. A recent multicenter trial (ZEPHIR study) including patients with HER2-positive MBC who had progressed after prior trastuzumab therapy and were due to receive trastuzumab emtansine – a recently approved antibody-drug conjugate [212] – has shown that pretreatment HER2 and metabolic imaging with ^{89}Zr-trastuzumab PET/CT and [^{18}F]FDG PET, followed by metabolic assessment with [^{18}F]FDG PET after one cycle of therapy, had a 100% NPV for therapeutic response after three cycles of therapy and also predicted time to treatment failure [213]. This study paves the way for other studies to assess the utility of combination imaging using PET and other modalities not only in determination of treatment efficacy in a number of clinical settings, such as the neoadjuvant and first-line metastatic settings, but also as a predictive tool in the pre-therapy setting [214].

Although studies of [^{18}F]FDG PET have shown that tumor glycolysis declines early in the course of treatment [215–217], it is likely that other pathways more closely tied to cellular growth and death may provide even earlier and more specific indications of therapeutic response. Imaging cellular proliferation in breast tumors is becoming increasingly enticing, especially given the recent approval of a new drug palbociclib, which inhibits cell cycle progression into S phase [218].

A number of PET tracers are being developed and studied [219] with much attention focused on thymidine analogs, since thymidine is a substrate for activity of the thymidine salvage pathway for DNA synthesis. ^{18}F has largely replaced the short half-life ^{11}C [220] for radiolabeling proliferation analogs (new ref see comments), with the most promise shown with ^{18}F-fluorothymidine (FLT). A recent phase II study showed some promise for its use in predicting pCR in the neoadjuvant setting [221]. Work on other proliferation targets such as the sigma-2 receptor ligand is ongoing [222, 223].

References

1. Siegel RL. Cancer statistics, 2015. CA Cancer J Clin. 2015;65(1):5–29.
2. Society, A.C. American Cancer Society. Cancer facts & figures 2015. Atlanta: American Cancer Society; 2015.
3. Writing Group for the Women's Health Initiative, I. Risks and benefits of estrogen plus progestin in healthy postmenopausal women: principal results from the women's health initiative randomized controlled trial. JAMA. 2002;288(3):321–33.

4. Berry DA, et al. Effect of screening and adjuvant therapy on mortality from breast cancer. N Engl J Med. 2005;353(17):1784–92.
5. DeVita VTJ, Rosenberg SA. Two hundred years of cancer research. N Engl J Med. 2012;366(23):2207–14.
6. Oeffinger KC, et al. Breast cancer screening for women at average risk: 2015 guideline update from the american cancer society. JAMA. 2015;314(15): 1599–614.
7. Salehi F, et al. Review of the etiology of breast cancer with special attention to organochlorines as potential endocrine disruptors. J Toxicol Environ Health B Crit Rev. 2008;11(3–4):276–300.
8. Howell A, et al. Risk determination and prevention of breast cancer. Breast Cancer Res: BCR. 2014;16(5): 446.
9. Colditz GA, Bohlke K. Priorities for the primary prevention of breast cancer. CA Cancer J Clin. 2014; 64(3):186–94.
10. Martino S, et al. Continuing outcomes relevant to evista: breast cancer incidence in postmenopausal osteoporotic women in a randomized trial of raloxifene. J Natl Cancer Inst. 2004;96(23):1751–61.
11. Goss PE, et al. Exemestane for breast-cancer prevention in postmenopausal women. N Engl J Med. 2011;364(25):2381–91.
12. Parkin DM, Boyd L, Walker LC. The fraction of cancer attributable to lifestyle and environmental factors in the UK in 2010. Br J Cancer. 2011;105(S2): S77–81.
13. Michailidou K, et al. Large-scale genotyping identifies 41 new loci associated with breast cancer risk. Nat Genet. 2013;45(4):353–61e2.
14. Barnes DR, Antoniou AC. Unravelling modifiers of breast and ovarian cancer risk for BRCA1 and BRCA2 mutation carriers: update on genetic modifiers. J Intern Med. 2012;271(4):331–43.
15. Pharoah PDP, et al. Polygenes, risk prediction, and targeted prevention of breast cancer. N Engl J Med. 2008;358(26):2796–803.
16. Gail MH, et al. Projecting individualized probabilities of developing breast cancer for white females who are being examined annually. J Natl Cancer Inst. 1989;81(24):1879–86.
17. Claus EB, Risch N, Thompson WD. Autosomal dominant inheritance of early-onset breast cancer. Implications for risk prediction. Cancer. 1994;73(3): 643–51.
18. Berry DA, et al. BRCAPRO validation, sensitivity of genetic testing of BRCA1/BRCA2, and prevalence of other breast cancer susceptibility genes. J Clin Oncol. 2002;20(11):2701–12.
19. Antoniou AC, et al. The BOADICEA model of genetic susceptibility to breast and ovarian cancers: updates and extensions. Br J Cancer. 2008;98 (8):1457–66.
20. Tyrer J, Duffy SW, Cuzick J. A breast cancer prediction model incorporating familial and personal risk factors. Stat Med. 2004;23(7):1111–30.
21. Moy L, et al. ACR appropriateness criteria stage I breast cancer: initial workup and surveillance for local recurrence and distant metastases in asymptomatic women. J Am Coll Radiol. 2014;11(12, Part A): 1160–8.
22. Fachal L, Dunning AM. From candidate gene studies to GWAS and post-GWAS analyses in breast cancer. Curr Opin Genet Dev. 2015;30:32–41.
23. Gail MH. Value of adding single-nucleotide polymorphism genotypes to a breast cancer risk model. J Natl Cancer Inst. 2009;101(13):959–63.
24. Schnitt SJ. Traditional and newer pathologic factors. J Natl Cancer Inst Monogr. 2001;30:22–6.
25. Symmans WF. A pathologist's perspective on emerging genomic tests for breast cancer. Semin Oncol. 2007;34(2 Suppl 3):S4–9.
26. Sotiriou C, Pusztai Gene-Expression L. Signatures in breast cancer. N Engl J Med. 2009;360(8):790–800.
27. Trop I, et al. Molecular classification of infiltrating breast cancer: toward personalized therapy. Radiographics. 2014;34(5):1178–95.
28. Perou CM, et al. Molecular portraits of human breast tumours. Nature. 2000;406(6797):747–52.
29. Sorlie T, et al. Gene expression patterns of breast carcinomas distinguish tumor subclasses with clinical implications. Proc Natl Acad Sci U S A. 2001;98: 10869–74.
30. Sorlie T, et al. Repeated observation of breast tumor subtypes in independent gene expression data sets. Proc Natl Acad Sci U S A. 2003;100: 8418–23.
31. Sotiriou C, et al. Breast cancer classification and prognosis based on gene expression profiles from a population-based study. Proc Natl Acad Sci U S A. 2003;100:10393–8.
32. Hu Z, et al. The molecular portraits of breast tumors are conserved across microarray platforms. BMC Genomics. 2006;7(1):1–12.
33. Walker RA. Immunohistochemical markers as predictive tools for breast cancer. J Clin Pathol. 2008;61 (6):689–96.
34. Ross JS, et al. Commercialized multigene predictors of clinical outcome for breast cancer. Oncologist. 2008;13(5):477–93.
35. Paik S, et al. A multigene assay to predict recurrence of tamoxifen-treated, node-negative breast cancer. N Engl J Med. 2004;351(27):2817–26.
36. Paik S, et al. Gene expression and benefit of chemotherapy in women with node-negative, estrogen receptor – positive breast cancer. J Clin Oncol. 2006;24(23): 3726–34.
37. Singletary SE, Connolly JL. Breast cancer staging: working with the sixth edition of the AJCC cancer staging manual. CA Cancer J Clin. 2006;56(1):37–47. quiz 50–1.
38. Edge SB, Compton CC. The American Joint Committee on cancer: the 7th edition of the AJCC cancer staging manual and the future of TNM. Ann Surg Oncol. 2010;17:1471–4. epub.

39. Edge SB, et al. AJCC cancer staging manual. 7th ed. New York: Springer; 2010.
40. Elmore JG, et al. Screening for breast cancer. JAMA. 2005;293(10):1245–56.
41. McDonald ES, et al. Baseline screening mammography: performance of full-field digital mammography versus digital breast tomosynthesis. Am J Roentgenol. 2015;205(5):1143–8.
42. Friedewald SM, et al. Breast cancer screening using tomosynthesis in combination with digital mammography. JAMA. 2014;311(24):2499–507.
43. Stavros AT, et al. Solid breast nodules: use of sonography to distinguish between benign and malignant lesions. Radiology. 1995;196(1):123–34.
44. Lehman CD, Schnall MD. Imaging in breast cancer: magnetic resonance imaging. Breast Cancer Res. 2005;7(5):215–9.
45. Lehman CD. Clinical indications: what is the evidence? Eur J Radiol. 2012;81 Suppl 1:S82–4.
46. Saslow D, et al. American Cancer Society guidelines for breast screening with MRI as an adjunct to mammography. CA Cancer J Clin. 2007;57(2):75–89.
47. Keating NL, et al. Surveillance testing among survivors of early-stage breast cancer. J Clin Oncol. 2007;25(9):1074–81.
48. Network NCC. NCCN clinical practice guidelines in oncology. Breast Cancer. Version 1. 2016. Available at https://www.nccn.org
49. Rhodes DJ, et al. Dedicated dual-head gamma imaging for breast cancer screening in women with mammographically dense breasts. Radiology. 2011;258(1):106–18.
50. Greene LR, Wilkinson D. The role of general nuclear medicine in breast cancer. J Med Radiat Sci. 2015;62(1):54–65.
51. Brem RF, Rechtman LR. Nuclear medicine imaging of the breast: a novel, physiologic approach to breast cancer detection and diagnosis. Radiol Clin. 2010;48(5):1055–74.
52. Mettler F, Guiberteau M. Essentials of nuclear medicine imaging. 6th ed. St. Louis: Mosby Elsevier; 2012.
53. Specht JM, Mankoff DA. Advances in molecular imaging for breast cancer detection and characterization. Breast Cancer Res: BCR. 2012;14(2):206.
54. Buscombe JR, et al. Uptake of Tc-99m MIBI related to tumour size and type. Anticancer Res. 1997;17(3B):1693–4.
55. Mankoff DA, et al. [Tc-99m]-sestamibi uptake and washout in locally advanced breast cancer are correlated with tumor blood flow. Nucl Med Biol. 2002;29(7):719–27.
56. Scopinaro F, et al. Technetium-99m sestamibi: an indicator of breast cancer invasiveness. Eur J Nucl Med. 1994;21(9):984–7.
57. O'Connor M, Rhodes D, Hruska C. Molecular breast imaging. Expert Rev Anticancer Ther. 2009;9(8):1073–80.
58. Hendrick RE. Radiation doses and cancer risks from breast imaging studies. Radiology. 2010;257(1):246–53.
59. Avril N, et al. Glucose metabolism of breast cancer assessed by ^{18}F-FDG PET: histologic and immunohistochemical tissue analysis. J Nucl Med. 2001;42(1):9–16.
60. Bos R, et al. Biologic correlates of ^{18}fluorodeoxyglucose uptake in human breast cancer measured by positron emission tomography. J Clin Oncol. 2002;20(2):379–87.
61. Scheidhauer K, Walter C, Seemann MD. FDG PET and other imaging modalities in the primary diagnosis of suspicious breast lesions. Eur J Nucl Med Mol Imaging. 2004;31 Suppl 1:S70–9.
62. Kumar RS, et al. Clinicopathologic factors associated with false negative FDG-PET in primary breast cancer. Breast Cancer Res Treat. 2006;98:267–74.
63. Rosen EL, Eubank WB, Mankoff DA. FDG PET, PET/CT, and breast cancer imaging. Radiographics. 2007;27 Suppl 1:S215–29.
64. Raylman RR, et al. The positron emission mammography/tomography breast imaging and biopsy system (PEM/PET): design, construction and phantom-based measurements. Phys Med Biol. 2008;53(3):637–53.
65. Berg WA, et al. Breast cancer: comparative effectiveness of positron emission mammography and MR imaging in presurgical planning for the ipsilateral breast. Radiology. 2011;258(1):59–72.
66. Rosen EL, et al. Detection of primary breast carcinoma with a dedicated, large-field-of-view FDG PET mammography device: initial experience. Radiology. 2005;234(2):527–34.
67. Berg WA, et al. High-resolution fluorodeoxyglucose positron emission tomography with compression ("positron emission mammography") is highly accurate in depicting primary breast cancer. Breast J. 2006;12(4):309–23.
68. Newman EA, Newman LA. Lymphatic mapping techniques and sentinel lymph node biopsy in breast cancer. Surg Clin North Am. 2007;87(2):353–64. viii.
69. Albertini J, et al. Lymphatic mapping and sentinel node biopsy in the patient with breast cancer. JAMA. 1996;276:1818–22.
70. Giuliano AE, et al. Lymphatic mapping and sentinel lymphadenectomy for breast cancer. Ann Surg. 1994;220(3):391–8. discussion 398–401.
71. Krag DN, et al. Surgical resection and radiolocalization of the sentinel lymph node in breast cancer using a gamma probe. Surg Oncol. 1993;2(6):335–9. discussion 340.
72. Lyman GH, et al. American Society of Clinical Oncology guideline recommendations for sentinel lymph node biopsy in early-stage breast cancer. J Clin Oncol. 2005;23(30):7703–20.
73. Langer I, et al. Morbidity of sentinel lymph node biopsy (SLN) alone versus SLN and completion axillary lymph node dissection after breast cancer surgery: a prospective Swiss multicenter study on 659 patients. Ann Surg. 2007;245(3):452–61.
74. Vanderveen KA, et al. Upstaging and improved survival of early breast cancer patients after

implementation of sentinel node biopsy for axillary staging. Ann Surg Oncol. 2006;13(11):1450–6.
75. Giuliano AE. Axillary dissection vs no axillary dissection in women with invasive breast cancer and sentinel node metastasis: a randomized clinical trial. JAMA. 2011;305(6):569–75.
76. Aarsvold JN, Alazraki NP. Update on detection of sentinel lymph nodes in patients with breast cancer. Semin Nucl Med. 2005;35(2):116–28.
77. Wallace AM, et al. Lymphoseek: a molecular imaging agent for melanoma sentinel lymph node mapping. Ann Surg Oncol. 2007;14(2):913–21.
78. Sugg SL, et al. Should internal mammary nodes be sampled in the sentinel lymph node era? Ann Surg Oncol. 2000;7:188–92.
79. Estourgie SH, et al. Lymphatic drainage patterns from the breast. Ann Surg. 2004;239(2):232–7.
80. Farrus B, et al. Incidence of internal mammary node metastases after a sentinel lymph node technique in breast cancer and its implication in the radiotherapy plan. Int J Radiat Oncol Biol Phys. 2004;60(3):715–21.
81. Paganelli G, et al. Internal mammary node lymphoscintigraphy and biopsy in breast cancer. Q J Nucl Med. 2002;46(2):138–44.
82. van Rijk MC, et al. Clinical implications of sentinel nodes outside the axilla and internal mammary chain in patients with breast cancer. J Surg Oncol. 2006; 94(4):281–6.
83. Yao MS, et al. Internal mammary nodal chain drainage is a prognostic indicator in axillary node-positive breast cancer. Ann Surg Oncol. 2007;14(10): 2985–93.
84. van der Ploeg IM, et al. Axillary and extra-axillary lymph node recurrences after a tumor-negative sentinel node biopsy for breast cancer using intralesional tracer administration. Ann Surg Oncol. 2008;15(4): 1025–31.
85. Manca G, et al. Sentinel lymph node mapping in breast cancer: a critical reappraisal of the internal mammary chain issue. Q J Nucl Med Mol Imaging. 2014; 58(2):114–26.
86. Utech CI, Young CS, Winter PF. Prospective evaluation of fluorine-18 fluorodeoxyclucose positron emission tomography in breast cancer for staging of the axilla related to surgery and immunocytochemistry. Eur J Nucl Med. 1996;23(12):1588–93.
87. Avril N, et al. Metabolic characterization of breast tumors with positron emission tomography using F-18 fluorodeoxyglucose. J Clin Oncol. 1996;14(6): 1848–57.
88. Veronesi P, Rodriguez-Fernandez J, Intra M. Controversies in the use of sentinel nodes: microinvasion, post surgery and after preoperative systemic treatment. Breast. 2007;16 Suppl 2:S67–70.
89. Pritchard KI, et al. Prospective study of 2-[^{18}F] fluorodeoxyglucose positron emission tomography in the assessment of regional nodal spread of disease in patients with breast cancer: an Ontario Clinical Oncology Group Study. J Clin Oncol. 2012;30(12):1274–9.
90. Jeong YJ. Additional value of F-18 FDG PET/CT for initial staging in breast cancer with clinically negative axillary nodes. Breast Cancer Res Treat. 2014;145(1): 137–42.
91. Mankoff DA, et al. [^{18}F]fluorodeoxyglucose positron emission tomography – computed tomography in breast cancer: when. . . and when not? J Clin Oncol. 2012;30(12):1252–4.
92. Perez EA, Foo ML, Fulmer JT. Management of locally advanced breast cancer. Oncology (Williston Park). 1997;11(9 Suppl 9):9–17.
93. Chia S, et al. Locally advanced and inflammatory breast cancer. J Clin Oncol. 2008;26(5):786–90.
94. Carlson RW, McCormick B. Update: NCCN breast cancer clinical practice guidelines. J Natl Compr Canc Netw. 2005;3 Suppl 1:S7–11.
95. Groheux D, et al. ^{18}F-FDG PET/CT in staging patients with locally advanced or inflammatory breast cancer: comparison to conventional staging. J Nucl Med. 2013;54(1):5–11.
96. Jung SY, et al. Factors associated with mortality after breast cancer metastasis. Cancer Causes Control. 2011; 23(1):103–12.
97. Manders K, et al. Clinical management of women with metastatic breast cancer: a descriptive study according to age group. BMC Cancer. 2006;6:179.
98. Plunkett TA, Smith P, Rubens RD. Risk of complications from bone metastases in breast cancer. Eur J Cancer. 2000;36(4):476–82.
99. Wei S, et al. Breast carcinomas with isolated bone metastases have different hormone receptor expression profiles than those with metastases to other sites or multiple organs. Ann Diagn Pathol. 2011; 15(2):79–83.
100. Crippa F, et al. Bone scintigraphy in breast cancer: a ten-year follow-up study. J Nucl Biol Med. 1993; 37(2):57–61.
101. Hamaoka T, et al. Bone imaging in metastatic breast cancer. J Clin Oncol. 2004;22(14):2942–53.
102. Savelli G, et al. Bone scintigraphy and the added value of SPECT (single photon emission tomography) in detecting skeletal lesions. Q J Nucl Med. 2001;45(1):27–37.
103. Even-Sapir E, et al. Role of SPECT in differentiating malignant from benign lesions in the lower thoracic and lumbar vertebrae. Radiology. 1993;187(1):193–8.
104. Han LJ. Comparison of bone single-photon emission tomography and planar imaging in the detection of vertebral metastases in patients with back pain. Eur J Nucl Med. 1998;25(6):635–8.
105. Sharma PP. Bone scintigraphy in breast cancer: added value of hybrid SPECT-CT and its impact on patient management. Nucl Med Commun. 2012;33(2):139–47.
106. Utsunomiya D, et al. Added value of SPECT/CT fusion in assessing suspected bone metastasis: comparison with scintigraphy alone and nonfused scintigraphy and CT. Radiology. 2006;238(1):264–71.
107. Palmedo HH. Whole-body SPECT/CT for bone scintigraphy: diagnostic value and effect on patient

management in oncological patients. Eur J Nucl Med Mol Imaging. 2014;41(1):59–67.
108. Uematsu T, et al. Comparison of FDG PET and SPECT for detection of bone metastases in breast cancer. AJR Am J Roentgenol. 2005;184(4):1266–73.
109. Fogelman I, et al. Positron emission tomography and bone metastases. Semin Nucl Med. 2005;35(2):135–42.
110. Even-Sapir E, Metser U, Flusser G, et al. Assessment of malignant skeletal disease: initial experience with F18-fluoride PET/CT and comparison between F18 fluoride PET and F18 fluoride PET/CT. J Nucl Med. 2004;45(2):272–8.
111. Schirrmeister H, et al. Early detection and accurate description of extent of metastatic bone disease in breast cancer with fluoride ion and positron emission tomography. J Clin Oncol. 1999;17(8):2381.
112. Withofs NN. ^{18}F-fluoride PET/CT for assessing bone involvement in prostate and breast cancers. Nucl Med Commun. 2011;32(3):168–76.
113. Damle NA. The role of ^{18}F-fluoride PET-CT in the detection of bone metastases in patients with breast, lung and prostate carcinoma: a comparison with FDG PET/CT and ^{99m}Tc-MDP bone scan. Jpn J Radiol. 2013;31(4):262–9.
114. Yoon S-H, et al. Usefulness of ^{18}F-fluoride PET/CT in breast cancer patients with osteosclerotic bone metastases. Nucl Med Mol Imaging. 2013;47(1):27–35.
115. Even-Sapir E, et al. The detection of bone metastases in patients with high-risk prostate cancer: ^{99m}Tc-MDP planar bone scintigraphy, single- and multi-field-of-view SPECT, ^{18}F-fluoride PET, and ^{18}F-fluoride PET/CT. J Nucl Med. 2006;47(2):287–97.
116. Kjölhede H, et al. Combined ^{18}F-fluorocholine and ^{18}F-fluoride positron emission tomography/computed tomography imaging for staging of high-risk prostate cancer. BJU Int. 2012;110(10):1501–6.
117. Langsteger WW. Fluorocholine (^{18}F) and sodium fluoride (^{18}F) PET/CT in the detection of prostate cancer: prospective comparison of diagnostic performance determined by masked reading. Q J Nucl Med Mol Imaging. 2011;55(4):448–57.
118. Hetzel M, et al. F-18 NaF PET for detection of bone metastases in lung cancer: accuracy, cost-effectiveness, and impact on patient management. J Bone Miner Res. 2003;18(12):2206–14.
119. Sharma PP. ^{18}F-Fluoride PET/CT for detection of bone metastasis in patients with renal cell carcinoma: a pilot study. Nucl Med Commun. 2014;35(12):1247–53.
120. Chakraborty DD. Comparison of ^{18}F fluoride PET/CT and ^{99m}Tc-MDP bone scan in the detection of skeletal metastases in urinary bladder carcinoma. Clin Nucl Med. 2013;38(8):616–21.
121. Yen R-F. The diagnostic and prognostic effectiveness of F-18 sodium fluoride PET-CT in detecting bone metastases for hepatocellular carcinoma patients. Nucl Med Commun. 2010;31(7):637–45.
122. ^{18}F-fluoride PET/CT versus ^{99m}Tc-MDP scanning for detecting bone metastases: a randomized, multicenter trial to compare two bone imaging techniques. Available from: https://clinicaltrials.gov/ct2/show/NCT00882609
123. ^{18}F – sodium fluoride pet imaging as a replacement for bone scintigraphy. Available at: https://clinicaltrials.gov/ct2/show/NCT01930812
124. Bastawrous S, et al. Newer PET application with an old tracer: role of ^{18}F-NaF skeletal PET/CT in oncologic practice. Radiographics. 2014;34(5):1295–316.
125. Grant FD, et al. Skeletal PET with ^{18}F-fluoride: applying new technology to an old tracer. J Nucl Med. 2008;49(1):68–78.
126. Even-Sapir E. Imaging of malignant bone involvement by morphologic, scintigraphic, and hybrid modalities. J Nucl Med. 2005;46(8):1356–67.
127. Hahn S, et al. Comparison of FDG-PET/CT and bone scintigraphy for detection of bone metastases in breast cancer. Acta Radiol. 2011;52(9):1009–14.
128. Ohta MM. Whole body PET for the evaluation of bony metastases in patients with breast cancer: comparison with ^{99}Tc^{m}-MDP bone scintigraphy. Nucl Med Commun. 2001;22(8):875–9.
129. Shie PP. Meta-analysis: comparison of F-18 Fluorodeoxyglucose-positron emission tomography and bone scintigraphy in the detection of bone metastases in patients with breast cancer. Clin Nucl Med. 2008;33(2):97–101.
130. Rong J, et al. Comparison of ^{18}FDG PET-CT and bone scintigraphy for detection of bone metastases in breast cancer patients. A meta-analysis. Surg Oncol. 2013;22(2):86–91.
131. Liu TT. A meta-analysis of ^{18}FDG-PET, MRI and bone scintigraphy for diagnosis of bone metastases in patients with breast cancer. Skeletal Radiol. 2011;40(5):523–31.
132. Cook GJ, et al. Detection of bone metastases in breast cancer by ^{18}FDG PET: differing metabolic activity in osteoblastic and osteolytic lesions. J Clin Oncol. 1998;16(10):3375–9.
133. Cook GJ, Azad GK, Goh V. Imaging bone metastases in breast cancer: staging and response assessment. J Nucl Med. 2016;57 Suppl 1:27S–33S.
134. Abe KK. Comparison of ^{18}FDG-PET with ^{99m}Tc-HMDP scintigraphy for the detection of bone metastases in patients with breast cancer. Ann Nucl Med. 2005;19(7):573–9.
135. Nakai T, et al. Pitfalls of FDG-PET for the diagnosis of osteoblastic bone metastases in patients with breast cancer. Eur J Nucl Med Mol Imaging. 2005;32(11):1253–8.
136. Morris PG, et al. Integrated positron emission tomography/computed tomography may render bone scintigraphy unnecessary to investigate suspected metastatic breast cancer. J Clin Oncol. 2010;28(19):3154–9.
137. Groheux D, et al. ^{18}F-FDG PET/CT for staging and restaging of breast cancer. J Nucl Med. 2016;57 Suppl 1:17S–26.
138. van der Hoeven JJ, et al. ^{18}F-2-fluoro-2-deoxy-d-glucose positron emission tomography in staging of

locally advanced breast cancer. J Clin Oncol. 2004;22 (7):1253–9.
139. Carkaci S, et al. Retrospective study of ^{18}F-FDG PET/CT in the diagnosis of inflammatory breast cancer: preliminary data. J Nucl Med. 2009;50(2):231–8.
140. Alberini J-L, et al. ^{18}F-fluorodeoxyglucose positron emission tomography/computed tomography (FDG-PET/CT) imaging in the staging and prognosis of inflammatory breast cancer. Cancer. 2009;115(21): 5038–47.
141. Walker GV, et al. Pretreatment staging positron emission tomography/computed tomography in patients with inflammatory breast cancer influences radiation treatment field designs. Int J Radiat Oncol Biol Phys. 2012;83(5):1381–6.
142. Cochet AA. ^{18}F-FDG PET/CT provides powerful prognostic stratification in the primary staging of large breast cancer when compared with conventional explorations. Eur J Nucl Med Mol Imaging. 2014; 41(3):428–37.
143. Groheux D, et al. Prognostic impact of ^{18}FDG-PET-CT findings in clinical stage III and IIB breast cancer. J Natl Cancer Inst. 2012;104(24):1879–87.
144. Vazquez B, Rousseau D, Hurd TC. Surgical management of breast cancer. Semin Oncol. 2007;34(3): 234–40.
145. Fisher B. From Halsted to prevention and beyond: advances in the management of breast cancer during the twentieth century. Eur J Cancer. 1999;35(14): 1963–73.
146. Gervasoni Jr JE, Sbayi S, Cady B. Role of lymphadenectomy in surgical treatment of solid tumors: an update on the clinical data. Ann Surg Oncol. 2007;14(9):2443–62.
147. Lucci A, et al. Surgical complications associated with sentinel lymph node dissection (SLND) plus axillary lymph node dissection compared with SLND alone in the American College of Surgeons Oncology Group Trial Z0011. J Clin Oncol. 2007;25 (24):3657–63.
148. Carlson RW, et al. NCCN task force report: adjuvant therapy for breast cancer. J Natl Compr Canc Netw. 2006;4 Suppl 1:S1–26.
149. Come SE, et al. Endocrine and targeted manipulation of breast cancer: summary statement for the Sixth Cambridge Conference. Cancer. 2008;112 Suppl 3:673–8.
150. Gralow JR. Optimizing the treatment of metastatic breast cancer. Breast Cancer Res Treat. 2005;89 Suppl 1:S9–15.
151. Perez EA, et al. Trastuzumab plus adjuvant chemotherapy for human epidermal growth factor receptor 2 – positive breast cancer: planned joint analysis of overall survival from NSABP B-31 and NCCTG N9831. J Clin Oncol. 2014;32(33):3744–52.
152. Moasser MM. Targeting the function of the HER2 oncogene in human cancer therapeutics. Oncogene. 2007;26(46):6577–92.
153. Slamon DJ, et al. Use of chemotherapy plus a monoclonal antibody against HER2 for metastatic breast cancer that overexpresses HER2. N Engl J Med. 2001;344(11):783–92.
154. Clark O, et al. Targeted therapy in triple-negative metastatic breast cancer: a systematic review and meta-analysis. Core Evid. 2014;9:1–11.
155. Lord CJ, Tutt ANJ, Ashworth A. Synthetic lethality and cancer therapy: lessons learned from the development of PARP inhibitors. Annu Rev Med. 2015; 66(1):455–70.
156. Baselga J, et al. Everolimus in postmenopausal hormone-receptor – positive advanced breast cancer. N Engl J Med. 2012;366(6):520–9.
157. Finn RS, et al. The cyclin-dependent kinase 4/6 inhibitor palbociclib in combination with letrozole versus letrozole alone as first-line treatment of oestrogen receptor-positive, HER2-negative, advanced breast cancer (PALOMA-1/TRIO-18): a randomised phase 2 study. Lancet Oncol. 2015;16(1):25–35.
158. Ma CX, et al. A phase II study of UCN-01 in combination with irinotecan in patients with metastatic triple negative breast cancer. Breast Cancer Res Treat. 2013;137(2):483–92.
159. Hu XC. Cisplatin plus gemcitabine versus paclitaxel plus gemcitabine as first-line therapy for metastatic triple-negative breast cancer (CBCSG006): a randomised, open-label, multicentre, phase 3 trial. Lancet Oncol. 2015;16(4):436–46.
160. Bellon JR, Katz A, Taghian A. Radiation therapy for breast cancer. Hematol Oncol Clin North Am. 2006;20(2):239–57. vii.
161. Ragaz J, et al. Adjuvant radiotherapy and chemotherapy in node-positive premenopausal women with breast cancer. N Engl J Med. 1997;337(14):956–62.
162. Feldman LD, et al. Pathological assessment of response to induction chemotherapy in breast cancer. Cancer Res. 1986;46:2578–81.
163. McCready DR, et al. The prognostic significance of lymph node metastases after preoperative chemotherapy for locally advanced breast cancer. Arch Surg. 1989;124:21–5.
164. Wolmark N, et al. Preoperative chemotherapy in patients with operable breast cancer: nine-year results from National Surgical Adjuvant Breast and Bowel Project B-18. J Natl Cancer Inst Monogr. 2001;30:96–102.
165. Eisenhauer EA, et al. New response evaluation criteria in solid tumours: revised RECIST guideline (version 1.1). Eur J Cancer. 2009;45(2):228–47.
166. Wahl RL, et al. Metabolic monitoring of breast cancer chemohormonotherapy using positron emission tomography: initial evaluation. J Clin Oncol. 1993;11(11):2101–11.
167. Mankoff DA, Dunnwald LK. Changes in glucose metabolism and blood flow following chemotherapy for breast cancer. PET Clin. 2005;1:71–82.
168. Avril N, Sassen S, Roylance R. Response to therapy in breast cancer. J Nucl Med. 2009;50 Suppl 1:55S–63.
169. Wang YY. Is ^{18}F-FDG PET accurate to predict neoadjuvant therapy response in breast cancer? A meta-analysis. Breast Cancer Res Treat. 2012;131(2):357–69.

170. Specht JM, et al. Tumor metabolism and blood flow as assessed by positron emission tomography varies by tumor subtype in locally advanced breast cancer. Clin Cancer Res. 2010;16(10):2803–10.
171. Groheux D, et al. HER2-overexpressing breast cancer: FDG uptake after two cycles of chemotherapy predicts the outcome of neoadjuvant treatment. Br J Cancer. 2013;109(5):1157–64.
172. Humbert OO. HER2-positive breast cancer: ^{18}F-FDG PET for early prediction of response to trastuzumab plus taxane-based neoadjuvant chemotherapy. Eur J Nucl Med Mol Imaging. 2014;41(8):1525–33.
173. Groheux D, et al. Triple-negative breast cancer: early assessment with ^{18}F-FDG PET/CT during neoadjuvant chemotherapy identifies patients who are unlikely to achieve a pathologic complete response and are at a high risk of early relapse. J Nucl Med. 2012;53 (2):249–54.
174. Humbert OO. Prognostic relevance at 5 years of the early monitoring of neoadjuvant chemotherapy using ^{18}F-FDG PET in luminal HER2-negative breast cancer. Eur J Nucl Med Mol Imaging. 2014;41 (3):416–27.
175. Groheux D, et al. Baseline tumor ^{18}F-FDG uptake and modifications after 2 cycles of neoadjuvant chemotherapy are prognostic of outcome in ER+/HER2 − breast cancer. J Nucl Med. 2015;56(6):824–31.
176. Dunnwald LK, et al. PET tumor metabolism in locally advanced breast cancer patients undergoing neoadjuvant chemotherapy: value of static versus kinetic measures of fluorodeoxyglucose uptake. Clin Cancer Res. 2011;17(8):2400–9.
177. Boellaard R. Need for standardization of ^{18}F-FDG PET/CT for treatment response assessments. J Nucl Med. 2011;52 Suppl 2:93S–100.
178. Groheux D, et al. Early metabolic response to neoadjuvant treatment: FDG PET/CT criteria according to breast cancer subtype. Radiology. 2015;277(2): 358–71.
179. Bassa P, et al. Evaluation of preoperative chemotherapy using PET with fluorine-18-fluorodeoxyglucose in breast cancer. J Nucl Med. 1996;37:931–8.
180. Burcombe RJ, et al. Evaluation of good clinical response to neoadjuvant chemotherapy in primary breast cancer using [^{18}F]-fluorodeoxyglucose positron emission tomography. Eur J Cancer. 2002;38(3):375–9.
181. Kim SJ, et al. Predictive value of [^{18}F]FDG PET for pathological response of breast cancer to neo-adjuvant chemotherapy. Ann Oncol. 2004;15(9):1352–7.
182. Emmering J, et al. Preoperative [^{18}F]FDG-PET after chemotherapy in locally advanced breast cancer: prognostic value as compared with histopathology. Ann Oncol. 2008;19:1573–7.
183. Couturier O, et al. Sequential positron emission tomography using [^{18}F]fluorodeoxyglucose for monitoring response to chemotherapy in metastatic breast cancer. Clin Cancer Res. 2006;12(21): 6437–43.
184. Dose Schwarz J, et al. Early prediction of response to chemotherapy in metastatic breast cancer using sequential ^{18}F-FDG PET. J Nucl Med. 2005;46(7):1144–50.
185. Gennari A, et al. Role of 2-[^{18}F]-fluorodeoxyglucose (FDG) positron emission tomography (PET) in the early assessment of response to chemotherapy in metastatic breast cancer patients. Clin Breast Cancer. 2000;1(2):156–61. discussion 162–3.
186. Mortazavi-Jehanno N, et al. Assessment of response to endocrine therapy using FDG PET/CT in metastatic breast cancer: a pilot study. Eur J Nucl Med Mol Imaging. 2011;39(3):450–60.
187. Lin NU, et al. Phase II study of lapatinib in combination with trastuzumab in patients with human epidermal growth factor receptor 2 – positive metastatic breast cancer: clinical outcomes and predictive value of early [^{18}F]fluorodeoxyglucose positron emission tomography imaging (TBCRC 003). J Clin Oncol. 2015;33(24):2623–31.
188. Coleman RE, et al. Bone scan flare predicts successful systemic therapy for bone metastases. J Nucl Med. 1988;29(8):1354–9.
189. Schneider JA, et al. Flare on bone scintigraphy following taxol chemotherapy for metastatic breast cancer. J Nucl Med. 1994;35(11):1748–52.
190. Wade AA, et al. Flare response in ^{18}F-fluoride ion PET bone scanning. Am J Roentgenol. 2006; 186(6):1783–6.
191. Cook GJ, Taylor B, Glendenning J, et al. Heterogeneity of treatment response in skeletal metastases from breast cancer in ^{18}F-fluoride and ^{18}F-FDG PET. Nucl Med Commun. 2015;36:515–16.
192. Hillner BE, et al. ^{18}F-fluoride PET used for treatment monitoring of systemic cancer therapy: results from the national oncologic PET registry. J Nucl Med. 2015;56(2):222–8.
193. Stafford SE, et al. Use of serial FDG PET to measure the response of bone-dominant breast cancer to therapy. Acad Radiol. 2002;9(8):913–21.
194. Specht JM, et al. Serial 2-[^{18}F]fluoro-2-deoxy-D-glucose positron emission tomography (FDG-PET) to monitor treatment of bone-dominant metastatic breast cancer predicts time to progression (TTP). Breast Cancer Res Treat. 2007;105(1):87–94.
195. Tateishi U, et al. Bone metastases in patients with metastatic breast cancer: morphologic and metabolic monitoring of response to systemic therapy with integrated PET/CT. Radiology. 2008;247(1):189–96.
196. Osborne CK, et al. The value of estrogen and progesterone receptors in the treatment of breast cancer. Cancer. 1980;46 Suppl 12:2884–8.
197. van Kruchten M, et al. PET imaging of oestrogen receptors in patients with breast cancer. Lancet Oncol. 2013;14(11):e465–75.
198. Mankoff DA. How imaging can impact clinical trial design: molecular imaging as a biomarker for targeted cancer therapy. Cancer J (Sudbury, Mass). 2015; 21(3):218–24.

199. Katzenellenbogen JA, Welch MJ, Dehdashti F. The development of estrogen and progestin radiopharmaceuticals for imaging breast cancer. Anticancer Res. 1997;17:1573–6.
200. Mintun MA, et al. Breast cancer: PET imaging of estrogen receptors. Radiology. 1988;169(1):45–8.
201. Peterson LM, et al. Quantitative imaging of estrogen receptor expression of breast cancer with PET and ^{18}F-fluoroestradiol. J Nucl Med. 2008;49:367–74. in press.
202. Fowler AM, et al. Imaging diagnostic and therapeutic targets: steroid receptors in breast cancer. J Nucl Med. 2016;57 Suppl 1:75S–80.
203. Clark AS. Using nuclear medicine imaging in clinical practice: update on PET to guide treatment of patients with metastatic breast cancer. Oncology (Williston Park). 2014;28(5):424–30.
204. Hammond MEH, et al. American Society of Clinical Oncology/College of American Pathologists guideline recommendations for immunohistochemical testing of estrogen and progesterone receptors in breast cancer. J Clin Oncol. 2010;28(16):2784–95.
205. Chung GG, et al. Quantitative analysis of estrogen receptor heterogeneity in breast cancer. Lab Invest. 2007;87(7):662–9.
206. Amir E, et al. Prospective study evaluating the impact of tissue confirmation of metastatic disease in patients with breast cancer. J Clin Oncol. 2012;30(6):587–92.
207. Dehdashti F, et al. Assessment of progesterone receptors in breast carcinoma by PET with 21-^{18}F-fluoro-16α,17α-[(R)-(1′-α-furylmethylidene)dioxy]-19-norpregn-4-Ene-3,20-dione. J Nucl Med. 2012;53(3):363–70.
208. Keen JC. The biology of breast carcinoma. Cancer. 2003;97 Suppl 3:825–33.
209. Linden HM, Dehdashti F. Novel methods and tracers for breast cancer imaging. Semin Nucl Med. 2013;43(4):324–9.
210. Dijkers EC, et al. Development and characterization of clinical-grade ^{89}Zr-trastuzumab for HER2/neu ImmunoPET imaging. J Nucl Med. 2009;50(6):974–81.
211. Dijkers EC. Biodistribution of ^{89}Zr-trastuzumab and PET imaging of HER2-positive lesions in patients with metastatic breast cancer. Clin Pharmacol Ther. 2010;87(5):586–92.
212. Verma S, et al. Trastuzumab emtansine for HER2-positive advanced breast cancer. N Engl J Med. 2012;367(19):1783–91.
213. Gebhart G, et al. Molecular imaging as a tool to investigate heterogeneity of advanced HER2-positive breast cancer and to predict patient outcome under trastuzumab emtansine (T-DM1): the ZEPHIR trial. Ann Oncol. 2016; 27(4):619–24.
214. Clark AS, DeMichele A, Mankoff D. HER2 imaging in the ZEPHIR study. Ann Oncol. 2016; 27(4):555–7.
215. Rousseau C, et al. Monitoring of early response to neoadjuvant chemotherapy in stage II and III breast cancer by [^{18}F]fluorodeoxyglucose positron emission tomography. J Clin Oncol. 2006;24(34):5366–72.
216. Schelling M, et al. Positron emission tomography using [^{18}F]fluorodeoxyglucose for monitoring primary chemotherapy in breast cancer. J Clin Oncol. 2000;18:1689–95.
217. Smith I, et al. Positron emission tomography using [^{18}F]-fluorodeoxy-D-glucose to predict the pathologic response of breast cancer to primary chemotherapy. J Clin Oncol. 2000;18:1676–88.
218. Migliaccio II. Cyclin-dependent kinase 4/6 inhibitors in breast cancer therapy. Curr Opin Oncol. 2014;26(6):568–75.
219. Kenny L, et al. Imaging early changes in proliferation at 1 week post chemotherapy: a pilot study in breast cancer patients with 3′-deoxy-3′-[^{18}F] fluorothymidine positron emission tomography. Eur J Nucl Med Mol Imaging. 2007;34(9):1339–47.
220. Kenny L. The use of novel PET tracers to image breast cancer biologic processes such as proliferation, DNA damage and repair, and angiogenesis. J Nucl Med. 2016;57 Suppl 1:89S–95.
221. Kostakoglu L, et al. A phase II study of 3′-deoxy-3′-^{18}F-fluorothymidine PET in the assessment of early response of breast cancer to neoadjuvant chemotherapy: results from ACRIN 6688. J Nucl Med. 2015;56(11):1681–9.
222. Dehdashti F, et al. Assessment of cellular proliferation in tumors by PET using ^{18}F-ISO-1. J Nucl Med. 2013;54(3):350–7.
223. Shoghi KI, et al. Quantitative receptor-based imaging of tumor proliferation with the sigma-2 ligand [^{18}F] ISO-1. PLoS One. 2013;8(9):e74188.

Diagnostic Applications of Nuclear Medicine: Lung and Mediastinal Tumors

22

Elite Arnon, Thida Win, Ora Israel, Ludmila Guralnik, and Simona Ben-Haim

Abstract

While CT and MRI provide high-resolution anatomic assessment of lung and mediastinal malignancies, [^{18}F]FDG imaging is superior in differentiating benign from malignant lymphadenopathy and in the detection of distant metastases. Pre-therapy assessment with [^{18}F]FDG can provide important prognostic information. In addition [^{18}F]FDG PET/CT can eliminate about half of futile thoracotomies and is therefore recommended for staging of lung and mediastinal tumors. [^{18}F]FDG imaging is also indicated in the diagnosis of recurrent disease and in monitoring treatment. [^{18}F]FDG PET/CT has been introduced for radiation planning, enabling refining treatment volumes to allow increased dose in target volume and reduced toxicity to nontarget tissues. Although [^{18}F]FDG is the most widely used tracer in oncology, other PET tracers are evaluated with specific clinical and research goals and may have a future role in the management of lung malignancies.

Keywords

Lung cancer • [^{18}F]FDG imaging in lung cancer • Lung and mediastinal tumor imaging • Staging of lung and mediastinal tumors

Glossary

[^{18}F]FDG	2-Deoxy-2-[^{18}F]fluoro-D-glucose
^{18}F-FLT	3′-deoxy-3′-^{18}F-fluorothymidine
^{18}F-MISO	^{18}F-Fluoromisonidazole
AJCC	American Joint Committee on Cancer
BAC	Bronchioloalveolar carcinoma

E. Arnon
Department of Nuclear Medicine, Rambam Health Care Campus, Haifa, Israel
e-mail: elite.arnon@gmail.com

T. Win
University College London, London, UK

University of Buckingham, Buckingham, UK

E&N Heartfordshire NHS Trust, Lister Hospital, Stevenage, UK
e-mail: thida.win@nhs.net

O. Israel
Department of Nuclear Medicine, Rambam Health Care Campus, Haifa, Israel

The Bruce Rappaport Faculty of Medicine, Technion-Israel Institute of Technology, Haifa, Israel
e-mail: o_israel@rambam.health.gov.il

L. Guralnik
The Bruce Rappaport Faculty of Medicine, Technion-Israel Institute of Technology, Haifa, Israel

Department of Radiolody, Rambam Health Care Campus, Haifa, Israel
e-mail: l_guralnik@rambam.health.gov.il

S. Ben-Haim (✉)
University College London and UCL Hospitals, NHS Trust, London, UK

Department of Nuclear Medicine, The Chaim Sheba Medical Center, Tel-Hashomer, Israel
e-mail: simona.ben-haim@sheba.health.gov.il

© Springer International Publishing Switzerland 2017
H.W. Strauss et al. (eds.), *Nuclear Oncology*,
https://doi.org/10.1007/978-3-319-26236-9_13

BS	Bone scintigraphy
CM	Coccidioidomycosis
CT	X-ray computed tomography
CTTA	CT texture analysis
CTV	Clinical tumor volume
CYP1A1	Gene encoding for a member of the cytochrome P450 superfamily of enzymes
DOTA	2-(4-Isothiocyanatobenzyl-1,4,7,10-tetra-azacyclododecane-1,4,7,10-tetraacetic acid (macrocyclic coupling agent to label compounds of biological interest with metal radionuclides)
DOTATATE	DOTA-Tyr^3-octreotate
DOTATOC	DOTA-octreotide
DWI	Diffusion-weighted imaging
EBUS	Endobronchial ultrasound
ECOG	Eastern Cooperative Oncology Group
EGFR	Epidermal growth factor receptor; the mutated form EGFRvIII plays a prominent role in tumorigenesis and pro-angiogenic signaling
EUS	Endoscopic ultrasound
GGO	Ground-glass opacity
GST mu	Gene encoding for the mu class of glutathione S-transferase
GTV	Gross tumor volume
HD	Hodgkin's disease
HIV	Human immunodeficiency virus
HRCT	High-resolution computed tomography
HU	Hounsfield units
LLL	Left lower lobe
M	Metastasis status according to the AJCC/UICC TNM staging system
MDCT	Multi-detector computed tomography
MinIP	Minimum intensity projections
MIP	Maximum intensity projection
MPM	Malignant pleural mesothelioma
MPR	Multiplanar reformations
MRI	Magnetic resonance imaging
MTV	Metabolic tumor volume
MVD	Microvessel density
N	Lymph node status according to the AJCC/UICC TNM staging system
NETs	Neuroendocrine tumors
NHL	Hodgkin's lymphoma
NLST	National lung screening trial
NOTA	2-(4,7-Bis(2-(tert-butoxy)-2-oxoethyl)-1,4,7-triazonan-1-yl) acetic acid, a bifunctional chelating agent for metal radionuclides
NPV	Negative predictive values
NSCLC	Non-small cell lung cancers
PET	Positron emission tomography
PET/CT	Positron emission tomography/Computed tomography
PET/MRI	Positron emission tomography/Magnetic resonance imaging
PFS	Progression free survival
PPV	Positive predictive values
PTV	Planning target organ volume
RECIST	Response evaluation criteria in solid tumors
RLL	Right lower lobe
RML	Right middle lobe
ROC	Receiver operator curve
RUL	Right upper lobe
SCLC	Small-cell lung cancer
SPN	Solitary pulmonary nodule
SRS	Somatostatin receptor scintigraphy
STT	Somatostatin
STTr	Somatostatin receptor
SUV	Standardized uptake value
SUV_{inc}	Increment in standardized uptake value in dual-phase acquisition
SUV_{max}	Standardized uptake value at point of maximum
T	Tumor status according to the AJCC/UICC TNM staging system
TB	Tuberculosis

TLG	Total lesion glycolysis
TNM	AJCC/UICC staging system based on parameters "T" (tumor status), "N" (lymph node status), and "M" (distant metastasis status)
UICC	Union Internationale Contre le Cancer (International Union Against Cancer)
WHO	World Health Organization

Contents

Epidemiology 641
Environmental and Genetic Factors 641
Underlying Molecular Biology Changes 642
Staging and Prognostic Stratification 642
Prognostic Stratification 642

Conventional Imaging Methods 643
Staging (TNM) 645
T Stage 646
N Stage 646
M Stage 647
Follow-Up Imaging 648
Mediastinal Tumors 649
Differential Diagnosis Between Lung Cancer and Lymphoma 651
Sarcoidosis 651
Histoplasmosis 652
Coccidioidomycosis 652
Tuberculosis 653

PET and PET/CT for Evaluation of Lung Cancer 654
Characterization of the Solitary Pulmonary Nodule 655
Location 657
Size 657
Solitary Pulmonary Nodule (SPN) 657
Other Lesions 659
[^{18}F]FDG Imaging for Preoperative Staging of NSCLC 659
Value of [^{18}F]FDG PET/CT in Patient Management 661
[^{18}F]FDG Imaging for Radiation Treatment Planning in NSCLC 662
Is Radical Therapy Suitable for the Patient? 663
Prognostic Value of SUV 663
[^{18}F]FDG Imaging for Assessment of Response to Therapy in NSCLC 663
[^{18}F]FDG Imaging in the Follow-Up of Lung Cancer 665
[^{18}F]FDG Imaging for Detection of NSCLC Recurrence 667
Small-Cell Lung Cancer (SCLC) 667
[^{18}F]FDG and Other PET Tracers for Imaging in Neuroendocrine Tumors 668
[^{18}F]FDG Imaging of Malignant Pleural Disease ... 669
[^{18}F]FDG Imaging of Mediastinal Tumors 671
PET/MRI Imaging of Lung and Thoracic Malignancies 673
PET Imaging of Lung and Thoracic Malignancies with Other Tracers 673

Conclusion 674

References 674

Epidemiology

Lung cancer is the leading cause of cancer death accounting for 29% of all cancer deaths in the USA [1]. It is estimated that in 2012, there were 58.7 new cases per 100,000 and 47.2 deaths per 100,000 per year from this disease in men and women [1]. Approximately 6.6% of men and women will be diagnosed with lung cancer at some point during their lifetime, based on 2010–2012 data [1]. Non-small cell lung cancers (NSCLC) are responsible for 85% of lung cancers. Major histologic types of NSCLC include squamous cell carcinoma (which typically arises in the bronchus), adenocarcinoma (originating in the periphery of the lung), and large-cell undifferentiated carcinoma. Small-cell lung carcinoma (SCLC) accounts for 15% of lung malignancies and typically arises centrally in association with a bronchus [1]. In the USA, adenocarcinoma is the most common histologic type of lung cancer, accounting for more than 40% of lung cancers, and has the worst prognosis among NSCLCs.

About 90% of lung cancer cases occur between the ages of 40 and 80, with a peak incidence in the fifth and sixth decades. Only 2% of cases are detected before the age of 40. At the time of diagnosis, 16% of patients have localized disease, 22% have regional spread, and approximately 57% have distant metastases.

Environmental and Genetic Factors

While approximately 10–15% of smokers develop lung cancer, cigarette smoking is linked to the majority of lung cancers in more than eight

out of ten cases (86%). About 15% of lung cancers occur in nonsmokers, but many of these patients have been exposed to secondhand smoke. The amount of smoking as well as the duration of being a smoker is directly correlated to the risk of developing lung cancer. Starting smoking at a young age is more harmful. Stopping smoking reduces the risk of lung cancer. Passive smoking increases the risk of lung cancer, but to a much lesser extent.

Additional factors which increase cancer risk include exposure to asbestos, radon gas, hydrocarbons, and metals such as chromium, nickel, and inorganic arsenic.

It is estimated that 8–14% of lung cancers are due to inherited factors. Relatives of lung cancer patients have a 2.4 times increased risk in developing lung cancers due to combination of genes.

Underlying Molecular Biology Changes

Lung cancer may arise from differentiated or undifferentiated cells, from either the central (SCLC and squamous cell carcinoma) or the peripheral (adenocarcinoma) airway compartment. The interaction between inhaled carcinogens and the epithelium of upper and lower airways leads to the formation of DNA adducts: pieces of DNA covalently bound to a cancer-causing chemical. In 2004, a locus on chromosome 6q23–25 was reported as conferring familial lung cancer susceptibility by family members affected by cancer [2].

The evidence for activated or inactivated carcinogens found in tobacco smoke is strongest in CYP1A1 polymorphisms and GST mu null [3].

Histological types depend on causative factors as well as cell origin. Smoking is linked with small cell, squamous cell, and adenocarcinoma. Nonsmokers usually develop adenocarcinoma. Lung cancers unrelated and related to smoking have different mutation profiles.

There are several signaling pathways in lung cancer. The main signaling pathways that may provide roadmaps for therapy include growth-promoting pathways (epidermal growth factor receptor/Ras/phosphatidylinositol 3-kinase), growth inhibitory pathways (p53/Rb/P14^{ARF}, STK11), apoptotic pathways (Bcl-2/Bax/Fas/FasL), DNA repair, and immortalization genes [4].

Staging and Prognostic Stratification

Only 15% of all lung cancer cases are diagnosed at an early stage, with a 5-year survival rate higher than 50%. Most of lung cancer cases are diagnosed at an advanced stage with distant metastases and a 5-year survival rate of about 4%. The overall 5-year survival rate for lung cancer is 17.4% [1]. Therefore, prognosis mainly depends on staging at the time of diagnosis.

To provide appropriate therapy, the histology of the lesion and determining whether the disease is localized, has regional involvement, or distant metastases are necessary. Staging of lung cancer uses the American Joint Committee on Cancer (AJCC) classification: T (tumor), N (lymph node involvement), and M (metastasis) staging system (Tables 1 and 2).

Prognostic Stratification

Although tumor stage is the main prognostic indicator, there are several additional factors affecting prognosis, including tumor histology, molecular genetics, comorbidity, socioeconomic background, age, gender, tumor heterogeneity, textural analysis, and standard uptake value (SUV) measured intensity of [^{18}F]FDG uptake [5–12]. In 554 patients with post-surgical follow-up, squamous cell carcinoma had the most favorable outcome and anaplastic small cell the least favorable [6]. However, in the subgroup of tumors <4 cm confined to the lung, SCLC had the highest percentage of 5-year survivors. In larger tumors, or in those with spread to the neighboring structures or lymph nodes, squamous cell was significantly more favorable. Histology did not affect survival in stage IV disease [6].

In a population-based cohort study in 5,683 first-time diagnosed lung cancer patients, the most common comorbid conditions included chronic pulmonary disease (52.5%), diabetes

Table 1 AJCC anatomic stage and prognostic groups for lung carcinoma

Group	T category	N category	M category
Occult carcinoma	TX	N0	M0
Stage 0	Tis	N0	M0
Stage IA	T1a	N0	M0
	T1b	N0	M0
Stage IB	T2a	N0	M0
Stage IIA	T2b	N0	M0
	T1a	N1	M0
	T1b	N1	M0
	T2a	N1	M0
Stage IIB	T2b	N1	M0
	T3	N0	M0
Stage IIIA	T1a	N2	M0
	T1b	N2	M0
	T2a	N2	M0
	T2b	N2	M0
	T3	N1	M0
	T3	N2	M0
	T4	N0	M0
	T4	N1	M0
Stage IIIB	T1a	N3	M0
	T1b	N3	M0
	T2a	N3	M0
	T2b	N3	M0
	T3	N3	M0
	T4	N2	M0
	T4	N3	M0
Stage IV	Any T	§Any N	M1a
	Any T	Any N	M1b

Used with the permission of Springer. The original source for this material is the *AJCC Cancer Staging Manual*, Seventh Edition (2010) published by Springer Science and Business Media LLC. www.springer.com

(15.7%), and congestive heart failure (12.9%). The presence of comorbid conditions was associated with worse survival [7]. Socioeconomic differences in survival are partly explained by social inequality in staging, treatment, and the presence of comorbidities [8].

Lung cancer mortality is strongly related to age, rising sharply from 45 to 49 years, with the highest mortality rates in men older than 85 years and women 80–84 years. Mortality rates are similar between men and women until the age of 50–54 and higher in men afterward up to a ratio of 21 men:10 women above 85 years [9]. Women had a higher incidence of adenocarcinoma and a higher incidence of stage IA disease as well as significantly better survival when compared to men (5-year survival 77.7% vs. 61.9% in adenocarcinoma and 59.3% vs. 53% in other lung tumors). No significant gender-related prognostic differences were found in non-adenocarcinoma [10].

Tumor heterogeneity, assessed by CT texture analysis (CTTA), and disease stage as determined by [^{18}F]FDG-PET are significant independent predictors of survival [11, 12].

Conventional Imaging Methods

Imaging plays an essential role in the detection, staging, and response assessment. CT is the modality of choice for lung cancer imaging,

Table 2 The AJCC definition of TNM for lung

TX	Primary tumor cannot be assessed, or tumor proven by the presence of malignant cells in sputum or bronchial washings but not visualized by imaging or bronchoscopy
T0	No evidence of primary tumor
Tis	Carcinoma in situ
T1	Tumor 3 cm or less in greatest dimension, surrounded by lung or visceral pleura, without bronchoscopic evidence of invasion more proximal than the lobar bronchus (i.e., not in the main bronchus)
T1a	Tumor 2 cm or less in greatest dimension
T1b	Tumor more than 2 cm but 3 cm or less in greatest dimension
T2	Tumor more than 3 cm but 7 cm or less or tumor with any of the following features (T2 tumors with these features are classified T2a if 5 cm or less)
	Involves main bronchus, 2 cm or more distal to the carina
	Invades visceral pleura (PL1 or PL2)
	Associated with atelectasis or obstructive pneumonitis that extends to the hilar region but does not involve the entire lung
T2a	Tumor more than 3 cm but 5 cm or less in greatest dimension
T2b	Tumor more than 5 cm but 7 cm or less in greatest dimension
T3	Tumor more than 7 cm or one that directly invades any of the following: parietal pleural (PL3), chest wall (including superior sulcus tumors), diaphragm, phrenic nerve, mediastinal pleura, parietal pericardium; or tumor in the main bronchus less than 2 cm distal to the carina[a] but without involvement of the carina; or associated atelectasis or obstructive pneumonitis of the entire lung or separate tumor nodule(s) in the same lobe
T4	Tumor of any size that invades any of the following: mediastinum, heart, great vessels, trachea, recurrent laryngeal nerve, esophagus, vertebral body, carina, separate tumor nodule(s) in a different ipsilateral lobe
	Regional lymph nodes (N)
NX	Regional lymph nodes cannot be assessed
N0	No regional lymph node metastases
N1	Metastasis in ipsilateral peribronchial and/or ipsilateral hilar lymph nodes and intrapulmonary nodes, including involvement by direct extension
N2	Metastasis in ipsilateral mediastinal and/or subcarinal lymph node(s)
N3	Metastasis in contralateral mediastinal, contralateral hilar, ipsilateral or contralateral scalene, or supraclavicular lymph node(s)
	Distant metastasis (M)
M0	No distant metastasis
M1	Distant metastasis
M1a	Separate tumor nodule(s) in a contralateral lobe; tumor with pleural nodules or malignant pleural (or pericardial) effusion[b]
M1b	Distant metastasis

Used with the permission of Springer. The original source for this material is the *AJCC Cancer Staging Manual,* Seventh Edition (2010) published by Springer Science and Business Media LLC. www.springer.com

[a]The uncommon superficial spreading tumor of any size with its invasive component Limited to the bronchial wall, which may extend proximally to the main bronchus, is also classified as T1a

[b]Most pleural (and pericardial) effusions with lung cancer are due to tumor. In a few patients, however, multiple cytopathologic examinations of pleural (pericardial) fluid are negative for tumor, and the fluid is nonbloody and is not an exudate. Where these elements and clinical judgment dictate that the effusion is not related to the tumor, the effusion should be excluded as a staging element and the patient should be classified as M0

whereas magnetic resonance imaging (MRI) is used for resolving specific questions, i.e., chest wall or mediastinal invasion, adrenal mass characterization, or differentiation between tumor recurrence and radiation fibrosis [13].

Multi-detector computed tomography (MDCT) devices provide high-quality images with short acquisition times [14]. Thin slices help avoid volume averaging and improve the display of anatomic structures. MDCT data can be reconstructed as

axial, sagittal, coronal, and oblique images, as well as multi-planar reformations (MPR), maximum and minimum intensity projections (MIP or MinIP), virtual bronchoscopy, and volume rendering. Low-dose CT can detect stage I lung tumors four to six times more frequent than conventional radiology [15]. Annual screening with low-dose CT can find lung cancers in their earliest stage, when the tumor is most easily treated. The National Lung Screening Trial (NLST) showed that screening with low-dose CT reduced the risk of death from lung cancer by 20% among persons 55–74 years of age who had a smoking history of at least 30 pack years. Recently this strategy is being adopted by several health systems [16, 17]. However, some lung cancers presenting as pulmonary nodules can be missed on CT [18] due to error in perception or misinterpretation. Subcentimeter nodules and low-density nodules, also known as ground-glass opacity (GGO), can be missed [19, 20].

Detection of a new solitary pulmonary nodule (SPN) in a patient with a history of lung cancer raises the possibility of recurrent disease. Features such as lesion size, location, contour, edge, and density (including the presence or absence of calcifications or fat) should be evaluated [21–23]. Unfortunately, none of these features alone establish benignity or malignancy. Specific combinations of features are more likely to be associated with either malignant or benign disease. For example, spiculated borders, ill-defined contours, the presence of bubble-like lucency, eccentric calcification, semisolid lesion, or GGOs are suggestive of malignancy, whereas a completely solid lesion with smooth and well-defined contours; total, central, or popcorn calcification; or inclusions of fat is indicative for benignity [24]. Because of the lack of specificity, more than 20% of SPNs are classified as indeterminate or suspicious after performing CT, and further investigation is required, either a repeat CT to evaluate change in size, PET/CT, or biopsy [23].

Evaluation of the growth rate is based on measurements of the nodule diameters on two consecutive examinations and calculating the doubling time. It can aid in the characterization, especially of indeterminate nodules. Inter- and intra-observer reproducibility of 2D diameter measurements is low [25–27]. Automated computation of the size of an SPN on 3D reconstruction has been shown to improve the ability to assess its growth [27], with the exception of nodules that are abutting the chest wall or vessels, where errors can occur [28]. Recently, the evaluation of the mass of an SPN, calculated by multiplying nodule volume and density, was proposed as a more accurate method. Mass measurements allow growth to be detected earlier and are subject to less variability [29, 30]. In solid SPNs the risk for malignancy can be evaluated by determining the degree of enhancement, which correlates with the degree of vascularity. Typically, malignant nodules enhance more than 20 HU, whereas benign nodules enhance less than 15 HU after intravenous administration of contrast media [31]. Dynamic perfusion CT can further evaluate features including blood volume, blood flow, permeability, mean transit time, and peak enhancement that can help assess the degree of vascularity of the nodule which correlates with malignancy [32]. Dual-energy CT has been suggested as a method of assessing the degree of enhancement with a single scan performed after the administration of contrast material and creating a virtual unenhanced image from the same dataset. Therefore, a single enhanced dual-energy CT scan allows measurement of the degree of enhancement as well as detection of calcifications. It may reduce radiation exposure to patients by avoiding baseline unenhanced scans and may also reduce measurement error due to different regions of interest during the subtraction of an unenhanced image from an enhanced one [33].

Staging (TNM)

Once the diagnosis of lung cancer has been established, the next important work-up step is the assessment of the anatomic extent of the tumor. Staging separates patients who are candidates for surgical resection from those with inoperable disease who should be treated with

chemotherapy and/or radiation. Staging is performed according to the recommendations of the International Staging System, and previously described evidence-based guidelines are used for clinical purposes [19] (Tables 1 and 2).

T Stage

Selection of the appropriate therapeutic approach requires measurement of tumor size and local extent (T stage) of the lesion. CT is an excellent tool for this purpose. The size of the lesion is easily measured, and its edges can be identified in most cases. However, the presence of atelectasis or consolidation distal to the tumor can complicate the identification of tumor margins. In the case of an intraluminal lesion, CT can be useful in identifying its proximal part, but another marker, such as the extent of hypermetabolism, is required to define the distal extent of the lesion. When the suspected lesion is surrounded by lung parenchyma, thin-section CT is crucial to determine whether the tumor invades the pleura [34]. In the presence of pleural invasion, the surgical approach cannot be modified. CT or MRI can be used to detect chest wall invasion but is not helpful in distinguishing chest wall invasion from fibrous adhesions. Reliable diagnosis of chest wall invasion can be made in the presence of rib destruction or of an obvious chest wall mass [35, 36]. The problem remains unresolved in the presence of contiguity of the tumor with the parietal pleura or of pleural thickening. The accuracy of CT for diagnosis of chest wall invasion is 39–87% [37–45]. Although MRI has superior soft tissue contrast resolution compared to CT, its sensitivity of 63–90% and specificity of 84–86% for diagnosis of chest wall invasion are low and similar to CT [46]. Respiratory dynamic MRI may potentially improve the accuracy of this modality [47]. MRI is superior to CT in the evaluation of chest wall involvement by superior sulcus or Pancoast tumors which almost invariably invade the extrathoracic soft tissue (subclavian vessels, brachial plexus, and vertebrae) [48–50]. Brachial plexus involvement and tumor extension into the spinal canal are contraindications to surgical resection, unlike vertebral body invasion. Invasion of the subclavian vessels, the common carotid, or the vertebral artery represents a relative contraindication to surgery. These vessels may need to be ligated, and CT and MRI can reveal significant atherosclerotic disease of the contralateral vessels, in which case the resection and ligation may not be feasible [51–53].

Nodularity of the pleura or pleural thickening associated with enhancement on CT is consistent with metastatic involvement. Thin-section CT is more sensitive in diagnosing pleural involvement [54–55].

In patients with bronchogenic carcinoma, CT allows accurate differentiation of potentially resectable T1–T3 lesions from unresectable T4 tumors. Mediastinal invasion cannot always be diagnosed on CT. MRI has inherent advantages including the fact that the delineation of mediastinal and hilar vessels does not require the administration of intravenous contrast. Improved soft-tissue characterization by MRI may be helpful in differentiating the tumor from other processes. However, MRI is costly and time consuming, and its spatial resolution is inferior to that provided by CT. Although neither MRI nor CT is capable of demonstrating minimal invasion of either the mediastinal pleura or mediastinal fat, significant obliteration of fat planes or compression or encasement of vessels in the mediastinum appears to be better demonstrated by MRI than CT [3, 54]. When using cardiac-gated T1-weighted MRI, the motion artifacts of the heart are reduced, and visualization of tumor invasion of the pericardium or heart is superior to CT [55]. The addition of contrast material in ECG-gated or breath-hold MR angiography improves the accuracy with higher sensitivity and specificity than contrast-enhanced CT and T1-weighted MR [54, 55].

N Stage

The most widely used diagnostic criterion of nodal metastases is lymph node size (short axis diameter). Other characteristics, such as shape, density, or contour, do not determine nodal

involvement. However, lymph node enlargement may also be due to reactive hyperplasia, and metastatic nodes are not necessarily enlarged. In a meta-analysis CT had a sensitivity of 57%, a specificity of 82%, and positive and negative predictive values (PPV and NPV) of only 56% and 83%, respectively, for mediastinal staging [55]. CT findings can exclude more than 40% of patients from potentially curative surgery and, on the other hand, lead to another almost 20% of patients will undergo unnecessary or non-curative surgery. CT should be seen as a tool pinpointing to suspicious enlarged nodes for histological confirmation. MRI is not sensitive for assessment of calcifications and is therefore not routinely used in the evaluation of lymph nodes although novel MRI sequences, including STIR turbo spin echo (SE) and diffusion-weighted imaging (DWI), have been used to differentiate metastatic from non-metastatic lymph nodes with a sensitivity and specificity that are superior to CT and comparable to [^{18}F]FDG-PET/CT [54, 55].

M Stage

Although in patients with early stage NSCLC the incidence of occult distant metastases is $<1\%$ [56], most clinicians prefer to conduct a metastatic survey in all patients [57]. The adrenals are currently evaluated by chest CT extended below the diaphragm, considering any adrenal mass with an attenuation value of <10 HU on non-enhanced CT to be consistent with an adenoma [58]. If an adrenal lesion remains indeterminate on a non-enhanced CT, MRI can be helpful [58]. The liver is often included in the chest CT. If a suspicious lesion is detected, dedicated CT, US, or MRI is required for its further characterization. Contrast-enhanced CT is the most commonly performed procedure in search of brain metastases in spite of the fact that MRI with contrast injection has a greater sensitivity than CT [59]. The utility of whole body MRI in the staging algorithm of lung cancer patients is considered, especially with advanced stage patients, due to the superiority in detecting brain metastases, determining mediastinal and chest wall invasion and lymph node metastases [60, 61].

TNM staging has a very important role in managing patients with lung cancer. Treatment options as well as prognosis vary for the different stages of disease. Tumor (T) staging is best accessed by either CT or MRI as these techniques offer better resolution and anatomical details. T stage depends on tumor size, location, and relationship to nearby structures. Five-year survival rates differ in relationship to the tumor size from 77% in T1a ($\leq$2 cm), 71% in T1b (2–3 cm), 58% in T2a (3–5 cm), 49% in T2b (5–7 cm), and 35% in T3 tumors ($>$7 cm) [34]. Data are now available showing the importance of [^{18}F]FDG imaging in TNM staging [35–37]. [^{18}F]FDG imaging also has a significant role in assessing involvement of the pleura. While pleural fluid cytology can be falsely negative in 30–40% of patients, [^{18}F]FDG imaging has a sensitivity of 89–95%, specificity of 67–94%, and accuracy of 91–92% for the detection of malignant pleural involvement [38, 39].

Locoregional lymph node spread represents an important factor in lung cancer management, especially in the absence of distant metastases. Patients with either negative or positive N1 (bronchopulmonary or hilar) nodes are considered for lung resection without further testing. Mediastinal lymph node-positive (ipsilateral [N2] or contralateral [N3]) patients are usually referred to confirmation biopsy either by mediastinoscopy, endoscopic ultrasound (EUS), or endobronchial ultrasound (EBUS). If positive on further tests, management is changed from surgery alone to a combined approach of surgery with chemo-/radiotherapy or combined chemo-/radiotherapy without surgery. [^{18}F]FDG imaging has an established high accuracy for nodal staging. The NICE study [40] suggested that [^{18}F]FDG-negative or a chain of [^{18}F]FDG-positive nodes would not necessarily need confirmation by other diagnostic testing.

The management of N2 disease varies. Most patients are regarded as not suitable for radical surgery alone, and neoadjuvant chemotherapy can be considered in a trial setting. Depending on the nodal station, some patients are better

Table 3 Treatment recommendations for non-small cell lung cancer

Stage	Standard management	Future directions	Survival
IA and B	Surgical resection	Adjuvant therapy (chemotherapy/radiation or combination); chemoprevention	75% (IA)
			55% (IB)
IIA and B	Surgical resection	Same as stage I	50% (IIA)
			40% (IIB)
IIIA	Chemoradiotherapy, surgical resection in selected patients	Neoadjuvant combined-modality therapy to downstage primary tumor	10–35%
IIIB	Chemoradiotherapy	Same as stage IIIA	5%
IV	Ciplatin-based chemotherapy, surgical resection if solitary metastatic lesion with resectable primary tumor	More efficacious single-agent and combination chemotherapy	<5%

served with radical radiotherapy. In other countries combined modality management is recommended for N2 disease. Proven N3 disease patients are usually not considered for radical treatment procedures. As indicated in the seventh edition of TNM classification, patients with single N1 disease have a 5-year survival of 48% as compared to 35% in patients with multiple N1, 34% for single N2, and 20% in patients with multiple N2 nodes [41].

In addition to T- and N staging, [^{18}F]FDG PET/CT imaging is useful for M staging where M0 = no metastasis and M1 = distant metastases. The presence of distant metastases usually changes patient management drastically with stage IV patients typically treated symptomatically and for palliation. Patients with good performance status (e.g., Zubrod/ECOG 0–2) are offered palliative chemotherapy, radiotherapy, and/or active supportive care. The 5-year survival rates in patients with involvement of ipsilateral nodes, pleural effusion, contralateral nodes, and distant metastases are 16%, 6%, 3%, and 1%, respectively [42].

Changes in lung cancer stage grouping were implemented in 2009 (Tables 1 and 2). The major changes include: stage T2 large size was upgraded from IB to IIA, and small T2 N1 was downgraded from IIB to IIA. According to this new TNM staging, the 5-year survival rates for NSCLC are 73% for stage IA, 58% for IB, 46% IIA, 36% IIB, 24% IIIA, 9% IIIB, and 13% for stage IV [42].

The same TNM classification is also suggested for SCLC. The 5-year survival rates for small-cell lung cancer are 38% for stage IA, 21% for IB, 38% IIA, 18% IIB, 13% IIIA, 9% IIIB, and 1% for stage IV [43].

Table 3 summarizes the treatment recommendations for non-small cell lung cancer.

Follow-Up Imaging

Lung cancer is usually followed up by serial CT scans. For patients receiving chemotherapy, assessment of treatment effectiveness is crucial. CT is the method of choice for measuring lesions before and after treatment. The World Health Organization (WHO) criteria and the Response Evaluation Criteria in Solid Tumors (RECIST) have created guidelines for the evaluation of tumor response to therapy. These guidelines provide a standard reporting system using uni- or bidimensional evaluation of tumor size to define its response to therapy as "complete response," "partial response," or "progressive disease" [62–64]. In recent years the introduction of molecular-targeted therapies, immunological agents, and stereotactic radiotherapy has necessitated the use of a new approach. There is growing evidence that target therapies induce effects that differ from those related to the classic cytotoxic treatment including intratumoral hemorrhage, changes in vascularity, or cavitation. More advanced imaging techniques such as DWI,

MR, and PET/CT that represent more adequately tumor biology and function are considered to evaluate response, including tumor volume, attenuation, or perfusion [65].

In patients treated with radiotherapy, CT can reveal postradiation pneumonitis and fibrosis and monitor tumor recurrence. In patients with nonspecific CT findings suspicious for recurrent cancer, sometimes difficult to differentiate from fibrosis, MRI using T2-weighted images or contrast-enhanced imaging can be helpful [66, 67].

Mediastinal Tumors

Mediastinal abnormalities are caused by a large number of processes that can involve various compartments of the mediastinum. Up to 50% of these processes are asymptomatic and discovered incidentally [68, 69]. The radiological armamentarium for evaluation of the mediastinum includes a wide variety of imaging modalities.

The standard posterior-anterior and lateral chest X-ray remains the initial diagnostic imaging tool [70]. It can reveal widening of the mediastinum, deformation of its contours, displacement of adjacent organs, and the presence and type of calcification. However, its ability to delineate the extent of mediastinal processes and their relationship to specific anatomic structure is limited.

CT plays a crucial role in the detection and, in particular, in the characterization of mediastinal abnormalities. Due to its excellent density resolution, CT is not only able to distinguish normal structures from pathological processes in the mediastinum but it can also characterize the latter based on their attenuation pattern and to accurately determine their origin and extent [71, 72]. Following the detection of a mediastinal abnormality on chest X-rays, CT should be the next step in the diagnostic work-up. A second common indication for CT is the detection of mediastinal pathology which is clinically suspected such as a suspected thymoma in patients with myasthenia gravis, thymic carcinoid in patients with ectopic corticotropin production, or an ectopic mediastinal parathyroid adenoma in patients with hypersecretion of parathyroid hormone production [73]. CT is also one of the main imaging modalities used for percutaneous biopsy guidance.

MRI is usually reserved for cases that need further clarification of CT findings and provides additional information regarding the nature, location, and extent of mediastinal disease. Based on its ability to distinguish between different tissues, MRI can confirm the cystic nature of a lesion that appears solid on CT. It can reveal small amounts of fat, favoring the diagnosis of fat-containing masses such as teratoma, hemangioma, or extramedullary hematopoiesis [74], and, in some cases, it can differentiate fibrosis from viable, recurrent tumor [71, 73]. Due to its ability to image vessels, MRI is used for the investigation of mediastinal pathology suspected to be of benign vascular origin, as well as for the assessment of invasion of a large artery or vein or their narrowing by a mediastinal tumor [74, 75]. MRI is helpful to evaluate mediastinal abnormalities, particularly in patients in whom administration of iodinated intravenous contrast medium is contraindicated. However, MRI is limited by reduced spatial resolution as compared with that of CT and by its inability to accurately detect calcifications [72, 74, 75]. In summary, CT is the modality of choice for evaluating suspected mediastinal pathology, whereas MRI is used as a problem-solving tool. Each modality has its own particular strengths; therefore CT and MRI do not compete, but are complementary in many clinical scenarios [71, 76, 77].

Differentiating malignant from benign tumors and grading of malignancy are essential for treatment planning as well as for defining patient prognosis. Unfortunately, the malignant or benign nature of a lesion cannot be confirmed using imaging criteria alone. Findings of irregular contours, necrotic or cystic component, heterogeneous enhancement, lymphadenopathy, and invasion of the great vessels are strongly suggestive of a malignant thymic tumor [78], whereas a unilocular, thin-walled, water-density lesion most probably represents a “true” cyst [78]. Nevertheless, further investigations are often required, including noninvasive tests, such as diffusion-weighted single-shot echo-planar MRI [79–81] or functional and metabolic nuclear medicine procedures, or invasive tests such as percutaneous or

video-assisted thoracoscopic biopsy, to obtain a definite diagnosis.

Thymomas, germ cell tumors, lymphomas, and neurogenic tumors account for the overwhelming majority of primary malignant mediastinal tumors in adults. Approximately 30–35% of thymomas, 20% of germ cell tumors, and 15% of nerve sheath tumors are invasive [68, 70, 71]. Radical excision is the standard of care for malignant thymic diseases and for lesions of neurogenic origin, whereas radiotherapy is the treatment of choice for seminoma. Non-seminomatous germ cell tumors are treated with a combination of surgery and chemotherapy, while a combination of chemo- and radiotherapy is administered in most cases of lymphoma [82–84].

Thymoma is the most common primary neoplasm located in the anterior mediastinum [85, 86]. It affects predominantly adults, with equal incidence in men and women, and is very rare in children [86]. Up to 50% of patients with thymoma suffer from myasthenia gravis, but some may also present with other thoracic complaints or can be entirely asymptomatic [86–88].

Thymoma is usually well defined, but it can be aggressive, penetrating the capsule and extending into the mediastinal fat, pleura, pericardium, lung, and great vessels [88, 89], and it can also cross the diaphragm, reaching the retroperitoneum [70]. Its size varies, ranging from small nodules to large masses [87]. Invasive thymoma can send drop metastases to the ipsilateral pleura and the pericardium [69]. Hematogenous metastases and lymphadenopathy are rare [87]. The presence of enlarged mediastinal lymph nodes in association with a dominant anterior mediastinal mass suggests the diagnosis of lymphoma or of thymic carcinoma rather than thymoma [86, 90].

Thymoma is not always detectable on chest X-rays. Contrast-enhanced MDCT is used for precise assessment of a mediastinal mass and its local invasion, aiding in the preoperative planning. Staging of thymoma is based on the widely accepted clinicopathological classification of Masaoca et al. [91] as well as on the WHO histological classification [92].

Although thymoma typically rises in the anterior-superior mediastinum, it can occur anywhere from the thoracic inlet to the cardiophrenic angle [93, 94]. Most tumors are unilateral [95], spherical or ovoid, and usually encapsulated soft tissue lesions outlined by adjacent mediastinal fat [96]. Up to 60% of thymomas demonstrate various degrees of invasion of adjacent structures [96] or encasement of vessels [97, 98]. While a lack of mediastinal fat obliteration does not necessarily exclude capsular penetration, when these planes are preserved, extensive invasion is unlikely [99]. Aggressive thymoma can present with pleural involvement even at diagnosis, and in cases with circumferential lung encasement, it may be indistinguishable from malignant mesothelioma [99]. Pleural effusion is not typical for patients with thymoma [89].

Thymoma can manifest heterogeneity on CT due to cystic degeneration, hemorrhage, or necrosis [98]. Calcifications can occur, are more frequent in aggressive subtypes, and exhibit a variety of patterns ranging from curvilinear calcification of tumor capsule or fibrous septa to punctuate or coarse calcifications within the tumor itself [87, 97–100].

Thymoma has no distinctive features on MRI, which only rarely provides additional important information to an optimally performed contrast-enhanced CT study [101]. MRI can be useful in the assessment of vascular involvement in patients who cannot tolerate intravenous iodine contrast injection or for clarifying equivocal CT findings. On dynamic MRI thymomas reach peak lesion enhancement earlier than other mediastinal neoplasms, earlier for lower stage as compared to higher-stage disease [102, 103]. Chemical shift MRI is lower in thymic hyperplasia as compared to thymoma. This is of significance in particular in patients with myasthenia gravis, who present with a homogeneous enlarged thymus on CT and MRI which can at times be indistinguishable from thymoma [103].

On T1-weighted MR images, thymoma has a similar signal intensity to muscle, while T2-weighted images show a high signal intensity. Thymomas showing a heterogeneous pattern and cystic changes present as areas of increase signal intensity on T2-weighted images [100, 103]. Hemorrhage is identified as an area of high signal

intensity on both T1- and T2-weighted or on STIR images [80]. Tumor capsule and fibrous septa show low signal intensity on both T1- and T2-weighted images [80]. The role of [^{18}F]FDG-PET/CT in thymoma is unclear. The majority of these lesions have SUVs <3 and a variable appearance on [^{18}F]FDG imaging. SUVs >5 suggest that the lesion may have a different etiology, such as lymphoma.

Differential Diagnosis Between Lung Cancer and Lymphoma

Although lymph node abnormalities depicted by CT are nonspecific, the patterns of thoracic lymphadenopathy can provide important clues in the differential diagnosis of their potential etiology. Nodal metastatic spread of lung cancer always follows a similar pathway. Tumors in the right lung involve initially almost exclusively ipsilateral mediastinal nodes, while left lung tumors have a higher propensity for contralateral spread [104]. Involvement of distal nodes may occur even when proximal nodes are spared. Nearly 30% of lung cancer patients have metastases to mediastinal lymph nodes without lobar or hilar lymph nodes being involved [105]. Lack of vessel invasion by enlarged lymph nodes may help in differentiating lymphoma from metastatic lung cancer [106].

Lymphoma is characterized by predominantly mediastinal nodal involvement. When present, hilar node involvement is usually asymmetric and accompanied by mediastinal disease [107]. Lymphoma tends to expand along or around, rather than invade adjacent structures.

Hodgkin's disease (HD) has a predilection for thoracic involvement found in up to 85% of patients, especially in the pre-vascular and paratracheal regions [108]. As a rule multiple sites show lymphomatous involvement although at times enlargement of a single nodal group can be encountered, usually indicating a nodular sclerosing histologic subtype [109]. HD typically spreads contiguously, involving adjacent lymph nodes, and only rarely skips nodal groups as described for lung cancer [109, 110]. HD also has a tendency to cause thymic involvement in association with mediastinal lymph node enlargement [111].

Thoracic disease is less common in non--Hodgkin's lymphoma (NHL) and is found in up to 50% of cases [112]. The pattern of nodal involvement is also somewhat different from other types of malignancy. Single-site lymph node enlargement is much more common in patients with NHL and occurs mainly in posterior or superior mediastinal or anterior diaphragmatic nodes [113]. Hilar node involvement is less common than for HD or lung cancer. Extranodal disease is frequently present and may involve the lungs, pleura, pericardium, and chest wall [112].

Sarcoidosis

Approximately 70% of patients with sarcoidosis present with a characteristic radiologic pattern including hilar and mediastinal lymphadenopathy with or without concomitant parenchymal abnormalities [114–116]. However, in up to one third of cases, radiological findings are nonspecific. The most frequent presentation is that of right paratracheal and bilateral hilar lymphadenopathy. The aortopulmonary, subcarinal, and retroazygous lymph nodes may be enlarged as well [117]. The posterior mediastinum is less commonly involved. Isolated lymphadenopathy in the anterior or posterior mediastinal compartments as well as unilateral hilar disease is more suggestive of lymphoma, metastatic lung cancer, or a granulomatous or infectious process rather than sarcoidosis. Lymph node calcification (occasionally with an eggshell pattern) can be found in up 25% of cases [118].

Parenchymal sarcoid can show a variety of radiographic patterns, including fine nodular, reticulo-nodular, or acinar lesions (poorly marginated, small to large nodules, or coalescent opacities), and only rarely focal lesions. Acinar opacities or interstitial granulomas may coalesce to give the appearance of the alveolar form of sarcoidosis, and an air bronchogram may be detected [118]. High-resolution CT (HRCT) findings include areas of ground-glass attenuation,

subpleural, or perivascular nodules, which appear as beading and irregular thickening of bronchovascular bundles and thickening of interlobular septa. The nodules, corresponding to coalescent interstitial granulomas, have irregular margins. The foci of ground-glass attenuation may represent areas of active alveolitis or diffuse microscopic interstitial granulomas [119–123]. Patients older than 50 years of age have a higher prevalence of solitary and multiple mass-like opacities in the lung at presentation [123]. In the presence of cavitation of parenchymal lesions, which occurs in less than 1% of patients with sarcoid, tuberculosis and fungal infections should be ruled out.

Histoplasmosis

Radiographic findings of thoracic histoplasmosis depend primarily on the clinical type of presentation and on the immune status of the host. A solitary pulmonary nodule is common in patients with an asymptomatic primary infection. The size of such nodules varies from a few millimeters to several centimeters. Most have well-defined margins and central, laminar, or diffuse calcification patterns. In some cases these nodules are slow growing, and in such cases histoplasmosis may be difficult to distinguish from malignancy.

Adenopathy is frequently seen in addition to parenchymal lung abnormalities, often with calcifications. The differential diagnosis of noncalcified mediastinal adenopathy includes sarcoidosis, lymphoma, and metastases. Enlarged lymph nodes may cause significant bronchial or tracheal compression or obstruction and may lead to esophageal obstruction as well [124].

In more severe cases, radiographs may show widely disseminated, diffuse, fairly discrete nodular shadows throughout the lungs, with individual lesions measuring 1–10 mm diameter. This form of disease is known as miliary histoplasmosis, and appearances are similar to miliary tuberculosis [125]. The infiltrates clear within 2–8 months; however, fibrotic lesions may calcify and persist for many years.

Lung cavitation is usually noted in patients with underlying obstructive lung disease and is similar to chronic active tuberculosis, with predominantly upper lobe disease, characterized by fibrosis, necrosis, cavitation, and granulomatous inflammation. Fibrosing mediastinitis can develop in some patients. It is important to define the extent of the fibrous mass in the mediastinum or hilum and to identify if it causes obstruction of the superior vena cava, pulmonary vessels, esophagus, trachea, or bronchi. Stippled or dense calcifications within the mass are present in most patients with fibrosing mediastinitis [126].

Coccidioidomycosis

Thoracic manifestations of primary coccidioidomycosis (CM) include parenchymal disease, lymphadenopathy, and pleural effusion [127]. Parenchymal consolidation, single or multiple, is the most common manifestation found in 75% of patients. It is segmental or subsegmental, usually unilateral and with a peri-hilar or basal distribution. It can resolve spontaneously within 1–2 weeks. Nodular lung disease is found in up to 20% of patients. The nodules are frequently well defined, simulating metastases, but may also present with ill-defined margins. They are 5–25 mm in diameter and have a parahilar and lower-lobe distribution. In approximately 20% of patients, hilar adenopathy is also present, usually unilateral and concomitant with parenchymal lesions. Mediastinal adenopathy is seen in the presence of severe and prolonged infection and is associated with a higher risk of dissemination. Pleural effusion occurs in less than 20% of patients, although pleuritic chest pain is more frequent, in 50–75% of cases [128].

Approximately 5% of patients may develop a persistent pulmonary disease such as pneumonia with or without adenopathy, nodules and cavities, bronchiectasis, empyema, or calcifications. Pulmonary nodules are the most common radiographic findings in persistent infection. They are, as a rule, single, well circumscribed and round, averaging 1.5–2 cm in diameter, and tend to occur

in the periphery of the middle and upper lobes of the lungs, in contrast to tuberculosis, when nodules develop mainly in the anterior segment of an upper lobe. CM-related nodules can remain stable for months and eventually regress. Only rarely is slow growth observed [128].

Calcification is much less frequent in CM than for tuberculosis and histoplasmosis. Therefore in the evaluation of these nodules, malignancy is a primary concern for the clinician. Cavitation may develop as a result of necrosis in an area of pneumonia or may be the result of the excavation of a nodule. Usually cavities appear as a single lesion, are located in the upper lobes, and can have thin or thick walls. Thin-walled cavities have a tendency to change in size, possibly reflecting check-valve communication with the bronchial tree. A rapid change in size of a cavity suggests coccidioidal infection rather than any other granulomatous process.

Disseminated CM may occur as a complication of the primary illness, a late complication of chronic disease, or may represent the reactivation of latent disease in susceptible individuals. Dissemination has a miliary pattern that resembles tuberculosis, although with less well-defined nodules. The differential diagnoses of this pattern also include other mycotic infections, silicosis, sarcoid, and metastatic disease. Hilar and mediastinal adenopathy is almost always associated with disseminated disease [128].

Tuberculosis

Primary lung tuberculosis (TB) has a nonspecific imaging presentation [129–132]. Common findings include segmental or lobar airspace consolidation, ipsilateral hilar and mediastinal lymphadenopathy, and/or pleural effusion.

Airspace consolidations tend to be homogeneous, with ill-defined margins, and usually occur in the lower and middle lobes and in the anterior segments of the upper lobes. Cavitation within parenchymal opacity is uncommon in primary infection. The lung opacity tends to become rounded with healing and continues to shrink until only a small nodule remains. Subsequently, the nodule may become calcified or ossified, resulting in a calcified granuloma.

Lymphadenopathy is a common manifestation of primary pulmonary TB. The presence of hilar and mediastinal lymphadenopathy helps in differentiating primary from postprimary TB where it is conspicuously absent. Lymphadenopathy may be the only manifestation of primary pulmonary TB without a concomitant parenchymal opacity. This is more common in patients with HIV infection. Adenopathy is mainly found in the ipsilateral hilar region in approximately 60% of children with primary TB, paratracheal adenopathy is found in 40%, and subcarinal lymphadenopathy in 80% of pediatric patients. In adults, lymphadenopathy is unusual in an immunocompetent host but is more frequent in blacks and Asians. Adenopathy is common in patients with an HIV infection. On contrast-enhanced CT involved lymph nodes demonstrate central hypoattenuation with peripheral rim enhancement. Sometimes the pattern of lymphadenopathy is indistinguishable from that of sarcoid or lymphoma. With an appropriate immune response or with adequate chemotherapy, enlarged necrotic lymph nodes may diminish in size and commonly calcify. Calcified lymph nodes and a granuloma represent the Ranke complex. Airway involvement is frequently present in primary TB due to bronchi compression by enlarged lymph nodes or endobronchial spread of infection, broncholithiasis, or bronchiectasis.

Parenchymal abnormalities of postprimary TB show a wide spectrum of findings [133], including patchy or confluent airspace opacities in the apical and posterior segments of the upper lobes and the superior segments of the lower lobes; cavities with a thick outer wall and a smooth inner contour and air-fluid levels [134]; tuberculomas appearing as discrete, sometimes calcified, nodules, typically within the upper lobes; and widespread ill-defined acinar shadows manifesting endobronchial spread, military (hematogenous) spread, appearing as circumscribed nodules less than 1–2 mm in diameter located diffusely throughout both lungs. In contrast to primary TB, lymphadenopathy is notably absent in patients with postprimary disease, with the exception of patients with HIV/AIDS infection.

Bronchiectasis may occur as well, as a consequence of fibrosis. Pleural involvement is more common in postprimary TB than in primary infection, including empyema or empyema necessitans.

PET and PET/CT for Evaluation of Lung Cancer

[^{18}F]FDG PET/CT has been used extensively in the differential diagnosis and characterization of single pulmonary lesions. While the overall performance of [^{18}F]FDG imaging for diagnosis of pulmonary malignancy is good, there are pitfalls and limitations that can lead to potential false-positive and false-negative findings. Inflammatory lesions such as sarcoid or tuberculosis can take up [^{18}F]FDG. While the pattern and, at times, intensity of uptake may be helpful to appropriately identify the etiology of the lesions, biopsy may be necessary to make a definitive diagnosis. False negatives may be due to small-size lesions or to the histological subtype of well-differentiated malignancies such as bronchioloalveolar carcinoma (BAC) or carcinoid [135], as well as sub-solid nodules, particularly GGOs, which often exhibit low glucose utilization rates and low-level metabolic activity and have therefore low or absent [^{18}F]FDG uptake. These are slow-growing tumors with less proliferative potential and longer mean doubling times as compared to NSCLC. The sensitivity of [^{18}F]FDG imaging for BAC is only around 50% [136]. On the other hand, multifocal BAC appearing as multiple nodules or GGOs is detected with a high sensitivity by [^{18}F]FDG imaging studies [137]. Indolent behavior, small size, and paucity of malignant cells all contribute to poor FDG avidity of sub-solid nodules [20]. Well-differentiated adenocarcinomas manifesting as GGOs can be falsely negative on [^{18}F]FDG PET/CT, whereas benign GGOs can be falsely positive [20, 138]. However, [^{18}F]FDG PET/CT is warranted in GGOs with a mixed solid component, more likely of being high-grade invasive tumors.

In spite of the abovementioned limitations, [^{18}F]FDG PET/CT has been reported to change management in 25–52% of patients with NSCLC and has a major role in reducing the number of futile thoracotomies [20, 139, 140]. Pretreatment [^{18}F]FDG PET/CT provides prognostic information. Pillot et al. have summarized the literature assessing the relationship between the SUV of the tumor and outcome [141], suggesting that the SUV is a powerful surrogate marker for outcome in NSCLC. Recently, Goodgame et al. retrospectively analyzed 136 patients with stage I NSCLC. Thirty-two patients had recurrence during a median follow-up of 46 months. In multivariate analysis a preoperative SUV_{max} of 5.5 or higher was an independent predictor of relapse and death in this group of patients [142]. Tann et al. conducted a retrospective study in 51 patients with stage I lung cancer, comparing [^{18}F]FDG PET/CT results to growth rates and tumor doubling times obtained from pretreatment chest CT examinations performed more than 25 days apart, and found that rapid, moderate, and slow doubling times correlated with SUV measurements [143]. Im et al. performed a meta-analysis of 13 studies and 1581 patients assessing the prognostic value of the volumetric parameters of [^{18}F]FDG PET/CT in patients with lung cancer [144]. Both the metabolic tumor volume (MTV) and total lesion glycolysis (TLG) were significant prognostic parameters in NSCLC. Patients with high MTV or high TLG had a poorer prognosis [145]. Recently it has been demonstrated in 102 NSCLC patients significantly higher [^{18}F]FDG uptake compared to EGFR and wild-type profiles [146]. If these preliminary results will be proven in large prospective trials, a single pretreatment [^{18}F]FDG PET/CT study may predict in future the rate of tumor growth and be used in an individualized approach to therapy.

Since most lung lesions are hypermetabolic (with the exception of low-grade BAC, carcinoid, and sub-solid nodules, as stated above), [^{18}F]FDG PET/CT imaging can provide important information for the management of patients with lung lesions. [^{18}F]FDG PET/CT is recommended as a component of initial evaluation in T1–T3 disease. [^{18}F]FDG imaging findings can play a pivotal role in determining whether a patient with T1 disease is resectable or whether patients with more advanced disease have metastases that may require specific therapy. In addition to defining whether pulmonary

nodules represent lung cancer, [^{18}F]FDG PET/CT can determine the number and location of hypermetabolic lesions in the chest and elsewhere and define tumor response to therapy.

A baseline study in patients with pulmonary nodules can help distinguish benign from malignant disease (Figs. 1 and 2). This is usually accomplished by evaluating a combination of the CT pattern of the lesion and its SUV (values >2 are suspicious, and values >4 require further evaluation, usually with biopsy). [^{18}F]FDG imaging studies can also detect other sites of hypermetabolism. If there are multiple hypermetabolic foci in addition to the nodule under investigation, the lesion is more likely to be neoplastic than inflammatory in etiology.

A baseline study in a patient with histologic evidence of lung cancer should evaluate the lung parenchyma, bronchus, lymph nodes (in the chest, neck, and abdomen), chest wall, pleura, liver, adrenal glands, and bone for hypermetabolic foci to stage the disease and address the question about the potential roles of surgery, radiotherapy, and chemotherapy in patient management.

Serial scans are helpful for surveillance, to detect recurrence, especially in patients with no clinical evidence of disease, and to determine the effectiveness of therapy, by detecting changes in lesion size and SUV, as well as detecting new lesions.

Characterization of the Solitary Pulmonary Nodule

A single pulmonary nodule is seen as an opacity in the lung parenchyma measuring <3 cm (larger lesions are masses) without associated adenopathy or atelectasis. Lung nodules can be caused by infection, inflammation, and neoplasms (about

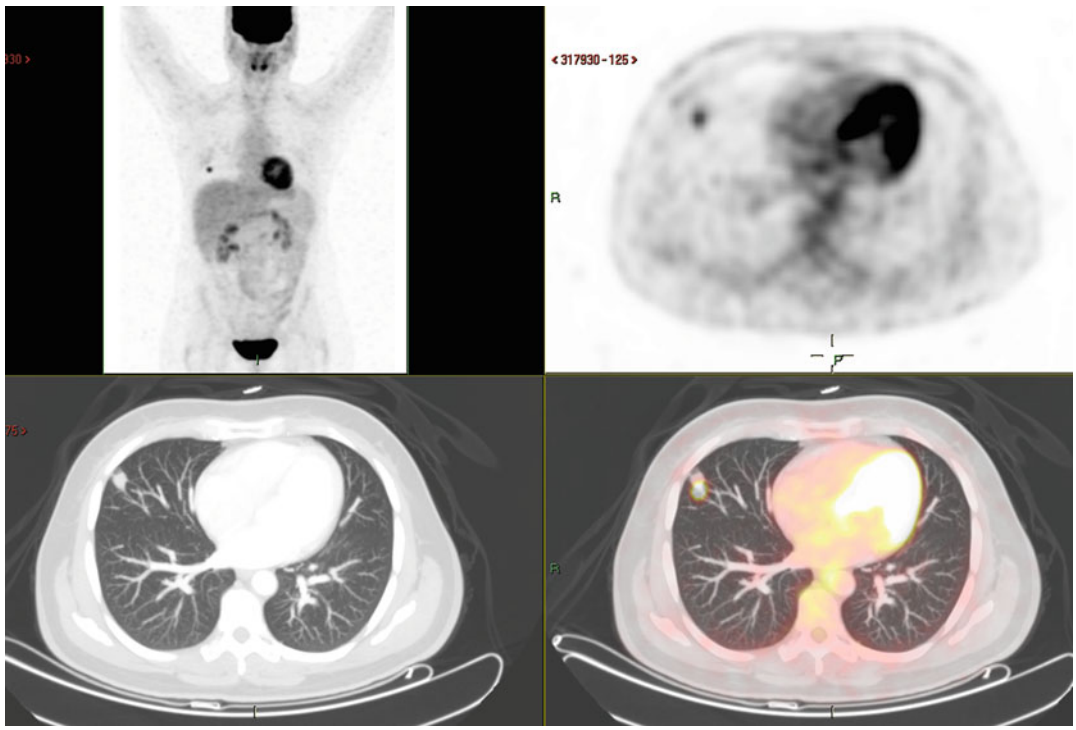

Fig. 1 A 54-year-old woman with a 1.1-cm RML nodule was referred to PET/CT for presurgical assessment. Selected transaxial CT, PET, and fused PET/CT slice and MIP image (*upper left*) show the [^{18}F]FDG-avid RML nodule (SUV_{max} 5.0). There is no hilar nor mediastinal [^{18}F]FDG-avid lymphadenopathy and no distant [^{18}F]FDG-avid disease, corresponding to T1aN0M0 disease by PET/CT. *RML* right middle lobe, *MIP* maximum intensity projection

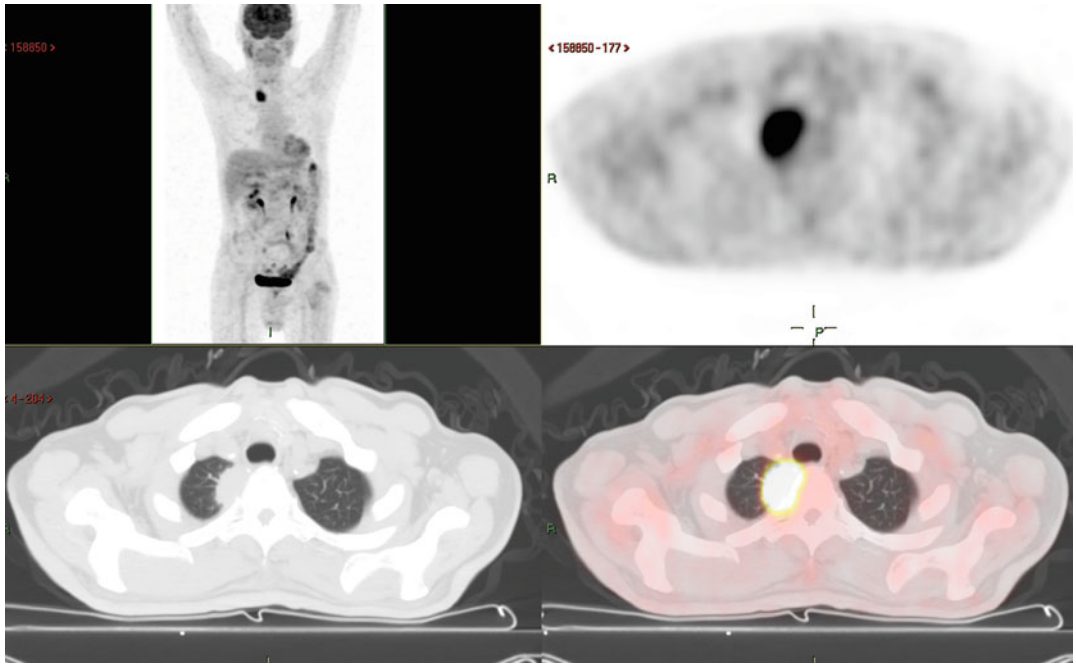

Fig. 2 A 73-year-old man with a 3-cm paravertebral RUL mass was referred to PET/CT for assessment prior to chemotherapy and radiotherapy. Selected transaxial CT, PET, and fused PET/CT slice and MIP image (*upper left*) show the [^{18}F]FDG-avid RUL mass (SUV_{max} 11.7), involving the intervertebral foramina of D2–D3. There is no hilar nor mediastinal [^{18}F]FDG-avid lymphadenopathy and no distant [^{18}F]FDG-avid disease, corresponding to T4N0M0 disease by PET/CT. *RUL* right upper lobe, *MIP* maximum intensity projection

80 different etiologies have been identified). CT alone, or with the addition of [^{18}F]FDG PET, allows the majority of pulmonary nodules to be categorized as benign or malignant. Lesions without spicules, with uniformly distributed dense calcification (>300 Hounsfield units, including the center of the nodule) and which have <15 HU enhancement with contrast administration, are radiographically benign. On the other hand, spiculated borders, indistinct margins, extension to pulmonary veins, focal retraction of adjacent pleura, heterogeneous composition, or enhancement of >25 HU following injection of intravenous contrast suggests malignancy. However, even after careful assessment by CT, distinguishing a malignant from a benign lesion is difficult. Lesions <7 mm diameter have <1% likelihood of malignancy [146]. Lesions 7–20 mm have a 15% incidence of malignancy, and lesions >20 mm have an 81% likelihood of malignancy. Determining the metabolic status of lesions >0.7 cm in diameter with FDG PET-CT can determine if these lesions are malignant or benign in ~90% of lesions. Lesions with SUV ≤2.0 have a low likelihood of malignancy, reducing the need for biopsy, lesions with SUV >4.0 are more likely malignant, and lesions between SUV 2.0 and SUV 4.0 are indeterminate. Nevertheless, an [^{18}F]FDG-negative lesion in a patient with high clinical suspicion for malignancy (e.g., history of smoking, exposure to asbestos, older age, and/or history of non-thoracic neoplasm) still needs to be biopsied to establish the etiology. In the presence of a low clinical suspicion in a patient who is at high risk for biopsy, follow-up by further imaging is usually indicated. If patients carry a high clinical risk, biopsy and histologic evaluation of the lesion are advisable if at all possible. While it could be argued that [^{18}F]FDG imaging is not indicated for diagnostic purposes in patients with a high clinical suspicion (as they would need biopsy or surgery), its main role in the management of these patients is to determine if disease is localized prior to possible surgical or radiation therapy.

In a meta-analysis of 1,474 pulmonary lesions of any size, Gould et al. [147] found a sensitivity of 96.8% and specificity of 77.8% for [^{18}F]FDG PET to distinguish malignant from benign etiologies. In another meta-analysis including five prospective studies, Hellwig et al. [148] reported a sensitivity of 93%, specificity of 87%, and PPV and NPV of 94% and 89%, respectively. The risk to miss malignancy was 11%. Cai et al. [149] showed that [^{18}F]FDG PET/CT is more accurate than helical dynamic CT for SPN characterization and therefore, where available, should be performed as a first-line evaluation. The semiquantitative criterion of a mean SUV $\geq$2.5 has been shown prospectively to have a sensitivity of 90–100% and specificity of 69–95% for diagnosis of malignancy [149, 150] (Fig. 1). In a prospective study in 585 patients, Bryant et al. [150] demonstrated that in nodules less than 2.5 cm in diameter, an SUV_{max} of 2.5 or less was associated in 24% of cases with malignancy, as compared to lesions with an SUV_{max} of 2.6–4 which have an 80% chance of malignancy, and lesions with an SUV above 4.1 with a 96% probability. In spite of these data, Hashimoto et al. [151] have recently shown that in SPNs with an SUV_{max} <2.5, visual analysis performs as well as semiquantitative measurements. The probability of malignancy in a visually evident lesion was 60%, but decreased significantly in lesions with no [^{18}F]FDG uptake.

Location

The location of the lesion is usually determined by CT or the CT component of PET/CT. The exact location of the tumor and its anatomical relationship to important structures such as the bronchi, pleura, pulmonary veins, and thoracic aorta, as well as defining the presence of mediastinal or chest wall invasion, are important in the decision-making process for further management.

Size

The size of the lesion is also determined by CT in most cases. However, in the presence of atelectasis distal to the tumor, the differential diagnosis between the tumor mass and the adjacent atelectasis may be difficult to determine on CT. The [^{18}F]FDG study can define which portion of the lesion is associated with metabolically active tumor, providing additional valuable information for staging. Precise measurement of tumor size is required for TNM classification (Table 1). Subclassification according to tumor size is a factor that has an impact on prognosis (Table 2). In addition, since in most patients there is an interval of few days to a few weeks between the initial staging CT and the [^{18}F]FDG study, exact measurement of the tumor size on the CT component of PET/CT study can help the clinician in determining the growth rate of the tumor.

Solitary Pulmonary Nodule (SPN)

SPN is defined as any nodule up to 3 cm in diameter. The majority of SPNs (60–70%) are benign in etiology. Lung cancer, however, is found in 20–30% of SPNs. [^{18}F]FDG imaging is a better predictor of malignancy in SPN than a combination of clinical and morphologic conventional imaging criteria [134, 144].

False-negative [^{18}F]FDG PET/CT (no uptake in a malignant SPN) is found in less than 5% of nodules 0.6–3 cm in diameter [38]. In the NY-ELCAP study, 378 nodules less than 5 mm in diameter were all nonmalignant on histopathology, therefore, suggesting the need for further follow-up only in nodules that are 5 mm in diameter or larger [152]. In nodules 5–10 mm in diameter, Bastarikka et al. [153] report a sensitivity of 69%, which increased to 95% in nodules of greater than 10 mm for the detection of malignancy by [^{18}F]FDG imaging. The authors also noted that uptake decreased when the size of the nodule was less than twice the system resolution (7–8 mm), and therefore different criteria may need to be applied for nodules less than 15 mm in diameter.

False-negative [^{18}F]FDG imaging results are usually due to the small size (less than 1 cm) of the SPN or the histology of a lesion [135] (Fig. 3). In a series of 36 patients with BAC, 50% of

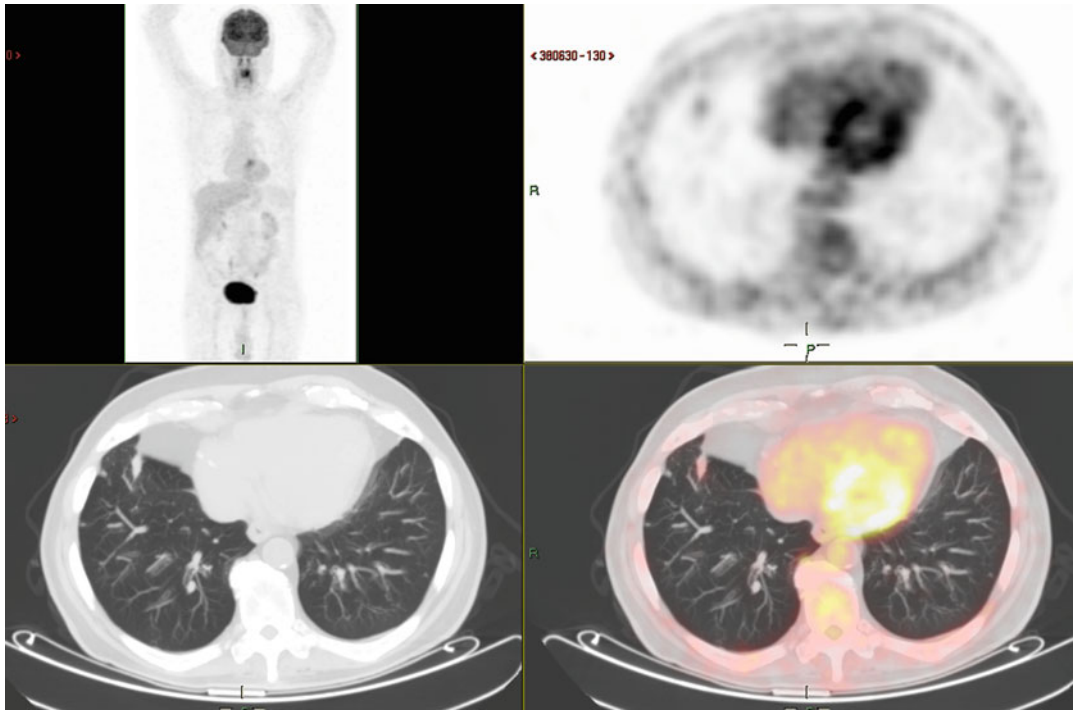

Fig. 3 A 73-year-old man with a 1.4-cm RUL nodule with a nonuniform border was referred to PET/CT for assessment. Selected transaxial CT, PET, and fused PET/CT slice and MIP image (*upper left*). Serial coronal PET slices and MIP image (lower right) show a low-grade [^{18}F]FDG-avid RUL nodule. CT showed additional subcentimeter nodules in RLL, RUL, and LLL, all below the resolution of PET. PET/CT findings are nonspecific, a tumor with low [^{18}F]FDG avidity could not be excluded, and further follow-up was recommended. *RUL* right upper lobe, *RLL* right lower lobe, *LLL* left lower lobe, *MIP* maximum intensity projection

patients had an SUV_{max} $\leq$2.5, and furthermore tumor FDG avidity predicted mortality [154].

Over 40% of SPNs are granulomas, including mycobacterial infection or histoplasmosis. The average SUV_{max} was 5.05 in patients with pulmonary mycobacterial infections (lesions >2 cm). Therapy resulted in a reduction of [^{18}F]FDG uptake to near negligible levels [155]. [^{18}F]FDG PET/CT has a promising role for evaluation of TB in high-risk immunocompromised patients with cancer [156, 157]. In an area with endemic histoplasmosis, inflammatory lesions were difficult to separate from NSCLC (mean SUV_{max} 3.2 in benign lesions vs. 8.5 in neoplastic lesions with significant overlap between groups) [158].

Nodal involvement with sarcoidosis can also be a confounding factor in evaluating the performance of [^{18}F]FDG imaging in SPNs. In one series, 95% of patients with sarcoidosis had pulmonary nodal uptake (SUV 8.6), and 66% of patients had parenchymal uptake (SUV 4.7) [159]. In cancer patients with biopsy-proven sarcoidosis, early metabolic response to systemic steroid treatment can help in the final differential diagnosis when both coexist [160]. Other inflammatory conditions such as pneumonia, pyogenic abscess, aspergillosis, Wegener's granulomatosis, and anthracosis may also need to be differentiated from lung cancer. In a patient with an [^{18}F]FDG-avid SPN and low clinical suspicion of malignancy, further investigation is indicated to determine the cause of tracer uptake.

Dual-phase [^{18}F]FDG studies at 1 and 2 h after tracer injection have been suggested to increase the sensitivity and specificity of [^{18}F]FDG imaging [161, 162]. Using an SUV cutoff of 2.5 and a

10% increase in SUV as a threshold of malignancy, Matthies et al. showed an improvement in sensitivity from 89% to 100%, associated however with a deterioration in specificity from 94% to 89% in single- and dual-phase PET studies, respectively, possibly due to differences in glucose-6 phosphatase and hexokinase levels within benign and malignant cells [161]. Chen et al. have assessed the increment in SUV (SUV_{inc}) from dual-phase [^{18}F]FDG PET in 187 consecutive patients with NSCLC and showed 3-year progression free survival (PFS) and overall survival of 61.6% and 87.8% in patients with $SUV_{inc} \leq 1$, compared to 21.1% and 46.2% in patients with $SUV_{inc} > 1$. The authors conclude that SUV_{inc} is a promising prognostic factor in NSCLC [162]. Of note, however, active granulomas, a frequent cause for false-positive [^{18}F]FDG studies, may also demonstrate the same increase in tracer uptake over time [155].

Other Lesions

[^{18}F]FDG PET/CT imaging can identify incidental lesions or entities such as inflammatory processes. However, it may be difficult to distinguish inflammation secondary to radiation therapy or recent interventional procedures from disease persistence or recurrence, especially if serial [^{18}F]FDG scans are used for surveillance (Fig. 4).

[^{18}F]FDG Imaging for Preoperative Staging of NSCLC

Accurate staging of NSCLC provides important prognostic information and determines the best treatment approach. Surgical resection is indicated for early stages of NSCLC and in N1 or N2 disease (ipsilateral mediastinal nodes), unless lymph node metastases are bulky, multilevel, or non-resectable. In N3 disease (contralateral mediastinal, scalene, or supraclavicular nodal metastases) as well as in patients with metastatic spread surgery is not indicated.

T Stage

Although CT can accurately detect tumor size and infiltration of adjacent structures, [^{18}F]FDG PET/CT predicts T stage in 82% of cases as compared to 68% and 76% for stand-alone CT and visually co-registered separately performed PET and CT, respectively [33–36, 163–166]. [^{18}F]FDG PET/CT may improve accuracy for detection of tumor invasion of the chest wall [163]. Changes in the therapeutic management due to PET/CT occur mainly in T3 and T4 tumors [164]. [^{18}F]FDG PET/CT has also an advantage in the assessment of tumor spread to the pleura. Pleural thickening and pleural nodularity can be detected on CT and MRI, but may also be encountered in benign disorders. However, [^{18}F]FDG PET/CT has a high PPV and NPV in the assessment of malignant pleural effusion [165]. In contrast to CT, [^{18}F]FDG PET/CT can help differentiate between tumor (usually avid) and peri-tumoral atelectasis (usually non-avid) and therefore has an impact on planning of surgical procedure or radiation therapy. The accurate information on tumor extent provided by [^{18}F]FDG PET/CT has been shown to cause changes in planning the radiation field in 30–40% of patients [167, 168].

N Stage

Based on the criterion that a node of $\geq$10 mm in the short axis diameter is metastatic, the sensitivity of CT has been reported in the range of 52–69% and the specificity between 69% and 82% [169]. Normal-size lymph nodes on CT have micrometastases in 15% of cases [170], while 30–40% of enlarged lymph nodes have no tumor cells [171]. [^{18}F]FDG imaging, on the other hand, has a sensitivity ranging between 79% and 85%, specificity of 89–92% [172], and a NPV above 90% [173] for the detection of metastatic mediastinal lymphadenopathy. False-negative results can occur in cases of micrometastases and false-positive findings in cases of inflammation. The PPV of [^{18}F]FDG imaging for evaluating the mediastinum ranges from 45% to 93% [174, 175]. Mediastinoscopy is therefore the standard of care for mediastinal staging. In cases of

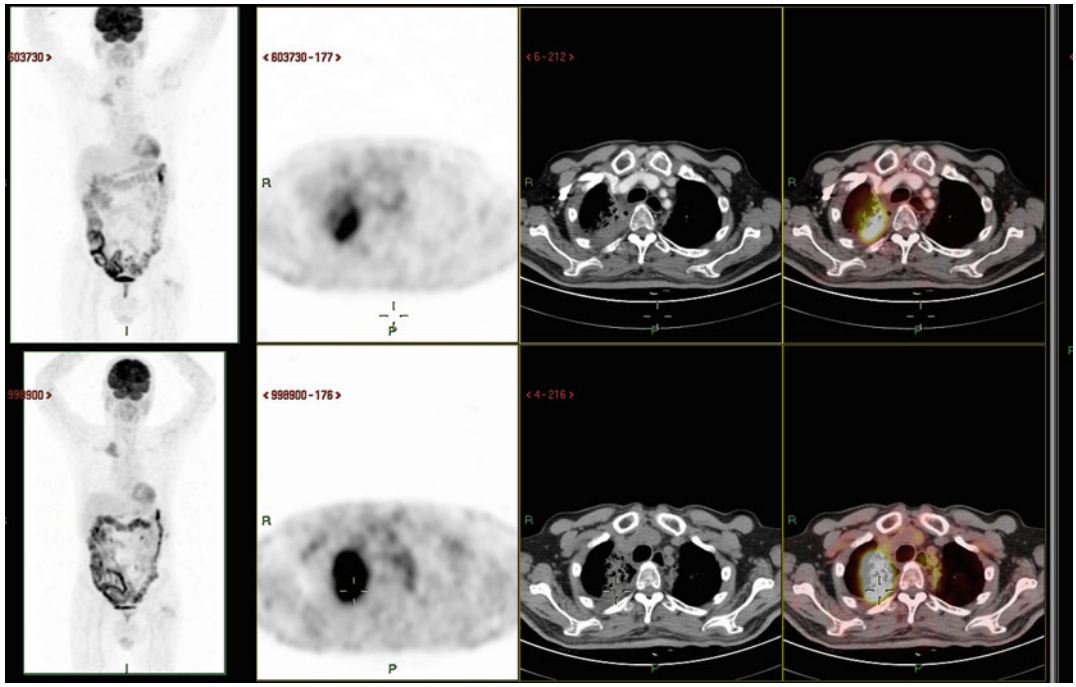

Fig. 4 A 73-year-old man with a paravertebral RUL adenocarcinoma, same patient as Fig. 5. Follow-up studies performed 2 months (*bottom row*) and 5 months (*upper row*) after completion of chemo- and radiation therapy. Selected transaxial CT, PET, and fused PET/CT slice and MIP image (*left*) show an [^{18}F]FDG-avid RUL mass which has reduced in size and in [^{18}F]FDG avidity compared to the first study. In addition there is a new [^{18}F]FDG-avid RUL infiltrate (SUV_{max} 4.8), reducing in size between the two studies, most likely representing post-radiotherapy pneumonitis, although a persistent residual and viable tumor within this infiltrate cannot be excluded. *RUL* right upper lobe, *MIP* maximum intensity projection

[^{18}F]FDG-positive mediastinal nodes, the study can further direct biopsy. Antoch et al. [33] assessed 27 NSCLC patients comparing CT and [^{18}F]FDG PET/CT with histopathology. PET/CT classified the tumor stage correctly in 26 patients, compared to 19 with CT. The accuracy for regional lymph node staging was 93% with PET/CT and 63% with CT. PET/CT also detected 17 distant metastases in four patients, compared to 14 metastases in four patients with CT [33]. Shim et al. prospectively recruited 106 patients with NSCLC who underwent tumor resection and lymph node dissection after [^{18}F]FDG PET/CT and CT. PET/CT correctly staged 86% of the primary tumors as compared to 79% by CT. PET/CT was more sensitive and more specific (85% vs. 70% and 84% vs. 69%, respectively) than CT for diagnosis of malignant regional nodes, with more false-positive findings and false-negative findings on CT [172].

M Stage

Distant metastases are found in 30–40% of patients with NSCLC at the time of presentation; most common sites are in the adrenal glands, liver, bones, and brain [176] (Fig. 5). Adrenal masses occur in about 10% of patients with bronchogenic cancer, and benign adenomas occur in 3–5% [58]. [^{18}F]FDG imaging is more sensitive than CT in the diagnosis of extrathoracic disease [176]. Sensitivities of 88–100% have been reported in characterizing adrenal lesions, with NPV and PPV of 98% and 94%, respectively [177, 178]. The sensitivity and specificity of [^{18}F]FDG imaging for detection of liver metastases from NSCLC are also high, reaching 100% [179]. Bone metastases are present in 20–30% of patients at the time of diagnosis. Although bone scintigraphy (BS) is highly sensitive, it has a less than optimal specificity [180]. In a recent meta-analysis, the sensitivity and specificity of [^{18}F]FDG PET/CT were

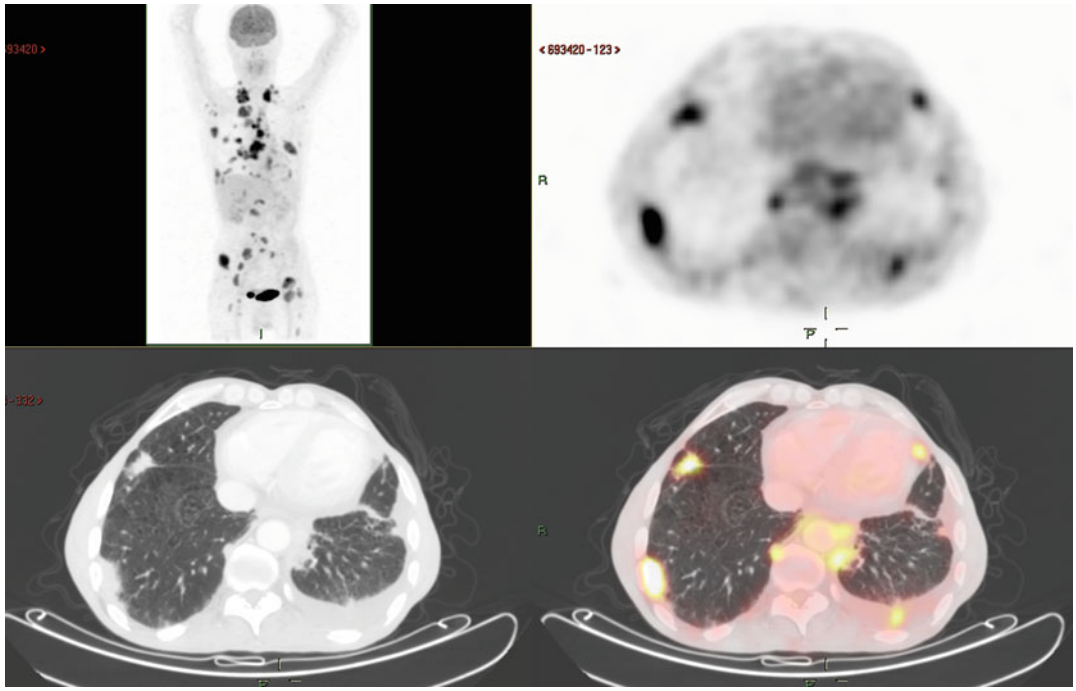

Fig. 5 A 65-year-old man was referred to [^{18}F]FDG PET/CT for evaluation of known metastatic lung cancer. Selected transaxial CT, PET, and fused PET/CT slice show 2.2-cm [^{18}F]FDG-avid RML nodules with spiculated margins, most likely the primary tumor (SUV_{max} 5.5). The MIP image (*upper left*) shows extensive [^{18}F]FDG-avid disease with involvement of the mediastinal and cervical lymph nodes, pleural plaques, pancreas, and extensive skeletal disease, consistent with stage IV disease. *RML* right middle lobe, *MIP* maximum intensity projection

92% and 98%, respectively, compared to 86% and 88% for BS [181]. Therefore, it has been suggested that BS can be eliminated in the staging workup of preoperative patients who undergo an [^{18}F]FDG PET/CT examination.

^{18}F-Fluoride-PET/CT was also assessed for the detection of bone metastases in NSCLC. In a prospective study [182] of 103 patients with lung cancer, receiver operator curve (ROC) analysis showed that the performance of ^{18}F-fluoride PET was better than that of the conventional BS. In 1,000 NSCLC patients with confirmed bone metastases, PET/CT had a better sensitivity (98.3% vs. 95.1%) and specificity (98.7% vs. 98.4%) as compared to planar BS [183]. Recently Kruger et al. [184] have correlated the findings on [^{18}F]FDG PET/CT to BS and ^{18}F-Fluoride studies in 126 patients with NSCLC including 34 patients with osteolytic metastatic bone lesions. [^{18}F]FDG PET/CT was superior to planar BS in the detection of these skeletal lesions, also leading to changes in patient management. ^{18}F-Fluoride detected more metastatic foci and was at least as sensitive as [^{18}F]FDG PET/CT [184].

[^{18}F]FDG imaging is less useful in the detection of brain metastases, due to high physiologic glucose utilization in normal brain tissue. [^{18}F]FDG PET/CT has an advantage in depicting unsuspected pancreatic metastases from lung cancer, particularly those that are not detected by CT alone [185]. Finally, [^{18}F]FDG imaging can also diagnose a synchronous second primary tumor, mainly of colorectal origin, detecting incidentalomas, unsuspected foci of increased tracer uptake in the gastrointestinal tract [185].

Value of [^{18}F]FDG PET/CT in Patient Management

Fisher et al. [186] assessed the clinical effect of [^{18}F]FDG PET/CT on preoperative staging of

NSCLC, comparing 98 patients who had PET/CT to 91 patients who had conventional staging. The primary end point was defined as the number of futile thoracotomies. There were 21/60 futile thoracotomies in the [^{18}F]FDG PET/CT group compared to 38/73 in the conventional imaging group. The number of justified thoracotomies and survival of patients were similar in the two groups. Therefore the use of [^{18}F]FDG PET/CT reduced the number of total and specifically of futile thoracotomies in these patients [186]. Similar findings were also reported by others, who have assessed the cost-effectiveness of lung cancer staging with [^{18}F]FDG PET/CT [139]. In a randomized prospective study, 188 patients had either conventional imaging including CT or had both conventional workup and [^{18}F]FDG imaging [187]. Patients who performed [^{18}F]FDG studies had a 51% reduction in unnecessary thoracotomies. Subedi et al. [188] assessed the clinical impact of [^{18}F]FDG PET/CT in 161 patients with suspected lung cancer. In this study the addition of PET/CT to the conventional evaluation of lung cancer excluded the presence of malignancy in 10% of patients with no uptake in the suspected lung lesion and revealed occult metastases in 16% of patients. [^{18}F]FDG PET/CT was a better predictor for T staging (64% vs. 58%) and N staging (78% vs. 65%) and influenced management decisions in 41% of patients, leading to a decrease in the number of thoracotomies performed for non-resectable disease [189].

[^{18}F]FDG Imaging for Radiation Treatment Planning in NSCLC

NSCLC patients with newly diagnosed stage IIIA or IIIB disease as well as patients with limited disease who are not suitable for surgery are candidates for radiation therapy [190]. It has been shown that [^{18}F]FDG imaging has a significant impact on defining the target volume in patients with lung cancer prior to radiation therapy [191]. Nestle et al. have reviewed the results in 661 patients with lung cancer in 18 trials that compared target volumes, gross tumor volume (GTV), clinical tumor volume (CTV), and planning target organ volume (PTV) using CT alone and [^{18}F]FDG PET/CT. All trials showed significant changes in target volumes when [^{18}F]FDG PET/CT was added due to better diagnosis of lymph node involvement and optimized differentiation between tumor and adjacent atelectasis [190]. In the past, due to diagnostic uncertainties, target volumes in lung cancer patients included large portions of unaffected tissue. High doses of irradiation were delivered with a high risk of irradiating normal lung and adjacent tissues. Due to the high NPV for the detection of mediastinal lymph nodes (>90%) and the delineation of the metabolically active tumor volume, [^{18}F]FDG PET/CT can influence the definition of the GTV for radiotherapy planning. The GTV can be reduced when [^{18}F]FDG-negative nodes or areas of atelectasis are excluded from the radiation treatment field or enlarged when previously unsuspected [^{18}F]FDG-avid nodes are detected. This can lead to a change in the GTV or dose to be delivered in up to two thirds of cases [192–198]. For example, omission of extensive nodal irradiation in patients with N2 disease with lower burden of nodal invasion resulted in a significant reduction of doses given to the lung, esophagus, heart, and spinal cord [195]. However, because of a false-positive rate that may reach 30%, depending on the patient population, ideally, pathological confirmation of [^{18}F]FDG-positive nodes should be obtained by mediastinoscopy or endoscopic ultrasound-guided fine-needle aspiration [197]. Importantly, the addition of [^{18}F]FDG imaging to CT reduces the inter-observer variability in definition of the GTV for NSCLC [199–204].

There are no large clinical trials assessing long-term consequences of [^{18}F]FDG-induced changes in the treatment plan. Isolated cases of nodal failure [205] and out-of-field recurrence [206] were reported. Large prospective trials of patient outcome are needed to assess the clinical impact of this strategy.

Is Radical Therapy Suitable for the Patient?

The outcome of the combined anatomic and metabolic data available from [^{18}F]FDG PET/CT imaging guides clinicians in the selection of the most suitable treatment modality. For example, an 80-year old patient with a single isolated [^{18}F]FDG-positive N2 node adjacent to a left upper lobe tumor would benefit more from radical radiotherapy rather than from neoadjuvant treatment followed by radical surgery.

[^{18}F]FDG imaging can also help in planning the surgical approach with respect to the extent of resection, by identifying [^{18}F]FDG-positive lesions in the mediastinum, chest wall invasion, peribronchial infiltration, or vascular invasion. [^{18}F]FDG imaging is also increasingly used for radiation treatment planning. It can help in decreasing the risk of radiation-related side effects such as pneumonitis and esophagitis by accurate definition of the tumor volume.

Prognostic Value of SUV

The importance of SUV measurements on the baseline [^{18}F]FDG study is very useful in lung tumors. SUV is a good prognostic indicator as well as a good indicator of response to treatment. In NSCLC patients an SUV_{max} of the primary tumor >7 [207] and >10 [208] had an independent prognostic impact, also showing that the median survival decreased with increasing mean SUV levels. Others also showed that the SUV_{max} was an independent predictor of disease free and overall survival [209, 210]. In a retrospective study in 100 patients, Downey et al. [211] showed that the 2-year survival rates were 68% for patients with a SUV_{max} above 9% and 96% in patients with SUV_{max} below 9. In patients with NSCLC, Cerfolio et al. [212] found the SUV_{max} to be an independent predictor of tumor aggressiveness and a more accurate predictor of tumor recurrence and survival as compared to TNM staging. Total lesion glycolysis (TLG) was also found to be a significant prognostic parameter in NSCLC [208].

[^{18}F]FDG Imaging for Assessment of Response to Therapy in NSCLC

Twenty to 40% of patients with NSCLC respond to treatment. Tumor progression after first-line chemotherapy occurs in up to one third of patients [154, 209]. Second-line treatment options can be offered to nonresponding patients if tumor response can be predicted early. Treatment response is mainly assessed with CT; however, there is evidence that [^{18}F]FDG PET/CT is more accurate, as volume reduction is often slower than metabolic response. [^{18}F]FDG imaging has been used to assess the changes in glucose metabolism occurring during treatment and thus for early prediction of tumor response [154, 155, 210, 211] (Fig. 6). The absolute SUV_{max} after treatment has been assessed as a predictor of overall survival. Patients with a posttreatment SUV_{max} of less than 4 survived for more than 56 months, as compared to only 19 months for a posttreatment $SUV_{max} \geq 4$ [212]. Changes in SUV may occur as early as 1 week after initiation of treatment [213]. Weber et al. assessed 57 patients with advanced NSCLC before and after the first cycle of platinum-based chemotherapy. Using a reduction of 20% in tumor SUV as a criterion for metabolic response, they found a close correlation between the change in SUV and tumor response to therapy. Median time to progression and overall survival were significantly longer for the 28 patients with a metabolic response (163 and 252 days) than for the metabolic nonresponders (54 and 151 days, respectively) [210]. In 56 patients with NSCLC who underwent [^{18}F]FDG imaging and CT before and after neoadjuvant chemotherapy followed by tumor resection, the change in SUV correlated much better with the percentage of nonviable tumor cells in the resected specimens than the change in size on CT. A decline of 80% or more in SUV predicted a complete pathological response with a sensitivity, specificity, and

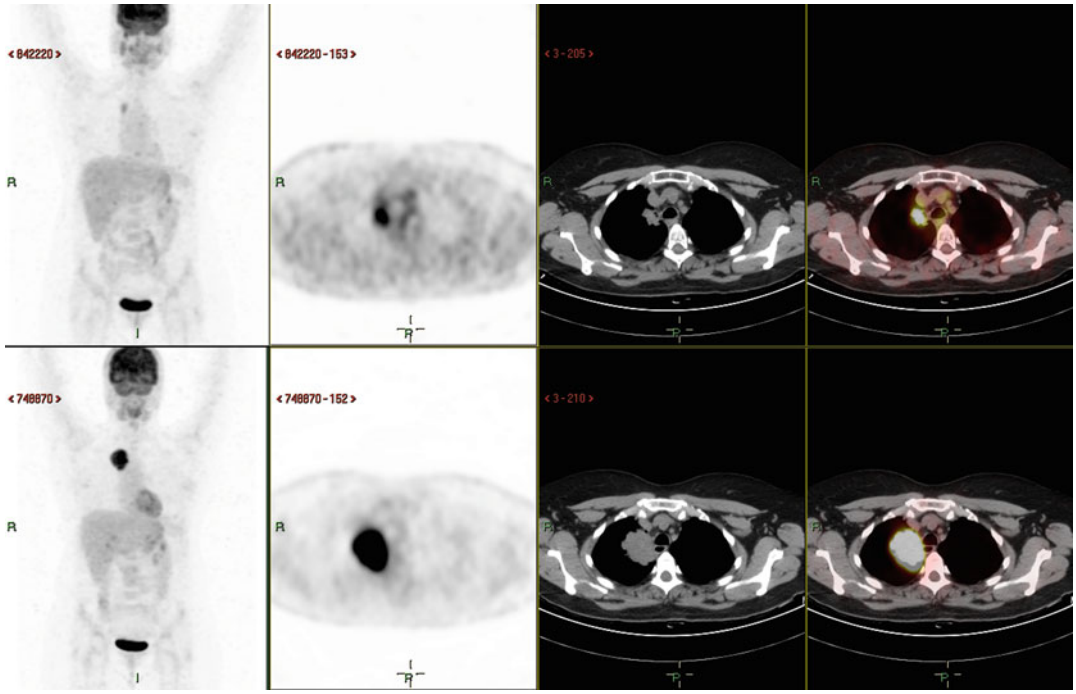

Fig. 6 A 52-year-old woman with a 5-cm RUL paramediastinal mass was referred to [^{18}F]FDG PET/CT for initial staging (*bottom row*) and for repeat PET/CT early after starting chemotherapy (*upper row*). Selected transaxial CT, PET, and fused PET/CT slices and MIP (*left*) show significant reduction in the size of the lesion (from 5 × 3 to 2.2 × 3 cm) and significantly reduced [^{18}F]FDG avidity during chemotherapy (SUV_{max} reduced from 13.5 to 5.6) consistent with a good partial metabolic response. *RUL* right upper lobe, *MIP* maximum intensity projection

accuracy of 90%, 100%, and 96%, respectively [211]. In a prospective study in 47 patients with stage III NSCLC, [18F]FDG imaging was performed before and after one and two cycles and at the end of induction chemotherapy [212]. At the end of therapy, nodal stage on CT was not predictive of outcome, but focal increase in [^{18}F]FDG uptake was associated with a twofold risk of death. A decline in SUV of 50% or more predicted survival. A similar trend was noted after one and two courses of chemotherapy [213]. Eschmann et al. performed [^{18}F]FDG imaging before and 2 weeks after completion of neoadjuvant radio- and chemotherapy and prior to resection in 70 patients with stage III NSCLC. A negative [^{18}F]FDG study or a reduction in SUV of more than 80% from baseline was the best predictors for good response to further treatment, whereas progressive disease on [^{18}F]FDG imaging studies correlated with an unfavorable outcome [214]. In 52 patients with advanced NSCLC who underwent baseline and follow-up [^{18}F]FDG PET/CT after four cycles of chemotherapy, a less than 50% decrease in TLG was identified as the optimal cutoff value to define disease progression, with 100% NPV for a 6 months of progression free survival (PFS). Almost all patients with a decrease in TLG less than 50% had early disease progression [215] (Fig. 7). A prospective multicenter study assessed 52 NSCLC patients who had a baseline and a second [^{18}F]FDG PET/CT during the fifth week of radio-chemotherapy or radiotherapy. SUV_{max} of 5.3 at the second study was the single predictive variable and had a sensitivity of 70% and specificity of 92% for predicting tumor progression or death at 1 year [216]. In 15 patients with stage I–III NSCLC requiring radiotherapy, [^{18}F]FDG PET/CT was performed at baseline, during, and after radiotherapy. There were 11 patients who achieved partial

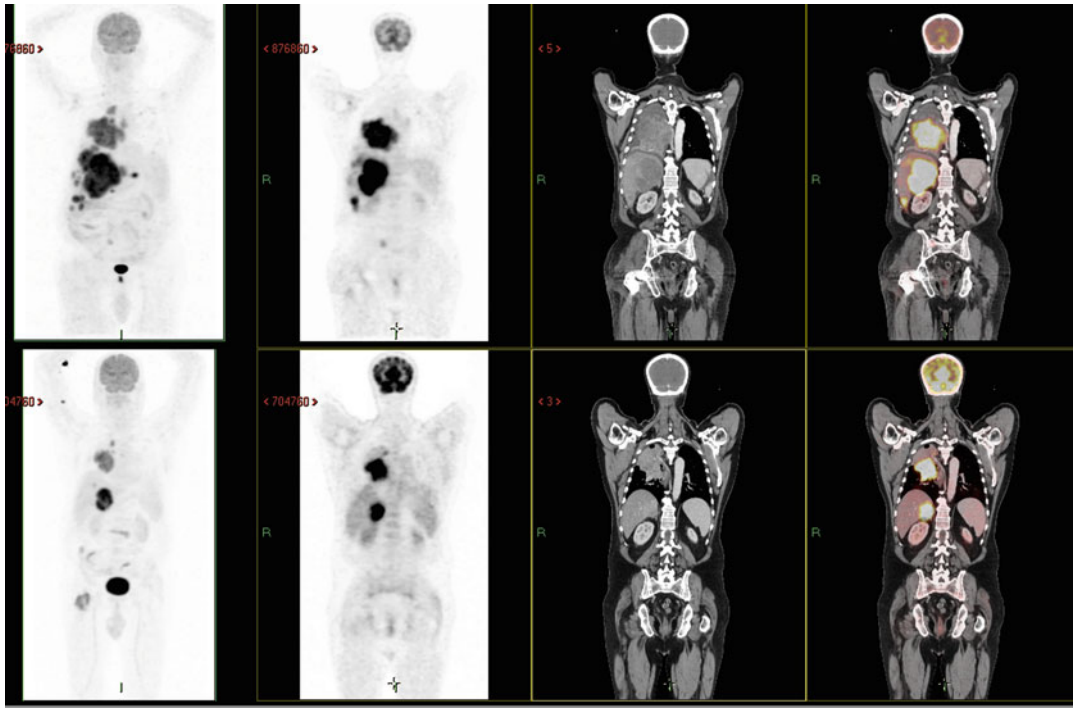

Fig. 7 A 74-year-old man with known metastatic NSCLC was referred to [^{18}F]FDG PET/CT for evaluation of right hip pain (*bottom row*) and for repeat PET/CT 4 months after completion of radiation therapy (*upper row*) due to increasing bone pain. Selected coronal PET, CT, and fused PET/CT slices and MIP (*left*) (*bottom row*) show the [^{18}F]FDG-avid right peri-hilar mass, mediastinal and right supraclavicular lymphadenopathy, liver metastases, and a right femoral lytic lesion. Following resection of right femoral lesion and radiotherapy (*upper row*), there is significant progression in [^{18}F]FDG-avid disease in the right lung, mediastinal nodes, left lung (not shown), and liver. *NSCLC* non-small cell lung cancer, *MIP* maximum intensity projection

response, two with complete response and two with stable disease. All [^{18}F]FDG-avid tumors showed a reduction in [^{18}F]FDG avidity from a mean SUV of 5.2 pre-therapy to 2.5 during radiation therapy and 1.7 post-radiotherapy [217] (Fig. 8). Increased [^{18}F]FDG due to posttreatment inflammation frequently occurs at 2–6 months after radiotherapy and may persist to about 12 months. It has to be considered when interpreting studies in patients treated with radiation [218].

Literature data thus indicate that a decrease in [^{18}F]FDG uptake usually correlates with the pathologic response and with improved survival. It needs to be emphasized, however, that there is not yet a consensus regarding the measurement of response and the degree of reduction in SUV that is required to define a metabolic response.

[^{18}F]FDG Imaging in the Follow-Up of Lung Cancer

After curative treatment follow-up is indicated to assure proper management of therapy-related complications or for early detection of tumor recurrence which is most likely to occur within the first 4 years with only 10% developing after 5 years or more [219]. A meta-analysis showed no significant benefits of follow-up of lung cancer after curative treatments. A nonsignificant trend for improved survival with intensive follow-up was identified in the curative-intent treatment subgroup [219]. The most recent guidelines published by the American College of Chest Physicians suggest that in patients who have undergone curative-intent surgical resection of NSCLC, chest CT should be

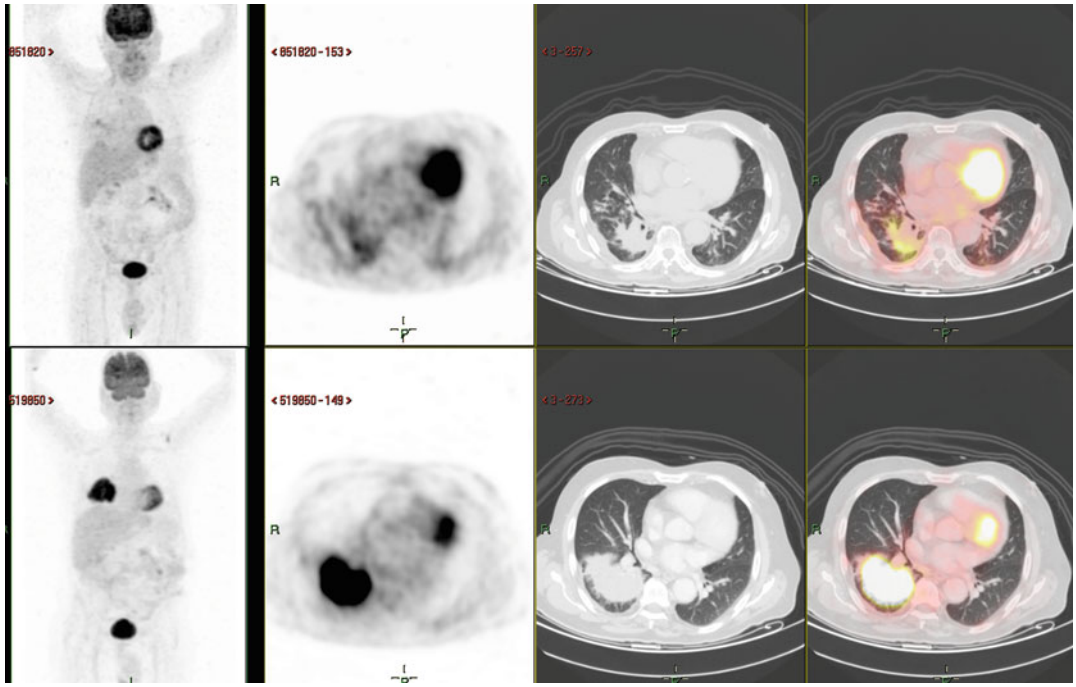

Fig. 8 A 82-year-old man with a 8-cm RLL mass was referred to [^{18}F]FDG PET/CT for initial staging (*bottom row*) and for repeat PET/CT 4 months after completion of radiation therapy (*upper row*). Selected transaxial CT, PET, and fused PET/CT slices and MIP (*left*) (*bottom row*) show the [^{18}F]FDG-avid RLL mass (SUV_{max} 19.7). There is no hilar nor mediastinal [^{18}F]FDG-avid lymphadenopathy and no distant [^{18}F]FDG-avid disease, corresponding to T3N0M0 disease by PET/CT. Following radiotherapy (*upper row*) there is significant reduction in the size of the lesion (from 8 to 4.8 cm) and significantly reduced [^{18}F]FDG avidity (SUV_{max} 3.0). Low-grade residual [^{18}F]FDG avidity is most likely due to post-radiotherapy inflammatory changes. *RLL* right lower lobe, *MIP* maximum intensity projection

performed every 6 months for the first 2 years after resection and every year thereafter [220]. It is further recommended that in NSCLC and carcinoid treated with curative intent, the original treating physicians participate in the decision-making process during follow-up. Routine surveillance with [^{18}F]FDG PET imaging, somatostatin receptor scintigraphy (SRS), or abdominal ultrasonography is not recommended [220].

[^{18}F]FDG PET-CT imaging is helpful in the management of advanced stage lung cancer. Advances in chemotherapy and availability of second- and third-line regimens (including less toxic drugs as well as oral chemotherapy) require a marker to define when these drugs are no longer effective and a change in therapy is necessary.

Changes in lesion size on CT and SUV on serial [^{18}F]FDG PET/CT studies provide information about the efficacy of therapy. Reduction in size and decrease in SUV suggest that therapy is effective. Increasing lesion size or failure of the SUV to decline by $\geq$25% after 6–8 weeks of treatment suggests failure of therapy. In patients who have a complete metabolic response, serial [^{18}F]FDG PET/CT surveillance imaging is very useful to detect recurrence and is more sensitive than stand-alone CT.

In a retrospective study of 261 lung cancer patients with 488 follow-up [^{18}F]FDG PET/CT studies performed $\geq$6 months after completion of initial treatment and followed for a median of 29.3 months, the median survival of [^{18}F]FDG-positive and [^{18}F]FDG-negative groups was 32.9 months and 81.6 months, respectively,

with similar differences in overall survival between the groups. Age and [^{18}F]FDG PET/CT results were the only factors associated with overall survival on multivariate analysis, regardless of the timing of the follow-up study [221]. The same group has assessed the value of the fourth and subsequent [^{18}F]FDG PET/CT studies performed during follow-up after completion of primary therapy in 1,171 patients. [^{18}F]FDG PET/CT identified recurrence or metastases in 43% of studies in patients with no previous evidence of disease and ruled out recurrence or metastases in 24% of studies with prior clinical suspicion of disease with an overall change in management in 28% of patients [222].

[^{18}F]FDG Imaging for Detection of NSCLC Recurrence

Early detection of recurrence can be difficult with CT. New findings can be related to tumor recurrence but can also be due to treatment. Differentiating treatment-induced fibrosis and necrosis from viable tumor may not be possible on CT [223, 224]. However, [^{18}F]FDG imaging can differentiate recurrent or persistent tumor from scar tissue with a sensitivity of 89–98% and specificity of 87–93% [225–227]. Since the results of [^{18}F]FDG studies performed less than 10 days after administration of chemotherapy may be misleading, it is advisable to perform the study at least 2 weeks after completion of therapy. Increased [^{18}F]FDG uptake in recent surgical scars, due to a healing inflammatory process, usually a linear pattern decreasing in intensity over time, can be differentiated from recurrence in the surgical field which has a more focal appearance with high intensity uptake [227].

Small-Cell Lung Cancer (SCLC)

SCLC which represents about 13% of all lung cancers is an aggressive malignancy with a rapid doubling time and early widespread metastases [228] (Fig. 9). Tumors are usually centrally located, often encasing mediastinal structures and compressing the tracheobronchial tree, presenting with large hilar and mediastinal nodes and often with distant metastases [43]. In the past patients with SCLC were staged as limited disease (tumor confined to the thorax) or extensive disease (contralateral lung and distant metastases) [229, 230]. Recently, however, the TNM staging has also been applied to SCLC [43] (Fig. 4). For accurate initial staging, NCCN guidelines suggest performing CT for assessment of the chest, liver, and adrenals and MRI for the brain. [^{18}F]FDG PET/CT is recommended only if limited disease is suspected.

The advantages of [18F]FDG PET-CT in SCLC appear to be similar to NSCLC. A prospective study of patients with extensive SCLC reported a sensitivity and specificity of 79% and 100% for standard staging, 93% and 83% for [^{18}F]FDG PET stand alone, and 93% and 100% respectively, for [^{18}F]FDG PET/CT. [^{18}F]FDG imaging is more accurate in nodal detection. [^{18}F]FDG-based selective nodal irradiation for limited disease SCLC resulted in a low rate of isolated nodal failures of 3% and low percentage of acute esophagitis [231]. These findings contradict results obtained using CT-based selective nodal irradiation, which showed isolated nodal failures in 11% of cases [231]. The low rate of isolated nodal failures and decreased esophageal toxicity supports the use of [^{18}F]FDG-based nodal irradiation for limited SCLC.

Response of SCLC to chemotherapy can be assessed as early as at the end of the first cycle of chemotherapy. Prognostic stratification was studied by Lee et al. [232] who reported that in patients with SCLC, high SUV_{max} was significantly related to poor prognostic factors and extensive disease. Furthermore, multivariate analysis indicated that high SUV_{max} was associated with poor survival outcomes compared with patients with low SUV_{max} (adjusted hazard ratio, 3.74). In a subgroup analysis, patients with limited disease and high SUV_{max} had a significantly shorter overall survival than patients with limited disease and low SUV_{max} (20.1 months vs. 35.3 months respectively; $p = 0.02$). Patients with extensive disease and high SUV_{max} had significantly shorter overall survival than patients

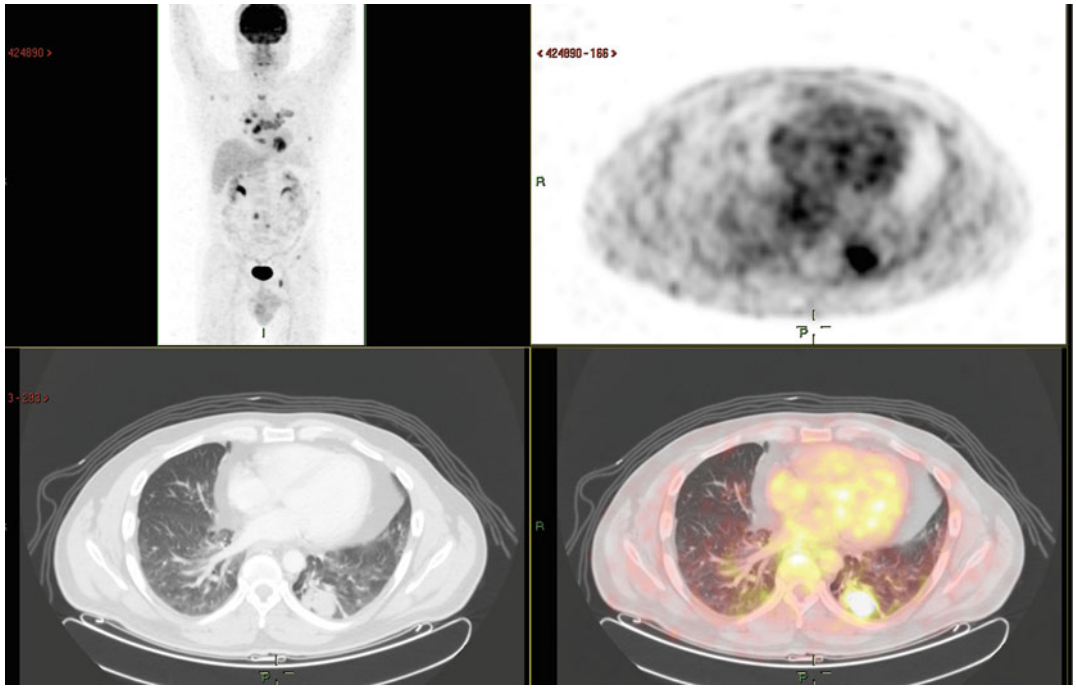

Fig. 9 A 52-year-old man was referred to [^{18}F]FDG PET/CT for staging of newly diagnosed small-cell lung cancer. Selected transaxial CT, PET, and fused PET/CT slice show a 4.5-cm [^{18}F]FDG-vid LLL mass. The MIP image (*upper left*) shows [^{18}F]FDG-avid mediastinal lymphadenopathy and skeletal involvement, consistent with stage IV disease. *LLL* left lower lobe, *MIP* maximum intensity projection

with extensive disease and low SUV_{max} (9.5 months vs. 17.7 months, respectively; $p = 0.007$). These findings were replicated in progression-free survival analysis. Therefore, it was concluded that in SCLC, metabolic tumor activity assessed by [^{18}F]FDG imaging is a significant prognostic factor and identifies subgroups of patients at higher risk of death in patients with both limited and extensive disease [232]. [^{18}F]FDG PET-CT also has a role in radiation treatment planning in patients with SCLC [233, 234]. In the current guidelines, [^{18}F]FDG PET-CT is not indicated for surveillance in SCLC.

[^{18}F]FDG and Other PET Tracers for Imaging in Neuroendocrine Tumors

Neuroendocrine tumors (NETs) vary in differentiation and glucose metabolism, and therefore [^{18}F]FDG imaging alone is unable to complete the phenotyping of this disease entity in individual patients [235]. [^{18}F]FDG imaging can detect NETs with a variable ability, even in the same patient [236]. Most NETs express a variety of somatostatin-subtype (STT) receptors, and the need for their thorough appreciation has guided the development of ligands successfully labelled with ^{68}Ga for specific imaging. Examples of such ligands are ^{68}Ga-DOTATATE and ^{68}Ga-DOTATOC, which target the SSTr2, SSTr4, and SSTr5 receptor subtypes [237–243]. Kayani et al. have recently compared ^{68}Ga-DOTATATE and [^{18}F]FDG using PET/CT in 18 patients with pulmonary NETs [243]. All typical carcinoids showed high ^{68}Ga-DOTATATE uptake (SUV_{max} 8.2 or higher) but 4 of 11 showed only minimal [^{18}F]FDG uptake (SUV_{max} 1.7–2.9), which could not discriminate tumor from distal atelectasis (Fig. 10). On the other hand, atypical carcinoids and high-grade tumors had less ^{68}Ga-DOTATATE uptake but were [^{18}F]FDG avid (SUV_{max} 11.7 or higher) [243].

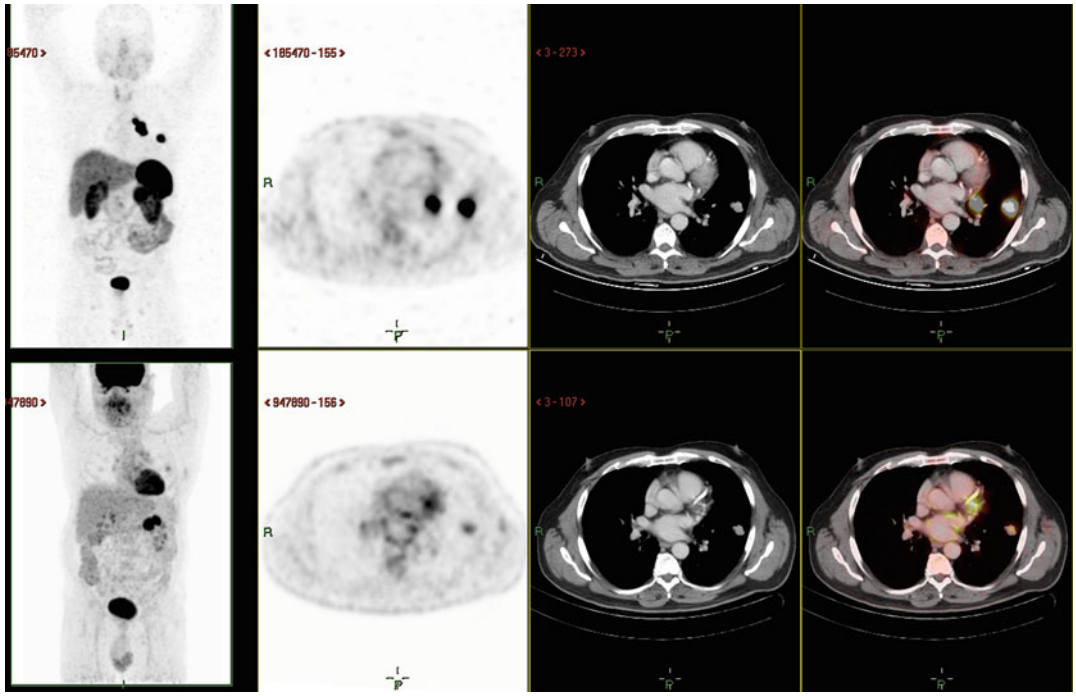

Fig. 10 A 61-year-old man was referred to PET/CT for evaluation of newly diagnosed carcinoid. PET/CT studies with [^{18}F]FDG (*bottom*) and with [^{68}Ga]DOTATATE (*top*) were performed. Selected transaxial CT, PET, fused PET/CT slice, and MIP (*left*) show non-[^{18}F]FDG-avid lingular, mediastinal, and left hilar lesions with somatostatin receptors. The patient underwent left upper lobectomy, confirming the diagnosis of carcinoid with lymph node involvement

[^{18}F]FDG Imaging of Malignant Pleural Disease

[^{18}F]FDG imaging has been used for the assessment of pleural masses and effusions. Pleural metastases of lung cancer are best diagnosed with CT, or the CT component of [^{18}F]FDG PET/CT study, since the lesions are as a rule below the resolution of PET [244]. In 25 patients with suspected malignant pleural effusions, Erasmus et al. found sensitivity, specificity, and PPV for [^{18}F]FDG PET/CT of 95%, 67%, and 95%, respectively [244]. Schaffler et al. have studied 92 patients and found a sensitivity, specificity, and PPV of 100%, 71%, and 63%, respectively [167].

Malignant pleural mesothelioma (MPM) is an aggressive tumor of mesothelial cell origin associated with asbestos exposure. Although it is a relatively rare neoplasm, its incidence is increasing worldwide due to widespread exposure to asbestos [245, 246]. Mesothelioma is seen more often in men (likely due to a higher incidence of exposure to asbestos) and occurs in the right hemithorax more often than the left. CT is the primary imaging modality [247–251]. Key findings include unilateral pleural effusion and nodular pleural and interlobar fissure thickening. Calcified pleural plaques are found in 20% of the patients, indicating previous asbestos exposure [251]. The invasion of adjacent structures, adenopathy, and the presence of bone, pulmonary, and distant metastases can occur in advanced stages of the disease [252, 253]. MRI provides detailed information in challenging cases [254] and can assist in differentiating malignant from benign pleural disease as well as in the assessment of chest wall and diaphragmatic involvement [255]. High signal intensity in relation to adjacent musculature on T2-WI, significantly enhancing on T1-WI, is suggestive of malignant disease. MRI has a 100% sensitivity

and 93% specificity for detection of pleural malignancy [256] and is superior to CT in delineating chest wall and diaphragm invasion, thus providing a better assessment of potential resectability [254, 255]. Dynamic contrast-enhanced MRI is a promising new technique that may reflect tumor histopathology [257] and may predict the therapeutic efficacy of chemotherapy in patients with MPM.

[^{18}F]FDG PET can provide additional diagnostic and prognostic information. SUVs are significantly higher in MPM as compared to benign diseases of the pleura such as inflammatory pleuritis and asbestos-related pleural thickening [258, 259] (Fig. 11). Not all areas of pleural thickening detected on CT correspond to areas of high metabolic activity, and [^{18}F]FDG imaging can be therefore a good guide to define the most appropriate sites for biopsy [260]. Benard et al. studied 28 patients with suspected and 22 with confirmed diagnosis of MPM. They found that the mean SUV measured on [^{18}F]FDG imaging studies correlated well with survival. Seven patients who died during follow-up had a mean SUV of 6.6 $\pm$ 2.9 as compared with 3.2 $\pm$ 1.6 in survivors [258].

Talc pleurodesis is a common palliative procedure since most patients develop pleural effusions. The inflammatory effect of pleurodesis affects both the CT and PET component where it is associated with higher SUV_{max} and TGV [261–263] (Fig. 12). Only few small studies were published with respect to response assessment in mesothelioma. Ceresoli et al. showed a decrease in 25% or more in tumor SUV_{max} correlated with time to progression and improved overall survival [264]. No correlation was observed between response on CT and time to tumor progression. Another small study showed that volume-based parameters on [^{18}F]FDG-PET, such as the metabolic tumor volume and TLG, were significantly correlated with patient outcome [265]. Recently Genenstreti et al. have assessed response to talc pleurodesis in eight patients with

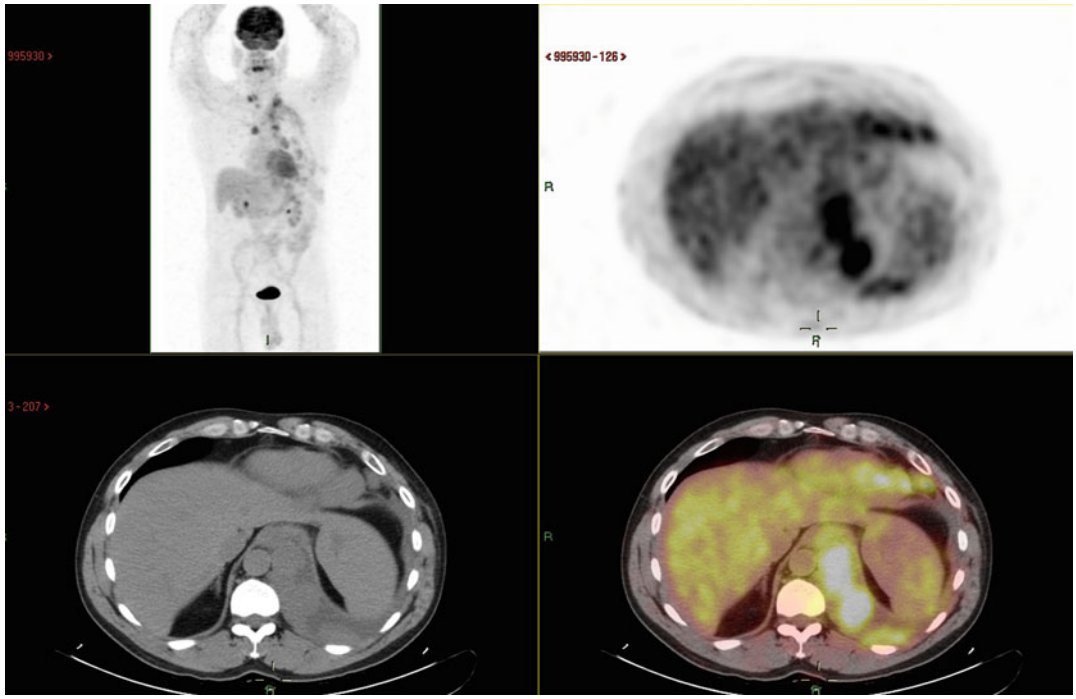

Fig. 11 A 45-year-old man with malignant pleural mesothelioma was referred to [^{18}F]FDG PET/CT for evaluation. Selected transaxial CT, PET, fused PET/CT slice, and MIP (*upper left*) show [^{18}F]FDG-avid soft tissue pleural masses and [^{18}F]FDG-avid mediastinal and right supraclavicular lymphadenopathy, consistent with metastatic involvement

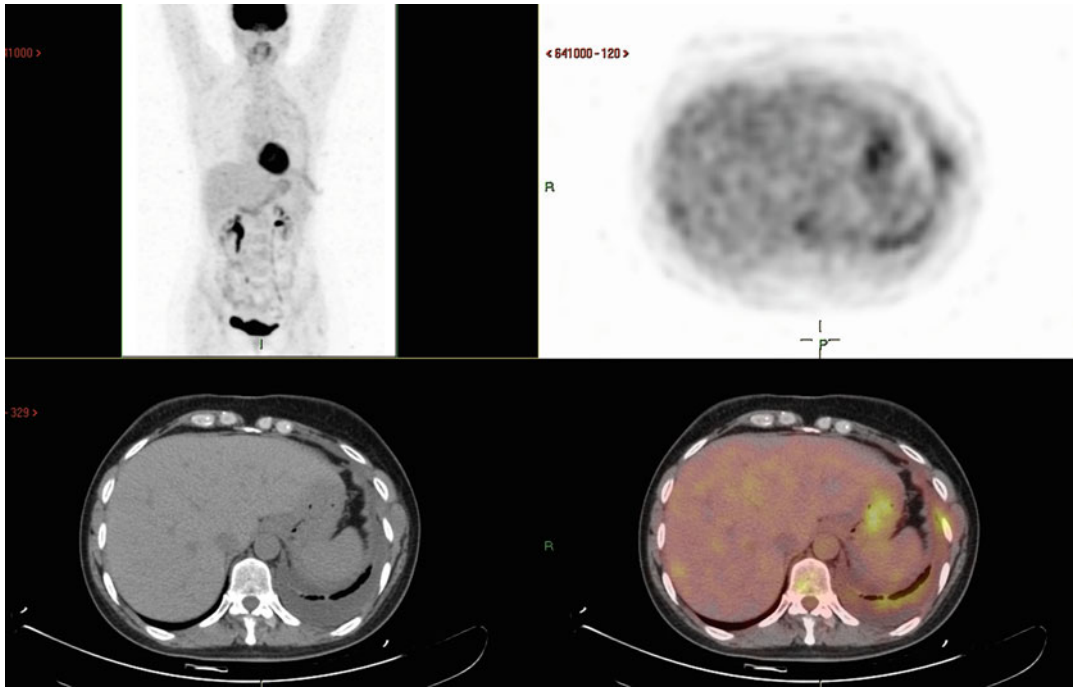

Fig. 12 A 57-year-old woman with malignant pleural mesothelioma after talc pleurodesis was referred to [^{18}F]FDG PET/CT for evaluation. Selected transaxial CT, PET, fused PET/CT slice, and MIP (*upper left*) show low-grade [^{18}F]FDG activity along the inner aspect of the left chest wall, corresponding to reactive changes after recent pleurodesis

MPM and showed that SUV mean corresponds better to modified RECIST and EORTC criteria as compared to SUV_{max} [266] (Fig. 13).

While [^{18}F]FDG imaging is at present under extensive investigation in patients with MPM, CT is the gold standard for response assessment in clinical trials in these patients. [^{18}F]FDG PET-CT was also assessed for radiation therapy planning in 13 patients with inoperable MPM, showing the usefulness of target volume delineation by PET/CT as compared to CT alone, which led to reducing the GTV, CTV, and PTVI by 47%, 39%, and 40%, respectively [267].

[^{18}F]FDG Imaging of Mediastinal Tumors

CT and MRI can identify mediastinal masses, show their extent, and diagnose correctly a variety of benign lesions. [^{18}F]FDG PET/CT may be helpful in the assessment of malignant as well as some of the benign masses. Luzzi et al. [268] evaluated [^{18}F]FDG PET/CT in the preoperative assessment of isolated anterior mediastinal lesions, especially for planning the operative strategy (biopsy or upfront resection), including 13 thymomas (six low grade and seven high grade), three lymphomas, and three with other primitive thymic tumors (one paraganglioma and two non-seminomatous germ cell tumors). The mean SUV of low-grade lesions was 3.3 ± 0.5 compared to 13.5 ± 7 in high-grade tumors ($p = 0.009$). The SUV in low-grade thymoma was significantly lower compared to lymphoma and to the other primitive anterior mediastinal tumors. Low SUV (less than 5) was associated with low-grade thymoma and minimal invasive thymoma. For lesions with an infiltrative pattern on CT and SUV above 5, open biopsy is mandatory to exclude mediastinal lymphomas or, in case of high-grade thymoma, to address neoadjuvant

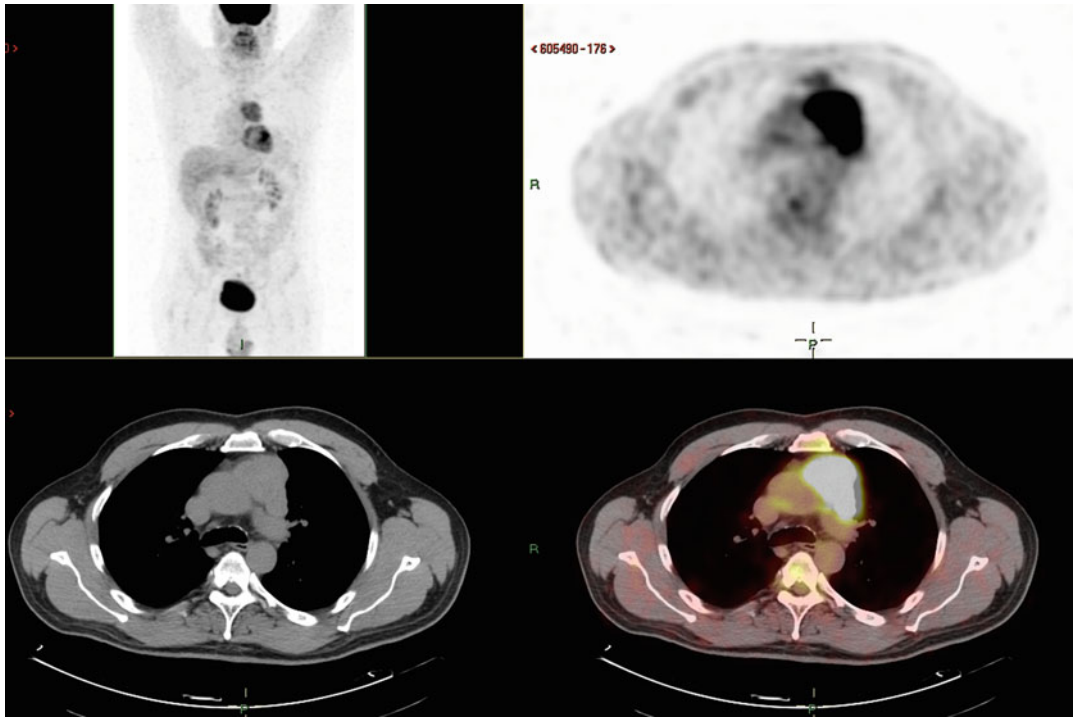

Fig. 13 A 62-year-old man with malignant invasive thymoma causing paresis of the left phrenic nerve was referred to [^{18}F]FDG PET/CT for evaluation before neoadjuvant chemotherapy and surgery. Selected transaxial CT, PET, fused PET/CT slice, and MIP (*upper left*) show a 6.7-cm [^{18}F]FDG-avid anterior mediastinal mass (SUV_{max} 4.0). B3 thymoma was confirmed at surgery

treatment [268]. Kumar et al. [269] reported on a mean SUV_{max} of 1.1 in thymic hyperplasia. Patients with low-risk thymoma had large tumors and a mean SUV_{max} of 3, while patients with high-risk thymoma had small tumors with a mean SUV_{max} of 2.1. The mean SUV_{max} in the entire group of thymomas was 2.3. All thymic carcinomas were large, with a mean SUV_{max} of 7. The difference between the mean SUV_{max} of thymic hyperplasia, thymoma, and thymic carcinoma was statistically significant, but not for high- and low-risk thymoma [269]. Sung et al. have assessed 33 patients with thymic epithelial tumors [270]. SUV_{max} of high- and low-risk thymomas were both significantly lower than that of thymic carcinomas. A homogenous [^{18}F]FDG uptake pattern was more common in thymic carcinomas, while thymomas showed heterogenous uptake [270]. Benveniste et al. have assessed whether [^{18}F]FDG PET/CT can assist in differentiating between early- (stage I–II) and advanced-stage (stages III and IV) thymoma before surgery, as patients with locally advanced tumors are treated with neoadjuvant chemotherapy before surgery [271]. [^{18}F]FDG uptake was significantly higher in patients with B3 thymoma compared to lower stages and was significantly higher in thymic carcinoma or carcinoid compared to thymoma [271]. Thomas et al. have evaluated 56 patients with unresectable advanced-stage thymic epithelial tumors who had [^{18}F]FDG PET/CT at baseline and after 6 weeks of treatment showing a close correlation between early response on [^{18}F]FDG PET/CT and subsequently diagnosed response by RECIST criteria. The authors conclude that [^{18}F]FDG PET/CT may be used for monitoring response to treatment in these patients [272].

Mediastinal sarcomas are rare, but can be [^{18}F]FDG avid [273]. The use of [^{18}F]FDG imaging in lymphoma is extensive and is covered in a separate chapter.

PET/MRI Imaging of Lung and Thoracic Malignancies

Increasing use of PET/MRI scanners in recent years does not expose the patient to the ionizing radiation of the CT scan, and provides new functional parameters, mainly lung perfusion, ventilation, blood flow, gas exchange, and respiratory motion. However, because of the low density of lung tissue artifacts at the air-tissue interfaces and because of respiratory and heart motion, MRI of the lungs is challenging.

The feasibility of PET/MRI in lung tumors has been confirmed in a pilot study in ten patients showing a similar overall performance with PET/CT [274]. While further recent studies showed an excellent agreement between PET/CT and PET/MRI in lung cancer patients with similar diagnostic accuracy, so far no specific advantage for PET/MRI was demonstrated [275–277]. The PET/MR protocol that has been used did not include specific brain and liver MR sequences which could have potentially improved the diagnostic value in some cases [277].

PET Imaging of Lung and Thoracic Malignancies with Other Tracers

While [^{18}F]FDG is the most widely used tracer in oncology, many biological targets can be imaged with other radiolabelled ligands. Uptake of [^{11}C]choline in tumors is an index of the rate of tumor-cell replication and has also been used to image lung cancer. Uptake of [^{18}F]FDG and [^{11}C]choline is similar in primary lung tumors [278, 279] but the latter can more accurately assess suspicious brain lesions, due to lower physiologic levels of tracer activity in the normal brain cortex.

Hypoxia is common in malignant tumors and influences the cell's ability to respond to therapy. The degree of hypoxia is therefore associated with tumor progression. Hypoxia also promotes angiogenesis by increasing the expression of growth factors such as the vascular endothelial growth factor. ^{60}Cu- or ^{64}Cu-labelled methylthiosemicarbazone (Cu-ATSM) has been used to assess tumor hypoxia [280]. This tracer is taken up and trapped in hypoxic cells but quickly washes out from normoxic cells. Dehdashti et al. [281] studied 14 patients with NSCLC before therapy with ^{60}Cu-ATSM-PET including eight who subsequently responded and six who had disease progression [281]. Pretreatment ^{60}Cu-ATSM uptake was predictive of response. The tumor/muscle uptake ratio was significantly lower in responders as compared to nonresponders. In the same group of patients, there was no significant difference in the degree of [^{18}F]FDG uptake between responders and nonresponders [278]. ^{18}F-fluoromisonidazole (^{18}F-MISO) is another specific tracer for hypoxia, with slower washout from normoxic cells compared to Cu-ATSM and was used in the initial studies of in vivo mapping of tumor hypoxia. Eschmann et al. [282] have assessed whether ^{18}F-MISO can predict tumor recurrence after radiation therapy in a group of patients including 14 with NSCLC. A tumor/muscle cutoff of 1.6 or a tumor/mediastinum cutoff of 2 differentiated patients with or without subsequent tumor recurrence.

Information on tumor cell proliferation can be obtained using the thymidine analog 3′-deoxy-3′-^{18}F-fluorothymidine (^{18}F-FLT). Thymidine incorporation into DNA is the gold standard for the assessment of proliferation, and ^{18}F-FLT has been therefore used to assess response to therapy. ^{18}F-FLT PET/CT in NSCLC correlated with tumor proliferation determined by Ki-67 labelling index and with tumor angiogenesis determined by tumor microvessel density (MVD) [283]. In 68 patients with known or suspected NSCLC who had ^{18}F-FLT PET/CT followed by surgery, ^{18}F-FLT SUV_{max} correlated with Ki-67 labelling index and with MVD. Survival of patients correlated with ^{18}F-FLT uptake and with Ki-67-labelling index, and both parameters correlated with MVD [283]. Everitt et al. studied 20 patients with stage I–III NSCLC at baseline and at weeks 2 and 4 during radical chemoradiotherapy with both FLT and [^{18}F]FDG PET/CT [284]. FLT was more sensitive for early treatment response. At the study performed at week 2, there was marked partial proliferative response in almost all tumors, whereas the metabolic tumor volume on [^{18}F]FDG PET-CT was

stable or showing only a moderate response in most patients, suggesting that chemoradiotherapy affects tumor cell proliferation more rapidly than cellular metabolism [284]. The prognostic significance of these differences is still unclear at present.

Integrin $\alpha_v\beta_3$ has a major role in angiogenesis and tumor growth. A recent pilot feasibility study in 17 lung cancer patients imaged with ^{18}F-Al-NOTA-PRGD2 (^{18}F-alfatide) showed that this tracer can successfully differentiate lung tumors from hamartoma but not from inflammatory changes [285]. Zheng et al. have recently assessed another integrin imaging tracer, ^{68}Ga-NOTA-PRGD2, in 91 patients with lung cancer and have reported sensitivity, specificity, and accuracy of 84%, 91%, and 86%, respectively, for the diagnosis of lung cancer. In addition, ^{68}Ga-NOTA-PRGD2 was more specific than [^{18}F]FDG PET-CT in the assessment of lymph node metastases, with positive and negative predictive values of 90% and 94% compared to 30% and 91% [286].

Conclusion

Although CT and MRI provide high-resolution anatomic assessment, [^{18}F]FDG imaging is superior in differentiating benign from malignant mediastinal lymphadenopathy and in the detection of distant metastases. Pre-therapy [^{18}F]FDG studies can provide important prognostic information. [^{18}F]FDG PET/CT can eliminate about half of futile thoracotomies and is therefore recommended for staging of lung and mediastinal tumors. [^{18}F]FDG imaging is also indicated in the diagnosis of recurrent disease and in monitoring treatment response. [^{18}F]FDG PET/CT has been introduced for radiation planning; optimizing delineation of treatment volumes, thus increasing the dose in target volumes; and reducing toxicity to nontarget tissues. Although [^{18}F]FDG is the most widely used tracer in oncology, other PET tracers are currently evaluated with specific clinical and mainly research goals and may have a role in future in the management of lung malignancies. PET/MRI has an overall similar performance to PET/CT in patients with lung cancer.

References

1. Howlader N, Noone AM, Krapcho M, et al., editors. SEER cancer statistics review, 1975–2012. Bethesda: National Cancer Institute. http://seer.cancer.gov/csr/1975_2012/, based on Nov 2014 SEER data submission, posted to the SEER web site, Apr 2015.
2. Bailey-Wilson JE, Amos CI, Pinney SM, Petersen GM, de Andrade M, Wiest JS, Fain P, Schwartz AG, You M, Franklin W, et al. A major lung cancer susceptibility locus maps to chromosome 6q23–25. Am J Hum Genet. 2004;75:460–74.
3. Schwartz AG. Genetic predisposition to lung cancer. Chest. 2004;125:86S–9S.
4. Brambilla E, Gazdar A. Pathogenesis of lung cancer signaling pathways: roadmap for therapies. Eur Respir J. 2009;33:1485–97.
5. Rami-Porta R, Bolejack V, Crowley J, et al. The IASLC lung cancer staging project. Proposals for the revisions of the T descriptors in the forthcoming eighth edition of the TNM classification folr lung cancer. J Thorac Oncol. 2015;10:990–1003.
6. Campobasso O, Invernizzi B, Berrino F. Survival rates of lung cancer according to histological type. Br J Cancer. 1974;29:240–6.
7. Islam KMM, Jiang X, Anggondowati T, Lin G, Ganti AK, et al. Comorbidity and survival in lung cancer patients. Cancer Epidemiol Biomarkers Prev. 2015; 24:1079–85.
8. Dalto SO, Stendig-Jessen M, Jakobsen E, Mellemgaard A, Osterlind K, Schutz J, Johansen C. Socioeconomic position and survival after lung cancer: Influence of stage, treatment and comorbidity among Danish patients with lung cancer diagnosed in 2004–2010. Acta Oncol. 2015;54:797–804.
9. http://www.cancerresearchuk.org/health-professional/cancer-statistics/statistics-per-cancer-type/lung-cancer/mortality
10. Sakurai H, Asamura H, Goya T, et al. Survival differences by gender for resected non-small cell lung cancer: a retrospective analysis of 12,509 cases in Japanese Lung Cancer Registry study. J Thorac Oncol. 2010;10:1594–601.
11. Ganesgan B, Panayiotou E, Burnand K, Dizdarevic S, Miles K. Thumour heterogeneity in non-small cell lung carcinoma assessed by CT texture analysis: a potential marker of survival. Eur Radiol. 2012; 22:796–802.
12. Ravanelli M, Farina D, Morassi M, Roca E, Cavalleri G, Tassi G, Maroldi R. Thexture analysis of advanced non-small cell lung cancer (NSCLC) on contrast-enhancer computer tomography: prediction of the response to first-line chemotherapy. Eur Radiol. 2013;23:3450–6.
13. Naidich DP, Webb RW, Muller NL, Krinsky GA, Zerhoun EA, Siegllman SS. Computed tomography and magnetic resonance of the thorax. 3rd ed. Philadelphia: Lippincott-Raven Publishers; 1999. p. 343–81.

14. Laurent F, Montaudon M, Corneloup O. CT and MRI of lung cancer. Respiration. 2006;73:133–42.
15. Henschke CI, McCauley DI, Yankelevich DF, et al. Early lung cancer action project: overall design and findings from baseline screening. Lancet. 1999; 354:99–105.
16. National Lung Screening Trial Research Team. The National Lung Screening Trial: overview and study design. Radiology. 2011;258:243–53.
17. Gould MK. Clinical practice. Lung-cancer screening with low-dose computed tomography. N Engl J Med. 2014;371:1813–20.
18. Swensen SJ, Jett JR, Sloan JA, et al. Screening for lung cancer with low dose spiral computed tomography. Am J Respir Crit Care Med. 2002;165:508–13.
19. Pfiser DG, Jonson DM, Azzoli CG, et al. American Society of Clinical Oncology treatment of unresectable non-small-cell lung cancer guideline: update 2003. J Clin Oncol. 2004;22:330–53.
20. Naidich DP, Rusinek H, McGuinness G, et al. Variables affecting pulmonary nodule detection with computed tomography:evaluation with three-dimensional computed simulation. J Thorac Imaging. 1993;8:291–9.
21. MacMahon H, Austin JH, Gamsu G, et al. Guidelines for management of small pulmonary nodules detected on CT scans: a statement from the Fleischner Society. Radiology. 2005;237:395–400.
22. Naidich DP, Bankier AA, MacMahon H, et al. Recommendations for the management of subsolid pulmonary nodules detected at CT: a statement from the Fleischner Society. Radiology. 2013;266:304–17.
23. Shaham D, Guralnik L. The solitary pulmonary nodule: radiologic considerations. Semin Ultrasound CT MRI. 2000;21:97–115.
24. Truong MT, Ko JP, Rossi SE, et al. Update in the evaluation of the solitary pulmonary nodule. RadioGraphics. 2014;34:1658–79.
25. McWilliams A, Tammemagi MC, Mayo JR, et al. Probability of cancer in pulmonary nodules detected on first screening CT. N Engl J Med. 2013;369:910–9.
26. Revel MP, Bissery A, Bienvenu M, et al. Are two dimensional CT measurements of small non-clacified pulmonary nodules reliable ? Radiology. 2004;231: 453–8.
27. Revel M-P, Merlin A, Peyrard S, et al. Software volumetric evaluation of doubling times for differentiating benign versus malignant pulmonary nodules. Am J Roentgenol. 2006;187:135–42.
28. Wormanns D, Kohl G, Klotz E, et al. Volumetric measurements of pulmonary nodules at multi-row detector CT: in vivo reproducibility. Radiology. 2004;14:86–92.
29. Hasegawa M, Sone S, Takashima S, et al. Growth rate of small lung cancers detected on mass CT screening. Br J Radiol. 2000;73:1252–9.
30. de Hoop B, Gietema H, van de Vorst S, Murphy K, van Klaveren RJ, Prokop M. Pulmonary ground-glass nodules: increase in mass as an early indicator of growth. Radiology. 2010;255:199–206.
31. Swensen SJ, Viggiano RW, Midthun DE, et al. Lung nodule enhancement at CT: multicenter study. Radiology. 2000;214:73–80.
32. Ohno Y, Nishio M, Koyama H, Miura S, Yoshikawa T, Matsumoto S, et al. Dynamic contrast-enhanced CT and MRI for pulmonary nodule assessment. Am J Roentgenol. 2014;202:515–29.
33. Chae EJ, Song JW, Krauss B, Song KS, Lee CW, Lee HJ, Seo JB. Dual-energy computed tomography characterization of solitary pulmonary nodules. J Thorac Imaging. 2010;25:301–10.
34. American Joint Committee on Cancer. AJCC cancer staging manual. 7th ed. New York: Springer; 2009.
35. Halpern BS, Schiepers C, Weber WA, et al. Presurgical staging of non-small cell lung cancer: positron emission tomography, integrated positron emission tomography/CT, and software image fusion. Chest. 2005;128:2289–97.
36. De Wever W, Ceyssens S, Mortelmans L, et al. Additional value pf PET-CT in the staging of lung cancer: comparison with CT alone, PET alone, and visual correlation of PET and CT. Eur Radiol. 2007;17: 23–32.
37. Pfannenberg AC, Aschoff P, Brechtel K, et al. Low dose non-enhanced CT versus standard dose contrast-enhanced CT in combined PET/CT protocols for staging and theray planning in non-small cell lung cancer. Eur J Nucl Med Mol Imaging. 2007;34:36–44.
38. Gupta NC, Rogers JS, Graeber GM, et al. Clinical role of F-18 flurodeoxyglucose positron emission tomography imaging in patients with lung cancer and suspected malignant pleural effusion. Chest. 2002; 122:1918–24.
39. Eramus JJ, Mcadams HP, Rossi SE, et al. FDG PET of pleural effusions in patients with non small cell lung cancer. AJR Am J Roentgenol. 2000;175:245–9.
40. http://guidance.nice.org.uk/CG24
41. Rami-Porta R, Crowley J, Goldstraw P. The revised TNM staging system for lung cancer. Ann Thorac Cardiovasc Surg. 2009;15:4–9.
42. Goldstraw P, Crowley J, Chansky K, et al. The IASLC Lung Cancer Staging Project: proposals for the revision of the TNM stage groupings in the fourth coming (seventh) edition of the TNM classification of malignant tumours. J Thorac Oncol. 2007;2:706–14.
43. Shephard FA, Crowley J, van Houtte P, et al. The international association for the study of lung cancer staging project: peoposals regarding the clinical staging of small cell lung cancer in the fourthcoming (seventh) edition of the tumour, node, metastasis classification for lung cancer. J Thorac Oncol. 2007;2: 1067–77.
44. Storto ML, Ciccotosto C, Guidotti A, et al. Neoplastic extension across pulmonary fissures: value of spiral computed tomography and multi-planar reformations. J Thorac Imaging. 1998;13:204–10.
45. Pearlberg JL, Sandler MA, Beute GH, et al. Limitations of CT in evaluation of neoplasms involving the chest wall. J Comput Assist Tomogr. 1987;11:290–3.

46. Padovani B, Mouroux J, Seksik L, et al. Chest wall invasion by bronchogenic carcinoma; evaluation with MRI imaging. Radiology. 1993;187:33–8.
47. Akata S, Kaiiwara N, Park J, et al. Evaluation of chest wall invasion by lung cancer using respiratory dynamic MRI. J Med Imaging Radiat Oncol. 2008; 52:36–9.
48. Kajiwara N, Akata S, Uchida O, et al. Cine MRI enables better therapeutic planning than CT in cases of possible lung cancer chest wall invasion. Lung Cancer. 2009;69:203–8.
49. McLoud TC, Swenson SJ. Lung carcinoma. Clin Chest Med. 1999;20:697–713.
50. White CS. MR evaluation of the pericardium and cardiac malignancies. Magn Reson Imaging Clin N Am. 1996;4:237–51.
51. Takahashi K, Furuse M, Hanaoka H, et al. Pulmonary vein and left atrial invasion by lung cancer: assessment by breath-hold gadolinium-enhanced three-dimensional MR angiography. J Comput Assist Tomogr. 2000;24:557–61.
52. Ohno Y, Adachi S, Motoyama A, et al. Multiphase ECG-triggered 3D contrast-enhanced MR angiography: utility for evaluation of hilar and mediastinal invasion of bronchogenic carcinoma. J Magn Reson Imaging. 2001;13:215–24.
53. Toloza EM, Harpole L, Detterbeck F, McCrory DC. Invasive staging of non-small cell lung cancer: a review of the current evidence. Chest. 2003;123: 147s–56s.
54. Sieren JC, Ohno Y, Koyama H, Sugimura K, McLennan G. Recent technological and application developments in computed tomography and magnetic resonance imaging for improved pulmonary nodule detection and lung cancer staging. J Magn Reson Imaging: JMRI. 2010;32:1353–69.
55. Henzler T, Goldstraw P, Wenz F, Pirker R, Weder W, Apfaltrer P, Meyer M, Buesing K, Crino L, Fennell D, Fink C, Grunenwald D, Manegold C, Pilz L, Schoenberg SO, Suresh S, Vansteenkiste J, Voigt W, Wängler B, Schmid-Bindert G. Perspectives of novel imaging techniques for staging, therapy response assessment, and monitoring of surveillance in lung cancer: summary of the Dresden 2013 Post WCLC-IASLC State-of-the-Art Imaging Workshop. J Thorac Oncol. 2015;10:237–49.
56. Silvestri GA, Littenberg B, Colice GL. The clinical evaluation for detecting metastatic lung cancer. A meta-analysis. Am J Respir Crit Care Med. 1995; 152:225–30.
57. Wong J, Haramati LB, Rosenshtein A, Yane M, Austin JH. Non-small cell lung cancer: practice patterns of extrathoracic imaging. Acad Radiol. 1999;6: 211–5.
58. Mayo-Smith WW, Boland GW, Noto RB, Lee MJ. State- of- the- art adrenal imaging. Radiographics. 2001;21:995–1012.
59. Suzuki K, Yamamoto M, Hasegawa Y, et al. Magnetic resonance imaging and computed tomography in the diagnoses of brain metastases of lung cancer. Lung Cancer. 2004;46:357–60.
60. Ohno Y, Koyama H, Nogami M, et al. Whole-body MR imaging vs. FDG-PET: comparison of accuracy of M-stage diagnosis for lung cancer patients. J Magn Reson Imaging. 2007;26:498–509.
61. Ohno Y, Koyama H, Onishi Y, et al. Non-small cell lung cancer: whole-body MR examination for M-stage assessment – utility for whole-body diffusion-weighted imaging compared with integrated FDG PET/CT. Radiology. 2008;248:643–54.
62. World Health Organization. WHO handbook for reporting results of cancer treatment: offset publication no. 48. Geneva: World Health Organization; 1979.
63. Therasse P, Arbuck SG, Eisenhauer EA, et al. New guidelines to evaluate the response to treatment in solid tumors. European Organization for Research and Treatment of Cancer, National Cancer Institute of the United States, National Cancer Institute of Canada. J Natl Cancer Inst. 2000;92:205–16.
64. Eisenhauer EA, Therasse P, Bogaerts J, et al. New response evaluation criteria in solid tumours: revised RECIST guideline (version 1.1). Eur J Cancer. 2009;45:228–47.
65. Nishino M, Hatabu H, Johnson BE, McLoud TC. State of the art: response assessment in lung cancer in the era of genomic medicine. Radiology. 2014; 271:6–27.
66. Bourgouin PM, McLoud TC, Fitzgibbon JF, et al. Differentiation of bronchogenic carcinoma from post-obstructive pneumonitis by magnetic resonance imaging: histopathologic correlation. J Thorac Imaging. 1991;6:22–7.
67. Ohno Y, Adachi S, Kono M, Kusumoto M, Motoyama A, Sugimura K. Predicting the prognosis of non-small cell lung cancer patient treated with conservative therapy using contrast-enhanced MR imaging. Eur Radiol. 2000;10:1770–81.
68. Wychulis AR, Payne WS, Clagett OT, Woolner LB. Surgical treatment of mediastinal tumors: a 40-year experience. J Thorac Cardiovasc Surg. 1971;62: 379–92.
69. Armstrong P, Wilson AG, Dee P, Hancell DM. Imaging of diseases of the chest. London: Mosby; 2000. p. 789–892.
70. Kohman IJ. Approach to the diagnosis and staging of mediastinal masses. Chest. 1993;103:328S–30S.
71. Naidich DP, Webb RW, Möller NL, Krinsky GA, Zerhoun EA, Sieglman SS. Computed tomography and magnetic resonance of the thorax. 3rd ed. Philadelphia: Lippincott-Raven Publishers; 1999. p. 37–159.
72. Tecce PM, Fishmann EK, Kuhlman JE. CT evaluation of the anterior mediastinum: spectrum of disease. Radiographics. 1994;14:973–90.
73. Brown LR, Aughenbaugh GL. Masses of the anterior mediastinum: CT and MR imaging. AJR Am J Roentegenol. 1991;157:1171–80.
74. Giron J, Fajadet P, Sans N, et al. Diagnostic approach to mediastinal masses. Eur J Radiol. 1998;27:21–42.

75. Ho VB, Prince HR. Thoracic MR aortography: imaging techniques and strategies. Radiographics. 1998; 18:287–309.
76. Shaham D, Skilakaki MG, Goitein O. Imaging of the mediastinum: applications for thoracic surgery. Thorac Surg Clin. 2004;14:25–42.
77. Tomiyama N, Honda O, Tsubamoto M, et al. Anterior mediastinal tumors: diagnostic accuracy of CT and MRI. Eur J Radiol. 2009;69:280–8.
78. Landwehr P, Shulte O, Lackner K. MR imaging of the chest: mediastinum and chest wall. Eur Radiol. 1999; 9:1737–44.
79. Whiten C, Khan S, Munneke G, Grubnik S. A diagnostic approach to mediastinal abnormalities. Radiographics. 2007;27:657–71.
80. Sadohara J, Fujimoto K, Müller NL, et al. Thymic epithelial tumors: comparison of CT and MR imaging findings of low-risk thymomas, high – risk thymomas and thymic carcinomas. EurJ Radiol. 2006;60:70–9.
81. Razek AA, Elmorsy A, Elshafey M, et al. Assesment of mediastinal tumors with diffusion weighted single-shot echo-planar MRI. J Magn Reson Imaging. 2009; 30:535–40.
82. Bacha EA, Chaplier AR, Mcchiarini P, et al. Surgery for invasive primary mediastinal tumors. Ann Thorac Surg. 1998;66:234–9.
83. Roviaro G, Rebuffat C, Varoli F, et al. Videothoracoscopic excision of mediastinal masses: indications and technique. Ann Thorac Surg. 1994;58: 1679–84.
84. Kantoff P. Surgical and medical management of germ cell tumors of the chest. Chest. 1993;103: 313S–33S.
85. Gawrychowsky J, Rokicki M, Gabriel A. Thymoma. The usefulness of some prognostic factors for diagnosis and treatment. Eur J Surg Oncol. 2000;26:203–8.
86. Wrigh CD, Mathisen DJ. Mediastinal tumors: diagnosis and treatment. World J Surg. 2001;25:204–9.
87. Strollo DC, Rosado-de-Christenson ML, Jett JR. Primary mediastinal tumors. Part 1: tumors of the anterior mediastinum. Chest. 1997;112:511–22.
88. Strollo DC, Rosado-de-Christenson ML. Tumors of the thymus. J Thorac Imaging. 1999;14:152–72.
89. Verstandig AG, Epstein DM, Miller Jr WT, et al. Thymoma. Report of 71 cases and a review. Crit Rev Diagn Imaging. 1992;33:201–30.
90. Rosado-de-Christenson ML, Strollo DC, Marom EM. Imaging of thymic epithelial neoplasms. Hematol Oncol Clin North Am. 2008;22:409–31.
91. Koga K, Matsuno Y, Noguchi M, et al. A review of 79 thymomas: modification of staging system and reappraisal of conventional division into invasive and non-invasive thymoma. Pathol Int. 1994;44: 359–67.
92. Travis WD, Brambilla E, Müller-Hermelink HK, Harris CC (Eds). Pathology & genetics: tumours of the lung, pleura, thymus and heart, World Health Organization classification of tumours. 10Lyon: IARC; 2004.
93. Huang T-W, Cheng Y-I, Tzoo C, et al. Middle mediastinal thymoma. Respirology. 2007;12:934–6.
94. Minniti S, Valentini M, Pinali L, et al. Thymic masses of the middle mediastinum. Report of two cases and review of the literature. J Thorac Imaging. 2004;19:192–5.
95. Jeong YJ, Lee KS, Kim J, et al. Does the thymic epithelial tumors enable us to differentiate histologic subtypes and predict prognosis? AJR Am J Roentgenol. 2004;183:283–9.
96. Tamiyama N, Müller NL, Elis SJ, et al. Invasive and noninvasive thymoma:distinctive CT features. J Comput Assist Tomgr. 2001;25:388–93.
97. Rosado-de-Christenson ML, Galobardes J, Moran CA. Thymoma: radiologic-pathologic correlation. Radiographics. 1992;12:151–68.
98. Santana L, Givica A, Camacho C. Best cases from AFIP. Thymoma. Radiographics. 2002;22:S95–102.
99. Zerhouni EA, Scott Jr WW, Baker RR, et al. Invasive thymomas: diagnosis and evaluation by computed tomography. J Comput Assist Tomogr. 1982;6:92–100.
100. Maher MM, Shepard JA. Imaging of thymoma. Semin Thorac Cardiovasc Surg. 2005;17:12–9.
101. Sakai F, Sone S, Kiyono K, et al. MR imaging of thymoma: radiologic-pathologic correlation. AJR Am J Roentgenol. 1992;158:751–6.
102. Sakai S, Muriyama S, Saeda H, et al. Differential diagnosis between thymoma and non-thymoma by dynamic MR imaging. Acta Radiol. 2002;43:262–8.
103. Inaka T, Takahashi K, Mineta M, et al. Thymic hyperplasia and thymic gland tumors:differentiation with with chemical shift MR imaging. Radiology. 2007; 243:869–76.
104. Nohl-Oser HC. An investigation of the anatomy of the lymphatic drainage of the lungs. Ann R Coll Surg Engl. 1972;51:157–76.
105. Libshitz HI, McKeenna RJ, Mountain CF. Patterns of mediastinal metastasis in bronchogenic carcinoma. Chest. 1986;90:229–32.
106. Glazer HS, Semenkovich JW, Gutierrez FR. Mediastinum. In: Lee JKT, Sagel SS, Stanley RJ, Heiken JP, editors. Computed body tomography with MRI correlation. 3rd ed. Philadelphia: Lippincot-Raven Publishers; 1998. p. 261–349.
107. Castellino RA, Blank N, Hoppe RT, Cho C. Hodgkin disease: contributions of chest CT in the initial staging evaluation. Radiology. 1986;160:603–5.
108. Filly R, Blank N, Castellino R. Radiographic distribution of intrathoracic disease in previously untreated patients with Hodgkin's disease and non- Hodgkin's lymphoma. Radiology. 1976;120:277–81.
109. Castellino RA. Hodgkin disease: practical concepts for the diagnostic radiologist. Radiology. 1986;157: 305–10.
110. Kaplan HS. Hodgkin's disease: unfolding concepts concerning its nature, management and prognosis. Cancer. 1980;45:2439–74.
111. Heron CW, Husband JE, Williams MP. Hodgkin disease: CT of the thymus. Radiology. 1988;167:647–51.

112. Castellino RA. The non-Hodgkin lymphomas: practical concepts for the diagnostic radiologist. Radiology. 1991;178:315–21.
113. Castellino RA, Hilton S, O'Brien JP, Portlock CS. Non-Hodgkin lymphoma: contribution of chest CT in the initial staging evaluation. Radiology. 1996; 199:129–32.
114. McLeod TC, Epler GR, Gaensler EA, et al. A radiographic classification for sarcoidosis: physiologic correlation. Invest Radiol. 1982;17:129–38.
115. Scadding JG, Mitchell DN (Eds). Sarcoidosis. London: Chapman and Hall; 1985.
116. Hillerdal G, Neu E, Osterman K, Schmekel B. Sarcoidosis: epidemiology and prognosis, a 15-year European study. Am Rev Respir Dis. 1984;130:29–32.
117. Patil SN, Levin DL. Distribution of thoracic lymphadenopathy in sarcoidosis using computed tomography. J Thorac Imaging. 1999;14:114–7.
118. Clarke D, Mitchell AW, Dick R, James GD. The radiology of sarcoidosis. Sarcoidosis. 1994;11:90–9.
119. Brauner MW, Grenier P, Mompoint D, et al. Pulmonary sarcoidosis: evaluation with high-resolution CT. Radiology. 1989;172:467–71.
120. Muller NL, Kullnig P, Miller RR. The CT findings of pulmonary sarcoidosis: analysis of 25 patients. AJR Am J Roentgenol. 1989;152:1179–82.
121. Johkoh T, Ikezoe J, Takeuchi N, et al. CT findings in "pseudoalveolar" sarcoidosis. J Comput Assist Tomogr. 1992;16:904–7.
122. Sider L, Horton Jr ES. Hilar and mediastinal adenopathy in sarcoidosis as detected by computed tomography. J Thorac Imaging. 1990;5:77–80.
123. Gotway MB, Tchao NK, Leung JW, et al. Sarcoidosis presenting as an enlarging solitary pulmonary nodule. J Thorac Imaging. 2001;16:117–22.
124. Conces DJ. Histoplasmosis. Semin Roentgenol. 1996;31:14–27.
125. McGuinness G, Naidich DP, Jagirdar J, et al. High resolution CT findings in miliary lung disease. J Comput Assist Tomogr. 1992;16:384–90.
126. Sherrick AD, Brown LR, Harms GF, Myers JL. The radiographic findings of fibrosing mediastinitis. Chest. 1994;106:484–9.
127. Einstein HE, Catanzaro A, Johnson R, et al. Pulmonary coccidioidomycosis. J Thorac Imaging. 1992;7:729–38.
128. Kim KI, Leung AN, Flint JD. Chronic pulmonary coccidioidomycosis: computed tomographic and pathologic findings in 18 patients. Can Assoc Radiol J. 1998;49:401–7.
129. Freudlich IM, Bragg DG. Granulomatous infections of the lung. In: A radiologic approach to diseases of the chest. Philadelphia: Williams & Wilkins; 1992. p. 263–87.
130. Harisinghani MG, McLoud TC, Shepard JA, et al. Tuberculosis from head to toe. Radiographics. 2000; 20:449–70.
131. Lee KS, Song KS, Lim TH, et al. Adult-onset pulmonary tuberculosis: findings on chest radiographs and CT scans. AJR Am J Roentgenol. 1993;160:753–8.
132. Eisenhuber E, Mostbeck G, Bankier A, Stadler A, Rumetshofer R. Radiologic diagnosis of lung tuberculosis. Radiologe. 2007;47:393–400.
133. Lee KM, Choe KH, Kim SJ. Clinical investigation of cavitary tuberculosis and tuberculous pneumonia. Korean J Intern Med. 2006;21:230–5.
134. Linh NN, Marks GB, Crawford AB. Radiographic predictors of subsequent reactivation of tuberculosis. Int J Tuberc Lung Dis. 2007;11:1136–42.
135. Fischer B, Mortenses J. The future in diagnosis and staging of lung cancer: positron emission tomography. Respiration. 2006;73:267–76.
136. Bunyarovich T, Coleman E. PET evaluation of lung cancer. J Nucl Med. 2006;47:451–69.
137. Lee KS, Kim Y, Han J, Ko EJ, Park CK, Primack SL. Bronchioalveolar carcinoma: clinical, histopathologic, and radiologic findings. Radiographics. 1997; 17:1345–57.
138. Nomori H, Watanabe K, Ohtsuka T, et al. Evaluation of F-18 fluorodeoxyglucose (FDG) PET scanning for pulmonary nodules less than 3 cm in diameter, with special reference to the CT images. Lung Cancer. 2004;45:19–27.
139. Sogard R, Fischer BMB, Mortensen J, Hogaard L, Lassen U. Preoperative staging of lung cancer with PET/CT:cost-effectiveness evaluation alongside a randomized controlled trial. Eur J Nucl Med Mol Imaging. 2011;38:802–9.
140. Takeuchi S, Khiewavan B, Fox PS, Swisher SG, Rohren EM, Bassett Jr RL, Macapinlac HA. Impact of initial PET/CT staging in terms of clinical stage management plan and prognosis in 592 patients with non-small cell lung cancer. Eur J Nucl Med Mol Imaging. 2014;41:906–14.
141. Pillot G, Siegel BA, Govindan R. Prognostic value of fluorodeoxy-glucose positron emission tomography in non-small cell lung cancer: a review. J Thorac Oncol. 2006;1:152–9.
142. Goodgame B, Pillot GA, Yang Z, et al. Prognostic value of preoperative positron emission tomography in resected stage I non-small cell lung cancer. J Thorac Oncol. 2008;3:130–4.
143. Tann M, Sandrasegaran S, Winer-Muram HT, Jennings SG, Welling ME, Fletcher JW. Can FDG-PET be used to predict growth of stage I lung cancer? Clin Radiol. 2008;63:856–63.
144. Im H-J, Pak K, Cheon GW, et al. Prognostic value of volumetric parameters in non-small-cell lung cancer: a meta-analysis. Eur J Nucl Med Mol Imaging. 2015; 42:241–51.
145. Caicedo C, Garcia-Velloso MJ, Lozano MD, et al. Role of [^{18}F]FDG PET in prediction of KRAS and EGFR mutation status in patients with advanced non-small-cell lung cancer. Eur J Nucl Med Mol Imaging. 2014;41:2058–65.
146. Swensen S, Jett J, Hartman T, Midthun D, Mandrekar S, Hillman S, Sykes AM, Aughenbaugh G, Bungum A, Allen K. CT screening for lung cancer. Radiology. 2005;235:259–65.

147. Gould MK, Maclean CC, Kuschne WG, et al. Accuracy of positron emission tomography for diagnosis of pulmonary nodules and mass lesions: a meta analysis. JAMA. 2001;285:914–24.
148. Hellwig D, Ukena D, Paulsen F, Bamberg M, Kirsch CM. Meta-analyysis of the efficacy of positron-emission tomography with F-18-fluorodeoxyglucose in lung tumors. Basis for discussion of the German Cobsensus Conference on PET in Oncology 2000. Pneumologie. 2001;55(8):367–77.
149. Cai Y-X, Fu X-N, Sun W, Zhang N. Stage I non-small cell lung cancer: a meta-analysis. PLoS One. 2013;8 (12):282366. doi:10.1371/journal/pone/0082366.
150. Bryant AS, Cerfolio RJ. The maximu, standardiszed uptake values on integrated FDG-PET/CT is useful in differentiating benign from malignant pulmonary nodules. Ann Thorac Surg. 2006;82:1016–20.
151. Hashimoto Y, Tsujikawa T, Kondo C, et al. Accuracy of PET for diagnosis of solid pulmonary lesions with ^{18}F-FDG uptake below the standardized uptake value of 2.5. J Nucl Med. 2006;47:426–31.
152. Bach PB. Inconsistencies in findings from the early lung cancer action project studies of lung cancer screening. J Natl Cancer Inst. 2011;103:1–5.
153. Bastarrica G, Garcia-Velloso MJ, Lozano MD, et al. Early lung cancer detection using spiral computed tomography and positron emission tomography. Am J Respir Crit Care Med. 2005;171:1378–83.
154. Raz DJ, Odisho AY, Franc BL, Jablons DM. Tumor fluoro-2-deoxy-D-glucose avidity on positron emission tomographic scan predicts mortality in patients with early-stage pure and mixed bronchioalveolar carcinoma. J Thorac Cardiovasc Surg. 2006;132: 1189–95.
155. Demura Y, Tsuchida T, Uesaka D, Umeda Y, Morikawa M, Ameshima S, Ishizaki T, Fujibayashi Y, Okazawa H. Usefulness of ^{18}F-fluorodeoxyglucose positron emission tomography for diagnosing disease activity and monitoring therapeutic response in patients with pulmonary mycobacteriosis. Eur J Nucl Med Mol Imaging. 2009;36:632–9.
156. Hofmeyer A, Lau WFE, Slavin MA. Mycobacterium tuberculosis infection in patients with cancer, the role of 18-fluorodeoxyglucose positron emission tomography for diagnosis and monitoring treatment response. Tuberculosis. 2007;87:459–63.
157. Lee JW, Kim BS, Lee DS, Chung J-K, Lee MC, Kim S, Kang WJ. ^{18}F-FDG PET/CT in mediatinal lymph node staging of non-small-cell lung cancer in a tuberculosis-endemic country: consideration of lymph-node calcification and distribution pattern to improve specificity. Eur J Nucl Med Mol imaging. 2009;36:1794–802.
158. Croft DR, Trapp J, Kernstine K, Kirchner P, Mullan B, Galvin J, Peterson MW, Gross T, McLennan G, Kern JA. FDG-PET imaging and the diagnosis of non-small cell lung cancer in a region of high histoplasmosis prevalence. Lung Cancer. 2002;36:297–30.
159. Keijsers RG, Grutters JC, van Velzen-Blad H, van den Bosch JM, Oyen WJ, Verzijlbergen FJ. ^{18}F-FDG PET patterns and BAL cell profiles in pulmonary sarcoidosis. Eur J Nucl Med Mol Imaging. 2010; 37:1181–8.
160. Aide N, Allouache D, Ollivier Y, de Raucourt S, Switsters O, Bardet S. Early 2′-deoxy-2′[^{18}F]fluoro-D-glucose PET metabolic response after corticosteroid therapy to differentiate cancer from sarcoidosis and sarcoid-like lesions. Mol Imaging Biol. 2009;11: 224–8.
161. Matthies A, Hickeson M, Cuchiara A, Alavi A. Dual time point ^{18}F-FDG PET for the evaluation of pulmonary nodules. J Nucl Med. 2002;43:871–5.
162. Chen HHW, Lee B-F, Su W-C, et al. The increment in standardized uptake value determined using dual-phase ^{18}F – FDG PET is a promising prognostic factor in non-small-cell lung cancer. Eur J Nucl Med Mol imaging. 2013;40:1478–85.
163. Lardinois D, Weder W, Hany TF, et al. Staging of non-small-cell lung cancer with integrated positron – emission tomography and computed tomography. N Engl J Med. 2003;348:2500–7.
164. Cerfolio RJ, Ohja B, Bryant AS, Raghuveer V, Mountz JM, Bartolucci AA. The accuracy of integrated PET-CT compared with dedicated PET alone for the staging of patients with nonsmall cell lung cancer. Ann Thorac Surg. 2004;78:1017–23.
165. Shim SS, Lee KS, Kim BT, et al. Non-small cell lung cancer: prospective comparison of integrated FDG PET/CT and CT alone for preoperative staging. Radiology. 2005;236:1011–9.
166. De Wever W, Stroobants S, Coolen J, Verschakelen JA. Integrated PET/CT in the staging of nonsmall cell lung cancer: technical aspects and clinical integration. Eur Respir J. 2009;33:201–12.
167. Schaffer GJ, Wolf G, Schoellnast H, et al. Non-small-cell lung cancer: evaluation of pleural abnormalities on CT scans with ^{18}F FDG PET. Radiology. 2004;231:858–65.
168. Nestle U, Walter K, Schmidt S, et al. ^{18}F-deoxyglucose positron emission tomography (FDG-PET) for the planning of radiotherapy in lung cancer: high impact in patients with atelectasis. Int J Radiat Oncol Biol Phys. 1999;44:593–7.
169. Dillemans B, Deneffe G, Verschakelen J, Decramer M. Value of computed tomography and mediastinoscopy in preoperative evaluation of mediastinal nodes in non-small cell lung cancer. A study of 569 patients. Eur J Cardiothorac Surg. 1994;8:37–42.
170. Shields TW. The significance of ipsilateral mediastinal lymph node metastatsis (N2 disease) in non-small cell carcinoma of the lung. A commentary. J Thorac Cardovasc Surg. 1990;99:48–53.
171. Berlangieri SU, Scott AM, Knight SR, et al. F-18 fluorodeoxyglucose positron emission tomography in the non-invasive staging of non-small cell lung cancer. Eur J Cardiothorac Surg. 1999;16(Suppl 1): S25–30.

172. Birim O, Kappetein AP, Stijnen T, Borges AJ. Meta-analysis of positron emission tomographic and computed tomographic imaging in detecting mediastinal lymph node metastases in nonsmall cell lung cancer. Ann Thorac Surg. 2005;79:375–82.
173. Schrevens L, Lorent N, Dooms C, VAnsteenkiste J. The role of PET scan in diagnosis, staging, and management of non-small cell lung cancer. Oncologist. 2004;9:633–43.
174. Pieterman RM, van Putten JWG, Meuzelaar JJ, et al. Preoperative staging of non-small cell lung cancer with positron emission tomography. N Engl J Med. 2000;343:254–61.
175. Gonzalez-Stawinski GV, Lemaire A, Merchant F, et al. A comparative analysis of positron emission tomography and mediastinoscopy in staging non-small cell lung cancer. J Thorac Cardiovasc Surg. 2003;126:1900–5.
176. Quint LE, Tummala S, Brisson LJ, et al. Distribution of distant metastases from newly diagnosed non-small cell lung cancer. Ann Thorac Surg. 1996;62:246–50.
177. Kumar R, Xiu Y, Yu JQ, et al. ^{18}F-FDG PET in evaluation of adrenal lesions in patients with lung cancer. J Nucl Med. 2004;45:2058–62.
178. Jana S, Zhang T, Milstein DM, ISasi CR, Blaufox MD. FDG-PET and CT characterization of adrenal lesions in patients with lung cancer. Eur J Nucl Med Mol Imaging. 2006;33:29–35.
179. Marom EM, McAdams HP, Erasmus JJ, et al. Staging non-small cell lung cancer with whole-body PET. Radiology. 1999;212:803–9.
180. Peterson JJ, Kransdorf MJ, O'Connor MI. Diagnosis of occult bone metastases: positron emission tomography. Clin Orthop Relat Res. 2003;415(Suppl): S120–8.
181. Qu X, Huang X, Yan W, Wu L, Dai K. A meta-analysis of ^{18}F-FDG-PET-CT, ^{18}F-FDG-PET, MRI and bone scintigraphy for diagnosis of bone metastases in patients with lung cancer. Eur J Radiol. 2012;81:1007–15.
182. Hetzel M, Arslandemir C, Konig HH, et al. F-18 NaF PET for detection of bone metastases in lung cancer: accuracy, cost effectiveness, and impact on patient management. J Bone Miner Res. 2003;18:206–14.
183. Song JW, Oh Y-M, Shim T-S, Kim WS, Ryu J-S, Choi C-M. Efficacy comparison between ^{18}F-FDG PET/CT and bone scintigraphy in detecting bony metastases of non-small-cell lung cancer. Lung Cancer. 2009;65:333–8.
184. Krüger S, Buck AK, Mottaghy FM, et al. Detection of bone metastases in patients with lung cancer: ^{99m}Tc-MDP planar bone scintigraphy, ^{18}F-fluoride PET or ^{18}F-FDG PET/CT. Eur J Nucl Med Mol Imaging. 2009;36:1807–12.
185. Vansteenkiste JF, Stroobants SG. The role of positron emission tomography with ^{18}F-fluoro-2-deoxy-D-glucose in respiratory oncology. Eur Respir J. 2001; 17:802–20.
186. Fischer B, Lassen U, Mortensen J, et al. Preoperative staging of lung cancer with combined PET-CT. N Engl J Med. 2009;361:32–9.
187. Van Tinteren H, Hoekstra OS, Smit EF, et al. Effectiveness of positron emission tomography in the preoperative assessment of patients with suspected non-small-cell lung cancer: the PLUS multicentre randomized trial. Lancet. 2002;359:1388–93.
188. Subedi N, Scarsbrook A, Darby M, Korde K, Mc Shane P, Muers MF. The clinical impact of integrated FDG PET-CT on management decisions in patients with lung cancer. Lung Cancer. 2009;64:301–7.
189. Delbeke D, Shöder H, Martin WH, Wahl RL. Hybrid imaging (SPECT/CT and PET/CT): improving therapeutic decisions. Semin Nucl Med. 2009;39:308–40.
190. Nestle U, Kremp S, Grosu A-L. Practical integration of [^{18}F]-FDG-PET and PET-CT in the planning of radiotherapy for non-small cell lung cancer (NSCLC): the technical basis, ICRU-target volumes, problems, perspectives. Radiother Oncol. 2006;81: 209–25.
191. Bradley J, Thorstad WL, Mutic S, et al. Impact of FDG-PET on radiation therapy volume delineation in non-small-cell lung cancer. Int J Radiat Oncol Biol Phys. 2004;59:78–86.
192. Deniaud-Alexandre E, Touboul E, Lerouge D, et al. Impact of computed tomography and ^{18}F-deoxyglucose coincidence detection emission tomography image fusion for optimization of conformal radiotherapy in non-small-cell lung cancer. Int J Radiat Oncol Biol Phys. 2005;63:1432–41.
193. Gondi V, Bradley K, Mehta M, et al. Clinical impact of ^{18}F fluorodeoxyglucose positron-emission tomography/computed tomography on radiotherapy planning in esophageal and non-small-cell lung cancer. Int J Radiat Oncol Biol Phys. 2007;67:187–95.
194. Kolodziejczyk M, Kepka L, Dziuk M, et al. Impact of [^{18}F]fluorodeoxyglucose PET-CT staging on treatment planning in radiotherapy incorporating elective nodal irradiation for non-small cell lung cancer: a prospective study. Int J Radiat Oncol Biol Phys. 2011;80:1008–14.
195. Mcmanus M, Nestle U, Rosenzweig KE, et al. Use of PET and PET-CT for radiation therapy planning: IAEA expert report 2006-2007. Radiother Oncol. 2009;91:85–94.
196. Pommier P, Touboul E, Chabaud S, Dussart S, Le Pechoux C, Giammarile F, Carrie C. Impact of ^{18}F-FDG PET on treatment strategy and 3D radiotherapy planning in non-small cell lung cancer: a prospective multicenter study. AJR Am J Roentgenol. 2010;195: 350–5.
197. Vila A, Sanchez-Reyes A, Conill C, et al. Comparison of positron emission tomography (PET) and computed tomography (CT) for better target volume definition in radiation therapy planning. Clin Transl Oncol. 2010;12:367–73.

198. De Ruysscher D, Kirsh C-M. PET scans in radiotherapy planning of lung cancer. Radiother Oncol. 2010. doi:10.1016/j.radonc.2010.07.002.
199. Caldwell CB, MAh K, Ung YC, et al. Observer variation in contouring gross tumor volume in patients with poorly defined non-small-cell lunf tumors on CT: the impact of ^{18}FDG-hybrid PET fusion. Int J Radiat Oncol Biol Phys. 2001;51:923–31.
200. Ciernik IF, Dizendorf E, Ciernik IF, et al. Radiation treatment planning with an integrated positron emission and computed tomography (PET/CT): a feasibility study. In J Radiat Oncol Biol Phys. 2003;57: 853–63.
201. Ashamalla H, Rafla S, Parikh K, et al. The contribution of integrated PET/CT to the evolving definition of treatment volumes in radiation treatment planning in lung cancer. Int J Tadiat Oncol Biol Phys. 2005;63:1016–23.
202. Fox JL, Rengan R, O'Meara W, et al. Does registration of PET and planning CT images decrease interobserver and intraobsrver variation in delineating tumor volumes for non-small-cell lung cancer? Int J Radiat Oncol Biol Phys. 2005;62:70–5.
203. Steenbakkers RJ, Duppen JC, Fitton I, et al. Reduction of observer variation using matched CT-PET for lung cancer delineation: a three-dimensional analysis. Int J Radiat Oncol Biol Phys. 2006;64:435–48.
204. Hanna GG, McAleese J, Carson KJ, et al. ^{18}F-FDG PET-CT simulation for non-small-cell lung cancer: effect in patients already staged by PET-CT. Int J Radiat Oncol Biol Phys. 2010;78:1040–51.
205. De Ruysscher D, Wanders S, van Haren E, et al. Selective mediastinal node irradiation based on FDG-PET scan data in patients with non-small cell lung cancer: a prospective clinical study. Int J Radiat Oncol Biol Phys. 2005;62:988–94.
206. Klopp AH, Chang JY, Tucker SL, et al. Intra-thoracic patterns of failure for non-small-cell lung cancer with positron-emission tomography/computed tomography-defined target delineation. Int J Radiat Oncol Biol Phys. 2007;69:1409–16.
207. Vansteeenkiste JF, Stroobants SG, De Leyn PR, et al. Prognostic importance of the standardized Uptake value on FDG PET scan in non small cell lung cancer: an analysis of 125 cases. J Clin Oncol. 1999;10:3201–6.
208. Ahuja V, Coleman RE, Herndon J, Patz EF. The prognostic significance of fluorodeoxyglucose positron emission tomography imaging for patients with non small cell lung carcinoma. Cancer. 1998;83:918–24.
209. Higashi K, Ueda Y, Arisaka Y, et al. FDG uptake as a biologic prognostic factor for recurrence in patients with surgically resected non-small cell lung cancer. J Nucl Med. 2002;43:39–45.
210. Jeong HJ, Min JJ, JM P, et al. Determination of the prognostic value of ^{18}F-fluorodexoyglucose uptake by using positron emission tomography in patients with non small cell lung cancer. Nucl Med Commun. 2002;23:865–70.
211. Downey RJ, Akhurst T, Gonen M, et al. Preoperative F-18 fluorodeoxyglucose-positron emission tomography maximal standardized uptake value predicts survival after lung cancer resection. J Clin Oncol. 2004; 22:3255–60.
212. Cerfolio R, Bryant A, Ohja B. The maximum standardised uptake values on positron emission tomography of non-small cell lung cancer predicts stage, recurrence and survival. J Thorac Cardiovasc Surg. 2005;130:151–9.
213. Weber WA, Petersen V, Schmidt B, et al. Positron-emission-tomography in non-small-cell lung cancer: prediction of response to chemotherapy by quantitative assessment of glucose use. J Clin Oncol. 2003; 21:2651–7.
214. Hoekstra CJ, Stroobants SG, Smit EF, et al. Prognostic relevance of response evaluation using [^{18}F]-2-fluoro-2-deoxy-D-glucose positron emission tomography in patients with locally advanced non-small-cell lung cancer. J Clin Oncol. 2005;23:8362–70.
215. Hellwig D, Graeter TP, Ukena D, et al. Value of F-18-fluorodeoxyglucose positron emission tomography after induction therapy of locally advanced bronchogenic carcinoma. J Thorac Cardiovasc Surg. 2004; 128:892–9.
216. Nahmias C, Hanna WT, Wahl LM, et al. Time course of early response to chemotherapy in non-small cell lung cancer patients with ^{18}F-FDG PET/CT. J Nucl Med. 2007;48:744–51.
217. Eschmann SM, Friedel G, Paulsen F, et al. ^{18}F-FDG PET for assessment of therapy response and pre-operative evaluation after neo-adjuvant radiochemotherapy in stage III non-small cell lung cancer. Eur J Nucl Med Mol Imaging. 2007;34:463–71.
218. Cerfolio RJ, Bryant AS, Winokur TS, Ohja B, Bartolucci AA. Repeat FDG-PET after neoadjuvant therapy is a predictor of pathologic response in patients with non-small cell lung cancer. Ann Thorac Surg. 2004;78:1903–9.
219. Moon SH, Cho S-H, Park LC, et al. Metabolic response evaluated by ^{18}F-FDG PET/CT as a potential screening tool in identifying a subgroup of patients with advanced non-small-cell lung cancer for immediate maintenance therapy after first-line chemotherapy. Eur J Nucl Med Mol Imaging. 2013;40:1005–13.
220. Vera P, Mezzani-Saillard S, Edet-Sanson A, et al. FDG PET during radiochemotherapy is predictive of outcome at 1 year in non-small-cell lung cancer patients: a prospective multicenter study (RTEP2). Eur J Nucl Med Mol Imaging. 2014;41:1057–65.
221. Lu F, Huang J, Sima CS, et al. Patterns of recurrence and second primary lung cancer in early-stage lung cancer survivors followed with routine computed tomography surveillance. J Thorac Cardiovasc Surg. 2013;145:75–81.
222. Calman L, Beaver K, Hind D, Lorigan P, Roberts C, Lloyd-Jones M. Survival benefits from follow-up of patients with lung cancer: a systematic

review and meta-analysis. J Thorac Oncol. 2011;6: 1993–2004.
223. Colt HG, Murgu SD, Korst RJ, Slatore CG, Unger M, Quadrelli S. Follow-up and surveillance of the patient with lung cancer after curative-intent therapy: diagnosis and management of lung cancer, 3rd ed: American College of Chest Physicians evidence-based clinical practice guidelines. Chest. 2013;143 (Suppl 5):e437S–54S.
224. Antoniou AJ, Marcus C, Tahari AK, Wahl RL, Subramaniam RM. Follow up or surveillance ^{18}F-FDG PET/CT and survival outcome in lung cancer patients. J Nucl Med. 2014;55:1062–8.
225. Marcus C, Paidpally V, Antoniou A, Zaheer A, Wahl RL, Subramaniam RM. ^{18}F-FDG PET/CT and lung cancer: value of fourth and subsequent follow-up scans for patient management. J Nucl Med. 2015;56: 204–8.
226. Hicks RJ, Lau E, Alam NZ, Chen RY. Imaging in the diagnosis and treatment of non-small cell lung cancer. Respirology. 2007;12:165–72.
227. Keidar Z, Haim N, Guralnik L, Wollner M, Bar-Shalom R, Ben-Nun A, Israel O. PET/CT using ^{18}F-FDG in suspected lung cancer recurrence: diagnostic value and impact on patient management. J Nucl Med. 2004;45:1640–6.
228. Nestle U, Hellwig D, Schmidt S, et al. 2-deoxy-2-[^{18}F]-fluoro-D-glucose positron emission tomography in target volume definition for radiotherapy of patients with non-small-cell lung cancer. Mol Imaging Biol. 2002;4:257–63.
229. Gilman MD, Aquino SL. State-of-the-art FDG-PET imaging of lung cancer. Semin Roentgenol. 2005;40:143–53.
230. Gorenberg M, Bar-Shalom R, Israel O. Patterns of FDG uptake in post-thoracotomy surgical scars in patients with lung cancer. Brit J Radiol. 2008;81:821–5.
231. Samson DJ, Seidenfeld J, Simon GR, et al. Evidence for management of small cell lung cancer: ACCP evidence-based clinical practice guidelines (2nd edition). Chest. 2007;132(3 Suppl):314S–23S.
232. Abrams J, Doyle LA, Aisner J. Staging, prognostic factors, and special considerations in small cell lung cancer. Semin Oncol. 1988;15:261–77.
233. Fischer BM, Mortensen J, Langer SW, et al. A prospective study of PET/CT in initial staging of small-cell lung cancer: comparison with CT, bone scintigraphy and bone marrow analysis. Ann Oncol. 2007;18:338–45.
234. Van Loon J, De Ruysscher D, Wanders R, et al. Selective nodal irradiation on basis of ^{18}FDG-PET scans in limited-disease small-cell lung cancer: a prospective study. Int J Radiat Oncol Biol Phys. 2010;77:329–36.
235. Lee YJ, Cho A, Cho BC, et al. High tumor metabolic activity as measured by fluorodeoxyglucose positron emission tomography is associated with poor prognosis in limited and extensive stage small-cell lung cancer. Clin Cancer Res. 2009;15:2426–32.
236. Kamel EM, Zwahlen D, Wyss MT, et al. Whole body ^{18}F-FDG-PET improves the management of patients with small cell lung cancer. J Nucl Med. 2003;44: 1911–7.
237. Van Loon J, Offermann C, Bosmans G, et al. 18FDG-PET based radiation planning of mediastinal lymph nodes in limnited disease small cell lung cancer changes radiotherapy fields: a planning study. Radiother Oncol. 2008;87:49–54.
238. Groves AM, Win T, Ben-Haim S, et al. Non-[^{18}F] FDG PET in clinical oncology. Lancet Oncol. 2007;8:822–30.
239. Groves AM, Mohan HK, Wegner EA, et al. Positron emission tomography using ^{18}F fluorodeoxyglucose to show thymic carcinoid. AJR Am J Roentgenol. 2004;182:511–4.
240. Ginj M, Zhang H, Waser B, et al. Somatostatin receptor antagonists are preferable to agonists for in vivo peptide receptor targeting of tumors. Proc Natl Acad Sci USA. 2006;103:16436–41.
241. Reubi JC, Waser B. Concomitant expression of several peptide receptors in neuroendocrine tumours: molecular basis for in vivo multireceptor tumour targeting. Eur J Nucl Med Mol Imaging. 2003;30:781–93.
242. Koukouraki S, Strauss LG, Georgoulias V, et al. Comparison of the pharmacokinetics of ^{68}Ga-DOTATOC and [^{18}F]FDG in patients with metastatic neuroendocrine tumours scheduled for ^{90}Y-DOTATOC therapy. Eur J Nucl Med Mol Imaging. 2006;33:1115–22.
243. Kayani I, Conry BG, Groves AM, Win T, Dickson J, Caplin M, Bomanji JB. A comparison of ^{68}Ga-DOTATATE and ^{18}F-FDG PET/CT in pulmonary neuroendocrine tumors. J Nucl Med. 2009;50:1927–32.
244. Shim SS, Lee KS, Kim BT, et al. Integrated PET/CT and the dry pleural dissemination of peripheral adenocarcinoma of the lung: diagnostic implications. J Comput Assist Tomogr. 2006;30:70–6.
245. Erasmus JJ, McAdams HP, Rossi SE, et al. FDG PET of pleural effusions in patients with non-small cell lung cancer. Am J Roentgenol. 2000;175:245–9.
246. Dunn MM. Asbestos and lung. Chest. 1989;95: 1304–8.
247. Robinson BW, Lake RA. Advances in malignant mesothelioma. N Engl J Med. 2005;353:1591–603.
248. Benamore RE, O'Doherty MJ, Entwisle JJ. Use of imaging in the management of malignant pleural mesothelioma. Clin Radiol. 2005;60:1237–47.
249. Gill RR, Gerbaudo VH, Sugarbaker DJ, et al. Current trends in radiologic management of malignant pleural mesothelioma. Semin Thorac Cardiovasc Surg. 2009; 21:111–20.
250. Marom EM, Erasmus JJ, Oass HI, et al. The role of imaging in malignant pleural mesothelioma. Semin Oncol. 2002;29:26–35.
251. Yamamuro M, Gerbaudo VH, Gill RR, et al. Morphologic and functional imaging of malignant pleural mesothelioma. Eur J Radiol. 2007;64:356–66.

252. Wang JZ, Reddy GP, Gotway MB, et al. Malignant pleural mesothelioma: evaluation with CT, MR imaging, and PET. Radiographics. 2004;24:105–19.
253. Kawashima A, Libshitz HI. Malignant pleural mesothelioma: CT manifestations in 50 cases. Am J Roentgenol. 1990;155:965–9.
254. Sahin AA, Coplu L, Selcuk ZT, et al. Malignant pleural mesothelioma caused by enviropmental exposure to asbestos or erionite in rural Turkey: Ct findings in 84 patients. AJR Am J Roentgenol. 1993;161:533–7.
255. Patz EF, Shaffer K, Piwnica-Worms DR, et al. Malignant pleural mesothelioma: value of CT and MR imaging in predicting resectability. AJR Am J Roentgenol. 1992;159:961–6.
256. Heelan RT, Rusch VW, Begg CB, et al. Staging of malignant pleural mesothelioma: comparison of CT and MR imaging. Am J Roetgenol. 1999;172: 1039–47.
257. Hierholzer J, Luo L, Bittner RC, et al. MRI and CT in the differential diagnosis of pleural disease. Chest. 2000;118:604–9.
258. Hatabu H, Tadamura E, Levin DL, et al. Quantitative assessment of pulmonary perfusion with dynamic contrast-enhanced MRI. Magn Reson Med. 1999;42: 1033–8.
259. Benard F, Sterman D, Smith RJ, Kaiser LR, Al-belda SM, Alavi A. Metabolic imaging of malignant pleural mesothelioma with fluorodeoxyglucose positron emission tomography. Chest. 1998;114:713–22.
260. Zhuang H, Pourdehnad M, Lambright ES, et al. Dual time point ^{18}F-FDG PET imaging for differentiating malignant from inflammatory processes. J Nucl Med. 2001;42:1412–7.
261. Ng DC, HAin SF, O'Doherty MJ, Dussek J. Prognostic value of FDG PET imaging in malignant pleural mesothelioma. J Nucl Med. 2000;41:1443–4.
262. Subramaniam RM, Wilcox B, Aubry MC, Jett J, Peller PJ. ^{18}F-fluoro-2-deoxy-D-glucose positron emission tomography and positron emission tomography/computed tomography imaging of malignant pleural mesothelioma. J Med Imaging Radiation Oncol. 2009;53:160–70.
263. Nowak AK, Armato III SG, Ceresoli GL, Yildirim H, Francis RJ. Imaging in pleural mesothelioma: a review of imaging research presented at the 9th international meeting of the international mesothelioma interest group. Lung Cancer. 2010;70:1–6.
264. Ceresoli GL, Chiti A, Zucali PA, Rodari M, et al. Early response evaluation in malignant pleural mesothelioma by positron emission tomography with [^{18}F]fluorodeoxyglucose. J Clin Oncol. 2006; 24:4587–93.
265. Lee HY, Hyun SH, Lee KS, et al. Volume-based parameter of ^{18}F-FDG PET/CT in malignant pleural mesothelioma: prediction of therapeutic response and prognostic implication. Ann Surg Oncol. 2010;17: 2787–94.
266. Genestreti G, Moretti A, Piciucchi S, et al. FDG PET/CT response evaluation in malignant pleural mesothelioma patients treated with talc pleurodesis and chmothrapy. J Cancer. 2012;3:241–5.
267. Phlivan B, Topkan E, Onal C, et al. Comparison of CT and integrated PET-CT based radiation therapy planning in patients with malignant pleural mesothelioma. Radiat Oncol. 2009;4:35.
268. Luzzi L, Campione A, Gorla A, et al. Role of fluorine-flurodeoxyglucose positron emission tomography/computed tomography in preoperative assessment of anterior mediastinal masses. Eur J Cardiothorac Surg. 2009;36:475–9.
269. Kumar A, Regmi SK, Dutta R, et al. Characterization of thymic masses using ^{18}F-FDG PET-CT. Ann Nucl Med. 2009;23:569–77.
270. Sung YM, Lee KS, Kim B-T, Choi JY, Shim YM, Yi CA. ^{18}F-FDG PET/CT of thymic epithelial tumors: usefulness for distinguishing and staging tumor subgroups. J Nucl Med. 2006;47:1628–34.
271. Benveniste MFK, Movan CA, Maelawi O, Fox PS, Swisher SG, Munden RF, Marom EM. FDG PET-CT aids in the preoperative assessment of patients with newly diagnosed thymic epithelial malignancies. J Thorac Oncol. 2013;8:502–10.
272. Thomas A, Mena E, Kurdziel K, et al. ^{18}F-fluorodeoxyglucose positron emission tomography in management of patients with thymic epithelial tumors. Clin Cancer Res. 2013;19:1487–93.
273. Katakura H, Fukuse T, Shiraishi I, et al. Mediastinal synovial sarcoma. Thorac Cardiovasc Surg. 2009;57: 183–5.
274. Schwenzer NF, Schraml C, Müller M, et al. Pulmonary lesion assessment: comparison of WB hybrid MR/PET and PET/CT imaging – pilot study. Radiology. 2012;264:551–8.
275. Heusch P, Buchbender C, Kohler J, et al. thoracic staging in lung cancer: prospective comparison of ^{18}F-FDG PET/MR imaging and ^{18}F-FDG PET/CT. J Nucl Med. 2014;55:373–8.
276. Fraioli F, Screaton NJ, James SM, et al. Non-small-cell lung cancer resectability: diagnostic value of PET/MR. Eur J Nucl Med Mol Imaging. 2015;52: 49–55.
277. Huellner MW, Barbosa FDG, Hausmann L, et al. TNM staging of NSCLC: Comparison of PET/MR and PET/CT. J Nucl Med. 2016;57:21–6.
278. Hara T, Inagaki K, Kosaka N, Morita T. Sensitive detection of mediastinal lymph node metastasis of lung cancer with ^{11}C-choline PET. J Nucl Med. 2000;41:1507–13.
279. Pieterman RM, Que TH, Elsinga PH, et al. Comparison of ^{11}C-choline and ^{18}F-FDG PET in primary diagnosis and staging of patients with thoracic cancer. J Nucl Med. 2002;43:167–72.
280. DeRoose CM, De A, Loening AM. Multimodality imaging of tumor xenografts and metastases in mice with combined small animal PET, small animal CT

and bioluminescence imaging. J Nucl Med. 2007;48: 295–303.
281. Dehdashti F, Mintun MA, Lewis JS, et al. In vivo assessment of tumor hypoxia in lung cancer with ^{60}Cu-ATSM. Eur J Nucl Med Mol Imaging. 2003;30:844–50.
282. Eschmann SM, Paulsen F, Reimold M, et al. Prognostic impact of hypoxia imaging with ^{18}F-misonidazole PET in Non-small cell lung cancer and head and neck cancer before radiotherapy. J Nucl Med. 2005;46: 253–60.
283. Yang W, Zhang Y, Fu Z, Sun X, Mu D, Yu J. Imaging proliferation of ^{18}F-FLT PET/CT correlates with the expression of microvessel density of tumour tissue in non-small-cell lung cancer. Eur J Nucl med Mol Imaging. 2012;39:1289–96.
284. Everitt SJ, Ball DL, Hicks RJ, et al. Differential ^{18}F-FDG and ^{18}F-FLT uptake on serial PET/CT imaging before and during definitive chemoradiation for non-small-cell lung cancer. J Nucl Med. 2014;55: 1069–74.
285. Gao S, Wu H, Li W, et al. A pilot study imaging integrin $\alpha_v\beta_3$ with RGD PET/CT in suspected lung cancer patients. Eur J Nucl Med Mol Imaging. 2015;42:2029–37.
286. Zheng K, Liang N, Zhang J, et al. ^{68}Ga-NOTA-PRGD2 PET/CT for integrin imaging in patients with lung cancer. J Nucl Med. 2015;56:1823–7.

Diagnostic Applications of Nuclear Medicine: Esophageal Cancers

23

Christopher G. Sakellis, Heather A. Jacene, and Annick D. Van den Abbeele

Abstract

Esophageal cancer is the eighth most commonly diagnosed malignancy worldwide. This chapter will review the epidemiology, environmental factors, genetic predisposition, and underlying biomolecular changes of the disease. The staging of esophageal cancer will be reviewed as well as the roles of conventional diagnostic imaging and nuclear imaging in this staging. Finally, the efficacy of these modalities in assessing response to the various treatments described in the chapter and in the long term surveillance for disease recurrence will be addressed.

Keywords

Esophageal cancer • Conventional diagnostic imaging • [^{18}F]FDG-PET/CT • [^{18}F]FDG-PET/MRI • Staging • Assessment of therapeutic response • Surveillance

Glossary

[^{18}F]FDG	2-Deoxy-2-[^{18}F]fluoro-D-glucose
AJCC	American Joint Committee on Cancer
APC	Gene encoding for adenomatous polyposis coli
c-myc	Gene encoding for a transcription factor (a multifunctional, nuclear phosphoprotein involved in cell cycle progression, apoptosis, and cellular transformation)
CT	X-ray computed tomography
erb B-2	Gene encoding for the receptor tyrosine-protein kinase erbB-2 (also known as CD340 or proto-oncogene Neu)
EUS	Endoscopic ultrasonography
GERD	Gastrointestinal reflux disease
GI	Gastrointestinal
Gy	Gray unit (ionizing radiation dose in the International System of Units, corresponding to the absorption of one joule of radiation energy per kilogram of matter)
HPV	Human papillomavirus

C.G. Sakellis • A.D. Van den Abbeele (✉)
Department of Imaging, Dana-Farber Cancer Institute, Boston, MA, USA

Department of Radiology, Brigham and Women's Hospital, Boston, MA, USA

Harvard Medical School, Boston, MA, USA

Center for Biomedical Imaging in Oncology, Dana-Farber Cancer Institute, Boston, MA, USA

Tumor Imaging Metrics Core, Dana-Farber/Harvard Cancer Center, Boston, MA, USA
e-mail: abbeele@dfci.harvard.edu

H.A. Jacene
Nuclear Medicine/PET-CT, Department of Imaging, Dana-Farber Cancer Institute and Department of Radiology, Brigham and Women's Hospital, Harvard Medical School, Boston, MA, USA

© Springer International Publishing Switzerland 2017
H.W. Strauss et al. (eds.), *Nuclear Oncology*,
https://doi.org/10.1007/978-3-319-26236-9_41

M	Metastasis status according to the AJCC/UICC TNM staging system
MBq	Mega-Becquerel (10^6 Becquerel)
MIP	Maximum intensity projection
MR	Magnetic resonance
N	Lymph node status according to the AJCC/UICC TNM staging system
p16	Protein encoded by the CDKN2A gene (also known as cyclin-dependent kinase inhibitor 2A or multiple tumor suppressor 1)
p53	Tumor protein p53, also known as cellular tumor antigen p53, phosphoprotein p53, tumor suppressor p53, antigen NY-CO-13, or transformation-related protein 53 (TRP53)
PERCIST	Positron emission tomography response criteria in solid tumors
PET	Positron emission tomography
PET/CT	Positron emission tomography/computed tomography
PET/MR	Positron emission tomography/magnetic resonance
Rb	Gene encoding for the retinoblastoma protein
RECIST	Response evaluation criteria in solid tumors
SSC	Squamous cell carcinoma
SUR	Standardized uptake ratio (ratio of tumor SUV and blood pool SUV)
SUV	Standardized uptake value
SUV_{max}	Standardized uptake value at point of maximum
T	Tumor status according to the AJCC/UICC TNM staging system
UICC	Union Internationale Contre le Cancer (International Union Against Cancer)
US	Ultrasonography

Contents

Epidemiology and Environmental Factors 686
Genetic Predisposition 687
Underlying Biomolecular Changes 687
Staging and Prognostic Classification 687
Conventional Diagnostic Imaging Staging 688
Nuclear Imaging Staging 689
Common Therapies 692
Assessing Efficacy of Treatment 693
Surveillance 694
References 695

Epidemiology and Environmental Factors

Esophageal cancer is the eighth most commonly diagnosed malignancy worldwide. It is also the sixth most common cause of cancer death, with a 5-year survival of approximately 15–20%. Over 16,000 new cases are estimated to be diagnosed in the United States in 2016, with over 15,000 deaths. Worldwide, over 450,000 new cases were diagnosed in 2012, with over 400,000 deaths. Esophageal cancer is three to four times more common among men than among women, with a lifetime risk in the United States of about 1 in 125 in men and about 1 in 435 in women [1, 2].

Over 95% of esophageal malignancies are squamous cell carcinoma (SCC) or adenocarcinoma, with lymphomas, sarcomas, neuroendocrine tumors, and metastatic disease largely accounting for the remainder. For most of the twentieth century, squamous cell carcinoma was the dominant histologic type, accounting for over 90% of cases and is still the dominant esophageal malignancy worldwide. However, over the past several decades in the Western world, the incidence of esophageal adenocarcinoma has risen significantly and now accounts for over 60% of esophageal cancers in the United States [3].

Esophageal SCC and adenocarcinoma differ in both typical tumor location and risk factors. Esophageal SCCs occur most frequently in the

mid to distal third of the esophagus, while adenocarcinomas are more prevalent in the distal third of the esophagus and gastroesophageal junction. Smoking and excessive alcohol intake are the major risk factors for esophageal SCC. The incidence of esophageal SCC increases with age, peaking in the seventh decade of life. Demographically, the incidence of esophageal SCC is three times higher in black people than in whites [4]. In the highest-risk region in the world for esophageal SCC, which stretches from Iran to China (the so-called esophageal cancer belt), major risk factors are poorly understood but are thought to include poor nutrition, diets lacking in fruits and vegetables, and the drinking of hot beverages [5]. Human papillomavirus (HPV), particularly subtypes 16 and 18, has also been implicated in the pathogenesis of esophageal SCC [6].

Esophageal adenocarcinomas arise from a region of metaplastic epithelium, commonly known as Barrett's esophagus, which replaces the squamous epithelium in the presence of gastrointestinal reflux disease (GERD) and progresses to dysplasia. Obesity and smoking are also known risk factors for esophageal adenocarcinoma [7]. The dramatic increase in incidence rates of esophageal adenocarcinoma in Western countries is in part tied to increases in the known risk factor of obesity. With regard to demographics, white people develop esophageal adenocarcinoma five times more often than black people, while men are affected eight times more often than women [8].

Genetic Predisposition

The role that hereditary factors play in the development of esophageal cancer remains unclear. However, familial aggregations have been described in regions with a high incidence of esophageal SCC, such as China [9]. Familial aggregations of Barrett's esophagus have also been described with regard to development of esophageal adenocarcinoma [10].

Genetic analysis of esophageal cancers has revealed frequent chromosomal losses, chromosomal gains, and occasional gene amplifications [11]. Gene polymorphism has also been studied. For example, polymorphisms of the epidermal growth factor gene have been found to be associated with a higher risk of esophageal adenocarcinoma, especially in patients with Barrett's esophagus [12].

Underlying Biomolecular Changes

A large number of molecular events have been implicated in the development and progression of both esophageal SCC and adenocarcinoma. Studies have indicated that activation of cyclin D1, erb B-2, and c-myc oncogenes and inactivation of p53, Rb, APC, and p16 tumor suppressor genes are frequently involved [13].

Barrett's esophagus develops when stratified squamous epithelium that normally lines the distal esophagus is replaced by metaplastic columnar epithelium as a result of chronic inflammation from GERD. Carcinogenesis in these metaplastic cells begins with genetic alterations that either activate some of the oncogenes and/or disable some of the tumor suppressor genes described above. It is thought that the first genetic changes that lead to adenocarcinoma in regions of Barrett's esophagus are abnormalities in p53 and p16 that permit proliferation of clones of premalignant and/or malignant cells [14].

Staging and Prognostic Classification

The TNM staging system of the American Joint Committee on Cancer (AJCC) and the International Union Against Cancer (UICC) is universally used. The most recent TNM staging system implemented in 2010 created separate histological stage groupings for esophageal SCCs and adenocarcinomas while maintaining similar definitions for tumor, nodal, and metastatic categories. For esophageal SCCs, staging is in part determined by the location of the superior edge of the primary tumor, with upper and middle esophageal malignancies arising above the lower border of the inferior pulmonary vein and lower esophageal malignancies arising below that level. Tumors

arising in the gastroesophageal junction and in the proximal 5 cm of the gastric cardia that extend to the gastroesophageal junction or esophagus (which includes almost all esophageal adenocarcinomas) are classified and staged as esophageal cancers.

Tumor (T) staging relates to the depth of invasion of the tumor in the esophageal wall and correlates with prognosis. While patients with disease limited to the mucosa/submucosa (T1) have a relatively high cure rate, patients with disease that has spread through the esophageal wall to the adventitia (T3) or to structures surrounding the esophagus (T4) have a much poorer prognosis. The T4 stage is further classified to indicate whether the cancer is invading adjacent structures such as the pleura, pericardium, or diaphragm (T4a) where surgical resection may still be possible or if it invades structures such as the aorta, carotid vessels, azygos vein, trachea, left main bronchus, or a vertebral body, which would preclude surgical resection (T4b).

Local lymph node invasion occurs relatively early in esophageal cancers because the esophageal lymphatics are located in the lamina propria, as opposed to being located beneath the muscularis mucosa elsewhere in the gastrointestinal tract [15]. For the nodal (N) staging system, regional lymph nodes for all esophageal cancers include the supraclavicular, upper paraesophageal, mediastinal, lower paraesophageal, diaphragmatic, pericardial, left gastric, and celiac stations. Data has demonstrated that the number of regional lymph nodes containing metastatic disease (positive nodes) is more important than the location of these positive nodes. N0 indicates no positive nodes, N1 indicates one to two positive nodes, N2 indicates three to six positive nodes, and N3 indicates seven or more positive nodes. These groupings are relatively arbitrary, and the presence of each additional positive lymph node is thought to increase risk and worsen prognosis.

Distant metastatic disease (M1) includes sites of malignancy not in direct contact with the esophagus and includes parenchymal (e.g., liver or lung) involvement and non-regional lymph node involvement, including the hilar and pulmonary lymph node stations.

Conventional Diagnostic Imaging Staging

Both esophageal SCC and adenocarcinoma have similar clinical presentations, with early esophageal cancer often presenting with nonspecific symptoms such as weight loss, hoarseness, and/or coughing. Dysphagia is usually described in more locally advanced cases.

The initial workup of these nonspecific symptoms suggesting esophageal disease usually consists of a barium swallow fluoroscopic examination and/or an upper GI endoscopy. While infiltrating or ulcerated mucosal masses visualized on endoscopy are nearly pathognomonic of esophageal cancer, biopsy is needed to confirm the diagnosis.

Once the diagnosis of a primary esophageal cancer is established via biopsy, the initial staging usually starts with a contrast-enhanced diagnostic CT scan of the chest and abdomen in order to evaluate the region of the primary tumor for local invasion of mediastinal structures and peritumoral lymph node metastases and to search for any distant metastases.

With regard to T staging, diagnostic CT scan is significantly limited in the identification of esophageal wall layers and is thus unable to accurately assess more superficial tumors (T1–T3). However, CT can provide important information on more invasive tumors, either by excluding the presence of T4 disease or by characterizing any adjacent mediastinal structures the tumor may invade and thus determining potential resectability (T4a vs. T4b disease). Regarding nodal metastases, CT scans have relatively poor diagnostic performance as they rely mostly on size criteria. Enlarged lymph nodes on CT may be reactive in nature, while normal-sized nodes may be positive for metastases [16]. Finally, while diagnostic CT can readily identify large distant metastases, it has limited sensitivity for smaller ones, particularly in the lungs, liver, and peritoneum.

Endoscopic ultrasonography (EUS) is also part of the initial staging workup for esophageal cancers. EUS uses high-frequency ultrasound to provide detailed images of the five layers of the

esophageal wall and the paraesophageal environment. EUS is still regarded as the most accurate imaging technique for locoregional staging of esophageal cancer. The overall accuracy of EUS for T staging is 80–90%, and it can accurately delineate both superficial (T1, T2) and invasive (T3, T4) tumors [17]. EUS is also effective in demonstrating peritumoral and paraesophageal metastatic lymph nodes. Findings suggestive of malignant lymph nodes include width greater than 10 mm, round shape, smooth border, and hypoechoic appearance. Of these, hypoechoic appearance and width greater than 10 mm appear to be the most specific for malignancy. When all four suspicious features are present in a visualized lymph node, there is an 80–100% chance of metastatic involvement [18]. Fine needle aspiration, which can be performed in conjunction with EUS, further increases the accuracy of diagnosing lymph node involvement. However, aspiration is only possible when the nodes are accessible and where the primary tumor does not block the path of the aspiration needle. EUS does have its limitations, most notably when there is a tumor-related stenosis in the esophagus that the ultrasound transducer cannot traverse. Since the entire tumor and more distal nodal stations are not visualized, EUS may understage the malignancy in these cases.

Nuclear Imaging Staging

Fluorodeoxyglucose-positron emission tomography/computed tomography ([^{18}F]FDG-PET/CT) has been shown to be of great value in the primary staging of esophageal cancer in conjunction with EUS. [^{18}F]FDG-PET/CT scanning has shown to add value to conventional staging methods consisting of both CT and EUS.

With regard to T staging, [^{18}F]FDG-PET/CT cannot accurately assess depth of tumor invasion. In fact, the sensitivity of [^{18}F]FDG-PET/CT in detecting biopsy-proven T1 tumors involving the mucosa and/or submucosa ranges approximately between 40% and 60%, likely due to the smaller size of the tumors and/or lower malignant cellularity (Fig. 1). [^{18}F]FDG-PET sensitivity for detection of more invasive tumors progressively rises from 83% in T2 tumors (involving the muscularis propria), to 97% in T3 tumors, to 100% in T4 tumors [19].

[^{18}F]FDG-PET/CT has demonstrated some advantages over traditional imaging in the staging of nodal metastases. Regional lymph nodes that are equivocal in size on diagnostic CT scan will be suspicious for metastatic sites of involvement if metabolically active on [^{18}F]FDG-PET/CT scan (Fig. 2). EUS does not evaluate for distal metastatic nodal disease. A meta-analysis performed by van Vliet et al. suggested that [^{18}F]FDG-PET/CT scanning is more sensitive for the detection of distant metastatic nodal disease than diagnostic CT alone [20]. However, with regard to regional nodal disease, [^{18}F]FDG-PET/CT has shown a similar, but slightly decreased, sensitivity when compared with EUS. This may be in part due to the [^{18}F]FDG uptake of lymph nodes in the immediate vicinity of the primary tumor being obscured by the primary tumor's uptake or by limitations in the spatial resolution of PET leading to false-negative results in small regional nodes (Fig. 3). Also, the [^{18}F]FDG uptake of the primary esophageal cancer has been shown to affect the detectability of nodal metastases, as they have similar histologies. Thus, if the primary lesion presents with a low baseline [^{18}F]FDG uptake, nodal metastases will have relatively low [^{18}F]FDG uptake as well, potentially resulting in a false-negative appearance [21].

The primary advantage [^{18}F]FDG-PET/CT demonstrates over EUS and diagnostic CT evaluation is in the detection of distant metastatic disease (M1). In addition to non-regional nodal metastases, distant metastatic disease includes parenchymal spread to the lungs and liver but may also include spread to more atypical sites difficult to evaluate on anatomic imaging such as the pleura, musculature, and skeleton (Fig. 4). Several studies have demonstrated that [^{18}F]FDG-PET and PET/CT have significantly higher sensitivities for the detection of distant metastatic disease than CT scans alone. [^{18}F]FDG-PET has been shown to upstage the disease in approximately 20% of patients first evaluated with CT/EUS, with the benefit of preventing unnecessary surgery [20, 22]. Another study

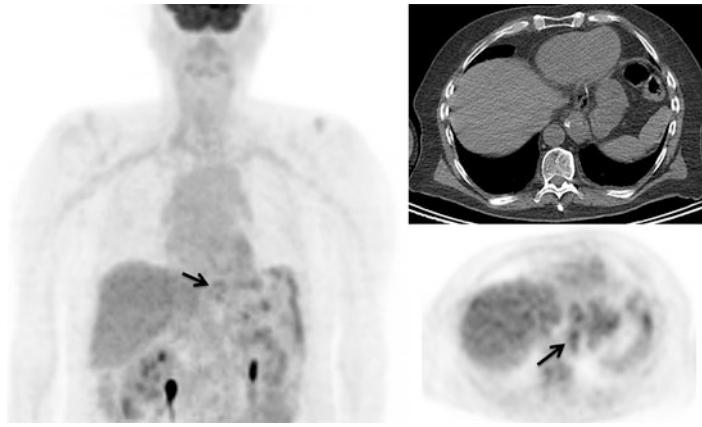

Fig. 1 [^{18}F]FDG-PET/CT of a 73 year old man with history of gastric bypass surgery presenting with recently diagnosed intramucosal adenocarcinoma of the distal esophagus in the background of Barrett's esophagus. The relatively mild associated uptake in the distal esophagus may relate to the primary tumor's small size and could even reflect inflammation in the setting of Barrett's esophagus. There is no evidence of regional or distant metastatic disease

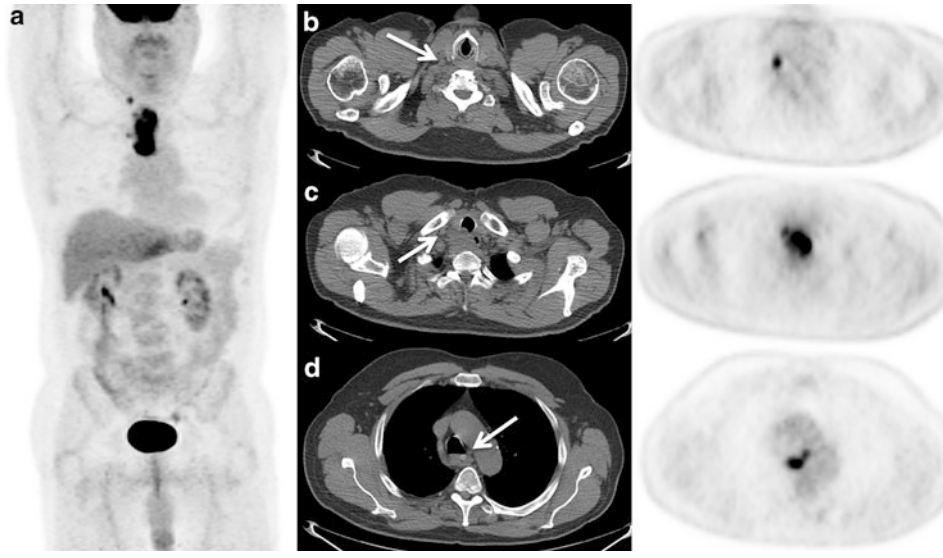

Fig. 2 (**a**) [^{18}F]FDG-PET/CT maximum intensity projection (MIP) image of a 67 year old man with newly diagnosed upper esophageal adenocarcinoma, represented by contiguous intense [^{18}F]FDG uptake in the upper thorax (*arrow*). (**b**) CT and PET images of an associated subcentimeter right supraclavicular lymph node (*arrow*). (**c**) CT and PET images of the primary tumor at the thoracic inlet and an associated subcentimeter node (*arrow*). (**d**) CT and PET images showing the more inferior extent of the primary tumor and an associated subcentimeter left paratracheal lymph node (*arrow*). The small [^{18}F]FDG-avid lymph nodes described in **b**, **c**, and **d** could all be considered equivocal on CT scan alone. The relatively intense [^{18}F]FDG uptake of these nodes on PET scan is strongly suggestive of regional nodal metastatic disease

demonstrated that staging with [^{18}F]FDG-PET significantly changed management in 38% of patients [23]. Given its superior sensitivity in detecting metastatic disease (and precluding expensive curative surgery), [^{18}F]FDG-PET combined with EUS, despite being more expensive, appears to be the more cost-effective method of staging patients compared to CT and EUS [24].

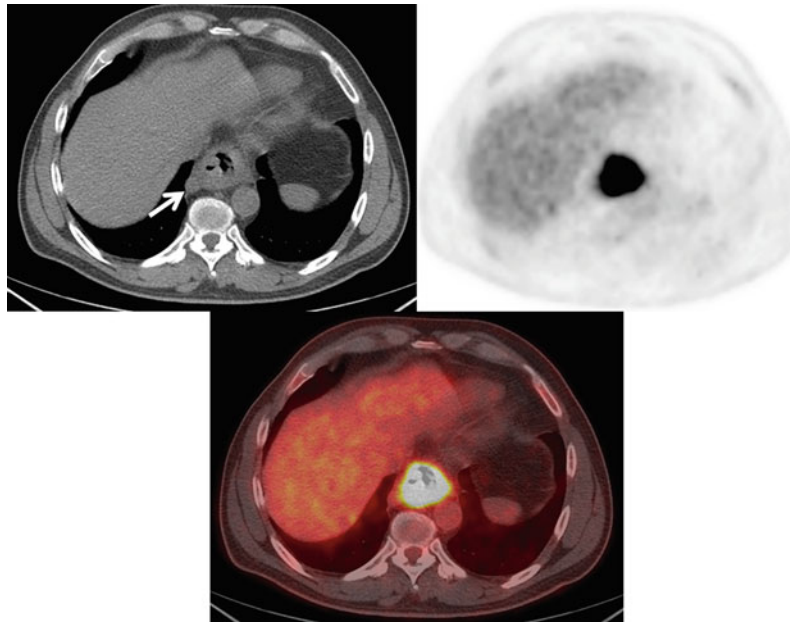

Fig. 3 [^{18}F]FDG-PET/CT scan of a 56 year old man with newly diagnosed distal esophageal adenocarcinoma. There is an enlarged paraesophageal lymph node immediately adjacent to the [^{18}F]FDG-avid primary tumor. This lymph node is likely a site of regional metastatic spread but is not significantly [^{18}F]FDG-avid, likely due to the dominance of the intense uptake (SUV_{max} 22) of the adjacent tumor

The potential prognostic value of the staging [^{18}F]FDG-PET/CT has been explored. Studies have suggested that patients with [^{18}F]FDG-avid nodal disease at baseline have a worse prognosis than those with undetectable nodal disease on [^{18}F]FDG-PET, suggesting that the PET N stage may be an appropriate parameter for determining whether to start a more aggressive treatment regimen than would be normally considered [25]. Several studies have investigated whether a relationship exists between the degree of [^{18}F]FDG uptake of the primary tumor, as measured by maximum standardized uptake value (SUV_{max}), and prognosis, with inconclusive results. A recent study reported that [^{18}F]FDG-PET provides independent prognostic information for overall survival and distant metastasis-free survival based on the staging tumor-to-blood standardized uptake ratio (SUR), a ratio of the tumor SUV and blood pool SUV. However, this parameter was not found to be prognostic with regard to locoregional tumor control [26]. Finally, studies evaluating intratumoral [^{18}F]FDG uptake heterogeneity, or "textural feature analysis," have suggested that baseline regional tumor uptake heterogeneity may predict poorer responses to traditional therapy. It is postulated that tumors exhibiting a heterogeneous, as opposed to a homogeneous, [^{18}F]FDG distribution may respond less favorably to uniformly distributed radiotherapy. Likewise, baseline tumor [^{18}F]FDG heterogeneity could also reflect underlying tumor neoangiogenesis, which if present, could reduce the effectiveness of conventional chemotherapy [27].

Although [^{18}F]FDG-PET/CT scanning is the mainstay of nuclear imaging for staging of esophageal cancer, initial investigations have been made into the utility of the newer and rapidly evolving hybrid modality of PET/MR. In one such study, EUS was once again found to demonstrate the highest accuracy in T staging, followed by PET/MR using [^{18}F]FDG, followed by diagnostic CT. While EUS appears to remain the gold standard for T staging, [^{18}F]FDG-PET/MR was somewhat

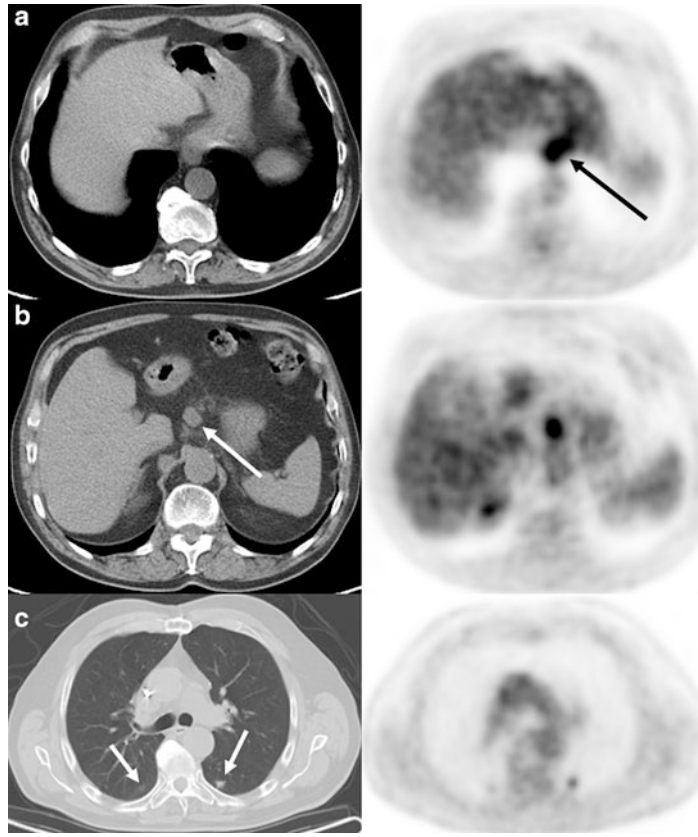

Fig. 4 (**a**) CT and PET images from an [^{18}F]FDG-PET/CT demonstrate a primary esophageal adenocarcinoma (*arrow*) arising at the gastroesophageal junction in a 74 year old man. (**b**) There is a single associated [^{18}F]FDG-avid celiac axis lymph node (*arrow*), which is considered regional disease. (**c**) There are bilateral [^{18}F]FDG-avid pulmonary nodules present (*arrows*) which are considered distant metastases (M1)

accurate in characterizing higher T stage lesions, and the MR images were able to identify esophageal wall layers, which are poorly evaluated on diagnostic CT scan and unable to be evaluated on non-contrast-enhanced [^{18}F]FDG-PET/CT. Furthermore, [^{18}F]FDG-PET/MR demonstrated the highest efficacy in diagnosing regional nodal metastases, followed by EUS, [^{18}F]FDG-PET/CT, and diagnostic CT, thought to be related to the excellent soft-tissue contrast of MR combined with the ability to quantitatively measure metabolic activity of the nodes. The diagnostic efficacy of M staging was not evaluated in this study, due to the time and cost involved in performing whole-body MR imaging over a large area comparable to [^{18}F]FDG-PET/CT imaging [28].

Common Therapies

The best option for curative treatment for patients with esophageal cancer is radical surgery consisting of esophagectomy with en bloc lymphadenectomy. The main contraindication for surgery is distant metastatic disease (M1) in which there are parenchymal metastases and/or distant metastatic lymph nodes or nodules. Unresectable invasive disease extending into the mediastinum (T4b) is also a contraindication for surgery. Despite improvements in perioperative care, esophagectomy carries significant morbidity and mortality risks and is thus contraindicated in patients with severe associated comorbid conditions (e.g., cardiovascular disease,

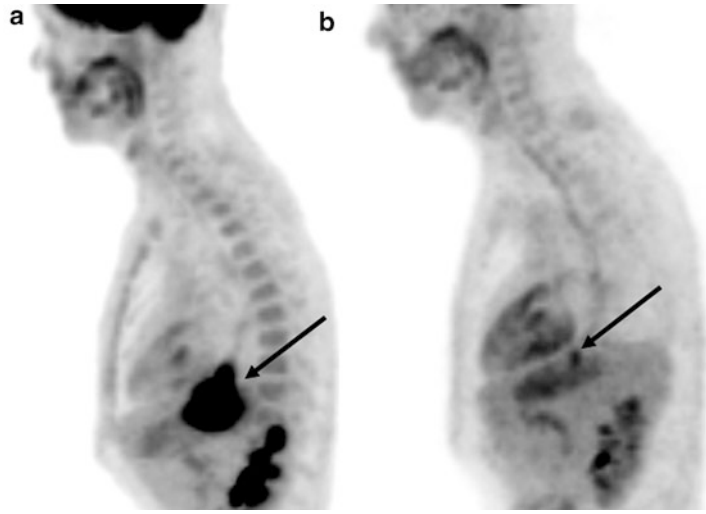

Fig. 5 (**a**) MIP images of [^{18}F]FDG-PET/CT scans performed on a patient with localized esophageal adenocarcinoma involving the gastroesophageal junction and gastric cardia. Baseline images prior to therapy show an intensely [^{18}F]FDG-avid mass with SUV_{max} 22. (**b**) Following completion of neoadjvant chemoradiotherapy, there is still some mild [^{18}F]FDG uptake at the gastroesophageal junction with SUV_{max} 3, but there has been a greater than 80% drop in uptake which has been shown to correlate with a more favorable long-term outcome. The patient went on to have an esophagectomy, and continued to be followed up with diagnostic CT. He is currently disease-free 6 years after the completion of trimodal therapy

respiratory disease). Medical care is reserved for nonsurgical candidates, with the main goal being the palliation of dysphagia, allowing patients to eat. Options include chemotherapy and/or radiotherapy, laser therapy, manual dilatation, metallic stenting, and photodynamic therapy.

After exclusion of distant metastases and/or unresectable locally invasive disease, the selection of the therapeutic regimen depends on the T stage. Localized tumors (T1/T2) have a high likelihood of curative resection, and primary esophagectomy is the most frequent treatment. In locally advanced tumors (T3/T4a, N^+), surgery is also the mainstay of therapy, but it has been shown that preoperative chemotherapy or chemoradiotherapy provides a survival benefit of 7–13% over surgery alone [29]. Neoadjuvant therapy typically consists of a combination of radiotherapy (approximately 45 Gy) and chemotherapy (commonly cisplatin and 5-fluorouracil). This combination therapy is usually administered over a 45-day period and is followed by esophageal resection after an interval of approximately 4 weeks. The goal of neoadjuvant therapy is to improve survival results related to surgery alone. Neoadjuvant chemotherapy is aimed at the eradication of lymphatic and/or hematogenous micrometastases and metastases, with improvement of survival. Neoadjuvant radiotherapy is aimed at shrinkage of the primary tumor, leading to an improved resectability rate.

Assessing Efficacy of Treatment

Many studies have shown that significant decrease in [^{18}F]FDG uptake of the primary tumor as well as resolution of [^{18}F]FDG-avid regional lymph nodes following neoadjuvant therapy correlates with favorable long-term prognosis following surgery. Complete metabolic response (defined as a reduction of SUV_{max} greater than 80%) after completion of preoperative chemotherapy has been shown to predict favorable long-term outcome (Figs. 5 and 6) [30].

PET response criteria in solid tumors (PERCIST) represent a standardized method for evaluation of metabolic tumor response. Under these criteria, progression on [^{18}F]FDG-PET scan is defined as an increase in [^{18}F]FDG uptake (as measured by SUV) of greater than 20% in a region 1 cm or larger

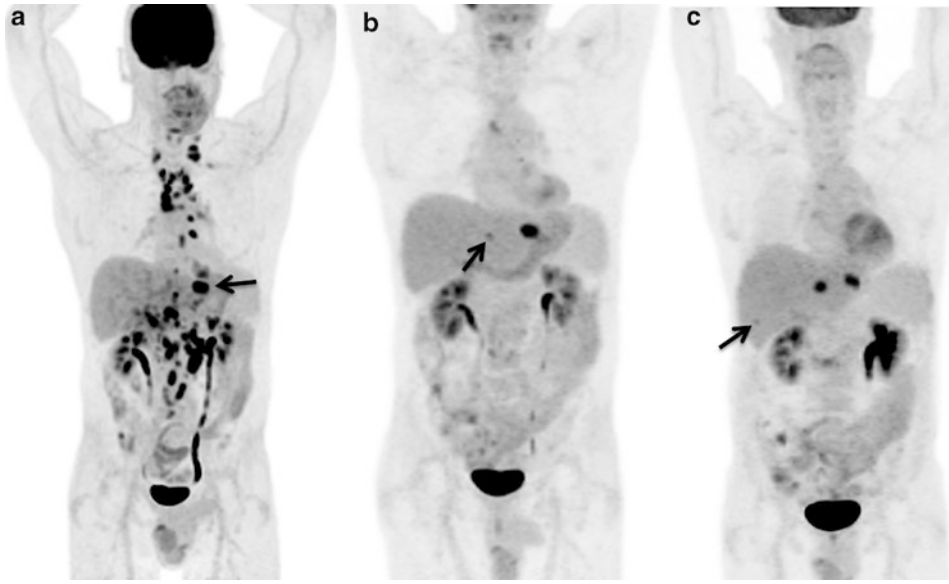

Fig. 6 [^{18}F]FDG-PET/CT MIP images of a 55 year old man who presented with metastatic gastroesophageal junction adenocarcinoma. (**a**) Baseline PET scan demonstrates the [^{18}F]FDG-avid primary tumor (*arrow*) along with extensive [^{18}F]FDG-avid metastatic lymphadenopathy above and below the diaphragm, in addition to liver metastases. (**b**) A follow up scan was performed two months after starting chemotherapy. There had been some response to treatment with significant decrease in size and uptake of the widespread lymphadenopathy and resolution of most of the liver metastases. The [^{18}F]FDG uptake of the primary tumor only decreased about 30% (from SUV_{max} 14.2 to 9.8), and there was persistent mild [^{18}F]FDG uptake in a single lesion in the caudate lobe of the liver (*arrow*), findings which did not suggest a favorable prognosis. (**c**) A follow up scan performed two months later demonstrated that the metabolic activity of the primary tumor had continued to slightly decrease but was still quite significant. There was also an increase in size and [^{18}F]FDG uptake of the caudate lesion as well as a new [^{18}F]FDG-avid lesion in the right hepatic lobe (*arrow*). These findings were consistent with progression of disease

in diameter, while response to treatment is defined as a decrease in uptake of greater than or equal to 30% [31]. Studies evaluating therapeutic response have compared PERCIST to RECIST (Response Evaluation Criteria in Solid Tumors), the more widely used solid tumor response metric based on changes in morphologic size [32]. One such study evaluating response to neoadjuvant therapy for locally advanced esophageal cancer demonstrated that PERCIST was found to be the strongest independent predictor of outcomes [33].

Surveillance

Even in those patients with esophageal cancer treated with curative intent, 5-year survival rates remain relatively poor, ranging from 34% to 47% [34]. Most recurrences occur within the first 2 years after surgery, with a median time to recurrence of slightly less than a year. Isolated distant systemic recurrences are diagnosed in about 50% of these patients, mainly involving the liver, lung, or bone. Locoregional recurrence (14%) or locoregional recurrence along with distant recurrence (35%) occurs less frequently [35]. After esophageal cancer recurs, very poor median survival rates of 3–9 months have been reported [36].

Because recurrences of esophageal cancer tend to occur at distant sites, [^{18}F]FDG-PET/CT may be useful in the postoperative surveillance period. In one recent meta-analysis, pooled estimates for [^{18}F]FDG-PET and [^{18}F]FDG-PET/CT scans calculated a high sensitivity (96%) and moderate specificity (78%) for detection of recurrent esophageal cancer after primary treatment with curative intent, indicating that [^{18}F]FDG-PET/CT is a valuable test in clinical

practice for surveillance of patients with esophageal cancer after surgery [37].

Endoscopic ultrasound is effective for the detection of locoregional recurrence with high sensitivity, but both endoscopy and ultrasound do not evaluate for the distant metastases that are of the most concern in this setting. Diagnostic CT scans can detect distant metastases but are limited in evaluating for recurrence at the site of resection due to anatomic distortion related to surgery and any prior radiotherapy. [^{18}F]FDG-PET/CT itself is somewhat limited in evaluating the resection site due to the possible presence of chronic inflammation associated with fibrotic scar tissue. As the false-positive rate on [^{18}F]FDG-PET/CT surveillance scans is not insignificant, histopathologic confirmation of suspected [^{18}F]FDG-avid lesions remains required.

Due to the limited amount of adequate treatment options after recurrent esophageal cancer is detected, presymptomatic surveillance with imaging is not universally performed. However, newer salvage chemotherapy regimens and surgical resection of isolated recurrent metastases have been associated with improved survival rates [38]. In this setting, [^{18}F]FDG-PET/CT may prove to be a reliable imaging modality for routine surveillance of treated esophageal cancer patients prior to development of symptoms given its high sensitivity.

References

1. Siegel RL, Miller KD, Jemal A. Cancer statistics, 2016. CA Cancer J Clin. 2016;66(1):7.
2. Torre LA, Bray F, Siegel RL, Ferlay J, Lortet-Tieulent J, Jemal A. Global cancer statistics, 2012. CA Cancer J Clin. 2015;65(2):87.
3. Pohl H, Sirovich B, Welch HG. Esophageal adenocarcinoma incidence: are we reaching the peak? Cancer Epidemiol Biomarkers Prev. 2010;19(6):1468.
4. Lagergren J. Adenocarcinoma of oesophagus: what exactly is the size of the problem and who is at risk? Gut. 2005;54 Suppl 1:i1–5.
5. Gholipour C, Shalchi RA, Abbasi M. A histopathological study of esophageal cancer on the western side of the Caspian littoral from 1994 to 2003. Dis Esophagus. 2008;21(4):322.
6. Shuyama K, Castillo A, Aguayo F, Sun Q, Khan N, Koriyama C, Akiba S. Human papillomavirus in high- and low-risk areas of oesophageal squamous cell carcinoma in China. Br J Cancer. 2007;96(10):1554.
7. Engel LS, Chow WH, Vaughan TL, Gammon MD, Risch HA, Stanford JL, et al. Population attributable risks of esophageal and gastric cancers. J Natl Cancer Inst. 2003;95(18):1404.
8. Hur C, Miller M, Kong CY, Dowling EC, Nattinger KJ, Dunn M, Feuer EJ. Trends in esophageal adenocarcinoma incidence and mortality. Cancer. 2013;119(6):1149–58.
9. Chang-Claude J, Becher H, Blettner M, Qiu S, Yang G, Wahrendorf J. Familial aggregation of oesophageal cancer in a high incidence area in China. Int J Epidemiol. 1997;26(6):1159.
10. Chak A, Lee T, Kinnard MF, Brock W, Faulx A, Willis J, Cooper GS, Sivak Jr MV, Goddard KA. Familial aggregation of Barrett's oesophagus, oesophageal adenocarcinoma, and oesophagogastric junctional adenocarcinoma in Caucasian adults. Gut. 2002;51(3):323.
11. Enzinger PC, Mayer RJ. Esophageal cancer. N Engl J Med. 2003;349(23):2241–52.
12. Lanuti M, Liu G, Goodwin JM, Zhai R, Fuchs BC, Asomaning K, Su L, Nishioka NS, Tanabe KK, Christiani DC. A functional epidermal growth factor (EGF) polymorphism, EGF serum levels, and esophageal adenocarcinoma risk and outcome. Clin Cancer Res. 2008;14(10):3216.
13. Kuwano H, Kato H, Miyazaki T, Fukuchi M, Masuda N, Nakajima M, et al. Genetic alterations in esophageal cancer. Surg Today. 2005;35(1):7–18.
14. Barrett MT, Sanchez CA, Prevo LJ, Wong DJ, Galipeau PC, Paulson TG, Rabinovitch PS, Reid BJ. Evolution of neoplastic cell lineages in Barrett oesophagus. Nat Genet. 1999;22(1):106.
15. Meltzer SJ. The molecular biology of esophageal carcinoma. Recent Results Cancer Res. 1996;142:1.
16. Yoon YC, Lee KS, Shim YM, Kim BT, Kim K, Kim TS. Metastasis to regional lymph nodes in patients with esophageal squamous cell carcinoma: CT versus FDG PET for presurgical detection - prospective study. Radiology. 2003;227:764–70.
17. Rosch T. Endosonographic staging of esophageal cancer: a review of literature results. Gastrointest Endosc Clin N Am. 1995;5(3):537.
18. Catalano MF, Sivak Jr MV, Rice T, Gragg LA, Van Dam J. Endosonographic features predictive of lymph node metastasis. Gastrointest Endosc. 1994;40(4):442.
19. Kato H, Miyazaki T, Nakajima M, Takita J, Kimura H, Faried A, et al. The incremental effect of positron emission tomography on diagnostic accuracy in the initial staging of esophageal carcinoma. Cancer. 2005;103(1):148–56.
20. van Vliet EP, Heijenbrok-Kal MH, Hunink MG, Kuipers EJ, Siersema PD. Staging investigations for oesophageal cancer: a meta-analysis. Br J Cancer. 2008;98(3):547.
21. Manabe O, Hattori N, Hirata K, Itoh K, Hosokawa M, Takahashi H, et al. Diagnostic accuracy of lymph node metastasis depends on metabolic activity of the

primary lesion in thoracic squamous esophageal cancer. J Nucl Med. 2013;54(5):670–6.
22. Heeren PA, Jager PL, Bongaerts F, van Dullemen H, Sluiter W, Plukker JT. Detection of distant metastases in esophageal cancer with ^{18}F-FDG PET. J Nucl Med. 2004;45(6):980–7.
23. Chatterton BE, Ho Shon I, Baldey A, Lenzo N, Patrikeos A, Kelley B, et al. Positron emission tomography changes management and prognostic stratification in patients with oesophageal cancer: results of a multicentre prospective study. Eur J Nucl Med Mol Imaging. 2009;36(3):354–61.
24. Wallace MB, Nietert PJ, Earle C, Krasna MJ, Hawes RH, Hoffman BJ, et al. An analysis of multiple staging management strategies for carcinoma of the esophagus: computed tomography, endoscopic ultrasound, positron emission tomography, and thoracoscopy/laparoscopy. Ann Thorac Surg. 2002;74(4):1026–32.
25. Yasuda, Higuchi I, Yano M, Miyata H, Yamasaki M, Takiguchi S, et al. The impact of ^{18}F-fluorodeoxyglucose PET positive lymph nodes on postoperative recurrence and survival in resectable thoracic esophageal squamous cell carcinoma. Ann Surg Oncol. 2012;19(2):652–60.
26. Bütof R, Hofheinz F, Zöphel K, Stadelmann T, Schmollack J, Jentsch C, et al. Prognostic value of pretherapeutic tumor-to-blood standardized uptake ratio in patients with esophageal carcinoma. J Nucl Med. 2015;56(8):1150–6.
27. Tixier, Le Rest CC, Hatt M, Albarghach N, Pradier O, Metges JP, et al. Intratumor heterogeneity characterized by textural features on baseline ^{18}F-FDG PET images predicts response to concomitant radiochemotherapy in esophageal cancer. J Nucl Med. 2011;52(3):369–78.
28. Lee G, I H, Kim SJ, Jeong YJ, Kim IJ, Pak K, et al. Clinical implication of PET/MR imaging in preoperative esophageal cancer staging: comparison with PET/CT, endoscopic ultrasonography, and CT. J Nucl Med. 2014;55(8):1242–7.
29. Gebski, Burmeister B, Smithers BM, Foo K, Zalcberg J, Simes J, et al. Survival benefits from neoadjuvant chemoradiotherapy or chemotherapy in oesophageal carcinoma: a meta-analysis. Lancet Oncol. 2007;8(3):226–34.
30. Kim MK, Ryu JS, Kim SB, Ahn JH, Kim SY, Park SI, et al. Value of complete metabolic response by ^{18}F-fluorodeoxyglucose-positron emission tomography in oesophageal cancer for prediction of pathologic response and survival after preoperative chemoradiotherapy. Eur J Cancer. 2007;43(9):1385–91.
31. Wahl RL, Jacene H, Kasamon Y, Lodge MA. From RECIST to PERCIST: evolving considerations for PET response criteria in solid tumors. J Nucl Med. 2009;50 Suppl 1:122S–50.
32. Eisenhauer EA, Therasse P, Bogaerts J, Schwartz LH, Sargent D, Ford R, et al. New response evaluation criteria in solid tumours: revised RECIST guideline (version 1.1). Eur J Cancer. 2009;45(2):228–47.
33. Yanagawa M, et al. Evaluation of response to neoadjuvant chemotherapy for esophageal cancer: PET response criteria in solid tumors versus response evaluation criteria in solid tumors. J Nucl Med. 2012;53(6):872–80.
34. Omloo JM, Lagarde SM, Hulscher JB, Reitsma JB, Fockens P, van Dekken H, et al. Extended transthoracic resection compared with limited transhiatal resection for adenocarcinoma of the mid/distal esophagus: five-year survival of a randomized clinical trial. Ann Surg. 2007;246(6):992–1000.
35. Mariette C, Balon JM, Piessen G, Fabre S, Van Seuningen I, Triboulet JP. Pattern of recurrence following complete resection of esophageal carcinoma and factors predictive of recurrent disease. Cancer. 2003;97(7):1616–23.
36. Abate E, DeMeester SR, Zehetner J, Oezcelik A, Ayazi S, Costales J, et al. Recurrence after esophagectomy for adenocarcinoma: defining optimal follow-up intervals and testing. J Am Coll Surg. 2010;210(4):428–35.
37. Goense L, van Rossum PS, Reitsma JB, Lam MG, Meijer GJ, van Vulpen M, et al. Diagnostic performance of ^{18}F-FDG FDG PET and PET/CT for the detection of recurrent esophageal cancer after treatment with curative intent: a systematic review and meta-analysis. J Nucl Med. 2015;56(7):995–1002.
38. Kubota K, Kuroda J, Yoshida M, Ohta K, Suwa T, Mafune K, et al. Surgical therapy and chemoradiotherapy for postoperative recurrent esophageal cancer. Hepatogastroenterology. 2013;60:1961–5.

Diagnostic Applications of Nuclear Medicine: Gastric Cancers

24

Christopher G. Sakellis, Heather A. Jacene, and Annick D. Van den Abbeele

Abstract

Gastric cancer is the fifth most common cancer worldwide. For the purposes of this chapter, gastric cancer will refer to gastric adenocarcinoma. The epidemiology, environmental factors, genetic predisposition, and underlying biomolecular changes of the disease will be reviewed. The staging of gastric cancer as well as the roles of conventional diagnostic imaging and nuclear imaging in this staging will be reviewed.

Finally, the efficacy of these modalities in assessing response to the various treatments described in the chapter and in the long-term surveillance for disease recurrence will be addressed.

Keywords

Gastric cancer • Gastric adenocarcinoma • Conventional diagnostic imaging • [^{18}F]FDG-PET/CT • ^{18}F-FLT-PET/CT • Staging • Assessment of therapeutic response • Surveillance

Glossary

[^{18}F]FDG	2-deoxy-2-[^{18}F]fluoro-D-glucose
^{18}F-FLT	3′-deoxy-3′-[^{18}F]fluorothymidine
AJCC	American Joint Committee on Cancer
APC	Gene encoding for adenomatous polyposis coli
c-met	Gene encoding for tyrosine-protein kinase Met, also known as hepatocyte growth factor receptor (HGFR)
CA 19–9	Carbohydrate antigen 19–9, a tumor-associated serum marker
CA 72–4	Tumor-associated glycoprotein 72 (TAG-72), a tumor-associated marker
CDH1	Gene encoding for cadherin, an adhesion molecule
CEA	Carcinoembryonic antigen, a tumor-associated marker
CT	X-ray computed tomography
EBV	Epstein-Barr virus
EUS	Endoscopic ultrasound
FDA	United States Food and Drug Administration
FIGC	Familial interstitial gastric cancer

C.G. Sakellis • A.D. Van den Abbeele (✉)
Department of Imaging, Dana-Farber Cancer Institute, Boston, MA, USA

Department of Radiology, Brigham and Women's Hospital, Boston, MA, USA

Harvard Medical School, Boston, MA, USA

Center for Biomedical Imaging in Oncology, Dana-Farber Cancer Institute, Boston, MA, USA

Tumor Imaging Metrics Core, Dana-Farber/Harvard Cancer Center, Boston, MA, USA
e-mail: abbeele@dfci.harvard.edu

H.A. Jacene
Nuclear Medicine/PET-CT, Department of Imaging, Dana-Farber Cancer Institute and Department of Radiology, Brigham and Women's Hospital, Harvard Medical School, Boston, MA, USA

© Springer International Publishing Switzerland 2017
H.W. Strauss et al. (eds.), *Nuclear Oncology*,
https://doi.org/10.1007/978-3-319-26236-9_14

GAPPS	Gastric adenocarcinoma and proximal polyposis of the stomach
GLUT1	Glucose transporter 1
HDGC	Hereditary diffuse gastric cancer
HER2	Human epidermal growth factor receptor 2
K-ras	Oncogene regulating signaling intracellular cascades
M	Metastasis status according to the AJCC/UICC TNM staging system
MIP	Maximum intensity projection
MRI	Magnetic resonance imaging
N	Lymph node status according to the AJCC/UICC TNM staging system
p53	Tumor protein p53, also known as cellular tumor antigen p53, phosphoprotein p53, tumor suppressor p53, antigen NY-CO-13, or transformation-related protein 53 (TRP53)
p73	Tumor-suppressor oncogene belonging to the p53 family of transcription factors
PERCIST	PET response criteria in solid tumors
PET	Positron emission tomography
PET/CT	Positron emission tomography/Computed tomography
RECIST	Response evaluation criteria in solid tumors
T	Tumor status according to the AJCC/UICC TNM staging system
TNM	AJCC staging system based on parameters "T" (tumor status), "N" (lymph node status), and "M" (distant metastasis status)
UICC	International Union Against Cancer (Union Internationale Contre le Cancer)

Contents

Epidemiology 698
Environmental Factors 699
Genetic Predisposition 699
Underlying Biomolecular Changes 699
Staging and Prognostic Classification 700
Conventional Diagnostic Imaging Staging 700
Nuclear Imaging Staging 702
Common Therapies 703
Assessing Efficacy of Treatment 704
Surveillance 705
References 706

Epidemiology

Gastric cancer is the fifth most common cancer worldwide and the third leading cause of cancer deaths [1]. For the purposes of this chapter, gastric cancer will refer to gastric adenocarcinoma and not the lymphomas, sarcomas, and carcinoid tumors that can also primarily arise in the stomach. Gastric cancer rates are highest in Eastern Asia, Latin America, and Eastern Europe. The American Cancer Society estimates about 26,000 new cases and about 11,000 deaths from the disease in the United States in 2016. Overall, gastric cancer affects older people (average age of diagnosis is 69), men more than women, and the average person has about a 1 in 111 risk of developing the disease in their lifetime [2].

The worldwide incidence of gastric cancer has declined over the past few decades, and this is thought to be related to several factors including increased use of refrigeration for food and increased use of antibiotics to treat infections.

The incidence of gastric cancer varies throughout different geographic regions and can even vary in incidence among different ethnic groups in the same region. Over 70% of gastric cancers arise in developing countries, and overall there is a higher gastric cancer risk associated with living at higher geographic latitudes [3].

There are two main histologic types of gastric adenocarcinoma which have different epidemiologies, pathogenesis, morphology, and genetics. The most common is called the "intestinal type" because it has morphology similar to adenocarcinomas arising elsewhere throughout the gastrointestinal tract. The other "diffuse" or infiltrative type is less differentiated than the intestinal type. Intestinal-type gastric cancer is more common in males and older age groups and is likely related to

environmental factors, as it is more prevalent in higher-risk areas. The diffuse type affects men and women equally, is more common in younger age groups, and has a worse prognosis [4]. While there has been a worldwide decrease in the incidence of intestinal-type cancers that parallels the overall decrease in gastric cancers, the decrease in the diffuse type has been slower, and it now accounts for approximately 30% of gastric cancers [5].

Environmental Factors

Geographic and ethnic differences in the incidence of gastric cancer around the world as well as trends in gastric cancer in certain populations over time suggest that environmental factors play a key role in its development. The fact that the generations born to people migrating from high-risk to low-risk countries subsequently develop a lower incidence of gastric cancer suggests that exposures to these environmental risk factors occur early in life [6].

Substantial evidence exists that the risk of gastric cancer increases with a high intake of salt and salt-preserved foods such as salted fish and cured meat. The declining incidence of gastric cancer over the past century has at least in part been attributed to the increase in availability of refrigeration, which precludes the use of salting to preserve foods. Refrigeration has also allowed for fresh fruits and vegetables to be more readily available to the public at large, providing an increased source of antioxidants which aid in cancer prevention. Dietary nitrates, obesity, low socioeconomic status, prior gastric surgery, and smoking are also associated with increased risk of gastric cancer.

Helicobacter pylori (*H. pylori*) has been characterized by the World Health Organization as a Group 1, or definite, carcinogen. If left untreated, *H. pylori* infection leads to chronic active gastritis, which is a risk factor for both the intestinal and diffuse types of gastric adenocarcinoma. In the development of intestinal-type tumors, it is thought that a cascade of histopathologic events occurs over the course of four or more decades from chronic active gastritis to atrophic gastritis to intestinal metaplasia to dysplasia and finally to invasive carcinoma [7].

Epstein-Barr virus (EBV) is also detected in 2–16% of gastric adenocarcinomas worldwide, but in contrast to *H. pylori* infection, its role in carcinogenesis is not understood [8].

Genetic Predisposition

The majority of genetic changes associated with gastric cancer are acquired, some of which are linked to *H. pylori* infection. Aggregation of gastric cancer within families occurs in approximately 10% of cases. However, true hereditary gastric cancer only accounts for 1–3% of total cases and is comprised of at least three syndromes: hereditary diffuse gastric cancer (HDGC), gastric adenocarcinoma and proximal polyposis of the stomach (GAPPS), and familial interstitial gastric cancer (FIGC) [9]. At this time, only HDGC is understood genetically. HDGC is associated with truncating mutations in the CDH1 gene which codes for the cell adhesion protein E-cadherin. These mutations have a high penetrance and are inherited in an autosomal dominant pattern [10].

Underlying Biomolecular Changes

With regard to the development of intestinal-type gastric carcinomas, many studies have implicated *H. pylori* in the multistage carcinogenic cascade from chronic active gastritis to adenocarcinoma. Initiation of this carcinogenesis process has been linked to mutagenic nitric oxides produced by inflammatory cells responding to the *H. pylori* infection which in turn induce abnormalities in the DNA of gastric epithelial cells [11]. In the various stages of gastric carcinogenesis, studies have described overexpression of oncogenes such as K-ras and c-met, as well as loss of tumor suppressor genes such as p53, p73, and APC [12].

The human epidermal growth factor receptor 2 gene (HER2) codes for a transmembrane tyrosine kinase receptor protein. Mutations which result in overexpression of HER2 have been linked with gastric cancer. HER2 overexpression has been found in approximately 20–30% of gastric cancers [13, 14].

Unlike the complex and poorly understood molecular pathways leading to the development of intestinal-type gastric cancers, diffuse-type carcinomas have the characteristic molecular abnormality of defective intracellular adhesions. In most cases, these result from loss of expression of the cell adhesion protein E-cadherin, which is coded by the same gene (CDH1) which is mutated in the HDGC syndrome described above [15].

Staging and Prognostic Classification

The TNM staging system of the American Joint Committee on Cancer (AJCC and the International Union Against Cancer (UICC) is the staging system for gastric cancer most often used in the Western hemisphere and now commonly in Asia as well.

Tumors arising in the proximal 5 cm of the stomach (gastric cardia) that extend to the gastroesophageal junction or esophagus are staged by the AJCC TNM system for esophageal adenocarcinoma. All other gastric cancers with a midpoint lying more than 5 cm distal to the gastroesophageal junction or within the gastric cardia but which do not extend into the gastroesophageal junction or esophagus are staged using the gastric staging system.

Tumor (T) staging is dependent on depth of tumor invasion and not its size. The T1 designation is divided into T1a (invasion of the lamina propria or muscularis mucosae) and T1b (invasion of the submucosa). T2 denotes invasion of the muscularis propria. T3 denotes invasion of the subserosal tissue without invasion of adjacent structures. T4 stage tumors are divided into those that extend beyond the serosa into the peritoneum (T4a) and those that extend into the peritoneum and invade adjacent structures (T4b). The adjacent structures of the stomach which can be involved in local extension include the spleen, transverse colon, liver, diaphragm, pancreas, abdominal wall, adrenal gland, kidney, small intestine, and retroperitoneum. Extensive T4b invasion of adjacent structures can make surgical resection of the tumor difficult and thus significantly decreases prognosis.

Nodal (N) staging is based on the number of regional lymph nodes containing metastatic disease (positive nodes). N0 refers to no regional positive nodes, N1 refers to one to two positive nodes, N2 refers to three to six positive nodes, and N3 refers to seven or more positive nodes. The more regional lymph nodes involved with metastatic disease, the worse the prognosis. The groups of lymph nodes which drain the wall of the stomach consist of stations along the greater curvature of the stomach, in the peripancreatic and splenic area, and along the lesser curvature of the stomach. These constitute the array of regional lymph nodes related to primary gastric cancers.

The presence of metastatic disease (M1) precludes surgical resection and has a dismal prognosis with a 5-year survival of only about 4–5% [3]. Distant nodal sites which constitute metastatic disease include the retropancreatic, portal, paraaortic, retroperitoneal, and mesenteric stations. Hematogenous metastases from gastric carcinoma most commonly involve the liver because the stomach is drained by the portal vein. Other less common sites of hematogenous spread include the lungs, adrenal glands, central nervous system, and skeleton. Ovarian metastases (Krukenberg tumor, Fig. 1) are thought to be due to hematogenous, peritoneal, and/or lymphatic spread [16]. Peritoneal metastases are an extremely unfavorable prognostic factor and are indicative of incurable disease. Positive peritoneal cytology is also classified as metastatic (M1) disease.

Tumor location, though not a part of the TNM staging, does influence prognosis, with more favorable outcomes for tumors located more distally in the stomach.

Conventional Diagnostic Imaging Staging

Gastric cancers most commonly present clinically with weight loss and persistent abdominal pain. In tumors arising in the proximal stomach, dysphagia is a common presenting symptom. Occult gastrointestinal bleeding with or without iron deficiency anemia is also observed.

The initial workup of patients suspected of having gastric disease is usually an upper gastrointestinal endoscopy, which can best obtain

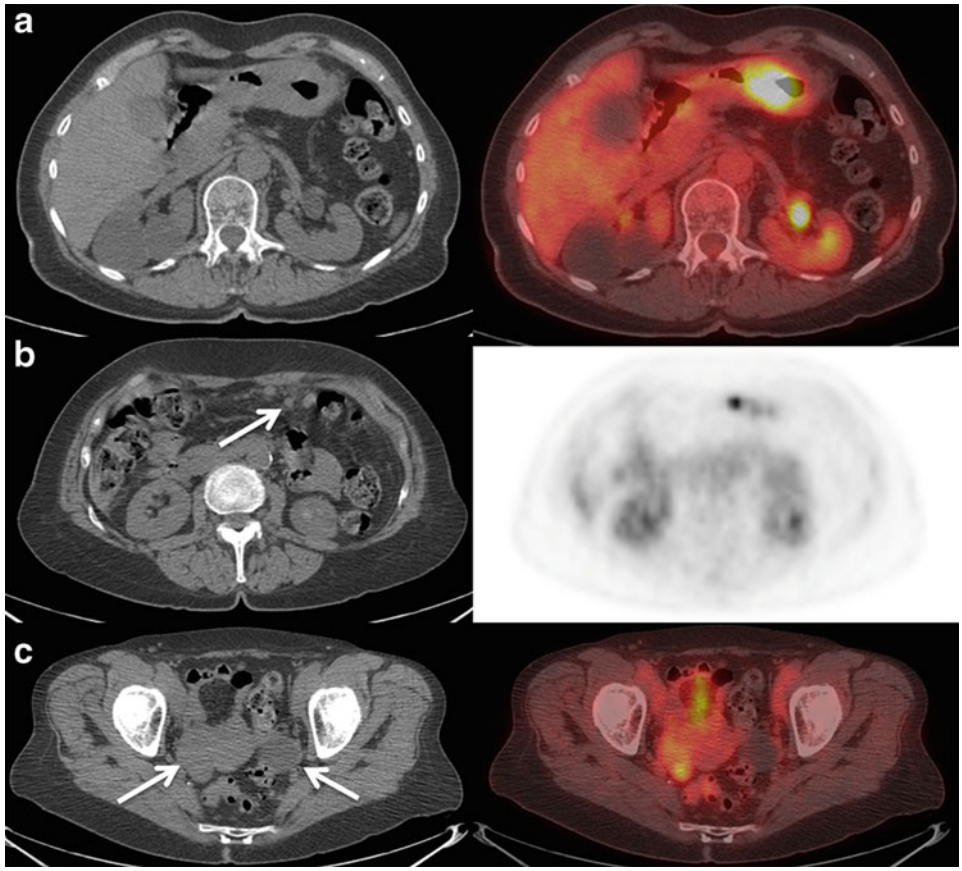

Fig. 1 (**a**) CT and fused images from an [^{18}F]FDG-PET/CT in a 65 year old woman with newly diagnosed gastric adenocarcinoma. The [^{18}F]FDG-avid primary tumor in the gastric body is demonstrated here. (**b**) CT and PET images of the mid-abdomen demonstrate [^{18}F]FDG-avid mesenteric nodules just to the *left* of midline (*arrow*) consistent with metastatic disease. (**c**) CT and fused images demonstrate large bilateral adnexal structures, solid and [^{18}F]FDG-avid on the *right* and more cystic with mild peripheral [^{18}F]FDG uptake associated with a more solid rim on the *left*. These findings were consistent with metastases to the ovaries (Krukenberg tumor)

anatomic location and tissue diagnosis of a gastric malignancy. Fluoroscopic barium studies are less often used due to false-negative results in up to 50% of cases and a low sensitivity for detection of early gastric cancers [17, 18]. However, barium studies may be more sensitive in detecting diffuse-type adenocarcinomas, which may present with widespread decreased distensibility of a "leather-flask" appearing stomach, termed linitis plastica, which is infiltrated by tumor. This appearance may be obvious radiographically but may look relatively normal on endoscopy.

Determination of the invasiveness of a gastric cancer is crucial to determine the ease of surgical resectability or if surgery is even feasible. Endoscopic ultrasound (EUS) is usually performed early in the preoperative evaluation after the diagnosis of gastric cancer is made. In a recent systemic review of studies comparing EUS staging with pathology, the sensitivity and specificity for EUS distinguishing T1 from T2 tumors were 85% and 90% respectively, while the sensitivity and specificity for EUS distinguishing T1/2 tumors from T3/4 tumors were 86% and 90%. For metastatic involvement of regional lymph nodes, the sensitivity and specificity were 83% and 67% respectively, findings which neither exclude nor confirm nodal positivity [19]. However, the ability to perform EUS-guided fine needle aspiration of suspicious nodes adds to the accuracy of nodal staging. Due

to the limited field of view of the ultrasound transducer, the utility of EUS in detecting metastatic disease is relatively poor.

Diagnostic contrast-enhanced CT scan of the chest, abdomen, and pelvis is usually also performed after diagnosis of a gastric cancer. CT is limited in assessing the depth of invasion, particularly with less invasive tumors (T1–T3). CT has been found to accurately assess T stage in only 50–70% of cases [20]. However, diagnostic CT is helpful in determining the extent of invasion of T4 lesions. A gastric mass that abuts an adjacent organ without evidence of an intervening fat plane is suggestive of parenchymal invasion. Coronal and sagittal reformatted CT images may help identify clear organ invasion that is equivocal when viewed in other imaging planes. On CT, positive nodes tend to be larger than 8–10 mm in short axis, have a round shape, are centrally necrotic, and have marked or heterogeneous enhancement. In addition, CT is helpful in identifying distant M1 nodes. However, CT is limited in that it has a low sensitivity in detecting normal-sized nodal metastases and distinguishing positive nodes from inflammatory lymphadenopathy. That being said, nodal staging is only slightly more accurate with EUS compared to CT [21].

MRI, though not routinely used in initial staging of gastric cancers, has demonstrated similar T staging accuracy as EUS [22].

Nuclear Imaging Staging

2-deoxy-2-[^{18}F]fluoro-D-glucose-positron emission tomography/computed tomography ([^{18}F]FDG-PET/CT) scans have been shown to be of some value in primary staging of gastric cancers. The [^{18}F]FDG-PET portion of the examination evaluates the metabolic activity of the primary malignancy and sites of metastasis, while the CT portion provides anatomic data.

While [^{18}F]FDG-PET/CT may demonstrate [^{18}F]FDG uptake associated with a primary gastric tumor, it is ultimately not very helpful in T staging due to its inability to accurately assess depth of tumor invasion and definitively identify adjacent organ invasion. In addition, primary gastric tumors, no matter the size, demonstrate variable levels of [^{18}F]FDG uptake. Large diffuse-type tumors with mucinous or signet ring histologies are relatively acellular and may only be minimally [^{18}F]FDG-avid (Fig. 2). In addition to low cellularity, these particular tumors also demonstrate low expression of glucose transporter 1 (GLUT1) protein that may further account for their relatively mild [^{18}F]FDG uptake [23].

[^{18}F]FDG-PET/CT is somewhat less sensitive than CT in the detection of regional lymph node metastases due to its relatively poor spatial resolution which makes discrimination of [^{18}F]FDG uptake associated with regional lymph nodes from the nearby primary tumor [^{18}F]FDG uptake difficult [24]. However, accurate characterization of these nodes may ultimately be unimportant in clinical planning, as they would all likely be removed at the time of surgery if the patient is a surgical candidate.

The major advantage of [^{18}F]FDG-PET/CT) over other anatomic imaging modalities is its ability to detect distant solid organ, peritoneal, and nodal metastases that would change the treatment strategy from curative to palliative (Fig. 3). A meta-analysis by Kinkel et al. designated [^{18}F]FDG-PET as the most sensitive imaging modality for this purpose [25]. For example, a small liver metastasis not identified on diagnostic CT may be visualized on [^{18}F]FDG-PET scan due to a high target-to-background ratio. Distant lymph nodes constituting M1 disease which may be equivocal in size and appearance on CT scan can be considered suspicious if [^{18}F]FDG-avid on PET scan.

Knowledge of the existence of peritoneal metastases at baseline associated with gastric cancer is important to avoid performing an unnecessary laparotomy. The ability of diagnostic CT to successfully identify peritoneal metastases can be limited by the small size of the tumor deposit(s), the presence of ascites, a paucity of intra-abdominal fat, and inadequate adjacent bowel enhancement. A few studies have reported that [^{18}F]FDG-PET has greater sensitivity than diagnostic CT in the evaluation of

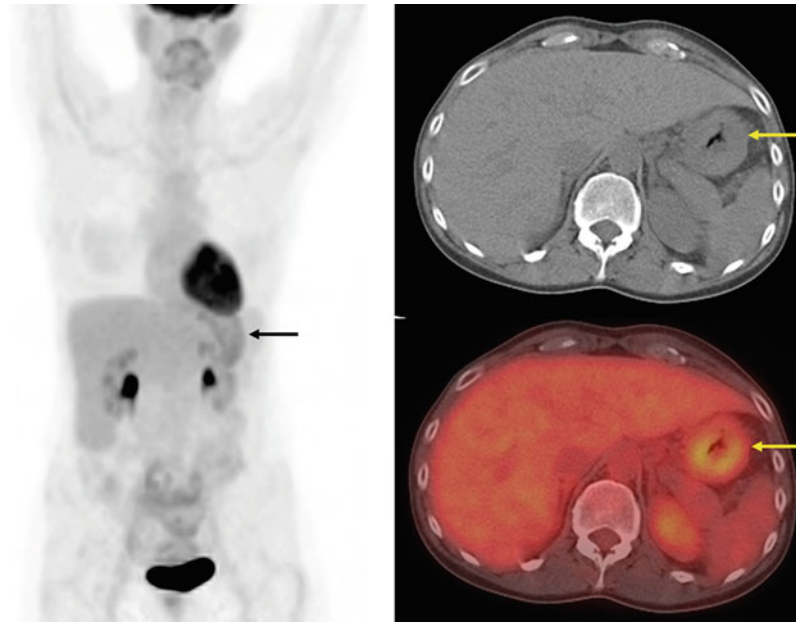

Fig. 2 [^{18}F]FDG-PET/CT scan of a 61 year old woman with recently diagnosed poorly differentiated signet ring gastric carcinoma (*arrows*). The tumor diffusely infiltrates the stomach, resulting in gastric wall thickening. Due to its relatively low cellularity, it demonstrates relatively mild FDG uptake

peritoneal carcinomatosis [26]. Indicators of peritoneal metastasis without definite associated CT correlates on [^{18}F]FDG-PET/CT include a pattern of diffuse uptake spreading throughout the abdomen and pelvis along the small and large bowel walls and/or discrete foci of [^{18}F]FDG uptake located randomly throughout the peritoneum, anteriorly in the mesentery, or dependently in the pelvis which are unrelated to solid viscera and may correlate with subtle ill-defined soft tissue density. However, the sensitivity of [^{18}F]FDG-PET scan for detection of peritoneal carcinomatosis was only calculated at around 50% [27] and is likely not significantly higher using [^{18}F]FDG-PET/CT due to the already low sensitivity for detecting small volume peritoneal carcinomatosis on CT alone as described above.

The intensity of [^{18}F]FDG uptake of primary gastric tumors has been found to correlate with HER2 status. Specifically, gastric adenocarcinomas that overexpress HER2 demonstrate relatively decreased [^{18}F]FDG uptake [28]. In this regard, the baseline [^{18}F]FDG-PET may be useful as a noninvasive means of determining HER2 status of gastric cancers and whether anti-HER2 therapies would be useful.

Common Therapies

Surgical resection of gastric cancers with regional lymphadenectomy offers the best chance for long-term survival for patients with localized disease. Early, minimally invasive (T1) gastric cancers can be cured by complete resection. The main contraindication for surgery is the presence of distant (M1) metastatic disease. Locally invasive disease (T4b) involving a major vascular structure such as the aorta or encasement and/or occlusion of the hepatic, celiac, or proximal splenic artery is also almost always a contraindication. Distal splenic artery involvement is not an absolute contraindication as the vessel can potentially be resected en bloc with the stomach, spleen, and distal pancreas. Diffuse-type infiltrative adenocarcinoma (linitis plastica) has an extremely poor prognosis and is considered a contraindication to curative resection by many surgeons.

Patients that are not candidates for curative resection may need palliative treatment for control of local symptoms such as nausea, pain, obstruction, perforation, or bleeding from the primary tumor. Nonsurgical palliation in these cases

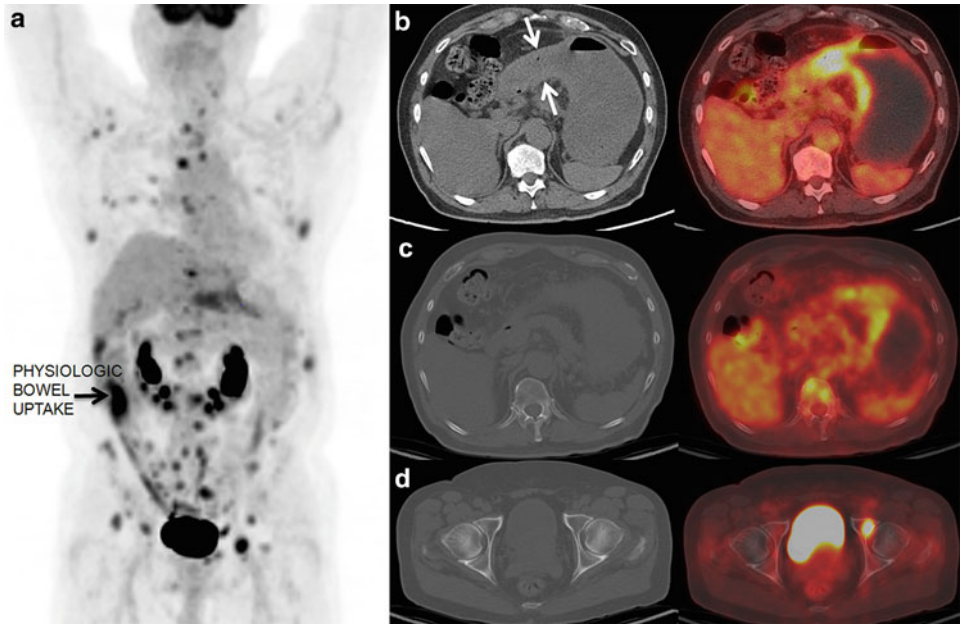

Fig. 3 (**a**) [^{18}F]FDG-PET/CT maximum intensity projection (MIP) image of a 75 year old man with a recently diagnosed infiltrative gastric adenocarcinoma. In addition to the uptake associated with the primary tumor (to be further described), there are innumerable [^{18}F]FDG-avid osseous metastases throughout the entire skeleton. There is no [^{18}F]FDG-avid lymphadenopathy or parenchymal metastatic disease. Of note, there was no mention of osseous metastases on the report of the diagnostic CT scan performed two weeks earlier. (Incidental note is made of a horseshoe kidney.) (**b**) CT and fused images of the stomach demonstrate [^{18}F]FDG-avid wall thickening involving a portion of the distal gastric body/proximal antrum consistent with the infiltrative primary malignancy. (**c**) There are two foci of [^{18}F]FDG uptake in the T12 vertebra. On CT, there may be some mild lucency associated with the sites of uptake. (**d**) There is an intense focus of uptake associated with the anterior left acetabulum associated with a tiny subtle lucency on CT. This PET/CT served to change the treatment strategy for this patient (from curative to palliative) due to the presence of widespread osseous metastatic disease which was obvious on the PET images but poorly appreciated on CT

includes stent placement, radiotherapy, and endoscopic laser therapy. In extreme cases which are highly symptomatic, palliative surgery is often performed.

Neoadjuvant chemotherapy or chemoradiotherapy is often recommended for patients with a more invasive primary tumor (T2 or higher) and/or with a high suspicion of regional nodal involvement on baseline imaging studies (N1+). Patients with bulky adenopathy suspicious for regional metastatic involvement which appears affixed to neighboring organs (such as the pancreatic head) may benefit from initial chemotherapy or chemoradiotherapy to shrink these findings and avoid a more complicated surgery (such as a Whipple procedure). The benefit of neoadjuvant therapy in patients determined to be unresectable at baseline but without distant metastatic disease (M0) is uncertain at this time.

Newer treatment options for inoperable gastric cancer include targeted therapies. In 2010, the monoclonal antibody trastuzumab (Herceptin) was approved by the FDA as a first-line treatment of HER2-overexpressing metastatic gastric cancers. Trastuzumab targets the extracellular domain of the HER2 protein and inhibits HER2 downstream cell signaling.

Assessing Efficacy of Treatment

[^{18}F]FDG-PET/CT may offer information on prognosis in patients with gastric cancer treated with preoperative chemotherapy. Patients responding

to preoperative chemotherapy per [^{18}F]FDG-PET/CT criteria have shown significantly improved survival compared with nonresponders [29]. Ott et al. demonstrated that a 35% decrease in [^{18}F]FDG uptake on PET scan performed 2 weeks after the start of preoperative chemotherapy predicted a favorable response with an accuracy of 85%. Two-year survival rate for those that responded using this criteria was 90% and was only 25% in nonresponders [30].

Wahl et al. delineated the [^{18}F]FDG-PET response criteria in solid tumors (PERCIST) which represent a standardized method for evaluation of metabolic tumor response. Under these criteria, progression on [^{18}F]FDG-PET scan is defined as an increase in [^{18}F]FDG uptake (as measured by standardized uptake value) of greater than 20% in a region 1 cm or larger in diameter, while response to treatment is defined as a decrease in uptake of greater than or equal to 30% [31].

As imaging of gastric cancers with [^{18}F]FDG-PET is somewhat limited because of the relative high number of primary tumors which are not significantly [^{18}F]FDG-avid, early evaluation of response to treatment is difficult [32]. Other PET radiotracers that may complement the information provided by [^{18}F]FDG have been investigated, including 3′-deoxy-3′-[^{18}F] fluorothymidine (^{18}F-FLT). ^{18}F-FLT is phosphorylated to fluorothymidine monophosphate by thymidine kinase I, leading to intracellular trapping. Thymidine kinase I concentration increases almost tenfold during DNA synthesis. Thus, ^{18}F-FLT uptake may accurately reflect cellular proliferation. In one such study, [^{18}F]FDG-PET imaging of pretreatment gastric cancer was compared to ^{18}F-FLT-PET imaging. In contrast to the standard [^{18}F]FDG-PET, FLT-PET was able to definitively detect all locally advanced gastric cancers. Even gastric tumors with histologies that typically demonstrate little to no [^{18}F]FDG uptake at baseline such as mucinous or signet ring adenocarcinomas demonstrated significant ^{18}F-FLT uptake [33].

Because many gastric cancers are not [^{18}F]FDG-avid on staging PET scans, repeat imaging following adjuvant treatment will likely not provide any additional useful information. Wahl et al. recommended the use of RECIST (Response Evaluation Criteria in Solid Tumors), the more widely used solid tumor response metric based on changes in morphologic size, to evaluate gastric cancers which are not significantly [^{18}F]FDG-avid at baseline [34]. After ^{18}F-FLT-PET showed promise in detection of gastric tumors which are typically not significantly [^{18}F]FDG-avid (as described above), Ott et al. [35] subsequently evaluated the performance of ^{18}F-FLT-PET versus [^{18}F]FDG-PET with regard to early response and prognosis in locally advanced gastric cancer treated with neoadjuvant chemotherapy. The only imaging parameter found to have a significant prognostic impact on survival was the ^{18}F-FLT uptake measured 2 weeks after the start of therapy [35]. However, caution was recommended in interpreting this result due to the small patient population and poor response rates. Further investigation is warranted at this time, but ^{18}F-FLT, in its role as a biomarker of cellular proliferation, may prove to be a predictive parameter and provide the molecular quantitative assessment of response to treatment that [^{18}F]FDG cannot provide in these particular gastric tumor subtypes.

Surveillance

As most deaths following surgical resection of gastric cancer are a result of distant recurrence, surveillance for recurrent disease is a key part of postsurgical management [36]. Although gastric tumor recurrence following surgery has a poor prognosis, early detection may be helpful in patients with minimal lymphadenopathy or small metastatic lesions who could have a more favorable response to subsequent salvage chemotherapy or radiotherapy. To detect gastric cancer recurrence following surgery, tumor markers (CEA, CA 19–9, CA 72–4) and endoscopy are commonly utilized. However, tumor markers cannot localize or quantify the recurrent disease, while endoscopy cannot detect extraluminal recurrence.

At present, the most frequently used method for detection of gastric cancer recurrence following surgery is a diagnostic CT scan. However, CT has several limitations. CT cannot reliably

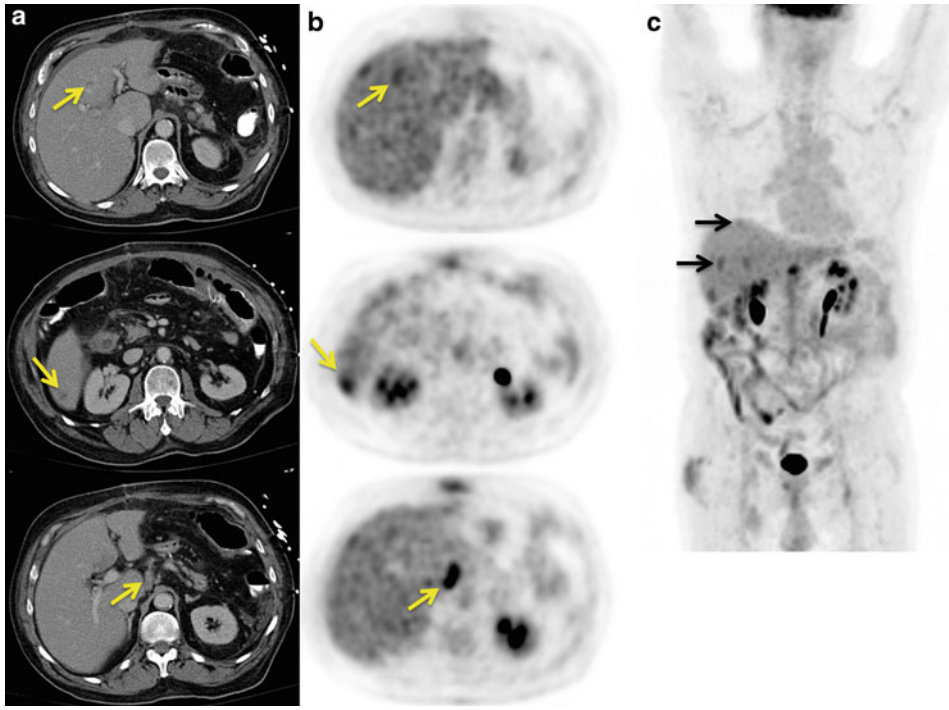

Fig. 4 (**a**) Diagnostic abdominal CT images of a 76 year old man with a history of gastric cancer treated with gastrectomy. There were two small new hypodense lesions observed in the liver and a gastrohepatic lymph node had slightly increased in size (*arrows*). (**b**) [^{18}F]FDG-PET/CT was ordered to further evaluate the somewhat equivocal findings on the CT scan. There was increased [^{18}F]FDG uptake associated with both liver lesions and the gastrohepatic lymph node was intensely [^{18}F]FDG-avid, findings consistent with new metastatic disease (*arrows*). (**c**) [^{18}F]FDG-PET/CT maximum intensity projection (MIP) image also demonstrates two additional foci of [^{18}F]FDG uptake in the liver without CT correlates which are also suspicious for metastatic disease (*arrows*)

differentiate treatment-induced morphologic changes from recurrent malignancy. Recurrence at the surgical anastomosis will look similar to nonspecific bowel wall thickening. [^{18}F]FDG-PET/CT) may help clarify equivocal CT findings in these cases, as recurrent tumor should have more conspicuous and focal [^{18}F]FDG uptake, while postoperative scar tissue should have only mild diffuse [^{18}F]FDG uptake. [^{18}F]FDG-PET/CT may also be more sensitive than CT alone in detecting distant recurrent metastatic disease following surgery, as it has shown to be in detecting distant disease prior to surgery (Fig. 4).

Postoperative surveillance of asymptomatic gastric cancer patients with [^{18}F]FDG-PET/CT has proven useful in detecting recurrent and/or metastatic disease, with a sensitivity of 84% and a specificity of 88% per a recent retrospective study conducted by Lee et al. [37]. Finally, as another recent study has demonstrated that sensitivity for detection of recurrent gastric cancer following surgical resection is greater in patients with initially [^{18}F]FDG-avid gastric cancers [38], surveillance FDG-PET/CT scans may be best utilized in patients with relatively high [^{18}F]FDG uptake associated with the primary tumor at baseline.

References

1. Ferlay J, Soerjomataram I, Dikshit R, Eser S, Mathers C, Rebelo M, et al. Cancer incidence and mortality worldwide: sources, methods, and major patterns in GLOBOCAN 2012. Int J Cancer. 2015;136(5): E359–86.
2. Siegel RL, Miller KD, Jemal A. Cancer statistics, 2016. CA Cancer J Clin. 2016;66(1):7.
3. Jemal A, Bray F, Center MM, Ferlay J, Ward E, Forman D. Global cancer statistics. CA Cancer J Clin. 2011;61(2):69.

4. Lauren P. The two histological main types of gastric carcinoma: diffuse and so-called intestinal-type carcinoma. An attempt at a histo-clinical classification. Acta Pathol Microbiol Scand. 1965;64:31.
5. Ikeda Y, Mori M, Kamakura T, Haraguchi Y, Saku M, Sugimachi K. Improvements in diagnosis have changed the incidence of histological types in advanced gastric cancer. Br J Cancer. 1995;72(2):424.
6. Haenszel W, Kurihara M. Studies of Japanese migrants. Mortality from cancer and other diseases among Japanese in the United States. J Natl Cancer Inst. 1968;40(1):43.
7. Correa P, Haenszel W, Cuello C, Tannenbaum S, Archer M. A model for gastric cancer epidemiology. Lancet. 1975;2(7924):58.
8. Takada K. Epstein-Barr virus and gastric carcinoma. Mol Pathol. 2000;53(5):255.
9. Oliveira C, Pinheiro H, Figueiredo J, Seruca R, Carneiro F. Familial gastric cancer: genetic susceptibility, pathology, and implications for management. Lancet Oncol. 2015;16(2):e60–70.
10. van der Post RS, Vogelaar IP, Carneiro F, Guilford P, Huntsman D, Hoogerbrugge N, et al. Hereditary diffuse gastric cancer: updated clinical guidelines with an emphasis on germline CDH1 mutation carriers. J Med Genet. 2015;52(6):361–74.
11. Pignatelli B. Inducible nitric oxide synthase, antioxidant enzymes and *Helicobacter pylori* infection in gastritis and gastric precancerous lesions in humans. Eur J Cancer Prev. 1998;7(6):439.
12. Smith MG, Hold GL, Tahara E, El-Omar EM. Cellular and molecular aspects of gastric cancer. World J Gastroenterol. 2006;12(19):2979.
13. Yano T, et al. Expression of HER2 in gastric cancer: comparison between protein expression and gene amplification using a new commercial kit. J Clin Oncol. 2004;22:14S.
14. Lordick F, et al. HER2-positive advanced gastric cancer: similar HER2-positivity levels to breast cancer. Eur J Cancer. 2007;5:271.
15. Graziano F, Humar B, Guilford P. The role of the E-cadherin gene (CDH1) in diffuse gastric cancer susceptibility: from the laboratory to clinical practice. Ann Oncol. 2003;14:1705.
16. Disaia P, Creasman W. Clinical gynecologic oncology. 5th ed. St. Louis: Mosby; 1997. p. 369–71.
17. Dooley CP, Larson AW, Stace NH, Renner IG, Valenzuela JE, Eliasoph J, et al. Double-contrast barium meal and upper gastrointestinal endoscopy. A comparative study. Ann Intern Med. 1984;101 (4):538–45.
18. Longo WE, Zucker KA, Zdon MJ, Modlin IM. Detection of early gastric cancer in an aggressive endoscopy unit. Am Surg. 1989;55(2):100.
19. Mocellin S, Pasquali S. Diagnostic accuracy of endoscopic ultrasonography (EUS) for the preoperative locoregional staging of primary gastric cancer. Cochrane Database Syst Rev. 2015;6(2): CD009944.
20. Abdalla EK, Pisters PW. Staging and preoperative evaluation of upper gastrointestinal malignancies. Semin Oncol. 2004;31(4):513.
21. Tsendsuren T, Jun SM, Mian XH. Usefulness of endoscopic ultrasonography in preoperative TNM staging of gastric cancer. World J Gastroenterol. 2006;12(1):43.
22. Kwee RM, Kwee TC. Imaging in local staging of gastric cancer: a systematic review. J Clin Oncol. 2007;25(15): 2107.
23. Kawamura T, Kusakabe T, Sugino T, Watanabe K, Fukuda T, Nashimoto A, et al. Expression of glucose transporter-1 in human gastric carcinoma: association with tumor aggressiveness, metastasis, and patient survival. Cancer. 2001;92(3):634–41.
24. Kim SK, Kang KW, Lee JS, Kim HK, Chang HJ, Choi JY, et al. Assessment of lymph node metastases using ^{18}F-FDG PET in patients with advanced gastric cancer. Eur J Nucl Med Mol Imaging. 2006;33(2):148–55.
25. Kinkel, Lu Y, Both M, Warren RS, Thoeni RF. Detection of hepatic metastases from cancers of the gastrointestinal tract by using noninvasive imaging methods (US, CT, MR, PET): a meta-analysis. Radiology. 2002;224(3):748–56.
26. Turkalow A, Yeung HW, Salmon AS, Macapinlac HA, Larson SM. Peritoneal carcinomatosis: role of ^{18}F-FDG PET. J Nucl Med. 2003;44(9):1407–12.
27. Yoshioka T, et al. Evaluation of ^{18}F-FDG PET in patients with advanced, metastatic, or recurrent gastric cancer. J Nucl Med. 2003;44(5):69.
28. Chen R, Zhou X, Liu J, Huang G. Relationship between ^{18}F-FDG PET/CT scans and HER2 expression in gastric cancer. J Nucl Med. 2016;57(7):1040–4.
29. Lowy AM, Mansfield PF, Leach SD, Pazdur R, Dumas P, Ajani JA. Response to neoadjuvant chemotherapy best predicts survival after curative resection of gastric cancer. Ann Surg. 1999;229(3):303–8.
30. Ott K, Herrmann K, Krause BJ, Lordick F. The value of PET imaging in patients with localized gastroesophageal cancer. Gastrointest Cancer Res. 2008;2 (6):287–94.
31. Wahl RL, Jacene H, Kasamon Y, Lodge MA. From RECIST to PERCIST: evolving considerations for PET response criteria in solid tumors. J Nucl Med. 2009;50 Suppl 1:122S–50.
32. Mochiki E, Kuwano H, Katoh H, Asao T, Oriuchi N, Endo K. Evaluation of ^{18}F-2-deoxy-2-fluoro-D-glucose positron emission tomography for gastric cancer. World J Surg. 2004;28(3):247–53.
33. Herrmann K, Ott K, Buck AK, Lordick F, Wilhelm D, Souvatzoglou M, et a. Imaging gastric cancer with PET and the radiotracers ^{18}F-FLT and ^{18}F-FDG: a comparative analysis. J Nucl Med. 2007;48(12):1945–50.
34. Eisenhauer EA, Therasse P, Bogaerts J, Schwartz LH, Sargent D, Ford R, et al. New response evaluation criteria in solid tumours: revised RECIST guideline (version 1.1). Eur J Cancer. 2009;45(2):228–47.
35. Ott W, Herrmann K, Schuster T, Langer R, Becker K, Wieder HA, et al. Molecular imaging of proliferation and glucose utilization: utility for monitoring response

and prognosis after neoadjuvant therapy in locally advanced gastric cancer. Ann Surg Oncol. 2011;18(12):3316–23.
36. Lacueva FJ, Calpena R. Gastric cancer recurrence: clues for future approaches to avoiding an old problem. J Clin Gastroenterol. 2001;32(1):3–4.
37. Lee JW, Lee SM, Son MW, Lee MS. Diagnostic performance of FDG PET/CT for surveillance in asymptomatic gastric cancer patients after curative surgical resection. Eur J Nucl Med Mol Imaging. 2016;43(5):881–8.
38. Kim SJ, Cho YS, Moon SH, Bae JM, Kim S, Choe YS, et al. Primary tumor ^{18}F-FDG avidity affects the performance of ^{18}F-FDG PET/CT for detecting gastric cancer recurrence. J Nucl Med. 2016;57(4):544–50.

Diagnostic Applications of Nuclear Medicine: Gastrointestinal Stromal Tumors

25

Christopher G. Sakellis, Heather A. Jacene, and Annick D. Van den Abbeele

Abstract

Gastrointestinal stromal tumor (GIST), although rare, is the most common mesenchymal gastrointestinal neoplasm. This chapter will review the epidemiology, environmental factors, genetic predisposition, and underlying biomolecular changes of the disease. The staging of GIST as well as the roles of conventional diagnostic imaging and nuclear imaging in this staging will be reviewed. Finally, the efficacy of these modalities in assessing response to the various treatments described in the chapter and in the long-term surveillance for disease recurrence will be addressed.

Keywords

Gastrointestinal stromal tumor (GIST) • Conventional diagnostic imaging • [^{18}F]FDG-PET/CT • Staging • Tyrosine kinase inhibitors • Assessment of therapeutic response • Surveillance

Glossary

[^{18}F]FDG	2-deoxy-2-[^{18}F]fluoro-D-glucose
ADC	Apparent diffusion coefficient
AFIP	Armed Forces Institute of Pathology
AJCC	American Joint Committee on Cancer
BRAF	Gene encoding for the B-Raf protein, a serine/threonine-protein kinase; the gene is also known as the proto-oncogene B-Raf and v-Raf murine sarcoma viral oncogene homolog B
CSF-1R	Colony-stimulating factor 1R
CT	X-ray computed tomography
DECT	Dual-energy CT
EORTC	European Organization for Research and Treatment of Cancer
EUS	Endoscopic ultrasound
FDA	United States Food and Drug Administration
GIST	Gastrointestinal stromal tumor
GLUT4	Glucose transporter 4
HPF	High-power fields

C.G. Sakellis • A.D. Van den Abbeele (✉)
Department of Imaging, Dana-Farber Cancer Institute, Boston, MA, USA

Department of Radiology, Brigham and Women's Hospital, Boston, MA, USA

Harvard Medical School, Boston, MA, USA

Center for Biomedical Imaging in Oncology, Dana-Farber Cancer Institute, Boston, MA, USA

Tumor Imaging Metrics Core, Dana-Farber/Harvard Cancer Center, Boston, MA, USA
e-mail: abbeele@dfci.harvard.edu

H.A. Jacene
Nuclear Medicine/PET-CT, Department of Imaging, Dana-Farber Cancer Institute and Department of Radiology, Brigham and Women's Hospital, Harvard Medical School, Boston, MA, USA

© Springer International Publishing Switzerland 2017
H.W. Strauss et al. (eds.), *Nuclear Oncology*,
https://doi.org/10.1007/978-3-319-26236-9_15

HU	Hounsfield units
IRA	Iodine-related attenuation
KIT	A proto-oncogene encoding for tyrosine-protein kinase Kit (or CD117), also known as mast/stem cell growth factor receptor (SCFR)
M	Metastasis status according to the AJCC/UICC TNM staging system
MRI	Magnetic resonance imaging
N	Lymph node status according to the AJCC/UICC TNM staging system
NCCN	National Comprehensive Cancer Network
NF1	Neurofibromatosis type 1
PDGFR	Platelet-derived growth factor receptor
PDGFRA	Platelet-derived growth factor receptor alpha
PET	Positron emission tomography
PET/CT	Positron emission tomography/ Computed tomography
RECIST	Response evaluation criteria in solid tumors
RET	A proto-oncogene encoding for a receptor tyrosine kinase for extracellular signalling molecules (from "rearranged during transfection")
RTK	Receptor tyrosine kinases
SCF	Stem cell factor
SDH	Succinate dehydrogenase
SURE	Sunitinib alternating with regorafenib
SUV_{max}	Standardized uptake value at point of maximum
SUV	Standardized uptake value
TKI	Tyrosine kinase inhibitor
TNM	AJCC/UICC staging system based on parameters "T" (tumor status), "N" (lymph node status) and "M" (distant metastasis status)
UICC	International Union Against Cancer (Union Internationale Contre le Cancer)
T	Tumor status according to the AJCC/UICC TNM staging system
TEK	Receptor tyrosine kinase
VEGFR	Vascular endothelial growth factor receptor

Contents

Epidemiology 710
Environmental Factors and Genetic Predisposition 711
Underlying Biomolecular Changes 711
Staging and Prognostic Stratification 711
Conventional Diagnostic Imaging Staging 712
Nuclear Imaging Staging 713
Traditional Therapies and GIST 713
Molecular Therapy and GIST 714
Assessing Response to Treatment 715
Assessing Resistance to Treatment 718
Surveillance 720
References 721

Epidemiology

Gastrointestinal stromal tumor (GIST) is the most common mesenchymal gastrointestinal neoplasm but is still a rare tumor, only accounting for about 1% of all gastrointestinal neoplasms [1, 2]. The incidence of the tumor in the United States is estimated to be 4,000–6,000 new cases per year [3].

GISTs are distinct from other mesenchymal gastrointestinal tumors like liposarcomas or leiomyosarcomas, as they are derived from cells in the myenteric plexus of the lamina propria within the gastrointestinal wall [4]. They can arise anywhere throughout the gastrointestinal tract, most commonly in the stomach (60%) and jejunum/ileum (30%), followed by the duodenum, rectum, colon, and esophagus in descending order [5]. Rarely, GISTs have been found to arise in the mesentery or retroperitoneum.

The majority of GISTs are sporadic, and in these cases, men and women are affected equally. There is no racial preference, and they rarely arise before 40 years of age, with a mean age at diagnosis in the seventh decade of life [6].

Environmental Factors and Genetic Predisposition

At this time, there are no known environmental or lifestyle-related causes of GIST. However, almost all GISTs have been found to be associated with sporadic activating mutations which promote tumor survival and growth.

Approximately 85% of GISTs have oncogenic gain-of-function mutations in one of two receptor tyrosine kinases (RTK): KIT or PDGFRA (platelet-derived growth factor receptor alpha) which play a central role in the pathogenesis of GIST [7–9]. KIT encodes for CD117, a transmembrane receptor tyrosine kinase protein. The most common mutation in KIT in GIST involves exon 11 (about 70% of cases), while other mutations have been found in exons 9 (10–20% of cases), 13, and 17 [10]. Various types of mutations have been described, most commonly in-frame deletions involving exon 11 and duplications in exon 9.

The activating mutations involving the PDGFRA gene which is homologous to KIT and also encodes a transmembrane receptor tyrosine kinase have been found in 5–10% of GISTs [8]. Single nucleotide substitutions are the most common mutations described in these PDGFRA-positive tumors. KIT-negative GISTs are more likely to have PDGFRA mutations than KIT-positive GISTs [11]. Approximately 10–15% of GISTs are considered wild type and are both KIT- and PDGFRA-negative [10].

Although rare, inherited predispositions have been found to account for 5% or less of all GISTs. Patients with neurofibromatosis type 1 (NF1) have a high incidence of GISTs, which are typically multiple, arise in the small intestine, and are both KIT- and PDGFRA-negative [12]. Overexpression of KIT can occur in these wild-type NF1-related GISTs, though the mechanism is unclear.

Pediatric GIST is rare, tends to arise in the setting of heritable syndromes, has a female predilection, and commonly presents with chronic gastrointestinal bleeding and multifocal gastric involvement. Unlike adult GISTs, pediatric GISTs lack KIT or PDGFRA mutations, commonly metastasize to the lymph nodes, and have a more indolent course. The Carney-Stratakis syndrome results from germline mutations in succinate dehydrogenase (SDH) genes and presents in children who go on to develop GISTs and paragangliomas [13]. Primary familial GIST syndrome is a very rare autosomal dominant phenomenon and involves a germline mutation in KIT with high penetrance. These patients tend to be younger, develop multiple tumors in the stomach and/or small bowel, and may display extra-gastrointestinal traits such as skin hyperpigmentation [14].

A subset (3–13%) of wild-type GISTs has also been found to possess mutations in the serine-threonine kinase BRAF [15].

Underlying Biomolecular Changes

CD117, a transmembrane receptor tyrosine kinase protein, is encoded for by the KIT gene and functions as a receptor for stem cell factor (SCF). In normal cells, CD117 is enzymatically inactive until it binds SCF, whereby it initiates a signaling cascade within the cell. When there is a "gain-of-function" mutation in the KIT gene, as seen in most GISTs, the mutated CD117 protein remains activated without the presence of its ligand SCF, and thus the signaling cascade continues unabated. The most common mutations of the KIT gene which occur in exon 11 specifically affect the intracellular juxtamembrane portion of CD117, which plays a role in inhibiting signal transduction in the absence of SCF [16]. Mutations in other exons of the KIT gene as well as mutations seen in GIST in the PDGFRA gene all result in constitutive kinase activation and unchecked cell signaling, which ultimately affects cell proliferation, apoptosis, chemotaxis, and metabolism, resulting in tumorigenesis.

Staging and Prognostic Stratification

The TNM (tumor-node-metastasis) staging system developed by the American Joint Committee on Cancer (AJCC) and the International Union Against Cancer (UICC) is used for GIST. Although the T, N, and M definitions are similar for all tumors, there are separate stage groups based on the location of the primary tumor.

Primary gastric and omental GISTs are grouped together in one scheme, while primary small bowel, esophageal, colorectal, and peritoneal GISTs are grouped in another. Based on the data of two large retrospective Armed Forces Institute of Pathology (AFIP) studies of GISTs with long-term follow-up, tumor-related mortality of small bowel GISTs was more than twice that of gastric GISTs [17, 18].

Tumor (T) staging includes an assessment of both tumor size and mitotic rate. As most GISTs are roughly ovoid, the greatest tumor diameter is relatively easy to assess. The size thresholds in assigning a T designation are 2, 5, and 10 cm. Depth of tumor invasion is not utilized as most GISTs have transmural extension at presentation. The mitotic rate of GIST is evaluated pathologically by determining the number of mitoses observed per 50 high-power fields (HPF) on microscopy. A low mitotic rate is defined as 5 or fewer mitoses per 50 HPF, while a high mitotic rate is over 5.

Based on AFIP data, GISTs smaller than 2 cm in size with low mitotic rates were found to have very low risk of recurrence but were still considered to have metastatic potential. In both gastric and small bowel GISTs, less than 3% of tumors less than 10 cm and with fewer than 5 mitoses per 50 HPF metastasized, while over 80% of tumors larger than 10 cm and with 5 or more mitoses per HPF metastasized. The more intermediate-risk gastric GISTs (greater than 10 cm with low mitotic rate/less than 10 cm with high mitotic rate) had relatively low metastatic potential (10–15%), while the intermediate-risk small bowel GISTs with the same characteristics had a much higher metastatic rate (greater than 50%) [17, 18]. The National Comprehensive Cancer Network (NCCN) guidelines stratify the risk of malignancy of GISTs as high, moderate, low, or very low based on the site of primary tumor, size, and anatomic location [19].

Nodal (N) staging evaluates for the presence of regional lymph node metastases, which are rarely seen outside of rare pediatric familial cases. The presence of no regional nodal metastases or an unknown nodal status is designated as N0.

Distant metastatic disease (M1) in GIST is tumor involvement outside the main tumor mass, most commonly in the mesentery or liver within the abdomen. Extra-abdominal metastases are rare, but can occur in the bone, subcutaneous tissue, and lung. Multiple synchronous gastrointestinal GISTs, usually seen in the setting of hereditary syndromes, should not be considered as metastatic disease, as all could be separate primary tumors.

The histology of GIST may affect prognosis. The three major histopathologic types are spindle cell (70%), epithelioid type (20%), and mixed cellularity (10%). Early data suggested that 5-year recurrence-free survival was significantly higher with spindle cell histology compared to epithelioid or mixed histology [20]. However, subsequent studies implied that the degree of cellularity of the GIST was a more important prognostic factor than histologic type [21].

At this time, it is not clear whether the presence or absence of KIT mutations affects the prognosis of a particular GIST. Specific types of KIT mutations, including those in exon 9, have been shown to be associated with more aggressive tumor behavior [22]. Specific mutations are not factored into the current TNM staging system.

Conventional Diagnostic Imaging Staging

Contrast-enhanced CT is the current imaging of choice for the initial diagnosis and staging of GISTs. Although tissue sampling is required to definitively diagnose a GIST, CT not only characterizes the size and extent of the primary tumor but also evaluates for any peritoneal seeding and/or more distant metastatic disease. With the aid of oral and intravenous contrast, features associated with the primary tumor such as ulceration and fistulization with the gastrointestinal lumen can be characterized.

Typically, at the time of presentation, primary GISTs appear as smoothly contoured, heterogeneously enhancing masses. Larger tumors may display internal heterogeneity due to associated necrosis, cystic degeneration, or hemorrhage. It is important that multiphasic CT imaging with

unenhanced, arterial phase, and portal venous phase images is performed when imaging the liver, as the surrounding hepatic parenchyma on delayed portal venous phase images performed alone may mask hypervascular hepatic metastases.

Though CT is better at globally evaluating the patient for metastatic disease, MRI has shown utility in evaluating disease, especially in specific fixed structures such as the liver or rectum. The higher soft-tissue contrast of MRI compared to CT often provides an advantage in determining the organ of origin of primary GISTs and in evaluating invasion or involvement of adjacent viscera and/or blood vessels.

Some MRI features of primary GISTs at baseline may be predictive of malignancy risk. The presence of intratumoral cystic change, which is more accurately assessed on MRI than CT, has been found to correlate with high-risk GISTs, as defined by the NCCN guidelines [23]. A similar correlation between the presence of low attenuation findings on CT and malignant potential has not been found, possibly because these findings can be more nonspecific on CT [24, 25]. On MRI, lower mean apparent diffusion coefficient (ADC) values have also been found to correlate with a higher malignant risk, possibly due to the higher cellularity (and associated diffusion restriction) of high-risk tumors [23].

Endoscopic ultrasound (EUS) has been considered for the diagnosis and management of very small GISTs (less than 2 cm). EUS-guided biopsy of the lesion can be performed at the time of evaluation. Certain high-risk EUS features of these very small GISTs have been described including irregular border, cystic spaces, ulceration, echogenic foci, and overall heterogeneity, which may prompt their surgical resection [26].

Nuclear Imaging Staging

2-deoxy-2-[^{18}F]fluoro-D-glucose-positron emission tomography/computed tomography ([^{18}F]FDG-PET/CT) scans are now commonly used in the baseline evaluation of biopsy-proven GIST. CT and [^{18}F]FDG-PET scans were initially shown to have comparable high sensitivity and positive predictive value in initial staging of GIST [27], while subsequent studies have demonstrated [^{18}F]FDG-PET/CT is slightly more sensitive than CT alone [28]. While contrast-enhanced CT provides superior anatomic definition compared to the nondiagnostic CT portion of a PET/CT exam, the PET portion of a [^{18}F]FDG-PET/CT may be more sensitive in detecting an unknown primary GIST and may more definitively characterize small findings on CT scan as sites of metastatic disease. [^{18}F]FDG-PET/CT scans may also better evaluate patients at baseline who have an allergy to intravenous contrast.

[^{18}F]FDG-PET allows for quantitation of tumor metabolism using measurements such as the maximum standardized uptake value (SUV_{max}). As PET has been shown to be superior in many ways to diagnostic CT in monitoring and quantifying therapeutic response to tyrosine kinase inhibitor (TKI) therapy (described below), especially early in the course of treatment, a baseline [^{18}F]FDG-PET scan should be obtained before starting any TKI administration to assess the baseline tumor metabolic activity and extent of tumor burden.

Traditional Therapies and GIST

Complete surgical resection is the treatment of choice for any patient with surgically resectable GIST and no metastases and offers the best chance for long-term disease-free survival. The goal of surgery is complete resection of the primary tumor with an intact pseudocapsule and negative microscopic margins on pathology. The resected tumor needs to be handled with care during removal, as tumor rupture will negatively impact survival due to the risk that it results in new intra-abdominal microscopic seeding of tumor.

The current consensus is that conventional cytotoxic chemotherapy is not useful for managing GIST. Several trials evaluating chemotherapeutic regimens in advanced GIST have reported very low response rates (0–5%) [29, 30].

Radiotherapy has been reported in the past to show no advantage in disease-free survival in several studies. A retrospective study analyzing patients treated at Massachusetts General Hospital

between 1973 and 1998 with incompletely resected GIST, some of whom were also treated with radiotherapy, concluded there was no support for its use [31]. GISTs are also commonly associated with mobile structures such as loops of small bowel and are more difficult to accurately target with radiotherapy.

Molecular Therapy and GIST

Until the early 2000s, the outcome for patients presenting with GISTs which were either advanced (surgically unresectable or marginally resectable) or who presented with metastatic disease was relatively bleak. After the discovery of the key role mutations in receptor tyrosine kinase genes, most notably KIT, played in GIST tumorogenesis, molecularly targeted agents known as tyrosine kinase inhibitors (TKIs) were developed to specifically treat GIST.

The first of these tyrosine kinase inhibitors used to treat GIST in clinical trials, and later the first to be approved by the FDA for treatment of advanced or metastatic GIST in 2002, was the small molecule imatinib mesylate. Imatinib inhibits the reaction that starts the cell signaling cascade of the KIT protein by competing with ATP for a binding site on its surface, thus inhibiting tumor progression. The drug is not cytotoxic like conventional chemotherapies. Instead it is cytostatic, and the NCCN guidelines recommend continuous administration of imatinib for metastatic GIST until there is evidence of progression [19]. The standard dose of imatinib is 400 mg, and it is able to be administered only once daily orally due to its circulating half-life of about 20 h.

In a large multicenter trial evaluating imatinib in the treatment of advanced and/or metastatic GISTs, tumors that were KIT-positive showed significant long-lasting response to the drug, with 85% surviving at 76 weeks after starting therapy [32]. However, in the same trial, 14% of the patients were found to have tumors resistant to imatinib, likely due to mutations in different proteins or in parts of the KIT protein structure that do not respond to imatinib binding. GIST patients with the most commonly observed KIT mutations in exon 11 have been found to respond to imatinib more favorably than those with KIT mutations involving exon 9 or wild-type GISTs [10]. This better response may be related to the fact that the binding site of imatinib is in close proximity to the portion of the KIT protein encoded by exon 11.

Dose escalation to 800 mg per day is the recommended first step in patients with unresectable or metastatic GIST that shows early evidence of progression on imatinib. GISTs with KIT mutations in exon 9 have also demonstrated a higher response rate and longer progression-free survival with this higher dose [10].

Preoperative imatinib therapy is recommended as a first-line therapy to reduce the size of large tumors. It is also recommended to reduce the size of tumors at sites where they may become adherent to adjacent tissue or organs and would initially require an extensive en bloc surgery with higher associated morbidity. For example, a duodenal GIST may initially require a pancreaticoduodenectomy, while a rectal GIST might require an abdominoperineal resection in which the rectal sphincter is unable to be spared. In cases like these, preoperative imatinib has been shown to lead to initially unresectable but localized GISTs becoming resectable and to less morbid organ- and function-preserving surgeries for initially marginally resectable tumors. Preoperative imatinib treatment has also been shown to reduce the risk of tumor rupture before or during surgery, which thus improves prognosis [33]. According to NCCN guidelines, preoperative imatinib should be monitored by imaging and continued until two consecutive restaging scans fail to demonstrate interval improvement in tumor burden [19].

Imatinib has been used as an adjuvant treatment following surgery. Even with complete surgical resection of GIST, it has high recurrence rate in the first 2 years after surgery. Imatinib was approved by the FDA in 2008 for treatment of GIST after complete surgical resection, as it was shown to significantly prolong survival in this setting. For patients who did not receive preoperative imatinib, imatinib following complete surgical resection is recommended for at least 36 months per the NCCN guidelines in patients who presented with higher-risk primary GISTs, namely, tumors

larger than 5 cm with more than 5 mitoses per 50 HPF [19]. For patients who did receive preoperative imatinib, the NCCN guidelines recommend that imatinib therapy is considered following complete surgical resection if there had been an objective response to preoperative therapy. However, the duration of this treatment is uncertain, although there have been single- and multicenter trials that have shown benefit in continuing imatinib treatment for 2 years after surgery [19].

Sunitinib was the second receptor TKI approved by the FDA for the treatment of GIST in 2006. It is indicated in patients who have developed resistance to imatinib or have progression of disease following escalation of the daily imatinib dose from 400 to 800 mg. Sunitinib is a less specific inhibitory drug than imatinib and is structurally distinct. It inhibits KIT and PDGFR like imatinib, but also acts to inhibit vascular endothelial growth factor receptors 1–3 (VEGFR1–3), Fms-related tyrosine kinase 3, colony-stimulating factor 1R (CSF-1R), and the RET receptor [34]. Sunitinib thus possesses an antiangiogenic effect in addition to an antitumoral effect. Patients either receive a continuous daily oral 37.5 mg dose of sunitinib or 4 weeks of a continuous 50 mg dose followed by 2 weeks off treatment [35]. There is evidence suggesting that GISTs with KIT exon 9 mutations, wild-type GISTs, and pediatric GISTs, tumors which are typically less responsive to imatinib, are more sensitive to sunitinib [36]. Sunitinib has been considered as a first-line therapy for these particular tumors.

Regorafenib is an oral multikinase inhibitor that was approved by the FDA in 2013 for the treatment of imatinib- and sunitinib-resistant GIST. Regorafenib inihibits the activity of several protein kinases including KIT, RET, BRAF, and PDGFR and has an antiangiogenic effect with inhibition of VEGFR1-3 and TEK. Regorafenib was shown to increase progression-free survival in a phase 3 trial of GIST patients who had progressed on imatinib and sunitinib [37].

In patients with wild-type GISTs, which lack both KIT and PDGRA mutations, but who do exhibit mutations in the BRAF kinase, treatment with BRAF inhibitors has shown some success. Falchook et al. reported the first case study of treatment of one such patient using a BRAF inhibitor, dabrafenib [38]. Other novel drugs have been investigated in the treatment of metastatic GIST resistant to imatinib and sunitinib. Sorafenib is a TKI that exhibits inhibitory action against several kinases and has demonstrated significant disease control rates in several studies [39].

In addition to treatment with novel drugs, regimens of two complementary TKIs given daily in a rapidly alternating regimen are currently under investigation (e.g., NCT02164240 Phase Ib Study of SUnitinib Alternating With REgorafenib in Patients With Metastatic and/or Unresectable GIST (SURE) at clinicaltrials.gov) in patients with metastatic GIST resistant to imatinib. It is hoped that these regimens provide a broader spectrum of activity with better tolerated side effects than treatment with a single agent.

Assessing Response to Treatment

The standard imaging modality used to assess response to treatment in GIST is a contrast-enhanced CT scan. Tumor size is not a useful metric for CT evaluation of response of GIST to imatinib therapy, as it is for monitoring response to conventional cytocidal therapy used in most other tumors. Imatinib is a cytostatic therapy, and a significant decrease in size of GIST metastases may take months to develop, even if the tumor is responding to the drug. In fact, there may be a paradoxical increase in size of tumors responding to treatment due to development of intratumoral hemorrhage and/or cystic changes (Fig. 1). The common way of assessing tumor response to therapy has been change in unidimensional size measurements using Response Evaluation Criteria in Solid Tumors (RECIST), where a partial response is defined as a 30% reduction in unidimensional measurements and progressive disease is defined as a 20% increase or the appearance of new lesions [40]. These definitions are obviously limited in the case of response of GIST to imatinib.

[^{18}F]FDG-PET and [^{18}F]FDG-PET/CT have proven valuable in assessing early response to

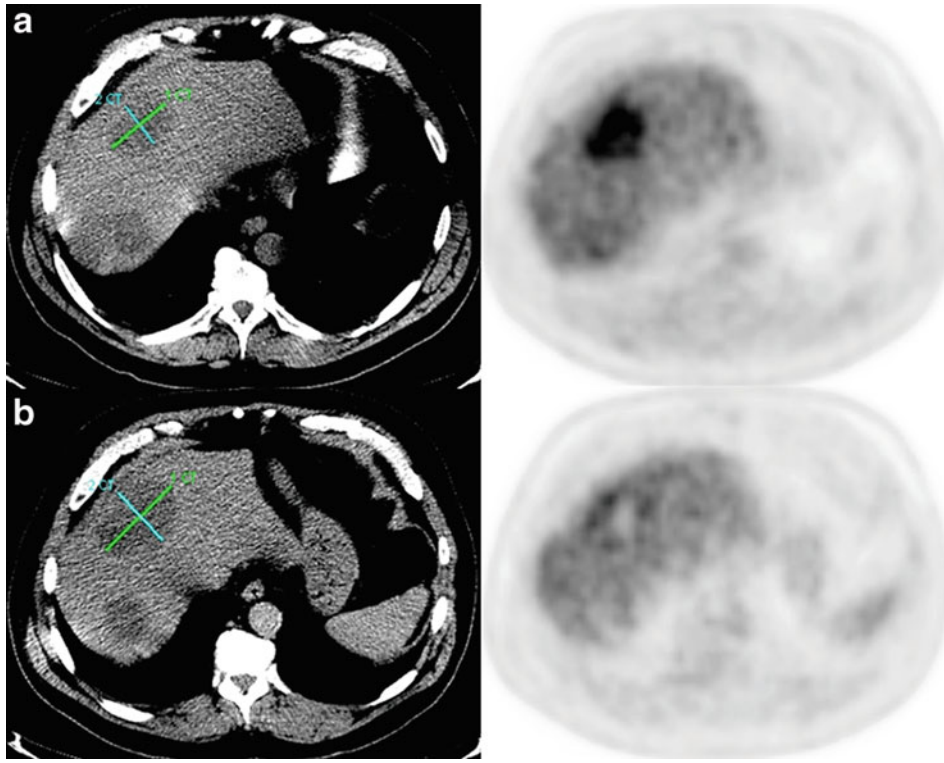

Fig. 1 (**a**) Baseline [^{18}F]FDG-PET/CT of 67 year old man with GIST demonstrating the dominant [^{18}F]FDG-avid hepatic metastasis. (**b**) PET/CT scan performed 2 months after start of imatinib demonstrates a slight increase in size of the dominant hepatic lesion, but a significant decrease in uptake and a decrease in associated density on CT scan. These findings are consistent with a significant metabolic response to therapy, despite the apparent increase in size of the dominant lesion

both neoadjuvant and systemic treatment in GIST, especially in the time before changes in size are demonstrated on CT. In one of the earliest trials assessing response to imatinib in GIST, [^{18}F]FDG-PET showed dramatic early decrease in [^{18}F]FDG uptake, and thus metabolic activity, in tumors which preceded anatomic changes by weeks or months (Fig. 2) [41]. A significant change in metabolic response can be observed on [^{18}F]FDG-PET in as little as hours after the start of imatinib therapy. This rapid response in metabolism was found to correspond at least in part with a decrease in glucose transporter 4 (GLUT4) expression in tumors on pathology prior to and following surgery in a study of patients receiving preoperative neoadjuvant imatinib [42].

The first phase 2 trial of imatinib [32] and many trials following it used criteria developed to assess metabolic response to treatment on [^{18}F]FDG-PET scans developed by the European Organization for Research and Treatment of Cancer (EORTC). Semiquantitative assessment of [^{18}F]FDG uptake is made using the maximum standardized uptake value (SUV_{max}) of tumor sites. The EORTC guidelines defined partial response as a greater than 25% decrease in SUV of tumor on a scan compared to the pretreatment baseline scan, with progressive disease demonstrating a greater than 25% increase in SUV or new [^{18}F]FDG-avid lesions [43]. The SUV_{max} is the most commonly used semiquantitative parameter for assessing response. When the EORTC guidelines for partial response to therapy have been met on early scans performed anywhere between 3 and 16 weeks after the start of imatinib therapy, several studies have demonstrated a correlation with more favorable outcome as defined

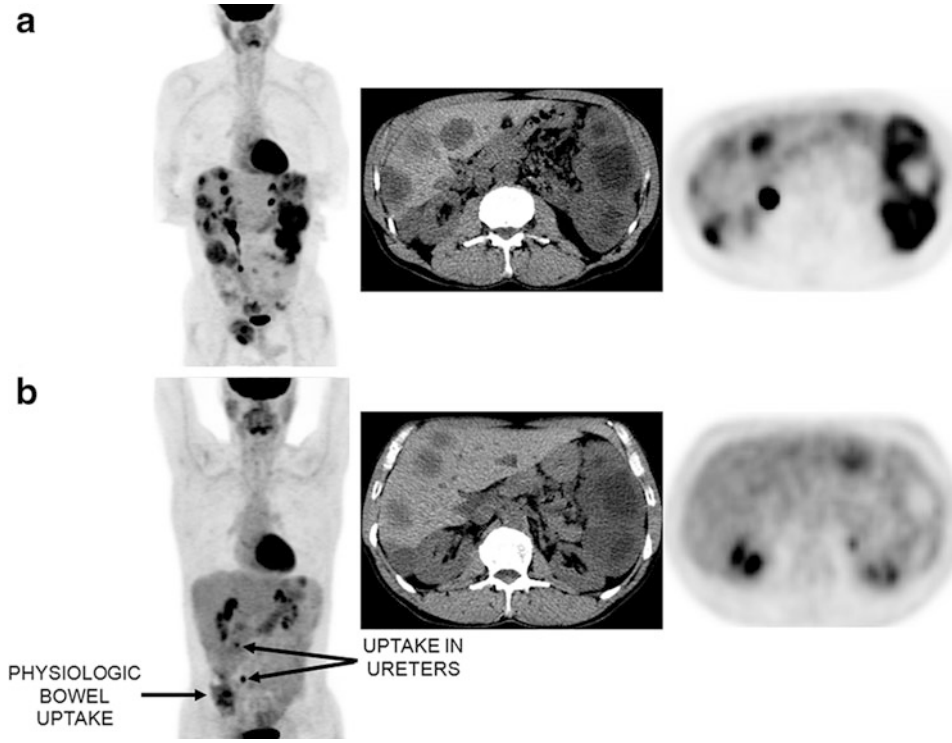

Fig. 2 (**a**) Baseline [^{18}F]FDG-PET/CT of 63 year old man with recently diagnosed metastatic gastrointestinal stromal tumor (GIST). There are multiple hepatic and peritoneal [^{18}F]FDG-avid lesions. (**b**) PET/CT scan performed 1 week later after the start of treatment with imatinib. Marked reduction of [^{18}F]FDG uptake is demonstrated in all lesions

by a longer time to treatment failure [44, 45]. Using a threshold of 40% reduction in baseline SUV_{max} on the first early PET scan has shown to be predictive of even longer time to treatment failure [46].

[^{18}F]FDG-PET has shown advantages over diagnostic CT in certain cases in assessing for treatment response in metastatic GIST. Imprecise timing of the administered intravenous contrast may cause a liver lesion to be inconspicuous on the baseline scan, while an enhancing mesenteric lesion at baseline associated with bowel loops may also be similarly obscured. If these lesions respond to treatment on follow-up CT scans, their resulting decrease in attenuation may make them newly conspicuous and may lead to them being misinterpreted as new lesions. An [^{18}F]FDG-PET/CT obtained at the same time as the follow-up diagnostic CT could help to properly characterize them as responding non-metabolically active lesions.

GIST has been found to have a characteristic pattern of response to imatinib treatment on CT scan. Heterogeneous high attenuation of tumor at baseline transitions to a more homogeneous pattern of lower attenuation (20–25 HU) during a response to treatment. These changes correlate histologically with a decrease in tumor vascularity and associated cystic and/or myxoid degeneration [47]. This change in attenuation usually occurs within 1–2 months [48]. Calcification and/or intratumoral hemorrhage can also occur, which leads to increased density and may mask response to therapy [49].

Alternative tumor response criteria on diagnostic CT proposed by Choi et al. (2007) incorporate change in tumor attenuation along with change in size and have been shown to have a similar

correlation to metabolic response to imatinib as [^{18}F]FDG uptake on [^{18}F]FDG-PET. The Choi criteria define treatment response as a decrease in tumor attenuation on CT of 15% and/or a reduction of tumor unidimensional diameter of 10%. While both the Choi and RECIST criteria were found to have a 100% specificity in identifying patients demonstrating metabolic response on [^{18}F]FDG-PET scan, the Choi criteria had a significantly higher sensitivity than the RECIST criteria, 97% versus 52% [50].

Dual-energy CT (DECT) allows for quantification of intratumoral intravenous iodinated contrast. DECT response criteria have been proposed and have been compared with the Choi CT criteria to determine whether they demonstrate better correlation with survival. DECT can quantify iodine-related attenuation (IRA), which can be considered a surrogate marker for perfusion and tumor vascularity. Meyer et al. compared DECT criteria to the Choi criteria in evaluating the response of GIST on tyrosine kinase inhibitor treatment [51]. The DECT criteria defined nonresponders as those with tumors that demonstrated an increase of 20% in both tumor size and IRA or a 50% increase in either tumor size or IRA, while responders were defined as all other patients. Those defined as responders by the DECT and Choi criteria demonstrated significantly longer progression-free survival than those defined as nonresponders. Of note, the DECT criteria, but not the Choi criteria, provided a statistically significant prediction of overall survival. One reason for this result was thought to be that intratumoral hemorrhage does not affect the quantification performed by DECT.

MRI has also been utilized in assessing the response of GIST to therapy. Some of the changes on MRI described in responding tumors are minimal to no contrast enhancement and T2 hyperintensity that may mimic that of cysts. Intratumoral hemorrhage can be more accurately differentiated from viable tumor on MRI than CT. Diffusion-weighted MRI images have also shown promise in characterizing early response to treatment. Diffusion-weighted MRI images demonstrate an increase ADC values compared to baseline values in tumors that are responding to treatment. Marked increase in the ADC values of lesions has been demonstrated on MRI just a week after the start of therapy and correlates with a favorable prognosis [52]. While early prognostic information provided by diffusion-weighted MRI may be on par with [^{18}F]FDG-PET/CT in localized GIST involvement, [^{18}F]FDG-PET/CT is better suited to evaluate the response of diffuse metastatic disease.

On all imaging modalities, the response of GIST to sunitinib and other TKIs is similar to the response seen on these modalities to imatinib. It should be kept in mind that sunitinib and certain other TKIs, unlike imatinib, have antiangiogenic effects on GIST which may result in intratumoral bleeding which may cause difficulty in CT interpretation. In these cases, [^{18}F]FDG-PET/CT may be helpful to rule out the presence of any metabolically active tumor, while MRI would better characterize any blood products.

[^{18}F]FDG-PET/CT continues to be utilized in trials involving novel TKIs due to its ability to identify early response to therapy and the positive prognostic significance of this early drop in metabolic activity.

Assessing Resistance to Treatment

Almost all patients treated with imatinib for metastatic or advanced GIST will inevitably develop resistance to the drug. This resistance can either develop early or late. Primary resistance is progression of disease within the first 6 months of imatinib treatment and has been found to occur in about 14% of patients [32]. There are several associations that have been described with primary resistance to imatinib including exon 9 KIT mutations, PDGFRA mutations, wild-type GISTs, and pediatric GISTs [53]. Response to initial imatinib therapy has been demonstrated consistently earlier on [^{18}F]FDG-PET/CT than on diagnostic CT, with decreases in metabolic

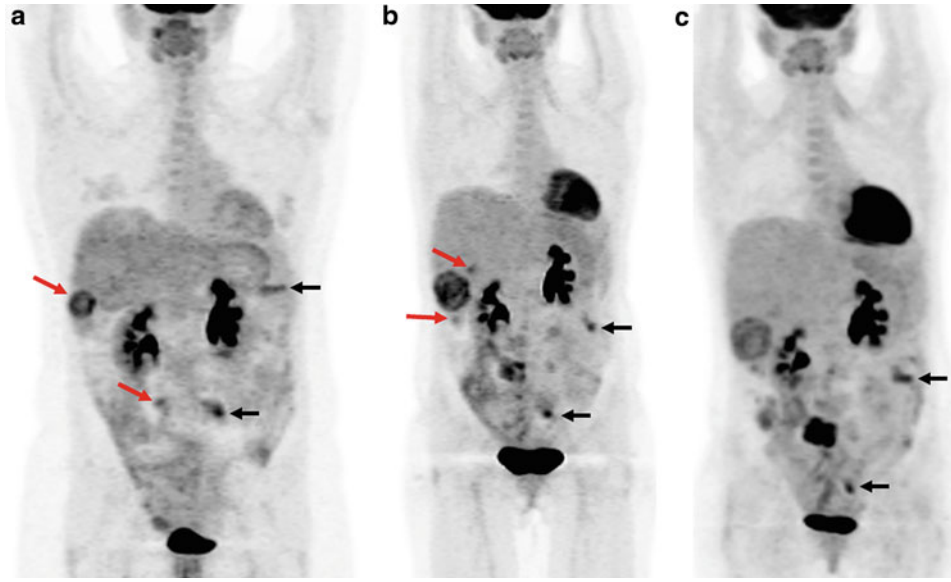

Fig. 3 (**a**) 44 year old man with metastatic GIST being treated with imatinib. [^{18}F]FDG uptake is demonstrated on PET scan in hepatic and mesenteric lesions (*red arrows*). *Black arrows* represent sites of colonic uptake unrelated to GIST without CT correlates. (**b**) Follow up PET scan after 6 weeks demonstrates an increase in size and uptake of the hepatic and mesenteric lesions, as well as two newly [^{18}F]FDG-avid hepatic metastases (*red arrow*), findings consistent with progression of disease. It was decided clinically to escalate the dose of imatinib. (**c**) Follow up PET scan after 3 weeks demonstrates a decrease in [^{18}F]FDG uptake in hepatic lesions, but an increase in uptake of the mesenteric lesion (*red arrow*). Although the hepatic disease did show response to the higher dose of imatinib, the mesenteric lesion continued to progress, indicating that this lesion had developed resistance to imatinib. (Of note, the focal sites of colonic uptake unrelated to GIST without CT correlates persist, and are highly suspicious for underlying adenomatous polyps)

activity often evident within the first week of treatment, while CT changes suggestive of response, including decrease in attenuation, may take up to a month or more to clearly develop. Therefore, [^{18}F]FDG-PET/CT may be of particular value in determining if a GIST has primary resistance to imatinib compared to other modalities. Lack of significant decrease in [^{18}F]FDG uptake from baseline of tumor on a [^{18}F]FDG-PET/CT scan performed during the first month of therapy is highly predictive of primary resistance, and this result should prompt clinicians to escalate the dose of imatinib [54]. If there is continued resistance demonstrated on scans after dose escalation, treatment with the second-line TKI sunitinib would be considered (Fig. 3).

Secondary resistance to imatinib occurs in patients who initially demonstrated a good response to treatment for at least 6 months. Secondary resistance to imatinib usually develops after a median of 2 years [55]. Usually secondary KIT mutations are responsible, often in exons [13, 14, 17] that code for portions of the intracytoplasmic portions of the KIT protein [36].

Findings of secondary resistance described on CT include new metastatic lesions and increase of size and/or attenuation of preexisting lesions. A characteristic pattern of tumor recurrence on CT or MRI is the so-called new "nodule-within-a-mass" appearance [56]. Here, recurrent tumor is defined as a new enhancing soft-tissue nodule or nodules on CT or MRI or within a cystic mass.

[^{18}F]FDG-PET/CT can identify secondary resistance by the reappearance of [^{18}F]FDG uptake within a previous lesion which was not

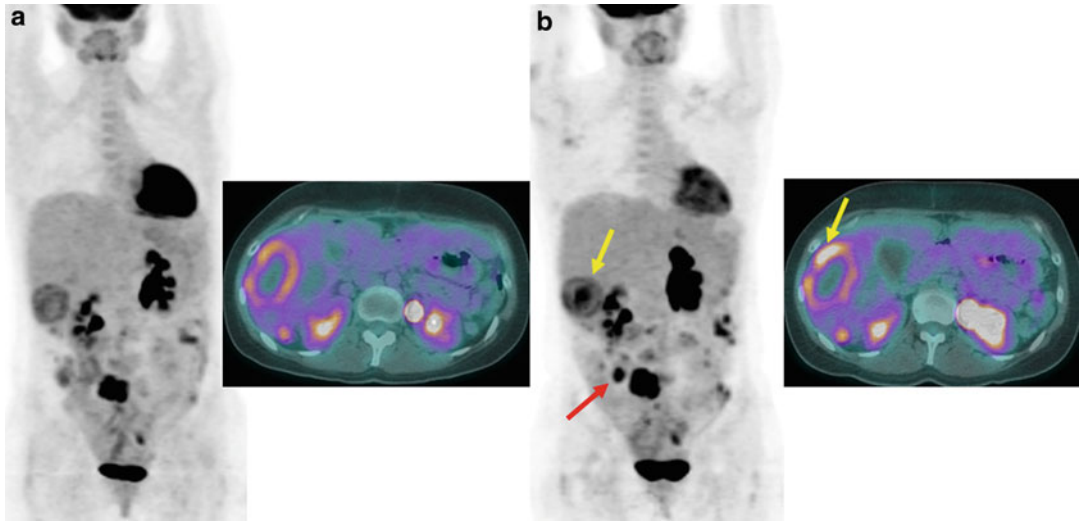

Fig. 4 (**a**) Same patient as in Fig. 3, undergoing treatment with escalated dose of imatinib. (**b**) Three week follow up PET scan not only demonstrates new [^{18}F]FDG uptake in another mesenteric lesion (*red arrow*) suggesting resistance to imatinib, but there is new increased [^{18}F]FDG uptake in the anterior aspect of the dominant hepatic lesion (*yellow arrow*), consistent with resistance to imatinib within a subpopulation of cells within an otherwise treated lesion. The clinical decision was made at this point to discontinue imatinib in anticipation of starting treatment with sunitinib

[^{18}F]FDG-avid on treatment. In patients with a large number of metastases, only a few lesions may demonstrate new [^{18}F]FDG uptake, yet this appearance would still be consistent with development of resistance. [^{18}F]FDG-PET/CT has the ability to demonstrate that resistance does not just arise throughout the entirety of discrete lesions. A small new focus of uptake within an otherwise photopenic lesion can suggest resistance developing within a subpopulation of cells within a single lesion (Fig. 4). These findings on [^{18}F]FDG-PET scans suggest that patients who develop secondary resistance have two biologically distinct populations of tumor, one that is still responding to imatinib and one which has developed mutations granting them resistance to the drug. This phenomenon was illustrated during a phase I/II clinical trial for sunitinib, where the trial protocol required patients to be off imatinib for a period of time (up to 3 weeks) before starting sunitinib. New baseline [^{18}F]FDG-PET scans were obtained with the patients taking neither drug. In addition to an increase in [^{18}F]FDG uptake seen in the lesions already determined to have imatinib-resistant GIST, a "flare" of new uptake was observed in many of the other previously non-[^{18}F]FDG-avid lesions (Fig. 5) [54]. Discontinuation of imatinib had lead to reactivation of glycolytic metabolism in the population of tumor cells that continued to respond to the drug.

Surveillance

GIST has a recurrence rate as high as 90% in the first 2 years, even after a successful complete surgical resection. GIST typically recurs in the liver or peritoneum. The current NCCN guidelines recommend contrast-enhanced CT for surveillance of GIST, especially in those initially characterized as high risk [19]. Patients are typically scanned in 3- to 6-month intervals. [^{18}F]FDG-PET/CT is usually only utilized when there is an ambiguous finding on CT or when treatment with a new TKI is considered and a baseline [^{18}F]FDG-PET scan is warranted.

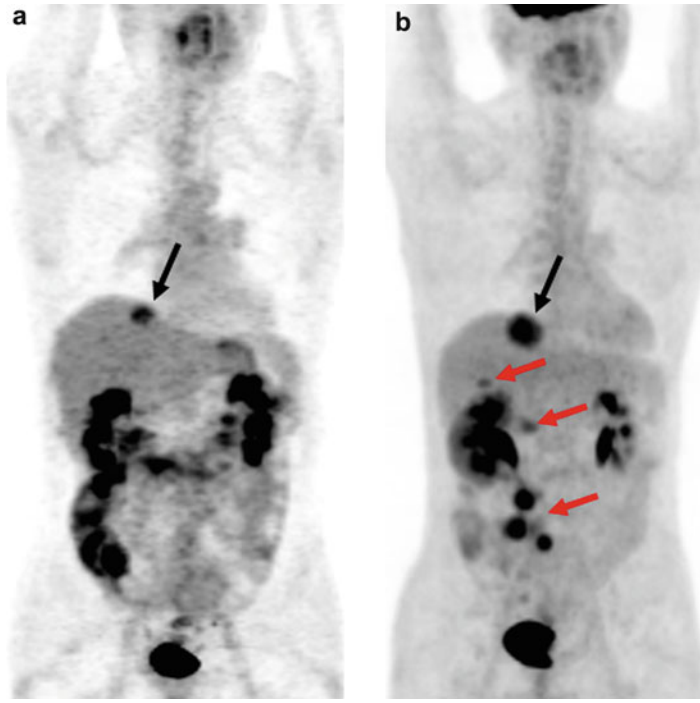

Fig. 5 (**a**) 48 year old man with metastatic GIST with development of a hepatic lesion resistant to imatinib (*black arrow*). (**b**) PET scan performed 3 weeks later prior to the start of sunitinib. Not only has the resistant lesion within the liver increased in [^{18}F]FDG uptake (*black arrow*), but there has been reactivation of metabolic activity in hepatic and mesenteric lesions which were previously responding to imatinib (*red arrows*)

In addition to detecting recurrent or progressive disease, surveillance scans can also identify side effects of TKI therapy. One of the more common side effects of imatinib seen on imaging is the third spacing of fluid within the body which can manifest as pleural effusions, pulmonary edema, ascites, and/or anasarca. As development of ascites would normally raise suspicion for the presence of new peritoneal disease, care must be taken in determining whether this is just a fluid overload-related side effect of the treatment. Other side effects of the various TKIs that may manifest on imaging include hepatic steatosis, hepatitis, pancreatitis, ischemic colitis, pneumatosis, and bowel perforation [57, 58].

References

1. Miettinen M, Lasota J. Gastrointestinal stromal tumors: definition, clinical, histological, immunohistological, and molecular genetic features and differential diagnosis. Virchow's Arch. 2001;438:1–12.
2. Miettinen M, et al. Evaluation of malignancy and prognosis of gastrointestinal stromal tumors: a review. Hum Pathol. 2002;33:478–83.
3. Ma GL, et al. Epidemiology of gastrointestinal stromal tumors in the era of histology codes: results of a population-based study. Cancer Epidemiol Biomarkers Prev. 2015;24:298.
4. Kindblom LG, Remotti HE, Aldenborg F, Meis-Kindblom JM. Gastrointestinal pacemaker cell tumor (GIPACT): gastrointestinal stromal tumors show phenotypic characteristics of the interstitial cells of Cajal. Am J Pathol. 1998;152:1259–69.
5. Miettinen M, Lasota J. Gastrointestinal stromal tumors: pathology and prognosis at different sites. Semin Diagn Pathol. 2006;23:70–83.
6. Tran T, Davila JA, El-Serag HB. The epidemiology of malignant gastrointestinal stromal tumors: an analysis of 1,458 cases from 1992 to 2000. Am J Gastroenterol. 2005;100:162.
7. Hirota S, Isozaki K, Moriyama Y, et al. Gain-of-function mutations of c-kit in human gastrointestinal stromal tumors. Science. 1998;279:577–80.
8. Heinrich MC, Corless CL, Duensing A, et al. PDGFRA activating mutations in gastrointestinal stromal tumors. Science. 2003;299:708–10.
9. Miettinen M, Lasota J. Gastrointestinal stromal tumors: review on morphology, molecular pathology, prognosis, and differential diagnosis. Arch Pathol Lab Med. 2006;130:1466–78.

10. Marrari A, Wagner AJ, Hornick JL. Predictors of response to targeted therapies for gastrointestinal stromal tumors. Arch Pathol Lab Med. 2012;136:483–9.
11. Corless CL, et al. PDGFRA mutations in gastrointestinal stromal tumors: frequency, spectrum, and in vitro sensitivity to imatinib. J Clin Oncol. 2005;23:5357.
12. Miettinen M, et al. Gastrointestinal stromal tumors in patients with neurofibromatosis 1: a clinicopathologic and molecular genetic study of 45 cases. Am J Surg Pathol. 2006;30:90.
13. Pappo AS, Janeway KA. Pediatric gastrointestinal stromal tumors. Hematol Oncol North Am. 2009;23:15.
14. Bachet JB, et al. Diagnosis, prognosis and treatment of patients with gastrointestinal stromal tumour (GIST) and germline mutation of KIT exon 13. Eur J Cancer. 2013;49:2531.
15. Agaram NP, et al. Novel V600E BRAF mutations in imatinib-naive and imatinib-resistant gastrointestinal stromal tumors. Genes Chromosomes Cancer. 2008; 47:886–96.
16. Corless CL, Fletcher JA, Heinrich MC. Biology of gastrointestinal stromal tumors. J Clin Oncol. 2004; 22:3813–25.
17. Miettinen M, Sobin LH, Lasota J. Gastrointestinal stromal tumors of the stomach: a clinicopathologic, immunohistochemical, and molecular genetic study of 1765 cases with long-term follow-up. Am J Surg Pathol. 2005;29:52.
18. Miettinen M, Makhlouf H, Sobin LH, Lasota J. Gastrointestinal stromal tumors of the jejunum and ileum: a clinicopathologic, immunohistochemical, and molecular genetic study of 906 cases before imatinib with long-term follow-up. Am J Surg Pathol. 2006;30: 477.
19. von Mehren M, et al. NCCN clinical practice guidelines in oncology. Soft tissue sarcoma. Version 2.2016. National Comprehensive Cancer Network website. http://www.nccn.org/professionals/physician_gls/f_guidelines.asp.
20. Singer S, et al. Prognostic value of KIT mutation type, mitotic activity, and histologic subtype in gastrointestinal stromal tumors. J Clin Oncol. 2002;20:3898.
21. Martin J, et al. Deletions affecting codons 557–558 of the c-KIT gene indicate a poor prognosis in patients with completely resected gastrointestinal stromal tumors: a study by the Spanish group for sarcoma research (GEIS). J Clin Oncol. 2005;23:6190.
22. Antonescu CR, et al. Association of KIT exon 9 mutations with nongastric primary site and aggressive behavior: KIT mutation analysis and clinical correlates of 120 gastrointestinal stromal tumors. Clin Cancer Res. 2003;9:3329.
23. Yu MH, et al. MRI features of gastrointestinal stromal tumors. AJR Am J Roentgenol. 2014;203:980–91.
24. Burkill GJ, et al. Malignant gastrointestinal stromal tumor: distribution, imaging features, and pattern of metastatic spread. Radiology. 2003;226:527–32.
25. Kim HC, et al. Small gastrointestinal stromal tumors with focal areas of low attenuation on CT: pathologic correlation. Clin Radiol. 2005;60:384–8.
26. Sepe PS, Brugge WR. A guide for the diagnosis and management of gastrointestinal stromal tumors. Nat Rev Gastroenterol Hepatol. 2009;6:363–71.
27. Gayed I, et al. The role of ^{18}F-FDG PET in staging and early prediction of response to therapy of recurrent gastrointestinal stromal tumors. J Nucl Med. 2004;45: 17–21.
28. Blodgett TM, et al. PET/CT: form and function. Radiology. 2007;242:360–85.
29. Edmonson JH, et al. Contrast of response to dacarbazine, mitomycin, doxorubicin, and cisplatin (DMAP) plus GM-CSF between patients with advanced malignant gastrointestinal stromal tumors and patients with other advanced leiomyosarcomas. Cancer Invest. 2002;20:605–12.
30. Trent JC, et al. A two-arm phase II study of temozolomide in patients with advanced gastrointestinal stromal tumors and other soft tissue sarcomas. Cancer. 2003;98:2693–9.
31. Pierie JEN, et al. The effect of surgery and grade on outcome of gastrointestinal stromal tumors. Arch Surg. 2001;136:383–9.
32. Demetri GD, et al. Efficacy and safety of imatinib mesylate in advanced gastrointestinal stromal tumors. N Engl J Med. 2002;347:472–80.
33. Eisenberg BL, et al. Phase II trial of neoadjuvant/adjuvant imatinib mesylate (IM) for advanced primary and metastatic/recurrent operable gastrointestinal stromal tumor (GIST): early results of RTOG 0132/ACRIN 6665. J Surg Oncol. 2009;99:42–7.
34. Demitri GD, et al. Efficacy and safety of sunitinib in patients with advanced gastrointestinal stromal tumor after failure of imatinib: a randomised controlled trial. Lancet. 2006;368:1329–38.
35. George S, et al. Clinical evaluation of continuous daily dosing of sunitinib malate in patients with advanced gastrointestinal stromal tumour after imatinib failure. Eur J Cancer. 2009;45:1959–68.
36. Heinrich MC, et al. Molecular correlates of imatinib resistance in gastrointestinal stromal tumors. J Clin Oncol. 2006;24:4764–74.
37. Demitri GD, et al. Efficacy and safety of regorafenib for advanced gastrointestinal stromal tumours after failure of imatinib and sunitinib (GRID): and international, multicentre, randomised, placebo-controlled, phase 3 trial. Lancet. 2013;381:295–302.
38. Falchook, et al. BRAF mutant gastrointestinal stromal tumor: first report of regression with BRAF inhibitor dabrafenib (GSK2118436) and whole exomic sequencing for analysis of acquired resistance. Oncotarget. 2013;4:310–5.
39. Park SH, et al. Sorafenib in patients with metastatic gastrointestinal stromal tumors who failed two or more prior tyrosine kinase inhibitors: a phase II study of

Korean gastrointestinal stromal tumors study group. Invest New Drugs. 2012;30:2377–83.
40. Therasse P, et al. New guidelines to evaluate the response to treatment in solid tumors. European organization for research and treatment of cancer, national cancer institute of the United States, national cancer institute of Canada. J Natl Cancer Inst. 2000;92: 205–16.
41. Van den Abbeele AD, et al. GIST Collaborative PET Study Group. ^{18}F-FDG-PET provides early evidence of biological response to STI571 in patients with malignant gastrointestinal stromal tumors (GIST). Proc Am Soc Clin Oncol. 2001;20:362a.
42. Van den Abbeele AD, et al. ACRIN 6665/RTOG 0132 phase II trial of neoadjuvant imatinib mesylate for operable malignant gastrointestinal stromal tumor: monitoring with ^{18}F-FDG PET and correlation with genotype and GLUT4 expression. J Nucl Med. 2011; 53:567–74.
43. Young H, et al. Measurement of clinical and subclinical tumour response using [^{18}F]-fluorodeoxyglucose and positron emission tomography: review and 1999 EORTC recommendations. European organization for research and treatment of cancer (EORTC) PET study group. Eur J Cancer. 1999; 35:1773–82.
44. Gayed I, et al. The role of ^{18}F-FDG PET in staging and early prediction of response to therapy of recurrent gastrointestinal stromal tumors. J Nucl Med. 2004;45: 17–21.
45. Goerres GW, et al. The value of PET, CT, and in-line PET/CT in patients with gastrointestinal stromal tumors: long term outcome of treatment with imatinib mesylate. Eur J Nuc Med Mol Imaging. 2005;32: 153–62.
46. Holdsworth CH, et al. CT and PET: Early prognostic indicators of response to imatinib mesylate in patients with gastrointestinal stromal tumor. AJR Am J Roentgenol. 2007;189:W324–30.
47. Abdulkader I, et al. Pathological changes related to imatinib treatment in a patient with a metastatic gastrointestinal stromal tumour. Histopathology. 2005;46: 470–2.
48. Hong X, et al. Gastrointestinal stromal tumor: role of CT in diagnosis and in response evaluation and surveillance after treatment with imatinib. Radiographics. 2006;26:481–95.
49. Tirumani SH, et al. Imatinib and beyond in gastrointestinal stromal tumors: a radiologist's perspective. AJR Am J Roentgenol. 2013;201:801–9.
50. Choi H, et al. Correlation of computed tomography and positron emission tomography in patients with metastatic gastrointestinal stromal tumor treated at a single institution with imatinib mesylate: proposal of new computed tomography response criteria. J Clin Oncol. 2007;25:1753–9.
51. Meyer M, et al. CT-based response assessment of advanced gastrointestinal stromal tumor: dual energy CT provides a more predictive imaging biomarker of clinical benefit than RECIST or Choi criteria. Eur J Radiol. 2013;82:923–8.
52. Tang L, et al. Gastrointestinal stromal tumors treated with imatinib mesylate: apparent diffusion coefficient in the evaluation of therapy response in patients. Radiology. 2011;258:729–38.
53. Benjamin RS, et al. Gastrointestinal stromal tumors II: medical oncology and tumor response assessment. Semin Oncol. 2009;36:302–11.
54. Van den Abbeele AD. The lessons of GIST—PET and PET/CT: a new paradigm for imaging. Oncologist. 2008;13:8–13.
55. Verwejj J, et al. Progression-free survival in gastrointestinal stromal tumors with high-dose imatinib: randomised trial. Lancet. 2004;354(9440):1127–34.
56. Shankar S, et al. Gastrointestinal stromal tumor: new nodule-within-a-mass pattern of recurrence after partial response to imatinib mesylate. Radiology. 2005;235: 892–8.
57. Howard, et al. Decade of molecular targeted therapy: abdominal manifestations of drug toxicities—what radiologists should know. AJR Am J Roentgenol. 2012;199:58–64.
58. Shingare, et al. Pneumatosis intestinalis and bowel perforation associated with molecular targeted therapy: an emerging problem and the role of radiologists in its management. AJR Am J Roentgenol. 2012;199:1259–65.

Diagnostic Applications of Nuclear Medicine: Tumors of the Liver and Biliary Tract

26

Mustafa Raoof, Steven M. Larson, and Yuman Fong

Abstract

In liver and biliary tumors, modern imaging techniques play an important role in therapeutic decision-making. Whether the decision involves determining if the tumor is resectable or how it is responding to treatment, nuclear imaging has the potential to facilitate the decision-making process. Here we cover various studies that investigate the comparative effectiveness of cross-sectional morphologic imaging alone and in combination with functional nuclear medicine imaging. Specifically, we discuss the role of nuclear imaging in the diagnosis, characterization, and treatment of patients with primary and secondary liver or biliary tract malignancies.

Keywords

Primary tumors • Hepatocellular carcinoma • Hepatoma • Gallbladder carcinoma • Cholangiocarcinoma • Biliary cancer • Colorectal metastases • Neuroendocrine metastases • [^{11}C]Acetate • 2-deoxy-2-[^{18}F]fluoro-D-glucose ([^{18}F]FDG) • PET/CT • MRI • CT scan • Staging • Resectability • Recurrence • Nuclear imaging • Diagnostic

Glossary

[^{18}F]FDG	2-deoxy-2-[^{18}F]fluoro-D-glucose
ACS	American Cancer Society
AFP	Alpha Fetoprotein
AI	Arterial infusion
CA	Cancer antigen
CA 19–9	Carbohydrate antigen 19–9, a tumor-associated marker
CEA	Carcinoembryonic antigen, a tumor-associated marker
CRC	Colorectal cancer
CT	X-ray computed tomography
DOTA	2-(4-Isothiocyanatobenzyl-1,4,7,10-tetra-azacyclododecane-1,4,7,10-tetraacetic acid (macrocyclic coupling agent to label compounds of biological interest with metal radionuclides)
DOTANOC	DOTA-1-Nal^3-octreotide
DOTATATE	DOTA-Tyr^3-octreotate
DOTATOC	DOTA-octreotide
FOLFOX	Chemotherapy regimen based on FOL– Folinic acid F – Fluorouracil OX – Oxaliplatin

M. Raoof • Y. Fong (✉)
Department of Surgery, City of Hope National Medical Center, Duarte, CA, USA
e-mail: yfong@coh.org

S.M. Larson
Molecular Imaging and Therapy Service, Memorial Sloan Kettering Cancer Center, New York, NY, USA
e-mail: larsons@mskcc.org

© Springer International Publishing Switzerland 2017
H.W. Strauss et al. (eds.), *Nuclear Oncology*,
https://doi.org/10.1007/978-3-319-26236-9_16

GBC	Gallbladder cancer
HCC	Hepatocellular carcinoma
HPB	Hepatopancreaticobiliary
IgG_4	Immunoglobulin G4
MIBG	Metaiodobenzylguanidine
MRCP	Magnetic Resonance Cholangiopancreatography
MRI	Magnetic Resonance Imaging
NCCN	National Comprehensive Cancer Network
NETs	Neuroendocrine Tumors
OS	Overall survival
PET	Positron emission tomography
PET/CT	Positron emission tomography/computed tomography
PFS	Progression-free survival
PSC	Primary sclerosing cholangitis
PTCS	Percutaneous transhepatic
SRS	Somatostatin receptor scintigraphy
SUV	Standardized uptake value
SUV_{max}	Standardized uptake value at point of maximum
TACE	Transcatheter arterial chemoembolization

Contents

Introduction 726

Metastatic Tumors 726
Colorectal Metastases 726
Neuroendocrine Metastases 729

Primary Tumors 730
Hepatocellular Carcinoma 730
Cholangiocarcinoma 735
Gallbladder Carcinoma 742

References 744

Introduction

The tumors arising from the liver are among some of the most frequent and lethal human tumors worldwide. The liver is also the most common site of metastases from gastrointestinal tumors via portal circulation and is thought to be a barrier to the disseminated spread of cancer to other organs. Multimodality treatment of liver tumors necessitates accurate imaging to guide management decisions. Traditionally, a high-resolution cross-sectional imaging study with a multidetector CT scan or an MRI with triple-phase contrast has been considered the gold standard. Several advances in imaging technologies specifically nuclear imaging of these tumors have significantly improved our ability to evaluate the true extent of disease. In this chapter we review the role of nuclear imaging in the complex and often challenging treatment of primary and secondary liver and biliary malignancies.

Metastatic Tumors

Colorectal Metastases

Colorectal cancer metastases are the most common malignant lesions of the liver. Approximately half of the patients diagnosed with colorectal cancer (CRC) will develop liver metastases. Historically, these patients were treated with chemotherapy that resulted in suboptimal response, and none of the patients survived beyond five years (Fig. 1). The management of CRC liver metastases has undergone a paradigm shift over the last two decades. Surgical resection of CRC metastases has resulted in overall survival that approaches 30% at five years for a selected group of patients. Improvements in the quality and safety of hepatic resections, combined with the widespread use of ablative technologies as well as with arterial infusion pump placement, have broadened the selection criteria for patients who can benefit from potentially curative therapies. [^{18}F]FDG-PET/CT scans can play an important role at every stage of the management of these complex patients.

a. Operative Planning and Resectability
   The role of PET/CT in staging of the primary lesion in colorectal cancer has been studied extensively. PET/CT scan is neither sufficient nor accurate for clinical staging of the primary lesion, and without evidence of distant metastases on contrast-enhanced cross-sectional imaging,

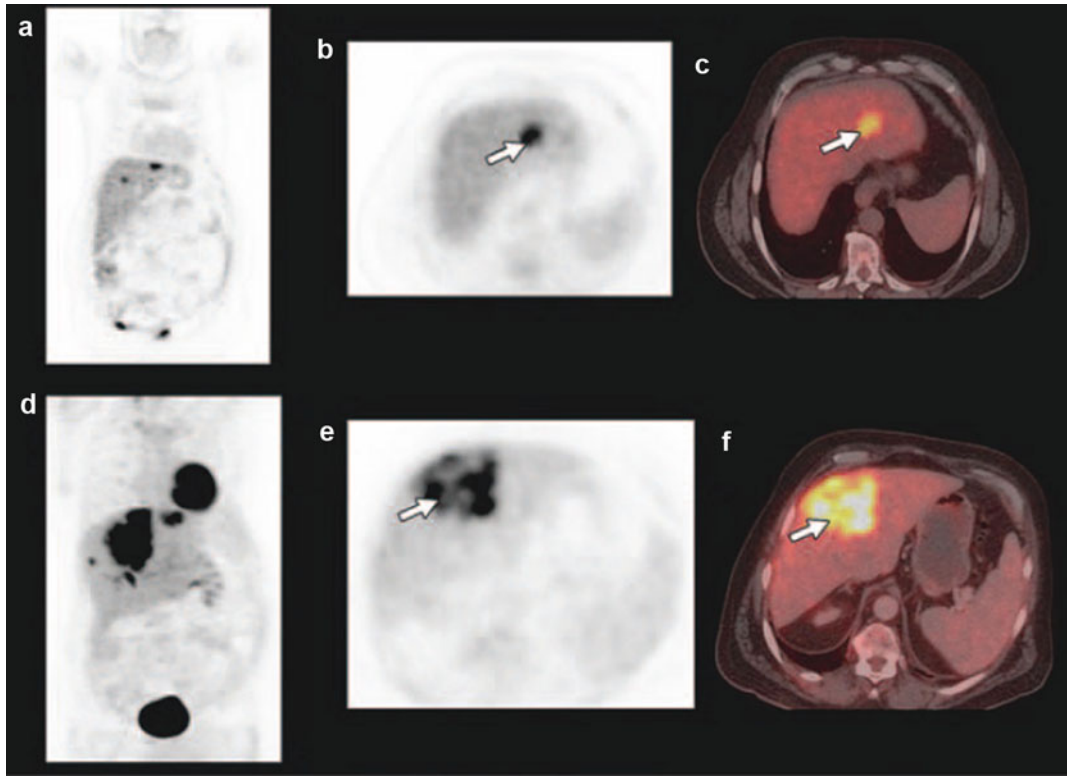

Fig. 1 71-year-old man with history of sigmoid colon cancer with surgical resection and chemotherapy for 6 months. (**a**) Patient's carcinoembryonic antigen levels started increasing after 6 months, and [^{18}F]FDG-PET/CT revealed hepatic metastasis. (**b**) Coronal PET shows two lesions (*arrow*) in segments 2 and 8. (**c**) Axial-fused PET/CT shows hypermetabolic lesion (*arrow*) in segment 2. (**d–f**) Patient underwent eight cycles of chemotherapy with FOLFOX-folinic acid, fluorouracil and oxaliplatin, and avastin, and subsequent PET-CT scans revealed progressive hepatic lesions (*arrow*, **e** and **f**) (Reprint with permission from Sacks A. et al. Value of PET-CT in the Management of Liver Metastases, Part 1. AJR Am J Roentgenol. 2011, Fig. 2, p. W259) [75]

the routine use of PET/CT is not justified. However, [^{18}F]FDG-PET scans are very accurate in detection of hepatic and extrahepatic disease. Pooled analysis from multiple studies demonstrates that the overall sensitivities of nonhelical CT, helical CT, 1.5-T MRI, and [^{18}F]FDG-PET in detecting liver metastases were 60.2%, 64.7%, 75.8%, and 94.6%, respectively [1]. Similar results were noted on a more recent analysis by Niekel et al., whereby the sensitivities of CT, MRI, and [^{18}F]FDG-PET were 83.6%, 88.2%, and 94.1%, respectively [2]. Similar sensitivity is noted for extrahepatic disease. A study by Kuehl et al. demonstrated an overall sensitivity of 95% for intrahepatic disease and 97% for extrahepatic disease [3].

Accurate staging of intrahepatic and extrahepatic disease is crucial in decision-making for these complex patients. A prospective study of patients with colorectal cancer metastatic to the liver demonstrated that a contrast-enhanced CT missed extrahepatic disease in one-third of the patients [4]. This number was reduced to 11% with the use of [^{18}F]FDG-PET scans. Similarly, another study reported that approximately one-third of the patients with a negative contrast-enhanced CT scan will have a positive finding on PET/CT scan [5]. [^{18}F]FDG-PET scans can be falsely positive in the setting of recent surgical resection or infection, and therefore, clinical correlation is vital when interpreting data from [^{18}F]FDG-PET scans.

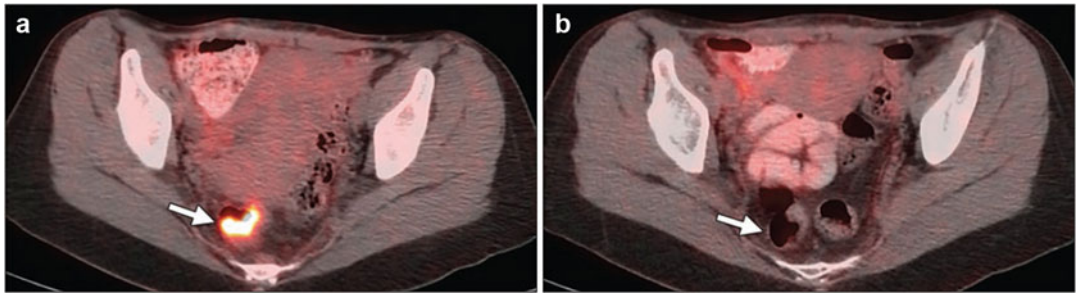

Fig. 2 [^{18}F]FDG PET/CT for initial staging and assessment of response to neoadjuvant therapy in 40-year-old woman with rectal adenocarcinoma. (**a**) Axial-fused PET/CT image obtained for initial staging shows metabolically active (standardized uptake value, 6.8) mass (*arrow*) in rectal wall. (**b**) Axial [^{18}F]FDG-PET/CT image obtained 3 months after staging PET/CT study (**a**) and after patient had undergone neoadjuvant chemotherapy shows lack of tracer uptake within rectal tumor (*arrow*), which suggests favorable response to therapy (Reprint with permission from Agarwal A. et al. FDG-PET-CT in the Management of Colorectal and Anal Cancers. AJR Am J Roentgenol. 2014, Fig. 2, p. 1116) [76]

In summary, PET/CT scans change the management choices in 30–40% of patients with colorectal liver metastases. The decision to obtain PET/CT scan preoperatively should be individualized. Patients with suspicious findings on contrast-enhanced CT or MRI or with extensive intrahepatic disease or those requiring extensive surgical resections with curative intent should be considered for an [^{18}F]FDG-PET scan.

b. Response to Therapies

Initial evidence supports the feasibility of PET scans in determining tumor response (Fig. 2). A study by Findlay et al. demonstrated that responsive lesions tend to grow slower at 5-week imaging intervals [6]. A recent meta-analysis of 15 studies with 867 patients demonstrated that a reduction in standardized uptake value (SUV) predicted overall survival. However, post-treatment SUV did not predict overall survival [7]. Additionally, [^{18}F]FDG-PET scans have been utilized increasingly to evaluate response to tumor-selective therapies such as radiofrequency or microwave ablation and selective radio- or trans-arterial chemoembolization.

[^{18}F]FDG-PET scans have the advantage of detecting metabolic response in a tumor that appears to be otherwise stable on cross-sectional imaging (Fig. 3). While several studies report the feasibility of this approach, whether a metabolic response is prognostic in these patients remains to be determined. Furthermore, neoadjuvant therapy lowers the sensitivity of [^{18}F]FDG-PET scans. A recent study reported a sensitivity of 65% for contrast-enhanced CT compared to 49% for [^{18}F]FDG-PET scan in detecting liver lesions after neoadjuvant chemotherapy [8]. For the same reason, there is no added value of [^{18}F]FDG-PET scan in detecting disappearing or vanishing liver metastases over a high-resolution contrast-enhanced CT or MRI.

c. Detecting Recurrence

Currently, National Comprehensive Cancer Network (NCCN) guidelines do not recommend routine use of PET/CT scans for surveillance, even in high-risk stage IV disease. This is likely the result of the lack of prospective studies that demonstrate the benefit of early detection of recurrence [9]. Theoretically, early detection would allow salvage curative resections, improving oncologic outcomes [10, 11]. A meta-analysis of 15 studies that included 510 patients demonstrated a 94% sensitivity and a 77.2% specificity of [^{18}F]FDG-PET scan in detecting recurrence for patients with rising CEA. This is more favorable than the sensitivity and specificity of contrast-enhanced CT scan at 51.3% and 90.2%, respectively [12], or that of plasma CEA levels alone, at 80% and 70%, respectively, in detecting recurrence [13]. Due to the unclear benefit of early

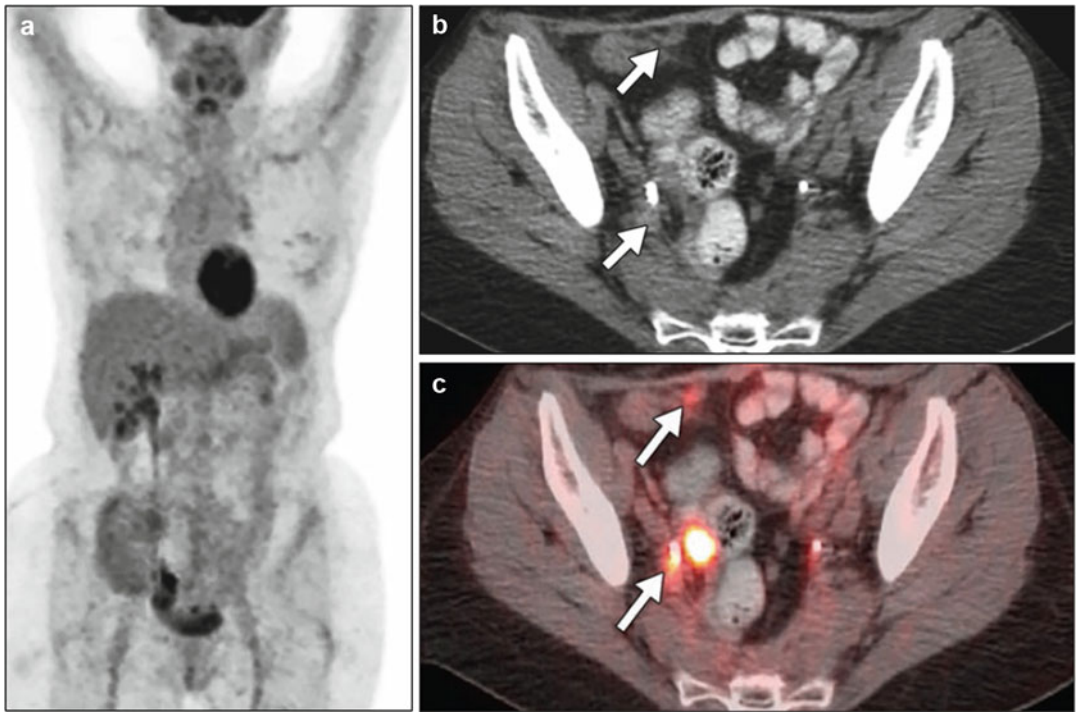

Fig. 3 Recurrence in 50-year-old woman with very low carcinoembryonic antigen (CEA) level who had undergone surgery and chemoradiation for treatment of adenocarcinoma of rectum. Patient underwent [^{18}F]FDG-PET/CT for restaging. (**a–c**) Anterior maximum intensity projection (**a**), axial CT (**b**), and fused PET/CT (**c**) images. Fused PET/CT image shows metabolically active (standardized uptake value, 10.02) malignant pelvic implants (*arrows*, **c**), whereas CT image shows ill-defined nonspecific soft tissue (*arrows*, **b**). CEA value at time of study was 1.8 ng/mL (Reprint with permission from Agarwal A. et al. FDG-PET-CT in the Management of Colorectal and Anal Cancers. AJR Am J Roentgenol. 2014, Fig. 5, p. 1117) [76]

detection on long-term survival and to the high cost of PET/CT scans, current consensus advises against the use of [^{18}F]FDG-PET scans for determining recurrence. However, an [^{18}F]FDG-PET scan should be considered in patients with continuously rising CEA over a 3-month interval with no visible disease on contrast-enhanced CT scan. We also consider [^{18}F]FDG-PET scan in CEA nonproducers who have suspicious findings for metastases on routine cross-sectional imaging.

Neuroendocrine Metastases

Neuroendocrine tumors (NETs) are rare with an incidence of 1.9–5.7 cases per 100,000 [14]. The majority of gastric, appendiceal, and rectal NETs are local. However, 65–95% of enteropancreatic NETs present with liver metastases [15, 16]. Liver metastases are the single most important prognostic determinant for patients with NETs. Morphologic combined with functional imaging plays an important role in diagnosis, determining resectability, and monitoring response to therapy and recurrence of liver metastases from NETs. However, the rarity of NETs makes it challenging to perform large prospective studies.

^{123}I-labeled noradrenalin analog metaiodobenzylguanidine (MIBG), ^{111}In-diethylenetriaminepentaacetic acid-octreotide somatostatin receptor scintigraphy (^{111}In-SRS), and [^{18}F]FDG-PET remain the most commonly used modalities for evaluating liver metastases from NETs. In a head-to-head comparison of the three modalities in a large prospective study of 96 patients, the overall sensitivity of ^{111}In-SRS, ^{123}I-MIBG scintigraphy, and [^{18}F]FDG-PET was 89%, 52%, and 58%,

respectively [17]. ^{111}In-SRS also exceeded ^{123}I-MIBG scintigraphy and [^{18}F]FDG-PET based on the number of lesions detected (393, 185, and 225, respectively). However, the sensitivity of [^{18}F]FDG-PET (92%) exceeded that of both ^{111}In-SRS (69%) and ^{123}I-MIBG scintigraphy (46%) for tumors with a proliferation index above 15%.

^{111}In-SRS relies on somatostatin receptor expression in NETs, which is seen in 60–90% of these tumors. Of these, 85% of NETs express somatostatin receptor subtype 2. There have been several attempts to improve on the ^{111}In-SRS introduced in 1990s, and the true benefit of these newer agents remains to be seen. Early experience with ^{68}Ga-labeled somatostatin analogues (DOTATOC, DOTATATE, or DOTANOC) suggests a lower cost and higher sensitivity in comparison to ^{111}In-SRS. Similarly, ^{64}Cu-DOTATATE somatostatin receptor scintigraphy was noted to be more sensitive than ^{111}In-SRS detecting additional lesions in 43% of the patients evaluated. Other radiotracers that have been used for functional imaging include ^{18}F-DOPA PET and [^{11}C]5-hydroxy-tryptophan ([^{11}C]5-HTP) PET. The role of these tracers and their comparative effectiveness remains to be studied [18].

In summary, we recommend that additional imaging should be strongly considered in patients with liver metastases from NETs on cross-sectional imaging to evaluate the true burden of disease and to determine resectability. ^{68}Ga-SRS appears to be more sensitive and cheaper than ^{111}In-SRS and should be utilized whenever available for low Ki67 (<15%) tumors. [^{18}F]FDG-PET should be preferred in evaluating tumors with high Ki67 (≥15%). Whether nuclear medicine imaging changes management over conventional morphologic imaging with high-resolution CT or MRI remains to be evaluated.

Primary Tumors

Hepatocellular Carcinoma

Hepatoma, also commonly referred to as hepatocellular carcinoma (HCC), is a neoplasm that arises from hepatic cells. Being one of the most common tumors worldwide, HCC is the fifth most frequent type of cancer, and it is the third most lethal [19, 20]. Due to the prevalence of hepatitis B or C infections in Asia compared to other world regions and to the expansion of hepatitis C infection in the USA, HCC cases are on the rise [21, 22]. Some patients with HCC still present normal liver function and may have a localized lesion when diagnosed; although those may be treated with partial resection, the 5-year survival rate is only 60–70% [23, 24]. Therapy for unresectable patients may require liver transplantation, although the majority of patients with HCC resort to nonoperative approaches, due to high-risk factors, including nonlocalized multiple intrahepatic lesions, extensive vascular invasion, or extrahepatic metastasis [25]. These therapeutic options include transcatheter arterial chemoembolization (TACE) and transcatheter arterial infusion chemotherapy (TAI) (Fig. 4).

Due to the complexity of HCC management, accurate staging of HCC is crucial in order to define treatment strategy. Conventional imaging modalities, including multiphase contrast-enhanced CT or MR imaging, are the current gold standard, with HCC tumors classically demonstrating late arterial enhancement with portal venous washout, obviating the need for tissue diagnosis. However, CT and MR scans frequently detect lesions that cannot be further defined, introducing uncertainty about the diagnosis or disease extent. Similarly, the therapeutic response of HCC to nonoperative therapy is usually assessed by conventional imaging modalities on the basis of changes in tumor size [26].

However, such criteria based on conventional imaging modalities have inherent limitation for accurate assessment of therapeutic response and tumor viability. Radiotracer imaging with or without concurrent high-resolution cross-sectional imaging provides a promising strategy to (i) improve our ability to detect subclinical disease, (ii) provide a functional insight into the behavior of tumors (i.e., glucose utilization), and (iii) probe molecular characteristics by utilizing targeted radiotracers. Each of these applications is reviewed below.

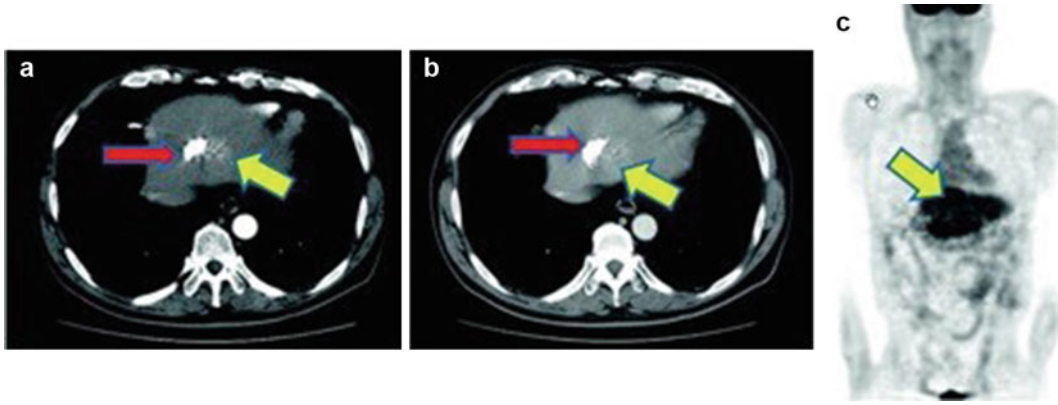

Fig. 4 A hepatoma recurrence after arterial chemoembolization. Contrast-enhanced CT at both arterial and portal phase shows a slight enhancement as suspected viable recurrent hepatoma, and a high [^{18}F]FDG accumulation is coincident with this stain (**a**–**c**; *large arrows*). [^{18}F]FDG-PET is to easily visualize viable hepatoma if the high-density area at CT image is difficult to distinguish with post-hemoembolized change (**a**, **b**; *small arrows*) [77]

a. 2-deoxy-2-[^{18}F]fluoro-D-glucose ([^{18}F]FDG)
The most common and widely available radiotracer for imaging [^{18}F]FDG has been investigated in patients with hepatocellular carcinomas [27, 28]. While [^{18}F]FDG-PET is considered as a sensitive modality to assess tumor viability and tumor detection for a multitude of histologies, its ability to detect hepatocellular carcinoma lesions within the liver is low [28–33]. Relatively low [^{18}F]FDG accumulation in liver cells is due to the presence of cytosolic glucose-6-phosphatase (G-6-Pase) which converts [^{18}F]FDG-6-P back to [^{18}F]FDG, which allows the tracer to diffuse out of liver cells [34, 35]. Moreover, well-differentiated HCCs demonstrate similar metabolic characteristics as adjacent liver tissue, making it very difficult to identify tumor lesions within the liver (Figs. 5 and 6) [34–36].

At present, the use of [^{18}F]FDG-PET scans for routine local staging and surveillance is not recommended. The overall sensitivity of [^{18}F]FDG-PET/CT in detecting HCC within the liver suffers, with a reported range of 50–65%. For this reason, [^{18}F]FDG-PET has been determined to be insufficiently sensitive to diagnose primary HCC. A study by Khan et al. found that the sensitivity of [^{18}F]FDG-PET in the diagnosis of HCC was 55%, compared with 90% for contrast-enhanced CT [31]. Another report, by Wudel et al. involving one of the largest series of [^{18}F]FDG-PET for HCC ($n = 91$), reported that the sensitivity of [^{18}F]FDG-PET for detection of HCC was 64% [37]. To improve the sensitivity of [^{18}F]FDG-PET to detect HCC, investigators have suggested a 2–3-h delay between [^{18}F]FDG injection and imaging instead of the conventional 1-h delay between injection and imaging [38]. The delayed [^{18}F]FDG-PET may differentiate HCC lesions showing persistent [^{18}F]FDG uptake from normal liver tissue with gradual washout of [^{18}F]FDG [38].

Seminal work by Torizuka et al. demonstrated that [^{18}F]FDG uptake in HCC directly correlates with the degree of differentiation of these tumors, with higher grade tumors demonstrating on average a twofold uptake increase compared to low-grade tumors [39]. Further, a recent study demonstrated that SUV ratios (SUV ratio of hepatoma to adjacent liver) directly correlates with tumor doubling time, providing important prognostic information that allows prediction of overall survival when adjusted for tumor size [40]. The role of [^{18}F]FDG-PET scans as a component of clinical prognostication tool remains to be further tested and validated.

With growing experience in the utilization of [^{18}F]FDG-PET scans in patients with HCC, another application has come to light. Limited, small sample studies demonstrate the superiority

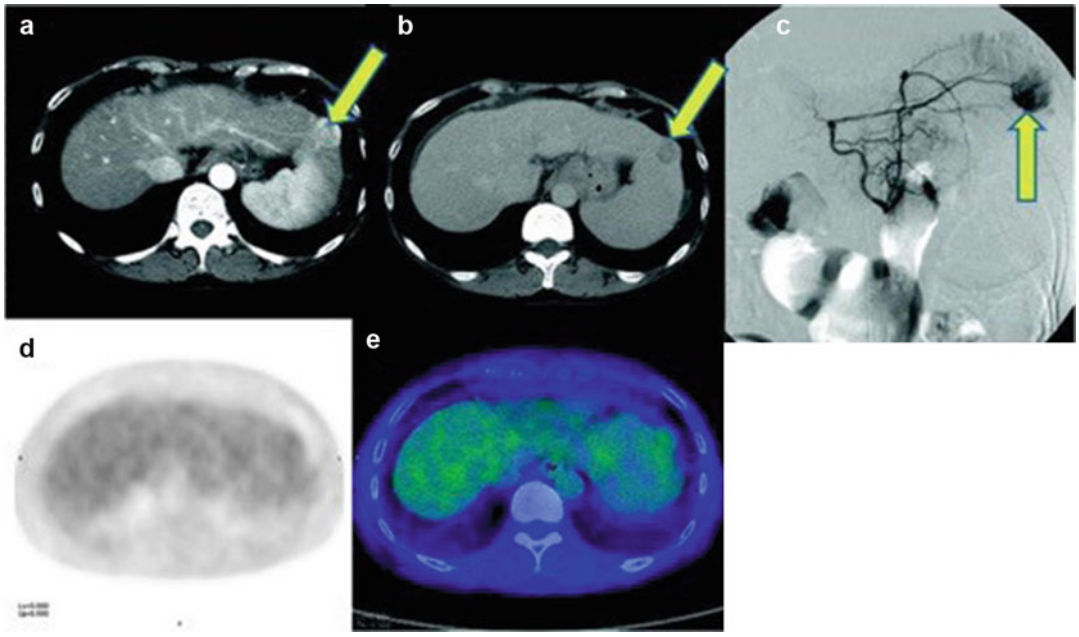

Fig. 5 *Normoglycolytic hepatoma*. Multiphase contrast-enhanced CT shows a tumor lesion, which has rich arterial perfusion but poor portal perfusion in left lobe (**a**, **b**; *yellow arrows*). Arterial angiography also shows early intense stain at same point (**c**; *yellow arrow*). These findings mean a typical classical hepatoma. However, PET/CT images do show only a normal [^{18}F]FDG accumulation on hepatoma (**d**, **e**) [77]

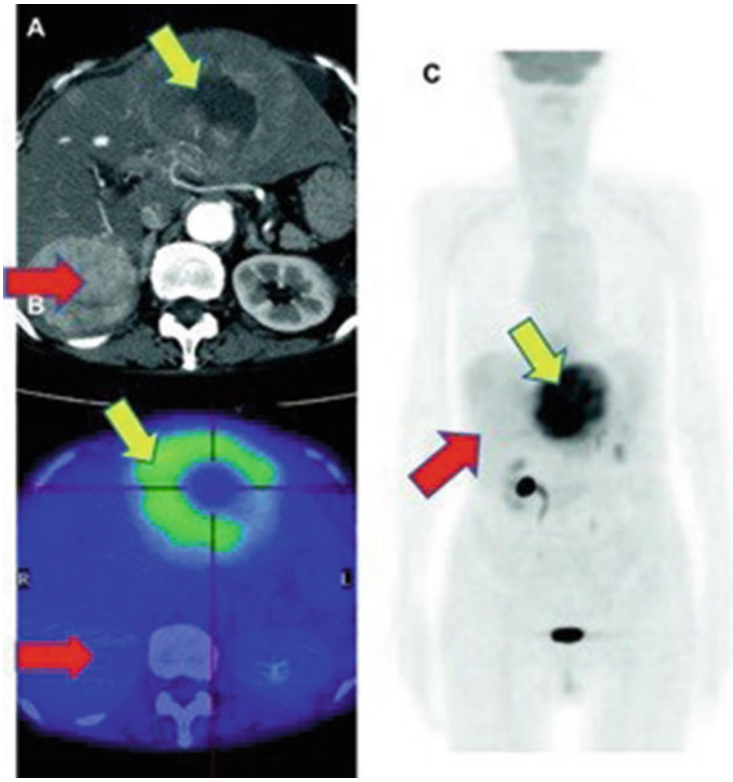

Fig. 6 *Synchronous double hepatomas*. Contrast-enhanced CT at arterial phase showed two of intrahepatic tumors. The heterogeneously stained tumor in the left lobe shows intense but heterogeneous accumulation of [^{18}F]FDG (**a**–**c**; *yellow arrows*). The other homogenously stained tumor in the right lobe shows [^{18}F]FDG normoaccumulation (**a**–**c**; *red arrows*). Both tumors were biopsied and proved that left-lobe hepatoma was poorly differentiated, but right-lobe one was well differentiated [77]

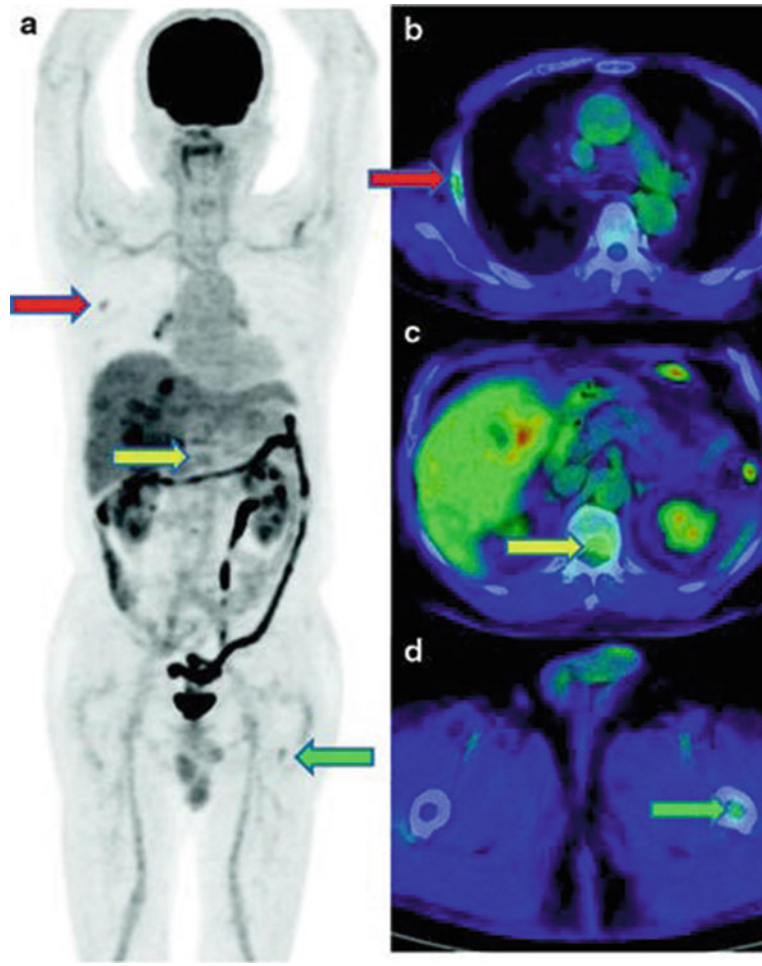

Fig. 7 *Multiple osseous metastases*. Slight [^{18}F]FDG accumulations are shown at the right thorax (**a**; *red arrow*), back (**a**; *yellow arrow*), and left femur (**c**; *green arrow*) on PET image. Fusion images disclose that these are, respectively, costal (**b**; *red arrow*), vertebral (**c**; *yellow arrow*), and femoral (**d**; *green arrow*) bone metastasis [77]

of detecting extrahepatic metastases with [^{18}F]FDG-PET scans in comparison to conventional MRI or CT (Figs. 7 and 8) [41]. In one study, 24 out of 87 patients with HCC had extrahepatic disease detectable by [^{18}F]FDG-PET [42]. Extrahepatic metastases in 10 out of the 24 patients were missed on conventional CT and MRI scans. The higher sensitivity of the [^{18}F]FDG-PET scan to detect metastatic disease versus localized disease is largely attributable to the higher grade of metastatic lesions. In particular, [^{18}F]FDG-PET scans are by far superior in the detection of bone metastases from HCC (sensitivity 83.3%, specificity 86.1%), in comparison to CT scan (sensitivity 41.6%, specificity 94.5%) and bone scintigraphy (sensitivity 52.7%, specificity 83.3%) [43].

Accurate assessment of treatment monitoring and outcome is another important role of [^{18}F]FDG-PET [29, 39, 44–46]. When the [^{18}F]FDG uptake in the lesion was higher or similar to the activity in the surrounding tissue, the presence of residual tumor was seen on histological confirmation. On the other hand, reduced [^{18}F]FDG uptake in the lesion makes it unlikely that there is residual tumor after TACE treatment [47, 48]. Similar findings have been reported in detecting local tumor progression following radiofrequency ablation of HCC. Kim et al. reported that, in HCC patients treated with

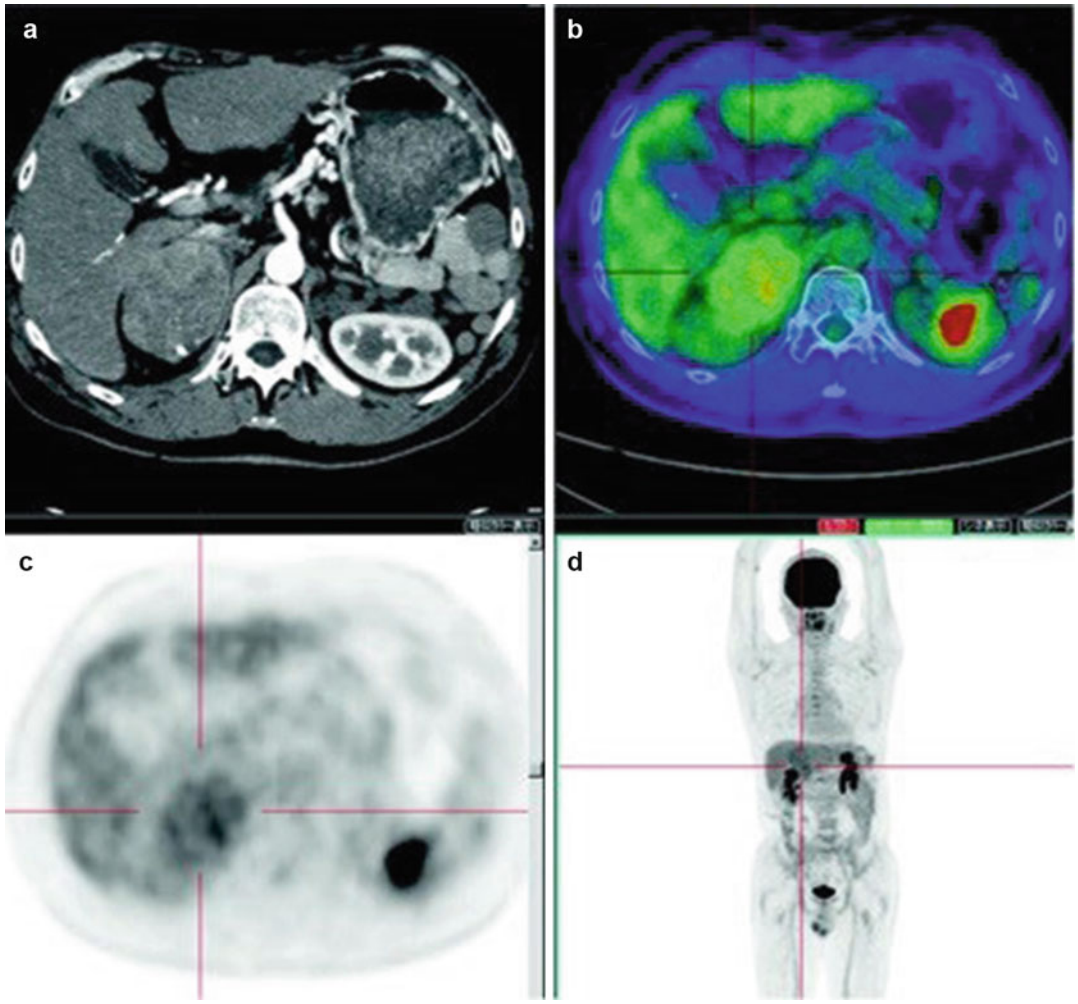

Fig. 8 *An adrenal metastasis of hepatoma*. A male with history of HCC therapy with AFP elevation but no intrahepatic recurrence. Contrast-enhanced CT at arterial phase shows early enhance on right enlarged adrenal gland (**a**). [^{18}F]FDG-PET/CT shows moderate hyperglycolysis at adrenal gland, so resection of this tumor disclosed metastatic hepatoma of adrenal gland (**b**). [^{18}F]FDG accumulation is slight and heterogeneous as well as general findings of hepatoma on PET (**c**, **d**) [77]

chemoradiation therapy, low [^{18}F]FDG uptake was associated with longer progression-free survival (PFS) and overall survival (OS) and that the high [^{18}F]FDG uptake group was more likely to have extrahepatic metastasis within 6 months [49].

b. [^{11}C]Acetate

To overcome the limited uptake and retention of [^{18}F]FDG in well-differentiated HCCs within the liver parenchyma, alternative radiotracers have been used. One such agent, [^{11}C]acetate, has been widely investigated with or without [^{18}F]FDG. Acetate, or acetic acid, is a molecule quickly picked up by cells and converted into acetyl-CoA by acetyl-CoA synthetase [50]. Acetyl-CoA feeds into the tricarboxylic acid cycle and it is utilized for cellular energy production. Alternatively, acetyl-CoA is an important substrate of anabolic pathways that lead to the synthesis of cholesterol, fatty acids, or amino acids. Tumor cells that overexpress fatty acid

synthetase or acetyl-CoA carboxylase generate [^{11}C]-labeled fatty acids and cholesterol, which are rapidly incorporated into the tumor cell membranes allowing for detection of tumor using [^{11}C]acetate-PET scans [50].

One of the first studies utilizing [^{11}C]acetate-PET scans in detecting HCC within the liver by Ho et al. included 39 patients with HCC [51]. Concurrent [^{18}F]FDG-PET scans were performed for comparison. Dual radiotracer imaging proved to be complimentary with a sensitivity of 98% and specificity of 86%. Well-differentiated lesions preferentially accumulate [^{11}C]acetate, whereas poorly differentiated lesions accumulate [^{18}F]FDG. A similar but considerably prospective study by Park et al. incorporated patients with localized as well as distant disease (n=90) [52]. [^{11}C]Acetate-PET offered superior sensitivity (75.4%) compared to [^{18}F]FDG-PET (60.9%). Dual-tracer imaging had a combined sensitivity of 82.7%. Of note, the ability to detect lesions by dual-tracer imaging is highly dependent on tumor size. For instance, tumors less than 2 cm are detected with a sensitivity of ~30% by combined radiotracer imaging.

The use of [^{11}C]acetate-PET in determining response to treatment remains to be studied. A feasibility study of [^{11}C]acetate in the monitoring of treatment response following Radiotherapy in patients with hepatocellular carcinoma is currently underway (NCT02549755). In conclusion, the early experience with dual-tracer PET imaging is very encouraging. More studies are needed to determine the utility of this modality in diagnosis, staging, surveillance, and response to therapy.

c. Tracers in Development

Targeted radiotracers hold the promise of enhanced sensitivity and specificity. Additionally, next-generation radiotracers could provide functional insight into the behavior of HCCs. This information can be crucial in selecting therapies as well as in assessing response to therapies. A recent study evaluated glypican 3-targeted [^{89}Zr] PET imaging for HCC [53]. Glypican 3 is expressed on the cell surface of up to 80% of HCCs, making it a suitable imaging target. Using this immune probe, tumors as small as 1 mm could be accurately identified in small animal studies with excellent specificity. Another study demonstrated that mouse extrahepatic hepatoma could be visualized by PET using copper-64 chloride as a tracer, based on increased copper uptake mediated by mouse copper transporter 1 (mCtr1). There was relatively less ^{64}Cu uptake in the hepatoma compared to the liver due to the presence of mCtr1 in normal liver cells. Choline is one of the components of phosphatidylcholine, an essential element of phospholipids in the cell membrane. HCC has significantly higher choline content than normal liver tissue. A prospective study aimed to compare the diagnostic performance of ^{18}F-fluorocholine and [^{18}F]FDG for detecting and staging hepatocellular carcinoma (HCC) in patients with chronic liver disease and suspected liver nodules [54]. This study demonstrated that ^{18}F-fluorocholine was significantly more sensitive (94%) than [^{18}F]FDG (59%) at detecting HCC, particularly in well-differentiated forms. The combined modality was thought to be superior.

In conclusion, [^{18}F]FDG-PET scan is inferior to multiphase CT or MRI in assessing true burden of hepatic disease. Liver HCC lesions that appear [^{18}F]FDG-avid tend to be poorly differentiated. Further, [^{18}F]FDG-PET can be considered in ruling out extrahepatic disease in patients undergoing transplantation or in analyzing burden of disease prior to systemic therapies. [^{11}C]Acetate scans are complimentary to [^{18}F]FDG-PET scans, and dual-tracer PET scans are expected to be more widely adapted in clinical practice as clinical experience accumulates. Development of targeted and functional radiotracers in proof-of-concept studies highlights the potential of these agents as promising tools in treatment of hepatocellular carcinomas.

Cholangiocarcinoma

Cholangiocarcinoma is a neoplasm that arises from cholangiocytes, the epithelial cells lining

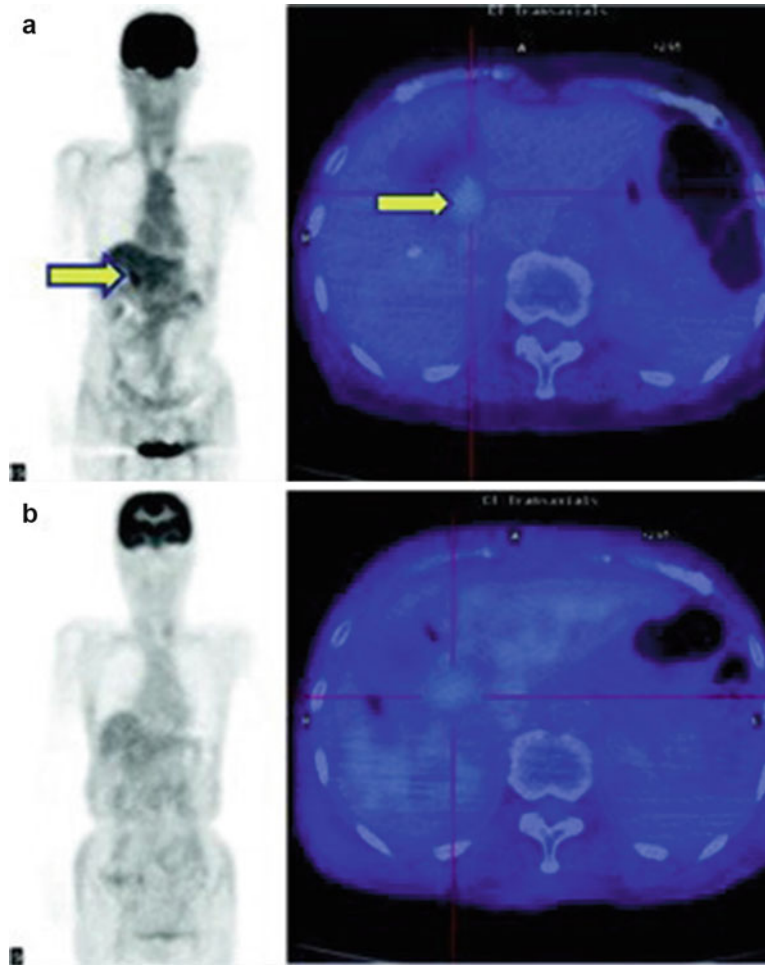

Fig. 9 Therapy monitor imaging of unresectable Klatskin tumor. [^{18}F]FDG abnormally accumulates primary tumor at hepatic hilum (**a**, **b**; *yellow arrows*). After external radiation (44 Gy) and brachytherapy (12 Gy) with concurrent hepatic arterial infusion (AI) together, [^{18}F]FDG accumulation became indistinct [77]

the bile ducts. The majority of lesions are adenocarcinoma. Carcinoma of the extrahepatic biliary tract is defined by the location of the tumor into Klatskin (hilar) tumor (Fig. 9), hepatic bile duct, common bile duct tumor, gallbladder cancer, and ampulla of Vater cancer [55]. Histopathological characterization of extrahepatic biliary cancer divides lesions into moderately differentiated, poorly differentiated, or undifferentiated adenocarcinoma [56]. Carcinoma of extrahepatic biliary tract is histopathologically divided into mass-forming (nodular), periductal-infiltrating (sclerosing), and intraductal (papillary) type (Fig. 10) [56]. These histopathological difference classifications give a great deal of influences at the situation using the radiological diagnosis. Although mass-forming types show vertical progression, while periductal-infiltrating lesions show horizontal progression, both of them progress invasively into surrounding structures. However, intraductal type including mucin-producing tumor progresses horizontally but noninvasively (Figs. 9 and 10) [56, 57].

In the USA, it is estimated that there have been 9760 new cases of cholangiocarcinoma in 2010 and 3320 deaths (ACS Cancer Facts 2010). Its incidence is annually 1–2 per 100,000 in the western world [58]. This rate is rising around the world, while in Japan the rate is decreasing in the twenty-first century. The annual number of deaths due to extrahepatic biliary cancer was

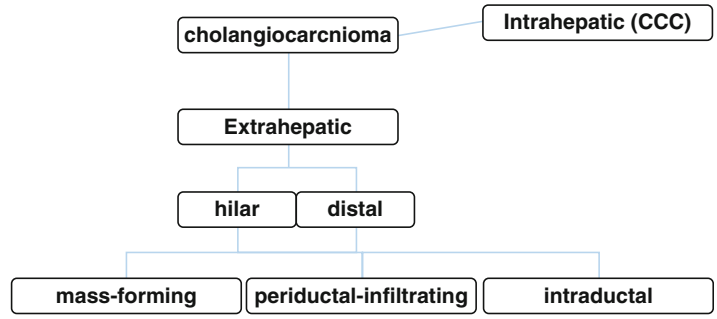

Fig. 10 Classification of cholangiocarcinoma [77]

about 3600 people in the USA. Statistics show that the 60s are the most frequent age, and the frequency in men is about twice than in women. Several known risk factors are described for cholangiocarcinoma, including primary sclerosing cholangitis [PSC, often associated with ulcerative colitis], Caroli's congenital abnormalities of the biliary tree (Caroli's disease syndrome, congenital hepatic fibrosis, and choledochal cysts), parasitic biliary infection (e.g., liver fluke, *Clonorchis*), and chronic typhoid fever [59]. It is thought that a long-term inflammation of the biliary tract or abnormal choledocholithiasis influences carcinogenesis, but there are a lot of unknown molecular carcinogenic processes [60].

The first clinical symptom is often painless jaundice, sometimes accompanied by pruritus, weight loss, and fever. Abdominal pain may occur in 30–50% of patients. Patients often have advanced disease at the time of diagnosis. In general, cholangiocarcinoma have a poor prognosis because complete resection is the only curative treatment. The 5-year survival rate after curative resection is still low (26–51%) [61]. For unresectable disease, chemotherapy with gemcitabine and cisplatin provides marginal benefit in overall survival [62].

Patients with cholangiocarcinoma typically present with painless jaundice that prompts an ultrasound (US) of the liver. Biliary dilation and elevated bilirubin necessitates multimodality imaging with endoscopic retrograde cholangiography, endoscopic US, and high-resolution triple-phase (arterial, venous, and delayed venous) contrast-enhanced cross-sectional imaging (CT or MRI). This provides adequate information to assess resectability of cholangiocarcinoma. Pathologic diagnosis is based on brushings and cytology. Often, surgical resection is warranted based on imaging findings in the absence of tissue diagnosis.

The role of [^{18}F]FDG-PET scan for imaging of biliary cancers is evolving (Figs. 11, 12, 13, and 14). Small, mostly retrospective series report a sensitivity ranging 91–95% for intrahepatic cholangiocarcinoma and 55–83% for extrahepatic cholangiocarcinoma [63–66]. Further, the diagnostic accuracy is higher for larger mass-forming lesions than periductal-infiltrating tumors. For instance, Anderson et al. reported that mass-forming or intraductally progressive (volume) type showed a higher proportion of patients with [^{18}F]FDG accumulation (17/20 patients) compared to the periductal-infiltrating (thin) type, which was found to be [^{18}F]FDG-positive in only 2/11 patients [63].

Obstructive jaundice typically leads to bactibilia, and some degree of cholangitis is usually present [57]. The utility of [^{18}F]FDG-PET scan is therefore limited by the high positive rates in the setting of acute cholangitis. It is also important to distinguish biliary cancer from autoimmune IgG_4-related cholangitis. As such, IgG_4-related disease is characterized by high serum IgG_4 concentrations and sclerosing inflammation (involving the parotid gland, pancreas, bile duct, and so on) with numerous IgG_4-positive plasma cells. However, [^{18}F]FDG-PET cannot help distinguish the two entities as autoimmune IgG_4-related cholangitis readily accumulates [^{18}F]FDG as well (Fig. 15). Involvement of multiple organs and elevated serum IgG_4

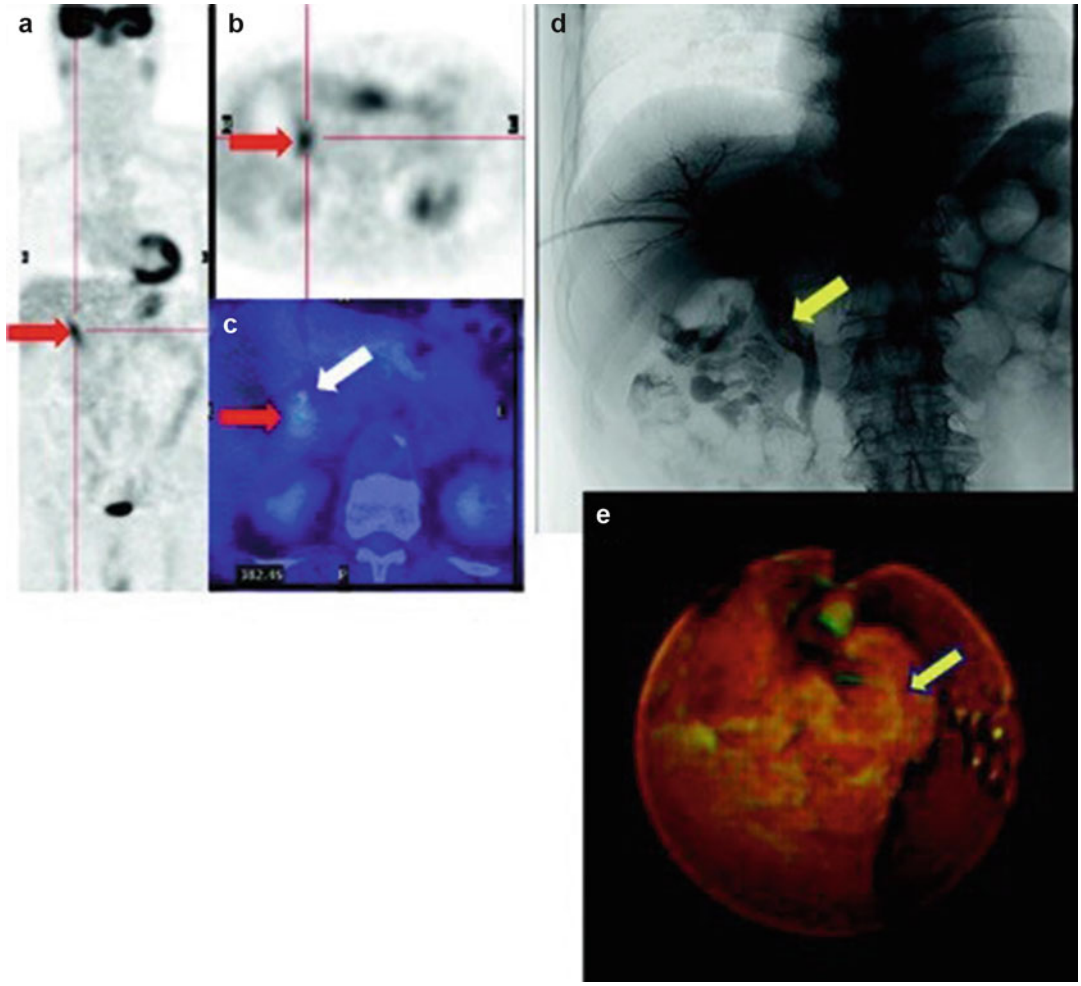

Fig. 11 Pretherapeutic extrahepatic bile duct (common bile duct) cancer. [^{18}F]FDG abnormally accumulates in the common bile duct (**a**–**c**; *red arrows*). And fusion image clearly discloses a local relationship between tumor and replaced drainage tube (**c**; *white arrow*). Cholangiography shows a filling defect on the dilated common bile duct (**d**; *yellow arrow*), and PTCS finding is mass-forming tumor (**e**; *yellow arrow*) [77]

should raise suspicion for autoimmune cholangitis rather than cholangiocarcinoma. Definitive diagnosis is only possible after surgical resection.

a. Preoperative Staging and Resectability
   Kim et al. analyzed their experience with 94 cholangiocarcinoma cases [65]. They reported a sensitivity of 95% for [^{18}F]FDG-PET/CT versus 100% for MRI/MRCP. High-resolution cross-sectional imaging provides vital information on the relationship of the tumor to the porta hepatic vasculature, allowing accurate assessment of resectability. [^{18}F]FDG-PET scan does not improve on this assessment given its low resolution. Accurate diagnosis of lymph node involvement is of clinical value for accurate staging in each patient. Again, [^{18}F]FDG-PET may have limited value for this purpose due to limited spatial resolution. One of the major limitations is that lymph node involvement is mainly seen in the adjacent areas of the primary tumor, therefore making it rather difficult to separate the lymph node lesion, without the use of PET/CT from the primary lesion by relatively low-resolution PET. In addition, it is rather difficult to

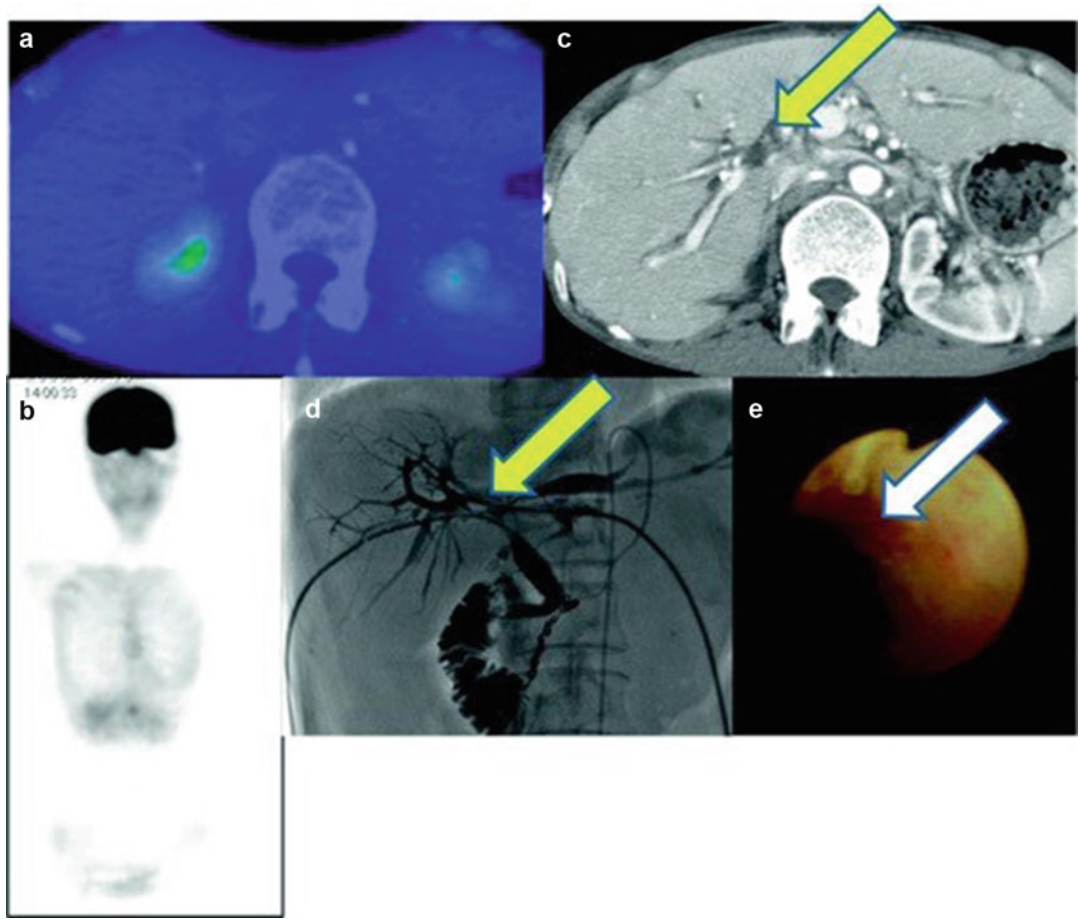

Fig. 12 Pretherapeutic Klatskin tumor. PET/CT does not show abnormal [^{18}F]FDG accumulation (**a**, **b**). Contrast-enhanced CT and cholangiography shows multiple filling defects (**c**, **d**; *yellow arrows*) because of tumor in hilum. PTCS shows focal mucosal redness (**e**; *white arrow*). Biopsy specimen proved periductal-infiltrating-type adenocarcinoma [77]

differentiate malignant invasion from the accompanied benign inflammatory lesions, which are often seen in biliary tracts. On the other hand, [^{18}F]FDG-PET has a high diagnostic value for detecting distant lymph node involvement, where previous reports showed a wide range of sensitivity (12–50%), specificity (80–100%), and overall accuracy (69–77%) [67]. However, among those, the relatively high specificity may prove to be of clinical value in identifying distant nodal involvement, as these patients are unlikely to benefit from aggressive surgical resection. It is estimated that [^{18}F]FDG-PET scans change patient management in 16–30% of patients with cholangiocarcinoma.

b. Detection of Recurrence

Patients with cholangiocarcinomas are currently evaluated by contrast-enhanced cross-sectional imaging for surveillance. A recent multicenter retrospective study in 50 patients with posttreatment surveillance of biliary cancer in Japan indicated that [^{18}F]FDG-PET provided high sensitivity (86%), specificity (91%), and overall accuracy (88%) for detecting tumor recurrence [68]. In addition, the [^{18}F]FDG-PET findings resulted in a change in management of 10 of the 50 patients

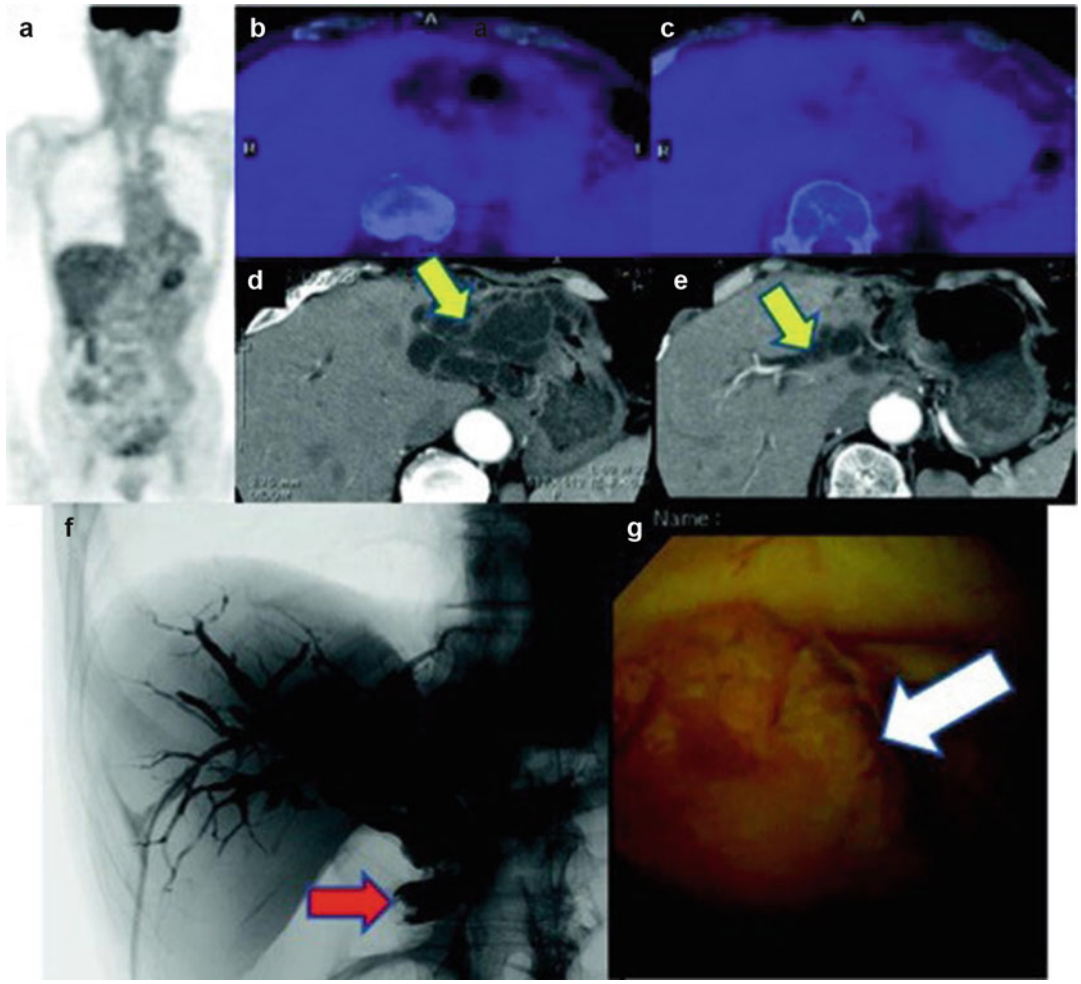

Fig. 13 Mucin-producing extrahepatic bile duct tumor. PET/CT does not show abnormal [^{18}F]FDG accumulation (**a**–**c**). Contrast-enhanced CT shows bile duct dilatation in bilateral lobe (**d**, **e**; *yellow arrows*). Cholangiography shows extra- and intrahepatic biliary dilatation and filling defect at lower common bile duct (**f**; *red arrow*). PTCS shows focal mucosal redness (**g**; *white arrow*). Biopsy specimen proved papillary-type, mucin-producing adenocarcinoma [77]

(20%) by initiating an unplanned treatment strategy ($n = 7$), by obviating the need for planned diagnostic procedures ($n = 2$), and by changing the treatment planning ($n = 1$) [68]. These multicenter studies confirmed the value of PET in patients with bile duct cancer after operation.

c. Risk Stratification

There are a number of established criteria for assessing prognosis of patients with bile duct cancer, including tumor histology and staging. Most of criteria may come from the findings during or after operation. PET and PET/CT may have a potential for selecting high-risk patients on the basis of tissue characterization. Furukawa et al. studied 69 patients with bile duct cancer [69]. These investigators found the [^{18}F]FDG uptake as a significant prognostic indicator. Those with SUV_{max} of higher than 6.3 on [^{18}F]FDG-PET were in the poor prognostic group, with a 3-year survival rate of 44.1%, whereas those with SUV_{max} of 6.3 or

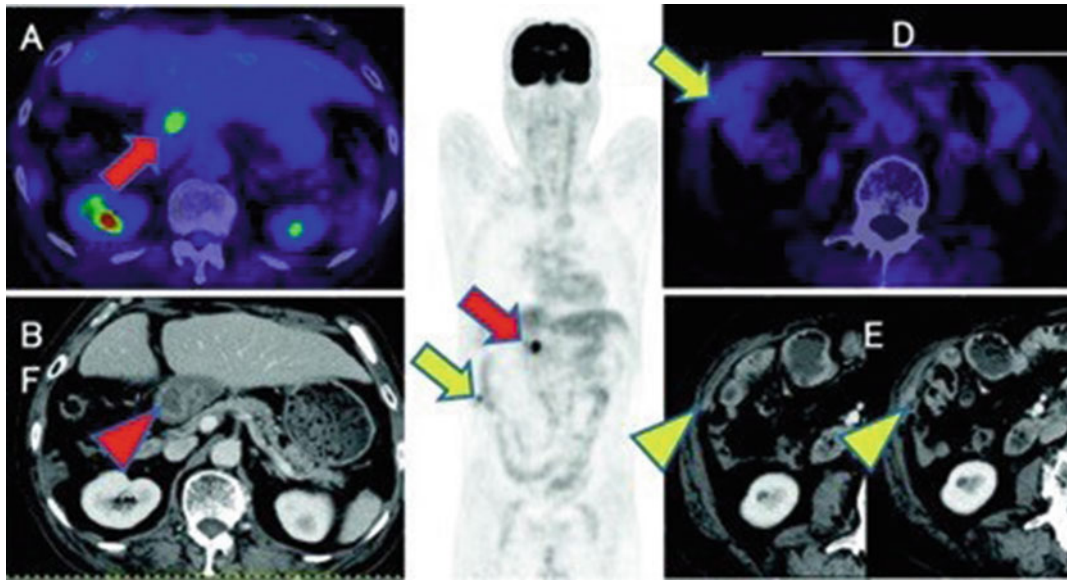

Fig. 14 Postoperative common bile duct cancer patient with CA19–9 elevation. Abnormal [^{18}F]FDG accumulations are shown at hepatic hilum (**a**, **c**; *red arrows*) and intra-abdominal space (**c**, **d**; *yellow arrows*). So these are highly suspected recurrent lesions including local recurrence and peritoneal dissemination. Coincidently, contrast-enhanced CT shows choledochojejunostomized wall (**b**; *red arrowhead*) and peritoneal small and increasing enhanced nodule (**e**, **f**; *yellow arrowheads*). But it is difficult to differentiate anastomosis and recurrence [77]

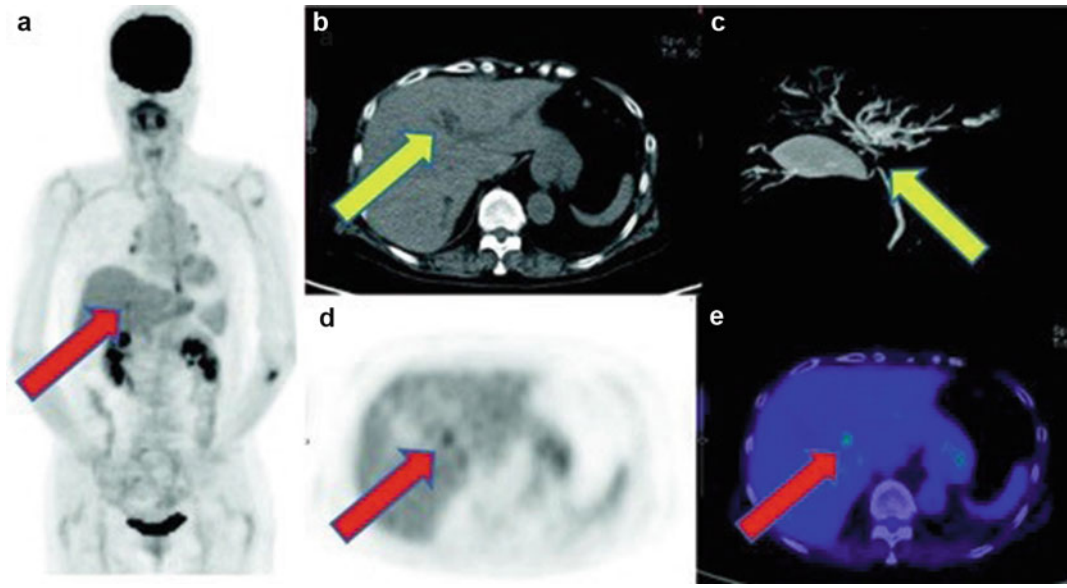

Fig. 15 IgG_4-related sclerosing cholangitis. Non-contrast CT and MRCP show intrahepatic bile duct dilatation due to hepatic hilar severe stenosis (**b**, **c**; *yellow arrows*). [^{18}F] FDG accumulates on the point of hepatic hilum (**a**, **d**, **e**; *red arrows*). But biopsy specimen proved no carcinoma cell but sclerosis cholangitis with plasmacyte and lymphocyte infiltration. His serum IgG_4 level was so high that IgG_4-related disease was confirmed [77]

less on [^{18}F]FDG-PET were in the better prognostic group, with a 3-year survival rate of 74.3% ($P = 0.012$). Kitamura et al. studied 73 patients with extrahepatic bile duct cancers to show SUV_{max} value of 5.7 as a significant cutoff point to differentiate poor prognosis from good prognosis subgroups [70]. They showed [^{18}F]FDG uptake value as an independent significant prognostic indicator on multivariate analysis.

Gallbladder Carcinoma

Gallbladder cancer (GBC) is a rare neoplasm that arises from the mucosal lining of the gallbladder. The American Cancer Society estimates approximately 10,000 cases of biliary origin cancers are diagnosed each year. Half of these originate in the gallbladder. Chronic inflammation is thought to be the main etiology in a majority of patients. For instance, the presence of gallstones increases the risk of GBC up to fivefold and predates the development of GBC in 75% of patients. Other causes of chronic inflammation predisposing to GBC can be autoimmune, i.e., primary sclerosing cholangitis and ulcerative colitis, or infectious, i.e., *Salmonella typhi* and *S. paratyphi*, liver flukes, and *Helicobacter pylori*. Genetic factors that may contribute are under active investigation. This hypothesis is based in the observation that the incidence of GBC is increased in certain genetic syndromes such as Gardner syndrome, neurofibromatosis type 1, and hereditary nonpolyposis colon cancer. The incidence of GBC in the USA has been decreasing since 1973. Internationally, a high incidence of GBC is noted in South America (Chile, Columbia, Peru, Bolivia, and Ecuador), South Asia (India), and East Asia (Korea and Japan).

Symptomatology occurs late in the course of the disease. Approximately 50% of patients have nodal disease at diagnosis. Increasingly, patients are incidentally discovered to have gallbladder cancer after a "routine" cholecystectomy for biliary colic or acute cholecystitis. Surgical resection is the only potentially curative treatment. Extent of surgical resection and resectability depends on accurate radiologic staging. A high-quality, contrast-enhanced cross-sectional imaging modality (CT or MRI) is the current standard. The role of PET scan is not clearly established for GBC and is not routinely recommended in the USA. However, mounting evidence from small studies may change this recommendation. The accuracy and utility of [^{18}F]FDG-PET in detecting regional and distant metastases in an otherwise resectable patient is discussed below. In addition, we discuss the role of [^{18}F]FDG-PET in the management of recurrent disease and the novel approaches being developed.

Preoperative PET/CT scans have been evaluated through small institutional experiences. The majority of these studies combine patients with GBC and cholangiocarcinoma, making it difficult to draw meaningful conclusions (Fig. 16). Butte et al. investigated 32 patients with incidental GBC following laparoscopic cholecystectomy [71]. While 13 patients had negative PET/CT results, 9 refused further resection, and only 1 of the 4 patients was resected, having residual disease on operative exploration. PET/CT changed management in 12 out of 32 patients (38%) demonstrating unexpected disseminated disease in 10 patients and localized resectable disease in 2 patients. Corvera et al. studied 31 patients with gallbladder cancer within their published series [66]. They demonstrated a sensitivity of 86% and a specificity of 50% for detection of the primary tumor, and a sensitivity of 87% and specificity of 89% for detection of nodal/distant disease, respectively. This resulted in a change in treatment for seven (23%) patients.

Shukla et al. evaluated the role of PET/CT in 24 patients with incidental gallbladder cancer prior to radical resection [72]. They demonstrated that PET/CT predicted resectability with a sensitivity of 100% but was not significantly superior to conventional CT. PET/CT demonstrated residual disease with a sensitivity of 28.5% and with a specificity of 80.9%. These results may have changed clinical management for two patients. One of the largest series analyzed data from 100 patients at a single institution [73]. Sixty-three patients were incidentally discovered to have GBC. In 73 patients, the PET/CT was concordant with contrast-enhanced imaging and did

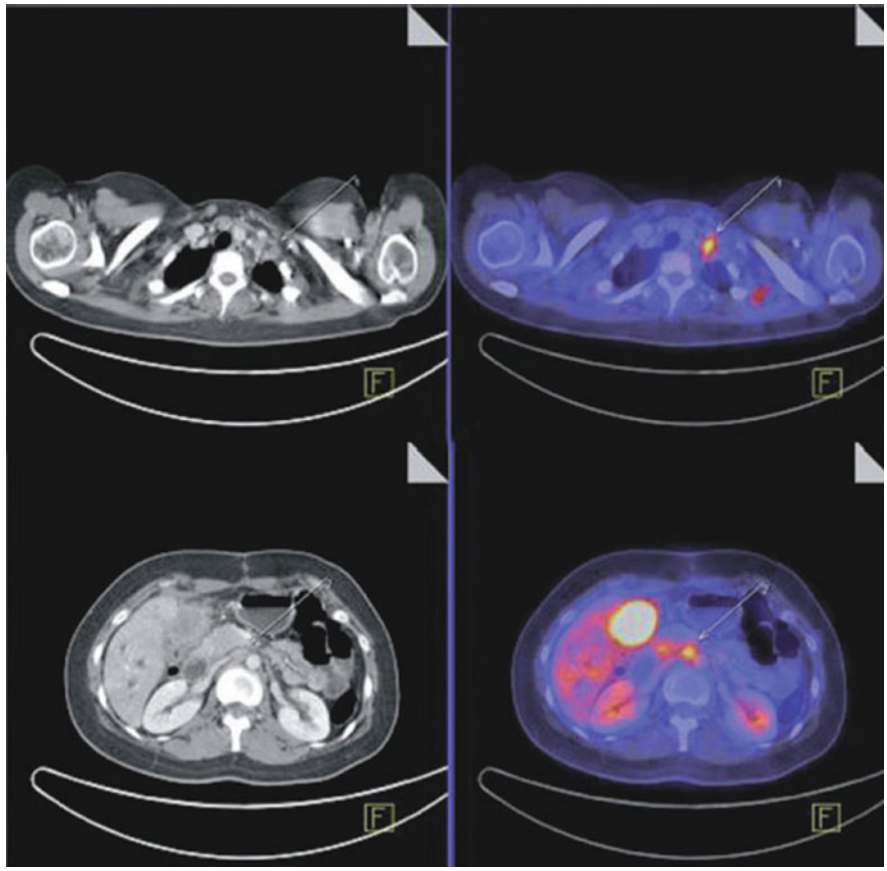

Fig. 16 An example of an [^{18}F]FDG PET/CT which showed evidence (positive finding) of disseminated disease (*arrow*) in a patient who was diagnosed with an incidental gallbladder carcinoma after cholecystectomy (Reprint with permission from Butte JM. et al. The role of PET/CT in patients with incidental gallbladder cancer. HPB. 2009, Fig. 3, p. 588) [71]

not add any information. In 3 patients, PET/CT detected metastatic disease not suspected on contrast-enhanced CT alone. In 12 patients, the CT scan was suspicious for locally advanced disease, and PET/CT helped confirm distant nodal disease (11 patients) or T4 disease (1 patient). Further, in two patients, CT was suspicious for distant metastases, but PET/CT ruled out that possibility, changing treatment choice. Taken together, PET/CT changed decision-making for 17 patients (17%). Improvement in conventional imaging has mitigated the benefit of PET/CT scans in recent years, with older studies reporting a higher proportion of patients where PET/CT appeared to change decision-making. The sensitivity of PET/CT in detecting distant metastases is 57%. This poor sensitivity is mainly because peritoneal disease tends to be less [^{18}F]FDG-avid (sensitivity 28%) versus nodal disease (70%). Given these results, routine preoperative [^{18}F]FDG-PET/CT is not recommended. A PET/CT scan may help prevent a potentially morbid operation in patients with suspicious nodal or distant lesions on cross-sectional imaging. False-positive result in these patients is thought to be low (specificity ~97–100%). Nonetheless, it must be kept in mind that equivocal or unexpected PET findings may prompt additional biopsies.

Kumar et al. evaluated the role of PET/CT in detecting recurrent GBC in 49 patients [74]. These investigators demonstrated a sensitivity and specificity of 97.6% and 90%, respectively, for

detecting recurrent disease. PET/CT was shown to be more specific than conventional imaging (100% vs. 50%) and resulted in a change in management for five patients (20%). More studies are needed to establish the role of PET/CT in recurrent GBC. The cost and resource utilization of unnecessary biopsies for false-positive findings needs to be investigated further.

In conclusion, [^{18}F]FDG-PET appears to be complimentary rather than definitive in many patients with GBC, and its role is limited in patients with negative CT/MRI and T1 disease. While the routine use of PET/CT in GBC is probably not cost effective, we believe that PET should be used when there are suspicious findings on CT/MRI, such as large tumors or questionable nodes. [^{18}F]FDG PET/CT should not be the imaging modality of choice when peritoneal-only disease is suspected as the sensitivity is low. Diagnostic laparoscopy has a higher yield in these patients.

References

1. Bipat S, van Leeuwen MS, Comans EF, Pijl ME, Bossuyt PM, Zwinderman AH, et al. Colorectal liver metastases: CT, MR imaging, and PET for diagnosis – meta-analysis. Radiology. 2005;237(1):123–31.
2. Niekel MC, Bipat S, Stoker J. Diagnostic imaging of colorectal liver metastases with CT, MR imaging, FDG PET, and/or FDG PET/CT: a meta-analysis of prospective studies including patients who have not previously undergone treatment. Radiology. 2010;257(3):674–84.
3. Kuehl H, Rosenbaum-Krumme S, Veit-Haibach P, Stergar H, Forsting M, Bockisch A, et al. Impact of whole-body imaging on treatment decision to radiofrequency ablation in patients with malignant liver tumors: comparison of [^{18}F]fluorodeoxyglucose-PET/computed tomography, PET and computed tomography. Nucl Med Commun. 2008;29(7):599–606.
4. Selzner M, Hany TF, Wildbrett P, McCormack L, Kadry Z, Clavien PA. Does the novel PET/CT imaging modality impact on the treatment of patients with metastatic colorectal cancer of the liver? Ann Surg 2004;240(6):1027–34; discussion 35-6.
5. Selzner M, Hany TF, Wildbrett P, McCormack L, Kadry Z, Clavien PA. Does the novel PET/CT imaging modality impact on the treatment of patients with metastatic colorectal cancer of the liver? Ann Surg 2004;240(6):1027–34; discussion 35-6.
6. Findlay M, Young H, Cunningham D, Iveson A, Cronin B, Hickish T, et al. Noninvasive monitoring of tumor metabolism using fluorodeoxyglucose and positron emission tomography in colorectal cancer liver metastases: correlation with tumor response to fluorouracil. J Clin Oncol. 1996;14(3):700–8.
7. Xia Q, Liu J, Wu C, Song S, Tong L, Huang G, et al. Prognostic significance of ^{18}FDG PET/CT in colorectal cancer patients with liver metastases: a meta-analysis. Cancer Imaging. 2015;15:19.
8. Lubezky N, Metser U, Geva R, Nakache R, Shmueli E, Klausner JM, et al. The role and limitations of 18-fluoro-2-deoxy-D-glucose positron emission tomography (FDG-PET) scan and computerized tomography (CT) in restaging patients with hepatic colorectal metastases following neoadjuvant chemotherapy: comparison with operative and pathological findings. J Gastrointest Surg. 2007;11(4):472–8.
9. Wolfort RM, Papillion PW, Turnage RH, Lillien DL, Ramaswamy MR, Zibari GB. Role of FDG-PET in the evaluation and staging of hepatocellular carcinoma with comparison of tumor size, AFP level, and histologic grade. Int Surg. 2010;95(1):67–75.
10. Chikamoto A, Tsuji T, Takamori H, Kanemitsu K, Uozumi H, Yamashita Y, et al. The diagnostic efficacy of FDG-PET in the local recurrence of hilar bile duct cancer. J Hepato-Biliary-Pancreat Surg. 2006;13(5):403–8.
11. Han AR, Gwak GY, Choi MS, Lee JH, Koh KC, Paik SW, et al. The clinical value of ^{18}F-FDG PET/CT for investigating unexplained serum AFP elevation following interventional therapy for hepatocellular carcinom. Hepato-Gastroenterology. 2009;56(93):1111–6.
12. Lu YY, Chen JH, Chien CR, Chen WT, Tsai SC, Lin WY, et al. Use of FDG-PET or PET/CT to detect recurrent colorectal cancer in patients with elevated CEA: a systematic review and meta-analysis. Int J Color Dis. 2013;28(8):1039–47.
13. Duffy MJ. Carcinoembryonic antigen as a marker for colorectal cancer: is it clinically useful? Clin Chem. 2001;47(4):624–30.
14. Lawrence B, Gustafsson BI, Chan A, Svejda B, Kidd M, Modlin IM. The epidemiology of gastroenteropancreatic neuroendocrine tumors. Endocrinol Metab Clin N Am 2011;40(1):1–18, vii.
15. Saxena A, Chua TC, Sarkar A, Chu F, Liauw W, Zhao J, et al. Progression and survival results after radical hepatic metastasectomy of indolent advanced neuroendocrine neoplasms (NENs) supports an aggressive surgical approach. Surgery. 2011;149(2):209–20.
16. Pape UF, Berndt U, Muller-Nordhorn J, Bohmig M, Roll S, Koch M, et al. Prognostic factors of long-term outcome in gastroenteropancreatic neuroendocrine tumours. Endocr Relat Cancer. 2008;15(4):1083–97.
17. Binderup T, Knigge U, Loft A, Mortensen J, Pfeifer A, Federspiel B, et al. Functional imaging of neuroendocrine tumors: a head-to-head comparison of somatostatin receptor scintigraphy, ^{123}I-MIBG scintigraphy, and ^{18}F-FDG PET. J Nucl Med. 2010;51(5):704–12.
18. Bodei L KM, Modlin I, Paganelli G. Nuclear medicine in the diagnosis and therapy of neuroendocrine tumors. In:

Akotlun C GS, editor. Nuclear oncology. Wolters Kluwer health, Alphen aan den Rijn, The Netherlands; 2013.
19. Parkin DM, Bray F, Ferlay J, Pisani P. Estimating the world cancer burden: Globocan 2000. Int J Cancer. 2001;94(2):153–6.
20. Pisani P, Parkin DM, Bray F, Ferlay J. Estimates of the worldwide mortality from 25 cancers in 1990. Int J Cancer. 1999;83(1):18–29.
21. Rocken C, Carl-McGrath S. Pathology and pathogenesis of hepatocellular carcinoma. Dig Dis. 2001;19 (4):269–78.
22. Esteves FP, Schuster DM, Halkar RK. Gastrointestinal tract malignancies and positron emission tomography: an overview. Semin Nucl Med. 2006;36(2):169–81.
23. Llovet JM, Fuster J, Bruix J. Intention-to-treat analysis of surgical treatment for early hepatocellular carcinoma: resection versus transplantation. Hepatology. 1999;30(6):1434–40.
24. Jonas S, Bechstein WO, Steinmuller T, Herrmann M, Radke C, Berg T, et al. Vascular invasion and histopathologic grading determine outcome after liver transplantation for hepatocellular carcinoma in cirrhosis. Hepatology. 2001;33(5):1080–6.
25. Cormier JN, Thomas KT, Chari RS, Pinson CW. Management of hepatocellular carcinoma. J Gastrointest Surg. 2006;10(5):761–80.
26. Therasse P, Arbuck SG, Eisenhauer EA, Wanders J, Kaplan RS, Rubinstein L, et al. New guidelines to evaluate the response to treatment in solid tumors. European Organization for Research and Treatment of Cancer, National Cancer Institute of the United States, National Cancer Institute of Canada. J Natl Cancer Inst. 2000;92(3):205–16.
27. Okazumi S, Isono K, Enomoto K, Kikuchi T, Ozaki M, Yamamoto H, et al. Evaluation of liver tumors using fluorine-18-fluorodeoxyglucose PET: characterization of tumor and assessment of effect of treatment. J Nucl Med. 1992;33(3):333–9.
28. Schroder O, Trojan J, Zeuzem S, Baum RP. Limited value of fluorine-18-fluorodeoxyglucose PET for the differential diagnosis of focal liver lesions in patients with chronic hepatitis C virus infection. Nuklearmedizin. 1998;37(8):279–85.
29. Delbeke D, Martin WH. PET and PET-CT for evaluation of colorectal carcinoma. Semin Nucl Med. 2004;34(3):209–23.
30. Trojan J, Schroeder O, Raedle J, Baum RP, Herrmann G, Jacobi V, et al. Fluorine-18 FDG positron emission tomography for imaging of hepatocellular carcinoma. Am J Gastroenterol. 1999;94(11):3314–9.
31. Khan MA, Combs CS, Brunt EM, Lowe VJ, Wolverson MK, Solomon H, et al. Positron emission tomography scanning in the evaluation of hepatocellular carcinoma. J Hepatol. 2000;32(5):792–7.
32. Jeng LB, Changlai SP, Shen YY, Lin CC, Tsai CH, Kao CH. Limited value of ^{18}F-2-deoxyglucose positron emission tomography to detect hepatocellular carcinoma in hepatitis B virus carriers. Hepato-Gastroenterology. 2003;50(54):2154–6.
33. Higashi T, Saga T, Nakamoto Y, Ishimori T, Fujimoto K, Doi R, et al. Diagnosis of pancreatic cancer using fluorine-18 fluorodeoxyglucose positron emission tomography (FDG PET) – usefulness and limitations in “clinical reality”. Ann Nucl Med. 2003;17(4):261–79.
34. Torizuka T, Tamaki N, Inokuma T, Magata Y, Sasayama S, Yonekura Y, et al. In vivo assessment of glucose metabolism in hepatocellular carcinoma with FDG-PET. J Nucl Med. 1995;36(10):1811–7.
35. Caraco C, Aloj L, Chen LY, Chou JY, Eckelman WC. Cellular release of [^{18}F]2-fluoro-2-deoxyglucose as a function of the glucose-6-phosphatase enzyme system. J Biol Chem. 2000;275(24):18489–94.
36. Seo S, Hatano E, Higashi T, Hara T, Tada M, Tamaki N, et al. Fluorine-18 fluorodeoxyglucose positron emission tomography predicts tumor differentiation, P-glycoprotein expression, and outcome after resection in hepatocellular carcinoma. Clin Cancer Res. 2007;13 (2 Pt 1):427–33.
37. Wudel LJ, Jr., Delbeke D, Morris D, Rice M, Washington MK, Shyr Y, et al. The role of [^{18}F] fluorodeoxyglucose positron emission tomography imaging in the evaluation of hepatocellular carcinoma. Am Surg 2003;69(2):117–24; discussion 24-6.
38. Lin WY, Tsai SC, Hung GU. Value of delayed ^{18}F-FDG-PET imaging in the detection of hepatocellular carcinoma. Nucl Med Commun. 2005;26(4): 315–21.
39. Torizuka T, Tamaki N, Inokuma T, Magata Y, Yonekura Y, Tanaka A, et al. Value of fluorine-18-FDG-PET to monitor hepatocellular carcinoma after interventional therapy. J Nucl Med. 1994;35(12): 1965–9.
40. Shiomi S, Nishiguchi S, Ishizu H, Iwata Y, Sasaki N, Tamori A, et al. Usefulness of positron emission tomography with fluorine-18-fluorodeoxyglucose for predicting outcome in patients with hepatocellular carcinoma. Am J Gastroenterol. 2001;96(6):1877–80.
41. Sugiyama M, Sakahara H, Torizuka T, Kanno T, Nakamura F, Futatsubashi M, et al. ^{18}F-FDG PET in the detection of extrahepatic metastases from hepatocellular carcinoma. J Gastroenterol. 2004;39(10): 961–8.
42. Yoon KT, Kim JK, Kim DY, Ahn SH, Lee JD, Yun M, et al. Role of ^{18}F-fluorodeoxyglucose positron emission tomography in detecting extrahepatic metastasis in pretreatment staging of hepatocellular carcinoma. Oncology. 2007;72(Suppl 1):104–10.
43. Kawaoka T, Aikata H, Takaki S, Uka K, Azakami T, Saneto H, et al. FDG positron emission tomography/computed tomography for the detection of extrahepatic metastases from hepatocellular carcinoma. Hepatol Res. 2009;39(2):134–42.
44. Weber WA. Use of PET for monitoring cancer therapy and for predicting outcome. J Nucl Med. 2005;46(6): 983–95.
45. Specht L. 2-[^{18}F]fluoro-2-deoxyglucose positron-emission tomography in staging, response evaluation,

and treatment planning of lymphomas. Semin Radiat Oncol. 2007;17(3):190–7.
46. Higashi T, Hatano E, Ikai I, Nishii R, Nakamoto Y, Ishizu K, et al. FDG PET as a prognostic predictor in the early post-therapeutic evaluation for unresectable hepatocellular carcinoma. Eur J Nucl Med Mol Imaging. 2010;37(3):468–82.
47. Shiomi S, Nishiguchi S, Ishizu H, Iwata Y, Sasaki N, Tamori A, et al. Usefulness of positron emission tomography with fluorine-18-fluorodeoxyglucose for predicting outcome in patients with hepatocellular carcinoma. Am J Gastroenterol. 2001;96(6):1877–80.
48. Dierckx R, Maes A, Peeters M, Van De Wiele C. FDG PET for monitoring response to local and locoregional therapy in HCC and liver metastases. Q J Nucl Med Mol Imaging. 2009;53(3):336–42.
49. Kim YK, Lee KW, Cho SY, Han SS, Kim SH, Kim SK, et al. Usefulness ^{18}F-FDG positron emission tomography/computed tomography for detecting recurrence of hepatocellular carcinoma in posttransplant patients. Liver Transpl. 2010;16(6):767–72.
50. Yun M, Bang SH, Kim JW, Park JY, Kim KS, Lee JD. The importance of acetyl coenzyme A synthetase for ^{11}C-acetate uptake and cell survival in hepatocellular carcinoma. J Nucl Med. 2009;50(8):1222–8.
51. Ho CL, Yu SC, Yeung DW. ^{11}C-acetate PET imaging in hepatocellular carcinoma and other liver masses. J Nucl Med. 2003;44(2):213–21.
52. Park JW, Kim JH, Kim SK, Kang KW, Park KW, Choi JI, et al. A prospective evaluation of ^{18}F-FDG and ^{11}C-acetate PET/CT for detection of primary and metastatic hepatocellular carcinoma. J Nucl Med. 2008;49 (12):1912–21.
53. Sham JG, Kievit FM, Grierson JR, Miyaoka RS, Yeh MM, Zhang M, et al. Glypican-3-targeted ^{89}Zr PET imaging of hepatocellular carcinoma. J Nucl Med. 2014;55(5):799–804.
54. Talbot JN, Fartoux L, Balogova S, Nataf V, Kerrou K, Gutman F, et al. Detection of hepatocellular carcinoma with PET/CT: a prospective comparison of ^{18}F-fluorocholine and ^{18}F-FDG in patients with cirrhosis or chronic liver disease. J Nucl Med. 2010;51(11): 1699–706.
55. Nakeeb A, Pitt HA, Sohn TA, Coleman J, Abrams RA, Piantadosi S, et al. Cholangiocarcinoma. A spectrum of intrahepatic, perihilar, and distal tumors. Ann Surg 1996;224(4):463–73; discussion 73-5.
56. Malhi H, Gores GJ. Cholangiocarcinoma: modern advances in understanding a deadly old disease. J Hepatol. 2006;45(6):856–67.
57. Kato T, Tsukamoto E, Kuge Y, Katoh C, Nambu T, Nobuta A, et al. Clinical role of ^{18}F-FDG PET for initial staging of patients with extrahepatic bile duct cancer. Eur J Nucl Med Mol Imaging. 2002;29 (8):1047–54.
58. Landis SH, Murray T, Bolden S, Wingo PA. Cancer statistics, 1998. CA Cancer J Clin. 1998;48(1):6–29.
59. Bergquist A, Ekbom A, Olsson R, Kornfeldt D, Loof L, Danielsson A, et al. Hepatic and extrahepatic malignancies in primary sclerosing cholangitis. J Hepatol. 2002;36(3):321–7.
60. Holzinger F, Z'Graggen K, Buchler MW. Mechanisms of biliary carcinogenesis: a pathogenetic multi-stage cascade towards cholangiocarcinoma. Ann Oncol. 1999;10(Suppl 4):122–6.
61. Washburn WK, Lewis WD, Jenkins RL. Aggressive surgical resection for cholangiocarcinoma. Arch Surg. 1995;130(3):270–6.
62. Kubicka S, Rudolph KL, Tietze MK, Lorenz M, Manns M. Phase II study of systemic gemcitabine chemotherapy for advanced unresectable hepatobiliary carcinomas. Hepato-Gastroenterology. 2001;48(39):783–9.
63. Anderson CD, Rice MH, Pinson CW, Chapman WC, Chari RS, Delbeke D. Fluorodeoxyglucose PET imaging in the evaluation of gallbladder carcinoma and cholangiocarcinoma. J Gastrointest Surg. 2004;8(1): 90–7.
64. Petrowsky H, Wildbrett P, Husarik DB, Hany TF, Tam S, Jochum W, et al. Impact of integrated positron emission tomography and computed tomography on staging and management of gallbladder cancer and cholangiocarcinoma. J Hepatol. 2006;45(1):43–50.
65. Kim JY, Kim MH, Lee TY, Hwang CY, Kim JS, Yun SC, et al. Clinical role of ^{18}F-FDG PET-CT in suspected and potentially operable cholangiocarcinoma: a prospective study compared with conventional imaging. Am J Gastroenterol. 2008;103(5): 1145–51.
66. Corvera CU, Blumgart LH, Akhurst T, DeMatteo RP, D'Angelica M, Fong Y, et al. ^{18}F-fluorodeoxyglucose positron emission tomography influences management decisions in patients with biliary cancer. J Am Coll Surg. 2008;206(1):57–65.
67. Breitenstein S, Apestegui C, Clavien PA. Positron emission tomography (PET) for cholangiocarcinoma. HPB (Oxford). 2008;10(2):120–1.
68. Kitajima K, Murakami K, Kanegae K, Tamaki N, Kaneta T, Fukuda H, et al. Clinical impact of whole body FDG-PET for recurrent biliary cancer: a multicenter study. Ann Nucl Med. 2009;23(8):709–15.
69. Furukawa H, Ikuma H, Asakura-Yokoe K, Uesaka K. Preoperative staging of biliary carcinoma using 18F-fluorodeoxyglucose PET: prospective comparison with PET+CT, MDCT and histopathology. Eur Radiol. 2008;18(12):2841–7.
70. Kitamura K, Hatano E, Higashi T, Seo S, Nakamoto Y, Narita M, et al. Prognostic value of ^{18}F-fluorodeoxyglucose positron emission tomography in patients with extrahepatic bile duct cancer. J Hepatobiliary Pancreat Sci. 2011;18(1):39–46.
71. Butte JM, Redondo F, Waugh E, Meneses M, Pruzzo R, Parada H, et al. The role of PET-CT in patients with incidental gallbladder cancer. HPB (Oxford). 2009;11 (7):585–91.
72. Shukla PJ, Barreto SG, Arya S, Shrikhande SV, Hawaldar R, Purandare N, et al. Does PET-CT scan have a role prior to radical re-resection for incidental

gallbladder cancer? HPB (Oxford). 2008;10(6): 439–45.
73. Leung U, Pandit-Taskar N, Corvera CU, D'Angelica MI, Allen PJ, Kingham TP, et al. Impact of pre-operative positron emission tomography in gallbladder cancer. HPB (Oxford). 2014;16(11):1023–30.
74. Kumar R, Sharma P, Kumari A, Halanaik D, Malhotra A. Role of ^{18}F-FDG PET/CT in detecting recurrent gallbladder carcinoma. Clin Nucl Med. 2012;37(5):431–5.
75. Sacks A, Peller PJ, Surasi DS, Chatburn L, Mercier G, Subramaniam RM. Value of PET/CT in the Management of Liver Metastases, Part 1. Am J Roentgenol. 2011;197(2):W256–W9.
76. Agarwal A, Marcus C, Xiao J, Nene P, Kachnic LA, Subramaniam RM. FDG PET/CT in the Management of Colorectal and Anal Cancers. Am J Roentgenol. 2014;203(5):1109–19.
77. Takei T, Boni G, Tamaki N, Saito H, Strauss HW. Tumors of the liver and biliary tract. In: Strauss HW, Mariani G, Volterrani D, Larson SM, editors. Nuclear oncology: pathophysiology and clinical applications. New York: Springer; 2012. p. 451–72.

Diagnostic Applications of Nuclear Medicine: Pancreatic Cancer

27

Elena Tabacchi, Cristina Nanni, Irene Bossert, Anna Margherita Maffione, and Stefano Fanti

Abstract

Pancreatic cancer can be assessed through a variety of imaging techniques including endoscopic ultrasonography (EUS), computed tomography (CT), endoscopic retrograde cholangiopancreatography (ERCP), magnetic resonance imaging (MRI), and magnetic resonance cholangiopancreatography (MRCP).

These imaging modalities are often effective in the evaluation of pancreatic cancers although sometimes they require the use of radiopharmaceuticals with positron and single-photon emission CT (PET and SPECT) imaging techniques. In this chapter the role of nuclear medicine with various radiolabeled compounds and the rationale for their use in endocrine and nonendocrine pancreatic tumors are discussed.

Keywords

Pancreatic cancer • Neuroendocrine tumor • Gastroenteropancreatic tumor • SPECT/CT • PET/CT • Somatostatin receptor scintigraphy • Somatostatin analogues • ^{111}In-pentetreotide • [^{18}F]FDG • ^{123}I-MIBG • ^{131}I-MIBG • ^{18}F-DOPA • ^{68}Ga-DOTA-peptides • Peptide radioreceptor therapy

Glossary

[^{18}F]FDG	2-deoxy-2-[^{18}F]fluoro-D-glucose
[^{18}F]FDOPA	*L*-3,4-Dihydroxy-6-[^{18}F] fluorophenylalanine
^{18}F-DOPA	2-^{18}F-Fluoro-L-3,4-dihydroxyphenylalanine
[^{11}C]5-HTP	[^{11}C]5-Hydroxy-L-tryptophan
^{18}F-FLT	3'-^{18}F-fluoro-3'-deoxythymidine
^{123}I-MIBG	meta-[^{123}I] iodobenzylguanidine
^{131}I-MIBG	meta-[^{131}I] iodobenzylguanidine
ACTHoma	Neuroendocrine tumor producing adrenocorticopic hormone
AJCC	American Joint Committee on Cancer
BRCA1	Breast cancer type 1 susceptibility protein
BRCA2	Breast cancer type 2 susceptibility protein
CA 19-9	Carbohydrate antigen 19-9

E. Tabacchi (✉) • C. Nanni (✉) • S. Fanti (✉)
Nuclear Medicine Unit, "S. Orsola-Malpighi" University Hospital, Bologna, Italy
e-mail: tabacchielena@libero.it

I. Bossert (✉)
Nuclear Medicine Unit, "S. Orsola-Malpighi" University Hospital, Bologna, Italy

Nuclear Medicine Service, "Fondazione Salvatore Maugeri" IRCCS, Pavia, Italy

A.M. Maffione (✉)
Nuclear Medicine Unit, Ospedale Santa Maria della Misericordia, Rovigo, Italy

© Springer International Publishing Switzerland 2017
H.W. Strauss et al. (eds.), *Nuclear Oncology*,
https://doi.org/10.1007/978-3-319-26236-9_17

CCK2	Cholecystokinin 2
CRHoma	Neuroendocrine tumor producing corticotropin-releasing hormone
CT	X-ray computed tomography
DM	Diabetes mellitus
DOPA	Dihydroxyphenylalanine
DOTA	1,4,7,10-Tetra-azacyclododecane-1,4,7,10-tetraacetic acid
DTPA	Diethylenetriaminepentaacetic acid
EDDA	Ethylenediamine-N,N'-bis(2-hydroxyphenyl)acetic acid
ENETS	European Neuroendocrine Tumor Society
ERCP	Endoscopic retrograde cholangiopancreatography
EUS	Endoscopic ultrasonography
FAMM	Multiple mole melanoma syndrome
FNA	Fine-needle aspiration
G-CSF	Granulocyte colony-stimulating factor
GEP-NET	Gastro-entero-pancreatic neuroendocrine tumor
GHRHoma	Neuroendocrine tumor producing growth hormone-releasing hormone
GI	Gastrointestinal
GLP-1	Exendin
GLP1R	Glucagon-like peptide 1 receptor
GTV	Gross tumor volume
hENT-1	Human equilibrative nucleoside transporter-1
HPF	High-power field
HYNIC	Hydrazidonicotinic acid/hydrazinonicotinamide
IPMN	Intraductal papillary mucinous neoplasm
LAN	Lanreotide
MDCT	Multi-detector row computed tomography
MIBG	Metaiodobenzylguanidine
MIP	Maximum intensity projection
MRCP	Magnetic resonance cholangiopancreatography
MRI	Magnetic resonance imaging
MTC	Medullary thyroid carcinoma
mTOR	Mammalian target of rapamycin
NCCN	National Comprehensive Cancer Network
NEC	Neuroendocrine carcinoma
NET	Neuroendocrine tumor
NOC	1-Nal^3-octreotide
PanIN	Pancreatic intraepithelial neoplasia
PC	Pancreatic cancer
PET	Positron emission tomography
PET/CT	Positron emission tomography/computed tomography
PET/MR	Integrated positron emission tomography/magnetic resonance system
pNEN	Pancreatic neuroendocrine neoplasm
pNET	Pancreatic neuroendocrine tumors
PRRT	Peptide receptor radionuclide therapy
R0	Surgery achieving negative microscopic resection margins
R1	Surgery achieving microscopic positive resection margins
R2	Surgery achieving residual macroscopic disease
RT	Radiation therapy
SPECT	Single-photon emission computed tomography
SPECT/CT	Single-photon emission computed tomography/computed tomography
SR	Somatostatin receptor
SRS	Somatostatin receptor scintigraphy
SSA	Somatostatin analogues
SSTR	Somatostatin receptors
SUV	Standardized uptake value
TATE	Octeotate
TNM	AJCC/UICC staging system based on parameters “T” (tumor status), “N” (lymph node status) and “M” (distant metastasis status)

TOC	Octreotide
UICC	Union Internationale Contre le Cancer (International Union Against Cancer)
US	Ultrasonography
VAP	Vapreotide
VIP	Vasoactive intestinal peptide
WHO	World Health Organization

Contents

Epidemiology of the Tumor 751

Environmental Factors and Genetic Predisposition 751

Clinical Manifestations and Diagnosis 752

Staging, Prognostic Classification, and Common Therapies 755

Diagnostic Imaging and Role of Nuclear Medicine 758
Primary Lesion Detection and Characterization 759
Pancreatic Cancer Staging 760
Therapy Response Evaluation 761
Prognostic Significance 762
Suspect of Relapse 762
Radiotherapy (RT) Planning 762
[^{18}F]FDG PET/CT-Guided Biopsy 764

Neuroendocrine Tumors 764
Somatostatin Receptor Scintigraphy 765
Metaiodobenzylguanidine (MIBG) Scintigraphy ... 765
Gastrin Receptor Scintigraphy 766
Glucagon-Like Peptide 1 Receptor Imaging 766
Vasoactive Intestinal Peptide Receptor Scintigraphy 766
PET/CT Using ^{68}Ga-DOTA-Labeled SSAs 766
[^{18}F]FDG PET/CT 766
^{18}F-DOPA PET/CT 768
[^{11}C]5-HTP 768

Future Directions and Ongoing Studies 768

References 768

Epidemiology of the Tumor

Pancreatic cancer (PC) is one of the five most lethal malignancies in the world [1], with an incidence rate equaling that of its mortality rate [2–4].

Its overall 5-year survival rate is 6%. Even after potentially curative surgery, survival rate does not increase significantly, with a 5-year survival rate raging from 10% to 25% [5–10].

Unfortunately, at the time of diagnosis, over 80% of all pancreatic tumors are unresectable [3].

Tumor detection at an earlier stage and development of effective therapies are the mainstay for reducing cancer death rate, even if the lack of a valid screening tool in terms of cost-efficacy makes this challenge difficult.

Environmental Factors and Genetic Predisposition

Less than 20% of familial pancreatic cancers can be attributed to a genetic syndrome [11], including hereditary cancer syndromes (like Peutz-Jeghers syndrome, familial atypical multiple mole melanoma, hereditary breast-ovarian cancer associated with BRCA1 and BRCA2 mutations, hereditary nonpolyposis colorectal carcinoma, and familial adenomatous polyposis) and syndromes related to inherited pancreatitis. Subjects presenting known familial adenomatous polyposis, BRCA1, or BRCA2 mutations have less than 5% increased relative risk [12] in comparison to the general population, while the risk in familial atypical multiple mole melanoma syndrome (FAMM) or Peutz-Jeghers is much greater [13]. The number of affected first-degree relatives and environmental factors can affect this genetic predisposition: some families with pancreatic cancer affecting at least two first-degree relatives and no association with genetic syndrome are currently defined as a "familial" pancreatic cancer kindred [14].

Hereditary pancreatitis and cystic fibrosis represent other syndromes that lead to an increased risk of pancreatic cancer. The remaining 80% of cases with an inherited predisposition remain under the generic term of familial pancreatic cancer with unclear genes identification.

Other epidemiological risk factors for pancreatic cancer include smoking [15], age (the risk increases with the age with a peak between 60 and 80 years) [1], race/ethnicity (more common in the African American population in comparison to the white population, probably as a result of socioeconomic factors and cigarette smoking) [1], gender (slightly more common in men than in women), chronic pancreatitis [16], long-standing

diabetes (long-standing DM is a modest risk factor for pancreatic cancer; conversely, new adult-onset diabetes mellitus can be a manifestation of pancreatic cancer [17]), partial gastrectomy [1], dietary risk factors (high meat intake, fried foods, nitrosamines) [1], and ABO blood groups (subjects with non-O-type blood are at modestly increased risk) [18].

Clinical Manifestations and Diagnosis

In the natural history of PC, symptoms at the time of diagnosis predict early death because symptoms are related to an advanced stage of disease: PC is diagnosed a median of 2 months after onset of symptoms, and death usually occurs 4–6 months following diagnosis. Delay in diagnosis is not uncommon due to nonspecific symptoms.

PC is considered a tumor with high propensity for metastatic dissemination so much that most patients with a history of resected PC subsequently die of metastatic disease [19].

To suspect PC on physical examination is a challenge for clinicians due to its retroperitoneal location. Disease-related symptoms depend on tumor location within the pancreas and on the degree of pancreatic involvement. First symptoms to appear include painless jaundice (in case of bile duct obstruction) and weight loss.

In advanced, metastatic disease, palpable lymph nodes, hepatomegaly, splenomegaly, ascites and peripheral edema (portal vein obstruction), palpable gallbladder (Courvoisier's sign), left supraclavicular lymphadenopathy (Virchow's node), or an abdominal mass might be appreciated [20].

Unfortunately, even laboratory findings in pancreatic cancer are nonspecific: raised liver enzymes and abnormalities in vitamin K-dependent clotting factors are related to biliary obstruction and malabsorption of fat-soluble vitamins, while impaired glucose tolerance or frank diabetes could be secondary to pancreatic duct obstruction and pancreatic atrophy (in as many as 70% of patients) [21].

Carbohydrate antigen 19-9 (CA 19-9) is the most commonly used serological marker in pancreatic cancer. Although it has a sensitivity of 80%, specificity is low (67.5%) because serum levels increase in many benign and malignant gastrointestinal conditions. For this reason, routine use as a diagnostic tool is not recommended, even if sequential evaluations may correlate with tumor growth. The presence of a normal CA 19-9, however, does not exclude recurrence [22–24].

Recent studies identified several promising biomarkers from saliva, stool, blood, and pancreatic juice, but their clinical utility must be validated [19].

Currently, available pancreatic imaging has a key-role in the characterization of pancreatic focal lesions, initial staging, surgical and therapeutic planning, and assessment of the treatment response using various imaging modalities, including ultrasonography (US), computed tomography (CT), magnetic resonance imaging (MRI), positron emission tomography (PET), and endoscopic ultrasonography (EUS) [25–35].

Multi-detector row computed tomography (MDCT) has a major role in the diagnosis and staging of pancreatic malignancies. MDCT of the pancreas is favorably complemented by EUS, which is more sensitive for the early detection of lesions, and allows relatively easy access to the pancreas for tissue diagnosis using fine-needle aspiration (FNA), as well as providing further important information for use in tumor staging [36]. MRI with magnetic resonance cholangiopancreatography (MRCP) and PET scanning can also contribute as secondary imaging modalities under selected circumstances, namely, when CT and EUS are not diagnostic.

Pancreatic epithelial neoplasms show a wide range of pathologic features: some of the entities are very uncommon or are regarded as variants of other entities from which they do not differ significantly in terms of treatment or prognosis. Thus, the wide and complex classification can be summarized into a shorter list of neoplasms which occur more frequently (Table 1) [37].

A particular group is represented by pancreatic neuroendocrine neoplasms (pNEN) which originate from neuroendocrine cells of the pancreas and account for less than 3% of all malignancies of the pancreas (increasing annual incidence in a range of 0.32–0.43/100,000) [38–40].

Table 1 List of pancreatic neoplasms which occur frequently

Exocrine neoplasms	Endocrine neoplasms	Epithelial neoplasms with multiple directions of differentiation	Epithelial neoplasms of uncertain direction of differentiation	Miscellaneous epithelial neoplasms
Serous cystic neoplasms	Microadenoma (<0.5 cm)	Mixed acinar-endocrine carcinoma	Solid-pseudopapillary neoplasm	Teratoma
Microcystic serous cystadenoma				
Macrocystic serous cystadenoma				
Solid serous adenoma				
von Hippel-Lindau-associated serous cystic neoplasm				
Serous cystadenocarcinoma				
Mucinous cystic neoplasms	Well-differentiated pancreatic endocrine neoplasm	Mixed acinar-ductal carcinoma		Lymphoepitelial cyst
With low-grade dysplasia				
With moderate dysplasia				
With high-grade dysplasia (carcinoma in situ)				
With an associated invasive carcinoma				
Intraductal neoplasms	Poorly differentiated endocrine carcinoma	Mixed ductal-endocrine carcinoma		Epidermoid cyst in intrapancreatic heterotopic spleen
Intraductal papillary mucinous neoplasms	Small cell carcinoma			
With low-grade dysplasia				
With moderate dysplasia	Large cell endocrine carcinoma			
With high-grade dysplasia (carcinoma in situ)				
With an associated invasive carcinoma				
Intraductal oncocytic papillary neoplasm				
Intraductal tubular neoplasms				
With low-grade dysplasia				

(*continued*)

Table 1 (continued)

Exocrine neoplasms	Endocrine neoplasms	Epithelial neoplasms with multiple directions of differentiation	Epithelial neoplasms of uncertain direction of differentiation	Miscellaneous epithelial neoplasms
With high-grade dysplasia (carcinoma in situ)				
With an associated invasive carcinoma				
Pancreatic intraepithelial neoplasia (PanIN)	Well-differentiated pancreatic endocrine neoplasm	Mixed acinar-ductal carcinoma		
PanIN-1A and PanIN-1B				
PanIN-2				
PanIN-3				
Invasive ductal adenocarcinoma		Pancreatoblastoma		
Tubular adenocarcinoma				
Adenosquamous carcinoma				
Colloid (mucinous noncystic) adenocarcinoma				
Hepatoid carcinoma				
Medullary carcinoma				
Signet ring cell carcinoma				
Undifferentiated carcinoma				
Anaplastic carcinoma				
Sarcomatoid carcinoma				
Carcinosarcoma				
Undifferentiated carcinoma with osteoclast-like giant cells				
Acinar cell neoplasms				
Acinar cell cystadenoma				
Acinar cell carcinoma				
Acinar cell cystadenocarcinoma				

Table 2 Clinical syndromes depending on the specific hormonal hypersecretion

Tumor subtype/ associated syndrome	Secretion products	Symptoms
Nonfunctional	Chromogranin A, pancreatic polypeptide, a-/β-human chorionic gonadotropin, calcitonin	Unspecific
Carcinoid syndrome	Serotonin	Diarrhea, flush, bronchial obstruction
Insulinoma	Insulin, proinsulin	Hypoglycemia
Gastrinoma/Zollinger-Ellison syndrome	Gastrin	Ulcerations, diarrhea
VIPoma	Vasoactive intestinal peptide	Diarrhea, hypokalemia
Glucagonoma	Glucagon	Necrolytic migratory erythema, diabetes mellitus
Somatostatinoma	Somatostatin	Diabetes mellitus, steatorrhea, cholelithiasis
GHRHoma	Growth hormone-releasing hormone	Acromegaly
CRHoma, ACTHoma	Corticotropin-releasing hormone, adrenocorticotropic hormone	Cushing's syndrome

For the most part, they are sporadic but they can also be part of rare hereditary syndromes like multiple endocrine neoplasia type 1 (with hyperparathyroidism and adenomas of the pituitary gland), von Hippel-Lindau syndrome, and tuberous sclerosis.

Pancreatic neuroendocrine neoplasms can be divided into functional and nonfunctional tumors. Functional tumors represent 10–55% of all pNEN with clinical syndromes depending on the specific hormonal hypersecretion [41, 42] (Table 2) and are most represented by insulinomas and gastrinomas. Carcinoid syndrome presenting with flush and/or diarrhea is only rarely seen (<5%) [41–44].

Nonfunctioning NETs may not present with clinical symptoms until they produce tumor mass effects at a late stage of tumor growth, so they are often diagnosed because of nonspecific abdominal symptoms or weight loss that leads the physician to make a referral for CT scanning of the abdomen.

Metastases are already present at the time of diagnosis in 60–70% of patients with the exception of insulinomas that are benign in 90% of the cases [45–48].

All pancreatic neuroendocrine tumors <2.0 cm in largest dimension with no evident local invasion or angioinvasion and no regional lymphatic or distant metastases are classified as "benign." Tumors confined to the pancreas and without metastases are said to be "uncertain" if the tumor size is >2.0 cm or local invasion has occurred (or both). Tumors with extended invasion of peripancreatic tissue or regional or distant tumor spread are classified as "malignant." These tumors can have heterogeneous microscopic findings, and immunohistochemical staining with markers (such as chromogranin A, synaptophysin, and neuron-specific enolase) can usually confirm the neuroendocrine origin [41].

Staging, Prognostic Classification, and Common Therapies

The staging system for pancreatic ductal adenocarcinoma is based on the AJCC/UICC TNM Staging System, 7th Edition (Tables 3 and 4) [49] which considers primary tumor extent (T stage), regional lymph node involvement (N stage), and presence of distant metastasis (M stage).

T stage includes: TX (primary tumor cannot be assessed), T0 (no evidence of primary tumor), Tis (carcinoma in situ, PanIN 3), T1 (tumor limited to the pancreas and no larger than 2 cm in greatest dimension), T2 (tumor limited to the pancreas but larger than 2 cm in greatest dimension), T3 (tumor

Table 3 TNM of the pancreatic ductal adenocarcinoma (From AJCC, 7th Edition)

Primary tumor (T)	
Tx	Primary tumor cannot be assessed
T0	No evidence of primary tumor
Tis	Carcinoma in situ
T1	Tumor limited to the pancreas, 2 cm or less in greatest dimension
T2	Tumor limited to the pancreas, more than 2 cm in greatest dimension
T3	Tumor extends beyond the pancreas but without involvement of the celiac axis or the superior mesenteric artery
T4	Tumor involves the celiac axis or the superior mesenteric artery (unresectable primary tumor)
Regional lymph nodes (N)	
Nx	Regional lymph nodes cannot be assessed
N0	No regional lymph node metastasis
N1	Regional lymph node metastasis
Distant metastasis (M)	
M0	No distant metastasis
M1	Distant metastasis

Table 4 Staging of the pancreatic adenocarcinoma based on TNM classification

AJCC staging for pancreatic cancer			
Stage	T	N	M
Stage 0	Tis	N0	M0
Stage IA	T1	N0	M0
Stage IB	T2	N0	M0
Stage IIA	T3	N0	M0
Stage IIB	T1	N1	M0
	T2	N1	M0
	T3	N1	M0
Stage III	T4	Any N	M0
Stage IV	Any T	Any N	M1

Table 5 Overall survival in pancreatic adenocarcinoma

Median survival (Mo)			
Stage	All patients	Non-resected	Resected
IA	10.0	6.8	24.1
IB	9.1	6.1	20.6
IIA	8.1	6.2	15.4
IIB	9.7	6.7	12.7
III	7.7	7.2	10.6
IV	2.5	2.5	4.5
Total	4.4	3.5	12.6

Adapted from Bilimoria et al. [53].

extends beyond the pancreas but it doesn't involve the celiac axis or the superior mesenteric artery), and T4 (tumor extends beyond the pancreas and involves the celiac axis or the superior mesenteric artery).

N stage includes N0 (no regional lymph node metastasis) and N1 (presence of regional lymph node metastasis); the M stage includes M0 (absence of distant metastasis) and M1 (presence of distant metastasis).

The survival rate of patients with any stage of pancreatic exocrine cancer is poor. Clinical trials are appropriate alternatives for treatment of patients with any stage of disease and should be considered prior to selecting palliative approaches. Surgical resection remains the primary modality when feasible because it can lead to long-term survival and provides effective palliation [50–52].

Treatment guidelines of pancreatic ductal adenocarcinoma differ according to the stage: stage II cancers are generally treated by surgery and adjuvant chemotherapy (with or without adjuvant radiation therapy); stage III disease is treated by chemotherapy with or without adjuvant radiation therapy; stage IV is controlled with a chemotherapy-only approach (Table 4). TNM staging correlates with overall survival as shown in Table 5 [53].

Some important prognostic factors are the histological grade (poorly differentiated cancers have the worst overall survival compared to well- or moderately differentiated pancreatic ductal adenocarcinoma) [54, 55]. Also, features such as stromal content and lymphovascular invasion are associated with a poorer outcome [56, 57]. Despite the prognostic importance of TNM staging, the selection of patient candidates for resection is made through the use of a "surgical staging" defined by Varadhachary et al. from the MD Anderson Cancer Center and slightly modified by the National Comprehensive Cancer Network (NCCN) (Table 6) [58–60].

According to these, localized pancreatic ductal adenocarcinomas are separated into three categories based on the relationship to the major visceral vessels as well as the prospect of achieving an upfront or initial complete resection.

Table 6 Surgical staging

Surgical staging criteria based on the MD Anderson criteria and NCCN guidelines				
Abutment, ≤180° involvement of circumference of the vessel; encasement, >180° involvement of circumference of the vessel				
Stage	Superior mesenteric artery	Celiac axis	Hepatic artery	Superior mesenteric vein/portal vein
Resectable	No abutment	No abutment	No abutment	No distortion
Borderline resectable	Abutment	Abutment; involvement of hepatic artery without expansion to celiac (NCCN)	Abutment/short segment encasement with option for reconstruction	Short segment occlusion with option for reconstruction
Locally advanced	Encasement	Encasement; abutment for pancreatic ductal adenocarcinoma of the head (NCCN)	Encasement and no option for reconstruction	Occluded and no option for reconstruction

Adapted from surgical staging guidelines proposed by Varadhachary et al. [59]; Evans et al. [60] and NCCN guidelines

The *resectable tumors* are usually removed with R0 resection (negative microscopic resection margins); the *borderline resectable ones* are usually resected with R1 resection margins (microscopic positive resection margins), and *locally advanced* tumors will most likely achieve R2 resection margins (residual macroscopic disease). Resection margins refer to the surgical or transected resection margins and comprise the transected pancreatic neck, the uncinate margin, the duodenum, and the bile duct [61].

Radical pancreatic surgery includes the Whipple procedure (pancreaticoduodenal resection for the head and uncinate process masses) and distal pancreatectomy for tumors of the body and tail of the pancreas. To obtain negative margins of the surgical specimen, total pancreatectomy could be necessary (with or without splenectomy) [62, 63].

Patients with locally advanced or metastatic disease are not suitable for surgery, and a single therapy with gemcitabine is generally regarded as first-line therapy even if numerous patients do not respond due to chemoresistance [64]. The variation in chemoresistance between individuals is partly related to the human equilibrative nucleoside transporter-1 (hENT-1) responsible for the intracellular uptake of gemcitabine [65].

Few combinations of gemcitabine with other cytotoxic agents have yet provided any significantly prolonged overall survival rates with more toxic effects compared with gemcitabine as monotherapy [66, 67].

Some patients have palliation of symptoms when treated by chemotherapy with gemcitabine or 5-fluorouracil [68–70].

The use of capecitabine and erlotinib in patients with gemcitabine refractory first-line treatment of advanced pancreatic cancer is associated with modest improvements in overall survival [71].

Pain-relieving procedures such as celiac or intrapleural block and palliative biliary bypass or stent placement must be considered.

Radiologists commonly use language in reports that could lead inexperienced clinicians to falsely assume a pancreatic ductal adenocarcinoma as unresectable [72]; for this reason, a multidisciplinary approach or surgical consultation in the evaluation of all patients with localized tumors is important.

Less than 20% of patients with pancreatic ductal adenocarcinoma are candidates for resection, and the majority of patients who undergo resection will still recur [56].

This is most likely due to occult metastases that had already occurred at the time of diagnosis although patients presented with clinical stage I or II.

At the moment, there are no effective screening tests to detect pancreatic ductal adenocarcinoma at a curable stage, and ongoing studies focus on

innovative molecular markers in serum and gastrointestinal secretions that could lead to early detection. The staging system based on regional and distant disease spread seems relatively crude: some patients without lymph node spread have rapid recurrence after resection, while many with lymph node spread have long-term survival [73]. It appears likely that genomic, transcriptomic, proteomic, and metabolomic signatures associated with a more aggressive biology will emerge and these will complement or replace the current staging system.

Pancreatic neuroendocrine neoplasms are classified based on histopathology according to the World Health Organization (WHO) classification (2010) [74], and an important part of this classification is the tumor grading (proliferative activity evaluated by Ki-67 index or by counting mitoses) that correlates with prognosis [75].

Neuroendocrine tumors with a proliferation index <2% usually show a slow growth, while neuroendocrine carcinomas with a proliferation index >20% usually have an aggressive behavior [45]. Also the size of the tumor affects the likelihood of metastasis: primary tumors of <2 cm only rarely metastasize. When possible, surgical resection of primary tumors with radical intent is recommended and that is the mainstay of therapy in insulinoma. If the primary tumor is a G1/2 pNET, surgical approaches also include metastases. Systemic treatment can be used for palliative care or as neoadjuvant approach to reduce tumor size before surgical treatment. For symptom control, functional tumors are primarily treated with somatostatin analogues (SSA) with the exception of gastrinomas that can be treated using proton-pump inhibitors alone for long periods. In insulinomas diazoxide is used to inhibit the release of insulin from the pancreas.

Antiproliferative SSA-based treatment can be used in functional and nonfunctional pNET with a proliferation index <10% [76]; streptozotocin-based chemotherapy is recommended according to the guidelines of the European Neuroendocrine Tumor Society (ENETS) in patients with progressive disease.

In patients with progressive disease while on chemotherapy, targeted therapies are used such as the multi-targeted receptor tyrosine kinase inhibitor sunitinib and the mammalian target of rapamycin (mTOR) inhibitor everolimus. Other treatment options are peptide receptor radionuclide therapy (PRRT) and other kinds of chemotherapy like temozolomide [46]. Diagnostic imaging, beside clinical assessment, has a major role in therapeutic decision in this setting of multidisciplinary treatment options.

Diagnostic Imaging and Role of Nuclear Medicine

Early detection of pancreatic cancer is pivotal to improve the patient's survival rate. The standard imaging technique for the initial evaluation of pancreatic cancer is contrast-enhanced computed tomography (CT) and/or magnetic resonance imaging (MRI) with magnetic resonance cholangiopancreatography (MRCP). Endoscopic ultrasound (EUS) allows further local staging and allows histologic confirmation by means of EUS-guided biopsy or fine-needle aspiration on the detected lesion. Although CT currently has a major role in the evaluation of pancreatic cancer, MRI with MRCP allows better detection of tumors at an earlier stage through a comprehensive analysis of the morphological changes of the pancreatic parenchyma and ductal system. The diagnosis could be improved using positron emission tomography techniques (PET/CT) in selected scenarios where CT and EUS are equivocal. It is essential for clinicians to understand the advantages and disadvantages of each imaging modality in order to select the correct imaging workup and pursue optimal treatment [77].

2-Deoxy-2-[^{18}F]fluoro-D-glucose-based positron emission tomography ([^{18}F]FDG PET) imaging allows the assessment of in vivo tissue metabolism and defines malignant tumors as hypermetabolic lesions hence lesions with an increased tracer uptake. The rationale for its use is based on the increased expression of membrane glucose transporters subsequent to an enhanced anaerobial glycolytic activity in cancer cells, which leads to a higher glucose demand. [^{18}F]FDG is carried into the cell by glucose transporters, as the normal glucose to be rapidly phosphorylated in a

biochemical form that causes its virtual trapping into the cell.

The CT component of [^{18}F]FDG PET/CT can be either a noncontrast CT (for anatomical localization of the abnormalities seen on PET and further attenuation correction of PET images) or a contrast-enhanced CT (a true diagnostic adjunct to PET) [33, 35].

Integrated PET and MR (PET/MR) scanners have recently become available. As MR has the inherent strength of superior soft-tissue contrast resolution, multiplanar imaging acquisition, and functional imaging capability, such as that seen in DCE-MR, DWI, MR spectroscopy, or elastography, PET/MR may exhibit superior diagnostic performance compared with PET/CT [78].

Since [^{18}F]FDG mimics glucose metabolism, there is physiologially a diffuse accumulation of this tracer in tissues such as the brain and liver. [^{18}F]FDG uptake in both normal tissues and tumor is influenced by a variety of patient-related factors like blood glucose levels, diabetes, recent meals, administration of granulocyte colony-stimulating factor (G-CSF), etc. For this reason, a proper prescan protocol is essential for diagnostic accuracy and reproducibility, including fasting for at least 6 h prior to the study, administering a dose of [^{18}F]FDG based on the patients height and weight in an optimal blood glucose range (usually $<$200 mg/dL), voiding prior to the study to avoid mistaking [^{18}F]FDG in the urine for pathologic uptake, minimizing patient motion prior to the study to reduce [^{18}F]FDG uptake in the muscles and misregistration during the acquisition phase, and maintaining moderate room temperatures to avoid uptake in brown fat [33, 35, 79].

Primary Lesion Detection and Characterization

PET alone is not considered a first-line examination to identify a primary pancreatic malignancy although some studies reported a relatively high sensitivity for pancreatic cancer (84–95%) [80–83].

Despite some intensely [^{18}F]FDG-avid tumors, pancreatic cancers do not usually show high [^{18}F]FDG uptake, with a mean SUV of only 6.7 as described in a study by Izhuishi et al. This value is only slightly higher than the mean SUV of the pancreas itself (2.0) [80]. Another limitation of PET is the identification of lesions $<$1 cm in size, and for this reason, MDCT remains the primary diagnostic modality for identifying a suspected pancreatic malignancy with a sensitivity approaching 97% and with a rapid exam execution, wide availability, and diagnostic accuracy. In most cases, MRI or endoscopic ultrasound is a better second-line modality than PET or PET/CT, such as in cases with a dilated pancreatic duct on MDCT without a discrete identifiable mass or an equivocal lesion on CT [84].

On the other hand, an important role for PET or PET/CT in primary diagnosis of a pancreatic mass is the differentiation of a pancreatic cancer from a focal chronic pancreatitis: Van Kouwen et al. described that 87% of chronic pancreatitis did not have any [^{18}F]FDG uptake while 24/26 patients with pancreatic cancer had focal uptake [85]. There is also evidence that PET may have a role in distinguishing pancreatic cancer from autoimmune pancreatitis: Lee et al. suggested that autoimmune pancreatitis showed diffuse uptake throughout the gland in more than 50% of cases (without focality contrarily to what happens in pancreatic cancer) and tended to be associated with abnormal uptake in the salivary glands and kidneys [86]. An advantage of using [^{18}F]FDG PET has been observed in the characterization of pancreatic cystic lesions with a sufficient amount of [^{18}F]FDG-avid tumor cells [87–89].

Sperti et al. [90] studied the usefulness of [^{18}F]FDG PET in differentiating malignant from benign pancreatic cysts in 50 patients concluding that [^{18}F]FDG PET was more accurate than CT (94% vs. 80% respectively).

Intraductal papillary mucinous neoplasms (IPMNs), are tumors characterized by the intraductal proliferation of neoplastic mucinous cells in the main pancreatic duct or in major branches, represent a diagnostic challenge: an accurate differentiation between IPMN with low-grade or moderate-grade dysplasia and malignant lesions (IPMN with high-grade dysplasia and invasive carcinoma) is essential to an appropriate treatment planning [91], and in this scenario PET/CT seems to be useful [92, 93].

Pancreatic Cancer Staging

PET/CT can be a valid tool in staging patients with localized lesions on CT that are at high risk for metastatic disease, including patients with locally advanced disease, borderline resectable tumors, or a severe increase of CA 19-9 [58]. PET/CT does not currently add much staging information in most patients with resectable disease [94, 95] (Fig. 1).

False-negative PET results can be observed in hyperglycemic patients or in subcentimeter lesions, whereas false-positive PET results can occur in some inflammatory states like pancreatitis (Fig. 2), infection of a pseudocyst, or local inflammation due to the placement of a biliary stent and the resulting accumulation of leukocytes with high metabolic activity [96–98]. Some studies including a meta-analysis in 2001 by Gambhir et al., a study by Zafra et al., and another one by Topkan et al. found that PET/CT changed management of patients with pancreatic adenocarcinoma respectively in 36%, 34%, and 36.6% of the studied populations [99–102]. Despite these results, a study by Izuishi et al. conducted in 2010 on 65 patients with pancreatic cancer found that 61.5% of patients had metastatic disease to the liver that was already confirmed on CT: hence PET did not change a single patient's staging. However, in the same study, PET detected a considerable number of nodal and bone metastases not found on CT. Nonetheless in these patients, already judged inoperable due to vascular involvement or liver metastases, PET/CT did not change management [80]. Another study by Lytras et al. found no real benefit from PET compared to CT in identifying either liver metastases or peritoneal carcinomatosis [98]. Although literature remains equivocal on whether PET truly changes patient outcomes and management, the majority of available data suggest that PET identifies some metastases not detected on CT. Thus PET/CT has become an accepted part of the imaging algorithm for patients with a new diagnosis of pancreatic cancer.

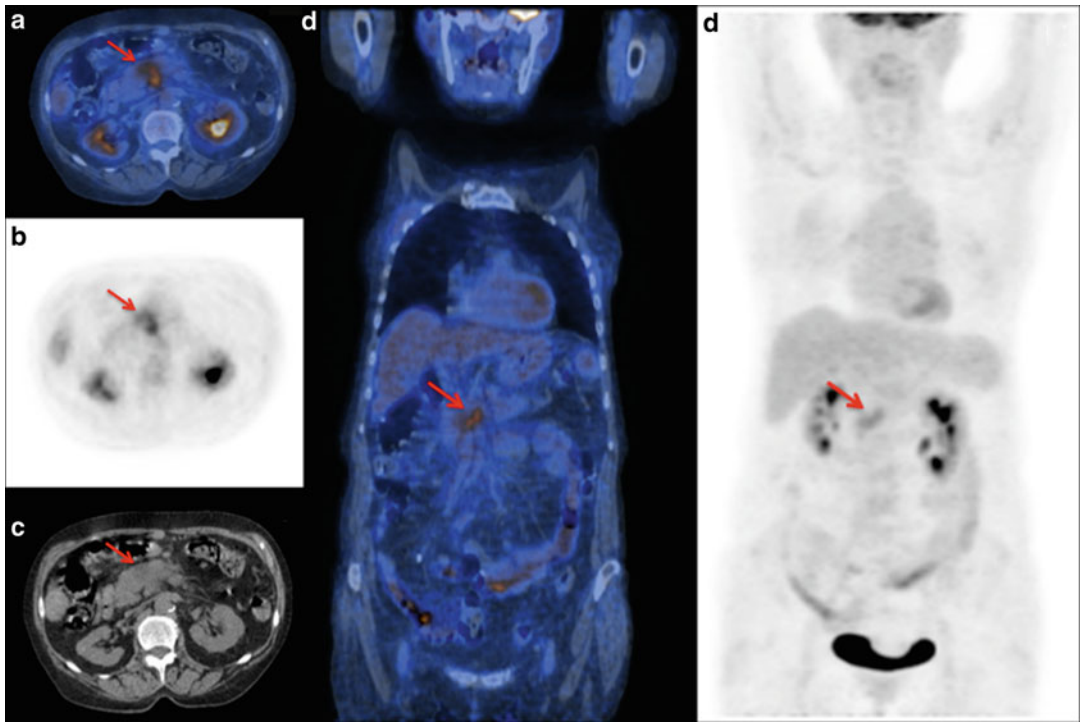

Fig. 1 Staging [^{18}F]FDG PET/CT. *Red flags*: pancreatic findings, pancreatic adenocarcinoma. (**a**) PET/CT, transaxial; (**b**) PET, transaxial; (**c**) CT, transaxial; (**d**) PET/CT, coronal; (**e**) MIP

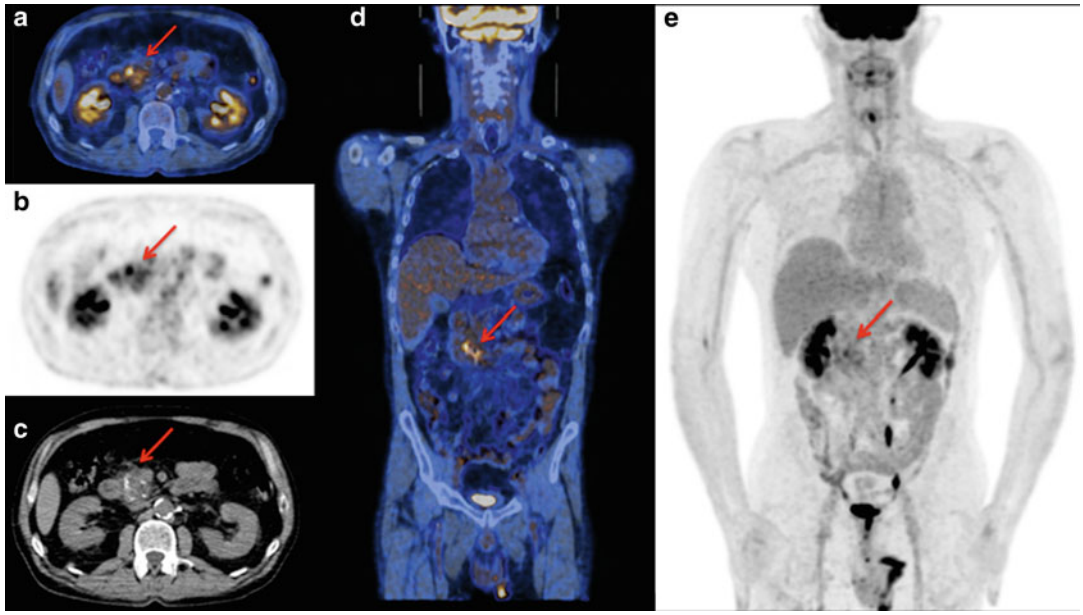

Fig. 2 False-positive [^{18}F]FDG PET/CT. *Red flags*: pancreatic findings, chronic pancreatitis. (**a**) PET/CT, transaxial; (**b**) PET, transaxial; (**c**) CT, transaxial; (**d**) PET/CT, coronal; (**e**) MIP

It should be emphasized that PET without a diagnostic contrast-enhanced CT is highly limited for staging, and a study by Imai et al. found that PET was as insensitive as CT for nodal metastases to the para-aortic chain (most likely due to PET's lack of sensitivity for lesions <1 cm) [103]. Furthermore, the role of PET in assessing local tumor spread and vascular involvement remains uncertain because the [^{18}F]FDG uptake within the primary mass can confound the assessment of the vascular margins where a degree of intrinsic [^{18}F]FDG blood activity is also present. For this reason, at the time, the resolution of PET is not considered sufficient to determine the vessels involvement, therefore the tumor resectability.

Therapy Response Evaluation

The identification of early responders to chemotherapy is important to avoid unnecessary toxicity in patients who will not respond (Fig. 3). Sometimes the metabolic response is not accompanied by changes in tumor size after chemoradiation therapy [104], and morphological response assessment by conventional imaging can be inaccurate (e.g., presence of fibrosis induced by treatments). In this scenario we can assume that the [^{18}F]FDG PET study can assess treatment response earlier and better compared with conventional imaging [105, 106].

In patients who are judged to be borderline resectable and are recommended to undergo neoadjuvant therapy, a baseline PET scan and CA 19-9 would allow the assessment of tumor metabolic response during therapy [107].

It is desirable to determine an appropriate time interval between end of treatment and time of posttherapy PET scan. Whereas oncologic therapies are expected to decrease the tumor metabolism, a treatment-induced inflammatory reaction can increase [^{18}F]FDG uptake. It has been demonstrated that also nonirradiated organs could show this inflammatory reaction probably via a cytokine interaction, and total [^{18}F]FDG uptake could fluctuate for more than 1 month [108].

However, perhaps because of its poor prognosis and short follow-up, there are no data on the right time interval between therapy and the PET study; therefore, we use the timing applied to other malignancies such as the head and neck (3 months from radiotherapy).

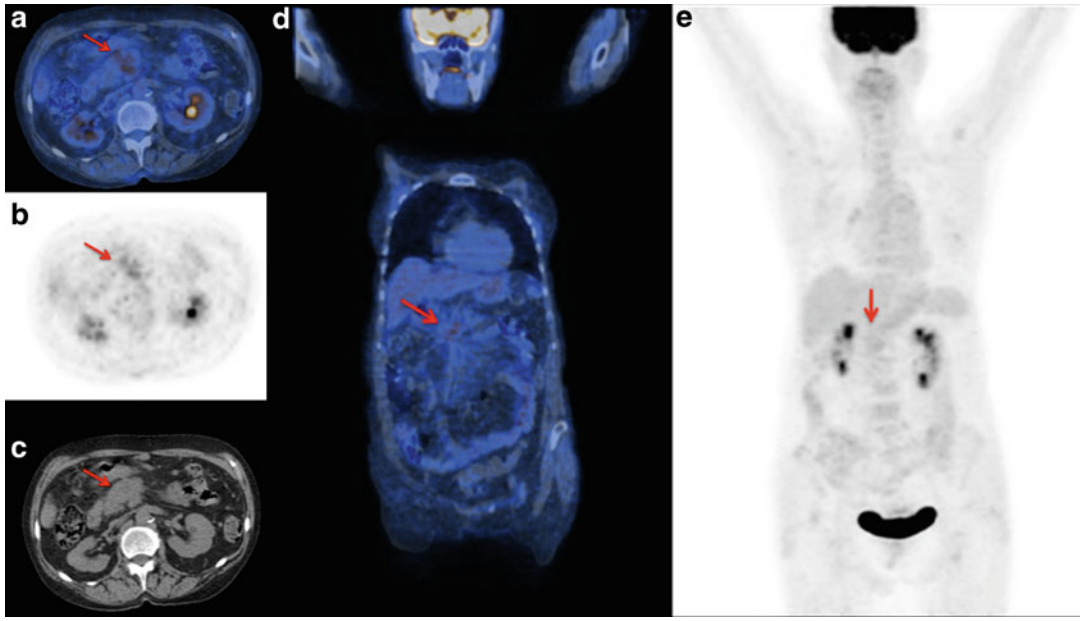

Fig. 3 Restaging [^{18}F]FDG PET/CT after 3 months from the end of radiotherapy in the same patient whose staging scan is represented in Fig. 1. *Red flags*: residual pancreatic cancer. (**a**) PET/CT, transaxial; (**b**) PET, transaxial; (**c**) CT, transaxial; (**d**) PET/CT, coronal; (**e**) MIP

[^{18}F]FDG PET/CT may predict survival by distinguishing between responders and nonresponders in order to plan the best treatment strategy [104, 105] and may be useful in differentiating recurrent disease from postsurgical/radiotherapy changes, especially if there is an increase in tumor marker levels with negative or equivocal conventional imaging findings [87, 109].

Prognostic Significance

Several studies have shown a correlation between higher metabolic activity of pancreatic carcinoma and poorer prognosis thus providing prognostic information [87].

Suspect of Relapse

An elevated CA 19-9 has a positive predictive value for pancreatobiliary malignancy of only 69%. This means that over 30% of those with an elevated CA 19-9 may have another tumor originating in another organ, or they may have no tumor at all. False-positive results have been associated with other pancreatobiliary disorders such as gallstones, pancreatitis, inflammatory bowel disease, other liver disorders, pulmonary diseases such as pneumonia, and hydronephrosis [110].

In this setting, when CA 19-9 is rising despite negative conventional imaging, [^{18}F]FDG PET could have a role in detecting sites of undetected recurrence, such as the local, liver, peritoneal dissemination, lung, distant lymph nodes metastasis (Fig. 4). [^{18}F]FDG PET could also exclude the presence of recurrence in cases of indeterminate findings by other imaging modalities [111].

Radiotherapy (RT) Planning

A well-established treatment option for patients with locally advanced pancreatic cancer is concurrent chemoradiotherapy, but, despite significant improvements in diagnostic imaging, chemotherapy, and radiotherapy, the outcome remains poor [112, 113].

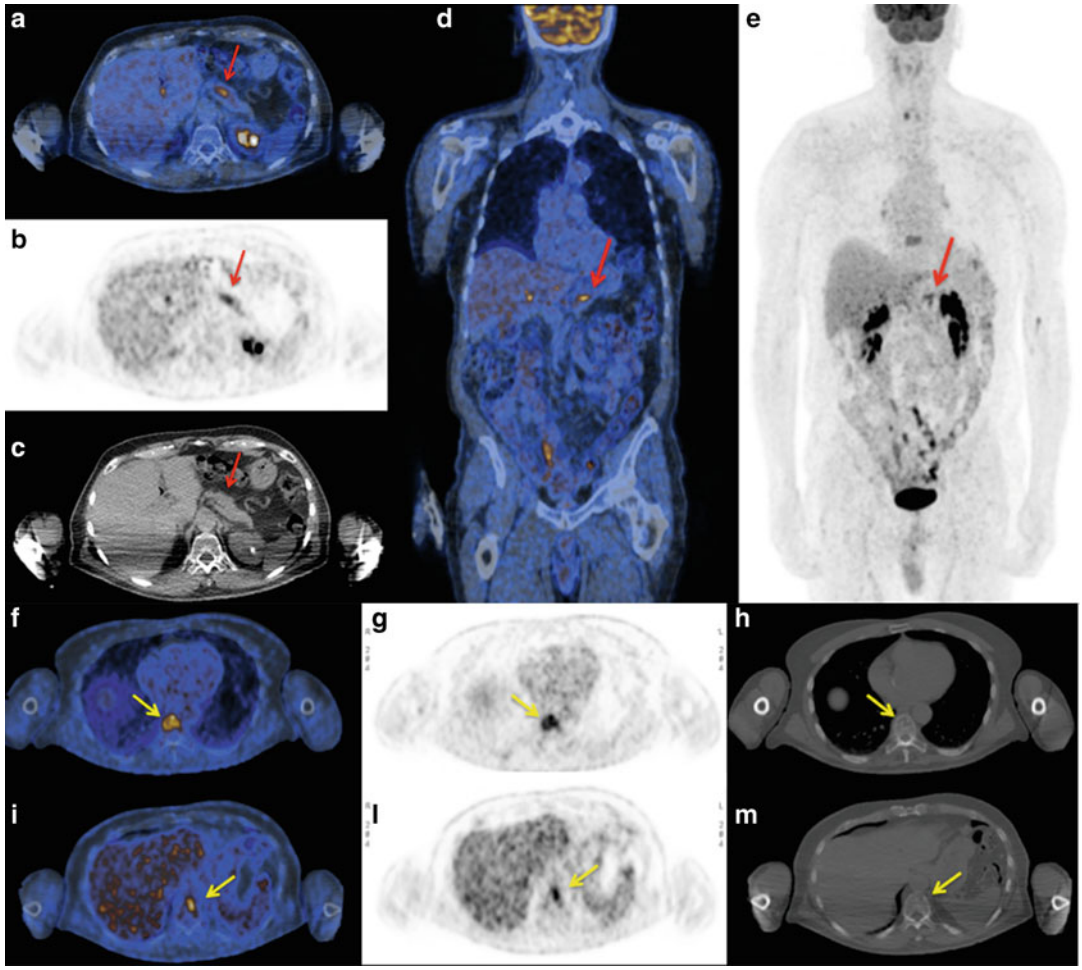

Fig. 4 (**a**) [^{18}F]FDG PET/CT in a patient with a history of pancreaticoduodenectomy and a suspect of relapse. *Red flags*: recurrence, pancreatic findings. *A* PET/CT, transaxial; *B* PET, transaxial; *C* CT, transaxial; *D* PET/CT, coronal; *E* MIP. (**b**) *Yellow flags*: bone recurrence. *F* I, PET/CT, transaxial; *G* L, PET, transaxial; *H* M, CT, transaxial

The accurate definition of target volumes and administration of appropriate radiation doses to these volumes represent a reasonable way to reduce local disease.

According to literature, the accuracy of target volume delineation, sometimes difficult with the use of conventional imaging alone (low accuracy on N and M staging), might be improved beyond the CT-based delineation by integrating PET and CT data. This integration allows an enlargement of the gross tumor volume (GTV) in 35.7% of cases due to detection of additional CT occult lymph node metastases and/or primary tumor extensions defined on the co-registered [^{18}F]FDG PET/CT with no evidence of increased toxicity [114].

Regarding resectable pancreatic cancer, in several surgical series, the outcome is proven to be affected by tumor size, status of resection margins, invasion of vascular and/or adjacent structures, degree of differentiation, performance status, CA 19-9, and C-reactive protein levels [115]. A few series indicate prognostic factors in locally advanced pancreatic cancer. A study by Parlak et al. [116] conducted on patients with locally advanced pancreatic cancer investigated the

potential prognostic value of the GTV delineated by co-registered contrast-enhanced CT and [^{18}F]FDG PET/CT-based RT on their outcome. This study suggests [^{18}F]FDG PET/CT-defined GTV may have a role in predicting outcome (in terms of overall survival, local regional progression free survival and progression free survival).

However, further evaluation in prospective clinical trials will be required to assess the real impact of change management induced by PET/CT on the overall survival of unresectable patients.

[^{18}F]FDG PET/CT-Guided Biopsy

PET/CT-guided biopsy combines the well-established value of anatomical information from CT with PET metabolic characterization [117] also in view of the fact that a lesion can present [^{18}F]FDG uptake with no anatomical alterations.

Malignant lesions can be heterogeneous and [^{18}F]FDG PET/CT is able to guide biopsy to the area of highest [^{18}F]FDG uptake [117, 118] (Fig. 5). The first studies on [^{18}F]FDG PET/CT-guided biopsy were published in 2008 by O'Sullivan et al. on musculoskeletal lesions [119] and subsequently other studies including that from Cerci et al. [120] in 2012 and Purandare et al. [121] in 2013 confirmed the value of PET/CT in guiding biopsy procedures.

When deciding on therapy, [^{18}F][^{18}F]FDG PET/CT-positive results should be confirmed by histology when possible: PET/CT-guided biopsy is feasible with reduced invasiveness, lower costs, and complication rate compared with surgical methods [122] and may optimize the diagnostic yield of image-guided interventions.

Neuroendocrine Tumors

Ultrasound, computed tomography, magnetic resonance, and nuclear medicine imaging play an important role also in the detection of clinically

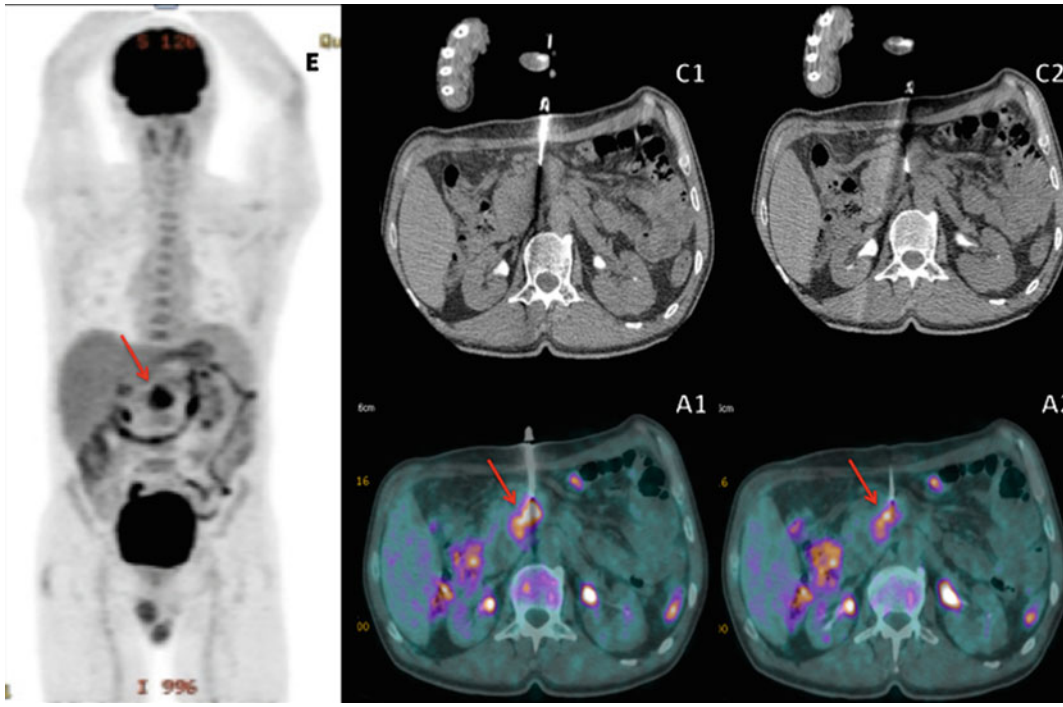

Fig. 5 [^{18}F]FDG PET/CT-guided biopsy. *Red flags*: pancreatic findings, site of biopsy. *A1* A2, PET/CT, transaxial; *C1* C2, CT, transaxial; *E* MIP (Images kindly provided by Juliano Cerci (Clinica Quanta, Curitiba, Brazil))

suspected or diagnosed pancreatic neuroendocrine tumors for staging.

Single photon and positron emitting radionuclides can be combined with various ligands (functionally active part) including somatostatin analogues [123]. Overexpression of subtypes of somatostatin receptors (SSTRs) in well- to moderately differentiated pNEN allows their in vivo characterization using single-photon emission computed tomography (SPECT) or positron emission tomography (PET) while for high-grade (more aggressive) pNEN, [^{18}F]FDG is preferred [124, 125].

The diagnosis of insulinomas poses a problem with somatostatin receptor analogues, and other tracers have been suggested as alternatives including ^{18}F-DOPA and GLP-1 (exendin labeled with either ^{111}In or ^{68}Ga) [126]. The major advantages of nuclear medicine imaging are the high sensitivity in detecting the primary tumor and metastases in unusual locations (whole body imaging), the high specificity in case of SSTR-positive lesions, and the assessment of SSTR positivity for therapeutic purposes. In order to add additional morphological informations, SPECT and PET should be combined with CT or MR imaging [127]. According to the ENETS guidelines, when initial SSTRs imaging is positive, patients should undergo SSTRs imaging for staging every 18–24 months [46].

Somatostatin Receptor Scintigraphy

Somatostatin is a peptide secreted by endocrine D cells in the gastrointestinal (GI) tract and pancreas, and it inhibits the release of endocrine and exocrine factors in the GI system itself [128].

Most GEP-NET cells have a high expression of high-affinity somatostatin receptors which are further classified into five subtypes (SSTR1, SSTR2, SSTR3, SSTR4, SSTR5) [129, 130]. More than 80% of GEP-NET express the subtype SSTR2 that binds the commercially available somatostatin analogues (SSAs) and the radiolabeled SSAs [129, 131].

^{111}In-DTPA-pentetreotide (Octreoscan®) is used for somatostatin receptor scintigraphy (SRS) [132]: it preferentially binds to SSTR2 with lower affinity to SSTR5 and SSTR3 [129, 133, 134]. Planar and single-photon emission computed tomography (SPECT) images are generally obtained 24 and 48 h after injection of this radiopharmaceutical. SRS has an overall sensitivity for well-differentiated GEP-NET of more than 80% and plays an important role in localization of primary GEP-NETs, their metastases and in monitoring treatment responses. SRS with ^{111}In-DTPA-pentetreotide can predict the clinical efficacy of current commercially available SSAs, and it is a useful tool to select patients for PRRT utilizing beta-radiation-emitting SSAs [135–138]. Physiological uptake of radiolabeled SSAs is shown in the pituitary gland, thyroid, kidneys, liver, and spleen [139]. False-positive results can derive from the presence of accessory spleen, infections, adrenal medullary tumors, and sometimes a specific uptake in the uncinate process of the pancreas [132]. The sensitivity is lower for small lesions (diameter <1 cm) due to insufficient tumor to background uptake ratio for nonmetastasized insulinomas due to low expression of SSTR2 [132, 140], and for NETs with high Ki-67 index [123].

Other radiolabeled SSAs (some still under investigation or already been used in few centers) are those labeled with ^{99m}Tc including ^{99m}Tc-depreotide (high affinity for SSTR2, SSTR3, and SSTR5) [141] and ^{99m}Tc-vapreotide (high affinity for SSTR2 and SSTR5 and low affinity for SSTR3 and SSTR4 [142]).

^{111}In-DOTA-lanreotide, ^{99m}Tc-HYNIC-TOC, and ^{99m}Tc-HYNIC-TATE are similar, in terms of SSTR affinity profile and results, to ^{111}In-pentetreotide [143–145].

Metaiodobenzylguanidine (MIBG) Scintigraphy

Radioiodinated MIBG, ^{123}I-MIBG (or ^{131}I-MIBG), is a guanethidine analogue with structural features similar to norepinephrine that at low concentrations is transported across the plasma membrane and accumulated in catecholamine-storing granules [146]. ^{123}I-MIBG (or ^{131}I-MIBG) scintigraphy has

a lower sensitivity than SRS for the imaging of NETs of the gastrointestinal tract (sensitivity about 50%) and pancreas (sensitivity <10%), but in patients with metastatic and inoperable GEP-NETs, high uptake on MIBG scintigraphy suggests a role for palliative treatment with ^{131}I-MIBG [147–150].

False-positive ^{123}I-MIBG scintigraphy is possible in adrenocortical adenoma, adrenocortical carcinoma, angiomyolipoma, and gastrointestinal stromal tumors [151].

Gastrin Receptor Scintigraphy

A high percentage of medullary thyroid carcinomas (MTCs) express the cholecystokinin 2 (CCK2) receptor, and many CCK2 receptor-binding radiopeptides have been developed for scintigraphy (^{111}In-DOTA-CCK, ^{99m}Tc-demogastrin, ^{111}In-DOTA-MG11), whereas for PET/CT imaging, ^{68}Ga-DOTA-minigastrin is used [152–154]. As GEP-NETs also express CCK2 receptors, this imaging modality was tested also in a variety of GEP-NETS (overall tumor detection reached 74% for ^{68}Ga-DOTA-minigastrin PET) [153].

Glucagon-Like Peptide 1 Receptor Imaging

Pancreatic beta-cells mainly express the glucagon-like peptide 1 receptor (GLP1R), and for this reason, it represents a target for imaging of insulinomas even if malignant insulinomas (unlike benign insulinomas) often lack GLP1R [155]. In many studies, GLP1R scintigraphy using ^{111}In-DOTA-exendin-4 successfully detected benign insulinomas, and this radiopharmaceutical is applied for the intraoperative localization of these benign tumors [155–159].

(Lys^{40}(Ahx-HYNIC-^{99m}Tc/EDDA)NH$_2$)-exendin-4 is another radiopeptide used for targeting the GLP1R and has been studied in medullary thyroid carcinomas (MTCs) and benign insulinomas [160, 161] [68].Ga-DOTA-exendin-3 is a promi sing tracer to visualize insulinomas on PET i maging [162].

Vasoactive Intestinal Peptide Receptor Scintigraphy

^{123}I-labeled vasoactive intestinal peptide (VIP) receptor scintigraphy generally shows lower sensitivity compared to SRS in GEP-NET localization, and for this reason, it is generally not recommended for the diagnostic workup of GEP-NETs [163–165].

PET/CT Using ^{68}Ga-DOTA-Labeled SSAs

^{68}Ga-DOTA-labeled SSAs (DOTANOC, DOTATATE, and DOTATOC) are used for the diagnostic workup of GEP-NETs (they allow for imaging 1–3 h within i.v. injection) and differ in their affinity spectrum toward the different SSTRs [132, 166–169]. ^{68}Ga-DOTATATE has high affinity for SSTR2, ^{68}Ga-DOTATOC for STTR2 and SSTR5, and ^{68}Ga-DOTANOC for SSTR2, SSTR3, and SSTR5 [132, 166–169] (Figs. 6 and 7). PET/CT with ^{68}Ga-DOTANOC, ^{68}Ga-DOTATATE, or ^{68}Ga-DOTATOC shows higher sensitivity for GEP-NET lesions in comparison with SRS SPECT-CT (more than 90%) due to better spatial resolution and SSTR binding affinity [132, 166–169].

There are new ^{68}Ga-DOTA-labeled SSAs for PET imaging that include ^{68}Ga-DOTAVAP and ^{68}Ga-DOTALAN [142].

[^{18}F]FDG PET/CT

High [^{18}F]FDG uptake is generally associated with more aggressive (poorly differentiated) GEP-NETs; thus, the use of this radiotracer can have an additional value in grade 3 neuroendocrine carcinomas (especially when SRS is negative) [123, 132, 170, 171].

[^{18}F]FDG PET has been used to predict the GEP-NET and lung-NET responses to PRRT with ^{177}Lu-octreotate: if [^{18}F]FDG PET after PRRT was negative, no tumor progression was found at follow-up. Patients with both a grade 2 NET and a positive [^{18}F]FDG PET finding showed a worse disease course after PRRT with subsequent changes in their therapeutic approach [172].

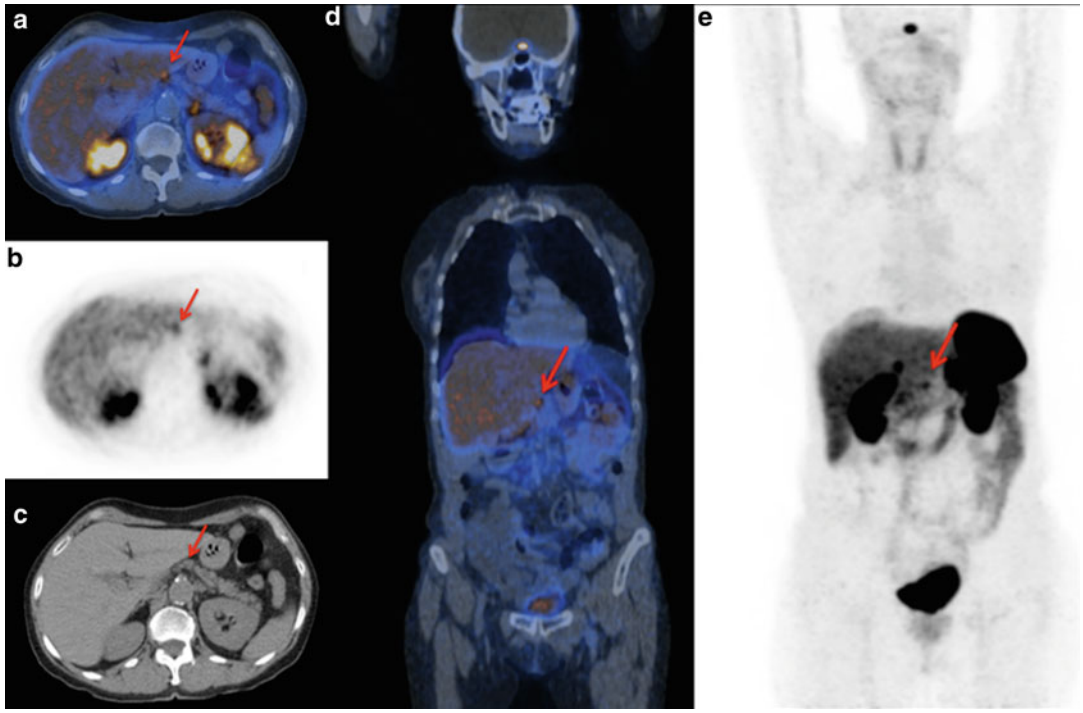

Fig. 6 Staging ^{68}Ga-DOTANOC PET/CT. *Red flags*: pancreatic findings. (**a**) PET/CT, transaxial; (**b**) PET, transaxial; (**c**) CT, transaxial; (**d**) PET/CT, coronal; (**e**) MIP

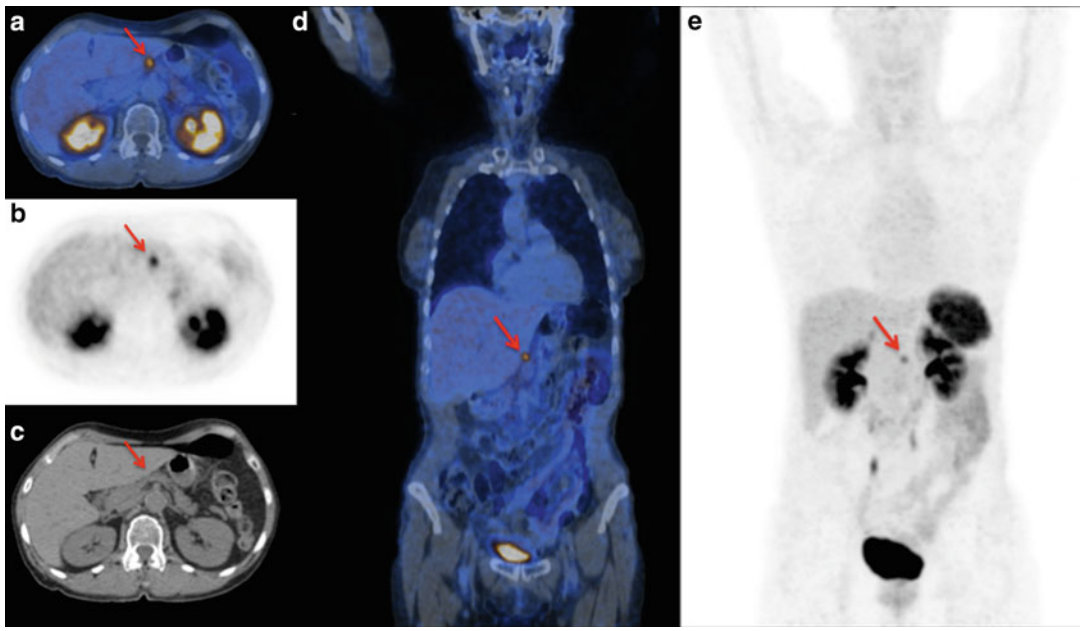

Fig. 7 ^{68}Ga-DOTANOC PET/CT to assess response to treatment after 2 months of therapy with somatostatin in the same patient as in Fig. 6. *Red flags*: pancreatic findings. (**a**) PET/CT, transaxial; (**b**) PET, transaxial; (**c**) CT, transaxial; (**d**) PET/CT, coronal; (**e**) MIP

^{18}F-DOPA PET/CT

The use of ^{18}F-L-3,4-dihydroxyphenylalanine (^{18}F-DOPA) PET/CT is based on co-secretion of dopamine and hormones or peptides by GEP-NET cells. In these cells, L-DOPA is converted by the enzyme L-DOPA decarboxylase to dopamine.

In comparison with SRS and [^{11}C]5-hydroxy-L-tryptophan ([^{11}C]5-HTP) PET and ^{18}F-DOPA PET showed the highest sensitivity (98%) for the detection of NETs of the gastrointestinal tract but not for those of the pancreas [132, 173].

[^{11}C]5-HTP

[^{11}C]5-HTP is a radiolabeled precursor in the synthesis of serotonin. The short half-life of the ^{11}C radiolabel and the complex synthesis limits the clinical use and the availability of [^{11}C]5-HTP PET. Compared with CT, SRS, and ^{18}F-DOPA PET, [^{11}C]5-HTP PET showed the highest sensitivity (96%) for the detection of pancreatic NETs [132, 173–176], and it is particularly useful for detecting small pancreatic NETs and early recurrences.

Future Directions and Ongoing Studies

New tracers such as [^{11}C]thymidine or the thymidine analogue 3'-^{18}F-fluoro-3'-deoxythymidine (^{18}F-FLT) could be a potential alternative to [^{18}F]FDG in prognosticating and characterizing pancreatic cancer: some studies have demonstrated that the quantification of the nuclear antigen Ki-67, a proliferation indicator, enables reliable differentiation between benign and malignant pancreatic tumors [177]; therefore, compounds that indicate proliferative activity, such as ^{18}F-FLT [178], should be more suitable for differentiating between malignancy and inflammatory processes than nonspecific metabolic markers such as [^{18}F]FDG [179].

It is apparent that PET techniques will gradually replace SPECT. New somatostatin receptors radioligands are being developed for clinical imaging, not only are somatostatin receptor agonists being studied but also receptor antagonists [180]. Other peptide receptors might be interesting target for receptor imaging like gastrin-releasing peptide or bombesin receptors [181–183].

References

1. Raimondi S, Maisonneuve P, Lowenfels AB. Epidemiology of pancreatic cancer: an overview. Nat Rev Gastroenterol Hepatol. 2009;6:699–708.
2. Hariharan D, Saied A, Kocher HM. Analysis of mortality rates for pancreatic cancer across the world. HPB (Oxford). 2008;10:58–62.
3. Hidalgo M. Pancreatic cancer. N Engl J Med. 2010; 362:1605–17.
4. Siegel R, Naishadham D, Jemal A. Cancer statistics, 2013. CA Cancer J Clin. 2013;63:11–30.
5. Klinkenbijl JH, Jeekel J, Sahmoud T, van Pel R, Couvreur ML, Veenhof CH, et al. Adjuvant radiotherapy and 5-fluorouracil after curative resection of cancer of the pancreas and periampullary region: phase III trial of the EORTC gastrointestinal tract cancer cooperative group. Ann Surg. 1999;230:776–82.
6. Klinkenbij JH, Jeekel J, Schmitz PI, Rombout PA, Nix GA, Bruining HA, et al. Carcinoma of the pancreas and periampullary region: palliation versus cure. Br J Surg. 1993;80:1575–8.
7. Neoptolemos JP, Stocken DD, Friess H, Bassi C, Dunn JA, Hickey H, et al. A randomized trial of chemoradiotherapy and chemotherapy after resection of pancreatic cancer. N Engl J Med. 2004;350: 1200–10.
8. Oettle H, Post S, Neuhaus P, Gellert K, Langrehr J, Ridwelski K, et al. Adjuvant chemotherapy with gemcitabine vs observation in patients undergoing curative-intent resection of pancreatic cancer: a randomized controlled trial. JAMA. 2007;17(297): 267–77.
9. Sohn TA, Yeo CJ, Cameron JL, Koniaris L, Kaushal S, Abrams R, et al. A Resected adenocarcinoma of the pancreas - 616 patients: results, outcomes, and prognostic indicators. J Gastrointest Surg. 2000;4:567–79.
10. Wagner M, Redaelli C, Lietz M, Seiler CA, Friess H, Büchler MW, et al. Curative resection is the single most important factor determining outcome in patients with pancreatic adenocarcinoma. Br J Surg. 2004;91:586–94.
11. Hruban RH, Canto MI, Goggins M, Schulick R, Klein AP. Update on familial pancreatic cancer. Adv Surg. 2010;44:293–311.
12. Goggins M, Canto M, Hruban R. Can we screen high-risk individuals to detect early pancreatic carcinoma? J Surg Oncol. 2000;74:243–8.

13. Templeton AW, Brentnall TA. Screening and surgical outcomes of familial pancreatic cancer. Surg Clin North Am. 2013;93:629–45.
14. Klein AP, Brune KA, Petersen GM, Goggins M, Tersmette AC, Offerhaus GJ. Prospective risk of pancreatic cancer in familial pancreatic cancer kindreds. Cancer Res. 2004;64:2634–8.
15. Lynch SM, Vrieling A, Lubin JH, Kraft P, Mendelsohn JB, Hartge P. Cigarette smoking and pancreatic cancer: a pooled analysis from the pancreatic cancer cohort consortium. Am J Epidemiol. 2009; 170:403–13.
16. Raimondi S, Lowenfels AB, Morselli-Labate AM, Maisonneuve P, Pezzilli R. Pancreatic cancer in chronic pancreatitis; aetiology, incidence, and early detection. Best Pract Res Clin Gastroenterol. 2010; 24:349–58.
17. Pannala R, Basu A, Petersen GM, Chari ST. New-onset diabetes: a potential clue to the early diagnosis of pancreatic cancer. Lancet Oncol. 2009;10:88–95.
18. Risch HA, Lu L, Wang J, Zhang W, Ni Q, Gao YT, et al. ABO blood group and risk of pancreatic cancer: a study in Shanghai and meta-analysis. Am J Epidemiol. 2013;177:1326–37.
19. Chari ST, Kelly K, Hollingsworth MA, Thayer SP, Ahlquist DA, Andersen DK. Early detection of sporadic pancreatic cancer: summative review. Pancreas. 2015;44:693–712.
20. Takhar AS, Palaniappan P, Dhingsa R, Lobo DN. Recent developments in diagnosis of pancreatic cancer. BMJ. 2004;18(329):668–73.
21. Saruc M, Pour PM. Diabetes and its relationship to pancreatic carcinoma. Pancreas. 2003;26:381–7.
22. Ozkan H, Kaya M, Cengiz A. Comparison of tumour marker CA 242 with CA 19-9 and carcinoembryonic antigen (CEA) in pancreatic cancer. Hepatogastroenterology. 2003;50:1669–74.
23. Willett CG, Daly WJ, Warshaw AL. CA 19-9 is an index of response to neoadjunctive chemoradiation therapy in pancreatic cancer. Am J Surg. 1996;172:350–2.
24. Yeo TP, Hruban RH, Leach SD, Wilentz RE, Sohn TA, Kern SE. Pancreatic cancer. Curr Probl Cancer. 2002;26:176–275.
25. Karmazanovsky G, Fedorov V, Kubyshkin V, Kotchatkov A. Pancreatic head cancer: accuracy of CT in determination of resectability. Abdom Imaging. 2005;30:488–500.
26. Miura F, Takada T, Amano H, Yoshida M, Furui S, Takeshita K. Diagnosis of pancreatic cancer. HPB (Oxford). 2006;8:337–42.
27. Brennan DD, Zamboni GA, Raptopoulos VD, Kruskal JB. Comprehensive preoperative assessment of pancreatic adenocarcinoma with 64-section volumetric CT. Radiographics. 2007;27:1653–66.
28. Morana G, Cancian L, Pozzi Mucelli R, Cugini C. Staging cancer of the pancreas. Cancer Imaging. 2010; 10(Spec no A):S137–41.
29. Appel BL, Tolat P, Evans DB, Tsai S. Current staging systems for pancreatic cancer. Cancer J. 2012;18: 539–49.
30. Fusaroli P, Kypraios D, Caletti G, Eloubeidi MA. Pancreatico-biliary endoscopic ultrasound: a systematic review of the levels of evidence, performance and outcomes. World J Gastroenterol. 2012;18:4243–56.
31. Sahani DV, Bonaffini PA, Catalano OA, Guimaraes AR, Blake MA. State-of-the-art PET/CT of the pancreas: current role and emerging indications. Radiographics. 2012;32:1133–58; discussion 1158–60.
32. Conrad C, Fernández-Del Castillo C. Preoperative evaluation and management of the pancreatic head mass. J Surg Oncol. 2013;107:23–32.
33. Shrikhande SV, Barreto SG, Goel M, Arya S. Multimodality imaging of pancreatic ductal adenocarcinoma: a review of the literature. HPB (Oxford). 2012;14:658–68.
34. Raman SP, Horton KM, Fishman EK. Multimodality imaging of pancreatic cancer-computed tomography, magnetic resonance imaging, and positron emission tomography. Cancer J. 2012;18:511–22.
35. Dibble EH, Karantanis D, Mercier G, Peller PJ, Kachnic LA, Subramaniam RM. PET/CT of cancer patients: part 1, pancreatic neoplasms. AJR Am J Roentgenol. 2012;199:952–67.
36. Kinney T. Evidence-based imaging of pancreatic malignancies. Surg Clin North Am. 2010;90:235–49.
37. Klimstra DS, Pitman MB, Hruban RH. An algorithmic approach to the diagnosis of pancreatic neoplasms. Arch Pathol Lab Med. 2009;133:454–64.
38. Lawrence B, Gustafsson BI, Chan A, Svejda B, Kidd M, Modlin IM. The epidemiology of gastroenteropancreatic neuroendocrine tumors. Endocrinol Metab Clin N Am. 2011;40:1–18.
39. Yao JC, Hassan M, Phan A, Dagohoy C, Leary C, Mares JE. One hundred years after "carcinoid": epidemiology of and prognostic factors for neuroendocrine tumors in 35,825 cases in the United States. J Clin Oncol. 2008;26:3063–72.
40. Zhou J, Enewold L, Stojadinovic A, Clifton GT, Potter JF, Peoples GE. Incidence rates of exocrine and endocrine pancreatic cancers in the United States. Cancer Causes Control. 2010;21:853–61.
41. Falconi M, Plockinger U, Kwekkeboom DJ, Manfredi R, Korner M, Kvols L. Well-differentiated pancreatic non-functioning tumors/carcinoma. Neuroendocrinology. 2006;84:196–211.
42. O'Toole D, Salazar R, Falconi M, Kaltsas G, Couvelard A, de Herder WW. Rare functioning pancreatic endocrine tumors. Neuroendocrinology. 2006; 84:189–95.
43. Modlin IM, Moss SF, Gustafsson BI, Lawrence B, Schimmack S, Kidd M. The archaic distinction between functioning and non-functioning neuroendocrine neoplasms is no longer clinically relevant. Langenbecks Arch Surg. 2011;396:1145–56.
44. Halfdanarson TR, Rabe KG, Rubin J, Petersen GM. Pancreatic neuroendocrine tumors (PNETs): incidence, prognosis and recent trend toward improved survival. Ann Oncol. 2008;19:1727–33.
45. Jensen RT, Cadiot G, Brandi ML, de Herder WW, Kaltsas G, Komminoth P, et al. ENETS Consensus

Guidelines for the management of patients with digestive neuroendocrine neoplasms: functional pancreatic endocrine tumor syndromes. Neuroendocrinology. 2012;95:98–119.
46. Pavel M, Baudin E, Couvelard A, Krenning E, Öberg K, Steinmüller T, et al. ENETS Consensus Guidelines for the management of patients with liver and other distant metastases from neuroendocrine neoplasms of foregut, midgut, hindgut, and unknown primary. Neuroendocrinology. 2012;95:157–76.
47. Heitz PU, Kommith P, Perren A, Klimstra DS, Dayal Y, Bordi C, et al. Pathology and genetics of tumours of endocrine organs. In: DeLellis DA, Lloyd RV, Heitz PU, editors. WHO classification of tumours. Pancreatic endocrine tumours: introduction. Lyon: IARC Press; 2004. p. 177–82.
48. Schindl M, Kaczirek K, Kaserer K, Niederle B. Is the new classification of neuroendocrine pancreatic tumours of clinical help? World J Surg. 2000;24:1312–8.
49. Edge SB, Byrd DR, Compton CC, Fritz AG, Greene FL, Trotti A. AJCC cancer staging manual (7th ed.). New York: Springer; 2010.
50. Yeo CJ, Cameron JL, Lillemoe KD, Sitzmann JV, Hruban RH, Goodman SN. Pancreaticoduodenectomy for cancer of the head of the pancreas. 201 patients. Ann Surg. 1995;221:721–31; discussion 731–3.
51. Conlon KC, Klimstra DS, Brennan MF. Long-term survival after curative resection for pancreatic ductal adenocarcinoma. Clinicopathologic analysis of 5-year survivors. Ann Surg. 1996;223:273–9.
52. Yeo CJ, Abrams RA, Grochow LB, Sohn TA, Ord SE, Hruban RH, et al. Pancreaticoduodenectomy for pancreatic adenocarcinoma: postoperative adjuvant chemoradiation improves survival. A prospective, single-institution experience. Ann Surg. 1997;225:621–33; discussion 633–6.
53. Bilimoria KY, Bentrem DJ, Ko CY, Ritchey J, Stewart AK, Winchester DP. Validation of the 6th edition AJCC pancreatic cancer staging system: report from the national cancer database. Cancer. 2007;110:738–44.
54. Wasif N, Ko CY, Farrell J, Wainberg Z, Hines OJ, Reber H. Impact of tumor grade on prognosis in pancreatic cancer: should we include grade in AJCC staging? Ann Surg Oncol. 2010;17:2312–20.
55. Rochefort MM, Ankeny JS, Kadera BE, Donald GW, Isacoff W, Wainberg ZA, et al. Impact of tumor grade on pancreatic cancer prognosis: validation of a novel TNMG staging system. Ann Surg Oncol. 2013;20:4322–9.
56. Winter JM, Cameron JL, Campbell KA, Arnold MA, Chang DC, Coleman J. 1423 pancreaticoduodenectomies for pancreatic cancer: a single-institution experience. J Gastrointest Surg. 2006;10:1199–210.
57. Erkan M, Michalski CW, Rieder S, Reiser-Erkan C, Abiatari I, Kolb A, et al. The activated stroma index is a novel and independent prognostic marker in pancreatic ductal adenocarcinoma. Clin Gastroenterol Hepatol. 2008;6:1155–61.
58. National Comprehensive Cancer Network (NCCN) practice guidelines in oncology. Pancreatic adenocarcinoma (version 1.2014). Available at: http://www.nccn.org/professionals/physician_gls/pdf/pancreatic.pdf.
59. Varadhachary GR, Tamm EP, Abbruzzese JL, Xiong HQ, Crane CH, Wang H, et al. Borderline resectable pancreatic cancer: definitions, management, and role of preoperative therapy. Ann Surg Oncol. 2006;13:1035–46.
60. Evans DB, Erickson BA, Ritch P. Borderline resectable pancreatic cancer: definitions and the importance of multimodality therapy. Ann Surg Oncol. 2010;17:2803–5.
61. Katz MH, Merchant NB, Brower S, Branda M, Posner MC, William Traverso L, et al. Standardization of surgical and pathologic variables is needed in multicenter trials of adjuvant therapy for pancreatic cancer: results from the ACOSOG Z5031 trial. Ann Surg Oncol. 2011;18:337–44.
62. Dalton RR, Sarr MG, van Heerden JA, Colby TV. Carcinoma of the body and tail of the pancreas: is curative resection justified? Surgery. 1992;111:489–94.
63. Brennan MF, Moccia RD, Klimstra D. Management of adenocarcinoma of the body and tail of the pancreas. Ann Surg. 1996;223:506–11; discussion 511–2.
64. Andersson R, Aho U, Nilsson BI, Peters GJ, Pastor-Anglada M, Rasch W, et al. Gemcitabine chemoresistance in pancreatic cancer: molecular mechanisms and potential solutions. Scand J Gastroenterol. 2009;44:782–6.
65. Damaraju VL, Damaraju S, Young JD, Baldwin SA, Mackey J, Sawyer MB. Nucleoside anticancer drugs: the role of nucleoside transporters in resistance to cancer chemotherapy. Oncogene. 2003;22:7524–36.
66. Di Marco M, Di Cicilia R, Macchini M, Nobili E, Vecchiarelli S, Brandi G. Metastatic pancreatic cancer: is gemcitabine still the best standard treatment? Oncol Rep. 2010;23:1183–92.
67. Sun C, Ansari D, Andersson R, Wu DQ. Does gemcitabine-based combination therapy improve the prognosis of unresectable pancreatic cancer? World J Gastroenterol. 2012;18:4944–58.
68. Rothenberg ML, Moore MJ, Cripps MC, Andersen JS, Portenoy RK, Burris 3rd HA. A phase II trial of gemcitabine in patients with 5-FU-refractory pancreas cancer. Ann Oncol. 1996;7:347–53.
69. Burris 3rd HA, Moore MJ, Andersen J, Green MR, Rothenberg ML, Modiano MR, et al. Improvements in survival and clinical benefit with gemcitabine as firstline therapy for patients with advanced pancreas cancer: a randomized trial. J Clin Oncol. 1997;15:2403–13.
70. Storniolo AM, Enas NH, Brown CA, Voi M, Rothenberg ML, Schilsky R. An investigational new drug treatment program for patients with gemcitabine: results for over 3000 patients with pancreatic carcinoma. Cancer. 1999;85:1261–8.
71. Kulke MH, Blaszkowsky LS, Ryan DP, Clark JW, Meyerhardt JA, Zhu AX, et al. Capecitabine plus

erlotinib in gemcitabine-refractory advanced pancreatic cancer. J Clin Oncol. 2007;25:4787–92.
72. Fong ZV, Tan WP, Lavu H, Kennedy EP, Mitchell DG, Koniaris LG, et al. Preoperative imaging for resectable periampullary cancer: clinicopathologic implications of reported radiographic findings. J Gastrointest Surg. 2013;17:1098–106.
73. Winter JM, Brennan MF, Tang LH, D'Angelica MI, Dematteo RP, Fong Y, et al. Survival after resection of pancreatic adenocarcinoma: results from a single institution over three decades. Ann Surg Oncol. 2012;19: 169–75.
74. Bosman FT, Carneiro F, Hruban RH, Theise ND. WHO classification of tumours of the digestive system. 4th ed. Lyon: IARC; 2010.
75. Rindi G, Falconi M, Klersy C, Albarello L, Boninsegna L, Buchler MW, et al. TNM staging of neoplasms of the endocrine pancreas: results from a large international cohort study. J Natl Cancer Inst. 2012;104:764–77.
76. Caplin ME, Pavel M, Ruszniewski P. Lanreotide in metastatic enteropancreatic neuroendocrine tumors. N Engl J Med. 2014;371:224–33.
77. Lee ES, Lee JM. Imaging diagnosis of pancreatic cancer. World J Gastroenterol. 2014;20:7864–77.
78. Torigian DA, Zaidi H, Kwee TC, Saboury B, Udupa JK, Cho ZH, et al. PET/MR imaging: technical aspects and potential clinical applications. Radiology. 2013; 267:26–44.
79. De Gaetano AM, Rufini V, Castaldi P, Gatto AM, Filograna L, Giordano A, et al. Clinical applications of ^{18}F-FDG PET in the management of hepatobiliary and pancreatic tumors. Abdom Imaging. 2012;37: 983–1003.
80. Izuishi K, Yamamoto Y, Sano T, Takebayashi R, Masaki T, Suzuki Y. Impact of 18-fluorodeoxyglucose positron emission tomography on the management of pancreatic cancer. J Gastrointest Surg. 2010;14:1151–8.
81. Lemke AJ, Niehues SM, Hosten N, Amthauer H, Boehmig M, Stroszczynski C, et al. Retrospective digital image fusion of multidetector CT and ^{18}F-FDG PET: clinical value in pancreatic lesions-a prospective study with 104 patients. J Nucl Med. 2004;45:1279–86.
82. Bang S, Chung HW, Park SW, Chung JB, Yun M, Lee JD, et al. The clinical usefulness of 18-fluorodeoxyglucose positron emission tomography in the differential diagnosis, staging, and response evaluation after concurrent chemoradiotherapy for pancreatic cancer. J Clin Gastroenterol. 2006;40:923–9.
83. Kauhanen SP, Komar G, Seppänen MP, Dean KI, Minn HR, Kajander SA, et al. A prospective diagnostic accuracy study of ^{18}F-fluorodeoxyglucose positron emission tomography/computed tomography, multidetector row computed tomography, and magnetic resonance imaging in primary diagnosis and staging of pancreatic cancer. Ann Surg. 2009;250:957–63.
84. Raman SP, Fishman EK, Lennon AM. Endoscopic ultrasound and pancreatic applications: what the radiologist needs to know. Abdom Imaging. 2013;38:1360–72.
85. van Kouwen MC, Jansen JB, van Goor H, de Castro S, Oyen WJ, Drenth JP. FDG-PET is able to detect pancreatic carcinomain chronic pancreatitis. Eur J Nucl Med Mol Imaging. 2005;32:399–404.
86. Lee TY, Kim MH, Park DH, Seo DW, Lee SK, Kim JS, et al. Utility of ^{18}F-FDG PET/CT for differentiation of autoimmune pancreatitis with atypical pancreatic imaging findings from pancreatic cancer. AJR Am J Roentgenol. 2009;193:343–8.
87. Pakzad F, Groves AM, Ell PJ. The role of positron emission tomography in the management of pancreatic cancer. Semin Nucl Med. 2006;36:248–56.
88. Pery C, Meurette G, Ansquer C, Frampas E, Regenet N. Role and limitations of ^{18}F-FDG positron emission tomography (PET) in the management of patients with pancreatic lesions. Gastroenterol Clin Biol. 2010;34:465–74.
89. Hong HS, Yun M, Cho A, Choi JY, Kim MJ, Kim KW, et al. The utility of F-18 FDG PET/CT in the evaluation of pancreatic intraductal papillary mucinous neoplasm. Clin Nucl Med. 2010;35:776–9.
90. Sperti C, Pasquali C, Decet G, Chierichetti F, Liessi G, Pedrazzoli S. F-18-fluorodeoxyglucose positron emission tomography in differentiating malignant from benign pancreatic cysts: a prospective study. J Gastrointest Surg. 2005;9:22–8.
91. Fassan M, Pizzi S, Sperti C, Pasquali C, Pedrazzoli S, Chierichetti F, et al. ^{18}F-FDG PET findings and GLUT-1 expression in IPMNs of the pancreas. J Nucl Med. 2008;49:2070.
92. Sperti C, Bissoli S, Pasquali C, Frison L, Liessi G, Chierichetti F, et al. 18-Fluorodeoxyglucose positron emission tomography enhances computed tomography diagnosis of malignant intraductal papillary mucinous neoplasms of the pancreas. Ann Surg. 2007;246:932–9.
93. Tomimaru Y, Takeda Y, Tatsumi M, Kim T, Kobayashi S, Marubashi S, et al. Utility of 2-[^{18}F]-fluoro-2-deoxy-D-glucose positron emission tomography in differential diagnosis of benign and malignant intraductal papillary mucinous neoplasm of the pancreas. Oncol Rep. 2010;24:613–20.
94. Javery O, Shyn P, Mortele K. FDG PET or PET/CT in patients with pancreatic cancer: when does it add to diagnostic CT or MRI? Clin Imaging. 2013;37: 295–301.
95. Nishiyama Y, Yamamoto Y, Yokoe K, Monden T, Sasakawa Y, Tsutsui K, et al. Contribution of whole body FDG-PET to the detection of distant metastasis in pancreatic cancer. Ann Nucl Med. 2005;19:491–7.
96. Bares R, Klever P, Hauptmann S, Hellwig D, Fass J, Cremerius U, et al. F18-fluorodeoxyglucose PET in vivo evaluation of pancreatic glucose metabolism for detection of pancreatic cancer. Radiology. 1994; 192:79–86.
97. Zimny M, Bares R, Fass J, Adam G, Cremerius U, Dohmen B, et al. Fluorine-18 fluorodeoxyglucose

positron emission tomography in the differential diagnosis of pancreatic carcinoma: a report of 106 cases. Eur J Nucl Med. 1997;24:678–82.
98. Lytras D, Connor S, Bosonnet L, Jayan R, Evans J, Hughes M, et al. Positron emission tomography does not add to computed tomography for the diagnosis and staging of pancreatic cancer. Dig Surg. 2005;22: 55–62.
99. Strobel K, Heinrich S, Bhure U, Soyka J, Veit-Haibach P, Pestalozzi BC, et al. Contrast-enhanced ^{18}F-FDG PET/CT: 1-stop-shop imaging for assessing the resectability of pancreatic cancer. J Nucl Med. 2008;49:1408–13.
100. Gambhir SS, Czernin J, Schwimmer J, Silverman DH, Coleman RE, Phelps ME. A tabulated summary of the FDG PET literature. J Nucl Med. 2001;42:1S–93.
101. Zafra M, Ayala F, Gonzalez-Billalabeitia E, Vicente E, Gonzalez-Cabezas P, García T, et al. Impact of whole-body ^{18}F-FDG PET on diagnostic and therapeutic management of medical oncology patients. Eur J Cancer. 2008;44:1678–83.
102. Topkan E, Parlak C, Yapar AF. FDG-PET/CT-based restaging may alter initial management decisions and clinical outcomes in patients with locally advanced pancreatic carcinoma planned to undergo chemoradiotherapy. Cancer Imaging. 2013;13:423–8.
103. Imai H, Doi R, Kanazawa H, Kamo N, Koizumi M, Masui T, et al. Preoperative assessment of para-aortic lymph node metastasis in patients with pancreatic cancer. Int J Clin Oncol. 2010;15:294–300.
104. Kuwatani M, Kawakami H, Eto K, Haba S, Shiga T, Tamaki N, et al. Modalities for evaluating chemotherapeutic efficacy and survival time in patients with advanced pancreatic cancer: comparison between FDG-PET, CT, and serum tumor markers. Intern Med. 2009;48:867–75.
105. Maisey NR, Webb A, Flux GD, Padhani A, Cunningham DC, Ott RJ, et al. FDG-PET in the prediction of survival of patients with cancer of the pancreas: a pilot study. World J Cancer. 2000;1166:287–93.
106. Higashi T, Sakahara H, Torizuka T, Nakamoto Y, Kanamori S, Hiraoka M, et al. Evaluation of intraoperative radiation therapy for unresectable pancreatic cancer with FDG PET. J Nucl Med. 1999;40: 1424–33.
107. Springett GM, Hoffe SE. Borderline resectable pancreatic cancer: on the edge of survival. Cancer Control. 2008;15:295–307.
108. Higashi T, Fisher SJ, Brown RS, Nakada K, Walter GL, Wahl RL. Evaluation of the early effect of local irradiation on normal rodent bone marrow metabolism using FDG; preclinical studies for PET. J Nucl Med. 2000;41:2026–35.
109. Ruf J, Lopez Hänninen E, Oettle H, Plotkin M, Pelzer U, Stroszczynski C, et al. Detection of recurrent pancreatic cancer: comparison of FDG-PET with CT/RM. Pancreatology. 2005;5:266–72.
110. Urban D, Catane R. Serum tumor markers in oncology. Isr Med Assoc J. 2009;11:103–4.
111. Higashi T, Saga T, Nakamoto Y, Ishimori T, Fujimoto K, Doi R, et al. Diagnosis of pancreatic cancer using fluorine-18 fluorodeoxyglucose positron emission tomography (FDG PET) – usefulness and limitations in "clinical reality". Ann Nucl Med. 2003; 17:261–79.
112. [No authors listed]. Radiation therapy combined with Adriamycin or 5-fluorouracil for the treatment of locally unresectable pancreatic carcinoma. Gastrointestinal Tumor Study Group. Cancer. 1985;56:2563–68.
113. Klaassen DJ, MacIntyre JM, Catton GE, Engstrom PF, Moertel CG, et al. Treatment of locally unresectable cancer of the stomach and pancreas: a randomized comparison of 5-fluorouracil alone with radiation plus concurrent and maintenance 5-fluorouracil – an Eastern Cooperative Oncology Group study. J Clin Oncol. 1985;3:373–8.
114. Topkan E, Yavuz AA, Aydin M, Onal C, Yapar F, Yavuz MN. Comparison of CT and PET-CT based planning of radiation therapy in locally advanced pancreatic carcinoma. J Exp Clin Cancer Res. 2008; 23:27–41.
115. Huguet F, Girard N, Guerche CS, Hennequin C, Mornex F, Azria D. Chemoradiotherapy in the management of locally advanced pancreatic carcinoma: a qualitative systematic review. J Clin Oncol. 2009;27: 2269–77.
116. Parlak C, Topkan E, Onal C, Reyhan M, Selek U. Prognostic value of gross tumor volume delineated by FDG-PET-CT based radiotherapy treatment planning in patients with locally advanced pancreatic cancer treated with chemoradiotherapy. Radiat Oncol. 2012;7:37.
117. Kobayashi K, Bhargava P, Raja S, Nasseri F, Al-Balas HA, Smith DD, et al. Image-guided biopsy: what the interventional radiologist needs to know about PET/CT. Radiographics. 2012; 32:1483–501.
118. Klaeser B, Mueller MD, Schmid RA, Guevara C, Krause T, Wiskirchen J. PET-CT-guided interventions in the management of FDG-positive lesions in patients suffering from solid malignancies: initial experiences. Eur Radiol. 2009;19:1780–5.
119. O'Sullivan PJ, Rohren EM, Madewell JE. Positron emission tomography-CT imaging in guiding musculoskeletal biopsy. Radiol Clin N Am. 2008;46: 475–86.
120. Cerci JJ, Pereira Neto CC, Krauzer C, Sakamoto DG, Vitola JV. The impact of coaxial core biopsy guided by FDG PET/CT in oncological patients. Eur J Nucl Med Mol Imaging. 2013;40:98–103.
121. Purandare NC, Kulkarni AV, Kulkarni SS, Roy D, Agrawal A, Shah S, et al. ^{18}F-FDG PET/CT-directed biopsy: does it offer incremental benefit? Nucl Med Commun. 2013;34:203–10.
122. Tomozawa Y, Inaba Y, Yamaura H, Sato Y, Kato M, Kanamoto T, et al. Clinical value of CT-guided needle biopsy for retroperitoneal lesions. Korean J Radiol. 2011;12:351–7.

123. Binderup T, Knigge U, Loft A, Mortensen J, Pfeifer A, Federspiel B, et al. Functional imaging of neuroendocrine tumors: a head-to-head comparison of somatostatin receptors scintigraphy, ^{123}I-MIBG scintigraphy, and ^{18}F-FDG PET. J Nucl Med. 2010; 51:704–12.
124. Ezziddin S, Logvinski T, Yong-Hing C, Ahmadzadehfar H, Fischer HP, Palmedo H, et al. Factors predicting tracer uptake in somatostatin receptor and MIBG scintigraphy of metastatic gastroenteropancreatic neuroendocrine tumors. J Nucl Med. 2006;47:223–33.
125. Kayani I, Bomanji JB, Groves A, Conway G, Gacinovic S, Win T, Dickson J, et al. Functional imaging of neuroendocrine tumors with combined PET/CT using ^{68}Ga-DOTATATE (DOTA-D-Phe^{1}, Tyr^{3}-octreotate) and ^{18}F-FDG. Cancer. 2008;112:2447–55.
126. Kauhanen S, Seppänen M, Minn H, Nuutila P. Clinical PET imaging of insulinoma and beta-cell hyperplasia. Curr Pharm Des. 2010;16:1550–60.
127. Sundin A, Vullierme MP, Kaltsas G, Plöckinger U, Mallorca Consensus Conference Participants, European Neuroendocrine Tumor Society. ENETS consensus guidelines for the standards of care in neuroendocrine tumors: radiological examinations. Neuroendocrinology. 2009;90:167–83.
128. Low MJ. Clinical endocrinology and metabolism: the somatostatin neuroendocrine system – physiology and clinical relevance in gastrointestinal and pancreatic disorders. Best Pract Res Clin Endocrinol Metab. 2004;18:607–22.
129. de Herder WW, Hofland LJ, van der Lely AJ, Lamberts SW, et al. Somatostatin receptors in gastroenteropancreatic neuroendocrine tumours. Endocr Relat Cancer. 2003;10:451–8.
130. Veenstra MJ, de Herder WW, Feelders RA, Hofland LJ. Targeting the somatostatin receptor in pituitary and neuroendocrine tumors. Expert Opin Ther Targets. 2013;17:1329–43.
131. de Herder WW, Lamberts SW. Somatostatin analog therapy in treatment of gastrointestinal disorders and tumors. Endocrine. 2003;20:285–90.
132. Sundin A. Radiological and nuclear medicine imaging of gastroenteropancreatic neuroendocrine tumours. Best Pract Res Clin Gastroenterol. 2012;26:803–18.
133. Kwekkeboom DJ, Kam BL, van Essen M, Teunissen JJ, van Eijck CH, Valkema R, et al. Somatostatin-receptor-based imaging and therapy of gastroenteropancreatic neuroendocrine tumors. Endocr Relat Cancer. 2010;17:R53–73.
134. de Herder WW, Kwekkeboom DJ, Feelders RA, van Aken MO, Lamberts SW, van der Lely AJ, et al. Somatostatin receptor imaging for neuroendocrine tumors. Pituitary. 2006;9:243–8.
135. Oberg K, Kvols L, Caplin M, Delle Fave G, de Herder W, Rindi G, et al. Consensus report on the use of somatostatin analogs for the management of neuroendocrine tumors of the gastroenteropancreatic system. Ann Oncol. 2004;15:966–73.
136. Lamberts SW, van der Lely AJ, de Herder WW, Hofland LJ. Octreotide. N Engl J Med. 1996;334: 246–54.
137. Bodei L, Mueller-Brand J, Baum RP, Pavel ME, Hörsch D, O'Dorisio MS, et al. The joint IAEA, EANM, and SNMMI practical guidance on peptide receptor radionuclide therapy (PRRNT) in neuroendocrine tumours. Eur J Nucl Med Mol Imaging. 2013;40:800–16.
138. Kwekkeboom DJ, Krenning EP, Lebtahi R, Komminoth P, Kos-Kudła B, de Herder WW, et al. ENETS consensus guidelines for the standards of care in neuroendocrine tumors: peptide receptor radionuclide therapy with radiolabeled somatostatin analogs. Neuroendocrinology. 2009;90:220–6.
139. Balon HR, Goldsmith SJ, Siegel BA, Silberstein EB, Krenning EP, Lang O, et al. Procedure guideline for somatostatin receptor scintigraphy with ^{111}In-pentetreotide. J Nucl Med. 2001;42:1134–8.
140. de Herder WW, Niederle B, Scoazec JY, Pauwels S, Kloppel G, Falconi M, et al. Well-differentiated pancreatic tumor/carcinoma: insulinoma. Neuroendocrinology. 2006;84:183–8.
141. Shah T, Kulakiene I, Quigley AM, Warbey VS, Srirajaskanthan R, Toumpanakis C, et al. The role of ^{99m}Tc-depreotide in the management of neuroendocrine tumours. Nucl Med Commun. 2008;29:436–40.
142. Heppeler A, Froidevaux S, Eberle AN, Maecke HR. Receptor targeting for tumor localisation and therapy with radiopeptides. Curr Med Chem. 2000;7: 971–94.
143. Smith-Jones PM, Bischof C, Leimer M, Gludovacz D, Angelberger P, Pangerl T, et al. DOTA-lanreotide: a novel somatostatin analog for tumor diagnosis and therapy. Endocrinology. 1999;140:5136–48.
144. Cwikla JB, Mikolajczak R, Pawlak D, Buscombe JR, Nasierowska-Guttmejer A, Bator A, et al. Initial direct comparison of ^{99m}Tc-TOC and ^{99m}Tc-TATE in identifying sites of disease in patients with proven GEP NETs. J Nucl Med. 2008;49:1060–5.
145. Gabriel M, Muehllechner P, Decristoforo C, von Guggenberg E, Kendler D, Prommegger R, et al. ^{99m}Tc-EDDA/HYNIC-Tyr^{3}-octreotide for staging and follow-up of patients with neuroendocrine gastro-entero-pancreatic tumors. Q J Nucl Med Mol Imaging. 2005;49:237–44.
146. Bombardieri E, Aktolun C, Baum RP, Bishof-Delaloye A, Buscombe J, Chatal JF, et al. ^{131}I/^{123}I-metaiodobenzylguanidine (MIBG), scintigraphy: procedure guidelines for tumour imaging. Eur J Nucl Med Mol Imaging. 2003;30:BP132–9.
147. Kaltsas G, Korbonits M, Heintz E, Mukherjee JJ, Jenkins PJ, Chew SL, et al. Comparison of somatostatin analog and meta-iodobenzylguanidine radionuclides in the diagnosis and localization of advanced neuroendocrine tumors. J Clin Endocrinol Metab. 2001;86:895–902.
148. Kaltsas G, Rockall A, Papadogias D, Reznek R, Grossman AB. Recent advances in radiological and

radionuclide imaging and therapy of neuroendocrine tumours. Eur J Endocrinol. 2004;151:15–27.
149. Buscombe JR, Cwikla JB, Caplin ME, Hilson AJ. Long-term efficacy of low activity meta-^{131}Iiodobenzylguanidine therapy in patients with disseminated neuroendocrine tumours depends on initial response. Nucl Med Commun. 2005;26:969–76.
150. Taal BG, Zuetenhorst H, Valdés Olmos RA, Hoefnagel CA. ^{131}I-MIBG radionuclide therapy in carcinoid syndrome. Eur J Surg Oncol. 2002;28:243.
151. Jacobson AF, Deng H, Lombard J, Lessig HJ, Black RR. ^{123}I-meta-iodobenzylguanidine scintigraphy for the detection of neuroblastoma and pheochromocytoma: results of a meta-analysis. J Clin Endocrinol Metab. 2010;95:2596–606.
152. Froberg AC, de Jong M, Nock BA, Breeman WA, Erion JL, Maina T, et al. Comparison of three radiolabelled peptide analogues for CCK-2 receptor scintigraphy in medullary thyroid carcinoma. Eur J Nucl Med Mol Imaging. 2009;36:1265–72.
153. Gotthardt M, Béhé MP, Beuter D, Battmann A, Bauhofer A, Schurrat T, et al. Improved tumour detection by gastrin receptor scintigraphy in patients with metastasised medullary thyroid carcinoma. Eur J Nucl Med Mol Imaging. 2006;33:1273–9.
154. Nock BA, Maina T, Béhé M, Nikolopoulou A, Gotthardt M, Schmitt JS, et al. CCK-2/gastrin receptor-targeted tumor imaging with ^{99m}Tc-labeled minigastrinanalogs. J Nucl Med. 2005;46:1727–36.
155. Wild D, Christ E, Caplin ME, Kurzawinski TR, Forrer F, Brändle M, et al. Glucagon-like peptide-1 versus somatostatin receptor targeting reveals 2 distinct forms of malignant insulinomas. J Nucl Med. 2011;52:1073–8.
156. Wild D, Mäcke H, Christ E, Gloor B, Reubi JC. Glucagon-like peptide 1-receptor scans to localize occult insulinomas. N Engl J Med. 2008;359:766–8.
157. Christ E, Wild D, Forrer F, Brändle M, Sahli R, Clerici T, et al. Glucagon-like peptide-1 receptor imaging for localization of insulinomas. J Clin Endocrinol Metab. 2009;94:4398–405.
158. Christ E, Wild D, Ederer S, Béhé M, Nicolas G, Caplin ME, et al. Glucagon-like peptide-1 receptor imaging for the localisation of insulinomas: a prospective multicentre imaging study. Lancet Diabetes Endocrinol. 2013;1:115–22.
159. Doherty GM, Doppman JL, Shawker TH, Miller DL, Eastman RC, Gorden P, et al. Results of a prospective strategy to diagnose, localize, and resect insulinomas. Surgery. 1991;110:989–96.
160. Pach D, Sowa-Staszczak A, Jabrocka-Hybel A, Stefańska A, Tomaszuk M, Mikołajczak R, et al. Glucagon-like peptide-1 receptor imaging with (Lys^{40}(Ahx-HYNIC-^{99m}Tc/EDDA)NH_2)–exendin-4 for the diagnosis of recurrence or dissemination of medullary thyroid cancer: a preliminary report. Int J Endocrinol. 2013;2013:384508.
161. Sowa-Staszczak A, Pach D, Mikołajczak R, Mäcke H, Jabrocka-Hybel A, Stefańska A, et al. Glucagon-like peptide-1 receptor imaging with (Lys^{40}(Ahx-HYNIC-^{99m}Tc/EDDA)NH_2)–exendin-4 for the detection of insulinoma. Eur J Nucl Med Mol Imaging. 2013;40:524–31.
162. Brom M, Oyen WJ, Joosten L, Gotthardt M, Boerman OC. ^{68}Ga-labelled exendin-3, a new agent for the detection of insulinomas with PET. Eur J Nucl Med Mol Imaging. 2010;37:1345–55.
163. Hessenius C, Bäder M, Meinhold H, Böhmig M, Faiss S, Reubi JC, et al. Vasoactive intestinal peptide receptor scintigraphy in patients with pancreatic adenocarcinomas or neuroendocrine tumours. Eur J Nucl Med. 2000;27:1684–93.
164. Virgolini I, Kurtaran A, Leimer M, Kaserer K, Peck-Radosavljevic M, Angelberger P, et al. Location of a VIPoma by iodine-123-vasoactive intestinal peptide scintigraphy. J Nucl Med. 1998;39:1575–9.
165. Virgolini I, Raderer M, Kurtaran A, Angelberger P, Banyai S, Yang Q, et al. Vasoactive intestinal peptide-receptor imaging for the localization of intestinal adenocarcinomas and endocrine tumors. N Engl J Med. 1994;331:1116–21.
166. Wild D, Bomanji JB, Benkert P, Maecke H, Ell PJ, Reubi JC, et al. Comparison of ^{68}Ga-DOTANOC and ^{68}Ga-DOTATATE PET/CT within patients with gastroenteropancreatic neuroendocrine tumors. J Nucl Med. 2013;54:364–72.
167. Haug AR, Cindea-Drimus R, Auernhammer CJ, Reincke M, Wängler B, Uebleis C, et al. The role of ^{68}Ga-DOTATATE PET/CT in suspected neuroendocrine tumors. J Nucl Med. 2012;53:1686–92.
168. Schraml C, Schwenzer NF, Sperling O, Aschoff P, Lichy MP, Müller M, et al. Staging of neuroendocrine tumours: comparison of ^{68}Ga-DOTATOC multiphase PET/CT and whole-body MRI. Cancer Imaging. 2013;13:63–72.
169. Ambrosini V, Campana D, Nanni C, Cambioli S, Tomassetti P, Rubello D, et al. Is ^{68}Ga-DOTA-NOC PET/CT indicated in patients with clinical, biochemical or radiological suspicion of neuroendocrine tumour? Eur J Nucl Med Mol Imaging. 2012;39:1278–83.
170. Binderup T, Knigge U, Loft A, Federspiel B, Kjaer A. ^{18}F-fluorodeoxy-glucose positron emission tomography predicts survival of patients with neuroendocrine tumors. Clin Cancer Res. 2010;16:978–85.
171. Abgral R, Leboulleux S, Déandreis D, Aupérin A, Lumbroso J, Dromain C, et al. Performance of ^{18}fluorodeoxyglucose-positron emission tomography and somatostatin receptor scintigraphy for high Ki67 (R10%) well-differentiated endocrine carcinoma staging. J Clin Endocrinol Metab. 2011;96:665–71.
172. Severi S, Nanni O, Bodei L, Sansovini M, Ianniello A, Nicoletti S, et al. Role of ^{18}FDG PET/CT in patients treated with ^{177}Lu-DOTATATE for advanced differentiated neuroendocrine tumours. Eur J Nucl Med Mol Imaging. 2013;40:881–8.

173. van Essen M, Sundin A, Krenning EP, Kwekkeboom DJ. Neuroendocrine tumours: the role of imaging for diagnosis and therapy. Nat Rev Endocrinol. 2014;10:102–14.
174. Rufini V, Baum RP, Castaldi P, Treglia G, De Gaetano AM, Carreras C, et al. Role of PET/CT in the functional imaging of endocrine pancreatic tumors. Abdom Imaging. 2012;37:1004–20.
175. Orlefors H, Sundin A, Ahlström H, Bjurling P, Bergström M, Lilja A, et al. Positron emission tomography with 5-hydroxytryptophan in neuroendocrine tumors. J Clin Oncol. 1998;16:2534–41.
176. Orlefors H, Sundin A, Garske U, Juhlin C, Oberg K, Skogseid B, et al. Whole-body ^{11}C-5-hydroxytryptophan positron emission tomography as a universal imaging technique for neuroendocrine tumors – comparison with somatostatin receptor scintigraphy and computed tomography. J Clin Endocrinol Metab. 2005;90:3392–400.
177. Buck AC, Schirrmeister HH, Guhlmann CA, Diederichs CG, Shen C, Buchmann I, et al. Ki-67 immunostaining in pancreatic cancer and chronic active pancreatitis: does in vivo FDG uptake correlate with proliferative activity? J Nucl Med. 2001;42:721–5.
178. Shields AF, Grierson JR, Dohmen BM, Machulla HJ, Stayanoff JC, Lawhorn-Crews JM, et al. Imaging proliferation in vivo with [F-18]FLT and positron emission tomography. Nat Med. 1998;4:1334–6.
179. von Forstner C, Egberts JH, Ammerpohl O, Niedzielska D, Buchert R, Mikecz P, et al. Gene expression patterns and tumor uptake of ^{18}F-FDG, ^{18}F-FLT, and ^{18}F-FEC in PET/MRI of an orthotopic mouse xenotransplantation model of pancreatic cancer. J Nucl Med. 2008;49:1362–70.
180. Wang X, Fani M, Schulz S, Rivier J, Reubi JC, Maecke HR. Comprehensive evaluation of a somatostatin-based radiolabelled antagonist for diagnostic imaging and radionuclide therapy. Eur J Nucl Med Mol Imaging. 2012;39:1876–85.
181. Marsouvanidis PJ, Maina T, Sallegger W, Krenning EP, de Jong M, Nock BA. ^{99m}Tc radiotracers based on human GRP(18–27): synthesis and comparative evaluation. J Nucl Med. 2013;54:1797–803.
182. Richter S, Wuest M, Krieger SS, Rogers BE, Friebe M, Bergmann R, et al. Synthesis and radiopharmacological evaluation of a high-affinity and metabolically stabilized ^{18}F-labeled bombesin analogue for molecular imaging of gastrin-releasing peptide receptor-expressing prostate cancer. Nucl Med Biol. 2013;40:1025–34.
183. Varasteh Z, Aberg O, Velikyan I, Lindeberg G, Sörensen J, Larhed M, et al. In vitro and in vivo evaluation of a^{18}F-labeled high affinity NOTA conjugated bombesin antagonist as a PET ligand for GRPR-targeted tumor imaging. PLoS ONE. 2013;8, e81932.

Diagnostic Applications of Nuclear Medicine: Colorectal Cancer

28

Ettore Pelosi, Désirée Deandreis, Laura Cassalia, and Daniele Penna

Abstract

Colorectal cancer is the fourth most common neoplastic disease (50–60% overall survival at 5 years); 90–95% of colorectal cancers are adenocarcinoma. Important prognostic factors include: whether the tumor is well differentiated, the extent of the primary tumor, and the presence of local and/or lymph node invasion. Two staging classifications for colorectal cancer are available: Dukes' classification and the TNM stage system by the American Joint Committee on Cancer/International Union Against Cancer (AJCC/UICC).

Contrast-enhanced computed tomography (CECT) of the chest, abdomen, and pelvis is used in pretreatment staging. Because of the high incidence of disease recurrence (30–40%), morphological imaging (CT, abdominal ultrasound) and serial measurements of serum markers (carcinoembryonic antigen, or CEA) are used in the follow-up. The use of [^{18}F]FDG-PET for early detection of primary colorectal cancer is limited due to the low sensitivity for small tumors as well as for mucinous lesions. False-positive PET findings are also reported in patients with inflammatory bowel disease (IBD) or previous diagnostic polipectomy. Although [^{18}F]FDG PET is more sensitive than CT in detecting regional lymph node involvement, CT is better at detecting liver metastases. As a result, the role of [^{18}F]FDG PET-CT for presurgical staging is unclear. [^{18}F]FDG-PET is useful as a complementary exam in selected patients with a high metastatic potential.

During restaging and follow-up, whole-body [^{18}F]FDG-PET/CT is recommended to localize recurrent disease in cases of elevated serum CEA and negative morphological imaging findings or indeterminate lesions. Combined PET/CT tomography improves the accuracy of the evaluation of colorectal cancer, especially in the visualization of abdomino-pelvic extrahepatic disease.

[^{18}F]FDG-PET may be useful to evaluate response to chemotherapy, although the optimum timing of the assessment of metabolic response remains unsettled. Moreover, new drugs targeted to angiogenesis or tyrosine kinase have opened new frontiers to the use of [^{18}F]FDG-PET in evaluating response because of their cytostatic rather than cytoreductive effect. In rectal cancer it is often difficult to evaluate response to radiotherapy by anatomic imaging due to residual

E. Pelosi (✉) • D. Penna
PET Center, Affidea IRMET, Torino, Italy
e-mail: ettore.pelosi@affidea.it; ettore.pelosi@gmail.com

D. Deandreis
Department of Medical Sciences Nuclear Medicine, University of Torino, Torino, Italy

L. Cassalia
Nuclear Medicine Unit, Department of Biomedical Sciences and of Morphologic and Functional Images, University of Messina, Messina, Italy

© Springer International Publishing Switzerland 2017
H.W. Strauss et al. (eds.), *Nuclear Oncology*,
https://doi.org/10.1007/978-3-319-26236-9_19

tissue mass, but [^{18}F]FDG-PET/CT can detect residual tumor by the metabolic activity. Finally, [^{18}F]FDG-PET has been proposed in the evaluation of response to local treatment of liver and lung metastases by radiofrequency ablation (RFA). In patients with unresectable liver metastases and/or advanced burden of liver disease, transarterial radioembolization with microspheres labeled with ^{90}Y is becoming a valid therapeutic alternative to chemoembolization and RFA.

Keywords

Colorectal cancer • [^{18}F]FDG-PET/CT in colorectal cancer • Diagnostic imaging in colorectal cancer • Staging and follow-up in colorectal cancer • Assessment of response to therapy in colorecatl cancer • Trans-arterial radioembolization with ^{90}Y-microspheres for liver metastases from colorecxtal cancer

Glossary

[^{18}F]FDG	2-deoxy-2-[^{18}F]fluoro-D-glucose
^{99m}Tc-HDP	^{99m}Tc-hydroxyethylenediphosphonate
AJCC	American Joint Committee on Cancer
BOmR	Best overall metabolic response
CEA	Carcinoembryonic antigen
CECT	Contrast-enhanced computed tomography
CI	Confidence interval
CMR	Complete metabolic response
CRC	Colorectal cancer
CRT	Chemoradiotherapy
CT	X-ray computed tomography
DOTA	1,4,7,10-tetraazacyclododecane-1,4,7,10-tetraacetic acid
EORTC	European Organization for Research and Treatment of Cancer
GI	Gastrointestinal
IBD	Inflammatory bowel disease
M	Metastasis status according to the AJCC/UICC TNM staging system
MRI	Magnetic resonance imaging
N	Lymph node status according to the AJCC/UICC TNM staging system
NOC	1-Nal^{3}-octreotide
NPV	Negative predictive value
PERCIST	Positron emission tomography response criteria in solid tumors
PET	Positron emission tomography
PET/CT	Positron emission tomography/computed tomography
PET/MRI	Positron emission tomography/magnetic resonance imaging
PMD	Progressive metabolic disease
PMR	Partial metabolic response
PPV	Positive predictive value
PREDIST	PET residual disease in solid tumor
PTV	Radiotherapy planning target volume
RECIST	Response evaluation criteria in solid tumors
RFA	Radiofrequency ablation
ROI	Region of interest
SMD	Stable metabolic disease
SN	Sensitivity
SP	Specificity
SUV	Standardized uptake value
T	Tumor status according to the AJCC/UICC TNM staging system
TLG	Total lesion glycolysis
TOC	Octreotide
TREUS	Transrectal ultrasound
TRG	Tumor regression grade
UICC	Union Internationale Contre le Cancer (International Union Against Cancer)

Contents

Overview of Colon-Rectal Cancer: Incidence and Mortality 779

Prognostic Factors 779

Staging Classification and Prognosis 780

Clinical Objectives in Colorectal Cancer 781

Current Role of Nuclear Medicine 781

Presurgical Staging of Primary Colorectal Cancer ... 782
Recurrent Colorectal Cancer 783
Treatment Response Evaluation 786

New Prospects 789
PET/MRI 789
Radiotherapy Volume Planning 790
Therapy with Transarterial ^{90}Y-Microspheres 790
Carcinoid Tumors 791

References 791

Overview of Colon-Rectal Cancer: Incidence and Mortality

Colorectal cancer is the fourth most common neoplastic disease, after prostate, lung, and breast cancer, and the second leading cause of death from cancer, with an estimated overall survival at 5 years of 50–60% in Western countries [1, 2]. There is considerable evidence for its correlation with saturated fat, low-fiber diet, obesity, and inflammatory bowel disease (IBD), as well as with genetic factors (familial adenomatous polyposis or the Lynch syndrome). Mortality rates have steadily decreased, particularly between 1980 and 2005, owing to improved surgical and adjuvant therapies (chemotherapy protocols and targeted molecular treatment) and more extensive screening programs with early diagnosis [3].

Despite improved prognosis and extensive primary and secondary prevention programs, about 150,000 new cases of colorectal cancer have been diagnosed in 2009 in the United States alone. Colorectal cancer remains a huge health problem [3].

Prognostic Factors

Some studies suggest a poorer prognosis in symptomatic patients due to local complications (e.g., locally extended cancer with obstruction and perforation) at diagnosis. Among patient characteristics, age less than 40 years at diagnosis is another factor of poor prognosis, because cancer is more aggressive in younger patients, with a high percentage of positive lymph nodes and aggressive histological features. As to histology, adenocarcinoma accounts for 90–95% of colorectal cancers. These tumors are classified into three groups according to the Dukes' grading system: grade 1, the most differentiated forms; grade 2, the intermediate forms; and grade 3, the less differentiated forms. The less differentiated forms carry a worse prognosis as they are locally more extensive, with a higher lymphatic affinity and metastatic potential. The remaining 5–10% of colorectal cancers include other histological variants such as colloid or mucinous adenocarcinomas, less frequently squamous cells, undifferentiated carcinomas, and carcinoid forms which usually arise in the rectum. The mucinous variant is also correlated with a more aggressive behavior and frequently with an advanced stage at diagnosis. Primary tumor extension at diagnosis expressed by local invasion and number of positive lymph nodes seems to be the most important prognostic factor, as curative treatment is possible only at the early stage of disease. Nearly 40% of patients present with a confined primary tumor at diagnosis, almost 40% with locally advanced disease, and the remaining 20% with metastatic spread. A localized tumor means that it is limited to the bowel wall, without lymphatic spread or peritoneal seeding when considering intraperitoneal sites (cecum, transverse colon, and sigmoid) or without extension to retroperitoneal lymph nodes, or to retroperitoneal tissue such as the kidneys, or to the ureter or the pelvis when considering extraperitoneal sites (ascending and descending colon and the majority of rectal localizations). Lymphatic spread usually occurs via the paracolic lymph node groups by the mesenteric the retroperitoneal lymph nodes in extraperitoneal localizations of colon cancer, and the perirectal lymph nodes in rectal cancer. Metastatic spread is often localized to the liver in colon cancer and in tumors of the upper rectum, whose venous system drains into the portal circulation. The distal rectum has a double drainage: to the portal system via the inferior mesenteric vein through the superior hemorrhoidal veins with metastatic spread to the liver, and to the inferior vena cava via the pelvic veins through the middle and inferior hemorrhoidal plexus; in the latter case case, lung metastases are more frequent. Bone lesions can be caused by metastatic spread through the vertebral venous

plexus and are more frequently located in the sacrum, coccyx, pelvis, and lumbar vertebrae.

Staging Classification and Prognosis

There are two different surgical staging classifications for colorectal cancer. Dukes' classification is a practical system that classifies tumors into three groups according to the extent of bowel wall penetration: (A) penetration into but not through the bowel wall, (B) penetration through the bowel wall, and (C) lymph node involvement regardless of bowel wall penetration. Stage D was later added to indicate disease extension beyond the limit of surgical resection and includes metastatic tumor. This system correlates easily with different prognoses for different stages. A 1984 meta-analysis by the Large Bowel Project, London, identified the number of positive lymph nodes as the most important factor [4]. A recent study by Fretwell et al. on 351 patients confirmed this result, showing that lymph node status is an independent prognostic factor [5].

The second system is the TNM classification, which has undergone several revisions with further modifications still in progress; the first unified and revised version was issued by the American Joint Committee on Cancer/International Union Against Cancer (AJCC/UICC) in 1987–1988 [6, 7]. This version takes into account tumor extension to the serosa and the number of positive lymph nodes calculated on at least 12 lymph nodes examined [8]. T is subdivided into T0 (absence of tumor in resected specimen), Tis (carcinoma in situ), T1 (submucosa invasion), T2 (muscolaris mucosa invasion), T3 (extension to subserosa or to nonperitoneal pericolic or perirectal tissue), and T4 (invasion of the peritoneal cavity or other organs). N is subdivided into N0 (tumor without lymph node involvement), N1 (tumor with one to three positive regional lymph nodes), N2 (tumor with four or more positive regional lymph nodes), and N3 (tumor with central positive lymph nodes). Based on the TNM classification, the AJCC/UICC identified a four-stage group (Table 1). Prognosis is closely correlated with stage: survival around 90% for Stage I, 80–70% for Stage II, 80–40% for Stage III, and around 10% for Stage IV (Table 2). The AJCC recommends recovering at least 12 lymph nodes for accurate analysis, where the number of lymph nodes recovered is itself a prognostic factor [9, 10]. Lymph node positivity at surgical resection is a known independent prognostic factor, and the cutoff of four lymph nodes in the TNM classification was based on statistical differences in prognosis between the two subgroups: overall 5-year survival of approximately 50% for patients with $\geq$4 metastatic lymph nodes at surgical staging versus approximately 70% for patients with less than four metastatic lymph nodes [4]. Furthermore, vascular or lymphatic invasion are adjunctive prognostic elements irrespective of the stage, since they increase the likelihood of lymph node or metastatic recurrence [11]. Other studies have demonstrated that peritoneal involvement could also be considered as a prognostic

Table 1 AJCC/UICC staging classification for colorectal cancer according to the TNM system

Stage I		Tis, N0, M0
Stage II	IIA	T3, N0, M0
	IIB	T4, N0, M0
Stage III	IIIA	T1-T2, N1, M0
	IIIB	T3-T4, N1, M0
	IIIC	Any T, N2, M0
Stage IV		Any T, any N, M1

Table 2 Prognosis based on AJCC staging classification of colon and rectal cancer released by American Cancer Society (results from study of National Cancer Institute's SEER database on 120,000 people diagnosed with colon cancer between 1991 and 2000)

Colon stage	5-year survival rate (%)	Rectal stage	5-year survival rate (%)
I	93	I	90
IIA	85	II	70
IIB	72	III	56
IIIA	83[a]	IV	7
IIIB	64		
IIIC	44		
IV	8		

[a]Uncertain result

factor independent of T and N stage [12]. Finally, other prognostic factors are molecular markers such as p53, p27, K-ras, thymidylate synthase, and mutations of mismatch repair genes, which can correlate with a more aggressive tumor. Furthermore, their abnormal expression can influence and predict tumor response to treatment [13–17]. Other cellular and tumor morphological parameters under study are the angiogenesis patterns, since anti-angiogenetic therapy constitutes a new chance of targeted treatment [18].

Clinical Objectives in Colorectal Cancer

The first objective in managing colorectal cancer patients is adequate and complete preoperative staging, which is routinely done by abdominal and thoracic contrast-enhanced computed tomography (CECT) to evaluate overall liver status. The purpose of primary tumor treatment is to be as curative and radical as possible, while exactly defining local disease extension. This is also important in cases with isolated metastatic spread. Surgery is usually the first choice treatment for localized disease and single and/or resectable metastases. In locally advanced disease, the use of neoadjuvant chemoradiation therapy appears to improve prognosis [19, 20]. Adjuvant treatment is indicated to limit tumor recurrence, based on initial tumor extension and prognostic factors (Stage III, lymph node metastases, poorly differentiated tumors, lymphovascular invasion). It ordinarily consists of systemic chemotherapy protocols based on 5-fluorouracil as first choice. On completion of treatment, close follow-up is essential because of the high percentage of disease recurrence after primary treatment (30–40%) [21]. Follow-up entails systematic evaluation by morphological imaging techniques (CT, abdominal ultrasounds) and systemic evaluation of serum markers (carcinoembryonic antigen, or CEA) to detect relapse or metastatic spread. Recurrence can be local, regional (lymph node localizations), peritoneal seeding, or metastatic liver/lung lesions, and it is closely correlated with primary tumor characteristics. The recurrence rate in locally advanced tumors is about 20% and rises to around 50% in the presence of initial lymph node involvement.

Current Role of Nuclear Medicine

Of the nuclear imaging modalities for managing patients with colorectal cancer, PET/CT with 2-deoxy-2-[^{18}F]fluoro-D-glucose ([^{18}F]FDG) is the most widely used. It is considered the most useful technique for achieving clinical objectives and has been added to standard imaging techniques as a new "strategic" tool in this scenario.

Several studies have demonstrated that whole-body [^{18}F]FDG-PET is an accurate noninvasive technique in staging/restaging several types of malignancies, and its usefulness has also been proved in the management of patients with colorectal cancer [22–24]. [^{18}F]FDG-PET is recognized as *appropriate* in restaging patients with suspected recurrence of colorectal cancer, elevated serum tumor markers such as CEA, and a negative or inconclusive standard diagnostic workup and in presurgical evaluation of patients with recurrence of disease and potentially resectable metastatic lesions.

In the preoperative initial staging of disease, [^{18}F]FDG-PET is considered *potentially useful* but not yet sufficiently demonstrated [25].

Finally, [^{18}F]FDG-PET in colorectal cancer holds promise for systematic follow-up and evaluation of response to therapy, especially in the evaluation of chemoradiation therapy in metastatic cancer (late and early response) or of local treatment efficacy such as radiofrequency ablation of liver metastases. Furthermore, because positivity and intensity of [^{18}F]FDG uptake are an expression of tumor aggressiveness, [^{18}F]FDG-PET is also considered as a prognostic tool [26].

Classic, standard nuclear imaging techniques such as ^{99m}Tc-HDP bone scan in disease staging and restaging are limited to the evaluation of secondary bone lesions. Finally, nuclear techniques such as treatment with intra-arterial ^{90}Y-microspheres for unresectable liver metastases are becoming increasingly available.

The current and potential uses of nuclear medicine techniques will be discussed in the following paragraphs.

Presurgical Staging of Primary Colorectal Cancer

Because few studies on a small number of patients are currently available, the role of [^{18}F]FDG-PET in the presurgical staging of primary disease remains controversial. Primary cancer is detected and studied by morphological imaging, oral contrast CT, and endo-ultrasonography which also allows for biopsy and histological confirmation [27, 28].

Several studies reported a high sensitivity of [^{18}F]FDG-PET (95–100%) in detecting the primary tumor, even when in situ [29–31]. The tumor's histopathological features and lesion diameter are closely correlated with these data. False-negative results have been reported in cases of mucinous carcinoma and of small tumor foci in tubulovillous polyps or villous adenoma [29, 30, 32]. Abdel-Nabi et al. reported false-positive PET findings (positive predictive value [PPV] 90%) in patients without colorectal cancer but with IBD or previous diagnostic polypectomy [29]. Although [^{18}F]FDG-PET appears to be more useful in detecting regional lymph node involvement and liver metastases, conflicting results have been reported. Abdel-Nabi and Kantorova both found higher sensitivity (78–88%) with PET than with contrast-enhanced abdominal/pelvic CT (38–67%) or ultrasonography (25%), with high specificity (96–100%) in detecting liver metastases [29, 30]. Furukawa reported that, when compared with multidetector helical CT for routine staging, [^{18}F]FDG-PET did not seem superior in terms of sensitivity and accuracy [31]. In this study, [^{18}F]FDG-PET accuracy in detecting lymph node involvement did not show a statistical difference in comparison with CECT accuracy (59% vs. 62%). Patel et al. in a systematic review reported that for extrahepatic lesions (three studies, 178 patients), PET/CT was more sensitive than CT, while specificity was similar (PET/CT sensitivity [SN] = 75–89% and specificity [SP] = 95–96% vs. CT SN = 58–64% and SP = 87–97%). For hepatic lesions (five studies; 316 patients), PET/CT had higher SN and SP than CT (PET/CT SN = 91–100% and SP = 75–100%; CT SN = 78–94% and SP = 25–98% [33].

Other studies confirmed low PET sensitivity (around 30%) primarily due to false-negative findings in cases of micrometastases or the presence of metastatic lymph nodes adjacent to the primary tumor [34]. In a review by Vriens et al., other more recent studies on a small group of patients showed that [^{18}F]FDG-PET can change patient management in 12–27% of cases when added to CT and/or pelvic magnetic resonance imaging (MRI) and ultrasonography, leading the bulk of cases to cancelation of surgery after unexpected metastatic lesions were detected, or to extension of the surgical plan or the radiotherapy field, or to neoadjuvant treatment after detection of pathological lymphadenopathy missed at morphological imaging [35–40].

In brief, the weighted mean change in the management of colorectal cancer calculated in the review was about 10.7% (95% confidence interval [CI] 7.6–14.5%) [41]. The discordant findings among the different studies can be explained by the patient selection bias, which showed a major impact of [^{18}F]FDG-PET in patients with a high metastatic potential, while in localized disease [^{18}F]FDG-PET added less additional information to the standard diagnostic workup (contrast-enhanced CT and colonoscopy).

What can be said at present is that the use of PET in staging primary colorectal cancer can lead to a change in clinical management when compared to standard diagnostic workup, but its systematic use in this application is not yet recognized.

We evaluated the role of [^{18}F]FDG-PET/CT in preoperative staging of rectal carcinoma and compared it to the conventional imaging techniques. With the collaboration of two PET centers and a total of four PET/CT scanners, 141 patients with diagnosis of rectal adenocarcinoma were studied from October 2006 to November 2014. For the evaluation of N stage, in 92/141 cases we found correlation between PET and conventional

imaging: 47/92 cases with evidence of lymph node metastases (N^+) and 45/92 without evidence of lymph node metastases (N^-). In the remaining 49 cases, PET and conventional imaging were discordant: in 38/49 PET did not identify small "mesorectal" lymph nodes (38/49); in 11 cases PET showed some "pelvic" unexpected lymph node metastases. In the M staging, in 106/141 patients (75%) we found correlation between PET and conventional imaging, with the same final stage of disease: in 46/106 patients without evidence of distant metastases (M^-) and in 60/106 with evidence of distant metastases (liver, lung, skeletal, peritoneal, adrenal). In the remaining 35/141 patients (25%), there was discordance between PET and conventional imaging in the M stage: in 9/35 cases PET identified unexpected metastases (three skeletal and six liver and/or lung; out of these we had one false positive case in the lung). In the remaining 26/35 patients, PET excluded distant metastases to the liver, spleen, and lung (out of these we had three lung false-negative findings and two liver false-negative findings). PET also identified seven cases of synchronous neoplasia (five in the colon, one gastric, and one thymoma). So, in our study PET showed high false-negative rate in the locoregional lymph nodes staging due to the spatial resolution limitations, but increased accuracy in the identification of lymph node metastases in less common areas; PET has also provided additional and/or complementary information regarding distant metastases; finally, PET identified unexpected neoplasia in 4% of patients. Considering the different and complementary information derived from PET and conventional imaging, at the moment we suggest the use of both techniques for rectal cancer staging [42, 43].

Recurrent Colorectal Cancer

The suspicion of colorectal cancer recurrence is oftentimes prompted by a rise in serum marker values (CEA) or abnormal findings at anatomical imaging (CECT, MRI) during follow-up and/or occurrence of new symptoms. [^{18}F]FDG-PET remains the mainstay of nuclear imaging in the follow-up of patients with colorectal cancer. In cases of elevated serum CEA values and negative morphological imaging findings, [^{18}F]FDG-PET is advised because of its ability to detect early disease and to reveal metabolic changes in normal-size structures before morphological findings appear. Literature data show that in about two out of three cases, whole-body [^{18}F]FDG-PET identifies recurrence of disease, making its use in an early phase of patient follow-up recommended [44]. Flamen et al. showed that [^{18}F]FDG-PET can detect disease recurrence in more than 80% of patients (43/50) [45]. In this study, disease recurrence missed at morphological imaging was located in the liver (27%), locally (20%), the lung (9%), other abdominal sites (36%), and other extra-abdominal non-pulmonary lesions (9%). These results were confirmed by both previous and more recent studies [46–48]. Lu et al. in a meta-analysis reported that 106 patients (106/510 = 20.8%) had true-negative [^{18}F]FDG-PET/CT results in detection of recurrent CRC when rising CEA. The pooled estimates of sensitivity and specificity and positive and negative likelihood ratios of [^{18}F]FDG-PET in the detection of tumor recurrence in CRC patients with elevated CEA were 90.3% (95% CI, 85.5–94.0%), 80.0% (95% CI, 67.0–89.6%), 2.88 (95% CI, 1.37–6.07%), and 0.12 (95% CI, 0.07–0.20%), respectively. The pooled estimates of sensitivity and specificity and positive and negative likelihood ratios of [^{18}F]FDG-PET/CT in the detection of tumor recurrence in CRC patients with elevated CEA were 94.1% (95% CI, 89.4–97.1%), 77.2% (95% CI, 66.4–85.9%), 4.70 (95% CI, 0.82–12.13%), and 0.06 (95% CI, 0.03–0.13%), respectively [49, 50]. Gade et al. showed in their study that PET/CT demonstrated recurrence with a sensitivity of 85.7%, a specificity of 94.7%, a positive predictive value of 93.8%, and a negative predictive value of 87.8% [51]. [^{18}F]FDG-PET is recommended when indeterminate lesions at conventional morphological imaging need to be characterized, in order to differentiate disease recurrence from scar tissue [52–55]. Identification of presacral recurrences in particular, which develop in a high percentage of patients, poses a considerable clinical challenge. Assessment with conventional pelvic imaging studies (CECT, transrectal ultrasound

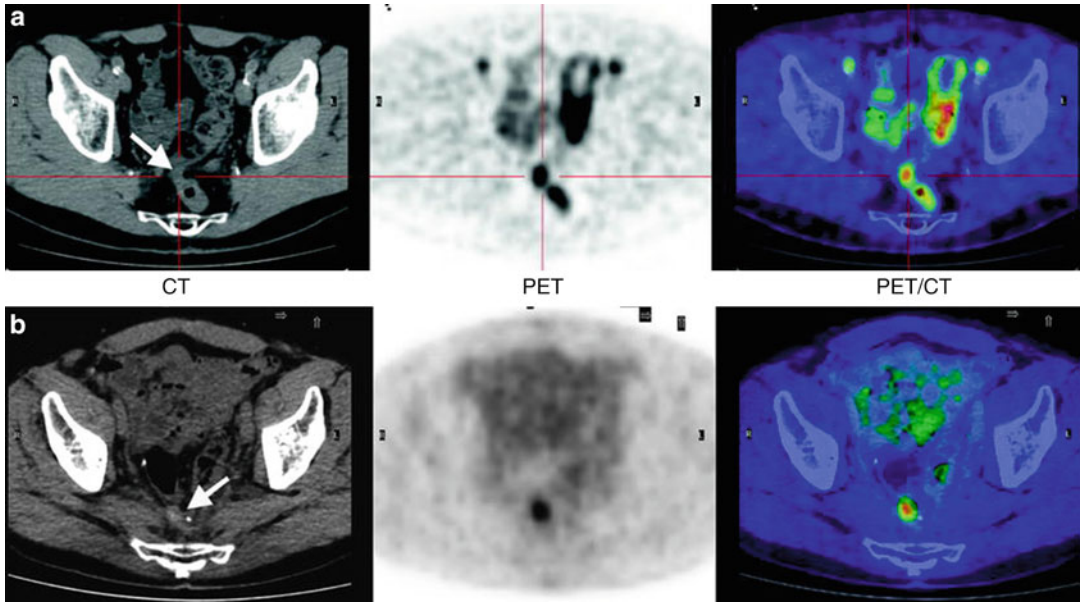

Fig. 1 Metabolic characterization of undetermined presacral lesions by [^{18}F]FDG-PET/CT. The nature of the lesions was confirmed by histological evaluation after the PET study. CT. (**a**, **b**) Suspected, undetermined presacral lesions at CT (*arrows*); PET. PET scan shows: (**a**, **b**) intense [^{18}F]FDG uptakes at the lesions level indicating disease recurrence; the fused PET/CT [^{18}F]FDG-PET images allows to easily localize and to characterize [^{18}F]FDG uptakes

[TREUS]) is problematic for differentiating post-surgical or radiotherapy residual fibrotic tissue from disease recurrence, which candidates the patient for further treatments (Fig. 1). Flamen et al. showed that [^{18}F]FDG-PET offers additional diagnostic value in 56% of cases compared to contrast-enhanced CT alone and in 20% of cases compared to contrast-enhanced CT in combination with TREUS [56]. Even-Sapir et al. demonstrated that PET/CT in patients with colorectal cancer who underwent abdominoperineal or anterior resection had 98% sensitivity, 96% specificity, 90% positive predictive value (PPV), 97% NPV, and 93% accuracy in distinguishing benign from malignant presacral abnormalities [57]. When recurrence is confirmed at morphological imaging, [^{18}F]FDG-PET is recommended to complete disease staging, because it can identify additional unexpected metastatic sites (upstaging) compared to CECT alone (Fig. 2). The general usefulness and the additional diagnostic value of [^{18}F]FDG-PET for this purpose were demonstrated in a meta-analysis by Huebner et al. showing that [^{18}F]FDG-PET leads to a change in clinical management in about 30% of patients with recurrent colorectal disease when added to standard imaging techniques in the evaluation of this patient subset [58]. In another study, Flamen et al. evaluated [^{18}F]FDG-PET and CECT performance in 103 patients with suspected recurrence of colorectal cancer [56]. [^{18}F]FDG-PET showed higher sensitivity than CECT in detecting metastatic lymph nodes in the abdominal cavity negative at CECT, especially those located in retroperitoneal and mesenteric sites. A statistically significant additional value of [^{18}F]FDG-PET was also found in the evaluation of extra-abdominal regions, where it identified unexpected metastases, most of which were located in the lung. Deleau et al. also reported a significant impact in the management of patients with CRC (40%) due to a higher sensitivity of PET than CT [59]. The literature reports discordant results for the evaluation of liver involvement. In the study by Flamen et al., no additional value of [^{18}F]FDG-PET in terms of sensitivity was found compared with normal CECT and/or MRI findings, but PET did allow to correctly classify anatomically

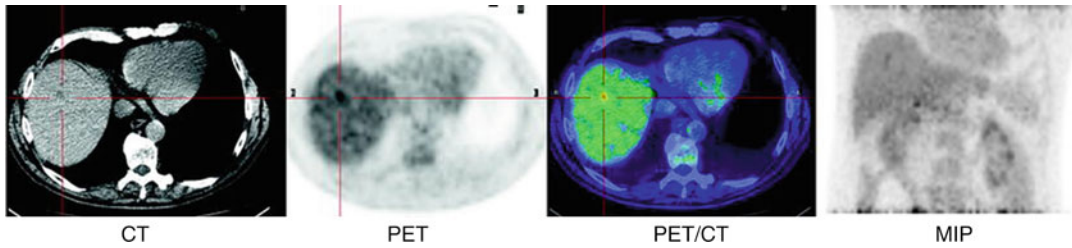

Fig. 2 Patient treated for primary colorectal cancer and referred for restaging. [^{18}F]FDG-PET/CT scan identified unexpected metastases in the liver not seen at CECT

undefined liver lesions [56]. Truant et al. showed that the sensitivity of [^{18}F]FDG-PET was equivalent to that of contrast-enhanced CT for hepatic sites (79% for both) and highly superior for extrahepatic abdominal sites (63% vs. 25%) [60]. A subsequent meta-analysis demonstrated that [^{18}F]FDG-PET can also be superior to conventional diagnostic techniques (CT, ultrasonography, MRI) in the detection of liver metastases (sensitivity around 90%) and that it can be considered as the most sensitive noninvasive imaging modality for the detection of hepatic metastases arising from gastrointestinal tract (GI) tumors, especially in colorectal cancer [61]. An interesting study by Sobhani et al. on 130 randomized patients undergoing complete follow-up (physical examination, biomarker assay, conventional imaging, and [^{18}F]FDG-PET) found that the time to recurrence detection was shorter for the patients studied by [^{18}F]FDG-PET than those who underwent conventional imaging (12.1 vs. 15.4 months), which led to the possibility to initiate a more curative treatment [62]. In a large group of patients ($n = 115$) presenting with recurrent colorectal cancer, Valk et al. reported that PET had a global sensitivity of 93% and a global specificity of 98% in detecting metastatic sites, compared with 69% and 96%, respectively, for CECT alone, confirming that [^{18}F]FDG-PET should be routinely performed in the follow-up of these patients. The most relevant finding emerging from this study was that PET identified unexpected metastases in 29% of patients presenting with only one site of recurrent disease at CECT, leading to an upstaging of disease [46]. Several studies later evaluated the impact of [^{18}F]FDG-PET or [^{18}F]FDG-PET/CT on the management of patients presenting with potentially curable liver metastases who underwent PET for complete restaging of disease [63–66]. McLeish et al. reported that hepatic metastases were identified on standard imaging in 232 (39.7%) patients, and [^{18}F]FDG-PET confirmed hepatic metastasis in 203 cases, including 22 cases with new lesions, and clarified presence of disease in 34/37 (92%) cases with equivocal standard imaging. In 54 patients, [^{18}F]FDG-PET was performed for disease assessment before hepatic resection. [^{18}F]FDG-PET had substantial management plan impact in 36/54 (66.7%) patients [67]. In this patient subset, PET allowed complete preoperative staging, determination of whether other neoplastic foci were present, and the choice of the most adequate treatment, thus avoiding unnecessary surgery. Lai et al. demonstrated that PET identified unexpected metastases in 25% of patients referred for presurgical staging to evaluate liver metastases resectability [63]. A 2005 review by Wiering et al. including all studies that had evaluated patients referred for presurgical staging for resectable liver metastases showed that [^{18}F]FDG-PET had sensitivity and specificity rates for liver lesions of 88% and 96.1%, respectively, and 91.5% and 95.4%, respectively, for extrahepatic lesions [68]. [^{18}F]FDG-PET resulted superior to CT in all cases but overall in detecting extrahepatic lesions. Patient management changed in about 32%, with cancelation of surgery and planning of systemic chemoradiation therapy in most cases. The review by Vriens et al. of 25 papers found a pooled mean management change of 22.3% in 1,060 patients [41]. With the introduction of combined PET/CT, the evaluation of many tumors and of colorectal cancer as well has improved even further, since it allows correlations between abnormal tissue metabolic changes detected at PET and anatomical

structures defined at CT, with accurate localization and characterization of lesions [69–71]. A review evaluating the potential of PET/CT in comparison with CECT, MRI, and PET alone suggested that, when available, [^{18}F]FDG-PET/CT appears to be the diagnostic tool of choice in early evaluation of recurrent colorectal disease [72]. Furthermore, the use of low-dose CT scanning to correct PET emission images for attenuation (instead of radioactive sources, as in the past) shortens the time needed to complete whole-body acquisition [73]. Still unclear is the influence of [^{18}F]FDG-PET on disease-free survival and overall survival in patients with recurrent colorectal cancer, owing to the difficulty of comparison between studies of different patient subgroups with different treatment plans; nonetheless, whole-body [^{18}F]FDG-PET has a key role in clinical practice and provides additional value to standard diagnostic workup and a high clinical impact [74].

In this subset of patients, [^{18}F]FDG-PET should be considered as an essential tool for better clinical management. Given its high NPV (around 95%), when a PET scan in this patient subgroup is negative, the presence of detectable disease recurrence could be excluded with [^{18}F]FDG-PET, though close clinical follow-up should still be undertaken. While there is considerable evidence for the usefulness of [^{18}F]FDG-PET, certain limitations to the technique deserve mention. [^{18}F]FDG-PET can produce false-positive findings at evaluation of abdominal recurrence when postsurgical inflammation and inflammatory disease are present (i.e., abscesses, colitis, rectal fistula). The physiological [^{18}F]FDG uptake in the GI and genitourinary tracts due to the excretion of the tracer itself can mimic but also hide pathological sites. The risk of false-negative findings is high in the presence of miliary liver metastatic spread, due to the physiological uptake of [^{18}F]FDG in the liver parenchyma and to a low lesion-to-background ratio or low [^{18}F]FDG uptake in diffuse peritoneal effusion. Besides anatomical sites, lesion size is another important factor affecting PET accuracy and may be responsible for false-negative results. This is true especially in lymph node or hepatic lesions <1 cm in diameter, near the technique's lower limit of effective spatial resolution. Finally, high patient blood glucose levels (>150 mg/dL) can deteriorate the [^{18}F]FDG-PET image quality, and some metastatic lesions, especially those in the liver, can be missed [75]. This is why blood glucose levels should be accurately kept under control with at least 6 h fasting before scanning. A meta-analysis by Huebner et al. evaluated the influence of false-positive and false-negative results on [^{18}F]FDG-PET sensitivity and specificity in patients with recurrent disease [58]. The final data showed that false positives had a greater impact than false negatives. In fact, the sensitivity of whole-body [^{18}F]FDG-PET resulted high (97%), with similar rates for the detection of liver (91–96%) and pelvic (94%) involvement. Specificity values in the evaluation of recurrence differed for total body (76%) and liver and pelvis (97–99%) due to the greater likelihood of false-positive results in extrahepatic and extrapelvic regions than in isolated organs. Furthermore, a study by Akhurst et al. [76] on a group of patients who underwent [^{18}F]FDG-PET for presurgical staging demonstrated that sensitivity was lower in those who received neoadjuvant chemotherapy due to the risk of the stunning phenomenon that leads to false-negative results when [^{18}F]FDG-PET is performed too early after the end of treatment.

Treatment Response Evaluation

The identification of responders to chemotherapy is of interest for selecting patients who may be expected to benefit from continued treatment and for selecting those who could be treated with other drugs. Evaluation of response to treatment is ordinarily based on morphological assessment of target lesions and of changes in lesion diameter over time. Currently, the Response Evaluation Criteria in Solid Tumors (RECIST) is the most widely used set of rules to define disease response to treatment: complete response is defined as disappearance of target lesions at morphological imaging; partial response, a minimum reduction of 30% in lesion diameter; disease progression, a minimum increase of 20% in lesion diameter or appearance of new lesions; and stable disease, neither partial response nor disease progression

[77]. With [^{18}F]FDG-PET came the need to have similar criteria for metabolic response, but consensus is still lacking. A significant decrease or increase in [^{18}F]FDG uptake in target lesions during treatment has always been considered as a sign of treatment response or disease progression, respectively; nevertheless, lacking standardized limits and standardized timing of response assessment, each study uses its own criteria. One limitation to [^{18}F]FDG-PET is its limited ability to detect minimal residual disease below the range of system spatial resolution. [^{18}F]FDG uptake is detectable in lesions measuring 5–10 mm in diameter, which correspond to about 10^8–10^9 tumor cells. But even with this limitation, a negative PET scan during or at the end of treatment is predictive of good prognosis since it indicates disease response. Furthermore, the interval required for a positive [^{18}F]FDG-PET/CT scan to become negative during treatment is a prognostic factor and a predictive element for final tumor response. If after 2 cycles of chemotherapy a PET scan is negative, as demonstrated in lymphomatous disease, the chances of obtaining remission at the end of the treatment are high, whereas the chances of remission with a few more chemotherapy cycles are lower if PET scans taken early at the beginning of treatment remain persistently positive [78–80]. Treatment response evaluated by [^{18}F]FDG-PET is clearly related to a better overall survival and disease-free survival in most types of tumors. Metabolic response to treatment is normally evaluated quantitatively by measuring variation in SUV_{max} (standardized uptake value), which is a more practical and reproducible way than with qualitative visual methods, even if many studies have employed the latter, with good stratification of subsequent prognosis [81–84].

Quantitative evaluation has to be reproducible, which means that pre-therapy and post-therapy scans have to be made in the same way, with the same scanner, similar injected activity, and the same patient preparation (body weight, blood glucose level) [85]. The problem is to determine which percentage in SUV_{max} reduction is considered significant for defining the clinical response. Many studies have proposed their own cutoff values (25–35%) for the drop in SUV_{max} [86, 87]. Recently, Wahl et al. have proposed the Positron Emission Tomography Response Criteria in Solid Tumors (PERCIST) as standardized criteria to define metabolic response to treatment. These criteria include standardized patient preparation: fasting at least 4–6 h before injection; serum glucose <200 mg/dL; insulin administration before [^{18}F]FDG-PET not indicated; image acquisition obtained 50–70 min after injection and reconstructed with the same software for baseline and post-therapeutic scan, with up to 15 min difference between the acquisition of the two scans; and SUV_{max} corrected for lean body mass as calculated by a region of interest (ROI) system of detection. Furthermore, it is recommended to choose up to five target lesions, two for organs with the highest [^{18}F]FDG uptake, better if about 2 cm in diameter. These target lesions will usually correspond to the target lesions considered by RECIST. Response to therapy is evaluated as a continuous variable expressed as the drop in the percentage of SUV_{max} between the pre- and post-therapeutic scans. Complete metabolic response is defined as the disappearance of all metabolic active tumor, with the target lesion showing the same uptake as the liver and indistinguishable from the surrounding background; a partial response, as a decrease of >30% in SUV_{max} of the most intense lesion; and progressive disease, an increase of >30% in SUV_{max} of the most intense lesion or a visible increase in the extent of [^{18}F]FDG uptake. Still debated is the number of chemotherapy cycles after which [^{18}F]FDG-PET has to be performed to evaluate the response and the delay in time between the last treatment and [^{18}F]FDG-PET; the PERCIST committee considers them as treatment-specific criteria. Several studies demonstrated that SUV_{max} begins to drop after only one cycle of chemotherapy, at which time early response can be detected [87, 88]. Based on previous studies, especially in lymphomatous disease, the suggested delay between the end of the treatment and the final [^{18}F]FDG-PET is around 10 days to 3 weeks for chemotherapy and 3 months after radiotherapy to avoid either the stunning risk or the occurrence of false-positive results, respectively [89]. [^{18}F]FDG-PET has been demonstrated to be a useful tool to evaluate

tumor response to treatment and to stratify patients for prognosis also in colorectal cancer [90]. Several studies have demonstrated the usefulness of performing [^{18}F]FDG-PET to evaluate response to neoadjuvant treatment, i.e., chemoradiation therapy with cytoreduction intent before surgery, during chemotherapy in advanced metastatic tumor, and after local treatment of liver metastases to detect complete/incomplete treatment [91, 92]. Maffione et al. correlated PERCIST criteria and a new criterion developed in their center that they named PET Residual Disease in Solid Tumor (PREDIST) with tumor regression grade (TRG) classification of pathologic response to neoadjuvant chemoradiotherapy (CRT) in patients affected by rectal cancer. [^{18}F]FDG-PET/CT scan is an accurate tool to preoperatively predict the response to CRT in patients with locally advanced rectal cancer. The novel proposed criterion (PREDIST) seems to be helpful to discriminate responders from nonresponders [93, 94]. Evaluation of response to radiotherapy is very difficult by anatomic imaging alone because residual tissue persists after irradiation, making it impossible for CT or MRI to distinguish persistent disease from fibrosis (accuracy 30–60%) [95–97]. A review by Wahl et al. of 19 studies published between 1992 and 2008 reported a NPV for [^{18}F]FDG-PET of 83–100% and a PPV of 77–100%, depending on the criteria used to define the response [77]. All these studies differed in the definition of response criteria, the delay between treatment and [^{18}F]FDG-PET acquisition, and clinical endpoints (metabolic response and histological verification vs. overall survival and disease-free survival). The studies considering histological confirmation of [^{18}F]FDG-PET findings as an endpoint demonstrated a significant correlation between [^{18}F]FDG-PET residual uptake and histological response (viable tumor cells). In the majority, a decrease in SUV_{max} after a median of 3–6 weeks after irradiation seemed to predict good response to radiotherapy. Most of the studies proposed quantitative evaluation of tumor response by using a decrease in SUV_{max} or SUV_{mean} after treatment, but with different cutoff values (30–60%); others proposed kinetic models which, although reproducible, are more difficult to perform in clinical practice. The study by Melton et al. in particular, which compared quantitative methods (decrease in SUV_{max} >70% and decrease in total lesion glycolysis [TLG]) versus qualitative visual methods, showed that for the evaluation of response to neoadjuvant treatment for colorectal cancer, the quantitative is more accurate than the qualitative method [98]. Of note, however, is the risk of false-positive results due to post-irradiation inflammatory processes and false-negative results due to minimal residual viable disease under the detection limits of [^{18}F]FDG-PET. A decrease in the SUV_{max} in patients undergoing treatment is not only the expression of tumor response, and the SUV_{max} itself is not only the expression of tumor absolute [^{18}F]FDG avidity: both need to be interpreted for their prognostic meaning. Some studies demonstrated that patients considered responders to [^{18}F]FDG-PET after chemoradiation therapy of the primary tumor had a better median overall survival and disease-free survival [84, 99–102]. Other studies demonstrated that the absolute SUV_{max} or SUV_{mean} can stratify patients with a better or worse overall survival, but at which cutoff is not yet clear. Calvo et al., for example, showed that patients with a pre-therapeutic tumor $SUV_{max} \leq 6$ had a better overall survival at 3 years after neoadjuvant and surgical treatment than those with a higher tumor SUV_{max} (92% vs. 60%) [103]. Riedl et al. proposed different ranges of SUV_{max} with different prognosis as expressed by median overall survival [104]. The role of [^{18}F]FDG-PET in the evaluation of systemic chemotherapy in advanced metastatic tumors is also under evaluation. A recent review by De Gesus Oei gives an overview of the results of five studies [105–110]. All such studies evaluated the response to treatment after a few cycles of chemotherapy in order to differentiate responder patients from nonresponders in order to optimize treatment. Maffione et al., also, reported that PET showed high accuracy in early prediction response during preoperative CRT. In the era of tailored treatment, early assessment of nonresponder patients allows modification of the subsequent strategy especially the timing and the type of surgical approach [111].

The problem is to define the correct timing for [^{18}F]FDG-PET so as to obtain a good correlation between global response and prognosis. These studies compared [^{18}F]FDG-PET findings at 1 or 2 weeks after the start of chemotherapy and then at 1–3 months. The majority demonstrated that the clinical correlation between metabolic response and treatment outcome was better detected at 1–3 months after the start of chemotherapy. Here, too, quantitative evaluation by SUV_{max} or SUV_{mean} is considered a better way to evaluate metabolic response than qualitative assessment. Furthermore, Dimitrakopoulou et al. demonstrated that the absolute SUV_{mean} of the most avid lesions at pre-therapeutic PET could predict response to treatment, a second-line chemotherapy in this study, thus supporting the concept that the higher the [^{18}F]FDG avidity as expressed by SUV_{max} or SUV_{mean}, the more resistant the lesions are to treatment [108]. The introduction of targeted therapy with anti-angiogenesis or anti-tyrosine kinase drugs for treating colorectal cancer has opened new frontiers to the use of [^{18}F]FDG-PET in evaluating response to treatment, given that this kind of therapy exhibits a cytostatic rather than a cytoreductive effect and that tumor metabolic change reflects response better than anatomic changes detectable by CT. Future, prospective studies are needed to elucidate this point [112, 113]. Skougaard et al. in their recent study compared European Organization for Research and Treatment of Cancer (EORTC) criteria with PET Response Criteria in Solid Tumors (PERCIST) for response evaluation of patients with metastatic colorectal cancer treated with a combination of the chemotherapeutic drug irinotecan and the monoclonal antibody cetuximab. A total of 61 patients and 203 PET/CT scans were eligible for response evaluation. With EORTC criteria, 38 had PMR, 16 had SMD, and 7 had PMD as their BOmR. With PERCIST, 34 had PMR, 20 had SMD, and 7 had PMD as their BOmR. There was agreement between EORTC criteria and PERCIST in 87% of the patients [114]. Finally, [^{18}F]FDG-PET has an important role in the evaluation of response to local treatment of liver and lung metastases by radiofrequency ablation (RFA), laser thermotherapy, or cryotherapy. [^{18}F]FDG-PET can detect incomplete treatment at a much earlier stage than CT and can better detect relapse of disease. After RFA, necrotic tissue and fibrotic scar formation in the treated lesion are frequently associated with inflammatory phenomena. Contrast enhanced CT does not reliably differentiate between persistent tumoral disease and inflammation. [^{18}F]FDG-PET shows different types of [^{18}F]FDG uptake in persistent active disease (focal and high [^{18}F]FDG uptake) versus inflammatory processes (more diffuse, circular, and mild uptake) (Fig. 3a–c). The review by De Gesus Oei looked at five studies [115–119]. All reported an NPV value for [^{18}F]FDG-PET of around 100% in an early stage (1–3 weeks after treatment), which means that [^{18}F]FDG-PET has to be performed early to define complete response to treatment. The wide range in PPV (80–97%) across the studies underlined again that, although [^{18}F]FDG-PET can detect relapse or persistent viable disease earlier than CT, there remains the risk of false-positive results due to inflammatory or infective phenomena.

New Prospects

PET/MRI

PET combined with magnetic resonance imaging (PET/MRI) seems to be a promising modality in different fields of tumor imaging. With the high soft tissue contrast of MRI and the superior ability of [^{18}F]FDG-PET to detect vital tumor tissue prior to morphological changes, the advent of combined PET/MRI will open new perspectives in noninvasive imaging. The combination of PET with MRI also opens up options to acquire multimodal molecular imaging parameters simultaneously. This may contribute to a more detailed characterization of molecular processes in vivo [120–122]. Some studies also report results for colorectal cancer. Paspulati et al. reported their initial experience showing a high diagnostic accuracy of PET/MRI in T staging of rectal cancer compared with PET/CT. In addition, PET/MRI shows at least comparable accuracy in N and M staging as well as restaging to PET/CT. However, the small sample size limits the possibility to

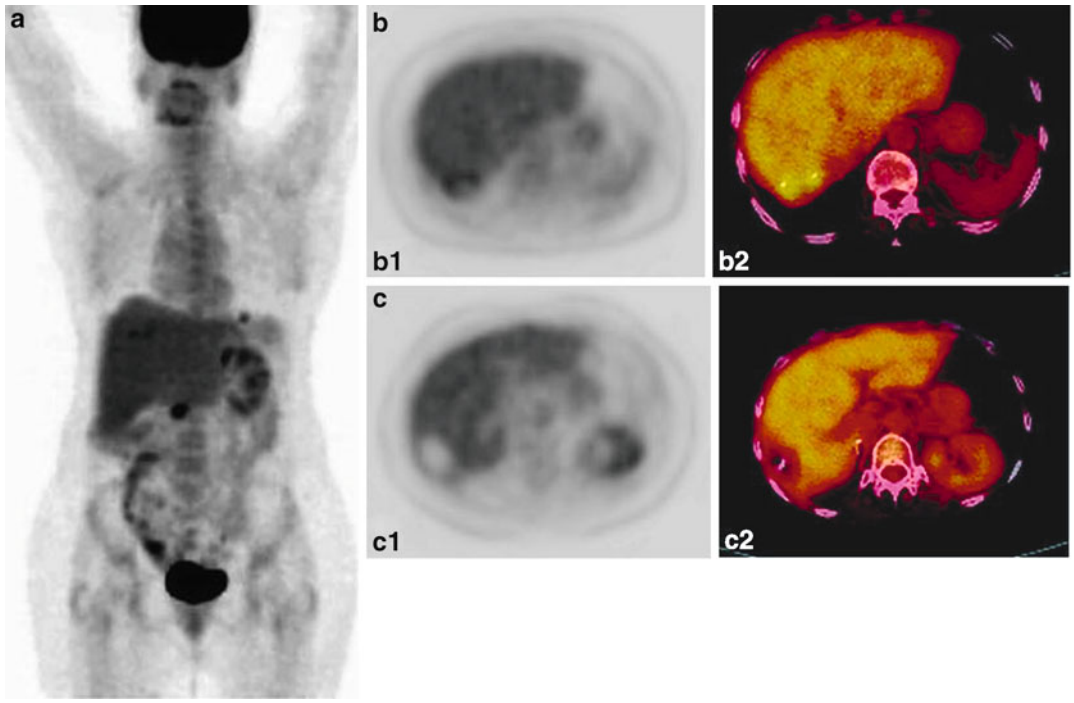

Fig. 3 Patient with colorectal cancer, liver metastases treated by RF, and abdominal lymphadenopathy. Evaluation of RF ablation efficacy by [^{18}F]FDG-PET. (**a**) MIP image, (**b1**) axial PET image showing physiological aspect of liver metastases after radiofrequency ablation (homogeneous and peripherical mild [^{18}F]FDG uptake), (**b2**) axial fusion image of the same lesion, (**c1**) axial PET image showing relapse of disease in liver metastases treated by RF ablation (heterogeneous and focal pattern of [^{18}F]FDG uptake), (**c2**) fusion axial image of the same lesion

assume these results as definitive. It is expected that PET/MRI would yield higher diagnostic accuracy than PET/CT considering the high soft tissue contrast provided by MRI compared with CT, but larger studies are necessary to fully assess the benefit of PET/MRI in colorectal cancer [123].

Radiotherapy Volume Planning

[^{18}F]FDG-PET is often used in clinical practice to identify target volume in radiotherapy treatment, especially in lung cancer [124–127]. Some studies also report results for colorectal cancer. Promising preliminary results in esophageal, pancreatic, and anorectal cancers and colorectal liver metastasis suggest that [^{18}F]FDG-PET might provide additional information useful in target volume delineation. Poor image resolution and a low sensitivity for lymph node detection currently limit its widespread implementation [128]. Ciernik et al. demonstrated that PET/CT-derived planning target volume (PTV) is as accurate as CT-derived PTV [129]. In the future, perhaps PET/CT alone will be sufficient for planning radiotherapy target volume.

Therapy with Transarterial ^{90}Y-Microspheres

In unresectable liver metastases and advanced liver metastases, radioembolization treatment with microspheres containing the beta emitter yttrium-90 is becoming a valid alternative to other treatments such as chemoembolization and radiofrequency. Microspheres are injected into an artery and, because of their diameter (20 to

60 μm), become entrapped by embolization in the microvascular tissues. The half-life of yttrium-90 is 64.1 h, and the administered dose is closely correlated with body surface area and tumor burden. Although few studies have evaluated its efficacy and feasibility to date, the results are promising in terms of tumor response and overall survival. A study by Whitney et al. evaluating application of this technique for liver metastases from different cancers, including colorectal cancer, demonstrated that it reduces tumor burden and can be followed by surgical resection of metastases [130]. In the bulk of studies, tumor response is based on CT according to RECIST, but there is also mounting evidence that [^{18}F]FDG-PET could be a useful tool and a more accurate technique even in this field to better characterize tumor response according to metabolic criteria. Necrosis, inflammatory, or fibrotic processes can lead to an increase in lesion size after treatment, which can be interpreted as disease progression at anatomic imaging [131–134]. Wong et al. showed that [^{18}F]FDG-PET detected more partial responses than CT, as clinically confirmed by the decrease in serum CEA levels [135]. In phase I–II studies, therapy with yttrium-90 microspheres can be combined with adjuvant chemotherapy to increase tumor radiosensitivity with good patient tolerability [136–139]. The most common side effects of this treatment are abdominal pain, transient hepatotoxicity with elevated transaminase, hyperbilirubinemia, and hypersplenism; occasional cases of important neutropenia possibly induced by bone marrow irradiation when combined with adjuvant chemotherapy have been reported [140]. Further studies on large-scale patient populations are needed to confirm these preliminary results.

Carcinoid Tumors

Endocrine tumors can be found in the GI tract and in the rectal tract in particular. Their management, treatment, and prognosis differ substantially from adenocarcinomas. Oftentimes, they are discovered after the onset of local symptoms such as rectorrhagy. Prognosis is closely correlated with tumor size and local extension. Frequently, a simple endoscopic resection is sufficient for obtaining complete remission; more complex surgery is chosen as first intention treatment for more advanced local tumors. Distant metastases are infrequent. Tumor extension is local in almost 70% of cases. Nuclear medicine offers an array of imaging techniques to study endocrine tumors, all of which are based on the affinity these tumors have for somatostatin receptors [141, 142]. Historically, ^{111}In-DTPA-octreotide scintigraphy is the most widely used technique to characterize the primary tumor and perform disease staging and follow-up of endocrine tumors. The sensitivity of this technique in endocrine tumor staging is between 60% and 100%, and it depends on tumor differentiation grade, somatostatin receptor density, origin, site, and size [143, 144]. Other approaches for evaluating intestinal endocrine tumor are now available: ^{18}F-DOPA-PET (^{18}F-6-fluoroDOPA), [^{11}C]HTP-PET ([^{11}C]5-hydroxytryptophane), ^{68}Ga-DOTA-TOC, and ^{68}Ga-DOTA-NOC, all tracers with an affinity for somatostatin receptors or that are involved in endogenous amine metabolism. Although several studies on small groups of patients have shown the superiority of these techniques over traditional somatostatin analog scintigraphy [145–147], further studies are needed to confirm their accuracy and to identify standard recommendations for their use [148–155].

References

1. Shike M, Winawer SJ, Greenwald PH, et al. Primary prevention of colorectal cancer. The WHO Collaborating Centre for the Prevention of Colorectal Cancer. Bull World Health Organ. 1990;68:377–85.
2. Jemal A, Siegel R, Ward E, et al. Cancer statistics, 2006. CA Cancer J Clin. 2006;56:106–30.
3. American Cancer Society. Cancer facts and figures 2009. Atlanta: American Cancer Society; 2009.
4. Phillips RKS, Hittinger R, Blesovsky L, et al. Large bowel cancer: surgical pathology and its relationship to survival. Br J Surg. 1984;71:604–10.
5. Fretwell V, Ang C, Tweedle E, et al. The impact of lymph node yield on Duke's B and C colorectal cancer survival. Colorectal Dis. 2010;12:995–1000.
6. International Union against Cancer. TNM classification of malignant tumors. 4th ed. Berlin: Springer; 1987.

7. American Joint Committee on Cancer. Manual for staging cancer. 3rd ed. Philadelphia: JB Lippincott; 1988. p. 75.
8. Compton C, Fenoglio-Preiser CM, Pettigrew N, et al. American joint committee on cancer prognostic factors consensus conference: colorectal working group. Cancer. 2000;88:1739–57.
9. Le Voyer TE, Sigurdson ER, Hanlon AL, et al. Colon cancer survival is associated with increasing number of lymph nodes analyzed: a secondary survey of intergroup trial INT-0089. J Clin Oncol. 2003;21: 2912–9.
10. Chang GJ, Rodriguez-Bigas MA, Skibber JM, et al. Lymph node evaluation and survival after curative resection of colon cancer: systematic review. J Natl Cancer Inst. 2007;99:433–41.
11. Coverlizza S, Risio M, Ferrari A, et al. Colorectal adenomas containing invasive carcinoma. Pathologic assessment of lymph node metastatic potential. Cancer. 1989;64:1937–47.
12. Shepherd NA, Baxter KJ, Love SB. The prognostic importance of peritoneal involvement in colonic cancer: a prospective evaluation. Gastroenterology. 1997; 112:1096–102.
13. Moerkerk P, Arends JW, van Driel M, et al. Type and number of Ki-ras point mutations relate to stage of human colorectal cancer. Cancer Res. 1994;54(13): 3376–8.
14. Johnston PG, Lenz HJ, Leichman CG, et al. Thymidylate synthase gene and protein expression correlate and are associated with response to 5-fluorouracil in human colorectal and gastric tumors. Cancer Res. 1995;55:1407–12.
15. Nemunaitis J, Cox J, Meyer W, et al. Irinotecan hydrochloride (CPT-11) resistance identified by K-ras mutation in patients with progressive colon cancer after treatment with 5-fluorouracil (5-FU). Am J Clin Oncol. 1997;20:527–9.
16. Yamachika T, Nakanishi H, Inada K, et al. A new prognostic factor for colorectal carcinoma, thymidylate synthase, and its therapeutic significance. Cancer. 1998;82:70–7.
17. Ahnen DJ, Feigl P, Quan G, et al. Ki-ras mutation and p53 over expression predict the clinical behavior of colorectal cancer: a Southwest Oncology Group study. Cancer Res. 1998;58:1149–58.
18. Chau I, Cunningham D. Treatment in advanced colorectal cancer: what, when and how? Br J Cancer. 2009;100:1704–19.
19. Arnoletti JP, Bland KI. Neoadjuvant and adjuvant therapy for rectal cancer. Surg Oncol Clin N Am. 2006;15:147–57.
20. Glynne-Jones R, Grainger J, Harrison M, Ostler P, Makris A. Neoadjuvant chemotherapy prior to preoperative chemoradiation or radiation in rectal cancer: should we be more cautious? Br J Cancer. 2006;94: 363–71.
21. Huguier M, Houry S, Barrier A. Local recurrence of cancer of the rectum. Am J Surg. 2001;182:437–9.
22. Reske SN, Kotzerke J. FDG-PET for clinical use. Results of the 3rd German Interdisciplinary Consensus Conference, "Onko-PET III", 21 July and 19 September 2000. Eur J Nucl Med. 2001;28: 1707–23.
23. Jerusalem G, Hustinx R, Beguin Y, et al. PET scan imaging in oncology. Eur J Cancer. 2003;39:1525–34.
24. Rohren EM, Turkington TG, Coleman RE. Clinical applications of PET in oncology. Radiology. 2004; 231:305–32.
25. ASR Regione Emilia Romagna. Indicazioni all'utilizzo della FDG-PET in oncologia. Analisi critica della letteratura scientifica. Dossier N. 124/ 2006. 5 Giugno 2007.
26. International Atomic Energy Agency. Appropriate use of FDG-PET for the management of cancer patients. Vienna: International Atomic Energy Agency; 2010. p. 75 (IAEA Human Health Series, ISSN 2075–3772; no. 9).
27. Pickhardt PJ. Recent developments in colorectal imaging. Curr Opin Gastroenterol. 2015;31:76–80.
28. Kekelidze M, D'Errico L, Pansini M, Tyndall A, Hohmann J. Colorectal cancer: current imaging methods and future perspectives for the diagnosis, staging and therapeutic response evaluation. World J Gastroenterol. 2013;19:8502–14.
29. Abdel-Nabi H, Doerr RJ, Lamonica DM, et al. Staging of primary colorectal carcinomas with fluorine-18 fluorodeoxyglucose whole-body PET: correlation with histopathologic and CT findings. Radiology. 1998;206:755–60.
30. Kantorova I, Lipska L, Belohlavek O, et al. Routine ^{18}F-FDG PET in preoperative staging of colorectal cancer: comparison with conventional staging and its impact on treatment decision making. J Nucl Med. 2003;44:1784–8.
31. Furukawa H, Ikuma H, Seki A, et al. Positron emission tomography scanning is not superior to whole body multidetector helical computed tomography in the preoperative staging of colorectal cancer. Gut. 2006;55:1007–11.
32. Whiteford MH, Whiteford HM, Yee LF, et al. Usefulness of FDG-PET scan in the assessment of suspected metastatic or recurrent adenocarcinoma of the colon and rectum. Dis Colon Rectum. 2000; 43:759–67.
33. Patel S, McCall M, Ohinmaa A, Bigam D, Dryden DM. Positron emission tomography/computed tomographic scans compared to computed tomographic scans for detecting colorectal liver metastases: a systematic review. Ann Surg. 2011;253:666–71.
34. Mukai M, Sadahiro S, Yasuda S, et al. Preoperative evaluation by whole-body ^{18}F-fluorodeoxyglucose positron emission tomography in patients with primary colorectal cancer. Oncol Rep. 2000;7:86–7.
35. Heriot AG, Hicks RJ, Drummond EG, et al. Does positron emission tomography change management in primary rectal cancer? A prospective assessment. Dis Colon Rectum. 2004;47:451–8.

36. Gearhart SL, Frassica D, Rosen R, et al. Improved staging with pretreatment positron emission tomography/computed tomography in low rectal cancer. Ann Surg Oncol. 2006;13:397–404.
37. Bassi MC, Turri L, Sacchetti G, et al. FDG-PET/CT imaging for staging and target volume delineation in preoperative conformal radiotherapy of rectal cancer. Int J Radiat Oncol Biol Phys. 2008;70:1423–6.
38. Davey K, Heriot AG, Mackay J, et al. The impact of 18-fluorodeoxyglucose positron emission tomography-computed tomography on the staging and management of primary rectal cancer. Dis Colon Rectum. 2008;51:997–1003.
39. Brush J, Boyd K, Chappell F, et al. The value of FDG positron emission tomography/computerised tomography (PET/CT) in pre-operative staging of colorectal cancer: a systematic review and economic evaluation. Health Technol Assess. 2011;15: 1–192.
40. De Vos N, Goethals I, Ceelen W. Clinical value of ^{18}F-FDG- PET-CT in the preoperative staging of peritoneal carcinomatosis from colorectal origin. Acta Chir Belg. 2014;114:370–5.
41. Vriens D, de Geus-Oei LF, van der Graaf WT, et al. Tailoring therapy in colorectal cancer by PET-CT. Q J Nucl Med Mol Imaging. 2009;53(2):224–44.
42. Penna D, Garcia JR, Arace P, Llinares E, Arena V, Riera E, Pelosi E. Could CE. CT/PET with ^{18}F-FDG represent the only examination in rectum adenocarcinoma staging? Clin Transl Imaging. 2015;3 Suppl 1: S70.
43. Riera E, Penna D, Llinares E, Arace P, Soler M, Arena V, Moragas M, Pelosi E, García JR. Rev Esp Med Nucl Imagen Mol. 2015;34 Suppl 1:78.
44. Flanagan FL, Dehdashti F, Ogunbiyi OA, et al. Utility of FDG-PET for investigating unexplained plasma CEA elevation in patients with colorectal cancer. Ann Surg. 1998;227:319–23.
45. Flamen P, Hoekstra OS, Homans F, et al. Unexplained rising carcinoembryonic antigen (CEA) in the postoperative surveillance of colorectal cancer: the utility of positron emission tomography (PET). Eur J Cancer. 2001;37:862–9.
46. Valk PE, Abella-Columna E, Haseman MK, et al. Whole-body PET imaging with [^{18}F]fluorodeoxyglucose in management of recurrent colorectal cancer. Arch Surg. 1999;134:503–11.
47. Simó M, Lomeña F, Setoain J, et al. FDG-PET improves the management of patients with suspected recurrence of colorectal cancer. Nucl Med Commun. 2002;23:975–82.
48. Shen YY, Liang JA, Chen YK, et al. Clinical impact of ^{18}F-FDG-PET in the suspicion of recurrent colorectal cancer based on asymptomatically elevated serum level of carcinoembryonic antigen (CEA) in Taiwan. Hepatogastroenterology. 2006;53:348–50.
49. Lu YY, Chen JH, Chien CR, Chen WT, Tsai SC, Lin WY, Kao CH. Use of FDG-PET or PET/CT to detect recurrent colorectal cancer in patients with elevated CEA: a systematic review and meta-analysis. Int J Colorectal Dis. 2013;28:1039–47.
50. Bu W, Wei R, Li J, Wang L, Shi C, Song J, Ma S, Chen H, Cong N. Association between carcinoembryonic antigen levels and the applied value of ^{18}F-fluorodeoxyglucose positron emission tomography/computed tomography in post-operative recurrent and metastatic colorectal cancer. Oncol Lett. 2014;8:2649–53.
51. Gade M, Kubik M, Fisker RV, Thorlacius-Ussing O, Petersen LJ. Diagnostic value of ^{18}F-FDG PET/CT as first choice in the detection of recurrent colorectal cancer due to rising CEA. Cancer Imaging. 2015;15:11.
52. Beets G, Penninckx F, Schiepers C, et al. Clinical value of whole-body positron emission tomography with [^{18}F]fluorodeoxyglucose in recurrent colorectal cancer. Br J Surg. 1994;81:1666–70.
53. Schiepers C, Penninckx F, De Vadder N, et al. Contribution of PET in the diagnosis of recurrent colorectal cancer: comparison with conventional imaging. Eur J Surg Oncol. 1995;21:517–22.
54. Ogunbiyi OA, Flanagan FL, Dehdashti F, et al. Detection of recurrent and metastatic colorectal cancer: comparison of positron emission tomography and computed tomography. Ann Surg Oncol. 1997;4: 613–20.
55. Kalff, Hicks RJ, Ware RE, et al. The clinical impact of 18F-FDG PET in patients with suspected or confirmed recurrence of colorectal cancer: a prospective study. J Nucl Med. 2002;43:492–9.
56. Flamen P, Stroobants S, Van Cutsem E, et al. Additional value of whole-body positron emission tomography with fluorine-18-2-fluoro-2-deoxy-D-glucose in recurrent colorectal cancer. J Clin Oncol. 1999; 17:894–901.
57. Even-Sapir E, Parag Y, Lerman H, et al. Detection of recurrence in patients with rectal cancer: PET/CT after abdominoperineal or anterior resection. Radiology. 2004;232:815–22.
58. Huebner RH, Park KC, Shepherd JE, et al. A meta-analysis of the literature for whole-body FDG PET detection of recurrent colorectal cancer. J Nucl Med. 2000;41:1177–89.
59. Deleau C, Buecher B, Rousseau C, Kraeber-Bodéré F, Flamant M, des Varannes SB, Frampas E, Galmiche JP, Matysiak-Budnik T. Clinical impact of fluorodeoxyglucose-positron emission tomography scan/computed tomography in comparison with computed tomography on the detection of colorectal cancer recurrence. Eur J Gastroenterol Hepatol. 2011;23: 275–81.
60. Truant S, Huglo D, Hebbar M, et al. Prospective evaluation of the impact of [^{18}F]fluoro-2-deoxy-D-glucose positron emission tomography of resectable colorectal liver metastases. Br J Surg. 2005;92: 362–9.
61. Kinkel K, Lu Y, Both M, et al. Detection of hepatic metastases from cancers of the gastrointestinal tract by using noninvasive imaging methods (US, CT, MR

Imaging, PET): a meta-analysis. Radiology. 2002; 224:748–56.
62. Sobhani I, Tiret E, Lebtahi R, et al. Early detection of recurrence by ^{18}FDG-PET in the follow-up of patients with colorectal cancer. Br J Cancer. 2008; 98:875–80.
63. Lai DT, Fulham M, Stephen MS, et al. The role of whole-body positron emission tomography with [^{18}F]fluorodeoxyglucose in identifying operable colorectal cancer metastases to the liver. Arch Surg. 1996;131:703–7.
64. Topal B, Flamen P, Aerts R, et al. Clinical value of whole-body emission tomography in potentially curable colorectal liver metastases. Eur J Surg Oncol. 2001;27:175–9.
65. Ruers TJ, Langenhoff BS, Neeleman N, et al. Value of positron emission tomography with [F-18] fluorodeoxyglucose in patients with colorectal liver metastases: a prospective study. J Clin Oncol. 2002;20:388–95.
66. Selzner M, Hany TF, Wildbrett P, et al. Does the novel PET/CT imaging modality impact on the treatment of patients with metastatic colorectal cancer of the liver? Ann Surg. 2004;240:1027–34.
67. McLeish AR, Lee ST, Byrne AJ, Scott AM. Impact of ^{18}F-FDG-PET in decision making for liver metastectomy of colorectal cancer. ANZ J Surg. 2012;82:30–5.
68. Wiering B, Krabbe PF, Jager GJ, et al. The impact of fluor-18-deoxyglucose-positron emission tomography in the management of colorectal liver metastases. Cancer. 2005;104:2658–70.
69. von Schulthess GK, Steinert HC, Hany TF. Integrated PET/CT: current applications and future directions. Radiology. 2006;238:405–22.
70. Kim JH, Czernin J, Allen-Auerbach MS, et al. Comparison between ^{18}F-FDG PET, in-line PET/CT, and software fusion for restaging of recurrent colorectal cancer. J Nucl Med. 2005;46:587–95.
71. Pelosi E, Messa C, Sironi S, et al. Value of integrated PET/CT for lesion localisation in cancer patients: a comparative study. Eur J Nucl Med Mol Imaging. 2004;31:932–9.
72. Vogel WV, Wiering B, Corstens FH, et al. Colorectal cancer: the role of PET/CT in recurrence. Cancer Imag. 2005;23(5 Suppl):S143–9.
73. Messa C, Bettinardi V, Picchio M, et al. PET/CT in diagnostic oncology. Q J Nucl Med Mol Imaging. 2004;48:66–75.
74. Ogawa S, Itabashi M, Kondo C, Momose M, Sakai S, Kameoka S. Prognostic value of total lesion glycolysis measured by ^{18}F-FDG-PET/CT in patients with colorectal cancer. Anticancer Res. 2015;35: 3495–500.
75. Crippa F, Gavazzi C, Bozzetti F, et al. The influence of blood glucose levels on [^{18}F]fluorodeoxyglucose (FDG) uptake in cancer: a PET study in liver metastases from colorectal carcinomas. Tumori. 1997; 83:748–52.
76. Akhurst T, Kates TJ, Mazumdar M, et al. Recent chemotherapy reduces the sensitivity of [^{18}F]fluorodeoxyglucose positron emission tomography in the detection of colorectal metastases. J Clin Oncol. 2005;23:8713–6.
77. Wahl R, Jacene H, Kasamon Y et al. From RECIST to PERCIST: evolving considerations for PET response criteria in solid tumors. J Nucl Med. 2009;50 (Suppl 1):122S–150S.
78. Kostakoglu L, Coleman M, Leonard JP, et al. PET predicts prognosis after 1 cycle of chemotherapy in aggressive lymphoma and Hodgkin's disease. J Nucl Med. 2002;43:1018–27.
79. Gallamini A, Rigacci L, Merli F, et al. The predictive value of positron emission tomography scanning performed after two courses of standard therapy on treatment outcome in advanced stage Hodgkin's disease. Haematologica. 2006;91:475–81.
80. Jerusalem G, Hustinx R, Beguin Y, et al. Evaluation of therapy for lymphoma. Semin Nucl Med. 2005;35:186–96.
81. Mac Manus MP, Hicks RJ, Matthews JP, et al. Positron emission tomography is superior to computed tomography scanning for response assessment after radical radiotherapy or chemoradiotherapy in patients with non small cell lung cancer. J Clin Oncol. 2003;21:1285–92.
82. Hicks RJ. The role of PET monitoring therapy. Cancer Imaging. 2005;5:51–7.
83. Duong CP, Hicks RJ, Wheil, et al. FDG PET status following chemo-radiotherapy provides high management impact and powerful prognostic stratification in oesophageal cancer. Eur J Nucl Med Mol Imaging. 2006;33:770–8.
84. Kalff V, Duong C, Drummond EG, et al. Findings on ^{18}F-FDG PET scans after neoadjuvant chemoradiation provides prognostic stratification in patients with locally advanced rectal carcinoma subsequently treated by radical surgery. J Nucl Med. 2006;47:14–22.
85. Shankar LK, Hoffman JM, Bacharach S, et al. Consensus recommendations for the use of ^{18}F-FDG as an indicator of therapeutic response in patients in National Cancer Institute Trials. J Nucl Med. 2006; 47:1059–66.
86. Weber WA, Ott K, Becker K, et al. Prediction of response to preoperative chemotherapy in adenocarcinomas of the esophagogastric junction by metabolic imaging. J Clin Oncol. 2001;19:3058–65.
87. Prior JO, Montemurro M, Orcurto MV, et al. Early prediction of response to sunitinib after imatinib failure by ^{18}F-fluorodeoxyglucose positron emission tomography in patients with gastrointestinal stromal tumor. J Clin Oncol. 2009;27:439–45.
88. Avril N, Sassen S, Schmalfeldt B, et al. Prediction of response to neoadjuvant chemotherapy by sequential F-18-fluorodeoxyglucose positron emission tomography in patients with advanced-stage ovarian cancer. J Clin Oncol. 2005;23:7445–53.

89. Juweid ME, Stroobants S, Hoekstra OS, et al. Imaging Subcommittee of International Harmonization Project in Lymphoma. Use of positron emission tomography for response assessment of lymphoma: consensus of the Imaging Subcommittee of International Harmonization Project in Lymphoma. J Clin Oncol. 2007;25:571–8.
90. Stokkel MP, Draisma A, Pauwels EK. Positron emission tomography with 2-[^{18}F]-fluoro-2-deoxy-D-glucose in oncology. Part IIIb: therapy response monitoring in colorectal and lung tumours, head and neck cancer, hepatocellular carcinoma and sarcoma. J Cancer Res Clin Oncol. 2001;127:278–85.
91. Zaniboni A, Savelli G, Pizzocaro C, Basile P, Massetti V. Positron emission tomography for the response evaluation following treatment with chemotherapy in patients affected by colorectal liver metastases: a selected review. Gastroenterol Res Pract. 2015;2015: 706808.
92. Altini C, Niccoli Asabella A, De Luca R, et al. Comparison of ^{18}F-FDG PET/CT methods of analysis for predicting response to neoadjuvant chemoradiation therapy in patients with locally advanced low rectal cancer. Abdom Imaging. 2015;40:1190–202.
93. Maffione AM, Ferretti A, Chondrogiannis S, et al. Proposal of a new ^{18}F-FDG PET/CT predictor of response in rectal cancer treated by neoadjuvant chemoradiation therapy and comparison with PERCIST criteria. Clin Nucl Med. 2013;38:795–7.
94. Maffione AM, Chondrogiannis S, Capirci C, et al. Early prediction of response by ^{18}F-FDG PET/CT during preoperative therapy in locally advanced rectal cancer: a systematic review. Eur J Surg Oncol. 2014;40(10):1186–94.
95. Rau B, Hunerbein M, Barth C, et al. Accuracy of endorectal ultrasound after pre operative radiochemotherapy in locally advanced rectal cancer. Surg Endosc. 1999;13:980–4.
96. Kwok H, Bisset IP, Hill GL. Preoperative staging of rectal cancer. Int J Colorectal Dis. 2000;15:9–20.
97. Bipat S, Glas AS, Slors FJ, et al. Rectal cancer: local staging and assessment of lymph nodes involvement with endoluminal US, CT and MR imaging-a meta-analysis. Radiology. 2004;232:773–83.
98. Melton GB, Lavely WC, Jacene HA, et al. Efficacy of preoperative combined 18-fluorodeoxyglucose positron emission tomography and computed tomography for assessing primary rectal cancer response to neoadjuvant therapy. J Gastrointest Surg. 2007;11:961–9.
99. Amthauer H, Denecke T, Rau B, et al. Response prediction by FDG-PET after neoadjuvant radiochemotherapy and combined regional hyperthermia of rectal cancer: correlation with endorectal ultrasound and histopathology. Eur J Nucl Med Mol Imaging. 2004;31:811–9.
100. Guillem JG, Moore HG, Akhurst T, et al. Sequential preoperative fluorodeoxyglucose-positron emission tomography assessment of response to preoperative chemoradiation: a means for determining long-term outcome of rectal cancer. J Am Coll Surg. 2004;199: 1–7.
101. Kristiansen C, Loft A, Berthelsen AK, et al. PET/CT and histopathologic response to preoperative chemoradiation therapy in locally advanced rectal cancer. Dis Colon Rectum. 2008;51:21–5.
102. Konski A, Li T, Sigurdson E, et al. Use of molecular imaging to predict clinical outcome in patients with rectal cancer after preoperative chemotherapy and radiation. Int J Radiat Oncol Biol Phys. 2009;74: 55–9.
103. Calvo FA, Domper M, Matute R, et al. ^{18}F-FDG positron emission tomography staging and restaging in rectal cancer treated with preoperative chemoradiation. Int J Radiat Oncol Biol Phys. 2004;58: 528–35.
104. Riedl CC, Akhurst T, Larson S, et al. ^{18}F-FDG PET scanning correlates with tissue markers of poor prognosis and predict mortality for patients after liver resection for colorectal metastases. J Nucl Med. 2007;48:771–5.
105. Findlay M, Young H, Cunningham D, et al. Noninvasive monitoring of tumor metabolism using fluorodeoxyglucose and positron emission tomography in colorectal cancer liver metastases: correlation with tumour response to fluorouracil. J Clin Oncol. 1996;14:700–8.
106. Bender H, Bangard N, Metten N, et al. Possible role of FDG-PET in the early prediction of therapy outcome in liver metastases of colorectal cancer hybridoma. Hybridoma. 1999;18:87–91.
107. Dimitrakopoulou-Strauss A, Strauss LG, Rudi J. PET-FDG as a predictor of therapy response in patients with colorectal carcinoma. Q J Nucl Med. 2003;47:8–13.
108. Dimitrakopoulou-Strauss A, Strauss LG, Burger C, et al. Prognostic aspect of ^{18}F-FDG PET kinetics in patients with metastatic colorectal carcinoma receiving FOLFOX chemotherapy. J Nucl Med. 2004;45:1480–7.
109. De Gesus Oei LF, van Laarhoven HW, Visser EP, et al. Chemotherapy response evaluation with FDG PET in patients with colorectal cancer. Ann Oncol. 2007;19:348–52.
110. De Gesus Oei LF, Vriens D, van Laarhoven WM, van der Graaf WTA, Oyen W. Monitoring and predicting response to therapy with ^{18}F-FDG PET in colorectal cancer: a systematic review. J Nucl Med. 2009;50: 43S–52.
111. Maffione AM, Marzola MC, Grassetto G, et al. Are PREDIST criteria better than PERCIST criteria as a PET predictor of preoperative treatment response in rectal cancer? Nucl Med Commun. 2014;35:890–2.
112. Funaioli C, Pinto C, Di Fabio F, et al. ^{18}FDG-PET evaluation correlates better than CT with pathological response in a metastatic colon cancer patient treated with bevacizumab-based therapy. Tumori. 2007;93: 611–5.

113. Brandi G, Nannini M, Pantaleo MA, et al. Molecular imaging suggests efficacy of bevacizumab beyond the second line in advanced colorectal cancer patients. Chemotherapy. 2008;54:421–4.
114. Skougaard K, Nielsen D, Jensen BV, Hendel HW. Comparison of EORTC criteria and PERCIST for PET/CT response evaluation of patients with metastatic colorectal cancer treated with irinotecan and cetuximab. J Nucl Med. 2013;54:1026–31.
115. Langenhoff BS, Oyen WJ, Jager GJ, et al. Efficacy of fluorine-18-deoxuglucose positron emission tomography in detecting tumor recurrence after local ablative therapy for liver metastases: a prospective study. J Clin Oncol. 2002;20:4453–8.
116. Donckier V, Van Laethem J, Goldman S, et al. F-18 fluorodeoxyglucose positron emission tomography as a tool for early recognition of incomplete tumor destruction after radiofrequency ablation of liver metastases. J Surg Oncol. 2003;84:215–23.
117. Joosten J, Jager G, Oyen W, et al. Cryosurgery and radiofrequency ablation for unresectable colorectal liver metastases. Eur J Surg Oncol. 2005;31:1152–9.
118. Veit P, Antoch G, Stergar H, et al. Detection of residual tumor after radiofrequency ablation of liver metastasis with dual modality PET/CT: initial results. Eur Radiol. 2006;16:80–7.
119. Denecke T, Steffen I, Hildebrandt B, et al. Assessment of local control after laser-induced thermotherapy of liver metastases from colorectal cancer: contribution of FDG PET in patients with clinical suspicion of progressive disease. Acta Radiol. 2007;48:821–30.
120. Von Schulthess GK, Kuhn FP, Kaufmann P, Veit-Haibach P. Clinical positron emission tomography/magnetic resonance imaging applications. Semin Nucl Med. 2013;43:3–10.
121. Sauter AW, Wehrl HF, Kolb A, Judenhofer MS, Pichler BJ. Combined PET/MRI: one step further in multimodality imaging. Trends Mol Med. 2010;16:508–15.
122. Gawlitza M, Purz S, Kubiessa K, Boehm A, Barthel H, Kluge R, Kahn T, Sabri O, Stumpp P. In vivo correlation of glucose metabolism, cell density and microcirculatory parameters in patients with head and neck cancer: initial results using simultaneous PET/MRI. PLoS ONE. 2015;10(8), e0134749. eCollection 2015.
123. Paspulati RM, Partovi S, Herrmann KA, Krishnamurthi S, Delaney CP, Nguyen NC. Comparison of hybrid FDG PET/MRI compared with PET/CT in colorectal cancer staging and restaging: a pilot study. Abdom Imaging. 2015;40:1415–25.
124. Nestle U, Kremp S, Grosu AL. Practical integration of [^{18}F]-FDG-PET and PET-CT in the planning of radiotherapy for non-small cell lung cancer (NSCLC): the technical basis, ICRU-target volumes, problems, perspectives. Radiother Oncol. 2006;81:209–25.
125. Grégoire V, Haustermans K, Geets X, et al. PET-based treatment planning in radiotherapy: a new standard? PET-based treatment planning in radiotherapy: a new standard? J Nucl Med. 2007;48 Suppl 1:68S–77.
126. MacManus M, Nestle U, Rosenzweig KE, et al. Use of PET and PET/CT for radiation therapy planning: IAEA expert report 2006–2007. Radiother Oncol. 2009;91:85–94.
127. Niyazi M, Landrock S, Elsner A, et al. Automated biological target volume delineation for radiotherapy treatment planning using FDG-PET/CT. Radiat Oncol. 2013;12:180.
128. Lambrecht M, Haustermans K. Clinical evidence on PET-CT for radiation therapy planning in gastrointestinal tumors. Radiother Oncol. 2010;96:339–46.
129. Ciernik IF, Huser M, Burger C, et al. Automated functional image-guided radiation treatment planning for rectal cancer. Int J Radiat Oncol Biol Phys. 2005;62:893–900.
130. Whitney R, Tatum C, Hahl M, et al. Safety of hepatic resection in metastatic disease to the liver after yttrium-90 therapy. J Surg Res. 2011;166:236–40.
131. Bienert M, McCook B, Carr BI, et al. ^{90}Y microsphere treatment of unresectable liver metastases: changes in ^{18}F-FDG uptake and tumour size on PET/CT. Eur J Nucl Med Mol Imaging. 2005;32:778–87.
132. Annunziata S, Treglia G, Caldarella C, Galiandro F. The role of ^{18}F-FDG-PET and PET/CT in patients with colorectal liver metastases undergoing selective internal radiation therapy with yttrium-90: a first evidence-based review. Sci World J. 2014;2014:879469.
133. Soydal C, Kucuk ON, Gecim EI, Bilgic S, Elhan AH. The prognostic value of quantitative parameters of ^{18}F-FDG PET/CT in the evaluation of response to internal radiation therapy with yttrium-90 in patients with liver metastases of colorectal cancer. Nucl Med Commun. 2013;34:501–6.
134. Gulec SA, Suthar RR, Barot TC, Pennington K. The prognostic value of functional tumor volume and total lesion glycolysis in patients with colorectal cancer liver metastases undergoing ^{90}Y selective internal radiation therapy plus chemotherapy. Eur J Nucl Med Mol Imaging. 2011;38:1289–95.
135. Wong CY, Salem R, Raman S, et al. Evaluating ^{90}Y-glass microsphere treatment response of unresectable colorectal liver metastases by [^{18}F]FDG PET: a comparison with CT or MRI. Eur J Nucl Med Mol Imaging. 2002;29:815–20.
136. Murthy R, Xiong H, Nunez R, et al. Yttrium 90 resin microspheres for the treatment of unresectable colorectal hepatic metastases after failure of multiple chemotherapy regimens: preliminary results. J Vasc Interv Radiol. 2005;16:937–45.
137. Sharma RA, Van Hazel GA, Morgan B, et al. Radioembolization of liver metastases from colorectal cancer using yttrium-90 microspheres with concomitant systemic oxaliplatin, fluorouracil, and leucovorin chemotherapy. J Clin Oncol. 2007;25:1099–106.

138. Dutton SJ, Kenealy N, Love SB, Wasan HS, Sharma RA, FOXFIRE Protocol Development Group and the NCRI Colorectal Clinical Study Group. FOXFIRE protocol: an open-label, randomised, phase III trial of 5-fluorouracil, oxaliplatin and folinic acid (OxMdG) with or without interventional Selective Internal Radiation Therapy (SIRT) as first-line treatment for patients with unresectable liver-only or liver-dominant metastatic colorectal cancer. BMC Cancer. 2014;14:497.
139. Gibbs P, Gebski V, Van Buskirk M, Thurston K, Cade DN, Van Hazel GA, SIRFLOX Study Group. Selective Internal Radiation Therapy (SIRT) with yttrium-90 resin microspheres plus standard systemic chemotherapy regimen of FOLFOX versus FOLFOX alone as first-line treatment of non-resectable liver metastases from colorectal cancer: the SIRFLOX study. BMC Cancer. 2014;14:897.
140. Van Hazel G, Blackwell A, Anderson J, et al. Randomised phase 2 trial of SIR-Spheres plus fluorouracil/leucovorin chemotherapy versus fluorouracil/leucovorin chemotherapy alone in advanced colorectal cancer. J Surg Oncol. 2004;88:78–85.
141. Maxwell JE, Howe JR. Imaging. Int J Endocrinol Oncol. 2015;2:159–68.
142. Van Binnebeek S, Karges W, Mottaghy FM. Functional imaging of neuroendocrine tumors. Methods Mol Biol. 2011;727:105–22.
143. Krenning EP, Kwekkeboom DJ, Bakker WH, et al. Somatostatin receptor scintigraphy with [^{111}In-DTPA-D-Phe^{1}]- and [^{123}I-Tyr^{3}]-octreotide: the Rotterdam experience with more than 1000 patients. Eur J Nucl Med. 1993;20:716–31.
144. Chiti A, Fanti S, Savelli G, Romeo A, et al. Comparison of somatostatin receptor imaging, computed tomography and ultrasound in the clinical management of neuroendocrine gastro-entero-pancreatic tumours. Eur J Nucl Med. 1998;25:1396–403.
145. Ambrosini V, Campana D, Tomassetti P, Fanti S. ^{68}Ga-labelled peptides for diagnosis of gastroenteropancreatic NET. Eur J Nucl Med Mol Imaging. 2012;39:s52–60.
146. Krausz Y, Freedman N, Rubinstein R, et al. ^{68}Ga-DOTA-NOC PET/CT imaging of neuroendocrine tumors: comparison with ^{111}In-DTPA-octreotide (OctreoScan). Mol Imaging Biol. 2011;13:583–93.
147. Santhanam P, Chandramahanti S, Kroiss A, Yu R, Ruszniewski P, Kumar R, Taïeb D. Nuclear imaging of neuroendocrine tumors with unknown primary: why, when and how? Eur J Nucl Med Mol Imaging. 2015;42:1144–55.
148. Lebtahi R, Cadiot G, Sarda L, et al. Clinical impact of somatostatin receptor scintigraphy in the management of patients with neuroendocrine gastroenteropancreatic tumors. J Nucl Med. 1997;38:853–8.
149. Hoegerle S, Altehoefer C, Ghanem N, et al. Whole-body ^{18}F DOPA PET for detection of gastrointestinal carcinoid tumors. Radiology. 2001;220:373–80.
150. Orlefors H, Sundin A, Garske U, et al. Whole-body ^{11}C-5-hydroxytryptophan positron emission tomography as a universal imaging technique for neuroendocrine tumors: comparison with somatostatin receptor scintigraphy and computed tomography. J Clin Endocrinol Metab. 2005;90:3392–400.
151. Montravers F, Grahek D, Kerrou K, et al. Can fluorodihydroxyphenylalanine PET replace somatostatin receptor scintigraphy in patients with digestive endocrine tumors? J Nucl Med. 2006;47:1455–62.
152. Ambrosini V, Tomassetti P, Castellucci P, et al. Comparison between ^{68}Ga-DOTA-NOC and ^{18}F-DOPA PET for the detection of gastro-entero-pancreatic and lung neuro-endocrine tumours. Eur J Nucl Med Mol Imaging. 2008;35:1431–8.
153. Ambrosini V, Campana D, Nanni C, et al. Is ^{68}Ga-DOTA-NOC PET/CT indicated in patients with clinical, biochemical or radiological suspicion of neuroendocrine tumour? Eur J Nucl Med Mol Imaging. 2012;39:1278–83.
154. Kroiss A, Putzer D, Decristoforo C, et al. ^{68}Ga-DOTA-TOC uptake in neuroendocrine tumour and healthy tissue: differentiation of physiological uptake and pathological processes in PET/CT. Eur J Nucl Med Mol Imaging. 2013;40:514–23.
155. Chiotellis A, Muller A, Mu L, Keller C, Schibli R, Krämer SD, Ametamey SM. Synthesis and biological evaluation of ^{18}F-labeled Fluoroethoxy tryptophan analogues as potential PET tumor imaging agents. Mol Pharm. 2014;11:3839–51.

Diagnostic Applications of Nuclear Medicine: Neuroendocrine Tumors

29

Lisa Bodei, Mark Kidd, Laura Gilardi, Duccio Volterrani, Giovanni Paganelli, Chiara M. Grana, and Irvin M. Modlin

Abstract

Neuroendocrine tumors (NETs) originate from neuroendocrine cells ubiquitously distributed throughout the body and occur mainly in the gastrointestinal and bronchopulmonary system. They are rare, are mostly sporadic, and comprise 0.66% of all neoplasia. Their incidence/prevalence is increasing based upon more sophisticated diagnostic strategies. Despite the majority being indolent, they are frequently metastatic at diagnosis. As a consequence their prognosis is often limited.

The European Neuroendocrine Tumor Society (ENETS) diagnostic and prognostic stratification criteria are based on histological typing, differentiation, grading (Ki67), and TNM staging. Although the general application of Ki67 is controversial, it remains embedded in therapeutic decision-making pending the implementation of molecular stratification systems.

Surgery is the only curative option. It is however effective in ~20% given the metastatic status of most lesions. Other therapeutic options include somatostatin analogs, interferon, "targeted" drugs, and peptide receptor radionuclide radiotherapy (PRRT).

NETs present a diagnostic and therapeutic challenge as their clinical presentation is protean, nonspecific, and late with hepatic metastases often present. Imaging plays a fundamental role in diagnosis, staging, treatment selection, and follow-up. Current modalities include morphologic techniques (CT, MRI), transabdominal ultrasound (US), and endoscopic (EUS) and intraoperative US (IOUS). Molecular imaging includes scintigraphy (^{111}In-pentetreotide or ^{99m}Tc-HYNIC-Tyr^3-octreotide), and, more

L. Bodei (✉)
Molecular Imaging and Therapy Service, Department of Radiology, Memorial Sloan Kettering Cancer Center, New York, NY, USA
e-mail: bodeil@mskcc.org

M. Kidd
Wren Laboratories, Branford, CT, USA
e-mail: mark@wrenlaboratories.com

L. Gilardi • C.M. Grana
Division of Nuclear Medicine, European Institute of Oncology, Milan, Italy
e-mail: laura.gilardi@ieo.it; chiara.grana@ieo.it

D. Volterrani
Regional Center of Nuclear Medicine, Department of Translational Research and Advanced Technologies in Medicine and Surgery, University of Pisa, Pisa, Italy
e-mail: duccio.volterrani@med.unipi.it

G. Paganelli
Nuclear Medicine and Radiometabolic Units, Istituto Scientifico Romagnolo per lo Studio e la Cura dei Tumori (IRST) IRCCS, Meldola, Italy
e-mail: giovanni.paganelli@irst.emr.it

I.M. Modlin
Wren Laboratories, Branford, CT, USA

Department of Surgery, Yale School of Medicine, New Haven, CT, USA
e-mail: imodlin@optonline.net

© Springer International Publishing Switzerland 2017
H.W. Strauss et al. (eds.), *Nuclear Oncology*,
https://doi.org/10.1007/978-3-319-26236-9_18

recently, PET with ^{68}Ga-labeled somatostatin analogs (SSA), ^{18}F-DOPA and [^{11}C]5-HTP; catecholamine metabolism is usually imaged with ^{123}I-metaiodobenzylguanidine. [^{18}F]FDG PET/CT has a prognostic role. A role for somatostatin receptor antagonists (better target/background ratio) as theranostics is currently proposed.

The major unmet needs are the development of more inclusive criteria for therapy monitoring, the validation of the recent PET techniques, and the integration of molecular biologic and metabolic information.

Keywords

Neuroendocrine tumors • Imaging • Scintigraphy • PET/CT

Glossary

[^{11}C]5-HTTP	[^{11}C]5-Hydroxytryptophan
^{18}F-DOPA	2-^{18}F-Fluoro-L-3,4-dihydroxyphenylalanine
[^{18}F]FDG	2-Deoxy-2-[^{18}F]fluoro-D-glucose
5-HIAA	5-Hydroxyindoleacetic acid, an end-metabolite of serotonin
5-HT	5-Hydroxytriptamin, also known as serotonin
AADC	Aromatic L-amino acid decarboxylase
AC	Atypical carcinoid
ACTH	Adrenocorticotropin hormone
AJCC	American Joint Committee on Cancer
APUD	Amine precursor uptake and decarboxylation
AUC	Area under the curve
BP	Bronchopulmonary
CEUS	Contrast-enhanced ultrasonography
CgA	Chromogranin A, a tumor-associated marker for neuroendocrine tumors
CT	X-ray computed tomography
CTC	Circulating tumor cell
CTGF	Connective tissue growth factor, also known as CCN2
DOTA	2-(4-Isothiocyanatobenzyl-1,4,7,10-tetra-azacyclododecane-1,4,7,10-tetraacetic acid (macrocyclic coupling agent to label compounds of biological interest with metal radionuclides)
DOTANOC	DOTA-Nal^3-octreotide
DOTATATE	DOTA-Tyr^3-Thr^8-octreotide
DOTATOC	DOTA-Tyr^3-octreotide
DTPA	Diethylenetriaminepentaacetic acid
DWI	Diffusion-weighted magnetic resonance imaging, an MR technique used to detect changes in the distribution of water molecules in selected regions
EANM	European Association of Nuclear Medicine
EC	Enterochromaffin
ECL	Enterochromaffin-like
EDDA	Ethylenediamine-N,N'-bis(2-hydroxyphenyl)acetic acid
ENETS	European Neuroendocrine Tumor Society
EPAS1	Gene encoding for the hypoxia-inducible factor 2-alpha (HIF-2α); the gene is also known as HIF2A
EUS	Endoscopic ultrasonography
FNAC	Fine needle aspiration cytology
FSH	Follicle-stimulating hormone
GEP	Originated in the gastroenteropancreatic tract
GH-RH	Growth-hormone releasing hormone
GH	Growth hormone
GIST	Gastrointestinal stromal tumor
GLP	Exendin, a glucagon-like protein
HPF	High-power field in optical microscopy
HYNIC	Hydrazidonicotinic acid/Hydrazinonicotinamide
IOUS	Intraoperative ultrasonography

LCNEC	Large-cell neuroendocrine carcinoma
LH	Luteinizing hormone
M	Metastasis status according to the AJCC/UICC TNM staging system
MAX	Gene encoding for the myc-associated factor X
MDCT	Multi-detector X-ray computed tomography
MEN	Multiple endocrine neoplasia
MIBG	*meta*-Iodobenzylguanidine
MRI	Magnetic resonance imaging
N	Lymph node status according to the AJCC/UICC TNM staging system
NE	Neuroendocrine
NEN	Neuroendocrine neoplasia
NET	Neuroendocrine tumor
NF1	Gene encoding for neurofibromin
NIH	United States National Institutes of Health
NKA	Gene encoding for Na^+/K^+ ATPase
NSE	Neuron-specific enolase
OS	Overall survival
p53	Tumor protein p53, also known as cellular tumor antigen p53, phosphoprotein p53, tumor suppressor p53, antigen NY-CO-13, or transformation-related protein 53 (TRP53)
PCC	Pheochromocytoma
PCR	Polymerase chain reaction
PET	Positron emission tomography
PET/CT	Positron emission tomography/Computed tomograhy
PFS	Progression-free survival
PGL	Paraganglioma
PPGL	Pheochromocytoma and paraganglioma
PRRT	Peptide receptor radionuclide therapy
PTH-RP	Parathyroid-hormone related protein
PTH	Parathyroid hormone
qPCR	Quantitative PCR
RECIST	Response evaluation criteria in solid tumors
RET	Proto-oncogene encoding for a receptor tyrosine kinase
SCLC	Small-cell lung cancer
SDHB	Gene encoding for succinate dehydrogenase B
SDHD	Gene encoding for succinate dehydrogenase D
SEER	Surveillance, Epidemiology, and End Results, a tumor registry of the National Institutes of Health
SIADH	Syndrome of inappropriate antidiuretic hormone secretion
SNMMI	Society of Nuclear Medicine and Molecular Imaging
SPECT	Single-photon computed tomography
SPECT/CT	Single-photon computed tomography/Computed tomography
SRS	Somatostatin receptor scintigraphy
SSA	Somatostatin analog
SSTR	Somatostatin receptor
SUV	Standardized uptake value
SUV_{max}	Standardized uptake value at point of maximum
T	Tumor status according to the AJCC/UICC TNM staging system
TC	Typical carcinoid
TMEM127	Gene encoding for a protein that acts as a tumor suppressor
TNM	AJCC/UICC staging system based on parameters "T" (tumor status), "N" (lymph node status), and "M" (distant metastasis status)
TSC	Gene encoding for the tuberous sclerosis factor, also known as hamartin
TSH	Thyroid stimulating hormone

UICC	Union Internationale Contre le Cancer (International Union Against Cancer)
US	Ultrasonography
VHL	von Hippel-Lindau
VIP	Vasoactive intestinal peptide
VMAT	Gene encoding for the vesicular monoamine transporter
WDHA	A syndrome characterized by watery diarrhea, hypokalemia, and achlorhydria
WHO	World Health Organization

Contents

Introduction 802

Neuroendocrine Tumors 803
Biomorphology 803
Incidence 804
Histopathological Classification 805
Clinical Symptomatology and Presentation 808

Biochemical Profile 810

Techniques 813
Radiological Techniques 813

^{18}F-DOPA 830

[^{11}C]5-HTP 832

[^{18}F]FDG 832

References 832

Introduction

Neuroendocrine tumors (NETs) represent a major diagnostic challenge since their clinical presentation is variable, nonspecific, and usually late, often when hepatic metastases are already present [1, 2]. Critical issues in diagnosis are the identification of primary tumor location and of regional and distant metastases. Plasma biomarkers, histopathology, and imaging are used to define these areas. Imaging includes radiological and nuclear medicine techniques to acquire information on tumor site, extent, and functionality. These include delineation of somatostatin receptor expression (somatostatin receptor imaging), neuroendocrine tumor metabolism (^{18}F-DOPA), and metabolic status ([^{18}F]FDG-PET). Histopathological examination of tumor biopsies provides further information but is limited by tumor heterogeneity and a paucity of molecular markers that accurately demarcate tumor biology. Although Ki67 is widely used, it is a monoanalyte, and controversy exists in regard to its accuracy and precise clinical application [2]. Biomarkers such as plasma chromogranin A (CgA) and urinary 5-hydroxyindoleacetic acid (5-HIAA) are currently most used. They are monoanalytes; the assays are suboptimal in terms of sensitivity and specificity and do not meet the NIH performance metrics for accurate biomarkers [3]. The recent reports of the high accuracy of the measurement of circulating mRNA neuroendocrine transcripts suggest that this strategy may facilitate early diagnosis and detection of lesions and may provide an accurate basis for prognostic determination and therapeutic recommendation [4, 5].

Imaging plays a central role in diagnosis, staging, treatment selection, and follow-up of NETs. Current diagnostic modalities include radiological techniques such as multi-detector CT (MDCT), MRI, transabdominal ultrasound (US), and endoscopic (EUS) and intraoperative US (IOUS). Nuclear medicine strategies or molecular imaging includes scintigraphy (including single photon emission computed tomography, SPECT) with ^{111}In-pentetreotide or ^{99m}Tc-HYNIC-Tyr^3-octreotide and, more recently, PET with ^{68}Ga-labeled somatostatin analogs (SSA), ^{18}F-DOPA, and [^{11}C]5-HTP [2]. Recently somatostatin receptor (SSR) antagonists have been investigated in clinical trials, based upon their better targeting properties [6]. No modality alone is entirely effective, and the overall sensitivity and specificity of diagnostic imaging is ~80–90% [2, 7]. Regardless of imaging modalities utilized, about 50% of NETs remain with an unknown primary site [2]. In order to optimize sensitivity and specificity, anatomic and functional techniques are generally combined [8, 9]. The development of hybrid scanners (SPECT/CT, PET/CT), whereby molecular and anatomic details are superimposed, has facilitated an increase diagnostic accuracy. Somatostatin receptor imaging (either with conventional ^{111}In-pentetreotide scintigraphy or with ^{68}Ga-SSA-PET/CT) is a prerequisite to evaluate the eligibility and also putative efficacy of peptide

receptor radionuclide therapy (PRRT) and, to a lesser extent, systemic treatment with unlabeled somatostatin analogs.

Despite substantial advances in the fields of anatomic and functional imaging, a number of critical unmet needs remain in NET imaging. These are the development of more inclusive criteria for NET progression, the delineation of therapeutic responses that can be applied to slow-growing tumors, the validation of the more recent functional techniques (such as somatostatin receptor PET), and the integration of novel molecular genomic, biologic, and metabolic information [10, 11].

Neuroendocrine Tumors

Neuroendocrine tumors (NETs) are relatively rare tumors originating from ubiquitous neuroendocrine cells distributed throughout the body. The term "neuroendocrine" relates to the hybrid morphological and biological nature of these cells, which have both endocrine secretory properties. Such cells synthesize, store, and secrete a variety of classic (circulating) hormones as well as local chemical messengers which function as neurotransmitters or neuromodulators [12, 13].

In 1907, the pathologist Siegfried Oberndorfer was the first to describe small tumors of the intestine that he referred to using the German diminutive for cancer, "Karzinoide," thereby erroneously suggesting a benign tumor. Although he subsequently reversed this conclusion, the incorrect concept of a benign neoplasm has unfortunately remained enshrined in medical oncological dogma. In 1914, Pierre Masson suggested the endocrine origin of these tumors, and thereafter Friedrich Feyrter in 1938 introduced the concept of diffuse endocrine system. In 1966, Anthony Pearse sought to unify the origin of all neuroendocrine tumors by expanding Feyrter's concept. He ascribed a series of common biochemical characteristics to embrace all such neoplasia using the term APUDoma (amine precursor uptake decarboxylation) and concluded all had a neural crest origin. Further studies by Bloom and Polak linked the immunohistochemical and secretory characteristics of NETs with their symptoms and formed the basis for the contemporary understanding of neuroendocrine neoplasia [14].

Biomorphology

(a) NE cells

The neuroendocrine system is composed of three major compartments: (1) neurons in the central and peripheral nervous system; (2) epithelial endocrine cells (often with neuronal features), dispersed individually in the gastroenteric and respiratory tracts, thyroid, thymus, skin, breast, larynx, kidney, urinary bladder, and prostate and in some instances assembled in units, such as the pancreatic islets of Langerhans or the renal juxtaglomerular apparatus (*polkissen* cells); and (3) the classic endocrine organs, such as the anterior pituitary, parathyroid glands, and adrenals [15]. Neuroendocrine cells regulate activity systemically or locally via endocrine or autocrine/paracrine mechanisms and thereby modulate metabolic, chemoreceptor, motility, and secretion functions [16].

Neuroendocrine cells, depending on their degree of differentiation, produce, store, and exocytose a number of bioactive agents, including gastrin; insulin; serotonin; somatostatin; glucagon; pancreatic polypeptide; VIP in gastroenteropancreatic (GEP) tract; catecholamines in the adrenal medulla; ACTH, GH, prolactin, FSH, LH, and TSH in the anterior pituitary; and PTH in parathyroid glands. The majority of these cells contain chromogranins (a constitutive secretory proteins and/or synaptophysin), which have by default become utilized as nonspecific biomarkers of the neuroendocrine cell system or its neoplasia [17].

(b) Neoplastic spectrum

The majority of neuroendocrine neoplasia (NEN) (>95%) are sporadic. Others, particularly of gastric and pancreatic origin, may be related to genetic conditions including multiple endocrine neoplasia type 1 (MEN1), neurofibromatosis (NF1), von Hippel–Lindau

(VHL) disease, tuberous sclerosis complex (TSC), or Carney's syndrome [18]. Overall, there are at least 13 different neuroendocrine cell types in the gastrointestinal tract (EC, ECL, gastrin, δ, etc.) and four in the pancreas (α, β, δ, PP) with individual anatomical localization and defined neuroendocrine secretory products. Germline mutations in five genes have been recognized to be responsible for familial pheochromocytomas: the von Hippel–Lindau gene (VHL), causing VHL syndrome; the RET gene, leading to multiple endocrine neoplasia (MEN) type 2; the neurofibromatosis type 1 gene (NF1), associated with von Recklinghausen's disease; and the genes encoding the B and D subunits of mitochondrial succinate dehydrogenase (SDHB and SDHD), which are associated with familial paragangliomas and pheochromocytomas. Hereditary GEP or bronchial NET and pituitary adenomas occur in MEN type 1.

Tumors may arise from each of the neuroendocrine cell types and can exhibit a wide spectrum of clinical and pathological behavior, ranging from asymptomatic to florid (flushing/diarrhea) or from indolent (e.g., gastric type I tumor) to highly aggressive growth (e.g., glucagonomas). Their natural history varies from torpid local invasion and fibrosis in the peritoneal cavity or heart to diffuse metastatic spread, most commonly to the liver and lungs [2]. Metastases are present overall in ~35% of all gastroenteropancreatic (GEP) NETs at presentation, ranging from <5 for type I gastric tumors to 60–80% for those originating in the small bowel and colon [2, 19].

Incidence

The Surveillance, Epidemiology, and End Results (SEER) database, containing 48,195 NENs from 1973 to 2006 [20], indicates that NETs constitute 0.66% of all malignancies in the United States and the incidence is increasing at a rate of 3–10% per year depending on the subtype (Fig. 1). Thus in 2004 NETs comprised 1.25% of all malignancies, as compared to 0.75% in 1994 [19, 20]. This increment is related to the technical progress of more sensitive diagnostic tools and to an

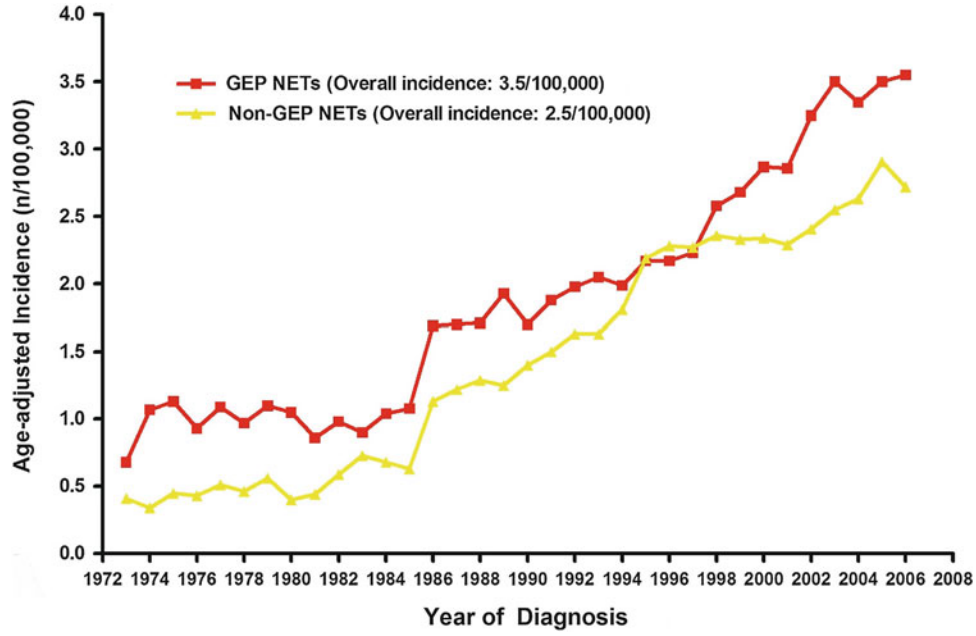

Fig. 1 Incidence of neuroendocrine neoplasms by anatomical location in the US population between 1973 and 2007

increased awareness among clinicians and pathologists [2, 21]. However, the greater frequency (1.22%) of NETs in a large autopsy series indicates that they are predominantly underdiagnosed [22]. It also suggests that there is a significant percentage that may have no clinical consequences during the lifetime of an individual. According to SEER, the most frequent site is the gastrointestinal tract (66%) followed by the bronchopulmonary system (25%). Other less frequent locations are the ovaries, testes, hepatobiliary, and pancreas (Fig. 2) [23].

The Rochester Epidemiology Project revealed that pheochromocytomas demonstrated an overall incidence in the white population of 0.8/100,000 cases per year over 30 years [24]. Of note was the observation that 0.5% of subjects with hypertension and 4% of those with an incidental adrenal mass harbor a pheochromocytoma [25].

Sporadic forms of pheochromocytoma are diagnosed in individuals aged 40–50 years, whereas hereditary forms are diagnosed at a younger age, often before 40. Pheochromocytoma is rare in children, but, when found, it is often extra-adrenal, multifocal, and associated with hereditary syndromes.

Histopathological Classification

NETs represent different pathological entities, depending on their organ and cell of origin, and have been considered as representing three categories: (a) those arising in neuroendocrine organs, such as medullary thyroid carcinomas, pancreatic endocrine tumors, pheochromocytomas, and paragangliomas; (b) those arising from dispersed neuroendocrine cells, such as bronchial or

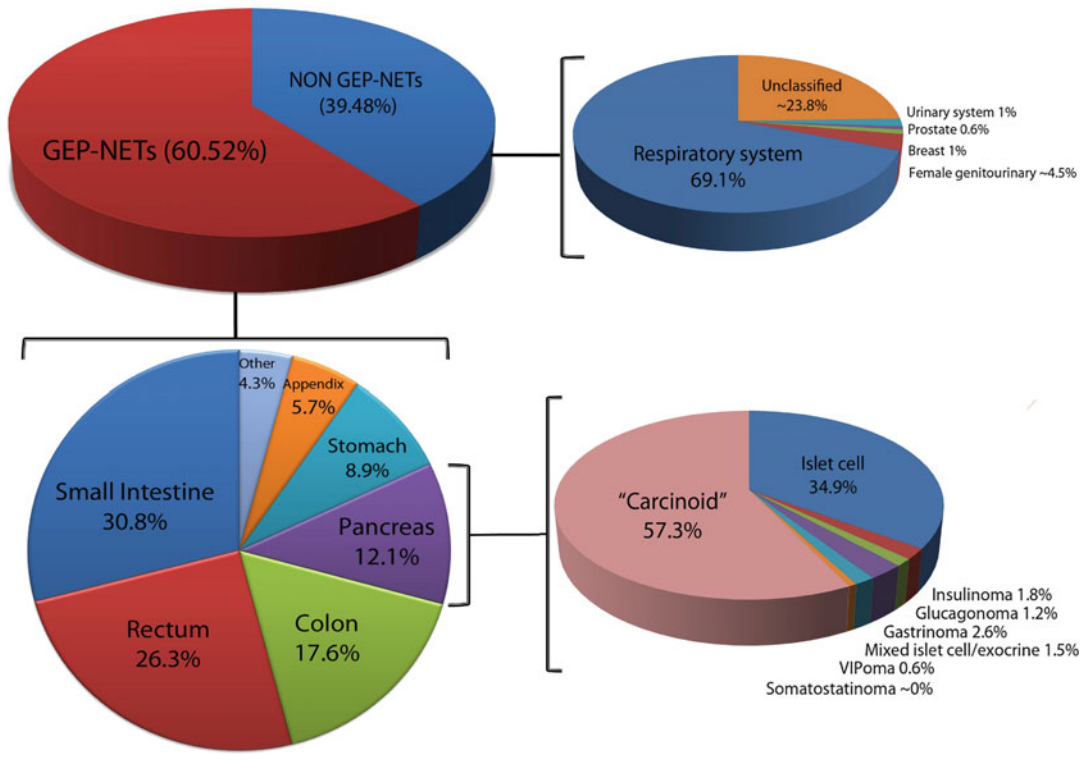

Fig. 2 Distribution of neuroendocrine tumors (n = 49,012) in the Surveillance, Epidemiology, and End Results (*SEER*) tumor registry database from 1973 to 2007, according to anatomical site and tumor type: total NETs (*top left*), gastroenteropancreatic (GEP)-NETs (*bottom left*), and pancreatic NETs (*bottom right*). Non-GEP-NETs are predominantly located in the respiratory system (~70 % are bronchopulmonary NETs; *top right*)

gastroenteric NETs; and (c) those arising from non-neuroendocrine organs, such as thymic carcinoids or cutaneous NETs.

NETs can be functioning or nonfunctioning, depending on the presence of a clinical symptomatology syndrome due to hypersecretion of bioactive amines or peptides. The 1963 classification of GEP-NETs, based on their embryologic origin (foregut, midgut, or hindgut) by Williams and Sandler [26], is used, though of minimal value, and has mostly been supplanted by the World Health Organization (WHO) classification system. The latter has defined these tumors based upon a number of morphological criteria including their degree of differentiation and site of origin [27]. The initial (2004) iteration identified well-differentiated neuroendocrine tumors (benign behavior or uncertain malignant potential), well-differentiated neuroendocrine carcinomas (low-grade malignancy), or poorly differentiated (small or large cell) neuroendocrine carcinomas of high-grade malignancy. The term "carcinoid" was reserved for "well-differentiated" tumors. Size, angioinvasion, proliferative activity, histologic differentiation, metastases, and hormonal activity (association with clinical syndromes or diseases) were included in the classification scheme. Histochemical indicators of prognosis include the degree of expression of the proliferation protein Ki-67 and the p53 tumor suppressor protein [28, 29]. ENETS and later WHO in 2010 further refined this classification to include the Ki-67 scoring index and the TNM classification system (Table 1) [30, 31]. The grading proposal stratifies tumors in G1, G2, and G3 and is based on the premise that *all* NETs are intrinsically malignant (Table 2) [32, 33]. The tumor grading, histopathology type and staging, reflects on the potential metastatic spread and, therefore, influences the choice of therapeutic options (surgery, biotherapy, and chemotherapy) [34]. Although the function of Ki-67 remains poorly characterized [35] and concerns remain regarding heterogeneity of expression and measurement techniques, it is used as a surrogate marker of proliferation [36]. In order to assure an optimal treatment of GEP-NETs, a standardized diagnostic procedure is required. The ENETS society has proposed diagnostic and prognostic stratification criteria, based on histological typing, differentiation, grading, and TNM staging. Immunostaining for the neuroendocrine markers synaptophysin and chromogranin and for the proliferation marker Ki67/MIB1 is considered mandatory, while immunostaining for hormones, receptors, and other markers is optional [34]. The recent development and introduction of a minimal data set for pathologists will add consistency and uniformity to the evaluation and classification of GEP-NENs [37].

This classification applies easily to GEP-NETs, while bronchopulmonary (BP) and thymic NETs

Table 1 WHO 2010 general neuroendocrine neoplasm categories: comparison with previous classifications

WHO 1980	WHO 2000	WHO 2010
I Carcinoid	1. Well-differentiated endocrine tumor (WDET)[a]	1. NET G1 (carcinoid)[b]
	2. Well-differentiated endocrine carcinoma (WDEC)[a]	2. NET G2[b]
	3. Poorly differentiated endocrine carcinoma/ small cell carcinoma (PDEC)	3. NEC (large cell or small cell type)[b, c]
II Mucocarcinoid	4. Mixed exocrine–endocrine carcinoma (MEEC)	4. Mixed adenoneuroendocrine carcinoma (MANEC)
III Mixed forms carcinoid – adenocarcinoma		
IV Pseudotumor lesions	5. Tumor-like lesions (TLL)	5. Hyperplastic and preneoplastic lesions

From Bosman et al. [151], with permission

[a]The difference between WDET and WDEC was defined according to staging features in the WHO 2000 classification. G2 NET does not necessarily translate into WDEC of the WHO 2000 classification

[b]Definition in parentheses for the International Classification of Diseases for Oncology (ICDO) coding

[c]"NET G3" has been used for this category but is not advised since NETs are by definition well differentiated

Table 2 WHO 2010 working principles for neuroendocrine neoplasms

Neoplasm definition to embrace all grades of endocrine tumors (low, intermediate, and high grade)
Neuroendocrine connotation recommended as description of shared neural–endocrine markers
Standard definition of neuroendocrine tumor (NET) for low- to intermediate-grade neoplasms and neuroendocrine carcinoma (NEC) for high grade
NET subdivision according to grade (ICDO codes 8240/3 and 8249/3); potential malignancy formalized
NEC subdivision in LCNEC and SC-NEC (ICDO codes 8013/3 and 8041/3)
Synonyms for NET: carcinoid, well-differentiated endocrine tumor/carcinoma; for NEC: poorly differentiated endocrine carcinoma, high-grade neuroendocrine carcinoma
TNM recommended (AJCC–UICC–WHO 2010)
For carcinoids only (excluded G3 neoplasms)
Blueprint from ENETS proposals 2006–2007 for the stomach, ileum, and colon but with significant differences for the appendix and pancreas (generate data)
Diagnosis by site according to the above uniform grading and staging parameters
Minimal histopathology report recommendation
Neoplasm definition as NET or NEC
Grade definition as G1–G3
pTNM definition (when possible)

From Bosman et al. [151], with permission

are still classified according to a proposal by Travis (Table 3). Travis recognized low-grade NETs – typical and atypical carcinoids – and high-grade NETs, large-cell neuroendocrine carcinoma (LCNEC) and small-cell lung cancer (SCLC). The most prevalent high-grade NET, accounting for 89% of cases according to the SEER database of National Cancer Institute, is SCLC [38–40].

A recent proposal of a three-tier grading system for BP-NETs has been published. It is based upon that currently utilized for GEP tumors and includes Ki67 index (with specific cut-offs) in addition to mitotic count and necrosis (Table 4) [41]. However, the utility of this new classification using Ki67 in BP-NETs requires prospective confirmation [42].

Pheochromocytomas and paragangliomas (PPGL) derive from sympathetic chromaffin tissue in the adrenal medulla and from the extra-adrenal paraganglial system of the thorax and abdomen. The frequency malignant propensity of chromaffin tumors, pheochromocytomas, and paragangliomas reflects the genetic background. Over 50% of PPGL can be attributed to genetic alterations [43]. These most frequently involve germline mutations of VHL or SDH genes (Table 5). The 2004 WHO classification recognized the common origin of PPGL from neuroectoderm and divided them into pheochromocytomas and paragangliomas, arising, respectively, in the adrenals or the extra-adrenal sympathetic tissue. Pheochromocytomas are usually considered as malignant only in the presence of metastases. These usually are found with decreasing frequency in the liver, lymph nodes, lung, and bone, either at diagnosis or during follow-up. This group has been colloquially defined by the so-called 10% rule, namely, 10% bilateral, 10% extra-adrenal, 10% familial, and 10% malignant [44]. Histopathological scoring criteria utilizing the presence of diffuse cellular growth, high cellularity, monotony, tumor cell spindling, atypical mitotic figures, high mitotic count, etc. failed to accurately assess the malignant potential due to inter- and intra-observer variation [45]. Malignant pheochromocytomas account for about 10% of all pheochromocytomas and are associated with capsular invasion and large tumor size (>5 cm in size and >80 g in weight) [46]. Genetically five autosomal dominant disorders are recognized: the paraganglioma (PGL) syndromes types 1–5 are characterized by a familial predisposition to PGLs, pheochromocytomas (PCCs), renal cell cancers, gastrointestinal stromal tumors and, rarely, pituitary adenomas. The different syndromes are based on five different/separate mutations of the SDH gene (SDHD=PGL1, SDHAF2=PGL2, SDHC=PGL3, SDHB=PGL4, and SDHA=PGL5) [47]. Malignant pheochromocytomas are evident in individuals with MEN2, > 90% of those in VHL disease, and ~90% of those in NF1 [48]. Malignant paragangliomas have a higher prevalence, 15–35% when associated with the SDHB gene mutations [49–51].

In addition to their hormonal profile, PPGL often exhibits neuroamine uptake mechanisms and/or specific receptors, such as cell membrane somatostatin receptors and norepinephrine

Table 3 The Travis 2004 classification of bronchopulmonary neuroendocrine tumors

Typical carcinoid
A tumor with carcinoid morphology and less than 2 mitoses per 2 mm^2 (10 high-power field (HPF)), lacking necrosis and 0.5 cm or larger
Atypical carcinoid
A tumor with carcinoid morphology with 2–10 mitoses per 2 mm2 (10 HPF*) OR necrosis (often punctate)
Large-cell neuroendocrine carcinoma
A tumor with a neuroendocrine morphology (organoid nesting, palisading, rosettes, trabeculae)
High mitotic rate: 11 or greater per 2 mm^2 (10 HPF), median of 70 per 2 mm^2 (10 HPF)
Necrosis (often large zones)
Cytologic features of a non-small cell carcinoma (NSCLC): large cell size, low nuclear to cytoplasmic ratio, vesicular or fine chromatin, and/or frequent nucleoli. Some tumors have fine nuclear chromatin and lack nucleoli, but qualify as NSCLC because of large cell size and abundant cytoplasm
Positive immunohistochemical staining for one or more neuroendocrine markers (other than neuron-specific enolase) and/or neuroendocrine granules by electron microscopy
Small cell carcinoma
Small size (generally less than the diameter of three small resting lymphocytes)
Scant cytoplasm
Nuclei: finely granular nuclear chromatin, absent or faint nucleoli
High mitotic rate (11 or greater per 2 mm^2 (10 HPF), median of 80 per 2 mm^2 (10 HPF)
Frequent necrosis often in large zones

From Travis et al. [152], with permission

Table 4 Proposed Grading system for bronchopulmonary neuroendocrine tumors

Grade	Mitotic count (10 HPF)[a]	Ki67 (%)[b]	Necrosis (%)[c]
G1	2	<4	No
G2	>2–47	4–<25	<10
G3	>47	≥25	>10

From Rindi et al. grading the neuroendocrine tumors of the lung: an evidence-based proposal. Endocr Relat Cancer. 2013, with permission

[a]10 HPF, ten high-power field=2 mm^2, to be assessed in at least 50 fields at 40× in areas of highest mitotic density

[b]Ki67%: MIB antibody, as percentage of 500–2,000 cells counted in areas of highest nuclear labeling

[c]Necrosis as % of sample: focal, presence of <10% of sample, diffuse, more than 10% of sample

transporter (vesicular monoamine transporter 1 and 2, VMAT 1 and 2), which are of critical relevance to their localization and treatment [52].

Clinical Symptomatology and Presentation

NETs, particularly those of GEP origin, exhibit protean symptomatology that is often overlooked. They may present with symptoms related to the inappropriate hypersecretion or paroxysmal bioactive peptide or amine. The large majority is nonfunctioning and such lesions are asymptomatic presenting late due to a mass effect (jaundice/pain). Thus, despite a sometime typical clinical scenario, such as the carcinoid syndrome, symptoms remain frequently unrecognized, and diagnosis is often tardy. Diagnostic delay is usually 5–7 years since the symptoms are considered as caused by other ubiquitous conditions (e.g., allergy, anxiety, menopause) as opposed to a tumor, or the paroxysmal nature of the symptoms leads to considerations of neurotic complaints or somatization [2]. NET is therefore often diagnosed late when metastasis (usually hepatic) has occurred; thus, curative surgery is no longer possible. Thus, despite the fact that the tumors tend to be well differentiated and slow growing, with a minority of aggressive forms, outcome is significantly diminished by delay in diagnosis.

Gastroenteropancreatic NETs

Gastric NETs (frequently referred to as gastric carcinoids) are typically multiple, small, and generally benign and derived from ECL cells. They are associated with hypergastrinemia and have

Table 5 Genetically related forms of pheochromocytoma and paraganglioma

Gene	Disease	Features
NF1	Neurofibromatosis type 1	Café-au-lait spots, neurofibromas, axillary and inguinal freckling, Lisch nodules, osseous lesions, optic gliomas, mainly pheochromocytomas
RET	Multiple endocrine neoplasia type 2	2A: Medullary thyroid cancer, primary hyperparathyroidism, PPGL
		2B: Medullary thyroid cancer, PPGL, Marfanoid habitus, mucocutaneous neuromas, gastrointestinal ganglioneuromatosis
VHL	von Hippel–Lindau disease	Central nervous system or retinal hemangioblastomas, renal cell carcinoma, PPGL, pancreatic neuroendocrine tumors and cysts, endolymphatic sac tumors, papillary cystadenoma of the epididymis and broad ligament
PGL1: SDHD	Hereditary paragangliomas	1. PGL5: SDHA
PGL2: SDHAF2		2. Head and neck paraganglioma
PGL3: SDHC		3. PPGL, rare renal cancers, GIST
PGL4: SDHB		4. PPGL, rare renal cancers, GIST
PGL5: SDHA		5. PPGL, GIST
1. TMEM127	Familial pheochromocytomas	1. Mainly pheochromocytomas, rare renal cancers
2. MAX		2. Mainly PPGL
EPAS1	Polycythemia paraganglioma	Polycythemia, PPGL, somatostatinoma
FH	Leiomyomatosis and renal cell	Cutaneous and uterine leiomyomas, type 2 papillary renal carcinoma, rare PPGL

GIST: gastrointestinal stromal tumors (Adapted from Favier et al. [43] with permission)

been classified as type I, associated with atrophic gastritis, or type II, in conjunction with MEN1 and/or the Zollinger–Ellison syndrome. Type I are very rarely malignant, whereas type II in 20–30% are malignant and metastatic. Type III gastric carcinoids not associated with hypergastrinemia and present as single, usually larger lesions often associated with metastatic disease.

Duodenal NETs frequently secrete gastrin and may be associated with Zollinger–Ellison syndrome, occasionally as part of MEN1. Intestinal NETs (the so-called classic "carcinoids," described by Oberndorfer) derive from enterochromaffin cells (EC cells). Symptoms are usually only evident after metastasis to the liver and are often paroxysmal and have been described as typical or atypical. Manifestations are protean and include cutaneous flushing, diarrhea, bronchospasm, tachycardia, and abdominal pain. Symptoms represent the overproduction and release in the systemic circulation of bioactive amines and peptides including mostly serotonin, histamine, and tachykinins. The classic carcinoid syndrome, however, is relatively uncommon (10–15%) [22]. A not insignificant percentage of carcinoids may be discovered when nonmetastatic due to emergency surgery for acute abdominal events relating to perforation, bleeding, or obstruction [53]. Colonic carcinoids are frequently large, nonfunctioning, and with a poor prognosis, while rectal lesions are small and rarely metastasize. Appendiceal carcinoids are usually identified early when they cause obstructive appendicitis and are mostly benign. A small percentage is malignant and metastatic usually manifesting with mucin producing diffuse peritoneal metastases and only occasionally functional [54].

NETs in the pancreas vary in size depending upon the time of identification and their symptomatology. Asymptomatic lesions usually present late unless identified by mass lesions obstructing the common bile duct or with bleeding and/or pain. Up

to 50% have synchronous local or liver metastatic disease. Functioning pancreatic islet cell tumors may present with syndromes related to the hyperproduction of insulin, gastrin, VIP, glucagon, or somatostatin. These tumors represent markedly different clinical and pathological entities depending upon their cell of origin and symptomatology. Insulinomas are often small and benign lesions causing hypoglycemia. Pancreatic gastrinomas are less common than in the duodenum but generally malignant, causing Zollinger–Ellison syndrome and in ~25% of cases are associated with MEN1. Glucagonomas present with mild diabetes and a characteristic rash (necrolytic migratory erythema). Finally, VIPomas may produce severe diarrhea, hypokalemia, and achlorhydria (WDHA syndrome). Rarely, a group of more malignant lesions may secrete ACTH, GH-RH, PTH-RP, and somatostatin [2].

Bronchopulmonary NETs

The majority of patients with BP-NETs have symptoms present with symptoms of cough, hemoptysis, and pneumonia (a classical triad), resulting from the lumen obstruction and ulceration of the tumor. Pathological classification predominantly divides the group into typical and atypical lesions although the criteria are sometimes difficult to ascertain. Typical carcinoids (TC) present characteristically as a central lesion, with signs and symptoms of bronchial obstruction, and exhibit a relatively benign/indolent biological behavior. Atypical carcinoids (AC) are frequently peripheral and functional. Their behavior may vary from indolent to aggressive, with lymphatic and hematogenous metastases. Less than 5% of BP-NETs exhibit hormonally related symptoms such as carcinoid syndrome, Cushing syndrome, acromegaly, or the syndrome of inappropriate antidiuretic hormone secretion (SIADH). Large-cell neuroendocrine cancers are aggressive and rare form of NET, usually metastatic at diagnosis, causing rapid clinical deterioration. Paraneoplastic syndromes are sporadic. Small-cell lung cancers (SCLCs) are particularly aggressive and are associated with early hematogenous and lymphatic metastasis. SCLCs are extremely chemosensitive but usually relapse. Mediastinal syndrome, caused by lymph node metastases, is a relatively common clinical presentation and is often accompanied by distant metastases, typically to the brain or bones. In many instances, they are associated with paraneoplastic syndromes, particularly Cushing syndrome and the syndrome of inappropriate antidiuretic hormone secretion (SIADH) [55–57].

Chromaffin Cell NETs

Most PPGLs, except those arising from the head and neck region, are associated with catecholamine hypersecretion [58]. The majority (80–85%) of pheochromocytomas arise from the adrenal medulla, while about 15–20% are extra-adrenal. Catecholamine-producing paragangliomas are usually located in the abdomen [45, 58]. The most frequent signs of catecholamine hypersecretion (pheochromocytoma has been described as “the great mimic”) are hypertension, tachycardia, headache, pallor, sweating, and feelings of panic or anxiety. Hyperglycemia, lactic acidosis, weight loss, nausea, fever, and flushing may also occur. Hypertension is usually paroxysmal, sometimes severe, leading to hypertensive emergencies, superimposed on a state of normal blood pressure or of hypertension. Sometimes blood pressure may be normal, when tumor load is limited or when dopamine is preferentially secreted. In rare cases of prevalent epinephrine secretion, patients may even present with hypotension [58].

Biochemical Profile

Serum or blood hormone assays are currently used for diagnosis in conjunction with histopathology and clinical evaluation. Numerous different peptides and amines (secretory unianalytes) have been proposed as biomarkers to identify and monitor disease status of NETs. In the past, the most common markers of NETs have been chromogranins A and B, pancreatic polypeptide, pancreastatin, and NSE [59]. The majority of biomarkers proposed for the diagnosis of these lesions have proven to exhibit a low sensitivity

and specificity, are difficult to measure accurately or easily, and are therefore mostly of research use, with the exceptions of the specific peptides gastrin, insulin, VIP, and glucagon in pancreatic NETs, which proved to be of clinical utility.

Recently the development of molecular multianalyte markers (mRNA transcripts) has provided evidence that this strategy is more sensitive and specific [4]. Transcript analysis in the blood provides >90% accuracy in the identification of NETs and the ability to define disease progression [60].

In the past, plasma CgA levels have been widely utilized as the default biomarker for all NETs. Although they are relatively sensitive (60–90%), their specificity is poor (10–30%). This reflects elevated levels in other NETs and other malignancies, spurious increases in individuals with impaired renal function or during administration of proton pump inhibitors [61]. CgA has mostly been used as the default measurement to confirm diagnosis and obtain information as to tumor burden and possible location of the tumor. Its interpretation is limited however by the fact that it is a secretory product and does not represent the diverse biological activity of the tumor (proliferation, metabolic status, etc.). Circulating CgA is elevated in ~60% of individuals with GEP-NETs, most frequently in subjects with gastrinomas (100%), followed by small-bowel "carcinoid" tumors (80%) and nonfunctioning pancreatic NETs (70%) [62]. Plasma CgA levels are considered more frequently elevated in well-differentiated tumors compared to poorly differentiated tumors of the midgut reflecting the observation that it is a secretory marker and dedifferentiated lesions rarely secrete. It has been proposed that CgA possesses some utility in predicting survival and in providing information on the efficacy of therapy; however, this is likely a surrogate of the fact that secretory capacity is inversely related to tumor differentiation [4]. Measurement of CgA is substantially limited by a lack of standardization of assays and a relatively low sensitivity/specificity in some clinical situations. Thus, CgAs measured at different time points in the disease or using different commercial assays are not comparable or provide information that is difficult to interpret. Moreover, measurement of urinary 5-HIAA levels or plasma 5-HT levels is cumbersome, insensitive, and difficult to quantify.

A recent Delphic consensus unanimously established that common biomarkers used for GEP-NETs are inadequate for BP-NETs and concluded that mRNA transcript analysis (NETest) was provided a greater opportunity for clinical utility [63]. The multianalyte-derived NET gene signature encompasses the expression of 51 genes, measured by qPCR that are assessed by four different prediction algorithms scaled to a disease/tumor activity (0–100%) score [64] using expression that specifically capture the hallmarks of neoplasia [65]. The expression of 51 NET marker genes includes analysis of clusters of biologically relevant genes that constitute the different "omes" (proliferome, metabolome, secretome, epigenome, and plurome) [64] which define the NET "fingerprint." This can be used to provide direct information about the tumor, its pathophysiology, and its state of evolution from stability to progression [66]. The test has a sensitivity and specificity of greater than 90% and significantly outperforms CgA measurement in every assessable parameter [67]. Clinically, gene expression is decreased following surgery and can be used to identify residual/recurrent disease [68]; it can also effectively monitor treatment protocols, e.g., somatostatin analog therapy [69, 70], and can predict disease progression Fig. 3 [71].

If a secretory phenotype is present, the diagnosis of chromaffin cell tumors is based on syndromic presentation, which triggers the assessment of plasma and urinary catecholamines and genetic testing [43]. Functioning chromaffin cell tumors secrete catecholamines, namely, norepinephrine, epinephrine, and dopamine. These agents are catabolized to metanephrines, which may be identifiable in high concentration in the urine. Urinary and plasma catecholamines, urinary metanephrines (normetanephrine and metanephrine), and urinary vanillylmandelic acid are usually measured for diagnosis. Currently, the plasma and 24-h urinary measurement of free metanephrines is the most sensitive method to accurately diagnose a pheochromocytoma/paraganglioma (96–100% and 92–99% sensitivity, respectively, and 87–92%

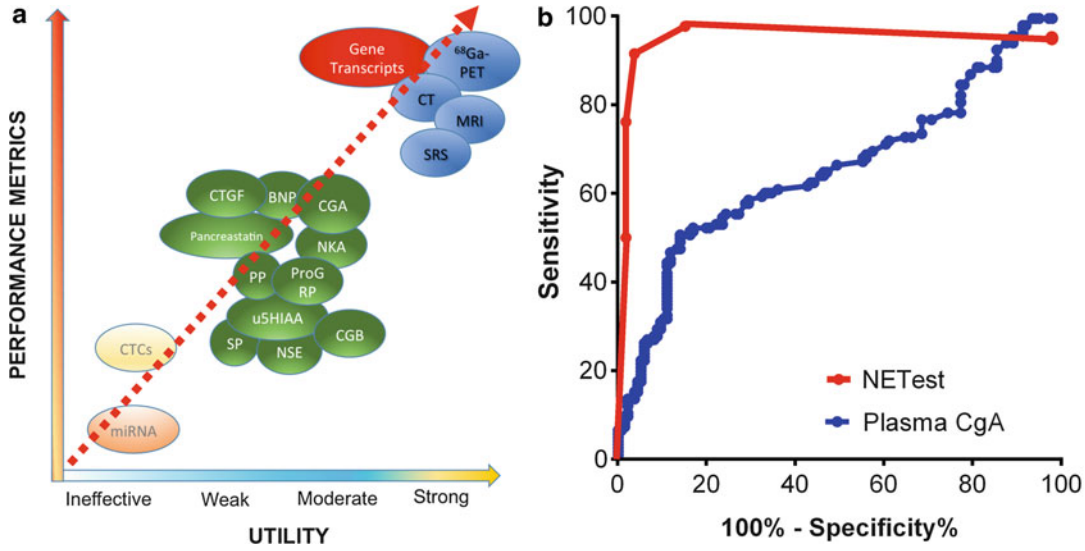

Fig. 3 Utility of biomarkers and imaging techniques in NET management. (**a**) The utility of current NET biomarkers and imaging based on published use and performance metrics. Overall clinical utility can be estimated by referencing the arrow (*red*) to the x any axes of metrics and utility. miRNA assessment (*orange*) has no rigorous utility or metrics available. CTC measurement (*yellow*) exhibits moderate metrics but has not been validated in NETs. Substance P, NSE, pancreatic polypeptide, NKA, pancreastatin, CTGF, and brain natriuretic peptide (*green*) all display variable performance metrics. Their overall utility is weak. Biomarkers including urinary 5-HIAA and CgA have moderate utility, but their metrics are highly variable. NET transcript analysis (*red*) exhibits high level metrics, and early clinical studies support its clinical utility. Imaging data derived from CT scan, MRI, somatostatin receptor scintigraphy, [^{18}F]FDG, and ^{68}Ga-SSA-PET/CT (*blue*) are included for comparison with current biomarkers. All imaging techniques have high utility, but the metrics exhibit a wide range from [^{18}F]FDG to ^{68}Ga-PET. *BNP* brain natriuretic peptide, *Ga-PET* ^{68}Ga-SSA-PET/CT, *PP* pancreatic polypeptide, *Pro-GRP* progastrin-releasing peptide, *SRS* somatostatin receptor scintigraphy, *u5-HIAA* urinary 5-HIAA. (**b**) Receiver operating characteristic curves for peripheral blood NET transcript analysis {polymerase chain reaction (PCR)} (*red*) compared to chromogranin A (CgA) (*blue*) for GEP-NETs. The NET transcript analysis area under the curve (AUC) was significantly more effective (AUC = 0.98, $p < 0.0001$) than CgA (AUC = 0.64, $p < 0.002$). In the efficacy analysis of NET, transcript analysis demonstrated that it was significantly more accurate than CgA ($p < 0.0001$)

and 64–72% specificity, respectively) [72]. Due to its low sensitivity and specificity, CgA is not used in chromaffin cell tumor assessment [73]. To avoid false-positive results, biochemical evaluation should not be performed if the patient is receiving drugs that can increase catecholamine levels. These agents include phenoxybenzamine and tricyclic antidepressants, monoaminooxidase inhibitors, calcium channel blockers, and caffeine. Biochemical evaluation of patients receiving these drugs is a major cause of false-positives. Dynamic tests, such as the clonidine test, are sometimes performed in norepinephrine-secreting tumors [74]. Head and neck paragangliomas are rarely hormonally active.

A key unmet need in the diagnostic assessment of NETs and chromaffin tumors is the availability of a blood test for early diagnosis or surveillance. The recent demonstration of specific NEN transcripts in plasma suggests that this strategy may enable early diagnosis and detection of lesions and even provide a basis for prognostic determination and therapeutic recommendation. Recent reports indicate that measurements of neuroendocrine blood transcripts are significantly more specific and reproducible than CgA measurement [5].

NET transcript analysis can identify PCC/PGL in 95–100%, and expression levels correlate with lesion extent, particularly extra-adrenal. Furthermore SDH mutations were associated with decreased expression of genes involved in metabolism providing a functional dimension to the assessment. In addition proliferation-associated

genes are elevated in progressive, metastatic disease; thus, measurement of circulating transcripts focusing on gene clusters has utility in identifying and differentiating disease activity in PGL/PCC tumors where other neuroendocrine biomarkers lack specificity [75].

Techniques

Radiological Techniques

Transabdominal ultrasonography (US) is usually the first examination to identify the location of the tumor. It is also used for needle guidance in case of fine needle aspiration cytology (FNAC) or core biopsy. To improve sensitivity, contrast-enhanced US (CEUS), endoscopic US (EUS), and intraoperative US (IOUS) are also used. Contrast-enhanced multi-detector CT (MDCT) and MRI are considered the fundamental methods for localizing the primary tumor and delineating its local extent, staging the locoregional and distant metastases, and restaging the patients after therapy [53]. Three-phase scans are performed to best delineate hypervascular and hypovascular lesions. Since NETs are typically hypervascular, CT and MRI are performed early after the bolus of contrast is injected (arterial phase) (Fig. 4). The sensitivity for pancreatic NETs ranges from 69% to 94% for CT and 74–94% for MRI and is >80% for EUS coupled with biopsy [53, 76–80]. The sensitivity for locating a primary small intestine NET is >90% for CT enteroclysis and 86–94% for MRI [81–83]. Although tumor arterial enhancement is homogeneous in small NETs, heterogeneous enhancement is more common in lesions larger than 3 cm. However, the degree, uniformity, and timing of enhancement can be highly variable, and other lesions, such as intrapancreatic accessory spleen, can be commonly mistaken for a NET. Vascular heterogeneity itself is considered to be a sign of malignancy since malignant lesions often have heterogeneous vascular structure, perfusion, and vascular permeability [84, 85].

Localization of GEP-NETs may be difficult since they often present as small lesions and their anatomic location is ubiquitous. EUS is mainly useful in the diagnosis and staging of small and intramural lesions of the duodenum, pancreas, stomach, and rectum and can detect up to 60% of duodenal and up to 100% of pancreatic lesions. EUS and IOUS have a detection rate of 92% for insulinomas. Although the diagnostic accuracy of US for the detection of pancreatic NETs is high, the best performance of US is for the diagnosis and follow-up of liver metastases (sensitivity and specificity are 88% and 95%, respectively) [27, 28].

GEP-NETs may metastasize systemically or locally into the bowel mesentery. Mesenteric disease can be identified on CT as a contrast-enhancing mass often containing calcifications [86]. Angio-CT has particular utility in the identification of the involvement of vascular structures (such as mesenteric arteries) that may preclude surgical resection [87]. However, CT and MR imaging cannot always differentiate tumors and mesenteric metastasis from intestinal structures. Lymphoma or retractile mesenteritis can also have a similar CT appearance [88].

The liver is the commonest site of NET metastases. The metastatic lesions are typically hypervascular, and most can be detected on CT or MR images acquired during the hepatic arterial phase. However, liver metastases may be hypovascular (Fig. 5). Moreover, larger metastases may show heterogeneous enhancement due to central necrosis. For liver metastases, MRI fast spin echo has a high sensitivity, while a single-shot sequence allows optimal distinction between hypervascular metastases from hemangiomas. Contrast-enhanced CT and MR imaging can also disclose occasional metastases to other intra-abdominal organs. Metastases to bone are easily missed on CT. Although MR imaging has a sensitivity of nearly 100%, the appearance of lesions may be identical to that of bone metastases from other primary tumors. Contrast-enhanced CT, MR imaging, and US are routinely used for monitoring lesions. Finally, video capsule and double-balloon enteroscopy can identify otherwise undetectable small intestine tumors [10].

Primary carcinoids of the lungs account for ~25–30% of all NETs. Most carcinoids (typical

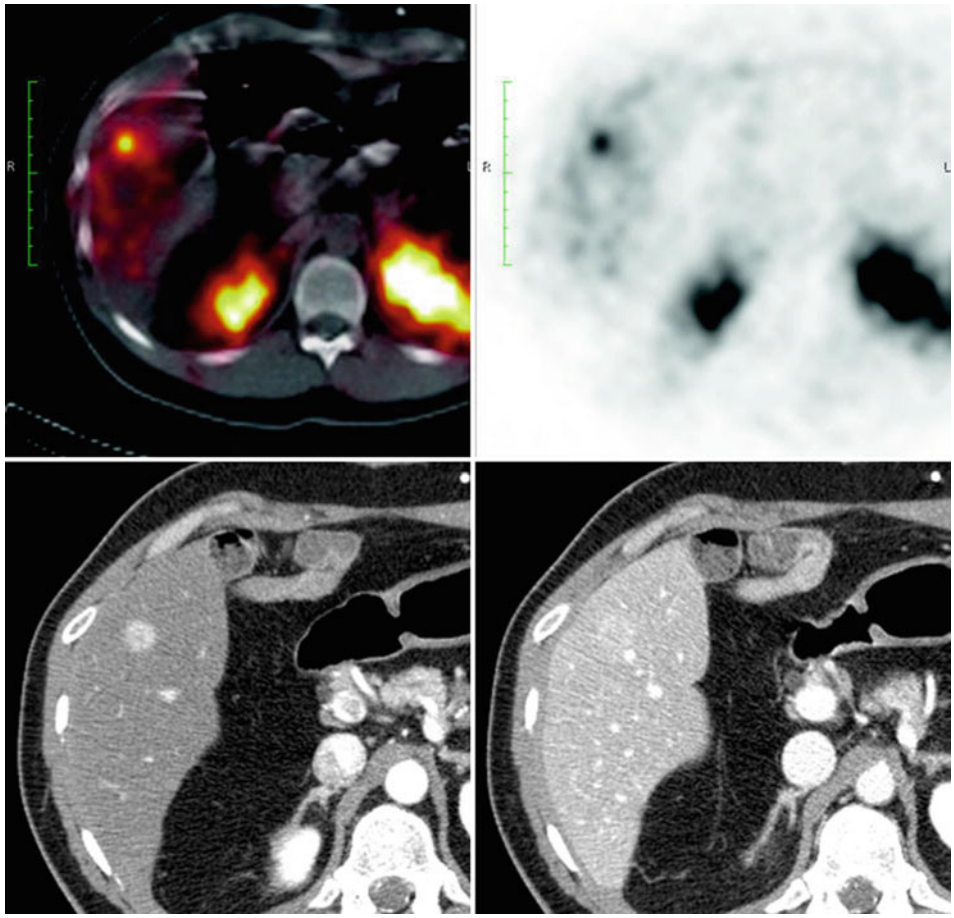

Fig. 4 Patient with a liver metastasis from an ileal neuroendocrine tumor. *Upper* images show SPECT/CT images demonstrating uptake of ^{111}In-pentetreotide within a liver metastasis. The *bottom left* image shows the metastasis with a typical contrast enhancement on CT during the arterial phase. The lesion enhancement decreases during the venous phase when compared to the liver parenchyma (*bottom right* image)

and atypical) are located close to central bronchi, although in about 16–40% (often atypical) are located in the peripheral lung. They typically show a spherical or ovoid shape with a well-defined border, but sometimes they develop along bronchi or pulmonary arteries. Punctate or diffuse calcifications are frequently observed on CT. Both typical and atypical carcinoids are usually hypervascular and demonstrate intense contrast enhancement (more than 30 HU). Atypical carcinoids are associated with hilar or mediastinal lymph node metastases. LCNEC, which is a poorly differentiated and high-grade NET, is morphologically intermediate between atypical carcinoid and SCLC. LCNEC and SCLC do not show any specific CT feature and can indistinguishable from the other common NSCLCs. However, CT plays a main role for staging and follow-up of all NETs of the lung.

CT and MRI are sensitive and specific for detecting adrenal pheochromocytomas (77–98% for CT and 95–100% for MRI). However, MRI and CT have a lower sensitivity (sensitivity of CT is 29%) for extra-adrenal lesions or metastases from malignant pheochromocytomas [46, 89]. In this setting, specificity may be decreased since

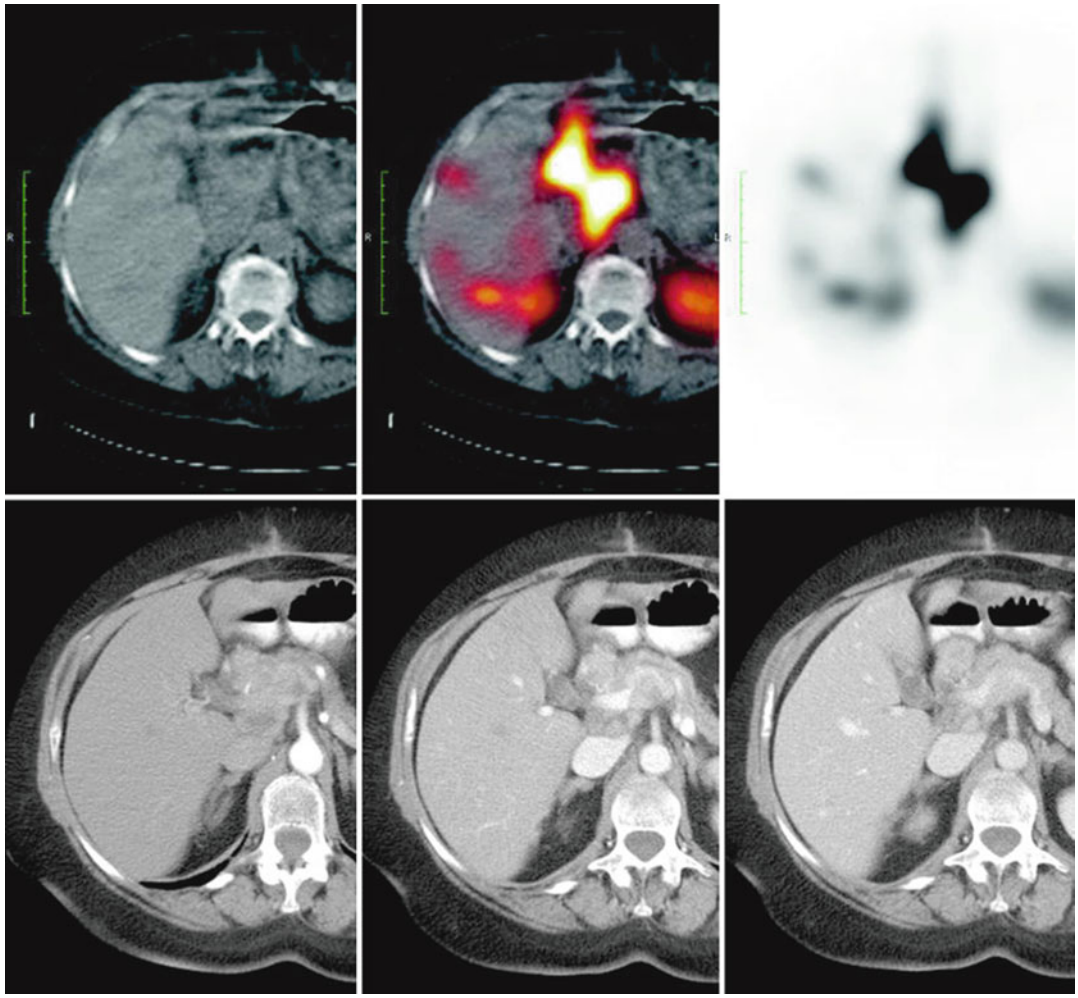

Fig. 5 Patient with a pancreatic NET and multiple liver metastases that result positive at SRS with ^{111}In-pentetreotide but negative at the three-phase contrast-enhanced CT

other tumors of neurogenic origin or mesodermal origin may resemble paragangliomas in both distribution and appearance [25] (Figs. 6 and 7).

Nuclear Medicine Techniques

Molecular imaging provides spectrum of information which includes somatostatin receptor status (e.g., ^{111}In-pentetreotide scintigraphy or ^{68}Ga-DOTA-SSA-PET/CT), metabolic activity ([^{18}F]FDG), and specific amine metabolism (e.g. ^{18}F-DOPA). As a result, further information regarding the biology of the lesion and the extent of disease may be generated, thus facilitating staging in molecular, metabolic, spatial, and functional dimensions.

Rationale of Nuclear Medicine Techniques

Somatostatin receptor imaging is used to obtain information as to the localization of disease and extent (staging and restaging) and to select patient for therapy with "cold" or radiolabeled somatostatin analogs [11, 90]. The rationale of somatostatin receptor imaging is the tumor cell receptor-mediated internalization of the receptor-radioanalog complex and its retention in the

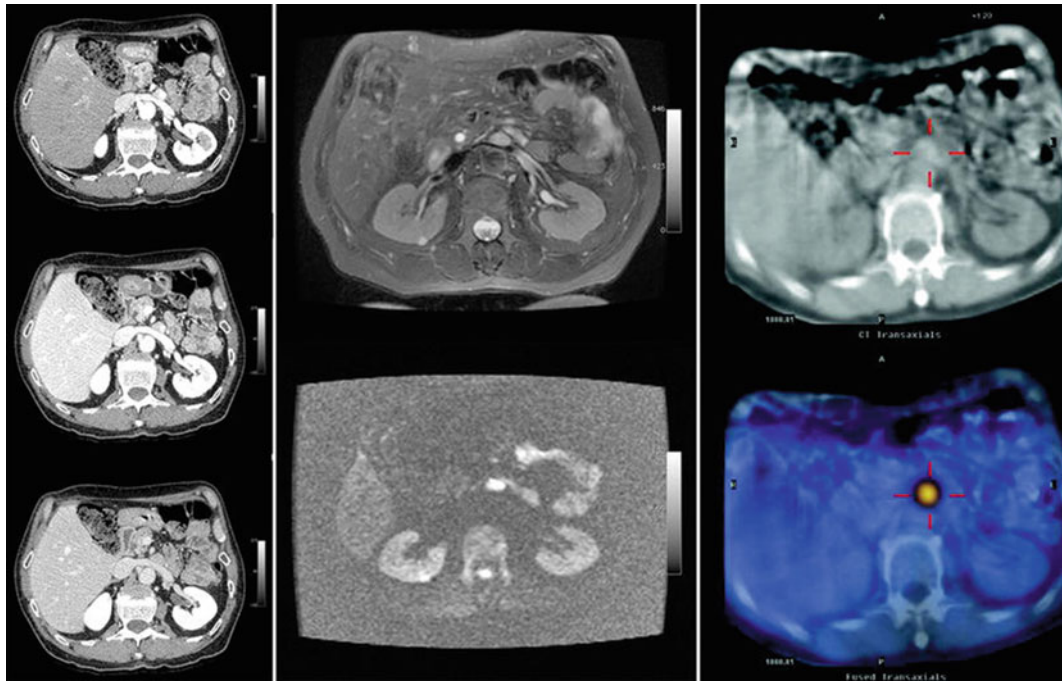

Fig. 6 Patient with an abdominal paraganglioma. The left images (from *top* to *bottom*) of a three-phase contrast-enhanced CT disclose a paraganglioma located in front of the left renal vein showing the typical contrast enhancement during the arterial phase (*top*). In the middle, MRI images show the same lesion hyperintense on T2-weighted image (*top*) and on DWI (*bottom*). The right images of a SPECT/CT study show the high uptake of ^{111}In-pentetreotide within the paraganglioma

Fig. 7 CT shows a lesion with contrast enhancement during the arterial phase along the left ureter suggesting a diagnosis of paraganglioma. Subsequent SRS and ^{123}I-MIBG scintigraphy were negative. After surgery, the lesion resulted to be a neurinoma at histopathology

cytoplasm. ^{111}In-pentetreotide or OctreoScan® represents the first approved radiopharmaceutical for NEN imaging and is the commonly used agent.

Somatostatin is a ubiquitous peptide that exists in either a 14-amino acid or a 28-amino acid form present in the hypothalamus, brainstem, gastrointestinal tract, and pancreas. SSTRs are found on cells of neuroendocrine origin as well as on activated lymphocytes. Six subtypes of SSTRs have been identified by molecular analysis (named sst1, sst2a, sst2b, sst3, sst4, and sst5), each exerting its action by inhibition of adenylyl cyclase activity. Each receptor subtype exhibits a different binding affinity for native somatostatin and for somatostatin analogs. Subtype 2 has the highest affinity (Kd 0.1–1 nM), whereas subtypes 3 and 5 are within the 10–100 nM range, and subtypes 1 and 4 exhibit a low affinity. Moreover, since SSTR2 is the most frequently expressed in NET tumors, it has proved to be the optimal target for imaging. A key advantage of somatostatin imaging efficacy is based upon the significant overexpression and hence high density of SSTRs in neuroendocrine neoplasia (80–2,000 fmol/mg protein compound) as compared to the relatively low expression within normal neuroendocrine tissue [91].

Currently, the majority of radiotracers used for SSTR imaging are based on octreotide, which is a long-acting analog of the human hormone, somatostatin. The presence of octreotide-binding sites (SSTRs) on tumors permits their in vivo visualization after injection of a radionuclide-labeled octreotide analog. Although ^{123}I-[Tyr^3]-octreotide was the initial imaging, radio compound utilized its relatively short effective half-life, and the high background of radioactivity within the abdomen limited its clinical application. The subsequent development of ^{111}In-[DTPA-D-Phe^1]-octreotide, or ^{111}In-pentetreotide, which exhibited greater stability and facilitated the acquisition of enhanced imaging characteristics in the delayed images. This compound is a registered trademark of Mallinckrodt Inc. with the name of OctreoScan®. Octreotide binds with high affinity to the SSTR2 and with moderate affinity to the SSTR3 and SSTR5 receptors. Subsequently since the early 2000s, the approach to the functional imaging of NENs has been substantially advanced by the introduction of octreotide derivatives, the DOTA-peptides, labeled with the positron emitter Gallium-68. The three most commonly used analogs are DOTA-Tyr^3-octreotide (DOTATOC), DOTA-Tyr^3-Thr^8-octreotide (DOTATATE), and DOTA-Nal^3-octreotide (DOTANOC). These analogs retain an octreotide-like affinity profile and, in particular, a high affinity for SSTR2. Only DOTANOC exhibits a substantial affinity for SSTR3 [91].

Initially NENs were referred to as APUD (amine precursor uptake and decarboxylation) tumors because of their ability to take up amino acids and transform them into biogenic amines by means of the enzyme aromatic amino acid decarboxylase. The terminology APUDoma was first used by Ilona Szij of Budapest and subsequently adopted by A. Pearse [13]. The amine uptake, decarboxylation characteristic remains a biological hallmark of chromaffin and neuroendocrine cells although the inelegant term for the tumors, APUDomas has over time evolved into the more commonly used acronym NETS. NET cells synthesize catecholamines in an enzymatic pathway, which initially converts the amino acid tyrosine into L-DOPA; thereafter, L-DOPA is decarboxylated to dopamine, oxidized to norepinephrine, and methylated to epinephrine, which is transported into synaptic vesicles. Reuptake of catecholamines occurs presynaptically by norepinephrine transporters present on the cell membrane [13]. Based upon this series of biochemical events, NETs can be imaged with ^{18}F-DOPA PET (6-L-^{18}F-dihydroxyphenylalanine) and [^{11}C]5-hydroxytryptophan ([^{11}C]5-HTP), which accumulate within cells due to the high activity of the aromatic amino acid L-DOPA decarboxylase. Thus, the tracer radioiodinated metaiodobenzylguanidine (MIBG) is internalized by the cell via the norepinephrine transporter and stored in neurosecretory vesicles by a catecholamine transporter (VMAT). ^{18}F-DOPA or ^{18}F-dopamine PET and ^{123}I/^{131}I-MIBG scintigraphy are highly sensitive for detecting tumors arising from the adrenal medulla. However, they can also be taken up by non-adrenomedullary NETs and paragangliomas [92, 93].

Metaiodobenzylguanidine (MIBG) is a norepinephrine analog that concentrates within secretory granules of catecholamine-producing cells. It is structurally similar to guanethidine. MIBG, like norepinephrine, is taken up by a cell membrane based active, sodium- and energy-dependent amine uptake mechanism (uptake-1), inserted into the cell membrane of chromaffin tissues, and then transported to the intracellular storage granules by an active uptake mechanism [94].

There are numerous drugs that reduce the sensitivity of the scintigraphy and frequently result in false negatives; this occurs through interference with the uptake, intracellular transport, granule storage, or the retention of MIBG [95]. To ensure optimal imaging, these pharmaceuticals should be temporarily withdrawn before the examination, for a time period of approximately five times longer their respective half-lives before imaging [58] (Table 6).

[^{18}F]FDG, a glucose analog, is transported into the cell via dedicated glucose transporters and thereafter phosphorylated by the cytoplasmic enzyme, hexokinase. The resulting compound cannot be further metabolized and is trapped within the cytoplasmic space. Since many tumors, particularly those of aggressive or accelerated proliferative nature, exhibit an increased glycolytic metabolism, they overexpress glucose transporters and have abundant hexokinase. This phenomenon provides the biological basis for the use of [^{18}F]FDG as a radiopharmaceutical to detect such tumors. The process of accelerated glycolytic metabolism is also however a common occurrence in activated inflammatory cells. Thus [^{18}F]FDG may also accumulate at sites of inflammation and constitute a potential cause of false positivity for malignancy [97].

Scintigraphy

Somatostatin Receptor Scintigraphy

Clinical Application

The radiolabeled somatostatin analog ^{111}In-pentetreotide (or ^{111}In-DTPA-D-Phe^{1}-octreotide or OctreoScan®) is the commonly used agent for somatostatin receptor scintigraphy (SRS) [98–101], although the ^{99m}Tc-labeled peptide ^{99m}Tc-EDDA-HYNIC-octreotide (Tektrotyd®) is used in several European countries [102]. The sensitivity of ^{111}In-pentetreotide scintigraphy has been well documented in the 1990s as >75% for gastroenteropancreatic (GEP-NETs) and bronchial tumors (BP-NETs, compared to other imaging modalities available (CT/MRI) [103]. Information from OctreoScan® images modified the therapeutic strategy in ~53% of cases by

Table 6 Pharmaceutical compounds that reduce the sensitivity of scintigraphy (Adapted with permission from [96])

Drugs	Mechanism of interference	Withdrawal before MIBG
Antiarrhythmics (e.g., amiodarone)	Uptake inhibition and depletion	Not easily feasible
Alpha–beta blockers (e.g., labetalol)	Uptake inhibition and depletion	3 days
Calcium channel blockers (e.g., amlodipine)	Increased uptake and retention	1–2 days
Alpha2 sympathomimetics (e.g., salbutamol)	Depletion of granules	1 day
Vasoconstrictor sympathomimetics (e.g., pseudoephedrine)	Uptake inhibition and depletion	1–2 days
Neuroleptics (e.g., haloperidol)	Uptake inhibition	1–15 days (short-acting formulations)
Antihistamine (e.g., promethazine)	Uptake inhibition	1 day
Opioid analgesics (e.g., tramadol)	Uptake inhibition	1 day
Tricyclic antidepressants (e.g., amitriptyline)	Uptake inhibition	2–8 days
Psychostimulants (amphetamines, cocaine)	Uptake inhibition and depletion	1–5 days

accurately staging NETs and especially by detection of metastatic disease [104, 105]. Currently, however the OctreoScan technique is regarded as suboptimal, with sensitivities <60%, compared with state-of-the-art morphological imaging (CT and MRI) [106]. Although MRI is considered to have the highest sensitivity for liver metastases, SRS is the most accurate imaging modality for "one-shot" detection of liver and extrahepatic metastases in patients with GEP-NETs [107] (Fig. 8). OctreoScan® is also utilized to monitor treatment efficacy. Changes in functional volume at scintigraphy are considered more useful than CT and RECIST (Response Evaluation Criteria in Solid Tumors) in monitoring tumor response after treatment and correlate well with later clinical response [108] (Fig. 9).

In BP-NETs, molecular imaging can help differentiate the etiology of bronchial masses [109]. Since most of thoracic NETs express somatostatin receptors, especially subtypes 2 and 5 (Fig. 10), ^{111}In-pentetreotide scintigraphy can detect most bronchial carcinoids >1 cm in diameter, including those associated with ectopic GH-RH secretion [110]. SRS is also helpful for radioguided surgery, allowing evaluation of the tumor bed after resection to detect any residual radioisotope uptake that might reflect the presence of residual tumor [111]. Since SSTRs are expressed on inflammatory cells, some degree of caution in the misinterpretation of early postsurgical changes should be considered.

Technique

The radiopharmaceutical should be prepared in accordance with the manufacturer's instructions and quality control performed with a calibrated ionization chamber. Radiochemical purity should be checked with thin-layer chromatography prior to patient administration. The amount of peptide injected in this preparation is 10 μg. To preserve diagnostic sensitivity, the recommended injected activity should be ~200 MBq (5.4 mCi). Lower activities can only be administered if acquisition parameters are adjusted accordingly [112]. At least two different sets of planar and/or whole body images should be acquired to facilitate the interpretation of the exam. Commonly adopted protocols include scans at 4 and 24 h or, optimally, 24 and 48 h postinjection and three-dimensional SPECT at 4, 24, and optionally at 48 h postinjection. Currently, the extensive use of SPECT/CT has reduced

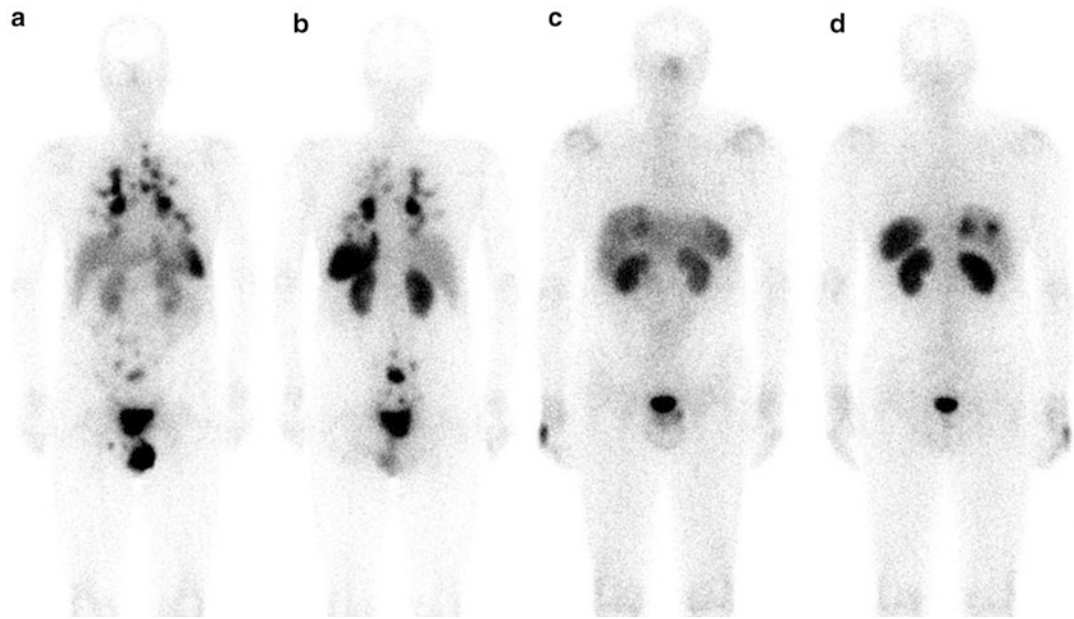

Fig. 8 SRS with ^{111}In-pentetreotide. On the *left* (**a**, **b**), a whole body scan shows a patient with an intestinal lesion, abdominal lymph nodes, and multiple lung metastases. On the *right* (**c**, **d**), a patient with liver metastases

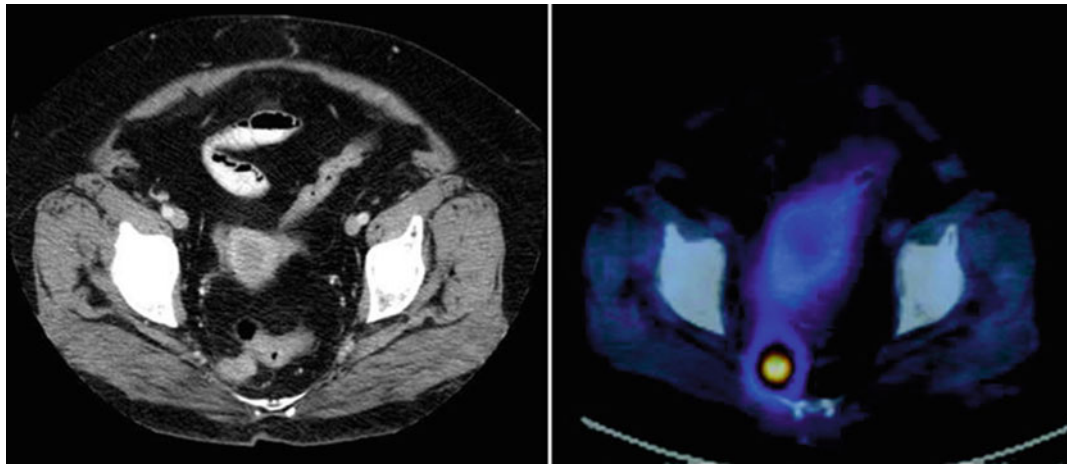

Fig. 9 SRS with ^{111}In-pentetreotide. Peritoneal relapse of a GEP-NET

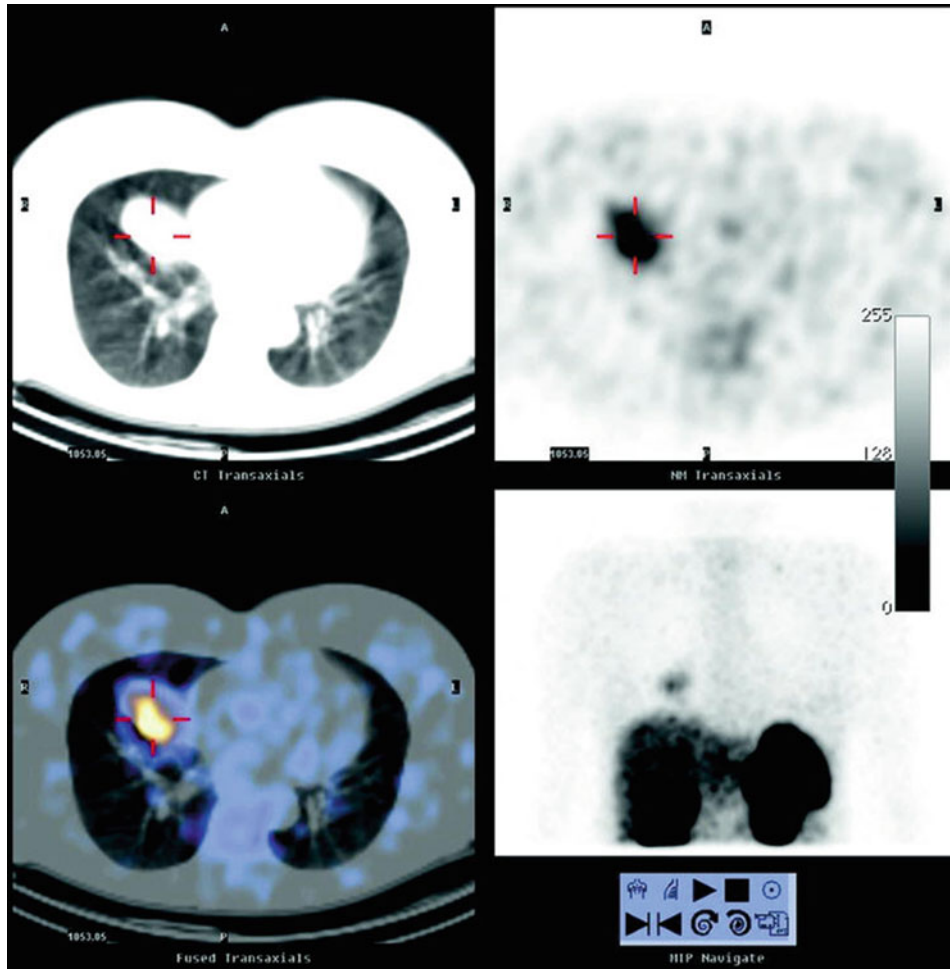

Fig. 10 Typical bronchial carcinoid. SRS with ^{111}In-pentetreotide shows an intense uptake of the tracer within a mass in the medium lobe

the need for the 4 and 48 h examinations, due to the increased specificity [100] (Fig. 11). Later images can also be acquired in case of equivocal findings. A gamma camera equipped with a medium-energy, parallel-hole collimator, with the window set for 20% on ^{111}In photopeaks (172 and 245 keV) should be used to acquire planar images, either spot or whole body. To achieve an acceptable

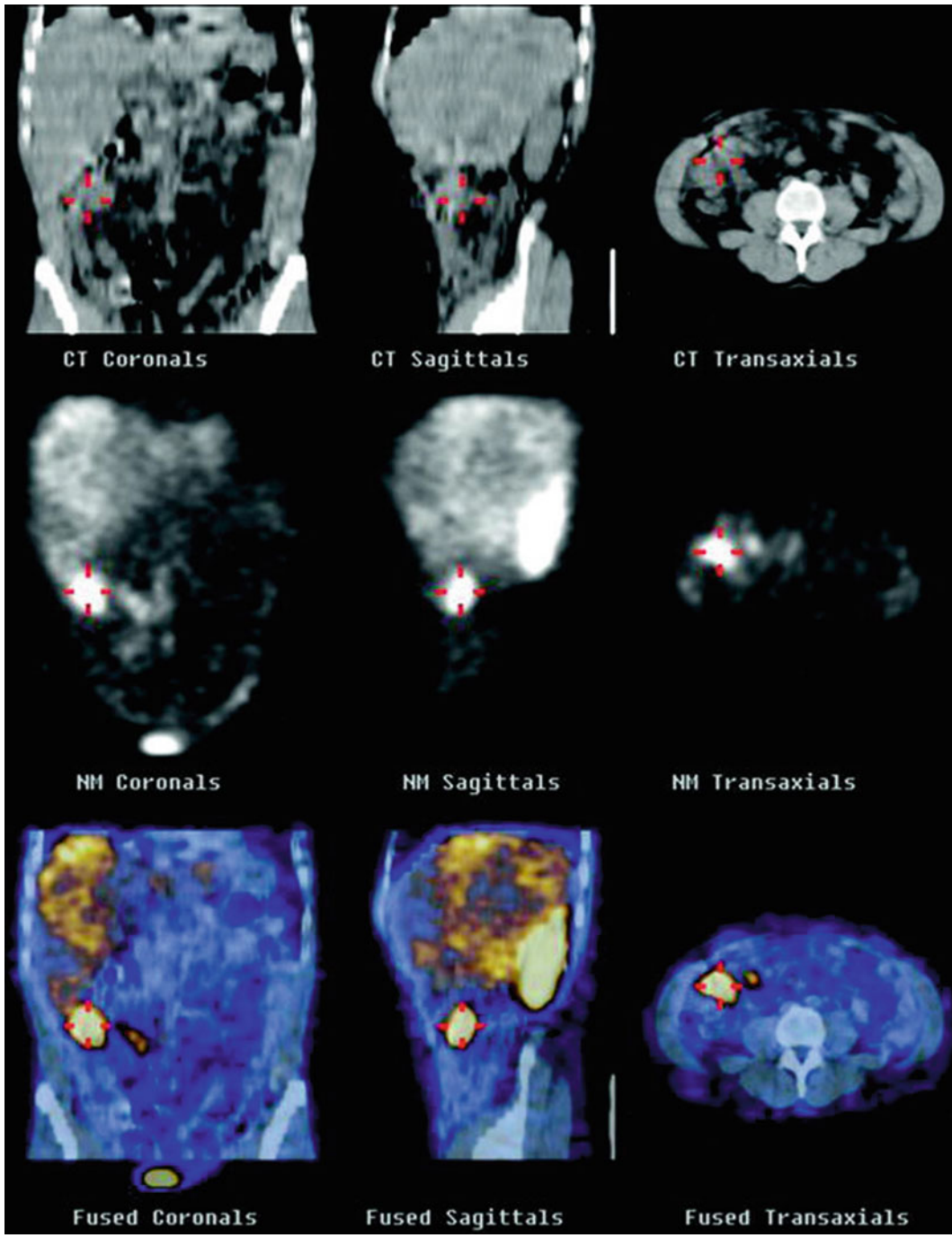

Fig. 11 SPECT/CT shows uptake of ^{111}In-pentetreotide within a NET of the ileum

sensitivity, planar images should be acquired for 10–15 min/image, using a 512 × 512 word matrix or 256 × 256 word matrix, whole body images into a 1,024 × 512 word matrix or 1,024 × 256 word matrix for a minimum of 30 min, corresponding to a maximum scanning speed of 3 cm/min. For precise details of the detailed scanning protocol, the SNMMI (Society of Nuclear Medicine and Molecular Imaging) or the EANM (European Association of Nuclear Medicine) procedure guidelines for ^{111}In-pentetreotide scintigraphy should be consulted [112].

After injection, plasma clearance is rapid, followed by a progressive accumulation in tissues. Elimination occurs mainly via the kidneys and, to a lesser extent, the hepatobiliary system. Physiologic areas of uptake are the spleen, the liver, and the kidneys. Normal scans also show variable uptake in the pituitary, thyroid, urinary bladder, and bowel [112]. The visualization of the kidneys is mainly due to filtration and proximal tubular reabsorption of the radiopeptide, while the uptake to the spleen, pituitary, and thyroid is receptor mediated (Fig. 12).

Preparation for the scan includes laxatives, to eliminate nonspecific activity in the bowel, and withdrawal of somatostatin analogs (short-acting analogs for at least 48 h, long-acting formulations for 4–6 weeks), although the latter point is still debated [112].

Interpretation

Assessment of images should be guided by clinical information. As a general rule, clearly outlined areas that show an isotope uptake higher than the normal liver distribution are classified as positive for receptor expression and thus considered to represent neuroendocrine malignancy. There are, however, alternative conditions that may be associated with increased somatostatin receptor expression and, hence, exhibit increased uptake. Possible sources of false positives include areas of chronic inflammation (such as radiation pneumonitis, sequelae of recent surgery), accessory spleens, gallbladder accumulation, focal stool aggregation, thyroid nodules, pulmonary granuloma, diffuse breast uptake, recent cerebrovascular infarction, arthritis, abscesses, and urine contamination [90].

False negatives imply the lack of visualization of NEN lesions, most commonly related to an incorrect methodology, such as low administered

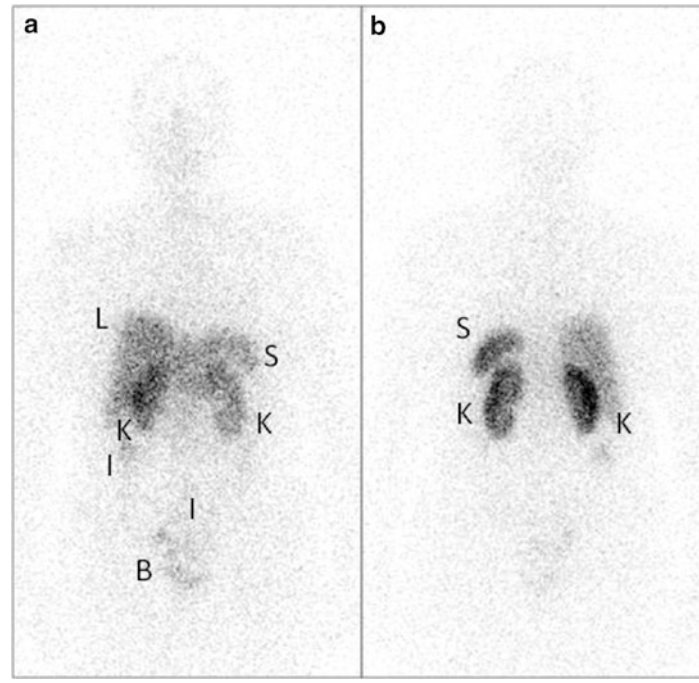

Fig. 12 Normal distribution of ^{111}In-pentetreotide, anterior (**a**) and posterior (**b**) whole body images, 24 h p.i., with physiological visualization of the liver (L), kidneys (K), and spleen (S) and of the activity eliminated in the urinary bladder (B) and the intestine (I)

activity, a too rapid (or too early) scan time, the absence of SPECT images, or lesions whose dimensions fall below the resolution limit of the gamma camera. Other possible causes may be competition for receptor uptake by recent analog therapy (although this issue is debated), alteration of receptor expression by recent chemotherapy, or truly receptor-negative disease (e.g., benign insulinomas, high-grade NETs). In some cases, normal accumulation in the liver may mask isointense metastases or those with a relatively low expression of somatostatin receptor density [101].

Metaiodobenzylguanidine

Clinical Application

Functional imaging with ^{123}I-MIBG is still the first choice among nuclear medicine methods available for chromaffin tumors although recent data suggest a superiority of ^{68}Ga-DOTA-SSA-PET/CT in pheochromocytomas and paragangliomas [113–117]. ^{123}I-MIBG has been used (labeled with ^{131}I or since 1980, with ^{123}I) for the specific imaging of tumors that originate from the neural crest (chromaffin tumors and NETs). Apart from its diagnostic utility, ^{131}I-MIBG has also been used (since 1984) for the therapy of chromaffin tumors and NETs [118]. In adrenal pheochromocytomas, ^{123}I-MIBG scintigraphy has sensitivity and specificity of 90% and 95%, respectively. Moreover, the combined sensitivity of catecholamine measurements and ^{123}I- MIBG scan approached 100% [119]. Thus a whole body scan ^{123}I-MIBG is particularly helpful in the preoperative identification of multiple primary lesions (relatively frequent in norepinephrine-secreting pheochromocytomas) or metastases from malignant tumors (Fig. 13).

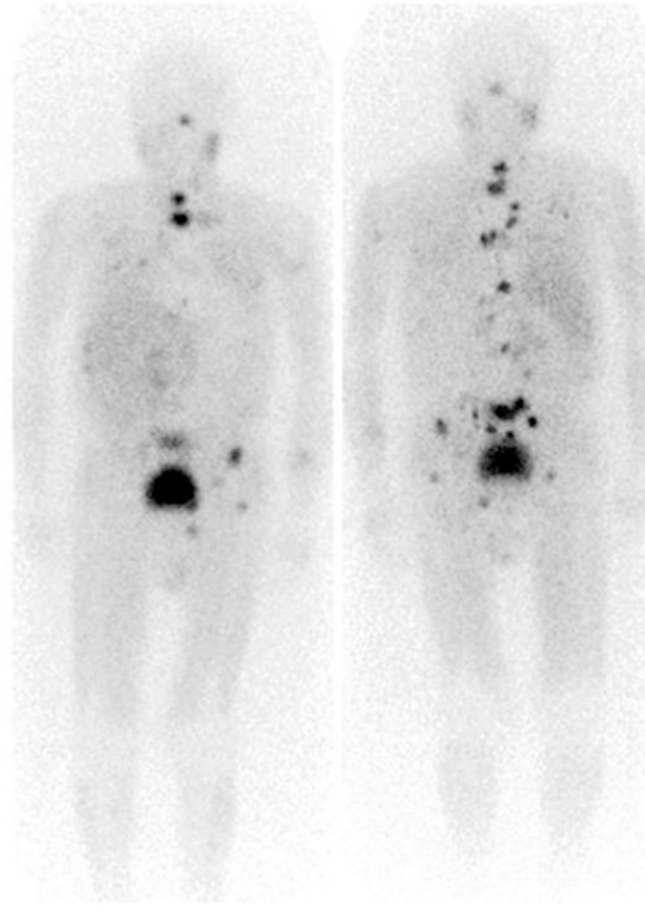

Fig. 13 ^{123}I-MIBG whole body scintigraphy. Multiple foci of tracer uptake indicating the presence of diffused bone metastases from a malignant pheochromocytoma

^{123}I-MIBG is of especial utility in the detection of recurrences since the radiotracer accumulates specifically within the tumor and is not affected by postsurgical or post-radiotherapy structural changes (Fig. 14). In extra-adrenal tumors, ^{123}I-MIBG imaging has a lower sensitivity (58%) than adrenal lesions (90–95%) [120]. Unlike abdominal and thoracic paragangliomas, ^{123}I-MIBG imaging has limited sensitivity for the detection of paragangliomas of the head and neck region (17–42%) [121].

Although both ^{131}I-MIBG and ^{123}I-MIBG are commercially available for diagnostic imaging, the former has been preferred since it is more widely available and economical. The physical characteristics of ^{131}I-MIBG, although not optimal for scintigraphic imaging (gamma energy 364 keV, half-life 8 days), facilitate delayed studies. Alternatively, the physical properties of ^{123}I (gamma energy 159 keV, half-life 13.3 h) provide better image quality, more favorable dosimetry, and the possibility of performing a SPECT study, rendering it the agent of choice. ^{123}I-MIBG has, however, been approved for US usage by the Food and Drug Administration [122].

Technique

Thyroid blockade with nonradioactive iodide or, alternatively, potassium perchlorate is necessary to avoid thyroid uptake of free radioiodine and consequent potential damage. A solution of saturated potassium iodide (1–2 mg/kg per day) is commonly used, beginning 1 day before injection and continuing for 3–5 days.

Administered activities are 37–74 MBq (1–2 mCi) for ^{131}I-MIBG and 370 MBq (10 mCi) for ^{123}I-MIBG. To avoid potential bioactive adverse events, ^{123}I- or ^{131}I-MIBG should be administered by slow intravenous injection.

^{131}I-MIBG scan is performed using a gamma camera equipped with a high-energy, parallel-hole collimator. Images are collected at 24 and 48 h after injection. If nonspecific activity is suspected in the kidneys or bowel, delayed images can be

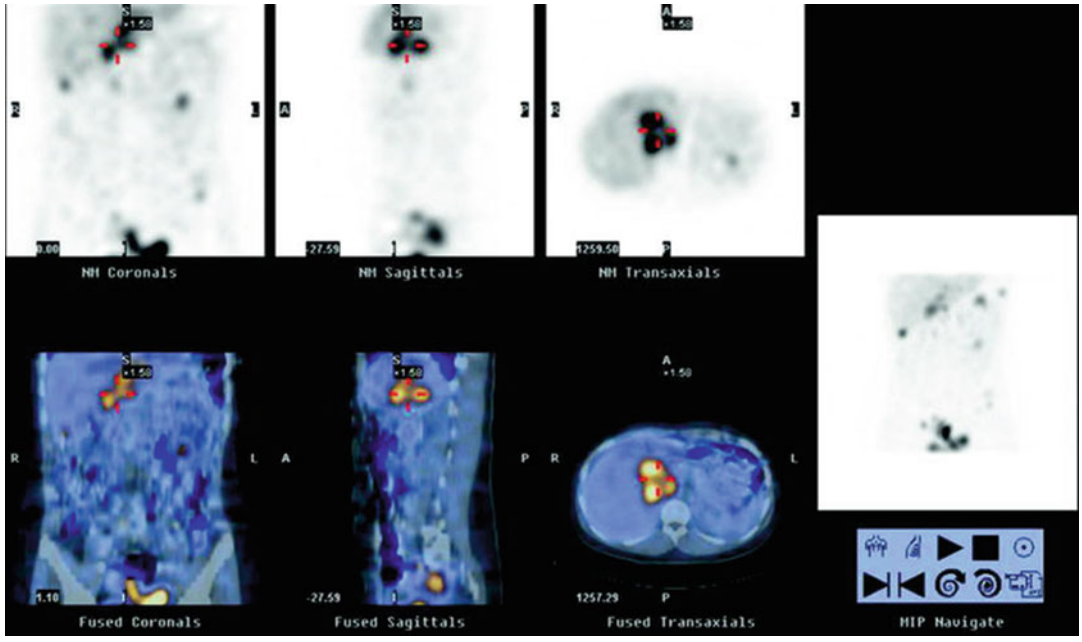

Fig. 14 Recurrence of adrenal pheochromocytoma. ^{123}I-MIBG SPECT/CT demonstrates a large lesion close to the site of the previous left adrenal resection. Patient history shows a laparoscopic surgery complicated by intense hemorrhage within the pheochromocytoma, producing the tumor seeding into the whole abdominal cavity (multiple other lesion are clearly shown in the MIP image on the *right*)

recorded after 72–120 h. Whole body and planar images of areas of interest are collected.

^{123}I-MIBG scan is performed with a medium-energy, collimator. Images are collected 6 and 24 h after injection and, if needed, 48 h post-injection. Whole body and spot images are recorded. The use of ^{123}I-MIBG allows SPECT imaging which is usually undertaken 24 h after administration. The use of hybrid SPECT/CT system further improves sensitivity [123]. Sub-optimal sensitivity can be caused by a small lesion size and and/or an extra-adrenal location. MIBG SPECT, evaluated side-by-side with contrast CT or MRI and/or hybrid imaging with SPECT/CT, provides an even more accurate anatomic localization of areas of MIBG uptake [120].

Interpretation

Normal findings, with either ^{123}I- or ^{131}I-MIBG, are the visualization of the lacrimal and salivary glands, heart, lungs, liver, spleen, urinary bladder, and, to some extent, bowel. Normal adrenal medulla is frequently visible with ^{123}I-MIBG but rarely with ^{131}I-MIBG. Any area of uptake located outside of these sites should be regarded as suspicious for malignancy (Fig. 15).

Physiologic accumulation of MIBG in the urinary tract or bowel can be a source of false-positive results. ^{123}I-MIBG SPECT evaluated with contrast CT or MRI or hybrid imaging with SPECT/CT allows more accurate anatomic localization of areas of uptake [124]. Rare causes of false-positive results such as the physiological accumulation of MIBG within the urinary tract or the bowel, which can mimic a tumor lesion, should also be considered. False negative results include lesions with dimensions below the spatial resolution of the gamma camera (~1 cm) or lesions whose uptake mechanisms have been altered by concomitant usage of drugs (Table 6).

PET/CT

Clinical Application

In the last 15 years, the approach to the molecular imaging of NETs has been revolutionized by the

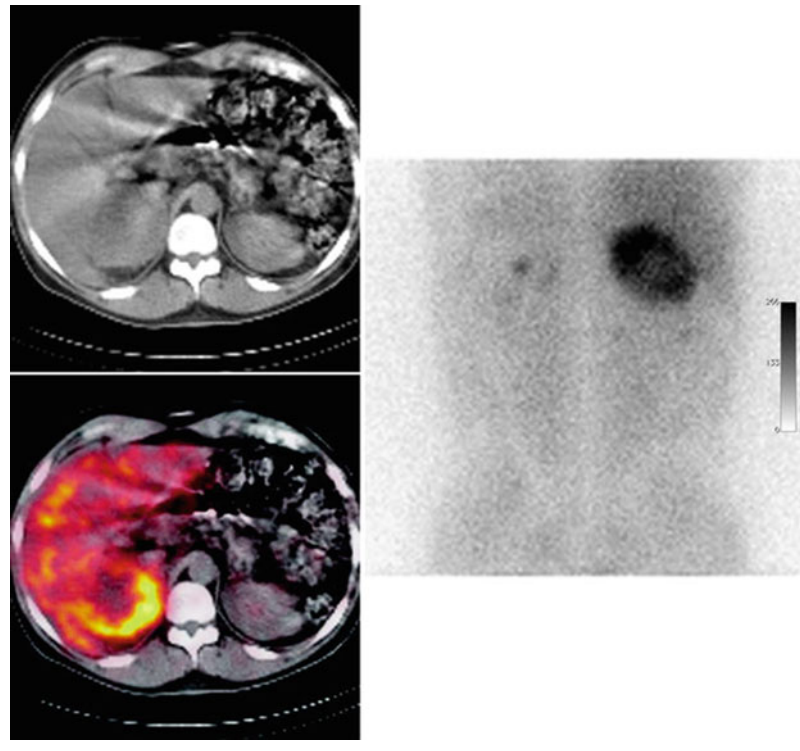

Fig. 15 ^{123}I-MIBG scintigraphy. The tracer uptake within a large tumor with central necrosis confirms the diagnosis of pheochromocytoma

introduction of PET with the Gallium-68 (^{68}Ga)-labeled octreotide derivatives, DOTATOC, DOTATATE, and DOTANOC (^{68}Ga-SSA-PET/CT) [125–127]. The overall sensitivity of ^{68}Ga-SSA-PET/CT for NETs is >90%, while the specificity ranges from 92% to 98% [106, 128, 129]. Copper-64 (^{64}Cu)-labeled SSA has also been evaluated for PET/CT of NETs with better imaging at later times (3–24 h p.i.) [130]. Compared to CT scan and receptor scintigraphy, PET exhibited the greatest sensitivity (97%) compared to CT (61%) and SRS (52%) for the detection of NET lesions, especially in patients with small tumors at a nodal or bone level. PET is also able to identify small lesions in unusual locations such as the breast, uterus, prostate, ovary, and kidney [106, 131]. PET with ^{68}Ga-DOTA-peptides is particularly useful in the early visualization of bone metastases, with a higher sensitivity, specificity, and accuracy than a CT scan. In a study of 84 patients (116 PET-positive lesions), only 84 (72.5%) were evident at conventional scintigraphy and only 58 (50%) at CT scan [106]. Recently, a study of 51 patients, 35 of which were GEP-NETs, among other SSTR2 positive tumors, demonstrated that PET/CT with ^{68}Ga-DOTATOC performed better than conventional somatostatin receptor scintigraphy or bone scintigraphy, resulting in a 97% sensitivity and 92% specificity [132].

Radiolabeled somatostatin receptor antagonists, characterized by a lack of internalization and a greater tumor uptake, were recently introduced in clinical trials due to their putative advantage of the much greater tumor-to-background ratio. Antagonists, such as ^{68}Ga-DOTA-JR11, have provided very interesting novel information in the largely explored SSR imaging [133].

Alternative PET tracers include ^{18}F-DOPA, which is a measure of neuroendocrine cell metabolism. This is a substrate utilized in the catecholamine synthesis pathway and is stored in the secretory granules [134]. The diagnostic performance of this compound appears however to be inferior to ^{68}Ga-DOTANOC [135]. [^{11}C]5-HTP, a serotonin precursor, which is the substrate for aromatic L-amino acid decarboxylase, is also utilized in research centers [92]. ^{18}F-DOPA PET was commonly used in the last decade, since it was the first PET modality to outperform ^{111}In-pentetreotide scintigraphy. In a variety of GEP-NETs, it exhibited high sensitivity and specificity for small-bowel carcinoid tumors (93% and 89%, respectively) compared to ^{111}In-pentetreotide [136]. In a prospective cohort of 53 patients with carcinoid tumors, ^{18}F-DOPA PET with carbidopa pretreatment demonstrated a per-patient sensitivity of 100%, detecting more lesions than conventional scintigraphy and CT scan [93]. The enthusiasm for the use of these alternative PET techniques has however been diminished by the increased availability of ^{68}Ga-DOTA-peptides and the demonstration of a superior sensitivity of somatostatin receptor PET with both ^{68}Ga-DOTANOC (71 vs. 45 lesions for ^{18}F-DOPA) and ^{68}Ga-DOTATATE (96% vs 56% for ^{18}F-DOPA) [135, 137]. A further limitation in their usage has been the fact that unlike somatostatin receptor imaging, these techniques do not possess a therapeutic counterpart.

[^{18}F]FDG-PET is usually not considered a primary diagnostic tool in well-differentiated NETs, because of its low sensitivity. Its optimal application is for imaging of high G2 NETs with Ki67 >15–20% for which SRS and ^{68}Ga-SSA-PET/CT may be less reliable [138]. [^{18}F]FDG-PET is generally recommended for neuroendocrine cancers (NEC) G3 tumors, although it has been reported as positive in 57% of G1 and 66% of G2 NETs [139]. The increased glucose metabolism, expressed as standardized uptake value (SUV), can provide predictive information in terms of overall survival (OS) and progression-free survival (PFS, SUV >3) [140]. Thus NETs that exhibit increased metabolic activity have a significantly lower disease control rate (100% vs 76%) and PFS (32 vs 20 months) after PRRT, compared to [^{18}F]FDG-negative tumors [139]. It has recently been proposed that [^{18}F]FDG can be used as an independent prognostic marker by applying a three-tier metabolic grading system based on the tumor-to-background ratio of uptake [141]. Finally, GLP1 receptor peptides for imaging of insulinomas (exendin analogs labeled with ^{68}Ga) are under investigation in clinical trials [142].

In bronchopulmonary NETs, ^{68}Ga-DOTA-SSA-PET/CT has surpassed OctreoScan in the

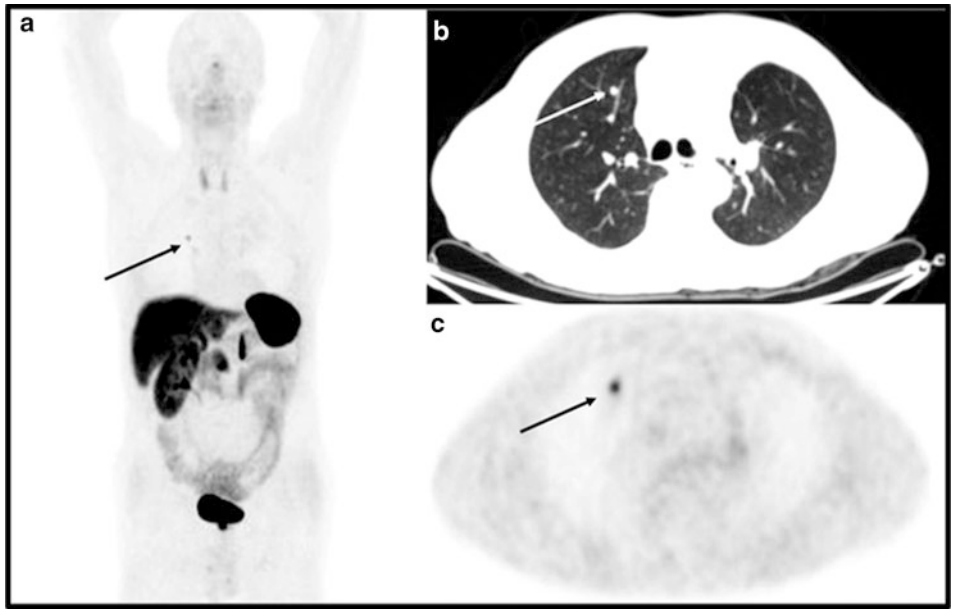

Fig. 16 ^{68}Ga-DOTATOC maximum intensity projection, CT, and PET images (**a**, **b,** and **c**, respectively) of a small typical bronchial carcinoid of the right upper lobe

assessment of small-volume disease, as well as mediastinal lymph node involvement and distant metastases (Fig. 16) [143].

[^{18}F]FDG-PET/CT in NETs of the lungs shows variable [^{18}F]FDG uptake according to tumor proliferation. A low [^{18}F]FDG uptake ($SUV_{max} < 2.5$) is evident in typical (low-grade) bronchial carcinoids [144]. Tumors of a higher grade than typical bronchial carcinoids can have high [^{18}F]FDG uptake. Atypical carcinoids can be more metabolically active and usually appear as a small pulmonary nodule with hilar or mediastinal lymph nodes showing high SUV. LCNECs usually exhibit high [^{18}F]FDG uptake, and PET/CT and stand-alone CT demonstrate high accuracy in prediction of the presence of hilar and mediastinal nodal involvement. However, PET/CT seems to be better than CT alone in detecting distant metastases and leading to the changes in the clinical management. An SUV_{max} greater than 13.7 predicts a short survival period, suggesting the use of PET/CT with [^{18}F]FDG not only in staging but also in assessing prognosis of LCNEC [145]. In SCLC, [^{18}F]FDG PET is valuable for initial staging to distinguish localized vs. metastatic disease, and [^{18}F]FDG PET/CT is also useful for prognosis, especially after treatment [146].

Early data addressing the combined use of [^{18}F]FDG and ^{68}Ga-DOTATOC appear to have clinical utility. Thus typical carcinoids, with high expression levels of SSRs, show high uptake on ^{68}Ga-DOTATOC PET/CT imaging but low [^{18}F]FDG uptake due to the low proliferative index. It has been proposed that increased avidity of [^{18}F]FDG and/or decreased avidity for ^{68}Ga-DOTATATE could identify aggressive tumors containing sites of possible dedifferentiation [144].

Data from a recent multi-center study of sporadic pheochromocytomas and paragangliomas indicate that PET/CT with ^{68}Ga-DOTATATE is superior to any other imaging modality, including [^{18}F]FDG PET/CT and CT/MRI, with a lesion-based detection rate of 97.6% versus 49.2% of [^{18}F]FDG PET/CT, 74.8% of ^{18}F-DOPA PET/CT, and 81.6% of CT/MRI [117]. In a group of 30 patients with pheochromocytomas and paragangliomas at initial diagnosis or relapse, ^{68}Ga-DOTATATE PET/CT exhibited the highest per lesion sensitivity (93% vs. 89% and 76%,

compared to ^{18}F-DOPA PET and conventional imaging). The highest sensitivity was identified in the detection of head and neck paragangliomas, especially in SDHD-related tumors [147]. Integration of this information with circulating mRNA from tumor may add further to the precise delineation of the biological behavior of these tumors.

Somatostatin Receptor PET/CT

Clinical Application

Somatostatin analogs labeled with ^{68}Ga (produced by a generator, therefore not requiring an in-house cyclotron) offer the advantage of both higher spatial resolution (about 4–5 mm) and signal-to-noise ratio as well as easier image quantification than SPECT (Fig. 17). Despite differences in receptor affinity, a clear clinical superiority of one of the three available compounds over the others has not been unambiguously demonstrated. A comparison of ^{68}Ga-DOTATOC versus ^{68}Ga-DOTATATE PET/CT in the same patients yielded comparable diagnostic accuracy for the two radiopeptides, with a potential advantage for ^{68}Ga-DOTATOC in the number of detected lesions and the higher SUV [148]. However, a recent comparison of ^{68}Ga-DOTATATE and ^{68}Ga-DOTANOC PET/CT imaging in the same patients with NETs showed higher SUV values and superiority of ^{68}Ga-DOTATATE on a lesion basis and a comparable diagnostic accuracy on a patient basis [149]. The inconclusive results on this issue may reflect the particular receptor configuration of the individual tumors. These novel radiopharmaceuticals are currently in use only as components of research projects, since none have yet been registered for use in routine clinical practice. The compound ^{68}Ga-DOTATATE was recently (2016) approved by FDA. It is of note that PET/CT with ^{68}Ga-DOTA-peptides offers several advantages over the

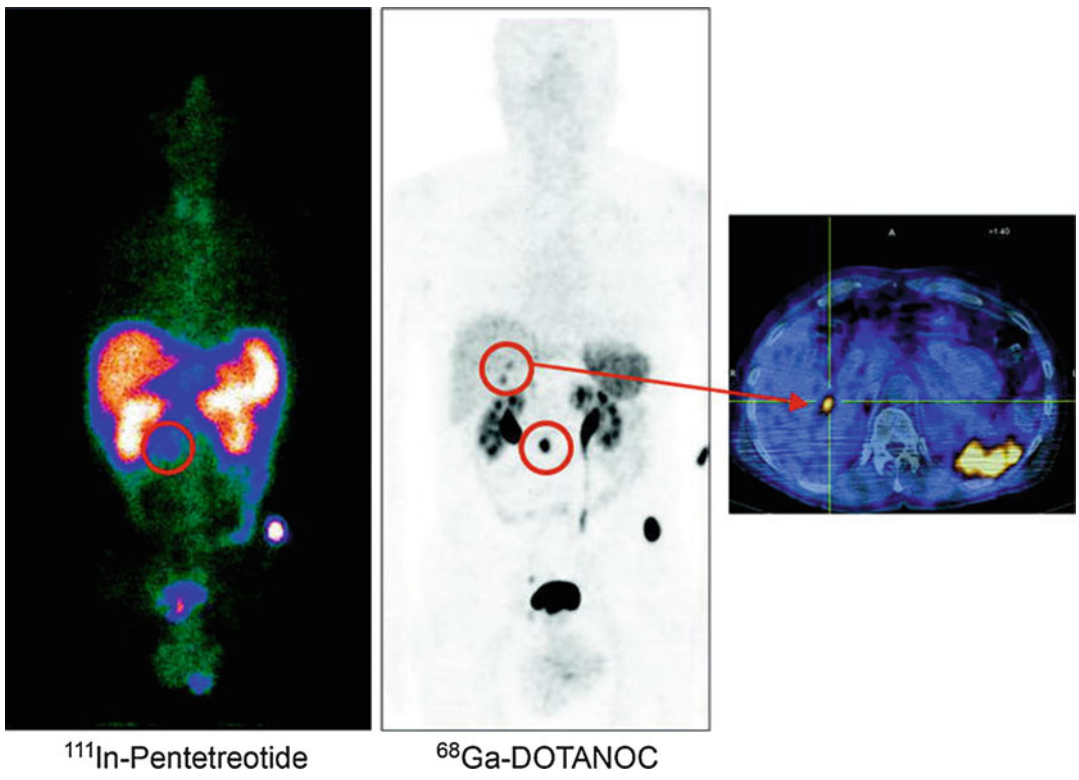

Fig. 17 Comparison between SRS with ^{111}In-pentetreotide and PET with ^{68}Ga-DOTANOC. The higher spatial resolution and signal-to-noise ratio of PET allow the identification of two small liver metastases which were not visualized by SRS

conventional scintigraphic technique. These include: the synthesis of the radiopeptide from the $^{68}Ge/^{68}Ga$ generator eluate is simple and economical and can also be undertaken in centers without an on-site cyclotron, the imaging can be performed as a single day procedure, the activity in a given region of interest can be semi-quantified as SUV, and the spatial resolution of the method is higher and allows an excellent quality of the images with the detection of small lesions <10 mm. A further potential advantage is the possibility of labeling the same peptide used for radionuclide therapy (whether DOTATOC, DOTATATE, or DOTANOC).

Technique

The recommended injected activity to obtain diagnostic quality images ranges from 100 to 300 MBq, depending on the tomographic characteristics and body weight. To avoid possible clinico-pharmacologic effects, the amount of the injected peptide should not exceed 50 μg [150]. The clearance of ^{68}Ga-DOTA-peptides from the blood is rapid. Arterial activity elimination is bi-exponential, and no radioactive metabolites are detected in serum and urine in the first 4 h. Maximal tumor activity accumulation is reached at 70 ± 20 min postinjection. Excretion occurs almost exclusively via the kidneys. The PET/CT acquisition begins 45–60 min after the intravenous administration of the radiopeptide, by means of a dedicated PET/CT scanner as a whole body image, preferably in a 3D mode. For a detailed description of the scanning protocol and image reconstruction, reference should be made to the EANM procedure guidelines for ^{68}Ga-DOTA-peptides [150]. The use of contrast media may further enhance detection. However, in standard usage, unenhanced PET/CT is considered sufficient. As for conventional scintigraphy, the normal findings include the visualization of the liver, the spleen, the pituitary, the thyroid, the kidneys, as well as the adrenal glands, salivary glands, the stomach wall, and the intestines (Fig. 18). Preparation is the same as for ^{111}In-pentetreotide.

Interpretation

The clinical interpretation of these images is easier than with single photon tomography, due to the better spatial resolution and the CT co-registration (Figs. 19 and 20). Criteria for defining areas of uptake as consistent with NET disease are the same as for ^{111}In-pentetreotide. In PET imaging, however, the head of the pancreas, in particular the uncinate process, may exhibit a variable physiologic uptake of ^{68}Ga-DOTA-peptides, related to the great concentration of pancreatic polypeptide cells [150]. This may represent a potential source of false-positive results that should not be ignored, since the pancreas and the duodenum are frequent sites of neuroendocrine malignancies. Other common non-NET-related sources of somatostatin receptor-mediated uptake (e.g., accessory spleens, sites of inflammation with lymphoid infiltrate, recent surgery, or urinary contamination) should be taken into consideration in the interpretation of the images (Fig. 21a–c).

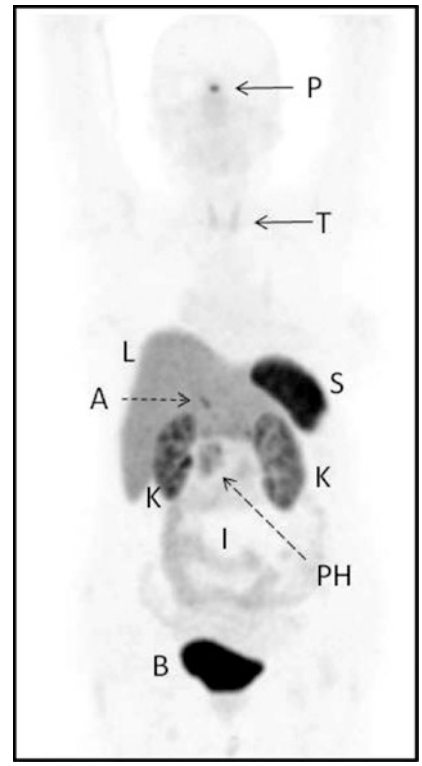

Fig. 18 Normal distribution of ^{68}Ga-DOTATOC (MIP, maximum intensity projection image) with physiological visualization of the pituitary (P), thyroid (T), liver (L), adrenals (A), kidneys (K), spleen (S), pancreatic head (PH) and of the elimination of the activity in the urinary bladder (B) and the intestine (I)

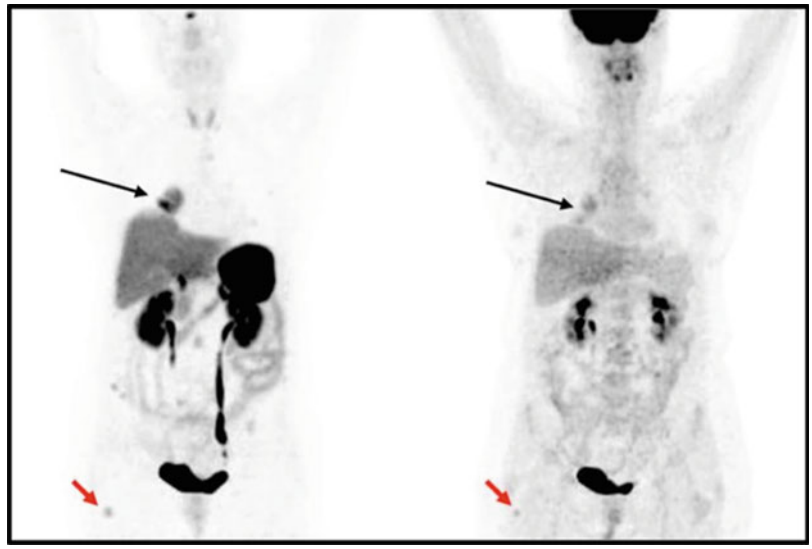

Fig. 19 ^{68}Ga-DOTATOC (*left*) and [^{18}F]FDG (*right*) PET/CT appearance of atypical bronchial carcinoid (*black arrows*). ^{68}Ga-DOTATOC maximum intensity projection image shows some bone metastases, while [^{18}F]FDG PET/CT detected only the one at the right femur (*red arrows*)

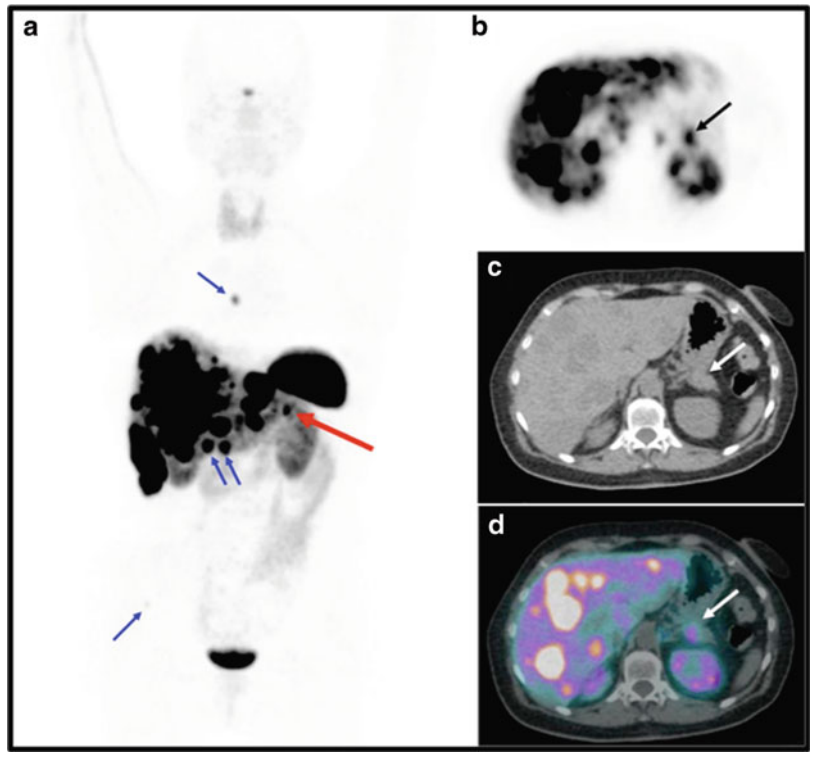

Fig. 20 Unknown primary NET with multiple liver lesions. ^{68}Ga-DOTATOC PET detected the primary tumor in the pancreatic tail (*red arrow* in **a**) and concomitant paracaval lymph nodes and bone metastases (*blue arrows* in **a**)

^{18}F-DOPA

NETs can be imaged with ^{18}F-DOPA PET/CT (Fig. 22). Oral co-administration of carbidopa, a peripheral inhibitor of AADC normally used in the treatment of Parkinson's disease, is routinely performed during ^{18}F-DOPA imaging to reduce the background activity, particularly in the pancreas, and to increase the tumor uptake and, ultimately, sensitivity [93]. Whole body imaging is initiated 30–90 min after injection of at least

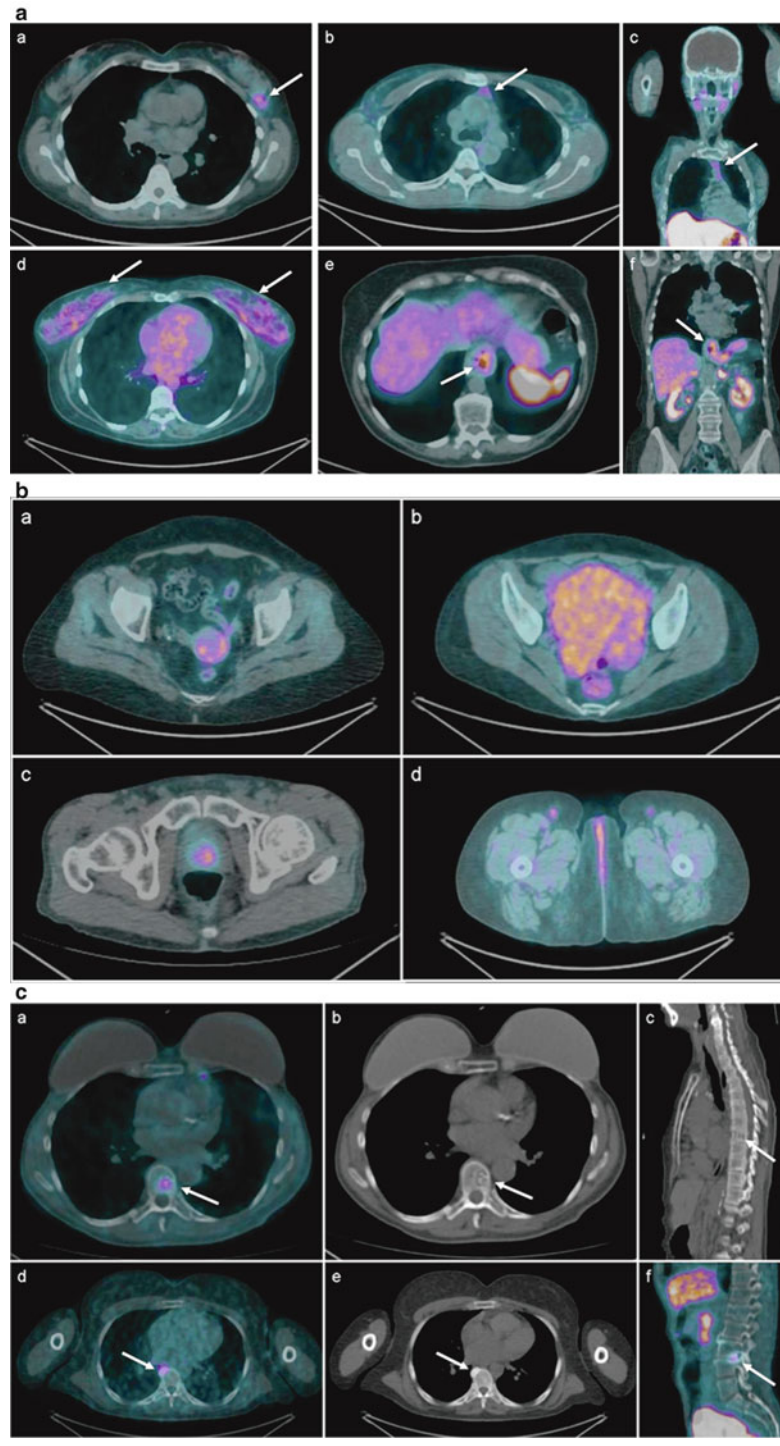

Fig. 21 Common non-NET-related findings at ^{68}Ga-DOTATOC PET/CT. **(A)** Common non-NET-related thoracic findings: Fused ^{68}Ga-DOTATOC PET/CT images of left breast fibroadenoma (*a*), breast physiologic radiotracer uptake (*d*), residual thymus (*b* and *c*), and hiatal hernia (*e* and *f*). **(B)** Common non-NET-related inguino-pelvic findings: fused ^{68}Ga-DOTATOC PET/CT images of physiologic radiotracer uptake in uterus and prostate (*a* and *c*, respectively), in uterus fibromatosis (*b*) and in reactive bilateral inguinal lymph nodes (*d*). **(C)** Common non-NET-related skeletal findings: ^{68}Ga-DOTATOC uptake in vertebral hemangioma (axial fused PET/CT, axial CT, and sagittal CT images *a*, *b*, and *c*, respectively), osteophyte (axial fused PET/CT and axial CT images *d* and *e*, respectively) and degenerative changes at L3–L4 passage (sagittal fused PET/CT image *f*)

100 MBq. Normal findings include the visualization of the kidneys, ureter, and bladder, with variable uptake in the gallbladder; intermediate uptake may be noted in the corpus striatum, myocardium, and liver and low uptake in the small intestine and muscles. There is also evidence of minimal uptake in the normal adrenal medulla [134].

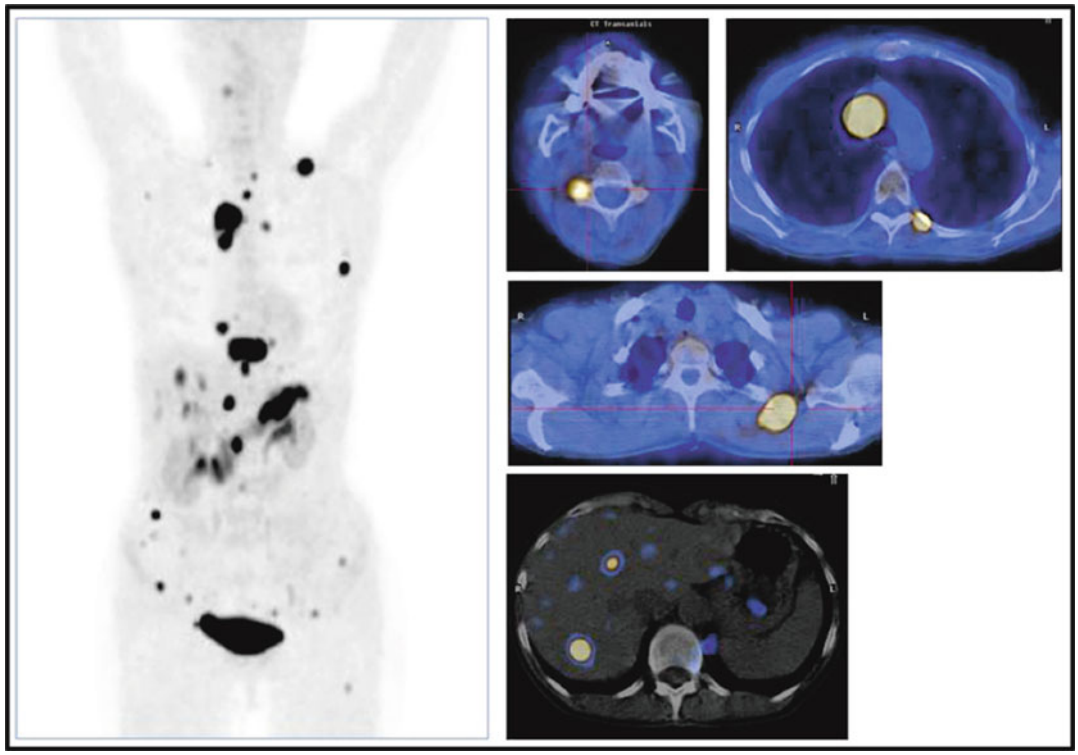

Fig. 22 ^{18}F-DOPA PET/CT in a patient affected by diffuse bone, lymph node, liver, and soft tissue metastases from a small bowel NEN (Courtesy of Prof. S. Fanti, University of Bologna)

[^{11}C]5-HTP

The serotonin precursor [^{11}C]5-HTP is used in some investigative centers to define the metabolism of the neuroendocrine cell and is thus considered a universal imaging method for NETs. Tomographic imaging is performed after intravenous injection of 370 MBq [92]. However, its widespread application is limited by the short half-life of ^{11}C, which requires an on-site cyclotron.

[^{18}F]FDG

For a detailed description of the scan methodology, reference should be made to the specific section on this subject.

References

1. Clark OH, Benson 3rd AB, Berlin JD, Choti MA, Doherty GM, Engstrom PF, et al. NCCN clinical practice guidelines in oncology: neuroendocrine tumors. J Natl Compr Cancer Netw: JNCCN. 2009;7(7):712–47.
2. Modlin IM, Oberg K, Chung DC, Jensen RT, de Herder WW, Thakker RV, et al. Gastroenteropancreatic neuroendocrine tumours. Lancet Oncol. 2008;9(1):61–72.
3. Duque M, Modlin IM, Gupta A, Saif MW. Biomarkers in neuroendocrine tumors. JOP: J Pancreas. 2013;14 (4):372–6.
4. Modlin IM, Drozdov I, Kidd M. The identification of gut neuroendocrine tumor disease by multiple synchronous transcript analysis in blood. PLoS ONE. 2013;8(5):e63364.
5. Kidd M, Drozdov I, Modlin I. Blood and tissue NET gene cluster analysis correlate, define Hallmarks and predict disease status. Endocr Relat Cancer. 2015;22 (4):561–75.
6. Wild D, Fani M, Fischer R, Del Pozzo L, Kaul F, Krebs S, et al. Comparison of somatostatin receptor agonist and antagonist for Peptide receptor

radionuclide therapy: a pilot study. J Nucl Med. 2014;55(8):1248–52.
7. Modlin IM, Latich I, Zikusoka M, Kidd M, Eick G, Chan AK. Gastrointestinal carcinoids: the evolution of diagnostic strategies. J Clin Gastroenterol. 2006;40 (7):572–82.
8. Gotthardt M, Dirkmorfeld LM, Wied MU, Rinke A, Behe MP, Schlieck A, et al. Influence of somatostatin receptor scintigraphy and CT/MRI on the clinical management of patients with gastrointestinal neuroendocrine tumors: an analysis in 188 patients. Digestion. 2003;68(2–3):80–5.
9. Oberg K. Diagnostic work-up of gastroenteropancreatic neuroendocrine tumors. Clinics (Sao Paulo). 2012;67 Suppl 1:109–12.
10. Sundin A. Radiological and nuclear medicine imaging of gastroenteropancreatic neuroendocrine tumours. Best Pract Res Clin Gastroenterol. 2012;26 (6):803–18.
11. Bodei L, Sundin A, Kidd M, Prasad V, Modlin IM. The status of neuroendocrine tumor imaging: from darkness to light? Neuroendocrinology. 2015;101(1):1–17.
12. Langley K. The neuroendocrine concept today. Ann N Y Acad Sci. 1994;733:1–17.
13. Pearse AG. The cytochemistry and ultrastructure of polypeptide hormone-producing cells of the APUD series and the embryologic, physiologic and pathologic implications of the concept. J Histochem Cytochem. 1969;17(5):303–13.
14. Kloppel G. Oberndorfer and his successors: from carcinoid to neuroendocrine carcinoma. Endocr Pathol. 2007;18(3):141–4.
15. Polak JM, Bloom SR. The diffuse neuroendocrine system. Studies of this newly discovered controlling system in health and disease. J Histochem Cytochem. 1979;27(10):1398–400.
16. Rehfeld JF. The new biology of gastrointestinal hormones. Physiol Rev. 1998;78(4):1087–108.
17. Polak JM, Bloom SR. Regulatory peptides of the gastrointestinal and respiratory tracts. Arch Int Pharmacodyn Ther. 1986;280(2 Suppl):16–49.
18. Metz DC, Jensen RT. Gastrointestinal neuroendocrine tumors: pancreatic endocrine tumors. Gastroenterology. 2008;135(5):1469–92.
19. Modlin IM, Lye KD, Kidd M. A 5-decade analysis of 13,715 carcinoid tumors. Cancer. 2003;97(4): 934–59.
20. The US National Cancer Institute, Surveillance Epidemiology and End Results (SEER) data base, 1973–2004. http://seer.cancer.gov/
21. Modlin IM, Champaneria MC, Chan AK, Kidd M. A three-decade analysis of 3,911 small intestinal neuroendocrine tumors: the rapid pace of no progress. Am J Gastroenterol. 2007;102(7):1464–73.
22. Berge T, Linell F. Carcinoid tumours. Frequency in a defined population during a 12-year period. Acta Pathol Microbiol Scand A Pathol. 1976;84(4): 322–30.
23. Gustafsson BI, Kidd M, Modlin IM. Neuroendocrine tumors of the diffuse neuroendocrine system. Curr Opin Oncol. 2008;20(1):1–12.
24. Beard CM, Sheps SG, Kurland LT, Carney JA, Lie JT. Occurrence of pheochromocytoma in Rochester, Minnesota, 1950 through 1979. Mayo Clin Proc. 1983;58(12):802–4.
25. Mittendorf EA, Evans DB, Lee JE, Perrier ND. Pheochromocytoma: advances in genetics, diagnosis, localization, and treatment. Hematol Oncol Clin North Am. 2007;21(3):509–25.
26. Williams ED, Sandler M. The classification of carcinoid tum ours. Lancet. 1963;1(7275):238–9.
27. DeLellis R, Lloyd R, Heitz P, editors EC. World Health Organization classification of tumours. Pathology and genetics of tumours of endocrine organs. Lyon: IARC Press; 2004.
28. Rorstad O. Prognostic indicators for carcinoid neuroendocrine tumors of the gastrointestinal tract. J Surg Oncol. 2005;89(3):151–60.
29. Hotta K, Shimoda T, Nakanishi Y, Saito D. Usefulness of Ki-67 for predicting the metastatic potential of rectal carcinoids. Pathol Int. 2006;56(10):591–6.
30. Ruszniewski P, Delle Fave G, Cadiot G, Komminoth P, Chung D, Kos-Kudla B, et al. Well-differentiated gastric tumors/carcinomas. Neuroendocrinology. 2006;84 (3):158–64.
31. Rindi G, Kloppel G, Couvelard A, Komminoth P, Korner M, Lopes JM, et al. TNM staging of midgut and hindgut (neuro) endocrine tumors: a consensus proposal including a grading system. Virchows Arch Int J Pathol. 2007;451(4):757–62.
32. Rindi G. The ENETS guidelines: the new TNM classification system. Tumori. 2010;96(5):806–9.
33. Bosman FT. WHO classification of tumours of the digestive system. 4th ed. Lyon: IARC Press; 2010.
34. Kloppel G, Couvelard A, Perren A, Komminoth P, McNicol AM, Nilsson O, et al. ENETS consensus guidelines for the standards of care in neuroendocrine tumors: towards a standardized approach to the diagnosis of gastroenteropancreatic neuroendocrine tumors and their prognostic stratification. Neuroendocrinology. 2009;90(2):162–6.
35. Scholzen T, Gerdes J. The Ki-67 protein: from the known and the unknown. J Cell Physiol. 2000;182 (3):311–22.
36. MacCallum DE, Hall PA. The location of pKi67 in the outer dense fibrillary compartment of the nucleolus points to a role in ribosome biogenesis during the cell division cycle. J Pathol. 2000;190(5):537–44.
37. Klimstra DS, Modlin IR, Adsay NV, Chetty R, Deshpande V, Gonen M, et al. Pathology reporting of neuroendocrine tumors: application of the Delphic consensus process to the development of a minimum pathology data set. Am J Surg Pathol. 2010;34 (3):300–13.
38. Bajetta E, Catena L, Procopio G, Bichisao E, Ferrari L, Della Torre S, et al. Is the new WHO classification of neuroendocrine tumours useful for

selecting an appropriate treatment? Ann Oncol. 2005;16(8):1374–80.
39. Beasley MB, Brambilla E, Travis WD. The 2004 World Health Organization classification of lung tumors. Semin Roentgenol. 2005;40(2):90–7.
40. Travis WD, Colby TV, Corrin B, Shimosato Y, Brambilla E. Histological classification of lung and pleural tumours, Histological typing of lung and pleural tumours. Berlin/Heidelberg: Springer; 1999. p. 21–4.
41. Rindi G, Klersy C, Inzani F, Fellegara G, Ampollini L, Ardizzoni A, et al. Grading the neuroendocrine tumors of the lung: an evidence-based proposal. Endocr Relat Cancer. 2014;21(1):1–16.
42. Caplin ME, Baudin E, Ferolla P, Filosso P, Garcia-Yuste M, Lim E, et al. Pulmonary neuroendocrine (carcinoid) tumors: European Neuroendocrine Tumor Society expert consensus and recommendations for best practice for typical and atypical pulmonary carcinoids. Ann Oncol. 2015;26(8):1604–20.
43. Favier J, Amar L, Gimenez-Roqueplo AP. Paraganglioma and phaeochromocytoma: from genetics to personalized medicine. Nat Rev Endocrinol. 2015;11(2):101–11.
44. Goldstein RE, O'Neill Jr JA, Holcomb 3rd GW, Morgan 3rd WM, Neblett 3rd WW, Oates JA, et al. Clinical experience over 48 years with pheochromocytoma. Ann Surg. 1999;229(6):755–64. discussion 64–6.
45. Wu D, Tischler AS, Lloyd RV, DeLellis RA, de Krijger R, van Nederveen F, et al. Observer variation in the application of the pheochromocytoma of the Adrenal Gland Scaled Score. Am J Surg Pathol. 2009;33(4):599–608.
46. Ilias I, Pacak K. A clinical overview of pheochromocytomas/paragangliomas and carcinoid tumors. Nucl Med Biol. 2008;35 Suppl 1:S27–34.
47. Benn DE, Robinson BG, Clifton-Bligh RJ. 15 years of paraganglioma: clinical manifestations of paraganglioma syndromes types 1–5. Endocr Relat Cancer. 2015;22(4):T91–103.
48. Amar L, Bertherat J, Baudin E, Ajzenberg C, Bressac-de Paillerets B, Chabre O, et al. Genetic testing in pheochromocytoma or functional paraganglioma. J Clin Oncol. 2005;23(34):8812–8.
49. Brouwers FM, Eisenhofer G, Tao JJ, Kant JA, Adams KT, Linehan WM, et al. High frequency of SDHB germline mutations in patients with malignant catecholamine-producing paragangliomas: implications for genetic testing. J Clin Endocrinol Metab. 2006;91(11):4505–9.
50. Chrisoulidou A, Kaltsas G, Ilias I, Grossman AB. The diagnosis and management of malignant phaeochromocytoma and paraganglioma. Endocr Relat Cancer. 2007;14(3):569–85.
51. Elder EE, Elder G, Larsson C. Pheochromocytoma and functional paraganglioma syndrome: no longer the 10% tumor. J Surg Oncol. 2005;89(3):193–201.
52. Faiss S, Scherübl H, Riecken EO, Wiedenmann B. Drug therapy in metastatic neuroendocrine tumors of the gastroenteropancreatic system. In: Kreuser E-D, Schlag PM, editors. New perspectives in molecular and clinical management of gastrointestinal tumors. Berlin/Heidelberg: Springer; 1996. p. 193–207.
53. Sundin A, Vullierme MP, Kaltsas G, Plockinger U, Mallorca Consensus Conference Participants, European Neuroendocrine Tumor Society. ENETS consensus guidelines for the standards of care in neuroendocrine tumors: radiological examinations. Neuroendocrinology. 2009;90(2):167–83.
54. Pahlavan PS, Kanthan R. Goblet cell carcinoid of the appendix. World J Surg Oncol. 2005;3:36.
55. Daddi N, Urbani M, Semeraro A, Capozzi R, Scarpelli G, Avenia N, et al. Surgical treatment of well differentiated neuroendocrine tumours of the lung. G Chir. 2008;29(5):246–9.
56. Ferolla P, Faggiano A, Avenia N, Milone F, Masone S, Giampaglia F, et al. Epidemiology of non-gastroenteropancreatic (neuro)endocrine tumours. Clin Endocrinol. 2007;66(1):1–6.
57. Fink G, Krelbaum T, Yellin A, Bendayan D, Saute M, Glazer M, et al. Pulmonary carcinoid: presentation, diagnosis, and outcome in 142 cases in Israel and review of 640 cases from the literature. Chest. 2001;119(6):1647–51.
58. Lenders JW, Eisenhofer G, Mannelli M, Pacak K. Phaeochromocytoma. Lancet. 2005;366(9486):665–75.
59. Oberg K. Circulating biomarkers in gastroenteropancreatic neuroendocrine tumours. Endocr Relat Cancer. 2011;18 Suppl 1:S17–25.
60. Modlin IM, Kidd M, Bodei L, Drozdov I, Aslanian H. The clinical utility of a novel blood-based multi-transcriptome assay for the diagnosis of neuroendocrine tumors of the gastrointestinal tract. Am J Gastroenterol. 2015;110(8):1223–32.
61. Modlin IM, Gustafsson BI, Moss SF, Pavel M, Tsolakis AV, Kidd M. Chromogranin A – biological function and clinical utility in neuro endocrine tumor disease. Ann Surg Oncol. 2010;17(9):2427–43.
62. Nobels FR, Kwekkeboom DJ, Coopmans W, Schoenmakers CH, Lindemans J, De Herder WW, et al. Chromogranin A as serum marker for neuroendocrine neoplasia: comparison with neuron-specific enolase and the alpha-subunit of glycoprotein hormones. J Clin Endocrinol Metab. 1997;82(8):2622–8.
63. Oberg K, Modlin IM, de Herder WW, Pavel M, Klimstra DS, Frilling A, et al. Biomarkers for neuroendocrine tumor disease: a Delphic Consensus assessment of multianalytes, genomics, circulating cells and monoanalytes. Lancet Oncol. 2015;16(9):e435–46.
64. Kidd M, Drozdov I, Modlin I. Blood and tissue neuroendocrine tumor gene cluster analysis correlate, define hallmarks and predict disease status. Endocr Relat Cancer. 2015;22(4):561–75.
65. Walenkamp A, Crespo G, Fierro Maya F, Fossmark R, Igaz P, Rinke A, et al. Hallmarks of gastrointestinal

neuroendocrine tumours: implications for treatment. Endocr Relat Cancer. 2014;21(6):R445–60.
66. Li SC, Essaghir A, Martijn C, Lloyd RV, Demoulin JB, Oberg K, et al. Global microRNA profiling of well-differentiated small intestinal neuroendocrine tumors. Mod Pathol. 2013;26(5):685–96.
67. Modlin I, Kidd M, Drozdov I, Aslanian H, Alaimo D, Callahan S et al., editors. A PCR-Based multigene transcript analysis blood test outperforms Chromogranin A in the detection of gastrointestinal and pancreatic neuroendocrine tumors and is unaffected by PPI use or hypertension. Neuroendocrinology: Karger Allschwilerstrasse 10, CH-4009, Basel, Switzerland; 2014.
68. Modlin IM, Frilling A, Salem RR, Alaimo D, Drymousis P, Wasan HS, et al. Blood measurement of neuroendocrine gene transcripts defines the effectiveness of operative resection and ablation strategies. Surgery. 2016;159(1):336–47.
69. Cwikla JB, Bodei L, Kolasinska-Cwikla A, Sankowski A, Modlin IM, Kidd M. Circulating transcript analysis (NETest) in GEP-NETs treated with somatostatin analogs defines therapy. J Clin Endocrinol Metab. 2015;100(11):E1437–45.
70. Bodei L, Kidd M, Modlin IM, Prasad V, Severi S, Ambrosini V, et al. Gene transcript analysis blood values correlate with Ga-DOTA-somatostatin analog (SSA) PET/CT imaging in neuroendocrine tumors and can define disease status. Eur J Nucl Med Mol Imaging. 2016;43(5):839–51.
71. Pavel M, Jann H, Prasad V, Drozdov I, Modlin IM, Kidd M. NET blood transcript analysis defines the crossing of the clinical rubicon: when stable disease becomes progressive. Neuroendocrinology. 2017;104 (2):170–182.
72. Grossman A, Pacak K, Sawka A, Lenders JW, Harlander D, Peaston RT, et al. Biochemical diagnosis and localization of pheochromocytoma: can we reach a consensus? Ann N Y Acad Sci. 2006;1073:332–47.
73. Boomsma F, Bhaggoe UM, Man in 't Veld AJ, Schalekamp MADH. Sensitivity and specificity of a new ELISA method for determination of chromogranin A in the diagnosis of pheochromocytoma and neuroblastoma. Clin Chim Acta. 1995;239 (1):57–63.
74. Eisenhofer G, Goldstein DS, Walther MM, Friberg P, Lenders JW, Keiser HR, et al. Biochemical diagnosis of pheochromocytoma: how to distinguish true- from false-positive test results. J Clin Endocrinol Metab. 2003;88(6):2656–66.
75. Darr R, Pamporaki C, Peitzsch M, Miehle K, Prejbisz A, Peczkowska M, et al. Biochemical diagnosis of phaeochromocytoma using plasma-free normetanephrine, metanephrine and methoxytyramine: importance of supine sampling under fasting conditions. Clin Endocrinol. 2014;80 (4):478–86.
76. Ichikawa T, Peterson MS, Federle MP, Baron RL, Haradome H, Kawamori Y, et al. Islet cell tumor of the pancreas: biphasic CT versus MR imaging in tumor detection. Radiology. 2000;216(1):163–71.
77. Rappeport ED, Hansen CP, Kjaer A, Knigge U. Multidetector computed tomography and neuroendocrine pancreaticoduodenal tumors. Acta Radiol. 2006;47(3):248–56.
78. Sahani DV, Bonaffini PA, Fernandez-Del Castillo C, Blake MA. Gastroenteropancreatic neuroendocrine tumors: role of imaging in diagnosis and management. Radiology. 2013;266(1):38–61.
79. Khashab MA, Yong E, Lennon AM, Shin EJ, Amateau S, Hruban RH, et al. EUS is still superior to multidetector computerized tomography for detection of pancreatic neuroendocrine tumors. Gastrointest Endosc. 2011;73(4):691–6.
80. Johanssen S, Boivin M, Lochs H, Voderholzer W. The yield of wireless capsule endoscopy in the detection of neuroendocrine tumors in comparison with CT enteroclysis. Gastrointest Endosc. 2006;63(4):660–5.
81. Kamaoui I, De-Luca V, Ficarelli S, Mennesson N, Lombard-Bohas C, Pilleul F. Value of CT enteroclysis in suspected small-bowel carcinoid tumors. AJR Am J Roentgenol. 2010;194(3):629–33.
82. Van Weyenberg SJ, Meijerink MR, Jacobs MA, Van der Peet DL, Van Kuijk C, Mulder CJ, et al. MR enteroclysis in the diagnosis of small-bowel neoplasms. Radiology. 2010;254(3):765–73.
83. Masselli G, Polettini E, Casciani E, Bertini L, Vecchioli A, Gualdi G. Small-bowel neoplasms: prospective evaluation of MR enteroclysis. Radiology. 2009;251(3):743–50.
84. Buetow PC, Parrino TV, Buck JL, Pantongrag-Brown L, Ros PR, Dachman AH, et al. Islet cell tumors of the pancreas: pathologic-imaging correlation among size, necrosis and cysts, calcification, malignant behavior, and functional status. AJR Am J Roentgenol. 1995;165(5):1175–9.
85. Kim SH, Lee JM, Lee JY, Han JK, Choi BI. Contrast-enhanced sonography of intrapancreatic accessory spleen in six patients. AJR Am J Roentgenol. 2007;188(2):422–8.
86. Buckley JA, Jones B, Fishman EK. Small bowel cancer. Imaging features and staging. Radiol Clin North Am. 1997;35(2):381–402.
87. Horton KM, Kamel I, Hofmann L, Fishman EK. Carcinoid tumors of the small bowel: a multitechnique imaging approach. AJR Am J Roentgenol. 2004;182 (3):559–67.
88. Seigel RS, Kuhns LR, Borlaza GS, McCormick TL, Simmons JL. Computed tomography and angiography in ileal carcinoid tumor and retractile mesenteritis. Radiology. 1980;134(2):437–40.
89. Ilias I, Pacak K. Current approaches and recommended algorithm for the diagnostic localization of pheochromocytoma. J Clin Endocrinol Metab. 2004;89(2): 479–91.
90. Kwekkeboom DJ, Kam BL, van Essen M, Teunissen JJ, van Eijck CH, Valkema R, et al. Somatostatin-receptor-based imaging and therapy of

gastroenteropancreatic neuroendocrine tumors. Endocr Relat Cancer. 2010;17(1):R53–73.
91. Reubi JC, Schar JC, Waser B, Wenger S, Heppeler A, Schmitt JS, et al. Affinity profiles for human somatostatin receptor subtypes SST1-SST5 of somatostatin radiotracers selected for scintigraphic and radiotherapeutic use. Eur J Nucl Med. 2000;27(3): 273–82.
92. Orlefors H, Sundin A, Garske U, Juhlin C, Oberg K, Skogseid B, et al. Whole-body ^{11}C-5-hydroxytryptophan positron emission tomography as a universal imaging technique for neuroendocrine tumors: comparison with somatostatin receptor scintigraphy and computed tomography. J Clin Endocrinol Metab. 2005;90(6):3392–400.
93. Koopmans KP, de Vries EG, Kema IP, Elsinga PH, Neels OC, Sluiter WJ, et al. Staging of carcinoid tumours with ^{18}F-DOPA PET: a prospective, diagnostic accuracy study. Lancet Oncol. 2006;7(9):728–34.
94. Wafelman AR, Hoefnagel CA, Maes RA, Beijnen JH. Radioiodinated metaiodobenzylguanidine: a review of its biodistribution and pharmacokinetics, drug interactions, cytotoxicity and dosimetry. Eur J Nucl Med. 1994;21(6):545–59.
95. Solanki KK, Bomanji J, Moyes J, Mather SJ, Trainer PJ, Britton KE. A pharmacological guide to medicines which interfere with the biodistribution of radiolabelled meta-iodobenzylguanidine (MIBG). Nucl Med Commun. 1992;13(7):513–21.
96. Bombardieri E, Aktolun C, Baum RP, Bishof-Delaloye A, Buscombe J, Chatal JF, et al. ^{131}I/^{123}I-metaiodobenzylguanidine (MIBG) scintigraphy: procedure guidelines for tumour imaging. Eur J Nucl Med Mol Imaging. 2003;30(12):Bp132–9.
97. Mankoff DA, Eary JF, Link JM, Muzi M, Rajendran JG, Spence AM, et al. Tumor-specific positron emission tomography imaging in patients: [^{18}F] fluorodeoxyglucose and beyond. Clin Cancer Res. 2007;13(12):3460–9.
98. Gibril F, Reynolds JC, Doppman JL, Chen CC, Venzon DJ, Termanini B, et al. Somatostatin receptor scintigraphy: its sensitivity compared with that of other imaging methods in detecting primary and metastatic gastrinomas. A prospective study. Ann Intern Med. 1996;125(1):26–34.
99. Chiti A, Fanti S, Savelli G, Romeo A, Bellanova B, Rodari M, et al. Comparison of somatostatin receptor imaging, computed tomography and ultrasound in the clinical management of neuroendocrine gastro-entero-pancreatic tumours. Eur J Nucl Med. 1998;25 (10):1396–403.
100. Krausz Y, Keidar Z, Kogan I, Even-Sapir E, Bar-Shalom R, Engel A, et al. SPECT/CT hybrid imaging with ^{111}In-pentetreotide in assessment of neuroendocrine tumours. Clin Endocrinol. 2003;59 (5):565–73.
101. Krenning EP, Kwekkeboom DJ, Bakker WH, Breeman WA, Kooij PP, Oei HY, et al. Somatostatin receptor scintigraphy with [^{111}In-DTPA-D-Phe^{1}]- and [^{123}I-Tyr^{3}]-octreotide: the Rotterdam experience with more than 1000 patients. Eur J Nucl Med. 1993;20 (8):716–31.
102. Parisella MG, Chianelli M, D'Alessandria C, Todino V, Mikolajczak R, Papini E, et al. Clinical indications to the use of ^{99m}Tc-EDDA/HYNIC-TOC to detect somatostatin receptor-positive neuroendocrine tumors. Q J Nucl Med Mol Imaging. 2012;56 (1):90–8.
103. Teunissen JJ, Kwekkeboom DJ, Valkema R, Krenning EP. Nuclear medicine techniques for the imaging and treatment of neuroendocrine tumours. Endocr Relat Cancer. 2011;18 Suppl 1:S27–51.
104. Schillaci O, Spanu A, Scopinaro F, Falchi A, Danieli R, Marongiu P, et al. Somatostatin receptor scintigraphy in liver metastasis detection from gastroenteropancreatic neuroendocrine tumors. J Nucl Med. 2003;44(3):359–68.
105. Perri M, Erba P, Volterrani D, Lazzeri E, Boni G, Grosso M, et al. Octreo-SPECT/CT imaging for accurate detection and localization of suspected neuroendocrine tumors. Q J Nucl Med Mol Imaging. 2008;52 (4):323–33.
106. Gabriel M, Decristoforo C, Kendler D, Dobrozemsky G, Heute D, Uprimny C, et al. ^{68}Ga-DOTA-Tyr^{3}-Octreotide PET in neuroendocrine tumors: comparison with somatostatin receptor scintigraphy and CT. J Nucl Med. 2007;48(4):508–18.
107. de Mestier L, Dromain C, d'Assignies G, Scoazec JY, Lassau N, Lebtahi R, et al. Evaluating digestive neuroendocrine tumor progression and therapeutic responses in the era of targeted therapies: state of the art. Endocr Relat Cancer. 2014;21(3):R105–20.
108. Gopinath G, Ahmed A, Buscombe JR, Dickson JC, Caplin ME, Hilson AJ. Prediction of clinical outcome in treated neuroendocrine tumours of carcinoid type using functional volumes on ^{111}In-pentetreotide SPECT imaging. Nucl Med Commun. 2004;25(3): 253–7.
109. Kumar A, Jindal T, Dutta R, Kumar R. Functional imaging in differentiating bronchial masses: an initial experience with a combination of ^{18}F-FDG PET-CT scan and ^{68}Ga DOTA-TOC PET-CT scan. Ann Nucl Med. 2009;23(8):745–51.
110. Tsagarakis S, Christoforaki M, Giannopoulou H, Rondogianni F, Housianakou I, Malagari C, et al. A reappraisal of the utility of somatostatin receptor scintigraphy in patients with ectopic adrenocorticotropin Cushing's syndrome. J Clin Endocrinol Metab. 2003;88(10):4754–8.
111. Rodriguez JA, Meyers MO, Jacome TH, Failla P, Harrison Jr LH. Intraoperative detection of a bronchial carcinoid with a radiolabeled somatostatin analog. Chest. 2002;121(3):985–8.
112. Bombardieri E, Ambrosini V, Aktolun C, Baum RP, Bishof-Delaloye A, Del Vecchio S, et al. ^{111}In-pentetreotide scintigraphy: procedure guidelines for tumour imaging. Eur J Nucl Med Mol Imaging. 2010;37(7):1441–8.

113. Cecchin D, Lumachi F, Marzola MC, Opocher G, Scaroni C, Zucchetta P, et al. A meta-iodobenzylguanidine scintigraphic scoring system increases accuracy in the diagnostic management of pheochromocytoma. Endocr Relat Cancer. 2006;13 (2):525–33.
114. Furuta N, Kiyota H, Yoshigoe F, Hasegawa N, Ohishi Y. Diagnosis of pheochromocytoma using [^{123}I]-compared with [^{131}I]-metaiodobenzylguanidine scintigraphy. Int J Urol: Off J Jpn Urol Assoc. 1999;6 (3):119–24.
115. Nakatani T, Hayama T, Uchida J, Nakamura K, Takemoto Y, Sugimura K. Diagnostic localization of extra-adrenal pheochromocytoma: comparison of ^{123}I-MIBG imaging and ^{131}I-MIBG imaging. Oncol Rep. 2002;9(6):1225–7.
116. Lynn MD, Shapiro B, Sisson JC, Beierwaltes WH, Meyers LJ, Ackerman R, et al. Pheochromocytoma and the normal adrenal medulla: improved visualization with I-123 MIBG scintigraphy. Radiology. 1985;155 (3):789–92.
117. Janssen I, Chen CC, Millo CM, Ling A, Taieb D, Lin FI, et al. PET/CT comparing ^{68}Ga-DOTATATE and other radiopharmaceuticals and in comparison with CT/MRI for the localization of sporadic metastatic pheochromocytoma and paraganglioma. Eur J Nucl Med Mol Imaging. 2016;43(10):1784–91.
118. Sisson JC, Shapiro B, Beierwaltes WH, Glowniak JV, Nakajo M, Mangner TJ, et al. Radiopharmaceutical treatment of malignant pheochromocytoma. J Nucl Med. 1984;25(2):197–206.
119. Guller U, Turek J, Eubanks S, Delong ER, Oertli D, Feldman JM. Detecting pheochromocytoma: defining the most sensitive test. Ann Surg. 2006;243(1):102–7.
120. Bhatia KSS, Ismail MM, Sahdev A, Rockall AG, Hogarth K, Canizales A, et al. ^{123}I-metaiodobenzylguanidine (MIBG) scintigraphy for the detection of adrenal and extra-adrenal phaeochromocytomas: CT and MRI correlation. Clin Endocrinol. 2008;69(2):181–8.
121. Milardovic R, Corssmit EP, Stokkel M. Value of ^{123}I-MIBG scintigraphy in paraganglioma. Neuroendocrinology. 2010;91(1):94–100.
122. Vallabhajosula S, Nikolopoulou A. Radioiodinated metaiodobenzylguanidine (MIBG): radiochemistry, biology, and pharmacology. Semin Nucl Med. 2011;41(5):324–33.
123. Rufini V, Calcagni ML, Baum RP. Imaging of neuroendocrine tumors. Semin Nucl Med. 2006;36 (3):228–47.
124. Rozovsky K, Koplewitz BZ, Krausz Y, Revel-Vilk S, Weintraub M, Chisin R, et al. Added value of SPECT/CT for correlation of MIBG scintigraphy and diagnostic CT in neuroblastoma and pheochromocytoma. AJR Am J Roentgenol. 2008;190 (4):1085–90.
125. Hofmann M, Maecke H, Borner R, Weckesser E, Schoffski P, Oei L, et al. Biokinetics and imaging with the somatostatin receptor PET radioligand ^{68}Ga-DOTATOC: preliminary data. Eur J Nucl Med. 2001;28(12):1751–7.
126. Al-Nahhas A, Fanti S. Radiolabelled peptides in diagnosis and therapy: an introduction. Eur J Nucl Med Mol Imaging. 2012;39 Suppl 1:S1–3.
127. Treglia G, Castaldi P, Rindi G, Giordano A, Rufini V. Diagnostic performance of Gallium-68 somatostatin receptor PET and PET/CT in patients with thoracic and gastroenteropancreatic neuroendocrine tumours: a meta-analysis. Endocrine. 2012;42(1):80–7.
128. Ambrosini V, Campana D, Tomassetti P, Fanti S. ^{68}Ga-labelled peptides for diagnosis of gastroenteropancreatic NET. Eur J Nucl Med Mol Imaging. 2012;39 Suppl 1:S52–60.
129. Srirajaskanthan R, Kayani I, Quigley AM, Soh J, Caplin ME, Bomanji J. The role of ^{68}Ga-DOTATATE PET in patients with neuroendocrine tumors and negative or equivocal findings on ^{111}In-DTPA-octreotide scintigraphy. J Nucl Med. 2010;51(6):875–82.
130. Pfeifer A, Knigge U, Binderup T, Mortensen J, Oturai P, Loft A, et al. ^{64}Cu-DOTATATE PET for neuroendocrine tumors: a prospective head-to-head comparison with ^{111}In-DTPA-octreotide in 112 patients. J Nucl Med. 2015.
131. Ambrosini V, Morigi JJ, Nanni C, Castellucci P, Fanti S. Current status of PET imaging of neuroendocrine tumours ([^{18}F]FDOPA, [^{68}Ga]tracers, [^{11}C]/[^{18}F]-HTP). Q J Nucl Med Mol Imaging. 2015;59(1):58–69.
132. Putzer D, Gabriel M, Henninger B, Kendler D, Uprimny C, Dobrozemsky G, et al. Bone metastases in patients with neuroendocrine tumor: ^{68}Ga-DOTA-Tyr^3-octreotide PET in comparison to CT and bone scintigraphy. J Nucl Med. 2009;50(8):1214–21.
133. Baumann T, Rottenburger C, Nicolas G, Wild D. Gastroenteropancreatic neuroendocrine tumours (GEP-NET) – imaging and staging. Best Pract Res Clin Endocrinol Metab. 2016;30(1):45–57.
134. Jager PL, Chirakal R, Marriott CJ, Brouwers AH, Koopmans KP, Gulenchyn KY. 6-L-^{18}F-fluorodihydroxyphenylalanine PET in neuroendocrine tumors: basic aspects and emerging clinical applications. J Nucl Med. 2008;49(4):573–86.
135. Ambrosini V, Tomassetti P, Castellucci P, Campana D, Montini G, Rubello D, et al. Comparison between ^{68}Ga-DOTA-NOC and ^{18}F-DOPA PET for the detection of gastro-entero-pancreatic and lung neuroendocrine tumours. Eur J Nucl Med Mol Imaging. 2008;35(8):1431–8.
136. Montravers F, Grahek D, Kerrou K, Ruszniewski P, de Beco V, Aide N, et al. Can fluorodihydroxyphenylalanine PET replace somatostatin receptor scintigraphy in patients with digestive endocrine tumors? J Nucl Med. 2006;47(9):1455–62.
137. Haug A, Auernhammer CJ, Wangler B, Tiling R, Schmidt G, Goke B, et al. Intraindividual comparison of ^{68}Ga-DOTA-TATE and ^{18}F-DOPA PET in patients with well-differentiated metastatic neuroendocrine tumours. Eur J Nucl Med Mol Imaging. 2009;36(5): 765–70.

138. Binderup T, Knigge U, Loft A, Mortensen J, Pfeifer A, Federspiel B, et al. Functional imaging of neuroendocrine tumors: a head-to-head comparison of somatostatin receptor scintigraphy, ^{123}I-MIBG scintigraphy, and ^{18}F-FDG PET. J Nucl Med. 2010;51(5):704–12.
139. Severi S, Nanni O, Bodei L, Sansovini M, Ianniello A, Nicoletti S, et al. Role of ^{18}FDG PET/CT in patients treated with ^{177}Lu-DOTATATE for advanced differentiated neuroendocrine tumours. Eur J Nucl Med Mol Imaging. 2013;40(6):881–8.
140. Binderup T, Knigge U, Loft A, Federspiel B, Kjaer A. ^{18}F-fluorodeoxyglucose positron emission tomography predicts survival of patients with neuroendocrine tumors. Clin Cancer Res. 2010;16(3):978–85.
141. Ezziddin S, Adler L, Sabet A, Poppel TD, Grabellus F, Yuce A, et al. Prognostic stratification of metastatic gastroenteropancreatic neuroendocrine neoplasms by ^{18}F-FDG PET: feasibility of a metabolic grading system. J Nucl Med. 2014.
142. Antwi K, Fani M, Nicolas G, Rottenburger C, Heye T, Reubi JC, et al. Localization of hidden insulinomas with ^{68}Ga-DOTA-Exendin-4 PET/CT: a pilot study. J Nucl Med. 2015;56(7):1075–8..
143. Ambrosini V, Castellucci P, Rubello D, Nanni C, Musto A, Allegri V, et al. ^{68}Ga-DOTA-NOC: a new PET tracer for evaluating patients with bronchial carcinoid. Nucl Med Commun. 2009;30(4):281–6.
144. Kayani I, Conry BG, Groves AM, Win T, Dickson J, Caplin M, et al. A comparison of ^{68}Ga-DOTATATE and ^{18}F-FDG PET/CT in pulmonary neuroendocrine tumors. J Nucl Med. 2009;50(12):1927–32.
145. Chong S, Lee KS, Chung MJ, Han J, Kwon OJ, Kim TS. Neuroendocrine tumors of the lung: clinical, pathologic, and imaging findings. Radiographics: Rev Publ Radiol Soc N Am Inc. 2006;26(1):41–57. discussion -8.
146. Pandit N, Gonen M, Krug L, Larson SM. Prognostic value of [^{18}F]FDG-PET imaging in small cell lung cancer. Eur J Nucl Med Mol Imaging. 2003;30(1):78–84.
147. Janssen I, Chen CC, Taieb D, Patronas NJ, Millo CM, Adams KT, et al. ^{68}Ga-DOTATATE PET/CT in the localization of head and neck paragangliomas compared with other functional imaging modalities and CT/MRI. J Nucl Med. 2016;57(2):186–91.
148. Poeppel TD, Binse I, Petersenn S, Lahner H, Schott M, Antoch G, et al. ^{68}Ga-DOTATOC versus ^{68}Ga-DOTATATE PET/CT in functional imaging of neuroendocrine tumors. J Nucl Med. 2011;52(12):1864–70.
149. Kabasakal L, Demirci E, Ocak M, Decristoforo C, Araman A, Ozsoy Y, et al. Comparison of ^{68}Ga-DOTATATE and ^{68}Ga-DOTANOC PET/CT imaging in the same patient group with neuroendocrine tumours. Eur J Nucl Med Mol Imaging. 2012;39(8):1271–7.
150. Virgolini I, Ambrosini V, Bomanji JB, Baum RP, Fanti S, Gabriel M, et al. Procedure guidelines for PET/CT tumour imaging with ^{68}Ga-DOTA-conjugated peptides: ^{68}Ga-DOTA-TOC, ^{68}Ga-DOTA-NOC, ^{68}Ga-DOTA-TATE. Eur J Nucl Med Mol Imaging. 2010;37(10):2004–10.
151. Bosman FT, Carneiro F, Hruban RH, et al. WHO classification of tumours of the digestive system. Lyon: IARC Press; 2010.
152. Travis WD, Brambilla E, Müller-Hermelink HK, Harris CC. Pathology and genetics: tumours of the lung, pleura, thymus and heart. Lyon: IARC; 2004.

Diagnostic Applications of Nuclear Medicine: Kidney and Bladder Cancer

30

Kirsten Bouchelouche

Abstract

Bladder cancer (BC) is the most common cancer in the urinary tract. It is a heterogeneous cancer, with 70% of patients presenting with superficial tumors which tend to recur but are generally not life threatening. Thirty percent present as muscle-invasive disease associated with a high risk of death from distant metastases. Renal cell carcinoma (RCC) is the most frequent type of kidney cancer in adults and the most lethal cancer in the urinary tract. It consists of three main histopathological RCC types, clear cell (65%), papillary (15–20%), and chromophobe (5%). There has been an important evolution in the understanding of the biology in both RCC and BC, which is important in cancer treatment strategies. Accurate imaging in both RCC and BC is still one of the mainstays of diagnosis, staging, and clinical management of the patients. The ability to identify metastatic disease preoperatively is of utmost importance in determining optimal treatment of the patient. The aim of this chapter, with focus on RCC and BC, is to give an overview of epidemiology of the tumors, environmental factors, genetic predisposition, underlying molecular biology changes, staging and prognostic stratification, overall performance of diagnostic imaging like computed tomography (CT) and magnetic resonance imaging (MRI) for the tumors, positron emission tomography (PET)/CT for staging/prognosis, and common therapies.

Keywords

Kidney cancer • Renal cell carcinoma • Bladder cancer • Urothelial cell carcinoma • PET/CT • Imaging

Glossary

[^{18}F]FDG	2-deoxy-2-[^{18}F]fluoro-D-glucose
^{18}F-FLT	^{18}F-Fluorothymidine
^{18}F-MISO	^{18}F-Fluoromisonidazole
5-FU	5-Fluorouracil
AJCC	American Joint Committee on Cancer
AUA	American Urological Association
BC	Bladder cancer
BCG	Bacillus Calmette-Guérin
CA	Cryoablation
CAIX	Carbonic anhydrase IX
ccRCC	Clear cell renal cell carcinoma
CEUS	Contrast-enhanced ultrasound
CI	Confidence interval
CIS	Carcinoma in situ
CSD	Cancer-specific death
CT	X-ray computed tomography
CTU	Computed tomography urography
DCE	Dynamic contrast-enhanced
DSS	Disease-specific survival
DW	Diffusion-weighted

K. Bouchelouche (✉)
Department of Nuclear Medicine and PET Centre, Aarhus University Hospital, Aarhus, Denmark
e-mail: kirsbouc@rm.dk

© Springer International Publishing Switzerland 2017
H.W. Strauss et al. (eds.), *Nuclear Oncology*,
https://doi.org/10.1007/978-3-319-26236-9_20

EAU	European Association of Urology
EBRT	External beam radiotherapy
EORTC	European Organisation for Research and Treatment of Cancer
FH	Gene encoding for fumarate hydratase (or fumarase)
FLCN	Gene encoding for the folliculin protein
FSP	Free survival progression
GLUT	Glucose transporter family
GSTM1	Gene encoding for glutathione S-transferase Mu 1
H&E	Hematoxylin and eosin
HIF	Hypoxia-inducible factor
HRAS	Gene encoding for the transforming protein p21
HU	Hounsfield units
IFN-α	Interferon-alpha
IL-2	Interleukin-2
ISUP	International Society of Urological Pathology
LN	Lymph node
LR	Likelihood ratio
mAb	Monoclonal antibody
MET	Gene encoding for a protein of the receptor tyrosine kinase family
mpMRI	Multiparametric MRI
MITF	Gene encoding for the melanogenesis associated transcription factor
MRI	Magnetic resonance imaging
MRVC	Magnetic resonance virtual cystoscopy
mTOR	Mammalian target of rapamycin
MVAC	Chemotherapy based on methotrexate, vinblastine, doxorubicin, and cisplatin
$Na^{18}F$	^{18}F-sodium fluoride
NAT2	Gene encoding for *N*-acetyltransferase 2 (or arylamine N-acetyltransferase)
NM	Lymph node metastasis
NPV	Negative predictive value
OS	Overall survival
PDGFR	Platelet-derived growth factor receptor
PET	Positron emission tomography
PET/CT	Positron emission tomography/Computed tomography
PET/MR	Integrated positron emission tomography/Magnetic resonance system
PFS	Progression-free survival
PLND	Pelvic lymph node dissection
PN	Partial nephrectomy
PPV	Positive predictive value
PS	Partial surgery
PTEN	Gene encoding for the phosphatase and tensin homolog protein
PTEN/MMAC1	Gene encoding for protein phosphatase
QF	Quality of life
RB1	Gene encoding for the retinoblastoma protein
RCC	Renal cell carcinoma
RECIST	Response evaluation criteria in solid tumors
RFA	Radiofrequency ablation
RFS	Recurrence-free survival
RN	Radical nephrectomy
RR	Response rate
SDH	Gene encoding for succinate dehydrogenase
SPECT/CT	Single-photon emission computed tomography/Computed tomography
TCC	Transitional cell carcinoma
TFE3	Gene encoding for the transcription factor E3
TFEB	Gene encoding for the transcription factor EB
TNM	AJCC staging system based on parameters "T" (tumor status), "N" (lymph node status), and "M" (distant metastasis status)
TS	Total survival
TSC	Tuberous sclerosis complex
TSC1	Gene encoding for the tuberous sclerosis 1 protein
TSC2	Gene encoding for the tuberous sclerosis 2 protein
TUR	Transurethral resection
TURB	Transurethral resection of bladder
UC	Urothelial carcinoma

UCB	Urothelial carcinoma of the bladder
US	Ultrasonography
UTUC	Upper tract urothelial carcinoma
VEGF	Vascular endothelial growth factor
VHL	von Hippel-Lindau
WHO	World Health organization

Contents

Introduction 841

Kidney Cancer 841
Epidemiology 841
Environmental and Genetic Factors 842
Symptoms and Diagnosis 844
Staging 845
Overall Performance of Diagnostic Imaging Other Than Nuclear Medicine for Kidney Cancer 846
[^{18}F]FDG PET/CT for Staging/Prognosis 849
PET Radiopharmaceuticals Other Than [^{18}F]FDG 853
Common Therapies 855

Bladder Cancer 857
Epidemiology of the Tumor 857
Environmental and Genetic Factors 858
Molecular Biology 861
Symptoms and Diagnosis 862
Staging and Prognostic Stratification 862
Overall Performance of Diagnostic Imaging Other Than Nuclear Medicine for the Tumor 863
[^{18}F]FDG PET/CT for Staging and Prognosis 865
PET Radiopharmaceuticals Other Than [^{18}F]FDG 868
Common Therapies 869

References 872

Introduction

In the urinary tract, bladder cancer (BC) is the most common cancer. Bladder cancer is a heterogeneous cancer, with 70% of patients presenting with superficial tumors, which tend to recur but are generally not life threatening, and 30% presenting as muscle-invasive disease associated with a high risk of death from distant metastases. A two-pathway model in BC has been proposed, taking into account both histopathological and molecular features. The main histological type in BC is urothelial carcinoma. Similar to BC, kidney cancer is not a single disease; it is made up of a number of different types of cancer, each with a different histology, a different clinical course, responding differently to therapy, and caused by a different gene. Renal cell carcinoma (RCC), the most frequent type of kidney cancer in adults and the most lethal cancer in the urinary tract, arises in the epithelium of the renal tubules and consists of three main histopathological entities. Clear cell RCC (ccRCC) is the dominant histology, accounting for approximately 65% of reported cases, followed by papillary and chromophobe RCC, accounting for approximately 15–20% and 5%, respectively [1]. Accurate imaging in both RCC and BC is one of the mainstays of diagnosis, staging, and therapeutic decision making. The ability to identify metastatic disease preoperatively is of utmost importance in determining treatment. The aim of this chapter, with focus on RCC and BC, is to give an overview of epidemiology of the tumors, environmental factors, genetic predisposition, underlying molecular biology changes, staging and prognostic stratification, overall performance of diagnostic imaging like computed tomography (CT) and magnetic resonance imaging (MRI) for the tumors, positron emission tomography (PET)/CT for staging/prognosis, and common therapies.

Kidney Cancer

Epidemiology

Kidney cancer was the 14th most frequently occurring cancer in women and the 9th most frequently occurring cancer in men worldwide in 2012 (Fig. 1). RCC is the most frequent type of kidney cancer in adults (>90% of cases) and accounts for 2–3% of all cancers in adults [2–4].

The incidence varies worldwide with the highest incidence in the developed countries (Fig. 2). Incidence worldwide is about 350,000 new cases per year and 140,000 deaths per year [3].

The incidence of RCC has steadily increased during the last three decades, with a trending

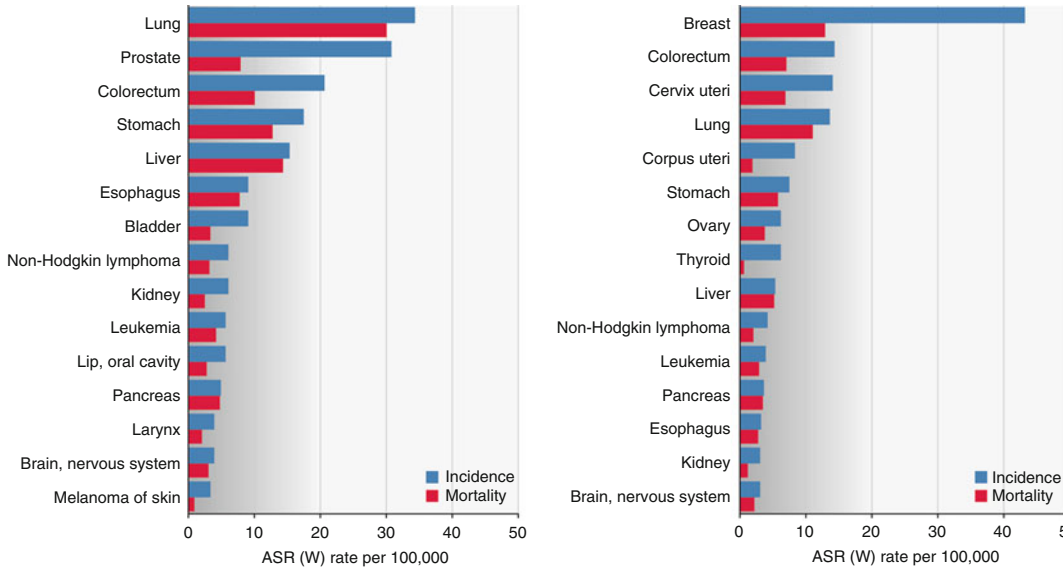

Fig. 1 Estimated age-standardized incidence and mortality rates in men (*left*) and women (*right*) (Reproduced from the public domain of the International Agency for Research on Cancer, GLOBOCAN database 2012, Cancer Incidence and Mortality Worldwide, available at http://globocan.iarc.fr)

increase in the incidence of this cancer by 2–3% per year [5]. However, in the same period, improvement in relative survival rates has been reported [3]. The factors contributing to this increase in incidence remain uncertain, but the widespread use of routine abdominal imaging and the detection of incidental, small solid renal tumors may contribute to this increase in incidence. Although most of the lesions in the kidneys detected incidentally are benign, up to 17% of the patients with RCC have distant metastases at the time of diagnosis [3]. RCC is a male-predominant (1.5:1.0 ratio) disease with a typical presentation in the sixth and seventh decades of life.

Environmental and Genetic Factors

Cigarette smoking and obesity are the strongest risk factors for RCC. Hypertension and family history also contribute to risk of disease [3]. As the world's population ages and the prevalence of risk factors (obesity, hypertension) increases, the burden of RCC is predicted to increase significantly. Classification of RCC has undergone dramatic changes over the past two decades. Improvements in these classification schemes are important, as pathologic variants differ not only in disease biology but also in clinical behavior, prognosis, and response to systemic therapy [6]. Each subtype harbors unique biology and thus responds differently to available treatment strategies. While RCC appears to arise from the nephron, different histological subtypes are believed to originate from different cells. Papillary and clear cell RCC (ccRCC) appear to arise from the proximal tubule, while oncocytoma and chromophobe tumors arise from the distal tubule [6]. The clear cell disease is so named because of the high lipid content in the cytoplasm which is dissolved during histological preparation methods leaving a clear cytoplasm. Clear cell RCC, papillary (types I and II), and chromophobe account for 85–90% of all renal malignancies (Fig. 3). The most common histological subtypes of RCC are clear cell (70–75%) and papillary (10–16%).

The International Society of Urological Pathology Vancouver Modification of WHO (2004) histological classification of kidney tumors is shown in Table 1.

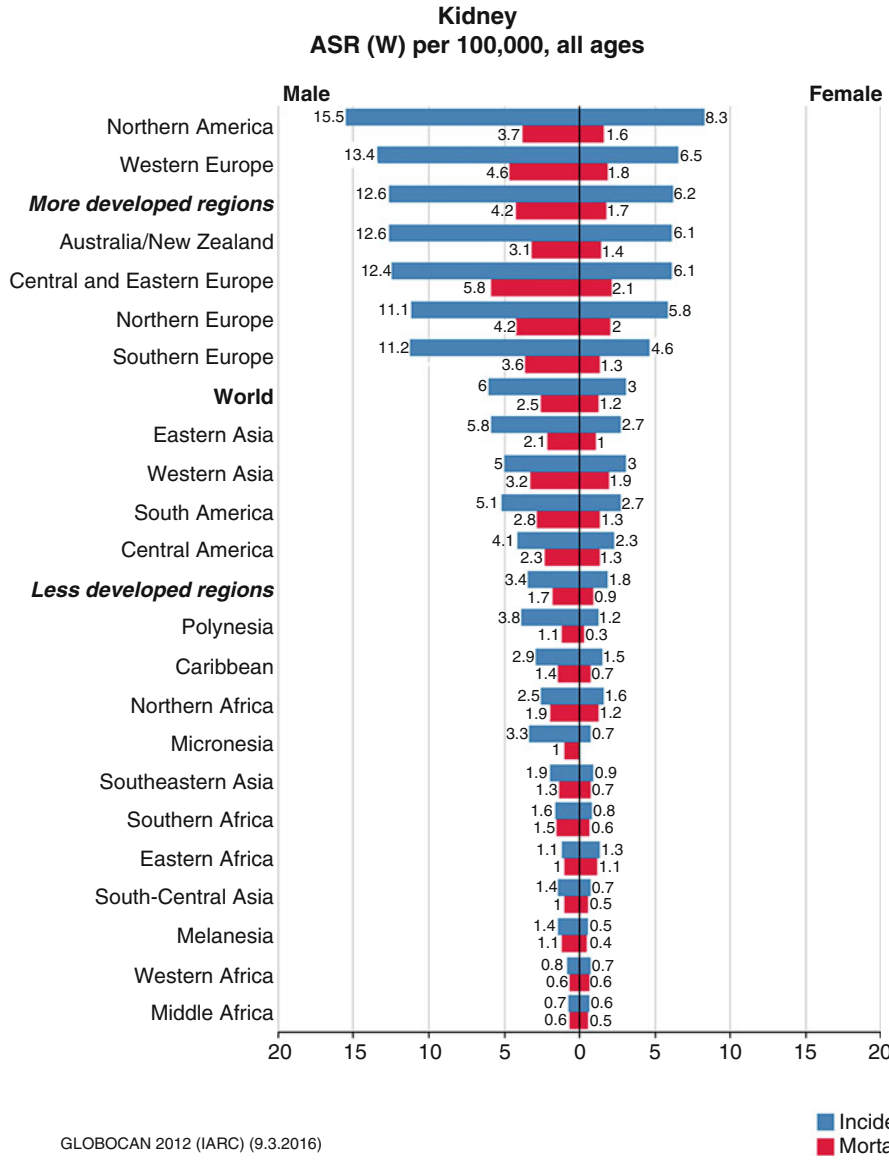

Fig. 2 Age-standardized incidence and mortality rates for kidney cancer by gender on different continents (Reproduced from the public domain of the International Agency for Research on Cancer, GLOBOCAN database 2012, Cancer Incidence and Mortality Worldwide, available at http://globocan.iarc.fr)

RCC can be sporadic or hereditary, and both types are often associated with structural alterations of chromosome 3 [3]. Familial RCC accounts for about 5% of cases of RCC. Most of these genetic conditions give rise to classic RCC subtypes, such as clear cell, papillary, and chromophobe tumors. Several autosomal dominant syndromes are described, each with a distinct genetic basis and phenotype [5]. Table 2 shows the hereditary RCC syndromes. The most common is von Hippel-Lindau (VHL) syndrome, which is characterized by the development of several vascular tumors, including ccRCC. The patients have a defect on one allele of the VHL

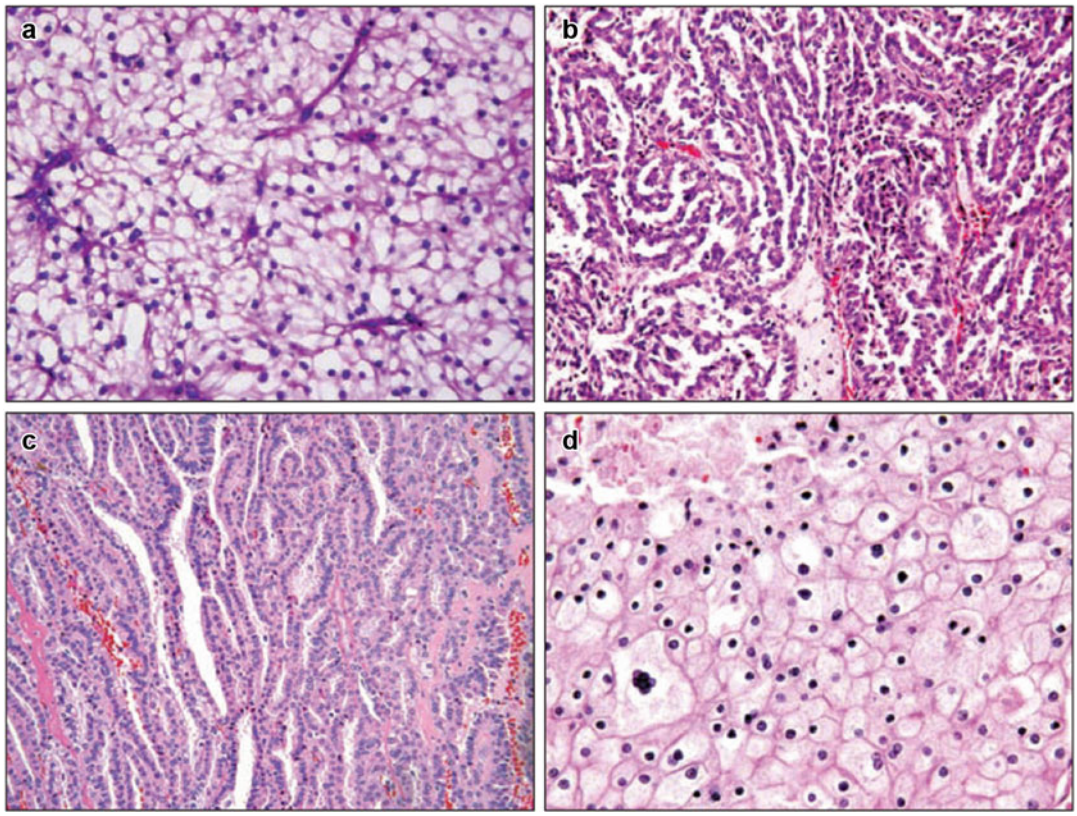

Fig. 3 Histopathological slides of renal cell carcinoma H&E staining. (**a**) Conventional ccRCC. Tumor shows large uniform cells with abundant cytoplasm that is rich in glycogen. (**b**) Papillary RCC type I. Tumor papillae are lined by short cuboidal cells with basophilic cytoplasm. Nuclei are small with few inconspicuous nucleoli. Collection of foamy histiocytes is present in middle of lower half of image. (**c**) Papillary RCC type II. Tumor shows papillae lined by columnar to pseudostratified cells that have striking eosinophilic cytoplasm. (**d**) Chromophobe RCC. Note sheet of tumor cells with focal necrosis (*upper left corner*). Tumor cells have abundant pale flocculent cytoplasm, prominent cell membranes, perinuclear halos, and wrinkled nuclei [7]

gene. Clear cell RCC in this syndrome tends to be early onset and multifocal. Most patients with sporadic (inherited) ccRCC have defects in both VHL alleles and dysfunction of the VHL protein [5]. In contrast, sporadic ccRCC tends to be late onset and unifocal. At least twelve well-studied genes are known to cause kidney cancer: VHL, MET, FLCN, fumarate hydratase, succinate dehydrogenase B, succinate dehydrogenase D, TFE3, TFEB, MITF, TSC1, TSC2, and PTEN. Each of these genes is involved in the cell's ability to sense oxygen, iron, nutrients, or energy; thus, it can be concluded that kidney cancer may fundamentally be a metabolic disease [8].

Symptoms and Diagnosis

RCC may remain clinically occult for most of its course. Symptoms usually do not appear until late, when the tumor may already be large and metastatic. The classic triad of flank pain, hematuria, and flank mass is uncommon (10%) and is indicative of advanced disease. Twenty-five to thirty percent of patients are asymptomatic, and their RCC is found on incidental imaging studies. The most common presentations are gross or microscopic hematuria (40%), flank pain (40%), and palpable mass in the flank or abdomen (25%). Only 30% of the patients are diagnosed on the basis of symptoms. RCC is a unique and

challenging tumor because of the frequent occurrence of paraneoplastic syndromes. The paraneoplastic events occur in 20% of patients and are largely related to secreted proteins, such as parathyroid hormone-related proteins (causing hypercalcemia), renin (causing hypertension), erythropoietin (causing erythrocytosis), and fever or wasting syndromes [5]. Prevalent use of ultrasonography and cross-sectional imaging is associated with increased incidental detection of many asymptomatic kidney tumors. Previously, biopsies of kidney tumors were not widely done due to concern about local tumor spread. The standard treatment was the removal of the kidney mass. The trend is now to perform a biopsy to establish the diagnosis of renal masses in patients that may be candidates for active surveillance and to select optimal targeted therapy in patients with metastatic disease [3]. Accuracy of biopsy for detecting malignancy is 38–100%. However, renal biopsies in the clinical management of renal masses are still underused.

Table 1 Renal cell tumors listed in the International Society of Urological Pathology Vancouver Modification [6]

ISUP Vancouver Modification of WHO (2004) histological classification of kidney tumors [8]
Renal cell tumors
Papillary adenoma
Oncocytoma
Clear cell RCC
Multilocular cystic cell of low malignant potential
Papillary RCC (types I and II)
Chromophobe RCC
Hybrid oncocytic/chromophobe tumor
Carcinoma of the collecting ducts of Bellini
Renal medullary carcinoma
MiT family translocation RCC [Xp11, t(6:11)]
Carcinoma associated with neuroblastoma
Mucinous tubular and spindle cell carcinoma
Clear cell tubulopapillary RCC
Hereditary leiomyomatosis RCC
RCC, unclassified

ISUP International Society of Urological Pathology, *MiT* microphthalmia transcription factor, *RCC* renal cell carcinoma, *WHO* World Health Organization

Staging

As in other malignant tumors, prognosis in RCC depends on tumor extent and metastases at the time of primary diagnosis. Since surgery is currently the only curative treatment for RCC, the prognosis greatly depends on the presurgical tumor stage. Therefore, preoperative imaging is most important for the planning of the surgical approach and strategy. The aim of any preoperative imaging in RCC is to differentiate benign from malignant lesions; to adequately assess tumor size, location, and organ

Table 2 Listing of known hereditary renal cell cancer syndromes [6]

Syndrome	Gene(s)	Chromosome location	Histology
von Hippel-Lindau syndrome	*VHL*	3p25	Clear cell
Hereditary papillary renal cell cancer	*MET*	7q31	Papillary type I
Hereditary leiomyomatosis and renal cancer	*FH*	1p42	Distinct from papillary type II
Birt-Hogg-Dubé syndrome	*FLCN*	17pp11	Hybrid oncocytic, chromophobe, oncocytoma
Tuberous sclerosis complex	*TSC1/2*	9q34/16p13	Clear cell, papillary, and chromophobe
Cowden syndrome	*PTEN*	10q23	Clear cell, papillary, and chromophobe
Hereditary pheochromocytoma and paraganglioma	*SDH B/C/D*	1p36/1q23/11q23	Clear cell, unclassified/eosinophilic variant
Chromosome 3 translocation renal cell	–	Translocations (3:6,3:8,3:11)	Clear cell
Unnamed	*MITF*	3p14	Not yet described

confinement; to identify lymph node (LN) and/or visceral metastases; and to reliably predict the presence and extent of any thrombus of the vena cava. There are two staging systems for RCC, both based on the degree of tumor spread beyond the kidney. The 40-year-old Robinson system is still used but has in most centers been replaced by the TNM staging system (Table 3), developed by the American Joint Committee on Cancer (AJCC) [5, 7, 9]. Furthermore, a clinical staging of RCC is used (Table 4) [7, 9].

Table 3 TNM staging of renal cell carcinoma [7]

Stage	Description
TX	Primary tumor cannot be assessed
T0	No evidence of primary tumor
T1	Tumor <7 cm in greatest dimension, limited to kidney
T1a	Tumor <4 cm in greatest dimension, limited to kidney
T1b	Tumor >4 cm but <7 cm in greatest dimension, limited to kidney
T2	Tumor ≥7 cm in greatest dimension, limited to kidney
T3	Tumor extends into major veins or invades adrenal gland or perinephric tissues, but not beyond Gerota's fascia
T3a	Tumor invades adrenal gland or perinephric tissues but not beyond Gerota's fascia
T3b	Tumor grossly extends into renal vein(s) or vena cava below diaphragm
T3c	Tumor grossly extends into vena cava above diaphragm
T4	Tumor invades beyond Gerota's fascia
NX	Regional lymph nodes cannot be assessed
N0	No regional lymph node metastasis
N1	Metastasis in a single regional lymph node
N2	Metastasis in more than one regional lymph node
MX	Distant metastasis cannot be assessed
M0	No distant metastasis
M1	Distant metastasis

Table 4 TNM groupings [7]

Stage grouping	T stage	N stage	M stage
I	T1	N0	M0
II	T2	N0	M0
III	T1	N1	M0
	T2	N1	M0
	T3	N0	M0
	T3	N1	M0
IV	T4	N0	M0
	T4	N1	M0
	Any T	N2	M0
	Any T	Any N	M1

Overall Performance of Diagnostic Imaging Other Than Nuclear Medicine for Kidney Cancer

The common utilization of abdominal ultrasound (US) or CT performed for other medical reasons has increased the number of incidentally detected renal tumors. Renal masses are classified as solid or cystic based on imaging findings. About 20% of masses are benign, 60% are probably indolent variants of RCC, and only 20% are potentially aggressive tumors [5, 9]. Important for differentiating malignant lesions is the presence of enhancement. US, CT, and MRI are used for detecting and characterizing renal masses, and most renal masses are diagnosed accurately by imaging alone. The aim of imaging is to characterize the renal mass and possible abdominal metastases, tumor extension, and venous involvement for staging. If malignant RCC is suspected, additional imaging is performed (i.e., CT of thorax, brain CT, total bone scan).

Ultrasound has been used for imaging of renal masses since it is easily repeatable, does not involve radiation exposure, and is cost-effective [10]. However, it requires operator experience, and the kidney cannot always be completely imaged, especially in large patients. Many RCCs are detected by abdominal US, but due to limitations in specificity and accuracy, it is necessary to use CT or MRI to confirm suspicious findings. US is inferior compared with CT, especially in smaller renal masses. The size of the lesions is an important factor. In lesions that are 0–5 mm, CT has a detection rate of 47%, as compared to US with a detection rate of 0 [11]. The detection rate increases with the size of the lesion. In lesions 10–35 mm, the detection rates are 80% and 82%, respectively [11]. US detection rate may be improved by the use of contrast-enhanced ultrasound (CEUS). A meta-analysis including 11 studies demonstrated that CEUS has a pooled

sensitivity of 88% and a pooled specificity of 80% for discriminating between malignant and benign renal masses [12]. However, microbubbles are not approved for use in the abdomen in many countries and thus are only of limited use. US may be used in patients undergoing radiofrequency ablation (RFA), and CEUS has demonstrated promising results in follow-up after RFA treatment [13].

Multislice CT has for many years been the gold standard for imaging of RCC and is widely used to differentiate benign from malignant lesions [14]. Renal oncocytoma and angiomyolipoma represent the most common benign lesions which have to be differentiated from RCC [14]. Imaging must be performed before and after administration of iodinated intravenous contrast medium to demonstrate enhancement. Enhancement with intravenous contrast correlates with malignant disease in about 80% of cases, although small renal tumors and those in young women are more likely to be benign [5]. Small ($\leq$4 cm) solid enhancing (becoming brighter on CT with contrast) renal masses must be considered highly suspicious for RCC [5]. Although RCC can appear as iso-, hyper-, or hypodense lesions on native CT scans, it usually demonstrates a significant contrast enhancement and intratumoral areas of necrosis following i.v. contrast application [14]. However, the management of these lesions has caused great controversy over the past decade. Benign lesions such as renal oncocytoma are most often homogeneous lesions exhibiting hypodensity compared to the normal renal parenchyma following i.v. contrast injection. The sensitivity and specificity of helical CT scans for differentiating conventional RCC from the other subtypes have been demonstrated to be 74% and 100% when 84 Hounsfield units (HU) is used as the cutoff value in the corticomedullary phase and 84% and 91% when 44 HU is used as the cutoff value in the excretory phase [15]. Triple-phase contrast abdominal CT is the current investigation of choice for the confirmation of diagnosis and staging in most instances [16]. In CT imaging, enhancement in renal masses is measured by comparing HU before and after contrast administration. To further increase diagnostic accuracy, evaluation should include images from the nephrographic phase, to discriminate between renal masses, which do not enhance to the same degree as the renal parenchyma. The nephrographic phase gives information about the glomeruli, the loop of Henle, and the collecting ducts. During this phase, medullary enhancement is similar to that of the cortex, so the kidney is seen more homogeneously on the images. Thus, this is the phase where it is easiest to detect lesions and characterize them in comparison with the arterial phase [10]. Multiphasic multidetector CT is able to distinguish ccRCC from oncocytoma, papillary RCC, and chromophobe RCC with accuracies of 77%, 85%, and 84%, respectively [17]. Figure 4 illustrates different RCCs on CT.

Venous tumor thrombus represents a significant problem in RCC, with 15–25% of patients having some degree of venous invasion [14]. Since an aggressive surgical approach is the mainstay in these patients, good presurgical planning depends on the preoperative evaluation of RCC with determination of tumor thrombus stage. Involvement of the renal vein and extension into the inferior vena cava below or above the diaphragm will change the surgery strategy [14]. Furthermore, the detection of visceral metastases appears to be crucial since it has been shown that even patients with metastatic disease might benefit from radical nephrectomy followed by systemic immunotherapy in the case of a good performance status and the presence of LN and pulmonary metastases only. Tumor staging is accomplished mainly with CT which allows for assessment of local invasiveness, LN involvement, or other metastases [5]. Abdominal CT provides information on: function and morphology of the contralateral kidney, primary tumor extension, venous involvement, enlargement of LNs, and conditions of the adrenal glands and other solid organs.

MRI. If the results of CT are indeterminate or in case of suspected pseudoenhancement, MRI may provide additional information on enhancement in renal masses, locally advanced malignancy, and venous involvement if the extent of the inferior vena cava tumor thrombus is poorly defined on CT. Exceptional circumstances where alternative imaging modalities would be preferred include contrast allergy, functional renal impairment, and pregnancy, where MRI may be used. The main

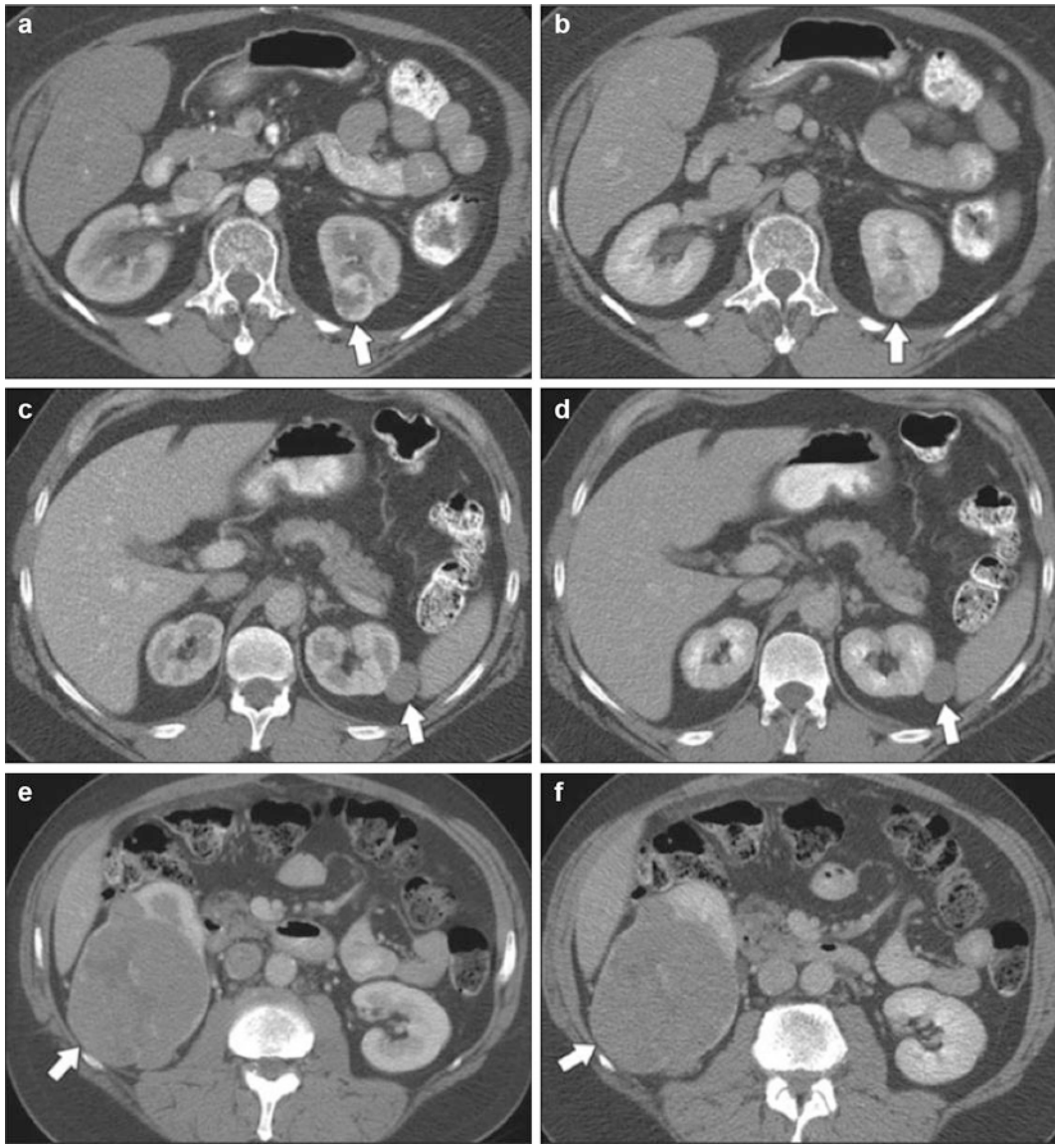

Fig. 4 CT appearances of various cell types of renal cell carcinoma. Conventional clear cell RCC (**a**, **b**). CT scans of TNM stage T1a tumor in corticomedullary and nephrogenic phases show typical hypervascularity of tumor (*arrow*, **a**) and subsequent washout (*arrow*, **b**). Papillary RCC (**c**, **d**). CT scans of TNM stage T1a tumor in corticomedullary (**c**) and nephrogenic (**d**) phases show typical hypovascularity of tumor (*arrow*). Chromophobe RCC (**e**, **f**). CT scans of TNM stage T2 tumor in corticomedullary (**e**) and nephrogenic (**f**) phases show hypovascularity of tumor (*arrow*) [7]

MRI feature indicating potential malignancy of a renal tumor is enhancement after i.v. gadolinium administration. However, enhancement at MRI cannot be measured as easily as enhancement at CT [18]. For the differentiation between thrombus and tumor thrombus in the renal vein and inferior vena cava, the use of gadolinium contrast is indicated, since the enhancement of the thrombus indicates a tumor [18]. Preoperative MRI accurately identifies the presence and nature of tumor thrombus with a sensitivity, specificity, and accuracy of 100%, 89%, and 92%, respectively [19]. The role of MRI in RCC imaging is still mainly in differentiating benign lesions versus malignant

lesion in patients who cannot undergo CT with i.v. iodinated contrast media or in cases with non-diagnostic CT results [18]. Both CT and MRI perform well in T staging of local tumor extent and M staging of distant metastases. However, both CT and MRI perform relatively poorly in N staging of lymphadenopathy [9, 14]. In patients with hereditary RCC who are worried about the radiation exposure of frequent CT scans, MRI may be offered as an alternative. Functional imaging with multiparametric MRI (mpMRI) is demonstrating promising results for discriminating RCC from benign lesions and for classifying RCC subtypes [20]. Especially, T2-weighted (T2W) MRI sequences have demonstrated promising results.

[^{18}F]FDG PET/CT for Staging/Prognosis

Primary diagnosis. Management of small renal tumors continues to change, and now urologists seek to incorporate new and important information as they plan surgery. For many years 2-deoxy-2-[^{18}F]fluoro-D-glucose ([^{18}F]FDG) PET/CT has been an important noninvasive imaging modality for the staging of many cancers. [^{18}F]FDG is a marker of increased glucose uptake. Many malignant neoplasms and their metastases are characterized by enhanced glucose utilization and therefore increased glucose uptake. As an analog of glucose, [^{18}F]FDG is taken up within tumor cells via GLUT and other transporters where it is phosphorylated by hexokinase but not further metabolized, leading to intracellular accumulation. PET imaging in combination with CT offers a high sensitivity scan for metabolic activity with precise anatomical localization. [^{18}F]FDG is excreted though the kidneys into the urine, and urine activity may mask tumors in urinary tract inclusive of the urinary bladder. The value of [^{18}F]FDG PET/CT in RCC is debated, especially for detecting primary renal tumors. Interference of excreted [^{18}F]FDG by the kidneys into the urinary tract accounts for the difficulty in identifying renal cancers that accumulate [^{18}F]FDG at levels that do not allow discrimination from normal urinary excretory tissue [21]. Forced diuresis coupled with parenteral hydration may improve the diagnostic accuracy of [^{18}F]FDG PET in various abdominopelvic malignancies, by enhancing urinary excretion of the tracer. However, the results from forced diuresis obtained in RCC are not convincing [22, 23]. Recently, early dynamic imaging and [^{18}F]FDG PET/CT have demonstrated promising results for evaluation of RCC [24]. In addition to the interference of background activity, the size and the [^{18}F]FDG avidity of the RCC may be partly responsible for the performance of [^{18}F]FDG PET/CT in RCC. Well-visualized tumors in kidneys on [^{18}F]FDG PET/CT are larger than non-visualized ones [22, 23]. In general RCCs have modest [^{18}F]FDG uptake due to lower metabolic state (Fig. 5). However, [^{18}F]FDG uptake is exquisitely seen in type II papillary RCC, especially when seen in the hereditary leiomyoma RCC syndrome [25]. Sarcomatoid tumors are also [^{18}F]FDG avid [25]. Benign renal tumors may also be FDG avid [25], and [^{18}F]FDG is not very useful on complex cystic renal masses, because of the low content of solid tissue in such lesions [26].

Various studies have confirmed that [^{18}F]FDG PET/CT offers little advantage over conventional imaging in the detection of primary RCC [21, 22, 28–32]. The sensitivity for detection of renal lesion is approx. 60% and the specificity approx. 90% [21, 22, 31, 33]. Contrast-enhanced CT and MRI have proven effective at detecting solid masses suspicious of RCC, but both modalities are nonspecific and cannot surely discriminate benign from malignant lesions. A negative [^{18}F]FDG PET/CT is not very useful clinically in these cases. Therefore, [^{18}F]FDG PET/CT only plays a minor role in the diagnosis of RCC. Diagnosis is generally made on CT and/or MRI and, if questions arise, a biopsy is usually recommended. [^{18}F]FDG may play an important role in particular subtypes of renal cancer, such as type II papillary and sarcomatoid (Fig. 6) [25, 34–36].

Primary staging. [^{18}F]FDG PET/CT is better to detect extrarenal rather than renal RCCs, as extrarenal lesions are not obscured by urinary [^{18}F]FDG activity [37]. In a meta-analysis, the pooled sensitivity and specificity were reported to be 79% and 90%, respectively, for detection of metastatic disease [33]. However, [^{18}F]FDG

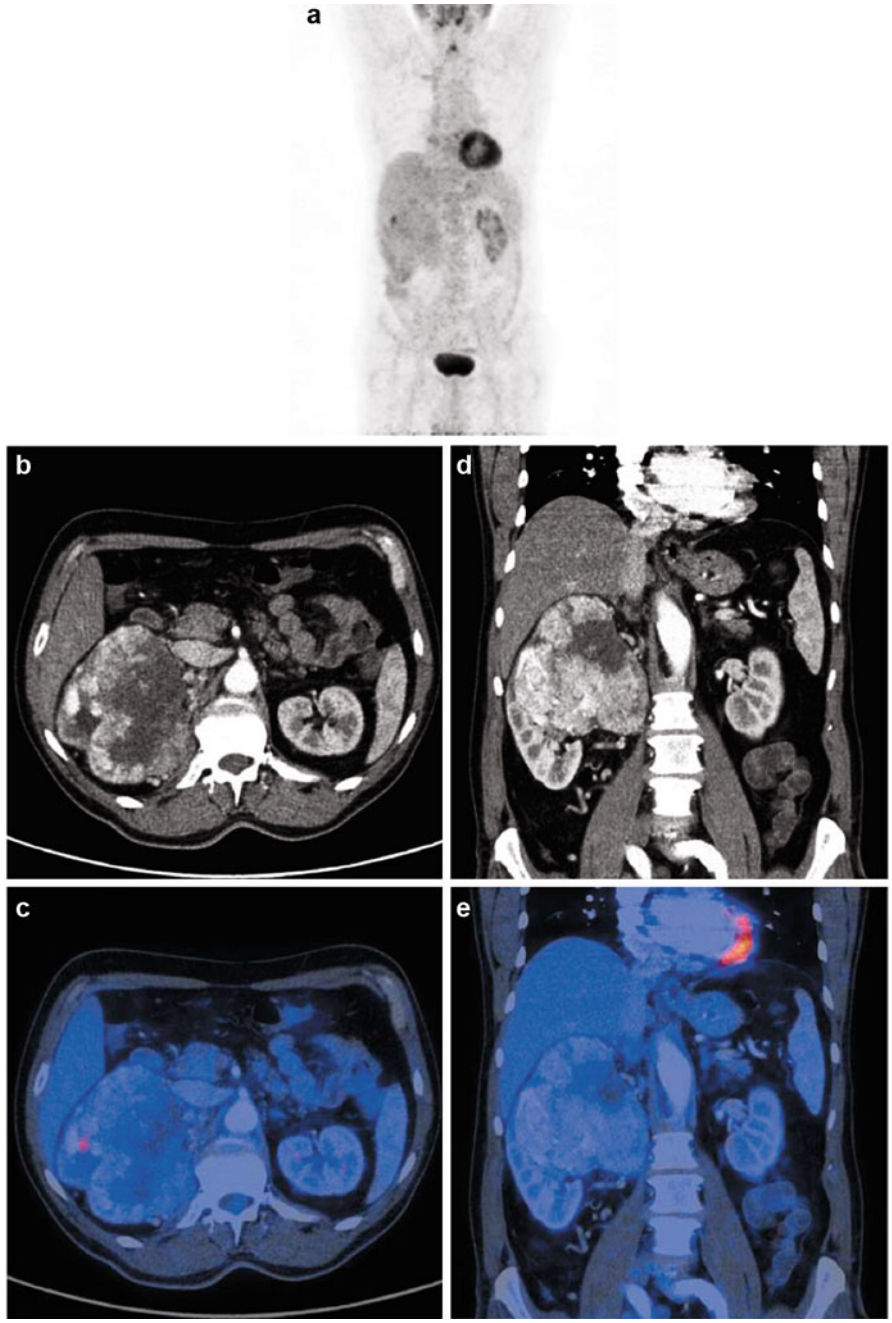

Fig. 5 Patient surviving more than 24 months after nephrectomy, classical RCC well differentiated with low level accumulation of [^{18}F]FDG (SUV_{max} 0–10). Whole-body MIP (**a**), CT images (**a**, **d**), and fused PET/CT images (**c**, **e**) [27]

PET/CT may not localize a small lesion as accurately as a larger one. In a study, the sensitivity of [^{18}F]FDG PET/CT increased from 76% to 92.9% when the lesion size increased from more than 1 to more than 2 cm [38]. In addition to lesion size, [^{18}F]FDG PET/CT may localize high-grade tumors more efficiently than low-grade ones [33]. In high-risk large tumors, [^{18}F]FDG

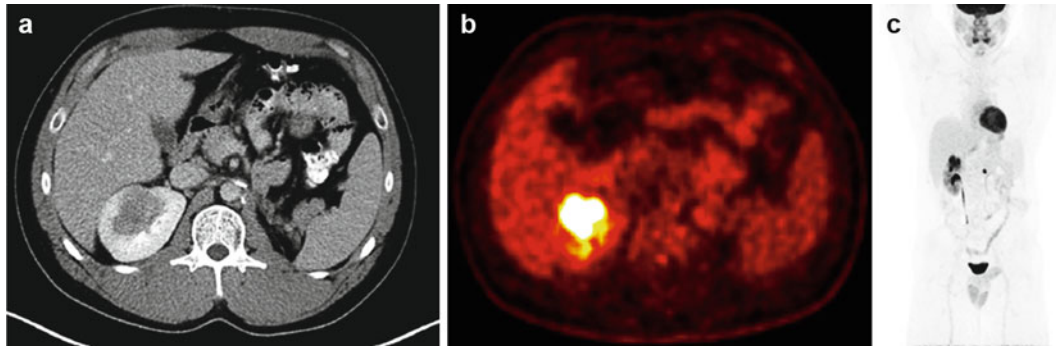

Fig. 6 Solitary renal cancer in the right upper pole. The patient had a type II papillary RCC in the right kidney (**a**) and was considered at high risk for metastatic disease. [^{18}F]FDG PET/CT demonstrates increased activity in the upper pole of the kidney corresponding to the mass on CT (**b**) and no evidence of metastatic disease elsewhere (**c**) [36]

PET/CT may be helpful for local staging in order to detect tumor thrombus in renal vein and inferior vena cava and discriminate between malignant or "bland" [39], which may help the surgeons in planning of the operation [40]. Furthermore, [^{18}F]FDG PET/CT may detect distant metastases with a higher accuracy than CT [22]. However, many of the primary RCCs detected by CT or MRI are small and with low risk of metastases. Thus, in general, [^{18}F]FDG PET/CT is not widely used for clinical primary staging of RCC.

Recurrent and metastatic disease. Early detection and management of metastatic disease have the potential to improve prognosis and quality of life. Several studies have used [^{18}F]FDG PET/CT for detection of recurrence and metastatic disease [21, 22, 37, 38, 41–44]. A meta-analysis found that [^{18}F]FDG PET can be useful in restaging and detection of metastatic disease, based on its acceptable sensitivity and specificity [45]. Similar results were demonstrated in another meta-analysis that only included studies using hybrid PET/CT scanners[33]. On a lesion-based analysis of three studies, the pooled sensitivity and specificity were 84% and 91%, respectively, for detection of extrarenal disease. On a scan-based analysis (n=7), the pooled sensitivity and specificity were 79% and 90%, respectively [33]. Figure 7 illustrates an example of [^{18}F]FDG PET/CT in BC and ccRCC.

Assessment of response to therapy. [^{18}F]FDG PET/CT in RCC is most often used in patients with metastatic disease treated with novel, targeted therapies [36]. Various molecular targeting therapies have become available for the treatment of advanced RCC. Agents targeting VEGF/PDGFR/mTOR pathway continue to be the mainstay of treatment in RCC [3]. Accurate prognostication is desirable for choosing the appropriate treatment for individual patients. Although tumor size measured according to the RECIST criteria have proven adequate for monitoring chemotherapy, for other cancers with modern targeted therapies, there is often little change in the size of the lesions, and some metastases even increase while the drug is prolonging survival [46]. Thus, [^{18}F]FDG activity may play a role in monitoring the efficacy of targeted therapies. Studies have demonstrated a correlation of sequential [^{18}F]FDG uptake on PET with the efficacy of VEGFR tyrosine kinase inhibitors [47–49]. In one study, time to progression in patients treated with the VEGFR inhibitor, sunitinib, was inversely correlated with [^{18}F]FDG uptake by the tumors [48]. Another study examined the relationship between [^{18}F]FDG uptake and the response in primary tumors to treatment with another VEGFR tyrosine kinase inhibitor, sorafenib, similarly demonstrating that those tumors with the highest avidity for [^{18}F]FDG tracer signal on PET were less likely to respond to therapy [49]. The decrease in [^{18}F]FDG accumulation of RCC lesions evaluated by PET/CT after treatment initiation with tyrosine kinase inhibitors is not influenced by the organs where the RCC metastasis is located [50]. Figure 8

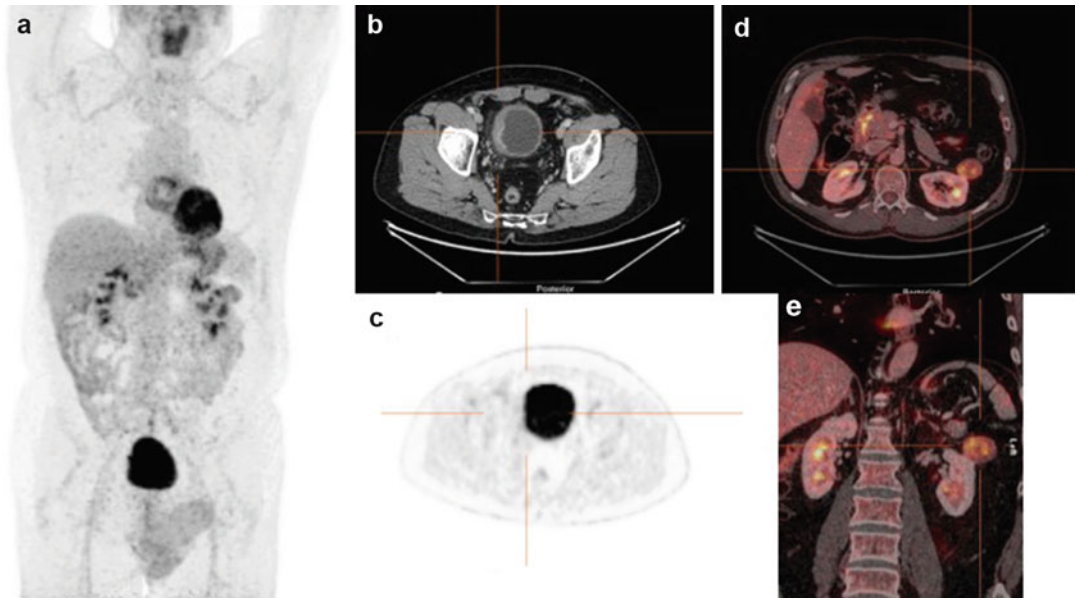

Fig. 7 Sixty-nine-year-old man with newly diagnosed muscle-invasive bladder cancer referred for primary staging with [^{18}F]FDG PET/CT. The bladder cancer is seen on CT in the right side of the bladder wall (**b**) but is not visible on PET (**a**, **c**) because of urinary excretion of [^{18}F]FDG that masks the tumor in the bladder. No lymph node metastases or distant metastases were seen (**a**). However, in the left kidney, a process measuring 3 × 4 cm with moderate [^{18}F]FDG uptake was seen on the fused PET/CT images (**d**, **e**). The patient was operated (laparoscopic cystectomy) for the bladder cancer. The process in the left kidney was removed with resection, and histology showed clear cell RCC. The case illustrates that tumor in the bladder often is masked on PET, because of urinary excretion of [^{18}F]FDG. Furthermore, some clear cell RCCs can be seen on PET/CT, most often with modest [^{18}F]FDG uptake, but not all clear cell RCCs are [^{18}F]FDG avid

demonstrates [^{18}F]FDG PET/CT in type II papillary RCC.

The prognosis for patients with RCC, where metastases are present at the time of diagnosis, is unfavorable. The median survival time given is between 10 and 21 months [51]. It is well known that prognoses for patients with RCC can vary, and the guidelines recommend risk-directed therapies using prognostic classifications based on a combination of clinical information and laboratory data. However, in this era of molecular targeting therapy, an index that expresses the biological activity of RCC directly, and prognosticates accurately, is desired for appropriate clinical decision making [52]. In one study the initial [^{18}F]FDG uptake in tumors correlated with prognosis, with patients whose renal tumors exhibit a SUV_{max} of greater than 10 having significantly worse survival than those with SUV_{max} less than 10 [27]. Recently, similar results were reported in a large study ($n = 101$), where pretreatment SUV_{max} assessed by [^{18}F]FDG PET was a useful prognostic marker for patients with advanced RCC, providing important information for clinical decision making [52]. Decreases in [^{18}F]FDG uptake on PET during therapy also correlate with prognosis [27, 46, 50].

Surveillance. In RCC, 20–40% of all patients relapse or develop metastases after radical nephrectomy with curative intent [53]. If this recurrence is diagnosed early, it can be treatable. Intensive surveillance imaging for recurrence of RCC following presumed curative surgical resection is driven by the widespread but unproven belief that early detection and treatment of asymptomatic disease may improve survival [54]. Defining the optimal surveillance regimen is challenging and must account for a number of complex patient and physician variables and interactions. The early detection of metastatic disease is the primary goal of postoperative surveillance for RCC. The imaging

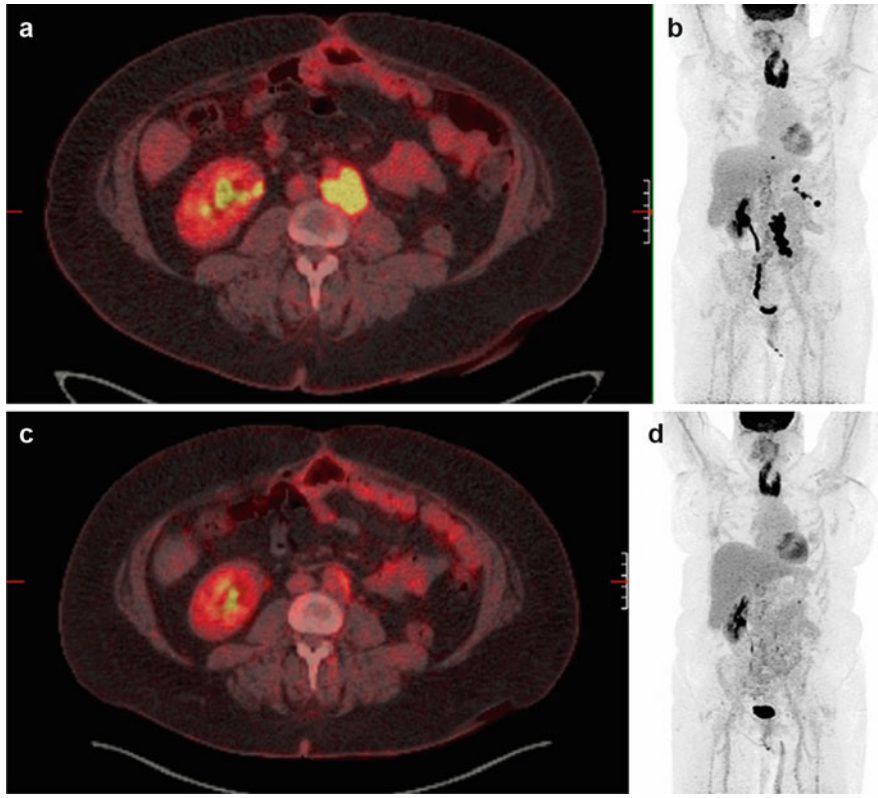

Fig. 8 Patient with type II papillary RCC associated with hereditary leiomyoma RCC syndrome, which has recurred after left nephrectomy. PET/CT with [^{18}F]FDG demonstrates intense uptake in the left para-aortic adenopathy on transverse PET/CT (**a**) and coronal projection image (**b**). After therapy with a combination of targeted therapies, the activity and size of the adenopathy have decreased dramatically (**c**, **d**). The patient has maintained a good response for 2 years [36]

methods used for follow-up can aid in the earlier detection of disease and in the appropriate administration of salvage therapy. A retrospective study assessed the efficacy of [^{18}F]FDG PET/CT for the surveillance of patients ($n = 63$) with a high risk of recurrence or metastasis after surgical treatment of RCC, compared to the conventional imaging methods [55]. The [^{18}F]FDG PET/CT accurately classified the presence of a recurrence or metastasis in 56 (89%) patients. [^{18}F]FDG PET/CT had an 89.5% sensitivity, 83.3% specificity, 77.3% positive predictive value, 92.6% negative predictive value, and 85.7% accuracy in detecting recurrence or metastasis, which was not significantly different from the results with conventional methods. Moreover, the accuracy of the [^{18}F]FDG PET/CT by nuclear grade and histological subtypes was not significantly different. The role of [^{18}F]FDG PET/CT in surveillance of RCC needs to be evaluated further in large prospective trials.

PET Radiopharmaceuticals Other Than [^{18}F]FDG

New radiotracers based upon compounds that are selectively accumulated by RCC or radiopharmaceuticals, which are not excreted in the urine, may be useful for imaging of RCC. Thus, other PET tracers than [^{18}F]FDG have been used in RCC in the past years including ^{18}F-fluoride (Na^{18}F), ^{124}I-eG250, [^{11}C]acetate, ^{18}F-MISO, and ^{18}F-fluorothymidine (^{18}F-FLT).

^{18}F-Fluoride. Bone is a common site of metastases in RCC, and bone metastases develop in more than 50% of patients with RCC during the

course of the disease [56]. About 80% of these bone metastases develop within 3 years of diagnosis [57]. For the moment, technetium ^{99m}Tc-methylene diphosphonate (^{99m}Tc-MDP) bone scan is the most commonly used modality for detection of bone metastases. However, as metastases from RCC are predominantly osteolytic, they may be missed on conventional ^{99m}Tc-MDP bone scan. Although Na^{18}F uptake, like ^{99m}Tc-MDP uptake, depends on the osteoblastic activity and the regional blood flow, the better spatial resolution with PET/CT may make Na^{18}F PET/CT more sensitive for detection of bone metastases. Yet, there has only been few reports using Na^{18}F PET/CT for detection of metastases in RCC. A recent report suggests that Na^{18}F PET is more sensitive than conventional ^{99m}Tc-MDP bone scan [58]. In the study, Na^{18}F PET/CT showed a sensitivity of 100%, specificity of 94.4%, positive predictive value (PPV) of 94.7%, negative predictive value (NPV) of 100%, and accuracy of 97.2% [58]. Na^{18}F PET/CT detected significant more lesions than bone scan. Na^{18}F is even able to detect lytic lesion [59]

^{124}I-cG250. Immuno-PET involves radiolabeling of monoclonal antibodies (mAbs) with positron emitters that bind to an antigen on tumor cells. In recent years, much focus has been on the chimeric antibody G250 (cG250), which reacts against carbonic anhydrase IX (CAIX). CAIX is overexpressed in ccRCC, and the G250 antigen is expressed on the cell surface of more than 90% of ccRCC whereas not expressed in normal kidney [60, 61]. CAIX is involved in cellular pH regulation and has been implicated in some pathogenic processes including tumor progression and is thought to play a role in regulating cell proliferation in response to hypoxic conditions [62]. High CAIX expression has been demonstrated in malignancies (renal, ovarian, colorectal, lung, brain, and bladder cancers). CAIX is associated with hypoxia and appears to be a marker of poor prognosis [63]. CAIX expression is regulated by the hypoxia-inducible factor 1α (HIF-1α). Mutation of the VHL genes leads to accumulation of HIF-1α and activation of downstream targets including CAIX [64]. Now CAIX is the best and most powerful diagnostic and predictive marker of ccRCC [63]. The half-life of common positron emitters, ^{11}C (20.4 min) and ^{18}F (109.7 min), is in general too short for use with a mAb in vivo. Positron emitters with longer half-lives, like ^{124}I (100 h) and ^{89}Zr (78 h), are better suited to the slow pharmacokinetics of radiolabeled mAbs. The optimal uptake of such antibody conjugates in tumors is normally several days post-injection for intact immunoglobulins [65]. In an ex vivo study, pairwise evaluation of ^{89}Zr-cG250 and ^{124}I-cG250 was performed. Superior PET images were obtained using ^{89}Zr-cG250, owing to the more prolonged trapping of the tracer in the tumor and simultaneous washout from normal tissues [66]. Recently, ^{124}I-cG250 PET/CT has been used to evaluate primary RCC [67, 68]. In the multicenter REDECT trial including 195 patients, ^{124}I-cG250 PET/CT showed a sensitivity of 86% and a specificity of 86% for ccRCC [68]. The results from the study were promising and demonstrated the potential use of ^{124}I-G250 PET as an imaging biomarker for malignancy. The PET agent may help noninvasively to distinguish ccRCC from other subtypes. Preoperative identification of tumor type could have important implications for the choice of treatment for RCC. Thus, ^{124}I-cG250 PET may be a useful diagnostic imaging tool in the future for clinical management of renal masses (Fig. 9). Imaging with ^{124}I-cG250 PET has the potential to change clinical management, in patients where a conservative approach (renal impairment, comorbid disease) may be appropriate in G250-negative tumors. These patients may be selected for nephron-sparing surgery or observed. Thus, ^{124}I-cG250 PET scan may be important value in risk stratification of patients with renal masses.

[^{11}C]Acetate, ^{18}F-MISO, and ^{18}F-FLT. The potential of [^{11}C]acetate as a metabolic tracer for RCC has been investigated in small studies [26, 69, 70]. Acetate is converted to acetyl coenzyme A in the mitochondria, followed by rapid clearance as carbon dioxide through the citric acid cycle. The results on [^{11}C]acetate PET are conflicting, and larger prospective studies are needed to clarify the role of [^{11}C]acetate PET/CT in RCC. However, the technical limitations of this agent (an on-site cyclotron is needed) are likely to inhibit its widespread

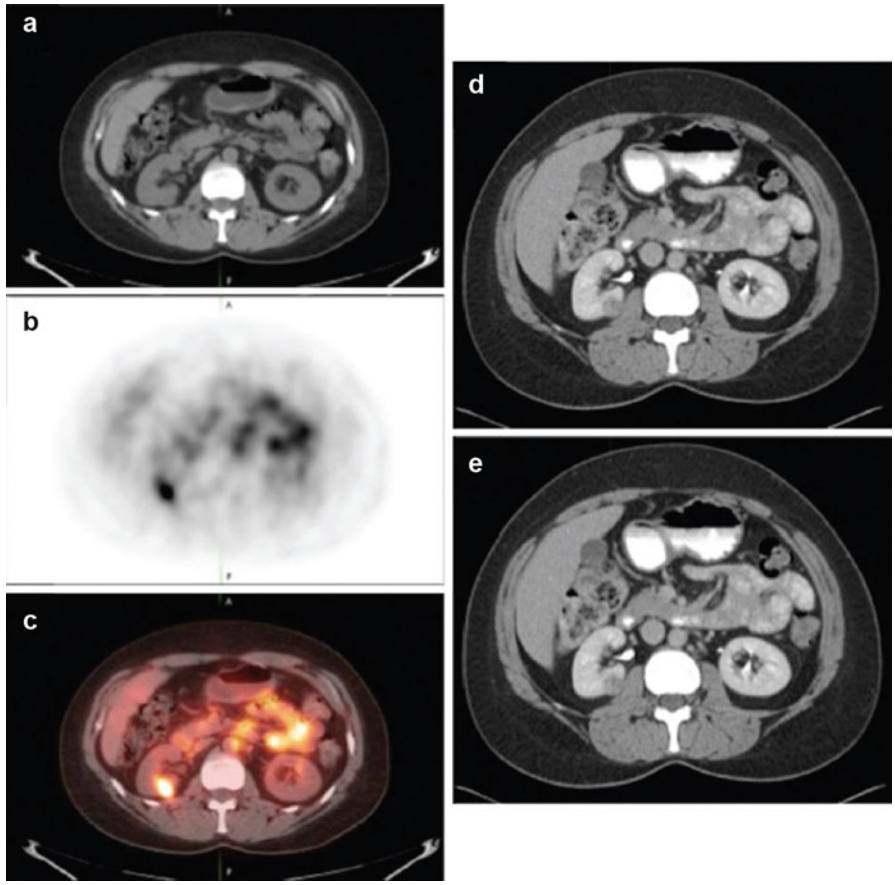

Fig. 9 Patient with a 1.0 cm right ccRCC (**a**). The mass is evident in the noncontrast CT image (**a**) from the PET/CT scan, positive on the ^{124}I-cG250 PET image, and is clearly evident on the fused PET/CT image (**c**). The mass was deemed to be positive on the contrast-enhanced CT scan of the parenchymal component (**d**) and excretory component (**e**) by Hounsfield criteria and qualitatively [68]

use. Radiolabeled nitroimidazole, ^{18}F-MISO, has emerged as noninvasive technique for assessing tumor hypoxia. Nitroimidazoles are effective against organisms thriving in hypoxic environments and are retained within hypoxic yet metabolically active cells. Thus, ^{18}F-MISO has been used in a number of malignant tumors, where hypoxia has been identified as a risk factor in the prognosis of the tumors. Because RCC is resistant to radiation and chemotherapy, it behaves like a tumor that contains hypoxic cell populations. A small study used ^{18}F-MISO PET in order to assess regional hypoxia in renal tumors [71]. A trend of increased ^{18}F-MISO uptake in RCC was demonstrated in RCC tumors as compared to normal tissue. However, although ^{18}F-MISO scans showed significant uptake in other solid tumors, there was only mild ^{18}F-MISO uptake in RCC. ^{18}F-FLT, which is radiopharmaceutical based on the nucleic acid thymidine and is able to measure cellular proliferation, has been used in few reports [72]. Larger studies are needed to evaluate the role of ^{18}F-FLT in RCC.

Common Therapies

The optimal treatment for RCC is surgery, especially when the tumor is located in the kidney with no LN involvement or metastasis. In advanced/metastatic RCC, most available treatments are palliative, and the patients usually die. In those cases,

the objective is to increase overall survival (OS), progression-free survival (PFS), response rate (RR), and quality of life (QF) of RCC patients [73]. Before target cell therapies became available, interleukin-2 (IL-2) and interferon-alpha (IFN-α) were the mainly used therapies for RCC, with low response, from 5% to 20% [73]. The treatment options for RCC include surgery, radiation therapy, chemotherapy, hormonal therapy, immunotherapy, targeted therapies, or combinations of these and some new approaches [74, 75]. Surgical treatment remains the mainstay of curative treatment for RCC and is recommended to achieve cure in localized RCC. In recent years, the explosion in laparoscopic and organ-sparing approaches has produced major shifts in the paradigm for surgical resection of RCC.

Surgical treatment. Operation may be performed as radical nephrectomy (RN) or as partial surgery (PN), i.e., nephron-sparing surgery. Radical nephrectomy includes the removal of the kidney, adrenal gland, perirenal fat, and Gerota's fascia and may be performed as open operation or as laparoscopic operation (standard laparoscopic or robot-assisted laparoscopic). Laparoscopic RN has a lower morbidity than open surgery [76]. Several studies have compared PN and RN for RCC (≤4 cm) and shown that RN was associated with increased mortality from any cause after adjusting for patient characteristics [77–79]. Thus, PN is recommended in patients with T1a tumors, and PN should be favored over RN in patients with T1b tumor when possible [80]. Ipsilateral adrenalectomy is only recommended when there is clinical evidence of invasion of the adrenal gland, and LN dissection is also only recommended if there is clinical evidence of LN invasion. PN is unsuitable in patients with locally advanced tumor growth and when PN is not feasible due to unfavorable tumor location. In these patients, the treatment is RN. Therapeutic alternatives to surgery include surveillance and ablative therapies. Two main ablative techniques, cryoablation (CA) and radiofrequency ablation (RFA), represent the currently available minimally invasive treatments for RCC. Other ablative techniques are used in experimental settings (microwave ablation, laser ablation, high-intensity focused ultrasound ablation). Population-based studies have compared the outcome of surgery (RN or PN) and nonsurgical management of renal tumors <4 cm and demonstrated a significant lower cancer-specific mortality for patients treated with surgery [81, 82]. However, this benefit is not seen in older patients (>75 years) in other studies [83, 84]. In active surveillance cohorts, the growth of small renal masses is low in most cases, and progression to metastatic disease is rare (1–2%) [85, 86]. Thus, in old patients and/or comorbid patients with small renal masses, active surveillance, RFA, and cryoablation can be offered.

Local advanced RCC is typically managed with radical nephrectomy, which will occasionally require en bloc resection of adjacent organs. Up to 40–60% of patients can be cured with such an aggressive approach [87]. Radical nephrectomy in the presence of metastatic disease (called debulking or cytoreductive nephrectomy) is often indicated as part of integrated management [75]. Lymph node dissection is performed in clinically positive LNs, for staging or local control. Tumor thrombus formation in inferior vena cava in RCC patients is an adverse prognostic factor [88]. These patients are operated with aggressive resection including the removal of the kidney and tumor thrombus if the patients have nonmetastatic disease. However, the best approach and management of these patients are still discussed [89].

Advanced/metastatic RCC is one of the most treatment-resistant malignancies [75].

The treatment may be local therapy (cytoreductive nephrectomy, embolization of the tumor), local therapy of metastases (bones, brain, etc.), or systemic therapy (immunotherapy, targeted therapies, monoclonal antibody against VEGF, mTOR inhibitors). Concerning local therapy of metastases, no general recommendation exists. The decision to resect metastases has to be decided in each patient and depends on the experience in the institution, risk profile, the patient's preference, etc. In some cases, stereotactic radiotherapy for bone metastases and stereotactic radiosurgery for brain metastases are offered for symptom relief. Chemotherapy is not considered effective in

patients with ccRCC. Chemotherapy is moderately effective only if 5-fluorouracil (5-FU) is combined with immunotherapeutic agents [90]. However, in one study IFN-α showed equivalent efficacy to IFN-α + IL-2 + 5-FU [91]. Overall, chemotherapy presently has little to no role in the treatment of metastatic RCC. Selected patients with metastatic disease may respond to immunotherapy, but many patients can be offered only palliative therapy for advanced disease. IL-2 and IFN-α have been used for more than 20 years. Despite this, the effectiveness of these two drugs is still controversial [75]. IFN-α monotherapy is inferior to targeted therapy in metastatic disease of RCC, but IL-2 monotherapy may be used in selected cases (ccRCC with only lung metastases). IL-2 has more side effects than IFN-α. Thus, immunotherapy is not routinely recommended as a first-line therapy in metastatic RCC.

New targeted therapies that have shown efficacy for advanced RCC include (1) tyrosine kinase inhibitors like sunitinib (Sutent®, Pfizer, New York, NY, USA), sorafenib (Nexavar®, Bayer, West Haven, CT, USA, and Onyx, Richmond, CA, USA), pazopanib (Votrient®, GlaxoSmithKline Pharma, London, UK), and axitinib (Inlyta®, Pfizer, New York, NY, USA); (2) monoclonal antibody against circulating VEGF like bevacizumab (Avastin®, Genentech, San Francisco, CA, USA); and (3) mTOR-inhibiting drug like temsirolimus (Torisel®, Wyeth, Collegeville, PA, USA) and everolimus (Afinitor®/Certican®/Votubia®, Novartis, Basel, Switzerland) [75, 92]. Other new treatments currently under investigations include stem cell transplantation, other interleukins, antiangiogenesis therapy, and vaccine therapy [93]. Sequential treatment with VEGF pathway-targeted therapies has become the standard treatment of metastatic RCC in many centers [75]. Figure 10 illustrates targeted therapies in RCC. Systemic treatment for metastatic RCC should be based on targeted agents, and sunitinib and pazopanib are recommended as a first-line therapy for advanced/metastatic ccRCC [80]. Bevacizumab + IFN-α is recommended as a first-line therapy for advanced/metastatic RCC in favorable-risk and intermediate-risk ccRCC and temsirolimus for first-line treatment in poor-risk RCC. Axitinib is second-line treatment for metastatic RCC. Everolimus is recommended for ccRCC patients who have failed VEGF-targeted therapy. Pazopanib and sorafenib are alternatives to axitinib as a second-line therapy. Sunitinib is a first-line therapy for non-clear cell metastatic RCC [80].

Bladder Cancer

Epidemiology of the Tumor

Bladder cancer (BC) is the ninth most commonly diagnosed cancer worldwide, with more than 380,000 new cases each year and more than 150,000 deaths per year. BC is the most common cancer in the urinary system [2] and is the sixth most common malignancy in men worldwide in 2012, following prostate, lung, colorectal, stomach, and liver cancer (Fig. 11). Recently, the overall and stage-specific age-adjusted 5-year survival and mortality rates of BC in the USA (period 1973–2009) were analyzed [94]. Although the analysis demonstrated statistically significant changes, the mortality rate associated with BC has not changed substantially in the last 30 years, indicating gaps between diagnosis and management of BC. Little or no change in BC control outcomes has been achieved during the study period [94]. Incidence of BC peaks in the sixth and seventh decades of life, although a trend toward presentation at younger ages has been suggested [95]. Because of long-term survival and the need for lifelong routine monitoring and treatment, the cost per patient of BC from diagnosis to death is the highest of all cancers in the USA [96]. Rates in males are three to four times those in females [97]. Incidence rates are high in many southern and eastern European countries, in parts of Africa and the Middle East, and in North America (Fig. 12) [97]. TCC accounts for over 90% of cases and is by far the most common epithelial tumor of the bladder [95]. The second most common cell type is squamous cell cancer (5%), and less than 2% are adenocarcinomas [95].

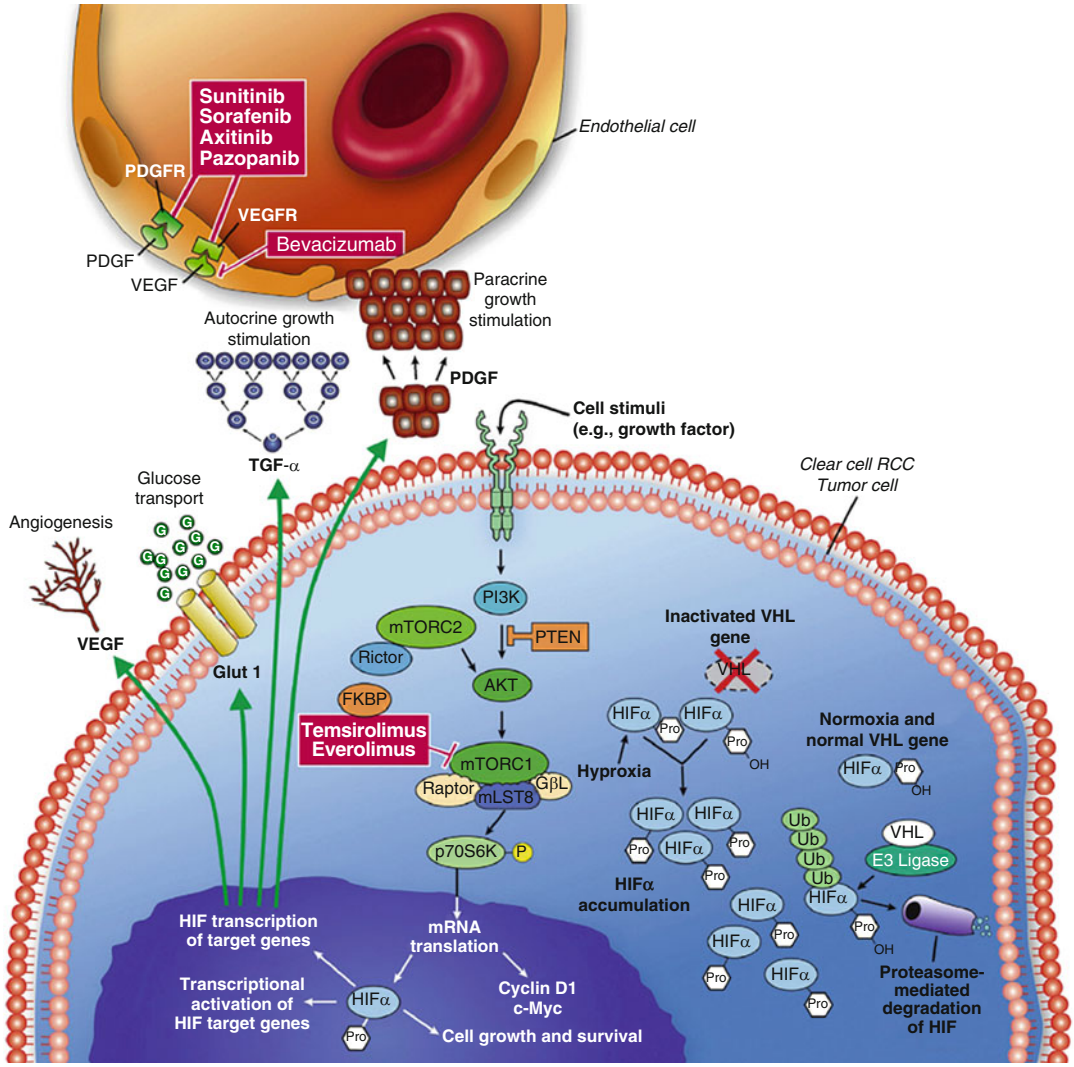

Fig. 10 The cellular pathways that are implicated in clear cell RCC carcinogenesis. Included are the seven US Food and Drug Administration-approved agents and where they act on this pathway [6]

Environmental and Genetic Factors

In bladder cancer, smoking is the most common risk factor and accounts for approximately half of all BCs [98]. Occupational exposure to aromatic amines and polycyclic aromatic hydrocarbons is an other important risk factor. The role of diet and environmental factors is less evident. In the recent years, there has been increasing evidence suggesting an influence of genetic predisposition on BC incidence.

Tobacco smoking. Several causative risk factors are associated with urothelial carcinoma (UC). Of these, smoking, especially cigarettes, is one of the most important factors and is consistently associated with the development of UC. While urothelial carcinoma of the bladder (UCB) and upper tract urothelial carcinoma (UTUC) are two distinct diseases [99], cigarette smoking is the most established risk factor for both [100]. Current smoking increases the risk of developing UCB and UTUC by as much as fourfold and sixfold,

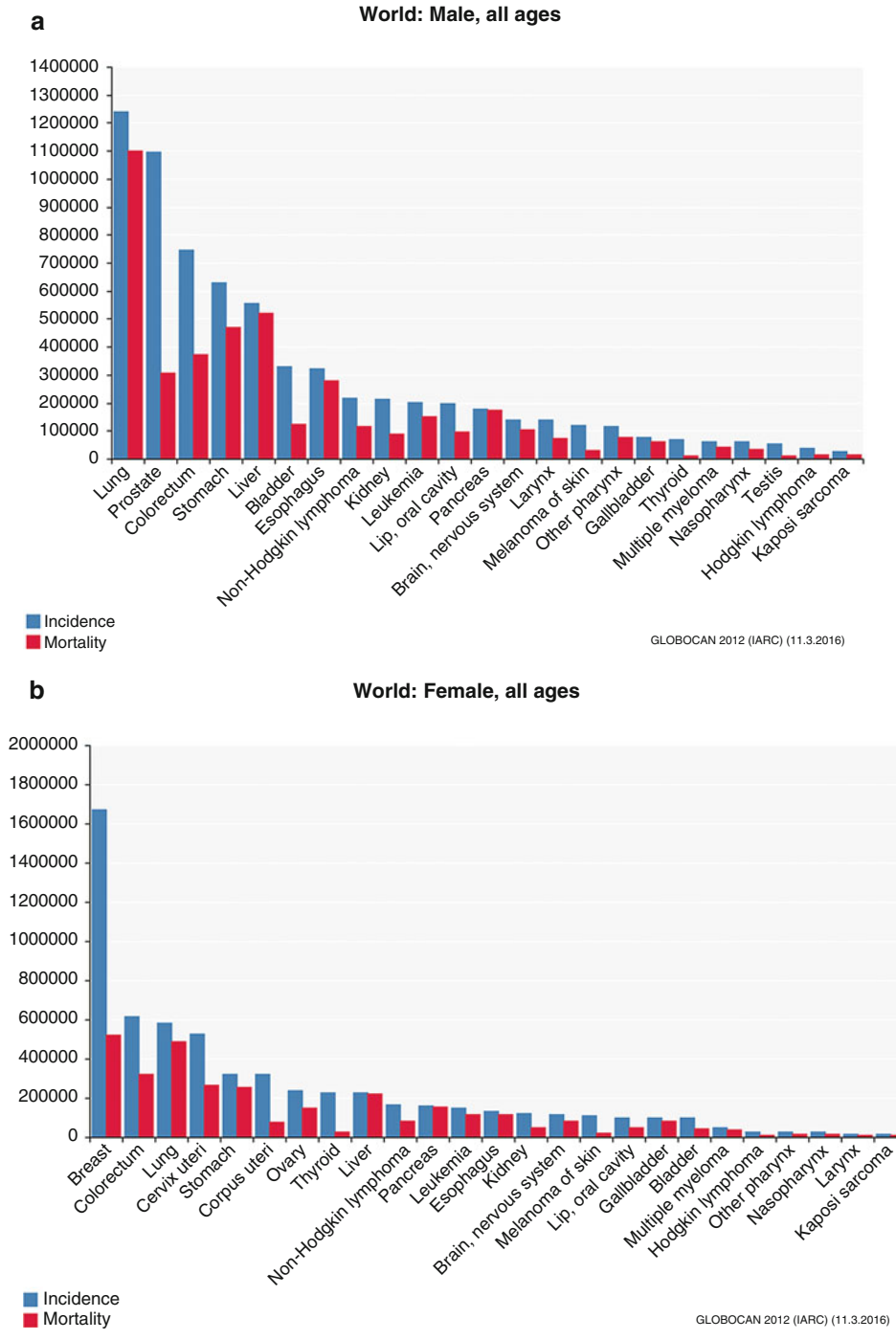

Fig. 11 Estimated age-standardized world incidence and mortality rates from different cancers in men (**a**) and women (**b**) (Reproduced from the public domain of the International Agency for Research on Cancer, GLOBOCAN database 2012, Cancer Incidence and Mortality Worldwide, available at http://globocan.iarc.fr)

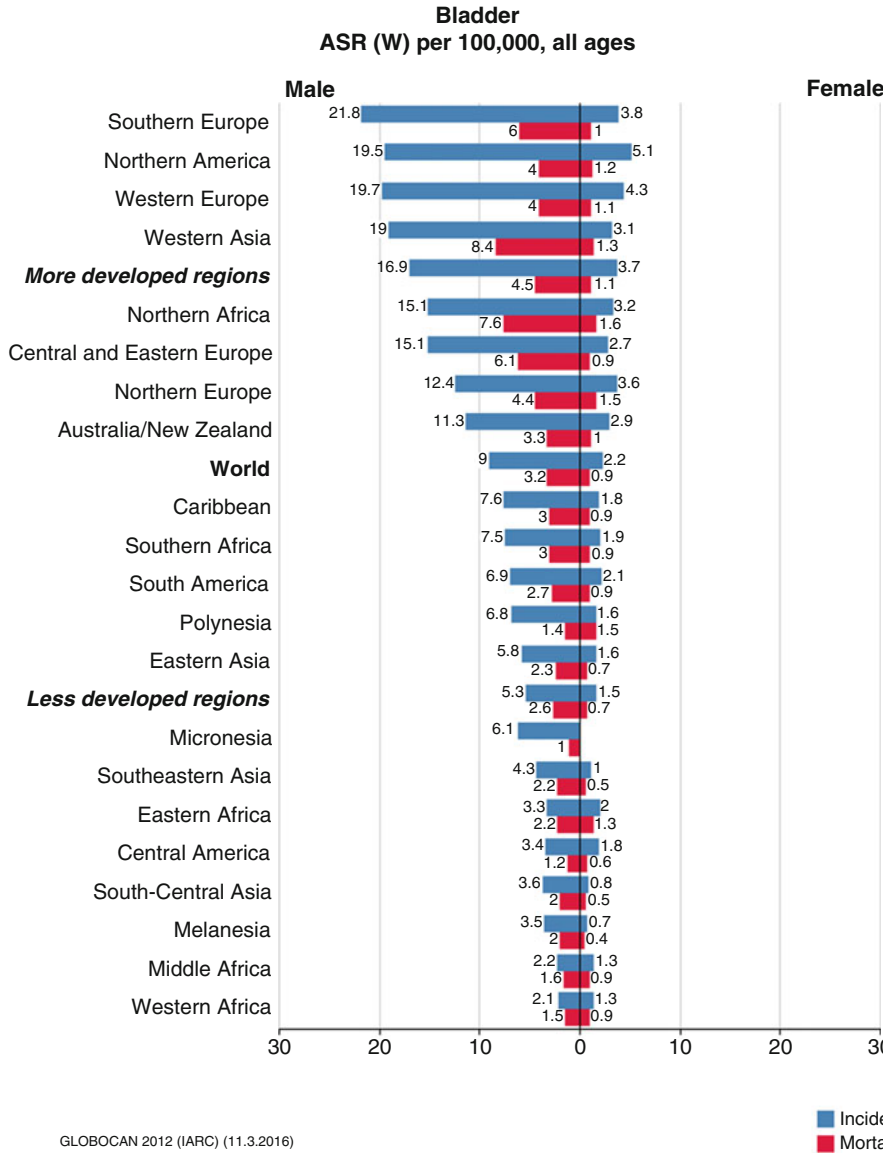

Fig. 12 Age-standardized incidence and mortality rates for bladder cancer by gender on different continents (Reproduced from the public domain of the International Agency for Research on Cancer, GLOBOCAN database 2012, Cancer Incidence and Mortality Worldwide, available at http://globocan.iarc.fr)

respectively [100], and 30–50% of all BC is caused by cigarette smoking [101]. The risk of developing UCB and UTUC increases with cumulative smoking exposure (i.e., number of smoked cigarettes/day and the duration of smoking), and it is independent of gender [100]. Tobacco smoking is causing 50–65% of male cases and 20–30% of female cases, and current cigarette smoking triples BC risk relative to never smoking [102]. A meta-analysis with 216 observational studies on cigarette smoking and BC demonstrated a significant association of BC for both current and former cigarette smokers [103]. The latency period is approximately 20–30 years. An increase in risk estimates for current smokers relative to never smokers has been demonstrated which may be due to changes in cigarette contents [102]. An immediate decrease in the risk of BC was observed

in those who stopped smoking [102]. The reduction was about 40% within 1–4 years of quitting cigarette smoking and 60% after 25 years of nonsmoking [104]. Thus, it is important to encourage people to stop smoking, since it would result in decreasing incidence of BC, both in men and women.

Exposure to chemicals. The second most important risk factor for BC is occupational exposure to chemicals, and work-related cases account for 20–25% of all BC [98]. The carcinogenic chemical compounds involved include aromatic amines (benzidine, 4-aminobiphenyl, 2-naphthylamine, 4-chloro-o-toluidine), polycyclic aromatic hydrocarbons, and chlorinated hydrocarbons, and it is likely to occur in occupations in which dyes, rubbers, textiles, paints, leathers, and chemicals are used [98, 105]. The risk of BC due to occupational exposure to carcinogenic aromatic amines is significantly greater after 10 years or more of exposure; the mean latency period normally exceeds 30 years. In recent years, the pattern extent and extent of occupational chemical exposure have changed because awareness has resulted in safety measurements in order to reduce carcinogenic chemical exposure [98]. Recent population-based studies demonstrated the occupational attribution for BC in men to be 7.1%, while no such attribution was discernible for women [106].

Genetic factors. There is growing evidence that genetic susceptibility factors and family associations may influence the incidence of BC. Genome-wide association studies of BC identified several susceptibility loci associated with BC risk. Several genetic changes have been related to risks of BC including *HRAS* mutation (Costello syndrome, facio-cutaneous-skeletal syndrome), *Rb1* mutation, *PTEN*/*MMAC1* mutation (Cowden syndrome), *NAT2* slow acetylator phenotype, and *GSTM1* null phenotype [107, 108]. With regard to gender, women have a lower BC incidence (up to fourfold) and a higher mortality rate than men [109].

Other factors. External beam radiotherapy for gynecologic cancer has been reported to increase rates of secondary bladder malignancies with relative risks of 2–4 [110]. Schistosoma haematobium bladder infections increase the risk of cancer (bilharzial bladder cancer) [111].

Exposure to arsenic in drinking water has also been recognized as a cause of BC [98]. Other dietary factors have been discussed, and many of these are still a topic of debate [98].

Molecular Biology

Improved treatment requires detailed understanding of UC pathogenesis and molecular biology. Expression-based analyses have identified distinct types of BC that have prognostic and therapeutic significance. Low-grade non-muscle-invasive BCs recur frequently but rarely progress to muscle invasion, whereas muscle-invasive BCs are usually diagnosed de novo and frequently metastasize [112]. Recent genome-wide expression and sequencing studies identify genes and pathways that are key drivers of UC and reveal a more complex picture with multiple molecular subclasses than through conventional grade and stage groupings. A two-pathway model has gained much attention, taking into account both histopathological and molecular features [112]. This model proposes that papillary noninvasive BC develops via epithelial hyperplasia and recruitment of a branching vasculature. Muscle-invasive BC is proposed to develop via flat dysplasia and CIS. The molecular characteristics of muscle-invasive BC and non-muscle-invasive BC are highly distinct. Figure 13 shows preneoplastic alterations in the bladder with tumor. These observations are leading to novel therapeutic approaches in BC [113]. This improved understanding of molecular features, disease pathogenesis, and heterogeneity provides new opportunities for prognostic application, disease monitoring, and personalized therapy of BC. Although noninvasive BC is not life threatening, its tendency to recur makes this disease more expensive to treat than other cancers, and disease monitoring and treatment are associated with considerable morbidity [112]. Key biomarker panels already are demonstrating promising results for application in noninvasive urine-based monitoring. For muscle-invasive BC, molecular profiling in the context of large clinical trials is required to confirm the ability of molecular signatures to stratify patients before treatment with conventional chemotherapy [112].

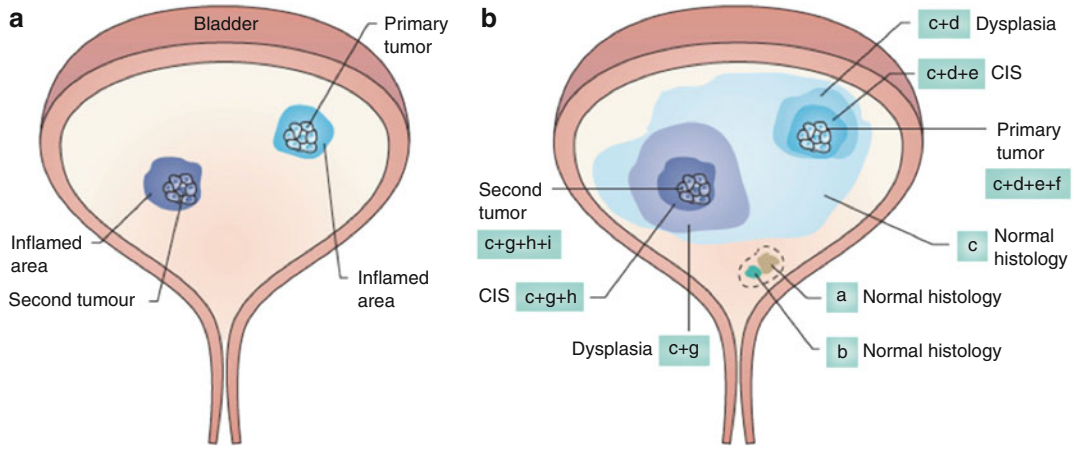

Fig. 13 Preneoplastic urothelial alterations in the tumor-bearing bladder. (**a**) A schematic of what the surgeon sees is shown. At presentation the primary tumor and an area of inflamed urothelium subsequently diagnosed as carcinoma in situ (CIS) are resected. During surveillance a second tumor and an associated area of CIS are visually identified and resected. (**b**) The molecular picture is shown. Large areas of urothelium have been replaced with altered cells. Different molecular events are indicated by letters. The primary tumor has developed within a large area of urothelium of normal appearance containing molecular alteration "c." Within this "field" of change, a dysplastic area (which also has normal appearance at cystoscopy) represents a subclone with "c + d" alterations; within this dysplastic area, a patch of CIS representing the immediate precursor to the overt tumor ("c + d + e + f") is recognized as an inflamed patch ("c + d + e"). A second tumor and CIS resected at a later date have also developed within the large altered field containing alteration "c" but differ in all other alterations (**g**–**i**). The possibility that tumors with independent initiating events may develop in some patients is indicated by patches "a" and "b," both of which may remain morphologically silent for many years. The dotted line indicates a urothelial patch as described by Gaisa et al. [124], which is putatively derived from a single stem cell. Despite independent tumor-initiating events, cells with alterations "a" and "b" are clonally related. The presence of large and clinically silent areas of preneoplastic urothelium emphasizes the need for novel approaches for local therapeutic targeting [112]

Symptoms and Diagnosis

Painless microscopic or gross hematuria is the initial symptom in over 80% of the patients with UC of the bladder, which is why UC needs to be excluded in patients presenting with these symptoms. The standard method of diagnosing papillary bladder cancer continues to be based on direct visualization of the bladder with cystoscopy and subsequent biopsy/resection [114, 115]. CIS is diagnosed by a combination of cystoscopy, urine cytology, and histological evaluation of multiple bladder biopsies [116]. Despite the development of several commercially available urinary markers for diagnosis and surveillance of BC, urinary cytology continues to play an important role in the diagnosis and surveillance of BC [117]. The specificity of cytology approaches 100%, whereas other markers generally outperform cytology with respect to sensitivity, especially for low-grade disease [114]. In an effort to improve the sensitivity of BC diagnosis, fluorescence cystoscopy continues to evolve. Several prospective randomized clinical trials have demonstrated increased detection of bladder tumors, particularly Ta tumors and CIS when using fluorescence cystoscopy [118–122].

Staging and Prognostic Stratification

Two different staging systems are used in classifying bladder tumors: the TNM and the Jewett-Strong-Marshall classification systems (Table 5) [123]. Until recently, the latter system was used extensively in the USA, but the TNM staging system (Table 6) has become the system of choice primarily because it has the advantage of distinguishing nodal involvement from locally advanced tumors and from distant metastatic spread

Table 5 The Jewett-Strong-Marshall classification of bladder cancer [123]

Class	Characteristic
O	Preinvasive
A	Submucosal invasion
B1	Superficial muscle
B2	Deep muscle
C	Extravesical spread
D1	Fixed to or invading prostate, uterus, vagina, or pelvic lymph nodes
D2	Spread to extrapelvic lymph nodes or distant metastases

Table 6 The TNM classification for bladder cancer [123]

Stage	Characteristic
Ta	Noninvasive papillary carcinoma
Tis	Carcinoma in situ: "flat tumor"
T1	Tumor invades subepithelial connective tissue
T2	Tumor invades muscle
T2a	Tumor invades superficial muscle (inner half)
T2b	Tumor invades deep muscle (outer half)
T3	Tumor invades perivesical tissue
T3a	Microscopically
T3b	Macroscopically (extravesical mass)
T4	Tumor invades any of the following: prostate, uterus, vagina, pelvic wall, abdominal wall
T4a	Tumor invades prostate or uterus or vagina
T4b	Tumor invades pelvic wall or abdominal wall
N0	No regional lymph node metastasis
N1	Metastasis in a single lymph node $\leq$2 cm in greatest dimension
N2	Metastasis in a single lymph node >2 cm but $\leq$5 cm in greatest dimension or multiple lymph nodes
N3	Metastasis in a lymph node >5 cm in greatest dimension
M0	No distant metastasis
M1	Distant metastasis

[123, 124]. Furthermore, a clinical staging for bladder cancer is used [123, 124]. The prognosis and treatment of BC depend on tumor grade and stage [125]. The overall 5-year survival rate is 82%. It is 94% for localized and superficial cancers, but it is only 6% for metastatic cancers [124]. Proper and accurate staging of the tumor is essential for optimal treatment of the patients [126].

Overall Performance of Diagnostic Imaging Other Than Nuclear Medicine for the Tumor

T staging. After diagnosing BC, it is necessary to determine whether the patient has a superficial or a muscle-invasive tumor (T1 vs. T2) since infiltration beyond the lamina propria will require more aggressive treatment than transurethral resection. Cystoscopy and biopsy at the time of initial examination reveals the tumor's cell type, grade, and depth of invasion. The primary tumor in the bladder may be detected either as a thickening of the bladder wall or as an intraluminal mass. Both CT and MRI may be used for assessment of local invasion, but they are unable to accurately detect microscopic invasion of perivesical fat (T2 versus T3a) [127–130]. The role of CT and MRI is therefore to detect T3b disease or higher. MRI has superior soft tissue contrast resolution compared with CT, but poorer spatial resolution. CT has sensitivities in the range of 79–89.7% and specificities ranging from 91% to 94.7% in detecting BC [124, 131–133]. CT is unable to differentiate between stages from Ta to T3a tumors but is useful for detection of perivesical fat invasion (T3b) and adjacent organs. The accuracy of CT to detect extravesical tumor extension varies from 55% to 92% and increases with more advanced disease [134, 135]. MRI is superior to CT for determining depth of bladder wall infiltration, while CT and MRI yield similar results in demonstrating invasion of perivesical structures [125, 136]. Dynamic contrast-enhanced (DCE) MRI may help differentiate bladder tumor from surrounding tissues or post-biopsy resection, because enhancement of the tumor occurs earlier than that of the normal bladder wall, due to neovascularization [137]. MRI imaging is considered by some to be the modality of choice for primary staging of urinary BC [136]. On MRI, the tumors appear slightly hyperintense relative to muscle on T2-weighted sequences and isointense relative to muscle on T1-weighted sequences (Fig. 14). Assessing small bladder primary tumors on CT and MRI can be difficult because underdistention of the bladder causes the appearance of bladder wall thickening, which can be mistaken as a tumor, and because

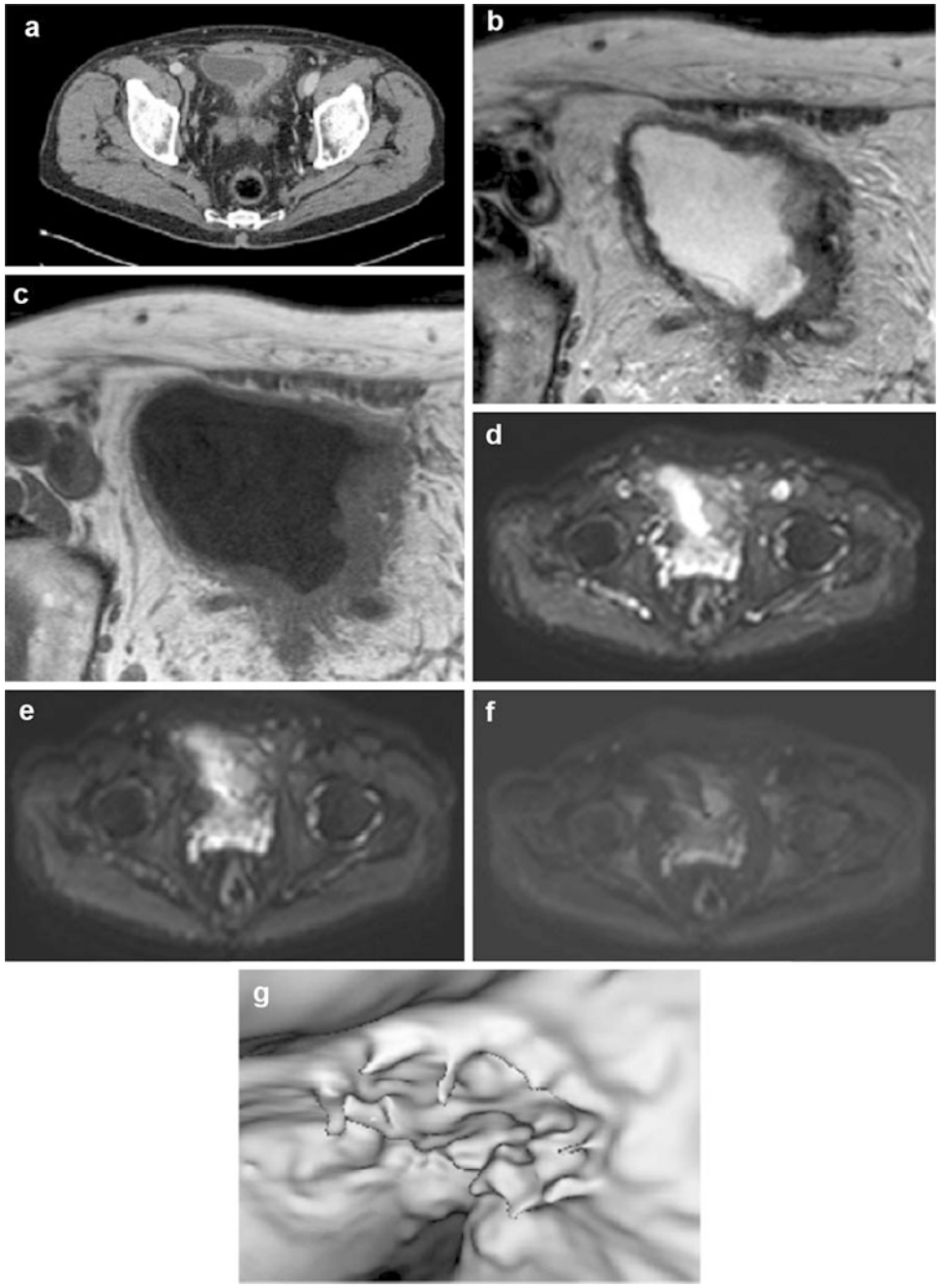

Fig. 14 Patient with known T2 N0 M0 bladder cancer (*left bladder wall*): (**a**) contrast-enhanced computed tomography (CT) scan, (**b**) axial T2-weighted image performed on a 3-T magnetic resonance imaging (MRI) unit showing a hypointense lesion, (**c**) corresponding T1 image, (**d**) axial diffusion-weighted (DW) MRI at b-value 0, (**e**) axial DW MRI at b-value 100, (**f**) axial DW MRI at b-value 750, and (**g**) magnetic resonance virtual cystoscopy (MRVC) of same tumor with three-dimensional reconstruction of tumor bed showing opening into adjacent diverticulum [130]

overdistension can flatten some tumors. Asymmetric wall thickening is often helpful in localizing the tumor. Currently, the most accurate method for differentiating T1 from T2 tumors is with a tissue specimen obtained from the muscularis propria of the tumor base during TUR [94, 126].

Excretory-phase CT urography is used for upper UTUC and has replaced conventional i.v. urography and ultrasound in high-risk patients. The sensitivity and specificity of CT urography for UTUC are 67–100% and 93–99%, respectively. For lesions detected on i.v. urography, biopsy is recommended to exclude false-positive results, to provide information about tumor grade, and for guiding therapy. Most often the biopsy is obtained endoscopically.

N staging. Accurate detection of LN metastases in BC is an essential component of the approach to treatment. Metastases are rarely associated with superficial disease. However, for muscle-invasive BC, additional imaging workup procedures are needed for accurate staging [125, 126]. CT and MRI reliably detect LN enlargement within the pelvis and abdomen in patients with BC. However, both techniques rely on size criteria. Metastases from BC frequently replace normal LNs, causing little if any enlargement, and high false-negative rates are recorded for both CT and MRI [123]. A commonly used criterion to diagnose pathologic adenopathy is a minimal axial diameter of 10 mm in oval-shaped nodes or 8 mm in round nodes [136, 138–140]. Lymph nodes tend to become rounded with metastatic involvement [138]. Microscopic metastatic deposits in normal-sized LNs can be missed, however, when only size criteria are used for diagnosis, thus leading to false-negative results and subsequent understaging using this threshold. For LN evaluation, the accuracy of CT ranges from 73% to 92%, with a tendency to understage nodal involvement [136]. The accuracy of MR imaging in staging LN metastases based on anatomic size criteria ranges from 73% to 90% and is comparable to that of CT [136]. Identification of metastases in LNs that are not enlarged continues to be an additional challenge for imaging. Currently, the preferred method for accurate N staging is pelvic lymphadenectomy [126]. However, recently promising results have been shown with lymphatic contrast agents for MRI [141]. After i.v. injection of highly lymphotropic superparamagnetic nanoparticles, the agents gain access to LNs by means of interstitial-lymphatic fluid transport. The nanoparticles are taken up by macrophages in healthy LNs, and therefore a lack of contrast uptake suggests the replacement of such normal macrophages by metastasis. In general, this requires two MRI examinations at two different time points: a baseline study and a second imaging after 24–36 h after administration of the iron oxide contrast medium. MR imaging with lymphatic contrast agents may improve nodal staging in patients with BC by depicting metastases even in normal-sized LNs [141].

M staging. Bladder cancer may also spread hematogenously. The incidence of distant metastases increases with increasing T and N stages [142]. Distant metastasis tends to occur late in the clinical course of BC and especially at the time of recurrence, with bones, lungs, brain, and liver being the most common sites. Both conventional abdominal/pelvic CT and CT urography (CTU), which may be combined with chest CT if needed, can be performed to detect distant metastases [125]. CT also may suggest adjacent visceral invasion, although MRI is superior because of better soft tissue contrast. A ^{99m}Tc-MDP bone scan may be used to assess the entire skeleton in the presence of metastases. The overall reported accuracy of CT in detecting and staging of BC varies from 64% to 97%, whereas that for perivesical invasion and for LN metastases range from 83% to 93% and 73–92%, respectively [138, 143]. The reported accuracy of MRI in overall staging of BC varies from 60% to 85%, depending on the sequence protocol and grouping of stages, whereas that of local staging varies from 73% to 96% [125, 138, 144]. The overall staging accuracy of gadolinium-enhanced MRI for staging extravesical extension in BC is 73–100%.

[^{18}F]FDG PET/CT for Staging and Prognosis

The treatment strategy of muscle-invasive BC is determined by tumor stage and grade. In clinical

practice CT and MRI are often the imaging modalities used. The aim of staging with imaging is to determine prognosis and provide information to guide treatment strategy. For staging of muscle-invasive BC, information on the extent of local tumor invasion, metastatic involvement of LNs, and spread of tumor to upper urinary tract or other distant organs (liver, lungs, bones, peritoneum, pleura, and adrenal glands) is required. The value of [^{18}F]FDG PET/CT in detecting localized tumor in the bladder is limited due to urinary excretion of radiotracer, which may mask tumor activity in the bladder wall. Several efforts have been made to overcome radioactivity interference in the urine, such as [^{18}F]FDG washout, early images, late images after voiding, dual-phase imaging, catheterization, bladder irrigation, and forced diuresis [36, 145–152]. Recently, a meta-analysis evaluated the diagnostic accuracy of [^{18}F]FDG PET/CT for detecting bladder cancer lesions [153]. Six studies met the inclusion criteria. The pooled sensitivity and specificity of PET or PET/CT for the detection of bladder cancer were 80.0% (95% CI, 71.0–87.0%) and 84.0% (95% CI, 69.0–93.0%), respectively. When compared with results of MRI and CT published by other studies, [^{18}F]FDG PET or PET/CT demonstrated no superiority in detecting local bladder lesions [153]. As a whole-body imaging, it was suggested that PET is more appropriate for the detection of metastasis.

NM staging. The sensitivity of CT and MRI for detection of LN metastases is low, since LN metastases rely on size criteria [145]. The specificity is also low since enlarged LN may be due to benign disease. Since [^{18}F]FDG PET may detect metabolic activity in normal size LNs, [^{18}F]FDG PET/CT has been used in clinical studies for primary NM staging [154–162]. [^{18}F]FDG PET/CT detects more malignant disease than conventional CT/MRI in 20–40% of patients [158, 159], and [^{18}F]FDG PET/CT may change the clinical management in up to 68% of the patients (Fig. 15) [159]. Upstaging is more frequent than downstaging [158]. Recently, a meta-analysis was performed to evaluate the diagnostic accuracy of [^{18}F]FDG PET/CT in detecting LN metastases [163]. Eight studies were included in the analysis [154, 160, 163–168]. The pooled sensitivity of [^{18}F]FDG PET/CT for detecting LN metastases was 56.5% (95% CI, 47.3–65.3%), specificity 95.4%

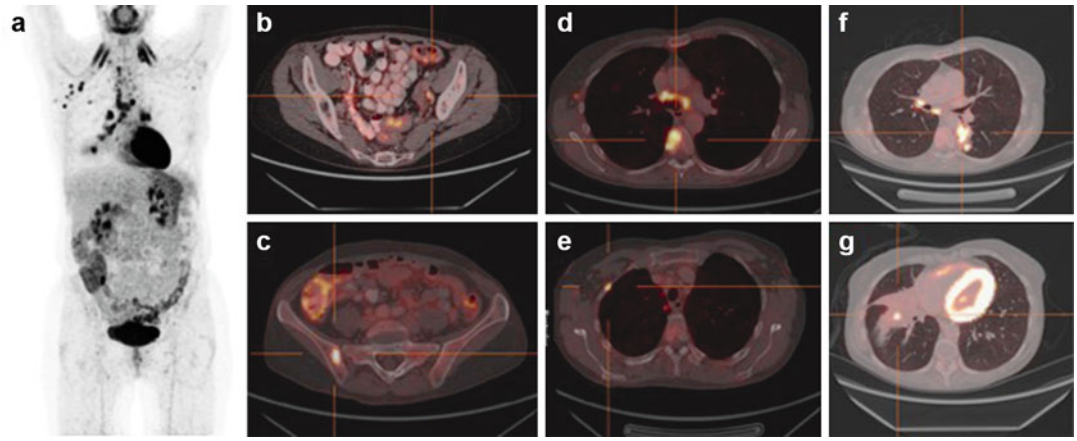

Fig. 15 Fifty-one-year-old woman with newly diagnosed muscle-invasive bladder cancer referred for staging with [^{18}F]FDG PET/CT. The tumor in the bladder is not visible on PET due to urinary excretion of [^{18}F]FDG (**a**). A metastasis in a not enlarged lymph node in left fossa obturatoria is seen on the axial fused PET/CT image (**b**). Several bone metastases are seen on the MIP (**a**) and on the axial fused PET/CT images in the right os ilium (**c**), in the spine (**d**), and in costae (**e**). Furthermore, PET/CT showed disseminated lung cancer in both the right and left lungs with metastases to the mediastinal lymph nodes (**f**, **g**). Histology showed non-small cell lung cancer, and the patient was treated with chemotherapy

(95% CI, 92.2–97.6%), positive LR 9.02 (95% CI, 4.48–18.16), and negative LR 0.50 (95% CI, 0.39–0.64). The pooled measures for CT alone in five of those studies were sensitivity 35%, specificity 95%, positive LR 4.91, and negative LR 0.7. The study concluded that [^{18}F]FDG PET/CT is better to detect LN metastases as compared to CT alone. With a pooled sensitivity of 35%, CT alone correctly identified 22% fewer patients with LN metastasis, as compared to [^{18}F]FDG PET/CT. Thus, [^{18}F]FDG PET/CT offered additional metabolic information, as compared to CT alone, and therefore is more accurate for staging BC. Another meta-analysis of [^{18}F]FDG PET/CT for the staging and restaging of BC found that the pooled sensitivity was 82%, the pooled specificity was 89%, and the global accuracy was 92% [169]. Six studies met the inclusion criteria [149, 151, 155, 159, 160, 170]. The pooled sensitivity and specificity of PET/CT for primary lesion detection of BC were 90% (95% CI, 70–99%) and 100% (95% CI, 74–100%), respectively. The pooled sensitivity and specificity of [^{18}F]FDG PET or PET/CT for staging or restaging (metastatic lesions) of BC were 82% (95% CI, 72–89%) and 89% (95% CI 81–95%), respectively. The study showed that the diagnostic accuracy of [^{18}F]FDG PET/CT is good in metastatic lesions of BC.

Recurrence. It is well known that muscle-invasive BC is a disease with a pattern of predominantly distant and early recurrences. Half of the patients with muscle-invasive BC relapse after radical cystectomy, and local occurrence accounts for 30% of relapses, whereas distant metastases are more common. The overall prognosis for recurrent and metastatic BC is poor. However, additional salvage and/or palliative therapies are prompted when recurrent disease is discovered. Accurate restaging is therefore important before additional costly and toxic therapies are considered [36]. There are few data available on the utility of [^{18}F]FDG PET or [^{18}F]FDG PET/CT in assessing for recurrence and metastatic disease in patients who have previously undergone treatment for their primary bladder tumor [149, 151, 170]. A study retrospectively assessed the diagnostic performance of [^{18}F]FDG PET/CT in the imaging evaluation of recurrent and metastatic BC [170]. In the study, 35 patients were previously treated for the primary disease. The metastatic sites detected in the study included the mediastinum, lung, and bone, and overall hybrid PET/CT diagnostic information was valuable in detecting, localizing, and characterizing the extent of metastatic disease. The complementary information provided by the combined PET/CT scanner affected the clinical management in 17% of patients, by prompting either additional therapy or a wait-and-watch strategy.

Response to therapy. Patients with BC and regional LN metastases could be targeted for neoadjuvant chemotherapy, and patients with distant metastases could be spared the unnecessary morbidity of radical cystectomy. Neoadjuvant cisplatin-based combination chemotherapy has demonstrated improved outcomes for muscle-invasive BC [171]. Since nonresponse rate to neoadjuvant chemotherapy is relatively high, monitoring the LN response to neoadjuvant chemotherapy may guide the selection of patients for further surgery. Conventional imaging modalities like CT and MRI are often ineffective in detection of therapy response in metastases because of difficulty in indentifying viable tumor in residual necrotic masses and small tumors in LNs of normal size. [^{18}F]FDG PET/CT has been used in the study for measuring therapy response to neoadjuvant chemotherapy in 19 patients with muscle-invasive BC [172]. Metabolic response was assessed according to European Organisation for Research and Treatment of Cancer (EORTC) recommendations based on the change in [^{18}F]FDG uptake on PET/CT. Radiological response was assessed on contrast-enhanced CT according to Response Evaluation Criteria in Solid Tumors (RECIST). All patients underwent pelvic lymph node dissection (PLND), and histopathological examination was the gold standard. Before neoadjuvant chemotherapy, increased [^{18}F]FDG uptake was seen in all 19 patients, which correlated the LN metastasis. Evaluating the LN response with PET/CT was feasible in all patients. PET/CT correctly distinguished responders from nonresponders (18 of 19 patients or 94.7% and 15 of 19 or 78.9%) and complete responders from patients with residual disease (13 of 19 or 68.4% and 12 of 19 or 63.2%, respectively). Although no definitive

conclusions can be drawn from these preliminary data, PET/CT may be feasible for evaluating the LN response to neoadjuvant chemotherapy and distinguishing responders from nonresponders [172]. However, this has to be investigated further in large prospective clinical trials.

Prognostic value. Few studies have investigated the prognostic value of [^{18}F]FDG PET/CT in BC. In a study, 43 chemotherapy-naïve patients underwent [^{18}F]FDG PET/CT before cystectomy [160]. Median follow-up was 14.9 months (range, 0.4–46.1 months). [^{18}F]FDG PET/CT demonstrated a positive predictive value (PPV) of 78% (7/9), a negative predictive value (NPV) of 91% (30/33), sensitivity of 70% (7/10), and specificity of 94% (30/32). Recurrence-free survival (RFS), disease-specific survival (DSS), and overall survival (OS) were all significantly poorer in the patients with positive [^{18}F]FDG PET/CT than in those with negative [^{18}F]FDG PET/CT. [^{18}F]FDG PET/CT detected occult metastatic disease in 7 of 42 patients with negative conventional preoperative evaluations (CT, ^{99m}Tc-MDP bone scan). PET findings were strongly correlated with survival in the study, and it was concluded that [^{18}F]FDG PET/CT may guide treatment strategy before radical cystectomy [160]. Recently, in a large bi-institutional study ($n = 211$), patients with muscle-invasive BC underwent [^{18}F]FDG PET/CT and CT for staging [173]. The patients were divided into two groups, a PET/CT-positive and a PET/CT-negative group. Data on staging and mortality were retrospectively analyzed from prospective databases. Median follow-up was 18 months. Patients with a positive PET/CT had a significantly shorter OS and DSS (median OS, 14 vs 50 months, $P = 0.001$; DSS, 16 vs 50 months, $P < 0.001$). In multivariate analysis, the presence of extravesical lesions on PET/CT was an independent prognostic indicator of mortality (OS, hazard ratio = 3.0, confidence interval 95% 1.7–5.1). This association was not statistically significant for conventional CT (hazard ratio = 1.6, 95% confidence interval 0.9–2.7). The study showed that the presence of extravesical metastatic disease on PET/CT might be considered an independent indicator of mortality [173].

PET Radiopharmaceuticals Other Than [^{18}F]FDG

Investigators have attempted to improve the sensitivity of PET by using tracers that are not excreted in urine. [^{11}C]choline, [^{11}C]acetate, and [^{11}C]methionine have been proposed for this purpose. Furthermore, Na^{18}F has been used for detection of bone metastases in muscle-invasive BC.

[^{11}C]Choline is an agent that is incorporated into tumor cells by conversion into [^{11}C]phosphorylcholine, which is trapped inside the cell [174]. This is followed by synthesis of phosphatidylcholine, a main component of cell membranes. The uptake of choline in tumors represents the rate of tumor cell proliferation. Minimal or no urinary excretion is seen with [^{11}C]choline. In the normal bladder wall, the uptake of choline is low, and [^{11}C]choline may visualize tumor in the bladder [175–177]. [^{11}C]choline PET/CT has also been used for primary NM staging of muscle-invasive BC [176, 178, 179]. In a recent study ($n = 59$), [^{11}C]choline PET/CT was used for detection of LN metastasis and compared the results with histological analysis [178]. [^{11}C]choline PET/CT overall detection rate was 62.7% (37/59 patients). On a regional-based analysis, [^{11}C]choline PET/CT was considered positive for primary cancer and/or local relapse in bladder bed in 54.2% of the patients (32/59). Considering LN metastasis detection, compared with histological analysis, [^{11}C]choline PET/CT showed in the whole population a sensitivity, specificity, positive predictive value, negative predictive value, and accuracy of 59%, 90%, 71%, 84%, and 81%, respectively. The authors concluded that PET/CT with [^{11}C]choline may provide additional diagnostic information in preoperative LN staging of patients with BC [178]. [^{11}C]choline may also be used for restaging of BC [178, 180]. A study ($n = 25$) reported that [^{11}C]choline PET/CT was sensitive, specific, and accurate, with good PPV and NPV for local relapse of 66.7%, 84.6%, 76%, 80%, and 73.3%, and 90%, 93.3%, 92%, 90%, and 93.3% for LNs and distant relapse, respectively [180]. In a relative small prospective study ($n = 44$), neither CT

nor [^{11}C]choline PET/CT could predict OS or CSD in BC patients treated with radical cystectomy [181]. However, larger cohorts are needed to clarify the prognostic value of [^{11}C]choline PET/CT in BC.

[^{11}C]Methionine uptake is proportional to the amino acid transport and to some extent protein synthesis [174]. In cancer, [^{11}C]methionine has been correlated with the amount of viable tumor tissue [182]. Tumor uptake of [^{11}C]methionine occurs rapidly (a peak at around 10 min followed by a plateau) [174]. [^{11}C]methionine undergoes rapid clearance from the blood pool and is primarily metabolized in the liver and pancreas with no significant renal excretion [174]. In a small study ($n = 22$), [^{11}C]methionine PET/CT was reported superior to [^{18}F]FDG for detection of tumor in the bladder; however, the sensitivity was only 78% (18/23) . In the study tracer uptake was proportional to tumor stage. In another study methionine PET was used for the evaluation of therapy response in 44 patients with varying stages of BC treated with chemotherapy [183]. In the study, the diagnostic accuracy of PET was poor, and the technique could not monitor the therapeutic effect of neoadjuvant chemotherapy, producing results that correlated with therapy outcome.

[^{11}C]Acetate has little or no urinary excretion. Three small studies have used acetate PET in BC patients. In one pilot study, [^{11}C]acetate PET/CT was used for primary staging of muscle-invasive BC patients before cystectomy with PLND and for response assessment after neoadjuvant chemotherapy in some of the patients [184]. The results indicate that acetate PET/CT may have good sensitivity for BC and LN metastases. However, false-positive uptake due to inflammation or granulomatous infection can occur, limiting the staging utility of [^{11}C]acetate PET/CT after prior intravesical BCG therapy [184]. A small study prospectively evaluated MRI, [^{11}C]acetate PET/CT, and CT for staging of BC [185]. MRI, [^{11}C]acetate PET/CT, and CT demonstrated similar levels of accuracy. For all modalities, a history of intravesical and/or systemic chemotherapy affected staging accuracy. [^{11}C]acetate PET/CT has been compared to [^{11}C]choline PET/CT in BC [186]. [^{11}C]acetate and [^{11}C]choline scans were performed within 1 week. The two tracers demonstrated equivalent results in the preoperative evaluation.

^{18}F-Fluoride. Lytic bone metastases of BC may be better detected using Na^{18}F PET scans compared with conventional ^{99m}Tc-MDP bone scan. In a prospective study, Na^{18}F PET/CT and ^{99m}Tc-MDP bone scan were compared in the detection of skeletal metastases in 48 patients with BC [187]. Both imaging modalities were performed within 48 h. Na^{18}F PET/CT identified bony metastases and changed the management in 17 of 48 patients (35%). The sensitivity, specificity, positive predictive value, negative predictive value, and accuracy of ^{99m}Tc-MDP planar bone scintigraphy were 82.35%, 64.51%, 56%, 86.95%, and 70.83%; of ^{99m}Tc-MDP SPECT/CT were 88.23%, 74.19%, 65.21%, 92%, and 79.16%; and of Na^{18}F PET/CT were 100%, 87.09%, 80.95%, 100%, and 91.66%, respectively. The study demonstrated that Na^{18}F PET/CT is superior to both ^{99m}Tc-MDP planar scintigraphy and ^{99m}Tc-MDP SPECT/CT for detection of bone metastases in BC.

Common Therapies

Treatment of Superficial Bladder Cancer

Most BCs are "non-muscle invasive" at the time of initial diagnosis. Roughly 70% of newly diagnosed BC is superficial disease [101]. They are either confined to the mucosa (stage Ta, CIS) or invade the lamina propria but not the muscularis propria (stage T1). Among the superficial cancer groups, approximately 70% present as Ta lesions, 20% as T1, and 10% as CIS [101]. Stage Ta tumors, especially those which are low grade, have a low risk of progression over time, and there is a trend toward more conservative management of these tumors. Therefore, in the majority of these patients, management can be limited to resection and subsequent observation [188]. Stage T1 tumors represent greater challenge to the urologist. Although these tumors are grouped into the category of "superficial," their risk of progression is much higher over time. The heterogeneity of T1 disease complicates its treatment. It remains a

challenge to determine which patient is at high risk of progression versus the patients who will do well with adjuvant intravesical therapy. The European Association of Urology (EAU) and American Urological Association (AUA) have similar recommendations for induction and maintenance treatment in patients based on clinical and pathologic risk factors [99, 189]. Low-risk patients (low-grade Ta) can be monitored on surveillance protocols. Conversely, those patients with high-risk superficial disease (CIS, T1, high-grade Ta, multiple tumors, and >3-cm tumors) should strongly be considered for adjuvant intravesical therapy.

Intravesical chemotherapy. Although TURB can remove a Ta and T1 tumor completely, recurrence of the disease is often seen and can progress to muscle-invasive BC. It is therefore important to consider adjuvant therapy in the patients. A single intravesical instillation of chemotherapy may be effective against circulating tumor cells resulting from TURB, on residual tumor cells at the resection site, and on overlooked tumors in the bladder [190–193]. Mitomycin, epirubicin, and doxorubicin have shown to be effective for that purpose [191–193]. The single intravesical chemotherapy instillation should be performed as soon as possible (within the first hours) after TURB. Chemotherapy in combination with hyperthermia seems to be a new promising treatment [194]. The need for further adjuvant chemotherapy depends on prognosis. In low-risk patients, the single intravesical instillation may be sufficient and is considered to be the standard therapy. In high-risk patients with a high likelihood of recurrence and/or progression, the single instillation is insufficient, and further instillations are recommended [195]. Intravesical bacillus Calmette-Guérin (BCG) immunotherapy maintenance therapy can also be used [196, 197], but more side effects are seen with BCG as compared to chemotherapy [198]. The length and frequency of chemotherapy instillations are still a topic of debate because of conflicting results [199]. Normally the chemotherapy lasts no longer than a year. A single postoperative instillation with chemotherapy is only indicated in low-risk disease. BCG is the treatment of choice for high-grade disease [194] and should be given as maintenance [194].

Intravesical BCG immunotherapy. Several meta-analyses have demonstrated that intravesical BCG immunotherapy is superior to TURB alone or TURB + chemotherapy for preventing recurrence of non-muscle-invasive BC [200–204]. The effect of BCG treatment is long lasting [205, 206]. Two meta-analyses have shown that BCG therapy prevents or delays the risk of progression of the bladder tumor [196, 206]. BCG represents the only agent known to reduce progression into muscle-invasive BC [189]. The addition of chemotherapy to maintenance BCG does not improve the efficacy [207]. Regarding BCG toxicity, BCG is clearly associated with more side effects as compared to intravesical chemotherapy [197]. Serious side effects are seen in less than 5% of the patients and can be treated effectively in nearly all cases [208]. Because major complications can be seen after systemic absorption of BCG, contraindications of BCG instillations should be followed. Absolute contraindications are during the first 2 weeks after TURB, in patients with visible hematuria, after traumatic catheterization, and in patients with symptomatic urinary tract infection [189]. Induction BCG therapy is given as 6-weekly schedule, and for optimal therapy, BCG must be given in a maintenance schedule. However, several different maintenance schedules are used. The optimal number of BCG induction instillations and duration of maintenance therapy is still unknown [209]. In BCG failures, cystectomy is recommended [194].

Treatment failure of non-muscle-invasive bladder cancer. According to EAU guidelines, it is reasonable to consider immediate radical cystectomy in patients with non-muscle-invasive BC tumors who have a high risk of progression: (1) T1 tumor, (2) G3 (high-grade) tumor, (3) CIS, and (4) multiple and recurrent and large (>3 cm) TaG1G2 tumors [210, 211]. Furthermore, cystectomy is strongly recommended in patients with BCG refractory tumors: (1) whenever muscle-invasive tumor is detected in follow-up; (2) if high-grade, non-muscle-invasive papillary tumor is present at 3 months; (3) if CIS (without concomitant papillary tumor) is present at both 3 and 6 months; (4) if high-grade tumor appears during BCG therapy; and (5) if there is high-grade recurrence after BCG [210].

Treatment of Muscle-Invasive Bladder Cancer

Surgery. The primary modality for treatment of clinically localized muscle-invasive BC is surgery, and developments in this field focus on minimizing the morbidity of surgery. Radical cystoprostatectomy with bilateral PLND remains the gold standard for management of muscle-invasive BC [114, 115, 210]. However, the precise limits of the LN dissection are debated [114]. Data from a large group of patients support the aggressive surgical management of invasive BC [212]. Recently, interest in the patient's quality of life has resulted in a trend toward bladder-preserving treatment modalities such as radio- and/or chemotherapy. The patients' performance status and age influence the choice of primary therapy, as well as the type of urinary diversion, with cystectomy being preferred in younger patients with good performance status and without concomitant disease [210, 213]. Long-term disease-free survival of up to 70% can be achieved in most patients with organ-confined disease [114, 212]. When there are metastatic involvements of LNs, orthotopic neobladder can still be considered in the case of N1 involvement (metastases in a single LN), but this is not the case of N2 or N3 tumors [214]. In men the standard radical cystectomy includes the removal of the bladder, prostate, seminal vesicles, distal ureters, and regional LNs. In women, standard radical cystectomy includes the removal of the bladder, entire urethra, adjacent vagina, uterus, distal ureters, and regional LNs [210]. Regional LNs consist of nodes below the bifurcation of the aorta [164, 210, 215–217]. The extent of LN dissection is not established yet. The standard lymphadenectomy includes the removal of LN up to the common iliac bifurcation, extended lymphadenectomy includes LNs in the region of the aortic bifurcation and presacral and common iliac vessel, and super-extended lymphadenectomy extends cranially to the level of the inferior mesenteric artery [210]. Cystectomy may be performed as open operation, laparoscopic cystectomy, or robotic-assisted laparoscopic cystectomy. Laparoscopic operation is a technically challenging procedure that requires high level of expertise in the institution [218–220]. Urinary diversion after radical cystectomy may be performed as (a) abdominal diversion, such as ureterocutaneostomy, ileal or colonic conduit, and various forms of continent pouch; (b) urethral diversion, which includes various forms of gastrointestinal pouches attached to the urethra as a continent; (c) orthotopic urinary diversion (neobladder, orthotopic bladder substitution); or (d) rectosigmoid diversions, such as uretero(ileo) rectostomy [210]. Currently, there is no particular type of urinary diversion that is generally recommended, but most institutions prefer ileal orthotopic neobladders and ileal conducts [210].

Neoadjuvant chemotherapy. The 5-year survival after standard radical cystectomy is only about 50% [210]. Neoadjuvant and adjuvant chemotherapy have been utilized in an attempt to improve outcomes for patients with high-risk muscle-invasive BC. Systematic chemotherapy using multidrug regimens is the standard therapy for metastatic disease, and the classic combination is the four-drug regimen MVAC (methotrexate, vinblastine, doxorubicin, and cisplatin) [115, 221, 222]. Neoadjuvant chemotherapy with cisplatin is recommended for T2-T4a, cN0 M0 bladder cancer, but is not recommended in patients who are ineligible for cisplatin-based combination chemotherapy [210]. Chemotherapy is delivered as early as possible, when the burden of micrometastatic disease is lowest as possible. The presence of micrometastases may be lower in small tumors compared to more extensive tumors. Neoadjuvant chemotherapy does not affect the outcome of surgical morbidity [223]. Currently, there is no available tool to select the patients who will benefit from neoadjuvant chemotherapy. Adjuvant chemotherapy after radical cystectomy is under debate in patients with pT3/T4 and/or LN-positive disease without detectable metastases (M0). According to EAU guidelines, adjuvant cisplatin combination chemotherapy can be offered to patients with pT3/T4 and/or pN+ disease if no neoadjuvant chemotherapy has been given [210].

Preoperative radiotherapy. Preoperative radiotherapy followed by cystectomy after 6 weeks has been investigated, but conflicting results exist. A meta-analysis of five randomized trials showed an odds ratio for the difference in 5-year survival

of 71% in favor of the preoperative radiotherapy, but when the largest study was excluded (because the patients did not receive the planned treatment), no significant difference was found, and it was concluded that the available clinical trial data do not support a role for routine use of preoperative radiation therapy in the treatment of muscle-invasive BC [224]. In the EAU guidelines, preoperative radiotherapy is not recommended to improve survival [210]. However, preoperative radiotherapy may result in downstaging after 4–6 weeks [210, 225, 226].

Unresectable tumors. Patients with locally advanced disease (T4b, invasion of pelvic or abdominal wall) are candidates for palliative radiotherapy. In patients with symptoms, palliative cystectomy may be an option. In muscle-invasive BC patients not suitable for radical cystectomy, transurethral resection of bladder tumor (TURB) may be performed, but TURB alone is not a curative treatment. External beam radiotherapy (EBRT) alone or chemotherapy alone is not recommended as a primary therapy for localized BC [210]. Multimodality bladder-preserving treatment combines TURB, radiation, and chemotherapy, and the aim is to obtain local tumor control. Multimodality treatment can be offered in selected and compliant patients, especially in patients where cystectomy is not an option [210].

Metastatic disease/recurrence. At the time of diagnosis of muscle-invasive BC, 10–15% of the patients have metastatic disease [227]. In patients treated with radical cystectomy, about 50% of the patients will get relapse, depending on the pathological stage of the primary tumor and LN metastases. About 30% are local relapse, and distant metastases are the most common site of recurrence. Distant metastases are most commonly seen in the LNs, lungs, liver, and bones. Patients with metastatic disease are treated with chemotherapy.

Surveillance. One of the distinguishing features of UC is that it has the highest recurrence rate for any cancer, thereby making rigorous post-treatment surveillance, often referred to as "urothelial surveillance," necessary in all patients. These tumors are also commonly multifocal. They involve any part of the urothelium in a seemingly random manner. An appropriate schedule for BC monitoring should be based on the natural timing of recurrence, probability and site of recurrence, functional monitoring after urinary diversion, and possible treatment of recurrence [210]. The follow-up of Ta, T1 tumors, and CIS is based on regular cystoscopy, and the time schedule of monitoring depends on tumor grade (CIS, Ta, T1) [189]. After TURB, patients should have cystoscopy and voided urine cytology every 3 months for 2 years, then six monthly for 2 years, and then once yearly indefinitely [95]. Upper tract imaging should be done every 12–24 months to establish whether a UC is present in the renal collecting system or ureters, because lifetime risk for the development of an upper tract tumor after a diagnosis of BC is about 5% [95].

References

1. Jonasch E, Futreal PA, Davis IJ, Bailey ST, Kim WY, Brugarolas J, et al. State of the science: an update on renal cell carcinoma. Mol Cancer Res. 2012;10:859–80.
2. Siegel RL, Miller KD, Jemal A. Cancer statistics, 2016. CA Cancer J Clin. 2016;66:7–30.
3. Capitanio U, Montorsi F. Renal cancer. Lancet. 2016;387:894–906.
4. Ljungberg B, Campbell SC, Choi HY, Jacqmin D, Lee JE, Weikert S, et al. The epidemiology of renal cell carcinoma. Eur Urol. 2011;60:615–21.
5. Rini BI, Campbell SC, Rathmell WK. Renal cell carcinoma. Curr Opin Oncol. 2006;18:289–96.
6. Shuch B, Amin A, Armstrong AJ, Eble JN, Ficarra V, Lopez-Beltran A, et al. Understanding pathologic variants of renal cell carcinoma: distilling therapeutic opportunities from biologic complexity. Eur Urol. 2015;67:85–97.
7. Ng CS, Wood CG, Silverman PM, Tannir NM, Tamboli P, Sandler CM. Renal cell carcinoma: diagnosis, staging, and surveillance. AJR Am J Roentgenol. 2008;191:1220–32.
8. Linehan WM, Rathmell WK. Kidney cancer. Urol Oncol. 2012;30:948–51.
9. Mueller-Lisse UG, Mueller-Lisse UL, Meindl T, Coppenrath E, Degenhart C, Graser A, et al. Staging of renal cell carcinoma. Eur Radiol. 2007;17:2268–77.
10. Sankineni S, Brown A, Cieciera M, Choyke PL, Turkbey B. Imaging of renal cell carcinoma. Urol Oncol. 2016;34:147–55.
11. Jamis-Dow CA, Choyke PL, Jennings SB, Linehan WM, Thakore KN, Walther MM. Small (< or = 3-cm) renal masses: detection with CT versus US and pathologic correlation. Radiology. 1996;198:785–8.

12. Wang C, Yu C, Yang F, Yang G. Diagnostic accuracy of contrast-enhanced ultrasound for renal cell carcinoma: a meta-analysis. Tumour Biol. 2014;35: 6343–50.
13. Kong WT, Zhang WW, Guo HQ, Qiu JL, Tang M, Jiang ZM, et al. Application of contrast-enhanced ultrasonography after radiofrequency ablation for renal cell carcinoma: is it sufficient for assessment of therapeutic response? Abdom Imaging. 2011;36:342–7.
14. Heidenreich A, Ravery V, European Society of Oncological U. Preoperative imaging in renal cell cancer. World J Urol. 2004;22:307–15.
15. Kim JK, Kim TK, Ahn HJ, Kim CS, Kim KR, Cho KS. Differentiation of subtypes of renal cell carcinoma on helical CT scans. AJR Am J Roentgenol. 2002;178:1499–506.
16. Bolton DM, Wong P, Lawrentschuk N. Renal cell carcinoma: imaging and therapy. Curr Opin Urol. 2007;17:337–40.
17. Young JR, Margolis D, Sauk S, Pantuck AJ, Sayre J, Raman SS. Clear cell renal cell carcinoma: discrimination from other renal cell carcinoma subtypes and oncocytoma at multiphasic multidetector CT. Radiology. 2013;267:444–53.
18. Nikken JJ, Krestin GP. MRI of the kidney-state of the art. Eur Radiol. 2007;17:2780–93.
19. Aslam Sohaib SA, Teh J, Nargund VH, Lumley JS, Hendry WF, Reznek RH. Assessment of tumor invasion of the vena caval wall in renal cell carcinoma cases by magnetic resonance imaging. J Urol. 2002; 167:1271–5.
20. Ramamurthy NK, Moosavi B, McInnes MD, Flood TA, Schieda N. Multiparametric MRI of solid renal masses: pearls and pitfalls. Clin Radiol. 2015;70: 304–16.
21. Ramdave S, Thomas GW, Berlangieri SU, Bolton DM, Davis I, Danguy HT, et al. Clinical role of F-18 fluorodeoxyglucose positron emission tomography for detection and management of renal cell carcinoma. J Urol. 2001;166:825–30.
22. Aide N, Cappele O, Bottet P, Bensadoun H, Regeasse A, Comoz F, et al. Efficiency of [^{18}F]FDG PET in characterising renal cancer and detecting distant metastases: a comparison with CT. Eur J Nucl Med Mol Imaging. 2003;30:1236–45.
23. Ozulker T, Ozulker F, Ozbek E, Ozpacaci T. A prospective diagnostic accuracy study of F-18 fluorodeoxyglucose-positron emission tomography/computed tomography in the evaluation of indeterminate renal masses. Nucl Med Commun. 2011;32:265–72.
24. Nakajima R, Abe K, Kondo T, Tanabe K, Sakai S. Clinical role of early dynamic FDG-PET/CT for the evaluation of renal cell carcinoma. Eur Radiol. 2016; 26:1852–62.
25. Makis W, Ciarallo A, Rakheja R, Probst S, Hickeson M, Rush C, et al. Spectrum of malignant renal and urinary bladder tumors on ^{18}F-FDG PET/CT: a pictorial essay. Clin Imaging. 2012;36:660–73.
26. Oyama N, Ito H, Takahara N, Miwa Y, Akino H, Kudo T, et al. Diagnosis of complex renal cystic masses and solid renal lesions using PET imaging: comparison of ^{11}C-acetate and ^{18}F-FDG PET imaging. Clin Nucl Med. 2014;39:e208–14.
27. Ferda J, Ferdova E, Hora M, Hes O, Finek J, Topolcan O, et al. ^{18}F-FDG-PET/CT in potentially advanced renal cell carcinoma: a role in treatment decisions and prognosis estimation. Anticancer Res. 2013;33:2665–72.
28. Ak I, Can C. F-18 FDG PET in detecting renal cell carcinoma. Acta Radiol. 2005;46:895–9.
29. Bachor R, Kotzerke J, Gottfried HW, Brandle E, Reske SN, Hautmann R. Positron emission tomography in diagnosis of renal cell carcinoma. Urol A. 1996;35: 146–50.
30. Montravers F, Grahek D, Kerrou K, Younsi N, Doublet JD, Gattegno B, et al. Evaluation of FDG uptake by renal malignancies (primary tumor or metastases) using a coincidence detection gamma camera. J Nucl Med. 2000;41:78–84.
31. Kang DE, White Jr RL, Zuger JH, Sasser HC, Teigland CM. Clinical use of fluorodeoxyglucose F 18 positron emission tomography for detection of renal cell carcinoma. J Urol. 2004;171:1806–9.
32. Fanti S, Nanni C, Ambrosini V, Gross MD, Rubello D, Farsad M. PET in genitourinary tract cancers. Q J Nucl Med Mol Imaging. 2007;51:260–71.
33. Wang HY, Ding HJ, Chen JH, Chao CH, Lu YY, Lin WY, et al. Meta-analysis of the diagnostic performance of [^{18}F]FDG-PET and PET/CT in renal cell carcinoma. Cancer Imaging. 2012;12:464–74.
34. Takahashi M, Kume H, Koyama K, Nakagawa T, Fujimura T, Morikawa T, et al. Preoperative evaluation of renal cell carcinoma by using ^{18}F-FDG PET/CT. Clin Nucl Med. 2015;40:936–40.
35. Nakhoda Z, Torigian DA, Saboury B, Hofheinz F, Alavi A. Assessment of the diagnostic performance of ^{18}F-FDG-PET/CT for detection and characterization of solid renal malignancies. Hell J Nucl Med. 2013;16:19–24.
36. Bouchelouche K, Choyke PL. PET/computed tomography in renal, bladder, and testicular cancer. PET Clin. 2015;10:361–74.
37. Bertagna F, Motta F, Bertoli M, Bosio G, Fisogni S, Tardanico R, et al. Role of F18-FDG-PET/CT in restaging patients affected by renal carcinoma. Nucl Med Rev Cent East Eur. 2013;16:3–8.
38. Majhail NS, Urbain JL, Albani JM, Kanvinde MH, Rice TW, Novick AC, et al. F-18 fluorodeoxyglucose positron emission tomography in the evaluation of distant metastases from renal cell carcinoma. J Clin Oncol. 2003;21:3995–4000.
39. Czarnecka AM, Kornakiewicz A, Kukwa W, Szczylik C. Frontiers in clinical and molecular diagnostics and staging of metastatic clear cell renal cell carcinoma. Future Oncol. 2014;10:1095–111.
40. Ravina M, Hess S, Chauhan MS, Jacob MJ, Alavi A. Tumor thrombus: ancillary findings on FDG

PET/CT in an oncologic population. Clin Nucl Med. 2014;39:767–71.
41. Jadvar H, Kherbache HM, Pinski JK, Conti PS. Diagnostic role of [F-18]-FDG positron emission tomography in restaging renal cell carcinoma. Clin Nephrol. 2003;60:395–400.
42. Nakatani K, Nakamoto Y, Saga T, Higashi T, Togashi K The potential clinical value of FDG-PET for recurrent renal cell carcinoma. Eur J Radiol. 2011;79: 29–35.
43. Safaei A, Figlin R, Hoh CK, Silverman DH, Seltzer M, Phelps ME, et al. The usefulness of F-18 deoxyglucose whole-body positron emission tomography (PET) for re-staging of renal cell cancer. Clin Nephrol. 2002;57:56–62.
44. Alongi P, Picchio M, Zattoni F, Spallino M, Gianolli L, Saladini G, et al. Recurrent renal cell carcinoma: clinical and prognostic value of FDG PET/CT. Eur J Nucl Med Mol Imaging. 2016;43:464–73.
45. Martinez de Llano SR, Delgado-Bolton RC, Jimenez-Vicioso A, Perez-Castejon MJ, Carreras Delgado JL, Ramos E, et al. Meta-analysis of the diagnostic performance of ^{18}F-FDG PET in renal cell carcinoma. Rev Esp Med Nucl. 2007;26:19–29.
46. Chen JL, Appelbaum DE, Kocherginsky M, Cowey CL, Rathmell WK, McDermott DF, et al. FDG-PET as a predictive biomarker for therapy with everolimus in metastatic renal cell cancer. Cancer Med. 2013;2:545–52.
47. Vercellino L, Bousquet G, Baillet G, Barre E, Mathieu O, Just PA, Desgrandchamps F, Misset JL, Hindie E, Moretti JL. ^{18}F-FDG PET/CT imaging for an early assessment of response to sunitinib in metastatic renal carcinoma: preliminary study. Cancer Biother Radiopharm. 2009;24:137–44.
48. Kayani I, Avril N, Bomanji J, Chowdhury S, Rockall A, Sahdev A, et al. Sequential FDG-PET/CT as a biomarker of response to sunitinib in metastatic clear cell renal cancer. Clin Cancer Res. 2011;17:6021–8.
49. Khandani AH, Cowey CL, Moore DT, Gohil H, Rathmell WK. Primary renal cell carcinoma: relationship between ^{18}F-FDG uptake and response to neoadjuvant sorafenib. Nucl Med Commun. 2012;33: 967–73.
50. Kakizoe M, Yao M, Tateishi U, Minamimoto R, Ueno D, Namura K, et al. The early response of renal cell carcinoma to tyrosine kinase inhibitors evaluated by FDG PET/CT was not influenced by metastatic organ. BMC Cancer. 2014;14:390.
51. Motzer RJ, Bander NH, Nanus DM. Renal-cell carcinoma. N Engl J Med. 1996;335:865–75.
52. Nakaigawa N, Kondo K, Tateishi U, Minamimoto R, Kaneta T, Namura K, et al. FDG PET/CT as a prognostic biomarker in the era of molecular-targeting therapies: max SUVmax predicts survival of patients with advanced renal cell carcinoma. BMC Cancer. 2015;16:67.
53. Janzen NK, Kim HL, Figlin RA, Belldegrun AS. Surveillance after radical or partial nephrectomy for localized renal cell carcinoma and management of recurrent disease. Urol Clin N Am. 2003;30:843–52.
54. Smaldone MC, Uzzo RG. Balancing process and risk: standardizing posttreatment surveillance for renal cell carcinoma. J Urol. 2013;190:417–8.
55. Park JW, Jo MK, Lee HM. Significance of ^{18}F-fluorodeoxyglucose positron-emission tomography/computed tomography for the postoperative surveillance of advanced renal cell carcinoma. BJU Int. 2009;103:615–9.
56. Jung ST, Ghert MA, Harrelson JM, Scully SP. Treatment of osseous metastases in patients with renal cell carcinoma. Clin Orthop Relat Res. 2003; 409:223–31.
57. Swanson DA, Orovan WL, Johnson DE, Giacco G. Osseous metastases secondary to renal cell carcinoma. Urology. 1981;18:556–61.
58. Sharma P, Karunanithi S, Chakraborty PS, Kumar R, Seth A, Julka PK, et al. ^{18}F-fluoride PET/CT for detection of bone metastasis in patients with renal cell carcinoma: a pilot study. Nucl Med Commun. 2014;35:1247–53.
59. Fuccio C, Spinapolice EG, Cavalli C, Palumbo R, D'Ambrosio D, Trifirò G. ^{18}F-fluoride PET/CT in the detection of bone metastases in clear cell renal cell carcinoma: discordance with bone scintigraphy. Eur J Nucl Med Mol Imaging. 2013;40:1930–1.
60. Oosterwijk E, Ruiter DJ, Hoedemaeker PJ, Pauwels EK, Jonas U, Zwartendijk J, et al. Monoclonal antibody G 250 recognizes a determinant present in renal-cell carcinoma and absent from normal kidney. Int J Cancer. 1986;38:489–94.
61. Stillebroer AB, Oosterwijk E, Oyen WJ, Mulders PF, Boerman OC. Radiolabeled antibodies in renal cell carcinoma. Cancer Imaging. 2007;7:179–88.
62. Pastorekova S, Ratcliffe PJ, Pastorek J. Molecular mechanisms of carbonic anhydrase IX-mediated pH regulation under hypoxia. BJU Int. 2008;101 Suppl 4:8–15.
63. Belldegrun AS, Bevan P. Carbonic anhydrase IX: role in diagnosis prognosis and cancer therapy. Introduction. BJU Int. 2008;101 Suppl 4:1.
64. Shuch B, Li Z, Belldegrun AS. Carbonic anhydrase IX and renal cell carcinoma: prognosis, response to systemic therapy, and future vaccine strategies. BJU Int. 2008;101 Suppl 4:25–30.
65. Brouwers A, Verel I, Van Eerd J, Visser G, Steffens M, Oosterwijk E, et al. PET radioimmunoscintigraphy of renal cell cancer using ^{89}Zr-labeled cG250 monoclonal antibody in nude rats. Cancer Biother Radiopharm. 2004;19:155–63.
66. Cheal SM, Punzalan B, Doran MG, Evans MJ, Osborne JR, Lewis JS, et al. Pairwise comparison of ^{89}Zr- and ^{124}I-labeled cG250 based on positron emission tomography imaging and nonlinear immunokinetic modeling: in vivo carbonic anhydrase IX receptor binding and internalization in mouse

xenografts of clear-cell renal cell carcinoma. Eur J Nucl Med Mol Imaging. 2014;41:985–94.
67. Divgi CR, Pandit-Taskar N, Jungbluth AA, Reuter VE, Gonen M, Ruan S, et al. Preoperative characterisation of clear-cell renal carcinoma using iodine-124-labelled antibody chimeric G250 (^{124}I-cG250) and PET in patients with renal masses: a phase I trial. Lancet Oncol. 2007;8:304–10.
68. Divgi CR, Uzzo RG, Gatsonis C, Bartz R, Treutner S, Yu JQ, et al. Positron emission tomography/computed tomography identification of clear cell renal cell carcinoma: results from the REDECT trial. J Clin Oncol. 2013;31:187–94.
69. Oyama N, Okazawa H, Kusukawa N, Kaneda T, Miwa Y, Akino H, et al. ^{11}C-acetate PET imaging for renal cell carcinoma. Eur J Nucl Med Mol Imaging. 2009;36:422–7.
70. Shreve P, Chiao PC, Humes HD, Schwaiger M, Gross MD. Carbon-11-acetate PET imaging in renal disease. J Nucl Med. 1995;36:1595–601.
71. Lawrentschuk N, Poon AM, Foo SS, Putra LG, Murone C, Davis ID, et al. Assessing regional hypoxia in human renal tumours using ^{18}F-fluoromisonidazole positron emission tomography. BJU Int. 2005;96:540–6.
72. Lawrentschuk N, Poon AM, Scott AM. Fluorine-18 fluorothymidine: a new positron emission radioisotope for renal tumors. Clin Nucl Med. 2006;31:788–9.
73. Duran M, Matheus W, Ferreira U, Clark O. Systematic review and meta-analysis of target therapies for the treatment of metastatic renal cancer. Int Braz J Urol. 2013;39:768–78.
74. Gattinoni L, Alu M, Ferrari L, Nova P, Del Vecchio M, Procopio G, et al. Renal cancer treatment: a review of the literature. Tumori. 2003;89:476–84.
75. Rini BI, Campbell SC, Escudier B. Renal cell carcinoma. Lancet. 2009;373:1119–32.
76. Gratzke C, Seitz M, Bayrle F, Schlenker B, Bastian PJ, Haseke N, et al. Quality of life and perioperative outcomes after retroperitoneoscopic radical nephrectomy (RN), open RN and nephron-sparing surgery in patients with renal cell carcinoma. BJU Int. 2009;104:470–5.
77. Huang WC, Elkin EB, Levey AS, Jang TL, Russo P. Partial nephrectomy versus radical nephrectomy in patients with small renal tumors – is there a difference in mortality and cardiovascular outcomes? J Urol. 2009;181:55–61. discussion 61–52.
78. Zini L, Perrotte P, Capitanio U, Jeldres C, Shariat SF, Antebi E, et al. Radical versus partial nephrectomy: effect on overall and noncancer mortality. Cancer. 2009;115:1465–71.
79. Thompson RH, Boorjian SA, Lohse CM, Leibovich BC, Kwon ED, Cheville JC, et al. Radical nephrectomy for pT1a renal masses may be associated with decreased overall survival compared with partial nephrectomy. J Urol. 2008;179:468–71. discussion 472–463.
80. Ljungberg B, Bensalah K, Canfield S, Dabestani S, Hoffmann F, Hora M, et al. EAU guidelines on renal cell carcinoma:2014 update. Eur Urol. 2015;67:913–24.
81. Zini L, Perrotte P, Jeldres C, Capitanio U, Duclos A, Jolivet-Tremblay M, et al. A population-based comparison of survival after nephrectomy vs nonsurgical management for small renal masses. BJU Int. 2009;103:899–904. discussion 904.
82. Sun M, Bianchi M, Trinh QD, Hansen J, Abdollah F, Hanna N, et al. Comparison of partial vs radical nephrectomy with regard to other-cause mortality in T1 renal cell carcinoma among patients aged >/=75 years with multiple comorbidities. BJU Int. 2013;111:67–73.
83. Sun M, Becker A, Tian Z, Roghmann F, Abdollah F, Larouche A, et al. Management of localized kidney cancer: calculating cancer-specific mortality and competing risks of death for surgery and nonsurgical management. Eur Urol. 2014;65:235–41.
84. Huang WC, Atoria CL, Bjurlin M, Pinheiro LC, Russo P, Lowrance WT, et al. Management of small kidney cancers in the new millennium: contemporary trends and outcomes in a population-based cohort. JAMA Surg. 2015;150:664–72.
85. Jewett MA, Mattar K, Basiuk J, Morash CG, Pautler SE, Siemens DR, et al. Active surveillance of small renal masses: progression patterns of early stage kidney cancer. Eur Urol. 2011;60:39–44.
86. Smaldone MC, Kutikov A, Egleston BL, Canter DJ, Viterbo R, Chen DY, et al. Small renal masses progressing to metastases under active surveillance: a systematic review and pooled analysis. Cancer. 2012;118:997–1006.
87. Margulis V, Sanchez-Ortiz RF, Tamboli P, Cohen DD, Swanson DA, Wood CG. Renal cell carcinoma clinically involving adjacent organs: experience with aggressive surgical management. Cancer. 2007;109:2025–30.
88. Haferkamp A, Bastian PJ, Jakobi H, Pritsch M, Pfitzenmaier J, Albers P, et al. Renal cell carcinoma with tumor thrombus extension into the vena cava: prospective long-term followup. J Urol. 2007;177:1703–8.
89. Kirkali Z, Van Poppel H. A critical analysis of surgery for kidney cancer with vena cava invasion. Eur Urol. 2007;52:658–62.
90. Stadler WM, Huo D, George C, Yang X, Ryan CW, Karrison T, et al. Prognostic factors for survival with gemcitabine plus 5-fluorouracil based regimens for metastatic renal cancer. J Urol. 2003;170:1141–5.
91. Gore ME, Griffin CL, Hancock B, Patel PM, Pyle L, Aitchison M, et al. Interferon alfa-2a versus combination therapy with interferon alfa-2a, interleukin-2, and fluorouracil in patients with untreated metastatic renal cell carcinoma (MRC RE04/EORTC GU 30012): an open-label randomised trial. Lancet. 2010;375:641–8.

92. Coppin C, Kollmannsberger C, Le L, Porzsolt F, Wilt TJ. Targeted therapy for advanced renal cell cancer (RCC): a cochrane systematic review of published randomised trials. BJU Int. 2011;108:1556–63.
93. Garcia Garzon JR, Bassa P, Llinares E, Soler M, Moragas M, Riera E. Metastatic renal cell cancer treated with antiangiogenic therapy monitoring by ^{18}F-FDG PET/CT. Clin Nucl Med. 2015;40:910–1.
94. Abdollah F, Gandaglia G, Thuret R, Schmitges J, Tian Z, Jeldres C, et al. Incidence, survival and mortality rates of stage-specific bladder cancer in United States: a trend analysis. Cancer Epidemiol. 2013;37:219–25.
95. Kaufman DS, Shipley WU, Feldman AS. Bladder cancer. Lancet. 2009;374:239–49.
96. Botteman MF, Pashos CL, Redaelli A, Laskin B, Hauser R. The health economics of bladder cancer: a comprehensive review of the published literature. Pharmacoeconomics. 2003;21:1315–30.
97. Parkin DM. The global burden of urinary bladder cancer. Scand J Urol Nephrol Suppl. 2008;218:12–20.
98. Burger M, Catto JW, Dalbagni G, Grossman HB, Herr H, Karakiewicz P, et al. Epidemiology and risk factors of urothelial bladder cancer. Eur Urol. 2013;63:234–41.
99. Green DA, Rink M, Xylinas E, Matin SF, Stenzl A, Roupret M, et al. Urothelial carcinoma of the bladder and the upper tract: disparate twins. J Urol. 2013;189:1214–21.
100. Crivelli JJ, Xylinas E, Kluth LA, Rieken M, Rink M, Shariat SF. Effect of smoking on outcomes of urothelial carcinoma: a systematic review of the literature. Eur Urol. 2014;65:742–54.
101. Kirkali Z, Chan T, Manoharan M, Algaba F, Busch C, Cheng L, et al. Bladder cancer: epidemiology, staging and grading, and diagnosis. Urology. 2005;66:4–34.
102. Freedman ND, Silverman DT, Hollenbeck AR, Schatzkin A, Abnet CC. Association between smoking and risk of bladder cancer among men and women. JAMA. 2011;306:737–45.
103. Gandini S, Botteri E, Iodice S, Boniol M, Lowenfels AB, Maisonneuve P, et al. Tobacco smoking and cancer: a meta-analysis. Int J Cancer. 2008;122:155–64.
104. Brennan P, Bogillot O, Cordier S, Greiser E, Schill W, Vineis P, et al. Cigarette smoking and bladder cancer in men: a pooled analysis of 11 case-control studies. Int J Cancer. 2000;86:289–94.
105. Pashos CL, Botteman MF, Laskin BL, Redaelli A. Bladder cancer: epidemiology, diagnosis, and management. Cancer Pract. 2002;10:311–22.
106. Rushton L, Bagga S, Bevan R, Brown TP, Cherrie JW, Holmes P, et al. Occupation and cancer in Britain. Br J Cancer. 2010;102:1428–37.
107. McDaniel AS, Zhai Y, Cho KR, Dhanasekaran SM, Montgomery JS, Palapattu G, et al. HRAS mutations are frequent in inverted urothelial neoplasms. Hum Pathol. 2014;45:1957–65.
108. Schroeder JC, Conway K, Li Y, Mistry K, Bell DA, Taylor JA. p53 mutations in bladder cancer: evidence for exogenous versus endogenous risk factors. Cancer Res. 2003;63:7530–8.
109. Fajkovic H, Halpern JA, Cha EK, Bahadori A, Chromecki TF, Karakiewicz PI, et al. Impact of gender on bladder cancer incidence, staging, and prognosis. World J Urol. 2011;29:457–63.
110. Kleinerman RA, Boice Jr JD, Storm HH, Sparen P, Andersen A, Pukkala E, et al. Second primary cancer after treatment for cervical cancer. An international cancer registries study. Cancer. 1995;76:442–52.
111. Kantor AF, Hartge P, Hoover RN, Narayana AS, Sullivan JW, Fraumeni Jr JF. Urinary tract infection and risk of bladder cancer. Am J Epidemiol. 1984;119:510–5.
112. Knowles MA, Hurst CD. Molecular biology of bladder cancer: new insights into pathogenesis and clinical diversity. Nat Rev Cancer. 2015;15:25–41.
113. Martin-Doyle W, Kwiatkowski DJ. Molecular biology of bladder cancer. Hematol Oncol Clin N Am. 2015;29:191–203. vii.
114. Barocas DA, Clark PE. Bladder cancer. Curr Opin Oncol. 2008;20:307–14.
115. Bischoff CJ, Clark PE. Bladder cancer. Curr Opin Oncol. 2009;21:272–7.
116. Kurth KH, Schellhammer PF, Okajima E, Akdas A, Jakse G, Herr HW, et al. Current methods of assessing and treating carcinoma in situ of the bladder with or without involvement of the prostatic urethra. Int J Urol. 1995;2 Suppl 2:8–22.
117. van Rhijn BW, van der Poel HG, van der Kwast TH. Urine markers for bladder cancer surveillance: a systematic review. Eur Urol. 2005;47:736–48.
118. Burger M, Grossman HB, Droller M, Schmidbauer J, Hermann G, Dragoescu O, et al. Photodynamic diagnosis of non-muscle-invasive bladder cancer with hexaminolevulinate cystoscopy: a meta-analysis of detection and recurrence based on raw data. Eur Urol. 2013;64:846–54.
119. Fradet Y, Grossman HB, Gomella L, Lerner S, Cookson M, Albala D, et al. A comparison of hexaminolevulinate fluorescence cystoscopy and white light cystoscopy for the detection of carcinoma in situ in patients with bladder cancer: a phase III, multicenter study. J Urol. 2007;178:68–73. discussion 73.
120. Grossman HB, Gomella L, Fradet Y, Morales A, Presti J, Ritenour C, et al. A phase III, multicenter comparison of hexaminolevulinate fluorescence cystoscopy and white light cystoscopy for the detection of superficial papillary lesions in patients with bladder cancer. J Urol. 2007;178:62–7.
121. Rink M, Babjuk M, Catto JW, Jichlinski P, Shariat SF, Stenzl A, et al. Hexyl aminolevulinate-guided fluorescence cystoscopy in the diagnosis and follow-up of patients with non-muscle-invasive bladder cancer: a critical review of the current literature. Eur Urol. 2013;64:624–38.
122. Malmstrom PU, Grabe M, Haug ES, Hellstrom P, Hermann GG, Mogensen K, et al. Role of

hexaminolevulinate-guided fluorescence cystoscopy in bladder cancer: critical analysis of the latest data and European guidance. Scand J Urol Nephrol. 2012;46:108–16.
123. MacVicar AD. Bladder cancer staging. BJU Int. 2000;86 Suppl 1:111–22.
124. Vikram R, Sandler CM, Ng CS. Imaging and staging of transitional cell carcinoma: part 1, lower urinary tract. AJR Am J Roentgenol. 2009;192:1481–7.
125. Beyersdorff D, Zhang J, Schoder H, Bochner B, Hricak H. Bladder cancer: can imaging change patient management? Curr Opin Urol. 2008;18:98–104.
126. Tsakiris P, de la Rosette J. Imaging in genitourinary cancer from the urologists' perspective. Cancer Imaging. 2007;7:84–92.
127. Lawrentschuk N, Lee ST, Scott AM. Current role of PET, CT, MR for invasive bladder cancer. Curr Urol Rep. 2013;14:84–9.
128. Takeuchi M, Sasaki S, Naiki T, Kawai N, Kohri K, Hara M, Shibamoto Y. MR imaging of urinary bladder cancer for T-staging: a review and a pictorial essay of diffusion-weighted imaging. J Magn Reson Imaging. 2013;38:1299–309.
129. Paik ML, Scolieri MJ, Brown SL, Spirnak JP, Resnick MI. Limitations of computerized tomography in staging invasive bladder cancer before radical cystectomy. J Urol. 2000;163:1693–6.
130. Hafeez S, Huddart R. Advances in bladder cancer imaging. BMC Med. 2013;11:104.
131. Knox MK, Cowan NC, Rivers-Bowerman MD, Turney BW. Evaluation of multidetector computed tomography urography and ultrasonography for diagnosing bladder cancer. Clin Radiol. 2008;63:1317–25.
132. Sadow CA, Silverman SG, O'Leary MP, Signorovitch JE. Bladder cancer detection with CT urography in an Academic Medical Center. Radiology. 2008;249:195–202.
133. Verma S, Rajesh A, Prasad SR, Gaitonde K, Lall CG, Mouraviev V, et al. Urinary bladder cancer: role of MR imaging. Radiographics. 2012;32:371–87.
134. Kundra V, Silverman PM. Imaging in oncology from the University of Texas M. D. Anderson Cancer Center. Imaging in the diagnosis, staging, and follow-up of cancer of the urinary bladder. AJR Am J Roentgenol. 2003;180:1045–54.
135. Kim B, Semelka RC, Ascher SM, Chalpin DB, Carroll PR, Hricak H. Bladder tumor staging: comparison of contrast-enhanced CT, T1- and T2-weighted MR imaging, dynamic gadolinium-enhanced imaging, and late gadolinium-enhanced imaging. Radiology. 1994;193:239–45.
136. Zhang J, Gerst S, Lefkowitz RA, Bach A. Imaging of bladder cancer. Radiol Clin N Am. 2007;45:183–205.
137. Rajesh A, Sokhi HK, Fung R, Mulcahy KA, Bankart MJ. Bladder cancer: evaluation of staging accuracy using dynamic MRI. Clin Radiol. 2011;66:1140–5.
138. Setty BN, Holalkere NS, Sahani DV, Uppot RN, Harisinghani M, Blake MA. State-of-the-art cross-sectional imaging in bladder cancer. Curr Probl Diagn Radiol. 2007;36:83–96.
139. Dorfman RE, Alpern MB, Gross BH, Sandler MA. Upper abdominal lymph nodes: criteria for normal size determined with CT. Radiology. 1991;180:319–22.
140. Barentsz JO, Engelbrecht MR, Witjes JA, de la Rosette JJ, van der Graaf M. MR imaging of the male pelvis. Eur Radiol. 1999;9:1722–36.
141. Deserno WM, Harisinghani MG, Taupitz M, Jager GJ, Witjes JA, Mulders PF, et al. Urinary bladder cancer: preoperative nodal staging with ferumoxtran-10-enhanced MR imaging. Radiology. 2004;233:449–56.
142. Knap MM, Lundbeck F, Overgaard J. Prognostic factors, pattern of recurrence and survival in a Danish bladder cancer cohort treated with radical cystectomy. Acta Oncol. 2003;42:160–8.
143. Kim JK, Park SY, Ahn HJ, Kim CS, Cho KS. Bladder cancer: analysis of multi-detector row helical CT enhancement pattern and accuracy in tumor detection and perivesical staging. Radiology. 2004;231:725–31.
144. Tekes A, Kamel I, Imam K, Szarf G, Schoenberg M, Nasir K, et al. Dynamic MRI of bladder cancer: evaluation of staging accuracy. AJR Am J Roentgenol. 2005;184:121–7.
145. Bouchelouche K, Turkbey B, Choyke PL. PET/CT and MRI in bladder cancer. J Cancer Sci Ther. 2012;30:S14.
146. Mertens LS, Bruin NM, Vegt E, de Blok WM, Fioole-Bruining A, van Rhijn BW, Horenblas S, Vogel WV. Catheter-assisted ^{18}F-FDG-PET/CT imaging of primary bladder cancer: a prospective study. Nucl Med Commun. 2012;33:1195–201.
147. Mertens LS, Fioole-Bruining A, Vegt E, Vogel WV, van Rhijn BW, Horenblas S. Detecting primary bladder cancer using delayed ^{18}F-2-fluoro-2-deoxy-D-glucose-positron emission tomography/computed tomography imaging after forced diuresis. Indian J Nucl Med. 2012;27:145–50.
148. Chondrogiannis S, Marzola MC, Colletti PM, Rubello D. Proposal of a new acquisition protocol for bladder cancer visualization with ^{18}F-FDG PET/CT. Clin Nucl Med. 2015;40:e78–80.
149. Anjos DA, Etchebehere EC, Ramos CD, Santos AO, Albertotti C, Camargo EE. ^{18}F-FDG PET/CT delayed images after diuretic for restaging invasive bladder cancer. J Nucl Med. 2007;48:764–70.
150. Yang Z, Cheng J, Pan L, Hu S, Xu J, Zhang Y, et al. Is whole-body fluorine-18 fluorodeoxyglucose PET/CT plus additional pelvic images (oral hydration-voiding-refilling) useful for detecting recurrent bladder cancer? Ann Nucl Med. 2012;26:571–7.
151. Harkirat S, Anand S, Jacob M. Forced diuresis and dual-phase F-fluorodeoxyglucose-PET/CT scan for restaging of urinary bladder cancers. Indian J Radiol Imaging. 2010;20:13–9.
152. Yildirim-Poyraz N, Ozdemir E, Uzun B, Turkolmez S. Dual phase ^{18}F-fluorodeoxyglucose positron

emission tomography/computed tomography with forced diuresis in diagnostic imaging evaluation of bladder cancer. Rev Esp Med Nucl Image Mol. 2013;32:214–21.
153. Wang N, Jiang P, Lu Y. Is fluorine-18 fluorodeoxyglucose positron emission tomography useful for detecting bladder lesions? A meta-analysis of the literature. Urol Int. 2014;92:143–9.
154. Swinnen G, Maes A, Pottel H, Vanneste A, Billiet I, Lesage K, Werbrouck P. FDG-PET/CT for the preoperative lymph node staging of invasive bladder cancer. Eur Urol. 2010;57:641–7.
155. Drieskens O, Oyen R, Van Poppel H, Vankan Y, Flamen P, Mortelmans L. FDG-PET for preoperative staging of bladder cancer. Eur J Nucl Med Mol Imaging. 2005;32:1412–7.
156. Bachor R, Kotzerke J, Reske SN, Hautmann R. Lymph node staging of bladder neck carcinoma with positron emission tomography. Urol A. 1999;38:46–50.
157. Kosuda S, Kison PV, Greenough R, Grossman HB, Wahl RL. Preliminary assessment of fluorine-18 fluorodeoxyglucose positron emission tomography in patients with bladder cancer. Eur J Nucl Med. 1997;24:615–20.
158. Mertens LS, Fioole-Bruining A, Vegt E, Vogel WV, van Rhijn BW, Horenblas S. Impact of ^{18}F-fluorodeoxyglucose (FDG)-positron-emission tomography/computed tomography (PET/CT) on management of patients with carcinoma invading bladder muscle. BJU Int. 2013;112:729–34.
159. Apolo AB, Riches J, Schoder H, Akin O, Trout A, Milowsky MI, et al. Clinical value of fluorine-18 2-fluoro-2-deoxy-D-glucose positron emission tomography/computed tomography in bladder cancer. J Clin Oncol. 2010;28:3973–8.
160. Kibel AS, Dehdashti F, Katz MD, Klim AP, Grubb RL, Humphrey PA, et al. Prospective study of [^{18}F] fluorodeoxyglucose positron emission tomography/computed tomography for staging of muscle-invasive bladder carcinoma. J Clin Oncol. 2009;27:4314–20.
161. Liu IJ, Lai YH, Espiritu JI, Segall GM, Srinivas S, Nino-Murcia M, et al. Evaluation of fluorodeoxyglucose positron emission tomography imaging in metastatic transitional cell carcinoma with and without prior chemotherapy. Urol Int. 2006;77:69–75.
162. Jensen TK, Holt P, Gerke O, Riehmann M, Svolgaard B, Marcussen N, et al. Preoperative lymph-node staging of invasive urothelial bladder cancer with ^{18}F-fluorodeoxyglucose positron emission tomography/computed axial tomography and magnetic resonance imaging: correlation with histopathology. Scand J Urol Nephrol. 2011;45:122–8.
163. Soubra A, Hayward D, Dahm P, Goldfarb R, Froehlich J, Jha G, et al. The diagnostic accuracy of ^{18}F-fluorodeoxyglucose positron emission tomography and computed tomography in staging bladder cancer: a single-institution study and a systematic review with meta-analysis. World J Urol. 2016;34:1229–37.
164. Jensen JB, Ulhoi BP, Jensen KM. Lymph node mapping in patients with bladder cancer undergoing radical cystectomy and lymph node dissection to the level of the inferior mesenteric artery. BJU Int. 2010;106:199–205.
165. Lodde M, Lacombe L, Friede J, Morin F, Saourine A, Fradet Y. Evaluation of fluorodeoxyglucose positron-emission tomography with computed tomography for staging of urothelial carcinoma. BJU Int. 2010;106:658–63.
166. Nayak B, Dogra PN, Naswa N, Kumar R. Diuretic ^{18}F-FDG PET/CT imaging for detection and locoregional staging of urinary bladder cancer: prospective evaluation of a novel technique. Eur J Nucl Med Mol Imaging. 2013;40:386–93.
167. Goodfellow H, Viney Z, Hughes P, Rankin S, Rottenberg G, Hughes S, et al. Role of fluorodeoxyglucose positron emission tomography (FDG PET)-computed tomography (CT) in the staging of bladder cancer. BJU Int. 2014;114:389–95.
168. Hitier-Berthault M, Ansquer C, Branchereau J, Renaudin K, Bodere F, Bouchot O, et al. ^{18}F-fluorodeoxyglucose positron emission tomography-computed tomography for preoperative lymph node staging in patients undergoing radical cystectomy for bladder cancer: a prospective study. Int J Urol. 2013;20:788–96.
169. Lu YY, Chen JH, Liang JA, Wang HY, Lin CC, Lin WY, et al. Clinical value of FDG PET or PET/CT in urinary bladder cancer: a systemic review and meta-analysis. Eur J Radiol. 2012;81:2411–6.
170. Jadvar H, Quan V, Henderson RW, Conti PS. [F-18]-fluorodeoxyglucose PET and PET-CT in diagnostic imaging evaluation of locally recurrent and metastatic bladder transitional cell carcinoma. Int J Clin Oncol. 2008;13:42–7.
171. Meeks JJ, Bellmunt J, Bochner BH, Clarke NW, Daneshmand S, Galsky MD, et al. A systematic review of neoadjuvant and adjuvant chemotherapy for muscle-invasive bladder cancer. Eur Urol. 2012;62:523–33.
172. Mertens LS, Fioole-Bruining A, van Rhijn BW, Kerst JM, Bergman AM, Vogel WV, et al. FDG-positron emission tomography/computerized tomography for monitoring the response of pelvic lymph node metastasis to neoadjuvant chemotherapy for bladder cancer. J Urol. 2013;189:1687–91.
173. Mertens LS, Mir MC, Scott AM, Lee ST, Fioole-Bruining A, Vegt E, et al. 18F-fluorodeoxyglucose – positron emission tomography/computed tomography aids staging and predicts mortality in patients with muscle-invasive bladder cancer. Urology. 2014;83:393–8.
174. Jana S, Blaufox MD. Nuclear medicine studies of the prostate, testes, and bladder. Semin Nucl Med. 2006;36:51–72.
175. de Jong IJ, Pruim J, Elsinga PH, Jongen MM, Mensink HJ, Vaalburg W. Visualisation of bladder cancer using ^{11}C-choline PET: first clinical

experience. Eur J Nucl Med Mol Imaging. 2002;29: 1283–8.
176. Gofrit ON, Mishani E, Orevi M, Klein M, Freedman N, Pode D, et al. Contribution of ^{11}C-choline positron emission tomography/computerized tomography to preoperative staging of advanced transitional cell carcinoma. J Urol. 2006;176:940–4. discussion 944.
177. Picchio M, Treiber U, Beer AJ, Metz S, Bossner P, van Randenborgh H, et al. Value of ^{11}C-choline PET and contrast-enhanced CT for staging of bladder cancer: correlation with histopathologic findings. J Nucl Med. 2006;47:938–44.
178. Ceci F, Bianchi L, Graziani T, Castellucci P, Pultrone C, Eugenio B, et al. ^{11}C-choline PET/CT and bladder cancer: lymph node metastasis assessment with pathological specimens as reference standard. Clin Nucl Med. 2015;40:e124–8.
179. Brunocilla E, Ceci F, Schiavina R, Castellucci P, Maffione AM, Cevenini M, et al. Diagnostic accuracy of ^{11}C-choline PET/CT in preoperative lymph node staging of bladder cancer: a systematic comparison with contrast-enhanced CT and histologic findings. Clin Nucl Med. 2014;39:e308–12.
180. Graziani T, Ceci F, Lopes FL, Chichero J, Castellucci P, Schiavina R, et al. ^{11}C-choline PET/CT for restaging of bladder cancer. Clin Nucl Med. 2015;40:e1–5.
181. Maurer T, Horn T, Souvatzoglou M, Eiber M, Beer AJ, Heck MM, et al. Prognostic value of ^{11}C-choline PET/CT and CT for predicting survival of bladder cancer patients treated with radical cystectomy. Urol Int. 2014;93:207–13.
182. Kubota R, Kubota K, Yamada S, Tada M, Takahashi T, Iwata R, et al. Methionine uptake by tumor tissue: a microautoradiographic comparison with FDG. J Nucl Med. 1995;36:484–92.
183. Letocha H, Ahlstrom H, Malmstrom PU, Westlin JE, Fasth KJ, Nilsson S. Positron emission tomography with L-methyl-^{11}C-methionine in the monitoring of therapy response in muscle-invasive transitional cell carcinoma of the urinary bladder. Br J Urol. 1994;74: 767–74.
184. Schoder H, Ong SC, Reuter VE, Cai S, Burnazi E, Dalbagni G, et al. Initial results with ^{11}C-acetate positron emission tomography/computed tomography (PET/CT) in the staging of urinary bladder cancer. Mol Imaging Biol. 2012;14:245–51.
185. Vargas HA, Akin O, Schoder H, Olgac S, Dalbagni G, Hricak H, et al. Prospective evaluation of MRI, ^{11}C-acetate PET/CT and contrast-enhanced CT for staging of bladder cancer. Eur J Radiol. 2012;81:4131–7.
186. Orevi M, Klein M, Mishani E, Chisin R, Freedman N, Gofrit ON. ^{11}C-acetate PET/CT in bladder urothelial carcinoma: intraindividual comparison with ^{11}C-choline. Clin Nucl Med. 2012;37:e67–72.
187. Chakraborty D, Bhattacharya A, Mete UK, Mittal BR. Comparison of ^{18}F fluoride PET/CT and ^{99m}Tc-MDP bone scan in the detection of skeletal metastases in urinary bladder carcinoma. Clin Nucl Med. 2013;38: 616–21.
188. Hall MC, Chang SS, Dalbagni G, Pruthi RS, Seigne JD, Skinner EC, et al. Guideline for the management of nonmuscle invasive bladder cancer (stages Ta, T1, and Tis): 2007 update. J Urol. 2007;178:231 4–30.
189. Babjuk M, Burger M, Zigeuner R, Shariat SF, van Rhijn BW, Comperat E, et al. EAU guidelines on non-muscle-invasive urothelial carcinoma of the bladder: update 2013. Eur Urol. 2013;64:639–53.
190. Oosterlinck W, Kurth KH, Schroder F, Bultinck J, Hammond B, Sylvester R. A prospective European Organization for Research and Treatment of Cancer Genitourinary Group randomized trial comparing transurethral resection followed by a single intravesical instillation of epirubicin or water in single stage Ta, T1 papillary carcinoma of the bladder. J Urol. 1993;149: 749–52.
191. Sylvester RJ, Oosterlinck W, van der Meijden AP. A single immediate postoperative instillation of chemotherapy decreases the risk of recurrence in patients with stage Ta T1 bladder cancer: a meta-analysis of published results of randomized clinical trials. J Urol. 2004;171:2186–90. quiz 2435.
192. Abern MR, Owusu RA, Anderson MR, Rampersaud EN, Inman BA. Perioperative intravesical chemotherapy in non-muscle-invasive bladder cancer: a systematic review and meta-analysis. J Natl Compr Cancer Netw. 2013;11:477–84.
193. Perlis N, Zlotta AR, Beyene J, Finelli A, Fleshner NE, Kulkarni GS. Immediate post-transurethral resection of bladder tumor intravesical chemotherapy prevents non-muscle-invasive bladder cancer recurrences: an updated meta-analysis on 2548 patients and quality-of-evidence review. Eur Urol. 2013;64:421–30.
194. van Lingen AV, Witjes JA. Current intravesical therapy for non-muscle invasive bladder cancer. Expert Opin Biol Ther. 2013;13:1371–85.
195. Huncharek M, McGarry R, Kupelnick B. Impact of intravesical chemotherapy on recurrence rate of recurrent superficial transitional cell carcinoma of the bladder: results of a meta-analysis. Anticancer Res. 2001; 21:765–9.
196. Bohle A, Bock PR. Intravesical bacille Calmette-Guerin versus mitomycin C in superficial bladder cancer: formal meta-analysis of comparative studies on tumor progression. Urology. 2004;63:682–6. discussion 686–687.
197. Sylvester RJ, van der Meijden AP, Lamm DL. Intravesical bacillus Calmette-Guerin reduces the risk of progression in patients with superficial bladder cancer: a meta-analysis of the published results of randomized clinical trials. J Urol. 2002; 168:1964–70.
198. Shang PF, Kwong J, Wang ZP, Tian J, Jiang L, Yang K, et al. Intravesical Bacillus Calmette-Guerin versus epirubicin for Ta and T1 bladder cancer. Cochrane Database Syst Rev. 2011;6:1–44.

199. Sylvester RJ, Oosterlinck W, Witjes JA. The schedule and duration of intravesical chemotherapy in patients with non-muscle-invasive bladder cancer: a systematic review of the published results of randomized clinical trials. Eur Urol. 2008;53:709–19.
200. Malmstrom PU, Sylvester RJ, Crawford DE, Friedrich M, Krege S, Rintala E, et al. An individual patient data meta-analysis of the long-term outcome of randomised studies comparing intravesical mitomycin C versus bacillus Calmette-Guerin for non-muscle-invasive bladder cancer. Eur Urol. 2009;56:247–56.
201. Shelley MD, Kynaston H, Court J, Wilt TJ, Coles B, Burgon K, et al. A systematic review of intravesical bacillus Calmette-Guerin plus transurethral resection vs transurethral resection alone in Ta and T1 bladder cancer. BJU Int. 2001;88:209–16.
202. Shelley MD, Wilt TJ, Court J, Coles B, Kynaston H, Mason MD. Intravesical bacillus Calmette-Guerin is superior to mitomycin C in reducing tumour recurrence in high-risk superficial bladder cancer: a meta-analysis of randomized trials. BJU Int. 2004;93:485–90.
203. Han RF, Pan JG. Can intravesical bacillus Calmette-Guerin reduce recurrence in patients with superficial bladder cancer? A meta-analysis of randomized trials. Urology. 2006;67:1216–23.
204. Bohle A, Jocham D, Bock PR. Intravesical bacillus Calmette-Guerin versus mitomycin C for superficial bladder cancer: a formal meta-analysis of comparative studies on recurrence and toxicity. J Urol. 2003; 169:90–5.
205. Jarvinen R, Kaasinen E, Sankila A, Rintala E, FinnBladder G. Long-term efficacy of maintenance bacillus Calmette-Guerin versus maintenance mitomycin C instillation therapy in frequently recurrent TaT1 tumours without carcinoma in situ: a subgroup analysis of the prospective, randomised FinnBladder I study with a 20-year follow-up. Eur Urol. 2009;56: 260–5.
206. Sylvester RJ, Brausi MA, Kirkels WJ, Hoeltl W, Calais Da Silva F, Powell PH, et al. Long-term efficacy results of EORTC genito-urinary group randomized phase 3 study 30911 comparing intravesical instillations of epirubicin, bacillus Calmette-Guerin, and bacillus Calmette-Guerin plus isoniazid in patients with intermediate- and high-risk stage Ta T1 urothelial carcinoma of the bladder. Eur Urol. 2010;57:766–73.
207. Houghton BB, Chalasani V, Hayne D, Grimison P, Brown CS, Patel MI, et al. Intravesical chemotherapy plus bacille Calmette-Guerin in non-muscle invasive bladder cancer: a systematic review with meta-analysis. BJU Int. 2013;111:977–83.
208. van der Meijden AP, Sylvester RJ, Oosterlinck W, Hoeltl W, Bono AV, Group EG-UTC. Maintenance Bacillus Calmette-Guerin for Ta T1 bladder tumors is not associated with increased toxicity: results from a European Organisation for Research and Treatment of Cancer Genito-Urinary Group Phase III Trial. Eur Urol. 2003;44:429–34.
209. Zlotta AR, van Vooren JP, Huygen K, Drowart A, Decock M, Pirson M, et al. What is the optimal regimen for BCG intravesical therapy? Are six weekly instillations necessary? Eur Urol. 2000;37: 470–7.
210. Witjes JA, Comperat E, Cowan NC, De Santis M, Gakis G, Lebret T, et al. EAU guidelines on muscle-invasive and metastatic bladder cancer: summary of the 2013 guidelines. Eur Urol. 2014;65:778–92.
211. van den Bosch S, Alfred Witjes J. Long-term cancer-specific survival in patients with high-risk, non-muscle-invasive bladder cancer and tumour progression: a systematic review. Eur Urol. 2011;60: 493–500.
212. Stein JP, Lieskovsky G, Cote R, Groshen S, Feng AC, Boyd S, et al. Radical cystectomy in the treatment of invasive bladder cancer: long-term results in 1,054 patients. J Clin Oncol. 2001;19:666–75.
213. Miller DC, Taub DA, Dunn RL, Montie JE, Wei JT. The impact of co-morbid disease on cancer control and survival following radical cystectomy. J Urol. 2003;169:105–9.
214. Lebret T, Herve JM, Yonneau L, Molinie V, Barre P, Lugagne PM, et al. After cystectomy, is it justified to perform a bladder replacement for patients with lymph node positive bladder cancer? Eur Urol. 2002;42:344–9. discussion 349.
215. Roth B, Wissmeyer MP, Zehnder P, Birkhauser FD, Thalmann GN, Krause TM, et al. A new multimodality technique accurately maps the primary lymphatic landing sites of the bladder. Eur Urol. 2010;57:205–11.
216. Vazina A, Dugi D, Shariat SF, Evans J, Link R, Lerner SP. Stage specific lymph node metastasis mapping in radical cystectomy specimens. J Urol. 2004;171: 1830–4.
217. Leissner J, Ghoneim MA, Abol-Enein H, Thuroff JW, Franzaring L, Fisch M, et al. Extended radical lymphadenectomy in patients with urothelial bladder cancer: results of a prospective multicenter study. J Urol. 2004;171:139–44.
218. Chade DC, Laudone VP, Bochner BH, Parra RO. Oncological outcomes after radical cystectomy for bladder cancer: open versus minimally invasive approaches. J Urol. 2010;183:862–9.
219. Kasraeian A, Barret E, Cathelineau X, Rozet F, Galiano M, Sanchez-Salas R, et al. Robot-assisted laparoscopic cystoprostatectomy with extended pelvic lymphadenectomy, extracorporeal enterocystoplasty, and intracorporeal enterourethral anastomosis: initial Montsouris experience. J Endourol. 2010;24:409–13.
220. Challacombe BJ, Bochner BH, Dasgupta P, Gill I, Guru K, Herr H, et al. The role of laparoscopic and robotic cystectomy in the management of muscle-invasive bladder cancer with special emphasis on

cancer control and complications. Eur Urol. 2011;60:767–75.
221. Winquist E, Kirchner TS, Segal R, Chin J, Lukka H, Genitourinary Cancer Disease Site Group CCOPiE-bCPGI. Neoadjuvant chemotherapy for transitional cell carcinoma of the bladder: a systematic review and meta-analysis. J Urol. 2004;171:561–9.
222. Vaughn DJ, Malkowicz SB. Neoadjuvant chemotherapy in patients with invasive bladder cancer. Urol Clin N Am. 2005;32:231–7.
223. Grossman HB, Natale RB, Tangen CM, Speights VO, Vogelzang NJ, Trump DL, et al. Neoadjuvant chemotherapy plus cystectomy compared with cystectomy alone for locally advanced bladder cancer. N Engl J Med. 2003;349:859–66.
224. Huncharek M, Muscat J, Geschwind JF. Planned preoperative radiation therapy in muscle invasive bladder cancer; results of a meta-analysis. Anticancer Res. 1998;18:1931–4.
225. Blackard CE, Byar DP. Results of a clinical trial of surgery and radiation in stages II and 3 carcinoma of the bladder. J Urol. 1972;108:875–8.
226. Anderstrom C, Johansson S, Nilsson S, Unsgaard B, Wahlqvist L. A prospective randomized study of preoperative irradiation with cystectomy or cystectomy alone for invasive bladder carcinoma. Eur Urol. 1983;9:142–7.
227. Rosenberg JE, Carroll PR, Small EJ. Update on chemotherapy for advanced bladder cancer. J Urol. 2005;174:14–20.

Diagnostic Applications of Nuclear Medicine: Prostatic Cancer

31

Emilio Bombardieri, Maria Grazia Sauta, Lucia Setti, Roberta Meroni, Gianluigi Ciocia, and Laura Evangelista

Abstract

Prostate cancer (PCa) is one of the most common cancers in the male population. Its incidence, mortality, and prevalence are different across different geographical areas, depending on the different approaches adopted for screening, early diagnosis, and availability of treatments. Digital rectal exploration (DRE) and the prostate-specific antigen (PSA) test are the most common clinical practice used for PCa screening.

The choice of treatment should be patient specific and risk adjusted. The therapeutic approaches for patients with PCa include different options: watchful waiting, radical prostatectomy, radiotherapy, hormone therapy, chemotherapy, immunotherapy, and treatment of bone metastases.

Keywords

Prostate cancer • Diagnostic imaging • Bone scan • SPECT/CT • PET/CT • Biomarkers for prostate cancer

Glossary

[^{11}C]CHO	[^{11}C]choline
[^{18}F]FDG	2-Deoxy-2-[^{18}F]fluoro-D-glucose
[^{18}F]FDHT	16β-[^{18}F]fluoro-5-dihydrotestosterone
^{18}F-CHO	^{18}F-fluoromethylcholine
^{18}F-DCFBC	*N*-[*N*-{(S)-1,3-dicarboxypropyl]carbamoyl} 4-^{18}F-fluorobenzyl-L-cysteine
^{18}F-DCFPyLis	2-[3-{1-Carboxy-5-[(6-[^{18}F] fluoro-pyridine-3-carbonyl)-amino]-pentil}-ureido]-pentanedioic acid
^{18}F-FACBC	*Anti*-1-amino-3-^{18}F-fluorocyclobutane-1-carboxylic acid, or ^{18}F-fluciclovine

E. Bombardieri (✉) • L. Setti
Nuclear Medicine Unit, "Humanitas Gavazzeni" Hospital, Bergamo, Italy
e-mail: emilio.bombardieri@gavazzeni.it; lucia.setti@gavazzeni.it

M.G. Sauta
Oncology Unit, "Humanitas Gavazzeni" Hospital, Bergamo, Italy
e-mail: maria_grazia.sauta@gavazzeni.it

R. Meroni
Radiology Unit, "Humanitas Gavazzeni" Hospital, Bergamo, Italy
e-mail: roberta.meroni@gavazzeni.it

G. Ciocia
Nuclear Medicine Unit, "Humanitas Gavazzeni" Hospital, Bergamo, Italy

Radiotherapy Unit, "Humanitas Gavazzeni" Hospital, Bergamo, Italy
e-mail: gianluigi.ciocia@gavazzeni.it

L. Evangelista
Nuclear Medicine and Molecular Imaging Unit, Veneto Institute of Oncology IOV - IRCCS, Padua, Italy
e-mail: laura.evangelista@ioveneto.it

© Springer International Publishing Switzerland 2017
H.W. Strauss et al. (eds.), *Nuclear Oncology*,
https://doi.org/10.1007/978-3-319-26236-9_43

^{18}F-NaF	^{18}F-sodium fluoride
3D CRT	Three-dimensional conformal radiotherapy
^{68}Ga-PSMA	Glu-urea-Lys-(Ahx)-[^{68}Ga(HBED-CC)]
^{99m}Tc-HMDP	^{99m}Tc-hydroxymethylene diphosphonate
^{99m}Tc-MDP	^{99m}Tc-methylene diphosphonate
ACP	American College of Physicians
ACS	American Cancer Society
ADT	Androgen deprivation therapy
AJCC	American Joint Committee on Cancer
ALP	Alkaline phosphatase
AS	Active surveillance
ASCO	American Society of Clinical Oncology
AUA	American Urological Association
BS	Bone scintigraphy
BSI	Bone scan index
CRPC	Castrate-resistant prostate cancer
CT	X-ray computed tomography
CTX	C-terminal telopeptide of type I collagen
CYP17	17-Alpha-monooxygenase, a crucial enzyme for the synthesis of testosterone from non-gonadal sources
DCE MRI	Dynamic contrast-enhanced magnetic resonance imaging
DRE	Digital rectal exploration
DWI	Diffusion-weighted imaging, an MR imaging technique
EBRT	External beam radiation therapy
ED	Effective dose
EMA	European Medicines Agency
ERG	ETS-related gene
ETS	E26 transformation-specific family
FDA	United States Food and Drug Administration
GLUT	Glucose transporter family
GS	Gleason score
HDR	High-dose rate radiotherapy
HIFU	High-intensity focused ultrasound
ICTP	Cross-linked carboxyterminal telopeptide of type I collagen
IGRT	Image-guided radiotherapy
IMRT	Intensity-modulated radiotherapy
LDR	Low-dose rate radiotherapy
LH	Luteinizing hormone
LHRH	Luteinizing hormone-releasing hormone
M	Metastasis status according to the AJCC/UICC TNM staging system
MR	Magnetic resonance
MRI	Magnetic resonance imaging
N	Lymph node status according to the AJCC/UICC TNM staging system
NCCN	National Comprehensive Cancer Network
NCCN	National Comprehensive Cancer Network
NOPR	United States National Oncologic PET Registry
NPV	Negative predictive value
p53	Tumor protein p53, also known as cellular tumor antigen p53, phosphoprotein p53, tumor suppressor p53, antigen NY-CO-13, or transformation-related protein 53 (TRP53)
PCa	Prostate cancer
PERCIST	Positron emission tomography response criteria in solid tumors
PET	Positron emission tomography
PET/CT	Positron emission tomography/computed tomography

PET/MR	Positron emission tomography/magnetic resonance
PET/MRI	Positron emission tomography/magnetic resonance imaging
PINP	Amino-terminal procollagen propeptide type I
PPV	Positive predictive value
PSA	Prostate-specific antigen
PSA	Prostate-specific antigen
PSMA	Prostate-specific membrane antigen
RANK	Receptor activator of nuclear factor kappa-B
RANKL	Receptor activator of nuclear factor kappa-B ligand, also known as tumor necrosis factor ligand superfamily member 11 (TNFSF11), TNF-related activation-induced cytokine (TRANCE), osteoprotegerin ligand (OPGL), and osteoclast differentiation factor (ODF)
RARP	Robot-assisted radical prostatectomy
RECIST	Response evaluation criteria in solid tumors
ROC	Receiver operating characteristic, a statistical analysis to assess the performance of a binary classifier
RT	Radiotherapy
SNMMI	Society of Nuclear Medicine and Molecular Imaging
SPECT	Single photon emission computed tomography
SPECT/CT	Single photon emission computed tomography/computed tomography
SRE	Skeletal related event
SUV	Standardized uptake value
SUV_{max}	Standardized uptake value at point of maximum
T	Tumor status according to the AJCC/UICC TNM staging system
TMPRSS2	Transmembrane protease, serine 2
TNM	AJCC/UICC staging system based on parameters "T" (tumor status), "N" (lymph node status) and "M" (distant metastasis status)
TRUS	Transrectal ultrasound
UICC	Union Internationale Contre le Cancer (International Union Against Cancer)
US	Ultrasonography
USPSTF	United States Preventive Services Task Force
WB	Whole body
WBS	Whole-body scan

Contents

Epidemiology 886

Prostate Cancer Screening 886

First Diagnosis 887

Pathology 887
Histopathological Type and Cancer Growth 887
TNM Classification 888
Histopathological Grade 888
Risk Stratification 888

Management Strategies for Prostate Cancer 888
Active Surveillance and Watchful Waiting 889
Radical Prostatectomy (With or Without Lymphadenectomy) 891
External Beam Radiation Therapy 892
Brachytherapy 892
High-Intensity Focused Ultrasound Therapy and Cryotherapy 893
Hormone Therapy 893
Chemotherapy 893
Immunotherapy 894
Treatment of Skeletal Metastases 894

Biochemical and Diagnostic Modalities 894
Laboratory Tests 894
Radiological Imaging 896
Nuclear Medicine Modalities 897

Clinical Considerations 914

References 915

Epidemiology

Prostate cancer (PCa) is one of the most common cancers in the male population. Its incidence, mortality, and prevalence are different across the geographical areas, depending on the different approaches adopted for screening, early diagnosis, and availability of treatments. Nearly 900,000 new PCa diagnoses are recorded per year on a global scale or 28.0 per 100,000 persons-year. According to national cancer registers, Australia and New Zealand reported the highest incidence rate, with 104.2 cases per 100,000 persons-year. A high incidence rate is observed also in Northern and West Europe, 73.1 and 93.1 per 100,000 persons-year, respectively. In Northern America, the incidence is similar, with 85.6 cases per persons-year. The lowest incidence rates are observed in Asia, with 7.2 per 100,000 persons-year (particularly in India and in China). The age-adjusted PCa mortality in Europe accounts for 12.00 per 100,000 persons-year, very similar to 9.9 per 100,000 persons-year in Northern America [1, 2].

Incidence and death rates have declined in the last 20 years, most likely as a consequence of decreased application of programs for widespread and "unselected" prostate-specific antigen (PSA) tests which have led to the overdiagnosis of small and localized tumors with a limited likelihood to spread locally or at distance. On the other hand, the increased public awareness for early detection and treatment together with better use of screening programs (i.e., in high-risk patients) has improved PCa mortality [3].

Little is known about the etiology of PCa, although some risk factors can play a role; age, family history, and genetics are the most important of such risk factors [4]. Recent studies demonstrated that also ethnicity, androgen status, diet, and lifestyle are relevant. More than two-thirds of all PCa cases occur in men older than 65 years. In first-degree relatives of affected men, the risk to develop PCa increases to threefold, and PCa tends to develop before the age of 55 [5–7].

Prostate Cancer Screening

Digital rectal exploration (DRE) and the prostate-specific antigen (PSA) test are the most common clinical practice biomarkers used for PCa screening. PSA is not specific for PCa, as it is elevated in benign prostatic hyperplasia, prostatitis, trauma, and urinary retention. Screening for PCa is a controversial issue. Screening offers the opportunity to find cancers at a more curable stage. On the other hand, the variability of the natural history of PCa should be considered, since some cases show an aggressive progression but many others are indolent and carry little threat about morbidity or mortality. Moreover, transrectal ultrasound (TRUS) has been associated with a high false-positive rate, making it unsuitable as a screening tool, although it has an established role in directing prostatic biopsies.

In the absence of a method to identify patients in whom the disease will have a rapid progression if left without therapy, any screening procedures result in some degree of overtreatment. Guidelines on PCa management have been issued by different scientific organizations: American Cancer Society (ACS), National Comprehensive Cancer Network (NCCN), US Preventive Services Task Force (USPSTF), American Urological Association (AUA), and American College of Physicians (ACP). The NCCN guidelines (revised in 2016) recommend considering the patient's history (including family history, medications, and any event of prostate disease) and emphasize the importance of physical examination. The clinician should then discuss the risks and benefits to obtain a baseline PSA and consider a baseline DRE to identify high-risk cancers associated with changes in PSA [8]. In asymptomatic patients, the guidelines recommend testing every 2–4 years for men aged 45–75 years with serum PSA values below 1 ng/mL. For men with PSA ranging between 1 and 3 ng/mL, PSA tests should occur at 1- to 2-year intervals. Biopsy should be considered in those men aged 45–75 years with serum PSA >3.0 ng/mL. However, the decision to perform a biopsy should not be based on the PSA cutoff threshold alone, but should be evaluated considering all clinical variables and the patient's preference.

First Diagnosis

Patients with abnormal DRE or elevated PSA levels should be further evaluated with prostate biopsy. The risk of being diagnosed with PCa increases with increasing PSA values, amounting to 34% for men with PSA values between 3 and 6 ng/mL and from 50% to 70% for those with PSA values >10 ng/mL. In younger subjects (<65 years), the cumulative risk is consistently lower than in older subjects. Patients with a free-to-total PSA ratio of <20% and PSA velocity >0.75 ng/mL/year have a higher risk of PCa and should also undergo prostate biopsy [9, 10].

Transrectal ultrasound (TRUS) imaging is the only imaging procedure to employ in this phase. TRUS-guided core biopsy has become the standard procedure to obtain tissue for histopathological examination. The fact that PCa is often multifocal and heterogeneous makes diagnosis based on a single biopsy difficult, as only a small amount of tissue is obtained with needle biopsy; thus, sampling errors are common. Initial biopsy guided by TRUS detected PCa in only 22–34% of the cases, and repeated biopsy is required in many patients. The likelihood of PCa diagnosis increases with the number of biopsy specimens; currently, at least ten biopsy cores are recommended, and 12–16 are obtained at some centers [11, 12].

Magnetic resonance imaging (MRI) is also important to diagnose PCa and to define its size and location. Cancers in patients with increased PSA and negative transrectal prostate biopsies can be diagnosed on MRI. MRI can specifically detect the anterior and apical tumors, which are usually missed on a TRUS-guided biopsy [13].

Pathology

Histopathological Type and Cancer Growth

Acinar adenocarcinoma is the most common type of PCa, representing over 95% of these cancers. Other rare tumors are basal cell, squamous cell, adeno-squamous carcinoma, and neuroendocrine carcinoma. Adenocarcinoma commonly originates from the peripheral zone of the gland (85%), less frequently from the transitional zone (10–15%), while only 5–10% of cases arise in the central zone [14, 15]. Most cancers are multifocal, with synchronous involvement of multiple zones of the prostate, which may be due to clonal and non-clonal tumors.

The clinical outcome of PCa is highly variable, since in some patients the tumor grows slowly, while in other patients, it can exhibit a very aggressive behavior with early metastasis and death. This is summarized by the "risk of progression" concept defined by the classes of risk, which can be obtained taking into account the extension (stage TNM), the Gleason score (GS), and PSA levels [16, 17]. PCa follows a multistep course of growth. The first step is known as "carcinoma in situ" when neoplastic cells are confined into a normal gland. Following the initial event, further mutations, including p53, can lead to progression and metastasis. Prostate cells are sensitive to activation of androgen receptors on their surface. Androgens bind to the receptor, an androgen-activated transcription factor that belongs to the steroid nuclear receptor family. The receptor translocates into the nucleus, where it binds to androgen response elements and modulates transcription and cell growth [18]. As the disease progresses from hormone dependent to castration resistance status, this system is altered. Two key changes include upregulation of the androgen receptor, which confers sensitivity to small amounts of androgen, and mutation of the receptor, which results in loss of specificity for androgens [19].

According to their original location in the prostate, locally advanced PCa in the transitional-zone tumors spread to the bladder neck, while the peripheral-zone tumors extend into the ejaculatory ducts and seminal vesicles. Penetration through the prostatic capsule and along the perineural or vascular spaces is a late event. PCa spreads to bone early, often without significant lymphadenopathy. At present, two predominant theories have been proposed: (1) the mechanic theory and (2) the seed-and-soil theory. Therefore, metastases can be caused by direct spread through the lymphatics and venous

spaces into the lower lumbar spine or/and are caused by the presence of tissue factors that allow preferential growth in certain tissues. Lung, liver, and adrenal metastases have also been documented.

TNM Classification

The standard staging system for newly diagnosed PCa is that of the American Joint Committee on Cancer (AJCC)/International Union Against Cancer (UICC). This system incorporates the anatomic extent of disease, including the primary tumor (T), regional lymph nodes (N), and distant metastases (M). The TNM staging system is widely used to stage PCa (Tables 1 and 2) [20]. Although imaging techniques are only occasionally useful for detecting/diagnosing PCa, they are mostly used for staging once a histological diagnosis is obtained. Usually a combination of the currently available imaging modalities is necessary for defining the most appropriate treatment strategies.

The 2010 update of this system incorporated the pretreatment serum PSA level and Gleason score/grade to subdivide patients into prognostic categories. This information about prognostic categories is also combined with patient's age; life expectancy; overall medical condition, including performance status and comorbidities; the presence or absence of symptoms; and patient preferences to make decisions for the optimal treatment for an individual patient.

Histopathological Grade

Gleason score (GS) is recommended as the grading system of choice, because it takes into account the inherent morphologic heterogeneity of PCa, and several studies have clearly established its prognostic value. A primary and a secondary pattern (the range of each is 1–5) are assigned and then summed-up to yield a total score. Scores of 2–10 are possible. It has been reported that high GS is associated with poor prognosis, although the behavior of cancer can be different in accordance with other histopathological variables (i.e., lymphovascular and neurovascular invasions, infiltrated margins, positive lymph nodes).

The majority of newly biopsy-diagnosed PCas are graded GS 6 or above. In a radical prostatectomy, if a tertiary pattern is present, it is commented upon but not reflected in the GS [9]:

- Gleason X: GS cannot be processed
- Gleason $\leq$6: well differentiated (slight anaplasia)
- Gleason 7: moderately differentiated (moderate anaplasia)
- Gleason 8–10: poorly differentiated/undifferentiated (marked anaplasia).

Risk Stratification

The initial management of patients with newly diagnosed PCa relies on multidisciplinary evaluation of the patient's conditions (age, life expectancy, performance status, comorbidities, presence or absence of symptoms, and consensus) and on a pretreatment assessment of the risk of locoregional recurrence or disseminated disease. Important factors in this assessment include clinical staging of the extent of disease (Tables 1 and 2), the pretreatment serum PSA, and GS in the pretreatment biopsy [19–21].

The categories of risk derived from the abovementioned information are summarized in Table 3. D'Amico's classification is the most commonly used, validated, and cited risk stratification for PCa.

Management Strategies for Prostate Cancer

The choice of treatment should be patient specific and risk adjusted and aims at improving cancer control while reducing the risks of treatment-related complications [8]. The therapeutic approaches for patients with PCa include (1) watchful waiting, (2) radical prostatectomy

Table 1 AJCC/UICC TNM classification of prostate cancer

Primary tumor (T)	
Clinical	
TX	Primary tumor cannot be assessed
T0	No evidence of primary tumor
T1	Clinically inapparent tumor neither palpable nor visible by imaging
T1a	Tumor incidental histologic finding in 5% or less of tissue resected
T1b	Tumor incidental histologic finding in more than 5% of tissue resected
T1c	Tumor identified by needle biopsy (e.g., because of elevated PSA)
T2	Tumor confined within prostate[a]
T2a	Tumor involves one-half of one lobe or less
T2b	Tumor involves more than one-half of one lobe, but not both lobes
T2c	Tumor involves both lobes
T3	Tumor extends through the prostate capsule[b]
T3a	Extracapsular extension (unilateral or bilateral) including microscopic bladder neck involvement
T3b	Tumor invades seminal vesicle(s)
T4	Tumor is fixed or invades adjacent structures other than seminal vesicles such as external sphincter, rectum, bladder, elevator muscles, and/or pelvic wall
Pathologic (pT)[c]	
pT2	Organ confined
pT2a	Unilateral, one-half of one side or less
pT2b	Unilateral, involving more than one-half of side, but not both sides
pT2c	Bilateral disease
pT3	Extraprostatic extension
pT3a	Extraprostatic extension or microscopic invasion of bladder neck[d]
pT3b	Seminal vesicle invasion
pT4	Invasion of rectum, elevator muscles, and/or pelvic wall
Regional lymph nodes (N)	
Clinical	
NX	Regional lymph nodes were not assessed
N0	No regional lymph node metastasis
N1	Metastasis in regional lymph node
Pathologic	
pNX	Regional nodes not sampled
pN0	No positive regional nodes
pN1	Metastasis in regional node(s)
Distant metastasis (M)[e]	
M0	No distant metastasis
M1	Distant metastasis
M1a	Non-regional lymph node(s)
M1b	Bone(s)
M1c	Other site(s) with or without bone disease

[a]Tumor found in one or both lobes by needle biopsy, but not palpable or reliably visible by imaging, is classified as T1c
[b]Invasion into the prostatic apex or into (but not beyond) the prostatic capsule is classified not as T3 but as T2
[c]There is no pathologic T1 classification
[d]Positive surgical margin should be indicated by an R1 descriptor (residual microscopic disease)
[e]When more than one site of metastasis is present, the most advanced category is used. pM1c is most advanced

(with or without lymphadenectomy), (3) radiotherapy, (4) hormonal therapy, (5) chemotherapy, (6) immunotherapy, and (7) treatment of bone metastases. The selection of a treatment should be taken on the basis of a multidisciplinary approach involving all specialists dealing with this pathology (Fig. 1).

Active Surveillance and Watchful Waiting

Active surveillance (AS) for patients with PCa consists in postponing the immediate therapy with a definitive treatment that should be started in case of the evidence of a consistent risk of disease progression. AS is an option for the initial management of selected men with localized, well-differentiated PCa thought to be at low risk for progression [22, 23]. This approach is based on the long natural history of PCa, and it is an attempt to balance the risks with the side effects of over-treatment against the possibility of disease progression and a lost opportunity for cure. In 2015, the Cancer Care Ontario organization (CCO) published a Clinical Practice Guideline on Active Surveillance for the Management of Localized Prostate Cancer. The ASCO Endorsement Panel reinforces these recommendations, also adding qualifying statements [24].

Table 2 AJCC anatomic stage and prognostic groups for prostate cancer. (Used with the permission of the American Joint Committee on Cancer (AJCC), Chicago, IL. The original source for this material is the AJCC Cancer Staging Manual, Seventh Edition (2010) published by Springer Science and Business Media LLC)

Group	T category	N category	M category	PSA[a]	Gleason score[a]
I	T1a–c	N0	M0	<10	≤6
	T2a	N0	M0	<10	≤6
	T1–2°	N0	M0	X	X
IIA	T1a–c	N0	M0	<20	7
	T1a–c	N0	M0	≥10 <20	≤6
	T2a	N0	M0	<20	≤7
	T2b	N0	M0	<20	≤7
	T2b	N0	M0	X	X
IIB	T2c	N0	M0	Any	Any
	T1–2	N0	M0	≥ 20	Any
	T1–2	N0	M0	Any	≥ 8
III	T3a–b	N0	M0	Any	Any
IV	T4	N0	M0	Any	Any
	Any T	N1	M0	Any	Any
	Any T	Any N	M1	Any	Any

[a]When either PSA or Gleason is not available, grouping should be determined by T stage and/or whichever of the either PSA or Gleason is available

Table 3 Categories of risk in prostate cancer patients

Very low risk: **clinically localized PCa**	Disease detected by prostate biopsy based upon serum PSA only, without detectable abnormality on digital rectal examination or imaging
	Grade group 1 (Gleason score ≤6), <3 positive cores, no core ≥50% involved
	Serum PSA <10 ng/mL
Low risk: **clinically localized PCa**	No apparent tumor in the prostate (i.e., diagnosis based upon a biopsy only, with no abnormal findings on imaging or palpation) or limited disease in one lobe of the prostate gland
	Serum PSA <10 ng/mL and grade group 1 (Gleason score ≤6)
Intermediate risk: **clinically localized PCa**	Tumor in the prostate involves more than one-half of one lobe of the prostate (T2b), or with bilateral disease (T2c), but without detectable extracapsular extension or seminal vesicle involvement
	Patients with T1 or T2a disease are classified as having intermediate-risk disease based upon a serum PSA between 10 and 20 ng/mL or a biopsy grade group 2 or 3 (Gleason score 7)
High risk: **clinically localized PCa**	Tumor with extracapsular extension (T3a)
	Serum PSA >20 ng/mL or a biopsy grade group 4 or 5 (Gleason score of 8–10)
Very high-risk PCa	Tumors with seminal vesicle involvement (T3b), tumor fixation (T4), or invasion of adjacent organs (T4)
	Primary Gleason pattern 5 or four or more cores with Gleason score 8–10 (grade groups 4 and 5) are classified as very high risk
Lymph node involvement	Patients with lymph node involvement are classified as having stage IV (metastatic) disease
Disseminated disease	Patients with disseminated metastases (M1) are classified as having stage IV (metastatic disease)

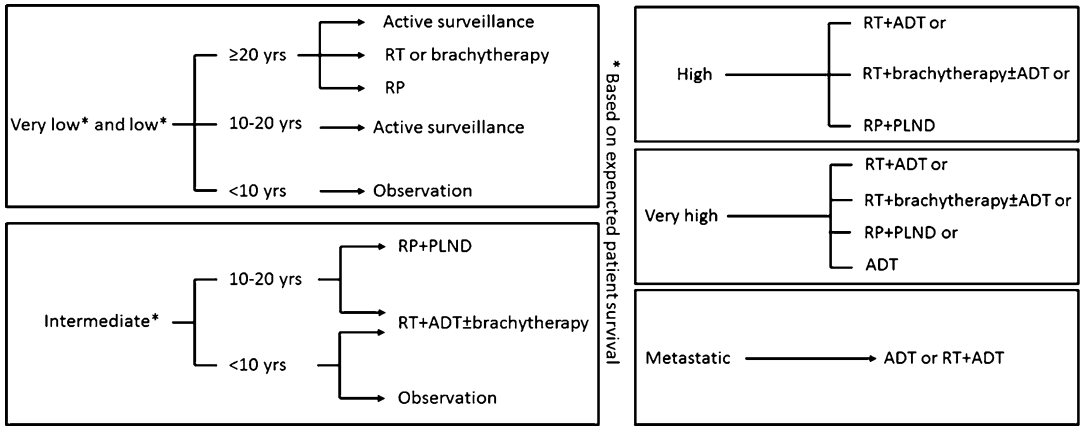

Fig. 1 A schematic illustration of treatment management in patients with PCa at different risk categories based on the anticipated years of survival (from NCCN guidelines, version 1.2016)

The distinction between AS and watchful waiting is important for clinical decision-making. AS, which carries a curative intent and involves regular monitoring with PSA, DRE, and biopsy, is appropriate for patients who have sufficient life expectancy and time to benefit from active treatment when disease progression is detected. For patients with a life expectancy of less than 5 years, watchful waiting (cessation of routine monitoring, with treatment initiated only if symptoms develop) is appropriate and further reduces the issue of overtreatment, including biopsies which carry a small but nonzero risk of infection and hospitalization. For most patients with low-risk (GS$\leq$6) localized PCa, AS is the recommended management strategy. However, since the ASCO Endorsement Panel recognizes that there is non-negligible disease heterogeneity, in selected patients with low-risk PCa, an immediate treatment instead of AS should be chosen, especially in young patients, with high-volume tumor, high GS, and African-American ethnicity, because these patients have a higher likelihood for disease progression during their lifetime.

The NCCN recommendation for follow-up schedule during AS includes PSA no more often than every 6 months unless clinically indicated, DRE no more often than every 12 months unless clinically indicated, and repeated prostate biopsy considered annually to assess for disease progression (biopsy should be repeated within 6 months of diagnosis if initial biopsy was <10 cores or assessment discordant, e.g., palpable tumor contralateral to the side of positive biopsy). A repetition of prostate biopsy is indicated when DRE changes or PSA increases, although neither parameter is very reliable for detecting PCa progression.

Radical Prostatectomy (With or Without Lymphadenectomy)

Radical prostatectomy is usually reserved to patients who are in good health and have tumor confined to the prostate gland (stage I and stage II) [25, 26]. There are two types of radical prostatectomy: retropubic and perineal prostatectomy. The perineal approach requires a separate incision for lymph node dissection. Laparoscopic lymphadenectomy is technically possible and accomplished with reduced morbidity [27]. For small, well-differentiated nodules, the incidence of positive pelvic lymph nodes is less than 20%, and pelvic node dissection may be omitted. With larger, less-differentiated tumors, pelvic lymph node dissection is more important. The value of pelvic lymph node dissection (i.e., open surgical or laparoscopic) in these cases is not therapeutic but spares patients

with positive nodes the morbidity of prostatectomy. In some cases, nerve-sparing surgery can be done. However, men with large tumors or tumors that are very close to the nerves may not be eligible for this surgery. This type of surgery may save the nerves that control erection. The advent of robotic prostate surgery offers several advantages over the traditional methods, yielding clinically superior results and reduced risk of complications and allowing a quicker recovery [28, 29]. The use of robot-assisted radical prostatectomy (RARP) for the management of localized PCa has increased dramatically in recent years. RARP is associated with improved perioperative outcomes, such as reduced blood loss and fewer transfusions. However, cancer control after RARP versus retropubic radical prostatectomy is equivalent, with similar incidences of positive surgical margins and comparable early oncological outcomes. RARP appears to provide advantages in recovery of continence, potency, and quality of life compared with retropubic radical prostatectomy [30].

External Beam Radiation Therapy

External beam radiation therapy (EBRT) is a good option as definitive treatment for patients with tumor at early or locally advanced stages and localized within the prostate. The evolution of radiotherapy techniques through three-dimensional conformal radiotherapy (3D CRT), intensity-modulated radiotherapy (IMRT), and image-guided radiotherapy (IGRT) has allowed more accurate and precise treatments and obtained significant improvements in the therapeutic ratio [31, 32]. These modalities make it possible to treat PCa with radical intent and can be an alternative to radical surgery. A critical issue in EBRT of PCa is that the therapeutic effective dose is limited by the dose delivered, since it has been shown that the biochemical disease-free survival increases with increasing radiation dose [33]. Some randomized trials have shown better results with higher doses (>70 Gy). EBRT can be combined also with hormone therapy, in a short or long course, depending on clinical stage [34]. An alternative to EBRT utilizes protons as the radiation source. The advantage of proton therapy is the reduced radiation exposure to normal tissues adjacent to the tumor, while maintaining a therapeutic dose to the lesion.

Suitable candidates for adjuvant radiation therapy are patients with multifocal disease, positive surgical margins, periprostatic tissue invasion (T3-T4), GS>7, or PSA >0.2 ng/mL after radical prostatectomy [35]. Immediate postoperative radiotherapy improves significantly the biochemical recurrence-free survival and local control, but not overall survival. EBRT is also indicated after surgery when increasing PSA levels or diagnostic imaging detects local or distant tumor localization (soft tissues and bone). In the scenario of radiation therapy, intense clinical investigations are ongoing to further optimize treatment of PCa, including dose escalation, moderate and extreme hypofractionation, optimal combination between radiotherapy and androgen deprivation therapy, and timing of postoperative RT [36].

Brachytherapy

Brachytherapy (also called seed implantation or interstitial radiation therapy) treats PCa with radiation from inside the prostate gland. There are two types of brachytherapy: (1) low-dose rate therapy (LDR) and (2) high-dose rate therapy (HDR) [37, 38]. Brachytherapy with LDR uses permanent implants of iodine-125 seeds, while HDR uses iridium-192 sources or cesium-137 sources that are removed after irradiation. LDR brachytherapy is safe and efficient and constitutes an alternative to surgery and EBRT, particularly in those patients with a prostate gland of small volume, clinical low risk, GS < 7, and a PSA <10 ng/mL. Recurrence-free survival at 5 years has been reported to range from 71% to 93% with a median follow-up between 36 and 120 months [39]. Differently from LDR, HDR brachytherapy should be performed in the presence of locally advanced PCa, often delivered as a boost in combination with EBRT.

High-Intensity Focused Ultrasound Therapy and Cryotherapy

High-intensity focused ultrasound (HIFU) therapy and cryotherapy, two sophisticated options for local treatment of PCa, can be performed both as primary treatment and as salvage treatment, after unsuccessful surgery or radiotherapy [40, 41]. At present, the diffusion of these techniques is limited. Therefore, despite some encouraging results, the overall clinical experience is limited to a few centers and data should be confirmed on larger series of patients. However, the clinical value of these techniques has a definite role, since both HIFU and cryotherapy can achieve precise ablation of small lesions (focal therapy) by treating a partial volume of the prostate gland.

Hormone Therapy

The growth of PCa cells is sustained by testosterone [42]. This is the reason why the treatment of PCa is based on suppression of this hormone [43]. This effect can be obtained by orchiectomy or by administering luteinizing hormone-releasing hormone (LHRH) agonists (leuprolide, goserelin, and buserelin) or LHRH antagonists (degarelix) that block LH production in the pituitary gland, thus inhibiting the synthesis of testosterone [44–46]. This strategy is called androgen deprivation therapy (ADT). LHRH agonists are indicated in the different phases of the disease and can be used alone or in combination with other drugs, in association with radiotherapy or after surgery. ADT has clinical and prognostic importance as adjuvant treatment after radical prostatectomy, if lymph nodes are positive for metastasis. For the treatment of extraprostatic cancer, ADT can be combined with EBRT, since clinical evidences demonstrated superiority of the combined treatment versus the single treatment. ADT should be considered as the first-choice therapy in patients with metastatic disease, with involvement of distant organs other than prostate gland and locoregional lymph node (e.g., bone, lung, or distant lymph nodes).

Another important type of hormone therapy is based on the use of antiandrogens (bicalutamide, flutamide, and cyproterone acetate), compounds that compete directly with circulating androgens for binding sites on their receptors within the prostate cells, thus promoting apoptosis and inhibiting PCa growth [47, 48]. Cyproterone acetate additionally blocks gonadotropin release by the pituitary, thus contributing to reduce the testosterone plasma levels. These drugs are administered as monotherapy or in combination with LHRH agonists.

Two new drugs have recently been made available in the armamentarium for hormone therapy: abiraterone acetate and enzalutamide, with different mechanisms of action. Abiraterone acetate is a potent inhibitor of the enzyme 17-alpha-monooxygenase (CYP17), which is essential for the synthesis of testosterone from nongonadal sources [49]. The inhibition of CYP17 (normally expressed in testicular, adrenal, and prostate tumor tissues) translates into reduced testosterone synthesis from cholesterol. Enzalutamide is a new generation antiandrogen with a higher affinity for the ligand binding the androgen receptor than the first-generation agents, such as bicalutamide [50]. This agent acts at three different steps: (1) it inhibits androgen binding to androgen receptors, (2) it inhibits androgen receptors from entering into the nucleus, and (3) it inhibits androgen receptors from binding to DNA.

Chemotherapy

Docetaxel belongs to the taxane family (antimitochondrial agents) and its use is mainly indicated in patients with metastatic PCa resistant to ADT. Docetaxel plus prednisone showed to be significantly superior to mitoxantrone in patients defined as castrate-resistant prostate cancer (CRPC) for all endpoints of efficacy, including overall survival [51, 52]. CRPC patients develop progression of disease (e.g., biochemical relapse or progression of metastases) in spite of low levels of circulating testosterone (<50 ng/dL). Another agent named

cabazitaxel, a new semisynthetic analogue of docetaxel, has been shown to be effective in metastatic CRPC patients, with significant survival benefit versus mitoxantrone [53].

Immunotherapy

Recently, some interesting results have been obtained with vaccines, such as GVAX, PROSTVAC-VF, and sipuleucel-T [54–56], and with novel anti-immune checkpoint inhibitors like ipilimumab [57–59]. Sipuleucel-T, approved by the FDA and EMA, is a dendritic vaccine obtained by isolating dendritic cells from patients, priming cells in vitro with prostate-specific acid phosphatase through a fusion protein and reinfusion of the activated cells in the patient. Ipilimumab is a fully human antibody that binds to the inhibitory cytotoxic T lymphocyte antigen 4 (CTLA-4), thereby enhancing antitumor immunity. The results achieved in PCa are so far of a very preliminary nature.

Treatment of Skeletal Metastases

Bone-modifying agents can modulate the activity of osteoclasts, osteoblasts, and osteocytes. Several bisphosphonates (e.g., zoledronic acid) and an inhibitor of the RANK/RANKL pathway (denosumab) have been approved for the treatment of bone metastases in solid tumors with the goal to reduce skeletal-related events [60]. Denosumab has been shown to have superior activity over zoledronic acid in delaying and preventing skeletal-related events in patients with skeletal metastases from metastatic CRPC. Overall, some clinical evidence supports the introduction of zoledronic acid in the treatment of hormone-sensitive metastatic PCa [61]. None of these agents, however, has induced an improvement in overall survival.

As a calcium analogue, the alpha emitter radium-223 ion (administered in the form of a chloride salt) is selectively taken up in osteoblastic areas, where it conveys high radiation energy within a short penetration range, thus resulting in irreparable DNA damage. Results of the ALSYMPCA trial indicate that, when used for the treatment of bone metastases, this radiopharmaceutical leads to an advantage in survival for metastatic CRPC patients who presented with symptoms [62, 63]. In addition to significant reduction in bone pain and better quality of life versus placebo, treatment with ^{223}Ra-dichloride caused a 30% reduction in the risk of death versus placebo and reduction of new skeletal related events (SRE) both in post-docetaxel and in chemo-naïve patients [64].

In the new therapeutic scenario for metastatic CRPC, the appropriate algorithm for use of the available drugs is still an area of open discussion. Abiraterone acetate and enzalutamide demonstrated significantly increased overall survival and progression-free survival in the post- and pre-docetaxel setting in patients with bone metastases, respectively. Moreover, a significant impact on the incidence and severity on bone-related adverse events was observed in patients receiving enzalutamide [50]. Also EBRT represents an effective palliative treatment for control of pain in patients with localized skeletal metastases. EBRT achieves significant clinical results in 60–80% of patients, with more than 50% of patients obtaining complete pain relief at the treated site [65–67].

For initial treatment of CRPC patients with skeletal metastases, NCCN Clinical Practice Guidelines recommend abiraterone, enzalutamide, and docetaxel (for rapidly progressing patients), radium-223 (for patients with bone metastases and no visceral metastases), or participation in clinical trials. Nevertheless, no consensus exists on the sequence of therapies to be employed alone or in combination after failure of initial therapy or first-line docetaxel. All agents plus cabazitaxel and salvage chemotherapy are options for second-line therapy. Figure 2 shows some examples of treatment strategies in PCa.

Biochemical and Diagnostic Modalities

Laboratory Tests

PSA is recognized as the first-choice tumor marker for PCa, since it has an absolute prostate specificity and is expressed by the majority of prostate cancers [50]. However, several nonneoplastic conditions

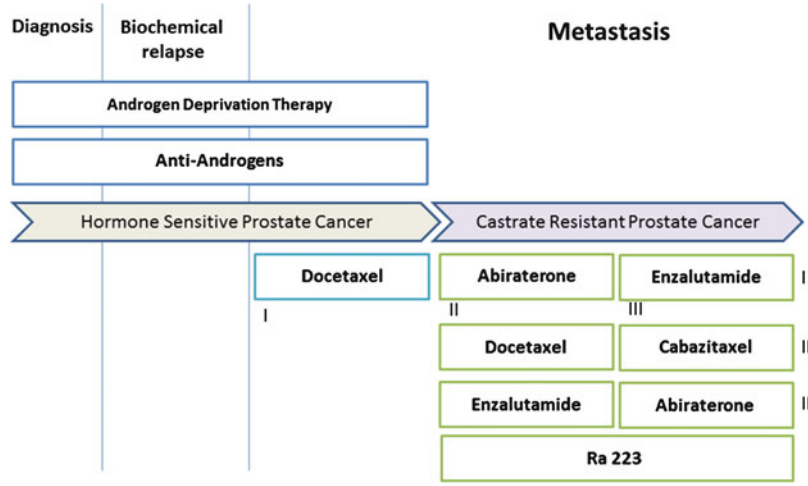

Fig. 2 Possible treatment strategies in different phases of PCa

of the prostate gland are associated with increased PSA levels; therefore, it has a lack of tumor specificity [68], which is the major drawback of PSA as a circulating marker for PCa. A number of patients with PCa have serum PSA levels below the cutoff of 4 ng/mL, even if about 15% of men with PSA below this threshold will have a biopsy-proven PCa. The probability of having a PCa rises as the PSA levels rise; the highest values correspond to the highest probability to have a PCa. Subjects with PSA levels ranging from 4 to 10 ng/mL have a 25% chance of having PCa (one out of four patients); when PSA concentrations are >10 ng/mL, the chance of having PCa is over 50–60%. Patients with a free-to-total PSA ratio <20% and PSA velocity >0.75 ng/mL per year have a higher risk of PCa. Different approaches were adopted in the past to optimize the sensitivity of the PSA test, for instance, by changing the cutoff threshold, variously elaborating on the PSA test (PSA density, PSA velocity), and investigating PSA isoforms (i.e., free PSA, conjugated PSA, pro-PSA). Novel biomarkers have also been explored, belonging to various molecular families (i.e., PCA-3, TMPRSS2-ERG gene fusions) [69, 70].

At variance with the use of PSA for the initial diagnosis, PSA is to be considered a strictly cancer-specific marker in patients in whom PCa has already been diagnosed and/or after primary treatments. In patients radically treated with curative intent, prostate tissue would not be represented anymore in the body, since it was fully removed by surgery or destroyed by radiotherapy. Then PSA should become undetectable in the serum after radical prostatectomy or should keep very low levels after radiotherapy. In these conditions, any significant and/or progressive increase of PSA values has to be considered cancer specific, particularly when the increase is constant over time. All patients with residual or relapsing PCa exhibit PSA changes, which therefore represent a clear biochemical sign of cancer presence [70–72]. There are two main characteristics of PSA as tumor marker: (a) a high proportion of prostate cancers produce PSA; (b) PSA is exclusively synthesized by prostatic tissue and this avoids any other analytical confounding noise that might mask PSA. Therefore, PSA is useful for monitoring patients radically treated, because the false-positive results are extremely rare in these conditions and any small increase of PSA may be considered to indicate cancer relapse.

Bony metastases are very frequents in PCa patients and are associated by high focal bone turnover with increased activity of osteolysis and/or osteogenesis. Markers of bone turnover might therefore be ideal to monitor progression of osteolytic or osteoblastic metastasis and/or to evaluate response to treatment. At present, bone alkaline phosphatase (bALP), total alkaline phosphatase (tALP), and amino-terminal procollagen propeptide type I (PINP) are considered as standard markers of bone formation, while cross-linked

C-terminal telopeptide of type I collagen (CTX) and cross-linked C-terminal telopeptide of type I collagen (ICTP) are utilized as markers of bone resorption [73–75]. The results from several studies conclude that in cancer patients with skeletal metastases, serum or urinary levels of bone turnover markers may be increased for various concomitant causes, in addition to skeletal metastases (e.g., age, vitamin D deficiency, and adjuvant hormone therapy). This makes it impossible to distinguish the contribution of the different components that determine high levels of bone markers; therefore, markers of bone turnover should not be considered as diagnostic tools for skeletal metastasis. Instead, markers of bone turnover can be considered as indicators of prognosis and parameters of progression. Some clinical investigations demonstrated a positive association between high levels of these markers and presence or progression of skeletal metastases from PCa [76, 77]. The highest diagnostic accuracy was described for b-ALP (72% sensitivity, 88% specificity), and the greatest diagnostic specificity was reported for PINP (92%). According to other reports, both baseline and on-study elevations in bone marker levels were associated with increased risks of SRE, disease progression and death [78–80]. In conclusion, clinical evidences confirm that all markers of bone turnover at present can be considered as parameters of prognosis or of response to therapy, but they have a very poor diagnostic value.

Radiological Imaging

Transrectal ultrasonography is used to look at the prostate when a patient has PSA abnormalities (e.g., high/increased levels, or altered free-to-total ratio, and/or high PSA velocity) or has abnormal DRE findings. TRUS has become the standard procedure to obtain material for histopathological examination [81]. Since early studies indicated that TRUS-guided single-spot biopsies detected PCa only in 22–34% of the cases, the current procedure is based on multiple sampling [14, 15]. The likelihood of PCa diagnosis increases with the number of biopsy specimens, and at least ten biopsy cores are recommended; 12–16 samples are obtained in some centers [17, 18]. Besides this recommendation, some US abnormalities do not correspond to a cancer lesion; therefore, the procedure can be affected by both false-negative and false-positive results. Attempts to improve its accuracy are based on the use of color Doppler, power US, and 3-D US. Moreover, TRUS can be used also to measure the size of the prostate gland, which can help in determining the PSA density, or can represent also a guide during some forms of treatment such as brachytherapy [82, 83].

CT scan has no value when the cancer is likely to be confined to the gland. Therefore, CT cannot be used for studying the prostate gland itself. However, CT can be helpful when spread to lymph nodes and adjacent structures is suspected (see Fig. 3), and for restaging patients. The role of CT scan in the current clinical routine consists in studying bone and soft tissues of the entire body, since it is the most available and reliable radiological whole-body method to detect and monitor lymph node, visceral, and skeletal metastases [84].

Magnetic resonance imaging (MRI) has recently emerged as the modality of choice for the detection of PCa after an inconclusive biopsy, for local staging, and for seminal vesicle evaluation. T2-weigted MRI sequences allow a precise definition of the local anatomy (see Fig. 4). The use of functional MRI sequences (namely, dynamic contrast-enhanced (DCE), diffusion-weighted imaging (DWI), and MRI spectroscopy) enables more accurate examinations [85, 86]. MRI associated with a systematic biopsy determines a better cancer detection also in patients with previous standard US-guided negative biopsies and elevated serum PSA [87, 88]. Although the bone itself does not have an MR signal, skeletal metastases are visualized by MRI through the detection of early changes in bone marrow that precede bone reaction to tumor invasion. MRI could represent an imaging technique of choice for detection and follow-up of bone metastases [89, 91]. New whole-body (WB) protocols have been adopted, and ad hoc WB-DWI sequences were developed to explore with multiparametric projections (MPR) areas that are difficult to analyze on standard anatomical imaging. In very few

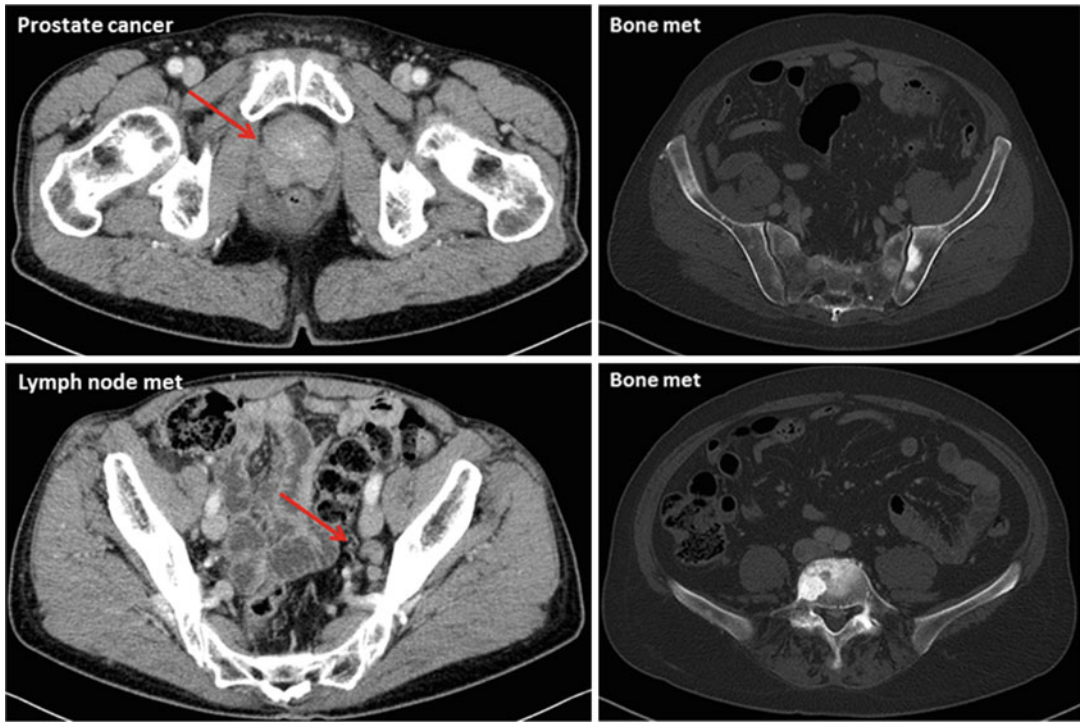

Fig. 3 CT images suggesting primary prostate cancer (*upper left panel*), pelvic lymph node involvement (*lower left panel*) in a 78-year-old patient with newly diagnosed PCa, before any treatment. Bone window CT images show bone metastases in the pelvis (*upper* and *lower right panels*)

centers, WB hybrid PET/MRI scanners have been introduced, for simultaneous acquisition and exact anatomical coregistration of PET and MRI. A limitation of this modality is that such sophisticated approaches are available in a limited number of specialized centers and these examinations are time-consuming, require specific expertise, and have an intrinsic high cost.

Nuclear Medicine Modalities

Nuclear medicine modalities can be classified according to the physical characteristics of the tracers (based on γ-emitting or β^+-emitting radionuclides), the type of detection (planar scintigraphy, SPECT, SPECT/CT, PET/CT,), the mechanism of accumulation of the agents (targeting bone or targeting cancer cells), and their availability in the clinical practice (already approved or experimental).

The choice of the best imaging strategy depends on several factors, such as availability and costs. Planar imaging and SPECT with bone targeting agents are the most commonly employed techniques, both for their availability and for economic reasons. PET/CT represents the more sophisticated technique that can be used with different radiotracers, both for bone and for cancer imaging.

Radiopharmaceuticals for PCa can be divided into two main groups: (1) targeting bone (^{99m}Tc-labeled diphosphonates and ^{18}F-fluoride) and (2) targeting cancer cells ([^{11}C]choline, ^{18}F-choline, [^{18}F]FDG, ^{68}Ga-PMSA-ligand, ^{18}F-FACBC, etc.).

^{99m}Tc-Biphosphonates Bone Scan, SPECT, and SPECT/CT

The commonest radiopharmaceuticals used to visualize bone metastases belong to the bisphosphonates family labeled with ^{99m}Tc, such as ^{99m}Tc-hydroxymetilendiphosphonic acid

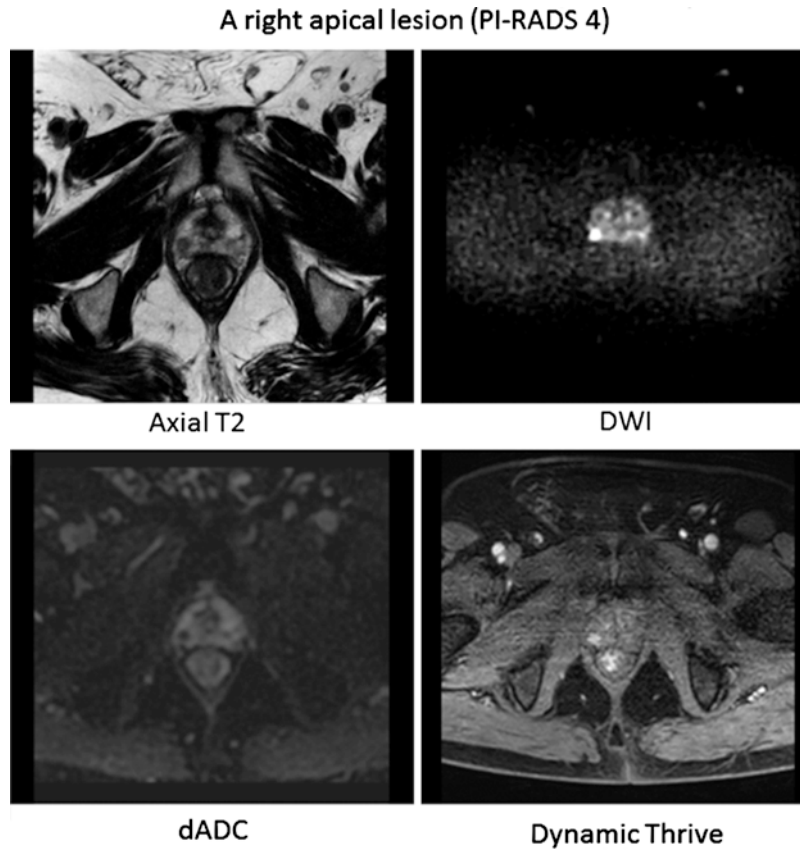

Fig. 4 MRI images obtained in a patient with PCa. A focal hypointense tumor focus in the right apical region of the prostate gland is shown in different sequences

(^{99m}Tc-HMDP), ^{99m}Tc-methylene diphosphonate (^{99m}Tc-MDP), and ^{99m}Tc-3,3-diphosphono-1,2-propanedicarboxylic acid (^{99m}Tc-MDP) [90–92]. ^{99m}Tc-MDP accumulates in the mineral component of bone: nearly two-thirds in the hydroxyapatite crystals and one-third in calcium phosphate. Its uptake is related to the osteoblastic activity, blood flow, and extraction efficiency. The vast majority of skeletal metastases from PCa are osteoblastic, lesions that can easily be depicted on a whole-body scan. Bone scintigraphy (BS) is the cornerstone of nuclear medicine for the assessment of the skeleton, particularly in oncology. The conventional whole-body scan (WBS) is recommended in the most important guidelines for PCa, because it is widely available, has low costs and high sensitivity, and is able to detect bone metastases several months before they are revealed by planar x-ray. In fact, more than 40% of trabecular bone has to be destroyed before the lesion becomes detectable by conventional x-ray [92, 93]. It is well known that the highest sensitivity of BS for PCa metastases is achieved in presence of osteoblastic lesions. BS can efficiently image both the osteoblastic and the mixed lesions, while the detection of osteolytic lesions is less efficient due to reduced calcium deposit and consequent poor uptake of the radiolabeled phosphonates. Another important notion to keep in mind is that BS cannot detect cancer invasion in the bone marrow per se, unless an osteoblastic reaction is activated.

The diagnostic sensitivity of BS in PCa patients varies from 75% to 95%; its specificity is relatively lower (from 60% to 75%), because metabolic bone reactions can also occur in benign conditions such as arthrosis, inflammation, and trauma [93–95]. The high variability reported across the clinical studies depends on differences between patient populations and pretest probability of bone metastases.

When is BS indicated in PCa patients? In asymptomatic newly diagnosed patients, we

have to consider the class of risk described above, in order to keep to a minimum the use of diagnostic investigations, especially in patients with a very low probability of having bone metastases. PSA levels represent the most common parameter to evaluate the probability of having bone metastases. Several retrospective studies indicate that PSA levels <20 ng/mL can exclude with a high probability the presence of bone metastases at BS, with a negative predictive value closed to 99% [96]. Conversely, WBS should be performed in PCa patients at high risk or very high risk (PSA >20 ng/mL or GS>8) (NCCN recommendations). In patients with intermediate risk, BS should be considered only in presence of clinical conditions suspected for bone metastases. In these patients, calculation of the pretest probability would be useful; several statistical approaches that produce complex nomograms are now available [97–101].

In patients with PCa after primary treatment (surgery or radiotherapy), the indications for bone imaging occur in two different situations: (a) symptomatic patients or biochemical recurrence (increase in PSA levels) and (b) patients under treatment, for monitoring response to therapy. In the first case, the physician faces the clinical problem to detect a possible cancer relapse with or without bone involvement, often driven by the appearance of clinical and/or biochemical symptoms based on the trend of rising PSA [102–107] (see Fig. 5). There are established cutoff values for PSA doubling time and PSA velocity (doubling time less than 2–3 months and velocity >5 ng/mL per year) suggesting the presence of bone metastases. Moreover, BS is often indicated to solve equivocal/non-diagnostic findings at radiological imaging.

In the second case, the goal is to describe changes in radiopharmaceutical uptake (i.e., intensity, size, or number) as an index to assess response to therapy. The use of BS to evaluate the response of bone metastases to therapy has recently been extensively discussed by Evangelista et al. reporting various important critical issues, such as timing of the scan, the possibility of false-positive results due to the flare phenomenon (a marked increase in multifocal skeletal tracer uptake as a result of a change in therapy within 2-3 months of the bone scan) the criteria of interpretation at different times during and after therapy, and other factors [108]. Of course, the flare phenomenon is the most important factor to consider; in spite of some existing standard criteria to carry out a correct interpretation of bone uptake, at present it still constitutes a limitation that affects the value of BS in assessing the response to therapy [46, 109–111]. It can be concluded that, in patients with bone metastases, WBS is more reliable for defining tumor progression than for measuring the changes of response to therapy.

A bone scan index (BSI) has been developed to quantitate the load of bone metastases from PCa. This index is calculated by considering the average weight of bones derived from a reference man and the fractional contribution of each bone expressed as a percentage of the entire skeleton [112]. Therefore, BSI represents the percentage of the skeletal mass occupied by metastases, and this value indicates the extent of bone involvement. BSI was demonstrated to represent a reproducible prognostic tool and can be used both for stratifying patients in treatment protocols and for assessing treatment response [113, 114]. Since calculation of the BSI is a very laborious and time-consuming procedure, various automated computer-assisted methods were developed, resulting in a clear improvement of accuracy and feasibility [115]. Significant correlation has been described between BSI and overall survival. However, BSI has not entered in the diagnostic routine and the general opinion is that BSI would be mainly adopted for clinical trials [116, 117].

SPECT can improve on the limited specificity of planar BS, as it enables better definition of particular skeletal areas, such as the spine, pelvis, hip, and knee. SPECT was shown to improve the sensitivity, specificity, negative predictive value (NPV), positive predictive value (PPV), and accuracy of conventional BS up to 92%, 91%, 94%, 82%, and 90%, respectively, over planar imaging [118–120]. In particular, hybrid SPECT/CT, by integrating the anatomical information from CT with the metabolic-functional information from SPECT, results in better interpretation of bone areas with increased tracer uptake, thus making it easier to distinguish benign from malignant lesions [121]. Several clinical studies on

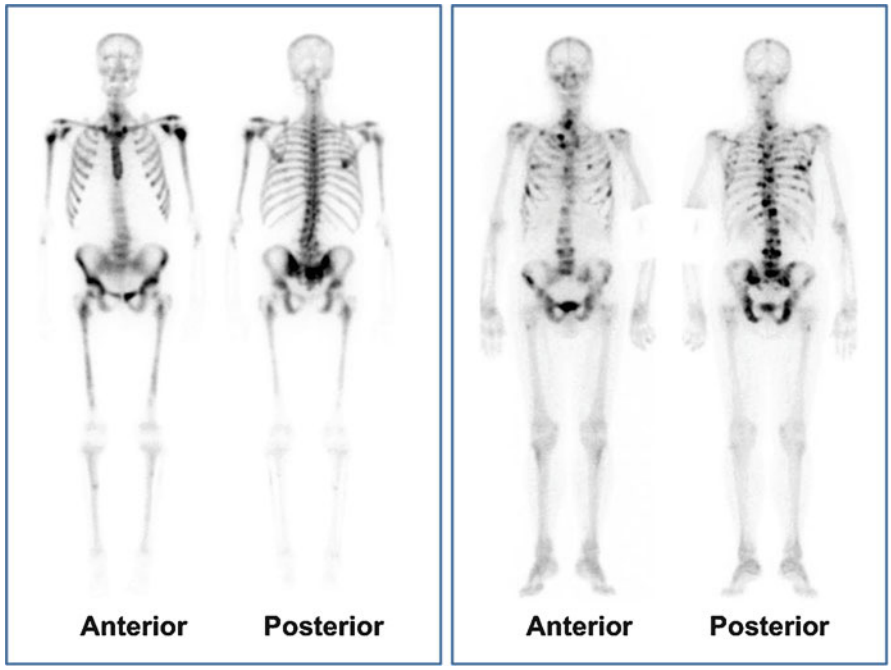

Fig. 5 Restaging BS in patients with biochemical PCA recurrence. (*Left*) A 65-year-old patient with a nonsurgical treated PCa with PSA 1,015 ng/mL, showing intensely increased tracer uptake in virtually all the skeletal segment ("super scan"). (*Right*) A 68-year-old patient with recurrent PCa, in whom the BS shows many areas of focally increased tracer uptake throughout several skeletal segments

scintigraphically equivocal lesions, the majority localized in the spine, demonstrated that SPECT/CT significantly improves the assessment of skeletal metastases from PCa [122–124]. Sharma et al. [125] showed that among 49 indeterminate lesions on planar BS, 96% were correctly classified with SPECT/CT and the patient management was changed in 61% [127]. Palmedo et al. compared SPECT/CT to ^{99m}Tc-HMDP BS and ^{99m}Tc-HMDP stand-alone SPECT in a series on PCa patients and found that SPECT/CT significantly improved specificity (94% versus 78%) and PPV (88% versus 59%) [126]. Although SPECT/CT has the advantage, over conventional BS, to allow a more detailed study of a limited region of the skeleton, its use in treatment monitoring is hampered by the hardware which prevents the WB acquisition in a reasonable time frame. In this regard, attempts have been undertaken to develop particular WB SPECT protocols enabling to image the entire body [127]. However, in spite of some particular multi-FOV methods reliable for the analysis of the WB scan, these modalities are not currently adopted in the clinical routine, due to their long acquisition time, limited compliance. Moreover, they do not solve the main drawback of conventional BS, which maintains a low diagnostic specificity and the inability to visualize the osteolytic lesions.

^{18}F- Fluoride PET/CT

^{18}F-Sodium fluoride (^{18}F-NaF) PET/CT detects skeletal metastatic disease by a mechanism of similar to that of ^{99m}Tc-HMDP. Clinical indications are the same as for ^{99m}Tc-HMDP WBS, including the detection of primary and secondary bone tumors, the evaluation of equivocal findings at radiological imaging, and the assessment of response to therapy [127, 128]. The clinical imaging protocol has been described by Segall et al. in the procedure guidelines published by the Society of Nuclear Medicine and Molecular Imaging (SNMMI) [129]. The recommended activity of ^{18}F-NaF is 1.5–3.7 MBq/kg (40–100 μCi/kg) up

Fig. 6 Mismatch between ^{18}F-fluoride PET/CT and BS in a 76-year-old patient with a significant increase in PSA (from 2 to 38 ng/mL) after radiotherapy. ^{18}F-fluoride PET/CT shows multiple sites of uptake in the skeleton, while the bone scan is negative

to a maximum of 370 MBq for oncologic imaging. Due to the lower injected activity and the physical decay characteristics, the total absorbed dose for ^{18}F-NaF PET is similar to that of the ^{99m}Tc-MDP BS [130, 131]. The kinetics of ^{18}F-NaF is characterized by a rapid plasma clearance and a high uptake in skeletal metastases with an especially favorable target-to-background ratio. Imaging quality of ^{18}F-NaF PET/CT is better than with ^{99m}Tc-MDP, with superior spatial resolution (4–5 mm versus 10–15 mm); imaging with ^{18}F-NaF is acquired earlier than with ^{99m}Tc-MDP (0.5–1 h versus approx. 3 h).

The overall diagnostic sensitivity of ^{18}F-NaF PET/CT is higher than that of conventional BS (Fig. 6). In a study by Even-Sapir et al. on 23 patients, patient-based sensitivity was 100% for ^{18}F-NaF PET/CT and 70% for BS, with 100% and 57% specificity, respectively. This advantage was reported also on a lesion-based analysis. Furthermore, the authors observed that PET/CT has significantly better sensitivity and specificity than SPECT/CT imaging [128]. A review article by Langsteger et al. on 22 patients with PCa found sensitivity, specificity, and accuracy values of 91%, 83%, and 88%, respectively, for skeletal metastases [132]. This superior sensitivity was reported also in other studies with ^{18}F-NaF PET/CT [133–136]. For example, Poulsen et al. described the superiority of ^{18}F-NaF PET/CT over conventional BS by studying 50 patients bearing 526 metastatic bone lesions from PCa; ^{18}F-NaF PET/CT had sensitivity, specificity, accuracy, and positive and negative predictive values of 93% versus 51%, 54% versus 82%, 81% versus 61%, 82% versus 86%, and 78% versus 43%, respectively [138].

Evangelista et al. confirmed that ^{18}F-NaF PET/CT has the highest weighted sensitivity (range of 81–100%) among the nuclear medicine modalities for the evaluation of bone metastases from PCa [108]. An important advantage of ^{18}F-NaF PET/CT is the ability to image both blastic and lytic skeletal metastatic lesions [137]. Despite the good performance of ^{18}F-NaF PET in detecting bone metastases (mainly in sensitivity), the interpretation of focal uptakes should be careful because of the increased number of false-positive results (which lowers specificity). A more accurate interpretation of the focal skeletal uptake can be achieved by semiquantitative

evaluation of uptake with the standardized uptake value (SUV) [143]. This approach has been employed by different authors, in particular for lesions located in the spine, demonstrating that SUV evaluation can play a role in better discriminating metastases from degenerative lesions [130, 138, 144, 145]. A large-cohort study based on data from the American National Oncologic PET Registry (NOPR) was carried out with the aim to elucidate the clinical impact of ^{18}F-NaF PET/CT on the management of patients. Results from 2,839 PET/CT scans performed in patients with different neoplastic diseases (68% prostate, 17% breast, 6% lung, 8% others) were evaluated. It was found that ^{18}F-NaF PET/CT induced changes of strategy in 40% of the cases [140]. Early diagnosis of cancer progression and early detection of metastatic lesions can lead to different successful treatments capable of altering prognosis. The prognostic impact of ^{18}F-NaF PET/CT was recently assessed by Apolo et al. in patients with bone metastases from PCa. A significant correlation was found between overall survival and modifications of SUV (besides the number of sites of skeletal uptake in the baseline PET scan) [137]. ^{18}F-NaF PET/CT was used in patients with bone metastases from PCa for evaluating the response to therapy and resulted in better performance than BS [139]. However, similar to conventional WBS, also the ^{18}F-NaF PET/CT findings can be affected by a "flare phenomenon" [141, 142].

There are sufficient data to demonstrate that PET/CT offers several advantages over conventional BS. However, PET/CT scanners are still less available than gamma cameras and the test is more expensive. ^{99m}Tc- MDP is easily and widely available, while the production of ^{18}F requires a cyclotron. Again, a conclusive and complete cost-effectiveness study on the clinical use ^{18}F-NaF PET/CT supported by a statistically significant number of tests is not available; for all these reasons, this modality is not still established worldwide in the current clinical practice.

[^{11}C]Choline and ^{18}F-Choline PET/CT

PET/CT with either [^{11}C]choline or ^{18}F-choline visualizes PCa using a metabolic tracer involved in phospholipid and in membrane metabolism, with the rationale that PCa is characterized by an upregulated choline transport, phosphorylation, and membrane metabolism. Choline (CHO) is phosphorylated to phosphoryl choline by the enzyme choline kinase; in this chemical form, it is trapped within the cancer cell [146, 147]. The radioisotopes used for labeling CHO are ^{11}C (half-life 20.4 min) or ^{18}F (half-life 109.7 min), to produce the imaging agents [^{11}C]CHO and ^{18}F-CHO, respectively.

Unfortunately, ^{18}F-CHO has a high urinary excretion, which may interfere with evaluation of tracer uptake in the prostate. On the other hand, [^{11}C]CHO has the disadvantage of a short physical half-life, thus making the [^{11}C]CHO PET scan feasible only in centers with an on-site cyclotron. An analog of [^{11}C]choline labeled with ^{18}F, ^{18}F-CHO can be distributed and utilized in centers without cyclotron facilities. Moreover, the emission energy of ^{18}F allows better detection with PET than ^{11}C [148, 149]. Nevertheless, [^{11}C]CHO and ^{18}F-CHO exhibit many similar characteristics, and for this reason, they are currently an established imaging modality to evaluate patients with PCa. [^{11}C]CHO is available in the USA with FDA approval (September 2012), while ^{18}F-CHO is available for routine clinical use in Europe. [^{11}C]CHO PET/CT imaging protocols are based on the i.v. bolus injection of 370–740 MBq. The effective dose (ED) is estimated to be approx. 0.3 Sv and the dose critical organ is the liver. The PET/CT scan starts 3–5 min after tracer injection and images are acquired for a total of 10–20 min with 2–5 min per bed position, depending on the PET camera. Similarly to ^{18}F-CHO, fasting is not strictly necessary, although many studies suggest to fast at least 4–6 h before PET scanning. For ^{18}F-CHO PET/CT imaging, patients receive an i.v bolus injection of 4.07 MBq/kg, whole-body imaging starting 60–90 min after tracer administration (see Fig. 7). Occasionally, for prostate bed evaluation, early static or dynamic pelvic images may be obtained 2 min after tracer administration [150–152].

Evangelista et al. analyzed the diagnostic effectiveness of radiolabeled choline PET/CT in different phases of patient management: in primary cancer localization, preoperative staging, and restaging and for the evaluation of therapy response [153]. The data suggest that the use of choline PET

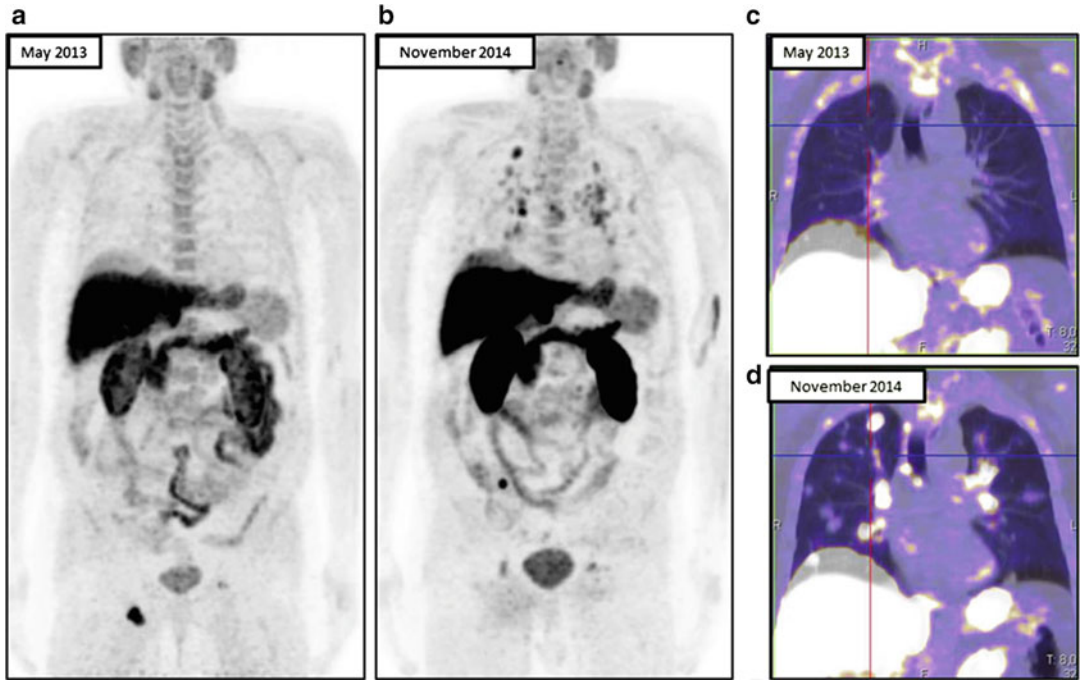

Fig. 7 ^{18}F-choline PET/CT for the detection of lymph node metastases in a 65-year-old patient with high-risk PCa. Radical prostatectomy was performed in 2011 (pT3bN1; GS = 9). The patient started Enantone in 2013 for disease progression in bone (**a**, **c**). Because of further increase in PSA level (36 ng/mL), the patient underwent PET/CT with ^{18}F-choline (**b**, **d**) that showed disease progression in the bone and lung

imaging for primary cancer detection in the preoperative phase is not supported by sufficiently convincing elements nor by a consistent number of observations. The region of the prostate gland can be successfully imaged by alternative radiological imaging modalities (US, MRI, CT), while preoperative evaluation of lymph node involvement with [^{11}C]CHO and ^{18}F-CHO PET/CT gave controversial results [154]. In a previous meta-analysis, Evangelista et al. had reported 49.2% pooled sensitivity with 95% pooled specificity for radiolabeled choline PET/CT in the detection of metastatic lymph node disease before a curative treatment. However, wide heterogeneity (between 22.7% and 78.4%) was reported across the studies [155]. Data from other studies showed sensitivity ranging from 33% to 45%, but confirmed high specificities when including larger patients' cohorts [156, 157]. The variability in the detection rate of lymph node metastasis was related to different biases, such as nonhomogeneity of GS, stage of disease, and other clinical factors. Therefore, despite good specificity, the current guidelines do not recommend choline PET imaging for lymph node staging of patients with primary PCa.

On the basis of clinical experience, the use of radiolabeled choline PET/CT in newly diagnosed patients should be limited to the detection of early osseous metastatic disease in high-risk patients [158]. When evaluating the value of ^{18}F-CHO PET/CT in the initial staging of 210 patients, Poulsen et al. found that a high focal bone uptake, consistent with bone metastasis, was seen in 18 patients. On the other hand, ^{18}F-CHO PET/CT has demonstrated some limitations in detecting densely sclerotic malignant lesions [159], since they are generally characterized by low metabolic activity.

At present, the best indication for [^{11}C]CHO or ^{18}F-CHO PET/CT consists in detecting PCa recurrence in patients already treated, but with biochemical recurrence (Fig. 8).

Krause et al. demonstrated a linear correlation between PSA values and the detection rates of

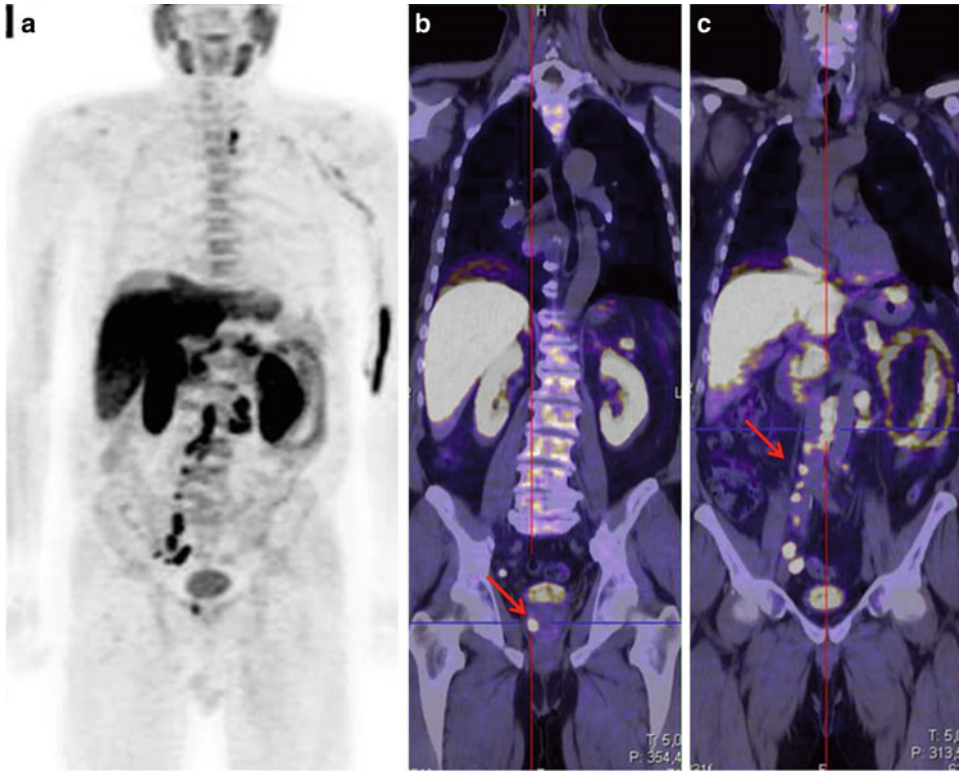

Fig. 8 Patient with increasing PSA after radical prostatectomy. This 72-year-old man had a high PSA level (36 ng/mL) at the time of initial diagnosis and underwent ^{18}F-choline PET/CT for staging. The MIP image (**a**) and coronal PET/CT images at two different depths demonstrate diffusion of the disease in the prostate (**b**) and in lymph nodes (**c**)

recurrences at radiolabeled choline PET/CT; this rate reached 75% in patients with PSA >3 ng/mL [160]. In patients with PSA values <1 ng/mL, recurrences were detected in approximately one out of three patients. The precise localization of the site of recurrence (local recurrence, recurrence as lymph node metastases, or systemic recurrence) is crucial for the choice of the subsequent treatment, as it directly influences personalized therapy. Graziani et al. published a retrospective analysis of 9,632 choline PET/CT scans performed for restaging in an academic center between 2007 and 2015. The inclusion criteria were radical prostatectomy, available levels of PSA, and proven biochemical relapse (PSA >0.2 ng/mL after radical prostatectomy or PSA >2 ng/mL above the nadir after primary EBRT with rising PSA levels); 3,203 patients matched the inclusion criteria and 4,426 scans were considered [161]. Overall, 52.8% of the [^{11}C]CHO PET/CT scans were positive. In patients with PSA levels between 1 and 2 ng/mL, 995 scans were performed and the positive rate was 44.7% with an incidence of distant findings of 19.2% and an incidence of oligometastatic disease of 37.7% These findings confirm the feasibility of [^{11}C]CHO PET/CT for detecting the site of metastatic disease in patients with confirmed biochemical recurrence.

Beheshti et al. investigated the ^{18}F-CHO PET/CT value for detecting bone metastases in patients with biochemical recurrence of disease and found that ^{18}F-CHO PET/CT had 79% sensitivity, 97% specificity, and 84% accuracy. The use of ^{18}F-CHO PET/CT for discovering skeletal metastases in general yields a detection rate

lower than conventional BS, but with greater specificity. The interpretation of focal uptakes with ^{18}F-CHO PET/CT leads to fewer false-positive and indeterminate findings and reduces the number of indeterminate lesions [162–166]. Beheshti et al. compared the diagnostic performance of ^{18}F-CHO and ^{18}F-fluoride PET/CT in 38 patients with biopsy-proven PCa for the detection of bone metastases. The authors found 81% sensitivity, 93% specificity, and 86% accuracy ^{18}F-fluoride, while the corresponding values were 74%, 99%, and 85%, respectively, for ^{18}F-CHO. In addition ^{18}F-CHO induced a change in the management in 2 out of 38 patients, due to the early detection of bone marrow metastases (bone invasion by cancer, before involvement of cortical bone) [134]. In a similar series of patients, Picchio et al. observed that [^{11}C]CHO PET/CT had lower sensitivity but higher specificity than BS in the detection of bone metastases in PCa patients with biochemical progression. The ranges of sensitivity, specificity, PPV, NPV, and accuracy for [^{11}C]CHO PET/CT were 89–89%, 98–100%, 96–100%, 94–96%, and 95–96%, respectively. For conventional bone scintigraphy, the corresponding values were 70–100%, 75–100%, 68–100%, 86–100%, and 83–90%. [^{11}C]CHO PET/CT and bone scan achieved a diagnostic concordance in 55 of 78 (71%) cases. This means that, in some selected cases, the combination of [^{11}C]CHO PET/CT with bone scan can provide additional useful information [164] (Fig. 9).

Sometimes patients with a single bone metastasis visualized by BS undergo [^{11}C]CHO PET/CT in order to obtain additional information about the extent of disease, both in bone and in other organs. In fact, some authors reported that PET/CT is able to depict multiple bone metastases and may provide images of bone lesions in up to 15% of patients with biochemical relapse after radical prostatectomy [167]. A recent article by Ceci et al. including 304 bone lesions from PCa found some differences in terms of SUV and PSA kinetics at [^{11}C]CHO PET/CT among osteoblastic lesions, osteolytic lesions, and bone marrow involvement. Osteoblastic lesions showed lower values of SUV_{max}, while osteolytic lesions had higher values. This interesting approach can represent an important proposal for classifying skeletal involvement [168] and may be of interest in terms of treatment choice and patient management.

Evaluation of response to treatment is a very critical issue, since in the clinical practice, this evaluation has a strategic role. The use of morphological and functional imaging criteria (e.g., with CT, PET, MRI) for assessing response to therapy is already well established, but its application and interpretation are, at present, still a matter of discussion (Fig. 10).

Radiolabeled CHO PET/CT has been proposed as biomarker for response evaluation in PCa patients, and the PERCIST criteria (PET response criteria in solid tumors) might be applied to this purpose. Furthermore, quantitative parameters such as the metabolically active tumor volume and SUV derivatives are under study, and some preliminary confirmations were obtained as prognostic parameters (related to overall survival) or as tool for assessing the efficacy of treatments [169–171].

^{68}Ga-PSMA-Ligand PET/CT and PSMA Derivates

The prostate-specific membrane antigen (PSMA) is a cell surface membrane-bound enzyme highly expressed in prostate carcinoma cells versus benign prostatic tissue. The localization of the catalytic site of PSMA in the extracellular domain allowed for the development of small specific inhibitors that are internalized after ligand binding [172, 173].

PSMA ligands have been labeled with different radionuclides enabling the use for PET imaging (^{89}Zr, ^{68}Ga, and ^{18}F), for single-photon scintigraphy (^{111}In, ^{99m}Tc), or for therapy (^{177}Lu, ^{90}Y) [174]. ^{111}In-capromab pendetide (a monoclonal agent against the intracellular epitope of PSMA) has been approved for clinical use to visualize PSMA expression by the FDA in 1996, with the trade name of ^{111}In-ProstaScint [175]. The use of this radiopharmaceutical has then been progressively abandoned in clinical practice, since the antibody cannot bind the intracellular domain of PSMA of intact cells, but only

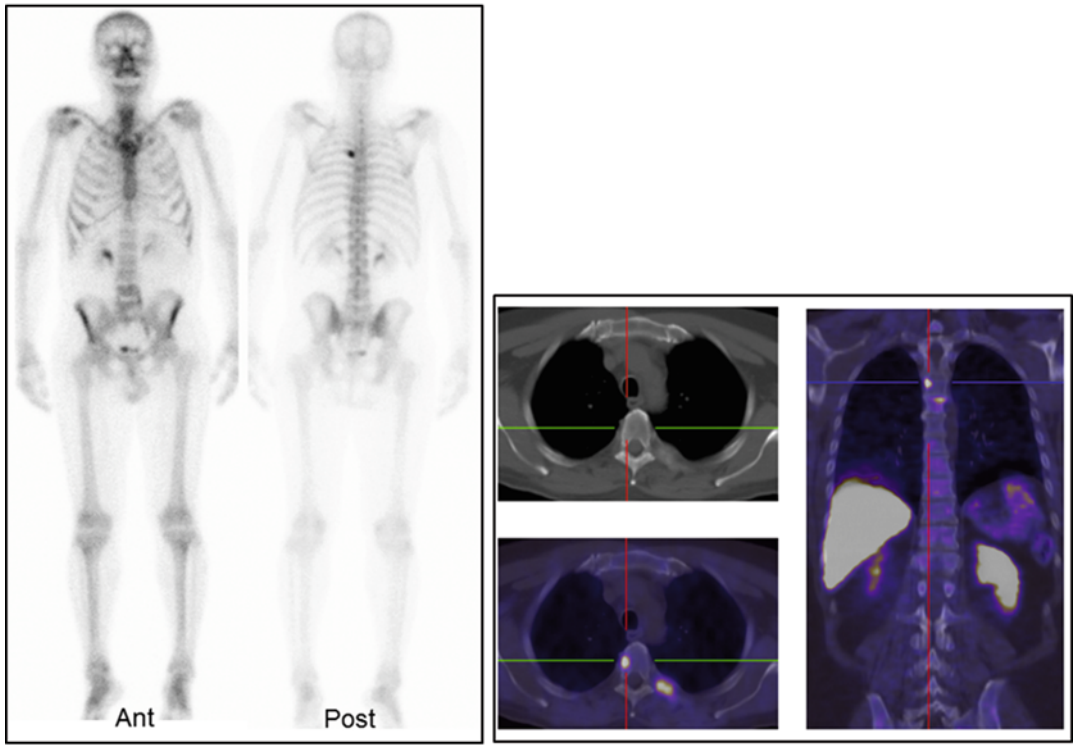

Fig. 9 Mismatch between BS and ^{18}F-choline PET/CT findings. (*Left*) The bone scan shows a single focus of uptake in the fourth left rib. (*Right*) ^{18}F-choline PET/CT confirms focal uptake in the fourth left rib but also in the right hemibody of T4

PSMA exposed in either apoptotic or dead cells. Therefore, the diagnostic performances of this immunoscintigraphic modality, in spite of some acceptable results, are not comparable with those that can be obtained with the most recent radiopharmaceuticals and novel PET/CT modalities for PCa assessment. Alternative monoclonal preparation probes targeting the extracellular domain of PSMA are under study, and a new ^{99m}Tc-labeled radiopharmaceuticals are being developed [176]. The ^{68}Ga-PSMA-ligand represents the most promising agent for the evaluation of patients with early biochemical recurrence of disease. Many studies have been published comparing the diagnostic performances of radiolabeled choline PET/CT with those of ^{68}Ga-PSMA-ligand PET/CT.

Preliminary studies demonstrated that PET/CT with the ^{68}Ga-PSMA-ligand (Glu-NH-CO-NH-Lys-(Ahx)-^{68}Ga(HBED-CC)), an inhibitor of the extracellular portion of PSMA molecule, resulted in significantly higher accuracy for the detection of early recurrence compared to ^{18}F-choline PET/CT [177]. These investigations also reported a higher tumor-to-background ratio for ^{68}Ga-PSMA-ligand PET/CT for the detection of suspected PCa metastases versus ^{18}F-choline PET/CT; moreover, highly promising performances were reported also at very low PSA levels.

Conversely, few data are available about the use of ^{68}Ga-PSMA-ligand PET/CT for the primary diagnosis of PCa. Fendler at al. recently evaluated the accuracy of this modality to localize cancer in the prostate and surrounding tissue at initial diagnosis. ^{68}Ga-PSMA-ligand PET/CT was able to detect invasion of the seminal vesicles and the extracapsular tumor spread [178].

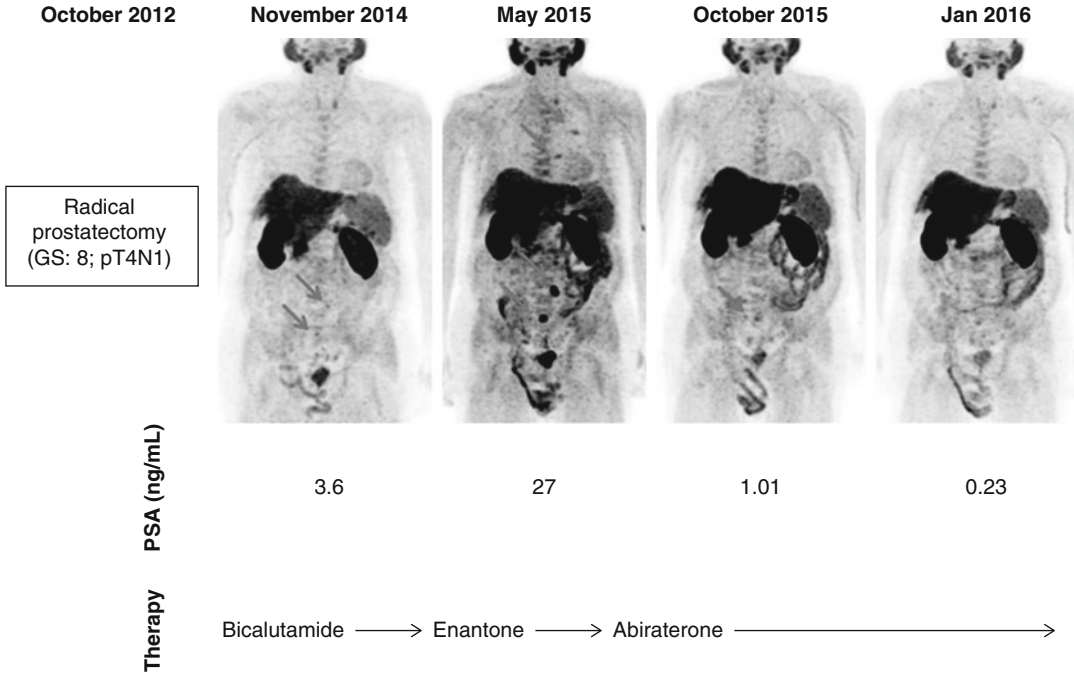

Fig. 10 Evaluation of response to therapy with ^{18}F-choline PET/CT. A 73-year-old with PCa shows progressively increasing PSA level during androgen deprivation therapy (bicalutamide). For this reason, therapy was switched to Enantone, then again to abiraterone acetate for further increasing serum PSA. The serial ^{18}F-choline PET/CT scans show a significant reduction in ^{18}F-choline uptake in the lymph nodes, after the start of treatments, particularly with abiraterone acetate

The combined use of ^{68}Ga-PSMA-ligand PET with multiparametric MRI can enable targeted fusion biopsies, especially in patients with a negative biopsy. At present, these preliminary experiences are too limited [179].

Interesting results were reported by Maurer et al. regarding primary staging of PCa patients. In a retrospective analysis on 130 consecutive patients with intermediate- and high-risk PCa who had radical prostatectomy with lymph node dissection, ^{68}Ga-PSMA-ligand PET/CT showed a 65.9% sensitivity and 98.9% specificity [180]. Conversely, Budaus et al. evaluated 30 PCa patients who underwent radical prostatectomy and lymph node dissection, using a preoperative ^{68}Ga-PSMA-ligand PET/CT for the identification of lymph node involvement, reporting overall sensitivity, specificity, PPV, and NPV of ^{68}Ga-PSMA-ligand PET/CT for the detection of lymph node metastasis of 33.3%, 100%, 100%, and 62.9%, respectively. Moreover, per site analysis revealed values of 27.3%, 100%, 100%, and 52.9% [181]. ^{68}Ga-PSMA-ligand PET/CT is able to detect visceral and skeletal lesions not visible by other modalities [182]. In recurrent disease, Afshar-Oromieh et al. studied 319 patients with PCa [177]. In this series, despite the non-homogeneous features of the patients' population (mean PSA 161 ng/mL, median PSA 4.59 ng/mL, 28 patients not treated with radical therapies), ^{68}Ga-PSMA-ligand PET/CT showed an overall detection rate of 82.8%. A detection rate of 50% was observed for serum PSA values <0.5 ng/mL and of 58% for PSA values ranging from 0.5 to 1 ng/mL. Interestingly, the detection rate was not influenced by the Gleason score or by ADT (Fig. 11).

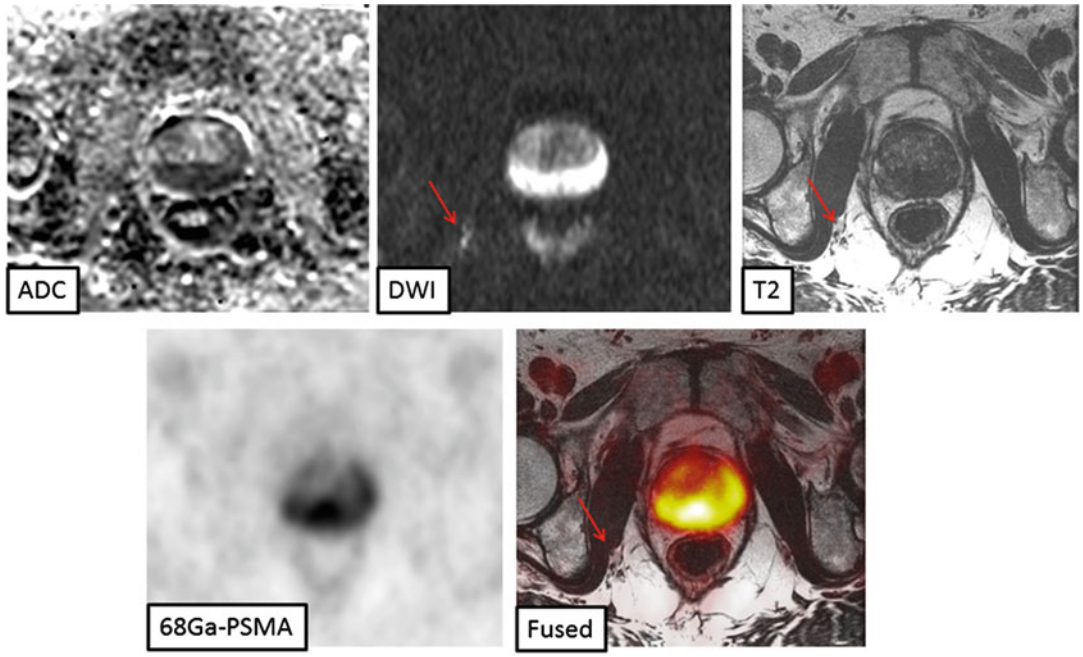

Fig. 11 A 59-year-old patient with PCa showing a slight increase in serum PSA level (0.6 ng/mL) after radical prostatectomy. The ^{68}Ga-PSMA-ligand PET/MRI shows significant tracer uptake in a right internal iliac lymph node (Images supplied by courtesy of Thomas A. Hope, Department of Radiology and Biomedical Imaging, University of California, San Francisco, California, USA)

In a cohort of 248 recurrent patients with median PSA of 1.99 ng/mL, Eiber et al. reported an overall positivity of 89.5% for ^{68}Ga-PSMA-ligand PET/CT [183]. Verburg et al. evaluated with ^{68}Ga-PSMA-ligand PET/CT the extent of disease in 151 patients with recurrent PCa. The imaging results were correlated to PSA levels, PSA doubling time, and GS [184]. In this study, the presence of recurrent lesions was correlated with absolute PSA levels and PSA kinetic. The detection rate resulted in 30% of GS values of less than 8 and 32% for values between 8 and 10. This finding confirms other data suggesting that PSMA overexpression is not directly related to GS and that fast PSA kinetics are more likely to be associated with a positive PSMA-ligand scan.

A critical review was recently published by Perera et al. [185]. Sixteen articles involving 1,308 patients were analyzed. ^{68}Ga-PSMA-ligand PET was positive in 40% of patients for primary staging and in 76% for biochemical recurrences. Positive ^{68}Ga-PSMA PET scans for biochemical recurrences increased with the pre-PET PSA value. For the PSA categories 0–0.2, 0.2–1, 1–2, and >2 ng/mL, the rates of positive scans were 42%, 58%, 76%, and 95%, respectively. A shorter PSA doubling time increased the PET/CT positivity. The conclusions indicate a favorable sensitivity and specificity profile, compared to choline-based imaging techniques, particularly in case of low PSA levels. New emerging indications for ^{68}Ga-PSMA-ligand PET/CT are in the management of radiotherapy [186].

At present, the most widely applied indication for ^{68}Ga-PSMA PET/CT is the detection of recurrent disease and restaging of treated patients. This modality seems to increase the rate of detection, even with serum PSA values <0.5 ng/mL [187]. Despite these promising findings, the results obtained up to now with ^{68}Ga-PSMA-ligand PET/CT have not been extensively validated

with either histology (biopsy of the areas of uptakes) or with lesion-directed imaging techniques characterized by high specificity. Furthermore, the overall clinical experience is still limited and derived from retrospective series and mostly from German institutions. For these reasons, further prospective studies and larger series of patients should be investigated in order to confirm the promising results.

A number of alternative radiopharmaceuticals to ^{68}Ga-PSMA-ligand are being explored, and the most interesting radiopharmaceuticals under development today are PSMA-ligand-based fluorinated compounds. The advantages of ^{18}F over ^{68}Ga are mainly based on the wider availability of the tracer without problems in production and distribution and better quality of imaging because of the favorable emission energy of ^{18}F for PET imaging. Two radiopharmaceuticals at present raise the interest of the nuclear medicine community: ^{18}F-DCFBC (N-[N-{(S)-1,3-dicarboxypropyl] carbamoyl} 4-^{18}F-fluorobenzyl-L-cysteine]) and ^{18}F-DCFPyLis (2-[3-{1-carboxy-5-[(6-[^{18}F]fluoro-pyridine-3-carbonyl)-amino]-pentil}-ureido]-pentanedioic acid). Both ^{18}F-DCFBC and ^{18}F-DCFPyLis exhibit favorable parameters in terms of radiation dosimetry, and biodistribution [188, 189]. Preliminary data in a limited series of patients suggest advantages of both tracers versus the current imaging modalities; however, these data require further confirmation in large-scale clinical trials [190, 191].

^{18}F-FACBC PET/CT

The anti 1-amino-3-^{18}F-fluorocyclobutane-1-carboxylic acid (^{18}F-FACBC or ^{18}F-fluciclovine) is a synthetic L-leucine analogue characterized by an excellent uptake in PCa cell lines [192]. The uptake is mediated through three L large-neutral amino acid sodium-independent systems, involving transporters related to proliferation and angiogenesis [193, 194]. ^{18}F-FACBC was initially evaluated in PCa patients with recurrence after radical treatment. This radiopharmaceutical has recently obtained FDA approval (May 2016).

Biodistribution and radiation dosimetry studies of ^{18}F-FACBC in healthy volunteers demonstrated that the organs with the highest initial uptake are the liver, red bone marrow, lung, and pancreas. Bone marrow demonstrates moderate and heterogeneous uptake, similarly as skeletal muscles [195–197]. A retrospective analysis by Kairemo et al. evaluated the role of ^{18}F-FACBC PET/CT in 26 patients with treated PCa related to PSA concentrations, PSA doubling time, and correlative images [198]. ^{18}F-FACBC PET/CT scans found 58 lesions: 12 (20.7%) were due to local relapse in the prostate bed and seminal vesicles, 9 (15.5%) were located in regional lymph nodes, 10 (17.2%) in distant lymph nodes, and 26 (44.8%) in the skeleton. The mean serum PSA level in ^{18}F-FACBC-positive patients was higher than in the negative patients (9.5 versus 1.9 ng/mL), and PSA doubling time was shorter in patients with metabolically active uptake.

Turkbey et al. carried out a study in 21 patients with localized PCa, benign prostate hyperplasia, and normal prostate, who underwent dynamic and static abdominopelvic ^{18}F-FACBC PET/CT and multiparametric MRI before robotic-assisted prostatectomy [198]. SUVs of ^{18}F-FACBC PET/CT were compared with the MR findings and histopathologic analysis was carried out. Sector-based comparison with histopathologic analysis revealed 67% sensitivity and 66% specificity for ^{18}F-FACBC PET/CT versus 73% and 79% for T2-weighted MRI. The sensitivity of combined PET and multiparametric MRI to localize tumors was 90%. The uptake of ^{18}F-FACBC was higher in intraprostatic tumor foci than in normal tissue; however, ^{18}F-FACBC uptake is similar in cancer as in benign prostate hyperplasia. Therefore, even though ^{18}F-FACBC turned out not to be specific for PCa, the combined use of PET/CT and MRI can enable a more accurate localization of cancer [199].

A retrospective analysis was performed in 53 patients with suspected recurrent prostate carcinoma and negative BS who underwent ^{18}F-FACBC PET/CT and diagnostic CT within 90 days. ^{18}F-FACBC PET/CT and CT were

positive in 41 (77.4%) and 10 (18.9%) patients, respectively. Positive rates were higher for ^{18}F-FACBC PET/CT than for CT, at all ranges of PSA concentration, PSA doubling time, and GS. ^{18}F-fluciclovine PET/CT had diagnostic performance superior to those of CT, both for detecting lesions in the prostate bed and for imaging metastases in extraprostatic regions. For 51 patients with a follow-up adequate enough to correctly evaluate the diagnostic performances in the prostate bed, the sensitivity, specificity, accuracy, PPV, and NPV were 88.6%, 56.3%, 78.4%, 81.6%, and 69.2% for ^{18}F-FACBC PET/CT and 11.4%, 87.5%, 35.3%, 66.7%, and 31.1% for CT, respectively. In 41 patients evaluated for lesions in extraprostatic regions, the corresponding values for ^{18}F-FACBC PET/CT were 46.2%, 100%, 65.9%, 100%, and 51.7%, respectively, versus 11.5%, 100%, 43.9%, 100%, and 39% for CT, respectively [200].

A prospective clinical trial was published by Shuster et al. who compared ^{18}F-FACBC PET/CT with ^{111}In-ProstaScint in 93 PCa patients with recurrent PCa [201]. ^{18}F-FACBC PET/CT was positive in 77 (82.8%) patients, including 49 (63.6%) in the prostate/bed only, 24 (31.2%) in the prostate/bed and in extraprostatic regions, and 4 (5.2%) only in extraprostatic regions. In 70 of 93 patients with a definitive consensus on extraprostatic disease, ^{18}F-FACBC demonstrated 55% sensitivity, 96.7% specificity, 72.9% accuracy, 95.7% PPV, and 61.7% NPV, figures significantly higher than with ^{111}In-ProstaScint scintigraphy.

In spite of very limited data published in the literature ^{18}F-FACBC has shown some favorable characteristics in comparison with CHO-PET/CT in terms of acquisition protocol, biodistribution, and image quality [199]. The very low excretion of this radiopharmaceutical in the urinary tract improves the detection of small lesions in the pelvis and namely in the prostatic region. The very rapid uptake in prostate cells and its very fast blood clearance allows the acquisition of images 4–5 min after the injection. The first study comparing ^{18}F-FACBC with [^{11}C]CHO PET/CT has been published by Nanni et al. who conclude that the detection rate with ^{18}F-FACBC PET/CT is better than with [^{11}C]CHO PET/CT, regardless of the PSA levels [202]. Therefore, this radiopharmaceutical may be useful for the primary diagnosis, staging and for restaging patients after treatment. Further studies are needed to confirm these preliminary results.

[^{18}F]FDG PET/CT

[^{18}F]FDG is a biomarker of the expression of glucose transporters (mainly GLUT-1) and hexokinase enzymatic activity in tissues [203]. GLUT-1 is overexpressed in poorly differentiated PCa cell lines [204]. The expression of GLUT-1 is modulated by androgens [205]; however, such enhanced expression occurs not only in PCa but also in benign prostatic hyperplasia. Furthermore, a strong correlation exists between GLUT-1 expression and GS [206–208].

Nevertheless, [^{18}F]FDG PET is not recommended for the diagnosis and staging of organ-confined PCa, nor for the detection of locally recurrent disease, because of the overlap of the intense activity accumulated in the urinary bladder on tumor uptake. Furthermore, [^{18}F]FDG is not a cancer-specific molecular probe and the tracer localizes in areas of wound healing, and inflammatory conditions [207–209]. However, [^{18}F]FDG uptake in PCa increases in advanced clinical disease high PSA levels, and elevated GS [210].

There is limited experience on the detection of lymph node metastases by [^{18}F]FDG PET/CT in patients with biochemical recurrence after potentially curative therapy [211, 212]. Chang et al. evaluated the performance of [^{18}F]FDG PET in 24 patients with rising serum PSA levels after treatment for PCa and who had negative findings on bone scan and equivocal CT results [213]. For the detection of metastatic pelvic lymph nodes, [^{18}F]FDG PET/CT showed 75% sensitivity, 100% specificity, 83.3% accuracy, 100% PPV, and 67.7% NPV. Schoder et al. reported that [^{18}F]FDG uptake was higher in patients with treatment failure and was associated with higher PSA levels [214]. Moreover, using ROC analysis, the authors found that the best compromise between the optimal

sensitivity and specificity would be reached for a PSA concentration of 2.4 ng/mL (80% and 70% respectively) and a PSA velocity of 1.3 ng/mL per year (71% and 77%, respectively). Since [^{18}F]FDG uptake is associated with metabolic activity, [^{18}F]FDG PET/CT can be useful for to assess tumor response to treatment. In a preclinical study, Zhang et al. evaluated immunodeficient mice harboring prostate tumor cell line CWR22 xenografts, by performing [^{18}F]FDG microPET to assess [^{18}F]FDG uptake before, during, and after treatment with a proteasome inhibitor (bortezomib). The reduction observed in [^{18}F]FDG uptake was more reliable than the reduction in tumor volume as a parameter of response to therapy [215].

Zukotynski et al. performed [^{18}F]FDG PET/CT, ^{18}F-NaF PET/CT, and standard ^{99m}Tc-MDP bone scintigraphy in nine patients with CRPC before and after 8 weeks of therapy with abiraterone and cabozantinib [216]. They found that the intensity of uptake of ^{18}F-NaF PET/CT in bone lesions did not predict response to treatment, while [^{18}F]FDG PET/CT enabled to stratify patients into three groups (widespread cancer [^{18}F]FDG-avid versus oligometastatic [^{18}F]FDG-avid versus non-[^{18}F]FDG-avid metastases). This approach could drive the choice of a tailored appropriate treatment. Another recent investigation showed that [^{18}F]FDG PET could be useful for assessing response to treatment with a mTOR inhibitor, everolimus, in combination with docetaxel [217]. Yu et al. compared [^{11}C]acetate and [^{18}F]FDG PET/CT for assessing treatment response to androgen deprivation therapy in eight patients with >3 PCa metastases on bone scintigraphy [218]. A lesion-by-lesion analysis of [^{18}F]FDG PET was performed by Morris et al. in 17 patients with progressive metastatic PCa with 134 skeletal lesions [219]. Ninety-five lesions (71%) were detected on both the [^{18}F]FDG PET and the bone scans, 31 lesions (23%) were only seen on the bone scan, and 8 lesions (6%) were seen only on [^{18}F]FDG PET scan. All metabolically active lesions on the [^{18}F]FDG PET were noted to be active on the follow-up bone scans (thus suggesting true-positive findings on PET). The authors concluded that the added value of [^{18}F]FDG is to identify metabolically active lesions from those scintigraphically quiescent. The extent and the intensity of [^{18}F]FDG uptake in metastatic lesions may also provide prognostic information. In fact, a >33% increase in the average SUV_{max} of metastatic lesions or the appearance of new lesions assigned patients to different groups: patients in progression versus patients with stable disease.

The prognostic value of bone scan and [^{18}F]FDG PET/CT was evaluated also by Meirelles et al. in a prospective trial in 43 men with metastatic CRPC [220]. This study demonstrated that the overall survival was inversely correlated with SUV_{max} obtained from the skeletal uptake. In patients with a median survival of 14.4 months SUV_{max} was >6.10, while it was ≤6.10 in patients with a median survival of 32.8 months. Although the BSI was also prognostic, in the multivariate analysis only SUV_{max} of [^{18}F]FDG uptake resulted an independent factor as a predictor of survival.

Vargas et al. evaluated 38 patients with metastatic CRPC who underwent CT, [^{18}F]FDG PET and ^{18}F-16β-fluoro-5-dihydrotestosterone (^{18}F-FDHT) PET/CT [221]. The number of lesions seen on CT, [^{18}F]FDG, and ^{18}F-FDHT PET was significantly associated with overall survival. However, in this trial, the association between tracer uptake and survival was demonstrated only with ^{18}F-FDHT, while it was not seen with the intensity of [^{18}F]FDG uptake.

On the contrary, a positive relationship was found by Jadvar et al. who showed in a multivariate analysis, after considering several confounding factors (such as age, PSA and serum AP levels, use of pain medication, prior chemotherapy, and GS at diagnosis) that the sum of SUV_{max} of up to 25 metabolically active lesions (lymph nodes, bone, and soft tissue metastases) was statistically significant as a predictor of overall survival [222].

The current clinical experience with [^{18}F]FDG PET/CT suggests this radiopharmaceutical has less to offer for clinical management compared

Table 4 Pros and cons of diagnostic imaging modalities and their current applications for PCa in clinical practice

	Pros	Cons	Current clinical indications
TRUS	1. Wide availability	1. Sensitivity is limited by the high number of isoechoic tumors originating in the peripheral zone	1. To guide prostate biopsies
	2. Possibility to perform biopsy	2. Reduced sensitivity in detecting transition zone tumors	2. To deliver local treatments such as brachytherapy
	3. No radiations	3. Inability to detect the anterior portion of the gland	3. To monitor cryotherapy treatment
CT	1. Wide availability	1. High radiation dose	1. Initial staging (for lymph node disease)
	2. Allows assessment of fine bone details and characterization of smaller lesions	2. Not used for systematic bone screening	2. Recurrence of disease
	3. Allows detection of lymph node and visceral metastases	3. Not useful for assessing response to therapy	3. Evaluation of response to therapy (RECIST criteria v. 1.1)
MRI	1. Good availability	1. Bone metastases outside vertebral spine or pelvic bones are not detected (in case of spinal MRI)	1. Active surveillance
	2. Earlier detection of tumor foci	2. Advanced diagnostic techniques only available in diagnostic imaging centers of excellence	2. Initial staging (for primary tumor and locoregional lymph node involvement)
	3. Better diagnostic performance in detection and characterization of bone lesions	3. Longer duration of examination, higher costs	3. Recurrence of disease (particularly in prostatic fossa)
	4. Highest diagnostic performance in detection and characterization of bone lesions		
	5. Allows detection of lymph node and visceral metastases		
	6. Possible role of DWI in assessment of response to therapy		
BS	1. Low cost	1. Low sensitivity for osteolytic lesions	1. Initial staging of disease (bone involvement)
	2. Wide availability	2. Does not detect bone marrow disease	2. Recurrence of disease (high PSA levels)
	3. Detection of bone metastases several months before they are revealed by planar x-ray	3. Poor sensitivity for osteolytic lesions without bone remodeling	3. Assessment of response to therapy
		4. Low specificity (false-positive findings in case of degenerative changes, inflammatory processes, trauma, mechanical stress, and Paget's disease)	
		5. Necessity of bone reactive changes to achieve the optimal sensitivity	
		6. Flare phenomenon due to some systemic treatments (also ^{223}Ra)	

(*continued*)

Table 4 (continued)

	Pros	Cons	Current clinical indications
SPECT	1. Improves the sensitivity of planar images	1. Limited field of view	1. See BS
		2. No improvement in terms of specificity over planar images	2. Not standardized
		3. As bone scan (*see above*)	
SPECT/CT	1. Improved sensitivity over planar images	1. Whole-body imaging with this modality is not currently standard practice	1. See BS
	2. Improved specificity over planar images	2. Resource implications of increased cost, specialist equipment, and specialist manpower hours	2. Not standardized
		3. Increased radiation dose than BS (from 3 to 5 mSv)	
		4. As bone scan (*see above*)	
^{18}F-fluoride PET/CT	1. The extraction of fluoride from the blood is rapid. The first-pass extraction is 100% vs. 64% for diphosphonates	1. Very sensitive to minimal degenerative changes	1. Restaging of disease (as an alternative to BS)
	2. Superior image quality and therefore high diagnostic accuracy	2. High costs	2. Assessment of response to therapy (in some clinical trials and as an alternative to BS)
	3. Rapid acquisition protocol (after 15 or 60 min from the injection)	3. Clinical impact when used to monitor treatment response is uncertain	
	4. As for ^{99m}Tc-diphosphonate is able to identify high bone turnover and remodeling	4. Flare phenomenon due to some systemic treatments (also ^{223}Ra)	
	5. Quantitative and automatic semiquantitative analyses of uptake in the lesions		
[^{18}F]FDG PET/CT	1. Can detect bone metastases at early stage of disease (bone marrow involvement)	1. Sclerotic metastases can be missed due to the relatively small amount of viable tumor tissue	1. Restaging of disease in patients with undifferentiated tumors (GS>8)
	2. In case of osteolytic lesion and in presence of aggressive prostatic cancer, tracer accumulation is higher for an increase in the glycolytic rate	2. [^{18}F]FDG uptake is limited in moderately or well-differentiated prostate cancer	
	3. Lack of FDG uptake in the osteoblastic lesion can be associated with the present of quiescent cells	3. Higher costs and increased radiation dose versus BS (from 3 to 5–7 mSv)	
	4. Superior image quality and therefore high diagnostic accuracy		
	5. Prognostic information		
	6. Quantitative and automatic semiquantitative analyses of uptake in the lesions		
[^{11}C]/^{18}F-CHO PET/CT	1. More specific for prostate cancer	1. Flare phenomena reported during the administration of abiraterone acetate and GCSF	1. Restaging of disease (based on PSA levels and PSA kinetic)
	2. Able to identify three patterns of bone disease (bone marrow	2. [^{11}C]CHO is not available in centers without an on-site cyclotron	2. Assessment of f response to therapy

(*continued*)

Table 4 (continued)

	Pros	Cons	Current clinical indications
	involvement, osteoblastic lesions, no active tumor)		
	3. No uptake in chronic degenerative bone disease	3. High costs and increased radiation dose versus BS (from 3 to 5–7 mSv)	
	4. Quantitative and automatic semiquantitative analysis of uptake in the lesions		
^{68}Ga-PSMA-ligand PET/CT	1. More specific for prostate cancer	1. PSMA expression is apparently differentially regulated by androgens	1. Restaging of disease (based on PSA levels and PSA kinetic)
	2. High detection rate, in the recurrence setting, for low PSA level	2. It is still considered an experimental imaging agent	
	3. Able to detect all sites of prostate cancer recurrences (lymph nodes, bone, visceral sites)	3. High costs and increased radiation dose versus BS (from 3 to 5–7 mSv)	
	4. No uptake in chronic degenerative bone disease	4. High costs for the production of the radiotracer	
	5. Quantitative and automatic semiquantitative analyses of uptake in the lesions		
^{18}F-FACBC PET/CT	1. More specific for prostate cancer	1. High uptake in the muscles	1. Restaging of disease (based on PSA levels and PSA kinetic)
	2. Higher detection rate, in the recurrence setting, than [^{11}C]CHO	2. It is still considered an experimental imaging agent	
	3. It is able to detect all sites of prostate cancer recurrences (lymph nodes, bone, and visceral sites)	3. High costs and increased radiation dose versus BS (from 3 to 5–7 mSv)	
	4. No uptake in chronic degenerative bone disease		
	5. Quantitative and automatic semiquantitative analysis of uptake in the lesions		

to more specific radiopharmaceuticals targeting PCa, although the intensity of [^{18}F]FDG uptake in lesions might be an independent predictor of overall survival [223].

Clinical Considerations

PCa is evolving both in terms of development of new therapeutic options and in terms of better definition of strategies for cancer cure and/or management. For this reason, a general overview of the available modalities of imaging in the different steps of PCa can be useful, as summarized in Table 4.

Based on the overall considerations reported in this chapter and on the current strategy of treatment for PCa patients, in closing this chapter, the author proposes a flow chart including a reasonable approach for the management of PCa patients, according to the state of the art of general knowledge on the diagnostic and therapeutic armamentarium currently available. (Fig. 12).

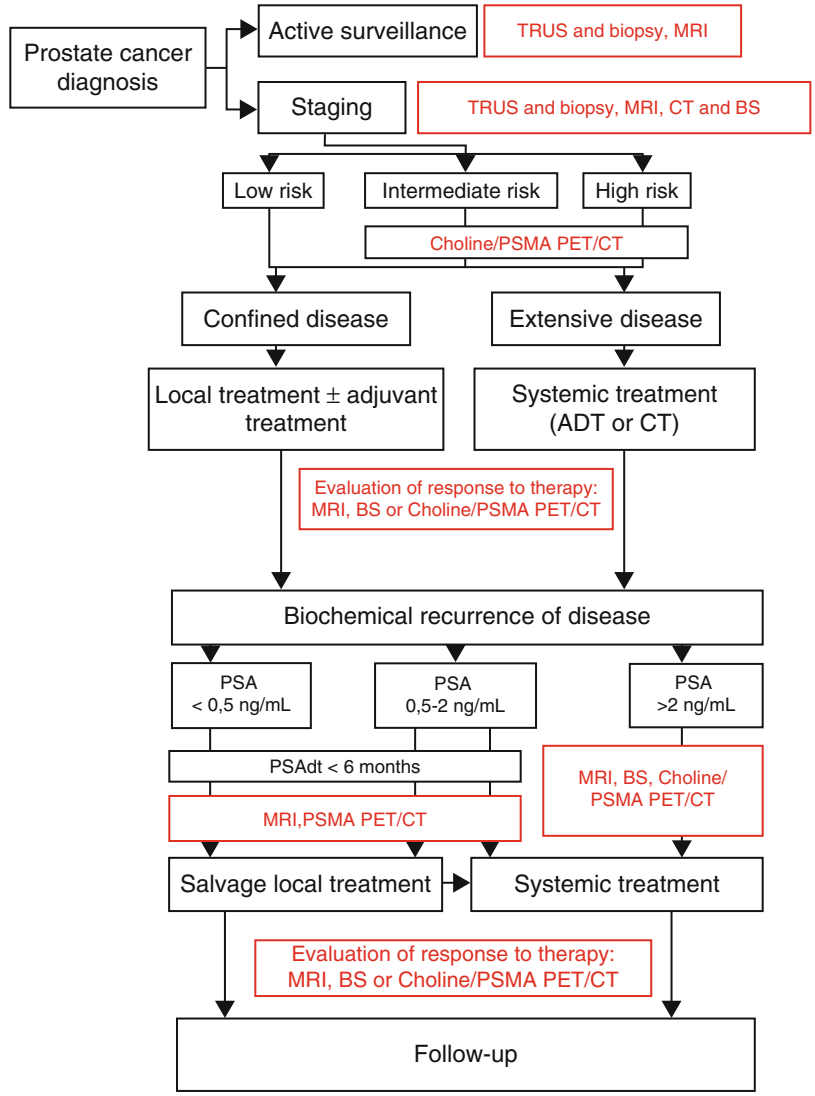

Fig. 12 A suggested diagnostic flow chart for patients with PCa. *TRUS* transrectal ultrasonography, *MRI* magnetic resonance imaging, *CT* computed tomography, *BS* bone scintigraphy, *PSMA* ^{68}Ga-PSMA-ligand PET/CT

Aknowledgments The authors are grateful to Dr. Thomas A. Hope, Department of Radiology and Biomedical Imaging, University of California (USA), for his scientific contribution and to Ms. Annaluisa De Simone Sorrentin for her kind editorial assistance.

References

1. Ferlay J, Soerjomataram I, Ervik M, et al. GLOBOCAN 2012 v1.0, cancer incidence and mortality worldwide: IARC cancer base No. 11 [internet]. Lyon: International Agency for Research on Cancer; 2013. Available from: http://globocan.iarc.fr. Last accessed on 12 June 2016.
2. Center MM, Jemal A, Lortet-Tieulent J, et al. International variation in prostate cancer incidence and mortality rates. Eur Urol. 2012;61:1079–92.
3. Siegel RL, Miller KD. Cancer statistics. CA Cancer J Clin. 2016;66:7–30.
4. Aly M, Wiklund F, Xu J, et al. Polygenic risk score improves prostate cancer risk prediction: results from the Stockholm-1 cohort study. Eur Urol. 2011;60:21–8.
5. Iwasaki M, Mameri CP, Hamada GS, Tsugane S. Secular trends in cancer mortality among Japanese immigrants in the state of São Paulo, Brazil, 1979–2001. Eur J Cancer Prev. 2008;17:1–8.
6. Couto E, Boffetta P, Lagiou P, et al. Mediterranean dietary pattern and cancer risk in the EPIC cohort. Br J Cancer. 2011;104:1493–9.

7. Fine SW, Al-Ahmadie HA, Gopalan A, et al. Anatomy of the anterior prostate and extraprostatic space: a contemporary surgical pathology analysis. Adv Anat Pathol. 2007;14:401–7.
8. NCCN National Comprehensive Cancer Network. Clinical practice guidelines in oncology version 2.2016 staging prostate cancer. http://www.nccn.org/professionals/physician_gls/f_guidelines.asp. Last accessed on 27 Feb 2016.
9. Wolf AM, Wender RC, Etzioni RB, et al. American Cancer Society guideline for the early detection of prostate cancer: update 2010. CA Cancer J Clin. 2010;60:70–98.
10. Hammerer PG, Kattan MW, Mottet N, Prayer-Galetti T. Using prostate-specific antigen screening and nomograms to asses risk and predict outcomes in the management of prostate cancer. BIU Int. 2006;98:11–9.
11. Boczko J, Messing E, Dogra V. Transrectal sonography in prostate evaluation. Radiol Clin N Am. 2006; 44:679–87.
12. Djavan B, Waldert M, Zlotta A, et al. Safety and morbidity of first and repeat transrectal ultrasound guided prostate needle biopsies: results of a prospective European prostate cancer detection study. J Urol. 2001;166:856–60.
13. Yacoub JH, Oto A, Miller FH. MR imaging of the prostate. In: Miller FH, editor. Adult body MR. Pennsylvania: Elsevier; 2014. p. 811–37.
14. Epstein JI, Algaba F, Allsbrook WC Jr, et al. Acinar adenocarcinoma. In: Eble JN, Sauter G, Epstein JI, editors. WHO classification of tumors, pathology & genetics. Tumors of the urinary system and male genital organs. Lyon: IARC Press; 2004. pp. 162–98.
15. Epstein JI, Allsbrook Jr WC, Amin MB, Egevad LL, ISUP Grading Committee. The 2005 International Society of Urological Pathology (ISUP) consensus conference on Gleason grading of prostatic carcinoma. Am J Surg Pathol. 2005;29:1228–42.
16. Schroder FH. Progress in understanding androgen-independent prostate cancer (AIPC): a review of potential endocrine-mediated mechanisms. Eur Urol. 2008;53:1129–37.
17. Ramsay AK, Leung HY. Signalling pathways in prostate carcinogenesis: potentials for molecular-targeted therapy. Clin Sci (Lond). 2009;117:209–28.
18. Klocker H, Culig Z, Eder IE, et al. Mechanism of androgen receptor activation and possible implications for chemoprevention trials. Eur Urol. 1999;35: 413–9.
19. Heidenreich A, Aus G, Bolla M, et al. EAU guidelines on prostate cancer. Eur Urol. 2008;53:68–80.
20. Sood A, Jeong W, Dalela D, et al. Role of robot-assisted radical prostatectomy in the management of high-risk prostate cancer. Indian J Urol. 2014;30:410–7.
21. AJCC cancer staging manual. 7th ed. Part IX: genitourinary sites. New York: Springer; 2010. p. 445–78.
22. Klein EA, Ciezki JP, Vogelzang N, Lee WR, Richie JP. Initial approach to low- and very low risk clinically localized prostate cancer. UpToDate www.uptodate.com. 2016.
23. Thompson I, Thrasher JB, Aus G, et al. Guideline for the management of clinically localized prostate cancer: 2007 update. J Urol. 2007;177:2106.
24. Chen RC, Rumble RB, Loblaw DA, et al. Active surveillance for the management of localized prostate cancer (Cancer Care Ontario Guideline): American Society of Clinical Oncology clinical practice guideline endorsement. J Clin Oncol. 2016;34:2182–90.
25. Catalona WJ, Bigg SW. Nerve-sparing radical prostatectomy: evaluation of results after 250 patients. J Urol. 1990;143:538–43.
26. Corral DA, Bahnson RR. Survival of men with clinically localized prostate cancer detected in the eighth decade of life. J Urol. 1994;151:1326–9.
27. Zincke H, Bergstralh EJ, Blute ML, et al. Radical prostatectomy for clinically localized prostate cancer: long-term results of 1,143 patients from a single institution. J Clin Oncol. 1994;12:2254–63.
28. Ko WJ, Hruby GW, Turk AT, Landman J, Badani KK. Pathological confirmation of nerve-sparing types performed during robot assisted radical prostatectomy. BJU. 2013;111:451–8.
29. Montorsi F, Wilson TG, Rosen RC, et al. Best practice in robot-assisted radical prostatectomy: recommendations of the Pasadena Consensus Panel. Eur Urol. 2012;62:368–81.
30. Carter SC, Shih YC, Hu JC. Robotic and standard open radical prostatectomy: oncological and quality-of-life outcomes. J Comp Eff Res. 2013;2:293–9.
31. Dal Pra A, Souhami L. Prostate cancer radiation therapy: a physicians perspective. Phys Med. 2016;32: 438–45.
32. Latorzeff I, Mazurier J, Boutry C, et al. Benefit of intensity modulated and image-guided radiotherapy in prostate cancer. Cancer Radiother. 2010;14:479–87.
33. Kupelian P, Kuban D, Thames H, et al. Improved biochemical relapse free survival with increased external radiation doses in patients with localized prostate cancer: the combined experience of nine institutions in patients treatment in 1994 and 1995. Int J Radiat Oncol Biol Phys. 2005;61:415–9.
34. Pasquir D, Ballereau C. Adjuvant and salvage radiotherapy after prostatectomy for prostate cancer: a literature review. Int J Radiat Oncol Biol Phys. 2008; 72:972–9.
35. Bottke D, Wiegel T. Adjuvant radiotherapy after radical prostatectomy; indications results and side effects. Urol Int. 2007;78:193–7.
36. Dulaney CR, Osula DO, Yang ES, Rais B. Prostate radiotherapy in the era of advanced imaging and precision medicine. Prostate Cancer. 2016;2016: 48917515. doi:10.1155/2016/4897515. Epub 2016 Feb 16.
37. Batterman JJ. Permanent prostate brachytherapy. In: Bolla M, van Poppel H, editors. Management of prostate cancer. Berlin: Springer; 2012. p. 113–28.

38. Bossi A, Verstaet R, Clamels L, Blanchard P. High-rate-dose-brachytherapy indications techniques and results. In: Bolla M, van Poppel H, editors. Management of prostate cancer. Berlin: Springer; 2012. p. 129–42.
39. Matchens S, Baumann R, Agemann G, et al. Long term results interstitial radiotherapy (LDR brachytherapy) in the treatment of patients with prostate cancer. World J Urol. 2006;24:289–95.
40. Tsivian M, Polascick TJ. Cryotherapy in management of prostate cancer. In: Bolla M, van Poppel H, editors. Management of prostate cancer. Berlin: Springer; 2012. p. 213–23.
41. Gelet A, Crouzet S, Rouviere O, Chapelon JY. High-Intensity Focused Ultrasound (HIFU) for prostate cancer. In: Bolla M, van Poppel H, editors. Management of prostate cancer. Berlin: Springer; 2012. p. 191–212.
42. Reznikov A. Hormonal impact on tumor growth and progression. Exp Oncol. 2015;37:162–72.
43. Lee RJ, Smith MR. Hormone therapy for prostate cancer. In: Chabner BA, Longo DL, editors. Cancer chemotherapy and biotherapy: principles and practice. 5th ed. Wolters Kluwer: Lippincott Williams & Wilkins; 2011.
44. Van den Berg RC, Van Casteren NJ, Van den Broek T, et al. Role of hormonal treatment in cancer patients with non metastatic disease recurrence after local curative treatment. A systematic review. Eur Urol. 2016; 69:802–20.
45. Heidenreich A, Bastina PJ, Bellmunt J, et al. EAU guidelines on prostate cancer part II: treatment of advanced, relapsing, and castration-resistant prostate cancer. Eur Urol. 2014;65:467–79.
46. Thomas C, Bogemann M, Konig F, et al. Advanced prostate cancer consensus conference (APCCC) 2015 in St. Gallen: critical review of recommendations on diagnosis and therapy of metastatic prostate cancer by a German expert panel. Urol A. 2016;55:772–82.
47. Helsen C, Kerkhofs S, Clinckemalie L, Spans L, Laurent M, Boonen S, et al. Structural basis for nuclear hormone receptor DNA binding. Mol Cell Endocrinol. 2012;348:411–7.
48. Gioeli DG. The promise of novel androgen receptor antagonist. Cell Cycle. 2010;9:440–1.
49. Attard G, Reid AH, A'Hern R, et al. Selective inhibition of CYP17 with abiraterone acetate is highly active in the treatment of castration-resistant prostate cancer. J Clin Oncol. 2009;27:3742–8.
50. Beer TM, Armstrong AJ, Rathkopf DE, et al. Enzalutamide in metastatic prostate cancer before chemotherapy. N Engl J Med. 2014;371:424–33.
51. Petrylak DP, Tangen CM, Hussain MH, et al. Docetaxel and estramustine compared with mitoxantrone and prednisone for advanced refractory prostate cancer. N Engl J Med. 2004;351:1513–20.
52. Tannock IF, de Wit R, Berry WR, et al. Docetaxel plus prednisone or mitoxantrone plus prednisone for advanced prostate cancer. N Engl J Med. 2004;351: 1502–12.
53. van Soest RJ, Nieuweboer AJ, de Morree ES, et al. The influence of prior novel androgen receptor targeted therapy on the efficacy of cabazitaxel in men with metastatic castration-resistant prostate cancer. Eur J Cancer. 2015;51:2562–9.
54. Kantoff PW, Higano CS, Shore ND, et al. Sipuleucel-T immunotherapy for castration-resistant prostate cancer. N Engl J Med. 2010;363:411–22.
55. Kantoff PW, Schuetz TJ, Blumenstein BA, et al. Overall survival analysis of a phase II randomized controlled trial a Poxviral based PSA-target immunotherapy in metastatic castraction-resistant prostate cancer. J Clin Oncol. 2010;28:1099–2005.
56. van den Eertwegh AJ, Versluis J, van den Berg HP, et al. Combined immunotherapy with granulocyte-macrophage colony-stimulating factor-transduced allogeneic prostate cancer cells and ipilimumab in patients with metastatic castraction-resistant prostate cancer: a phase I dose-escalation trial. Lancet Oncol. 2012;13: 509–17.
57. Kwon ED, Drake CG, Scher HI, et al. Ipilimumab versus placebo after radiotherapy in patients with metastatic castration-resistant prostate cancer that had progressed after docetaxel chemotherapy (CA184-043): a multicentre, randomised, double-blind, phase 3 trial. Lancet Oncol. 2014;15:700–12.
58. Quinn DI, Shore ND, Egawa S, et al. Immunotherapy for castration-resistant prostate cancer: progress and new paradigms. Urol Oncol. 2015;33:245–50.
59. Slovin SF, Higano CS, Hamid O, et al. Ipilimumab alone or in combination with radiotherapy in metastatic castration-resistant prostate cancer: results from an open-label, multicenter phase I/II study. Ann Oncol. 2013;24:1813–8.
60. Saad F, McKiernan J, Eastham J. Rationale for zoledronic acid therapy in men with hormone-sensitive prostate cancer with or without bone metastasis. Urol Oncol. 2006;24:4–12.
61. James MD, Sydes MR, Mason MD. Docetaxel (DOC) +/− zoledronic acid for hormone –naive prostate cancer: first available results from STAMPEDE and treatment effects within subgroups (NCT00268476). Eur J Cancer. 2015;51:S719.
62. Sartor O, Coleman R, Nilsson S, et al. Effect of radium-223 dichloride on symptomatic skeletal events in patients with castration-resistant prostate cancer and bone metastases: results from a phase 3, double-blind, randomised trial. Lancet Oncol. 2014;15:738–46.
63. Parker C, Nilsson S, Heinrich D, et al. Alpha emitter radium-223 and survival in metastatic prostate cancer. N Engl J Med. 2013;369:213–23.
64. Parker C, Gillessen S, Heidenreich A, Committee EG, et al. Cancer of the prostate: ESMO Clinical Practice Guidelines for diagnosis, treatment and follow-up. Ann Oncol. 2015;26:69–77.

65. Chow E, Harris K, Fan G, Tsao M, Sze WM. Palliative radiotherapy trials for bone metastases: a systematic review. J Clin Oncol. 2007;25:1423–36.
66. Lutz S, Berk L, Chang E, et al. Palliative radiotherapy for bone metastases: an ASTRO evidence-based guideline. Int J Radiat Oncol Biol Phys. 2011;79: 965–76.
67. Fairchild A, Barnes E, Ghosh S, et al. International patterns of practice in palliative radiotherapy for painful bone metastases: evidence-based practice? Int J Radiat Oncol Biol Phys. 2009;75:1501–10.
68. Sandblom G, Ladjevardi S, Garmo H, Varenhorst E. The impact of prostate-specific antigen level at diagnosis on the relative survival of 28,531 men with localized carcinoma of the prostate. Cancer. 2008; 112:813–9.
69. Roehrborn CG, McConnell J, Bonilla J, et al. Serum prostate specific antigen is a strong predictor of future prostate growth in men with benign prostatic hyperplasia. PROSCAR long-term efficacy and safety study. J Urol. 2000;163:13–20.
70. Yang Z, Yu L, Wang Z. PCA3 and TMPRSS2-ERG gene fusions as diagnostic biomarkers for prostate cancer. Chin J Cancer Res. 2016;28:65–71.
71. Freedland SJ, Moul JW. Prostate specific antigen recurrence after definitive therapy. J Urol. 2007;177: 1985–91.
72. Briganti A, Suardi N, Gallina A, et al. Predicting the risk of bone metastasis in prostate cancer. Cancer Treat Rev. 2014;40:3–11.
73. Onukwugha E, Yong C, Mullins CD, et al. Skeletal-related events and mortality among older men with advanced prostate cancer. J Geriatr Oncol. 2014;5: 281–9.
74. Costa L, Demers LM, Gouveia-Oliveira A, et al. Prospective evaluation of the peptide-bound collagen type I cross-links N-telopeptide and C-telopeptide in predicting bone metastases status. J Clin Oncol. 2002;20:850–6.
75. Koizumi M, Yonese J, Fukui I, Ogata E. The serum level of the amino-terminal propeptide of type I procollagen is a sensitive marker for prostate cancer metastasis to bone. BJU Int. 2001;87:348–51.
76. Koopmans N, de Jong IJ, Breeuwsma AJ, van der Veer E. Serum bone turnover markers (PINP and ICTP) for the early detection of bone metastases in patients with prostate cancer: a longitudinal approach. J Urol. 2007;178:849–53.
77. Zafeirakis AG, Papatheodorou GA, Limouris GS. Clinical and imaging correlations of bone turnover markers in prostate cancer patients with bone only metastases. Nucl Med Commun. 2010;31:249–53.
78. Coleman RE, Major P, Lipton A, et al. Predictive value of bone resorption and formation markers in cancer patients with bone metastases receiving the bisphosphonate zoledronic acid. J Clin Oncol. 2005; 23:4925–35.
79. Cook RJ, Coleman R, Brown J, et al. Markers of bone metabolism and survival in men with hormone-refractory metastatic prostate cancer. Clin Cancer Res. 2006;12(11 Pt 1):3361–7.
80. Smith MR, Cook RJ, Coleman R, et al. Predictors of skeletal complications in men with hormone-refractory metastatic prostate cancer. Urology. 2007;70: 315–9.
81. Gomella LG, El Gabry EA, Strup S, et al. Ultrasound contrast agent for prostate imaging and biopsy. Urol Oncol. 2001;6:189–92.
82. Morelli G, Pagni R, Mariani C. Results of vardenafil mediated power Doppler ultrasound contrast enhanced ultrasounds and systematic random biopsies to detect prostate cancer. J Urol. 2011;185:2126–31.
83. Wink M, Frauscher F, Cosgrove D, et al. Contrast enhanced ultrasound and prostate cancer a multicenter European research coordination project. Eur Urol. 2008;54:982–93.
84. Taneja SS. Imaging in the diagnosis and management of prostate cancer. Rev Urol. 2004;6:101–3.
85. Dickinson L, Ahmed HU, Allen C, et al. Clinical application of multiparametric MRI within the prostate cancer diagnostic pathway. Urol Oncol. 2013;31: 281–4.
86. Guneyli S, Erdem CZ, Erdem L. Magnetic resonance imaging in prostate cancer. Clin Imaging. 2016;40: 601–9.
87. Presti JC. Repeat prostate biopsy. When, where and how. Urol Oncol. 2009;27:312–4.
88. Hambrock T, Somford DM, Hoeks C. Magnetic resonance imaging guided prostate biopsy in men with repeat negative biopsies and increased prostate specific antigen. J Urol. 2010;183:520–7.
89. Pasougly V, Michoux N, Peeters F, et al. Whole body 3D T1 weighted MR imaging in patients with prostate cancer. Feasibility and evaluation in screening for metastatic disease. Radiology. 2015;275:155–66.
90. Fogelman I. Diphosphonate bone scanning agents – current concepts. Eur J Nucl Med. 1982;7:506–9.
91. Fogelman I, Bessent RG, Cohen HN, et al. Skeletal uptake of diphosphonate. Method for prediction of post-menopausal osteoporosis. Lancet. 1980;2: 667–70.
92. Love C, Din AS, Tomas MB, et al. Radionuclide for bone imaging: an illustrative review. Radiographics. 2003;23:341–58.
93. Bombardieri E, Aktoloun C, Baum RP, et al. Bone scintigraphy: procedure guidelines. Eur J Nucl Med Mol Imaging. 2003;30:BP99–106.
94. Bombardieri E, Setti L, Kirienko M, et al. Which metabolic imaging, besides bone scan with ^{99m}Tc-phosphonates, for detecting and evaluating bone metastases in prostatic cancer patients? An open discussion. Q J Nucl Med Mol Imaging. 2015;59: 381–99.
95. Gnanasegaran G, Cook G, Adamson K, Fogelman I. Patterns, variants, artifacts, and pitfalls in conventional radionuclide bone imaging and SPECT/CT. Semin Nucl Med. 2009;39:380–95.

96. Iagaru A, Mittra E, Dick DW, Gambhir SS. Prospective evaluation of ^{99m}Tc MDP Scintigraphy, ^{18}F NaF PET/CT, and ^{18}F FDG PET/CT for detection of skeletal metastases. Mol Imaging Biol. 2012;14:252–9.
97. Briganti A, Passoni N, Ferrari M, et al. When to perform bone scan in patients with newly diagnosed prostate cancer: external validation of the currently available guidelines and proposal of a novel risk stratification tool. Eur Urol. 2010;57:551–8.
98. Passoni NM, Di Trapani E, Suardi N, et al. Clinical and diagnostic assessment for therapeutic decisions in prostate cancer. Q J Nucl Med Mol Imaging. 2012;56: 321–30.
99. Lee CT, Oesterling JE. Using prostate-specific antigen to eliminate the staging radionuclide bone scan. Urol Clin N Am. 1997;24:389–94.
100. Chybowski FM, Keller JJ, Bergstralh EJ, Oesterling JE. Predicting radionuclide bone scan finding in patients with mewly diagnoses untreated prostate cancer: PSA is superior to all other clinical parameters. J Urol. 1991;145:313–8.
101. Kattan MW, Eastham JA, Stapleton AM, Wheeler TM, Scardino PT. A preoperative nomogram for disease recurrence following radical prostatectomy for prostate cancer. J Natl Cancer Inst. 1998;90: 766–71.
102. Boorjian SA, Karnes RJ, Rangel LJ, Bergstralh EJ, Blute ML. Mayo Clinic validation of the D'Amico risk group classification for predicting survival following radical prostatectomy. J Urol. 2008;179: 1354–60.
103. Lughezzani G, Briganti A, Karakiewicz PI, et al. Predictive and prognostic models in radical prostatectomy candidates: a critical analysis of the literature. Eur Urol. 2010;58:687–700.
104. Choi WW, Williams SB, Gu X, et al. Overuse of imaging for staging low risk prostate cancer. J Urol. 2011;185:1645–9.
105. Pucar D, Sella T, Schoder H. The role of imaging in the detection of prostate cancer local recurrence after radiation therapy and surgery. Curr Opin Urol. 2008; 18:87–97.
106. D'Amico AV, Whittington R, Malkowicz SB, et al. Biochemical outcome after radical prostatectomy external beam radiation therapy, or interstitial radiation therapy for clinically localized prostate cancer. JAMA. 1998;280:969–74.
107. Dotan ZA, Bianco Jr FJ, Rabbani F, et al. Pattern of PSA failure dictates the probability of a positive bone scan in patients with an increasing PSA after radical prostatectomy. J Clin Oncol. 2005;23:1962–8.
108. Evangelista L, Bertoldo F, Boccardo F, et al. Diagnostic imaging to detect and evaluate response to therapy in bone metastases from prostate cancer: current modalities and new horizons. Eur J Nucl Med Mol Imaging. 2016;43:1546–62.
109. Messiou C, Cook G, de Souza MN. Imaging metastatic bone disease from carcinoma of the prostate. Br J Cancer. 2009;101:1225–32.
110. Levenson RM, Sauerbrunn BJ, Bates HR, et al. Comparative value of bone scintigraphy and radiography in monitoring tumour response in systemically treated prostatic carcinoma. Radiology. 1983;146: 513–8.
111. Pollen JJ, Witztum KF, Ashburn WL. The flare phenomenon on radionuclide bone scan in metastatic prostate cancer. AJR Am J Roentgenol. 1984; 142:773–6.
112. Imbriaco M, Larson SM, Yeung HW, et al. A new parameter for measuring metastatic bone involvement by prostate cancer: the bone scan index. Clin Cancer Res. 1998;4:1765–72.
113. Mitsui Y, Shiina H, Yamamoto Y, et al. Prediction of survival benefit using an automated bone scan index in patients with castration-resistant prostate cancer. BJU Int. 2012;110:E628–34.
114. Dennis ER, Jia X, Mezheritskiy IS, et al. Bone scan index: a quantitative treatment response biomarker for castration-resistant metastatic prostate cancer. J Clin Oncol. 2012;10:519–24.
115. Kaboteh R, Damber JE, Gjersson P, et al. Bone scan index: a prognostic imaging for high risk prostate cancer patients receiving primary hormonal therapy. EJNMMI Res. 2013;3:9.
116. Poulsen MH, Rasmussen J, Edenbrandt L, et al. Bone scan index predicts outcome in patients with metastatic hormone-sensitive prostate cancer. BJU Int. 2016;117:748–53.
117. Reza M, Bjartell A, Ohisson M, et al. Bone scan index as a prognostic imaging biomarker during androgen deprivation therapy. EJNMMI Res. 2014;4:58.
118. Sarikaya I, Sarikaya A, Holder LE. The role of single photon emission computed tomography in bone imaging. Semin Nucl Med. 2001;31:3–16.
119. Sedonja I, Budihna NV. The benefit of SPECT when added to planar scintigraphy in patients with bone metastases in the spine. Clin Nucl Med. 1999;24: 407–13.
120. Savelli G, Maffioli L, Maccauro M, De Deckere E, Bombardieri E. Bone scintigraphy and the added value of SPECT (single photon emission tomography) in detecting skeletal lesions. Q J Nucl Med. 2001;45:27–37.
121. Romer W, Nomayr A, Uder M, Bautz W, Kuwert T. SPECT-guided CT for evaluating foci of increased bone metabolism classified as indeterminate on SPECT in cancer patients. J Nucl Med. 2006;47:1102–6.
122. Gnanasegaran G, Barwick T, Adamson K, et al. Multislice SPECT/CT in benign and malignant bone disease: when the ordinary turns into the extraordinary. Semin Nucl Med. 2009;39:431–42.
123. Helyar V, Mohan HK, Barwick T, et al. The added value of multislice SPECT/CT in patients with equivocal bony metastasis from carcinoma of the prostate. Eur J Nucl Med Mol Imaging. 2010;37:706–13.
124. Ndlovu X, George R, Ellmann A, Warwick J. Should SPECT-CT replace SPECT for the evaluation of equivocal bone scan lesions in patients with

underlying malignancies? Nucl Med Commun. 2010;31:659–65.
125. Sharma P, Dhull VS, Reddy RM, et al. Hybrid SPECT-CT for characterizing isolated vertebral lesions observed by bone scintigraphy: comparison with planar scintigraphy, SPECT, and CT. Diagn Interv Radiol. 2013;19:33–40.
126. Palmedo H, Marx C, Ebert A, et al. Whole-body SPECT/CT for bone scintigraphy: diagnostic value and effect on patient management in oncological patients. Eur J Nucl Med Mol Imaging. 2014;41:59–67.
127. Schirrmeister H, Guhlmann A, Elsner K, et al. Sensitivity in detecting osseous lesions depends on anatomic localization: planar bone scintigraphy versus ^{18}F PET. J Nucl Med. 1999;40:1623–9.
128. Even-Sapir E, Metser U, Mishani E, et al. The detection of bone metastases in patients with high-risk prostate cancer: ^{99m}Tc-MDP planar bone scintigraphy, single and multi-field-of-view SPECT, ^{18}F-fluoride PET, and ^{18}F-fluoride PET/CT. J Nucl Med. 2006;47:287–97.
129. Segall G, Delbeque D, Stabin MG, et al. SNM practice guidelines of sodium ^{18}F-fluoride PET/CT bone scan. J Nucl Med. 2010;52:1813–20.
130. Grant FD, Fahey FH, Packard AB, et al. Skeletal PET with ^{18}F-fluoride: applying new technology to an old tracer. J Nucl Med. 2008;49:68–78.
131. Beheshti M, Mottaghy FM, Payche F, et al. ^{18}F-NaF PET/CT: EANM procedure guidelines for bone imaging. Eur J Nucl Med Mol Imaging. 2015;42:1767–77.
132. Langsteger W, Heinisch M, Fogelman I. The role of fluorodeoxyglucose, ^{18}F-dihydroxyphenylalanine, ^{18}F-choline, and ^{18}F-fluoride in bone imaging with emphasis on prostate and breast. Semin Nucl Med. 2006;36:73–92.
133. Park-Holohan SJ, Blake GM, Fogelman I. Quantitative studies of bone using ^{18}F-fluoride and ^{99m}Tc-methylene diphosphonate: evaluation of renal and whole-blood kinetics. Nucl Med Commun. 2001;22:1037–44.
134. Beheshti M, Vali R, Waldenberger P, et al. Detection of bone metastases in patients with prostate cancer by ^{18}F fluorocholine and ^{18}F fluoride PET-CT: a comparative study. Eur J Nucl Med Mol Imaging. 2008;35:1766–74.
135. Araz M, Aras G, Kucuk ON. The role of ^{18}F-NaF PET/CT in metastatic bone disease. J Bone Oncol. 2015;4:92–7.
136. Fox JJ, Schoder H, Larson SM. Molecular imaging of prostate cancer. Curr Opin Urol. 2012;22:320–7.
137. Apolo AB, Lindenberg L, Shih JH, et al. Prospective study evaluating Na^{18}F-positron emission tomography/computed tomography (NaF-PET/CT) in predicting clinical outcomes and survival in advanced prostate cancer. J Nucl Med. 2016;57:886–92.
138. Poulsen MH, Petersen H, Hoilund-Carlsen PF, et al. Spine metastases in prostate cancer: comparison of technetium-99m-MDP whole-body bone scintigraphy, [^{18}F]choline positron emission tomography (PET)/computed tomography (CT) and [^{18}F]NaF PET/CT. BJU Int. 2014;114:818–23.
139. Zukotynski KA, Kim CK, Gerbaudo VH, et al. ^{18}F-FDG-PET/CT and ^{18}F-NaF-PET/CT in men with castrate-resistant prostate cancer. Am J Nucl Med Mol Imaging. 2015;5:72–82.
140. Hillner BE, Siegel BA, Hanna L, et al. ^{18}F-fluoride PET used for treatment monitoring of systemic cancer therapy: results from the National Oncologic PET Registry. J Nucl Med. 2015;56:222–8.
141. Jadvar H, Desai B, Ji L, et al. Prospective evaluation of ^{18}F-NaF and ^{18}F-FDG PET/CT in detection of occult metastatic disease in biochemical recurrence of prostate cancer. Clin Nucl Med. 2012;37:637–43.
142. Wade AA, Scott JA, Kuter I, Fischman AJ. Flare response in ^{18}F-fluoride in PET bone scanning. AJR Am J Roentgenol. 2006;186:1783–6.
143. Muzahir S, Jeraj R, Liu G, et al. Differentiation of metastatic vs degenerative joint disease using semiquantitative analysis with ^{18}F-NaF PET/CT in castrate resistant prostate cancer patients. Am J Nucl Med Mol Imaging. 2015;5:162–8.
144. Rosen RS, Fayad L, Wahl RL. Increased ^{18}F-FDG uptake in degenerative disease of the spine: characterization with ^{18}F-FDG PET/CT. J Nucl Med. 2006;47:1274–80.
145. Sabbah N, Jackson T, Mosci C, et al. ^{18}F-sodium fluoride PET/CT in oncology: an atlas of SUVs. Clin Nucl Med. 2015;40:e228–31.
146. Podo F. Tumour phospholipid metabolism. NMR Biomed. 1999;12:413–39.
147. Janardhan S, Srivani P, Sastry GN. Choline kinase: an important target for cancer. Curr Med Chem. 2006;13:1169–86.
148. De Grado TR, Coleman RE, Wang S, et al. Synthesis and evaluation of ^{18}F-F-labeled choline as an oncologic tracer for PET: initial findings in prostate cancer. Cancer Res. 2001;61:110–7.
149. Hara T, Kosaka N, Kishi H. PET imaging of prostate cancer using carbon-11-choline. J Nucl Med. 1998;39:990–5.
150. Tolvanen T, Yli-Kerttula T, Ujula T, et al. Biodistribution and radiation dosimetry of ^{11}C-choline: a comparison between rat and human data. Eur J Nucl Med Mol Imaging. 2010;37:874–83.
151. Bauman G, Belhocine T, Kovacs M, et al. ^{18}F-fluorocholine for prostate cancer imaging: a systematic review of the literature. Prostate Cancer Prostatic Dis. 2012;15:45–55.
152. Chondrogiannis S, Marzola MC, Grassetto GB, et al. New acquisition protocol of ^{18}F-choline PET/CT in prostate cancer patients: review of the literature about methodology and proposal of standardization. Biomed Res Int. 2014;2014:215650. doi:10.1155/2014/. Epub 2014 June 10.
153. Evangelista L, Briganti A, Fanti S, et al. New clinical indications for ^{18}F/^{11}C-choline, new tracers for

positron emission tomography and a promising hybrid device for prostate cancer staging: a systematic review of the literature. Eur Urol. 2016;70:161–75.
154. McCarthy M, Slew T, Campbell A, et al. ^{18}F-fluoromethylcholine (FCH) PET imaging in patients with castration-resistant prostate cancer: prospective comparison with standard imaging. Eur J Nucl Med Mol Imaging. 2011;38:14–22.
155. Evangelista L, Guttila A, Zattoni F, et al. Utility of choline positron emission tomography/computed tomography for lymph node involvement identification in intermediate-to high-risk prostate cancer: a systematic literature review and meta-analysis. Eur Urol. 2013;63:1040–8.
156. Beheshti M, Broiger G, Vali R, et al. ^{18}F choline PET/CT in the preoperative staging of prostate cancer in patients with intermediate or high risk of extracapsular disease: a prospective study of 130 patients. Radiology. 2010;254:925–33.
157. Schiavina RSV, Castellucci P, Picchio M, et al. ^{11}C-choline positron emission tomography/computerized tomography for preoperative lymph node staging in intermediate-risk and high-risk prostate cancer: comparison with clinical staging nomograms. Eur Urol. 2008;54:392–401.
158. De Bari B, Alongi F, Lestrade L, Giammarile F. Coline-PET in prostate cancer management: the point of view of the radiation oncologist. Crit Rev Oncol Hematol. 2014;91:234–47.
159. Poulsen MH, Bouchelouche K, Hoilund-Carlsen PF, et al. ^{18}F-fluoromethylcholine (FCH) positron emission tomography/computed tomography (PET/CT) for lymph node staging of prostate cancer: a prospective study of 210 patients. BJU Int. 2012;110:1666–71.
160. Krause BJ, Souvatzoglou M, Treiber U. Imaging of prostate cancer with PET/CT and radioactively labelled choline derivates. Urol Oncol. 2013;31:427–35.
161. Graziani T, Ceci F, Castellucci P, et al. ^{11}C-choline PET/CT for restaging prostate cancer. Results form 4,426 scans in a single-centre patient series. Eur J Nucl Med Mol Imaging. 2016. Epub ahead of print. 43(11):1971–79.
162. Beheshti M, Vali R, Waldenberger P, et al. The use of F-18 choline PET in the assessment of bone metastases in prostate cancer: correlation with morphological changes on CT. Mol Imaging Biol. 2010;12:98–107.
163. Kjolhede H, Ahlgren G, Almquist H, et al. Combined ^{18}F-fluorocholine and ^{18}F-fluoride positron emission tomography/computed tomography imaging for staging of high-risk prostate cancer. BJU Int. 2012;110:1501–6.
164. Picchio M, Spinapolice EG, Fallanca F, et al. ^{11}C-choline PET/CT detection of bone metastases in patients with PSA progression after primary treatment for prostate cancer: comparison with bone scintigraphy. Eur J Nucl Med Mol Imaging. 2012;39:13–26.
165. Langsteger W, Haim S, Knauer M, et al. Imaging of bone metastases in prostate cancer: an update. Q J Nucl Med Mol Imaging. 2012;56:447–58.
166. von Eyben FE, Kairemo K. Meta-analysis of ^{11}C-choline and ^{18}F-choline PET/CT for management of patients with prostate cancer. Nucl Med Commun. 2014;35:221–30.
167. Fuccio C, Castellucci P, Schiavina R, Guidalotti PL, Gavaruzzi G, Montini GC, et al. Role of ^{11}C-choline PET/CT in the re-staging of prostate cancer patients with biochemical relapse and negative results at bone scintigraphy. Eur J Radiol. 2012;81:893–6.
168. Ceci F, Castellucci P, Graziani T, et al. ^{11}C-choline PET/CT identifies osteoblastic and osteolytic lesions in patients with metastatic prostate cancer. Clin Nucl Med. 2015;40:265–70.
169. Wahl RL, Jacene H, Kasamon Y, Lodge MA. From RECIST to PERCIST: evolving considerations for PET response criteria in solid tumors. J Nucl Med. 2009;50:122S–50.
170. Kwee SA, Lim J, Watanabe A, et al. Prognosis related to metastatic burden measured by ^{18}F-fluorocholine PET/CT in castration resistant prostate cancer. Eur J Nucl Med Mol Imaging. 2014;55:905–10.
171. Oprea-Lager DE, Kramer G, van de Ven PM, van den Eertwegh AJ, van Moorselaar RJ, Schober P, et al. Repeatability of quantitative ^{18}F-fluoromethylcholine PET/CT studies in prostate cancer. J Nucl Med. 2016;57:721–7.
172. Sweat SD, Pacelli A, Murphy GP, Bostwick DG. Prostate-specific membrane antigen expression is greatest in prostate adenocarcinoma and lymph node metastases. Urology. 1998;52:637–40.
173. Silver DA, Pellicer I, Fair WR, Heston WD, Cordon-Cardo C. Prostate-specific membrane antigen expression in normal and malignant human tissues. Clin Cancer Res. 1997;3:81–5.
174. Morigi JJ, Stricker PD, van Leeuwen PJ, et al. Prospective comparison of ^{18}F-fluoromethylcholine versus ^{68}Ga-PSMA PET/CT in prostate cancer patients who have rising PSA after curative treatment and are being considered for targeted therapy. J Nucl Med. 2015;56:1185–90.
175. Manyak MJ. Indium 111 capromab pendetide in the management of recurrent prostate cancer. Exp Rev Anticancer Ther. 2008;18:175–81.
176. Pandit-Taskar N, O'Donoghue JA, Durack JC. A phase I/II sudy for analytical validation of ^{89}Zr-J591 ImmunoPET as a molecular imaging agent for metastatic prostate cancer. Clin Cancer Res. 2015;21:5277–85.
177. Afshar-Oromieh A, Zechmann CM, Malcher A, et al. Comparison of PET imaging with a ^{68}Ga-labelled PSMA ligand and ^{18}F-choline-based PET/CT for the diagnosis of recurrent prostate cancer. Eur J Nucl Med Mol Imaging. 2013;41:11–20.
178. Fendler WP, Schmidt DF, Wenter V, et al. ^{68}Ga-PSMA-HBED-CC PET/CT detects location and extent of primary prostate cancer. J Nucl Med. 2016;57:1720–5.
179. Zettinig O, Shaha A, Hennesperger C, et al. Multimodal image-guided prostate fusion biopsy based on

automatic deformable registration. Int J Comput Assist Surg. 2015;10:1997–2007.
180. Maurer T, Gschwend JE, Rauscher I, et al. Diagnosic efficacy of ^{68}Ga-PSMA PET compared to conventional imaging in lymph node staging of 130 consecutive patients with intermediate high-risk prostate cancer. J Urol. 2016;195:1436–43.
181. Budaus L, Leyh-Bannurah SR, Salomoin G, et al. Intial experience of ^{68}Ga PSMA PET/CT imaging in high risk prostate cancer patients prior to radical prostatectomy. Eur Urol. 2016;69:393–6.
182. Queiroz MA, Viana P, Santos A, et al. Clinical impact of ^{68}Ga-PSMA PET/CT in a patient with biochemical recurrence of prostate cancer. Clin Nucl Med. 2016; 41:e417–9. Epub ahead of print.
183. Eiber M, Maurer T, Souvatzoglou M, et al. Evaluation of hybrid ^{68}Ga-PSMA-ligand PET/CT in 248 patients with biochemical recurrence after radical prostatectomy. J Nucl Med. 2015;56:668–74.
184. Verburg FA, Pfister D, Heidenreich A, et al. Extent of disease in recurrent prostate cancer determined by [^{68}Ga]PSMA-HBED-CC PET/CT in relation to PSA levels, PSA doubling time and Gleason score. Eur J Nucl Med Mol Imaging. 2016;43:397–403.
185. Perera M, Papa N, Christidis D, et al. Sensitivity, specificity and predictors of positive ^{68}Ga-prostate-specific membrane antigen positron emission tomography in advanced prostate cancer: a systematic review and meta-analysis. Eur Urol. 2016;70:926–37.
186. Sterzing F, Kratochwil C, Fiedler H, et al. ^{68}Ga-PSMA-11 PET/CT: a new technique with high potential for the radiotherapeutic management of prostate cancer patients. Eur J Nucl Med Mol Imaging. 2016; 43:34–41.
187. Maurer T, Eiber M, Schwaiger M, et al. Current use of PSMA-PET in prostate cancer management. Nat Rev Urol. 2016;13:226–35.
188. Cho SY, Gage KL, Mease RC, et al. Biodistribution, tumor detection, and radiation dosimetry of ^{18}F-DCFBC, a low-molecular-weight inhibitor of prostate-specific membrane antigen, in patients with metastatic prostate cancer. J Nucl Med. 2012;53:1883–91.
189. Chen Y, Pullambhatla M, Foss CA, et al. 2-(3-{1-Carboxy-5-[(6-[^{18}F]fluoro-pyridine-3-carbonyl)-amino]-pentyl}-ureido)-pentanedioic acid, [^{18}F]DCFPyL, a PSMA-based PET imaging agent for prostate cancer. Clin Cancer Res. 2011;17:7645–53.
190. Rowe SP, Macura KJ, Ciarallo A, et al. Comparison of prostate-specific membrane antigen-based ^{18}F-DCFBC PET/CT to conventional imaging modalities for detection of hormone-naïve and castration-resistant metastatic prostate cancer. J Nucl Med. 2016;57:46–53.
191. Rowe SP, Mana-Ay M, Javadi MS, et al. PSMA-based detection of prostate cancer bone lesions with ^{18}F-DCFPyL PET/CT: a sensitive alternative to ^{99m}Tc-MDP bone scan and Na^{18}F PET/CT? Clin Genitourin Cancer. 2016;14:e115–8.
192. Oka S, Hattori R, Kurosaki F, et al. A preliminary study of anti-1-amino-3^{18}F-fluorocyclobutyl-1 carboxylic acid for the detection of prostate cancer. J Nucl Med. 2007;48:46–55.
193. Sorensen J, Owenius R, Lax M, et al. Regional distribution and kinetics of ^{18}F fluciclovine (anti-^{18}FFABC) a tracer of aminoacid transport, in subject with primary prostate cancer. Eur J Nucl Med Mol Imaging. 2013; 40:394–402.
194. Okudaira H, Shikano N, Nishii R, et al. Putative transport mechanism and intracellular fate of trans-1-amino-3-^{18}F-fluorocyclobutanecarboxylic acid in human prostate cancer. J Nucl Med. 2011;52:822–9.
195. McParland BJ, Wall A, Johansson S, Sørensen J. The clinical safety, biodistribution and internal radiation dosimetry of [^{18}F]fluciclovine in healthy adult volunteers. Eur J Nucl Med Mol Imaging. 2013;40:1256–64.
196. Nye JA, Schuster DM, Yu W, Camp VM, Goodman MM, Votaw JR. Biodistribution and radiation dosimetry of the synthetic nonmetabolized amino acid analogue anti-^{18}F-FACBC in humans. J Nucl Med. 2007; 48:1017–20.
197. Asano Y, Inoue Y, Ikeda Y, et al. Phase I clinical study of NMK36: a new PET tracer with the synthetic amino acid analogue anti-[^{18}F]FACBC. Ann Nucl Med. 2011;25:414–8.
198. Kairemo K, Rasulova N, Partanen K, et al. Preliminary clinical experience of trans-1-amino-3-^{18}F-fluocyclobutanecarboxylic acid (anti-^{18}F-FACBC)-PET/CT image in prostate cancer patients. Biomed Res Int. 2014;2014:305182. doi:10.1155/2014/305182. Epib 2014 Jun 1.
199. Turkbey B, Mena E, Shih J, et al. Localized prostate cancer detection with ^{18}F-FACBC PET/CT: comparison with MR imaging and histopathologic analysis. Radiology. 2014;3:849–56.
200. Odewole OA, Tade FI, Nieh PT, et al. Recurrent prostate cancer detection with anti-3 ^{18}F FACB PET/CT: comparison with CT. Eur J Nucl Med Mol Imaging. 2016;43:1773–83.
201. Schuster DM, Nieh PT, Jani AB, et al. Anti-3-[^{18}F] FACBC positron emission tomography-computerized tomography and ^{111}In-capromab pendetide single photon emission computerized tomography-computerized tomography for recurrent prostate carcinoma: results of a prospective clinical trial. J Urol. 2014;191:1446–53.
202. Nanni C, Schiavina R, Brunocilla E, et al. ^{18}F-fluciclovine PET/CT for the detection of prostate cancer relapse: a comparison to ^{11}C-choline PET/CT. Clin Nucl Med. 2015;40:386–91.
203. Macheda ML, Rogers S, Bets JD. Molecular and cellular regulation of glucose transport (GLUT) proteins in cancer. J Cell Physiol. 2005;202:654–62.
204. Effert P, Beniers AJ, Tamimi Y, et al. Expression of glucose transporter 1 (GLUT-1) in cell lines and clinical specimen from human prostate adenocarcinoma. Anticancer Res. 2004;24:3057–63.

205. Kukuk D, Reischl G, Raguin O, et al. Assessment of PET tracer uptake in hormone-independent and hormone-dependent xenograft prostate cancer mouse models. J Nucl Med. 2011;52:1654–6.
206. Jadvar H, Ye W, Groshen S. ^{18}F-fluorodeoxyglucose PET-CT of the normal prostate gland. Ann Nucl Med. 1998;22:787–93.
207. Jadvar H. Imaging evaluation of prostate cancer with ^{18}F-fluorodeoxyglucose PET/CT: utility and limitations. Eur J Nucl Med Mol Imaging. 2013;40:S5–10.
208. Liu IJ, Zafar MB, Lai YH, et al. Fluorodeoxyglucose PET studies in diagnosis and staging of clinically organ-confined prostate cancer. Urology. 2001;57: 108–11.
209. Kao PF, Chou YH, Iai CW. Diffuse FDG uptake in acute prostatitis. Clin Nucl Med. 2008;33:308–10.
210. Oyama N, Akino H, Suzuki Y, et al. The increased accumulation of ^{18}F-fluoredeoxyglucose in untreated prostate cancer. Jpn J Clin Oncol. 1999;29:623–9.
211. Morris NJ, Akhurst T, Osman I, et al. Fluorinated deoxyglucose PET imaging in progressive metastatic prostate cancer. Urology. 2002;59:913–8.
212. Jadvar H, Pinski J, Conti P. FDG PET in suspected recurrent and metastatic prostate cancer. Oncol Rep. 2003;10:1485–8.
213. Chang CH, Wu HC, Tsai JJ, et al. Detecting metastatic pelvic lymph nodes by ^{18}F-2 deoxyglucose positron tomography in patients with PSA relapse after treatment with localized prostate cancer. Urol Int. 2003; 70:311–5.
214. Schoder H, Hermann K, Gonen M, et al. ^{18}F Fluorodeoxyglucose positron emission tomography for detection of disease in patients with PSA relapse after radical prostatectomy. Clin Cancer Res. 2005; 11:4761–9.
215. Zhang Y, Saylor M, Wen S, et al. Longitudinally quantitative 2-deoxy-2-[^{18}F]fluoro-D-glucose micro positron emission tomography imaging for efficacy of new anticancer drugs: a case study with bortezomib in prostate cancer murine model. Mol Imaging Biol. 2006;8:300–8.
216. Zukotynski KA, Kim CK, Gerbaudo VH, et al. ^{18}FF-FDG-PET/CT and ^{18}F-NaF-PET/CT in men with castrate-resistant prostate cancer. Am J Nucl Med Mol Imaging. 2014;5:72–82.
217. Courtney KD, Manola JB, Elfiky AA, et al. A phase I study of everolimus and docetaxel in patients with castration-resistant prostate cancer. Clin Genitourin Cancer. 2015;13:113–23.
218. Yu EY, Muzi M, Hackenbracht JA, et al. C-11-acetate and F-18 FDG PET for men with prostate cancer bone metastases: relative findings and response to therapy. Clin Nucl Med. 2011;36:192–8.
219. Morris MJ, Akhurst T, Larson SM, et al. Fluorodeoxyglucose positron emission tomography as an outcome measure for castrate metastatic prostate cancer treated with antimicrotubule chemotherapy. Clin Cancer Res. 2005;11:3210–6.
220. Meirelles GS, Schoder H, Ravizzini GC, et al. Prognostic value of baseline [^{18}F] fluorodeoxyglucose positron emission tomography and ^{99m}Tc-MDP bone scan in progressing metastatic prostate cancer. Clin Cancer Res. 2010;16:6093–9.
221. Vargas HA, Wassberg C, Fox JJ, et al. Bone metastases in castration-resistant prostate cancer: associations between morphologic CT patterns, glycolytic activity, and androgen receptor expression on PET and overall survival. Radiology. 2014;271:220–9.
222. Jadvar H, Desai B, Ji L, et al. Baseline ^{18}F-FDG PET/CT parameters as imaging biomarkers of overall survival in castrate-resistant metastatic prostate cancer. J Nucl Med. 2013;54:1195–2001.
223. Jadvar H, Groshen SG, Quinn DI. Association of overall survival with glycolytic activity of castrate-resistant prostate cancer metastases. Radiology. 2015; 274:624–5.

Diagnostic Applications of Nuclear Medicine: Testicular Cancer

32

Abedallatif AlSharif, Serena Chiacchio, and Giampiero Giovacchini

Abstract

Testicular cancer is the most common solid-non hematological cancer diagnosed in young adult men. Personal history of testicular cancer is a major risk factor for developing testicular cancer. Testicular germ cell tumors are the most common tumors, these are further divided into seminomas and non seminomatous germ cell tumors. Tumors generally present as painless testicular mass, the first investigation is testicular ultrasound followed by serum biomarkers. MRI can be used as a problem solver only in equivocal cases. Radical orchiectomy provides therapy as well as pathological T staging. CT scan is the primary investigation for assessing lymph node status and for evaluation of distant metastasis. [^{18}F]FDG PET/CT is not recommended for diagnosis of primary testicular cancer with reported unsatisfactory negative predictive value. Nevertheless PET/CT offers several advantages over CT particularly for patients with equivocal CT findings and in patients who exhibit elevated tumor markers and negative CT scan. In addition, [^{18}F]FDG PET/CT is especially useful for evaluation of post chemotherapy residual masses in metastatic seminoma. [^{18}F]FDG PET/CT is, however, not routinely indicated for post chemotherapy evaluation of non seminomatous germ cell tumors because of high false negative rate in teratomas.

Keywords

PET/CT • Testicular cancer • Seminoma • Germ cell tumor • Non germ cell tumor • Teratoma

Glossary

[^{18}F]FDG	2-Deoxy-2-[^{18}F]fluoro-D-glucose
AFP	α-Fetoprotein
AJCC	American Joint Committee on Cancer
Beta-hCG	Beta-human chorionic gonadotropin
BRAF	Gene encoding for the B-Raf protein, a serine/threonine-protein kinase (also known as the proto-oncogene B-Raf and v-Raf murine sarcoma viral oncogene homolog B)

A. AlSharif (✉)
Department of Radiology and Nuclear Medicine, University of Jordan, Jordan University Hospital, Amman, Jordan
e-mail: abedsharif@ju.edu.jo; alsharifabedallatif@gmail.com

S. Chiacchio
Regional Center of Nuclear Medicine, University Hospital of Pisa, Pisa, Italy
e-mail: chiacchioserena@gmail.com

G. Giovacchini
Nuclear Medicine Department, "S. Andrea" Hospital, La Spezia, Italy
e-mail: giampiero.giovacchini@as5.liguria. it

© Springer International Publishing Switzerland 2017
H.W. Strauss et al. (eds.), *Nuclear Oncology*,
https://doi.org/10.1007/978-3-319-26236-9_21

C-KIT	Proto-oncogene encoding for tyrosine-protein kinase Kit (or CD117), also known as mast/stem cell growth factor receptor (SCFR)
CT	X-ray computed tomography
CXCR4	Gene encoding for C-X-C chemokine receptor type 4 (CXCR-4), also known as fusin or CD184 (cluster of differentiation 184)
EGFR	Epidermal growth factor receptor; the mutated form EGFRvIII plays a prominent role in tumorigenesis and proangiogenic signaling
GCT	Germ cell tumor
IGD	In greatest dimension
IGF	Insulin-like factor
LDH	Lactate dehydrogenase
M	Metastasis status according to the AJCC/UICC TNM staging system
MRI	Magnetic resonance imaging
N	Lymph node status according to the AJCC/UICC TNM staging system
NCCN	National Comprehensive Cancer Network
NSGCT	Nonseminomatous germ cell tumor
p53	Tumor protein p53, also known as cellular tumor antigen p53, phosphoprotein p53, tumor suppressor p53, antigen NY-CO-13, or transformation-related protein 53 (TRP53)
PET	Positron emission tomography
PET/CT	Positron emission tomography/Computed tomography
RAS	Oncogene regulating signaling cascades
SDF-1	Gene encoding for the stromal cell-derived factor 1, also known as C-X-C motif chemokine 12 (CXCL12)
SNP	Single nucleotide polymorphism
SPECT	Single-photon emission tomography
SPECT/CT	Single-photon emission tomography/Computed tomography
T	Tumor status according to the AJCC/UICC TNM staging system
TGCT	Testicular germ cell tumor
TNM	AJCC/UICC staging system based on parameters "T" (tumor status), "N" (lymph node status), and "M" (distant metastasis status)
UICC	Union Internationale Contre le Cancer (International Union Against Cancer)
ULN	Upper limit of normal range
US	Ultrasonography
WHO	World Health Organization

Contents

Epidemiology of Testicular Cancer 927
Risk Factors 927
Genetic Predisposition 927
Underlying Molecular Biology Changes 928
Histopathology of Testicular Cancer 928
Serum Biomarkers 929
Clinical Presentation, Staging, and Prognostic Stratification 929
Overall Performance of Diagnostic Imaging Other than Nuclear Medicine 931
Nuclear Imaging for Diagnosis and Staging 933
Common Therapies 936
Assessing the Efficacy of Treatment(s) 938
Surveillance in Seminomas 938
Pure Seminoma Stage IA and IB 939
Pure Seminomas Stages IIA and IIB 939
Follow-Up for Stages IIA and Non-bulky IIB Pure Seminoma After Radiotherapy Treatment 939
Follow-Up of Bulky Stages II A, IIB, IIC, and III Treated with Chemotherapy 939
Follow-Up of Pure Seminoma Bulky Stage II and Stage III After Chemotherapy 940
Surveillance in NSGCT 940

Follow-Up for Nonseminoma Stage IA 940
Follow-Up for Nonseminoma Stage IB 940
Follow-Up for Nonseminoma Stages IIA and IIB and Metastatic Nonseminoma 940

References 940

Epidemiology of Testicular Cancer

The incidence of testicular cancer was estimated at 5.6 cases per 100,000 men in the United States in 2011, with a rising trend over the past decades in the United States and in the Western world in general [1]. Testicular cancer can affect men at all ages; its incidence peaks at ages between 25 and 29 years, with 14.3 cases diagnosed per 100,000 men per year in this age group. With this incidence, testicular cancer is the most common solid non-hematological cancer diagnosed in young adult men. There is a wide variability of incidence of testicular cancer among different races, the highest rates being reported among Caucasians and the lowest rates among Blacks and Asians. In the United States, the incidence of testicular cancer in White Americans is fivefold more common than in Black Americans and fourfold more common than in Asians [1].

Risk Factors

Personal history of prior testicular cancer is a major risk factor for developing testicular cancer, as there is actually a 12-fold increase in the risk of developing another testicular cancer in patients with prior cancer in the contralateral testicle [2]. In addition, 2% of germ cell testicular cancers is bilateral at presentation. History of surgically uncorrected undescended testicle increases the risk for developing testicular cancer by up to eightfold; this risk remains high in cases where surgical correction was performed after puberty [2]. There is a growing body of evidence suggesting that exposure to toxic substances increases the risk of testicular cancer. The main substances with a potential association with testicular cancer include organic chlorides, polychlorinated biphenyls, polyvinyl chlorides, phthalates, marijuana, and tobacco [1]. Prenatal exposure to estrogens has been suggested as a risk factor as well, although this notion remains controversial [1]. Male infertility increases the risk of developing testicular cancer by nearly threefold, an observation that suggests a common etiology between testicular cancer and the testicular dysgenesis syndrome, Hiwi protein and chromosome 12 aneuploidy, DNA mismatch repair, and Y chromosome instability [1]. Microcalcifications are often seen on testicular ultrasonography; although this finding is not known to be a risk factor per se, testicular tumors are more likely to be found in young men with microcalcifications than in those without [1, 3].

Histologically, the presence of intratubular germ cell tumor (carcinoma in situ) is considered to be a well-established risk factor for testicular cancer. Intratubular germ cell tumors are frequently seen in surgical specimens of orchiectomy and in the contralateral testis of patients with history of testicular cancer [1].

Genetic Predisposition

There is evidence that family history of testicular cancer is a significant risk factor for developing the disease, and it has been estimated that sons or brothers of patients with testicular cancer are at a six- to tenfold higher risk of developing the cancer themselves. It is not clear, however, whether this familial risk factor is genetic or environmental. Furthermore, linkage analysis studies have failed to identify any significant genetic linkage in these cases of familial testicular germ cell tumors (TGCTs) [1, 4].

In sporadic cases, the most common genetic alteration in patients with infertility is a deletion of 1.6 Mb (deletion gr/gr) in the AZF region of the Y chromosome, which doubles the risk for developing TGCTs [5]. In addition, at least 25 single nucleotide polymorphism (SNPs) associated with genetic predisposition in several chromosomal regions have been identified in patients with TGCTs; these SNPs most likely increase genetic susceptibility to develop TGCT [5]. Although these SNPs may be biologically

significant, they account for less than 20% of the familial risk of TGCTs [5].

Underlying Molecular Biology Changes

A number of molecular alterations have been described in testicular germ cell tumors. C-KIT mutations are the most common single-nucleotide variations, with 10% of all TGCTs and 20% of seminomas harboring a C-KIT mutation microsatellite instability (MSI); BRAF mutations are associated with chemo-refractory TGCT. One study has shown evidence for epidermal growth factor receptor (EGFR) amplification as a possible genetic aberration associated with chemoresistance [6]. A small subset of TGCTs (predominantly seminomas) have mutations in this RAS oncogene family, but these mutations are of unclear clinical and pathobiologic significance. TP53 mutations are not common in TGCTs; however, overexpression of wild-type p53 may be seen at immunohistochemistry [5, 7].

Genomic DNA methylation studies have shown a contrast in methylation patterns between TGCT tissue and normal tissue, as well as between seminoma and normal tissue (generally decreased/hypomethylated) versus nonseminomatous TGCT (generally methylated) [5, 7].

Skakkebæk proposed a model that suggests that fetal gonocytes beyond normal development in spermatogonia could present abnormal cell division mediated by a receptor/SCF kit, a paracrine circuit leading to uncontrolled proliferation of gonocytes. The subsequent invasive growth is mediated by stimulation of postnatal and pubertal gonadotropins [5, 8]. A second model proposed by Chaganti and Houldsworth suggests that aberrant chromatid exchange during meiotic division could lead to block p53-dependent apoptotic response and to cell cycle reset, therefore to genomic instability [5, 9].

Several molecular mediators in the testicular microenvironment have recently been associated with the transition from germ cell tumor in situ to an aggressive phenotype of TGCT cells. Several data indicate that the IGF-1/IGF1R and SDF-1/CXCR4 signaling pathways are important mediators in the pathogenesis of TGCTs and also in the acquisition of phenotypic features associated with metastatic ability, such as proliferation, differentiation, migration, cellular survival, and angiogenesis [5].

Histopathology of Testicular Cancer

Testicular germ cell tumors (TGCTs) are the most common testicular cancers, as this group constitutes approximately 95% of all testicular cancers. TGCTs arise from the germinal epithelium in seminiferous tubules. Other rare sites of GCTs are the pineal gland, neurohypophysis, mediastinum, and retroperitoneum [1, 7, 10].

TGCTs are currently subdivided according to the 2004 World Health Organization (WHO) classification into seminomas and nonseminomatous germ cell tumors (NSGCTs). Pure seminomas are the most common TGCTs, accounting for approximately 50% of all TGCTs. Typically, seminomas occur in older men when compared with NSGCT; the mean age of patients at presentation is 40 years, and more than 80% occur after the age of 30. The clinical and pathological diagnosis of a seminoma is restricted to pure seminoma histology and a normal serum concentration of α-fetoprotein (AFP). Seminomas are chemo- and radiosensitive, and these tumors are characterized by a high 5-year survival – reaching approximately 95% [1, 7].

NSGCTs are clinically more aggressive than pure seminomas and often include multiple cell types including embryonal cell carcinomas, choriocarcinomas, yolk sac tumors, and teratomas. Approximately one-third of TGCTs contain mixed features of seminomas and NGCTs; when both features of seminomas and NSGCT are present, clinical management is adopted according to guidelines for nonseminoma tumors. These mixed neoplasms are actually the second most common testicular cancer after seminomas [1, 7, 10].

Pure embryonal carcinomas are only occasionally encountered, whereas choriocarcinomas and yolk sac tumors are rarely seen after puberty. Yolk sac tumor is the most common testicular cancer in boys younger than 2 years. Pure choriocarcinomas

are exceedingly rare; in contrast to other TGCTs, choriocarcinomas usually present with symptoms of metastasis rather than as a testicular mass. Teratomas are further classified into mature or immature type, depending on cell differentiation. Rarely, a teratoma histologically resembles a somatic cancer, such as sarcoma or adenocarcinoma, and is then referred to as a teratoma with malignant transformation. Pure teratoma is uncommon in the postpubertal setting, accounting for fewer than 5% of all TGCTs. In children, prepubertal pure teratoma comprises nearly one-third of the testicular tumors; mature prepubertal teratomas are benign and do not metastasize. Postpubertal teratomas may be associated with metastasis in approximately one-third of the cases and typically contain other TGCT components [1, 7, 10].

Non-germ cell tumors are rare and comprise approximately 5% of testicular cancers; they include Leydig cell, Sertoli cell, and granulosa cell tumors. In men older than 60 years, lymphoma is the most common testicular malignancy. Other rare testicular tumors include leukemia, sarcoma, leiomyoma, vascular tumors, fibromas, and neurofibromas [7, 10, 11].

Serum Biomarkers

The serum tumor markers α-fetoprotein (AFP), lactate dehydrogenase (LDH), and beta-human chorionic gonadotropin (beta-hCG) are critical in the diagnosis and management of TGCTs. These serum tumor-associated markers should be evaluated before and after treatment, as well as throughout follow-up. Serum tumor markers are very useful for monitoring all stages of nonseminomas and in monitoring metastatic seminomas. AFP is a serum tumor marker produced by nonseminomatous cells (i.e., embryonal carcinoma, yolk sac tumor) and may be seen at any stage. The half-life of AFP (a glycoprotein that can be considered as the fetal precursor of serum albumin) in serum is 5–7 days. In the absence of testicular malignancy, AFP elevation can occur in infants under 1-year-old, during liver dysfunction (hepatitis, cirrhosis, hepatocellular carcinoma), and in other non-testicular malignancies (liver, pancreatic, gastric, lung). In testicular cancer, AFP is never associated with pure seminoma [12–14].

In patients with choriocarcinomas, beta-hCG is always elevated; it is also elevated in up to 10% of patients with pure seminomas and in some patients with seminomatous or other nonseminomatous tumors. Elevations of beta-hCG must be interpreted with caution, as its serum levels can be abnormally increased in patients with hypogonadism or in marijuana users; its half-life in serum is 1–3 days. LDH (an enzyme with a half-life in serum of 5–7 days) is a less specific marker than either AFP or beta-hCG; it can be elevated in both seminomas and NSGCTs, and high serum levels typically indicate bulky or extensive disease [13, 14].

Clinical Presentation, Staging, and Prognostic Stratification

A testicular tumor typically presents as a painless testicular mass. After history taking and physical examination, the first-line diagnostic test is testicular ultrasound (US), which remains the cornerstone of primary imaging in patients with testicular cancer and should be performed on both testicles. Once a suspected tumor is confirmed, the measurement of serum tumor markers including AFP, beta-hCG, and LDH is the next step for diagnosis and staging. Patients with confirmed testicular tumor must undergo computed tomography (CT) examination of the chest, abdomen, and pelvis as an integral part of the staging evaluation. Bone scan or spine MRI is indicated only in patients with bone pain. Brain MRI is indicated in patients with symptoms, in patients with lung metastasis, and in patients with high beta-hCG levels [14, 15].

Radical inguinal orchiectomy provides therapy-oriented as well as diagnostic and staging information. In particular, orchiectomy provides definitive histopathology information regarding tumor subtype and is considered curative for nearly 80% of low-stage seminomas and for approximately 60–70% of low-stage NSGCTs [14, 15].

The correct interpretation of serum biomarkers, in conjunction with correct histopathology reading and interpretation of CT images, is the mainstays of

Table 1 TNM classification of testicular cancer

pT: primary tumor[a]	
pTX	Primary tumor cannot be assessed
pT0	No evidence of primary tumor (e.g., histologic scar in the testis)
pTis	Intratubular germ cell neoplasia (testicular intraepithelial neoplasia)
pT1	Tumor limited to the testis and epididymis without vascular/lymphatic invasion; tumor may invade tunica albuginea, but not tunica vaginalis
pT2	Tumor limited to the testis and epididymis with vascular/lymphatic invasion or tumor extending through into the tunica albuginea with involvement of tunica vaginalis
pT3	Tumor invades the spermatic cord with or without vascular/lymphatic invasion
pT4	Tumor invades the scrotum with or without vascular/lymphatic invasion
N: regional lymph nodes (clinical)	
NX	Regional lymph nodes cannot be assessed
N0	No regional lymph node metastasis
N1	Metastasis with a lymph node mass ≤2 cm IGD or multiple lymph nodes, none >2 cm IGD
N2	Metastasis with a lymph node mass >2 cm but not >5 cm IGD or multiple lymph nodes with any one mass >2 cm but not >5 cm IGD
N3	Metastasis with a lymph node mass >5 cm IGD
pN: pathologic lymph nodes	
pNX	Regional lymph nodes cannot be assessed
pN0	No regional lymph node metastasis
pN1	Metastasis with a lymph node mass ≤2 cm IGD and ≤5 positive nodes, none >2 cm IGD
pN2	Metastasis with a lymph node mass >2 cm but not >5 cm IGD; or >5 nodes positive, none >5 cm IGD; or evidence of extranodal tumor extension
pN3	Metastasis with a lymph node mass >5 cm IGD
M: distant metastasis	
MX	Distant metastasis cannot be assessed
M0	No distant metastasis
M1	Distant metastasis
M1a	Nonregional lymph node(s) or lung
M1b	Other sites
S: serum tumor markers	
SX	Serum marker studies not available or not performed
S0	Serum marker levels within normal limits
S1	LDH <1.5 × ULN and hCG <5,000 mIU/mL and AFP <1,000 ng/mL
S2	LDH 1.5–10 × ULN or hCG 5,000–50,000 mIU/mL or AFP 1,000–10,000 ng/mL
S3	LDH >10 × ULN or hCG >50,000 mIU/mL or AFP >10,000 ng/mL

IGD in greatest dimension, *LDH* lactate dehydrogenase, *hCG* human chorionic gonadotropin, *AFP* α-fetoprotein, *ULN* upper limit of normal range

[a]Except for pTis and pT4, for which radical orchiectomy is not always necessary for classification purposes, the extent of the primary tumor is classified after radical orchiectomy. In other circumstances, TX is used if no radical orchiectomy has been performed

patient staging and prognostic stratification. Tables 1 and 2 summarize TNM staging of testicular cancer [14–16]. The pathologic T stage of the tumor is assigned according to the presence or absence of lymphovascular invasion and depth of invasion (tunica vaginalis, spermatic cord, scrotal involvement). During human development, the gonads are formed in the abdomen at the lumbar level, approximately at 21 weeks after conception; the testicles begin migration to the inguinal canal and then descend into the scrotum by 30 weeks after conception. As a result, blood supply and lymphatic channels drain to the abdominal retroperitoneal nodes, and typically not to the pelvis, unless scrotal violation has occurred. Metastasis from testicular cancer occurs via predictable lymphatic channels to retroperitoneal lymph nodes for right- or left-sided primary tumors (pT) [17–19]. Right-sided tumors typically spread to the aortocaval lymph nodes inferior to the renal hilar vessels, while left-sided tumors commonly spread to the left para-aortic lymph nodes. Para-aortic and aortocaval lymph nodes at the level of the kidneys are usually the first lymph node stations affected by metastasis from testicular cancer. While the spread from the right to the left retroperitoneal lymph nodes is seen frequently, the spread from left to right has never been reported [17–19].

Similarly as in other solid cancers, sentinel lymph node biopsy has been suggested as an approach to reduce the morbidity associated with de novo lymph node dissection, which currently

Table 2 Stage grouping for testicular cancer

Stage	T	N	M	Serum tumor marker
Stage 0	pTis	N0	M0	S0, SX
Stage I	pT1–T4	N0	M0	SX
Stage IA	pT1	N0	M0	S0
Stage IB	pT2–T4	N0	M0	S0
Stage IS	Any patient/TX	N0	M0	S1–3
Stage II	Any patient/TX	N1–N3	M0	SX
Stage IIA	Any patient/TX	N1	M0	S0, S1
Stage IIB	Any patient/TX	N2	M0	S0, S1
Stage IIC	Any patient/TX	N3	M0	S0, S1
Stage III	Any patient/TX	Any N	M1a	SX
Stage IIIA	Any patient/TX	Any N	M1a	S0, S1
Stage IIIB	Any patient/TX	N1–N3	M0	S2
	Any patient/TX	Any N	M1a	S2
Stage IIIC	Any patient/TX	N1–N3	M0	S3
	Any patient/TX	Any N	M1a	S3
	Any patient/TX	Any N	M1b	Any S

constitutes the recognized standard of care for proper N staging of patients with stage I testicular cancer. Funicular block using 2% lidocaine is followed by intratesticular injection of 60–100 MBq ^{99m}Tc-nanocolloidal albumin in 0.2 mL. Early dynamic anterior and lateral images for 10 min are then acquired; subsequently, delayed images at 2 h, preferably with SPECT/CT technique, are obtained (see Fig. 1). Intraoperatively, sentinel lymph nodes are localized and resected under the guidance of a handheld gamma probe; the additional use of a dedicated portable gamma camera can also be useful. As in other types of solid cancers, the identification of early metastasis in sentinel lymph nodes offers proper early treatment (elective lymph node dissection of the affected lymphatic basin) while avoiding overtreatment in patients without metastatic disease. Using this technique, no recurrences developed after a median follow-up of 21 months in patients with stage I testicular cancer and negative sentinel lymph nodes [20].

Distant hematogenous metastasis is rare in testicular cancer, ranging from an uncommon event seen in patients with choriocarcinomas to even less frequent occurrence in yolk sac tumors. Distant hematogenous spread may be seen in the lung, liver, brain, bones, kidney, adrenal gland, gastrointestinal tract, or spleen [1, 14, 15].

A prognostic staging system is used to assist treatment recommendations for patients with metastatic testicular cancer. This system was developed by the International Germ Cancer Collaborative Group in 1997 and classifies patients into either good, intermediate, or poor prognostic groups on the basis of histology, site of primary tumor, metastatic disease, and serum tumor markers (see Tables 2 and 3) [14–16, 21].

Overall Performance of Diagnostic Imaging Other than Nuclear Medicine

Scrotal ultrasound (US) examination is the initial primary imaging procedure for any patient with suspected testicular tumor. US can distinguish between intratesticular lesions (which are commonly malignant) and extra-testicular lesions (which are usually benign). Tumors typically present as a hypoechoic lesion, which can be heterogeneous with calcific or cystic changes particularly in NSGCT; in addition, blood flow is increased within the tumor or at its fibrous septa on Doppler

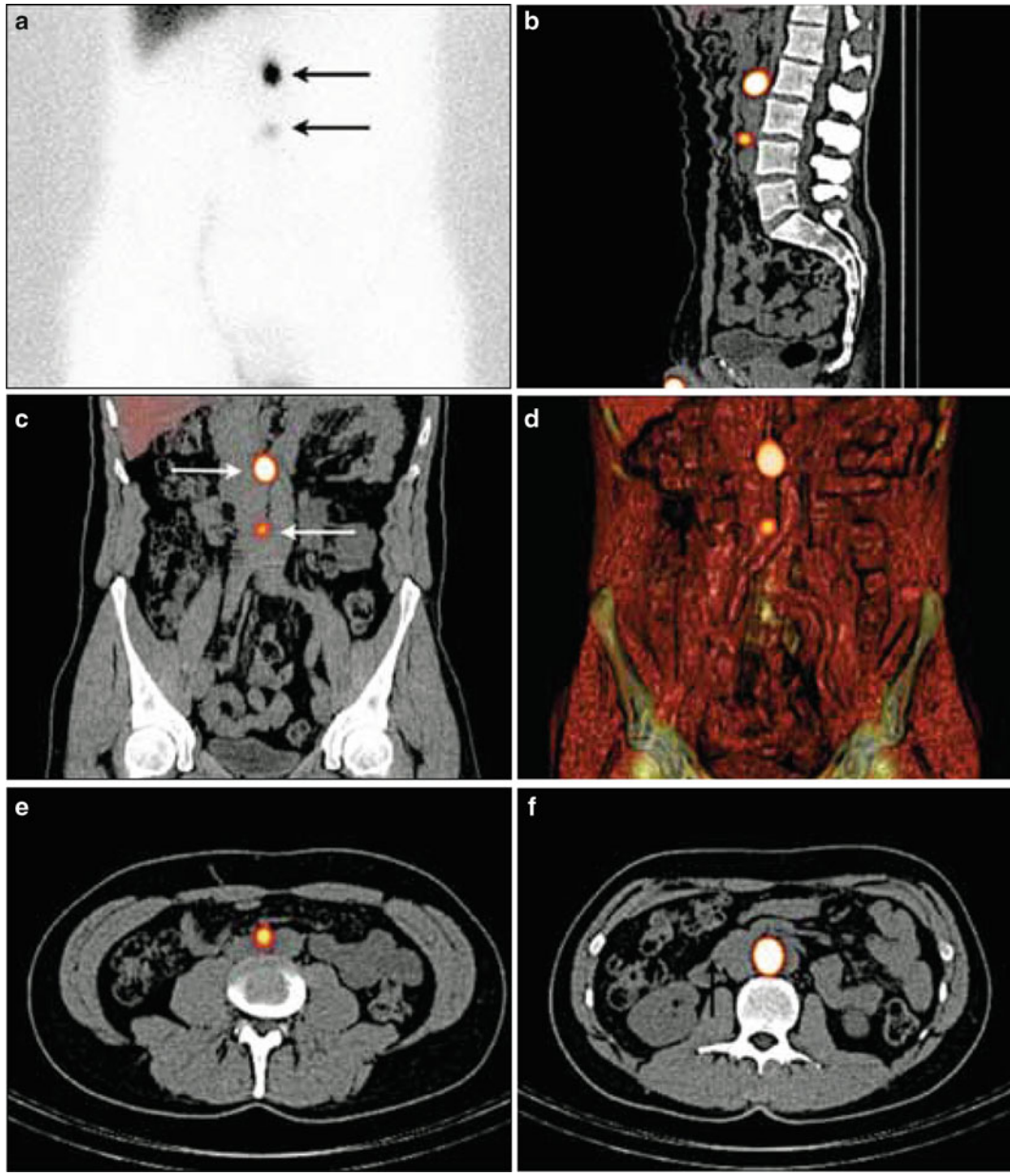

Fig. 1 Preoperative lymphoscintigraphy in a 42-year-old patient with cancer in the right testicle; abdominal CT showed no enlarged lymph nodes. ^{99m}Tc-nanocolloidal albumin (87 MBq) was injected intratumorally under ultrasound guidance. Static planar imaging was acquired about 30 min postinjection, a ^{57}Co flood source being placed beneath the patient's body in order to delineate the body outline; SPECT/CT was acquired about 2 h postinjection. (**a**) Early planar anterior image showing lymphatic drainage to two abdominal sentinel lymph nodes (*arrows*). (**b**) Sagittal SPECT/CT image fusion showing the injection site (at the very *bottom* of the image) and both sentinel nodes along the great abdominal vessels. (**c**, **d**) The coronal SPECT/CT image fusion and 3D volume-rendered image reveal that both sentinel lymph nodes are located interaortocavally (*arrows*). (**e**, **f**) Axial SPECT/CT fused images provide additional information about anatomic location of the two sentinel lymph nodes. Both nodes were harvested laparoscopically and were tumor-free at histopathology (Reproduced with permission from Brouwer et al. [53])

imaging. Overall, US has a high reported sensitivity (92–98%) in detecting testicular cancer, with a specificity of 95–99.8%. False-positive US findings have been reported in patients with testicular infarction, hematoma, or infection as these conditions may also present as mass-like structures with variable blood flow on Doppler images [22–25].

Testicular microlithiasis is a common finding on US examination, with an incidence of 5% in young healthy adults; this is 1,000 times greater than the incidence of testicular malignancy. Testicular microlithiasis in an otherwise normal testicular US scan does not predispose to testicular malignancy. However, clustering of more than ten microlithiasis lesions in certain areas of the testis is associated with an increased risk of developing testicular cancer, and these areas may contain foci of carcinoma in situ [24–28].

Sonoelastography is a new US technique that quantifies the stiffness of tissues; real-time sonoelastography has high sensitivity and specificity for discriminating malignant from benign lesions of the testis, as most malignant testicular lesions demonstrate heterogeneous color pattern with increased stiffness values [28–30].

MRI is usually the second imaging modality of choice for testicular lesions, as it can be considered as a problem-solver procedure when the primary diagnosis is still equivocal after US examination. Low T2 signal intensity with intra-tumoral septal enhancement after contrast administration is more compatible with seminomas, whereas heterogeneous signal intensity on both T1- and T2-weighted images with cystic and necrotic components and a heterogeneous enhancement pattern indicates NSGCT [31]. The sensitivity and specificity of MRI in differentiating benign from malignant intratesticular lesions were reported at 100% and 87.5%, respectively [24, 25, 28]. This diagnostic performance can be further improved by the addition of diffusion-weighted images to routine MRI examinations, with reported sensitivity of 93.3%, specificity of 90%, positive predictive value of 87.5%, and negative predictive value of 94.7% in the characterization of intratesticular masses [32]. Furthermore, MRI can provide useful preoperative information regarding T staging, with reported accuracy of 92.8% [29, 31].

Whereas surgical pathology determines the T stage of the tumor, imaging provides both N and M components of the staging system. CT is the primary imaging technique used in staging testicular cancer, as the scan can efficiently detect lymph node metastasis in addition to distant metastasis involving the liver and lungs. Metastatic lymph nodes are identified based on size criteria, with malignant nodes usually considered to be 8–10 mm or greater in diameter. Using size criteria, abdominopelvic CT offers sensitivity of approximately 70–80%; this criterion is, however, suboptimal because testicular cancer has a high propensity for nodal micrometastases [30]. In 1997, Hilton et al. assessed preoperative CT images in 70 patients who underwent retroperitoneal lymphadenectomy and found that using 10 mm or larger as a cutoff for positive lymph nodes, the sensitivity was only 37% (with 100% specificity); of course, sensitivity improves using 4 mm as cutoff (reaching approximately 93%), associated however with reduced specificity (57%) [33]. In another study, Hudolin et al. adopted a cutoff criterion of 7–8 mm and reported 70% sensitivity and 80% specificity in patients with testicular cancer who underwent retroperitoneal lymphadenectomy [34].

It is currently recommended that lymph nodes 8 mm or larger should be considered suspicious, especially in higher-risk patients who have lymphovascular invasion, which constitute a high proportion of embryonal subtype or T category $\geq$ II [25]. In addition to size criteria, lymph nodes from NSGCT may appear heterogeneous with cystic changes [28]. Because of the growing concern regarding the frequent use of CT in young male patients, more recently MRI has been shown to be equivalent to CT scan in detecting metastatic retroperitoneal lymph nodes, when assessed by experienced specialists [35].

Nuclear Imaging for Diagnosis and Staging

There is at present no sufficient evidence justifying a recommendation to use [^{18}F]FDG PET/CT for diagnosis or staging of testicular cancer. A meta-analysis on the accuracy of the diagnostic

Table 3 Prognostic-based staging system for metastatic germ cell cancer (International Germ Cell Cancer Collaborative Group)

Group	Type	Criteria
Good prognosis	Nonseminoma (56% of cases)	All of the following criteria:
	5-year PFS 89%	Testis/retroperitoneal primary
	5-year survival 92%	No nonpulmonary visceral metastases
		AFP <1,000 ng/mL
		hCG <5,000 mIU/mL (1,000 ng/mL)
		LDH <1.5 × ULN
	Seminoma (90% of cases)	All of the following criteria:
	5-year PFS 82%	Any primary site
	5-year survival 86%	No nonpulmonary visceral metastases
		Normal AFP
		Any hCG
		Any LDH
Intermediate prognosis	Nonseminoma (28% of cases)	All of the following criteria:
	5-year PFS 75%	Testis/retroperitoneal primary
	5-year survival 80%	No nonpulmonary visceral metastases
		AFP 1,000–10,000 ng/mL or
		hCG 5,000–50,000 mIU/mL or
		LDH 1.5–10 × ULN
	Seminoma (10% of cases)	All of the following criteria:
	5-year PFS 67%	Any primary site
	5-year survival 72%	Nonpulmonary visceral metastases
		Normal AFP
		Any hCG
		Any LDH
Poor prognosis	Nonseminoma (16% of cases)	Any of the following criteria:
	5-year PFS 41%	Mediastinal primary
	5-year survival 48%	Nonpulmonary visceral metastases
		AFP >10,000 ng/mL or
		hCG >50,000 mIU/mL (10,000 ng/mL) or
		LDH >10 × ULN
	Seminoma	No patients classified as poor prognosis

Prechemotherapy serum tumor markers should be assessed immediately before administration of chemotherapy (same day)

PFS progression-free survival, *AFP* α-fetoprotein, *hCG* human chorionic gonadotropin, *LDH* lactate dehydrogenase, *ULN* upper limit of normal range

[^{18}F]FDG PET in testicular cancer has recently been published; the analysis included a total of 16 published studies, with an overall 957 [^{18}F]FDG PET scans in 807 patients. Pooled sensitivity and specificity were 75% and 87%, respectively [36]. This reported sensitivity, with a negative likelihood ratio of 0.31, is unsatisfactory to confidently exclude testicular malignancy. False-negative studies are mostly explained by small tumor volume and micrometastases; in addition, teratomas do not demonstrate significant metabolic activity on [^{18}F]FDG PET [36]. Furthermore positive findings have occasionally been reported, due to infective/inflammatory processes [36, 37].

Nevertheless, as a functional/metabolic imaging procedure (see Fig. 2), [^{18}F]FDG PET offers in principle several advantages over CT, which uses mere size criteria to define metastatic lymph node

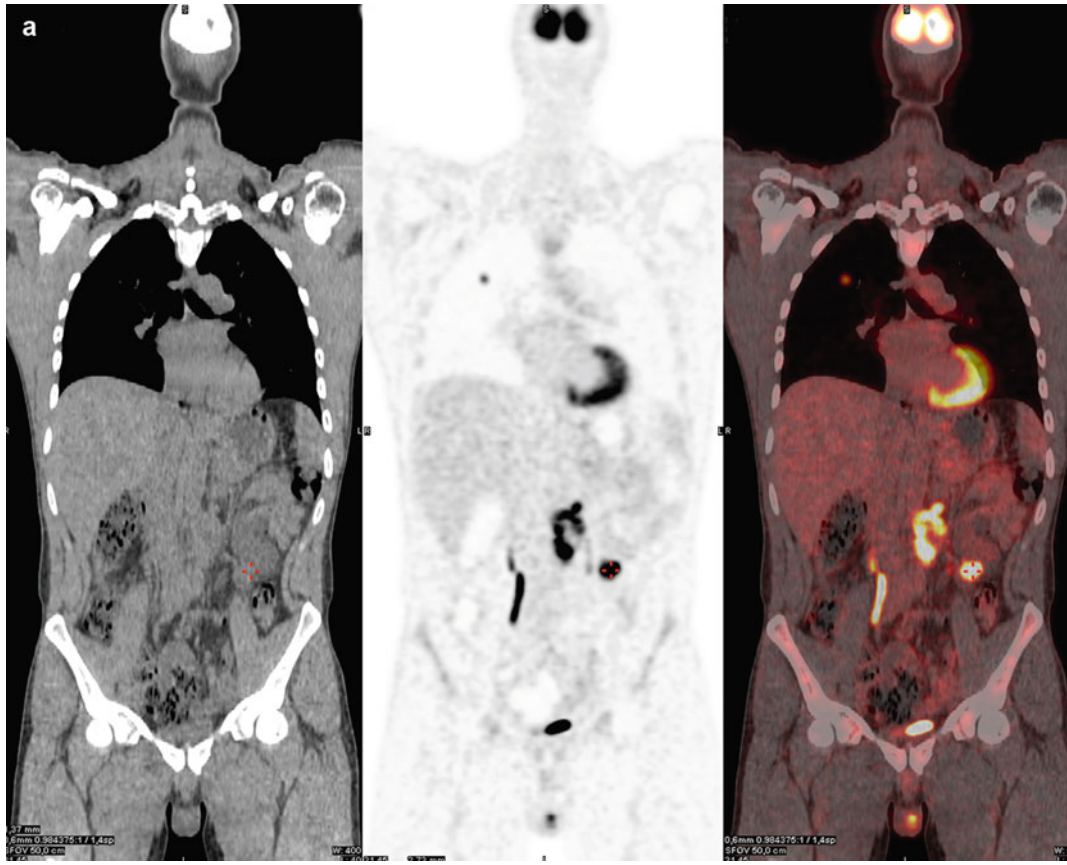

Fig. 2 (continued)

involvement. [^{18}F]FDG PET/CT can be especially useful in patients with a negative CT scan who exhibit elevated tumor markers or in patients with equivocal findings on the CT scan [38–40].

In a recent study by Gary Cook, [^{18}F]FDG PET was used at initial staging of 16 patients (ten with seminoma, five with NSGCTs, and one with mixed GCT). In 11 patients, the PET/CT scans were performed to clarify equivocal staging diagnostic CT results, usually with para-aortic lymph nodes that were in the expected drainage of the primary tumor but were less than the 1 cm cutoff size value required to be classified as positive on CT. In addition, five patients with normal primary staging CT scans but high-risk disease underwent [^{18}F]FDG PET/CT scans to aid decisions for surveillance versus adjuvant chemotherapy [41]. Eight of the 11 patients with equivocal CT scans had true-negative [^{18}F]FDG PET/CT scans, while three patients had a true-positive [^{18}F]FDG PET scan. These findings are in line with previous reports that have concluded that [^{18}F]FDG PET is most useful in patients with equivocal CT scans [38–40]. The five high-risk patients with normal staging CT scans had negative [^{18}F]FDG PET/CT scans, but two subsequently relapsed. This finding is also in line with a previous report that prospectively investigated whether [^{18}F]FDG PET could correctly detect high-risk patients without occult metastatic disease [42]. It is concluded that [^{18}F]FDG PET/CT is helpful when primary staging CT scans are equivocal, but it is insufficiently sensitive to predict relapse in high-risk patients with normal CT scans [41, 42].

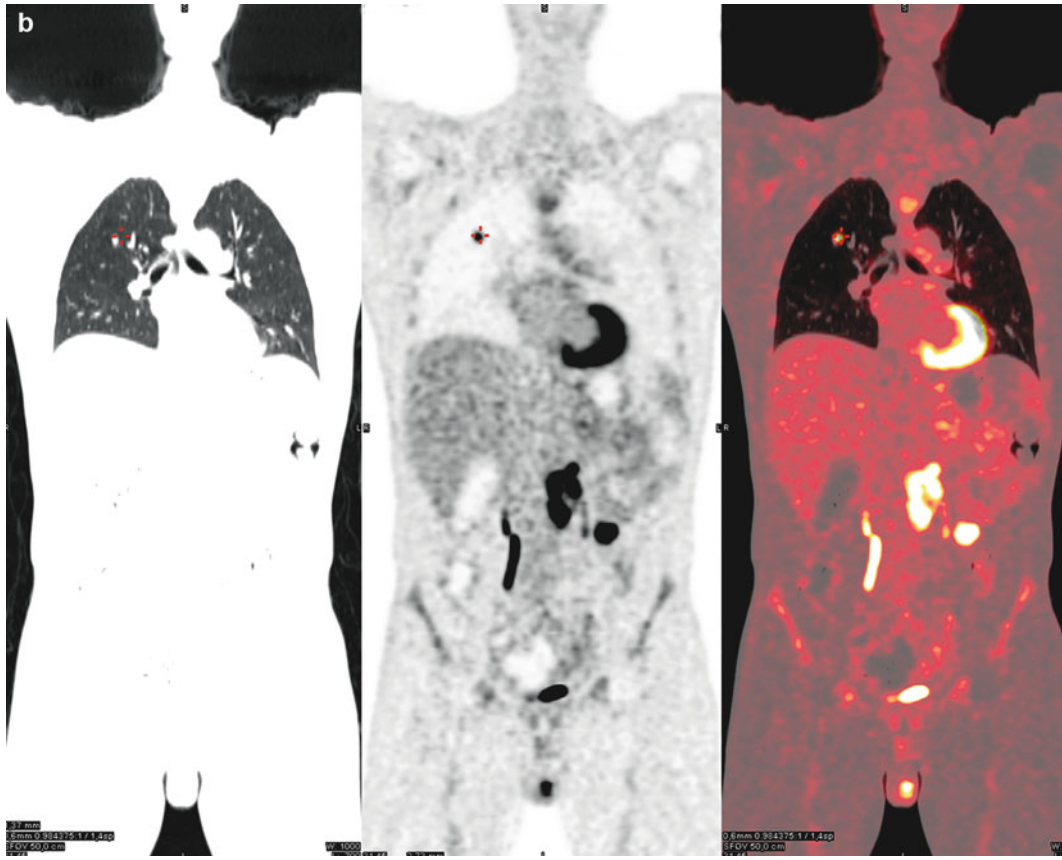

Fig. 2 (continued)

Common Therapies

Management of testicular cancer involves a multidisciplinary team including urologists, medical oncologists, radiation oncologists, and pathologists. As mentioned previously, the survival rate of testicular cancer approaches 97%; however, this high cure rate is achievable in excellent clinical settings, where diagnosis, treatment facilities, and specialized experience are available [14, 15].

One of the important points to emphasize when counseling patients with a new diagnosis of testicular cancer is that it is generally a treatable and highly curable disease. Sperm banking should be offered to the patients prior to commencement of therapy. Over 80% of men with stage I seminoma are cured by radical orchiectomy. Staging procedures reveal that 15–20% of stage I seminomas have subclinical metastatic disease, usually in the retroperitoneum, and will relapse after orchiectomy alone. The decision regarding adjuvant therapy (one cycle of adjuvant carboplatin or adjuvant radiotherapy course) should be based on discussion with the patient, after explaining advantages and disadvantages based on the individual patient's situation. Most clinicians set reduced treatment long-term toxicity as a management goal in patients with stage I seminoma. The overall cancer-specific survival rate under surveillance performed by experienced centers is 97–100% for stage I seminoma [14, 15, 43].

Patients with stage I NSGCT have subclinical metastases in 30% of the cases; they will usually

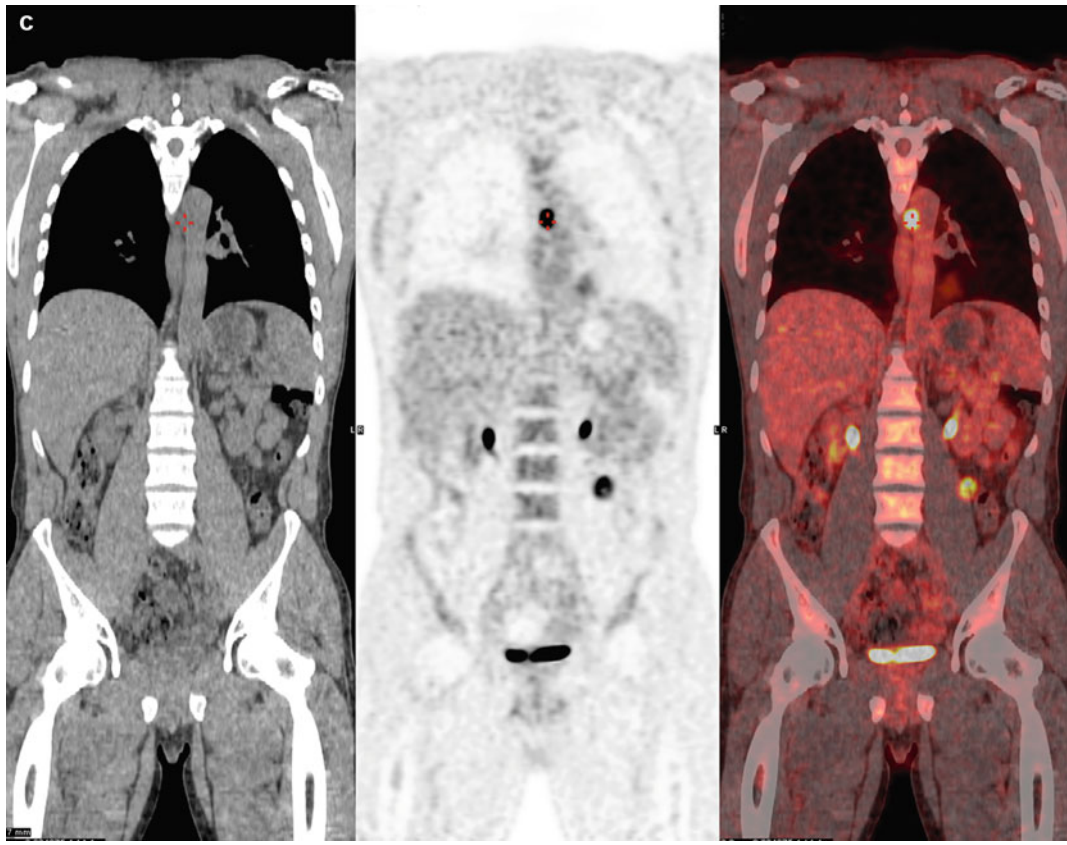

Fig. 2 [^{18}F]FDG PET/CT performed for staging in a 35-year-old male patient after incidental discovery of a mass in the right lung with associated enlarged mediastinal lymph nodes; this had originally been interpreted on CT as possible primary lung cancer with metastatic spread to mediastinal lymph nodes, although with a somewhat atypical pattern. In addition to the expected foci of increased [^{18}F]FDG uptake in the chest lesions, the PET/CT scan detected a distinct focus of increased tracer uptake in the left testicle, subsequently confirmed to be a primary seminomatous testicular cancer. (**a**) Coronal sections of the CT component (*left*), the PET component (*center*), and corresponding fused hybrid PET/CT image (*right*), showing increased [^{18}F]FDG uptake in the left testicle, in left common iliac lymph nodes, and in the mass of the right lung. (**b**) Same sections as in (**a**), but with the CT component being displayed with the imaging window for the lung. (**c**) Coronal sections of the CT component (*left*), the PET component (*center*), and corresponding fused hybrid PET/CT image (*right*) in a more posterior plane than in (**a**) and (**b**); in addition to the still visible increased [^{18}F]FDG uptake in the left common iliac lymph nodes, there is distinct tracer uptake in the aortopulmonary space

relapse if surveillance alone is undertaken after orchiectomy, mostly within the first year. The treating clinician should discuss with the patients the advantages and disadvantages of each treatment option; surveillance is usually offered to non-risk compliant patients [14, 15].

First-line treatment of stage II or stage III TGCT depends on histology of the primary tumor and on prognostic groups (see Table 3). To date, the standard treatment of stage IIA/B seminoma has been radiotherapy, with reported recurrence rates of 9–24% [14, 15]. Alternatively, these patients may undergo three courses of chemotherapy with bleomycin, etoposide, and cisplatin (BEP) or four courses with etoposide with cisplatin. Stage IIA/B NSGCT with elevated tumor markers should receive chemotherapy followed by residual tumor resection if indicated. Stage IIA/B NSGCT patients without elevated tumor markers can be managed by primary retroperitoneal lymphadenectomy or surveillance. Chemotherapy is the standard treatment of

metastatic TGCTs with varying chemotherapy protocols according to histology and prognostic stratification [14, 15].

Assessing the Efficacy of Treatment(s)

[^{18}F]FDG PET/CT is especially useful for evaluation of post-chemotherapy residual masses and metastatic seminoma, an occurrence observed in an average 25% of cases [24, 25, 28]. Several studies have reported that [^{18}F]FDG PET is superior to CT in predicting viable tumor in seminoma residuals after chemotherapy, with accuracy greater than 90% [24, 25, 28, 44, 45].

When the residual lymph node mass is larger than 3 cm in its long axis, particularly in cases with pure seminomas, surgical treatment is usually recommended [46]. However, the prospective SEMPET study has suggested that [^{18}F]FDG PET/CT can confidently differentiate residual disease from fibrosis [44]. When [^{18}F]FDG PET is negative, then there is no need to perform surgery, and the patient is put under surveillance. False-positive [^{18}F]FDG PET scans are infrequent if scans are scheduled more than 2 months after chemotherapy [15]. A retrospective validation of the SEMPET trial including 127 patients yielded sensitivity, specificity, negative predictive value, and positive predictive values of [^{18}F]FDG PET at 50%, 77%, 91%, and 25%, respectively [47]. To reduce the post-chemotherapy false-positive cases, it is currently recommended to repeat the [^{18}F]FDG PET scan at least after six additional weeks. Repeating [^{18}F]FDG PET is a helpful strategy particularly if residual disease is considered unlikely from the clinical point of view; it is also helpful to guide biopsy in those patients who otherwise can also be falsely classified as negative. If the repeat scan is not performed, the residual mass must then be biopsied [15, 39, 41, 47, 48].

[^{18}F]FDG PET is not routinely indicated for post-chemotherapy staging in NSGCT [15]. Residual masses after completion of first-line chemotherapy are found in approximately 40% of patients, even after normalization of serum tumor markers [49]. Histology of the resected lesions reveals necrosis in 40%, vital carcinoma in 20%, and mature teratoma in 40% of cases [50]. Mature teratomas are completely chemoresistant; in addition, they carry the risk of subsequent malignant transformation, and as mentioned previously, they are usually not [^{18}F]FDG avid. Therefore, tumor resection is mandatory for all patients with residual masses >1.0 cm along the short axis on CT images [15]. In a prospective trial of 121 stage IIC or III NSGCT patients, [^{18}F]FDG PET was performed after completion of chemotherapy, and the results were correlated with histopathology, CT scan, and serum tumor markers [51]. Prediction of tumor viability with [^{18}F]FDG was correct in 56% of the cases, therefore, with an accuracy that was not better than CT (55%) or tumor markers (56%). Sensitivity and specificity of [^{18}F]FDG PET were 70% and 48%, respectively. The positive predictive values were not significantly different (55%, 61%, and 59% for CT, serum tumor markers, and PET, respectively). Judging only vital carcinoma as a true malignant finding, the negative predictive value increased to 83% for [^{18}F]FDG PET. As mentioned previously, the presence of vital carcinoma and mature teratoma is common in residual masses in patients with NSGCT; this prospective, histology controlled study demonstrated that [^{18}F]FDG PET does not yield a clear additional clinical benefit with respect to the standard diagnostic procedures (CT and serum tumor markers) for predicting tumor viability in residual masses [51]. [^{18}F]FDG PET, on the other hand, can be used to localize post-chemotherapy hypermetabolic tissue and therefore serve as a guide for biopsy or surgical intervention.

Surveillance in Seminomas

The National Comprehensive Cancer Network (NCCN) has recently published clinical practice guidelines in testicular cancer, describing in details surveillance of testicular cancer according to stage of disease, histopathological findings, and treatment plan. Since a detailed discussion of the

proposed surveillance plan is beyond the scope of this chapter, we summarize here the relevant recommendation particularly regarding seminomas, where [^{18}F]FDG PET plays a major role for clinical decision-making [14].

Pure Seminoma Stage IA and IB

The relapse rate seen in these patients is 15–20% at 5 years; the risk of relapse is highest in the first 2 years, and most of the relapses are first detected in infradiaphragmatic lymph nodes. Surveillance is considered as the preferred option for patients with pT1–pT3; if surveillance is not possible, adjuvant chemotherapy or radiotherapy should be considered.

Follow-Up During Active Surveillance

It includes a medical history and physical examination, with measurement of post-orchiectomy serum tumor markers every 3–6 months for the first year, every 6–12 months for years 2–3, and annually thereafter. There is controversy regarding how many imaging studies should be performed in patients during active surveillance. The NCCN Panel recommends abdominal/pelvic CT every 3, 6, and 12 months for the first year; every 6–12 months for years 2 and 3; and then every 12–24 months for years 4 and 5. No initial relapses in the lung have been reported for patients with stage I seminoma managed by active surveillance; therefore, according to the NCCN Panel, routine chest imaging during surveillance is only indicated for patients with thoracic symptoms.

Follow-Up After Adjuvant Treatment

The risk of recurrence 5 years after adjuvant treatment is $<0.3\%$ annually. Follow-up of patients treated with adjuvant therapy includes a history and physical examination, with measurement of post-orchiectomy serum tumor markers performed every 6–12 months for the first 2 years and annually thereafter. The NCCN Panel recommends performing abdominal and pelvic CT scans annually for 3 years in patients treated with radiotherapy or carboplatin. Chest x-rays should be obtained only when clinically indicated.

Pure Seminomas Stages IIA and IIB

Follow-Up for Stages IIA and Non-bulky IIB Pure Seminoma After Radiotherapy Treatment

The recommended follow-up after radiation therapy for patients with stage IIA and non-bulky IIB tumors includes a history and physical examination, with measurement of post-orchiectomy serum tumor markers performed every 3 months for year 1 and then every 6 months for years 2 through 5. Chest x-ray is recommended every 6 months for the first 2 years. An abdominal CT scan is recommended at 3 months, then at 6 and 12 months in year 1, and then annually for years 2 and 3 after radiotherapy and as clinically indicated thereafter.

Follow-Up of Bulky Stages II A, IIB, IIC, and III Treated with Chemotherapy

After chemotherapy these patients are evaluated with serum tumor markers and a CT scan of the chest, abdomen, and pelvis. Patients are then classified according to the presence or absence of a residual mass and the status of serum tumor markers. Patients with normal markers and either no residual mass or residual mass of 3 cm or less need no further treatment. They should undergo surveillance as pure seminoma bulky stage II and stage III after chemotherapy. In cases of residual tumor >3 cm and normal marker levels, the NCCN Panel recommends an [^{18}F]FDG PET scan in these patients approximately 6 weeks after chemotherapy in order to decide whether to continue with surveillance or resume treatment. If the PET scan is negative, no further treatment is needed; however, the patient should undergo follow-up as discussed in pure seminoma bulky stage II and stage III after chemotherapy. In cases with a positive [^{18}F]FDG PET scan, retroperitoneal lymph node dissection

(RPLND) may be considered if technically feasible; alternatively, second-line chemotherapy is indicated.

Follow-Up of Pure Seminoma Bulky Stage II and Stage III After Chemotherapy

The NCCN Panel recommends follow-up schedules for patients with bulky stage II or stage III disease *after* treatment with chemotherapy *and* either no or $\leq$3 cm residual mass and normal tumor markers, including history and physical examination plus measurement of post-orchiectomy serum tumor markers every 2 months for the first year, every 3 months for the second year, every 6 months for the third and fourth years, and annually for year 5. An abdominal/pelvic CT scan is recommended at 3 and 6 months and then as clinically indicated. The [^{18}F]FDG PET scan may be performed if clinically indicated. Chest x-ray is recommended every 2 months during the first year, every 3 months during the second year, and annually during years 3 through 5. Chest CT is preferred over chest x-ray in patients with thoracic symptoms.

The NCCN Panel notes that patients with PET-negative result and tumor residual mass measuring >3 cm after chemotherapy should undergo an abdominopelvic CT scan every 6 months for the first year and then annually for 5 years.

Surveillance in NSGCT

Follow-Up for Nonseminoma Stage IA

In the updated NCCN Guidelines, the long-term follow-up tests for stage IA patients electing primary surveillance, post-RPLND, or post-chemotherapy include serum marker assessment, chest x-ray, and an abdominal CT scan.

Follow-Up for Nonseminoma Stage IB

In the updated NCCN Guidelines, the long-term routine follow-up tests for the selected patients with T2 disease undergoing surveillance and for those who underwent chemotherapy include serum marker assessment, chest x-ray, and an abdominal/pelvic CT scan. The frequency of these tests varies depending on the adjuvant management strategy.

Follow-Up for Nonseminoma Stages IIA and IIB and Metastatic Nonseminoma

After primary treatment, the subsequent management depends on tumor marker levels and the residual masses detected on CT scan; lesions less than 1.0 cm may still harbor residual disease and therefore must be interpreted with caution. [^{18}F]FDG PET scans have limited negative predictive value in patients with residual masses, but still might be useful in guiding multimodality treatment [52].

References

1. Gonzalez-Exposito R, Merino M, Aguayo C. Molecular biology of testicular germ cell tumors. Clin Transl Oncol. 2016;18:550–6.
2. Fosså SD, Chen J, Schonfeld SJ, et al. Risk of contralateral testicular cancer: a population-based study of 29,515 U.S. men. J Natl Cancer Inst. 2005;97:1056–66.
3. Heller HT, Oliff MC, Doubilet PM, O'Leary MP, Benson CB. Testicular microlithiasis: prevalence and association with primary testicular neoplasm. J Clin Ultrasound. 2014;42:423–6.
4. Crockford GP, Linger R, Hockley S, et al. Genome-wide linkage screen for testicular germ cell tumour susceptibility loci. Hum Mol Genet. 2006;15:443–5.
5. Gonzalez-Exposito R, Merino M, Aguayo C. Molecular biology of testicular germ cell tumors. Clin Transl Oncol. 2016;18:550–6.
6. Madani A, Kemmer K, Sweeney C, et al. Expression of kit and epidermal growth factor receptor in chemotherapy refractory non-seminomatous germ cell tumors. Ann Oncol. 2003;14:873–80.
7. Howitt BE, Berney DM. Tumors of the testis: morphologic features and molecular alterations. Surg Pathol Clin. 2015;8:687–716.
8. Skakkebaek NE, Rajpert-De Meyts E, et al. Germ cell cancer and disorders of spermatogenesis: an environmental connection? APMIS. 1998;106:3–11.
9. Chaganti RS, Houldsworth J. The cytogenetic theory of the pathogenesis of human adult male germ cell tumors. APMIS. 1998;106:80–3.

10. Ulbright TM, Tickoo SK, Berney DM, Srigley JR. Members of the IIiDUPG. Best practices recommendations in the application of immunohistochemistry in testicular tumors: report from the International Society of Urological Pathology consensus conference. Am J Surg Pathol. 2014;38:e50–9.
11. Leite KR, Garicochea B, Srougi M, et al. Monoclonality of asynchronous bilateral lymphoma of the testis. Eur Urol. 2000;38:774–7.
12. Nazeer T, Ro JY, Amato RJ, Park YW, Ordonez NG, Ayala AG. Histologically pure seminoma with elevated alpha-fetoprotein: a clinicopathologic study of ten cases. Oncol Rep. 1998;5:1425–9.
13. Weissbach L1, Bussar-Maatz R, Mann K. The value of tumor markers in testicular seminomas. Results of a prospective multicenter study. Eur Urol. 1997;32: 16–22.
14. Motzer RJ, Jonasch E, Agarwal N, et al. Testicular cancer, version 2.2015. J Natl Compr Canc Netw. 2015;13:772–99.
15. Albers P, Albrecht W, Algaba F, et al. Guidelines on testicular cancer: 2015 update. Eur Urol. 2015;68: 1054–68.
16. Sobin LH, Gospodarowicz MK, Wittekind C, editors. TNM classification of malignant tumors. 7th ed. Oxford: Wiley-Blackwell; 2009. p. 249–54.
17. Ray B, Hajdu SI, Whitmore Jr WF. Proceedings: distribution of retroperitoneal lymph node metastases in testicular germinal tumors. Cancer. 1974;33: 340–8.
18. Donohue JP, Zachary JM, Maynard BR. Distribution of nodal metastases in nonseminomatous testis cancer. J Urol. 1982;128:315–20.
19. Weissbach L, Boedefeld EA. Localization of solitary and multiple metastases in stage II nonseminomatous testis tumor as basis for a modified staging lymph node dissection in stage I. J Urol. 1987;138:77–82.
20. Brouwer OR, Valdés Olmos RA, Vermeeren L, Hoefnagel CA, Nieweg OE, Horenblas S. SPECT/CT and a portable gamma-camera for image-guided laparoscopic sentinel node biopsy in testicular cancer. J Nucl Med. 2011;52:551–4.
21. Mead GM, Stenning SP. The International Germ Cell Consensus Classification: a new prognostic factor-based staging classification for metastatic germ cell tumours. Clin Oncol. 1997;9:207–9.
22. Guthrie JA, Fowler RC. Ultrasound diagnosis of testicular tumours presenting as epididymal disease. Clin Radiol. 1992;46:397–400.
23. Schwerk WB, Schwerk WN, Rodeck G. Testicular tumors: prospective analysis of real-time US patterns and abdominal staging. Radiology. 1987;164:369–74.
24. Meyts ER, McGlynn KA, Okamoto K, Jewett MA, Bokemeyer C. Testicular germ cell tumours. Lancet. 2016;387(10029):1762–74.
25. Coursey Moreno C, Small WC, Camacho JC, et al. Testicular tumors: what radiologists need to know – differential diagnosis, staging, and management. Radiographics. 2015;35:400–15.
26. Höbarth K, Szabo N, Klingler HC, Kratzik C. Sonographic appearance of testicular microlithiasis. Eur Urol. 1993;24:251–5.
27. Richenberg J, Belfield J, Ramchandani P, et al. Testicular microlithiasis imaging and follow-up: guidelines of the ESUR scrotal imaging subcommittee. Eur Radiol. 2015;25:323–30.
28. Secil M, Altay C, Basara I. State of the art in germ cell tumor imaging. Urol Oncol. 2016;34:156–64.
29. Kreydin EI, Barrisford GW, Feldman AS, Preston MA. Testicular cancer: what the radiologist needs to know. AJR Am J Roentgenol. 2013;200:1215–25.
30. Correas JM, Drakonakis E, Isidori AM, et al. Update on ultrasound elastography: miscellanea. Prostate, testicle, musculo-skeletal. Eur J Radiol. 2013;82:1904–12.
31. Tsili AC, Argyropoulou MI, Giannakis D, Sofikitis N, Tsampoulas K. MRI in the characterization and local staging of testicular neoplasms. AJR Am J Roentgenol. 2010;194:682–9.
32. Algebally AM, Tantawy HI, Yousef RR, Szmigielski W, Darweesh A. Advantage of adding diffusion weighted imaging to routine MRI examinations in the diagnostics of scrotal lesions. Pol J Radiol. 2015;80:442–9.
33. Hilton S, Herr HW, Teitcher JB, Begg CB, Castéllino RA. CT detection of retroperitoneal lymph node metastases in patients with clinical stage I testicular nonseminomatous germ cell cancer: assessment of size and distribution criteria. AJR Am J Roentgenol. 1997;169:521–5.
34. Rajpert-De Meyts E, McGlynn KA, Okamoto K, Jewett MA, Bokemeyer C. Testicular germ cell tumours. Lancet. 2016;387(10029):1762–74.
35. Sohaib SA, Koh DM, Barbachano Y, et al. Prospective assessment of MRI for imaging retroperitoneal metastases from testicular germ cell tumours. Clin Radiol. 2009;64:362–7.
36. Zhao JY, Ma XL, Li YY, et al. Diagnostic accuracy of ^{18}F-FDG-PET in patients with testicular cancer: a meta-analysis. Asian Pac J Cancer Prev. 2014;15: 3525–31.
37. Mansberg R, Ho B, Bui C. Positive FDG PET/CT of recurrent testicular tumour due to orchitis. Mol Imaging Radionucl Ther. 2014;23:28–30.
38. Lassen U, Daugaard G, Eigtved A, Højgaard L, Damgaard K, Rørth M. Whole-body FDG-PET in patients with stage I non-seminomatous germ cell tumours. Eur J Nucl Med Mol Imaging. 2003;30: 396–402.
39. Tsatalpas P, Beuthien-Baumann B, Kropp J, et al. Diagnostic value of ^{18}F-FDG positron emission tomography for detection and treatment control of malignant germ cell tumors. Urol Int. 2002;68:157–63.
40. De Wit M, Brenner W, Hartmann M, et al. [^{18}F]-FDG-PET in clinical stage I/II non-seminomatous germ cell tumours: results of the German multicentre trial. Ann Oncol. 2008;19:1619–23.
41. Cook GJ, Sohaib A, Huddart RA, Dearnaley DP, Horwich A, Chua S. The role of ^{18}F-FDG PET/CT in

the management of testicular cancers. Nucl Med Commun. 2015;36:702–8.
42. Huddart RA, O'Doherty MJ, Padhani A, NCRI Testis Tumour Clinical Study Group, et al. ^{18}Fluorodeoxyglucose positron emission tomography in the prediction of relapse in patients with high-risk, clinical stage I nonseminomatous germ cell tumors: preliminary report of MRC Trial TE22 – the NCRI Testis Tumour Clinical Study Group. J Clin Oncol. 2007;25:3090–5.
43. Tandstad T, Smaaland R, Solberg A, et al. Management of seminomatous testicular cancer: a binational prospective population-based study from the Swedish Norwegian Testicular Cancer Study Group. J Clin Oncol. 2011;29:719–25.
44. De Santis M, Becherer A, Bokemeyer C, et al. 2-^{18}fluorodeoxy-D-glucose positron emission tomography is a reliable predictor for viable tumor in postchemotherapy seminoma: an update of the prospective multicentric SEMPET trial. J Clin Oncol. 2004;22:1034–9.
45. Becherer A, De Santis M, Karanikas G, et al. FDG PET is superior to CT in the prediction of viable tumour in post-chemotherapy seminoma residuals. Eur J Radiol. 2005;54:284–8.
46. Stattaus J, Bockisch A, Forsting M, Müller SP. Value of imaging for lymph node metastases from renal cell, bladder, prostate, penile, and testicular cancers. Urologe A. 2005;44:614–24.
47. Bachner M, Loriot Y, Gross-Goupil M, et al. 2-^{18}Fluoro-deoxy-D-glucose positron emission tomography (FDG-PET) for postchemotherapy seminoma residual lesions: a retrospective validation of the SEMPET trial. Ann Oncol. 2012;23:59–64.
48. Hinz S, Schrader M, Kempkensteffen C, et al. The role of positron emission tomography in the evaluation of residual masses after chemotherapy for advanced stage seminoma. J Urol. 2008;179:936–40.
49. Gerl A, Clemm C, Schmeller N, et al. Sequential resection of residual abdominal and thoracic masses after chemotherapy for metastatic nonseminomatous germ cell tumours. Br J Cancer. 1994;70:960–5.
50. Hartmann JT, Schmoll HJ, Kuczyk MA, et al. Postchemotherapy resections of residual masses from metastatic non-seminomatous testicular germ cell tumors. Ann Oncol. 1997;8:531–8.
51. Oechsle K, Hartmann M, Brenner W, et al. [^{18}F] Fluorodeoxyglucose positron emission tomography in nonseminomatous germ cell tumors after chemotherapy: the German multicenter positron emission tomography study group. J Clin Oncol. 2008;26:5930–5.
52. Quak E, Kovacs I, Oyen WJ, van der Graaf WT. FDG-PET/CT in a patient with poor-risk non-seminoma testis with mature teratoma and secondary gliosarcoma: multimodality imaging for guiding multimodality treatment. Nucl Med Mol Imaging. 2015;49:237–40.
53. Brouwer OR, Meinhart W, Horenblas S, Valdés Olmos RA. Preoperative and intraoperative lymphatic mapping for radioguided sentinel node biopsy in cancers of the male reproductive system. In: Mariani G, Manca G, Orsini F, Vidal-Sicart S, Valdés Olmos RA, editors. Atlas of lymphoscintigraphy and sentinel node mapping – a pictorial case-based approach. Milan: Springer-Verlag Italia; 2013. p. 269–83.

Diagnostic Applications of Nuclear Medicine: Penile Cancer

33

Serena Chiacchio, Abedallatif AlSharif, Zia Saad, Giampiero Giovacchini, and Jamshed Bomanji

Abstract

Penile carcinomas are rare in most developed countries; in contrast, this cancer is not infrequent in the tropical and subtropical regions of Latin America, Asia, and Africa. In addition, penile cancer is common in regions with high prevalence of human papilloma virus infection. More than 95% of penile carcinomas are of the squamous cell type; other histologic types include basal cell carcinoma, melanoma, and sarcoma. Penile carcinoma usually spreads through lymphatic channels to the superficial and deep inguinal lymph nodes; subsequently iliac lymph nodes are involved. The presence and extent of metastatic disease in inguinal nodes is the single most important prognostic factor in patients with penile cancer. Primary evaluation of penile cancer is based on physical examination including inguinal lymph node palpation. Ultrasound and MRI can provide information on tumor invasion of the corpora cavernosa if organ preservation is planned. Ultrasound can be used to evaluate nonpalpable inguinal lymph nodes, whereas pelvic CT scan can be used to assess pelvic lymph nodes. Lymphoscintigraphy, preferably with SPECT/CT imaging, and subsequently sentinel lymph node biopsy is gaining popularity in clinical practice, especially in patients with nonpalpable lymph nodes; sensitivity reported for this local staging approach ranges from 70% to 86%. Assessment of distant metastases should be performed in patients with positive inguinal nodes; this includes abdomen and pelvis CT, chest X-ray, or thoracic CT. [^{18}F]FDG PET/CT can be used for initial staging of penile cancer with pooled sensitivity and specificity of 80.9% and 92.4% respectively; this staging technique is particularly advocated for patients with positive lymph nodes. [^{18}F]FDG PET/CT can also be employed to monitor the efficacy of induction chemotherapy. Follow-up of penile cancer is based mainly on clinical evaluation, while radionuclide imaging techniques have rarely been used for restaging purposes during regular follow-up.

Keywords

Penile cancer • Imaging • [^{18}F]FDG PET/CT

S. Chiacchio (✉)
Regional Center of Nuclear Medicine, University Hospital of Pisa, Pisa, Italy
e-mail: chiacchioserena@gmail.com

A. AlSharif
Department of Radiology and Nuclear Medicine, University of Jordan, Jordan University Hospital, Amman, Jordan

Z. Saad • J. Bomanji
Institute of Nuclear Medicine, University College London Hospitals, NHS Foundation Trust, University College Hospital, London, UK

G. Giovacchini
Nuclear Medicine Department, "S. Andrea" Hospital, La Spezia, Italy

© Springer International Publishing Switzerland 2017
H.W. Strauss et al. (eds.), *Nuclear Oncology*,
https://doi.org/10.1007/978-3-319-26236-9_44

Glossary	
[^{18}F]FDG	2-Deoxy-2-[^{18}F]fluoro-D-glucose
AIDS	Acquired immune deficiency syndrome
AJCC	American Joint Committee on Cancer
CDKN2A	Gene encoding for cyclin dependent kinase inhibitor 2A, also encoding for proteins p16INK4A and p14ARF
CI	Confidence interval
CpG	5′-C-phosphate-G-3′ sequence in DNA, where cytosine and guanine are separated by only one phosphate
CT	X-ray computed tomography
EAU	European Association of Urology
HPV	Human papilloma virus
KAI1/CD82	Member of the tetraspanin family classified as metastasis suppressor gene
LOH	Loss of heterozygosity
MR	Magnetic resonance
MRI	Magnetic resonance imaging
p53	Tumor protein p53, also known as cellular tumor antigen p53, phosphoprotein p53, tumor suppressor p53, antigen NY-CO-13, or transformation-related protein 53 (TRP53)
PET	Positron emission tomography
PET/CT	Positron emission tomography/computed tomography
PUVA	Therapy with psoralen plus ultraviolet light to treat atopic dermatitis
Rb	Gene encoding for the retinoblastoma protein
SCC Ag	Squamous cell carcinoma antigen
SCC	Squamous cell carcinoma
SLN	Sentinel lymph node
SLNB	Sentinel lymph node biopsy
SPECT	Single-photon emission computed tomography
SPECT/CT	Single-photon emission computed tomography/computed tomography
TNM	AJCC/UICC staging system based on parameters "T" (tumor status), "N" (lymph node status) and "M" (distant metastasis status)
US	Ultrasonography
WHO	World Health Organization

Contents

Epidemiology and Environmental Factors 944

Risk Factors and Association with Other Conditions 945

Prevention 946

Genetic Predisposition 946

Underlying Molecular Biological Changes 946

Staging and Prognostic Stratification 946
Grading 947
Pathologic Prognostic Factors 947
Lymphatic Involvement 948

Performance of Diagnostic Imaging Other Than Nuclear Medicine 949
Primary Lesion 949
Regional Lymph Nodes 949

Distant Metastases 949

Performance of Nuclear Imaging for Staging and Prognosis 950

Staging 951

Follow-Up and Restaging 953

Treatment Options for Penile Cancer 953

References 955

Epidemiology and Environmental Factors

Penile carcinomas are rare in most developed nations including in Europe and the USA where the rate is less than 1 per 100,000 men per year. Incidence is also affected by race and ethnicity in North America [1, 2], with the highest incidence of penile cancer found in white Hispanics (1.01 per 100,000), followed by a lower incidence in

Alaskan, Native American Indians (0.77 per 100,000), blacks (0.62 per 100,000), and white non-Hispanics (0.51 per 100,000), respectively.

In contrast, penile cancer is not infrequent in the tropical or subtropical regions of Latin America, Asia, and Africa. In South America, Southeast Asia, and parts of Africa, the incidence of penile cancer is much higher and can represent 1–2% [2, 3] of all malignant diseases in men. The annual age-adjusted incidence is 0.7–3.0 per 100,000 men in India, 8.3 per 100,000 men in Brazil, and even higher in Uganda, where it is the most commonly diagnosed cancer in men [3, 4].

Penile cancer is common in regions with a high prevalence of human papilloma virus (HPV) infection, and therefore much knowledge about penile cancer comes from research in countries with a high incidence of the disease. HPV infection in the population may account for the wide variability in incidence observed across countries, as the HPV infection prevalence varies considerably worldwide. Whereas at least one third of cases can be attributed to HPV-related carcinogenesis, there are no clear data linking penile cancer to HIV infection or AIDS.

In the USA, the overall age-adjusted incidence rate decreased between 1973 and 2002 from 0.84 per 100,000 in 1973–1982 to 0.69 per 100,000 in 1983–1992 and further declined to 0.58 per 100,000 in 1993–2002 [1, 2]. In European countries, the overall incidence has remained stable from the 1980s until today [5]. Recently, an increased incidence has been reported from Denmark [6] and the UK, where a longitudinal study has confirmed a 21% increase in incidence over the period 1979–2009 [7].

Risk Factors and Association with Other Conditions

The incidence of penile cancer increases with age [3] and have a peak during the sixth decade of life, although this disease can indeed occur in younger men [8].

Infection by the human papilloma virus is an important risk factor in the development of penile cancer. DNA of HPV has been identified in 70–100% of intraepithelial neoplasias and in 40–50% of invasive penile cancer tissue samples. The HPV virus plays an important role in oncogenesis through the interaction with oncogenes and tumor suppressor genes (p53, Rb genes) [9, 10]. The rate of HPV positive differs between different histological subtypes of penile cancer. This suggests that HPV is a cofactor in the carcinogenesis of some variants of penile SCC, while other variants of penile cancer are not related to HPV [2]. HPV subtypes most commonly found associated with penile cancer are types 16 and 18 [11]. The risk of penile cancer is also increased in patients with *condyloma acuminata* [12]. It is not clear whether HPV-associated penile cancer differs in prognosis from non-HPV-associated penile cancer. A significantly better 5-year disease-specific survival has been reported for HPV-positive versus HPV-negative cases (93% vs. 78%) in one study [13], while no difference in lymph node metastases and 10-year survival rate was reported in another study [14].

No direct association between the incidence of penile cancer and that of cervical cancer has been established yet, except the coexistent link with the prevalence of HPV infections [2, 15, 16]. In particular, female sexual partners of patients with penile cancer do not have an increased incidence of cervical cancer.

Other known risk factors for penile carcinoma include conditions such as phimosis, chronic inflammations leading to balanoposthitis and *lichen sclerosus et atrophicus*, sexual history (multiple partners, early age at first intercourse), history of condylomata, and smoking [9–17].

Around 25–60% of phimosis patients develop penile cancer at some stage of their lives [18]. The phimosis causes retention of desquamated epidermal cells and urinary products, collectively called "smegma," which leads to chronic inflammation of prepuce and glans penis causing balanitis. Sexual promiscuity which plays a major role in sexually transmitted diseases also poses increased risk of developing penile cancers.

Some, but not all, observational studies also suggest that male newborn circumcision is associated with a decreased risk of penile cancer [19, 20]. According to one study, the risk among

uncircumcised men was found to be 3.2 times higher [21], while according to another published data, if the relationship is causal, the number needed to treat is about 909 circumcisions to prevent a single case of invasive penile cancer [22]. In addition, the treatment of psoriasis by ultraviolet light in the region was also found to increase significantly the risk of cancer development [23].

Prevention

Circumcision is a precautionary measure taken by a few healthy adult subpopulations, although no published literature has shown clear advantage in adult circumcision. Similarly, smegma is blamed to be a strong risk factor, but again without any definite correlation having been published so far. Practicing better hygiene, however, has shown to decrease the risk of chronic recurrent inflammation, which is in some situations a precursor of squamous cell carcinoma (SCC).

Raising the awareness regarding sexual health and protective sex can also be considered an effective preventive measure to both privileged and poor socioeconomic countries.

There is at present no recommendation for the use of HPV vaccination in boys due to a different HPV-associated risk pattern in penile and anal cancer; furthermore, the epidemiological effects of HPV vaccination and its acceptance in girls will have to be assessed before any further recommendations can be made [24, 25]. The newer available vaccines against HPV 16 and 18 have shown to be effective with protection for around 5 years; however, their true efficacy in the long term has not yet been established [26].

Due to high rates of developing SCC of the genitalia after psoralen plus ultraviolet light A (PUVA) therapy, genitalia shielding and serial checkups should be in place [27].

Genetic Predisposition

To date no genetic predisposition to penile cancers has been identified.

Underlying Molecular Biological Changes

So far only few datasets are available linking chromosomal abnormalities in penile SCC (the predominant histological type of penile cancer) to biological pattern and patient outcomes [2, 10]. The alterations in DNA copy number found in penile carcinoma are comparable to those found in SCC of other origins. Lower copy numbers and alteration numbers in penile SCC have been linked to poorer survival. Alterations in the locus 8q24 seem to play a major role and have also been assumed to be involved in the carcinogenesis of other neoplasms such as prostate cancer [28, 29]. Telomerase activity has been demonstrated in invasive penile carcinoma [30]. It has also been reported that aneuploidy changes according to tumor grade [31].

Epigenetic alterations evaluating the methylation pattern of CpG islands in *CDKN2A* have been described as well [32]. *CDKN2A* encodes for two tumor suppressor proteins (p16INK4A and p14ARF) that control cell growth through the Rb and p53 pathways. Poetsch at al. showed that 62% of invasive SCCs of the penis displayed allelic loss of p16 and 42% promoter hypermethylation. Tumors immunohistochemically negative for p16 showed hypermethylation of and/or copy number neutral loss of heterozygosity (LOH) near the p16INK4A locus; furthermore, p16 negativity was linked to greater probability of lymph node metastasis and to poor prognosis [33]. Allelic loss of the p53 gene is a frequent event in penile SCC (42%) and has been linked to poor prognosis [34]. Another factor influencing lymph node metastasis is the metastasis-suppressor protein KAI1/CD82; in particular, decreased expression of this protein favors lymph node metastasis [35].

Staging and Prognostic Stratification

The TNM classification of penile cancer is shown in Tables 1 and 2. Ultrasound (US) is useful in evaluating suspected penile masses and has been advised for primary penile cancer deemed to invade the corpora cavernosa [36]; SCC usually

Table 1 AJCC TNM classification of penile cancer

Definitions of TNM	
Primary tumor (T)	
TX	Primary tumor cannot be assessed
T0	No evidence of primary tumor
Tis	Carcinoma in situ
Ta	Noninvasive verrucous carcinoma[a]
T1a	Tumor invades subepithelial connective tissue without lymph-vascular invasion and is not poorly differentiated (i.e., grades 3–4)
T1b	Tumor invades subepithelial connective tissue with lymph-vascular invasion or is poorly differentiated
T2	Tumor invades corpus spongiosum or cavernosum
T3	Tumor invades urethra
T4	Tumor invades other adjacent structures
Regional lymph nodes (N)	
Clinical stage definition[b]	
cNX	Regional lymph nodes cannot be assessed
cN0	No palpable or visibly enlarged inguinal lymph nodes
cN1	Palpable mobile unilateral inguinal lymph node
cN2	Palpable mobile multiple or bilateral inguinal lymph nodes
cN3	Palpable fixed inguinal nodal mass or pelvic lymphadenopathy unilateral or bilateral
Pathologic stage definition[c]	
pNX	Regional lymph nodes cannot be assessed
pN0	No regional lymph node metastasis
pN1	Metastasis in a single inguinal lymph node
pN2	Metastasis in multiple or bilateral inguinal lymph nodes
pN3	Extranodal extension of lymph node metastasis or pelvic lymph node(s) unilateral or bilateral
Distant metastasis (M)	
M0	No distant metastasis
M1	Distant metastasis[d]
Histopathological grading	
GX	Grade of differentiation cannot be assessed
G1	Well differentiated
G2	Moderately differentiated
G3-4	Poorly differentiated/undifferentiated

Used with the permission of the American Joint Committee on Cancer (AJCC), Chicago, Illinois. The original source for this material is the AJCC Cancer Staging Manual, Eighth Edition (2014) published by Springer Science and Business Media LLC. www.springer.com

[a]Broad pushing penetration (invasion) is permitted; destructive invasion is against this diagnosis

[b]Clinical stage definition based on palpation and imaging

[c]Pathologic stage definition based on biopsy or surgical excision

[d]Lymph node metastasis outside of the true pelvis in addition to visceral or bone sites

presents as a hypoechoic lesion with heterogeneous appearance. However, US evaluation is unreliable in the presence of microscopic invasion. On MR imaging, penile carcinoma is often a solitary, ill-defined mass infiltrating the adjacent corpora, hypo-intense on both T1- and T2-weighted images [37]. The local extent, the depth of tumor invasion, and the extension to adjacent structures can be accurately depicted using MRI, and this information is valuable for surgical planning [38].

Both clinical examination and conventional imaging techniques, including US, CT, and MRI, are unreliable in accurately detecting lymph node metastases [36]. Hence, prophylactic inguinal lymphadenectomy is often recommended, particularly in high-risk patients, with the expectation to improve survival. However, the morbidity of groin dissection is high, with complication rates between 30% and 50%, thus stimulating interest in the search for other techniques able to noninvasively assess the lymph node status and possibly reduce the need for groin dissection [39].

Grading

Tumor grade has been included into the penile cancer TNM classification because of its prognostic relevance. However, tumor grading of penile cancer according to Broder's classification has been shown to be highly observer dependent and is therefore no longer used, similarly as has occurred for the WHO grading system [40]. The currently recommended grading according to the pTNM system is reported in Table 1.

Pathologic Prognostic Factors

More than 95% of penile malignancies are of the SCC type (see Fig. 1). SCC displays multiple subtypes with different prognostic features. Other

Table 2 AJCC anatomic stages and prognostic groups for penile cancer

Group	T category	N category	M category
Stage 0	Tis	N0	M0
	Ta	N0	M0
Stage I	T1a	N0	M0
Stage II	T1b	N0	M0
	T2	N0	M0
	T3	N0	M0
Stage IIIa	T1–3	N1	M0
Stage IIIb	T1–3	N2	M0
Stage IV	T4	Any N	M0
	Any T	N3	M0
	Any T	Any N	M1

Used with the permission of the American Joint Committee on Cancer (AJCC), Chicago, IL. The original source for this material is the AJCC Cancer Staging Manual, Eighth Edition (2014) published by Springer Science and Business Media LLC. www.springer.com

histologic types include basal cell carcinoma, melanoma, and sarcoma. The glans penis is the most common site of SCC (48%) [41].

Lymphatic Involvement

Penile carcinoma usually spreads through penile lymphatic channels to regional lymph nodes, especially the superficial and deep inguinal nodes, and subsequently to the iliac nodes. Presence and degree of lymph node involvement is the most important prognostic factor for penile carcinoma. The prevalence of nodal disease is related to the stage of the primary lesion and occurs in 20% of T1 penile cancers and in 47–66% of T2–T4 tumors [42, 43]. Between 30% and 60% of patients with penile carcinoma have palpable inguinal nodes, but nearly half of these are linked to inflammatory reaction [44]. Some tumors metastasize directly to deep inguinal nodes.

Basaloid tumors are poorly differentiated subtypes of SCC, are infiltrative, and frequently metastasize to inguinal lymph nodes. The prognosis for survival in patients with lymph node metastases is closely correlated with the number and location of involved lymph nodes and with the presence of extranodal extension [9, 45]. Involvement of deep

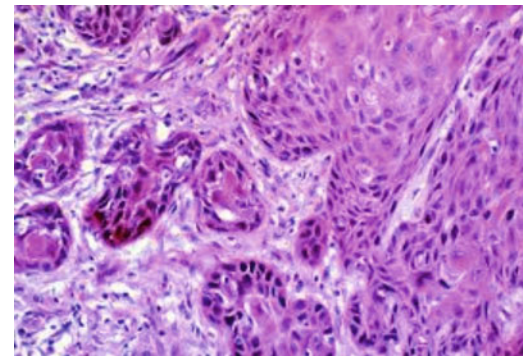

Fig. 1 Penile cancer: typical histopathologic pattern of a squamous cell cancer (also called "spinocellular" cancer) of the penis. Hematoxylin and eosin staining; original magnification approximately 250×

inguinal nodes is more ominous than involvement of superficial inguinal nodes. The 5-year overall and disease-free survival rates are as high as 80% for unilateral, superficial inguinal lymph node involvement with no more than one node (N1), only 10–20% for bilateral or pelvic lymph nodes involved (N2/N3), and less than 10% in the presence of extranodal extension [9, 41].

Hungerhuber et al. recommend prophylactic lymphadenectomy for high-risk patients [46]. Chaux et al. proposed a "prognostic index" based on findings in 193 patients; this index incorporates several pathological parameters (such as grade, deepest anatomical level, perineural invasion) and permits scoring in a ranking system that can be used to predict the likelihood of inguinal lymph node metastases and the likelihood of 5-year survival [47]. Low scores confer a 95% chance of 5-year survival, intermediate scores a 65%, and high scores a 45% likelihood of 5-year survival.

Widespread dissemination occurs in 20–40% of the patients; distant metastases occur most frequently in the lung, liver, and skeleton. Histopathologic features affecting patients' outcome are multiple. Poorer prognosis is related to histological grade, patterns of growth, perineural and vascular invasion, corpus cavernosum invasion, and histological subtype of SCC [41]. For example, verrucous carcinomas are well differentiated, have an expansile border, and are essentially nonmetastatic.

Performance of Diagnostic Imaging Other Than Nuclear Medicine

While penile cancer can be cured in over 80% of all cases, it is a life-threatening disease with poor prognosis once metastatic spread has occurred. Furthermore, local treatment, although potentially lifesaving, can be mutilating and devastating for the psychological well-being of the patient. Therefore, the treatment of patients with penile cancer requires a careful diagnosis and adequate staging before treatment decisions can be made [2].

Primary Lesion

Penile carcinoma is often a clinically obvious lesion, but can be hidden under a phimosis. Physical examination of a patient with penile cancer should include palpation of the penis with a view to examining the extent of local invasion.

Ultrasound can give information about infiltration of the corpora [48, 49]. Magnetic resonance imaging (MRI) in combination with an artificial erection induced by prostaglandin E1 can also be used for excluding tumor invasion of the corpora cavernosa if organ preservation is planned and preoperative decisions are needed [37, 50].

Regional Lymph Nodes

Careful palpation of both groins for the detection of enlarged inguinal lymph nodes must be part of the initial physical examination of patients with penile cancer.

- *Palpable inguinal nodes*

  Palpable lymph nodes are highly suspicious for the presence of lymph node metastases. Physical examination should note the number of palpable nodes on each side and whether these are fixed or mobile. Additional inguinal imaging does not alter management and is usually not required. A pelvic CT scan can be performed in order to assess the pelvic lymph nodes.

- *Non-palpable inguinal nodes*

  The management of clinically node-positive groin in penile cancer is clear-cut with radical inguinal lymph node dissection being the surgical option. It is known that lymph node metastases have an inverse prognostic outcome for these patients. In clinically node-negative groin with occult metastases, the dilemma remains whether to perform lymphadenectomy (with the associated risk of high morbidity) or to continue close observations. In the absence of palpable abnormalities, the likelihood of the presence of micrometastatic disease is about 25%. However, current imaging techniques are not reliable in detecting micrometastases. Inguinal ultrasound (7.5 MHz) can reveal abnormal lymph nodes with some enlargement. The longitudinal/transverse diameter ratio and the absence of the lymph node hilum have been reported to be relatively specific for lymph node metastasis [51]. Conventional CT or MRI scans similarly cannot detect micrometastases reliably [38]. Imaging studies are therefore not helpful in staging clinically normal inguinal regions. An exception can be represented by obese patients, in whom palpation is unreliable or not possible. The further diagnostic management of patients with normal inguinal nodes should be guided by pathological risk factors. Several series have identified lymph-vascular invasion, local stage, and grade as risk factors predicting the likelihood of lymphatic metastasis [52, 53]. Nomograms are unreliable as they cannot achieve an over 80% accuracy. Invasive lymph node staging is required in patients at intermediate or high risk of lymphatic spread.

Distant Metastases

An assessment of distant metastases should be performed in patients with positive inguinal nodes [44, 54, 55]. Computed tomography of the abdomen and pelvis and a chest X-ray are recommended, although thoracic CT will be more sensitive than a plain chest X-ray, and in symptomatic M1 patients a bone scan is also advisable,

as per guidelines of the European Association of Urology (EAU) [2, 56].

There is no established tumor marker for penile cancer. The squamous cell carcinoma antigen (SCC Ag) is increased in less than 25% of penile cancer patients. In one study, SCC Ag was not a predictor for occult metastatic disease, but it was a prognostic indicator of disease-free survival in lymph node-positive patients [57].

Performance of Nuclear Imaging for Staging and Prognosis

Due to its low incidence, penile cancer is best managed at specialized centers. Imaging with CT or MRI can neither accurately detect occult metastases nor predict on tumor characteristics reliably. Lymphoscintigraphy to visualize lymphatic drainage, especially its early dynamic sequence to look for sentinel lymph node(s) (the first node in a given lymphatic pathway from the primary tumor), has been a standard technique for over a decade [58, 59]. This imaging procedure (the preliminary phase of sentinel lymph node biopsy) is recommended for patients without palpable inguinal lymph nodes by the latest guidelines both of the EAU [2] and of the National Cancer Comprehensive Network (Version 1.2014, at www.nccn/guideline/urological/english/penile.pdf, last accessed March 5, 2016). However, it has not yet been sufficiently utilized in Europe or the USA in patients with penile cancers to identify non-palpable metastasis, despite the well-known notion that only 20–25% of clinically negative inguinal nodes harbor metastatic disease [60]. Nevertheless, sentinel lymph node biopsy (SLNB) as a diagnostic procedure in patients with malignancies, especially SCC, has proven to be of tremendous advantage for the detection of subclinical lymph node metastases [61, 62]. The technique of SLNB with the primary penile tumor has become standardized for the identification of a patient population with subclinical or clinically negative groin (see Fig. 2); when metastasis is found in sentinel

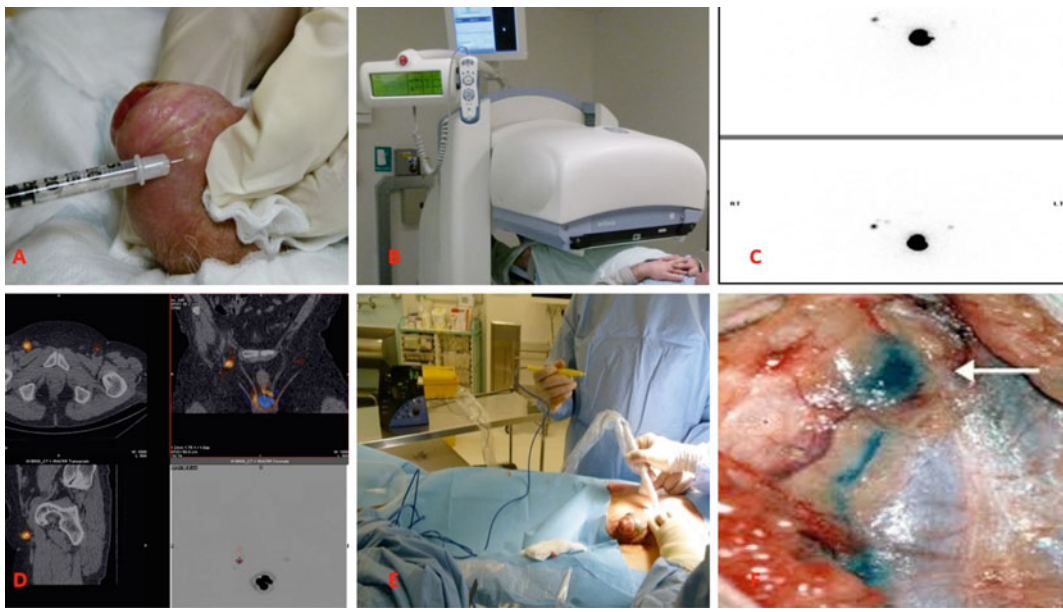

Fig. 2 Pictorial sequence of sentinel lymph node biopsy in penile cancer. (**a**) Interstitial injection of the radiocolloid (^{99m}Tc-nanocolloidal albumin) proximally to the primary tumor. (**b**) Imaging with dual-head gamma camera imaging. (**c**) Planar imaging: early (*top*) and delayed (*bottom*), showing lymphatic drainage to both right and left inguinal lymph nodes. (**d**) Fused SPECT/CT images in the three axial planes (maximum intensity projection image in the *bottom right panel*). (**e**) Intraoperative localization of sentinel lymph node(s) with the gamma probe (after *blue dye* injection). (**f**) Probe-positive sentinel node localized (*white arrow*) demonstrating in-transit *blue dye*

lymph node(s), then elective lymph node dissection is currently recommended [63, 64]. Recent data indicate that correct application of this treatment algorithm can confer an effective survival benefit to patients with penile SCC [65].

Staging

Early detection plays a vital role in disease control, and appropriate diagnostic modalities must be used in order to accurately identify the cancer and its progression. The use of imaging in combination with biopsy is an effective mean in determining disease stage and grade [26]. One of the most important factors that affect the outlook for people with penile cancer is whether nearby lymph nodes contain cancer cells or not.

The management of the regional lymph nodes is of critical importance to both quantity and quality of life for these patients. Importance of inguinal and pelvic nodes cannot be overlooked in this uncommon malignancy, and the final management of penile cancer relies on the timely and appropriate management of the inguinal and pelvic lymph nodes. In fact, the presence and extent of metastatic disease in the inguinal lymph nodes is the single most important prognostic indicator in patients with penile cancer. In particular, the 5-year survival rate is approximately 95% when no metastasis is present in inguinal lymph nodes, while it is 80% when metastatic disease is limited to a single inguinal lymph node, and it drops to 40% if there are two or more metastatic inguinal lymph nodes; in addition, the 5-year survival rate is virtually 0% when metastatic disease at diagnosis involves pelvic lymph nodes [66].

Penile lymphatic drainage follows a well-validated pattern, draining to superficial inguinal nodes (above the fascia lata) and to deep inguinal nodes surrounding the saphenofemoral junction. After these two basins/regions, it flows to pelvic nodes following the ipsilateral iliac and obturator vessels. The pattern of lymphatic drainage can be accurately depicted by lymphoscintigraphy following interstitial injection of a suitable radiopharmaceutical (typically a ^{99m}Tc-labeled colloid) around the tumor. This imaging procedure constitutes an essential component of radioguided biopsy of the sentinel lymph node (SLN). Seminal work with SLN biopsy was originally described by Cabañas in the late 1970s [67]; nevertheless, his pioneering intuition of the clinical relevance of the SLN tumor status was based on the incorrect assumption of a fixed anatomic location of the SLN, a concept that was later corrected after lymphoscintigraphic demonstration of a certain degree of variability in lymphatic drainage patterns from the penis and following the currently accepted definition of the SLN as the first lymph node encountered on a direct drainage pathway from the primary tumor [68, 69]. In this regard, there can be more than one single pathway of direct lymphatic drainage from the penis. In fact, both *unilateral* (Fig. 3) and *bilateral* drainage patterns are recognized and could be either a physiological variant, secondary to previous inguinal surgeries, or could be due to extensive metastatic infiltration (a recent concept) [70]. The advanced hybrid SPECT/CT systems are at present gaining popularity in clinical practice. The value of lymphoscintigraphy can be greatly enhanced by performing a tomographic acquisition 2 h post-injection and by correlating scintigraphic findings to regional morphology assessed with CT; with this combined approach, the sensitivity of SPECT may be as high as 95% [38, 70].

The eventual survival criteria in patients presenting with penile cancer rests with the detection and complete resection of nodal metastases. This resection can be curative even in advanced disease, but carries with it a significant burden of morbidity that has led the thrust to develop protocols and techniques to maximize detection and minimize morbidity and unnecessary surgery.

The sensitivity of sentinel lymph node (SLN) biopsy in patients with penile cancer with non-palpable lymph nodes ranges between 70% and 86% [71, 72]. In patients with clinically palpable nodes, SLN biopsy is less useful due to the possibility of false-negative results as a result of massive invasion of lymphatic pathways by cancer cells.

PET/CT with [^{18}F]FDG has also been used for initial staging of penile cancer [73–75]. In a systematic review and meta-analysis of the literature,

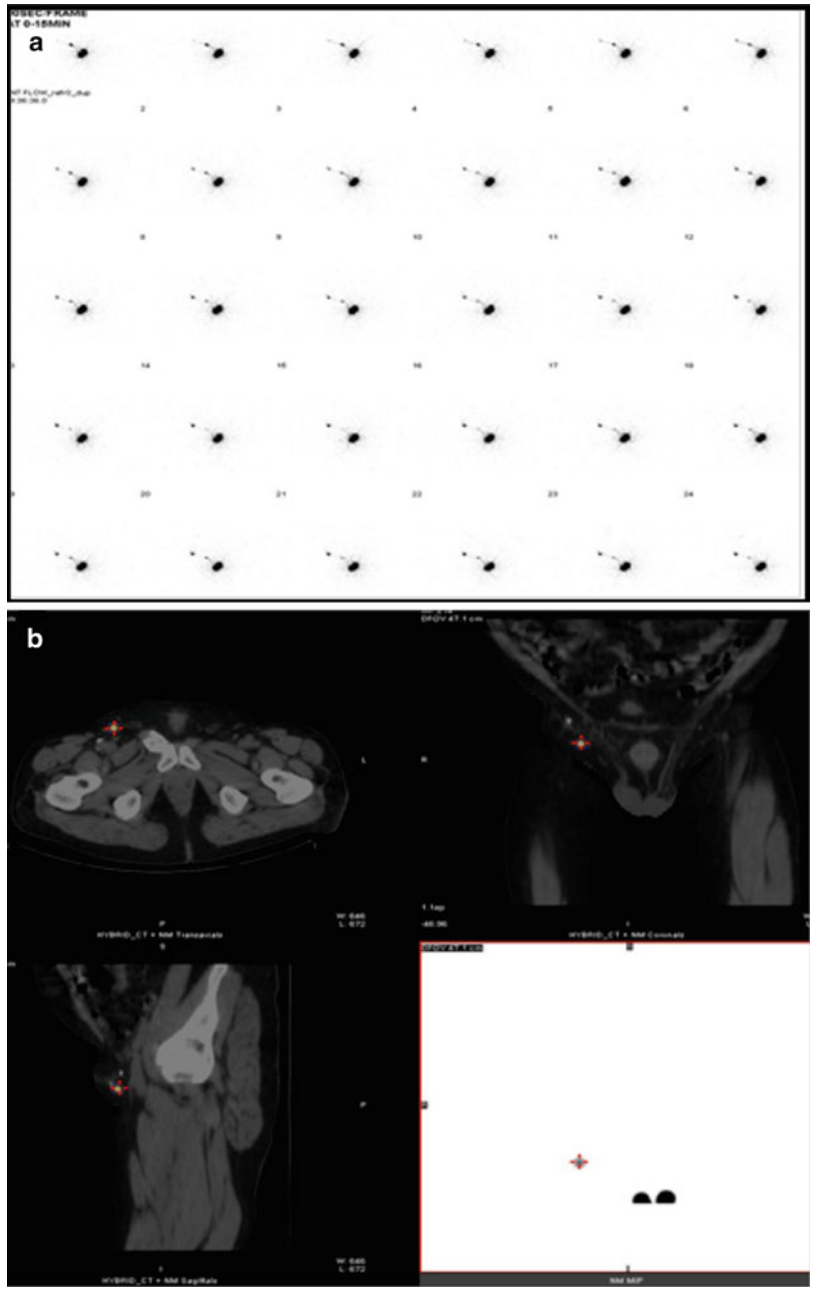

Fig. 3 Dynamic sentinel lymph node biopsy following intradermal peritumoral injection of ^{99m}Tc-nanocolloidal albumin in a patient with penile cancer. (**a**) Dynamic acquisition for approximately 15 min, showing unilateral lymphatic drainage to the right groin. (**b**) Fused SPECT/CT images in the axial, coronal, and sagittal planes (*upper left*, *upper right*, and *lower left* images, respectively), confirming visualization of a single lymph node in the right groin

overall pooled sensitivity and specificity of [^{18}F]FDG PET/CT were 80.9% (95% CI: 69.589.4%) and 92.4% (95% CI: 86.8–96.2%), respectively. However, sensitivity for clinically negative patients was only 56.5% (95% CI: 34.5–76.8%), considerably lower than in patients with palpable inguinal lymph nodes (96.4%, with 95% CI 81.7–99.9%) [76]. The authors concluded therefore that the routine use of [^{18}F]FDG PET/CT is not justified in patients without palpable inguinal lymph nodes, while patients with palpable lymph nodes may benefit from this imaging procedure. Nevertheless, [^{18}F]FDG PET/CT can occasionally be useful to evaluate also sub-centimeter lymph

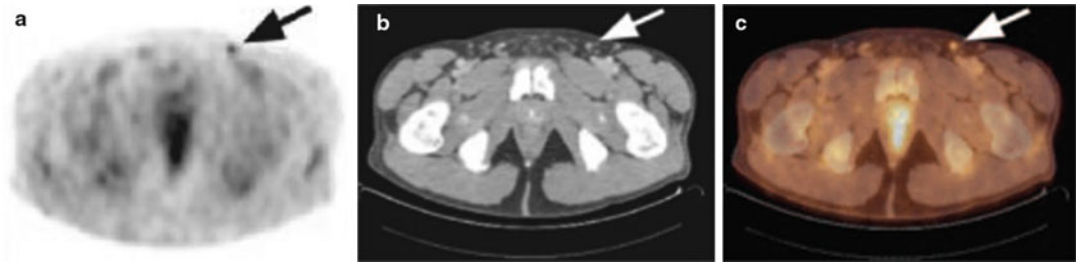

Fig. 4 [^{18}F]FDG PET/CT in a 61-year-old patient with newly diagnosed penile SCC (T2; G3) with clinically negative inguinal lymph nodes. Axial sections at the level of the groin: (**a**) PET component; (**b**) CT component; (**c**) fused PET/CT image. Despite the small size (maximum diameter was 8 mm by CT estimate), metastasis in a left inguinal lymph node showed distinct focal [^{18}F]FDG uptake (*arrows*) (Reprinted with permission of the Society of Nuclear Medicine)

nodes that would be deemed as negative both clinically and on morphological imaging alone (Fig. 4). A more recent study has explored the diagnostic performance of combined [^{18}F]FDG PET/CT and sentinel lymph node biopsy in a group of 129 patients, showing a combined sensitivity of 94.4% (95% CI: 81–99%) and a false-negative rate as low as 5.6% (95% CI: 1–11.9%) [77].

Since distant metastasis is detected in 20% of the patients with cytological positive inguinal disease, routine use of [^{18}F]FDG PET/CT at initial staging has been advocated for patients with positive lymph nodes (see Fig. 5), as integration of PET/CT scanning into preoperative staging algorithms may avoid surgical staging in selected patients [74, 76]. Since bone metastases are rare, bone scintigraphy is not yet commonly used in newly diagnosed penile SCC.

Follow-Up and Restaging

Most relapses are seen during the first 2 years after primary treatment, while late recurrences are uncommon [41]. Conservative treatment and surveillance are recommended for pN0 disease, at 2–4 month intervals in the first 2 years, 3–6 months in the third year, and 6–12 months thereafter. Follow-up is based mainly on clinical evaluation, while radionuclide imaging techniques have rarely been used for restaging purposes during regular follow-up. Whereas it has been shown that [^{18}F]FDG PET may be used for assessing the metabolic response to induction chemotherapy in patients with positive inguinal lymph nodes, in fact, changes in glucose metabolism preceded morphological changes, thus indicating that functional assessment is more sensitive than morphological assessment. However, the implications of such findings on long-term survival are still unknown [52].

Treatment Options for Penile Cancer

The primary tumor and regional lymph nodes are usually treated separately [78]. The front-line treatment for managing the primary lesion remains surgical; however, the options are corresponding to the stage and grade of the disease. The gold standard remains partial or total penectomy with local control rates of above 90%, but carries very high psychosexual morbidity [79]. In the light of the new EAU guidelines, margins of up to 1–2 cm are enough to provide the same control rates [2].

- *Treatment option for carcinoma in situ*
  It ranges from topical use of 5% 5-fluorouracil cream for 6 weeks, laser, circumcision, resurfacing glans penis to total glansectomy in case of urethral involvement [79].
- *Treatment options for T1*
  This group requires careful selection of patients and close surveillance as it involves wide local excision with primary closure or split skin graft (depending on the size of lesion) in case where there is no urethral involvement and complete amputation for recurrences [80].

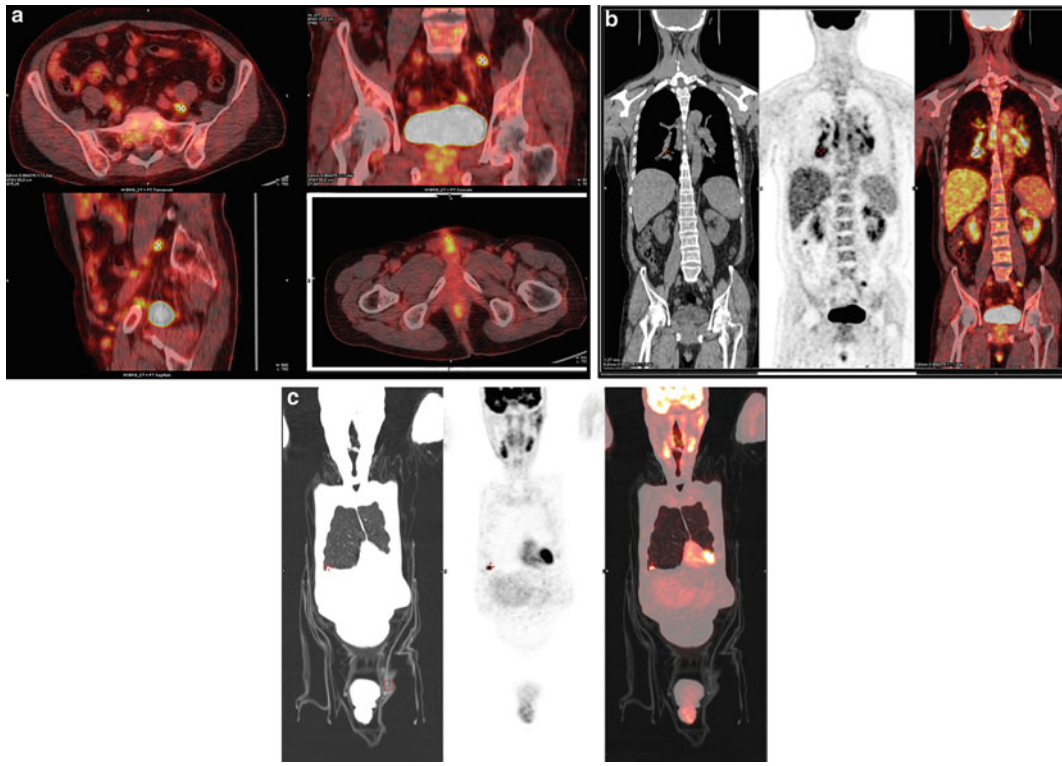

Fig. 5 Fused images obtained at various plane levels after i.v. injection of [^{18}F]FDG and PET/CT performed for staging purposes in a 48-year-old patient with newly diagnosed penile carcinoma. (**a**) Besides increased metabolic activity at the primary tumor site (axial section shown in *lower right panel*), this patient had clinically silent metastatic disease in left common iliac lymph nodes (axial section shown in *upper left panel*, coronal section in *upper right panel*, and sagittal section in *lower left panel*). (**b**) Coronal sections of the CT component (*left panel*), of the PET component (*center panel*), and corresponding fused PET/CT image (*right panel*) demonstrating metastatic disease in mediastinal and para-hilar lymph nodes (bilaterally). (**c**) Coronal sections of the CT component (*left panel*), of the PET component (*center panel*), and corresponding fused PET/CT image (*right panel*) demonstrating a pulmonary metastasis in the right anterior costophrenic space

- *Treatment options for T2*

  According to the new TNM stage classification, the previous two T2 stages (T2a, involvement of corpus spongiosum, and T2b, involvement of corpus cavernosa) have been amalgamated into one stage, which is T2. T2 has higher lymph node metastases, and if corpus cavernosa is involved, then conservative surgery is not an option. Therefore, in most cases partial penectomy is carried out unless the tumor has proximal extension warranting total penectomy with phalloplasty.
- *Radiotherapy*

  Radiotherapy either by conventional external beam therapy or brachytherapy is commonly indicated for patients with tumors of less than 4 cm in size. Due to their high rate of complications and morbidity secondary to urethral stenosis, fibrosis, or even penile necrosis leading to amputation, the EAU guidelines restricted its use for T1–T2 tumors of glans penis or penile sulcus and for palliative use in advanced metastatic disease [56, 80].
- *Chemotherapy*

  Chemotherapeutic regimens such as combination of bleomycin, methotrexate, and cisplatin have played positive role when used as neoadjuvant therapy. A new agent, cetuximab, has shown its promise in head and neck SCC, and due to close cross resemblance of SCC

prevalent in penis, anal canal, and vulva, the efficacy of this agent is presumed to be high [81].

Since tumors are often localized in the penis at the time of diagnosis, they can be treated either by local excision or circumcision, laser ablation, brachytherapy, external radiation, or partial penectomy. Preservation of the penis is a concern for most patients, but more proximal or advanced lesions require total penectomy. With adequate treatment of the primary tumor, however, the rate of local recurrence is very low [82].

The management of inguinal metastasis is crucial, as distant metastases are rare in the absence of inguinal metastases. The standard recommendation for patients with palpable lymph nodes is bilateral inguinal lymphadenectomy. Inguinal lymphadenectomy, however, is associated with high morbidity, including severe lymphedema, wound infection, etc. The decision to opt either for imaging coupled with minimally invasive sentinel lymph node sampling or to predict nodal disease on the basis of primary tumor characteristics and pathology imposes significant challenge.

In patients with non-palpable lymph nodes, decision-making is based on risk stratification and recommendations that vary between surveillance, SLN biopsy, and radical inguinal lymph node dissection. Patients with high risk of distant disease are treated using a multimodality approach. Possible strategies in this setting include neoadjuvant chemotherapy followed by surgery (penectomy and bilateral groin dissection), or chemoradiotherapy, either cytoreductive or adjuvant.

In case of inoperable advanced penile cancer with distant metastasis, [^{18}F]FDG PET/CT has been employed to monitor the efficacy of induction chemotherapy, by performing the scan at baseline, then after two cycles of therapy [83]; although a relatively small group of patients was studied, the [^{18}F]FDG PET/CT findings were compared with CT data and with histopathological analysis. The preliminary results so obtained suggest that the metabolic tumor response is more reliable than morphologic imaging with CT to monitor the efficacy of induction chemotherapy in patients with penile cancer.

References

1. Backes DM, Kurman RJ, Pimenta JM, et al. Systematic review of human papillomavirus prevalence in invasive penile cancer. Cancer Causes Control. 2009;20:449–57.
2. Hakenberg OW, Comperat E, Minhas S, et al. Guidelines on penile cancer. European Association of Urology 2014. https://uroweb.org/guidelines/. Last accessed 5 Mar 2016.
3. Parkin DM, Whelan SL, Ferlay J, et al. Cancer incidence in five continents, IARC scientific publications. No. 155, vol. VIII. Lyon: IARC; 2002.
4. Parkin DM, Bray F. The burden of HPV-related cancers. Vaccine. 2006;24 Suppl 3:S3/11–25.
5. Chaux A, Netto GJ, Rodríguez IM, et al. Epidemiologic profile, sexual history, pathologic features, and human papillomavirus status of 103 patients with penile carcinoma. World J Urol. 2013;31:861–7.
6. Baldur-Felskov B, Hannibal CG, Munk C, et al. Increased incidence of penile cancer and high-grade penile intraepithelial neoplasia in Denmark 1978–2008: a nationwide population-based study. Cancer Causes Control. 2012;23:273–80.
7. Arya M, Li R, Pegler K, et al. Long-term trends in incidence, survival and mortality of primary penile cancer in England. Cancer Causes Control. 2013;24:2169–76.
8. Barnholtz-Sloan JS, Maldonado JL, Pow-sang J, et al. Incidence trends in primary malignant penile cancer. Urol Oncol. 2007;25:361–7.
9. Bleeker MC, Heideman DA, Snijders PJ, Horenblas S, Dillner J, Meijer CJ. Penile cancer: epidemiology, pathogenesis and prevention. World J Urol. 2009;27:141–50.
10. Kayes O, Ahmed HU, Arya M, et al. Molecular and genetic pathways in penile cancer. Lancet Oncol. 2007;8:420–9.
11. Muñoz N, Castelisague X, de Gonzalez AB, et al. HPV in the etiology of human cancer. Vaccine. 2006;24 Suppl 3:S3/1–10.
12. Nordenvall C, Chang ET, Adami HO, et al. Cancer risk among patients with condylomata acuminata. Int J Cancer. 2006;119:888–93.
13. Lont AP, Kroon BK, Horenblas S, et al. Presence of high risk human papillomavirus DNA in penile carcinoma predicts favorable outcome in survival. Int J Cancer. 2006;119:1078–81.
14. Bezerra AL, Lopes A, Santiago GH, et al. Human papillomavirus as a prognostic factor in carcinoma of the penis: analysis of 82 patients treated with amputation and bilateral lymphadenectomy. Cancer. 2001;91:5–21.
15. Philippou P, Shabbir M, Ralph DJ, et al. Genital lichen sclerosus/balanitis xerotica obliterans in men with penile carcinoma: a critical analysis. BJU Int. 2013;111:970–6.
16. D'Hauwers KW, Depuydt CE, Bogers JJ, et al. Human papillomavirus, lichen sclerosus and penile cancer: a study in Belgium. Vaccine. 2012;30:6573–7.

17. Dillner J, von Krogh G, Horenblas S, Meijer CJ. Etiology of squamous cell carcinoma of the penis. Scand J Urol Nephrol Suppl. 2000;34:89–93.
18. Pow-Sang MR, Ferreira U, Pow-Sang JM, Nardi AC, Destefano V. Epidemiology and natural history of penile cancer. Urology. 2010;76(2 Suppl 1):S2–6.
19. Schoen EJ, Oehrli M, Colby C, et al. The highly protective effect of newborn circumcision against invasive penile cancer. Pediatrics. 2000;105:E36.
20. Fetus and Newborn Committee, Canadian Paediatric Society. Neonatal circumcision revisited. CMAJ. 1996; 154:769–80.
21. Maden C, Sherman KJ, Beckmann AM, et al. History of circumcision, medical conditions, and sexual activity and risk of penile cancer. J Natl Cancer Inst. 1993; 85:19–24.
22. Christakis DA, Harvey E, Zerr DM, et al. A trade-off analysis of routine newborn circumcision. Pediatrics. 2000;105(1 Pt 3):246–9.
23. Stern RS. Genital tumors among men with psoriasis exposed to psoralens and ultraviolet A radiation (PUVA) and ultraviolet B radiation. The photochemotherapy follow-up study. N Engl J Med. 1990; 322:1093–7.
24. Newman PA, Logie CH, Doukas N, et al. HPV vaccine acceptability among men: a systematic review and meta-analysis. Sex Transm Infect. 2013;89:568–74.
25. Fisher H, Trotter CL, Audrey S, et al. Inequalities in the uptake of human papillomavirus vaccination: a systematic review and meta-analysis. Int J Epidemiol. 2013; 42:896–908.
26. Lawindy SM, Rodriguez AR, Horenblas S, Spiess PE. Current and future strategies in the diagnosis and management of penile cancer. Adv Urol. 2011;2011: 593751.
27. Minhas S, Manseck A, Watya S, Hegarty PK. Penile cancer – prevention and premalignant conditions. Urology. 2010;76(2 Suppl 1):S24–35.
28. Fromont G, Godet J, Peyret A, et al. 8q24 amplification is associated with Myc expression and prostate cancer progression and is an independent predictor of recurrence after radical prostatectomy. Hum Pathol. 2013; 44:1617–23.
29. Alves G, Heller A, Fiedler W, et al. Genetic imbalances in 26 cases of penile squamous cell carcinoma. Genes Chromosom Cancer. 2001;31:48–53.
30. Alves G, Fiedler W, Guenther E, et al. Determination of telomerase activity in squamous cell carcinoma of the penis. Int J Oncol. 2001;18:67–70.
31. Kayes OJ, Loddo M, Patel N, et al. DNA replication licensing factors and aneuploidy are linked to tumor cell cycle state and clinical outcome in penile carcinoma. Clin Cancer Res. 2009;15:7335–44.
32. Gunia S, Erbersdobler A, Hakenberg OW, et al. p16 (INK4a) is a marker of good prognosis for primary invasive penile squamous cell carcinoma: a multiinstitutional study. J Urol. 2012;187:899–907.
33. Poetsch M, Hemmerich M, Kakies C, et al. Alterations in the tumor suppressor gene p16(INK4A) are associated with aggressive behavior of penile carcinomas. Virchows Arch. 2011;458:221–9.
34. Gunia S, Kakies C, Erbersdobler A, et al. Expression of p53, p21 and cyclin D1 in penile cancer: p53 predicts poor prognosis. J Clin Pathol. 2012;65:232–6.
35. Protzel C, Kakies C, Kleist B. et al J. Downregulation of the metastasis suppressor protein KAI1/CD82 correlates with occurrence of metastasis, prognosis and presence of HPV DNA in human penile squamous cell carcinoma. Virchows Arch. 2008;452:369–75.
36. Kochhar R, Taylor B, Sangar V. Imaging in primary penile cancer: current status and future directions. Eur Radiol. 2010;20:36–47.
37. Kayes O, Minhas S, Allen C, Hare C, Freeman A, Ralph D. The role of magnetic resonance imaging in the local staging of penile cancer. Eur Urol. 2007;51:1313–8.
38. Mueller-Lisse UG, Scher B, Scherr MK, Seitz M. Functional imaging in penile cancer: PET/computed tomography, MRI, and sentinel lymph node biopsy. Curr Opin Urol. 2008;18:105–10.
39. Spiess PE, Izawa JI, Bassett R, et al. Preoperative lymphoscintigraphy and dynamic sentinel node biopsy for staging penile cancer: results with pathological correlation. J Urol. 2007;177:2157–61.
40. Gunia S, Burger M, Hakenberg OW, et al. Inherent grading characteristics of individual pathologists contribute to clinically and prognostically relevant interobserver discordance concerning Broders' grading of penile squamous cell carcinomas. Urol Int. 2013;90:207–13.
41. Misra S, Chaturvedi A, Misra NC. Penile carcinoma: a challenge for the developing world. Lancet Oncol. 2004;5:240–7.
42. Hughes B, Leijte J, Shabbir M, Watkin N, Horenblas S. Noninvasive and minimally invasive staging of regional lymph nodes in penile cancer. World J Urol. 2009;27:197–203.
43. Hughes BE, Leijte JA, Kroon BK, et al. Lymph node metastasis in intermediate-risk penile squamous cell cancer: a two-centre experience. Eur Urol. 2010;57: 688–92.
44. Ornellas AA, Seixas AL, Marota A, Wisnescky A, Campos F, de Moraes JR. Surgical treatment of invasive squamous cell carcinoma of the penis: retrospective analysis of 350 cases. J Urol. 1994; 151:1244–9.
45. Pandey D, Mahajan V, Kannan RR. Prognostic factors in node-positive carcinoma of the penis. J Surg Oncol. 2006;93:133–8.
46. Hungerhuber E, Schlenker B, Karl A, et al. Risk stratification in penile carcinoma: 25-year experience with surgical inguinal lymph node staging. Urology. 2006; 68:621–5.
47. Chaux A, Caballero C, Soares F, et al. The prognostic index: a useful pathologic guide for prediction of nodal

metastases and survival in penile squamous cell carcinoma. Am J Surg Pathol. 2009;33:1049–57.
48. Bertolotto M, Serafini G, Dogliotti L, et al. Primary and secondary malignancies of the penis: ultrasound features. Abdom Imaging. 2005;30:108–12.
49. Lont AP, Besnard AP, Gallee MP, et al. A comparison of physical examination and imaging in determining the extent of primary penile carcinoma. BJU Int. 2003;91:493–5.
50. Petralia G, Villa G, Scardino E, et al. Local staging of penile cancer using magnetic resonance imaging with pharmacologically induced penile erection. Radiol Med. 2008;113:517–28.
51. Krishna RP, Sistla SC, Smile R, et al. Sonography: an underutilized diagnostic tool in the assessment of metastatic groin nodes. J Clin Ultrasound. 2008;36:212–7.
52. Graafland NM, Lam W, Leijte JA, et al. Prognostic factors for occult inguinal lymph node involvement in penile carcinoma and assessment of the high-risk EAU subgroup: a two-institution analysis of 342 clinically node-negative patients. Eur Urol. 2010;58:742–7.
53. Alkatout I, Naumann CM, Hedderich J, et al. Squamous cell carcinoma of the penis: predicting nodal metastases by histologic grade, pattern of invasion and clinical examination. Urol Oncol. 2011;29:774–81.
54. Horenblas S, van Tinteren H, Delemarre JF, et al. Squamous cell carcinoma of the penis. III. Treatment of regional lymph nodes. J Urol. 1993;149:492–7.
55. Zhu Y, Zhang SL, Ye DW, et al. Predicting pelvic lymph node metastases in penile cancer patients: a comparison of computed tomography, Cloquet's node, and disease burden of inguinal lymph nodes. Onkologie. 2008;31:37–41.
56. Pizzocaro G, Algaba F, Horenblas S, et al. EAU penile cancer guidelines 2009. Eur Urol. 2010;57:1002–12.
57. Zhu Y, Ye DW, Yao XD, et al. The value of squamous cell carcinoma antigen in the prognostic evaluation, treatment monitoring and followup of patients with penile cancer. J Urol. 2008;180:2019–23.
58. Leijte JAP, Kroon BK, Valdés Olmos RA, Nieweg OE, Horenblas S. Reliability and safety of current dynamic sentinel node biopsy for penile carcinoma. Eur Urol. 2007;52:170–7.
59. Hadway P, Smith Y, Corbishley C, Heenan S, Watkin NA. Evaluation of dynamic lymphoscintigraphy and sentinel lymph-node biopsy for detecting occult metastases in patients with penile squamous cell carcinoma. BJU Int. 2007;100:561–5.
60. Ficarra V, Zattoni F, Cunico SC, et al. Lymphatic and vascular embolizations are independent predictive variables of inguinal lymph node involvement in patients with squamous cell carcinoma of the penis: Gruppo Uro-Oncologico del Nord Est (Northeast Uro-Oncological Group) Penile Cancer data base data. Cancer. 2005;103:2507–16.
61. Saad Z, Buscombe J. Sentinel lymph node: established and new areas of use. Clin Transl Imaging. 2015;3:225–36.
62. Belhocine T, Pierard G, De Labrassinne M, Lahaye T, Rigo P. Staging of regional nodes in AJCC stage I and II melanoma: ^{18}FDG PET imaging versus sentinel node detection. Oncologist. 2002;7:271–8.
63. Protzel C, Alcaraz A, Horenblas S, Pizzocaro G, Zlotta A, Hakenberg OW. Lymphadenectomy in the surgical management of penile cancer. Eur Urol. 2009;55:1075–88.
64. Horenblas S. Sentinel lymph node biopsy in penile carcinoma. Semin Diagn Pathol. 2012;29:90–5.
65. Djajadiningrat RS, Graafland NM, van Werkhoven E, et al. Contemporary management of regional nodes in penile cancer – improvement of survival? J Urol. 2014;191:68–73.
66. Zhu Y, Ye D-W. Lymph node metastases and prognosis in penile cancer. Chin J Cancer Res. 2012;24:90–6.
67. Cabañas RM. An approach for the treatment of penile carcinoma. Cancer. 1977;39:456–66.
68. Ollila DW, Brennan MB, Giuliano AE. The role of intraoperative lymphatic mapping and sentinel lymphadenectomy in the management of patients with breast cancer. Adv Surg. 1999;32:349–64.
69. Nieweg OE, Tanis PJ, Kroon BBR. The definition of a sentinel node. Ann Surg Oncol. 2001;9:538–41.
70. Leijte JA, van der Ploeg IM, Valdés Olmos RA, Nieweg OE, Horenblas S. Visualization of tumor blockage and rerouting of lymphatic drainage in penile cancer patients by use of SPECT/CT. J Nucl Med. 2009;50:364–7.
71. Spiess PE, Hernandez MS, Pettaway CA. Contemporary inguinal lymph node dissection: minimizing complications. World J Urol. 2009;27:205–12.
72. Crawshaw JW, Hadway P, Hoffland D, et al. Sentinel lymph node biopsy using dynamic lymphoscintigraphy combined with ultrasound-guided fine needle aspiration in penile carcinoma. Br J Radiol. 2009;82:41–8.
73. Scher B, Seitz M, Reiser M, et al. ^{18}F-FDG PET/CT for staging of penile cancer. J Nucl Med. 2005;46:1460–5.
74. Graafland NM, Leijte JA, Valdés Olmos RA, Hoefnagel CA, Teertstra HJ, Horenblas S. Scanning with ^{18}F-FDG-PET/CT for detection of pelvic nodal involvement in inguinal node-positive penile carcinoma. Eur Urol. 2009;56:339–45.
75. Schlenker B, Scher B, Tiling R, et al. Detection of inguinal lymph node involvement in penile squamous cell carcinoma by ^{18}F-fluorodeoxyglucose PET/CT: a prospective single-center study. Urol Oncol. 2012;30:55–9.
76. Sadeghi R, Gholami H, Zakavi SR, Kakhki VR, Horenblas S. Accuracy of ^{18}F-FDG PET/CT for diagnosing inguinal lymph node involvement in penile squamous cell carcinoma: systematic review and meta-analysis of the literature. Clin Nucl Med. 2012;37:436–41.
77. Jakobsen JK, Alslev L, Ipsen P, et al. DaPeCa-3: promising results of sentinel node biopsy combined with

^{18}F-fluorodeoxyglucose positron emission tomography/computed tomography in clinically lymph node-negative patients with penile cancer – a national study from Denmark. BJU Int. 2016;118:102–11.
78. Pagliaro LC, Crook J. Multimodality therapy in penile cancer: when and which treatments? World J Urol. 2009;27:221–5.
79. Rossari JR, Vora T, Gil T. Advances in penile cancer management. Curr Opin Oncol. 2010;22: 226–35.
80. Horenblas S, van Tinteren H. Squamous cell carcinoma of the penis. IV. Prognostic factors of survival: analysis of tumor, nodes and metastasis classification system. J Urol. 1994;151:1239–43.
81. Gold KA, Lee H-Y, Kim ES. Targeted therapies in squamous cell carcinoma of the head and neck. Cancer. 2009;115:922–35.
82. Culkin DJ, Beer TM. Advanced penile carcinoma. J Urol. 2003;170:359–65.
83. Graafland NM, Valdés Olmos RA, Teertstra HJ, Kerst JM, Bergman AM, Horenblas S. ^{18}F-FDG PET/CT for monitoring induction chemotherapy in patients with primary inoperable penile carcinoma: first clinical results. Eur J Nucl Med Mol Imaging. 2010;37:1474–80.

Diagnostic Applications of Nuclear Medicine: Vulvar Cancer

34

Sonia Mahajan, Weining Ma, and Neeta Pandit-Taskar

Abstract

Vulvar cancer is an uncommon malignancy in females and is less frequently seen as compared to cervical or endometrial cancer. Human papillomavirus (HPV) infection, chronic lichen simplex infection, and genital warts are considered some of the predisposing factors. While metastases occur in late-stage disease (usually via lymphatic spread), many lesions are seen in the early stages. Anatomic imaging is the mainstay of evaluation for local extent. [^{18}F]FDG PET imaging has incremental value for evaluation of equivocal lesions, assessing nodal status and detecting distant metastasis. Lymphoscintigraphy for sentinel node mapping is useful for surgical planning and limiting postoperative morbidity from extensive nodal dissection. This review summarizes the current status and emerging trends in imaging vulvar cancer using radiopharmaceuticals.

Keywords

Vulvar cancer • Vulvar cancer imaging • [^{18}F]FDG • PET/CT in vulvar cancer • Lymphoscintigraphy • Sentinel node mapping

Glossary

[^{18}F]FDG	2-deoxy-2-[^{18}F]fluoro-D-glucose
AJCC	American Joint Committee on Cancer
CT	X-ray computed tomography
FIGO	International Federation of Gynecology and Obstetrics
GOG	Gynecologic Oncology Group
GROINSS V	GROningen INternational Study on Sentinel Lymph Nodes in Vulvar Cancer
HPE	Histopathology exam
HPV	Human papillomavirus
ICG	Indocyanine green
ILN	Inguinal lymph nodes
LN	Lymph node
LSG	Lymphoscintigraphy
M	Metastasis status according to the AJCC/UICC TNM staging system
MIP	Maximum intensity projection
MRI	Magnetic resonance imaging
N	Lymph node status according to the AJCC/UICC TNM staging system
NA	Not available
NCCN	National Comprehensive Cancer Network
NIRF	Near-infrared fluorescent imaging
NPV	Negative predictive value

S. Mahajan • W. Ma • N. Pandit-Taskar (✉)
Department of Radiology, Memorial Sloan Kettering Cancer Center, New York, NY, USA
e-mail: pandit-n@mskcc.org

© Springer International Publishing Switzerland 2017
H.W. Strauss et al. (eds.), *Nuclear Oncology*,
https://doi.org/10.1007/978-3-319-26236-9_22

OS	Overall survival
p16	Gene encoding the cyclin-dependent kinase inhibitor 2A, also known as multiple tumor suppressor 1
p53	Gene encoding for tumor protein p53, also known as cellular tumor antigen p53, phosphoprotein p53, tumor suppressor p53, antigen NY-CO-13, or transformation-related protein 53 (TRP53)
PET	Positron emission tomography
PET/CT	Positron emission tomography/Computed tomography
PPV	Positive predictive value
SCC	Squamous cell carcinoma
SLN	Sentinel lymph node
SN	Sensitivity
SPECT	Single-photon emission computed tomography
SPECT/CT	Single-photon emission computed tomography/Computed tomography
SUV	Standardized uptake value
SUV_{max}	Standardized uptake value at point of maximum
T	Tumor status according to the AJCC/UICC TNM staging system
TNM	AJCC/UICC staging system based on parameters "T" (tumor status), "N" (lymph node status), and "M" (distant metastasis status)
UICC	Union Internationale Contre le Cancer (International Union Against Cancer)
US	Ultrasound
VIN	Vulvar intraepithelial neoplasia

Contents

Introduction 960
Introduction and Epidemiology 960
References 977

Introduction

Introduction and Epidemiology

Vulvar carcinoma comprises of about 0.4% of all new cancer cases and approximately 5.4% of all gynecologic cancers with 5,950 estimated new cases in the USA in 2016 [1]. It accounts for approximately 0.2% of all cancer-related deaths. Based on 2009–2013 statistics, the number of new cases of vulvar cancer was 2.4 per 100,000 women per year, and the number of age-adjusted deaths was 0.5 per 100,000 women per year [1]; a steady increase in vulvar cancer incidence has been noted over the past 40 years [2].

The median age for vulvar cancer at diagnosis is 65–70 years and that for vulvar intraepithelial neoplasia (VIN) is 45–50 years. It has slightly higher preponderance in whites and Native Americans compared to Asians and blacks. The higher incidence of VIN in women younger than 55 years is probably related to human papillomavirus HPV16 infection. An increasing incidence of vulvar cancers involving clitoral and periurethral region [2] has been noted that is generally associated with worse prognosis as compared to those not involving these regions [3]. A majority of vulvar cancers are usually detected in early clinical stages (59.2%) that are associated with a high 5-year survival rate of about 85.8% as against 55.4% for those with regional metastasis and 15.5% for those with distant metastatic disease. The age of the patient and characteristics of the tumor including size of the lesion, depth of invasion, cellular differentiation and grade, nodal status, and extranodal extension are independent prognostic variables associated with vulvar cancer with lymph nodal status the most important factor [4, 5].

Environmental factors and genetic predisposition: Cigarette smoking is considered a cofactor of HPV in the development of vulvar squamous cell carcinoma [6]. Certain studies have linked smoking to immunosuppression, and although the exact mechanism underlying the association is unknown, it is also postulated that the presence of nicotine, cotinine, and other

constituents may be seen in cervical mucus which affect the presence of cervical Langerhans cells and T lymphocytes [6]. Active smokers have about greater than threefold increased risk of developing vulvar SCC compared to nonsmokers, while former smokers may have little or no increased risk [7].

Persistent infection with HPV, an encapsulated DNA virus, is a known risk factor for hyperplasias associated with low-risk HPV types as well as for premalignant lesions caused by high-risk HPV types such as 16, 18, 31, 33, and 45 [8]. While the mechanism of such association is not fully known, it appears to be related to disruption of cellular gene functions caused by insertion of HPV genomes into host genomes [9]. It has been noted that following infection there is replication of viral DNA in basal cells with stable retention of multiple copies in preneoplastic lesions (episomal state). The viral DNA then integrates with the genome of the cell, and transcription of specific viral gene products occurs in invasive state [9, 10], some of which directly interfere with function of p53 and pRB.

The p16 and p53 expression has also been associated with variable presentation and prognosis [11, 12]. Diffuse p16 expression has been associated with younger age at presentation and basaloid and warty subtypes, while p53 immunopositivity is negatively associated with VIN [11]. Nonneoplastic epithelial cell disorders of vulva such as lichen sclerosis, squamous hyperplasia, and other dermatoses may develop cellular atypia or VIN in about 10% cases. Higher p53 mutations are more likely associated with HPV-negative tumors and point mutations more likely in metastatic lesions, suggesting a role in disease progression [12].

Prevention of HPV infections by vaccines can help decrease the incidence of vulvar intraepithelial neoplasias, genital warts, and cervical cytological abnormalities [13–15]. General recommendation is to offer vaccination to adolescents/young adults in three-dose series at 0, 2, and 6 months interval [16–18].

Histopathologic categories of vulvar cancer (Table 1): The most common histology of vulvar cancer is squamous cell carcinoma that forms more than 90% of the total, followed by vulvar melanoma that accounts for 2–4% of primary vulvar malignancies [19, 20]. The squamous cell carcinomas are further divided as keratinizing, warty, or basaloid. Keratinizing subtype is more commonly (60–80%) seen in postmenopausal women, is generally well to moderately differentiated, and is not associated with VIN or HPV, while warty or basaloid subtypes occur more commonly in pre- or perimenopausal women and are associated with VIN [21]. Verrucous carcinoma is a variant of SCC that is slow growing and less aggressive and rarely metastasizes though can be locally invasive. Basal cell carcinomas present in about 2% of patients who generally have other lesions in the body. The lesion may appear as discoloration or plaque and may be indolent. Sarcomatous lesions are less frequent and occur in less than 2% of patients. These are associated with poor prognosis and higher recurrence is seen in those with high-grade histology and large tumor size (>5 cm). Paget's disease of the vulva is rare

Table 1 Histological variants of vulvar carcinoma [21–23]

1. Squamous cell carcinoma
(a) Invasive
(b) Squamous variant of Bartholin gland carcinoma
2. Malignant melanoma
3. Anaplastic carcinoma
4. Vulvar intraepithelial neoplasia – high grades II and III (4% develop invasive cancer)
5. Paget's disease (5–10% are associated with underlying adenocarcinoma)
6. Adenocarcinoma
(a) Invasive
(b) Adenocarcinoma variant of Bartholin gland carcinoma
7. Other tumors
(a) Transitional cell variant of Bartholin gland carcinoma
(b) Adenoid cystic carcinoma – variant of Bartholin gland carcinoma
(c) Primary mammary adenocarcinoma
(d) Verrucous carcinoma
(e) Basal cell carcinoma
(f) Histiocytosis X
(g) Sebaceous carcinoma
(h) Sarcomas

(<1%) and presents as an eczematoid well-demarcated lesion. It can be multifocal and may be associated with invasive adenocarcinoma in deeper tissues.

Staging and Prognosis

The clinical staging of vulvar cancer is generally performed based on the International Federation of Gynecology and Obstetrics (FIGO) classification [24, 25] (Table 2). The classification is based on lesion size, tumor grade, and depth of invasion [24]. Vulvar melanomas are staged similar to cutaneous melanomas (Table 3). Staging of vulvar melanomas is based on Breslow's and modified Clark's classification [27].

Early-stage disease (stage I) has a very good overall 5-year survival (84.0%) as against FIGO stage II, III, and IV patients with overall survival (OS) of approximately 74.6%, 47.8%, and 9.4%, respectively. Nodal metastasis is correlated with worse prognosis; pooled data showed a 5-year OS of 84.5% for patients without LN metastasis and 30.1% for patients with three or more LN metastasis [28]. Inguinal and/or femoral node involvement is the most significant prognostic factor for survival in patients with vulvar cancer [29]. Other factors like tumor size and thickness, depth of invasion, and lympho-vascular space invasion also adversely affect prognosis. The presence of high mitotic rate, aneuploidy, infiltrative growth pattern, and basaloid histologic pattern is correlated with poor prognosis [30, 31]. Extranodal extension, defined as the extension of tumor from the node to adjacent soft tissue, is also associated with adverse outcomes. In a meta-analysis, Luchini et al. showed significant increase in all-cause mortality, cancer-specific mortality, and recurrence in patients with extranodal extension of tumor as compared to those without [32].

Clinical presentation and management: Vulvar cancer can present in various forms either as subtle nonspecific presenting symptoms or as a frank ulcerating lesions or mass. Patients most commonly present with chronic itching or pain in introitus. The lesion may appear like lichen sclerosis, contact dermatitis, or warts and can be overlooked as inflammatory or benign condition. Patients may have skin changes including discoloration or thickening. Lesions may appear like plaques or exophytic or fungating growths. A chronic condition of the vulva that recurs or does not respond to treatment should be therefore further investigated and preferably biopsied [33]. Diagnosis is usually made with wedge biopsy; however, excision biopsy is preferred for lesions that are <1 cm. Clinical examination helps to rule out multifocal or multicentric involvement, while colposcopic examination is required to know the extent [34].

Surgical excision is the mainstay of management of vulvar cancer. Radical vulvectomy with wide excision of the vulva up to the deep fascia of the thigh and urogenital diaphragm is performed in order to achieve a tumor-free margin ≥1 cm to minimize local recurrence. Unilateral or bilateral inguinal nodes may be sampled and dissected based on extent of the primary lesion. Lesions in the midline or crossing the midline may spread to bilateral inguinal nodes seen in up to 3–5% of cases; however, the rates vary with inclusion of other factors such as tumor size and depth of invasion [30, 35]. Pelvic node involvement is not common and occurs in about 5% of patients [36]. T1 lesions without extension to adjacent perineal structures (i.e., urethra, vagina, and/or anus) may be effectively treated by wide local excision [37]. NCCN guidelines for SCC of vulva [38] recommend wide local resection followed by observation for early-stage T1 and smaller T2 lesions less than or equal to 4 cm that have ≤1 mm invasion. For lesions greater than 1 mm invasion, radical local resection or modified radical vulvectomy is recommended. For midline lesions, bilateral inguinofemoral groin lymph node dissection should be considered with or without sentinel lymph node detection. For a lesion that is lateral (≥2 cm from midline), ipsilateral lymph node dissection with or without sentinel lymph node detection is performed. T2 lesions with extension to adjacent perineal structures are best treated with radical vulvectomy or hemivulvectomy. In locally advanced disease, neoadjuvant radiation and chemotherapy is administered; residual tumor, if present, is surgically excised [38, 39].

Table 2 FIGO (2009) and AJCC classification [26]

FIGO stage	Description
I	Tumor confined to the vulva
Ia	Lesions ≤2 cm in size, confined to the vulva or perineum and with stromal invasion ≤1 mm, no nodal metastases
Ib	Lesions >2 cm in size or with stromal invasion >1 mm, confined to the vulva or perineum, with negative nodes
II	Tumor of any size with extension to adjacent perineal structures (lower third of the urethra, lower third of the vagina, anus) with negative nodes
III	Tumor of any size with or without extension to adjacent perineal structures (lower third of the urethra, lower third of the vagina, anus) with positive inguinofemoral nodes
IIIa	With 1 lymph node metastasis (≥5 mm) or with 1–2 lymph node metastases (<5 mm)
IIIb	With 2 or more lymph node metastasis (≥5 mm) or with 3 or more lymph node metastases (<5 mm)
IIIc	Positive lymph nodes with extracapsular spread
IV	Tumor invades other regional (upper two thirds of the urethra, upper two thirds of the vagina) or distant structures
IVa	Tumor invades either upper urethral/vaginal mucosa, bladder mucosa, rectal mucosa, fixed to pelvic bone, or fixed/ulcerated inguinofemoral lymph nodes
IVb	Any distant metastases including pelvic lymph nodes
TNM staging	
Primary tumor (T)	
Tx – Primary tumor cannot be assessed	
T0 – No evidence of primary tumor	
Tis – Carcinoma in situ (preinvasive)	
T1a – Lesions ≤2 cm, confined to the vulva or perineum and with stromal invasion ≤1 mm (FIGO IA)	
T1b – Lesions >2 cm or any size with stromal invasion >1 mm, confined to the vulva or perineum (FIGO IB)	
T2 – Tumor of any size with extension to adjacent perineal structures (distal third of the urethra, distal third of the vagina, anal involvement) (FIGO II)	
T3 – Tumor of any size with extension to any of the following proximal two thirds of the urethra, proximal two thirds of the vagina, bladder mucosa, or rectal mucosa or fixed to pelvic bone (FIGO IVA)	
Regional lymph nodes (N)	
Nx – Regional lymph nodes cannot be assessed	
N0 – No regional lymph node metastasis	
N1a – 1 or 2 lymph node metastases, each <5 mm (FIGO IIIA)	
N1b – 1 regional lymph node metastasis ≥5 mm (FIGO IIIA)	
N2a – 3 or more lymph node metastases, each <5 mm (FIGO IIIB)	
N2b – 2 or more regional lymph node metastases ≥5 mm (FIGO IIIB)	
N2c – Regional lymph node metastasis with extracapsular spread (FIGO IIIC)	
N3 – Fixed or ulcerated regional lymph node metastasis (FIGO IVA)	
Distant metastasis (M)	
M0 – No distant metastases	
M1 – Distant metastases (including to pelvic lymph nodes) (FIGO IVB)	

Role of Imaging

Diagnosis of vulvar cancer initiated based on clinical history and examination; a suspicious lesion is biopsied. Imaging plays a limited role in the evaluation of primary disease. For evaluation of disease extent and treatment planning, contrast-enhanced CT or MRI or PET with 2-deoxy-2-[^{18}F] fluoro-D-glucose be used based on clinical need and suspicion. In patients with locally advanced disease, chest radiograph, CT, and/or MRI is recommended to establish staging (Fig. 1). Assessment of inguinofemoral region is critical

Table 3 Breslow's classification and Clark's classification

Stage	Depth
Breslow's classification	
Stage I	Less than or equal to 0.75 mm
Stage II	0.76–1.50 mm
Stage III	1.51–2.25 mm
Stage IV	2.26–3.0 mm
Stage V	Greater than 3.0 mm
Clark's classification	
Level 1	Melanoma confined to the epidermis (melanoma in situ)
Level 2	Invasion into the papillary dermis
Level 3	Invasion to the junction of the papillary and reticular dermis
Level 4	Invasion into the reticular dermis
Level 5	Invasion into the subcutaneous fat

for management and to segregate patients for nodal sampling and surgical dissection prior to treatment with chemotherapy and/or radiation.

MRI is useful in evaluating the local extent of disease in patients with advanced tumor, especially for assessment of extent in the perineum and extension to the vagina or anus, and therefore useful for surgical planning. The tumor is best visualized in T2-weighted sequences and may be seen as a mass or skin thickening with intermediate to high signal intensity. The extent of the lesion is better visualized on contrast-enhanced fat-suppressed T1-weighted images. MRI may also be useful to assess the depth of tumor invasion and local extent, especially involvement of the clitoris or urethral meatus [40]. MRI provides accurate assessment of lymph node metastasis [41, 42] and is highly specific in identifying abnormal lymph nodes by using size criteria and morphology. However, the sensitivity is low ranging between 40% and 50% [37]. Using short/long axis (S/L) ratio as a quantitative marker for diagnosing lymph node metastasis, a higher sensitivity of 87% and specificity of 81% have been reported [37].

Ultrasound (US) is used mainly to detect abnormal inguinal lymph nodes or for ultrasound-guided biopsy of suspicious lymph nodes. Focused ultrasound imaging is performed using a high-frequency transducer (linear 8–18 MHz). Abdominopelvic CT scans may be useful in detecting local and distant lymph nodes or other distant metastases and are generally used in conjunction with US and MRI for staging or restaging based on patient's clinical presentation and suspicion.

Radiopharmaceutical imaging: Of the various techniques and tracers available, [^{18}F]FDG-PET/CT imaging and lymphoscintigraphy are primarily used for imaging and evaluation of patients with vulvar cancer. Currently, the role of [^{18}F]FDG PET/CT has not been fully established though early data suggests a complimentary role and advantages in assessing distant disease [43, 44].

[^{18}F]FDG PET Imaging

Generally vulvar cancer shows avid uptake of [^{18}F]FDG (Figs. 2 and 3). For initial staging, FDG PET is more often used to detect distant metastatic disease while assessment of nodal disease is less critical. Anatomic imaging provides superior details in determining local extent, and [^{18}F]FDG PET may play a complimentary role in evaluating equivocal findings on conventional imaging, especially in assessing nodal disease in non-enlarged or borderline-sized nodes (Fig. 4). In a small prospective study in vulvar SCC ($n = 15$, stages IB–IV), [^{18}F]FDG PET was performed prior to surgery and compared with results of groin dissection (Table 4). All patients showed avid uptake in primary tumors [45]. [^{18}F]FDG PET showed suspicious nodes in six out of nine groins (in four out of five patients) that were pathologically positive. In a single patient, [^{18}F]FDG PET was also positive for pelvic nodes that were further treated with radiation. Other distant sites that showed uptake included adrenal gland adenoma and physiologic prominent uptake in the cecum.

In a prospective study that analyzed CT, MRI, and [^{18}F]FDG PET imaging in 23 patients, [^{18}F]FDG PET showed high uptake in the primary tumor with an average SUV of 11; however, the values ranged between 2.4 and 28.5. In 2/17 patients, [^{18}F]FDG had a positive impact on management by either detecting a distant metastasis or excluding pelvic metastasis [46]. For those evaluated for recurrence, 2/14 had unknown metastatic sites detected on [^{18}F]FDG PET as compared to

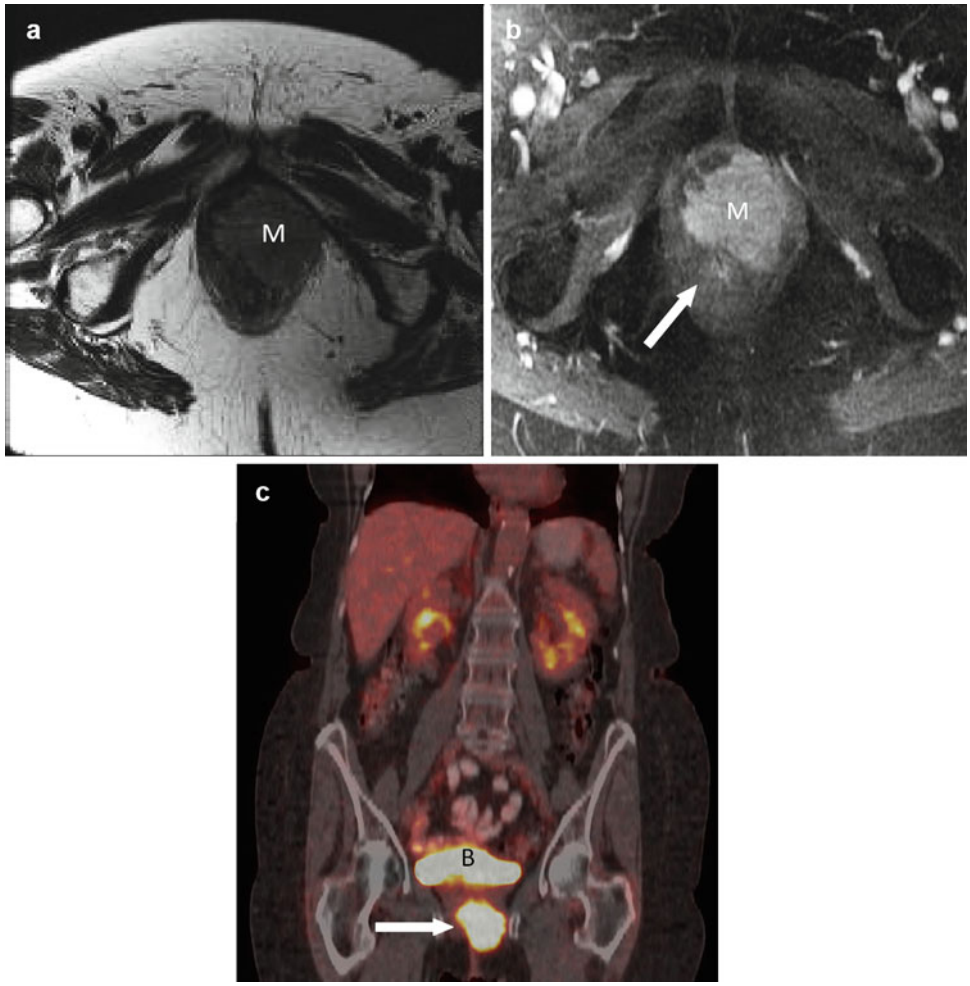

Fig. 1 MR pelvis (**a**) axial T2-weighted (**b**) gadolinium-enhanced T1 image shows a left vulvar soft tissue mass (*M*); T2 mildly hyperintense with homogenous enhancement invading through the pelvic floor with involvement of posterolateral urethral, lower vaginal, and anal walls (*white arrow*). (**c**) Coronal fused PET/CT image showed [^{18}F]FDG avid (SUV_{max} 10.8) left vulvar mass (*white arrow*), *B*: urinary bladder. HPE revealed moderately differentiated invasive SCC

other conventional imaging. However in this study, the overall accuracy and specificity of [^{18}F]FDG PET imaging were lower as compared to CT and/or MRI [46]. In evaluating the role of [^{18}F]FDG PET in staging prior to planned radical vulvectomy and inguinofemoral lymphadenectomy, imaging analysis in 20 patients showed high uptake in vulvar lesions ranging from 2.5 to 14.7 and uptake of 2.4–3.0 in groin nodes [47]. In a very small study ($n = 8$), [^{18}F]FDG localized to all primary well-differentiated SCC of the vulva; the nodal uptake was higher (SUV range of 3.5–15) in metastatic nodes versus reactive nodes (SUV range of 1.7–3.1) [48].

[^{18}F]FDG PET has been evaluated for assessing nodal status especially the involvement of inguinofemoral lymph nodes and as a noninvasive tool for preoperative assessment [45–48] (Figs. 5 and 6). Kamran and colleagues evaluated the usefulness of [^{18}F]FDG PET in categorizing

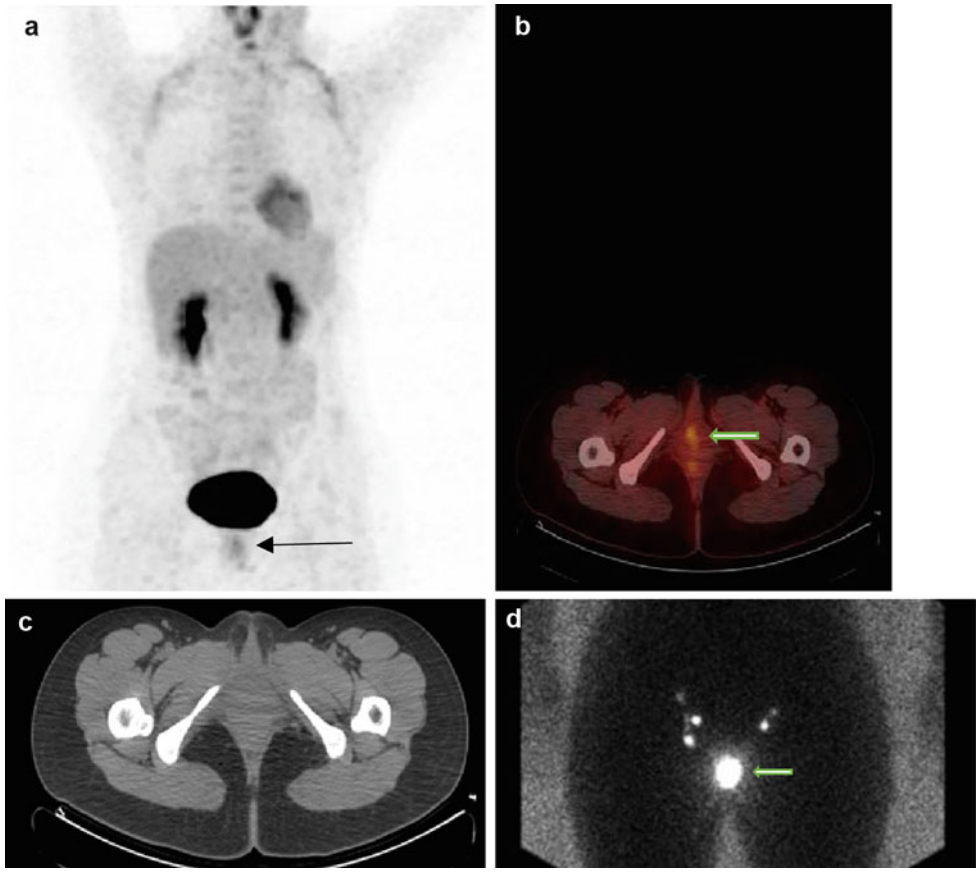

Fig. 2 Primary vulvar carcinoma (VIN III). A 28-year-old with biopsy-proven high-grade squamous intraepithelial lesion (**a)** MIP (*black arrow*) and **(b)** axial fused PET/CT image of pelvis show minimal asymmetric [^{18}F]FDG uptake in the perineum (SUV_{max} 1.9) (*white arrow*); no gross disease is seen on the noncontrast CT (**c**). No other metastatic lesion was seen in the rest of the body. **(e)** Patient underwent presurgical lymphoscintigraphy. LSG planar and SPECT images, following ^{99m}Tc-sulfur colloid injection intradermally, show lymph nodes in bilateral groin region and pelvis (*arrow*, injection site)

stage III disease accurately and in comparison to histopathology; while the specificity was high (100%), the sensitivity and overall accuracy were low for nodal assessment. In this small study, it was noted that there were larger, multiple, and bilateral nodal metastases in those with a more avid primary tumor versus those with a less avid primary tumor. Due to low negative predictive value (NPV) of [^{18}F]FDG the low-risk patients could not be reliably identified; however, the high PPV suggested that it could be a useful guide in proceeding with a full lymphadenectomy [47]. This however needs to be evaluated in a more systematic and larger group.

Cohn and colleagues evaluated [^{18}F]FDG PET for detecting groin nodal metastasis in correlation with pathologic finding and detected higher sensitivity for nodal detection on a per patient basis as against nodal basin-based analysis (80% vs 67%); however, the specificity was higher in site-specific analysis (95% vs 90%). The positive and negative predictive values for nodal detection were about 80–90%. The overall sensitivity was however less optimal to preclude surgical lymphadenectomy using [^{18}F]FDG data only [45]. Similar result, though with lower sensitivity, was noted by Kamran et al.; [^{18}F]FDG PET had sensitivity of 50% only, though high

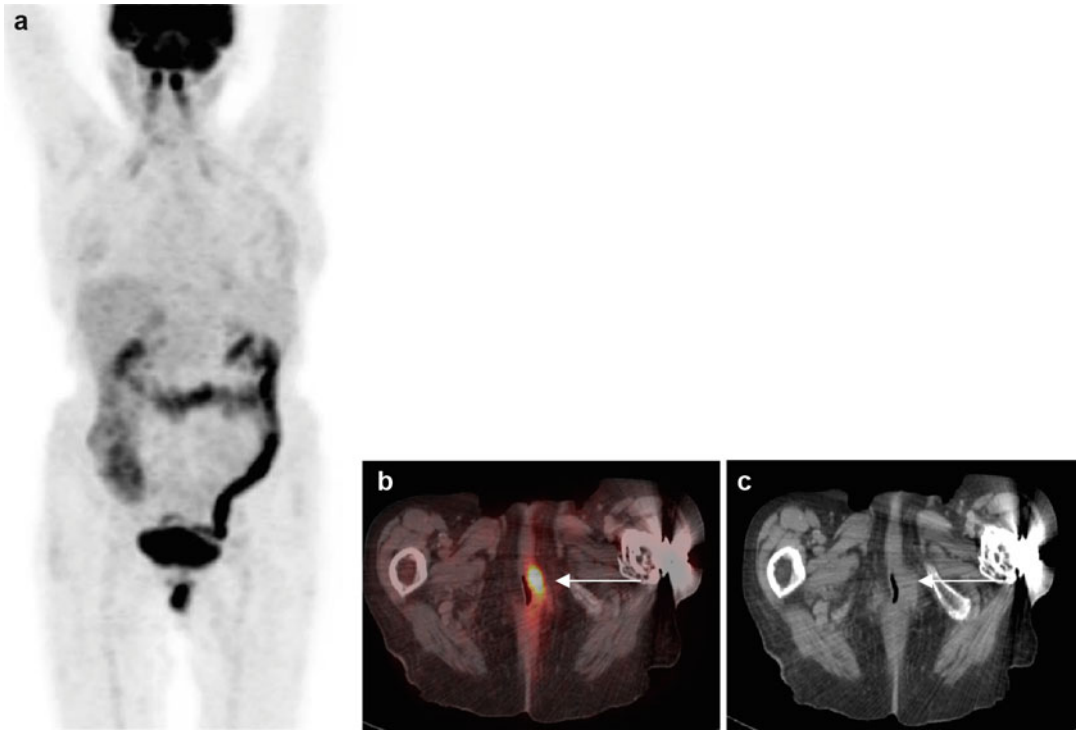

Fig. 3 Primary vulvar carcinoma. A 76-year-old with left vulvar lesion that shows intense [^{18}F]FDG uptake on MIP (**a**) and fused PET/CT images (**b**, SUV_{max} 10.7). The lesion measured 2.8 × 1.6 cm as seen on axial CT (**c**). No other metastatic lesion was seen in the rest of the body (**a**)

specificity of 100% was seen with a positive predictive value of 100 [47].

In those with high-risk disease, [^{18}F]FDG PET can help detect metastatic disease especially to the distant sites (Fig. 6) and affect management change. A recent study that analyzed the impact of [^{18}F]FDG PET/CT in the management of 54 patients with vulvar cancer showed a change in prognosis in 54% of which 33% (18/54) had improved prognosis and 20% (11/54) had worse prognosis [49]. Though the data is combined with vaginal cancer patients, it appears that additional disease sites were detected by [^{18}F]FDG PET in lungs and adrenals that contributed to worsening of prognostic outlook with an overall change in management in 36% of the combined population.

Recurrences are common in vulvar cancer patients. In a study of 502 patients, reported rates were 22% for stage I, 35.8% for stage II, and about 44–45% for stage III and IV disease with higher recurrences seen in the inguinal region as against pelvic regions [29]. [^{18}F]FDG PET/CT may play a role in restaging and planning treatment in recurrent disease (Fig. 7). Extent of local, groin, and other sites of disease helps guide salvage or palliative therapy in individual cases. The data is limited for systematic evaluation of the use of [^{18}F]FDG PET in restaging as well as for the assessment of treatment response (Figs. 7 and 8) and would need well-designed studies.

Lymphoscintigraphy

The concept of sentinel lymph node (SLN) mapping was initially developed by Cabanas in 1977 for penile cancers [50] which was extended to map nodes in melanoma using isosulfan blue dye intraoperatively [51]. Later, radionuclide scintigraphy was used in conjunction with blue dye that yielded superior results in nodal

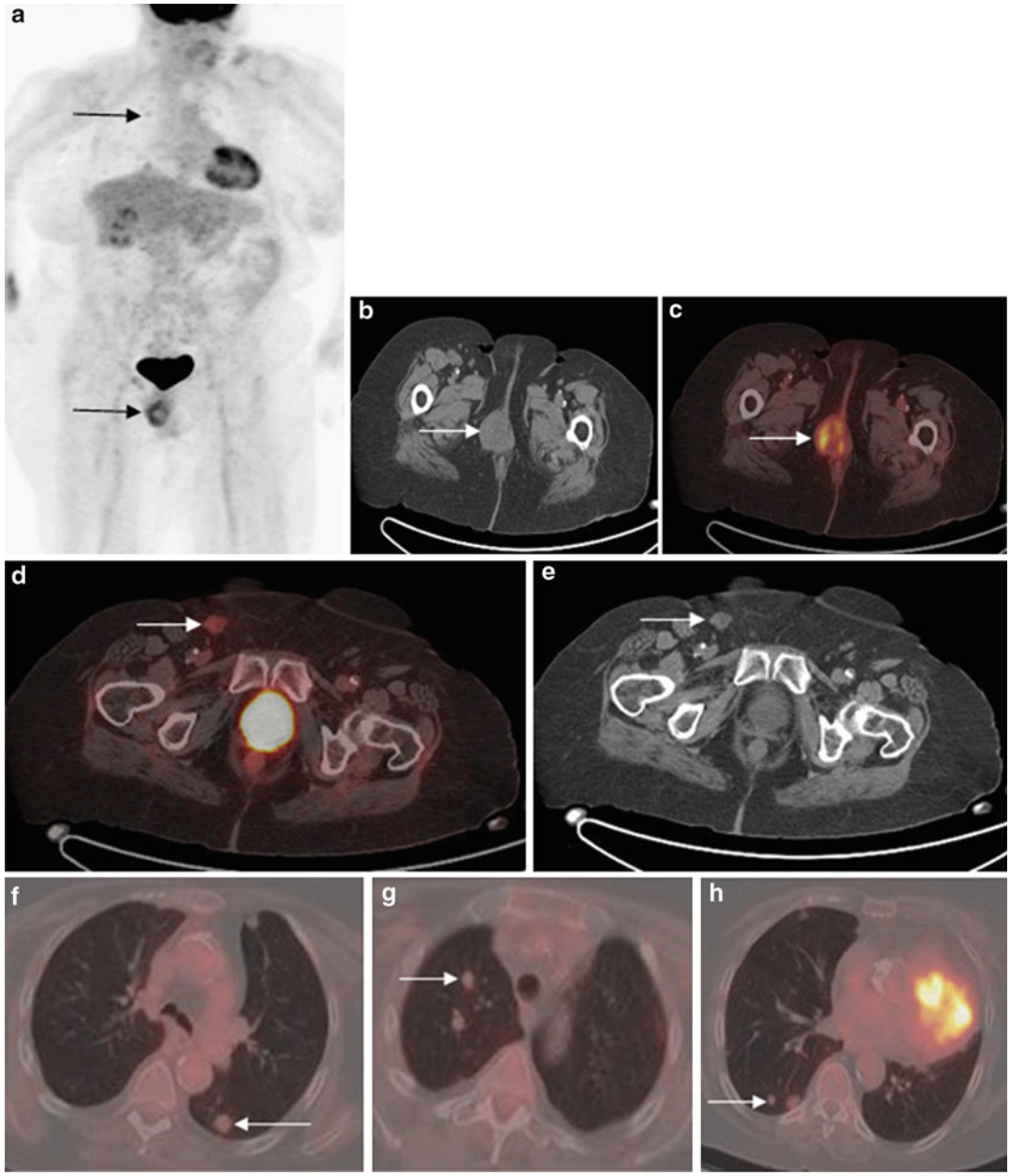

Fig. 4 Patient with vulvar carcinoma referred for staging of the disease. Whole-body MIP (**a**, *black arrow*) image shows increased [^{18}F]FDG uptake in the primary lesion seen on CT (**b**, *white arrow*) and fused PET/CT image (**c**, SUV_{max} 4.7). Additional uptake is seen in inguinal lymph nodes (**d**, **e**, *white arrow*) (SUV_{max} 1.1). On whole-body PET/CT, multiple suspicious lesions showing mildly increased [^{18}F]FDG uptake were noted in both lungs (**f**, **g**, **h,** *white arrows*)

localization in breast cancer and melanoma [52, 53]. Extensive nodal dissection can lead to significant morbidity which can be considerably alleviated by sentinel node technique.

SLN with filtered ^{99m}Tc sulfur colloid is performed as a single-day procedure either on the day of surgery or a day prior to surgery. Intradermal, subcutaneous, or intratumoral injections may

Table 4 [^{18}F]FDG PET in vulvar cancer – literature

Author, year	Type	Indication	Number of patients/stage	Comparative imaging (CT or MRI)	Histopathology confirmation (yes/no)	Sensitivity/ specificity/ accuracy
Lin et al., 2015	Prospective	Primary staging ($n = 17$), response assessment ($n = 7$), restaging ($n = 14$) (38 PET studies)	23: SCC ($n = 15$) stages I–IV, adenocarcinoma ($n = 2$), melanoma ($n = l$), Paget's disease ($n = 4$), small cell ca ($n = l$)	CT/MRI	Yes	ILN: [^{18}F] FDG– 92%/91%/ 91%; CT/MRI – 92%/ 100%/97%
Kamran et al., 2014	Retrospective	Staging: detection of inguinal and femoral LN	20 SCC stage I/II ($n = 8$), III ($n = 12$)	No	Yes	50%/ 100%/70%
Cohn et al., 2002	Prospective	Staging: detection of groin lymph node metastases	15 SCC stage IB ($n = 3$), M ($n = 7$), Nl ($n = l$), IVA ($n = 4$)	No	Yes	Per patient basis – 80%/90%/ NA. Per groin basis – 67%/ 95%/NA
Dolanbay et al., 2015	Prospective	Staging: assessment of inguinofemoral lymph nodes	8 SCC stage IB ($n = 4$), IIIB ($n = 4$)	No	Yes	100%/ 100%/NA

SCC squamous cell carcinoma, *ILN* inguinal lymph nodes

be performed. The intradermal injection is administered at the periphery of the lesion, approximately at the four corners of the lesion or post biopsy scar site. Dynamic images are obtained soon after the injection in the anterior projection. This is followed by static images in anterior, posterior, and lateral projections. A SPECT/CT may be performed, and is increasingly used, to localize the nodal site especially if there is a suspicion of localization of a deeper node. Blue dye (isosulfan blue) is injected intraoperatively as the transit is fast; many times the initial nodes may not be visualized. Handheld gamma probes have been used for detecting "hot nodes" for removal during surgery. In vivo and ex vivo counts are done over the node. Generally, nodes with counts more than ten times the background levels are considered sentinel.

SLN mapping is increasingly being used in gynecological cancers including vulvar cancer (Table 5) to prevent morbidity from en bloc inguinofemoral dissection. Standard treatment of vulvar SCC in those with T1–2, N0–1, and M0 tumor includes surgical excision of the tumor with unilateral or bilateral nodal dissection of the inguinofemoral nodal basins. The recurrence rate in the groin in those with pathologic negative nodes is less than 2%, and even in those with positive nodes on pathology, recurrence rates range between 5% and 10% [54, 55]. Total lymphadenectomy is associated with postoperative sequelae including cellulitis and lymphedema that results in increased morbidity and lower quality of life. SLN mapping is useful in allowing sampling of nodes and planning lymphadenectomies.

In an observational multicenter study (GROningen INternational Study on Sentinel lymph nodes in Vulvar cancer – GROINSS V), 276/403 patients with early-stage disease (T1/T2, primary lesion <4 cm, and clinically non-suspicious inguinofemoral LN) had negative SLN and did

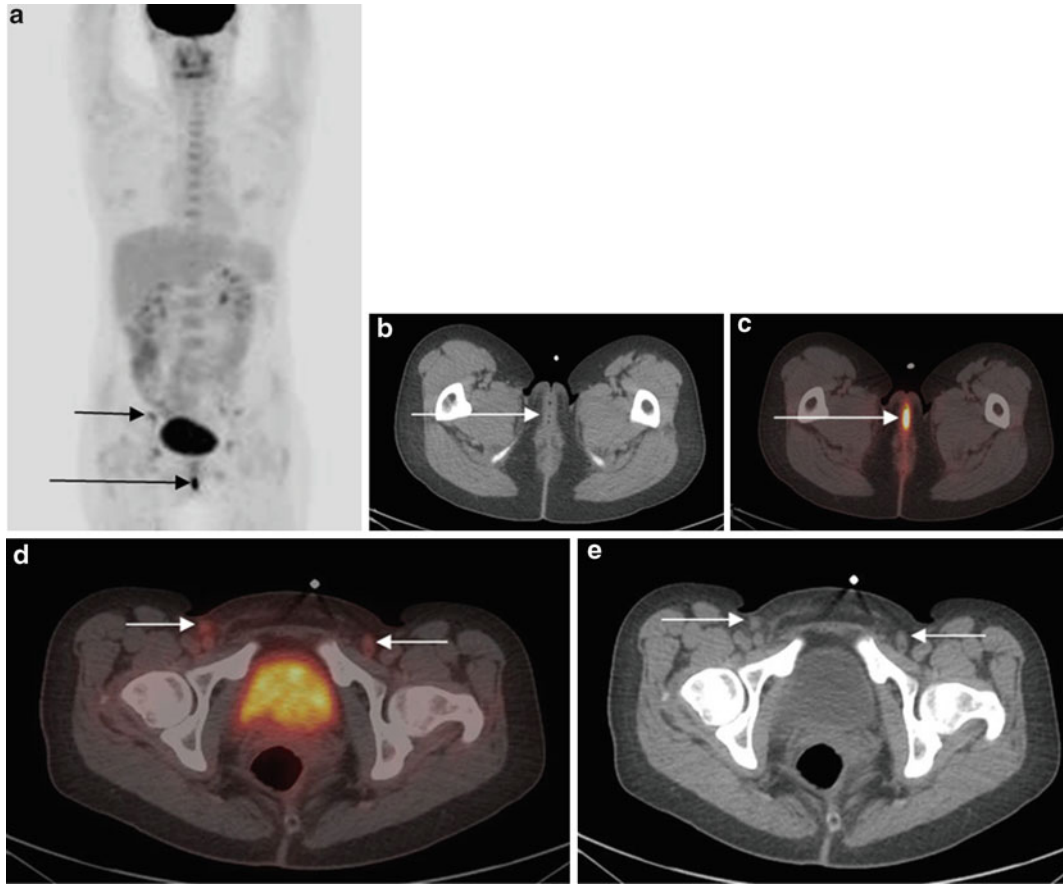

Fig. 5 A 36-year-old woman with history of recurrent vulvar carcinoma referred for restaging. (**a)** Whole-body MIP image shows [^{18}F]FDG uptake in the perineum (SUV_{max} 8.8) (*long arrow*) localizing to thickening in vulvar region noted on CT (**b**, *white arrow*) and fused PET/CT image (**c**, *white arrow*). Additional foci of uptake are seen in bilateral inguinal regions (MIP image a, *short arrow*) (**d**, **e**, SUV_{max} 2.5 on the left side) which were considered equivocal. The patient underwent radical vulvectomy with bilateral inguinal lymph node dissection; histopathology showed invasive squamous cell carcinoma vulva and negative nodes. (Teaching point: faint uptake in nodes is nonspecific and may be related to reactive uptake; however, assessment is best correlated with clinical suspicion)

not undergo lymphadenectomy. Groin recurrence rate was 3% at 2 years. Low incidence rates of short- and long-term morbidity were reported in patients who had negative SLN versus patients who underwent lymphadenectomy following positive SLN procedure, such as wound breakdown (11.7% vs 34%) and cellulitis (4.5% vs 21.3%). Incidence rates of long-term morbidities such as lymphedema and recurrent erysipelas were also more common in patients who underwent SLN with lymphadenectomy as compared to the group with only SLN (25.2% and 16.2% vs 1.9% and 0.4%, respectively) [56].

Histopathological sampling guided by SLN mapping using blue dye and ^{99m}Tc-sulfur colloid has been reported to be an effective method to detect inguinofemoral LN involvement in patients with early-stage disease with primary lesions less

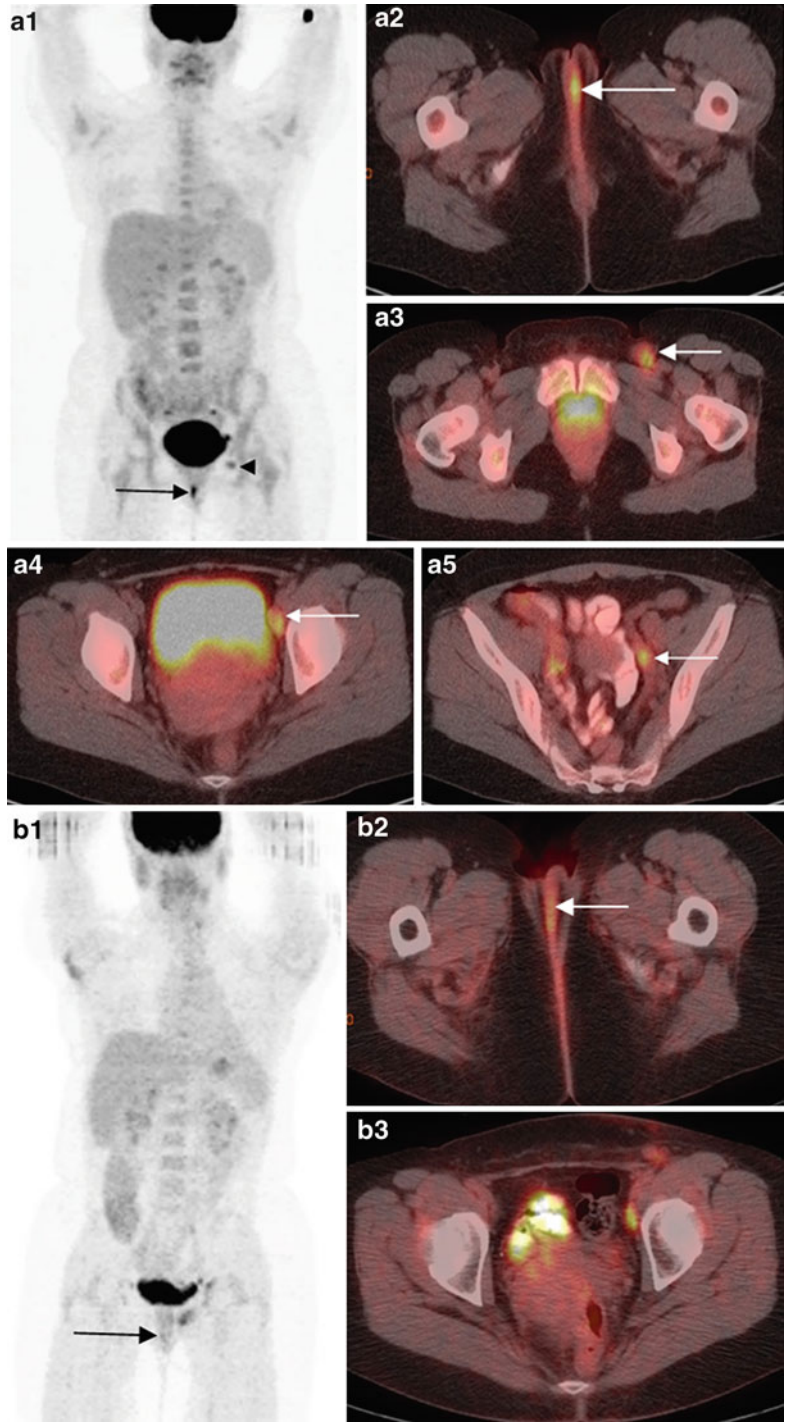

Fig. 6 (continued)

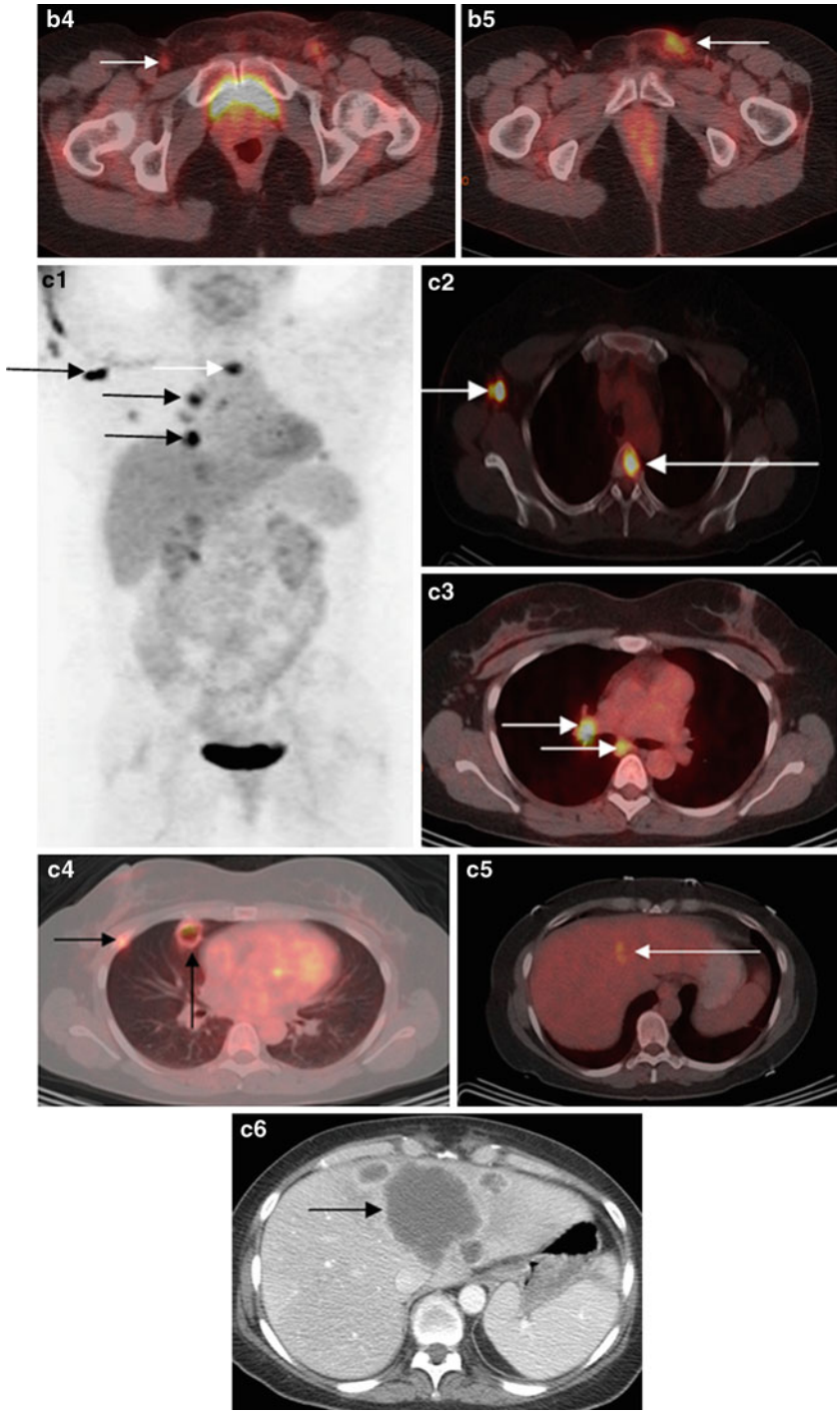

Fig. 6 (continued)

than 4 cm in size [57]. In a GOG 173 study, false-negative predictive value of SLN in those with primary lesion measuring less than 4 cm was only 2% but was higher at 7.4% for lesions measuring 4–6 cm. On a patient-based analysis, SN of the SLN procedure was 91.7% and false NPV was 3.7% [56, 57].

Using lymphoscintigraphy and intraoperative gamma probe, Decesare and colleagues reported sensitivity and NPV of 100% in a small number of patients [58]. In a slightly larger study, using the same technique, SN of SLN detection was 90% [59]. Using a combination of ^{99m}Tc-nanocolloid and blue patent dye to identify the sentinel node [60], de Hullu et al. noted superior (100%) localization of sentinel nodes by ^{99m}Tc-nanocolloid as against 56% with blue dye. A number of studies subsequently [61–63] have reported high detection rates using both blue dye and radiocolloid scintigraphy with sensitivity ranging between 90% and 100%. ^{99m}Tc-phytate also has been used for mapping with comparable results [64]. With midline vulvar cancer, the drainage is often to bilateral nodes that may miss detection [65] and bilateral lymphadenectomy is recommended. In a GOG 173 study, Coleman and colleagues studied the significance of SLN in those with larger tumors measuring 2–6 cm, lateral, midline, or lateral ambiguous tumors; many of these may have bilateral lymphatic drainage necessitating bilateral inguinal nodal dissection. In 234 patients with early-stage disease, lymphoscintigraphy however detected only unilateral drainage in 32 of 105 patients with midline tumor, which prevented nodal dissection on the contralateral side. Also larger tumors showed more ambiguous drainage suggesting value of SLN mapping in this subgroup of patients [66].

SPECT/CT imaging is more sensitive and combines the tracer localization with anatomic details providing a superior three-dimensional localization, thereby facilitating surgical excision (Fig. 9). It is reported to identify sentinel nodes in higher number of patients [67]. In a prospective study of 40 patients with direct comparison of planar vs SPECT/CT imaging, a higher number of nodes were detected with SPECT/CT; mean nodes/patient for SPECT were 8.7 vs 5.9 for planar imaging. In 17.5%, aberrant lymph drainage was noted with localization to gluteal, paravaginal, vesical, paravesical, and retrovesical regions [67]. Overall sensitivity and NPV was 100% for inguinofemoral nodal SLN detection in correlation with histopathology. About 71% (5/7) of patients with aberrant nodal drainage had midline tumors, highlighting the importance of SLN mapping in midline tumors. Similar experience in small number of patients was reported by another group [68]. Overall, the existing data documents feasibility and usefulness of LSG in vulvar cancer.

There has also been increasing interest in the use of fluorescent dyes like indocyanine green (ICG) [69] for evaluation of nodes based on

Fig. 6 A 41-year-old with vulvar SCC was initially referred for pretreatment evaluation of the primary disease and extent Panel **a**: Whole-body MIP image **a1** (*arrow*) shows abnormal uptake in vulvar region also noted on fused images **a2** (SUV_{max} 7.8). Increased uptake was also seen in left inguinal node (**a3**, SUV_{max} 4.3) as well as in left obturator node (**a4**, SUV 8.0). Foci of increased uptake superiorly in bilateral pelvis corresponded to physiologic uptake in bilateral adnexa (**a5**). Panel **b**: The patient was treated with chemoradiation and a follow-up [^{18}F]FDG scan showed resolution of focal uptake in the vulva (**b1**, **b2** *arrows*) as well as decreased uptake in the inguinal and obturator nodes (**b3**). Heterogeneous uptake in the mons pubis corresponding to ill-defined infiltrative changes and mildly avid right inguinal node (**b4**, **b5**) was likely post-radiation changes. Patient underwent partial vulvectomy and left inguinal node dissection. Panel **c**: Patient returned for routine follow-up imaging after 6 months. The scan showed several new lesions suspicious for metastatic disease including T3 vertebra (SUV_{max} 8) (**c2** *long arrow*), right axillary (**c2** *short arrow*), subcarinal and hilar lymph nodes (**c3**, *arrows*), and right lung lower lobe (**c4**, SUV_{max} 10.4). Mild focal uptake was also noted in the liver (**c5**, SUV_{max} 4.4), suspicious for metastatic lesion. Lung lesion was positive for malignant disease, and while the liver lesion was negative on biopsy, a follow-up CT revealed a large lesion in the same region and additional lesions in the liver, positive for metastatic disease (**c6**, *arrows*). Teaching point: [^{18}F]FDG PET can help detect unknown distant metastatic sites and early lesions

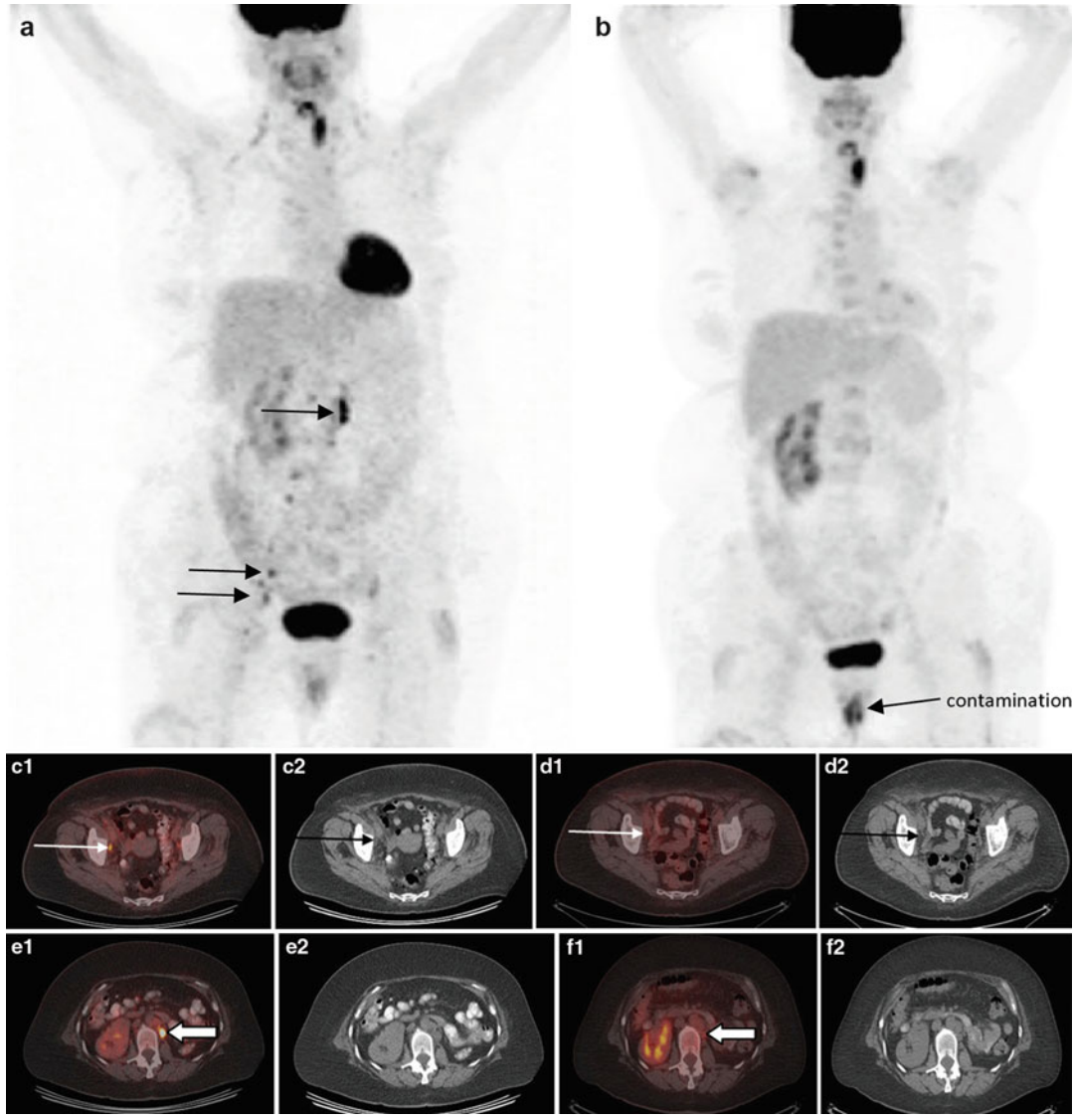

Fig. 7 Patient with poorly differentiated adenosquamous vulvar carcinoma referred for follow-up evaluation of extent of disease. Patient was prior treated with radical vulvectomy and nodal dissection. Whole-body MIP showed foci of increased [^{18}F]FDG uptake in the pelvis and abdomen (**a**, *arrows*) localizing to right obturator lymph node (**c1**, **c2** SUV_{max} 4.5) and left para-aortic lymph node (**e1**, **e2** SUV_{max} 11.6 *thick arrow*). Patient was treated with chemoradiation; a follow-up PET/CT to assess response showed complete resolution of disease and pelvic lymph nodes (**d1**, **d2** *arrows*) with partial response in para-aortic lymph node (**f1**, **f2** SUV_{max} 3.3, *thick arrow*)

near-infrared fluorescent imaging (NIRF). The faster transit and change in color that can be easily detected by the surgeon using infrared light are significant advantages of the use of fluorescent dyes. In a pilot study of ten patients with early-stage SCC of vulva, SLN were mapped using ^{99m}Tc-nanocolloid blue dye, and ICG to evaluate the feasibility of ICG SLN mapping. While largest numbers of nodes were mapped using nano-colloid, ICG mapped most of the SLN with added advantage of transcutaneous localization, especially in leaner patients [70].

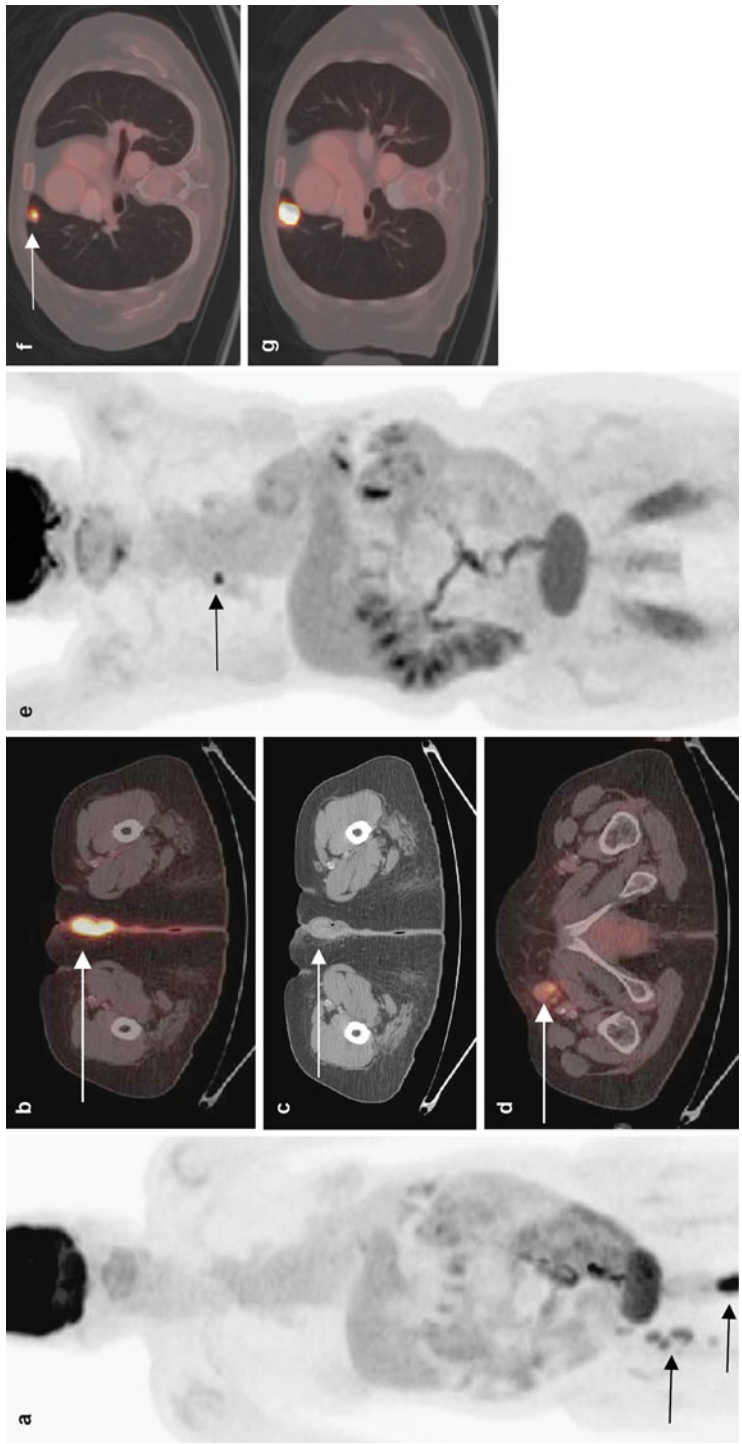

Fig. 8 A 72-year-old female with vulvar adenocarcinoma was referred for pretreatment evaluation of disease. Whole-body MIP image (**a**) showed abnormal uptake in the vulvar region (*arrows* **a**, **b**, **c**, SUV_{max} 9.0) and inguinal lymph nodes (**d**, SUV_{max} 4.9). A 6-month follow-up scan post chemoradiotherapy showed resolution of all the disease sites seen previously in the vulvar region and inguinofemoral nodes. However, a new focal uptake was noted in the right chest (**e**, *black arrow*) localizing to a nodule in the right lung upper lobe (**f**, SUV_{max} 5.9), which showed progression (**g**, SUV_{max} 12.6) on further follow-up imaging obtained after 3 months and was positive on pathology for metastatic disease

Table 5 Lymphoscintigraphy in vulvar cancer

Author and year	Type	Number of patients: FIGO staging	Histopathology confirmation (yes/no)	Comparison with blue dye (detection rate)	Sensitivity of LSG
de Hullu et al., 2000	Prospective	59: SCC stage I ($n = 25$), II ($n = 34$)	Yes	Yes (60%)	100%
Van der Zee et al., 2008	Prospective	403: SCC stage I	Yes	Yes	94.10%
Lindell et al., 2010	Retrospective	77: SCC stage I/II ($n = 76$), IVA ($n = 1$)	Yes	Yes (94% blue dye alone $n = 17$) (98% LSG and blue dye $n = 60$)	NA
Levenback et al., 2012	Prospective	452: SCC stage I	Yes	Yes (92.4%)	By patient basis 91.7%, by groin basis 92.1%
Klapdor et al., 2015	Prospective	40: SCC stage IA ($n = 5$), IB ($n = 26$), II ($n = 8$), III ($n = 1$)	Yes	Yes	100%
Collarino et al., 2015	Prospective	83: SCC stage IB ($n = 51$), II ($n = 9$), III ($n = 18$), IVA ($n = 2$), melanoma ($n = 2$), adenocarcinoma (n=l)	Yes	Yes	96.30%
Bogliolo et al., 2015	Retrospective	45: SCC stage I ($n = 14$), II ($n = 31$)	Yes	No	90%

SCC squamous cell carcinoma, *LSG* lymphoscintigraphy, *NA* not available

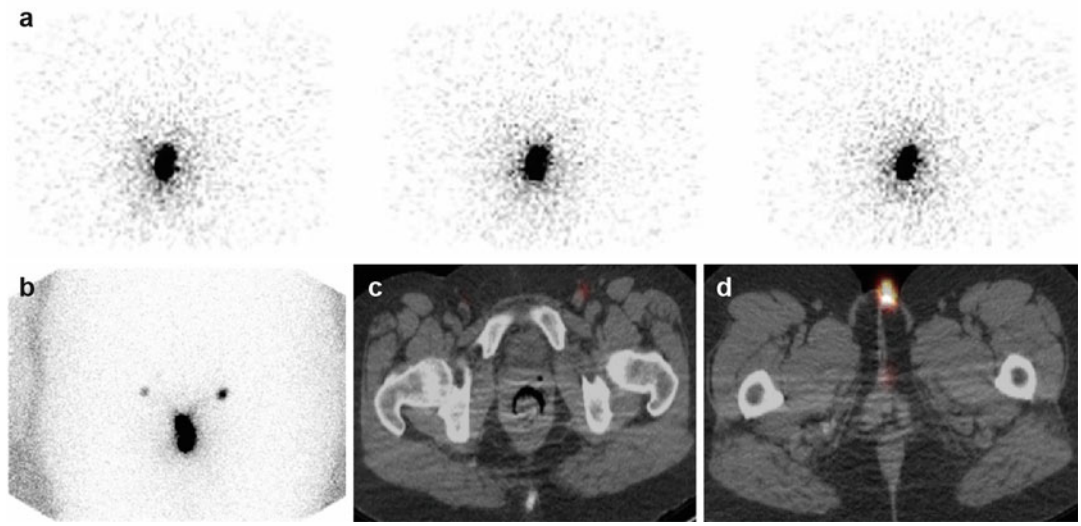

Fig. 9 Patient with vulvar cancer. LSG with ^{99m}Tc-sulfur colloid shows tracer at the site of injection and no significant transit elsewhere in dynamic imaging (**a**). Static image **b** shows tracer at injection site and bilateral groins, localizing to inguinal regions on SPECT/CT (**c**). Fused image **d** shows tracer at the site of vulvar lesion

References

1. sheet., S.s.f. National Cancer Institute. http://seer.cancer.gov/statfacts/html/vulva.html. Cited 25 Dec 2015.
2. Lanneau GS, et al. Vulvar cancer in young women: demographic features and outcome evaluation. Am J Obstet Gynecol. 2009;200(6):645.e1. 5.
3. Hinten F, et al. Clitoral involvement of squamous cell carcinoma of the vulva: localization with the worst prognosis. Eur J Surg Oncol. 2015;41(4):592–8.
4. Rouzier R, et al. Local relapse in patients treated for squamous cell vulvar carcinoma: incidence and prognostic value. Obstet Gynecol. 2002;100(6):1159–67.
5. Paladini D, et al. Prognostic-significance of lymph-node variables in squamous-cell carcinoma of the vulva. Cancer. 1994;74(9):2491–6.
6. Hussain SK, et al. Cervical and vulvar cancer risk in relation to the joint effects of cigarette smoking and genetic variation in interleukin 2. Cancer Epidemiol Biomarkers Prev. 2008;17(7):1790–9.
7. Daling JR, et al. Cigarette smoking and the risk of anogenital cancer. Am J Epidemiol. 1992;135(2):180–9.
8. Santegoets LA, et al. Different DNA damage and cell cycle checkpoint control in low- and high-risk human papillomavirus infections of the vulva. Int J Cancer. 2012;130(12):2874–85.
9. Wentzensen N, Vinokurova S, von Knebel Doeberitz M. Systematic review of genomic integration sites of human papillomavirus genomes in epithelial dysplasia and invasive cancer of the female lower genital tract. Cancer Res. 2004;64(11):3878–84.
10. Santegoets LA, et al. HPV related VIN: highly proliferative and diminished responsiveness to extracellular signals. Int J Cancer. 2007;121(4):759–66.
11. Dong F, et al. Squamous cell carcinoma of the vulva: a subclassification of 97 cases by clinicopathologic, immunohistochemical, and molecular features (p16, p53, and EGFR). Am J Surg Pathol. 2015;39(8):1045–53.
12. Lee YY, et al. Carcinoma of the vulva: HPV and p53 mutations. Oncogene. 1994;9(6):1655–9.
13. Preti M, et al. VIN usual type-from the past to the future. Ecancermedicalscience. 2015;9:531.
14. Hampl M, et al. Effect of human papillomavirus vaccines on vulvar, vaginal, and anal intraepithelial lesions and vulvar cancer. Obstet Gynecol. 2006;108(6):1361–8.
15. Giuliano AR, et al. Efficacy of quadrivalent HPV vaccine against HPV Infection and disease in males. N Engl J Med. 2011;364(5):401–11.
16. Dunne EF, et al. Recommendations on the use of quadrivalent human papillomavirus vaccine in Males-Advisory Committee on Immunization Practices (ACIP), 2011 (Reprinted from MMWR, vol 60, pg 1705, 2011). Jama-J Am Med Assoc. 2012;307(6):557–9.
17. Markowitz LE, et al. Quadrivalent human papillomavirus vaccine: recommendations of the Advisory Committee on Immunization Practices (ACIP). MMWR Recomm Rep. 2007;56(RR-2):1–24.
18. Centers for Disease, C. and Prevention. National and state vaccination coverage among adolescents aged 13–17 years – United States, 2011. MMWR Morb Mortal Wkly Rep. 2012;61(34):671–7.
19. Sideri M, et al. Squamous vulvar intraepithelial neoplasia: 2004 modified terminology, ISSVD Vulvar Oncology Subcommittee. J Reprod Med. 2005;50(11):807–10.
20. Eifel PJ, Berek JS, Markman MA. Cancer of the cervix, vagina, and vulva. Cancer: principles and practice of oncology. 9th ed. Philadelphia: Lippincott; 2011. p. 1311–44.
21. Medeiros F, Nascimento AF, Crum CP. Early vulvar squamous neoplasia: advances in classification, diagnosis, and differential diagnosis. Adv Anat Pathol. 2005;12(1):20–6.
22. Brown L, editor. Pathology of the vulva and vagina. London: Springer; 2013. p. 113–272.
23. Fuh KC, Berek JS. Current management of vulvar cancer. Hematol Oncol Clin North Am. 2012;26(1):45–62.
24. Pecorelli S. Revised FIGO staging for carcinoma of the vulva, cervix, and endometrium. Int J Gynaecol Obstet. 2009;105(2):103–4.
25. AJCC cancer staging manual. Springer International Publishing; 2017.
26. Berek J, HN. Berek & Hacker's gynecologic oncology. 2010.
27. Verschraegen CF, et al. Vulvar melanoma at the M. D. Anderson Cancer Center: 25 years later. Int J Gynecol Cancer. 2001;11(5):359–64.
28. Zhou J, Shan G. The prognostic role of FIGO stage in patients with vulvar cancer: a systematic review and -meta-analysis. Curr Med Res Opin. 2016;32(6):1121–30.
29. Maggino T, et al. Patterns of recurrence in patients with squamous cell carcinoma of the vulva. A multicenter CTF study. Cancer. 2000;89(1):116–22.
30. Homesley HD, et al. Prognostic factors for groin node metastasis in squamous cell carcinoma of the vulva (a Gynecologic Oncology Group study). Gynecol Oncol. 1993;49(3):279–83.
31. Landrum LM, et al. Gynecologic Oncology Group risk groups for vulvar carcinoma: improvement in survival in the modern era. Gynecol Oncol. 2007;106(3):521–5.
32. Luchini C, et al. Prognostic implications of extranodal extension in node-positive squamous cell carcinoma of the vulva: a systematic review and meta-analysis. Surg Oncol. 2016;25(1):60–5.
33. Sagdeo A, et al. The diagnostic challenge of vulvar squamous cell carcinoma: clinical manifestations and unusual human papillomavirus types. J Am Acad Dermatol. 2014;70(3):586–8.
34. Kuppers V, et al. Risk factors for recurrent VIN. Role of multifocality and grade of disease. J Reprod Med. 1997;42(3):140–4.
35. Gonzalez Bosquet J, et al. Patterns of inguinal groin metastases in squamous cell carcinoma of the vulva. Gynecol Oncol. 2007;105(3):742–6.
36. Hacker NF, et al. Radical vulvectomy and bilateral inguinal lymphadenectomy through separate groin incisions. Obstet Gynecol. 1981;58(5):574–9.
37. Tantipalakorn C, et al. Outcome and patterns of recurrence for International Federation of Gynecology and

Obstetrics (FIGO) stages I and II squamous cell vulvar cancer. Obstet Gynecol. 2009;113(4):895–901.
38. Guidelines, N. https://www.nccn.org/professionals/physician_gls/pdf/vulvar.pdf. 2016.
39. Trope C, et al. Bleomycin alone or combined with mitomycin C in treatment of advanced or recurrent squamous cell carcinoma of the vulva. Cancer Treat Rep. 1980;64(4–5):639–42.
40. Kim KW, et al. Update on imaging of vulvar squamous cell carcinoma. AJR Am J Roentgenol. 2013;201(1):W147–57.
41. Sohaib SA, et al. MR imaging of carcinoma of the vulva. AJR Am J Roentgenol. 2002;178(2):373–7.
42. Kataoka MY, et al. The accuracy of magnetic resonance imaging in staging of vulvar cancer: a retrospective multi-centre study. Gynecol Oncol. 2010;117(1):82–7.
43. Basu S, Li G, Alavi A. PET and PET-CT imaging of gynecological malignancies: present role and future promise. Expert Rev Anticancer Ther. 2009;9(1):75–96.
44. Grigsby PW. Role of PET in gynecologic malignancy. Curr Opin Oncol. 2009;21(5):420–4.
45. Cohn DE, et al. Prospective evaluation of positron emission tomography for the detection of groin node metastases from vulvar cancer. Gynecol Oncol. 2002;85(1):179–84.
46. Lin G, et al. Computed tomography, magnetic resonance imaging and FDG positron emission tomography in the management of vulvar malignancies. Eur Radiol. 2015;25(5):1267–78.
47. Kamran MW, et al. Whole-body [^{18}F]fluoro-2-deoxyglucose positron emission tomography scan as combined PET-CT staging prior to planned radical vulvectomy and inguinofemoral lymphadenectomy for squamous vulvar cancer: a correlation with groin node metastasis. Eur J Gynaecol Oncol. 2014;35(3):230–5.
48. Dolanbay, M, et al. F-18 fluoro-D-glucose (FDG)-positron emission tomography (PET)/computed tomography (CT) in planning of surgery and sentinel lymph node screening in vulvar cancers. Arch Gynecol Obstet. 2016;293:1319–24.
49. Robertson NL, et al. The impact of FDG-PET/CT in the management of patients with vulvar and vaginal cancer. Gynecol Oncol. 2016;140(3):420–4.
50. Cabanas RM. An approach for the treatment of penile carcinoma. Cancer. 1977;39(2):456–66.
51. Morton DL, et al. Technical details of intraoperative lymphatic mapping for early stage melanoma. Arch Surg. 1992;127(4):392–9.
52. Krag D, et al. The sentinel node in breast cancer – a multicenter validation study. N Engl J Med. 1998;339(14):941–6.
53. Harlow SP, et al. Gamma probe guided biopsy of the sentinel node in malignant melanoma: a multicentre study. Melanoma Res. 2001;11(1):45–55.
54. Burger MP, et al. The importance of the groin node status for the survival of T1 and T2 vulval carcinoma patients. Gynecol Oncol. 1995;57(3):327–34.
55. De Hullu JA, et al. Vulvar carcinoma. The price of less radical surgery. Cancer. 2002;95(11):2331–8.
56. Van der Zee AG, et al. Sentinel node dissection is safe in the treatment of early-stage vulvar cancer. J Clin Oncol. 2008;26(6):884–9.
57. Levenback CF, et al. Lymphatic mapping and sentinel lymph node biopsy in women with squamous cell carcinoma of the vulva: a gynecologic oncology group study. J Clin Oncol. 2012;30(31):3786–91.
58. Decesare SL, et al. A pilot study utilizing intraoperative lymphoscintigraphy for identification of the sentinel lymph nodes in vulvar cancer. Gynecol Oncol. 1997;66(3):425–8.
59. Bogliolo S, et al. Sentinel node mapping with radiotracer alone in vulvar cancer: a five year single-centre experience and literature review. Eur J Gynaecol Oncol. 2015;36(1):10–5.
60. de Hullu JA, et al. Sentinel lymph node identification with technetium-99m-labeled nanocolloid in squamous cell cancer of the vulva. J Nucl Med. 1998;39(8):1381–5.
61. de Hullu JA, et al. Sentinel lymph node procedure is highly accurate in squamous cell carcinoma of the vulva. J Clin Oncol. 2000;18(15):2811–6.
62. Merisio C, et al. Radioguided sentinel lymph node detection in vulvar cancer. Int J Gynecol Cancer. 2005;15(3):493–7.
63. Lindell G, et al. Evaluation of preoperative lymphoscintigraphy and sentinel node procedure in vulvar cancer. Eur J Obstet Gynecol Reprod Biol. 2010;152(1):91–5.
64. Tavares MG, et al. The use of ^{99m}Tc-phytate for sentinel node mapping in melanoma, breast cancer and vulvar cancer: a study of 100 cases. Eur J Nucl Med. 2001;28(11):1597–604.
65. Louis-Sylvestre C, et al. Sentinel node localization should be interpreted with caution in midline vulvar cancer. Gynecol Oncol. 2005;97(1):151–4.
66. Coleman RL, et al. Is bilateral lymphadenectomy for midline squamous carcinoma of the vulva always necessary? An analysis from Gynecologic Oncology Group (GOG) 173. Gynecol Oncol. 2013;128(2):155–9.
67. Klapdor R, et al. SPECT/CT for SLN dissection in vulvar cancer: improved SLN detection and dissection by preoperative three-dimensional anatomical localisation. Gynecol Oncol. 2015;138(3):590–6.
68. Kraft O, Havel M. Detection of sentinel lymph nodes in gynecologic tumours by planar scintigraphy and SPECT/CT. Mol Imaging Radionucl Ther. 2012;21(2):47–55.
69. Darin MC, et al. Role of indocyanine green in sentinel node mapping in gynecologic cancer: is fluorescence imaging the new standard? J Minim Invasive Gynecol. 2016;23(2):186–93.
70. Crane LM, et al. Intraoperative near-infrared fluorescence imaging for sentinel lymph node detection in vulvar cancer: first clinical results. Gynecol Oncol. 2011;120(2):291–5.

Diagnostic Applications of Nuclear Medicine: Uterine Cancers

35

Neeta Pandit-Taskar, Sonia Mahajan, and Weining Ma

Abstract

Cervical and uterine malignancies are a significant health issue for women worldwide. Uterine cancers are the most common gynecological cancers, although ovarian cancers have the highest mortality. The primary modalities for anatomic imaging are ultrasound, computed tomography (CT), and magnetic resonance imaging (MRI). These imaging tools are used for the diagnosis, staging, and posttherapy follow-up for detection of recurrent disease; however, they lack biologic information. Positron emission tomography (PET) with [^{18}F] fluoro-2-deoxy-D-glucose ([^{18}F]FDG) imaging plays a critical role in the evaluation of cervical and uterine malignancies. A number of studies have established the role of [^{18}F]FDG PET in the staging and prognosis of advanced cervical cancer. PET/MRI scanners with newer technology are available and in future may be the mainstay in assessment of gynecologic malignancies.

Radionuclide lymphoscintigraphy is an established technique for sentinel lymph node (SNL) mapping in vulvar cancer. For cervical and endometrial cancer, it can help prevent morbidities that follow lymphadenectomies and there is convincing evidence that SLN mapping can be useful in early-stage disease.

In this chapter, we discuss the role of nuclear imaging, especially [^{18}F]FDG PET scanning, and summarize the initial experiences with PET/MRI in cervical and uterine cancers; we also discuss the use of lymphoscintigraphy in gynecological cancers.

Keywords

FDG PET/CT • Cervical cancer • Endometrial cancer • Lymphoscintigraphy

Glossary

[^{18}F]FDG	2-Deoxy-2-[^{18}F]fluoro-D-glucose
^{18}F-FMISO	^{18}F-fluoromisonidazole, 1-fluoro-3-(2-nitroimidazol-1-yl)-propan-2-ol
ADC	Apparent diffusion coefficient, a parameter of magnetic resonance imaging
AJCC	American Joint Committee on Cancer
ceCT	Contrast-enhanced computed tomography
CI	Confidence interval
CIN	Cervical intraepithelial neoplasia
CT	X-ray computed tomogaphy
DES	Diethylstilbestrol
EC	Endometrial cancer

N. Pandit-Taskar (✉)
Department of Radiology, Memorial Sloan Kettering Cancer Center, New York, NY, USA

Department of Radiology, Weill Cornell Medical College, New York, NY, USA
e-mail: pandit-n@mskcc.org

S. Mahajan • W. Ma
Department of Radiology, Memorial Sloan Kettering Cancer Center, New York, NY, USA

© Springer International Publishing Switzerland 2017
H.W. Strauss et al. (eds.), *Nuclear Oncology*,
https://doi.org/10.1007/978-3-319-26236-9_45

FDA	United States Food and Drug Administration
FIGO	International Federation of Obstetrics and Gynecology
GLUT	Glucose transporter family
HIV	Human immunodeficiency virus
HK	Hexokinase
HPV	Human papilloma virus
IMRT	Intensity-modulated radiation therapy
IVP	Intravenous pyelography
LACC	Locally advanced cervical cancer
LSG	Lymphoscintigraphy
M	Metastasis status according to the AJCC/UICC TNM staging system
MIP	Maximum intensity projection
MRI	Magnetic resonance imaging
MTV	Metabolic tumor volume
N	Lymph node status according to the AJCC/UICC TNM staging system
NPV	Negative predictive value
OS	Overall survival
PALN	Para-aortic lymph nodes
PET	Positron emission tomography
PET/CT	Positron emission tomography/Computed tomography
PET/MRI	Positron emission tomography/Magnetic resonance imaging
PFS	Progression-free survival
PLN	Pelvic lymph nodes
PPV	Positive predictive value
SCC	Squamous cell carcinoma
SNL	Sentinel lymph node
SPECT	Single-photon emission computed tomography
SPECT/CT	Single-photon emission computed tomography/Computed tomography
SUV	Standardized uptake value
SUV_{max}	Standardized uptake value at point of maximum
T	Tumor status according to the AJCC/UICC TNM staging system
TLG	Total lesion glycolysis
UICC	Union Internationale Contre le Cancer (International Union Against Cancer)
US	Ultrasonography

Contents

Cervical Cancer 980
Epidemiology and Prevalence 980
Pathophysiology and Clinical Presentation 981
Diagnosis of Cervical Cancer 982
Role of Conventional Imaging 983
[^{18}F]FDG PET Imaging 984
Primary Cervical Cancer 984
[^{18}F]FDG PET in Staging of Cervical Cancer 987
Pelvic and Para-Aortic Lymph Node Assessment at Initial Staging, in Locally Advanced and Advanced Cervical Cancer 991
Prognostic Value of PET/CT 992
[^{18}F]FDG PET in Cervical Cancer: Impact on Management and Treatment Planning 994
[^{18}F]FDG PET in Recurrent Cervical Cancer 994

Endometrial Cancers 999
Epidemiology and Prevalence 999
Pathophysiology and Clinical Presentation 1002
Role of Conventional Imaging 1003
Role of [^{18}F]FDG PET in Endometrial Carcinoma 1003
Lymphoscintigraphy 1009

References 1014

Cervical Cancer

Epidemiology and Prevalence

Cervical cancer is the second most common cancer in women worldwide and the third most common gynecologic cancer in the United States with 12,990 new cases and 4,120 deaths predicted in 2016 [1]. Cervical cancer was once a leading cause of cancer death for women in the United States; however, the prevalence and mortality have decreased significantly in the past few decades largely as a result of effective screening with the Papanicolaou (Pap) smear test. A continuous decline in the death rate has been observed, at a rate of nearly 0.8% each year. Cervical cancer is uncommon in women younger than 20 years, and most often occurs in women younger than 50 years although about 15–20% cases may occur in women over 65 years. It is more common in Black and Hispanic women compared

with non-Hispanic White women. The 5-year relative survival rate for early-stage invasive cervical cancer is 91.3%, while the overall 5-year survival rate for all stages is about 67.5% [1] (Fig. 1).

Cervical cancer is associated with several risk factors such as human papilloma virus (HPV), cigarette smoking, chlamydia, and human immunodeficiency virus (HIV) infection, long-term use of oral contraceptives or exposure to diethylstilbestrol (DES), diet low in fruits and vegetables, low socioeconomic status, multiple pregnancies, and younger age at first pregnancy. The most important risk factor for cervical cancer is HPV infection. The high-risk viral types are HPV 16, HPV 18, HPV 31, HPV 33, and HPV 45, with about two thirds of all cervical cancers being associated with HPV 16 and 18 [2]. Vaccines have been developed to help prevent infection with some types of HPV; currently three HPV vaccines have been approved for use in the United States by the Food and Drug Administration (FDA) [2].

Pathophysiology and Clinical Presentation

There are generally no symptoms in women with precancerous lesions and early cervical lesions.

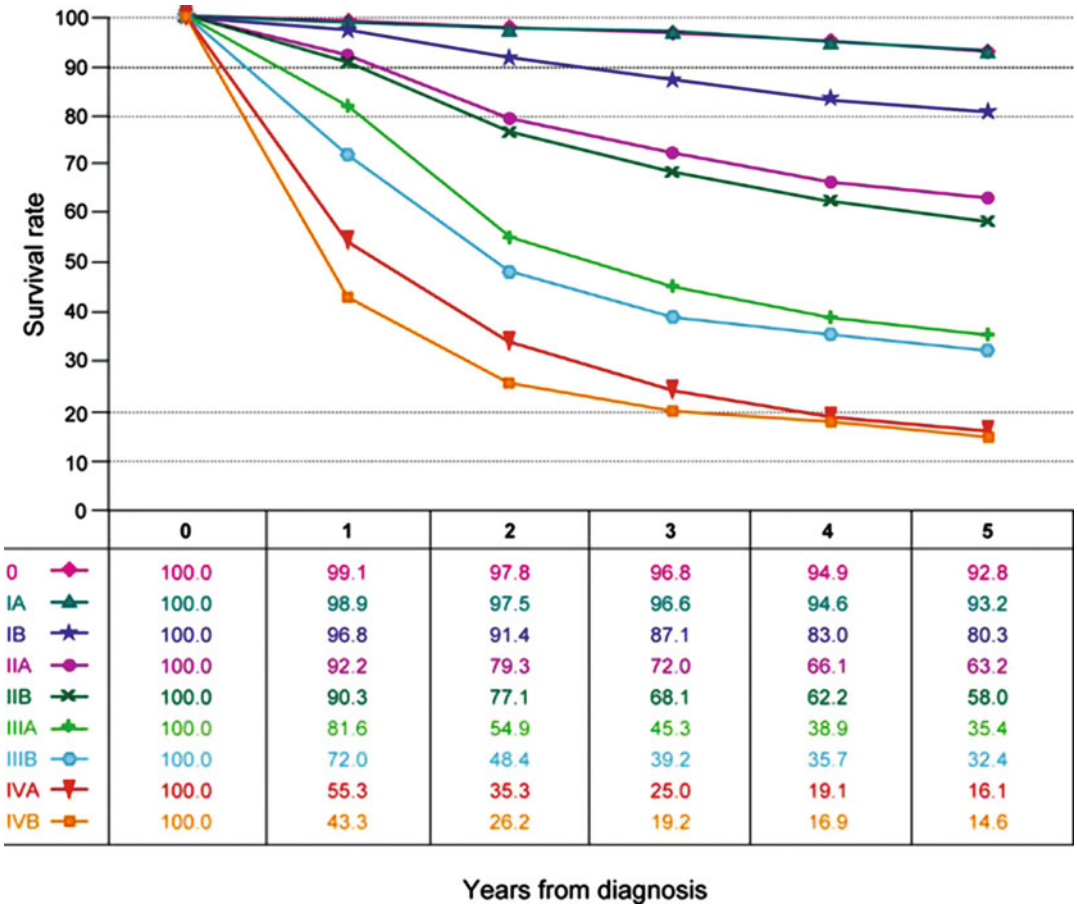

	0	1	2	3	4	5
0	100.0	99.1	97.8	96.8	94.9	92.8
IA	100.0	98.9	97.5	96.6	94.6	93.2
IB	100.0	96.8	91.4	87.1	83.0	80.3
IIA	100.0	92.2	79.3	72.0	66.1	63.2
IIB	100.0	90.3	77.1	68.1	62.2	58.0
IIIA	100.0	81.6	54.9	45.3	38.9	35.4
IIIB	100.0	72.0	48.4	39.2	35.7	32.4
IVA	100.0	55.3	35.3	25.0	19.1	16.1
IVB	100.0	43.3	26.2	19.2	16.9	14.6

Fig. 1 Observed survival rates for 15,070 cases with carcinoma of the cervix uterus. Data from the National Cancer Data Base (Commission on Cancer of the American College of Surgeons and the American Cancer Society) diagnosed in years 2000–2002. Stage 0 includes 7,119 patients; Stage IA, 1,530; Stage IB, 2,249; Stage IIA 453; Stage IIB, 1,518; Stage IIIA, 191; Stage IIIB, 1,009; Stage IVA, 213; and Stage IVB, 788. (Used with the permission of the American Joint Committee on Cancer (AJCC), Chicago, IL. The original source for this material is the AJCC Cancer Staging Manual, Seventh Edition (2010) published by Springer Science and Business Media LLC. http://www.springer.com)

Abnormal postmenopausal vaginal bleeding, including postcoital bleeding, intermenstrual bleeding, menorrhagia and spotting between periods, abnormal discharge, painful coitus, and bleeding after vaginal examination are some of the symptoms that are associated with advanced stages and invasive cancers. In some advanced-stage cases, symptoms of bowel obstruction or urinary tract obstruction may be found at presentation [3].

Cervical intraepithelial neoplasia (CIN) is a precursor lesion of cervical cancer and is graded into three groups based on cellular dysplasia: CIN 1 with minor dysplasia; CIN 2 with moderate dysplasia; and CIN 3 or carcinoma in-situ with severe dysplasia. Up to 40% of CIN 3 lesions could develop into invasive cervical cancer if left untreated.

Histologically, 80–90% of all cervical malignancies are squamous cell carcinoma (SCC) (Table 1), with 25% well-differentiated, keratinizing, large-cell SCC histology while 70% are moderately differentiated, non keratinizing, large-cell SCC. Small-cell undifferentiated carcinomas account for only about 5% of cases, but are associated with a poor prognosis. Adenocarcinomas arise from endocervical-type cells and constitute 5–20% of all cervical malignancies. The histologic patterns of adenocarcinoma include well-differentiated mucinous adenocarcinoma, papillary adenocarcinoma, and clear-cell types. Poorly differentiated and aggressive histologic subtypes of cervical adenocarcinoma are associated with a poorer prognosis compared with SCC. Miscellaneous, uncommon, or rare cancers of the cervix include variants of SCC and adenocarcinomas, mixed carcinomas, small-cell carcinoma, sarcoma, lymphoma, melanoma, and metastatic tumors. The most common metastases arise from endometrial primary tumors while others include the ovary, colon, and breast primaries [3–4].

Preinvasive lesions can be treated with electrocoagulation, conization, cryotherapy, laser ablation, or local surgery, while invasive cancers require surgery (total hysterectomy, modified radical hysterectomy, or radical trachelectomy), radiation or chemotherapy, or combination therapy. The survival rate for women with localized cancer is about 91% at 5 years. However, it is lower for women with advanced disease with relative 1-year and 5-year survival rates of 88% and 73%, respectively. The 5-year survival rate is 57% when tumor has spread to surrounding tissues or organs and/or the regional lymph nodes and is only 16.8% in the presence of distant metastatic disease [1].

Diagnosis of Cervical Cancer

The Pap test is a very effective screening test that has led to the detection of a large number of cervical cancers at early stages. The American Cancer

Table 1 Pathological types of cervical cancer

1. Squamous cell carcinoma
a. Carcinoma in situ (CIN)
b. Microinvasive carcinoma
c. Invasive squamous cell carcinoma
2. Variants of squamous cell carcinoma
a. Verrucous carcinoma
b. Papillary squamous and transitional carcinoma
c. Lymphoepithelioma-like carcinoma
3. Adenocarcinoma
a. Early invasive
b. Mucinous adenocarcinoma
i. Endocervical variant
ii. Intestinal type, signet ring and colloid variants
iii. Minimal deviation variant (adenoma malignum)
iv. Well-differentiated villoglandular variant
c. Endometrioid adenocarcinoma
d. Clear cell adenocarcinoma
e. Serous adenocarcinoma
f. Mesonephric adenocarcinoma
g. Microcystic endocervical adenocarcinomas
4. Other epithelial tumors
a. Adenosquamous carcinoma
b. Glassy cell carcinoma
c. Adenoid cystic carcinoma
d. Adenoid basal epithelioma
e. Neuroendocrine tumors
f. Carcinoid tumors
5. Mixed epithelial and mesenchymal tumors
a. Mullerian adenosarcomas
6. Other malignant tumors
a. Sarcomas
b. Secondary tumors

Society recommends screening for cervical cancer to start approximately 3 years after a woman begins to have vaginal intercourse, but no later than 21 years of age [2]. For women between 21 and 29 years of age, the Pap test is recommended every 3 years. At 30 or more years of age, both a Pap test and an HPV test should be performed every 5 years, or a Pap test only every 3 years. In women who have three normal test results in a row, screening may be performed every 2–3 years. Women with a higher risk such as those with HIV infection or a weak immune system may need to get screened more frequently. Women aged 65 years and older, who have had three or more consecutive normal Pap tests in the past 10 years and have not had any precancerous histology (CIN 2 or 3) detected in the previous 20 years, may choose to stop cervical cancer screening. Screening after total hysterectomy is not necessary, unless surgery was done for cervical cancer [2].

Patients with suspicious findings on Pap smear or patients with high-risk HPV strains could be further evaluated with colposcopy or colposcopy-directed biopsies of the suspicious areas and if necessary with conization to establish the diagnosis [2–5]. Those diagnosed with cervical cancer should undergo clinical staging with imaging and detailed pathology followed by surgical staging.

Role of Conventional Imaging

Patients are staged clinically according to the International Federation of Gynecologic and Obstetrics (FIGO) staging system (Table 2). Conventional imaging studies recommended for clinical staging include chest x-ray, barium enema, and intravenous urogram. However, ultrasound (US), computed tomography (CT), magnetic resonance imaging (MRI), and positron emission tomography (PET) are increasingly being used. Intravenous pyelography (IVP) and barium enema are usually restricted for selective patients.

Surgical staging is generally done to assess pelvic and para-aortic lymph node (PALN) involvement, critical for further treatment and follow-up. Establishing the local extent of the primary tumor is very important and, while involvement of pelvic or para-aortic lymph nodes may not affect the FIGO staging, it identifies patients with a worse prognosis [6–9]. Spread of cervical cancer occurs initially by direct extension to local structures and regional lymphatics, later disseminating hematogenously to distant organs, such as the lung, bone, liver, and brain. Nodal metastasis sequentially involves first the pelvic lymph nodes followed by para-aortic and supraclavicular lymph nodes. Scalene nodes can also be involved in up to 17% of the cases, seen more commonly in patients who have para-aortic nodal disease [6, 10–11]. Bone metastasis occurs infrequently and therefore bone scans are not routinely indicated. Bone scans are indicated in patients with bone pain. For initial staging, imaging is critical to define the local extent of cervical cancer and detect local *and* distant nodal metastatic disease. Abdominal and pelvic CT provides high-resolution anatomic detail and is an integral part of routine staging. Disease in the cervix, uterus, parametrium and adnexa, as well as pelvic and abdominal nodes and extrapelvic disease sites, can be assessed with high sensitivity [12]. Evaluation of microscopic disease, however, is limited since the anatomic changes are subtle, thereby reducing the sensitivity of CT. In high-risk cases, CT of the chest is performed to detect lung and mediastinal disease.

MRI has superior soft tissue characterization and is preferred for assessment of the local extent of tumors (Figs. 2, 3, and 4). MRI can help predict endometrial involvement in about 84–96% of the cases compared with 55–80% for CT and has a high negative predictive value (NPV) [12–14]. Para-aortic nodal metastasis can be detected with high specificity; however, the sensitivity is only 50% [14]. Staging using physical examination, colposcopy, lesion biopsy, and cystoscopy or sigmoidoscopy may understage up to 30% of stage I and II cases and up to 40% of stage III cases. Conversely, it may overstage approximately 64% of patients with stage IIIB disease [8–9, 15–17]. Accurate assessment of tumor size, especially in endocervical location, parametrial and pelvic sidewall invasion, lymph node and distant metastases is extremely important for prognosis. Although CT is an integral part of the clinical staging, useful to evaluate both local extent and metastatic disease [18], CT is limited, especially in early stage [9] disease. Additional

Table 2 TNM and FIGO classification of carcinoma of the cervix

TNM categories (FIGO stage)	Description
TX	Primary tumor cannot be assessed
T0	No evidence of primary tumor
Tis[a]	Carcinoma in situ (preinvasive carcinoma)
T1 I	Cervical carcinoma confined to uterus (extension to corpus should be disregarded)
T1a[b] **(IA)**	Invasive carcinoma diagnosed only by microscopy. Stromal invasion with a maximum depth of 5.0 mm measured from the base of the epithelium and a horizontal spread of 7.0 mm or less. Vascular space involvement, venous or lymphatic, does not affect classification
T1a1 (IA1)	Measured stromal invasion 3.0 mm or less in depth and 7.0 mm or less in horizontal spread
T1a2 (IA2)	Measured stromal invasion more than 3.0 mm and not more than 5.0 mm with a horizontal spread 7.0 mm or less
T1b (IB)	Clinically visible lesion confined to the cervix or microscopic lesion greater than T1a/IA2
T1b1 (IB1)	Clinically visible lesion 4.0 cm or less in greatest dimension
T1b2 (IB2)	Clinically visible lesion more than 4.0 cm in greatest dimension
T2 (II)	Cervical carcinoma invades beyond uterus but not to pelvic wall or to lower third of vagina
T2a (IIA)	Tumor without parametrial invasion
T2a1 (IIA1)	Clinically visible lesion 4.0 cm or less in greatest dimension
T2a2 (IIA2)	Clinically visible lesion more than 4.0 cm in greatest dimension
T2b (IIB)	Tumor with parametrial invasion
T3 (III)	Tumor extends to pelvic wall and/or involves lower third of vagina, and/or causes hydronephrosis or nonfunctioning kidney
T3a (IIIA)	Tumor involves lower third of vagina, no extension to pelvic wall
T3b (IIIB)	Tumor extends to pelvic wall and/or causes hydronephrosis or nonfunctioning kidney
T4 (IVA)	Tumor invades mucosa of bladder or rectum, and/or extends beyond true pelvis (bullous edema is not sufficient to classify a tumor as T4)
Nodal stage	
NX	Regional lymph nodes cannot be assessed
N0	No regional lymph node metastasis
N1 (IIIB)	Regional lymph node metastasis
Metastasis	
M0	No distant metastasis
M1 (IVB)	Distant metastasis (including peritoneal spread, involvement of supraclavicular, mediastinal, or para-aortic lymph nodes, lung, liver, or bone)

[a]Note: FIGO no longer includes stage 0 (Tis)
[b]All microscopically visible lesions, even with superficial invasion are T1b/IB

imaging with MRI and [^{18}F]FDG PET/CT can provide critical information for management of disease.

[^{18}F]FDG PET Imaging

PET/CT is useful in the staging of cervical cancer patients to assess local extent, pelvic nodal involvement, and detect distant metastases. This information is useful for planning surgery and/or for radiation therapy planning. It is useful in assessing response to neoadjuvant therapy and for identification of persistent/recurrent disease after treatment.

Primary Cervical Cancer

[^{18}F]FDG avidly localizes in cervical cancer. The uptake of [^{18}F]FDG in cervical cancer appears to be related to high GLUT-1 expression in tumor cells; however, there is no established correlation of PET/CT-based standardized uptake value (SUV) or GLUT-1 expression with the initial

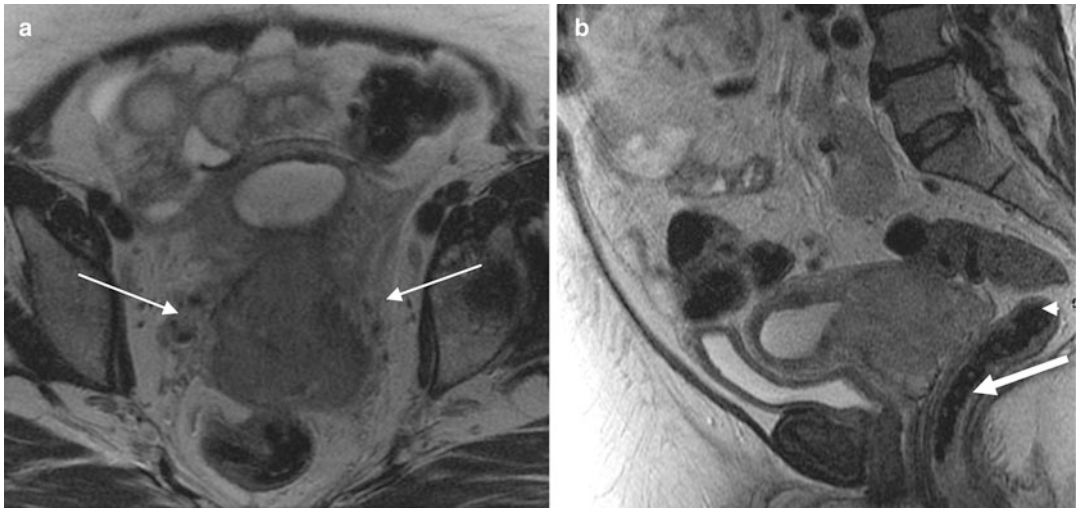

Fig. 2 Magnetic resonance imaging of the pelvis: axial T2-weighted (**a**) and sagittal T2-weighted images (**b**) show a large soft tissue mass in the cervix invading the parametrium bilaterally (*white arrows*), involving the upper third of the vagina (*thick arrow*), and abutting the anterior wall of the rectosigmoid colon (*arrow head*). No bladder or lower vaginal invasion is noted. Biopsy revealed well- to moderately differentiated squamous cell carcinoma

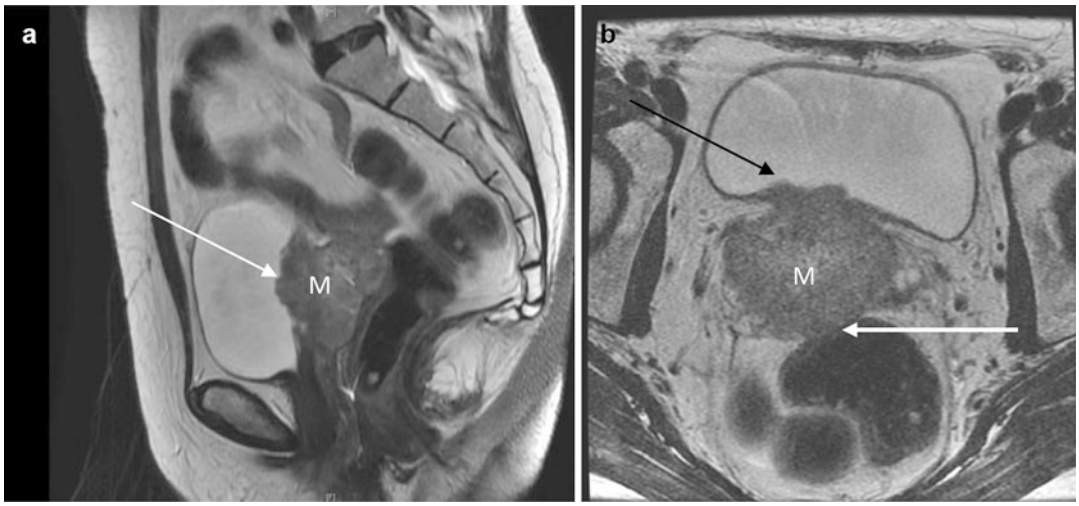

Fig. 3 Magnetic resonance imaging of the pelvis: (**a**) sagittal T2-weighted image shows a soft tissue mass (*M*) arising from cervical stump, status after prior supracervical hysterectomy for cervical cancer, invading posterior bladder wall (*black arrows*); (**b**) axial T2-weighted image shows cervical stump of recurrent mass again invading the posterior bladder wall (*black arrow*) and possibly invading anterior rectal wall, with obliteration of fat planes (*white arrow*). Surgical pathology showed squamous cell carcinoma, moderately or poorly differentiated

grade of histologic differentiation and FIGO staging. Higher GLUT-1 expression is seen in recurrent or persistent disease than in metastatic lymph nodes [19]. Similarly, a higher PET positivity has been noted in pathologically positive nodes with higher expression of GLUT-1 and HK-II [20].

Although most primary cervical cancers accumulate [^{18}F]FDG (Fig. 5), poorly differentiated and squamous cell histology tumors are more [^{18}F]FDG avid. In 240 patients with stage I–IV disease, a significant difference in uptake was seen in well vs. poorly differentiated lesions with a mean

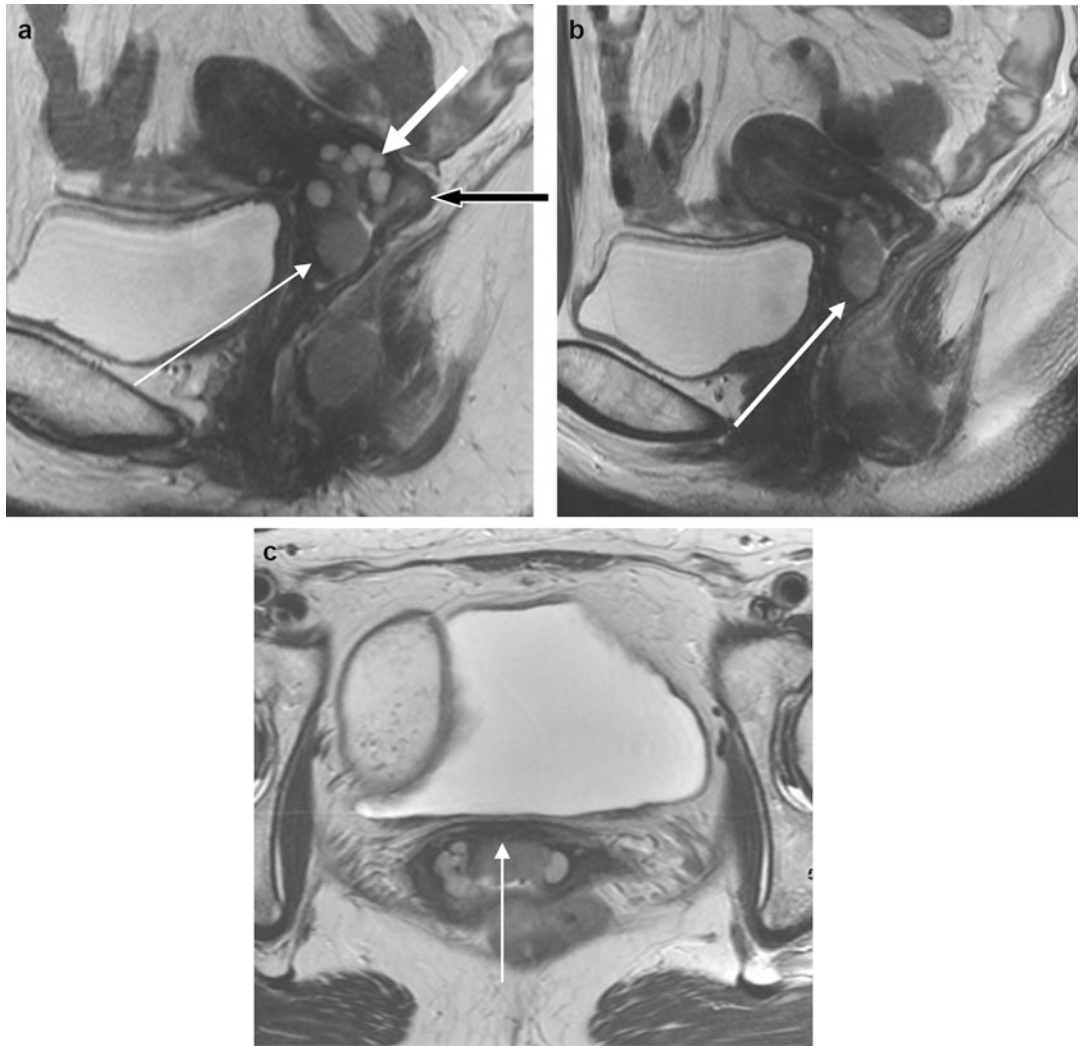

Fig. 4 Magnetic resonance imaging of the pelvis: (**a**, **b**) sagittal T2-weighted and axial T2-weighted images (**c**) show intermediate T2 signal intensity of cervical lesion consistent with cervical cancer (*white thin arrows*). The bulk of the lesion within the ventral aspect of the cervical canal demonstrates deep stromal invasion, without extension involving the parametrium. Then tumor extends into the posterior aspect of the cervix into the posterior fornix of the vagina (**a**, *black arrow*). Multiple nabothian cysts are seen in the cervical canal (**a**, *white thick arrow*). The tumor abuts the internal cervical os and no extension into the lower uterine segment is seen

SUV_{max} of 8.58 for well-differentiated, 11.56 for moderately differentiated, and 12.23 for poorly differentiated tumors [19]. Higher uptakes were seen in squamous cell histology (average SUV_{max} of 11.91, range 2.50–50.39) than in non-squamous histology (average SUV_{max} of 8.05, range 2.83–13.92). A higher SUV_{max} is associated with an increased risk of nodal involvement: Patients with $SUV_{max} < 5$ had 24% nodal involvement compared with 59% for patients with SUV_{max} 5–14, and 72% for those with $SUV_{max} > 14$ [19]. Similar findings were noted for 43 patients with cervical cancer (stage IB–IVB) where, using a cut-off SUV_{max} value of 13.5 for defining high- vs. low-uptake groups, it was noted that lymph node metastasis, predominantly pelvic, was more commonly seen in the high SUV_{max} group (73%, 16/22) than in the low SUV_{max} group (38%, 8/21) [21].

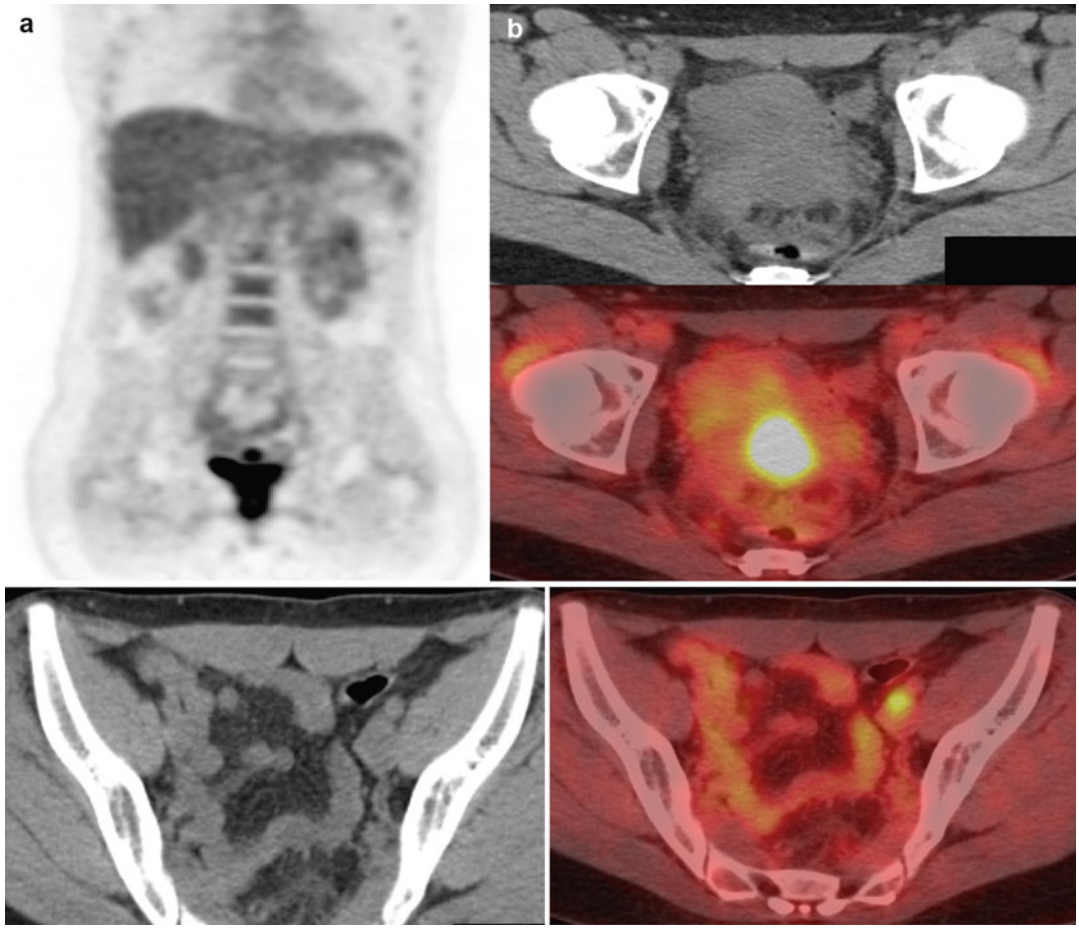

Fig. 5 (**a**, **b**) Primary carcinoma of the cervix: extent of disease at diagnosis. A 50-year-old woman with cervical cancer. [^{18}F]FDG PET/CT showed abnormal uptake (SUV_{max} 13.6) in the cervix and uptake in left external iliac node

Early studies used dedicated PET scanners without CT capability [22]. Fusion imaging with PET/CT scanners improves localization and hence diagnosis thereby leading to a decrease in equivocal results. This is especially relevant for gynecologic malignancies where peritoneal and serosal bowel implants may be obscured by physiological [^{18}F]FDG activity. Early studies showed the increased accuracy of hybrid PET and CT imaging compared with side-by-side reading of CT and PET. These studies demonstrated improved accuracy in detecting nodal involvement and lesions adjacent to the chest or abdominal wall or bowel [23]. The hybrid method also improved characterization of physiological and inflammatory uptake [24].

In 13 primary and metastatic uterine cervical cancer patients, PET/CT provided more definite lesion localization in 30% and additional definite lesion characterization in 20% of patients compared with PET alone. There was higher diagnostic accuracy with PET/CT than with PET alone on a lesion-based analysis (92% vs. 78%), although no difference was noted for evaluation of metastatic disease [25].

[^{18}F]FDG PET in Staging of Cervical Cancer

Clinical studies have shown the usefulness of PET/CT in staging cervical cancer (Table 3). While

Table 3 Carcinoma of the cervix: staging/para-aortic and pelvic nodal assessment on [^{18}F]FDG PET

Author and year	Type	Stage	Number of patients; Histology	Comparative imaging (CT or MRI)	Histopathology confirmation (Yes/No)	Sensitivity/specificity/accuracy
Driscoll et al. 2015	Prospective	IA ($n = 9$), IB1 ($n = 38$)	47; SCC ($n = 31$), Adenocarcinoma ($n = 14$), Adenosquamous ($n = 2$)	MRI (negative)	Yes	Patient based: 0%/100%/96% Node based: 0%/100%/99%
Gouy et al. 2013	Prospective	IB2 ($n = 79$), IIA ($n = 10$), IIB ($n = 121$), IIIA ($n = 6$), IIIB ($n = 16$), IVA ($n = 5$)	237; SCC ($n = 199$), Adenocarcinoma ($n = 35$), Adenosquamous ($n = 1$), Clear cell ($n = 1$), Glassy cell ($n = 1$)	MRI/CT/PET (negative)	Yes	NA/NA, False-negative rate – 12%
Leblanc et al. 2011	Prospective	IB2 ($n = 43$), IIA ($n = 9$), IIB ($n = 46$), IIIA ($n = 2$), IIIB ($n = 13$), IVA ($n = 10$), recurrent ($n = 2$)	125; SCC ($n = 109$), Adenocarcinoma ($n = 14$), Clear cell ($n = 2$)	MRI and CT (negative)	Yes	LN size >5 mm: 42%/93%, LN size <5 mm: 22%/91%
Lv et al. 2014	Retrospective	IA1 ($n = 3$), IA2 ($n = 14$), IB1 ($n = 19$), IB2 ($n = 15$), IIA ($n = 26$), IIB ($n = 10$)	87; SCC ($n = 69$), Adenocarcinoma ($n = 12$), Neuroendocrine ($n = 2$), Clear cell ($n = 4$)	MRI	Yes	Node based – [^{18}F]FDG: 91%/NA/98% MRI: 37.3%/NA/95%. Patient based – [^{18}F]FDG: 100%/NA/94.3% MRI: 44%/NA/69%
Perez-Medina et al. 2013	Prospective	IB2 ($n = 17$), IIA2 ($n = 3$), IIB ($n = 18$), IIIA ($n = 3$), IIIB ($n = 8$), IVA ($n = 3$)	52; SCC ($n = 38$), Adenocarcinoma ($n = 13$), Clear cell ($n = 1$)	MRI	Yes	FDG: 77.7%/94.1%/NA MRI: 66.7%/94.1%/NA

Monteil et al. 2011	Prospective	IA ($n = 1$), IB1 ($n = 10$), IB2 ($n = 4$), IIB ($n = 22$), IIIB ($n = 2$), IVA ($n = 1$)	40; SCC ($n = 28$), Adenocarcinoma ($n = 12$)	MRI	Yes	Pelvic LN metastases – [^{18}F]FDG: 33%/92%/81%, MRI: 67%/84%/81% Para-aortic LN metastases – [^{18}F] FDG: 100%/77%/70%, MRI: 60%/73%/70%
Ramirez et al. 2011	Prospective	IB2 ($n = 16$), IIA ($n = 12$), IIB ($n = 16$), IIIA ($n = 4$), IIIB ($n = 12$)	60; SCC ($n = 48$), Adenocarcinoma ($n = 9$), Neuroendocrine ($n = 2$), Transitional cell ($n = 1$)	CT/MRI (negative)	Yes	36%/96%/NA In patients with positive pelvic LN: 45%/91%/NA
Nogami et al. 2015	Prospective	IA ($n = 5$), IB ($n = 62$), IIA ($n = 2$), IIB ($n = 1$)	70; SCC ($n = 41$), Adenosquamous($n = 2$), Mucinous adenocarcinoma ($n = 20$), Glassy cell ($n = 2$), Serous adenocarcinoma ($n = 1$), Endometroid ($n = 1$), Endometroid adenocarcinoma ($n = 3$)	None	Yes	Case based – 33.3%, 92.7% LN based – 30.6%, 98.9%
Yang, 2016	Retrospective	IB1 ($n = 56$), IB2 ($n = 17$), IIA1 ($n = 35$), IIA2 ($n = 5$)	113; NA	No	Yes	53.8%/95%/94.7%

NA not available, *SCC* squamous cell carcinoma

the reported sensitivity is variable ranging from 38% to 86%, a definite advantage of [^{18}F]FDG PET is the ability to detect (a) involvement of lymph nodes that are benign using size criteria and (b) distant metastases that were not detected by other imaging modalities [26], especially defining pelvic and distant nodal status [27–29]. In a retrospective analysis ($n = 41$) [^{18}F]FDG PET showed 100% accuracy in detecting disease for initial staging, while for restaging, sensitivity and specificity were 82% and 97%, respectively [22]. MRI facilitates an excellent evaluation of local tumor and parametrial involvement, while PET is more useful for the evaluation of pelvic lymph nodes; however, microscopic disease is missed by both modalities [30]. An additional advantage of PET/CT over MRI includes the ability to image larger scanning areas allowing for an estimation of thoracic or suprathoracic disease in a single study. Tran and colleagues detected supraclavicular nodal involvement in about 8% of patients with a 100% positive predictive value (PPV) [11].

The sensitivity and accuracy of [^{18}F]FDG for detection of lesions are higher for advanced disease but lower in early-stage disease including stage IA2–IIA, although abnormal lymph nodes may be detected better with [^{18}F]FDG PET than with CT [31–34].

[^{18}F]FDG PET is more sensitive than CT or MRI for detecting lymph node metastases [27–28, 32, 34–37]. Using a cut-off SUV_{max} value of 2.5 on PET/CT and 1 cm or greater lesion size on MRI, higher sensitivity and accuracy for detecting lymph node metastases were noted with [^{18}F]FDG PET compared with MRI (91% and 98%, respectively, vs. 37.3% and 95%, respectively). MRI yielded negative findings for 63% of positive lymph nodes diagnosed, and 56% (19/34) of patients were inappropriately classified. MRI also gave false-positive results in 16 lymph nodes [37]. However, the sensitivity for micrometastasis in early cervical cancer is low for both; in 120 patients who had a normal MRI for pelvic nodes, PET had low sensitivity for detection of micrometastasis;, all PET-undetected nodes had micrometastasis with a mean tumor focus of 4.0 × 3.0 mm (range 0.5 × 0.5 to 7 × 6 mm) [32]. Other groups have reported a false-negative lymph node detection rate for [^{18}F]FDG PET between 13% and 32% cases, although detection was overall better compared with CT [33, 38–39]. Higher sensitivity with MRI (93%) has been reported using iron oxide nanoparticles for contrast-enhanced imaging for nodal detection than when using the conventional size criteria (29%) [40].

In a study of 22 patients with stage IB–IVA cervical cancer, Choi et al. found that PET/CT had a higher sensitivity (57%) than MRI (33%) for lymph node detection, and that nodal size was critical for detection. In their study, the short-axis dimension of metastatic lymph nodes was 11.8 ± 3.5 mm while that of nonmetastatic nodes was (6.5 ± 4.6 mm); understandably, the detection of lymph node metastases was higher for areas of larger involvement. Regionwise, the overall sensitivity of MRI for detecting lymph node metastases (32.0%) appears to be lower than PET, with a detection rate of 42.9% and 54.5% for tumor diameters of 5–10 mm and >10 mm, respectively [41]. Some studies report a high number of false negatives (8/10 or 80%) in lesions smaller than 10 mm in diameter, noted on thin-slice examination of the pathological specimen [32]. Overall reported sensitivities for disease detection in cervical cancer are widely variable, possibly due to differences in the completeness of surgical staging and the number of lymph nodes removed.

The value of PET/CT in early-stage cervical cancer is limited and while not recommended as a routine evaluation for staging [32–33, 42–43], it has a high specificity especially for detecting nodal disease, although small-volume disease may be missed. In a study by Sironi et al., 47 patients with stage IA and IB disease were evaluated preoperatively. The overall patient-based sensitivity and specificity of PET/CT was 73% and 97%, respectively. The overall node-based specificity was 99.7% and while the overall sensitivity was lower (72%), a 100% sensitivity was seen for lymph nodes larger than 0.5 cm in diameter [44].

In a recent retrospective analysis of 113 patients, [^{18}F]FDG PET/CT showed high accuracy in preoperative staging (94.7%) and was superior to clinical staging. Six patients were upstaged based on [^{18}F]FDG findings. Nodal staging had lower sensitivity (53.8%) but was more specific (95%)

[45]. The study evaluated use of metabolic tumor volume (MTV) for predicting stromal invasion and showed that an MTV cut-off of 8.76 had a sensitivity of 75.0% and specificity of 76.2% for predicting stromal invasion and may be a useful parameter. This, however, needs to be established in a larger study.

In a prospective study of 120 patients with newly diagnosed cervical cancer with FIGO stage ≥IB, [^{18}F]FDG PET/CT had 75% sensitivity and 96% specificity for nodal status in those who underwent surgery [46]. For para-aortic nodal disease, the PPV was 94%, NPV 100%, sensitivity 100% and specificity 99%, while for distant metastasis PPV was 63%, NPV 100%, sensitivity 100%, and specificity 94%. This highlights the ability to decide on the management of patients: Those with PET-positive nodes can be offered radio/chemotherapy instead of surgery, and patients with para-aortic nodal involvement may be treated with extended-field radiotherapy [46]. In comparison with MRI, [^{18}F]FDG PET shows higher sensitivity for the detection of para-aortic nodes and may be useful in guiding PALN dissection [47].

False-positive findings on [^{18}F]FDG PET may be seen for lymph nodes with granulomatous involvement or in reactive nodes especially in sites such as the axilla and groin, which may raise concern for metastatic disease and lead to further evaluation. The limitations of [^{18}F]FDG PET also include false-negative results related to low spatial resolution and micrometastasis, and false-positive results related to bowel uptake and urinary artifacts. Distant metastases are uncommon in sites like the neck or mediastinum, while metastases in the liver, lung, omentum, or bones are seen in more aggressive and higher-stage disease [46].

Pelvic and Para-Aortic Lymph Node Assessment at Initial Staging, in Locally Advanced and Advanced Cervical Cancer

The rate of PALN involvement in locally advanced cervical cancer (LACC) is 15–20%, and it carries a poor prognosis with an overall survival (OS) rate of only 17% [48–49]. Early studies using [^{18}F]FDG PET with 12 or more subjects and with a clinical follow-up of 6 months or longer, or histopathology as the reference standards, showed a pooled sensitivity of 79% (95% CI, 65–90%) and a pooled specificity of 99% (96–99%) for detection of pelvic or para-aortic lymph node metastasis in patients with newly diagnosed cervical cancer [27–29, 44, 50]. In comparisons of PET with MRI with CT, PET was superior to both [31, 33, 50]. CT had a pooled sensitivity of 47% (95% CI, 21–73%) and MRI had a pooled sensitivity of 72% (95% CI, 53–87%) and a pooled specificity of 96% (95% CI, 92–98%).

Sugawara et al. in a study of 21 patients with cervical cancer of stages IB to IVA, reported a sensitivity of 86% for [^{18}F]FDG PET in pelvic lymph node and PALN metastasis detection, which was higher than CT (57% sensitivity) [51]. Rose et al. studied presurgical patients with stages IIB–IVA and reported a sensitivity of 75% and specificity of 92% for [^{18}F]FDG PET in depicting PALN metastasis. In these studies there was overall higher sensitivity (100%) for PLN detection than for PALN metastases [27].

In prospective studies comparing [^{18}F]FDG PET imaging for PALN metastasis with histopathology after para-aortic lymphadenectomy, the pooled sensitivity of PET for the detection of PALN metastasis was 84% (95% CI, 68–94%) and the pooled specificity was 95% (89–98%) [33, 52–54]. Pooled data from 15 studies on [^{18}F]FDG PET in cervical cancer showed 84% sensitivity (range 68–98%) and 95% specificity (range 89–98%) for PALN metastasis, with a 79% sensitivity (range 65–90%) and 99% specificity (range 96–99%) for PLN metastasis [55].

In a meta-analysis of PALN detection, data from ten studies involving 385 patients showed the overall specificity of [^{18}F]FDG PET to be as high as 97% (95% CI, 93–99%), but with a low overall sensitivity that was highly variable among the studies (average 34%; 95% CI, 10–72%). In the five studies with a prevalence of PALN metastasis greater than 15%, the estimated sensitivity and specificity were 73% (95% CI, 53–87%) and 93% (95% CI, 86–97%), respectively. With this diagnostic performance and assuming a 15%

prevalence, the calculated false-positive and false-negative rates were 35% and 5%, respectively. This suggests a greater value of PET in those with high clinical probability of PALN metastasis than when used for patients with a low risk of PALN involvement [35]. [^{18}F]FDG PET may be of value in patients with normal CT or MRI of the abdomen [52–53, 56]. In a small-sized study of patients with locally advanced (FIGO stage IIB-IVA) cervical squamous cancer with normal, conventional CT findings, PET/CT scans were done prospectively, followed by surgery. Based on histopathological confirmation, the accuracy, sensitivity, specificity, PPV, and NPV of PET/CT for PALN metastasis were 75%, 50%, 83.3%, 50%, and 83.3%, respectively. Change of management based on PET/CT findings occurred for four of 16 (25%) patients [56]. Compared with the histopathological analysis of pelvic and para-aortic nodes from 22 patients, two of the four para-aortic metastatic nodes were missed on preoperative PET/CT imaging [31]. The false-negative rate for detection of PALN involvement by PET can vary between 4% and 17%, most likely related to small lesions and micrometastasis, which should be considered before planning radiation treatment. In 98 patients with LACC (stage IB2–IVA), 8.4% of patients with negative PET/CT findings had metastatic disease within PALN; all of the patients also had no evidence of extrapelvic disease detected on preoperative CT or MRI. Nodal metastases of 5 mm or smaller were found in four patients and larger than 1 cm in the other four patients [57]. Similar results were noted from other studies, which found a low sensitivity (33–36%) for the detection of microscopic involvement and disease in small nodes [58–59]. Of the 27 patients with positive pelvic nodes but negative PALN on PET/CT, six patients (22%) had histopathologically positive PALN. PALN dissection should be part of pretherapeutic staging for every LACC patient before undergoing definitive concurrent chemoradiotherapy [57–60].

For pelvic nodal assessment, the use of [^{18}F]FDG PET imaging for routine staging prior to radical hysterectomy and PLN dissection is still controversial, although the high specificity and NPV of [^{18}F]FDG PET may be helpful in planning the appropriate surgical procedure [61]. In a retrospective review, PET/CT was found to have limited sensitivity (36.4%) but high specificity for predicting PLN metastasis. With a median number of harvested lymph nodes of 29 (range 13–57), 17 (50.0%) had PLN metastases. The overall region-specific sensitivity and specificity of PET/CT was 36.4% and 98.8%, respectively [61].

Overall, PET is of value in nodal assessment and can also guide management. While microscopic disease and small nodes may be missed, the clinical significance and impact of such findings in conjunction with normal conventional imaging remains to be determined in view of systemic therapy that may be instituted.

Prognostic Value of PET/CT

High uptake of [^{18}F]FDG in the primary disease may influence the outcome and is linked to survival and recurrence. In 44 patients with FIGO clinical stage IB–IIA, SUV_{max} was significantly higher in patients with deep stromal invasion, lymph-vascular space invasion, and a tumor size of more than 4 cm. An SUV_{max} greater than or equal to 13.4 correlated with a reduced disease-free survival rate and was a significant independent predictor of recurrence. If validated in larger studies, the uptake and cut-off may be used in planning a more aggressive multimodal treatment [62].

Recent studies have evaluated and shown prognostic value of volume-based quantification of tumor [^{18}F]FDG uptake in patients with cervical cancer. In a comparison between MRI and PET findings, quantitative MRI parameters such as mean apparent diffusion coefficient (ADC) on pretreatment diffusion-weighted MRI, MTV (with threshold 42%), and total lesion glycolysis (TLG) from PET/CT showed a significant correlation with adverse prognostic factors such as advanced FIGO stage and lymph node metastases, disease-free survival, and OS, while no correlation was found for the SUV_{max} value of the lesions [63]. Chung et al. demonstrated that preoperative MTV more than or equal to 23.4 ml was a better predictor of disease-free survival and recurrence in patients with early-stage disease [64]. In 73 patients (stage IB1–IVA), a primary tumor TLG cut-off value of 7,600 was

better than SUV_{max} for identifying patients with higher risk of recurrence [65]. Overall, there is variation in the TLG and MTV cut-off values correlated with prognostic factors. Several studies have shown TLG cut-off values of 215 or 562 to be an independent predictor of recurrence-free survival [66–67]. In a more recent study, lower values of MTV larger than 5.6 ml and TLG greater than 21.6 ml were significantly associated with OS and progression-free survival (PFS) [68].

Nodal uptake and extent detected by [^{18}F]FDG PET in cervical cancer also stratifies patients for recurrence and survival outcomes. Assessment of PALN metastasis is prognostically important and is related to PFS in advanced cervical cancer. The presence of nodal disease on the [^{18}F]FDG PET scan can help predict cause-specific survival, prognosis, and OS. In a study of 47 patients with FIGO stage IIIB cervical cancer who were evaluated before therapy, the 3-year cause-specific survival was highest for patients without nodal metastasis at 73%, lower for those with only PLN metastasis at 58%, 29% for patients with pelvic and PALN disease, and the lowest (0%) for those with pelvic, para-aortic, and supraclavicular lymph node metastasis [69]. Similar findings were noted in a larger prospective study of patients with newly diagnosed cervical cancer patients ($n = 560$, stage IA2–IVA) that showed decreased survival with nodal involvement for all stages and an increased risk of recurrence with the number and site of distant nodal metastasis being the highest for supraclavicular nodal involvement and lowest for pelvic nodal disease only [70]. Distant nodal uptake is linked to an adverse prognosis. Involvement of the supraclavicular node or scalene nodes can be seen in about 0–17% of patients, more commonly in those who have para-aortic node disease [71–72] with a PPV as high as 100% [72]. Therefore, PET findings might help in selecting suitable patients for curative primary and/or salvage treatment. In a follow-up study by the same group, recurrence-free survival, disease-specific survival, and OS were correlated with PET-based cervical tumor volume, SUV_{max}, and lymph node status. Lymph node status had the highest influence on patient outcome, followed by cervical tumor volume [73].

A number of studies have shown an adverse effect on outcomes and higher recurrence rates in patients with PALN disease. In a retrospective study of 336 patients, OS at 2 years was significantly lower for patients who were surgically or imaging positive for PALN on PET or CT compared with those who were negative for PALN disease by surgery or imaging [10]. [^{18}F]FDG uptake in nodes on PET studies has also been correlated with outcomes. SUV_{max} in PALN is also a significant prognostic factor; in 70 patients with FIGO stage I–IV, SUV_{max} greater than or equal to 3.3 for PALN was a significant adverse factor [74]. SUV_{max} values of PLN have been correlated with PALN recurrence and survival after chemoradiotherapy; an SUV_{max} cut-off value of 3.85 or more was found to be an independent risk factor and those with SUV_{max} greater than 3.85 had significantly worse PFS than those with lower SUV_{max} [75]. The definitive SUV_{max} cut-off that can be universally applied clinically is not yet definite, as others have noted higher SUV_{max} cut-off values of up to 7.5 correlating with recurrences [76].

In multivariate analysis, the detection of nodes by imaging was independently associated with a poorer prognosis compared with those detected at surgery only [77]. A recent meta-analysis including 14 studies ($n = 1{,}150$) summarized the findings on prognostic indicators in imaging. While there is variation in the methodology and descriptions of SUV_{max} cut-off and some studies have found no significant correlation [78–80], the majority of data support the association of a higher risk of recurrence and poor outcomes with a higher SUV_{max} of the primary or nodal lesions [81]. Only limited studies have shown the value of SUV_{max} in PLN and PALN as a single independent predictor of outcomes [82–84]. Outcomes following chemoradiation therapy were found to be best for patients without PALN by surgical and radiographic imaging. In multivariate analysis, detection of metastatic lymph nodes by imaging was independently associated with a poorer prognosis for disease progression compared with nodal positivity at surgery only [77].

In patients with LACC, PET and MRI were compared with FIGO staging for impact on outcomes measured by OS, relapse-free survival,

time to failure, local failure, nodal failure, and distant failure. In 206 patients the OS rate was 59% at 5 years. Local failure was mostly associated with adenocarcinoma, and involvement of the corpus on MRI was significantly associated with nodal involvement. Nodal status on PET was a major predictor of outcome in LACC undergoing chemoradiation and was superior to FIGO staging, while MRI tumor volume was a predictor of locoregional relapse [85].

[^{18}F]FDG PET in Cervical Cancer: Impact on Management and Treatment Planning

[^{18}F]FDG PET/CT can alter management by detecting nodal disease or unknown metastatic sites (Figs. 6 and 7) [71, 86–87]. Patients with cervical cancer whose CT and MRI studies showed metastases limited to para-aortic, inguinal, and/or supraclavicular lymph nodes were prospectively evaluated for the impact of the addition of PET or PET/CT on management. PET had a positive clinical impact in 21 (44.7%) of the 47 patients, including detection of additional curable sites ($n = 8$), down-staging ($n = 6$), offering metabolic biopsy ($n = 4$), or change of treatment to palliation ($n = 3$) [71]. In a more recent study, [^{18}F]FDG PET led to a major change in management in 32% patients owing to the detection of more extensive local nodal involvement, occult metastatic disease, synchronous tumors, or exclusion of otherwise equivocal lymph nodes on MRI [87].

An accurate status of nodal involvement is critical for treatment planning. For those patients with PET-negative lymph nodes, there is no benefit of combined treatment with radiation therapy and chemotherapy vs. radiation therapy alone [88]. PET/CT maximizes patient triage to correct therapy in pretreatment of early-stage disease; combined MRI and PET/CT spares patients unnecessary trimodality therapy [89].

[^{18}F]FDG PET has been useful for management and therapy planning in about 14–35% of cases [90–91]. Pretherapeutic assessment with [^{18}F]FDG PET is useful in guiding therapy [50, 87]. PET/CT led to modifications of the radiotherapy dose or field in 32–34% and to major alterations in treatment plans in 23% of patients with widespread disease, with a reported minor impact in 8% of patients [50, 87].

Pretreatment [^{18}F]FDG PET improves the detection of extrapelvic metastasis, mainly PALN, and helps select patients for extended-field radiotherapy [92]. [^{18}F]FDG PET has been increasingly used for radiation treatment planning with intensity-modulated radiation therapy (IMRT) and brachytherapy enabling the use of higher radiation doses while sparing adjacent normal organs and tissues [93–94]. The concept of prophylactic extended radiotherapy based on PET guidance has been examined; the rate of para-aortic failure in patients with only pelvic node involvement was 2.5%. The study shows that routine application of extended-field IMRT with concurrent chemotherapy can lower the rates of PALN relapse [95].

Persistent uptake of [^{18}F]FDG after therapy is linked to poor outcome and the need for more aggressive treatment and follow-up [96]. The ratio of posttreatment vs. pretreatment SUV_{max} is, as expected, lower for those who achieve complete response and have better outcomes; a cut-off SUV_{max} of 4.0 yielded a sensitivity and specificity of 92% and 94%, respectively [96].

[^{18}F]FDG PET in Recurrent Cervical Cancer

[^{18}F]FDG PET has a high sensitivity in the detection of recurrent disease (Figs. 8 and 9; Table 4). The overall sensitivity and specificity for detection of recurrence are reported to be 86% and 94%, respectively [97–102]. While detection of small-volume disease is limited, owing to the lack of resolution, peritoneal disease can be detected when metabolically active [103]. [^{18}F]FDG PET increases physician confidence and decision-making in cases with equivocal findings on conventional imaging [104]. However, some have questioned the cost-effectiveness of [^{18}F]FDG PET in this clinical scenario and further data are needed [105].

Combining PET with contrast-enhanced CT (ceCT) may improve detection, although the

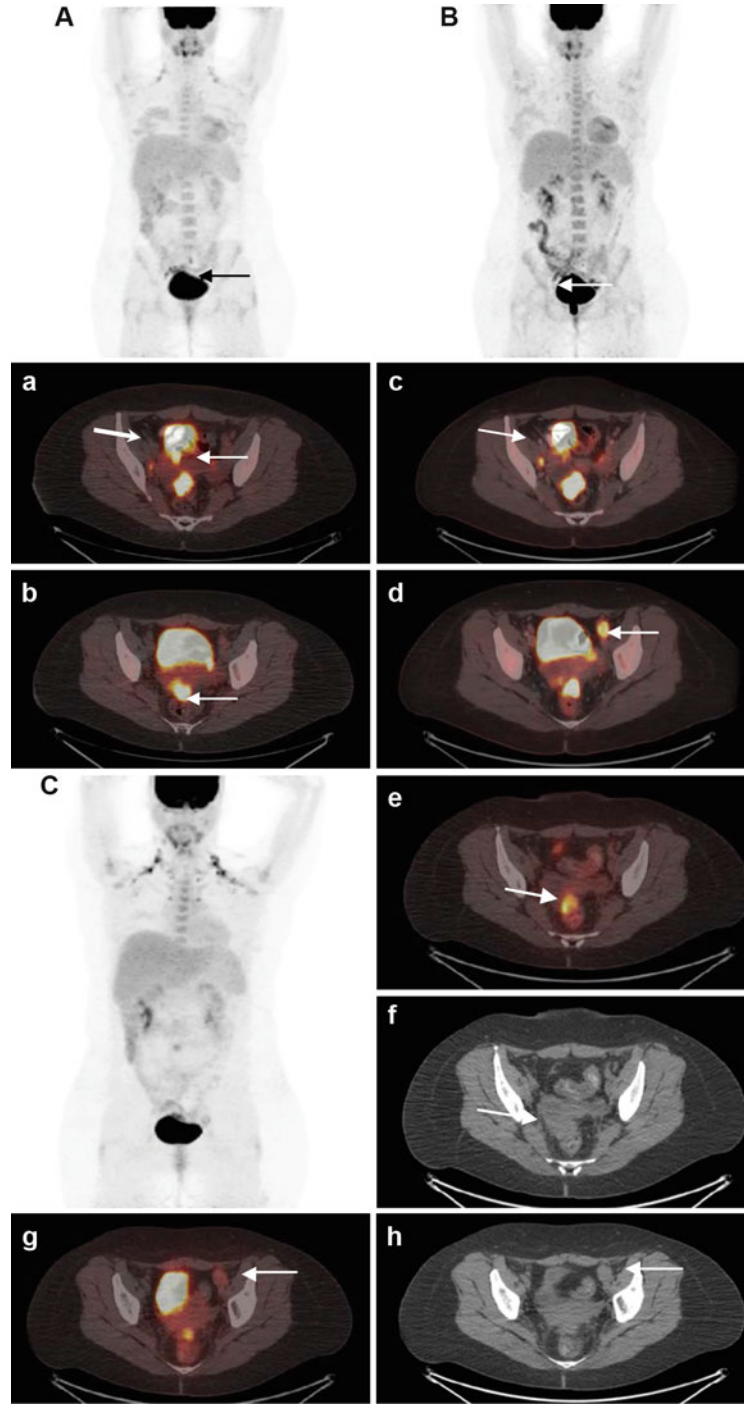

Fig. 6 A 22-year-old female patient diagnosed with invasive squamous cell carcinoma of the cervix was evaluated for recurrence. [^{18}F]FDG PET/CT scan (**A**, *black arrow*) shows uptake in the cervix consistent with a recurrence. Additional uptake was noted in the right external iliac node (SUV_{max} 5.1) (**a**, **b** *white arrow*, SUV 13.3) that was confirmed on pathology. She was treated with chemotherapy. A follow-up scan at the end of treatment showed an increase in size of an external iliac node (MIP – **B**, *black arrows* and **c**, *white arrows*, SUV 8.5) and depicted a new left abdominal anterior peritoneal nodule (**d**, *arrow*, SUV 7.8). The patient was treated with pelvic and para-aortic radiotherapy and chemotherapy. Follow-up PET/CT scan (**C**) showed metabolic resolution of right external iliac node, partial metabolic response in pelvic sidewall metastases (**e**, **f** *arrows* SUV_{max} 7.4), and peritoneal nodules (**g**, **h** *arrows* SUV_{max} 2.93)

increment in value may not be significant depending on the distribution of the disease. In 100 women with either uterine cervical ($n = 55$) or endometrial cancer ($n = 45$), while there was no significant difference in sensitivity or specificity between contrast-enhanced and low-dose CT [99], PET/ceCT led to better delineation of equivocal lesions; four equivocal regions by PET/low-dose

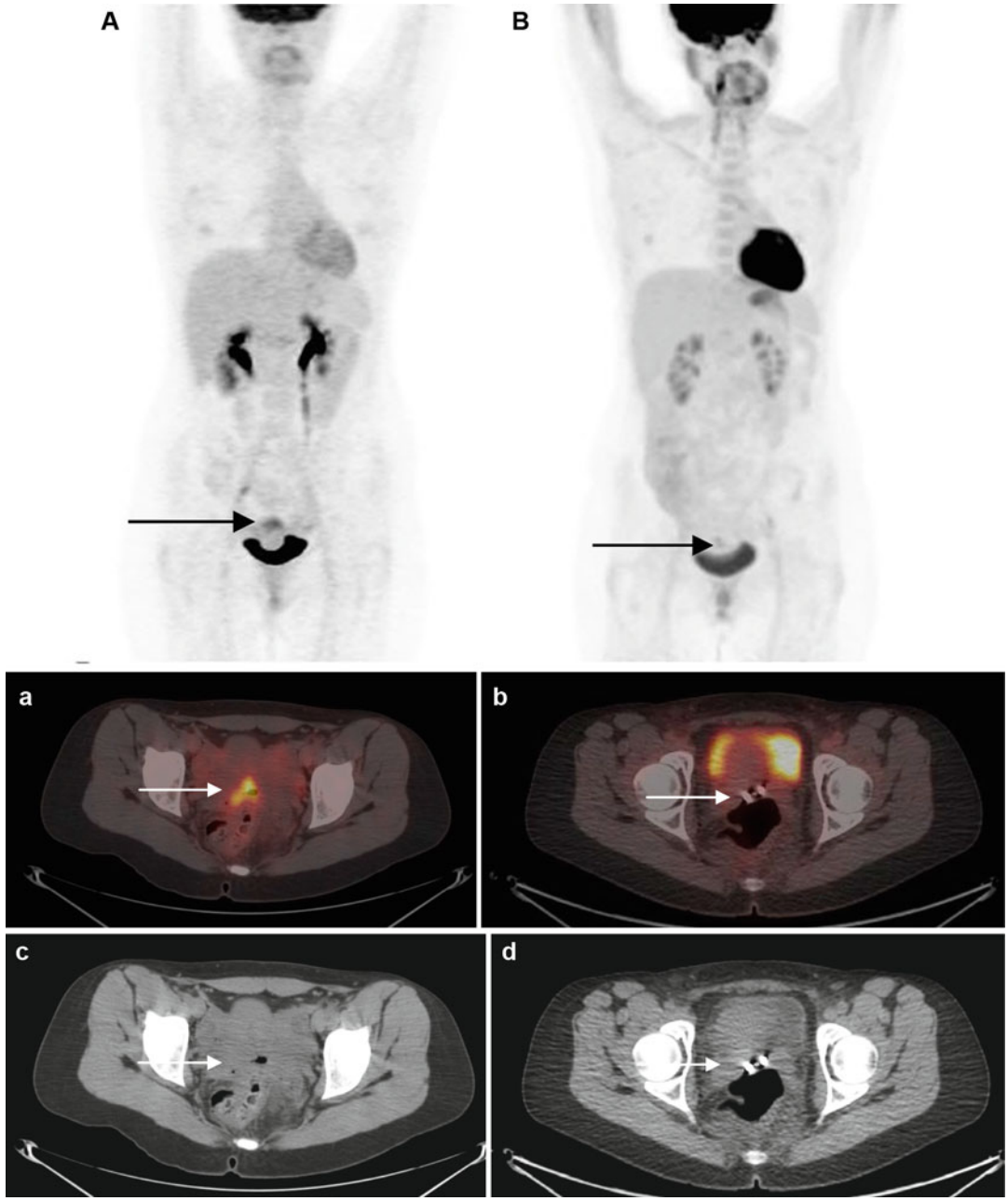

Fig. 7 A 33-year-old female patient with poorly differentiated invasive squamous cell carcinoma of the cervix. [^{18}F]FDG PET/CT maximum intensity projection (MIP; **A**) shows abnormal uptake in the pelvis (*black arrow*) corresponding to primary lesion in the cervix (**a**, **b** *white arrows*, SUV_{max} 6.2). The patient was treated with chemoradiotherapy. On follow-up PET/CT scan, whole-body MIP (**B**) shows resolution of the primary lesion in the cervix (**c**, **d** *white arrows*) suggestive of complete metabolic response to therapy

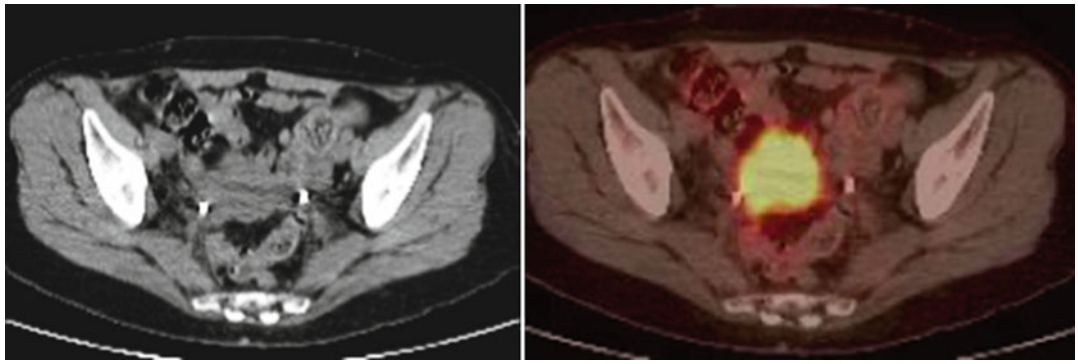

Fig. 8 A 32-year-old woman with carcinoma of the cervix, stage IIa, treated with chemoradiation therapy, was referred for PET/CT evaluation of residual disease and restaging. Focal ^{18}[F]FDG PET uptake is seen in the cervix consistent with residual/recurrent disease

CT (local recurrence, PLN metastasis, liver metastasis and muscle metastasis) were correctly interpreted as positive by PET/ceCT [99]

[^{18}F]FDG PET has a high sensitivity for detecting recurrence; the sensitivity in asymptomatic women is lower than that for symptomatic women (80% vs. 100%) [101, 106] and in those with rising markers with normal conventional imaging enabling institution of early therapy or management [107]. [^{18}F]FDG PET is not routinely performed or recommended for surveillance. In asymptomatic patients treated with radiation, [^{18}F]FDG PET can help in early detection of recurrent disease, or help confirm disease in those with abnormal serum tumor marker values. In such patients, the sensitivity for the detection of extrapelvic lymph node metastases was extremely high (100%); by contrast, the sensitivity and specificity for lung and bone lesions were 75.0% (12/16) and 33.3% (1/3), respectively [108]. Chang et al. [109] reported the detection of disease in 94% of patients with normal conventional imaging, leading to institution of earlier therapy.

[^{18}F]FDG PET has the advantage of facilitating the identification of extrapelvic metastases with high sensitivity and specificity [110] and plays a complimentary role to conventional imaging. In 150 patients who had findings suggestive of recurrence on CT or MRI, or elevated serum squamous cell carcinoma antigen SCC-Ag levels, an additional benefit from [^{18}F]FDG PET over CT–MRI was seen in 73.8% of patients; in particular, [^{18}F]FDG PET CT led to the correction of false-negative findings on CT-MRI in 74.2% and of false-positive findings on CT-MRI in 25.8% of cases. About 75.4% of these lesions were extrapelvic. In 26.2% patients, CT-MRI findings were discrepant from [^{18}F]FDG PET, which was able to confirm false-negative lesions in nine patients and exclude disease in 19; most of these lesions were extrapelvic.

[^{18}F]FDG PET provides useful prognostic information in patients with recurrent disease [104, 111]. The most significant prognostic factor was the presence of more than three [^{18}F]FDG-positive lesions. The median survival for those with more than three PET-positive lesions was shorter than for those with a normal scan or fewer lesions on PET [111]. Similarly, posttreatment [^{18}F]FDG PET/CT is also useful for prognosis and planning management. In a retrospective study involving 276 patients, the 5-year PFS and OS in patients with negative scan findings for recurrence were significantly better than those with positive scan findings (98.6% vs. 17.8%, $p < 0.0001$ for PFS, 99.3% vs. 85.3%, $p = 0.0015$ for OS) [112].

Increasingly, [^{18}F]FDG PET is being used for radiation treatment planning in recurrent cervical cancers. Using PET/CT, radiation dose to various organs like the stomach, liver, and colon could be significantly reduced, while radiation to other structures such as the spinal cord, kidneys, and small intestine was possible but depended on the beam sparing [113]. PET/CT-guided treatment planning for IMRT and brachytherapy allows for dose escalation without harming the surrounding

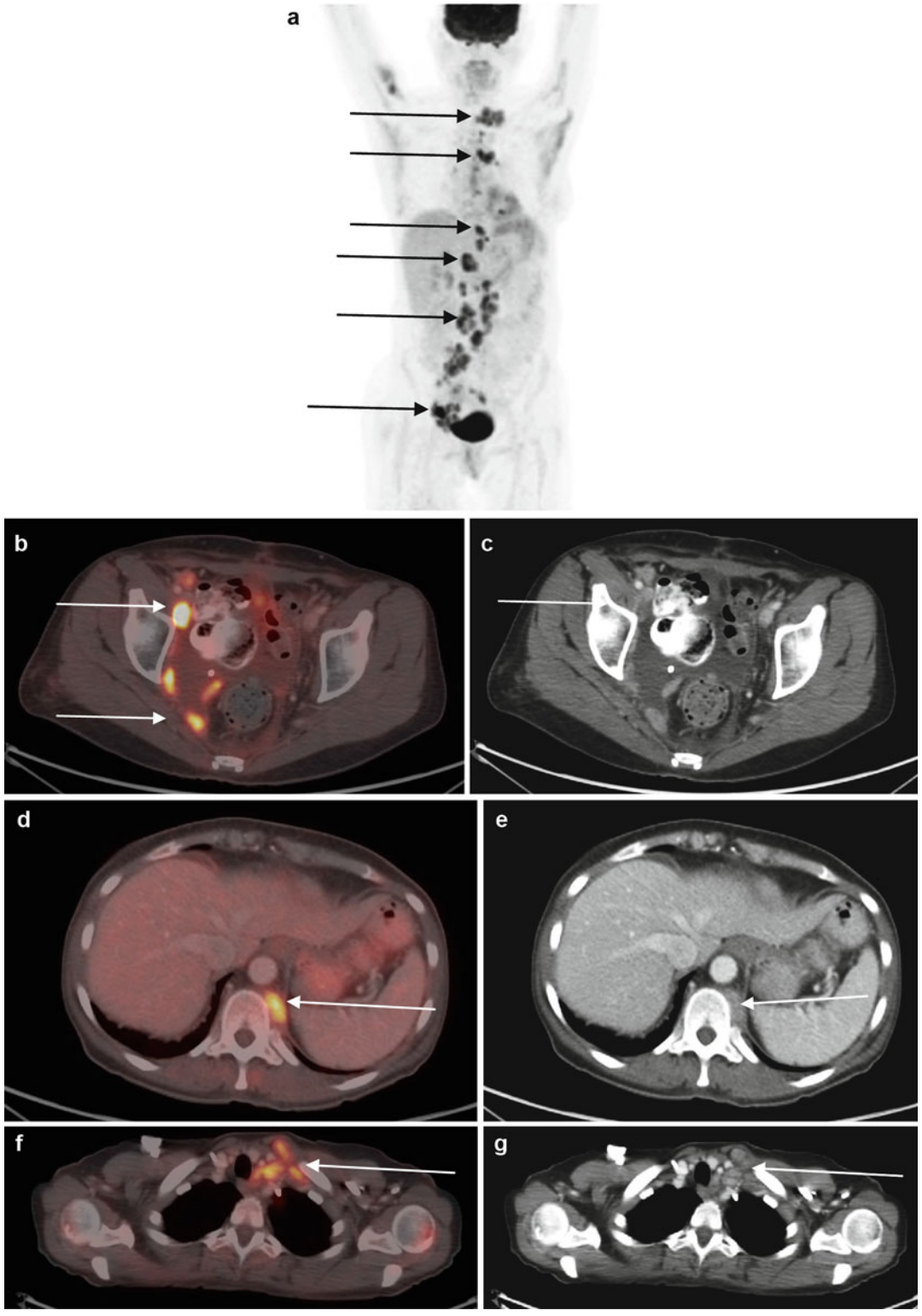

Fig. 9 (continued)

tissues [93–94]. Such escalated treatments may have better outcomes [114, 115], and a similar approach has been effectively used by others [95, 116].

Hypoxia is known to be a limiting factor in response to therapy (especially radiation therapy), and is increasingly recognized as an important aspect of treatment planning. It is associated with an increased likelihood of local recurrence and distant metastasis and heralds poor response to therapy [117–118]. The phenomenon has also been recognized in cervical and uterine cancers and is associated with a more aggressive tumor phenotype [111]. Tumor hypoxia can be measured through the tumor PO_2 levels using oxygen probes; however, this technique is invasive and needs special instruments and technical expertise.

A number of PET tracers are under investigation for noninvasive assessment of tumor hypoxia. Radiocopper-labeled diacetyl-bis(*N*(4)-methylthiosemicarbazone) [^{64}Cu-ATSM] has been described as a potential tracer for imaging hypoxia [119–120]. In cervical cancer, an inverse correlation between outcome and uptake of ^{64}Cu-ATSM has been shown [121]. Hypoxic tumors have a significantly increased risk of nodal or distant metastases, and noninvasive methods of metabolic imaging would be critical in providing guidance for management. Another tracer for hypoxia evaluation is [^{18}F-] fluoromisonidazole (^{18}F-MISO), which has been extensively evaluated in cervical cancer. The feasibility of combined [^{18}F]FDG and ^{18}F-MISO PET/MRI was recently evaluated in LACC. Combined metabolic [^{18}F]FDG and hypoxia PET imaging with ^{18}F-MISO in conjunction with MRI can help identify discordant areas and tumor heterogeneity and also help direct radiation dose escalation to the hypoxic regions [122].

There is an emerging role of PET/MRI in gynecologic tumors. In cervical cancer, it can improve the detection of nodal involvement compared with PET/CT [123–124] and helps in better assessment of local disease extent for staging [125]. MRI has superior soft tissue contrast resulting in better characterization of lesions with PET/MRI [126]. An additional advantage includes the reduction in radiation dosage. While the sensitivity is high, PET/MRI is likely to show more false-positive lesions. In a total of 79 patients where 553 nodal groups were assessed, PET/MRI detected an additional six positive nodal groups compared with PET/CT; however, it gave false-positive results in eight nodal groups [124]. In comparison with MRI alone, PET/MRI can help identify more disease (92% vs. 100%, respectively) and shows better characterization of lesions (88.8% vs. 98.9%, respectively) [127]. Specifically, PET/MRI is superior in the characterization and detection of lesions in the liver, peritoneum, and lymph nodes; however, it is limited in the assessment of lung lesions compared with PET/CT [128, 129].

Endometrial Cancers

Epidemiology and Prevalence

Endometrial cancer is the most common female pelvic malignancy, and the fourth most common cancer in women after breast, gastrointestinal, and lung cancer. It is more common in postmenopausal women, in Western countries, and is linked to exposure to unopposed estrogen. In 2016, 60,050 new cases and 10,470 deaths were predicted. The overall 5-year survival rate is estimated to be 81.7% – 95.4% for patients with localized disease, 68.7% for those with regional spread, and 16.8% for distant metastatic disease

Fig. 9 A 60-year-old female patient with invasive squamous cell carcinoma of the cervix, after total abdominal hysterectomy with bilateral salpingo-oophorectomy (TAH/BSO) and chemoradiotherapy, referred for evaluation of recurrent disease. Whole-body MIP (**a**, *black arrows*) shows multiple foci of increased [^{18}F]FDG uptake in the neck, chest, abdomen, and pelvis localizing to disease in the surgical bed (**b**), consistent with recurrence. [^{18}F]FDG-avid lesions are also noted in the peritoneum (**b**, **c** *white arrows*, SUV_{max} 11.3) and retrocrural lymph node (**d**, **e** *white arrows*, SUV_{max} 7.05); additional lesions are noted in retroperitoneal nodes, mediastinal nodes, including prominent uptake in left upper paratracheal node. Additional distant nodes are also noted in the left axillary and left supraclavicular regions (**f**, **g** *white arrows*, SUV_{max} 5.6)

Table 4 FDG PET in cervical cancer

Author and Year	Design	Number of patients; disease stage evaluated	Pathology	Indication	Comparative imaging (CT or MRI)	Histopathology confirmation (yes/no)	Sensitivity/ specificity/ accuracy	Cut-off SUV_{max} identified on posttreatment PET scan (yes/no)/value	Median follow-up time (range) months	PFS/OS
Havrilesky et al. 2003	Retrospective	28; IB ($n = 7$), IIA ($n = 1$), IIB ($n = 10$), IIIB ($n = 9$), IVB ($n = 1$)	SCC ($n = 23$), Adenocarcinoma ($n = 4$), Unknown ($n = 1$)	Recurrence	None	Yes	85.7%/86.7%/ NA	No/NA	14.3 (3.6–235)	NA
Ryu et al. 2003	Retrospective	249; IB ($n = 100$), IIA ($n = 49$), IIB ($n = 83$), III/IV ($n = 17$)	SCC ($n = 226$), Adenocarcinoma ($n = 10$), Adenosquamous ($n = 5$), Others ($n = 8$)	Recurrence in asymptomatic/ negative CI	Yes	Yes	90.3%/76.1%/ NA	No/NA	30 (6–282)	NA
Unger et al. 2004	Retrospective	47; IB($n = 29$), IIA ($n = 4$), IIB($n = 9$), IIIA($n = 1$), IIIB ($n = 4$)	NA	Recurrence	None	Yes	Asymptomatic: 80%/100%/NA Symptomatic: 100%/85.7%/ NA	No/NA	16.4 (6–33)	NA
Sironi et al. 2007	Prospective	25; Cervical Ca ($n = 12$; Stage IIB ($n =6$), IIIA ($n =5$), IIIB ($n =1$), Endometrial Ca ($n = 13$; Stage IC ($n =1$), IIB ($n =8$), IIIA ($n =3$), IIIB ($n =1$)	NA	Recurrence	CT/MRI	Yes	Patient based 92.9%/100%/ 96%, Lesion based 94.7%/ 99.5%/99%	No/NA	15.3 (12–23)	NA

van der Veldt et al. 2008	Retrospective	40; Stage IB ($n = 13$), IIA ($n = 3$), IIB ($n = 6$), IIIA ($n = 1$), IIIB ($n = 13$), IVA ($n = 1$), IVB ($n = 1$), Unknown ($n = 2$)	SCC ($n = 25$), Adenocarcinoma ($n = 11$), Large cell ($n = 2$), Glassy cell ($n = 1$), Unknown ($n = 1$)	Recurrence	CT/MRI	Yes	92%/93%/NA	No/NA	18 (10–37)	NA
Kitajima et al. 2008	Prospective	52; Stage I ($n = 12$), II ($n = 15$), III ($n = 21$), IV ($n = 4$)	SCC ($n = 42$), Adenocarcinoma ($n = 8$), Adenosquamous cell carcinoma ($n = 2$)	Recurrence	None	Yes	FDG PET/CT 92%/92.6%/ 92.3%, PET 80%/77.8%/ 78.8%	No/NA	17 (12–25)	NA
Pallardy et al. 2010	Retrospective	40; I ($n = 7$), II ($n = 16$), III ($n = 13$), IV ($n = 4$)	SCC ($n = 39$), Adenosquamous ($n = 1$)	Recurrence	Yes	Yes	FDG PET/CT94%/ 75%/92.5% CI 42.5%/71.5%/ 47.5%	No/NA	25 (3–312)	NA
Chung HH et al. 2012	Retrospective	276; IA2 ($n = 30$), IB ($n = 134$), II ($n = 86$), III ($n = 11$), IV ($n = 15$)	SCC ($n = 235$), Adenocarcinoma ($n = 27$), Adenosquamous ($n = 8$), Others ($n = 6$)	Recurrence	None	Yes	94.7%, 87.8%, 90.2%	Yes/5.25	49 (6–345)	5 years −98.62%/ 99.31%
Choi et al. 2014	Retrospective	136; IB1 ($n = 2$), IB2 ($n = 1$), IIA ($n = 5$), IIB ($n = 97$), IIIA ($n = 2$), IIIB ($n = 15$), IVA ($n = 7$), IVB ($n = 7$)	SCC ($n = 124$), Adenocarcinoma ($n = 9$), Other ($n = 3$)	Residual disease	MRI	No	92%/95%/NA	Yes/4	NA	NA

SCC squamous cell carcinoma, *PFS* progression-free survival, *OS* overall survival, *CI* conventional imaging, *NA* not available

[1]. There is a slight increase in death rates annually, at a rate of 1.2% per year.

Pathophysiology and Clinical Presentation

Endometrial cancer results in abnormal bleeding in about 80% of patients. About 15% of postmenopausal women presenting with abnormal bleeding have endometrial carcinoma [3–4]. Uterine cancer most commonly presents as polypoid fungating masses in the endometrial cavity causing asymmetric enlargement of the uterus. Invasion occurs directly into the myometrium, while distant spread of the tumor occurs through blood vessels or lymphatics. Prognostic factors include histology, tumor grade, depth of endometrial invasion, extension into the cervix or vascular space or adnexa, and pelvic or aortic node involvement. Surgical staging is definitive and nodal sampling is routinely performed. Clinical staging is commonly based on the FIGO classification (Table 5).

The most common histological type is adenocarcinoma (Table 6), which is seen as areas of irregular glands lined by malignant columnar epithelial cells. Although most adenocarcinomas are well-differentiated, areas of squamous differentiation can occur and are prominent in adenoacanthomas. Squamous areas that are poorly differentiated and show cytologic features of malignancy are seen in adenosquamous carcinoma. Endometrial carcinomas are graded according to their degree of histologic differentiation. Well-differentiated carcinomas are grade 1. The presence of large solid areas qualifies the tumors as grade 2, and poor differentiation is grade 3; both grades 2 and 3 carry a worse prognosis. Papillary serous adenocarcinoma is a variant that resembles ovarian serous carcinoma and has a worse prognosis than adenocarcinoma.

Leiomyosarcoma is a rare uterine neoplasm, accounting for 3% of all uterine malignancies and the most common uterine sarcoma arising from smooth muscle of the myometrium. These are generally bulky, fleshy masses that commonly occur in older women and have a high incidence of local recurrence and hematogenous metastases. Hemorrhage and necrosis are seen, with marked

Table 5 AJCC and FIGO staging for endometrial cancer

Stage I: cancer confined to the corpus uteri
IA: invasion to less than 50% of the myometrium
IB: invasion to greater than 50% of the myometrium
Stage II: cancer involves stromal connective tissue of the cervix but has not extended outside the uterus[a]
Stage III: extension beyond the uterus but not beyond the true pelvis
IIIA: tumor invades serosa and/or adnexa and/or positive peritoneal cytology
IIIB: vaginal involvement (direct extension or metastasis) or parametrial involvement
IIIC: metastases to pelvic and/or para-aortic lymph nodes
IIIC1: pelvic lymph node involvement
IIIC2: para-aortic lymph node involvement (with or without pelvic nodes)
Stage IV: involves the bladder or bowel mucosa or has metastasized to distant sites
IVA: tumor invasion of bladder and/or bowel mucosa
IVB: distant metastases, including intra-abdominal and/or inguinal lymph nodes
Grading:
G1: no more than 5% of a nonsquamous or nonmorular solid growth pattern
G2: 6–50% of a nonsquamous or nonmorular solid growth pattern
G3: >50% of a nonsquamous or nonmorular solid growth pattern
FIGO staging
Tumor limited to corpus
Stage IA; G123: tumor limited to endometrium
Stage IB; G123: invasion to less than 50% of the myometrium
Stage IC; G123: invasion to greater than 50% of the myometrium
Tumor extends beyond the uterus, within the pelvis
Stage II; G123: cervical stromal invasion
Extension beyond the uterus but not beyond the true pelvis
Stage IIIA; G123: tumor invades serosa and/or adnexa and/or positive peritoneal cytology
Stage IIIB; G123: vaginal metastases
Stage IIIC; G123: metastases of pelvic and/or para-aortic lymph nodes
Extension to bladder, intestinal mucosa or distant metastasis
Stage IVA; G123: tumor invasion of bladder and/or bowel mucosa
Stage IVB; distant metastases including intra-abdominal and/or inguinal lymph nodes

[a]Endocervical glandular involvement should only be considered as stage I and no longer as stage II

Table 6 Endometrial carcinoma: histopathologic types

1. Endometrioid adenocarcinoma
a. Papillary villoglandular
b. Adenocarcinoma with squamous differentiation
c. Secretory
d. Ciliated cell
2. Mucinous adenocarcinoma
3. Serous carcinoma
4. Clear cell carcinoma
5. Squamous carcinoma
6. Undifferentiated carcinoma
7. Mixed cell type
8. Secondary tumors

cytologic pleomorphism and atypia with a high rate of mitotic cells, which is diagnostic.

Role of Conventional Imaging

The diagnosis is generally made by obtaining an endometrial biopsy specimen [130]. Transvaginal ultrasonography may be used initially to evaluate those who cannot undergo biopsy. Ultrasound allows for a quick early preliminary examination that may be performed on patients with abnormal bleeding. A thickened and heterogeneous endometrium suggesting the presence of hyperplasia, polyps, or suspicious lesions may be noted that can be further evaluated by biopsy. In premenopausal women, the thickness of the endometrium varies with menstrual phase; however, a thickness of more than or equal to 5 mm in postmenopausal patients with bleeding should be considered abnormal and investigated further [131]. Recent studies, however, advocate the use of a 3–4-mm cut-off [132–134].

Chest imaging/CT of the chest may be performed for initial assessment to exclude disease. MRI is helpful in evaluating the disease extent to the cervix. MRI and CT of the abdomen and pelvis are performed before surgery to assess the presence of extrauterine disease [135]. MRI is sensitive in detecting myometrial invasion and involvement of the lower uterine segments, and it should be considered for the presurgical evaluation of patients who are suspected to have gross cervical involvement, thus affecting further management. CT and/or MRI of the abdomen and pelvis is specifically helpful in evaluating endometrial stromal tumors to assess the extent of the primary tumor and the presence of extrauterine disease including pelvic and para-aortic nodal involvement [135].

Role of [^{18}F]FDG PET in Endometrial Carcinoma

Increased uterine [^{18}F]FDG uptake is commonly seen in young premenopausal patients related to cyclical changes in the endometrium. Intense uptake is frequently detected during active menstruation, while focal endometrial uptake is common in the late follicular and early luteal phases (Fig. 10) [136]. Careful interpretation is needed especially when focal uterine uptake is noted in close proximity to a known cervical tumor so as to differentiate physiological activity from uterine invasion. Variable [^{18}F]FDG uptake has also been demonstrated in different benign pathologies of the uterus such as fibroids and polyps (Fig. 11) [137].

[^{18}F]FDG accumulates in uterine tumors [138–139] (Table 7). Presurgical assessment with [^{18}F]FDG PET for staging in high-grade endometrial cancer allows for the detection of extrapelvic sites of disease and distant metastasis (Fig. 12). Preoperative [^{18}F]FDG PET/CT detects primary lesions with a high sensitivity. In high-risk malignancy, while there is lower sensitivity for detection of nodal disease (57.1%), the detection of distant disease is high (sensitivity 100%). The specificity, however, is high for both nodal disease (100%) and distant disease (96%) [140].

[^{18}F]FDG PET/CT is more useful than MRI for assessing lymph node metastasis [141]. In a prospective multicenter study, the diagnostic performance of PET/CT, MRI, and transvaginal ultrasound was assessed preoperatively in 318 women with endometrial cancer. For lymph node metastases, the sensitivity and specificity were 74% and 93%, respectively, for PET/CT while for MRI it was 59% and 93%, respectively [141].

The SUV_{max} of [^{18}F]FDG PET correlates with histological grade, tumor size, and glucose transporter GLUT-1 expression. In 44 patients, the mean SUV_{max} of the primary endometrial cancer tumors was 17.6 (range, 3.04–34.74) [142]. In

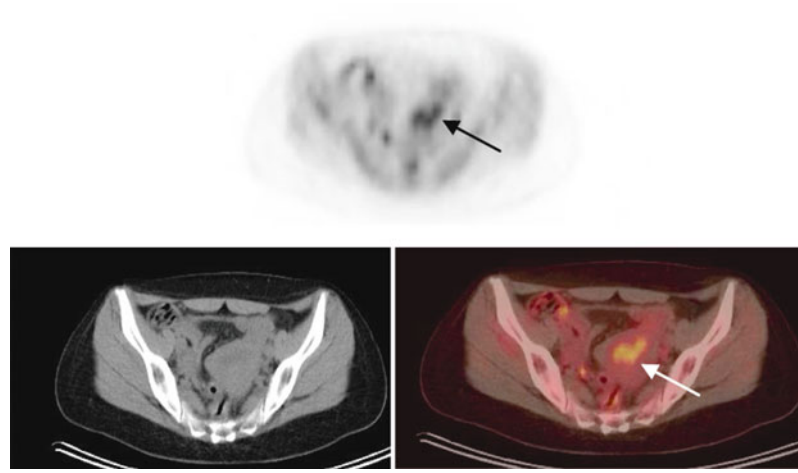

Fig. 10 Physiologic uptake in the uterus. Woman with lung malignancy imaged with [^{18}F]FDG PET for restaging. Uptake is seen in the uterine cavity (*arrows*). Patient was menstruating at the time of the scan, consistent with physiologic uptake

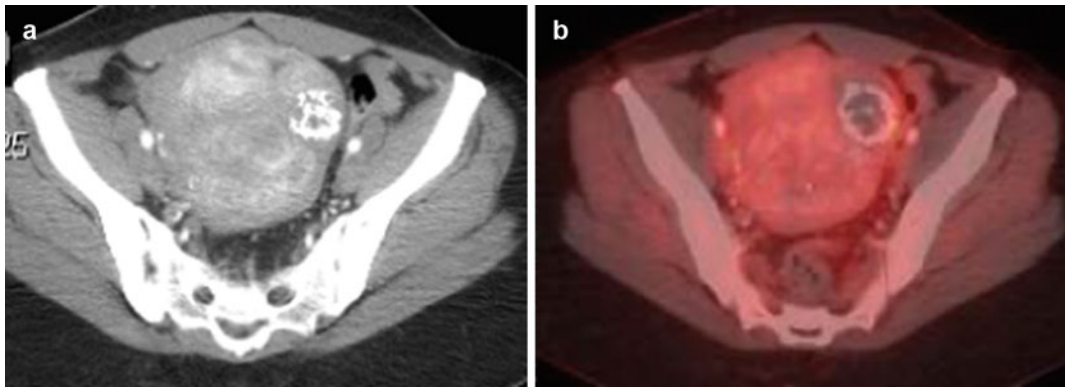

Fig. 11 Variable uptake in uterine fibroids. CT images (**a**) show heterogeneously enlarged uterus with lesions that have calcification consistent with fibroids. [^{18}F]FDG PET/CT (**b**) shows no uptake in the region of calcified fibroid and mild heterogeneous activity associated with remainder of the enlarged uterus

106 patients, the SUV_{max} of the primary tumor was inversely correlated with disease-free survival and OS rates. A mean SUV_{max} cut-off of 16.4 of the primary tumor was found to delineate prognostic groups [143].

In patients with high clinical risk and early-stage endometrial cancer, [^{18}F]FDG PET has a high NPV that can serve as a guide in selecting patients for lymphadenectomy and thus minimize operative and surgical complications in others. PLN metastases were found at histopathological analysis in nine of 37 patients (24.3%). Patient-based sensitivity and specificity of [^{18}F]FDG PET for detection of nodal disease were 77.8% and 100.0%, respectively, while nodal lesion site-based sensitivity and specificity were 66.7% and 99.4%, respectively [144]. In more recent and larger studies, high PPV and NPV for pelvic lymph node metastases have been reported, up to 93% and 94%, respectively [145]. The specificity for nodal detection was also high ranging between 91% and 99% [146–147].

Preoperative [^{18}F]FDG PET with ceCT is superior to conventional imaging in detecting metastatic disease, but it is limited in the assessment of small lymph nodes. In 45 patients with endometrial carcinoma, the overall node-based sensitivity and specificity were 51.1% and 99.8%, respectively. For smaller lymph nodes, the sensitivity was only 12.5% for nodes below 4 mm, 66.7% (16/24) for nodes 5–9 mm in size, and 100.0% for nodes 10 mm or larger(5/5) [148].

Table 7 Role of [^{18}F]FDG PET CT in endometrial cancer

Author and year	Type	Disease stage evaluated	Indication	Number of cases	Comparative imaging (CT or MRI)	Histopathology confirmation (yes/no)	Sensitivity/specificity/accuracy
Antonsen et al. 2013	Prospective	Atypical endometrial hyperplasia ($n = 18$), I	Staging	318	MR, TV 2D US	Yes	For myometrial invasion [^{18}F]FDG – 93%/49%/61% MRI -
Kitajima et al. 2009	Prospective	Endometrial: Stage I ($n = 12$), II ($n = 8$), III ($n = 10$) Cervical: I ($n = 7$), II ($n = 8$)	Staging	45 (30 Endometrial and 15 cervical carcinoma)	None	Yes	Overall: 51.1%/99.8%/98.7% Pelvic LN: 52.2%/99.8%/ 98.9% Para-aortic LN: 50%/ 99.7%/98.3%
Nakamura et al. 2011	Prospective	IA ($n = 18$), IB ($n = 31$), IC ($n = 18$), IIA ($n = 3$), IIB ($n = 11$), IIIA ($n = 9$), IIIB ($n = 1$), IIIC ($n = 11$), IVB ($n = 4$)	Staging	106	None	Yes	For LN metastasis 96.8%/ 69.2%/93.4%
Husby et al. 2015	Prospective	I ($n = 96$), II ($n = 17$), III ($n = 12$), IV ($n = 4$)	Staging	129	None	Yes	For lymph node metastases 77–85%/91–96%/89–93%
Nogami et al. 2015	Prospective	I ($n = 36$), II ($n = 5$), III ($n = 10$), IV ($n = 2$)	Staging	53	MRI	Yes	Patient based – 50%/93.9%/NA LN based – 45%/99.4%/NA
Signorelli et al. 2015	Prospective	IA ($n = 36$), IB ($n = 17$), II ($n = 7$), IIIA ($n = 7$), IIIB ($n = 4$), IIIC1 ($n = 10$), IIIC2 ($n = 7$), IVB ($n = 5$)	Staging	93	None	Yes	73.7%/98.7%/93.6%
Sharma et al. 2012	Retrospective	I ($n = 63$), II ($n = 26$), III ($n = 10$), IV ($n = 2$)	Recurrent disease	101	CT/MRI	Yes	88.9%/93.6%/94.1%

TV 2DUS transvaginal 2D ultrasonography, *NA* not available

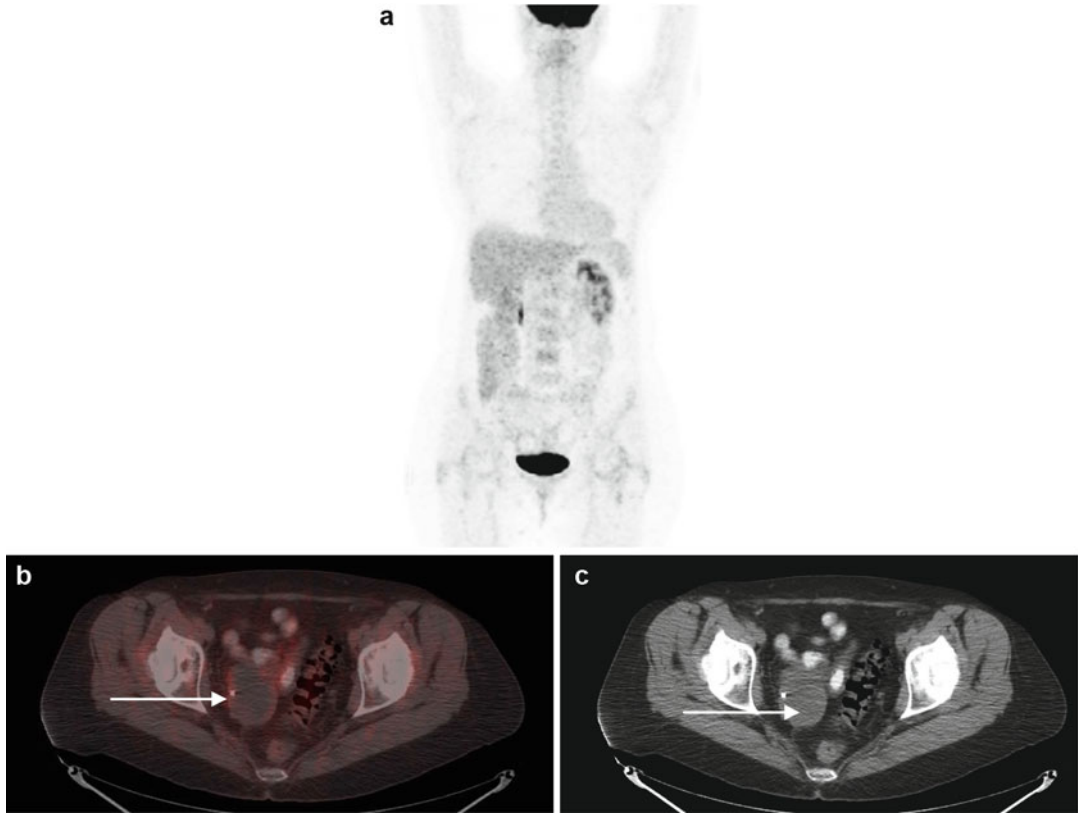

Fig. 12 A 50-year-old female patient with a history of recurrent endometrial adenocarcinoma was noted to have a pelvic lesion on CT. The patient was treated with chemoradiation, but the lesion persisted, although there was a decrease in size. The patient was referred for PET/CT imaging for response evaluation and to rule out extrapelvic disease. The scan revealed a mildly [^{18}F]FDG-avid (**b**, **c**, *white arrow*, SUV_{max} 2.8) pelvic mass adjacent to the urinary bladder with central necrosis. No other [^{18}F]FDG-avid lesions were noted elsewhere (MIP, **a**). Patient underwent surgery; pathology confirmed necrotic tumor. Teaching point: [^{18}F]FDG PET has lower uptake and sensitivity for necrotic or cystic lesions and will be generally photopenic. [^{18}F]FDG PET helped rule out other disease sites

In uterine cancers [^{18}F]FDG PET is useful for postsurgical monitoring and surveillance for recurrent disease (Figs. 13, 14, and 15). Belhocine and colleagues retrospectively analyzed findings from 34 women (41 scans) with suspected recurrence based upon tumor markers or findings of other radiographic imaging. PET confirmed recurrence in 88% of the cases; it also helped localize the site of disease and detected asymptomatic recurrences in 12% of patients. Moreover, in nine of 26 patients (35%) additional metastatic sites were detected with PET, a finding which significantly altered the treatment choice [149]. Similar results were noted in a larger study involving 101 posttherapy patients; the reported sensitivity and specificity were 89% and 94%, respectively [150].

Earlier studies in a small number of patients showed superior results with [^{18}F]FDG PET compared with conventional imaging or tumor markers for recurrent disease. In 21 patients with 30 studies, PET showed 100% sensitivity and 88% specificity, compared with 85% sensitivity and 86% specificity for conventional imaging, or 100% sensitivity and 70.6% specificity with tumor markers. [^{18}F]FDG-PET affected the patient management in one third of the cases, and patients with negative PET results had a trend to show longer disease-free courses [151]. The combination of [^{18}F]FDG PET with

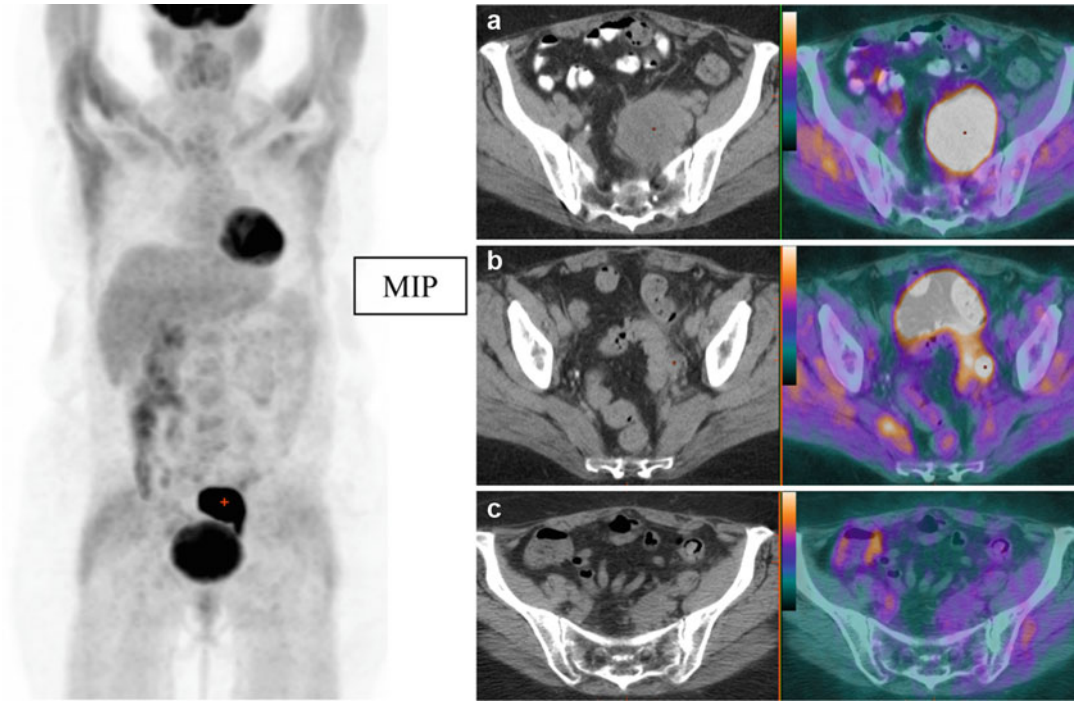

Fig. 13 A 57-year-old female patient with endometrial carcinoma was referred for evaluation of recurrent disease. MIP images show large area of abnormal activity superior to the bladder. Axial CT and fused [^{18}F]FDG PET/CT images show large left pelvic mass consistent with recurrent disease (**a**) and a node (**b**). Follow-up study shows resolution of [^{18}F]FDG avidity and a decreased size of the pelvic mass (**c**) after chemoradiation

ceCT is superior in categorizing the lesions as malignant vs. benign in comparison with low-dose CT owing to decreasing equivocal results, although no significant difference was noted in overall accuracy [99]. In a more recent follow-up study of 35 patients, PET/CT was compared with manually fused PET/MRI; while no significant difference was noted in diagnosing primary tumors, PET/MRI detected the extent of disease better than PET/CT (83% vs. 53.3%, respectively) [152].

Metabolic parameters derived from preoperative [^{18}F]FDG PET/CT can help in the characterization of endometrial carcinomas. In 129 patients, preoperative [^{18}F]FDG PET-derived MTV, using an absolute SUV_{max} threshold of 2.5, and TLG significantly correlated with deep myometrial invasion, lymph node metastases, and high histological grade. The potential cut-off value of MTV for predicting deep myometrial invasion and lymph node metastases was 30 ml (85% sensitivity, 76% specificity) [146]. A similar evaluation in patients with recurrent disease ($n = 84$) calculated an MTV cut-off of 17.5 ml (75% sensitivity, 58% specificity) and a TLG of 56.43 g (75% sensitivity, 53% specificity) as useful parameters [153].

Uterine sarcomas constitute less than 5% of the uterine corpus malignancies, and, based on the type of cell they developed from, belong to three groups: endometrial stromal sarcomas, uterine leiomyosarcomas, and uterine carcinosarcomas. These tumors are very aggressive and have high mortality. MRI is presently the most accurate imaging modality for these lesions. Leiomyosarcomas are [^{18}F]FDG avid [154]. When compared with MRI in five patients, PET was positive in all five patients vs. four for MRI. The uptake in most cases was high, with a mean SUV of 4.5. In 53 patients with either uterine sarcomas, endometrial carcinomas, or leiomyomas, [^{18}F]FDG uptake (SUV_{max}) was higher in uterine sarcomas and endometrial carcinomas than for leiomyomas; however, there

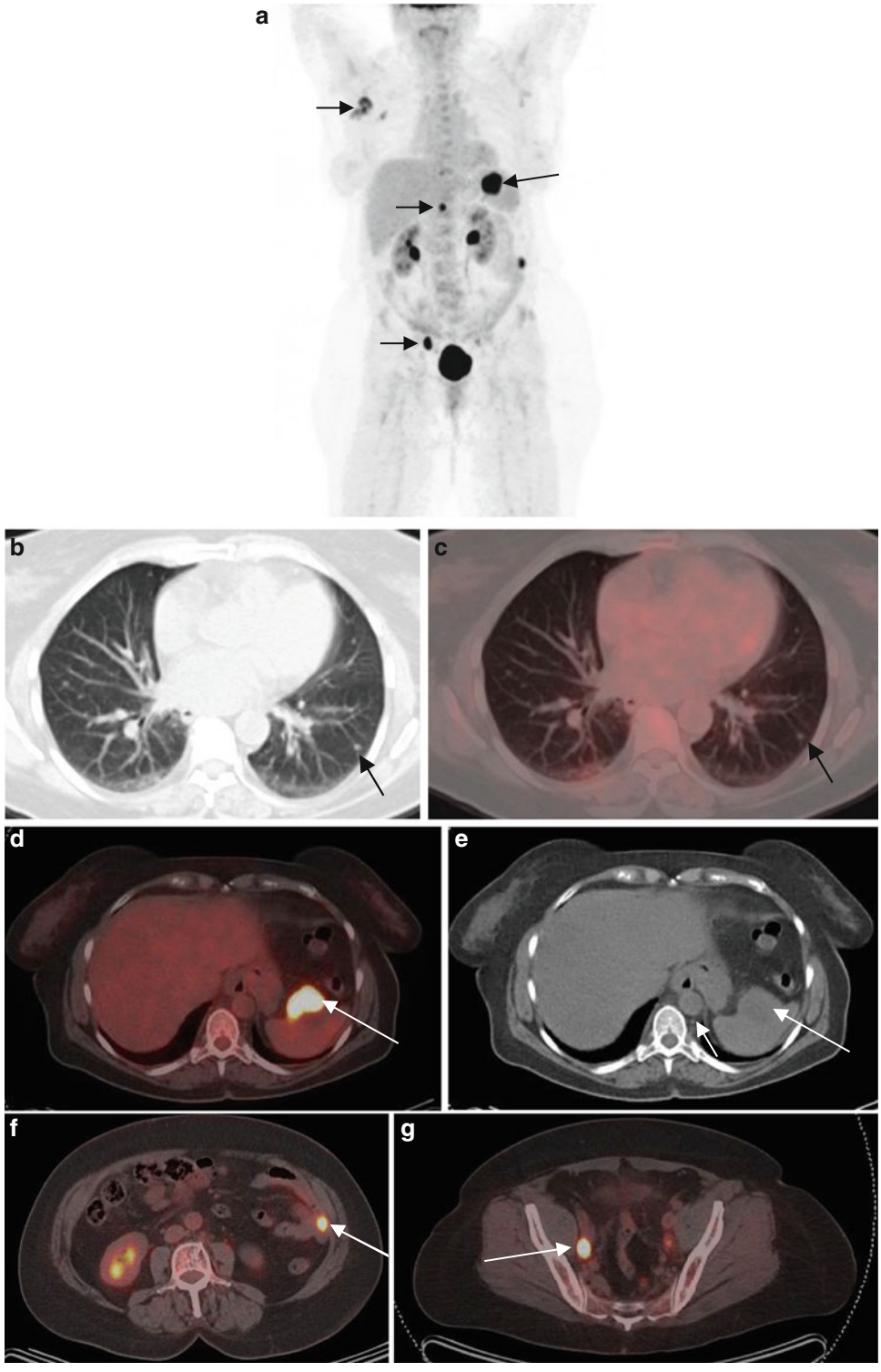

Fig. 14 (continued)

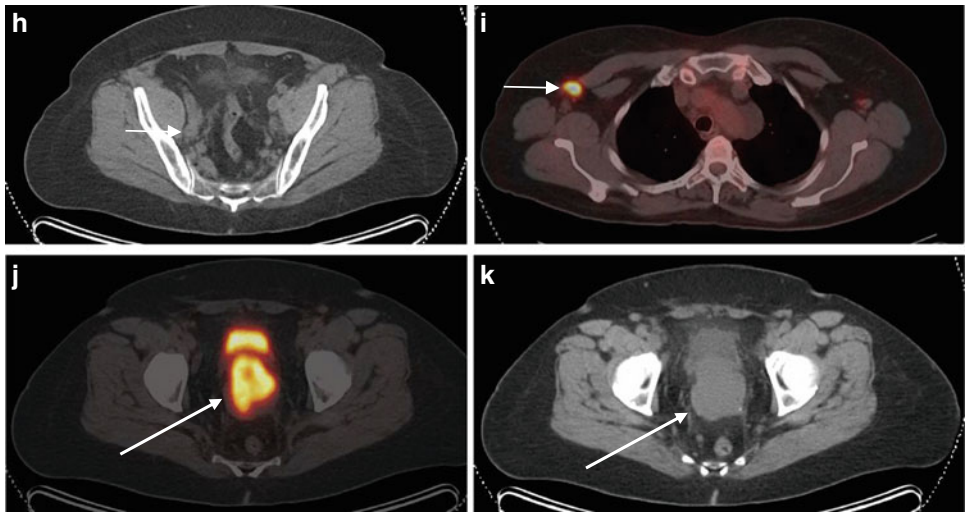

Fig. 14 A 61-year-old female patient with endometrioid adenocarcinoma referred for [^{18}F]FDG PET/CT for restaging. The patient had presented with vaginal spotting and slightly elevated CA-125 markers (~43 ng/mL); CT imaging showed new subcentimeter pulmonary nodules, limited in the PET assessment, negative for uptake in the lungs (**b**, **c**; *arrows*). PET/CT MIP (**a**, *black arrows*) demonstrated splenic hilar implant (**d**, **e,** *arrows*, SUV_{max} 20.1), peritoneal nodules (**f**, *arrow*; SUV_{max} 10.1), and pelvic nodes (**g**, **h**, *arrows*, SUV_{max} 16.9). Additionally PET/CT showed suspicious lesions in bilateral axillary nodes (**i**, *arrow*, SUV_{max} 7.4 on the right) and a bilobed mass in the vaginal cuff (**j**, **k** *arrow*; SUV_{max} 31.3), which was later confirmed to be recurrent disease on histopathology. Teaching point: [^{18}F]FDG PET/CT helps identify distant sites of disease involvement. Small lesions including subcentimeter lesions may be limited in assessment due to size

was no significant difference in SUVs among endometrial carcinomas, carcinosarcomas, and leiomyosarcomas [155]. The diagnostic accuracy for leiomyosarcomas was only 73%. Sarcomas had higher GLUT-1 expression than endometrial carcinomas (EC). However, frequently, the uptake in leiomyomas can be very high, too, making it difficult to distinguish malignant from benign lesions based on uptake alone (Fig. 16).

In summary, the role of [^{18}F]FDG PET is primarily in the evaluation of nodes or lesions in cases of equivocal conventional imaging and for detection of pelvic and distant disease in high-grade disease and high-risk patients.

Lymphoscintigraphy

Sentinel node mapping for cervical and uterine malignancies has been evaluated over the past decade for its feasibility and accuracy in early cervical and uterine cancers, and more clinical data are emerging of its use to prevent morbidity associated with nodal dissections [156–167]. Vascular and neural injuries with pain and paresthesia, formation of lymphoceles and seromas, and late and chronic sequelae of lymphedema associated with lymphadenectomies cause significant morbidity.

Lymph node status in cervical and endometrial cancer remains the most important prognostic factor for recurrence and survival and a major decision criterion for adjuvant therapy [168–169]. In cervical cancer of stage IA1, the rate of lymphatic/vascular invasion is less than 1% [170]. Pelvic node metastases are detected in 0–4.8% of patients with stage IA disease, in 0–17% of those with stage IB disease, and in approximately 20–40% of stage II cervical cancers [49, 171]. In stage I and occult stage II endometrial cancers, the incidence of lymph node metastases is approximately 10% [172]. Accurate assessment of the disease status of pelvic and paraaortic lymph nodes preoperatively is suboptimal and requires surgical staging [31]. Routinely performed extensive nodal dissection in patients who otherwise have a low likelihood of nodal metastasis suggests

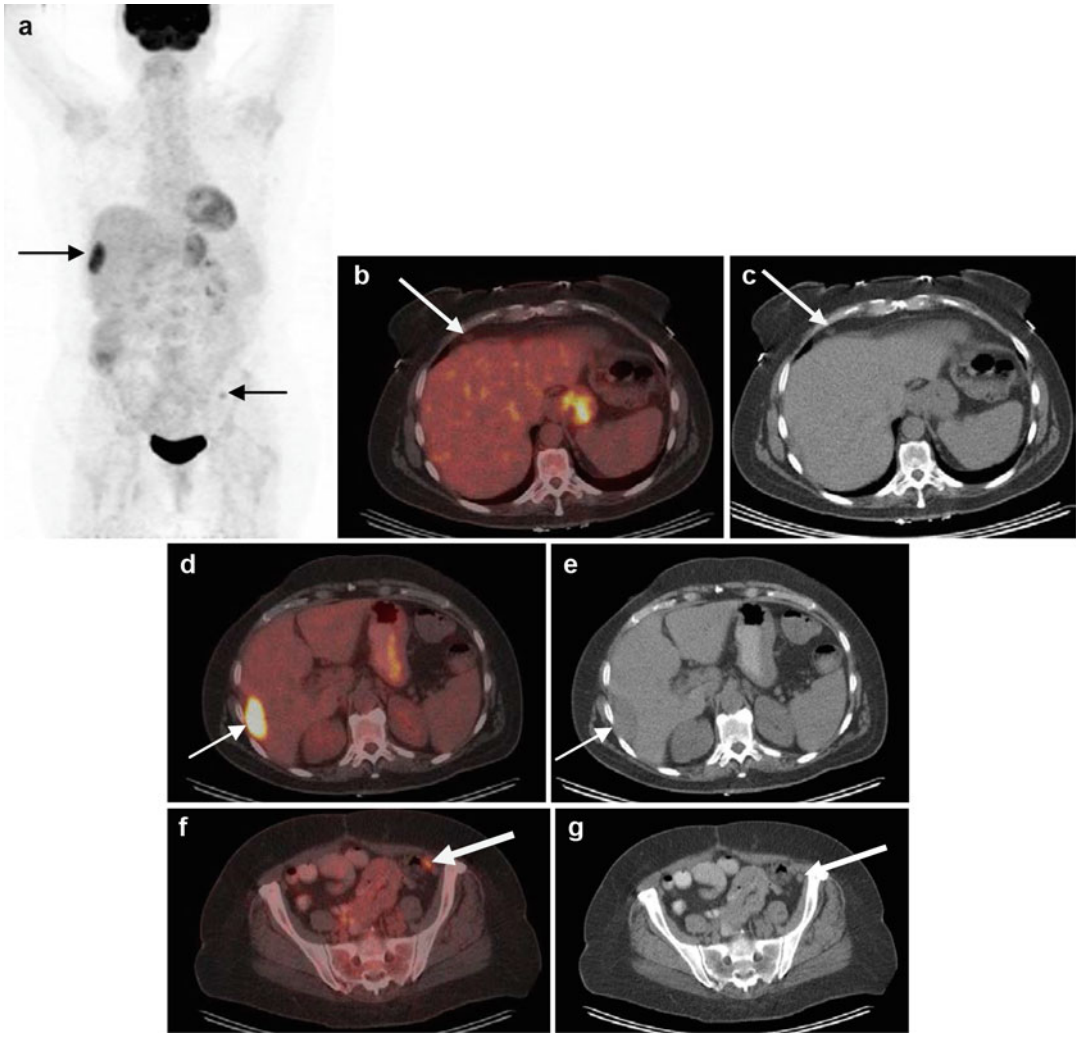

Fig. 15 A 59-year-old patient with stage I endometrioid adenocarcinoma, previously submitted to TAH/BSO, with suspected recurrence underwent [^{18}F]FDG PET/CT for restaging. MIP images (**a**, *black arrows*) revealed hypermetabolic implants in the parahepatic region (**d**, **e,** *arrows* SUV_{max} 9.5) and left paracolic gutter (**f**, **g,** *arrows* SUV_{max} 3.3). A small supradiaphragmatic lymph node was also noted (*white arrow* **b**, **c**). No other lesions were noted elsewhere. The patient underwent surgery and all the [^{18}F]FDG-positive lesions were confirmed metastasis. Teaching point: [^{18}F]FDG PET excluded extensive disease and distant organ metastasis that would have otherwise required systemic therapy

that a number of patients undergo dissection without clinical benefit and with a potential for increased complications and morbidity [173–174]. The incidence of nodal metastasis is low in patients presenting with a low-grade endometrioid adenocarcinoma [175] and the overall prognosis is excellent [176]. The use of lymphatic mapping and SLN identification in these patients may help reduce the morbidity of surgery without compromising the identification of patients who require adjuvant treatment [157, 177–179, 180–181].

Lymphoscintigraphy (LSG) is a noninvasive and convenient technique that can be performed either on the day of surgery or 1 day before surgery to map the nodal drainage. Various injection techniques of radiolabeled colloids have been applied for nodal mapping in cervical and endometrial cancers. Generally, they involve injecting

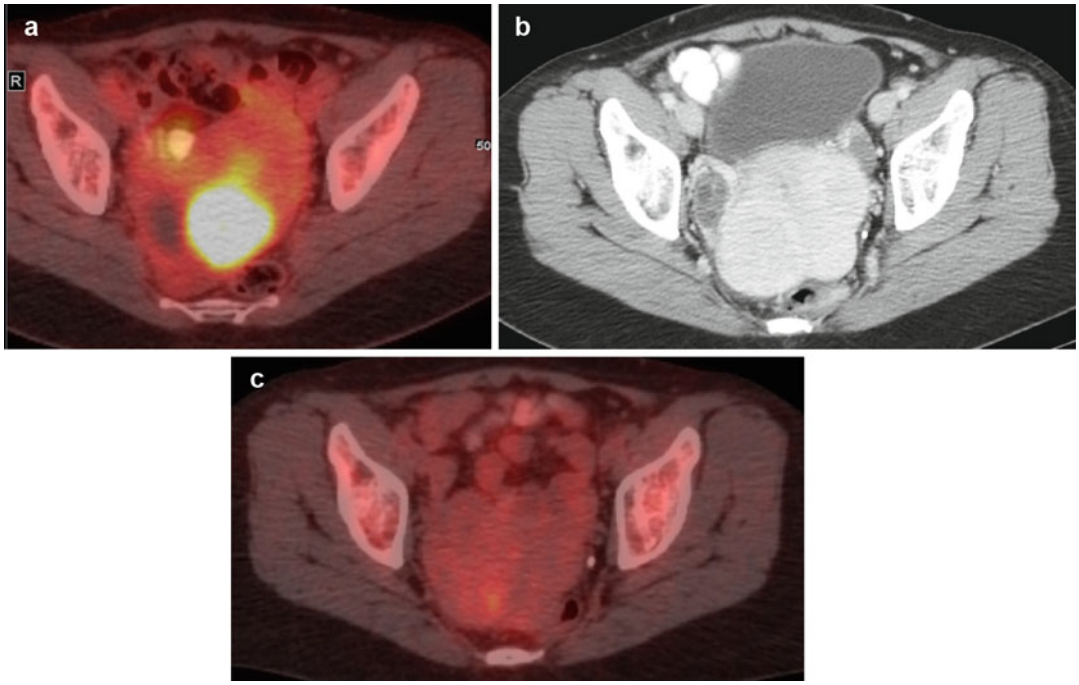

Fig. 16 PET/CT fused image in a patient with non-gynecologic malignancy. Intense [^{18}F]FDG uptake (**a**, SUV_{max} 8.5) seen in the uterus localizing to posteriorly lying fibroid on CT image (**b**), which increased in comparison with prior study 1 year earlier (**c**). MRI and further evaluation confirmed intense uptake within the dominant intramural posterior leiomyomata. Teaching point: Fibroids may show variable uptake and intensity may vary with time. It is difficult to distinguish between benign and malignant lesions based on [^{18}F]FDG uptake alone

1–2 mCi of radiocolloid in 1–1.5 mL volume at the site of the lesion; filtered ^{99m}Tc-sulfur colloid is generally used in the United States, while ^{99m}Tc-albumin nanocolloid is has been more commonly applied in Europe and elsewhere. More recently, ^{99m}Tc-tilmanocept, a node-seeking tracer that targets the mannose receptor CD206 has been approved for use in a variety of tumors [182–183]. More recently, fluorescent dyes such as indocyanine green have been explored in both cervical and endometrial cancer, providing an advantage of better intraoperative visualization of SLN with infrared light [184–185].

For cervical cancer, submucosal injection of tracer is carried out around the lesion or in four quadrants of the cervix using a 3.5-inch-long spinal needle. Imaging is acquired immediately after injection, and dynamic flow and static imaging in anterior, posterior, and lateral images are obtained. Handheld gamma probes have been used to detect "hot nodes" for removal during surgery. In vivo and ex vivo counts are recorded over the node. Generally, those with counts more than ten times the background levels are considered sentinel. The optimal site to inject radiotracer during LSG in patients with endometrial cancers is not well established and various techniques have been used including cervical, fundal, or hysteroscopic injections for SLN mapping [157, 178, 186–187]. Cervical injection for SLN mapping has several advantages over the other methods such as being easily accessible, less invasive, and having fewer chances of being influenced by anatomic variation in the uterus that may affect fundal injection and tumor infiltration [188].

External iliac and obturator nodes are more frequently seen on LSG, and bilateral nodal drainage is common. Using LSG alone, the detection rate is between 80% and 93% while combined blue dye and colloid scintigraphy increases the

detection rate with a reported range of 78–100% [157, 179, 178]. False-negative rates are very low, with an overall rate of less than 1% and a high NPV reported up to 100% [177].

Single photon emission computed tomography (SPECT) provides three-dimensional imaging information that, when combined with CT imaging (fusion imaging), can help to improve localization of SLNs (Fig. 17). This is more helpful in endometrial and cervical cancers, owing to the complex pelvic anatomy. Detection of SLNs with the hand-held probe requires experience. If the site of cervical injection is close to the sites of SLN basins in the pelvis, detecting the SLN uptake can be difficult because of scatter from the site of injection in the cervix. The closer the injected radiolabeled colloid is to the nodal sites, the more likely the interference with the hand-held

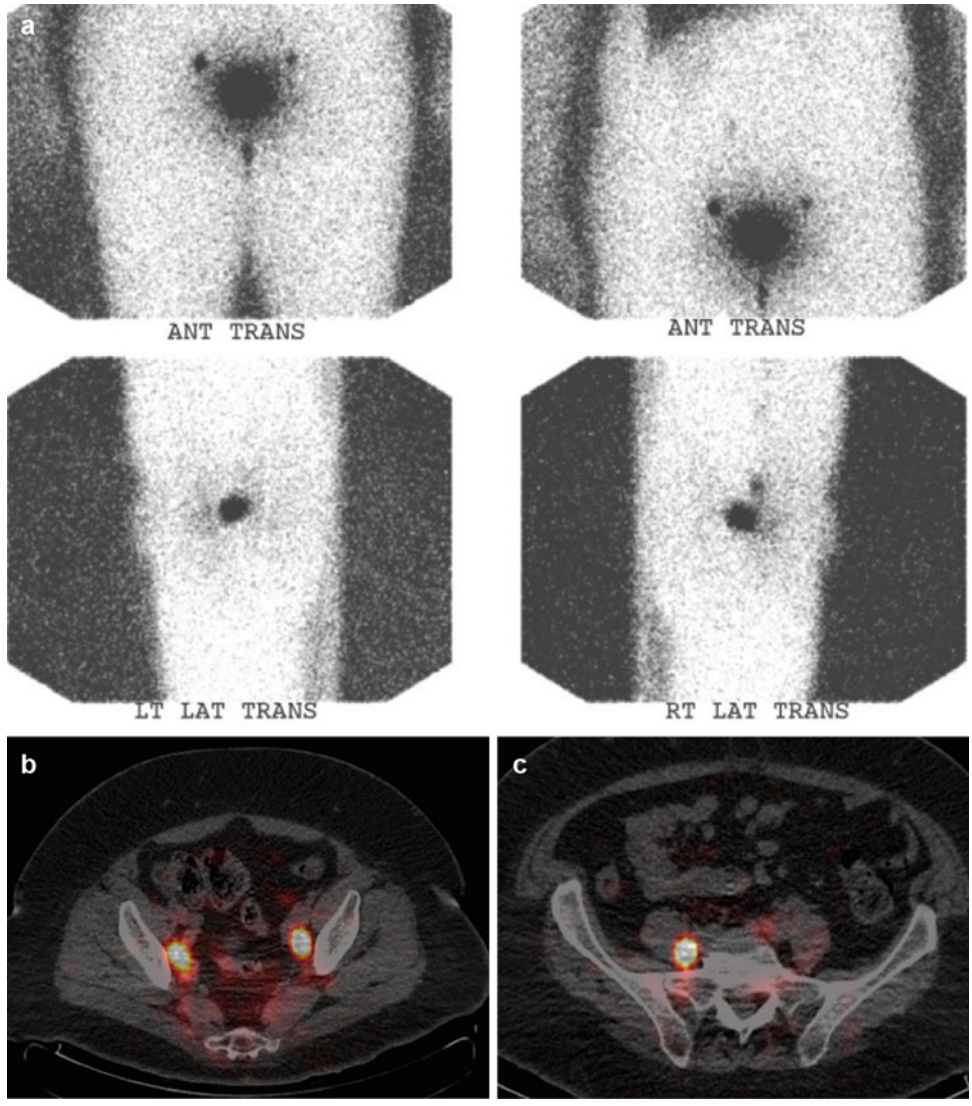

Fig. 17 Cervical carcinoma patient referred for lymphoscintigraphy. Planar images (**a**) show intense tracer activity in the injection site in the cervix. Two foci are seen superolaterally to the injection site localizing to the external iliac nodal region on SPECT/CT images (**b**). Additional focus seen faintly in the right side on planar images that localizes to the right common iliac nodal region on SPECT/CT (**c**)

probe. For similar reasons, a nodal basin like the parametrium (that is closer to the injection site) would be difficult to assess both by planar imaging and by probe counting. This is also true for blue dye, since the blue dye diffuses easily into the parametrium and can make it difficult to identify parametrial SLNs.

Several studies have shown that SPECT imaging for SLN detection in endometrial and cervical cancer is superior to planar imaging and improves the sensitivity of detection and localization of SLN [188]. Using SPECT imaging, there was increased sensitivity of SLN detection, with a 100% detection rate using SPECT/CT compared with either planar LSG, hand-held probe, or blue dye alone (75%, 92.5%, and 82.5%, respectively, for endometrial cancer and 70%, 90%, and 90%, respectively, for cervical cancer), as well as compared with combined imaging plus probe and blue dye injection (94.2%). A recent meta-analysis of data from eight studies ($n = 208$) for SLN in early-stage cervical cancer showed an overall SLN detection rate of 98.6% for SPECT/CT vs. 85.3% for planar LSG, although bilateral nodal site localization was similar (69% vs. 67%) [189]. Accurate anatomic localization of SLNs preoperatively can also aid in probe-directed surgery and in reducing operator-dependent variation and time involved in surgery. SPECT/CT helps achieve faster intraoperative localization and SLN removal; an average time advantage of 25 min in lymph node retrieval was noted with the use of SPECT/CT [190]. Similarly, in a group of 59 patients with early-stage cervical cancer, Klapdor et al. demonstrated a detection rate of 84.3% for planar imaging and 92.2% for SPECT/CT [191–192].

A similar advantage of SPECT/CT was shown in SLN mapping in early-stage endometrial cancer: The detection rate for planar imaging ranges between 50% and 67% while with SPECT/CT the range is 84–91% [193] [186]. With SPECT/CT, fewer false-positive findings are seen and localization of para-aortic and pelvic nodes is superior to planar imaging [188, 194], leading to a change in location in 37% of patients and in 22% of nodal sites compared with planar imaging. A recent study of 136 women with low-to-intermediate-risk endometrial carcinoma detected SLN with micrometastasis that resulted in upstaging of 22 patients and a higher risk group identified in ten cases, influencing management [195].

Certain limitations and potential issues with SPECT must be understood; for example, detection of multiple nodes can occur depending on the time of imaging, injection volume, and rate. Therefore, all these parameters should be standardized. Nodal localization may be seen on both sides of the pelvis, the first most intense node on each side may be regarded as the SLN; however, more data are needed to establish this clearly. With the current data, there is incremental value in using SPECT/CT and it should be employed in conjunction with planar imaging whenever possible and especially in patients with negative findings on planar imaging, to enhance SLN detection and localization.

LSG can identify patients with an atypical drainage pattern and identify unusual sites of SLN. In a prospective SENTICOL study comprising 139 patients with early-stage cervical disease, about 57% patients were noted to have atypical sites of SLN localization using LSG compared with 38% by intraoperative mapping. About 49% of patients with atypical SLN sites on LSG also had atypical sites detected by intraoperative mapping. In 13 patients, a parametrial SLN was seen with LSG only; 3% of patients also showed common iliac and para-aortic SLNs with LSG only [196].

In the SENTI-ENDO study, SLN mapping was performed on 118 of 133 patients with early endometrial cancers, for whom delayed imaging was performed at 120 min after injection (long protocol) vs. 90 min after injection (short protocol).The overall detection rate of LSG was 74.6% (88/118) with no significant difference in overall detection rate; however, a higher detection of para-aortic SLN was seen in patients imaged with the long protocol [197].

In summary, the feasibility of LSG in cervical and endometrial cancers has been documented. The overall detection rates with LSG are high and superior when used in conjunction with blue dye. Recent developments and the increasing use of fluorescent dyes may influence the future applications and use of LSG.

References

1. National Cancer Institute Surveillance E. End Results (NCI SEER) program. http://www.seer.cancer.gov; 2013.
2. American Cancer Society. Cancer facts and figures. http://www.cancer.org
3. Chi DBR, Rubin SC. Gynecologic malignancies. Cancer management: a multidisciplinary approach. 4th ed. Melville: PRR; 1999.
4. Young RC, Fuks Z, Hoskins WJ. In: DeVita VT, Hellman S, Rosenberg St., editors. Cancer: principles and practice of oncology. vol. 9. Philadelphia: J B Lippincott; 2011.
5. http://www.FIGO.org
6. Toita T, et al. Prognostic value of cervical size and pelvic lymph node status assessed by computed tomography for patients with uterine cervical cancer treated by radical radiation therapy. Int J Radiat Oncol Biol Phys. 1995;33(4):843–9.
7. Van Nagell Jr JR, Roddick Jr JW, Lowin DM. The staging of cervical cancer: inevitable discrepancies between clinical staging and pathologic findinges. Am J Obstet Gynecol. 1971;110(7):973–8.
8. Kamura T, et al. Multivariate analysis of the histopathologic prognostic factors of cervical cancer in patients undergoing radical hysterectomy. Cancer. 1992;69(1):181–6.
9. Walsh JW, Goplerud DR. Prospective comparison between clinical and CT staging in primary cervical carcinoma. AJR Am J Roentgenol. 1981;137(5):997–1003.
10. Vandeperre A, et al. Para-aortic lymph node metastases in locally advanced cervical cancer: comparison between surgical staging and imaging. Gynecol Oncol. 2015;138(2):299–303.
11. Tran BN, et al. Occult supraclavicular lymph node metastasis identified by FDG-PET in patients with carcinoma of the uterine cervix. Gynecol Oncol. 2003;90(3):572–6.
12. Hricak H, et al. Invasive cervical carcinoma: comparison of MR imaging and surgical findings. Radiology. 1988;166(3):623–31.
13. Togashi K, et al. Cervical cancer. J Magn Reson Imaging. 1998;8(2):391–7.
14. Kim SH, et al. Preoperative staging of uterine cervical carcinoma: comparison of CT and MRI in 99 patients. J Comput Assist Tomogr. 1993;17(4):633–40.
15. Lagasse LD, et al. Results and complications of operative staging in cervical cancer: experience of the Gynecologic Oncology Group. Gynecol Oncol. 1980;9(1):90–8.
16. LaPolla JP, et al. The influence of surgical staging on the evaluation and treatment of patients with cervical carcinoma. Gynecol Oncol. 1986;24(2):194–206.
17. Yen TC, et al. ^{18}F-FDG uptake in squamous cell carcinoma of the cervix is correlated with glucose transporter 1 expression. J Nucl Med. 2004;45(1):22–9.
18. Schneider A, Hertel H. Surgical and radiographic staging in patients with cervical cancer. Curr Opin Obstet Gynecol. 2004;16(1):11–8.
19. Kidd EA, et al. Cervical cancer histology and tumor differentiation affect ^{18}F-fluorodeoxyglucose uptake. Cancer. 2009;115(15):3548–54.
20. Tong SY, et al. Correlation between FDG uptake by PET/CT and the expressions of glucose transporter type 1 and hexokinase II in cervical cancer. Int J Gynecol Cancer. 2012;22(4):654–8.
21. Yilmaz M, et al. FDG PET-CT in cervical cancer: relationship between primary tumor FDG uptake and metastatic potential. Nucl Med Commun. 2010;31(6):526–31.
22. Wong TZ, Jones EL, Coleman RE. Positron emission tomography with 2-deoxy-2-[^{18}F]fluoro-D-glucose for evaluating local and distant disease in patients with cervical cancer. Mol Imaging Biol. 2004;6(1):55–62.
23. Metser U, et al. Tumor lesion detection: when is integrated positron emission tomography/computed tomography more accurate than side-by-side interpretation of positron emission tomography and computed tomography? J Comput Assist Tomogr. 2005;29(4):554–9.
24. Kitajima K, et al. Performance of FDG-PET/CT for diagnosis of recurrent uterine cervical cancer. Eur Radiol. 2008;18(10):2040–7.
25. Tatsumi M, et al. Imaging uterine cervical cancer with FDG-PET/CT: direct comparison with PET. Mol Imaging Biol. 2009;11(4):229–35.
26. Sugawara Y, et al. Evaluation of FDG PET in patients with cervical cancer. J Nucl Med. 1999;40(7):1125–31.
27. Rose PG, et al. Positron emission tomography for evaluating para-aortic nodal metastasis in locally advanced cervical cancer before surgical staging: a surgicopathologic study. J Clin Oncol. 1999;17(1):41–5.
28. Roh JW, et al. Role of positron emission tomography in pretreatment lymph node staging of uterine cervical cancer: a prospective surgicopathologic correlation study. Eur J Cancer. 2005;41(14):2086–92.
29. Park W, et al. The usefulness of MRI and PET imaging for the detection of parametrial involvement and lymph node metastasis in patients with cervical cancer. Jpn J Clin Oncol. 2005;35(5):260–4.
30. Park W, et al. The usefulness of MRI and PET imaging for the detection of parametrial involvement and lymph node metastasis in patients with cervical cancer. Jpn J Clin Oncol. 2005;35(5):260–4.
31. Choi HJ, et al. Comparison of the accuracy of magnetic resonance imaging and positron emission tomography/computed tomography in the presurgical detection of lymph node metastases in patients with uterine cervical carcinoma: a prospective study. Cancer. 2006;106(4):914–22.
32. Chou HH, et al. Low value of [^{18}F]-fluoro-2-deoxy-D-glucose positron emission tomography in primary staging of early-stage cervical cancer before radical hysterectomy. J Clin Oncol. 2006;24(1):123–8.
33. Reinhardt MJ, et al. Metastatic lymph nodes in patients with cervical cancer: detection with MR

imaging and FDG PET. Radiology. 2001;218(3): 776–82.
34. Loft A, et al. The diagnostic value of PET/CT scanning in patients with cervical cancer: a prospective study. Gynecol Oncol. 2007;106(1):29–34.
35. Kang S, et al. Diagnostic value of ^{18}F-FDG PET for evaluation of paraaortic nodal metastasis in patients with cervical carcinoma: a metaanalysis. J Nucl Med. 2010;51(3):360–7.
36. Belhocine T, et al. Contribution of whole-body 18FDG PET imaging in the management of cervical cancer. Gynecol Oncol. 2002;87(1):90–7.
37. Lv K, et al. Role of ^{18}F-FDG PET/CT in detecting pelvic lymph-node metastases in patients with early-stage uterine cervical cancer: comparison with MRI findings. Nucl Med Commun. 2014;35(12): 1204–11.
38. Wright JD, et al. Preoperative lymph node staging of early-stage cervical carcinoma by F-18 -fluoro-2-deoxy-D-glucose-positron emission tomography. Cancer. 2005;104(11):2484–91.
39. Lai CH, Yen TC, Chang TC. Positron emission tomography imaging for gynecologic malignancy. Curr Opin Obstet Gynecol. 2007;19(1):37–41.
40. Rockall AG, et al. Diagnostic performance of nanoparticle-enhanced magnetic resonance imaging in the diagnosis of lymph node metastases in patients with endometrial and cervical cancer. J Clin Oncol. 2005;23(12):2813–21.
41. Roh JW, et al. Role of positron emission tomography in pretreatment lymph node staging of uterine cervical cancer: a prospective surgicopathologic correlation study. Eur J Cancer. 2005;41(14): 2086–92.
42. Williams AD, et al. Detection of pelvic lymph node metastases in gynecologic malignancy: a comparison of CT, MR imaging, and positron emission tomography. AJR Am J Roentgenol. 2001;177(2):343–8.
43. Belhocine T, et al. Staging of primary cervical cancers: the role of nuclear medicine. Crit Rev Oncol Hematol. 2003;46(3):275–84.
44. Sironi S, et al. Lymph node metastasis in patients with clinical early-stage cervical cancer: detection with integrated FDG PET/CT. Radiology. 2006;238(1): 272–9.
45. Yang Z, et al. ^{18}F-FDG PET/CT can correct the clinical stages and predict pathological parameters before operation in cervical cancer. Eur J Radiol. 2016;85 (5):877–84.
46. Loft A, et al. The diagnostic value of PET/CT scanning in patients with cervical cancer: a prospective study. Gynecol Oncol. 2007;106(1):29–34.
47. Monteil J, et al. Lymph node assessment with ^{18}F-FDG-PET and MRI in uterine cervical cancer. Anticancer Res. 2011;31(11):3865–71.
48. Leblanc E, et al. Therapeutic value of pretherapeutic extraperitoneal laparoscopic staging of locally advanced cervical carcinoma. Gynecol Oncol. 2007;105(2): 304–11.
49. Michel G, et al. Lymphatic spread in stage Ib and II cervical carcinoma: anatomy and surgical implications. Obstet Gynecol. 1998;91(3):360–3.
50. Akkas BE, Demirel BB, Vural GU. Clinical impact of ^{18}F-FDG PET/CT in the pretreatment evaluation of patients with locally advanced cervical carcinoma. Nucl Med Commun. 2012;33(10):1081–8.
51. Sugawara Y, et al. Evaluation of FDG PET in patients with cervical cancer. J Nucl Med. 1999;40(7): 1125–31.
52. Lin WC, et al. Usefulness of ^{18}F-fluorodeoxyglucose positron emission tomography to detect para-aortic l ymph nodal metastasis in advanced cervical cancer with negative computed tomography findings. Gynecol Oncol. 2003;89(1):73–6.
53. Yeh LS, et al. Detecting para-aortic lymph nodal metastasis by positron emission tomography of 18F-fluorodeoxyglucose in advanced cervical cancer with negative magnetic resonance imaging findings. Oncol Rep. 2002;9(6):1289–92.
54. Rose PG, et al. Positron emission tomography for evaluating para-aortic nodal metastasis in locally advanced cervical cancer before surgical staging: a surgicopathologic study. J Clin Oncol. 1999;17(1): 41–5.
55. Havrilesky LJ, et al. FDG-PET for management of cervical and ovarian cancer. Gynecol Oncol. 2005;97 (1):183–91.
56. Yildirim Y, et al. Integrated PET/CT for the evaluation of para-aortic nodal metastasis in locally advanced cervical cancer patients with negative conventional CT findings. Gynecol Oncol. 2008;108(1):154–9.
57. Uzan C, et al. Analysis of morbidity and clinical implications of laparoscopic para-aortic lymphadenectomy in a continuous series of 98 patients with advanced-stage cervical cancer and negative PET-CT imaging in the para-aortic area. Oncologist. 2011;16(7):1021–7.
58. Leblanc E, et al. Accuracy of 18-fluoro-2-deoxy-D-glucose positron emission tomography in the pretherapeutic detection of occult para-aortic node involvement in patients with a locally advanced cervical carcinoma. Ann Surg Oncol. 2011;18(8):2302–9.
59. Ramirez PT, et al. Laparoscopic extraperitoneal paraaortic lymphadenectomy in locally advanced cervical cancer: a prospective correlation of surgical findings with positron emission tomography/computed tomography findings. Cancer. 2011;117(9):1928–34.
60. Perez-Medina T, et al. Prospective evaluation of 18-fluoro-2-deoxy-D-glucose positron emission tomography for the discrimination of paraaortic nodal spread in patients with locally advanced cervical carcinoma. Int J Gynecol Cancer. 2013;23(1):170–5.
61. Chung HH, et al. Role of integrated PET-CT in pelvic lymph node staging of cervical cancer before radical hysterectomy. Gynecol Obstet Investig. 2009;67(1): 61–6.
62. Lee YY, et al. The prognostic significance of the SUVmax (maximum standardized uptake value for

F-18 fluorodeoxyglucose) of the cervical tumor in PET imaging for early cervical cancer: preliminary results. Gynecol Oncol. 2009;115(1):65–8.
63. Micco M, et al. Combined pre-treatment MRI and ^{18}F-FDG PET/CT parameters as prognostic biomarkers in patients with cervical cancer. Eur J Radiol. 2014;83(7):1169–76.
64. Chung HH, et al. Prognostic value of metabolic tumor volume measured by FDG-PET/CT in patients with cervical cancer. Gynecol Oncol. 2011;120(2):270–4.
65. Yoo J, et al. Prognostic significance of volume-based metabolic parameters in uterine cervical cancer determined using ^{18}F-fluorodeoxyglucose positron emission tomography. Int J Gynecol Cancer. 2012;22 (7):1226–33.
66. Hong JH, et al. Prognostic value of total lesion glycolysis measured by ^{18}F-FDG PET/CT in patients with locally advanced cervical cancer. Nucl Med Commun. 2016;37(8):843–8.
67. Herrera F, et al. [^{18}F]FDG-PET/CT metabolic parameters as useful prognostic factors in cervical cancer patients treated with chemo-radiotherapy. Radiat Oncol, 2016. 11: p. 43.
68. Krhili, et al. Use of metabolic parameters as prognostic factors during concomitant chemoradiotherapy for locally advanced cervical cancer. Am J Clin Oncol. 2017;40(3):250–55.
69. Singh AK, et al. FDG-PET lymph node staging and survival of patients with FIGO stage IIIb cervical carcinoma. Int J Radiat Oncol Biol Phys. 2003;56 (2):489–93.
70. Kidd EA, et al. Lymph node staging by positron emission tomography in cervical cancer: relationship to prognosis. J Clin Oncol. 2010;28(12):2108–13.
71. Chao A, et al. Positron emission tomography in evaluating the feasibility of curative intent in cervical cancer patients with limited distant lymph node metastases. Gynecol Oncol. 2008;110(2):172–8.
72. Qiu JT, et al. Supraclavicular lymph node metastases in cervical cancer. Eur J Gynaecol Oncol. 2007;28 (1):33–8.
73. Kidd EA, et al. FDG-PET-based prognostic nomograms for locally advanced cervical cancer. Gynecol Oncol. 2012;127(1):136–40.
74. Yen TC, et al. Standardized uptake value in para-aortic lymph nodes is a significant prognostic factor in patients with primary advanced squamous cervical cancer. Eur J Nucl Med Mol Imaging. 2008;35(3):493–501.
75. Kim, D.H., et al. Maximum standardized uptake value of pelvic lymph nodes in [^{18}F]-fluorodeoxyglucose positron emission tomography is a prognostic factor for para-aortic lymph node recurrence in pelvic node-positive cervical cancer treated with definitive chemoradiotherapy. Int J Gyn Cancer. 2016;26 (7):1274–80.
76. Onal C, et al. Prognostic value of ^{18}F-fluorodeoxyglucose uptake in pelvic lymph nodes in patients with cervical cancer treated with definitive chemoradiotherapy. Gynecol Oncol. 2015;137(1):40–6.
77. Gold MA, et al. Surgical versus radiographic determination of para-aortic lymph node metastases before chemoradiation for locally advanced cervical carcinoma: a Gynecologic Oncology Group Study. Cancer. 2008;112(9):1954–63.
78. Crivellaro, et al. ^{18}F–FDG PET/CT can predict nodal metastases but not recurrence in early stage uterine cervical cancer. Gynecol Oncol. 2012;127(1):131–5.
79. Kim BS, et al. The prognostic value of the metabolic tumor volume in FIGO stage IA to IIB cervical cancer for tumor recurrence: measured by F-18 FDG PET/CT. Nucl Med Mol Imaging. 2011;45(1):36–42.
80. Kidd EA, Grigsby PW. Intratumoral metabolic heterogeneity of cervical cancer. Clin Cancer Res. 2008;14(16):5236–41.
81. Sarker A, et al. Prognostic implications of the SUVmax of primary tumors and metastatic lymph node measured by ^{18}F-FDG PET in patients with uterine cervical cancer: a meta-analysis. Clin Nucl Med. 2016;41(1):34–40.
82. Chung HH, et al. Preoperative PET/CT FDG standardized uptake value of pelvic lymph nodes as a significant prognostic factor in patients with uterine cervical cancer. Eur J Nucl Med Mol Imaging. 2014;41(4):674–81.
83. Yen TC, et al. Standardized uptake value in para-aortic lymph nodes is a significant prognostic factor in patients with primary advanced squamous cervical cancer. Eur J Nucl Med Mol Imaging. 2008;35(3):493–501.
84. Nakamura K, et al. Maximum standardized lymph node uptake value could be an important predictor of recurrence and survival in patients with cervical cancer. Eur J Obstet Gynecol Reprod Biol. 2014; 173:77–82.
85. Narayan K, et al. Patterns of failure and prognostic factor analyses in locally advanced cervical cancer patients staged by positron emission tomography and treated with curative intent. Int J Gynecol Cancer. 2009;19(5):912–8.
86. Belhocine T, et al. Contribution of whole-body ^{18}FDG PET imaging in the management of cervical cancer. Gynecol Oncol. 2002;87(1):90–7.
87. Fleming S, et al. Clinical impact of FDG PET-CT on the management of patients with locally advanced cervical carcinoma. Clin Radiol. 2014;69(12):1235–43.
88. Grigsby PW, et al. Lack of benefit of concurrent chemotherapy in patients with cervical cancer and negative lymph nodes by FDG-PET. Int J Radiat Oncol Biol Phys. 2005;61(2):444–9.
89. Pandharipande PV, et al. MRI and PET/CT for triaging stage IB clinically operable cervical cancer to appropriate therapy: decision analysis to assess patient outcomes. AJR Am J Roentgenol. 2009;192 (3):802–14.
90. Yoshida Y, et al. Metabolic monitoring of advanced uterine cervical cancer neoadjuvant chemotherapy by using [F-18]-Fluorodeoxyglucose positron emission tomography: preliminary results in three patients. Gynecol Oncol. 2004;95(3):597–602.

91. Sandvik RM, et al. Positron emission tomography-computed tomography has a clinical impact for patients with cervical cancer. Dan Med Bull. 2011;58(3): A4240.
92. Tsai CS, et al. A prospective randomized trial to study the impact of pretreatment FDG-PET for cervical cancer patients with MRI-detected positive pelvic but negative para-aortic lymphadenopathy. Int J Radiat Oncol Biol Phys. 2010;76(2):477–84.
93. Malyapa RS, et al. Physiologic FDG-PET three-dimensional brachytherapy treatment planning for cervical cancer. Int J Radiat Oncol Biol Phys. 2002;54(4):1140–6.
94. Mutic S, et al. PET-guided IMRT for cervical carcinoma with positive para-aortic lymph nodes-a dose-escalation treatment planning study. Int J Radiat Oncol Biol Phys. 2003;55(1):28–35.
95. Vargo JA, et al. Extended field intensity modulated radiation therapy with concomitant boost for lymph node-positive cervical cancer: analysis of regional control and recurrence patterns in the positron emission tomography/computed tomography era. Int J Radiat Oncol Biol Phys. 2014;90(5):1091–8.
96. Choi J, et al. The role of ^{18}F-FDG PET/CT in assessing therapy response in cervix cancer after concurrent chemoradiation therapy. Nucl Med Mol Imaging. 2014;48(2):130–6.
97. Havrilesky LJ, et al. FDG-PET for management of cervical and ovarian cancer. Gynecol Oncol. 2005;97 (1):183–91.
98. Havrilesky LJ, et al. The role of PET scanning in the detection of recurrent cervical cancer. Gynecol Oncol. 2003;90(1):186–90.
99. Kitajima K, et al. Low-dose non-enhanced CT versus full-dose contrast-enhanced CT in integrated PET/CT studies for the diagnosis of uterine cancer recurrence. Eur J Nucl Med Mol Imaging. 2010;37 (8):1490–8.
100. Spottswood SE, et al. Peritoneal carcinomatosis from cervical cancer detected by F-18 FDG positron emission tomography. Clin Nucl Med. 2005;30(1):56–9.
101. Unger JB, et al. Detection of recurrent cervical cancer by whole-body FDG PET scan in asymptomatic and symptomatic women. Gynecol Oncol. 2004;94(1):212–6.
102. Weber TM, et al. Cervical carcinoma: determination of recurrent tumor extent versus radiation changes with MR imaging. Radiology. 1995;194(1):135–9.
103. Spottswood SE, et al. Peritoneal carcinomatosis from cervical cancer detected by F-18 FDG positron emission tomography. Clin Nucl Med. 2005;30(1):56–9.
104. van der Veldt AA, et al. Clarifying the diagnosis of clinically suspected recurrence of cervical cancer: impact of ^{18}F-FDG PET. J Nucl Med. 2008;49 (12):1936–43.
105. Auguste P, et al. Evaluating PET-CT in routine surveillance and follow-up after treatment for cervical cancer: a cost-effectiveness analysis. BJOG. 2014;121(4):464–76.
106. Mittra E, et al. Efficacy of ^{18}F-FDG PET/CT in the evaluation of patients with recurrent cervical carcinoma. Eur J Nucl Med Mol Imaging. 2009;36 (12):1952–9.
107. Chang TC, et al. Positron emission tomography for unexplained elevation of serum squamous cell carcinoma antigen levels during follow-up for patients with cervical malignancies: a phase II study. Cancer. 2004;101(1):164–71.
108. Sakurai H, et al. FDG-PET in the detection of recurrence of uterine cervical carcinoma following radiation therapy–tumor volume and FDG uptake value. Gynecol Oncol. 2006;100(3):601–7.
109. Chang WC, et al. Usefulness of FDG-PET to detect recurrent cervical cancer based on asymptomatically elevated tumor marker serum levels–a preliminary report. Cancer Investig. 2004;22(2):180–4.
110. Yen TC, et al. Comparative benefits and limitations of ^{18}F-FDG PET and CT-MRI in documented or suspected recurrent cervical cancer. Eur J Nucl Med Mol Imaging. 2006;33(12):1399–407.
111. Pallardy A, et al. Clinical and survival impact of FDG PET in patients with suspicion of recurrent cervical carcinoma. Eur J Nucl Med Mol Imaging. 2010; 37(7):1270–8.
112. Chung HH, et al. Predictive role of post-treatment [^{18}F]FDG PET/CT in patients with uterine cervical cancer. Eur J Radiol. 2012;81(8):e817–22.
113. Esthappan J, et al. Treatment planning guidelines regarding the use of CT/PET-guided IMRT for cervical carcinoma with positive paraaortic lymph nodes. Int J Radiat Oncol Biol Phys. 2004;58 (4):1289–97.
114. Dolezelova H, et al. The impact of PET with ^{18}FDG in radiotherapy treatment planning and in the prediction in patients with cervix carcinoma: results of pilot study. Neoplasma. 2008;55(5):437–41.
115. Kidd EA, et al. Clinical outcomes of definitive intensity-modulated radiation therapy with fluorodeoxyglucose-positron emission tomography simulation in patients with locally advanced cervical cancer. Int J Radiat Oncol Biol Phys. 2010;77(4):1085–91.
116. Dyk P, et al. Cervical gross tumor volume dose predicts local control using magnetic resonance imaging/diffusion-weighted imaging-guided high-dose-rate and positron emission tomography/computed tomography-guided intensity modulated radiation therapy. Int J Radiat Oncol Biol Phys. 2014;90(4):794–801.
117. Fyles AW, et al. Oxygenation predicts radiation response and survival in patients with cervix cancer. Radiother Oncol. 1998;48(2):149–56.
118. Hockel M, et al. Association between tumor hypoxia and malignant progression in advanced cancer of the uterine cervix. Cancer Res. 1996;56(19):4509–15.
119. Fujibayashi Y, et al. Copper-62-ATSM: a new hypoxia imaging agent with high membrane permeability and low redox potential. J Nucl Med. 1997;38 (7):1155–60.
120. Vavere AL, Lewis JS. Cu-ATSM: a radiopharmaceutical for the PET imaging of hypoxia. Dalton Trans. 2007;43:4893–902.

121. Dehdashti F, et al. Assessing tumor hypoxia in cervical cancer by positron emission tomography with ^{60}Cu-ATSM: relationship to therapeutic response-a preliminary report. Int J Radiat Oncol Biol Phys. 2003;55(5):1233–8.
122. Pinker K, et al. Multiparametric [^{18}F]fluorodeoxyglucose/[^{18}F]fluoromisonidazole positron emission tomography/magnetic resonance imaging of locally advanced cervical cancer for the non-invasive detection of tumor heterogeneity: a pilot study. PLoS One. 2016;11(5):e0155333.
123. Lee SI, Catalano OA, Dehdashti F. Evaluation of gynecologic cancer with MR imaging, ^{18}F-FDG PET/CT, and PET/MR imaging. J Nucl Med. 2015;56(3):436–43.
124. Kim SK, et al. Additional value of MR/PET fusion compared with PET/CT in the detection of lymph node metastases in cervical cancer patients. Eur J Cancer. 2009;45(12):2103–9.
125. Queiroz MA, et al. PET/MRI and PET/CT in advanced gynaecological tumours: initial experience and comparison. Eur Radiol. 2015;25(8):2222–30.
126. Fraum TJ, Fowler KJ, McConathy J. PET/MRI: emerging clinical applications in oncology. Acad Radiol. 2016;23(2):220–36.
127. Grueneisen J, et al. Simultaneous positron emission tomography/magnetic resonance imaging for whole-body staging in patients with recurrent gynecological malignancies of the pelvis: a comparison to whole-body magnetic resonance imaging alone. Investig Radiol. 2014;49(12):808–15.
128. Beiderwellen K, et al. [^{18}F]FDG PET/MRI vs. PET/CT for whole-body staging in patients with recurrent malignancies of the female pelvis: initial results. Eur J Nucl Med Mol Imaging. 2015;42(1):56–65.
129. Zhang S, et al. Defining PET tumor volume in cervical cancer with hybrid PET/MRI: a comparative study. Nucl Med Commun. 2014;35(7):712–9.
130. Burke WM, et al. Endometrial cancer: a review and current management strategies: part I. Gynecol Oncol. 2014;134(2):385–92.
131. Goldstein RB, et al. Evaluation of the woman with postmenopausal bleeding: Society of Radiologists in Ultrasound-Sponsored Consensus Conference statement. J Ultrasound Med. 2001;20(10):1025–36.
132. Timmermans A, et al. Endometrial thickness measurement for detecting endometrial cancer in women with postmenopausal bleeding: a systematic review and meta-analysis. Obstet Gynecol. 2010;116(1):160–7.
133. Tirumani SH, Shanbhogue AK, Prasad SR. Current concepts in the diagnosis and management of endometrial and cervical carcinomas. Radiol Clin N Am. 2013;51(6):1087–110.
134. Wong AS, et al. Reappraisal of endometrial thickness for the detection of endometrial cancer in postmenopausal bleeding: a retrospective cohort study. BJOG. 2016;123(3):439–46.
135. www.nccn.org/professionals/physician_gls/f_guidelines.asp., NCCN guidelines.
136. Nishizawa S, Inubushi M, Okada H. Physiological ^{18}F-FDG uptake in the ovaries and uterus of healthy female volunteers. Eur J Nucl Med Mol Imaging. 2005;32(5):549–56.
137. Lerman H, et al. Normal and abnormal ^{18}F-FDG endometrial and ovarian uptake in pre- and postmenopausal patients: assessment by PET/CT. J Nucl Med. 2004;45(2):266–71.
138. Lentz SS. Endometrial carcinoma diagnosed by positron emission tomography: a case report. Gynecol Oncol. 2002;86(2):223–4.
139. Nakahara T, et al. F-18 FDG uptake in endometrial cancer. Clin Nucl Med. 2001;26(1):82–3.
140. Picchio M, et al. High-grade endometrial cancer: value of [^{18}F]FDG PET/CT in preoperative staging. Nucl Med Commun. 2010;31(6):506–12.
141. Antonsen SL, et al. MRI, PET/CT and ultrasound in the preoperative staging of endometrial cancer – a multicenter prospective comparative study. Gynecol Oncol. 2013;128(2):300–8.
142. Nakamura K, et al. The SUVmax of ^{18}F-FDG PET correlates with histological grade in endometrial cancer. Int J Gynecol Cancer. 2010;20(1):110–5.
143. Nakamura K, et al. The measurement of SUVmax of the primary tumor is predictive of prognosis for patients with endometrial cancer. Gynecol Oncol. 2011;123(1):82–7.
144. Signorelli M, et al. Role of the integrated FDG PET/CT in the surgical management of patients with high risk clinical early stage endometrial cancer: detection of pelvic nodal metastases. Gynecol Oncol. 2009;115(2):231–5.
145. Signorelli M, et al. Staging of high-risk endometrial cancer with PET/CT and sentinel lymph node mapping. Clin Nucl Med. 2015;40(10):780–5.
146. Husby JA, et al. Metabolic tumor volume on ^{18}F-FDG PET/CT improves preoperative identification of high-risk endometrial carcinoma patients. J Nucl Med. 2015;56(8):1191–8.
147. Nogami Y, et al. The efficacy of preoperative positron emission tomography-computed tomography (PET-CT) for detection of lymph node metastasis in cervical and endometrial cancer: clinical and pathological factors influencing it. Jpn J Clin Oncol. 2015;45(1):26–34.
148. Kitajima K, et al. Accuracy of integrated FDG-PET/contrast-enhanced CT in detecting pelvic and paraaortic lymph node metastasis in patients with uterine cancer. Eur Radiol. 2009;19(6):1529–36.
149. Belhocine T, et al. Usefulness of ^{18}F-FDG PET in the post-therapy surveillance of endometrial carcinoma. Eur J Nucl Med Mol Imaging. 2002;29(9):1132–9.
150. Sharma P, et al. Carcinoma endometrium: role of 18-FDG PET/CT for detection of suspected recurrence. Clin Nucl Med. 2012;37(7):649–55.
151. Saga T, et al. Clinical value of FDG-PET in the follow up of post-operative patients with endometrial cancer. Ann Nucl Med. 2003;17(3):197–203.

152. Kitajima K, et al. Fusion of PET and MRI for staging of uterine cervical cancer: comparison with contrast-enhanced ^{18}F-FDG PET/CT and pelvic MRI. Clin Imaging. 2014;38(4):464–9.
153. Shim SH, et al. Metabolic tumour volume and total lesion glycolysis, measured using preoperative ^{18}F-FDG PET/CT, predict the recurrence of endometrial cancer. BJOG. 2014;121(9):1097–106. discussion 1106.
154. Umesaki N, et al. Positron emission tomography with ^{18}F-fluorodeoxyglucose of uterine sarcoma: a comparison with magnetic resonance imaging and power Doppler imaging. Gynecol Oncol. 2001;80(3):372–7.
155. Nagamatsu A, et al. Use of ^{18}F-fluorodeoxyglucose positron emission tomography for diagnosis of uterine sarcomas. Oncol Rep. 2010;23(4):1069–76.
156. Cibula D, Oonk MH, Abu-Rustum NR. Sentinel lymph node biopsy in the management of gynecologic cancer. Curr Opin Obstet Gynecol. 2015;27(1):66–72.
157. Abu-Rustum NR, et al. Sentinel lymph node mapping for grade 1 endometrial cancer: is it the answer to the surgical staging dilemma? Gynecol Oncol. 2009;113(2):163–9.
158. Dargent D, Martin X, Mathevet P. Laparoscopic assessment of the sentinel lymph node in early stage cervical cancer. Gynecol Oncol. 2000;79(3):411–5.
159. Diaz JP, et al. Sentinel lymph node biopsy in the management of early-stage cervical carcinoma. Gynecol Oncol. 2011;120(3):347–52.
160. Frumovitz M, et al. Lymphatic mapping and sentinel node biopsy in women with high-risk endometrial cancer. Gynecol Oncol. 2007;104(1):100–3.
161. Khoury-Collado F, et al. Sentinel lymph node mapping for endometrial cancer improves the detection of metastatic disease to regional lymph nodes. Gynecol Oncol. 2011;122(2):251–4.
162. Lantzsch T, et al. Sentinel node procedure in Ib cervical cancer: a preliminary series. Br J Cancer. 2001;85(6):791–4.
163. Malur S, et al. Sentinel lymph node detection in patients with cervical cancer. Gynecol Oncol. 2001;80(2):254–7.
164. Niikura H, et al. Sentinel lymph node detection in early cervical cancer with combination 99mTc phytate and patent blue. Gynecol Oncol. 2004;94(2):528–32.
165. Pelosi E, et al. Preliminary study of sentinel node identification with ^{99m}Tc colloid and blue dye in patients with endometrial cancer. Tumori. 2002;88(3):S9–10.
166. van Dam PA, et al. Intraoperative sentinel node identification with Technetium-99m-labeled nanocolloid in patients with cancer of the uterine cervix: a feasibility study. Int J Gynecol Cancer. 2003;13(2):182–6.
167. Verheijen RH, et al. Sentinel node detection in cervical cancer. Obstet Gynecol. 2000;96(1):135–8.
168. Barlin JN, et al. The importance of applying a sentinel lymph node mapping algorithm in endometrial cancer staging: beyond removal of blue nodes. Gynecol Oncol. 2012;125(3):531–5.
169. Cibula D, et al. Prognostic significance of low volume sentinel lymph node disease in early-stage cervical cancer. Gynecol Oncol. 2012;124(3):496–501.
170. Elliott P, et al. Early invasive (FIGO stage IA) carcinoma of the cervix: a clinico-pathologic study of 476 cases. Int J Gynecol Cancer. 2000;10(1):42–52.
171. Sakuragi N, et al. Incidence and distribution pattern of pelvic and paraaortic lymph node metastasis in patients with Stages IB, IIA, and IIB cervical carcinoma treated with radical hysterectomy. Cancer. 1999;85(7):1547–54.
172. Creasman WT, et al. Surgical pathologic spread patterns of endometrial cancer. A Gynecologic Oncology Group Study. Cancer. 1987;60(8 Suppl):2035–41.
173. Vogelzang, et al. Comprehensive textbook of genitourinary oncology. Philadelphia: Lippincott Williams & Wilkins. 3rd ed. p. 816.
174. Kitchener H, et al. Efficacy of systematic pelvic lymphadenectomy in endometrial cancer (MRC ASTEC trial): a randomised study. Lancet. 2009;373(9658):125–36.
175. Chi DS, et al. The incidence of pelvic lymph node metastasis by FIGO staging for patients with adequately surgically staged endometrial adenocarcinoma of endometrioid histology. Int J Gynecol Cancer. 2008;18(2):269–73.
176. Abu-Rustum N, et al. What is the incidence of isolated paraaortic nodal recurrence in grade 1 endometrial carcinoma? Gynecol Oncol, 2008. 111(1): p. 46–48.
177. Abu-Rustum NR. Sentinel lymph node mapping for endometrial cancer: a modern approach to surgical staging. J Natl Compr Cancer Netw. 2014;12(2):288–97.
178. Kadkhodayan S, et al. Lymphatic mapping and sentinel node biopsy in endometrial cancer–a feasibility study using cervical injection of radiotracer and blue dye. Nucl Med Rev Cent East Eur. 2014;17(2):55–8.
179. van de Lande J, et al. Sentinel lymph node detection in early stage uterine cervix carcinoma: a systematic review. Gynecol Oncol. 2007;106(3):604–13.
180. Ballester M, et al. Detection rate and diagnostic accuracy of sentinel-node biopsy in early stage endometrial cancer: a prospective multicentre study (SENTIENDO). Lancet Oncol. 2011;12(5):469–76.
181. How J, et al. Accuracy of sentinel lymph node detection following intra-operative cervical injection for endometrial cancer: a prospective study. Gynecol Oncol. 2012;127(2):332–7.
182. Tausch C, Baege A, Rageth C. Mapping lymph nodes in cancer management – role of ^{99m}Tc-tilmanocept injection. Onco Targets Ther. 2014;7:1151–8.
183. Surasi DS, O'Malley J, Bhambhvani P. ^{99m}Tc-tilmanocept: a novel molecular agent for lymphatic mapping and sentinel lymph node localization. J Nucl Med Technol. 2015;43(2):87–91.
184. Ruscito I, et al. Sentinel node mapping in cervical and endometrial cancer: indocyanine green versus other

conventional dyes-a meta-analysis. Ann Surg Oncol. 2016;23(11):3749–56.
185. Beavis A, et al. Sentinel lymph node detection rates using indocyanine green in women with early-stage cervical cancer. Gynecol Oncol. 2016;143(2): 302–6.
186. Naaman Y, et al. The Added Value of SPECT/CT in Sentinel Lymph Nodes Mapping for Endometrial Carcinoma. Ann Surg Oncol. 2016;23(2):450–5.
187. Solima E, et al. Diagnostic accuracy of sentinel node in endometrial cancer by using hysteroscopic injection of radiolabeled tracer. Gynecol Oncol. 2012; 126(3):419–23.
188. Pandit-Taskar N, et al. Single photon emission computed tomography SPECT-CT improves sentinel node detection and localization in cervical and uterine malignancy. Gynecol Oncol. 2010;117(1): 59–64.
189. Hoogendam JP, et al. ^{99m}Tc SPECT/CT versus planar lymphoscintigraphy for preoperative sentinel lymph node detection in cervical cancer: a systematic review and metaanalysis. J Nucl Med. 2015;56(5):675–80.
190. Hoogendam JP, et al. Preoperative sentinel node mapping with ^{99m}Tc-nanocolloid SPECT-CT significantly reduces the intraoperative sentinel node retrieval time in robot assisted laparoscopic cervical cancer surgery. Gynecol Oncol. 2013;129(2):389–94.
191. Klapdor R, et al. Value and advantages of preoperative sentinel lymph node imaging with SPECT/CT in cervical cancer. Int J Gynecol Cancer. 2014;24 (2):295–302.
192. Diaz-Feijoo B, et al. Change in clinical management of sentinel lymph node location in early stage cervical cancer: the role of SPECT/CT. Gynecol Oncol. 2011;120(3):353–7.
193. Buda A, et al. Integration of hybrid single-photon emission computed tomography/computed tomography in the preoperative assessment of sentinel node in patients with cervical and endometrial cancer: our experience and literature review. Int J Gynecol Cancer. 2012;22(5):830–5.
194. Kraft O, Havel M. Detection of sentinel lymph nodes in gynecologic tumours by planar scintigraphy and SPECT/CT. Mol Imaging Radionucl Ther. 2012; 21(2):47–55.
195. Raimond E, et al. Impact of sentinel lymph node biopsy on the therapeutic management of early-stage endometrial cancer: results of a retrospective multicenter study. Gynecol Oncol. 2014;133(3):506–11.
196. Bats AS, et al. Contribution of lymphoscintigraphy to intraoperative sentinel lymph node detection in early cervical cancer: analysis of the prospective multicenter SENTICOL cohort. Gynecol Oncol. 2015; 137(2):264–9.
197. Frati A, et al. Contribution of lymphoscintigraphy for sentinel lymph node biopsy in women with early stage endometrial cancer: results of the SENTI-ENDO study. Ann Surg Oncol. 2015;22(6):1980–6.

Diagnostic Applications of Nuclear Medicine: Ovarian Cancer

36

Neeta Pandit-Taskar, Sonia Mahajan, and Weining Ma

Abstract

Ovarian malignancies are a leading cause of death in women in the United States and a significant health issue for women worldwide. Anatomic imaging with ultrasound, computed tomography, and magnetic resonance is a main tool for the diagnosis, staging, and follow-up of recurrent disease; however, it lacks biologic information. Nuclear imaging, primarily positron emission tomography (PET) with 2-deoxy-2-[^{18}F]fluoro-D-glucose ([^{18}F]FDG), has been increasingly used for the detection of cancer. Encouraging data have emerged in recent years that support the use of [^{18}F]FDG PET in a variety of clinical settings in ovarian cancer management.

Keywords

Ovarian cancer • Imaging • Staging • Prognosis • Response to therapy

Glossary

[^{18}F]FDG	2-[^{18}F]fluoro-2-deoxy-D-glucose
AJCC	American Joint Committee on Cancer
BRCA1	Breast cancer type 1 susceptibility protein
BRCA2	Breast cancer type 2 susceptibility protein
CA-125 U/mL	A tumor-associated marker for ovarian cancer (also known as carbohydrate antigen 125 or mucin 16)
CT	X-ray computed tomography
CTce	Contrast-enhanced computed tomography
FIGO	International Federation of Obstetrics and Gynecology
GLUT	Glucose transporter family
LBMI	Large bowel mesentery implants
LI	Labeling index
M	Metastasis status according to the AJCC/UICC TNM staging system
MIB-1	Marker of cell proliferation based on an antibody against an epitope of the nuclear protein different from that recognized by the Ki-67 antibody
MRI	Magnetic resonance imaging
MTV	Metabolic tumor volume
N	Lymph node status according to the AJCC/UICC TNM staging system

N. Pandit-Taskar (✉)
Molecular Imaging and Therapy Service, Department of Radiology, Memorial Sloan Kettering Cancer Center, New York, NY, USA

Department of Radiology, Weill Cornell Medical College, New York, NY, USA
e-mail: pandit-n@mskcc.org

S. Mahajan • W. Ma
Molecular Imaging and Therapy Service, Department of Radiology, Memorial Sloan Kettering Cancer Center, New York, NY, USA

© Springer International Publishing Switzerland 2017
H.W. Strauss et al. (eds.), *Nuclear Oncology*,
https://doi.org/10.1007/978-3-319-26236-9_46

NPV	Negative predictive value
PET	Positron emission tomography
PET/CT	Positron emission tomography/computed tomography
PFS	Progression-free survival
PPV	Positive predictive value
RO	Right ovary
SLL	Second look laparotomy
SUV	Standardized uptake value
SUV_{max}	Standardized uptake value at point of maximum
T	Tumor status according to the AJCC/UICC TNM staging system
TAHBSO	Total abdominal hysterectomy with bilateral salpingo oophorectomy
TLG	Total lesion glycolysis
TNM	AJCC staging system based on parameters "T" (tumor status), "N" (lymph node status), and "M" (distant metastasis status)
TVUS	Transvaginal ultrasound
UICC	Union Internationale Contre le Cancer (International Union Against Cancer)
US	Ultrasonography

Contents

Ovarian Cancer 1022
Pathogenesis 1022
Pathology 1022
Staging 1024
Diagnosis of Ovarian Cancer 1024
Role of Conventional Imaging in Primary Ovarian Cancer 1024
[^{18}F]FDG PET Imaging 1026
Normal Variants and Limitations 1026
Impact on Management at Staging 1034
Imaging in Recurrent Ovarian Cancer 1034
Impact on Management of Recurrent Disease 1040
Role in Assessment Before Second-Look Laparotomy or Secondary Debulking 1042
Response Assessment and Prognostication 1043
References 1043

Ovarian Cancer

The American Cancer Society estimated 22,280 new cases of ovarian cancer and 14,240 deaths related to ovarian cancer in 2016 in the United States [1]. Ovarian cancer is the ninth most common non-skin-related cancer in women and the fifth most common cause of cancer deaths in women. Ovarian cancer is an insidious disease, and patients often present with an advanced stage of disease. Despite clinical advances and improved surgical techniques, it remains a form of gynecologic malignancy with the highest mortality (Fig. 1). Ovarian cancer represents the second most common gynecologic malignancy and leads to more than half of all deaths related to gynecologic cancer. There is no fully reliable screening tumor marker, but CA-125 U/mL has proven useful. Treatment with surgical debulking is critical. Surgery is usually followed by chemotherapy. However, there is high recurrence rate, and the overall 5-year survival rate for advanced disease is only 17% [2].

Pathogenesis

The pathogenesis of ovarian cancer is multifactorial [1–3]. About 5–10% of ovarian cancers are familial and include three distinct hereditary patterns: breast–ovarian cancers (genetically linked to mutations in the *BRCA1* and *BRCA2* tumor suppressor genes), site-specific ovarian cancer, and ovarian and nonpolyposis colon cancers or Lynch syndrome II. The remaining 90% of ovarian cancers are sporadic.

Pathology

Ovarian neoplasms are classified according to their histogenesis (Table 1). Tumor derived from surface epithelium is most common with almost 90% of ovarian cancers originating from germinal epithelium. Other tumors include germ cell neoplasms, stromal neoplasms, and metastases, which comprise the remaining 10%. Epithelial ovarian cancer subtypes include serous, endometrioid, mucinous, clear

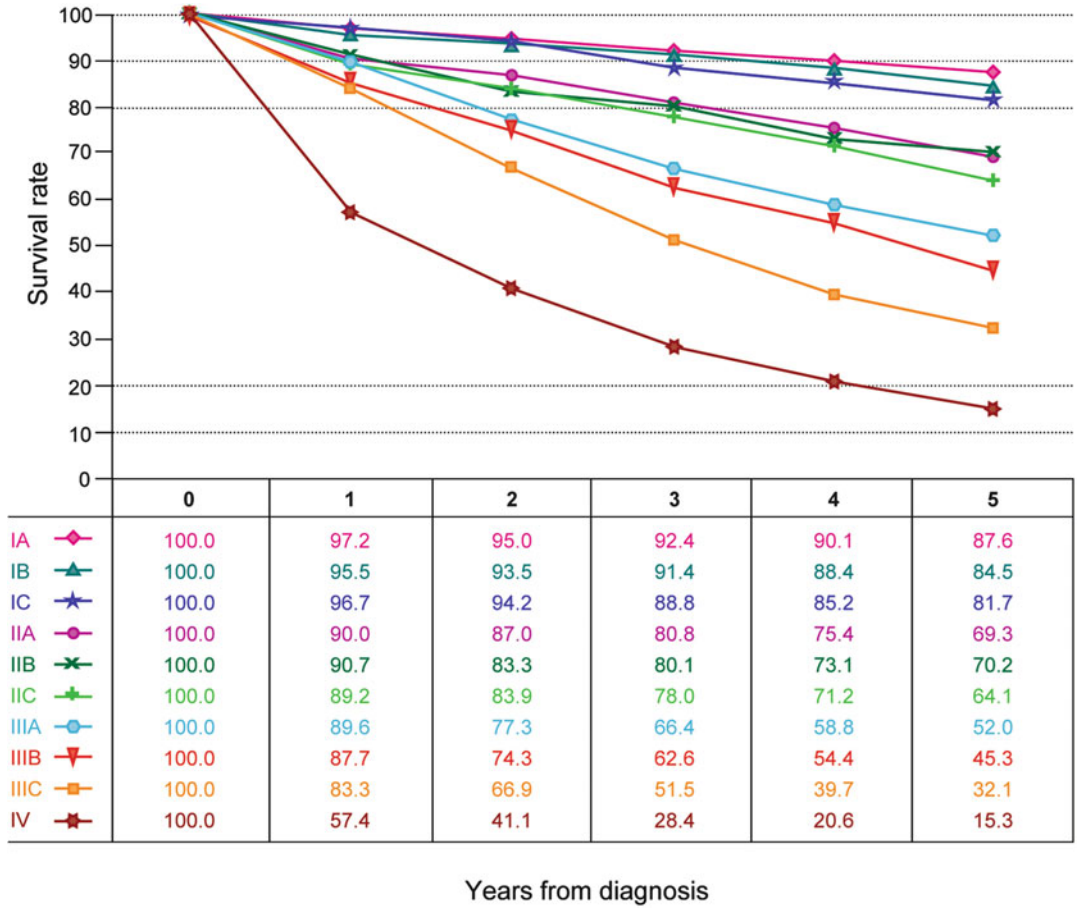

	0	1	2	3	4	5
IA	100.0	97.2	95.0	92.4	90.1	87.6
IB	100.0	95.5	93.5	91.4	88.4	84.5
IC	100.0	96.7	94.2	88.8	85.2	81.7
IIA	100.0	90.0	87.0	80.8	75.4	69.3
IIB	100.0	90.7	83.3	80.1	73.1	70.2
IIC	100.0	89.2	83.9	78.0	71.2	64.1
IIIA	100.0	89.6	77.3	66.4	58.8	52.0
IIIB	100.0	87.7	74.3	62.6	54.4	45.3
IIIC	100.0	83.3	66.9	51.5	39.7	32.1
IV	100.0	57.4	41.1	28.4	20.6	15.3

Fig. 1 Observed survival rates for 11,738 cases of primary ovarian epithelial cancer. Data from the National Cancer Database (Commission on Cancer of the American College of Surgeons and the American Cancer Society), diagnosed in the period 1998–2002. Stage 0 includes 60 patients; stage IA, 1, 415; stage IB, 160; stage IC, 878; stage IIA, 211; stage IIB, 304; stage IIC, 473; stage IIIA, 284; stage IIIB, 425; stage IIIC, 3,815; and stage IV, 3,773 (Used with the permission of the American Joint Committee on Cancer [AJCC], Chicago, IL. The original source for this material is the *AJCC Cancer Staging Manual*, Seventh Edition (2010) published by Springer Science and Business Media LLC. http://www.springer.com)

cell, undifferentiated, and Brenner types. Serous tumors are the most common, accounting for approximately 40% of primary ovarian neoplasms and 40% of primary cancers. They occur in the age group of 15–50 years. Benign neoplasms tend to occur in younger women than malignant neoplasms. Serous tumors are frequently bilateral; 25% of benign, 30% of low malignant potential (borderline), and 70% of malignant serous tumors are bilateral. Mucinous tumors account for 20% of ovarian neoplasms and occur commonly in the age group of 15–50 years. These are mostly benign and more commonly unilateral. Mucinous cystadenocarcinoma accounts for 10% of ovarian cancers [2, 3].

Endometrioid carcinoma accounts for 20% of malignant ovarian neoplasms and is frequently bilateral. It is defined by its microscopic resemblance to endometrial carcinoma. Associated endometriosis is found in about 25% of cases. In some cases, concurrent endometrial carcinoma is present, raising the question of whether the ovarian neoplasm is metastatic or a second independent primary. An origin from endometriosis has been demonstrated for some endometrioid carcinomas; however, the frequency with which this

Table 1 Ovarian cancer: histologic types

Tumor type	% of all tumors
Epithelial tumors	75
Serous tumors	40
Benign serous cystadenoma	
Serous tumor of low malignant potential	
Serous cystadenocarcinoma	
Mucinous tumors	20
Benign mucinous cystadenoma	
Mucinous tumor of low malignant potential	
Mucinous cystadenocarcinoma	
Endometrioid tumors	5
Carcinoma	
Clear cell carcinoma	2
Brenner tumors	2
Undifferentiated carcinoma	5–10
Germ cell tumors	20
Teratoma	15
Dysgerminoma	5
Yolk sac carcinoma	Rare
Embryonal carcinoma	Very rare
Choriocarcinoma	Very rare
Gonadal stromal tumors	5
Granulosa–theca cell	2
Fibrothecoma	3
Sertoli–Leydig cell	Rare
Mixed germ and stromal cell	**Rare**
Metastatic neoplasms	**Common**

occurs is probably low, and in most cases the tumor is believed to represent endometrioid differentiation of a neoplasm derived from the celomic epithelium. Endometrioid carcinomas grossly appear as solid and cystic masses that frequently show areas of hemorrhage and necrosis. Microscopically, the cells resemble endometrial carcinoma. Squamous metaplasia is seen in 50% of cases [2, 3].

Staging

Staging is surgically based. Both the International Federation of Obstetrics and Gynecology (FIGO) and the TNM classification of ovarian cancer are based on the intraoperative findings [4–6] (Table 2). Early-stage ovarian cancer is treated with comprehensive staging laparotomy, whereas advanced but operable disease is treated with primary cytoreductive surgery (debulking) followed by adjuvant therapy. Patients with unresectable disease may benefit from neoadjuvant (preoperative) chemotherapy before debulking. Factors that generally indicate inoperable disease include: invasion of the pelvic sidewall, rectum, sigmoid colon, or bladder; tumor deposits greater than 1–2 cm in the porta hepatis; intersegmental fissure of the liver, lesser sac, gastrosplenic ligament, gastrohepatic ligament, subphrenic space, mesenteric root, and presacral space; suprarenal adenopathy; and hepatic parenchymal, pleural, or pulmonary metastases.

Diagnosis of Ovarian Cancer

Pelvic or transvaginal ultrasonography and CA-125 U/mL tumor marker levels are used in combination for identification of ovarian carcinoma in early stages. There is some evidence that supports the use of these screening tools in high-risk populations, i.e., women with genetic predisposition or positive family history [6, 7]. The impact of such routine screening on reducing the mortality of patients with ovarian carcinoma is not yet clearly established.

In women presenting with a suspected ovarian mass, confirmation should be obtained pathologically by either biopsy or laparoscopic removal [6].

Role of Conventional Imaging in Primary Ovarian Cancer

Ovarian cancer usually presents as: unilateral or bilateral adnexal complex cystic masses with a thick, irregular wall; thick septations greater than 3 mm in thickness; and mural nodularity, papillary projections, or a solid component with variable degree of necrosis. Advanced stages of ovarian cancers are often associated with pelvic organ invasion, ascites, and peritoneal carcinomatosis.

Ultrasound (US) is usually an initial imaging modality for detection and characterization of

Table 2 International Federation of Obstetrics Gynecology (FIGO) and TNM staging for ovarian cancer

Primary tumor (T)			
TNM	FIGO		
Tx			Primary tumor cannot be assessed
T0			No evidence of primary tumor
T1	I		Tumor limited to the ovaries (one or both)
T1a	IA		Tumor limited to one ovary; capsule intact, no tumor on surface; negative washings
T1b	IB		Tumor limited to both ovaries; rest same as IA
T1c	IC		Tumor limited to one or both ovaries with any of the following: surgical spill; capsule rupture; tumor on ovarian surface; malignant cells in ascites or peritoneal washings
		IC1	Tumor limited to one or both ovaries with surgical spill
		IC2	Tumor limited to one or both ovaries with ruptured capsule or tumor on ovarian surface
		IC3	Tumor limited to one or both ovaries with malignant cells in ascites or peritoneal washings
T2	II		Tumor involving one or both ovaries with pelvic extension
T2a	IIA		Extension and/or implants on uterus and/or fallopian tube
T2b	IIB		Extension and/or implants on other pelvic tissues
T2c[a]	IIC		[a]
T3	III		Tumor involving one or both ovaries with histologically or cytologically confirmed peritoneal spread outside pelvis and/or metastasis to retroperitoneal lymph nodes
T3a[a]	IIIA		Positive retroperitoneal lymph nodes and/or microscopic metastases outside pelvis
		IIIA1	Positive retroperitoneal lymph nodes
		IIIA1(i)	Size $\leq$10 mm
		IIIA1(ii)	Size >10 mm
	IIIA2		Microscopic peritoneal spread outside pelvis and/or retroperitoneal lymph nodes
T3b	IIIB		Macroscopic peritoneal spread (metastases $\leq$2 cm) and/or positive retroperitoneal lymph nodes. Including extension to liver/splenic capsule
T3c	IIIC		Macroscopic peritoneal spread (metastases >2 cm) and/or positive retroperitoneal lymph nodes. Including extension to liver/splenic capsule
Regional lymph nodes (N)			
TNM	FIGO		
Nx			Regional lymph nodes cannot be assessed
N0			No regional lymph node metastasis
N1	IIIC		Regional lymph node metastasis
Distant metastasis (M)			
TNM	FIGO		
M0			No distant metastasis
M1[a]	IV		Distant metastasis (excluding peritoneal metastasis)
	IVA		Pleural effusion with positive cytology
	IVB		Hepatic and/or splenic parenchymal metastasis, metastasis to extra-abdominal organs (including inguinal lymph nodes and lymph nodes outside of the abdominal cavity)

[a]Changes made to FIGO staging criteria have not yet been resolved by TNM system. FIGO stage IIC has been eliminated

adnexal masses and pelvic ascites (Figs. 2 and 3). Computed tomography (CT) is the imaging modality of choice for preoperative staging. Magnetic resonance imaging (MRI) better characterizes adnexal lesions (Fig. 4) and is especially helpful in cases with inconclusive US findings and those with complex changes or involvement of nodes and adjacent organs (Fig. 5); it is also the modality of choice for evaluation of pelvic side wall invasion (Fig. 6). MRI increases the specificity of detection for indeterminate lesions on US and decreases the incidence of resections for

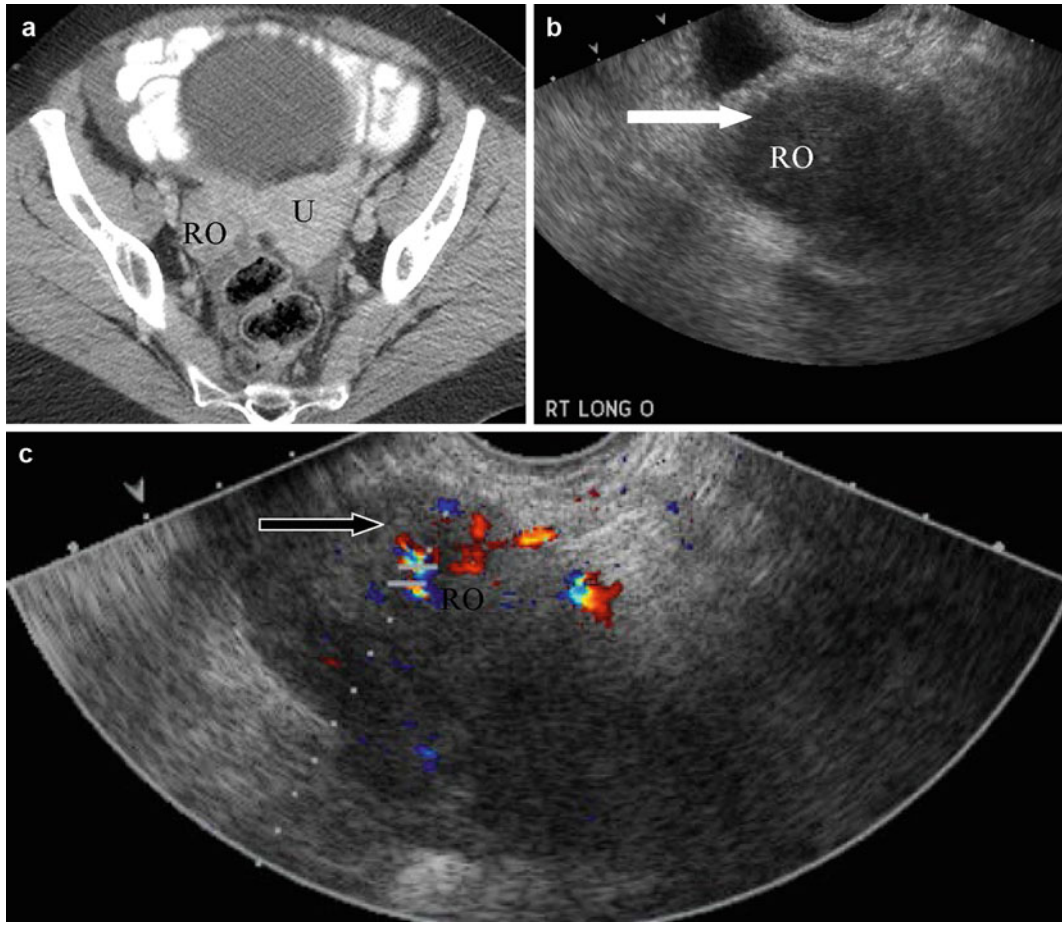

Fig. 2 (**a**) Contrast-enhanced axial computed tomography of the pelvis shows prominent right ovary (*RO*) and adjacent uterus (*U*). (**b**, **c**) Transvaginal pelvic ultrasound shows right ovarian hypoechoic solid mass (*white arrow*) with internal vascularity (*black arrow*) on color Doppler image (**c**). Surgical pathology analysis of the right ovary proved to be metastatic signet ring cell adenocarcinoma of the stomach

benign lesions (Fig. 7). CT is more useful in staging and treatment planning once malignancy is proven (Fig. 8).

[^{18}F]FDG PET Imaging

Normal Variants and Limitations

Increased uptake of 2-deoxy-2-[^{18}F]fluoro-D-glucose ([^{18}F]FDG) can be seen in some benign lesions and physiological conditions. Functional uptake in ovaries related to cyclical changes and maturing or growing follicles is frequently seen [8] (Fig. 9). This is commonly noted in younger females of reproductive age. Physiologic ovarian uptake may also be seen during cyclical variation in premenopausal females. Increased ovarian uptake may be seen in nonmalignant lesions such as serous and mucinous cyst adenoma, dermoid cyst, endometriosis, inflammation, teratoma, and schwannoma [9, 10]. An absolute standardized uptake value (SUV) to distinguish benign from malignant lesions is not known, but in general malignant lesions show higher uptake although a significant overlap is seen. Cutoff SUV_{max} values ranging between 2.75 and 3 have been suggested to distinguish benign from malignant lesions. In an

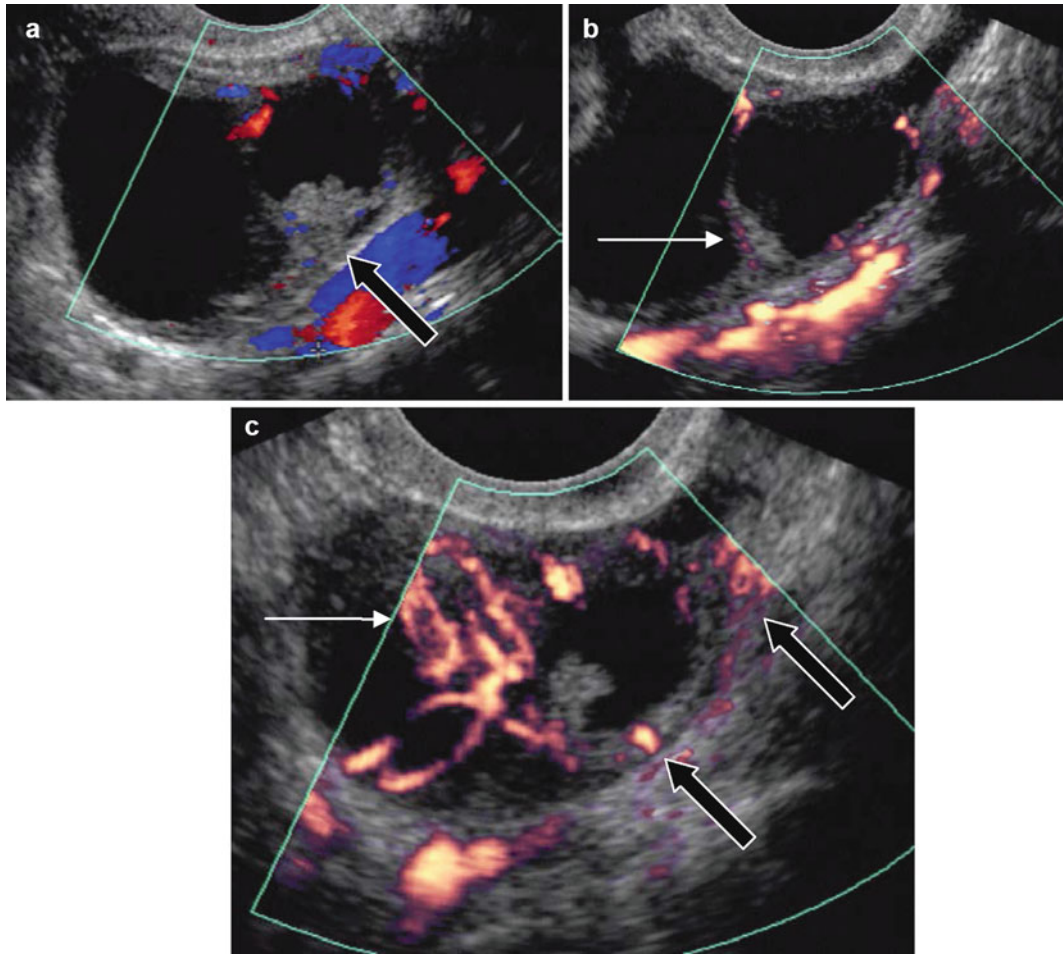

Fig. 3 (**a**) Transvaginal pelvic ultrasound color Doppler images show a left ovarian complex cystic mass containing vascular thick septations (*white arrows*) and vascular solid components (*black arrows*); (**b**, **c**). Surgical pathology analysis from the left ovarian cystectomy showed papillary serous tumor, a borderline tumor

analysis of 160 patients, Tanizaki et al. demonstrated that a cutoff SUV_{max} of 2.9 had a sensitivity and specificity of 80.6% and 94.6%, respectively, for differentiating between benign and malignant ovarian tumors [11]. Only three of 79 cases (3.8%) with benign tumors were PET positive (SUV_{max} >2.9). Castellucci et al. suggested a cutoff SUV_{max} of 3 (sensitivity and specificity of 87% and 100%, respectively) [12], and Kitajima et al. found that a cutoff SUV_{max} of 2.75 (sensitivity and specificity of 86.3% and 73.7%, respectively) [13] could help distinguish benign/borderline from malignant ovarian masses. Contrary to these findings, Lerman and colleagues determined an SUV of 7.9 for determining benign versus malignant uptake, with a sensitivity of 57% and a specificity of 95% [14]. The SUV for those with ovarian cancer was on average 9.1 ± 4 and in premenopausal females without known ovarian malignancy it was 5.7 ± 1.5. This variation may likely be due to differences in the sample size of patients that were evaluated. Increased ovarian uptake in postmenopausal patients is associated with malignancy and should be further evaluated when visualized. It is therefore important that any uptake in the ovaries be correlated with clinical history and corresponding CT findings.

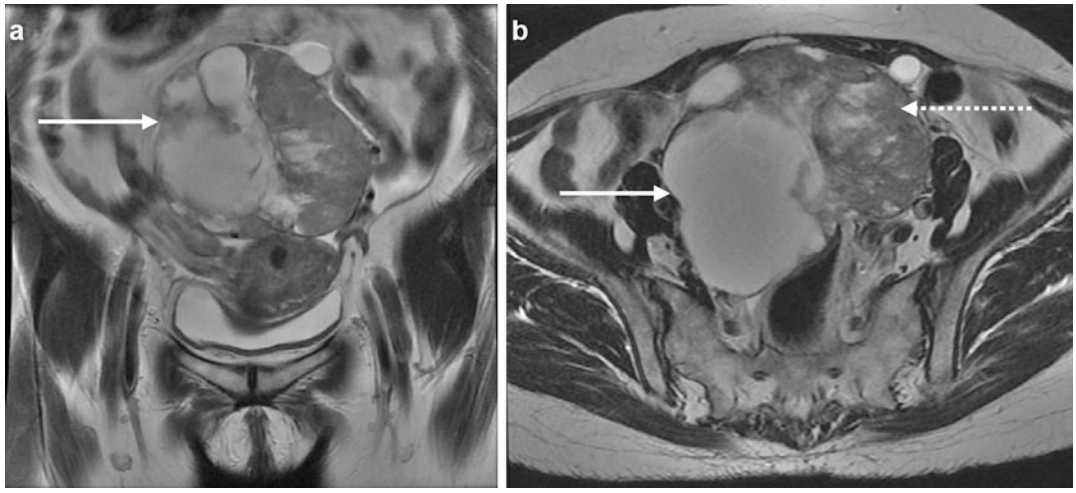

Fig. 4 Magnetic resonance imaging of the pelvis. (**a**) Coronal T2-weighted and (**b**) axial T2-weighted images show a large pelvic multiloculated/septated complex cystic mass (*white arrow*) containing a large soft tissue component (*dashed white arrow*), probably arising from the left adnexa. Histopathology revealed bilateral ovarian high-grade serous carcinoma

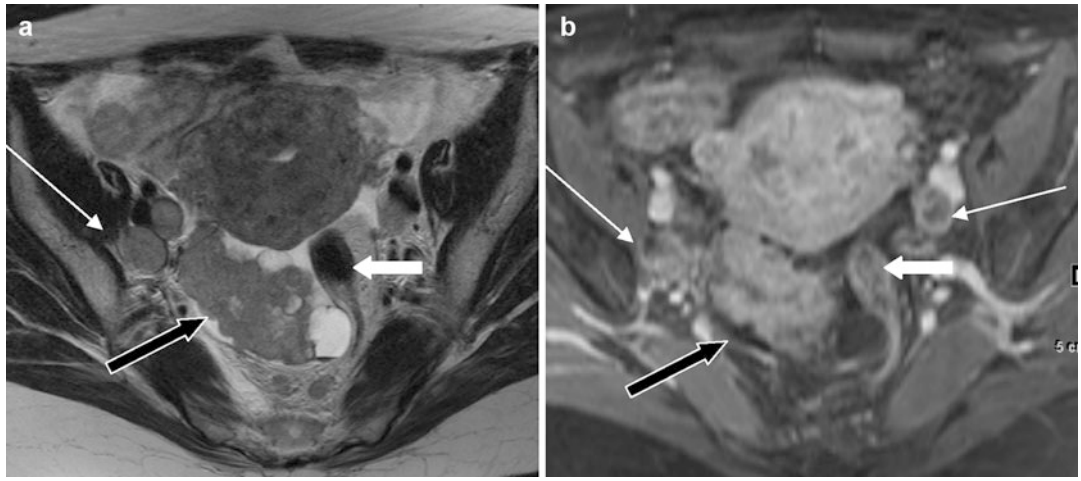

Fig. 5 Magnetic resonance imaging of the pelvis. (**a**) Axial T2-weighted and (**b**) gadolinium-enhanced axial T1-weighted images show a large right adnexal mass containing an enhancing component (*black arrows*) that is inseparable from the rectum (*small white arrow*), bilateral external iliac enlarged lymph nodes (*large white arrows*), and pelvic ascites. Pathology confirmed high-grade serous carcinoma

Demonstration of a functional ovarian cyst on CT and correlation with menstrual history can help in identifying functional cysts. Focal uptake in the pelvis can also be seen related to fallopian tubes predominantly in premenopausal women at mid-menstrual cycle, owing to the influence of estrogen on the fallopian tubes [15] (Fig. 10).

In the primary diagnosis and staging of ovarian cancer, the role of [^{18}F]FDG PET is limited by size resolution. Although [^{18}F]FDG-avid ovarian uptake in postmenopausal women is considered suggestive of malignancy, PET/CT is not recommended for primary cancer detection because of the high false–positive rates

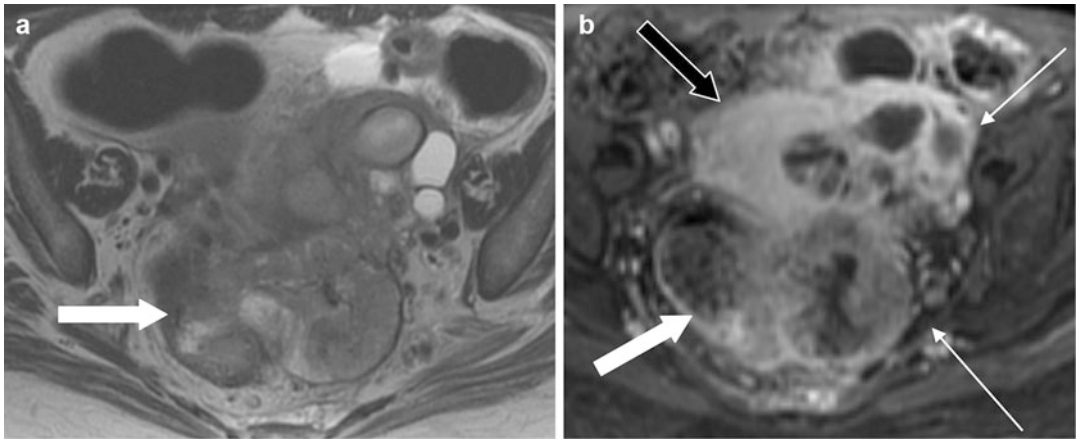

Fig. 6 Patient with high grade papillary serous carcinoma. MRI Pelvis (**a**) axial T2-weighted and (**b**) Gadolinium-enhanced axial T1 weighted images showed a left adnexal complex mixed cystic and solid mass invading adjacent rectum (small white arrows), uterus (black arrow) and left pelvic side wall (large white arrows).

[16]. Most primary lesions show high [^{18}F]FDG activity (Fig. 11) although detection of small lesions and peritoneal deposits is still limited. Earlier studies using only PET reported a positive predictive value (PPV) of 86–96% and a negative predictive value (NPV) of 76% with an overall accuracy of about 90% [17, 18]. PET does seem to add incremental value to conventional imaging in staging ovarian cancer either through confirmation of disease or exclusion of distant disease [19] (Fig. 12).

Most epithelial tumors show intense accumulation of [^{18}F]FDG. There was no positive correlation of SUV with clinical stage, tumor grade, cell proliferation, and glucose metabolism in 17 patients suspected of having ovarian epithelial cancer . Intensity of GLUT-1 expression, MIB-1 LI, and histologic grading score showed statistically significant positive correlations with [^{18}F]FDG uptake. GLUT-1 transporter expression was the strongest parameter to predict positive [^{18}F]FDG uptake [20]. For distinguishing malignant from benign pelvic lesions, [^{18}F]FDG PET/CT is similar to transvaginal ultrasound (TVUS) in sensitivity; however, it is more specific (100% vs. 61%). In staging ovarian cancer, PET/CT appears to be superior to CT alone. When correlated with final pathological staging, PET was concordant in 22 of 32 (69%) patients as compared with CT, which was concordant in 17 of 32 (53%) patients. Staging was modified correctly suing PET, leading to upstaging four out of six patients by detecting distant metastasis in the liver, pleura, mediastinum, and left supraclavicular lymph nodes [12].

A prospective study by Hynninen et al. found that PET/CT provided incremental information to CT in the detection of intra-abdominal disease, particularly mesenteric and subdiaphragmatic peritoneal disease, and was more effective for detection of extra-abdominal disease. In 35 patients with ovarian cancer, the overall site-based sensitivity, specificity, and accuracy for [^{18}F]FDG PET/CT were 51%, 89%, and 64% and for CT 41%, 92%, 57% [21]. Dauwen et al. assessed the value of [^{18}F]FDG PET/CT in evaluating suspicious ovarian masses. In comparison with CT, [^{18}F]FDG PET had higher specificity (77% vs. 38% for CT) for detecting malignant tumors and extra-abdominal metastases [22].

[^{18}F]FDG PET/CT has a low diagnostic value in differentiating between borderline malignant or benign tumors and other malignant ovarian tumors. The reported sensitivity and specificity of [^{18}F]FDG PET/CT in detecting malignant lesions are as high as 100% and 85.0%, respectively, while the rates for borderline tumors are only 71.4% and 81.3%, respectively. The SUV_{max} of borderline tumors is generally lower than that of malignant tumors and is very similar to benign

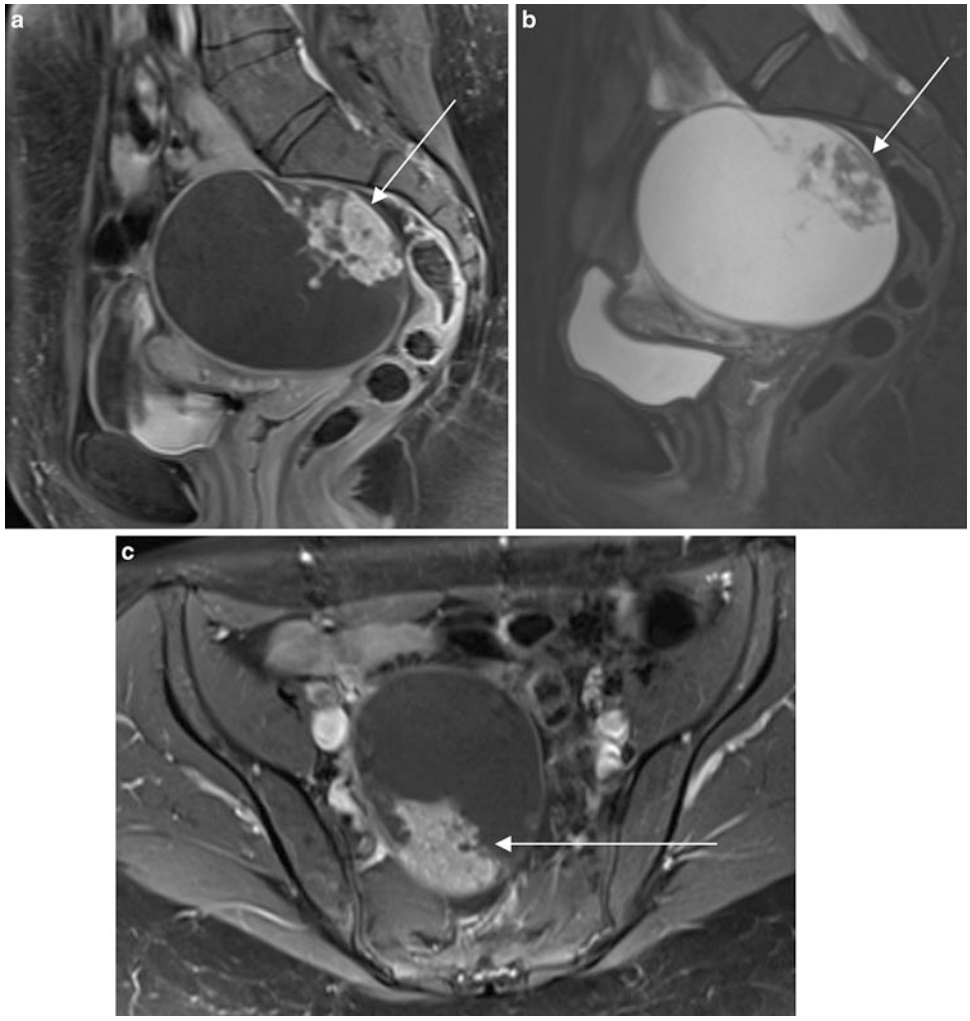

Fig. 7 MRI pelvis (**a**) Gadolinium-enhanced sagittal T1 weighted (**b**) sagittal T2 weighted and (**c**) Gadolinium-enhanced axial T1 weighted images showed a right adnexal large complex cystic mass containing an enhancing solid component (large white arrows). Surgical pathology revealed right ovarian Sertoli Leydig cell tumor (right ovarian sex cord stromal tumor).

tumors, making it difficult to conclusively reach the diagnosis [23]. Mucinous tumors and germ cell tumors are also generally less avid. It is important to be aware of this variation so that false negatives can be recognized. In a retrospective study of 98 patients, PET/CT had high sensitivity and specificity in detecting primary tumors. PET/CT yielded true-positive findings in 87 of 94 patients and true-negative findings in four of four patients with benign lesions [24]. PET/CT can be a useful adjunct to conventional imaging, especially in equivocal cases. It has incremental value in staging through detection of disease in normal-sized or small nodes and metastatic disease especially at distant sites. In comparison with Doppler US, CT, or MRI, PET/CT was concordant with surgical staging in 78% of patients and revealed 15 (15.8%) cases of unpredicted extra-abdominal lymph node metastasis in 95 patients with ovarian cancer. Furthermore, PET/CT was more specific in distinguishing malignant from benign lesion, although overall sensitivity did not

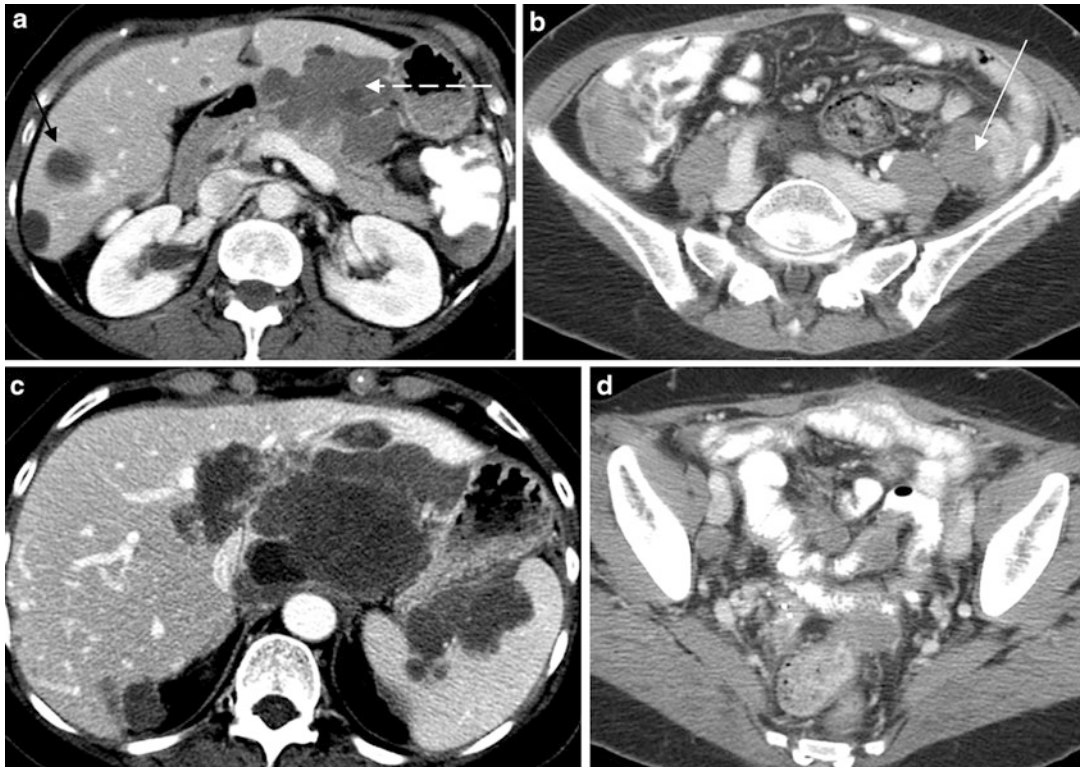

Fig. 8 Contrast enhanced axial CT abdomen and pelvis of 58 yo woman who presented with intermittent abdominal pain and increased CA-125 U/mL (~169.9) showed (**a**) hepatic metastases [black arrow], perihepatic implant (dashed white arrow), (**b**) serosal implant in the left paracolic gutter (white arrow) (**c**) perisplenic implant (white arrow), (**d**) right external iliac lymph node (white arrow) and minimal pelvic ascites (black arrow). Histopathology was positive for high grade ovarian adenocarcinoma.

vary significantly between the three modalities. In detecting malignant lesions in the extra-ovarian pelvis and the abdomen, the sensitivity was similar (94.6% vs. 94.1%), but specificity was significantly higher for PET/CT at 82.8% than for CT at 71.4% [25]. In detecting malignant nodes, including the bilateral pelvic and the para-aortic lymph nodes, both the sensitivity and specificity of PET/CT were higher (83.8%, 92.6%, respectively) than for CT and/or MRI combined (62.5%, 83.6%, respectively). PET/CT was shown to have higher accuracy than pelvic US, CT, or MRI (0.749; $p = 0.013$). False-negative findings on PET/CT included bowel mucosal invasion, small peritoneal seeding, and adjacent adnexal invasion [25]. Physiologic activity in the bowel and low resolution are known to lead to false negatives. Unknown supradiaphragmatic metastases were found in 15 cases of which ten (66.6%) were supraclavicular lymph node metastasis [25]. Michielsen et al. evaluated the role of whole-body diffusion-weighted MRI in staging and compared it with CT and [^{18}F]FDG PET/CT in 32 patients with suspected ovarian cancer. Comparable accuracy was similar for all modalities; however, the specificity for characterizing primary lesions was the highest with MRI [26]. PET/CT is valuable in staging as it can detect unexpected sites and can lead to stage migration [27]. In a large prospective study of 101 patients with primary ovarian cancer, Risum and colleagues reported a high sensitivity of PET/CT in detecting malignant pelvic tumor of ~100% (57/57) with a specificity of 92.5% (37/40) and an incremental value in staging. In three of five patients (60%) with stage IV disease, metastases were found only on PET/CT, located in an inguinal

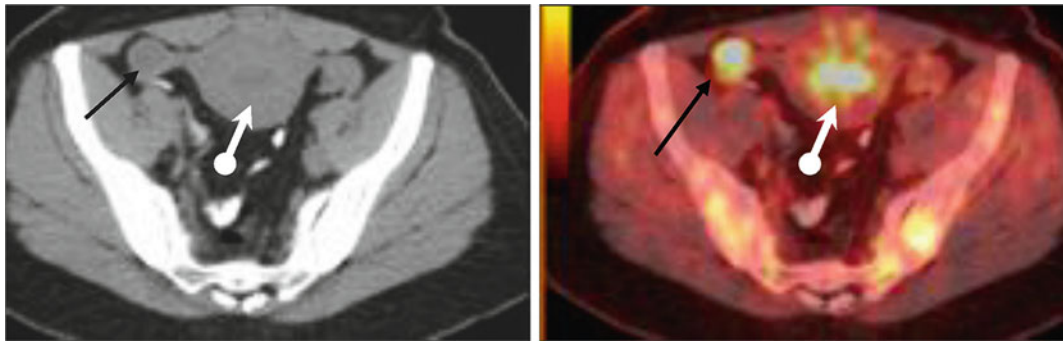

Fig. 9 Physiologic [^{18}F]FDG uptake in the right ovary and uterine cavity (*arrows*). No abnormality was detected on follow-up. Findings consistent with uptake related to cyclical changes in the uterus and corpus luteal cyst in the right ovary

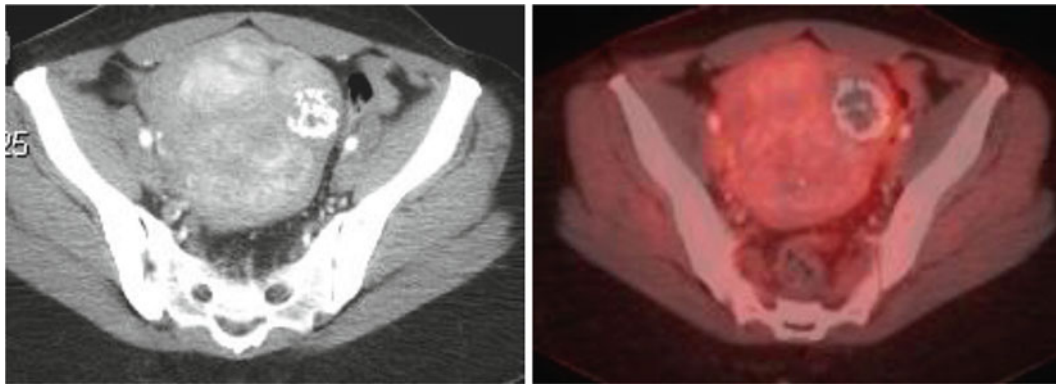

Fig. 10 Variable uptake in uterine fibroids. CT images (*left*) show heterogeneously enlarged uterus with lesions that have calcificationconsistent with fibroids. [^{18}F]FDG PET/CT (*right*) shows no uptake in the region of calcified fibroid and mild heterogeneous activity associated with the remainder of the enlarged uterus

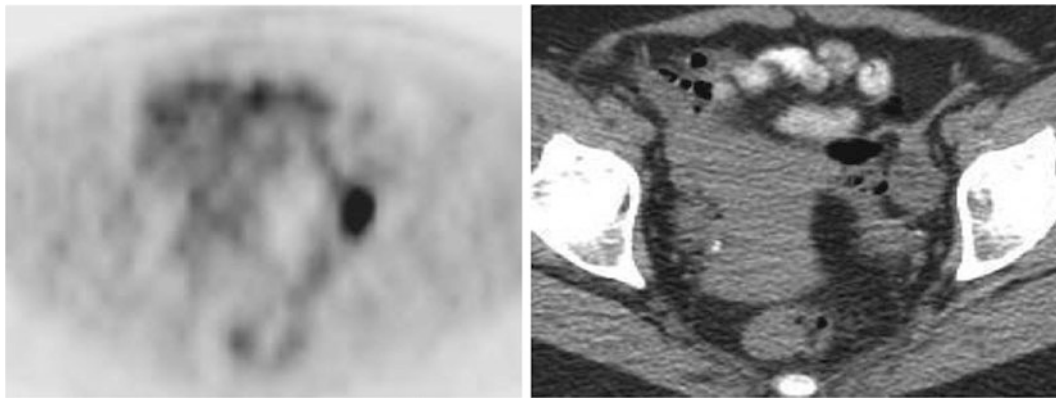

Fig. 11 A 60-year-old woman with breast cancer and elevated CA-125 U/mL level referred for evaluation of a left ovarian cyst. PET/CT shows intense [^{18}F]FDG uptake in the mildly enlarged left ovary. Pathology showed poorly differentiated serous adenocarcinoma of the left ovary

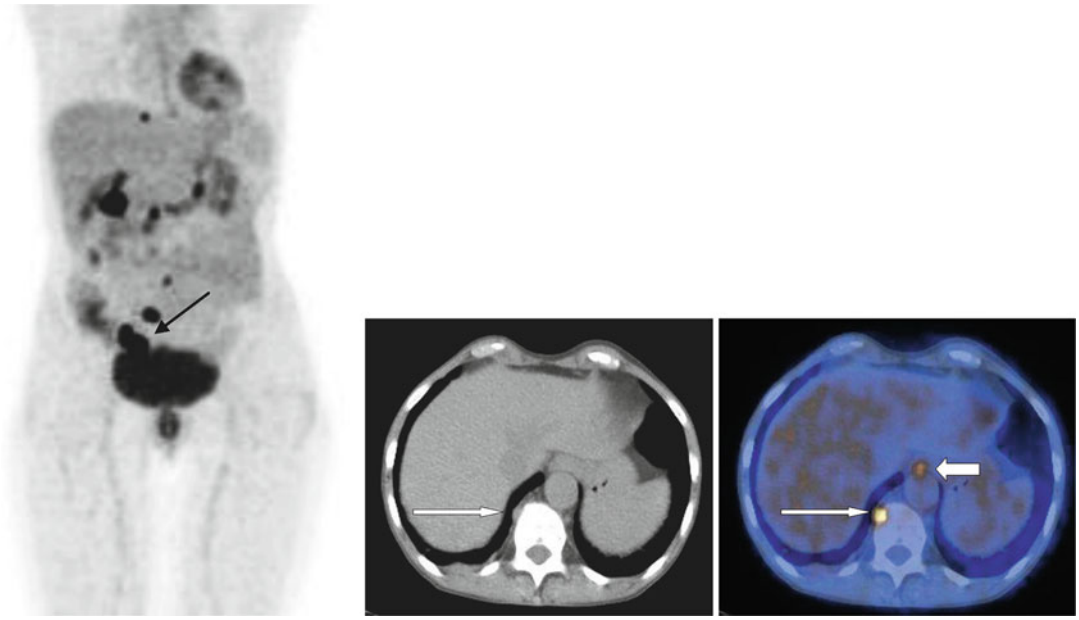

Fig. 12 A 56-year-old woman with ovarian cancer referred for staging. Uptake is seen in the primary tumor in the pelvis and pelvic adenopathy (*black arrow*). [^{18}F]FDG PET images show uptake in the right retrocrural (*white long arrow*) and preaortic (*white short arrow*) node that were not suspicious based on size criteria

lymph node and in a supraclavicular lymph node [28]. In limited studies, a combination of PET with contrast-enhanced CT (CTce) was shown to improve detection. A comparison of modalities (CTce vs. PET/CTce) in 40 patients showed improvement in overall lesion-based sensitivity from 37.6% (32/85) to 69.4% (59/85), while the specificity between CTce and PET/CTce was comparable (97.1% and 97.5%, respectively) [29].

[^{18}F]FDG PET/CT is useful in detecting lymph node involvement in patients with ovarian cancer. In a meta-analysis of 18 studies analyzing 882 patients, the diagnostic performance of CT, MRI, and PET was compared. [^{18}F]FDG PET or [^{18}F]FDG PET/CT was more accurate than CT and MRI in the detection of lymph node metastasis in patients with ovarian cancer (sensitivity and specificity were 73.2% and 96.7% for [^{18}F]FDG, 42.6% and 95% for CT, and 54.7% and 88.3% for MRI, respectively) [30]. Nodal staging in 68 patients (stage IA–IIIC) revealed a sensitivity of 83.3%, a specificity of 98.2%, and an NPV of 96.5% for [^{18}F]FDG PET/CT; however, the sample size was small with nodal disease found in only 12 patients. All false–negative results were seen in patients with a nodal size less than 5 mm. Sensitivity in detecting pelvic nodes (63.6%) was lower compared with that for para-aortic nodes (82.3%), which is likely attributable to the difficulty in assessing the pelvic region because of anatomic location close to the ovarian primary tumor [31].

[^{18}F]FDG PET/CT may be limited in detecting small lesions and peritoneal disease. De Iaco et al. compared the sensitivity of [^{18}F]FDG PET with histopathology for detecting peritoneal disease in 40 patients with ovarian cancer. PET/CT yielded positive results in 268 of 360 quadrants, with a sensitivity and specificity of 78% and 68%, respectively, and a PPV of 95%. False–negative results were seen in those with adhesions and in lesions smaller than 5 mm such as in carcinomatosis [32]. Some have found PET/CT comparable to MR and multidetector CT in assessing peritoneal carcinomatosis and have reported an added value of PET in detecting small peritoneal implants in patients with ascites due to a better separation of bowel loops, allowing for easier

distinction between physiological intestinal activity and pathological uptake [33].

Impact on Management at Staging

Primary treatment for ovarian cancer is primary cytoreduction, which when performed optimally has prognostic value. Presence of disease outside the abdomen can have significant implications in further management of ovarian cancer. Detecting distant metastases is therefore critical. The current FIGO staging system allows for the use of any imaging modality to evaluate metastatic disease. A number of studies have shown the value of PET and PET/CT in detecting previously unrecognized distant metastases [28, 29, 34, 35].

[^{18}F]FDG PET/CT can help identify disease in sites that may prevent primary cytoreductive surgery; in six of 21 cases, [^{18}F]FDG PET detected previously unknown hepatic hilar infiltration (4/6) and disease in the mesenteric root (2/6) that was confirmed at surgical exploration [36].

PET/CT, through more accurate staging, provides prognostic information. Of 201 patients with primary ovarian cancer, the overall survival and prognostic variables were analyzed in 66 patients ($n = 64$, stage III; $n = 2$, stage IV). Using PET/CT, 51% (39/66) of the patients were diagnosed as having stage III and 41% (27/66) as having stage IV disease. With a median follow-up of 30.2 months and using univariate analysis, a lower stage on PET/CT was a significant prognostic variable besides optimal debulking and performance status; however, it was not an independent prognostic factor. The study was somewhat limited owing to the lack of histological correlation for distant metastatic sites detected on PET [27].

Preoperative PET/CT may help predict surgical outcomes. In a prospective study of 179 patients, the predictive value of ten parameters of preoperative PET/CT findings were evaluated for optimal versus suboptimal cytoreduction [37]. In 77% of women undergoing incomplete cytoreduction, PET/CT showed large bowel mesentery implants or ascites. In 31% of women undergoing incomplete cytoreduction, PET/CT showed pleural effusion, and in 89%, PET/CT showed peritoneal carcinomatosis that were predictors of incomplete cytoreduction. Using multivariate analysis, large bowel mesentery implants was the only independent predictor of incomplete cytoreduction, and no predictor of suboptimal cytoreduction was found. PET/CT can be a useful supplementary imaging modality before surgery in primary ovarian cancer and may also have a role in the appropriate selection of patients for neoadjuvant chemotherapy [38].

Imaging in Recurrent Ovarian Cancer

Approximately 50% of patients with ovarian cancer will present with recurrence after cytoreductive surgery and first-line chemotherapy. The presentation is pelvic masses, recurrence at the vaginal cuff or pelvic side wall, peritoneal tumor implants, malignant ascites, lymphadenopathy, or distant metastases including of the lung, pleura, liver, or bone (Figs. 13 and 14). CT is the most commonly used modality for detection of recurrent tumor (Fig. 15), while MRI provides superior information on the local extent of disease including evaluation of the involvement of other organs, the pelvic side wall, and vascular invasion.

In general clinical practice, [^{18}F]FDG PET has been a secondary imaging modality after CT and MRI, with [^{18}F]FDG PET indicated only in cases with equivocal findings by other imaging modalities or cases with negative findings on other imaging in the presence of rising tumor markers.

There are significant data published on the utility of [^{18}F]FDG PET in recurrent ovarian cancer including in the surveillance and assessment of patients with rising tumor markers as well as in management decisions (Table 3). [^{18}F]FDG PET has been shown to be superior to CT or MRI in the detection of recurrent disease, with reported sensitivity and specificity of 83–91% and 66–93% for [^{18}F]FDG PET, respectively, versus 45–91% and 46–84% for CT or MRI [39, 40]. [^{18}F]FDG PET helps identify disease in those with rising CA-125 U/mL levels. In a retrospective study by Dragosavac et al., PET/CT detected disease in 42 of 45 patients and unsuspected lesions in 20 of 45 patients; 11 of these patients had normal conventional imaging. [^{18}F]FDG PET/CT was

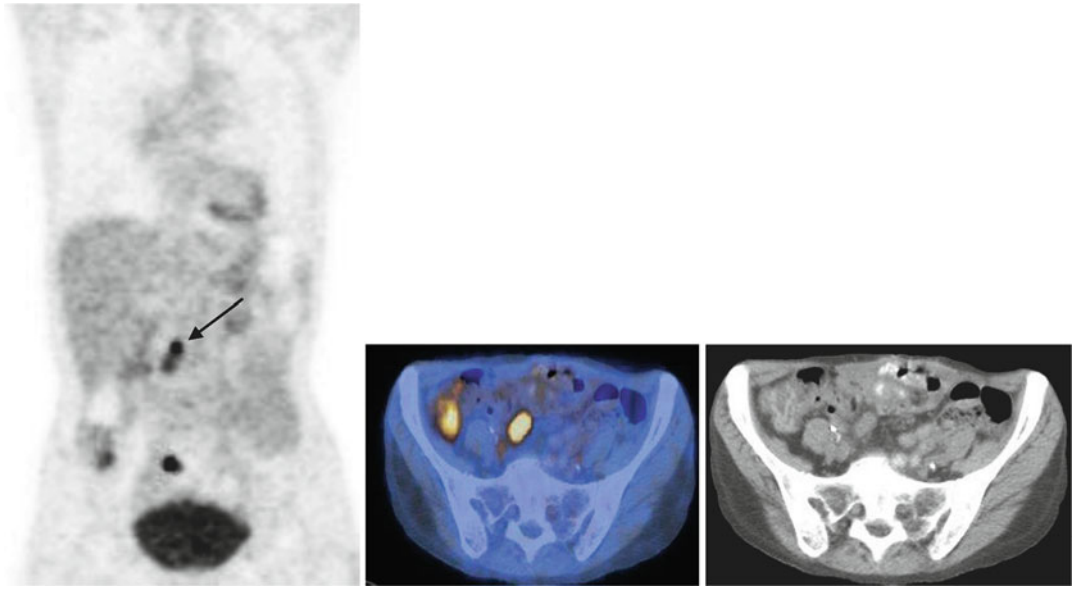

Fig. 13 Recurrence of ovarian carcinoma. A 62-year-old woman with ovarian cancer, submitted to total abdominal hysterectomy with bilateral salpingo-oophorectomy, referred for evaluation of metastatic disease. Whole-body images show focal [^{18}F]FDG uptake in the pelvis and mid-abdomen localizing to the nodes in common iliac region and para-aortic region (*arrow*)

true negative in the remaining three patients. A limitation of this study was the lack of histopathological confirmation of the lesions, although the conclusion was supported by concurrent clinical data and follow-up [41].

The role of [^{18}F]FDG PET has, however, been uncertain owing to variable results. Its role is limited in the detection of microscopic and small-volume disease where earlier studies reported low sensitivity in detecting disease. A study by Rose et al. of 17 ovarian cancer patients reported poor results for [^{18}F]FDG PET [42]. The study was done with patients who had optimal primary cytoreduction, using PET only, and most of the lesions not detected were smaller than 6 mm. In 36 patients, Kim et al. observed an overall significant difference in lesion-based sensitivity for PET/CT (66%) and MRI (86%). MRI was, however, more accurate than PET in detecting peritoneal lesions, with the overall lesion-based sensitivity and accuracy of PET/CT being 43% and 86% and that for MRI being 75% and 94%, respectively [43]. For peritoneal implants that are slightly larger, the results have been variable, although some authors have reported equivalent or higher sensitivity for [^{18}F]FDG PET. In a recent study, the sensitivity of PET/CT was better than MRI in detecting small to medium-sized peritoneal implants (<2 cm); the reported sensitivity was 95.4% for [^{18}F]FDG versus 50% for MRI (for sizes of 0.5–1 cm) [44]. In a meta-analysis of 29 studies involving 1,651 patients, the pooled sensitivity and specificity of [^{18}F]FDG were 88.6% and 90.3%, respectively, for detection of recurrence in ovarian carcinoma [45].

Detection is improved with combined PET/CT than with PET alone (Figs. 16 and 17). Reported sensitivities for the detection of peritoneal disease range between 57% and 88%, although with higher specificity for PET than for CT (94% vs. 77%, respectively). In these studies, the combined sensitivity ranged from 88% to 100% and the specificity from 79% to 93% [46–50].

[^{18}F]FDG PET can help in the early detection of disease in patients who are asymptomatic with normal CA-125 U/mL levels as well as in those with rising CA-125 U/mL levels and normal conventional imaging including CT scan or MRI [50–52].

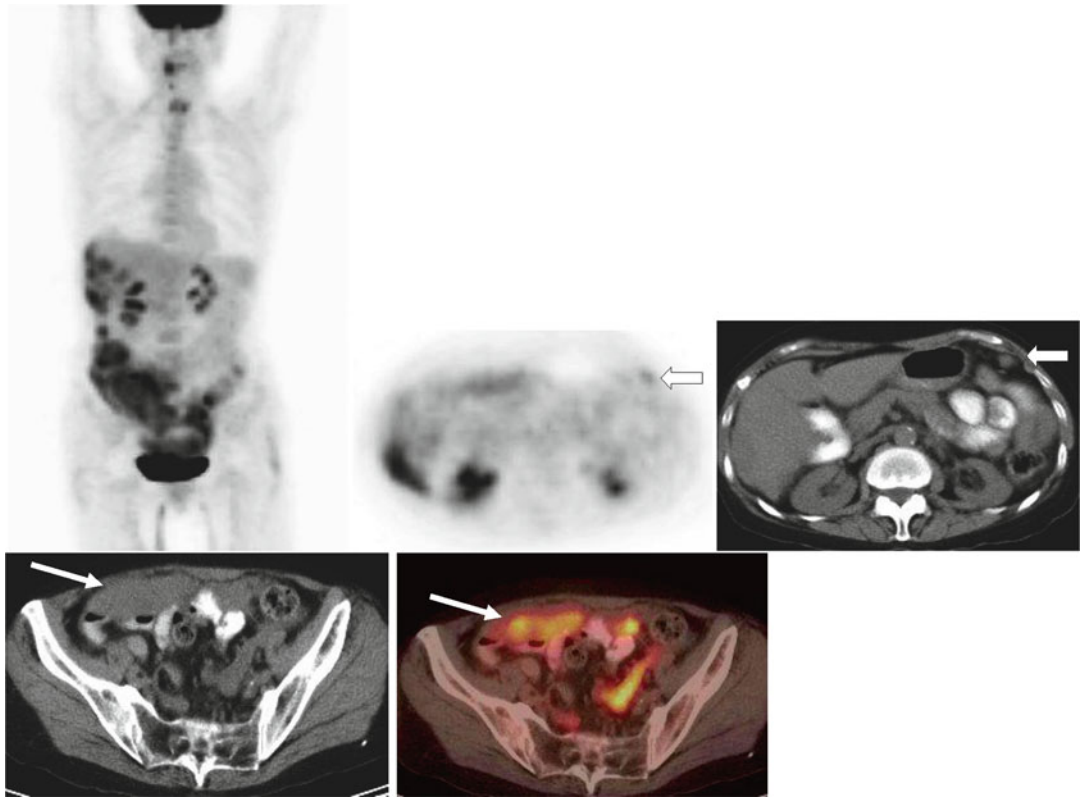

Fig. 14 A 64-year-old woman with ovarian carcinoma and rising CA-125 U/mL level referred for assessment of disease extent. [^{18}F]FDG uptake is seen in the lower anterior pelvic peritoneal lesion, small peritoneal implant in the left abdomen (*white short arrow*), and right perihepatic implants

Fig. 15 Contrast-enhanced axial computed tomography of the abdomen in a 68-year-old woman with recurrent ovarian carcinoma shows omental disease (caking; *white arrow*) and small loculated ascites (*black arrow*) in the left hemiabdomen. Pathology showed high-grade serous ovarian carcinoma

A single study reported a sensitivity of 100% with a specificity of 85% for this modality; however, this was a study with a very small number of patients who underwent exploratory laparotomy ($n = 22$) or diagnostic laparoscopy ($n = 15$) [50]. In a meta-analysis, Gu et al. compared data from 34 studies to evaluate the accuracy of CA-125 U/mL, PET alone, PET/CT, CT, and MRI in diagnosing recurrent

Table 3 Performance of [^{18}F]FDG PET in the assessment of recurrent ovarian carcinoma

Author and year	Type	FIGO stage	Total number of patients studied	Comparative imaging (CT or MRI)	Number of cases with negative/equivocal CT and MRI findings	Histopathology confirmation (yes/no)	Sensitivity/specificity/accuracy
Rusu et al. (2015)	Retrospective	II ($n = 1$), III ($n = 41$)	42	CT	23	Yes	[^{18}F]FDG: 92.2%/100%/92.5%; CT: 60.8%/NA/52.8%
Dragosavac et al. (2013)	Retrospective	I ($n = 2$), II ($n = 3$), III ($n = 34$), IV ($n = 6$)	45	US/CT/MRI	23	Yes	[^{18}F]FDG: 100%/100%/NA
Antunovic et al. (2012)	Retrospective	NA	121	US/CT/MRI	41	Yes	[^{18}F]FDG: 82%/87%/83%; CA-125 U/mL: 59%/80%/63%; conventional imaging: 69%/47%/66%
Sanli et al. (2012)	Retrospective; Assessed detection of peritoneal implants by [^{18}F]FDG PET	NA	47	MRI	NA	Yes	**Overall**:
							[^{18}F]FDG: 97.5%/100%/97.8%; MRI; 95%/85.7%/93.6%
							For implants 0.5-1 cm: [^{18}F]FDG: 95.4%/100%/97.8%; MRI: 50%/100%/78.7%
							For implants >3 cm: [^{18}F]FDG: 100%/100%/100%; MRI: 87.5%/100%/97.8%
Pan et al. (2011)	Prospective	I ($n = 7$), III ($n = 23$), IV ($n = 7$)	37	None	NA	Yes	[^{18}F]FDG: 100%/84%/94%; CA-125 U/mL: 58%/100%/72%; CA15-3: 29%/100%/54%
Bilici et al. (2010)	Retrospective	I ($n = 8$), II ($n = 6$), III ($n = 43$), IV ($n = 3$)	60	CT	20	Yes	[^{18}F]FDG – 95.5%/93.3%/95%. CT – 55.5%/66.6%/58.3%

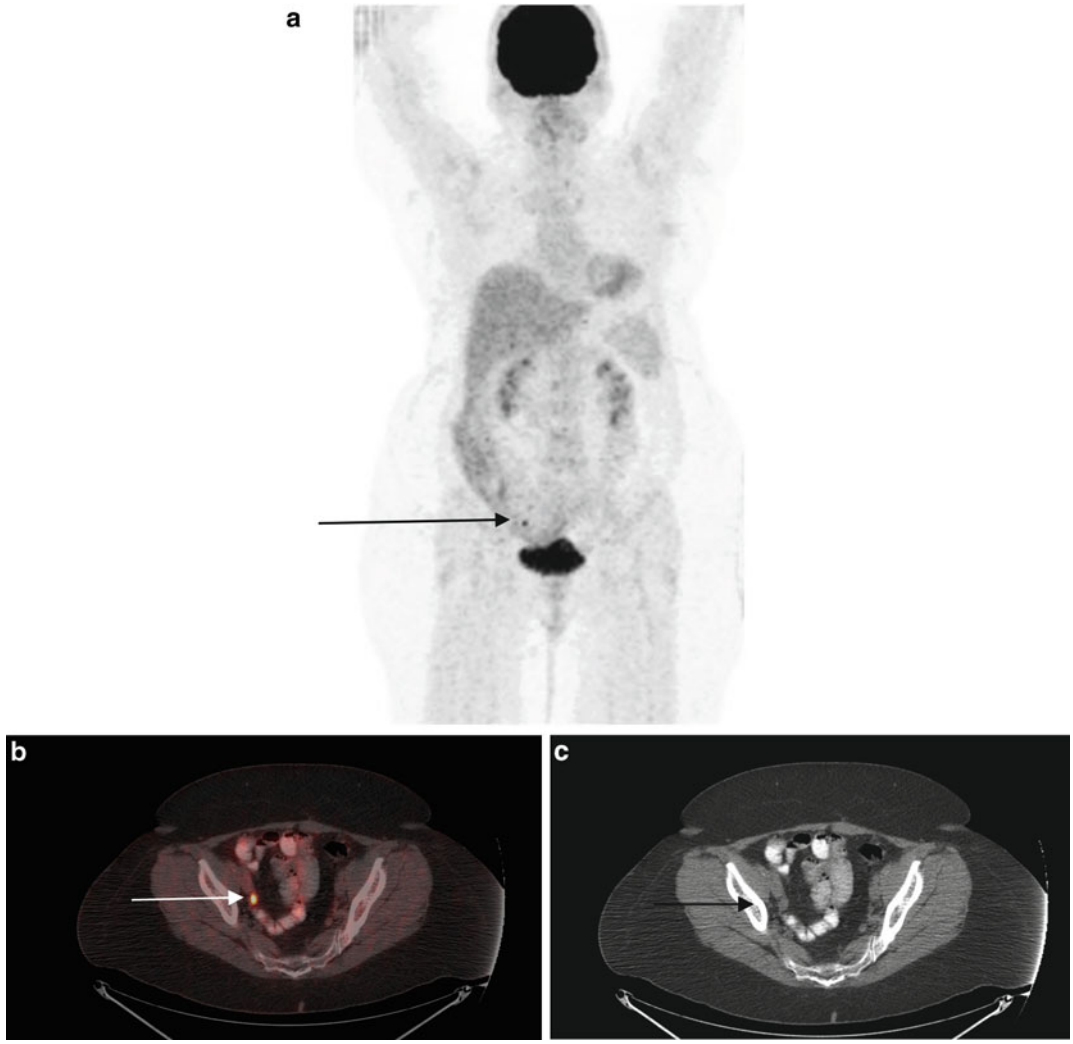

Fig. 16 A 67-year-old patient with papillary serous adenocarcinoma of the left ovary, who underwent status post total abdominal hysterectomy/bilateral salpingo-oophorectomy, was referred for PET/CT for restaging in view of rising CA-125 U/mL levels (34 U/ml). The patient was clinically asymptomatic and had normal findings on conventional imaging. Maximum intensity projection image (**a**, *arrow*) shows focal abnormal [^{18}F]FDG uptake in the right side of the pelvis localizing to a right para-iliac soft tissue nodule measuring 1.5 × 1.1 cm (**b**, **c** *arrows*; SUV_{max}, 7.3), likely a lymph node. No other metabolically active lesion was noted elsewhere. Pathology findings were positive for metastatic carcinoma

ovarian carcinoma. Pooled data showed the highest specificity for CA-125 U/mL at 0.93 (95% CI: 0.89–0.95), while PET/CT had the highest pooled sensitivity at 0.91 (95% CI: 0.88–0.94). There was significant heterogeneity among studies and evidence of publication bias. The pooled sensitivity of PET alone was 0.88 (95% CI, 0.84–0.92), not statistically significant from PET/CT [47]. The combined pooled data supported the use of PET/CT as a supplement to current surveillance techniques, particularly for those patients with an increasing CA-125 U/mL level and normal CT or MRI findings.

Similar results were seen for PET in more recent studies of patients who were clinically disease-free [46, 49]. PET compared with

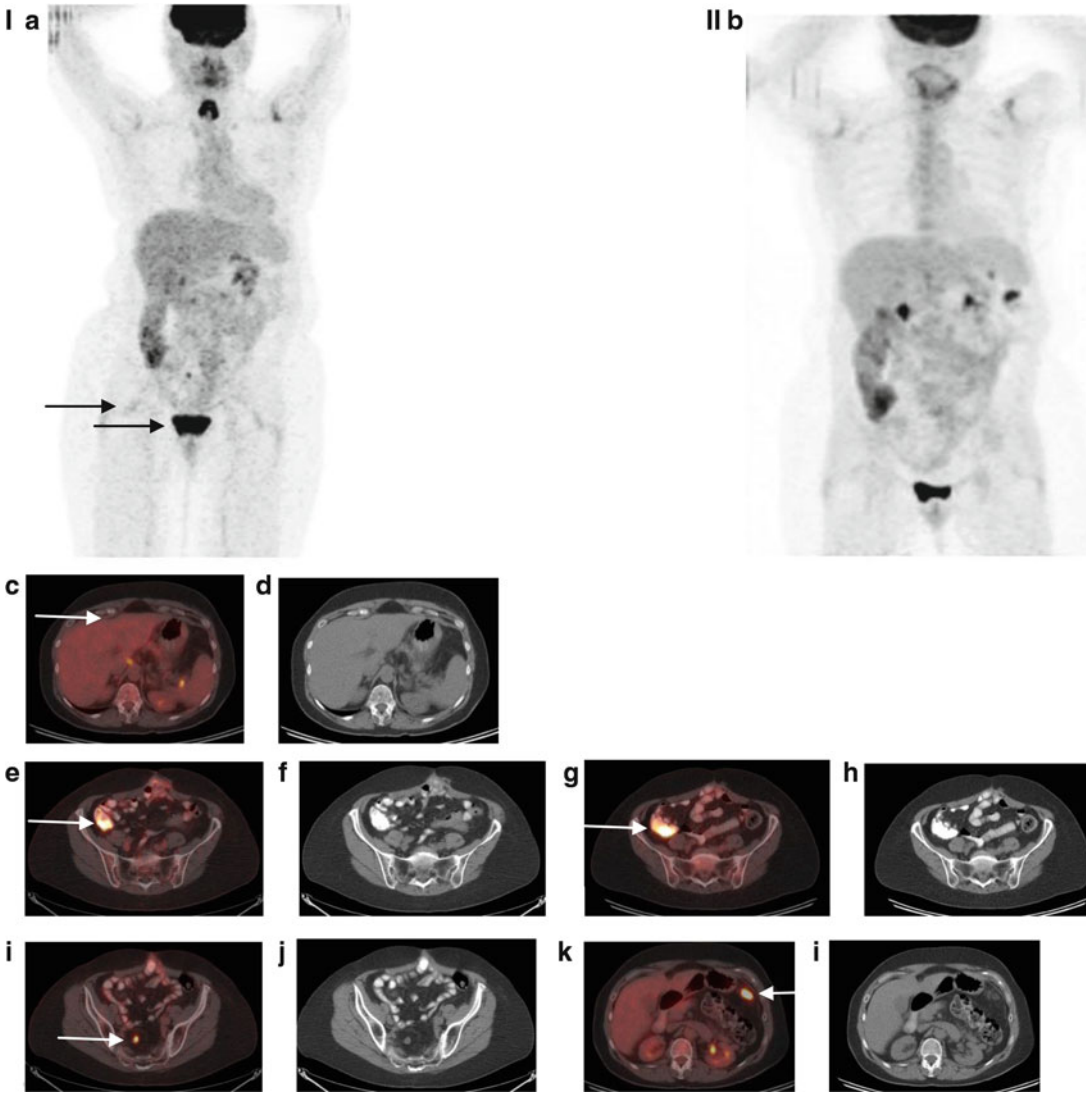

Fig. 17 A 66-year-old patient with ovarian carcinoma, who underwent and status post primary (total abdominal hysterectomy/bilateral salpingo-oopherectomy) and secondary (partial resection of transverse colon/omentectomy) cytoreduction was referred for restaging in view of rising CA-125 U/mL levels (from 11 U/mL to17 U/mL in 3 months). PET/CT (*panel I*) shows a peritoneal nodule in the pelvis (**a**, **b** *arrow*; SUV_{max}: 6.2) suggestive of recurrence. The patient was treated with chemotherapy. A follow-up PET/CT (panel II), however, shows progression (**g**, **h** *arrow*) with appearance of new peritoneal nodules in the perihepatic portacaval region (**c**, **d** *arrow*; SUV_{max}: 4.2) and in the left upper abdominal peritoneum (**e**, **f** *arrows*; SUV_{max}: 8.2)

conventional imaging and serum CA-125 U/mL levels showed superior results than conventional imaging, with a sensitivity of 86.9% and a specificity of 78.8% versus 53.3% and 81.8%, respectively. [^{18}F]FDG PET detected disease in 23 patients with positive serum CA-125 U/mL levels but who had normal findings on other imaging modalities and in 11 patients with negative serum CA-125 U/mL levels and normal findings with other imaging modalities [46]. Murakami and colleagues reported the detection of disease using PET in 46 patients (51%); in eight of 41 patients (19.5%) with normal CA-125 U/mL levels, disease was seen with PET only. The

sensitivity of the combination of PET and CA-125 U/mL was highest at 97.8%. PET detected intraperitoneal and retroperitoneal metastases and normal-sized nodal metastases and was able to detect recurrence at relatively low titers of CA-125 U/mL [49]. In a more recent study, Antunovic et al. evaluated 121 patients for recurrence using [^{18}F]FDG PET/CT and conventional imaging with a sensitivity of 82% and 70%, respectively. Of these patients, only 55 had serum CA-125 U/mL levels greater than 35 U/mL, whereas 52 patients presented with CA-125 U/mL levels in the normal reference range [51]. The detection rates with [^{18}F]FDG PET are generally higher with a greater increase in the CA-125 U/mL level; the reported detection rates were around 53% for CA-125 U/mL levels less than 30 U/mL compared with 89% for CA-125 U/mL levels greater than 286 U/mL [52].

PET/CT may be considered for the evaluation of patients suspected of having recurrent disease [6].

Impact on Management of Recurrent Disease

The use of PET/CT in conjunction with conventional imaging has potential impact on management [53]. It has also been suggested that the combination of PET/CT and staging laparoscopy has a significant effect on the multimodal approach through its complementary role in the assessment of disease (Fig. 18).

Fagotti and colleagues evaluated [^{18}F]FDG PET and staging laparoscopy in identifying surgically treatable or untreatable patients in 70 recurrent ovarian cancer cases [54]. The sensitivity and specificity of PET were 93.0% and 55.6%, respectively, versus 95.0% and 64.0% for staging laparoscopy. Combined radiological and laparoscopic evaluation improved all parameters, with an NPV of 88.9% and a sensitivity of 95.3%.

[^{18}F]FDG PET/CT may be helpful in optimizing the selection of patients for site-specific treatment, including radiation treatment planning and selection of optimal surgical candidates. In a retrospective review of 39 ovarian cancer patients, [^{18}F]FDG PET/CT detected disease in three patients with clinical symptoms of recurrence but normal CA-125 U/mL levels, while in four patients with no clinical evidence of recurrent disease, PET was true negative in all cases [55]. PET/CT facilitated the accurate localization of disease, guided treatment, and helped avoid surgery in four patients in whom additional disease was detected in unresectable anatomic areas. In five of eight patients, PET confirmed the presence of disease following treatment [55]. In another study, PET/CT led to a change in the clinical management in 44% of cases when PET/CT information was added to conventional follow-up findings [56]. For 32 patients, both CTce and PET/CT were performed: PET/CT yielded positive findings in 91% of cases compared with 63% for CT. Intermodality changes in management were indicated for 14 of 32 (44%) patients undergoing PET, with the decision changed from observation in five, further examinations in three, and chemotherapy in six additional patients [56].

In a larger study of 132 women, the combination of CTce with PET improved the diagnosis, resulting in a change of management for 51 of the 132 patients (39%). In comparison, CTce alone changed management in 12% while PET/CT (non-contrast) affected management in only 2% of cases [57]. For patient-based analysis, the sensitivity, specificity, and accuracy of PET/ceCT was the highest and significantly different at 78.8%, 90.9%, and 84.8%, respectively, whereas those of PET/non-contrast-enhanced CT were 74.2%, 90.9%, and 82.6%, respectively, and those of CTce were 60.6%, 84.8%, and 72.7%, respectively [57].

Similar results were reported by Chung and colleagues in their study where PET/CT modified the diagnostic or treatment plan for 19 patients (24.7%), by leading to the use of previously unplanned therapeutic procedures in 11 (57.9%) and the avoidance of previously planned diagnostic procedures in eight (42.1%) patients [58].

In 56 women with elevated CA-125 U/mL levels of more than 35 IU/mL, all but one had a positive finding on PET/CT. PET/CT altered the known disease distribution in 40 scans (64%). Overall, PET/CT showed less disease in six scans (9%) and more disease in 34 scans (52%). Regardless of the value of CA-125 U/mL, PET/CT identified a subgroup of women with

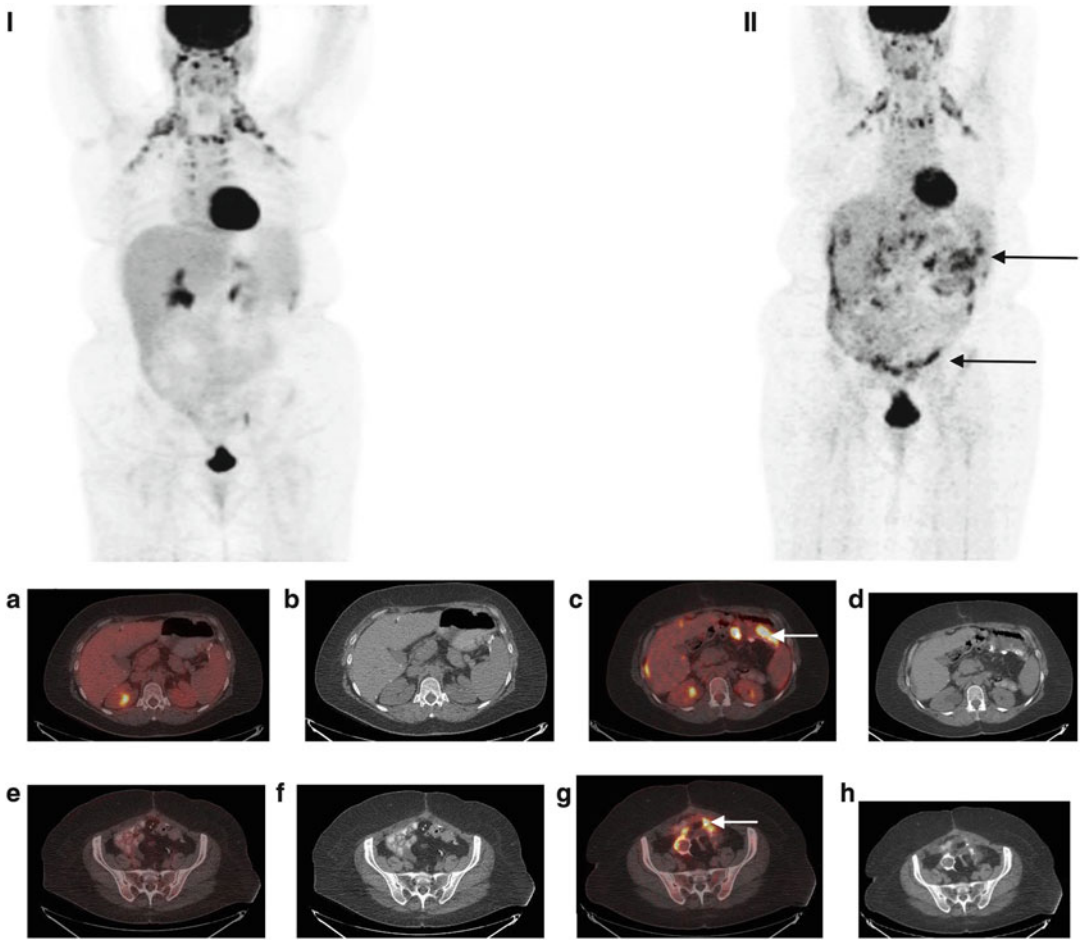

Fig. 18 A 58-year-old patient with stage-III high-grade papillary serous carcinoma who underwent status post partial primary cytoreduction and chemotherapy. PET/CT performed after completion of therapy (*panel I*) does not show evidence of any [^{18}F]FDG-avid disease (**a**–**d**). In view of rising CA-125 U/mL levels 4 months later, the patient was referred for PET/CT scan (*panel II, arrows*) revealing hypermetabolic disease in the peritoneum (**e**–**h** *arrows*) and retroperitoneal lymph nodes. No other distant metastases were seen in the whole-body scan. She was started on chemotherapy and underwent a second debulking procedure

apparently localized disease or no definite evidence of disease. This group had improved survival compared with women shown to have systemic disease. PET/CT resulted in a major change of management plan in 34 patients (58%) [59]. In a recent study, [^{18}F]FDG PET/CT changed the management of 31 patients (51.6%), leading to the use of previously unplanned treatment procedures in 19 patients (61.2%) and the avoidance of previously planned therapeutic procedures in 12 patients (38.8%) [60].

When pre- and post-PET/CT questionnaires completed by the oncologists were examined for the impact of PET/CT results on decision-making, there was a statistically significant change in the decision-making for ten patients (34%, $p < 0.0001$). PET had positive findings in 93% of patients compared with the CT scan (76%) and it modified the disease distribution for 16 patients (55%; $p < 0.001$) compared with CT [61].

In a recent prospective, multicenter, cohort study where referring doctors were asked to specify a management plan pre- and post-PET imaging, PET/CT affected management in 60% of cases (49% high, 11% medium impact) and identified 168 more lesions than conventional imaging

that were mostly nodal or peritoneal sites of disease. Patients in whom more disease was detected with PET/CT were more likely to experience disease progression in the following 12 months [62].

Role in Assessment Before Second-Look Laparotomy or Secondary Debulking

At second-look laparotomy (SSL), about 36–73% of patients are found to have persistent ovarian cancer [42]. Even patients with negative results from second-look procedures have a relapse rate of 30–50% with a mean interval of 24 months. About 60% of recurrence is in the peritoneal cavity [63]. Careful monitoring of the patients is therefore mandatory. SLL is performed on patients without clinical evidence of disease in order to assess tumor response. If SLL cannot confirm presence of disease, then adjunctive therapy is discontinued while reductive surgery is performed on those with residual disease before further chemotherapy [64, 65]. Some feel that the clinical impact of the diagnostic SLL is limited because even when there is no disease (negative SLL), 40–60% of patients relapse within 5 years [66, 67]. Additional drawbacks include invasive surgical procedure, associated complications and morbidity, risk of anesthesia, and all the associated expenses leading to an overall more costly management [67].

Prior to cytoreductive surgery, [^{18}F]FDG PET/CT may be helpful in confirming discrete macroscopic disease in those cases where conventional imaging is unable to detect disease or has equivocal results. It can also help localize the sites of disease so that surgery or biopsy can be directed better. This is useful in cases where detection by conventional imaging fails because of postsurgical changes. Use of a PET probe in the operating room can aid identification and localization of disease sites for resection and help establish the completeness of surgical resection. In a feasibility study, intraoperative gamma probe detection, specimen PET/CT, and postoperative PET/CT verified complete resection of the clinical and hypermetabolic lesions and helped identify disease sites when the extent of disease was not fully apparent intraoperatively by gross palpation or inspection. The intraoperative gamma probe also helped characterize extensive, unresectable disease in the porta hepatis and celiac axis of a patient, much of which was not recognized with the initial intraoperative survey [68]. This, however, needs to be validated in larger studies.

[^{18}F]FDG PET is cost-effective for the evaluation of recurrent disease and helps guide surgical management; reported change may be affected in about 50–60% patients [40, 69]. In their study of 42 patients, Rusu et al. noted a change in therapeutic procedures in 30 out of 53 (56.6%) cases, leading to a change from surgical intervention to conservative treatment in 11, while three patients were eligible for surgery contrary to the prior plan of either systemic treatment or observation [40].

The high NPV of PET scanning may be useful for avoiding second-look surgery, and by better selection of patients for secondary cytoreductive surgery [^{18}F]FDG PET may be a substitute for second-look surgery [70–72]. In a prospective evaluation of 60 patients, Risum and colleagues compared [^{18}F]FDG PET/CT with abdominal/TVUS and CT performed before secondary cytoreductive surgery. All patients had a CA-125 U/mL level greater than 50 U/mL or more than 15% over the baseline level. The sensitivities of US, CT, and PET/CT for diagnosing recurrence were 66%, 81%, and 97%, respectively. The specificity of US, CT, and PET/CT for diagnosing recurrence was 90% for all three modalities. PET/CT detected recurrence in ten (50%) of 20 patients without evidence of recurrence on CT. Multiple versus solitary tumors were found using PET/CT on 27 of 39 (69%) patients compared with 19 of 39 (48%) by CT [72].

Smith et al. demonstrated a reduction in unnecessary invasive staging procedures and healthcare costs following the introduction of [^{18}F]FDG PET. PET led to a decrease in unnecessary laparotomies from 70% to 5%; 35% of patients underwent the less-invasive laparoscopy instead of laparotomy [71]. Mansueto and colleagues also reported on the cost-effectiveness of using PET/CT in recurrent disease through accurate detection of disease sites and its ability to direct the clinical

management [70]. The study compared treatment strategies based on CT only, PET/CT for those with normal CT scans, and PET/CT for all cases. The expected costs, avoided surgery, and incremental cost-effectiveness ratio were calculated to identify the most cost-effective strategy. PET/CT reoriented physician choice in 31% of patients submitted to PET/CT after a negative CT scan, and in 62% of patients who always underwent PET/CT –irrespective of the CT findings. While applying PET/CT in all cases adds to the cost, it is offset by cases where surgery is avoided. In this study, surgery was avoided in three cases [70].

PET/CT offers a noninvasive method for assessing and predicting full resectability of recurrent disease when planning cytoreductive surgery and hyperthermic intraperitoneal chemotherapy [73]. In 206 patients with recurrent ovarian cancer who were evaluated with either [^{18}F]FDG PET or conventional imaging ($n = 103$ each), those who had secondary cytoreductive surgery guided by PET/CT had fewer residual lesions and showed prolonged overall survival (43 months vs. 22 months) and progression-free survival (median 20 months vs. 9 months, respectively) compared with those who underwent conventional imaging [74]. When compared with a scoring system based on clinical parameters of resectability, PET/CT showed a higher sensitivity of 100% and an NPV of 100%, although overall specificity at 60% was low. A very good prediction of full resectability was shown for patients undergoing concordant PET/CT and clinical scoring, with a sensitivity of 100% (63–100), specificity of 75% (20–96%), PPV of 89%, and NPV of 100%. PET/CT can provide complimentary information to clinical parameters or score and may be a noninvasive tool for the assessment of resectability [75].

Response Assessment and Prognostication

Limited data exist on the role of monitoring treatment response. In a small study of ovarian cancer patients receiving neoadjuvant therapy, response using [^{18}F]FDG PET was retrospectively analyzed in eight patients and compared with histopathological parameters to identify responders or nonresponders. Posttherapy SUV in responders was significantly lower than that in nonresponders, and an SUV cutoff of 3.8 on posttherapy scans differentiated responders and nonresponders, with a sensitivity of 90%, a specificity of 63.6%, and an accuracy of 76.2%; a percent change in SUV of 65 as the cutoff showed a sensitivity of 90%, a specificity of 81.8%, and an accuracy of 85.7% for differentiating responders from nonresponders [76]. More data and studies are needed to consolidate and define the role of [^{18}F]FDG PET in assessing treatment response.

Quantitative PET parameters may be useful for prognostication and assessing treatment outcomes although their role is yet to be fully understood and defined in routine practice. Metabolic tumor volume (MTV) and total lesion glycolysis (TLG) are some parameters associated with outcomes of surgery and prognosis. In 175 patients with primary disease, TLG was an independent prognostic factor for progression-free interval [77]. For presurgical staging, MTV and TLG values were inversely associated with clinical outcome. Patients with values higher than the cutoff value of 70 for MTV and 563 for TLG were associated with worse outcome and shorter progression-free interval compared with those with lower values [78]. Similar results were also shown in patients with recurrent disease [79, 80]. While there are data available on this topic, many of the studies are limited owing to their retrospective design and small cohort of patients. The use of such parameters and relevance in routine practice remains to be established.

References

1. American Cancer Society. 2016. http://www.cancer.org
2. Chi DBR, Rubin SC, et al. Gynecologic malignancies. In: CLR P, Hoskins WJ, Wagman LD, editors. Cancer management: a multidisciplinary approach. Melville: PRR Inc; 1999. p. 361–430.
3. Young RC, Fuks FZ, Hoskins WJ. Cancer of the ovary. In: Devita VT, editor. Cancer: principles and practice of oncology. Philadelphia: J. B Lippincott Co.; 2011.
4. http://www.FIGO.org

5. Prat J. Staging classification for cancer of the ovary, fallopian tube, and peritoneum. Int J Gynaecol Obstet. 2014;124(1):1–5.
6. NCCN. Practice guidelines: ovarian cancer. 2016. https://www.nccn.org/professionals/physician_gls/f_guidelines.asp
7. Morgan Jr RJ, et al. Ovarian cancer, version 1.2016, NCCN clinical practice guidelines in oncology. J Natl Compr Canc Netw. 2016;14(9):1134–63.
8. Subhas N, et al. Imaging of pelvic malignancies with in-line FDG PET-CT: case examples and common pitfalls of FDG PET. Radiographics. 2005;25(4):1031–43.
9. Fenchel S, et al. Asymptomatic adnexal masses: correlation of FDG PET and histopathologic findings. Radiology. 2002;223(3):780–8.
10. Grab D, et al. Classification of asymptomatic adnexal masses by ultrasound, magnetic resonance imaging, and positron emission tomography. Gynecol Oncol. 2000;77(3):454–9.
11. Tanizaki Y, et al. Diagnostic value of preoperative SUV_{max} on FDG-PET/CT for the detection of ovarian cancer. Int J Gynecol Cancer. 2014;24(3):454–60.
12. Castellucci P, et al. Diagnostic accuracy of ^{18}F-FDG PET/CT in characterizing ovarian lesions and staging ovarian cancer: correlation with transvaginal ultrasonography, computed tomography, and histology. Nucl Med Commun. 2007;28(8):589–95.
13. Kitajima K, et al. FDG-PET/CT for diagnosis of primary ovarian cancer. Nucl Med Commun. 2011;32(7):549–53.
14. Lerman H, et al. Normal and abnormal ^{18}F-FDG endometrial and ovarian uptake in pre- and postmenopausal patients: assessment by PET/CT. J Nucl Med. 2004;45(2):266–71.
15. Yun M, et al. Physiologic ^{18}F-FDG uptake in the fallopian tubes at mid cycle on PET/CT. J Nucl Med. 2010;51(5):682–5.
16. Iyer, V.R., Lee S.I., MRI, CT, and PET/CT for ovarian cancer detection and adnexal lesion characterization. AJR Am J Roentgenol, 2010. 194(2) 311–321.
17. Hubner KF, et al. Assessment of primary and metastatic ovarian cancer by positron emission tomography (PET) using 2-[^{18}F]deoxyglucose (2-[^{18}F]FDG). Gynecol Oncol. 1993;51(2):197–204.
18. Schroder W, et al. The role of ^{18}F-fluoro-deoxyglucose positron emission tomography (^{18}F-FDG PET) in diagnosis of ovarian cancer. Int J Gynecol Cancer. 1999;9(2):117–22.
19. Yoshida Y, et al. Incremental benefits of FDG positron emission tomography over CT alone for the preoperative staging of ovarian cancer. AJR Am J Roentgenol. 2004;182(1):227–33.
20. Kurokawa T, et al. Expression of GLUT-1 glucose transfer, cellular proliferation activity and grade of tumor correlate with [F-18]-fluorodeoxyglucose uptake by positron emission tomography in epithelial tumors of the ovary. Int J Cancer. 2004;109(6):926–32.
21. Hynninen J, et al. A prospective comparison of integrated FDG-PET/contrast-enhanced CT and contrast-enhanced CT for pretreatment imaging of advanced epithelial ovarian cancer. Gynecol Oncol. 2013;131(2):389–94.
22. Dauwen H, et al. PET/CT in the staging of patients with a pelvic mass suspicious for ovarian cancer. Gynecol Oncol. 2013;131(3):694–700.
23. Yamamoto Y, et al. Preoperative evaluation of pelvic masses with combined ^{18}F-fluorodeoxyglucose positron emission tomography and computed tomography. Int J Gynaecol Obstet. 2008;102(2):124–7.
24. Zytoon AA, et al. High impact of FDG-PET/CT in diagnostic strategies for ovarian cancer. Acta Radiol. 2013;54(3):340–8.
25. Nam EJ, et al. Diagnosis and staging of primary ovarian cancer: correlation between PET/CT, Doppler US, and CT or MRI. Gynecol Oncol. 2010;116(3):389–94.
26. Michielsen K, et al. Whole-body MRI with diffusion-weighted sequence for staging of patients with suspected ovarian cancer: a clinical feasibility study in comparison to CT and FDG-PET/CT. Eur Radiol. 2014;24(4):889–901.
27. Risum S, et al. Does the use of diagnostic PET/CT cause stage migration in patients with primary advanced ovarian cancer? Gynecol Oncol. 2010;116(3):395–8.
28. Risum S, et al. The diagnostic value of PET/CT for primary ovarian cancer – a prospective study. Gynecol Oncol. 2007;105(1):145–9.
29. Kitajima K, et al. Diagnostic accuracy of integrated FDG-PET/contrast-enhanced CT in staging ovarian cancer: comparison with enhanced CT. Eur J Nucl Med Mol Imaging. 2008;35(10):1912–20.
30. Yuan Y, et al. Computer tomography, magnetic resonance imaging, and positron emission tomography or positron emission tomography/computer tomography for detection of metastatic lymph nodes in patients with ovarian cancer: a meta-analysis. Eur J Radiol. 2012;81(5):1002–6.
31. Signorelli M, et al. Detection of nodal metastases by ^{18}F-FDG PET/CT in apparent early stage ovarian cancer: a prospective study. Gynecol Oncol. 2013;131(2):395–9.
32. De Iaco P, et al. FDG-PET/CT in advanced ovarian cancer staging: value and pitfalls in detecting lesions in different abdominal and pelvic quadrants compared with laparoscopy. Eur J Radiol. 2011;80(2):e98–103.
33. Schmidt S, et al. Peritoneal carcinomatosis in primary ovarian cancer staging: comparison between MDCT, MRI, and ^{18}F-FDG PET/CT. Clin Nucl Med. 2015;40(5):371–7.
34. Hicks RJ, Ware RE, Lau EW. PET/CT: will it change the way that we use CT in cancer imaging? Cancer Imaging. 2006;6:S52–62.
35. Fruscio R, et al. Preoperative ^{18}F-FDG PET/CT in the management of advanced epithelial ovarian cancer. Gynecol Oncol. 2013;131(3):689–93.
36. Alessi A, et al. FDG-PET/CT to predict optimal primary cytoreductive surgery in patients with advanced ovarian cancer: preliminary results. Tumori. 2016;102(1):103–7.

37. Risum S, et al. Prediction of suboptimal primary cytoreduction in primary ovarian cancer with combined positron emission tomography/computed tomography – a prospective study. Gynecol Oncol. 2008; 108(2):265–70.
38. Risum S, et al. Positron emission tomography/computed tomography predictors of overall survival in stage IIIC/IV ovarian cancer. Int J Gynecol Cancer. 2012;22(7):1163–9.
39. Delbeke D, Martin WH. Positron emission tomography imaging in oncology. Radiol Clin North Am. 2001; 39(5):883–917.
40. Rusu D, et al. Clinical and Survival Impact of FDG PET in Patients with Suspicion of Recurrent Ovarian Cancer: A 6-Year Follow-Up. Front Med (Lausanne). 2015;2:46.
41. Dragosavac S, et al. Staging recurrent ovarian cancer with ^{18}FDG PET/CT. Oncol Lett. 2013;5(2):593–7.
42. Rose PG, et al. Positive emission tomography for evaluating a complete clinical response in patients with ovarian or peritoneal carcinoma: correlation with second-look laparotomy. Gynecol Oncol. 2001;82(1):17–21.
43. Kim CK, et al. Detection of recurrent ovarian cancer at MRI: comparison with integrated PET/CT. J Comput Assist Tomogr. 2007;31(6):868–75.
44. Sanli Y, et al. Diagnostic value of PET/CT is similar to that of conventional MRI and even better for detecting small peritoneal implants in patients with recurrent ovarian cancer. Nucl Med Commun. 2012;33(5): 509–15.
45. Limei Z, et al. Accuracy of positron emission tomography/computed tomography in the diagnosis and restaging for recurrent ovarian cancer: a meta-analysis. Int J Gynecol Cancer. 2013;23(4):598–607.
46. Garcia-Velloso MJ, et al. Diagnostic accuracy of FDG PET in the follow-up of platinum-sensitive epithelial ovarian carcinoma. Eur J Nucl Med Mol Imaging. 2007;34(9):1396–405.
47. Gu P, et al. CA 125, PET alone, PET-CT, CT and MRI in diagnosing recurrent ovarian carcinoma: a systematic review and meta-analysis. Eur J Radiol. 2009; 71(1):164–74.
48. Iagaru AH, et al. ^{18}F-FDG PET/CT evaluation of patients with ovarian carcinoma. Nucl Med Commun. 2008;29(12):1046–51.
49. Murakami M, et al. Whole-body positron emission tomography and tumor marker CA125 for detection of recurrence in epithelial ovarian cancer. Int J Gynecol Cancer. 2006;16(Suppl 1):99–107.
50. Pan HS, et al. Combined positron emission tomography-computed tomography and tumor markers for detecting recurrent ovarian cancer. Arch Gynecol Obstet. 2011;283(2):335–41.
51. Antunovic L, et al. Revisiting the clinical value of ^{18}F-FDG PET/CT in detection of recurrent epithelial ovarian carcinomas: correlation with histology, serum CA-125 U/mL assay, and conventional radiological modalities. Clin Nucl Med. 2012;37(8):e184–8.
52. Palomar A, et al. Value of FDG PET/CT in patients with treated ovarian cancer and raised CA125 serum levels. Mol Imaging Biol. 2012;14(1):123–9.
53. Chen YM, et al. Is there an impact of ^{18}F-FDG PET/CT on the surveillance and clinical management of recurrent ovarian cancer? Research based on a large sample in a single PET/CT center. Nucl Med Commun. 2014;35(4):347–52.
54. Fagotti A, et al. A treatment selection protocol for recurrent ovarian cancer patients: the role of FDG-PET/CT and staging laparoscopy. Oncology. 2008;75(3–4):152–8.
55. Thrall MM, et al. Clinical use of combined positron emission tomography and computed tomography (FDG-PET/CT) in recurrent ovarian cancer. Gynecol Oncol. 2007;105(1):17–22.
56. Mangili G, et al. Integrated PET/CT as a first-line re-staging modality in patients with suspected recurrence of ovarian cancer. Eur J Nucl Med Mol Imaging. 2007;34(5):658–66.
57. Kitajima K, et al. Performance of integrated FDG-PET/contrast-enhanced CT in the diagnosis of recurrent ovarian cancer: comparison with integrated FDG-PET/non-contrast-enhanced CT and enhanced CT. Eur J Nucl Med Mol Imaging. 2008;35(8):1439–48.
58. Chung HH, et al. Role of [^{18}F]FDG PET/CT in the assessment of suspected recurrent ovarian cancer: correlation with clinical or histological findings. Eur J Nucl Med Mol Imaging. 2007;34(4):480–6.
59. Simcock B, et al. The impact of PET/CT in the management of recurrent ovarian cancer. Gynecol Oncol. 2006;103(1):271–6.
60. Bilici A, et al. Clinical value of FDG PET/CT in the diagnosis of suspected recurrent ovarian cancer: is there an impact of FDG PET/CT on patient management? Eur J Nucl Med Mol Imaging. 2010; 37(7):1259–69.
61. Soussan M, et al. Impact of FDG PET-CT imaging on the decision making in the biologic suspicion of ovarian carcinoma recurrence. Gynecol Oncol. 2008; 108(1):160–5.
62. Fulham MJ, et al. The impact of PET-CT in suspected recurrent ovarian cancer: a prospective multi-centre study as part of the Australian PET Data Collection Project. Gynecol Oncol. 2009;112(3):462–8.
63. Lurain JR. Second-look laparotomy and other reoperations for ovarian cancer. In: Sciarra JJ, editor. Gynecology and obstetrics. Philadelphia: Lippincott Williams & Wilkins; 2004.
64. Rubin SC, et al. Ten-year follow-up of ovarian cancer patients after second-look laparotomy with negative findings. Obstet Gynecol. 1999;93(1):21–4.
65. Rubinstein E, Knudsen JB. Clinical aspects of second-look laparotomy in ovarian cancer. Ann Chir Gynaecol. 1986;75(3):177–9.
66. Obermair A, Sevelda P. Impact of second look laparotomy and secondary cytoreductive surgery at second-look laparotomy in ovarian cancer patients. Acta Obstet Gynecol Scand. 2001;80(5):432–6.

67. Sijmons EA, Heintz AP. Second-look and second surgery: second chance or second best? Semin Surg Oncol. 2000;19(1):54–61.
68. Cohn DE, et al. Novel perioperative imaging with ^{18}F-FDG PET/CT and intraoperative ^{18}F-FDG detection using a handheld gamma probe in recurrent ovarian cancer. Gynecol Oncol. 2008;110(2):152–7.
69. Ebina Y, et al. Impact of FDG PET in optimizing patient selection for cytoreductive surgery in recurrent ovarian cancer. Eur J Nucl Med Mol Imaging. 2014; 41(3):446–51.
70. Mansueto M, et al. Positron emission tomography/computed tomography introduction in the clinical management of patients with suspected recurrence of ovarian cancer: a cost-effectiveness analysis. Eur J Cancer Care (Engl). 2009;18(6):612–9.
71. Smith GT, et al. Cost analysis of FDG PET for managing patients with ovarian cancer. Clin Positron Imaging. 1999;2(2):63–70.
72. Risum S, et al. Influence of 2-(^{18}F) fluoro-2-deoxy-D-glucose positron emission tomography/computed tomography on recurrent ovarian cancer diagnosis and on selection of patients for secondary cytoreductive surgery. Int J Gynecol Cancer. 2009;19(4):600–4.
73. Pfannenberg C, et al. ^{18}F-FDG-PET/CT to select patients with peritoneal carcinomatosis for cytoreductive surgery and hyperthermic intraperitoneal chemotherapy. Ann Surg Oncol. 2009;16(5):1295–303.
74. Peng P, et al. Benefits of fluorine-18 fludeoxyglucose positron emission tomography in secondary cytoreductive surgery for patients with recurrent epithelial ovarian cancer. Br J Radiol. 2015;88(1052): 20150109.
75. Lenhard SM, et al. Predictive value of PET-CT imaging versus AGO-scoring in patients planned for cytoreductive surgery in recurrent ovarian cancer. Eur J Obstet Gynecol Reprod Biol. 2008;140(2):263–8.
76. Nishiyama Y, et al. Monitoring the neoadjuvant therapy response in gynecological cancer patients using FDG PET. Eur J Nucl Med Mol Imaging. 2008;35(2):287–95.
77. Lee JW, et al. The role of metabolic tumor volume and total lesion glycolysis on ^{18}F-FDG PET/CT in the prognosis of epithelial ovarian cancer. Eur J Nucl Med Mol Imaging. 2014;41(10):1898–906.
78. Chung HH, et al. Prognostic value of preoperative metabolic tumor volume and total lesion glycolysis in patients with epithelial ovarian cancer. Ann Surg Oncol. 2012;19(6):1966–72.
79. Kim CY, et al. Quantitative metabolic parameters measured on F-18 FDG PET/CT predict survival after relapse in patients with relapsed epithelial ovarian cancer. Gynecol Oncol. 2015;136(3):498–504.
80. Mayoral M, et al. Prognostic value of ^{18}F-FDG PET/CT volumetric parameters in recurrent epithelial ovarian cancer. Rev Esp Med Nucl Imagen Mol. 2016;35(2):88–95.

Diagnostic Applications of Nuclear Medicine: Sarcomas

37

Janet F. Eary

Abstract

Sarcomas most commonly occur in the muscles, bones, fat, and connective tissues. These tumors constitute approximately 1% of cancers in adults and about 20% of pediatric cancer. The American Joint Committee on Cancer (AJCC) criteria are often used clinically for staging soft tissue sarcoma patients. Bone tumor staging follows the schemes utilized for other tumors. Adverse prognostic factors include deep tumor location, largest dimension >5 cm, locally recurrent disease, proximal lower extremity site, and presence of metastasis.

Imaging studies, including plain films, chest X-ray, CT with and without contrast, MRI, and [^{18}F]FDG PET, are used in combination to stage and restage sarcoma patients. Serial imaging studies, especially [^{18}F]FDG PET scans, can identify treatment response to neoadjuvant chemo- and radiation therapy. The bone scan with ^{99m}Tc-MDP is still routinely used because of its sensitivity in detection of bone metastases and to occasionally identify metastatic lesions in soft tissues. ^{18}F-Fluoride is increasingly being used as a sensitive bone scanning agent for metastatic surveys.

[^{18}F]FDG PET/CT can reliably distinguish low-grade from high-grade soft tissue sarcoma based on the SUV. Special features and [^{18}F]FDG uptake are related to specific histologic types. Moreover, by identifying areas of increased uptake within a lesion, [^{18}F]FDG PET can be helpful to localize a site for diagnostic biopsy. [^{18}F]FDG PET has been used for tumor staging identifying bone and soft tissue metastases and nodal metastases. A high-resolution contrast chest CT is preferred to visualize small lung metastases.

Keywords

Sarcoma imaging • Imaging in sarcoma • Staging in sarcoma • [^{18}F]FDG PET in sarcoma

Glossary

[^{18}F]FDG	2-Deoxy-2-[^{18}F]fluoro-D-glucose
^{99m}Tc-HDP	^{99m}Tc-hydroxyethylenediphosphonate
^{99m}Tc-MDP	^{99m}Tc-methylenediphosphonate
AJCC	American Joint Committee on Cancer
CT	X-ray computed tomography
EWS-FL1	Ewing's sarcoma fusion gene encoding for a transcriptional activator
FNCLCC	Fédération Nationale des Centres de Lutte Contre le Cancer
G	Histologic tumor grade
GIST	Gastrointestinal stromal tumor

J.F. Eary (✉)
Cancer Imaging Program, National Cancer Institute, National Institutes of Health, Bethesda, MD, USA
e-mail: janet.eary@nih.gov

© Springer International Publishing Switzerland 2017
H.W. Strauss et al. (eds.), *Nuclear Oncology*,
https://doi.org/10.1007/978-3-319-26236-9_23

M	Metastasis status according to the AJCC TNM staging system
MFH	Malignant fibrous histiocytoma
MRI	Magnetic resonance imaging
N	Lymph node status according to the AJCC TNM staging system
NF	Neurofibromatosis
PET	Positron emission tomography
PET/CT	Positron emission tomography/computed tomography
PET/MR	Positron emission tomography/magnetic resonance
PNET	Primitive neuroectodermal tumor/peripheral neuroepithelioma
RECIST	Response evaluation criteria in solid tumors
SUV	Standardized uptake value
SUV_{max}	Standardized uptake value at point of maximum
T	Tumor status according to the AJCC TNM staging system

Contents

Disease Overview 1048

Approaches to Staging 1050

Radiopharmaceuticals 1052
^{99m}Tc-MDP 1052
^{201}TI-Chloride 1054
^{18}F-Fluoride 1054

Sarcoma Treatment 1055
[^{18}F]FDG in Sarcoma Restaging and Treatment Response 1055

References 1061

Disease Overview

Sarcoma is a cancer that originates from the mesenchymal body tissues [1]. These comprise the connective, muscle, fat, bone, cartilage, peripheral nerve, and blood vessel tissues. Sarcomas most commonly occur in the muscles, bone, fat, and connective tissue. While the bone marrow is also derived from mesenchymal tissues, in clinical practice the hematologic malignancies are considered separately from the solid tumors, or sarcomas. Sarcomas are a complex group of tumors that have many different clinical manifestations, but they most often present as a mass.

Sarcomas occur in children and adults. Although the overall cancer incidence is much lower for children, sarcomas account for about one fifth of pediatric cancers. In adults, on the other hand, sarcomas constitute about 1% of cancers [2]. In the USA approximately 10,000 people are diagnosed with sarcomas each year and approximately 3,700 people per year succumb to their disease [2]. The median age of adult sarcoma patients is 59–60 years. There are approximately 30 common sarcoma subtypes that occur in both adults and younger age groups [3]. Most adult sarcomas are the soft tissue types, while bone tumors and cartilage tumors occur less frequently. Women comprise approximately 60% of sarcoma patients [3]. The majority of childhood sarcomas are bone sarcomas which have different clinical presentations, age preponderance, and outcomes compared to childhood soft tissue sarcomas.

The complexity of clinical presentations and diagnoses for sarcomas are based on their pathological characteristics. As these tumors are derived from mesenchymal elements, the tumors at presentation may have histologic and tissue marker characteristics that identify their tissue of origin. They can arise in any mesenchymal tissues. Some sarcomas appear to have no cell of origin identified in normal tissues, supporting the theory that sarcomas form and may differentiate according to surrounding tissue signals or other environmental and genetic factors. There are more than 50 histologic subtypes of sarcoma [4]. They most commonly occur in the extremities and trunk regions. Table 1 lists the mesenchymal tissues, while Table 2 lists the most common soft tissue sarcoma subtypes in adults. Table 3 lists the most common pediatric sarcomas. Bone tumors predominate in the pediatric population.

Adults with sarcomas have approximately a 50% 5-year overall survival rate [1]. Patients with poor outcomes succumb to metastatic disease, local recurrence, or both. Local recurrence after resection occurs in 25% of patients with soft tissue sarcomas,

Table 1 Mesenchymal Tissues

Muscle
Smooth muscle
Skeletal muscle
Connective tissue
Fat tissue
Peripheral nerves
Blood vessels

Table 2 Common soft tissue sarcoma subtypes

Leiomyosarcoma
Rhabdomyosarcoma
Subtypes
Alveolar (pediatric)
Embryonal (pediatric)
Pleomorphic (adult)
Fibrosarcoma
Malignant fibrous histiocytoma (MFH)
Liposarcoma
Subtypes
Well differentiated
Myxoid
Round cell
Pleomorphic
De-differentiated
Malignant peripheral nerve sheath tumor
Malignant schwannoma
Angiosarcoma
Hemangiopericytoma
Lymphangiosarcoma
Pleomorphic sarcoma
Synovial sarcoma
Alveolar soft part sarcoma
Gastrointestinal stromal tumor

Table 3 Common pediatric sarcomas

Osteosarcoma
Conventional types
Chondroblastic
Fibroblastic
Osteoblastic
Parosteal
Telangiectatic (vascular)
Small cell
Periosteal
High-grade surface types
Secondary
Chondrosarcomas
Central, primary, secondary
Peripheral
Mesenchymal
Clear cell
Ewing sarcoma
Extraosseous Ewing sarcoma
Askin tumor (chest wall primary tumor)
Peripheral primitive neuroectodermal tumor/peripheral neuroepithelioma (PNET)
Giant cell tumor
Malignant giant cell tumors
Notochordal tumors (i.e., chordoma)

an event that portends eventual metastatic spread [1]. Typically, pulmonary metastases are the leading site, followed by bone and other soft tissue locations. Disease prognostic factors include patient age, tumor grade (a risk assessment based on histopathological characteristics), tumor depth (superficial or deep), size, histologic subtype, surgical margin status at resection, and disease status (primary or recurrent disease) [1].

Adverse prognostic factors affecting patient survival with soft tissue sarcomas are deep tumor location, a tumor greatest dimension of 5 cm or larger, locally recurrent disease, proximal lower extremity site, and microscopic or grossly involved tumor margins at surgical resection [1]. Sixty percent of adult soft tissue sarcomas occur in the extremities. The proximal lower extremity is a common location for soft tissue sarcomas in adults, which increases risk for poor outcome because of its association with other poor risk factors. Poor risk factors include depth beneath the fascial plane and large tumor growth before diagnosis. In most patients, once metastases occur, survival time diminishes rapidly, despite salvage combination therapy regimens [4]. There are a number of treatment protocols for adults with sarcomas. Patients with low-grade, small sarcomas are likely to proceed to tumor resection with the possibility of adjuvant radiation. Those with high-grade large tumors are often treated with doxorubicin-based neoadjuvant chemotherapy with or without radiation followed by resection and adjuvant therapy. Surgical resection ranges from simple excision with wide margins to complex limb salvage procedures.

Experimental therapy clinical trials for sarcoma are now incorporating targeted therapy agents,

which may influence imaging considerations in the future for clinical care. Adult bone tumors are most often cartilaginous histologic types. Usually, only high-grade tumors are metastatic. The intermediate-grade and low-grade cartilage tumors have high morbidity rates due to repeated local recurrence and poor responses to neoadjuvant chemotherapy. The bone tumors are less frequent in older adults, and osteosarcomas and Ewing's sarcomas are typically seen in younger adults. They are rarely observed in adults over age 50. Bone sarcomas are metaphyseal tumors that primarily spread to the lungs. Risk factors for osteosarcoma include prior radiation therapy and germ line mutations [5]. There are a few soft tissue sarcoma histologic types that can also occur in the bone. Synovial sarcoma is a common example of a cancer that is more biologically consistent with its soft tissue tumor counterparts. As in the soft tissue sarcomas, prognostic factors include the presence of metastases at presentation and chemotherapy resistance. Treatment for the bone sarcomas in adults is similar to the soft tissue sarcomas. Neoadjuvant doxorubicin-based chemotherapy is given and is followed by surgical resection and additional chemotherapy. Five-year survival depends largely on the level of chemotherapy resistance, which is approximately 60%. The lower-grade osteosarcomas are treated with wide local excision and limb salvage procedures. They typically recur in about 5% of cases; however, these recurrences decrease 5-year survival significantly if the tissue recurrence degenerates into a higher-grade or undifferentiated tumor type.

Pediatric sarcomas are dominated by the osteosarcomas and Ewing's sarcomas. The osteosarcomas have a peak incidence in patients in their second decade of life, and the age range begins at approximately 10 years. They predominately present in the extremities, and 15–20% of patients have pulmonary metastases at the time of diagnosis. In addition to prior radiation, the list of possible predisposing factors includes germ line p53 mutations, growth abnormalities, trauma, fetal and parental X-ray exposure. Metastases present at the time of diagnosis are prognostic of poor outcome. Treatment with intensive neoadjuvant chemotherapy results in 60–80% 5-year survival [5]. The treatment response rate and overall survival rate for pediatric sarcomas are significantly higher than that for adults with osteosarcomas.

Ewing's sarcomas are also a bone tumor of adolescence with a peak incidence around the age of 15 years [5]. They most commonly present as a painful mass in the extremities and are often metastatic at presentation. Bone metastases (15–30% of patients), lung metastases, and soft tissue involvement adjacent to the primary tumor mass are common. Presumably, these tumors arise from postsynaptic neural crest precursors and are synonymous with the peripheral neuroectodermal tumors (PNETs), which occur more predominantly in soft tissues [5]. The presence of the EWS-FL1 fusion protein in the tumor confers poor prognosis. There are no known risk factors for causing these tumors, and they are rarely associated with other syndromes.

Patients with sarcoma have highly variable characteristics and clinical outcomes. Sarcomas are often multidrug resistant [6, 7]. The multidrug resistance systems are tissue transporters that remove toxins from tissues. Normally occurring in tissue epithelial linings in the intestines, kidneys, and blood-brain and placental barriers, their activity is unregulated in sarcomas [8–10]. This is a major cause of increased treatment failure and disease progression. The pathobiological basis of multidrug resistance activity and other sarcoma characteristics are complexities that are likely a result of a substantial variety of genetic abnormalities. These consist of broad categories of tumor-specific translocations that contribute to tumor diagnostic criteria and to sarcoma subtypes that have genetic and chromosomal instability [11]. Sarcomas in all body locations present unique challenges for diagnosis and management. These challenges have presented opportunities for evaluation and validation of new imaging techniques.

Approaches to Staging

Because sarcomas are difficult to risk stratify for outcome, staging systems have been devised to improve patient treatment and outcome. The American Joint Committee on Cancer (AJCC) criteria are often used clinically for staging soft tissue sarcoma patients (Tables 4 and 5). This system undergoes periodic analyses and revisions. The current AJCC

Table 4 AJCC definition of TNM and stage grouping for soft tissue sarcoma

Primary tumor (T)	
TX	Primary tumor cannot be assessed
T0	No evidence of primary tumor
T1	Tumor 5 cm or less in greatest dimension[a]
T1a	Superficial tumor
T1b	Deep tumor
T2	Tumor more than 5 cm in greatest dimension[a]
T2a	Superficial tumor
T2b	Deep tumor
Regional lymph nodes (N)	
NX	Regional lymph nodes cannot be assessed
N0	No regional lymph node metastasis
N1[b]	Regional lymph node metastasis
Distant metastasis (M)	
M0	No distant metastasis
M1	Distant metastasis

[a]Superficial tumor is located exclusively above the superficial fascia without invasion of the fascia; deep tumor is located either exclusively beneath the superficial fascia, superficial to the fascia with invasion of or through the fascia, or both superficial yet beneath the fascia

[b]Presence of positive nodes (N1) in M0 tumors is considered Stage III

Table 5 AJCC anatomic stage and prognostic groups for soft tissue sarcoma

Group	T category	N category	M category	
Stage IA	T1a	N0	M0	G1, GX
	T1b	N0	M0	Gl.GX
Stage IB	T2a	N0	M0	Gl.GX
	T2b	N0	M0	G1, GX
Stage IIA	T1a	N0	M0	G2, G3
	T1b	N0	M0	G2, G3
Stage IIB	T2a	N0	M0	G2
	T2b	N0	M0	G2
Stage III	T2a, T2b	N0	M0	G3
	Any T	Nl	M0	AnyG
Stage IV	Any T	Any N	Ml	AnyG

soft tissue sarcoma system stratifies patient tumor by size (T1≤5 cm, T2≥5 cm). Additionally, the tumor is characterized by histologic grade (I–III), the presence or absence of nodal and distant metastasis, and special location descriptions. Revisions that have been suggested include categories for very large tumors (T3≥15 cm), specific primary tumor sites, tumor margin status, histologic subtypes, the presence or absence of tumor local recurrence, and specific markers for biologic aggressiveness.

Sarcoma groups are incorporating these parameters in clinical practice more routinely each year. The pathologic tumor grade is an important component of any tumor staging system; however, there are pitfalls that exist in its application to individual patient tumors. The most widely used sarcoma grading system is the FNCLCC designed by the French Fédération Nationale des Centres de Lutte Contre le Cancer [12]. Even with well-defined grading systems, there are several challenges with grading soft tissue sarcomas. Tumors for which it is difficult to assign histologic grade because of their rare characteristics include tumors where the grade applied does not provide additional prognostic information beyond what is conferred from accurately determining the tumor histologic subtype. These include differentiated liposarcomas, the tumors that are considered "ungradable"; the epithelioid, clear cell, and angiosarcomas; and those where the histologic grade does not predict outcome well, such as the malignant peripheral nerve sheath tumors [13]. These findings reflect the heterogeneity of biological behavior in the sarcomas, and they provide the stimulus for incorporation of newer systems that integrate tumor characteristics from a number of different sources that identify patient risk for malignant behavior more accurately.

A comparative analysis of the AJCC, the Memorial Sloan Kettering Cancer Center system, and the Surgical Staging System of the Musculoskeletal Tumor Society soft tissue sarcoma staging systems found that schemes that include tumor depth, grade, and size are most predictive of tumor relapse in patients with extremity tumors. Wunder et al. suggest that these systems can be used to identify patients that are most likely to benefit from participation in adjuvant therapy trials [14].

Bone tumor staging follows the schemes utilized for other tumors, with a few notable exceptions. The primary tumor is assessed by whether it is confined to cortex (T1) or if it extends beyond this bone structure (T2) [15]. The tumor histologic type and grade predominate the staging criteria for prognosis. The presence or absence of distant metastases is also significant. As with soft tissue

sarcoma staging, bone sarcoma staging includes a careful examination of the lungs to discover metastases, which are often present at the time of initial diagnosis. Inclusion of nomograms for improved prognosis has also been developed, and their use may help to improve selection of multimodality treatment for bone sarcoma patients [16].

Imaging plays an increasingly important role in sarcoma staging. All types of examinations – including plain films, chest X-ray, CT with and without contrast, MRI, and [^{18}F]FDG PET – are now used routinely in combination to stage sarcoma patients and to restage patients when treatment decisions are contemplated. The bone scan is still used routinely because of its sensitivity in detection of bone metastases, although most sarcomas predominantly metastasize to the lungs. If necrosis or ossification is present in the lung metastasis, the lesion may appear as a focal region of low-level uptake in the pulmonary parenchyma. It is rare, however, to detect lung metastasis on a bone scan that is not visible on CT. Several types commonly have associated bone metastases, such as the osteosarcomas, Ewing's sarcomas, and highly undifferentiated tumors. Imaging methods and their uses in sarcoma management are discussed more thoroughly in the following sections.

Radiopharmaceuticals

Disease staging in sarcoma involves all aspects of imaging the body with radiopharmaceuticals. Since these tumors vary considerably in their presentation, local recurrence rates, and patterns of metastatic spread, different imaging studies that provide complementary information for disease staging are used in clinical practice. These are for characterizing the extent of tumor; presence of bony, lymph node; and soft tissue metastases. Some tumor types involve multifocal primary disease presentation, synchronous tumors, and skip metastases. In most sarcoma clinics, a combination of nonspecific, highly sensitive, and tissue-specific imaging agents is used in diagnosis, staging, response, and restaging aspects of patient management.

^{99m}Tc-MDP

The bone scan is widely used in oncology for staging the skeleton for the presence of bony metastases. Sarcoma metastases generally show osteoblastic behavior and are less likely to show lytic metastases. For soft tissue masses, the bone scan is also a standard part of disease staging. Patients with bony metastases show increased uptake in typical metastatic disease patterns in the axial skeleton and extremities. The presence or absence of uptake is often diagnostic in separating benign or locally aggressive tumors from malignant types. Bone scans also have special utility in primary bone tumors. These tumors form malignant osteoid matrices that are undergoing disordered calcification; therefore, they are ^{99m}Tc-MDP avid (Fig. 1). Both the osteosarcomas and some chondrosarcomas with osteoblastic differentiation contain malignant osteoid. Ewing's sarcomas cause bone destruction and reaction that result in bone scan positivity. Primary bone tumors have frequent bone metastases and can present with skip lesions in the affected bone. The osteosarcomas also frequently have bone metastases, but bone scan positive appearance in multiple sites is also common in Ewing's sarcoma. In this latter group of tumors, metastases are often present at the time of diagnosis.

The bone scan is a sensitive method for identifying osteosarcoma pulmonary metastases (Fig. 2). These are often highly ^{99m}Tc-MDP avid. Some clinicians use the relative decrease in ^{99m}Tc-MDP uptake in pulmonary metastases as an indicator of treatment response and suitability for wedge resection metastasectomy. In osteosarcoma patients with limited pulmonary metastasis, this procedure has been shown to increase disease-free survival [17]. The ^{99m}Tc-MDP scan has been reported to contribute to the diagnosis of bone-forming malignant tumors by revealing unusual sites and presentations. The ^{99m}Tc-MDP bone scan is also a means of monitoring treatment response. A decrease in malignant osteoid matrix calcification indicates a response to treatment in this cellular portion of the tumor. The bone scan appearance in metastatic

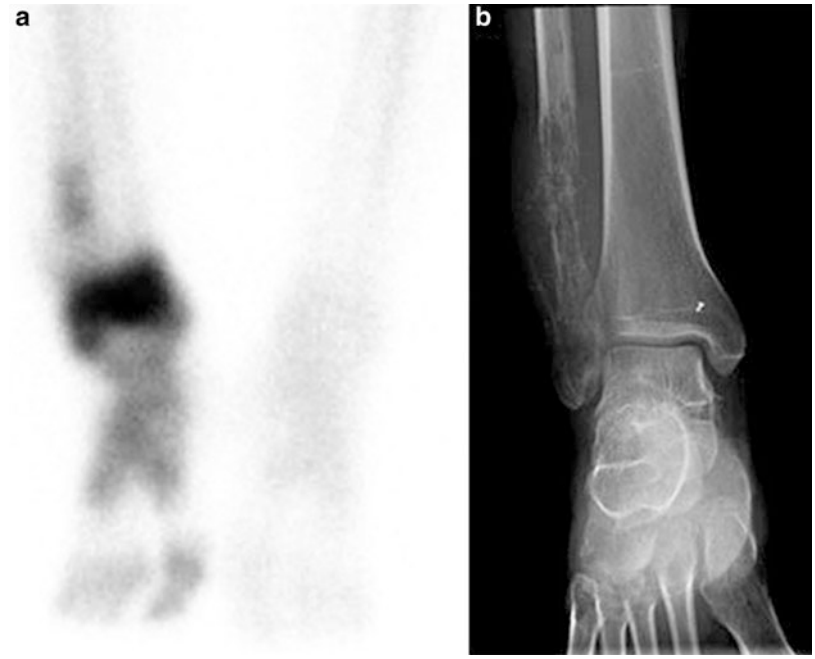

Fig. 1 (**a**) Bone scintigraphy with ^{99m}Tc-MDP of the right ankle showing a Ewing's sarcoma. There is marked uptake in the proximal foot. (**b**) Plain x-ray image of the right ankle shows fibular involvement with soft tissue extension

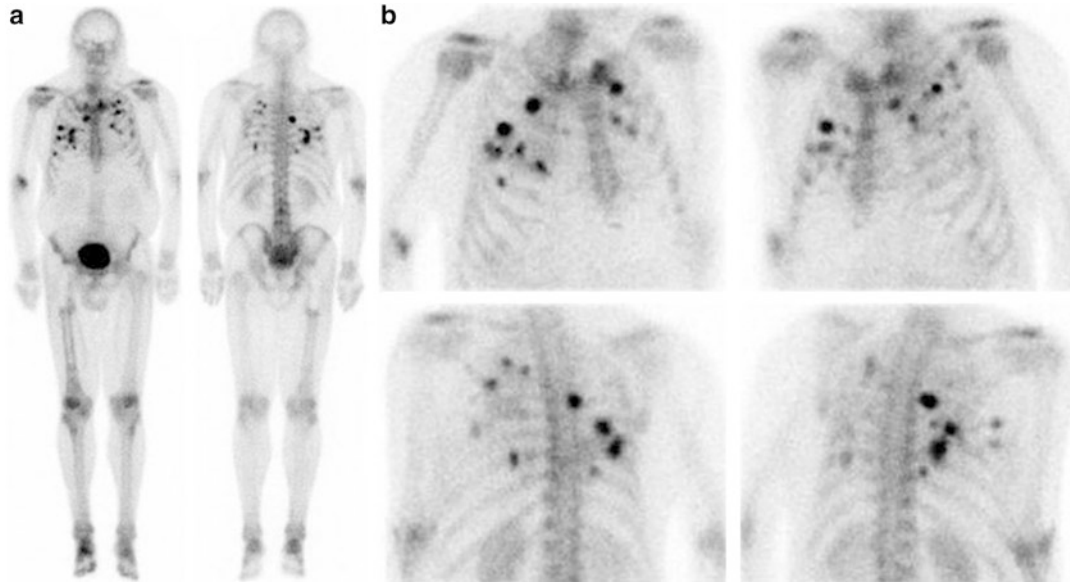

Fig. 2 Bone scan in a patient with active osteosarcoma pulmonary metastases

disease, as with other tumors, can also underestimate the extent and severity of skeletal metastases. In these cases, the metastases involving the bone may only be apparent when a cortical reaction occurs. Subsequent other whole-body surveys such as CT or [^{18}F]FDG PET may provide a complimentary picture of the extent of diseased skeleton [18].

^{201}TI-Chloride

^{201}TI-Chloride as a nonspecific tumor imaging agent has been described for use in many tumors, including sarcoma. Most often, higher uptake is noted in malignant tumors, while lower uptake more frequently signifies benign neoplasms. Soft tissue, bone, and cartilaginous tumors have all shown positivity [19]. Typical high-grade tumor features, such as central necrosis, can also be noted in ^{201}Tl-chloride imaging; this finding is predictive of decreased survival [20].

^{18}F-Fluoride

^{18}F-Fluoride is increasingly being used as a sensitive bone scanning agent for metastatic surveys for many cancers. Recent imaging study results indicate that a combination of [^{18}F]FDG and ^{18}F-fluoride may provide a more complete visualization of bone metastases than either agent alone. This is also the case for sarcomas; however, the use of ^{18}F-fluoride may extend beyond the detection of metastases in bone sarcomas. Since the hallmark of these tumors is new bone formation, uptake of ^{18}F-fluoride will likely change in response to therapy. A particular use may be in evaluating activity in lung metastases since it is common practice to resect lung metastases when they are quiescent after successful chemotherapy. Figure 3 shows a whole-body ^{18}F-fluoride bone scan.

[^{18}F]FDG and Sarcoma Diagnosis

Positron emission tomography (PET) with 2-deoxy-2-[^{18}F]fluoro-D-glucose ([^{18}F]FDG) has been evaluated for use in sarcoma imaging. Imaging in primary cancers has several critical aspects for patient treatment planning. It is used to determine the biological behavior of the tumor, often determining if the tumor is benign or malignant; however, sarcomas include numerous tumors that do not fit well with either category because they can be locally aggressive, yet rarely metastatic. Using a combination of tumor histopathology from biopsy and imaging data is helpful in determining the tumor grade, which is the propensity of the tumor to behave aggressively.

Fig. 3 Whole Body [F^{18}]Fluoride PET bone scan

Several retrospective studies and meta-analyses describe the utility of [^{18}F]FDG PET in sarcoma clinical practice. It is recommended as a part of the clinical work-up for a patient undergoing diagnosis, disease staging, and treatment planning [21–32]. Numerous studies describe [^{18}F]FDG PET utility in both soft tissue and bone tumors as well as rhabdomyosarcomas and Ewing's tumors in the pediatric population [33–37].

Tumor grade describes the probability of a tumor to exhibit malignant biological behavior. This implies patient outcome and survival. Following early studies in mixed sarcoma populations, additional studies have correlated patient prognosis with [^{18}F]FDG PET tumor uptake measures prior to therapy. These have established [^{18}F]FDG PET imaging in sarcomas as an independent biomarker for tumor risk stratification [30, 38–44]. Additional refinements in imaging techniques such as tumor uptake measures by dual-time point imaging, reporting tumor SUV_{max} versus total lesion glycolysis, necrosis volume, and combination with MR

imaging characteristics may provide improvements in prognostic capabilities [45–51].

Several prospective and retrospective studies have described histologic type determined from the utility of [^{18}F]FDG PET in sarcoma diagnosis. In soft tissue sarcoma, this imaging can reliably distinguish low-grade from high-grade tumors [52–54]. There is less ability to discriminate benign from low-grade tumors or intermediate-grade types from either high-grade or low-grade processes. Low-grade tumors are often difficult to distinguish through histologic criteria as well. Combinale et al. found that [^{18}F]FDG PET could be used to identify malignant transformation in patients with neurofibromatosis type 1 (NF1) [55]. This finding implies that [^{18}F]FDG PET could be used for other benign mesenchymal tumor conditions such as enchondromatoses and Paget's disease where malignant transformation is a potential occurrence in existing masses. [^{18}F]FDG PET has been used for effective tumor staging. It can be used to identify bone and soft tissue metastases and nodal metastases in those types where they occur (epithelioid and synovial sarcomas). While lung metastases are the most common site of metastases in patients with high-grade tumors, these are often small and are not visualized on [^{18}F]FDG PET. For this reason, a complete staging examination for both soft tissue and bony sarcomas also consists of a high-resolution contrast chest CT scan.

Additionally, special features and [^{18}F]FDG uptake are related to specific histologic types. For example, the atypical lipomas and the low-grade liposarcomas may have very similar tissue features and biological behavior. They often result in repeated local recurrence; nevertheless, in a large mass, the [^{18}F]FDG appearance can be significant for identifying small areas of high-grade de-differentiation, which can lead to a much worse outcome than the low-grade majority of the tumor mass composition. Figure 4 shows several [^{18}F]FDG PET examples of primary sarcoma tumors.

The [^{18}F]FDG image can also be helpful in identifying areas for diagnostic biopsy. Soft tissue sarcomas can be highly heterogeneous in their histologic characteristics, a feature which often confers heterogeneity in [^{18}F]FDG spatial uptake distribution. These unique tumor features may account for high levels of treatment resistance and variable responses to multimodality therapy. Spatial heterogeneity in sarcoma uptake has been shown to be independently predictive of patient outcome. This finding reported by Eary et al. found that baseline [^{18}F]FDG in diagnostic scans and tumor grade were somewhat weaker in outcome prediction, suggesting that new methods for incorporating [^{18}F]FDG tumor uptake distribution and for incorporating SUV into diagnostic methods for sarcomas can provide significant tumor prognostic information [56]. Additional image analyses such as texture feature extraction may also provide important diagnostic and prognostic information [57]. Figure 5 shows several tumors with high levels of [^{18}F]FDG uptake heterogeneity.

Sarcoma Treatment

Soft tissue sarcoma treatment plans are determined primarily by tumor grade. Large intermediate-grade and high-grade soft tissue sarcomas often receive neoadjuvant doxorubicin-based chemotherapy with or without preoperative radiation. After resection, if a response was obtained based on percent tumor necrosis in the resected tumor, adjuvant therapy is started. If an adequate response was not obtained, an alternative regimen usually replaces the ineffective treatment. Bone tumors are also treated through clinical protocols that have varying durations for neoadjuvant treatment, depending on patient age. Pediatric patients receive the most intense therapy, which yields good long-term outcome rates. Ewing's sarcoma patients also participate in protocol studies, and therapy with bone marrow transplant is considered in some advanced cases.

[^{18}F]FDG in Sarcoma Restaging and Treatment Response

A review of cancer treatment response for sarcoma as with other cancers begins with consideration of the pathological basis of the tumor process. Sarcomas are complex pathobiologic processes that may exhibit a wide range of blood flow, cell proliferation rate, cell viability, inflammation, pH, oxygenation, and numerous other processes. Because of these

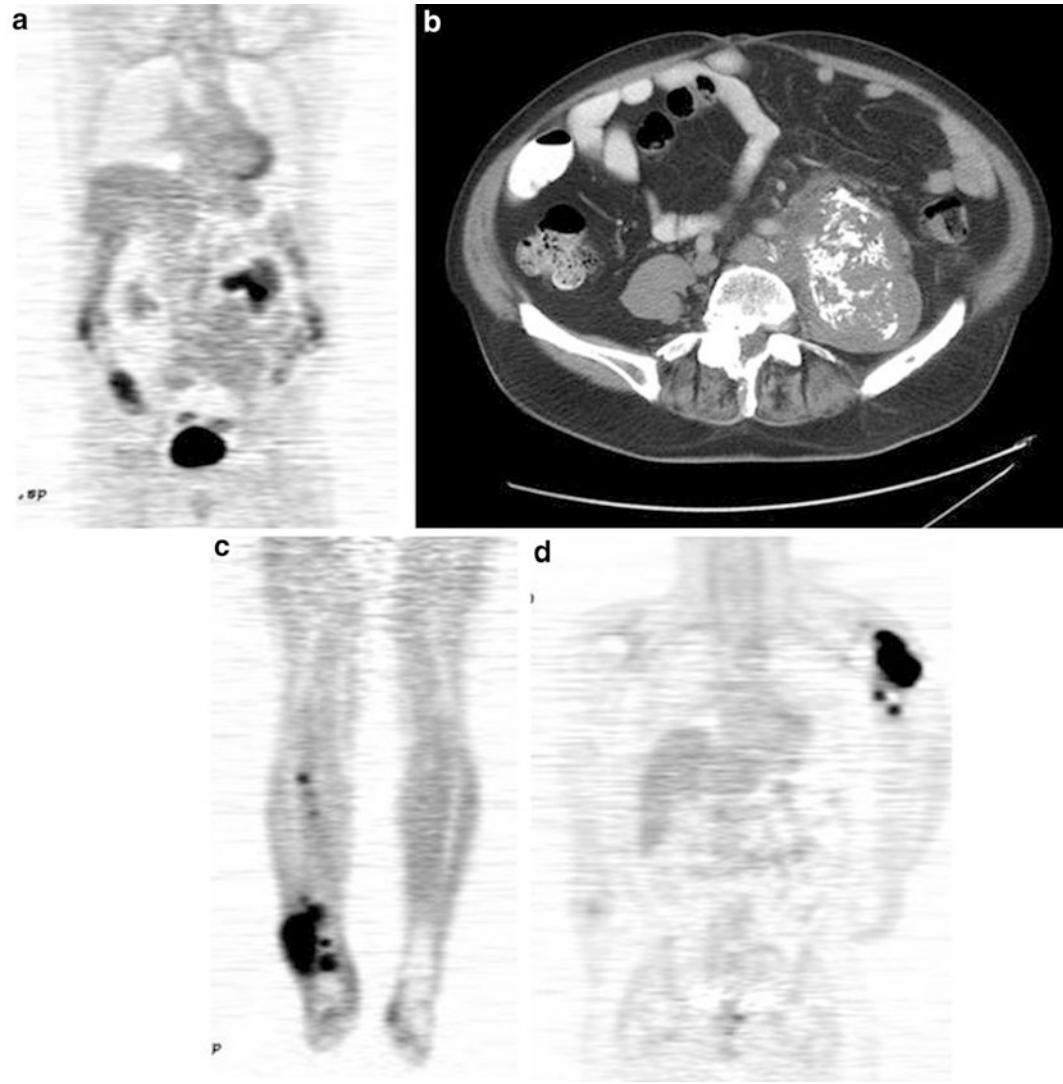

Fig. 4 Primary sarcoma presentations. (**a** and **b**) [^{18}F]FDG PET and contrast CT of a patient with an unusual calcifying abdominal liposarcoma. (**c**) [^{18}F]FDG PET right ankle Ewing's sarcoma, [**d**] [^{18}F]FDG PET left proximal humerus high grade undifferentiated soft tissue sarcoma with nodular extensions

processes, treatment response can differ significantly from a standard treatment combination or from treatments with different mechanisms of action. The ability of [^{18}F]FDG PET to identify treatment response is an important goal for the sarcoma patient population.

These tumors often do not change size in response to neoadjuvant chemotherapy because they can be composed of tissue elements that do not change in tumor response or undergo very slow changes in size reduction, such as in bone, cartilage, scar, and myxoid areas. Consequently, the RECIST criteria for treatment response do not apply well to this group, and [^{18}F]FDG has an advantage, as described by Evelevitch [58]. In this work, a 60% decrease in tumor [^{18}F]FDG uptake compared to baseline had a sensitivity of 100% and a specificity of 71% for histologic response, whereas RECIST criteria for response applied to the same group showed a sensitivity of 25% and a specificity of 100% [59, 60]. In sarcoma clinical practice, tumor treatment response assessments must provide information on the nature and timing of response.

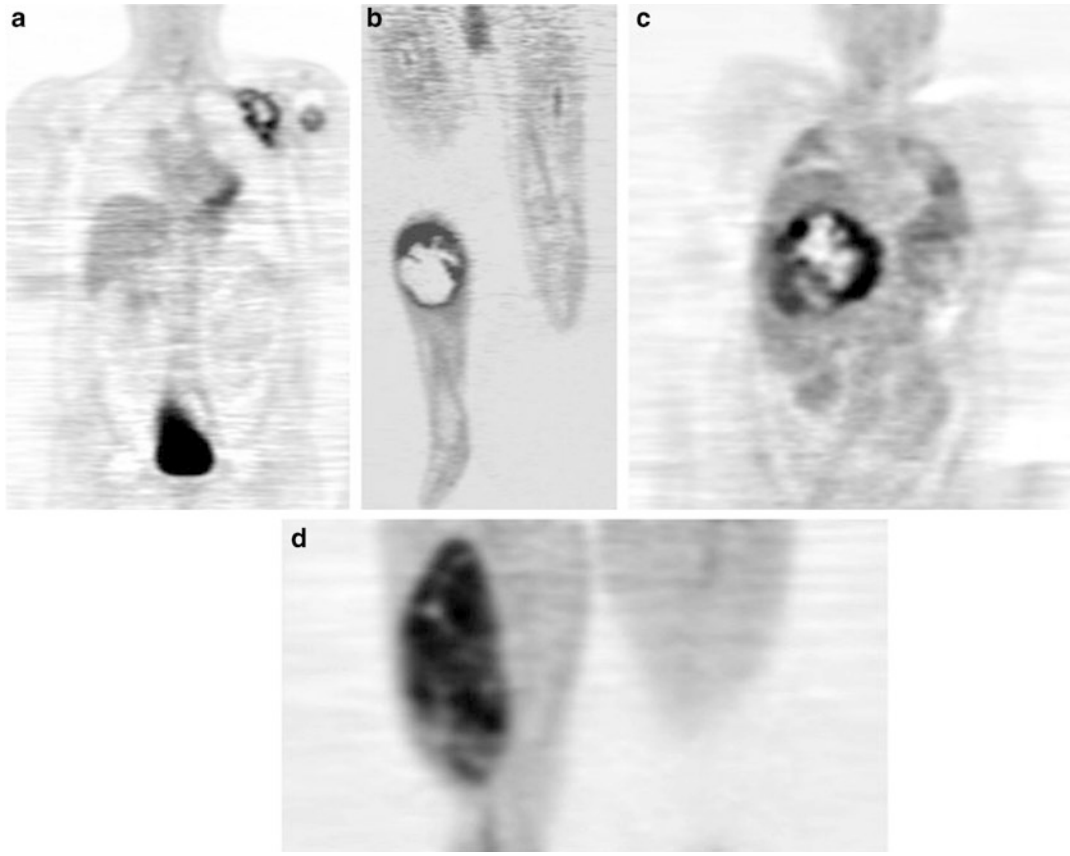

Fig. 5 (**a-d**) Primary sarcomas with high levels of spatial heterogeneity in [^{18}F]FDG uptake

Since clinical and histopathological response evaluations can be subjective, imaging tumor response quantitatively can provide clinically relevant objective information for treatment planning. For sarcoma patients where treatment choices are limited and often highly toxic, newer therapies that are directed at specific molecular targets may be cytostatic and result in tumor growth arrest, which can be observed effectively with [^{18}F]FDG PET. These changes may indicate effective therapy for a patient, as opposed to direct cell killing mechanisms and tumor shrinkage, and they may indicate improved patient outcome [61].

Tumor cellular necrosis fraction is considered the hallmark of treatment response to chemotherapy in sarcomas; however, overinterpretation of tumor cellular necrosis in a tumor specimen may result in cases where necrosis was present as a distinguishing feature of the primary tumor. Figure 6 shows an example of a primary sarcoma where significant necrosis is present prior to therapy. Scarring is a common treatment response and is also common in radiation treatment. Compared to necrosis, scarring as a treatment response is metabolically active and can cause significant [^{18}F]FDG uptake. In cases where granulation tissue formation precedes scarring, the inflammatory cells present may also elevate the apparent tumor bed tissue metabolism. Activated white cells can show as much as a tenfold difference in [^{18}F]FDG uptake, complicating image interpretation. An important part of treatment response interpretation in sarcoma is identifying the treatment agent mechanism, tumor subtype, and timing of the scan observation in relation to the course and type of treatment. Early after therapy, observations may reveal very different findings from those obtained after the biological mechanisms involved in

Fig. 6 Primary pelvic sarcoma with a large central area of tumor necrosis at presentation

treatment response have reached a more static state. Radiation responses to tumor and surrounding tissues may have very different timescales in relation to the end of the final therapy response. Early detection of treatment response that indicates improved patient outcome with newer therapies is an area of active research.

Many groups advocate the use of the [^{18}F]FDG PET tumor SUV to measure sarcoma uptake and to monitor treatment response [58, 61]. If the [^{18}F]FDG PET study is performed in a standard and consistent manner, the SUV is a robust value for comparison of one imaging study to another in the same patient at a later time and between patients in different groups. The optimum parameters for [^{18}F]FDG imaging in cancer were described in a report of a National Cancer Institute consensus committee where standard techniques for the use of [^{18}F]FDG as a biomarker for cancer treatment are presented [62]. The use of [^{18}F]FDG PET as a biomarker or surrogate endpoint for patient outcome is the basis for clinical research studies that determine the sensitivity and specificity of the method for following response to treatment and for assessing normal tissue damage as a result of treatment. Few effective treatment strategies exist for sarcoma, yet there is a great potential for new therapy strategies. [^{18}F]FDG PET can be a powerful tool for noninvasive treatment effectiveness evaluation [63–66].

The most dramatic example of [^{18}F]FDG PET as a biomarker for treatment response assessment is in gastrointestinal stromal tumors (GISTs) treated with Gleevec. GISTs are [^{18}F]FDG avid and can yield impressive PET images. Goerres et al. found that median survival of patients who demonstrated an [^{18}F]FDG PET response was 100% at 2 years compared to a group with residual tumor uptake after treatment. The study also demonstrated ability to separate patients by time to tumor progression based on [^{18}F]FDG tumor uptake levels [67].

Early response to Gleevec in the GIST population detected by [^{18}F]FDG PET has also been shown. As much as a 65% decrease in tumor [^{18}F]FDG uptake was demonstrated at the end of 1 week of effective therapy, and as high as a 95% response detected by 1 month after treatment initiation has been found by other groups. Response detection using CT criteria was less accurate, including no significant CT responses noted in [^{18}F]FDG-responsive patients [68–73]. [^{18}F]FDG PET imaging for GIST patients at baseline to observe for maximum tumor activity levels and for accurate staging is recommended. Repeat imaging is suggested in the first month after therapy initiation to observe response and to predict treatment effect. Another image may be helpful if treatment resistance is suspected and if a new baseline tumor uptake and location for treatment observation need to be established. [^{18}F]FDG imaging for GIST treatment response evaluation has been incorporated into the guidelines for GIST management determined by an international consensus conference [74].

Treatment response in other sarcomas using [^{18}F]FDG PET has been demonstrated in a number of studies. Soft tissue sarcomas represent the majority of sarcomas that occur in adults. Treatment response imaging for this group of patients is emerging [75–79]. In an extremity soft tissue sarcoma group treated with adriamycin-based neoadjuvant chemotherapy, Scheutze et al. showed that

separating patients by their [^{18}F]FDG response (>40%) showed a significant difference in survival for each of the groups [80]. Patients in the [^{18}F]FDG PET nonresponse group had a 90% risk of disease recurrence at 4 years compared to [^{18}F]FDG responders. These data, and that of others, may indicate the effectiveness and survival increase in soft tissue sarcoma patients treated with neoadjuvant chemotherapy prior to tumor resection. Figure 7 shows an example of a patient who had a treatment response documented by [^{18}F]FDG PET for neurofibrosarcoma in the base of the neck. This imaging technique may be useful for patients who have tumor resistance during the course of therapy and, therefore, might benefit from treatment intensification or early resection.

A similar finding was shown in Ewing's sarcoma population reported by Hawkins et al. [81]. Patients whose tumors increased SUV ratios between the baseline and pre-resection (after neoadjuvant chemotherapy) scans had significantly improved survival. In the future, good responders may be identified for less toxic treatment protocols. Studies in imaging osteosarcoma for treatment response have also been conducted. Early studies by Schulte et al. showed that changes in tumor [^{18}F]FDG uptake correlated with tumor necrosis levels in patients treated with neoadjuvant chemotherapy. Implications for limb salvage surgery were described because such complex tumor resection procedures might not be considered in nonresponders [82]. Others have recently shown similar results for [^{18}F]FDG imaging in osteosarcoma [83, 84].

Pediatric sarcomas are usually bony tumors, but they have been separated in studies because the treatment for pediatric patients differs compared to protocols for adults. Similar to their findings in Ewing's sarcomas in this mixed group of osteosarcoma and Ewing's sarcoma patients, Hawkins et al. found that the ratios in [^{18}F]FDG uptakes correlated with histologic response [85]. Noting a need for prospective imaging studies to be conducted in the pediatric sarcoma populations, both Franzius et al. and McCarville et al. published data on small pediatric sarcoma subgroups to demonstrate the clinical utility of [^{18}F]FDG imaging [86, 87]. The latter group included a rhabdomyosarcoma subgroup, a tumor subtype where most patients are treated under cooperative group therapy protocols. Correlation of longer survival with [^{18}F]FDG changes in response to therapy in a large pooled patient group retrospective study in patients with rhabdomyosarcomas has been published showing similar results.

[^{18}F]FDG imaging in treatment response can make a significant contribution to sarcoma patient care in identifying clinically relevant responses, or a lack thereof, and in providing predictive information for patient outcome. Although sarcomas are a less

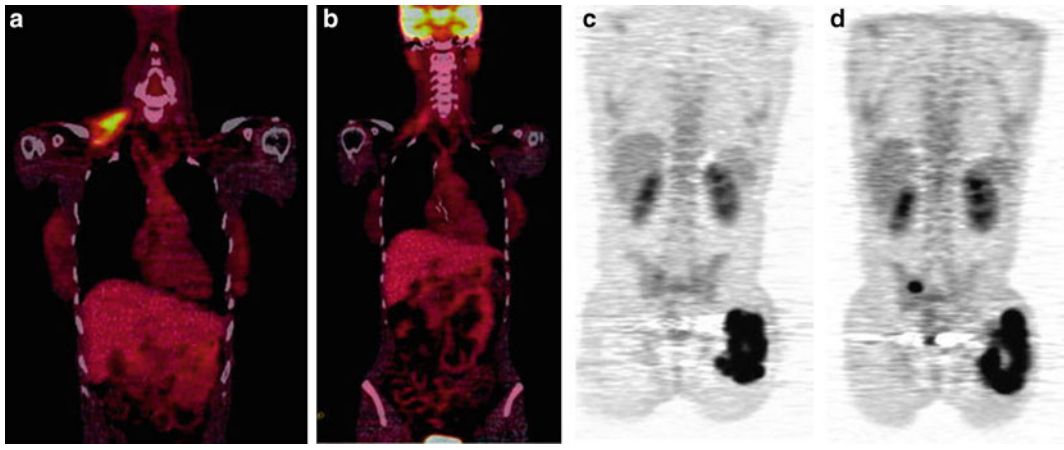

Fig. 7 Two examples of sarcoma tumor treatment [^{18}F]FDG PET responses. Shown in (**a**) is a patient with a right neck base malignant nerve sheath prior to neoadjuvant chemotherapy. (**b**) Response in base of neck tumor. (**c**) [^{18}F]FDG PET image of a patient with a large high grade proximal thigh tumor. (**d**) Lack of response, with sacral metastasis development

frequent form of malignancy in the population, they affect the entire human age span, and they constitute a large number of affected individuals in aggregate. Currently, treatment for the more aggressive high-grade tumors and for locally recurrent low-grade tumors often results in less than optimum treatment outcomes. Future clinical trials for newer treatment combinations for sarcoma patients will benefit from the incorporation of [^{18}F]FDG PET imaging treatment response information as a part of their treatment strategies, as they have for patients with other cancer types. For the individual patient, [^{18}F]FDG PET can provide critical information about treatment response and indicate further treatment planning. Increasingly for patients with standard therapy refractory disease, [^{18}F]FDG PET has been effective in identifying response to newer combination treatments and experimental therapy clinical trials. Recent experience described by Andreou et al. demonstrated that [^{18}F]FDG PET SUV_{max} in soft tissue sarcoma response to combination neoadjuvant isolated limb perfusion and TNF was correlated with response [88]. Similar imaging results have been reported in trials with sunitinib in extraskeletal myxoid chondrosarcoma [89], desmoid tumors with imatinib [90], insulin-like growth factor 1 in Ewing's sarcoma [91], and regional hyperthermia for soft tissue sarcomas [92]. Often these imaging observed responses predicted overall survival [93, 94].

Although currently there are no specific recommendations for [^{18}F]FDG PET in sarcoma patient care, the findings from the previously summarized reports indicate that baseline [^{18}F]FDG PET is important for contributing information for disease grade and staging that complements other imaging and histologic diagnostic information. This information aids in treatment planning and sets the baseline quantitation for tumor metabolic activity for treatment response assessment. Treatment response assessment with [^{18}F]FDG PET recommendations would be similar to those in other solid tumors. Approximately every 3 months on treatment, or when a change in treatment is envisioned, [^{18}F]FDG PET imaging results can be especially helpful when complete response or treatment nonresponse is suspected, as it provides objective information on tumor viability. Table 6 describes suggestions for sarcoma evaluation and treatment response imaging.

Table 6 Suggested lines of imaging procedures for sarcomas in patient care

Staging	***Soft tissue sarcomas***	***Bone sarcomas***
	MR of tumor region	MR and plain x-ray of tumor area
	[^{18}F]FDG PET	[^{18}F]FDG PET and ^{18}F-fluoride PET
	Whole body	Whole body
	^{99m}Tc-MDP bone scan	^{99m}Tc-MDP bone scan
	Whole body	Whole body
	Lung CT with contrast	Lung CT with contrast
Treatment response		
	MR of tumor region	MR of tumor region
	[^{18}F]FDG PET	[^{18}F]FDG PET and ^{18}F-fluoride PET
	Whole body	Whole body
	^{99m}Tc-MDP bone scan	^{99m}Tc-MDP bone scan
	Whole body if positive at baseline	If lungs positive at baseline
	Lung CT with contrast	Lung CT with contrast

PET/MR imaging experience in sarcomas is emerging. Current reports indicate that potential utility in sarcoma surgical resection planning may be improved with the better tumor edge detection provided by this imaging combination [95].

Other PET radiopharmaceuticals that are more specific than [^{18}F]FDG for biologically relevant aspects of sarcomas are under investigation in the sarcoma population. Determination of levels of tumor hypoxia is a measurement with clinical significance for many tumors, including sarcoma [96, 97]. Hypoxia is known to confer resistance to both radiotherapy and chemotherapy in sarcomas. Most sarcomas have some level of hypoxia present that confers treatment resistance. Newer therapies that target hypoxic tumor tissues after identification of these regions may improve patient outcome. PET radiopharmaceuticals designed to quantify tumor proliferation will also play an important role in sarcoma patient diagnosis and treatment assessment [98, 99]. Since sarcomas are a highly variable group of tumors, with similarly variable clinical outcomes, their cellular proliferation levels likely indicate increased risk of metastasis and poor clinical

outcome. Sarcoma patients are likely to benefit from these more biologically specific imaging techniques that may provide insight regarding treatment effectiveness. Molecular imaging research efforts in PET are directed toward identifying tumor characteristics that can be used to define patient risk for aggressive disease behavior and for noninvasive treatment monitoring.

References

1. Pisters PW, Leung DH, Woodruff J, et al. Analysis of prognostic factors in 1,041 patients with localized soft tissue sarcomas of the extremities. J Clin Oncol. 1996;14:1679–89.
2. Gadgeel SM, Harlan LC, Zeruto CA, et al. Patterns of care in a population-based sample of soft tissue sarcoma patients in the United States. Cancer. 2009; 115:2744–54.
3. Salas S, Stoeckle E, Collin F, et al. Superficial soft tissue sarcomas (S-STS): a study of 367 patients from the French Sarcoma Group (FSG) database. Eur J Cancer. 2009;45:2091–102.
4. Engellau J, Bendahl PO, Persson A, et al. Improved prognostication in soft tissue sarcoma: independent information from vascular invasion, necrosis, growth pattern, and immunostaining using wholetumor sections and tissue microarrays. Hum Pathol. 2005;36: 994–1002.
5. Eary JF. PET-CT and SPECT-CT of malignant bone tumors and PET and PET-CT in soft tissue sarcomas. In: von Schulthess GK, editor. Molecular anatomic imaging: PET-CT and SPECT-CT integrated modality imaging. 2nd ed. Schmid DT, CD-ROM editor. Philadelphia: Lippincott Williams & Wilkins; 2007. p. 443–9,456–67.
6. Coley HM, Verrill MW, Gregson SE, et al. Incidence of P-glycoprotein overexpression and multidrug resistance (MDR) reversal in adult soft tissue sarcoma. Br J Cancer. 2000;36:881–8.
7. Komdeur R, Plaat BE, van der Graaf WT, et al. Expression of P-glycoprotein, multidrug resistance-associated protein 1, and lung resistance-related protein in human soft tissue sarcomas before and after hyperthermic isolated limb perfusion with tumor necrosis factor-alpha and melphalan. Cancer. 2001; 91:1940–8.
8. Komdeur R, Plaat BE, van der Graaf WT, et al. Expression of multidrug resistance proteins, P-gp, MRP1 and LRP, in soft tissue sarcomas analyzed according to their histological type and grade. Eur J Cancer. 2003;39:909–16.
9. Komdeur R, Molenaar WM, Zwart N, et al. Multidrug resistance proteins in primary and metastatic soft-tissue sarcomas: down-regulation of P-glycoprotein during metastatic progression. Anticancer Res. 2004;24: 291–5.
10. Oda Y, Saito T, Tateishi N, et al. ATP-binding cassette superfamily transporter gene expression in human soft tissue sarcomas. Int J Cancer. 2005;114:854–62.
11. Helman LJ, Meltzer P. Mechanisms of sarcoma development. Nat Rev Cancer. 2003;3:685–94.
12. Coindre JM, Terrier P, Guillou L, et al. Predictive value of grade for metastasis development in the main histologic types of adult soft tissue sarcomas: a study of 1240 patients from the French Federation of Cancer Centers Sarcoma Group. Cancer. 2001;91:1914–26.
13. Deyrup AT, Weiss SW. Grading of soft tissue sarcomas: the challenge of providing precise information in an imprecise world. Histopathology. 2006;48:42–50.
14. Wunder JS, Healey JH, Davis AM, Brennan MF. A comparison of staging systems for localized extremity soft tissue sarcoma. Cancer. 2000;88:2721–30.
15. International Union Against Cancer, Spiess B, Beahrs OH, Hermanek P, Hutter RVP, Scheibe O, Sobin LH, Wagner G, editors. TNM Atlas: illustrated guide to the TNM/pTNM classification of malignant tumors. 3rd ed., 2nd rev. Berlin: Springer; 1992.
16. Kim MS, Lee SY, Lee TR, et al. Prognostic nomogram for predicting the 5-year probability of developing metastasis after neoadjuvant chemotherapy and definitive surgery for AJCC stage IT extremity osteosarcoma. Ann Oncol. 2009;20:955–60.
17. Antunes M, Bernardo J, Salete M, et al. Excision of pulmonary metastases of osteogenic sarcoma of the limbs. Eur J Cardiothorac Surg. 1999;15:592–6.
18. Iagaru A, Goris ML. Rhabdomyosarcoma diffusely metastatic to the bone marrow: suspicious findings on ^{99m}Tc-MDP bone scintigraphy confirmed by ^{18}F-FDG PET/CT and bone marrow biopsy. Eur J Nucl Med Mol Imaging. 2008;35:1746.
19. Goto Y, Ihara K, Kawauchi S, et al. Clinical significance of thallium-201 scintigraphy in bone and soft tissue tumors. J Orthop Sci. 2002;7:304–12.
20. McCarville MB, Barton EH, Cameron JR, et al. The cause and clinical significance of central tumor photopenia on thallium scintigraphy of pediatric osteosarcoma of the extremity. AJR Am J Roentgenol. 2007;188:572–8.
21. Jackson T, Mosci C, von Eyben R, et al. Combined ^{18}F-NaF and ^{18}F-FDG PET/CT in the evaluation of sarcoma patients. Clin Nucl Med. 2015;40:720–4.
22. Amini B, Jessop AC, Ganeshan DM, et al. Contemporary imaging of soft tissue sarcomas. J Surg Oncol. 2015;111:496–503.
23. Costelloe CM, Chuang HH, Madewell JE. FDG PET/CT of primary bone tumors. AJR Am J Roentgenol. 2014;202: W521–31.
24. Choi YY, Kim JY, Yang SO. PET/CT in benign and malignant musculoskeletal tumors and tumor-like conditions. Semin Muscoloskelet Radiol. 2014;18: 133–48.
25. Quartuccio N, Fox J, Kuk D, et al. Pediatric bone sarcoma: diagnostic performance of ^{18}F-FDG PET/CT versus conventional imaging for initial staging and follow-up. AJR Am J Roentgenol. 2015;204: 153–60.

26. Fuglø HM, Jørgensen SM, Loft A, et al. The diagnostic and prognostic value of ^{18}F-FDG PET/CT in the initial assessment of high-grade bone and soft tissue sarcoma. A retrospective study of 89 patients. Eur J Nucl Med Mol Imaging. 2012;39:1416–24.
27. Etchebehere EC, Hobbs BP, Milton DR, et al. Assessing the role of ^{18}F-FDG PET and ^{18}F-FDG PET/CT in the diagnosis of soft tissue musculoskeletal malignancies: a systematic review and meta-analysis. Eur J Nucl Med Mol Imaging. 2016;43:860–70.
28. Quartuccio N, Treglia G, Salsano M, et al. The role of Fluorine-18-Fluorodeoxyglucose positron emission tomography in staging and restaging of patients with osteosarcoma. Radiol Oncol. 2013;47:97–102.
29. Kubo T, Furuta T, Johan MP, Ochi M. Prognostic significance of ^{18}F-FDG PET at diagnosis in patients with soft tissue sarcoma and bone sarcoma; systematic review and meta-analysis. Eur J Cancer. 2016;58: 104–11.
30. Sheikhbahaei S, Marcus C, Hafezi-Nejad N, et al. Value of FDG PET/CT in patient management and outcome of skeletal and soft tissue sarcomas. PET Clin. 2015;10:375–93.
31. Fendler WP, Chalkidis RP, Ilhan H, et al. Evaluation of several FDG PET parameters for prediction of soft tissue tumour grade at primary diagnosis and recurrence. Eur Radiol. 2015;25:2214–21.
32. Liu F, Zhang Q, Zhu D, et al. Performance of positron emission tomography and positron emission tomography/computed tomography using fluorine-18-fluorodeoxyglucose for the diagnosis, staging, and recurrence assessment of bone sarcoma: a systematic review and meta-analysis. Medicine (Baltimore). 2015;94:e1462.
33. Norman G, Fayter D, Lewis-Light K, et al. An emerging evidence base for PET-CT in the management of childhood rhabdomyosarcoma: systematic review. BMJ Open. 2015;5:e006030.
34. Eugene T, Corradini N, Carlier T, et al. ^{18}F-FDG-PET/CT in initial staging and assessment of early response to chemotherapy of pediatric rhabdomyosarcomas. Nucl Med Commun. 2012;33:1089–95.
35. Johnsen B, Boye K, Rosendahl K, et al. F-18-FDG PET-CT in children and young adults with Ewing sarcoma diagnosed in Norway during 2005–2012: a national population-based study. Clin Physiol Funct Imaging. 2016;36(6):441–446.
36. Newman EN, Jones RL, Hawkins DS. An evaluation of [F-18]-fluorodeoxy-D-glucose positron emission tomography, bone scan, and bone marrow aspiration/biopsy as staging investigations in Ewing sarcoma. Pediatr Blood Cancer. 2013;60:1113–7.
37. Guimarães JB, Rigo L, Lewin F, Emerick A. The importance of PET/CT in the evaluation of patients with Ewing tumors. Radiol Bras. 2015;48:175–80.
38. Eary JF, O'Sullivan F, Powitan Y, et al. Sarcoma tumor FDG uptake measured by PET and patient outcome: a retrospective analysis. Eur J Nucl Med Mol Imaging. 2002;29:1149–54.
39. Andersen KF, Fuglo HM, Rasmussen SH, et al. Semi-quantitative calculations of primary tumor metabolic activity using F-18 FDG PET/CT as a predictor of survival in 92 patients with high-grade bone or soft tissue sarcoma. Medicine (Baltimore). 2015;94:e1142.
40. Casey DL, Wexler LH, Fox JJ, et al. Predicting outcome in patients with rhabdomyosarcoma: role of [^{18}F] fluorodeoxyglucose positron emission tomography. Int J Radiat Oncol Biol Phys. 2014;90:1136–42.
41. Fendler WP, Chalkidis RP, Ilhan H, et al. Evaluation of several FDG PET parameters for prediction of soft tissue tumour grade at primary diagnosis and recurrence. Eur Radiol. 2015;2598:2214–21.
42. Chang KJ, Lim I, Park JY, et al. The role of ^{18}F-FDG PET/CT as a prognostic factor in patients with synovial sarcoma. Nucl Med Mol Imaging. 2015;49:33–41.
43. Skamene SR, Rakheja R, Dahlstrom KR, et al. Metabolic activity measured on PET/CT correlates with clinical outcomes in patients with limb and girdle sarcomas. J Surg Oncol. 2014;109:410–4.
44. Yoshikawa K, Shimada M, Kurita N, et al. Efficacy of PET-CT for predicting the malignant potential of gastrointestinal stromal tumors. Surg Today. 2013;43: 1162–7.
45. Byun BH, Kim SH, Lim SM, et al. Prediction of response to neoadjuvant chemotherapy in osteosarcoma using dual-phase^{18}F-FDG PET/CT. Eur Radiol. 2015;25:2015–24.
46. Choi ES, Ha SG, Kim HS, et al. Total lesion glycolysis by ^{18}F-FDG PET/CT is a reliable predictor of prognosis in soft-tissue sarcoma. Eur J Nucl Med Mol Imaging. 2013;40:1839–42.
47. Hong SP, Lee SE, Choi YL, et al. Prognostic value of ^{18}F-FDG PET/CT in patients with soft tissue sarcoma: comparisons between metabolic parameters. Skelet Radiol. 2014;43:641–8.
48. Rakheja R, Makis W, Tulbah R, et al. Necrosis on FDG PET/CT correlates with prognosis and mortality in sarcomas. AJR Am J Roentgenol. 2013;201:170–7.
49. Byun BH, Kong CB, Lim I, et al. Combination of ^{18}F-FDG PET/CT and diffusion-weighted MR imaging as a predictor of histologic response to neoadjuvant chemotherapy: preliminary results in osteosarcoma. J Nucl Med. 2013;54:1053–9.
50. Byun BH, Kong CB, Lim I, et al. Early response monitoring to neoadjuvant chemotherapy in osteosarcoma using sequential ^{18}F-FDG PET/CT and MRI. Eur J Nucl Med Mol Imaging. 2014;41:1553–62.
51. Nose H, Otsuka H, Otomi Y, et al. Correlations between F-18 FDG PET/CT and pathological findings in soft tissue lesions. J Med Invest. 2013;60 (3–4):184–90.
52. Eary JF, Conrad EU, Bruckner JD, et al. Quantitative [F-18]fluorodeoxyglucose positron emission tomography in pretreatment and grading of sarcoma. Clin Cancer Res. 1998;4:1215–20.
53. Nieweg OE, Pruirn J, van Ginkel RJ, et al. Fluorine-18-fluorodeoxyglucose PET imaging of soft-tissue sarcoma. J Nucl Med. 1996;37:257–61.

54. Griffet LK, Dehdashti F, McGuire AH, et al. PET evaluation of soft-tissue masses with f!uorine-18 fluoro-2-deoxy-D-glucose. Radiology. 1992;182:185–94.
55. Combemale P, Valeyrie-Allanore L, Giammarile F, et al. Utility of ^{18}F-FDG PET with a semi-quantitative index in the detection of sarcomatous transformation in patients with neurofibromatosis type 1. PLoS ONE. 2014;9(2), e85954.
56. Eary JF, O'Sullivan F, O'Sullivan J, Conrad EU. Spatial heterogeneity in sarcoma ^{18}F-FDG uptake as a predictor of patient outcome. J Nucl Med. 2008;49: 1973–9.
57. Vallières M, Freeman CR, Skamene SR, El Naqa I. A radiomics model from joint FDG-PET and MRI texture features for the prediction of lung metastases in soft-tissue sarcomas of the extremities. Phys Med Biol. 2015;60:5471–96.
58. Evilevitch V, Weber WA, Tap WD, et al. Reduction of glucose metabolic activity is more accurate than change in size at predicting histopathologic response to neoadjuvant therapy in high-grade softtissue sarcomas. Clin Cancer Res. 2008;14:715–20.
59. Benjamin RS, Choi H, Macapinlac HA, et al. We should desist using RECIST, at least in GIST. J Clin Oncol. 2007;25:1760–4.
60. Schuetze SM, Baker LH, Benjamin RS, Canetta R. Selection of response criteria for clinical trials of sarcoma treatment. Oncologist. 2008;13 Suppl 2:32–40.
61. Kelloff GJ, Hoffman JM, Johnson B, et al. Progress and promise of FDG-PET imaging for cancer patient management and oncologic drug development. Clin Cancer Res. 2005;11:2785–808.
62. Shankar LK, Hoffman JM, Bacharach S, et al. Consensus recommendations for the use of ^{18}F-FDG PET as an indicator of therapeutic response in patients in National Cancer Institute Trials. J Nucl Med. 2006;47:1059–66.
63. Benz MR, Allen-Auerbach MS, Eilber FC, et al. Combined assessment of metabolic and volumetric changes for assessment of tumor response in patients with soft-tissue sarcomas. J Nucl Med. 2008;49:1579–84.
64. Weber WA. Use of PET for monitoring cancer therapy and for predicting outcome. J Nucl Med. 2005;46: 983–95.
65. Jerusalem G, Belhocine TZ. Metabolic monitoring of chemosensitivity with ^{18}FDG PET. Methods Mol Med. 2005;111:417–40.
66. Larson SM, Erdi Y, Akhurst T, et al. Tumor treatment response based on visual and quantitative changes in global tumor glycolysis using PET-FDG imaging. The visual response score and the change in total lesion glycolysis. Clin Positron Imaging. 1999;2:159–71.
67. Goerres GW, Stupp R, Barghouth G, et al. The value of PET, CT and in-line PET/CT in patients with gastrointestinal stromal tumors: long-term outcome of treatment with imatinib mesylate. Eur J Nucl Med Mol Imaging. 2005;32:153–62.
68. Stroobants S, Goeminne J, Seegers M, et al. ^{18}FDG-Positron emission tomography for the early prediction of response in advanced soft tissue sarcoma treated with imatinib mesylate (Glivec). Br J Cancer. 2003; 39:2012–20.
69. Van den Abbeele AD, Badawi RD. Use of positron emission tomography in oncology and its potential role to assess response to imatinib mesylate therapy in gastrointestinal stromal tumors (GISTs). Eur J Cancer. 2002;38 Suppl 15:S60–5.
70. Antoch G, Kanja J, Bauer S, et al. Comparison of PET, CT, and dual-modality PET/CT imaging for monitoring of imatinib (STI571) therapy in patients with gastrointestinal stromal tumors. J Nucl Med. 2004;45:357–65.
71. Gayed I, Vu Y, Iyer R, et al. The role of ^{18}F-FDG PET in staging and early prediction of response to therapy of recurrent gastrointestinal stromal tumors. J Nucl Med. 2004;45:17–21.
72. Jager PL, Gietma JA, van der Graaf WT. Imatinib mesylate for the treatment of gastrointestinal stromal tumours: best monitored with FDG PET. Nucl Med Commun. 2004;25:433–8.
73. McAuliffe JC, Hunt KK, Lazar AJ, et al. A randomized, phase II study of preoperative plus postoperative imatinib in GIST: evidence of rapid radiographic response and temporal induction of tumor cell apoptosis. Ann Surg Oncol. 2009;16:910–9.
74. Blay JY, Bonvalot S, Casali P, et al. Consensus meeting for the management of gastrointestinal stromal tumors. Report of the GIST Consensus Conference of 20–21 March 2004, under the auspices of ESMO. Ann Oncol. 2005;16:566–78.
75. Schuetze SM. Imaging and response in soft tissue sarcomas. Hematol Oncol Clin N Am. 2005;19:471–87.
76. Schuetze SM. Utility of positron emission tomography in sarcomas. Curr Opin Oncol. 2006;18:369–73.
77. Hicks RJ. Functional imaging techniques for evaluation of sarcomas. Cancer Imaging. 2005;5:58–65.
78. Khamly KK, Hicks RJ, McArthur GA, Thomas DM. The promise of PET in clinical management and as a sensitive test for drug cytotoxicity in sarcomas. Expert Rev Mol Diagn. 2008;8:105–19.
79. Toner GC, Hicks RJ. PET for sarcomas other than gastrointestinal stromal tumors. Oncologist. 2008;13 Suppl 2:22–6.
80. Schuetze SM, Rubin BP, Vernon C, et al. Use of positron emission tomography in localized extremity soft tissue sarcoma treated with neoadjuvant chemotherapy. Cancer. 2005;103:339–48.
81. Hawkins DS, Schuetze SM, Butrynski JE, et al. [^{18}F] Fluorodeoxyglucose positron emission tomography predicts outcome for Ewing sarcoma family of tumors. J Clin Oncol. 2005;23:8828–34.
82. Schulte M, Brecht-Krauss D, Werner M, et al. Evaluation of neoadjuvant therapy response of osteogenic sarcoma using FDG PET. J Nucl Med. 1999;40:1637–43.
83. Sato J, Yanagawa T, Dobashi Y, et al. Prognostic significance of ^{18}F-FDG uptake in primary osteosarcoma after but not before chemotherapy: a possible association with autocrine motility factor/phosphoglucose isomerase expression. Clin Exp Metastasis. 2008;25:427–35.

84. Ye Z, Zhu J, Tian M, et al. Response of osteogenic sarcoma to neoadjuvant therapy: evaluated by ^{18}F-FDG-PET. Ann Nucl Med. 2008;22:475–80.
85. Hawkins DS, Rajendran JG, Conrad 3rd EU, et al. Evaluation of chemotherapy response in pediatric bone sarcomas by [F-18]-fluorodeoxy-n-glucose positron emission tomography. Cancer. 2002;94:3277–84.
86. Franzius C, Schober O. Assessment of therapy response by FDG PET in pediatric patients. Q J Nucl Med. 2003;47:41–5.
87. McCarville MB, Christie R, Daw NC, et al. PET/CT in the evaluation of childhood sarcomas. AIR Am J Roentgenol. 2005;184:1293–304.
88. Andreou D, Boldt H, Pink D, et al. Prognostic relevance of ^{18}F-FDG PET uptake in patients with locally advanced, extremity soft tissue sarcomas undergoing neoadjuvant isolated limb perfusion with TNF-α and melphalan. Eur J Nucl Med Mol Imaging. 2014;41:1076–83.
89. Stacchiotti S, Dagrada GP, Morosi C, et al. Extraskeletal myxoid chondrosarcoma: tumor response to sunitinib. Clin Sarcoma Res. 2012;2:22.
90. Kasper B, Dimitrakopoulou-Strauss A, Pilz LR, et al. Positron emission tomography as a surrogate marker for evaluation of treatment response in patients with desmoid tumors under therapy with imatinib. Biomed Res Int. 2013;2013:389672.
91. Hyun OJ, Luber BS, Leal JP, et al. Response to early treatment evaluated with ^{18}F-FDG PET and PERCIST 1.0 predicts survival in patients with Ewing sarcoma family of tumors treated with a monoclonal antibody to the insulin-like growth factor 1 receptor. J Nucl Med. 2016;57:735–40.
92. Fendler WP, Lehmann M, Todica A, et al. PET response criteria in solid tumors predicts progression-free survival and time to local or distant progression after chemotherapy with regional hyperthermia for soft-tissue sarcoma. J Nucl Med. 2015;56:530–7.
93. Herrmann K, Benz MR, Czernin J, et al. ^{18}F-FDG-PET/CT Imaging as an early survival predictor in patients with primary high-grade soft tissue sarcomas undergoing neoadjuvant therapy. Clin Cancer Res. 2012;18:2024–31.
94. Dharmarajan KV, Wexler LH, Gavane S, et al. Positron emission tomography (PET) evaluation after initial chemotherapy and radiation therapy predicts local control in rhabdomyosarcoma. Int J Radiat Oncol Biol Phys. 2012;84:996–1002.
95. Loft A, Jensen KE, Löfgren J, et al. PET/MRI for preoperative planning in patients with soft tissue sarcoma: a technical report of two patients. Case Rep Med. 2013;2013:791078.
96. Krohn KA, Link JM, Mason RP. Molecular imaging of hypoxia. J Nucl Med. 2008;49 Suppl 2:129S–48.
97. Rajendran JG, Wilson DC, Conrad EU, et al. [^{18}F] FMISO and [^{18}F]FDG PET imaging in soft tissue sarcomas: correlation of hypoxia, metabolism and VEGF expression. Eur J Nucl Med Mol Imaging. 2003; 30:695–704.
98. Tatum JL, Kelloff GJ, Gillies RJ, et al. Hypoxia: importance in tumor biology, noninvasive measurement by imaging, and value of its measurement in the management of cancer therapy. Int J Radiat Biol. 2006; 82:699–757.
99. Kelloff GJ, Krohn KA, Larson SM, et al. The progress and promise of molecular imaging probes in oncologic drug development. Clin Cancer Res. 2005;11:7967–85.

Suggested Reading

Helman U, Meltzer P. Mechanisms of sarcoma development. Nat Rev Cancer. 2003;3:685–94.
Kelloff GJ, Hoffman JM, Johnson B, et al. Progress and promise of FDG-PET imaging for cancer patient management and oncologic drug development. Clin Cancer Res. 2005a;11:2785–808.
Pisters PW, Leung DH, Woodruff J, Shi W, Brennan MF. Analysis of prognostic factors in 1,041 patients with localized soft tissue sarcomas of the extremities. J Clin Oncol. 1996;14:1679–89.
Schuetze SM, Baker LH, Benjamin RS, Canetta R. Selection of response criteria for clinical trials of sarcoma treatment. Oncologist. 2008;13 Suppl 2:32–40.

Diagnostic Applications of Nuclear Medicine: Malignant Melanoma

38

Andrew M. Scott, Marika Ciprotti, and Sze-Ting Lee

Abstract

Malignant melanoma was diagnosed in approximately 74,000 patients in 2015 in the USA. Melanoma accounts for about 3% of all skin cancers. Major parameters that impact prognosis include Breslow thickness, ulceration, tumor location, growth pattern, histological subtype, patient's age, gender, and tumor status of regional lymph nodes. Melanomas are staged using the American Joint Committee on Cancer (AJCC) TNM system, which has incorporated the histological status of SLN into its latest staging system version of cutaneous malignant melanoma.

In early stage melanoma (AJCC I–II), sentinel lymph node biopsy (SLNB) is the standard of care for nodal staging. Lymphoscintigraphy with SPECT/CT improves the detection of SLN. In AJCC stage I–II melanoma, [^{18}F]FDG PET/CT has poor sensitivity for the detection of nodal metastases but it is sensitive for the detection of distant metastases. In patients with AJCC stage III (regional nodal involvement) or stage IV disease (systemic metastases), [^{18}F]FDG PET/CT is useful to identify metastatic disease. PET imaging in melanoma patients should include the arms and legs, especially in patients whose primary lesions arise on extremities. False-negative results can occur with small skin and brain metastases, and lesions adjacent to the heart, kidneys, or urinary bladder.

Although [^{18}F]FDG PET/CT is more specific in the diagnosis of melanoma pulmonary metastases, chest CT is more sensitive. Most PET false negatives in recurrent disease are typically less than 1 cm in diameter and are mainly pulmonary and hepatic in location, or in the brain. [^{18}F]FDG PET/CT is useful in treatment monitoring of metastatic melanoma and in posttherapy surveillance.

Keywords

Melanoma • Imaging in melanoma • Malignant melanoma • Staging of melanoma • Sentinel lymph node biopsy in melanoma

Glossary

[^{18}F]FDG	2-Deoxy-2-[^{18}F]fluoro-D-glucose
^{18}F-FLT	3′-^{18}F-fluoro-3′-deoxythymidine
AJCC	American Joint Committee on Cancer
APC	Antigen-presenting cell

A.M. Scott (✉) • S.-T. Lee
Olivia Newton-John Cancer Research Institute and La Trobe University, Melbourne, VIC, Australia

Department of Molecular Imaging and Therapy, Austin Health, Melbourne, VIC, Australia
e-mail: Andrew.Scott@onjcri.org.au

M. Ciprotti
Global Clinical Research Oncology, Bristol-Myers Squibb, London, UK

© Springer International Publishing Switzerland 2017
H.W. Strauss et al. (eds.), *Nuclear Oncology*,
https://doi.org/10.1007/978-3-319-26236-9_24

bFGF	Basic fibroblast growth factor
BRAF	RAF serine-/threonine-specific protein kinase
Breslow thickness	A prognostic factor in cutaneous melanoma, based on description of how deeply tumor cells have invaded the skin (also called "Breslow depth")
c-KIT	A proto-oncogene encoding for tyrosine-protein kinase Kit (or CD117), also known as mast/stem cell growth factor receptor (SCFR)
CDK4	Cyclin-dependent kinase 4
CDKN2A	Cyclin-dependent kinase inhibitor 2A
ceCT	Contrast-enhanced computed tomography
CI	Confidence interval
Clark level	A staging system for cutaneous melanoma based on description of the level of anatomic invasion of the melanoma in the skin (generally used in conjunction with Breslow's depth)
COT	A mitogen-activated protein serine/threonine kinase involved in T-cell activation
CR	Complete response
CT	X-ray computed tomography
ERK	Extracellular signal-regulated kinase
FDA	United States Food and Drug Administration
GLUT	Glucose transporter family
HR	Hazard ratio, a statistical parameter used in survival analysis
IDO	Indoleamine 2,3-dioxygenase
IFN	Interferon
IGFR1	Insulin-like growth factor 1
LAG-3	Lymphocyte-activation gene 3
LDH	Lactate dehydrogenase
LS	Lymphoscintigraphy
M	Metastasis status according to the AJCC/UICC TNM staging system
MAGE	Melanoma-associated antigen gene
MAPK	Mitogen-activated protein kinase
MHC	Major histocompatibility complex
MRI	Magnetic resonance imaging
N	Lymph node status according to the AJCC/UICC TNM staging system
NCCN	National Comprehensive Cancer Network
NRAS	Oncogene encoding for a membrane protein that shuttles between the Golgi apparatus and the plasma membrane
ORR	Overall response rate
OS	Overall survival
PD-L1	Programmed death ligand
PDGF	Platelet-derived growth factor
PET	Positron emission tomography
PET/CT	Positron emission tomography/computed tomography
PFS	Progression-free survival
PFS	Progression-free survival
PI3K	Phosphatidylinositol 3-kinase
PlGF	Placental growth factor
PTEN	Gene encoding for the phosphatase and tensin homolog protein, a tumor suppressor (PTEN deletions indicate a poor prognosis)
RAF	Rapidly accelerated fibrosarcoma, related to retroviral oncogenes
RECIST	Response evaluation criteria in solid tumors
S-100	A low-molecular-weight calcium-binding protein expressed in melanomas, but also in other benign and malignant conditions
SLN	Sentinel lymph node
SLNB	Sentinel lymph node biopsy
SLNE	Sentinel lymph node excision
SPECT	Single photon emission computed tomography

SPECT/CT	Single photon emission computed tomography/computed tomography
SUV	Standardized uptake value
SUV_{max}	Standardized uptake value at point of maximum
T	Tumor status according to the AJCC/UICC TNM staging system
TGF	Transforming growth factor
TIM-3	T-cell immunoglobulin and mucin-domain containing-3
UICC	Union Internationale Contre le Cancer (International Union Against Cancer)
UV	Ultraviolet
VEGF	Vascular endothelial growth factor
WHO	World Health Organization

Contents

Epidemiology 1067

Risk Factors 1067

Pathogenesis 1068
Ras/Raf/MEK/Erk Pathway 1068
Immune Regulation 1068
Angiogenesis 1069

Tumor Histology 1069

Staging Systems for Melanoma 1069
Breslow Staging, AJCC Classification 1069

Treatment for Localized Melanoma 1070

Prognostic Factors 1070

Adjuvant Therapy 1073

Treatment of Metastatic Malignant Melanoma 1073
Targeted Therapies Against BRAF Mutations 1074
Immunotherapy 1074
Novel Targets and Combination Therapies 1076
c-KIT Inhibitors 1076
Antiangiogenic Therapy 1076
Apoptotic Therapy 1077

Role of Nuclear Medicine in Melanoma Patients 1077
Initial Staging of Primary Melanoma 1077

Conclusions 1097

References 1097

Epidemiology

Malignant melanoma is an increasingly common public health problem in many countries. It most often arises from the melanocytes found in the basal layer of the skin, although it can also derive from noncutaneous melanocytes such as those lining the choroidal layer of the eye, gastrointestinal and genitourinary mucosal surfaces, or the meninges. It accounts for about 3% of all skin cancers, with an annual increase in the order of 3–7% per year for fair-skinned Caucasian populations [1].

According to the World Health Organization (WHO), the number of melanoma cases worldwide is increasing faster than that of any other type of cancer. The highest incidence of melanoma occurs in Australia and New Zealand where the annual incidence rates are more than two to three times higher than those found in Canada, the USA, and the UK [2]. In Australia, it is the fourth most common cancer. Recently reported statistical data suggest that the risk of an individual being diagnosed with melanoma skin cancer by their 85th birthday is 1 in 18 (1 in 14 males and 1 in 23 females) [3]. In Europe, approximately 100,300 people were estimated to be diagnosed with melanoma in 2012. In the same year, 22,200 Europeans were estimated to have died from the disease [4]. In 2015, an estimated 73,870 patients were diagnosed with melanoma in the USA, and approximately 9,940 of them died of the disease [5]. Data from the USA and Europe show that the lifetime risk of developing malignant melanoma has increased from 1 in 800 individuals in 1960 to 1 in 74 individuals in 2000.

Risk Factors

The factors associated with an increased risk of developing melanoma remain incompletely understood, but people with a family history of melanoma, multiple benign or atypical nevi, and a previous melanoma are at the greatest risk for cutaneous melanoma. Inherited mutations in the cyclin-dependent kinase inhibitor 2A (CDKN2A) and cyclin-dependent kinase 4 (CDK4) genes,

which have been documented in some families with hereditary melanoma, confer a 60–90% lifetime risk of melanoma. Overall, CDKN2A mutations have been observed in approximately 25–40% of the members of melanoma-prone families. In addition, around one-half of families with three or more cases of melanoma show evidence of linkage to the 9p21 region [6]. According to the Surveillance, Epidemiology, and End Results Program of the National Cancer Institute (SEER), the rate of subsequent cutaneous melanomas among persons with a history of melanoma was more than ten times the rate of a first cutaneous melanoma among the general population [7].

Immunosuppression, sun sensitivity, and exposure to ultraviolet radiation are also associated with an increased risk of cutaneous melanoma. Sensitivity to ultraviolet light is associated with variations in particular genes (polymorphisms) that affect both the defensive response of the skin to ultraviolet light and the risk of melanoma. A defensive measure to ultraviolet lights includes the tanning response, and variations in pigmentation and tanning response are associated with variations in susceptibility to melanoma [8]. Unlike the more common skin cancers, which are associated with total cumulative exposure to ultraviolet radiation, melanomas are associated with intense intermittent exposure, specifically with exposures that induce sunburn during adolescence [9]. Differences in the amount of exposure to ultraviolet (UV) radiation by geographic latitude may also contribute to the wide geographic variation in melanoma incidence rates. Educational efforts to promote recognition of early lesions (including ABCD criteria for asymmetry, border irregularity, unevenness of distribution of color, and a diameter that is greater than 6 mm or increasing in size) and avoidance of sun exposure have not prevented these increases in incidence and mortality.

Pathogenesis

Understanding of the pathogenesis of melanoma is crucial to develop new markers for diagnosis and prognosis and identify new targets for rational therapy.

Ras/Raf/MEK/Erk Pathway

One of the most studied molecular pathways in melanoma is the intracellular Ras-regulated Raf/MEK/ERK and MAPK signal cascade. Melanocytes require this cascade to maintain a balance between proliferation and differentiation. There is a strong link between dysregulation of this pathway and uncontrolled cell proliferation and survival. Dysregulation of the MAPK signaling pathway through constitutive activation is a frequent event in multiple human cancers [10]. Mutations of the PTEN tumor suppressor have also been reported in up to 25% of melanomas, and alterations of the PI3K pathway, in conjunction with dysregulation of the MAPK pathway, play an essential role in melanoma development and progression.

BRAF is a RAF serine-/threonine-specific protein kinase and has been identified as a common oncogene in many cancers, particularly melanoma where it regulates many cellular responses, such as proliferation, survival, and invasion/metastasis. BRAF mutations occur in about 60% of melanomas occurring on skin without signs of chronic sun-induced damage, but infrequent in melanomas that occur on skin showing evidence of chronic sun-induced damage as well as on sun-protected skin such as the palms, soles, or subungual sites, and on mucosal membranes. Recent studies have shown that over 90% of BRAF mutations occur in codon 600, usually resulting in a valine to glutamate substitution (designated V600E) [11].

Immune Regulation

The immune system plays a vital role in regulating the growth of tumors and immune-regulation of T-cells is an essential link in understanding the pathophysiology of melanoma. When naïve T cells are presented tumor antigens complexed with MHC molecules by antigen-presenting cells (APCs), they mature into effector cells. However, a second costimulatory signal is required to induce activation. This signal is provided by the interaction of B7 molecule on the surface of APCs with the T-cell CD28 receptor. However the immune-checkpoint protein cytotoxic T lymphocyte antigen 4 (CTLA-

4), which is upregulated on CD-8$^+$ T cells after activation, can bind to B7 molecule and replace the activation signal with an inhibitory signal.

Once activated (priming phase), the CD-8$^+$ T cell matures and travels from peripheral lymphoid organs to peripheral tissues to carry out its cytotoxic effector function against tumor cells (effector phase). During this phase, binding the MHC-antigen complex is sufficient to induce effector functions, without the need of a costimulatory signal. An inhibitory pathway consisting of the expression of the programmed death 1 (PD-1) receptor on the T-cell surface may lead to the inactivation of the T-cell after binding to the programmed death ligand 1 (PD-L1) on tumor tissue. Tumor cells can upregulate PD-L1 on their surface to evade immune-mediated destruction [12]. The traditional approach to immunotherapy has focused on increasing the frequency of tumor-specific T cells (i.e., vaccines, interleukin-2), improving the presentation of tumor antigens to the immune system, or trigger innate immune activation and inflammation in the tumor microenvironment (i.e., interferons) [12]. More recently, a better understanding of immune regulatory mechanisms has led to the development of agents that can modulate immune checkpoints (i.e., CTLA-4, PD-1, PD-L1) and effectively overcome tumor-induced immunesuppressive mechanisms.

Angiogenesis

Angiogenesis is a fundamental physiological process by which new vascular networks are formed from pre-existing capillaries. Many tumors overexpress multiple angiogenic factors such as vascular endothelial growth factor (VEGF), which is strongly associated with new vasculature formation in melanoma, and its overexpression is correlated with a poor prognosis [13, 14]. Although VEGF is only expressed in 32% of primary melanomas, its expression level in metastases [15, 16] is increased. Several other angiogenic factors have been implicated in the pathology of human melanomas, such as IL-8, placental growth factor (PlGF), basic fibroblast growth factor (bFGF), platelet-derived growth factor (PDGF)-AA, and PDGF-BB [17, 18]. Innovative antiangiogenic strategies in oncology drug development are currently being explored with monoclonal antibodies and small-molecule kinase inhibitors.

Tumor Histology

Melanoma often arises from precursor pigmented lesions, which demonstrate changes in shape, color, and irregular borders, or develop ulceration. The most common form is superficial spreading melanoma (up to 70% of cases), where lesions may be flat or elevated, demonstrate change in color or border, and is most commonly seen in the legs and trunk. Nodular melanoma (10–20% of cases) typically grows rapidly, is elevated, and also occurs mainly on the legs and trunk. Lentigo maligna melanoma usually occurs on sun-exposed areas such as the face, more typically seen in darker-skinned patients, and is seen in 5–15% of cases. Acral melanoma most commonly occurs on the sole of the feet, or palm and nail beds, and is seen in 2–8% of patients. Superficial spreading melanoma, lentigo maligna melanoma, and acral melanoma are also characterized by an early in situ phase of radial growth, prior to deeper extension, which is associated with a worse prognosis. Microscopic examination of melanomas demonstrates sheets of malignant cells which may be associated with pigment cells and various infiltrative cells including lymphocytes. The extent and depth of malignant cell infiltration, ulceration, mitotic rate, and morphologic appearance all influence diagnosis, treatment, and prognosis; hence, full excision and careful pathologic examination are critical in the initial diagnosis and management of melanoma patients.

Staging Systems for Melanoma

Breslow Staging, AJCC Classification

The histologic pattern and depth of infiltration of the primary melanoma, together with the site and extent of metastatic disease, have a significant impact on treatment selection and prognosis [19,

20]. Clinical and histologic variables that have been shown to impact on prognosis include Breslow thickness (the total vertical height of the lesion: <1 mm, 5-year survival >95%; 1–2 mm, 5-year survival 80–95%; 2.1–4 mm, 5-year survival 60–75%; >4 mm, 5-year survival 37–50%), Clark Level (depth of penetration: Level I, confined to the epidermis; Level II, invasion of the upper dermis; Level III, invasion of the papillary dermis but to the junction of the reticular dermis; Level IV, invasion of the reticular dermis; Level V, invasion of deep subcutaneous tissue), ulceration, tumor location, growth pattern, histological subtype, patient age, gender, and tumor status of regional lymph nodes [21]. Clinical studies exploring risk factors and their impact on prognosis have clearly shown that the metastatic involvement of lymph node(s) draining the primary tumor, also called sentinel lymph node(s) (SLN), is the most powerful prognostic factor in early stage melanoma patients [22, 23]. The American Joint Committee on Cancer (AJCC) has recently incorporated the histological status of SLN into its latest staging system version of cutaneous malignant melanoma (Tables 1 and 2).

Melanoma may metastasize through local extension, via lymphatics prior to first draining lymph node (in-transit metastases) to regional lymph nodes, or systemic metastases to distant sites. AJCC stage I–II melanomas usually develop regional nodal metastases as the initial first site of metastatic disease; of those patients who develop nodal metastases, the majority will also present with satellite/in-transit disease or distant metastases [24]. Apart from lymph nodes, the most common sites for metastatic disease are skin, lung, liver, and brain, although almost any site in the body may be affected [24–26]. The patterns of spread of disease are dependent on tumor site and thickness, with approximately one-third of melanomas from the lower extremities metastasize locally to satellite/in-transit metastases, whereas nearly one-third of melanomas from the trunk and upper extremities disseminated directly to distant sites [24]. In contrast, head and neck primary melanomas develop local, regional, and distant metastases in nearly the same proportions (about one-third). Distant metastases were most often observed in men (mainly trunk melanomas), while locoregional metastases were rather detected in women, who have an increased incidence of lower limb melanomas.

Treatment for Localized Melanoma

Surgical excision is the primary treatment for melanoma. Several randomized, controlled trials have determined appropriate resection margins according to the thickness of the primary melanoma. For melanoma in situ, margins of 0.5–1 cm around the visible lesion or biopsy scar are recommended. Resection margins of 1–2 cm are recommended for 1–4 mm thickness primary lesions, and 2–3-cm margins if the primary lesion is >4.0 mm thick.

Regional lymph node spread of melanoma, or intransit disease, may occur at the time of initial presentation, or usually within 3 years of initial diagnosis. Lymph node resection is usually performed for regional nodal disease. Local radiation treatment may also be performed for regional lymph node metastases, depending on the extent of disease and success of initial surgery, and is also commonly used for in-transit disease.

Prognostic Factors

Patients with melanoma can be stratified into various risk groups: those with stage IA disease who carry a very low risk of recurrence and a 5-year survival of approximately 95%; those with stage IB and IIA disease, who have an intermediate risk and a 5-year survival from 65% to 90%; those with IIB, IIC, and IIIA disease who have a higher risk; and those with stage IIIB and IIIC disease who carry a very high risk of recurrence and a 5-year survival from 45% to 70%.

Over the past 10 years, there has been a debate focused on the optimal diagnostic, prognostic, and therapeutic strategies for cutaneous melanoma. It is important to identify and evaluate prognostic factors that can accurately categorize patients into different risk groups for distant metastatic disease. Currently, the most useful prognostic factors in clinical practice

Table 1 AJCC definitions of TNM for malignant melanoma

Primary tumor (T)	
TX	Primary tumor cannot be assessed (e.g., curettaged or severely regressed melanoma)
T0	No evidence of primary tumor
Tis	Melanoma in situ
Tl	Melanomas 1.0 mm or less in thickness
T2	Melanomas 1.01–2.0 mm
T3	Melanomas 2.01–4.0 mm
T4	Melanomas more than 4.0 mm

Note: a and b subcategories of T are assigned based on ulceration and number of mitoses per mm^2 as shown below

T classification	Thickness (mm)	Ulceration status/mitoses
Tl	<1.0	(a) w/o ulceration and mitosis <l/mm^2
		(b) with ulceration or mitoses >l/mm^2
T2	1.01–2.0	(a) w/o ulceration
		(b) with ulceration
T3	2.01–4.0	(a) w/o ulceration
		(b) with ulceration
T4	>4.0	(a) w/o ulceration
		(b) with ulceration

Regional lymph nodes (N)	
NX	Patients in whom the regional nodes cannot be assessed (e.g., previously removed for another reason)
NO	No regional metastases detected
Nl-3	Regional metastases based upon the number of metastatic nodes and presence or absence of intralymphatic metastases (intransit or satellite metastases)

Note: N1–3 and a–c subcategories assigned as shown below

N classification	No. of metastatic nodes	Nodal metastatic mass
Nl	1 node	(a) Micrometastasis[a]
		(b) Macrometastasis[b]
N2	2–3 nodes	(a) Micrometastasis[a]
		(b) Macrometastasis[b]
		(c) Intransit met(s)
		Satellite(s) without metastatic nodes
N3	4 or more metastatic nodes, or matted nodes, or intransit met(s)/satellite(s) *with* metastatic node(s)	

[a]Micrometastases are diagnosed after sentinel lymph node biopsy and completion lymphadenectomy (if performed)

[b]Macrometastases are defined as clinically detectable nodal metastases confirmed by therapeutic lymphadenectomy or when nodal metastasis exhibits gross extracapsular extension

Distant metastasis (M)	
M0	No detectable evidence of distant metastases
M1a	Metastases to skin, subcutaneous or distant lymph nodes
Mlb	Metastases to lung
Mlc	Metastases to all other visceral sites or distant metastases to any site combined with an elevated serum LDH

Note: Serum LDH is incorporated into the M category as shown below

Used with the permission of the American Joint Committee on Cancer (AJCC), Chicago, IL. The original source for this material is the *AJCC Cancer Staging Manual,* Seventh Edition (2010) published by Springer Science and Business Media LLC www.springer.com

M classification	Site	Serum LDH
M1a	Distant skin, subcutaneous or nodal mets	Normal
Mlb	Lung metastases	Normal
Mlc	All other visceral metastases	Normal
	Any distant metastasis	Elevated

Table 2 AJCC anatomic stage and prognostic groups for melanoma

Clinical staging[a]				Pathologic staging[b]			
Group	T category	N category	M category	Group	T category	N category	M category
Stage 0	Tis	N0	M0	0	Tis	N0	M0
Stage IA	T1a	N0	M0	IA	T1a	N0	M0
Stage IB	T1b	N0	M0	IB	T1b	N0	M0
	T2a	N0	M0		T2a	N0	M0
Stage IIA	T2b	N0	M0	IIA	T2b	N0	M0
	T3a	N0	M0		T3a	N0	M0
Stage IIB	T3b	N0	M0	IIB	T3b	N0	M0
	T4a	N0	M0		T4a	N0	M0
Stage IIC	T4b	N0	M0	IIC	T4b	N0	M0
Stage III	Any T	≥N1	M0	IIIA	T1–4a	N1a	M0
					T1–4a	N2a	M0
				IIIB	T1–4b	N1a	M0
					T1–4b	N2a	M0
					T1–4a	N1b	M0
					T1–4a	N2b	M0
					T1–4a	N2c	M0
				IIIC	T1–4b	N1b	M0
					T1–4b	N2b	M0
					T1–4b	N2c	M0
					Any T	N3	M0
Stage IV	Any T	Any N	M1	IV	Any T	Any N	M1

Used with the permission of the American Joint Committee on Cancer (AJCC), Chicago, IL. The original source for this material is the AJCC Cancer Staging Manual, Seventh Edition (2010) published by Springer Science and Business Media LLC www.springer.com

[a]Clinical staging includes microstaging of the primary melanoma and clinical/radiologic evaluation for metastases. By convention, it should be used after complete excision of the primary melanoma with clinical assessment for regional and distant metastases

[b]Pathologic staging includes microstaging of the primary melanoma and pathologic information about the regional lymph nodes after partial or complete lymphadenectomy. Pathologic stage 0 or stage IA patients are the exception; they do not require pathologic evaluation of their lymph nodes

for localized melanoma are Breslow thickness, presence of lymph node involvement, and ulceration.

Sentinel lymph node biopsy (SLNB) is important for planning therapy, although it has failed to show any benefit in overall survival (OS). There has been no consensus on which patient categories benefit from SLNB. The National Comprehensive Cancer Network recommends that SLNB should be considered for patients with high-risk stage IA melanoma and discussed and offered to patients with stage IB–IIC melanomas [27]. SLNB can identify patients who may benefit from more extensive staging investigations and, based on pathology results, may be suitable for adjuvant therapy [28].

Thickness and ulceration of melanoma are highly correlated with each other, and studies have shown that the incidence of melanoma ulceration rises with increasing tumor thickness, ranging from 6–12.5% for thin melanomas to 63–72.5% for thick (>4.0 mm) lesions. The presence of ulceration is associated with decreased survival in all tumor thickness categories. Thin (<1.0 mm) ulcerated tumors have approximately a 4% decreased 5-year survival rate compared to nonulcerated tumors. This survival decrement is as high as 22% in thick (>4.0 mm) tumors [21]. Furthermore, the tumor mitotic rate is an additional independent prognostic factor that has emerged as more powerful than ulceration in several studies [29–31]. A better understanding of prognostic factors together with accurate staging in cutaneous melanoma allows the identification

of patients whose risk of recurrence is sufficiently high to justify adjuvant systemic treatment.

Adjuvant Therapy

Attempts to reduce the incidence of recurrent melanomas with adjuvant therapy have been studied in more than 100 randomized controlled trials [32, 33]. However, adjuvant treatment has historically been challenging, with fewer options available. The role of chemotherapy remains unclear with no tangible benefit in terms of prolonged OS.

Until recently, interferon was the only FDA approved adjuvant option in over 20 years. High-dose interferon (IFN) was evaluated in three large United States cooperative group trials. The data from ECOG 1684, which led to FDA approval of IFN for the treatment of patients with resected stage IIB and stage III melanoma, showed a 5-year relapse-free survival improvement and suggested a statistically significant benefit in overall survival at a median follow-up of 6.9 years [34]. However, at 12.6 years of follow-up, the OS was not significantly different between the two groups, even though the relapse-free survival benefit was confirmed. A pooled analysis of three large randomized trials of high-dose IFN confirmed a consistent and significant effect on recurrence-free survival in patients with high-risk resected melanoma, but did not find a statistically significant improvement in OS [35]. High-dose IFN is approved in the USA and Canada, but it is not currently accepted worldwide due to its considerable toxic effects and to the fact that the benefit occurs in only a minority of the patients at risk. A large phase-III trial (EORTC18991) compared the treatment with pegylated interferon-a2b for up to 5 years with observation in Stage III patients. The results indicated a significant impact on relapse free survival without a significant improvement of distant metastasis-free survival or OS [36]. Based on this data, pegylated interferon alfa received approval by the FDA in March 2011 for the adjuvant treatment of stage III disease. Efforts to improve the efficacy and toxicity profiles of interferon have also included the use of lower-dose regimens, and combination with various drugs and vaccines [37–39].

Due to the only marginally effective adjuvant therapies with interferons and the recent successes of novel immunotherapeutic agents in metastatic melanoma, several clinical trials using these agents were initiated. In October 2015, Ipilimumab was approved by FDA for use in the adjuvant setting for patients with stage III melanoma. The approval was based on the results from the EORTC 18071 study, which randomly assigned 951 patients to ipilimumab or placebo [40]. Adjuvant ipilimumab significantly improved recurrence-free survival for patients with completely resected high-risk stage III melanoma.

Various phase III studies are currently testing the potential role of other immunotherapies (anti-PD1 antibodies MAGE 3 vaccine), as well as BRAF and MEK inhibitors (vemurafenib, dabrafenib, trametinib) in the adjuvant setting. Decisions regarding adjuvant therapy for neoplastic diseases represent a balancing of risk of disease recurrence against the relative value of the agent used in terms of its activity, toxicity, and cost.

Treatment of Metastatic Malignant Melanoma

Approximately 2–5% of new patients with melanoma present with metastatic disease, and 30% of patients initially diagnosed as localized or regional disease develop distant metastasis [41]. The prognosis for patients with advanced visceral metastatic melanoma in the pretargeted and pre-immunotherapy era was particularly poor with 3-year survival rate of only 6–12% [42]. At that time, the only standard first line treatment was dacarbazine despite its limited clinical benefit. The response rate observed with single-agent dacarbazine chemotherapy did not exceed 12% [43] and no other chemotherapeutic agents either alone or in combination have proved superior to single-agent dacarbazine chemotherapy [43]. With the recent development of targeted therapies and immunotherapies which have demonstrated better efficacy than conventional chemotherapy,

the therapeutic landscape for metastatic melanoma is rapidly changing.

Targeted Therapies Against BRAF Mutations

About half of patients with metastatic melanoma harbor an activating mutation in BRAF, the most common being BRAF V600E [44].

Vemurafenib is a selective BRAF inhibitor that targets the V600 mutant forms of the BRAF and was the first BRAF inhibitor to gain FDA approval in August 2011. A phase 2 trial (BRIM2) involving patients with previously treated BRAF V600E mutant stage IV melanoma showed a response rate of 53%, with a median duration of response of 6.7 months [44]. A subsequent phase 3 randomized trial (BRIM3) of previously untreated patients compared vemurafenib with dacarbazine. This study demonstrated an improvement in progression free survival (PFS) (6.9 months vs. 1.6 months), OS (13.6 months vs. 9.7 months), and overall response rate (57% vs. 8.6%) [45].

Following vemurafenib, two additional agents targeting BRAF-mutated disease have been approved by the FDA.

Dabrafenib has shown similar results to those with vemurafenib in phase I/II studies [46, 47]. A Phase III randomized trial compared dabrafenib with dacarbazine in previously untreated patients with BRAFV600E-mutated metastatic melanoma. Dabrafenib significantly improved PFS (5.1 months vs. 2.7 months, HR = 0.30, $P < 0.001$) and response rates (53% vs. 19%) compared with dacarbazine [48]. These results have led to FDA approval in May 2013.

Trametinib is an oral small-molecule inhibitor of MEK 1 and MEK 2, which are downstream of BRAF in the MAP kinase signal transduction pathway. In the open-label phase III trial (METRIC) that led to FDA approval in May 2013, 322 patients with BRAF V600E/K-mutant metastatic melanoma were randomized to receive either trametinib or chemotherapy with either dacarbazine or paclitaxel [49]. The median PFS was improved to 4.8 months in the trametinib group, as compared to 1.4 months in the chemotherapy group (HR = 0.45, 95% CI: 0.33–0.63; $P < 0.001$). The OS rate at 6 months was 81% in the trametinib group and 67% in the chemotherapy group (HR = 0.54, 95% CI: 0.32–0.92; $P = 0.01$), despite 65% of patients in the chemotherapy arm crossing over to the trametinib arm.

Numerous studies are being conducted so as to find methods of overcoming or delaying the resistance. In January 2014, FDA approved the first combination of a BRAF inhibitor dabrafenib and a MEK inhibitor trametinib to treat patients with unresectable or metastatic melanoma with BRAF V600E or V600K mutation. A phase 3 study tested the combination of dabrafenib with trametinib versus dabrafenib and placebo [50]. The median PFS was longer in the combination therapy group compared to the dabrafenib only group (9.3 vs. 8.8 months with HR of 0.75, $P = 0.03$). In the patient population with elevated LDH levels, the median PFS was longer in the combination therapy group compared to monotherapy (7.1 vs. 3.8 months). Interestingly, the BRAF and MEK inhibitor combination demonstrated not only a potential reduction in drug resistance but also a lower incidence of skin toxicity and secondary cancers.

Another combination of Cobimetinib and vemurafenib was associated with a significant improvement in PFS among patients with BRAF V600 mutated metastatic melanoma and was approved by the FDA in November 2015 [51].

Immunotherapy

Although melanoma has historically been considered as one of the most immunogenic types of cancer, clinically translated immunotherapies including treatment with interleukin-2, interferon alpha therapy, vaccination with peptide-pulsed dendritic cells, or adoptive T-cell therapies had not led to a statistically significant improvement in OS until recent years. Three immune-therapeutic agents (ipilimumab, pembrolizumab, and nivolumab) have been approved since 2011 and they have each produced survival advantage in patients with metastatic melanoma.

Ipilimumab, a monoclonal antibody binding to the CTLA-4 receptor expressed in activated T cells,

was the first agent to demonstrate an OS benefit in the treatment of advanced melanoma. It received FDA approval in March 2011. Approval was based on a phase III study of 676 previously treated metastatic melanoma patients [52] who were randomized to receive ipilimumab plus a gp100 vaccine versus ipilimumab alone versus the vaccine alone in a 3:1:1 ratio. OS was significantly longer for patients treated with the combination (10 months; HR = 0.68; $P < 0.001$) or ipilimumab alone (10.1 months; HR = 0.66; $P < 0.003$) versus gp100 alone (6.4 months). A second phase III study compared dacarbazine with or without ipilimumab in previously untreated melanoma patients [53]. The addition of ipilimumab to dacarbazine significantly improved the OS compared with dacarbazine alone (11.2 vs. 9.1 months; $P < 0.05$). However, the trial employed a dose of Ipilimumab more than three times higher than currently licensed.

Pembrolizumab, an anti-PD-1 monoloclonal antibody, was approved by FDA in September 2014 for the treatment of patients with unresectable or metastatic melanoma with disease progression after treatment with ipilimumab or BRAF-inhibitor in case of BRAF-positive disease. KEYNOTE-001 was an open label phase Ib study randomizing 655 patients (342 ipilimumab treated (IPI-T) and 313 ipilimumab naive (IPI-N)) with unresectable or metastatic melanoma to receive pembrolizumab 2 mg/kg or 10 mg/kg IV once every 3 weeks or 10 mg/kg every 2 weeks [54]. At the time of analysis, ORR was 34% (29% IPI-T, 38% IPI-N), with a 6% complete remission (CR) rate; median PFS was 5.2 months (IPI-T, 4.9 months (3.0–5.5); IPI-N, 5.4 months (3.1–6.9)) and the 1-year OS rate was 67%. KEYNOTE-002 was a phase 2 randomized study which demonstrated an improvement in PFS in the pembrolizumab 2 mg/kg arm (HR of 0.57 [95% CI: 0.45, 0.73]; $P < 0.001$) and in the pembrolizumab 10 mg/kg arm (HR of 0.50 [95% CI: 0.39, 0.64]; $P < 0.001$) when compared to investigator-choice chemotherapy in 540 patients with advanced melanoma who were previously treated with ipilimumab and, if BRAF V600 mutation positive, a BRAF or MEK inhibitor [55]. The phase 3 KEYNOTE-006 study randomized 834 patients with advanced melanoma to receive pembrolizumab (10 mg/kg every 2 or 3 weeks) or ipilimumab [56]. In the planned interim analysis of the coprimary endpoints, pembrolizumab demonstrated superior PFS and OS compared to ipilimumab. Following the results from this study, FDA approved (December 2015) an expanded indication for pembrolizumab to include the first-line treatment of patients with unresectable or metastatic melanoma regardless of BRAF status.

Nivolumab is a monoclonal antibody that targets the PD-1 protein and was initially approved by FDA in December 2014 for patients who progressed after treatment with ipilimumab and in patients whose tumors express BRAF V600 mutation. The indication for nivolumab was then expanded to include the first-line treatment of unresectable or metastatic melanoma. The approvals were based on the results from two phase 3 trials: Checkpoint 037 and Checkmate 066. Checkpoint 037 enrolled 272 patients with metastatic melanoma who had received prior anti-CTLA-4 therapy and a BRAF inhibitor if a V600 mutation was present [57]. Patients were randomly assigned to nivolumab or chemotherapy (either dacarbazine or carboplatin plus paclitaxel). Nivolumab led to a greater proportion of patients achieving an objective response (31.7% vs. 10.6%) and fewer toxic effects than with alternative available chemotherapy regimens. In the previously untreated setting, 418 patients without BRAF mutation were randomly assigned to nivolumab or dacarbazine [58]. OS was significantly increased in those treated with nivolumab (1-year survival rate 73% vs. 42%). PFS was also increased with nivolumab (median 5.1 vs. 2.2 months), as was the ORR (40% vs. 14%).

Finally, the combination of nivolumab and ipilimumab has been recently (September 2015) approved in the USA for the treatment of patients with BRAF V600 wild-type and BRAF V600 mutation-positive unresectable or metastatic melanoma based on findings from the phase 2 CheckMate-069 study and from the phase 3 CheckMate-067 trial. This marks the first approval for an immunotherapy combination for patients with cancer. The phase 3 CheckMate-067 study, where 945 previously untreated patients with advanced melanoma were assigned to nivolumab alone, nivolumab plus ipilimumab, or ipilimumab alone, showed a median PFS of 11.5 months for the nivolumab plus ipilimumab regimen and 6.9 months for nivolumab

monotherapy, versus 2.9 months for ipilimumab monotherapy [59]. The combined regimen demonstrated a 58% reduction in the risk of disease progression vs. ipilimumab (HR: 0.42; $P < 0.0001$), while nivolumab monotherapy demonstrated a 43% risk reduction versus ipilimumab monotherapy (HR: 0.57; $p < 0.0001$).

Novel Targets and Combination Therapies

The advent of new treatment options has resulted in various novel combination approaches involving targeted therapies, immunotherapies, as well as other treatment modalities (i.e., chemotherapy, radiotherapy). Resistance to BRAF inhibitors develops in the majority of patients within 6–8 months and can be mediated by a number of different mechanisms occurring along the MAPK pathway (e.g., mutations in MEK, NRAS, overexpression of COT) or via bypass signalling pathways (e.g., activation of PI3K/AKT signalling, loss of PTEN, RTK overexpression, IGFR1). In addition to the combinations that have already been approved, other targeted combinations to overcome resistance are currently being evaluated.

Another possible way of overcoming the resistance to BRAF inhibitors is the combination of immunotherapeutic agents and BRAF inhibitors. A phase I/II trial combining vemurafenib and ipilimumab was conducted by Ribas et al. [60]. While the combination was shown not to be feasible due to hepatotoxicity leading to discontinuation of the study, sequential administration was shown to be safe, with some potential for efficacy. Clinical trials evaluating combinations of PD1 pathway inhibitors with BRAF inhibitors such as vemurafenib (NCT01656642), or dabrafenib and with MEK inhibitor trametinib (NCT02224781) are underway. Furthermore, preliminary safety data from the combination trial of MEDI4736 (a PDL1-specific mAb), dabrafenib and trametinib appear promising [61].

Combining immunological agents may also improve response rates and the duration of response by stimulating an antitumor immunological memory regardless of BRAF-mutational status. Dual blockade of PD-1 and CTLA-4 with nivolumab and ipilimumab has proven benefit in advanced melanoma, although it is associated with higher toxicity than either monotherapy. The combination of ipilimumab with the oncolytic virus, T-VEC, another immunotherapy, also obtained a very promising ORR of 55%, with a good safety profile. Novel immunomodulatory candidates for rational combination with immune checkpoint inhibitors are at various stages of clinical development. Early phase studies involve the combination of nivolumab with other immunomodulating antibodies targeting inhibiting receptors, such as LAG-3 or TIM-3, and with antibodies targeting activating receptors, such as CD 137 or OX-40. Other strategies are also being explored, such as agents that may block the inhibition of natural killer cell activity (i.e., KIRs, C-type lectins, CD244 and CD48, ILT family) or target the tumor microenvironment (i.e., IDO, TGFβ).

c-KIT Inhibitors

Mutations in c-KIT are seen in up to 6% of cutaneous melanomas, although the frequency may be higher in mucosal and acral lesions. In an open-label, single-arm, phase II clinical trial 51 patients with mutations were identified out of the 295 screened and 28 patients were treated with imatinib [62]. The authors did find an association between clinical response and mutation pattern. Further clinical studies using other CKIT inhibitors such as dasatinib and nilotinib are in progress and results are pending.

Antiangiogenic Therapy

Blockade of the VEGF pathway has been achieved by many different approaches, including blocking antibodies targeted against VEGF or its receptors, soluble decoy receptors that prevent VEGF from binding to its normal receptors (VEGF trap), as well as small-molecule inhibitors of the tyrosine kinase activity of the VEGFRs. Bevacizumab is a potent antibody against the VEGF and has been shown to be effective for the treatment of various

advanced cancers. Bevacizumab has also been studied in phase II trials in metastatic melanoma [63, 64]. Prolonged disease stabilization and response rates have been demonstrated in one-quarter of metastatic melanoma patients after the addition of bevacizumab to low-dose IFN, and dacarbazine [65]. In addition, the combination of temsirolimus and bevacizumab demonstrated an objective clinical response in patients with BRAF/RAS–wild-type melanomas suggesting that the combination of an angiogenesis inhibitor with an mTOR inhibitor may be promising in a subset of melanoma patients who lack activating mutations in both BRAF and RAS and for whom no targeted therapies are currently available [66]. Further trials of bevacizumab combined with chemotherapy, immunotherapy, and other targeted therapies are ongoing in melanoma patients, and numerous other antiangiogenic agents are currently in clinical trials or in development.

Apoptotic Therapy

The Bcl-2 protein is one of the most important inhibitors of apoptosis, and it is overexpressed in approximately 90% of melanomas. Drug resistance in melanoma has been partially attributed to overexpression of Bcl-2. Oblimersen sodium is a Bcl-2 antisense oligonucleotide that selectively targets Bcl-2 RNA for degradation. Although promising results were seen in an initial phase III trial which demonstrated significant increases in PFS and response rate when oblimersen was combined with dacarbazine [67], these findings were not confirmed in a second trial.

Role of Nuclear Medicine in Melanoma Patients

Initial Staging of Primary Melanoma

Staging Nodal Metastases

Lymphoscintigraphy. In early stage melanoma (AJCC I–II), SLNB has become the standard of care for staging the regional draining lymph nodes, which are typically the first site of possible metastatic spread of disease [28, 68]. Compelling evidence from the literature indicates that SNLB is the procedure of choice for detection of occult regional lymph node metastases, particularly in patients presenting with an intermediate Breslow thickness lesion (1–4 mm) [22, 23] (see also ▶ Chap. 48, "Radioguided Surgery for Malignant Melanoma" of this book). Preoperative lymphoscintigraphy is normally performed, followed by intraoperative detection with blue dye and/or a gamma probe [69]. Precise identification of sentinel lymph node (SLN) site(s) is essential, as there may be true nodal sites, intransit nodes, and alternate drainage basins in some situations (Fig. 1). Lymphoscintigraphy has been shown to be highly sensitive and specific (>90%) for the detection of SLN, thus assisting surgical biopsy and decisions regarding subsequent therapeutic options.

Lymphoscintigraphy for SLN detection must be performed with transmission scans, and/or with hybrid SPECT/CT systems, to precisely define the location of sentinel nodes and eliminate false-positive results. All nodes demonstrating uptake must be evaluated by detailed histology, as a SLN may not be the lymph node which demonstrates the highest tracer uptake, and different drainage basins may occur from a single primary melanoma site (Fig. 2). Intransit and aberrant metastatic lymph nodes occur in 14–22% of cases [69]. Status of the sentinel lymph node is an important prognostic factor for disease-free and overall survival. In the Multicenter Selective Lymphadenectomy Trial (MSLT-1), patients who had immediate lymph node dissection following positive SLNB had a higher survival rate than those who underwent delayed lymphadenectomy [28].

Anatomic correlation of the lymphoscintigram with SPECT/CT improves the accuracy of lymphoscintigraphy by defining anatomical site and excluding false-positive results, compared to planar gamma camera imaging. In one study of patients with primary melanoma located in the head and neck or trunk region, SPECT/CT identified "hot" nodes missed on planar images including nodes invaded by metastases in 43% of cases [69]. These SLNs identified by SPECT/CT were nodes hidden by the injection-site-scattered radiation, deeply located or intransit nodes. Multiple draining basins were clearly identified in 50%

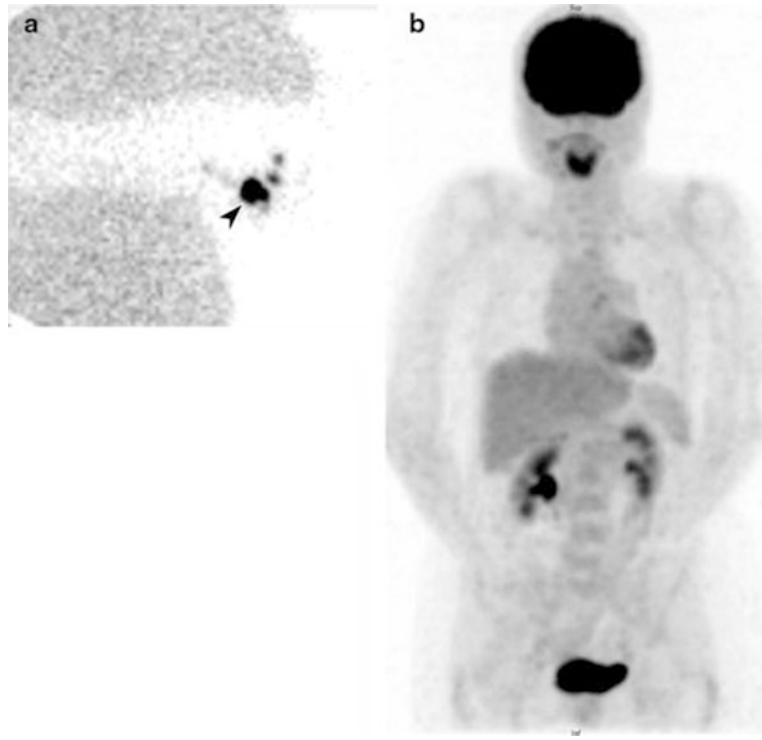

Fig. 1 Lymphoscintigraphy of primary melanoma of the right thumb. Right axillary lymph node (*arrow*) identified on sentinel lymph node scintigraphy with transmission scan (**a**) and negative whole-body staging [^{18}F]FDG PET scan (**b**)

patients with trunk melanoma and in 33% patients with head and neck malignancy. Further validation of lymphoscintigraphy with SPECT/CT in clinical studies is ongoing and may help to provide additional information on improvement in outcomes of patients evaluated preoperatively with this investigation.

[^{18}F]FDG PET. In patients with AJCC stage I–II melanoma, multiple studies with [^{18}F]FDG PET alone, and PET/CT, have shown a poor sensitivity for the detection of metastatic disease in draining lymph nodes. Cumulative data from over 800 patients with early stage melanoma show that PET has a low sensitivity for detecting SLN metastases (Table 3) [68, 70–87]. The small size of involved lymph nodes, which are often <5 mm in size, is a major factor in detection of disease, as most metastatic melanoma sites are [^{18}F]FDG-avid. In an early study by Crippa et al., the sensitivity of PET significantly varied with the size of lymph node metastases [88]. The sensitivity of PET was only 23% for lymph nodes <5 mm and increased to 83% and 100% for lymph nodes with a size of 6–10 and >10 mm, respectively. In another study exploring the impact of spatial resolution of PET scanners with typical size of metastatic lymph nodes, a spatial resolution of 4–6 mm resulted in less than 50% of lymph nodes being potentially detectable [89]. Other studies have confirmed the small size of metastatic disease in SLN and corresponding low sensitivity for PET and PET/CT for AJCC stage I–II disease [68, 70–87] (Table 3).

There is a potential role for [^{18}F]FDG PET in patients with apparent AJCC stage I–II disease but higher risk of metastatic disease, including those with intermediate/high-risk lesions (Breslow ≥ 1 mm, regression, ulceration) or high-risk lesions (Breslow >4 mm). These patients have a prevalence of regional lymph node or distant metastases at the time of initial presentation of $>10\%$. For example, in one study of 43 patients with intermediate/high-risk melanomas, extensive staging identified disease resulting in early treatment in 12 patients (28%) [81]. The analysis of melanomas for gene signatures that are associated with a worse prognosis is the subject of ongoing research, and this may also in the future identify

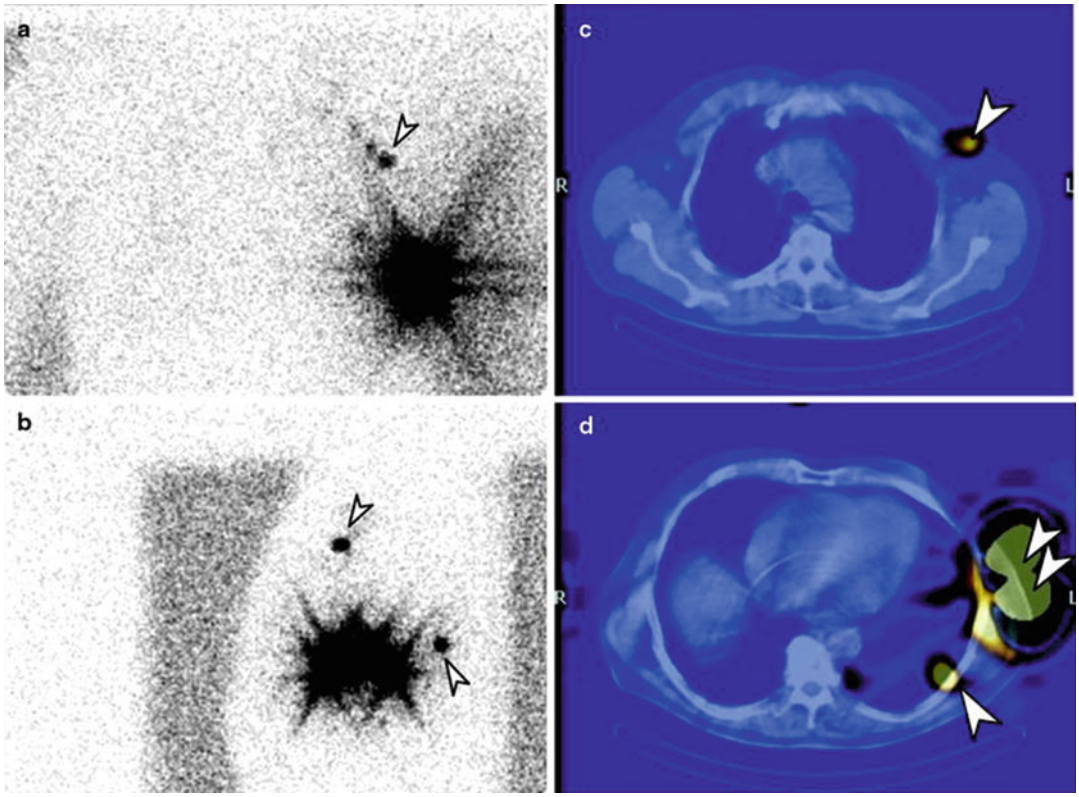

Fig. 2 Lymphoscintigraphy of primary melanoma of the left chest. Planar transmission scan images in the anterior (**a**) and lateral (**b**) projections. SPECT/CT confirms two separate SLN, one lateral to left pectoral muscle (**c**) and one in left midthoracic intercostal space (**d**) (Courtesy of Dr Martin Cherk, Alfred Hospital, Melbourne, Australia)

patients who would benefit from more extensive staging procedures such as PET [69].

These results have led to [^{18}F]FDG PET not being recommended for the routine detection of regional nodal involvement in AJCC I–II melanoma patients. However, PET in initial staging may have a role in situations where AJCC stage I–II patients are considered at higher risk of distant metastatic disease, such as in intermediate-high-risk or high-risk primary lesions, multiple melanomas, or unusual gene signatures in melanoma lesions [90].

Staging of Metastatic Disease

Initial Staging

Melanoma patients presenting with AJCC stage III disease (regional nodal involvement) are at higher risk of presenting with systemic metastases, and as this can impact on therapy, accurate staging is essential (Fig. 3). [^{18}F]FDG PET has been shown to be more accurate than conventional imaging techniques in identifying metastatic disease in stage III patients in a number of reported studies [91–97] (Figs. 4, 5, and 6). In a recent large prospective study evaluating 251 patients with PET/CT prior to surgery for known metastatic melanoma and nodal involvement, lymph node metastases were visualized in 91% of patients by PET, and 92% by CT, although in this series most lymph nodes were large [97]. Systemic metastases were suspected in 32% of patients by PET and in 24% by CT. Upstaging by PET was correct in 27% and in 24% by CT, and more bone and soft tissue sites were detected by PET compared to CT. [^{18}F]FDG PET and CT performed at initial diagnosis for patients with confirmed stage III melanoma conferred survival benefits for both the patients

Table 3 Studies using [^{18}F]FDG PET in regional lymph node staging in early-stage cutaneous melanoma

Study	Study type	Patients	AJCC stage	Clinical use of PET	Reference test	Sensitivity
Wagner et al. [68]	Prospective	70	I–III	Detection of sentinel node metastases	SLNB	PET: Sensitivity 7.7% (stage I–II), 40% (stage III)
Klein et al. [70]	Prospective	17	I–II	Detection of sentinel node metastases	LS/SLNB or clinical follow-up (20 months)	PET: Sensitivity 67%
Acland et al. [71]	Prospective	50	T2–T4 or lymphatic invasion	Detection of regional lymph node metastases	LS/SLNB and clinical follow	PET: Sensitivity 0% SLNB: Sensitivity 100%
Kokoska et al. [72]	Prospective	18	T1–T4 N0 M0	Detection of sentinel node metastases	LS/SLNE	PET: Sensitivity 40%
Belhocine et al. [73]	Prospective	21	T2–T4 N0 M0	Detection of sentinel node metastases	LS/SLNE	PET: Sensitivity 14% SLNB: Sensitivity 86%
Havenga et al. [74]	Prospective	53	T2–T4 N0	Prediction of sentinel node metastases	LS/SLNB	PET: Sensitivity 15% SLNB: Sensitivity 100%
Longo et al. [75]	Prospective	25	T2–T4 N0 M0	Prediction of regional lymph involvement	LS/SLNB	PET: Sensitivity 22% LM/LS: Sensitivity 100%
Schafer et al. [76]	Prospective	40	T2–T4 N0 M0	Detection of regional lymph node metastases	SLNB	PET: Sensitivity 0%
Fink et al. [77]	Prospective	48	T2–T4 N0 M0	Prediction of regional lymph involvement	LS/SLNB	PET: Sensitivity 13% SLNB: Sensitivity 100%
Hafner et al. [78]	Prospective	100	T2–T4	Detection of regional lymph node metastases	LS/SLNB	PET: Sensitivity 8% SLNB: Sensitivity 100%
Libberecht et al. [79]	Retrospective	5	T2–T3 or local recurrence	Detection of regional lymph node metastases	LS/SLNB	PET: Sensitivity 0%

(*continued*)

Table 3 (continued)

Study	Study type	Patients	AJCC stage	Clinical use of PET	Reference test	Sensitivity
Wagner et al. [80]	Prospective	144	T2–T4 N0 M0 or TxN2cM0	Detection of regional lymph node metastases	LS/SLNB	PET: Sensitivity 8% SLNB: Sensitivity 97.5%
Vereecken et al. [81]	Prospective	43	T2–T4 or T1 with regression and/or ulceration	Preoperative staging	LS/SLNB	PET: Sensitivity 40%
Clark et al. [82]	Retrospective	64	T2–T4	Detection of regional lymph node metastases	LS/SLNB	PET: Sensitivity 10.5%
Kell et al. [83]	Retrospective	37	Breslow > 0.75 mm N0 M0	Detection of regional lymph node metastases	LS/SLNB	PET/CT: Sensitivity 22%
Maubec et al. [84]	Prospective	19	T4 N0 M0	Detection of regional lymph node metastases	LS/SLNB	PET: Sensitivity 0% SLNB: Sensitivity 87.5%
Constantinidou et al. [85]	Retrospective	30	Breslow > 1 mm	Preoperative staging	LS/SLNB	PET or PET/CT: Sensitivity 0%
Singh et al. [86]	Prospective	52	T2–T4 N0 M0	Detection of regional lymph node metastases	LS/SLNB	PET/CT: Sensitivity 14.3% SLNB: Sensitivity 100%
Klode et al. [87]	Retrospective	61	T2–T4 N0 M0	Detection of regional lymph node metastases	LS/SLNE	PET/CT: Sensitivity 5.9%

LS lymphoscintigraphy, *SLNB* sentinel lymph node biopsy, *SLNE* sentinel lymph node excision, *LM* lymph node mapping

who were negative for disseminated disease and those whose disease was upstaged because of distant metastases, which they attributed to the early detection of occult subclinical metastases and subsequent modifications in treatment decisions [98]. The use of PET in assessing systemic metastatic disease in this patient group is also included in established clinical guidelines [90].

In patients with known or suspected AJCC stage IV disease (systemic metastases), [^{18}F]FDG PET also has an important role in identifying metastatic disease sites and extent (Tables 4 and 5), which can impact on initial treatment, including surgical options and decisions regarding chemotherapy/biologic therapy [69, 90] (Fig. 7). The majority of melanoma metastases are [^{18}F]FDG-avid, provided lesions are >5–6 mm in size. The exceptions are brain metastases, which may be difficult to identify due to gray matter [^{18}F]FDG uptake, and hepatic metastases of uveal melanoma, which have been shown to be negative on [^{18}F]FDG PET in up to 59% of cases and which do not appear to be related to GLUT-1 expression [111].

Melanoma patients should have whole-body PET imaging, including arms/legs in patients whose primary lesions arise on extremities

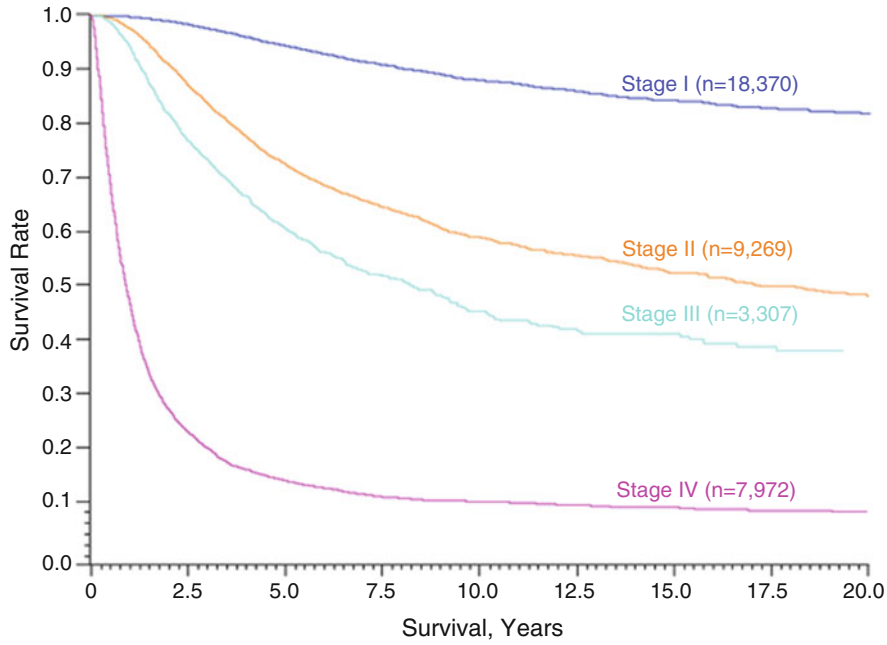

Fig. 3 Fifteen-year survival curves for patients with localized melanoma (stages I and II), regional metastases (stage III), and distant metastases (stage IV). The numbers in parentheses are the numbers of patients from the AJCC Melanoma Staging Database used to calculate the survival rates. The differences between the curves are highly significant ($p < 0.0001$). (Used with the permission of the American Joint Committee on Cancer (AJCC), Chicago, IL. The original source for this material is the *AJCC Cancer Staging Manual* Seventh Edition (2010) published by Springer Science and Business Media LLC www.springer.com)

(Figs. 5 and 6). Reported studies have shown the value of whole-body imaging in melanoma patients, where primary lesions were in the limbs. In one retrospective study of 153 patients, abnormal PET findings in the legs were observed in 53 (35%) of patients; in these 53 patients, 72% also had distant metastases detected. Only patients with primary melanoma of the legs had PET findings justifying inclusion of the legs in the whole-body PET scan [112]. Published guidelines support the use of whole-body PET with extremities in patients with primary melanoma of the arms or legs and full images of the head in patients with primary scalp melanoma [113]. False-negative results can occur with small skin and brain metastases, and lesions adjacent to the heart, kidneys, or urinary bladder. Furthermore, while PET is more specific in the diagnosis of melanoma pulmonary metastases, chest CT is more sensitive. [^{18}F]FDG PET/CT provides an improved technique for assessing pulmonary disease (see later section), although it should be performed in conjunction with brain MR imaging to optimally identify brain metastases.

Recurrent Metastatic Disease

Identifying metastatic disease is critically important in melanoma patients, as the median survival after the appearance of distant metastases is approximately 6 months. An additional consideration is that treatment decisions are based on site and extent of disease [21]. While a comprehensive clinical history and physical examination may assist in identifying possible recurrent disease, particularly in stage III and IV patients, accurate staging is vitally important to guide decisions regarding surgery (which may extend survival) or radiotherapy in patients with recurrent disease [114, 115]. It has been shown that conventional staging investigations (CT chest, abdomen, brain MRI with or without bone scan) have limited sensitivity and specificity for the detection of

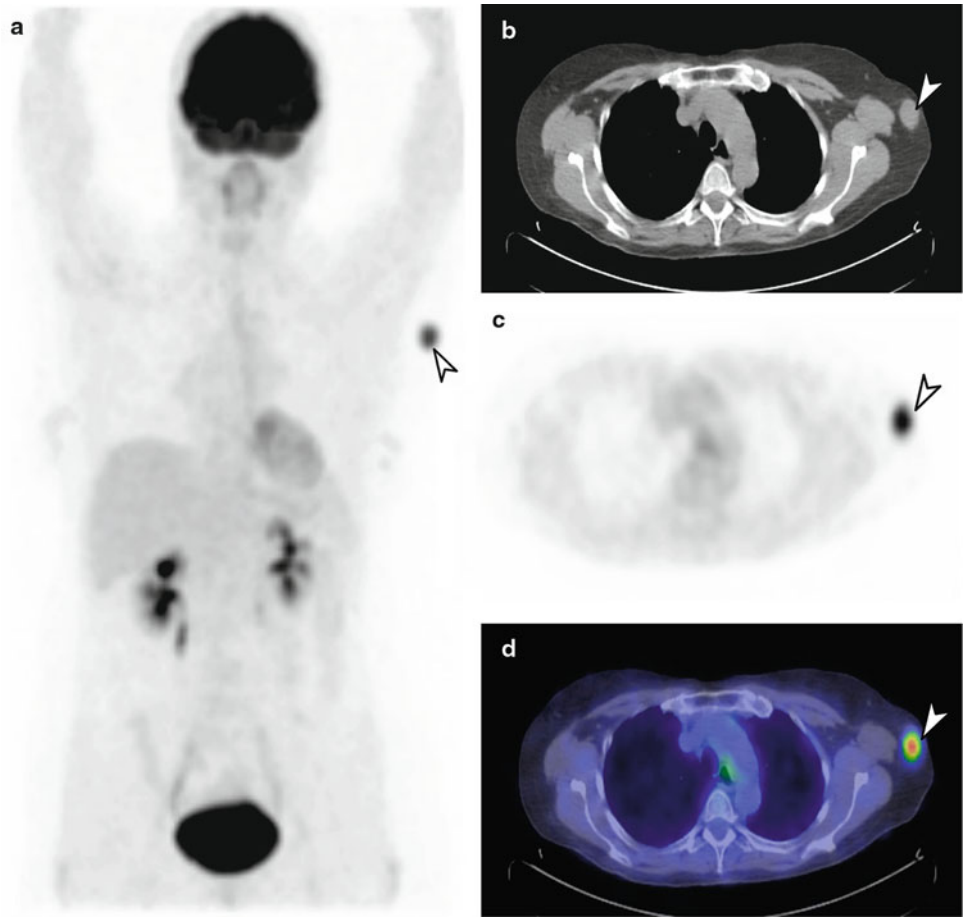

Fig. 4 [^{18}F]FDG PET/CT staging of biopsy-proven left axillary melanoma metastasis. Whole-body PET image (**a**) shows a solitary metastatic lymph node in the left axilla (*arrow*), with no distant metastatic disease. Also seen on axial CT (**b**), PET (**c**), and fused PET/CT (**d**) images

melanoma metastases and have been estimated in patients with stage II–IV melanoma to have a sensitivity of 57–81% and a specificity of 45–87%, respectively, on the basis of single melanoma lesions [92, 93, 95]. In a further study of 347 patients with clinical stage III melanoma, CT scans identified twice as many false positives as true-positive melanoma lesions [116].

In published studies (Table 4) and meta-analyses of the literature, the reported sensitivity, specificity, and accuracy of [^{18}F]FDG PET in detecting recurrent melanoma ranges from 70% to 100% [94, 96, 117]. PET is particularly sensitive and specific for detecting soft tissue and lymph node metastases that are not assessable by clinical examination and have not been demonstrated by CT [92, 93, 96, 99] (Fig. 8). [^{18}F]FDG PET has also been shown to detect disease up to 6 months earlier than conventional techniques. In studies directly comparing PET to conventional imaging in patients with recurrent melanoma, PET has had superior accuracy for the detection of both locoregional and distant metastases [96, 100] (Figs. 9, 10, 11, and 12). In patients with pulmonary metastases, PET-staged patients have also been shown to have improved survival compared to patients staged with conventional imaging techniques [118]. In a prospective, multicenter study of [^{18}F]FDG PET in 134 patients with known or suspected recurrent metastatic melanoma, PET identified an additional 189 lesions in 55.2% of patients, principally in soft tissue, bone, and nodal

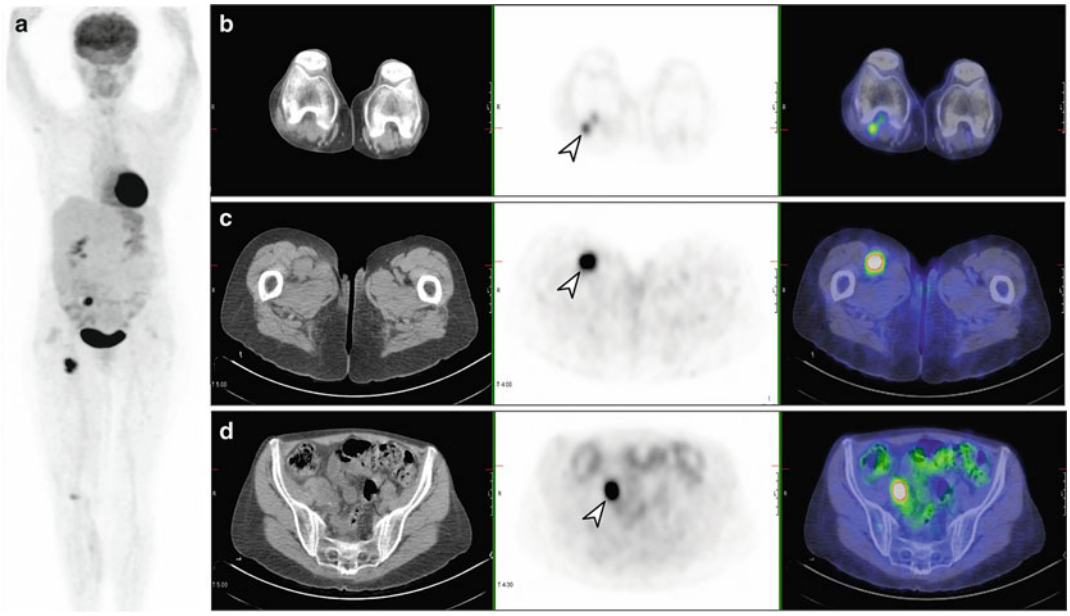

Fig. 5 [^{18}F]FDG PET/CT staging postresection of primary melanoma from right calf. Whole-body PET image (**a**) shows local and distant lymph node involvement in right popliteal (**b**), femoral (**c**), and iliac (**d**) lymph nodes

sites [110]. Most PET false negatives in recurrent disease are typically less than 1 cm in diameter and are mainly pulmonary and hepatic in location, or in the brain (Fig. 13). The majority of these false negatives can be detected by CT scanning or MRI for brain metastases. Therefore, PET should complement rather than replace CT/MRI scanning in patients with suspected recurrent disease. Most CT false negatives are located in the abdomen, suggesting that PET can especially assist in the staging of this region.

Unsuspected additional primary tumors may be detected with [^{18}F]FDG PET. In one series of 92 patients with stage IV melanoma staged with [^{18}F]FDG PET, seven new primary tumors were detected, emphasizing the importance of considering differential diagnoses and obtaining a tissue diagnosis particularly at the time of the first relapse [96].

[^{18}F]FDG PET

[^{18}F]FDG PET/CT is superior to PET alone in the assessment of metastatic melanoma, with improved detection of nodal spread and distant metastases, although some false positives are seen [101, 107–109, 119–121] (Fig. 14). PET/CT has a significant impact on the interpretation of suspicious metastatic lesions, and the false-negative and false-positive rates of standalone PET can be reduced through the use of PET/CT, particularly by providing clarity for normal [^{18}F]FDG uptake variants. Precise anatomic localization of sites of [^{18}F]FDG uptake can define a patient's suitability for surgery as well as pinpoint metastases. [^{18}F]FDG PET/CT is also helpful for the staging of unusual sites of primary melanoma such as ocular melanoma and vaginal melanoma (Fig. 15). In addition, [^{18}F]FDG PET/CT can assist in identifying incidental metastatic melanoma in patients with other malignancies, although this is an unusual finding.

The use of contrast-enhanced CT as part of the [^{18}F]FDG PET/CT study has also been evaluated in melanoma patients. In a study of 56 patients evaluated with contrast-enhanced [^{18}F]FDG PET/CT, lymph node detection was poor (38% vs. 23% for CT), and the detection of systemic metastases was slightly improved, although no statistically significant difference was seen [101]. The precise role of contrast-

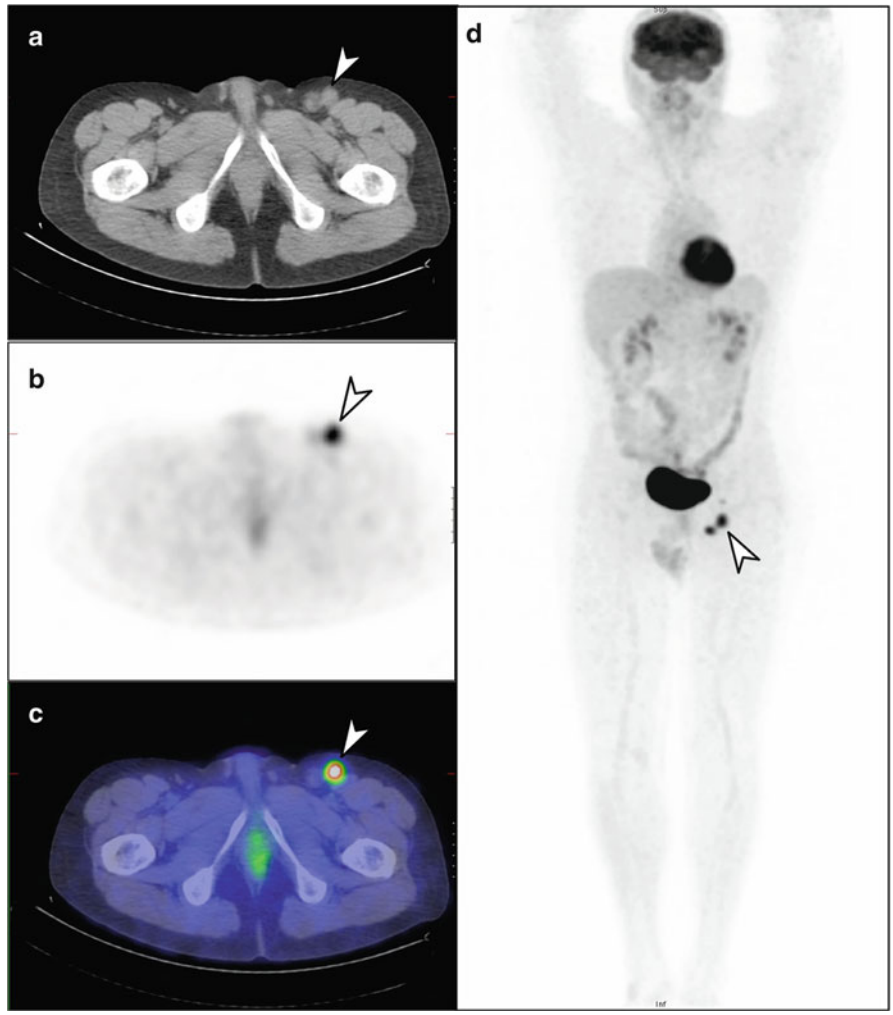

Fig. 6 Staging [^{18}F]FDG PET/CT scan of left heel primary melanoma. (**a**) Transaxial PET, (**b**) CT, and (**c**) PET/CT images show metastatic lymph nodes in the left inguinofemoral region (*arrow*), also seen on (**d**) whole-body PET image, without other metastatic disease identified

enhanced CT with [^{18}F]FDG PET/CT in melanoma is still to be determined. In a study comparing [^{18}F]FDG PET/CT with whole-body MRI in stage III/IV patients, PET/CT was found to be more accurate (86.7% compared to 78.8%), particularly for nodal and skin/subcutaneous metastases, whereas MRI was more accurate for liver, bone, and brain metastases. Changes in treatment were implemented in 64% of patients due to imaging findings, indicating the potential clinical value of combined [^{18}F]FDG PET/CT and organ-specific MRI in melanoma patients [122].

Monitoring Treatment Response

Whole-body [^{18}F]FDG PET can also play a useful role in the treatment monitoring of metastatic melanoma. This is particularly relevant in patients with unresectable regional or distant metastatic disease who are enrolled in immunotherapy, chemotherapy, or biologic therapy protocols. PET has been shown to accurately detect early metabolic response to conventional and experimental therapies in patients with metastatic melanoma (Fig. 16). Therefore, the timely incorporation of whole-body PET into clinical trial protocols may help improve the efficacy of

Table 4 Selected studies of [^{18}F]FDG PET in staging distant metastatic melanoma

Study	Patients	Study type	Clinical use of [^{18}F]FDG PET	Results
Crippa et al. [88]	38	Prospective	Detection of lymph node metastases	Sensitivity 100% of metastases ≥10 mm, 83% of metastases 6–10 mm, and 23% of metastases ≤5 mm
Swetter et al. [99]	104	Retrospective	Initial staging; known or suspected recurrent disease; routine surveillance	Sensitivity 84% Specificity 97%
Harris et al. [96]	92	Retrospective	Detection of metastases	Sensitivity 92% Specificity 88%
Wagner et al. [80]	144	Prospective	Preoperative detection of metastases in patients with Breslow > 1.0 mm, local disease recurrence, or solitary intransit metastases	Sensitivity for detection regional lymph node 21% and specificity 97%. Sensitivity for detection of distant metastatic disease 4% and specificity 86%
Brady et al. [100]	103	Prospective	Detection of metastases in patients with stage IIC, III, IV melanoma	Sensitivity PET versus CT 68% versus 48%. Specificity 92% versus 95%
Bastiaannet et al. [97]	251	Prospective	Detection of metastases in patients with palpable and proven lymph nodes metastases	27% patients correctly upstaged by PET and 24% by CT. PET had an additional value over CT in 14%, and CT over PET in 9%. PET detected more metastatic sites, particularly bone and subcutaneous
Veit-Haibach et al. [101]	56	Prospective	Initial staging after resection of the primary melanoma	Sensitivity N-stage: PET/ceCT[a] and PET-only 38.5%; CT-only 23.1% Sensitivity M-stage: PET/ceCT 41.7%, PET-only 33.3%, CT-only 25.0%
Aukema et al. [102]	70	Prospective	Detection of metastases in patients with palpable lymph nodes	PET/CT: Sensitivity 87% PET/CT: Specificity 98%

[a]PET/ceCT: [^{18}F]FDG PET and combined contrast enhanced CT

Table 5 Studies of management impact of [^{18}F]FDG PET in melanoma patients

Study	Type	Patients	AJCC stage	Clinical use of [^{18}F]FDG PET	Reference test	Change in management after PET
Steinert et al. [91]	Prospective	33	II ($n = 10$) IV ($n = 23$)	Initial staging and restaging in stage IV	Histopathology or conventional imaging	PET: treatment changes in 4 of 29 assessable patients (14%)
Damian et al. [92]	Retrospective	100	I–II ($n = 6$) III–IV ($n = 94$)	Preoperative staging, evaluation of disease status and response to treatment	Clinical examination, histopathology, and conventional imaging	PET: treatment changes in 22 patients (22%)
Rinne et al. [93]	Prospective	100	II ($n = 52$) III–IV ($n = 48$)	Initial staging and restaging for recurrent disease	Conventional imaging	PET: treatment changes in 8 patients (8%)

(*continued*)

Table 5 (continued)

Study	Type	Patients	AJCC stage	Clinical use of [^{18}F]FDG PET	Reference test	Change in management after PET
Tyler et al. [94]	Prospective	95	III	Preoperative staging, restaging and response to treatment	Clinical examination and conventional imaging	PET: treatment changes in 15 patients (16%)
Mijnhout et al. [103]	Prospective	58	II ($n = 4$) III–IV ($n = 54$)	Preoperative staging	Conventional imaging	PET: treatment changes in 23 patients (40%)
Stas et al. [95]	Retrospective	84	IV	Restaging for suspected recurrence or progression	Clinical examination and conventional imaging	PET: treatment changes in 26 patients (31%)
Gulec et al. [104]	Retrospective	49	II ($n = 3$) III–IV ($n = 46$)	Evaluation of extent of disease	Clinical examination and conventional imaging	PET: treatment changes in 24 patients (49%)
Fuster et al. [105]	Retrospective	156	I–II ($n = 98$) III–IV ($n = 58$)	Restaging for suspected recurrent disease	Conventional imaging	PET: treatment changes in 36% of patients
Harris et al. [96]	Retrospective	92	I–II ($n = 8$) III–IV ($n = 84$)	Staging and assessment of response	Clinical follow-up and conventional imaging	PET: treatment changes in 40 patients (32%)
Bastiaannet et al. [106]	Prospective	251	III	Staging	CT	PET: treatment changes in 43 patients (17%)
Brady et al. [100]	Prospective	103	II ($n = 12$) III–IV ($n = 91$)	Preoperative staging	CT	PET: treatment changes in 14 patients (14%)
Reinhardt et al. [107]	Retrospective	250	I–II ($n = 110$) III–IV ($n = 140$)	Initial staging, therapy control, restaging, and follow-up	CT	PET/CT: treatment changes in 121 patients (48%)
Falk et al. [108]	Retrospective	60	I–II ($n = 35$) III–IV ($n = 25$)	Initial staging, therapy control, recurrence staging, follow-up	Histopathology, conventional images and clinical follow-up	PET/CT: treatment changes in 35 patients (28%)
Lagaru et al. [109]	Retrospective	106	I–II ($n = 76$) III–IV ($n = 30$)	Disease restaging	Clinical examination and histopathology	PET/CT: treatment changes in 4 of the 30 patients with stage III–IV (13%)
Fulham et al. [110]	Prospective, multicenter	134	IV	Restaging prior to possible surgery	Clinical examination, pathology, and follow-up	PET changed management in 83 patients (62%)

(*continued*)

Table 5 (continued)

Study	Type	Patients	AJCC stage	Clinical use of [^{18}F]FDG PET	Reference test	Change in management after PET
Veit-Haibach et al. [101]	Prospective	56	I–II ($n = 38$) III–IV ($n = 18$)	Initial staging	Clinical examination and histopathology	PET/CT: treatment changes in 6 patients (11%)
Aukema et al. [102]	Prospective	70	III	Staging before lymph node dissection	Histopathology and/or additional images and/or clinical follow-up	PET/CT: treatment changes in 26 patients (37%)

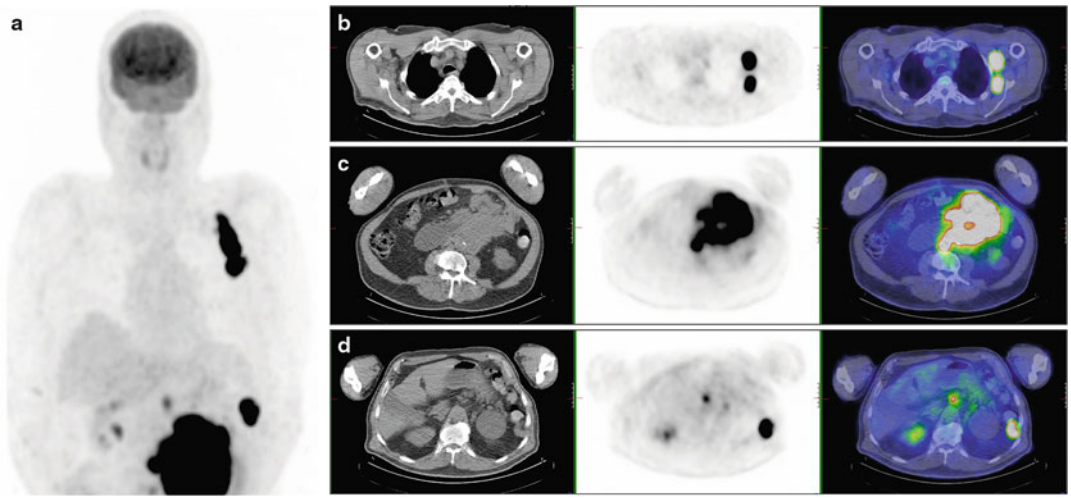

Fig. 7 [^{18}F]FDG PET/CT for staging of melanoma. Whole-body PET image (**a**) shows multiple metastases in left axillary lymph nodes (**b**), abdominal mass (**c**), parasplenic mass, para-aortic lymph node, and mesenteric mass (**d**)

treatment regimens including dosage and scheduling optimization.

In a study of 25 patients with stage IV melanoma, [^{18}F]FDG PET/CT and S-100B (tumor marker) was evaluated after 2–3 cycles of chemotherapy. [^{18}F]FDG PET/CT and CT showed a good correlation with overall response, with a trend for OS to be better in PET initial responders versus nonresponders, and PFS was significantly longer in PET responders versus nonresponders [123]. Brain metastases were better detected with MRI/CT and were often the sites of subsequent relapse. Other studies have also confirmed the utility of [^{18}F]FDG PET in assessing treatment response to chemotherapy and biologic agents [121, 124, 125] (Fig. 17).

Early data suggest that [^{18}F]FDG PET may be suitable for monitoring treatment response to mutation-driven therapies such as vemurafenib and dabrafenib. Mutated BRAF kinase has been shown to activate signaling pathways that up-regulate glucose metabolism, facilitating tumor growth [126]. The inhibition of this pathway by BRAF inhibitors could theoretically be visualized

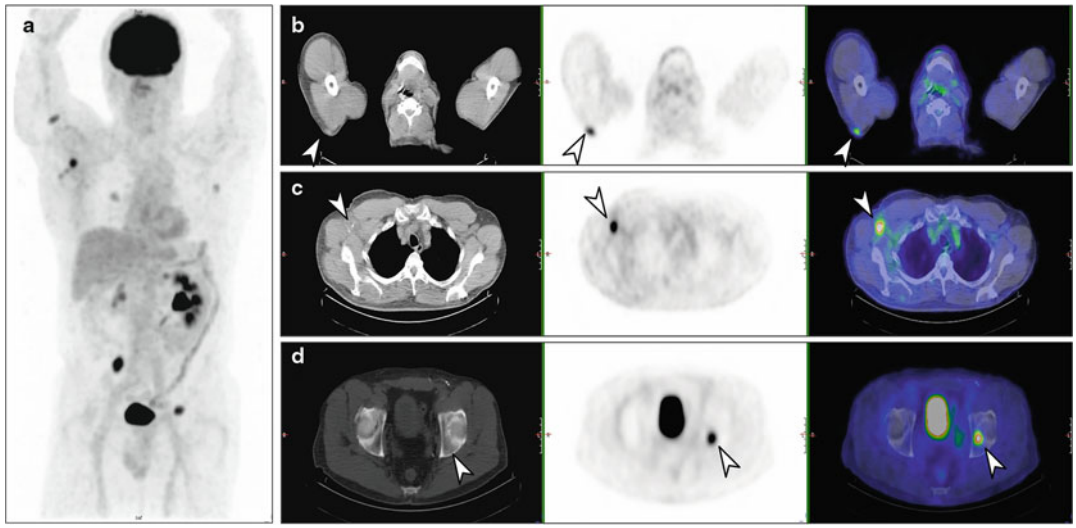

Fig. 8 [^{18}F]FDG PET/CT for postoperative restaging in a patient presenting with a seroma postresection of metastatic melanoma in the right axilla. Multiple locoregional and distant metastatic lesions identified on the whole-body PET scan (**a**), which on axial PET/CT include a cutaneous lesion over right deltoid (**b**), local metastasis in right axilla (**c**), and left acetabulum metastasis (**d**)

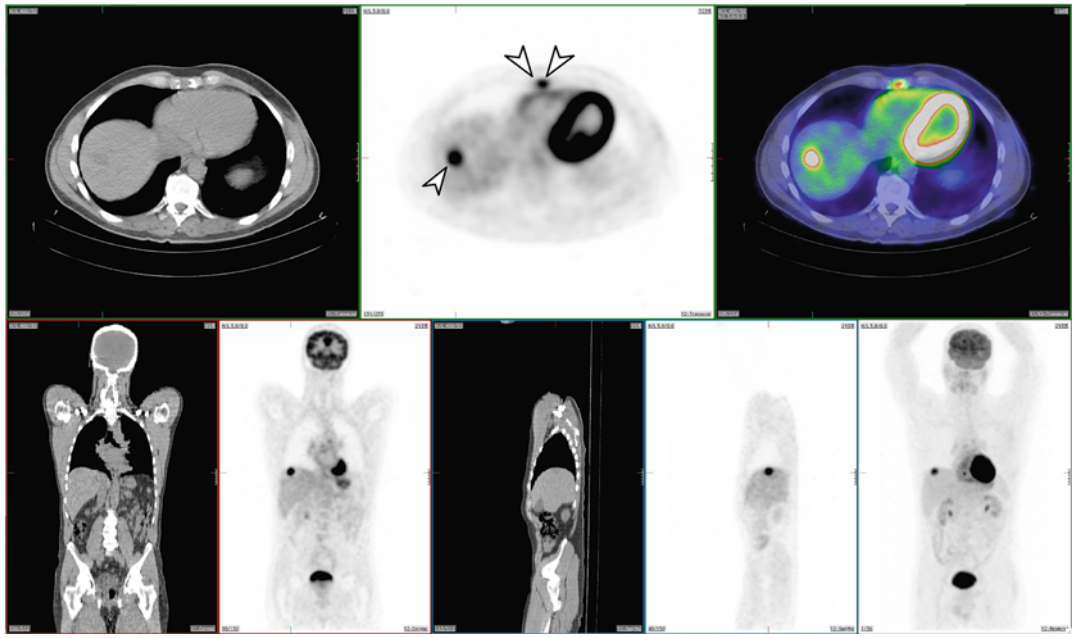

Fig. 9 [^{18}F]FDG PET/CT for restaging following resection of left chest and axillary metastatic melanoma lymph nodes, and new liver lesion on CT scan. Two metastatic lesions are identified, in the liver (*arrow*), and the lower sternum (*double arrows*)

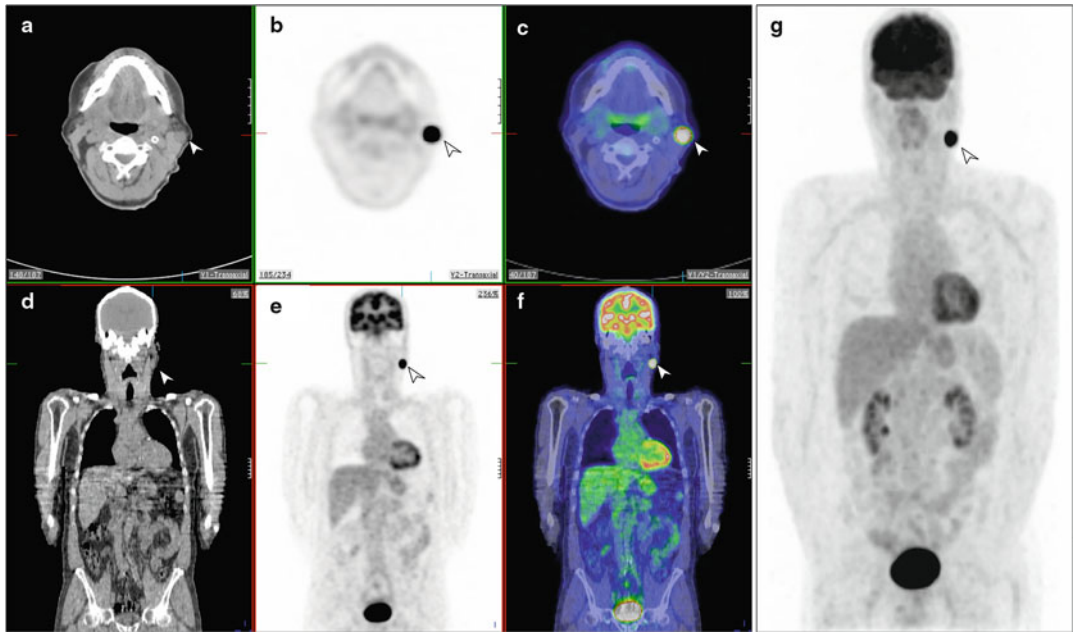

Fig. 10 [^{18}F]FDG PET/CT for restaging of possible left neck nodal recurrence. Axial CT/PET fused images (**a**–**c**) and coronal (**d**–**f**) and whole-body PET image (**g**) show a single metastasis in a left submandibular lymph node (*arrow*)

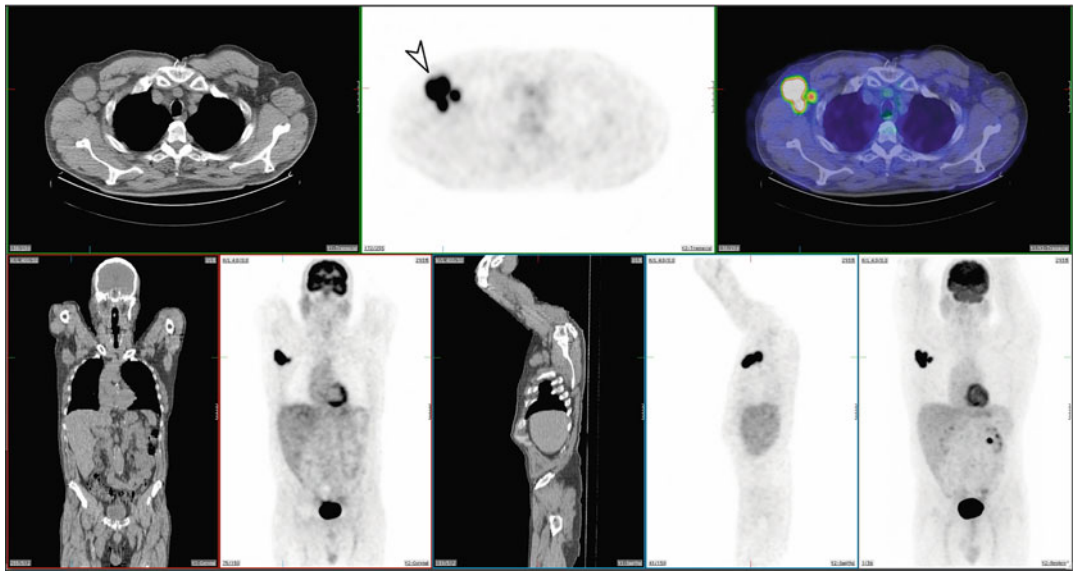

Fig. 11 Locoregional recurrent disease in melanoma patient. [^{18}F]FDG PET/CT shows recurrent metastatic involvement of right axillary lymph nodes (*arrow*), with no evidence of distant metastatic disease

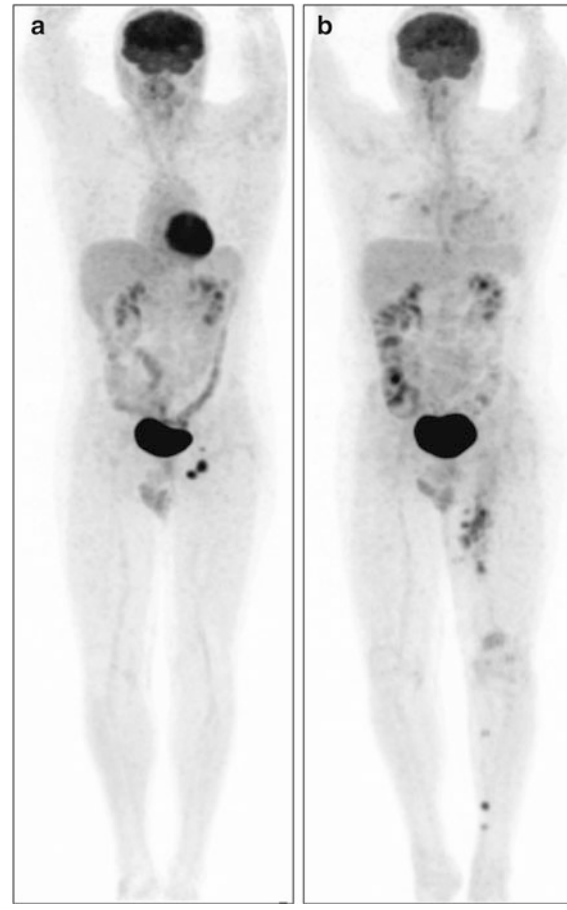

Fig. 12 [^{18}F]FDG PET/CT for restaging posttreatment. (**a**) Whole-body PET shows left inguinal nodal metastasis in a patient with a left lower leg primary melanoma. A whole-body PET scan performed 6 months postresection of left inguinal nodes shows new intransit and left upper leg and inguinal node metastases and new lung metastases (**b**)

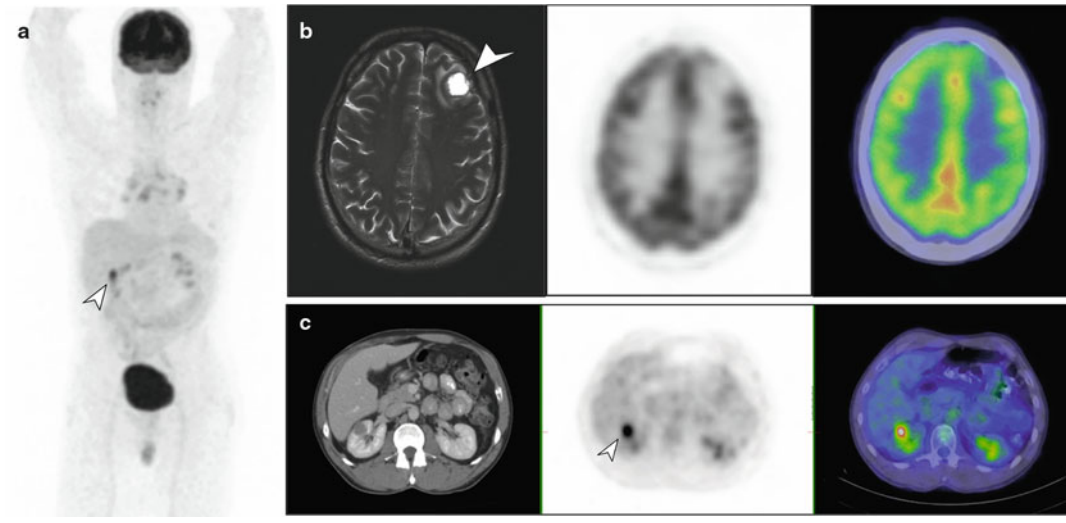

Fig. 13 Restaging [^{18}F]FDG PET/CT prior to cerebral metastasectomy in a patient with known metastatic melanoma. (**a**) Whole-body PET shows a lesion in the right abdomen, localized to the right kidney (*arrow*) on axial PET/CT (**c**). The left frontal lobe metastasis seen on MRI was not [^{18}F]FDG avid (**b**)

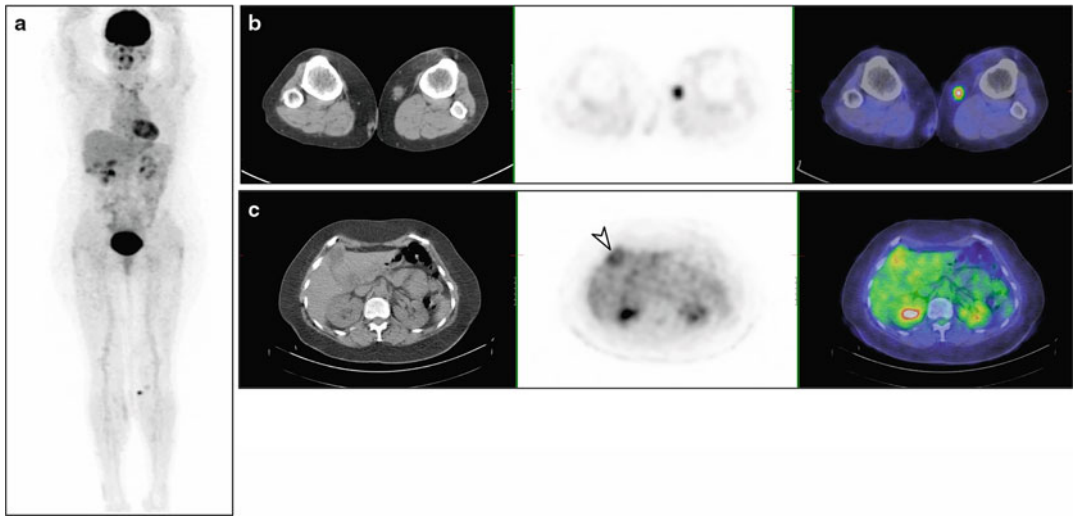

Fig. 14 False-positive [^{18}F]FDG PET/CT scan for liver metastasis. Fifty-year-old lady with melanoma in the left ankle resected 15 years ago presents with intransit recurrence in the left knee for restaging. Whole-body PET (**a**) and PET/CT show increased [^{18}F]FDG uptake in left medial knee intransit metastasis (**b**) and increased [^{18}F]FDG uptake in a 4-cm liver lesion (**c** *arrow*). The liver lesion was biopsied and diagnosed as a hepatic adenoma, with no features of melanoma on immunohistotyping

using [^{18}F]FDG PET (Figs. 18, 19, and 20). In one study the intrapatient heterogeneity of response in metastatic melanoma treated with dabrafenib was evaluated with [^{18}F]FDG PET, and compared with clinical outcomes. They reported that [^{18}F]FDG PET/CT showed responses in all patients, with 26% showing a homogeneous PET response and 74% exhibiting a heterogeneous PET response. Heterogeneity was associated with a shorter time to progression (3.0 months vs. 7.4 months for PET homogeneous responders) [127]. In a phase I study, [^{18}F]FDG PET/CT was found to be a useful marker of an early biologic response to vemurafenib [128]. There was a trend for patients with greater reductions in uptake of [^{18}F]FDG to have longer PFS and the study showed a positive correlation between percentage of injected dose in all identified disease and target-lesion SUV_{max}, although no relationship was found between the reduction in target lesion SUV_{max} and best response according to RECIST.

[^{18}F]FDG PET/CT is commonly used in evaluating melanoma treatment response to immunotherapy, although there are no published studies that have rigorously assessed its role. Several case reports have described the radiologic features of the immune-related adverse reactions and highlighted the challenges of monitoring immunotherapy response, such as the presence of inflammatory cells which are known to be [^{18}F]FDG-avid and can mimic tumor FDG uptake in lymph nodes. [^{18}F]FDG PET/CT may have a role to in the early detection of immune-related adverse events and in directing earlier treatment [129, 130].

Management Impact of [^{18}F]FDG PET/CT

Information on the direct impact of [^{18}F]FDG PET on the clinical management of patients with melanoma strongly supports its role in the surveillance of patients for recurrent disease. In the majority of cases, this involves alteration of decision-making regarding the surgical treatment of recurrent disease (Table 5). Surgery can be curative for stage III disease and is the only therapy that influences survival in patients with stage IV disease [131] (see Figs. 4 and 5). Up to one-quarter of patients with metastatic disease are candidates for potentially curative surgical resection, and 20% of patients who achieve a curative resection become long-term survivors [132].

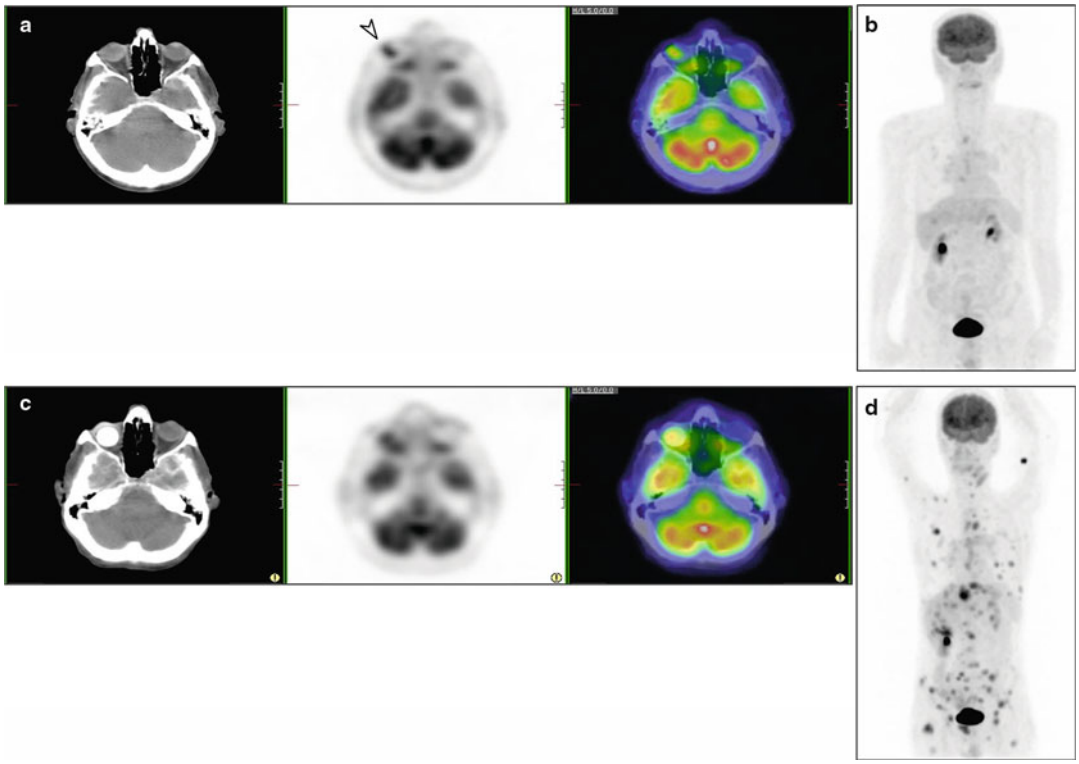

Fig. 15 Ocular melanoma staged with [^{18}F]FDG PET/CT. Primary melanoma of the right eye (*arrow*) seen on axial PET/CT images (**a**) with an involved solitary subcarinal lymph node seen on whole-body PET images (**b**). The patient represented 9 months later with biopsy-proven cervical nodal metastasis for restaging. Recurrent disease is evident on PET/CT around the right eye prosthesis (**c**), and widespread distant metastatic disease is seen in pulmonary, liver, mediastinal, skeletal, and subcutaneous sites (**d**)

Retrospective studies of patients with predominantly stage III and IV disease have suggested that the PET result influences the management of 13–49% of patients [92, 95, 96, 104, 107, 109, 121]. In two prospective studies, the PET result changed patient management 16% of the time in one series of 95 patients with stage III disease and contributed to a change in therapy in 40% of a second series of 58 patients with suspected recurrent melanoma [94, 103]. In a study of 92 patients with primarily stage IV disease, management impact was seen following [^{18}F]FDG PET scans in 40 patient studies (32%), particularly assisting in the selection of patients for surgery [96]. In a recent prospective multicenter study of 134 patients with known or suspected metastatic melanoma evaluated with PET prior to surgery, clinical management was changed in 62% of patients, and the pre-PET surgical plan was reduced by 33%. In addition, patients with additional [^{18}F]FDG-avid lesions were more likely to have progressive disease within 12 months of the initial PET scan [110]. It should be noted that PET can miss small-volume disease and/or micrometastatic disease, as evidenced by some false-negative PET studies and by the number of patients who relapse soon after surgery. It is clear that [^{18}F]FDG PET can assist in appropriate selection of patients for surgery, which in turn can lead to improved progression-free survival, although further studies are required to establish if this may also lead to improved overall survival.

Surveillance

Surveillance follow-up of patients with melanoma is guided by risk factors, patient history, and institutional guidelines. The natural history of melanoma and the likelihood of recurrent disease provide guidance about the frequency and

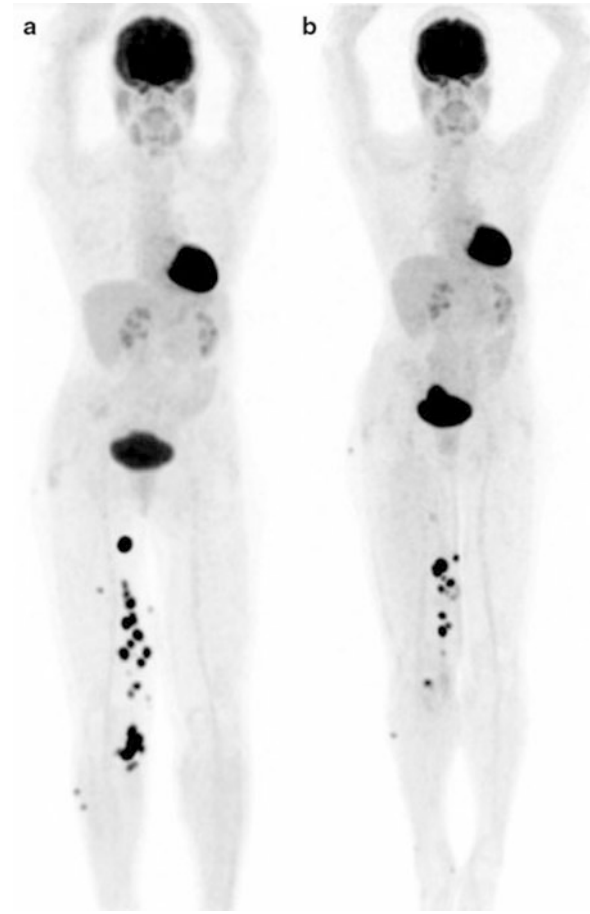

Fig. 16 [^{18}F]FDG PET/CT assessment of treatment response. Initial staging whole-body PET scan (**a**) shows intransit disease in the right leg (**a**). Posttreatment whole-body PET scan performed after resection of the primary lesion and radiotherapy (**b**) shows a partial metabolic response, with persistent intransit disease

duration of follow-up required. In patients with stage I–II melanoma, most recurrences occur within 2 years after initial diagnosis. In a study of 340 patients with stage III melanoma, the sites of relapse were principally systemic in IIIB and IIIC patients, and most relapses occurred within 2–3 years [133]. In stage IV patients, metastatic recurrence usually occurs within 2 years. Melanoma patients with asymptomatic and locoregional recurrences that are subsequently treated have been shown to have improved survival compared to those with symptomatic and distant recurrences [134]. In addition, the type of metastases (i.e., visceral vs. nonvisceral), the number of metastatic sites, and the evolution of metastatic burden over time are significant prognostic factors in treated melanoma patients [135]. Thus, regular follow-up is required for at least 2 years for most melanoma patients, extending to 5 years or more for long-term survivors.

The selection of follow-up investigations in melanoma patients includes blood tests, CT and MRI, and [^{18}F]FDG PET. Blood tests including serum lactate dehydrogenase (LDH) and S-100B have been explored as markers of possible recurrence, but as yet have not achieved routine use. In asymptomatic melanoma patients CT and MRI are of limited value for detecting nodal and visceral metastases [114]. The role of [^{18}F]FDG PET in routine surveillance is also unclear. In one study of 38 patients (AJCC II–III), the ability of PET to uncover silent metastases from melanoma was estimated at 34%, thereby avoiding futile and cost-prohibitive interventions [136]. In a cost-effectiveness study exploring the use of [^{18}F]FDG PET/CT versus whole-body CT for

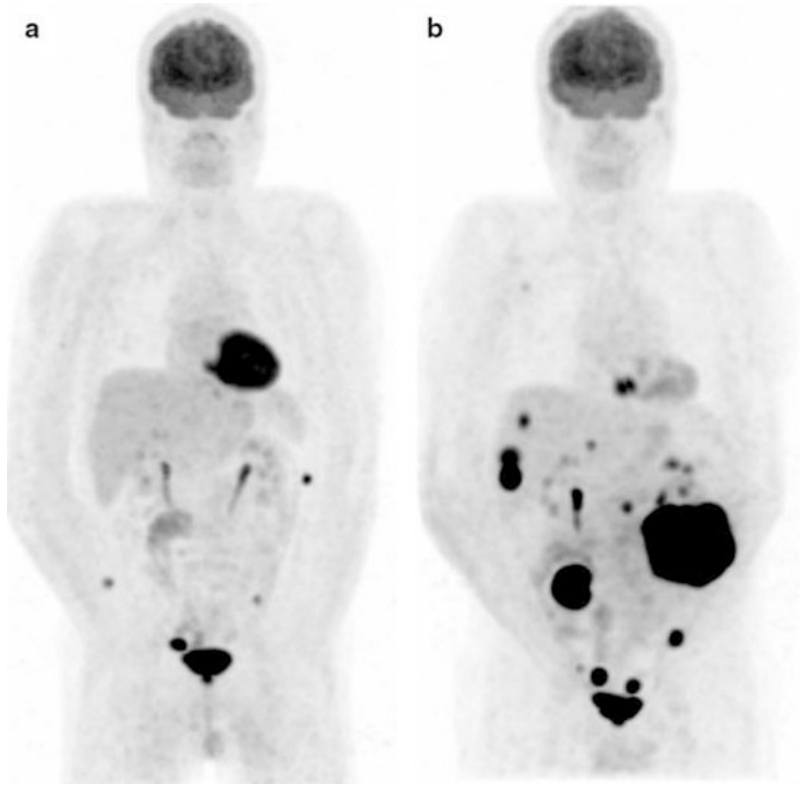

Fig. 17 [^{18}F]FDG PET/CT assessment of treatment response to chemotherapy. The patient had a history of metastatic melanoma and right axillary dissection and underwent chemotherapy for systemic disease. Whole-body PET image before treatment (**a**), and 6 months later (**b**) shows progressive metastatic disease despite treatment

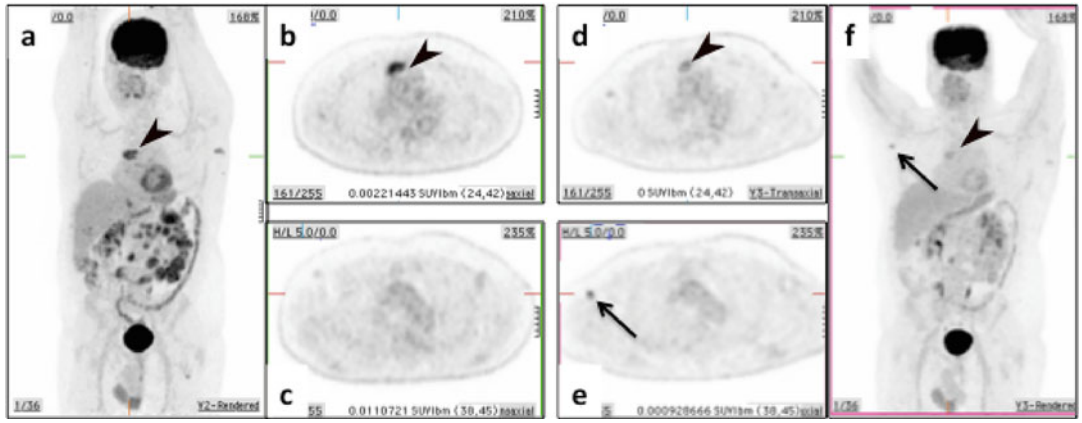

Fig. 18 [^{18}F]FDG PET/CT assessment of treatment response to combination BRAF/MEK1 inhibitor treatment (dabrafenib/trametinib). The patient had [^{18}F]FDG-avid disease in the abdomen and mediastinum seen on baseline (**a**, **b**); with posttreatment scans showing a partial metabolic response to treatment (**d**, **f**) and the appearance of a [^{18}F]FDG-avid node in the right axilla (**c**, **e**) due to reactive node rather than progressive disease

surveillance of melanoma patients with suspected pulmonary metastases, [^{18}F]FDG PET/CT was found to be less costly and resulted in 20% less futile surgeries and a potential survival benefit at 10 years [137]. The likelihood of PET detecting recurrent disease is higher in patients with symptoms and recent treatment of metastatic disease, and in these clinical scenarios, PET is more likely

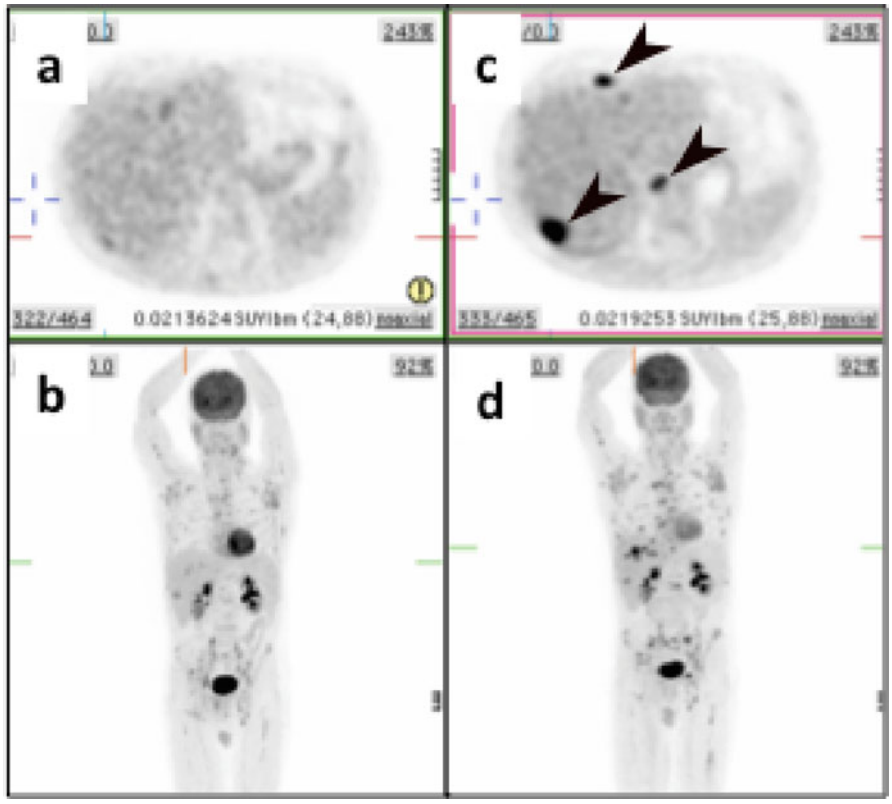

Fig. 19 [^{18}F]FDG PET/CT assessment of treatment response to combination BRAF/MEK1 inhibitor treatment (dabrafenib/trametinib). Baseline study (**a**, **b**), with progressive metabolic disease noted in the liver on follow-up study (**c**, **d**)

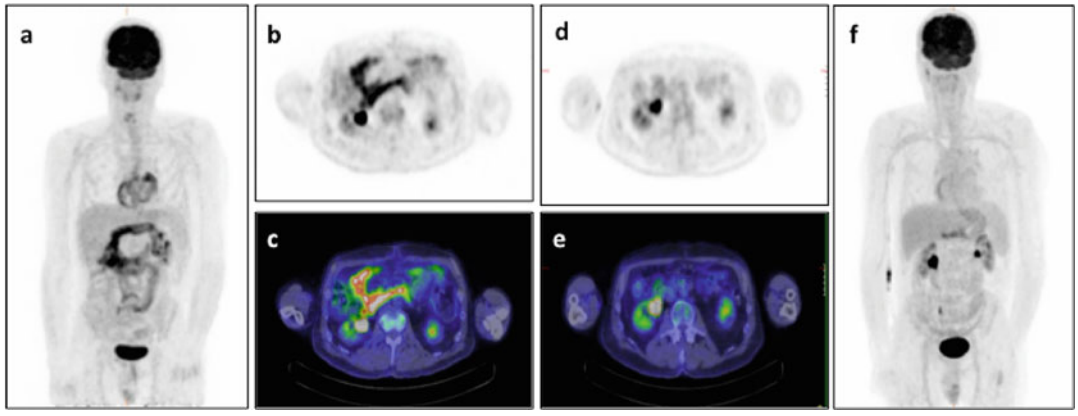

Fig. 20 [^{18}F]FDG PET/CT assessment of treatment response to nivolumab. Baseline study (**a**–**c**) showing treatment related enteritis which resolved with steroid treatment (**d**–**f**)

to detect sites of recurrence compared to other investigations. The use of [^{18}F]FDG PET for surveillance is yet to be formally established in practice guidelines, and its use should be guided by individual patient history and clinical suspicion of recurrence.

Non-[^{18}F]FDG PET Tracers in Melanoma

[^{18}F]FDG PET has gained wide acceptance in patients with malignant melanoma, in particular, for staging, restaging, and therapy monitoring. However, the detection of metastatic lesions in the brain may be difficult due to the high background; elsewhere in the body there may be false-positive sites due to nonmalignant lesions such as inflammation or infection. In view of this, a number of other PET tracers have been evaluated in melanoma patients.

In a study of ^{18}F-fluorothymidine (^{18}F-FLT) PET in 10 patients with clinical stage III melanoma, ^{18}F-FLT PET had a sensitivity of 88% and a specificity of 60% for metastatic disease when compared with histopathological evaluation. The detection limit for lymph node metastases was approximately 6 mm, which is similar to the [^{18}F]FDG and a consequence of the spatial resolution of the PET camera. It is still unlikely that ^{18}F-FLT PET could be a suitable alternative to [^{18}F]FDG PET in melanoma patients with stage III disease [138].

Another PET compound receiving particular interest in melanoma is [^{18}F]fluoro-L-dopa (^{18}F-DOPA). Experimental studies have shown that ^{18}F-DOPA is incorporated into melanin and therefore represents an indicator of melanogenesis [139]. In a study of 11 pretreated patients with metastatic melanoma studied with ^{18}F-DOPA [^{15}O]water and [^{18}F]FDG PET, ^{18}F-DOPA PET was found to provide different information from [^{18}F]FDG PET because its uptake was not perfusion dependent, and the detectability of metastases was enhanced when both tracers were used (combined sensitivity of 95%). ^{18}F-DOPA PET could therefore be helpful to increase the accuracy of PET for therapy management in those patients with treated metastases and negative [^{18}F]FDG findings [140].

^{18}F-Galacto RGD (specific for a beta-integrin found in tumor vasculature and on melanoma cells) is another PET tracer that has been investigated in a clinical setting. In a study of 19 patients, 7 of whom had malignant melanoma, most known lesions were identified; however, intensity of uptake varied, most likely related to differing levels of a b-integrin found in tumors [141]. Additional PET tracers including ^{18}F-*N*-(2-(diethylamino)ethyl)-6-fluoronicotinamide have been shown to have promise in preclinical studies [142]. Further studies are required to define the utility of non-[^{18}F]FDG PET tracers in melanoma.

Conclusions

Nuclear medicine has a pivotal role to play in the management of patients with melanoma, including initial staging, restaging, assisting in therapy selection, treatment response assessment, and surveillance. Lymphoscintigraphy has a major role in sentinel node identification, and SPECT/CT provides improved lesion detection and anatomical localization in this clinical setting. In initial staging, [^{18}F]FDG PET has an important role in detecting extent of metastatic spread beyond microscopic locoregional nodal involvement and has a potential role in evaluating AJCC stage II patients with thick primary tumors or high risk factors and in patients with stage III disease. Published guidelines clearly indicate the importance of PET in staging patients with stage IV disease and assisting in treatment decisions. Studies comparing PET with [^{18}F]FDG PET/CT have convincingly shown the improved accuracy of [^{18}F]FDG PET/CT over PET alone. In restaging, PET may be indicated where there are suspicious clinical symptoms, intransit disease or palpable lymphadenopathy, or other suggestions of possible locoregional or metastatic disease. PET clearly impacts on patient management and can guide treatment decisions. Although there is controversy over the role of PET in surveillance, the sensitivity of [^{18}F]FDG PET/CT makes it valuable in patients with high-risk disease. The use of new PET tracers may assist in more accurate staging of disease in the future and assist in developing biologic therapies targeted to specific oncogenic pathways in melanomas.

References

1. Diepgen TL, Mahler V. The epidemiology of skin cancer. Br J Dermatol. 2002;146 Suppl 61:1–6.
2. Ferlay J, Soerjomataram I, Ervik M, Dikshit R, Eser S, Mathers C, et al. GLOBOCAN 2012 v1.0, Cancer incidence and mortality worldwide: IARC

CancerBase No. 11 [Internet]. Lyon: International Agency for Research on Cancer; 2013.
3. Australian Institute of Health and Welfare. Cancer in Australia: an overview, 2014. Canberra: Australian Government; 2014.
4. European Network of Cancer Registries No. 4, November 2003.
5. American Cancer Society. Cancer facts & figures 2009. Atlanta: American Cancer Society; 2009.
6. Bishop DT, Demenais F, Goldstein AM, et al. Geographical variation in the penetrance of CDKN2A mutations for melanoma. J Natl Cancer Inst. 2002;94:894–903.
7. Goggins WB, Tsao H. A population-based analysis of risk factors for a second primary cutaneous melanoma among melanoma survivors. Cancer. 2003; 97:639–43.
8. Miller AJ, Mihm Jr MC. Melanoma. N Engl J Med. 2004;351:998–1012.
9. Gilchrest BA, Eller MS, Geller AC, Yaar M. The pathogenesis of melanoma induced by ultraviolet radiation. N Engl J Med. 1999;340:1341–8.
10. Haluska FG, Tsao H, Wu H, Haluska FS, Lazar A, Goel V. Genetic alterations in signaling pathways in melanoma. Clin Cancer Res. 2006;12(7 Pt 2): 2301s–7.
11. Davies H, Bignell GR, et al. Mutations of the BRAF gene in human cancer. Nature. 2002;417:949–54.
12. Disis ML. Mechanism of action of immunotherapy. Semin Oncol. 2014;41 Suppl 5:S3–13.
13. Carmeliet P, Jain RK. Angiogenesis in cancer and other diseases. Nature. 2000;407(6801):249–57.
14. Ferrara N. Vascular endothelial growth factor: basic science and clinical progress. Endocr Rev. 2004;25:581–611.
15. Salven P, Heikkila P, Joensuu H. Enhanced expression of vascular endothelial growth factor in metastatic melanoma. Br J Cancer. 1997;76:930–4.
16. Bayer-Garner IB, Hough Jr AJ, Smoller BR. Vascular endothelial growth factor expression in malignant melanoma: prognostic versus diagnostic usefulness. Mod Pathol. 1999;12:770–4.
17. Barnhill RL, Xiao M, Graves D, Antoniades HN. Expression of platelet-derived growth factor (PDGF)-A, PDGF-B and the PDGF-alpha receptor, but not the PDGF-beta receptor, in human malignant melanoma in vivo. Br J Dermatol. 1996;135: 898–904.
18. Rofstad EK, Halsor EF. Vascular endothelial growth factor, interleukin 8, platelet-derived endothelial cell growth factor, and basic fibroblast growth factor promote angiogenesis and metastasis in human melanoma xenografts. Cancer Res. 2000;60:4932–8.
19. Jost LM. ESMO minimum clinical recommendations for diagnosis, treatment and follow-up of cutaneous malignant melanoma. Ann Oncol. 2003;14:1012–3.
20. American Joint Committee on Cancer (AJCC). TNM staging system for melanoma. 7th ed. New York: Springer; 2010.
21. Balch CM, Soong SJ, Gershenwald JE, et al. Prognostic factors analysis of 17,600 melanoma patients: validation of the American Joint Committee on Cancer melanoma staging system. J Clin Oncol. 2001;19:3622–34.
22. Morton DL, Thompson JF, Essner R. Validation of the accuracy of intraoperative lymphatic mapping and sentinel lymphadenectomy for early-stage melanoma: a multicenter trial. Multicenter Selective Lymphadenectomy Trial Group. Ann Surg. 1999; 230:453–63.
23. Gershenwald JE, Thompson W, Mansfield PF, et al. Multi-institutional melanoma lymphatic mapping experience: the prognostic value of sentinel lymph node status in 612 stage I or II melanoma patients. J Clin Oncol. 1999;17:976–83.
24. Meier F, Will S, Ellwanger U, Schlagenhauff B, Schittek B, Rassner G, Garbe C. Metastatic pathways and time courses in the orderly progression of cutaneous melanoma. Br J Dermatol. 2002;147:62–70.
25. Leiter U, Meier F, Schittek B, Garbe C. The natural course of cutaneous melanoma. J Surg Oncol. 2004;86:172–8.
26. Manola J, Atkins M, Ibrahim J, Kirkwood J. Prognostic factors in metastatic melanoma: a pooled analysis of Eastern Cooperative Oncology Group trials. J Clin Oncol. 2000;18:3782–93.
27. NCCN Clinical Practice Guidelines in Oncology™ Melanoma. V.2.2016.
28. Morton DL, Thompson JF, Cochran AJ, et al. Sentinel-node biopsy or nodal observation in melanoma. N Engl J Med. 2006;355:1307–17.
29. Barnhill RL, Katzen J, Spatz A, Fine J, Berwick M. The importance of mitotic rate as a prognostic factor for localized cutaneous melanoma. J Cutan Pathol. 2005;32:268–73.
30. Azzola MF, Shaw HM, Thompson JF, et al. Tumor mitotic rate is a more powerful prognostic indicator than ulceration in patients with primary cutaneous melanoma. Cancer. 2003;97:1488–98.
31. Thompson JF, Shaw HM. Is sentinel lymph node biopsy appropriate in patients with thin melanomas: too early to tell? Ann Surg Oncol. 2006;13:279–81.
32. Nathan FE, Mastrangelo MJ. Adjuvant therapy for cutaneous melanoma. Semin Oncol. 1995;22: 647–61.
33. Santinami M, Maurichi A, Patuzzo R, Pennacchioli E, Cascinelli N. Impact of clinical trials on the treatment of melanoma. Surg Oncol Clin N Am. 2001; 10: 935–47.
34. Kirkwood JM, Strawderman MH, Ernstoff MS, et al. Interferon alpha-2b adjuvant therapy of high-risk resected cutaneous melanoma: the Eastern Cooperative Oncology Group Trial EST 1684. J Clin Oncol. 1996;14:7–17.
35. Kirkwood JM, Manola J, Ibrahim J, et al. A pooled analysis of Eastern Cooperative Oncology Group and intergroup trials of adjuvant high-dose interferon for melanoma. Clin Cancer Res. 2004;10:1670–7.

36. Eggermont AM, Suciu S, Santinami M, et al. Adjuvant therapy with pegylated interferon alpha-2b versus observation alone in resected stage III melanoma: final results of EORTC 18991, a randomized phase III trial. Lancet. 2008;372:117–26.
37. Grob JJ, Dreno B, de la Salmoniere P, et al. Randomised trial of interferon alpha-2a as adjuvant therapy in resected primary melanoma thicker than 1.5 mm without clinically detectable node metastases. French Cooperative Group on Melanoma. Lancet. 1998;351:1905–10.
38. Mitchell MS, Abrams J, Thompson JA, et al. Randomized trial of an allogeneic melanoma lysate vaccine with low-dose interferon alpha-2b compared with high-dose interferon alpha-2b for resected stage III cutaneous melanoma. J Clin Oncol. 2007;25: 2078–85.
39. Kevin B, Kima KB, Sewa S, et al. A randomized phase III trial of biochemotherapy versus interferon-α-2b for adjuvant therapy in patients at high risk for melanoma recurrence. Melanoma Res. 2009;19:42–9.
40. Eggermont AM, Chiaron-Sileni V, Grob JJ, et al. Adjuvant ipilimumab versus placebo after complete resection of high risk stage III melanoma (EORTC 18071): a randomized, double blind, phase III trial. Lancet Oncol. 2015;16:522–30.
41. NCCN Clinical Practice Guidelines in Oncology Melanoma v.2.2009.
42. Balch CM, Gershenwald JE, Soong S-J, et al. Final version of 2009 AJCC melanoma staging and classification. J Clin Oncol. 2009;27:6199–206.
43. Blesa JMG, Pulido EG, Pulla MP, Cande VA. Treatment options for metastatic melanoma. A systematic review. Cancer Ther. 2009;7:188–99.
44. Sosman JA, Kim KB, Schuchter L, et al. Survival in BRAF V600-mutant advanced melanoma treated with vemurafenib. N Engl J Med. 2012;366:707–14.
45. Chapman PB, Hauschild A, Robert C, et al. Improved survival with vemurafenib in melanoma with BRAF V600E mutation. N Engl J Med. 2011; 364:2507–16.
46. Trefzer U, Minor D, Ribas A, et al. BREAK-2: a phase IIA trial of the selective BRAF kinase inhibitor GSK2118436 in patients with BRAF mutation-positive (V600E/K) metastatic melanoma. Pigment Cell Melanoma Res. 2011;24:1020.
47. Falchook GS, Long GV, Kurzrock R, et al. Dabrafenib in patients with melanoma, untreated brain metastases, and other solid tumours: a phase 1 dose-escalation trial. Lancet. 2012;379:1893–901.
48. Hauschild A, Grob JJ, Demidov LV, et al. Dabrafenib in BRAF-mutated metastatic melanoma: a multicentre, open-label, phase 3 randomised controlled trial. Lancet. 2012;380(9839):358–65.
49. Flaherty KT, Robert C, Hersey P, et al. Improved survival with MEK inhibition in BRAF-mutated melanoma. N Engl J Med. 2012;367:107–14.
50. Long GV, Stroyakovskiy D, Gogas H, et al. Combined BRAF and MEK inhibition versus BRAF inhibition alone in melanoma. N Engl J Med. 2014;371:1877–88.
51. Larkin J, Ascierto PA, Dreno B, et al. Combined vemurafenib and cobimetinib in BRAF-mutated melanoma. N Engl J Med. 2014;371:1867–76.
52. Hodi FS, O'Day SJ, McDermott DF, et al. Improved survival with ipilimumab in patients with metastatic melanoma. N Engl J Med. 2010;363:711–23.
53. Robert C, Thomas L, Bondarenko I, et al. Ipilimumab plus dacarbazine for previously untreated metastatic melanoma. N Engl J Med. 2011;364:2517–26.
54. Daud A, Robert C, Hodi S, et al. Long-term efficacy of pembrolizumab (MK-3475) in a pooled analysis of 655 patients with advanced melanoma enrolled in KEYNOTE-001. ASCO Annual meeting; 2015.
55. Ribas A PI, et al. A randomized controlled comparison of pembrolizumab and chemotherapy in patients with ipilimumab refractor melanoma. In: Society of Melanoma Research Conference; 2014.
56. Robert C, Schachter J, Long GV, et al. Pembrolizimab versus ipilimumab in advanced melanoma. N Engl J Med. 2015;372:2521–32.
57. Weber JS, D'Angelo SP, Minor D, et al. Nivolumab versus chemotherapy in patients with advanced melanoma who progressed after anti-CTLA-4 treatment (CheckMate 037): a randomized, controlled, open-label phase # trial. Lancet Oncol. 2015;16:375–84.
58. Robert C, Long GV, Brady B, et al. Nivolumab in previously untreated melanoma without BRAF mutation. N Engl J Med. 2015;372:320–30.
59. Larkin J, Chiarion-Sileni V, Gonzales R, et al. Combined nivolumab and ipilimumab or monotherapy in intreated melanoma. N Engl J Med. 2015;372: 2521–32.
60. Ribas A, Hodi FS, Callahan M, Konto C, Wolchok J. Hepatotoxicity with combination of vemurafenib and ipilimumab. N Engl J Med. 2013;368:1365–6.
61. Ribas A, et al. Phase I study combining anti-PD-L1 (MEDI4736) with BRAF (dabrafenib) and/or MEK (trametinib) inhibitors in advanced melanoma. J Clin Oncol. 2015;33(Suppl):3003.
62. Carvajal RD, Antonescu CR, Wolchok JD, et al. KIT as a therapeutic target in metastatic melanoma. JAMA. 2011;305:2327–34.
63. Varker A, Biber J, Kefauver C, et al. A randomized phase 2 trial of bevacizumab with or without daily low-dose interferon alpha-2b in metastatic malignant melanoma. Ann Surg Oncol. 2007;14:2367–76.
64. Perez DG, Suman VJ, Fitch TR, et al. Phase 2 trial of carboplatin, weekly paclitaxel, and biweekly bevacizumab in patients with unresectable stage IV melanoma: a North Central Cancer Treatment Group study, N047 A. Cancer. 2009;115:119–27.
65. Vihinen PP, Hernberg M, Vuoristo MS, et al. A phase II trial of bevacizumab with dacarbazine and daily low-dose interferon-alpha2a as first line treatment in metastatic melanoma. Melanoma Res. 2010; 20: 318–25.

66. Slingluff Jr CR, Petroni GR, Molhoek KR, et al. Clinical activity and safety of combination therapy with temsirolimus and bevacizumab for advanced melanoma: a phase II trial (CTEP 7190/Mel47). Clin Cancer Res. 2013;19:3611–20.
67. Bedikian AY, Millward M, Pehamberger H, et al. Bcl-2 antisense (oblimersen sodium) plus dacarbazine in patients with advanced melanoma: the Oblimersen Melanoma Study Group. J Clin Oncol. 2006; 24: 4738–45.
68. Wagner JD, Schauwecker D, Davidson D, Coleman 3rd JJ, Saxman S, Hutchins G, Love C, Hayes JT. Prospective study of fluorodeoxyglucose-positron emission tomography imaging of lymph node basins in melanoma patients undergoing sentinel node biopsy. J Clin Oncol. 1999;17:1508–15.
69. Belhocine T, Scott AM, Even-Sapir E, Essner R. The role of nuclear medicine in the management of cutaneous malignant melanoma. J Nucl Med. 2006; 47:957–67.
70. Klein M, Freedman N, Lotem M, et al. Contribution of whole body F-18-FDG-PET and lymphoscintigraphy to the assessment of regional and distant metastases in cutaneous malignant melanoma. A pilot study. Nuklearmedizin. 2000;39:56–61.
71. Acland KM, Healy C, Calonje E, et al. Comparison of positron emission tomography scanning and sentinel node biopsy in the detection of micrometastases of primary cutaneous malignant melanoma. J Clin Oncol. 2001;19:2674–8.
72. Kokoska MS, Olson G, Kelemen PR, et al. The use of lymphoscintigraphy and PET in the management of head and neck melanoma. Otolaryngol Head Neck Surg. 2001;125:213–20.
73. Belhocine T, Pierard G, De Labrassinne M, Lahaye T, Rigo P. Staging of regional node in AJCC stage I and II melanoma: [^{18}F]FDG PET imaging versus sentinel node detection. Oncologist. 2002;7:271–8.
74. Havenga K, Cobben DC, Oyen WJ, et al. Fluorodeoxyglucose-positron emission tomography and sentinel lymph node biopsy in staging primary cutaneous melanoma. Eur J Surg Oncol. 2003;29:662–4.
75. Longo MI, Lazaro P, Bueno C, Carreras JL, Montz R. Fluorodeoxyglucose-positron emission tomography imaging versus sentinel node biopsy in the primary staging of melanoma patients. Dermatol Surg. 2003;29:245–8.
76. Schafer A, Herbst RA, Beiteke U, et al. Sentinel lymph node excision (SLNE) and positron emission tomography in the staging of stage I–II melanoma patients. Hautarzt. 2003;54:440–7.
77. Fink AM, Holle-Robatsch S, Herzog N, et al. Positron emission tomography is not useful in detecting metastasis in the sentinel lymph node in patients with primary malignant melanoma stage I and II. Melanoma Res. 2004;14:141–5.
78. Hafner J, Schmid MH, Kempf W, Burg G, Kunzi W, Meuli-Simmen C, et al. Baseline staging in cutaneous malignant melanoma. Br J Dermatol. 2004;150:677–86.
79. Libberecht K, Husada G, Peeters T, Michiels P, Gys T, Molderez C. Initial staging of malignant melanoma by positron emission tomography and sentinel node biopsy. Acta Chir Belg. 2005;105:621–5.
80. Wagner JD, Schauwecker D, Davidson D, et al. Inefficacy of F-18 fluorodeoxy-D-glucose-positron emission tomography scans for initial evaluation in early-stage cutaneous melanoma. Cancer. 2005; 104:570–9.
81. Vereecken P, Laporte M, Petein M, Steels E, Heenen M. Evaluation of extensive initial staging procedure in intermediate/high-risk melanoma patients. J Eur Acad Dermatol Venereol. 2005;19:66–73.
82. Clark PB, Soo V, Kraas J, Shen P, Levine EA. Futility of fluorodeoxyglucose F-18 positron emission tomography in initial evaluation of patients with T2 to T4 melanoma. Arch Surg. 2006;141:284–8.
83. Kell MR, Ridge JA, Joseph N, Sigurdson ER. PET/CT imaging in patients undergoing sentinel node biopsy for melanoma. Eur J Surg Oncol. 2007; 33:911–3.
84. Maubec E, Lumbroso J, Masson F, et al. F-18 fluorodeoxy-D-glucose positron emission tomography scan in the initial evaluation of patients with a primary melanoma thicker than 4 mm. Melanoma Res. 2007;17:147–54.
85. Constantinidou A, Hofman M, O'Doherty M, Acland KM, Healy C, Harries M. Routine positron emission tomography and positron emission tomography/computed tomography in melanoma staging with positive sentinel node biopsy is of limited benefit. Melanoma Res. 2008;18:56–60.
86. Singh B, Ezziddin S, Palmedo H, et al. Preoperative [^{18}F]-FDG-PET/CT imaging and sentinel node biopsy in the detection of regional lymph node metastases in malignant melanoma. Melanoma Res. 2008;18:346–52.
87. Klode J, Dissemond J, Grabbe S, Hillen U, Poeppel T, Boeing C. Sentinel lymph node excision and PET-CT in the initial stage of malignant melanoma: a retrospective analysis of 61 patients with malignant melanoma in American Joint Committee on cancer stages I and II. Dermatol Surg. 2010;36:439–45.
88. Crippa F, Leutner M, Belli F, et al. Which kinds of lymph node metastases can FDG PET detect? A clinical study in melanoma. J Nucl Med. 2000;41:1491–4.
89. Mijnhout GS, Hoekstra OS, van Lingen A, van Diest PJ, Adèr HJ, Lammertsma AA, Pijpers R, Meijer S, Teule GJJ. How morphometric analysis of metastatic load predicts the (un)usefulness of PET scanning: the case of lymph node staging in melanoma. J Clin Pathol. 2003;56:283–6.
90. Fletcher JW, Djulbegovic B, Soares HP, et al. Recommendations on the use of [^{18}F]FDG PET in oncology. J Nucl Med. 2008;49:480–508.
91. Steinert HC, Huch Boni RA, Buck A, et al. Malignant melanoma: staging with whole-body positron emission tomography and 2-[F-18]-fluoro-2-deoxy-D-glucose. Radiology. 1995;195:705–9.

92. Damian DL, Fulham MJ, Thompson E, Thompson JF. Positron emission tomography in the detection and management of metastatic melanoma. Melanoma Res. 1996;6:325–9.
93. Rinne D, Baum RP, Hor G, Kaufmann R. Primary staging and follow-up of high risk melanoma patients with whole-body [^{18}F]fluorodeoxyglucose positron emission tomography: results of a prospective study of 100 patients. Cancer. 1998;82:1664–71.
94. Tyler DS, Onaitis M, Kherani A, et al. Positron emission tomography scanning in malignant melanoma. Cancer. 2000;89:1019–25.
95. Stas M, Stroobants S, Dupont P, et al. [^{18}F]FDG PET scan in the staging of recurrent melanoma: additional value and therapeutic impact. Melanoma Res. 2002;12:479–90.
96. Harris MT, Berlangieri SU, Cebon JS, Davis ID, Scott AM. Impact of 2-deoxy-2[F-18]fluoro-D-glucose positron emission tomography on the management of patients with advanced melanoma. Mol Imaging Biol. 2005;7:304–8.
97. Bastiaannet E, Wobbes T, Hoekstra OS, et al. Prospective comparison of [^{18}F]FDG PET/CT in patients with melanoma and palpable lymph node metastases: diagnostic accuracy and impact on treatment. J Clin Oncol. 2009;27:4774–80.
98. Niebling MG, Bastiaannet E, Hoekstra OS, Bonenkamp JJ, Koelemij R, Hoekstra HJ. Outcome of clinical stage III melanoma patients with FDG-PET and whole-body CT added to the diagnostic workup. Ann Surg Oncol. 2013;20:3098–105.
99. Swetter SM, Carroll LA, Johnson DL, Segall GM. Positron emission tomography is superior to computed tomography for metastatic detection in melanoma patients. Ann Surg Oncol. 2002;9:646–53.
100. Brady MS, Akhurst T, Spanknebel K, et al. Utility of preoperative [^{18}]F-fluorodeoxyglucose-positron emission tomography scanning in high-risk melanoma patients. Ann Surg Oncol. 2006;13:525–32.
101. Veit-Haibach P, Vogt FM, Jablonka R, et al. Diagnostic accuracy of contrast enhanced FDG-PET/CT in primary staging of cutaneous malignant melanoma. Eur J Nucl Med Mol Imaging. 2009;36:910–8.
102. Aukema TS, Valdés Olmos RA, Wouters WJM, et al. Utility of preoperative [^{18}F]FDG PET/CT and brain MRI in melanoma patients with palpable lymph node metastases. Ann Surg Oncol. 2010;17:2773–8.
103. Mijnhout GS, Comans EF, Raijmakers P, et al. Reproducibility and clinical value of [^{18}F]-fluorodeoxyglucose positron emission tomography in recurrent melanoma. Nucl Med Commun. 2002;23:475–81.
104. Gulec SA, Faries MB, Lee CC, et al. The role of fluorine-18 deoxyglucose positron emission tomography in the management of patients with metastatic melanoma: impact on surgical decision making. Clin Nucl Med. 2003;28:961–5.
105. Fuster D, Chiang S, Johnson G, Schuchter LM, Zhuang H, Alavi A. Is [^{18}F]FDG PET more accurate than standard diagnostic procedures in the detection of suspected recurrent melanoma? J Nucl Med. 2004;45:1323–7.
106. Bastiaannet E, Oyen WJ, Meijer S, et al. Impact of [^{18}F]fluorodeoxyglucose positron emission tomography on surgical management of melanoma patients. Br J Surg. 2006;93:243–9.
107. Reinhardt MJ, Joe AY, Jaeger U, et al. Diagnostic performance of whole body dual modality [^{18}F]FDG PET/CT imaging for N- and M-staging of malignant melanoma: experience with 250 consecutive patients. J Clin Oncol. 2006;24:1178–87.
108. Falk MS, Truitt AK, Coakley FV, Kashani-Sabet M, Hawkins RA, Franc B. Interpretation, accuracy and management implications of FDG PET/CT in cutaneous malignant melanoma. Nucl Med Commun. 2007;28:273–80.
109. Lagaru A, Quon A, Johnson D, Gambhir SS, McDougall IR. 2-Deoxy-2-[F-18]fluorodeoxyglucose positron emission tomography/computed tomography in the management of melanoma. Mol Imaging Biol. 2007;9:50–7.
110. Fulham MJ, Kelley B, Ramshaw J, Scott AM. Impact of FDG PET on the management of patients with suspected or proven metastatic melanoma prior to surgery: a prospective, multi-centre study as part of the Australian PET Data Collection Project. J Nucl Med. 2007;48 Suppl 2:191P.
111. Strobel K, Bode B, Dummer R, et al. Limited value of [^{18}F]FDG PET/CT and S-100B tumour marker in the detection of liver metastases from uveal melanoma compared to liver metastases from cutaneous melanoma. Eur J Nucl Med Mol Imaging. 2009;36:1774–82.
112. Loffler M, Weckesser M, Franzius Ch, Nashan D, Schober O. Malignant melanoma and [^{18}F]FDG PET: should the whole body scan include the legs? Nuklearmedizin. 2003;42:167–72.
113. Coleman RE, Delbeke D, Guiberteau MJ, et al. Concurrent PET/CT with an integrated imaging system: intersociety dialogue from the Joint Working Group of the American College of Radiology, the Society of Nuclear Medicine, and the Society of Computed Body Tomography and Magnetic Resonance. J Nucl Med. 2005;46:1225–39.
114. Hofmann U, Szedlak M, Rittgen W, Jung EG, Shadendorf D. Primary staging and follow-up in melanoma patient-monocenter evaluation of methods, costs and patient survival. Br J Cancer. 2002;87:151–7.
115. Weiss M, Loprinzi CL, Creagan ET, Dalton RJ, Novotny P, O'Fallon JR. Utility of follow-up tests for detecting recurrent disease in patients with malignant melanomas. JAMA. 1995;274:1703–5.
116. Kuvshinoff BW, Kurtz C, Coit DG. Computed tomography in evaluation of patients with stage III melanoma. Ann Surg Oncol. 1997;4:252–8.
117. Jiménez-Requena F, Delgado-Bolton RC, Fernández-Pérez C, et al. Meta-analysis of the performance of

[^{18}F]FDG PET in cutaneous melanoma. Eur J Nucl Med Mol Imaging. 2010;37:284–300.
118. Dalrymple-Hay MJ, Rome PD, Kennedy C, Fulham M, McCaughan BC. Pulmonary metastatic melanoma – the survival benefit associated with positron emission tomography scanning. Eur J Cardiothorac Surg. 2002;21:611–4.
119. Schöder H, Larson SM, Yeung HW. PET/CT in oncology: integration into clinical management of lymphoma, melanoma, and gastrointestinal malignancies. J Nucl Med. 2004;45 Suppl 1:72S–81.
120. Mottaghy FM, Sunderkotter C, Schubert R, et al. Direct comparison of [^{18}F]FDG PET/CT with PET alone and with side-by-side PET and CT in patients with malignant melanoma. Eur J Nucl Med Mol Imaging. 2007;34:1355–64.
121. Macapinlac HA. The utility of 2-deoxy-2-[^{18}F]fluoro-D-glucose positron emission tomography and combined positron emission tomography and computed tomography in lymphoma and melanoma. Mol Imaging Biol. 2004;6:200–7.
122. Pfannenberg C, Aschoff P, Schanz S, et al. Prospective comparison of [^{18}F]fluorodeoxyglucose positron emission tomography/computed tomography and whole-body magnetic resonance imaging in staging of advanced melanoma. Eur J Cancer. 2007; 43:557–64.
123. Strobel K, Dummer R, Steinert HC, et al. Chemotherapy response assessment in stage IV melanoma patients-comparison of [^{18}F]FDG-PET/CT, CT, brain MRI, and tumor marker S-100B. Eur J Nucl Med Mol Imaging. 2008;35:1786–95.
124. González AB, Jiménez RB, Delgado PJR, et al. Biochemotherapy in the treatment of metastatic melanoma in selected patients. Clin Transl Oncol. 2009;11:382–6.
125. Hofman MS, Constantinidou A, Acland K, Healy C, Harries M, O'Doherty M, Melanoma Group. Assessing response to chemotherapy in metastatic melanoma with FDG PET: early experience. Nucl Med Commun. 2007;28:902–6.
126. Zheng B, Jeong JH, Asara JM, et al. Oncogenic B-RAF negatively regulates the tumor suppressor LKB1 to promote melanoma cell proliferation. Mol Cell. 2009;33:237–47.
127. Carlino MS, Saunders CA, Haydu LE, et al. [^{18}F]-labelled fluorodeoxyglucose-positron emission tomography (FDG-PET) heterogeneity of response is prognostic in dabrafenib treated *BRAF* mutant metastatic melanoma. Eur J Cancer. 2013;49:395–402.
128. McArthur GA, Puzanov I, Amaravadi R, et al. Marked, homogeneous, and early [^{18}F]fluorodeoxyglucose-positron emission tomography responses to vemurafenib in *BRAF*-mutant advanced melanoma. J Clin Oncol. 2012;30:1628–34.
129. Koo PJ, Klingensmith WC, Lewis KD, Bagrosky BM, Gonzalez R. Anti-CTLA4 antibody therapy related complications on FDG PET/CT. Clin Nucl Med. 2014;39:e93–6.
130. van der Hiel B, Blank CU, Haanen JB, Stokkel MP. Detection of early onset of hypophysitis by [^{18}F]FDG PET-CT in a patient with advanced stage melanoma treated with ipilimumab. Clin Nucl Med. 2013;38:e182–4.
131. Brand C, Ellwanger U, Stroebel W, et al. Prolonged survival of 2 years or longer for patients with disseminated melanoma: an analysis of related prognostic factors. Cancer. 1997;70:2345–53.
132. Meyer T, Merkel S, Goehl J, Hohenberger W. Surgical therapy for distant metastases of malignant melanoma. Cancer. 2000;89:1983–91.
133. Romano E, Scordo M, Dusza SW, Coit DG, Chapman PB. Site and timing of first relapse in stage III melanoma patients: implications for follow-up guidelines. J Clin Oncol. 2010;28:3042–7.
134. Poo-Hwu W-J, Ariyan S, Lamb L, et al. Follow-up recommendations for patients with American Joint Committee on cancer stages I–III malignant melanoma. Cancer. 1999;88:2252–8.
135. Soong SJ, Harrison RA, McCarthy WH, Urist MM, Balch CM. Factors affecting survival following local, regional, or distant recurrence from localized melanoma. J Surg Oncol. 1998;67:228–33.
136. Eigtved A, Andersson AP, Karin Dahlstrøm K, et al. Use of fluorine-18 fluorodeoxyglucose positron emission tomography in the detection of silent metastases from malignant melanoma. Eur J Nucl Med. 2000;27:70–5.
137. Krug B, Crott R, Roch I, et al. Cost-effectiveness analysis of FDG PET-CT in the management of pulmonary metastases from malig- nant melanoma. Acta Oncol. 2010;49:192–200.
138. Cobben DC, Jager PL, Elsinga PH, Maas B, Suurmeijer AJ, Hoekstra HJ. ^{18}F-3-fluoro-3-deoxy-**l**-thymidine: a new tracer for staging of metastatic melanoma? J Nucl Med. 2003;44:1927–32.
139. Ishiwata K, Kubota K, Kubota R, Iwata R, Takahashi T, Ido T. Selective 2-[^{18}F]fluorodopa uptake for melanogenesis in murine metastatic melanomas. J Nucl Med. 1991;32:95–101.
140. Dimitrakopoulou-Strauss A, Strauss LG, Burger C. Quantitative PET studies in pretreated melanoma patients: a comparison of 6-[^{18}F]fluoro-**l**-dopa with ^{18}F-FDG and 15O-water using compartment and non-compartment analysis. J Nucl Med. 2001;42:248–56.
141. Beer AJ, Haubner R, Sarbia M, et al. Positron emission tomogra- phy using [^{18}F]-Galacto-RGD identifies the level of integrin a_vb_3 expression in man. Clin Cancer Res. 2006;12:3942–9.
142. Greguric I, Taylor SR, Denoyer D, et al. Discovery of [^{18}F]N-(2-(diethylamino)ethyl)-6-fluoronicotinamide: a melanoma positron emission tomography imaging radiotracer with high tumor to body contrast ratio and rapid renal clearance. J Med Chem. 2009;52: 5299–302.

Diagnostic Applications of Nuclear Medicine: Pediatric Cancers

39

Thomas Pfluger, Andrea Ciarmiello, Giampiero Giovacchini, Françoise Montravers, Hubert Ducou Le Pointe, Judith Landman-Parker, Martina Meniconi, and Christiane Franzius

Abstract

Pediatric cancers are defined as cancers occurring before the age of 15 years and account for only 2% of all cancers. Intracranial tumors are the most common solid neoplasms in children. Although [^{18}F]FDG uptake is associated with more malignant and aggressive tumor types, [^{18}F]FDG-PET is not routinely used for the clinical management of pediatric brain tumors. PET/MRI coregistration/image fusion improves localization of the lesion. [^{18}F]FDG-PET is also helpful to differentiate indolent and active components of the lesion and to improve the diagnostic yield of stereotactic biopsies and the accuracy of the radiosurgical dosimetry planning.

Lymphomas account for 10–15% of all childhood malignancies and are the third most common cause of cancer. Non-Hodgkin's lymphoma is more frequent. Staging of Hodgkin's lymphoma (HL) is performed according to the Cotswold revision of the Ann Arbor classification. Non-Hodgkin's lymphoma in childhood is significantly different from adults. The predominant subtypes are Burkitt's lymphoma, large B-cell lymphoma, and primary mediastinal B-cell lymphomas, followed by lymphoblastic lymphoma and anaplastic large-cell lymphoma. Most cases are extensive at diagnosis, corresponding to stages 3 and 4 of the St. Jude Children's Research Hospital

T. Pfluger (✉)
Department of Nuclear Medicine, Ludwig-Maximilians-University of Munich, Munich, Germany
e-mail: thomas.pfluger@med.uni-muenchen.de

A. Ciarmiello
Nuclear Medicine Department, Institute of Nuclear Medicine, S. Andrea Hospital, La Spezia, Italy
e-mail: andrea.ciarmiello@asl5.liguria.it

G. Giovacchini
Nuclear Medicine Department, S. Andrea Hospital, La Spezia, Italy
e-mail: giampiero.giovacchini@asl5.liguria.it

F. Montravers
Department of Nuclear Medicine, Tenon Hospital, Assistance Publique Hôpitaux de Paris, Pierre et Marie Curie University, Paris, France
e-mail: francoise.montravers@aphp.fr

H.D. Le Pointe
Department of Radiology, Armand-Trousseau Hospital, Assistance Publique Hôpitaux de Paris, Pierre et Marie Curie University, Paris, France

J. Landman-Parker
Department of Pediatric Oncology, Armand-Trousseau Hospital, Assistance Publique Hôpitaux de Paris, Pierre et Marie Curie University, Paris, France

M. Meniconi
Regional Center of Nuclear Medicine, University of Pisa, Pisa, Italy
e-mail: martina.meniconi@tiscali.it

C. Franzius
Nuclear Medicine and PET/CT Centre Bremen, Bremen, Germany

Centre of Modern Diagnostics (ZEMODI), MRI and MR/PET, Bremen, Germany
e-mail: christiane-franzius@t-online.de

© Springer International Publishing Switzerland 2017
H.W. Strauss et al. (eds.), *Nuclear Oncology*,
https://doi.org/10.1007/978-3-319-26236-9_25

classification (Murphy staging). Contrast-enhanced diagnostic CT (ce-CT) or MRI together with thoracic CT remains mandatory at least at diagnosis (performed either simultaneously with [^{18}F]FDG-PET by using hybrid PET/CT or PET/MRI scanners or separately). Diagnostic CT reliably detects enlarged lymph nodes, and contrast media are required to accurately distinguish lymphadenopathy. Diagnostic CT also allows detailed evaluation of the pulmonary parenchyma, pleura, and pericardium. Ultrasonography has a definite role in both initial evaluation and follow-up of superficial lymph nodes and is an effective method to detect testicular infiltration and to explore liver and spleen. Chest radiography remains useful in HL to classify disease as "bulky" or "nonbulky." MRI is superior to ce-CT for evaluation of the bone marrow, liver, soft tissue, and central nervous system.

^{67}Ga-citrate scintigraphy and bone scintigraphy have been replaced by [^{18}F]FDG-PET/CT or PET/MRI, which depicts nodal and extranodal disease as well as focal bone marrow disease. The role of [^{18}F]FDG-PET is well established to stage HL before treatment. Early response assessment can be evaluated by interim PET in HL. When interim PET is negative, no other examination needs to be performed at the end of therapy in the absence of clinical signs. Systematic [^{18}F]FDG-PET is not indicated during follow-up.

In non-Hodgkin's lymphoma, [^{18}F]FDG avidity is high for Burkitt's lymphoma, large B-cell lymphoma, lymphoblastic lymphoma, and anaplastic large-cell lymphoma. The main indications for [^{18}F]FDG-PET in children with non-Hodgkin's lymphoma are inconclusive. However, [^{18}F]FDG-PET appears to be a useful tool for characterization of residual masses, as no reliable CT or MRI criteria are available for distinguishing residual disease from fibrosis or necrosis.

Wilms' tumor is the most common renal malignancy in childhood. The diagnostic workup includes a CT or MRI scan of the abdomen and pelvis, lymph nodes, and intra-abdominal or pelvic tumor deposits. A Doppler ultrasound is recommended to evaluate if there is a tumoral thrombus in the renal vein and inferior vena cava. For the detection of bilateral disease and the assessment of nephroblastomatosis representing premalignant lesions, MRI is the imaging modality of choice. ^{123}I-MIBG scintigraphy can be very helpful for the differentiation of neuroblastoma from Wilms' tumor. There is no major role for [^{18}F]FDG-PET in these patients.

Neuroblastoma accounts for about 8% of pediatric malignancies and is responsible for 15% of cancer deaths in children. It arises from the neural crest cells, and the tumor is usually situated in the adrenal gland or anywhere else along the sympathetic nervous system chain. Staging is crucial in order to choose the appropriate treatment. Imaging of neuroblastoma consists of ultrasonography, computed tomography (CT), magnetic resonance imaging (MRI), and ^{123}I-MIBG scintigraphy. ^{123}I-MIBG is sensitive and specific for the detection of neuroblastoma involvement. [^{18}F]FDG-PET is less sensitive than ^{123}I-MIBG scintigraphy in neuroblastoma patients. However, in any case of a discrepancy between ^{123}I-MIBG scintigraphy and morphological imaging (CT and/or MRI), [^{18}F]FDG-PET should be considered for further tumor evaluation.

Sarcomas are a heterogeneous group of neoplasms with different tumor biology, malignancy, and therapeutic options. The two major groups of primary bone tumors in children and adolescents are osteosarcomas and the Ewing family of tumors. As regards soft-tissue sarcomas, the most common histologic entities in children and adolescents are rhabdomyosarcoma, extraosseous Ewing sarcoma and peripheral neuroectodermal tumor, synovial sarcoma, neurofibrosarcoma, fibrosarcoma, and leiomyosarcoma. Langerhans cell histiocytosis (LCH) is a proliferation of Langerhans-type histiocytes. Despite its clonal origin, there is no definitive proof of malignancy. Primary bone tumors are best classified using a conventional planar x-ray. Local CT and MRI supply further information on tumor

localization and extension. Bone scintigraphy is very sensitive in the detection of osseous metastases of osteosarcoma, and even soft-tissue metastases are often visible on the bone scan.[^{18}F]FDG-PET has a high accuracy in detecting primary sarcomas and its metastases, with the exception of pulmonary metastases. Therefore, a thoracic CT is additionally necessary for staging sarcomas.

Keywords

Pediatric cancer imaging • Sarcoma imaging in the pediatric population • Neuroblastoma imaging in children • Wilms' tumor imaging in children • Lymphoma imaging in children • Intracranial tumor imaging in children

Glossary

[^{11}C]HED	[^{11}C]Hydroxyephedrine
[^{11}C]MET	[^{11}C]Methionine
^{153}Sm-EDTMP	^{153}Sm-ethylenediaminetetramethylene phosphonic acid
^{18}F-DOPA	2-^{18}F-Fluoro-L-3,4-dihydroxyphenylalanine
[^{18}F]FDG	2-Deoxy-2-[^{18}F]fluoro-D-glucose
^{18}F-FET	*O*-(2-^{18}F-Fluoroethyl)-L-Tyrosine, a tyrosine analog
^{68}Ga-DOTA-TOC	^{68}Ga-DOTA-Tyr^{3}-octreotide
^{99m}Tc-MDP	^{99m}Tc-methyldiphosphonate
ACCIS	European Automated Childhood Cancer Information System
ce-CT	Contrast-enhanced diagnostic CT
CNS	Central nervous system
CT	X-ray computed tomography
DOTA	2-(4-Isothiocyanatobenzyl-1,4,7,10-tetra-azacyclododecane-1,4,7,10-tetraacetic acid (macrocyclic coupling agent to label compounds of biological interest with metal radionuclides)
EGFR	Epidermal growth factor receptor
GCSF	Granulocyte colony-stimulating factor
Gy	Gray unit (ionizing radiation dose in the International System of Units, corresponding to the absorption of one joule of radiation energy per kilogram of matter)
HL	Hodgkin's lymphoma
LCH	Langerhans cell histiocytosis
LGAs	Low-grade astrocytomas
MIBG	*meta*-iodobenzylguanidine
MRI	Magnetic resonance imaging
NE	Norepinephrine
NHL	Non-Hodgkin's lymphoma
PD	Progressive disease
PET	Positron emission tomography
PET/CT	Positron emission tomography/Computed tomography
PET/MRI	Positron emission tomography/Magnetic resonance imaging system
PNET	Peripheral neuroectodermal tumor
RECIST	Response evaluation criteria in solid tumors
SEER	Surveillance, epidemiology and end results
SPECT	Single-photon emission computed tomography
SPECT/CT	Single-photon emission computed tomography/Computed tomography
SUV	Standardized uptake values
WHO	World Health Organization

Contents

Pediatric Brain Tumors 1107
Epidemiology 1107
Symptoms 1108
[^{18}F]FDG PET Scan 1108
Experience with [^{18}F]FDG-PET 1108

Childhood Lymphoma 1110
Hodgkin's Lymphoma 1110

Role of Nuclear Medicine Techniques 1111
[^{18}F]FDG-PET/CT and PET/MRI 1111
Indications for [^{18}F]FDG-PET/CT 1112
Non-Hodgkin's Lymphoma 1114

Limitations of [^{18}F]FDG-PET 1116
False-Negative Results 1116
Physiologic Uptake, Pitfalls, and False-Positive Results 1116
False-Positive Results Can Also Be Treatment Induced 1116
Prospects 1118

Wilms' Tumor 1119

Neuroblastoma 1120
MIBG Scintigraphy 1121
Bone Scintigraphy 1122
Positron-Emission Tomography 1122

Morphological and Multimodality Imaging 1125

Conclusion 1128

Pediatric Osseous and Soft-Tissue Sarcomas 1128
Bone Sarcomas 1128
Soft-Tissue Sarcomas 1128
Langerhans Cell Histiocytosis 1128

Role of Imaging 1129
Three-Phase Bone Scintigraphy 1129

Langerhans Cell Histiocytosis 1129

References 1130

Cancer in children is much less common than in adults. Pediatric cancers, defined as cancers occurring before the age of 15 years, account for only 2% of all cancers [1]. Nevertheless, cancer is the second most common cause of death in children in developed countries. However, improvement of treatment strategies has increased the probability of survival. For example, EUROCARE data showed an 8% reduction in the relative risk of death when comparing the 2000–2002 time span to the 1995–1999 period. Also in the interval from 1995 to 2002, pediatric cancer patients had an overall 5-year survival of 81% in Europe and the USA (Table 1) [2].

The most common tumors among the under 15-year-olds are leukemias, at 34%, brain tumors, at 23%, and lymphomas, at 12%, according to the International Classification of Childhood Cancer [2]. The most frequent single diagnoses are acute lymphoblastic leukemia, astrocytoma, neuroblastoma, non-Hodgkin's lymphoma, and nephroblastoma. There is considerable variation between countries. Incidence rates range from 130 (British Isles) to 160 cases (Scandinavian countries) per million children. Incidence rates have shown an increase over time since the middle of the last century. In Europe, the yearly increase averages 1.1% for the 1978–1997 period and ranges from 0.6% for the leukemias to 1.8% for soft-tissue sarcomas [2].

Nuclear medicine is important in the diagnosis, staging, and long-term surveillance of a number of pediatric cancers. Skeletal scintigraphy is used to evaluate primary skeletal cancers, such as osteosarcoma and Ewing sarcoma, and nonskeletal

Table 1 Five-year survival rates for childhood cancer (0–14 years) according to ACCIS (European Automated Childhood Cancer Information System 1988–1997) and SEER (US-Surveillance, Epidemiology and End Results 1985–1999)

Cancer group	ACCIS (%)	SEER (%)
Total	72	75
Leukemias	73	74
Lymphomas and reticuloendothelial neoplasms	84	83
CNS and miscellaneous intracranial and intraspinal neoplasms	64	66
Sympathetic nervous system tumors	59	66
Retinoblastoma	93	95
Renal tumors	84	90
Hepatic tumors	57	56
Malignant bone tumors	61	68
Soft-tissue sarcomas	65	73
Germ cell, trophoblastic, and other gonadal neoplasms	84	87
Carcinomas and other malignant epithelial neoplasms	89	89
Others and unspecified malignant neoplasms	74	–

From Kaatsch [2], with permission

cancers, such as neuroblastoma, medulloblastoma, rhabdomyosarcoma, and retinoblastoma. Meta-iodobenzylguanidine scintigraphy is valuable in examinations of children with neuroblastoma, and [^{18}F]FDG-PET/CT is useful in lymphoma, thymoma, and embryonal cell tumors. Recent years have witnessed a growing role of [^{18}F]FDG-PET/CT in the management of children with cancer. The conventional staging evaluation of these children includes magnetic resonance imaging (MRI) or CT for detection of the primary tumor and regional nodal beds, chest CT for detection of pulmonary metastases, and technetium-99m methyldiphosphonate (^{99m}Tc-MDP) bone scan for detection of bone metastases. The Response Evaluation Criteria in Solid Tumors (RECIST), introduced in 2000 as an alternative to the World Health Organization (WHO) criteria, provides a standard, reproducible, and objective method of assessing the efficacy of solid tumor therapies [3]. Unfortunately, they rely on changes in unidimensional tumor measurements to define tumor response or progression. In this regard, it must be emphasized that solid malignancies, such as bone sarcomas and cystic soft-tissue sarcomas, may respond well to chemotherapy without substantially changing in size. Furthermore, sarcomas do not shrink or grow in a uniform manner; therefore, unidimensional measurements may not accurately reflect response or progression of the tumor. Tumors that respond poorly to therapy may be followed for months before a unidimensional measurement increases significantly. Meanwhile, patients are exposed to toxic but ineffective chemotherapy and are likely to have a diminished probability of survival. [^{18}F]FDG-PET, on the other hand, provides a three-dimensional assessment of viable tumor tissue based on metabolic activity. A decrease in tumor glucose uptake after treatment suggests a reduction in the number of viable tumor cells or a decrease in metabolism of the tumor tissue. Therefore, [^{18}F]FDG-PET may offer a more sensitive evaluation of the response or progression of some pediatric solid malignancies than anatomic imaging modalities [4]. It should be noted that virtually all stand-alone PET scanners have recently been replaced with integrated hybrid PET/CT scanners that intrinsically allow the combination of the functional PET data with the morphological data of CT. Hybrid PET/CT imaging has shown clear advantages over PET imaging alone, by improving correction for tissue attenuation as well as by providing better anatomical resolution and correlation, thus resulting in better characterization and localization of the lesion and in reduction of the doubtful results [5, 6].

Interest is growing also in the use of hybrid PET/MRI scanners, although the diffusion of this technology is currently still limited by high cost and complexity of operation. Nevertheless, this novel imaging modality is emerging as an especially attractive technique for application in pediatric patients, because it does not involve the radiation burden pertaining to the CT component of the PET/CT scanners. This feature is particularly relevant in children with cancer, who frequently need to perform periodic diagnostic tests [7, 8]. Although several studies have shown the feasibility of PET/MRI in pediatric oncology, clear diagnostic advantages over PET/CT have not been established, also because of the paucity of studies comparing head-to-head in the same patients (especially in the pediatric age group) the diagnostic performances of PET/MRI with those of PET/CT [9–13]. Further validation studies are therefore needed [14, 15].

Pediatric Brain Tumors

Epidemiology

Intracranial tumors are the most common solid neoplasms in children and the second most common malignancy of childhood after leukemia. Among children younger than 19 years, the prevalence rate for all pediatric brain tumors was 9.5 per 10,000, while the incidence rate was 29.1 cases per 1,000,000 [16].

Pediatric brain tumors differ from adult tumors on various grounds. About 60–70% of all pediatric brain tumors, including astrocytomas, medulloblastomas, and ependymomas, develop in the infratentorial compartment. The remaining 30–40% of tumors are supratentorial and consist of gliomas, optic pathway tumors, hypothalamic tumors, and

craniopharyngiomas. The reason why pediatric brain tumors have a propensity to occur in the posterior fossa has not yet been elucidated.

In contrast to those that occur in adults, most gliomas that occur in children are low-grade gliomas. Moreover, in the pediatric age mixed (glioneuronal) and atypical (xanthoastrocytoma) tumors are frequent as also frequent are lesions with very low or questionable evolving potential (hamartoma). Young age is a favorable prognostic factor for malignant gliomas. In adults, the majority of high-grade gliomas are primary and show amplification of the epidermal growth factor receptor (EGFR) gene, which encodes a tyrosine kinase involved in cell replication. In contrast, in pediatric patients high-grade gliomas more commonly derive from low-grade gliomas and often have mutations in TP53 (a gene encoding for p53 protein) but seldom display amplification of EGFR [17, 18].

Many types of supratentorial pediatric brain tumors are well delineated; they have a moderate tendency to infiltrate neighboring tissue and are usually amenable to total resection. However, some pediatric brain tumors may not be accessible surgically because they are close to vital brain structures. This typically occurs for medulloblastoma, a primitive neuroectodermal tumor that originates from the cerebellum, close to the brainstem and to the fourth ventricle.

Finally, 5–10% of brain tumors in childhood are thought to be linked to a genetic predisposition, while such proportion is much lower in adults. Hereditary brain tumors occur in some familial cancer syndromes, such as the Li-Fraumeni syndrome. At variance, hereditary brain tumors in adult subjects are associated with rare hereditary syndromes, such as tuberous sclerosis, neurofibromatosis types 1 and 2, and familial adenomatous polyposis.

Symptoms

The diagnosis of brain tumor may be challenging in children because tumor signs and symptoms may resemble those of more common inflammatory or infectious diseases. Recurrent bouts of headache, nausea, or vomiting without focal deficits are frequently observed in children. For medulloblastoma early symptoms are secondary to increased intracranial pressure due to blockage of the fourth ventricle. The child typically becomes lethargic, with repeated episodes of vomiting and morning headache. In more advanced stages, the child develops stumbling gait, frequent falls, diplopia, papilledema, and sixth cranial nerve palsy.

[^{18}F]FDG PET Scan

The preparation and acquisition procedures are very similar to those adopted for adult studies. Systemic sedation with benzodiazepines may be necessary for very young children, to ensure compliance during the scan. Dynamic scans are rarely performed.

The most important issue in pediatric PET scanning is to limit the radiation burden. The procedure guidelines of the Society of Nuclear Medicine and Molecular Imaging recommend an administered activity of [^{18}F]FDG ranging from 5 to 10 MBq per kg of body weight, from a minimum activity of 37 MBq to a maximum of 750 MBq [19]; nevertheless, with the high sensitivity of modern PET/CT scanners, lower activities can be administered without reducing diagnostic quality of the PET scans. Good hydration and early urine voiding are recommended to reduce bladder toxicity. The absorbed dose to the brain in infants is about 0.24 $\pm$ 0.05 mGy/MBq, a higher value than in adult subjects, because of the higher glucose consumption in the infant brain than in the adult brain [20].

Experience with [^{18}F]FDG-PET

The very first study in a relatively large population of pediatric patients with brain tumor was reported by Hoffman et al. in 1992 [21]. They studied 17 pediatric patients with posterior fossa brain tumors with [^{18}F]FDG-PET. [^{18}F]FDG uptake was visually ranked by two observers, and the results were correlated to tumor histology. Increased [^{18}F]FDG uptake was associated with more malignant and

aggressive tumor types. Heterogeneity of [^{18}F]FDG uptake was associated with previous therapy, including radiation therapy and chemotherapy. The authors concluded that [^{18}F]FDG-PET would likely be an important adjunct in the management of pediatric posterior fossa tumors and predicted a rapid dissemination of PET technology for pediatric applications [21].

Nevertheless, PET has not become routinely used for the clinical management of pediatric brain tumors. Literature remains relatively scarce on this matter, and the difference between adult and pediatric studies cannot be merely attributed to differences in prevalence of the disease [21].

Borgwardt et al. studied 38 untreated pediatric patients with primary CNS tumors using PET with [^{18}F]FDG and, when possible, (n = 16), with ^{15}O-water at rest. Image processing included coregistration to MRI in all patients. The [^{18}F]FDG uptake in tumors was semiquantitatively estimated with a region-of-interest approach. They found a positive correlation between [^{18}F]FDG uptake and malignancy grading. On the other hand, there was no correlation between blood flow as measured with ^{15}O-water and histological grade, a finding that was attributed to some uncoupling between glucose metabolism and blood flow. Image fusions based on digital PET/MRI coregistration improved the information on the tumor location in 90% of cases. The results of the PET scan altered management in 77% of the patients [12].

Pirotte et al. reported their experience at the Erasme Hospital Pediatric Center, where between 1995 and 2005 they examined with [^{18}F]FDG-PET about 400 pediatric patients with brain tumor. In their retrospective analysis, they included 126 patients in whom pre- and postoperative MR imaging showed limitations for assessing the evolving nature of an incidental lesion, selecting targets for biopsy, and delineating tumor tissue for surgical resection. In this group of patients (about one-third of the whole case series), PET was expected to be most useful. They found that PET was helpful on several grounds, i.e., to (1) take a more appropriate decision in incidental lesions by detecting tumor/evolving tissue, (2) better differentiate indolent and active components of the lesion, (3) improve target selection and diagnostic yield of stereotactic biopsies, especially when performed in eloquent areas such as the brainstem or the pineal region, (4) provide prognostic information, (5) better delineate ill-defined tumor borders, (6) increase the number of tumor resections and the amount of tumor tissue surgically removed, (7) improve detection of tumor residues in the operative cavity at the early postoperative stage, (8) facilitate the decision of early second-look surgery for optimizing the radical resection, and (9) improve the accuracy of the radiosurgical dosimetry planning [22].

Utriainen et al. used PET [^{18}F]FDG and [^{11}C]MET to ascertain whether metabolic characteristics could be used as an index of clinical aggressiveness. SUV (standardized uptake values) for both tracers were compared with histopathology and selected histochemical features. The accumulation of both [^{18}F]FDG and [^{11}C]MET was significantly higher in high-grade than in low-grade tumors, but a considerable overlap was found. High-grade tumors showed higher proliferative activity and vascularity than the low-grade tumors. In univariate analysis, [^{18}F]FDG SUV, [^{11}C]MET SUV, and apoptotic index were independent predictors of event-free survival [22].

Kruer et al. [23] examined with [^{18}F]FDG-PET a cohort of 46 children/adolescents with low-grade astrocytomas (LGAs, WHO grade 1 or 2) in order to identify LGAs at risk for progressive disease (PD); they found that tumors with [^{18}F]FDG hypermetabolism were significantly more likely to demonstrate aggressive behavior and PD.

Galldiks et al. [24] investigated the diagnostic accuracy of [^{11}C]MET-PET to distinguish between tumorous and nontumorous lesions in 39 children and adolescents. [^{11}C]MET-PET was able to distinguish brain tumors and nontumorous brain lesions with a high sensitivity (83%) and specificity (92%). The authors suggested that [^{11}C]MET-PET may be helpful when results of routine anatomic diagnostic imaging are not sufficient enough to obtain a treatment decision and planning.

In pediatric patients with central nervous system (CNS) germinomas, the diagnostic utility of [^{11}C]MET was also recently demonstrated by Okochi et al. [25].

Despite these promising results, both [^{18}F]FDG and [^{11}C]MET PET are still not routinely used for clinical evaluation of pediatric brain tumors. The physiologic high [^{18}F]FDG uptake of the normal brain cortex limits tumor detection, especially in low-grade gliomas [26], whereas the short half-life (20 min) of [^{11}C]MET limits its application to centers with an on-site cyclotron.

In the last few years, new fluorinated tracers have emerged as alternative radiolabeled compounds for characterizing pediatric brain tumors. Among them, ^{18}F-DOPA was found to be a multitargeted molecule in children, since it can be used for primary/recurrent brain tumors [27, 28], for neuroblastoma diagnosis, prognosis, and surveillance [29], including detection of CNS metastasis [30], and in nontumoral conditions such as congenital hyperinsulinism [31], with a potential impact on healthcare cost optimization.

Recent findings suggest that also ^{18}F-FET imaging is able to detect metabolic active tumor tissue within diffuse tumors or pretreated lesions [32] and can be used for target selection and to guide surgical treatment in pediatric brain tumors [33].

Childhood Lymphoma

Lymphoma accounts for 10–15% of all childhood malignancies and is the third most common cause of cancer, after leukemia and brain tumors. Non-Hodgkin's lymphoma (NHL) is more frequent than Hodgkin's lymphoma (HL) (about 60% and 40%, respectively) [34].

Hodgkin's Lymphoma

HL, exceptional before the age of 5 years (median age: 14 years), usually presents with asymptomatic enlarged lymph node(s). The malignant cell in HL is the Reed-Sternberg cell, located in the tumor masses within a background of inflammatory cells and fibrosis. Four histologic subtypes of HL are described: lymphocytic predominance, mixed cellularity, lymphocytic depletion, and nodular sclerosis. Nodular sclerosis is the most common subtype, affecting 60% of children, whereas the lymphocytic depletion subtype is very rare. During therapy, residual masses are frequent and usually correspond to fibrosis and/or necrosis [35], especially in the nodular sclerosis subtype of HL because of its abundant fibrotic component [36]. Extent of disease at staging must be evaluated as accurately as possible because treatment is related not only to stage but also to each site of disease in order to plan conformal radiotherapy when it is indicated.

According to the Cotswold revision of the Ann Arbor classification, stage I is defined as involvement of a single lymph node region. Stage II has involvement of two or more lymph node regions on the same side of the diaphragm. Stage III has involvement of lymph node regions on both sides of the diaphragm. Stage IV has extranodal involvement, such as bone, liver, or lung disease. Involvement of the spleen is considered to be lymph node involvement. Each stage is also classified by the presence or absence of symptoms. "A" indicates that the patient is asymptomatic; "B" indicates that the patient has at least one of the following systemic symptoms: inexplicable weight loss of more than 10% within the last 6 months, unexplained persisting or recurrent temperature above 38 °C, and/or drenching night sweats. "E" stage is defined as involvement of a single extranodal site contiguous or proximal to known nodal sites. Clinical and imaging evaluation must be performed at the end of therapy to confirm that therapy has been fully effective and has achieved complete response.

Major therapeutic progress has been made in HL, with current cure rates ranging from 90% to 95% for all stages [37, 38]. Most treatment regimens for childhood HL consist of chemotherapy with or without radiotherapy, with current efforts to reduce the use of radiotherapy and late effects related to cumulative doses of cytotoxic agents [39].

Treatments for pediatric HL can induce important long-term side effects on both quality of life and on life expectancy per se; for these reasons, many studies aim at defining protocols capable of minimizing treatment-related toxicity without compromising the cure rate [40, 41].

Non-Hodgkin's Lymphoma

NHL in childhood is significantly different from NHL in adults, as, in almost every case, it corresponds to high-grade malignancies with frequent invasion of the bone marrow and central nervous system [42]. In children, the predominant subtypes are Burkitt's lymphoma, large B-cell lymphoma, and primary mediastinal B-cell lymphomas, followed by lymphoblastic lymphoma and anaplastic large-cell lymphoma [43]. NHL is very rare before the age of 2 years and has a peak incidence at the age of 7 years. NHL requires urgent treatment, consisting of combination chemotherapy (without radiotherapy) and neuromeningeal prophylaxis of recurrences by intrathecal chemotherapy. Most cases are extensive at diagnosis, corresponding to stages 3 and 4 of the St. Jude Children's Research Hospital classification (Murphy staging) [44].

Stage I disease is defined as a single tumor or nodal area outside of the abdomen and mediastinum. Stage II is a single tumor with regional lymph node involvement, two or more tumors or nodal areas on one side of the diaphragm, or a primary gastrointestinal tract tumor (completely resected) with or without regional node involvement. Stage III consists of tumors or lymph node areas on both sides of the diaphragm, or any primary intrathoracic (mediastinal, pleural, or thymic disease) or extensive intra-abdominal disease, or any paraspinal or epidural disease. Stage IV includes central nervous system and/or bone marrow involvement, regardless of other sites of involvement. Residual masses after treatment are less frequent in NHL than in HL but more frequently correspond to a persistent active disease [45].

The prognosis of childhood NHL has improved over the past 20 years with a 2-year event-free survival of 95% for B-cell lymphoma (Burkitt's lymphoma and large-cell lymphoma) [46, 47], 75% for lymphoblastic lymphoma [48], and 70% for anaplastic large-cell lymphoma [49].

Role of Nuclear Medicine Techniques

^{67}Ga-citrate scintigraphy and bone scintigraphy have largely been replaced by [^{18}F]FDG-PET/CT or – recently – PET/MRI. Compared to ^{67}Ga-citrate scintigraphy, [^{18}F]FDG-PET detects more disease sites [50, 51], especially in the abdomen, where the diagnostic performance of gallium scintigraphy is limited by physiologic bowel uptake. The other advantage of [^{18}F]FDG-PET over ^{67}Ga-citrate scintigraphy is same-day imaging with PET (in contrast with imaging over 2 or 3 days for gallium) and a more favorable dosimetry [51]. Bone scintigraphy is also less sensitive than [^{18}F]FDG-PET to detect bone and bone marrow involvement [52].

[^{18}F]FDG-PET/CT and PET/MRI

The majority of PET systems now consist of hybrid PET/CT scanners which use the CT portion of the examination for attenuation correction and anatomic localization of lesions identified on PET. Low-dose CT (typically 5 mA at 80 kVp for attenuation correction/anatomic correlation, which may be increased to several hundred mA for thin slice diagnostic quality contrast-enhanced CT) that is usually performed with PET has been shown to be more accurate in adults with lymphoma than PET alone [53]. However, contrast-enhanced diagnostic CT (ce-CT) or MRI with thoracic CT remains mandatory at least at diagnosis (performed either simultaneously with PET or separately).

Diagnostic CT and MRI reliably detect enlarged lymph nodes, and contrast media are required to accurately distinguish lymphadenopathy from other structures, especially in the abdomen and pelvis due to the lack of retroperitoneal fat in children [54]. Diagnostic CT also allows detailed evaluation of the pulmonary parenchyma, pleura, and pericardium.

[^{18}F]FDG-PET/CT must also be considered in relation to:

- Ultrasonography, which has a definite role in both initial evaluation and follow-up of superficial lymph nodes. It is also the best method to detect testicular infiltration [54] and an effective imaging method to explore liver and spleen [54].
- Chest radiography, which remains useful in HL to classify disease as "bulky" or "nonbulky," which constitutes an important prognostic factor. Disease is classified as "bulky" when the ratio of the largest tumor diameter to chest diameter is greater than one-third.
- MRI is superior to ce-CT for evaluation of the bone marrow [55], liver, soft tissue, and central nervous system [56]. MRI is currently performed as a complement to other imaging modalities, but its role as a whole-body imaging technique is under evaluation for pediatric and adolescent lymphoma staging [57]. However, whole-body MRI is increasingly performed by using hybrid PET/MRI scanners instead of PET/CT scanners in children [11].

[^{18}F]FDG-PET frequently detects nodal and extranodal disease sites that are missed by conventional staging methods and improves the characterization of lesions that are equivocal on other types of imaging. [^{18}F]FDG-PET is especially accurate to detect bone marrow disease, even in the case of negative iliac crest bone marrow biopsy.

Various studies in adults indicate that [^{18}F]FDG-PET for the detection of bone marrow involvement is superior not only to conventional imaging modalities but also to bone marrow trephine biopsy [51, 58, 59]. This appears to be true also in children [51, 60–64], bone marrow biopsy being now not yet indicated in HL and replaced by [^{18}F]FDG-PET [65]. When bone marrow involvement is detected by PET, it is often not detected by diagnostic CT and must be confirmed by another modality, preferably MRI or bone scan when MRI is not available. In contrast, [^{18}F]FDG-PET/CT can understage disease, especially in the case of lung sites (more reliably detected by diagnostic CT than by PET) [64] and because some lesions, even large lesions, may not be [^{18}F]FDG avid, while other lesions take up [^{18}F]FDG. Careful comparison of functional and morphologic imaging therefore remains essential.

Indications for [^{18}F]FDG-PET/CT

The role of [^{18}F]FDG-PET in childhood lymphoma has been specifically assessed in short series [6, 50, 52, 61, 64–76] and review articles [51, 77–80]. The objectives of [^{18}F]FDG-PET are different in HL and NHL and will be discussed separately.

Hodgkin's Lymphoma

HL has a reported [^{18}F]FDG avidity of 97–100% (defined as at least one [^{18}F]FDG-avid HL site detected, on a per-patient basis), according to four studies, comprising a total of 489 patients (adults and children), with an unspecified proportion of children [81–84]. No difference in intensity of [^{18}F]FDG uptake is observed according to HL subtypes [85], and the intensity of uptake at diagnosis does not appear to have any prognostic value.

[^{18}F]FDG-PET at staging must be performed before starting chemotherapy, as [^{18}F]FDG uptake very rapidly reflects the metabolic response to chemotherapy. In children with aggressive disease, [^{18}F]FDG-PET must also be performed before corticosteroid therapy, as HL is a malignancy comprising a large background of inflammatory cells [86, 87].

Initial Staging

In adults, [^{18}F]FDG-PET/CT and -PET/MRI is useful for pretreatment staging. PET/CT cannot replace diagnostic ce-CT, but it can provide complementary information, potentially resulting in a modification of disease stage (usually upstaging) in about 15–20% of adult patients, with an impact on management in about 5–15% [88]. In children, [^{18}F]FDG-PET modified the stage in 10–23% of patients [51] (Fig. 1). Apart from its role in staging and radiation therapy planning pretreatment, [^{18}F]FDG-PET/CT or PET/MRI is also essential because it provides a

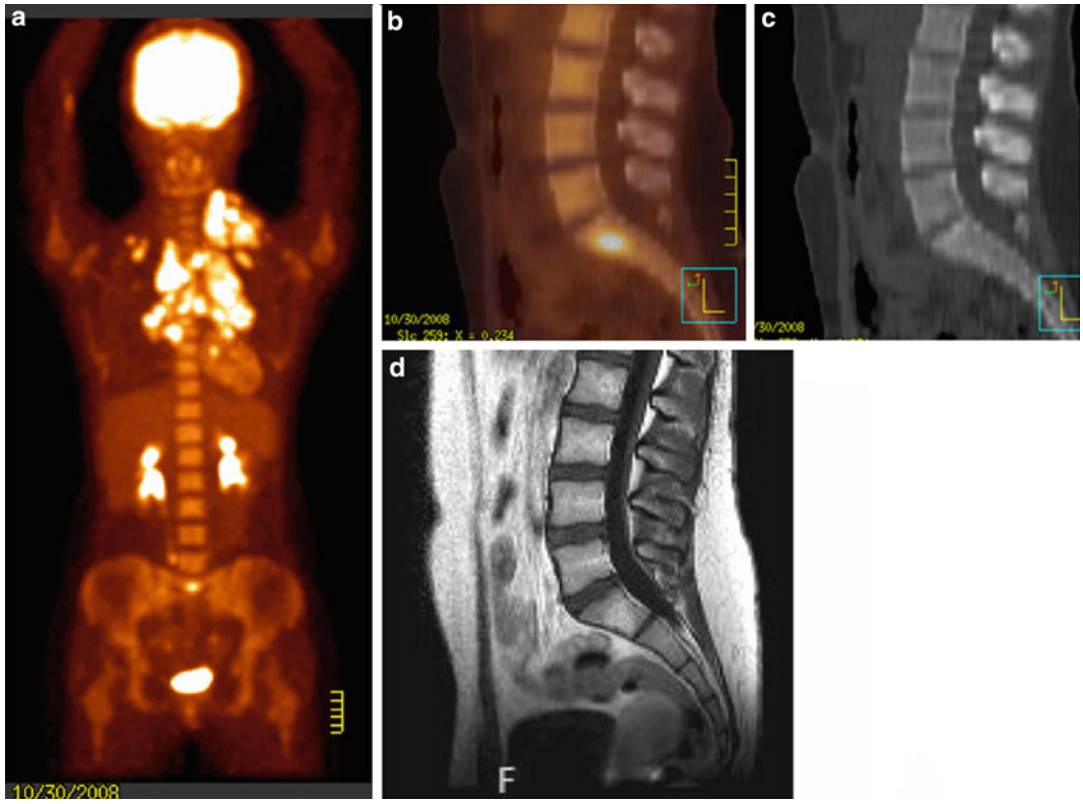

Fig. 1 Hodgkin's lymphoma in a 14-year-old girl, classified stage II before [^{18}F]FDG-PET/CT with extensive supradiaphragmatic lymph node involvement. [^{18}F]FDG-PET/CT showed an unexpected focus in the sacral bone marrow (**a**, **b**), with no abnormality on CT (**c**). Bone marrow involvement was confirmed by MRI (**d**), leading to upstaging of the disease from stage II to stage IV

reference, facilitating interpretation of subsequent treatment evaluation with PET, as recurrences usually occur in previously involved lesions, and de novo sites of uptake observed during follow-up must be primarily suspected to be false-positive [89].

Monitoring of Response to Therapy

As HL is a curable disease, it is essential to ensure that therapy has been fully effective at the end of treatment. [^{18}F]FDG-PET/CT or PET/MRI is routinely performed for this purpose, usually after completion of chemotherapy and before radiotherapy, as a negative [^{18}F]FDG-PET is a reliable indicator of complete remission [88] (Fig. 2). The metabolic information provided by [^{18}F]FDG-PET at the end of therapy is very important, as assessment of response by morphologic imaging modalities is particularly difficult, due to the generally slow and protracted regression of the size of enlarged lymph nodes [51]. Moreover, in HL, malignant cells comprise only a small fraction of the tumor volume, which is mostly composed of reactive infiltrating cells not directly affected by antineoplastic therapy [90].

Early response assessment can also be evaluated by [^{18}F]FDG, as PET has been shown to be an effective prognostic tool in adults with HL [90]. In pediatric HL interim [^{18}F]FDG-PET/CT, after two to three cycles of standard chemotherapy, has shown high negative predictive value, and therefore an early negative scan is a reliable indicator for therapy response [67, 76]. Interim PET must not modify the scheduled therapy except in the context of a controlled clinical trial [91]. When interim PET is negative, no other PET needs to be performed at the end of therapy in the absence of clinical signs [92].

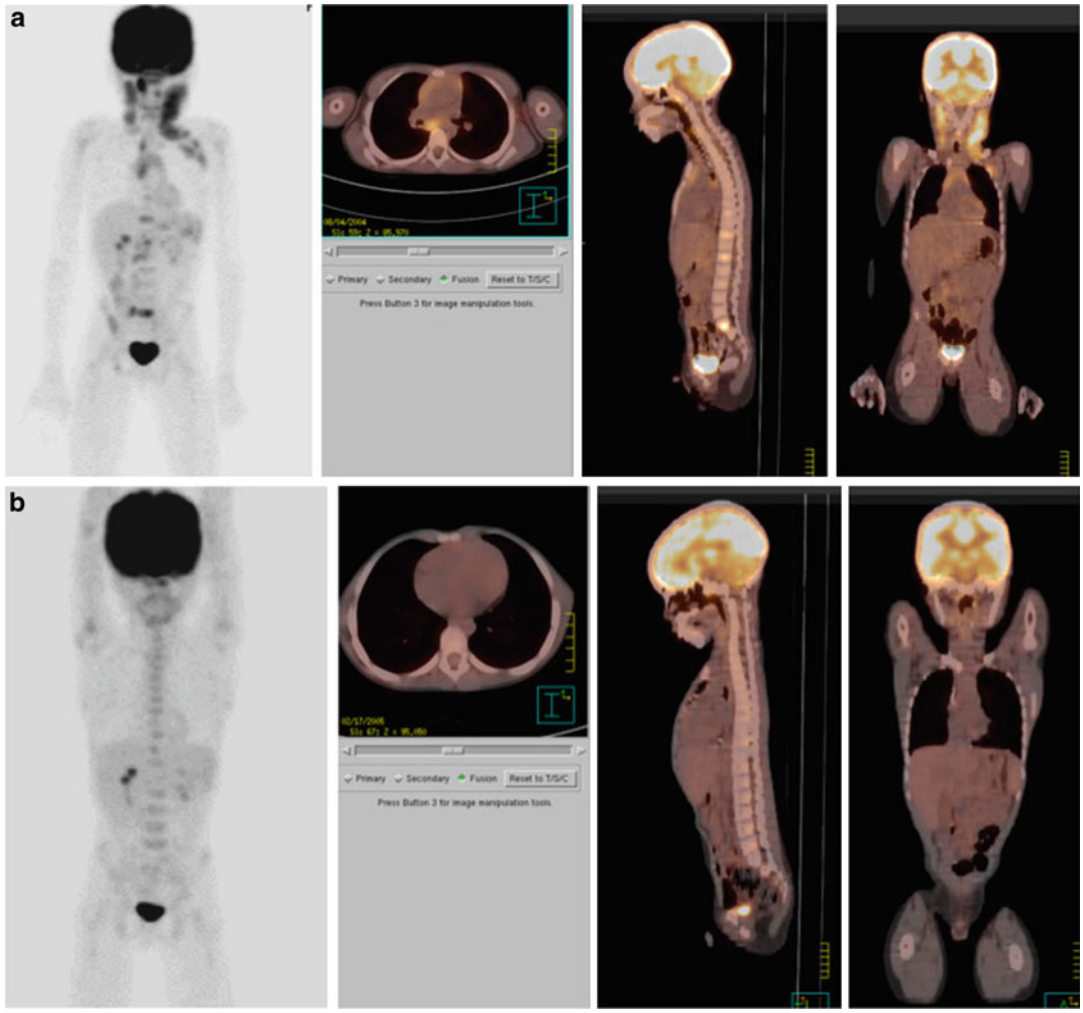

Fig. 2 Hodgkin's lymphoma stage IV (lymph node and bone marrow involvement) in an 8-year-old boy. [^{18}F]FDG-PET/CT at staging (**a**) and after completion of chemotherapy and before radiotherapy (**b**), with metabolic complete response. Persistent clinical remission 4 years after the end of therapy

Systematic [^{18}F]FDG-PET/CT is not indicated during follow-up because it can result in false positives [93], thus contributing to an increase in costs and radiation exposure in the absence of evident benefits [94–96]; therefore, [^{18}F]FDG-PET/CT must only be performed in the case of suspected recurrence.

Non-Hodgkin's Lymphoma

In contrast with HL, [^{18}F]FDG uptake cannot be considered to be constant in NHL. In adult NHL, [^{18}F]FDG uptake tends to be more intense in higher-grade lymphomas than in lower-grade lymphomas [97], and some low-grade NHL, especially T-cell lymphoma, present inconstant [^{18}F]FDG uptake [81]. As most NHLs in children are high-grade and aggressive tumors, it can be assumed that false-negative PET at staging would probably be very rare. However, no study has specifically assessed [^{18}F]FDG uptake according to the various subtypes of NHL in children. According to three studies [82, 83], based on a mixed population of adults and children, [^{18}F]FDG avidity (defined as

at least one [^{18}F]FDG-avid lymphoma site detected on a per-patient basis) was 100% for Burkitt's lymphoma (24/24), 97% for large B-cell lymphoma (294/303), 100% for lymphoblastic lymphoma (6/6), and 100% for anaplastic large-cell lymphoma (24/24), corresponding to the most frequent subtypes of NHL encountered in children. However, in a limited experience of [^{18}F]FDG-PET performed for NHL in 18 children, two false-negative [^{18}F]FDG-PET scans were reported in patients with anaplastic T-small-cell lymphoma, an uncommon subtype of anaplastic T-cell lymphoma [98].

[^{18}F]FDG-PET staging is frequently difficult to organize in a timely fashion and rarely performed due to the urgency of therapy for NHL in children. Moreover, and in contrast with HL, in which all disease sites must be precisely detected in order to plan therapy, the detection of all involved sites is less important in NHL, as treatment consists of high-dose intensive chemotherapy without radiotherapy. Nevertheless, an exception can be staging of Burkitt's lymphoma; in fact, since this subtype frequently occurs as a single site of disease, [^{18}F]FDG-PET can confirm the absence of other site of disease and thus be of help in choosing the initial therapy.

[^{18}F]FDG-PET is therefore rarely performed at staging in NHL and is not performed routinely during follow-up.

The main indications for [^{18}F]FDG-PET in children with NHL are inconclusive results of conventional imaging modalities, that is, suspicion of recurrence (Fig. 3) or characterization of residual masses after treatment [99]. [^{18}F]FDG-PET performed for these purposes can be difficult to interpret firstly because a reference [^{18}F]FDG-PET is usually not available for comparison (and there is no absolute certainty that the NHL subtype is able to take up [^{18}F]FDG). [^{18}F]FDG-PET can also be falsely positive in the presence of inflammation and/or necrosis, very frequent after surgery and chemotherapy for gut involvement in Burkitt's lymphoma [100].

However, [^{18}F]FDG-PET appears to be a useful tool for characterization of residual masses, as no reliable CT or MRI criteria are available for

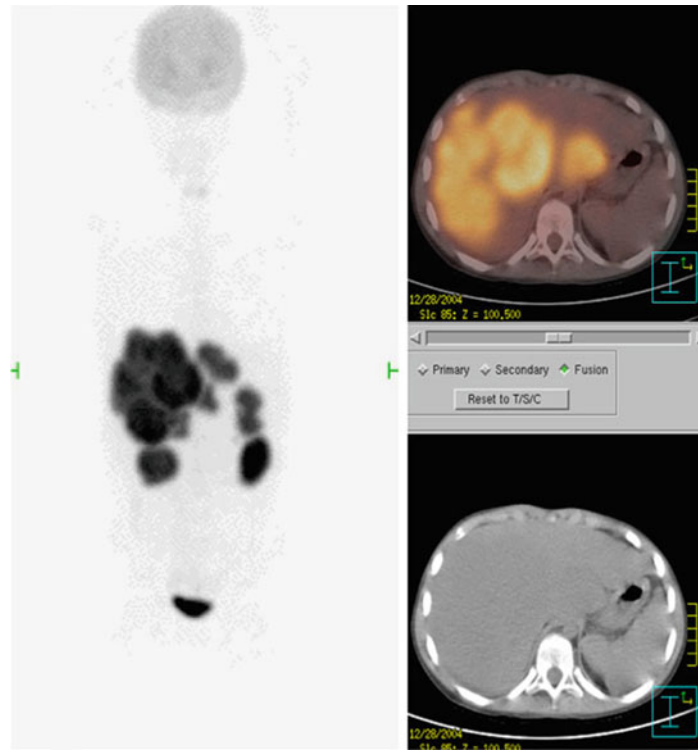

Fig. 3 Liver recurrence of Burkitt's NHL. Note the very high intensity of [^{18}F]FDG uptake by liver lesions, higher than physiologic brain uptake

distinguishing residual disease from fibrosis or necrosis [101]. In the presence of a posttreatment residual mass, negative [^{18}F]FDG-PET has been shown to be a reliable indicator of complete clinical remission [51, 79].

Limitations of [^{18}F]FDG-PET

False-Negative Results

It must be remembered that, even with the most recent PET scanners, [^{18}F]FDG-PET is unable to detect low-grade metabolic lesions measuring less than about 5 mm. Very small lung nodules, with minimal increased metabolic rates, are therefore more reliably detected by diagnostic CT than by PET [64]. During follow-up, persistence of microscopic active disease within residual masses also cannot be detected by PET. Hyperglycemia may also induce false-negative results by reducing [^{18}F]FDG uptake in the tumor [51].

Physiologic Uptake, Pitfalls, and False-Positive Results

Certain physiologic sites of [^{18}F]FDG uptake in children must be recognized. For example, physiologic [^{18}F]FDG uptake may be observed in the endometrium (during menstruations) and in the ovaries (usually at mid-cycle) in adolescent girls and should not be confused with residual or recurrent tumor in pelvic lymph nodes [102, 103]. Due to the increasing resolution of PET systems, some normal structures can now appear to be slightly active on PET, for example, spinal cord, especially in the two sites of physiologic anatomic enlargement, that is, cervical and lumbar regions [104].

In children thymus uptake of [^{18}F]FDG is frequent, physiologic, and enhanced by treatment. The physiologic appearance of thymus uptake is usually easily recognized because it is diffuse and moderately active and frequently has an inverted "V" shape. Sometimes, especially in the presence of an accessory gland, differentiation of normal thymic activity from tumor or inflammation may be difficult or impossible, and PET must then be compared with MRI, which is able to differentiate thymic tissue from recurrent lymphoma [51]. Characterization of the mass can be particularly difficult when ectopic thymic tissue is located in the neck [105].

Brown fat activation is also frequently seen in children. Brown fat is normally distributed in the neck, around the diaphragm, in the perinephric space, and in para-aortic and intercostal regions [102]. Brown fat activation is more easily recognized with hybrid PET/CT scanners (Fig. 4), as [^{18}F]FDG uptake corresponds to low density structures on CT. Nevertheless, even after comparison with CT images, interpretation remains difficult when brown fat activation occurs in previously involved sites. Brown fat activation can be prevented by keeping children warm prior to [^{18}F]FDG administration and during uptake, but these measures may not be sufficient. Benzodiazepine pretreatment may also reduce this activation [101]. More recently, beta-blockers have been shown to be particularly effective and can be used with the agreement of pediatric oncologists [106].

False-positive results are relatively frequent because [^{18}F]FDG is not specific for malignancy and increased uptake can occur in benign conditions associated with increased glycolysis, such as infection, inflammation, granulomatous disease, and more rarely benign tumors (e.g., Fig. 5).

In children and adolescents, false-positive results can be related to infectious mononucleosis [107] or vaccination. [^{18}F]FDG-PET was positive in draining axillary nodes close to the vaccination site in all ten patients recently vaccinated against the pandemic H1N1 virus [108].

False-Positive Results Can Also Be Treatment Induced

In patients treated with low-dose-involved field radiation, [^{18}F]FDG uptake can be slightly increased even months after therapy [102], but the uptake observed in a context of acute radiation pneumonitis can be intense [102].

Granulocyte colony-stimulating factor (GCSF) is a useful adjunct in patients receiving

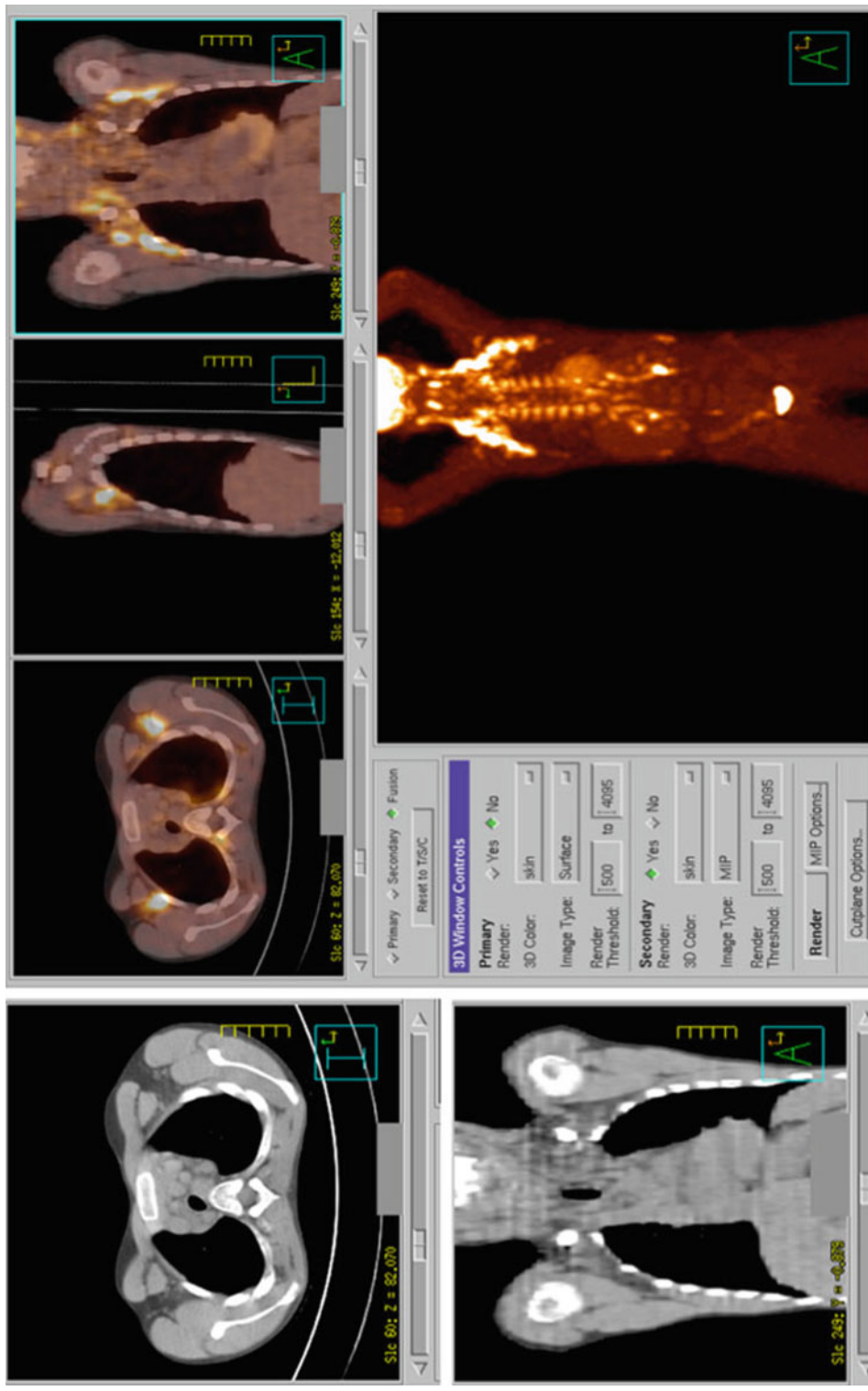

Fig. 4 Extensive brown fat activation. Correlative [^{18}F]FDG PET and CT imaging easily identifies the low density of fat on CT images

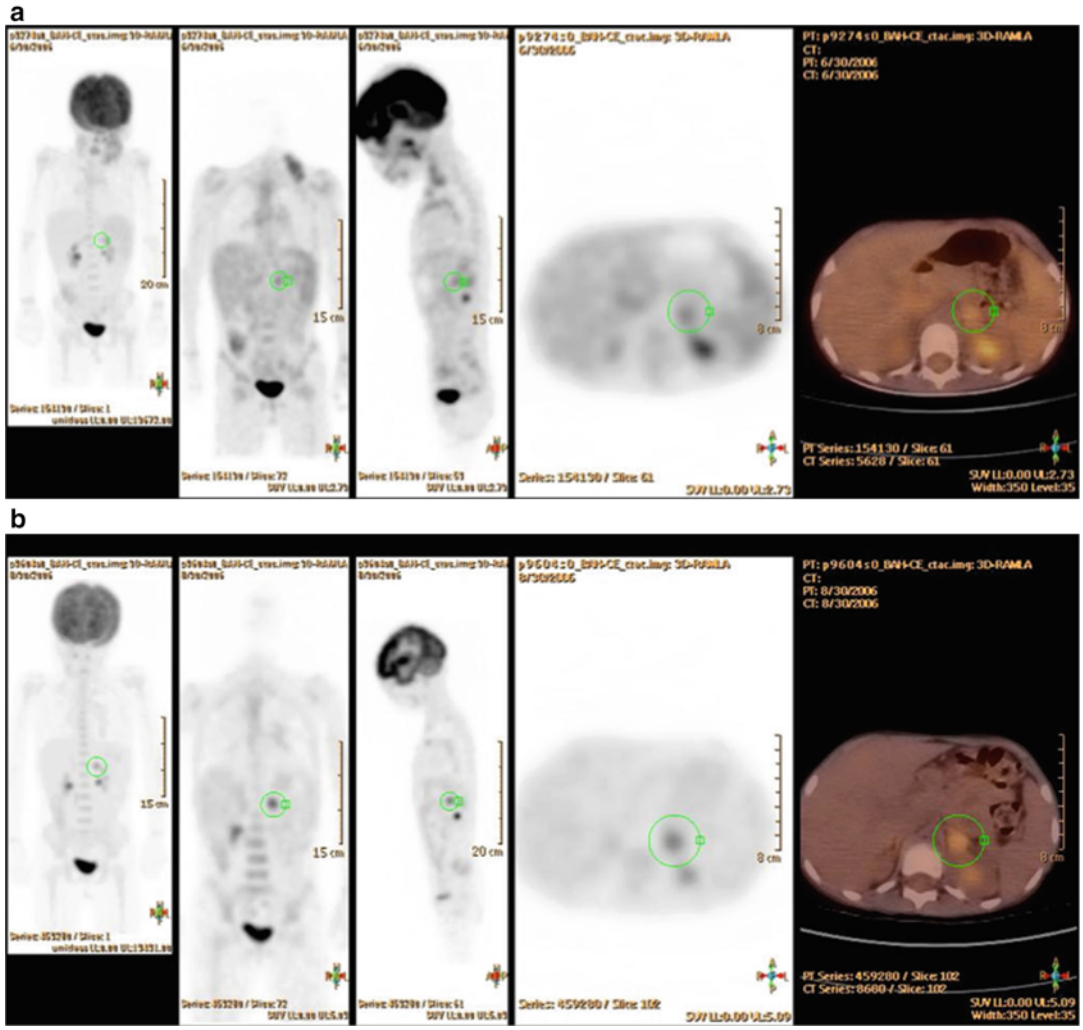

Fig. 5 Unexpected [^{18}F]FDG uptake in the left adrenal gland in a 5-year-old girl with stage II HL (supradiaphragmatic lymph node involvement), at staging (**a**) and persistent after chemotherapy (**b**) although all supradiaphragmatic sites became [^{18}F]FDG negative. This adrenal uptake was suspected to be a false-positive finding, which was confirmed at surgery. The adrenal lesion was benign, corresponding to a leiomyoma

myelosuppressive chemotherapy. Administration of hematopoietic growth factors can induce reconversion from fatty marrow to red marrow, resulting in increased [^{18}F]FDG uptake in the spine, pelvis, and long bones and in the spleen [102]. Increased activity in the spleen has also been observed both during and after GCSF treatment [102]. However, this very diffuse and homogeneous uptake is usually easy to recognize and typically declines after discontinuation of treatment but can remain increased for up to 4 weeks post-therapy [102].

Prospects

[^{18}F]FDG-PET/CT or PET/MRI is already an integral part of the management of childhood HL for staging, adaptation of conformal radiotherapy, and assessment of therapy and suspected

recurrence. [^{18}F]FDG-PET/CT is the subject of a major ongoing European study (Euronet) designed to minimize late toxicity of therapy without compromising the cure rate. Patients who obtain a good early response to two cycles of chemotherapy (complete remission or partial remission and negative [^{18}F]FDG-PET) do not receive radiotherapy [51].

Nevertheless, the actual role of [^{8}F]FDG-PET in the management of childhood NHL has not yet been defined. Although various studies have addressed this issue, the data are still scarce; furthermore, most of the studies are retrospective, and most of them include also patients with LH, therefore resulting in some heterogeneity in the data [109].

The role of [^{18}F]FDG-PET in childhood NHL is currently under evaluation in a trial in France, designed to address several major issues: Does NHL histology affect PET staging and PET response? What is the optimal timing of interim PET during NHL treatment? Should children with poor early PET be considered for treatment intensification?

Wilms' Tumor

Wilms' tumor is the most common renal malignancy in childhood [110]. The 5-year survival rate currently is about 91.9% [111]. Therapy follows multimodality approaches, including surgery/nephrectomy, chemotherapy, and radiation treatment. In general, recurrent disease manifests as local relapse in the lungs, regional lymph nodes, distal urinary tract, and liver but may also occur elsewhere [110]. Two histopathologic findings are described: the favorable and the anaplastic.

Imaging studies are mainly used to define the origin and anatomic extent of the tumor, determine the status of metastatic disease, survey therapy, and detect relapse. So far, the diagnostic workup of newly diagnosed Wilms' tumor includes a CT or MRI scan of the abdomen and pelvis, lymph nodes, and intra-abdominal or pelvic tumor deposits. A Doppler ultrasound is recommended to evaluate if there is a tumor thrombus in the renal vein and inferior vena cava [110]. For the detection of bilateral disease and the assessment of nephroblastomatosis representing premalignant lesions, MRI is the imaging modality of choice (Fig. 6) [112]. In cases with unclear definition of the organ of origin (the kidney, adrenal gland, sympathetic trunk), ^{123}I-MIBG scintigraphy can be very helpful for the differentiation of neuroblastoma versus Wilms' tumor (Fig. 7).

Fig. 6 Four-year-old boy with bilateral Wilms' tumor and nephroblastomatosis. Transversal fat-suppressed T1-weighted image after contrast enhancement reveals bilateral nephroblastoma (*arrows*) and a right-sided nephroblastomatosis lesion (*arrowheads*)

Chemotherapy is usually used prior to surgery. Therefore, a reliable response assessment using noninvasive imaging even prior to definite surgery is needed to modify therapy and to gain prognostic information [113].

Although [^{18}F]FDG-PET was successfully used to image Wilms' tumor for the first time [113] in the 1990s and [^{18}F]FDG uptake is usually consistent with a metabolically active tumor, no difference in uptake can distinguish between favorable and unfavorable histological findings [110]. Only a few years later, it became known that [^{18}F]FDG-PET did not provide additional information during the first diagnostic workup but appeared helpful in the follow-up [113].

PET/CT scans of patients with extensive disease were studied in a follow-up setting. [^{18}F]FDG-PET was reported to detect metastatic

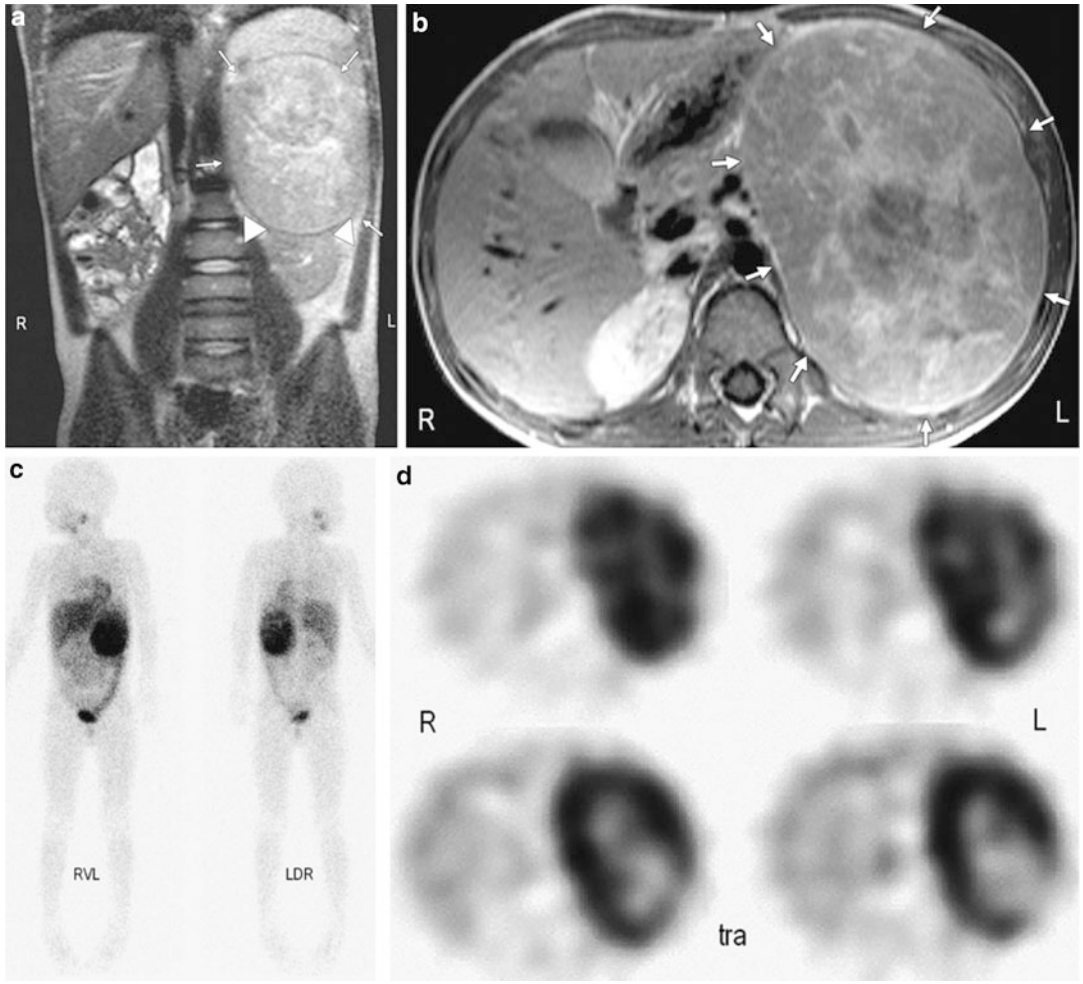

Fig. 7 Six-year-old boy with large neuroblastoma originating from left adrenal gland. **(a)** Coronal T2-weighted image reveals large mass in left abdomen (*arrows*) with appearance typical of Wilms' tumor with pseudocapsule and apparent origin from kidney (*arrowheads*). **(b)** Corresponding transverse T1-weighted image depicts large mass (*arrows*). **(c)** Strong focal uptake by mass visible on ^{123}I-MIBG scintigrams led to correct differential diagnosis of neuroblastoma. *RVL* right side, ventral view, left side, *LDR* left side, dorsal view, right side. **(d)** Transverse (*tra*) SPECT reconstructions that correlate to MRIs show tumor extent and central tumor necrosis

lesions that would have been missed by the conventional imaging [110–114]. Nevertheless, [^{18}F]FDG-PET failed to visualize small pulmonary metastases [102]. Consequently, PET/CT with the increased spatial resolution of the CT component seems to be the modality of choice in defining tumor involvement and evaluating therapy in patients with extended disease, in particular for tumors that are not amenable to surgical resection [110]. Whether PET/CT is useful for primary diagnosis of Wilms' tumors is yet to be determined. Therefore, [^{18}F]FDG-PET/CT does not seem to be of great importance for staging patients with Wilms' tumor with limited disease [113].

Neuroblastoma

Neuroblastoma, an embryonic tumor, is the most frequent extracranial solid malignancy in pediatric patients (about 8% of pediatric malignancies) and remains, despite treatment intensification,

responsible for approximately 15% of cancer deaths in children [115–118]. It arises from the neural crest cells, which form the adrenal medulla and the sympathetic nervous system [119]. The tumor is usually situated in the adrenal gland or anywhere else along the sympathetic nervous system chain [115]. At diagnosis, roughly 50% of patients have distant hematogenous metastases [120]. Neuroblastoma presents a wide spectrum clinical behavior and survival rates; therefore, staging is crucial in order to choose the appropriate treatment [121].

The therapeutic spectrum depends upon clinical stage and consists of supportive care with no treatment (stage IVS), definitive excision if possible, or chemotherapy before and after surgery. The treatment approaches are partially combined with total-body irradiation and ^{131}I-MIBG therapy, followed by autologous bone marrow transplantation [118, 120, 122, 123].

Imaging of neuroblastoma consists of sonography, computed tomography (CT), MRI, and radionuclide examinations such as bone scintigraphy, ^{123}I-MIBG scintigraphy, positron-emission tomography (PET) with different tracers (primarily [^{18}F] FDG), and recently hybrid imaging (PET/CT and SPECT/CT) [124, 125, 200–206].

MIBG Scintigraphy

Radiolabeled MIBG was originally developed in the late 1970s as a norepinephrine (NE) analog for imaging of the adrenal medulla [126, 127]. With the amount of radioiodinated MIBG administered for diagnostic imaging, uptake is mediated primarily by the NE transporter located on the surface of sympathetic neurons [128, 129]. Based on this mechanism, both ^{123}I-MIBG and ^{131}I-MIBG have been proven effective agents for scintigraphic imaging of tumors arising from the embryonologic precursors of the sympathetic nervous system, particularly the neural crest tumors neuroblastoma and pheochromocytoma [130, 131].

Scintigraphy with ^{123}I- or ^{131}I-labeled MIBG has become a well-established method in the diagnosis and staging of neuroblastoma [132–134] because of its high specificity, which is reported in the literature to be between 90% and 100% [122, 135, 136].

Moreover MIBG scintigraphy is used to determine eligibility for ^{131}I-MIBG therapy, as the presence of MIBG-avid disease must be ascertained prior to treatment.

For diagnosis, ^{123}I-labeled MIBG is superior to ^{131}I-MIBG [137]. Due to more favorable dosimetric properties, a higher activity of ^{123}I-MIBG can be administered enabling to obtain SPECT acquisitions that may increase sensitivity and provide more precise anatomical localization of the disease especially after coregistration with radiological modalities such as CT scan or MRI [138].

Reasons for false-negative studies are not entirely clear: it may be related to modifications of the active uptake mechanism due to differentiation of tumor cells or to pharmacologic interference [139–141]. Pharmacological interference: ((1) tricyclic antidepressants and related drugs – should be avoided for 6 weeks prior to the study: (a) amitriptyline and derivatives (Elavil, Endep, Etrafon, Triavil, Amitril, Emitrip, Enovil), (b) amoxapine (Asendin), (c) loxapine, (d) doxepin (Adapin, Sinequan), (e) imipramine and derivatives (Tofranil, Imavate, Janimine, Presamine, SK-Pramine, Tipramine). (2) Antihypertensives – should be avoided for 2 weeks prior to the study: (a) labetalol (Normodyne, Trandate), (b) calcium channel blockers, (c) reserpine (Serpasil, Sandril). (3) Sympathetic amines – should be avoided for 2 weeks prior to the study: (a) pseudoephedrine (Halofed, Sudafed, Sudrin, others), (b) phenylpropanolamine HCL (Propagest, Sucrets Cold Decongestant, Entex, others), (c) phenylephrine HCL (Neo-Synephrine, Alconefrin, Rhinail, others), (d) ephedrine, (4) cocaine – should be avoided at all times and for 2 weeks prior to the study) is probably the most frequent cause of a false-negative study. False-negative MIBG findings have been described in children with ganglioneuroblastoma, where the ganglioneuroma elements were predominant, suggesting that uptake is influenced by histology and the degree of tumor cell maturation, whereas no relationship with the secretion of catecholamines could be assessed [139]. However, other studies in

children with completely negative MIBG scans at diagnosis did not find any correlation with histopathology, biological factors, or stage of disease [132]. On the other hand, in recent studies it could be shown that there is a correlation between a high MIBG uptake and an unfavorable histopathology [142]. Furthermore, combined MIBG scintigraphy and tumor marker analysis can predict unfavorable histopathology of neuroblastic tumors with high accuracy [143].

When looking at lesion-based evaluations, bone and bone marrow lesions are identified more consistently than soft-tissue lesions. Overall sensitivities range between 60% and 70% [133, 144, 145].

Physiological distribution of MIBG is present in the heart and salivary glands because of their sympathetic innervation, while other systems (urinary tract, gastrointestinal system) represent excretion routes of the tracer [146]. Most of false-positive MIBG findings are due to a nonspecific radioactivity accumulation in the urinary tract, and/or gastrointestinal structures, and not to specific MIBG uptake by nonneuroblastic cells [145, 147–154]. Using SPECT/CT to acquire MIBG images reduces the likelihood of false-positive scans.

Bone Scintigraphy

In the literature, usefulness of bone scintigraphy for the staging of neuroblastoma is under discussion. When comparing MIBG and bone scintigraphy in patients with confirmed neuroblastoma, it was found that ^{99m}Tc-MDP and MIBG scans were concordant for the presence or absence of skeletal disease. However, nearly twofold greater number of skeletal lesions was evident on MIBG scanning. In patients with histological evidence of bone marrow involvement, each study suggested skeletal lesions in approximately 70%. In addition, no patients with normal bone scans had MIBG scans indicating bone involvement. In conclusion, both MIBG and ^{99m}Tc-MDP are useful for the detection of skeletal neuroblastoma. ^{123}I-MIBG is the better agent for characterizing the extent of disease, and ^{99m}Tc-MDP is a valuable adjunctive agent that provides skeletal landmarks for comparison [155].

Therefore, bone scintigraphy with ^{99m}Tc-diphosphonates could be important to check for bone metastases when neuroblastoma does not concentrate radioiodinated MIBG. However, in primary staging in particular, whole-body MRI will replace bone scintigraphy as has been shown by several studies demonstrating that whole-body MRI has a higher sensitivity than skeletal scintigraphy in children for the detection of bone marrow metastases [156] and shows a higher number of bone lesions than standard skeletal scintigraphy in children and young adults with malignancies [157].

However, MRI has poor specificity for metastatic osteomedullary infiltration which is most important for follow-up evaluation. False-positive results of MRI for bone marrow infiltration persisted even months after successful treatment completion in children with stage 4 neuroblastoma who had normal ^{123}I-MIBG scans and bone marrow biopsy at the end of treatment [158].

Positron-Emission Tomography

Despite the high diagnostic accuracy of ^{123}I-MIBG imaging, there are several disadvantages of this modality such as limited spatial resolution, limited sensitivity in small lesions, need for two or – in the case of SPECT – even more acquisition sessions, and a delay between the start of the examination and result. Furthermore, MIBG imaging is not sufficient for operative or biopsy planning in most of the cases. The majority of these disadvantages can potentially be overcome with PET [159] due to its higher spatial resolution and the possibility of a whole-body tomography versus SPECT (that has a more limited field of view). PET or PET/CT is completed in one examination within 30–60 min after injection versus ^{123}I-MIBG scintigraphy and SPECT or SPECT/CT that require at least 18–24 h to achieve tumor-to-background ratios adequate for imaging. The resulting shorter scanning time of PET has the potential for reducing the number of sedations in small children.

The use of [^{18}F]FDG-PET in the evaluation of pediatric neuroblastoma is increasing, although its role remains less clear. Questions remain regarding when and in which patients [^{18}F]FDG-PET is most useful. Three studies have compared MIBG scintigraphy and [^{18}F]FDG-PET in neuroblastoma [160–162]. In these studies, MIBG was labeled with either ^{131}I or ^{123}I. These authors demonstrated that most neuroblastomas concentrate [^{18}F]FDG. However, they found that [^{18}F]FDG is inferior to MIBG in the evaluation of neuroblastoma because of its lower tumor-to-nontumor uptake ratio (especially after therapy) and because of [^{18}F]FDG uptake in nontumor sites (such as bone marrow, thymus, and bowel), causing potential false-positive or false-negative results. They concluded that [^{18}F]FDG was most beneficial in tumors that failed to accumulate or weakly accumulated MIBG [162]. In another study, 92 [^{18}F]FDG-PET scans were performed in conjunction with staging evaluations including ^{123}I-MIBG scans, bone scans, CT (or MRI) scans, urine catecholamine, and bone marrow examinations. In this study, PET was equal or superior to MIBG scans for identifying neuroblastoma in soft-tissue and extracranial skeletal structures, for revealing small lesions, and for delineating the extent and localizing sites of disease [161]. Their results showed that [^{18}F]FDG-PET and bone marrow sampling are sufficient to monitor for progressive disease in patients whose primary tumor has been resected and in whom cranial vault lesions are absent or resolved [161].

The third study found stage-dependent results for both modalities [160]. [^{18}F]FDG was superior in depicting stage 1 and 2 neuroblastoma. [^{18}F]FDG also better depicted disease in stages 3 and 4 when tumors did not accumulate ^{123}I-MIBG or did so only weakly. Furthermore, [^{18}F]FDG can better delineate disease extent in the chest, abdomen, and pelvis and should always be considered when ^{123}I-MIBG reveals less disease than suggested by clinical symptoms or conventional imaging modalities (Fig. 8) [119].^{123}I-MIBG was superior in stage 4 neuroblastoma, primarily because of the better detection of bone or marrow metastases. This was especially true during initial chemotherapy or under treatment with granulocyte colony-stimulating factor, conditions associated with marked increase in bone marrow uptake, which can either mask or mimic metastatic disease [160].

However, in all these comparative studies, there is a consensus that [^{18}F]FDG-PET should be considered if there is a discrepancy between morphological imaging and ^{123}I-MIBG scintigraphy [163].

As [^{18}F]FDG is a marker for the viability of malignancies in general, more specific PET tracers have been developed for imaging the sympathetic nervous system like hydroxyephedrine labeled with carbon-11 ([^{11}C]HED) [164, 165]. The aromatic portion of HED is less lipophilic than that of MIBG, and while HED bears closer structural similarity to norepinephrine, it is not metabolized as is norepinephrine. Biodistribution studies in experimental animals and humans have shown selective uptake in organs with rich sympathetic innervation, including the heart and adrenal medulla. When HED is labeled with ^{11}C, its distribution can be portrayed in vivo using PET. In a study, neuroblastomas were located by PET scanning with [^{11}C]HED in all seven participants [165]. The uptake of [^{11}C]HED into neuroblastomas was rapid; tumors were evident on images within 5 min post-intravenous injection. Those lesions in the field of view of the PET camera were also identified on ^{123}I-MIBG scintigraphic images. In two patients, however, tumor deposits in the abdomen were better visualized with ^{123}I-MIBG scintigraphy due to relatively less hepatic accumulation of ^{123}I-MIBG than [^{11}C]HED. The authors concluded that PET scanning with [^{11}C]HED for neuroblastoma results in high-quality functional images of the tumors that can be obtained within minutes following injection [165].

Furthermore, [^{11}C]HED PET/CT was shown to be feasible in tumors of the sympathetic nervous system [166]. In this study, [^{11}C]HED PET/CT detected more tumor lesions than ^{123}I-MIBG SPECT/CT, but not in neuroblastoma, where one large local relapse was missed with [^{11}C]HED in contrast to ^{123}I-MIBG. Moreover, tumor-to-background contrast of [^{11}C]HED in

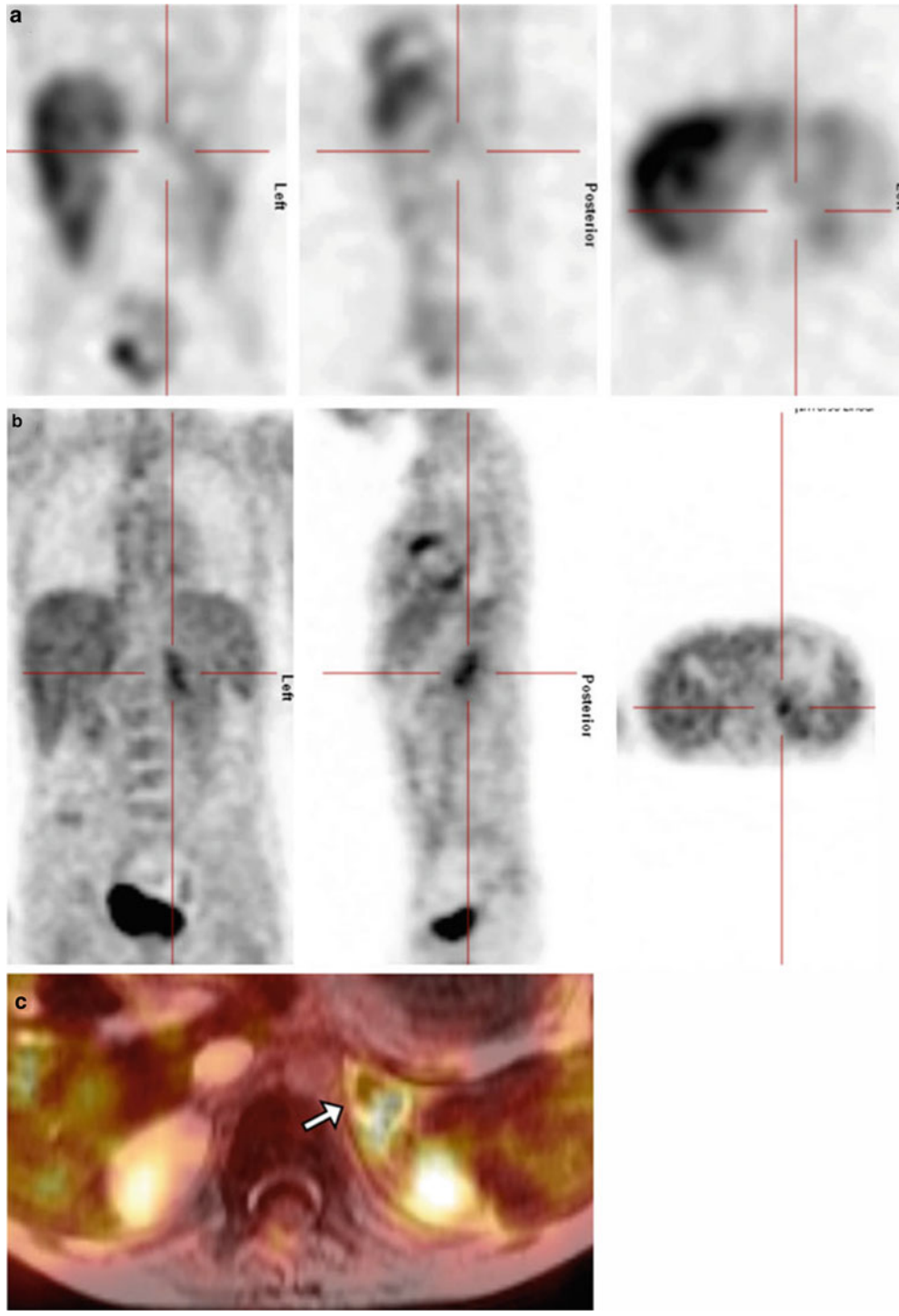

Fig. 8 A 7-year-old boy with a histologically proven recurrent neuroblastoma in the region of the left adrenal gland. **(a)** ^{123}I-MIBG SPECT does not show any pathological uptake in the left adrenal region (*crosshair*) leading to a false-negative result. **(b)** [^{18}F]FDG-PET clearly demonstrates an increased glucose metabolism in the respective region (*crosshair*) suspect for recurrent disease. **(c)** Image fusion between [^{18}F]FDG-PET and MRI shows increased [^{18}F]FDG uptake within a contrast-enhancing soft-tissue mass (*arrow*)

lesions can be higher, equal, or lower compared with ^{123}I-MIBG [166]. The relatively high physiologic liver uptake of [^{11}C]HED may impede the detection of small liver metastases. Some of these shortcomings may be avoided by using PET/CT with ^{18}F-labeled tracers (half-life: 110 min), such as ^{18}F-DOPA which has been used for imaging of a variety of neuroendocrine tumors [167–169]. However, there are a few studies reporting the results of ^{18}F-DOPA PET in pediatric neuroblastoma [29, 170–172], and there are no comparative studies between [^{11}C]HED PET and ^{18}F-DOPA PET [166]. Attention is currently being paid to the role of ^{18}F-DOPA-PET in pediatric neuroblastoma, as well as that of PET with ^{124}I-MIBG, ^{68}Ga-DOTA-TOC (or other radiolabeled somatostatin analogs), because new, highly sensitive and specific PET tracers would be of great clinical interest for imaging during initial staging and for assessing response to therapy, in the perspective of individualizing therapeutic strategies.

Morphological and Multimodality Imaging

The major limitation of morphological imaging (CT and/or MRI) is in the assessment of the viability of morphologically detectable lesions. On the other hand, functional imaging (MIBG or PET) often lacks in distinguishing physiological changes versus tumor lesions. Ideally, multimodality imaging helps to increase diagnostic safety for defining the adequate therapeutic consequence [173].

In contrast to CT, MRI has several advantages in the diagnosis of neuroblastoma: high sensitivity in detecting bone marrow abnormalities [158], lack of ionizing radiation, high intrinsic soft-tissue contrast resolution [125], depiction of internal structure [174], and exact definition of intraspinal tumor extension (Fig. 9) or diaphragmatic involvement of thoracic tumors [124, 175]. All these factors are decisive, especially in primary diagnosis and for operative or biopsy planning [176]. In a comparative study, the benefit of a combined analysis with MRI and ^{123}I-MIBG scintigraphy in pediatric neuroblastoma lesions was assessed. In this study, ^{123}I-MIBG scintigraphy, MRI, and combined analysis showed a sensitivity of 69%, 86%, and 99% and a specificity of 85%, 77%, and 95%, respectively. On MRI, 15 false-positive findings were recorded: post-therapeutic reactive changes ($n = 10$) (Fig. 10), benign adrenal tumors ($n = 3$), and enlarged lymph nodes ($n = 2$). On ^{123}I-MIBG scintigraphy, ten false-positive findings occurred: ganglioneuromas ($n = 2$), benign liver tumors ($n = 2$), and physiologic uptake ($n = 6$). Thirteen neuroblastoma metastases and two residual masses under treatment with chemotherapy were judged to be false-negative findings on MRI. Two primary or residual neuroblastomas and one orbital metastasis were misinterpreted as Wilms' tumor, reactive changes after surgery, and rhabdomyosarcoma on MRI. Thirty-two bone and bone marrow metastases (Fig. 11), six other neuroblastoma metastases, and one adrenal neuroblastoma showed no ^{123}I-MIBG uptake. On combined imaging, one false-negative (bone metastasis) and three false-positive (two ganglioneuromas and one pheochromocytoma) findings remained. In conclusion, MRI showed a higher sensitivity and ^{123}I-MIBG scintigraphy a higher specificity. However, integrated imaging showed an increase in both sensitivity and specificity [145].

With regard to a combined PET/CT or PET/MRI approach, hybrid imaging significantly improved the characterization of abnormal [^{18}F]FDG foci in children with cancer, mainly by excluding the presence of active malignancy in sites of increased tracer activity [9, 10, 177].

The CT component of the PET/CT acquisition is not very sensitive for the detection of malignant marrow infiltrations, which can be diffuse rather than focal or multifocal, in particular, in patients with neuroblastoma, rhabdomyosarcoma, and Ewing sarcoma [178, 179]. Thus, in patients with a high suspicion for bone and bone marrow metastases, additional imaging modalities such as MRI may be needed (Fig. 11) [180, 181], or acquisition using a PET/MRI hybrid scanner.

PET/CT also has been shown to be superior to PET alone by allowing precise CT localization of metabolic abnormalities shown on PET and superior to CT alone by allowing metabolic

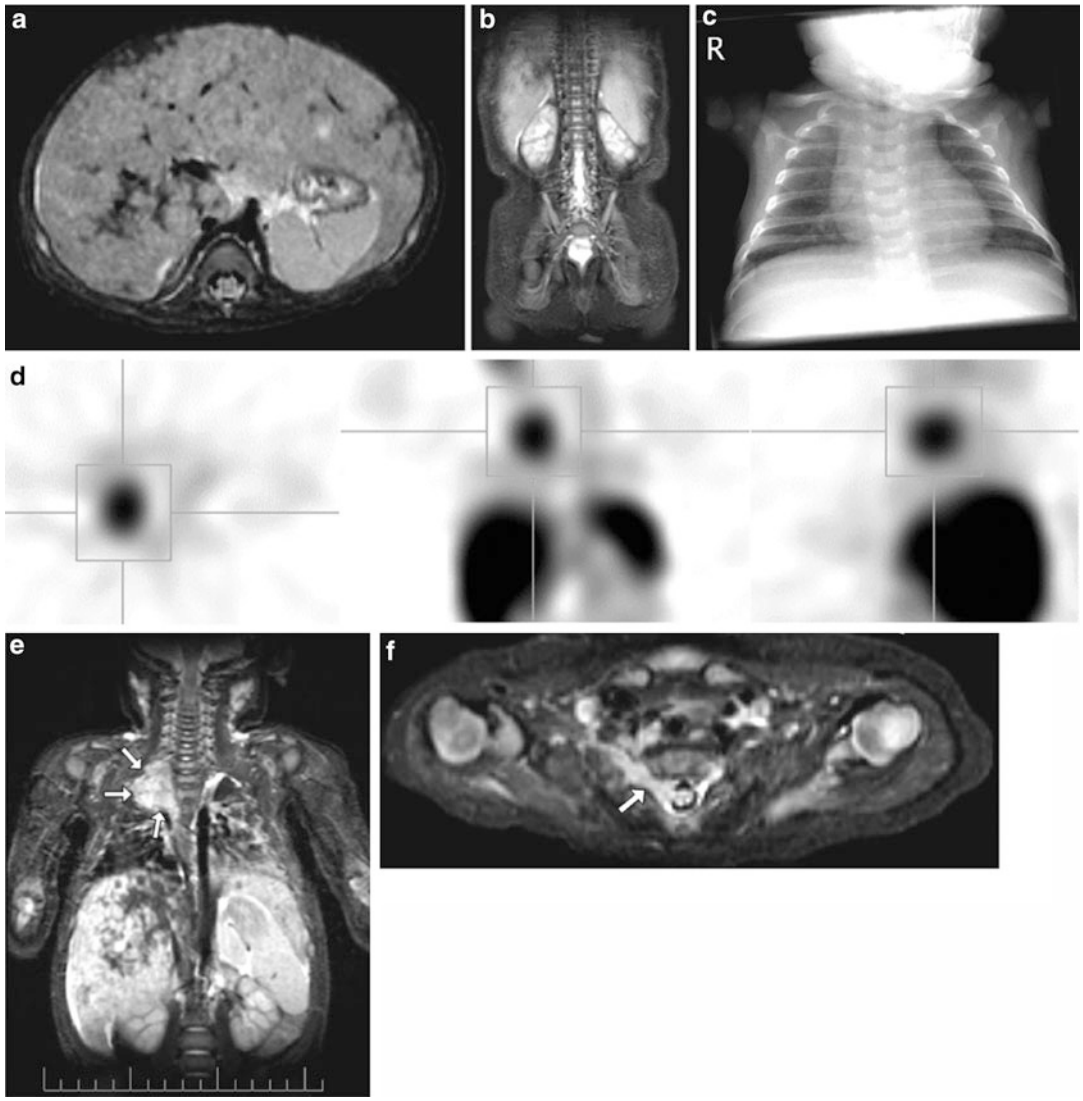

Fig. 9 A 2-month-old suckling with a stage IV neuroblastoma. Clinical and ultrasound findings did not demonstrate a primary tumor. (**a)** Transversal T2-weighted MRI of the abdomen demonstrated diffuse liver metastases. (**b)** Coronal T1-weighted MRI did not show a primary in the adrenal glands or the sympathetic trunk of the abdomen. (**c)** Chest x-ray could not detect a neuroblastoma in the thorax. (**d)** SPECT reconstructions of ^{123}I-MIBG scintigraphy clearly depict the right paravertebral primary as well as diffuse liver metastases. However, exact extent of the tumor and intraspinal involvement cannot be assessed. (**e**, **f)** Coronal and transversal T1-weighted MRI demonstrate the exact extent of the primary and tumor growth through intervertebral foramina (*arrows*) which is decisive for further therapy planning

characterization of abnormal and normal findings shown on CT, thereby increasing diagnostic confidence and reducing equivocal image interpretations [177, 182–185].

Concerning the added value of ^{123}I-MIBG SPECT/CT compared to contrast-enhanced CT, it was observed that all equivocal cases on CT were solved by SPECT/CT, related to the high specificity of ^{123}I-MIBG for tumoral tissue, and concluded that during follow-up of children with MIBG-positive neuroblastoma at diagnosis, SPECT/CT should be performed first and, if

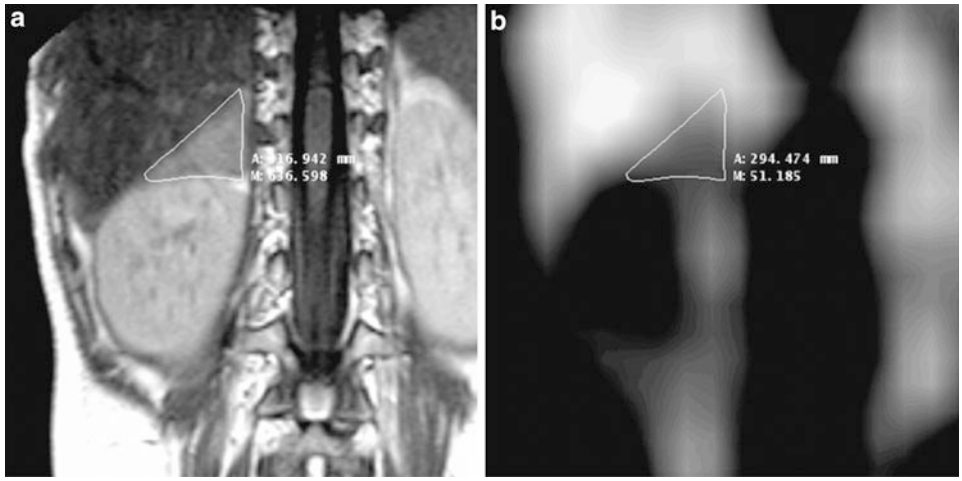

Fig. 10 A 4-year-old boy with reactive changes 6 months after resection of stage II neuroblastoma of the right adrenal gland. (**a)** Coronal T1-weighted MRI demonstrated a contrast-enhancing tumor (region of interest) suspect of residual or recurrent viable tumor tissue. Differentiation between residual tumor and reactive changes is not possible with MRI (false-positive finding). (**b)** Coronal SPECT reconstructions of ^{123}I-MIBG scintigraphy reveal a negative finding. True-negative diagnosis was confirmed by follow-up control examinations over 2 years

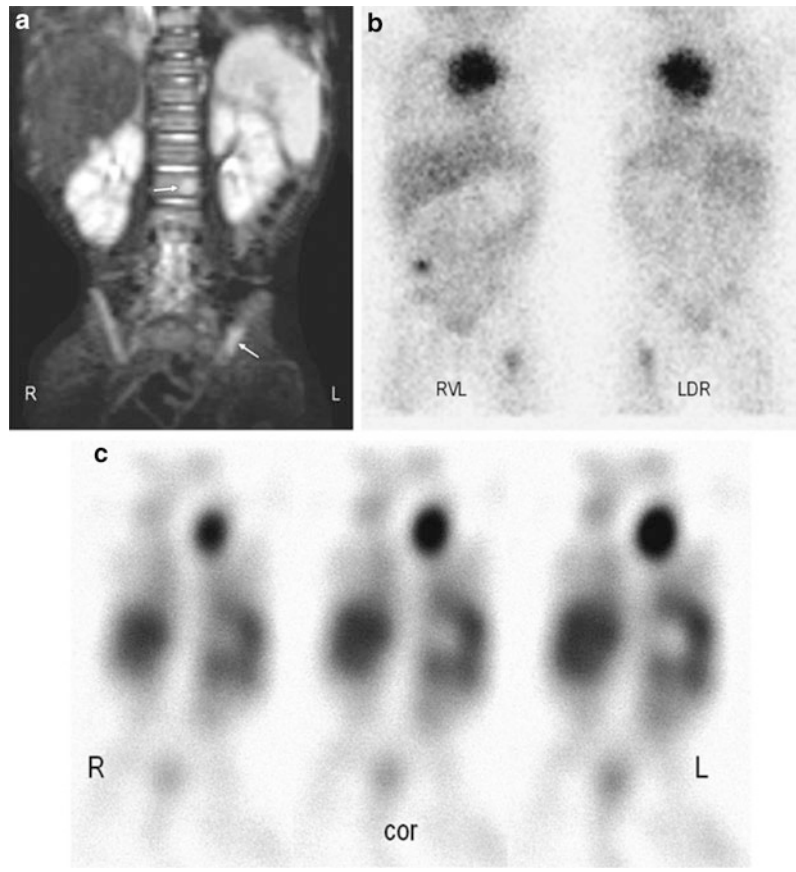

Fig. 11 An 8-month-old girl with stage IV neuroblastoma who presented with multiple bony metastases. (**a)** MRI from STIR sequence shows high signal in two bone marrow metastases in left iliac bone and second lumbar vertebra (*arrows*) (true-positive findings). (**b)** In corresponding regions, planar ^{123}I-MIBG scintigrams show no uptake (false-negative findings). Strong uptake can be seen in mediastinal primary tumor as well as in a left-sided femoral bone metastasis. *RVL* right side, ventral view, left side, *LDR* left side, dorsal view, right side. (**c)** Corresponding coronal (*cor*) SPECT reconstructions of ^{123}I-MIBG scintigraphy support findings of planar images

negative, contrast-enhanced CT could be discarded. Inversely, single positive/equivocal ^{123}I-MIBG foci without concordant morphological changes may need histological confirmation [186].

Conclusion

There is strong evidence that ^{123}I-MIBG scintigraphy (planar images and SPECT) remains the method of choice for the noninvasive staging of children with neuroblastoma. PET imaging using [^{18}F]FDG or the more specific tracer [^{11}C]HED has not definitely proven to be superior to ^{123}I-MIBG.

With regard to multimodality imaging, it has been shown that a combined approach with ^{123}I-MIBG/MRI, ^{123}I-MIBG/CT, and PET/CT has the potential to increase diagnostic sensitivity and specificity as compared to single modalities. Unfortunately, PET/CT represents no one-stop shop for the evaluation of pediatric neuroblastoma as PET cannot surpass ^{123}I-MIBG scintigraphy, and CT cannot replace MRI especially in primary diagnosis (delineation of the infiltration of the spinal canal and detection of bone marrow edema).

Concerning the state-of-the-art diagnostic strategy in neuroblastoma imaging, it is important to differentiate between primary diagnosis and follow-up controls.

In primary diagnosis, ^{123}I-MIBG scintigraphy (i.e., whole-body staging, differential diagnosis) and MRI (i.e., operability, bone marrow metastases) are indispensable. In case of any discrepancy between these two modalities, further staging should be performed with [^{18}F]FDG-PET/CT or -PET/MRI.

In follow-up examinations, ^{123}I-MIBG scintigraphy is most important in MIBG-positive neuroblastoma as specificity of morphological imaging is very low here. In ^{123}I-MIBG-negative neuroblastoma or equivocal MIBG findings, [^{18}F]FDG-PET/CT or -PET/MRI represents the imaging modalities of choice.

Pediatric Osseous and Soft-Tissue Sarcomas

Sarcomas are a heterogeneous group, combining various tumor entities with different tumor biology, malignancy, and therapeutic options. There are different age patterns in different tumor entities. Some entities such as embryonal rhabdomyosarcomas, osteosarcomas, or Ewing tumors are mainly or exclusively found in childhood and adolescence. The metastatic spread of sarcomas is mainly hematogenous to the lungs and the bones. However, in soft-tissue sarcomas, also lymphatic spread occurs. The presence or absence of metastases and the tumor histology and grade mainly influence the treatment.

Bone Sarcomas

The two major groups of primary bone tumors in children and adolescents are osteosarcomas and the Ewing family of tumors.

Soft-Tissue Sarcomas

Soft-tissue sarcomas in children are a heterogeneous group of malignant tumors that originate in the soft tissues and have a predominantly mesenchymal origin. The most common histologic entities in children and adolescents are rhabdomyosarcoma (embryonal and alveolar, 61%), extraosseous Ewing sarcoma and peripheral neuroectodermal tumor (PNET, 8%), synovial sarcoma, neurofibrosarcoma, fibrosarcoma, and leiomyosarcoma.

Langerhans Cell Histiocytosis

Langerhans cell histiocytosis (LCH) is a proliferation of Langerhans-type histiocytes. Despite its clonal origin, there is no definitive proof of malignancy. The term “LCH” replaces a number of synonyms that have been used in the past to describe various conditions: histiocytosis X, Abt-Letterer-

Siwe syndrome, Hand-Schüller-Christian disease, and eosinophilic granuloma.

Role of Imaging

Three-Phase Bone Scintigraphy

Primary Bone Tumors and Tumor-Like Lesions

Even in the age of cross-sectional imaging, primary bone tumors are best classified using a conventional planar x-ray. CT and MRI supply further information on tumor localization and extension. A three-phase bone scan with increased tracer uptake in all three phases supports a presumptive diagnosis of a primary malignant bone tumor. However, the pattern is not specific since acute inflammation shows the same tracer pattern. Additionally, some benign lesions demonstrate a clearly increased tracer uptake in all three phases, for example, osteoid osteoma. A normal or only marginally increased blood pool phase and a moderately increased bone phase suggest a benign lesion.

After chemotherapy of primary bone tumors, bone scintigraphy can be used for therapy control. A decrease in tracer uptake in the blood pool phase and in the bone phase of more than 30% indicates a good response [187, 188]. However, even in good responders there might be an increased tracer uptake during chemotherapy due to the flare phenomenon. Therefore, therapy response should be assessed by bone scintigraphy more than 6 weeks after the end of chemotherapy.

Osseous Metastases

Although bone metastases are usually visualized by ^{99m}Tc-diphosphonate bone scan 3–6 months earlier than by plain x-ray films [189], the specificity of skeletal scintigraphy is only 60–70%. Therefore, verification of abnormal findings is often necessary. Many studies have demonstrated the superiority of MRI in comparison to bone scintigraphy in the detection of osseous metastases, especially in the vertebral column [190].

A distinctive feature of osteosarcoma and its metastases is the capability to produce premature osseous matrix, the point of chemoadsorption of the radiolabeled phosphonates. Therefore, skeletal scintigraphy is very sensitive in the detection of osseous metastases of osteosarcoma, and even soft-tissue metastases are often visible on the bone scan [191–193]. Because of this characteristic feature, therapy with bone-seeking radiopharmaceuticals can be applied in patients with osteosarcoma. Despite highly efficacious chemotherapy, patients with osteosarcomas still have a poor prognosis if adequate surgical control cannot be obtained. These patients may benefit from therapy with radiolabeled phosphonates, such as samarium-153 ethylenediaminetetramethylene phosphonic acid (^{153}Sm-EDTMP) [194].

For a more extensive discussion of osseous and soft-tissue sarcomas, see chapter ▶ Chap. 37, "Diagnostic Applications of Nuclear Medicine: Sarcomas".

Langerhans Cell Histiocytosis

No large-scale studies have yet been done on the use of [^{18}F]FDG-PET, [^{18}F]FDG-PET/CT, or PET/MRI of LCH. One multicase report with three patients found that coincidence [^{18}F]FDG-PET was better able to distinguish between active and healed bony LCH lesions than plain x-ray or bone scans [195]. This observation is supported by a study on various pediatric tumor entities including LCH [196]. Another small study in three patients with cerebral LCH involvement demonstrated that [^{18}F]FDG-PET could detect intracerebral foci of increased or decreased glucose metabolism [197]. Like the authors of a single case-report [198], Calming et al. conclude that [^{18}F]FDG-PET is useful for the evaluation of disease activity during follow-up.

In a comparative study, Mueller et al. evaluated 53 LCH lesions in 21 combined MRI and [^{18}F]FDG-PET studies (15 patients). They concluded that the retrospective analysis suggests a pivotal role of [^{18}F]FDG-PET in lesion follow-up due to a lower number of false-positive findings

after chemotherapy. MRI showed a higher sensitivity and is indispensable for primary staging, evaluation of brain involvement, and biopsy planning. Combined MRI/PET analysis improved sensitivity by decreasing the false-negative rate during primary staging indicating a future role of simultaneous whole-body PET/MRI for primary investigation of pediatric histiocytosis [199].

References

1. Connolly LP, Drubach LA, Ted Treves S. Applications of nuclear medicine in pediatric oncology. Clin Nucl Med. 2002;27:117–25.
2. Kaatsch P. Epidemiology of childhood cancer. Cancer Treat Rev. 2010;36:277–85.
3. Therasse P, Arbuck SG, Eisenhauer EA, et al. New guidelines to evaluate the response to treatment in solid tumors. European Organization for Research and Treatment of Cancer, National Cancer Institute of the United States, National Cancer Institute of Canada. J Natl Cancer Inst. 2000;92:205–16.
4. McCarville MB. PET-CT imaging in pediatric oncology. Cancer Imaging. 2009;9:35–43.
5. Yeung HW, Schöder H, Gonen M, Larson SM. Clinical value of combined positron emission tomography/computed tomography imaging in the interpretation of 2-deoxy-2-[F-18]fluoro-D-glucose–positron emission tomography studies in cancer patients. Mol Imaging Biol. 2005;7:229–35.
6. Kleis M, Heike Daldrup-Link H, Matthay K, et al. Diagnostic value of PET/CT for the staging and restaging of pediatric tumors. Eur J Nucl Med Mol Imaging. 2009;36:23–36.
7. Schwenzer NF, Pfannenberg C, Reischl G, et al. Application of MR/PET in oncologic imaging. Rofo. 2012;184:780–7.
8. Hirsch FW, Sattler B, Sorge I, et al. PET/MR in children: initial clinical experience in paediatric oncology using an integrated PET/MR scanner. Pediatr Radiol. 2013;43:860–75.
9. Aghighi M, Pisani LJ, Sun Z, Klenk C, Madnawat H, Fineman SL, Advani R, Von Eyben R, Owen D, Quon A, Moseley M, Daldrup-Link HE. Speeding up PET/MR for cancer staging of children and young adults. Eur Radiol. 2016;26:4239–48.
10. Sher AC, Seghers V, Paldino MJ, et al. Assessment of sequential PET/MRI in comparison with PET/CT of Pediatric lymphoma: a prospective study. AJR Am J Roentgenol. 2016;206:623–31.
11. Ponisio MR, McConathy J, Laforest R, Khanna G. Evaluation of diagnostic performance of whole-body simultaneous PET/MRI in pediatric lymphoma. Pediatr Radiol. 2016;46:1258–1268.
12. Eiber M, Takei T, Souvatzoglou M, et al. Performance of whole-body integrated ^{18}F-FDG PET/MR in comparison to PET/CT for evaluation of malignant bone lesions. J Nucl Med. 2014;55:191–7.
13. Schäfer JF, Gatidis S, Schmidt H, et al. Simultaneous whole-body PET/MR imaging in comparison to PET/CT in pediatric oncology: initial results. Radiology. 2014;273:220–31.
14. Purz S, Sabri O, Viehweger A, et al. Potential pediatric applications of PET/MR. J Nucl Med. 2014;55 Suppl 2:32S–9.
15. Spick C, Herrmann K, Czernin J. ^{18}F-FDG PET/CT and PET/MRI perform equally well in cancer: evidence from studies on more than 2,300 patients. J Nucl Med. 2016;57:420–30.
16. Jadvar H, Connolly LP, Fahey FH, Shulkin BL. PET and PET/CT in pediatric oncology. Semin Nucl Med. 2007;37:316–31.
17. Packer RJ. Childhood brain tumors: accomplishments and ongoing challenges. J Child Neurol. 2008;23:1122–7.
18. Packer RJ, Vezina G. Management of and prognosis with medulloblastoma: therapy at a crossroads. Arch Neurol. 2008;65:1419–24.
19. Schelbert HR, Hoh CK, Royal HD, et al. Procedure guideline for tumor imaging using fluorine-18-FDG. Society of Nuclear Medicine. J Nucl Med. 1998;39:1302–5.
20. Stauss J, Franzius C, Pfluger T, et al. Guidelines for ^{18}F-FDG PET and PET-CT imaging in paediatric oncology. Eur J Nucl Med Mol Imaging. 2008;35:1581–8.
21. Hoffman JM, Hanson MW, Friedman HS, et al. FDG-PET in pediatric posterior fossa brain tumors. J Comput Assist Tomogr. 1992;16:62–8.
22. Borgwardt L, Hojgaard L, Carstensen H, et al. Increased fluorine-18 2-fluoro-2-deoxy-D-glucose (FDG) uptake in childhood CNS tumors is correlated with malignancy grade: a study with FDG positron emission tomography/magnetic resonance imaging coregistration and image fusion. J Clin Oncol. 2005;23:3030–7.
23. Kruer MC, Kaplan AM, Etzl MM Jr, et al. The value of positron emission tomography and proliferation index in predicting progression in low-grade astrocytomas of childhood. J Neurooncol. 2009;95:239–45.
24. Galldiks N, Kracht LW, Berthold F, et al. [^{11}C]-L-methionine positron emission tomography in the management of children and young adults with brain tumors. J Neurooncol. 2010;96:231–9.
25. Okochi Y, Nihashi T, Fujii M, et al. Clinical use of ^{11}C-methionine and ^{18}F-FDG-PET for germinoma in central nervous system. Ann Nucl Med. 2014;28:94–102.
26. Uslu L, Donig J, Link M, et al. Value of ^{18}F-FDG PET and PET/CT for evaluation of pediatric malignancies. J Nucl Med. 2015;56:274–86.
27. Morana G, Piccardo A, Milanaccio C, et al. Value of ^{18}F-3,4-dihydroxyphenylalanine PET/MR image fusion in pediatric supratentorial infiltrative

astrocytomas: a prospective pilot study. J Nucl Med. 2014;55:718–23.
28. Morana G, Piccardo A, Garrè ML, et al. Multimodal magnetic resonance imaging and ^{18}F-L-dihydroxyphenylalanine positron emission tomography in early characterization of pseudoresponse and nonenhancing tumor progression in a pediatric patient with malignant transformation of ganglioglioma treated with bevacizumab. J Clin Oncol. 2013;31: e1–5.
29. Piccardo A, Puntoni M, Lopci E, et al. Prognostic value of ^{18}F-DOPA PET/CT at the time of recurrence in patients affected by neuroblastoma. Eur J Nucl Med Mol Imaging. 2014;41:1046–56.
30. Piccardo A, Morana G, Massollo M, et al. Brain metastasis from neuroblastoma depicted by ^{18}F-DOPA PET/CT. Nucl Med Mol Imaging. 2015;49:241–2.
31. Ribeiro MJ, De Lonlay P, Delzescaux T, et al. Characterization of hyperinsulinism in infancy assessed with PET and ^{18}F-fluoro-L-DOPA. J Nucl Med. 2005;46:560–6.
32. Dunkl V, Cleff C, Stoffels G, et al. The usefulness of dynamic O-(2-^{18}F-fluoroethyl)-L-tyrosine PET in the clinical evaluation of brain tumors in children and adolescents. J Nucl Med. 2015;56:88–92.
33. Misch M, Guggemos A, Driever PH, et al. ^{18}F-FET-PET guided surgical biopsy and resection in children and adolescence with brain tumors. Childs Nerv Syst. 2015;31:261–7.
34. Pastore G, Magnani C, Verdecchia A, et al. Survival of childhood lymphomas in Europe, 1978–1992: a report from the EUROCARE study. Eur J Cancer. 2001;37:703–10.
35. Weihrauch MR, Re D, Scheidhauer K, et al. Thoracic positron emission tomography using ^{18}F-fluorodeoxyglucose for the evaluation of residual mediastinal Hodgkin disease. Blood. 2001;98:2930–4.
36. Brisse H, Pacquement H, Burdairon E, Plancher C, Neuenschwander S. Outcome of residual mediastinal masses of thoracic lymphomas in children: impact on management and radiological follow-up strategy. Pediatr Radiol. 1998;28:444–50.
37. Oberlin O. Present and future strategies of treatment in childhood Hodgkin's lymphomas. Ann Oncol. 1996;7 Suppl 4:73–8.
38. Schwartz CL. The management of Hodgkin disease in the young child. Curr Opin Pediatr. 2003;15:10–6.
39. Landman-Parker J, Pacquement H, Leblanc T, et al. Localized childhood Hodgkin's disease: response-adapted chemotherapy with etoposide, bleomycin, vinblastine, and prednisone before low-dose radiation therapy-results of the French Society of Pediatric Oncology Study MDH90. J Clin Oncol. 2000;18: 1500–7.
40. Yeh JM, Diller L. Pediatric Hodgkin lymphoma: trade-offs between short- and long-term mortality risks. Blood. 2012;120:2195–202.
41. Hay AE, Meyer RM. Balancing risks and benefits of therapy for patients with favorable-risk limited-stage Hodgkin lymphoma: the role of doxorubicin, bleomycin, vinblastine, and dacarbazine chemotherapy alone. Hematol Oncol Clin North Am. 2014;28:49–63.
42. Mann G, Attarbaschi A, Burkhardt B, et al. Clinical characteristics and treatment outcome of infants with non-Hodgkin lymphoma. Br J Haematol. 2007;139: 443–9.
43. Reiter A. Diagnosis and treatment of childhood non-Hodgkin lymphoma. Hematology ASH Education Book. 2007;1:285–296.
44. Murphy SB, Fairclough DL, Hutchison RE, Berard CW. Non-Hodgkin's lymphomas of childhood: an analysis of the histology, staging, and response to treatment of 338 cases at a single institution. J Clin Oncol. 1989;7:186–93.
45. Patte C. Non-Hodgkin's lymphoma. Eur J Cancer. 1998;34:359–62. discussion 62–3.
46. Patte C, Auperin A, Gerrard M, et al. Results of the randomized international FAB/LMB96 trial for intermediate risk B-cell non-Hodgkin lymphoma in children and adolescents: it is possible to reduce treatment for the early responding patients. Blood. 2007;109: 2773–80.
47. Cairo MS, Gerrard M, Sposto R, et al. Results of a randomized international study of high-risk central nervous system B non-Hodgkin lymphoma and B acute lymphoblastic leukemia in children and adolescents. Blood. 2007;109:2736–43.
48. Grenzebach J, Schrappe M, Ludwig WD, et al. Favorable outcome for children and adolescents with T-cell lymphoblastic lymphoma with an intensive ALL-type therapy without local radiotherapy. Ann Hematol. 2001;80 Suppl 3:B73–6.
49. Brugieres L, Le Deley MC, Rosolen A, et al. Impact of the methotrexate administration dose on the need for intrathecal treatment in children and adolescents with anaplastic large-cell lymphoma: results of a randomized trial of the EICNHL Group. J Clin Oncol. 2009;27:897–903.
50. Mody RJ, Bui C, Hutchinson RJ, Frey KA, Shulkin BL. Comparison of ^{18}F Flurodeoxyglucose PET with Ga-67 scintigraphy and conventional imaging modalities in pediatric lymphoma. Leuk Lymphoma. 2007; 48:699–707.
51. Shankar A, Fiumara F, Pinkerton R. Role of FDG PET in the management of childhood lymphomas-case proven or is the jury still out? Eur J Cancer. 2008;44:663–73.
52. Shulkin BL, Goodin GS, McCarville MB, et al. Bone and [^{18}F]fluorodeoxyglucose positron-emission tomography/computed tomography scanning for the assessment of osseous involvement in Hodgkin lymphoma in children and young adults. Leuk Lymphoma. 2009;50:1794–802.
53. Allen-Auerbach M, Quon A, Weber WA, et al. Comparison between 2-deoxy-2-[^{18}F]fluoro-D-glucose

positron emission tomography and positron emission tomography/computed tomography hardware fusion for staging of patients with lymphoma. Mol Imaging Biol. 2004;6:411–6.
54. Toma P, Granata C, Rossi A, Garaventa A. Multimodality imaging of Hodgkin disease and non-Hodgkin lymphomas in children. Radiographics. 2007;27:1335–54.
55. Rahmouni A, Montazel JL, Divine M, et al. Bone marrow with diffuse tumor infiltration in patients with lymphoproliferative diseases: dynamic gadolinium-enhanced MR imaging. Radiology. 2003;229:710–7.
56. Haque S, Law M, Abrey LE, Young RJ. Imaging of lymphoma of the central nervous system, spine, and orbit. Radiol Clin North Am. 2008;46:339–61.
57. Punwani S, Taylor SA, Bainbridge A, et al. Pediatric and adolescent lymphoma: comparison of whole-body STIR half-Fourier RARE MR imaging with an enhanced PET/CT reference for initial staging. Radiology. 2010;255:182–90.
58. Moog F, Bangerter M, Diederichs CG, et al. Extranodal malignant lymphoma: detection with FDG PET versus CT. Radiology. 1998;206:475–81.
59. Carr R, Barrington SF, Madan B, et al. Detection of lymphoma in bone marrow by whole-body positron emission tomography. Blood. 1998;91:3340–6.
60. Agrawal K, Rai Mittal B, Bansal D, Varma N, et al. Role of F-18 FDG PET/CT in assessing bone marrow involvement in pediatric Hodgkin's lymphoma. Ann Nucl Med. 2013;27:146–51.
61. Montravers F, McNamara D, Landman-Parker J, et al. [^{18}F]FDG in childhood lymphoma: clinical utility and impact on management. Eur J Nucl Med Mol Imaging. 2002;29:1155–65.
62. Hermann S, Wormanns D, Pixberg M, et al. Staging in childhood lymphoma: differences between FDG-PET and CT. Nuklearmedizin. 2005;44:1–7.
63. Furth C, Denecke T, Steffen I, et al. Correlative imaging strategies implementing CT, MRI, and PET for staging of childhood Hodgkin disease. J Pediatr Hematol Oncol. 2006;28:501–12.
64. Kabickova E, Sumerauer D, Cumlivska E, et al. Comparison of ^{18}F-FDG-PET and standard procedures for the pretreatment staging of children and adolescents with Hodgkin's disease. Eur J Nucl Med Mol Imaging. 2006;33:1025–31.
65. Purz S, Mauz-Körholz C, Körholz D, et al. [^{18}F] Fluorodeoxyglucose positron emission tomography for detection of bone marrow involvement in children and adolescents with Hodgkin's lymphoma. J Clin Oncol. 2011;29:3523–8.
66. Wickmann L, Luders H, Dorffel W. 18-FDG-PET-findings in children and adolescents with Hodgkin's disease: retrospective evaluation of the correlation to other imaging procedures in initial staging and to the predictive value of follow up examinations. Klin Padiatr. 2003;215:146–50.
67. Furth C, Steffen IG, Amthauer H, et al. Early and late therapy response assessment with [^{18}F]fluorodeoxyglucose positron emission tomography in pediatric Hodgkin's lymphoma: analysis of a prospective multicenter trial. J Clin Oncol. 2009;27:4385–91.
68. Lopci E, Burnelli R, Ambrosini V, et al. ^{18}F-FDG PET in pediatric lymphomas: a comparison with conventional imaging. Cancer Biother Radiopharm. 2008; 23:681–90.
69. Miller E, Metser U, Avrahami G, et al. Role of ^{18}F-FDG PET/CT in staging and follow-up of lymphoma in pediatric and young adult patients. J Comput Assist Tomogr. 2006;30:689–94.
70. Riad R, Omar W, Kotb M, et al. Role of PET/CT in malignant pediatric lymphoma. Eur J Nucl Med Mol Imaging. 2010;37:319–29.
71. Depas G, De Barsy C, Jerusalem G, et al. ^{18}F-FDG PET in children with lymphomas. Eur J Nucl Med Mol Imaging. 2005;32:31–8.
72. Hernandez-Pampaloni M, Takalkar A, Yu JQ, et al. F-18 FDG-PET imaging and correlation with CT in staging and follow-up of pediatric lymphomas. Pediatr Radiol. 2006;36:524–31.
73. Amthauer H, Furth C, Denecke T, et al. FDG-PET in 10 children with non-Hodgkin's lymphoma: initial experience in staging and follow-up. Klin Padiatr. 2005;217:327–33.
74. Rhodes MM, Delbeke D, Whitlock JA, et al. Utility of FDG-PET/CT in follow-up of children treated for Hodgkin and non-Hodgkin lymphoma. J Pediatr Hematol Oncol. 2006;28:300–6.
75. Bakhshi S, Radhakrishnan V, Sharma P, et al. Pediatric nonlymphoblastic non-Hodgkin lymphoma: baseline, interim, and posttreatment PET/CT versus contrast-enhanced CT for evaluation – a prospective study. Radiology. 2012;262:956–68.
76. Ilivitzki A, Radan L, Ben-Arush M, et al. Early interim FDGPET/CT prediction of treatment response and prognosis in pediatric Hodgkin disease: added value of low-dose CT. Pediatr Radiol. 2013;43:86–92.
77. Korholz D, Kluge R, Wickmann L, et al. Importance of F18-fluorodeoxy-D-2-glucose positron emission tomography (FDG-PET) for staging and therapy control of Hodgkin's lymphoma in childhood and adolescence – consequences for the GPOH-HD 2003 protocol. Onkologie. 2003; 26:489–93.
78. Hudson MM, Krasin MJ, Kaste SC. PET imaging in pediatric Hodgkin's lymphoma. Pediatr Radiol. 2004; 34:190–8.
79. Kluge R, Kurch L, Montravers F, Mauz-Körholz C. FDG PET/CT in children and adolescents with lymphoma. Pediatr Radiol. 2013;43:406–17.
80. London K, Cross S, Onikul E, et al. ^{18}F-FDG PET/CT in paediatric lymphoma: comparison with conventional imaging. Eur J Nucl Med Mol Imaging. 2011;38:274–84.

81. Weiler-Sagie M, Bushelev O, Epelbaum R, et al. ^{18}F-FDG avidity in lymphoma readdressed: a study of 766 patients. J Nucl Med. 2010;51:25–30.
82. Tsukamoto N, Kojima M, Hasegawa M, et al. The usefulness of ^{18}F-fluorodeoxyglucose positron emission tomography (^{18}F-FDG-PET) and a comparison of ^{18}F-FDG-PET with ^{67}gallium scintigraphy in the evaluation of lymphoma: relation to histologic subtypes based on the World Health Organization classification. Cancer. 2007;110:652–9.
83. Elstrom R, Guan L, Baker G, et al. Utility of FDG-PET scanning in lymphoma by WHO classification. Blood. 2003;101:3875–6.
84. Rigacci L, Vitolo U, Nassi L, et al. Positron emission tomography in the staging of patients with Hodgkin's lymphoma. A prospective multicentric study by the Intergruppo Italiano Linfomi. Ann Hematol. 2007;86:897–903.
85. Dobert N, Menzel C, Berner U, et al. Positron emission tomography in patients with Hodgkin's disease: correlation to histopathologic subtypes. Cancer Biother Radiopharm. 2003;18:565–71.
86. Kasamon YL, Jones RJ, Wahl RL. Integrating PET and PET/CT into the risk-adapted therapy of lymphoma. J Nucl Med. 2007;48 Suppl 1:19S–27.
87. Montravers F, Landman-Parker J, Grahek D, et al. FDG PET in childhood Hodgkin's lymphoma. Reports on the false-negative, false-positive and unexpected results during a five-year experience. J Nucl Med. 2006;47:144P.
88. Juweid ME. Utility of positron emission tomography (PET) scanning in managing patients with Hodgkin lymphoma. Hematol Am Soc Hematol Educ Prog. 2006;259–65:510–1.
89. van Quarles Ufford H, Hoekstra O, de Haas M, et al. On the added value of baseline FDG-PET in malignant lymphoma. Mol Imaging Biol. 2010;12:225–32.
90. Hutchings M, Barrington SF. PET/CT for therapy response assessment in lymphoma. J Nucl Med. 2009;50 Suppl 1:21S–30.
91. Hasenclever D, Kurch L, Mauz-Körholz C, et al. qPET – a quantitative extension of the Deauville scale to assess response in interim FDG-PET scans in lymphoma. Eur J Nucl Med Mol Imaging. 2014;41:1301–8.
92. Strobel K, Schaefer NG, Renner C, et al. Cost-effective therapy remission assessment in lymphoma patients using 2-[fluorine-18]fluoro-2-deoxy-D-glucose-positron emission tomography/computed tomography: is an end of treatment exam necessary in all patients? Ann Oncol. 2007;18:658–64.
93. Meany HJ, Gidvani VK, Minniti CP. Utility of PET scans to predict disease relapse in pediatric patients with Hodgkin lymphoma. Pediatr Blood Cancer. 2007;48:399–402.
94. Nievelstein RA, Quarles van Ufford HM, Kwee TC, et al. Radiation exposure and mortality risk from CT and PET imaging of patients with malignant lymphoma. Eur Radiol. 2012;22:1946–54.
95. Rathore N, Eissa HM, Margolin JF. Pediatric Hodgkin lymphoma: are we over-scanning our patients? Pediatr Hematol Oncol. 2012;29:415–23.
96. Voss SD. Surveillance imaging in pediatric Hodgkin lymphoma. Curr Hematol Malig Rep. 2013;8:218–25.
97. Moog F, Bangerter M, Diederichs CG, et al. Lymphoma: role of whole-body 2-deoxy-2-[F-18]fluoro-D-glucose (FDG) PET in nodal staging. Radiology. 1997;203:795–800.
98. Montravers F, Landman-Parker J, Kerrou K, et al. Impact of FDG PET on the management of childhood non-Hodgkin lymphoma: a five-year experience. J Nucl Med. 2006;47:87P.
99. Sher AC, Seghers V, Paldino MJ, et al. The role of FDG-PET/CT in the evaluation of residual disease in paediatric non-Hodgkin lymphoma. Br J Haematol. 2015;168:845–53.
100. Riad R, Omar W, Sidhom I, et al. False-positive F-18 FDG uptake in PET/CT studies in pediatric patients with abdominal Burkitt's lymphoma. Nucl Med Commun. 2010;31:232–8.
101. Palestro CJ, Rini JN, Tomas MB. Lymphoma. In: Charron M, editor. Practical pediatric PET imaging. New York: Springer Science; 2006. p. 220–42.
102. Kaste SC, Howard SC, McCarville EB, et al. ^{18}F-FDG-avid sites mimicking active disease in pediatric Hodgkin's. Pediatr Radiol. 2005;35:141–54.
103. Shammas A, Lim R, Charron M. Pediatric FDG PET/CT: physiologic uptake, normal variants, and benign conditions. Radiographics. 2009;29:1467–86.
104. Kamoto Y, Sadato N, Yonekura Y, et al. Visualization of the cervical spinal cord with FDG and high-resolution PET. J Comput Assist Tomogr. 1998;22:487–91.
105. Saggese D, Ceroni Compadretti G, Cartaroni C. Cervical ectopic thymus: a case report and review of the literature. Int J Pediatr Otorhinolaryngol. 2002;66:77–80.
106. Soderlund V, Larsson SA, Jacobsson H. Reduction of FDG uptake in brown adipose tissue in clinical patients by a single dose of propranolol. Eur J Nucl Med Mol Imaging. 2007;34:1018–22.
107. Lustberg MB, Aras O, Meisenberg BR. FDG PET/CT findings in acute adult mononucleosis mimicking malignant lymphoma. Eur J Haematol. 2008;81:154–6.
108. Panagiotidis E, Exarhos D, Housianakou I, et al. FDG uptake in axillary lymph nodes after vaccination against pandemic (H1N1). Eur Radiol. 2010;20:1251–3.
109. Bhojwani D, McCarville MB, Choi JK, et al. The role of FDG-PET/CT in the evaluation of residual disease in paediatric non-Hodgkin lymphoma. Br J Haematol. 2015;168:845–53.
110. Moinul Hossain AK, Shulkin BL, et al. FDG positron emission tomography/computed tomography studies of Wilms' tumor. Eur J Nucl Med Mol Imaging. 2010;37:1300–8.

111. Smith MA, Seibel NL, Altekruse SF, et al. Outcomes for children and adolescents with cancer: challenges for the twenty-first century. J Clin Oncol. 2010;28:2625–34.
112. Pfluger T, Leinsinger G, Sander A, et al. Magnetic resonance imaging of benign and premalignant tumors in childhood. Radiologe. 1999;39:685–94.
113. Misch D, Steffen IG, Schonberger S, et al. Use of positron emission tomography for staging, preoperative response assessment and posttherapeutic evaluation in children with Wilms tumour. Eur J Nucl Med Mol Imaging. 2008;35:1642–50.
114. Shulkin BL, Chang E, Strouse PJ, et al. PET FDG studies of Wilms tumors. J Pediatr Hematol Oncol. 1997;19:334–8.
115. Belgaumi AF, Kauffman WM, Jenkins JJ, et al. Blindness in children with neuroblastoma. Cancer. 1997;80:1997–2004.
116. Kropp J, Hofmann M, Bihl H. Comparison of MIBG and pentetreotide scintigraphy in children with neuroblastoma. Is the expression of somatostatin receptors a prognostic factor? Anticancer Res. 1997;17:1583–8.
117. Schmidt M, Simon T, Hero B, Schicha H, Berthold F. The prognostic impact of functional imaging with ^{123}I-mIBG in patients with stage 4 neuroblastoma >1 year of age on a high-risk treatment protocol: results of the German Neuroblastoma Trial NB97. Eur J Cancer. 2008;44:1552–8.
118. Taggart D, Dubois S, Matthay KK. Radiolabeled metaiodobenzylguanidine for imaging and therapy of neuroblastoma. Q J Nucl Med Mol Imaging. 2008;52:403–18.
119. Custodio CM, Semelka RC, Balci NC, et al. Adrenal neuroblastoma in an adult with tumor thrombus in the inferior vena cava. J Magn Reson Imaging. 1999;9:621–3.
120. DuBois SG, Matthay KK. Radiolabeled metaiodobenzylguanidine for the treatment of neuroblastoma. Nucl Med Biol. 2008;35 Suppl 1:S35–48.
121. Boubaker A, Bischof Delaloye A, Bischof Delaloye A. Nuclear medicine procedures and neuroblastoma in childhood. Their value in the diagnosis, staging and assessment of response to therapy. Q J Nucl Med. 2003;47:31–40.
122. Parisi MT, Greene MK, Dykes TM, et al. Efficacy of metaiodobenzylguanidine as a scintigraphic agent for the detection of neuroblastoma. Invest Radiol. 1992;27:768–73.
123. de Kraker J, Hoefnagel KA, Verschuur AC, et al. Iodine-131-metaiodobenzylguanidine as initial induction therapy in stage 4 neuroblastoma patients over 1 year of age. Eur J Cancer. 2008;44:551–6.
124. Hugosson C, Nyman R, Jorulf H, et al. Imaging of abdominal neuroblastoma in children. Acta Radiol. 1999;40:534–42.
125. Sofka CM, Semelka RC, Kelekis NL, et al. Magnetic resonance imaging of neuroblastoma using current techniques. Magn Reson Imaging. 1999;17:193–8.
126. Valk TW, Frager MS, Gross MD, et al. Spectrum of pheochromocytoma in multiple endocrine neoplasia. A scintigraphic portrayal using ^{131}I-meta-iodobenzylguanidine. Ann Intern Med. 1981;94:762–7.
127. Wieland DM, Brown LE, Tobes MC, et al. Imaging the primate adrenal medulla with [^{123}I] and [^{131}I] meta-iodobenzylguanidine: concise communication. J Nucl Med. 1981;22:358–64.
128. Sisson JC, Wieland DM. Radiolabeled meta-iodobenzylguanidine: pharmacology and clinical studies. Am J Physiol Imaging. 1986;1:96–103.
129. Guilloteau D, Chalon S, Baulieu JL, et al. Comparison of MIBG and monoamines uptake mechanisms: pharmacological animal and blood platelets studies. Eur J Nucl Med. 1988;14:341–4.
130. Rufini V, Calcagni ML, Baum RP. Imaging of neuroendocrine tumors. Semin Nucl Med. 2006;36:228–47.
131. Howman-Giles R, Shaw PJ, Uren RF, Chung DK. Neuroblastoma and other neuroendocrine tumors. Semin Nucl Med. 2007;37:286–302.
132. Biasotti S, Garaventa A, Villavecchia GP, et al. False-negative metaiodobenzylguanidine scintigraphy at diagnosis of neuroblastoma. Med Pediatr Oncol. 2000;35:153–5.
133. Piccardo A, Lopci E, Conte M, et al. PET/CT imaging in neuroblastoma. Q J Nucl Med Mol Imaging. 2013;57:29–39.
134. Sharp SE, Parisi MT, Gelfand MJ, et al. Functional-metabolic imaging of neuroblastoma. Q J Nucl Med Mol Imaging. 2013;57:6–20.
135. Troncone L, Rufini V, Montemaggi P, et al. The diagnostic and therapeutic utility of radioiodinated meta-iodobenzylguanidine (MIBG). 5 years of experience. Eur J Nucl Med. 1990;16:325–35.
136. Gelfand MJ. Meta-iodobenzylguanidine in children. Semin Nucl Med. 1993;23:231–42.
137. Shulkin BL, Shapiro B, Francis IR, et al. Primary extra-adrenal pheochromocytoma: positive I-123 MIBG imaging with negative I-131 MIBG imaging. Clin Nucl Med. 1986;11:851–4.
138. Boubaker A, Bischof Delaloye A. MIBG scintigraphy for the diagnosis and follow-up of children with neuroblastoma. Q J Nucl Med Mol Imaging. 2008;52:388–402.
139. Hadj-Djilani NL, Lebtahi NE, Delaloye AB, et al. Diagnosis and follow-up of neuroblastoma by means of iodine-123 metaiodobenzylguanidine scintigraphy and bone scan, and the influence of histology. Eur J Nucl Med. 1995;22:322–9.
140. Khafagi FA, Shapiro B, Fig LM, et al. Labetalol reduces iodine-131 MIBG uptake by pheochromocytoma and normal tissues. J Nucl Med. 1989;30:481–9.
141. Solanki KK, Bomanji J, Moyes J, et al. A pharmacological guide to medicines which interfere with the biodistribution of radiolabelled meta-iodobenzylguanidine (MIBG). Nucl Med Commun. 1992;13:513–21.

142. Fendler WP, Wenter V, Thornton HI, et al. Combined scintigraphy and tumor marker analysis predicts unfavorable histopathology of neuroblastic tumors with high accuracy. PLoS One. 2015;10(7):e0132809.
143. Fendler WP, Melzer HI, Walz C, et al. High ^{123}I-MIBG uptake in neuroblastic tumours indicates unfavourable histopathology. Eur J Nucl Med Mol Imaging. 2013;40:1701–10.
144. Gordon I, Peters AM, Gutman A, et al. Skeletal assessment in neuroblastoma – the pitfalls of iodine-123-MIBG scans. J Nucl Med. 1990;31:129–34.
145. Pfluger T, Schmied C, Porn U, et al. Integrated imaging using MRI and ^{123}I metaiodobenzylguanidine scintigraphy to improve sensitivity and specificity in the diagnosis of pediatric neuroblastoma. AJR Am J Roentgenol. 2003;181:1115–24.
146. Geatti O, Shapiro B, Shulkin B, et al. Gastrointestinal iodine-131-meta-iodobenzylguanidine activity. Am J Physiol Imaging. 1988;3:188–91.
147. Granata C, Carlini C, Conte M, et al. False positive MIBG scan due to accessory spleen. Med Pediatr Oncol. 2001;37:138–9.
148. McGarvey CK, Applegate K, Lee ND, Sokol DK. False-positive metaiodobenzylguanidine scan for neuroblastoma in a child with opsoclonus-myoclonus syndrome treated with adrenocorticotropic hormone (ACTH). J Child Neurol. 2006;21:606–10.
149. Moralidis E, Arsos G, Papakonstantinou E, et al. ^{123}I-Metaiodobenzylguanidine accumulation in a urinoma and cortex of an obstructed kidney after surgical resection of an abdominal neuroblastoma. Pediatr Radiol. 2008;38:118–21.
150. Bahar RH, Mahmoud S, Ibrahim A, al-Gazzar AH. A false positive I-131 MIBG due to dilated renal pelvis: a case report. Clin Nucl Med. 1988;13:900–2.
151. Bonnin F, Lumbroso J, Tenenbaum F, et al. Refining interpretation of MIBG scans in children. J Nucl Med. 1994;35:803–10.
152. Pirson AS, Krug B, Tuerlinckx D, et al. Additional value of I-123 MIBG SPECT in neuroblastoma. Clin Nucl Med. 2005;30:100–1.
153. Rufini V, Fisher GA, Shulkin BL, et al. Iodine-123-MIBG imaging of neuroblastoma: utility of SPECT and delayed imaging. J Nucl Med. 1996;37:1464–8.
154. Gelfand MJ, Elgazzar AH, Kriss VM, et al. Iodine-123-MIBG SPECT versus planar imaging in children with neural crest tumors. J Nucl Med. 1994;35:1753–7.
155. Shulkin BL, Shapiro B, Hutchinson RJ. Iodine-131-metaiodobenzylguanidine and bone scintigraphy for the detection of neuroblastoma. J Nucl Med. 1992;33:1735–40.
156. Daldrup-Link HE, Franzius C, Link TM, et al. Whole-body MR imaging for detection of bone metastases in children and young adults: comparison with skeletal scintigraphy and FDG PET. AJR Am J Roentgenol. 2001;177:229–36.
157. Mentzel HJ, Kentouche K, Sauner D, et al. Comparison of whole-body STIR-MRI and ^{99m}Tc-methylene-diphosphonate scintigraphy in children with suspected multifocal bone lesions. Eur Radiol. 2004;14:2297–302.
158. Lebtahi N, Gudinchet F, Nenadov-Beck M, et al. Evaluating bone marrow metastasis of neuroblastoma with iodine-123-MIBG scintigraphy and MRI. J Nucl Med. 1997;38:1389–92.
159. Mueller WP, Coppenrath E, Pfluger T. Nuclear medicine and multimodality imaging of pediatric neuroblastoma. Pediatr Radiol. 2013;43:418–27.
160. Sharp SE, Shulkin BL, et al. ^{123}I-MIBG scintigraphy and ^{18}F-FDG PET in neuroblastoma. J Nucl Med. 2009;50:1237–43.
161. Kushner BH, Yeung HW, Larson SM, et al. Extending positron emission tomography scan utility to high-risk neuroblastoma: fluorine-18 fluorodeoxyglucose positron emission tomography as sole imaging modality in follow-up of patients. J Clin Oncol. 2001;19:3397–405.
162. Shulkin BL, Hutchinson RJ, Castle VP, et al. Neuroblastoma: positron emission tomography with 2-[fluorine-18]-fluoro-2-deoxy-D-glucose compared with metaiodobenzylguanidine scintigraphy. Radiology. 1996;199:743–50.
163. Melzer HI, Coppenrath E, Schmid I, et al. ^{123}I-MIBG scintigraphy/SPECT versus ^{18}F-FDG PET in paediatric neuroblastoma. Eur J Nucl Med Mol Imaging. 2011;38:1648–58.
164. Rosenspire KC, Haka MS, Van Dort ME, et al. Synthesis and preliminary evaluation of carbon-11-meta-hydroxyephedrine: a false transmitter agent for heart neuronal imaging. J Nucl Med. 1990;31:1328–34.
165. Shulkin BL, Wieland DM, Baro ME, et al. PET hydroxyephedrine imaging of neuroblastoma. J Nucl Med. 1996;37:16–21.
166. Franzius C, Hermann K, Weckesser M, et al. Whole-body PET/CT with ^{11}C-meta-hydroxyephedrine in tumors of the sympathetic nervous system: feasibility study and comparison with ^{123}I-MIBG SPECT/CT. J Nucl Med. 2006;47:1635–42.
167. Becherer A, Szabo M, Karanikas G, et al. Imaging of advanced neuroendocrine tumors with ^{18}F-FDOPA PET. J Nucl Med. 2004;45:1161–7.
168. Hoegerle S, Nitzsche E, Altehoefer C, et al. Pheochromocytomas: detection with ^{18}F DOPA whole body PET–initial results. Radiology. 2002;222:507–12.
169. Mamede M, Carrasquillo JA, Chen CC, et al. Discordant localization of 2-[^{18}F]-fluoro-2-deoxy-D-glucose in 6-[^{18}F]-fluorodopamine- and [^{123}I]-meta-iodobenzylguanidine-negative metastatic pheochromocytoma sites. Nucl Med Commun. 2006;27:31–6.
170. Piccardo A, Lopci E. Potential role of ^{18}F-DOPA PET in neuroblastoma. Clin Transl Imaging. 2016. doi:10.1007/s40336-016-0162-2.
171. Lu MY, Liu YL, Chang HH, et al. Characterization of neuroblastic tumors using ^{18}F-FDOPA PET. J Nucl Med. 2013;54:42–9.

172. Lopci E, Piccardo A, Nanni C, et al. ^{18}F-DOPA PET/CT in neuroblastoma: comparison of conventional imaging with CT/MR. Clin Nucl Med. 2012; 37:e71–8.
173. Pfluger T, Melzer HI, Mueller WP, et al. Diagnostic value of combined ^{18}F-FDG PET/MRI for staging and restaging in paediatric oncology. Eur J Nucl Med Mol Imaging. 2012;39:1745–55.
174. Muller MF, Krestin GP, Willi UV. Abdominal tumors in children. A comparison between magnetic resonance tomography (MRT) and ultrasonography (US). Rofo. 1993;158:9–14.
175. Daldrup HE, Link TM, Wortler K, et al. MR imaging of thoracic tumors in pediatric patients. AJR Am J Roentgenol. 1998;170:1639–44.
176. Kaste SC. Issues specific to implementing PET-CT for pediatric oncology: what we have learned along the way. Pediatr Radiol. 2004;34:205–13.
177. Bar-Sever Z, Keidar Z, Ben-Barak A, et al. The incremental value of ^{18}F-FDG PET/CT in paediatric malignancies. Eur J Nucl Med Mol Imaging. 2007;34:630–7.
178. Olson PN, Everson LI, Griffiths HJ. Staging of musculoskeletal tumors. Radiol Clin North Am. 1994;32: 151–62.
179. Silberstein EB, Saenger EL, Tofe AJ, et al. Imaging of bone metastases with ^{99m}Tc-Sn-EHDP (diphosphonate), ^{18}F, and skeletal radiography. A comparison of sensitivity. Radiology. 1973;107:551–5.
180. Hahn K, Charron M, Shulkin BL. Role of MR imaging and iodine 123 MIBG scintigraphy in staging of pediatric neuroblastoma. Radiology. 2003;227:908. author reply 08-9.
181. Shah Syed GM, Naseer H, Usmani GN, Cheema MA. Role of iodine-131 MIBG scanning in the management of paediatric patients with neuroblastoma. Med Princ Pract. 2004;13:196–200.
182. Moon L, McHugh K. Advances in paediatric tumour imaging. Arch Dis Child. 2005;90:608–11.
183. Nanni C, Rubello D, Castellucci P, et al. ^{18}F-FDG PET/CT fusion imaging in paediatric solid extracranial tumours. Biomed Pharmacother. 2006;60:593–606.
184. Yeung HW, Schoder H, Smith A, et al. Clinical value of combined positron emission tomography/computed tomography imaging in the interpretation of 2-deoxy-2-[F-18]fluoro-D-glucose-positron emission tomography studies in cancer patients. Mol Imaging Biol. 2005;7:229–35.
185. Brodeur GM, Pritchard J, Berthold F, et al. Revisions of the international criteria for neuroblastoma diagnosis, staging, and response to treatment. J Clin Oncol. 1993;11:1466–77.
186. Rozovsky K, Koplewitz BZ, Krausz Y, et al. Added value of SPECT/CT for correlation of MIBG scintigraphy and diagnostic CT in neuroblastoma and pheochromocytoma. AJR Am J Roentgenol. 2008;190: 1085–90.
187. Erlemann R, Sciuk J, Bosse A, et al. Response of osteosarcoma and Ewing sarcoma to preoperative chemotherapy: assessment with dynamic and static MR imaging and skeletal scintigraphy. Radiology. 1990;175:791–6.
188. Knop J, Delling G, Heise U, Winkler K. Scintigraphic evaluation of tumor regression during preoperative chemotherapy of osteosarcoma. Skeletal Radiol. 1990;19:165–72.
189. O'Mara RE. Bone scanning in osseous metastatic disease. JAMA. 1988;229:1915–7.
190. Algra PR, Bloem JL, Tissing H, et al. Detection of vertebral metastases: comparison between MR imaging and bone scintigraphy. Radiographics. 1991;11:219–32.
191. Grant F, Fahey F, Packard A, et al. Skeletal PET with F-18-fluoride: applying new technology to an old tracer. J Nucl Med. 2008;49:68–78.
192. Petersen M. Radionuclide detection of primary pulmonary osteogenic sarcoma: a case report and review of the literature. J Nucl Med. 1990;31:1110–4.
193. Othman S, El-Desouki M. Bone scan appearance in aggressive osteogenic sarcoma with pleural, lung, bone, and soft-tissue metastases. Clin Nucl Med. 2003;28:926.
194. Anderson PM. Sm-153-EDTMP therapy with stem cell support in patients. In: Bruland OS, editor. Towards the eradication of osteosarcoma metastases. Norway: The Norwegian Radium Hospital; 1998. p. 87–8.
195. Binkovitz L, Olshefski R, Adler B. Coincidence FDG-PET in the evaluation of Langerhans' cell histiocytosis: preliminary findings. Pediatr Radiol. 2003;33:598–602.
196. Daldrup-Link HE, Franzius C, Rummeney EJ, et al. Whole body MRI for detection of bone marrow metastases in pediatric patients: comparison with skeletal scintigraphy and FDG-PET. Am J Roentgenol. 2001;177:229–36.
197. Calming U, Bemstrand C, Mosskin M, Elander S, Ingvar M, Henter J. Brain F-18-FDG PET scan in central nervous system Langerhans cell histiocytosis. J Pediatr. 2002;141:435–40.
198. Buchler T, Cervinek L, Belohlavek O, et al. Langerhans cell histiocytosis with central nervous system involvement: follow-up by FDG-PET during treatment with cladribine. Pediatr Blood Cancer. 2005;44:286–8.
199. Mueller WP, Melzer HI, Schmid I, et al. The diagnostic value of ^{18}F-FDG PET and MRI in paediatric histiocytosis. Eur J Nucl Med Mol Imaging. 2013;40:356–63.
200. Taggart DR, Han MM, Quach A, et al. Comparison of iodine-123 metaiodobenzylguanidine (MIBG) scan and [^{18}F]fluorodeoxyglucose positron emission tomography to evaluate response after iodine-131 MIBG therapy for relapsed neuroblastoma. J Clin Oncol. 2009;27:5343–9.
201. McDowell H, Losty P, Barnes N, Kokai G. Utility of FDG-PET/CT in the follow-up of neuroblastoma which became MIBG-negative. Pediatr Blood Cancer. 2009;52:552.

202. Shore RM. Positron emission tomography/computed tomography (PET/CT) in children. Pediatr Ann. 2008;37:404–12.
203. Murphy JJ, Tawfeeq M, Chang B, Nadel H. Early experience with PET/CT scan in the evaluation of pediatric abdominal neoplasms. J Pediatr Surg. 2008;43:2186–92.
204. Colavolpe C, Guedj E, Cammilleri S, et al. Utility of FDG-PET/CT in the follow-up of neuroblastoma which became MIBG-negative. Pediatr Blood Cancer. 2008;51:828–31.
205. Roca I, Simo M, Sabado C, de Toledo JS. PET/CT in paediatrics: it is time to increase its use! Eur J Nucl Med Mol Imaging. 2007;34:628–9.
206. Franzius C, Riemann B, Vormoor J, et al. Metastatic neuroblastoma demonstrated by whole-body PET-CT using ^{11}C-HED. Nuklearmedizin. 2005;44: N4–5.

Part III

Radionuclide Therapy

Radionuclide Therapy of Lymphomas 40

Heather A. Jacene, Sree Harsha Tirumani, and Richard L. Wahl

Abstract

Radioimmunotherapy is an effective therapy for NHL in a variety of settings and is well tolerated. Current studies continue to investigate the role of NHL at various time points in the management of patients with NHL. The limited clinical use of RIT seems to have been driven by economics rather than by a lack of clinical effectiveness. As new radiolabeled agents and indications and nonradioactive agents are being investigated, probably in parallel with nonradioactive agents, close collaborations between medical oncologists and nuclear medicine physicians/radiologists are paramount for optimal integration of these agents into the overall treatment schema for patients with lymphoma.

Radioimmunotherapy (RIT) for treatment of non-Hodgkin lymphoma (NHL) has been undergoing investigations since the early 1990s and became available for clinical use to treat relapsed/refractory NHL in the early 2000s. Since then, the indications for the use of RIT in NHL have been expanded. RIT for NHL is an effective therapy; however, the use in clinical practice has been limited as there are multiple other competing nonradioactive therapies for NHL, several developed in the past few years.

This chapter will provide a review of the current and possible future roles of RIT in patients with lymphoma.

Keywords

Radioimmunotherapy • RIT • Zevalin • Bexxar • Lymphoma

Glossary

[^{18}F]FDG	2-deoxy-2-[^{18}F]fluoro-D-glucose
AML	Acute myelogenous leukemia
CR	Complete response
CHOP	Chemotherapy regimen based on cyclophosphamide,doxorubicin, vincristine, and prednisone
DLBCL	Diffuse large B-cell lymphoma
FDA	United States Food and Drug Administration
Gy	Gray unit (ionizing radiation dose in the International System of Units, corresponding to the absorption of one joule of radiation energy per kilogram of matter)
HACA	Human anti-chimeric antibodies

H.A. Jacene (✉) • S.H. Tirumani
Nuclear Medicine/PET-CT, Department of Imaging, Dana-Farber Cancer Institute and Department of Radiology, Brigham and Women's Hospital, Harvard Medical School, Boston, MA, USA
e-mail: hjacene@partners.org

R.L. Wahl (✉)
Mallinkrodt Institute of Radiology, Washington University School of Medicine, St. Louis, MO, USA
e-mail: wahlr@mir.wustl.edu

© Springer International Publishing Switzerland 2017
H.W. Strauss et al. (eds.), *Nuclear Oncology*,
https://doi.org/10.1007/978-3-319-26236-9_47

HAMA	Human anti-mouse antibodies
IPI	International prognostic index
MDS	Myelodysplastic syndrome
MTD	Maximum tolerated dose
NHL	Non-Hodgkin's lymphoma
PFS	Progression-free survival
PR	Partial response
R	Rituximab
RIT	Radioimmunotherapy
SWOG	Southwest Oncology Group

Contents

Rationale and Mechanism of Action 1142

Efficacy and Safety of RIT in Recurrent NHL 1142

Front-Line and Consolidation Therapy with RIT 1144

Logistics of RIT Regimens and Practical Considerations 1145

Repeat Therapies 1148

Barriers to the Use of RIT 1149

Other Settings for RIT 1149

[^{18}F]FDG-PET for Evaluation of Response to RIT 1150

Other Radiolabeled Monoclonal Antibodies and Strategies 1151

References 1152

Rationale and Mechanism of Action

The rationale for the use of radioimmunotherapy (RIT) in cancer is that radiolabeled monoclonal antibodies will specifically target and irradiate tumor cells while sparing normal tissues. The specific tumor targeting of RIT theoretically allows higher doses of radiation to be delivered to tumor compared to external beam radiation because there are less effects of the radiation on normal tissues with RIT. Two radiolabeled anti-CD20 monoclonal antibodies, yttrium-90 (^{90}Y)-ibritumomab tiuxetan and iodine-131 (^{131}I)-tositumomab, are approved by the United States Food and Drug Administration (FDA) for the treatment of NHL as part of the Zevalin® (Spectrum Pharmaceuticals, Irvine, CA [1]) and Bexxar® (GlaxoSmithKline [2]) therapeutic regimens, respectively.

^{90}Y-ibritumomab tiuxetan is composed of the radioisotope ^{90}Y and the murine monoclonal antibody ibritumomab. ^{131}I-tositumomab is composed of the ^{131}I radioisotope and the murine monoclonal antibody tositumomab. Both components contribute to the drugs' mechanism of action. The antibodies recognize slightly different epitopes of the extracellular domain of the CD20 antigen, which is found on the surface of pre-B lymphocytes, mature B-lymphocytes, and >90% of B-cell NHLs [3, 4]. Formation of the antibody-antigen complex results in induction of apoptosis, complement-dependent cytotoxicity, and antibody-dependent cytotoxicity [5, 6]. The radioisotopes emit β^- radiations, which deposit enough energy in the tumor to result in cell death. Because the distribution of the radiolabeled antibody within a tumor can be heterogeneous [7], an additional advantage of RIT is that the β^- emissions of the radiolabel can also target the surrounding malignant cells via the cross-fire effect and thus result in killing of residual microscopic disease in cells that the unlabeled antibody did not reach.

Efficacy and Safety of RIT in Recurrent NHL

In clinical trials investigating ^{90}Y-ibritumomab tiuxetan and ^{131}I-tositumomab in patients with recurrent NHL, overall response rates ranged from 60% to 83%, with complete response (CR) rates of 15–52% [8–15]. The median duration of response with RIT ranges from 6 to 16 months for all responders, but seems to be associated with the quality of the initial response. At the time of publication of several studies, the median duration of response for patients who achieved a CR was much longer than for those achieving a less robust response, and had not yet been reached. Higher response rates were reported for RIT compared to the unlabeled anti CD-20 antibody. In a cross-over study of ^{131}I-tositumomab, 42% of patients non-responsive to unlabeled tositumomab achieved a CR after receiving a therapeutic dose of ^{131}I-tositumomab [16]. Again, a partial explanation for the improved overall response rates with the

radioactive monoclonal antibodies is that the addition of the radioactivity probably allows more cells to be targeted and killed due to the cross-fire effect.

Although the initial results of the studies investigating RIT in recurrent NHL (mostly follicular) were excellent, the initial studies preceded the widespread use of the anti CD-20 mouse-human chimeric antibody, rituximab. These trials included mostly patients who were rituximab-naïve and studies were needed to show efficacy of RIT in the group of patients previously treated with unlabeled rituximab. Rituximab is now a routine component of B-cell lymphoma regimens. Two important studies showed excellent efficacy (overall response rates, 65–74%; complete response rates, 15–42%), durations of response, and progression-free survival (6.8–12.4 months) of RIT in patients with a prior history of rituximab therapy compared to the prior studies of rituximab-naïve patients [8, 13]. In addition, responses to radioimmunotherapy were seen in patients who appeared to be refractory to rituximab therapy.

Numerous prognostic factors have been evaluated in an attempt to identify which patients are most likely to respond to RIT. In individual studies, factors reported to be associated with response are low-grade follicular histology, non-bulky disease, no bone marrow involvement, fewer prior regimens, normal serum lactate dehydrogenase levels, lower IPI, higher total body radiation dose, and no prior history of transplant [8–15]. Of all of these, low-grade follicular histology and non-bulky disease at the time of treatment are the most reliable predictors, especially in patients who had received no or minimal prior therapy for lymphoma.

In patients with NHL, RIT is generally well tolerated. The most common adverse events are serious cytopenias, notably declines in platelets and white blood cells, which are experienced by a majority of patients. Sixty to 70% of patients enrolled in clinical trials developed grade III/IV thrombocytopenia and/or neutropenia. Count nadirs typically occurred between 4 and 7 weeks post-RIT, and cytopenias may last for approximately 30 days. Consequently, monitoring of complete blood counts is required for at least 10–12 weeks post-therapy. Hematologic support is required for ~15–32% of patients after RIT [1, 2]. Notably, count nadirs occur later than typically seen with cytotoxic chemotherapies.

Additional non-hematologic short-term side effects are usually mild and may include fatigue, asthenia, nausea, and fever. There are several long-term side effects of which prescribing nuclear medicine physicians/radiologists, oncologists and patients must also be aware of [1, 2, 17, 18]. In patients with recurrent NHL treated with RIT, human anti-mouse or chimeric antibodies are found in 4–11%. Acute side effects due to HAMA/HACA (such as serum sickness-like illness) are not typically seen in this population due to a history of prior therapies and relative immune compromise, but could affect future treatment decisions (treatment with additional monoclonal antibody, eligibility for clinical trials) or interfere with certain laboratory evaluations. In studies in which ^{131}I-tositumomab RIT has been used as the initial therapy of lymphoma, HAMA rates have been even higher. Hypothyroidism has been reported to occur in ~18% of patients who receive ^{131}I-tositumomab, despite attempted thyroid blockade prior to therapy with cold iodine; this occurrence is probably less frequent with careful attention to thyroid blockade.

Secondary myelodysplastic syndrome/acute myelogenous leukemia (MDS/AML) has been reported in 2–4% of patients with recurrent NHL who received RIT [1, 2, 17, 18]. Nevertheless, the patients in these studies were heavily pretreated; thus, the role of RIT versus exposure to prior cytotoxic agents and a history of NHL in the development of MDS/AML remains unresolved. Czuczman et al. [17] retrospectively reviewed the data from 746 patients previously treated with ^{90}Y-ibritumomab tiuxetan from 1996 to 2002 who were participating in clinical trials and compassionate use trials. Nineteen patients (2.5%) developed MDS/AML at a median of 5.6 years (1.4–13.9 years) after RIT. The annualized incidences of MDS/AML after NHL diagnosis (0.3% per year) and after treatment (0.7% per year) were not more than expected in heavily pretreated patients with NHL. At a median follow-up of 5.1 years, no cases of MDS/AML were reported in 76 patients with untreated follicular NHL treated with ^{131}I-tositumomab as front-line therapy [19]. This patient population

is generally at higher risk for the development of MDS/AML and should be monitored carefully.

Front-Line and Consolidation Therapy with RIT

RIT has also been investigated in front-line and consolidation settings. In both instances, single doses of RIT are effective and can produce long-term remissions. In 76 untreated patients with follicular NHL, Kaminski et al. reported a 95% overall response rate and 75% complete response rate to a single dose of ^{131}I-tositumomab [19]. The estimated median progression-free survival rate at 5 years was 59% and progression-free survival was 6.1 years, with 5 years of follow-up. The relapse rate decreased progressively with time from the first RIT, and the long-term observations suggest that the quality of initial response may be important for subsequent relapse. HAMA was seen with greater frequency in this patient population.

A pivotal, multicenter phase III trial of ^{90}Y-ibritumomab tiuxetan by Morschhauser et al. (FIT trial) led to the approval of ^{90}Y-ibritumomab tiuxetan in the United States in the consolidation setting in 2009 [20] and long-term follow-up results have since been published [21]. Patients with untreated advanced follicular NHL received first-line chemotherapy, and if a response (complete, complete unconfirmed, or partial) was attained, patients were randomized to no treatment or ^{90}Y-ibritumomab tiuxetan consolidation. In the updated results of the FIT trial and similar to the initial publication, median progression-free survival (PFS) was significantly longer for patients in the ^{90}Y-ibritumomab tiuxetan consolidation arm ($n = 207$) versus the no treatment arm ($n = 202$) (4.1 years versus 1.1 years, $p < 0.001$) [21]. More patients in the ^{90}Y-ibritumomab tiuxetan arm who achieved a PR to first-line chemotherapy converted to CR/CRu than in the no treatment arm (77.2% versus 17.5%, $p < 0.001$) [20] and in long-term follow-up the benefit of ^{90}Y-ibritumomab tiuxetan was better in this group than in those who achieved a CR. Time to next treatment was 8.1 years in the ^{90}Y-ibritumomab tiuxetan arm versus 3 years in the control arm ($p < 0.001$) [21]. Response rates to second-line therapy and 8-year overall survival rates were the same in both arms, which the authors attributed to salvage therapy [21]. The major criticism of this study is the lack of a comparison arm with maintenance rituxumab, which has also been shown to improve PFS, and the lack of rituximab in the chemotherapy alone arms in this trial [22, 23]. Press et al. with the Southwest Oncology Group (SWOG) reported similar encouraging results in a phase II study using ^{131}I-tositumomab in the consolidation setting after six cycles of CHOP. In 90 patients, the overall and complete response rates were 91% and 69%, respectively, and 5-year progression-free survival was 67%. These outcomes were higher versus historical studies with CHOP alone [24]. Based on these results, a phase III study of CHOP/rituximab versus CHOP/^{131}I-tositumomab was conducted in patients with previously untreated follicular lymphoma (SWOG S0016). Patients were randomly assigned to six cycles of CHOP with rituximab ($n = 267$) or six cycles of CHOP and a single dose of therapeutic ^{131}I-tositumomab ($n = 265$). After a median of 4.9 years of follow-up, no difference in PFS or OS survival was seen between the CHOP-R and CHOP-RIT groups [25]. The Spanish intergroup PETHEMA/GELTAMO/GELCAB conducted a randomized phase II trial comparing consolidation with ^{90}Y-ibritumomab tiuxetan ($n = 63$) and maintenance rituximab ($n = 61$) after a response to R-CHOP in patients with grades 1-3a follicular lymphoma. Thirty-six month PFS survival was higher in the maintenance rituximab group than the RIT group (86% versus 64%, $p = 0.01$) [26]. Overall survival was similar between the two arms at the time of follow-up in that study. Overall, it seems that consolidation or maintenance anti-CD20 therapy is helpful in terms of PFS and the optimal regimen remains to be determined. Press et al. also raised additional questions about maintenance rituximab versus RIT and a combination of these to further optimize PFS [25].

As in the recurrent setting, RIT is also very well tolerated in the front-line and consolidation settings. Hematologic side effects were again the most common, but more modest compared to the recurrent setting [19–21]. One difference is the

occurrence of HAMA (~50% in Kaminski's initial treatment with RIT study [19]) and the observation of associated clinical symptoms. A flu-like illness (fever, chills, myalgias, arthalgias) developed in 26% of patients with HAMA [19]. Symptoms were moderate and resolved without sequelae in 3–4 days. An association with shorter progression-free survival was suggested in post-hoc analysis for patients who developed very high HAMA levels (>5 times the lowest level found in the first 7 weeks). No cases of MDS/AML were reported by Kaminski et al. using ^{131}I-tositumomab [19]; however, in the long-term follow-up of the FIT trial, the annualized incidence of rate of MDS/AML was higher in the ^{90}Y-ibritumomab tiuxetan consolidation arm than controls (0.50% versus 0.07%, $p = 0.42$) [21]. The eight patients who developed MDS/AML received various subsequent treatments, and a common cytogenetic abnormality (−7 and/or 5q deletion) was found in six. The rate of MDS/AML was similar to those reported in other studies investigating RIT and non-RIT treatment [17, 25], but certainly raises a concern given that all eight patients with MDS/AML were in the RIT arm.

Logistics of RIT Regimens and Practical Considerations

The logistics of administering RIT, including determining which patients are eligible for treatment, are described and reviewed in the agents package inserts as well as by Wahl, Wagner et al. and by Goldsmith [1, 2, 27–29].

First, patient eligibility for RIT must be determined. This is largely determined by indication and the ability to safely administer the agents. Patients must have CD20$^+$ lymphoma and the currently approved indications are listed in Table 1. The use of RIT has been evaluated for other indications (i.e., diffuse large B-cell lymphoma, less common indolent lymphomas, mantle cell lymphoma). In these cases, RIT is best administered in the clinical trial setting and on an individual basis in close consultation with the referring oncologist, and with full informed consent of the patient who is made aware of the potential risks and benefits.

The minimum laboratory requirements for treatment are shown in Table 2. The minimum recommended platelet requirement is 100,000/mm^3 and absolute neutrophil requirement is 1,500/mm^3. The prescribed therapeutic activities for both ^{90}Y-ibritumomab tiuxetan and ^{131}I-tositumomab are based on platelet count (Table 2). Patients with a prior history of transplant can be treated safely, although reduced doses of RIT may be considered [10, 30, 31]. In order to avoid extensive and prolonged toxicity to the bone marrow, patients should have <25% of the marrow involved with lymphoma at the time of RIT. Traditionally, this is ascertained by marrow biopsy within 6–8 weeks before RIT, but [^{18}F]FDG PET may provide complementary information as well. Pertinent medical history also includes, but is not limited to, allergies to medications, reactions to prior administrations of monoclonal antibody therapy, and concurrent medications (e.g., anti-platelet and anti-clotting agents).

There are additional considerations for ^{131}I-tositumomab. Creatinine levels should be assessed because free radioiodine is renally excreted and there is potential for a high radiation dose to the uro-epithelium in a patient with renal obstruction. Radiation safety issues, including home environment, must also be assessed and this may play a role in deciding which agent to use for RIT (discussed below). Radiation safety precautions to be followed are reproduced in the review article by Goldsmith [27].

Table 1 Clinical indications for radioimmunotherapy of lymphomas

^{131}I-tositumomab	^{90}Y-ibritumomab tiuxetan
CD20$^+$ relapsed or refractory low-grade, follicular, or transformed NHL, including patients with rituximab-refractory NHL	Relapsed or refractory low-grade or follicular B-cell NHL
	Previously untreated follicular NHL who achieve partial or complete response to first-line chemotherapy

Table 2 General eligibility and dosing for radioimmunotherapy of lymphomas

General eligibility criteria	For both agents:
	Tumor-expressing CD20
	Platelet count $\geq$100,000/mm^3
	Absolute neutrophil count $\geq$1,500/mm^3
	<25% lymphomatous marrow involvement
	Other pertinent medical history:
	Medications
	Allergies
	Absence of infusion reactions to prior antibody therapy
	For ^{131}I-tositumomab:
	Baseline creatinine level
	Ability to follow radiation safety precautions
Therapeutic dosing of RIT	
Platelet count $\geq$150,000/mm^3	
^{90}Y-ibritumomab tiuxetan	0.4 mCi/kg
^{131}I-tositumomab	75 cGy total body radiation dose
Platelet count =100,000–150,000/mm^3	
^{90}Y-ibritumomab tiuxetan	0.3 mCi/kg
^{131}I-tositumomab	65 cGy total body radiation dose

Until very recently, the regimens for both ^{90}Y-ibritumomab tiuxetan and ^{131}I-tositumomab consisted of two steps in the United States. For both regimens, the first step consisted of imaging studies and the second step consisted of the administration of the therapeutic radiolabeled antibody. The schemas for each are shown in Fig. 1, and although similar, the major difference is the method for determining the amount of radioactivity to administer for the therapeutic dosage.

Because ^{90}Y is a pure β^- emitter, imaging studies are performed with ^{111}In-ibritumomab tiuxetan (185 MBq, or 5 mCi). The purpose is to assure normal biodistribution of the tracer and avoid inadvertently delivering high radiation doses to normal organs. The incidence of abnormal biodistribution studies with ^{111}In-ibritumomab tiuxetan is low [30]. In the United States, the requirement for ^{111}In-ibritumomab tiuxetan imaging prior to therapeutic ^{90}Y-ibritumomab was removed by the Food and Drug Administration in late 2011. Kylstra et al. presented a meta-analysis of five clinical trials and 9 years of post-approval safety data [32]. There was no difference in incidence of serious adverse events or bone marrow failure in countries performing imaging (United States/Japan) and not performing imaging (rest of world) [32]. The amount of ^{90}Y radioactivity to administer for the therapeutic dosage is calculated based on platelet count and patient weight because, despite some patient-to-patient variability, only modest correlations between pharmacokinetic/dosimetric parameters using ^{111}In-ibritumomab tiuxetan and hematologic toxicity have been demonstrated [31, 33].

Although biodistribution is also assessed, imaging before therapeutic ^{131}I-tositumomab is performed (with 185 MBq ^{131}I-tositumomab) mainly to determine patient-specific kinetics. The amount of radioactivity (in mCi) to achieve a desired total body radiation dose is then calculated based on this patient-specific kinetics, and a single therapeutic amount of ^{131}I-tositumomab is administered [34–36].

Prior to administration of both the tracer and therapeutic doses of ^{90}Y-ibritumomab tiuxetan and ^{131}I-tositumomab, unlabeled anti-CD20 antibody (rituximab and tositumomab, respectively) is given to increase the tumor radiation dose relative to normal tissue radiation dose, as well as to increase the serum half-life of the radiolabeled antibody [37]. There has been some suggestion

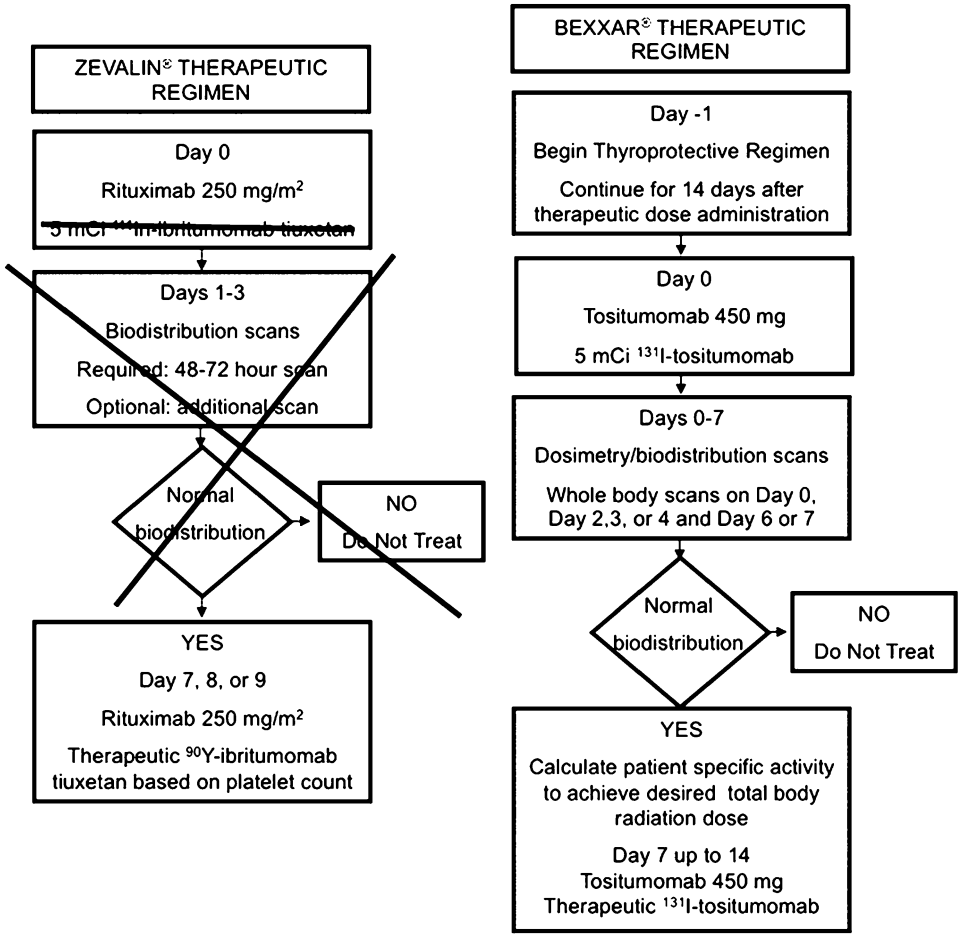

Fig. 1 Schemes for Zevalin® and Bexxar® therapeutic regimens adapted from prescribing information. The infusions of unlabeled and labeled antibody are administered intravenously and preceded by pre-medications to decrease infusion reactions and side effects. Biodistribution with ^{111}In-ibritumomab tiuxetan is no longer required in the United States prior to therapy with ^{90}Y-ibritumomab tiuxetan (Zevalin®)

that administration of unlabeled antibody may, in some settings, block available tumor CD-20 positive sites and prevent the radiolabeled antibody from binding to tumor [38]. There is some logic to this, and it is noted that in the initial studies showing improved tumor dosimetry with pre-dosing, clinical efficacy of RIT in the recurrent and consolidation settings were performed mostly in rituximab-naïve patients. Regardless, no clinical data yet supports that prior rituximab, or unlabeled tositumomab pre-dosing, decreases the clinical efficacy of RIT [39], and further work on this issue is needed.

There are currently no randomized controlled trials comparing ^{90}Y-ibritumomab tiuxetan and ^{131}I-tositumomab. The clinical efficacy and safety profiles of the single agents, ^{90}Y-ibritumomab tiuxetan and ^{131}I-tositumomab, are similar in the clinical trials reported so far. From a practical standpoint, once a patient is determined to be a candidate for RIT, either agent may be used. However, as of February 2014, commercial production of ^{131}I-tositumomab was discontinued, thus limiting the clinical choice.

Prior to 2014, we used both ^{131}I-tositumomab and ^{90}Y-ibritumomab tiuxetan routinely. When a

patient was felt to be a candidate for RIT, one of the agents was chosen based on patient and disease characteristics as well as referring physician preference and familiarity. Differences in the physical properties of the agents and resultant studies, although very limited, helped to guide our decision process [40, 41].

Song et al. [41] performed a Monte-Carlo based dosimetric analysis and found that when compared to ^{90}Y, ^{131}I has a narrower distribution of tumor absorbed doses of radiation and is predicted to be more efficacious in the treatment of lung nodules, particularly those with radii less than 2 cm, presumably because of the shorter path length of ^{131}I (0.8 mm) compared to ^{90}Y (5.3 mm) [27]. This may be of particular relevance in small tumor foci near normal structures, if these findings can be extrapolated beyond the lungs [41].

We also retrospectively evaluated our clinical experience with ^{90}Y-ibritumomab tiuxetan and ^{131}I-tositumomab from 2002 to 2006 and found less severe declines in platelet count with ^{131}I-tositumomab (which is based on patient-specific dosimetry) than with ^{90}Y-ibritumomab tiuxetan (for which dosimetry measures are not performed) [40]. We suggested that ^{131}I-tositumomab may be a more appropriate choice for patients with limited bone marrow reserve or lung metastases, or conditions which might alter the biological clearance rate of the radioantibodies; however, large, randomized, prospective trials would be needed for further evaluation.

The entire patient and clinical situation must be considered when assessing appropriateness for RIT, including radiation safety regulations at the institution and the ability of the patient to follow radiation safety precautions. The choice of RIT agents is currently limited to ^{90}Y-ibritumomab tiuxetan due to commercial availability in the United States. In Australia, ^{131}I-rituximab is available for treatment in select patients.

Subsequent therapies have been well tolerated after RIT. Multiple cycles (up to seven) of chemotherapy and radiation therapy have been given post-RIT [42, 43]. Autologous and allogeneic transplants have been performed after RIT, with adequate stem cell collection occurring after RIT. The toxicity of various subsequent therapies has not been shown to be different after RIT.

Repeat Therapies

Neither ^{90}Y-ibritumomab tiuxetan nor ^{131}I-tositumomab are approved by the FDA for repeat dosing, but repeat dosing for both agents has been studied to a limited extent. A consideration for repeat dosing is the induction of a host immunologic response, because both ^{90}Y-ibritumomab tiuxetan and ^{131}I-tositumomab are mouse antibodies. The chance of developing human anti-mouse antibodies (HAMA) is higher with tositumomab/^{131}I-tositumomab because the pre-dose (and larger protein load) of antibody is also mouse antibody, whereas the pre-dose for ^{90}Y-ibritumomab tiuxetan is the human/mouse chimeric antibody rituximab. Most patients with follicular NHL who receive RIT have also received prior therapies and are somewhat immunocompromised, thus probably decreasing the chance of developing HAMA.

Kaminski et al. reported on 28 of 32 patients with relapsed follicular NHL who received a second dose of ^{131}I-tositumomab after previously responding to ^{131}I-tositumomab for at least 3 months [44]. The median duration of response in this population was similar for the first and second doses of ^{131}I-tositumomab and 10 of the 18 re-responders had a longer duration of response with the repeat dose, 5 of which lasted longer than 1.5 years. Hematologic toxicity was similar after the first and second doses of ^{131}I-tositumomab. Ten percent of patients developed HAMA and 12% had an elevated thyroid-stimulating hormone [44].

A retrospective study was done describing experience with ^{90}Y-ibritumomab tiuxetan re-treatment. Eighteen patients were identified from the Biogen-IDEC database. Similar to ^{131}I-tositumomab, the safety and efficacy profiles after the second course of ^{90}Y-ibritumomab tiuxetan were overall similar to the first. There are also several case reports of individuals tolerating and benefiting from repeat doses of RIT [45–47]. These data suggest that, in selected patients, repeat treatment with RIT may be beneficial.

Others have evaluated administering ^{90}Y-ibritumomab tiuxetan with fractionated or sequential schedules. A phase II study evaluated fractionated ^{90}Y-ibritumomab tiuxetan for initial therapy of follicular lymphoma [48]. Seventy-four patients were enrolled: 55 received both doses of ^{90}Y-ibritumomab tiuxetan 8–12 weeks apart and 17 received only a single dose of ^{90}Y-ibritumomab tiuxetan due to hematologic toxicity, treating physician preference, HAMA, or premorbid condition. Overall response rate was 94.4% with CR/CRu rate of 58.3% after the initial dose, and nine patients improved their response after the second dose. Estimated 3-year overall survival was 95%, and median PFS was 3.35 years. Toxicity was primarily hematologic, as expected, with slightly higher percentage of grade 3–4 toxicity and duration of toxicity with the second dose [48].

Witzig et al. performed a phase I study to determine the maximally tolerated dose (MTD) of two rapidly sequenced doses of ^{90}Y-ibritumomab tiuxetan given 12–24 weeks apart [49]. Eighteen patients were enrolled and dose-limiting hematologic toxicity was seen in the cohort receiving 0.3 mCi/kg for the second dose of ^{90}Y-ibritumomab tiuxetan. The authors concluded that the MTD for the second dose of ^{90}Y-ibritumomab tiuxetan was 0.2 mCi/kg [49]. Consideration of the time from last treatment, response to last treatment, baseline and previous hematologic toxicity and time to recovery, and bone marrow tumor burden are all important considerations in the repeat setting, which again is not an FDA indication.

Barriers to the Use of RIT

Radiolabeled anti-CD20 antibody therapy for low-grade follicular lymphoma is effective and it has a predictable and very tolerable safety profile. Nevertheless, despite improvement in response rates compared to unlabeled rituximab and anti-lymphoma activity in patients with rituximab-refractory disease, these agents are not widely applied in the clinical setting. Limited drug sales led to the discontinuation of production of the ^{131}I-tositumomab agent in 2014. Schaefer et al. conducted two surveys in the United States to identify barriers to use of RIT [50, 51]. The first was an eight-question survey sent to medical oncologists, and 5% (216 of 4,239) responded [51]. The three top concerns were bone marrow damage and limiting future therapies, late side effects and too many effective nonradioactive alternatives. Contrary, the literature supports that subsequent therapies are well tolerated after RIT. There were some differences in concerns amongst oncologists practicing in academic versus nonacademic settings. Nonacademic oncologists had significantly greater concerns regarding adverse economic effects on their own practice, lack of referral centers, complicated referral process and lack of interest by Nuclear Medicine specialists. Despite these concerns, 37% thought that RIT would grow in use in the United States [51].

The second survey was sent to nuclear medicine physicians and radiation oncologists; 4.6% (613 of 13,221) responded [50]. About 40% did not treat NHL with RIT. The biggest concerns among this group was that referring providers wanted to treat patients themselves with nonradioactive drugs, and the cost of RIT. Those who thought RIT had a negative future believed that the procedure was time consuming, had concerns about the dosimetry procedure and radiation safety, and the high-cost. Those from academic centers had less concerns about these issues than those in nonacademic settings [50].

Other Settings for RIT

In addition to non-follicular NHL subtypes, the use of RIT is under investigation in several additional clinical situations. In the transplant setting, standard and high dose (myeloablative) RIT has been included in conditioning regimens. The approaches have varied from institution to institution, but results from multiple phase II trials have shown that the addition of RIT is tolerable without increasing toxicity, and the efficacy results have shown promise. They are reviewed

by Gisselbrecht et al. [52]. A phase III intergroup study comparing Rituxan/BEAM ($n = 113$) versus BEXXAR/BEAM ($n = 111$) conditioning prior to autologous stem cell transplant for persistent or relapsed chemosensitive DLBCL showed similar 2-year PFS and OS between the groups [53].

[^{18}F]FDG-PET for Evaluation of Response to RIT

[^{18}F]FDG uptake in tumors typically drops significantly following RIT [54–60] (Fig. 2). Large declines in [^{18}F]FDG uptake tend to be seen in patients with the longest progression-free survival [55, 56].

Semi-quantitative parameters on pre-RIT PET have been evaluated as possible predictors of response. In 1991, Okada et al. reported that patients with the worse prognoses after chemotherapy and/or radiotherapy had higher levels of [^{18}F]FDG uptake [57]. Several subsequent studies have not shown a correlation between pre-RIT SUV_{max} corrected for whole body or lean body weight of the hottest tumor and response [54, 55]; however, a trend for this was very recently reported by Cazaentre et al. [54]. In this study, Cazaentre et al. [54] also found that pre-RIT total lesion glycolysis (a measure of [^{18}F]FDG uptake and tumor volume) was higher for those who did not respond to RIT compared to those who did. Tumor volume has previously been shown to be a prognostic factor for response to RIT and may be more indicative of disease state than the metabolic activity of a single lesion. In a study of 59 patients with follicular NHL treated with ^{90}Y-ibritumomab tiuxetan, post-RIT PET response was the only independent predictive factor for progression-free survival in the multivariate analysis [56].

The optimal timing to obtain a PET scan after RIT is still being defined. We, and others, have performed PET scanning 2–3 months after RIT with several interesting observations. At this time point, it is possible to identify those with a complete response, those with progressive disease (most commonly due to new lesions) and in such instances, management decisions are clear [55, 58]. However, [^{18}F]FDG-PET cannot adequately predict the subsequent outcome of the group of patients who achieves a partial response by the revised IWG at 12 weeks. Some patients

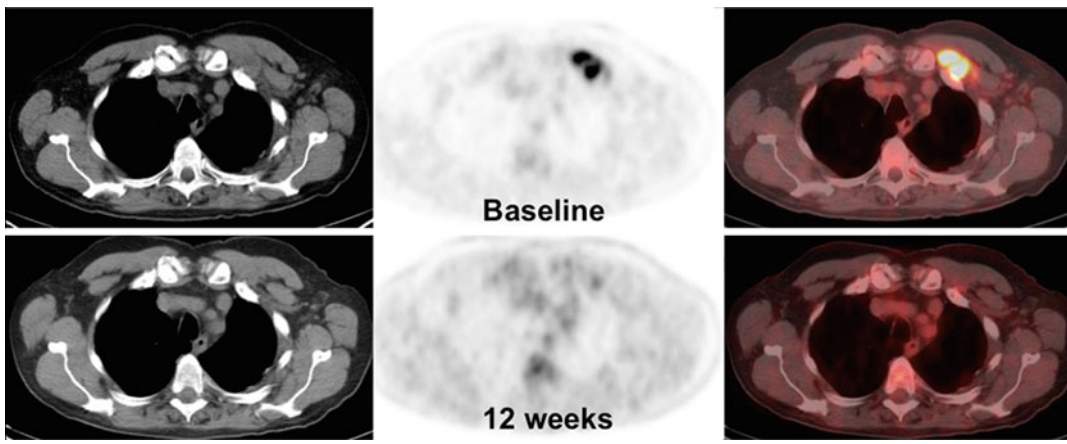

Fig. 2 A 62-year-old man with a history of transformed non-Hodgkin's lymphoma (NHL). He received five regimens for low-grade NHL and then progressed with transformation to diffuse large B-cell lymphoma after R-CHOP. He was referred for radioimmunotherapy (RIT). At the time of therapy, his platelet count was 180,000/mm^3 and the absolute neutrophil count was 3,320/mm^3. He received 0.4 mCi/kg ^{90}Y-ibritumomab tiuxetan. The baseline PET/CT scan shows intense [^{18}F]FDG uptake in left supraclavicular lymph nodes (A: *top row*). At 12 weeks after therapy, the [^{18}F]FDG uptake in lymph nodes resolved, which is consistent with complete response to RIT. The duration of response was 10 months. (*Left*: CT; *Center*: PET; *Right*: Fused PET/CT)

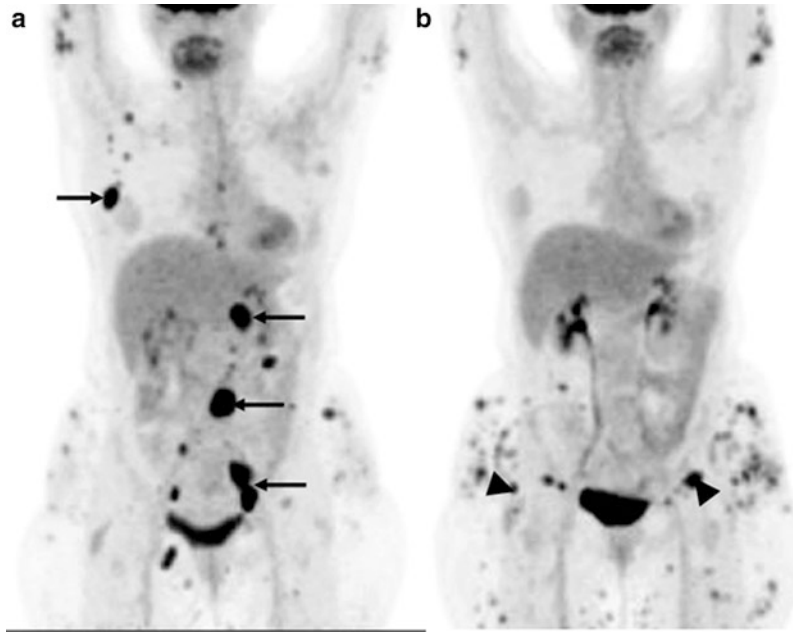

Fig. 3 A 59-year-old woman with a long history of stage 4 splenic marginal zone lymphoma status post splenectomy and multiple treatments with local external beam radiation and single-agent rituximab was referred for radioimmunotherapy and treated with a 75 cGy total body radiation dose of ^{131}I-tositumomab. The pre-RIT PET/CT scan (**a**) shows multiple foci of abnormal [^{18}F]FDG uptake in right axillary, upper abdominal, para-aortic, iliac, and inguinal lymph nodes, which is consistent with active lymphoma. There were also numerous subcutaneous nodules present indicating lymphoma. Post-RIT (**b**), many of the large lymph nodes resolved (e.g., *arrows*); however, new lymph node lesions (*arrowheads*) and subcutaneous lesions were seen, suggesting overall progressive disease. The patient refused further systemic chemotherapy but has received further external beam radiation to sites causing local symptoms

may have a continued response, warranting further observation, while others may progress necessitating treatment. Several authors have found longer response durations and time to progression with patients who have a response seen on PET scans performed even earlier, at 4–6 weeks post-RIT [59, 61]. Further prospective studies in larger numbers of patients are needed.

The use of [^{18}F]FDG-PET for evaluating response to RIT has helped to demonstrate an interesting pattern of relapse after RIT. In our own study, we found that progressive disease was only due to "new" lesions in a majority of patients (11/12) who progressed at 12 weeks (Fig. 3) [55]. Aviles et al. found that bulky disease was a negative factor for achieving a CR to RIT, but if a CR was achieved, the site of bulky disease was not at increased risk for recurrence [62]. Lymphoma is more likely to recur outside initial radiation ports after external beam radiation therapy; whereas, recurrence is more likely at initial sites and less frequently at new sites after chemotherapy alone. These data suggest that the quality of the initial response may predict long-term outcome and that progressive disease/relapse may be more likely to occur at new sites of disease rather than at sites of previous involvement.

Other Radiolabeled Monoclonal Antibodies and Strategies

Several other radiolabeled monoclonal antibodies are currently under investigation [63, 64]. ^{90}Y-veltuzumab (Immunomedics, Inc, Morris Plains, NJ) is a humanized anti-CD20 monoclonal antibody. The potential benefit of the humanized

antibody is less HAMA formation. Initial phase I/II clinical studies have been reported with the unlabeled antibody [65] and the therapeutic activity of the radiolabeled agent in animal models of NHL is reported [64].

Epratuzumab is an anti-CD22 monoclonal antibody. CD22 is a B-cell marker found on 60–80% of B-cell malignancies. Epratuzumab has been radiolabeled with ^{131}I and ^{90}Y radioisotopes [64]. In a pilot study of 11 patients with refractory B-cell lymphomas, six patients responded to ^{131}I-epratuzumab, three with a complete response [66]. More responses were seen with follicular and transformed NHL than DLBCL, and toxicity was higher in patients with decreased marrow reserve. A potential disadvantage with ^{131}I-epratuzumab is internalization and a short intracellular half-life. Better tumor dosimetry has been reported for ^{90}Y-epratuzumab. Using a fractionated schedule of ^{90}Y-epratuzumab in 16 patients with NHL, the same group reported overall response rates of 62% and CR rates of 25% [66]. Epratuzumab has also been labeled with Rhenium-186 and administration is feasible in phase I trials [67].

The group at Fred Hutchinson Cancer Research Center in Seattle (WA, USA) has demonstrated therapeutic activity of ^{131}I-anti-CD45 antibodies in NHL B-cell and T-cell xenograft models, with minimal toxicity [68, 69].

In addition to targeting various isotopes, improving approaches and schedules for administration of RIT are areas of active investigation. These approaches were recently reviewed by Sharkey et al. [64]. In the pre-targeting approach, bispecific antibodies recognize both the tumor target and a radiolabeled hapten-peptide. The unlabeled bispecific antibody is given first and allowed to bind to the target. Several days later, the radiolabeled hapten-peptide is given which binds the bispecific antibody. Pre-targeting should help to decrease the serum half-life of the radiolabel in the blood and subsequently exposure of non-tumor hematopoietic tissue and toxicity. Combinations of antibodies targeting different surface antigens may also help to increase the amount of tumor targeting and circumvent the issue of "tumor blocking" by unlabeled antibody.

References

1. [insert] Zp. Irvine, CA: Spectrum Pharmaceuticals, Inc; 2013.
2. [insert] Bp. Seattle, WA: GlaxoSmithKline; 2012.
3. Anderson KC, Bates MP, Slaughenhoupt BL, Pinkus GS, Schlossman SF, Nadler LM. Expression of human B cell-associated antigens on leukemias and lymphomas: a model of human B cell differentiation. Blood. 1984;63:1424–33.
4. Tedder TF, Boyd AW, Freedman AS, Nadler LM, Schlossman SF. The B cell surface molecule B1 is functionally linked with B cell activation and differentiation. J Immunol. 1985;135:973–9.
5. Cardarelli PM, Quinn M, Buckman D, Fang Y, Colcher D, King DJ, et al. Binding to CD20 by anti-B1 antibody or F(ab')$_2$ is sufficient for induction of apoptosis in B-cell lines. Cancer Immunol Immunother. 2002;51:15–24.
6. Stashenko P, Nadler LM, Hardy R, Schlossman SF. Characterization of a human B lymphocyte-specific antigen. J Immunol. 1980;125:1678–85.
7. Brown RS, Kaminski MS, Fisher SJ, Chang AE, Wahl RL. Intratumoral microdistribution of [^{131}I]MB-1 in patients with B-cell lymphoma following radioimmunotherapy. Nucl Med Biol. 1997;24:657–63.
8. Horning SJ, Younes A, Jain V, Kroll S, Lucas J, Podoloff D, et al. Efficacy and safety of tositumomab and iodine-131 tositumomab (Bexxar) in B-cell lymphoma, progressive after rituximab. J Clin Oncol. 2005;23:712–9.
9. Kaminski MS, Estes J, Zasadny KR, Francis IR, Ross CW, Tuck M, et al. Radioimmunotherapy with iodine ^{131}I tositumomab for relapsed or refractory B-cell non--Hodgkin lymphoma: updated results and long-term follow-up of the University of Michigan experience. Blood. 2000;96:1259–66.
10. Kaminski MS, Zasadny KR, Francis IR, Milik AW, Ross CW, Moon SD, et al. Radioimmunotherapy of B-cell lymphoma with [^{131}I]anti-B1 (anti-CD20) antibody. N Engl J Med. 1993;329:459–65.
11. Kaminski MS, Zelenetz AD, Press OW, Saleh M, Leonard J, Fehrenbacher L, et al. Pivotal study of iodine I 131 tositumomab for chemotherapy-refractory low-grade or transformed low-grade B-cell non--Hodgkin's lymphomas. J Clin Oncol. 2001;19:3918–28.
12. Vose JM, Wahl RL, Saleh M, Rohatiner AZ, Knox SJ, Radford JA, et al. Multicenter phase II study of iodine-131 tositumomab for chemotherapy-relapsed/refractory low-grade and transformed low-grade B-cell non--Hodgkin's lymphomas. J Clin Oncol. 2000;18:1316–23.
13. Witzig TE, Flinn IW, Gordon LI, Emmanouilides C, Czuczman MS, Saleh MN, et al. Treatment with ibritumomab tiuxetan radioimmunotherapy in patients with rituximab-refractory follicular non-Hodgkin's lymphoma. J Clin Oncol. 2002;20:3262–9.
14. Witzig TE, Gordon LI, Cabanillas F, Czuczman MS, Emmanouilides C, Joyce R, et al. Randomized

controlled trial of yttrium-90-labeled ibritumomab tiuxetan radioimmunotherapy versus rituximab immunotherapy for patients with relapsed or refractory low-grade, follicular, or transformed B-cell non-Hodgkin's lymphoma. J Clin Oncol. 2002;20:2453–63.
15. Witzig TE, White CA, Wiseman GA, Gordon LI, Emmanouilides C, Raubitschek A, et al. Phase I/II trial of IDEC-Y2B8 radioimmunotherapy for treatment of relapsed or refractory $CD20^+$ B-cell non-Hodgkin's lymphoma. J Clin Oncol. 1999;17:3793–803.
16. Davis TA, Kaminski MS, Leonard JP, Hsu FJ, Wilkinson M, Zelenetz A, et al. The radioisotope contributes significantly to the activity of radioimmunotherapy. Clin Cancer Res. 2004;10:7792–8.
17. Czuczman MS, Emmanouilides C, Darif M, Witzig TE, Gordon LI, Revell S, et al. Treatment-related myelodysplastic syndrome and acute myelogenous leukemia in patients treated with ibritumomab tiuxetan radioimmunotherapy. J Clin Oncol. 2007;25:4285–92.
18. Witzig TE, White CA, Gordon LI, Wiseman GA, Emmanouilides C, Murray JL, et al. Safety of yttrium-90 ibritumomab tiuxetan radioimmunotherapy for relapsed low-grade, follicular, or transformed non-hodgkin's lymphoma. J Clin Oncol. 2003;21:1263–70.
19. Kaminski MS, Tuck M, Estes J, Kolstad A, Ross CW, Zasadny K, et al. ^{131}I-tositumomab therapy as initial treatment for follicular lymphoma. N Engl J Med. 2005;352:441–9.
20. Morschhauser F, Radford J, Van Hoof A, Vitolo U, Soubeyran P, Tilly H, et al. Phase III trial of consolidation therapy with yttrium-90-ibritumomab tiuxetan compared with no additional therapy after first remission in advanced follicular lymphoma. J Clin Oncol. 2008;26:5156–64.
21. Morschhauser F, Radford J, Van Hoof A, Botto B, Rohatiner AZ, Salles G, et al. ^{90}Yttrium-ibritumomab tiuxetan consolidation of first remission in advanced-stage follicular non-Hodgkin lymphoma: updated results after a median follow-up of 7.3 years from the international, randomized, phase III first-line indolent trial. J Clin Oncol. 2013;31:1977–83.
22. Hochster H, Weller E, Gascoyne RD, Habermann TM, Gordon LI, Ryan T, et al. Maintenance rituximab after cyclophosphamide, vincristine, and prednisone prolongs progression-free survival in advanced indolent lymphoma: results of the randomized phase III ECOG1496 study. J Clin Oncol. 2009;27:1607–14.
23. Salles G, Seymour JF, Offner F, Lopez-Guillermo A, Belada D, Xerri L, et al. Rituximab maintenance for 2 years in patients with high tumour burden follicular lymphoma responding to rituximab plus chemotherapy (PRIMA): a phase 3, randomised controlled trial. Lancet. 2011;377(9759):42–51.
24. Press OW, Unger JM, Braziel RM, Maloney DG, Miller TP, Leblanc M, et al. Phase II trial of CHOP chemotherapy followed by tositumomab/iodine I-131 tositumomab for previously untreated follicular non-Hodgkin's lymphoma: five-year follow-up of Southwest Oncology Group Protocol S9911. J Clin Oncol. 2006;24:4143–9.
25. Press OW, Unger JM, Rimsza LM, Friedberg JW, LeBlanc M, Czuczman MS, et al. Phase III randomized intergroup trial of CHOP plus rituximab compared with CHOP chemotherapy plus ^{131}iodine-tositumomab for previously untreated follicular non-Hodgkin lymphoma: SWOG S0016. J Clin Oncol. 2013;3:314–20.
26. Lopez-Guillermo A, Canales M, Dlouhy I, Briones J, Caballero D, Sancho J, et al. A randomized phase II study comparing consolidation with a single dose of ^{90}Y-Ibritumomab tiuxetan (Zevalin) (Z) vs. maintenance with rituxumab (R) for two years in patients with newly diagnosed follicular lymphoma (FL) responding to R-CHOP. Preliminary results at 36 months from randomization. Blood. 2013;122:P369.
27. Goldsmith SJ. Radioimmunotherapy of lymphoma: Bexxar and Zevalin. Semin Nucl Med. 2010;40:122–35.
28. Wagner Jr HN, Wiseman GA, Marcus CS, Nabi HA, Nagle CE, Fink-Bennett DM, et al. Administration guidelines for radioimmunotherapy of non-Hodgkin's lymphoma with ^{90}Y-labeled anti-CD20 monoclonal antibody. J Nucl Med. 2002;43:267–72.
29. Wahl RL. Tositumomab and ^{131}I therapy in non-Hodgkin's lymphoma. J Nucl Med. 2005;46 Suppl 1:128S–40.
30. Jacobs SA, Vidnovic N, Joyce J, McCook B, Torok F, Avril N. Full-dose ^{90}Y ibritumomab tiuxetan therapy is safe in patients with prior myeloablative chemotherapy. Clin Cancer Res. 2005;11(19 Pt 2):7146s–50.
31. Vose JM, Bierman PJ, Loberiza Jr FR, Bociek RG, Matso D, Armitage JO. Phase I trial of ^{90}Y-ibritumomab tiuxetan in patients with relapsed B-cell non-Hodgkin's lymphoma following high-dose chemotherapy and autologous stem cell transplantation. Leuk Lymphoma. 2007;48:683–90.
32. Kylstra JW, Huang M, Emmanouilidis C, Hagenbeek A, Wiseman G, Von Schilling C, editors. Discriminatory power of the 111-Indium scan (111-In) in the prediction of altered biodistribution of radioimmunoconjugate in the 90-Yttrium ibritumomab tiuxetan therapeutic regimen: data from 5 trials and 9 years of clinical experience in 45 countries. Annals of oncology. Oxford: Oxford University Press; 2011.
33. Conti PS, White C, Pieslor P, Molina A, Aussie J, Foster P. The role of imaging with ^{111}In-ibritumomab tiuxetan in the ibritumomab tiuxetan (Zevalin) regimen: results from a Zevalin Imaging Registry. J Nucl Med. 2005;46:1812–8.
34. Kaminski MS, Fig LM, Zasadny KR, Koral KF, DelRosario RB, Francis IR, et al. Imaging, dosimetry, and radioimmunotherapy with iodine 131-labeled anti-CD37 antibody in B-cell lymphoma. J Clin Oncol. 1992;10:1696–711.
35. Kaminski MS, Zasadny KR, Francis IR, Fenner MC, Ross CW, Milik AW, et al. Iodine-131-anti-B1 radioimmunotherapy for B-cell lymphoma. J Clin Oncol. 1996;14:1974–81.

36. Wahl RL, Kroll S, Zasadny KR. Patient-specific whole-body dosimetry: principles and a simplified method for clinical implementation. J Nucl Med. 1998;39 (8 Suppl):14S–20.
37. Buchsbaum DJ, Wahl RL, Glenn SD, Normolle DP, Kaminski MS. Improved delivery of radiolabeled anti-B1 monoclonal antibody to Raji lymphoma xenografts by predosing with unlabeled anti-B1 monoclonal antibody. Cancer Res. 1992;52:637–42.
38. Gopal AK, Press OW, Wilbur SM, Maloney DG, Pagel JM. Rituximab blocks binding of radiolabeled anti-CD20 antibodies (Ab) but not radiolabeled anti-CD45 Ab. Blood. 2008;112:830–5.
39. Illidge TM, Bayne M, Brown NS, Chilton S, Cragg MS, Glennie MJ, et al. Phase 1/2 study of fractionated ^{131}I-rituximab in low-grade B-cell lymphoma: the effect of prior rituximab dosing and tumor burden on subsequent radioimmunotherapy. Blood. 2009;113:1412–21.
40. Jacene HA, Filice R, Kasecamp W, Wahl RL. Comparison of ^{90}Y-ibritumomab tiuxetan and ^{131}I-tositumomab in clinical practice. J Nucl Med. 2007;48:1767–76.
41. Song H, Du Y, Sgouros G, Prideaux A, Frey E, Wahl RL. Therapeutic potential of ^{90}Y- and ^{131}I-labeled anti-CD20 monoclonal antibody in treating non-Hodgkin's lymphoma with pulmonary involvement: a Monte Carlo-based dosimetric analysis. J Nucl Med. 2007;48:150–7.
42. Ansell SM, Ristow KM, Habermann TM, Wiseman GA, Witzig TE. Subsequent chemotherapy regimens are well tolerated after radioimmunotherapy with yttrium-90 ibritumomab tiuxetan for non-Hodgkin's lymphoma. J Clin Oncol. 2002;20:3885–90.
43. Dosik AD, Coleman M, Kostakoglu L, Furman RR, Fiore JM, Muss D, et al. Subsequent therapy can be administered after tositumomab and iodine I-131 tositumomab for non-Hodgkin lymphoma. Cancer. 2006;106:616–22.
44. Kaminski MS, Radford JA, Gregory SA, Leonard JP, Knox SJ, Kroll S, et al. Re-treatment with I-131 tositumomab in patients with non-Hodgkin's lymphoma who had previously responded to I-131 tositumomab. J Clin Oncol. 2005;23:7985–93.
45. Peyrade F, Italiano A, Fontana X, Peyrottes I, Thyss A. Retreatment with ^{90}Y-labelled ibritumomab tiuxetan in a patient with follicular lymphoma who had previously responded to treatment. Lancet Oncol. 2007;8:849–50.
46. Rana TM. Post Bexxar relapse in NHL responds to Zevalin and can be safely accomplished. [Abstract]. Proc Am Soc Clin Oncol. 2003;22:613. #2465.
47. Tsai DE, Maillard I, Schuster SJ, Nasta SD, Porter DL, Klumpp TR, et al. Use of ibritumomab tiuxetan anti-CD20 radioimmunotherapy in a non-Hodgkin's lymphoma patient previously treated with a yttrium-90-labeled anti-CD22 monoclonal antibody. Clin Lymphoma. 2003;4:56–9.
48. Illidge TM, Mayes S, Pettengell R, Bates AT, Bayne M, Radford JA, et al. Fractionated ^{90}Y-ibritumomab tiuxetan radioimmunotherapy as an initial therapy of follicular lymphoma: an international phase II study in patients requiring treatment according to GELF/BNLI criteria. J Clin Oncol. 2014;32:212–8.
49. Witzig TE, Wiseman WG, Geyer SM, et al. A phase I trial of two-sequential doses of ZEVALIN radioimmunotherapy for relapsed low grade B-cell non--Hodgkins lymphoma [Abstract]. Blood. 2003;102:406a. #1475.
50. Schaefer NG, Huang P, Buchanan JW, Wahl RL. Radioimmunotherapy in non-Hodgkin lymphoma: opinions of nuclear medicine physicians and radiation oncologists. J Nucl Med. 2011;52:830–8.
51. Schaefer NG, Ma J, Huang P, Buchanan J, Wahl RL. Radioimmunotherapy in non-Hodgkin lymphoma: opinions of U.S. medical oncologists and hematologists. J Nucl Med. 2010;51:987–94.
52. Gisselbrecht C, Vose J, Nademanee A, Gianni AM, Nagler A. Radioimmunotherapy for stem cell transplantation in non-Hodgkin's lymphoma: in pursuit of a complete response. Oncologist. 2009;14 Suppl 2:41–51.
53. Vose JM, Carter S, Burns LJ, Ayala E, Press OW, Moskowitz CH, et al. Phase III randomized study of rituximab/carmustine, etoposide, cytarabine, and melphalan (BEAM) compared with iodine-131 tositumomab/BEAM with autologous hematopoietic cell transplantation for relapsed diffuse large B-cell lymphoma: results from the BMT CTN 0401 trial. J Clin Oncol. 2013;31:1662–8.
54. Cazaentre T, Morschhauser F, Vermandel M, Betrouni N, Prangere T, Steinling M, et al. Pre-therapy ^{18}F-FDG PET quantitative parameters help in predicting the response to radioimmunotherapy in non-Hodgkin lymphoma. Eur J Nucl Med Mol Imaging. 2010;37:494–504.
55. Jacene HA, Filice R, Kasecamp W, Wahl RL. ^{18}F-FDG PET/CT for monitoring the response of lymphoma to radioimmunotherapy. J Nucl Med. 2009;50:8–17.
56. Lopci E, Burnelli R, Ambrosini V, Nanni C, Castellucci P, Biassoni L, et al. ^{18}F-FDG PET in pediatric lymphomas: a comparison with conventional imaging. Cancer Biother Radiopharm. 2008;23: 681–90.
57. Okada J, Yoshikawa K, Itami M, Imaseki K, Uno K, Itami J, et al. Positron emission tomography using fluorine-18-fluorodeoxyglucose in malignant lymphoma: a comparison with proliferative activity. J Nucl Med. 1992;33:325–9.
58. Storto G, De Renzo A, Pellegrino T, Perna F, De Falco T, Erra P, et al. Assessment of metabolic response to radioimmunotherapy with ^{90}Y-ibritumomab tiuxetan in patients with relapsed or refractory B-cell non-Hodgkin lymphoma. Radiology. 2010; 254:245–52.

59. Torizuka T, Zasadny KR, Kison PV, Rommelfanger SG, Kaminski MS, Wahl RL. Metabolic response of non-Hodgkin's lymphoma to ^{131}I-anti-B1 radioimmunotherapy: evaluation with FDG PET. J Nucl Med. 2000;41:999–1005.
60. Ulaner GA, Colletti PM, Conti PS. B-cell non-Hodgkin lymphoma: PET/CT evaluation after ^{90}Y-ibritumomab tiuxetan radioimmunotherapy – initial experience. Radiology. 2008;246:895–902.
61. Bodet-Milin C, Kraeber-Bodere F, Dupas B, Morschhauser F, Gastinne T, Le Gouill S, et al. Evaluation of response to fractionated radioimmunotherapy with ^{90}Y-epratuzumab in non-Hodgkin's lymphoma by ^{18}F-fluorodeoxyglucose positron emission tomography. Haematologica. 2008;93:390–7.
62. Aviles A, Neri N, Delgado S, Perez F, Nambo MJ, Cleto S, et al. Residual disease after chemotherapy in aggressive malignant lymphoma: the role of radiotherapy. Med Oncol. 2005;22:383–7.
63. Castillo J, Winer E, Quesenberry P. Newer monoclonal antibodies for hematological malignancies. Exp Hematol. 2008;36:755–68.
64. Sharkey RM, Karacay H, Goldenberg DM. Improving the treatment of non-Hodgkin lymphoma with antibody-targeted radionuclides. Cancer. 2010;116 (4 Suppl):1134–45.
65. Morschhauser F, Leonard JP, Fayad L, Coiffier B, Petillon MO, Coleman M, et al. Humanized anti-CD20 antibody, veltuzumab, in refractory/recurrent non-Hodgkin's lymphoma: phase I/II results. J Clin Oncol. 2009;27:3346–53.
66. Linden O, Hindorf C, Cavallin-Stahl E, Wegener WA, Goldenberg DM, Horne H, et al. Dose-fractionated radioimmunotherapy in non-Hodgkin's lymphoma using DOTA-conjugated, ^{90}Y-radiolabeled, humanized anti-CD22 monoclonal antibody, epratuzumab. Clin Cancer Res. 2005;11:5215–22.
67. Postema EJ, Raemaekers JM, Oyen WJ, Boerman OC, Mandigers CM, Goldenberg DM, et al. Final results of a phase I radioimmunotherapy trial using ^{186}Re-epratuzumab for the treatment of patients with non-Hodgkin's lymphoma. Clin Cancer Res. 2003;9 (10 Pt 2):3995S–4002.
68. Gopal AK, Pagel JM, Fromm JR, Wilbur S, Press OW. ^{131}I anti-CD45 radioimmunotherapy effectively targets and treats T-cell non-Hodgkin lymphoma. Blood. 2009;113:5905–10.
69. Pagel JM, Hedin N, Subbiah K, Meyer D, Mallet R, Axworthy D, et al. Comparison of anti-CD20 and anti-CD45 antibodies for conventional and pretargeted radioimmunotherapy of B-cell lymphomas. Blood. 2003;101:2340–8.

Radionuclide Therapy of Leukemias and Multiple Myeloma

41

Martina Sollini, Sara Galimberti, Roberto Boni, and Paola Anna Erba

Abstract

Monoclonal antibodies (MAbs) raised against cancer antigens may mediate antibody-dependent cell-mediated cytotoxicity. This form of cancer control arises from cytolysis of a target cell by effector lymphocytes, such as cytotoxic T lymphocytes or natural killer cells. However, most of these antibodies have low/moderate efficacy for tumor control. Antibodies targeting hormone receptors expressed by cancer have shown greater tumor control compared with other cell membrane targets. Moreover, the labeling of these antibodies with a toxin can potentiate their efficacy for tumor control. In this way, the antibody becomes an invaluable targeting vector for delivery of the toxin to the cancer cells. The toxin/antibody complex is called an immunoconjugate. Different molecules, chemicals, or radioisotopes can serve as toxins; toxins may have long half-lives in the body (e.g., ricin), thus increasing the toxicity to both the cancer cells and normal tissues.

Beta emitting radioisotopes, predominantly iodine-131, have had only modest success in radioimmunotherapy. More recently, high-linear-energy transfer (LET) radiation in the form of alpha particles has been studied: alpha radiation is ideal for killing isolated cancer cells in transit in the vascular and lymphatic systems and regressing tumors by disruption of tumor capillary networks by targeting and killing tumor capillary endothelial cells.

Over the past 20 years, the development of alpha-immunoconjugates has enabled targeted alpha therapy (TAT) to progress from in vitro studies, through in vivo experiments, to clinical trials. The dose to normal tissues limits the injected dose and that received by the tumor. However, TAT can achieve cancer regression within the maximum tolerance dose for normal tissue. TAT was originally thought to be an ideal therapy for "liquid" cancers, e.g., leukemia and micrometastases, as the short half-lives of the radioisotopes were sufficient to target these cancer cells and the short range ensured that the targeted cancer cells received the highest radiation dose. Different antibodies have been developed and tested in clinical trials as conditioning treatment, but none of them have yet been approved for RIT in MM. Additionally, bone-seeking radiopharmaceuticals are being evaluated in MM patients in the transplant setting.

M. Sollini
Department of Biomedical Sciences, Humanitas University, Rozzano, Milan, Italy
e-mail: martina.sollini@cancercenter.humanitas.it

S. Galimberti
Hematology Unit, University of Pisa, Pisa, Italy
e-mail: sara.galimberti@do.med.unipi.it

R. Boni • P.A. Erba (✉)
Regional Center of Nuclear Medicine, Department of Translational Research and New Technology in Medicine, University of Pisa, Pisa, Italy
e-mail: paola.erba@unipi.it

© Springer International Publishing Switzerland 2017
H.W. Strauss et al. (eds.), *Nuclear Oncology*,
https://doi.org/10.1007/978-3-319-26236-9_48

Keywords

Leukemia • Multiple myeloma • Hematological malignancies • Therapy • Radioimmunotherapy

Glossary

[^{18}F]FDG	2-Deoxy-2-[^{18}F]fluoro-D-glucose
ADCC	Antibody-dependent cell-mediated cytotoxicity
ALL	Acute lymphocytic leukemia
alloHSCT	Allogeneic hematopoietic stem cell transplantation
AML	Acute myeloid leukemia
APL	Acute promyelocytic leukemia
ASCO	American Society of Clinical Oncology
ASCT	Autologous stem cell transplantation
ATO	Arsenic trioxide
ATP	Adenosine 5′-triphosphate
ATRA	All-trans retinoic acid
BCP-ALL	B-cell precursor acute lymphoblastic leukemia
BCR	B-cell receptor
BMT	Bone marrow transplantation
BR	Bendamustine plus rituximab
BTK	Bruton's tyrosine kinase
CBF	Core binding factor
cDNAs	Complementary deoxyribonucleic acid
Clb	Chlorambucil
CLL	Chronic lymphocytic leukemia
CML	Chronic myeloid leukemia
CNS	Central nervous system
CR	Complete response
CRAB	Hypercalcemia, renal failure, anemia, bone lesions
CT	Computed tomography
CTD	Cyclophosphamide/thalidomide/dexamethasone
CVAD	Cyclophosphamide, vincristine, doxorubicin, dexamethasone
DCF	Deoxycoformycin
DIC	Disseminated intravasal coagulation
DNA	Deoxyribonucleic acid
DOTA	1,4,7,10-Tetraazacyclododecane-1,4,7,10-tetraacetic acid
DOTMP	1,4,7,10-Tetraazacyclododecane-1,4,7,10-tetramethylene-phosphonic acid
DSF	Disease free survival
DTPA	Diethylenetriaminepentaacetic acid
DVD	Doxorubicin liposomal-vincristine-dexamethasone
EBRT	External beam radiotherapy
EDTMP	Ethylenediamine tetra(methylene phosphonic acid)
EMA	European Medicines Agency
ESMO	European Society of Clinical Oncology
FCR	Chemotherapy regimen based on fludarabine cyclophosphamide, and rituximab
GMMG	German Multicenter Myeloma Group
GVHD	Graft versus host disease
Gy	Gray unit (ionizing radiation dose in the International System of Units, corresponding to the absorption of one joule of radiation energy per kilogram of matter)
HAMA	Human anti-mouse antibody
HCL	Hairy cell leukemia
HCL-V	Hairy cell leukemia variant
HD	High-dose
HLA	Human leucocyte antigen
HLA-DR	Human Leukocyte Antigen-antigen D related
HOVON	Dutch-Belgian Hemato-Oncology Cooperative Group
HR	High risk
IFN-α	Interferon-α
IMiDs	Immunomodulatory drugs
ITD	Internal tandem duplications
KIR	Killer immunoglobulin-like Receptor
LAIP	Leukemia-associated immunophenotype
LET	Linear energy transfer

MAbs	Monoclonal antibodies
MDACC	MD Anderson Cancer Center
MDR	Multidrug resistance
MDS	Myelodysplastic syndrome
MM	Multiple myeloma
MP	Melphalan and prednisone
MPR	Melphalan/prednisone/lenalidomide
MPT	Melphalan/prednisone/thalidomide
MRD	Minimal residual disease
mRNAs	Messenger ribonucleic acid
MTD	Maximum tolerable dose
NHL	Non-Hodgkin lymphomas
NLS	Nuclear localiation signal peptide
NMRI	Naval Medical Research Institute
NOD	Non-obese diabetic
NPM	Nucleophosmin
OR	Odd ratio
OS	Overall survival
PAD	Bortezomib, doxorubicin, and dexamethasone
PCR	Polymerase chain reaction
PET	Positron emission tomography
PFS	Progression-free survival
Ph+	Philadelphia positive
PRIT	Pretargeted radioimmunotherapy
R	Rituximab
RANKL	Receptor activator of nuclear factor kappa-B ligand
RIC	Dose-reduced chemotherapy intensity
RIT	Radio-immunotherapy
RT	Reverse transcriptase
RVD	Lenalidomide-bortezomib-dexamethasone
SCID	Severe combined immunodeficiency
SCT	Stem cell transplantation
SLL	Small lymphocytic leukemia
SPECT	Single-photon emission computed tomography
SR	Standard risk
TAT	Targeted alpha therapy
TBI	Total body irradiation
TD	Thalidomide-dexamethasone
TKI	Tyrosine kinase inhibitor
TRM	Treatment-related mortality
VAD	Chemotherapy regime based on vincristine, adriamycin, doxorubicin
VCD	Bortezomib-cyclophosphamide-dexamethasone
VMP	Bortezomib/melphalan/prednisone
VP	Bortezomib-prednisone
VTD	Velcade-thalidomide-dexamethasone
VTP	Bortezomib-thalidomide-prednisone
WBC	White blood cells

Contents

Radioimmunotherapy of Leukemia 1159

Treatment of Acute Lymphocytic Leukemia (ALL) in Adults 1160

Treatment of Chronic Lymphocytic Leukemia 1163
Treatment of Hairy Cell Leukemia 1166

Treatment of Acute Myeloid Leukemia (AML) 1169

Treatment of Chronic Myeloid Leukemia (CML) 1172

Therapies with Radiolabeled Antibodies 1173
Therapies with Radiolabeled Anti-CD33 mAb 1173
Therapies with Radiolabeled Anti-CD45 mAb 1176
Therapies with Radiolabeled Anti-CD66 mAb 1177
Treatment of Multiple Myeloma 1178

Radioimmunotherapy in Multiple Myeloma 1182
Radiotherapy with Bone-Seeking Radionuclides 1184

References 1185

Radioimmunotherapy of Leukemia

Radiolabeled antibodies with affinity for hematopoietic cells may be used for myeloablative radioimmunotherapy (RIT) to increase the radiation dose to the bone marrow spearing normal cells prior to autologous stem cell transplantation (ASCT) in patients with leukemia.

This strategy relies on a well-known side effect of treatments with radiolabeled antibodies: accumulation in the bone marrow which is evident even in the presence of low burden bone marrow disease or when the targeted antigen is co-expressed on healthy hematopoietic cells. In these cases, ASCT may be required to limit severe therapy-induced cytopenia and to prevent complications such as severe infections or bleeding [1–3].

Treatment of Acute Lymphocytic Leukemia (ALL) in Adults

When the diagnosis is established, treatment should start immediately. The outcome of ALL is strictly related to the age of patient, with probability of success from 80% to 90% in childhood ALL, decreasing to <10% in elderly/frail ALL patients [4].

Currently, the use of monoclonal antibodies is a promising approach in the treatment of ALL. There are four types of monoclonal antibodies developed for ALL: (1) those destroying neoplastic cells by the antibody-dependent cell-mediated cytotoxicity (ADCC), such as rituximab, ofatumumab (anti-CD20), alemtuzumab (anti-CD52), and epratuzumab (anti-CD22); (2) antibodies conjugated with a drug, such as inotuzumab ozogamicin (anti-CD22 plus calicheamicin); (3) antibodies conjugated with a toxin, such as combotox (anti-CD22 combined with ricin A); and (4) bispecific antibodies T-cell engaging, such as blinatumomab (anti-CD19/CD3).

Epratuzumab added to conventional therapy (clofarabine and cytarabine) increased CR to 52% of patients versus 17% of the control arm [5].

Inotuzumab ozogamicin improved overall response rate (81% vs. 33%), with an evident advantage by achieving eradication of minimal residual disease (MRD) [6].

In a recent phase-3 trial, adults with relapsed or refractory ALL were randomized to receive either inotuzumab ozogamicin or standard intensive chemotherapy: the rate of CR was significantly higher in the inotuzumab ozogamicin group (81% vs. 29%), with an advantage also in terms of PFS (median, 5 vs. 2 months), but comparable OS [7].

In a series of relapsed ALL patients, blinatumomab induced 33% of CR and 82% of MRD negativity, but up to 70% of cases presented fever, hypotension, cerebellar symptoms, or encephalopathy [8].

Despite the existence of studies and meta-analyses comparing chemotherapy and allogeneic transplantation (alloSCT) [9], the indications for alloSCT in adult ALL patients in first CR is not defined and requires update. This is due to the improving results with conventional and targeted chemotherapy regimens on one hand and to the decreasing mortality and broader availability of alloSCT on the other. Several attempts have been made to provide evidence-based guidelines for indication of alloSCT [10–13]: some studies reported that alloSCT when performed in first remission was superior to the conventional chemotherapy, but other authors suggest it is useful only in a second remission. A pre-phase treatment with corticosteroids (usually prednisone or dexamethasone) alone, or in combination with another drug (e.g., vincristine, cyclophosphamide), is often given together with allopurinol (sometimes rasburicase to prevent the tumor lysis syndrome) and hydration for ~5–7 days as well as intrathecal prophylaxis. Interestingly, the response to this pre-phase therapy defines the chemosensitivity of the disease, with good responders to prednisone having a better outcome [14].

Supportive therapy should be initiated whenever necessary in particular to treat infections or to maintain circulating levels of platelets/erythrocytes. Severe neutropenia (<500/μL) is often seen at diagnosis and is most frequent (>80%) during induction therapy, causing infections and infection-related death [4]. The goal of induction therapy is the achievement of a complete response (CR) or, even better, a molecular CR or a good molecular response, usually obtained within 6–16 weeks from start of chemotherapy.

Most regimens are centered on vincristine, corticosteroids, and anthracyclines (daunorubicin, doxorubicin, idarubicin), sometimes with cyclophosphamide or cytarabine.

There are no randomized trials comparing different induction regimens; however, in 6617 patients from 14 studies, the weighted mean for

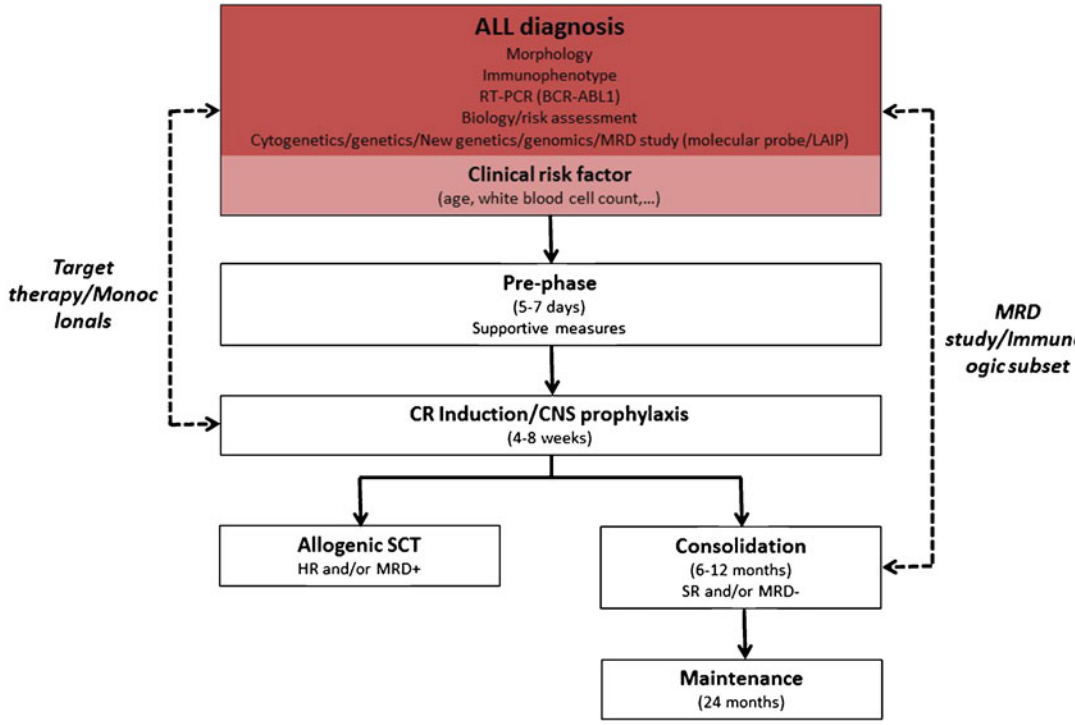

Fig. 1 Diagnosis and risk assessment in adult ALL for achievement of CR and risk-oriented post-remission therapy. Major diagnostic subsets are identified within 1–2 days to allow start of pre-phase therapy, identify cases eligible to targeted therapy (TKI in Ph+ ALL), and set up the MRD study. Pre-phase therapy allows for management/prevention of metabolic/infectious/hemorrhagic complications before the start of induction therapy and checks HLA identity between patient and siblings. Induction/early consolidation therapy (incorporating CNS prophylaxis) aims to induce CR with a deep MRD response, to support subsequent risk- and MRD-oriented therapy with/without allogeneic SCT. *ALL* acute lymphoblastic leukemia, *RT-PCR* reverse transcriptase polymerase chain reaction, *MRD* minimal residual disease, *LAIP* leukemia-associated immunophenotype, *WBC* white blood cells, *CR* complete remission, *CNS* central nervous system, *SR* standard risk, *HR* high risk, *SCT* stem cell transplantation, *TKI* tyrosine kinase inhibitor, *Ph+* Philadelphia positive, *HLA* human leucocyte antigen (Modified from Holzer et al. [4])

the CR rate was 83% (62–92%) [15]. Using current approaches, the CR rate had increased to 80–90% [4], according to the risk score. There are two prevalent approaches: one includes 2 cycles of induction followed by the consolidation [4] and represents the most frequently adopted in Europe. A schematic treatment algorithm in adult ALL according to ESMO Clinical Practice Guidelines [4] is reported in Fig. 1.

The second approach uses two different alternating intensive chemotherapy cycles, identical for induction and consolidation, accounting for a total of eight cycles, such as the hyper-CVAD (cyclophosphamide, vincristine, doxorubicin, dexamethasone) protocol, preferentially used in the United States [4].

Effective prophylaxis to prevent CNS relapse is an essential part of ALL therapy: treatment modalities include CNS irradiation and intrathecal methotrexate, eventually combined with steroids or cytarabine and systemic HD therapy with either methotrexate and/or cytarabine. The combination of these measures reduces CNS relapses from 10% to <5%. Patients with CNS involvement (mostly of the leptomeninges) at diagnosis are treated with the standard chemotherapy regimen and additional intrathecal applications until there is complete blast clearance in the spinal fluid [4].

The rationale to use systemic high-dose (HD) therapy in the post-remission consolidation is to reach sufficient drug levels in sanctuary sites (e.g., CNS). Most protocols employ 6–8 cycles containing either HD methotrexate or HD cytarabine ± L-asparaginase [4].

Maintenance therapy usually consists of daily 6-mercaptopurine and weekly methotrexate; in some treatment regimens, repeated cycles of vincristine, dexamethasone, or other drugs in monthly or longer intervals are given. Treatment duration of 2.5–3 years is optimal and is usually recommended [4]. Omission of maintenance worsens outcome significantly in BCP-ALL, less in T-ALL [16], and probably not in B-ALL [17].

Nevertheless, relapses are still a major clinical challenge, especially in adults: indeed, there is no universally accepted treatment, and evidence based on randomized, controlled trials is still lacking [4]. The most commonly used regimens in Europe are fludarabine- and anthracycline-containing regimens, such as FLAG-Ida (fludarabine, high-dose ara-C, granulocyte colony-stimulating factor, and idarubicin). Despite its common use and inclusion as "standard of care" arm in several trials for relapsed ALL, there is remarkably a small number of publications in relapsed ALL [18]. Clofarabine-based regimens including cytarabine, cyclophosphamide, or etoposide are also commonly used based mostly on data in childhood ALL [19]. Liposomal vincristine [20] is licensed for the treatment of relapsed ALL. These standard chemotherapy approaches are applicable in BCP-ALL as well as in T-ALL.

Additionally, nelarabine has been licensed for this indication: it offered 31% CRs, with median DFS and OS of 20 weeks, thus demonstrating that nelarabine is well tolerated and has significant antitumor activity in relapsed or refractory T-ALL [21].

Advances have also been made in the setting of Ph'+ ALL, because of the use of tyrosine kinase inhibitors, such as imatinib, dasatinib, and ponatinib [4].

The Italian group GIMEMA treated frontline elderly ALL patients with imatinib 800 mg daily, associated to steroids without further chemotherapy: 100% obtained CR, with a median BCR-ABL1 reduction of 2 logs. No major toxicities occurred and the median survival from diagnosis was 20 months [22].

In another GIMEMA protocol, patients with Ph'+ ALL received dasatinib induction therapy for 84 days combined with steroids for the first 32 days and intrathecal chemotherapy: also in this case, all patients achieved CR by the first month, with 20-month OS of 69% and DFS of 51%. The reduction of BCR-ABL1 levels to <10–3 did significantly an impact on DFS [23].

Dasatinib was used in combination with low-intensity chemotherapy (vincristine and dexamethasone, followed by consolidation with dasatinib, reduced doses of sequential cytarabine and methotrexate for 6 months) in patients older than 55 years. CR rate was 96%, and 65% of patients achieved a 3-log reduction in BCR-ABL1 transcript levels during consolidation, with 5-year OS of 36% [24].

The MDACC recently published about the combination of the HyperCVAD regimen and ponatinib: 2-year event-free survival was 81%, with an 8% incidence of cardiovascular/thrombotic events [25].

Although targeted therapies are used increasingly in hematologic malignancies, RIT is not extensively used in ALL, even though this radiosensitive tumor expresses CD22, potentially a good target for this approach. Positive results have been published using ^{90}Y-epratuzumab tetraxetan [26].

Chevallier et al. [27] published results of a standard 3 + 3 phase I study which evaluated ^{90}Y-DOTA-epratuzumab RIT in refractory or relapsed CD22-positive B-cell acute lymphoblastic leukemia (with CD22 expression on at least 70% of blast cells). Treatment protocol included one cycle of ^{90}Y-DOTA-epratuzumab on days 1 and 8 at one of four dose levels: 92.5 MBq/m^2 (level 1), 185 MBq/m^2 (level 2), 277.5 MBq/m^2 (level 3), and 370 MBq/m^2 (level 4). Seventeen patients were treated (5 at level 1, 3 at level 2, 3 at level 3, and 6 at level 4): one dose-limiting toxic effect (aplasia lasting 8 weeks) occurred at level 4, but the MTD was not reached. The most common grade 3–4 adverse events were pancytopenia and infections. Authors concluded recommending the dose of 370 MBq/m^2 for two doses 1 week apart per cycle.

RIT using murine ^{131}I-anti-CD52 mAb has been used in the conditioning regimen for allogeneic hematopoietic stem cell transplantation in recurrent refractory CD52-positive ALL preceded by ^{124}I-labeled anti-CD52-mAb PET to evaluate dosimetry [28].

A patient with Ph'+ B-ALL in third relapse received RIT with ^{90}Y-labeled anti-CD22 epratuzumab tetraxetan; 7 weeks after initiating therapy, the patient became BCR-ABL1 negative by quantitative PCR lasting at 6 months before alloSCT. Although with limited clinical data, ^{90}Y-epratuzumab tetraxetan may be a promising therapeutic option for CD22+ B-ALL [26].

Treatment of Chronic Lymphocytic Leukemia

The first decision to be made in CLL is whether the patient requires therapy. A schematic treatment algorithm in adult CLL according to ESMO Clinical Practice Guidelines [29] is shown in Fig. 2.

Previous studies have shown that early treatment with chemotherapeutic agents does not translate into a survival advantage in patients with early-stage CLL. The standard treatment of patients with early disease is a watch-and-wait strategy. Blood cell counts and clinical examinations should be carried out every 3–6 months [29]. In Binet stage A and B with active disease or Binet stage C, Rai 0–II with active disease or Rai III–IV, treatment should be initiated in patients with symptomatic, active disease. Active disease is defined as significant B symptoms (weight loss, sweating, itching); cytopenias not caused by autoimmune phenomena and symptoms or complications from lymphadenopathy, splenomegaly, or hepatomegaly; lymphocyte doubling time of $<$6 months (only in patients with more than 30×10^9/L lymphocytes), as well as autoimmune anemia and/or thrombocytopenia poorly responsive to conventional (steroid) therapy. The presence of del(17p) or TP53 mutation without the abovementioned conditions is not an indication for treatment by itself [29].

In physically fit patients (physically active, with no major health problems, normal renal

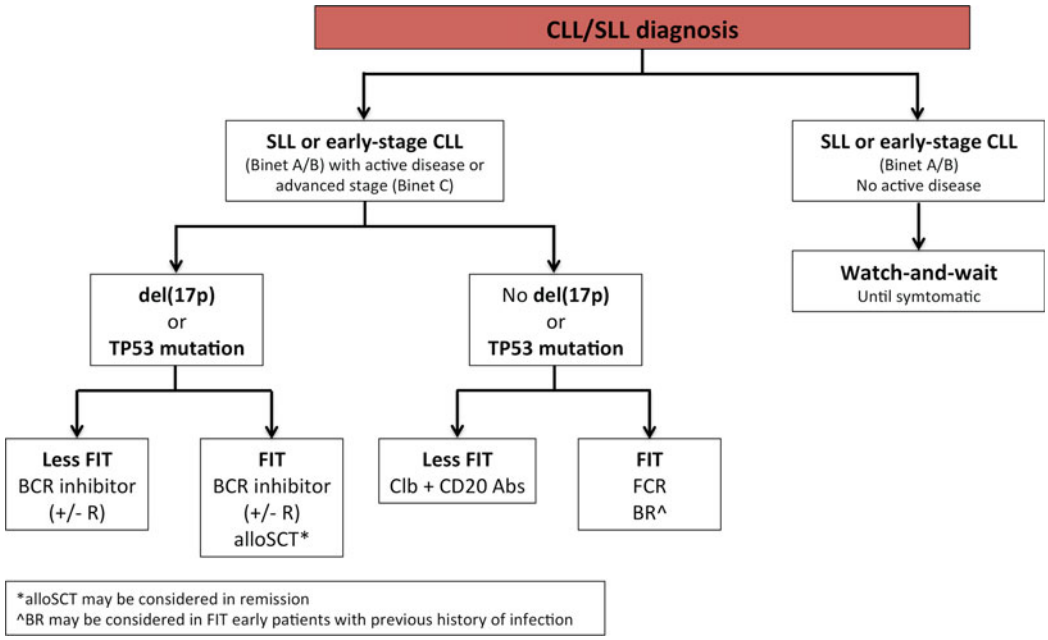

Fig. 2 Algorithm for frontline treatment in CLL. *CLL* chronic lymphocytic leukemia; *SLL* small lymphocytic leukemia; *BCR* B-cell receptor; *R* rituximab; *alloHSCT* allogeneic hematopoietic stem cell transplantation; *FCR* fludarabine, cyclophosphamide, and rituximab; *BR* bendamustine plus rituximab; *Clb* chlorambucil (Modified from Eichhorst et al. [29])

function) without TP53 deletion/mutation, fludarabine, cyclophosphamide, and rituximab (FCR) therapy is the standard first-line therapy with significantly improved OS [29, 30]. Combinations based on other purine analogues, such as cladribine [31] or pentostatin [32], have shown similar activity, but it is uncertain whether they can replace fludarabine in the FCR regimen. In fit but elderly patients, FCR was shown to be associated with a higher rate of severe infections when compared with bendamustine plus rituximab (BR) [29]. Therefore, in this group of patients, therapy with BR may be considered, although it produces fewer complete remissions than FCR [29]. In patients with relevant comorbidity, who are usually older, but without TP53 deletion/mutation, the combination of chlorambucil plus an anti-CD20 antibody (rituximab, ofatumumab, or obinutuzumab) prolongs progression-free survival when compared with monotherapy and is therefore the standard approach [33]. In a head-to-head comparison of chlorambucil-based combinations, the type II antibody obinutuzumab (GA-101) was superior to the type I antibody rituximab with regard to PFS, complete remission, and minimal residual disease remissions [29].

Nevertheless, patients with TP53 deletion/mutation have a poor prognosis even after FCR therapy [30]: therefore, it is recommended to treat them with novel inhibitors (ibrutinib, idelalisib plus rituximab) in frontline and at relapse.

Ibrutinib, an inhibitor of Bruton's kinase, in 17p CLL patients induced objective responses in more than 80% of cases, with 2-year PFS of 60%, comparing favorably with historical treatments that offered a median PFS of 1 year [34].

Idelalisib, a BCL2 inhibitor, in combination with rituximab was able to offer 82% of overall responses and median PFS of 17 months [35].

For fit patients responding to inhibitor treatment, the option of alloSCT can be discussed, using individual and transplant-related risk factors [36].

Maintenance therapy in CLL patients with higher risk of relapse may have some benefit, but are not generally recommended [29].

At relapse, the same regimen used as first-line may be repeated if the relapse occurs at least 24 months after chemoimmunotherapy and if TP53 deletion/mutation was excluded [29]. If relapse occurs before or in case of refractory disease, the therapeutic regimen should be changed with ibrutinib or rituximab combined with idelalisib [29, 37, 38]. A schematic treatment algorithm in adult CLL according to ESMO Clinical Practice Guidelines [29] is reported in Fig. 3.

Fit patients achieving the second remission should proceed to alloSCT [36]. On the contrary, autologous stem cell transplantation is not advantageous in CLL, but could be offered to patients achieving a good response after new drugs [29, 39].

Radiation therapy in CLL is indicated in case of large, bulky lymphoid masses causing compression symptomatology, especially if patients are unresponsive to chemotherapy. Splenic irradiation has been performed in patients with painful splenic enlargement or cytopenias related to hypersplenism, but splenectomy remains preferable. Following splenectomy, major improvements in blood counts can be achieved in 50–90% of patients [40]. Total body irradiation was used in the 1970s (response rates of 80–90%) [41] but no longer recommended since comparative studies of TBI with chemotherapy demonstrated a higher response rate with chemotherapy.

Radioimmunotherapy for the treatment of CLL has been limited by frequent extensive bone marrow involvement. Lym-1 is a radioimmunoconjugate consisting of a ^{131}I-labeled mouse IgG_k. The antibody recognizes a 31–35 kDa antigen presumed to be a polymorphic variant of the HLA-DR antigen and thought to be specific for B cells [42–46]. In a phase Ia trial including 10 patients, the antibody was well tolerated, but not active enough [47]. Repeated administration of ^{131}I-Lym-1 showed a dose-limiting thrombocytopenia in up to 28% of patients, but tumor regression was documented in some cases.

^{90}Y-ibritumomab tiuxetan and ^{131}I-tositumomab have also been used in patients with CLL excluding patients with bone marrow involvement >25% because of safety concerns. Nevertheless, Kaminski et al. [48] reported their experience in 14 patients with SLL and a median of four prior chemotherapeutic regimens, with responses occurring in

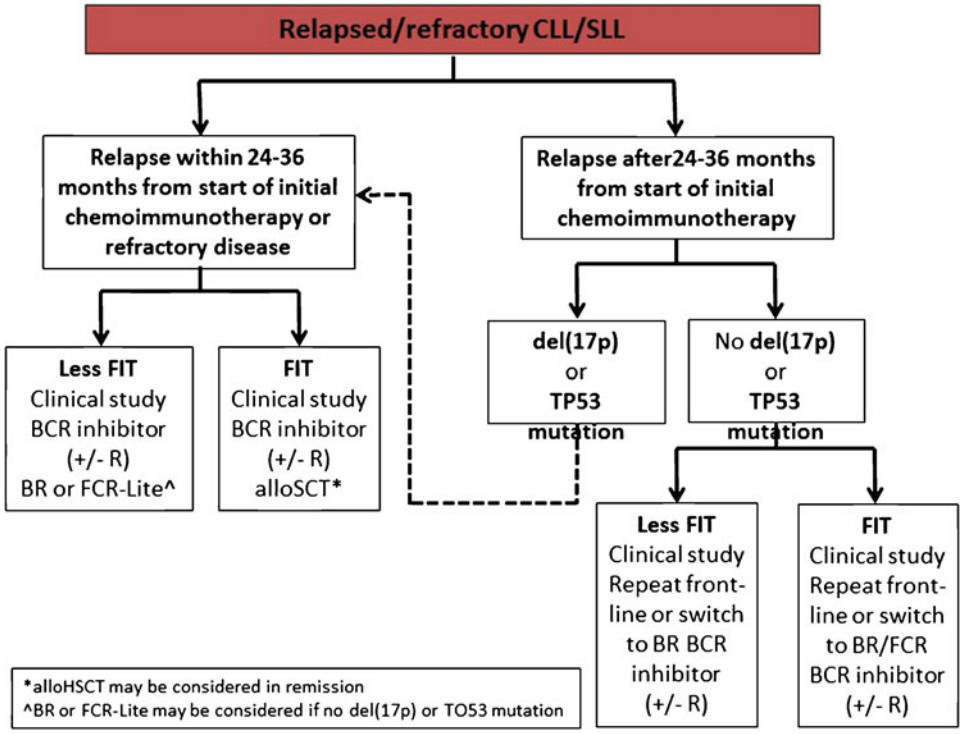

Fig. 3 Algorithm for relapse treatment in CLL. *CLL* chronic lymphocytic leukemia; *SLL* small lymphocytic leukemia; *BCR* B-cell receptor; *R* rituximab; *BR* bendamustine plus rituximab; *FCR* fludarabine, cyclophosphamide, and rituximab; *alloSCT* allogeneic hematopoietic stem cell transplantation (Modified from Eichhorst et al. [29])

64% of patients (including 21% complete remissions). The median duration of response was 24.7 months.

An interesting strategy under development is the reduction of bone marrow involvement prior to RIT therapy since the use of RIT in CLL is limited by the extent of bone marrow involvement. Thus, reducing the number of CLL cells in the bone marrow prior to RIT by the administration of an agent that is effective in clearing the bone marrow, such as anti-CD52 antibody (alemtuzumab), is a potentially interesting strategy.

Furthermore, ^{188}Re-alemtuzumab has been proposed by De Decker et al. [49] in an in vitro (HuT-78 cell line) and murine study (female NMRI mice) showing excellent receptor binding as well as a fast clearance from blood ($t_{1/2\alpha}$=4.79 h) and slower clearance from the body ($t_{1/2\beta}$=55.45 h). Mean radiation dose estimates, calculated for the human adults using the residence times derived from mice biodistribution data, identified the kidney (0.159–3.26 mGy/MBq), heart (0.0705–0.132 mGy/MBq), and liver (0.0602–0.220 mGy/MBq) as critical organs. The effective dose for the human reference adult was estimated to be approximately 0.0486–0.195 mSv/MBq [49, 50].

The ^{177}Lu-DOTA-HH1 (anti-CD37 monoclonal antibody) has been tested in nude mice to evaluate the toxicity profile; results demonstrated that ^{177}Lu-DOTA-HH1 was well tolerated at dosages about ten times above those considered relevant for RIT in patients with CLL and other non-Hodgkin lymphomas (NHL) [51].

^{131}I-tositumomab has been used in patients in complete/partial response after induction chemotherapy; 3 months after RIT, complete response was achieved (50%) or sustained (25%), and one third of patients cleared the minimal residual disease. Hematologic toxicities were anemia (6%), neutropenia (81%), and thrombocytopenia (50%);

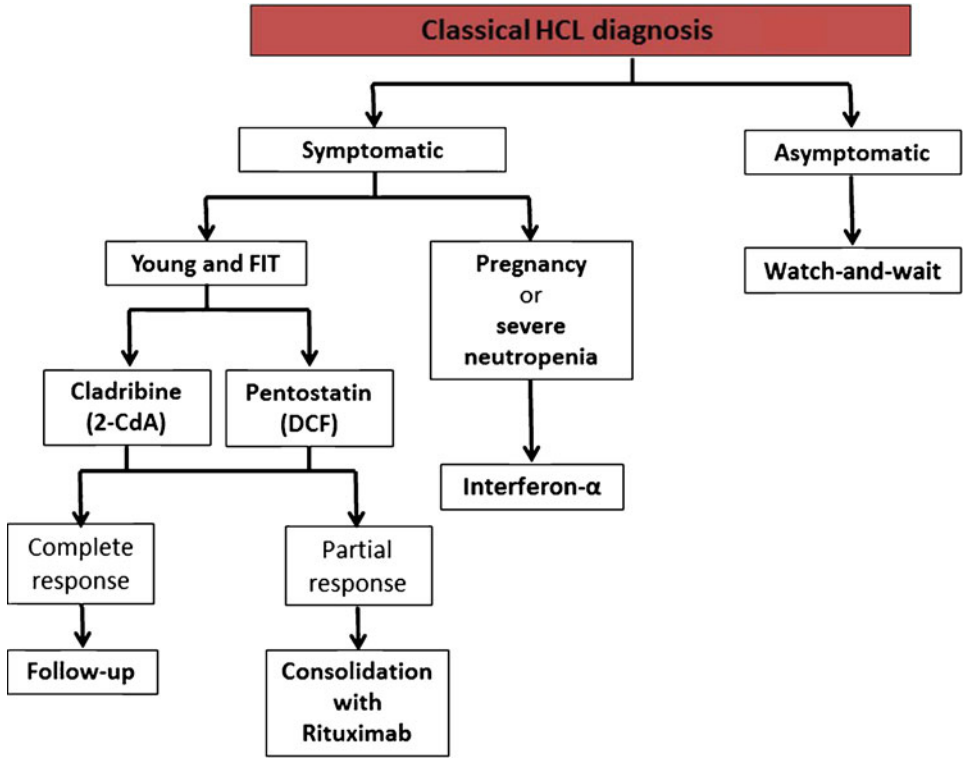

Fig. 4 Therapeutic algorithm for newly diagnosed classical hairy cell leukemia (Modified from Robak et al. [56])

12% of patients developed myelodysplastic syndromes 17 and 20 months after consolidation [52].

Fourteen patients with relapsed CLL either in partial remission or in complete remission but with disease documented by flow cytometry were treated with ^{90}Y ibritumomab tiuxetan. Grade 3 or 4 hematologic toxicity was seen in 92% of evaluable patients. In addition, myelosuppression was prolonged, with a median duration of grade 3–4 thrombocytopenia of 37 days. Five patients had persistent thrombocytopenia 3 months post-therapy. Even in patients with CLL and limited marrow involvement, the use of RIT results in unacceptable hematologic toxicity [53].

Treatment of Hairy Cell Leukemia

As with CLL, treatment for HCL is not indicated in asymptomatic patients; patients should be closely monitored with a complete history, physical examination, and complete blood cell count every 3–6 months. In contrast to CLL, asymptomatic patients, who may be diagnosed by chance, are rare, and in practice most patients need treatment shortly after diagnosis, either because of symptoms or to correct cytopenias. Treatment should be initiated in patients with symptomatic disease manifested by bulky or progressive, symptomatic splenomegaly or cytopenias (hemoglobin <10 g/dl and/or platelets $<100 \times 10^9$/L and/or neutrophils $<1 \times 10^9$/L), recurrent or severe infections, and/or systemic symptoms [54–56]. A schematic treatment algorithm in classical HCL (diagnosis and relapsed) and HCL variant according to ESMO Clinical Practice Guidelines [56] is reported in Figs. 4, 5, and 6, respectively.

Purine analogues, cladribine (2-CdA) or pentostatin (DCF), are recommended as initial treatment of symptomatic HCL patients who are young and fit. 2-CdA, subcutaneous or intravenous, induces durable and unmaintained response in 87–100% patients, including CR in 85–91%, after a single course of therapy [56]. Grade 3–4

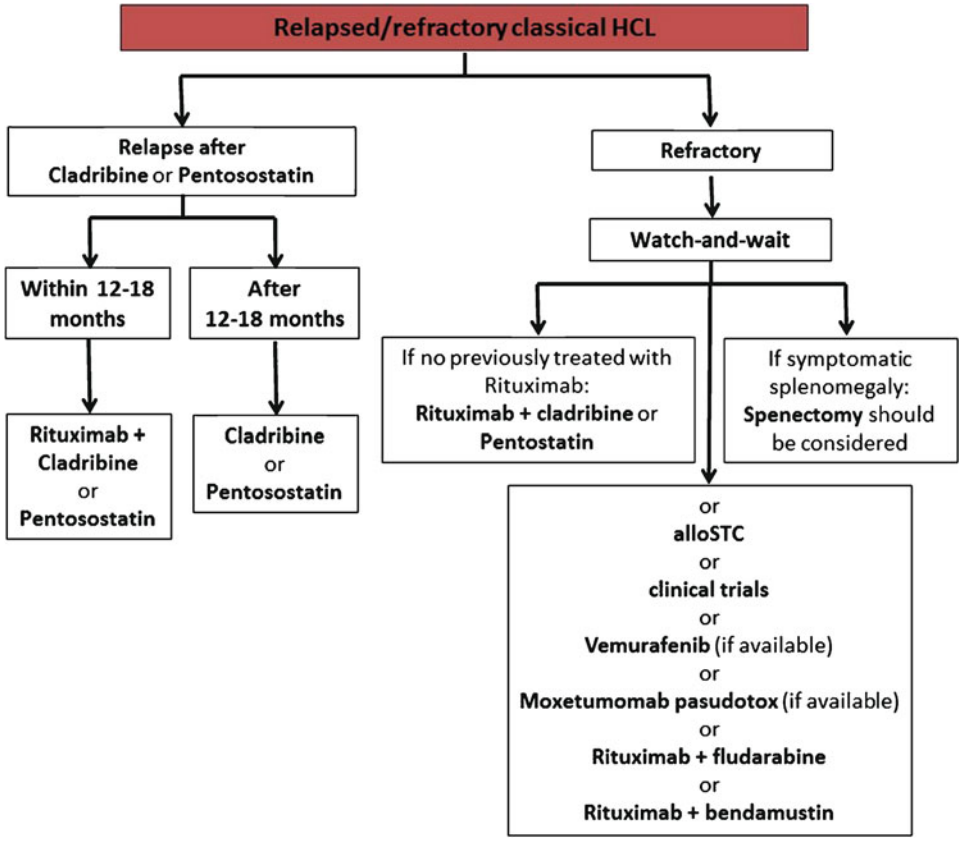

Fig. 5 Therapeutic algorithm for refractory/relapsed classical hairy cell leukemia (Modified from Robak et al. [56])

toxicities, largely represented by neutropenia and infections, were less frequent when low doses were used (0.5 mg/kg vs. 0.7 mg/kg), with similar OR [57]. A CR following 2-CldA administration is durable even without maintenance therapy [58]. In patients demonstrating a partial remission after the first course of 2-CldA, a second course should be repeated to achieve CR at least 6 months after the end of the first course, with or without rituximab [59]. Similarly to 2-CdA, DCF induces a high rate of long-lasting CR. In patients with a normal creatinine clearance, DCF is usually given at a dose of 4 mg/m^2 i.v. every second week until CR, plus one or two consolidating injections [60]. After 8–9 courses, the full blood count usually normalizes, and the bone marrow biopsy should be performed to confirm a CR. If a CR is documented, one or two further cycles are indicated [58]. DCF and 2-CdA appear to induce similar high response rates, duration of response, recurrence rates, and adverse events [58]. However, no randomized, direct comparison between the two drugs has been performed [56]. The advantage of DCF over interferon-α (IFN-α) in HCL patients has been confirmed in a multicenter, randomized trial [61]. The use of IFN-α in the treatment of HCL is limited since purine analogues produce higher and more durable remissions and are more convenient to patients [56]. However, IFN-α may still have a place in the treatment of HCL in pregnancy. It can also be used in patients presenting with very severe neutropenia [56, 62]. Relapsed patients can be successfully retreated with 2-CdA or DCF if relapse occurs after 12–18 months [63]. The alternative nucleoside analogue can be used in early relapse within 2 years after the first-line treatment [64]. The ability to attain CR decreases with each

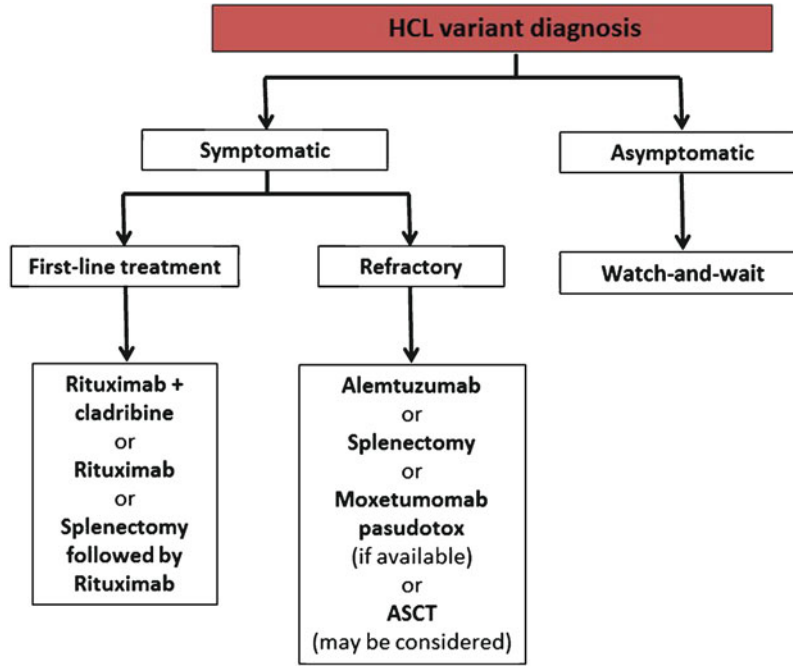

Fig. 6 Therapeutic algorithm for newly diagnosed variant hairy cell leukemia (Modified from Robak et al. [56])

course of therapy, but CR duration appears to be similar after first-, second-, or third-line therapy [58, 65]. Rituximab given weekly (dose of 375 mg/m^2 for 4–8 doses) can be used in early relapsed patients [66–68]; however, rituximab alone is inferior to purine analogues and is not the treatment of choice. Outcomes for patients with recurrent HCL appear to be better when a combination of rituximab and 2-CdA or DCF is used rather than the purine analogue alone [69, 70]. Concurrent therapy of rituximab and purine analogues induces higher response rates, and higher rates of toxic events than in the sequential administration [71]. IFN-α is also a possible option for selected patients relapsing after purine analogue therapy [72, 73]. Patients refractory to purine analogue therapy should be enrolled whenever possible on clinical trials that use new agents.

Oral fludarabine (dose of 40 mg/m^2) for five consecutive days in combination with rituximab for four cycles can be a therapeutic option in relapsed or refractory patients previously treated with 2-CdA [56].

Bendamustine (70–90 mg/m^2) combined with rituximab is another therapeutic option in multiple relapsed/refractory HCL and could be considered in HCL patients after the failure of standard therapies [74].

Other promising drugs active in purine analogue refractory HCL patients include moxetumomab pasudotox, an anti-CD22 recombinant immunotoxin, and vemurafenib, a BRAF V600E inhibitor [56, 75, 76]. A phase I trial of moxetumomab pasudotox in relapsed/refractory HCL induced an 86% OR rate and a 46% CR [58, 59].

Recently, the efficacy of vemurafenib was assessed in a cohort of 21 HCL patients treated outside of clinical trials: vemurafenib improved blood counts in all patients by 1.5–2 months, with a CR rate of 40% and a median EFS of 17 months [77].

The therapeutic potential of the Bruton's tyrosine kinase (BTK) inhibitor ibrutinib also needs to be taken into consideration in a relapse setting, given the proven in vitro activity of this drug in hairy cells [78].

Splenectomy may be indicated in patients with resistant massive symptomatic splenomegaly (>10 cm below the costal margin) with accompanied low-level bone marrow infiltration (OR rates of 60–100%) [62, 79]. Splenectomized patients respond better and faster to the subsequent

chemotherapy. Splenectomy can also be considered when progressive HCL develops during pregnancy and in patients refractory to nucleoside analogues and IFN-α [62]. Systemic therapy should not be performed earlier than 6 months after splenectomy to reach full benefits of this treatment [64]. Allogeneic stem cell transplantation has a potential role in younger, heavily pretreated HCL patients who have had multiple relapses and are refractory to purine analogues and rituximab [80, 81]. In pregnant woman, treatment is indicated only when truly warranted, and the appropriate therapy depends on the stage of pregnancy, the rate of disease progression, and the response to previous therapies. IFN-α shows good tolerance, uncomplicated pregnancy, and normal child development [82].

Splenectomy is another option to consider, should INF-α fail, especially in early gestation when the risks are lower [83, 84]. Administration of 2-CdA and rituximab is not indicated in pregnancy because of the risk of teratogenic effects, although successful pregnancy has also been reported [56, 85].

The results of the treatment of hairy cell leukemia variant (HCL-V) with purine analogues are poor [56, 86]. In addition, the majority of HCL-V patients required more than 1 cycle to maintain a response. Using DCF, PR was observed in 8/15 (54%) patients, and no CR was achieved; rituximab alone, or splenectomy followed by rituximab, can also induce CR in HCL-V [87–89]. However, administration of 2-CdA immediately followed by rituximab appears to be more effective than 2-CdA alone or rituximab alone and should be considered as the initial treatment of HCL-V patients [56, 69, 90].

Alternatively, case reports suggest that alemtuzumab is an active agent in treating HCL-V, even in patients who have relapsed after rituximab [91]. Splenectomy induces clinical responses in some patients with HCL-V and is recommended because it corrects cytopenias, removes the bulk of the tumor, and may improve response to purine nucleoside analogues [56, 92]. Splenic irradiation could be performed in elderly patients with a high surgical risk of splenectomy [56]. Although limited data, clinical case reports support the use of moxetumomab pasudotox in patients with HCL-V and the use of autologous or allogeneic hematopoietic cell transplantation in refractory patients [56, 75, 93].

Treatment of Acute Myeloid Leukemia (AML)

Whenever possible, AML treatment should be offered in clinical trials and given only in experienced centers offering an adequate multidisciplinary infrastructure as well as a suitably high case load. Treatment should be planned with curative intent whenever possible. Intensive chemotherapy of AML is divided into an induction phase, consolidation, and (rarely) maintenance. Potential candidates for alloSCT (scheduled for the consolidation phase) must be identified early at diagnosis or during induction chemotherapy. Treatment of acute promyelocytic leukemia (APL) differs in several important aspects from therapy of all other AML types [94].

Patients with excessive leukocytosis at presentation and with clinical signs of leukostasis may require emergency leukapheresis coordinated with the start of chemotherapy. These patients are at particular risk of a tumor lysis syndrome under induction chemotherapy and need appropriate monitoring. In these cases, a single injection of rasburicase may be considered to prevent hyperuricemia and hence renal failure, but data are insufficient to support a firm recommendation in this respect.

In respect of a common induction regimen, the strategy of consolidation eventually followed by autologous or allogeneic transplantation depends on the cytogenetic/molecular features of disease. Induction chemotherapy usually includes an anthracycline and cytarabine in the well-known “3+7” regimen. Data on dose escalation of daunorubicin to improve AML outcome look promising, but longer follow-up is required to support a firm recommendation [95–101]. Consolidation therapy in AML is warranted once patients have reached clinical and hematological remission. There is no consensus on a

single "best" post-remission treatment schedule. In good-risk AML patients in first remission, who have a relapse risk of 35% or less, alloSCT is not justified because its toxic effect and/or the risk of mortality exceed the benefit. Also, these patients may receive salvage therapy including alloSCT in second remission. Good-risk AML patients (including NPM-mutated AML with absence of internal tandem duplications of FLT3 (FLT3-ITD), core binding factor (CBF) AML, and bi-allelic mutant CEBPα AML), as well as patients who are unsuitable for alloSCT for other reasons, should receive at least one cycle of intensive consolidation chemotherapy preferably incorporating intermediate or high-dose cytarabine [94].

Patients in intermediate- and poor-risk groups with an HLA-identical sibling may be candidates for alloSCT, provided their age and performance status allow for such treatment [102–112]. Newer data suggest that alloSCT may no longer be mandatory in intermediate-risk patients, but these data need to be confirmed [96]. Patients in these risk groups without a family donor may qualify for alloSCT with an HLA-matched unrelated donor identified through an international donor registry. In fact, peripheral stem cells harvested from unrelated HLA-matched donors have become the most frequently used source of stem cells. If a killer immunoglobulin-like receptor (KIR) mismatch is present, haploidentical transplant may be considered. Conditioning regimens for alloSCT with dose-reduced chemotherapy intensity (RIC) may be used for patients in the upper age range (particularly those >50 years of age), but there is some evidence that RIC may also be used in adults at a younger age.

The role of high-dose chemotherapy with autologous stem transplantation in AML is still controversial. Recent data suggest that it may be a good option (and thus an alternative to alloSCT) in patients in the intermediate-risk group [100]. While it may prolong time to relapse or remission duration, its potential to prolong overall survival is uncertain [104, 106, 107].

Patients with significant comorbidity and elderly are often not eligible for intensive treatment; they should receive best supportive care or palliative systemic treatment. Nevertheless, recently demethylating agents have been approved for patients with 20–30% of blasts (5-azacytidine) or aged more than 65 years (decitabine) [94].

A recent retrospective study evaluated the efficacy of 5-azacitidine in a cohort of 130 elderly patients ineligible for intensive chemotherapy: patients received 5-azacitidine for a median of four cycles, with overall response rate of 36% and 37% of hematologic improvement. Median OS was 18 months for responders and 12 months for nonresponders [113].

Decitabine has been reported to offer 18%–24% of CRs, but no overall survival benefit [114].

Excessive leukocytosis due to spilling of malignant blasts into the periphery may be reduced with cytoreductive agents such as hydroxyurea or low-dose cytarabine, which, however, also can reduce also normal blood cell counts and red cells, neutrophils, or platelets. Treatment of infections due to neutropenia and transfusions to improve anemia or thrombocytopenia are important additional measures. Erythropoietin is of questionable value in patients with anemia due to extensive infiltration of the marrow with leukemia. In severely neutropenic patients, hematopoietic growth factors may be tried when neutropenic fever or infections are a problem; however, there is no evidence to support their continuous use [94, 95, 98, 104, 112].

Resistance to therapy (refractory or relapsed AML) is the major cause of treatment failure, rather than mortality due to infections and other treatment-related complications. Patients failing to respond to one or two cycles of induction are considered refractory and can be candidates for alloSCT, albeit with limited chances of success and at the cost of considerable morbidity from this procedure. For patients unsuited to this approach, best supportive care or palliative systemic treatment is often a reasonable option with, at least, limited toxic effect. The prognosis of such patients is often dismal regardless of treatment attempts. Patients presenting with relapse after a first remission may be offered intensive re-induction, with better chances of success in patients with a longer interval from first remission. Patients in second or subsequent remission

may still qualify for alloSCT with a family or unrelated HLA-matched donor or with cord blood-derived stem cells [94].

Suspicion of or established diagnosis of acute promyelocytic leukemia (APL) must trigger a distinctive therapy program [115–118]: oral all-trans retinoic acid (ATRA) should immediately be started, because of the high risk of bleeding caused by the disseminated intravasal coagulation (DIC) [94]. Risk assessment of APL is based on white blood cell count at presentation, where patients with a WBC count $>10 \times 10^9$/L fare worse. APL induction chemotherapy consists of ATRA as a differentiating agent and idarubicin. The use of arsenic trioxide (ATO) in first-line APL therapy is promising, but long-term results are not yet available.

However, the results of ATRA-ATO combination without chemotherapy look promising, particularly in good-risk APL: in the GIMEMA APL0406 study, adults between 18 and 71 years with low- or intermediate-risk APL were randomly assigned to receive ATRA-ATO or ATRA-chemotherapy. All patients achieved CR in the ATO arm versus 97% in the chemotherapy group, with a significant advantage in terms of 4-years EFS (97% vs. 80%) and OS (99% vs. 92%) [119].

The need for daily i.v. application of ATO over a prolonged period of time, electrolyte as well as cardiac problems (including potentially fatal torsade-de-pointe ventricular arrhythmias), and case reports on secondary cancers after ATO must all be considered [120].

RIT could potentially circumvent multidrug resistance and yield remissions in drug-resistant AML. The choice of the most suitable radionuclide to label specific antibodies is based on purely clinical considerations such as the type of disease, the degree of leukemic bone marrow infiltration, and the presence of extramedullary burden. Furthermore, the decision to combine different radioimmunoconjugates may also be applied to improve the therapeutic efficacy if compared to monotherapies [121].

Radiolabeled antibodies with specificity for the antigens CD33, CD45, and CD66 have been developed and studied for myeloablative radioimmunotherapy in patients with AML or MDS. CD33 is an antigen expressed from the promyelocyte stage to the stage of mature myeloid cell and in most AML blasts. The CD45 antigen is expressed on almost all leucocytes (except plasma cells) and on 80–95% of leukemic blasts of the myeloid and lymphoid line. The CD66 antigen belongs to the group of nonspecific cross-reacting antigens and is present from the promyelocyte stage to the mature granulocyte stage, rarely on myeloid leukemic blasts. Nevertheless, none of the antibodies currently tested in clinical trials for myeloablative RIT (Table 1) are approved for this purpose. The only commercially available antibody is ^{99m}Tc-BW250/183 (IgG1; NCA 95, scintimun, besilesomab; CIS Bio International, Schering, Switzerland), but it is registered for the scintigraphic diagnosis of infections only. Preliminary results suggest that myeloablative RIT may

Table 1 examples of antibodies developed and tested in clinical trials for leukemia and multiple myeloma

Type of antibodies	Antigen specificity	Clinical indications	Radiolabeling
M195 (IgG_{2a}, murine)	CD33	AML	^{131}I
HuM195 (IgG_{2a}, humanized)	CD33	AML	^{90}Y, ^{213}Bi, ^{131}I
Lintuzumab (whole antibody, humanized)	CD33	AML	^{225}Ac
p67 (IgG, murine)	CD33	AML	^{131}I
BC8 (IgG_1, murine)	CD45	AML, MM	^{131}I
YTH24.5 (IgG_{2b}, rat)	CD45	AML, CML, ALL	^{99m}Tc (dosimetry)
YAML568 (IgG_{2a}, rat)	CD45	AML, MM	^{90}Y
BW250/183 (IgG_1; murine)	CD66b	AML, MM	^{90}Y, ^{188}Re
Lym-1 (IgG_K, murine)	HLA-DR	CCL	^{131}I
Ibritumomab tiuxetan (IgG_1, murine)	CD20	CLL	^{90}Y
Tositumomab (IgG_{2a}, murine)	CD20	CLL	^{131}I

close the gap between benefit and toxicity of conditioning therapies. When myeloablative RIT is used to condition patients scheduled for transplantation, it provides high-energy doses into the bone marrow thus inducing hypoplasia/aplasia, the rate of relapse is decreased, and normal organs that do not express the target antigen are spared from toxicity. Additionally, myeloablative RIT does not significantly increase the rate of therapy-related mortality. Generally, RIT is employed in younger patients in good general condition in addition to dose-escalated conditioning, while in patients >55 years and/or with comorbidities, it should be added to reduce the intensity of "standard" conditioning therapies [121]. ^{188}Re-alemtuzumab RIT followed by fludarabine (150 mg/m^2), busulfan (8 mg/kg), and alemtuzumab (75 mg) has been evaluated before alloSCT in a phase II trial enrolling 22 patients with advanced myeloid malignancies. The extramedullary toxicity in the first 100 days posttransplantation was limited, and all patients engrafted with complete donor chimerism. The probability of OS at 2 years was 40%. A comparison with a younger historical cohort having received the same dose of fludarabine and busulfan but neither radioimmunotherapy nor alemtuzumab showed no difference in outcome. Although the use of alemtuzumab reduced the incidence of acute graft-versus-host disease, it was associated with a relapse incidence of 40% despite the incorporation of RIT. These data confirmed the feasibility of combined RIT and reduced-intensity conditioning in elderly patients [50]. Current clinical trials for myeloablative RIT are designed to obtain an individual dosimetric study either to calculate the therapy doses or, in dose-escalating protocols, to ensure not to exceed the dose-limiting organ doses. For monotherapy in patients with AML or MDS and a low tumor load, the radiolabeled anti-CD66 mAb is considered the optimal choice, and the use of DTPA-derived chelators is suggested to improve the biodistribution profile (increased bone marrow/liver doses ratio). In patients with extensive bone marrow infiltration with blast cells or significant extramedullary disease, anti-CD33 and anti-CD45 radioimmunoconjugates are preferred [121].

Low linear energy transfer (LET)-ionizing radiation is an important form of therapy for acute leukemias. Ionizing radiation is also a potential source of DNA damage. High LET-ionizing radiation produces structurally different forms of DNA damage and has emerged as potential treatment of metastatic and hematopoietic malignancies. Haro et al. [122] created a stable myeloid leukemia HL60 cell line radioresistant to both γ-rays or α-particles to understand possible mechanisms in radioresistance. Cross-resistance to each type of ionizing radiation was observed, but resistance to clustered, complex α-particle damage was substantially lower than that to equivalent doses of γ-rays. The resistant phenotype was driven by changes in apoptosis, late G2/M checkpoint accumulation that was indicative of increased genomic instability, stronger dependence on homology-directed repair, and more robust repair of DNA double-strand breaks and sublethal-type damage induced by γ-rays, but not by α-particles. The more potent cytotoxicity of α-particles warrants their continued investigation as therapies for leukemia and other cancers [122].

The key properties of the alpha particles generated by ^{225}Ac are the following: (i) limited range in tissue of a few cell diameters, (ii) high linear energy transfer leading to dense radiation damage along each alpha track, (iii) a 10-day half-life, and (iv) four net alpha particles emitted per decay [123].

Treatment of Chronic Myeloid Leukemia (CML)

The introduction of tyrosine kinase inhibitors at the beginning of 2000s revolutionized the outcome of patients affected by CML, improving survival from the 40% to 90%, with a good quality of life [124]. TKIs interfere with the ATP-binding site in the BCR-ABL1 pocket blocking its uncontrolled tyrosine kinase activity. Imatinib was the first TKI to be introduced in the clinical practice on the basis of a randomized trial versus IFN-α and low-dose arabinosylcytosine (IRIS study); thus, IFN and hydroxyurea are not still recommended in treatment of CML patients.

Now, second-generation TKIs offering faster and more complete responses are available. After onset of mutations of the ABL1 that often abrogated the efficacy of the TKI, other third-generation TKIs have been designed; thus, today five different compounds are available. Each of them has a specific toxicity profile, with increased cardiovascular events for nilotinib and ponatinib, increased pleural effusion for dasatinib, diarrhea for bosutinib, and fluid retention for imatinib [125]. Consequently, European and American guidelines suggest if and when TKIs have to be changed, but not which one has to be used in the first line [126].

Moreover, no substantial progress has been made in the treatment of blast-phase disease; allogeneic transplantation is now reserved to patients failing at least 2 TKIs.

Projected annual 3–5-year survival rates range from 38% to 80%, with the higher values reported from more experienced centers. BMT in accelerated and/or blast-phase disease is relatively unsatisfactory; nonetheless, 15% to 20% of patients may become long-term survivors.

A recent multi-institutional randomized trial compared the use of bone marrow with peripheral blood stem cells from HLA-identical siblings for relatively favorable patients with a variety of hematologic neoplasms, including CML, undergoing transplantation. Hematologic recovery was more rapid and the 2-year OS significantly increased (70% vs. 45% of BMT). Drug treatment is superior to allogeneic stem cell transplantation in first-line therapy of CML, because of transplant-related mortality. Thus, initial allogeneic SCT cannot be recommended anymore [127].

Therapies with Radiolabeled Antibodies

Therapies with Radiolabeled Anti-CD33 mAb

Schwartz et al. [128] conducted a dose-escalation study with fractionated doses of ^{131}I-M195 (185–7.77 MBq/m^2) in 24 patients with relapsed/refractory myeloid leukemia. Post therapy whole-body scintigraphy demonstrated marked uptake of the antibody into all involved areas in every patient. A significant decrease of bone marrow blasts was observed in 83% of cases, with sufficient bone marrow cytoreduction allowing subsequent ASCT in 33% of the patients. These data suggest that a safe leukemic cytoreduction may be achieved with ^{131}I-M195, and it may be useful as part of a myeloablative conditioning regimen. Nevertheless, in 37% of patients, human anti-mouse antibody (HAMA) was produced, preventing effective retreatment with the same murine M195 MaAb. To avoid immunogenicity leading to HAMA development [128], humanized MoAbs for the treatment of leukemia have been developed (Hu-M195). Caron et al. [129] evaluated the biodistribution profile and leukemia cell targeting, as well as safety concerning especially immunogenicity, in 13 patients with AML and CML treated with increased doses of ^{131}I-Hu-M195. The pharmacokinetics of Hu-M195 were very similar to M195 with serum $t_{½-a}$ more rapid than that of the murine M195, probably because of the rapid targeting of Hu-M195 to leukemia cells (Hu-M195 affinity is 8 times higher compared to the murine form). Additionally, the amount of antibody binding to splenic targets during the "first pass" may contribute to the shorter serum $t_{½-a}$. Whole-body scintigraphy also confirmed the rapid and specific binding of radiolabeled Hu-M195 to the target areas. A similar trial was reported by Appelbaum et al. [130] in patients with advanced AML using ^{131}I-labeled p67, a murine IgG targeting CD33. However, their results were not satisfactory since the administration of a single dose of ^{131}I-p67 due to its short marrow residence times; this was presumably due to the modulation of the antigen-antibody complex with subsequent rapid release of ^{131}I from the marrow space [130, 131]. In fact, to be effective for myeloablation, antibodies should be retained longer in the bone marrow, as in the case of ^{131}I-M195 and ^{131}I-HuM195 that presented a bone marrow retention of at least 3 days [132].

Sgouros et al. [133] analyzed imaging data obtained from the phase I trial of ^{131}I-HuMl95: response to RIT was influenced by tumor burden, antibody clearance kinetics, and the antibody-antigen interaction. Compartmental modeling

analysis provided biodistribution data for absorbed dose calculations to tissues not directly sampled, to determine the optimum therapeutic dose of radiolabeled antibody for a given patient [134]. The results demonstrated a large inter- and intrapatient variability, such differences suggesting that dosimetry based upon the activity concentration at a single site may not adequately assess the potential for marrow toxicity in any patient. Red marrow dosimetry is important only if it provides a better index of potential marrow toxicity than other more easily determined parameters, such as whole-body absorbed dose or administered activity. Marrow dose estimation is critical since the biological clearance rate, fractional uptake in marrow, radionuclide half-life, and emission characteristics are accounted for in assessing absorbed dose. Both the variability in regional bone marrow radiosensitivity and the effect of treatment before absorbed dose estimates, are directly related to complication treatment-induced.

To determine the possible use of RIT in the conditioning phase, Jurcic et al. [135] associated the myeloablative action of ^{131}I-M195 or ^{131}I-HuM195 (4.4–14 GBq) to cyclophosphamide and busulfan in 30 patients with refractory/relapsed AML de novo or secondary to CML: no significant toxicities were reported and complete remissions were observed in 93% of patients; 19% of patients were alive and disease-free after 4.5–8 years.

A median survival of 4.9 months was also reported by Burke et al. [132] with the same treatment schedule and dose of ^{131}I-M195 or ^{131}I-HuM195 (4.5–16.17 MBq) combined with busulfan and cyclophosphamide; moreover, imaging confirmed good targeting of the radioimmunoconjugate to all areas of leukemic involvement, including vertebrae, pelvis and long bones, liver, and spleen. The bone marrow-absorbed radiation dose was calculated to range between 0.27 and 1.47 Gy. When comparing the performance of ^{131}I-M195 with that of ^{131}I-HuM195, this latest offers some advantages, including the ability to mediate antibody-dependent cellular cytotoxicity and complement-mediated cytotoxicity, the lack of immunogenicity, and the modest intrinsic antileukemic activity.

Nevertheless, ^{131}I-labeled anti-CD33 in the setting of myeloablative RIT does not represent the optimal compound: in fact, radioiodination of antibodies decreases their ability to bind to the antigen (about 1/3 of the tyrosine residues binding ^{131}I are located in the hypervariable regions) and thus prevents the delivery of high radiation doses to the bone marrow. Furthermore, the relatively long half-life of ^{131}I delays transplantation, since the radionuclide retained within the bone marrow must decay totally in order to prevent injury to the grafted hematopoietic stem cells; finally, ^{131}I requires hospitalization in a radioprotected ward. Radiometals such as ^{90}Y and ^{188}Re have been evaluated as alternatives to ^{131}I: such radioisotopes offer better retention by target cells after internalization of antigen-antibody complexes, while the higher energy of their β emissions permits a lower effective dose, and the absence of γ emission reduces radioprotection restrictions [132].

Jurcic et al. [136] conducted a phase I trial to determine the safety and biological activity of ^{90}Y-HuM195 (185–1036 MBq, as a single administration). Biodistribution and dosimetry studies were also performed after the administration of ^{111}In-HuM195 (370 MBq). Dose-limiting toxicity (leucopenia G4) was seen at 11 MBq/kg. Scintigraphy showed uptake of ^{111}In-HuM195 in the bone marrow, liver, and spleen within 1 hour of administration and for at least 3 days. Radiation doses to the bone marrow and liver were 0.29–0.70 Gy and 0.12–0.30 Gy, respectively. ^{90}Y-HuM195 may overcome the limitations of ^{131}I-anti-CD33 conjugates, being safer but still retaining a significant antileukemic activity.

The first clinical trial with ^{213}Bi was conducted at Memorial Sloan Kettering Cancer Center in New York in collaboration with the National Institutes of Health and the Institute for Transuranium Elements in Karlsruhe [137].In this study, 18 patients with relapsed and refractory acute myelogenous leukemia or chronic myelomonocytic leukemia were treated with 10.4 to 37.0 MBq/kg of ^{213}Bi-HuM195. Fourteen of fifteen evaluable patients (93%) had reductions in circulating blasts, and 14 of 18 patients (78%) had reductions in the percentage of bone marrow blasts. No significant extramedullary toxicity was seen. Jurcic et al.

demonstrating the safety, feasibility, and antileukemic effects of ^{213}Bi-HuM195 provided the first proof-of-concept for systemic radiometal-based RIT in patients with relapsed/refractory AML or CML [137]. Based on the encouraging results of this pioneering study, another phase I/II study was conducted to determine the maximum tolerated dose and efficacy of ^{213}Bi-HuM195 after partially cytoreductive chemotherapy with cytarabine. Thirty-one patients with newly diagnosed (n = 13) or relapsed/refractory (n = 18) AML were treated: significant reduction in marrow blasts was seen at all dose levels and complete remissions, and partial responses were seen in 6/25 patients (24%) who received doses of ≥37 MBq/kg. Myelosuppression was tolerable, and no significant extramedullary toxicity was observed [138].

Sgouros et al. [139] analyzed the results of a phase I trial, demonstrating that ^{213}Bi-HuM195 rapidly localized to areas of leukemic involvement and all patients developed myelosuppression with absorbed dose ratios 1000 times greater than with β-emitting radioimmunoconjugates. Moreover, 93% of evaluable patients had a reduction in circulating blasts, while 78% of patients had reductions in the percentage of bone marrow blasts [137]. Kolbert et al. [140] developed a method to provide a "whole-body" assessment of the pharmacokinetics of ^{213}Bi-HuM195 in the patients enrolled in this phase I trial: images were acquired after multiple injections of ^{213}Bi-HuM195 with progressively increasing antibody concentration, over 2–4 days. A linear expression to the counts in each pixel was applied to obtain parametric rate images defining clearance and uptake rates in each organ. Planar images of antibody distribution showed significant uptake in the liver, spleen, and bone marrow. The generated rate images displayed different patterns (i.e., with negative values in the liver and spleen and positive values in bone marrow), reflecting clearance and uptake rates rather than total accumulation. The inter-patient comparison developed with this method showed that rate image patterns varied based on patient-specific conditions, such as the amount of disease and previous therapies. Maximum-tolerated dose has been established for ^{213}Bi-immunoconjugates in AML at about 37 MBq/kg [137].

Miederer et al. [141] analyzed the pharmacokinetics profile, dosimetry, and toxicity of the targetable atomic generator ^{225}Ac-HuM195 in nonhuman primates and found severe renal toxicity and anemia at a cumulative activity of 377 kBq/kg. The longer blood $t_{1/2}$ and the lack of target cell antigens in cynomolgus monkeys may increase toxicity compared with the human setting, where an activity level of 28 kBq/kg may be a safe starting dose (no toxicity at 6 months).

More recently, Maguire et al. [142] described three strategies to stably chelate ^{225}Ac and evaluated ^{225}Ac-HuM195 in a mouse model of leukemia (NSG) which demonstrated a lower dose-limiting toxicity (2.22 kBq) than other mouse models. Despite this aspect possibly related to the immunocompromised state of NSG mouse or to the lack of circulating antibody, reductions in tumor growth rate and a significant difference between specific and control antibodies was observed. These observations supported the hypothesis that in immunocompetent hosts, higher or repeated doses may be used, and consequently a greater absolute therapeutic effect can be achieved.

Kersemans et al. [143] recently demonstrated that ^{111}In-HuM195 and ^{111}In-M195 modified with peptides harboring nuclear-localizing sequences may decrease cell growth and clonogenic survival for both drug-resistant AML cell lines and primary AML patient specimens expressing MDR transporters, through the emission of Auger electrons, after CD33-mediated internalization. More than 99% of the Auger electrons emitted by ^{111}In have a range of less than 1 μm, which obviates the cross-fire effect and yields high-linear-energy transfer comparable to that of highly cytotoxic a-emitters (i.e., 50–100 keV/mm). Targeted Auger electron RIT using ^{111}In-NLSHuM195 and ^{111}In-NLS-M195 may be able to overcome resistance [143, 144].

^{211}At has been shown to be a promising, highly cytotoxic RIT in CD33-positive AML and kills tumor cells more efficiently than calicheamicin-conjugated antibody. Labeling techniques leading to higher chemical yield and specific activities have been evaluated to increase ^{211}At-anti-CD33 therapeutic effects [145].

Clinical experience with ^{225}Ac therapy is currently still limited. The ongoing phase I clinical trial was initiated at Memorial Sloan Kettering Cancer Center with a primary goal to define both safety and the MDT of ^{225}Ac RIT in advanced AML patients through a dose-escalation series. The trial has been successful in demonstrating that ^{225}Ac RIT targeted by lintuzumab had anti-leukemic activity across all dose levels and it is now being investigated in a multicenter USA phase I/II trial in combination with low-dose cytarabine for elderly AML patients [146].

A study of combined modalities for treating AML has been recently completed at the Memorial Sloan Kettering Cancer Center using chemotherapy to reduce the cancer load followed by RIT (^{213}Bi- or ^{225}Ac-immunoconjugates) [147].

^{213}Bi-anti-CD33 exhibits its cytotoxic effects specifically in CD33-expressing AML cells via induction of the intrinsic, mitochondrial pathway of apoptosis. The abrogation of chemo- and radioresistances and the reactivation of apoptotic pathways seem to be promising for the treatment of patients with so far untreatable resistant AML and underline the importance of this emerging therapeutic approach of targeted alpha-therapies [148].

Therapies with Radiolabeled Anti-CD45 mAb

^{131}I-BC8 (2.8–22.6 GBq) prior to transplantation in combination with cyclophosphamide and fractionated total body EBRT (12 Gy) has been used by Matthews et al. [149] in patients with advanced acute leukemia or MDS after first complete remission. Bone marrow doses obtained with this compound were up to 30 Gy, with maximum liver doses of 7 Gy [149].

A comparative study of the biodistribution and biokinetics of two other immunoconjugates, ^{99m}Tc-BW250/183 and ^{99m}Tc-YTH24.5, in patients with AML, CML, and ALL was performed by Buchmann et al. [150], who concluded that YTH24.5 is not appropriate for myeloablation because of its unfavorable biodistribution profile. Thus, YTH24.5 has been modified from IgG_{2b} to IgG_{2a}; this compound, named anti-CD45 MoAb YAML568, demonstrated a significant improvement of the bone marrow/liver dose ratio. Although the biodistribution and dosimetry of YAML568 are less favorable than those of BW250/183, the former represents an alternative option for leukemia patients with a high medullary tumor load or with extramedullary disease.

To improve the efficacy of RIT, Kletting et al. [151] developed a physiologically based pharmacokinetic model to describe the biodistribution of ^{90}Y-labeled anti-CD45 antibody YAML568. Dosimetric estimates in patients receiving unlabeled antibody before the injection of ^{111}In-labeled anti-CD45 MoAb (121±21 MBq), demonstrated that the preload with cold antibody increased selective delivery of radioactivity to the target organ as well as reducing toxicity to normal tissue [151, 152]. The method is in principle applicable also to RIT with other antibodies to decrease nonspecific binding of the labeled antibody to the liver or spleen. Validation of this model is still under evaluation.

Additionally, the conjugation with (Ab)-streptavidin and DOTA-biotin labeled with β-emitting radionuclides has been explored in AML as a strategy to decrease relapse and RIT toxicity, suggesting that anti-CD45 RIT may be highly effective and minimally toxic for treatment of AML [153].

In theory total body irradiation may be replaced by RIT in hematopoietic cell transplantation conditioning regimens, leading to positive outcomes on transplant overall survival. Anti-CD45 RIT can increase the dose of cytotoxic radiation targeted to malignant cells, while sparing normal organs. Opportunities for further optimization of CD45-targeted RIT exist, including alternate radioisotopes with different physical properties and energy characteristics. The continued combinations of innovative preclinical studies and supportive clinical trials suggest that CD45-targeted RIT will continue to develop as a critical option for improving hematopoietic cell transplantation outcomes for hematological malignancies [154].

Mawad et al. [155] used RIT with ^{131}I-anti-CD45 antibody (332–1561 mCi) combined with fludarabine and total body irradiation (2 Gy) to

improve hematopoietic cell transplantation success in advanced AML or high-risk MDS patients. Marrow doses were arbitrarily capped at 43 Gy to avoid radiation-induced stromal damage; no graft failure or evidence of stromal damage was observed. Graft-versus-host disease was observed in the majority of patients treated. Six patients (40%) were still alive after a median of 5 years (range 4.2–8.3 years), with 1-year OS of 73%. Moreover, the arbitrary limit of 43 Gy to the marrow may be unnecessarily conservative, and continued escalation of targeted radioimmunotherapy doses may be feasible to further reduce relapse [155]. The relative therapeutic efficacy and toxicity of the anti-CD45 RIT employing ^{90}Y and ^{177}Lu in a syngeneic, disseminated murine myeloid leukemia (B6SJLF1/J) model has been compared. ^{90}Y-DOTA-30F11 RIT demonstrated a dose-dependent survival benefit and was associated with transient, mild myelotoxicity without hepatic or renal toxicity. Conversely, ^{177}Lu- anti-CD45 RIT yielded no long-term survivors. Thus, in this murine leukemia model, ^{90}Y was more effective than ^{177}Lu for anti-CD45 RIT of AML [156]. Efficacy and toxicity of anti-CD45 RIT using ^{211}At were positively evaluated in a disseminated murine AML model suggesting that ^{211}At-anti-CD45 RIT in conjunction with hematopoietic stem cell transplantation may be a promising therapeutic option for AML [157].

Very recently, Orozco et al. [158] evaluated a conditioning regimen employing ^{90}Y-anti-CD45 RIT replacing total body irradiation (TBI) before haploidentical alloSCT in a murine model, suggesting the possible introduction of RIT in clinical practice.

A phase II trial evaluated ^{131}I-BC8, fludarabine, TBI, and donor stem cell transplant followed by cyclosporine and mycophenolate mofetil in patients with advanced AML or myelodysplastic syndrome is currently ongoing [147].

Therapies with Radiolabeled Anti-CD66 mAb

The anti-CD66 MoAb ^{188}Re-BW250/183 (8.2±4.1 GBq) was employed in very poor prognosis childhood leukemia: the protocol consisted in a conditioning regimen including RIT, high-dose chemotherapy, and, optionally, total body EBRT before allogeneic transplantation. In this setting, the kidney was the dose-limiting organ (doses higher than the liver), and doses to the bone marrow were in the 5.5–30 Gy range. The results of this study were disappointing, since after a follow-up of 5–8 months, 6/7 patients died [159]. Subsequently, the same antibody and schedule were applied to adult AML or MDS presenting bone marrow infiltration <25% and high risk of relapse: RIT was administered at a mean activity of 11.1 GBq, associated with conventional conditioning therapy with cyclophosphamide combined with either total body EBRT (12 Gy) or busulfan. The majority of patients received T-cell depleted graft, while others had autologous transplantation. Mean bone marrow dose was 14.9 Gy, with moderate acute toxicity; the kidney was the dose-limiting organ; 18-month DFS was 45% [160, 161]. Patients with >50–60% bone marrow infiltration were excluded from treatment with ^{188}Re-BW250/183 because specific marrow doses were lower than the non-specific doses to the liver (Buchmann, unpublished data), probably due to low number of binding sites on the normal hematopoietic cells. Associating ^{188}Re-BW250/183 to conditioning regimens in patients receiving BMT did not significantly increase the incidence of acute graft-versus-host disease compared to the conventional conditioning therapies [162].

A phase I/II study with the anti-CD66 MoAb BW250/183, labeled with either ^{188}Re or ^{90}Y in adult patients with AML and MDS, demonstrated the feasibility and safety of RIT also in reduced dose-intensity conditioning regimens prior to allo-SCT. Bone marrow doses were 21.9±8.4 Gy, with a significantly higher dose for ^{90}Y- versus ^{188}Re-labeling. Comparison of biodistribution profile of ^{188}Re- and ^{90}Y-BW250/183 suggested a more favorable profile of the ^{90}Y-labeled MoAb, especially concerning the kidney doses. Kidney toxicity was observed in 6.4% of patients after intensified conditioning with ^{188}Re-BW250/183, but none in patients treated with ^{90}Y-BW250/18. Following these results, ^{90}Y was coupled to the

antibody via the chelator MX-DTPA, and further improvements had also recently been reported by Orchard et al. [163], with the use of different DTPA derivatives, such as the chelator 2B3M-DTPA [164]. Intraindividual dosimetric evaluation between PET and conventional scintigraphy, using ^{18}F- and ^{99m}Tc-labeled anti-CD66, respectively, in a patient with high-risk leukemia, displayed a similar distribution pattern, with high preferential uptake in bone marrow. Nevertheless, urinary excretion of radioactivity after administration of ^{18}F-anti-CD66 was faster, and bone marrow uptake was lower than after administration of ^{99m}Tc-anti-CD66 [165].

The combination of reduced-intensity conditioning, ^{188}Re-anti-CD66 RIT, and in vivo T-cell depletion was successfully applied in elderly patients with AML or MDS; a prospective phase II protocol evaluated if a dose reduction of alemtuzumab (from 75 mg to 50 mg) would improve leukemia-free survival by reducing the incidence of relapse. Fifty-eight patients received RIT followed by fludarabine (150 mg/m^2) and busulfan (8 mg/kg) combined with standard (75 mg; n = 26) or low (50 mg; n = 32) dose of alemtuzumab. The overall incidence of engraftment and the disease-free and overall survival did not differ, and the dose reduction had no positive impact on overall outcome [166].

In vitro studies showed that the human polynucleotide kinase/phosphatase inhibitor A12B4C3 radiosensitized AML cells to the DNA-damaging effects of ^{111}In-NLS-7G3 (which recognizes the CD123$^+$/CD131$^-$ phenotype displayed by leukemia stem cells), suggesting that the combination treatment may improve the effectiveness of Auger electron RIT of AML targeting the leukemia stem cells subpopulation [167].

The CSL360 is a chimeric IgG_1 monoclonal antibody that recognizes CD123 (IL-3 receptor α-subchain) expressed in the absence of CD131 (β-subchain), an epitope that is displayed by leukemia stem cells (LSCs) and has been evaluated for RIT of AML in a model mouse (NOD/SCID mice). Additionally, microSPECT/CT has been used to assess engraftment of primary human AML specimens into NOD/SCID mice. The targeting of ^{111}In-DTPA-NLS-CSL360 to sites of AML engraftment in the NOD/SCID mouse model is encouraging for future RIT studies [168, 169].

Treatment of Multiple Myeloma

Targeted therapies employing anti-CD45, anti-CD66, and anti-CD138 antibodies against hematopoietic or bone marrow stromal cells radiolabeled with beta-emitting radiopharmaceuticals have been developed for myeloablative RIT in MM. The CD45 antigen is overexpressed in clonogenic myeloma stem cells, and the CD66 antigen is expressed in all the intermediate stages from promyelocyte to the mature granulocyte, while anti-CD138 (syndecan-1), a heparan sulfate proteoglycan, is constantly expressed on tumor cells in MM. Different antibodies have been developed and tested in clinical trials as conditioning treatment, but none of them have yet been approved for RIT in MM (Table 1) [121]. Typically, bone marrow toxicity represents the major and dose-limiting side effect of all RIT regimens proposed so far. In fact, the radiolabeled antibodies can accumulate in the bone marrow irrespective of the severity of bone marrow infiltration or when an antibody cross-reacting with healthy hematopoietic cells is employed. Bone marrow doses of 2–8 Gy induce moderate myelosuppression, while doses >8–10 Gy induce relevant hypoplasia or aplasia. Thus, ASCT or supportive care is often required to prevent life-threatening complications. When RIT is used in the setting of conditioning regimens prior to stem cell transplantation, myelotoxicity takes on a "positive" role since it contributes to the destruction of plasma cells infiltrating the bone marrow. This option has been proposed to overcome the relative toxicity of intensified chemo- and EBRT, given the selective mechanism of action of radiolabeled antibodies. The maximum bone marrow dose applied in this clinical setting is generally limited to 35–40 Gy to avoid stromal cell damage that may affect engraftment of the transplanted stem cells. The anti-CD45 monoclonal antibody YAML568 is an option for patients with MM. Orchard et al. [163] published promising

data obtained in patients with MM treated in a dose-escalated phase I trial with ^{90}Y-labeled 2B3M-DTPA anti-CD66 BW250/183 followed by ASCT, thus prompting an ongoing phase II trial. Myeloablative RIT as conditioning treatment in patients with MM still remains difficult. It is assumed that there is a progenitor myeloma stem cell that is CD45 positive and circulates as an isolated single cell in peripheral blood. Taking these considerations into account, patients with MM should be treated beneficially with an anti-CD45 monoclonal antibody labeled with a combination of alpha-emitters (to damage the single progenitor cells circulating in the blood, the myeloma cells, and myeloma progenitor cells in the margin of the marrow) and beta-emitters (to enhance the effect in the bone marrow). Furthermore, malignant plasma cells may build clusters in the bone marrow, thus making tumor targeting more difficult. Therefore, RIT protocols should include only patients with a diffuse pattern of bone marrow infiltration and clusters <1 mL [121]. Before going into the details of the main application of RIT in MM, we will provide a brief overview on the current treatment options in MM.

When only one osteolytic bone lesion is seen in the presence of 10% or more clonal plasma cells, no clear indication is present for systemic therapy if no other criteria are met for active myeloma. This circumstance is rare, and we recommend that patients could be given radiation therapy and observed. Clinical trials to determine the value of adjuvant systemic therapy for these patients are being planned [170]. Treatment should be initiated in all patients with active myeloma fulfilling the CRAB criteria and in those symptomatic due to the underlying disease [171]. A major discriminant among the different treatment options for high-risk patients is the possibility to perform high-dose chemotherapy regimens plus either autologous stem cell transplantation (ASCT) or allogeneic bone marrow transplantation (Fig. 7). Initial treatment for newly diagnosed MM (induction therapy) was historically performed with high-dose melphalan. Given the possibility of such initial therapy to adversely affect the ability to collect stem cells and considering the recent introduction of new class of drugs in transplant eligible patients, thalidomide/lenalidomide and bortezomib-based regimens are currently preferred to single agent dexamethasone and VAD (vincristine, adriamycin, doxorubicin), with strong recommendation for the use of bortezomib-containing regimens in high-risk patients. Oral combinations of melphalan and prednisone (MP) plus novel agents or lenalidomide and steroid are considered as standards of care for elderly patients (non-transplant setting) [171] (Fig. 8). The two following options are recommended (level IA): melphalan/prednisone/thalidomide (MPT) [173] and bortezomib/melphalan/prednisone (VMP) [174]; both are approved in this setting by the European Medicines Agency

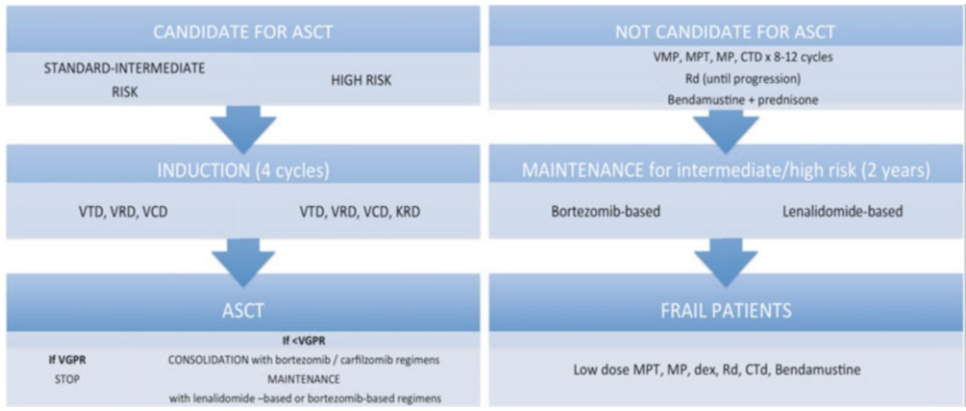

Fig. 7 Treatment options for multiple myeloma (Adapted from Rajkumar et al. [170] and Moreau et al. [171])

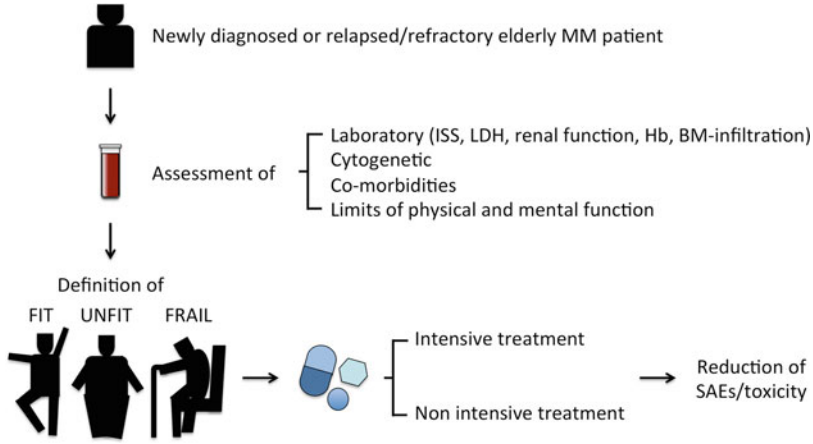

Fig. 8 Special considerations prior to therapy in elderly or frail patients. In multiple myeloma patients with newly diagnosed or refractory disease, a detailed geriatric and functional assessment helps to define more precisely "fit" *versus* "frail" patients and to evaluate patients' risk for treatment toxicity and treatment discontinuation. These definitions of fit, unfit, and frail patients are anticipated to influence selection of therapeutics, as well as the correct allocation to intensive or nonintensive treatment should reduce side effects/SAEs and treatment toxicity (Modified from Terpos et al. [172])

(EMA). Bendamustine plus prednisone is another regimen that is also approved by the EMA in patients who have clinical neuropathy at time of diagnosis precluding the use of thalidomide (MPT regimen) or bortezomib (VMP regimen) [175]. Melphalan/prednisone/lenalidomide (MPR) allowed 81% of patients to achieve at least a partial response, and to about half of them to achieve a very good partial response, to 24% to reach a CR, with 12-month EFS of 92% and OS of 100% [176]. Moreover, in a randomized trial comparing MPR followed by lenalidomide as maintenance versus MPR without maintenance versus MP, MPR-R significantly prolonged progression-free survival (median, 31 months) as compared with MPR (median, 14 months) and MP (median, 13 months), but without any significant impact on OS. At least a very good partial response was reported in 33% in the MPR-R and MPR groups versus 12% in the MP group. Even in this trial, OS was not different among the 3 arms [177]. Cyclophosphamide/thalidomide/dexamethasone (CTD) combination has also been compared with MP and is superior in terms of response rates, but does not induce a clear survival advantage over MP [178]. In patients in good clinical condition (e.g., fit patients), induction followed by high-dose therapy with autologous stem cell transplantation (ASCT) is the standard treatment (level IIb) [171]. ASCT improves complete response and prolongs median overall survival by approximately 24 months, though with an intrinsic mortality rate ranging from 1% to 2%. Response rates to induction therapy have been significantly increased by the use of novel agent-based combinations. Bortezomib-dexamethasone, which is superior to the classical VAD regimen (vincristine, adriamycin, and high-dose dexamethasone) [179], has become the backbone of induction therapy before ASCT (level IIb) [171]. The addition of a third agent to bortezomib-dexamethasone, e.g., thalidomide (VTD), doxorubicin (DVD or PAD), lenalidomide (RVD), or cyclophosphamide (VCD), has shown to offer higher response rates in phase II trials [180]. Three prospective studies have already shown that VTD is superior to TD or bortezomib-dexamethasone [181–183]. Based on response rates, depth of response, and PFS as surrogate markers for outcome, three-drug combinations including at least bortezomib and dexamethasone are currently the standard of care before ASCT. Three to four courses are recommended before proceeding to stem cell collection [171]. Melphalan (200 mg/m^2 i.v.) is the standard preparative regimen before ASCT [184]

(level IIb) [171]. Peripheral blood progenitor cells are the preferred source of stem cells, rather than BM [171]. Tandem ASCT has been evaluated before the era of novel agents. The benefit of tandem ASCT was observed in patients that were not reaching very good partial response after the first ASCT [185]. In a recent study phase III (Hovon 65-GMMG HD4 trial) in the context of bortezomib induction and maintenance treatment, OS was better in the GMMG group, which carried out tandem ASCT in contrast to HOVON (single ASCT) [186]. Nevertheless, the trial was not powered to compare single versus double high-dose melphalan. Ongoing trials running both in Europe and the USA comparing prospectively single versus tandem ASCT in the era of novel agents will solve this important issue. Allogeneic stem cell transplantation should only be carried out in the context of a clinical trial and only in patients with good response before transplant [171]. Myeloablation as part of radioimmunotherapy (RIT, see above) can be used 10–14 days before transplantation to reduce the dose of the conditioning treatment. Ongoing studies aim at assessing whether the conditioning regimen can be improved by the addition of bone-seeking radiopharmaceuticals such as ^{166}Ho-DOTMP or ^{153}Sm-EDTMP. A second sequential ASCT has been investigated as additional consolidation therapy to further reduce disease burden. Such tandem ASCT seems to be beneficial for patients who have failed to achieve good partial response after the first ASCT. Allogeneic stem cell transplantation is not recommended as part of initial therapy, but can be considered in young patients at high risk achieving a good response after the first ASCT. Indeed, notwithstanding the new conditioning strategies and the possibility of employing sibling or unrelated donors, the treatment-related mortality (TRM) rate is still about 10–20%, in addition to the high probability of graft versus host disease (GVHD) [187]. Thus far, in the era of novel agent-based induction therapy, there is still not enough evidence that consolidation therapy should be systematically applied [171]; even some studies suggest that consolidation after ASCT could be advantageous in terms of OS and PFS [188]. In elderly patients following induction, three randomized trials have explored the benefit of maintenance therapy in terms of OS using either immunomodulatory drugs (IMiDs) or bortezomib: MP versus MPR versus MPR-R [177], bortezomib-melphalan-prednisone-thalidomide/bortezomib-thalidomide versus VMP [189], VMP versus VTP followed by either bortezomib-prednisone (VP) or VP maintenance [190]. Due to the trial design, the benefit in OS is not well established. Therefore, systematic maintenance therapy is not recommended in elderly patients [171]. In young patients following ASCT, phase III randomized trials have demonstrated that maintenance therapy with IMiDs, either thalidomide or lenalidomide, prolongs PFS [191, 192], but the OS benefit is still unclear. Bortezomib maintenance is also under evaluation [186]. These three agents are not approved in this setting; therefore, systematic maintenance therapy is not recommended [171]. The choice of therapy in the relapse setting depends on several parameters, such as age; performance status; comorbidities; the type, efficacy, and tolerance of the previous treatment; the number of prior treatment lines; the available remaining treatment options; and the interval since the last therapy [171]. The EMA has approved lenalidomide in combination with dexamethasone [193, 194] and bortezomib either alone as single agent [195] or in combination with pegylated doxorubicin [196]. Thalidomide and bendamustine are effective drugs, often used, but not approved [197]. Triplet combinations have proved effective in phase II trials, but only one single randomized trial has shown the superiority of VTD over TD for PFS in patients relapsing following ASCT [198]. In young patients, a second ASCT may be considered, provided the patient responded well to the previous ASCT and had a PFS of more than 24 months [199]. In the relapse setting, allogeneic SCT should only be carried out in the context of a clinical trial. When possible, patients should be offered participation in clinical trials. Pomalidomide, the third-in-class IMiD, and carfilzomib [197] are now available in Europe also. Moreover, monoclonal antibodies, such as daratumumab and elotuzumab, are very promising options: daratumumab as single agent offered overall response to one third of patients refractory either to IMIDs or to bortezomib, with median duration of response of 7.4 months and 12 months OS of 65% and good tolerability [200].

Intravenous elotuzumab, in combination with lenalidomide and dexamethasone, offered to more than 90% of resistant patients a response and to more than 40% a very good partial response [201]. In a recently published phase 3 trial, refractory or relapsed MM patients were randomized to receive ixazomib (oral proteasome inhibitor) plus lenalidomide and dexamethasone or placebo plus lenalidomide and dexamethasone. PFS was 21 months in the ixazomib group versus 15 months in the control group, with similar percentage of serious adverse events [202]. Finally, histone-deacetylase inhibitors, such as panobinostat, have been licensed in association with bortezomib for relapsed patients: in the PANORAMA 2 trial, panobinostat was administered to relapsed MM patients in combination with bortezomib and dexamethasone (overall response rate of 34%, with PFS of 6 months for responsive cases) [203]. Supportive care with bisphosphonates can decrease bone pain as wells as reduce the progression of osteolytic lesions and prevent pathologic fractures. The exact time of start and optimal duration of treatment are still under investigation. However, according to ASCO recommendations, such therapy should be started in the presence of significant bone loss or of pathological spine fractures (lower bone density leads to weaker bones) and should continue for no longer than 2 years [204, 205]. A fully humanized mAb to RANKL (denosumab, which binds and inhibits the RANK ligand thus reducing bone resorption markers) is still under clinical investigation. Erythropoietin or darbepoetin is useful in patients with persistent symptomatic anemia. Indication for prophylactic antibiotic therapy in patients undergoing chemotherapy is still debated, while it should be considered in all patients receiving high-dose steroid therapy [205]. Intravenous immunoglobulin administration is indicated if patients have recurrent severe infections associated with severe hypogammaglobulinemia. Plasmapheresis is useful in patients with the hyperviscosity syndrome. Vertebroplasty and kyphoplasty generally result in rapid and long-lasting reduction of bone pain and improvement in functional activity in patients with vertebral compression fractures. The standard treatments for cord or cauda equina compression are steroids and radiation therapy, whereas surgical decompression is rarely necessary. Radiotherapy is generally used for the treatment of painful bone lesions or to prevent complications and is performed at least once in about 70% of patients with MM. Typically, doses <30 Gy are preferred, to avoid permanent side effects which could jeopardize subsequent chemotherapy or ASCT [205, 206]. Among the radionuclide therapies for MM, CXCR4-targeted radiotherapy with pentixather appears to be a promising novel treatment option in combination with cytotoxic chemotherapy and autologous stem cell transplantation, especially for patients with advanced MM as recently reported in a first in human experience [207].

Radioimmunotherapy in Multiple Myeloma

In 1999 Couturier O. et al. [208] evaluated RIT in MM targeting a specific monoclonal antibody (B-B4) coupled to ^{213}Bi by a chelating agent (pentaacetic triamine diethylene *p*-aminobenzyl acid). The efficacy of alpha-RIT was assessed in vitro by analysis of thymidine incorporation, cell mortality, apoptosis of myeloma cells, and the study of nonspecific irradiation of hematopoietic cell lines not recognized by B-B4-pentaacetic triamine diethylene *p*-aminobenzyl acid immunoconjugate. B-B4 has been shown to induce apoptotic death of more than 40% of myeloma cells at a dose of 7.4 kBq/10^5 cells. Similarly, Burtun et al. [209] explored the biochemical nature and potential of MUC1 as antigenic target in MM. MA5 mAb was strongly reactive with 6/8 human MM cell lines as shown by flow cytometry. In 7/8 MM patient samples (bone marrow and/or peripheral blood), reactivity was found in 10–90% of the cells, whereas normal control (n = 5) and leukemia and lymphoma (n = 5) cells showed only 0–6% reactivity. ^{125}I-labeled MA5 whole-cell binding studies showed quantitatively similar amounts of binding between strongly positive MM lines and high-MUC1-expressing breast carcinoma lines. MM cell lines were positive for mRNA expression (Northern blotting and reverse transcription-PCR), with strong similarity in the sizes of the mRNAs and cDNAs.

Finally, biodistribution experiments were carried out with ^{131}I-labeled MA5 versus a nonbinding control ^{125}I-labeled mAb in a MM xenograft model. Selective MM tumor uptake of the MA5 mAb was demonstrated, with a potential for delivering a tumor radiation absorbed dose of 8540 cGy/mCi of injected dose compared with 3099 cGy/mCi of tumor-absorbed dose delivered by nonspecific antibody. Results of a direct comparison between B-B4 and MA5 labeled with iodine-131 and bismuth-213 in vitro have been demonstrated that B-B4 RIT might be more effective than MA5 and suggested that alpha-RIT might be more suitable than beta-RIT for treating single-cell tumor models [210]. Different mechanisms (cell cycle synchronization, DNA damage, and apoptosis) that might underlie potential synergy between chemotherapy (paclitaxel or doxorubicin) and RIT with alpha radionuclides have been analyzed in three different MM cell lines (LP1, RMI 8226, and U266). Cells were treated with ^{213}Bi-B-B4 24 hours after paclitaxel (1 nmol/L) or doxorubicin (10 nmol/L) treatment; radiation enhancement ratio showed that paclitaxel and doxorubicin were synergistic with alpha RIT. After a 24-h incubation, paclitaxel and doxorubicin arrested all cell lines in the G2-M phase of the cell cycle. Doxorubicin combined with alpha RIT increased tail DNA in the RPMI 8226 cell line but not the LP1 or U266 cell lines compared with doxorubicin alone or alpha RIT alone. Neither doxorubicin nor paclitaxel combined with alpha RIT increased the level of apoptosis induced by either drug alone or alpha RIT alone. Both cell cycle arrest in the G2-M phase and an increase in DNA double-strand breaks could lead to radiosensitization of cells by doxorubicin or paclitaxel, but apoptosis would not be involved in radiosensitization mechanisms [211].

In myeloma xenografts models, treatment with ^{213}Bi-anti-CD38-MAb suppressed tumor growth via induction of apoptosis in tumor tissue and significantly prolonged survival compared to controls [212, 213].

In order to define where alpha-RIT stands in MM treatment, melphalan was compared with alpha-RIT using a ^{213}Bi-anti-CD38-MAb in a syngeneic MM mouse model. Fifty percent of untreated mice died by day 63 after MM engraftment. In mice treated with melphalan alone, 200 μg improved median survival. No animal was cured after melphalan treatment, whereas 60% of the mice survived with RIT alone at day 22 after tumor engraftment, with only slight and reversible hematological radiotoxicity. No therapeutic effect was observed with alpha-RIT 25 days after engraftment. Melphalan and alpha-RIT combination does not improve overall survival compared to RIT alone, resulting in increased leukocyte and red blood cell toxicity. Based on these data, alpha-RIT seems to be a good alternative to melphalan, while their association provides no benefit [214].

To promote an efficient and long-lasting antitumor response, combining α-RIT (^{213}Bi-radiolabeled anti-CD138 antibody) and adoptive T-cell transfer (ovalbumin-specific CD8+ T cells) have been evaluated in an animal model. Animals treated with the combination had significant tumor growth control and an improved survival compared to control mice or the ones that received RIT alone or adoptive T-cell transfer alone [215].

Pretargeting with biotin may improve RIT efficacy. A comparison between conventional RIT using anti-CD38-MAb and streptavidin-biotin pretargeted RIT (PRIT) demonstrated more favorable results for PRIT. Particularly, PRIT demonstrated better biodistribution with a very high tumor-to-blood ratio (638:1 24 h after PRIT; ratios never exceeded 1:1 with conventional RIT). Objective remissions were observed within 7 days in 100% of the mice treated with PRIT (800–1200 μCi of anti-CD38 pretargeted ^{90}Y-DOTA-biotin), including 100% of complete remissions by day 23. Furthermore, 100% of animals bearing NCI-H929 multiple myeloma tumor treated with 800 μCi of anti-CD38 pretargeted ^{90}Y-DOTA-biotin achieved long-term myeloma-free survival (>70 days) compared with none of the control animals [216].

More recently, preliminary biodistribution and dosimetry results were obtained in refractory MM patients in a phase I/II RIT study using ^{131}I-B-B4. Four patients at the fourth relapse received 370 MBq (20 mg/m^2) of ^{131}I-B-B4: each patient underwent three-point images (day 0, day 1, and day 3–4) to assess doses absorbed by organs and

the bone marrow. Images obtained 1 h after ^{131}I-B-B4 injection showed high bone marrow and liver uptake without kidney uptake. The bone marrow uptake confirmed the bone marrow involvement as detected by [^{18}F]FDG-PET/CT. Absorbed doses were calculated at 2.03 ± 0.3 mGy/MBq for the liver, 1.10 ± 0.9 mGy/MBq for the kidney, and 0.52 ± 0.20 mGy/MBq for the bone marrow. Grade III thrombocytopenia was documented in two cases (highest bone marrow-absorbed doses), and no grade IV hematological toxicity was observed. One patient experienced partial response, with 60% reduction of M-spike on serum electrophoresis, and total relief of pain, lasting for 1 year. This proof-of-concept study based on dosimetry demonstrated the feasibility of the anti-CD138 antibody RIT [217]. Animal model studies confirmed the efficacy of ^{213}Bi-labeled anti-mCD138 for the treatment of residual disease in the case of MM, with only moderate and transient toxicity [213].

Promising results have been reported also by using ^{131}I-Radretumab. Radretumab is a fully human antibody binding the extradomain-B splice variant of fibronectin. Strong extradomain-B expression in almost all lymphoma subtypes and in the bone marrow from MM patients has also been reported [218].

Based on these preclinical data, a phase I/II study was performed in patients with solid tumors and hematological malignancies. Two MM patients were treated with 3.7 GBq and 1.85 GBq of ^{131}I-Radretumab, respectively, achieving disease stabilization lasting few months [219].

The newly synthetized te2a-Ph-NCS has been conjugated to a new anti-CD138 mAb (9E7.4) to evaluate its in vivo behavior and potentiality as bifunctional chelating agents and to explore a first attempt of PET-phenotypic imaging in MM (^{64}Cu-9E7.4-CSN-Ph-te2a). Animal experiments were carried out on 5 T33-Luc(+) tumor bearing mice: a millimetric bone uptake was localized in the sacroiliac myeloma. Nonspecific uptakes were observed at 2 h postinjection, but, unlike for the tumor, a significant decrease was observed at 20 h postinjection [220].

Very recently, the therapeutic efficacy of RIT in the 5 T33 murine MM model using 9E7.4 labeled either with ^{213}Bi for α-RIT or ^{177}Lu for β-RIT has been evaluated. α-RIT performed with 3.7 MBq of ^{213}Bi-9E7.4 increased median survival to 80 days compared to untreated control (37 days) and effected cure in 45% of animals. β-RIT performed with 18.5 MBq of ^{177}Lu-9E7.4 mAb was well tolerated and significantly increased mouse survival (54 vs. 37 days in the control group); however, no mice were cured with this treatment [221].

Radiotherapy with Bone-Seeking Radionuclides

Bone-seeking radiopharmaceuticals, although used more widely in the palliation of bone pain for patients with metastases from prostate or breast cancer, are also being evaluated in MM patients in the transplant setting.

In vitro studies showed that myeloma cell lines treated with ^{153}Sm-EDTMP showed a 50% decrease in clonogenic activity and mice who received treatment improved median survival from 18 to 25 days ($p<0.001$) [222].

A phase II trial using high-dose ^{153}Sm-EDTMP conducted at the Mayo Clinic included 46 patients treated with melphalan 200 mg/m^2 and 40 Gy of ^{153}Sm-EDTMP: engraftment was comparable to that seen after conventional ASCT. No dose-related toxicity or cases of thrombotic thrombocytopenic purpura, radiation nephritis, or bladder toxicity were observed with a median follow-up of 14.2 months [223].

In another study, the clinical impact and quality of life after treatment with ^{153}Sm-EDTMP (2 GBq every 12 weeks) and zoledronic acid (4 mg every 28 days) for symptomatic refractory MM were evaluated in elderly patients. A single course of ^{153}Sm-EDTMP plus zoledronic acid prolonged duration of the clinical response (reduction of MM-related symptoms). No significant hematological or non-hematological side effects were observed [224]. This combination is therefore safe and may be useful in the setting of refractory bone pain for MM patients with bone disease. It is currently ongoing a phase I/II trial which evaluates the efficacy and side effects of ^{153}Sm-

lexidronam pentasodium when given together with zoledronic acid or pamidronate [147]. More recent studies also showed that many of the newer agents (including bortezomib, thalidomide, and arsenic trioxide) have a radiosensitizing effect, possibly through inhibitory effects on the NF-κB pathway that usually upregulates the anti-apoptotic signaling following exposure to ionizing radiation [222, 225, 226].

Very interesting results were obtained by a phase I dose-escalation study assessing the safety, tolerability, and efficacy of ^{153}Sm-lexidronam combined with bortezomib (as radiosensitizing agent) for patients with relapsed/refractory MM: the maximum tolerated was not reached and no dose-limiting toxicities were observed. Responses occurred in five (21%) patients, including three (12.5%) complete and two (8.3%) minimal responses. These results suggested that bortezomib combined with ^{153}Sm-lexidronam is a well-tolerated regimen and it might be effective in patients with relapsed or refractory MM [227].

Results of a phase I/II trial evaluating the side effects and best activity of samarium ^{153}Sm-lexidronam when given together with high-dose melphalan in patients with MM undergoing stem cell transplant are not available [147]. However, therapy with ^{186}Re-HEDP used as part of an intensified conditioning regimen before allogeneic stem cell transplantation has been reported in two patients with advanced ALL during the second partial or third complete remission [228]. After a pre-therapeutic dynamic scintigraphy with ^{99m}Tc-Mag3 showing normal renal function, a dynamic bone scintigraphy with ^{99m}Tc-MDP was used to calculate the expected bone marrow and kidney doses, with effective doses equal to 2.1 Gy and 1.6 Gy, respectively. No unexpected complications occurred after completing conditioning and allogeneic stem cell transplantation, and no deterioration of renal function was noticed. The authors therefore concluded that ^{186}Re-HEDP is expected to increase the total additional bone marrow dose without inducing clinically significant nephrotoxicity; in these conditions, doses near 10 Gy to the bone marrow can be achieved.

References

1. Richman CM, Denardo SJ, O'Donnell RT, Yuan A, Shen S, Goldstein DS, et al. High-dose radioimmunotherapy combined with fixed, low-dose paclitaxel in metastatic prostate and breast cancer by using a MUC-1 monoclonal antibody, m170, linked to indium-111/yttrium-90 via a cathepsin cleavable linker with cyclosporine to prevent human. Clin Cancer Res. 2005;11:5920–5927.
2. Behr TM, Griesinger F, Riggert J, Gratz S, Béhé M, Kaufmann CC, et al. High-dose myeloablative radioimmunotherapy of mantle cell non-Hodgkin lymphoma with the iodine-131-labeled chimeric anti-CD20 antibody C2B8 and autologous stem cell support. Results of a pilot study. Cancer. 2002;94:1363–72.
3. Nademanee A, Forman S, Molina A, Fung H, Smith D, Dagis A, et al. A phase 1/2 trial of high-dose yttrium-90-ibritumomab tiuxetan in combination with high-dose etoposide and cyclophosphamide followed by autologous stem cell transplantation in patients with poor-risk or relapsed non-Hodgkin lymphoma. Blood. 2005;106:2896–902.
4. Hoelzer D, Bassan R, Dombret H, Fielding A, Ribera JM, Buske C. Acute lymphoblastic leukaemia in adult patients: ESMO Clinical Practice Guidelines for diagnosis, treatment and follow-up. Ann Oncol. 2016;27(suppl 5):v69–v82.
5. Advani AS, Mcdonough S, Coutre S, Wood B, Radich J, Mims M, et al. SWOG S0910: a phase 2 trial of clofarabine/cytarabine/epratuzumab for relapsed/refractory acute lymphocytic leukaemia. Br J Haematol. 2014;165:504–9.
6. Kantarjian H, Thomas D, Jorgensen J, Kebriaei P, Jabbour E, Rytting M, et al. Results of inotuzumab ozogamicin, a CD22 monoclonal antibody, in refractory and relapsed acute lymphocytic leukemia. Cancer. 2013;119:2728–36.
7. Kantarjian HM, DeAngelo DJ, Stelljes M, Martinelli G, Liedtke M, Stock W, et al. Inotuzumab ozogamicin versus standard therapy for acute lymphoblastic leukemia. N Engl J Med. 2016;375:740–53.
8. Benjamin JE, Stein AS. The role of blinatumomab in patients with relapsed/refractory acute lymphoblastic leukemia. Ther Adv Hematol. 2016;7:142–56.
9. Nishiwaki S, Miyamura K, Ohashi K, Kurokawa M, Taniguchi S, Fukuda T, et al. Impact of a donor source on adult philadelphia chromosome-negative acute lymphoblastic leukemia: a retrospective analysis from the adult acute lymphoblastic leukemia working group of the japan society for hematopoietic cell transplantation. Ann Oncol. 2013;24:1594–602.
10. Oliansky D, Camitta B, Gaynon P, Nieder M, Parson S, Pulsipher M, et al. The role of cytotoxic therapy with hematopoietic stem cell transplantation in the treatment of pediatric acute lymphoblastic leukemia: update of the 2005 evidence-based review.

ASBMT Position Statement. Biol Blood Marrow Translant. 2012;18:979–81.
11. Marks DI, Woo KA, Zhong X, Appelbaum FR, Bachanova V, Barker JN, et al. Unrelated umbilical cord blood transplant for adult acute lymphoblastic leukemia in first and second complete remission: a comparison with allografts from adult unrelated donors. Haematologica. 2014;99:322–8.
12. Atsuta Y, Suzuki R, Nagamura-Inoue T, Taniguchi S, Takahashi S, Kai S, et al. Disease-specific analyses of unrelated cord blood transplantation compared with unrelated bone marrow transplantation in adult patients with acute leukemia. Blood. 2009;113: 1631–8.
13. Goldstone A, Richards S, Lazarus H, Tallman M, Buck G, Fielding A, et al. In adults with standard-risk acute lymphoblastic leukemia, the greatest benefit is achieved from a matched sibling allogeneic transplantation in first complete remission. Blood. 2008;111:1827–33.
14. Annino L, Vegna ML, Camera A, Specchia G, Visani G, Fioritoni G, et al. Treatment of adult acute lymphoblastic leukemia (ALL): long-term follow-up of the GIMEMA ALL 0288 randomized study. Blood. 2002;99:863–71.
15. Bassan R, Hoelzer D. Modern therapy of acute lymphoblastic leukemia. J Clin Oncol. 2011;29:532–43.
16. Marks DI, Paietta EM, Moorman AV, Richards SM, Buck G, Dewald G, et al. T-cell acute lymphoblastic leukemia in adults: clinical features, immunophenotype, cytogenetics, and outcome from the large randomized prospective trial. Leukemia. 2009; 114:5136–45.
17. Hoelzer D, Walewski J, Döhner H, Viardot A, Hiddemann W, Spiekermann K, et al. Improved outcome of adult Burkitt lymphoma/leukemia with rituximab and chemotherapy: report of a large prospective multicenter trial. Blood. 2014;124:3870–9.
18. Specchia G, Pastore D, Carluccio P, Liso A, Mestice A, Rizzi R, et al. FLAG-IDA in the treatment of refractory/relapsed adult acute lymphoblastic leukemia. Ann Hematol. 2005;84:792–5.
19. Hijiya N, Thomson B, Isakoff MS, Silverman LB, Steinherz PG, Borowitz MJ, et al. Phase 2 trial of clofarabine in combination with etoposide and cyclophosphamide in pediatric patients with refractory or relapsed acute lymphoblastic leukemia. Blood. 2011;118:6043–9.
20. O'Brien S, Schiller G, Lister J, Damon L, Goldberg S, Aulitzky W, et al. High-dose vincristine sulfate liposome injection for advanced, relapsed, and refractory adult philadelphia chromosome-negative acute lymphoblastic leukemia. J Clin Oncol. 2013;31:676–83.
21. DeAngelo DJ, Yu D, Johnson JL, Coutre SE, Stone RM, Stopeck AT, et al. Nelarabine induces complete remissions in adults with relapsed or refractory T-lineage acute lymphoblastic leukemia or lymphoblastic lymphoma: Cancer and Leukemia Group B study 19801. Blood. 2007;109:5136–42.
22. Vignetti M, Fazi P, Cimino G, Martinelli G, Di Raimondo F, Ferrara F, et al. Imatinib plus steroids induces complete remissions and prolonged survival in elderly Philadelphia chromosome-positive patients with acute lymphoblastic leukemia without additional chemotherapy: results of the Gruppo Italiano Malattie Ematologiche dell'Adu. Blood. 2007;109:3676–8.
23. Foà R, Vitale A, Vignetti M, Meloni G, Guarini A, De Propris MS, et al. Dasatinib as first-line treatment for adult patients with Philadelphia chromosome-positive acute lymphoblastic leukemia. Blood. 2011;118: 6521–8.
24. Rousselot P, Coude MM, Gokbuget N, Gambacorti Passerini C, Hayette S, Cayuela J-M, et al. Dasatinib and low-intensity chemotherapy in elderly patients with Philadelphia chromosome-positive ALL. Blood. 2016;15–6.
25. Jabbour E, Kantarjian H, Ravandi F, Thomas D, Huang X, Faderl S, et al. Combination of hyper-CVAD with ponatinib as first-line therapy for patients with Philadelphia chromosome-positive acute lymphoblastic leukaemia: a single-centre, phase 2 study. Lancet Oncol. 2015;16:1547–55.
26. Chevallier P, Bodet-Milin C, Robillard N, Eugene T, Menard A, Le Houerou C, et al. BCR-ABL1 molecular remission after ^{90}Y-epratuzumab tetraxetan radioimmunotherapy in CD22+ Ph+ B-ALL: proof of principle. Eur J Haematol. 2013;91:552–6.
27. Chevallier P, Eugene T, Robillard N, Isnard F, Nicolini F, Escoffre-Barbe M, et al. ^{90}Y-labelled anti-CD22 epratuzumab tetraxetan in adults with refractory or relapsed CD22-positive B-cell acute lymphoblastic leukaemia: a phase 1 dose-escalation study. Lancet Haematol. 2015;2:e108–17.
28. Putzer D, Dobrozemsky G, Haubner R, Clausen J, Nachbaur D, Virgolini I. ^{124}I-anti-CD52 dosimetry before radioimmunotherapy as part of conditioning for stem cell transplantation in acute leukemia. Clin Nucl Med. 2012;37:390–2.
29. Eichhorst B, Robak T, Montserrat E, Ghia P, Hillmen P, Hallek M, et al. Chronic lymphocytic leukaemia: ESMO Clinical Practice Guidelines for diagnosis, treatment and follow-up. Ann Oncol. 2015;26:v78–84.
30. Hallek M, Fischer K, Fingerle-Rowson G, Fink AM, Busch R, Mayer J, et al. Addition of rituximab to fludarabine and cyclophosphamide in patients with chronic lymphocytic leukaemia: a randomised, open-label, phase 3 trial. Lancet (London, England). 2010;376:1164–74.
31. Robak T, Jamroziak K, Gora-Tybor J, Stella-Holowiecka B, Konopka L, Ceglarek B, et al. Comparison of cladribine plus cyclophosphamide with fludarabine plus cyclophosphamide as first-line therapy for chronic lymphocytic leukemia: a phase III randomized study by the Polish Adult Leukemia Group (PALG-CLL3 Study). J Clin Oncol. 2010;28:1863–9.

32. Kay NE, Geyer SM, Call TG, Shanafelt T, Zent C, Jelinek D, et al. Combination chemoimmunotherapy with pentostatin, cyclophosphamide, and rituximab shows significant clinical activity with low accompanying toxicity in previously untreated B chronic lymphocytic leukemia. Blood. 2007;109:405–411.
33. Goede V, Fischer K, Busch R, Engelke A, Eichhorst B, Wendtner CM, et al. Obinutuzumab plus chlorambucil in patients with CLL and coexisting conditions. N Engl J Med. 2014;370:1101–10.
34. Varma G, Johnson T, Advani R. Bruton's tyrosine kinase inhibitors in chronic lymphocytic leukemia and lymphoma. Clin Adv Hematol Oncol. 2016;14:543–54.
35. Keating GM. Idelalisib: a review of its use in chronic lymphocytic leukaemia and indolent non-Hodgkin's lymphoma. Target Oncol. 2015;10:141–51.
36. Dreger P, Schetelig J, Andersen N, Corradini P, van Gelder M, Gribben J, et al. Managing high-risk CLL during transition to a new treatment era: stem cell transplantation or novel agents? Blood. 2014;124:3841–9.
37. Byrd JC, Brown JR, O'Brien S, Barrientos JC, Kay NE, Reddy NM, et al. Ibrutinib versus ofatumumab in previously treated chronic lymphoid leukemia. N Engl J Med. 2014;371:213–23.
38. Furman RR, Sharman JP, Coutre SE, Cheson BD, Pagel JM, Hillmen P, et al. Idelalisib and rituximab in relapsed chronic lymphocytic leukemia. N Engl J Med. 2014;370:997–1007.
39. Brion A, Mahé B, Kolb B, Audhuy B, Colombat P, Maisonneuve H, et al. Autologous transplantation in CLL patients with B and C Binet stages: final results of the prospective randomized GOELAMS LLC 98 trial. Bone Marrow Transplant. 2012;47:542–8.
40. Seymour JF, Cusack JD, Lerner SA, Pollock RE, Keating MJ. Case/control study of the role of splenectomy in chronic lymphocytic leukemia. J Clin Oncol. 1997;15:52–60.
41. Rubin P, Bennett JM, Begg C, Bozdech MJ, Silber R. The comparison of total body irradiation vs chlorambucil and prednisone for remission induction of active chronic lymphocytic leukemia: an ECOG study. Part I: total body irradiation-response and toxicity. Int J Radiat Oncol Biol Phys. 1981;7:1623–32.
42. DeNardo GL, Lewis JP, DeNardo SJ, O'Grady LF. Effect of Lym-1 radioimmunoconjugate on refractory chronic lymphocytic leukemia. Cancer. 1994;73:1425–32.
43. Epstein AL, Marder RJ, Winter JN, Stathopoulos E, Chen FM, Parker JW, et al. Two new monoclonal antibodies, Lym-1 and Lym-2, reactive with human B-lymphocytes and derived tumors, with immunodiagnostic and immunotherapeutic potential. Cancer Res. 1987;47:830–40.
44. DeNardo GL, DeNardo SJ, O'Grady LF, Levy NB, Adams GP, Mills SL. Fractionated radioimmunotherapy of B-cell malignancies with ^{131}I-Lym-1. Cancer Res. 1990;50:1014s–6s.
45. DeNardo SJ, DeNardo GL, O'Grady LF, Hu E, Sytsma VM, Mills SL, et al. Treatment of B cell malignancies with ^{131}I Lym-1 monoclonal antibodies. Int J Cancer Suppl. 1988;3:96–101.
46. DeNardo GL, DeNardo SJ, O'Grady LF, Mills SL, Lewis JP, Macey DJ. Radiation treatment of B cell malignancies with immunoconjugate. Front Radiat Ther Oncol. 1990;24:194–201-3.
47. Hu E, Epstein AL, Naeve GS, Gill I, Martin S, Sherrod A, et al. A phase 1a clinical trial of LYM-1 monoclonal antibody serotherapy in patients with refractory B cell malignancies. Hematol Oncol. 1989;7:155–66.
48. Kaminski MS, Zelenetz AD, Press OW, Saleh M, Leonard J, Fehrenbacher L, et al. Pivotal study of iodine I 131 tositumomab for chemotherapy-refractory low-grade or transformed low-grade B-cell non-Hodgkin's lymphomas. J Clin Oncol. 2001;19:3918–28.
49. De Decker M, Bacher K, Thierens H, Slegers G, Dierckx RA, De Vos F. In vitro and in vivo evaluation of direct rhenium-188-labeled anti-CD52 monoclonal antibody alemtuzumab for radioimmunotherapy of B-cell chronic lymphocytic leukemia. Nucl Med Biol. 2008;35:599–604.
50. Lauter A, Strumpf A, Platzbecker U, Schetelig J, Wermke M, Radke J, et al. ^{188}Re anti-CD66 radioimmunotherapy combined with reduced-intensity conditioning and in-vivo T cell depletion in elderly patients undergoing allogeneic haematopoietic cell transplantation. Br J Haematol. 2010;148:910–7.
51. Repetto-Llamazares AHV, Larsen RH, Giusti AM, Riccardi E, Bruland ØS, Selbo PK, et al. ^{177}Lu-DOTA-HH1, a novel anti-CD37 radio-immunoconjugate: a study of toxicity in nude mice. PLoS One. 2014;9:e103070.
52. Shadman M, Gopal AK, Kammerer B, Becker PS, Maloney DG, Pender B, et al. Radioimmunotherapy consolidation using ^{131}I-tositumomab for patients with chronic lymphocytic leukemia or small lymphocytic lymphoma in first remission. Leuk Lymphoma. 2015;1–5.
53. Jain N, Wierda W, Ferrajoli A, Wong F, Lerner S, Keating M, et al. A phase 2 study of yttrium-90 ibritumomab tiuxetan (Zevalin) in patients with chronic lymphocytic leukemia. Cancer. 2009;115:4533–9.
54. Grever MR. How I treat hairy cell leukemia. Blood. 2010;115:21–8.
55. Cornet E, Delmer A, Feugier P, Garnache-Ottou F, Ghez D, Leblond V, et al. Recommendations of the SFH (French Society of Haematology) for the diagnosis, treatment and follow-up of hairy cell leukaemia. Ann Hematol. 2014;93:1977–83.
56. Robak T, Matutes E, Catovsky D, Zinzani PL, Buske C. Hairy cell leukaemia: ESMO Clinical Practice Guidelines for diagnosis, treatment and follow-up. Ann Oncol. 2015;26:v100–7.
57. Lauria F, Cencini E, Forconi F. Alternative methods of cladribine administration. Leuk Lymphoma. 2011;52 Suppl 2:34–7.

58. Else M, Dearden CE, Matutes E, Garcia-Talavera J, Rohatiner AZS, Johnson SAN, et al. Long-term follow-up of 233 patients with hairy cell leukaemia, treated initially with pentostatin or cladribine, at a median of 16 years from diagnosis. Br J Haematol. 2009;145:733–40.
59. Dearden CE, Else M, Catovsky D. Long-term results for pentostatin and cladribine treatment of hairy cell leukemia. Leuk Lymphoma. 2011;52 Suppl 2:21–4.
60. Flinn IW, Kopecky KJ, Foucar MK, Head D, Bennett JM, Hutchison R, et al. Long-term follow-up of remission duration, mortality, and second malignancies in hairy cell leukemia patients treated with pentostatin. Blood. 2000;96:2981–6.
61. Grever M, Kopecky K, Foucar MK, Head D, Bennett JM, Hutchison RE, et al. Randomized comparison of pentostatin versus interferon alpha-2a in previously untreated patients with hairy cell leukemia: an intergroup study. J Clin Oncol. 1995;13:974–82.
62. Habermann TM, Rai K. Historical treatments of in hairy cell leukemia, splenectomy and interferon: past and current uses. Leuk Lymphoma. 2011;52 Suppl 2:18–20.
63. Naik RR, Saven A. My treatment approach to hairy cell leukemia. Mayo Clin Proc. 2012;87:67–76.
64. Jones G, Parry-Jones N, Wilkins B, Else M, Catovsky D. Revised guidelines for the diagnosis and management of hairy cell leukaemia and hairy cell leukaemia variant*. Br J Haematol. 2012;156:186–95.
65. Zinzani PL, Pellegrini C, Stefoni V, Derenzini E, Gandolfi L, Broccoli A, et al. Hairy cell leukemia: evaluation of the long-term outcome in 121 patients. Cancer. 2010;116:4788–92.
66. Hagberg H, Lundholm L. Rituximab, a chimaeric anti-CD20 monoclonal antibody, in the treatment of hairy cell leukaemia. Br J Haematol. 2001;115: 609–11.
67. Nieva J, Bethel K, Saven A. Phase 2 study of rituximab in the treatment of cladribine-failed patients with hairy cell leukemia. Blood. 2003;102:810–3.
68. Forconi F, Toraldo F, Sozzi E, Amato T, Raspadori D, Lauria F. Complete molecular remission induced by concomitant cladribine–rituximab treatment in a case of multi-resistant hairy cell leukemia. Leuk Lymphoma. 2007;48:2441–3.
69. Ravandi F, O'Brien S, Jorgensen J, Pierce S, Faderl S, Ferrajoli A, et al. Phase 2 study of cladribine followed by rituximab in patients with hairy cell leukemia. Blood. 2011;118:3818–23.
70. Else M, Dearden CE, Matutes E, Forconi F, Lauria F, Ahmad H, et al. Rituximab with pentostatin or cladribine: an effective combination treatment for hairy cell leukemia after disease recurrence. Leuk Lymphoma. 2011;52 Suppl 2:75–8.
71. Else M, Osuji N, Forconi F, Dearden C, Del Giudice I, Matutes E, et al. The role of rituximab in combination with pentostatin or cladribine for the treatment of recurrent/refractory hairy cell leukemia. Cancer. 2007;110:2240–7.
72. Hoffman MA. Interferon-alpha is a very effective salvage therapy for patients with hairy cell leukemia relapsing after cladribine: a report of three cases. Med Oncol. 2011;28:1537–41.
73. Seymour JF, Estey EH, Keating MJ, Kurzrock R. Response to interferon-alpha in patients with hairy cell leukemia relapsing after treatment with 2-chlorodeoxyadenosine. Leukemia. 1995;9:929–32.
74. Burotto M, Stetler-Stevenson M, Arons E, Zhou H, Wilson W, Kreitman RJ. Bendamustine and rituximab in relapsed and refractory hairy cell leukemia. Clin Cancer Res. 2013;19:6313–21.
75. Kreitman RJ, Tallman MS, Robak T, Coutre S, Wilson WH, Stetler-Stevenson M, et al. Phase I trial of anti-CD22 recombinant immunotoxin moxetumomab pasudotox (CAT-8015 or HA22) in patients with hairy cell leukemia. J Clin Oncol. 2012;30:1822–8.
76. Samuel J, Macip S, Dyer MJS. Efficacy of vemurafenib in hairy-cell leukemia. N Engl J Med. 2014;370:286–8.
77. Dietrich S, Pircher A, Endris V, Peyrade F, Wendtner C-M, Follows GA, et al. BRAF inhibition in hairy cell leukemia with low dose vemurafenib. Blood. 2016; 127:2847–55.
78. Sivina M, Kreitman RJ, Arons E, Ravandi F, Burger JA. The bruton tyrosine kinase inhibitor ibrutinib (PCI-32765) blocks hairy cell leukaemia survival, proliferation and B cell receptor signalling: a new therapeutic approach. Br J Haematol. 2014;166:177–88.
79. Jansen J, Hermans J. Splenectomy in hairy cell leukemia: a retrospective multicenter analysis. Cancer. 1981;47:2066–76.
80. Kiyasu J, Shiratsuchi M, Ohtsuka R, Sada E, Idutsu K, Nagasawa E, et al. Achievement of complete remission of refractory hairy cell leukemia by rituximab progressing after allogeneic hematopoietic stem cell transplantation. Int J Hematol. 2009;89: 403–5.
81. Zinzani PL, Bonifazi F, Pellegrini C, Casadei B, Argnani L, Motta MR, et al. Hairy cell leukemia: allogeneic transplantation could be an optimal option in selected patients. Clin Lymphoma Myeloma Leuk. 2012;12:287–9.
82. Baer MR, Ozer H, Foon KA. Interferon-alpha therapy during pregnancy in chronic myelogenous leukaemia and hairy cell leukaemia. Br J Haematol. 1992;81: 167–9.
83. Stiles GM, Stanco LM, Saven A, Hoffmann KD. Splenectomy for hairy cell leukemia in pregnancy. J Perinatol. 1998;18:200–1.
84. Adeniji BA, Fallas M, Incerpi M, Hamburg S, Katz R, Ogunyemi D. Laparoscopic splenectomy for hairy cell leukemia in pregnancy. Case Rep Med. 2010; 2010. pii: 136823. doi: 10.1155/2010/136823.
85. Daver N, Nazha A, Kantarjian HM, Haltom R, Ravandi F. Treatment of hairy cell leukemia during pregnancy: are purine analogues and rituximab viable therapeutic options. Clin Lymphoma Myeloma Leuk. 2013;13:86–9.

86. Robak T. Hairy-cell leukemia variant: recent view on diagnosis, biology and treatment. Cancer Treat Rev. 2011;37:3–10.
87. Matutes E, Wotherspoon A, Catovsky D. The variant form of hairy-cell leukaemia. Best Pract Res Clin Haematol. 2003;16:41–56.
88. Narat S, Gandla J, Dogan A, Mehta A. Successful treatment of hairy cell leukemia variant with rituximab. Leuk Lymphoma. 2005;46:1229–32.
89. Yoshida T, Mihara K, Sugihara S, Arihiro K, Mino T, Sasaki N, et al. Splenectomy followed by administration of rituximab is useful to treat a patient with hairy cell leukemia-variant. Ann Hematol. 2013;92:711–3.
90. Kreitman RJ, Wilson W, Calvo KR, Arons E, Roth L, Sapolsky J, et al. Cladribine with immediate rituximab for the treatment of patients with variant hairy cell leukemia. Clin Cancer Res. 2013;19: 6873–81.
91. Telek B, Batár P, Udvardy M. Successful alemtuzumab treatment of a patient with atypical hairy cell leukaemia variant. Orv Hetil. 2007;148: 1805–7.
92. Zinzani PL, Lauria F, Buzzi M, Raspadori D, Gugliotta L, Bocchia M, et al. Hairy cell leukemia variant: a morphologic, immunologic and clinical study of 7 cases. Haematologica. 1990;75:54–7.
93. Busemann C, Schüler F, Krüger W, Kiefer T, Wuppermann M, Androshchuk M, et al. Late extramedullary relapse after allogeneic transplantation in a case of variant hairy cell leukaemia. Bone Marrow Transplant. 2010;45:1117–8.
94. Fey MF, Buske C. Acute myeloblastic leukaemias in adult patients: ESMO Clinical Practice Guidelines for diagnosis, treatment and follow-up. Ann Oncol. 2013;24 Suppl 6:vi138–43.
95. Estey EH. Acute myeloid leukemia: 2013 update on risk-stratification and management. Am J Hematol. 2013;88:318–27.
96. Burnett AK, Goldstone A, Hills RK, Milligan D, Prentice A, Yin J, et al. Curability of patients with acute myeloid leukemia who did not undergo transplantation in first remission. J Clin Oncol. 2013;31: 1293–301.
97. Roboz GJ. Current treatment of acute myeloid leukemia. Curr Opin Oncol. 2012;24:711–9.
98. Döhner H, Estey EH, Amadori S, Appelbaum FR, Büchner T, Burnett AK, et al. Diagnosis and management of acute myeloid leukemia in adults: recommendations from an international expert panel, on behalf of the European LeukemiaNet. Blood. 2010;115: 453–74.
99. Löwenberg B, van Putten W, Theobald M, Gmür J, Verdonck L, Sonneveld P, et al. Effect of priming with granulocyte colony-stimulating factor on the outcome of chemotherapy for acute myeloid leukemia. N Engl J Med. 2003;349:743–52.
100. Pfirrmann M, Ehninger G, Thiede C, Bornhäuser M, Kramer M, Röllig C, et al. Prediction of postremission survival in acute myeloid leukaemia: a post-hoc analysis of the AML96 trial. Lancet Oncol. 2012;13:207–14.
101. Pabst T, Vellenga E, van Putten W, Schouten HC, Graux C, Vekemans M-C, et al. Favorable effect of priming with granulocyte colony-stimulating factor in remission induction of acute myeloid leukemia restricted to dose escalation of cytarabine. Blood. 2012;119:5367–73.
102. Burnett AK, Hills RK, Milligan DW, Goldstone AH, Prentice AG, McMullin M-F, et al. Attempts to optimize induction and consolidation treatment in acute myeloid leukemia: results of the MRC AML12 trial. J Clin Oncol. 2010;28:586–95.
103. Koreth J, Schlenk R, Kopecky KJ, Honda S, Sierra J, Djulbegovic BJ, et al. Allogeneic stem cell transplantation for acute myeloid leukemia in first complete remission: systematic review and meta-analysis of prospective clinical trials. JAMA. 2009;301:2349–61.
104. Stone RM. Acute myeloid leukemia in first remission: to choose transplantation or not? J Clin Oncol. 2013;31: 1262–6.
105. Cornelissen JJ, van Putten WLJ, Verdonck LF, Theobald M, Jacky E, Daenen SMG, et al. Results of a HOVON/SAKK donor versus no-donor analysis of myeloablative HLA-identical sibling stem cell transplantation in first remission acute myeloid leukemia in young and middle-aged adults: benefits for whom? Blood. 2007;109:3658–66.
106. Burnett AK, Goldstone AH, Stevens RM, Hann IM, Rees JK, Gray RG, et al. Randomised comparison of addition of autologous bone-marrow transplantation to intensive chemotherapy for acute myeloid leukaemia in first remission: results of MRC AML 10 trial. UK Medical Research Council Adult and Children's Leukaemia Working Parties. Lancet (London, England). 1998;351:700–8.
107. Zittoun RA, Mandelli F, Willemze R, de Witte T, Labar B, Resegotti L, et al. Autologous or allogeneic bone marrow transplantation compared with intensive chemotherapy in acute myelogenous leukemia. European Organization for Research and Treatment of Cancer (EORTC) and the Gruppo Italiano Malattie Ematologiche Maligne dell'Adulto (GIMEMA) Leukemia Cooperative Groups. N Engl J Med. 1995;332: 217–23.
108. Mayer RJ, Davis RB, Schiffer CA, Berg DT, Powell BL, Schulman P, et al. Intensive postremission chemotherapy in adults with acute myeloid leukemia. Cancer and Leukemia Group B. N Engl J Med. 1994;331:896–903.
109. Basara N, Schulze A, Wedding U, Mohren M, Gerhardt A, Junghanss C, et al. Early related or unrelated haematopoietic cell transplantation results in higher overall survival and leukaemia-free survival compared with conventional chemotherapy in high-risk acute myeloid leukaemia patients in first complete remission. Leukemia. 2009;23:635–40.
110. Bradstock KF, Matthews JP, Lowenthal RM, Baxter H, Catalano J, Brighton T, et al. A randomized

trial of high-versus conventional-dose cytarabine in consolidation chemotherapy for adult de novo acute myeloid leukemia in first remission after induction therapy containing high-dose cytarabine. Blood. 2005;105:481–8.
111. Breems DA, Löwenberg B. Acute myeloid leukemia and the position of autologous stem cell transplantation. Semin Hematol. 2007;44:259–66.
112. Thomas X, Suciu S, Rio B, Leone G, Broccia G, Fillet G, et al. Autologous stem cell transplantation after complete remission and first consolidation in acute myeloid leukemia patients aged 61–70 years: results of the prospective EORTC-GIMEMA AML-13 study. Haematologica. 2007;92:389–96.
113. Tombak A, Ucar MA, Akdeniz A, Tiftik EN, Sahin DG, Akay OM, et al. The role of azacitidine in the treatment of elderly patients with AML-results of a retrospective multicenter study. Turkish J Hematol. 2016;1–2.
114. Ganetsky A. The role of decitabine for the treatment of acute myeloid leukemia. Ann Pharmacother. 2012;46:1511–7.
115. Sanz MA, Grimwade D, Tallman MS, Lowenberg B, Fenaux P, Estey EH, et al. Management of acute promyelocytic leukemia: recommendations from an expert panel on behalf of the European LeukemiaNet. Blood. 2009;113:1875–91.
116. Fenaux P, Chastang C, Chevret S, Sanz M, Dombret H, Archimbaud E, et al. A randomized comparison of all transretinoic acid (ATRA) followed by chemotherapy and ATRA plus chemotherapy and the role of maintenance therapy in newly diagnosed acute promyelocytic leukemia. The European APL Group. Blood. 1999;94:1192–200.
117. Sanz MA, Lo-Coco F. Modern approaches to treating acute promyelocytic leukemia. J Clin Oncol. 2011;29:495–503.
118. de Botton S, Fawaz A, Chevret S, Dombret H, Thomas X, Sanz M, et al. Autologous and allogeneic stem-cell transplantation as salvage treatment of acute promyelocytic leukemia initially treated with all-trans-retinoic acid: a retrospective analysis of the European acute promyelocytic leukemia group. J Clin Oncol. 2005;23:120–6.
119. Platzbecker U, Avvisati G, Cicconi L, Thiede C, Paoloni F, Vignetti M, et al. Improved outcomes with retinoic acid and arsenic trioxide compared with retinoic acid and chemotherapy in non-high-risk acute promyelocytic leukemia: final results of the randomized Italian-German APL0406 trial. J Clin Oncol. 2016;15–6.
120. Lo-Coco F, Avvisati G, Vignetti M, Thiede C, Orlando SM, Iacobelli S, et al. Retinoic acid and arsenic trioxide for acute promyelocytic leukemia. N Engl J Med. 2013;369:111–21.
121. Buchmann I, Meyer RG, Mier W, Haberkorn U. Myeloablative radioimmunotherapy in conditioning prior to haematological stem cell transplantation: closing the gap between benefit and toxicity? Eur J Nucl Med Mol Imaging. 2009;36:484–98.
122. Haro KJ, Scott AC, Scheinberg DA. Mechanisms of resistance to high and low linear energy transfer radiation in myeloid leukemia cells. Blood. 2012;120:2087–97.
123. Scheinberg DA, McDevitt MR. Actinium-225 in targeted alpha-particle therapeutic applications. Curr Radiopharm. 2011;4:306–20.
124. Ferdinand R, Mitchell SA, Batson S, Tumur I. Treatments for chronic myeloid leukemia: a qualitative systematic review. J Blood Med. 2012;3:51–76.
125. Kalmanti L, Saussele S, Lauseker M, Müller MC, Dietz CT, Heinrich L, et al. Safety and efficacy of imatinib in CML over a period of 10 years: data from the randomized CML-study IV. Leukemia. 2015;29:1123–32.
126. Muller Lutz P, Carsten MT. Indikationen zur allogenen Stammzelltransplantation bei myeloischen Neoplasien. Dtsch Arztebl Int. 2015;112:262–70.
127. Hehlmann R, Berger U, Pfirrmann M, Heimpel H, Hochhaus A, Hasford J, et al. Drug treatment is superior to allografting as first-line therapy in chronic myeloid leukemia. Blood. 2007;109:4686–92.
128. Schwartz MA, Lovett DR, Redner A, Finn RD, Graham MC, Divgi CR, et al. Dose-escalation trial of M195 labeled with iodine 131 for cytoreduction and marrow ablation in relapsed or refractory myeloid leukemias. J Clin Oncol. 1993;11:294–303.
129. Caron PC, Jurcic JG, Scott AM, Finn RD, Divgi CR, Graham MC, et al. A phase 1B trial of humanized monoclonal antibody M195 (anti-CD33) in myeloid leukemia: specific targeting without immunogenicity. Blood. 1994;83:1760–8.
130. Appelbaum FR. Immunobiologic therapies for myelodysplastic syndrome. Best Pract Res Clin Haematol. 2004;17:653–61.
131. Matthews DC. Immunotherapy in acute myelogenous leukemia and myelodysplastic syndrome. Leukemia. 1998;12 Suppl 1:S33–6.
132. Burke JM, Caron PC, Papadopoulos EB, Divgi CR, Sgouros G, Panageas KS, et al. Cytoreduction with iodine-131-anti-CD33 antibodies before bone marrow transplantation for advanced myeloid leukemias. Bone Marrow Transplant. 2003;32:549–56.
133. Sgouros G, Jureidini IM, Scott AM, Graham MC, Larson SM, Scheinberg DA. Bone marrow dosimetry: regional variability of marrow-localizing antibody. J Nucl Med. 1996;37:695–8.
134. Sgouros G, Graham MC, Divgi CR, Larson SM, Scheinberg DA. Modeling and dosimetry of monoclonal antibody M195 (anti-CD33) in acute myelogenous leukemia. J Nucl Med. 1993;34:422–30.
135. Jurcic JG, Caron PC, Nikula TK, Papadopoulos EB, Finn RD, Gansow OA, et al. Radiolabeled anti-CD33 monoclonal antibody M195 for myeloid leukemias. Cancer Res. 1995;55:5908s–10s.
136. Jurcic J, Divgi C, McDevitt M, Ma D, Sgouros G, Finn R, et al. Potential for myeloablation with yttrium-90-HuM195 (anti-CD33) in myeloid leukemia [abstract]. J Clin Oncol. 2000;19:8a.

137. Jurcic JG, Larson SM, Sgouros G, McDevitt MR, Finn RD, Divgi CR, et al. Targeted alpha particle immunotherapy for myeloid leukemia. Blood. 2002;100:1233–9.
138. Rosenblat TL, McDevitt MR, Mulford DA, Pandit-Taskar N, Divgi CR, Panageas KS, et al. Sequential cytarabine and alpha-particle immunotherapy with bismuth-213-lintuzumab (HuM195) for acute myeloid leukemia. Clin Cancer Res. 2010;16:5303–11.
139. Sgouros G, Ballangrud AM, Jurcic JG, McDevitt MR, Humm JL, Erdi YE, et al. Pharmacokinetics and dosimetry of an alpha-particle emitter labeled antibody: ^{213}Bi-HuM195 (anti-CD33) in patients with leukemia. J Nucl Med. 1999;40:1935–46.
140. Kolbert KS, Hamacher KA, Jurcic JG, Scheinberg DA, Larson SM, Sgouros G. Parametric images of antibody pharmacokinetics in Bi213-HuM195 therapy of leukemia. J Nucl Med. 2001;42:27–32.
141. Miederer M, McDevitt MR, Sgouros G, Kramer K, Cheung N-K V, Scheinberg DA. Pharmacokinetics, dosimetry, and toxicity of the targetable atomic generator, ^{225}Ac-HuM195, in nonhuman primates. J Nucl Med. 2004;45:129–37.
142. Maguire WF, McDevitt MR, Smith-Jones PM, Scheinberg DA. Efficient 1-step radiolabeling of monoclonal antibodies to high specific activity with ^{225}Ac for α-particle radioimmunotherapy of cancer. J Nucl Med. 2014;55:1492–8.
143. Kersemans V, Cornelissen B, Minden MD, Brandwein J, Reilly RM. Drug-resistant AML cells and primary AML specimens are killed by ^{111}In-anti-CD33 monoclonal antibodies modified with nuclear localizing peptide sequences. J Nucl Med. 2008;49:1546–54.
144. Chen P, Wang J, Hope K, Jin L, Dick J, Cameron R, et al. Nuclear localizing sequences promote nuclear translocation and enhance the radiotoxicity of the anti-CD33 monoclonal antibody HuM195 labeled with ^{111}In in human myeloid leukemia cells. J Nucl Med. 2006;47:827–36.
145. Petrich T, Korkmaz Z, Krull D, Frömke C, Meyer GJ, Knapp WH. In vitro experimental ^{211}At-anti-CD33 antibody therapy of leukaemia cells overcomes cellular resistance seen in vivo against gemtuzumab ozogamicin. Eur J Nucl Med Mol Imaging. 2010;37:851–61.
146. Baidoo KE, Yong K, Brechbiel MW. Molecular pathways: targeted α-particle radiation therapy. Clin Cancer Res. 2013;19:530–7.
147. Home – ClinicalTrials.gov..https://clinicaltrials.gov/
148. Friesen C, Roscher M, Hormann I, Leib O, Marx S, Moreno J, et al. Anti-CD33-antibodies labelled with the alpha-emitter Bismuth-213 kill CD33-positive acute myeloid leukaemia cells specifically by activation of caspases and break radio- and chemoresistance by inhibition of the anti-apoptotic proteins X-linked inhibitor of apoptosis protein and B-cell lymphoma-extra large. Eur J Cancer. 2013;49:2542–54.
149. Matthews DC, Appelbaum FR, Eary JF, Fisher DR, Durack LD, Bush SA, et al. Development of a marrow transplant regimen for acute leukemia using targeted hematopoietic irradiation delivered by ^{131}I-labeled anti-CD45 antibody, combined with cyclophosphamide and total body irradiation. Blood. 1995;85:1122–31.
150. Buchmann I, Kull T, Glatting G, Bunjes D, Hale G, Kotzerke J, et al. A comparison of the biodistribution and biokinetics of ^{99m}Tc-anti-CD66 mAb BW 250/183 and ^{99m}Tc-anti-CD45 mAb YTH 24.5 with regard to suitability for myeloablative radioimmunotherapy. Eur J Nucl Med Mol Imaging. 2003;30:667–73.
151. Kletting P, Bunjes D, Reske S, Glatting G. Improving anti-CD45 antibody radioimmunotherapy using a physiologically based pharmacokinetic model. J Nucl Med. 2009;50:296–302.
152. Kletting P, Kull T, Bunjes D, Luster M, Reske SN, Glatting G. Optimal preloading in radioimmunotherapy with anti-cD45 antibody. Med Phys. 2011;38:2572–8.
153. Pagel JM, Kenoyer AL, Bäck T, Hamlin DK, Wilbur DS, Fisher DR, et al. Anti-CD45 pretargeted radioimmunotherapy using bismuth-213: high rates of complete remission and long-term survival in a mouse myeloid leukemia xenograft model. Blood. 2011;118:703–11.
154. Orozco JJ, Zeller J, Pagel JM. Radiolabeled antibodies directed at CD45 for conditioning prior to allogeneic transplantation in acute myeloid leukemia and myelodysplastic syndrome. Ther Adv Hematol. 2012;3:5–16.
155. Mawad R, Gooley TA, Rajendran JG, Fisher DR, Gopal AK, Shields AT, et al. Radiolabeled anti-CD45 antibody with reduced-intensity conditioning and allogeneic transplantation for younger patients with advanced acute myeloid leukemia or myelodysplastic syndrome. Biol Blood Marrow Transplant. 2014;20:1363–8.
156. Orozco JJ, Balkin ER, Gooley TA, Kenoyer A, Hamlin DK, Wilbur DS, et al. Anti-CD45 radioimmunotherapy with ^{90}Y but not ^{177}Lu is effective treatment in a syngeneic murine leukemia model. PLoS One. 2014;9:e113601.
157. Orozco JJ, Bäck T, Kenoyer A, Balkin ER, Hamlin DK, Wilbur DS, et al. Anti-CD45 radioimmunotherapy using ^{211}At with bone marrow transplantation prolongs survival in a disseminated murine leukemia model. Blood. 2013;121:3759–67.
158. Orozco JJ, Kenoyer A, Balkin ER, Gooley TA, Hamlin DK, Wilbur DS, et al. Anti-CD45 radioimmunotherapy without TBI before BMT facilitates persistent haploidentical donor engraftment in a murine model. Blood. 2015;127:352–9.
159. Buchmann I, Schulze A, Sparber M, et al. Myeloablative radioimmunotherapy with Re-188-anti-CD66-mAb in paediatric leukaemia patients: a phase I-trial. J Nucl Med. 2002;43:37P.

160. Buchmann I, Bunjes D, Kotzerke J, Martin H, Glatting G, Seitz U, et al. Myeloablative radioimmunotherapy with Re-188-anti-CD66-antibody for conditioning of high-risk leukemia patients prior to stem cell transplantation: biodistribution, biokinetics and immediate toxicities. Cancer Biother. Radiopharm. 2002;17:151–63.
161. Bunjes D, Buchmann I, Duncker C, Seitz U, Kotzerke J, Wiesneth M, et al. Rhenium 188-labeled anti-CD66 (a, b, c, e) monoclonal antibody to intensify the conditioning regimen prior to stem cell transplantation for patients with high-risk acute myeloid leukemia or myelodysplastic syndrome: results of a phase I-II study. Blood. 2001;98:565–72.
162. Buchmann I, Bunjes D, Kotzerke J, Martin H, Glatting, Seitz U, et al. Myeloablative radioimmunotherapy with Re-188-anti-CD66-mAb before stem cell transplantation does not increase cytokine levels (abstract). J Nucl Med. 2002;43:314P.
163. Orchard K, Cooper M, Lewington V, Tristan M, Zivanovic M, Thom J, et al. Targeted radiotherapy in haematopoietic stem cell transplantation: results of a phase I trial using an yttrium-90-labelled anti-CD66 murine monoclonal antibody demonstrating consistent BM targeting. Bone Marrow Transpl. 2006;37: S45.
164. Camera L, Kinuya S, Garmestani K, Wu C, Brechbiel MW, Pai LH, et al. Evaluation of the serum stability and in vivo biodistribution of CHX-DTPA and other ligands for yttrium labeling of monoclonal antibodies. J Nucl Med. 1994;35:882–9.
165. Neumaier B, Mottaghy FM, Buck AK, Glatting G, Blumstein NM, Mahren B, et al. Short communication: ^{18}F-immuno-PET: determination of anti-CD66 biodistribution in a patient with high-risk leukemia. Cancer Biother Radiopharm. 2008;23:819–24.
166. Schneider S, Strumpf A, Schetelig J, Wunderlich G, Ehninger G, Kotzerke J, et al. Reduced-intensity conditioning combined with ^{188}Rhenium radioimmunotherapy before allogeneic hematopoietic stem cell transplantation in elderly patients with acute myeloid leukemia: the role of in vivo T cell depletion. Biol Blood Marrow Transplant. 2015;21:1754–60.
167. Zereshkian A, Leyton J V, Cai Z, Bergstrom D, Weinfeld M, Reilly RM. The human polynucleotide kinase/phosphatase (hPNKP) inhibitor A12B4C3 radiosensitizes human myeloid leukemia cells to Auger electron-emitting anti-CD123 ^{111}In-NLS-7G3 radioimmunoconjugates. Nucl Med Biol. 2014;41:377–83.
168. Leyton J V, Williams B, Gao C, Keating A, Minden M, Reilly RM. MicroSPECT/CT imaging of primary human AML engrafted into the bone marrow and spleen of NOD/SCID mice using 111In-DTPA-NLS-CSL360 radioimmunoconjugates recognizing the CD123+ / CD131- epitope expressed by leukemia stem cells. Leuk Res. 2014;38:1367–73.
169. Leyton JV, Hu M, Gao C, Turner PV, Dick JE, Minden M, et al. Auger electron radioimmunotherapeutic agent specific for the CD123+/CD131- phenotype of the leukemia stem cell population. J Nucl Med. 2011;52:1465–73.
170. Rajkumar SV, Dimopoulos MA, Palumbo A, Blade J, Merlini G, Mateos MV, et al. International Myeloma Working Group updated criteria for the diagnosis of multiple myeloma. Lancet Oncol. Elsevier Ltd. 2014;15:e538–48.
171. Moreau P, San Miguel J, Ludwig H, Schouten H, Mohty M, Dimopoulos M, et al. Multiple myeloma: ESMO clinical practice guidelines for diagnosis, treatment and follow-up. Ann Oncol. 2013;24 Suppl 6: vi133–7.
172. Terpos E, Kleber M, Engelhardt M, Zweegman S, Gay F, Kastritis E, et al. European myeloma network guidelines for the management of multiple myeloma-related complications. Haematologica. 2015;100: 1254–66.
173. Fayers PM, Palumbo A, Hulin C, Waage A, Wijermans P, Beksaç M, et al. Thalidomide for previously untreated elderly patients with multiple myeloma : meta-analysis of 1685 individual patient data from six randomized clinical trials myeloma : meta-analysis of 1685 individual-patient data from six randomized. Blood. 2011;118:1239–48.
174. San Miguel JF, Schlag R, Khuageva NK, Dimopoulos MA, Shpilberg O, Kropff M, et al. Bortezomib plus melphalan and prednisone for initial treatment of multiple myeloma. N Engl J Med. 2008;359:906–17.
175. Pönisch W, Mitrou PS, Merkle K, Herold M, Assmann M, Wilhelm G, et al. Treatment of Bendamustine and Prednisone in patients with newly diagnosed multiple myeloma results in superior complete response rate, prolonged time to treatment failure and improved quality of life compared to treatment with Melphalan and Prednisone—a randomized phase III study of the East German Study Group of Hematology and Oncology (OSHO). J Cancer Res Clin Oncol. 2006;132:205–12.
176. Palumbo A, Falco P, Corradini P, Falcone A, Di Raimondo F, Giuliani N, et al. Melphalan, prednisone, and lenalidomide treatment for newly diagnosed myeloma: a report from the GIMEMA – Italian Multiple Myeloma Network. J Clin Oncol. 2007;25:4459–65.
177. Palumbo A, Hajek R, Delforge M. Continuous lenalidomide treatment for newly diagnosed multiple myeloma. N Engl J Med. 2012;366:1759–69.
178. Morgan GJ, Davies FE, Gregory WM, Russell NH, Bell SE, Szubert AJ, et al. Cyclophosphamide, thalidomide, and dexamethasone (CTD) as initial therapy for patients with multiple myeloma unsuitable for autologous transplantation. Blood. 2011;118:1231–8.
179. Harousseau JL, Attal M, Avet-Loiseau H, Marit G, Caillot D, Mohty M, et al. Bortezomib plus

dexamethasone is superior to vincristine plus doxorubicin plus dexamethasone as induction treatment prior to autologous stem-cell transplantation in newly diagnosed multiple myeloma: results of the IFM 2005-01 phase III trial. J Clin Oncol. 2010;28:4621–9.
180. Moreau P, Avet-Loiseau H, Harousseau JL, Attal M. Current trends in autologous stem-cell transplantation for myeloma in the era of novel therapies. J Clin Oncol. 2011;29:1898–906.
181. Cavo M, Tacchetti P, Patriarca F, Petrucci MT, Pantani L, Galli M, et al. Bortezomib with thalidomide plus dexamethasone compared with thalidomide plus dexamethasone as induction therapy before, and consolidation therapy after, double autologous stem-cell transplantation in newly diagnosed multiple myeloma: a randomised phase 3. Lancet. 2010;376:2075–85.
182. Rosinol L, Oriol A, Teruel AI, Hernandez D, Lopez-Jiménez J, De La Rubia J, et al. Superiority of bortezomib, thalidomide, and dexamethasone (VTD) as induction pretransplantation therapy in multiple myeloma: a randomized phase 3 PETHEMA/GEM study. Blood. 2012;120:1589–96.
183. Moreau P, Avet-loiseau H, Facon T, Attal M, Tiab M, Hulin C, et al. Bortezomib plus dexamethasone versus reduced-dose bortezomib, thalidomide plus dexamethasone as induction trthalidomide plus dexamethasone as induction treatment before autologous stem cell transplantation in newly diagnosed multiple myeloma. Blood. 2012;118:5752–8.
184. Moreau P, Facon T, Attal M, Hulin C, Michallet M, Maloisel F, et al. Comparison of 200 mg/m^2 melphalan and 8 Gy total body irradiation plus 140 mg/m^2 melphalan as conditioning regimens for peripheral blood stem cell transplantation in patients with newly diagnosed multiple myeloma: final analysis of the Intergroupe Francop. Blood. 2002;99:731–5.
185. Attal M, Harousseau J-L, Facon T, Guilhot F, Doyen C, Fuzibet J-G, et al. Single versus double autologous stem-cell transplantation for multiple myeloma. N Engl J Med. 2003;349:2495–502.
186. Sonneveld P, Schmidt-Wolf IGH, Van Der Holt B, El Jarari L, Bertsch U, Salwender H, et al. Bortezomib induction and maintenance treatment in patients with newly diagnosed multiple myeloma: results of the randomized phase III HOVON-65/ GMMG-HD4 trial. J Clin Oncol. 2012;30:2946–55.
187. Stewart AK. Reduced-intensity allogeneic transplantation for myeloma: reality bites. Blood. 2009;113:3135–6.
188. Krishnan A, Vij R, Keller J, Dhakal B, Hari P. Moving beyond autologous transplantation in multiple myeloma: consolidation, maintenance, allogeneic transplant, and immune therapy. Am Soc Clin Oncol Educ B. 2016;36:210–21.
189. Palumbo A, Bringhen S, Rossi D, Cavalli M, Ria R, Gentilini S, et al. Overall survival benefit for bortezomib-melphalan-prednisone-thalidomide followed by maintenance with bortezomib-thalidomide (VMPT-VT) versus bortezomib-melphalan-prednisone (VMP) in newly diagnosed multiple myeloma patients. Blood. 2012;120 (Suppl):200.
190. Mateos M, Oriol A, Martínez-lópez J, Gutiérrez N, Teruel A, López A, et al. Maintenance therapy with bortezomib plus thalidomide or bortezomib plus prednisone in elderly multiple myeloma patients included in the GEM2005MAS65 trial. Blood. 2012;120: 2581–8.
191. Attal V, Marit G, Caillot D, Moreau P, Facon T, Stoppa AM, et al. Lenalidomide maintenance after stem-cell transplantation for multiple myeloma. N Engl J Med. 2012;366:1782–91.
192. McCarthy PL, Owzar K, Hofmeister CC, Hurd DD, Hassoun H, Richardson PG, et al. Lenalidomide after stem-cell transplantation for multiple myeloma. N Engl J Med. 2012;366:1770–81.
193. Weber DM, Chen C, Niesvizky R, Wang M, Belch A, Stadtmauer EA, et al. Lenalidomide plus dexamethasone for relapsed multiple myeloma in North America. N Engl J Med. 2007;357:2133–42.
194. Dimopoulos M, Spencer A, Attal M, Prince HM, Harousseau J-L, Dmoszynska A, et al. Lenalidomide plus dexamethasone for relapsed or refractory multiple myeloma. N Engl J Med. 2007;357:2123–32.
195. Richardson PG, Sonneveld P, Schuster MW, Irwin D, Stadtmauer EA, Facon T, et al. Bortezomib or high-dose dexamethasone for relapsed multiple myeloma. N Engl J Med. 2005;352:2487–98.
196. Orlowski RZ, Nagler A, Sonneveld P, Bladé J, Hajek R, Spencer A, et al. Randomized phase III study of pegylated liposomal doxorubicin plus bortezomib compared with bortezomib alone in relapsed or refractory multiple myeloma: combination therapy improves time to progression. J Clin Oncol. 2007;25:3892–901.
197. Moreau P. The future of therapy for relapsed/refractory multiple myeloma: emerging agents and novel treatment strategies. Semin Hematol. Elsevier Inc.; 2012;49:S33–46.
198. Garderet L, Iacobelli S, Moreau P, Dib M, Lafon I, Niederwieser D, et al. Superiority of the triple combination of bortezomib-thalidomide- dexamethasone over the dual combination of thalidomide-dexamethasone in patients with multiple myeloma progressing or relapsing after autologous transplantation: The MMVAR/IFM 2005-04 random. J. Clin. Oncol. 2012;30:2475–82.
199. Lemieux E, Hulin C, Caillot D, Tardy S, Dorvaux V, Michel J, et al. Autologous stem cell transplantation: an effective salvage therapy in multiple myeloma. Biol Blood Marrow Transplant. Elsevier Inc. 2013; 19:445–9.
200. Lonial S, Weiss BM, Usmani SZ, Singhal S, Chari A, Bahlis NJ, et al. Daratumumab monotherapy in

patients with treatment-refractory multiple myeloma (SIRIUS): an open-label, randomised, phase 2 trial. Lancet. 2016;387:1551–60.
201. Richardson PG, Jagannath S, Moreau P, Jakubowiak AJ, Raab MS, Facon T, et al. Elotuzumab in combination with lenalidomide and dexamethasone in patients with relapsed multiple myeloma: final phase 2 results from the randomised, open-label, phase 1b–2 dose-escalation study. Lancet Haematol. 2015;2:e516–27.
202. Moreau P, Masszi T, Grzasko N, Bahlis NJ, Hansson M, Pour L, et al. Oral ixazomib, lenalidomide, and dexamethasone for multiple myeloma. N Engl J Med. 2016;374:1621–34.
203. Richardson PG, Schlossman RL, Alsina M, Weber DM, Coutre SE, Gasparetto C, et al. PANORAMA 2: panobinostat in combination with bortezomib and dexamethasone in patients with relapsed and bortezomib-refractory myeloma. Blood. 2013;122:2331–7.
204. Berenson JR, Hillner BE, Kyle RA, Anderson K, Lipton A, Yee GC, et al. American Society of Clinical Oncology clinical practice guidelines: the role of bisphosphonates in multiple myeloma. J Clin Oncol. 2002;20:3719–36.
205. Roodman GD. Skeletal imaging and management of bone disease. Hematology Am Soc Hematol Educ Program. 2008;313–9.
206. Kapadia SB. Multiple myeloma: a clinicopathologic study of 62 consecutively autopsied cases. Medicine (Baltimore). 1980;59:380–92.
207. Herrmann K, Schottelius M, Lapa C, Osl T, Poschenrieder A, Hänscheid H, et al. First-in-human experience of CXCR4-directed endoradiotherapy with ^{177}Lu- and ^{90}Y-labeled pentixather in advanced-stage multiple myeloma with extensive intra- and extramedullary disease. J Nucl Med. 2016;57:248–51.
208. Couturier O, Faivre-Chauvet A, Filippovich I V, Thédrez P, Saï-Maurel C, Bardiès M, et al. Validation of ^{213}Bi-alpha radioimmunotherapy for multiple myeloma. Clin Cancer Res. 1999;5:3165 s–70 s.
209. Burton J, Mishina D, Cardillo T, Lew K, Rubin A, Goldenberg DM, et al. Epithelial mucin-1 (MUC1) expression and MA5 anti-MUC1 monoclonal antibody targeting in multiple myeloma. Clin Cancer Res. 1999;5:3065 s–72 s.
210. Supiot S, Faivre-Chauvet A, Couturier O, Heymann MF, Robillard N, Kraeber-Bodéré F, et al. Comparison of the biologic effects of MA5 and B-B4 monoclonal antibody labeled with iodine-131 and bismuth-213 on multiple myeloma. Cancer. 2002;94:1202–9.
211. Supiot S, Gouard S, Charrier J, Apostolidis C, Chatal J-F, Barbet J, et al. Mechanisms of cell sensitization to alpha radioimmunotherapy by doxorubicin or paclitaxel in multiple myeloma cell lines. Clin Cancer Res. 2005;11:7047 s–52 s.
212. Teiluf K, Seidl C, Blechert B, Gaertner FC, Gilbertz K-P, Fernandez V, et al. α-Radioimmunotherapy with ^{213}Bi-anti-CD38 immunoconjugates is effective in a mouse model of human multiple myeloma. Oncotarget. 2015;6:4692–703.
213. Chérel M, Gouard S, Gaschet J, Saï-Maurel C, Bruchertseifer F, Morgenstern A, et al. ^{213}Bi radioimmunotherapy with an anti-mCD138 monoclonal antibody in a murine model of multiple myeloma. J Nucl Med. 2013;54:1597–604.
214. Gouard S, Pallardy A, Gaschet J, Faivre-Chauvet A, Bruchertseifer F, Morgenstern A, et al. Comparative analysis of multiple myeloma treatment by CD138 antigen targeting with bismuth-213 and Melphalan chemotherapy. Nucl Med Biol. 2014;41 Suppl:e30–5.
215. Ménager J, Gorin J-B, Maurel C, Drujont L, Gouard S, Louvet C, et al. Combining α-radioimmunotherapy and adoptive T cell therapy to potentiate tumor destruction. PLoS One. 2015;10:e0130249.
216. Green DJ, Orgun NN, Jones JC, Hylarides MD, Pagel JM, Hamlin DK, et al. A preclinical model of CD38-pretargeted radioimmunotherapy for plasma cell malignancies. Cancer Res. 2014;74:1179–89.
217. Rousseau C, Ferrer L, Supiot S, Bardiès M, Davodeau F, Faivre-Chauvet A, et al. Dosimetry results suggest feasibility of radioimmunotherapy using anti-CD138 (B-B4) antibody in multiple myeloma patients. Tumour Biol. 2012;33:679–88.
218. Sauer S, Erba PA, Petrini M, Menrad A, Giovannoni L, Grana C, et al. Expression of the oncofetal ED-B-containing fibronectin isoform in hematologic tumors enables ED-B-targeted ^{131}I-L19SIP radioimmunotherapy in Hodgkin lymphoma patients. Blood. 2009;113:2265–74.
219. Erba PA, Sollini M, Orciuolo E, Traino C, Petrini M, Paganelli G, et al. Radioimmunotherapy with radretumab in patients with relapsed hematologic malignancies. J Nucl Med. 2012;53:922–7.
220. Halime Z, Frindel M, Camus N, Orain P-Y, Lacombe M, Chérel M, et al. New synthesis of phenyl-isothiocyanate C-functionalised cyclams. Bioconjugation and ^{64}Cu phenotypic PET imaging studies of multiple myeloma with the te2a derivative. Org Biomol Chem. 2015;13:11302–14.
221. Fichou N, Gouard S, Maurel C, Barbet J, Ferrer L, Morgenstern A, et al. Single-dose anti-CD138 radioimmunotherapy: bismuth-213 is more efficient than lutetium-177 for treatment of multiple myeloma in a preclinical model. Front Med. 2015;2:76.
222. Goel A, Dispenzieri A, Greipp PR, Witzig TE, Mesa RA, Russell SJ. PS-341-mediated selective targeting of multiple myeloma cells by synergistic increase in ionizing radiation-induced apoptosis. Exp Hematol. 2005;33:784–95.
223. Dispenzieri A, Wiseman GA, Lacy MQ, Hayman SR, Kumar SK, Buadi F, et al. A Phase II study of ^{153}Sm-EDTMP and high-dose melphalan as a peripheral

blood stem cell conditioning regimen in patients with multiple myeloma. Am J Hematol. 2010;85:409–13.
224. Abruzzese E, Iuliano F, Trawinska MM, Di Maio M. ^{153}Sm: its use in multiple myeloma and report of a clinical experience. Expert Opin Investig Drugs. 2008;17:1379–87.
225. Ansiaux R, Baudelet C, Jordan BF, Beghein N, Sonveaux P, De Wever J, et al. Thalidomide radiosensitizes tumors through early changes in the tumor microenvironment. Clin Cancer Res. 2005;11:743–50.
226. Monzen H, Griffin RJ, Williams BW, Amano M, Ando S, Hasegawa T. Study of arsenic trioxide-induced vascular shutdown and enhancement with radiation in solid tumor. Radiat Med. 2004;22:205–11.
227. Berenson JR, Yellin O, Patel R, Duvivier H, Nassir Y, Mapes R, et al. A phase I study of samarium lexidronam/bortezomib combination therapy for the treatment of relapsed or refractory multiple myeloma. Clin Cancer Res. 2009;15:1069–75.
228. Döbert N, Martin H, Kranert WT, Menzel C, Klein SA, Mose S, et al. Re-186 HEDP conditioning therapy in patients with advanced acute lymphoblastic leukemia before allogeneic bone marrow transplantation. Clin Nucl Med. 2003;28:738–42.

Radionuclide Therapy of Thyroid Tumors

42

Rossella Elisei, Laura Agate, Sara Mazzarri, Valeria Bottici, Federica Guidoccio, Eleonora Molinaro, Giuseppe Boni, Marco Ferdeghini, and Giuliano Mariani

Abstract

When indicated, ablation of postsurgical thyroid remnants with ^{131}I-iodide constitutes a unicum with surgery as the primary form of treatment for differentiated thyroid cancer (DTC) derived from the follicular epithelium. According to the most recent guidelines, thyroid remnant ablation is indicated in DTC patients with a moderate to high risk of recurrence. Patients are prepared with low-iodine diet and with either withdrawal of replacement therapy with L-thyroxine (l-T4) for a period sufficient to achieve serum TSH levels >30 μIU/mL (usually within 4–6 weeks) or administration of exogenous human recombinant (rhTSH). Administered activities of ^{131}I-iodide vary considerably between 1.11 and 3.7 GBq (30–100 mCi), according to the estimated risk of recurrence. A whole-body scan (^{131}I-WBS, preferably completed with SPECT/CT acquisitions at selected sites) is performed 4–7 days after ^{131}I-iodide administration, as it can detect lymph node involvement or unexpected metastases. Therapy with ^{131}I-iodide causes in some instances side effects that are usually mild, transient, and well manageable. More important side effects (e.g., a radiation-induced second malignancy) can be expected only after repeated administrations of radioiodide for therapy of recurrent metastatic disease and for very high cumulative doses.

The major diagnostic modalities employed to follow patients with DTC treated with remnant ablation are measurement of serum Tg, ^{131}I-WBS, and neck US. Additional diagnostic imaging (e.g., CT, MRI) is applicable in selected circumstances; in fact, although CT and MRI can in principle localize very small lesions in the neck, chest, and bones, the features of such lesions are rarely specific for recurrent/metastatic DTC.

If lymph node metastasis is suspected on the basis of imaging findings, a FNAC should be performed, also assaying Tg in the needle washing. Serum Tg levels that become detectable or show an increasing trend during follow-up indicate the need for further evaluation, possibly with additional ^{131}I-iodide therapy in case of small metastatic lesions (<1 cm in size) with a relatively high radioiodine uptake. In case of bigger lymph node metastasis, surgery is preferable – possibly followed by adjuvant radioiodine therapy. External beam radiation therapy (EBRT) has little role in treatment of recurrent/metastatic DTC, except in case of tumors

R. Elisei (✉) • L. Agate • V. Bottici • E. Molinaro
Endocrine Unit, Department of Clinical and Experimental Medicine, University of Pisa, Pisa, Italy
e-mail: rossella.elisei@med.unipi.it

S. Mazzarri • F. Guidoccio • G. Boni • G. Mariani
Regional Center of Nuclear Medicine, Department of Translational Research and Advanced Technologies in Medicine and Surgery, University of Pisa, Pisa, Italy

M. Ferdeghini
Nuclear Medicine Unit, Department of Diagnostics and Public Health, University of Verona, Verona, Italy

© Springer International Publishing Switzerland 2017
H.W. Strauss et al. (eds.), *Nuclear Oncology*,
https://doi.org/10.1007/978-3-319-26236-9_49

exhibiting a trend to dedifferentiation. Patients with recurrent DTC may develop poorly differentiated lesions that cannot concentrate radioiodide. In these patients [^{18}F]FDG PET/CT has an important prognostic role and is useful to determine the sites and extent of these metastases. When DTC becomes refractory to ^{131}I-iodide therapy, metastatic and progressive lesions can be treated with tyrosine kinase inhibitors (TKI) such as sorafenib and lenvatinib.

Radionuclide therapy has no role in the treatment of anaplastic or poorly differentiated thyroid cancers, because these tumors cannot concentrate radioiodide; in these patients therapy is based on surgery (whenever possible – also with simple debulking/palliative purposes), chemotherapy, and EBRT. Prognosis of these patients is very poor.

Surgery is the first-choice option for the treatment of patients with medullary thyroid cancer (MTC). Follow-up is based on monitoring of biochemical tumor recurrence (rising serum calcitonin and/or CEA levels) and on diagnostic imaging with radiopharmaceuticals that are commonly used for the whole spectrum of neuroendocrine tumors: ^{123}I-MIBG, radiolabeled somatostatin analogs (^{111}In-DTPA-pentetreotide, ^{68}Ga-DOTA-NOC/TATE) in addition to the overall tumor-imaging agent [^{18}F]FDG. Radionuclide therapy of recurrent/metastatic DTC can include ^{131}I-MIBG and ^{90}Y- or ^{177}Lu-DOTA-TOC/NOC/TATE. As in the case of radioiodide-refractory DTC, treatment of advanced recurrent/metastatic MTC can include novel targeted therapies such as TKIs.

Keywords

Differentiated thyroid cancer • Ablation of post-surgical remnants • Therapy with ^{131}I-iodide • Recombinant TSH • Whole-body scintigraphy • SPECT/CT • Neck ultrasound • [^{18}F]FDG PET • ^{124}I-iodide PET

Glossary

[^{18}F]FDG	2-Deoxy-2-[^{18}F]fluoro-D-glucose
^{123}I-MIBG	^{123}I-*meta*-Iodobenzylguanidine
^{131}I-MIBG	^{131}I-*meta*-Iodobenzylguanidine
^{131}I-WBS	Whole-body scintigraphy with ^{131}I-iodide
^{18}F-DOPA	2-^{18}F-Fluoro-L-3,4-dihydroxyphenylalanine
AJCC	American Joint Committee on Cancer
APUD	Amine precursor uptake and decarboxylation
ATA	American Thyroid Association
ATC	Anaplastic thyroid cancer
BRAF	Gene encoding for the B-Raf protein, a serine/threonine-protein kinase; the gene is also known as the proto-oncogene B-Raf and v-Raf murine sarcoma viral oncogene homolog B
CCK-BR	Gastrin/cholecystokinin B receptor
CEA	Carcinoembryonic antigen, a tumor-associated serum marker
CP	Chemotherapy based on carboplatinum and plaxitaxel
Ct	Calcitonin
CT	X-ray computed tomography
DMSA	Dimercaptosuccinic acid, a metal-chelating agent
DOTA-NOC	DOTA-1-Nal^3-octreotide
DOTA-TATE	DOTA-Tyr^3-octreotate
DOTA-TOC	DOTA-octreotide
DOTA	1,4,7,10-Tetra-azacyclododecane-1,4,7,10-tetraacetic acid
DTC	Well-differentiated thyroid cancer
DTPA	Diethylenetriaminepentaacetic acid, a metal-chelating agent
EBRT	External beam radiation therapy
EGF	Epidermal growth factor
EGFR	Epidermal growth factor receptor; the mutated form EGFRvIII plays a prominent role in tumorigenesis and pro-angiogenic signalling
EMA	European Medicines Agency
FDA	United States Food and Drug Administration

FNAC	Fine-needle aspiration cytology
FT3	Free circulating form of the thyroid hormone triiodothyronine
FT4	Free circulating form of the thyroid hormone tetraiodothyronine
FTC	Follicular thyroid tumor
Gy	Gray unit (ionizing radiation dose in the International System of Units, corresponding to the absorption of one joule of radiation energy per kilogram of matter)
l-T4	Levo-thyroxine (or tetraiodothyronine)
M	Metastasis status according to the AJCC/UICC TNM staging system
MEK	Mitogen-activated protein kinase
MEN	Multiple endocrine neoplasia
MIBG	*meta*-Iodobenzylguanidine
MRI	Magnetic resonance imaging
MTC	Medullary thyroid cancer
N	Lymph node status according to the AJCC/UICC TNM staging system
NIS	Na^+/I^- symporter
ORR	Overall response rate
PDGFRα	Platelet-derived growth factor receptor α
PDTC	Poorly differentiated thyroid cancer
PET	Positron emission tomography
PET/CT	Positron emission tomography/Computed tomography
PFS	Progression-free survival
PTC	Papillary thyroid tumor
RECIST	Response evaluation criteria in solid tumors
RET	A proto-oncogene encoding for a receptor tyrosine kinase for extracellular signalling molecules (from "rearranged during transfection")
rhTSH	Recombinant human TSH
RT-PCR	Reverse transcriptase polymerase chain reaction
SPECT	Single-photon emission tomography
SPECT/CT	Single-photon emission tomography/Computed tomography
T	Tumor status according to the AJCC/UICC TNM staging system
T3	Triiodothyronine
Tg	Thyroglobulin
TgAb	Anti-Tg autoantibodies
TKI	Thymidine kinase inhibitor
TNM	AJCC/UICC staging system based on parameters "T" (tumor status), "N" (lymph node status), and "M" (distant metastasis status)
TSH	Thyroid stimulating hormone, or thyrotropin
UICC	Union Internationale Contre le Cancer (International Union Against Cancer)
US	Ultrasonography
VEGF	Vascular endothelial growth factor
VEGFR	Vascular endothelial growth factor receptor
WBS	Whole-body scintigraphy

Contents

Primary Treatment of Differentiated Thyroid Cancer 1200
Surgery 1200
Adjuvant Ablation of Postsurgical Remnants with ^{131}I-Iodide 1201
Side Effects of Radioiodide Therapy 1206

Evaluation of Success of Thyroid Remnant Ablation 1208

Levothyroxine Therapy 1208

Follow-Up 1210
Measurement of Serum Tg 1210
Whole-Body Scintigraphy with ^{131}I-Iodide 1212
Neck Ultrasound 1212
Other Diagnostic Procedures 1213

Management of Locoregional Recurrences 1216

Management of Distant Metastases 1216

Advanced DTC Refractory to Radioiodide Treatment 1222
Reinduction of the Ability to Take Up Iodine 1222
Conventional Chemotherapy 1222
New Targeted Therapies 1222
External Beam Radiation Therapy 1224
Treatment of Anaplastic Thyroid Cancer 1224
Initial Treatment of Medullary Thyroid Cancer 1225
Follow-Up of Medullary Thyroid Cancer 1225
Radionuclide Imaging in Recurrent MTC 1226
Treatment for Recurrent or Persistent MTC ... 1229
References 1231

Treatment of thyroid cancers derived from the follicular epithelium that are either poorly differentiated or plain anaplastic relies on the main pillars of the vast majority of biologically aggressive tumors, i.e., surgery (whenever possible with curative intent – but frequently only for palliative purposes), chemotherapy, and new targeted therapies. In this scenario, there is very little or no role for therapy with radiopharmaceuticals. Whereas, radiopharmaceuticals have multiple important roles for treatment and follow-up of more differentiated forms of thyroid cancer derived from either the follicular epithelium (papillary and follicular thyroid cancer) or from the parafollicular C cells (medullary thyroid cancer). The focus of this chapter is on treatment and follow-up of differentiated thyroid cancers.

Primary Treatment of Differentiated Thyroid Cancer

Surgery

Unlike follicular thyroid cancer (FTC, which usually presents as a solitary nodule), papillary thyroid cancer (PTC) frequently exhibits multifocal growth. Until recently, total thyroidectomy was always indicated as initial treatment when the diagnosis of PTC was known before surgery, e.g., when the ultrasound (US) findings had been typical for cancer, or fine needle aspiration cytology (FNAC) had shown a Thy 4 or Thy 5 pattern. In fact, given the high rate of multifocality and bilaterality of PTC, total thyroidectomy results in lower recurrence rates than lobectomy or subtotal thyroidectomy [1]. However, with the wide diffusion of neck ultrasound and the possibility to detect early possible recurrence in the residual lobe, simple lobectomy is nowadays indicated when the PTC is in a single nodule and of small size [2]. The main reason for this choice is the lower prevalence of complications after lobectomy than after total thyroidectomy, either vocal cord palsy and/or hypoparathyroidism.

When locoregional disease is not detected preoperatively (as assessed by, e.g., US examination of the neck [3] or by preoperative FNAC), the prevailing consensus is that there is no need to routinely perform lateral lymph node dissection in patients with DTC. Conversely, some authors suggest central lymph node dissection for primary surgery in lymph node-positive PTC, in order to abrogate the serum levels of thyroglobulin (Tg) – which would then become a tumor-associated marker [4]. However, since total thyroidectomy and systematic lymph node dissection in the central, and especially in the lateral neck, have been linked to higher surgical morbidity, there is no universal consensus on the necessity to perform central neck dissection by principle. In this regard, recently published studies demonstrate that the outcome of patients treated with prophylactic central neck dissection is characterized by a higher proportion of postsurgical hypoparathyroidism – but with the same long-term clinical outcome of those treated only with total thyroidectomy [5, 6]. Nevertheless, if neck lymph node metastases, either in the central or lateral compartment, are diagnosed by US examination before thyroidectomy, surgery must include lateral neck dissection [7]. Selective excision of confirmed lymph node metastases (the so-called "cherry picking" or "node plucking" technique) is justified only in those patients with thyroid cancer who have already had systematic dissections of the respective neck area(s) during prior operations [8].

Adjuvant Ablation of Postsurgical Remnants with ^{131}I-Iodide

The rationale of performing radioiodide therapy of DTC after surgery in order to ablate postsurgical thyroid remnants is based on the selective ability of thyroid cells to concentrate iodine, which is then utilized to synthesize Tg and thyroid hormones. This capacity (which is maintained by DTC tumor cells to a much lesser extent than in normal thyroid cells) is significantly enhanced by TSH stimulation, a condition that can be achieved either by discontinuing replacement/suppressive hormonal therapy with L-thyroxine or by administering exogenous rhTSH (see further below); full benefits of the diagnostic and therapeutic uses of ^{131}I-iodide can be achieved on the basis of this property.

Ablation of postsurgical thyroid remnants with ^{131}I-iodide is indicated in DTC to eliminate any residual, macroscopically normal thyroid tissue left after total or near-total thyroidectomy [9–11]. This therapeutic strategy ensues four major benefits:

1. Since 50% of PTCs are multifocal, ^{131}I-iodide ablation may decrease the recurrence and mortality rates, by destroying postoperative microscopic residual tumor foci.
2. ^{131}I-iodide ablation of normal appearing residual thyroid tissue facilitates the early detection of recurrences based on sequential measurements of serum Tg. In this regard, it should be noted that thyroid remnants synthesize and secrete Tg that is indistinguishable from Tg possibly produced by residual thyroid cancer cells.
3. ^{131}I-iodide ablation makes it possible to perform a highly sensitive diagnostic whole-body scan (^{131}I-WBS) 4–7 days after administration of the ablative ^{131}I activity, which may reveal previously undetected metastatic tumor lesions, as identified by foci of uptake outside the thyroid bed (see example in Fig. 1).
4. By reducing/ablating the mass of normal thyroid tissue, any subsequent therapeutic use of ^{131}I-iodide in case of recurrent/metastatic DTC will be more effective.

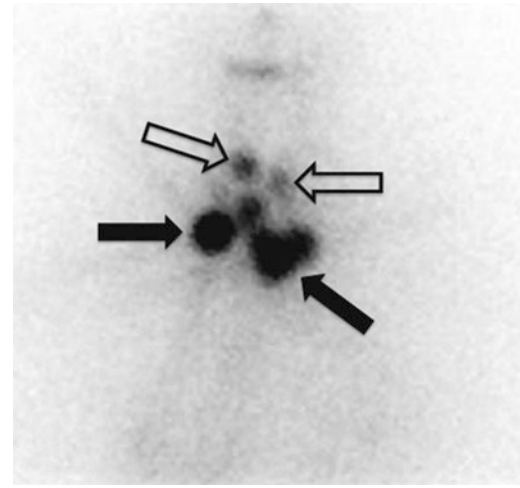

Fig. 1 Spot planar imaging of the upper chest and neck region (anterior view) obtained 7 days after administration of 3.7 GBq (100 mCi) ^{131}I-iodide for thyroid remnant ablation in a patient treated for PTC. In addition to at least two obvious thyroid tissue remnants with intense radioiodide uptake (*solid black arrows*), there are at least two areas with lower intensity uptake (indicated by *open arrows*), corresponding to lymph node metastases that were previously unknown; subsequent characterization by FNAC with assay of Tg in the needle washing confirmed the presence of metastasis (From Volterrani et al. [301], with permission of Springer Science+Business Media)

However, since the indication for ablation with ^{131}I-iodide is based on prognostic factors and no benefits from radioiodine ablation for patients with intrathyroidal tumors <1.5 cm has been demonstrated [10, 12–14], the prevailing consensus is that these "low-risk" thyroid cancer patients should not undergo postsurgical radioiodine ablation. In this regard, the most recent US guidelines for the treatment of thyroid cancer do not recommend as mandatory the use of ^{131}I-iodide thyroid remnant ablation in patients with lymph node-negative, unifocal intrathyroidal microcarcinomas (T1aN0M0) [2]. Also in patients with larger tumors (>1.5 cm), with multifocal tumors, or with extension beyond the thyroid capsule or with lymph node metastasis, the so-called "intermediate-risk" cases, the benefits of ablation with ^{131}I-iodide continue to be debated [10, 13–16]. Therefore, in these patients the use of radioiodine

for the purpose of ablating normal remnant tissue should be "selective" and debated case by case, although the prevailing consensus is that these conditions should indeed be treated [17]. In patients with high-risk DTC, there is instead a clear need for ^{131}I-iodide treatment to prolong disease-free and overall survival (Table 1).

Even if a real clinical benefit of ^{131}I-iodide remnant ablation is not fully recognized for lower-risk tumors, its role in making easier the follow-up of DTC patients in any risk category has been proposed for many years as one of the rationales to perform it. In fact, since either normal and/or neoplastic thyroid tissue may be responsible for Tg production in patients with thyroid remnants, serum Tg measurement will be more useful for detecting persistent/recurrent disease after all sources of Tg secretion alternative to tumor tissue (i.e., normal thyroid remnants) have been eliminated. Any detectable serum Tg level after total thyroidectomy and successful remnant ablation should therefore indicate the presence of residual tumor. Nevertheless, over the years it has been recognized that the trend of increase of serum Tg is more important than the absolute value to follow up these patients [18], especially when combined with a neck US scan performed by expert endocrinologists or radiologists [19].

On the other hand, also the diagnostic ^{131}I-WBS is more sensitive and specific after radioiodine ablation of normal thyroid remnants; furthermore, imaging with radioiodide WBS and US evaluation of the neck are the only reliable diagnostic modalities in patients in whom the assay of serum Tg is unreliable because of the presence of circulating anti-Tg antibodies.

Although ^{131}I-iodide can be very successful in achieving all of the above objectives, many factors may affect the degree of success of ^{131}I-iodide thyroid remnant ablation. These include, but are not limited to, the extent of surgery, percent radioiodide uptake in normal residual thyroid tissue, volume of normal residual thyroid tissue, prescribed activity of ^{131}I-iodide, geometrical shape of normal residual thyroid tissue, effective half-life of ^{131}I in the normal residual thyroid tissue, patient's compliance with low-iodine diet, serum level of TSH, prior use of diagnostic ^{131}I-iodide with possible stunning, and definition of successful radioiodine ablation.

The kinetics of radioiodine accumulation in DTC cells differs from that in normal thyroid tissue. In the latter, uptake of radioiodide is approximately 1% of the administered activity per gram of tissue, with a biological half-life of about 8 days; whereas, in the tumor tissue uptake of ^{131}I-iodide varies from 0.5% to 0.001% of administered activity per gram, with half-lives ranging from a few days to a few hours [20]. This difference explains why, following administration of any given activity of ^{131}I-iodide, the amount of radiation delivered to the tumor is small compared to that delivered to normal thyroid tissue. A quantitative dosimetric approach determines the therapeutic activity required to deliver a sufficient dose of radiation to treat and can also predict the outcome of ^{131}I-iodide therapy. The recommended radiation dose for ablation of thyroid remnants is 300 Gy [9].

It should also be considered that the dosimetric burden must not exceed the maximum permissible irradiation to the whole body and particularly to the bone marrow (2 Gy); to this purpose, an empiric estimate has been suggested, i.e., to administer ^{131}I-iodide activities such that whole-body retention at 48 h post-administration should not exceed 4.44 GBq (or 120 mCi). Furthermore, particular attention should be paid to dosimetric estimates in patients with diffuse lung metastases, in whom radioiodine might cause pulmonary fibrosis over certain values of accumulation/retention; in these patients the estimated whole-body

Table 1 Indications for radioiodide treatment in DTC patients

Risk category	TNM (6th ed.)	Benefits	Indication to ^{131}I-iodide
Low	T1aN0M0	None	No
Intermediate	T1b-T2N0M0 T1-2N1M0	Could reduce relapses	Yes/no[a]
High	T1-2N0-1MI, T3-4 N0-1, and/or M0-1	Reduces relapse and death	Yes

European Consensus: Pacini et al. [303]
[a]"Yes": European Consensus; "no": ATA guidelines

retention of ^{131}I at 48 h should not exceed 2.96 GBq (80 mCi) [21, 22]. Nevertheless, at the same time, therapeutic activity to be administered should be calculated so as to ensure the delivery of an effective dose to the tumor lesions; if this condition cannot be achieved because of low radioiodine uptake, then it would be appropriate to consider therapies alternative to radioiodine therapy, such as surgery (whenever possible), EBRT, and/or chemotherapy [9, 22].

Administration of ^{131}I-iodide in activities prefixed according to certain thresholds irrespective of pretreatment dosimetric estimates is still the most widely employed approach. Its main advantage is simplicity, although probably not being the optimal solution for all cases; in fact, any prefixed activity may be excessive in some cases and insufficient in others. For ablation purposes, a single administration of either 1.11 or 3.7 GBq (30 or 100 mCi) of ^{131}I-iodide ensues complete destruction of the remnants in 90% of the cases when uptake of a tracer amount of radioiodide in the residue is <2% (which translates into a residual thyroid tissue mass <2 g), while ablation is successful in only two-thirds of the cases when uptake is >2% (i.e., a residual thyroid mass >2 g) [9].

Accurate individual patient-tailored dosimetric estimates require a set of information on the target tissue. Considering that the radiation dose is basically delivered energy per mass, such information includes the volume (or mass) of the target tissue and the retention kinetics of ^{131}I-iodide in that target. While imaging techniques can provide volumetric estimates of the target tissue, the kinetics of uptake and retention of radioiodide can be derived from serial measurements following administration of a tracer activity of ^{131}I-iodide (such as, e.g., 3.7 MBq); since such measurements are usually limited to only 24 h (or 48 h at the latest) post-administration, certain assumptions derived from standard pharmacokinetic models are adopted for describing the kinetics of radioiodide retention from the last time point onward. Although preferable in principle to more simplistic empiric approaches, from a practical standpoint, the approach of administering ^{131}I-iodide activities based on pretreatment dosimetric estimates has four major drawbacks, which apply not only to the remnant ablation case but also to the case of radioiodide therapy of recurrent/metastatic lesions from DTC:

1. The estimated volume in which radioiodide is concentrated is in general only an approximation derived from, e.g., US evaluation; moreover, this volume cannot be measured in patients with metastases that are too small for viewing by imaging techniques, as is the case for diffuse lung metastases that are not discernible as separate lesions by chest x-ray or CT.
2. The biological half-life of ^{131}I-iodide in the target tissues differs from one patient to another, and even between different metastatic lesions in any given patient, or in different periods; thus, dosimetric estimates based on standard models may have a wide range of approximation.
3. The intestinal absorption of ^{131}I-iodide can vary even over short intervals of time, such as those occurring between administration of the tracer activity for the dosimetric study and administration of the actual therapeutic activity.
4. Dose distribution in a certain tumor target tissue can be heterogeneous, as shown by the typical patchy distribution of radioiodide visualized on tissue autoradiographs. In this case, voxel dosimetry could be useful for predicting the possibility of either whole or partial ablation of tumor tissue. In this regard, 3D dosimetry makes it possible to obtain the so-called dose-volume histogram, a map of the different absorbed dose values in different portions of the target tissue [23].

Thyroid remnant ablation with ^{131}I-iodide must be performed under adequate TSH stimulation, which is necessary in order to increase the uptake of radioiodine by follicular thyroid cells. After the effectiveness and safety of the use of rhTSH have been recognized [24], ablation of thyroid remnants can be performed by administering ^{131}I-iodide after two i.m. injections of

0.9 mg of rhTSH performed 24 and 48 h before the treatment [25]. If rhTSH administration is unfortunately not available, a period of L-thyroxine (l-T4) withdrawal of at least 4 weeks is required; in this case, serum TSH should be >30 μIU/mL before radioiodide is given; otherwise, the withdrawal period is prolonged for another 1–2 weeks. The main drawback of this traditional modality of patient's preparation for radioiodide therapy is the development of hypothyroidism symptoms after about 2–3 weeks from hormone withdrawal and continuing for other 2–3 weeks after the reintroduction of the l-T4 therapy. Replacing l-T4 with T3 for 2 weeks before complete hormonal withdrawal and taking T3 with l-T4 during the 2–3 weeks after the radioiodine treatment can be useful to limit the hypothyroidism symptoms, because of the much faster metabolic clearance of T3 versus that of T4 (biologic half-life about 10 h versus 7 days, respectively). However, T3 requires a three times per day administration, and many patients experience tachycardia soon after its consumption.

The use of rhTSH (Thyrogen®) is approved in the USA and Europe for pre-therapeutic stimulation before administering radioiodide for ablation of thyroid tissue remnants after near-total or total thyroidectomy for DTC, in patients without evidence of distant metastases. Very recently two independent multi-center randomized studies, one performed in France [26] and one in the UK [27], have clearly demonstrated that low-risk and intermediate-risk DTC patients can successfully be ablated when treated either with 1.11. or 3.7 GBq ^{131}I-iodide (30 or 100 mCi) and regardless of the type of TSH stimulation (i.e., obtained after withdrawal of LT4 therapy or after rhTSH administration). After these studies, the use of rhTSH for remnant ablation has been approved in combination with activities ranging from 30 to 100 mCi of ^{131}I-iodide.

Irrespective of the modality of TSH stimulation (i.e., through increased endogenous secretion following l-T4 withdrawal or through administration of exogenous rhTSH), an important component of patient's preparation for radioiodide therapy is to ensure that the pool of native iodide in the body fluids is reduced as much as possible. In fact, reducing competition from unlabeled iodide for uptake of radioiodide in the thyroid cells increases the chances for the radioactive iodide atoms to be accumulated in the thyroid cells or in the DTC cells. Depletion of the iodide pool in the body is achieved by following a low-iodine diet (Table 2A) for at least 2 weeks before radioiodide administration. This is of particular relevance in countries with normal-high levels of iodine in the population while it is not mandatory in countries with median-low levels of iodine. Patients should also avoid excessive iodine intake through other sources, such as drugs, iodinated contrast agents, etc. (Table 2B) for list of products/drugs with high-iodine content) [28, 29].

Very recently, the question of whether the iodine content expressed as urinary iodine content can represent a limitation to the success of radioiodine therapy has been questioned. However, the absence of iodine contamination should always be verified by measuring urinary iodine content, preferably normalized as iodine/creatinine ratio (i.e., as microgram of iodine per gram of creatinine, μg/g); in case this value is greater than 250 μg/g [29], ^{131}I-iodide therapy should be delayed until the body stores of iodine have decreased [30]. Assessing urinary iodine might be relevant especially in those patients who have a negative post-ablation/therapy scan despite evidence of residual/recurrent disease as assessed by serum Tg. In women of childbearing age, pregnancy must be excluded before administering radioiodine for therapy.

Although the issue of thyroid stunning (characterized by a reduction of therapeutic radioiodide uptake consequent to prior administration of a diagnostic activity of ^{131}I-iodide) was recognized more than 50 years ago [31, 32], it still is a matter of debate, and its clinical significance and even its existence have been questioned [33]. The frequency of thyroid stunning, a condition that potentially compromises the therapeutic efficacy and outcome of radioiodide treatment, appears to increase with increasing activities of radioiodide administered in the diagnostic phase [34, 35]. Indeed, the exposure of follicular thyroid cells

Table 2 High-iodine content foods/products, to be limited/avoided before scintigraphy or therapy with radioiodide in patients with DTC

A) Food Products	Amount of time it should be avoided before therapy
Iodized salt, sea salt	2 weeks
Milk or other dairy products, including ice cream, cheese, yogurt, etc.	2 weeks
Eggs	2 weeks
Seafood, including fish, shellfish, kelp, or seaweed	2 weeks
Foods that contain the additives carrageenan, agar-agar, and algin alginates	2 weeks
Cured and corned foods (ham, lox, corned beef, sauerkraut)	2 weeks
Breads made with iodinated dough conditioners	2 weeks
Foods and medications containing red food dyes	2 weeks
Chocolate	2 weeks
Molasses	2 weeks
Soy products (soy sauce, soy milk)	2 weeks
B) Drugs with high content of iodine possibly interfering with 131-I uptake	
Lugol's solution	3 weeks
Potassium iodide solution	3 weeks
Topical iodine (e.g., surgical skin preparation)	3 weeks
Iodinated radiographic contrast agents:	
Intravenous (water soluble)	4 weeks (with normal renal function)
Lipophilic (rarely used)	>4 weeks
Amiodarone	>3 months
In addition, restaurant food should be avoided, because there is no way to know whether they use iodized salt	3 weeks

(or of follicular-derived tumor cells) to sublethal doses of radiation from ^{131}I-iodide (as it might be caused by radioiodide administered for a diagnostic ^{131}I-WBS, usually in the order of 185 MBq) may decrease the efficiency of subsequent treatment with ^{131}I-iodide [36, 37]. This effect is associated with nonablative radiation doses (up to 10 Gy) that reduce by as much as 50% the ability of the tissue to concentrate and store radioiodide [32]. Although reduced radioiodide uptake in thyroid tissue on the post-ablation ^{131}I-WBS evaluated by visual analysis has been reported [36], quantitative studies have failed to definitely confirm the occurrence of stunning [38, 39]. Furthermore, there is no conclusive evidence that stunning does indeed lead to a higher rate of unsuccessful ablations.

As to the possible mechanisms that have been proposed to explain thyroid stunning, reduced expression of the sodium/iodide symporter (NIS) [40] seems to be the main determinant of this event, as it is involved in the response to irradiation-induced DNA damage [41, 42]. Because of the fear of this effect, a diagnostic ^{131}I-WBS is usually not recommended before thyroid remnant ablation with ^{131}I-iodide. If a diagnostic ^{131}I-iodide scan prior to ablation therapy is deemed useful (e.g., in patients with suspected metastases or to evaluate the size of the remnants), then it is recommended to administer no more than 74 MBq of ^{131} I-iodide and to perform ablation within 48–72 h. Alternatively, ^{123}I-iodide can be used for scintigraphic pre-ablation assessments [43], as the low-energy Auger electrons emitted by this radionuclide are devoid of any stunning effect on thyroid follicular cells. For radiodosimetric purposes using simplified models, uptake of radioiodide in the thyroid remnant can be measured (and scintigraphy of the neck can be performed) by administering a very low activity of ^{131}I-iodide, such as 1.85 or 3.7 MBq (50 or 100 μCi).

A ^{131}I-WBS performed 4–7 days after treatment with ^{131}I-iodide for thyroid remnant ablation is extremely useful to evaluate the distribution and the sites of radioiodide uptake. Scintigraphic detection of focal areas of radioiodide uptake outside the thyroid bed demonstrates the presence of metastatic disease, so that additional treatments must be considered, either further radiometabolic therapy (at an adequate interval, e.g., at least 6 months after ablation) or surgery. Similarly as with the post-ablation scan, the presence of additional metastatic foci has been reported in 10–26% of patients in the post-therapy scan compared to those detected in the diagnostic scan, leading to change the management strategy in 9–15% of the patients [44, 45]. Post-ablation SPECT/CT fusion imaging provides

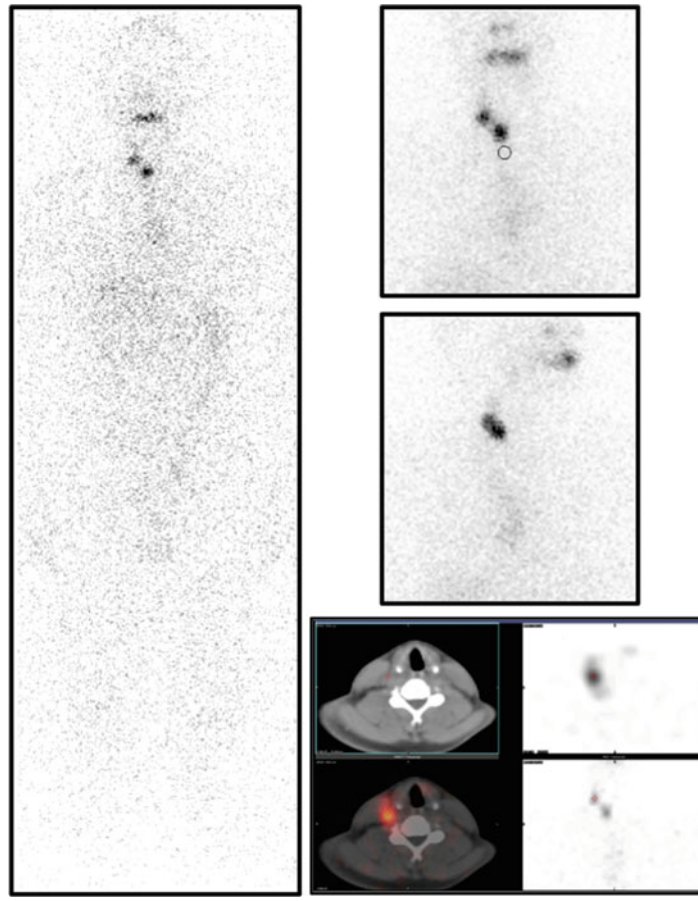

Fig. 2 ^{131}I-WBS and SPECT/CT acquisitions of the cervical region obtained 8 days after administration of 3.7 GBq (100 mCi) ^{131}I-iodide for thyroid remnant ablation in a 21-year-old man who had been submitted 2 months earlier to thyroidectomy because of a PTC occupying virtually the entire right thyroid lobe (4.5 cm in maximum diameter, pT3). The planar whole-body scan (*left panel*) reveals two foci of uptake in the right paramedian aspect of the neck; spot acquisitions in the anterior view (*upper right panel*) and right oblique view (*middle right panel*) confirm the presence of the two foci of uptake, one more intense, almost central just above the sternal notch (indicated by the *open circle*), and one less intense, more laterally and superiorly; the inferior focus of intense uptake was interpreted as representing postsurgical thyroid remnant, while the focus of uptake located more laterally and superiorly was interpreted as possibly representing lymph node metastasis. *Right lower panel*: CT component (*upper left*), SPECT component (*upper right*), and fused SPECT/CT image (*lower left*) of axial section centered on the focus of less intense uptake (MIP image, *lower right*). Although performed with a low-definition system, the CT component suggests that the focus of less intense uptake corresponds to an enlarged lymph node. Subsequent characterization by FNAC with assay of Tg in the needle washing confirmed the presence of metastasis

superior diagnostic information, concerning especially lymph node involvement, than planar ^{131}I-WBS or even stand-alone SPECT (see examples in Figs. 2 and 3) [46–58]. SPECT/CT plays therefore an important role in the evaluation of disease after ablation therapy, as it may alter management of these patients, either by upstaging or by downstaging the disease in about 25% of the cases [49].

Side Effects of Radioiodide Therapy

Short-term side effects of therapy with ^{131}I-iodide for thyroid remnant ablation are usually minimal and transient [59, 60]. Nausea and gastric pain occur frequently after ^{131}I-iodide treatment and last a few days; these symptoms can be prevented/treated by administering proton-pump

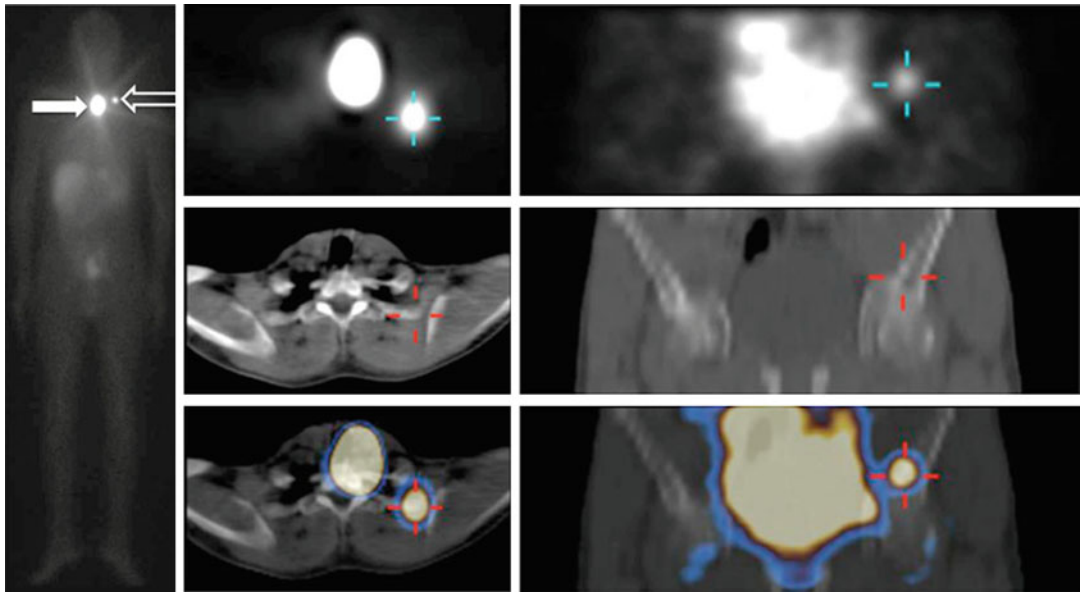

Fig. 3 *Left panel*: Post-ablation ^{131}I-WBS in a 33-year-old man previously submitted to thyroidectomy and left cervical lymphadenectomy because of PTC of the left lobe (follicular variant) with presurgical diagnosis of lymph node metastasis; serum Tg under rhTSH stimulation was 94 ng/mL at the time of administering ^{131}I-iodide. Besides intense uptake in the thyroid remnant, there was an area of focal uptake in the left cervical region (interpreted as a lymph node metastasis in the ^{131}I-WBS), while important bladder activity hampered correct interpretation of the pelvic region. *Center panel*: Representative transverse SPECT/CT section of the cervical region (SPECT component at the *top*, CT component in the *middle*, and SPECT/CT fusion at the *bottom*): the focal area of uptake was actually bone metastasis located in the posterior arc of a left rib. *Right panel*: Representative coronal SPECT/CT section of the pelvic region (SPECT component at the *top*, CT component in the *middle*, and SPECT/CT fusion at the *bottom*): the distinct focal area of uptake lateral to radioactivity accumulation in the bladder represented metastasis in the left iliac bone (From Mariani et al. [302], with permission)

inhibitors or similar drugs. Sialoadenitis is also frequent, with pain and enlargement of the salivary glands but rarely leading to permanent xerostomia; for prophylaxis, patients are advised to drink large quantities of fluids and to stimulate salivary secretion with lemon juice. Loss or change of taste is reported by the majority of patients receiving therapy with ^{131}I-iodide, but usually lasts only a few days. When large thyroid remnants are present and completion thyroidectomy is not feasible, steroids should be given to prevent swelling in the neck due to radiation-induced inflammation.

As to the long-term side effects, the overall relative risk of a second primary tumor is increased only in patients treated with high cumulative activities of ^{131}I-iodide, an occurrence that is encountered in patients with recurrent/metastatic DTC. In particular, a significantly greater risk of leukemia or other second primary tumor has been reported for patients treated with cumulative activities exceeding 22 GBq (or 600 mCi) of ^{131}I-iodide, especially if radioiodide therapy has been associated with external radiotherapy [61]. On the other hand, controversial reports continue to fuel the ongoing debate on the possibility that treatment of DTC with radioiodide per se at any administered activity increases the risk of second primary malignancies [62, 63]. In particular, Bhattacharyya and Chien analyzed the incidence of second primary malignancies in a total of 29,231 DTC patients, 18,882 of whom had been treated and 10,349 had not been treated with radioiodide (with mean follow-up of 55.5 and 61.8 months, respectively). According to univariate analysis, patients treated with ^{131}I-iodide actually had significantly fewer second primary malignancies than the untreated patients (4.8% versus 6.1%, $P < 0.001$), while

radioiodide therapy did not exhibit a statistically significant hazard ratio on multivariate analysis [64]. On the other hand, in a more recent meta-analysis, Sawka et al. confirmed an increased relative risk for leukemia in DTC patients treated with radioiodide versus those nontreated with radioiodide (relative risk of 2.5, with $P = 0.024$); the overall relative risk for all second primary malignancies pooled together in DTC survivors treated with radioiodide was 1.19 ($P = 0.010$), without however a significantly increased risk for any specific type of tumor [65]. It is also noteworthy to emphasize that some reports support the notion that, although the incidence of second primary malignancies is indeed increased in patients with DTC, this increase is not linked to long-term effects of radioiodide therapy but rather to some not yet identified genetic factors [66, 67].

Considering that many patients with DTC are women in their reproductive age, one of the concerns for radioiodide therapy is the possibility of long-term adverse effects on fertility and on the outcomes of pregnancies posttreatment. In this regard, a recent study based on 2,673 pregnancies in DTC patients who had been treated with radioiodide concluded that there is no evidence that exposure to radioiodine affects the outcome of subsequent pregnancies and offspring [68].

Radioiodine treatment may result in transient impairment of male gonadal function, consisting in a reduction of motility and reduced sperm count in a variable number of patients [69]. Changes in the germinal epithelium and Leydig cell function (with consequent increase in serum FSH levels) are usually transient and may have some clinical significance in subjects with a preexisting impairment of fertility [70]. Permanent damage to the germinal epithelium with the consequent increased risk of infertility is related to cumulative dose, and it may become permanent following delivery of high-radiation doses [70, 71]. The use of sperm banks should be considered in young men who will be treated with high activities (14 GBq or more) or with pelvic metastases [72, 73].

Radiation fibrosis may develop in patients with diffuse lung metastases who have received repeated excessive activities (over 5.55 MBq or 150 mCi) of radioiodide at short intervals, especially if less than 6 months [74, 75].

Evaluation of Success of Thyroid Remnant Ablation

The success of thyroid remnant ablation is usually evaluated 6–12 months after radioiodine therapy based on the following criteria [25, 76]:

1. Negative radioiodine uptake in the thyroid bed ("no visible uptake in the thyroid bed" or, if visible, uptake <0.1%, an arbitrarily set threshold) on diagnostic ^{131}I-WBS.
2. RhTSH-stimulated serum Tg levels <1 ng/mL in the absence of detectable anti-Tg antibodies (although a 2 ng/mL threshold is frequently adopted in the clinical routine, and the FDA recommends the 2.5 ng/mL threshold).
3. Absence of suspicious findings on neck US.

Levothyroxine Therapy

Endocrine function of the excised thyroid gland can only be replaced by administration of thyroid hormones; l-T4 is the medication of choice for such long-term replacement. The thyroid gland produces both tetraiodothyronine (or thyroxine, T4), which contains four atoms of iodide, and triiodothyronine (T3), which contains three atoms of iodide and is the true biologically active hormone; T4 (which has a biological half-life of 7 days) constitutes about 75–80% of thyroidal hormone production, while T3 (which has a biological half-life of 20–30 h) constitutes the remainder 20–25% [77–79]. These hormones have two isomers, which can be levo- (l) or dextro-rotatory (d): the levo-rotatory isoform (i.e., l-T4 in the case of T4) is the active variant. Since l-T4 is physiologically converted to the active hormone, T3, in the peripheral tissues, in a steady state, the oral administration of l-T4 mimics physiological conditions and stabilizes serum T3 levels [80].

There are two main goals for l-T4 treatment in PTC and FTC patients after thyroidectomy:

1. To correct postoperative hypothyroidism
2. To suppress the endogenous secretion of TSH (which is a potent growth factor for follicular thyroid cells as well as for follicular-derived tumor cells), at least until the evidence that the patient has been cured is achieved

In contrast, both ATC and MTC, which are constituted by TSH-independent cells, do not benefit from TSH suppression and only require l-T4 replacement therapy to correct postoperative hypothyroidism. The optimal daily l-T4 dose for suppressing TSH secretion ranges between 1.6 and 2.8 μg/kg body weight. However, it is recognized that this dose must be tailored on an individual basis, since it is only roughly correlated with body weight and age. Younger patients, especially children, and patients with a high lean body mass usually require higher doses per kg of body weight [81]. By contrast, older patients require lower l-T4 daily doses, and further reductions are needed for subjects with concurrent heart disease [82]. Since l-T4 has a blood half-life of about 7 days, a single daily dose is usually sufficient. After oral administration, up to 80% of l -T4 is absorbed in the gut, subject however to some interindividual variability [83]. Food intake can reduce l-T4 absorption; therefore, patients are usually advised to take their l-T4 dose on an empty stomach, preferably early in the morning 20–30 min before breakfast. However, recently new l-T4 formulations have been produced whose absorption does not require fasting [84, 85]. Nevertheless, several substances are known to interfere with l-T4 absorption in the gut, including commonly used components such as dietary fiber and coffee. Furthermore, several commonly used drugs, such as bile acid sequestrants, ferrous sulfate, sucralfate, calcium carbonate, aluminum-containing antacids, phosphate binders, raloxifene, and proton-pump inhibitors, have been shown to interfere with the absorption of l-T4 [83, 86, 87]. In addition, several chronic diseases, such as regional enteritis, pancreatic disease, and cirrhosis, may be associated with decreased l-T4 absorption [88, 89]. Patients should be also aware that, since bioavailability of the drug may vary in different preparations, it is preferable that they do not change not only their usual l-T4 daily dosage but also the commercial brands too frequently, since this may change the hormone levels in their blood. If this happens, a reassessment of the daily dosage should be performed 45–50 days after the changing of the therapy.

The effectiveness of l-T4 therapy in DTC patients must be monitored by measuring serum TSH with an ultrasensitive assay [75]. In addition to monitoring serum TSH (which should be suppressed, i.e., less than 0.1 μIU/mL), the serum levels of free T3 (FT3) and free T4 (FT4) must also be measured; even when the TSH suppression is required, both FT3 and FT4 levels should be in the normal range in order to avoid possible iatrogenic thyrotoxicosis [80, 90]. A major concern for patients and physicians is the possibility that (despite the normal FT3 levels) normal to high levels of l-T4 may have negative effects on some target organs during long-term suppressive therapy [91–95]. In this regard, the bone and heart are considered organs at major risk. However, when patients are monitored as described above, l-T4 suppressive therapy is safe and devoid of any long-term adverse effects. It is also important to emphasize that l-T4 suppressive therapy in children has no adverse effect on bone maturation, final height, and pubertal development. Since a 25% increase in the FT4 level is usually observed when blood is drawn 3–4 h after ingestion of l-T4, patients should be instructed not to take their medication the morning before blood testing.

An important issue for DTC patients is for how long l-T4 therapy must be continued on a TSH-suppressive dose. There is no doubt that patients with evidence of persistent or recurrent disease or at a high risk of recurrence should be kept on suppressive therapy in order to decrease the risk of recurrence [96]. However, in patients with favorable prognostic factors and evidence of complete cure (i.e., a negative ^{131}I-WBS and undetectable TSH-stimulated serum Tg in the absence of anti-Tg autoantibodies), the dose of l-T4 may be decreased with the aim of maintaining serum TSH levels between 0.1 and 0.5 μU/ml. Currently, low-risk patients who are cured with initial treatment constitute more than

80% of the cases. Long-term suppressive therapy is thus maintained only in patients with persistent disease or, less commonly, in those at high risk of recurrence [88]. The age and the general health conditions must be also considered in the decision to continue a TSH-suppressive l-T4 therapy or to reduce it for a better balance between a real efficacy in reducing the risk of recurrence and the risk of developing severe side effects such as atrial fibrillation [93, 97].

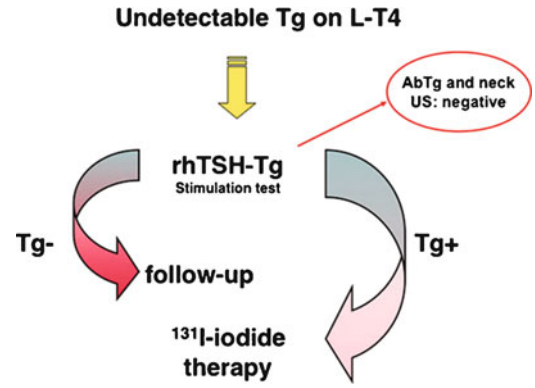

Fig. 4 Suggested algorithm of follow-up in patients with DTC previously treated with total thyroidectomy and post-surgical remnant ablation with ^{131} I-iodide. When serum Tg on l-T4 suppressive therapy is undetectable, an rhTSH stimulation test for Tg should be performed to confirm the absence of recurrent/metastatic disease. A negative rhTSH stimulation test (*left arm* of the diagram) does not require further therapy, and the patient is included in a regular follow-up program. A positive rhTSH stimulation test (*right arm* of the diagram) indicates instead the presence of recurrent/metastatic disease and should be treated with further therapy with ^{131}I-iodide; localization of the sites of recurrence and/or metastasis is usually possible in the post-therapy WBS (preferably integrated with SPECT/CT) acquired between 5 and 10 days after administration of radioiodide therapy

Follow-Up

The aims of follow-up for patients treated with surgery and with radioiodide remnant ablation for DTC are twofold:

1. To maintain adequate l-T4 therapy
2. To discover the persistence or recurrence of thyroid cancer early on (see Fig. 4)

Follow-up is virtually lifelong because, especially in DTC patients, recurrences can occur even 10–20 years after apparently successful initial treatment [13, 14, 98]. The major diagnostic modalities employed for the follow-up of DTC patients are measurement of serum Tg, ^{131}I-WBS, and neck US examination. Evaluation of these parameters at 6–12 month intervals enables the clinicians to assess the clinical status of the patients and to identify early those patients who need additional treatment(s) [99, 100].

Measurement of Serum Tg

Since Tg is produced exclusively by normal or neoplastic thyroid follicular cells, it constitutes an excellent tumor marker after removal of the thyroid gland. In fact, serum Tg should be undetectable after total thyroidectomy and successful thyroid remnant ablation. Whereas, when the serum Tg levels of these patients remain detectable or rise, they indicate the presence of persistent or recurrent disease [101]. Tg is produced by virtually all papillary and follicular cancer tissues, as demonstrated by immunohistochemistry using anti-Tg antibodies [102] or, more recently, by molecular biology techniques such as RT-PCR [103]. There are two major limitations with regard to the measurement of serum Tg as a tumor marker for DTC:

1. The presence of circulating anti-Tg autoantibodies (TgAb) may interfere with the measurement of serum Tg. According to the method used for assaying serum Tg, TgAb may cause false-positive results (i.e., when employing a radioimmunoassay method) or false-negative results (i.e., when employing an immunoradiometric assay method) [14]. It should also be noted that even noncompetitive immunometric assays based on detection techniques other than radioactivity counting can be affected by circulating heterophilic autoantibodies [104]. In patients with circulating TgAb, who account for about 20–25% of all patients with DTC [105], serum

Tg measurement alone cannot be relied upon if not correlated to the assay of serum TgAb.

2. Since TSH is a growth factor for both normal follicular cells and follicular-derived cancer cells, the production of Tg (therefore its level in circulating blood) is kept to a minimum under l-T4 suppressive therapy. Therefore, undetectable serum Tg levels under l-T4 suppressive therapy (which would indicate cure of the disease) must be confirmed by a TSH stimulation test. Nowadays, Tg stimulation is performed by administering exogenous rhTSH rather than by discontinuing administration of suppressive l-T4 so as to induce hypothyroidism; in fact, the latter is an uncomfortable condition that, though only temporary, may profoundly impact the quality of life of many patients [106]. The protocol for performing rhTSH administration to stimulate serum Tg (i.e., the rhTSH stimulation Tg test) is illustrated in Fig. 5.

An rhTSH-stimulated serum Tg measurement is usually obtained 6–12 months after total or near-total thyroidectomy and ^{131}I-iodide ablation in DTC patients with undetectable serum Tg (<0.1 ng/mL when using the newer-generation, ultrasensitive assays) on l-T4 suppression therapy. The resulting change in serum Tg levels at the peak of rhTSH stimulation (48–72 h after the last of two 0.9-mg doses in the euthyroid state) versus baseline is recorded. According to the cutoff of serum Tg chosen (which may vary in different institutions, but is usually set at 2 ng/mL although the FDA recommends 2.5 ng/mL), the following situations may be encountered [107]:

1. Serum Tg remains undetectable (<0.1 ng/mL); up to 65% of the low-risk patients have no rise in serum Tg concentrations after rhTSH.
2. Serum Tg rises between 1 and 2 ng/mL; this occurs in about 20% of low-risk patients and necessitates further periodic rhTSH stimulation tests, perhaps as often as once yearly. Neck US plays an important diagnostic role in this group. In some patients, the high TSH-stimulated serum Tg level will spontaneously decline over one or more years [108], while in others it will steadily rise, and metastases will become apparent [109].
3. Serum Tg rises above 2 ng/mL; this occurs in about 20% of low-risk patients and usually indicates a substantial thyroid remnant or residual cancer. Patients with this pattern usually require further imaging evaluation to localize the source of the Tg.

With the introduction and wide clinical acceptance of the ultrasensitive Tg assays [110], the rhTSH stimulation test can be avoided when the basal serum Tg is <0.1 ng/mL and reserved to those cases with a serum Tg level on the gray zone (i.e., from 0.1 to 1 ng/mL). In fact, in this latter group, the stimulation test can clearly distinguish the true "positive" cases (about 25%) that require further investigation from negative

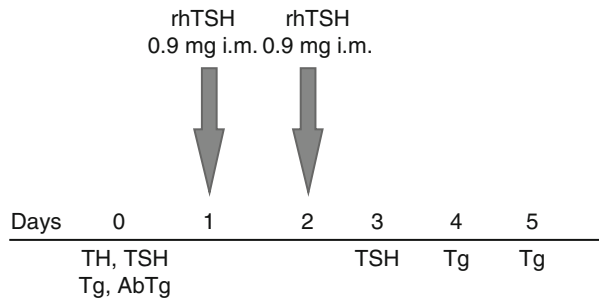

Fig. 5 Outline of rhTSH administration for the Tg stimulation test: before the administration of rhTSH (day 1), blood is taken for assaying thyroid hormones (TH), TSH, Tg, and Tg-antibodies (TgAb). Two i.m. injections of rhTSH are given at day 1 and 2: at day 3 serum TSH must be assayed again to verify the correct stimulus, while serum Tg levels must be measured at days 4 and 5

cases for which the clinical remission of the disease can be defined [111].

Whole-Body Scintigraphy with ^{131}I-Iodide

A ^{131}I-WBS performed 6–12 months after thyroid remnant ablation is useful in the follow-up of patients with high- or intermediate-risk for persistent disease, although its diagnostic sensitivity is lower than that of the serum Tg stimulation test [112]. Similarly as for the Tg stimulation test, radioiodide scintigraphy is performed under TSH stimulation (following either l-T4 withdrawal or administration of rhTSH); images are usually acquired 72 h after administration of 185 MBq (5 mCi) of ^{131}I-iodide if patients have been prepared with l-T4 withdrawal or 48 h in case of preparation with rhTSH. When there is high risk of persistent/recurring disease (such as detectable serum Tg levels with suppressed TSH levels), ^{123}I-iodide can be used instead of ^{131}I-iodide in order not to jeopardize with a possible stunning effect the efficacy of subsequent radioiodide therapy. In this instance, images are usually acquired 48 or 24 h after administering i.v. 185 MBq of ^{123}I-iodide depending on preparation of the patient, i.e., with l-T4 withdrawal or with rhTSH stimulation, respectively [113, 114].

Diagnostic radioiodide WBS is not necessary in low-risk patients who are clinically free of disease, with undetectable (<0.1 ng/mL) serum Tg, while on l-T4 suppressive therapy and whose neck US examination is negative [112], provided they have not circulating TgAb possibly interfering with the serum Tg assay (see above).

Serum Tg levels that become detectable upon TSH stimulation indicate the need for further treatment therapy with ^{131}I-iodide [115, 116]. In the last years, a cut off of 10 ng/ml of rhTSH stimulated serum Tg has been identified as convenient to decide to treta again with 131–I. Clearly, a positive serum Tg stimulation test does not provide per se any information on topographic location of persistent/recurring disease nor on the ability of tumor lesions to concentrate radioiodide (therefore on their susceptibility to be treated with further ^{131}I-iodide therapy). Such information would instead be provided by a positive radioiodide WBS. On the other hand, some patients with DTC may have persistent/recurring disease (as demonstrated by their abnormal serum Tg levels), yet their tumor lesions may have lost the ability to concentrate and retain radioiodide, either as a biologic feature of some DTC histologic types [117, 118] or at some point in the evolution of the disease after having been treated with ^{131}I-iodide therapy [119].

Whereas, if stimulated serum Tg remains undetectable (in the absence of serum TgAb), the patient can be considered as cured [120]. The diagnostic ^{131}I-WBS plays an important role when it is not possible to rely neither on baseline nor on stimulated serum Tg because of a positive serum TgAb titer [99]. In this regard, some role as a surrogate tumor marker can be played also by the TgAb titer itself, which should decline and disappear when the disease is cured (as a consequence of reduced/absent antigenic stimulation on TgAb production), while it usually persists elevated or increases even further in case of persistent or recurring disease [105, 121].

Neck Ultrasound

Neck US examination is nowadays a fundamental component of follow-up evaluation in all DTC patients, especially those at high risk for recurrent disease and those with suspicious clinical findings. Metastatic lymph nodes can be detected with neck US in the lateral and, even though to a lesser degree, in the central neck compartments. The US features of metastatic lymph nodes differ in a number of respects from those of possibly enlarged but benign lymph nodes. In particular, benign lymph nodes are usually smaller, thin, or oval in shape and have a conspicuous hilus, while lymph nodes with metastasis are roundish in shape, may display microcalcification, are hypoechoic, and do

not have a visible hilus [3]. However, if a lymph node metastasis is suspected, an FNA should be performed and the aspirate sent both for cytology and for Tg measurement [122].

Other Diagnostic Procedures

Other imaging modalities can be used in patients with evidence of elevated serum Tg but negative post-therapeutic ^{131}I-WBS and neck US. These include CT or MRI of the chest and neck; bone scintigraphy; scintigraphy with single-photon-emitting, nonspecific tumor-seeking agents (such as ^{201}Tl-chloride, ^{99m}Tc-Sestamibi, or ^{99m}Tc-tetrofosmin) [123]; and positron emission tomography (PET). Although CT and MRI can in principle localize very small lesions (2–5 mm) in the neck, chest, and bones, the morphologic features of such lesions are rarely specific for recurrent/metastatic DTC [124, 125].

PET with the glucose analog [^{18}F]fluoro-2-deoxyglucose ([^{18}F]FDG) is emerging as a powerful diagnostic and prognostic imaging technique in DTC patients with non-iodine-avid recurrences and/or metastases [126, 127]. Enhanced glucose metabolism is a nonspecific feature of many tumor cells that is directly correlated with their proliferative activity, therefore with the degree of biological aggressiveness of the tumor. Considering that DTCs are in general characterized by low biological aggressiveness, PET with [^{18}F]FDG does not play a relevant diagnostic role in DTC patients whose tumor lesions concentrate radioiodide as a thyroid-specific differentiation feature. Nevertheless, the incidental detection of well-DTCs during [^{18}F]FDG PET performed in patients with other malignancies has been the object of several reports (see ▶ Chap. 19, "Diagnostic Applications of Nuclear Medicine: Thyroid Tumors" of this book) [128–136].

Radioiodide remains therefore the radiopharmaceutical of choice for diagnostic and/or localizing purposes in most patients with DTC as well as for therapy when using ^{131}I as the radionuclide. However, some DTCs do exhibit a clinical pattern characterized by higher biological aggressiveness, either at some late time after primary treatment or even earlier in the course of the disease; these biological features are usually associated with poor differentiation that can be identified also on histopathologic analysis. The biologic pattern thereby DTC recurrences/metastases that lose the thyroid-specific iodide-trapping properties and exhibit enhanced aggressiveness become more [^{18}F]FDG avid (see clinical example in Fig. 6) has been termed "flip- flop" mechanism (Fig. 7) [126, 137]. [^{18}F]FDG PET-positive thyroid cancers have a worse prognosis than PET-negative tumors [138, 139]; this information may be useful to adapt management of patients to their individual clinical condition. Nevertheless, the flip-flop paradigm should not be considered as a rigid concept implying evolution of DTC toward less differentiated, aggressive forms; in fact, even well-differentiated classical variants of PTC can occasionally show avid uptake of [^{18}F]FDG, yet maintaining a nonaggressive pattern of tumor growth (see ▶ Chap. 19, "Diagnostic Applications of Nuclear Medicine: Thyroid Tumors" of this book).

Although [^{18}F]FDG PET can be performed while the patient is on thyroxine treatment, TSH stimulates the expression of GLUT on cell membranes; thus [^{18}F]FDG uptake by DTC cells is higher under TSH stimulation [140–142]. The clinical counterpart of these biological events translates into greater sensitivity of the [^{18}F]FDG PET scan in the TSH-stimulated than in the TSH-suppressive state [143–149]. Metastatic lymph nodes even smaller than 1 cm can be detected by [^{18}F]FDG PET, although small lung metastases identified by CT can occasionally be missed on the PET scan. Although highly useful in certain clinical settings, [^{18}F]FDG PET cannot systematically replace WBS with radioiodide in all DTC patients and should be performed preferentially in patients with a negative high-dose ^{131}I-WBS and a high likelihood of persistent or recurrent disease.

Although the use of ^{124}I-iodide in patients with DTC was described over 50 years ago [150], it is only recently that sufficient evidence has

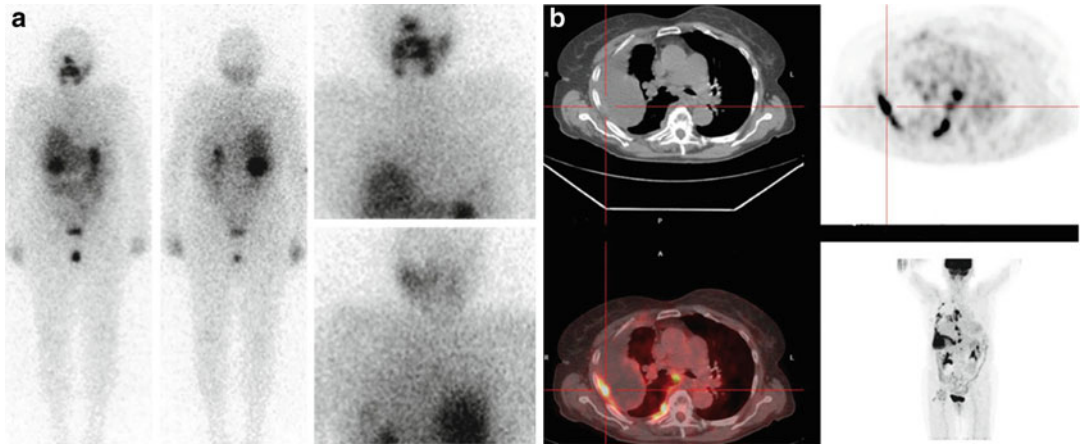

Fig. 6 (**a**) Anterior and posterior whole-body and spot images obtained 8 days after administration of 7.4 GBq (200 mCi) ^{131} I-iodide in a patient who had been submitted 17 years previously to thyroidectomy because of metastasis from DTC in a cervical lymph node. Histology had revealed two papillary cancers (columnar cell variant) measuring only 1 mm each. The patient was subsequently treated with several cycles of ^{131} I-iodide therapy totalling 35.5 GBq (960 mCi), with progressive loss of the iodine-trapping capability in metastatic lesions gradually spreading from cervical lymph nodes to the lung and pleura. Despite high levels of serum Tg and x-ray evidence of metastasis in the chest, the post-therapy scan does not reveal any focal area of abnormal ^{131} I-iodide uptake; nevertheless, scintigraphic visualization of the liver indicates some degree of radioiodide uptake in metastatic lesions, with subsequent release of radioiodinated hormones that are then metabolization in the liver. (**b**) Whereas PET/CT reveals high uptake of [^{18}F]FDG in pleuropulmonary lesions that are obvious also in the CT images (From Volterrani et al. [301], with permission of Springer Science+Business Media)

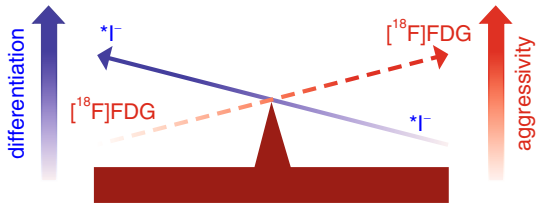

Fig. 7 Diagrammatic representation of the so-called "flip-flop" phenomenon that can be observed in patients with DTC, e.g., a somewhat inverse correlation between radioiodide uptake by tumor lesions (an index of cell differentiation generally associated with relatively low biologic aggressivity) and uptake of [^{18}F]FDG (an index of cell dedifferentiation almost invariably associated with high biologic aggressivity) (From Volterrani et al. [301], with permission of Springer Science+Business Media)

accumulated to propose clinical application of ^{124}I-iodide PET/CT to improve lesion detection in recurrent and/or metastatic DTC disease [151]. In fact, ^{124}I-iodide PET/CT provides images of higher spatial and contrast resolution (translating into higher target-to-background ratios) compared to planar or SPECT imaging with either ^{131}I- or ^{123}I-iodide [152] (see example in Fig. 8), thus resulting in superior accuracy combined with lower radiation exposure [153–155].

^{124}I-iodide PET/CT shows a 97% overall lesion detectability compared to 83% with the ^{131}I-WBS scan [156]. In particular, local lymph node and distant metastases that were undetected on the ^{131}I-iodide WBS are detected by ^{124}I-iodide PET/CT in 12% and 4% of the cases, respectively [157]. The superiority of ^{124}I-iodide PET/CT over ^{131}I-WBS has recently been confirmed also by Van Nostrand et al. who reported that, in 32% of patients with DTC, PET with ^{124}I-iodide identified 50% more foci of radioiodide uptake than planar scintigraphy with ^{131}I-iodide [158].

When restaging patients with recurrent DTC as shown by rising serum Tg levels, yet with a negative US of the neck, the combination of ^{124}I-iodide PET/CT with [^{18}F]FDG PET results in improved sensitivity (91%) compared with

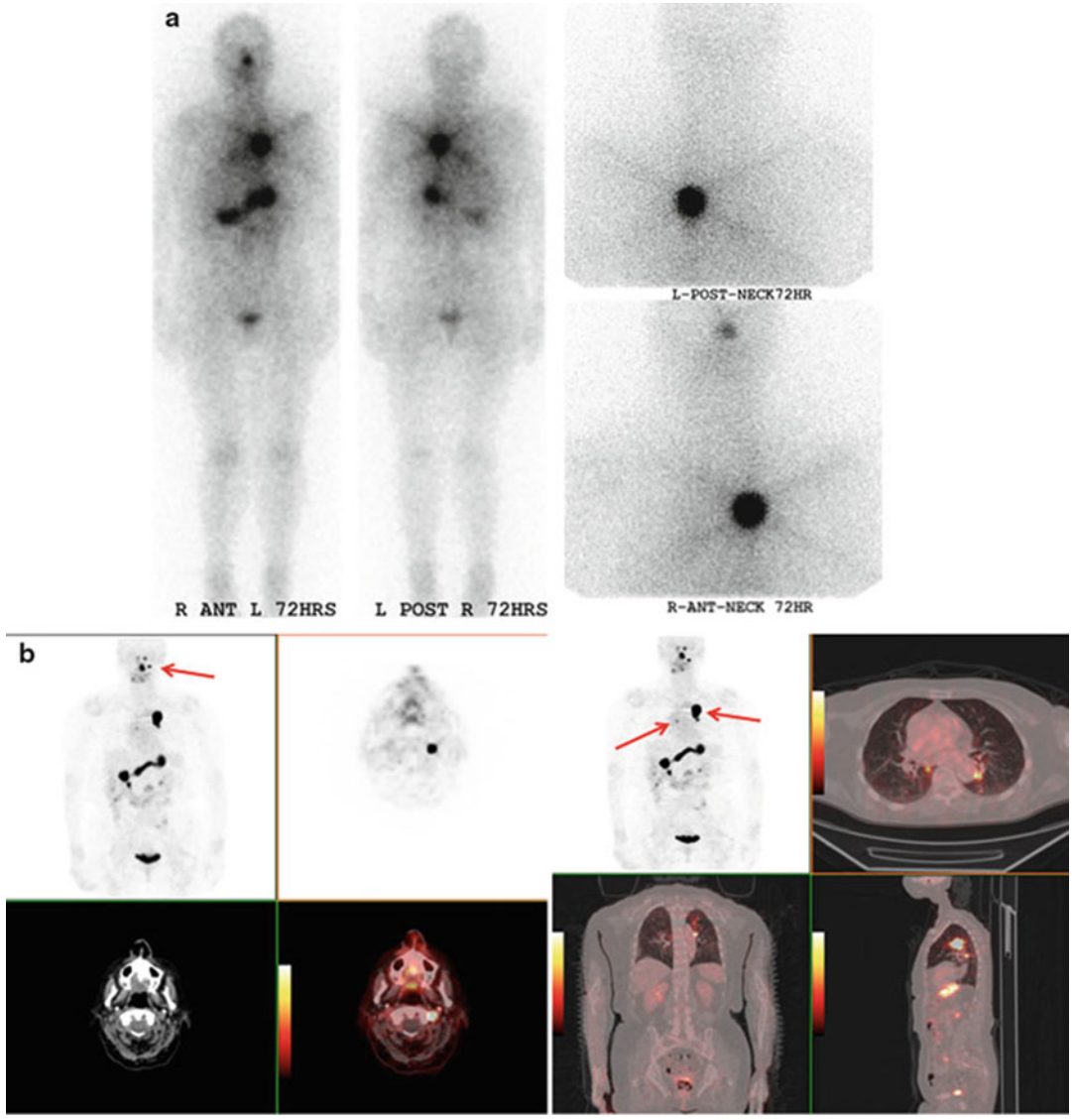

Fig. 8 Seventy-six-year-old woman with DTC (classified histologically as well differentiated). After total thyroidectomy she was treated with 7.4 GBq (200 mCi) ^{131}I-iodide, with evidence on post-therapeutic ^{131}I-WBS of pulmonary radioiodine-avid disease (**a**). Serum Tg progressively increased over time, with no evidence of disease progression on the CT scan and a negative [^{18}F]FDG PET/CT. PET/CT with ^{124} I-iodide showed high uptake in a voluminous mediastinal adenopathy, in two lung lesions and in a cervical left node (**b**). She was then retreated with 5.55 GBq ^{131} I-iodide (150 mCi), and the post-therapeutic ^{131}I-WBS showed high uptake only in the mediastinal adenopathy, but no uptake in the lung lesions or in the cervical region (Courtesy of Dr. Ravinder Grewal, Division of Nuclear Medicine, Memorial Sloan-Kettering Cancer Center, New York, NY, USA)

each PET imaging technique alone (80% and 70%, respectively) [159]. Nevertheless, although highly promising in principle, in patients with suspicion of diffuse lung metastases, quantitative analysis based on the lung/background ratio does not invariably allow to define an unequivocal diagnosis [160]. Furthermore, "shine-through" activity near the trachea, which is present in 17% of patients, can induce incorrect interpretation of imaging in this location [161].

Management of Locoregional Recurrences

Although recurrences are usually identified during the first year postprimary treatment, they may develop later on in the course of follow-up [13, 14]. In case of local recurrence, mortality at 30 years is 12%. Detection of a local or regional recurrence dictates complete workup to evaluate its extent and to search for distant metastases. Early detection of local relapse increases the survival rates of patients, especially if the recurring lesions are operable and/or radioiodine avid [10, 21].

In patients with local or locoregional recurrence, treatment with ^{131}I-iodide is often effective, as shown by a 50% reduction in the rate of further subsequent recurrences and in mortality at 30 years [11]. Therapy with radioiodide ensues complete response in 75–80% of the patients with regional lymph node metastasis, provided the radiation dose absorbed by the tumor tissue is at least 80–100 Gy, a target that is, however, difficult to achieve when the tumor lesion is large (i.e., greater than 1 cm in maximum diameter). Therefore, in case of bulkier recurrences, but still limited to lymph nodes (as shown by morphologic imaging, such as US, CT, and/or MRI), the first therapeutic option should be surgery, whenever possible [162]. In fact, surgical removal of metastatic lymph node(s) can successfully prevent further recurrence in 62% of the patients [163]. In this clinical setting, ^{131}I-iodide can play a role as adjuvant therapy.

Whereas, in case of small lymph node metastasis with high radioiodide uptake, the initial therapeutic approach can be based on administration of radioiodide [162]. The ^{131}I activity to be administered can be based on dosimetric estimates aiming at releasing the maximal safe dose to the patient, yet with a radiation dose >85 Gy to the lymph node(s), as well as to metastatic lesions at other sites (see example in Fig. 9). Alternatively, an empiric activity based on average estimates and prior experience can be administered, usually 3.7–5.5 GBq of ^{131}I-iodide.

As mentioned above, response to ^{131}I-iodide therapy is better in tumor foci smaller than 1 cm in diameter. In young patients with metastatic DTC, response to treatment with radioiodide is generally favorable concerning both locoregional recurrences and distant metastases. Indeed, radioiodide uptake was still detectable after three ^{131}I-iodide treatments in only 24% of patients who initially had small lymph node metastases and who then underwent surgery [109]. In contrast, treatment with ^{131}I-iodide is less effective in patients with larger tumor lesions, radioiodide uptake being still detectable after repeated ^{131}I-iodide treatments in 80% of the cases [164–166].

Even when lymph node metastases from DTC lose the ability to concentrate radioiodide, they may continue to be palpable or detectable by US examination. Nevertheless, although imaging modalities, such as US, CT, and MRI, generally have high sensitivity, their interpretation may be difficult in previously dissected areas, because of anatomic distortion and scar tissue. In contrast, ^{131}I-WBS may demonstrate neoplastic foci more specifically. Furthermore, a ^{131}I-WBS performed after administration of a large (i.e., therapeutic) amount of ^{131}I-iodide may detect new previously unrecognized lesions in up to 60–80% of the cases and remains the most sensitive diagnostic/localizing imaging modality in patients with functioning metastases from DTC [165].

Small and not growing cervical lymph nodes should not necessarily be treated. A “wait-and-see” strategy is nowadays suggested in these cases since the neck US can easily allow to monitor these lesions and be ready to perform a surgical treatment or any other appropriate therapeutic strategy [167]. When a significant increase in number or size is detected.

Management of Distant Metastases

Distant metastases occur in a subgroup of patients with DTC and can be discovered from 2 to 3 up to more than 10 years after initial treatment. This observation indicates that follow-up must continue throughout the patient’s life. In general, early detection of distant metastases is based on

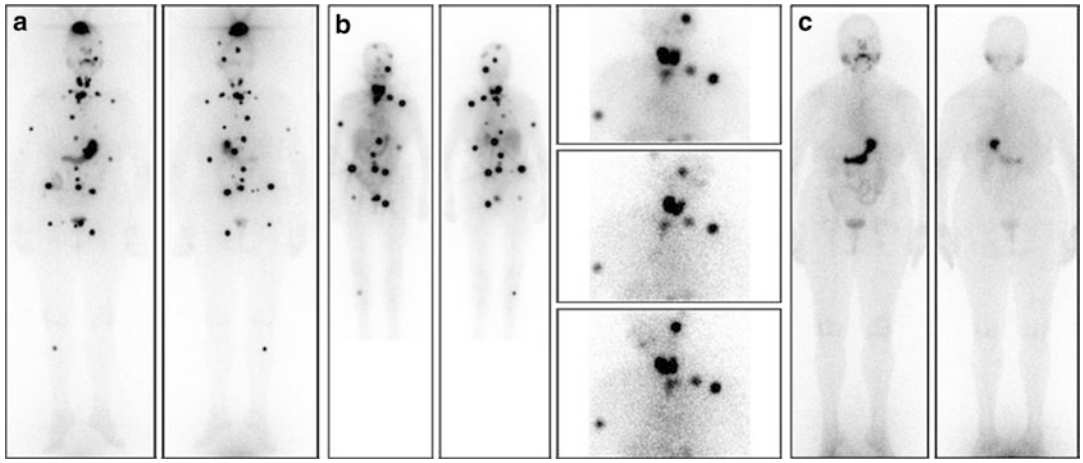

Fig. 9 Seventy-five-year-old patient referred to our center after histology of a lesion removed from the lumbar spine had revealed metastasis from DTC (well differentiated). The patient had been submitted 3 years previously to total thyroidectomy because of multinodular goiter (histology was not available). A dosimetric study was performed with ^{123}I-iodide (and converted into ^{131}I-equivalent data), scanning the patient until 72 h post-administration with both whole-body and spot acquisitions (including SPECT/CT at selected areas). In addition to uptake in the postsurgical remnant, diagnostic scintigraphy revealed numerous bone metastases scattered throughout virtually all the skeleton, including two bulky lesions in the skull (**a**); the peak of serum Tg at this time was 3,810 ng/mL after stimulation with rhTSH. The dosimetric study yielded very favorable estimates for the absorbed radiation dose, i.e., 63.5 mGy corresponding to an average absorbed dose of 250 Gy per lesion based on administration of 3.7 GBq ^{131}I-iodide. The two bulky lesions in the skull were removed surgically, and radioiodide was administered for therapy. The post-therapeutic ^{131}I-WBS scan acquired 10 days later confirmed high uptake in the metastatic bone lesions, with only some residual uptake in the skull (**b**). At the 1-year follow-up, serum Tg was undetectable with suppressed TSH, peaking at 0.6 ng/mL following rhTSH stimulation; the WBS performed with ^{131}I-iodide was completely negative (**c**). Six years later, follow-up continues to be negative (From Volterrani et al. [301], with permission of Springer Science+Business Media)

the combined use of serum Tg measurement and ^{131}I-WBS.

Most distant metastases from DTC are located in the lung (50–60%) or bones (20–30%). Liver, brain, and skin metastases, which are much more rare, are found in about 3% of patients at the time of the identification of a diffuse metastatic disease. They may also occur late after initial discovery of lung metastasis during the course of distant dissemination. In this latter instance, they yield a prognostic indication of rapid evolution of the disease (concerning especially skin metastases, a rather poor prognostic factor for survival). Metastases at multiple sites are present in about 10% of the patients with metastatic disease [165, 168]. The site of metastatic disease depends on a number of factors. Metastases in the lungs are more frequently observed in patients with PTC and in younger patients; indeed, they are virtually the only sites of distant metastases in children [169, 170]. In contrast, bone metastases are more frequently observed in patients with FTC and in older patients [165].

DTC patients with metastatic disease should undergo complete diagnostic workup. An ^{131}I-WBS performed after the administration of a therapeutic activity of ^{131}I-iodide (3.7 GBq, or 100 mCi) may clarify the extent and location of metastatic disease. In particular, a ^{131}I-WBS so performed often reveals lung metastases not visible on plain chest x-rays nor on CT. In this regard, only about half the patients with normal chest x-rays, who have diffuse uptake of ^{131}I-iodide in the lungs, have peripheral micronodular lung metastases detectable in the CT scan [171, 172]. X-rays are required also for patients with bone metastases that are painful and accumulate radioiodide, although it is either CT or MRI that helps

to delineate more precisely the extent of these metastatic lesions. MRI is particularly useful in the workup of metastases of the spine and base of the skull. Since most bone metastases from DTC are hypervascularized, arterial embolization may help to facilitate subsequent surgical removal [173–177].

Conventional therapeutic strategies such as surgery, radioiodide, external beam radiation therapy (EBRT), and systemic therapy with the new "targeted" therapies can all be used to treat metastatic DTC. The therapeutic strategy must be tailored to the individual patient by considering the number, size, location, and iodine avidity of the metastatic sites. Surgery should be considered with curative intent in patients with a single or few brain metastases. Lung metastases are often multiple, and surgical excision or pulmonary resection is rarely curative; in these conditions, surgery can prevent or delay the onset of clinical symptoms. Palliative surgery is required for bone metastases, ideally before orthopedic or neurological complications arise, especially when the risk of complications, such as vertebral collapse, is high [178]. Although no controlled studies have been performed on patients with metastatic thyroid cancer, diffuse metastatic bone disease may benefit from systemic therapy with zoledronate, similarly as it happens in patients with bone metastasis deriving from other solid tumors [179].

In approximately two-thirds of the patients, distant metastases from DTC concentrate radioiodide, a factor that facilitates their detection and treatment. Since accumulation of radioiodide may be higher in small lesions with a relatively low uptake than in bulky metastases with higher uptake, therapy with ^{131}I-iodide can ablate small foci of neoplastic tissue, whereas it can seldom ablate large tumor deposits [165]. A radiation dose higher than 80 Gy should be delivered to achieve cure; instead, the chances of success are remote in case of radiation doses lower than 35 Gy [9]. Although based on empiric estimates that do not take into account uptake measurements for each lesion in each individual patient, recommended therapeutic activities that should satisfy such desired radiation dose threshold are generally in the range of 3.7–5.5 GBq (100–150 mCi) of ^{131}I-iodide in adults and approximately 37 MBq/kg body weight (or 1 mCi/kg) in young children [180–183]. Higher activities, i.e., 7.4 GBq (200 mCi), or more have instead been recommended in patients with bone metastases [183]. In patients with diffuse, small lung metastases that are not visible on x-rays, a dosimetric approach is not feasible, as the mass of neoplastic tissue cannot be estimated. In these cases, some centers adopt the so-called Benua–Leeper approach, which is based on the maximum tolerable absorbed dose to the organ at risk [184]. For therapy with ^{131}I-iodide, the organ at risk is the red bone marrow; 2 Gy is the maximum limit that the red marrow can absorb. The maximum tolerable administered activity (i.e., the activity that would imply a 2 Gy dose to the red marrow) can be calculated using simple parameters, such as the blood kinetics following administration of a tracer activity of ^{131}I-iodide [185].

The outcome of ^{131}I-iodide therapy in patients with pulmonary metastases from DTC is variable from patient to patient (see examples in Figs. 10 and 11) and not obviously related to the initial total uptake of radioiodide in the lungs. Neoplastic masses are probably smaller in patients with lower uptake. Subsequent treatments with ^{131}I-iodide are given 6 months later for 1–2 years and then annually until there is no more evidence of residual radioiodide uptake on post-therapeutic ^{131}I-WBS. Of course, between two treatment courses, l-T4 TSH-suppressive therapy is continued with the aim of reducing serum TSH to levels not stimulating tumor growth.

Although there is virtually no limit to the cumulative ^{131}I-iodide activity that can be given to patients with distant metastases, the risk of second primary malignancies (especially leukemia) rises slightly for cumulative administered activities higher than 22.2 GBq (600 mCi) [61, 62]. Furthermore, it should be considered that higher cumulative activities are presumably of little benefit because of the progressive loss of iodine-trapping property of metastatic lesions [186].

As mentioned in ► Chap. 19, "Diagnostic Applications of Nuclear Medicine: Thyroid Tumors" with reference to postsurgical ablation of thyroid remnants, radioiodide therapy of

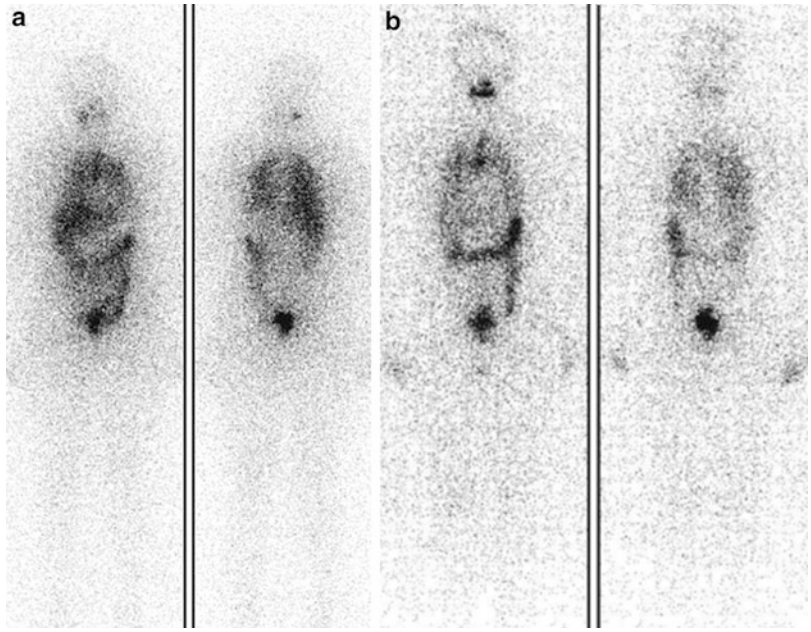

Fig. 10 ^{131}I-WBS images obtained in two separate occasions 7–10 days after administration of ^{131}I-iodide for therapy of pulmonary metastases in a patient already treated for DTC with total thyroidectomy and radioiodide remnant ablation. (**a**) October 2005 (at the age of 25 years): diffuse uptake in the pulmonary parenchyma, indicating miliary-type metastatic involvement (serum Tg 21 ng/mL under endogenous TSH stimulation achieved with l -T4 withdrawal). (**b**) June 2009: progressive improvement of the pulmonary metastatic involvement following repeated therapies totalling 28.5 GBq (770 mCi) of ^{131} I-iodide (serum Tg 8 ng/mL under endogenous TSH stimulation achieved with l-T4 withdrawal); thymic uptake of radioiodide (frequently seen in younger patients) is now more evident in the post-therapy scan (From Volterrani et al. [301], with permission of Springer Science + Business Media)

recurrent/metastatic lesions from DTC must be performed under TSH stimulation, with a minimum threshold conventionally set at a serum TSH level of 30 μIU/mL. These high TSH levels can be obtained through withdrawal of l-T4 therapy, with resulting transient hypothyroidism; unfortunately, the use of recombinant human TSH has not been approved yet for the preparation of patients with metastatic DTC before therapy with ^{131}I-iodide (except in case of failure of the pituitary to produce TSH), although there is evidence that it can produce the same result as the withdrawal of the l-T4 [187–189]. However, when a severe consequence of the hypothyroidism can be envisaged, the rhTSH may be employed inside the "compassionate" program or, in some countries, as "off label." It should be also considered that the use of rhTSH greatly reduces the exposure of the body (i.e., bone marrow) to the possible damage from radioiodine exposure [190, 191].

Pre-therapy evaluation with a diagnostic ^{131}I-WBS (performed by administering 185 MBq ^{131}I-iodide) is useless in patients with known metastases, since the results of this evaluation will not alter the therapeutic strategy and, because of the possible "stunning" effect, may actually interfere with the uptake of the subsequent therapeutic activity of ^{131}I-iodide. Instead, a ^{131}I-WBS performed 4–7 days after administration of a therapeutic activity of ^{131}I-iodide may clarify both the distribution and metabolic activity of metastases, including those that had gone undetected prior to ^{131}I-iodide therapy (see Fig. 12). Alternatively, the use of ^{123}I-iodide can be envisaged in the pre-therapy phase (either for diagnostic/localization purposes and/or for dosimetric estimates), since this radionuclide does not induce a stunning effect.

Furthermore, one of the main advantages perceived with the use of ^{124}I-iodide PET/CT in patients with DTC candidate to therapy with

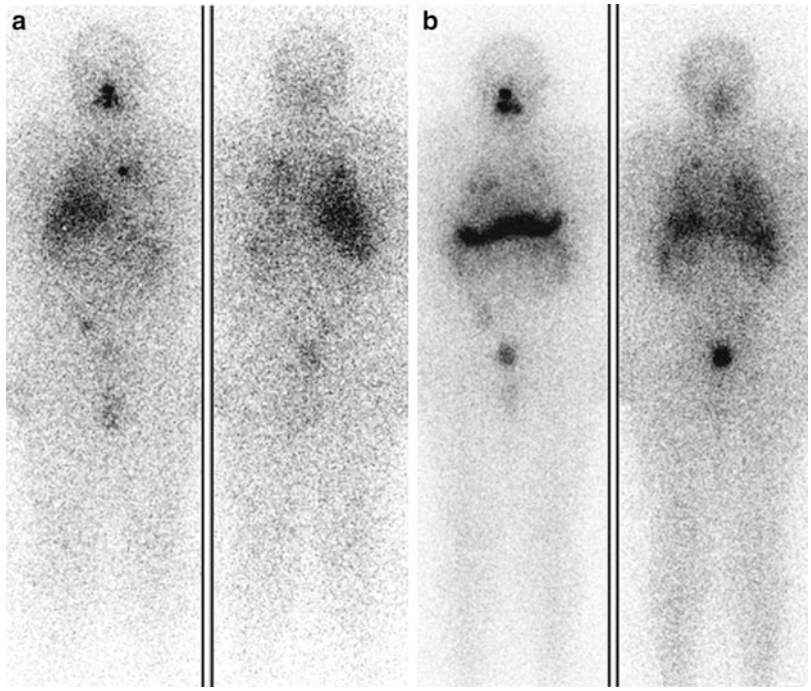

Fig. 11 ^{131}I-WBS images obtained in two separate, sequential occasions 7–10 days after administration of ^{131}I-iodide for therapy of pulmonary metastases (with predominantly macronodular pattern) in a patient already treated for DTC with total thyroidectomy and radioiodide remnant ablation. (**a**) September 2006: besides a pattern of diffuse metastatic involvement, radioiodide uptake can clearly be seen also with a macronodular pattern, more obvious in the left para-hilar region (serum Tg 251 ng/mL under stimulation with rhTSH). (**b**) July 2007: partial regression of the left para-hilar lesion, but development of macronodular lesions in the right lung (serum Tg 1,918 ng/mL under stimulation with rhTSH) (From Volterrani et al. [301], with permission of Springer Science+Business Media)

^{131}I-iodide – whenever this procedure is available – is the possibility of accurate quantification of radioiodide uptake as a basis for more accurate dosimetric estimates than with the single-photon-emitting radionuclides [192, 193]. In fact, lesion dosimetry based on planar gamma camera or SPECT images may result in inaccurate estimates of the absorbed dose due to the difficulty of measuring the target lesion volumes (especially for small lesions) and of reliably measuring radioiodine uptake using ^{131}I-iodide as the tracer (due to low spatial resolution and imaging sensitivity). The feasibility of calculating the mean absorbed dose in patients using ^{124}I-iodide PET images was described in 1999 [194], after reports on preliminary quantitative phantom studies [152].

Accurate lesion quantification for dosimetry estimates is possible using the approach of recovery coefficients (RCs), a method that allows to correct the activity concentration in the lesions imaged for partial-volume effect and for the prompt gamma coincidence effect due to the complex decay scheme of ^{124}I-iodide [195]. Several protocols for dosimetry estimates have used serial PET measurements from three to five time points, combining imaging scans at 4, 24, 48, 72, and 96 h post-administration (more rarely until 144 h) [192, 193]. The five-point protocol is certainly the most accurate approach, although even a simplified two-point protocol (i.e., 24 and 96 h) can be employed for determining the lesion absorbed dose per administered ^{131}I-iodide activity (LDpA) within a 20% uncertainty compared to the more complex protocol [196].

As a quantitative tomographic imaging modality, PET/CT with ^{124}I-iodide is especially useful to

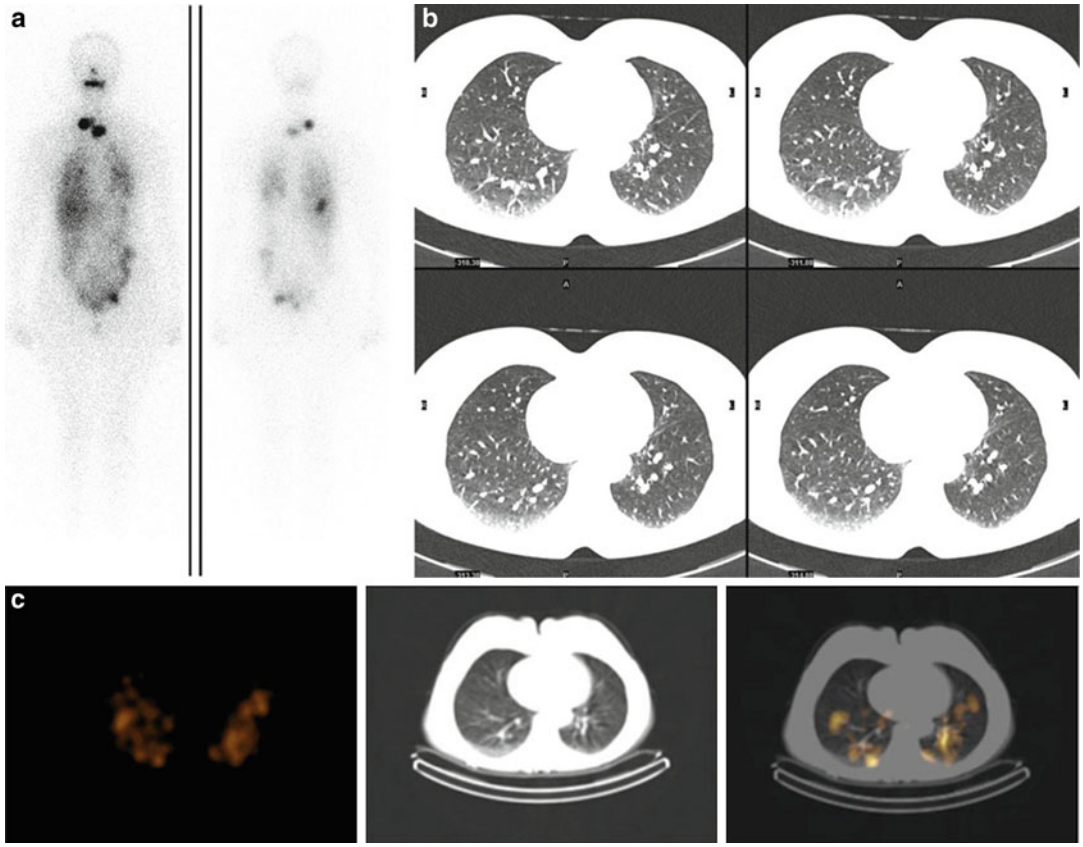

Fig. 12 Fifty-three-year-old patient with follicular variant of PTC infiltrating the thyroid capsule. US examination prior to remnant ablation with ^{131}I-iodide revealed metastasis in cervical lymph nodes; 4.8 GBq (130 mCi) of radioiodide was administered upon stimulation with rhTSH (with ensuing 219 ng/mL peak Tg level). Post-therapy WBS (**a**) showed radioiodide uptake in the metastatic cervical lymph nodes, as well as a pattern of diffuse uptake in the lungs indicating presence of metastasis that was unrecognized before therapy and was undetectable on diagnostic CT (**b**, with transaxial sections at different levels). SPECT/CT (**c**) better characterized the pulmonary areas that, despite not being associated with abnormalities on the CT component, were the site of lung metastasis from DTC

calculate the mean dose for normal organs using a three-dimensional internal dosimetry software, and the results of which are comparable with those obtained with OLINDA dosimetry [197]. Widely variable values have been reported for the mean absorbed dose estimated with ^{124}I-iodide PET, ranging 0.4–49 Gy/Bq (absorbed dose distribution from 0.3 to a maximum of 4,000 Gy). This is probably the result of the wide range in the ^{124}I effective half-life values observed in recurrent/metastatic lesions from DTC, that is, between 22 and 65 h in one report [194], between 14 and 43 h in another study [188], and between 6 and 80 h in a more recent report [196]. As per today's knowledge, ^{124}I-iodide PET dosimetry certainly constitutes an important tool in pre-therapy evaluation of patients with DTC [198], to be possibly used in the clinical routine whenever available [199]. However, evidence-based long-term data on the clinical impact of such accurate dosimetric calculations have not yet been published.

When radioiodide uptake is no longer demonstrable on post-therapeutic WBS, treatment with ^{131}I-iodide should be discontinued. EBRT and local treatments (thermoablation, laser-therapy, etc.) may be considered as first approach when radioiodide is no more effective and surgical

removal of metastases is not feasible. However, since the growth rate of DTC metastases is usually slow, a "wait-and-see" approach with six monthly controls seems warranted in this setting [18, 162]. Instead, if the lesions are rapidly growing and fulfilling the Response Evaluation Criteria in Solid Tumors (RECIST) criteria, a targeted therapy can be initiated [200].

Advanced DTC Refractory to Radioiodide Treatment

About 15% of DTCs become radioiodide refractory after several courses of ^{131}I-iodide treatments because of tumor dedifferentiation. In these patients, other therapeutic strategies must be defined. Among these, the approaches most commonly adopted in the past attempted at inducing "redifferentiation" of the "dedifferentiated" TC cells.

Reinduction of the Ability to Take Up Iodine

The possibility to restore the ability to take up iodine in radioiodine-refractory DTC has been recently explored. Treatment with all-trans-retinoic acid has proven effective in re-differentiating neoplastic cell clones in patients with acute promyelocytic leukemia, thus making them susceptible to chemotherapy [201]. This favorable experience has prompted similar attempts with retinoic acid in patients with non-iodine-avid metastatic DTC, aimed primarily at restoring the ability to trap iodine by acting on the NIS system [202, 203]. Several studies have been performed which demonstrated the ability of retinoic acid to reinduce iodine uptake [203–209]. Despite all these efforts, the final result is that retinoic acid can work, but only on a relatively low percentage of dedifferentiated DTCs, determining just a small control of tumor growth.

Recently, selumetinib, a new drug able to block the activity of MEK, has been demonstrated to be able to both reinduce the ability concentrate iodine in dedifferentiated DTC and determine an objective tumor size reduction as documented by CT scan [210]. Clinical trials on the effect of selumetinib on metastatic radioiodine-refractory DTC are ongoing in different academic centers throughout the USA.

Conventional Chemotherapy

When DTCs are metastatic, non-iodide-avid and rapidly growing, conventional therapies such as EBRT and chemotherapy are only minimally effective. The only chemotherapy agent that appeared to be effective in patients with metastatic DTC is doxorubicin [211]. Although a 33% response rate has been reported with doxorubicin as a single agent (60 mg/m^2 every 3–4 weeks), this observation has not been confirmed by subsequent studies, in which response rates ranged from 0% to 22% (all responses being partial and lasting only few months, without any survival benefit) [212, 213]. In two studies where doxorubicin was combined with cisplatin, the response rates were similar as those observed with doxorubicin alone, but at the expense of major toxicity [214, 215]. Although an increased response rate has been observed in patients treated with cisplatin plus epirubicin after TSH stimulation relative to non-stimulated patients treated with the same drugs [216], these promising results should be confirmed in larger series. With the introduction of new targeted therapies based on tyrosine kinase inhibitors (TKIs), the use of conventional chemotherapeutic agents is strictly limited to those few cases that cannot be treated with TKIs [2].

New Targeted Therapies

Following the discovery of oncogenic mutations involved in the pathogenesis of PTC and MTC, several novel targeted drugs have been developed in the last decade for treating these patients. These biological agents inhibit tumor growth by blocking physiological processes such as angiogenesis (i.e., they act as antivascular agents) and/or intracellular signaling. Most of them are

tyrosine kinase inhibitors (TKIs) and are able to partially inhibit multiple kinases and signaling pathways alike. Since the RET oncogene plays an important pathogenic role in both PTC and MTC, its inhibition may be relevant for controlling tumor growth. Motesanib (AMG706), vandetanib (Caprelsa®), imatinib (Gleevec®), sorafenib (Nexavar®), lenvatinib (Lenvima®), and cabozantinib (Cometriq®) are all RET inhibitors that effectively block tumor growth in vitro [217]. It is worth noting that all these TKIs have multiple targets, and they act also against VEGFR1-3, PDGFRβ, and others. In many cases the anti-VEGFR action is the most significant, and the antiangiogenic effect highly contributes to shrinkage of the tumoral mass. Sorafenib is the only known TKI agent able to block the serine kinase BRAF that is mutated in about 40% of PTCs. Motesanib has been the first TKI tested in a phase II/III trial, in which it was shown to induce partial responses in patients with progressive advanced metastatic DTC [218] and MTC [219]. Unfortunately, motesanib was not submitted to the authorities for the approval in the treatment of advanced DTC. Recently, the results of the phase III study (ZETA trial), which explored the activity of vandetanib in the treatment of advanced MTC, have been published showing a significant prolongation of progression-free survival (PFS) in patients with progressing MTC [220].

Cabozantinib has been also tested for the treatment of advanced MTC showing progressing disease, according to RECIST criteria, in the prior 14 months (EXAM study). The study, a multicenter, randomized, and international phase III study, clearly demonstrated that patients treated with this drug had a longer PFS time and a greater objective response rate (ORR) [221]. Based on these results, cabozantinib has been approved by both FDA and EMA for the treatment of advanced and progressive MTC. Interestingly, cabozantinib showed good results also in patients who had previously been treated with vandetanib and entered into progression after initial response; this observation implies the possibility of efficaciously using cabozantinib as a second-line treatment in progressive MTC [222].

Sorafenib, which is being used for the treatment of advanced hepatocellular and renal cell cancer since several years, has been recently approved by both FDA and EMA for the treatment of advanced and progressive DTC. Approval was promoted by the excellent results obtained in a phase III trial (DECISION study) in which patients treated with sorafenib showed a significantly longer PFS with respect to those treated with placebo [223]. As for the majority of TKIs, the efficacy of sorafenib in controlling tumor growth has a limited time span (mean 10.8 months); for this reason, other TKIs have been explored for the treatment of advanced DTC. The very promising results of a phase II study regarding the use of vandetanib in advanced DTC [224] are now being better explored in a phase III study (VERIFY trial) that is still ongoing. Recently, another TKI, Lenvima, has been approved both in the USA and in Europe, for the treatment of advanced, metastatic, and progressive DTC and PDTC. The phase III study (SELECT study) [225] showed promising results regarding both PFS and ORR in patients treated with the drug with respect to those treated with placebo. Most interestingly, both the FTC subgroup and the group of older patients (>65 years) showed also a significant prolongation of the overall survival. Moreover, lenvatinib showed excellent results also in patients who had previously been treated with other TKIs and entered into progression.

All TKIs have very important side effects that must be taken into consideration before starting the treatment. Fortunately, most of these side effects can be controlled with other drugs, as in the case of hypertension or diarrhea or allergies, while others require a dose reduction. In many cases the dose reduction is a reasonable compromise between the drug efficacy and the drug toxicity [226].

Despite the approval of two TKIs for MTC and two for DTC/PDTC, it is still necessary to identify other drugs with different actions, for example, nivolumab, a humanized IgG_4 anti-programmed death-ligand 1 (anti-PD-1) monoclonal antibody, or other biologically logical combinations of therapeutic targets in order to maximize synergistic effectiveness. In this regard, the American

Thyroid Association guidelines for the treatment of either DTC or MTC clearly indicate that patients with advanced disease should be offered to participate in clinical trial with TKIs or to be treated with TKIs already approved – rather than with conventional chemotherapy [162, 227].

External Beam Radiation Therapy

The role of EBRT for the treatment of recurrent DTC confined to the neck remains controversial [228]. There are no prospective randomized controlled trials to confirm a therapeutic value, which is so far suggested by retrospective analyses only. Although some authors have reported that EBRT was rather ineffective [211, 229], other data support the view that this modality of treatment may actually improve local control in selected patients. In particular, EBRT may be warranted in patients older than 40 years with PTC and extrathyroidal invasion without significant ^{131}I-iodide uptake in the neck. In these patients, EBRT may destroy neoplastic cells unresponsive to radioiodine therapy. Indeed, the analysis of patients with recurrent PTC showed that locally invasive carcinoma, in contrast to lymph node recurrence, often did not concentrate iodine [211]. Patients with inoperable gross residual disease after surgery also appear to benefit from EBRT, which can be combined with ^{131}I-iodide therapy to treat a poorly differentiated tumor component. In these patients, a combination of EBRT with low-dose doxorubicin (10 mg/m^2 per week) may improve tumor response [230]. The most common acute complications of EBRT are transient esophagitis and tracheitis. Long-term complications are neck fibrosis, decreased salivary flow, and consequent parodontitis. Arterial thrombosis, brachial plexus neuropathy, laryngeal necrosis, or radiation-induced tumors (soft tissue sarcomas) have been observed in about 5% of the patients [231]. These severe complications clearly demonstrate that EBRT should be offered only to those patients with non-iodine-avid tumors who are technically inoperable or too ill to tolerate major resections. EBRT can be used as palliative therapy for some bone metastases (especially if they cannot be treated with surgery), to control local pain. Similarly, EBRT could be indicated for diffused brain metastases.

Treatment of Anaplastic Thyroid Cancer

Multimodality treatment of ATC includes surgery, EBRT, and combination chemotherapy; nevertheless, despite all therapeutic attempts, median survival does not exceed 1 year. The possibility to perform radical surgery should always be considered in patients with newly diagnosed ATC, since this option somewhat improves survival of these patients [232, 233]. If total thyroidectomy is not possible, at least debulking of the tumoral mass to improve the local symptoms should be performed, whenever possible [234]. Tracheostomy is performed for impending airway obstruction, but not as a prophylactic approach. Radiometabolic therapy with ^{131}I-iodide does not apply to ATC, because the original follicular cells have lost all features of differentiation, among which the ability to concentrate and retain iodine. In some instances, neoadjuvant hyperfractionated EBRT and chemotherapy with doxorubicin followed by surgery can achieve local control of the disease prior to surgery [235, 236].

Several chemotherapy regimens either with single agents or with various combinations (such as doxorubicin, etoposide, cisplatin, bleomycin, and vincristine) have been attempted [237–239], but none of these approaches has shown adequate control of the disease. ATC cells are particularly chemoresistant, possibly through a mechanism of multidrug resistance mediated by overexpression of the P-glycoprotein [236, 239].

Novel therapeutic strategies based on molecular approaches are under investigation, such as RET proto-oncogene or BRAF-targeting drugs [240, 241]. Inhibition of the EGFR and VEGFR signaling pathways have also been shown to inhibit tumor growth and angiogenesis in experimental ATC models, thus opening a new avenue to the treatment options available for ATC [242, 243]. Recently, new drugs have been explored for the treatment of ATC such as combretastatin, a "vascular disrupting agent" that inhibits the

polymerization of tubulin of cytoskeleton with a selective action on newly formed tumoral endothelial cells. Combretastatin has been shown to have direct antitumor effects in vivo and in vitro, by destabilizing spindles and inducing apoptosis; the end result is the disruption of neovascular endothelial cells with interruption of blood flow to the tumor. A phase II/III study showed a clinical advantage of the use of combretastatin associated with chemotherapy (carboplatinum and placlitaxel [CP]) with respect to chemotherapy alone. In fact, the 1-year survival for CP/combretastatin versus CP alone was 26% versus 9%, respectively [244].

New therapeutic approaches are being explored with lenvatinib in vitro (using ATC cell lines) and in animal models (xenografted mice) [245], and a phase II/III international multicenter study is planned to start soon.

Initial Treatment of Medullary Thyroid Cancer

Wide consensus has been reached on the concept that total thyroidectomy and lymph node dissection of the central neck compartment is the treatment of choice for MTC; therefore, a definite presurgical diagnosis of MTC is crucial for planning this surgical approach, and any effort to achieve such diagnosis should be undertaken [246]. In this regard, measuring calcitonin (Ct) concentration in the washout of the needle used for FNAC of a suspected thyroid nodule may be useful for diagnosing MTC [247]. This approach is of particularly useful also to ascertain the nature of enlarged neck lymph nodes, especially before thyroidectomy, in order to better plan the surgical approach or the most appropriate therapeutic strategies [247]. The possibility of avoiding central node neck dissection in RET gene carriers who undergo prophylactic thyroidectomy and who do not yet have evidence of clinical and/or biochemical disease has been well defined in the more recent MTC guidelines [248].

Cure and survival rates in patients with MTC strongly correlate with age and with the stage at diagnosis. Elevated serum CEA levels (above 5–10 ng/mL) preoperatively are correlated with a bigger tumor size and greater number of lymph node metastases, thus reflecting the burden of disease. Postoperative hypercalcitoninemia indicates persistent MTC, which occurs in 30–55% of the patients after primary surgical treatment, particularly when the tumor is not more confined to the thyroid [249]. Instead, rising serum Ct levels after the initial decline to biochemically free disease following surgery indicate recurrent disease, an occurrence observed in 5–12% of patients after total thyroidectomy [250].

Follow-Up of Medullary Thyroid Cancer

MTC patients are followed by monitoring the serum Ct and CEA levels and by neck US examination. Evaluating these biochemical and clinical parameters every 6–12 months allows the clinicians to assess the clinical status of the patients and to discover early those who need medical treatment. Overall survival is closely related to postsurgical recurrences and/or to the appearance of distant metastases, events that reduce the 10-year survival rate to 40%.

Serum Ct is the most specific and sensitive marker for MTC, both before and after thyroidectomy. It is a small polypeptide hormone (32 amino acids) normally produced almost exclusively by the parafollicular C cells. Ten years after the recognition of MTC as a distinct histologic type of thyroid cancer, high levels of Ct have been demonstrated to be present both in the tumoral tissue and in the serum of patients with MTC [251, 252]. Elevated baseline serum levels of Ct are diagnostic for MTC [252]. Routine measurement of serum Ct in patients with nodular thyroid disease allows the preoperative diagnosis of unsuspected sporadic MTC [246]. In this regard, assaying serum Ct facilitates the early diagnosis of MTC, usually when the tumor is still at stage I, thus favoring successful surgical treatment [253]. Ct doubling time in serum is the most sensitive biomarker for MTC progression. On the other hand, normal postoperative CEA levels are sometimes observed in patients with metastatic disease. Nevertheless,

serum CEA may be used as a surrogate tumor-associated marker in those MTCs that do not secrete Ct [254]. There are some recent evidences that elevated levels of serum Ca 19.9 in patients with advanced MTC represent a prognostic factor for poor survival [255, 256].

Accurate identification of the sites of recurrences is essential for patient management. Diagnostic imaging workup for the evaluation of local relapse or of regional recurrence includes US of the cervical region, CT scan, and MRI.

Radionuclide Imaging in Recurrent MTC

The role of nuclear medicine in patients with MTC is important mostly in the postoperative workup, to detect residual or recurrent tumor. Nevertheless, radiopharmaceuticals can also be employed for therapy of recurrent/metastatic MTC (see below). Diagnostic agents for MTC include both single-photon-emitting and positron-emitting radiopharmaceuticals. Of particular interest among the former group is pentavalent ^{99m}Tc-labeled dimercaptosuccinic acid (^{99m}Tc(V)-DMSA), a nonspecific tumor-seeking agent that has been used to evaluate many types of cancers including breast tumors, head and neck cancers, osteosarcomas, and hepatocellular carcinoma. Although the exact mechanism of ^{99m}Tc(V)-DMSA uptake in tumor cells is still poorly understood, it seems to be mediated by the sodium phosphate cotransporter type III [257]. Concerning MTC, this radiopharmaceutical has been used to localize the site of disease in patients whose serum Ct levels increase, yet who are clinically free of disease. Scintigraphy with ^{99m}Tc(V)-DMSA has sensitivity up to 70%, associated however with low specificity because of its accumulation also at inflammatory sites [258, 259]. It should also be noted that this radiopharmaceutical is not currently commercially available in most countries, although it can be prepared according to relatively easy to perform in-house formulations.

Scintigraphy with the nonspecific tumor-seeking agent ^{99m}Tc-Sestamibi has overall 56% sensitivity for detecting recurrent MTC in patients with serum Ct levels in excess of 6 ng/mL; this imaging procedure is especially useful for postoperative evaluation of cervical and mediastinal regions, where a high target-to-background ratio can be observed [260] (Fig. 13). ^{99m}Tc-Sestamibi scintigraphy has improved sensitivity when combined with CT scan and/or other imaging procedures.

Scintigraphy with the somatostatin analog ^{111}In-pentetreotide (OctreoScan®) is not extensively employed for the evaluation of MTC patients, because the distribution of somatostatin receptors is not homogeneous among different tumor lesions and generally lower than in other neuroendocrine tumors [261]; these features explain the wide range in sensitivities reported for OctreoScan® scintigraphy, from 35% to 75% [262, 263]. The highest sensitivity is reported in patients with neck and mediastinal lymph node involvement, while it is lowest for distant metastases [264]. An important indication for somatostatin-receptor scintigraphy with OctreoScan® is for pretreatment evaluation in patients candidate to therapy with radiolabeled somatostatin analogs.

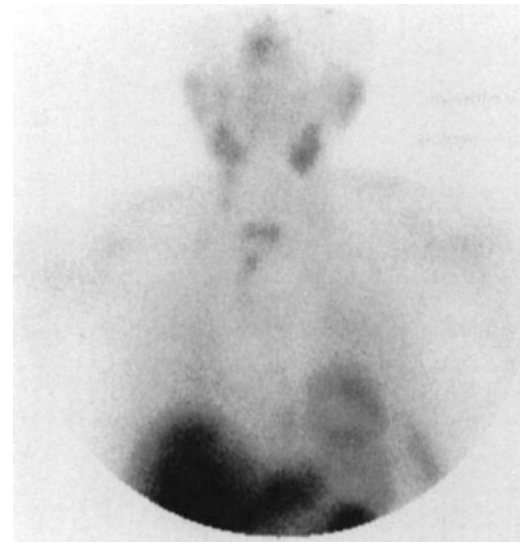

Fig. 13 Planar scan with ^{99m}Tc-Sestamibi of the neck and chest in a patient who had undergone total thyroidectomy because of medullary thyroid cancer 2 years earlier. During follow-up serum calcitonin reached 6.24 ng/mL. This spot view demonstrates the presence of three mediastinal lesions and two cervical lesions (*right side*) (From Learoyd et al. [260], with permission)

^{123}I-metaiodobenzylguanidine (^{123}I-MIBG, structurally similar to norepinephrine) accumulates in tumors arising from the neural crest. Scintigraphy with ^{123}I-MIBG has very high sensitivity (about 95%) in patients with MTC [265], with an especially high accuracy for staging patients with MEN II and familial MTC. Instead, the sensitivity of ^{123}I-MIBG scintigraphy in patients with increased serum Ct but who are clinically free of disease is only 38% [266] (Fig. 14).

Ligands for the gastrin/cholecystokinin B receptor (CCK-BR) constitute a new class of peptides that can be radiolabeled and utilized for diagnosis or for therapy of CCK-BR-expressing tumors; among these, MTCs express the CCK-BR in almost 90% of the cases [267]. ^{111}In-labeled derivatives of gastrin (^{111}In-DTPA-D-Glu^{1}-minigastrin) showed excellent targeting of CCK-BR-expressing tumors, with 94% sensitivity [268, 269]. Minigastrin may also be labeled with ^{90}Y or with ^{177}Lu for therapeutic purposes [270, 271].

Immunoscintigraphy with radiolabeled monoclonal anti-CEA antibody provides high sensitivity (75–100%) to detect recurrent MTC in patients with aggressively growing forms of this tumor [272]. However, this radiopharmaceutical is not commercially available.

The diagnostic performance of single-photon-emitting radiopharmaceuticals is in general unsatisfactory in MTC patients, due to variable tracer uptake and to relatively low spatial resolution. Instead, PET imaging agents can be successfully employed in MTC (see example in Fig. 15).

[^{18}F]FDG PET suffers from several limitations in the case of MTC, because these tumors are generally characterized by a metabolic activity that is only slightly increased with respect to normal cells, while their degree of differentiation and secretory profile are quite variable. Indeed, [^{18}F]FDG PET sensitivity in patients with MTC is associated with Ct serum levels higher than 500 pg/mL, Ki-67 scores higher than 2.0%, and short Ct doubling time in serum [273]. In particular, sensitivity of [^{18}F]FDG PET in patients with Ct levels below 500 pg/mL is only 20%, while it is 78% in patients with more elevated serum Ct levels (1,000 pg/mL) [274]. On the other hand, the diagnostic performance of [^{18}F]FDG PET in detecting lymph node involvement in the cervical and mediastinal regions is higher than that of

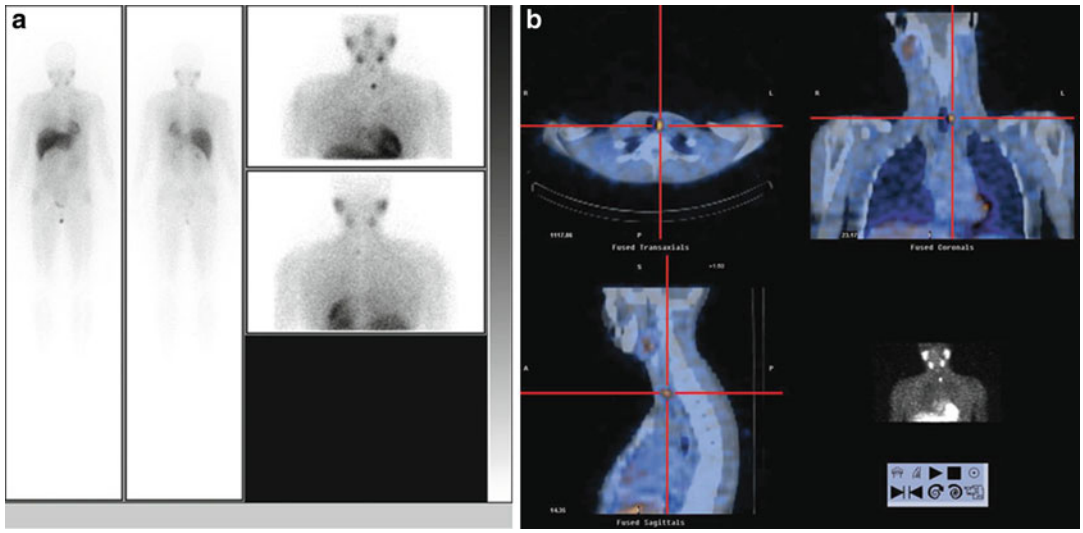

Fig. 14 Scintigraphy with ^{123}I-MIBG in a patient already submitted to thyroidectomy because of medullary thyroid carcinoma; investigation performed because of progressively rising serum Ct levels. (**a**) Planar whole-body images and spot acquisition on the chest and neck (both acquisitions in the anterior and the posterior views), showing local recurrence in the neck. (**b**) SPECT/CT of the 3neck (fused SPECT/CT images in the three planes), showing exact topographic localization (left thyroidal postsurgical bed) of the lesion detected in the planar images

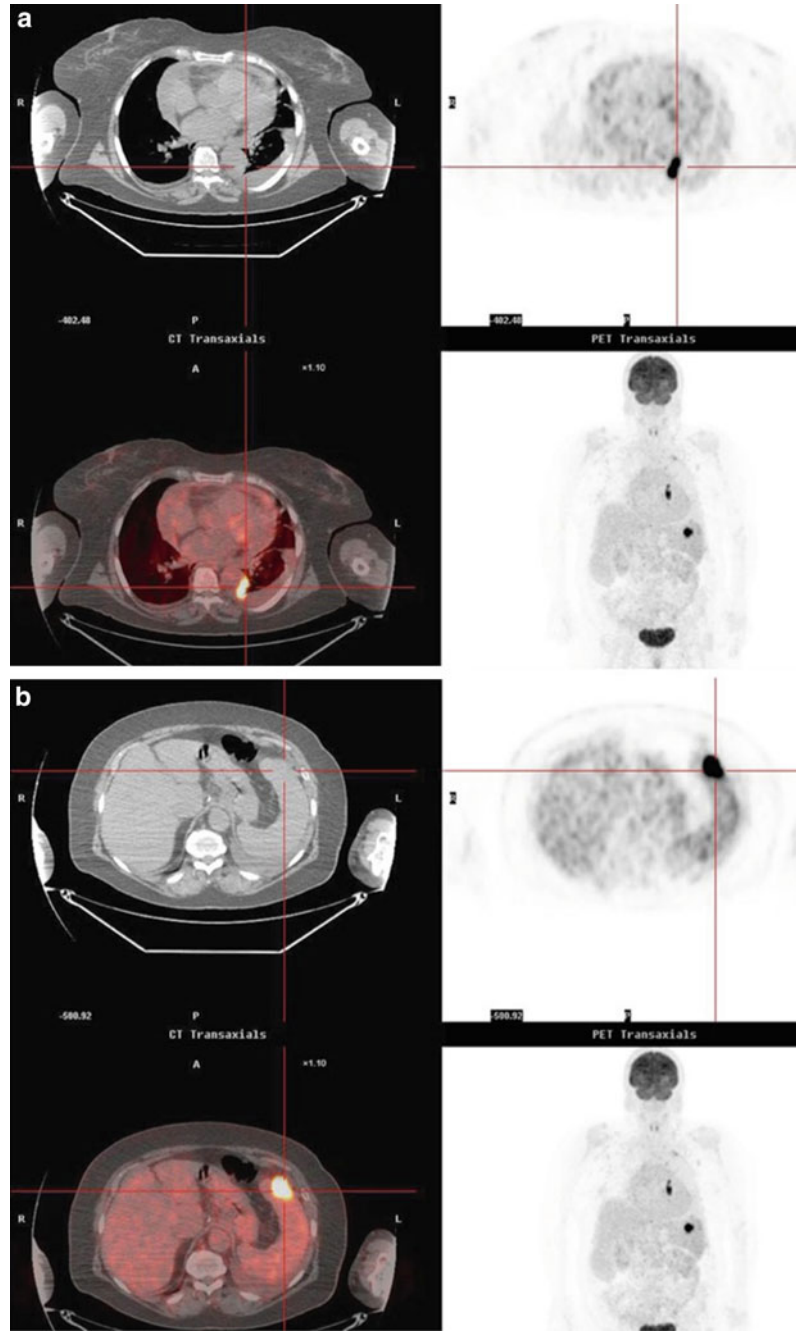

Fig. 15 [^{18}F]FDG PET/CT in a patient developing distant metastases from MTC, about 18 months after surgery of the primary tumor. (**a**) Left pleural metastasis of disease. **b** Splenic metastasis

other imaging methods (CT, MRI, and ^{131}I-MIBG scintigraphy) with sensitivity ranging from 76% to 96% [275]; nevertheless, sensitivity of PET with [^{18}F]FDG is low for small pulmonary metastases and for detecting bone involvement [276].

PET with ^{18}F-DOPA or with ^{68}Ga-labeled somatostatin analogs has recently been proposed for patients with MTC. Concerning in particular the former PET agent, it should be considered that the C cells are neuroendocrine cells belonging to the APUD system, i.e., they have the property to

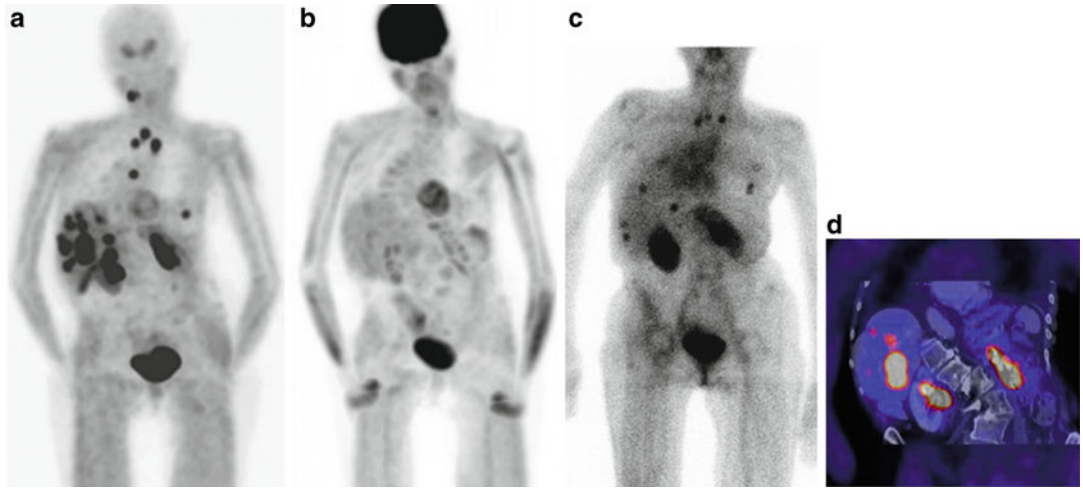

Fig. 16 Comparative imaging of a 68-year-old woman with metastatic medullary thyroid cancer related to a MEN 2A syndrome. Her Ct doubling time was 91 months (Ct, 27,190 ng/L), and her CEA doubling time was 151 months (CEA, 1,460 mg/L). (**a**) ^{18}F-DOPA PET shows the largest number of lesions, located in the neck, upper mediastinum, left thorax, liver, and skeleton. (**b**) [^{18}F]FDG PET shows only physiologic uptake but no tumor lesions. (**c**) ^{99m}Tc(V)-DMSA shows lesions in the upper mediastinum, left thorax, liver, and skeleton, although with much smaller number of lesions. (**d**) ^{18}F-DOPA PET/CT fusion slice shows liver lesions (From Koopmans et al. [278], with permission)

uptake and decarboxylate monoamine precursors. Therefore, 6-L-^{18}F-fluorodihydroxyphenylalanine (^{18}F-DOPA), an intermediate in the catecholamine synthesis pathway, can successfully be employed for PET imaging. Indeed, PET with ^{18}F-DOPA is more accurate than other imaging modalities in patients with MTC, in particular for detecting recurrent disease and lymph node involvement (with up to 81% sensitivity), even in patients with long serum Ct doubling times [277–279] (Fig. 16). In general, PET with [^{18}F] FDG offers important clinical information in patients with predominantly aggressive tumors such as the sporadic form of MTC.

Other promising PET agents to image neuroendocrine tumors include somatostatin analogs labeled with ^{68}Ga through the DOTA chelator (such as ^{68}Ga-DOTA-TOC, ^{68}Ga-DOTA-TATE, ^{68}Ga-DOTA-NOC) [280] (Fig. 17). However, the diagnostic role of ^{68}Ga-DOTA-peptides is still under extensive investigation and validation, because of controversial reports probably linked to the fact that even well-differentiated MTCs show a variable and often low somatostatin-receptor subtype expression [281].

Treatment for Recurrent or Persistent MTC

Local or regional recurrence of MTC in the neck and mediastinum can be effectively treated with surgical removal, possibly followed by EBRT when neck involvement is extensive [282]. Nevertheless, biochemical cure (i.e., normalization of serum Ct and/or CEA levels) is observed in only 5–35% of the cases; these patients are at high risk of developing distant metastases [250]. The main cause of MTC-related death is distant metastasis, which affects more frequently the lungs, bones, and liver, more rarely the brain and skin [283]. The 5-year survival rate of patients with distant metastases is 25% [284], with low response rates elicited by any of the therapeutic options available. Combination chemotherapy induces a response in only 20% of the cases [285–287], while Interferon-α and somatostatin analogs only induce transient improvement of the symptoms [288]. Bone metastases can be treated with surgery, EBRT, and/or bisphosphonates. In patients with predominant metastasis in the liver,

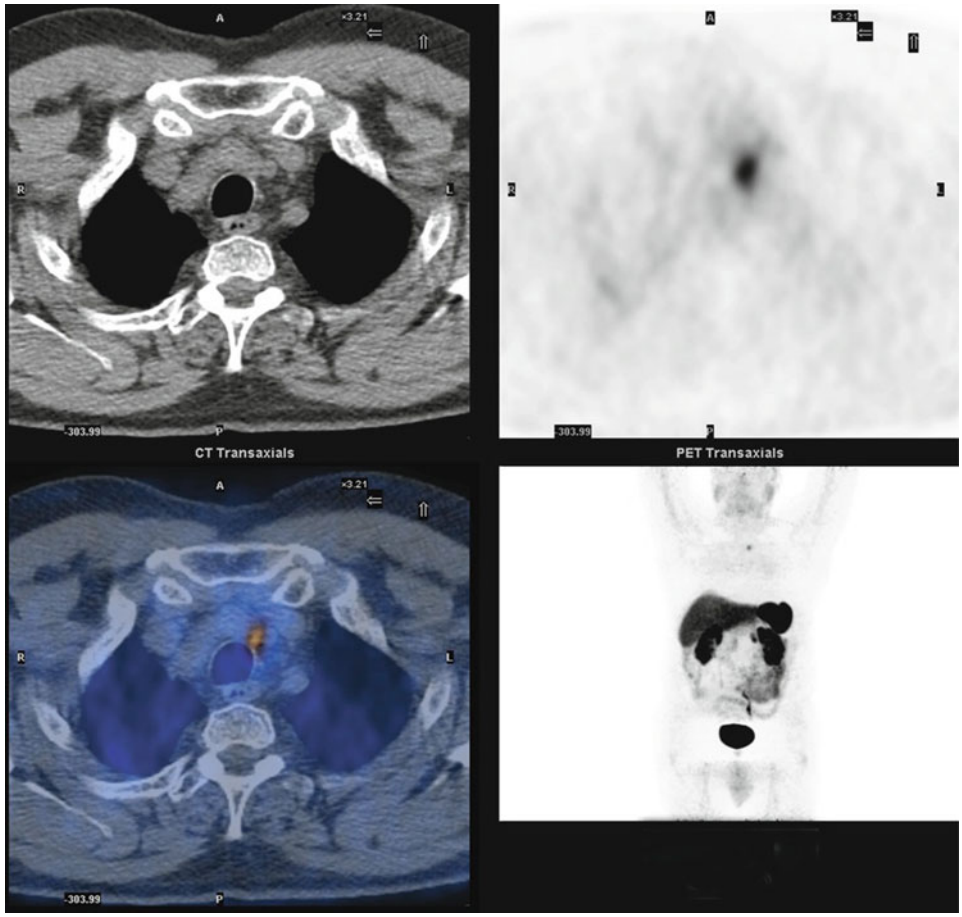

Fig. 17 PET/CT with ^{68}Ga-DOTA-TOC in a patient previously submitted to thyroidectomy because of MTC but with rising serum Ct levels. The images demonstrate uptake of the radiolabeled somatostatin analog in a metastatic lesion located in the upper mediastinum, in the left pretracheal region. The MIP image in the *right lower* panel demonstrates physiologic distribution of the ^{68}Ga-labeled peptide in the remainder of the body (Courtesy of Prof. Stefano Fanti, Nuclear Medicine Division, "S. Orsola – Malpighi" University Hospital, Bologna, Italy)

chemoembolization has proven effective in reducing the tumor mass [289].

Radiolabeled anti-CEA antibodies have been used for radioimmunotherapy in addition to surgical treatment and have been shown to induce long-term disease stabilization and significantly prolonged survival in high-risk MTC patients [290, 291].

More recently, radionuclide therapy with the radiolabeled somatostatin analog ^{90}Y-DOTA-Tyr^3-octreotide (^{90}Y-DOTA-TOC) has been tested in metastatic MTC. This therapy has resulted in favorable biochemical response in about one-third of the patients (irrespective of the result of the pre-therapeutic scintigraphy), associated with a long-term survival benefit [292]. Further studies are in progress to investigate the effect of other radiolabeled somatostatin analogs, including ^{177}Lu-DOTA-TATE and other radiopeptides, among which gastrin-like ligands, on the survival of patients with advanced metastatic MTC [267, 293–295]. Mostly due to the limited number of patients enrolled in each study, at present there is no clear evidence for a definite clinical benefit from such therapies for patients with advanced metastatic MTC.

Molecular targets represent the new frontier for treating patients with metastatic MTC [296]. In

particular, the RET gene is a promising target for therapy in patients with familial MTC as well as for some patients with sporadic MTC. Several inhibitors of the RET kinase activity (i.e., sorafenib, motesanib, sunitinib), which are active also against the VEGF receptor (thus causing cytostatic rather than cytotoxic effects), have been evaluated in the last decade [296–298]. In particular, results of the ZETA® phase III study showed a promising therapeutic potential of a new molecule named vandetanib, so that in April 2011 and in February 2012, the FDA and EMA, respectively, approved the use of vandetanib (Caprelsa®, AstraZeneca, USA) in patients with unresectable locally advanced or metastatic MTC [298]. Vandenatib seems to exert its antiangiogenic activity through three combined mechanisms, i.e., inhibition of VEGF, EGF, and RET. More recently, another multitarget TKI, cabozantinib (Cometriq®, Exelixis, USA), has been approved by both the FDA and EMA for the treatment of advanced and progressive metastatic MTC. Cabozantinib is also an antiangiogenic drug active against RET, MET (hepatocyte growth factor receptor), and VEGFR2 and less effective against VEGFR1, VEGFR3, KIT, and other tyrosine kinase receptors [299]. Its ability to block cell growth has been explored in a phase III study (EXAM study) [300] that demonstrated a significant prolongation of progression-free survival in the group of MTC patients treated with cabozantinib with respect to those treated with placebo. At present, vandetanib and cabozantinib represent the two options for the treatment of advanced and progressive MTC.

References

1. Bilimoria KY, Bentrem DJ, Ko CY, Stewart AK, Winchester DP, Talamonti MS, Sturgeon C. Extent of surgery affects survival for papillary thyroid cancer. Ann Surg. 2007;246:375–81.
2. Haugen BR, Alexander EK, Bible KC, et al. 2015 American Thyroid Association management guidelines for adult patients with thyroid nodules and differentiated thyroid cancer: the American Thyroid Association Guidelines Task Force on Thyroid Nodules and Differentiated Thyroid Cancer. Thyroid. 2016;26:1–133.
3. Leboulleux S, Girard E, Rose M, et al. Ultrasound criteria of malignancy for cervical lymph nodes in patients followed up for differentiated thyroid cancer. J Clin Endocrinol Metab. 2007;92:3590–4.
4. Sywak M, Cornford L, Roach P, et al. Routine ipsilateral level VI lymphadenectomy reduces postoperative thyroglobulin levels in papillary thyroid cancer. Surgery. 2006;140:1000–5.
5. Ywata de Carvalho A, Chulam TC, Kowalski LP. Long-term results of observation vs prophylactic selective level VI neck dissection for papillary thyroid carcinoma at a cancer center. JAMA Otolaryngol Head Neck Surg. 2015;141:599–606.
6. Nixon IJ, Wang LY, Ganly I, et al. Outcomes for patients with papillary thyroid cancer who do not undergo prophylactic central neck dissection. Br J Surg. 2016;103:218–25.
7. Palazzo FF, Gosnell J, Savio R, et al. Lymphadenectomy for papillary cancer: changes in practice over four decades. Eur J Surg Oncol. 2006; 32:340–4.
8. Carty SE, Cooper DS, Doherty GM, et al. Consensus statement on the terminology and classification of central neck dissection for thyroid cancer. Thyroid. 2009;19:1153–8.
9. Maxon 3rd HR, Englaro EE, Thomas SR, et al. Radioiodine-131 therapy for well-differentiated thyroid cancer – a quantitative radiation dosimetric approach: outcome and validation in 85 patients. J Nucl Med. 1992;33:1132–6.
10. Mazzaferri EL, Jhiang SM. Long-term impact of initial surgical and medical therapy on papillary and follicular thyroid cancer. Am J Med. 1994;97:418–28.
11. Van Nostrand D. The benefits and risks of I-131 therapy in patients with well-differentiated thyroid cancer. Thyroid. 2009;19:1381–91.
12. DeGroot LJ, Kaplan EL, McCormick M, Straus FH. Natural history, treatment, and course of papillary thyroid carcinoma. J Clin Endocrinol Metab. 1990; 71:414–24.
13. Tubiana M, Schlumberger M, Rougier P, et al. Long-term results and prognostic factors in patients with differentiated thyroid carcinoma. Cancer. 1985;55: 794–804.
14. Baudin E, Travagli JP, Ropers J, et al. Microcarcinoma of the thyroid gland: the Gustave-Roussy Institute experience. Cancer. 1998;83:553–9.
15. Simpson WJ, Panzarella T, Carruthers JS, et al. Papillary and follicular thyroid cancer: impact of treatment in 1578 patients. Int J Radiat Oncol Biol Phys. 1988;14:1063–75.
16. Grebe SK, Hay ID. Follicular cell-derived thyroid carcinomas. Cancer Treat Res. 1997;89:91–140.
17. Ruel E, Thomas S, Dinan M, et al. Adjuvant radioactive iodine therapy is associated with improved survival for patients with intermediate-risk papillary thyroid cancer. J Clin Endocrinol Metab. 2015;100:1529–36.
18. Elisei R, Agate L, Viola D, et al. How to manage patients with differentiated thyroid cancer and a rising

serum thyroglobulin level. Endocrinol Metab Clin North Am. 2014;43:331–44.
19. Wang LY, Roman BR, Palmer FL, et al. Effectiveness of routine ultrasonographic surveillance of patients with low-risk papillary carcinoma of the thyroid. Surgery. 2016;159:1390–5.
20. Remy H, Borget I, Leboulleux S, et al. ^{131}I effective half-life and dosimetry in thyroid cancer patients. J Nucl Med. 2008;49:1445–50.
21. Mazzaferri EL, Kloos RT. Clinical review 128: current approaches to primary therapy for papillary and follicular thyroid cancer. J Clin Endocrinol Metab. 2001;86:1447–63.
22. Sgouros G, Song H, Ladenson PW, Wahl RL. Lung toxicity in radioiodine therapy of thyroid carcinoma: development of a dose-rate method and dosimetric implications of the 80-mCi rule. J Nucl Med. 2006;47:1977–84.
23. Bolch WE, Bouchet LG, Robertson JS, et al. MIRD pamphlet No. 17: the dosimetry of nonuniform activity distributions – radionuclide S values at the voxel level. J Nucl Med. 1999;40(Suppl):11S–36.
24. Haugen BR, Pacini F, Reiners C, et al. A comparison of recombinant human thyrotropin and thyroid hormone withdrawal for the detection of thyroid remnant or cancer. J Clin Endocrinol Metab. 1999;84: 3877–85.
25. Pacini F, Ladenson PW, Schlumberger M, et al. Radioiodine ablation of thyroid remnants after preparation with recombinant human thyrotropin in differentiated thyroid carcinoma: results of an international, randomized, controlled study. J Clin Endocrinol Metab. 2006;91:926–32.
26. Schlumberger M, Catargi B, Borget I, et al. Strategies of radioiodine ablation in patients with low-risk thyroid cancer. N Engl J Med. 2012;366:1663–73.
27. Mallick U, Harmer C, Yap B, et al. Ablation with low-dose radioiodine and thyrotropin alfa in thyroid cancer. N Engl J Med. 2012;366:1674–85.
28. Silberstein EB, Alavi A, Balon HR, et al. Procedure guideline for therapy of thyroid disease with iodine-131. J Nucl Med. 2002;43:856–61.
29. Park II JT, Hennessey JV. Two-week low iodine diet is necessary for adequate outpatient preparation for radioiodine rhTSH scanning in patients taking levothyroxine. Thyroid. 2004;14:57–63.
30. Regalbuto C, Gullo D, Vigneri R, Pezzino V. Measurement of iodine before ^{131}I in thyroid cancer. Lancet. 1994;344:1501–2.
31. Rawson RW, Rall JE, Peacock W. Limitations in the treatment of cancer of the thyroid with radioactive iodine. Trans Assoc Am Physicians. 1951;64:179–98.
32. Bajén MT, Mañé S, Muñoz A, Ramòn GJ. Effect of diagnostic dose of 185 MBq ^{131}I on postsurgical thyroid remnants. J Nucl Med. 2000;41:2038–42.
33. McDougall IR, Iagaru A. Thyroid stunning: fact or fiction? Semin Nucl Med. 2011;41:105–12.
34. Park HM. Stunned thyroid after high dose ^{131}I imaging. Clin Nucl Med. 1992;17:501–2.
35. Sisson JC, Avram AM, Lawson SA, et al. The so-called stunning of thyroid tissue. J Nucl Med. 2006;47:1406–12.
36. Park HM, Perkins OW, Edmondson JW, Schnute RB, Manatunga A. Influence of diagnostic radioiodines on the uptake of ablative dose of iodine-131. Thyroid. 1994;4:49–54.
37. Muratet JP, Giraud P, Daver A, et al. Predicting the efficacy of first iodine-131 treatment in differentiated thyroid carcinoma. J Nucl Med. 1997;38:1362–8.
38. McDougall IR. 74 MBq radioiodine ^{131}I does not prevent uptake of therapeutic doses of ^{131}I (i.e. it does not cause stunning) in differentiated thyroid cancer. Nucl Med Commun. 1997;18:505–12.
39. Cholewinski SP, Yoo KS, Klieger PS, O'Mara RE. Absence of thyroid stunning after diagnostic whole-body scanning with 185 MBq ^{131}I. J Nucl Med. 2000;41:1198–202.
40. Nordén MM, Larsson F, Tedelind S, et al. Down-regulation of the sodium/iodide symporter explains ^{131}I-induced thyroid stunning. Cancer Res. 2007;6: 7512–7.
41. Medvedec M. Thyroid stunning in vivo and in vitro. Nucl Med Commun. 2005;26:731–5.
42. Caudill CM, Zhu Z, Ciampi R, et al. Dose-dependent generation of RET/PTC in human thyroid cells after in vitro exposure to gamma-radiation: a model of carcinogenic chromosomal rearrangement induced by ionizing radiation. J Clin Endocrinol Metab. 2005;90:2364–9.
43. de Geus-Oei LF, Oei HY, Hennemann G, Krenning EP. Sensitivity of ^{123}I whole-body scan and thyroglobulin in the detection of metastases or recurrent differentiated thyroid cancer. Eur J Nucl Med Mol Imaging. 2002;29:768–74.
44. Sherman SI, Tielens ET, Sostre S, et al. Clinical utility of posttreatment radioiodine scans in the management of patients with thyroid carcinoma. J Clin Endocrinol Metab. 1994;78:629–34.
45. Fatourechi V, Hay ID, Mullan BP, et al. Are post-therapy radioiodine scans informative and do they influence subsequent therapy of patients with differentiated thyroid cancer? Thyroid. 2000;10:573–7.
46. Chen L, Luo Q, Shen Y, et al. Incremental value of ^{131}I SPECT/CT in the management of patients with differentiated thyroid carcinoma. J Nucl Med. 2008;49:1952–7.
47. Wong KK, Zarzhevsky N, Cahill JM, et al. Incremental value of diagnostic ^{131}I SPECT/CT fusion imaging in the evaluation of differentiated thyroid carcinoma. AJR Am J Roentgenol. 2008;191:1785–94.
48. Aide N, Heutte N, Rame JP, et al. Clinical relevance of single-photon emission computed tomography/computed tomography of the neck and thorax in post-ablation ^{131}I scintigraphy for thyroid cancer. J Clin Endocrinol Metab. 2009;94:2075–84.

49. Schmidt D, Szikszai A, Linke R, et al. Impact of ^{131}I SPECT/spiral CT on nodal staging of differentiated thyroid carcinoma at the first radioablation. J Nucl Med. 2009;50:18–23.
50. Spanu A, Solinas ME, Chessa F, et al. ^{131}I SPECT/CT in the follow-up of differentiated thyroid carcinoma: incremental value versus planar imaging. J Nucl Med. 2009;50:184–90.
51. Kohlfuerst S, Igerc I, Lobnig M, et al. Posttherapeutic ^{131}I SPECT-CT offers high diagnostic accuracy when the findings on conventional planar imaging are inconclusive and allows a tailored patient treatment regimen. Eur J Nucl Med Mol Imaging. 2009;36: 886–93.
52. Akram K, Parker JA, Donohoe K, Kolodny G. Role of single photon emission computed tomography/computed tomography in localization of ectopic parathyroid adenoma: a pictorial case series and review of the current literature. Clin Nucl Med. 2009;34:500–2.
53. Barwick T, Murray I, Megadmi H, et al. Single photon emission computed tomography (SPECT)/computed tomography using Iodine-123 in patients with differentiated thyroid cancer: additional value over whole body planar imaging and SPECT. Eur J Endocrinol. 2010;162:1131–9.
54. Mustafa M, Kuwert T, Weber K, et al. Regional lymph node involvement in T1 papillary thyroid carcinoma: a bicentric prospective SPECT/CT study. Eur J Nucl Med Mol Imaging. 2010;37:1462–6.
55. Grewal RK, Tuttle RM, Fox J, et al. The effect of posttherapy ^{131}I SPECT/CT on risk classification and management of patients with differentiated thyroid cancer. J Nucl Med. 2010;51:1361–7.
56. Wong KK, Sisson JC, Koral KF, et al. Staging of differentiated thyroid carcinoma using diagnostic ^{131}I SPECT/CT. AJR Am J Roentgenol. 2010;195:730–6.
57. Avram AM. Radioiodine scintigraphy with SPECT/CT: an important diagnostic tool for thyroid cancer staging and risk stratification. J Nucl Med Technol. 2014;42:170–80.
58. Al Balooshi B, Vinjamuri S. Should all patients with differentiated thyroid carcinoma undergo ^{131}I SPECT-CT scanning rather than ^{131}I whole-body scanning? Nucl Med Commun. 2015;36:540–52.
59. Allweiss P, Braunstein GD, Katz A, Waxman A. Sialadenitis following I-131 therapy for thyroid carcinoma: concise communication. J Nucl Med. 1984; 25:755–8.
60. Alexander C, Bader JB, Schaefer A, et al. Intermediate and long-term side effects of high-dose radioiodine therapy for thyroid carcinoma. J Nucl Med. 1998;39:1551–4.
61. de Vathaire F, Schlumberger M, Delisle MJ, et al. Leukaemias and cancers following iodine-131 administration for thyroid cancer. Br J Cancer. 1997;75:734–9.
62. Rubino C, de Vathaire F, Dottorini ME, et al. Second primary malignancies in thyroid cancer patients. Br J Cancer. 2003;89:1638–44.
63. de Vathaire F. The carcinogenic effects of radioiodine therapy for thyroid carcinoma. Nat Clin Pract Endocrinol Metab. 2008;4:180–1.
64. Bhattacharyya N, Chien W. Risk of second primary malignancy after radioactive iodine treatment for differentiated thyroid carcinoma. Ann Otol Rhinol Laryngol. 2006;115:607–10.
65. Sawka AM, Thabane L, Parlea L, et al. Second primary malignancy risk after radioactive iodine treatment for thyroid cancer: a systematic review and meta-analysis. Thyroid. 2009;19:451–7.
66. Verkooijen RB, Smit JW, Romijn JA, Stokkel M. The incidence of second primary tumors in thyroid cancer patients is increased, but not related to treatment of thyroid cancer. Eur J Endocrinol. 2006;155:801–6.
67. Subramanian S, Goldstein DP, et al. Second primary malignancy risk in thyroid cancer survivors: a systematic review and metaanalysis. Thyroid. 2007;17: 1277–88.
68. Garsi J-P, Schlumberger M, Rubino C, et al. Therapeutic administration of ^{131}I for differentiated thyroid cancer: radiation dose to ovaries and outcome of pregnancies. J Nucl Med. 2008;49:845–52.
69. Wichers M, Benz E, Palmedo H, et al. Testicular function after radioiodine therapy for thyroid carcinoma. Eur J Nucl Med. 2000;27:503–7.
70. Rosário PW, Barroso AL, Rezende LL, et al. Testicular function after radioiodine therapy in patients with thyroid cancer. Thyroid. 2006;16:667–70.
71. Pacini F, Gasperi M, Fugazzola L, et al. Testicular function in patients with differentiated thyroid carcinoma treated with radioiodine. J Nucl Med. 1994;35:1418–22.
72. Hyer S, Vini L, O'Connell M, et al. Testicular dose and fertility in men following I^{131} therapy for thyroid cancer. Clin Endocrinol (Oxf). 2002;56:755–8.
73. Krassas GE, Pontikides N. Male reproductive function in relation with thyroid alterations. Best Pract Res Clin Endocrinol Metab. 2004;18:183–95.
74. Hebestreit H, Biko J, Drozd V, et al. Pulmonary fibrosis in youth treated with radioiodine for juvenile thyroid cancer and lung metastases after Chernobyl. Eur J Nucl Med Mol Imaging. 2011;38:1683–90.
75. Reiners C, Biko J, Haenscheid H, et al. Twenty-five years after Chernobyl: outcome of radioiodine treatment in children and adolescents with very high-risk radiation-induced differentiated thyroid carcinoma. J Clin Endocrinol Metab. 2013;98:3039–48.
76. Pilli T, Brianzoni E, Capoccetti F, et al. A comparison of 1850 (50 mCi) and 3700 MBq (100 mCi) 131-iodine administered doses for recombinant thyrotropin-stimulated postoperative thyroid remnant ablation in differentiated thyroid cancer. J Clin Endocrinol Metab. 2007;92:3542–6.
77. Bianchi R, Mariani G, Molea N, et al. Peripheral metabolism of thyroid hormones in man. I. Direct measurement of the conversion rate of thyroxine to 3,5,3′-triiodothyronine. J Clin Endocrinol Metab. 1983;56:1152–63.

78. Bianchi R, Pilo A, Mariani G, Molea N, Cazzuola F, Ferdeghini M, Bertelli P. Comparison of plasma and urinary methods for the direct measurement of thyroxine to 3,5,3′-triiodothyronine conversion in man. J Clin Endocrinol Metab. 1984;58:993–1002.
79. Pilo A, Iervasi G, Vitek F, Ferdeghini M, Cazzuola F, Bianchi R. Thyroidal and peripheral production of 3,5,3′-triiodothyronine in humans by multicompartmental analysis. Am J Physiol. 1990;258: E715–26.
80. Bartalena L, Martino E, Pacchiarotti A, et al. Factors affecting suppression of endogenous thyrotropin secretion by thyroxine treatment: retrospective analysis in athyreotic and goitrous patients. J Clin Endocrinol Metab. 1987;64:849–55.
81. Santini F, Pinchera A, Marsili A, et al. Lean body mass is a major determinant of levothyroxine dosage in the treatment of thyroid diseases. J Clin Endocrinol Metab. 2005;90:124–7.
82. Sawin CT, Geller A, Hershman JM, Castelli W, Bacharach P. The aging thyroid. The use of thyroid hormone in older persons. JAMA. 1989;261:2653–5.
83. Hays MT, Hsu L, Kohatsu S. Transport of the thyroid hormones across the feline gut wall. Thyroid. 1992;2:45–56.
84. Vita R, Saraceno G, Trimarchi F, Benvenga S. A novel formulation of L-thyroxine (L-T4) reduces the problem of L-T4 malabsorption by coffee observed with traditional tablet formulations. Endocrine. 2013;43:154–60.
85. Cappelli C, Pirola I, Daffini L, et al. A double-blind placebo-controlled trial of liquid thyroxine ingested at breakfast: results of the TICO study. Thyroid. 2016; 26:197–202.
86. Uzzan B, Nicolas P, Perret G, Vassy R, Tod M, Petitjean O. Effects of troleandomycin and josamycin on thyroid hormone and steroid serum levels, liver function tests and microsomal monooxygenases in healthy volunteers: a double blind placebo-controlled study. Fundam Clin Pharmacol. 1991;5:513–26.
87. Liwanpo L, Hershman JM. Conditions and drugs interfering with thyroxine absorption. Best Pract Res Clin Endocrinol Metab. 2009;23:781–92.
88. Centanni M, Gargano L, Canettieri G, et al. Thyroxine in goiter, Helicobacter pylori infection, and chronic gastritis. N Engl J Med. 2006;354:1787–95.
89. Checchi S, Montanaro A, Pasqui L, et al. l-Thyroxine requirement in patients with autoimmune hypothyroidism and parietal cell antibodies. J Clin Endocrinol Metab. 2008;93:465–9.
90. Marcocci C, Golia F, Bruno-Bossio G, et al. Carefully monitored levothyroxine suppressive therapy is not associated with bone loss in premenopausal women. J Clin Endocrinol Metab. 1994;78:818–23.
91. Jennings PE, O'Malley BP, Griffin KE, Northover B, Rosenthal FD. Relevance of increased serum thyroxine concentrations associated with normal serum triiodothyronine values in hypothyroid patients receiving thyroxine: a case for "tissue thyrotoxicosis". Br Med J (Clin Res Ed). 1984;289:1645–7.
92. Ross DS. Monitoring l-thyroxine therapy: lessons from the effects of l-thyroxine on bone density. Am J Med. 1991;91:1–4.
93. Do Cao C, Wémeau JL. Risk-benefit ratio for TSH-suppressive Levothyroxine therapy in differentiated thyroid cancer. Ann Endocrinol (Paris). 2015;76 (1 Suppl):1S47–52.
94. Kim CW, Hong S, Oh SH, et al. Change of bone mineral density and biochemical markers of bone turnover in patients on suppressive levothyroxine therapy for differentiated thyroid carcinoma. J Bone Metab. 2015;22:135–41.
95. Mendonça Monteiro de Barros G, Madeira M, Vieira Neto L, et al. Bone mineral density and bone microarchitecture after long-term suppressive levothyroxine treatment of differentiated thyroid carcinoma in young adult patients. J Bone Miner Metab. 2016;34:417–21.
96. Cooper DS, Specker B, Ho M, et al. Thyrotropin suppression and disease progression in patients with differentiated thyroid cancer: results from the National Thyroid Cancer Treatment Cooperative Registry. Thyroid. 1998;8:737–44.
97. Biondi B, Filetti S, Schlumberger M. Thyroid-hormone therapy and thyroid cancer: a reassessment. Nat Clin Pract Endocrinol Metab. 2005;1:32–40.
98. Mazzaferri EL, Jhiang SM. Differentiated thyroid cancer long-term impact of initial therapy. Trans Am Clin Climatol Assoc. 1995;106:151–68.
99. Schlumberger M. Can iodine-131 whole-body scan be replaced by thyroglobulin measurement in the post-surgical follow-up of differentiated thyroid carcinoma? J Nucl Med. 1992;33:172–3.
100. Mazzaferri EL. Changing paradigms in the follow-up of patients with differentiated thyroid cancer: an alternative to [^{18}F]fluorodeoxyglucose positron emission tomographic scanning. Endocr Pract. 2003;9:324–6.
101. Van Herle AJ. Serum thyroglobulin levels in patients with differentiated thyroid carcinoma. Ann Radiol (Paris). 1977;20:743–5.
102. Watanabe K, Koizumi N, Ozaki O, et al. Immunohistochemical studies on thyroid peroxidase and thyroglobulin in 13 human thyroid tumors and 7 Graves' goiters. Endocr J. 1993;40:683–90.
103. Elisei R, Vivaldi A, Agate L, et al. Low specificity of blood thyroglobulin messenger ribonucleic acid assay prevents its use in the follow-up of differentiated thyroid cancer patients. J Clin Endocrinol Metab. 2004;89:33–9.
104. Spencer CA, Lopresti JS. Measuring thyroglobulin and thyroglobulin autoantibody in patients with differentiated thyroid cancer. Nat Clin Pract Endocrinol Metab. 2008;4:223–33.
105. Pacini F, Mariotti S, Formica N, et al. Thyroid autoantibodies in thyroid cancer: incidence and relationship with tumour outcome. Acta Endocrinol (Copenh). 1988;119:373–80.

106. Pacini F, Molinaro E, Lippi F, et al. Prediction of disease status by recombinant human TSH-stimulated serum Tg in the postsurgical follow-up of differentiated thyroid carcinoma. J Clin Endocrinol Metab. 2001;86:5686–90.
107. Mazzaferri EL, Robbins RJ, Spencer CA, et al. A consensus report of the role of serum thyroglobulin as a monitoring method for low-risk patients with papillary thyroid carcinoma. J Clin Endocrinol Metab. 2003;88:1433–41.
108. Lamartina L, Montesano T, Trulli F, et al. Papillary thyroid carcinomas with biochemical incomplete or indeterminate responses to initial treatment: repeat stimulated thyroglobulin assay to identify disease-free patients. Endocrine. 2015, Dec 14. [Epub ahead of print].
109. Pacini F, Cetani F, Miccoli P, et al. Outcome of 309 patients with metastatic differentiated thyroid carcinoma treated with radioiodine. World J Surg. 1994; 18:600–4.
110. Schlumberger M, Hitzel A, Toubert ME, et al. Comparison of seven serum thyroglobulin assays in the follow-up of papillary and follicular thyroid cancer patients. J Clin Endocrinol Metab. 2007;92: 2487–95.
111. Chindris AM, Diehl NN, Crook JE, Fatourechi V, Smallridge RC. Undetectable sensitive serum thyroglobulin (<0.1 ng/ml) in 163 patients with follicular cell-derived thyroid cancer: results of rhTSH stimulation and neck ultrasonography and long-term biochemical and clinical follow-up. J Clin Endocrinol Metab. 2012;97:2714–23.
112. Pacini F, Capezzone M, Elisei R, et al. Diagnostic 131-iodine whole-body scan may be avoided in thyroid cancer patients who have undetectable stimulated serum Tg levels after initial treatment. J Clin Endocrinol Metab. 2002;87:1499–501.
113. Gerard SK, Cavalieri RR. I-123 diagnostic thyroid tumor whole-body scanning with imaging at 6, 24, and 48 hours. Clin Nucl Med. 2002;27:1–8.
114. Yan W, Roach PJ, Bautovich GJ, et al. Timing of iodine-123 scintigraphy following use of recombinant human thyrotropin in differentiated thyroid carcinoma. Clin Nucl Med. 2007;32:375–7.
115. Pacini F, Lippi F, Formica N, et al. Therapeutic doses of iodine-131 reveal undiagnosed metastases in thyroid cancer patients with detectable serum thyroglobulin levels. J Nucl Med. 1987;28:1888–91.
116. Pineda JD, Lee T, Ain K, et al. Iodine-131 therapy for thyroid cancer patients with elevated thyroglobulin and negative diagnostic scan. J Clin Endocrinol Metab. 1995;80:1488–92.
117. Elisei R, Pinchera A, Romei C, et al. Expression of thyrotropin receptor (TSH-R), thyroglobulin, thyroperoxidase, and calcitonin messenger ribonucleic acids in thyroid carcinomas: evidence of TSH-R gene transcript in medullary histotype. J Clin Endocrinol Metab. 1994;78:867–71.
118. Arturi F, Russo D, Schlumberger M, et al. Iodide symporter gene expression in human thyroid tumors. J Clin Endocrinol Metab. 1998;83:2493–6.
119. Schlumberger MJ. Papillary and follicular thyroid carcinoma. N Engl J Med. 1998;338:297–306.
120. Pacini F. Follow-up of differentiated thyroid cancer. Eur J Nucl Med Mol Imaging. 2002;29 Suppl 2:492–4966.
121. Chiovato L, Latrofa F, Braverman LE, et al. Disappearance of humoral thyroid autoimmunity after complete removal of thyroid antigens. Ann Intern Med. 2003;139:346–51.
122. Pacini F, Fugazzola L, Lippi F, et al. Detection of thyroglobulin in fine needle aspirates of nonthyroidal neck masses: a clue to the diagnosis of metastatic differentiated thyroid cancer. J Clin Endocrinol Metab. 1992;74:1401–4.
123. Haugen BR, Lin EC. Isotope imaging for metastatic thyroid cancer. Endocrinol Metab Clin North Am. 2001;30:469–92.
124. Reading CC, Gorman CA. Thyroid imaging techniques. Clin Lab Med. 1993;13:711–24.
125. Gross ND, Weissman JL, Talbot JM, et al. MRI detection of cervical metastasis from differentiated thyroid carcinoma. Laryngoscope. 2001;111:1905–9.
126. Feine U, Lietzenmayer R, Hanke JP, et al. Fluorine-18-FDG and iodine-131-iodide uptake in thyroid cancer. J Nucl Med. 1996;37:1468–72.
127. Dietlein M, Scheidhauer K, Voth E, et al. Fluorine-18 fluorodeoxyglucose positron emission tomography and iodine-131 whole-body scintigraphy in the follow-up of differentiated thyroid cancer. Eur J Nucl Med. 1997;24:1342–8.
128. Ramos CD, Chisin R, Yeung HW, et al. Incidental focal thyroid uptake on FDG positron emission tomographic scans may represent a second primary tumor. Clin Nucl Med. 2001;26:193–7.
129. Are C, Hsu JF, Schoder H, et al. FDG-PET detected thyroid incidentalomas: need for further investigation? Ann Surg Oncol. 2007;14:239–47.
130. Salvatori M, Melis L, Castaldi P, et al. Clinical significance of focal and diffuse thyroid diseases identified by ^{18}F-fluorodeoxyglucose positron emission tomography. Biomed Pharmacother. 2007;61:488–93.
131. Shie P, Cardarelli R, Sprawls K, et al. Systematic review: prevalence of malignant incidental thyroid nodules identified on fluorine-18 fluorodeoxyglucose positron emission tomography. Nucl Med Commun. 2009;30:742–8.
132. Ohba K, Nishizawa S, Matsushita A, et al. High incidence of thyroid cancer in focal thyroid incidentaloma detected by ^{18}F-fluorodexyglucose positron emission tomography in relatively young healthy subjects: results of 3-year follow-up. Endocr J. 2010;57:395–401.
133. Chen W, Li G, Parsons M, et al. Clinical significance of incidental focal versus diffuse thyroid uptake on FDG-PET imaging. PET Clin. 2007;2:321–9.
134. Nayan S, Ramakrishna J, Gupta MK. The proportion of malignancy in incidental thyroid lesions on 18-FDG

PET study: a systematic review and meta-analysis. Otolaryngol Head Neck Surg. 2014;151:190–200.
135. Agrawal K, Weaver J, Ul-Hassan F, et al. Incidence and significance of incidental focal thyroid uptake on ^{18}F-FDG PET study in a large patient cohort: retrospective single-centre experience in the United Kingdom. Eur Thyroid J. 2015;4:115–22.
136. Demir Ö, Köse N, Özkan E, et al. Clinical significance of thyroid incidentalomas identified by ^{18}F-FDG PET/CT: correlation of ultrasonograpy findings with cytology results. Nucl Med Commun. 2016;37:715–20.
137. Feine U, Lietzenmayer R, Hanke JP, et al. ^{18}FDG whole-body PET in differentiated thyroid carcinoma. Flip-flop in uptake patterns of ^{18}FDG and ^{131}I. Nuklearmedizin. 1995;34:127–34.
138. Wang W, Larson SM, Fazzari M, et al. Prognostic value of [^{18}F]fluorodeoxyglucose positron emission tomographic scanning in patients with thyroid cancer. J Clin Endocrinol Metab. 2000;85:1107–13.
139. Robbins RJ, Wan Q, Grewal RK, et al. Real-time prognosis for metastatic thyroid carcinoma based on 2-[^{18}F]fluoro-2-deoxy- D-glucose-positron emission tomography scanning. J Clin Endocrinol Metab. 2006;91:498–505.
140. Hosaka Y, Tawata M, Kurihara A, et al. The regulation of two distinct glucose transporter (GLUT1 and GLUT4) gene expressions in cultured rat thyroid cells by thyrotropin. Endocrinology. 1992;131:159–65.
141. Sisson JC, Ackermann RJ, Meyer MA, Wahl RL. Uptake of 18-fluoro-2-deoxy-D-glucose by thyroid cancer: implications for diagnosis and therapy. J Clin Endocrinol Metab. 1993;77:1090–4.
142. Blaser D, Maschauer S, Kuwert T, Prante O. In vitro studies on the signal transduction of thyroidal uptake of ^{18}F-FDG and ^{131}I-Iodide. J Nucl Med. 2006;47:1382–8.
143. Moog F, Linke R, Manthey N, et al. Influence of thyroid-stimulating hormone levels on uptake of FDG in recurrent and metastatic differentiated thyroid carcinoma. J Nucl Med. 2000;41:1989–95.
144. van Tol KM, Jager PL, Piers DA, et al. Better yield of ^{18}fluorodeoxyglucose-positron emission tomography in patients with metastatic differentiated thyroid carcinoma during thyrotropin stimulation. Thyroid. 2002; 12:381–7.
145. Petrich T, Borner AR, Otto D, et al. Influence of rhTSH on [^{18}F]fluoro-deoxyglucose uptake by differentiated thyroid carcinoma. Eur J Nucl Med Mol Imaging. 2002;29:641–7.
146. Chin BB, Patel P, Cohade C, et al. Recombinant human thyrotropin stimulation of fluoro-D-glucose positron emission tomography uptake in well-differentiated thyroid carcinoma. J Clin Endocrinol Metab. 2004;89:91–5.
147. Leboulleux S, Schroeder PR, Busaidy NL, et al. Assessment of the incremental value of recombinant thyrotropin stimulation before 2-[^{18}F]-fluoro-2-deoxy-D-glucose positron emission tomography/computed tomography imaging to localize residual differentiated thyroid cancer. J Clin Endocrinol Metab. 2009;94:1310–6.
148. Vera P, Kuhn-Lansoy C, Edet-Sanson A, et al. Does recombinant human thyrotropin-stimulated positron emission tomography with [^{18}F]fluoro-2-deoxy-D-glucose improve detection of recurrence of well-differentiated thyroid carcinoma in patients with low serum thyroglobulin? Thyroid. 2010;20:15–23.
149. Prestwich RJ, Viner S, Gerrard G, et al. Increasing the yield of recombinant thyroid-stimulating hormone-stimulated 2-(18-fluoride)-flu-2-deoxy-D-glucose positron emission tomography-CT in patients with differentiated thyroid carcinoma. Br J Radiol. 2012;85:e805–13.
150. Phillips AF, Haybittle JL, Newbery GR. Use of iodine-124 for the treatment of carcinoma of the thyroid. Acta Unio Int Contra Cancrum. 1960;16: 1434–8.
151. Freudenberg LS, Jentzen W, Stahl A, et al. Clinical applications of ^{124}I-PET/CT in patients with differentiated thyroid cancer. Eur J Nucl Med Mol Imaging. 2011;38(Supp 1):S48–56.
152. Pentlow KS, Graham MC, Lambrecht RM, et al. Quantitative imaging of iodine-124 with PET. J Nucl Med. 1996;37:1557–62.
153. Phan HT, Jager PL, Paans AM. The diagnostic value of ^{124}I-PET in patients with differentiated thyroid cancer. Eur J Nucl Med Mol Imaging. 2008;35: 958–65.
154. Kist JW, de Keizer B, Stokkel MP, et al. Recurrent differentiated thyroid cancer: towards personalized treatment based on evaluation of tumor characteristics with PET (THYROPET Study): study protocol of a multicenter observational cohort study. BMC Cancer. 2014;14:405. doi:10.1186/1471-2407-14-405.
155. Binse I, Poeppel TD, Ruhlmann M, et al. Imaging with ^{124}I in differentiated thyroid carcinoma: is PET/MRI superior to PET/CT? Eur J Nucl Med Mol Imaging. 2016;43:1011–7.
156. Freudenberg LS, Antoch G, Jentzen W, et al. Value of ^{124}I-PET/CT in staging of patients with differentiated thyroid cancer. Eur Radiol. 2004;14:2092–8.
157. Capoccetti F, Criscuoli B, Rossi G, et al. The effectiveness of ^{124}I PET/CT in patients with differentiated thyroid cancer. Q J Nucl Med Mol Imaging. 2009;53:536–45.
158. Van Nostrand D, Moreau S, Bandaru VV, et al. ^{124}I positron emission tomography versus ^{131}I planar imaging in the identification of residual thyroid tissue and/or metastasis in patients who have well-differentiated thyroid cancer. Thyroid. 2010;20: 879–83.
159. Freudenberg LS, Antoch G, Frilling A, et al. Combined metabolic and morphologic imaging in thyroid carcinoma patients with elevated serum thyroglobulin and negative cervical ultrasonography: role of ^{124}I-PET/CT and FDG-PET. Eur J Nucl Med Mol Imaging. 2008;35:950–7.

160. Freudenberg LS, Jentzen W, Müller SP, Bockisch A. Disseminated iodine-avid lung metastases in differentiated thyroid cancer: a challenge to ^{124}I PET. Eur J Nucl Med Mol Imaging. 2008;35:502–8.
161. Abdul-Fatah SB, Zamburlini M, Halders SG, et al. Identification of a shine-through artifact in the trachea with ^{124}I PET/CT. J Nucl Med. 2009;50:909–11.
162. Cooper DS, Doherty GM, Haugen BR, et al. Revised American Thyroid Association management guidelines for patients with thyroid nodules and differentiated thyroid cancer. Thyroid. 2009;19:1167–214.
163. Al-Saif O, Farrar WB, Bloomston M, et al. Long-term efficacy of lymph node reoperation for persistent papillary thyroid cancer. J Clin Endocrinol Metab. 2010;95:2187–94.
164. Coburn M, Teates D, Wanebo HJ. Recurrent thyroid cancer. Role of surgery versus radioactive iodine (I^{131}). Ann Surg. 1994;219:587–93.
165. Schlumberger M, Challeton C, De Vathaire F, et al. Radioactive iodine treatment and external radiotherapy for lung and bone metastases from thyroid carcinoma. J Nucl Med. 1996;37:598–605.
166. Baudin E, Schlumberger M. Metastasis of differentiated cancers of the thyroid. Ann Endocrinol (Paris). 1997;58:326–9.
167. Urken ML, Milas M, Randolph GW, et al. Management of recurrent and persistent metastatic lymph nodes in well-differentiated thyroid cancer: a multifactorial decision-making guide for the Thyroid Cancer Care Collaborative. Head Neck. 2015;37:605–14.
168. Ozata M, Suzuki S, Miyamoto T, et al. Serum thyroglobulin in the follow-up of patients with treated differentiated thyroid cancer. J Clin Endocrinol Metab. 1994;79:98–105.
169. Ceccarelli C, Pacini F, Lippi F, et al. Thyroid cancer in children and adolescents. Surgery. 1988;104:1143.
170. Vassilopoulou-Sellin R, Klein MJ, Smith TH, et al. Pulmonary metastases in children and young adults with differentiated thyroid cancer. Cancer. 1993;71:1348–52.
171. Piekarski JD, Schlumberger M, Leclere J, et al. Chest computed tomography (CT) in patients with micronodular lung metastases of differentiated thyroid carcinoma. Int J Radiat Oncol Biol Phys. 1985;11:1023–7.
172. Schlumberger M, Arcangioli O, Piekarski JD, et al. Detection and treatment of lung metastases of differentiated thyroid carcinoma in patients with normal chest X-rays. J Nucl Med. 1988;29:1790–4.
173. Sumimura J, Nakagawa K, Kawamura J, et al. Thyroid cancer metastasis to the lumbar spine successfully treated by embolization and radioiodine. A case report. Nippon Geka Gakkai Zasshi. 1990;91:910–3.
174. Court C, Noun Z, Gagey O, Nordin JY. Surgical treatment of metastases from thyroid cancer in the axial skeleton. A retrospective study of 18 cases. Acta Orthop Belg. 2000;66:345–52.
175. Smit JW, Links TP, Hew JM, et al. Embolization of skeletal metastases in patients with differentiated thyroid carcinoma. Ned Tijdschr Geneeskd. 2000;144:1406–10.
176. Van Tol KM, Hew JM, Jager PL, et al. Embolization in combination with radioiodine therapy for bone metastases from differentiated thyroid carcinoma. Clin Endocrinol (Oxf). 2000;52:653–9.
177. van Tol KM, Hew JM, Links TP. Images in thyroidology. Embolization of a bone metastasis of follicular thyroid carcinoma. Thyroid. 2000;10:621–2.
178. Marcocci C, Pacini F, Elisei R, et al. Clinical and biologic behavior of bone metastases from differentiated thyroid carcinoma. Surgery. 1989;106:960–6.
179. Coleman R, Cook R, Hirsh V, et al. Zoledronic acid use in cancer patients: more than just supportive care? Cancer. 2011;117:11–23.
180. Klain M, Ricard M, Leboulleux S, et al. Radioiodine therapy for papillary and follicular thyroid carcinoma. Eur J Nucl Med Mol Imaging. 2002;29:479–85.
181. Franzius C, Dietlein M, Biermann M, et al. Procedure guideline for radioiodine therapy and 131 iodine whole-body scintigraphy in paediatric patients with differentiated thyroid cancer. Nuklearmedizin. 2007;46:224–2231.
182. Jarzab B, Handkiewicz-Junak D, Wloch J. Juvenile differentiated thyroid carcinoma and the role of radioiodine in its treatment: a qualitative review. Endocr Relat Cancer. 2005;12:773–803.
183. Van Nostrand D, Wartofsky L. Radioiodine in the treatment of thyroid cancer. Endocrinol Metab Clin North Am. 2007;36:807–22.
184. Benua RS, Leeper RD. A method and rationale for treating metastatic thyroid carcinoma with the largest safe dose of I-131. In: Medeiros-Neto G, Gaitan G, editors. Frontiers in thyroidology. New York: Plenum; 1986. p. 1317–21.
185. Traino AC, Ferrari M, Cremonesi M, Stabin MG. Influence of total-body mass on the scaling of S-factors for patient-specific, blood-based red-marrow dosimetry. Phys Med Biol. 2007;52:5231–48.
186. Durante C, Haddy N, Baudin E, et al. Long-term outcome of 444 patients with distant metastases from papillary and follicular thyroid carcinoma: benefits and limits of radioiodine therapy. J Clin Endocrinol Metab. 2006;91:2892.
187. Lippi F, Capezzone M, Angelini F, et al. Radioiodine treatment of metastatic differentiated thyroid cancer in patients on l-thyroxine, using recombinant human TSH. Eur J Endocrinol. 2001;144:5–11.
188. Jarzab B, Handkiewicz-Junak D, Roskosz J, et al. Recombinant human TSH-aided radioiodine treatment of advanced differentiated thyroid carcinoma: a single-centre study of 54 patients. Eur J Nucl Med Mol Imaging. 2003;30:1077–86.
189. Luster M, Lippi F, Jarzab B, et al. rhTSH-aided radioiodine ablation and treatment of differentiated thyroid

carcinoma: a comprehensive review. Endocr Relat Cancer. 2005;12:49–64.
190. Taïeb D, Sebag F, Farman-Ara B, Portal T, Baumstarck-Barrau K, Fortanier C, et al. Iodine biokinetics and radioiodine exposure after recombinant human thyrotropin-assisted remnant ablation in comparison with thyroid hormone withdrawal. J Clin Endocrinol Metab. 2010;95:3283–90.
191. Vallejo Casas JA, Mena Bares LM, Gálvez MA, et al. Treatment room length-of-stay and patient throughput with radioiodine thyroid remnant ablation in differentiated thyroid cancer: comparison of thyroid-stimulating hormone stimulation methods. Nucl Med Commun. 2011;32:840–6.
192. Eschmann SM, Reischl G, Bilger K, et al. Evaluation of dosimetry of radioiodine therapy in benign and malignant thyroid disorders by means of iodine-124 and PET. Eur J Nucl Med. 2002;29:760–7.
193. Freudenberg LS, Jentzen W, Görges R, et al. ^{124}I-PET dosimetry in advanced differentiated thyroid cancer: therapeutic impact. Nuklearmedizin. 2007; 46:121–8.
194. Erdi YE, Macapinlac H, Larson SM, et al. Radiation dose assessment for I-131 therapy of thyroid cancer using I-124 PET imaging. Clin Positron Imaging. 1999;2:41–6.
195. Jentzen W, Weise R, Kupferschläger J, et al. Iodine-124 PET dosimetry in differentiated thyroid cancer: recovery coefficient in 2D and 3D modes for PET/CT systems. Eur J Nucl Med Mol Imaging. 2008;35: 611–23.
196. Jentzen W, Freudenberg L, Eising EG, et al. Optimized ^{124}I PET dosimetry protocol for radioiodine therapy of differentiated thyroid cancer. J Nucl Med. 2008;49:1017–723.
197. Kolbert KS, Pentlow KS, Pearson JR, et al. Prediction of absorbed dose to normal organs in thyroid cancer patients treated with ^{131}I by use of ^{124}I PET and 3-dimensional internal dosimetry software. J Nucl Med. 2007;48:143–9.
198. Lassmann M, Hänscheid H, Verburg FA, Luster M. The use of dosimetry in the treatment of differentiated thyroid cancer. Q J Nucl Med Mol Imaging. 2011;55: 107–15.
199. Jentzen W, Verschure F, van Zon A, et al. PET assessment of response of bone metastases to initial radioiodine treatment of differentiated thyroid cancer. J Nucl Med. 2016;57:1499–1504.
200. Schlumberger M, Brose M, Elisei R, et al. Definition and management of radioactive iodine-refractory differentiated thyroid cancer. Lancet Diabetes Endocrinol. 2014;2:356–8.
201. Sanz MA, Lo-Coco F. Modern approaches to treating acute promyelocytic leukemia. J Clin Oncol. 2011;29: 495–503.
202. Schmutzler C, Schmitt TL, Glaser F, et al. The promoter of the human sodium/iodide-symporter gene responds to retinoic acid. Mol Cell Endocrinol. 2002;189:145–55.
203. Schmutzler C, Köhrle J. Retinoic acid redifferentiation therapy for thyroid cancer. Thyroid. 2000;10:393–406.
204. Simon D, Körber C, Krausch M, et al. Clinical impact of retinoids in redifferentiation therapy of advanced thyroid cancer: final results of a pilot study. Eur J Nucl Med Mol Imaging. 2002;29:775–82.
205. Coelho SM, Corbo R, Buescu A, et al. Retinoic acid in patients with radioiodine non-responsive thyroid carcinoma. J Endocrinol Invest. 2004;27:334–9.
206. Courbon F, Zerdoud S, Bastie D, et al. Defective efficacy of retinoic acid treatment in patients with metastatic thyroid carcinoma. Thyroid. 2006;16:1025–31.
207. Zhang Y, Jia S, Liu Y, et al. A clinical study of all-trans-retinoid-induced differentiation therapy of advanced thyroid cancer. Nucl Med Commun. 2007;28:251–5.
208. Fernández CA, Puig-Domingo M, Lomeña F, et al. Effectiveness of retinoic acid treatment for redifferentiation of thyroid cancer in relation to recovery of radioiodine uptake. J Endocrinol Invest. 2009;32:228–33.
209. Handkiewicz-Junak D, Roskosz J, Hasse-Lazar K, et al. 13-cisretinoic acid re-differentiation therapy and recombinant human thyrotropin-aided radioiodine treatment of non-functional metastatic thyroid cancer: a single-center, 53-patient phase 2 study. Thyroid Res. 2009;2:8. doi:10.1186/1756-6614-2-8.
210. Ho AL, Grewal RK, Leboeuf R, et al. Selumetinib-enhanced radioiodine uptake in advanced thyroid cancer. N Engl J Med. 2013;368:623–32.
211. Samaan NA, Schultz PN, Hickey RC, et al. The results of various modalities of treatment of well differentiated thyroid carcinomas: a retrospective review of 1599 patients. J Clin Endocrinol Metab. 1992;75:714–20.
212. Matuszczyk A, Petersenn S, Bockisch A, et al. Chemotherapy with doxorubicin in progressive medullary and thyroid carcinoma of the follicular epithelium. Horm Metab Res. 2008;40:210–3.
213. Sherman SI. Cytotoxic chemotherapy for differentiated thyroid carcinoma. Clin Oncol (R Coll Radiol). 2010;22:464–8.
214. Shimaoka K, Schoenfeld DA, DeWys WD, et al. A randomized trial of doxorubicin versus doxorubicin plus cisplatin in patients with advanced thyroid carcinoma. Cancer. 1985;56:2155–60.
215. Williams SD, Birch R, Einhorn LH. Phase II evaluation of doxorubicin plus cisplatin in advanced thyroid cancer: a Southeastern Cancer Study Group Trial. Cancer Treat Rep. 1986;70:405–7.
216. Santini F, Bottici V, Elisei R, et al. Cytotoxic effects of carboplatinum and epirubicin in the setting of an elevated serum thyrotropin for advanced poorly differentiated thyroid cancer. J Clin Endocrinol Metab. 2002;87:4160.
217. Sherman SI. Early clinical studies of novel therapies for thyroid cancers. Endocrinol Metab Clin North Am. 2008;37:511–24.

218. Sherman SI, Wirth LJ, Droz JP, et al. Motesanib diphosphate in progressive differentiated thyroid cancer. N Engl J Med. 2008;359:31–42.
219. Schlumberger MJ, Elisei R, Bastholt L, et al. Phase II study of safety and efficacy of motesanib in patients with progressive or symptomatic, advanced or metastatic medullary thyroid cancer. J Clin Oncol. 2009; 27:3794–801.
220. Chau NG, Haddad RI. Vandetanib for the treatment of medullary thyroid cancer. Clin Cancer Res. 2013;19: 524–9.
221. Elisei R, Schlumberger MJ, Muller SP, et al. Cabozantinib in progressive medullary thyroid cancer. J Clin Oncol. 2013;31:3639–46.
222. Viola D, Cappagli V, Elisei R. Cabozantinib (XL184) for the treatment of locally advanced or metastatic progressive medullary thyroid cancer. Future Oncol. 2013;9:1083–92.
223. Brose MS, Nutting CM, Jarzab B, et al. Sorafenib in radioactive iodine-refractory, locally advanced or metastatic differentiated thyroid cancer: a randomised, double-blind, phase 3 trial. Lancet. 2014;384(9940):319–28.
224. You YN, Lakhani V, Wells Jr SA. New directions in the treatment of thyroid cancer. J Am Coll Surg. 2007;205(4 Suppl):S45–8.
225. Schlumberger M, Tahara M, Wirth LJ, et al. Lenvatinib versus placebo in radioiodine-refractory thyroid cancer. N Engl J Med. 2015;372:621–30.
226. Brose MS, Frenette CT, Keefe SM, Stein SM. Management of sorafenib-related adverse events: a clinician's perspective. Semin Oncol. 2014;41 Suppl 2:S1–16.
227. Kloos RT, Eng C, Evans DB, et al. Medullary thyroid cancer: management guidelines of the American Thyroid Association. Thyroid. 2009;19:565–612.
228. O'Connell ME, A'Hern RP, Harmer CL. Results of external beam radiotherapy in differentiated thyroid carcinoma: a retrospective study from the Royal Marsden Hospital. Eur J Cancer. 1994;30:733–9.
229. Taylor T, Specker B, Robbins J, et al. Outcome after treatment of high-risk papillary and non-Hurthle-cell follicular thyroid carcinoma. Ann Intern Med. 1998;129:622–7.
230. Kim JH, Leeper RD. Treatment of locally advanced thyroid carcinoma with combination doxorubicin and radiation therapy. Cancer. 1987;60:2372–5.
231. Zackrisson B, Mercke C, Strander H, et al. A systematic overview of radiation therapy effects in head and neck cancer. Acta Oncol (Stockholm). 2003;42: 443–61.
232. Ain KB. Anaplastic thyroid carcinoma: a therapeutic challenge. Semin Surg Oncol. 1999;16:64–9.
233. Chiacchio S, Lorenzoni A, Boni G, et al. Anaplastic thyroid cancer: prevalence, diagnosis and treatment. Minerva Endocrinol. 2008;33:341–57.
234. Haigh PI, Ituarte PH, Wu HS, et al. Completely resected anaplastic thyroid carcinoma combined with adjuvant chemotherapy and irradiation is associated with prolonged survival. Cancer. 2001;91:2335–42.
235. Tennvall J, Lundell G, Wahlberg P, et al. Anaplastic thyroid carcinoma: three protocols combining doxorubicin, hyperfractionated radiotherapy and surgery. Br J Cancer. 2002;86:1848–53.
236. Are C, Shaha AR. Anaplastic thyroid carcinoma: biology, pathogenesis, prognostic factors, and treatment approaches. Ann Surg Oncol. 2006;13:453–64.
237. Biganzoli L, Gebbia V, Maiorino L, et al. Thyroid cancer: different outcomes to chemotherapy according to tumour histology. Eur J Cancer. 1995;31A:2423–4.
238. Heron DE, Karimpour S, Grigsby PW. Anaplastic thyroid carcinoma: comparison of conventional radiotherapy and hyperfractionation chemoradiotherapy in two groups. Am J Clin Oncol. 2002;25:442–6.
239. Chang HS, Nam KH, Chung WY, Park CS. Anaplastic thyroid carcinoma: a therapeutic dilemma. Yonsei Med J. 2005;46:759–64.
240. Blagosklonny MV, Giannakakou P, Wojtowicz M, et al. Effects of p53-expressing adenovirus on the chemosensitivity and differentiation of anaplastic thyroid cancer cells. J Clin Endocrinol Metab. 1998;83:2516–22.
241. Dziba JM, Marcinek R, Venkataraman G, et al. Combretastatin A4 phosphate has primary antineoplastic activity against human anaplastic thyroid carcinoma cell lines and xenograft tumors. Thyroid. 2002;12:1063–70.
242. Kim S, Prichard CN, Younes MN, et al. Cetuximab and irinotecan interact synergistically to inhibit the growth of orthotopic anaplastic thyroid carcinoma xenografts in nude mice. Clin Cancer Res. 2006;12: 600–7.
243. Prichard CN, Kim S, Yazici YD, et al. Concurrent cetuximab and bevacizumab therapy in a murine orthotopic model of anaplastic thyroid carcinoma. Laryngoscope. 2007;117:674–9.
244. Sosa JA, Balkissoon J, Lu SP, et al. Thyroidectomy followed by fosbretabulin (CA4P) combination regimen appears to suggest improvement in patient survival in anaplastic thyroid cancer. Surgery. 2012;152: 1078–87.
245. Tohyama O, Matsui J, Kodama K, et al. Antitumor activity of lenvatinib (e7080): an angiogenesis inhibitor that targets multiple receptor tyrosine kinases in preclinical human thyroid cancer models. J Thyroid Res. 2014;2014:638747. doi:10.1155/2014/638747.
246. Elisei R, Bottici V, Luchetti F, et al. Impact of routine measurement of serum calcitonin on the diagnosis and outcome of medullary thyroid cancer: experience in 10,864 patients with nodular thyroid disorders. J Clin Endocrinol Metab. 2004;89:163–8.
247. Boi F, Maurelli I, Pinna G, et al. Calcitonin measurement in wash-out fluid from fine needle aspiration of neck masses in patients with primary and metastatic medullary thyroid carcinoma. J Clin Endocrinol Metab. 2007;92:2115–8.
248. Wells Jr SA, Asa SL, Dralle H, et al. Revised American Thyroid Association guidelines for the

management of medullary thyroid carcinoma. Thyroid. 2015;25:567–610.
249. Gharib H, McConahey WM, Tiegs RD, et al. Medullary thyroid carcinoma: clinicopathologic features and long-term follow-up of 65 patients treated during 1946 through 1970. Mayo Clin Proc. 1992;67:934–40.
250. Modigliani E, Cohen R, Campos JM, et al. Prognostic factors for survival and for biochemical cure in medullary thyroid carcinoma: results in 899 patients. The GETC Study Group. Groupe d'étude des tumeurs à calcitonine. Clin Endocrinol. 1998;48:265–73.
251. Hamada S, Ishikawa N, Yoshi M, et al. Roles of circulating carcinoembryonic antigen and calcitonin in diagnosis of medullary thyroid carcinoma: a comparative study. Endocrinol Jpn. 1976;23:505–10.
252. Calmettes C, Moudktar MS, Milhaud G. Correlation between calcitonin and carcinoembryonic antigen levels in medullary carcinoma of the thyroid. Biomedicine. 1977;27:52–4.
253. Pacini F, Fontanelli M, Fugazzola L, et al. Routine measurement of serum calcitonin in nodular thyroid diseases allows the preoperative diagnosis of unsuspected sporadic medullary thyroid carcinoma. J Clin Endocrinol Metab. 1994;78:826–9.
254. van Veelen W, de Groot JW, Acton DS, et al. Medullary thyroid carcinoma and biomarkers: past, present and future. J Intern Med. 2009;266:126–40.
255. Milman S, Whitney KD, Fleischer N. Metastatic medullary thyroid cancer presenting with elevated levels of CA 19-9 and CA 125. Thyroid. 2011;21:913–6.
256. Elisei R, Lorusso L, Romei C, et al. Medullary thyroid cancer secreting carbohydrate antigen 19-9 (Ca 19-9): a fatal case report. J Clin Endocrinol Metab. 2013;98:3550–4.
257. Chopra A. [^{99m}Tc]-Pentavalent dimercaptosuccinic acid. Molecular Imaging and Contrast Agent Database (MICAD) [Internet]. Bethesda: National Center for Biotechnology Information (US); 2004–2010; 2011.
258. Clarke S, Lazarus C, Maisey M. Experience in imaging medullary thyroid carcinoma using ^{99m}Tc(V) dimercaptosuccinic acid (DMSA). Henry Ford Hosp Med J. 1989;37:167–8.
259. Bozkurt MF, Ugur O, Banti E, et al. Functional nuclear medicine imaging of medullary thyroid cancer. Nucl Med Commun. 2008;29:934–42.
260. Learoyd DL, Roach PJ, Briggs GM, et al. Technetium-^{99}m-sestamibi scanning in recurrent medullary thyroid carcinoma. J Nucl Med. 1997;38:227–30.
261. Papotti M, Kumar U, Volante M, et al. Immunohistochemical detection of somatostatin receptor types 1–5 in medullary carcinoma of the thyroid. Clin Endocrinol (Oxf). 2001;54:641–9.
262. Baudin E, Lumbroso J, Schlumberger M, et al. Comparison of octreotide scintigraphy and conventional imaging in medullary thyroid carcinoma. J Nucl Med. 1996;37:912–6.
263. Behr TM, Behe M, Becker W. Diagnostic applications of radiolabeled peptides in nuclear endocrinology. Q J Nucl Med. 1999;43:268–80.
264. Endo K, Shiomi K, Kasagi K, Konishi J, Torizuka K, Nakao K, Tanimura H. Imaging of medullary thyroid cancer with ^{131}I-MIBG. Lancet. 1984;2:233.
265. Castellani MR, Seregni E, Maccauro M, et al. MIBG for diagnosis and therapy of medullary thyroid carcinoma: is there still a role? Q J Nucl Med Mol Imaging. 2008;52:430–40.
266. Rufini V, Castaldi P, Treglia G, et al. Nuclear medicine procedures in the diagnosis and therapy of medullary thyroid carcinoma. Biomed Pharmacother. 2008;62:139–46.
267. Gotthardt M, Behe MP, Beuter D, et al. Improved tumour detection by gastrin receptor scintigraphy in patients with metastasised medullary thyroid carcinoma. Eur J Nucl Med Mol Imaging. 2006;33:1273–9.
268. Behr TM, Behe MP. Cholecystokinin-B/Gastrin receptor-targeting peptides for staging and therapy of medullary thyroid cancer and other cholecystokinin-B receptor-expressing malignancies. Semin Nucl Med. 2002;32:97–109.
269. Behe M, Behr TM. Cholecystokinin-B (CCK-B)/gastrin receptor targeting peptides for staging and therapy of medullary thyroid cancer and other CCK-B receptor expressing malignancies. Biopolymers. 2002;66:399–418.
270. Reubi JC. CCK receptors in human neuroendocrine tumors: clinical implications. Scand J Clin Lab Invest Suppl. 2001;234:101–4.
271. Ocak M, Helbok A, von Guggenberg E, et al. Influence of biological assay conditions on stability assessment of radiometal-labelled peptides exemplified using a ^{177}Lu-DOTA-minigastrin derivative. Nucl Med Biol. 2011;38:171–9.
272. Barbet J, Peltier P, Bardet S, et al. Radioimmunodetection of medullary thyroid carcinoma using indium-111 bivalent hapten and anti-CEA x anti-DTPA-indium bispecific antibody. J Nucl Med. 1998;39:1172–8.
273. Faggiano A, Grimaldi F, Pezzullo L, et al. Secretive and proliferative tumor profile helps to select the best imaging technique to identify postoperative persistent or relapsing medullary thyroid cancer. Endocr Relat Cancer. 2009;16:225–31.
274. Ong SC, Schoder H, Patel SG, et al. Diagnostic accuracy of ^{18}F-FDG PET in restaging patients with medullary thyroid carcinoma and elevated calcitonin levels. J Nucl Med. 2007;48:501–7.
275. Szakall Jr S, Esik O, Bajzik G, et al. ^{18}F-FDG PET detection of lymph node metastases in medullary thyroid carcinoma. J Nucl Med. 2002;43:66–71.
276. Conti PS, Durski JM, Bacqai F, Grafton ST, Singer PA. Imaging of locally recurrent and metastatic thyroid cancer with positron emission tomography. Thyroid. 1999;9:797–804.
277. Hoegerle S, Altehoefer C, Ghanem N, et al. ^{18}F-DOPA positron emission tomography for tumour detection in patients with medullary thyroid

carcinoma and elevated calcitonin levels. Eur J Nucl Med. 2001;28:64–71.
278. Koopmans KP, de Groot JWB, Plukker JTM, et al. ^{18}F-Dihydroxyphenylalanine PET in patients with biochemical evidence of medullary thyroid cancer: relation to tumor differentiation. J Nucl Med. 2008;49:524–31.
279. Beheshti M, Pocher S, Vali R, et al. The value of ^{18}F-DOPA PET-CT in patients with medullary thyroid carcinoma: comparison with ^{18}F-FDG PET-CT. Eur Radiol. 2009;19:1425–34.
280. Antunes P, Ginj M, Zhang H, et al. Are radiogallium labelled DOTA-conjugated somatostatin analogues superior to those labelled with other radiometals? Eur J Nucl Med Mol Imaging. 2007;34:982–93.
281. Ambrosini V, Marzola MC, Rubello D, Fanti S. ^{68}Ga-somatostatin analogues PET and ^{18}F-DOPA PET in medullary thyroid carcinoma. Eur J Nucl Med Mol Imaging. 2010;37:46–8.
282. Schlumberger M, Carlomagno F, Baudin E, et al. New therapeutic approaches to treat medullary thyroid carcinoma. Nat Clin Pract Endocrinol Metab. 2008; 4:22–32.
283. Modigliani E. Medullary thyroid carcinoma. Curr Ther Endocrinol Metab. 1994;5:112–7.
284. Bergholm U, Bergstrom R, Ekbom A. Long-term follow-up of patients with medullary carcinoma of the thyroid. Cancer. 1997;79:132–8.
285. Droz JP, Schlumberger M, Rougier P, et al. Chemotherapy in metastatic nonanaplastic thyroid cancer: experience at the Institut Gustave-Roussy. Tumori. 1990;76:480–3.
286. Wu LT, Averbuch SD, Ball DW, et al. Treatment of advanced medullary thyroid carcinoma with a combination of cyclophosphamide, vincristine, and dacarbazine. Cancer. 1994;73:432–6.
287. Nocera M, Baudin E, Pellegriti G, et al. Treatment of advanced medullary thyroid cancer with an alternating combination of doxorubicin-streptozocin and 5 FU-dacarbazine. Groupe d'Etude des Tumeurs à Calcitonine (GETC). Br J Cancer. 2000;83:715–8.
288. Modigliani E, Cohen R, Joannidis S, et al. Results of long-term continuous subcutaneous octreotide administration in 14 patients with medullary thyroid carcinoma. Clin Endocrinol (Oxf). 1992;36:183–6.
289. Fromigue J, De Baere T, Baudin E, et al. Chemoembolization for liver metastases from medullary thyroid carcinoma. J Clin Endocrinol Metab. 2006; 91:2496–9.
290. Kraeber-Bodere F, Bardet S, et al. Radioimmunotherapy in medullary thyroid cancer using bispecific antibody and iodine 131-labeled bivalent hapten: preliminary results of a phase I/II clinical trial. Clin Cancer Res. 1999;5:3190–8.
291. Chatal JF, Campion L, Kraeber-Bodere F, et al. Survival improvement in patients with medullary thyroid carcinoma who undergo pretargeted anti-carcinoembryonic-antigen radioimmunotherapy: a collaborative study with the French Endocrine Tumor Group. J Clin Oncol. 2006;24:1705–11.
292. Iten F, Müller B, Schindler C, et al. Response to [^{90}Yttrium-DOTA]-TOC treatment is associated with long-term survival benefit in metastasized medullary thyroid cancer: a phase II clinical trial. Clin Cancer Res. 2007;13:6696–702.
293. Kwekkeboom DJ, de Herder WW, Kam BL, et al. Treatment with the radiolabeled somatostatin analog [^{177}Lu-DOTA^{0}, Tyr^{3}]octreotate: toxicity, efficacy, and survival. J Clin Oncol. 2008;26:2124–30.
294. Lapa C, Werner RA, Schmid JS, et al. Prognostic value of positron emission tomography-assessed tumor heterogeneity in patients with thyroid cancer undergoing treatment with radiopeptide therapy. Nucl Med Biol. 2015;42:349–54.
295. Vaisman F, de Castro PH, Lopes FP, et al. Is there a role for peptide receptor radionuclide therapy in medullary thyroid cancer? Clin Nucl Med. 2015; 40:123–7.
296. Castellone MD, Carlomagno F, Salvatore G, Santoro M. Receptor tyrosine kinase inhibitors in thyroid cancer. Best Pract Res Clin Endocrinol Metab. 2008;22: 1023–8.
297. Wells Jr SA, Gosnell JE, Gagel RF, et al. Vandetanib for the treatment of patients with locally advanced or metastatic hereditary medullary thyroid cancer. J Clin Oncol. 2010;28:767–72.
298. Wells Jr SA, Robinson BG, Gagel RF, et al. Vandetanib in patients with locally advanced or metastatic medullary thyroid cancer: a randomized, double-blind phase III trial. J Clin Oncol. 2012;30:134–41.
299. Frank-Raue K, Fabel M, Delorme S, et al. Efficacy of imatinib mesylate in advanced medullary thyroid carcinoma. Eur J Endocrinol. 2007;157:215–20.
300. Mitsiades CS, McMillin D, Kotoula V, et al. Antitumor effects of the proteasome inhibitor bortezomib in medullary and anaplastic thyroid carcinoma cells in vitro. J Clin Endocrinol Metab. 2006;91:4013–21.
301. Volterrani D, Erba PA, Mariani G. Fondamenti di Medicina Nucleare – Tecniche e Applicazioni. Milan: Springer; 2010.
302. Mariani G, Bruselli L, Kuwert T, et al. A review on the clinical uses of SPECT/CT. Eur J Nucl Med Mol Imaging. 2010;37:1959–85.
303. Pacini F, Schlumberger M, Dralle H, et al. European consensus for the management of patients with differentiated thyroid carcinoma of the follicular epithelium. Eur J Endocrinol. 2006;154:787–803. Erratum in: Eur J Endocrinol. 2006;155:385.

Neuroendocrine Tumors: Therapy with Radiolabeled Peptides

43

Lisa Bodei, Laura Gilardi, Duccio Volterrani, Giovanni Paganelli, Chiara M. Grana, Mark Kidd, and Irvin M. Modlin

Abstract

Treatment of neuroendocrine tumors (NETs) is typically multidisciplinary and should be individualized according to the tumor histology, lesion extent, patient performance status, and symptoms. Surgery is the only potentially curative option. NET liver metastases are typically hypervascular, and chemoembolization or bland embolization of the hepatic artery, performed mechanically by microspheres or chemically with cytotoxic agents, can lead to significant necrosis. Medical therapy is directed at the control of symptoms and/or reducing tumor growth. Strategies range from the use of bioactive agents (somatostatin analogues or interferon) to conventional chemotherapy. PRRT uses radiolabeled somatostatin analogue peptides to treat unresectable or metastasized NETs. The therapeutic strategy of PRRT has been utilized for more than two decades and is accepted as an effective therapeutic modality in the treatment of inoperable or metastatic GEP, bronchopulmonary, and other NETs. PRRT with either ^{90}Y-DOTATOC or ^{177}Lu-DOTATATE is generally extremely well tolerated, with modest toxicity to the target organs, such as the kidneys and bone marrow. The chapter illustrates the efficacy and safety features of these compounds.

Keywords

Neuroendocrine tumors • PRRT • Therapy • ^{177}Lu-DOTATATE • ^{90}Y-DOTATOC

Glossary

[^{18}F]FDG	2-Deoxy-2-[^{18}F]fluoro-D-glucose
5-FU	5-Fluorouracil
BED	Bioeffective radiation dose

L. Bodei (✉)
Molecular Imaging and Therapy Service, Department of Radiology, Memorial Sloan Kettering Cancer Center, New York, NY, USA
e-mail: bodeil@mskcc.org

L. Gilardi • C.M. Grana
Division of Nuclear Medicine, European Institute of Oncology, Milan, Italy
e-mail: laura.gilardi@ieo.it; chiara.grana@ieo.it

D. Volterrani
Regional Center of Nuclear Medicine, Department of Translational Research and Advanced Technologies in Medicine and Surgery, University of Pisa, Pisa, Italy
e-mail: duccio.volterrani@med.unipi.it

G. Paganelli
Nuclear Medicine and Radiometabolic Units, "Istituto Scientifico Romagnolo per lo Studio e la Cura dei Tumori" (IRST) IRCCS, Meldola, Italy
e-mail: giovanni.paganelli@irst.emr.it

M. Kidd
Wren Laboratories, Branford, CT, USA
e-mail: mark@wrenlaboratories.com

I.M. Modlin
Wren Laboratories, Branford, CT, USA

Department of Surgery, Yale School of Medicine, New Haven, CT, USA
e-mail: imodlin@optonline.net

© Springer International Publishing Switzerland 2017
H.W. Strauss et al. (eds.), *Nuclear Oncology*,
https://doi.org/10.1007/978-3-319-26236-9_50

BP	Bronchopulmonary
CEA	Carcinoembryonic antigen, a tumor-associated marker
CgA	Chromogranin A, a tumor-associated marker for neuroendocrine tumors
CI	Confidence interval
CR	Complete response
CT	X-ray computed tomography
DOTA	2-(4-Isothiocyanatobenzyl-1,4,7,10-tetra-azacyclododecane-1,4,7,10-tetraacetic acid (macrocyclic coupling agent to label compounds of biological interest with metal radionuclides)
DOTATATE	DOTA-Tyr^3-Thr^8-octreotide
DOTATOC	DOTA-Tyr^3-octreotide
FDA	United States Food and Drug Administration
GEP	Originated in the gastroenteropancreatic tract
GFR	Glomerular filtration rate
Gy	Gray unit (ionizing radiation dose in the International System of Units, corresponding to the absorption of one joule of radiation energy per kilogram of matter)
KPS	Karnofsky performance status
LCNEC	Large-cell neuroendocrine carcinoma
MDS	Myelodysplastic syndrome
MEN	Multiple endocrine neoplasia
MIRD	Medical internal radiation dose
MR	Mixed response
MRI	Magnetic resonance imaging
mTOR	Mammalian target of rapamycin
NEN	Neuroendocrine neoplasia
NET	Neuroendocrine tumor
NSE	Neuron-specific enolase
OLINDA	Organ level internal dose assessment/Exponential modeling
OS	Overall survival
PET	Positron emission tomography
PET/CT	Positron emission tomography/Computed tomography
PFS	Progression-free survival
PR	Partial response
PRRT	Peptide receptor radionuclide therapy
QoL	Quality of life
RECIST	Response evaluation criteria in solid tumors
SCLC	Small-cell lung cancer
SD	Stabilization of disease
SPECT	Single-photon computed tomography
SPECT/CT	Single-photon computed tomography/Computed tomography
SSA	Somatostatin analog
SSTR	Somatostatin receptor
SUV	Standardized uptake value
SUV_{max}	Standardized uptake value at point of maximum
SWOG	Southwest Oncology Group, an organization supported by the National Cancer Institute of the United States to conduct clinical trials in adult cancers
TTP	Time to progression
VEGF	Vascular endothelial growth factor
WHO	World Health Organization

Contents

Therapy with Radiolabeled Peptides 1245
Overall Therapeutic Strategy 1245

Peptide Receptor Radionuclide Therapy (PRRT) 1246

PRRT Safety 1251

Renal Toxicity 1252

Hematological Toxicity 1253
Dosimetry in PRRT 1254
PRRT Efficacy 1256

Conclusions 1262

References 1263

Therapy with Radiolabeled Peptides

Overall Therapeutic Strategy

Treatment of neuroendocrine tumors (NETs) is typically multidisciplinary and should be individualized according to the tumor histology, lesion extent, patient performance status, and symptoms. An optimal management strategy includes a clinical assessment of the patient followed by characterization of the primary tumor and thereafter delineation of the grade and stage of the lesion [1]. Whenever possible and clinically/technically feasible, removal of the primary tumor should be undertaken to prevent the consequences of local events (bleeding, obstruction, perforation) and locoregional invasion and reduce the likelihood of metastatic spread. Surgery is the only potentially curative option; however, effective en bloc resections can only be obtained in 20% of cases due to the frequent presence of metastatic disease [2]. The surgical options include en bloc removal of the primary tumor, resection of hepatic metastases, radiofrequency ablation, and, in selected cases, hepatic or even enteric transplantation [3]. Tumors located in the head of the pancreas or in the duodenum are resected using the Kausch–Whipple pancreaticoduodenectomy procedure, while neuroendocrine tumors (carcinoids) of the distal ileum are managed by ileal resection and/or right hemicolectomy [4]. For bronchial carcinoids, lung resection surgery, including lymphadenectomy, is the option of choice. In the situation of more aggressive categories of thoracic NETs (large cell and small cell neuroendocrine carcinomas, LCNEC and SCLC, respectively), surgery is seldom feasible, and the outcomes are quite poor [5]. Liver transplantation for GEP-NETs remains controversial and can be proposed in selected situations (Milan criteria) when the liver is the sole site of disease, usually in a setting of stable metastases from intestinal NETs and low Ki67 index [6]. The definitive treatment for pheochromocytoma/paraganglioma is surgical. Laparoscopic removal of intra-adrenal and extra-adrenal pheochromocytomas is regarded as the surgical technique of choice [7]. Operative mortality is less than 1%, if adequate preparation with alpha and beta blockade is undertaken in the event of catecholamine-secreting tumors [8, 9]. Cortex-sparing adrenalectomy can be performed in hereditary, frequently bilateral, tumors, while malignant and diffusely spread tumors are approached utilizing conventional transabdominal resection. Interventional radiology techniques are helpful to treat multiple or dominant metastatic hepatic lesions not amenable to surgical resection. NET liver metastases are typically hypervascular, and chemoembolization or bland embolization of the hepatic artery, performed mechanically by microspheres or chemically with cytotoxic agents, can lead to significant necrosis. More recently radioembolization with ^{90}Y-labeled microspheres have been reported to have excellent results [10–12]. Other ablative techniques employed in routine approach to liver metastases include "umbrella" radiofrequency ablation, cryoablation, and high-intensity focused ultrasound (HIFU) ablation [13, 14]. Medical therapy is directed at the control of symptoms and/or reducing tumor growth. Strategies range from the use of bioactive agents (somatostatin analogues (SSAs) or interferon) to conventional chemotherapy. In functional tumors such as gastrinomas or insulinomas, symptomatic treatment with proton pump inhibitors or anti-hypoglycemic agents, respectively, is effective. More recently, a variety of novel agents (everolimus, sunitinib, and bevacizumab) with putative molecular targets (e.g., mTOR, VEGF) have been introduced with varying degrees of efficacy [15]. Everolimus and sunitinib have been approved by FDA for the treatment of pancreatic NETs. Early reports of efficacy have been tempered by concerns regarding adverse advents [16]. Traditional chemotherapy has little place in well-differentiated NETs, since most of them are indolent. Nevertheless, several studies have reported efficacy of the combination capecitabine + temozolomide in pancreatic NETs [17, 18].

Somatostatin analogue biotherapy is regarded as a basic therapeutic agent for the management of NETs. The over expression of somatostatin receptors (SSTR) on NETs allows effective

targeting and hence effective treatment of symptoms due to hyper or paroxysmal secretion of bioactive peptides and amines. There is some inhibitory effect growth of primary and metastatic lesions, but it is limited and difficult to predict or define given limitations in imaging sensitivity and suboptimal biomarker availability [19]. All SSTR subtypes bind somatostatin (both 14- and 28-amino-acid isoforms) and its analogues with varying degrees of efficacy. Somatostatin has an extremely short plasma half-life (about 2 min) and cannot be used for clinical purposes. Octreotide and lanreotide are two somatostatin analogues with high affinity for sst 2 receptor, moderately high affinity for sst 5, and intermediate affinity for sst 3 [20]. Somatostatin analogues are generally well tolerated, and long-acting formulations effectively control symptoms in up to 70% of patients, although tachyphylaxis frequently occurs [21]. Objective partial responses are identifiable in less than 10% [22]. Individuals with a clinical syndrome (flushing and diarrhea) have a reduced survival (5-year survival of 21%, 38 months median survival from the first facial flushing, 23 months from the biological diagnosis). Thus, SSA therapy, which reduces symptomatology and its sequelae, improves quality of life and decreases tumor growth, has merit, and is widely used as an initial therapeutic strategy [23]. An Italian multicenter trial [24] in NETs of various origins (using octreotide 0.5–1 mg t.i.d.) demonstrated symptomatic and biochemical responses in 73% and 77% of patients, respectively, with only 3% objective (partial) responses in carcinoids. The use of high-dose lanreotide (up to 12 mg/day) gave similar biochemical and symptomatic responses, as well as similar tumor responses (partial responses in 5% of patients) [25]. In the medical treatment of advanced SCLC, both octreotide and lanreotide were able to reduce growth factors, such as IGF-1, but did not show any antitumor efficacy [26–29]. Recently, an agonist with broader SSR affinity (pasireotide) has been introduced in the clinical practice to overcome resistance to octreotide or lanreotide. Current efficacy data appear limited and substantial adverse events have limited its utility [30].

Peptide Receptor Radionuclide Therapy (PRRT)

Neuroendocrine cells are typically regulated by numerous hormones, acting via specific receptors on the membrane surface. These receptors are usually 7-transmembrane domain G-protein-coupled receptors. The presence of a suitable density of internalizing somatostatin receptors (SSTR) on the cell surface of NETs is the basis for a somatostatin receptor-targeted therapy. Agonists binding to somatostatin receptors are internalized into endosomes and activate post-receptor mechanisms, such as adenyl cyclase, phospholipase, and ion channels, that are responsible for activation of the biological/pharmacological events within the cell. The receptor is either recycled on the membrane surface or entrapped into lysosomes for degradation. This retention into the lysosomes enables a radionuclide-based peptide diagnosis and/or therapy, depending on the radionuclide utilized (Figs. 1, 2, and 3 [31]).

Peptide receptor radionuclide therapy (PRRT) uses radiolabeled peptides to treat unresectable or metastasized NETs. The radiopharmaceutical is concentrated in the tumor cell, where the sensitive targets, such as DNA, can be attained. To estimate the radioactivity concentration in tumors, all PRRT protocols include a baseline assessment of the SSTR density, obtained in vivo with the conventional ^{111}In-pentetreotide scintigraphy or ^{68}Ga-SSA-PET/CT. The information obtained with these exams is used to determine the probability of clinical efficacy. It has been established that an uptake greater than that of kidneys and/or spleen (on planar scintigraphic images) is correlated with an objective response in ~60% of individuals [32]. The quantification of this uptake utilizing ^{68}Ga-DOTATOC PET/CT has indicated that a SUV_{max} threshold of >16 has sensitivity and specificity of 95% and 60%, respectively, in the prediction of tumor response [33].

PRRT consists in the systemic administration of a radiolabeled somatostatin analogue, in sequential cycles up to a cumulative activity that is calculated on renal irradiation. Cycles are usually administered

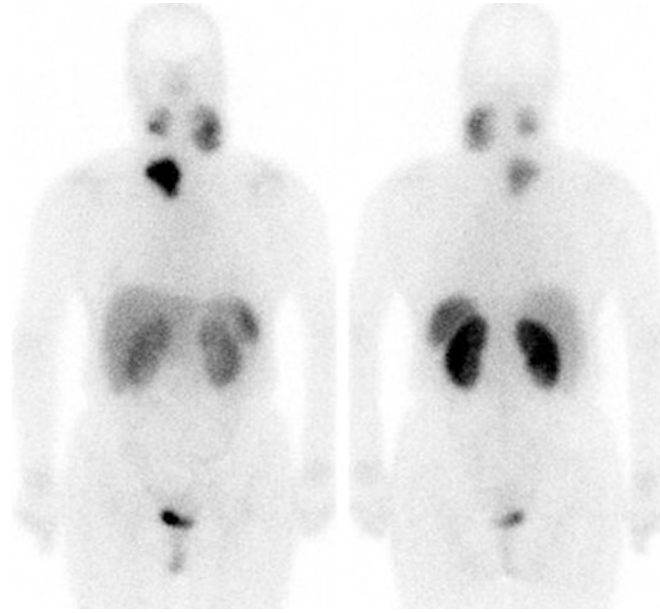

Fig. 1 Somatostatin receptor scintigraphy with ^{111}In-pentetreotide in a patient with multiple neck paragangliomas

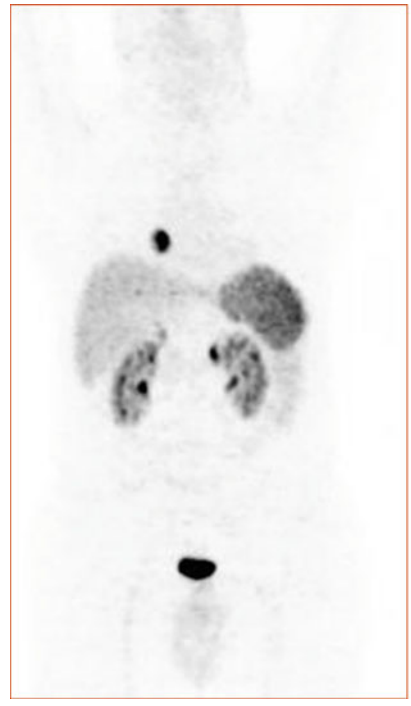

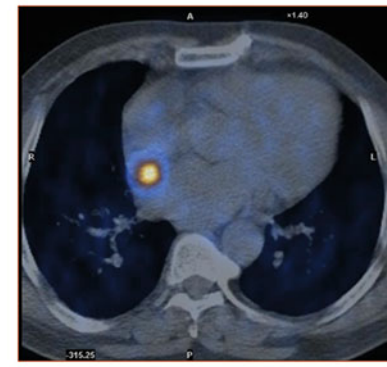

Fig. 2 PET/CT with ^{68}Ga-DOTANOC. Suspect relapse of paraganglioma in a patient who had previously undergone a pararenal paraganglioma excision. PET discloses a paraganglioma within the thorax, close to the superior vena cava. Subsequent surgery confirmed the PET finding

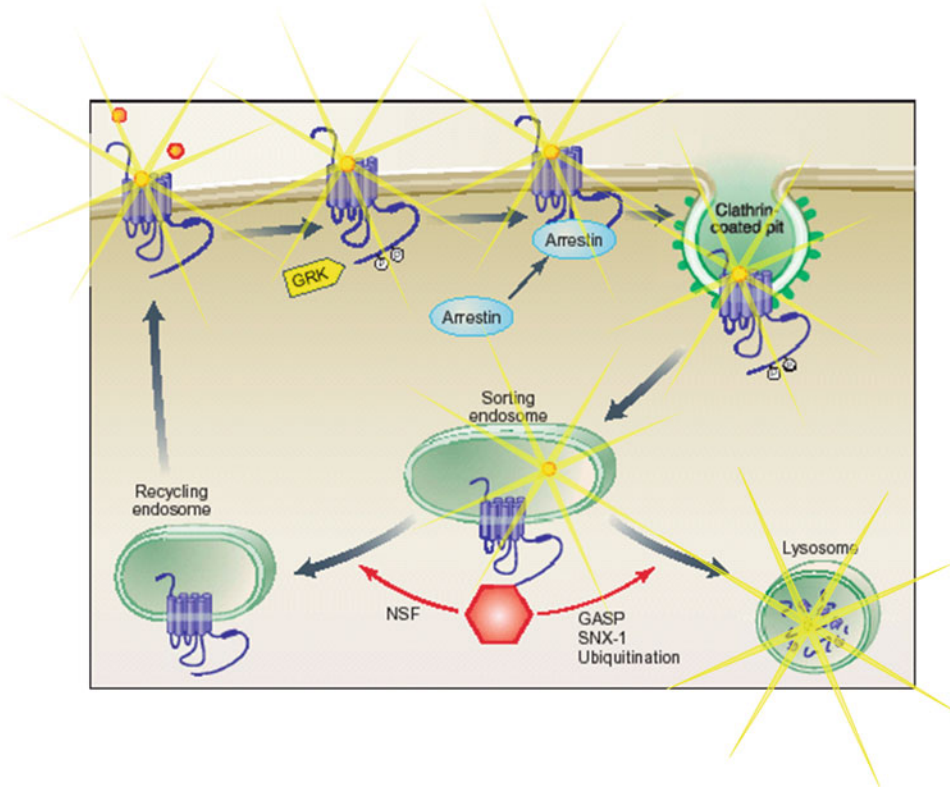

Fig. 3 Peptide receptor radionuclide therapy rationale: the internalization and intracellular retention of a suitably radiolabeled peptide (Adapted from Gray et al. [31])

6–12 weeks apart in order to ameliorate any potential hematological toxicity. To mitigate any renal risk, PRRT is usually accompanied by the coadministration of nephroprotective amino acids, such as lysine and arginine that diminish the renal absorbed dose by 50–60% [34].

Given the high first-pass extraction of the radiopeptides, the technique of intrahepatic arterial administration has been investigated with some success in clinical trials, although further information is needed to rigorously define its efficacy and safety [35].

The therapeutic strategy of PRRT has been utilized for more than two decades and is accepted as an effective therapeutic modality in the treatment of inoperable or metastatic GEP, bronchopulmonary, and other NETs [36]. It was initially utilized in 1992 at Erasmus University, Rotterdam, as a logical step following the introduction by this group of somatostatin receptor scintigraphy with [^{111}In-DTPA^{0}-D-Phe^{1}]-octreotide or ^{111}In-pentetreotide [37]. The two most commonly used radiopeptides for PRRT, ^{90}Y-octreotide and ^{177}Lu-octreotate, produce disease-control rates of 68–94% (SWOG or RECIST based) (Table 1) [34, 41, 42, 44, 50, 51]. In addition to tumor volume reduction, biochemical and symptomatic responses are commonly (up to 70%) observed [52]. The resulting progression-free survival (PFS) and overall survival (OS) rates compare favorably with SSAs, chemotherapy, and more recent usage of "targeted" therapies such as everolimus and sunitinib [32, 43]. The preliminary results of the current phase III randomized trial (NETTER-1) unequivocally indicated the clear advantage of ^{177}Lu-octreotate over high-dose SSAs in midgut NETs, in terms of PFS, OS, and objective response [53].

PRRT with ^{111}In-octreotide was initiated in the 1990s by Eric Krenning and coworkers at

Table 1 Review of the efficacy of PRRT with ^{90}Y-DOTATOC and ^{177}Lu-DOTATATE

	Schedule	Patients	CR	PR	DCR	Progression at baseline	Response criteria	Outcome (median PFS or TTP)
^{90}Y-octreotide	7.4 GBq/sqm in 4 cycles [38]	36 GEP	4%	20%	92%	100%	WHO	Not assessed
	2.96–5.55 GBq/cycle × 2 [39]	21 GEP	0%	28%	71%	n.a.	WHO	TTP 10 m
	0.93–2.78 GB/sqm/cycle [40]	58 GEP	0%	9%	71%	81%	SWOG	TTP 29 m
	4.4 GBq/cycle × 3 [41]	90 SI	0%	4%	74.4%	100%	SWOG	PFS 16 m
	1–10 cycles (median 2), various activity [42]	821 GEP	0.2%	38%	n.a.	n.a.	RECIST	n.a.
^{177}Lu-octreotate	27.8–29.6 GBq in 3–4 cycles [43]	310 GEP	2%	28%	81%	43%	SWOG	PFS 33 months
	3.7–29.2 GBq in 4–6 cycles of 3.7–7.4 GBq [44]	39 GEP	3%	31%	88%	76%	RECIST	TTP 36 months
	Mean 25.5 GBq in 5 cycles, normal subjects; mean 17.8 GBq in risk patients [45]	52 P	8%	21%	81%	88%	SWOG	PFS 20 months in reduced dosage, not reached in full dosage
	32 GBq in 4 cycles [46]	68 P	0%	60.3%	85.3%	67.6%	SWOG	PFS 34 months
	Median 25.7 vs. 18.4 GBq (normal vs. risk patients) [47]	43 SI	7%	0%	84%	100%	SWOG	PFS 36 months
	32 GBq in 4 cycles [48]	61 SI	0%	13.1%	91.8%	75.4%	SWOG	PFS 33 months
	27.8–29.6 GBq in 3–4 cycles vs. octreotide LAR 60 mg/month [49]	201 SI	19% (Lu) vs 3% (LAR) CR + PR		20% (Lu) vs 58% (LAR)	100%	RECIST	PFS not reached (Lu) vs. 8.4 months (LAR)

Modified from Bodei et al. [36], with permission

Erasmus University, in Rotterdam. A subsequent multicenter trial demonstrated some clinical benefit due to the Auger and conversion electrons emitted by indium-111 in close proximity to the cell nucleus. Despite these premises, partial remissions were unusual [54]. Higher-energy and longer-range emitters, such as pure β-emitter Yttrium-90 (E_{max} 2.27 MeV, R_{max} 11 mm, $T_{1/2}$ 64 h), were considered more suitable for therapeutic purposes. Therefore, a new analogue, Tyr^3-octreotide, with a similar pattern of affinity for somatostatin receptors, was developed. This analogue exhibited high hydrophilicity, simple labeling with ^{111}In and ^{90}Y, and tight binding to the macrocyclic chelator DOTA (1,4,7,10-tetraazacyclododecane- N,N′,N″,N‴-tetraacetic acid), to form ^{90}Y-[DOTA]^0-Tyr^3-octreotide or ^{90}Y-DOTATOC [55]. As a consequence of this optimization in 2000, the newer analogue {octreotate (Tyr^3,Thr^8-octreotide)}, with six to ninefold higher affinity for SSTR2, was introduced into clinical practice. The chelated analogue [DOTA]^0-Tyr^3-octreotate or DOTATATE can be labeled with the β–γ-emitter lutetium-177 ($E_{\beta max}$ 0.49 MeV, $R_{\beta max}$ 2 mm, $T_{1/2}$ 6.7 days) (Fig. 4).

In principle, Auger electron emitters represent an attractive alternative to β-particle emitters for cancer therapy if they can be placed

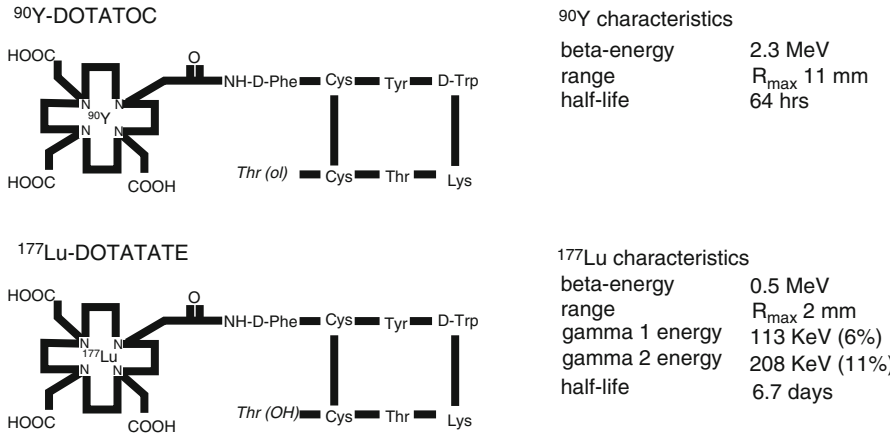

Fig. 4 Chemical structures of ^{90}Y-DOTATOC and ^{177}Lu-DOTATATE, the most used radiopeptides for PRRT. Note the substitution of a natural Thr in the eight octreotide amino acid in ^{177}Lu-DOTATATE. This modification increases the affinity for the SSTR2 receptor by six to nine fold

intracellularly, especially in close proximity to (or within) the nuclear DNA. Incorporation of Auger electron emitters into the DNA is a particularly efficient source of irradiation, capable of inducing cell death with virtually no damage to the surrounding cells. However, nuclear translocation of radiolabelled somatostatin analogues has never been clearly demonstrated so far, and PRRT is currently performed primarily with β-emitters to maximize ionization in the region of the nucleus [56, 57].

The most widely used radiopeptides are ^{90}Y-DOTATOC and ^{177}Lu-DOTATATE based upon their optimal pharmacokinetic considerations. Yttrium-90 has a higher β-particle emission compared to lutetium-177. The analysis of the residence times for DOTATATE and DOTATOC, calculated by means of the ^{177}Lu-labeled peptides, indicated that residence times for DOTATATE are significantly longer in kidney and tumor (ratios DOTATATE:DOTATOC = 1.4 and 2.1, respectively). This property enables the delivery of higher tumor doses although a similar increase in renal exposure occurs [58]. Based upon this consideration (higher tumor dose), ^{177}Lu appears of more benefit for labeling DOTATATE; while given the higher renal dose burden, ^{90}Y appears more useful in labeling DOTATOC.

A high expression of somatostatin receptors is a critical variable for determining the inclusion criteria of an individual for effective PRRT. As opposed to other treatments, the unique opportunity to identify and quantify the target (SSTR) prior to initiation of therapy informs the likelihood of success with PRRT [59]. Assessment of SSTR expression enables the possibility of quantification of the absorbed dose [32]. These values as well as the evaluation functioning somatostatin receptor overexpression can be accurately determined by somatostatin receptor imaging with either ^{111}In-pentetreotide or ^{68}Ga-SSA-PET/CT (Fig. 5). While immunohistochemistry for sst 2 can provide information on receptor status, it should be regarded as representing a "photographic image" taken at the moment of bioptic sampling and provides no information in respect of the actual internalizing capacity and the possible evolution with time of receptor density.

The development of molecular tools, such as transcript analysis of specific circulating NET mRNA signature, has demonstrated exciting possibilities in facilitating prediction of outcome (efficacy, tolerability). Such information is of considerable clinical utility in determining the most effective multidisciplinary sequencing of extensive and expensive therapies, particularly since conventional (morphologic/functional) imaging and biomarkers have been demonstrated to have substantial limitations in predicting effective therapy or defining progression and outcome. The

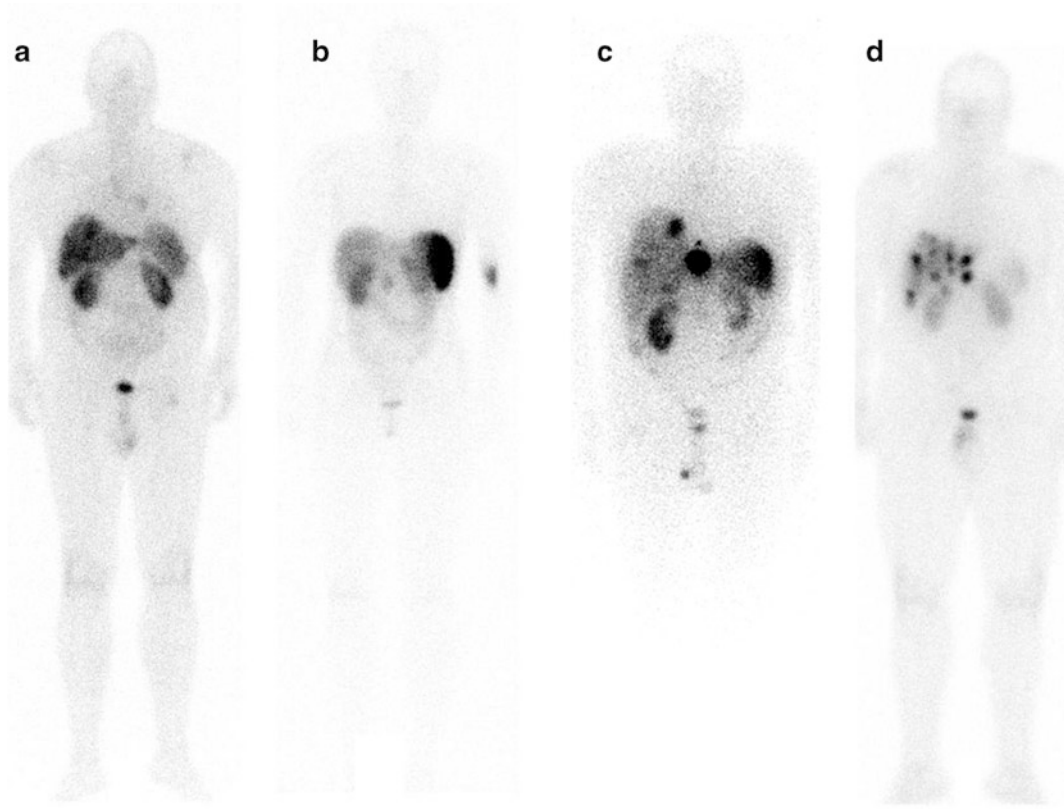

Fig. 5 Tumors candidates to PRRT are those with an uptake on planar images at least equal to the one of the normal liver (grade 1, image **b**), higher than that (grade 2, image **c**) or higher than the one of kidneys and spleen, the "hottest" organs at ^{111}In-pentetreotide scintigraphy (grade 3, image **d**)

introduction into clinical practice of measurement of circulating multianalyte 51-gene NET molecular signature has demonstrated significant advantage in early detection of residual disease of surgery-treated patient or in the assessment of somatostatin analogue response [60, 61]. Preliminary results indicate highly effective prediction of response to PRRT and accurate monitoring of therapeutic efficacy [62].

PRRT Safety

PRRT with either ^{90}Y-DOTATOC or ^{177}Lu-DOTATATE is generally extremely well tolerated, with modest toxicity to the target organs, such as the kidneys and bone marrow. Toxicity may be divided into acute, subacute, and long term. Acute side effects include mild nausea (25%), more rarely vomiting, related to the coadministration of renal protective amino-acid solutions, which is easily controlled or prevented by proper antinausea preparations, and abdominal pain (10%) [63]. Subacute effects comprise mild to moderate fatigue, depending also on the extent of disease, which is common in the 7–10 days following the therapy and mild (grade 1) alopecia, which is frequently reported after ^{177}Lu-DOTATATE [64]. The most common subacute side effect is hematologic toxicity, which is mild (WHO grades 1 or 2) and transient in 85–90% of patients [36]. Severe (grades 3 and 4) toxicity occurs in 10–15% of patients irrespective of the radiopeptide; however, this is usually reversible and rarely requires transfusion or granulocyte support [63, 65]. Chronic and permanent effects in the

kidneys and the bone marrow, such as renal function loss and reduction of bone marrow reserve, are rare and generally mild. The likelihood of such adverse events is significantly ameliorated if the necessary precautions, such as renal protection with amino acids and dosage adaptation to the clinical scenario, are undertaken. Secondary myeloproliferative diseases (myelodysplastic syndrome and leukemia) are extremely rare but have been noted [34, 38, 42, 64, 66, 67] (Table 2). Whether they represent a specific toxicity or susceptibility to an as yet unidentified genomic predisposition remains to be determined.

Renal Toxicity

The kidneys are considered the critical "at risk" organs in PRRT, particularly after ^{90}Y-DOTATOC administration. Proximal tubular reabsorption of the radiopeptide and the subsequent retention in the interstitium result in renal irradiation. Nephrotoxicity is increased in patients with preexisting long-standing and poorly controlled hypertension or diabetes. Given the high kidney retention of radiopeptides, positively charged molecules, such as L-lysine and/or L-arginine, are used to competitively inhibit the proximal tubular reabsorption of the radiopeptide. This leads to a reduction in the renal dose by 9–53% [70, 71] and can be further reduced by ~40% by prolonging infusion over 10 h and up to 65% by prolonging it over 2 days after radiopeptide administration. This time frame covers almost the entire renal elimination phase of the isotope [72, 73]. Kidney radiation toxicity is typically evident several months after irradiation due to the slow repair characteristics of renal cells (Fig. 6). The accepted renal tolerated dose is 23–25 Gy, as proposed by the National Council on Radiation Protection and Measurements (NCRPM). It has however more been determined that 23 Gy to the kidneys causes detrimental deterministic effects in 5% of patients within 5 years [75, 76].

Long-term evaluation of renal toxicity in a cohort ($n = 28$) undergoing PRRT with ^{90}Y-DOTATOC and dosimetric analysis showed that, of the 23 treated with ^{90}Y-octreotide, a low (28 Gy BED) threshold was observed with risk factors (mainly long-standing hypertension and/or poorly controlled diabetes), in comparison to 40 Gy in the absence of such risk factors [74]. These observations are consistent with the evidence that a higher and more persistent decline in creatinine clearance and the consequent development of renal toxicity are more likely to occur in the presence of preexisting risk factors [76]. The reason for the more frequent association of ^{90}Y-PRRT with renal function reduction is intrinsic to the specific physical characteristics of the ^{90}Y radionuclide, namely, the much more extensive intrarenal particle penetration.

In a retrospective series ($n = 1{,}109$) treated with ^{90}Y-octreotide, 103 subjects (9.2%) experienced grade 4–5 permanent renal toxicity [42]. Multivariate regression analysis indicated that the initial kidney uptake was predictive of severe renal toxicity. However, this relatively high

Table 2 Summary of long-term tolerability of PRRT with ^{90}Y-DOTATOC and ^{177}Lu-DOTATATE

	Patients	Follow-up (months)	Renal toxicity	MDS	Acute leukemia	Reference
^{90}Y-octreotide	40	19	10% grade 1	0	0	[39]
	39	6	3% grade 2	0	0	[38]
	58	18	3% grade 4	1	0	[40]
	1,109	23	9,2% grade 3/4	1	1	[42]
	358	30	2.8%	7 (1.95%)	5 (1.4%)	[68]
^{177}Lu-octreotate	504	19	0.4% grade 4	3	0	[43]
	51	29	24% grade 1	0	0	[44]
	74	21	1.3% grade 3/4	3	0	[67, 69]
	290	30	0%	6 (2.06%)	2 (0.69%)	[68]

Modified from Bodei et al. [36], with permission

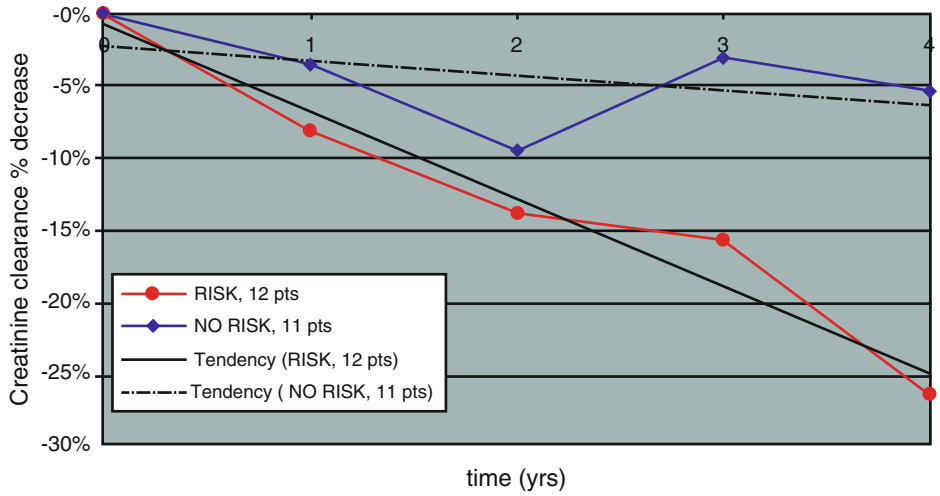

Fig. 6 The influence of risk factor on the course of renal parameters. Patients with risk factors for delayed renal toxicity (mainly longstanding and poorly controlled hypertension and diabetes) had more marked and persistent reduction in creatinine clearance and a lower bioeffective dose (BED) threshold for renal toxicity than did patients without risk factors (Adapted from Bodei et al. [74])

incidence was possibly related to the high administered activities per cycle (3.7 GBq/m^2 body surface, namely, activities of about 6.4 GBq per cycle in a standard male). In addition, subjects with preexisting impairment of renal function were not excluded from PRRT, and infusion of protective amino acids was not a routine procedure in the initial phases of the study [77].

Recently, the results of an analysis of long-term tolerability of PRRT ($n = 807$) treated with ^{90}Y-octreotide, ^{177}Lu-octreotate, or the combination (^{177}Lu, 34.4%; ^{90}Y, 44.4%; ^{177}Lu + ^{90}Y, 19.5%) have provided additional information on the issue of PRRT tolerability. The large numbers included in this analysis allowed clarification of the exact role for preexistent clinical parameters (such as diabetes, hypertension, and chemotherapy) in the determination of toxicity. Nephrotoxicity (transient and persistent) was detectable in 279 (34.6%) and was severe in 1.5%. ^{90}Y-peptides or the combination of ^{90}Y/^{177}Lu-peptides showed greater nephrotoxicity than ^{177}Lu-peptides alone. However, <30% of toxicities could be modeled by clinical parameters of which hypertension and anemia were identifiable as the most relevant risk factors. These results suggest that an individual susceptibility to radiation-associated disease, possibly of genetic origin, might play a determinant role [68].

An accurate assessment of glomerular filtration rate (GFR), as a measure of renal function (scintigraphic Gates' method), was carried out after PRRT ($n = 74$) with a median of 21 months (range 12–50) follow-up. The evaluation included potential risk factors, such as diabetes mellitus, hypertension, and chemotherapy. Results confirmed an alteration in GFR, with a relative yearly reduction of 1.8 ± 19%. Sixteen patients experienced a more pronounced reduction (>10 ml/min/year). However, toxicity was only evident in one. None of the described clinical factors, including the cumulative administered activity, contributed significantly to the decline of renal function [69].

Hematological Toxicity

PRRT is generally well tolerated. Hematologic toxicity is typically mild (WHO grades 1–2) and transient within few weeks from treatment completion. Severe, grade 3 or 4, toxicity may occur in <15% patients, with either ^{90}Y-DOTATOC or ^{177}Lu-DOTATATE, and are also generally

reversible within 2–3 months. In ~50% recovery may be longer (mean 12 months in a series of 203 ^{177}Lu-octreotate-treated patients) [63, 67]. Tumor diffusion in the bone marrow is a common feature in these cases [78]. PRRT is well tolerated, and severe, grade 3 or 4, hematological toxicity only occurred in <13% of patients treated with ^{90}Y-DOTATOC and ~10% of those treated with ^{177}Lu-DOTATATE (Table 2) [38–40, 43].

Sporadic cases of myelodysplastic syndrome (MDS) or even overt acute leukemia have been reported in ~2% [63]. Although predicted absorbed doses are lower than the conventional threshold for toxicity, both acute and permanent bone marrow damage remain a cause for concern, particularly when repeated radionuclide administrations are planned or the patients undergo several potentially myelotoxic treatments [36]. Dose-finding phase I studies indicate that the maximum cumulative administrable activity per cycle of ^{90}Y-octreotide, with renal protection, is 5.18 GBq, as determined by dose-limiting hematological toxicity [39]. Investigations employing the dose-limiting toxicity method were abandoned, since published data identified that 7.4 GBq could be safely used as a maximum activity per cycle [79]. This dosage was based on the experience of thyroid cancer therapy with ^{131}I, a radionuclide with physical characteristics similar to ^{177}Lu [65].

In data from a cohort with GEP-NENs ($n = 33$) treated in a salvage study, toxicity results were encouraging. Thus, re-treatment with median 18 GBq of ^{177}Lu-octreotate (two to four cycles, up to a median cumulative activity of 44.3 GBq: range 30–84) resulted in neither severe nephrotoxicity nor MDS during the follow-up (37 ± 16 months from initial PRRT and 23 ± 7 months from the start of salvage PRRT) [80].

An analysis of 203 patients treated with four intended cycles of 8 GBq each at 3-month intervals included the assessment of risk factors, including bone metastases, chemotherapy, or cumulative administered activity. The incidence of MDS was 1.4%. Myelosuppression was almost invariably reversible, and the cumulative administered activity and initial cytopenia were identified as the most important risk factors for myelotoxicity [67].

An analysis of a large group of 807 subjects treated with ^{90}Y-octreotide, ^{177}Lu-octreotate, or the combination showed that MDS occurred in 2.35%. This study also noted that commonly considered risk factors, such as prior chemotherapy, were associated with toxicity in up to 30%. Associated clinical features, such as platelet toxicity grade and the increasing duration of PRRT, were relevant. This led to speculation that unidentified individual susceptibilities, presumably of a genetic basis, could better explain the radiation-associated disease at the low marrow doses commonly obtained with PRRT [68].

Recent studies demonstrated that ^{177}Lu-octreotate can be safely utilized even in the presence of diffuse bone metastases, with severe bone replacement and potential elevated exposure of bone marrow. Significant G3/G4 reversible hematological toxicity occurred in 35% ($n = 4$) of 11 patients. Toxicity either resolved spontaneously ($n = 1$) or was controlled by support therapy ($n = 3$). A return to baseline values was obtained in 23 months after completion of PRRT [81].

Dosimetry in PRRT

Measuring the radiation burden to normal organs and malignant lesions is necessary to select the appropriate dose for therapy. The potential risk of kidney and red marrow toxicity limits the amount of radioactivity that may be administered. Indeed, when tumor masses are irradiated with suitable doses, volume reduction may be observed [82].

Techniques for radio-dosimetric estimates are illustrated in detail in ▶ Chap. 13, "Radiobiology and Radiation Dosimetry in Nuclear Medicine" of this book. Briefly, they include the generation of time–activity curves in normal organs and tumor lesions, based on data obtained from serial images recorded using a diagnostic activity of ^{111}In-pentetreotide or ^{86}Y-DOTATOC PET for ^{90}Y-DOTATOC PRRT or with ^{177}Lu-DOTATATE directly [83, 84] (Table 3).

Radiation dosimetry of normal organs and malignant lesions provides an insight for optimizing the delivery of radiation, allowing

Table 3 Absorbed radiation dose estimates following PRRT with ^{90}Y-DOTATOC and ^{177}Lu-DOTATATE. Values are organ absorbed doses per unit activity (Gy/GBq); mean ± SD or median (range)

	^{90}Y-DOTATOC		^{177}Lu-DOTATATE	
Organ	Dose (Gy/GBq)	Reference	Dose (Gy/GBq)	Reference
Red marrow	0.03 ± 0.01	Cremonesi et al. [84]	0.07 ± 0.01	Kwekkeboom et al. [101]
	0.17 ± 0.02	Forrer et al. [85]	0.04 (0.02–0.06)	Cremonesi et al. [83]
	0.09 (0.03–0.18)	Rodrigues et al. [89]	0.04 ± 0.02	Wehrmann et al. [90]
	0.05 ± 0.00	Förster et al. [87]	0.02 ± 0.03	Krenning et al. [86]
	0.06 ± 0.02	Helisch et al. [88]		
	0.12 ± 0.02	Menda et al. [100]		
Kidneys	6.05 (unprotected)	Kwekkeboom et al. [101]	1.65 ± 0.47 (unprotected); 0.88 ± 0.19 (protected)	Kwekkeboom et al. [101]
	3.84 ± 2.02 (unprotected)	Cremonesi et al. [84]	0.62 (0.45–17.74)	Cremonesi et al. [83]
	2.84 ± 0.64	Forrer et al. [85]	0.9 ± 0.3	Wehrmann et al. [90]
	2.44 (1.12–4.5)	Rodrigues et al. [89]	(0.32–1.67)	Sandstrom et al. [94]
	2.73 ± 1.41	Helisch et al. [88]		
	1.71 ± 0.89 (1.20–5.10)	Jamar et al. [75]		
	2.24 ± 0.84 (1.1–3.8)	Menda et al. [100]		

Adapted with permission from Bodei et al. [59]

maximization of the absorbed dose to the tumor while minimizing the dose delivered to normal organs. Absorbed doses are largely dependent on the administered activity, radionuclide used, and individual organ mass. Absorbed or biological effective doses in organs are calculated from the spatial activity distribution of the radionuclide as a function of time. This distribution is obtained from planar scintigraphy, SPECT/CT, or PET/CT images. The computer codes used to derive the dose vary from a simple and reproducible method based on standard phantoms, such as MIRD, OLINDA, which may not necessarily represent the organ anatomy of a single individual, to accurate but complicated and time-consuming codes utilizing personalized Monte Carlo simulations [91, 92].

Dosimetry is an obligatory procedure in planning external radiotherapy, yet the prediction of the dose–response relationship in nuclear medicine therapy remains inaccurate. This is due to the large variability in the individual organ volume, diversity of biodistribution and tumor uptake among individuals, the lack of uniform tissue distribution of the radioactivity, the inaccuracy of the absorbed dose to the kidneys in predicting renal toxicity, and, finally, the difficulty in modeling organs such as the bone marrow. These variables when summated render the accurate prediction of toxicity difficult [83, 93]. As a consequence, dosimetry is not widely performed, and skepticism among clinicians is pervasive. However, dosimetry is the only form of personalization that takes into account the actual radiation dose – namely, the effector of the desired effect – delivered to the target tissue and therefore represents a worthwhile area for development and its refinement.

The initial clinical studies that assessed the individual tolerance to radiopeptides identified clinical factors that could modify the renal dose threshold for radiopeptides, suggesting a consequent modification of the PRRT schedule [74]. Subsequently, based on the conventional dose thresholds of tolerance of the bone marrow and kidneys, Sandström et al. demonstrated that the same scheme of PRRT (four cycles of 200 mCi each of ^{177}Lu-octreotate) could result in different absorbed doses at the targets. Thus conversely, a substantial number of patients could tolerate higher cumulative activities or number of cycles – hence higher tumor doses and, potentially, efficacy. On the contrary a not irrelevant number of patients could tolerate lower cumulative activities

or number of cycles – possibly inefficient to control the tumor [94]. This represents a major step toward a dosimetry-based personalized treatment.

PRRT Efficacy

Experience with ^{111}In-Octreotide

Objective responses were rare due to the short range of the emission (0.0025 μm) of the particles. Among 40 patients treated with cumulative doses of 20–160 GBq, 1 partial remission, 6 minor remissions, and 14 stabilization of disease were reported. Mild hematological toxicity was observed, but three cases of myelodysplastic syndrome (MDS) or leukemia occurred in those treated with high activities (>100 GBq) and high estimated bone marrow doses (about 3 Gy). In a separate GEP-NETs study ($n = 27$), partial responses occurred in 2 of 26 patients with measurable disease. Renal insufficiency was reported in one patient, although possibly not treatment-related [54, 95].

Experience with ^{90}Y-DOTATOC

GEP-NET Tumors

All the published results derive from phase I to II trials and reflect heterogenous patient selection, inclusion criteria, treatment schemes, and dosages (cumulative activities ranged from 2 to 32 GBq). This has diminished the ability to derive rigorous conclusions. Complete and partial remissions were registered in 10–30% of patients, a higher rate than that obtained with ^{111}In-pentetreotide (~5%). In the initial report, 29 persons were treated with a dose-escalation scheme consisting of four or more cycles of ^{90}Y-DOTATOC with cumulative activities of 6.12 ± 1.35 GBq/m^2. Twenty showed disease stabilization, two had partial remission, four had minor remission, and three progressed [96]. In a subsequent study ($n = 39$) four equal intravenous injections were administered with a total of 7.4 GBq/m^2 of ^{90}Y-DOTATOC. The objective response rate was 23%, with complete remission in 2, partial remission in 7, and stabilization in 27. Pancreatic NETs ($n = 13$) exhibited a higher objective response rate (38%). A significant reduction of clinical symptoms was recorded in 83% of patients with diarrhea, in 46% of patients with flushing, in 63% of patients with wheezing, and in 75% of patients with pellagra [38]. Toxicity was generally mild and involved the kidney and the bone marrow. However, renal insufficiency was reported in five individuals who did not receive renal protection during the therapy. Severe hematological toxicity occurred in individuals receiving high cumulative activities [72].

In cohorts receiving up to an administered activity of 5.55 GBq per cycle, reversible grade 3 hematological toxicity was noted in 43% of patients injected with 5.18 GBq, which was defined as the maximum tolerated dose per cycle. None developed acute or delayed kidney toxicity, although follow-up was short. Partial and complete responses were reported in 28% of 87 patients with NETs [39].

In the multicenter phase 1 study, 60 patients received escalating activities of up to 14.8 GBq/m2 in four cycles or up to 9.3 GBq/m^2 in a single dose, without reaching the maximum tolerated single administration. All patients received renal protection. Three patients suffered dose-limiting toxicity: one with hepatic toxicity, one grade 4 thrombocytopenia, and one MDS. Four of 54 patients (8%) treated with the maximum allowed dose underwent a partial response, and 7 patients (13%) had minor responses. The median time to progression in the 44 patients showing stable disease, minor or partial response, was 30 months [97].

A multicenter study evaluated the role of ^{90}Y-octreotide in 90 patients with symptomatic, metastatic "carcinoids" (small bowel NENs). The data identified stabilization of tumor response (SWOG criteria) in 74% as well as a durable amelioration of symptoms related to the tumor mass and the hypersecretion of bioactive amines [41]. This trial reported a PFS of 16 months and an overall survival of 27 months.

Figure 7 illustrates an example of objective response to ^{90}Y-DOTATOC in a patient affected by gross liver metastases from a resected pancreatic insulinoma treated with 23 GBq in seven cycles.

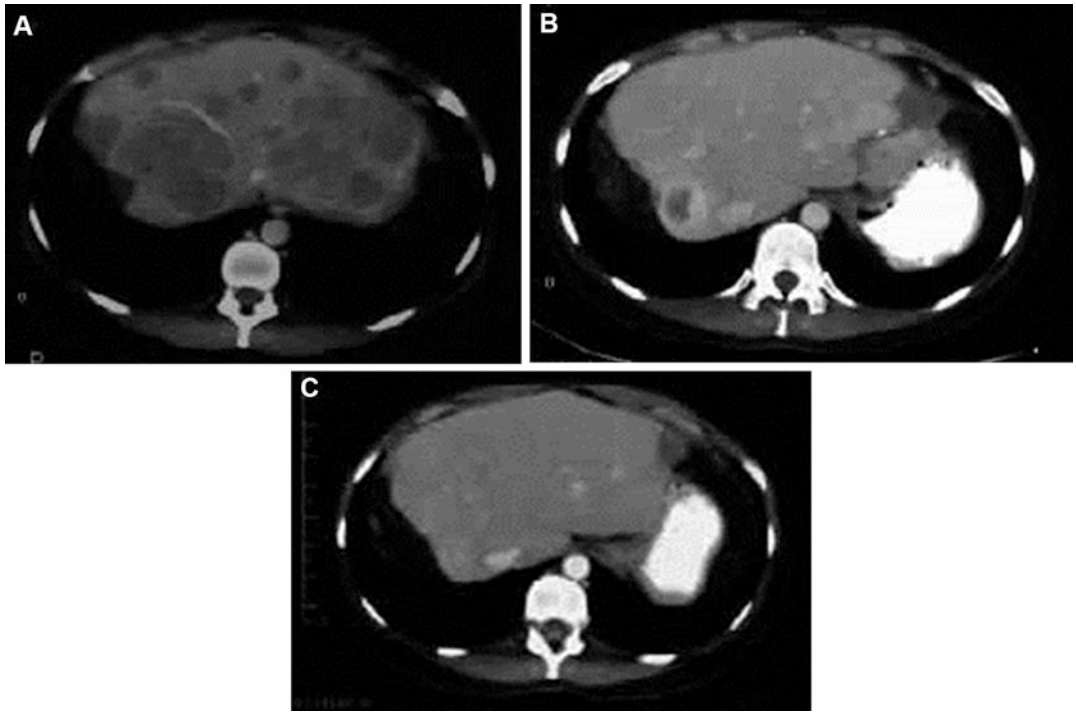

Fig. 7 Illustrates an example of objective response to ^{90}Y-DOTATOC in a patient affected by massive liver metastases from a resected insulinsecreting pancreatic neuroendocrine tumor after treatment, treated with ^{90}Y-DOTATOC (23 GBq in seven cycles) (**a**–**c** CT scans)

In respect of survival after ^{90}Y-DOTATOC, a phase I–II study of GEP-NETs ($n = 58$) treated with 1.7–32.8 GBq reported a clinical benefit (including stabilization and minor response) in 57% (with true objective response in 20%), a median overall survival of 36.7 months (vs. 12 months in the historic group treated with ^{111}In-pentetreotide), and a median progression-free survival of 29.3 months. Characteristically, patients stable at baseline had a better overall survival than those progressive at baseline, while the extent of disease at baseline was an additional predictive factor for survival [40].

A favorable clinical response after ^{90}Y-DOTATOC, as determined by a scoring system that included weight, patient-assessed health score, Karnofsky score, and tumor-related symptoms, was reported in 14/21 patients who were treated with 13.3 GBq in three cycles [98].

More recently, the Basel group published the results of an open-label phase II trial in 1,109 patients with different NET lesions (GEP, BP, and other endocrine tumors, such as medullary thyroid cancer, paraganglioma, and neuroblastoma) treated with ^{90}Y-octreotide, divided into multiple cycles of 3.7 GBq/m^2 each. Objective morphologic responses (RECIST criteria) were observed in 378 (34.1%), biochemical responses in 172 (15.5%), and symptomatic responses in 329 (29.7%). In this series, the NEN groups were 265 small bowel and 342 pancreatic tumors. The rates of objective response were 26.8% and 47%, respectively. A longer survival was correlated with tumor and symptomatic response. The best predictor of survival was tumor uptake at baseline determined by OctreoScan® [42].

Other Endocrine and EndocrineRegulated Tumors

Limited experiences in the treatment of medullary and follicular thyroid carcinomas, lymphoproliferative disorders, pheochromocytomas, and paragangliomas have been reported. ^{90}Y-DOTATOC (7.5–19.2 GBq in two to eight

cycles) was administered to 21 patients with metastatic medullary thyroid carcinoma with positive OctreoScan®, progressive after conventional treatments. Two patients (10%) obtained a complete response (CR), as evaluated by CT, MRI, and/or ultrasound, while a stabilization of disease (SD) was observed in 12 (57%); 7 (33%) failed to respond to therapy. The duration of the response ranged from 3 to 40 months. Using biochemical parameters (calcitonin and CEA), a complete response was observed in one patient (5%), while partial response occurred in five (24%) and stabilization in three (14%). Twelve had progression (57%). Complete responses were observed in those with lower tumor burden and calcitonin values at the time of the enrolment. Medullary thyroid cancers showed a lower response rate compared to classic GEP-NETs; nevertheless, patients with smaller tumors and higher uptake of the radiopeptide tended to respond better [99].

In a phase I study involving 17 children and young adults (2–24-year-old) affected by SSTR-positive tumors (including neuroblastomas, MEN2B, and gliomas), patients were treated with ^{90}Y-DOTATOC (1.1–1.85 GBq/m^2 per cycle for a total of three cycles, administered 6 weeks apart). Partial response according to the Pediatric Oncology Group criteria was observed in 12%, while 29% exhibited minor responses; the most obvious clinical benefit was overall improved quality of life. Thus, PRRT with ^{90}Y-DOTATOC is effective and well tolerated also in young patients [100].

Experience with ^{177}Lu-DOTATATE in GEP-NETs

The somatostatin analogue [DOTA^0, Tyr^3, Thr^8]-octreotide or DOTATATE has a ninefold higher affinity for the SSTR2 compared with [DOTA^0, Tyr^3]octreotide in vitro. Radiolabeling with the β/γ-emitter lutetium-177 yielded tumor regressions and prolonged animal survival in a rat model [55]. The compound ^{177}Lu-octreotate was thereafter investigated in several clinical phase I and II studies [43, 44, 101, 102] and shown to have enhanced efficacy and greater manageability, due to a lower dosimetric burden to the kidney. An additional advantage is provided by the possibility of obtaining both scintigraphic images and dosimetric studies simultaneously since ^{177}Lu exhibits gamma photon co-emission. Currently this compound represents the most frequently used radiopeptide for PRRT.

In a preliminary report by the Rotterdam group, GEP-NETs ($n = 35$) were treated with 3.7, 5.6, or 7.4 GBq of ^{177}Lu-DOTATATE per cycle, up to a final cumulative activity of 22.2–29.6 GBq. Complete and partial responses were noted in 38% with no serious adverse events observed [79].

In a larger study ($n = 131$) of somatostatin, receptor-positive tumors were treated up to a cumulative activity of 22.2–29.6 GBq of ^{177}Lu-DOTATATE. One developed renal insufficiency, and another hepatorenal syndrome. Severe hematological toxicity occurred in <2% of the administrations. In the 125 evaluated patients, complete remission was observed in 3 (2%), partial remission in 32 (26%), minor response in 24 (19%), and stable disease in 44 (35%), while 22 (18%) progressed. Better responses were more frequent in the case of a high uptake on baseline OctreoScan® scintigraphy and when a limited number of liver metastases were present, while progression was significantly more frequent in those with a low performance score and extensive disease at enrollment. Median time to progression was more than 36 months, comparing favorably to chemotherapy. A categorization of objective response showed again that pancreatic tumors tended to respond better than other GEP tumors, although pancreatic gastrinomas tended to relapse in a shorter interval (median TTP 20 months vs. >36 in the rest of GEP tumors). In addition, ^{177}Lu-DOTATATE significantly improved the global health/QoL and various function and symptom scales in individuals with metastatic disease. The effect was more frequent in patients obtaining tumor regression but, surprisingly, was observed also in progressing patients [51, 103]. Of note was the fact that there was no significant decrease in QoL in individuals asymptomatic prior to therapy [52].

An enlargement of the previous series to 504 subjects treated with ^{177}Lu-DOTATATE was undertaken. Efficacy was evaluated in 310, along

with the confirmation of the occurrence of complete and partial remissions in 2 and 28% of cases, demonstrated a survival benefit of 40–72 months, compared to historical controls treated with chemotherapy. Reported prognostic factors for predicting tumor remission (CR, PR, or MR) as treatment outcome were uptake on the OctreoScan® ($P < 0.01$) and Karnofsky performance status (KPS) > 70 ($P < 0.05$). The degree of uptake at OctreoScan® is crucial and can be regarded roughly as a surrogate of the future absorbed dose provided by the therapy. Response benefit was more frequent in individuals with limited liver involvement and a high uptake on baseline ^{111}In-pentetreotide scintigraphy. Conversely, progression was significantly more frequent in those with a low performance score and extensive disease at enrolment. Categorization of objective responses identified that pancreatic NENs tended to respond better than other GEP-NENs and that functioning tumors, e.g., pancreatic gastrinomas, tended to relapse after a shorter interval (median time to progression 20 months vs. >36 in the remaining GEP-NENs) [43].

Figure 8 illustrates an example of objective response in a patient with liver and bone metastases from ileal neuroendocrine carcinoma treated with ^{177}Lu-DOTATATE (24 GBq in five cycles).

It is interesting to note that a small proportion of patients, responding to PRRT with either SD or mixed response at the first evaluation 3 months after therapy completion, showed a further objective response at 6 and 12 months of follow-up [43]. These observations allow speculation on the possible radiobiological implications, such as a "bystander effect," triggered by the low dose rate, protracted irradiation of lutetium-177.

The results of a phase I–II escalation dose study aimed at defining toxicity and efficacy of ^{177}Lu-octreotate were published in 2011 [44]. A cohort ($n = 51$) with unresectable/metastatic NENs, mainly of GEP origin, were divided into two dosage groups. One group received escalating activities, from 3.7 to 5.18 GBq and the second from 5.18 to 7.4 GBq, with dosimetry-based cumulative activities up to 29 GBq. Partial and complete responses were observed in 15 (32.6%). The median time to progression was 36 months, with an overall survival of 68% at 36 months. Nonresponders and patients with extensive tumor involvement were noted to have a lower survival [44].

Efficacy in Skeletal Involvement

It was generally considered, at the beginning of the PRRT experience, that bone metastases were less responsive to PRRT and that therefore these patients should receive additional therapies to treat skeletal locations. Despite the fact that neither SWOG nor RECIST criteria however include the evaluation of bone metastases, more recent studies indicate that PRRT is efficient in bone metastases. In a retrospective series ($n = 68$) treated with ^{177}Lu-octreotate (four intended cycles, 8.1 GBq each, at 3-month intervals; followed up for a median of 48 months). The observed objective response rate was comparable to other studies of PRRT in GEP-NENs, with 2.9% and 33.8% complete and partial responses, respectively. The median PFS was 35 months. Individuals with PRRT-responsive bone metastases exhibited longer overall survivals (median 56 vs. 39 months). In this group, high neuron-specific enolase (NSE) values and Ki67 > 10% were associated with a shorter overall survival. Of note was the observation that Karnofsky performance status and multifocal bone metastatic disease did not limit the efficacy of PRRT [104].

Efficacy in Different Types of NETs

Pancreatic NETs

Recent advances on pathobiological and molecular genomics have indicated that pancreatic and small intestine NETs are two separate entities. Therefore, current studies have tended to address the role of PRRT in single-system pathologies.

A prospective phase II study used ^{177}Lu-octreotate in a cohort ($n = 52$) with advanced well-/moderately differentiated pancreatic NETs. Based on the reported existence of putative risk factors for renal toxicity (hypertension and diabetes), patients were divided into two groups treated with different levels of activity. Thus, a full dose (21–28 GBq) was compared to a reduced dose

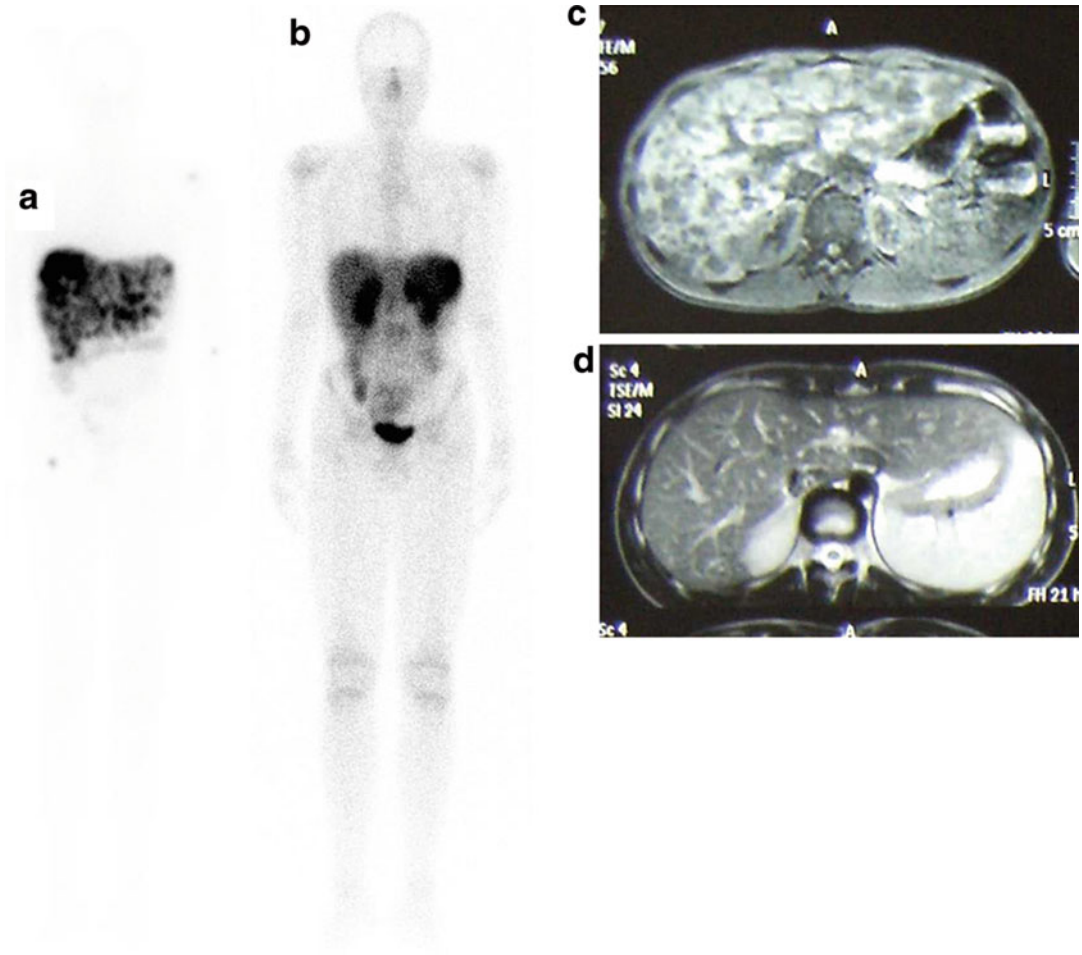

Fig. 8 Serial functional and morphologic imaging in a young male patient affected by liver and bone metastases from ileal neuroendocrine carcinoma treated with ^{177}Lu-DOTATATE (24 GBq in five cycles). Basal evaluation (**a** ^{177}Lu-DOTATATE scintigraphy; **c** MRI) showed extensive liver involvement. Final evaluation (**b** ^{177}Lu DOTATATE scintigraphy; **d** MRI) showed an almost complete response

(11–20 GBq) for a normal and risk subset of subjects, respectively. Both regimens resulted in antitumor efficacy. PFS was not reached at the time of the analysis in the cohort treated with the full-dose regimen, while it was 20 months in individuals treated with a reduced dose. This suggests the full-dose scheme should be recommended, when possible [45].

A recent retrospective study evaluated a cohort with metastatic pancreatic NENs ($n = 68$, 52% at their first systemic treatment) treated with ^{177}Lu-octreotate (four intended cycles, 8 GBq each, at 3-month intervals). In this group 68% were in progression at enrolment. Partial responses were noted in 60%, with a median PFS of 34 months. Multivariate analysis indicated that G1 tumors had a longer PFS. Reduced performance status (KPS $\leq$ 70), a high liver burden ($\geq$25% of volume), and increased NSE (>15 ng/ml) were associated with a poorer prognosis [56]. To better define the predictors of long-term outcome, the same group undertook a multivariate analysis in a cohort of metastatic GEP-NENs ($n = 74$) who had previously undergone PRRT with

^{177}Lu-octreotate (four cycles, 7.9 GBq each, at 3-month intervals). A Ki67 index >10%, a Karnofsky performance status ≤70, a tumor burden in the liver ≥25%, and a baseline NSE >15 ng/ml were independent predictors of shorter survival. However, even individuals with Ki67 > 10% benefited from PRRT, with a median PFS of 19 months as opposed to 26 months for the entire cohort [102].

A separate study by van Vliet E et al. considered non-resectable or borderline resectable or oligometastatic (≤3 liver metastases) non-functioning pancreatic NETs ($n = 29$). This group was treated with ^{177}Lu-octreotate with neo-adjuvant intent. After PRRT, successful surgery could be undertaken in nine individuals (31%) [Whipple procedure ($n = 6$), pylorus-preserving pancreaticoduodenectomy ($n = 1$), and splenopancreatectomy ($n = 1$)]. PFS was significantly longer in those in whom surgery could be undertaken (69 vs. 49 months). A further comparison with 90 plurimetastatic subjects treated in the same fashion provided a PFS of 25 months [105]. This study supports the proposal of early treatment and the possibility of downstaging tumors with PRRT.

Small Intestinal NETs

A phase II study of PRRT in progressive G1-G2 tumors ($n = 43$) from the Meldola group applied the same principle of reducing cumulative activities (median 25.7 vs. 18.4 GBq) in patients at risk for delayed renal or hematological toxicity. Both activities proved to be safe and effective (84% disease-control rate (SWOG criteria) and PFS of 36 months) in all. Of note is the observation that [^{18}F]FDG-PET-negative patients exhibited a significantly longer PFS than those with an [^{18}F]FDG-positive scan [47].

A more recent study by the Bonn group utilized the standard approach and described the benefit of ^{177}Lu-octreotate in a uniformly treated group (four cycles of 7.9 GBq each). The cohort ($n = 61$) included unresectable small intestine tumors, in progression or with uncontrolled symptoms, which were treated and followed for 62 months. Disease control rate was 91.8% (SWOG criteria). Median PFS was 33 months, OS was 61. Objective response was significantly associated with longer survival. Independent predictors of shorter PFS were functionality and high plasma CgA levels >600 ng/mL at baseline [48].

The recent phase III study of small intestine NETs using ^{177}Lu-DOTATATE named NETTER-1 was undertaken by a bicontinental multicentric group sponsored by Advanced Accelerator Applications (AAA). This randomized trial compared ^{177}Lu-DOTATATE vs. high-dose octreotide in patients with inoperable, progressive, midgut carcinoid tumors. Preliminary results indicate that ^{177}Lu-octreotate significantly improves PFS (PFS not reached vs. 8.4 months; hazard ratio 0.21) [49].

Efficacy of Repeated Treatments: Salvage Therapy

The Rotterdam group published the results of salvage therapy with ^{177}Lu-DOTATATE in NET patients with progressive disease after initial response to PRRT with the same agent administered with cumulative activities of 22.2–29.6 GBq. A total of 32 patients received two additional cycles of ^{177}Lu-DOTATATE totaling 15 GBq, with ensuing new objective response in 8 (two partial and six minor responses) and stabilization of disease in 8; median time to progression in those responding was 17 months. Although the rate of response was lower than that observed after primary treatment and tumor response lasted for shorter periods, salvage therapy represents a valuable option in individuals with advanced disease, who have relapsed after responding to a first course of PRRT [106].

A more recent analysis by the Meldola group included 26 subjects in progression after an initial treatment with ^{90}Y-octreotide. All patients had preserved kidney and hematological parameters and received an intended cumulative activity of 14.8–18.5 GBq of ^{177}Lu-octreotide in four or five cycles. Disease control rate was 84.6%, the median PFS 22 months (95% CI 16 months – not reached) and was comparable to that obtained after ^{90}Y-octreotide (28 months; 95% CI 20–36 months). Tumor burden and number of liver metastases were significant negative prognostic factors [107].

Efficacy of PRRT in Combination with Chemotherapy or Biomolecular Agents

This concept is consistent with recent combinatorial therapeutic trends in oncology. A variety of different studies have demonstrated feasibility and efficacy. However, adequately powered, optimally randomized, and rigorously analyzed studies are required to define the exact benefit of this approach.

A phase II study of NET patients with progressive disease ($n = 33$) used a regimen including four cycles of ^{177}Lu-DOTATATE (7.8 GBq) plus the radiosensitizer chemotherapy agent capecitabine (1,650 mg/m^2), for the following 2 weeks. No additional toxicity was observed, while objective response (according to RECIST criteria) was achieved in 24%, stable disease in 70%, and disease progression in 6% [108].

A more recent adaptation of the chemo-radiotherapy protocol utilized 5-fluorouracil (5-FU) as opposed to its oral prodrug capecitabine. A retrospective analysis of patients with progressive disease ($n = 68$) or uncontrollable symptoms from NETs reported that the combination strategy (median cumulative activity of ^{177}Lu-octreotate 31 GBq and 200 mg/m2/24 h 5-FU, from 4 days before to 3 weeks after PRRT cycle 2–4) resulted in 70% benefit for at least 6 months for symptomatic patients and 68% disease-control rate in progressive disease. Non-pancreatic primary site, dominant liver metastases lesions <5 cm, and the use of 5-FU were associated with objective response [109].

A combination of ^{177}Lu-octreotate with capecitabine and temozolomide was studied in a phase I–II trial of advanced low-grade NETs ($n = 35$), with the aim of evaluating safety and efficacy. Standard dosages (7.8 GBq) of ^{177}Lu-octreotate every 8 weeks were combined with 14 days of capecitabine 1,500 mg/m2 and, in successive cohorts, to escalating doses of temozolomide (100, 150, and 200 mg/m^2 in the last 5 days of each capecitabine cycle). Treatment was well tolerated without dose-limiting toxicities. Complete responses were observed in 15%, partial response in 38%, and stable disease in 38%. Responses tended to be higher in gastropancreatic than in small intestine primaries. Median PFS was 31 months [110].

An alternative combination phase I study evaluated the combination of everolimus with ^{177}Lu-octreotate in subjects with advanced GEP-NETs ($n = 16$). Standard PRRT (four cycles of 7.8 GBq each) was administered in cohorts of patients receiving escalating doses of everolimus (from 5 to 10 mg daily for 24 weeks). The maximum tolerated dose of everolimus was 7.5 mg (hematological and renal toxicity). The overall response rate was 44%, with no progression over the period of treatment. The optimal response occurred in pancreatic NENs, where four of five patients achieved 80% reduction of disease [111].

Efficacy of Combinations of ^{90}Y- and ^{177}Lu-Peptides

Protocols combining both ^{177}Lu- and ^{90}Y-peptides have been assessed with the purpose of exploiting the different physical properties of each radionuclide. Theoretically, this approach should result in a synergistic effect and allow simultaneous treatment of both large lesions (exploiting the higher energy and penetration range of the particles emitted by ^{90}Y) and small lesions (exploiting the lower energy and penetration range of ^{177}Lu). Combined ^{90}Y- and ^{177}Lu-PRRT was undertaken in a Danish cohort of 69 subjects treated in Basel. Complete responses were noted in 5 (7.4%), partial remissions in 11 (16.2%), and stabilization in 42 (61.8%). The median PFS was 29 months. Pancreatic NENs responded better than small bowel tumors [66]. However, to ascertain if this strategy is advantageous in terms of response and tolerability over more conventional PRRT protocols, validation is required in adequately powered and randomized trials with long-term follow-up, rather than empirically designed single-armed ^{177}Lu and ^{90}Y protocols [112, 113].

Conclusions

PRRT has become a well-established effective therapeutic modality for inoperable or metastatic GEP, bronchopulmonary, and other NETs over the last two decades. Experience with ^{90}Y-octreotide and ^{177}Lu-octreotate from phase I to II studies and

the preliminary results of the phase III studies in intestinal NETs suggest antitumor activity and a consistent survival benefit. PRRT is overall well tolerated by the majority with only moderate toxicity if the necessary precautions are undertaken. The two most commonly used radiopeptides, ^{90}Y-octreotide and ^{177}Lu-octreotate, produce significant objective response rates, with positive impact on PFS and OS. In addition, both biochemical and symptomatic responses are commonly observed. Molecular analysis of nephro- and hematotoxicity genes in cohorts of treated patients is likely to further improve the prediction of toxicity [36].

References

1. Modlin IM, Oberg K, Chung DC, Jensen RT, de Herder WW, Thakker RV, et al. Gastroenteropancreatic neuroendocrine tumours. Lancet Oncol. 2008;9(1):61–72.
2. Modlin IM, Latich I, Zikusoka M, Kidd M, Eick G, Chan AK. Gastrointestinal carcinoids: the evolution of diagnostic strategies. J Clin Gastroenterol. 2006;40 (7):572–82.
3. Doherty G. Surgical treatment of neuroendocrine tumors (including carcinoid). Curr Opin Endocrinol Diabetes Obes. 2013;20(1):32–6.
4. Norton JA. Endocrine tumours of the gastrointestinal tract. Surgical treatment of neuroendocrine metastases. Best Pract Res Clin Gastroenterol. 2005;19(4): 577–83.
5. Rea F, Rizzardi G, Zuin A, Marulli G, Nicotra S, Bulf R, et al. Outcome and surgical strategy in bronchial carcinoid tumors: single institution experience with 252 patients. Eur J Cardiothorac Surg. 2007; 31(2):186–91.
6. van Vilsteren FG, Baskin-Bey ES, Nagorney DM, Sanderson SO, Kremers WK, Rosen CB, et al. Liver transplantation for gastroenteropancreatic neuroendocrine cancers: defining selection criteria to improve survival. Liver Transplant. 2006;12(3):448–56.
7. Vargas HI, Kavoussi LR, Bartlett DL, Wagner JR, Venzon DJ, Fraker DL, et al. Laparoscopic adrenalectomy: a new standard of care. Urology. 1997; 49(5):673–8.
8. Niemann U, Hiller W, Behrend M. 25 years experience of the surgical treatment of phaeochromocytoma. Eur J Surg = Acta Chir. 2002;168(12): 716–9.
9. Pacak K. Preoperative management of the pheochromocytoma patient. J Clin Endocrinol Metab. 2007; 92(11):4069–79.
10. Kennedy AS, Dezarn WA, McNeillie P, Coldwell D, Nutting C, Carter D, et al. Radioembolization for unresectable neuroendocrine hepatic metastases using resin ^{90}Y-microspheres: early results in 148 patients. Am J Clin Oncol. 2008;31(3):271–9.
11. O'Toole D, Ruszniewski P. Chemoembolization and other ablative therapies for liver metastases of gastrointestinal endocrine tumours. Best Pract Res Clin Gastroenterol. 2005;19(4):585–94.
12. Orgera G, Krokidis M, Cappucci M, Gourtsoyianni S, Tipaldi MA, Hatzidakis A, et al. Current status of interventional radiology in the management of Gastro-Entero-Pancreatic Neuroendocrine Tumours (GEP-NETs). Cardiovasc Intervent Radiol. 2015;38(1):13–24.
13. Dubinsky TJ, Cuevas C, Dighe MK, Kolokythas O, Hwang JH. High-intensity focused ultrasound: current potential and oncologic applications. AJR Am J Roentgenol. 2008;190(1):191–9.
14. Mazzaglia PJ, Berber E, Siperstein AE. Radiofrequency thermal ablation of metastatic neuroendocrine tumors in the liver. Curr Treat Options Oncol. 2007;8(4):322–30.
15. Stevenson R, Libutti SK, Saif MW. Novel agents in gastroenteropancreatic neuroendocrine tumors. JOP: J Pancreas. 2013;14(2):152–4.
16. Pavel M, Unger N, Borbath I, Ricci S, Hwang TL, Brechenmacher T, et al. Safety and QOL in patients with advanced NET in a phase 3b expanded access study of everolimus. Target Oncol. 2016;19:19.
17. O'Toole D, Hentic O, Corcos O, Ruszniewski P. Chemotherapy for gastro-enteropancreatic endocrine tumours. Neuroendocrinology. 2004;80 Suppl 1:79–84.
18. Strosberg JR, Fine RL, Choi J, Nasir A, Coppola D, Chen DT, et al. First-line chemotherapy with capecitabine and temozolomide in patients with metastatic pancreatic endocrine carcinomas. Cancer. 2011;117(2):268–75.
19. Lamberts SW, van der Lely AJ, de Herder WW, Hofland LJ. Octreotide. N Engl J Med. 1996;334(4): 246–54.
20. Reubi JC, Schar JC, Waser B, Wenger S, Heppeler A, Schmitt JS, et al. Affinity profiles for human somatostatin receptor subtypes SST1-SST5 of somatostatin radiotracers selected for scintigraphic and radiotherapeutic use. Eur J Nucl Med. 2000;27(3):273–82.
21. Hofland LJ, Lamberts SW. The pathophysiological consequences of somatostatin receptor internalization and resistance. Endocr Rev. 2003;24(1):28–47.
22. Saltz L, Trochanowski B, Buckley M, Heffernan B, Niedzwiecki D, Tao Y, et al. Octreotide as an antineoplastic agent in the treatment of functional and nonfunctional neuroendocrine tumors. Cancer. 1993;72(1): 244–8.
23. Plockinger U, Wiedenmann B. Neuroendocrine tumors. Biotherapy. Best Pract Res Clin Endocrinol Metab. 2007;21(1):145–62.
24. di Bartolomeo M, Bajetta E, Buzzoni R, Mariani L, Carnaghi C, Somma L, et al. Clinical efficacy of octreotide in the treatment of metastatic neuroendocrine tumors. A study by the Italian Trials in Medical Oncology Group. Cancer. 1996;77(2):402–8.

25. Eriksson B, Renstrup J, Imam H, Oberg K. High-dose treatment with lanreotide of patients with advanced neuroendocrine gastrointestinal tumors: clinical and biological effects. Ann Oncol: Off J Eur Soc Med Oncol/ESMO. 1997;8(10):1041–4.
26. Marschke Jr RF, Grill JP, Sloan JA, Wender DB, Levitt R, Mailliard JA, et al. Phase II study of high-dose somatostatin analogue in patients either previously treated or untreated who have extensive-stage small cell lung cancer. Am J Clin Oncol. 1999;22(1): 15–7.
27. Rinke A, Muller HH, Schade-Brittinger C, Klose KJ, Barth P, Wied M, et al. Placebo-controlled, double-blind, prospective, randomized study on the effect of octreotide LAR in the control of tumor growth in patients with metastatic neuroendocrine midgut tumors: a report from the PROMID Study Group. J Clin Oncol. 2009;27(28):4656–63.
28. Fazio N, de Braud F, Delle Fave G, Oberg K. Interferon-alpha and somatostatin analog in patients with gastroenteropancreatic neuroendocrine carcinoma: single agent or combination? Ann Oncol. 2007;18 (1):13–9.
29. Yao JC, Hoff PM. Molecular targeted therapy for neuroendocrine tumors. Hematol Oncol Clin North Am. 2007;21(3):575–81. x.
30. Alonso-Gordoa T, Capdevila J, Grande E. GEP-NETs update: biotherapy for neuroendocrine tumours. Eur J Endocrinol/Eur Fed Endocr Soc. 2015;172(1): R31–46.
31. Gray JA, Roth BL. Cell biology. A last GASP for GPCRs? Science. 2002;297(5581):529–31.
32. Kwekkeboom DJ, Kam BL, van Essen M, Teunissen JJ, van Eijck CH, Valkema R, et al. Somatostatin-receptor-based imaging and therapy of gastroenteropancreatic neuroendocrine tumors. Endocr Relat Cancer. 2010;17(1):R53–73.
33. Kratochwil C, Stefanova M, Mavriopoulou E, Holland-Letz T, Dimitrakopoulou-Strauss A, Afshar-Oromieh A, et al. SUV of [^{68}Ga]DOTATOC-PET/CT predicts response probability of PRRT in neuroendocrine tumors. Mol Imaging Biol. 2015;17(3):313–8.
34. Bodei L, Ferone D, Grana CM, Cremonesi M, Signore A, Dierckx RA, et al. Peptide receptor therapies in neuroendocrine tumors. J Endocrinol Invest. 2009;32(4):360–9.
35. Kratochwil C, López-Benítez R, Mier W, Haufe S, Isermann B, Kauczor HU, Choyke PL, Haberkorn U, Giesel FL. Hepatic arterial infusion enhances DOTATOC radiopeptide therapy in patients with neuroendocrine liver metastases. Endocr Relat Cancer. 2011;18(5):595–602.
36. Bodei L, Kwekkeboom DJ, Kidd M, Modlin IM, Krenning EP. Radiolabeled somatostatin analogue therapy of gastroenteropancreatic cancer. Semin Nucl Med. 2016;46(3):225–38.
37. Krenning EP, Kooij PP, Bakker WH, Breeman WA, Postema PT, Kwekkeboom DJ, et al. Radiotherapy with a radiolabeled somatostatin analogue, [^{111}In-DTPA-D-Phe^{1}]-octreotide. A case history. Ann N Y Acad Sci. 1994;733:496–506.
38. Waldherr C, Pless M, Maecke HR, Schumacher T, Crazzolara A, Nitzsche EU, et al. Tumor response and clinical benefit in neuroendocrine tumors after 7.4 GBq ^{90}Y-DOTATOC. J Nucl Med. 2002; 43(5):610–6.
39. Bodei L, Cremonesi M, Zoboli S, Grana C, Bartolomei M, Rocca P, et al. Receptor-mediated radionuclide therapy with ^{90}Y-DOTATOC in association with amino acid infusion: a phase I study. Eur J Nucl Med Mol Imaging. 2003;30(2):207–16.
40. Valkema R, Pauwels S, Kvols LK, Barone R, Jamar F, Bakker WH, et al. Survival and response after peptide receptor radionuclide therapy with [^{90}Y-DOTA^{0},Tyr^{3}] octreotide in patients with advanced gastroenteropancreatic neuroendocrine tumors. Semin Nucl Med. 2006;36(2):147–56.
41. Bushnell Jr DL, O'Dorisio TM, O'Dorisio MS, Menda Y, Hicks RJ, Van Cutsem E, et al. ^{90}Y-edotreotide for metastatic carcinoid refractory to octreotide. J Clin Oncol. 2010;28(10):1652–9.
42. Imhof A, Brunner P, Marincek N, Briel M, Schindler C, Rasch H, et al. Response, survival, and long-term toxicity after therapy with the radiolabeled somatostatin analogue [^{90}Y-DOTA]-TOC in metastasized neuroendocrine cancers. J Clin Oncol. 2011; 29(17):2416–23.
43. Kwekkeboom DJ, de Herder WW, Kam BL, van Eijck CH, van Essen M, Kooij PP, et al. Treatment with the radiolabeled somatostatin analog [^{177}Lu-DOTA^{0}, Tyr^{3}]octreotate: toxicity, efficacy, and survival. J Clin Oncol. 2008;26(13):2124–30.
44. Bodei L, Cremonesi M, Grana CM, Fazio N, Iodice S, Baio SM, et al. Peptide receptor radionuclide therapy with ^{177}Lu-DOTATATE: the IEO phase I–II study. Eur J Nucl Med Mol Imaging. 2011;38(12):2125–35.
45. Sansovini M, Severi S, Ambrosetti A, Monti M, Nanni O, Sarnelli A, et al. Treatment with the radiolabelled somatostatin analog Lu-DOTATATE for advanced pancreatic neuroendocrine tumors. Neuroendocrinology. 2013;97(4):347–54.
46. Ezziddin S, Khalaf F, Vanezi M, Haslerud T, Mayer K, Al Zreiqat A, et al. Outcome of peptide receptor radionuclide therapy with ^{177}Lu-octreotate in advanced grade 1/2 pancreatic neuroendocrine tumours. Eur J Nucl Med Mol Imaging. 2014;41(5): 925–33.
47. Paganelli G, Sansovini M, Ambrosetti A, Severi S, Monti M, Scarpi E, Donati C, Ianniello A, Matteucci F, Amadori D. ^{177}Lu-Dota-octreotate radionuclide therapy of advanced gastrointestinal neuroendocrine tumors: results from a phase II study. Eur J Nucl Med Mol Imaging. 2014;41(10):1845–1851.
48. Sabet A, Dautzenberg K, Haslerud T, Aouf A, Sabet A, Simon B, et al. Specific efficacy of peptide receptor radionuclide therapy with ^{177}Lu-octreotate in advanced neuroendocrine tumours of the small intestine. Eur J Nucl Med Mol Imaging. 2015;42(8):1238–46.

49. http://www.adacap.com/wp-content/uploads/2015/09/2015-09-27-Press-Release-NETTER-1-results-ENG-FINAL-FINAL1.pdf
50. Kwekkeboom DJ, Mueller-Brand J, Paganelli G, Anthony LB, Pauwels S, Kvols LK, et al. Overview of results of peptide receptor radionuclide therapy with 3 radiolabeled somatostatin analogs. J Nucl Med: Off Publ Soc Nucl Med. 2005;46 Suppl 1:62s–6.
51. Kwekkeboom DJ, Teunissen JJ, Bakker WH, Kooij PP, de Herder WW, Feelders RA, et al. Radiolabeled somatostatin analog [^{177}Lu-DOTA^{0},Tyr^{3}]octreotate in patients with endocrine gastroenteropancreatic tumors. J Clin Oncol. 2005;23(12):2754–62.
52. Khan S, Krenning EP, van Essen M, Kam BL, Teunissen JJ, Kwekkeboom DJ. Quality of life in 265 patients with gastroenteropancreatic or bronchial neuroendocrine tumors treated with [^{177}Lu-DOTA^{0}, Tyr^{3}]octreotate. J Nucl Med. 2011;52(9):1361–8.
53. Strosberg J, Wolin EM, Chasen B, Kulke M, Bushnell Jr DL, Caplin M, et al. ^{177}Lu-Dotatate significantly improves progression-free survival in patients with midgut neuroendocrine tumours: results of the phase III NETTER-1 trial. Eur J Cancer (Oxford, England: 1990). 2015;51(Supplement S3):S710.
54. Valkema R, De Jong M, Bakker WH, Breeman WA, Kooij PP, Lugtenburg PJ, et al. Phase I study of peptide receptor radionuclide therapy with [In-DTPA]octreotide: the Rotterdam experience. Semin Nucl Med. 2002;32(2):110–22.
55. De Jong M, Bakker WH, Breeman WA, Bernard BF, Hofland LJ, Visser TJ, et al. Pre-clinical comparison of [DTPA^{0}] octreotide, [DTPA^{0}, Tyr^{3}] octreotide and [DOTA^{0}, Tyr^{3}] octreotide as carriers for somatostatin receptor-targeted scintigraphy and radionuclide therapy. Int J Cancer. 1998;75(3):406–11.
56. Bodei L, Kassis AI, Adelstein SJ, Mariani G. Radionuclide therapy with iodine-125 and other auger-electron-emitting radionuclides: experimental models and clinical applications. Cancer Biother Radiopharm. 2003;18(6):861–77.
57. Cescato R, Schulz S, Waser B, Eltschinger V, Rivier JE, Wester HJ, et al. Internalization of sst2, sst3, and sst5 receptors: effects of somatostatin agonists and antagonists. J Nucl Med. 2006;47(3):502–11.
58. Esser JP, Krenning EP, Teunissen JJ, Kooij PP, van Gameren AL, Bakker WH, et al. Comparison of [^{177}Lu-DOTA^{0},Tyr^{3}]octreotate and [^{177}Lu-DOTA^{0}, Tyr^{3}]octreotide: which peptide is preferable for PRRT? Eur J Nucl Med Mol Imaging. 2006;33 (11):1346–51.
59. Bodei L, Mueller-Brand J, Baum RP, Pavel ME, Hörsch D, O'Dorisio MS, et al. The joint IAEA, EANM, and SNMMI practical guidance on peptide receptor radionuclide therapy (PRRNT) in neuroendocrine tumours. Eur J Nucl Med Mol Imaging. 2014;40(5):800–16.
60. Modlin IM, Frilling A, Salem RR, Alaimo D, Drymousis P, Wasan HS, et al. Blood measurement of neuroendocrine gene transcripts defines the effectiveness of operative resection and ablation strategies. Surgery. 2016;159(1):336–47.
61. Cwikla JB, Bodei L, Kolasinska-Cwikla A, Sankowski A, Modlin IM, Kidd M. Circulating transcript analysis (NETest) in GEP-NETs treated with Somatostatin Analogs defines Therapy. J Clin Endocrinol Metab. 2015;100(11):E1437–45.
62. Bodei L, Kidd M, Modlin IM, Prasad V, Severi S, Ambrosini V, et al. Gene transcript analysis blood values correlate with Ga-DOTA-somatostatin analog (SSA) PET/CT imaging in neuroendocrine tumors and can define disease status. Eur J Nucl Med Mol Imaging. 2016;43(5):839–51.
63. Kwekkeboom DJ, Krenning EP. Peptide receptor radionuclide therapy in the treatment of neuroendocrine tumors. Hematol Oncol Clin North Am. 2016; 30(1):179–91.
64. Bodei L, Modlin IM, Luster M, Forrer F, Cremonesi M, Hicks RJ, et al. Myeloid neoplasms after chemotherapy and PRRT: myth and reality. Endocr Relat Cancer. 2016;23(8):C1–7.
65. Bergsma H, Konijnenberg MW, Kam BL, Teunissen JJ, Kooij PP, de Herder WW, et al. Subacute haematotoxicity after PRRT with ^{177}Lu-DOTA-octreotate: prognostic factors, incidence and course. Eur J Nucl Med Mol Imaging. 2016;43(3):453–63.
66. Pfeifer AK, Gregersen T, Gronbaek H, Hansen CP, Muller-Brand J, Herskind Bruun K, et al. Peptide receptor radionuclide therapy with ^{90}Y-DOTATOC and ^{177}Lu-DOTATOC in advanced neuroendocrine tumors: results from a Danish cohort treated in Switzerland. Neuroendocrinology. 2011;93(3): 189–96.
67. Sabet A, Ezziddin K, Pape UF, Ahmadzadehfar H, Mayer K, Poppel T, et al. Long-term hematotoxicity after peptide receptor radionuclide therapy with ^{177}Lu-octreotate. J Nucl Med. 2013;54(11): 1857–61.
68. Bodei L, Kidd M, Paganelli G, Grana CM, Drozdov I, Cremonesi M, et al. Long-term tolerability of PRRT in 807 patients with neuroendocrine tumours: the value and limitations of clinical factors. Eur J Nucl Med Mol Imaging. 2015;42(1):5–19.
69. Sabet A, Ezziddin K, Pape UF, Reichman K, Haslerud T, Ahmadzadehfar H, et al. Accurate assessment of long-term nephrotoxicity after peptide receptor radionuclide therapy with ^{177}Lu-octreotate. Eur J Nucl Med Mol Imaging. 2014;41(3):505–10.
70. Bernard BF, Krenning EP, Breeman WA, Rolleman EJ, Bakker WH, Visser TJ, et al. D-lysine reduction of indium-111 octreotide and yttrium-90 octreotide renal uptake. J Nucl Med. 1997;38(12):1929–33.
71. Brans B, Bodei L, Giammarile F, Linden O, Luster M, Oyen WJ, et al. Clinical radionuclide therapy dosimetry: the quest for the "Holy Gray". Eur J Nucl Med Mol Imaging. 2007;34(5):772–86.
72. de Jong M, Krenning E. New advances in peptide receptor radionuclide therapy. J Nucl Med. 2002; 43(5):617–20.

73. Bodei L, Cremonesi M, Grana C, Rocca P, Bartolomei M, Chinol M, et al. Receptor radionuclide therapy with ^{90}Y-[DOTA]^{0},Tyr^{3}-octreotide (^{90}Y-DOTATOC) in neuroendocrine tumours. Eur J Nucl Med Mol Imaging. 2004;31(7):1038–46.
74. Bodei L, Cremonesi M, Ferrari M, Pacifici M, Grana CM, Bartolomei M, et al. Long-term evaluation of renal toxicity after peptide receptor radionuclide therapy with ^{90}Y-DOTATOC and ^{177}Lu-DOTATATE: the role of associated risk factors. Eur J Nucl Med Mol Imaging. 2008;35(10):1847–56.
75. Jamar F, Barone R, Mathieu I, Walrand S, Labar D, Carlier P, et al. ^{86}Y-DOTA^{0}-D-Phe^{1},Tyr^{3}-octreotide (SMT487) – a phase 1 clinical study: pharmacokinetics, biodistribution and renal protective effect of different regimens of amino acid co-infusion. Eur J Nucl Med Mol Imaging. 2003;30(4):510–8.
76. Valkema R, Pauwels SA, Kvols LK, Kwekkeboom DJ, Jamar F, de Jong M, et al. Long-term follow-up of renal function after peptide receptor radiation therapy with ^{90}Y-DOTA^{0},Tyr^{3}-octreotide and ^{177}Lu-DOTA^{0},Tyr^{3}-octreotate. J Nucl Med. 2005;46 Suppl 1:83s–91.
77. Cybulla M, Weiner SM, Otte A. End-stage renal disease after treatment with ^{90}Y-DOTATOC. Eur J Nucl Med. 2001;28(10):1552–4.
78. Hubble D, Kong G, Michael M, Johnson V, Ramdave S, Hicks RJ. ^{177}Lu-octreotate, alone or with radiosensitising chemotherapy, is safe in neuroendocrine tumour patients previously treated with high-activity ^{111}In-octreotide. Eur J Nucl Med Mol Imaging. 2010;37(10):1869–75.
79. Kwekkeboom DJ, Bakker WH, Kam BL, Teunissen JJ, Kooij PP, de Herder WW, et al. Treatment of patients with gastro-entero-pancreatic (GEP) tumours with the novel radiolabelled somatostatin analogue [^{177}Lu-DOTA^{0},Tyr^{3}]octreotate. Eur J Nucl Med Mol Imaging. 2003;30(3):417–22.
80. Sabet A, Haslerud T, Pape UF, Sabet A, Ahmadzadehfar H, Grunwald F, et al. Outcome and toxicity of salvage therapy with ^{177}Lu-octreotate in patients with metastatic gastroenteropancreatic neuroendocrine tumours. Eur J Nucl Med Mol Imaging. 2014;41(2):205–10.
81. Sabet A, Khalaf F, Yong-Hing CJ, Sabet A, Haslerud T, Ahmadzadehfar H, et al. Can peptide receptor radionuclide therapy be safely applied in florid bone metastases? A pilot analysis of late stage osseous involvement. Nuklearmedizin Nucl Med. 2014;53(2):54–9.
82. Pauwels S, Barone R, Walrand S, Borson-Chazot F, Valkema R, Kvols LK, et al. Practical dosimetry of peptide receptor radionuclide therapy with ^{90}Y-labeled somatostatin analogs. J Nucl Med. 2005;46 Suppl 1:92s–8.
83. Cremonesi M, Ferrari M, Bodei L, Tosi G, Paganelli G. Dosimetry in peptide radionuclide receptor therapy: a review. J Nucl Med. 2006;47(9):1467–75.
84. Cremonesi M, Botta F, Di Dia A, Ferrari M, Bodei L, De Cicco C, et al. Dosimetry for treatment with radiolabelled somatostatin analogues. A review. Q J Nucl Med Mol Imaging. 2010;54(1):37–51.
85. Forrer F, Uusijärvi H, Waldherr C, Cremonesi M, Bernhardt P, Mueller-Brand J, Maecke HR. A comparison of ^{111}In-DOTATOC and ^{111}In-DOTATATE: biodistribution and dosimetry in the same patients with metastatic neuroendocrine tumours. Eur J Nucl Med Mol Imaging. 2004;31(9):1257–1262.
86. Forrer F, Krenning EP, Kooij PP, Bernard BF, Konijnenberg M, Bakker WH, et al. Bone marrow dosimetry in peptide receptor radionuclide therapy with [^{177}Lu-DOTA^{0},Tyr^{3}]octreotate. Eur J Nucl Med Mol Imaging. 2009;36(7):1138–1146.
87. Förster GJ, Engelbach MJ, Brockmann JJ, Reber HJ, Buchholz HG, Mäcke HR, et al. Preliminary data on biodistribution and dosimetry for therapy planning of somatostatin receptor positive tumours: comparison of ^{86}Y-DOTATOC and ^{111}In-DTPA-octreotide. Eur J Nucl Med. 2001;28(12):1743–1750.
88. Helisch A, Förster GJ, Reber H, Buchholz HG, Arnold R, Göke B, et al. Pre-therapeutic dosimetry and biodistribution of ^{86}Y-DOTA-Phe^{1}-Tyr^{3}-octreotide versus ^{111}In-pentetreotide in patients with advanced neuroendocrine tumours. Eur J Nucl Med Mol Imaging. 2004;31(10):1386–1392.
89. Rodrigues M, Traub-Weidinger T, Li S, Ibi B, Virgolini I. Comparison of ^{111}In-DOTA-D-Phe^{1}-Tyr^{3}-octreotide and ^{111}In-DOTA-lanreotide scintigraphy and dosimetry in patients with neuroendocrine tumours. Eur J Nucl Med Mol Imaging. 2006;33(5):532–540.
90. Wehrmann C, Senftleben S, Zachert C, Müller D, Baum RP. Results of individual patient dosimetry in peptide receptor radionuclide therapy with ^{177}Lu-DOTA-TATE and ^{177}Lu DOTA-NOC. Cancer Biother Radiopharm. 2007;22(3):406–416.
91. Stabin MG, Brill AB. State of the art in nuclear medicine dose assessment. Semin Nucl Med. 2008;38(5):308–20.
92. Wierts R, de Pont CD, Brans B, Mottaghy FM, Kemerink GJ. Dosimetry in molecular nuclear therapy. Methods (San Diego, Calif). 2011;55(3):196–202.
93. Cremonesi M, Ferrari M, Di Dia A, Botta F, De Cicco C, Bodei L, et al. Recent issues on dosimetry and radiobiology for peptide receptor radionuclide therapy. Q J Nucl Med Mol Imaging. 2011;55(2):155–67.
94. Sandstrom M, Garske-Roman U, Granberg D, Johansson S, Widstrom C, Eriksson B, et al. Individualized dosimetry of kidney and bone marrow in patients undergoing ^{177}Lu-DOTA-octreotate treatment. J Nucl Med. 2013;54(1):33–41.
95. Anthony LB, Woltering EA, Espenan GD, Cronin MD, Maloney TJ, McCarthy KE. Indium-111-pentetreotide prolongs survival in gastroenteropancreatic malignancies. Semin Nucl Med. 2002;32(2):123–32.
96. Otte A, Herrmann R, Heppeler A, Behe M, Jermann E, Powell P, et al. Yttrium-90 DOTATOC: first clinical results. Eur J Nucl Med. 1999;26(11):1439–47.

97. De Jong M, Valkema R, Jamar F, Kvols LK, Kwekkeboom DJ, Breeman WA, et al. Somatostatin receptor-targeted radionuclide therapy of tumors: preclinical and clinical findings. Semin Nucl Med. 2002;32(2):133–40.
98. Bushnell D, O'Dorisio T, Menda Y, Carlisle T, Zehr P, Connolly M, et al. Evaluating the clinical effectiveness of ^{90}Y-SMT 487 in patients with neuroendocrine tumors. J Nucl Med. 2003;44(10):1556–60.
99. Bodei L, Handkiewicz-Junak D, Grana C, Mazzetta C, Rocca P, Bartolomei M, et al. Receptor radionuclide therapy with ^{90}Y-DOTATOC in patients with medullary thyroid carcinomas. Cancer Biother Radiopharm. 2004;19(1):65–71.
100. Menda Y, O'Dorisio MS, Kao S, Khanna G, Michael S, Connolly M, et al. Phase I trial of ^{90}Y-DOTATOC therapy in children and young adults with refractory solid tumors that express somatostatin receptors. J Nucl Med. 2010;51(10):1524–31.
101. Kwekkeboom DJ, Bakker WH, Kooij PP, Konijnenberg MW, Srinivasan A, Erion JL, et al. [^{177}Lu-DOTA^{0}-Tyr^{3}]octreotate: comparison with [^{111}In-DTPAo]octreotide in patients. Eur J Nucl Med. 2001;28(9):1319–25.
102. Ezziddin S, Attassi M, Yong-Hing CJ, Ahmadzadehfar H, Willinek W, Grunwald F, et al. Predictors of long-term outcome in patients with well-differentiated gastroenteropancreatic neuroendocrine tumors after peptide receptor radionuclide therapy with ^{177}Lu-octreotate. J Nucl Med. 2014;55(2):183–90.
103. Teunissen JJ, Kwekkeboom DJ, Krenning EP. Quality of life in patients with gastroenteropancreatic tumors treated with [^{177}Lu-DOTA^{0},Tyr^{3}]octreotate. J Clin Oncol: Off J Am Soc Clin Oncol. 2004;22(13):2724–9.
104. Sabet A, Khalaf F, Haslerud T, Al-Zreiqat A, Sabet A, Simon B, et al. Bone metastases in GEP-NET: response and long-term outcome after PRRT from a follow-up analysis. Am J Nucl Med Mol Imaging. 2013;3(5):437–45.
105. van Vliet EI, van Eijck CH, de Krijger RR, Nieveen van Dijkum EJ, Teunissen JJ, Kam BL, et al. Neoadjuvant Treatment of Nonfunctioning Pancreatic Neuroendocrine Tumors with [^{177}Lu-DOTA^{0},Tyr^{3}]Octreotate. J Nucl Med. 2015;56(11):1647–1653.
106. van Essen M, Krenning EP, Kam BL, de Herder WW, Feelders RA, Kwekkeboom DJ. Salvage therapy with ^{177}Lu-octreotate in patients with bronchial and gastroenteropancreatic neuroendocrine tumors. J Nucl Med: Off Publ Soc Nucl Med. 2010;51(3):383–90.
107. Severi S, Sansovini M, Ianniello A, Bodei L, Nicolini S, Ibrahim T, et al. Feasibility and utility of re-treatment with ^{177}Lu-DOTATATE in GEP-NENs relapsed after treatment with ^{90}Y-DOTATOC. Eur J Nucl Med Mol Imaging. 2015;42(13):1955–1963.
108. van Essen M, Krenning EP, Kam BL, de Herder WW, van Aken MO, Kwekkeboom DJ. Report on short-term side effects of treatments with ^{177}Lu-octreotate in combination with capecitabine in seven patients with gastroenteropancreatic neuroendocrine tumours. Eur J Nucl Med Mol Imaging. 2008;35(4):743–8.
109. Kong G, Thompson M, Collins M, Herschtal A, Hofman MS, Johnston V, et al. Assessment of predictors of response and long-term survival of patients with neuroendocrine tumour treated with peptide receptor chemoradionuclide therapy (PRCRT). Eur J Nucl Med Mol Imaging. 2014;41(10):1831–1844.
110. Claringbold PG, Price RA, Turner JH. Phase I-II study of radiopeptide ^{177}Lu-octreotate in combination with capecitabine and temozolomide in advanced low-grade neuroendocrine tumors. Cancer Biother Radiopharm. 2012;27(9):561–9.
111. Claringbold PG, Turner JH. NeuroEndocrine tumor therapy with lutetium-177-octreotate and everolimus (NETTLE): a phase I study. Cancer Biother Radiopharm. 2015;30(6):261–9.
112. de Jong M, Breeman WA, Valkema R, Bernard BF, Krenning EP. Combination radionuclide therapy using ^{177}Lu- and ^{90}Y-labeled somatostatin analogs. J Nucl Med. 2005;46 Suppl 1:13s–7.
113. Kunikowska J, Krolicki L, Hubalewska-Dydejczyk A, Mikolajczak R, Sowa-Staszczak A, Pawlak D. Clinical results of radionuclide therapy of neuroendocrine tumours with ^{90}Y-DOTATATE and tandem ^{90}Y/^{177}Lu-DOTATATE: which is a better therapy option? Eur J Nucl Med Mol Imaging. 2011;38(10):1788–97.

Neuroendocrine Tumors: Therapy with ^{131}I-MIBG

44

Jorge A. Carrasquillo and Clara C. Chen

Abstract

Metaiodobenzylguanidine (MIBG) is an analog of guanethidine which has been used for imaging a variety of neuroendocrine tumors (NETs). While ^{131}I-MIBG is approved by the FDA for imaging, it is not yet approved for therapy, whereas it is approved for therapy by the EMA. Thus, in the United States ^{131}I-MIBG used for therapy trials is either made in accordance with USP regulations or used under an investigational new drug application (IND).

Procedure guidelines for the use of ^{131}I-MIBG in therapy have been published. ^{131}I-MIBG is used mostly to treat pheochromocytoma/paraganglioma (PHEO/PARA), carcinoid tumors, and neuroblastoma. Preparation of patients prior to treatment with ^{131}I-MIBG includes discontinuing therapy with drugs known to interfere with uptake of MIBG by tumor cells and blocking thyroid uptake of radioiodine. Because patients may have nausea and vomiting after administration of MIBG, antiemetics are often administered prior to therapy and in the first 3 days post-administration. To minimize the bladder dose, hydration is encouraged. Candidates for ^{131}I-MIBG therapy should have a reasonable performance status and a life expectancy of at least 3 months. Acceptable hematopoietic parameters are required prior to MIBG therapy. There are no uniform guidelines for selecting or excluding patients from consideration for ^{131}I-MIBG therapy. Most investigators require tumor localization on a diagnostic MIBG scan. Other selection criteria often include evidence of disease progression or symptoms.

^{131}I-MIBG is administered i.v. by pump through a plastic indwelling catheter or central line. Slow administration is a precaution to minimize pharmacologic effects from the unlabeled MIBG. There is no standard activity for therapy. Most studies use fixed activities based on empirical evidence of limited toxicity. Others have used fixed activities adjusted to body weight based on dose escalation studies. Some studies use estimates of dose to radiosensitive organs to define a safe upper limit.

Response assessment may be performed as early as 2 months, but more frequently at 3–6-month intervals unless the patient is known to have fast-growing disease. Follow-up typically involves anatomic and functional imaging with ^{123}I-MIBG or [^{18}F]FDG. The frequency of retreatment is variable, ranging from every 4 weeks to every 6 months.

J.A. Carrasquillo (✉)
Molecular Imaging and Therapy Service, Memorial Sloan-Kettering Cancer Center, New York, NY, USA
e-mail: carrasj1@mskcc.org

C.C. Chen
Division of Nuclear Medicine, Department of Radiology and Imaging Sciences, Clinical Center, National Institutes of Health, Bethesda, MD, USA
e-mail: cchen1@cc.nih.gov

© Springer International Publishing Switzerland (outside the USA) 2017

H.W. Strauss et al. (eds.), *Nuclear Oncology*,
https://doi.org/10.1007/978-3-319-26236-9_26

PHEO/PARA are tumors that originate in the chromaffin tissue of the adrenal medulla and sympathetic nervous system and often secrete catecholamines. Some PHEO/PARA are related to genetic defects and are associated with an increased incidence of malignant and/or extra-adrenal disease. The lymph nodes, bone, liver, and lung are the most common sites of metastases.

The optimal therapy for PHEO/PARA consists of surgical resection when feasible. In patients in whom a surgical cure is not possible, chemotherapy regimens have been developed. However, given the often suboptimal response to chemotherapy, other therapeutic modalities such as ^{131}I-MIBG are now being applied. Although many patients benefit from ^{131}I-MIBG treatment, complete response rates are low. It appears that the response of soft tissue disease to MIBG therapy is superior to that of bone and that patients with smaller volume disease are more likely to respond than those with high-volume disease. Biochemical catecholamine response has often been reported after treatment. Responses vary in duration, with reported 5-year survivals between 45% and 85%. Low-, medium-, or high-dose activities of ^{131}I-MIBG have been used in PHEO/PARA, but there have been no systematic comparisons between these groups. However, there is some evidence that higher activities $>$500 mCi or myeloablative regimens are associated with higher response rates. The use of high specific activity ^{131}I-MIBG for therapy seems to reduce acute side effects. Few data have been published regarding combined chemotherapy with ^{131}I-MIBG therapy in this patient group.

Carcinoids are slow-growing NETs that often secrete substances leading to hormonal syndromes. The most frequent sites for carcinoids are the gastrointestinal tract (73.7%) and the bronchopulmonary system (25.1%).

Initial staging and follow-up relies on CT and MRI to evaluate for nodal and metastatic liver disease. Imaging with ^{111}In-pentetreotide or, more recently, with ^{68}Ga-somatostatin analogs is performed. Scintigraphy with ^{123}I-/^{131}I-MIBG is also often performed and a published review reported a sensitivity of 70%. At presentation, the best management is surgical resection, or in cases with metastatic disease, debulking for palliation. Unfortunately, metastatic disease at presentation is frequent, and no consistently effective therapeutic strategies are available. Symptomatic tumor response is often seen following therapy with cold octreotide analogs, whereas objective tumor regression is rare. Interferon may also result in symptomatic improvement. Multiple chemotherapy regimens have been utilized with none showing objective tumor responses greater than 15%. The uptake of ^{131}I-MIBG in carcinoid led to the use of this radiopharmaceutical therapeutically. Recently, radiolabeled octreotide analogs have recently been utilized and shown a higher overall accumulation in carcinoids than MIBG.

Although carcinoid patients rarely have a complete response to ^{131}I-MIBG therapy, objective response rates of 11–27.5% and symptomatic response rates ranging from 38% to 92% have been reported. Biochemical responses are less common. Median 5-year survivals of 42–78% have been reported after ^{131}I-MIBG therapy in carcinoid. Initial single activities of $>$14.8 GBq (400 mCi) have been recommended to improve survival and symptomatic improvement. Studies combining ^{131}I-MIBG with chemotherapy or biologic therapy are rare.

Neuroblastoma is a tumor that arises from primordial neural crest cells and is almost exclusively found in infants and young children. It is the most common tumor of childhood. Therapy relies on induction chemotherapy, surgery, and radiotherapy (given that this is a radiosensitive tumor), followed by consolidation of remission with autologous stem cell transplant (ASCT) or *cis*-retinoic acid with or without antibody immunotherapy. High-risk patients often relapse and are resistant to conventional therapy. ^{131}I-MIBG therapy has been utilized as first-line therapy, combined with chemotherapy or biologic therapy for consolidation, and as palliative therapy for patients with multiple relapses. Several ^{131}I-MIBG dosing strategies have been pursued. Most ^{131}I-MIBG trials have selected patients

with advanced disease that have failed first-line therapy, while others have incorporated ^{131}I-MIBG into multiprong treatment strategies. Several trials demonstrated that repeated doses of ^{131}I-MIBG could be administered safely. Partial objective responses have been reported in up to 40% of patients, but complete response rates are usually much lower (seldom over 10%). Because many trials were not prospective, reporting criteria in terms of outcome were variable, and the parameters measured in terms of duration of response have been inconsistent and include survival, overall response, and event-free survival (EFS).

The most significant toxicity associated with ^{131}I-MIBG therapy in both children and adults is hematologic. Nadirs in children have been reported to occur approximately 28 days after a single ^{131}I-MIBG administration (range 9–42). When chemotherapy is combined with ^{131}I-MIBG therapy, this nadir may occur earlier and is felt to be predominantly driven by the chemotherapy. Patients treated with high activities of ^{131}I-MIBG ($\geq$444–666 MBq/kg (12–18 mCi/kg)) may require bone marrow transplant because of significant and prolonged marrow toxicity, particularly in heavily pretreated subjects. Because higher doses induce considerable neutropenia, significant infections are occasionally encountered.

Myelodysplasia (MDS)/acute myelocytic leukemia have been reported in patients who have received both chemotherapy and large amounts of ^{131}I-MIBG. Secondary malignancies have been also reported. The occurrence of secondary malignancies and bone marrow disorders indicates that these patients require close follow-up, especially those with prolonged survival. Hypothyroidism can also occur. Common systemic/constitutional toxicity associated with large doses of ^{131}I-MIBG includes asthenia, nausea, and vomiting. Although ^{131}I-MIBG localizes in normal organs such as the heart, lung, kidney, liver, and adrenals, complications related to cardiac, renal, liver, or adrenal insufficiency have been very limited. Pulmonary complications are most frequently related to infectious disorders.

Keywords

^{131}I-MIBG therapy • Meta-iodobenzylguanidine • Pheochromocytoma • Paraganglioma • Carcinoids • Neuroblastoma

Glossary

[^{18}F]FDG	2-deoxy-2-[^{18}F]fluoro-D-glucose
^{18}F-DOPA	2-^{18}F-Fluoro-L-3,4-dihydroxyphenylalanine
ARDS	Acute respiratory distress syndrome
ASCT	Autologous stem cell transplantation
BOOP	Bronchiolitis obliterans organizing pneumonia
CISP	Cis platinum
CR	Complete response
CT	X-ray computed tomography
CTX	Cytoxan
CVD	Chemotherapy regimen based on Cyclophosphamide, vincristine, and dacarbazine
DOTATATE	1,4,7,10- tetra-azacyclododecane-1,4,7,10-tetraacetic acid -(Tyr^3)-octreotate
DOTATOC	1,4,7,10-tetra-azacyclododecane-1,4,7,10-tetraacetic acid0-Phe1-Tyr^3) octreotide
EANM	European Association of Nuclear Medicine
EFS	Event-free survival
eGFR	Estimated glomerular filtration rate
EMA	European Medicines Agency
FDA	United States Food and Drug Administration
FH	Gene encoding for a member of the pseudo-hypoxic pathway family
G-CSF	Granulocyte colony stimulating factor
GEP	Gastroenteropancreatic
GFR	Glomerular filtration rate
GI	Gastrointestinal

Gy	Gray unit (ionizing radiation dose in the International System of Units, corresponding to the absorption of one joule of radiation energy per kilogram of matter)
HIF2A	Gene encoding for a member of the pseudo-hypoxic pathway family
ID	Injected dose
IND	Investigational new drug
KI	Potassium iodide
MAX	Gene encoding for a member of the tyrosine kinase signaling pathway family
MDS	Myelodisplastic syndrome
MEN	Gene encoding for a member of the tyrosine kinase signaling pathway family
MEN	Multiple endocrine neoplasia
MIBG	Metaiodobenzylguanidine
MIRD	Medical Internal Radiation Dose
MRI	Magnetic resonance imaging
MSKCC	Memorial Sloan-Kettering Cancer Center
MYCN	Gene encoding for a member of the MYC family of transcription factors
NA	Not available
NB	Neuroblastoma
NET	Neuroendocrine tumor
NF1	Gene encoding for a member of the tyrosine kinase signaling pathway family
NRC	Nuclear regulatory commission
OS	Overall survival
PARA	Paraganglioma
PD	Progressive disease
PFS	Progression-free survival
PHEO	Pheochromocytoma
PR	Partial response
RET	Gene encoding for a member of the tyrosine kinase signaling pathway family
RFA	Radiofrequency ablation
SD	Stable disease
SDHAF2	Gene encoding for a member of the pseudo-hypoxic pathway family
SDHB	Gene encoding for one of four subunits of the succinate dehydrogenase (SDH) enzyme
SDHx	Gene encoding for a member of the pseudo-hypoxic pathway family
SSKI	Saturated solution of potassium iodide
SUV	Standardized uptake value
T3	3-5-3'-Triiodothyronine, a thyroid hormone
TMEM127	Gene encoding for a member of the tyrosine kinase signaling pathway family
TSH	Thyroid stimulating hormone
TTP	Time to progression
UCSF	University of San Francisco
USP	United States Pharmacopeia
VHL	Von Hippel Lindau
VNC	Vincristine
VP-16	Etoposide
WBC	White blood cell
WHO	World Health Organization

Contents

^{131}I-MIBG Preparation 1273
Logistical Issues 1273

Patient Preparation 1274

Thyroid Blockade 1275
Additional Precautions 1276
Patient Eligibility 1276

Patient Selection Criteria 1277

Activity/Dose Selection 1278
Dosimetry 1278
Evaluation of Response 1281

Pheochromocytoma/Paraganglioma 1288

Carcinoid 1291

Neuroblastoma 1293

Toxicity 1297

Summary 1299

References 1299

Metaiodobenzylguanidine (MIBG), also known as iobenguane, was developed at the University of Michigan by Wieland et al. [202]. As an analog of guanethidine, MIBG shares structural features with norepinephrine, binds to the norepinephrine transporter, and is internalized. Having entered the cell, MIBG is transported to secretory granules via vesicular monoamine transporters [101] or, in some cells without many granules, localizes in the cytoplasm [106, 171, 177]. For imaging purposes, MIBG is labeled with ^{131}I or ^{123}I. For diagnostic imaging, ^{123}I is superior to ^{131}I [57], and imaging methods are described in imaging guidelines [15].

Radiolabeled MIBG has been used for imaging a variety of neuroendocrine tumors (NETs) and other disorders [26, 156]. The sensitivity for tumor detection of pheochromocytoma/paraganglioma (PHEO/PARA) and neuroblastoma (NB) tends to be higher than for other NETs. Given the excellent localization often seen with radioiodinated MIBG (Fig. 1a), therapy with ^{131}I-MIBG has been evaluated. In this chapter, we focus on the therapeutic use of MIBG in the three most frequently treated tumors: PHEO/PARA, carcinoid, and neuroblastoma.

^{131}I-MIBG Preparation

Procedure guidelines for the use of ^{131}I-MIBG in therapy have been published [65]. The specific activity of the ^{131}I-MIBG used for imaging typically is low (123 MBq/mg, or 3.33 mCi/mg), while the specific activity of the ^{131}I-MIBG used for therapy is higher, ranging from 1.11 to 1.85 GBq/mg (30–50 mCi/mg) [41, 51, 70, 85, 118, 170]. At these specific activities, approximately 1 in every 2,000 molecules of MIBG will be labeled with ^{131}I. Therefore, for an activity of 18.5 GBq (500 mCi), a total of 10–17 mg of MIBG is administered. Even higher specific activity ^{131}I-MIBG has been developed, in the range of 92.5 GBq/mg (2,500 mCi/mg) [80, 112, 113]. Theoretical and preclinical studies in small animals have shown that higher specific activity results in greater tumor uptake and higher tumor to normal tissue ratios than lower specific activity reagents [112, 114]. However, a study with high specific activity MIBG resulted in higher activity in heart but not in tumor xenografts [189]. Limited studies in humans using high specific activity ^{131}I-MIBG have also failed to show higher tumor targeting [145], including phase I clinical trials with high specific activity ^{131}I-MIBG, and have not clearly confirmed an advantage in terms of tumor targeting, although its safety has been documented [36]. Even if high specific activity ^{131}I-MIBG does not have a clear advantage over low specific activity material in terms of tumor targeting, administration of lower mass amounts of MIBG over a shorter period of time with a lower incidence of nausea, vomiting, and hypertension may be possible [6]. It should be noted that while ^{131}I-MIBG was approved by the FDA for imaging, it has yet to be approved for therapy in the USA. Thus, for therapy trials in the United States, ^{131}I-MIBG is either made in accordance with USP regulations or used under an investigational new drug application (IND). Whereas, the use of ^{131}I-MIBG for therapy has been approved by the EMA as well as by regulatory authorities in other countries.

Logistical Issues

At present, there are few centers performing ^{131}I-MIBG therapy. One major impediment is that the radiopharmaceutical is not yet FDA approved for therapeutic use, as previously described above. Other impediments relate to the safe handling of large amounts of therapeutic materials. In establishing an ^{131}I-MIBG therapy program, there needs to be adequately trained staff to carry out the treatment safely and within regulatory compliance with NRC mandates, and a significant institutional commitment is necessary [167]. In addition to radiation safety-related issues, a dedicated multimodality group of physicians that deal with the relevant diseases are necessary to provide optimal patient care. High-activity administration in the range of 18 mCi/kg, as is often used in patients with neuroblastoma, has its own safety challenges that must be appropriately addressed, especially when dealing with small children [32].

Patient Preparation

Proper preparation of patients is required prior to treatment with ^{131}I-MIBG. A variety of drugs are known to interfere with uptake of MIBG by tumor cells and should be discontinued prior to therapy, including labetalol, tricyclic antidepressants, reserpine, and some sympathomimetics (Table 1) [5, 76, 97, 133, 172]. A detailed list of drugs that may interfere has been compiled [172] and recommendations of which to avoid have been proposed [87]. When possible, these drugs are eliminated or substituted prior to therapy with ^{131}I-MIBG. The amount of time necessary for

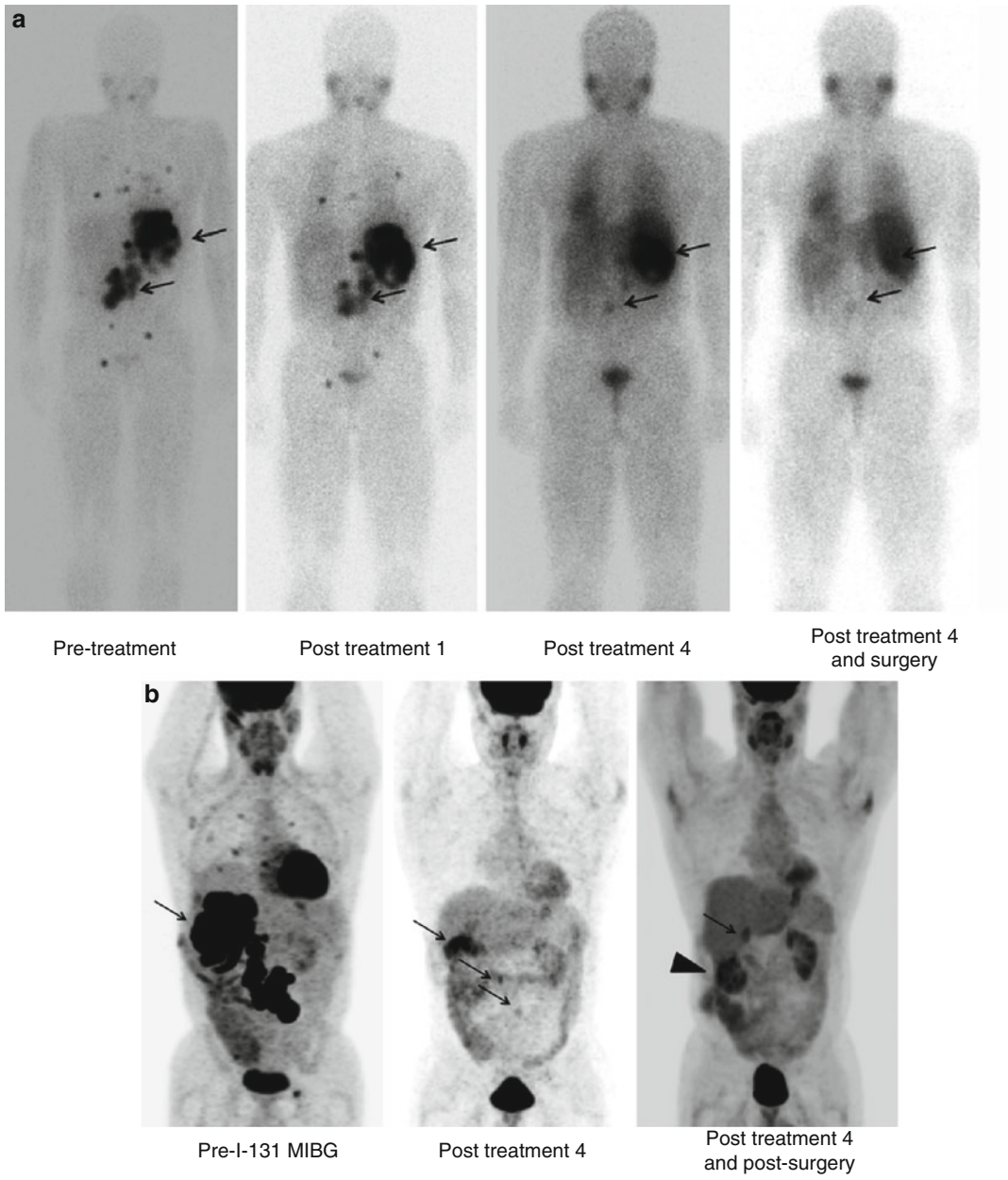

Fig. 1 (continued)

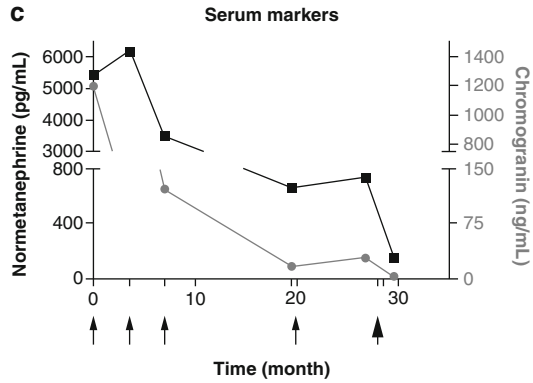

Fig. 1 (**a**) Serial ^{123}I-MIBG posterior whole-body images from a patient with unresectable primary PHEO of the right adrenal (*upper arrows*) and metastatic disease to retroperitoneal nodes (*lower arrows*), spine, pelvis, ribs, and bilateral lung metastases are also present. He received four treatments consisting of 204, 211, 215, and 243 mCi of ^{131}I-MIBG over a 14-month period. The initial posttreatment scan 1 showed some decrease in retroperitoneal nodes and disappearance of some lung and bone lesions. Posttreatment 4, all lung and bone lesions had disappeared, and retroperitoneal nodes had resolved or improved markedly. The adrenal mass had decreased in size and intensity and was resected for palliative reasons. (**b**) Anterior [^{18}F]FDG PET/CT MIP images of the same patient as in Fig. 1a, showing extensive [^{18}F]FDG avid PHEO uptake in the primary adrenal tumor (*arrow*) and retroperitoneal, bone, and lung metastases. After four treatments (cumulative activity of 873 mCi ^{131}I-MIBG) (*middle panel*), residual [^{18}F]FDG activity was only seen in the right adrenal bed and retroperitoneal nodes (*two lower arrows*). The adrenal mass had shrunk considerably and become largely necrotic. Because persistent mild elevation of normetanephrines was observed and this was the site of largest disease, this residual adrenal mass was resected. [^{18}F]FDG PET 6 months postsurgery (*right panel*) showed small residual uptake in the surgical bed and two small hypermetabolic nodes in the abdomen (not clearly seen in this MIP image). Note that the activity in the right upper quadrant (*arrowhead*) represents kidney, not tumor. (**c**) Biochemical parameters may be used to track response in PHEO. This is the same patient shown in Fig. 1a and b who had elevated chromogranin and normetanephrine levels pretreatment. The *arrows* represent the four ^{131}I-MIBG treatments, totaling 873 mCi. Although chromogranins started to improve after the first treatment, it was not until after the second treatment that metanephrines started to improve. Chromogranin levels were in the normal range at the time of the fourth treatment, but normetanephrine levels did not normalize until after surgery (*arrowhead*)

withdrawal is related to their half-life [172]. In PHEO/PARA patients, hypertension can usually be controlled with oral phenoxybenzamine and atenolol as they do not block ^{131}I-MIBG uptake in vivo. In addition, nifedipine can be added to antihypertensive regimens since interference has not been observed [11]. As a practical matter, patients generally undergo a diagnostic ^{123}I-MIBG study on their current drug regimen to assess targeting of MIBG prior to considering therapy [209].

Thyroid Blockade

Although USP release criteria require >95% ^{131}I bound to MIBG, ^{131}I-MIBG preparations all contain a small amount of free radioiodine. In the interval between manufacture and dose administration, there is a time-dependent breakdown, with the release of free iodine [197] into solution. In addition, a small amount of free iodide may be generated in vivo from metabolism [115]. Therefore, blocking the thyroid is necessary to prevent thyroid damage from radioiodine. A variety of regimens using potassium iodide (KI), saturated solution of potassium iodide (SSKI), or Lugol's solution have been used for this purpose. Several studies have shown the efficacy and timing of cold iodine administration to block thyroid uptake of radiolabeled iodine [176, 208]. The dose of KI recommended by the FDA for use during radiation emergencies is 130 mg of KI (100 mg iodine) per day for adults and is scaled down for children (http://www.fda.gov/downloads/Drugs/GuidanceComplianceRegulatoryInformation/Guidances/ucm080542.pdf).

Table 1 Drugs that interfere with MIBG uptake[a]

	Documented in patients	Documented in vitro
Antihypertensives	Labetalol [97, 133], phenoxybenzamine [172][b]	Propranolol but not other beta-blocker [5], guanethidine, reserpine, nifedipine, verapamil
Opioids	Cocaine [209]	
Tricyclic antidepressants	Imipramine [139]	Amitriptyline derivatives
Sympathomimetics		Phenylpropanolamine, amphetamines, pseudoephedrine, phenylephrine
Antipsychotic		Phenothiazines, haloperidol

[a]For detailed list of drugs that have the potential to interfere, see Solanski et al. [172] and Giammarile et al. [65]
[b]Phenoxybenzamine at low doses does not interfere; i.v. administration at high doses is reported to interfere

This regimen is in line with what others have suggested for blockade prior to diagnostic MIBG scanning [173]. Typically, the dose of KI prior to ^{131}I-MIBG therapy is higher than 130 mg. Thyroid blockade usually starts 1 day prior to administration of the ^{131}I-MIBG [150, 183, 205], although some protocols start up to 5–7 days prior [59, 61]. However, this appears to be unnecessary [176, 208]. The amount of KI has ranged from 120 to 200 mg/day with smaller amounts for children [13, 64, 65, 104, 148, 166]. The length of blockade has ranged from 7 to 45 days [17, 41, 59, 61, 64, 153, 183, 206]. Some have used more intensive regimens including thyroid suppression with thyroid hormone, in order to decrease TSH [37, 52, 61]. In pediatric populations, some regimens add potassium perchlorate and T3 to lower the TSH [81]. A report analyzing various phase I and II studies in children utilized an oral loading dose of 6 mg/kg of KI solution 8–12 h prior to ^{131}I-MIBG infusion, then 1 mg/kg every 4 h on days 0–6, and 1 mg/kg/day through day 45 post-infusion. Potassium perchlorate was also given as an additional oral blocking agent for 5 days post-infusion with a loading dose of 8 mg/kg and then 2 mg/kg every 6 h on days 0–4, beginning 4 h after the start of ^{131}I-MIBG infusion.

The EANM guidelines suggest starting iodide blockade 24–48 h prior to treatment and continuing for 10–15 days and do not recommend thyroxine administration [65]. Pharmacokinetic studies of radioiodinated ^{131}I-MIBG have shown that there is less than 10% in blood at 1 h post-administration [122] and that >80% of radiolabeled MIBG is released from the body over 4–5 days [36, 198, 199]. MIBG clears from the body with a terminal effective half-life of 37 h [45]. Therefore, it is reasonable to stop administering iodide for thyroid blockade 14 days after treatment. In spite of these blocking measures, it is not unusual to see some uptake of ^{131}I in the normal thyroid with some series showing that only 52% of subjects had no visualization of the thyroid posttreatment [17, 153].

SSKI and Lugol's are well tolerated. Infrequent side effects include sialadenitis, gastrointestinal disturbances, allergic-like reactions, and minor rashes. Thyroidal side effects include iodine-induced thyrotoxicosis, which is more common in older people and in iodine-deficient areas, and hypothyroidism, particularly in iodine-sufficient areas.

Additional Precautions

Because patients may have nausea and vomiting after administration of ^{131}I-MIBG, antiemetics such as ondansetron are often administered prior to therapy and in the first 3 days post-administration. Since the major route of ^{131}I-MIBG excretion is renal, the bladder is exposed to high concentrations of radioactivity. To minimize the radiation dose to the bladder, hydration is encouraged. Some investigators administer 3 L/m^2 or 150 mL/h for several days [68, 107]. In small children, urinary catheterization is often performed to decrease both the radiation dose and the potential for contamination [82, 107, 205].

Patient Eligibility

Candidates for ^{131}I-MIBG therapy should have a reasonable performance status (Karnofsky >60)

and a life expectancy of at least 3 months, unless they have intractable bone pain. Reasonable hematopoietic parameters (WBC >3,000/μL, platelets >100 K/μL) are required prior to ^{131}I-MIBG therapy, especially when stem cells are not available [65]. The degree of acceptable liver function required has not been well established, although some have used bilirubin ≤2.5 and liver enzymes ≤2.5 times the upper limit of normal as criteria [70]. Kidney glomerular filtration rate >30 mL/min or serum creatinine ≤2.5 the upper limit of normal are also desirable [65, 70]. Recently, it has been found that patients with nephrotic syndrome receiving large activities of ^{131}I-MIBG may be prone to bronchiolitis obliterans organizing pneumonia (BOOP) or acute distress respiratory distress syndrome (ARDS), and a recommendation has been made to limit the cumulative activity in these patients to less than 800 mCi of ^{131}I-MIBG [70].

^{131}I-MIBG is administered by pump i.v. through an indwelling catheter or central line. A variety of infusion times have been used, ranging from 1 to 2 h [164, 161, 150, 148, 23]. Six and even 24 h infusions have also been evaluated [81, 99, 181]. Slow administration is a precaution to minimize pharmacologic effects from the unlabeled MIBG, although some have administered the therapy over 30–60 min without sequela [14, 148, 23]. Our practice at MSKCC is to administer the drug over ~45 min. When high specific activity material is given, the infusion rate has been shortened to 15–30 min, since the total mass of MIBG is reduced [89, 36]. Monitoring of vital signs during the administration is recommended since patients may develop a hypertensive response. This can be particularly significant in PHEO/PARA patients and requires slowing of the infusion or pharmacologic intervention.

Administering therapy on an inpatient versus outpatient basis depends on multiple considerations. In many countries, there are policies or regulations that define the limits of administered activity for outpatient treatment. In the USA, patients must be given oral and written instructions to ensure that there is less than 500 mrem exposure to caregivers or other household members when they return home. Several groups have confirmed that this exposure rate to caregivers can be achieved. Caregiver exposures of 30–125 mrem with activities up to 5.55 GBq (150 mCi) were observed by Hoefnagel et al., and a median exposure of 60 mrem/3.7 GBq (60 mrem/100 mCi) was reported [61, 77]. With a higher median activity of 16.2 GBq (437.8 mCi), radiation exposure to caregivers was within regulatory range with median dose to them of 302 mrem [58]. At MSKCC, we perform most adult MIBG therapy as outpatients, although internal policies require that patients receiving >9.25 GBq (>250 mCi) ^{131}I-MIBG be inpatients. In children, most groups are more conservative and will hospitalize for ease of treatment, monitoring, and radiation safety considerations. Furthermore, in order to reduce bladder radiation, a Foley catheter is often placed for 3 days to minimize bladder dose and avoid contamination.

Patient Selection Criteria

There are no uniform guidelines for selecting or excluding patients from consideration for ^{131}I-MIBG therapy. Most investigators require demonstration of tumor localization on a diagnostic MIBG scan, although it is not always stated whether all known lesions were MIBG avid [70, 141, 148, 150, 165, 180]. Criteria for deciding how much tumor localization is required range from >20 cGy/37 MBq (>20 cGy/mCi) [165], 5 Gy/3.7 GBq (5 Gy/100 mCi) [104], visual localization above background, higher than two times background [70], and >1% of ID in tumor [13, 137]. Requiring a positive diagnostic MIBG scan is required since not all tumors take up MIBG. Furthermore, this also helps to avoid the presence of interfering medication.

Other selection criteria often include evidence of disease progression or symptoms [141, 148]. Patients need to follow radiation safety precautions; thus, a Karnofsky performance status of greater than 60% is advisable. Patients must not be pregnant or breast-feeding and must agree to birth control, although it is not known for exactly how long. Sperm banking or ovum harvest may be considered in younger patients.

Activity/Dose Selection

Various approaches have been utilized to select the dose for ^{131}I-MIBG therapy. Most studies have used fixed activities based on empirical evidence of limited toxicity [28, 37, 40, 61, 64, 72, 77, 81, 85, 110, 117, 120, 161, 164, 186]. Others have used fixed activities adjusted to body weight based on dose escalation studies [63, 70, 82, 94, 99, 121, 124, 126, 155]. Yet others have performed dosimetry analysis using a diagnostic scan and have calculated activities to deliver less than 2–4 Gy to blood or whole body [50, 62, 107].

There is also no standardized practice in terms of frequency of ^{131}I-MIBG therapy administration. If the patient responds to treatment or is stable and has no dose-limiting toxicity, the therapy is usually repeated. The frequency of retreatment is variable, ranging from a minimum of every 4 weeks to 6 months and requiring adequate recovery from toxicity [13, 40, 64, 72, 77, 92, 110]. Some investigators tailor the frequency based on tumor growth rate, with fast-growing tumors treated every 2.5–3 months and slower-growing tumors every 6 months [23]. Others perform three treatments and then reassess whether to proceed [23, 148]. High-activity therapy often requires longer intervals between treatments to allow marrow recovery; lower activities are much better tolerated. High-activity regimens delivering 18 mCi/kg on two occasions have shown the feasibility of stem cell rescue with 50–71% of patients achieving platelet transfusion independence [82, 91].

Thus, there are no predefined limits in terms of repeated treatments. In patients with PHEO/PARA (Table 2), patients have received 1–11 treatments with ^{131}I-MIBG [14, 64, 104]. Krempf et al. observed that 1–8 treatments were needed before a response was observed and no patient had a complete biochemical response until at least three treatments were given [104]. Similarly, Sisson et al. reported variable responses in patients ($n = 5$) receiving 2–4 treatments and suggested a minimum tumor dose of 150 Gy (15,000 rad) [168]. Those utilizing very large doses have found that continued response may be seen many months after treatment and sometimes wait a year before considering retreatment [68].

The cumulative activity administered has ranged up to 118.1 GBq (3,191 mCi) in PHEO/PARA (Table 2), 78.1 GBq (2,112 mCi) in carcinoids (Table 4), and 89.3 GBq (2,414 mCi) or 31.325 GBq/kg (35.8 mCi/kg) in neuroblastoma (Tables 6 and 7).

Dosimetry

Several studies have reviewed the pharmacokinetics of ^{131}I-MIBG. The pharmacokinetics of carrier-free ^{131}I-MIBG in adults has been reported [36] – with alpha $T_{1/2}$ of 3 h and beta $T_{1/2}$ of 38.3 h. In adults, the mean urinary excretion was 27.4% in the first 6 h, 49.8% in 24 h, and 80.3% in 120 h. Detailed pharmacokinetics in children with neuroblastoma has been published [100, 198, 199]. A terminal biologic $T_{1/2}$ in serum of 45.8 h is reported. In addition, at 24 h there was a cumulative urinary excretion of 32%, 71% at 48 h, and 65% at 6 days. MIRD dosimetry of ^{131}I-MIBG [88, 185] identifies the main target organs as the liver, myocardium, and gonads. Dosimetry of no-carrier added ^{131}I-MIBG is somewhat different, with higher radiation dose per mCi to most normal organs than those described in the package insert for low specific activity ^{131}I-MIBG [36]. While some of these dosimetry differences can be related to the specific activity, differences in methodology where self-irradiation is not considered likely plays a large role; dosimetry estimates performed from diagnostic scans in NB patients are often significantly different from those estimated from the therapy dose. Fielding et al. found that estimates from the diagnostic scan would have resulted in under dosing 65% of the patients. Nonetheless, this was more reproducible than weight-based dosing [21, 50]. Using dosimetry from diagnostic scans, Lashford et al. predicted therapy doses to within −20–30% of that seen with the therapeutic dose [107]. It is not known what the required doses are to obtain biochemical or tumor responses. Estimates of radiation-absorbed dose to tumor vary considerably between patients and diseases. For

Table 2 PHEO/PARA: treatment schema (administered activities are listed here in mCi; multiply by 37 for conversion to MBq)

Author	# patients	Single administration (mCi)	Cumulative (mCi)	# Doses
Shapiro et al. [164]	28	97–301 (mean 181)	111–916 (mean 479)	1–6
Fischer [52]	14	64–210	200–1,135 (median 559)	1–6
Bestagno et al. [10]	6	100–200	147–1,022	1–6
Krempf et al. [104]	15	78.4–250 (mean 127)	300–2,322 (mean 624)	2–11 (median 3.5)
Lumbroso et al. [110], Schlumberger et al. [161]	11	100–200	100–711 (mean 200)	1–6 (median 2)
Loh et al. [109]	116[a]	96–300 (mean 158)	96–2,322 (mean 490)	1–11 (mean 3.3)
Hartley et al. [72]	6	200	200–1,200 (mean 640)	1–6 (median 2.5)
Mukherjee et al. [137]	15	100–300 (mean 188)	200–1,592 (592 median)	1–7 (mean 3.4)
Safford et al. [158]	33	391 mean	70–1,223 (mean 549)	1–6 (median 1)
Bomanji et al. [14]	6	220–357 (mean 304)	342–987 (mean 910)	1–3
Rose et al. [155]	12	5.6–18.3 mCi/kg (median 11.5 mCi/kg and 800)	386–1,717 (median 1,015)	1–3 (median 1.5)
Gedik et al. [64]	19	100–700 (median 200)	183–2,200 median (800)	1–10 (median 3)
Gonias et al. [70]	50	6–19 mCi/kg (492–1,160), 500 if no stem cells (median 818)	492–3,191	1–3 (median 1)
Castellani et al. [28]	12	124–149 (median 149)	149–1,800 (median 1,065)	Up to 10 (median 7)
	16	200–350 (median 268)	249–1,546 (median 651)	Up to 6 (median 2)
Shilkrut et al. [166]	10	150 (mean 145)	100–600 (mean 310)	1–4 (median 2.1)
Rachh et al. [154]	12	NA[b]	199–513 (mean 319)	1–5(median 2)
Sze et al. [179]	14	Around 195	Mean 576	Median 2
Wakabayashi et al. [200]	26	1.9–5.8 mCi/kg (median 200)	NA	1–6 (median 2)
Yoshinaga et al. [207]	48	100–300 (median 3.5 mCi/kg)	NA	1–4 (median 2)
Rutherford et al. [157]	22	135–305 (mean 270)	270–1,369 (mean 544)	1–5 (median 2)

[a]Combination of several series from different institutions
[b]Not available

instance, tumor dose estimates of 10–40 cGy/37 MBq (10–40 cGy/mCi) have been reported [36, 164], with cumulative doses ranging from 10 to 198 Gy [77, 104, 109, 168] in patients with PHEO/PARA. The impression has been that cumulative doses 60–100 Gy are beneficial [104, 168]. Other studies suggested that doses of 150 Gy were necessary to obtain tumor response [168]. Because there is large variability in determining tumor dose due to inherent problems in quantification of single-photon emitters, many studies use estimates of dose to whole body as a

Table 3 PHEO/PARA: response

Author	# patients	Objective CR (%)	Objective CR/PR (%)	Biochemical CR (%)	Biochemical CR/PR (%)	Symptomatic CR (%)	Symptomatic CR/PR (%)	Duration of response or survival
Shapiro et al. [164]	28	0	7	0	18	NA	NA	Median PFS 18 months
Fischer [52]	14	0	14	NA	NA	NA	100	NA
Krempf et al. [104]	15	0	33	27	47	NA	NA	Median TTP 36 months
Lumbroso et al. [110], Schlumberger et al. [161]	20	0	15	0	15	0	71	Median OS 16 months
Bomanji et al. [13]	5	0	60	75	75	80	80	Median OS > 50 months
Loh et al. [109]	116[a]	4	30	13	45	NA	76	Median PFS 19 months
Mukherjee et al. [137]	15	0	62	22	89	7	93	5-year survival 85%
Hartley et al. [72]	6	0	0	25	50	NA	NA	Median TTP 12 months
Safford et al. [158]	33	NA	38	NA	60	NA	86	Median survival 4.7 years 5-year survival 45% Median OS 56 months
Bomanji et al. [14]	6	0	83	25		50	83	Median OS > 30.5 months
Rose et al. [155]	12	18	36	22	56	50	90	15 months PFS Median symptomatic improvement 43 months
Gedik et al. [64]	19	0	47	17	67	62	89	Median PFS 24 months Median OS 42 months
Gonias et al. [70][a] After first treatment	50	9[b] 17[c]	27[b] 50[c]	19	35	NA	NA	64% 5-year OS 47% 5 EFS
Castellani et al. [28]	Group 1 12/28 Group 2 16/28	8.3 12.5	33 25	33 29	89 67	NA	NA	Group 1 median response duration 1.9 years Group 2 median response duration 2.3 years
Shilkrut et al. [166]	10	0	30	NA	50	NA	50	Median PFS 17.5 months
Sze et al. [179]	14	0	NA	NA	NA	NA		5 years survival 68%
Wakabayashi et al. [200]	26	0	0	0	24	0	52	5 years survival 50%
Yoshinaga et al. [207]	48	0	2	NA	NA	NA	NA	NA
Rutherford et al. [157]	22	5	19	5	10	5	23%	Median survival from date of first treatment was 11.1 years

CR complete response, *PR* partial response, *OS* overall survival, *PFS* progression-free survival, *EFS* event-free survival, *TTP* time to progression

[a]Review of the literature from multiple centers

[b]After first treatment

[c]After second treatment combination of several series from different institutions

Table 4 Carcinoid: treatment schema (administered activities are listed here in mCi; multiply by 37 for conversion to MBq)

Author	# patients	Single administration (median) (mCi)	Cumulative (mCi)	# doses
Taal et al. [180]	30	200	200–600	1–3 (mean 1.8)
Pathirana et al. [150]	12	200 Initial single dose		1
Mukherjee et al. [137]	18	70–220 (median 190)	200–1,592 (median 600)	1–8 (median 3.2)
Sywak et al. [178]	58	2.5 mCi/kg capped at 150	Median 182	Mean 2.8
Nguyen et al. [141]	32[a]	157–554 (median 381)	157–554 (median 381)	1
Pasieka et al. [148]	13[a]	2.5 mCi/kg (median 149)	85–2,112 (median 594)	1–7
Safford et al. [159]	98	77–500 (median 306)	77–1,076 (median 401)	1–3 (mean 1.2)
Buscombe et al. [23]	25[a]	54–91	54–635 (median 300)	1–11
Nwosu et al. [143]	48[a]	200 Each cycle	200–800 (mean ~362)	1–4 (mean 1.8)
Ezziddin et al. [47]	31[a]	300	300–1,200 (median 600)	1–4 (median 2)

[a]Included some non-carcinoids

safe upper limit [50, 164]. Whole-body doses ranged from 50 to 231 cGy [85, 164]. New methods to evaluate the biodistribution and residence time of ^{131}I-MIBG are now feasible using the surrogate positron emitting reagent ^{124}I-MIBG [73, 84, 144].

Evaluation of Response

Response assessment may be performed as early as 2 months [14] but more frequently at 3–6-month intervals unless the patient is known to have fast-growing disease [64, 70, 166, 205]. Follow-up typically involves anatomic imaging such as CT or MRI to evaluate changes in lesion size. Functional imaging is performed using ^{123}I-MIBG [43] and, in known [^{18}F]FDG avid lesions (Fig. 1b), changes in SUV may be an indication of response, although limited studies have been reported [149]. In hormone-secreting tumors, biochemical parameters can be used to assess response (Fig. 1c).

Following therapy, response is usually evaluated at 8–24 weeks. As in many cancers, response is determined using size measurement criteria, most often using WHO criteria [27, 141, 148, 181]. WHO criteria for complete response include the disappearance of all lesions and negative ^{123}I-MIBG scans; partial response is a 50% or greater reduction of all measurable disease; and progression is the appearance of new lesions or an increase of 25% or more in tumor size. In PHEO/PARA, because most patients have elevated catecholamines, levels of these and their metabolites are also used to gauge response. Biochemical CR is defined as complete normalization of biochemical markers, partial response typically by $\geq$50% drop but not normalization, and progression by $\geq$20% increase in these levels (Fig. 1c).

In neuroblastoma, posttreatment diagnostic ^{123}I-MIBG scintigraphy is routinely used to assess response (Fig. 2) [43, 91]. Interestingly, Johnson et al. noted that in four patients with CR based on negative ^{123}I-MIBG imaging following their initial treatment, a post-therapy ^{131}I-MIBG scan performed after a second treatment showed residual disease [91]; this is probably related to the higher sensitivity of tumor detection on post-therapy scans that have shown to be more sensitive for tumor detection [204]. These authors suggest that ^{131}I-MIBG therapy could be used to consolidate first remission in patients with newly diagnosed high-risk neuroblastoma. Patients

Table 5 Carcinoid: response

Author	# Patients	Objective CR (%)	Objective CR/PR (%)	Biochemical CR (%)	Biochemical CR/PR (%)	Symptomatic CR (%)	Symptomatic CR/PR (%)	Duration of response or survival
Hoefnagel [74]	52[a]	4	15	NA	NA	NA	65	NA
Taal et al. [180]	30	0	0	0	13	0	60	3-year survival 22% Median OS 29 months Median symptom response 8 months
Pathirana et al. [150]	12	0	17	NA	NA	58	83	Mean symptom response 15.4 months
Pasieka et al. [148]	13[b]	8	15	0	15	0	92	Mean symptom response 17 months
Safford et al. [159]	98	0	15	6	37	NA	49	5-year survival 22% Median OS 2.3 years
Sywak et al. [178]	58	NA	NA	NA	NA	NA	NA	5-year survival 63% Median OS 8.3 years
Buscombe et al. [23]	25[c]	0	35	NA	NA	NA	NA	Median PFS 14.5 months Median OS 18 months
Nwosu et al. [143]	48[d]	0	28	NA	37	NA	56	Median survival of symptomatic responder 59 months Nonresponder 22 months
Ezziddin et al. [47]	31[e]	NA	10	NA	NA	27	82	PFS 34 month, median OS 47 month, 5 year survival 31%

CR complete response, *PR* partial response, *OS* overall survival, *PFS* progression-free survival, *NA* not available
[a]Worldwide experience summary up to 1994
[b]Included 4 non-carcinoid
[c]17 With carcinoid, 8 non-carcinoids
[d]Included 30 GEP, 6 pulmonary NET, 12 unknown primary
[e]20 carcinoids, 11 other tumors survival data for carcinoids

undergoing high-dose therapy invariably have significant hematologic toxicity, and stem cell harvesting is routinely performed in these patients [91]. The parameter that determines if the patient needs stem cell transplant is the duration and resistance of the hematologic toxicity to respond to supportive treatment. When transplantation is required, it is usually not performed for at least 3 weeks post- ^{131}I-MIBG treatment [82, 124, 205].

Table 6 ^{131}I-MIBG therapy in neuroblastoma (administered activities are listed here in mCi; multiply by 37 for conversion to MBq)

Study	# Patients	Stage	Single treatment (mCi)	Number of treatments	Cumulative dose (mCi)	PR	CR	Measurement of response duration
Treuner et al. [184]	6	3–4	35–210 (median 85)	2–5 (median 3)	150–590 (median 234)	33%	17%	Median PFS 5.1
Troncone et al. [186]	7	3–4	70–184 (median 122)	1–4 (median 2)	80–296 (median 178)	43%	14%	NA
Hoefnagel et al. [77]	16[a]	High risk/4	40.5–200	1–6 (median 3)	59–1,100 (median 300)	42%	17%	NA
Klingebiel et al. [99]	47	3–4	1.7–30 mCi/kg (8.9 mCi/kg)	1–6	88–1,033	Stage 3 36% Stage 4 25%	Stage 3 39% Stage 4 22%	Stage 3: survival at 28 months 32% Stage 4: survival at 28 months 12%
Garaventa et al. [61]	31	Resistant/ recurrent	68–162 based on body weight	1–5 (median 3)	76–646	13%	6% 23% biochemistry	Median TTP 4–9 months
Hor [81]	15	3–4	To deliver 1 Gy	1–6 (median 3)	8.8 mCi/kg	13%	0%	Median survival ~12 months
Hoefnagel et al. [79]	53	Stage 3 and 4	100–200	1	100–200	43%	13%	Response lasted 2–38 months
Lumbroso et al. [110]	26	3–4	30–108 (median 70)	1–5	NA	0	0	NA
Lashford et al. [107]	25	3–4	64–327 (based on 1,2, 2.5 Gy whole body)	1	64–327	33%	0	Median survival 12 months
Hutchinson et al. [85]	14	3–4	60–220 (median 154)	1–3 (median 1)	60–293 (median 210)	0%	0%	Median survival 5.65 months
De Kraker et al. [40] Cfirst line	33	2,3,4	200 with repeat 100	2–7 (median 3)	NA	54%	3%	NA

(*continued*)

Table 6 (continued)

Study	# Patients	Stage	Single treatment (mCi)	Number of treatments	Cumulative dose (mCi)	PR	CR	Measurement of response duration
Matthay et al. [121]	30	3–4	90–803 2.6–18.2 mCi/kg	1	90–803	30%	3%	Median survival 6 months
Garaventa et al. [59]	43	3–4	68–149 (median 100) based on body weight	1–5 (median 3)	NA	28%	2%	Stage 3: 5-year EFS 92% Stage 4: 5-year EFS 40%
Kang et al. [94]	20	2–4	3.8–14.1 mCi/kg (9.5 mCi/kg)	1–3	27.6–30.5 mCi/kg	31%	0%	Pain relief 1–3 months
Howard et al. [82]	28	4	Median 17.3 (2.6–19.3 mCi/kg)	1–4 (median 2)	346–2,414 (median 860 or 35.8 mCi/kg)	36%	4%	Median survival 12 months
Matthay et al. [124] Phase II	164	Progressive/ relapsed/ refractory	12 mCi/kg or 18 mCi/kg if stem cells	1	NA	19% 29%	6% 8%	OS at 2 years 29% EFS at 1 year 18%
de Kraker et al. [41] First line	44	High risk	200 initial with repeat 100–150	1–5 (median 3)	350–950 (median 500)	63%	2%	Median EFS 10 months OS15 month 5 year OS 14.6%

Matthay et al. [123] Phase I	21	Refractory/ relapsed	Dose escalation-based 4,6, 8 Gy red marrow	2	Double dose (day 0 and 14) 22–51 mCi/kg (4–8 Gy marrow)	10%	0%	OS at 18 months 48% PFS 0.55 year
Johnson et al. [91]	76	Relapsed	Intent 18 mCi/kg × 2	1–2	Double dose 36 mCi/kg	First treatment 23.7% Second treatment 17.1%	First treatment 6.6% Second treatment 12.2%	OS 60% at median 18 month OS for those with CR 22 month
Polishchuk et al. [151]	39 (10–17 years) 16 pts. >18	Recurrent or refractory	11.9 mCi/kg (range,2.6–18.8 mCi/ kg)	1–4 (median 1)	10–17y/o 17.8 mCi/kg >18 y/o 16.9 mCi/kg (range, 9.0–43.0 mCi/kg),	10–17 y/o 39% >18 y/o 44%	10–17 y/o 0% >18 y/o 13%	5 years OS 14.6%
Schoot et al. [163]	21[b]	Stage 1–3	First 5.8–20.6 mCi/kg (median 13.4 mCi/kg Second 5.9–16.3 mCi/ kg(median 12.4 mCi/ kg)	1–7 (median 2)	NA	4	16	10 years OS 90.5%

CR complete response, *PR* partial response, *OS* overall survival, *PFS* progression-free survival, *EFS* event-free survival, *TTP* time to progression

[a]Include neuroblastoma only

[b]In some patients combined with chemo and or surgery

Table 7 ^{131}I-MIBG therapy plus chemotherapy in neuroblastoma (administered activities are listed here in mCi; multiply by 37 for conversion to MBq)

Study	# patients	Stage	Single treatment (mCi)	Number of treatments	Cumulative dose (mCi)	PR	CR	Measurement of response duration	Chemotherapy
Corbett et al. [38]	5	Advanced/ relapsed	200–303	1	200–303	NA	NA	NA	Carboplatin, melphalan or etoposide, vincristine
Mastrangelo et al. [118]	4	4	100–120	2	200–250	25%	50%	Two only lasted <3.5 months and one at least 5 months	CISP, CTX
Voute et al. [196]	No O_2: 36 hyperbaric O_2:27	4	200 mCi followed by 100 mCi	2–7 (median 3) 2–12 (median 3)	NA	NA	NA	No O_2: survival at 28 months—12% O_2: survival at 28 months–32%	No chemo, hyperbaric
Gaze et al. [63]	5	4	2 Gy whole body (179–277)	1	179–277	20	80%	OS 23 months	Melphalan, whole-body XRT(12.6–14.4 Gy), and stem cells
Klingebiel et al. [98]	11	4	7.8–22 mCi/kg (median 15.7 mCi/kg) 195–302	1	195–302 (median 297)	18%	36%	Mean PFS 2.15 years	Melphalan, carboplatin etoposide, and anti-GD2 mAb after MIBG
Miano et al. [126]	17	3–4	4.1–11.1 mCi/kg (median 7 mCi/kg)	1	NA	35	12	NA	Busulfan and melphalan
Mastrangelo et al. [120]	21 (16 with MIBG)	3–4	200	1	200	75%	0%	PFS median 12 months	CISP, VP16 VNC. CTX then MIBG
Yanik et al. [205]	12	Metastatic or localized	132–484 (median 212 or 12 mCi/kg)	1	132–484	17%	50%	Median survival 12.8 months	Carboplatin, etoposide, melphalan
Gaze et al. [62]	8	4	12 mCi/kg (median 243) Second dose to deliver total 4 Gy	2	318–609 (median 431)	NA	NA	NA	Topotecan

Mastrangelo et al. [119]	Group 1 = 5 Group 2 = 8	Stage 4 and 3	Group 1 168–200 (mean 178) Group 2,109–200 (mean164)	1	Same	Group 1 80% Group 2 75%		Group 1 20% Group 2 13%	Both group; Carboplatinum, cyclophosphamide, etoposide, doxorubicin, vincristine Group 2 additional busulfan, mephalan, and G-CSF
DuBois et al. [42]	24	Relapse or refractory	Dose escalation 8,12,15,18 mCi/kg (median 16.5)	1–3 (Median 1)	8–36 mCi/kg	17	9	NA	Vincristine and irinotecan
Kraal et al. [103]	16	High risk	First 10.6 (6.9–12.6) mCi/kg Second 10.6 (6.9–12.6) mCi/kg	2	25 (14.3–29.4) mCi/kg	56	0	10 year OS	Topotecan[a]
DuBois et al. [43]	27	Relapse or refractory	8,12,15 and 18 mCi/kg	1–2	Same	12		NA	Vorinostat
Yanik et al. [206]	50	Cohort 1 refractory and relapse Cohort 2 partial responder	8–12 mCi/kg based on GFR	1	8–12 mCi/kg	2.4% 12.5%	7.3% 25%	3 years (EFS) 20% ± 7% OS 62% ± 8%	Carboplatin, etoposide, mephalan,local XRT
Modak et al. [129]	19	Recurrent or refractory	12–18.7 (median 18)	1	Same	0	0	Median OS 23.7 ± 9.1 Median time to progression 6.5 ± 2	Arsenic trioxide

CR complete response, *PR* partial response, *OS* overall survival, *PFS* progression-free survival, *EFS* event-free survival
[a]After MIBG and topotecan therapy pts. underwent standard induction treatment surgery or ASCT

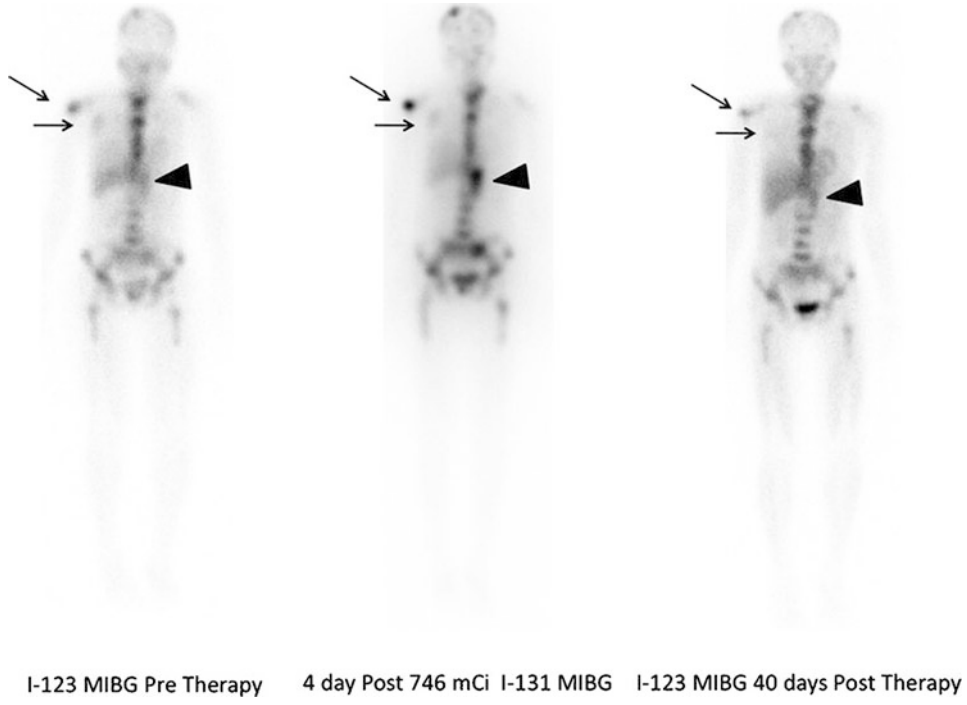

Fig. 2 A 26-year-old woman with neuroblastoma. ^{123}I-MIBG diagnostic scan (*left panel*) pre-therapy shows extensive bone disease (*arrows*) and left adrenal mass (*arrowhead*). After receiving 27.6 GBq (746 mCi) ^{131}I-MIBG, she was imaged at 4 days (*middle panel*). This showed excellent targeting of sites of disease. A follow-up ^{123}I-MIBG scan (*right panel*) showed that in spite of excellent tumor targeting, there was little response with only minor decreases in uptake in the left scapula and humerus compared to baseline

Pheochromocytoma/Paraganglioma

PHEO/PARA are tumors that originate in chromaffin tissue of the adrenal medulla or sympathetic nervous system. The incidence of PHEO/PARA is estimated to be ~1–2 per million [9, 49], although in autopsy series an incidence of 1 in 2,031 cases has been reported [125]. These tumors are most often found in the adrenal and in this location are referred to as PHEO. If they occur outside of the adrenal they are referred to as PARA. Three percent of adrenal "incidentalomas" are PHEO [95]. These tumors often secrete catecholamines, and consequently, patients present with hypertension and other symptoms of adrenergic excess. In some instances, however, these tumors are nonfunctional and presentation is related to mass effect or incidental discovery.

Traditionally, PHEO/PARA were known as the "10% tumor" due to the thought that they were 10% bilateral, 10% metastatic, 10% extra-adrenal, 10% non-hypertensive, and 10% inherited. However, in the last decade, it has become increasingly clear that this rule no longer holds, as was explicitly pointed out by Elder et al. in 2005 [46]. While the majority of PHEO/PARA are still thought to be sporadic, up to 35–40% of PHEO/PARA are now estimated to be related to genetic defects, and 15% or more with somatic mutations [39, 116, 147]. With ever expanding genetic testing, mutations are now frequently found in patients with apparently sporadic disease, no family history, and a non-syndromic presentation [1, 140]. Since 2002, when SDHx mutations were first associated with PHEO/PARA [3, 8], at least 17 genetic mutations have been identified to date, as well as somatic mutations occurring in the same susceptibility genes as the genetic ones [22, 147]. Depending on the mutation, two major pathways have been recognized: a pseudo hypoxic pathway referred to as Cluster 1 (including

SDHx, SDHAF2 VHL, HIF2A, and *FH*) and a tyrosine kinase signaling pathway (including *MEN*, *RET*, *NF1*, *MAX*, and *TMEM127*) referred to as Cluster 2 [39].

While most PHEO/PARA are benign, up to 26% or more are malignant [152, 210], with higher rates in certain inherited forms of disease [39, 116, 147]. In addition, extra-adrenal tumors which are also more prevalent in certain inherited PHEO/PARA are often malignant [1, 7, 140, 210]. In particular, SDHB related PHEO/PARA are known to have a high risk for metastases [66]. Pathologically it is difficult to differentiate benign from malignant tumors because of lack of robust morphological and histological criteria [182]. Therefore, in order to classify PHEO/PARA as malignant, one must find disease in sites where this tissue is not normally present [33]. The most common sites of metastatic disease include lymph nodes, bone, liver, and lung [18].

The most sensitive tests to confirm the diagnosis of PHEO/PARA are plasma-free metanephrines or urinary fractionated metanephrines, with sensitivities of 97% and 99%, respectively [30, 108]. The diagnostic imaging modalities most often used for staging are CT and MRI; functional imaging modalities are also useful, including radiolabeled MIBG (Fig. 1a), ^{18}F-fluorodopamine PET, ^{18}F-DOPA PET, [^{18}F]FDG PET (Fig. 1b), ^{111}In-pentetreotide scintigraphy [26, 146, 213], and ^{68}Ga-DOTA-somatostatin analog-scans (REF below). ^{68}Ga-DOTATATE has recently been approved by the FDA.

The optimal therapy for PHEO/PARA consists of surgical resection when feasible. Even in patients with metastatic disease, surgical debulking is often used with palliative intent, although no controlled studies have been performed to show an effect on survival. Patients with benign disease have normal overall survival after complete surgical resection, whereas patients with malignant disease typically have an overall 5-year survival of less than 50% [31, 90, 160]. Nonetheless, it is recognized that there is a subset of patients with malignant disease who have a more indolent course and may live >20 years with limited therapy [135]. Patients that are asymptomatic and have slow growth rates may opt for observation until symptoms require therapy.

Averbuch et al. evaluated the use of cyclophosphamide, vincristine, and dacarbazine (CVD) for metastatic disease [4]. In 14 patients with malignant PARA, they observed a complete or partial response in 57%, with median duration of 21 months. A second analysis of this data expanded to 18 patients was performed with long-term follow-up of 22 years [83]. A CR was present in 11% of the patients, 44% had a partial response, and 72% had a biochemical response with a median duration of 20 months. Nonetheless, 16 of the 18 patients died of their disease and one was lost to follow-up. Patients that responded had a median survival of 3.8 years compared to 1.8 years for nonresponders. The common toxicities were myelosuppression, peripheral neuropathy, and gastrointestinal toxicity. Overall, the treatment was well tolerated as evidenced by the ability to administer a median of 23 cycles. These authors conclude that the treatment is not for all patients with metastatic disease but can be considered when patients are symptomatic or tumor shrinkage is desirable. Results in other small series or case reports have shown similar findings, with remissions typically lasting less than 2 years [162]. CVD have become the most often used first-line chemotherapy regimen for metastatic disease, although other regimens have also been utilized [60, 175]. Given the suboptimal response to chemotherapy, newer therapeutic modalities such as ^{131}I-MIBG therapy are being applied in patients with PHEO/PARA, and guidelines have been published [65], but others believe 60–100 Gy is adequate [104, 186]. Patients with disease limited to the liver have also been treated successfully with RFA ablation [192]. In patients with rapidly progressive disease, chemotherapy with the CVD regimen is often used first.

There has not been a systematic evaluation comparing regimens using low, mid, or high doses of ^{131}I-MIBG in PHEO/PARA. Initial reports, first by Vetter et al. [193] and followed shortly by a report of treatment of five patients at the University of Michigan [168] appeared in the early 1980s. In the latter report, five patients were treated with total activities ranging from

9.99 to 17.91 GBq (270–484 mCi), resulting in 35–180 Gy to tumor [168]. A significant reduction in tumor size was observed in a few patients. Since then, a variety of dose ranges have been used. Individual doses ranging from low activity (2.96–7.4 GBq or 80–200 mCi), intermediate (up to 18.5 GBq, or 500 mCi), to high activities that are often weight based (444–666 GBq/kg, or 12–18 mCi/kg) have been used (Table 2). Strategies using low-intermediate activity rely on repeat treatment, with which cumulative doses as high as 85.1 GBq (2.3 Ci) have been achieved, although median cumulative activities are generally in the 18.5–37 GBq (500–1,000 mCi) range (Table 2). Even higher total doses have been achieved using high activities doses The UCSF group has been a proponent of high doses with stem cell support, based on a phase I dose escalation trial [54, 70, 155]. Activities >12 mCi/kg usually require having stem cells available for transplantation.

A meta-analysis of publications from 1983 to 1997 on 116 patients treated with ^{131}I-MIBG has been reported [109]. These studies used a mean single activity of 5.85 GBq (range 3.55–11.1 GBq) or mean 158 mCi (range 96–300 mCi) with a mean of 3.3 (1–11) repeated treatments, resulting in cumulative activities of 3.55–85.9 GBq (mean of 18.1 GBq) and 96–2,322 mCi (mean of 490 mCi). Although these retrospective studies had different methodologies, clear therapeutic results were observed using what are now regarded as relatively low activities. Of the 116 patients, 4% had an objective CR and 26% had partial response (PR). Biochemical catecholamine response demonstrated complete normalization in 13% of 96 patients, 32% had >50% improvement, and 76% of 99 patients had improvement in symptoms.

Other reports describe results with low (median below 7.4 GBq or 200 mCi) [28, 64, 166], intermediate (median above ≥7.4 GBq or above 200 mCi) [14, 28, 72, 158], and high activities (>44.4 MBq/kg or >12 mCi/kg) (Table 3) [70, 155]. A retrospective review of the Duke experience in 33 patients treated with ^{131}I-MIBG with cumulative activities ranging from 2.59 to 45.3 GBq or 70–1,223 mCi (mean individual activity 14.47 GBq or 391 mCi) demonstrated an objective response rate of 38%, a symptomatic response rate of 86%, and a biochemical response rate of 60%. Responders had a median survival of 4.7 years compared to 1.7 years for nonresponders. Patients receiving high-activity therapy (>18.5 GBq or 500 mCi) had a survival advantage with median survival of 3.8 years versus 2.6 years for the low-activity group [158].

A prospective study using high-dose therapy, median individual activity of 30.27 GBq (818 mCi), showed a CR of 8% and objective response in 36%. In this group, the majority of the patients only received a single administration, with a small proportion receiving two or three treatments. Because of the expected myelotoxicity, peripheral stem cells were harvested, although some patients recovered adequate marrow function and did not require stem cell infusion [70].

The use of high specific activity ^{131}I-MIBG for therapy was recently evaluated in a phase I clinical trial [36]. In a group of 11 patients receiving no-carrier added ^{131}I-MIBG, no side effects were observed related to the injection. Estimated tumor doses ranged from 11 to 40 rad/37 MBq (11–40 rad/mCi). In this phase I study, activities ranged from 222 to 333 MBq/kg (6–9 mCi/kg) with a maximum activity of 24.98 GBq (675 mCi).

When comparing objective responses in different studies where patients received median activity of approximately 7.4, 14.47, or 30.27 GBq (200, 391, or 818 mCi), the observed response rates overlap, in the range of 20–40% (Table 3) [64, 70, 158]. Within a single institution, Castellani et al. reviewed patients treated with a median activity of 5.51 GBq (149 mCi) versus 9.92 GBq (268 mCi). Their conclusion was that in these ranges, higher activities could deliver the desired dose faster, with a modest increase in toxicity and similar overall response rates [28].

Several protocols have combined chemotherapy with ^{131}I-MIBG therapy in neuroblastoma, but there has been only one such prospective report in patients with PHEO [170]. In this small series, six patients underwent dosimetry and were scheduled to receive three ^{131}I-MIBG treatments at 3-month intervals with activities estimated to deliver 85–90 cGy to the whole body per single

administration. The patients would then start the CVD chemotherapy regimen [4]. Three of the six patients had improvement in tumor following ^{131}I-MIBG therapy. Two patients completed 9 months of sequential chemotherapy with further improvement and were considered to have partial response. Toxicity from ^{131}I-MIBG was minimal but forced reduction of chemotherapy doses in some patients.

The most frequent sites of metastatic disease include the lymph nodes, bone, lung, and liver [18]. There is suggestion that soft tissue disease response to ^{131}I-MIBG therapy is superior to that of the bone [69, 104, 168]. It also appears that patients with smaller volume disease following surgical resection are more likely to respond.

In summary, high-quality data on the use of ^{131}I-MIBG therapy in PHEO/PARA is limited, with few prospective trials, and there is currently no consensus on an optimal dosing strategy. Differences in patient selection and follow-up may account for differences in response rates and survival. It is clear that many patients will benefit from treatment, and objective responses are often observed, but complete response rates are low, ranging from 0% to 18%. The duration of responses is also variable, with 5-year survivals between 45% and 85% [137, 158]. There is some suggestion that higher activities >18.5 GBq (500 mCi) or myeloablative regimens may be associated with higher response rates. However, there are no direct comparisons to determine if fractionated smaller activities, that are associated with lesser toxicity, result in different overall survival. Nonetheless, the ease of performing this therapy, the evidence of objective responses, symptomatic improvement, biochemical improvement, and the limited toxicity and few late effects compared to other chemotherapy and external beam regimens make this an acceptable strategy in patients with metastatic PHEO/PARA.

Carcinoid

^{131}I-MIBG is used most frequently to treat neuroblastoma and PHEO/PARA. The third largest experience is with carcinoid tumors (Tables 4 and 5) [148, 23]. Carcinoids are slow-growing NETs that often secrete substances leading to hormonal syndromes. These tumors are rare, with incidence in the range of two cases per 100,000 [67, 132]. The most frequent sites for carcinoids are the gastrointestinal (GI) tract (73.7%) and the bronchopulmonary system (25.1%). Within the GI tract, most occur in the small bowel (28.7%), appendix (18.9%), rectum (12.6%), and stomach (6%). Although 45% exhibit metastases at the time of diagnosis, the overall 5-year survival is 50–67% [131, 132]. Higher incidences of carcinoids are found in patients with MEN1, VHL, and neurofibromatosis. In 2000, recognizing the heterogeneity of presentation, prognosis, and outcome, the WHO developed a classification system for NET reflecting a better understanding of cell biology, therapeutic implications, and pathology [174]. Three types of NET were defined: (1) well-differentiated NET (benign behavior, low grade), (2) well-differentiated neuroendocrine carcinoma (low-grade malignant), and (3) poorly differentiated neuroendocrine carcinoma (high-grade malignant). However, this classification is relatively new, and most reports of ^{131}I-MIBG therapy in carcinoid have not incorporated this classification.

Initial staging and follow-up relies on conventional imaging, such as CT and MRI, to evaluate for nodal or metastatic liver disease. Because these tumors often express somatostatin receptors, functional imaging with ^{111}In-pentetreotide or, more recently, with ^{68}Ga-somatostatin analogs is performed [26]. Before ^{111}In-pentetreotide was available, ^{131}I/^{123}I-MIBG scintigraphy was often performed following an initial report by Fischer et al. [53]. These tumors also express norepinephrine transporters, as do PHEO/PARA. Reports have shown that ^{131}I-MIBG has a lower sensitivity for the detection of carcinoid than for pheochromocytoma [26]. A review of 275 carcinoid patients demonstrated a sensitivity of 70% for tumor detection with ^{131}I-MIBG [74].

At presentation, the best management is surgical removal for curative intent, or in cases with metastatic disease, debulking for palliation. Unfortunately, metastatic disease at presentation

is frequent, and no consistently effective therapeutic strategies are available. Symptomatic tumor response is often seen following therapy with octreotide analogs [2], whereas objective tumor regression is rare [130]. Interferon may also result in symptomatic improvement in 58–65% of patients [130]. Multiple single and multi-agent chemotherapy regimens have been utilized, with none showing objective tumor response greater than 15%, and newer molecularly targeted reagents are now being evaluated [130]. Because liver metastases are commonly present, interventional radiology techniques including embolization and ablation with radiofrequency or cryoablation are often utilized [105, 130].

The uptake and accumulation of ^{131}I-MIBG in carcinoid raised the possibility of using the radiopharmaceutical for treating these tumors [78]. More recently, ^{111}In-, ^{90}Y-, and ^{177}Lu-octreotide or other somatostatin analogs have been utilized since somatostatin reagents have higher overall accumulation in carcinoid and gastroenteropancreatic tumors [93]. In this chapter, we focus on the use of ^{131}I-MIBG therapy of carcinoid, since radiolabeled somatostatin analog therapy is discussed in the chapter "▶ Neuroendocrine Tumors" by Dr. Bodei of this book.

Hoefnagel et al. treated five patients with ^{131}I-MIBG which produced some symptomatic responses [78]. Numerous additional reports have since followed (Table 4). Activities have ranged from ~2 to 20.5 GBq (54–554 mCi), with most series having median single activity <7.4 GBq (<200 mCi). As in PHEO/PARA, patients are often treated repetitively (1–11 treatments, median 1.2–3 treatments) until toxicity or lack of response is seen. Cumulative activities have ranged from 2 to 78.14 GBq (54–2,112 mCi), with median activities between 6.73 and 21.98 GBq (182–594 mCi). In contrast to neuroblastoma and PHEO/PARA, no series have included marrow ablative doses and stem cell transplant in carcinoid patients.

Although carcinoid patients rarely have a complete response to ^{131}I-MIBG therapy, measurable objective response rates of 11–27.5% have been reported (Table 5). The cumulative experience in 52 patients treated up to 1994 reported a 15% objective response rate and 65% symptomatic response. Multiple publications suggest that symptomatic response rates range from 38% to 92%, with partial symptomatic improvement more common than complete relief [137, 150, 159]. Patients whose symptomatic disease is resistant to octreotide or chemotherapy may benefit from ^{131}I-MIBG [159]. Biochemical responses are seen less commonly than symptomatic responses and range from 13% to 73% (Table 5), with complete biochemical normalization being infrequent [137, 148, 159]. For instance, Taal et al. observed that 60% of patients had symptomatic improvement, whereas only 13% had decreases in biochemical markers [180]. It is not well understood why only some patients with symptomatic response also show biochemical response [148, 180]. Symptomatic responses last a median of 8–17 months [148, 150, 180].

Because evaluation and outcome reporting is not standardized, the exact advantage in terms of survival is difficult to gauge from the literature. Median 5-year survivals of 42–78% have been reported [137, 159]. This is in the same overall survival range for carcinoid patients undergoing other, non-^{131}I-MIBG treatments [131, 132]. The largest series of 98 patients was reported by Duke University [159]. Their median initial activity was 11.32 GBq (306 mCi), although over time, this increased, and they now recommend initial single activities of >14.8 GBq (>400 mCi). Patients receiving >14.8 GBq (>400 mCi) survived an average of 4.69 years compared to 1.86 years for those receiving <14.8 GBq (<400 mCi). Most of these patients received only a single treatment. The authors also noted that patients that had symptomatic improvement had a 5.76-year survival compared to 2.09 years for those that did not. Interestingly, in those with biochemical improvement, survival was not significantly different from those without biochemical response (4.11 years versus 3.42 years). In this study, 49% of progressive metastatic carcinoid patients had improvement in symptoms. Similarly, others have also reported high rates ranging from 56% to 92% (Table 5). Nwosu et al. also found that patients with symptomatic improvement had a longer

survival of 59 months compared to 22 months in those without improvement [143].

Few studies have directly compared ^{131}I-MIBG treatment to untreated controls or patients undergoing other therapies. Sywak et al. reported a 5-year survival of 63% in patients treated with ^{131}I-MIBG compared to 47% for those not receiving it [178]. In these patients, further deaths occurred over time, with a 10-year survival of 38% in the ^{131}I-MIBG treatment group versus 33% in the no treatment control. In a separate report, Taal et al. compared ^{131}I-MIBG therapy to nonradioactive MIBG therapy and the median survival times were similar, approximately 28 months from start of treatment. Interestingly, they found a symptomatic response rate in both groups of 60%, although responses lasted longer with ^{131}I-MIBG than with nonradioactive MIBG (8 months versus 4–5 months) [180].

Studies combining ^{131}I-MIBG with chemotherapy or biologic therapy are rare. Zuetenhorst et al. evaluated whether interferon or cold MIBG increased the uptake of ^{131}I-MIBG in carcinoid tumors [212]. They found a 10% increase in ^{131}I-MIBG uptake in 19% of the patients receiving interferon and a 10% increase in 83% receiving cold MIBG. Unfortunately, no objective responses or synergistic effect from combined treatments with ^{131}I-MIBG were observed.

Another approach that may result in improved response is direct intra-arterial injection of the radiopharmaceutical. This approach delivered a 69% higher dose of ^{131}I-MIBG to the targeted tumor [20], but the therapeutic consequences of this approach are still to be determined.

With the advent of improved somatostatin analogs that exhibit better targeting of carcinoids than MIBG, the role of ^{131}I-MIBG therapy in this disease has diminished. ^{90}Y- and ^{177}Lu-labeled DOTATOC and DOTATATE have already demonstrated promising results [24, 190]. Nonetheless, in octreotide negative patients or those with borderline renal function, ^{131}I-MIBG remains a useful palliative option.

Case reports and smaller series have been reported on therapy of other NETs (non-PHEO/PARA carcinoid and neuroblastoma). For example, in a review article, the experience in 52 patients with medullary thyroid carcinoma was presented. There was a 38% objective response rated and palliation in 22% of the patients [74]. Treatment of 38 patients with gastroenteropancreatic tumors with a median of 6.8 GBq (range 1.6–10.57 GBq) of ^{131}I-MIBG has been reported. At 3–6 month following single treatment, 75%, 67%, and 63% of patients showed either a partial response (PR) or stable disease (SD) on radiological, biochemical, and symptomatic criteria, respectively. Overall survival from the date of the first therapy was 4 years $\pm$ 0.69 years, with 29% of patients alive at 10 years [138].

In summary, this modality is safe in patients with carcinoid, and there is evidence of objective, symptomatic, and biochemical benefit, although rarely complete responses are reported. There is a lack of prospective well-designed trials to compare with other modalities. Many carcinoid patients failing surgical resection or local ablation procedures are treated with radiolabeled somatostatin rather than ^{131}I-MIBG because of better targeting with somatostatin analogs. Nonetheless, in patients in whom radiolabeled somatostatin may be contraindicated (e.g., poor renal function) or not available, ^{131}I-MIBG is a reasonable strategy for symptomatic palliation.

Neuroblastoma

Neuroblastoma is a tumor that arises from primordial neural crest cells and is almost exclusively found in infants and young children. It is the most common tumor of childhood with an incidence rate of 9.5 per million [71]. Prognostic markers include age, stage at presentation, and MYCN amplification status [127]. The 5-year survival is 83% for infants, 55% for children 1–4 years, and 40% for older children [71]. Children less than 1 year may present with a self-limited disease with spontaneous remission (stage 4S). These children have an excellent long-term prognosis with 70–97% survival [142]. Stage 4 disease consists of dissemination to the distant lymph nodes, bone, bone marrow, liver, skin, and/or other organs. In patients younger than 18 months and without

MYCN amplification, these tumors have more favorable prognosis and are usually treated with intermediate dose chemotherapy without autologous stem cell transplant (ASCT). Patients at high risk are those >18 months old with stage 4 disease and those with MYCN amplification. Therapy for these patients usually relies on induction chemotherapy, surgery, and radiotherapy (given that this is a radiosensitive tumor) followed by consolidation of remission with ASCT or *cis*-retinoic acid with or without antibody immunotherapy [127]. High-risk patients often relapse and are resistant to conventional therapy. Newer strategies include immunotherapy such as anti-GD2 antibodies [127]. ^{131}I-MIBG therapy has also been utilized, and several retrospective studies and a few phase I and II studies have been reported. ^{131}I-MIBG applications have included palliative therapy for patients with multiple relapses, first-line therapy, localized symptomatic inoperable disease, and combined therapy with chemotherapy or biologic therapy for consolidation.

Patient preparation for ^{131}I-MIBG therapy is simple and similar to that described above, where patients are taken off drugs that may interfere with uptake or release of MIBG [172]. The patient's thyroid is blocked with an age-appropriate dose of KI. A diagnostic ^{123}I-MIBG scan is obtained to document MIBG uptake, which is typically seen in 93–97% of neuroblastoma patients [86, 194].

Several ^{131}I-MIBG dosing strategies have been pursued in patients with neuroblastoma (Tables 6 and 7). Fixed activities are most commonly used, usually consisting of single 3.7–7.4 GBq (100–200 mCi) administrations that are repeated at a similar activity. Treatment regimens such as this that are not weight based have been repeated up to seven times with cumulative activities of up to 1.1 Ci. Another strategy is based on activity per body weight where phase I dose escalation trials have been performed using single activities of 96–666 MBq/kg (2.6–18 mCi/kg), number of doses ranging from 1 to 7 [61, 77, 94, 99, 121]. Typically, activities above 444 MBq/kg (12 mCi/kg) require preharvesting of stem cells because of marked hematologic toxicity. Other groups have based dosing on a delivered whole-body radiation dose, where the goal is to deliver 1–4 Gy to the whole body based on a dosimetric study or on an initial ^{131}I-MIBG therapy study [62, 81, 107]. Using these strategies, whole-body doses of 2 Gy can be administered without bone marrow support. Typically, the large myeloablative strategies utilize high doses, delivering 666 MBq/kg (∼18 mCi/kg) [124] or large whole-body radiation doses, >4 Gy [21, 62]. A high-dose study that allowed up to 8 Gy fractionated marrow dose recommended a maximum cumulative activity of 1.33 GBq/kg (36 mCi/kg) [123]. In addition, some have utilized a combination of strategies coupled to the concomitant administration of chemotherapy (Table 7).

Response criteria have been developed for the objective assessment in patients with neuroblastoma [19]. Most ^{131}I-MIBG trials have selected patients with advanced disease that have failed first-line therapy, while others have incorporated ^{131}I-MIBG into a multiprong dosing strategy (Tables 6 and 7). Initial trials were focused on feasibility and toxicity and represented single center, poorly controlled trials [61, 81, 184, 186]. Nonetheless, these trials demonstrated that repeated administrations of ^{131}I-MIBG could be given safely in patients with advanced disease who had failed conventional therapy. Overall, evidence of objective response was often observed (Table 6) with several trials reporting partial responses of up to ∼40% in patients who had failed other treatments. The incidence of objective complete response was usually much lower and seldom over 10%. In Tables 6 and 7, objective response rates are utilized although it is recognized that symptomatic or biochemical improvements are also important outcome measures [61, 94, 110, 184, 187]. Because many of these trials were not prospective, reporting criteria in terms of outcome were variable, and the parameters measured in terms of duration of response are inconsistent and include survival, overall response, and event-free survival (EFS).

Early studies such as those of Garaventa et al. reported their experience in patients with stage 3 or 4 neuroblastoma who had not achieved a complete response following conventional therapy. These patients received 1–5 treatments of 2.52–5.51 GBq (68–149 mCi) ^{131}I-MIBG and

had a 30% objective response rate with 2% achieving a CR. The 5-year EFS was 40% for stage 4 and 92% for stage 3 [61]. In a retrospective review, Kang et al. treated 20 patients, the majority of whom had residual or recurrent disease, with submyeloablative doses (median single activity of ^{131}I-MIBG 351 MBq/kg (9.5 mCi/kg) and cumulative activities of 1.02–1.13 GBq/kg, or 27.6–30.5 mCi/kg) [94]. These patients experienced a 31% objective partial response rate and effective symptomatic relief.

A formal phase I study was reported by Matthay et al. in patients with stage 3–4 relapsed neuroblastoma receiving escalating activities of 111–666 MBq/kg (3–18 mCi/kg) [121]. In patients receiving >444 MBq/kg (>12 mCi/kg), stem cells were harvested because of the significant bone marrow toxicity that was expected. Dose-limiting toxicity requiring stem cell transplant was observed in patients receiving 555 and 666 MBq/kg (15–18 mCi/kg). After transplant, a significant proportion of the patients did not achieve platelet independence before death (49–150 days posttransplant), although neutrophils recovered. Thirty-seven percent of patients had objective responses, 3% achieved CR, and median survival for all patients was 6 months.

In a phase I trial, Lashford et al. treated patients with advanced chemoresistant neuroblastoma using escalating whole-body doses of 1, 2, or 2.5 Gy based on a diagnostic scan [107]. Overall, the activity ranged from 2.37 to 12.1 GBq (64–327 mCi) with activities >5.29–9.18 GBq (143–248 mCi) required to deliver 2.5 Gy to the whole body. In this study, 56% of the measured post-therapy whole-body doses were a median of 10% lower than the prescribed dose. Whole-body doses of 1 Gy were well tolerated. However, 31% of patients receiving 2 Gy developed grade 3 or 4 thrombocytopenia, and at 2.5 Gy, 80% developed grade 3 or 4 thrombocytopenia and 40% developed grade 3 or 4 neutropenia. A 33% objective response was seen, similar to the range of results seen by Matthay et al. [124].

While most studies have administered more than one therapeutic dose of ^{131}I-MIBG (Table 6), there have been several studies using a single administration [79, 107, 121, 124]. The response rates reported in these trials are in the range of 25–46% (Table 6). Although single large amounts of ^{131}I-MIBG may target sites of disease well, this does not guarantee response to treatment (Fig. 2). Several studies have also repeated large doses of ^{131}I-MIBG. Howard et al. delivered high-cumulative doses of ^{131}I-MIBG by administering a median of 1.325 GBq/kg (35.8 mCi/kg). This was delivered in a median of two sessions (range 1–4) [82]. These treatments resulted in a response rate of ~40% with median overall survival of 12 months. Matthay et al. used two sequential administrations of ^{131}I-MIBG totaling 0.81–1.89 GBq/kg (22–51 mCi/kg) delivered over 14 days, with a response rate of 10% and overall survival of 48% at 18 months [123]. A compassionate use report in 53 subjects with relapsed neuroblastoma administered tandem doses of 18 mCi/kg to 41 patients with the second dose administered at 6 weeks (within 100 days). In these patients, stem cell support was available. Response rates are shown in Table 6 [91]. In these patients, 30% response rate was seen to initial treatment with a further 29% response on repeat treatment. While one report suggests that the greatest benefit occurs after the first of multiple treatments [82], this has not been adequately studied. A report using ^{131}I-MIBG in conjunction with chemotherapy concluded that two administrations were optimal, whereas reports in patients with pheochromocytoma have indicated that it may take more than one treatment before objective responses are noted.

Most studies have used ^{131}I-MIBG therapy in the setting of resistant or recurrent disease at the time of relapse or in conjunction with chemotherapy regimens. One group used it as first-line therapy with intent to obtain better results at time of tumor surgery with less toxicity than that of conventional approaches. Hoefnagel et al. treated 31 patients with stages 3 and 4 disease with an initial activity of 7.4 GBq (200 mCi) followed by 2–6 treatments with 3.7 GBq (100 mCi) treatments [75]. This regimen was well tolerated and resulted in an overall 71% response rate in primary tumors and 81% in metastatic lesions. Initial ^{131}I-MIBG resulted in successful surgical resection of >95% of tumor in 70% of the patients. Furthermore, they observed a greater than 50% drop in

catecholamines in 70% of patients. The same group reported on their expanded experience in 41 patients treated with frontline ^{131}I-MIBG using the same regimen of 7.4 GBq (200 mCi) followed by 3.7 GBq (100 mCi) every 4 weeks, with cumulative total doses of 12.95–35.15 GBq (350–950 mCi). In this study, an objective partial response rate of 63% was observed along with a 2% complete response rate [41]. Their conclusion was that the optimal response appeared to occur after two treatments. This was part of a planned therapy regimen that was to be followed by surgery and chemotherapy, and the overall response rate after surgery was 73%.

A retrospective study focused on patients with stage 1–3 with localized inoperable disease causing compromised organ dysfunction or respiratory effects [163]. These patients received a regimen previously described by the group consisting of a fixed dose of 5.5–7.4 GBq (200 or 150 mCi) followed by a second dose of 3.7–5.5 GBq (150 or 100 mCi), with adjustments based on weight. That study concluded that ^{131}I-MIBG therapy is an effective treatment modality for unresectable localized neuroblastoma causing or in danger of causing organ or respiratory dysfunction and offers a good alternative to chemotherapy if urgent treatment is needed. Toxicity was mainly hematologic and mostly well tolerated.

There is some data to suggest that older patients with NB have improved response rates compared to younger patients [55, 96]. Neuroblastoma is predominantly seen in young children. In a retrospective study a total of 39 patients were treated with median large cumulative doses of 720 mCi (17.8 mCi/kg) ^{131}I-MIBG for those 10–17 years old and 857 mCi (16.9 mCi/kg) for those $\geq$18 years old. The overall response rate was 39% for those 10–17 years old and 56% for those $\geq$18 years old. Overall survival rates at 3 years were 32.8% and 43.2%, respectively.

In a retrospective analysis of 218 patients, 72 had refractory disease and 146 patients had relapsed disease. These patients were then treated with 6.3–20.9 mCi/kg ^{131}I-MIBG. Less favorable outcomes were seen in patients with relapsed disease, with 24% of relapsed patients having progressive disease compared to only 9% of refractory patients, and 39% of relapsed patients had stable disease compared to 59% of refractory patients. Among all patients, the 24-month OS was 47.0%. The 24-month OS for refractory patients was significantly higher at 65.3%, compared to 38.7% for relapsed patients ($p < 0.001$) [211].

Sixteen patients with high-risk neuroblastoma were treated with two upfront courses of ^{131}I-MIBG combined with topotecan. An overall response rate of 57% was noted with a response in 94% of primary tumors but only 34% of bone marrow disease. Further treatment with induction chemotherapy, surgery, or ASCT resulted in additional responses [103].

Because of the response rate to ^{131}I-MIBG as a single agent in relapsed or refractory neuroblastoma, several investigators have used ^{131}I-MIBG prior to chemotherapy, attempting to improve the remission status prior to myeloablative chemotherapy and ASCT. In one such study, eight refractory NB patients were administered ^{131}I-MIBG treatment at doses of 16–19 mCi/kg i.v. followed by autologous stem cell transplant approximately 2 weeks later. Some patients received local radiation to primary tumors and/or residual sites of disease. After 6–8 weeks, the patients received myeloablative treatment with busulfan and mephalan followed by ASCT [56]. Seven of the eight patients were alive 10 months after ASCT, demonstrating that combined therapy was possible and engraftment was achieved. One patient died of sinusoidal obstructive syndrome at day 50. Two patients had PR and three had CR. Other investigators have aimed to combine ^{131}I-MIBG with arsenic, based on preclinical studies that have shown a radiosensitizing effect. A group of 19 recurrent or refractory NB patients were treated with ^{131}I-MIBG and arsenic. By international research criteria, 12 patients had no response while 7 had progressive disease (PD), including six out of eight who entered the study with PD. Objective improvements in semiquantitative MIBG scores were observed in six patients. Five-year overall survival for NB was 37 $\pm$ 11%. The adverse drug-related side effects were similar to those for ^{131}I-MIBG alone [129]. Overall, the addition of arsenic had no additional effect on toxicity.

Full courses of irinotecan and vincristine have been administered with high-dose ^{131}I-MIBG with stem cell transplant in the setting of a dose escalation phase I [42]. Significant responses were observed in 26% when a combination of MIBG, CT, and bone marrow was used for assessment. Furthermore, responses were seen in 43% of seven patients receiving more than one therapy cycle.

Other pharmaceuticals that may enhance the therapeutic effect of ^{131}I-MIBG have been combined, taking advantage of potentially synergistic mechanisms and pathways. Vorinostat, a histone deacetylase inhibitor and radiosensitizer [136], also increases density of norepinephrine receptors [134]. Based on these preclinical studies, ^{131}I-MIBG has been combined with vorinostat in a dose escalation trial. This combination resulted in an overall 12% response rate and 17% response rate at the highest dose level [43].

There is no consensus on how to best incorporate ^{131}I-MIBG in the treatment of high-risk patients. It is clear that ^{131}I-MIBG has efficacy in advanced neuroblastoma, but research continues as to how best to incorporate its use as part of a multimodal approach to therapy, taking advantage of synergies of mechanism of actions and to some extent non-overlapping toxicities. There is also ongoing work using improved reagents with ^{131}I-MIBG at high specific activity [36] and work using ^{211}At-MIBG [188]. Furthermore, future imaging may be used to select candidates that may benefit from the combination of ^{131}I-MIBG and peptide receptor radionuclide therapy such as ^{177}Lu-/^{90}Y-labeled somatostatin analogs [25].

Toxicity

The most significant toxicity associated with ^{131}I-MIBG therapy in both children and adults is hematologic. There is a larger drop in platelets than white blood cells, likely related to binding of MIBG to platelets [48]. These drops in counts are dependent on the administered activity and are minor when activities in the range of 7.4 GBq (200 mCi) are used [47], whereas doses >444 MBq/kg (12 mCi/kg) cause hematologic toxicity. Grade 3 or 4 thrombocytopenia is observed in 80–87% of patients, requiring platelet transfusion and/or growth factors [70, 91, 124]. After whole-body doses up to 2.5 Gy in children with neuroblastoma, grade 3 or 4 thrombocytopenia was seen in 80% [107]. The nadir in children has been reported to occur at approximately 28 days after a single administration (range 9–42) [107]. When chemotherapy is combined with ^{131}I-MIBG therapy, nadirs may occur earlier and are felt to be predominantly driven by the chemotherapy [120].

In patients with upfront ^{131}I-MIBG treatment receiving median activities of 441 MBq/kg as a first dose and a repeated median dose of 328 MBq/kg, the main toxicity was also hematologic with grade 4 thrombocytopenia in 1% of patients after first treatment and 3% after the second [12]. This is lower than that seen in patients with multiple prior treatments. Other predictors of increased marrow toxicity include whole-body or marrow absorbed dose, extensive marrow/bone involvement, and prior stem cell transplantation [12, 44, 59, 169].

Children and adults treated with activity ≥444–666 MBq/kg (12–18 mCi/kg) may require bone marrow transplant because of significant and prolonged marrow toxicity [44, 91]. Howard et al. reported thrombocytopenia requiring platelet transfusion in 78% and 82% of patients after the first and second infusion, respectively, while only 50% had grade 4 neutropenia that was usually transient. Ten patients required stem cell transplant. Nonetheless, in this and other trials, there are patients who fail to engraft adequately at these high levels of activity [44, 82]. In this and other trials, stem cells are transplanted when severe neutropenia is present, requiring growth factors, or when the patient requires platelet transfusion more than 2 times a week [82, 124]. In other cases, stem cells are routinely transplanted at 21 days post high-dose ^{131}I-MIBG [206]. With tandem therapy of 18 mCi/kg, 85% of patients receiving two treatments required stem cell support, which typically was administered a median of 15 days after the second therapy dose [91]. Gaze et al. used dosimetry to deliver 4 Gy to the whole body

[62]. These doses often required transplant that was performed 14 days post last ^{131}I-MIBG treatment and when the estimated whole-body retention of ^{131}I was less than 0.8 mCi. In patients receiving ^{131}I-MIBG and myeloablative chemotherapy, the stem cells were infused 21 days after MIBG and 7 days after the chemotherapy [205]. At a mean activity of 381 mCi, Safford et al. reported that 12% of patients had enough hematopoietic depression to required hospitalization [158]. Because neutropenia is infrequent with low activity, the incidence of infections is low. As expected with higher activity that induces considerable neutropenia, significant infections are occasionally encountered [107, 124, 205]. In addition, when high-dose ^{131}I-MIBG is given with myeloablative chemotherapy, a high incidence of febrile neutropenia was observed in 70% of treated patients [206]. With tandem high-dose treatment, 29% of patients remained thrombocytopenic and transfusion dependent in spite of stem cell transplant. Toxicity was similar for adult patients, young adolescent receiving high-dose therapy compared to younger patients [151]. Combined chemotherapy and high-dose ^{131}I-MIBG results in hematotoxicity similar to when ^{131}I-MIBG is given alone, but other toxicities are new/more prominent when combined with chemotherapy; for example, when irinotecan, vincristine, and MIBG therapy were combined, diarrhea was frequently seen [42].

Myelodysplasia (MDS)/acute myelocytic leukemia have been reported in patients who have received both chemotherapy and large amounts of ^{131}I-MIBG. In adult PHEO patients, a ~4% incidence was reported with high-dose therapy [42, 70]. MDS has also been reported after therapy in patients with medullary thyroid carcinoma and carcinoid tumors [29]. MDS in children receiving ^{131}I-MIBG is also reported [59, 79]. The timeline for MDS after ^{131}I-MIBG is typically >2 years [28, 70]. The UCSF group reviewed their experience in 95 patients with neuroblastoma as well as a review of the literature. In their patients, the cumulative incidence of MDS was 3.9% at 60-month post-therapy [201]. A further review of the literature only yielded three additional patients out of 500 treated with ^{131}I-MIBG. The authors felt that alkylating chemotherapy agents played a significant role. Garaventa et al. reviewed 119 patients treated with a mean of two therapy regimens using activity estimated at ~240 MBq/kg (6.5 mCi/kg) where whole-body doses were usually less than 200 cGy. At follow-up, 78 patients had died and five secondary malignancies were reported at a median of 3 years (1–15 years) including acute monolymphoblastic leukemia, chronic myelomonocytic leukemia, angiomatoid malignant fibrous histiocytoma, malignant schwannoma, and rhabdomyosarcoma [60]. This occurrence of secondary malignancy and bone marrow disorders indicates that these patients require close follow-up, especially in patients with prolonged survival.

The thyroid is routinely protected with iodine-containing solutions (see above). Nonetheless, hypothyroidism has been reported. The incidence of hypothyroidism has ranged from 11% to 32% [41, 61, 164, 166, 205]. One investigator reported that 48% of treated patients developed hypothyroidism [59]. In children receiving high-dose ^{131}I-MIBG (~18 mCi/kg), there was a high baseline incidence of elevated TSH in 24% of patients [153]. In the latter report, the 2-year cumulative incidence rates of hypothyroidism was 35 ± 14% in those with baseline thyroid dysfunction and 10 +/± 5% in those without baseline abnormal thyroid function, possibly attributed to the KI and potassium perchlorate regimen. In patients with neuroblastoma, the incidence of non-visualization of the thyroid in post-therapy images ranges from 52% to 59% [35, 153]. In adults, the incidence of hypothyroidism is lower [150, 190]. There have also been reports of thyroid cancer attributed to ^{131}I-MIBG [191].

Common systemic/constitutional toxicity associated with large doses of radiation from ^{131}I-MIBG is often observed (6–67% of patients) including asthenia, nausea, and vomiting. Nausea and/or vomiting may start as early as 8–12 h and last a week; this appears to be more frequent in patients with larger liver metastatic burdens [64, 104, 109, 158, 164]. While some have reported a low incidence [47, 61, 109, 158], other have encountered it more frequently, sometimes in >40% of the patients [12, 164]. In our institution, ondansetron

is administered prophylactically starting immediately before treatment and continued for several days. This regimen minimizes the incidence of nausea and vomiting due to therapy. Salivary gland tenderness and short-term dysfunction have been reported [128].

Although ^{131}I-MIBG localizes in normal organs such as the heart, lung, liver, and adrenal, there have been very limited complications related to cardiac, renal, liver, or adrenal insufficiency. Pulmonary toxicity is most frequently related to infectious disorders. Nonetheless, infrequent reports of ARDS, bronchiolitis obliterans, and other serious pulmonary disorders have been described [12, 70, 82, 126]. Mild changes in liver function have been encountered [41, 137, 150], but severe hepatic dysfunction is rare [13, 16, 107]. Sinusoidal obstructive syndrome has been reported when ^{131}I-MIBG is combined with chemotherapy, that was though to be mainly related to the chemotherapy component [206]. In children receiving a median dose of 18.2 mCi/kg ^{131}I-MIBG, there were 20 patients who developed grade 3 or 4 liver toxicity, although there suggestion of causality with ^{131}I MIBG in only eight cases [153]. Changes in glomerular filtration rate have been documented, but the induction of renal failure is unlikely [41]. Drops in hormone levels such as corticosteroids and testosterone have been reported, as well as primary ovarian failure [34, 195].

Hypertension can occur and cases of hypertensive crises have been reported in PHEO patients [72, 154]. Hypertension can also occur following administration of ^{131}I-MIBG therapy in patients with neuroblastoma [102, 111]. Hypertension was reported in 5% of 50 patients receiving 110 infusions of ^{131}I-MIBG, more commonly in those with pre-existing hypertension, including hypertensive crises with seizure [102]. In this report, a $>$15 mm Hg rise was seen in 12% of the patients. Most adverse hypertensive events occur between 20 and 25 h post-administration [12, 102, 203]. Risk factors for a hypertensive response not only include pre-existing hypertension but also younger age and eGFR prior to treatment [203]. When therapy is administered, antihypertensive medication should be available, particularly in patients with PHEO [54], and observation over 48 h has been suggested. In 218 administrations of ^{131}I-MIBG, the administration of antihypertensive medication (nifedipine) was only required in 2.8% of patients [203].

Summary

Therapeutic ^{131}I-MIBG is safe and well tolerated in both children and adults with few side effects, when used in low-to-moderate doses in patients with PHEO/PARA, carcinoid, and neuroblastoma. Myeloablative doses are associated with more toxicity but are still relatively well tolerated. The role of ^{131}I-MIBG has been best characterized in patients with PHEO/PARA where symptomatic and biochemical improvements are frequently observed. In patients with carcinoid, studies have also shown that, in selected patients, good palliative results can be obtained. In both carcinoid and PHEO/PARA, objective partial responses are often seen and can be long lasting. In neuroblastoma, good responses, albeit often temporary, have also been obtained with ^{131}I-MIBG. In neuroblastoma, most studies have been used with therapeutic rather than palliative intent. It is clear that new, combined approaches must be developed if ^{131}I-MIBG is to find more general use and to have greater impact on quality of life or survival in neuroblastoma, PHEO/PARA, and carcinoid.

References

1. Amar L, Bertherat J, et al. Genetic testing in pheochromocytoma or functional paraganglioma. J Clin Oncol. 2005;23(34):8812–8.
2. Arnold R, Trautmann ME, et al. Somatostatin analogue octreotide and inhibition of tumour growth in metastatic endocrine gastroenteropancreatic tumours. Gut. 1996;38(3):430–8.
3. Astuti D, Latif F, et al. Gene mutations in the succinate dehydrogenase subunit SDHB cause susceptibility to familial pheochromocytoma and to familial paraganglioma. Am J Hum Genet. 2001;69(1):49–54.
4. Averbuch SD, Steakley CS, et al. Malignant pheochromocytoma: effective treatment with a combination of cyclophosphamide, vincristine, and dacarbazine. Ann Intern Med. 1988;109(4):267–73.
5. Babich JW, Graham W, et al. Effect of adrenergic receptor ligands on metaiodobenzylguanidine uptake

and storage in neuroblastoma cells. Eur J Nucl Med. 1997;24(5):538–43.
6. Barrett JA, Joyal JL, et al. Comparison of high-specific-activity ultratrace $^{123/131}$I-MIBG and carrier-added $^{123/131}$I-MIBG on efficacy, pharmacokinetics, and tissue distribution. Cancer Biother Radiopharm. 2010;25(3):299–308.
7. Bausch B, Borozdin W, et al. Clinical and genetic characteristics of patients with neurofibromatosis type 1 and pheochromocytoma. N Engl J Med. 2006; 354(25):2729–31.
8. Baysal BE, Willett-Brozick JE, et al. Prevalence of SDHB, SDHC, and SDHD germline mutations in clinic patients with head and neck paragangliomas. J Med Genet. 2002;39(3):178–83.
9. Beard CM, Carney JA, et al. Incidence of pheochromocytoma. J Hum Hypertens. 1989;3(6):481.
10. Bestagno M, Pizzocaro C, et al. Results of [^{131}I]meta-iodobenzylguanidine treatment in metastatic carcinoid. J Nucl Biol Med. 1991;35(4):343–5.
11. Blake GM, Lewington VJ, et al. Modification by nifedipine of I-131-meta-iodobenzylguanidine kinetics in malignant pheochromocytoma. Eur J Nucl Med. 1988;14(7–8):345–8.
12. Bleeker G, Schoot RA, et al. Toxicity of upfront ^{131}I-metaiodobenzylguanidine (^{131}I-MIBG) therapy in newly diagnosed neuroblastoma patients: a retrospective analysis. Eur J Nucl Med Mol Imaging. 2013;40 (11):1711–7.
13. Bomanji J, Britton KE, et al. Treatment of malignant pheochromocytoma, paraganglioma and carcinoid-tumors with ^{131}I-metaiodobenzylguanidine. Nucl Med Commun. 1993;14(10):856–61.
14. Bomanji JB, Wong W, et al. Treatment of neuroendocrine tumours in adults with ^{131}I-MIBG therapy. Clin Oncol. 2003;15(4):193–8.
15. Bombardieri E, Aktolun C, et al. ^{131}I/^{123}I-metaiodobenzylguanidine (MIBG) scintigraphy: procedure guidelines for tumour imaging. Eur J Nucl Med Mol Imaging. 2003;30(12):BP132–9.
16. Bongers V, deKlerk JMH, et al. Acute liver necrosis induced by iodine-131-MIBG in the treatment of metastatic carcinoid tumors. J Nucl Med. 1997;38(7): 1024–6.
17. Brans B, Monsieurs M, et al. Thyroidal uptake and radiation dose after repetitive I-131-MIBG treatments: influence of potassium iodide for thyroid blocking. Med Pediatr Oncol. 2002;38(1):41–6.
18. Bravo EL. Evolving concepts in the pathophysiology, diagnosis, and treatment of pheochromocytoma. Endocr Rev. 1994;15(3):356–68.
19. Brodeur GM, Pritchard J, et al. Revisions of the international criteria for neuroblastoma diagnosis, staging, and response to treatment. J Clin Oncol. 1993;11(8): 1466–77.
20. Brogsitter C, Pinkert J, et al. Enhanced tumor uptake in neuroendocrine tumors after intraarterial application of ^{131}I-MIBG. J Nucl Med. 2005;46(12):2112–6.
21. Buckley SE, Saran FH, et al. Dosimetry for fractionated ^{131}I-mIBG therapies in patients with primary resistant high-risk neuroblastoma: preliminary results. Cancer Biother Radiopharm. 2007;22(1): 105–12.
22. Burnichon N, Vescovo L, et al. Integrative genomic analysis reveals somatic mutations in pheochromocytoma and paraganglioma. Hum Mol Genet. 2011; 20(20):3974–85.
23. Buscombe JR, Cwikla JB, et al. Long-term efficacy of low activity meta-[I-131]iodobenzylguanidine therapy in patients with disseminated neuroendocrine turmours depends on initial response. Nucl Med Commun. 2005;26(11):969–76.
24. Bushnell Jr DL, O'Dorisio TM, et al. ^{90}Y-edotreotide for metastatic carcinoid refractory to octreotide. J Clin Oncol. 2010;28(10):1652–9.
25. Bushnell DL, Madsen MT, et al. Feasibility and advantage of adding ^{131}I-MIBG to ^{90}Y-DOTATOC for treatment of patients with advanced stage neuroendocrine tumors. EJNMMI Res. 2014;4(1):38. doi: 10.1186/s13550-014-0038-2.
26. Carrasquillo JA, Chen CC. Molecular Imaging of Neuroendocrine Tumors. Semin Oncol. 2010;37(6): 662–79.
27. Castellani MR, Chiti A, et al. Role of ^{131}I-metaiodobenzylguanidine (MIBG) in the treatment of neuroendocrine tumours – Experience of the National Cancer Institute of Milan. Q J Nucl Med. 2000;44(1): 77–87.
28. Castellani MR, Seghezzi S, et al. ^{131}I-MIBG treatment of pheochromocytoma: low versus intermediate activity regimens of therapy. Q J Nucl Med Mol Imaging. 2010;54(1):100–13.
29. Castellani MR, Seregni E, et al. MIBG for diagnosis and therapy of medullary thyroid carcinoma: is there still a role? Q J Nucl Med Mol Imaging. 2008;52(4): 430–40.
30. Chen H, Sippel RS, et al. The North American Neuroendocrine Tumor Society consensus guideline for the diagnosis and management of neuroendocrine tumors pheochromocytoma, paraganglioma, and medullary thyroid cancer. Pancreas. 2010;39(6):775–83.
31. Chrisoulidou A, Kaltsas G, et al. The diagnosis and management of malignant phaeochromocytoma and paraganglioma. Endocr Relat Cancer. 2007;14(3): 569–85.
32. Chu BP, Horan C, et al. Feasibility of administering high-dose ^{131}I-MIBG therapy to children with high-risk neuroblastoma without lead-lined rooms. Pediatr Blood Cancer. 2016;63(5):801–7.
33. Clarke MR, Weyant RJ, et al. Prognostic markers in pheochromocytoma. Hum Pathol. 1998;29(5):522–6.
34. Clement SC, Kraal K, et al. Primary ovarian insufficiency in children after treatment with ^{131}I-metaiodobenzylguanidine for neuroblastoma: report of the first two cases. J Clin Endocrinol Metab. 2014; 99(1):E112–6.

35. Clement SC, van Eck-Smit BLF, et al. Long-term follow-up of the thyroid gland after treatment with ^{131}I-metaiodobenzylguanidine in children with neuroblastoma: importance of continuous surveillance. Pediatr Blood Cancer. 2013;60(11):1833–8.
36. Coleman RE, Stubbs JB, et al. Radiation dosimetry, pharmacokinetics, and safety of ultratrace (TM) iobenguane I-131 in patients with malignant pheochromocytoma/paraganglioma or metastatic carcinoid. Cancer Biother Radiopharm. 2009;24(4): 469–75.
37. Colombo L, Lomuscio G, et al. Preliminary results of [^{131}I]metaiodobenzylguanidine treatment in metastatic malignant pheochromocytoma. J Nucl Biol Med. 1991;35(4):300–4.
38. Corbett R, Pinkerton R, et al. [^{131}I]metaiodobenzylguanidine and high-dose chemotherapy with bone marrow rescue in advanced neuroblastoma. J Nucl Biol Med. 1991;35(4):228–31.
39. Dahia PLM. Pheochromocytoma and paraganglioma pathogenesis: learning from genetic heterogeneity. Nat Rev Cancer. 2014;14(2):108–19.
40. De Kraker J, Hoefnagel CA, et al. First line targeted radiotherapy, a new concept in the treatment of advanced stage neuroblastoma. Eur J Cancer. 1995;31A(4):600–2.
41. de Kraker J, Hoefnagel KA, et al. Iodine-131-metaiodobenzylguanidine as initial induction therapy in stage 4 neuroblastoma patients over 1 year of age. Eur J Cancer. 2008;44(4):551–6.
42. DuBois SG, Chesler L, et al. Phase I study of vincristine, irinotecan, and ^{131}I-metaiodobenzylguanidine for patients with relapsed or refractory neuroblastoma: a new approaches to neuroblastoma therapy trial. Clin Cancer Res. 2012;18(9):2679–86.
43. DuBois SG, Groshen S, et al. Phase I study of vorinostat as a radiation sensitizer with ^{131}I-metaiodobenzylguanidine (^{131}I-MIBG) for patients with relapsed or refractory neuroblastoma. Clin Cancer Res. 2015;21(12):2715–21.
44. DuBois SG, Messina J, et al. Hematologic toxicity of high-dose iodine-131-metaiodobenzylguanidine therapy for advanced neuroblastoma. J Clin Oncol. 2004;22(12):2452–60.
45. Ehninger G, Klingebiel T, et al. Stability and pharmacokinetics of m-[^{131}I]iodobenzylguanidine in patients. Cancer Res. 1987;47(22):6147–9.
46. Elder EE, Elder G, et al. Pheochromocytoma and functional paraganglioma syndrome: no longer the 10% tumor. J Surg Oncol. 2005;89(3):193–201.
47. Ezziddin S, Sabet A, et al. Long-term outcome and toxicity after dose-intensified treatment with ^{131}I-MIBG for advanced metastatic carcinoid tumors. J Nucl Med. 2013;54(12):2032–8.
48. Feldman JM, Frankel N, et al. Platelet uptake of the pheochromocytoma-scanning agent ^{131}I-metaiodobenzylguanadine. Metabolism. 1984;33(5): 397–9.
49. Fernandezcalvet L, Garciamayor RVG. Incidence of pheochromocytoma in South Galicia, Spain. J Intern Med. 1994;236(6):675–7.
50. Fielding SL, Flower MA, et al. Dosimetry of iodine-131 metaiodobenzylguanidine for treatment of resistant neuroblastoma – results of a UK study. Eur J Nucl Med. 1991;18(5):308–16.
51. Fielding SL, Flower MA, et al. The treatment of resistant neuroblastoma with ^{131}I-mIBG – alternative methods of dose prescription. Radiother Oncol. 1992;25(1):73–6.
52. Fischer M. Therapy of pheochromocytoma with [^{131}I] metaiodobenzylguanidine. J Nucl Biol Med. 1991; 35(4):292–4.
53. Fischer M, Kamanabroo D, et al. Scintigraphic imaging of carcinoid-tumors with ^{131}I-metaiodobenzylguanidine. Lancet. 1984;2(8395):165.
54. Fitzgerald PA, Goldsby RE, et al. Malignant pheochromocytomas and paragangliomas: a phase II study of therapy with high-dose ^{131}I-metaiodobenzylguanidine (^{131}I-MIBG). Ann N Y Acad Sci. 2006;1073:465–90.
55. Franks LM, Bollen A, et al. Neuroblastoma in adults and adolescents – an indolent course with poor survival. Cancer. 1997;79(10):2028–35.
56. French S, DuBois SG, et al. ^{131}I-MIBG followed by consolidation with busulfan, melphalan and autologous stem cell transplantation for refractory neuroblastoma. Pediatr Blood Cancer. 2013;60(5):879–84.
57. Furuta N, Kiyota H, et al. Diagnosis of pheochromocytoma using [^{123}I]-compared with [^{131}I]-metaiodobenzylguanidine scintigraphy. Int J Urol. 1999;6 (3):119–24.
58. Gains JE, Walker C, et al. Radiation exposure to comforters and carers during paediatric molecular radiotherapy. Pediatr Blood Cancer. 2015;62(2):235–9.
59. Garaventa A, Bellagamba O, et al. ^{131}I-metaiodobenzylguanidine (^{131}I-MIBG) therapy for residual neuroblastoma: a mono-institutional experience with 43 patients. Br J Cancer. 1999;81(8):1378–84.
60. Garaventa A, Gambini C, et al. Second malignancies in children with neuroblastoma after combined treatment with ^{131}I-metaiodobenzylguanidine. Cancer. 2003;97(5):1332–8.
61. Garaventa A, Guerra P, et al. Treatment of advanced neuroblastoma with ^{131}I-meta-iodobenzylguanidine. Cancer. 1991;67(4):922–8.
62. Gaze MN, Chang YC, et al. Feasibility of dosimetry-based high-dose ^{131}I-meta-iodobenzylguanidine with topotecan as a radiosensitizer in children with metastatic neuroblastoma. Cancer Biother Radiopharm. 2005;20(2):195–9.
63. Gaze MN, Wheldon TE, et al. Multimodality megatherapy with [^{131}I]metaiodobenzylguanidine, high-dose melphalan and total-body irradiation with bone-marrow rescue – feasibility study of a new strategy for advanced neuroblastoma. Eur J Cancer. 1995;31A(2):252–6.
64. Gedik GK, Hoefnagel CA, et al. ^{131}I-MIBG Therapy in metastatic phaeochromocytoma and

paraganglioma. Eur J Nucl Med Mol Imaging. 2008; 35(4):725–33.
65. Giammarile F, Chiti A, et al. EANM procedure guidelines for ^{131}I-meta-iodobenzylguanidine (^{131}I-mIBG) therapy. Eur J Nucl Med Mol Imaging. 2008;35(5): 1039–47.
66. Gimenez-Roqueplo AP, Favier J, et al. Mutations in the SDHB gene are associated with extra-adrenal and/or malignant phaeochromocytomas. Cancer Res. 2003;63(17):5615–21.
67. Godwin JD. Carcinoid tumors – analysis of 2837 cases. Cancer. 1975;36(2):560–9.
68. Goldsby RE, Fitzgerald PA. Meta I-131 iodobenzylguanidine therapy for patients with metastatic and unresectable pheochromocytoma and paraganglioma. Nucl Med Biol. 2008;35:S49–62.
69. Goncalves E, Ninane J, et al. Familial pheochromocytoma – successful treatment with ^{131}I-MIBG. Med Pediatr Oncol. 1990;18(2):126–30.
70. Gonias S, Goldsby R, et al. Phase II study of high-dose ^{131}I-metaiodobenzylguanidine therapy for patients with metastatic pheochromocytoma and paraganglioma. J Clin Oncol. 2009;27(25):4162–8.
71. Goodman M, Gurney J, et al. Sympathetic nervous system tumors. Cancer incidence and survival among children and adolescents: United States SEER Program 1975–1995, National Cancer Institute, SEER Program. R. LAG, S. MA and G. JG. Bethesda, NIH Pub. No. 99-4649. Bethesda, 1999. p. 65–72.
72. Hartley A, Spooner D, et al. Management of malignant phaeochromocytoma: a retrospective review of the use of MIBG and chemotherapy in the West Midlands. Clin Oncol. 2001;13(5):361–6.
73. Hartung-Knemeyer V, Rosenbaum-Krumme S, et al. Malignant pheochromocytoma imaging with ^{124}I-mIBG PET/MR. J Clin Endocrinol Metab. 2012; 97(11):3833–4.
74. Hoefnagel CA. Metaiodobenzylguanidine and somatostatin in oncology – role in the management of neural crest tumors. Eur J Nucl Med. 1994;21(6): 561–81.
75. Hoefnagel CA, De Kraker J, et al. ^{131}I-MIBG as a first-line treatment in high-risk neuroblastoma patients. Nucl Med Commun. 1994;15(9):712–7.
76. Hoefnagel CA, Schornagel J, et al. [^{131}I]Meta-iodobenzylguanidine therapy of malignant pheochromocytoma: interference of medication. J Nucl Biol Med. 1991;35(4):308–12.
77. Hoefnagel CA, Jager FCAD, et al. The role of I-131-MIBG in the diagnosis and therapy of carcinoids. Eur J Nucl Med. 1987;13(4):187–91.
78. Hoefnagel CA, Jager FCAD, et al. Diagnosis and treatment of a carcinoid-tumor using iodine-131 metaiodobenzylguanidine. Clin Nucl Med. 1986;11 (3):150–2.
79. Hoefnagel CA, Voute PA, et al. [^{131}I]meta-iodobenzylguanidine therapy after conventional therapy for neuroblastoma. J Nucl Biol Med. 1991;35(4): 202–6.
80. Hoefnagel CA, Voute PA, et al. Radionuclide diagnosis and therapy of neural crest tumors using I-131 metaiodobenzylguanidine. J Nucl Med. 1987;28(3): 308–14.
81. Hor G, Maul FD, et al. Outcome of [^{131}I]meta-iodobenzylguanidine therapy of neuroblastoma: seven years after. J Nucl Biol Med. 1991;35(4):207–15.
82. Howard JP, Maris JM, et al. Tumor response and toxicity with multiple infusions of high dose ^{131}I-MIBG for refractory neuroblastoma. Pediatr Blood Cancer. 2005;44(3):232–9.
83. Huang H, Abraham J, et al. Treatment of malignant pheochromocytoma/paraganglioma with cyclophosphamide, vincristine, and dacarbazine recommendation from a 22-year follow-up of 18 patients. Cancer. 2008;113(8):2020–8.
84. Huang SY, Bolch WE, et al. Patient-specific dosimetry using pretherapy [^{124}I-]m-iodobenzylguanidine ([^{124}I]mIBG) dynamic PET/CT imaging before [^{131}I] mIBG targeted radionuclide therapy for neuroblastoma. Mol Imaging Biol. 2015;17(2):284–94.
85. Hutchinson RJ, Sisson JC, et al. 131-I-meta-iodobenzylguanidine treatment in patients with refractory advanced neuroblastoma. Am J Clin Oncol Canc Clin Trials. 1992;15(3):226–32.
86. Jacobson AF, Deng HW, et al. ^{123}I-meta-iodobenzylguanidine scintigraphy for the detection of neuroblastoma and pheochromocytoma: results of a meta-analysis. J Clin Endocrinol Metab. 2010;95(6): 2596–606.
87. Jacobson AF, Travin MI. Impact of medications on MIBG uptake, with specific attention to the heart: comprehensive review of the literature. J Nucl Cardiol. 2015;22(5):980–93.
88. Jacobsson L, Mattsson S, et al. Biokinetics and dosimetry of ^{131}I-metaiodobenzylguanidine (MIBG) Fourth International Radiopharmaceutical Dosimetry Symposium, Oakridge; 1992.
89. James O, Coleman RE. Radioiodinated MIBG in paraganglioma and pheochromocytoma: previous results and early experiences using no-carrier-added MIBG. Nucl Med Biol. 2008;35:S63–76.
90. John H, Ziegler WH, et al. Pheochromocytomas: can malignant potential be predicted? Urology. 1999; 53(4):679–83.
91. Johnson K, McGlynn B, et al. Safety and efficacy of tandem ^{131}I-metaiodobenzylguanidine infusions in relapsed/refractory neuroblastoma. Pediatr Blood Cancer. 2011;57(7):1124–9.
92. Kaltsas GA, Mukherjee JJ, et al. Treatment of metastatic pheochromocytoma and paraganglioma with ^{131}I-meta-iodobenzylguanidine (MIBG). Endocrinologist. 2003;13(4):321–33.
93. Kaltsas GA, Mukherjee JJ, et al. The value of radiolabelled MIBG and octreotide in the diagnosis and management of neuroendocrine tumours. Ann Oncol. 2001;12:S47–50.
94. Kang TI, Brophy P, et al. Targeted radiotherapy with submyeloablative doses of ^{131}I-MIBG is effective for

disease palliation in highly refractory neuroblastoma. J Pediatr Hematol Oncol. 2003;25(10):769–73.
95. Kasperlik-Zaluska AA, Roslonowska E, et al. 1,111 Patients with adrenal incidentalomas observed at a single endocrinological center – incidence of chromaffin tumors. Ann N Y Acad Sci. 2006;1073:38–46.
96. Kaye JA, Warhol MJ, et al. Neuroblastoma in adults. Three case reports and a review of the literature. Cancer. 1986;58(5):1149–57.
97. Khafagi FA, Shapiro B, et al. Labetalol reduces iodine-131 MIBG uptake by pheochromocytoma and normal-tissues. J Nucl Med. 1989;30(4):481–9.
98. Klingebiel T, Bader P, et al. Treatment of neuroblastoma stage 4 with ^{131}I-meta-iodo-benzylguanidine, high-dose chemotherapy and immunotherapy. A pilot study. Eur J Cancer. 1998;34(9):1398–402.
99. Klingebiel T, Berthold F, et al. Metaiodobenzylguanidine (mIBG) in treatment of 47 patients with neuroblastoma: results of the German neuroblastoma trial. Med Pediatr Oncol. 1991;19(2):84–8.
100. Klingebiel T, Treuner J, et al. [^{131}I]-Meta-iodobenzylguanidine in the treatment of metastatic neuro-blastoma – clinical, pharmacological and dosimetric aspects. Cancer Chemother Pharmacol. 1989;25(2):143–8.
101. Kolby L, Bernhardt P, et al. Uptake of meta-iodobenzylguanidine in neuroendocrine tumours is mediated by vesicular monoamine transporters. Br J Cancer. 2003;89(7):1383–8.
102. Kosmin MA, Bomanji JB, et al. Hypertension complicating ^{131}I-meta-iodobenzylguanidine therapy for neuroblastoma. Eur J Nucl Med Mol Imaging. 2012;39(4):597–601.
103. Kraal K, Tytgat GAM, et al. Upfront treatment of high-risk neuroblastoma with a combination of ^{131}I-MIBG and topotecan. Pediatr Blood Cancer. 2015;62(11):1886–91.
104. Krempf M, Lumbroso J, et al. Use of m-[^{131}I] iodobenzylguanidine in the treatment of malignant pheochromocytoma. J Clin Endocrinol Metab. 1991;72(2):455–61.
105. Kvols LK, Turaga KK, et al. Role of interventional radiology in the treatment of patients with neuroendocrine metastases in the liver. J Natl Compr Cancer Netw. 2009;7(7):765–72.
106. Lashford LS, Hancock JP, et al. Metaiodobenzylguanidine (metaiodobenzylguanidine) uptake and storage in the human neuroblastoma cell-line SK-N-BE(2C). Int J Cancer. 1991;47(1):105–9.
107. Lashford LS, Lewis IJ, et al. Phase I/II study of iodine 131 metaiodobenzylguanidine in chemoresistant neuroblastoma – a United-Kingdom childrens cancer study-group investigation. J Clin Oncol. 1992;10(12):1889–96.
108. Lenders JWM, Pacak K, et al. Biochemical diagnosis of pheochromocytoma – which test is best? JAMA. 2002;287(11):1427–34.
109. Loh KC, Fitzgerald PA, et al. The treatment of malignant pheochromocytoma with iodine-131 metaiodobenzylguanidine (^{131}I-MIBG): a comprehensive review of 116 reported patients. J Endocrinol Invest. 1997;20(11):648–58.
110. Lumbroso J, Schlumberger M, et al. [^{131}I]meta-iodobenzylguanidine therapy in 20 patients with malignant pheochromocytoma. J Nucl Biol Med. 1991;35(4):288–91.
111. Madre C, Orbach D, et al. Hypertension in childhood cancer: a frequent complication of certain tumor sites. J Pediatr Hematol Oncol. 2006;28(10):659–64.
112. Mairs RJ, Cunningham SH, et al. No-carrier-added iodine-131-MIBG – evaluation of a therapeutic preparation. J Nucl Med. 1995;36(6):1088–95.
113. Mairs RJ, Gaze MN, et al. Carrier-free ^{131}I-meta-iodobenzylguanidine – comparison of production from meta-diazobenzylguanidine and from meta-trimethylsilylbenzylguanidine. Nucl Med Commun. 1994;15(4):268–74.
114. Mairs RJ, Russell J, et al. Enhanced tumor uptake and in-vitro radiotoxicity of no-carrier-added [^{131}I] metaiodobenzylguanidine – implications for the targeted radiotherapy of neuroblastoma. Eur J Cancer. 1995;31A(4):576–81.
115. Mangner TJ, Tobes MC, et al. Metabolism of iodine-131 metaiodobenzylguanidine in patients with metastatic pheochromocytoma. J Nucl Med. 1986;27(1):37–44.
116. Martucci VL, Pacak K. Pheochromocytoma and paraganglioma: diagnosis, genetics, management, and treatment. Curr Probl Cancer. 2014;38(1):7–41.
117. Mastrangelo R, Tornesello A, et al. Role of I-131-metaiodobenzylguanidine in the treatment of neuroblastoma. Med Pediatr Oncol. 1998;31(1):22–5.
118. Mastrangelo R, Tornesello A, et al. A new approach in the treatment of stage-IV neuroblastoma using a combination of [^{131}I]metaiodobenzylguanidine (MIBG) and cisplatin. Eur J Cancer. 1995;31A(4):606–11.
119. Mastrangelo S, Rufini V, et al. Treatment of advanced neuroblastoma in children over 1 year of age: the critical role of ^{131}I-metaiodobenzylguanidine combined with chemotherapy in a rapid induction regimen. Pediatr Blood Cancer. 2011;56(7):1032–40.
120. Mastrangelo S, Tornesello A, et al. Treatment of advanced neuroblastoma: feasibility and therapeutic potential of a novel approach combining 131-I-MIBG and multiple drug chemotherapy. Br J Cancer. 2001;84(4):460–4.
121. Matthay KK, DeSantes K, et al. Phase I dose escalation of ^{131}I-metaiodobenzylguanidine with autologous bone marrow support in refractory neuroblastoma. J Clin Oncol. 1998;16(1):229–36.
122. Matthay KK, Panina C, et al. Correlation of tumor and whole-body dosimetry with tumor response and toxicity in refractory neuroblastoma. treated with ^{131}I-MIBG. J Nucl Med. 2001;42(11):1713–21.
123. Matthay KK, Quach A, et al. Iodine-131-meta-iodobenzylguanidine double infusion with autologous stem-cell rescue for neuroblastoma: a new

approaches to neuroblastoma therapy phase I study. J Clin Oncol. 2009;27(7):1020–5.
124. Matthay KK, Yanik G, et al. Phase II study on the effect of disease sites, age, and prior therapy on response to iodine-131-metaiodobenzylguanidine therapy in refractory neuroblastoma. J Clin Oncol. 2007;25(9):1054–60.
125. McNeil AR, Blok BH, et al. Phaeochromocytomas discovered during coronial autopsies in Sydney, Melbourne and Auckland. Aust N Z J Med. 2000;30(6): 648–52.
126. Miano M, Garaventa A, et al. Megatherapy combining I^{131} metaiodobenzylguanidine and high-dose chemotherapy with haematopoietic progenitor cell rescue for neuroblastoma. Bone Marrow Transplant. 2001;27(6):571–4.
127. Modak S, Cheung NK. Neuroblastoma: therapeutic strategies for a clinical enigma. Cancer Treat Rev. 2010;36(4):307–17.
128. Modak S, Pandit-Taskar N, et al. Transient sialoadenitis: a complication of ^{131}I-metaiodobenzylguanidine therapy. Pediatr Blood Cancer. 2008;50(6):1271–3.
129. Modak S, Zanzonico P, et al. Arsenic trioxide as a radiation sensitizer for ^{131}I-metaiodobenzylguanidine therapy: results of a phase II study. J Nucl Med. 2016;57(2):231–7.
130. Modlin IM, Latich I, et al. Therapeutic options for gastrointestinal carcinoids. Clin Gastroenterol Hepatol. 2006;4(5):526–47.
131. Modlin IM, Lye KD, et al. A 5-decade analysis of 13,715 carcinoid tumors. Cancer. 2003;97(4):934–59.
132. Modlin IM, Sandor A. An analysis of 8305 cases of carcinoid tumors. Cancer. 1997;79(4):813–29.
133. Morais J, Lemarec H, et al. Metaiodobenzylguanidine scintigraphy of a patient with pheochromocytoma on labetalol therapy. Clin Nucl Med. 1992;17(4):308–11.
134. More SS, Itsara M, et al. Vorinostat increases expression of functional norepinephrine transporter in neuroblastoma in vitro and in vivo model systems. Clin Cancer Res. 2011;17(8):2339–49.
135. Mornex R, Badet C, et al. Malignant pheochromocytoma – a series of 14 cases observed between 1966 and 1990. J Endocrinol Invest. 1992;15(9):643–9.
136. Mueller S, Yang XD, et al. Cooperation of the HDAC inhibitor vorinostat and radiation in metastatic neuroblastoma: efficacy and underlying mechanisms. Cancer Lett. 2011;306(2):223–9.
137. Mukherjee JJ, Kaltsas GA, et al. Treatment of metastatic carcinoid tumours, phaeochromocytoma, paraganglioma and medullary carcinoma of the thyroid with ^{131}I-meta-iodobenzylguanidine (^{131}I-mIBG). Clin Endocrinol (Oxf). 2001;55(1):47–60.
138. Mulholland N, Chakravartty R, et al. Long-term outcomes of ^{131}Iodine mIBG therapy in metastatic gastrointestinal pancreatic neuroendocrine tumours: single administration predicts non-responders. Eur J Nucl Med Mol Imaging. 2015;42(13):2002–12.
139. Nakajo M, Shapiro B, et al. Salivary-gland accumulation of meta-[^{131}I]iodobenzylguanidine. J Nucl Med. 1984;25(1):2–6.
140. Neumann HPH, Bausch B, et al. Germ-line mutations in nonsyndromic pheochromocytoma. N Engl J Med. 2002;346(19):1459–66.
141. Nguyen C, Faraggi M, et al. Long-term efficacy of radionuclide therapy in patients with disseminated neuroendocrine tumors uncontrolled by conventional therapy. J Nucl Med. 2004;45(10):1660–8.
142. Nickerson HJ, Matthay KK, et al. Favorable biology and outcome of stage IV-S neuroblastoma with supportive care or minimal therapy: a children's cancer group study. J Clin Oncol. 2000;18(3):477–86.
143. Nwosu AC, Jones L, et al. Assessment of the efficacy and toxicity of ^{131}I-metaiodobenzylguanidine therapy for metastatic neuroendocrine tumours. Br J Cancer. 2008;98(6):1053–8.
144. Ott RJ, Tait D, et al. Treatment planning for ^{131}I-mIBG radiotherapy of neural crest tumors using ^{124}I-mIBG positron emission tomography. Br J Radiol. 1992;65(777):787–91.
145. Owens J, Bolster AA, et al. No-carrier-added ^{123}I-MIBG: an initial clinical study in patients with phaeochromocytoma. Nucl Med Commun. 2000; 21(5):437–40.
146. Pacak K, Eisenhofer G, et al. Diagnostic imaging of pheochromocytoma. Pheochromocytoma. 2004;31: 107–20.
147. Pacak K, Wimalawansa SJ. Pheochromocytoma and paraganglioma. Endocr Pract. 2015;21(4):406–12.
148. Pasieka JL, McEwan AJB, et al. The palliative role of ^{131}I-MIBG and ^{111}In-octreotide therapy in patients with metastatic progressive neuroendocrine neoplasms. Surgery. 2004;136(6):1218–26.
149. Patel D, Mehta A, et al. Total ^{18}F-FDG PET/CT metabolic tumor volume is associated with postoperative biochemical response in patients with metastatic pheochromocytomas and paragangliomas. Ann Surg. 2016;263(3):582–7.
150. Pathirana AA, Vinjamuri S, et al. ^{131}I-MIBG radionuclide therapy is safe and cost-effective in the control of symptoms of the carcinoid syndrome. Eur J Surg Oncol. 2001;27(4):404–8.
151. Polishchuk AL, DuBois SG, et al. Response, survival, and toxicity after iodine-131-metaiodobenzylguanidine therapy for neuroblastoma in preadolescents, adolescents, and adults. Cancer. 2011;117(18):4286–93.
152. Proye C, Vix M, et al. High-incidence of malignant pheochromocytoma in a surgical unit – 26 cases out of 100 patients operated from 1971 to 1991. J Endocrinol Invest. 1992;15(9):651–63.
153. Quach A, Ji LY, et al. Thyroid and hepatic function after high-dose ^{131}I-metaiodobenzylguanidine (^{131}I-MIBG) therapy for neuroblastoma. Pediatr Blood Cancer. 2011;56(2):191–201.
154. Rachh SH, Abhyankar S, et al. I-131 metaiodobenzylguanidine therapy in neural crest tumors:

varying outcome in different histopathologies. Nucl Med Commun. 2011;32(12):1201–10.
155. Rose B, Matthay KK, et al. High-dose ^{131}I-meta-iodobenzylguanidine therapy for 12 patients with malignant pheochromocytoma. Cancer. 2003;98(2):239–48.
156. Rufini V, Shulkin B. The evolution in the use of MIBG in more than 25 years of experimental and clinical applications. Q J Nucl Med Mol Imaging. 2008;52(4):341–50.
157. Rutherford MA, Rankin AJ, et al. Management of metastatic phaeochromocytoma and paraganglioma: use of iodine-131-meta-iodobenzylguanidine therapy in a tertiary referral centre. QJM. 2015;108(5):361–8.
158. Safford SD, Coleman E, et al. Iodine-131 meta-iodobenzylguanidine is an effective treatment for malignant pheochromocytoma and paraganglioma. Surgery. 2003;134(6):956–62.
159. Safford SD, Coleman RE, et al. Iodine-131 meta-iodobenzylguanidine treatment for metastatic carcinoid – results in 98 patients. Cancer. 2004;101(9):1987–93.
160. Samaan NA, Hickey RC, et al. Diagnosis, localization, and management of pheochromocytoma – pitfalls and follow-up in 41 patients. Cancer. 1988; 62(11):2451–60.
161. Schlumberger M, Gicquel C, et al. Malignant pheochromocytoma: clinical, biological, histologic and therapeutic data in a series of 20 patients with distant metastases. J Endocrinol Invest. 1992;15(9):631–42.
162. Scholz T, Eisenhofer G, et al. Current treatment of malignant pheochromocytoma. J Clin Endocrinol Metab. 2007;92(4):1217–25.
163. Schoot RA, Bleeker G, et al. The role of ^{131}I-meta-iodobenzylguanidine (MIBG) therapy in unresectable and compromising localised neuroblastoma. Eur J Nucl Med Mol Imaging. 2013;40(10):1516–22.
164. Shapiro B, Sisson IC, et al. Radiopharmaceutical therapy of malignant pheochromocytoma with [^{131}I]meta-iodobenzylguandine: results from ten years of experience. J Nucl Biol Med. 1991;35(4):269–76.
165. Shapiro B, Sisson JC, et al. Malignant pheochromocytoma – clinical, biochemical and scintigraphic characterization. Clin Endocrinol (Oxf). 1984;20(2):189–203.
166. Shilkrut M, Bar-Deroma R, et al. Low-dose iodine-131 metaiodobenzylguanidine therapy for patients with malignant pheochromocytoma and paraganglioma single center experience. Am J Clin Oncol-Canc Clin Trials. 2010;33(1):79–82.
167. Shusterman S, Grant FD, et al. Iodine-131-labeled meta-iodobenzylguanidine therapy of children with neuroblastoma: program planning and initial experience. Semin Nucl Med. 2011;41(5):354–63.
168. Sisson JC, Shapiro B, et al. Radiopharmaceutical treatment of malignant pheochromocytoma. J Nucl Med. 1984;25(2):197–206.
169. Sisson JC, Shapiro B, et al. Predictors of toxicity in treating patients with neuroblastoma by radiolabeled metaiodobenzylguanidine. Eur J Nucl Med. 1994; 21(1):46–52.
170. Sisson JC, Shapiro B, et al. Treatment of malignant pheochromocytomas with ^{131}I-metaiodobenzylguanidine and chemotherapy. Am J Clin Oncol-Canc Clin Trials. 1999;22(4):364–70.
171. Smets LA, Janssen M, et al. Pharmacokinetics and intracellular-distribution of the tumor-targeted radiopharmaceutical m-iodo-benzylguanidine in SK-N-SH neuroblastoma and PC-12 pheochromocytoma cells. Int J Cancer. 1991;48(4):609–15.
172. Solanki KK, Bomanji J, et al. A pharmacological guide to medicines which interfere with the biodistribution of radiolabeled metaiodobenzylguanidine (meta-iodobenzylguanidine). Nucl Med Commun. 1992; 13(7):513–21.
173. Solanki KK, Bomanji JB, et al. Thyroid blocking policy – revisited. Nucl Med Commun. 2004;25(11):1071–6.
174. Solcia E, Kloppel G, et al. Histological typing of endocrine tumours. In: Solcia E, Kloppel G, Sobin LH, editors. WHO international histological classification of tumours. Heidelberg: Springer; 2000. p. 1–5.
175. Srimuninnimit V, Wampler GL. Case report of metastatic familial pheochromocytoma treated with cisplatin and 5-fluorouracil. Cancer Chemother Pharmacol. 1991;28(3):217–9.
176. Sternthal E, Lipworth L, et al. Suppression of thyroid radioiodine uptake by various doses of stable iodide. N Engl J Med. 1980;303(19):1083–8.
177. Streby KA, Shah N, et al. Nothing but NET: a review of norepinephrine transporter expression and efficacy of ^{131}I-mIBG therapy. Pediatr Blood Cancer. 2015;62 (1):5–11.
178. Sywak MS, Pasieka JL, et al. ^{131}I-meta-iodobenzylguanidine in the management of metastatic midgut carcinoid tumors. World J Surg. 2004;28(11):1157–62.
179. Sze WCC, Grossman AB, et al. Sequelae and survivorship in patients treated with ^{131}I-MIBG therapy. Br J Cancer. 2013;109(3):565–72.
180. Taal BG, Hoefnagel CA, et al. Palliative effect of metaiodobenzylguanidine in metastatic carcinoid tumors. J Clin Oncol. 1996;14(6):1829–38.
181. Taal BG, Zuetenhorst H, et al. [^{131}I]MIBG radionuclide therapy in carcinoid syndrome. Eur J Surg Oncol. 2002;28(3):243.
182. Tischler AS, Kimura N, et al. Pathology of pheochromocytoma and extra-adrenal paraganglioma. Pheochromocytoma. K. Pacak and G. Eisenhofer. Oxford: Blackwell Publishing; 2006; 1073:557–70.
183. Treuner J, Klingebiel T, et al. Treatment of neuroblastoma with metaiodobenzylguanidine – results and side-effects. Med Pediatr Oncol. 1987;15(4): 199–202.
184. Treuner J, Klingebiel T, et al. Clinical-experiences in the treatment of neuroblastoma with ^{131}I-metaiodobenzylguanidine. Pediatr Hematol Oncol. 1986;3(3):205–16.
185. Tristam M, Alaamer AS, et al. Iodine-131-meta-iodobenzylguanidine dosimetry in cancer therapy: risk versus benefit. J Nucl Med. 1996;37(6):1058–63.

186. Troncone L, Riccardi R, et al. Treatment of neuroblastoma with ^{131}I-metaiodobenzylguanidine. Med Pediatr Oncol. 1987;15(4):220–3.
187. Troncone L, Rufini V, et al. [^{131}I]metaiodobenzylguanidine treatment of malignant pheochromocytoma: experience of the Rome group. J Nucl Biol Med. 1991;35(4):295–9.
188. Vaidyanathan G, Affleck DJ, et al. A kit method for the high level synthesis of [^{211}At]MABG. Bioorg Med Chem. 2007;15(10):3430–6.
189. Vaidyanathan G, Friedman HS, et al. Localisation of [^{131}I]MIBG in nude mice bearing SK-N-SH human neuroblastoma xenografts: effect of specific activity. Br J Cancer. 1996;73(10):1171–7.
190. Van Essen M, Krenning EP, et al. Peptide receptor radionuclide therapy with radiolabelled somatostatin analogues in patients with somatostatin receptor positive tumours. Acta Oncol. 2007;46(6):723–34.
191. van Santen HM, Tytgat GAM, et al. Differentiated thyroid carcinoma after ^{131}I-MIBG treatment for neuroblastoma during childhood: description of the first two cases. Thyroid. 2012;22(6):643–6.
192. Venkatesan AM, Locklin J, et al. Radiofrequency ablation of metastatic pheochromocytoma. J Vasc Interv Radiol. 2009;20(11):1483–90.
193. Vetter H, Fischer M, et al. ^{131}I-meta-iodobenzylguanidine in treatment of malignant phaeochromocytomas. Lancet. 1983;2(8341):107.
194. Vik TA, Pfluger T, et al. ^{123}I-mIBG scintigraphy in patients with known or suspected neuroblastoma: results from a prospective multicenter trial. Pediatr Blood Cancer. 2009;52(7):784–90.
195. Voute PA, Hoefnagel CA, et al. Radionuclide therapy of neural crest tumors. Med Pediatr Oncol. 1987;15(4):192–5.
196. Voute PA, Vanderkleij AJ, et al. Clinical-experience with radiation enhancement by hyperbaric-oxygen in children with recurrent neuroblastoma stage-IV. Eur J Cancer. 1995;31A(4):596–600.
197. Wafelman AR, Hoefnagel CA, et al. Radiochemical purity, at expiry, and radiochemical stability of iodine-131 labelled meta-iodobenzylguanidine concentrates for intravenous infusion. Nuklearmedizin. 1996;35(4):122–5.
198. Wafelman AR, Hoefnagel CA, et al. Renal excretion of iodine-131 labelled meta-iodobenzylguanidine and metabolites after therapeutic doses in patients suffering from different neural crest-derived tumours. Eur J Nucl Med. 1997;24(5):544–52.
199. Wafelman AR, Nortier YL, et al. Renal excretion of meta-iodobenzylguanidine after therapeutic doses in cancer patients and its relation to dose and creatinine clearance. Nucl Med Commun. 1995;16(9):767–72.
200. Wakabayashi H, Taki J, et al. Prognostic values of initial responses to low-dose ^{131}I-MIBG therapy in patients with malignant pheochromocytoma and paraganglioma. Ann Nucl Med. 2013;27(9):839–46.
201. Weiss B, Vora A, et al. Secondary myelodysplastic syndrome and leukemia following ^{131}I-metaiodobenzylguanidine therapy for relapsed neuroblastoma. J Pediatr Hematol Oncol. 2003;25(7):543–7.
202. Wieland DM, Swanson DP, et al. Imaging the adrenal-medulla with an ^{131}I-labeled antiadrenergic agent. J Nucl Med. 1979;20(2):155–8.
203. Wong T, Matthay KK, et al. Acute changes in blood pressure in patients with neuroblastoma treated with ^{131}I-metaiodobenzylguanidine (MIBG). Pediatr Blood Cancer. 2013;60(9):1424–30.
204. Yang JG, Codreanu I, et al. I-131 MIBG post-therapy scan is more sensitive than I-123 MIBG pretherapy scan in the evaluation of metastatic neuroblastoma. Nucl Med Commun. 2012;33(11):1134–7.
205. Yanik GA, Levine JE, et al. Pilot study of iodine-131-metaiodobenzylguanidine in combination with myeloablative chemotherapy and autologous stem-cell support for the treatment of neuroblastoma. J Clin Oncol. 2002;20(8):2142–9.
206. Yanik GA, Villablanca JG, et al. ^{131}I-metaiodobenzylguanidine with intensive chemotherapy and autologous stem cell transplantation for high-risk neuroblastoma. A new approaches to neuroblastoma therapy (NANT) phase II study. Biol Blood Marrow Transplant. 2015;21(4):673–81.
207. Yoshinaga K, Oriuchi N, et al. Effects and safety of I-131-metaiodobenzylguanidine (MIBG) radiotherapy in malignant neuroendocrine tumors: Results, from a multicenter observational registry. Endocr J. 2014;61(12):1171–80.
208. Zanzonico PB, Becker DV. Effects of time of administration and dietary iodine levels on potassium iodide (KI) blockade of thyroid irradiation by ^{131}I from radioactive fallout. Health Phys. 2000;78(6):660–7.
209. Zaplatnikov K, Menzel C, et al. Drug interference with MIBG uptake in a patient with metastatic paraganglioma. Br J Radiol. 2004;77(918):525–7.
210. Zarnegar R, Kebebew E, et al. Malignant pheochromocytoma. Surg Oncol Clin N Am. 2006;15(3):555–71.
211. Zhou MJ, Doral MY, et al. Different outcomes for relapsed versus refractory neuroblastoma after therapy with ^{131}I-metaiodobenzylguanidine (I-131-MIBG). Eur J Cancer. 2015;51(16):2465–72.
212. Zuetenhorst JM, Olmos RAV, et al. Interferon and meta-iodobenzylguanidin combinations in the treatment of metastatic carcinoid tumours. Endocr Relat Cancer. 2004;11(3):553–61.
213. Janssen I, Blanchet EM, et al. Superiority of [^{68}Ga]-DOTATATE PET/CT to other functional imaging modalities in the localization of SDHB-Associated metastatic pheochromocytoma and paraganglioma. Clin Cancer Res. 2015;21(17):3888–95.

Targeted Radionuclide Therapy for Bone Metastasis

45

Neeta Pandit-Taskar and Chaitanya R. Divgi

Abstract

Bone metastases markedly reduce the quality of life due to bone pain, pathologic fractures, loss of mobility, and hypercalcemia. A graded three-step approach, as recommended by the World Health Organization (WHO), is used to treat pain according to its severity. Nonsteroidal anti-inflammatory drugs are used in patients with mild to moderate pain. When pain persists or increases, a weak opioid such as codeine or hydrocodone is added. Higher doses or more potent opioids are used if the pain persists or becomes more severe. Bisphosphonates (BPs) are useful in the treatment of osteoporosis and metastatic disease by decreasing the resorption of the bone. BPs bind to bone mineral and directly interfere with the activation of osteoclasts. They are internalized by osteoclasts and inhibit specific biochemical and metabolic pathways in these cells; they also reduce skeletal complications and reduce the rate of development of new lesions and delay progression in bone metastases. External beam radiation therapy given as a single or multifractionated dose is an effective treatment and provides early relief, especially for localized bone pain due to bone metastasis. Therapy with bone-seeking radiopharmaceuticals is effective for reducing pain in patients with widespread, painful bone metastases from various malignancies particularly prostate cancer. A variety of radiopharmaceuticals have been used and tested, including many beta-emitting nuclides and alpha emitting radium-223 (^{223}Ra) dichloride. Each of these agents target the bone by chemical bonding or adsorbing to the trabecular surface of the bone, the metal-chelated radiotracer to the trabecular surface, while ^{32}P-sodium orthophosphate and ^{89}Sr-chloride distribute more widely throughout the bone. ^{89}Sr-chloride and ^{153}Sm-EDTMP are two FDA-approved beta-emitting radiopharmaceuticals that have largely replaced ^{32}P-sodium orthophosphate in the treatment of metastatic bone pain in the United States. More recently, alpha-emitting ^{223}Ra-dichloride has been used in symptomatic castration-resistant prostate cancer (CRPC). The onset of pain relief commonly occurs within 7–21 days. Re-treatment is possible after allowing for marrow recovery; however, multiple therapies require consideration of cumulative marrow toxicity.

^{89}Sr-chloride and ^{153}Sm-EDTMP have been used extensively, primarily for the treatment of bone pain from breast and prostate cancer due to the presence of osteoblastic

N. Pandit-Taskar (✉)
Department of Radiology, Memorial Sloan Kettering Cancer Center, New York, NY, USA

Department of Radiology, Weill Cornell Medical College, New York, NY, USA
e-mail: pandit-n@mskcc.org

C.R. Divgi
Jenkintown, PA, USA
e-mail: divgic@gmail.com

© Springer International Publishing Switzerland 2017
H.W. Strauss et al. (eds.), *Nuclear Oncology*,
https://doi.org/10.1007/978-3-319-26236-9_27

disease that enables high uptake of the agents. Radionuclide therapy may be used alone or in combination with chemotherapy or radiation therapy to enhance pain relief and delay onset of new pain; consideration needs to be directed to overlapping or cumulative toxicities especially in the marrow that may require supportive treatment. Patients most suitable for bone pain therapy are those with multiple sites of bone metastases confirmed by a bone scan showing focal sites of increased radiopharmaceutical uptake and those who have symptoms related to osseous disease that requires increased doses of pain medication or is refractory to pain medication. ^{223}Ra is an alpha-emitting radionuclide that accumulates in the bone as it is analogous to calcium. The high linear energy transfer of alpha radiation leads to double-strand DNA breaks within the cells. While effective for pain palliation, it has also shown survival benefit in those with metastatic osseous disease from prostate cancer. However, it is currently approved for use only in symptomatic CRPC patients who have no other visceral diseases.

Keywords

Bone metastasis • Bone pain palliation • Radium-223 dichloride • Strontium-89 chloride • Samarium-153 EDTMP • Phosphorus-32 • Bone targeted radionuclide therapy • Radiopharmaceutical therapy for bone metastases

Glossary

^{153}Sm-EDTMP	^{153}Sm- Ethylenediamine Tetramethylene Phosphoric Acid
^{117m}Sn-DTPA	^{117m}Sn-Diethylenetriamine-pentaacetic acid
[^{18}F]FDG	2-deoxy-2-[^{18}F]fluoro-D-glucose
^{186}Re-HEDP	^{186}Re Hydroxyethylidene diphosphonate
AEs	Adverse events
ALARA	As low as reasonably achievable
ALP	Alkaline phosphatase
ALSYMPCA	Alpharadin in Symptomatic Prostate Cancer Patients
ATP	Adenosine triphosphate
BPs	Bisphosphonates
CD	Cluster of differentiation
CPFS	Clinical progression-free survival
CRPC	Castration-resistant prostate cancer
DLT	Dose-limiting toxicity
DNA	Deoxyribonucleic acid
DOTMP	1,4,7,10 - tetra-azacyclododecane -1,4,7,10-tetramethylene phosphonic acid
DTPMP	Diethylenetriamine pentakis (methylphosphonic acid)
EBRT	External beam radiation therapy
ECM	Extracellular matrix
ER	Estrogen receptor
FDA	United States Food and Drug Administration
FPPS	Farnesyl pyrophosphate synthase
GFAP	Glial fibrillary acidic protein
GFR	Glomerular filteration rate
GI	Gastro-intestinal
GMP	Good manufacturing practices
GTP	Guanosine Triphosphate
Gy	Gray unit (ionizing radiation dose in the International System of Units, corresponding to the absorption of one joule of radiation energy per kilogram of matter)
ICER	Incremental cost-effectiveness ratio
IMRT	Intensity modulated radiotherapy
IV	Intravenous
LDH	Lactate dehydrogenase

LET	Linear energy transfer
^{99m}Tc-MDP	^{99m}Tc-Methylene Diphosphonate
MTD	Maximum tolerated dose
NCCN	National Comprehensive Cancer Network
NRC	Nuclear Regulatory Commission
NSAIDs	Nonsteroidal anti-inflammatory drugs
OPGL	Osteoprotegerin ligand
OS	Overall survival
PFS	Progression-free survival
PGA	Physician's global assessment
PSA	Prostate-specific antigen
PTHrP	Parathyroid hormone-related protein
QALY	Quality-adjusted life-year
QOL	Quality of life
RANK	Receptor activator of nuclear factor kappa-B
RANKL	Receptor activator of nuclear factor kappa-B ligand
RP	Radiopharmaceutical
RT	Radiotherapy
SAE	Serious adverse event
SBRT	Stereotactic body radiation therapy
SEP	Sum of effect product
SRE	Skeletal relevant events
TGF-β	Transforming growth factor-beta
TNF	Tumor necrosis Factor
TTHMP	Tri-ethylenetetraminehexa-methylene phosphonic acid
ULN	Upper limit of normal
uNTX-1	Urinary N-telopeptide of type 1
VAS-AUPC	Visual analog scale-area under the pain curve
WBC	White blood cell
WHO	World Health Organization
XRT	External radiation therapy
ZA	Zoledronic acid

Contents

Introduction 1309
Pathophysiology of Metastasis 1310
Prevention of Bone Resorption 1311
Radiation Therapy 1312
Radiopharmaceutical Therapy 1312
Mechanism of Action 1312
^{32}P 1313
^{89}Sr-Chloride 1313
^{153}Sm-EDTMP (Lexidronam) 1317
Therapy with Alpha Emitter Radium-223 Dichloride ($^{223}RaCl_2$) 1322
Other Agents 1327
Rhenium-Labeled Radiopharmaceuticals: ^{186}Re-HEDP and ^{188}Re-HEDP (Etidronate) 1327
^{117m}Sn-Pentetate and ^{177}Lu-EDTMP 1328
Patient Identification and Referral 1329
Administration of Radiopharmaceutical Agent 1329
Summary 1330
References 1330

Introduction

Bone metastases are commonly seen in the advanced stages of a number of malignancies, including cancers of the prostate, breast, lung, thyroid, bladder, melanoma, kidney, and myeloma [1, 2]. Overall, the skeleton is the third most common site of metastasis, and it is estimated that one of every five patients with metastatic disease will have symptomatic osseous involvement [3]. Skeletal metastases markedly reduce the quality of life due to bone pain and pathologic fractures and loss of mobility. Analgesic medications are used in a graded three-step approach (recommended by WHO) to treat metastatic osseous pain according to severity [4]. Usually, nonsteroidal anti-inflammatory drugs (NSAIDs) including aspirin, ibuprofen, and naproxen are used in patients with mild to moderate pain. When pain persists or increases while on

NSAIDS, a weak opioid such as codeine or hydrocodone is added. Higher doses or more potent opioids such as morphine, hydromorphone, or fentanyl are used if the pain persists or becomes more severe. The National Comprehensive Cancer Network (NCCN) guidelines recommend treatment based on an initial comprehensive assessment of severity of pain, pathophysiology of causes, cancer pain syndromes, and skeletal-related events. General management includes initiation of analgesic NSAIDS, and corticosteroids are added if associated inflammation is a factor. Localized radiotherapy or systemic radionuclide treatment may be added as needed for local or diffuse disease pain, respectively. Continuous pain is treated with regular doses of pain medication with small doses of opioids given additionally for breakthrough pain. Opioid dosage and type may be changed when pain persists or increases [5]. Bisphosphonates and RANKL-inhibiting monoclonal antibody, denosumab, are approved medications useful to prevent bone resorption and skeletal-related events.

Narcotics may reduce the pain, but can cause significant side effects including constipation and/or drowsiness, as well as physical and psychological dependence (addiction). When a patient has pain from a localized bone metastasis, external beam radiation therapy is often used. In patients with symptomatic widespread skeletal metastases, therapy with bisphosphonates and bone-seeking radiopharmaceuticals helps reduce pain.

Pathophysiology of Metastasis

Metastasis occurs when tumor cells detach from the tumor mass and migrate to a new location where the tumor cells adhere to endothelial cells, with subsequent invasion and colonization of the metastatic site [6, 7]. Chemical mediators, such as cadherins, integrins, immunoglobulins, E- and P-selectins, and CD 44, are involved in this complex process. Tumor cell adherence to the extracellular matrix (ECM) is mediated by integrins, while cell-cell adhesions are mediated by cadherins [8].The activation of integrins is accompanied by the activation of proteases that together help to degrade the ECM, forming a pathway for invasion. Matrix metalloproteinases, plasmin, urokinase, cathepsins, and heparinases promote tumor invasion [6]. An embolus of tumor cells bound to coagulation factors like fibrinogen, fibrin, thrombin and tissue factor gets trapped in capillary beds. The endothelial cell E- and P-selectins contribute to tumor cell arrest and initiate adhesion to the endothelium. E-selectin, produced de novo by activated endothelium, also facilitates the process. In vitro, E-selectin mediates binding of colon carcinoma cell line to endothelial cells. It has also been associated with breast cancer metastasis. P-selectin is likely involved in binding of cells in a range of tumors, including those of the lung, melanoma, and colon [9–14]. Greater endothelial tumor cell adhesion involves cadherins or immunoglobulin-like cell adhesion molecules [15].

Invasiveness is mediated by a number of enzyme systems including serine proteases like matrix metalloproteinase and urokinase plasminogen activation systems. Tumor cell motility, critical for the development of distant metastases, appears to be mediated by a number of factors, including growth factors, hyaluronans, components of matrix, and other host- or tumor-secreted factors (e.g., cytokinins such as autotoxin and hepatocyte growth) [16–18].

Metastatic involvement of the bone meets the "seed and soil theory of metastasis" hypothesis proposed by Paget, which holds that interactions between tumor cells and their environment influence why certain tumors metastasize to the bone. The dissemination pattern can sometimes be explained by anatomic predisposition. For example, prostate cancer has propensity to spread to the pelvis and vertebrae because of the venous plexus of Batson.

Osteoblastic metastases occur due to mediators that stimulate osteoblast proliferation or differentiated osteoblast function. Prostate cancer cells express transforming growth factor-beta (TGF-β), which has a bone stimulatory effect; fibroblast growth factors can stimulate osteoblast proliferation and increased bone formation, as well as other proteins that are growth factors

belonging to the TGF-β family, the most potent stimulants of in vivo bone formation [19–21]. The loss of bone mineral in osteolytic lesions is mediated predominantly by increased osteoclast activity. Numerous factors produced either by tumor cells, e.g., parathyroid hormone-related protein (PTHrP), or the bone matrix stimulate this resorptive action of osteoclasts, leading to increased destruction of the bone. Higher PTHrP in primary breast tumors predicts the subsequent development of bone metastasis [22].

Metastatic osseous disease often leads to debilitating pain. Anatomic factors and chemical mediators contribute to this pain; tumor in the bone may cause expansion, periosteal stress, or nerve compression. Bone cancer pain may also occur due to interaction with and sensitization of the nervous system [23]. Peripheral sensitization results in increased release of substance P from nociceptors even with minor stimulation, leading to allodynia and hyperalgesia. Central sensitization of dorsal horn of the spinal cord also leads to increased sensitivity to pain. Increased astrocytosis, enhanced expression of c-Fos (a marker of neuronal activity), and the presence of the prohyperalgesic peptide dynorphin have been seen in the spinal cord. Prostaglandins are associated with inflammation and cancer pain [24]. Upregulation of glial fibrillary acidic protein (GFAP) occurs, and isoenzyme cyclooxygenase-2 (Cox-2) has also been found in tumor cells [25].

Low intra- and extracellular pH in tumors can also contribute to pain [23]. Neuropathic pain may occur due to entrapment or injury to nerves by tumor growth.

Prevention of Bone Resorption

Bone metastasis is linked to bone destruction caused by osteoclastic activity that can be prevented by the use of bisphosphonates [26, 27]. Proliferation, survival, and activity of osteoclasts are regulated by osteoprotegerin ligand (OPGL), which belongs to the TNF family of molecules. Osteoblasts and activated T cells are key sources of OPGL that act via binding to RANK receptors expressed on osteoclast precursors and mature osteoclasts [28]. RANK-ligand inhibition has been shown to be effective and is approved as a therapy to reduce osteoclastic activity in skeletal metastases.

Bisphosphonates are a class of agents in which two phosphonate groups are linked via phosphoether bonds to a carbon core. BPs bind with high affinity to calcium in the bone mineral matrix, hence the avidity for bones, and are thought to act primarily by inhibiting osteoclast-mediated bone resorption. BPs bind to bone mineral and directly interfere with the activation of osteoclasts; they get internalized in the osteoclasts and inhibit their action by interfering with specific biochemical and metabolic pathways. BPs inhibit ATP-dependent intracellular enzymes or enzymes of the mevalonate pathway, preventing formation of proteins required for modification of GTP-binding proteins. The key target is farnesyl pyrophosphate synthase (FPPS) [29]. Another mechanism may be stimulating osteoblasts to produce osteoclast inhibitory factors [30].

BPs act by decreasing the resorption of the bone [31] and have become an important part of management of osseous metastases [32], especially those with significant osteolytic component such as breast cancer and multiple myeloma [33, 34] by significantly reducing skeletal complications, lowering the rate of development of new lesions, and delaying progression in bone metastases [34]. Increasing evidence is emerging regarding their potential to prevent disease recurrence and metastases [35] and possible effect on survival [36]. Zoledronic acid (ZA) has been shown to be effective for the treatment of bone metastases in patients with metastatic prostate, lung, renal cell, and other carcinomas [37, 38].

In prostate cancer, the use of ZA has been shown to reduce pain and the number and rate of skeletal-related morbidities [39]. The use of BPs in conjunction with other agents in prostate cancer may improve efficacy [40]. Osteoclast inhibition via a human monoclonal antibody denosumab that targets RANKL is useful in preventing bone resorption and increases bone mineral density. In

patients with nonmetastatic prostate cancer, it showed a lower incidence of vertebral fractures in comparison to placebo [41, 42]. Also in comparison to ZA, it showed an increased time to skeletal related events [43]. As with BP, osteonecrosis of the jaw is a common side effect as well as increased hypocalcemia that needs active calcium supplementation [44]. Recent guidelines suggest denosumab as a first-line treatment for prevention of skeletal-related events in metastatic prostate cancer [45].

Radiation Therapy

External beam radiation therapy (EBRT) is the treatment of choice for localized bone pain due to bone metastasis and is very effective in providing early and rapid pain relief that may be seen as early as 48 h after the commencement of therapy. Radiation destroys viable tumor cells, resulting in shrinkage of tumor, and enables osteoblastic repair of damaged bone.

Local radiotherapy to a small area may be given as a single or multifractionated dose. The choice of one over the other is still controversial, however. While single-fraction dose is convenient and less expensive for patients, there is concern that the equivalent biologic dose may be smaller compared to multifractionated method, leading to an inferior response in pain palliation [46]. Re-treatments may be required more with single-fraction therapy than with multifractionated therapy [47]. Single-fraction treatment doses vary, though a minimum of 8 Gy is preferred, and higher pain responses are seen with this dose as compared to lower doses [48]. Varied fractionation schemes including a single 8 Gy and 20 Gy in five fractions, 24 Gy in six fractions, and 30Gy in ten fractions can result in similar results for pain relief [49]. For repeat treatments of spinal metastasis, SBRT, IMRT, and proton beam therapy are more suitable, although re-treatment carries a higher risk of radiation myelitis. For those with severe pain or spinal compression in sites previously irradiated, surgical intervention should be considered for palliative purposes. Survival benefit from aggressive local therapy of oligometastasis is not yet proven.

Radiopharmaceutical Therapy

Advanced cancers, especially prostate and breast cancer, often cause skeletal metastases that may cause significant pain at multiple sites. Systemic antitumor therapy like chemotherapy and hormone therapy is used to treat and prevent the spread of metastatic disease; however, the benefit in advanced disease may be limited, and symptomatic pain relief usually requires pain-relieving medication. In patients with painful osseous metastatic disease, refractory to conventional analgesia, radiopharmaceutical therapy has played a key role in pain palliation.

The radioisotope's half-life should be long enough to enable cytocidal doses of radiation to be delivered. Radiopharmaceuticals that have been used to target bone metastasis include the beta-emitting nuclide phosphorus-32 (^{32}P) sodium phosphate or orthophosphate, strontium-89 (^{89}Sr) chloride, samarium-153 ethylenediamine tetramethylene phosphoric acid (^{153}Sm-EDTMP), rhenium-186 and rhenium-188 hydroxyethylidene diphosphonate (^{186}Re-HEDP and ^{188}Re-HEDP), lutetium-177 ethylenediamine tetramethylene phosphonic acid (^{177}Lu-EDTMP), and ^{117m}Sn diethylenetriaminepentaacetic acid (^{117m}Sn-DTPA), as well as radium-223 dichloride, an alpha-emitting radiopharmaceutical (Table 1). Bone pain palliation therapy with radiopharmaceuticals is a cost-effective systemic therapy to relieve pain from skeletal metastases with a consequent decrease in morbidity and an improvement in quality of life [50–52].

Mechanism of Action

^{32}P orthophosphate, ^{89}Sr-chloride, and ^{223}Ra dichloride have direct affinity for the bone. On the other hand, ^{153}Sm, ^{186}Re, ^{188}Re, and ^{177}Lu are

Table 1 Radiolabeled agents for targeting bone metastasis

Isotope	Compound	Half-life (days)	Emission	Maximum energy MeV	γ-energy MeV (%)	Soft tissue range mm (maximum)
^{177}Lu	^{177}Lu-EDTMP	6.7	β^-	0.497	0.208 (11)	–
^{32}P	^{32}P-phosphate	14.3	β^-	1.71	–	**8**
^{89}Sr	^{89}Sr-chloride	50.5	β^-	1.46	0.91 (0.01)	**2.4**
^{223}Ra	^{223}Ra-dichloride	11.4	α	5.78	0.269 (13.6%) 0.324 (3.9%); 0.154 (6.04%)	**0.1 mm**
^{186}Re	^{186}Re-HEDP	3.7	β^-	1.07	0.137 (9)	**2.4**
^{188}Re	^{188}Re-HEDP	0.7	β^-	2.12	–	**3**
^{153}Sm	^{153}Sm-EDTMP	1.9	β^-	0.81	0.103 (28)	**0.6**
^{117m}Sn	^{117m}Sn-DTPA	13.6	Conversion electron	–	–	**0.3**

targeted to the bone by complexing the radionuclide to phosphonate complexes like EDTMP (lexidronam) or HEDP (etidronate). The sources of radiation within the bone differ depending on the radiopharmaceutical. The metallic-chelated radiotracers tend to chemically absorb to the trabecular surface, whereas ^{32}P-sodium orthophosphate, ^{89}Sr-chloride, and ^{223}Ra dichloride distribute more widely throughout the bone because of the natural distribution of phosphate and the fact that strontium behaves very much like calcium in the body, as both are members of Periodic Table Family II. Due to the heterogeneity of radiopharmaceutical uptake, spicule thickening, and tumor and marrow distribution, there is variation in dosimetry between the various agents [53].

^{32}P

^{32}P was the radionuclide initially used in the treatment of bone pain, and it remained the most widely used agent until the 1980s [54]. It is a reactor-produced, pure beta-emitting radionuclide with a physical half-life of 14.3 days and emission of an energetic beta particle of 1.71 MeV. Its high energy allows a maximum tissue range of 8 mm and an average range of 3 mm and is available in both oral and injectable forms. The mechanism of action appears to be DNA damage from decay to ^{32}S with subsequent tumor cell death.

Its uptake in malignant tissue was demonstrated by Lawrence and colleagues who used it to treat leukemia [55, 56]. The pain response rates for ^{32}P therapy are reported between 59 and 93% for prostate cancer and 52–94% for breast cancer with overall response rates of 77% and 84%, respectively [57, 58]. No dose-response relationship was seen. Pain palliation is usually observed within 14 days with a range of 2 days–4 weeks. The long beta particle range results in significant radiation to the bone marrow, with frequent hematopoietic side effects [59]. Dose-dependent pancytopenia occurs at around 4–5 weeks, with recovery by 6–7 weeks.

^{89}Sr-Chloride

^{89}Sr-chloride is an FDA-approved radiopharmaceutical that has been extensively used in the treatment of metastatic bone pain and largely replaced ^{32}P in the United States. It belongs to the II-A family of the Periodic Table of Elements, the same family as calcium. ^{89}Sr has a physical

half-life of 50.5 days and emits a beta particle with a maximum energy of 1.46 MeV, with a maximum beta particle range of 7.2 mm and an average soft tissue range of 2.4 mm. It has very low gamma emissions (0.01% abundant gamma emission with a 0.91 MeV photopeak) precluding external imaging. Following an intravenous administration, it is rapidly concentrated in the bones, primarily in osteoblastic areas. About 80% of free ^{89}Sr is excreted through the kidneys and 20% through the gastrointestinal system. Its biological half-life is 4–5 days with biexponential clearance, such that 20% remains in the body, mostly in the bone, at 90 days [60].

The administered activity is generally 40–60 μCi/kg or 4 mCi. The onset of pain relief commonly occurs within 7–21 days, and the mean duration of relief is about 2–6 months. Transient increased bone pain (flare) may occur in about 10–15% of patients and is usually seen within 24–120 h posttreatment. This is usually mild, self-limited, and controlled with analgesics. A flare also usually heralds a good treatment response [61]. Hematologic toxicity is usually mild and reversible, and there is a minimal decrease in red cell counts. In various studies, platelet and white cell counts may drop by an average of 30–40% from the pretreatment level, though nadirs as low as 25–30% of pretreatment values have been seen [62–64].

^{89}Sr has been extensively used, mainly in the treatment of bone pain from breast and prostate cancer, with 60–80% of patients respectively obtaining some relief of bone pain [65–68]. An early phase I/II studies treated 38 patients (45 treatments) with 1–4.5 mCi or 16–70 μCi/kg of ^{89}Sr. All patients had an increasing need for pain medication and highly variable performance status at baseline. One patient had complete pain relief, and 18 patients had an overall 25% reduction in narcotic use lasting at least 1 month, and/or a 20% improvement in Karnofsky scale rating was seen after 48% of treatments [62]. A multicenter study in 83 prostatic carcinoma patients showed an effectiveness of ^{89}Srin relieving bone pain even in those who had failed to respond to conventional therapies. About 75% experienced pain relief and 22% became pain-free at treatment dose of 1.5 MBq/kg or more. Symptomatic improvement was seen as early as 6 weeks and the mean duration of effect was 6 months [61]. A clear benefit over placebo was seen in a prospective randomized double-blind controlled study [68]. A dose-response relationship may exist between the dose of ^{89}Sr administered and complete relief of pain due to skeletal metastases [65]. Early studies on combination treatment with chemotherapy suggested that a low dose of carboplatin may have an enhanced effect on pain relief [69]. Multiple doses combined with low-dose docetaxel are also feasible and may have antitumor activity [70]. Pain relief and performance improvement was achieved in 76% and 40% of patients, respectively, and a prostate-specific antigen (PSA) decrease of 75% or more from baseline was seen in 32% of evaluable patients [70].

Repeated therapy with ^{89}Sr is effective in relieving pain, though the response rate and duration of response may be lower than after first treatment. Re-treatment is permitted after 90 days; however, detailed reassessment and close follow-up is recommended because multiple therapies may lead to cumulative marrow toxicity [71–77]. Quilty et al. compared ^{89}Sr-chloride with radiation therapy in patients with prostate cancer. Individuals treated with ^{89}Sr experienced a longer time to onset of new painful sites than those who received radiation therapy alone, and fewer patients reported new pain sites after strontium therapy than after local or hemibody radiotherapy. However, there was no survival benefit [78]. When given as an adjuvant to external beam radiation, ^{89}Sr-chloride improved pain relief and delayed bone disease progression in hormone-resistant prostate cancer [79]. In a randomized phase III study, 126 hormone-refractory prostate cancer patients were treated with a higher dose (400 MBq) of ^{89}Sr-chloride as adjunct to radiation therapy while a comparable number received placebo. Patients who received ^{89}Sr-chloride had better response to pain control with reduced need for analgesia. Delayed progression of disease was noted as evidenced by lower requirement for subsequent radiotherapy; some showed lower tumor marker levels. Patients receiving strontium-89

also showed enhanced quality of life by some measures. Even with higher dose (10.8 mCi), the hematologic toxicity was reversible; however, no effect was noted on survival improvement [79] (Table 2).

^{89}Sr-chloride therapy given concurrently with chemotherapy may enhance pain relief and delay the onset of new painful metastases [80]. The role of ^{89}Sr in combination with a variety of chemotherapeutic agents has shown response rates (complete plus partial response) of between 55 and 80%. In a randomized trial in patients with hormone-refractory prostate cancer, cisplatin administered with ^{89}Sr-chloride showed better overall pain relief (91% vs. 63%), longer median duration of pain relief (120 days vs. 60 days), lower incidence of new sites of pain (14% vs. 30%), and lower progression of bone metastasis (27% vs. 64%) as compared to those with ^{89}Sr and placebo, respectively. Importantly, there were no significant differences in toxicities between the groups. There was no therapeutic effect noted as measured by PSA change and survival [81].

In patients with progressive bone metastases, hormonal therapy or chemotherapy alone is unable to provide durable control in pain

Table 2 ^{89}Sr-chloride clinical studies

Author, date	Disease	# of patients	Activity/dose	Major endpoints	Results
Ma et al. (2008)	Prostate cancer	116	40–60 μCi/kg	Toxicity, pain relief, PSA, ALP, LDH	84% with pain reduction. Decrease in bone markers
Tu et al. (2005)	Androgen-independent prostate cancer	34	55 μCi/kg and docetaxel +Sr or docetaxel alone	Long-term survival from prior study (Tu et al. 2001)	No bone marrow failure at 6 months; follow-up other treatments
Nilsson et al. (2005)	Androgen-independent prostate cancer	35	55 μCi/kg 5-FU, epirubicin, and mitomycin C	Double-blind randomization; toxicity, PSA, ALP	Higher toxicity in chemotherapy group while mild toxicity in ^{89}Sr group. Significant reduction in intensity and frequency of pain after 3 weeks in both groups
Baczyk et al. (2003)	Prostate cancer	70	4 mCi	Toxicity, pain relief, PSA, ALP, LDH	88% with pain reduction
Tu et al. (2001)	Androgen-independent prostate cancer	34/103	55 μCi/kg and docetaxel or docetaxel alone	Toxicity, PSA, ALP, survival	Overall 60% with >50% PSA decrease; 52% with complete pain reduction
Dafermou et al. (2001)	Prostate cancer	527	4 mCi	Toxicity, pain relief, PSA, ALP, LDH	60% with pain reduction
Turner et al. (2011)	Prostate cancer	93	4 mCi	elief, PSA, ALP, LDH	63% with pain reduction
Kraeber-Bodeara et al. (2000)	Prostate cancer	94	4 mCi	Toxicity, pain relief, PSA, ALP, LDH	78% with pain reduction
Porter et al. (1993)	Endocrine-resistant prostate cancer	126	10.8 mCi adjuvant therapy with ^{89}Sr vs. placebo	Pain relief, markers, QOL, cost	Significant improvement in pain and bone markers for those treated with ^{89}Sr vs. placebo
Quilty et al. (1994)	Prostate cancer	294	5.35 mCi	Local or hemibody radiation vs. ^{89}Sr	Pain relief up to 3 months: 63.6% after hemibody RT, 66.1% after ^{89}Sr. Fewer new pain sites after ^{89}Sr than RT. Average 30–40% decrease in platelet and WBC after ^{89}Sr

symptoms. It is likely that tumor cells that metastasize to the bone are intrinsically resistant or can withstand such treatments as a result of either continued exposure to factors in the bone microenvironment or secretion of factors that enhance the cell. For metastatic prostate cancer, initial therapy for metastatic disease involves androgen withdrawal, to which most patients respond. Relapse is usually seen accompanied by a change in phenotype that renders the tumor cells "castration resistant" and disease continues to progress despite conventional antiandrogen therapy.

Systemic therapy for castration-resistant prostate cancer (CRPC) has evolved considerably in the past decade, with the initial taxane-based therapy approved for metastatic CRPC followed by recent approval of nonsteroidal antiandrogens (enzalutamide) and androgen synthesis inhibitors (abiraterone) showing survival benefit. Multimodality therapy is therefore of interest, and more studies have emerged that evaluate various regimens.

Combined ^{89}Sr-chloride and chemotherapy may result in survival benefit in androgen-independent prostate cancer. A significant increase in both disease-free and median overall survival was seen in those who received ^{89}Sr and doxorubicin (27.7 months) compared to those who received doxorubicin alone (16.8 months) [82, 83]. In a randomized phase II trial, 103 patients received induction chemotherapy using ketoconazole and doxorubicin alternating with estramustine and vinblastine. Patients who did not progress following induction were randomized either to ^{89}Sr with doxorubicin or to doxorubicin only. Patients who received the bone-targeted therapy had a 14-month progression-free survival as opposed to a 7-month progression-free survival achieved by the patients who received chemotherapy alone. More importantly, patients treated with the strontium achieved an overall survival of 27.7 months as opposed to 16.8 months for those who received chemotherapy alone [83]. Although the trial was not powered to make direct comparisons of the two arms, the data do suggest that combinations of chemotherapy and treatments directed at bone metastases should be pursued. In a subgroup analysis of randomized phase II trial in which patients were administered either doxorubicin alone or doxorubicin with ^{89}Sr, patients who received the combination appeared to have an improvement in both disease-free and overall survival [82]. There is no conclusive data on survival benefit with ^{89}Sr monotherapy in metastatic bone disease though a significant decrease in PSA or pain may be accompanied by a longer survival [84, 85].

Small studies using docetaxel and ketoconazole with other chemotherapy agents like estramustine, paclitaxel, and vinblastine in prostate cancer have shown feasibility [81, 86]. A small randomized phase III trial (35 patients per arm) was conducted in which patients were randomized to either ^{89}Sr and cisplatin or ^{89}Sr alone. Chemotherapy enhanced the palliative effects of strontium (91% vs. 63%, $p < 0.01$) and increased the duration (134 days vs. 68 days, $p = 0.002$) of these effects. In addition, a lower proportion of patients who received both therapies progressed in the bone than in those who received strontium only (27% vs. 64%, $p = 0.01$). However, there was no significant therapeutic effect seen (PSA or survival), which is not surprising given that cisplatin as a single agent is not active in prostate cancer and given the small size of the study.

A more recent TRAPEZE trial performed in the UK compared the outcomes from administration of docetaxel alone vs. docetaxel plus ^{89}Sr or ZA, or both, and had a minimum follow-up of 12 months. Primary outcome measures such as clinical progression-free survival (CPFS) were collected, including progression of pain, skeletal-related events, or death. About 349/757 patients (46%) completed docetaxel treatment. A benefit of ^{89}Sr on CPFS was noted. While ZA had no significant effect on CPFS, it did have a significant effect on SRE-free intervals and fewer skeletal-related events in about a third of patients ($P = 0.01$). Neither ZA nor ^{89}Sr had a significant effect on OS [87].

The treatment can also be safely administered with conventional radiation therapy, ideally given just prior to or on the day of RT [88]. Concurrent administration may be more effective in preventing skeletal-related events. In a randomized

study comparing ^{89}Sr vs. placebo in patients with advanced castrate-sensitive prostate cancer, all had a follow-up treatment with androgen deprivation therapy and ZA and docetaxel. The treatment was found to be safe and feasible, though survival benefit could not be clearly defined in this small study [89].

While RP therapy is most effective in prostate cancer, it is also effective in breast cancer patients with bone metastases. Sciuto et al. observed pain relief in 84% of patients, with duration of pain relief ranging from 2 to 14 months [90]. Other studies in breast cancer have also reported pain relief in about 60–80% of patients, with duration of response between 3 and 12 months. Good relief (in 83% of patients) was also seen in patients re-treated with ^{89}Sr [72, 91]. Responses are better in patients with osteoblastic lesions and in those with limited involvement and higher performance status [92]. Clinical cases showing a decrease in the disease burden have been reported [93].

^{89}Sr has also been used successfully in other cancers, though large studies evaluating the effectiveness for pain control and survival are lacking [94, 95].

^{89}Sr-chloride is cost-effective, as the need for radiotherapy narcotic analgesic use and hospitalization is reduced [96]. A quality of life (QOL) and cost per additional quality-adjusted life-year (QALY) analysis were more favorable for ^{89}Sr than non-generic ZA; however, the use of generic ZA was most cost-effective [97]. Addition of both ZA and ^{89}Sr to standard chemotherapy was cost-effective and led to a small improvement in QALY with a modest increase in cost. The incremental cost-effectiveness ratios (ICER) were lower than the threshold for conventional willingness-to-pay per QALY thresholds for both ZA and ^{89}Sr [98].

^{153}Sm-EDTMP (Lexidronam)

^{153}Sm is a fission product with a half-life of 46.3 h. The radionuclide emits a beta particle with a maximum energy of 0.81 MeV, a mean energy of 0.23 MeV, an average soft tissue range of 0.6 mm, and a 28% abundant gamma emission with a photopeak of 0.103 MeV. Gamma emissions of ^{153}Sm allow gamma camera imaging to confirm the targeting of lesions [99, 100] as demonstrated on bone scans.^{153}Sm-EDTMP is usually administered at a dose of 1 mCi/kg.

^{153}Sm-EDTMPis made by complexing ^{153}SmCl acid with the calcium salt of EDTMP. It is a stable complex that selectively accumulates in skeletal tissue in association with hydroxyapatite. It accumulates in high concentration in areas of high bone turnover such as such as bone metastases [99, 100] (Fig. 1). Bone metastasis may contain 3–5 times more ^{153}Sm-EDTMP than healthy bone tissue; hence, the amount of drug retained in the body is related to the extent of metastases rather than the administered activity. About 50–60% of the administered dose localizes to bone in 2–3 h, with 30–50% excretion in urine and with larger relative amounts of activity deposited in bone in subjects with impaired renal function [100] or with widespread metastases.

^{153}Sm-EDTMP is cleared rapidly from the blood; 4–34% of the dose remains in the serum 1 h after administration [101]. An initial rapid phase is followed by a slower second phase with T1/2b that may range from 8.1 to 17.1 h. Urinary excretion is the main route of elimination, with the majority cleared at 6–8 h [101]. The low energy of the beta particle reduces the radiation burden to the bone marrow compared to ^{89}Sr. Hematological side effects are generally reversible and mild.

In an early study of dose escalation, Farhangi and colleagues studied 22 patients, giving escalating doses of ^{153}Sm-EDTMP from 0.1 to 1.0 mCi/kg (3.7–37 MBq/kg) [101]. The therapy was well tolerated with transient grade 1 myelotoxicity observed in 34.5% of cases; those with extensive metastases were more likely to have myelotoxicity. A later study in 52 prostate cancer patients used escalated doses from 0.5 to 3.0 mCi/kg (18.5–111 MBq/kg) [102]. Treatment at higher doses was also well tolerated, and maximum tolerated dose (MTD) was determined to be 2.5 mCi/kg (92.5 MBq/kg). Bone marrow suppression is generally mild (grade 1, 2) and reversible. Platelets and leukocytes may decrease about 10–40% from the pretreatment values, generally reaching nadir at 3–4 weeks. The recovery of both is

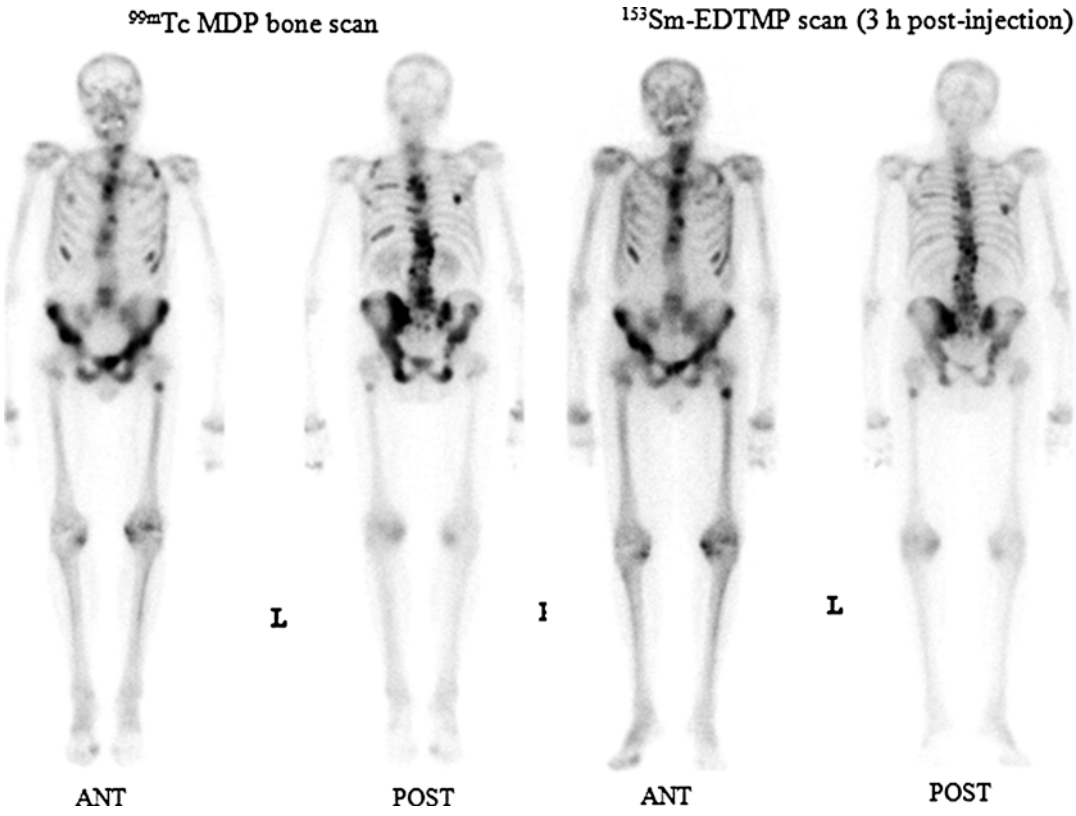

Fig. 1 Whole-body imaging: ^{99m}Tc-MDP bone scan and ^{153}Sm-EDTMP scan. Bone scan (*left*) shows multiple areas of abnormal uptake in the bones consistent with metastatic disease; targeting of all sites by ^{153}Sm-EDTMP is seen on whole-body scans (*right*)

generally complete, reaching the pretreatment values by 6–8 weeks [67, 103].

Multiple studies have shown the efficacy of ^{153}Sm-EDTMP therapy in pain palliation with the average response in variable malignancies between 62 and 74% [104, 105] (Table 3). A statistically insignificant trend toward improved survival was seen in those treated with higher doses than those treated with lower doses. Placebo-controlled studies have shown significant pain reduction with ^{153}Sm-EDTMP in a variety of cancers including CRPC [106]. ^{153}Sm-EDTMP showed an improved overall efficacy in pain relief of 77.8% compared to 44.4% with pamidronate alone, though transient myelotoxicity was also higher [107]. It has been suggested that prior treatment with pamidronate does not affect ^{153}Sm-EDTMP skeletal uptake [108].

Pain relief is generally noted within 5–10 days and can last up to 4 months. Repeated dosing of ^{153}Sm-EDTMP is feasible if pain returns or increases [109]. As with ^{89}Sr-chloride, transient exacerbation of the preexisting pain (flare) after ^{153}Sm-EDTMP has been seen in 12–20% of patients [110]. A change in whole-body uptake values for ^{99m}Tc-MDP on follow-up scanning after samarium therapy may be seen [100], though some studies suggest no change in bone scan appearance [101].

In a randomized dose-controlled study, 114 patients received either 18.5 MBq/kg or 37 MBq/kg of the ^{153}Sm-EDTMP. At 4 weeks, pain relief was better with the higher dose (55% vs. 70%). In patient-rated efficacy assessments including degree of pain, level of daytime discomfort, quality of sleep, and pain relief, improvement

Table 3 ^{153}Sm-EDTMP clinical studies

Author, date	Disease	# of patients	Activity	# ^{153}Sm injections	Chemotherapy	Major endpoints	Results
Resche et al. (1997)	Phase III dose-controlled study – CRPC and breast ($n = 36$)	114	18.5 MBq/kg vs. 37 MBq/kg	1	NA	Efficacy, toxicity, optimal dose	VAS-AUPC, PGA scores better for 37 mB/kg dose at 4 weeks, with responses seen up to 16 weeks. Response in up to 80%
Alberts et al. (1997)	Phase I/II, dose escalation	82	27.75–55.55–111 MBq/kg	1 or more	NA	Efficacy, toxicity	Pain control at all doses in 78–95% patients; duration of pain control 40–56 days, greater at higher doses. No dose-response relationship seen. Multiple doses are feasible but cause higher toxicity limiting treatment to only 38%
Serafini et al. (1998)	Double-blind placebo-controlled study; prostate cancer	118	18.5 MBq/kg vs. 37 MBq/kg	1	NA	VAS-AUPC, efficacy, toxicity, optimal dose	Pain response: Gr.1 in 20–40%; Gr.2 in 55–60%; Gr.3 in 62–72%; better responses at higher dose; no grade 4 toxicity
Tian et al. (1999)	Various malignancies (lung, breast, esophagus, prostate, GI, renal, others). Phase III, randomized study	105	18.5 MBq/kg vs. 37 MBq/kg	1	NA	Pain score, SEP, PGA, efficacy, toxicity	Effective pain response and palliation in 84%; temporary myelosuppression was the main SE; side effects were not dose-related
Sartor et al. (2004)	CRPC, phase III randomized trial – ^{153}Sm vs. nonradioactive Sm	152	37 MBq/kg	1	NA	Safety, efficacy	Pain relief noted within 1–2 weeks; reductions in opioid use noted at 3–4 weeks. Hematologic toxicity was mild; nadir WBC and platelet count seen at 3–4 weeks, recover at 8 weeks. No grade 4 hematologic toxicity
Suttmann et al. (2008)	Hormone-resistant prostate cancer	12	37MBq/kg	1	Docetaxel 35 mg/m^2	Toxicity, pain relief, PSA, ALP	50% with at least 50% PSA drop; pain reduction in 58%; decrease in bone markers

(*continued*)

Table 3 (continued)

Author, date	Disease	# of patients	Activity	# ^{153}Sm injections	Chemotherapy	Major endpoints	Results
Morris et al. (2009)	CRCP	28	18.5 MBq/kg; 27.75 MBq/kg; 37 MBq/kg	1–6; Average 2.9	Docetaxel (65, 70, 75, 75, 75 mg/m^2) +^{153}Sm; both multiple doses; average docetaxel dose #: 5.6 (range 1–13 doses)	Toxicity, PSA, ALP	Overall 54% with >50% PSA decrease; significant decrease in bone markers
Fizazi et al. (2009)	CRCP	43	37 MBq/kg	1	Consolidation docetaxel 20 mg/m^2 ×6	Toxicity, PSA-PFS survival; pain relief	5% grade 2 thrombocytopenia; median PSA-PFS was 6.4 months
Tu et al. (2009)	CRCP	18	37 MBq/kg	2	Docetaxel 25, 30, 35 mg/m^2 ×2	Toxicity	Mild toxicity with transient myelosuppression. Five patients (28%) with Gr.3 and no Gr. ≥ 4 hematologic toxicities
Lin et al. (2011)	CRCP	13	37 MBq/kg	2	Docetaxel 50, 75 mg/m^2 ×4	Toxicity	Transient myelosuppression, 35 episodes Gr. 3/4 neutropenia. One DLT Gr. 3 thrombocytopenia in cohorts 3 and 4. 8/13 (62%) with PSA drop >50%
Valicenti et al. (2011)	High-risk M0 prostate cancer; phase I		Dose escalation; phase I 9.25–74 MBq/kg	28	Postoperative hormone and radiation therapy (46.8 Gy pelvic region; 23.4 Gy prostate)	Toxicity	At 23 months median follow-up, 7% experienced Gr.3 hematologic toxicity. No increased toxicity seen at 74 MBq/kg dose vs. lower doses
Barai et al. (2015)	CRPC	44	37 MBq/kg	1	Plus capecitabine (1650 mg/m^2) orally for 8 days or placebo	Safety, pain/ analgesia	Improved pain control in study arm with capecitabine vs. placebo; low side effects

Abbreviations: *PGA* physician's global assessment, *VAS-AUPC* visual analog scale-area under the pain curve, *CRPC* castration-resistant prostate cancer, *SEP* sum of effect product, *PSA* prostate-specific antigen, *ALP* alkaline phosphatase, *PFS* progression-free survival, *DLT* dose-limiting toxicity

was seen in all patients. Among the subsets of patients examined, female patients with breast cancer receiving 1.0 mCi/kg had the most noticeable improvement. A predictable level of dose-related marrow suppression was seen with platelet and WBC nadirs at 3 or 4 weeks that recovered by 8 weeks [105].

Repeat therapy is feasible and safe and produces pain relief of similar magnitude as the first treatment. Hematologic toxicity may be cumulative, and larger decreases in blood counts may be noted with multiple dosing. No increase in frequency or severity of adverse events has been reported with repeated dosing. The treatment option should be considered in those whom bone pain recurs after an initial dose if baseline hematologic criteria are adequate [111].

In an early phase II study, re-treatment with ^{153}Sm-EDTMP was studied in 15 patients with treatment dose based on prospective evaluation of marrow dose limited to 2 Gy [109]. The re-treatment median radiation-absorbed dose to red marrow was 1.9 Gy at a median of 9 weeks (range 6–38) given after initial treatment. Pain control was seen in 13 patients (87%). A higher median duration of pain control (24 weeks) and survival (9 months) was seen in the re-treated group as against 8 weeks and 4 months, respectively, in those treated with a single dose [109]. Additional toxicity seen in the re-treated patients was confined to anemia, requiring blood transfusion in 9 of the 15 patients (60%).

In a prospective study with 202 patients treated with 37 MBq/kg of ^{153}Sm, 55 received $\geq$2 doses of ^{153}Sm-EDTMP. Pain scores, adverse events, and hematologic parameters were assessed after each dose. Common side effects included mild, transient suppression of platelets and white blood cell counts with nadir levels at 4 weeks post-treatment approximately half that at baseline. Recovery was generally seen by week 8 in 90% of patients. Temporary grade 3 thrombocytopenia occurred in 11, 12, and 17% of patients after the first, second, and third dose administration, respectively. Grade 3 leukopenia occurred in less than 7% of patients independent of the number of administrations. Significant decreases in pain scores ($P < 0.001$) were observed at week 4 after each of the first three doses and maintained at week 8 after the first two doses ($P < 0.003$), but not the third. Decreases in pain scores were observed in 70, 63, and 80% of patients, respectively, at week 4 after the first three administrations [111].

No significant data exists on the survival benefit of using ^{153}Sm alone. While studies showed a trend toward survival benefit, this was generally seen with higher doses or multiple dosing. In a randomized dose-controlled study, survival benefit was noted in breast cancer patients at larger dose of only 37 MBq/kg of ^{153}Sm-EDTMP; however, no confirmatory controlled trial has been conducted [105].

There is an increasing effort to utilize RP to improve patient outcomes. A particular focus has been in CRPC. In a small study, a single dose of samarium at the 37 MBq/kg (1 mCi/kg) dose level combined with six weekly infusions of 35 mg/m^2 docetaxel was given in 12 patients. With a mean follow-up of 11.4 (range, 1.1–25.8) months, overall 1-year survival was 48.6%, and median survival was 11.5 months. A PSA response of >50% was seen in 50% of patients and pain relief was seen in 58.3% of patients [112].

In a phase I study, patients were treated with a combination of escalating doses of ^{153}Sm-EDTMP and docetaxel; this combination was found to be safely administered at full doses over repeated cycles. Patients were assigned to six different cohorts based on increasing doses first of docetaxel and then of ^{153}Sm-EDTMP. Cycle 1 toxicity was used to define dose-limiting toxicity (DLT). The key aspect of this study was a starting dose of docetaxel at 65 mg/m^2, well within therapeutic range [113] escalated to 75 mg/m^2 in subsequent cohorts. Similarly, the starting dose of the ^{153}Sm-EDTMP was 0.5 mCi/kg in the combination, which escalated to the full FDA-approved dose of 1.0 mCi/kg. Dose reductions were imposed for both drugs in the event of hematologic or serious nonhematologic toxicities. Patients were removed from the study if they required more than two dose reductions. Twenty-eight men were treated in six cohorts. MTD was not reached because full doses of both agents were well tolerated, even when using an every-6-weeks

dosing schedule of ^{153}Sm-EDTMP. Patients received an average of 5.6 docetaxel doses (range, 1–13 doses) and 2.9 ^{153}Sm-EDTMP doses (range, 1–6 doses). Fifteen patients demonstrated a more than 50% decline in PSA, and some responses were also seen in the small group of patients with taxane-resistant disease [113]. Longer follow-up of these patients showed a median biochemical or radiographic progression-free survival of 7.0 months and an overall survival of 14.3 months. Nine patients (30%) did not recover platelet counts to >100 K/mm^3 after a median of three cycles to allow for additional treatment, with four patients experiencing prolonged thrombocytopenia. The most common reasons for trial discontinuation were progressive disease and hematologic toxicity [114].

Tu and colleagues also used a concurrent combination of weekly docetaxel with repeated ^{153}Sm-lexidronam in patients with CRPC. Eighteen patients were treated in three cohorts comprising two cycles of weekly docetaxel at 25, 30, and 35 mg/m^2, respectively, on days 1, 8, and 15 of a 28-day cycle in combination with ^{153}Sm-EDTMP (1 mCi/kg) on day 1 [115]. Failure to recover by day 56 of either combination cycle was considered unacceptable toxicity. Most toxicity was mild, with transient grade 3 myelosuppression in five patients (28%) and no grade 3 or more nonhematologic toxicities.

In a phase II study, Fizazi and colleagues treated 43 patients with docetaxel and ^{153}Sm-EDTMP as a consolidation therapy docetaxel 20 mg/m^2/week for 6 weeks with ^{153}Sm-EDTMP (37 MBq/kg) given in week 1 [116]. The PSA response was the primary endpoint, and pain response was assessed secondarily using a visual analog scale. A PSA response was obtained in 77% of patients and the pain response rate was 69%. The median PSA-PFS was 6.4 months. Median survival was 29 months, 1-year survival rate was 77%, while the 2-year survival rate was 56%.

Concurrent 6-month administration of four doses of docetaxel at doses of 75 mg/m^2 in a standard 3-week schedule with two doses of 37 MBq/kg ^{153}Sm-EDTMP given at 3-month intervals has also been shown to be feasible [117] as well as the combination with radiosensitizer capecitabine. A randomized prospective study with 44 patients with bone metastasis from various primary malignancies was carried out. The test group received a single dose of 1 mCi/kg ^{153}Sm-EDTMP plus capecitabine (1650 mg/m^2) orally for 8 days, while the control group received 1 mCi/kg ^{153}Sm-EDTMP dose plus placebo for the 8 days. A follow-up of 12 weeks showed significant improvement in degree of pain relief experienced by patients treated with concurrent capecitabine than those who did not receive capecitabine (pain score of 1.29 ± 1.05 and 3.59 ± 2.77, respectively). No significant differences in toxicity were seen between the two groups [118].

Samarium-153 EDTMP may be useful in patients with osteosarcoma. Early evaluation in a mouse model showed localization and significant effect on tumor [119]. In unresectable osteosarcoma cases, high-dose therapy with about 150 MBq/kg dose of Sm was found to be feasible and potentially useful [120–122]. Initial small experience of combined treatment with gemcitabine showed feasibility; however, pain response was not significant, so larger data sets and studies may be needed to establish this [123].

Therapy with Alpha Emitter Radium-223 Dichloride ($^{223}RaCl_2$)

Radium-223 (^{223}Ra) is an alpha particle-emitting radionuclide that has been approved by the US FDA for treatment of symptomatic bone metastatic disease from CRPC, with no visceral metastasis. ^{223}Ra decays ($t_{1/2}$ = 11.4 days) to stable lead, producing four α-particles and a chain of short-lived daughter radionuclides. In the decay of ^{223}Ra, 94% of the total decay energy is released as α-particles (Fig. 2). The noble gas first daughter ^{219}Rn has a $t_{1/2}$ of ~4 s, in contrast to the long-lived radon daughters from the other naturally occurring radium isotopes. ^{223}Ra can be produced efficiently in large amounts. The precursor ^{227}Ac ($t_{1/2}$ = 21.7 years) can be used as a long-term operating generator for ^{223}Ra [124, 125]. Actinium-227 is produced by neutron irradiation of

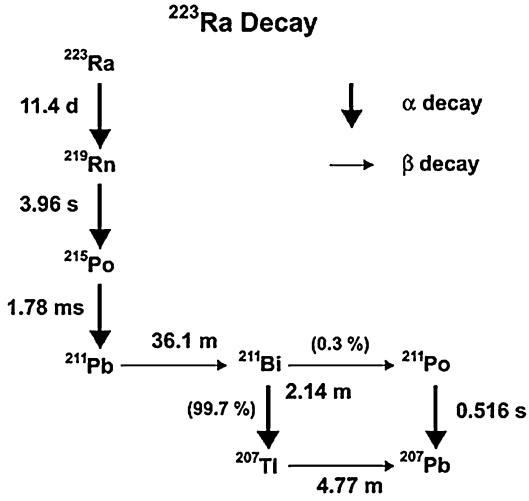

Fig. 2 ^{223}Radium decay

natural ^{226}Ra and decays via thorium-227 (half-life 18.7 days) to ^{223}Ra. The long $t_{1/2}$ of ^{223}Ra provides sufficient time for its preparation, distribution (including long-distance shipment), and administration to patients. Its low γ-irradiation is favorable from the point of view of handling, radiation protection, and treatment on an outpatient basis in the United States.

Alpha particles from the first three nuclides in the decay chain are emitted almost instantaneously. They are therefore likely to contribute to the radiation dose in the vicinity of the site of ^{223}Ra decay. Hence, ^{223}Ra has the potential to deliver a therapeutically relevant tumor dose from a relatively small amount of administered activity without causing unacceptable doses to nontargeted tissue.

The intrinsic bone-targeting properties of ^{223}Ra are similar to that of other alkaline earth elements, like calcium.^{223}Ra emits α-particles with high linear energy transfer (LET) alpha radiation and a limited range of less than 100 μm. These radiation characteristics generate highly localized and effective radiation zones with a high probability of inducing DNA double-strand breaks in cells. An α-emitter localized in or near bone metastases will deliver most radiation at the site of the lesion, thereby reducing exposure of surrounding normal tissues, especially marrow leading to less myelotoxicity. Initial assessment in animal models shows a significant ^{223}Ra antitumor effect in nude rats. All tumor-bearing control animals showed signs of induced paralysis 20–30 days after tumor cell injection, whereas rats treated with 110 kBq/kg showed a significantly increased symptom-free survival ($p < 0.05$). Approximately 40% of the treated rats were alive beyond the 67-day follow-up period compared to none in the control group [126].

Following an intravenous injection, ^{223}Ra clears rapidly from the blood and concentrates in increasing amounts in the bones. The major route of elimination is through the gut via the small intestine; only 1–5% radioactivity is seen in the urine in 48 h. The kidney and bladder exposure is low [127] (Table 4). On imaging, early radioactivity in the gut decreases and is thought to be within the gut contents, as it is seen to move with time on delayed imaging. There is no specific retention seen in other normal organs such as the heart, liver, gallbladder, stomach, or spleen. The highest radiation-absorbed doses are in the GI tract, bone, and red marrow [127, 128]. Imaging of lesions is possible (Fig. 3); however it is limited by low gamma counts and is not routinely recommended. Dosimetric estimations have been attempted but are not predictive of response due to high variations [129].

Initial studies showed promising results in patients with CRPC and potential application to other cancers such as breast, lung, and kidney cancer. In a dose escalation study, 31 patients with bone metastases from breast and prostate cancer received single and multiple doses of $^{223}RaCl_2$. The single-dose escalation ranged from 46 to 250 kBq/kg b.w., and multiple doses escalated from 50 kBq/kg to 125 kBq/kg including five or two doses at 3 or 6 weeks, respectively. Pain relief was observed in more than 50% of patients [127]. When the pain score data was pooled from all dose groups, a statistically significant decrease in pain score after treatment ($p < 0.05$) occurred during the 8-week observation period. Decreases in mean total alkaline phosphatase (ALP) values after injections of ^{223}Ra were observed in all dose groups.

Table 4 ^{223}Radium-dichloride clinical studies

Author, date	Disease	# of patients	Activity (kBq/kg); dose	Major endpoints	Results
Nilsson et al. (2005)	Breast, prostate. Phase I	25 (10 breast/ 15 prostate)	46, 93, 163, 213, or 250 ×1	Toxicity, ALP	Mild myelosuppression with nadirs at 2–4 weeks; few Gr. 3/4 SE; diarrhea, nausea, and vomiting were common SE, seen more at higher doses. Greater decrease in ALP in prostate vs. breast patients; about 52% reported pain relief by 7 days
Nilsson et al. (2007)	Prostate cancer; randomized phase II double-blind	64	50 vs. placebo q 4 weeks ×4	ALP, SRE, PSA progression, OS	Greater decrease in bone ALP post-^{223}Ra (median 65.6% vs. 9.3% in placebo arm); longer time to first SRE, time to PSA progression, median OS and OS with ^{223}Ra vs. placebo
Nilsson et al. (2012)	Prostate cancer; randomized phase II double-blind	100	5, 25, 50, or 100 x 1	Pain	Significant dose-response for pain seen as early as 2 weeks; higher pain response at largest dose (40% at 5 kBq/g vs. 56% at 50kbq/kg vs. 71% at 100 kBq/kg). Significant improvement in brief pain inventory functional index in all dose groups
Nilsson et al. (2013)	Prostate cancer; randomized phase II double-blind	64	50 q 4 weeks ×4 vs. placebo after XRT	Long-term safety, treatment-related AEs; 2-year survival	30% treated with ^{223}Ra were alive after 2 yrs. vs. 13% in placebo group; longer median OS (65 vs. 46 weeks) for ^{223}Ra and placebo group, respectively
Parker et al. (2013)	Prostate cancer; randomized phase III double-blind ALSYMPCA	921	50 vs. placebo q 4 weeks ×6	OS, SRE, PSA response, ALP, toxicity, QOL	^{223}Ra arm showed survival benefit as against placebo (median, 14.9 mos vs. 11.3 mos); low myelosuppression and adverse events rates
Sartor et al. (2014)	Prostate cancer; results from phase III, double-blind, randomized ALSYMPCA	921	50 vs. placebo q 4 weeks ×6	OS, SRE, QOL analysis	Symptomatic SRE in ^{223}Ra arm 33% vs. 38% in placebo; longer time to first symptomatic SRE with ^{223}Ra vs. placebo (median 15.6 vs. 9.8 months); reduced risk for EBRT and cord compression with ^{223}Ra; no significant reduced risk for pathologic bone fracture or tumor-related surgical intervention
Vogelzang et al. (2016)	Post-ad hoc analysis of hematologic toxicity from ALSYMPCA	901	50 q 4 weeks ×6	Hematologic toxicity	Gr.3/4 thrombocytopenia more common in ^{223}Ra vs. placebo patients (6% vs. 2%). Predictors of Gr.2 or more toxicity: disease extent,

(*continued*)

Table 4 (continued)

Author, date	Disease	# of patients	Activity (kBq/kg); dose	Major endpoints	Results
					PSA, hemoglobin, and decreased platelets
Saad et al. (2016)	CRPC, single-arm phase IIIb	696	50/55 q 4 weeks ×6 and concomitant medications	Safety, efficacy, OS	All grade SAE in 35%; Gr.3/4 SE included anemia (5%); thrombocytopenia (2%); neutropenia (1%); longer OS in those with baseline higher than ULN of ALP and Hb >10

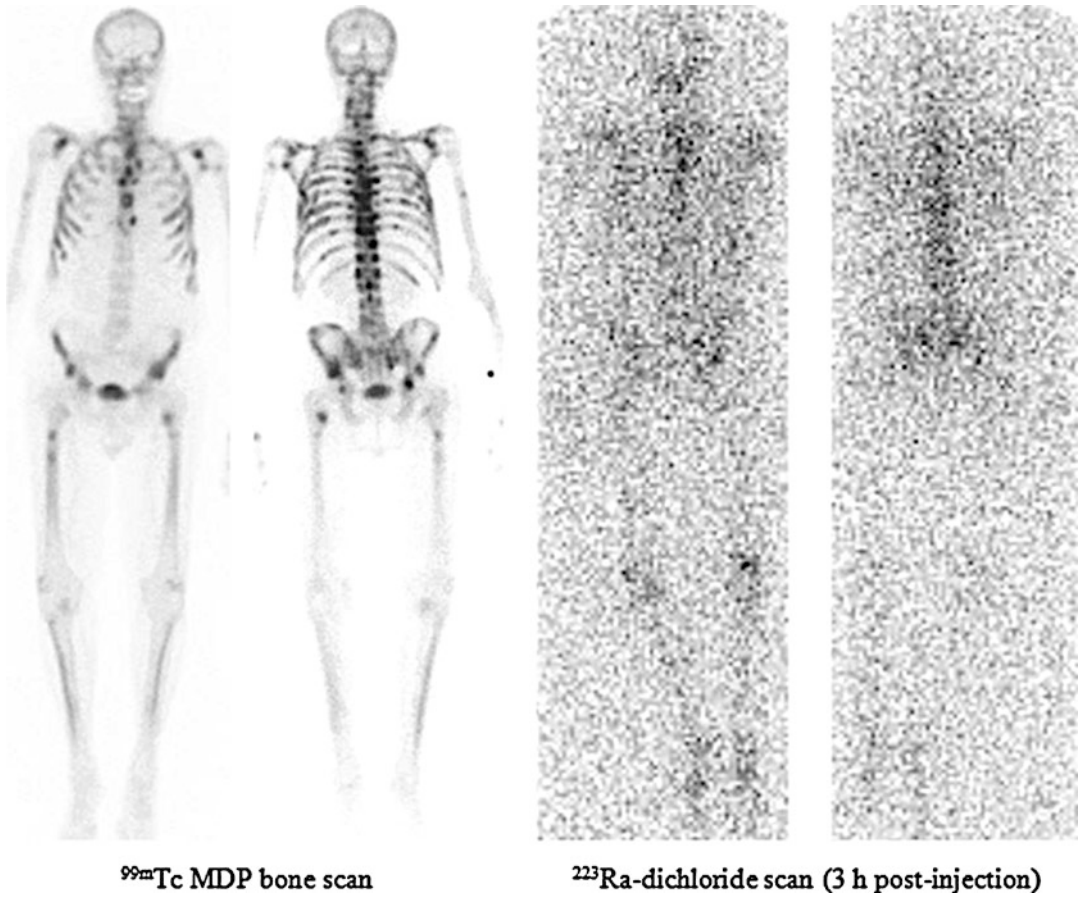

Fig. 3 Whole-body imaging: ^{99m}Tc-MDP bone scan and ^{223}Ra-dichloride scan. Bone scan (*left*) shows multiple areas of abnormal uptake in the bones consistent with metastatic disease; targeting of all sites by ^{223}Ra-dichloride is seen on whole-body scans (*right*)

In a follow-up randomized, multicenter phase II study, 33 patients received four doses of 50 kBq/kg (0.0014 mCi/kg) at 4-week intervals while 31 patients received placebo. Primary efficacy endpoint was decrease in serum bone markers; PSA response and time to PSA

progression were also monitored. Interim analysis showed a statistically significant decrease in bone alkaline phosphatase (~66%) from baseline compared with placebo (9.3%) [130]. Follow-up data for overall survival from the phase II study showed an increase in median survival time from 46 to 65 weeks for the $^{223}RaCl_2$ group vs. the placebo. At 2 years, 10 of 33 of patients (30%) treated with $^{223}RaCl_2$ were alive compared to 4 of 31 of placebo patients (13%), showing a trend for survival benefit with $^{223}RaCl_2$ [131].

A pivotal multicenter randomized, double-blind, placebo-controlled phase III study (ALSYMPCA) showed survival benefit from the use of radium dichloride in patients with CRPC. The efficacy and safety of ^{223}Ra-dichloride was compared with placebo in 921 patients receiving best standard-of-care treatment including local radiotherapy, corticosteroids, antiandrogens, estrogens, estramustine, or ketoconazole. All patients were allowed to continue androgen deprivation therapy. Patients received either ^{223}Ra at a dose of 50 kBq/kg or placebo every 4 weeks for up to six doses. Interim analysis in 809 patients showed improved survival with ^{223}Ra as compared to placebo (median time of 14.0 months vs. 11.2 months); this was confirmed in the final analysis of all 921 patients (median survival 14.9 months vs. 11.3 months). The myelosuppression rates and adverse events were low [132]. $^{223}RaCl_2$ treatment was also found to be helpful in patients who had not received prior docetaxel with the median overall survival of 16.1 months in this subgroup compared to placebo, with a median OS of 11.5 months. $^{223}RaCl_2$ was approved by the FDA in May 2013 and is currently marketed as Xofigo.

Single and multiple injections of $^{223}RaCl_2$ have been found to be safe and well tolerated, with manageable myelotoxicity and no indication of long-term toxicity. In general, most AEs seen are mild to moderate in severity and included nausea, bone pain, diarrhea, and fatigue. The most commonly reported serious adverse event (SAE) was bone pain, which was considered related to disease itself and not directly a result of the treatment. No dose-limiting hematotoxicity or increased risk of neutropenia was observed upon multiple administrations of $^{223}RaCl_2$ [127].

Multivariate analyses to assess baseline risk factors for hematologic toxicities in 901 patients treated in the phase III study with either $^{223}RaCl_2$($n = 600$) or placebo ($n = 301$) showed slightly higher incidence of grade 3/4 thrombocytopenia (6%) with $^{223}RaCl_2$ vs. 2% in placebo-treated patients. However, a greater number of patients completed all six cycles of treatment in the $^{223}RaCl_2$ arm (65%) compared to 48% in the control arm. The extent of disease with involvement of six or more sites and elevated PSA at baseline were predictors for grade 2–4 anemia; baseline hemoglobin and platelet levels and prior treatment with docetaxel were predictors for thrombocytopenia. The number of injections of $^{223}RaCl_2$ was not found to be significantly associated with cumulative hematologic toxicity [133].

A phase IIIb study performed following the ALSYMPCA trial as part of the early access program prior to regulatory approval of $^{223}RaCl_2$, evaluated safety and survival. Asymptomatic CRPC patients were also included; patients with two or more skeletal metastases by imaging were eligible. An additional criterion for inclusion was the absence of visceral disease (lymph node metastases <3 cm were allowed). Dosing was similar to the ALSYMPCA trial, though based on recalibration; some received a 55 kBq/kg dose. Other concomitant anticancer therapies were allowed. A total of 696 patients were treated; 403 (58%) received all six doses. About 523/696 (75%) patients had adverse events; 281 (40%) were treatment-related. Grade 3 or greater hematologic toxicity was seen in 1–5%. The median overall survival was 16 months. Median overall survival was longer in patients with nonelevated baseline alkaline phosphatase concentration, hemoglobin levels of 10 g/dL or greater, good performance status, and no pain at baseline. The study also showed safety of combined $RaCl_2$ and antiandrogen therapy and noted a higher median overall survival in patients who received concomitant denosumab, abiraterone, and/or enzalutamide [134]. A detailed analysis of quality of life (QOL) data from the ALSYMPCA trial showed that improved

survival was associated with a higher percentage of patients with meaningful improvement in QOL and a slower decline in QOL over time.

A follow-up evaluation of ALSYMPCA patients who had follow-up chemotherapy showed that generally the interval to start chemotherapy was later for those who were treated with ^{223}Ra than for placebo patients, though the duration of chemotherapy received was similar. There was low incidence of grade 3–4 hematologic toxicity in both groups; however, a greater decrease in platelet count from the baseline prior to chemotherapy was noted in ^{223}Ra vs. placebo patients. No significant difference was noted in median OS between those who had prior ^{223}Ra vs. placebo dose (16.0 and 15.8 months, respectively). The data suggests that subsequent treatment with chemotherapeutic agents is effective and safe in those treated with ^{223}Ra, as well as those who were not chemotherapy naïve prior to ^{223}Ra [135].

Other trials in prostate cancer are under way to assess feasibility and efficacy in different clinical states of prostate cancer and in combination with chemotherapy and antiandrogen therapy. Interim results of the "ERADICATE" trial assessing the efficacy of ^{223}Ra-dichloride with concurrent abiraterone acetate and prednisone in 36 symptomatic CRPC patients showed improvement of symptoms with decreased pain, significant improvement in QOL, and enhanced quality of sleep [136].

Data on ^{223}Ra in other malignancies such as breast cancer is emerging. Early studies in mouse models have shown decreased osteolysis and tumor growth leading to improvement in survival [137]. Safety and short-term efficacy of ^{223}Ra in breast cancer have been reported in a small study with 23 patients. This was an open-label, phase IIa nonrandomized study in breast cancer patients with progressive bone metastasis who were not candidates for endocrine therapy; patients were treated with 50 kBq/kg IV of ^{223}Ra every 4 weeks for four cycles. ^{223}Ra significantly reduced urinary N-telopeptide of type 1 (uNTX-1) and serum bone alkaline phosphatase. Metabolic response with decrease in [^{18}F]FDG avidity was seen in 50/155 lesions following two treatments. The overall metabolic response rate at the end of four cycles of treatment or week 17 was 41.5% [138].

Randomized studies evaluating the role of ^{223}Ra in estrogen receptor (ER)-positive breast cancer patients with and without combination therapies such as exemestane or everolimus have been initiated (NCT02258464, NCT02258451); exploratory studies in other malignancies such as lung cancer and myeloma are under way. It should be noted that the "bone tropism" of prostate cancer metastases may make it preferentially suitable for such therapy.

Other Agents

With the availability of alpha therapy with ^{223}Ra, the development of other bone-seeking agents has declined in recent years. These agents remain investigative and the subject of research interest. Specific advantages and clinical applications are yet to be established with these agents.

Rhenium-Labeled Radiopharmaceuticals: ^{186}Re-HEDP and ^{188}Re-HEDP (Etidronate)

Two rhenium isotopes (^{186}Re and ^{188}Re) (Table 1) linked to bisphosphonates have been tested in patients, but have not gained regulatory approval for clinical use in the US or European Union [84]. ^{186}Re has a physical half-life of 3.7 days, emits a beta particle with a maximum energy of 1.07 MeV and a mean energy of 0.349 MeV, and has an average range of 0.5 mm in dense bone and 1.1 mm in soft tissue. It has low abundance (9%) of 137 keV gamma emissions. ^{186}Re is conjugated to 1-hydroxyethylidene-1,1-diphosphonate (^{186}Re-HEDP/^{186}Re(Sn)HEDP or etidronate) complex, which attaches to hydroxyapatite crystals by forming hydroxide bridges.

^{186}Re-HEDP has a plasma half-life of 41.0 ± 6.0 h [84] with about 70% of the activity excreted in the urine in 24 h in subjects with no evidence of bone metastases. The maximum tolerated activity is 2960 MBq in patients with metastatic prostate cancer. The bone marrow-absorbed dose is about

1.04 mGy/MBq [85]. A number of initial studies reported safety and efficacy for the use of ^{186}Re-HEDP in bone pain palliation. A study by Sciuto et al. with ^{186}Re-HEDP showed an overall pain palliation rate of 92% in breast cancer patients [69]. Pain relief was established early, and tumor-/bone marrow-absorbed dose ratio was 14:1, suggesting clinical relevance in patients with more compromised bone marrow reserve. Typical marrow recovery times ranged from 4 to 6 weeks. A small study in breast cancer patients ($n = 12$) showed an MTD of 2405 MBq (65 mCi), limited primarily by thrombocytopenia [139].

An evaluation of pain response and hematologic toxicity in prostate and breast cancer patients receiving single or multiple therapies with ^{186}Re-HEDP while on ZA treatments showed a slightly greater decrease in WBC, hemoglobin, and platelet levels. However, only platelets showed a significant decrease compared to baseline levels after repeat therapies. Pain responses were seen in all patients, and improvements were seen after therapies even with multiple doses [140]. A single study has shown a baseline hemoglobin level to be predictive of pain response [141]. High-dose therapy has been tested in a preliminary phase I study in 25 patients with progressive hormone-refractory prostate cancer with bone metastasis. Doses ranging between 2500 and 5000 MBq (67.6–135 mCi) of ^{186}Re-hydroxyethylidene diphosphonate were administered, followed by reinfusion of peripheral blood stem cells 14 days later. Five of 25 patients (20%) showed a PSA drop at 4 weeks [142]. The concept, however, has not been evaluated in larger studies, and other forms of treatment are now available that are less intensive.

^{188}Re is a generator-produced isotope that may be "milked" on demand from a ^{188}W/^{188}Re generator. A kit is available for conjugating it to HEDP. Methods have been developed to obtain a high yield of GMP-radiolabeled agent [143, 144].^{188}Re has a beta energy of 2.1 MeV with a gamma emission of 155 keV (15% abundance) that allows for imaging. The high beta energy has the potential to kill tumor cells. The physical half-life is 16.8 h. The biodistribution of ^{188}Re (Sn)HEDP is identical to ^{186}Re(Sn)HEDP with rapid urinary excretion; 60 ± 12% of administered activity is in the urine by 48 h, which varies with renal function and extent of osteoblastic metastases [145].

Limited data exists on the use of this agent in the treatment of bone pain. An initial study demonstrated pain palliation in 60–75% of prostate cancer patients receiving a dose of 2.6 GBq or higher [146]. Pain responses in breast and prostate cancer patients are noted and similar to other agents [147]. The possibility of repeated therapy at low cost has led to the agent being investigated for use in developing countries. The effectiveness of repeated therapy using ^{188}Re-HEDP has been demonstrated in 64 patients with progressive, hormone-resistant prostate cancer [148]. A QOL assessment following treatment in prostate ($n = 45$) and breast cancer ($n = 47$) patients showed a significant decrease in pain visual analog scale and overall pain response of 69%and an overall QOL response rate of 68% after a single injection of ^{188}Re-HEDP. The responses were similar even after repeated therapies [149].

^{117m}Sn-Pentetate and ^{177}Lu-EDTMP

^{117m}Sn-pentetate emits conversion electrons with therapeutic potential; their high LET and very short range in soft tissue (0.2–0.3 mm) may explain lower myelosuppression with ^{117m}Sn-pentetate as compared to other agents.

^{117m}Sn is injected as the pentetate (DTPA) chelate and has no affinity for hydroxyapatite. The mechanism of localization is unclear and is postulated to occur via precipitation of stannous oxide on bone surfaces and possibly involving hydrolysis reaction with hydroxyapatite. The uptake pattern is similar to 99mTc-MDP. There is biexponential clearance related to a soft tissue component (22%) with clearance average half-life of 1.45 d and the second bone phase (77.6%) that showed no biologic clearance. Urinary clearance was not very high, with 11.4% excreted in urine within 24 h and 22.4% in 14 days [150]. Studies have estimated that the pain palliation rate is approximately 75%. No apparent dose-response relationship is evident; at doses more than 12 mCi

Table 5 Common indications and contraindications for radiopharmaceutical therapy of bone metastasis

Indications	Contraindications
Multiple painful osseous metastases for bone pain palliation agents	Pregnancy; breastfeeding
Symptomatic castration-resistant metastatic prostate cancer without visceral metastasis	Acute/chronic renal failure
	Acute spinal cord suppression – needs external radiation therapy
	Hb <10.0 g/L
	Total white cell count $<3.0 \times 10^9$/L
	Granulocytes <2000/mL; platelets $<60 \times 10^9$/L
	GFR <30 mL/min

(per 70 kg body weight), pain palliation has been noted as early as <1 week after treatment [151]. ^{117m}Sn-DTPA is not currently approved for clinical use.

^{177}Lu has been explored as a potential radionuclide for bone pain palliation chelated to EDTMP [152], DTPMP, or TTHMP with stability for up to 14 days [153] and also with DOTMP, which shows the longest stability up to 40d [154]. ^{177}Lu has a half-life of 6.71 days and is both a beta and gamma emitter [155]. Preliminary studies have shown dose-related pain responses at low (1295 MBq/35 mCi; 55% pain response) as well as high dose (2590 MBq/75 mCi; 80% pain response). Pain response was seen prominently by 2 weeks, and toxicities at both levels were low. The low dose was found sufficient for adequate treatment of bone pain in breast cancer and hormone-refractory prostate cancer [156]. A prospective comparison of ^{177}Lu-EDTMP with ^{153}Sm-EDTMP carried out in 32 patients with bone pain showed comparable pain responses, improvement of symptoms, and QOL between the two [157].

These studies are preliminary and encouraging; however, more studies in focused clinical states are needed to establish its role and to define its specific clinical application, especially with an increasing array of currently available approved agents.

Patient Identification and Referral

Patients are generally referred for radiopharmaceutical bone pain palliation by medical or radiation oncologists or pain medicine physicians.

Table 6 Checklist prior to administration of radiopharmaceutical

Positive bone scan (within 6–12 weeks)
Symptoms: worsening bone pain despite pain medication or other related to metastatic disease
Exclude cord compression
H/o chemotherapy, external beam radiation within 6 weeks before therapy with bone-targeting radiopharmaceutical: assessment and planning
Evaluate for extent of disease: for $^{223}RaCl_2$, exclude visceral metastasis
Get informed consent
Labs:
Obtain blood counts as close as possible to treatment – preferably within 2 weeks prior
Ensure adequate blood cell count levels

A detailed history should be taken to evaluate patient eligibility based on performance status, presence of other systemic illness like renal failure, and any symptoms that may suggest vertebral fracture or acute cord compression. Cord compression is an emergency that warrants immediate radiation therapy and/or sometimes surgery. RPs have no place in the management of spinal cord compression or pathological fracture (Tables 5 and 6).

Administration of Radiopharmaceutical Agent

Once eligibility is established, the patient is usually treated in an outpatient setting. Patient identifiers are checked, and informed consent is obtained for administration of systemic radiopharmaceutical therapy after discussing the possibility

of transiently increased pain due to flare response. An intravenous line is inserted and checked for good blood return and free flow of the saline flush. Care must be taken to prevent extravasation of tracer, which may cause tissue necrosis. Patient weight is checked and used to calculate the treatment dose for ^{153}Sm-EDTMP and ^{223}Ra. The radiopharmaceutical is injected as a slow intravenous injection over a period of 1–2 min and flushed with 10–20 ml of saline. In the United States, the use and administration of these RPs fall under the guidelines of the Nuclear Regulatory Commission (NRC).

Radiation level in the patient at surface and 1 m is checked. The patient is instructed about radiation safety precautions (Table 7). For those administering the dose, contamination control involves employing universal body fluid precautions when working with the patient. Federal guidelines [158] do not require patient-specific ALARA (as low as reasonably achievable) instructions for patients receiving up to 140 mCi of ^{153}Sm-EDTMP. In addition, no limit is placed on patients receiving the pure beta emitter ^{89}Sr because of minimal exposure to members of the public. Alpha emitters generally pose no major radiation exposure concern for outpatient treatments. The nuclear medicine physician or a radiation safety officer typically discusses detailed radiation safety precautions after reviewing individual patient specifics.

Table 7 Suggested radiation safety specifications for beta-emitting therapy to treat painful bone metastases

Radiation safety specifications
1. Many of the agents are primarily removed from the body via urine or stool. Practice good hygiene when using the toilet: Sit down to urinate to reduce possibility of contamination Flush toilet twice after use Wipe any spilled urine with a tissue and flush it away Avoid soiling underclothing or areas around toilet bowls Wash hands thoroughly after using the toilet
2. Wash clothes and bed linens if they become soiled. Wash them separately from other clothes
3. If cut, wash away blood. Wipe spilled blood with tissue and flush it away
4. There is generally no medically significant exposure to other people; no requirement for isolation or limiting interaction with others
5. Eat a normal diet

The patient usually follows up with the referring physician, who evaluates the patient's clinical response and obtains blood counts at recommended intervals (usually weekly for the first 6–10 weeks and more frequently if there is evidence of toxicity, although a drop in counts is uncommon before 7–14 days after treatment). Blood counts, notably platelet and white blood cell counts, should be obtained until all counts are normal; return to pretreatment baseline may not always occur.

Summary

Bone pain palliation therapy with radiopharmaceuticals is a cost-effective systemic therapy to relieve pain from skeletal metastases with a consequent decrease in morbidity and an improvement in quality of life. Both beta- and alpha-emitting agents are effective in improving symptoms and quality of life. ^{223}Ra has been approved by the FDA for specific use in symptomatic CRPC with no visceral metastasis, and studies are under way to evaluate its role in other clinical states and in combination with other therapies. Beta emitters have been available for many years for bone pain palliation in metastatic disease. RPs should be considered in patients with widespread osteoblastic metastases causing multiple painful skeletal sites. Bone-seeking radiopharmaceuticals as part of a multimodality regimen may also slow disease progression. Repeat therapies should be carefully administered when blood counts have returned to safe levels. Combination therapy with other agents is possible with careful planning and follow-up for additional toxicities.

References

1. Coleman RE. Metastatic bone disease: clinical features, pathophysiology and treatment strategies. Cancer Treat Rev. 2001;27(3):165–76.
2. Frassica FJ, Gitelis S, Sim FH. Metastatic bone disease: general principles, pathophysiology, evaluation, and biopsy. Instr Course Lect. 1992;41:293–300.

3. Hage WD, Aboulafia AJ, Aboulafia DM. Incidence, location, and diagnostic evaluation of metastatic bone disease. Orthop Clin North Am. 2000;31(4):515–28.vii.
4. WHO. World health organization. Cancer pain relief. Geneva: World Health Organization; 1986. http://www.WHO.int/cancer/palliative/painladder/en/.
5. NCCN practice guidelines: adult cancer pain. 2016. https://www.nccn.org/professionals/physician_gls/f_guidelines.asp.
6. Steeg PS. Tumor metastasis: mechanistic insights and clinical challenges. Nat Med. 2006;12(8):895–904.
7. Steeg PS. Targeting metastasis. Nat Rev Cancer. 2016;16(4):201–18.
8. Choong PF. The molecular basis of skeletal metastases. Clin Orthop Relat Res. 2003;415(Suppl):S19–31.
9. Zhao Y, Wang Y, Liu J. P-selectin and tumor metastasis. Zhonghua Jie He He Hu Xi Za Zhi. 2001;24(9):568–70.
10. Yeatman TJ, Nicolson GL. Molecular basis of tumor progression: mechanisms of organ-specific tumor metastasis. Semin Surg Oncol. 1993;9(3):256–63.
11. Tang DG, Honn KV. Adhesion molecules and tumor metastasis: an update. Invasion Metastasis. 1994;14(1–6):109–22.
12. Laubli H, Borsig L. Selectins promote tumor metastasis. Semin Cancer Biol. 2010;20(3):169–77.
13. Kim YJ, et al. P-selectin deficiency attenuates tumor growth and metastasis. Proc Natl Acad Sci U S A. 1998;95(16):9325–30.
14. Coupland LA, Chong BH, Parish CR. Platelets and P-selectin control tumor cell metastasis in an organ-specific manner and independently of NK cells. Cancer Res. 2012;72(18):4662–71.
15. Koukoulis GK, Patriarca C, Gould VE. Adhesion molecules and tumor metastasis. Hum Pathol. 1998;29(9):889–92.
16. Blair JM, et al. Mechanisms of disease: roles of OPG, RANKL and RANK in the pathophysiology of skeletal metastasis. Nat Clin Pract Oncol. 2006;3(1):41–9.
17. Rabbani SA, et al. Over-production of parathyroid hormone-related peptide results in increased osteolytic skeletal metastasis by prostate cancer cells in vivo. Int J Cancer. 1999;80(2):257–64.
18. Orr FW, et al. Tumor-bone interactions in skeletal metastasis. Clin Orthop Relat Res. 1995;312:19–33.
19. Parfitt AM. Targeted and nontargeted bone remodeling: relationship to basic multicellular unit origination and progression. Bone. 2002;30(1):5–7.
20. Parfitt AM. Bone remodeling, normal and abnormal: a biological basis for the understanding of cancer-related bone disease and its treatment. Can J Oncol. 1995;5(Suppl 1):1–10.
21. Raisz LG. Physiology and pathophysiology of bone remodeling. Clin Chem. 1999;45(8 Pt 2):1353–8.
22. Powell GJ, et al. Localization of parathyroid hormone-related protein in breast cancer metastases: increased incidence in bone compared with other sites. Cancer Res. 1991;51(11):3059–61.
23. Mantyh PW, et al. Molecular mechanisms of cancer pain. Nat Rev Cancer. 2002;2(3):201–9.
24. Pareek TK, et al. Cyclin-dependent kinase 5 modulates nociceptive signaling through direct phosphorylation of transient receptor potential vanilloid 1. Proc Natl Acad Sci USA. 2007;104(2):660–5.
25. Sabino MA, et al. Simultaneous reduction in cancer pain, bone destruction, and tumor growth by selective inhibition of cyclooxygenase-2. Cancer Res. 2002;62(24):7343–9.
26. Heidenreich A, Ohlmann CH. Ibandronate: its pharmacology and clinical efficacy in the management of tumor-induced hypercalcemia and metastatic bone disease. Expert Rev Anticancer Ther. 2004;4(6):991–1005.
27. Heidenreich A, Hofmann R, Engelmann UH. The use of bisphosphonate for the palliative treatment of painful bone metastasis due to hormone refractory prostate cancer. J Urol. 2001;165(1):136–40.
28. Honore P, et al. Osteoprotegerin blocks bone cancer-induced skeletal destruction, skeletal pain and pain-related neurochemical reorganization of the spinal cord. Nat Med. 2000;6(5):521–8.
29. Russell RG. Bisphosphonates: from bench to bedside. Ann N Y Acad Sci. 2006;1068:367–401.
30. Vitte C, Fleisch H, Guenther HL. Bisphosphonates induce osteoblasts to secrete an inhibitor of osteoclast-mediated resorption. Endocrinology. 1996;137(6):2324–33.
31. Finley RS. Bisphosphonates in the treatment of bone metastases. Semin Oncol. 2002;29(1 Suppl 4):132–8.
32. Liu J, et al. Bisphosphonates in the treatment of patients with metastatic breast, lung, and prostate cancer: a meta-analysis. Medicine (Baltimore). 2015;94(46):e2014.
33. Van Acker HH, et al. Bisphosphonates for cancer treatment: mechanisms of action and lessons from clinical trials. Pharmacol Ther. 2016;158:24–40.
34. Berenson JR, et al. Zoledronic acid reduces skeletal-related events in patients with osteolytic metastases. Cancer. 2001;91(7):1191–200.
35. Strobl S, et al. Adjuvant bisphosphonates and breast cancer survival. Annu Rev Med. 2016;67:1–10.
36. Rennert G, et al. Oral bisphosphonates and improved survival of breast cancer. Clin Cancer Res. 2017;23(7):1684–89.
37. Lebret T, et al. The use of bisphosphonates in the management of bone involvement from solid tumours and haematological malignancies – A European survey. Eur J Cancer Care (Engl). 2017 Jul;26(4). doi: 10.1111/ecc.12490.
38. Hendriks LE, et al. Effect of bisphosphonates, denosumab, and radioisotopes on bone pain and quality of life in patients with non-small cell lung cancer and bone metastases: a systematic review. J Thorac Oncol. 2016;11(2):155–73.
39. Saad F. The role of bisphosphonates in the management of prostate cancer. Curr Oncol Rep. 2006;8(3):221–7.
40. Berry S, et al. The use of bisphosphonates in men with hormone-refractory prostate cancer: a systematic

review of randomized trials. Can J Urol. 2006;13(4): 3180–8.
41. Smith MR, et al. Denosumab for the prevention of skeletal complications in metastatic castration-resistant prostate cancer: comparison of skeletal-related events and symptomatic skeletal events. Ann Oncol. 2015;26(2):368–74.
42. Smith MR, et al. Denosumab in men receiving androgen-deprivation therapy for prostate cancer. N Engl J Med. 2009;361(8):745–55.
43. Fizazi K, et al. Denosumab versus zoledronic acid for treatment of bone metastases in men with castration-resistant prostate cancer: a randomised, double-blind study. Lancet. 2011;377(9768):813–22.
44. Gartrell BA, et al. Toxicities following treatment with bisphosphonates and receptor activator of nuclear factor-kappaB ligand inhibitors in patients with advanced prostate cancer. Eur Urol. 2014;65(2): 278–86.
45. Cookson MS, et al. Castration-resistant prostate cancer: AUA guideline amendment. J Urol. 2015;193(2): 491–9.
46. Sze WM, et al. Palliation of metastatic bone pain: single fraction versus multifraction radiotherapy – A systematic review of randomised trials. Clin Oncol (R Coll Radiol). 2003;15(6):345–52.
47. Chow E, et al. Palliative radiotherapy trials for bone metastases: a systematic review. J Clin Oncol. 2007;25(11):1423–36.
48. Jeremic B, et al. A randomized trial of three single-dose radiation therapy regimens in the treatment of metastatic bone pain. Int J Radiat Oncol Biol Phys. 1998;42(1):161–7.
49. Lo, S.S et al. Expert panel on Radiation Oncology Bone metastases et al. ACR appropriateness criteria. (R) spinal bone metastases. J Palliat Med. 2013;16(1): 9–19.
50. Gaultney J, et al. Results of a dutch cost-effectiveness model of radium-223 in comparison to cabazitaxel, abiraterone, and enzalutamide in patients with metastatic castration resistant prostate cancer previously treated with docetaxel. Value Health. 2015;18(7): A459.
51. Macedo A, et al. Cost-effectiveness of samarium-153-EDTMP for the treatment of pain due to multiple bone metastases in hormone-refractory prostate cancer versus conventional pain therapy, in Portugal. Acta Medica Port. 2006;19(5):421–6.
52. McEwan AJ, et al. A retrospective analysis of the cost effectiveness of treatment with Metastron (^{89}Sr-chloride) in patients with prostate cancer metastatic to bone. Nucl Med Commun. 1994; 15(7):499–504.
53. Silberstein EB. Dosage and response in radiopharmaceutical therapy of painful osseous metastases. J Nucl Med. 1996;37(2):249–52.
54. Silberstein EB, Elgazzar AH, Kapilivsky A. Phosphorus-32 radiopharmaceuticals for the treatment of painful osseous metastases. Semin Nucl Med. 1992;22(1):17–27.
55. Lawrence JH, Low-Beer BV, Carpender JW. Chronic lymphatic leukemia; a study of 100 patients treated with radioactive phosphorus. J Am Med Assoc. 1949;140(7):585–8.
56. Lawrence JH, Dobson RL, et al. Chronic myelogenous leukemia; a study of 129 cases in which treatment was with radioactive phosphorus. J Am Med Assoc. 1948;136(10):672–7.
57. Maxfield Jr JR, et al. The use of radioactive phosphorus and testosterone in metastatic bone lesions from breast and prostate. South Med J. 1958;51(3):320–7.
58. Cheung A, et al. Evaluation of radioactive phosphorus in the palliation of metastatic bone lesions from carcinoma of the breast and prostate. Radiology. 1980;134(1):209–12.
59. Silberstein EB. The treatment of painful osseous metastases with phosphorus-32-labeled phosphates. Semin Oncol. 1993;20(3 Suppl 2):10–21.
60. Blake GM, et al. Sr-89 therapy: strontium kinetics in disseminated carcinoma of the prostate. Eur J Nucl Med. 1986;12(9):447–54.
61. Laing AH, et al. Strontium-89 chloride for pain palliation in prostatic skeletal malignancy. Br J Radiol. 1991;64(765):816–22.
62. Silberstein EB, et al. Strontium-89 therapy for the pain of osseous metastases. J Nucl Med. 1985;26(4):345–8.
63. McEwan AJ. Unsealed source therapy of painful bone metastases: an update. Semin Nucl Med. 1997;27(2): 165–82.
64. Baumrucker S. Palliation of painful bone metastases: Strontium-89. Am J Hosp Palliat Care. 1998;15(2): 113–5.
65. Mertens WC, Stitt L, Porter AT. Strontium 89 therapy and relief of pain in patients with prostatic carcinoma metastatic to bone: a dose response relationship? Am J Clin Oncol. 1993;16(3):238–42.
66. Blake GM, et al. Strontium-89 therapy: measurement of absorbed dose to skeletal metastases. J Nucl Med. 1988;29(4):549–57.
67. McEwan AJ. Use of radionuclides for the palliation of bone metastases. Semin Radiat Oncol. 2000;10(2): 103–14.
68. Lewington VJ, et al. A prospective, randomised double-blind crossover study to examine the efficacy of strontium-89 in pain palliation in patients with advanced prostate cancer metastatic to bone. Eur J Cancer. 1991;27(8):954–8.
69. Sciuto R, et al. Radiosensitization with low-dose carboplatin enhances pain palliation in radioisotope therapy with strontium-89. Nucl Med Commun. 1996;17(9):799–804.
70. Tu SM, et al. Strontium-89 combined with doxorubicin in the treatment of patients with androgen-independent prostate cancer. Urol Oncol. 1996;2(6):191–7.
71. Giammarile F, et al. Bone pain palliation with ^{85}SR therapy. J Nucl Med. 1999;40(4):585–90.

72. Fuster D, et al. Usefulness of strontium-89 for bone pain palliation in metastatic breast cancer patients. Nucl Med Commun. 2000;21(7):623–6.
73. Jager PL, et al. Treatment with radioactive ^{89}strontium for patients with bone metastases from prostate cancer. BJU Int. 2000;86(8):929–34.
74. Kraeber-Bodere F, et al. Treatment of bone metastases of prostate cancer with strontium-89 chloride: efficacy in relation to the degree of bone involvement. Eur J Nucl Med. 2000;27(10):1487–93.
75. Giammarile F, et al. Bone pain palliation with strontium-89 in cancer patients with bone metastases. Q J Nucl Med. 2001;45(1):78–83.
76. Windsor PM. Predictors of response to strontium-89 (Metastron) in skeletal metastases from prostate cancer: report of a single centre's 10-year experience. Clin Oncol (R Coll Radiol). 2001;13(3):219–27.
77. Kasalicky J, Krajska V. The effect of repeated strontium-89 chloride therapy on bone pain palliation in patients with skeletal cancer metastases. Eur J Nucl Med. 1998;25(10):1362–7.
78. Quilty PM, et al. A comparison of the palliative effects of strontium-89 and external beam radiotherapy in metastatic prostate cancer. Radiother Oncol. 1994;31(1):33–40.
79. Porter AT, McEwan AJ. Strontium-89 as an adjuvant to external beam radiation improves pain relief and delays disease progression in advanced prostate cancer: results of a randomized controlled trial. Semin Oncol. 1993;20(3 Suppl 2):38–43.
80. Sciuto R, et al. Effects of low-dose cisplatin on ^{89}Sr therapy for painful bone metastases from prostate cancer: a randomized clinical trial. J Nucl Med. 2002;43(1):79–86.
81. Akerley W, et al. A multiinstitutional, concurrent chemoradiation trial of strontium-89, estramustine, and vinblastine for hormone refractory prostate carcinoma involving bone. Cancer. 2002;94(6):1654–60.
82. Tu SM, et al. Therapy tolerance in selected patients with androgen-independent prostate cancer following strontium-89 combined with chemotherapy. J Clin Oncol. 2005;23(31):7904–10.
83. Tu SM, et al. Bone-targeted therapy for advanced androgen-independent carcinoma of the prostate: a randomised phase II trial. Lancet. 2001;357(9253):336–41.
84. Kuroda I, et al. Strontium-89 for prostate cancer with bone metastases: the potential of cancer control and improvement of overall survival. Ann Nucl Med. 2014;28(1):11–6.
85. Zyskowski A, et al. Strontium-89 treatment for prostate cancer bone metastases: does a prostate-specific antigen response predict for improved survival? Australas Radiol. 2001;45(1):39–42.
86. Amato RJ, et al. Bone-targeted therapy: phase II study of strontium-89 in combination with alternating weekly chemohormonal therapies for patients with advanced androgen-independent prostate cancer. Am J Clin Oncol. 2008;31(6):532–8.
87. James ND, et al. Clinical outcomes and survival following treatment of metastatic castrate-refractory prostate cancer with docetaxel alone or with strontium-89, zoledronic acid, or both: the TRAPEZE randomized clinical trial. JAMA Oncol. 2016;2(4):493–9.
88. Heianna J, et al. Concurrent use of strontium-89 with external beam radiotherapy for multiple bone metastases: early experience. Ann Nucl Med. 2015;29(10):848–53.
89. Bilen MA, et al. Randomized phase 2 study of bone-targeted therapy containing strontium-89 in advanced castrate-sensitive prostate cancer. Cancer. 2015;121(1):69–76.
90. Sciuto R, et al. Metastatic bone pain palliation with 89-Sr and 186-Re-HEDP in breast cancer patients. Breast Cancer Res Treat. 2001;66(2):101–9.
91. Pons F, et al. Strontium-89 for palliation of pain from bone metastases in patients with prostate and breast cancer. Eur J Nucl Med. 1997;24(10):1210–4.
92. Baziotis N, et al. Strontium-89 chloride in the treatment of bone metastases from breast cancer. Oncology. 1998;55(5):377–81.
93. Heianna J, et al. Tumor regression of multiple bone metastases from breast cancer after administration of strontium-89 chloride (Metastron). Acta Radiol Short Rep. 2014;3(4):2047981613493412.
94. Zenda S, et al. Strontium-89 (Sr-89) chloride in the treatment of various cancer patients with multiple bone metastases. Int J Clin Oncol. 2014;19(4):739–43.
95. Maeda O, et al. A patient with esophageal cancer with bone metastasis who achieved pain relief with repetitive administration of strontium-89 chloride. Clin J Gastroenterol. 2014;7(5):387–91.
96. McEwan AJ, et al. A retrospective analysis of the cost effectiveness of treatment with Metastron in patients with prostate cancer metastatic to bone. Eur Urol. 1994;26(Suppl 1):26–31.
97. James N, et al. TRAPEZE: a randomised controlled trial of the clinical effectiveness and cost-effectiveness of chemotherapy with zoledronic acid, strontium-89, or both, in men with bony metastatic castration-refractory prostate cancer. Health Technol Assess. 2016;20(53):1–288.
98. Andronis L, et al. Cost-effectiveness of zoledronic acid and strontium-89 as bone protecting treatments in addition to chemotherapy in patients with metastatic castrate-refractory prostate cancer: results from the TRAPEZE trial (ISRCTN 12808747). BJU Int. 2017;119(4):522–9.
99. Singh A, et al. Human pharmacokinetics of samarium-153 EDTMP in metastatic cancer. J Nucl Med. 1989;30(11):1814–8.
100. Eary JF, et al. Samarium-153-EDTMP biodistribution and dosimetry estimation. J Nucl Med. 1993;34(7):1031–6.
101. Farhanghi M, et al. Samarium-153-EDTMP: pharmacokinetic, toxicity and pain response using an

escalating dose schedule in treatment of metastatic bone cancer. J Nucl Med. 1992;33(8):1451–8.
102. Collins C, et al. Samarium-153-EDTMP in bone metastases of hormone refractory prostate carcinoma: a phase I/II trial. J Nucl Med. 1993;34(11):1839–44.
103. Sartor O. Overview of samarium Sm 153 lexidronam in the treatment of painful metastatic bone disease. Rev Urol. 2004;6(Suppl 10):S3–S12.
104. Serafini AN, et al. Palliation of pain associated with metastatic bone cancer using samarium-153 lexidronam: a double-blind placebo-controlled clinical trial. J Clin Oncol. 1998;16(4):1574–81.
105. Resche I, et al. A dose-controlled study of ^{153}Sm-ethylenediaminetetramethylenephosphonate (EDTMP) in the treatment of patients with painful bone metastases. Eur J Cancer. 1997;33(10):1583–91.
106. Sartor O, et al. Samarium-153-Lexidronam complex for treatment of painful bone metastases in hormone-refractory prostate cancer. Urology. 2004;63(5):940–5.
107. Wang RF, et al. A comparative study of samarium-153-ethylenediaminetetramethylene phosphonic acid with pamidronate disodium in the treatment of patients with painful metastatic bone cancer. Med Princ Pract. 2003;12(2):97–101.
108. Marcus CS, et al. Lack of effect of a bisphosphonate (pamidronate disodium) infusion on subsequent skeletal uptake of Sm-153 EDTMP. Clin Nucl Med. 2002;27(6):427–30.
109. Turner JH, et al. A phase II study of treatment of painful multifocal skeletal metastases with single and repeated dose samarium-153 ethylenediaminetetramethylene phosphonate. Eur J Cancer. 1991;27(9):1084–6.
110. Turner JH, et al. A phase I study of samarium-153 ethylenediaminetetramethylene phosphonate therapy for disseminated skeletal metastases. J Clin Oncol. 1989;7(12):1926–31.
111. Sartor O, et al. Safety and efficacy of repeat administration of samarium Sm-153 lexidronam to patients with metastatic bone pain. Cancer. 2007;109(3):637–43.
112. Suttmann H, et al. Combining Sm-153-lexidronam and docetaxel for the treatment of patients with hormone-refractory prostate cancer: first experience. Cancer Biother Radiopharm. 2008;23(5):609–18.
113. Morris MJ, et al. Phase I study of samarium-153 lexidronam with docetaxel in castration-resistant metastatic prostate cancer. J Clin Oncol. 2009;27(15):2436–42.
114. Autio KA, et al. Repetitively dosed docetaxel and ^{153}samarium-EDTMP as an antitumor strategy for metastatic castration-resistant prostate cancer. Cancer. 2013;119(17):3186–94.
115. Tu SM, et al. Phase I study of concurrent weekly docetaxel and repeated samarium-153 lexidronam in patients with castration-resistant metastatic prostate cancer. J Clin Oncol. 2009;27(20):3319–24.
116. Fizazi K, et al. Phase II trial of consolidation docetaxel and samarium-153 in patients with bone metastases from castration-resistant prostate cancer. J Clin Oncol. 2009;27(15):2429–35.
117. Lin J, et al. Phase I trial with a combination of docetaxel and ^{153}Sm-lexidronam in patients with castration-resistant metastatic prostate cancer. Urol Oncol. 2011;29(6):670–5.
118. Barai S, et al. Effects of low-dose capecitabine on Samarium-153-EDTMP therapy for painful bone metastases. Indian J Nucl Med. 2015;30(2):111–5.
119. Winderen M, et al. Pronounced therapeutic effect of samarium 153-ethylenediaminetetramethylene phosphonate in an orthotopic human osteosarcoma tibial tumor model. J Natl Cancer Inst. 1995;87(3):221–2.
120. Franzius C, et al. High-activity samarium-153-EDTMP therapy followed by autologous peripheral blood stem cell support in unresectable osteosarcoma. Nuklearmedizin. 2001;40(6):215–20.
121. Franzius C, et al. High-dose samarium-153 ethylene diamine tetramethylene phosphonate: low toxicity of skeletal irradiation in patients with osteosarcoma and bone metastases. J Clin Oncol. 2002;20(7):1953–4.
122. Anderson PM, et al. High-dose samarium-153 ethylene diamine tetramethylene phosphonate: low toxicity of skeletal irradiation in patients with osteosarcoma and bone metastases. J Clin Oncol. 2002;20(1):189–96.
123. Anderson PM, et al. Gemcitabine radiosensitization after high-dose samarium for osteoblastic osteosarcoma. Clin Cancer Res. 2005;11(19 Pt 1):6895–900.
124. Henriksen G, et al. Ra-223 for endoradiotherapeutic applications prepared from an immobilized Ac-227/Th-227 source. Radiochim Acta. 2001;89(10):661–6.
125. Biersack HJ, et al. Radium-223 in prostate cancer. N Engl J Med. 2013;369(17):1659.
126. Henriksen G, et al. Significant antitumor effect from bone-seeking, alpha-particle-emitting ^{223}Ra demonstrated in an experimental skeletal metastases model. Cancer Res. 2002;62(11):3120–5.
127. Nilsson S, et al. First clinical experience with alpha-emitting radium-223 in the treatment of skeletal metastases. Clin Cancer Res. 2005;11(12):4451–9.
128. Carrasquillo JA, et al. Phase I pharmacokinetic and biodistribution study with escalating doses of ^{223}Ra-dichloride in men with castration-resistant metastatic prostate cancer. Eur J Nucl Med Mol Imaging. 2013;40(9):1384–93.
129. Kairemo K, et al. Evaluation of alpha-therapy with radium-223-dichloride in castration resistant metastatic prostate cancer-the role of gamma scintigraphy in dosimetry and pharmacokinetics. Diagnostics (Basel). 2015;5(3):358–68.
130. Nilsson S, et al. Bone-targeted radium-223 in symptomatic, hormone-refractory prostate cancer: a randomised, multicentre, placebo-controlled phase II study. Lancet Oncol. 2007;8(7):587–94.

131. Nilsson S, et al. Two-year survival follow-up of the randomized, double-blind, placebo-controlled phase II study of radium-223 chloride in patients with castration-resistant prostate cancer and bone metastases. Clin Genitourin Cancer. 2013;11(1):20–6.
132. Parker C, et al. Alpha emitter radium-223 and survival in metastatic prostate cancer. N Engl J Med. 2013;369 (3):213–23.
133. Vogelzang NJ, et al. Hematologic safety of radium-223 dichloride: baseline prognostic factors associated with myelosuppression in the ALSYMPCA trial. Clin Genitourin Cancer. 2017;15(1):42–52.
134. Saad F, et al. Radium-223 and concomitant therapies in patients with metastatic castration-resistant prostate cancer: an international, early access, open-label, single-arm phase 3b trial. Lancet Oncol. 2016;17(9): 1306–16.
135. Sartor O, et al. Chemotherapy following radium-223 dichloride treatment in ALSYMPCA. Prostate. 2016;76(10):905–16.
136. Shore ND, et al. Interim results from ERADICATE: an open-label phase 2 study of radium Ra 223 dichloride with concurrent administration of abiraterone acetate plus prednisone in castration-resistant prostate cancer subjects with symptomatic bone metastases. Clin Adv Hematol Oncol. 2016;14(4 Suppl 5):3–7.
137. Suominen MI, et al. Survival benefit with radium-223 dichloride in a mouse model of breast cancer bone metastasis. J Natl Cancer Inst. 2013;105(12):908–16.
138. Coleman R, et al. A phase IIa, nonrandomized study of radium-223 dichloride in advanced breast cancer patients with bone-dominant disease. Breast Cancer Res Treat. 2014;145(2):411–8.
139. de Klerk JM, et al. Phase 1 study of rhenium-186-HEDP in patients with bone metastases originating from breast cancer. J Nucl Med. 1996;37(2):244–9.
140. Zafeirakis A, et al. Management of metastatic bone pain with repeated doses of rhenium 186-HEDP in patients under therapy with zoledronic acid: a safe and additively effective practice. Cancer Biother Radiopharm. 2009;24(5):543–50.
141. van der Poel HG, et al. Serum hemoglobin levels predict response to strontium-89 and rhenium-186-HEDP radionuclide treatment for painful osseous metastases in prostate cancer. Urol Int. 2006;77(1):50–6.
142. O'Sullivan JM, et al. High activity rhenium-186 HEDP with autologous peripheral blood stem cell rescue: a phase I study in progressive hormone refractory prostate cancer metastatic to bone. Br J Cancer. 2002;86(11):1715–20.
143. Lange R, et al. Applying quality by design principles to the small-scale preparation of the bone-targeting therapeutic radiopharmaceutical rhenium-188-HEDP. Eur J Pharm Sci. 2016;90:96–101.
144. ter Heine R, et al. Bench to bedside development of GMP grade rhenium-188-HEDP, a radiopharmaceutical for targeted treatment of painful bone metastases. Int J Pharm. 2014;465(1–2):317–24.
145. Liepe K, et al. Dosimetry of ^{188}Re-hydroxyethylidene diphosphonate in human prostate cancer skeletal metastases. J Nucl Med. 2003;44(6):953–60.
146. Palmedo H, et al. Dose escalation study with rhenium-188 hydroxyethylidene diphosphonate in prostate cancer patients with osseous metastases. Eur J Nucl Med. 2000;27(2):123–30.
147. Liepe K, Runge R, Kotzerke J. Systemic radionuclide therapy in pain palliation. Am J Hosp Palliat Care. 2005;22(6):457–64.
148. Palmedo H, et al. Repeated bone-targeted therapy for hormone-refractory prostate carcinoma: tandomized phase II trial with the new, high-energy radiopharmaceutical rhenium-188 hydroxyethylidenediphosphonate. J Clin Oncol. 2003;21(15):2869–75.
149. Lange R, et al. Treatment of painful bone metastases in prostate and breast cancer patients with the therapeutic radiopharmaceutical rhenium-188-HEDP. Clinical benefit in a real-world study. Nuklearmedizin. 2016; 55(5):188–95.
150. Krishnamurthy GT, et al. Tin-117m(4^+)DTPA: pharmacokinetics and imaging characteristics in patients with metastatic bone pain. J Nucl Med. 1997;38(2): 230–7.
151. Srivastava SC, et al. Treatment of metastatic bone pain with tin-117m Stannic diethylenetriaminepentaacetic acid: a phase I/II clinical study. Clin Cancer Res. 1998;4(1):61–8.
152. Ando A, et al. ^{177}Lu-EDTMP: a potential therapeutic bone agent. Nucl Med Commun. 1998;19(6):587–91.
153. Chakraborty S, et al. ^{177}Lu labelled polyaminophosphonates as potential agents for bone pain palliation. Nucl Med Commun. 2002;23(1):67–74.
154. Das T, et al. ^{177}Lu-labeled cyclic polyaminophosphonates as potential agents for bone pain palliation. Appl Radiat Isot. 2002;57(2):177–84.
155. Chakraborty S, et al. ^{177}Lu-EDTMP: a viable bone pain palliative in skeletal metastasis. Cancer Biother Radiopharm. 2008;23(2):202–13.
156. Yuan J, et al. Efficacy and safety of 177Lu-EDTMP in bone metastatic pain palliation in breast cancer and hormone refractory prostate cancer: a phase II study. Clin Nucl Med. 2013;38(2):88–92.
157. Thapa P, et al. Clinical efficacy and safety comparison of ^{177}Lu-EDTMP with ^{153}Sm-EDTMP on an equidose basis in patients with painful skeletal metastases. J Nucl Med. 2015;56(10):1513–9.
158. Guideline. Medical use of byproduct material. Title 10, code of federal regulations. http://www.rc.gov/reading-rm/doccollections/cfr/part035/part035-0075.html.

Radionuclide Therapy of Tumors of the Liver and Biliary Tract

46

Giuseppe Boni, Federica Guidoccio, Duccio Volterrani, and Giuliano Mariani

Abstract

The liver represents a frequent site for both primary cancer and metastatic disease, In these circumstances, liver-directed therapies as cytoreduction via surgery or in situ ablative techniques may influence the natural history of the disease progression and improve clinical outcomes.

Radioembolization (RE) is a selective internal radiotherapy technique in which ^{131}I-lipiodol or 90Y microspheres are infused through the hepatic arteries. It is based on the fact that primary and secondary hepatic tumors are vascularized mostly by arterial blood flow whereas the normal liver perfusion is mostly from the portal network. This enables high radiation doses to be delivered, sparing the surrounding non-malignant liver parenchyma.

Although there are some clinical evidences that RE may play an important role in the management of hepatocellular carcinoma of intermediate or advanced stage and in liver-dominant metastatic colorectal cancer and metastatic neuroendocrine tumors, further randomised clinical trials are mandatory to better assess the potential beneficial and harmful outcomes of trans-arterial radioembolisation either as a monotherapy or in combination with other systemic or locoregional therapies.

In this chapter we discuss some technical aspects, patient selection, current clinical evidence, and future directions of radioembolisation for primary and secondary liver cancer.

Keywords

Hepatocellular carcinoma • Selective internalradiation therapy • Radioembolization • Liver • Neoplasm • Metastasis

Glossary

[^{18}F]FDG	2-Deoxy-2-[^{18}F]fluoro-D-glucose
5-FU	5-Fluorouracil, a chemotherapy agent
^{68}Ga-DOTANOC	^{68}Ga-DOTA-1-Nal^3-octreotide
^{99m}Tc-HSA	^{99m}Tc-human serum albumin
^{99m}Tc-MAA	^{99m}Tc-macroaggregated albumin
$^{99m}TcO_4^-$	^{99m}Tc-pertechnetate
AFP	Alpha-fetoprotein, a circulating serum marker of hepatocellular carcinoma (and of testicular germ-cell cancer as well)

G. Boni (✉) • F. Guidoccio • D. Volterrani • G. Mariani
Regional Center of Nuclear Medicine, Department of Translational Research and Advanced Technologies in Medicine and Surgery, University of Pisa, Pisa, Italy
e-mail: g.boni@med.unipi.it; bonigb@yahoo.it; federica.guidoccio@gmail.com; duccio.volterrani@med.unipi.it; dvolterrani@gmail.com; giuliano.mariani@med.unipi.it; giuliano.mariani11@gmail.com

© Springer International Publishing Switzerland 2017
H.W. Strauss et al. (eds.), *Nuclear Oncology*,
https://doi.org/10.1007/978-3-319-26236-9_51

Bq	Becquerel unit
BSA	Body surface area
CA 19–9	Carbohydrate antigen 19–9, a tumor-associated serum marker
ce-CT	Contrast-enhanced x-ray computed tomography
CI	Confidence interval
CR	Complete response
CRC	Colorectal cancer
CT	X-ray computed tomography
DEB	Drug-eluting bead
DOTA	1,4,7,10-Tetra-azacyclododecane-1,4,7,10-tetraacetic acid
EASL	European Association for the Study of the Liver
ECOG	Eastern Cooperative Oncology Group
eV	Electron volt
GBq	Giga-Becquerel (10^9 Becquerel)
Gy	Gray unit (ionizing radiation dose in the International System of Units, corresponding to the absorption of one joule of radiation energy per kilogram of matter)
HCC	Hepatocellular carcinoma
HDD	4-Hexadecyl 2,2,9,9-tetramethyl-4,7-diaza-1,10-decanethiol, a chelating agent
ICC	Intrahepatic cholangiocarcinoma
IRE	Irreversible electroporation
keV	Kiloelectron volt (10^3 eV)
LSF	Lung shunt fraction
MBq	Mega-Becquerel (10^6 Becquerel)
MeV	Megaelectron volt (10^6 eV)
MIP	Maximum intensity projection
MIRD	Medical Internal Radiation Dose
MR	Magnetic resonance
MRI	Magnetic resonance imaging
NET	Neuroendocrine tumor
PET	Positron emission tomography
PET/CT	Positron emission tomography/computed tomography
PFS	Progression-free survival
PR	Partial response
PVT	Portal vein thrombosis
RE	Radioembolization
RECIST	Response evaluation criteria in solid tumors
RFA	Radiofrequency ablation
RILD	Radiation-induced liver diseases
ROI	Region of interest
SD	Stable disease
SIRT	Selective internal radiation therapy
SPECT/CT	Single-photon emission computed tomography/computed tomography
SUV	Standardized uptake value
SUV_{max}	Standardized uptake value at point of maximum
TACE	Transcatheter arterial chemoembolization
TARE	Transarterial radioemobilization
VIPoma	Neuroendocrine tumor producing vasoactive intestinal peptide
WHO	World Health Organization

Contents

Introduction 1339

Rationale of Radioembolization Therapy for Liver Tumors 1340

Radioactive Lipiodol 1340

^{90}Y-Microspheres 1341

Patient Selection 1341

Assessment of Arterial Anatomy 1342

Pretreatment Imaging with ^{99m}Tc-MAA 1342

Radiodosimetric Aspects 1343

^{90}Y-Microsphere Administration 1347

Posttreatment Scan 1347

Patient Follow-Up and Assessment of Response to Therapy 1348

^{90}Y-Microsphere Radioembolization Combined with Other Therapies 1348

Clinical Indications 1351

Primary Liver Tumors 1351
Hepatocellular Carcinoma 1351
Intrahepatic Cholangiocarcinoma 1352

Metastatic Liver Tumors 1353
Metastatic Colorectal Carcinoma 1353
Metastatic Neuroendocrine Tumors 1354

Absolute and Relative Contraindications 1354

Early and Late Toxicities 1354

Perspectives on Radioembolization for Primary and Metastatic Liver Tumors 1355

References 1355

Introduction

Both primary tumors and metastatic malignancies can arise in the liver. Hepatocellular carcinoma (HCC) is the fifth most common malignancy worldwide, and its incidence is rising [1]. In addition, the liver is one of the most common sites for hematogenous metastases from different solid tumors primarily arising in other tissues/organs, most importantly colorectal cancer (CRC). About 15–25% of all CRCs may present synchronous hepatic metastases or develop metachronous metastatic involvement of the liver disease during the course of the disease [2].

Although significant survival benefit can be achieved with curative resection or liver transplantation in selected cases [3], less than 15% of the patients with newly diagnosed HCC are candidates for surgical procedures with curative intents. Although various treatments have been proposed for the remaining patients, definite agreement has not been reached on which option offers the greatest survival benefit associated with the least toxicity.

External beam radiation therapy has a limited role in the treatment of HCC due to the relatively high radiosensitivity of normal hepatic tissue [4]. In fact, exposure of the liver to radiation doses greater than 40 Gy may result in a clinical syndrome called "radiation-induced liver disease" (RILD) or radiation hepatitis. This syndrome, which occurs weeks to months following therapy, includes elevated liver enzymes, anicteric hepatomegaly, and ascites [4, 5].

Minimally invasive, percutaneous ablative treatments include radiofrequency ablation (RFA), microwave ablation, cryoablation, and irreversible electroporation (IRE) that have become widely accepted as potentially curative therapies for either HCC or metastatic liver disease [6]. In particular, these ablative techniques are useful for treating patients who do not meet the criteria for surgery but in whom curative treatment is desired.

Transcatheter arterial chemoembolization (TACE) is the mainstay of catheter-based locoregional therapies for unresectable primary liver cancer; its use is expanding and includes liver metastatic disease from other malignancies [7]. Conventional TACE typically involves the injection of chemotherapeutic agents mixed with lipiodol and embolic particles into the branch of the hepatic artery that feeds the tumor [8]. TACE with drug-eluting beads (DEB) involves the injection of DEBs into the tumor-feeding artery, offering simultaneous delivery of chemotherapy and embolization with sustained and controlled drug release over time [9]. Both TACE and DEB-TACE are effective as palliative treatments for primary and metastatic liver cancers [10, 11].

There are substantial differences in the treatment strategies for primary or metastatic malignancies of the liver. While locoregional treatments are a mainstay in primary liver cancers [12], transcatheter techniques such TACE or DEB-TACE are not commonly used for patients with metastatic liver disease.

The recent successful development of transarterial radioembolization (TARE) with ^{90}Y-labeled particles has revived interest in an approach to locoregional treatment of liver tumors with radionuclides that had been introduced earlier with the use of lipiodol containing ^{131}I but had shown little benefit for long-term survival (see further below). This technique is also defined as "selective internal

radiation therapy" (SIRT); therefore, the acronyms TARE and SIRT can be employed in an interchangeable manner.

Rationale of Radioembolization Therapy for Liver Tumors

In order to deliver the highest possible therapeutic doses to the tumor while sparing normal liver parenchyma, techniques based on minimally invasive intra-arterial administration of therapeutic radionuclides have been developed, an approach that takes advantage of the dual blood supply to the liver. Normal hepatic tissue derives greater than 70% of its blood supply from the portal system, whereas blood to malignant tissue is preferentially supplied by the arterial system. High tumoricidal doses can thus be selectively delivered to the tumor lesions (more than 70 Gy, usually 200–300 Gy) through locoregional administration of agents emitting β^- particles (labeled with either ^{131}I, ^{90}Y, ^{188}Re, or ^{166}Ho), with low levels of associated damage for the non-affected liver and therefore a minimal risk of inducing RILD [13–17].

Radioactive Lipiodol

Upon injection into the hepatic artery of patients with HCC, the iodinated oil ^{131}I-lipiodol (a suspension of lipidic particles) follows the preferential blood flow toward the tumor; the radiolabeled micellae are then retained by pinocytosis both in the tumor cells and in the endothelial cells of the arteries feeding the tumor [18]. Following this route of administration (which is performed under angiographic monitoring), more than 75% of the injected ^{131}I-lipiodol remains in the liver, while the remainder distributes mainly to the lungs. Release of free radioiodine results in some accumulation of radioactivity in the thyroid gland. Dose to the thyroid gland can be minimized by pretreatment with sodium iodide. Tumor/non-tumor uptake ratios in the liver are generally higher than 5, and more than 10% of the injected radioactivity remains within the tumor with an effective half-life greater than 6 days, longer than in the normal liver tissue [14, 15, 19]. Administered activity can be either a fixed amount of 2.4 GBq (65 mCi) or defined on the basis of patient-specific dosimetric estimates. Due to the long half-life of ^{131}I-lipiodol in the tumor, current legislation in some countries requires hospitalization for about 1 week, for the purpose of radioprotection of the general population.

Treatment is in general well tolerated, and serious adverse effects are very rare, while generic asthenia is commonly reported; hematologic toxicity is exceptionally rare, although blood cell counts may be altered due to the cirrhosis-related hypersplenism often present in these patients. Interstitial pneumopathy due to trapping and retention of the radiolabeled particle suspension is reported as the main risk of this treatment [20].

Both retrospective studies [21–23] and prospective trials [21, 24, 25] have demonstrated the safety of ^{131}I-lipiodol therapy, while the objective response rate is reported in the 40–50% range. In particular, a randomized controlled trial comparing ^{131}I-lipiodol therapy versus best supportive care in a group of 27 HCC patients with portal thrombosis demonstrated that survival at 3 months was 71% in the treatment arm versus 10% in the best supportive care arm (with median overall survivals of 26 weeks and 10 weeks, respectively) [24].

In the adjuvant setting, the efficacy of ^{131}I-lipiodol therapy was tested in a phase II study involving 28 patients [26]. Median time to recurrence was 28 months (range 12–62 months) in the 16 patients who were apparently disease-free at follow-up; overall survival in the responding patients was 86% at 3 years and 65% at 5 years. In a recently published phase III study, 21 patients without evidence of residual disease after potentially curative resection for HCC received 1,850 MBq of ^{131}I-lipiodol intra-arterially as adjuvant therapy, while 22 patients treated with surgery alone served as the control group [27]. The recurrence rate in the patients treated with surgery alone was 63.6%, while it was 47.6% in those receiving adjuvant radioembolization. The 5-year, 7-year, and 10-year disease-free survivals were 61.9%,

52.4%, and 47.6%, respectively, in the adjuvant therapy group, significantly higher than the values in the corresponding control group (31.8% with $P = 0.0397$, 31.8% with $P = 0.0224$, and 27.3% with $P = 0.0892$, respectively). Also, overall survivals in the treated group (66.7% at both 5 and 7 years, 52.4% at 10 years) were higher than in the control group (36.4% with $P = 0.0433$ at 5 years, 31.8% with $P = 0.0243$ at 7 years, and 27.3% with $P = 0.0905$ at 10 years, respectively). When compared with chemoembolization, embolization with ^{131}I-lipiodol has yielded similar results in terms of efficacy but better tolerance [23].

More recently lipiodol labeled with ^{188}Re using 4-hexadecyl 2,2,9,9-tetramethyl-4,7-diaza-1,10-decanethiol (HDD) as the chelating agent [28] was shown to be a promising agent for radioembolization in patients with inoperable large and/or multifocal HCCs. ^{188}Re has potentially favorable physical characteristics, such as a shorter half-life than ^{131}I (16.9 h versus 8 days), a β^- emission of high energy with ensuing good tumoricidal effect ($E_{max} = 2.1$ MeV), and a 155-keV γ emission favorable for gamma-camera imaging (for the purpose of dosimetric estimates). Furthermore, the relatively short-lived ^{188}Re can be obtained through a generator system based on its parent radionuclide (^{188}W) that has a physical half-life of 69 days, suitable for distribution logistics.

Therapy of HCC with ^{188}Re-HDD-lipiodol results in higher tumor-killing efficacy than ^{131}I-lipiodol, yet combined with lower toxicity. The ^{188}Re-labeled agent represents therefore an excellent alternative to the ^{131}I-labeled agent [29].

Promising results of both safety and clinical response following therapy with ^{188}Re-HDD-lipiodol were obtained in a multicenter study performed in 93 patients with inoperable HCC [30]. Treatment was well tolerated, and an objective response (including either tumor regression of some degree or stabilization of disease that was in progression prior to therapy) was observed in 66/93 patients (71%); out of these 66 objective responses, there were 5 cases with complete ablation of the tumor mass, 17 cases of partial response, and 23 cases with stabilization of disease.

^{90}Y-Microspheres

Intra-arterial radioembolization with ^{90}Y-labeled particles was approved in 2002 for the treatment of liver tumors, both primary malignancies and metastatic lesions originated by other tumors [31]. ^{90}Y is a pure β^- emitter that decays to stable ^{90}Zr and has a physical half-life of 64.2 h. The average energy of β^- emission is 0.936 MeV, with a mean tissue penetration of 2.5 mm and a maximum tissue range of 10 mm. The physical properties of ^{90}Y allow the delivery of high-radiation doses to hepatic malignancies, when administered with this technique, while minimally affecting the non-affected surrounding liver parenchyma.

Two types of microspheres labeled with ^{90}Y are currently available, made, respectively, of glass (TheraSphere®, MDS Nordion, Ottawa, Ontario, Canada) and of resin (SIR-Spheres®, Sirtex Medical, Sydney, Australia). These two preparations differ in some important respects [32]. TheraSphere® consists of particles 20–30 μm in diameter, each one carrying 2,500 Bq of ^{90}Y (high specific activity); about 1.2 million microspheres is injected intra-arterially for a single treatment, corresponding to a total administered activity of about 3 GBq (81 mCi). SIR-Spheres® consists instead of particles 20–60 μm in diameter, each one carrying 50 Bq of ^{90}Y (low specific activity); 40–80 million microspheres are injected for a single treatment to achieve a similar total administered activity of 3 GBq [32].

Patient Selection

After the diagnosis of inoperable liver tumor has been made on the basis of proper imaging and biopsy, the pretreatment functional status of the liver is evaluated by routine blood chemistry workup. Patients with an ECOG performance status of greater than two are not considered ideal candidates for this treatment.

An inadequate liver function reserve with total bilirubin >2.0 mg/dL and serum albumin <3 g/dL is considered a contraindication to treatment with

^{90}Y-microspheres. In case of concomitant renal failure, care must be taken to avoid or minimize the use of iodinated contrast medium during angiography (see further below).

Pretreatment evaluation for TARE/SIRT with ^{90}Y-microspheres is based on cross-sectional imaging and arteriograms in the individual patient, with the fundamental prerequisite that the patient has liver-dominant unresectable disease. The workup should include CT or MR imaging of the liver for assessment of tumoral and non-tumoral volume, portal vein patency, and extent of extrahepatic disease. Distribution of the tumor disease is typically characterized as unilobar or bilobar; however, the correlation of tumor lesions with hepatic arterial supply is variable and can only be ascertained through arteriography. Ascites indicates poor hepatic reserve or peritoneal metastasis, both of which bear poor prognosis.

The final decision-making about treatment with ^{90}Y-microsphere TARE/SIRT for each individual patient should be achieved after careful consideration of all functional and anatomic parameters within a multidisciplinary team involving interventional radiologists, surgical oncologists, medical oncologists, nuclear medicine physicians, radiation oncologists, medical physicists, and radiation safety experts.

Assessment of Arterial Anatomy

Pretreatment angiography (an essential requisite for the therapeutic procedure) is performed to assess the vascular anatomy of the liver, patency of the portal vein, and presence of artero-portal shunting and/or shunting to extrahepatic territories, the most important of which is the liver-to-lung shunt (see further below). Abnormal blood flow spreading the radiolabeled microspheres outside the liver vasculature is prevented by prophylactic embolization of some vessels identified during angiography, such as the gastroduodenal artery and the right gastric artery [5]. This is a safe and effective procedure to minimize the risks of hepato-enteric flow. Mesenteric angiography is necessary to ensure that blood supply to the lesions has been adequately identified, as incomplete/inaccurate definition of the pattern of blood supply to the tumor may lead to incomplete/ineffective targeting of the tumor lesion.

Pretreatment Imaging with ^{99m}Tc-MAA

During pretreatment angiography, ^{99m}Tc-macroaggregated serum albumin ((^{99m}Tc-MAA) or alternatively ^{99m}Tc-HSA-microspheres) is injected into the hepatic artery to confirm that the radiolabeled particles home in the tumor lesion(s), as well as to assess for the presence of shunting to the splanchnic and/or pulmonary vascular bed. To this purpose, scintigraphy of the lung and upper abdomen by either planar and/or SPECT/CT imaging (i.e., the optimal imaging technique) is routinely performed (Figs. 1, 2, and 3) [33]. Images can be acquired within 4 h of the administration of ^{99m}Tc-HSA-microspheres, while the optimal time window for imaging after administration of ^{99m}Tc-MAA is within 1 h post-administration. In fact, albumin macroaggregates undergo a relatively fast intrahepatic degradation, with possible redistribution of radioactivity (constituted either by smaller fragments and/or free $^{99m}TcO_4^-$) from the capillary bed of the liver to the capillary bed of the lung. As a consequence, the liver-to-lung shunt fraction can be overestimated at later time points after administration [34], or radioactivity accumulation at other sites (e.g., free $^{99m}TcO_4^-$ accumulating in the stomach) can be misinterpreted as shunting to extrahepatic sites. In order to avoid such occurrence, sodium perchlorate is administered orally about 30 min before ^{99m}Tc-MAA injection [35].

It is crucial to correlate the ^{99m}Tc-MAA scintigraphic images to the angiography pattern, as topographic proximity of the duodenum and stomach to the liver may decrease the ability to identify extrahepatic shunting by scintigraphy alone, especially if based solely on planar imaging. Based on ROI technique, the lung shunt fraction (LSF) is calculated and employed to estimate the radiation dose delivered to the lungs for any given amount of radioactivity, so that appropriate adjustments in the administered activity can be made to minimize the risk of radiation pneumonitis (see further below).

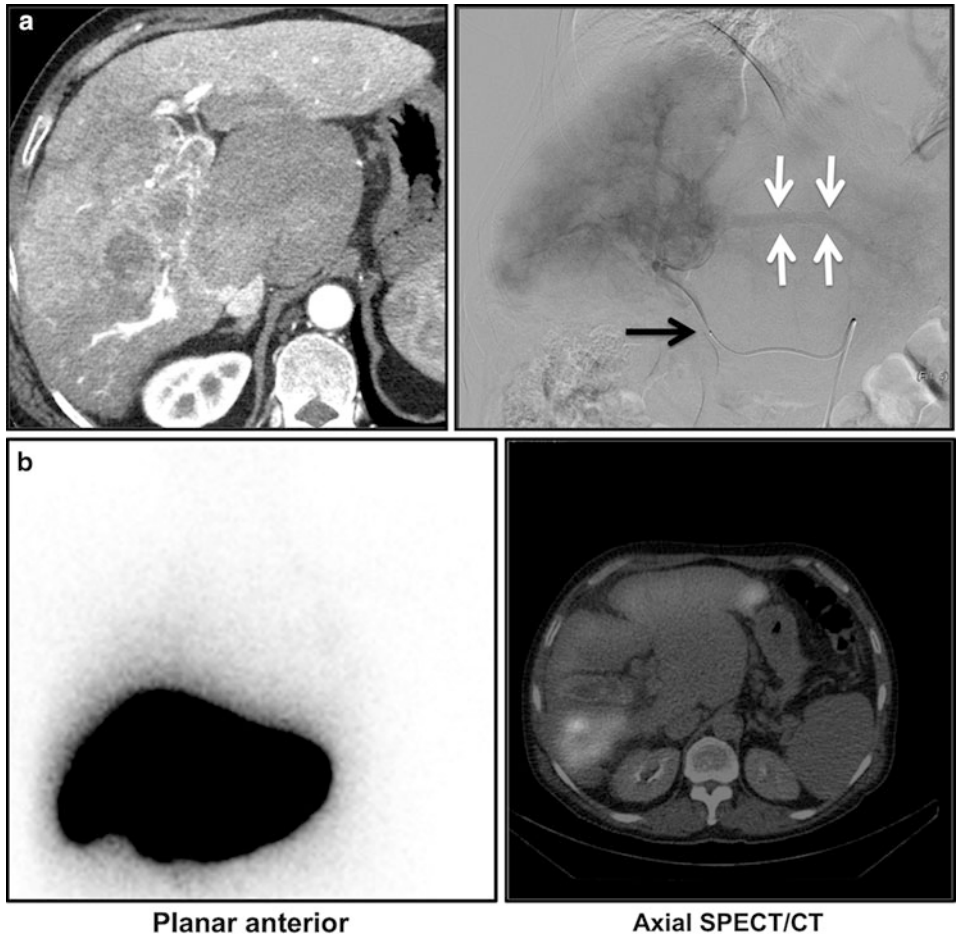

Fig. 1 Angiographic and scintigraphic pretreatment evaluation of a 67-year-old patient with a large, infiltrating hepatocellular carcinoma (HCC) candidate to radioembolization therapy with ^{90}Y-microspheres. (**a**) *Left panel* shows contrast-enhanced CT *demonstrating massive infiltration of segment 1 by a large HCC, with extension to the adjacent liver segments. Right panel* shows an early phase of digital subtraction angiography through the hepatic artery (catheter indicated by *black arrow*); there is intense diffuse enhancement of the left branches of the portal vein, with a wide-lumen artero-portal fistula (indicated by *white arrows*). (**b**) *Left panel* shows planar scintigraphy acquired after trans-arterial injection of ^{99m}Tc-MAA (anterior view) demonstrating widespread diffusion of the injected particles to virtually the entire liver. *Right panel* shows the fused axial SPECT/CT image, which better defines the intrahepatic distribution of ^{99m}Tc-MAAs, mostly to both the right and the left lobes of the liver, while there is minimal perfusion of the main site of the tumor. On the basis of the angiographic and scintigraphic characterization, this patient was excluded from trans-arterial radioembolization with ^{90}Y-microspheres, because this treatment would have exposed the non-tumor liver parenchyma to excessive, unjustified radiation doses without actually an expected benefit for what concerns tumor therapy

Radiodosimetric Aspects

The choice of the most appropriate ^{90}Y activity to be delivered into the tumor target and to the normal liver parenchyma requires adequate knowledge of many factors, mainly the liver function and reserve, that are frequently influenced by concomitant pathologies (i.e., cirrhosis) or by prior chemotherapy and/or external beam radiation therapy.

The main complications possibly linked to ^{90}Y-microsphere radioembolization are caused by excessive irradiation of nontarget tissue. In

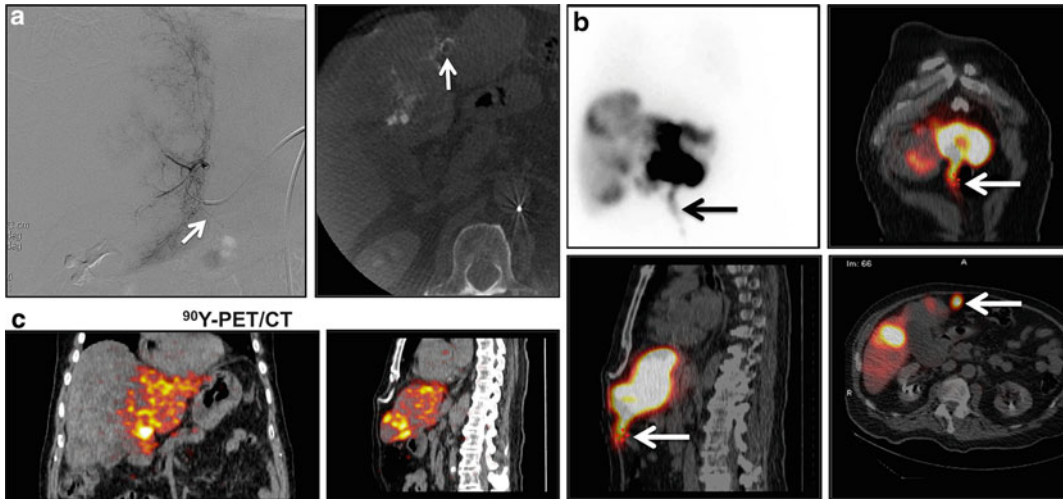

Fig. 2 Angiographic and scintigraphic pretreatment evaluation of a 75-year-old man with metastasis from an urothelial carcinoma in both lobes of the liver, with posttreatment PET/CT acquisition based on internal pair production during decay of ^{90}Y. Selective angiography was performed by injecting contrast medium separately into the right, the median, and the left branches of the hepatic artery. (**a**) *Left panel* shows digital subtraction angiography obtained upon injection into the median hepatic artery, revealing a thin branch (indicated by the *white arrow*) identified as a patent falciform artery. *Right panel* shows the corresponding contrast-enhanced CT phase (falciform artery indicated by *white arrow*). (**b**) Scintigraphy acquired after trans-arterial ^{99m}Tc-MAA injection clearly demonstrate the abnormal arterial branch (indicated by *arrows*) in the planar anterior view (*upper left panel*) as well as in the fused SPECT/CT images (coronal in *upper right*, sagittal in *lower left*, axial in *lower right panels*, respectively). During the subsequent trans-arterial treatment phase, an ice pack was positioned on the cutaneous projection of the falciform artery before injecting the ^{90}Y-microspheres, in order to induce vasoconstriction and thus reduce as much as possible inadvertent deposition of the radiolabeled particles in the periumbilical region, which would have caused delivery of a high-radiation dose to this region. The procedure was uneventful, and the post-treatment PET/CT acquisition based on internal pair production of ^{90}Y (**c**) showed excellent tumor targeting without visualization of the area fed by the patent falciform artery (fused coronal image in *left panel*, fused sagittal image in *right panel*)

this regard, the key limiting factor is the lower tolerance to radiation of normal liver parenchyma relative to the dose required to destroy the tumor target. The maximum external beam acceptable cumulative dose to the whole liver is 35 Gy (based on prior experience with external beam radiation therapy) [36], while the estimated dose to destroy a solid tumor is more than 70 Gy. Above the 35 Gy threshold radiation dose to the liver parenchyma, the risk of liver failure rises sharply.

The other absolute and relative contraindications for the procedure are related to the possible flow/reflux of part of the ^{90}Y-microspheres to arteries feeding the wall of the gastrointestinal tract and to excessive lung radiation due to a high hepato-pulmonary shunt, frequently observed in HCC as well as in metastatic disease with a large tumor burden. In this case, the administration of therapeutic amounts of ^{90}Y-microspheres increases the risk of clinically relevant radiation pneumonitis.

To warrant the safety of the procedure, it is crucial to quantify the lung shunt fraction (LSF) as detected in the pretreatment evaluation with the ^{99m}Tc-MAA scan, in order to calculate the expected radiation dose to the lungs. Previous data extrapolated from the large body of experience accumulated with external beam radiation therapy indicate that the highest tolerable dose to the lungs is 30 Gy for a single administration and less than 50 Gy as the cumulative dose for multiple treatments [36].

The LSF value is routinely calculated by ROI analysis of the planar scans acquired after ^{99m}Tc-MAA administration in the pretreatment phase, using the geometric mean of the lung and liver

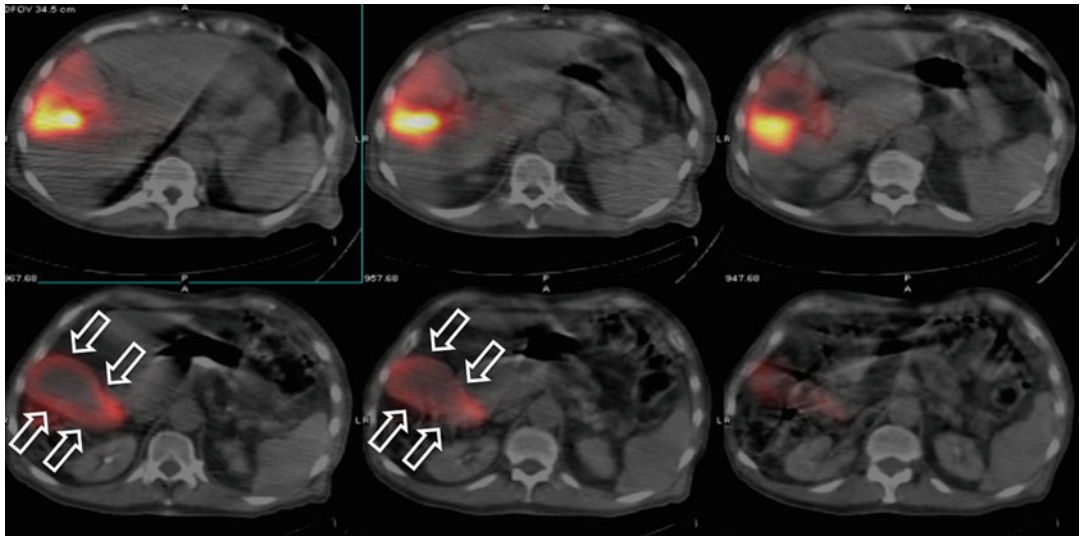

Fig. 3 Scintigraphic pretreatment evaluation (fused axial SPECT/CT images at various levels) of a 72-year-old patient with a tumor lesion between segments 5 and 6 of the liver. Trans-arterial ^{99m}Tc-MAA injection results in satisfactory distribution to the tumor lesion but also in scintigraphic visualization of the gallbladder wall, due to flow of the radiolabeled particles through the cholecystic artery. Therapy with ^{90}Y-microsperes was not performed, because of the fear of causing necrotizing radiation-induced cholecystitis. In patients with vascular patterns similar to this (as those regarding the mesenteric artery feeding the gastric wall), further attempt to ^{90}Y-microsphere radioembolization therapy must be preceded by coil embolization of the arteries feeding extrahepatic territories

counts, respectively, in the anterior and posterior views, according to the following equation:

$$LSF(\%) = \frac{\text{Lung Counts}}{\text{Lung Counts} + \text{Liver Counts}} \times 100$$

Radioembolization with ^{90}Y-microspheres has no restrictions for any LSF value <10%, whereas an LSF value >20% constitutes per se an absolute contraindication to treatment. Activity adjustments can be adopted for LSF values between 10% and 20%, that is, a 20% reduction in administered activities for LSF values included between 10% and 15% and a 40% reduction for LSF values included between 15% and 20% (see Fig. 4).

Different models have been proposed and can be employed to calculate the ^{90}Y activity to be administered that would allow delivery of the highest dose to the tumor while sparing normal liver tissue. The so-called partition model (based on the MIRD approach) takes into account three different compartments for radiation dose estimates, i.e., the liver tumor, the non-tumoral liver, and the lungs [37]. The basic assumption is that the LSF and the relative distribution of ^{99m}Tc-MAAs in the tumor and non-tumor liver compartments (expressed as T/N ratio) reliably predicts distribution of the ^{90}Y-microspheres that will be administered during another interventional radiology procedure performed a few days later by the same radiologist trying to replicate exactly the same position of the intra-arterial catheter as during ^{99m}Tc-MAA administration. The activity of ^{90}Y-microspheres to be administered can be estimated using the LSF derived from the ^{99m}Tc-MAA scintigraphic images. This approach is adopted routinely when administering the glass ^{90}Y-microspheres and has been shown to yield safe and reproducible estimates regarding expected toxicity and clinical outcomes.

When using the resin ^{90}Y-microspheres, two additional methods can be employed to estimate the activity to be administered, i.e., empiric method and the body surface area (BSA) method. The empiric method is based on the volume of the liver occupied by the tumor tissue expressed as a fraction of the overall liver volume, as estimated by

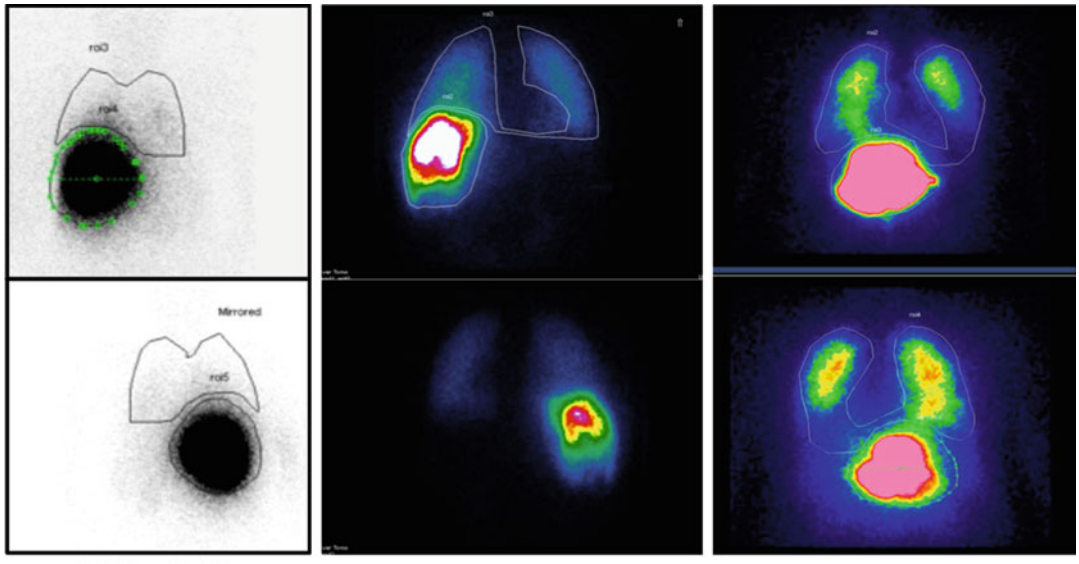

Fig. 4 Representative examples in three different patients of estimation of the lung shunt fraction (LSF) as derived from planar gamma-camera imaging after trans-arterial injection of ^{99m}Tc-MAA. For each patient, the anterior and posterior views are displayed, with delineation of regions of interest (ROI) for the liver and for the lung fields, respectively; each ROI is first manually drawn on the anterior view, and then it is flipped on the horizontal axis to match the posterior view. The geometric means of the ROI counts from the two orthogonal views are utilized to calculate the LSF value according to the equation described in the text. The LSF value calculated for the patient in *left panel* resulted to be 6.4%; the ^{90}Y-microsphere activity injected in this patient was therefore the full amount planned on the basis of the dosimetric estimate. A 20% reduction for administered ^{90}Y-microsphere activity was instead applied to the patient in the *center panel* (whose LSF was 12%), while the patient represented in *right panel* was excluded from treatment because of a LSF exceeding 20%

cross-sectional imaging (either CT or MRI). A ^{90}Y-microsphere activity of 2 GBq is recommended for a tumor/liver fraction <0.25, increasing to 2.5 GBq for tumor fractions between 0.25 and 0.5 and increasing further to 3 GBq for tumor fractions >0.5 (keeping in mind that a value above 0.7 constitutes per se an absolute contraindication to treatment).

The body surface area (*BSA*, expressed in square meters) method uses the following equation to calculate the ^{90}Y-microsphere activity (A) to be administered:

$$A(GBq) = (BSA - 0.2) + \frac{\text{tumor volume}}{\text{total liver volume}}$$

Although these two methods based on clinically derived data of intraoperative activity calculations are routinely used in some centers, they are not optimal in certain situations, in particular when the target is well identified and the total volume of the three compartments is accurately known. Moreover, it has been demonstrated that both the BSA method and the empiric method frequently overestimate the activity to be administered to the patient [38, 39]. Therefore, the use of the MIRD partition model should be recommended when administering the resin ^{90}Y-microspheres.

Patient-specific dosimetry requires accurate evaluation of the liver and tumor mass (usually derived from anatomic imaging such as CT) and of ^{99m}Tc-MAA biodistribution based on scintigraphic imaging. However, the predictive value of ^{99m}Tc-MAA scintigraphy as to the distribution of ^{90}Y-microspheres in the liver is still a matter of debate [40–42]. Parameters that may induce some

discordance between the distribution of ^{99m}Tc-MAAs and that of the ^{90}Y-microspheres include interval differences in catheter position during injection in the two separate occasions, physiologic changes in hepatic blood flow, tumor histopathology, and tumor load, size, and morphology differences between the ^{99m}Tc-MAA particles and the ^{90}Y-microspheres [42]. These factors may all limit the concordance between ^{99m}Tc-MAA distribution as assessed in the pretreatment procedure and actual distribution of the ^{90}Y-microspheres administered for therapy [41].

Although the ability of ^{99m}Tc-MAA to predict radiation dosimetry expected from ^{90}Y-microsphere administration is far from ideal, most of the retrospective studies based on ^{99m}Tc-MAA scintigraphy for these estimates have shown a definite dose-response correlation with a threshold value from 120 to 205 Gy [43, 44] and even up to 500 Gy [45]. However, no prospective studies have confirmed these observations, and no single cutoff value that ensures tumor response has been identified as yet.

The dosimetry-based methods utilized to calculate the activity to be administered during radioembolization are described in detail in ► Chap. 13, "Radiobiology and Radiation Dosimetry in Nuclear Medicine" of this book.

^{90}Y-Microsphere Administration

During the radioembolization session, the vessel perfusing the tumor is reached under fluoroscopic guidance, and the ^{90}Y-microsphere suspension is injected into the artery feeding the target lesion. A delivery system that allows the administration in a step-by-step manner is useful to avoid early full embolization of the vasculature that prevents infusion of the total estimated activity. The infusion is usually done with alternating injections of iodinated contrast medium and sterile water/glucose solution when using the resin ^{90}Y-microspheres or of saline solution during infusion of the glass ^{90}Y-microspheres. Continuous fluoroscopy monitoring ensures that no stasis occurs during infusion and also serves to confirm that the flow of microspheres is similar to that observed during the prior angiographic workup.

According to topography of the tumor, treatment can be either selective (i.e., directed to one liver lobe) or super-selective (directed to one liver segment).

Posttreatment Scan

Early posttreatment assessment of the pattern of ^{90}Y-microsphere deposition by high-quality imaging is necessary to exclude radioactivity accumulation in gastrointestinal tract and to evaluate the radiation-absorbed dose delivered to the tumor.

A post-therapy planar and SPECT/CT scan based on the bremsstrahlung emission generated by the high-energy β^- particles of ^{90}Y helps to confirm correct deposition of the radiolabeled microspheres in the tumor lesions [46]. However, the low-resolution and poor-quality imaging obtained from the bremsstrahlung emission does not allow an accurate quantification of microsphere distribution, especially when dealing with small lesions.

More recently imaging with ^{90}Y PET has been used to assess the distribution of the microspheres [47] (Fig. 5). PET imaging is made possible by the fact that, despite the commonly held notion that ^{90}Y is a pure β^- emitter, in reality, a certain fraction of ^{90}Y decays (even if extremely small, i.e., 32 per million) occur through internal pair production that generates 511 keV annihilation photons. The annihiliation radiation generated from these emissions can be imaged by PET. In the case of radioembolization of liver tumors with ^{90}Y-microspheres, the therapeutic agent remains concentrated in a relatively small volume at the administration site; therefore, even the extremely small fraction of ^{90}Y decays occurring through internal pair production are sufficient to acquire clinically useful PET images for validation and dosimetric purposes [48–51]. The better resolution images provided by PET may allow easy detection of extrahepatic distribution of ^{90}Y-microspheres and assessment of the absorbed dose delivered during the radioembolization procedure [47, 48].

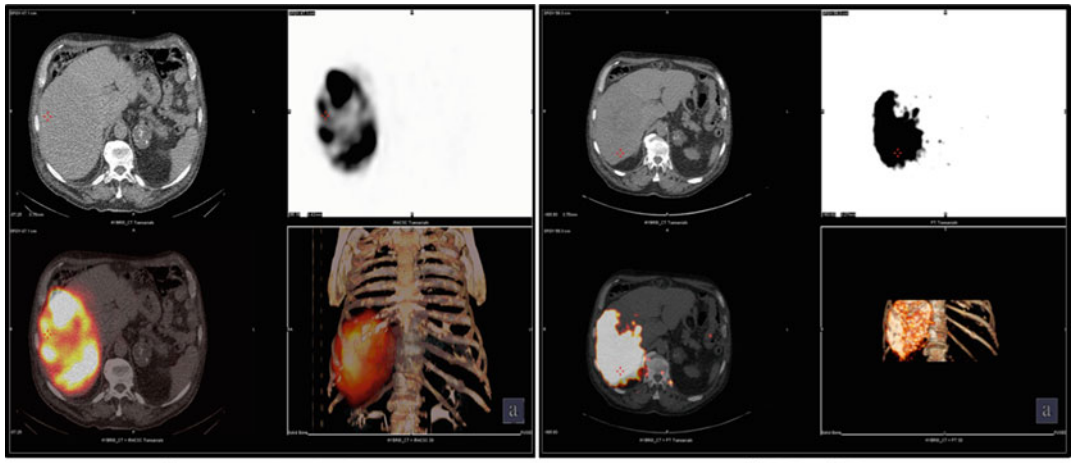

Fig. 5 Good correspondence in the patterns of intrahepatic distribution of radiolabeled particles injected into the right hepatic artery between pretreatment ^{99m}Tc-MAA SPECT/CT (*left*) and posttreatment ^{90}Y-PET/CT (*right*). For SPECT/CT, the MIP image is displayed in *upper right panel*, the axial CT image in *upper left panel*, the fused axial SPECT/CT image in *lower left panel*, and the 3D surface volumetric rendering in *lower right panel*. Similar displays for PET/CT: MIP image in *upper right panel*, axial CT image in *upper left panel*, fused PET/CT image in *lower left panel*, and 3D surface volumetric rendering in *lower right panel*

Radioembolization with ^{90}Y-microspheres can be performed as an outpatient procedure, and the patient can be discharged from the hospital on the same day of treatment or on the following day.

Patient Follow-Up and Assessment of Response to Therapy

Tumor response to radioembolization is monitored both clinically and radiologically. Routine follow-up includes blood chemistry to monitor possible toxicity due to treatment; in the case of HCC, measurement of the serum levels of the tumor-associated marker AFP serves to assess evolution of the malignant disease. Contrast CT is performed at 1 month posttreatment, while additional CT scans are performed every 3 months to assess response to treatment or progression of disease. Although tumor response to therapy can be assessed by classical RECIST criteria, specific criteria set by the World Health Organization (WHO) and by the European Association for the Study of the Liver (EASL) based on size parameters and on necrosis parameters, respectively, are employed to assess response in the target lesions [13, 52].

In metabolic assessment with [^{18}F]FDG-PET provides useful prognostic information in response of either primary or metastatic liver tumors to trans-arterial radioembolization with ^{90}Y-microspheres [40, 53–55]. The superiority of functional metabolic imaging with PET versus the conventional morphology-based criteria such as RECIST for early assessment of tumor response to radioembolization with ^{90}Y-microspheres has been demonstrated in different clinical settings such as HCC [56, 57], intrahepatic cholangiocellular carcinoma [55] (Fig. 6), metastatic CRC [58, 59] (Figs. 7 and 8), and liver metastases from breast cancer [60] and metastatic neuroendocrine malignancies (the latter using ^{68}Ga-DOTANOC as the PET tracer) [61] (Fig. 9).

^{90}Y-Microsphere Radioembolization Combined with Other Therapies

Radioembolization with ^{90}Y-microspheres is a valid therapeutic option per se, preferably in patients with early stage inoperable liver-

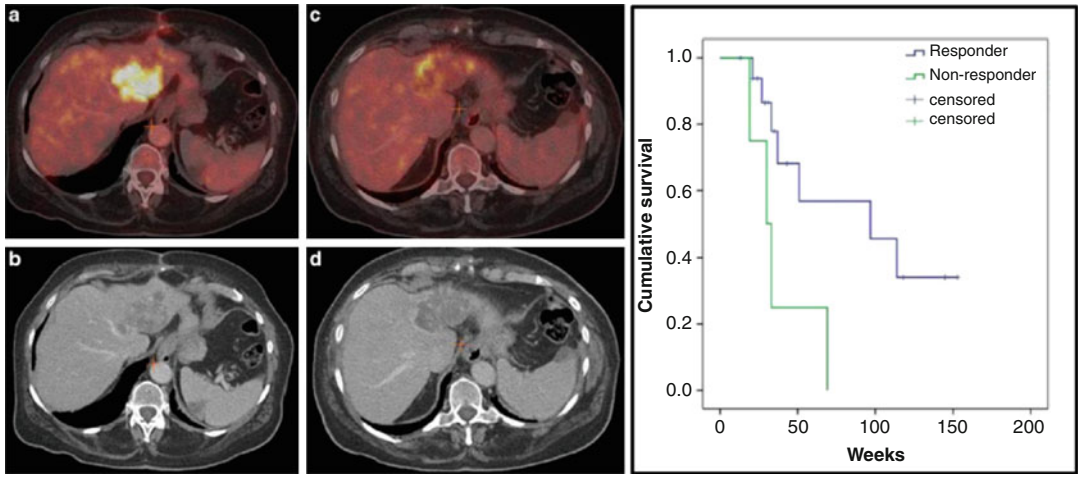

Fig. 6 *Left panel*: response to trans-arterial therapy with ^{90}Y-microspheres in a patient with intrahepatic cholangiocarcinoma. (**a**) Axial fused pre-therapeutic [^{18}F]FDG-PET/CT image; (**b**) corresponding slice of diagnostic CT; (**c**) axial fused post-therapeutic [^{18}F]FDG-PET/CT image; (**d**) corresponding slice of diagnostic CT. The SUV_{max} declined by 70% 3 months after radioembolization, and the serum levels of CA 19-9 fell from 85.2 to 49.2 U/mL; the patient was still alive 12 months after radioembolization without evidence of progression within the liver. *Right panel*: Kaplan-Meier survival curves as a function of ΔSUV_{2SD}. Responders (*blue line*) had a significantly ($P < 0.05$) longer survival than nonresponders (*green line*) (Modified and reproduced with permission from: Haug et al. [55])

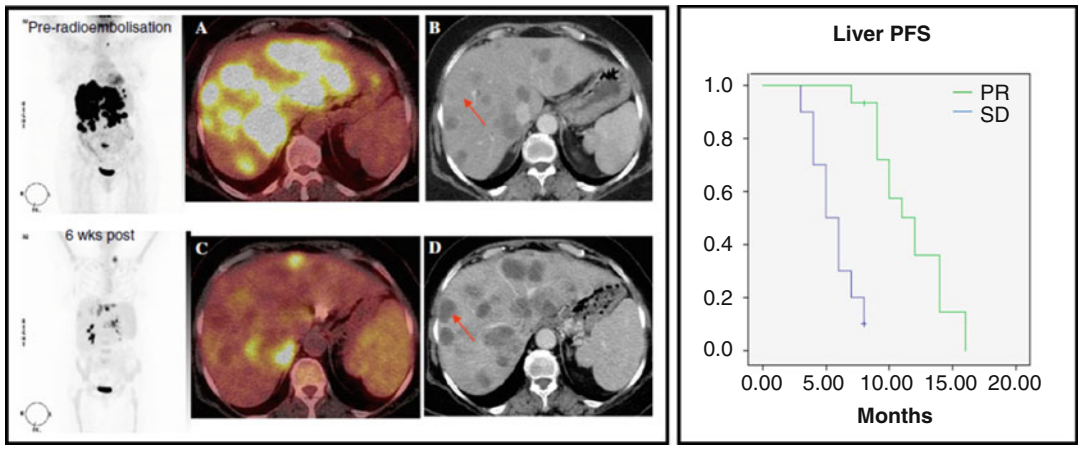

Fig. 7 *Left panel*: coronal PET (*left*), axial fused [^{18}F]FDG-PET/CT images (**a**, **c**), and axial contrast-enhanced CT (ce-CT) images (**b**, **d**) in a patient with metastatic colorectal cancer before and 6 weeks after radioembolization with ^{90}Y-microspheres. (**a**) Baseline PET/CT shows increased [^{18}F]FDG uptake in metastases in segments I, II, IVa, VII, and VIII. (**b**) The ce-CT image before radioembolization shows some of the metabolically active metastases as low-attenuation lesions, but several of them are isointense compared to the liver parenchyma and are difficult to delineate, such as the lesions in segment VIII (*arrow*). (**c**) PET/CT after radioembolization shows an excellent partial response (PR) with marked reduction in the intensity and extent of uptake in the metastatic lesions. (**d**) Post-radioembolization ce-CT shows multiple new low-attenuation lesions, which are more apparent as they have become necrotic, such as the metastasis in segment VIII (*arrow*). This ce-CT image was incorrectly reported as showing disease progression. *Right panel*: Kaplan-Meier plots of progression-free survival (PFS) in relation to responses seen on [^{18}F]FDG-PET/CT. Patients who had a PR or stable disease on [^{18}F]FDG-PET/CT had median PFS of 12 and 5 months, respectively (Modified and reproduced with permission from: Zerizer et al. [58])

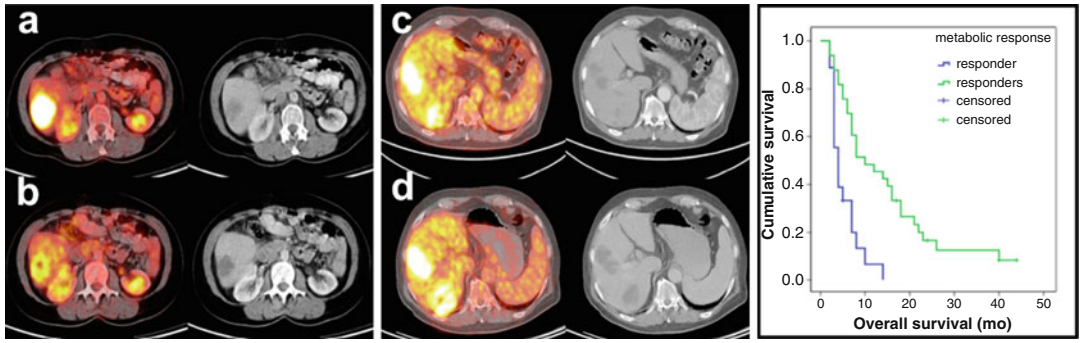

Fig. 8 *Left panel*: axial fused [^{18}F]FDG-PET/CT images before (**a**) and 4 weeks after (**b**) trans-arterial radioembolization with ^{90}Y-microspheres of a patient with metastatic colorectal cancer; the marked metabolic response was associated with a survival of 12 months after treatment. *Center panel*: Axial fused [^{18}F]FDG-PET/CT images before (**a**) and 4 weeks after (**b**) trans-arterial radioembolization with ^{90}Y-microspheres of a patient with metastatic colorectal cancer; this metabolic nonresponder survived 5 months after treatment (Modified and reproduced with permission from: Sabet et al. [59])

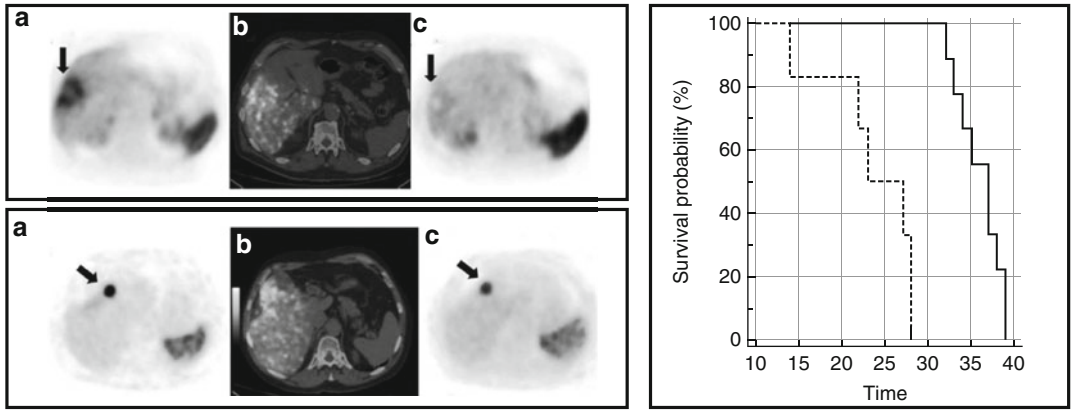

Fig. 9 *Left upper panel*: (**a**) ^{68}Ga-DOTANOC PET axial slice acquired before trans-arterial radioembolization with ^{90}Y-microspheres shows intense tracer accumulation in a patient with a large metastasis from a neuroendocrine neoplasm in the right hepatic lobe (*arrow*). (**b**) Fused unenhanced CT slice and ^{90}Y PET axial slice acquired after administration of ^{90}Y-microspheres shows radioactivity accumulation in the tumor mass with a necrotic core surrounded by a hot circular region. (**c**) ^{68}Ga-DOTANOC PET axial slice acquired 6 weeks after radioembolization shows significant reduction of tracer uptake in the tumor uptake (*arrow*), consistent with a molecular response (ΔT/S was −73.4%); overall survival was 34 months. *Left lower panel*: (**a**) ^{68}Ga-DOTANOC PET axial slice acquired before trans-arterial radioembolization with ^{90}Y-microspheres shows intense tracer accumulation in a patient with a metastasis from neuroendocrine neoplasm in hepatic segment IV (*arrow*). (**b**) Fused unenhanced CT slice and ^{90}Y-PET slice acquired after administration of ^{90}Y-microspheres shows radioactivity accumulation in the tumor mass. (**c**) ^{68}Ga-DOTANOC PET/CT axial slice acquired 6 weeks after treatment shows substantially unchanged tumor uptake (*arrow*), consistent with no response (ΔT/S was −24.6%). Overall survival was 23 months. *Right panel*: Kaplan-Meier survival analysis in relation to ΔT/S measured 6 weeks after radioembolization. Patients with ΔT/S less than −50% (*dashed line*) had significantly lower ($P < 0.001$) survival than those with ΔT/S more than −50% (*solid line*) (Modified and reproduced with permission from: Filippi et al. [61])

predominant malignancies. Nevertheless, it can be used also in combination with systemic molecular/chemotherapies in patients presenting with an intermediate or even advanced stage of HCC [62] or with unresectable liver-predominant metastases from colorectal cancer. Moreover, thanks

to its ability to downsize/downgrade the disease, SIRT/TARE may be used as neoadjuvant therapy also in patients with HCC not meeting the criteria for resection, percutaneous ablation, or transplantation.

The clinical situations in which patients with nonresectable/ablatable HCC can be used with radioembolization combined with other therapies can be summarized as follows:

- Before planned resection or transplantation [63], radioembolization may be considered as a neoadjuvant treatment to reduce the tumor burden and simplify surgery or to stop/slow down tumor progression in order to keep patients on the transplant waiting list or to improve the long-term outcome – even achieving in some cases downstaging of the disease [64]. In selected clinical situations where the non-tumoral liver is too small in terms of functional reserve (thus hindering any type of resection), lobar or segmental selective radioembolization may lead to ipsilateral lobar of segmental parenchymal hypotrophy and contralobar hypertrophy (ranging from 21% to 35%) allowing subsequent surgery [65].
- As an alternative option when other ablative treatments cannot be applied. ^{90}Y-microsphere radioembolization as well trans-arterial chemoembolization may improve the survival in patients with poor prognosis with portal vein occlusion, who are often excluded from a targeted therapy [66].
- In combination with systemic therapies. Although preliminary data suggest a synergistic beneficial effect of ^{90}Y-microsphere radioembolization when combined with sorafenib (with associated tolerable toxicity) [67–70], large-scale multicenter trials are still ongoing to confirm these data and to define the safety profile and the impact of the combination on survival of this combination regimen.
- In patients with unresectable liver-predominant metastases from colorectal cancer, preliminary results of the SIRFLOX study indicate that radioembolization combined with systemic therapy as first-line treatment can lead to downstaging of the disease in a significant proportion of cases and to improved PFS for the liver lesions (but not overall PFS, while the follow-up phase is ongoing for overall survival) [71].
- As a second-line treatment and in the salvage setting for liver-predominant metastatic colorectal cancer, there are clinical evidences that combination of radioembolization and systemic chemotherapy using radiosensitizing drugs (i.e., oxaliplatin, 5-FU, and irinotecan) is safe, with preliminary results indicating a 79% response rate [72].

Clinical Indications

Radioembolization with ^{90}Y-microspheres has shown to be an effective procedure with significant impact on survival of patients with either primary or secondary liver malignancies.

Primary Liver Tumors

Hepatocellular Carcinoma

Radioembolization as a treatment option has been extensively investigated for the most common primary liver malignancy, i.e., HCC, especially after Geschwind and coworkers published their landmark comprehensive analysis on the use of ^{90}Y-microspheres for HCC. Besides demonstrating overall clinical safety and benefit of this therapy, the study also indicated better survival as treatment was employed earlier in the course of disease, i.e., in Okuda stage I (63% for 1-year survival and 628-day median survival) rather than in Okuda stage II patients (51% for 1-year survival and 384-day median survival, with $P = 0.02$) [73].

The response rates to radioembolization with ^{90}Y-microspheres may vary widely not only because of variable tumor biology but also because of differences in evaluation times or in treatment intensity. Tumor shrinkage after therapy may take months to occur, with a median time to response of approximately 6 months according to WHO criteria [74]. Nevertheless, response in

tumor size is not an adequate parameter to define all the antitumor effects of therapy. When combining different response criteria, such as tumor size and arterial contrast enhancement with the EASL response criteria, the overall tumor response rates vary between 40% and 90%, with a disease control rate in targeted lesion of 80–100%. According to changes in vascular enhancement, time to response occurs in the treated tumor lesions earlier than response in tumor size, around 2 months after ^{90}Y-microsphere radioembolization [74].

Surgery is the optimal standard of care with curative intents for patients with HCC; however, resection is possible only for lesions limited in size and number and if the liver function is well preserved; the latter is not a frequent condition considering that most HCCs originate in patients with liver cirrhosis. On the other hand, patients with a single lesion <5 cm in diameter, or with ≤ 3 lesions, all <3 cm without extrahepatic metastases or portal vein thrombosis (PVT), are eligible for liver transplantation. Nevertheless, orthotopic liver transplantation has had a limited role in the management of patients with HCC due both to limited availability of donor organs and to dropout of patients because of tumor progression. Since radioembolization has been shown to slow the progression of HCC, this procedure may allow patients more time to wait for donor organs and thus increases their chance of undergoing liver transplant [75–77].

Patients whose disease is too advanced to meet transplant criteria, but do not have malignant PVT or metastatic HCC, are good candidates for radioembolization. In fact, radioembolization has been shown to downstage the disease so that 56% of the patients who were initially stratified as non-eligible for transplant according to Milan criteria then become eligible for transplant after therapy; 8 out of 34 downstaged patients actually underwent subsequent liver transplantation, with 84%, 54%, and 27% overall survivals, respectively, at 1, 2, and 3 years. In addition to downstaging, radioembolization also prolongs overall survival of these patients [75–77].

Survival benefit following radioembolization has been observed also in patients with malignant vascular involvement, with a 70% response rate according to EASL criteria [78]. The presence of distant metastases contraindicates treatment, as a survival benefit has not been demonstrated for this subset of patients.

Intrahepatic Cholangiocarcinoma

Resection has a modest survival benefit in patients who have resectable intrahepatic cholangiocarcinoma (ICC). Some improvement in survival has been observed after trans-arterial chemoembolization, but toxicity associated with this treatment remains high. On the other hand, while radioembolization has been shown to be an effective treatment for HCC, its role in the management of ICC patients has not been extensively investigated. Nevertheless, a pilot study in 24 patients with biopsy-proven ICC has shown favorable tumor response and favorable survival outcomes following therapy with ^{90}Y-microspheres, especially for patients with better ECOG performance status [79].

A recent systematic review on the use of TARE in the treatment of ICC identified 12 studies including a total of 73 patients. PR and SD at 3 months were reported in 28% and 54% of patients, respectively. In a pooled analysis, the overall weighed median survival was 15.5 months, and downstaging to surgery was achieved in seven patients [80]. The combination of TARE and chemotherapy as a strategy for downstaging ICC to achieve resectability has recently been proposed, with encouraging initial data [81]. However, when comparing different locoregional treatments for ICC, TARE may not be the most effective approach. In a comparative analysis, TARE performed second in terms of tumor response to intra-arterial chemotherapy but was more effective than TACE or DEB-TACE both in terms of tumor response and in terms of overall survival. In fact, overall survival was 22.8 months for intra-arterial chemotherapy, 13.9 months for

TARE, 12.4 months for TACE, and 12.3 months for DEB-TACE. Nevertheless, intra-arterial chemotherapy had the highest toxicity [82]. Despite the lack of randomized controlled trials, locoregional treatments appear to be somewhat more effective than the current standard chemotherapy regimens with oxaliplatin and gemcitabine [83]. For patients with unresectable ICC, trans-arterial radioembolization with ^{90}Y-microspheres seems to be best suited for patients who are not eligible for intra-arterial chemotherapy.

[^{18}F]FDG-PET is the best independent predictor for patient outcome after radioembolization treatment, based on reduction in the metabolically active tumor volume at 3 months after therapy [55].

Metastatic Liver Tumors

Extrahepatic metastasis and comorbidities limit the role of surgical resection in patients with secondary liver tumors [84]. The use of radioembolization in these patients has been extensively investigated, either as a single treatment or in adjunct to systemic chemotherapy.

Metastatic Colorectal Carcinoma

Liver metastases from colorectal carcinoma (CRC) are resectable in less than 10% of the patients [84]. Radioembolization has been shown to be effective in the treatment of metastatic CRC to the liver. Candidates for radioembolization are those patients who have unresectable liver metastases and are on systemic chemotherapy or have failed to respond to first- or second-line chemotherapy. In these patients, [^{18}F]FDG-PET has been shown to be more sensitive than CT for assessing tumor response to radioembolization [54, 85]. Furthermore, reduction of the hepatic metastatic load can be assessed quantitatively by [^{18}F]FDG-PET, by evaluating the percent change of total liver SUV after treatment [53, 54].

Most of the studies on ^{90}Y-microsphere TARE reported so far have been conducted in patients with chemorefractory liver-predominant metastatic CRC. A systematic review of 20 studies including a total of 979 patients treated with resin ^{90}Y-microspheres has demonstrated the overall safety and efficacy of TARE for unresectable, chemorefractory metastatic CRC, with a median time to intrahepatic progression of 9 months and overall survival of 12 months [86].

In a randomized controlled clinical trial involving 74 patients, the combination of systemic therapy with radioembolization resulted in significantly better tumor response (44% objective response versus 17.6% in the control group), longer time to progression, and longer survival than systemic chemotherapy alone [87]; furthermore, the safety profile of the combined regimen was acceptable [87], and dose escalation studies have shown improved tumor response with increasing doses [88].

Several prospective trials have investigated the efficacy of TARE in combination with systemic chemotherapy versus systemic chemotherapy alone. In an early study, TARE combined with systemic 5-fluorouracil (5-FU) induced better objective response rates than 5-FU alone: 73% versus 0%, with time to progression of 18.6 months versus 3.6 months and overall survival of 29.4 months versus 12.8 months [89]. More recent prospective studies have evaluated chemotherapy regimen more up-to-date than 5-FU. In a first-line setting, TARE combined with FOLFOX4 achieved a 90% PR rate [90], while TARE with irinotecan in a second-line setting after failure of previous chemotherapy reported an overall 87% response rate, with 48% PR and 39% SD [91]. In the SIRFLOX study, a randomized clinical trial including 530 patients, the results of mFOLFOX 6 with or without bevacizumab were compared with TARE + mFOLFOX 6 with or without bevacizumab. While there was no difference in progression-free survival, there was a significant difference in progression-free survival in the liver, favoring the combination with TARE (20.5 months) over chemotherapy alone (12.6 months, with $P = 0.002$). Objective response rates were somewhat better with the combination therapy than with chemotherapy

alone (76.4% versus 68.1%, but without reaching statistical significance, with $P = 0.113$) [92].

Also the recently published results obtained by Hong and coworkers show that radioembolization is safe and effective as a salvage therapy in the management of metastatic CRC when compared with chemoembolization [93].

A recent systematic review on TARE in unresectable, chemorefractory metastatic CRC includes 20 studies for a total of 979 patients enrolled after failure of two to five lines of chemotherapy. TARE achieved CR, PR, and SD in 0% (range 0–6%), 31% (range 0–73%), and 40.5% (range 17–76%) of patients, respectively. The median time to intrahepatic progression was 9 months (range 6–16), and median overall survival was 12 months (range 8.3–36) [94]. In a large multicenter trial, overall survival was strongly dependent on previous treatments; in particular, median survival after ^{90}Y-microsphere radioembolization was 13 months (95% CI 10.5–14.6) when TARE was performed as second-line treatment, 9 months (95% CI 7.8–11.0) for third-line treatment, and 8.1 months (95% CI 6.4–9.3) for fourth-line treatment and over, respectively, with $P < 0.001$ [95].

Metastatic Neuroendocrine Tumors

Several neuroendocrine tumors, such as carcinoids, VIPomas, gastrinomas, and somatostatinomas, metastasize to the liver. These lesions are often well arterialized and represent a target for transarterial therapies, similarly to patients with HCC. The goals of treatment in these patients are both control of symptoms and survival. Systemic chemotherapy and ablative procedures have all been shown to produce modest benefit in these patients. Patients with unresectable disease are considered candidates for radioembolization. The results obtained in a multicenter study including 148 patients have shown that radioembolization of metastatic neuroendocrine tumors to the liver is safe and effective, with very high response rates: any response in 95.1% of patients and progressive disease in only 4.9% of the patients. Response rates were even longer than 2 years, especially in non-pancreatic NETs [96, 97].

Absolute and Relative Contraindications

Two absolute contraindications exist for therapy with ^{90}Y-microspheres intra-arterially. The main contraindication is represented by a pretreatment ^{99m}Tc-MAA scan demonstrating significant hepatopulmonary shunting. This occurrence would in fact result in the delivery of a radiation dose to the lungs greater than 30 Gy with a single infusion or as much as 50 Gy for multiple infusions. The second contraindication is the inability to prevent deposition of the radiolabeled microspheres in the gastrointestinal tract. Relative contraindications include reduced pulmonary function, inadequate functional liver reserve, serum creatinine >2.0 mg/dL, and platelet count $<75 \times 10^9$/L. When such relative contraindications exist, clinical judgment should be exercised for determining whether or not a patient is appropriate to undergo the procedure, taking into consideration either ^{90}Y-microspheres or ^{131}I-lipiodol [98].

Early and Late Toxicities

The most common clinical toxicity observed with ^{90}Y-microsphere therapy is a mild post-embolic syndrome. Similarly as observed with other embolic treatments such as trans-arterial chemoembolization, this syndrome includes fatigue, vague abdominal discomfort, pain, and fever [99, 100]. Other toxicities that can occur as a result of nontarget radiation (and should therefore be avoided by adequate pre-therapy procedures and by accurate treatment planning) include the following: cholecystitis, gastric ulceration, gastroduodenitis, pancreatitis, radiation pneumonitis, and RILD [75, 78, 79, 101]. By adopting meticulous planning, careful selection of patients, and proper techniques, the majority of these toxicities can be mitigated. Finally, a common hematologic toxicity observed in the immediate post-radioembolization period is represented by lymphopenia, not an unexpected finding considering the sensitivity of lymphocytes to radiation. Despite this possible occurrence, no infectious complications have been reported [13, 33, 52–54, 99–102].

Perspectives on Radioembolization for Primary and Metastatic Liver Tumors

A growing body of evidence supports the use of TARE with ^{90}Y-microspheres as an effective monotherapy in patients with HCC. Future avenues to be explored concern the scenario of combination therapies with systemic and locoregional agents, specifically sorafenib and TARE, in the adjuvant or neoadjuvant setting. Although the mechanisms of action for the two therapeutic approaches can in principle be considered as complementary one to the other from the pathophysiologic point of view, there are currently scarce data confirming the actual clinical benefit of regimens based on this combination.

In the only prospective study so far reported for combination therapy of TARE with sorafenib, the rate of objective responses was 25%, somewhat disappointing with respect to that expected on the basis of the underlying rationale. Moreover, 39% of the patients could not complete the prescribed dose of sorafenib due to important side effects [67]. On the other hand, initial safety results in the first 40 patients enrolled in a randomized controlled clinical trial comparing TARE with resin ^{90}Y-microspheres followed by sorafenib with sorafenib only indicate a similar tolerance for the two treatment arms [69]. Long-term outcome data from ongoing randomized controlled clinical trials such as SORAMIC, SARAH, or SIRveNIB (based on the use of resin ^{90}Y-microspheres) or STOP-HCC (using glass ^{90}Y-microspheres) have not been published yet.

Regarding treatment of metastatic disease, there is the need of randomized controlled clinical trials comparing TARE with up-to-date chemotherapy regimens, since the few data so far available have been obtained in studies comparing the efficacy of therapy with resin ^{90}Y-microspheres versus chemotherapeutic regimen that are now obsolete or the studies lack survival data. An ongoing randomized controlled clinical phase III trial evaluates treatment with glass ^{90}Y-microspheres and second-line chemotherapy after failure of first-line chemotherapy in comparison to second-line chemotherapy alone for metastatic CRC; 360 patients have been enrolled in this trial, and the first results of the analysis are expected to be released soon.

The FOXFIRE global is an international phase III study assessing the value of additional resin ^{90}Y-microspheres in the setting of first-line treatment with FOLFOX6m (NCT01721954). Enrollment of 530 patients has been completed, and the preliminary results are encouraging, with significantly prolonged PFS in the liver by competing risk analysis, from a median of 12.6 months for control patients to 20.5 months ($P = 0.002$) for patients receiving resin ^{90}Y-microspheres; this translates into a 31% reduction in the risk of disease progression in the liver. Pooling the data of studies with similar designs (SIRFLOX, FOXFIRE, and FOXFIRE global) from over 1,100 patients will provide sufficient statistical power to assess the survival benefit derived from the addition of resin ^{90}Y-microspheres to current chemotherapy regimens. Survival data from the three combined studies are expected to be released in 2017.

Further ongoing studies evaluate the role of TARE in uveal melanoma with liver metastasis (SIRUM trial, NCT01473004) or the combination of TARE and pasireotide and everolimus in liver metastatic neuroendocrine tumors (NCT01469572) [103].

References

1. El-Serag HB. Epidemiology of viral hepatitis and hepatocellular carcinoma. Gastroenterology. 2012; 142:1264–73.
2. van der Pool AE, Damhuis RA, Ijzermans JN, de Wilt JH, Eggermont AM, Kranse R, Verhoef C. Trends in incidence, treatment and survival of patients with stage IV colorectal cancer: a population-based series. Colorectal Dis. 2012;14:56–61.
3. Mazzaferro V, Regalia E, Doci R, Andreola S, Pulvirenti A, Bozzetti F, et al. Liver transplantation for the treatment of small hepatocellular carcinomas in patients with cirrhosis. N Engl J Med. 1996;334:693–9.
4. Ingold JA, Reed GB, Kaplan HS, Bagshaw MA. Radiation hepatitis. Am J Roentgenol Radium Ther Nucl Med. 1965;93:200–8.
5. Lawrence TS, Robertson JM, Anscher MS, Jirtle RL, Ensminger WD, Fajardo LF. Hepatic toxicity resulting from cancer treatment. Int J Radiat Oncol Biol Phys. 1995;31:1237–48.
6. Yu H, Burke CT. Comparison of percutaneous ablation technologies in the treatment of malignant liver tumors. Semin Interv Radiol. 2014;31:129–37.

7. Stuart K. Chemoembolization in the management of liver tumors. Oncologist. 2003;8:425–37.
8. Geschwind JFH. Chemoembolization for hepatocellular carcinoma: where does the truth lie? J Vasc Interv Radiol. 2002;13:991–4.
9. Varela M, Real MI, Burrel M, Forner A, Sala M, Brunet M, et al. Chemoembolization of hepatocellular carcinoma with drug eluting beads: efficacy and doxorubicin pharmacokinetics. J Hepatol. 2007;46: 474–81.
10. Llovet JM, Real MI, Montana X, Planas R, Coll S, Aponte J, et al. Arterial embolisation or chemoembolisation versus symptomatic treatment in patients with unresectable hepatocellular carcinoma: a randomised controlled trial. Lancet. 2002;359(9319):1734–9.
11. Kettenbach J, Stadler A, Katzler IV, Schernthaner R, Blum M, Lammer J, et al. Drug-loaded microspheres for the treatment of liver cancer: review of current results. Cardiovasc Intervent Radiol. 2008;31: 468–76.
12. European Association for the Study of the Liver, European Organisation for Research and Treatment of Cancer. EASLEORT clinical practice guidelines: management of hepatocellular carcinoma. J Hepatol. 2012;56:908–43.
13. Salem R, Lewandowski RJ, Atassi B, Gordon SC, Gates VL, Barakat O, et al. Treatment of unresectable hepatocellular carcinoma with use of ^{90}Y microspheres (TheraSphere): safety, tumor response, and survival. J Vasc Interv Radiol. 2005;16:1627–39.
14. Raoul JL, Bourguet P, Bretagne JF, Duvauferrier R, Coornaert S, Darnault P, et al. Hepatic artery injection of I-131-labelled lipiodol. I. Biodistribution study results in patients with hepatocellular carcinoma. Radiology. 1988;168:541–5.
15. Nakajo M, Kobayashi H, Shimabukuro K, Shirono K, Sakata H, Taguchi M, et al. Biodistribution and in vivo kinetics of iodine-131 lipiodol infused via the hepatic artery of patients with hepatic cancers. J Nucl Med. 1988;29:1066–77.
16. Smits ML, Nijsen JF, van den Bosch MA, Lam MG, Vente MA, Huijbregts JE, et al. Holmium-166 radioembolization for the treatment of patients with liver metastases: design of the phase I HEPAR trial. J Exp Clin Cancer Res. 2010;29:70.
17. Nowicki ML, Cwikla JB, Sankowski AJ, Shcherbinin S, Grimmes J, Celler A, et al. Initial study of radiological and clinical efficacy radioembolization using ^{188}Re-human serum albumin (HSA) microspheres in patients with progressive, unresectable primary or secondary liver cancers. Med Sci Monit. 2014;20:1353–62.
18. Bhattacharya S, Dhillon AP, Winslet MC, Davidson BR, Shukla N, Gupta SD, et al. Human liver cancer cells and endothelial cells incorporate iodised oil. Br J Cancer. 1996;73:877–81.
19. Madsen MT, Park CH, Thakur ML. Dosimetry of iodine-131 ethiodol in the treatment of hepatoma. J Nucl Med. 1988;29:1038–44.
20. Monsieurs MA, Bacher K, Brans B, Vral A, De Ridder L, Dierckx RA, et al. Patient dosimetry for ^{131}I-lipiodol therapy. Eur J Nucl Med Mol Imaging. 2003;30:554–61.
21. Bhattacharya S, Novell JR, Dusheiko GM, Hilson AJ, Dick R, Hobbs KE. Epirubicin-lipiodol chemotherapy versus ^{131}iodine-lipiodol radiotherapy in the treatment of unresectable hepatocellular carcinoma. Cancer. 1995;76:2202–10.
22. Yoo HS, Park CH, Lee JT, Kim KW, Yoon CS, Suh JH, et al. Small hepatocellular carcinoma: high dose internal radiation therapy with superselective intra-arterial injection of I-131-labeled Lipiodol. Cancer Chemother Pharmacol. 1994;33:S128–33.
23. Leung WT, Lau WY, Ho S, et al. Selective internal radiation therapy with intra-arterial iodine-131-lipiodol in inoperable hepatocellular carcinoma. J Nucl Med. 1994;35:1313–8.
24. Raoul JL, Guyader D, Bretagne JF, Duvauferrier R, Bourguet P, Bekhechi D, et al. Randomized controlled trial for hepatocellular carcinoma with portal vein thrombosis: intra-arterial iodine-131-iodized oil versus medical support. J Nucl Med. 1994;35:1782–7.
25. Boucher E, Garin E, Guillygomac'h A, Olivie D, Boudjema K, Raoul JL. Intra-arterial injection of iodine-131-labeled lipiodol for treatment of hepatocellular carcinoma. Radiother Oncol. 2007;82:76–82.
26. Partensky C, Sassolas G, Henry L, Paliard P, Maddern GJ. Intra-arterial iodine 131-labeled lipiodol as adjuvant therapy after curative liver resection for hepatocellular carcinoma: a phase 2 clinical study. Arch Surg. 2000;135:1298–300.
27. Lau WY, Lai EC, Leung TW, Yu SC. Adjuvant intra-arterial iodine-131-labeled lipiodol for resectable hepatocellular carcinoma: a prospective randomized trial-update on 5-year and 10-year survival. Ann Surg. 2008;247:43–8.
28. Lee YS, Jeong JM, Kim YJ, Chung JW, Park JH, Suh YG, et al. Synthesis of ^{188}Re-labelled long chain alkyl diaminedithiol for therapy of liver cancer. Nucl Med Commun. 2002;23:237–42.
29. De Ruyck K, Lambert B, Bacher K, Gemmel F, De Vos F, Vral A, et al. Biologic dosimetry of ^{188}Re-HDD/lipiodol versus ^{131}I-lipiodol therapy in patients with hepatocellular carcinoma. J Nucl Med. 2004;45: 612–8.
30. Kumar A, Srivastava DN, Chau TT, Long HD, Bal C, Chandra P, et al. Inoperable hepatocellular carcinoma: transarterial ^{188}Re HDD-labeled iodized oil for treatment. Prospective multicenter clinical trial. Radiology. 2007;243:509–19.
31. Sato K, Lewandowski RJ, Bui JT, Omary R, Hunter RD, Kulik L, et al. Treatment of unresectable primary and metastatic liver cancer with yttrium-90 microspheres (TheraSphere): assessment of hepatic arterial embolization. Cardiovasc Intervent Radiol. 2006;29: 522–9.
32. Salem R, Thurston KG. Radioembolization with ^{90}Yttrium microspheres: a state-of-the-art

brachytherapy treatment for primary and secondary liver malignancies. Part 1: technical and methodologic considerations. J Vasc Interv Radiol. 2006;17: 1251–78.
33. Hamami ME, Poeppel TD, Müller S, Heusner T, Bockisch A, Hilgard P, Antoch G. SPECT/CT with ^{99m}Tc-MAA in radioembolization with ^{90}Y microspheres in patients with hepatocellular cancer. J Nucl Med. 2009;50:688–92.
34. Grosser OS, Rufi J, Kupitz D, Pethe A, Ulrich G, Genseke P, et al. Pharmacokinetics of ^{99m}Tc-MAA- and ^{99m}Tc-HSA microspheres used in preradioembolization dosimetry: influence on the liver–lung shunt. J Nucl Med. 2016;57:925–7.
35. Sabet A, Ahmadzadehfar H, Muckle M, Haslerud T, Wilhelm K, Biersack HJ, et al. Significance of oral administration of sodium perchlorate in planning liver-directed radioembolisation. J Nucl Med. 2011; 52:1063–7.
36. Dale RG. Dose-rate effects in targeted radiotherapy. Phys Med Biol. 1996;41:1871–84.
37. Ho S, Lau WY, Leung TW, Chan M, Chan KW, Lee WY, et al. Partition model for estimating radiation doses from yttrium-90 microspheres in treating hepatic tumors. Eur J Nucl Med. 1996;23:947–52.
38. Kennedy AS, Dezarn WA, McNeillie P, Overton C, England M, Sailer SL. Fractionation, dose selection, and response of hepatic metastases of neuroendocrine tumors after ^{90}Y-microsphere brachytherapy. Brachytheraphy. 2006;5:103–4.
39. Kennedy AS, Dezarn WA, McNeillie P, Overton C, England M, Sailer SL. Dose selection of resin ^{90}Y-micrspheres for liver brachytherapy: a single center review. Brachytheraphy. 2006;5:104.
40. Flamen P, Vanderlinden B, Delatte P, Ghanem G, Ameye L, Van Den Eyden M, et al. Multimodality imaging can predict the metabolic response of unresectable colorectal liver metastases to radioembolisation therapy with yttrium-90 labeled resin microspheres. Phys Med Biol. 2008;53:6591–693.
41. Jiang M, Fischman A, Nowakowski FS, et al. Segmental perfusion differences on paired Tc-99m macroaggregated albumin (MAA) hepatic perfusion imaging and yttrium-90 (Y-90) bremsstrahlung imaging studies in SIR-sphere radioembolization: associations with angiography. J Nucl Med Radiat Ther. 2012;3:122.
42. Wondergem M, Smits MLJ, Elschot M, de Jong HWAM, Verkooijen HM, van den Bosch MAAJ, Nijsen JFW, Lam MGEH. ^{99m}Tc-Macroaggregated albumin poorly predicts the intrahepatic distribution of ^{90}Y resin microspheres in hepatic radioembolization. J Nucl Med. 2013;54:1294–301.
43. Lau WY, Sangro B, Chen PJ, Cheng SQ, Chow P, Lee RC, et al. Treatment for hepatocellular carcinoma with portal vein tumor thrombosis: the emerging role for radioembolization using yttrium-90. Oncology. 2013;84:311–8.
44. Garin E, Lenoir L, Rolland Y, Edeline J, Mesbah H, Laffont S, et al. Dosimetry based on ^{99m}Tc-macroaggregated albumin SPECT/CT accurately predicts tumor response and survival in hepatocellular carcinoma patients treated with ^{90}Y-loaded glass microspheres: preliminary results. J Nucl Med. 2012;53: 255–63.
45. Mazzaferro V, Sposito C, Bhoori S, Romito R, Chiesa C, Morosi C, et al. Yttrium-90 radioembolization for intermediate-advanced hepatocellular carcinoma: a phase 2 study. Hepatology. 2013;57:1826–37.
46. Ahmadzadehfar H, Muckle M, Sabet A, Wilhelm K, Kuhl C, Biermann K, et al. The significance of bremsstrahlung SPECT/CT after yttrium-90 radioembolisation treatment in the prediction of extrahepatic side effects. Eur J Nucl Med Mol Imaging. 2011;39:309–15.
47. Lhommel R, Goffette P, del Eynde V, Jamar F, Pauwels S, Bilbao JI, et al. Yttrium-90 TOF PET scan demonstrates high-resolution biodistribution after liver SIRT. Eur J Nucl Med Mol Imaging. 2009;36:1696.
48. Lhommel R, van Elmbt L, Goffette P, Van den Eynde M, Jamar F, Pauwels S, et al. Feasibility of ^{90}Y TOF PET-based dosimetry in liver metastasis therapy using SIR-spheres. Eur J Nucl Med Mol Imaging. 2010;37:1654–62.
49. Kao YH, Tan EH, Lim KY, Eng CE, Goh SW. Yttrium-90 internal pair production imaging using first generation PET/CT provides high resolution images for qualitative diagnostic purposes. Br J Radiol. 2012;85: 1018–9.
50. Wright CL, Zhang J, Tweedle MF, Knopp MV, Hall NC. Theranostic imaging of yttrium-90. Biomed Res Int. 2015;2015:481279.
51. Gnesin S, Canetti L, Adib S, Cherbuin N, Silva-Monteiro M, Bize P, et al. Partition model based ^{99m}Tc-MAA SPECT/CT predictive dosimetry compared to ^{90}Y TOF PET/CT post treatment dosimetry in radioembolisation of hepatocellular carcinoma: a quantitative agreement comparison. J Nucl Med. 2016;57:1672–8.
52. Riaz A, Memon K, Miller FH, Nikolaidis P, Kulik LM, Lewandowski RJ, et al. Role of the EASL, RECIST, and WHO response guidelines alone or in combination for hepatocellular carcinoma: radiologic-pathologic correlation. J Hepatol. 2011;54:695–704.
53. Wong CY, Qing F, Savin M, Campbell J, Gates VL, Sherpa KM, et al. Reduction of metastatic load to liver after intraarterial hepatic yttrium-90 radioembolization as evaluated by [^{18}F]fluorodeoxyglucose positron emission tomographic imaging. J Vasc Interv Radiol. 2005;16:1101–6.
54. Miller FH, Keppke AL, Reddy D, Huang J, Jin J, Mulcahy MF, Salem R. Response of liver metastases after treatment with yttrium-90 microspheres: role of size, necrosis, and PET. AJR Am J Roentgenol. 2007; 188:776–83.
55. Haug AR, Heinemann V, Bruns CJ, Hoffmann R, Jakobs T, Bartenstein P, Hacker M. ^{18}F-FDG PET independently predicts survival in patients with cholangiocellular carcinoma treated with ^{90}Y microspheres. Eur J Nucl Med Mol Imaging. 2011;38:1037–45.

56. Sabet A, Ahmadzadehfar H, Bruhman J, Sabet A, Meyer C, Wasmuth JC, et al. Survival in patients with hepatocellular carcinoma treated with ^{90}Y-microsphere radioembolization. Prediction by ^{18}F-FDG PET. Nuklearmedizin. 2014;53:39–45.
57. Hartenbach M, Weber S, Albert NL, Hartenbach S, Hirtl A, Zacherl MJ, et al. Evaluating treatment response of radioembolization in intermediate-stage hepatocellular carcinoma patients using ^{18}F-fluoroethylcholine PET/CT. J Nucl Med. 2015;56:1661–6.
58. Zerizer I, Al-Nahhas A, Towey D, Tait P, Ariff B, Wasan H, et al. The role of early ^{18}F-FDG PET/CT in prediction of progression-free survival after ^{90}Y radioembolization: comparison with RECIST and tumour density criteria. Eur J Nucl Med Mol Imaging. 2012;39:1391–9.
59. Sabet A, Meyer C, Aouf A, Sabet A, Ghamari S, Pieper CC, et al. Early post-treatment FDG PET predicts survival after ^{90}Y microsphere radioembolization in liver-dominant metastatic colorectal cancer. Eur J Nucl Med Mol Imaging. 2015;42:370–6.
60. Haug AR, Tiega Donfack BP, Trumm C, Zech CJ, Michl M, Laubender RP, et al. ^{18}F-FDG PET/CT predicts survival after radioembolization of hepatic metastases from breast cancer. J Nucl Med. 2012;53:371–7.
61. Filippi L, Scopinaro F, Pelle G, Cianni R, Salvatori R, Schillaci O, et al. Molecular response assessed by ^{68}Ga-DOTANOC and survival after ^{90}Y microsphere therapy in patients with liver metastases from neuroendocrine tumours. Eur J Nucl Med Mol Imaging. 2016;43:432–40.
62. Fidelman N, Kerlan Jr RK. Transarterial chemoembolization and ^{90}Y radioembolization for hepatocellular carcinoma: review of current applications beyond intermediate-stage disease. AJR Am J Roentgenol. 2015;205:742–52.
63. Braat AJ, Huijbregts JE, Molenaar IQ, Borel Rinkes IH, van den Bosch MA, Lam MG. Hepatic radioembolization as a bridge to liver surgery. Front Oncol. 2014;4:199.
64. Lewandowski RJ, Donahue L, Chokechanachaisakul A, Kulik L, Mouli S, Caicedo J, et al. ^{90}Y radiation lobectomy: outcomes following surgical resection in patients with hepatic tumors and small future liver remnant volumes. J Surg Oncol. 2016;114:99–105.
65. Teo JY, Allen Jr JC, Ng DC, Choo SP, Tai DW, Chang JP, et al. A systematic review of contralateral liver lobe hypertrophy after unilobar selective internal radiation therapy with Y90. HPB (Oxford). 2016;18:7–12.
66. Johnson GE, Monsky WL, Valji K, Hippe DS, Padia SA. Yttrium-90 radioembolization as a salvage treatment following chemoembolization for hepatocellular carcinoma. J Vasc Interv Radiol. 2016;27:1123–9.
67. Chow PK, Poon DY, Khin MW, Singh H, Han HS, Goh AS, Asia-Pacific Hepatocellular Carcinoma Trials Group, et al. Multicenter phase II study of sequential radioembolization-sorafenib therapy for inoperable hepatocellular carcinoma. PLoS One. 2014;9(3), e90909.
68. Kulik L, Vouche M, Koppe S, Lewandowski RJ, Mulcahy MF, Ganger D, et al. Prospective randomized pilot study of Y90 +/− sorafenib as bridge to transplantation in hepatocellular carcinoma. J Hepatol. 2014;61:309–17.
69. Ricke J, Bulla K, Kolligs F, Peck-Radosavljevic M, Reimer P, Sangro B, et al. Safety and toxicity of radioembolization plus Sorafenib in advanced hepatocellular carcinoma: analysis of the European multicentre trial SORAMIC. Liver Int. 2015;35:620–6.
70. Lorenzin D, Pravisani R, Leo CA, Bugiantella W, Soardo G, Carnelutti A, et al. Complete remission of unresectable hepatocellular carcinoma after combined sorafenib and adjuvant yttrium-90 radioembolization. Cancer Biother Radiopharm. 2016;31:65–9.
71. Sangha BS, Nimeiri H, Hickey R, Salem R, Lewandowski RJ. Radioembolization as a treatment strategy for metastatic colorectal cancer to the liver: what can we learn from the SIRFLOX trial? Curr Treat Options Oncol. 2016;17:26.
72. Dutton SJ, Kenealy N, Love SB, Wasan HS, Sharma RA, FOXFIRE Protocol Development Group and the NCRI Colorectal Clinical Study Group. FOXFIRE protocol: an open-label, randomised, phase III trial of 5-fluorouracil, oxaliplatin and folinic acid (OxMdG) with or without interventional selective internal radiation therapy (SIRT) as first-line treatment for patients with unresectable liver-only or liver-dominant metastatic colorectal cancer. BMC Cancer. 2014;14:497.
73. Geschwind JF, Salem R, Carr BI, Soulen MC, Thurston KG, Goin KA, et al. Yttrium-90 microspheres for the treatment of hepatocellular carcinoma. Gastroenterology. 2004;127:S194–205.
74. Salem R, Lewandowsky RJ, Mulcahy MF, Riaz A, Ryu RK, Ibrahim S, et al. Radioembolisation for hepatocellular carcinoma using Yttrium-90 microspheres. a comprehensive report of long term outcomes. Gastroenterology. 2010;138:52–64.
75. Kulik LM, Atassi B, van Holsbeeck L, Souman T, Lewandowski RJ, Mulcahy MF, et al. Yttrium-90 microspheres (TheraSphere®) treatment of unresectable hepatocellular carcinoma: downstaging to resection, RFA and bridge to transplantation. J Surg Oncol. 2006;94:572–86.
76. Tohme S, Sukato D, Chen HW, Amesur N, Zajko AB, Humar A, et al. Yttrium-90 radioembolization as a bridge to liver transplantation: a single-institution experience. J Vasc Interv Radiol. 2013;24:1632–8.
77. Abdelfattah MR, Al-Sebayel M, Broering D, Alsuhaibani H. Radioembolization using yttrium-90 microspheres as bridging and downstaging treatment for unresectable hepatocellular carcinoma before liver transplantation: initial single-center experience. Transplant Proc. 2015;47:408–11.

78. Kulik LM, Carr BI, Mulcahy MF, Lewandowski RJ, Atassi B, Ryu RK, et al. Safety and efficacy of ^{90}Y radiotherapy for hepatocellular carcinoma with and without portal vein thrombosis. Hepatology. 2007;41:71–81.
79. Ibrahim SM, Mulcahy MF, Lewandowski RJ, Sato KT, Ryu RK, Masterson EJ, et al. Treatment of unresectable cholangiocarcinoma using yttrium-90 microspheres: results from a pilot study. Cancer. 2008;113:2119–28.
80. Al-Adra DP, Gill RS, Axford SJ, Shi X, Kneteman N, Liau SS. Treatment of unresectable intrahepatic cholangiocarcinoma with yttrium-90 radioembolization: a systematic review and pooled analysis. Eur J Surg Oncol. 2015;41:120–7.
81. Rayar M, Sulpice L, Edeline J, Garin E, Levi Sandri GB, Meunier B, et al. Intra-arterial yttrium-90 radioembolization combined with systemic chemotherapy is a promising method for downstaging unresectable huge intrahepatic cholangiocarcinoma to surgical treatment. Ann Surg Oncol. 2015;22:3102–8.
82. Boehm LM, Jayakrishnan TT, Miura JT, Zacharias AJ, Johnston FM, Turaga KK, et al. Comparative effectiveness of hepatic artery based therapies for unresectable intrahepatic cholangiocarcinoma. J Surg Oncol. 2015;111:213–20.
83. Valle J, Wasan H, Palmer DH, Cunningham D, Anthoney A, Maraveyas A, et al. Cisplatin plus gemcitabine versus gemcitabine for biliary tract cancer. N Engl J Med. 2010;362:1273–81.
84. Welsh JS, Kennedy AS, Thomadsen B. Selective internal radiation therapy (SIRT) for liver metastases secondary to colorectal adenocarcinoma. Int J Radiat Oncol Biol Phys. 2006;66:S62–73.
85. Wong CY, Salem R, Raman S, Gates VL, Dworkin HJ. Evaluating ^{90}Y-glass microsphere treatment response of unresectable colorectal liver metastases by [^{18}F]FDG PET: a comparison with CT or MRI. Eur J Nucl Med Mol Imaging. 2002;29:815–20.
86. Van den Eynde M, Flamen P, El Nakadi I, Liberale G, Delatte P, Larsimont D, Hendlisz A. Inducing resectability of chemotherapy refractory colorectal liver metastasis by radioembolization with yttrium-90 microspheres. Clin Nucl Med. 2008;33:697–9.
87. Gray B, Van Hazel G, Hope M, Burton M, Moroz P, Anderson J, et al. Randomised trial of SIR-spheres plus chemotherapy vs. chemotherapy alone for treating patients with liver metastases from primary large bowel cancer. Ann Oncol. 2001;12:1711–20.
88. Goin JE, Dancey JE, Hermann GA, Sickles CJ, Roberts CA, MacDonald JS. Treatment of unresectable metastatic colorectal carcinoma to the liver with intrahepatic Y-90 microspheres: a dose-ranging study. World J Nucl Med. 2003;2:216–25.
89. Van Hazel G, Blackwell A, Anderson J, Price D, Moroz P, Bower G, Cardaci G, Gray B. Randomised phase 2 trial of SIR-Spheres plus fluorouracil/leucovorin chemotherapy versus fluorouracil/leucovorin chemotherapy alone in advanced colorectal cancer. J Surg Oncol. 2004;88:78–85.
90. Sharma RA, Van Hazel GA, Morgan B, Berry DP, Blanshard K, Price D, Bower G, et al. Radioembolization of liver metastases from colorectal cancer using yttrium-90 microspheres with concomitant systemic oxaliplatin, fluorouracil, and leucovorin chemotherapy. J Clin Oncol. 2007;25:1099–106.
91. van Hazel GA, Pavlakis N, Goldstein D, Olver IN, Tapner MJ, Price D, et al. Treatment of fluorouracil-refractory patients with liver metastases from colorectal cancer by using yttrium-90 resin microspheres plus concomitant systemic irinotecan chemotherapy. J Clin Oncol. 2009;27:4089–95.
92. Gibbs P, Heinemann V, Sharma NK, Findlay MPN, Ricke J, Gebski V, SIRFLOX Study Group, et al. SIRFLOX: randomized phase III trial comparing firstline mFOLFOX6 ± bevacizumab (bev) versus mFOLFOX6 + selective internal radiation therapy (SIRT) ± bev in patients (pts) with metastatic colorectal cancer (mCRC). J Clin Oncol. 2015;33(Suppl):3502.
93. Hong K, McBride JD, Georgiades CS, Reyes DK, Herman JM, Kamel IR, et al. Salvage therapy for liver-dominant colorectal metastatic adenocarcinoma: comparison between transcatheter arterial chemoembolization versus yttrium-90 radioembolization. J Vasc Interv Radiol. 2009;20:360–7.
94. Saxena A, Bester L, Shan L, Perera M, Gibbs P, Meteling B, et al. A systematic review on the safety and efficacy of yttrium-90 radioembolization for unresectable, chemorefractory colorectal cancer liver metastases. J Cancer Res Clin Oncol. 2014;140:537–47.
95. Kennedy AS, Ball D, Cohen SJ, Cohn M, Coldwell DM, Drooz A, et al. Multicenter evaluation of the safety and efficacy of radioembolization in patients with unresectable colorectal liver metastases selected as candidates for ^{90}Y resin microspheres. J Gastrointest Oncol. 2015;6:134–42.
96. Rhee TK, Lewandowski RJ, Liu DM, Mulcahy MF, Takahashi G, Hansen PD, et al. ^{90}Y radioembolization for metastatic neuroendocrine liver tumors: preliminary results from a multi-institutional experience. Ann Surg. 2008;247:1029–35.
97. Kennedy AS, Dezarn WA, McNeillie P, Coldwell D, Nutting C, Carter D, et al. Radioembolization for unresectable neuroendocrine hepatic metastases using resin ^{90}Y-microspheres: early results in patients. Am J Clin Oncol. 2008;31:271–9.
98. Giammarile F, Bodei L, Chiesa C, Flux G, Forrer F, Kraeber-Bodere F, et al. EANM procedure guideline for the treatment of liver cancer and liver metastases with intra-arterial radioactive compounds. Eur J Nucl Med Mol Imaging. 2011;38:1393–406.
99. Shepherd FA, Rotstein LE, Houle S, Yip TC, Paul K, Sniderman KW. A phase I dose escalation trial of

yttrium-90 microspheres in the treatment of primary hepatocellular carcinoma. Cancer. 1992;70:2250–4.
100. Yan ZP, Lin G, Zhao HY, Dong YH. An experimental study and clinical pilot trials on yttrium-90 glass microspheres through the hepatic artery for treatment of primary liver cancer. Cancer. 1993;72:3210–5.
101. Lau WY, Leung WT, Ho S, Cotton LA, Ensminger WD, Shapiro B. Treatment of inoperable hepatocellular carcinoma with intrahepatic arterial yttrium-90 microspheres: a phase I and II study. Br J Cancer. 1994;70:994–9.
102. Andrews JC, Walker SC, Ackermann RJ, Cotton LA, Ensminger WD, Shapiro B. Hepatic radioembolization with yttrium-90 containing glass microspheres: preliminary results and clinical follow-up. J Nucl Med. 1994;35:1637–44.
103. Mahnken AH. Current status of transarterial radioembolization. World J Radiol. 2016;8:449–59.

Part IV

Radioguided Surgery

Radioguided Surgery for Breast Cancer

47

Francesco Giammarile, Federica Orsini, Renato A. Valdés Olmos, Sergi Vidal-Sicart, Armando E. Giuliano, and Giuliano Mariani

Abstract

Sentinel lymph node biopsy is the standard surgical procedure for staging clinically tumor-free regional nodes in patients with early-stage breast cancer. This technique has spared the additional morbidity of axillary lymph node dissection without compromising diagnostic accuracy and prognostic information. However, it is still important to discuss current techniques and some controversies. Current data indicate that the combined radiocolloid injection approach (both superficial and deep injections) results in a higher identification rate of sentinel lymph nodes. Routine preoperative scintigraphic imaging helps the intraoperative search for sentinel lymph nodes and is vital for detecting extra-axillary or aberrant nodes, as well as for patients who have had prior core breast biopsy or surgery. SPECT/CT imaging, in addition to conventional lymphoscintigraphy, leads to improved preoperative visualization and localization of sentinel lymph nodes, especially if performed for specific indications. The combined use of radioactive tracers and blue dyes is more effective in detecting sentinel lymph nodes than either modality used alone and is therefore recommended for routine use.

Intraoperative imaging with portable gamma cameras is being increasingly employed, enhancing the reliability of the gamma probe by adding clear imaging of the surgical fields, especially when the injection site is close to the lymphatic basin. Portable gamma cameras can also be useful during radioguided occult lesion localization procedures in patients with non-palpable breast lesions.

F. Giammarile (✉)
Nuclear Medicine and Diagnostic Imaging Section, Division of Human Health, Department of Nuclear Sciences and Applications, International Atomic Energy Agency, Vienna, Austria
e-mail: F.Giammarile@iaea.org

F. Orsini
Nuclear Medicine Unit, "Maggiore della Carità" University Hospital, Novara, Italy

R.A. Valdés Olmos
Nuclear Medicine Section and Interventional Molecular Imaging Laboratory, Department of Radiology, Leiden University Medical Centre, Leiden, The Netherlands

Diagnostic Oncology Division, Nuclear Medicine Department, Netherlands Cancer Institute – Antoni van Leeuwenhoek Hospital, Amsterdam, CX, The Netherlands

S. Vidal-Sicart
Nuclear Medicine Department, Hospital Clínic Barcelona, Barcelona, Catalonia, Spain

Institut d'Investigació Biomèdica August Pi i Sunyer (IDIBAPS), Barcelona, Spain

A.E. Giuliano
Surgical Oncology, Samuel Oschin Comprehensive Cancer Institute, Cedars-Sinai, Los Angeles, CA, USA

G. Mariani
Regional Center of Nuclear Medicine, Department of Translational Research and Advanced Technologies in Medicine and Surgery, University of Pisa, Pisa, Italy

© Springer International Publishing Switzerland 2017
H.W. Strauss et al. (eds.), *Nuclear Oncology*,
https://doi.org/10.1007/978-3-319-26236-9_28

Advances in radiopharmaceuticals and computer technology make it possible to integrate optical, hybrid tracers and 3D rendering systems that facilitate intraoperative sentinel lymph node identification.

Keywords

Breast cancer • Sentinel lymph node biopsy • Nuclear medicine • Axillary lymph node dissection • Radiocolloid injection • Radioguided occult lesion localization

Glossary

[^{18}F]FDG	2-Deoxy-2-[^{18}F]fluoro-D-glucose
^{99m}Tc-MAA	^{99m}Tc-macroaggregated albumin
ALND	Axillary lymph node dissection
ART	Axillary radiotherapy
ASCO	Americal Society of Clinical Oncology
CT	X-ray computed tomography
DCIS	Ductal carcinoma in situ
FOV	Field of view
GOSTT	Guided intraoperative scintigraphic tumor targeting
H&E	Hematoxylin and eosin staining
ICG	Indocyanine green
IHC	Immunohistochemistry staining
IMC	Lymph nodes of the internal mammary chain
IMN	Internal mammary lymph nodes
LEHR	Low-energy high-resolution
LEUHR	Low-energy ultra-high resolution
LN	Lymph node
MRI	Magnetic resonance imaging
NACT	Neoadjuvant systemic chemotherapy
PET	Positron emission tomography
PET/CT	Positron emission tomography/computed tomography
ROLL	Radioguided occul lesion localization
SLN	Sentinel lymph node
SLNB	Sentinel lymph node biopsy
SNOLL	Sentinel node occult lesion localization (a combined procedure of simultaneous SLNB and ROLL in the same surgical session)
SPECT	Single photon emission computed tomography
SPECT/CT	Single photon emission computed tomography/computed tomography
SPIO	Superparamagnetic iron oxide
US	Ultrasonography

Contents

Introduction 1364
General Background 1364
Breast Cancer 1365
Sentinel Lymph Node in Breast Cancer 1367
Pathophysiological Aspects 1367
Indications 1367
Procedures 1367
Image Interpretation 1375
Procedures in the Surgical Suite 1376
Clinical Controversial Aspects 1380
Primary Localizing Techniques 1383
Radioprotection 1385
Future Perspectives 1386
Concluding Remarks 1388
References 1388

Introduction

General Background

Radioguided surgery constitutes a wide range of procedures which involve close collaboration between different specialties (nuclear medicine and surgery, often pathology) [1].

"Radioguided surgery" includes a set of pre-, intra-, and postoperative techniques and procedures that are designed to optimize oncologic surgery. All these technologies and applications can be encompassed in the recently coined concept of guided intraoperative scintigraphic tumor targeting (GOSTT) [2]. The basic feature that most obviously characterizes GOSTT is the preoperative administration of a radiopharmaceutical (either interstitially or systemically), associated with the intraoperative use of a handheld radioactivity counting probe (most often the so-called gamma probe) that facilitates the task of the

surgeon – that is, the identification and removal of the target tissue, either a lymph node or the tumor itself – by virtue of preferential radioactivity accumulation in the target tissue. Intraoperative exploration of the surgical field with the gamma probe (which has recently evolved to allow intraoperative imaging as well) is made possible by a set of preoperative techniques employed by the nuclear medicine physician to achieve accumulation of the radiopharmaceutical in the specific target lesion. In this scenario, the most recent advances are based on growing interaction among different components of the complex armamentarium now available to the imaging community (including hybrid imaging, hybrid imaging agents, and/or virtual navigation systems) and to the surgical community (including robot-assisted surgery) [2–6].

The concentration of a radiopharmaceutical in a target lesion can be achieved by three main mechanisms: (1) interstitial administration of an adequate radiopharmaceutical, typically a radiocolloid, that scintigraphically depicts the pattern of lymphatic drainage from the site of a solid epithelial tumor, i.e., performing lymphoscintigraphy to identify the sentinel lymph node (s) (SLN) of the tumor; (2) systemic administration of a radiopharmaceutical that preferentially accumulates in the target lesion, e.g., ^{99m}T-sestamibi for localization of parathyroid adenomas or [^{18}F]FDG for [^{18}F]FDG-avid tumor lesions; and (3) direct intralesional administration of a radiopharmaceutical such as ^{99m}Tc-macroaggregated human albumin (^{99m}Tc-MAA, comprised of particles that, by virtue of their relatively large size, are virtually indefinitely retained at the injection site) for the so-called radioguided occult lesion localization (ROLL) for non-palpable breast tumors.

In the last few years, GOSTT applications have rapidly expanded especially to perform sentinel lymph node biopsy (SLNB). The sentinel lymph node (SLN) procedure is a diagnostic staging procedure that is applied in a variety of tumor types. The procedure aims to determine the tumor status of the SLN(s). Although historically the term "sentinel lymph node" was used to describe a group of nodes seen in patients with penile carcinoma [7], an SLN is currently defined as the first lymph node on a direct drainage pathway from the primary tumor [8, 9]. The concept is based on the premise that lymph flow from the primary tumor travels sequentially to the SLN and then onto the other regional lymph nodes (Fig. 1). The SLN is the node most likely to harbor metastases.

The histopathologic status of this node should reflect the histopathologic status of the entire nodal basin, and additional treatment of the nodal basin (e.g., surgery) is routinely performed in case of metastatic involvement of the SLN – although the presence per se of metastatic tumor cells in the SLN is not the only factor determining lymph node dissection of the basin of interest (see further below in this chapter). A negative SLN, however, would justify a wait-and-see policy avoiding unnecessary elective lymph node dissections and the associated morbidity, hospital stay, and costs.

In addition to being continually applied in patients with breast cancer and cutaneous melanoma, radioguided SLNB is being explored in patients with a wide variety of other solid epithelial cancers. In particular, malignancies where the feasibility and/or clinical impact of radioguided SLNB is increasingly being investigated include head and neck cancers, gynecological cancers (vulvar, cervical, and endometrial), gastrointestinal cancers (esophagus, stomach, colorectal, anus), prostate cancer, non-small cell lung cancer, differentiated thyroid carcinoma, and others [10–15].

Breast Cancer

Breast cancer is the most frequent cancer diagnosed in women worldwide [16]. In patients with breast cancer, accurate lymph node (LN) staging is essential for both prognosis (of early-stage disease) and treatment both for regional control of disease and for adjuvant therapies [17].

Clinical examination (i.e., palpation) is not accurate enough for assessing the axillary status, and preoperative imaging modalities including PET/CT with [^{18}F]FDG and ultrasound have low sensitivity, especially in case of micrometastatic disease [18–24]. Thus, in breast cancer, the traditional staging approach has been axillary LN dissection (ALND). However, ALND results in a

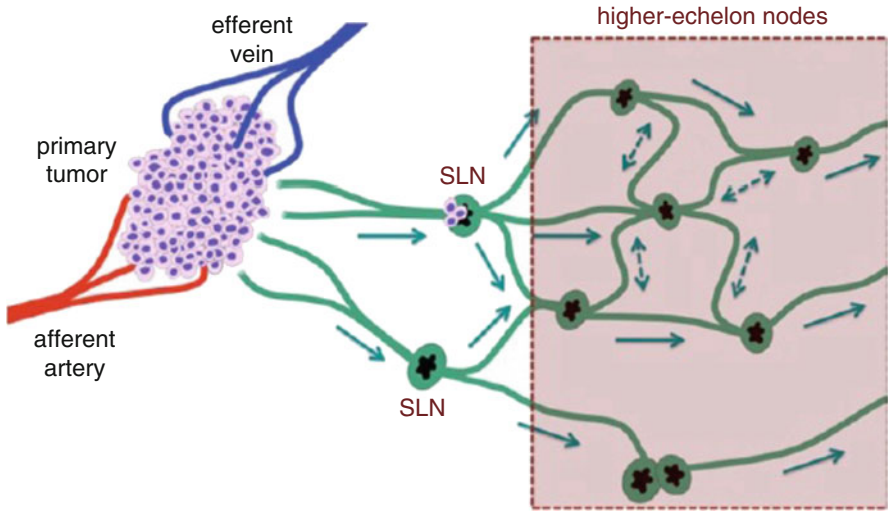

Fig. 1 Schematic representation of the sentinel lymph node concept. Assuming that lymph drainage from a solid tumor proceeds in an orderly way from lower-echelon to higher-echelon lymph nodes, the first node (s) encountered in such pathway, that is, the sentinel node (s), should be the site where tumor cells migrating through lymphatic channels are most likely to be entrapped and possibly originate metastasis before spreading to higher-echelon lymph nodes. As illustrated in the figure, even in any given lymphatic basin, there can be more than one sentinel lymph node, as lymph can drain from the site of the primary tumor via different lymphatic channels toward the same basin. The diagram also illustrates the complex interconnections that can exist at higher levels, with variable directions of lymph flow at intermediate levels within the general pattern of overall centripetal flow. The pattern of lymph flow is even more complex when considering that lymph from the tumor site can drain to more than one lymphatic basin, each one repeating the basic pattern represented here for a single basin

high incidence (about 25–30%) of postoperative complications that can reduce quality of life, such as delayed wound healing; lymphedema; peripheral nerve injury or even brachial plexus injury, with sensory/motor impairment; and pain. Furthermore, in early breast cancer, nearly 80% of axillary dissections reveal no metastasis and, therefore, could have been avoided [25].

Based on the definition of SLNs as those regional nodes that directly drain lymph from the primary tumor, SLNs are the first nodes to potentially receive the seeding of lymph-borne metastatic cells [26, 27]. After the initial description by Morton et al. of a method of SLNB in the management of melanoma patients, more than two decades ago [28, 29], SLN mapping and biopsy were applied in breast cancer [30, 31]. Since then, SLN mapping and biopsy have become routine techniques in breast cancer management, contributing to the development of less invasive surgical procedures [32–44]. Sentinel node biopsy is extremely accurate and effective. A systematic review showed an axillary 0.6% relapse rate in negative SLN patients and no benefits to completion ALND in terms of survival after negative SLNB [42, 45]. Thus, when the SLN is free of metastasis, the patient can be spared an ALND that until a few years ago was considered the standard staging procedure for breast cancer [31, 46, 47].

Despite the widespread application of SLNB for early-stage breast cancer, there is significant variation in performance characteristics reported for such procedures. Differences in institutional experience and in lymphatic mapping techniques are two of the main contributing factors to variations in the proportions of successful mappings [48–50]. The ranges of rates for false-negative findings and for SLN identifications emphasize the variability of this procedure. Learning curves for this technical procedure also vary [48]. Nevertheless, once a multidisciplinary team is experienced with the procedure, reasonable levels of accuracy are achieved, with identification rates of more than 95% reported routinely [25, 47, 51–54].

Sentinel Lymph Node in Breast Cancer

Pathophysiological Aspects

The breast embryologically originates from ectodermal tissue, as a skin appendage, and therefore shares a pattern of lymphatic drainage with the overlying skin. The mammary gland is interposed between the superficial (subdermal) and the deep (subcutaneous) lymphatic plexuses, the two systems being interconnected by a dense network of lymphatic vessels (Fig. 2a). Lymphatic vessels surrounding the mammary lobules predominantly drain to the subareolar Sappey's plexus, which is part of the superficial plexus of the skin. Most of the lymph produced in the breast is therefore drained to the subareolar region, progressing then toward the ipsilateral axillary nodes (Fig. 2b). A small fraction of the lymph produced in the breast (about 3%) is instead drained to lymph nodes of internal mammary chain, while an even smaller amount drains to other lymph nodes such as the intercostal, pectoral muscles, contralateral breast, or even abdominal nodes [55].

By following these routes of drainage, lymph and cancer cells entering the lymph space spread initially to the first node, which is the SLN. If the SLN is free of metastasis, the probability of tumor cells skipping that lymph node and metastasizing to second- or third-echelon nodes is an exceptionally rare event [39, 46, 56–64].

Indications

The main objective of SLN mapping and SLNB in breast cancer patients is axillary staging. These procedures are an appropriate alternative to routine staging axillary LN dissection for patients with early-stage biopsy-proven breast carcinoma without cytologically or histologically proven axillary lymph node metastases [65]. Appropriately identified patients with negative SLN biopsy do not need to undergo axillary LN dissection.

Currently, the SLNB procedure is recognized as the standard treatment for stage I and stage II breast cancer patients [40, 66, 67]. In these stages, the results showed that SLNB has a positive LN rate similar to that observed after ALND [40, 68, 69], yet with a significant reduction in morbidity [68] and similar gold standard (i.e., axillary LN recurrence rates at 5 years) [40]. The technique is validated if SLNs are found in more than 95% of the cases (i.e., the probability of detecting tumor cells in non-sentinel nodes is less than 5%). False-negative rates are higher in grade 3 lesions and when a single SLN is harvested, compared to cases where multiple SLNs are harvested [70].

The recognized indications for SLNB, together with recommendations as to whether an SLN procedure is the established standard of care, are listed in Table 1 [71].

Procedures

Generally, the procedure for SLN mapping and SLNB involves interstitial tracer injection, preoperative scintigraphic imaging, and intraoperative gamma probe localization for surgical removal of the detected LNs. Although there is consensus on some broad aspects of SLN protocols for breast cancer, consensus does not exist on all details. Controversies exist with regard to the particle size of the radiotracer, the optimal route for injection, timing and type of scintigraphy and intraoperative detection, and whether or not extra-axillary LNs should be considered for harvesting and analysis. The specific radiotracer and technique used are additionally guided by local availabilities, regulations, and practices [71].

Procedures in Nuclear Medicine

Three main parameters define an optimal tracer administration technique for radioguided SLNB: injection site, injected volume, and injected activity. A fourth parameter to be taken into account is the time elapsed between injection and surgery, as it specifically influences the amount of radioactivity to be injected [72, 73].

Radiopharmaceuticals

Several ^{99m}Tc-based agents have been used for radioguided SLNB for breast cancer (see Table 2) [74]. The radiopharmaceuticals most widely used

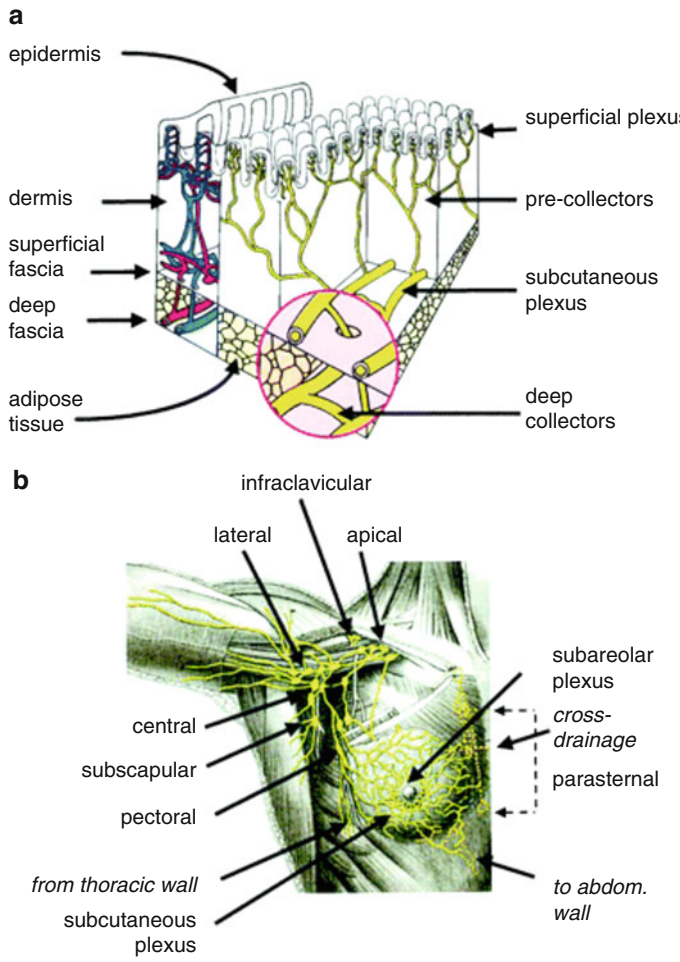

Fig. 2 (**a**) Schematic structure of cutaneous blood and lymph vessels. For easier comprehension, the lymph and blood vessel networks (which are actually embedded in each other) are represented separately, respectively, on the *right* (*yellow*) and on the *left* (*red* and *blue*). Due to its embryologic origin in the ectoderm, the mammary gland can be placed in an ideal space between the subcutaneous plexus and the deep lymphatic collectors (magnified insert in the figure). Branches of the periductal plexus drain lymph mostly toward the skin surface (via the subareolar plexus), while a minor component drains toward the deep collectors (which in turn drain toward the internal mammary chain). Radiocolloids injected intradermally over the mammary gland drain to the subcutaneous plexus that also receives most of the lymph draining from the mammary gland. (**b**) Pathways of the lymphatic vessels and lymph node stations draining the mammary gland. Most of the lymph produced in the breast drains to the subareolar plexus, then merges with the subcutaneous plexus of overlying skin, and flows mostly toward the axilla. Lymph from deeper portion of mammary gland drains either through the same pathway or through deep lymphatics that reach the parasternal, internal mammary chain (and even the contralateral side). *abdom* abdominal (From [38] with permission)

are ^{99m}Tc-sulfur colloid (particle size: 15–5,000 nm, but usually filtered to select a more restricted range of particles' size), ^{99m}Tc-nanocolloid (5–100 nm), and ^{99m}Tc-antimony trisulfide (3–30 nm).

The ideal radiotracer should show rapid transit to SLNs with prolonged retention in the nodes. In general, the drainage, distribution, and clearance of radioactive colloids by the lymphatic system may vary and are dependent on the size of the particles. Small particles are drained and cleared first; large particles are drained and cleared last and may be retained longer at the injection site.

Table 1 Recommendations on the use of SLN biopsy (Modified from [71])

Clinical circumstance	Use of SLN biopsy
T1 or T2 tumor	Established
T3 or T4 tumor	Controversial
Multicentric or multifocal tumor	Controversial
Inflammatory breast cancer	Not recommended
DCIS with mastectomy	Established
DCIS without mastectomy, but with suspected or proven microinvasion	Established
DCIS without mastectomy	Controversial
Suspicious, palpable axillary nodes	Controversial
Older age	Established
Obesity	Established
Male breast cancer	Established
Pregnancy	Controversial
Evaluation of internal mammary lymph nodes	Controversial
Prior diagnostic or excisional breast biopsy	Controversial
Prior axillary surgery	Controversial
Prior non-oncologic breast surgery	Controversial
After preoperative systemic therapy	Controversial
Before preoperative systemic therapy	Established

Controversial indications are those for which SLN biopsy is not universally accepted or for which the evidence behind the practice is limited or entirely missing. *DCIS* ductal carcinoma in situ

Table 2 Radiopharmaceutical characteristics (Modified from [74])

^{99m}Tc-based agents	Particle size max (nm)	Particle size mean (nm)
Sulfur colloid	350–5,000	100–220 (filtered)
Antimony trisulfide	80	3–30
Sulfide nanocolloid (Lymphoscint®)	80	10–50
Nanocolloidal albumin (Nanocoll®)	100	5–80
Rhenium sulfide nanocolloid (Nanocis®)	500	50–200
Tin colloid	800	30–250
Labeled dextran	800	10–400
Hydroxyethyl starch	1,000	100–1,000
Stannous phytate	1,200	200–400
Tilmanocept (Lymphoseek®)	~7 (equivalence)	~7 (equivalence)

Studies have shown that the success rate of identification of axillary SLNs is not significantly affected by the particle size of the radiotracer [38, 75–77]. Thus, the selection of radiotracer is based more on local availability than on differences in SLN detection. However, there is general agreement that a 100–200nm sized radiocolloid should be considered the best compromise between fast lymphatic drainage and optimal retention in SLNs [78].

New tracers have been developed in recent years. The tracer most recently made commercially available is Lymphoseek®, which is composed of a dextran backbone with multiple glucose and mannose residues attached to DTPA for ^{99m}Tc-labeling. The potential advantages of its small molecular size (7.1 nm) and the receptor-targeted nature of the mannose moieties in ^{99m}Tc-Tilmanocept include rapid transit from the primary site to the SLN as well as selective accumulation in that node, with limited pass-through to second-echelon nodes [79–82].

Activities and Volumes

Literature supports the use of small volumes with high specific activity to improve SLN detection. Nevertheless, consensus on the activity to be administered in an SLN procedure has not been reached. Activities as low as 3.7 MBq (0.1 mCi) [83] and as high as 370 MBq (10 mCi) [84] have been used. In current practice, a total injected activity of 5–30 MBq (depending on the elapsed time between scintigraphy and surgery) is generally considered sufficient for surgery planned for the same day. Prior day injection has been shown to be technically feasible by adequately increasing the amount of radioactivity injected (up to 150 MBq) [85].

Injection of large volumes may disrupt local lymphatics; therefore, a quantity of 0.2–0.5 mL should be injected. Moreover, the syringe should also contain a sufficient amount of air to clear any dead space within the syringe and the needle.

Injection Procedure

The injection site of the mapping agent is another controversial issue, mainly because lymphatic

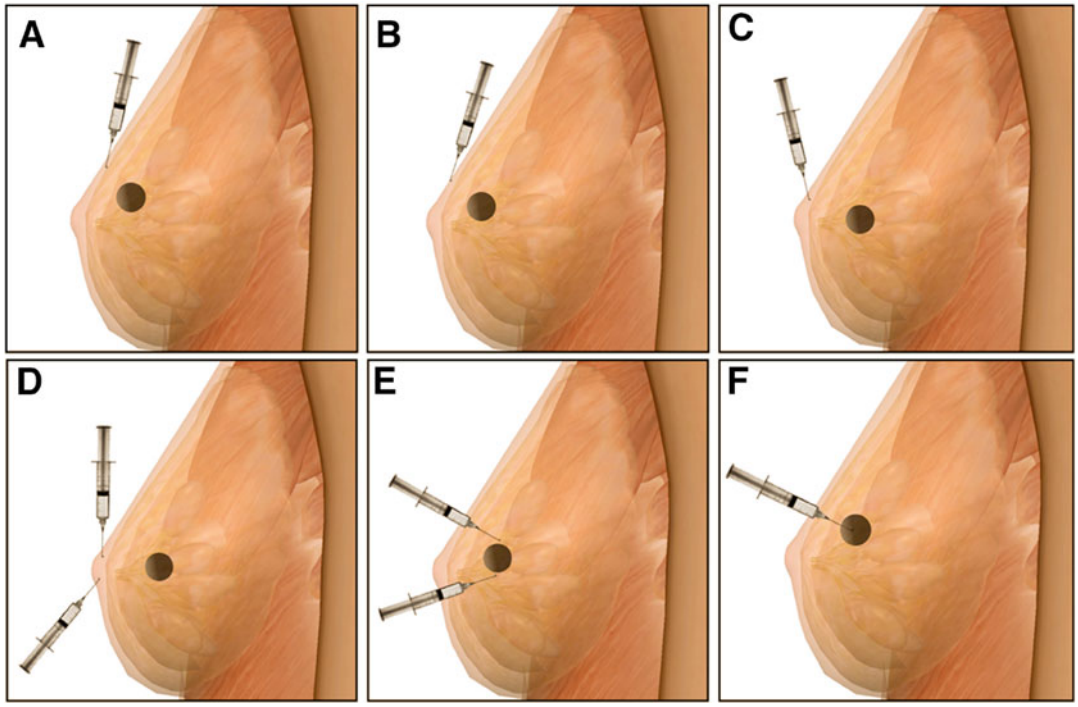

Fig. 3 Modalities of interstitial radiocolloid injection for SLNM in breast cancer. Superficial injections (**a**–**d**) and deep injections (**e**, **f**): intradermal (**a**), subcutaneous (**b**), subareolar (**c**), periareolar (**d**), peritumoral (**e**), and intratumoral (**f**)

drainage of the breast is not completely understood [86]. The most commonly used injection sites can be classified into two categories: deep (intratumoral and peritumoral) and superficial (intradermal, subdermal, subareolar, and periareolar) injection (see Fig. 3).

All injection modalities enable axillary sentinel nodes to be identified accurately, and satisfactory SLN detection rates have been reported for all injection approaches [87]. Lymphatic circulation within solid tumors (including breast cancer) is generally grossly abnormal, disrupted, and inefficient. Thus, intratumoral administration requires the injection of high activities (up to 370 MBq or 10 mCi) and large volumes (even up to over 1 mL). Injection of such large volumes can substantially increase interstitial pressure at the injection site, thus possibly altering the pattern of lymphatic drainage and forcing drainage routes different from those prevailing in baseline conditions. Furthermore, most of the injected radioactivity is retained at the injection site, often causing interference – the so-called "shine-through" effect – in scintigraphic and intraoperative sentinel lymph node detection. Finally, the slow drainage from the tumor can cause poor scintigraphic visualization of the lymphatic channels and possibly lead to failure of lymphoscintigraphic imaging and of intraoperative identification of the sentinel lymph node.

All the above considerations explain why, at present, most nuclear medicine centers prefer peritumoral or superficial injections versus the originally proposed intratumoral route of administration, although the high reproducibility of intratumoral injection has been well demonstrated [88].

Lymphatic circulation in the peritumoral area is normal and actually represents the entrance site to lymph vessels of cancer cells detached from the growing edge of the tumor, which eventually gives rise to lymph nodal metastasis. Indeed, any drainage pattern from any quadrant of the breast can occur, and most of the lymph from the breast flows toward the nodal basins with a direct course, not necessarily passing through the subareolar

plexus [87, 89]. Peritumoral injection is considered the gold standard for accurate SLN detection, because the tracer is injected near the same lymph vessels draining the tumor and is able to reveal extra-axillary drainage [90]. However, the validity of this approach has been questioned especially in non-palpable and multicentric tumors. Peritumoral administration is usually performed by depositing two aliquots on each side of the tumor, while intra-/subdermal administration is performed in or just under the skin overlying the tumor. Intradermal injection should produce a small wheal. More than one injection could be performed in adjacent sites. Periareolar administration is generally performed with two to four aliquots, each one at the edge of the areola at Sappey's plexus.

The rationale of intra-/subdermal administration stems from the fact that lymph is drained from the intra-/subdermal space to the subcutaneous plexus, which is the merging point for lymph originating from the underlying breast parenchyma (see Fig. 2a). Thus, a tracer injected intra-/subdermally displays the same pathways of lymphatic drainage as the underlying breast gland and of cancer cells entering the lymphatic space. Similar considerations apply to the periareolar route of administration: the lymph produced in the breast flows to the periareolar Sappey's plexus, before draining to axillary LNs (see Fig. 2b).

Superficial injection sites have numerous advantages, including simplicity, shorter time between injection and SLN identification, and increased radiotracer nodal uptake which may result in improved nodal identification rates. Nevertheless, superficial injection allows almost exclusive identification of axillary nodes. The use of peritumoral injections requires careful investigation of a patient's prior imaging and medical records, particularly if the tumor is non-palpable. Tumor location and injection sites may be identified by ultrasound and/or x-ray stereotactic guidance. If a tumor is in the upper outer quadrant, the relatively intense activity at the injection site may make it difficult to localize of a nearby SLN with less intense uptake [91, 92].

Regardless of the injection site, after injection, the patient is asked to gently massage the breast to facilitate lymphatic drainage of the tracer. Massage can also be employed if the passage of activity from the injection site is delayed at any time during the study [93, 94].

Results of multiple studies support the validity of both the deep and the superficial injection approaches; in particular, all injection modalities enable axillary SLN to be identified accurately, and satisfactory SLN detection rates have been reported for all injection approaches [87]. A clinical trial comparing the injection routes demonstrated, in 400 breast cancer patients, the superior intraoperative gamma probe localization of the axillary SLNs for the intradermal route (100%) compared to the subareolar route (95%) and the intraparenchymal route (90%) [95]. A preferential drainage to the same few axillary SLNs has been postulated for most of the breast tissue and its overlying skin, after merging initially to the retroareolar Sappey plexus; therefore, accurate identification of *axillary* SLNs is supposed not to be affected by the injection route [93, 94, 96, 97]. Thus, if the goal is axillary staging only, a superficial tracer injection (periareolar, subareolar, subdermal, intradermal) may be preferable to a deep injection (peritumoral, intratumoral) due to better and quicker visualization of axillary SLNs [98]. On the other hand, an important advantage of deep injection is the improved detection of extra-axillary SLNs: after peritumoral administration, lymphoscintigraphy shows drainage to the internal mammary chain in 20–30% of the cases, while this fraction is much lower (<3%) after intra-/subdermal or periareolar administration [66, 99, 100]. Thus, if one's aim is to stage extra-axillary nodal basins as well as the axilla, deep injection is recommended.

The superficial routes of administration are generally preferred in the case of superficial, easily palpable tumors and the peritumoral route for deeply seated tumors. The periareolar route can be used mainly in upper quadrant tumors to avoid possible cross talk owing to the short distance between the peritumoral depot and the axillary SLNs and is particularly recommended in cases of non-palpable or multifocal tumors [101, 102].

The combination of both injection techniques (deep and superficial) in the same patient may improve SLN detection [90].

Imaging Procedures

Lymphatic mapping allows determination of the number of LNs that are on a direct drainage pathway and to locate the SLNs [71] [103]. Preoperative imaging is strongly recommended due to variability in breast lymphatic drainage into the axilla and extra-axillary nodes [104]. Thus, preoperative lymphatic mapping has the potential to both improve accuracy (especially in extra-axillary LN) and reduce morbidity relative to the use of handheld gamma probes alone [34, 71]. Preoperative imaging also serves as quality control on the use of the appropriate tracer, failure of the injection, failure of the radiopharmaceutical, and management of the appropriate breast and axilla – injection of the proper side (L/R). Reasons not to use preoperative lymphoscintigraphy are logistical or because there is no definite evidence of a higher intraoperative success rate in the harvesting of axillary SLNs [105, 106].

Timing: In order to identify all SLNs and to avoid confusion with radiocolloid stasis in a lymphatic vessel, images are acquired with an adequate delay after injection. This delay may vary according to the radiopharmaceutical used, the injection site, and the patient's characteristics (lymphatic drainage can be slower in elderly or overweight patients). While smaller particles allow quick visualization of SLNs, larger particles have slow transit in the lymphatic system that tends to minimize visualization of non-sentinel second-tier nodes (lymph nodes downstream of SLNs) [107]. After superficial tracer administration, lymphatic drainage and subsequent lymph node visualization is usually quicker than after peritumoral injection (20–30 min compared to 2–3 h on average). After 15–18 h, during surgery, the amount of radiocolloid migrated to LNs represents about 1% of the injected activity after superficial administration, while it is about 0.1% after peritumoral administration.

SLNs are generally visualized within 1–2 h, and the patient should be in the operating theater within 2–30 h of radiocolloid injection, depending on the facility's schedule [71, 107]. In the event a surgery is scheduled for early morning, injection and imaging may be safely performed the afternoon prior to the surgery [108].

Gamma camera parameters: A single- or dual-head gamma camera system with large field-of-view (FOV) detectors is generally used to acquire planar emission and, if desired, single-photon computed tomographic (SPECT) or SPECT/computed tomographic (SPECT/CT) images. Low-energy, high-resolution, or low-energy high-resolution collimators should be used. The energy window should be 15% (±5%) centered on the 140 keV photopeak of ^{99m}Tc.

Image acquisition: Dynamic (flow) imaging is not often used in SLN procedures for breast cancer, but can provide information useful for SLN localization.

Planar (static) imaging should be performed 15–30 min, and 2–4 h post injection, and as needed thereafter up to 18–30 h. At least two, preferably all three, of the following images should be acquired: anterior, 45° anterior oblique, and lateral. Each image is typically 3–5 min in duration. For a system with large FOV detectors, the pixel size is recommended to be approximately 2 mm and the matrix size 256 × 256 with zoom 1 or, rarely, 128 × 128 with zoom 2. If 2 mm pixel size is not feasible on the system, the smallest pixel size available should be used.

Figure 4 shows different patterns of lymphatic drainage and SLN distribution as obtained by planar scintigraphic imaging in preparation for radioguided SLNB. Although conventional planar imaging certainly enables to identify the draining pattern to SLNs, it does not provide the exact anatomic location of the detected LNs, an information that is instead very useful intraoperatively [109]. By combining tomographic functional lymphoscintigrams registered with anatomic data from CT, SPECT/CT imaging provides better contrast and resolution than planar imaging and has the possibility to correct for attenuation and scatter. Fused SPECT/CT imaging considerably improves the topographic localization of the SLN within an anatomical landscape, thus providing a valuable surgical road map [110].

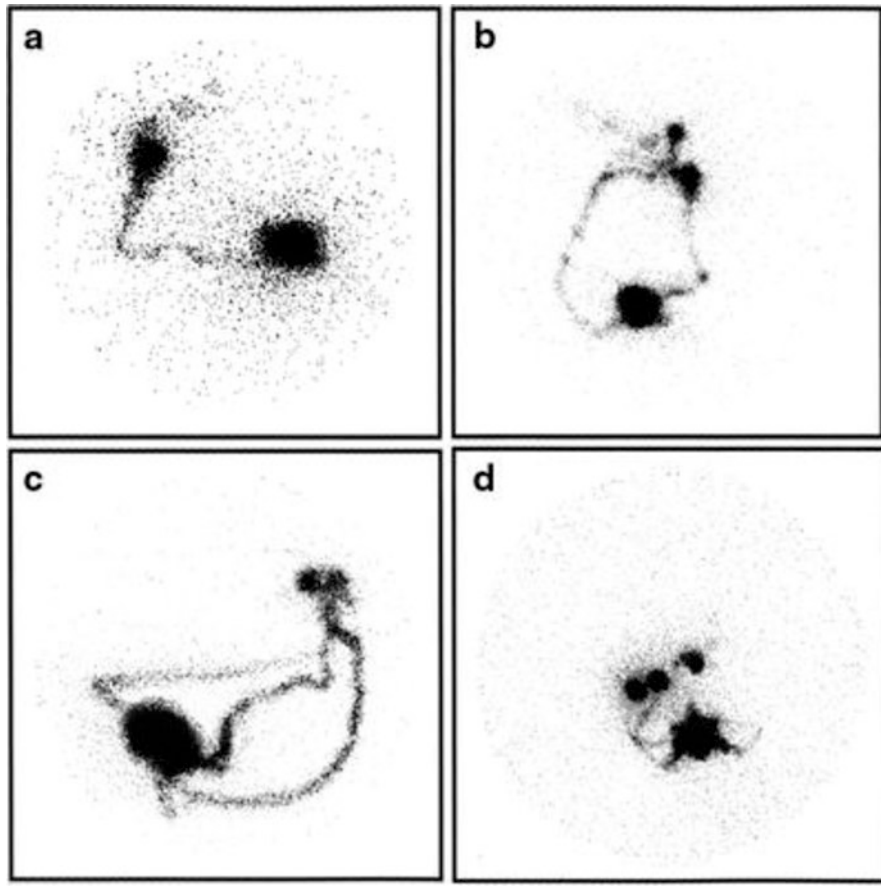

Fig. 4 Variable lymphoscintigraphic patterns visualized between 30 and 60 min after intradermal injection of ^{99m}Tc-nanocolloidal albumin in patients with breast cancer. (**a**) Single lymphatic vessel leading to a single sentinel lymph node, with faint visualization of subsequent-tier lymph nodes (right anterior oblique view). (**b**) Two separate lymphatic vessels widely diverging in their initial pathway, eventually leading to two separate but adjacent sentinel lymph nodes, with faint visualization of subsequent-tier nodes (left anterior oblique view). (**c**) Three separate lymphatic vessels widely diverging in their initial pathway, eventually leading to two separate but very close sentinel nodes (left anterior oblique view). (**d**) Multiple lymphatic vessels leading to at least three separate sentinel lymph nodes (right anterior oblique view) (From [38] with permission)

SPECT acquisition for SLN detection should be performed with a dual-detector SPECT system equipped with LEHR or LEUHR collimators. Acquisition parameters should include matrix size of 128 × 128 (4–5 mm pixels) and 120 or 128 projections over 360° with 20−25 s/projection.

Both low-dose CT (140 kVp, 2.5 mA) and conventional CT (140 kVp, 30–150 mA) can provide useful anatomical detail that can be used for anatomical localization and, if desired, attenuation correction.

Mapping of all direct tumor-draining LNs requires knowledge of the number and location of these SLNs, which will be provided by SPECT/CT in addition to planar images. SPECT/CT imaging provides significant information in the large majority of patients, with useful preoperative complimentary information to the surgeons: better location, reduced surgical time, and greater confidence of the surgeons with the technique [111].

It has been shown that SPECT/CT images can detect additional SLNs not visualized on planar images in a substantial number of patients in whom the conventional images are difficult to interpret [110–112]. In the majority of cases, the surgical team appreciates the anatomic

information provided by the fused SPECT/CT images and the surgical time is reduced [113]. However, because the current conventional approach based on combined radiocolloid and blue dye injection, preoperative planar scintigraphic imaging, and intraoperative gamma probe counting has proven very successful (with SLN detection rates over 95%), the added value of SPECT/CT imaging seems to be limited to a small fraction of breast cancer patients undergoing SLNB. Current recognized indications for SPECT/CT imaging in breast cancer patients are non-visualization of SLNs at conventional imaging, obesity, and presence of extra-axillary SLNs or otherwise unusual drainage (e.g., in cases of previous breast surgery) [71]. SPECT/CT imaging might also be performed if the conventional images are difficult to interpret (e.g., if contamination is suspected or an SLN is located near to the injection area) [112, 113].

When acquiring planar imaging, a ^{57}Co flood source can be positioned between the patient's body and the collimator in order to obtain some reference anatomic landmarks in the scintigraphic image (see Fig. 5). Alternatively, the body contour can be delineated by moving a ^{57}Co point source during scintigraphic acquisition (see Fig. 6). SPECT/CT acquisitions obviate the problem of identifying anatomic landmarks as a reference for topographic location of the SLN(s) (see Figs. 7 and 8) [109, 114–118].

Surface marks that provide a method to triangulate SLNs and to estimate their depths are desired by some surgeons. Surface locations should be marked on the skin with a small spot of indelible ink, and the depth of the node should

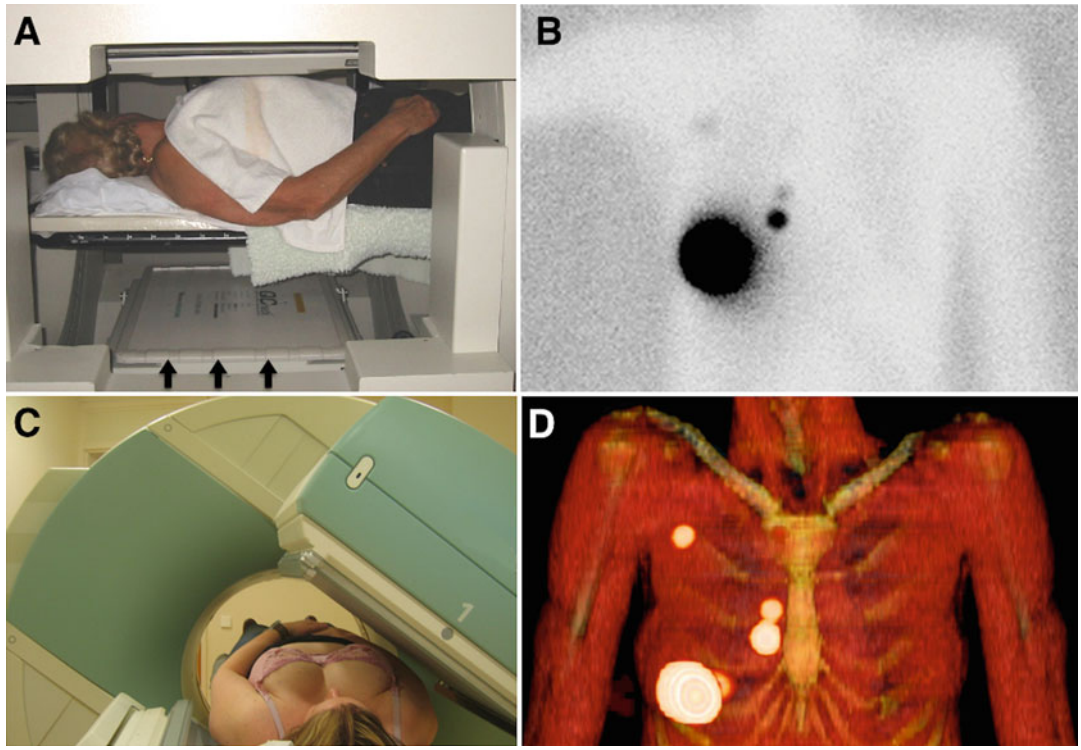

Fig. 5 Anatomical information in lymphatic mapping. (**a**) The use of a ^{57}Co flood phantom placed opposite to the gamma camera head (*black arrows*) provides body contour delineation in the anterior planar image (**b**) in a patient with cancer of the right breast and drainage to the right axilla and right internal mammary chain. In the same patient, subsequent SPECT/CT acquisition (**c**) leads to anatomically identify the axillary and parasternal sentinel lymph nodes after reconstruction of the fused SPECT/CT using volume rendering (**d**)

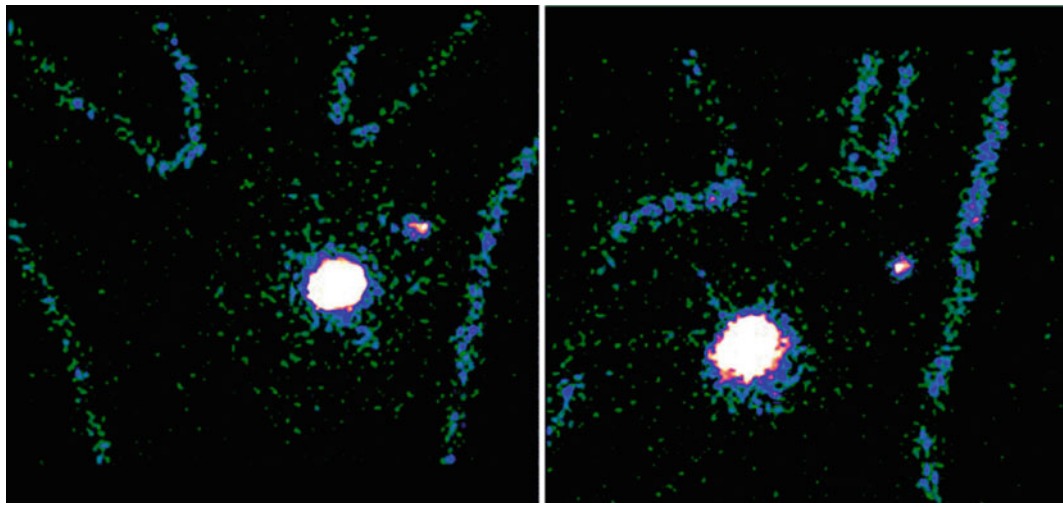

Fig. 6 Body contour delineation obtained by moving a ^{57}Co point source along the body of the patient during acquisition of the planar scintigraphic images. In this patient with cancer of the left breast, ^{99m}Tc-nanocolloidal albumin was injected at four spots periareorally. Images acquired both in the anterior projection (*left panel*) and in the left anterior oblique projection (*right panel*) visualize migration of the radiocolloid to a single sentinel lymph node in the axilla

be described. When marking the skin in the imaging process, an attempt should be made to position the patient's arm in the same position as it will be placed during surgery.

Image Interpretation

Early and delayed lymphoscintigraphic planar images identify SLNs in a majority of cases [71]. Major criteria to identify LNs as SLNs are the time of appearance and, occasionally, visualization of lymphatic channels (if dynamic imaging was performed). Usually, SLNs cannot be readily distinguished from second-tier LNs. The SLN is not necessarily the hottest node, although that is often the case. Separate lymphatic channels that drain to different LNs identify each of those as distinct SLNs, even though they may be located in the same anatomic region. When drainage to more than one anatomic region is seen, each of those regions has at least one SLN.

In current protocols SPECT/CT is performed following delayed planar images. This sequential acquisition is helpful to clarify the role of both modalities. For imaging interpretation the major criteria to identify LNs visualized on lymphoscintigraphy as SLNs are the visualization of lymphatic ducts, the time of appearance, the lymph node basin, and the intensity of lymph node uptake [105, 119]. Following these criteria visualized radioactive lymph nodes may be classified as:

(A) Definitively SLNs: this category concerns all LNs draining from the site of the primary tumor through their own lymphatic vessel or a single radioactive LN in a certain lymphatic basin.
(B) Highly probable SLNs: this category includes LNs appearing between the injection site and a first draining node or LNs with increasing uptake appearing in other lymph node stations.
(C) Less probable SLNs: all higher-echelon LNs may be included in this category.

Axillary LNs represent the main basin for breast lymphatic drainage, but different patterns can also occur in some cases. Drainage to the internal mammary basin is present in up to 35–40% of patients after intratumoral/peritumoral radiocolloid injection. Other unusually located SLNs are also observed in a non-negligible fraction of patients:

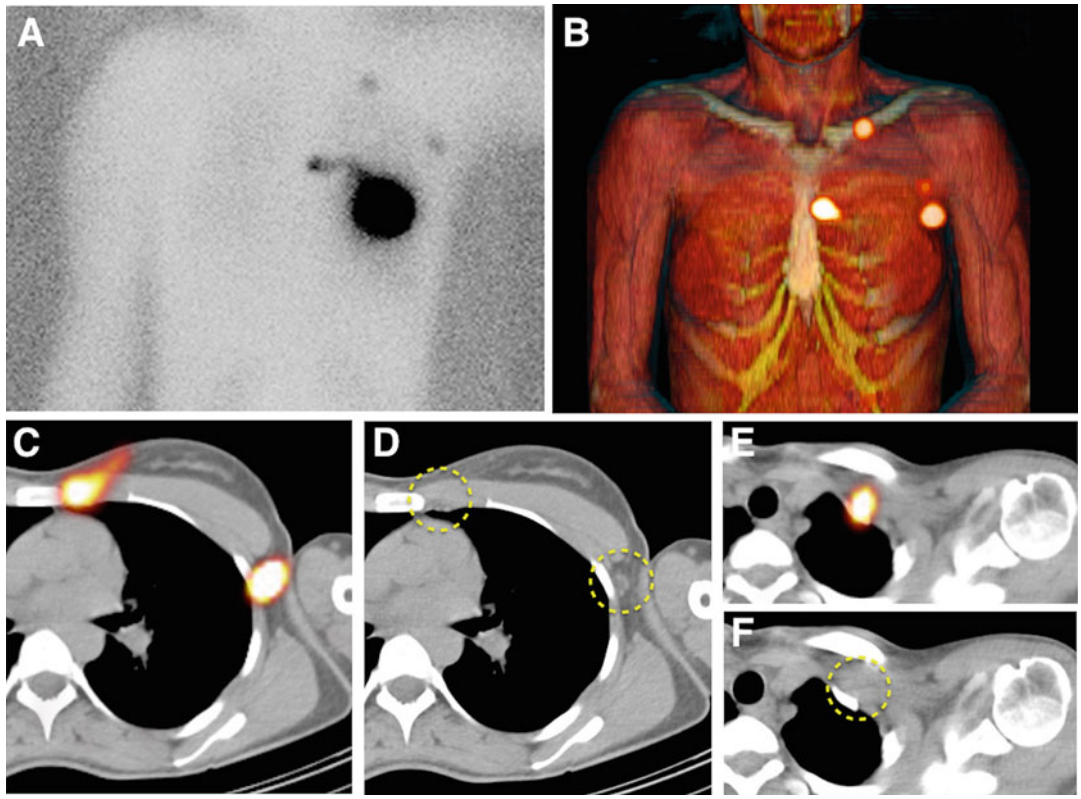

Fig. 7 Anatomical sentinel lymph node localization in breast cancer. Following deep injection of ^{99m}Tc-nanocolloidal albumin in the left breast, lymphatic drainage to the axilla, periclavicular area, and internal mammary chain is observed on anterior planar image (**a**) and on SPECT/CT fused imaging displayed with volume rendering (**b**). Lymph nodes are subsequently localized in the second intercostal space, level I of the left axilla, and behind the left clavicle (**c**–**f**)

intramammary (prepectoral) in 6%, interpectoral in 2%, and infraclavicular in 3% [120, 121].

The report to the referring physician should describe the orientations of the images acquired, the radiopharmaceutical, the method of administration, the amount and volume of activity injected, the location of the SLNs on each image, and any source of error or inaccuracy of the procedure.

The images and report should be available by the time the patient arrives in the surgical suite – in electronic form or as hard copy. If this is not possible, the critical information should be relayed directly to the surgeon. A close working relationship between the imaging department and the surgeon is critical for accurate dissemination of information regarding numbers and locations of sentinel lymph nodes.

Procedures in the Surgical Suite

Blue Dye Lymph Node Localization

Regarding the use of blue dye for optical guidance during surgery, there is general agreement that combined administration of radiocolloid and blue dye using both superficial injection and deep injection enhances SLN detection [38, 94, 97]. A possible advantage of the combined technique is where macrometastasis in the SLN may inhibit tracer accumulation [122, 123].

Blue dye can be injected around the primary tumor 10–20 min prior to surgery in a volume of 2–5 mL. The site of injection can be gently massaged after the administration or if the drainage of activity from the injection site is delayed at any time during the study [94]. Within 5–15 min, the

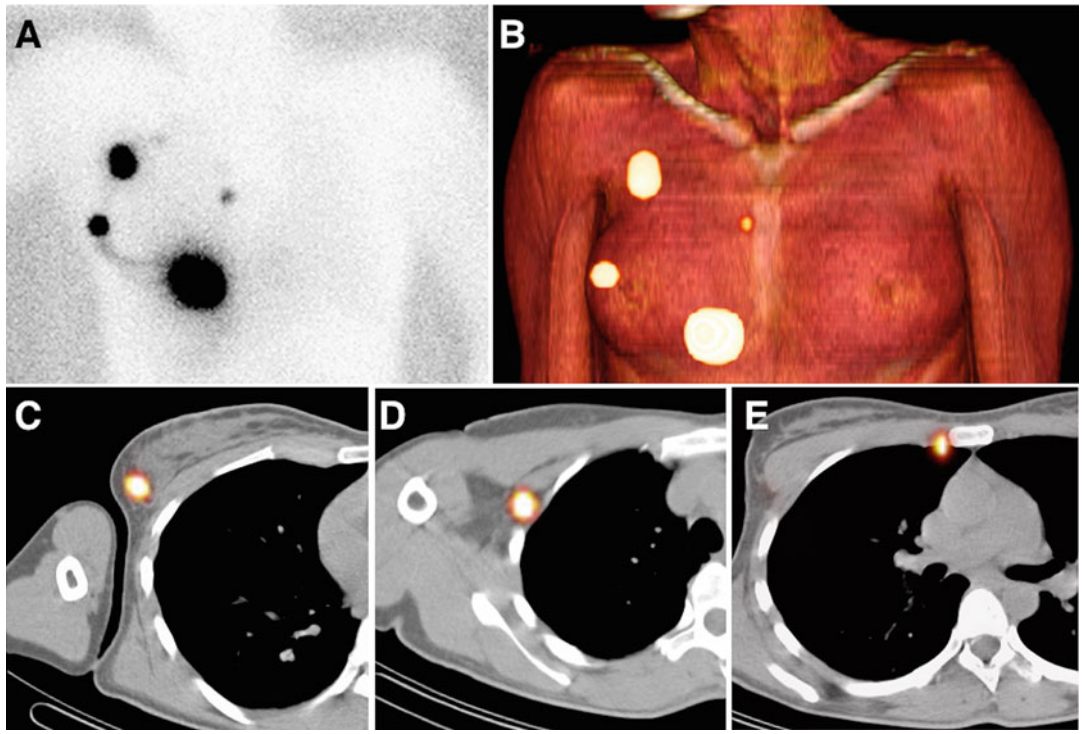

Fig. 8 Multidirectional lymphatic drainage after deep injection of ^{99m}Tc-nanocolloidal albumin on anterior planar image (**a**) in a patient with breast cancer in the medial inferior quadrant of the right breast. SPECT/CT with volume rendering (**b**) and axial fused SPECT/CT sections (**c**–**e**) depict ipsilateral sentinel lymph nodes in the breast, in the axilla, and in the internal mammary chain

SLNs are colored. Washout is evident after approximately 45 min.

Multiple studies have established the validity of blue dyes as markers for SLNs with reasonably high detection rates (ranging from 75% to 80%) [124]; nevertheless such rates are slightly lower than those achieved with radiocolloids. In most cases, the same SLNs are detected by the two methods. Disadvantages of using blue dyes are as follows: (i) impossibility to evaluate extra-axillary nodes, (ii) temporary blue tattooing of the skin or areola (for patients with breast conservation surgery), and (iii) induction of anaphylactic reactions (which require resuscitation in 0.5–1.0% of patients and that contraindicate its use in pregnant women) [124–131].

Radioguided Surgery

Intraoperative detection of SLNs is usually radioguided by a gamma-detection probe. Such probes should be designed and constructed to be suitable for intraoperative use, in order to be able to detect the SLN from the skin surface as well as within the exposed surgical cavity [26]. The probe is placed in a sterile bag to be used in the sterile surgical field. A display capable of providing clear instantaneous and cumulative counts is a major requirement. It is helpful if the instantaneous count rate is fed to an audio signal that conveys count rate information.

The count rates obtained with the gamma probe during surgery are recorded per unit time with the probe in the surgical field, over the node before excision (in vivo) and after excision (ex vivo). A background tissue count is also recorded with the probe pointing away from the injection site, nodal activity, or other physiological accumulation sites (i.e., liver) [71].

Just before starting surgery and with the patient positioned on the operating table, using the

images and skin markings as guides, the gamma probe scans the axilla or any other region where tracer accumulation has been visualized in order to confirm correct identification and localization of the SLN(s) and to select the optimum location for incision. This task requires the sensitivity of the detector to be sufficient to identify a weakly active SLN when attenuated by, typically, up to 5 cm of soft tissue. The surgeon then introduces the probe through the skin incision to guide dissection to the hot node(s). Discriminating activity counts within the SLN from those originating from nearby sites requires the probe to be well collimated with a small angle of view. The detector should offer a high level of shielding against radiation hitting the side of the probe assembly. However, when working with the probe, it is important to direct the probe away from activity at the injection sites.

When a hot SLN has been removed, the surgical bed should be checked to confirm removal of the hot node(s) and to evaluate remaining activity. Owing to the limited spatial resolution of the gamma camera, LNs closer than approximately 15–20 mm may appear on lymphoscintigraphy as one single hot spot; so, in some cases another hot node may still be present at a close location after removal of the hottest SLN. In this regard, the use of SPECT/CT imaging is very helpful because it may provide information about the actual presence of a cluster of LNs rather than a single SLN. When other sources of activity are found in the lymphatic basin, the decision of whether to remove them will depend upon the report from lymphoscintigraphy and the working definition of "nodes to remove" [132, 133]. In principle, SLNB requires the removal of all SLNs receiving direct lymphatic drainage from the site of the primary tumor. In practice, this is not always achieved. In cases with multiple radiolabeled LNs, it is often difficult to distinguish between SLNs and second-tier LNs. The issue of how many SLNs should be biopsied when multiple radioactive LNs are found is still debated. In this regard, while removing too few nodes may miss potential metastases in regional LNs, indiscriminate removal of all radioactive axillary nodes may cause morbidity similar to that experienced after conventional ALND (in addition to the unnecessarily increased burden for histopathological analysis).

Several operational definitions of the SLN have evolved over time in order to decide exactly which nodes should be removed to maximize the likelihood of locating the "true" biologic SLN and to minimize the superfluous removal of non-SLNs. Some authors base SLN identification on the absolute number of counts per second recorded for the presumed nodes, while others consider the ratio of the "in vivo" or "ex vivo" radioactive counts in the SLNs relative to background or to neighboring non-SLNs. Empiric thresholds corresponding to (i) 10% or 20% of the counting rate in the first LN removed (which is usually the most radioactive) or (ii) at least ten times the background count, taken at a location remote from the injection site, are widely reported in the literature [98, 134–137]. It is generally accepted that removing more than five LNs from the axilla does not result in marked improvement in the sensitivity of axillary SLNB [138–143]. If blue dye is used, it can be a useful adjunct for aiding SLN localization and harvesting. Blue dye generally results in a lower SLN detection rate than radiotracers, but it can be used in addition to radiocolloids. Following injection, the blue dye drains to the SLNs, staining the channels, which can be followed to the first-echelon nodes. Direct visualization and dissection of these channels facilitate SLN localization.

Deeply located SLNs are difficult to detect intraoperatively because of tissue attenuation; furthermore, the large amount of radioactivity retained at the injection site may cause nearby located SLNs to be hidden because of the shine-through effect. Patients who have undergone previous breast surgery or radiation may demonstrate nodes in locations not typically seen in patients without a history of prior surgery. The lymphatic duct to the original SLN may be obstructed by tumor growth or the original SLN may be entirely replaced by disease. Consequently, lymphatic drainage may be either diverted to a non-sentinel node or no lymph

nodes may be visualized, increasing false-negative results.

The use of SPECT/CT images can help localization of focal activity [144] as can the use of intraoperative imaging with portable gamma cameras; the latter imaging equipment is generally used simply to verify that all radioactive lymph nodes of interest are removed [4]. Finally, to minimize false-negative results, the open axilla should be palpated and suspicious lymph nodes harvested, even if these are neither hot nor blue.

SLN Non-visualization or Failed Intraoperative Detection

It is important to consider that when an SLN is not detected intraoperatively, this corresponds to a failure of the method and not to a false-negative case (better defined as when an axillary relapse is observed despite a prior negative SLNB). The majority of patients with preoperative lymphoscintigraphic SLN non-visualization will have at least one SLN detected intraoperatively, either by a gamma probe alone or by a gamma probe combined with blue dye. While logistically difficult in most centers, a second radiocolloid injection, following perhaps a different injection route, may be useful to visualize previously non-visualized SLNs.

In approximately 1–2% of the patients, SLNs will not be detected preoperatively or intraoperatively, and the status of axillary LNs cannot be determined. Old age, obesity, tumor location other than in the upper outer quadrant and non-visualization of SLNs on preoperative lymphoscintigraphy may be associated with failed SLN localization [142]. The significance of preoperative scintigraphic SLN non-visualization is not yet known. Some studies have suggested that patients with unsuccessful axillary mapping may have an increased risk of metastatic axillary involvement [145]. There is no definitive consensus on what to do if an SLN cannot be visualized. However, current standards of care recommend axillary LN dissection when intraoperative SLN identification is not achieved [146].

New approaches and strategies have been proposed in case of failure to visualize SLN(s) with conventional lymphoscintigraphy. Recently, Pouw et al. demonstrated in a large cohort of patients that SPECT/CT provided SLN visualization in 23.2% of cases with non-visualization of the SLN on planar imaging (66/284). In those patients receiving reinjection after persistent SPECT/CT non-visualization, the SLN visualization rate reached 62.1% (36/58). Thus, an adjustment of the clinical protocols (logistically not easy) may be proposed when no SLN is visualized during planar imaging [147].

Histopathology of SLNs

Detailed histopathological analysis of the SLN is the standard procedure on which to base selection of the postoperative management strategy of breast cancer patients. By focusing on only a few lymph nodes rather than on 15–20 nodes as generally harvested during an axillary dissection, the pathologist can completely dissect and examine at 50–100 μm intervals each SLN. However, protocols for SLN analysis have not yet been standardized; therefore, high variability in procedures still exists among different centers.

Immunohistochemistry (IHC) considerably improves sensitivity by identifying micrometastases and even isolated tumor cells, which are generally missed with conventional hematoxylin and eosin (H&E) staining alone [148, 149]. Methods for molecular biology analysis, such as those based on the reverse transcription polymerase chain reaction, are also being used for SLN analysis, although they are generally characterized by relatively poor reproducibility and longer time for analysis. Nevertheless, equipment for fast, even intraoperative, analysis has recently been made commercially available; a potential disadvantage of such new techniques is that the whole SLN is usually homogenized and processed for molecular analysis, without parallel conventional histopathologic analysis being conducted [150, 151].

Different procedures for intraoperative SLN analysis have been developed, including the touch imprint of one or more slices (relatively low sensitivity, but very high specificity), staining of one or several intraoperative frozen sections, and even IHC for cytokeratins as the most exhaustive method. In this case, if the SLN has

metastasis, it is possible to perform ALND immediately. On the other hand, if complete intraoperative histopathologic evaluation of the SLN is not performed, it is necessary to wait for definitive histology usually obtained within a week. If metastases are detected, ALND may be performed with a second procedure.

No significant difference exists in terms of 5-year survival rate between patients with SLN-positive and those with SLN-negative metastases by IHC. Consequently, it would seem that SLN micrometastases identified only by IHC are clinically insignificant and that IHC staining of SLNs appears to be unnecessary. IHC should be limited to particular cases, such as infiltrating lobular carcinoma, for which it is difficult to detect SLN metastases with H&E staining alone [78, 152, 153].

Qualifications and Responsibilities of Personnel

SLN studies should only be performed by surgeons and nuclear medicine specialists who have received specific training in such procedures [154].

An initial supervised learning phase is recommended to harmonize and optimize interaction between these specialists. The most important parameters to test such a multidisciplinary team are (a) percentage of SLNBs successfully identified and (b) percentage of false negatives.

It is often considered that 20–40 procedures under guidance are sufficient in order to implement radioguided SLNB into the routine clinical practice of a given hospital. These numbers, however, are highly variable, and SLNB should only be introduced to clinical practice where the team demonstrates high identification rate and accuracy [40, 71, 78, 98, 155, 156].

Clinical Controversial Aspects

T3–T4 Tumors

The evidence regarding the safety of sentinel node biopsy is mainly based on studies including T1 and small T2 tumors only [71, 78, 157–160]. However, a few reports suggest that false-negative rate and axillary recurrence reported in larger tumors are similar [63, 161].

Multiple (Multifocal/Multicentric) Tumors

Multifocal breast cancer is defined as separate foci of ductal carcinoma more than 2 cm apart within the same quadrant, while multicentric breast cancer indicates the presence of separate independent foci of carcinoma in different quadrants [101]. Until recently, SLNB was contraindicated in patients with multicentric and multifocal breast cancer because it was believed that it was difficult to localize the true SLN, and a negative SLNB would not exclude the possibility of positive LN metastasis in basins draining from other regions of the breast. However, most of the mammary gland can actually be considered as a single unit with lymph drainage to only a few designated lymph nodes in the axilla [93, 162]. In this regard, the efficacy of SLNB in patients with multifocal/multicentric cancer has been shown to be equal to that in patients with unicentric breast cancer. This means that the presence of multiple tumors should not affect lymphatic drainage and the possibility to perform SLNB with superficial injection [163, 164]. Nevertheless, it should be noted that the prevalence of axillary metastases seems higher in multifocal or multicentric tumors. Furthermore, high false-negative rates have been reported [165]. However, even if there are limited and heterogenic data on the efficacy and safety of SLNB in multiple breast cancer [102, 166], the reported axillary recurrence rates are acceptable, and the SLNb may be performed in patients with multifocal or multicentric tumors [63, 101, 163].

Ductal Carcinoma In Situ (DCIS) and Breast-Conserving Surgery

By definition, DCIS does not metastasize to regional lymph nodes. However, controversy exists over the use of SLNB in patients with preoperative diagnosis of DCIS [167]. In fact, core needle/vacuum-assisted minimally invasive biopsy may be affected by sampling error; invasive disease is found at surgery in about 15–30% of patients with DCIS [168, 169]. Because of the low prevalence of metastatic involvement and the feasibility of SLNB after breast-conserving surgery, SLNB should not be considered a standard procedure in the treatment of all patients with

DCIS, but only recommended in those patients undergoing mastectomy [170–172]. However, wide local excision before SLNB can alter lymphatic drainage, especially to the internal mammary nodes (IMNs) [173, 174]. Thus, SLNB could also be an option in women treated with breast-conserving surgery when there is a high risk of invasive cancer at final diagnosis (i.e., palpability of the lesion or presence of a mammographic mass) [175].

Suspicious Palpable Axillary Nodes

Palpable axillary LN may be tumor negative in up to 40% of the patients [176, 177]. The proportion is lower when considering suspected LN identified by noninvasive techniques during preoperative staging (US, CT, MRI, or [^{18}F]FDG-PET). In any case, axillary ultrasound with fine needle aspiration cytology or core needle biopsy from the suspicious nodes is a widely accepted policy. In that case, SLNB can be performed in patients with palpable LNs, if negative in the preoperative diagnosis. However, the suspicious, palpable LNs should be harvested for histopathological evaluation, even when neither hot nor blue.

Evaluation of Internal Mammary and Other Extra-Axillary Nodes

Although the IMNs, in the same way as the axilla, are a first-echelon nodal drainage site in breast cancer, the importance of their treatment has long been debated [71, 178]. Randomized trials have failed to demonstrate a survival benefit from surgical internal mammary chain (IMC) dissection, and several retrospective studies have shown that IMNs are rarely the first site of recurrence [179–184]. However, the recent widespread adoption of SLNB has stimulated a critical reappraisal of such early results. Furthermore, the virtually systematic application of adjuvant systemic and/or locoregional radiotherapy encourages reexamination of the significance of IMN metastases [185]. There is strong evidence that postmastectomy radiotherapy to chest wall and nodal basins (including IMC) reduces both recurrence and breast cancer mortality in axilla-positive patients, even when systemic therapy is given [186]. However, internal mammary radiation remains controversial, mainly because of the difficulties in selecting patients at risk of occult internal mammary involvement [187, 188].

It is generally recognized that mapping of IMNs requires deep injection of the lymphatic mapping agent, either peritumorally or intratumorally [99, 100, 189]. Moreover, the fused SPECT/CT images represent a further technical solution to increase the identification rate of IMNs. Nevertheless, the rates of detection and intraoperative harvesting of IMNs are much lower than those for axillary LNs. Visualization of the IMNs has been detected in approximately one third of patients with breast cancer receiving deep radiocolloid injection, of which about 63–92% could be harvested during surgery, and 11–27% of them had metastases [178, 190–192].

In conclusion, there is no doubt that IMN metastasis has prognostic significance similar to prognostic importance to axillary nodal involvement [193–195]. However, the significance of IMN biopsy is not clear. There is evidence that IMN mapping leads to upstage migration and to modifications of treatment planning with respect to radiotherapy and systemic therapy, but more evidence is necessary to support the idea that IMN mapping will improve the outcome of treatment and survival, perhaps because IMN drainage at lymphoscintigraphy is more difficult to demonstrate than axillary drainage [178, 196]. Thus, an "integrated and multidisciplinary technique" is required to evaluate IMN drainage [192, 197].

Previous Surgery

Although the lymph drainage is probably changed in patients who have undergone previous breast surgery, current data indicate that lymphatic mapping is feasible with accuracies comparable to the results obtained in the general population [198–200].

Prior excisional biopsy: The lymph drainage pattern may be altered in patients who have undergone prior procedures, as non-axillary drainage has been identified more often in reoperative SLNB than in primary SLNB. In 73% of such patients, migration to the regional nodal drainage basins has been noted in ipsilateral axillary, supraclavicular, internal mammary, interpectoral, and

contralateral axillary nodes [173, 201–203]. However, there is evidence that sentinel node biopsy performed in the area of previous breast biopsy is not affected significantly by the prior procedure as regards success of the second procedure [204, 205].

Prior other breast surgeries: SLNB can be performed in patients undergoing breast surgery due to a local recurrence after breast conservation surgery in patients with DCIS. Although plastic surgery for breast augmentation or reduction requires major tissue movements, it does not contraindicate the SLN procedure [206, 207].

Prior axillary surgery: A second SLNB can be performed in patients with a local recurrence after breast conservation surgery and negative axillary SLN biopsy, although the success rate may be lower when compared with a primary SLN biopsy. Furthermore, extra-axillary SLNs are visualized more frequently in this group of patients. Encouraging results have been reported regarding axillary recurrences but, due to the rarity of the cases, the evidence is not solid. On the other hand, there is no evidence that these patients benefit from diagnostic axillary lymph node dissection [208].

Axillary Lymph Node Dissection

Review of surveillance, epidemiology, and end-result data has shown that the use of ALND for SLN metastasis has decreased in recent years [53, 209]. Actually, the management of breast cancer continues to advance toward more minimally invasive approaches, and the role of ALND for patients whose SLNs contain metastases is likely to become less important in the future. Cancer biology is much better understood now than it was when ALND was introduced. Consequently, the decision to administer systemic therapy is influenced by a variety of patient- and tumor-related factors, with lymph node tumor status influencing [210–212], but not necessarily dictating the use of chemotherapy [213–215].

Indeed, a high rate of locoregional control is achieved with modern multimodality therapy, including axillary radiotherapy (ART), even without ALND. Likewise, no significant difference is observed in disease-free survival or in overall survival between SLN plus ALND and SLN-only groups for selected patients with early nodal metastases, suggesting that ALND might not be required for all SLN-positive breast cancer women [216–219].

Thus, the ASCO Update Committee recommended that clinicians should avoid ALND in cases of women affected by early-stage breast cancer with one or two SLN metastases, who will receive breast-conserving surgery with conventionally fractionated whole-breast radiotherapy. Instead, clinicians might offer ALND to women suffering from early-stage breast cancer with nodal metastases found on SLNB who will receive mastectomy [43, 44, 50, 220–222].

Neoadjuvant Chemotherapy

Neoadjuvant systemic chemotherapy (NACT) is established for locally advanced breast cancer and is increasingly used for early-stage disease as well [223, 224]. Debate is ongoing on whether SLNB is accurate enough after NACT or whether it should be performed before starting NACT. Performing SLNB before or after primary systemic treatment has advantages and disadvantages in both cases. Before NACT, SLNB yields a more precise axillary staging, with useful information about possible nodal spread. Nevertheless, the procedure can postpone the beginning of treatment, and two surgeries may be necessary. After NACT, SLNB may lead to an underestimation of the initial stage of the disease because the tumor regression pattern in the axilla is unknown [225–227]. On the other hand, axillary nodal status after NACT is a highly significant prognostic factor. Pathologic complete response in the axilla can be achieved in up to 40% of patients. These patients can be spared ALND and the associated morbidity. Available data show that SLNB following NACT in cN0 patients is acceptable [226, 228–238].

A second issue concerns the possibility to perform SLNB in patients with initial node-positive disease who are downstaged by NACT to cN0. At present, SLNB may not be routinely recommended after NACT in patients with prior metastatic nodes. Changes in approach and patient selection would be necessary to support

the use of SLN surgery as an alternative to ALND in this patient population [160, 239–243].

Pregnancy

Many studies have demonstrated that prenatal doses from sentinel node imaging, when properly performed, are low enough that they do not significantly increase the risk of prenatal death, malformation, or mental impairment (see further below in the "Radioprotection" section) [244–247]. Thus, pregnancy is not an absolute contraindication for SLNB, in patients with early lesions and clinically/US negative axilla, but it is recommended to reduce the time interval between lymphoscintigraphy and surgery in order to reduce the injected activity (i.e., using a single day protocol). Furthermore, since small quantities of the radioactive colloid may be excreted with breast milk, lactation should be suspended for 24 h after radiopharmaceutical administration. It is also important to consider that vital dyes may have some contraindications in pregnancy [248–250]. Pregnant women with breast cancer should be followed by a multidisciplinary team and be clearly informed about the potential risks of radioactive tracers balanced against the risk of delaying therapy or omitting nodal staging [248, 251].

Primary Localizing Techniques

ROLL

Screening programs for breast cancer have led to an increase in detection of non-palpable breast tumors. Current approaches to breast cancer surgery aim at removing the lesion with an adequate clearance margin while, at the same time, accurately assessing the risk of distant metastases. Effective localization procedures are required to ensure complete excision of small non-palpable lesions detected on either symptomatic mammography or screening mammography. Several localization techniques have been developed for this purpose.

Hook-wire localization of non-palpable lesions has been the most widely used preoperative technique for many years. Although this is a reasonably effective technique, it involves a number of disadvantages. First, the entry site of the wire is often not at the ideal location for surgical incision at the time of operation. This may lead to additional unnecessary dissection and suboptimal cosmetic results. In addition, the wire must be placed on the day of operation, necessitating the coordination of radiology and operative schedules. The most important disadvantage, however, is the inaccuracy of localizing the target lesion percutaneously and during dissection. This results in high rates of reoperation for tissue margins involved in carcinoma [252, 253].

Intraoperative US imaging without preoperative wire localization has been used to map excision of non-palpable breast lesions; however, this technique has limitations, as it is feasible only in patients whose breast lesion is visible at US imaging [254–259].

The "radioguided occult lesion localization" (ROLL) approach [260–262] has gained popularity for non-palpable tumor lesions, including breast cancer. ROLL involves injection, into the center of the lesion, of a small amount of radioactive tracer that does not migrate from the site of interstitial injection, typically ^{99m}Tc-MAA. Injection is performed on the same day or on the day before surgery, under mammographic or US guidance (activity injected ranges from 2 to 150 MBq). Surgeons identify the lesion intraoperatively as a hot spot by using a handheld gamma probe, which allows accurate lesion localization and removal with minimal excision of healthy tissue (the skin incision is made at the site with highest counts or at a site suitable for oncoplastic breast surgery). After specimen resection, residual activity in the surgical field must be checked to avoid the possibility of missing some residual involved tissue [263]. This technique enables a good cosmetic outcome.

ROLL is a well-tolerated and feasible technique for localizing early-stage breast cancer in the course of breast-conserving surgery and is a suitable replacement for wire-guided localization [264–268]. Reported advantages of the ROLL technique include (i) easy and precise intraoperative localization of the breast lesion; (ii) complete lesion resection, with free margins and reduced needs for second operations; (iii) an

Table 3 Studies comparing ROLL and hook-wire techniques [266]

Authors	*n* (ROLL–hook wire)	Detection (%)	Free margins (ROLL versus hook wire) (%)	*p*
Gallegos, 2004	132 (65–67)	100	83 versus 64	0.014
Macmillan, 2004	95 (48–47)	100	61 versus 72	NS
Nadeem, 2004	130 (65–65)	100	83 versus 57	0.001
Thind, 2005	140 (70–70)	100	84 versus 60	0.002
Zgajnar, 2004	143 (51–92)	100	70 versus 44	
Rönkä, 2005	78 (64–14)	100	89 versus 79	0.05
Fraile, 2005	233 (65–168)	100	80 versus 70	NS
Strnad, 2006	33 (21–12)	100	Hook wire < ROLL	NS

increased capacity to center the lesion within the specimen; and (iv) a surgical approach (skin incision) that is independent from the intralesional radiotracer injection procedure [269–273]. Some potential pitfalls have been described; these are related to possible radiotracer spillage, contamination of the skin, or the injection path or ductal diffusion, as well as the presence of microcalcifications or DCIS [270, 271]. However, a systematic review of the ROLL technique concluded that this approach compares favorably to conventional wire localization for non-palpable breast lesions (Table 3) [267].

It is important to notice that radiation doses at the injection site and patient and staff absorbed doses are maintained well within the recommended limits established by the International Commission on Radiological Protection (ICRP) [274]. Finally, the possibility of performing ROLL after systemic intravenous administration of ^{99m}Tc-sestamibi (as a nonspecific, tumor-seeking agent) on the day of surgery has also been described [275].

SNOLL

As ROLL is an excellent technique enabling the removal of small breast cancers, the possibility to simultaneously perform SLNB without compromising oncological safety and the SLN detection rate is very important. Different techniques have been described to identify the SLNs in combination with ROLL, the so-called sentinel node occult lesion localization (SNOLL) [269, 276–284].

An intratumoral injection of ^{99m}Tc-MAA for ROLL of a tumor may be associated with a subdermal injection of ^{99m}Tc-nanocolloid for SLN mapping and SLNB. When the lesions are located near to the areola, intraoperative interference between the tracers could be avoided by elevation of the dermis and the subdermal area after skin incision [276]. Another possibility is to use a single intratumoral injection for both ROLL and SNOLL in the same session [280]. As a single procedure for localization of breast lesions and sentinel nodes, SNOLL may improve the entire surgical procedure. The majority of the studies published so far show a high percentage of successful tumor resection and intraoperative SLN localization with reduced failure [267, 269, 276, 279–284].

Radioactive Seeds

Alternatives to hook-wire localization of occult breast lesions include carbon trace as well as the use of sealed radioactive seeds. The seeds are essentially the same as the ones used in brachytherapy for cancer of the prostate, namely, a 4.5–0.8 mm titanium capsule containing a ceramic cylinder enriched with ^{125}I-iodine. Iodine-125 has a long decay time (half-life of 59.4 days) and emits low-energy photons (27 keV). The use of one or two seeds with this low photon energy has a negligible effect on the surrounding tissue. The radioactive seed is placed in the center of the breast lesion using an 18 G needle fixed in a needle holder under mammographic or ultrasonographic guidance; after successful positioning, the exact location is confirmed by mammography. During surgery, excision of the lesion is guided by using a handheld gamma probe [285].

If a SNOLL technique is scheduled, the ^{99m}Tc-colloid is subsequently injected, around the tumor or through a superficial route. Thus, the handheld gamma probe can be switched between the 27 keV energy window of the ^{125}I source and the 140 keV of ^{99m}Tc, allowing discrimination between the emissions of the two radioisotopes. Effective seed removal is verified by the absence of ^{125}I activity in the breast and its presence in the specimen. X-ray of the surgical specimen may confirm the presence of the seed and the relation of the lesion to the resection margins.

It has been shown that radioguided seed localization in non-palpable breast lesions is at least equivalent to the hook-wire technique in terms of ease of procedure, removing the target lesion, volume of breast tissue excised, obtaining negative margins, avoiding a second operative intervention, and allowing for simultaneous axillary staging [285–289].

Added Value of Intraoperative Portable Gamma Cameras

Recently, several types of portable or handheld mini gamma cameras have become available for clinical practice; while some of these portable gamma cameras are not specifically designed for radioguided surgery, other models are focused on different applications of SLNB [4, 5, 290, 291].

Appropriate use of a portable gamma camera enhances the reliability of the gamma probe by adding a clear image of the surgical field. The use of an intraoperative imaging device implies the possibility to better plan the surgical approach, to localize surgical targets in complex anatomical areas, to monitor the lymphatic basin before and after removal of the hot nodes, and, above all, to verify the correct SLN excision. Moreover, the use of point sources (e.g., ^{133}Ba or ^{125}I) facilitates SLN localization, as these sources can be depicted separately on the screen of the portable gamma camera, thus functioning as a pointer in the search for the SLNs. Nevertheless, their role in breast cancer surgery is still to be clarified. Intraoperative imaging using a portable gamma camera might be useful only when no conventional gamma camera is available for preoperative imaging, in particular in cases with extra-axillary drainage. Portable gamma cameras have also been used with promising results in other GOSTT environments regarding breast cancer, such as in ROLL or SNOLL procedures [290–296].

An interesting recent development of intraoperative imaging consists in combining conventional gamma probes with position and orientation tracking systems such as the so-called freehand SPECT, which permits a virtual reconstruction in a 3D environment (see Fig. 9) [4, 5, 293]. All these technologies will play an increasing role in the future extension of the GOSTT concept, in order to provide a better roadmap for radioguided surgery [2, 5].

Radioprotection

Nuclear medicine, surgery, and pathology professionals are involved if a radiopharmaceutical is used in a sentinel node procedure. Each involved practitioner (nuclear physician, surgeon, personnel in the surgical suite, pathologist) and the patient undergoing SLN and/or ROLL procedures are exposed to radiation. The exposures received by each, when radioactive activities standard for SLN procedures are administered, are well below recommended limits for both public and occupational exposures.

Estimates of radiation exposures for patients [244, 297–302], surgeons [299–301, 303–309], and pathologists [299–311] have been reported by several investigators. Table 4 presents a summary and interpretation of most of the available data. The estimates in the second column were extracted or derived from information in the included references. The values in the third column assume that SLN procedures were conducted on 100 patients in a year and assume that each patient was injected with an activity of 18.5 MBq. Columns four and five are International Commission on Radiological Protection (ICRP) recommended public and occupational limits [310].

Repeated measurements have clearly demonstrated that exposures to patients and personnel involved in radioguided SLN procedures (surgeon, nurse, pathologist) are minimal. Since exposures in SLN procedures of all nonnuclear medicine personnel are sufficiently low, none

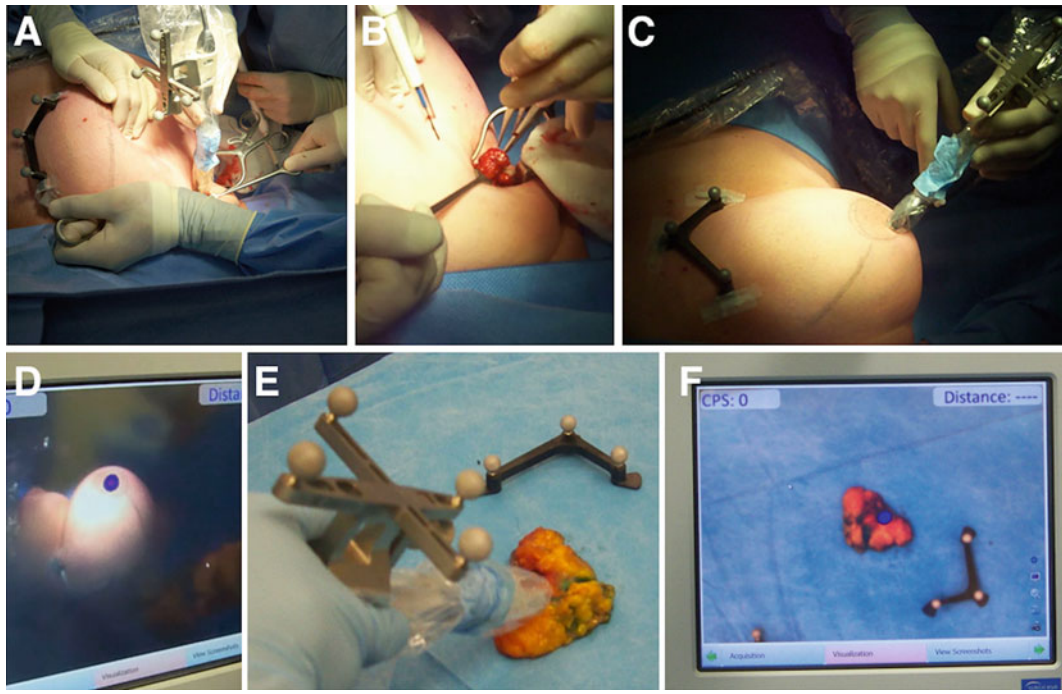

Fig. 9 Radioguided sentinel lymph node and occult lesion localization (SNOLL) in a patient with breast cancer using a single intratumoral injection of ^{99m}Tc-nanocolloidal albumin. Using a freehand SPECT probe (**a**), first the axillary sentinel lymph node is removed (**b**). Subsequently, the primary lesion is detected (**c**) following an image-guided procedure (**d**). Finally, the freehand SPECT probe (**e**) is used to visualize the primary tumor in relation to the margins of the specimen (**f**)

need be monitored routinely for occupational radiation exposure. Low patient effective doses and very low fetus/uterus equivalent doses [244, 299, 312–314] indicate that exposure to radiation is not a contraindication for an SLN procedure on any patient, including pregnant women. However, prudence dictates care should be exhibited when conducting an SLN procedure on any patient. For patients who are breastfeeding, nursing should be suspended for 24 h following radiopharmaceutical administration. Obviously, when using a ^{57}Co flood transmission source or SPECT/CT imaging, the total exposure is the emission-generated dose plus the transmission-generated dose [315].

Although the dose absorbed at the injection site can be relevant (see Table 4), there are no known negative consequences at the injection site. In fact, the site is often, though not always, excised. Furthermore, the radiation dose caused by the radionuclide-based procedure is very small relative to that received from postoperative radiation therapy.

Because exposures in SLN procedures of all nonnuclear medicine personnel are sufficiently low, none need be monitored routinely for radiation exposure. Finally, contamination with residual radioactivity of material from the operating room (surgical gauzes, liquids, and biological tissues of the patient) is minimal already at the time of surgery. Due to the fast physical decay of ^{99m}Tc, it is sufficient to wait only a few hours before disposal of operating room material to ensure an almost nonexistent radioactivity exposure to personnel [299].

Future Perspectives

The possibility of combining currently used radiotracers with other imaging agents opens new avenues for further developments. In this regard, hybrid tracers containing both a radioactive and a fluorescence label have recently been introduced (see Fig. 10), thus enabling the direct

Table 4 Ranges of estimates of radiation exposures (Modified from [71])

Radiation exposure	Range of estimates (mSv/MBq)	×18.5 MBq	×100 patients/ year (mSv/year)	Public limit (mSv/year)	Occupational limit (mSv/year)
Injection site absorbed dose	1–50	<925			
Injected breast equivalent dose	0.03–0.8	<15			
Patient effective dose	0.002–0.03	<0.56		<1	
Fetus/uterus equivalent dose	0.00003–0.0009	<0.017		<1	
Surgeon lens-of-eye equivalent dose	0.00009		<0.17	<15	<150
Surgeon hand equivalent dose	0.0004–0.01		<19	<50	<500
Surgeon effective dose	0.00004–0.0003		<0.56	<1	<20
Pathologist lens-of-eye equivalent dose	0.00001–0.00003		<0.056	<15	<150
Pathologist hand equivalent dose	0.00001–0.001		<1.9	<50	<500
Pathologist effective dose	0.000004–0.0002		<0.37	<1	<20

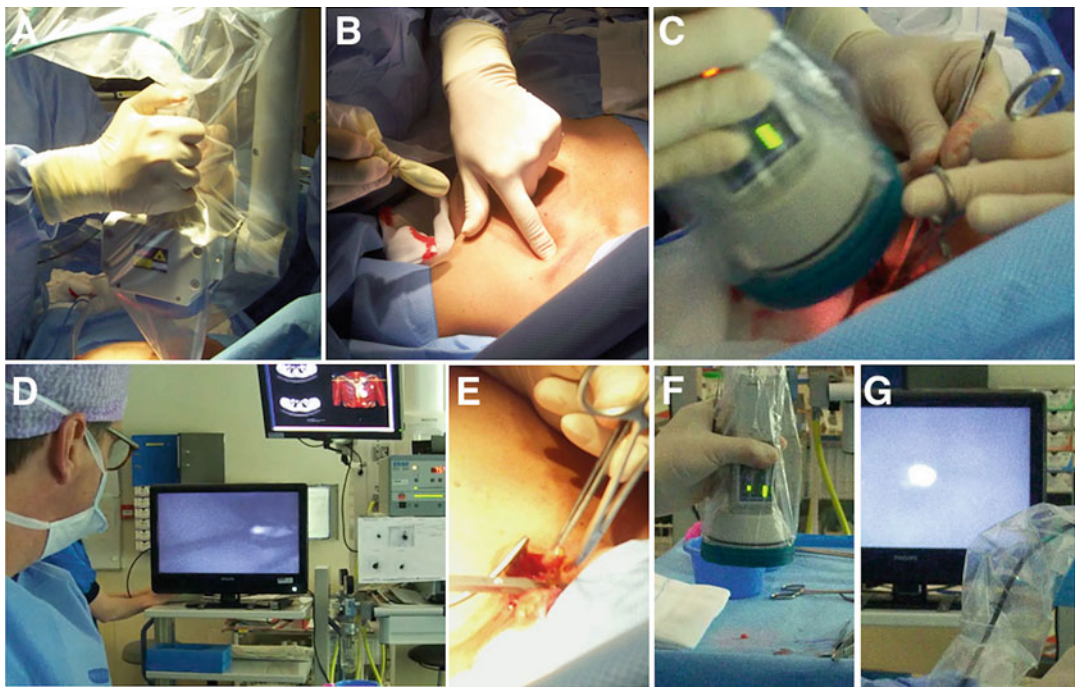

Fig. 10 Resection of an infraclavicular sentinel lymph node in a patient with high-risk breast cancer using the hybrid tracer ICG-^{99m}Tc-nanocolloid. The sentinel lymph node is first located on the skin projection using a portable gamma camera (**a**) and a handheld gamma probe (**b**). Subsequently, a portable near-infrared camera (**c**) is used to depict the fluorescence signal on the screen (**d**). This enables to remove the node (**e**) and to perform ex vivo control of the fluorescence signal (**f**, **g**)

integration of conventional preoperative imaging with intraoperative radio- and fluorescence guidance to the SLN via one single tracer injection [54].

Competitive methods are emerging: the techniques for SLNB that are not radioactivity-dependent or that refine the existing method (i.e., indocyanine green fluorescence, contrast-enhanced ultrasound using microbubbles, and superparamagnetic iron oxide nanoparticles) are particularly interesting [316–332]. In particular, the SentiMAG Multicentre Trial demonstrated that the magnetic technique with superparamagnetic iron oxide (SPIO) is feasible for SLNb, with an identification rate that is not inferior to the standard technique [333–337]. Recently, it has been shown that the SLN status can be evaluated with high accuracy preoperatively using contrast-enhanced color Doppler ultrasonography [338, 339].

However, a systematic review suggested that these new methods have clinical potential but yield high levels of false-negative results and presently cannot challenge the existing standard procedure. Further assessment of these techniques against the standard dual technique in randomized trials is thus needed [340].

Concluding Remarks

The development and wide acceptance of SLNB has deeply affected the management of breast cancer. Several technical and clinical controversies have been raised during the development of this technique. The resolution of these controversies should result in the standardization of the procedure and in the expansion of the number of patients evaluated with SLNB in the future. The modern approach in breast cancer care, which includes more detailed screening diagnostics, pathological evaluation, improved planning of surgical and radiation therapy, and more effective systemic treatment, emphasizes the need for ongoing re-evaluation of the "standard" locoregional therapy [341, 342].

References

1. Mariani G, Giuliano AE, Strauss HW, editors. Radioguided surgery – a comprehensive team approach. New York: Springer; 2008.
2. Zaknun JJ, Giammarile F, Valdés Olmos R, et al. Changing paradigms in radioguided surgery and intraoperative imaging: the GOSTT concept. Eur J Nucl Med Mol Imaging. 2012;39:1–3.
3. Chin PT, Welling MM, Meskers SC, et al. Optical imaging as an expansion of nuclear medicine: cerenkov-based luminescence vs fluorescence-based luminescence. Eur J Nucl Med Mol Imaging. 2013;40:1283–91.
4. Vidal-Sicart S, Rioja ME, Paredes P, et al. Contribution of perioperative imaging to radioguided surgery. Q J Nucl Med Mol Imaging. 2014;58:140–60.
5. Valdés Olmos RA, Vidal-Sicart S, Giammarile F, et al. The GOSTT concept and hybrid mixed/virtual/augmented reality environment radioguided surgery. Q J Nucl Med Mol Imaging. 2014;58:207–15.
6. KleinJan GH, van den Berg NS, de Jong J, et al. Multimodal hybrid imaging agents for sentinel node mapping as a means to (re)connect nuclear medicine to advances made in robot-assisted surgery. Eur J Nucl Med Mol Imaging. 2016;43:1278–87.
7. Cabañas RM. An approach for the treatment of penile carcinoma. Cancer. 1977;39:456–66.
8. Ollila DW, Brennan MB, Giuliano AE. The role of intraoperative lymphatic mapping and sentinel lymphadenectomy in the management of patients with breast cancer. Adv Surg. 1999;32:349–64.
9. Nieweg OE, Tanis PJ, Kroon BBR. The definition of a sentinel node. Ann Surg Oncol. 2001;9:538–41.
10. Mariani G, Manca G, Valdés Olmos RA, Orsini F, Vidal-Sicart S, editors. Atlas of lymphoscintigraphy and sentinel node mapping – a pictorial case-based approach. Milan: Springer; 2013.
11. de Bree R, Nieweg OE. The history of sentinel node biopsy in head and neck cancer: from visualization of lymphatic vessels to sentinel nodes. Oral Oncol. 2015;51:819–23.
12. Smith B, Backes F. The role of sentinel lymph nodes in endometrial and cervical cancer. J Surg Oncol. 2015;112:753–60.
13. Yashiro M, Matsuoka T. Sentinel node navigation surgery for gastric cancer: overview and perspective. World J Gastrointest Surg. 2015;27(7):1–9.
14. Jakobsen JK. Sentinel node biopsy in uro-oncology: a history of the development of a promising concept. Urol Oncol. 2015;33:486–93.
15. Shersher DD, Liptay MJ. Status of sentinel lymph node mapping in non-small cell lung cancer. Cancer J. 2015;21:17–20.

16. Siegel RL, Miller KD, Jemal A. Cancer statistics. CA Cancer J Clin. 2015;65:5–29.
17. Zurrida S, Veronesi U. Milestones in breast cancer treatment. Breast J. 2015;21:3–12.
18. Veronesi U, De Cicco C, Galimberti VE, et al. A comparative study on the value of FDG-PET and sentinel node biopsy to identify occult axillary metastases. Ann Oncol. 2007;18:473–8.
19. Liu Y. Role of FDG PET-CT in evaluation of locoregional nodal disease for initial staging of breast cancer. World J Clin Oncol. 2014;5:982–9.
20. Futamura M, Asano T, Kobayashi K, et al. Prediction of macrometastasis in axillary lymph nodes of patients with invasive breast cancer and the utility of the SUV lymph node/tumor ratio using FDG-PET/CT. World J Surg Oncol. 2015;13:49.
21. Krammer J, Schnitzer A, Kaiser CG, et al. ^{18}F-FDG PET/CT for initial staging in breast cancer patients – is there a relevant impact on treatment planning compared to conventional staging modalities? Eur Radiol. 2015;25:2460–9.
22. Boone BA, Huynh C, Spangler ML, et al. Axillary lymph node burden in invasive breast cancer: a comparison of the predictive value of ultrasound-guided needle biopsy and sentinel lymph node biopsy. Clin Breast Cancer. 2015;15:e243–8.
23. Hyun SJ, Kim EK, Yoon JH, et al. Adding MRI to ultrasound and ultrasound-guided fine-needle aspiration reduces the false-negative rate of axillary lymph node metastasis diagnosis in breast cancer patients. Clin Radiol. 2015;70:716–22.
24. You S, Kang DK, Jung YS, et al. Evaluation of lymph node status after neoadjuvant chemotherapy in breast cancer patients: comparison of diagnostic performance of ultrasound, MRI and ^{18}F-FDG PET/CT. Br J Radiol. 2015;88(1052):20150143.
25. Beek MA, Verheuvel NC, Luiten EJ, et al. Two decades of axillary management in breast cancer. Br J Surg. 2015;102:1658–64.
26. Keshtgar MRS, Ell PJ. Sentinel lymph node detection and imaging. Eur J Nucl Med. 1999;26:57–67.
27. Chatterjee A, Serniak N, Czerniecki BJ. Sentinel lymph node biopsy in breast cancer: a work in progress. Cancer J. 2015;21:7–10.
28. Morton DL, Wen DR, Wong JH, et al. Technical details of intraoperative lymphatic mapping for early stage melanoma. Arch Surg. 1992;127:392–9.
29. Nieweg OE, Uren RF, Thompson JF. The history of sentinel lymph node biopsy. Cancer J. 2015;21:3–6.
30. Krag DN, Weaver D, Alex JC, Fairbank JT. Surgical resection and radiolocalization of sentinel lymph node in breast cancer using a gamma probe. Surg Oncol. 1993;2:335–9.
31. Giuliano AE, Kirgan D, Guenther JM. Lymphatic mapping and sentinel lymphadenectomy for breast cancer. Ann Surg. 1994;220:391–401.
32. Noguchi M, Katev N, Miyazaki I. Diagnosis of axillary lymph node metastases in patients with breast cancer. Breast Cancer Res Treat. 1996;40:283–93.
33. Taylor A, Murray D, Herda S, et al. Dynamic lymphoscintigraphy to identify the sentinel and satellite nodes. Clin Nucl Med. 1996;21:755–8.
34. Pijpers R, Meijer S, Hoekstra OS, et al. Impact of lymphoscintigraphy on sentinel node identification with technetium-99m-colloid albumin in breast cancer. J Nucl Med. 1997;38:366–8.
35. Giuliano AE. Lymphatic mapping and sentinel node biopsy in breast cancer. JAMA. 1997;277:791–2.
36. Veronesi U, Paganelli G, Galimberti V, et al. Sentinel node biopsy to avoid axillary dissection in breast cancer patients with clinically negative lymph-nodes. Lancet. 1997;349:1864–7.
37. International Breast Cancer Consensus Conference. Image-detected breast cancer: state of the art diagnosis and treatment. International Breast Cancer Consensus Conference. J Am Coll Surg. 2001;193:297–302.
38. Mariani G, Moresco L, Viale G, et al. Radioguided sentinel lymph node biopsy in breast cancer surgery. J Nucl Med. 2001;42:1198–215.
39. Veronesi U, Paganelli G, Viale G, et al. A randomized comparison of sentinel-node biopsy with routine axillary dissection in breast cancer. N Engl J Med. 2003;349:546–53.
40. Veronesi U, Paganelli G, Viale G, et al. Sentinel-lymph-node biopsy as a staging procedure in breast cancer: update of a randomized controlled study. Lancet Oncol. 2006;7:983–90.
41. Benson JR, Della Rovere GQ, Axilla Management Consensus Group. Management of the axilla in women with breast cancer. Lancet Oncol. 2007;8:331–48.
42. Giuliano AE, Gangi A. Sentinel node biopsy and improved patient care. Breast J. 2015;21:27–31.
43. Lopez Penha TR, van Roozendaal LM, Smidt ML, et al. The changing role of axillary treatment in breast cancer: who will remain at risk for developing arm morbidity in the future? Breast. 2015;24:543–7.
44. Layeequr Rahman R, Crawford SL, Siwawa P. Management of axilla in breast cancer – the saga continues. Breast. 2015;24:343–53.
45. Pepels MJ, Vestjens JH, de Boer M, et al. Safety of avoiding routine use of axillary dissection in early stage breast cancer: a systematic review. Breast Cancer Res Treat. 2011;125:301–13.
46. Atalay C. New concepts in axillary management of breast cancer. World J Clin Oncol. 2014;10:895–900.
47. Sledge GW, Mamounas EP, Hortobagyi GN, et al. Past, present, and future challenges in breast cancer treatment. J Clin Oncol. 2014;32:1979–86.

48. Buscombe J, Paganelli G, Burak ZE, European Association of Nuclear Medicine Oncology Committee and Dosimetry Committee, et al. Sentinel node in breast cancer procedural guidelines. Eur J Nucl Med Mol Imaging. 2007;34:2154–9.
49. Lizarraga IM, Weigel RJ. Axillary lymph node dissection for breast cancer: primum non nocere. Eur J Surg Oncol. 2015;41:955–7.
50. van den Hoven I, Voogd AC, Roumen RM. A paradigm shift in axillary breast cancer treatment; from "treat all-except" toward "treat none-unless". Clin Breast Cancer. 2015;15:399–402.
51. Galimberti V, Manika A, Maisonneuve P, et al. Long-term follow-up of 5262 breast cancer patients with negative sentinel node and no axillary dissection confirms low rate of axillary disease. Eur J Surg Oncol. 2014;40:1203–8.
52. Han HJ, Kim JR, Nam HR, et al. Clinical outcomes after sentinel lymph node biopsy in clinically node-negative breast cancer patients. Radiat Oncol J. 2014;32:132–7.
53. Joyce DP, Manning A, Carter M, et al. Meta-analysis to determine the clinical impact of axillary lymph node dissection in the treatment of invasive breast cancer. Breast Cancer Res Treat. 2015;153: 235–40.
54. Tsujimoto M. Recent advances in sentinel node biopsy in breast surgery. Breast Cancer. 2015;22:211.
55. Suami H, Pan WR, Taylor GI. Historical review of breast lymphatic studies. Clin Anat. 2009;22:531–6.
56. Torrenga H, Fabry H, van der Sijp JR, et al. Omitting axillary lymph node dissection in sentinel node negative breast cancer patients is safe: a long term follow-up analysis. J Surg Oncol. 2004;88:4–7.
57. Carlo JT, Grant MD, Knox SM, et al. Survival analysis following sentinel lymph node biopsy: a validation trial demonstrating its accuracy in staging early breast cancer. BUMC Proc. 2005;18:103–7.
58. Fuhrman GM, Gambino J, Bolton JS, et al. Five-year follow-up after sentinel node mapping for breast cancer demonstrates better than expected treatment outcomes. Am Surg. 2005;71:564–9.
59. Sanjuàn A, Vidal-Sicart S, Zanón G, et al. Clinical axillary recurrence after sentinel node biopsy in breast cancer: a follow-up study of 220 patients. Eur J Nucl Med Mol Imaging. 2005;32:932–6.
60. Smidt ML, Janssen CM, Kuster DM, et al. Axillary recurrence after a negative sentinel node biopsy for breast cancer: incidence and clinical significance. Ann Surg Oncol. 2005;12:29–33.
61. Veronesi U, Galimberti V, Mariani L, et al. Sentinel node biopsy in breast cancer: early results in 953 patients with negative sentinel node biopsy and no axillary dissection. Eur J Cancer. 2005;41: 197–8.
62. de Kanter AY, Menke-Pluymers MM, Wouters MW, et al. Five-year follow-up of sentinel node negative breast cancer patients. Eur J Surg Oncol. 2006;32: 282–6.
63. Veronesi U, Galimberti V, Paganelli G, et al. Axillary metastases in breast cancer patients with negative sentinel nodes: follow-up of 3,548 cases. Eur J Cancer. 2009;45:1381–8.
64. Veronesi U, Viale G, Paganelli G, et al. Sentinel lymph node biopsy in breast cancer: ten-year results of a randomized control study. Ann Surg. 2010;251: 595–600.
65. Kaufmann M, Morrow M, von Minckwitz G, et al. Locoregional treatment of primary breast cancer: consensus recommendations from an International Expert Panel. Cancer. 2010;116:1184–91.
66. van der Ploeg IM, Nieweg OE, van Rijk MC, et al. Axillary recurrence after a tumour-negative sentinel node biopsy in breast cancer patients: a systematic review and meta-analysis of the literature. Eur J Surg Oncol. 2008;34:1277–84.
67. Krag DN, Anderson SJ, Julian TB, et al. Sentinel-lymph-node resection compared with conventional axillary-lymph-node dissection in clinically node-negative patients with breast cancer: overall survival findings from the NSABP B-32 randomised phase 3 trial. Lancet Oncol. 2010;11:927–33.
68. Purushotham AD, Upponi S, Klevesath MB, et al. Morbidity after sentinel lymph node biopsy in primary breast cancer: results from a randomized controlled trial. J Clin Oncol. 2005;23:4312–21.
69. Mansel RE, Fallowfield L, Kissin M, et al. Randomized multicenter trial of sentinel node biopsy versus standard axillary treatment in operable breast cancer: the ALMANAC Trial. J Natl Cancer Inst. 2006;98:599–609.
70. Goyal A, Newcombe RG, Chhabra A, Mansel RE, ALMANAC Trialists Group. Factors affecting failed localisation and false-negative rates of sentinel node biopsy in breast cancer – results of the ALMANAC validation phase. Breast Cancer Res Treat. 2006;99: 203–8.
71. Giammarile F, Alazraki N, Aarsvold JN, et al. The EANM and SNMMI practice guideline for lymphoscintigraphy and sentinel node localization in breast cancer. Eur J Nucl Med Mol Imaging. 2013;40:1932–47.
72. Mount MG, White NR, Nguyen CL, et al. Evaluating one day versus two days preoperative lymphoscintigraphy protocols for sentinel lymph node biopsy in breast cancer. Am Surg. 2015;81:454–7.
73. Wang H, Heck K, Pruitt SK, et al. Impact of delayed lymphoscintigraphy for sentinel lymph node biopsy for breast cancer. J Surg Oncol. 2015;111:931–4.
74. Wilhelm AJ, Mijnhout GS, Franssen EJF. Radiopharmaceuticals in sentinel lymph-node detection – an overview. Eur J Nucl Med. 1999;26:S36–42.
75. Clarke D, Khoni N, Mansel ER. Sentinel node biopsy in breast cancer. ALMANAC trial. World J Surg. 2001;25:819–22.
76. Burak WE, Agnese DM, Povoski SP. Advances in the surgical management of early stage invasive breast cancer. Curr Probl Surg. 2004;41:877–936.

77. Bourgeois P. Scintigraphic investigations of the lymphatic system: the influence of injected volume and quantity of labeled colloidal tracer. J Nucl Med. 2007;48:693–5.
78. Lyman GH, Giuliano AE, Somerfield MR, et al. American Society of Clinical Oncology guideline recommendations for sentinel lymph node biopsy in early-stage breast cancer. J Clin Oncol. 2005;23:7703–20.
79. Vera DR, Wallace AM, Hoh CK. A synthetic macromolecule for sentinel node detection: ^{99m}Tc-DTPA-mannosyl-dextran. J Nucl Med. 2001;42:951–9.
80. Wallace AM, Han LK, Povoski SP, et al. Comparative evaluation of [^{99m}Tc]tilmanocept for sentinel lymph node mapping in breast cancer patients: results of two phase 3 trials. Ann Surg Oncol. 2013;20:2590–9.
81. Dambros Gabbi MC, Masiero PR, Uchoa D, et al. Comparison between preoperative and intraoperative injection of ^{99m}Tc Dextran-500 for sentinel lymph node localization in breast cancer. Am J Nucl Med Mol Imaging. 2014;4:602–10.
82. Baker JL, Pu M, Tokin CA, et al. Comparison of [^{99m}Tc]tilmanocept and filtered [^{99m}Tc]sulfur colloid for identification of SLNs in breast cancer patients. Ann Surg Oncol. 2015;22:40–5.
83. McCarter MD, Yeung H, Yeh S, et al. Localization of the sentinel node in breast cancer: identical results with same-day and day-before isotope injection. Ann Surg Oncol. 2001;8:682–6.
84. van der Ent FW, Kengen RA, van der Pol HA, Hoofwijk AG. Sentinel node biopsy in 70 unselected patients with breast cancer: increased feasibility by using 10 mCi radiocolloid in combination with a blue dye tracer. Eur J Surg Oncol. 1999;25:24–9.
85. Gray RJ, Pockaj BA, Roarke MC. Injection of ^{99m}Tc-labeled sulfur colloid the day before operation for breast cancer sentinel lymph node mapping is as successful as injection the day of operation. Am J Surg. 2004;188:685–9.
86. Suami H, Pan WR, Mann GB, Taylor GI. The lymphatic anatomy of the breast and its implications for sentinel lymph node biopsy: a human cadaver study. Ann Surg Oncol. 2008;15:863–71.
87. Ahmed M, Purushotham AD, Horgan K, et al. Meta-analysis of superficial versus deep injection of radioactive tracer and blue dye for lymphatic mapping and detection of sentinel lymph nodes in breast cancer. Br J Surg. 2015;102:169–81.
88. Tanis PJ, Valdés Olmos RA, Muller SH, Nieweg OE. Lymphatic mapping in patients with breast carcinoma: reproducibility of lymphoscintigraphic results. Radiology. 2003;228:546–51.
89. Tanis PJ, Nieweg OE, Valdes Olmos RA, Kroon BB. Anatomy and physiology of lymphatic drainage of the breast from the perspective of sentinel node biopsy. J Am Coll Surg. 2001;192:399–409.
90. Hindie E, Groheux D, Espie M, et al. Sentinel node biopsy in breast cancer. Bull Cancer. 2009;96:713–25.
91. Pelosi E, Bello M, Griors M, et al. Sentinel lymph node detection in patients with early-stage breast cancer: comparison of periareolar and subdermal/peritumoral injection techniques. J Nucl Med. 2004;45:220–5.
92. Chakera AH, Friis E, Hesse U, et al. Factors of importance for scintigraphic non-visualization of sentinel nodes in breast cancer. Eur J Nucl Med Mol Imaging. 2005;32:286–93.
93. Nieweg OE, Estourgie SH, van Rijk MC, Kroon BB. Rationale for superficial injection techniques in lymphatic mapping in breast cancer patients. J Surg Oncol. 2004;87:153–6.
94. Noguchi M, Inokuchi M, Zen Y. Complement of peritumoral and subareolar injection in breast cancer sentinel lymph node biopsy. J Surg Oncol. 2009;100:100–5.
95. Povoski SP, Olsen JO, Young DC, et al. Prospective randomized clinical trial comparing intradermal, intraparenchymal, and subareolar injection routes for sentinel lymph node mapping and biopsy in breast cancer. Ann Surg Oncol. 2006;13:1412–21.
96. Linehan DC, Hill ADK, Akhurst T, et al. Intradermal radiocolloid and intraparenchymal blue dye injection optimize sentinel node identification in breast cancer patients. Ann Surg Oncol. 1999;6:286–93.
97. Pesek S, Ashikaga T, Krag LE, Krag D. The false-negative rate of sentinel node biopsy in patients with breast cancer: a meta-analysis. World J Surg. 2012;36:2239–51.
98. Martin 2nd RC, Edwards MJ, Wong SL, et al. Practical guidelines for optimal gamma probe detection of sentinel lymph nodes in breast cancer: results of a multi-institutional study. Surgery. 2000;128:139–44.
99. Paganelli G, Galimberti V, Trifirò G, et al. Internal mammary node lymphoscintigraphy and biopsy in breast cancer. Q J Nucl Med. 2002;46:138–44.
100. Krynyckyi BR, Chun H, Kim HH, et al. Factors affecting visualization rates of internal mammary sentinel nodes during lymphoscintigraphy. J Nucl Med. 2003;44:1387–93.
101. Kumar R, Jana S, Heiba SI, et al. Retrospective analysis of sentinel node localization in multifocal multicentric, palpable, or non palpable breast cancer. J Nucl Med. 2003;44:7–10.
102. Knauer M, Konstantiniuk P, Haid A, et al. Multicentric breast cancer: a new indication for sentinel node biopsy – a multi-institutional validation study. J Clin Oncol. 2006;24:3374–80.
103. Uren RF, Howman-Giles R, Chung D, Thompson JF. Imaging sentinel lymph nodes. Cancer J. 2015;21:25–32.
104. Moncayo VM, Aarsvold JN, Alazraki NP. Lymphoscintigraphy and sentinel nodes. J Nucl Med. 2015;56:901–7.
105. McMasters KM, Wong SL, Tuttle TM, et al. Preoperative lymphoscintigraphy for breast cancer does not improve the ability to identify axillary sentinel lymph nodes. Ann Surg. 2000;231:724–31.
106. Marchal F, Rauch P, Morel O, et al. Results of preoperative lymphoscintigraphy for breast cancer are

predictive of identification of axillary sentinel lymph nodes. World J Surg. 2006;30:55–62.
107. De Cicco C, Cremonesi M, Luini A, et al. Lymphoscintigraphy and radioguided biopsy of the sentinel axillary node in breast cancer. J Nucl Med. 1998;39: 2080–4.
108. Babiera GV, Delpassand ES, Breslin TM, et al. Lymphatic drainage patterns on early versus delayed breast lymphoscintigraphy performed after injection of filtered Tc-99m sulfur colloid in breast cancer patients undergoing sentinel lymph node biopsy. Clin Nucl Med. 2005;30:11–5.
109. Lerman H, Metser U, Lievshitz G, et al. Lymphoscintigraphic sentinel node identification in patients with breast cancer: the role of SPECT-CT. Eur J Nucl Med Mol Imaging. 2006;33:329–37.
110. Keidar Z, Israel O, Krausz Y. SPECT/CT in tumor imaging: technical aspects and clinical applications. Semin Nucl Med. 2003;33:205–18.
111. Vermeeren L, van der Ploeg IM, Valdés Olmos RA, et al. SPECT/CT for preoperative sentinel node localization. J Surg Oncol. 2010;101:184–90.
112. van der Ploeg IM, Nieweg OE, Kroon BB, et al. The yield of SPECT/CT for anatomical lymphatic mapping in patients with breast cancer. Eur J Nucl Med Mol Imaging. 2009;36:903–9.
113. Jimenez-Heffernan A, Ellman A, et al. Results of a prospective International Atomic Energy Ahency (IAEA) sentinel node trial on the value of SPECT/CT over planar imaging in various malignancies. J Nucl Med. 2015;56:1338–44.
114. Even-Sapir E, Lerman H, Lievshitz G, et al. Lymphoscintigraphy for sentinel node mapping using a hybrid SPECT/CT system. J Nucl Med. 2003; 44:1413–20.
115. Lerman H, Lievshitz G, Zak O, et al. Improved sentinel node identification by SPECT/CT in overweight patients with breast cancer. J Nucl Med. 2007;48: 201–6.
116. Valdés Olmos RA, Rietbergen DD, Vidal-Sicart S, et al. Contribution of SPECT/CT imaging to radioguided sentinel lymph node biopsy in breast cancer, melanoma, and other solid cancers: from "open and see" to "see and open". Q J Nucl Med Mol Imaging. 2014;58:127–39.
117. Serrano-Vicente J, Rayo-Madrid JI, Domínguez-Grande ML, et al. Role of SPECT-CT in breast cancer sentinel node biopsy when internal mammary chain drainage is observed. Clin Transl Oncol. 2016;18:418–25.
118. Tomiguchi M, Yamamoto-Ibusuki M, Yamamoto Y, et al. Prediction of sentinel lymph node status using single-photon emission computed tomography (SPECT)/computed tomography (CT) imaging of breast cancer. Surg Today. 2016;46:214–23.
119. Vidal-Sicart S, Brouwer OR, Valdés Olmos RA. Evaluation of the sentinel lymph node combining SPECT/CT with the planar image and its importance for the surgical act. Rev Esp Med Nucl. 2011;30:331–7.
120. Uren RF, Howman-Giles R, Chung D, Thompson JF. Nuclear medicine aspects of melanoma and breast lymphatic mapping. Semin Oncol. 2004;31: 338–48.
121. van Rijk MC, Tanis PJ, Nieweg OE, et al. Clinical implications of sentinel nodes outside the axilla and internal mammary chain in patients with breast cancer. J Surg Oncol. 2006;94:281–6.
122. Estourgie SH, Nieweg OE, Valdés Olmos RA, et al. Eight false-negative sentinel lymph node procedures in breast cancer: what went wrong? Eur J Surg Oncol. 2003;29:336–40.
123. O'Reilly EA, Prichard RS, Al Azawi D, et al. The value of isosulfan blue dye in addition to isotope scanning in the identification of the sentinel lymph node in breast cancer patients with a positive lymphoscintigraphy: a randomized controlled trial (ISRCTN98849733). Ann Surg. 2015;262:243–8.
124. Anan K, Mitsuyama S, Kuga H, et al. Double mapping with subareolar blue dye and peritumoral green dye injections decreases the false negative rate of dye only sentinel node biopsy for early breast cancer: 2 site injection is more accurate than 1-site injection. Surgery. 2006;139:624–9.
125. Albo D, Wayne JD, Hunt KK, et al. Anaphylactic reactions to isosulfan blue dye during sentinel lymph node biopsy for breast cancer. Am J Surg. 2001;182:393–8.
126. Borgen PI. Isosulfan blue dye reactions during sentinel lymph node mapping for breast cancer. Anesth Analg. 2002;95:385–8.
127. Montgomery LL, Thorne AC, Van Zee KJ, et al. Incidence of anaphylactoid reactions to isosulfan blue dye during breast carcinoma lymphatic mapping in patients treated with preoperative prophylaxis: results of a surgical prospective clinical practice protocol. Cancer. 2005;104:692–9. Dal.
128. Scherer K, Studer W, Figueiredo V, Bircher AJ. Anaphylaxis to isosulfan blue and cross-reactivity to patent blue V: case report and review of the nomenclature of vital blue dyes. Ann Allergy Asthma Immunol. 2006;96:497–500.
129. Rodier JF, Velten M, Wilt M, et al. Prospective multicentric randomized study comparing periareolar and peritumoral injection of radiotracer and blue dye for the detection of sentinel lymph node in breast sparing procedures: FRANSENODE trial. J Clin Oncol. 2007;25:3664–9.
130. Varghese P, Abdel-Rahman AT, Akberali S, et al. Methylene blue dye – a safe and effective alternative for sentinel lymph node localization. Breast J. 2008; 14:61–7.
131. Iqbal FM, Basit A, Salem F, Vidya R. Feeling blue, going green and finding other attractive alternatives: a case of biphasic anaphylaxis to patent blue and a literature review of alternative sentinel node localisation methods. BMJ Case Rep. 2015;pii: bcr2015213107. doi: 10.1136/bcr-2015-213107.

132. Chung A, Yu J, Stempel M, et al. Is the "10% rule" equally valid for all subsets of sentinel-node-positive breast cancer patients? Ann Surg Oncol. 2008;15:2728.
133. Liu LC, Lang JE, Jenkins T, et al. Is it necessary to harvest additional lymph nodes after resection of the most radioactive sentinel lymph node in breast cancer? J Am Coll Surg. 2008;207:853–8.
134. Morton DL, Bostick PJ. Will the true sentinel node please stand? Ann Surg Oncol. 1999;6:12–4.
135. Nathanson SD. Will the true sentinel node please stand? Ann Surg Oncol. 1999;6:514–6.
136. McMasters KM, Reintgen DS, Ross MI, et al. Sentinel lymph node biopsy for melanoma: how many radioactive nodes should be removed? Ann Surg Oncol. 2001;8:192–7.
137. Manca G, Romanini A, Pellegrino D, et al. Optimal detection of sentinel lymph node metastases by intraoperative radioactive threshold and molecular analysis in patients with melanoma. J Nucl Med. 2008;49:1769–75.
138. Aarsvold JN, Alazraki NP. Update on detection of sentinel lymph nodes in patients with breast cancer. Semin Nucl Med. 2005;35:116–28.
139. Goyal A, Newcombe RG, Mansel RE, Axillary Lymphatic Mapping Against Nodal Axillary Clearance (ALMANAC) Trialists Group. Clinical relevance of multiple sentinel nodes in patients with breast cancer. Br J Surg. 2005;92:438–42.
140. Serrano Vicente J, Infante de la Torre JR, Domínguez Grande ML, et al. Optimization of sentinel lymph node biopsy in breast cancer by intraoperative axillary palpation. Rev Esp Med Nucl. 2010;29:8–11.
141. Ban EJ, Lee JS, Koo JS, et al. How many sentinel lymph nodes are enough for accurate axillary staging in t1-2 breast cancer? J Breast Cancer. 2011;14:296–300.
142. Cheng G, Kurita G, Kurita S, et al. Current status of sentinel lymph-node biopsy in patients with breast cancer. Eur J Nucl Med Mol Imaging. 2011;38:562–75.
143. Schuman S, Walker G, Avisar E. Processing sentinel nodes in breast cancer: when and how many? Arch Surg. 2011;146:389–93.
144. Uren RF, Howman-Giles R, Chung DK, et al. SPECT/CT scans allow precise anatomical location of sentinel lymph nodes in breast cancer and redefine lymphatic drainage from the breast to the axilla. Breast. 2012;21:480–6.
145. Brenot-Rossi I, Houvenaeghel G, Jacquemier J, et al. Nonvisualization of axillary sentinel node during lymphoscintigraphy: is there a pathologic significance in breast cancer? J Nucl Med. 2003;44:1232–7.
146. Leidenius MH, Krogerus LA, Toivonen TS, et al. The sensitivity of axillary staging when using sentinel node biopsy in breast cancer. Eur J Surg Oncol. 2003;29:849–53.
147. Pouw B, Hellingman D, Kieft M, et al. The hidden sentinel node in breast cancer: reevaluating the role of SPECT/CT and tracer reinjection. Eur J Surg Oncol. 2016;42:497–503.
148. Krishnamurthy S, Meric-Bernstam F, Lucci A, et al. A prospective study comparing touch imprint cytology, frozen section analysis, and rapid cytokeratin immunostain for intraoperative evaluation of axillary sentinel lymph nodes in breast cancer. Cancer. 2009;115:1555–62.
149. Dixon JM, Rutgers E, Hunt KK. Intraoperative assessment of axillary lymph nodes in patients with breast cancer. BMJ. 2014;349:g6803.
150. Bernet L, Cano R, Martinez M, et al. Diagnosis of the sentinel lymph node in breast cancer: a reproducible molecular method: a multicentric Spanish study. Histopathology. 2011;58:863–9.
151. Castellano I, Macrì L, Deambrogio C, et al. Reliability of whole sentinel lymph node analysis by one-step nucleic acid amplification for intraoperative diagnosis of breast cancer metastases. Ann Surg. 2012;255:334–42.
152. Goldhirsch A, Wood WC, Coates AS, et al. Strategies for subtypes – dealing with the diversity of breast cancer: highlights of the St. Gallen International Expert Consensus on the Primary Therapy of Early Breast Cancer. Ann Oncol. 2011;22:1736–47.
153. Shimazu K, Noguchi S. Clinical significance of breast cancer micrometastasis in the sentinel lymph node. Surg Today. 2016;46:155–60.
154. Morita ET, Chang J, Leong SP. Principles and controversies in lymphoscintigraphy with emphasis on breast cancer. Surg Clin North Am. 2000;80:1721–39.
155. Giuliano AE, Jones RC, Brennan M, Statman R. Sentinel lymphadenectomy in breast cancer. J Clin Oncol. 1997;15:2345–50.
156. Krag D, Weaver D, Ashikaga T, et al. The sentinel node in breast cancer – a multi-center validation study. N Engl J Med. 1998;339:941–6.
157. Tausch C, Konstantiniuk P, Kugler F, Austrian Sentinel Node Study Group, et al. Sentinel lymph node biopsy after preoperative chemotherapy for breast cancer: findings from the Austrian Sentinel Node Study Group. Ann Surg Oncol. 2008;15:3378–83.
158. Zervoudis S, Iatrakis G, Tomara E, et al. Main controversies in breast cancer. World J Clin Oncol. 2014;5:359–73.
159. Assi H, Sbaity E, Abdelsalam M, Shamseddine A. Controversial indications for sentinel lymph node biopsy in breast cancer patients. Biomed Res Int. 2015;2015:405949.
160. Manca G, Rubello D, Tardelli E, et al. Sentinel lymph node biopsy in breast cancer: indications, contraindications, and controversies. Clin Nucl Med. 2016;41:126–33.
161. Meretoja TJ, Leidenius MH, Heikkilä PS, Joensuu H. Sentinel node biopsy in breast cancer patients

with large or multifocal tumors. Ann Surg Oncol. 2009;16:1148–55.
162. Zavagno G, Rubello D, Franchini Z, et al. Axillary sentinel lymph nodes in breast cancer: a single lymphatic pathway drains the entire mammary gland. Eur J Surg Oncol. 2005;31:479–84.
163. Goyal A, Newcombe RG, Mansel RE, et al. Sentinel lymph node biopsy in patients with multifocal breast cancer. Eur J Surg Oncol. 2004;30:475–9.
164. Gentilini O, Trifirò G, Soteldo J, et al. Sentinel lymph node biopsy in multicentric breast cancer. The experience of the European Institute of Oncology. Eur J Surg Oncol. 2006;32:507–10.
165. Spillane AJ, Brennan ME. Accuracy of sentinel lymph node biopsy in large and multifocal/multicentric breast carcinoma – a systematic review. Eur J Surg Oncol. 2011;37:371–85.
166. Giard S, Chauvet MP, Penel N, et al. Feasibility of sentinel lymph node biopsy in multiple unilateral synchronous breast cancer: results of a French prospective multi-institutional study (IGASSU 0502). Ann Oncol. 2010;21:1630–5.
167. Francis AM, Haugen CE, Grimes LM, et al. Is sentinel lymph node dissection warranted for patients with a diagnosis of ductal carcinoma in situ? Ann Surg Oncol. 2015;22:4270–9.
168. Bruening W, Fontanarosa J, Tipton K, et al. Systematic review: comparative effectiveness of core-needle and open surgical biopsy to diagnose breast lesions. Ann Intern Med. 2010;152:238–46.
169. Brennan ME, Turner RM, Ciatto S, et al. Ductal carcinoma in situ at core-needle biopsy: meta-analysis of underestimation and predictors of invasive breast cancer. Radiology. 2011;260:119–28.
170. Intra M, Rotmensz N, Veronesi P, et al. Sentinel node biopsy is not a standard procedure in ductal carcinoma in situ of the breast: the experience of the European Institute of Oncology on 854 patients in 10 years. Ann Surg. 2008;247:315–9.
171. Virnig BA, Tuttle TM, Shamliyan T, Kane RL. Ductal carcinoma in situ of the breast: a systematic review of incidence, treatment, and outcomes. J Natl Cancer Inst. 2010;102:170–8.
172. Kotani H, Yoshimura A, Adachi Y, et al. Sentinel lymph node biopsy is not necessary in patients diagnosed with ductal carcinoma in situ of the breast by stereotactic vacuum-assisted biopsy. Breast Cancer. 2016;23:190–4.
173. Taback B, Nguyen P, Hansen N, et al. Sentinel lymph node biopsy for local recurrence of breast cancer after breast-conserving therapy. Ann Surg Oncol. 2006;13:1099–104.
174. Tunon-de-Lara C, Chauvet MP, Baranzelli MC, et al. The role of sentinel lymph node biopsy and factors associated with invasion in extensive DCIS of the breast treated by mastectomy: The Cinnamome prospective multicenter study. Ann Surg Oncol. 2015;22:3853–60.
175. Schneider C, Trocha S, McKinley B, et al. The use of sentinel lymph node biopsy in ductal carcinoma in situ. Am Surg. 2010;76:943–6.
176. Specht MC, Fey JV, Borgen PI, Cody 3rd HS. Is the clinically positive axilla in breast cancer really a contraindication to sentinel lymph node biopsy? J Am Coll Surg. 2005;200:10–4.
177. Usmani S, Ahmed N, Saleh NA, et al. The clinical utility of combining pre-operative axillary ultrasonography and fine needle aspiration cytology with radionuclide guided sentinel lymph node biopsy in breast cancer patients with palpable axillary lymph nodes. Eur J Radiol. 2015;84:2515–20.
178. Kim H, Shin MJ, Kim SJ, et al. The relation of visualization of internal mammary lymph nodes on lymphoscintigraphy to axillary lymph node metastases in breast cancer. Lymphat Res Biol. 2014;12:295–300.
179. Veronesi U, Valagussa P. Inefficacy of internal mammary nodes dissection in breast cancer surgery. Cancer. 1981;47:170–5.
180. Meier P, Ferguson DJ, Karrison T. A controlled trial of extended radical mastectomy. Cancer. 1985;55:880–91.
181. Lacour J, Le MG, Hill C, et al. Is it useful to remove internal mammary nodes in operable breast cancer? Eur J Surg Oncol. 1987;13:309–14.
182. Meier P, Ferguson DJ, Karrison T. A controlled trial of extended radical versus radical mastectomy. Ten-year results. Cancer. 1989;63:188–95.
183. Morimoto T, Monden Y, Takashima S, et al. Five-year results of a randomized clinical trial comparing modified radical mastectomy and extended radical mastectomy for stage II breast cancer. Surg Today. 1994;24:210–4.
184. Veronesi U, Marubini E, Mariani L, et al. The dissection of internal mammary nodes does not improve the survival of breast cancer patients. 30-year results of a randomised trial. Eur J Cancer. 1999;35:1320–5.
185. Madsen EV, Aalders KC, van der Heiden-van der Loo M, et al. Prognostic significance of tumor-positive internal mammary sentinel lymph nodes in breast cancer: a multicenter cohort study. Ann Surg Oncol. 2015;22:4254–62.
186. McGale P, Taylor C, Correa C, et al. Effect of radiotherapy after mastectomy and axillary surgery on 10-year recurrence and 20-year breast cancer mortality: meta-analysis of individual patient data for 8135 women in 22 randomised trials. Lancet. 2014;383:2127–35.
187. Hennequin C, Fourquet A. Controversy about internal mammary chain irradiation in breast cancer. Cancer Radiother. 2014;18:351–5.
188. Poortmans PM, Collette S, Kirkove C, et al. Internal mammary and medial supraclavicular irradiation in breast cancer. N Engl J Med. 2015;373:317–27.
189. Estourgie SH, Tanis PJ, Nieweg OE, et al. Should the hunt for internal mammary chain sentinel nodes begin? An evaluation of 150 breast cancer patients. Ann Surg Oncol. 2003;10:935–41.

190. Paredes P, Vidal-Sicart S, Zanón G, et al. Clinical relevance of sentinel lymph nodes in the internal mammary chain in breast cancer patients. Eur J Nucl Med Mol Imaging. 2005;32:1283–7.
191. Bourre JC, Payan R, Collomb D, et al. Can the sentinel lymph node technique affect decisions to offer internal mammary chain irradiation? Eur J Nucl Med Mol Imaging. 2009;36:758–64.
192. Manca G, Volterrani D, Mazzarri S, et al. Sentinel lymph node mapping in breast cancer: a critical reappraisal of the internal mammary chain issue. Q J Nucl Med Mol Imaging. 2014;58:114–26.
193. Singletary SE, Allred C, Ashley P, et al. Revision of the American Joint Committee on Cancer staging system for breast cancer. J Clin Oncol. 2002;20: 3628–36.
194. Edge SB, Compton CC. The American Joint Committee on Cancer: the 7th edition of the AJCC cancer staging manual and the future of TNM. Ann Surg Oncol. 2010;17:1471–4.
195. Noushi F, Spillane AJ, Uren RF, Gebski V. Internal mammary node metastasis in breast cancer: predictive models to determine status and management algorithms. Eur J Surg Oncol. 2010;36:16–22.
196. Leidenius MH, Krogerus LA, Toivonen TS, et al. The clinical value of parasternal sentinel node biopsy in breast cancer. Ann Surg Oncol. 2006;13:321–6.
197. Ozmen V, Ozcinar B, Bozdogan A, et al. The effect of internal mammary lymph node biopsy on the therapeutic decision and survival of patients with breast cancer. Eur J Surg Oncol. 2015;41:1368–72.
198. Bergkvist L, Frisell J, Liljegren G, et al. Multicentre study of detection and false-negative rates in sentinel node biopsy for breast cancer. Br J Surg. 2001;88:1644–8.
199. Intra M, Trifirò G, Viale G, et al. Second biopsy of axillary sentinel lymph node for reappearing breast cancer after previous sentinel lymph node biopsy. Ann Surg Oncol. 2005;12:895–9.
200. Newman EA, Cimmino VM, Sabel MS, et al. Lymphatic mapping and sentinel lymph node biopsy for patients with local recurrence after breast-conservation therapy. Ann Surg Oncol. 2006;13:52–7.
201. Port ER, Garcia-Etienne CA, Park J, et al. Reoperative sentinel lymph node biopsy: a new frontier in the management of ipsilateral breast tumor recurrence. Ann Surg Oncol. 2007;14:2209–14.
202. Tasevski R, Gogos AJ, Mann GB. Reoperative sentinel lymph node biopsy in ipsilateral breast cancer relapse. Breast. 2009;18:322–6.
203. Kaur P, Kiluk JV, Meade T, et al. Sentinel lymph node biopsy in patients with previous ipsilateral complete axillary lymph node dissection. Ann Surg Oncol. 2011;18:727–32.
204. Luini A, Galimberti V, Gatti G, et al. The sentinel node biopsy after previous breast surgery; preliminary results on 543 patients treated at EIO. Breast Cancer Res Treat. 2005;89:159–63.
205. Leidenius MH, Vironen JH, von Smitten KA, Heikkilä PS, Joensuu HJ. The outcome of sentinel node biopsy in breast cancer patients with preoperative surgical biopsy. Surg Oncol. 2009;99:420–3.
206. Heuts EM, van der Ent FW, Kengen RA, et al. Results of sentinel node biopsy not affected by previous excisional biopsy. Eur J Surg Oncol. 2006;32:278–81.
207. Rodriguez Fernandez J, Martella S, Trifirò G, et al. Sentinel node biopsy in patients with previous breast aesthetic surgery. Ann Surg Oncol. 2009;16:989–92.
208. Kothari MS, Rusby JE, Agusti AA, MacNeill FA. Sentinel lymph node biopsy after previous axillary surgery: a review. Eur J Surg Oncol. 2012;38:8–15.
209. Rescigno J, Zampell JC, Axelrod D. Patterns of axillary surgical care for breast cancer in the era of sentinel lymph node biopsy. Ann Surg Oncol. 2009;16: 687–96.
210. Goldhirsch A, Glick JH, Gelber RD, Senn HJ. Meeting highlights: international consensus panel on the treatment of primary breast cancer. J Natl Cancer Inst. 1998;90:1601–8.
211. Abrams JS. Adjuvant therapy for breast cancer – results from the USA consensus conference. Breast Cancer. 2001;8:298–304.
212. Fu Y, Chung D, Cao MA, Apple S, Chang H. Is axillary lymph node dissection necessary after sentinel lymph node biopsy in patients with mastectomy and pathological N1 breast cancer? Ann Surg Oncol. 2014;21:4109–23.
213. van de Vijver MJ, He YD, van't Veer LJ, et al. A gene-expression signature as a predictor of survival in breast cancer. N Engl J Med. 2002;347:1999–2009.
214. Paik S, Tang G, Shak S, et al. Gene expression and benefit of chemotherapy in women with node-negative, estrogen receptor-positive breast cancer. J Clin Oncol. 2006;24:3726–34.
215. Albain KS, Barlow WE, Shak S, et al. Prognostic and predictive value of the 21-gene recurrence score assay in postmenopausal women with node-positive, oestrogen-receptor-positive breast cancer on chemotherapy: a retrospective analysis of a randomised trial. Lancet Oncol. 2010;11:55–65.
216. Donker M, van Tienhoven G, Straver ME, et al. Radiotherapy or surgery of the axilla after a positive sentinel node in breast cancer (EORTC 10981–22023 AMAROS): a randomised, multicentre, open-label, phase 3 non-inferiority trial. Lancet Oncol. 2014;15: 1303–10.
217. Li CZ, Zhang P, Li RW, et al. Axillary lymph node dissection versus sentinel lymph node biopsy alone for early breast cancer with sentinel node metastasis: a meta-analysis. Eur J Surg Oncol. 2015;41:958–66.
218. Marrazzo A, Boscaino G, Marrazzo E, et al. Breast cancer subtypes can be determinant in the decision making process to avoid surgical axillary staging: a retrospective cohort study. Int J Surg. 2015;21:156–61.
219. van Roozendaal LM, de Wilt JH, van Dalen T, et al. The value of completion axillary treatment in sentinel

node positive breast cancer patients undergoing a mastectomy: a Dutch randomized controlled multicentre trial (BOOG 2013-07). BMC Cancer. 2015; 15:610.
220. Khatcheressian JL, Hurley P, Bantug E, et al. Breast cancer follow-up and management after primary treatment: American Society of Clinical Oncology clinical practice guideline update. J Clin Oncol. 2013;31: 961–5.
221. García-Fernández A, Chabrera C, García-Font M, et al. Breast cancer patients undergoing sentinel node biopsy: additional axillary tumor burden as a function of the total number of excised sentinel nodes – a multicenter study. Clin Breast Cancer. 2015;15:490–7.
222. van la Parra RF, de Wilt JH, Mol SJ, et al. Is SLN biopsy alone safe in SLN positive breast cancer patients? Breast J. 2015;21:621–6.
223. Kaufmann M, von Minckwitz G, Mamounas EP, et al. Recommendations from an international consensus conference on the current status and future of neoadjuvant systemic therapy in primary breast cancer. Ann Surg Oncol. 2012;19:1508–16.
224. Manguso N, Gangi A, Giuliano AE. Neoadjuvant chemotherapy and surgical management of the axilla in breast cancer: a review of current data. Oncology (Williston Park). 2015;29:733–8.
225. Schwartz GF, Giuliano AE, Veronesi U, Consensus Conference Committee. Proceedings of the consensus conference on the role of sentinel lymph node biopsy in carcinoma of the breast. Breast. 2002;11:362–73.
226. Veronesi P, Gentilini O, Rodriguez-Fernandez J, Magnoni F. Breast conservation and sentinel lymph node after neoadjuvant systemic therapy. Breast. 2009;18:590–2.
227. Patten DK, Zacharioudakis KE, Chauhan H, et al. Sentinel lymph node biopsy after neo-adjuvant chemotherapy in patients with breast cancer: are the current false negative rates acceptable? Breast. 2015;24:318–20.
228. Schwartz GF, Meltzer AJ. Accuracy of sentinel node biopsy following neoadjuvant (induction) chemotherapy for carcinoma of the breast. Breast J. 2003;9:374–9.
229. Mamounas EP, Brown A, Anderson S, et al. Sentinel node biopsy after neoadjuvant chemotherapy in breast cancer: results from National Surgical Adjuvant Breast and Bowel Project Protocol B-27. J Clin Oncol. 2005;23:2694–702.
230. Tanaka Y, Maeda H, Ogawa Y, et al. Sentinel node biopsy in breast cancer patients treated with neoadjuvant chemotherapy. Oncol Rep. 2006;15:927–31.
231. Xing Y, Foy M, Cox DD, et al. Meta-analysis of sentinel lymph node biopsy after preoperative chemotherapy in patients with breast cancer. Br J Surg. 2006;93:539–46.
232. Kelly AM, Dwamena B, Cronin P, Carlos RC. Breast cancer sentinel node identification and classification after neoadjuvant chemotherapy – systematic review and metaanalysis. Acad Radiol. 2009;16:551–63.
233. van Deurzen CH, Vriens BE, Tjan-Heijnen VC, et al. Accuracy of sentinel node biopsy after neoadjuvant chemotherapy in breast cancer patients: a systematic review. Eur J Cancer. 2009;45:3124–30.
234. Dixon JM, Cody 3rd HS. Role of sentinel node biopsy in patients having neoadjuvant chemotherapy. Eur J Surg Oncol. 2010;36:511–3.
235. Gilardi L, De Cicco C, Colleoni M, et al. Investigation of ^{18}F-FDG PET in the selection of patients with breast cancer as candidates for sentinel node biopsy after neoadjuvant therapy. Eur J Nucl Med Mol Imaging. 2010;37:1834–41.
236. Tan VK, Goh BK, Fook-Chong S, et al. The feasibility and accuracy of sentinel lymph node biopsy in clinically node-negative patients after neoadjuvant chemotherapy for breast cancer – a systematic review and meta-analysis. J Surg Oncol. 2011;104:97–103.
237. Reimer T, Hartmann S, Stachs A, Gerber B. Local treatment of the axilla in early breast cancer: concepts from the national surgical adjuvant breast and bowel project B-04 to the planned intergroup sentinel mamma trial. Breast Care (Basel). 2014;9:87–95.
238. Lyman GH. Appropriate role for sentinel node biopsy after neoadjuvant chemotherapy in patients with early-stage breast cancer. J Clin Oncol. 2015;33:232–4.
239. Rubio IT. Sentinel lymph node metastasis after neoadjuvant treatment in breast cancer: any size matters? World J Clin Oncol. 2015;6:202–6.
240. van der Heiden-van der Loo M, de Munck L, Sonke GS, et al. Population based study on sentinel node biopsy before or after neoadjuvant chemotherapy in clinically node negative breast cancer patients: identification rate and influence on axillary treatment. Eur J Cancer. 2015;51:915–21.
241. van Nijnatten TJ, Schipper RJ, Lobbes MB, et al. The diagnostic performance of sentinel lymph node biopsy in pathologically confirmed node positive breast cancer patients after neoadjuvant systemic therapy: a systematic review and meta-analysis. Eur J Surg Oncol. 2015;41:1278–87.
242. Thorat MA. Sentinel lymph node assessment in breast cancer patients receiving neo-adjuvant chemotherapy: to biopsy before or after? Int J Cancer. 2016; 138:267–70.
243. Mocellin S, Goldin E, Marchet A, Nitti D. Sentinel node biopsy performance after neoadjuvant chemotherapy in locally advanced breast cancer: a systematic review and meta-analysis. Int J Cancer. 2016;138: 472–80.
244. Pandit-Taskar N, Dauer LT, Montgomery L, et al. Organ and fetal absorbed dose estimates from ^{99m}Tc-sulfur colloid lymphoscintigraphy and sentinel node localization in breast cancer patients. J Nucl Med. 2006;47:1202–8.
245. Khera SY, Kiluk JV, Hasson DM, et al. Pregnancy-associated breast cancer patients can safely undergo lymphatic mapping. Breast J. 2008;14:250–4.

246. Gentilini O, Cremonesi M, Toesca A, et al. Sentinel lymph node biopsy in pregnant patients with breast cancer. Eur J Nucl Med Mol Imaging. 2010;37:78–83.
247. Gropper AB, Calvillo KZ, Dominici L, et al. Sentinel lymph node biopsy in pregnant women with breast cancer. Ann Surg Oncol. 2014;21:2506–11.
248. Filippakis GM, Zografos G. Contraindications of sentinel lymph node biopsy: are there any really? World J Surg Oncol. 2007;5:10.
249. Barthelmes L, Goyal A, Newcombe RG, et al. Adverse reactions to patent blue V dye – the NEW START and ALMANAC experience. Eur J Surg Oncol. 2010;36:399–403.
250. Bezu C, Coutant C, Salengro A, et al. Anaphylactic response to blue dye during sentinel lymph node biopsy. Surg Oncol. 2011;20:e55–9.
251. Rovera F, Chiappa C, Coglitore A, et al. Management of breast cancer during pregnancy. Int J Surg. 2013;11:S64–8.
252. Chan BK, Wiseberg-Firtell JA, Jois RH, Jensen K, Audisio RA. Localization techniques for guided surgical excision of non-palpable breast lesions. Cochrane Database Syst Rev. 2015;12:CD009206.
253. Tóth D, Varga Z, Sebő É, Török M, Kovács I. Predictive factors for positive margin and the surgical learning curve in non-palpable breast cancer after wire-guided localization – prospective study of 214 consecutive patients. Pathol Oncol Res. 2016;22:209–15.
254. Rahusen FD, Bremers AJ, Fabry HF, van Amerongen AH, Boom RP, Meijer S. Ultrasound-guided lumpectomy of nonpalpable breast cancer versus wire-guided resection: a randomized clinical trial. Ann Surg Oncol. 2002;9:994–8.
255. Bennett IC, Greenslade J, Chiam H. Intraoperative ultrasound-guided excision of nonpalpable breast lesions. World J Surg. 2005;29:369–74.
256. James TA, Harlow S, Sheehey-Jones J, et al. Intraoperative ultrasound versus mammographic needle localization for ductal carcinoma in situ. Ann Surg Oncol. 2009;16:1164–9.
257. Krekel NM, Zonderhuis BM, Schreurs HW, et al. Ultrasound-guided breast-sparing surgery to improve cosmetic outcomes and quality of life. A prospective multicentre randomised controlled clinical trial comparing ultrasound-guided surgery to traditional palpation-guided surgery (COBALT trial). BMC Surg. 2011;11:8.
258. Ahmed D, Douek M. Intra-operative ultrasound versus wire-guided localization in the surgical management of non-palpable breast cancers: systematic review and meta-analysis. Breast Cancer Res Treat. 2013;140:435–46.
259. Yu CC, Chiang KC, Kuo WL, et al. Low re-excision rate for positive margins in patients treated with ultrasound-guided breast-conserving surgery. Breast. 2013;22:698–702.
260. De Cicco C, Pizzamiglio M, Trifirò G, et al. Radioguided occult lesion localisation (ROLL) and surgical biopsy in breast cancer. Technical aspects. Q J Nucl Med. 2002;46:145–51.
261. Paganelli G, Luini A, Veronesi U. Radioguided occult lesion localization (ROLL) in breast cancer: maximizing efficacy, minimizing mutilation. Ann Oncol. 2002;13:1839–40.
262. Paganelli G, Veronesi U. Innovation in early breast cancer surgery: radio-guided occult lesion localization and sentinel node biopsy. Nucl Med Commun. 2002;23:625–7.
263. Landman J, Kulawansa S, McCarthy M, et al. Radioguided localisation of impalpable breast lesions using 99m-technetium macroaggregated albumin: lessons learnt during introduction of a new technique to guide preoperative localisation. J Med Radiat Sci. 2015;62:6–14.
264. Rovera F, Frattini F, Marelli M, et al. Radio-guided occult lesion localization versus wire-guided localization in non-palpable breast lesions. Int J Surg. 2008;1:S101–3.
265. van der Ploeg IM, Hobbelink M, van den Bosch MA, et al. 'Radioguided occult lesion localisation' (ROLL) for non-palpable breast lesions: a review of the relevant literature. Eur J Surg Oncol. 2008;34:1–5.
266. Sajid MS, Parampalli U, Haider Z, Bonomi R. Comparison of radioguided occult lesion localization (ROLL) and wire localization for non-palpable breast cancers: a meta-analysis. J Surg Oncol. 2012;105:852–8.
267. Ahmed M, Douek M. Sentinel node and occult lesion localization (SNOLL): a systematic review. Breast. 2013;22:1034–40.
268. Aydogan F, Velidedeoglu M, Kilic F, Yilmaz H. Radio-guided localization of clinically occult breast lesions: current modalities and future directions. Expert Rev Med Devices. 2014;11:53–63.
269. Monti S, Galimberti V, Trifirò G, et al. Occult breast lesion localization plus sentinel node biopsy (SNOLL): experience with 959 patients at the European Institute of Oncology. Ann Surg Oncol. 2007;14:2928–31.
270. Mariscal Martínez A, Solà M, de Tudela AP, et al. Radioguided localization of nonpalpable breast cancer lesions: randomized comparison with wire localization in patients undergoing conservative surgery and sentinel node biopsy. AJR Am J Roentgenol. 2009;193:1001–9.
271. Vernet-Tomas Mdel M, Ortega M, Vidal S, et al. Factors affecting surgical margins in nonpalpable breast tumors excised with the radioguided occult lesion localization approach. J Obstet Gynaecol Res. 2011;37:422–7.
272. Ahmed M, van Hemelrijck M, Douek M. Systematic review of radioguided versus wire-guided localization in the treatment of non-palpable breast cancers. Breast Cancer Res Treat. 2013;140:241–52.
273. Postma EL, Koffijberg H, Verkooijen HM, et al. Cost-effectiveness of radioguided occult lesion localization (ROLL) versus wire-guided localization (WGL) in breast conserving surgery for nonpalpable breast cancer: results from a randomized controlled multicenter trial. Ann Surg Oncol. 2013;20:2219–26.

274. Rampaul RS, Dudley NJ, Thompson JZ, et al. Radioisotope for occult lesion localisation (ROLL) of the breast does not require extra radiation protection procedures. Breast. 2003;12:150–2.
275. Duarte GM, dos Santos CC, Torresan RZ, et al. Radioguided surgery using intravenous ^{99m}Tc sestamibi associated with breast magnetic resonance imaging for guidance of breast cancer resection. Breast J. 2006;12:202–7.
276. De Cicco C, Trifirò G, Intra M, et al. Optimised nuclear medicine method for tumour marking and sentinel node detection in occult primary breast lesions. Eur J Nucl Med Mol Imaging. 2004;31:349–54.
277. Fraile M, Mariscal A, Lorenzo C, et al. Radio-guided occult lesion localization combined with sentinel node biopsy in women with breast cancer. Cir Esp. 2005;77:36–9.
278. Strnad P, Rob L, Halaska MG, et al. Radioguided occult lesion localisation in combination with detection of the sentinel lymph node in non-palpable breast cancer tumours. Eur J Gynaecol Oncol. 2006;27:236–8.
279. Intra M, De Cicco C, Gentilini O, et al. Radioguided localisation (ROLL) of non-palpable breast lesions and simultaneous sentinel lymph node biopsy (SNOLL): the experience of the European Institute of Oncology. Eur J Nucl Med Mol Imaging. 2007;34:957–8.
280. van Rijk MC, Tanis PJ, Nieweg OE, et al. Sentinel node biopsy and concomitant probe-guided tumor excision of nonpalpable breast cancer. Ann Surg Oncol. 2007;14:627–32.
281. Lavoué V, Nos C, Clough KB, et al. Simplified technique of radioguided occult lesion localization (ROLL) plus sentinel lymph node biopsy (SNOLL) in breast carcinoma. Ann Surg Oncol. 2008;15:2556–61.
282. Thind CR, Tan S, Desmond S, et al. SNOLL. Sentinel node and occult (impalpable) lesion localization in breast cancer. Clin Radiol. 2011;66:833–9.
283. Bordea C, Plesca M, Condrea I, et al. Occult breast lesion localization and concomitant sentinel lymph node biopsy in early breast cancer (SNOLL). Chirurgiae (Bucur). 2012;107:722–9.
284. Follacchio GA, Monteleone F, Anibaldi P, et al. A modified sentinel node and occult lesion localization (SNOLL) technique in non-palpable breast cancer: a pilot study. J Exp Clin Cancer Res. 2015;34:113.
285. Jakub JW, Gray RJ, Degnim AC, et al. Current status of radioactive seed for localization of non palpable breast lesions. Am J Surg. 2010;199:522–8.
286. Sung JS, King V, Thornton CM, et al. Safety and efficacy of radioactive seed localization with I-125 prior to lumpectomy and/or excisional biopsy. Eur J Radiol. 2013;82:1453–7.
287. Jackson L, Bourke AG, Abdul Aziz F, Taylor D. Radioactive seed localisation to guide removal of impalpable lymph nodes (radioguided occult lesion localisation using iodine-125 seeds, "ROLLIS"). BMJ Case Rep. 2014; pii: bcr-2013-203267. doi: 10.1136/bcr-2013-203267.
288. Parvez E, Cornacchi SD, Hodgson N, et al. A cosmesis outcome substudy in a prospective, randomized trial comparing radioguided seed localization with standard wire localization for nonpalpable, invasive, and in situ breast carcinomas. Am J Surg. 2014;208:711–8.
289. van der Noordaa ME, Pengel KE, Groen E, et al. The use of radioactive iodine-125 seed localization in patients with non-palpable breast cancer: a comparison with the radioguided occult lesion localization with 99m technetium. Eur J Surg Oncol. 2015;41:553–8.
290. Vermeeren L, Valdés Olmos RA, Klop WM, et al. A portable gamma-camera for intraoperative detection of sentinel nodes in the head and neck region. J Nucl Med. 2010;51:700–3.
291. Bricou A, Duval MA, Charon Y, Barranger E. Mobile gamma cameras in breast cancer care – a review. Eur J Surg Oncol. 2013;39:409–16.
292. Bluemel C, Cramer A, Grossmann C, et al. iROLL: does 3-D radioguided occult lesion localization improve surgical management in early-stage breast cancer? Eur J Nucl Med Mol Imaging. 2015;42:1692–9.
293. Engelen T, Winkel BM, Rietbergen DD, et al. The next evolution in radioguided surgery: breast cancer related sentinel node localization using a freehand SPECT-mobile gamma camera combination. Am J Nucl Med Mol Imaging. 2015;5:233–45.
294. Lombardi A, Nigri G, Scopinaro F, et al. High-resolution, handheld camera use for occult breast lesion localization plus sentinel node biopsy (SNOLL): a single-institution experience with 186 patients. Surgeon. 2015;13:69–72.
295. Taylor D, Landman J. 'Rolling out radioguided occult lesion localisation for breast tumours': moving from ROLL to ROLLIS. J Med Radiat Sci. 2015;62:175–6.
296. Bricou A, Duval MA, Bardet L, et al. Is there a role for a handheld gamma camera (TReCam) in the SNOLL breast cancer procedure? Q J Nucl Med Mol Imaging. 2015 Mar 31 [Epub ahead of print].
297. Bergqvist L, Strand SE, Persson B, et al. Dosimetry in lymphoscintigraphy of Tc-99m antimony sulfide colloid. J Nucl Med. 1982;23:698–705.
298. Cremonesi M, Ferrari M, Sacco E, et al. Radiation protection in radioguided surgery of breast cancer. Nucl Med Commun. 1999;20:919–24.
299. Waddington WA, Keshtgar MRS, Taylor I, et al. Radiation safety of the sentinel node technique in breast cancer. Eur J Nucl Med. 2000;27:377–91.
300. Law M, Cheng KC, Wu PM, et al. Patient effective dose from sentinel lymph node lymphoscintigraphy in breast cancer: a study using a female humanoid phantom and thermoluminescent dosimeters. Br J Radiol. 2003;76:818–23.

301. Law M, Chow LW, Kwong A, Lam CK. Sentinel lymph node technique for breast cancer: radiation safety issues. Semin Oncol. 2004;31:298–303.
302. Sata S, Knesaurek K, Krynyckyi BR. Effective dose in sentinel lymph node imaging. Br J Radiol. 2004;77:709. author reply 709.
303. Glass EC, Basinski JE, Krasne DL, Giuliano AE. Radiation safety considerations for sentinel node techniques. Ann Surg Oncol. 1999;6:10–1.
304. Miner TJ, Shriver CD, Flicek PR, et al. Guidelines for the safe use of radioactive materials during localization and resection of the sentinel lymph node. Ann Surg Oncol. 1999;6:75–82.
305. Stratmann SL, McCarty TM, Kuhn JA. Radiation safety with breast sentinel node biopsy. Am J Surg. 1999;178:454–7.
306. Morton R, Horton PW, Peet DJ, Kissin MW. Quantitative assessment of the radiation hazards and risks in sentinel node procedures. Br J Radiol. 2003;76:117–22.
307. de Kanter AY, Arends PP, Eggermont AM, Wiggers T. Radiation protection for the sentinel node procedure in breast cancer. Eur J Surg Oncol. 2003;29:396–9.
308. Klausen TL, Chakera AH, Friis E, et al. Radiation doses to staff involved in sentinel node operations for breast cancer. Clin Physiol Funct Imaging. 2005;25:196–202.
309. Nejc D, Wrzesień M, Piekarski J, et al. Sentinel node biopsy in patients with breast cancer – evaluation of exposure to radiation of medical staff. Eur J Surg Oncol. 2006;32:133–8.
310. Ckarke RH, Bines W. Evolution of ICRP recommendations 1977, 1990, 2007 – Publications 26 to 60 to 103. OECD NEA, No 6920, 2011. http://www.oecd-nea.org/rp/reports/2011/nea6920-ICRP-recommendations.pdf
311. Singleton M, Firth M, Stephenson T, et al. Radiation-guided breast sentinel lymph node biopsies – is a handling delay for radiation protection necessary? Histopathology. 2012;61:277–82.
312. Gentilini O, Cremonesi M, Trifirò G, et al. Safety of sentinel node biopsy in pregnant patients with breast cancer. Ann Oncol. 2004;15:1348–51.
313. Keleher A, Wendt 3rd R, Delpassand E, et al. The safety of lymphatic mapping in pregnant breast cancer patients using Tc-99m sulfur colloid. Breast J. 2004;10:492–5.
314. Spanheimer PM, Graham MM, Sugg SL, et al. Measurement of uterine radiation exposure from lymphoscintigraphy indicates safety of sentinel lymph node biopsy during pregnancy. Ann Surg Oncol. 2009;16:1143–7.
315. Law M, Ma WH, Leung R, et al. Evaluation of patient effective dose from sentinel lymph node lymphoscintigraphy in breast cancer: a phantom study with SPECT/CT and ICRP-103 recommendations. Eur J Radiol. 2012;81:717–20.
316. Winter A, Woenkhaus J, Wawroschek F. A novel method for intraoperative sentinel lymph node detection in prostate cancer patients using superparamagnetic iron oxide nanoparticles and a handheld magnetometer: the initial clinical experience. Ann Surg Oncol. 2014;21:4390–6.
317. Rubio IT, Diaz-Botero S, Esgueva A, et al. The superparamagnetic iron oxide is equivalent to the Tc99 radiotracer method for identifying the sentinel lymph node in breast cancer. Eur J Surg Oncol. 2015;41:46–51.
318. Pitsinis V, Provenzano E, Kaklamanis L, et al. Indocyanine green fluorescence mapping for sentinel lymph node biopsy in early breast cancer. Surg Oncol. 2015;24:375–9.
319. Koslow Mautner S, Cody 3rd HS. Sentinel node biopsy after neoadjuvant chemotherapy for node-positive breast cancer: does axillary ultrasound improve performance? J Clin Oncol. 2015;33:3375–8.
320. Toh U, Iwakuma N, Mishima M, et al. Navigation surgery for intraoperative sentinel lymph node detection using indocyanine green (ICG) fluorescence real-time imaging in breast cancer. Breast Cancer Res Treat. 2015;153:337–44.
321. Tian P, Zhang W, Zhao H, et al. Intraoperative detection of sentinel lymph node metastases in breast carcinoma by Fourier transform infrared spectroscopy. Br J Surg. 2015;102:1372–9.
322. Stoffels I, Dissemond J, Pöppel T, et al. Intraoperative fluorescence imaging for sentinel lymph node detection: prospective clinical trial to compare the usefulness of indocyanine green vs Technetium Tc 99m for identification of sentinel lymph nodes. JAMA Surg. 2015;150:617–23.
323. Piñero-Madrona A, Torró-Richart J, de León-Carrillo J, et al. Superparamagnetic iron oxide as a tracer for sentinel node biopsy in breast cancer: a comparative non-inferiority study. Eur J Surg Oncol. 2015;41:991–7.
324. Kuijs VJ, Moossdorff M, Schipper RJ, et al. The role of MRI in axillary lymph node imaging in breast cancer patients: a systematic review. Insights Imaging. 2015;6:203–15.
325. Tsuyuki S, Yamaguchi A, Kawata Y, Kawaguchi K. Assessing the effects of neoadjuvant chemotherapy on lymphatic pathways to sentinel lymph nodes in cases of breast cancer: usefulness of the indocyanine green-fluorescence method. Breast. 2015;24:298–301.
326. Kida K, Ishikawa T, Yamada A, et al. A prospective feasibility study of sentinel node biopsy by modified indigo carmine blue dye methods after neoadjuvant chemotherapy for breast cancer. Eur J Surg Oncol. 2015;41:566–70.
327. Samorani D, Fogacci T, Panzini I, et al. The use of indocyanine green to detect sentinel nodes in breast cancer: a prospective study. Eur J Surg Oncol. 2015;41:64–70.

328. Caudle AS, Yang WT, Mittendorf EA, et al. Selective surgical localization of axillary lymph nodes containing metastases in patients with breast cancer: a prospective feasibility trial. JAMA Surg. 2015;150: 137–43.
329. Inoue T, Nishi T, Nakano Y, et al. Axillary lymph node recurrence after sentinel lymph node biopsy performed using a combination of indocyanine green fluorescence and the blue dye method in early breast cancer. Breast Cancer. 2016;23:295–300.
330. Nakagawa M, Morimoto M, Takechi H, et al. Preoperative diagnosis of sentinel lymph node (SLN) metastasis using 3D CT lymphography (CTLG). Breast Cancer. 2016;23:519–24.
331. Sugie T, Kinoshita T, Masuda N, et al. Evaluation of the clinical utility of the ICG fluorescence method compared with the radioisotope method for sentinel lymph node biopsy in breast cancer. Ann Surg Oncol. 2016;23:44–50.
332. Benson J. Indocyanine green fluorescence for sentinel lymph node detection in early breast cancer. Ann Surg Oncol. 2016;23:6–8.
333. Pouw JJ, Grootendorst MR, Bezooijen R, et al. Preoperative sentinel lymph node localization in breast cancer with superparamagnetic iron oxide MRI: the SentiMAG multicentre trial imaging subprotocol. Br J Radiol. 2015;88:20150634.
334. Li C, Meng S, Yang X, et al. Sentinel lymph node detection using magnetic resonance lymphography with conventional gadolinium contrast agent in breast cancer: a preliminary clinical study. BMC Cancer. 2015;15:213.
335. Ahmed M, Anninga B, Goyal S, et al. Magnetic sentinel node and occult lesion localization in breast cancer (MagSNOLL Trial). Br J Surg. 2015;102:646–52.
336. Ghilli M, Carretta E, Di Filippo F, et al. The superparamagnetic iron oxide tracer: a valid alternative in sentinel node biopsy for breast cancer treatment. Eur J Cancer Care (Engl). 2015 Sep 14 [Epub ahead of print].
337. Motomura K, Izumi T, Tateishi S, et al. Superparamagnetic iron oxide-enhanced MRI at 3 T for accurate axillary staging in breast cancer. Br J Surg. 2015;17 [Epub ahead of print].
338. Dellaportas D, Koureas A, Contis J, et al. Contrast-enhanced color Doppler ultrasonography for preoperative evaluation of sentinel lymph node in breast cancer patients. Breast Care (Basel). 2015;10:331–5.
339. Rautiainen S, Sudah M, Joukainen S, et al. Contrast-enhanced ultrasound-guided axillary lymph node core biopsy: diagnostic accuracy in preoperative staging of invasive breast cancer. Eur J Radiol. 2015;84:2130–6.
340. Ahmed M, Purushotham AD, Douek M. Novel techniques for sentinel lymph node biopsy in breast cancer: a systematic review. Lancet Oncol. 2014;15:e351–62.
341. Chung A, Gangi A, Amersi F, et al. Not performing a sentinel node biopsy for older patients with early-stage invasive breast cancer. JAMA Surg. 2015;150:683–4.
342. Jacobson GM, Partin JF, Salkeni MA. Optimal management of sentinel lymph node positive biopsy patients in early breast cancer. Ann Transl Med. 2015;3:87.

Radioguided Surgery for Malignant Melanoma

48

Sergi Vidal-Sicart, Federica Orsini, Francesco Giammarile, Giuliano Mariani, and Renato A. Valdés Olmos

Abstract

Melanoma is one of the most aggressive and therapy-resistant cancers, and currently, its incidence is increasing worldwide. The metastatic involvement of lymph nodes is of utmost importance for prognosis in patients with intermediate-thickness melanoma. Other prognostic factors include tumor thickness, presence of ulceration, and mitotic rate.

Radioguided surgery has a prominent role in melanoma, because the sentinel lymph node approach is nowadays a choice procedure for regional lymphatic staging of these patients. Sentinel lymph node biopsy sensitivity is superior than that of PET/CT for the detection of lymphatic micrometastases in early stages of the disease.

The sentinel lymph node approach involves a preoperative lymphoscintigraphy and the use of a handheld gamma probe and vital dyes. Presurgical lymphoscintigraphy constitutes the "roadmap" for guiding surgeons toward draining lymph nodes potentially harboring metastasis and is extremely useful for localizing unpredictable drainage patterns that otherwise would be unnoticed. In recent years, new refinements have been added to this approach in order to improve clinical results. In particular, SPECT/CT imaging increases the sentinel lymph node identification rate and overcomes some of the limitations of planar imaging. New tracers are now available and new intraoperative devices can be added to the classical ones. In general, this radioguided approach is cost-effective, although there is a scarcity of data and the different factors involved in the whole procedure are not equally considered by different analyses that have so far been performed.

S. Vidal-Sicart (✉)
Nuclear Medicine Department, Hospital Clínic Barcelona, Barcelona, Catalonia, Spain

Institut d'Investigació Biomèdica August Pi i Sunyer (IDIBAPS), Barcelona, Spain
e-mail: svidal@clinic.ub.es

F. Orsini
Nuclear Medicine Unit, "Maggiore della Carità" University Hospital, Novara, Italy

F. Giammarile
Nuclear Medicine and Diagnostic Imaging Section, Division of Human Health, Department of Nuclear Sciences and Applications, International Atomic Energy Agency, Vienna, Austria
e-mail: F.Giammarile@iaea.org

G. Mariani
Regional Center of Nuclear Medicine, Department of Translational Research and Advanced Technologies in Medicine and Surgery, University of Pisa, Pisa, Italy

R.A. Valdés Olmos
Nuclear Medicine Section and Interventional Molecular Imaging Laboratory, Department of Radiology, Leiden University Medical Centre, Leiden, The Netherlands

Diagnostic Oncology Division, Nuclear Medicine Department, Netherlands Cancer Institute – Antoni van Leeuwenhoek Hospital, Amsterdam, CX, The Netherlands

© Springer International Publishing Switzerland 2017
H.W. Strauss et al. (eds.), *Nuclear Oncology*,
https://doi.org/10.1007/978-3-319-26236-9_53

Keywords

Melanoma • Sentinel node • Lymphoscintigraphy • Radiotracer • Blue dyes • Handheld gamma probe • Portable gamma camera • SPECT/CT • Fluorescence • Hybrid tracers • PET/CT

Glossary

[^{18}F]FDG	2-Deoxy-2-[^{18}F]fluoro-D-glucose
AJCC	American Joint Committee on Cancer
Bq	Becquerel unit
Breslow thickness	A prognostic factor in cutaneous melanoma, based on description of how deeply tumor cells have invaded the skin (also called "Breslow depth")
Clark level	A staging system for cutaneous melanoma based on description of the level of anatomic invasion of the melanoma in the skin (generally used in conjunction with Breslow's depth)
CT	X-ray computed tomography
eV	Electron volt
FDA	United States Food and Drug Administration
GOSTT	Guided intraoperative scintigraphic tumor targeting
HMB-45	Homatropine methylbromide 45, a monoclonal antibody that reacts against an antigen present in melanomas
ICG	Indocyanine green
keV	Kiloelectron volt (10^3 eV)
MART-1	Melanoma antigen recognized by T cells 1, also known as Melan A
MBq	Mega-Becquerel (10^6 Becquerel)
MRI	Magnetic resonance imaging
MSS	Melanoma-specific survival
NCCN	National Comprehensive Cancer Network
NIR	Near-infrared
PCR	Polymerase chain reaction
PET	Positron emission tomography
PET/CT	Positron emission tomography/computed tomography
ROLL	Radioguided occult lesion localization
S-100	A low-molecular-weight calcium-binding protein expressed in melanomas, but also in other benign and malignant conditions
SLN	Sentinel lymph node
SLNB	Sentinel lymph node biopsy
SPECT	Single-photon emission computed tomography
SPECT/CT	Single-photon emission computed tomography/computed tomography
US	Ultrasonography
UV	Ultraviolet

Contents

Introduction 1403

The Clinical Problem 1403

Lymphatics in Cutaneous Melanoma 1404

Indications and Advantages of SLN Biopsy in Melanoma 1405

Technical Issues 1407
Radiotracers 1407
Activity and Injection 1409
Presurgical Lymphoscintigraphy 1409
Additional SPECT/CT Imaging 1412

Surgery 1414

Sentinel Lymph Node Analysis and Its Importance for Clinical Decision 1415

Refinements for the Classical Technique 1417

Portable Gamma Cameras 1417

Freehand SPECT 1418

Fluorescent and Hybrid Tracers 1419

Particular Issues for SLN Mapping in Melanoma 1422
In-Transit, Aberrant, or Ectopic Lymph Nodes 1422
Head and Neck Location 1423

Cost-Effectiveness of SLN Biopsy in Melanoma 1424

Role of PET/CT Imaging for Radioguided Surgery 1426

References 1427

Introduction

Melanoma is one of the most aggressive and therapy-resistant cancers. Moreover, it currently is a global health problem because its incidence is increasing worldwide [1].

In recent years the melanoma incidence stands for 10–14 cases/100,000 inhabitants in Central Europe and 6–10/100,000 inhabitants in Southern Europe. In the USA the incidence has risen to 10–25/10,000 inhabitants, and Australia and New Zealand have the highest incidence with 60 cases/100,000 inhabitants [2].

According to the American Cancer Society, more than 76,000 new cases of melanoma are currently diagnosed in the USA each year, and about 9,500 people are expected to die of metastatic disease [3].

There are several risk factors related for the development of melanoma (history of sunburn, previous melanoma within the family, high UV exposure, and red or blonde hair), and the appearance of regional or distant metastases is an ominous prognostic factor for the disease [4, 5].

Thus, the prognosis for a patient depends on the stage of the disease. In the case of early melanomas (<0.76-mm Breslow thickness), surgical wide excision is sufficient and there is no need for further invasive staging. Accurate evaluation is important in cases of a more advanced primary tumor. In general, lymph node metastases often occur first, and for this reason, the regional nodal status is the most important prognostic factor and stratifies the patients for adjuvant therapy [6, 7].

The metastatic involvement of lymph nodes is of utmost importance for prognosis in patients with intermediate-thickness melanoma (AJCC stage I or II). Other prognostic factors include tumor thickness, presence of ulceration, and the recently added mitotic rate. The Clark level of invasion was omitted from the recent AJCC classification [5, 8–10].

The Clinical Problem

The clinical outcome for patients with intermediate-thickness melanoma relies on adequate surgical control of the primary melanoma site and on the accuracy of regional and systemic staging at diagnosis. It is well known that physical examination of lymph nodes is inaccurate in up to 40% of patients. Noninvasive diagnostic imaging procedures (CT, MRI, US) have been employed to rule out nodal involvement, but despite their use, their findings are not sufficiently accurate so as to avoid invasive techniques, also because small lymph node metastases cannot reliably be detected with any imaging modalities. Approximately 20% of patients with a melanoma with a Breslow thickness >1 mm may have clinically occult lymph node metastasis, therefore making histopathologic assessment of the regional lymph nodes mandatory [11].

The traditional surgical approach to cutaneous melanoma is based on elective, or prophylactic, regional lymph node dissection to reveal these occult metastases. Randomized studies, however, showed no clear survival advantages when performing regional lymphadenectomy, a surgical procedure frequently associated with morbidity, such as lymphedema, nerve injury, wound infection or dehiscence, etc. [12].

In 1992 Morton et al. reported the results of a seminal study carried out in 223 patients with melanoma to test the concept of intraoperative identification of the sentinel lymph node (SLN) using blue dye as a minimally invasive surgical alternative for nodal staging. By employing this approach to perform SLN biopsy, these authors were able to detect clinically occult nodal metastasis, thus identifying a subgroup of patients who could actually benefit from complete lymphadenectomy [13].

The procedure assumes orderly diffusion of melanoma metastasis through the lymphatic system, and the SLN is defined as the first node on a direct lymphatic drainage pathway from the primary tumor [6, 14]. According to this hypothesis, tumor involvement or lack of involvement of the SLN predicts the overall nodal status with a high accuracy [15].

Shortly thereafter, radionuclide-based techniques were introduced to perform lymphatic mapping, by injecting a suitable radiocolloid agent around the melanoma. Following such interstitial administration of the radiopharmaceutical, scintigraphy allows the identification of SLNs in the lymph node basin and this or these nodes is/are harvested during surgery with the aid of a handheld gamma probe during surgery. This approach, which constitutes the mainstay of radioguided SLN biopsy as it is currently employed, overcomes some drawbacks intrinsic in the dye approach. The feature that characterizes radioguided surgery is the use of a radiotracer to "mark" the desired tissues and the intraoperative utilization of a handheld gamma probe that facilitates the task of the surgeon, that is, identification and removal of the target tissue, either a lymph node or the tumor itself – as in other applications of radioguided surgery. Intraoperative exploration of the surgical field with the handheld probe is made possible by the preoperative techniques employed by the nuclear medicine physician to achieve accumulation of the radiopharmaceutical in the specific target lesion. This is the most common method utilized to perform a SLN biopsy, because radiocolloid alone has been shown to be very safe and to have a low false-negative rate [16, 17]. Currently, this approach is widely validated and has been adapted to additional applications for SLN biopsy in other types of cancers, such as breast, urologic, gynecologic, and head and neck cancers [18–21].

Radiotracers allow scintigraphic visualization with gamma camera of the physiology of lymphatic drainage, thereby changing the paradigm of "open and see" (blue dyes) to "see (scintigraphy) to open." In fact, preoperative lymphoscintigraphy constitutes the "roadmap" for guiding surgeons toward subsidiary lymph node sites of potential metastasis and is extremely useful for localizing unpredictable drainage patterns that otherwise would be unnoticed. The value of lymphoscintigraphy lies in different factors, as summarized in Table 1.

Table 1 Lymphoscintigraphy features for lymphatic mapping

Identification of the radioactive lymph nodes (although not all radioactive lymph nodes are SLNs nor the SLN is necessarily the most radioactive lymph node)
Identification of the lymphatic drainage basin(s) from the tumor site
Identification of the SLN and of second-tier lymph nodes
Identification of the aberrant or in-transit SLNs (lymph nodes localized outside the common drainage areas and those between the primary tumor and the region of lymph node drainage, respectively)
Confirmation of true radiotracer uptake versus false-positive uptake (originated from cutaneous folds, lymphatic dilatations, and lymphangiomas)

Nuclear medicine techniques and radioguided surgery are continuously evolving with the implementation of technological imaging advances. Even after 20 years of use, this technique of SLN biopsy may, sometimes, be challenging, especially in patients with high body mass index or in complex anatomical areas (e.g., the abdomen or head and neck). With the aim of finding more efficient methods to improve the preoperative and intraoperative images, hybrid fluorescent–radioactive tracers or more specific tracers, which enable high-quality preoperative lymphoscintigraphy and SPECT/CT imaging, have been developed. Moreover, intraoperative portable imaging technologies, such as freehand SPECT and small portable gamma cameras, have been introduced into the armamentarium available for improving intraoperative SLN identification procedure [22].

Lymphatics in Cutaneous Melanoma

The lymphatic system presents a high density of vessels in the dermis, especially in the layers between 50 and 200 μm below the epidermis. This density varies in different regions of the body, the highest vessel density being observed

in the head and neck area and the lowest in the limbs.

Moreover, the velocity of lymphatic flow is not the same in all regions of the body and varies depending on the area of the skin. Thus, the average lymph flow velocity in the head and neck region is 1.5 cm/min, it increases in the posterior trunk to 3.9 cm/min, and even higher in the forearm and hand (5.5 cm/min). The highest velocity of lymph flow is seen from the lower limb (10.2 cm/min) [23].

On the other hand, the lymphatic drainage from the primary tumor is quite predictable when this tumor is located in the extremities. So, a melanoma located in the lower limb drains usually to the ipsilateral groin, while from the upper limb, it drains to the homolateral axilla. Computer analysis from a large lymphoscintigraphic database provided new important insights into the skin lymphatic drainage. In particular, it was demonstrated that lymphatic drainage of the skin is likely to be entirely symmetric. There are well-defined areas of the skin that nearly always drain to the ipsilateral axilla, groin, cervical level II, and preauricular node fields [24].

However, the drainage patterns from lesions in the head and neck area or in the trunk are less predictable. The concepts developed by Sappey in the nineteenth century about skin lymphatic drainage went largely unaltered until the last quarter of twentieth century, when new information became available from lymphatic mapping studies using lymphoscintigraphy. In fact, the more recent lymphoscintigraphic findings have modified the concept of Sappey, that is, that lymphatic watersheds with ambiguous skin drainage are limited to a narrowband about 2.5 cm on either side of the midline of the trunk (for right–left drainage) and/or the line between the umbilicus and the level of the second lumbar vertebra on the back (for cranial or caudal drainage, respectively) [25, 26].

Instead, the width of the area of ambiguous drainage has been extended to more than 20 cm instead of the original 5 cm (Fig. 1), because lymphatic drainage is highly variable among different patients and Sappey's concepts would predict drainage to the wrong node basin in 30% of patients [27, 28].

Indications and Advantages of SLN Biopsy in Melanoma

SLN biopsy is a minimally invasive procedure, which should be indicated or considered for patients with the following characteristics:

- A risk of presenting occult metastasis >10%, which justifies the procedure.
- The tumoral status of the SLN is useful for decision-making.
- The prognostic information provided by the SLN biopsy is valuable for the patient and the physician (even for a decision to include patients in clinical trials).

The indication for SLN biopsy in melanoma should be offered and discussed to all patients with melanomas ≥1.0 mm in thickness, clinically negative regional lymph nodes on physical examination, fulfilling the abovementioned criteria and in whom the morbidity and risk are considered to be acceptable. However, SLN biopsy can also be offered to patients with melanomas ≤1.0 mm with some characteristics which increase the possibility of micrometastasis in the regional node basin (the presence of ulceration, mitotic index ≥1/mm^2, and/or Clark IV/V invasion, especially in tumors >0.75 mm in thickness) [29].

Analysis of the AJCC database demonstrated an inverse correlation between the mitotic index and survival. Then, the greater the mitotic value, the shorter the survival. In patients with melanomas from 0.5 to 1.0 mm in thickness and with <1 mitosis/mm^2, the 10-year survival was 93%. In the same group, this figure decreased to 87% when >1 mitosis/mm^2 was present [30].

On the other hand, SLN biopsy may be considered in patients with melanocytic lesions with unknown metastatic potential. The NCCN guidelines are similar in regard to melanomas with a thickness >1 mm. However, the presence of ≥1 mitosis/mm^2, which upstages IA to IB tumors, is not taken into account for indicating SLN biopsy in melanomas <1 mm in thickness. SLN biopsy is not recommended in lesions with a thickness

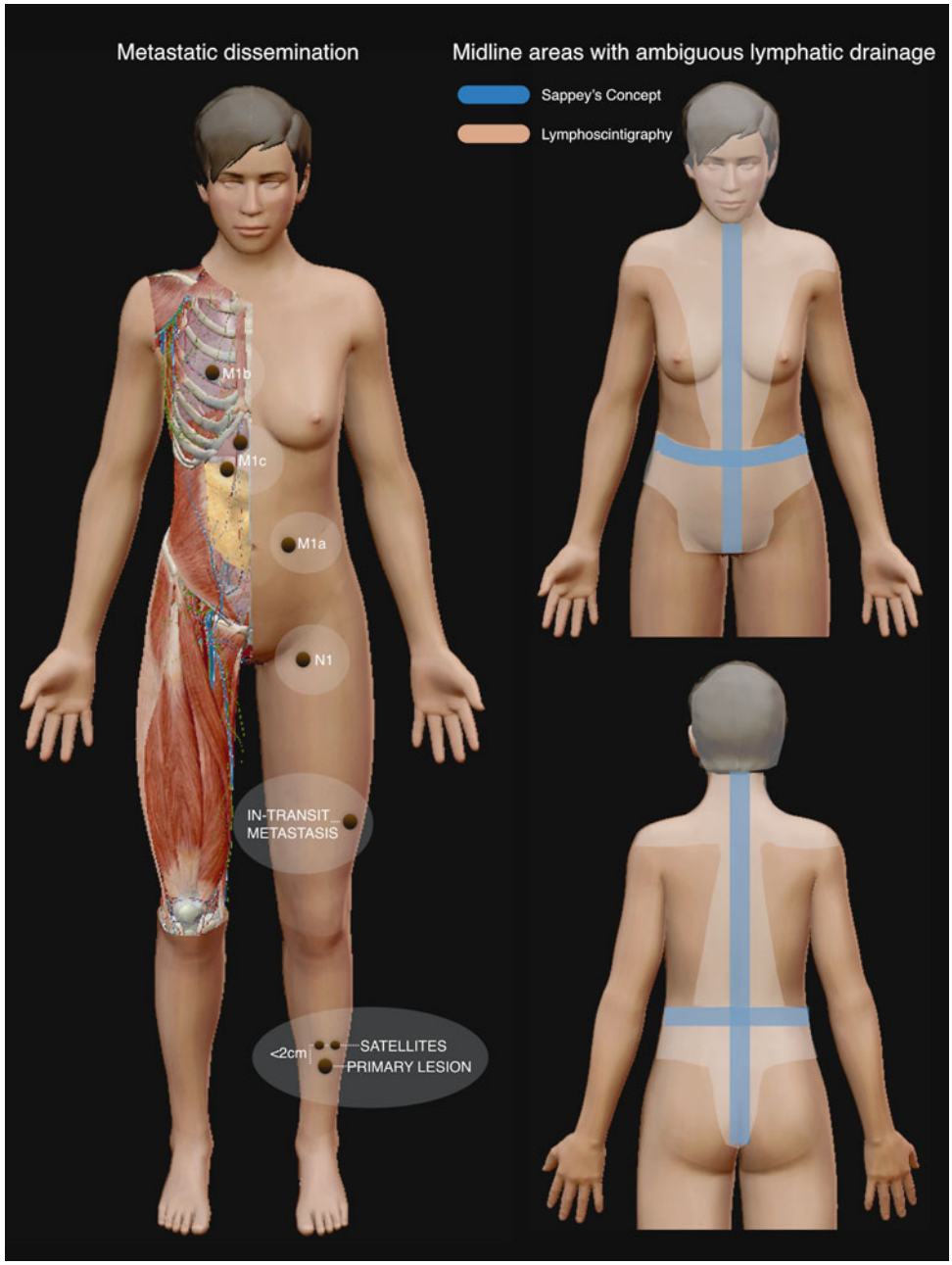

Fig. 1 On the *left*, metastatic dissemination in melanoma: *N1*, metastasis in draining lymph node basin; *M1a*, distant skin, subcutaneous, or nodal metastases; *M1b*, lung metastases; *M1c*, all other visceral metastases. On the *right*, midline areas with ambiguous lymphatic drainage according to the classical skin watershed Sappey's concept (*blue*) and its extension according to lymphoscintigraphy (slightly *brown*)

<0.75 mm, while in tumors between 0.76 and 1 mm thick, the option to perform or not SLN biopsy should be discussed with the patient, since the proportion of metastasis is low in these patients (<6%) and its clinical impact is modest [31, 32].

Although no direct therapeutic advantage has been demonstrated for the SLN approach, the final

report of the MSLT-I trial, which compared long-term outcome of SLN biopsy-positive patients with that of patients who developed regional lymphatic metastases in the observation group, showed a significant benefit in the arm of SLN biopsy with a 10-year melanoma-specific survival (MSS) advantage of 20.6%. Thus, it was concluded that SLN biopsy-based management prolongs MSS for patients with nodal metastases in the intermediate-thickness melanoma group. In addition, the information provided by the SLN may be useful for advising patients about inclusion in clinical studies.

Thus, SLN biopsy-based staging of intermediate-thickness or even thick primary melanomas provides important prognostic information and identifies patients with nodal metastases who may benefit from immediate complete lymphadenectomy [33–35].

However, some criticism has been raised about this statement. According to van Akkooi, if both groups are equally compared, the MSS difference is minimal between groups (81.4% against 78.3%, respectively). There are some reasons to be considered in the critical analysis of these data (the false-negative rate, difference in nodal positivity between groups, and tumor load of metastasis, as well as an adequate statistical analysis). Moreover, the center that treated patients should be included as a potential confounding factor, because the results may differ significantly due to the diverse experience of each multidisciplinary medical team [36].

Finally, there is a certain time delay between melanoma excision and wide local excision for adequate margins and SLN biopsy. This delay is due to several factors, including surgical scheduling, preoperative evaluation, need for further diagnostic tests, etc. The influence of this delay over the prognosis of the patient is not clear. Parrett et al. studied the time effect to perform SLN biopsy on node metastatic invasion, recurrence, and mortality. The study showed no significant differences in survival if SLN biopsy was performed within 40 days or beyond 40 days after excision of the primary tumor [37].

Tejera-Vaquerizo et al. reported surprising findings in a multicentric retrospective observational study with 1963 melanoma patients scheduled to SLN biopsy. The main outcome was disease-free survival and melanoma-specific survival. A delay of more than 40 days was associated with better 5-year disease-free survival (80.1% vs. 73.8%; $P = 0.0839$) and better 5-year melanoma-specific survival (89.5% vs. 82%; $P = 0.0002$). These results raise important issues, and the implication that early SLN biopsy reduces MMS needs to be further and prospectively explored. On the other hand, a delay in the procedure did not worsen the prognosis in any case [38].

Technical Issues

Radiotracers

The term "colloid" indicates a class of macromolecules with similar chemical and biological behaviors. These particles vary between 5 and 1,000 nm in size. Colloids circulating in the lymph or blood are removed from the circulation by macrophages, located in the bone marrow, spleen, liver, and lymph nodes.

Following their arrival to lymph nodes through the afferent lymphatic channels draining from the injection site, these particles are phagocytized by macrophages located in the node sinusoids. Therefore, retention of radiocolloids in the lymph node is a physiological process, and it does not indicate the presence or absence of metastatic involvement in the node [28].

The speed of lymphatic drainage from the injection site and the amount retained in the SLN depend on the size of the radiocolloids. Small-sized radiocolloids (less than about 100 nm) migrate quite fast from the injection site through the lymphatic system and best visualize the lymphatic vessels. Lymphoscintigraphy can be completed in a relatively short time (within 45–60 min after injection). However, more than one lymph node, often as many as three to four, can be visualized along a single lymphatic draining channel. This may result in a misleading identification of the SLN, unless there are sequential or dynamic images acquired after injection. Intermediate-sized particles (50–200 nm) migrate more slowly from the primary lesion, but exhibit a more prolonged retention in the SLN. Larger-sized

radiocolloids are retained more efficiently in the SLN, and lymphoscintigraphy usually visualizes one to two nodes only; nevertheless, migration of larger particles from the interstitial administration site is very slow, so that a longer time can be necessary to complete lymphoscintigraphy. Altogether, the choice of radiopharmaceutical varies according to geographic region and is usually guided by local legislation and the agent's commercial availability [39].

Radiotracers for SLN lymphoscintigraphy include ^{99m}Tc-antimony trisulfide (particle size 3–40 nm) with a wide application in Australia, ^{99m}Tc-sulfur colloid (100–400 nm, mostly used in North America), and ^{99m}Tc-nanocolloidal albumin (<80 nm, predominantly used in Europe). It has been suggested that the optimal particle size for SLN detection is between 100 and 200 nm. There is no specific consensus regarding the activity to inject, which should be adapted to the local logistics and to the time lapse between the injection and surgery. Activities usually range from 5 to 120 MBq, depending on the specific 1-day or 2-day protocol employed. It has been demonstrated that both procedures are equally effective for SLN detection [40, 41].

Recently, a new agent, ^{99m}Tc-tilmanocept, has been prospectively evaluated in two non-randomized phase III trials in comparison with vital blue dye. These trials showed ^{99m}Tc-tilmanocept to have a very high rate of SLN identification [42, 43]. This new radiotracer was approved by the US Food and Drug Administration (FDA) in 2013 and by the European Medicines Agency in 2014. ^{99m}Tc-tilmanocept (Lymphoseek®) is a mannosyl diethylene triamine pentaacetate (DTPA) dextran with a molecular size of 7 nm. However, its accumulation in SLNs is not dependent on particle size as with the other colloids. Tilmanocept binds to CD206 mannose receptors expressed by reticuloendothelial tissue including macrophages and dendritic cells within lymph nodes, which present it to T-cell lymphocytes. The advantages of this tracer include rapid clearance from the injection site and low migration to second-echelon nodes (see Fig. 2) [44, 45].

In the PET/CT era, there is a scarcity of PET tracers dedicated to lymphatic mapping. However, some preliminary reports have been published on the use of ^{89}Zr-nanocolloidal albumin for lymphatic mapping with PET imaging; the results reported are similar to those observed with ^{99m}Tc-nanocolloid.

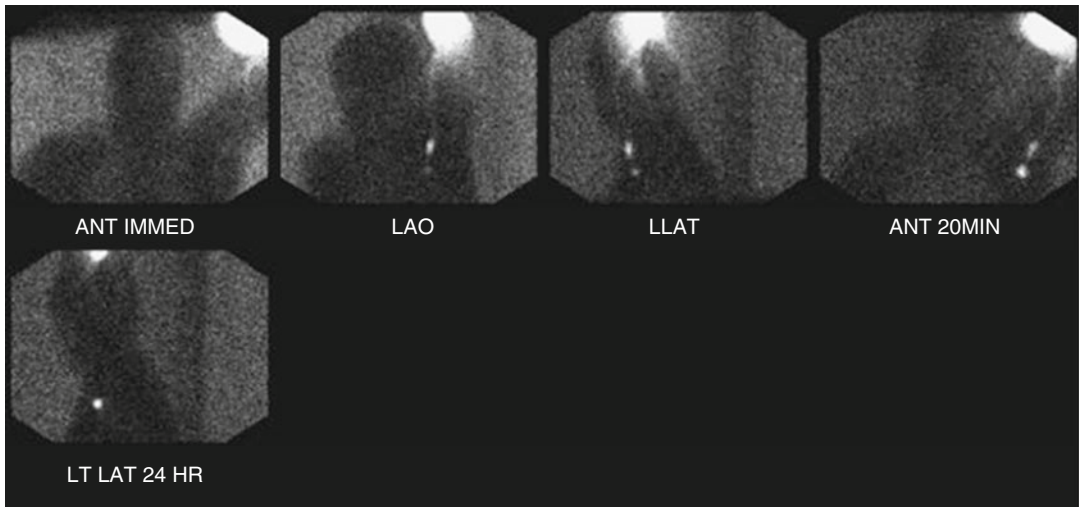

Fig. 2 Lymphoscintigraphy with ^{99m}Tc-Tilmanocept obtained in a patient scheduled for SLN biopsy for a 0.95-mm nonulcerated melanoma of the left forearm (site of injection visible in the first image, *top row*). A single axillary lymph node was visualized 20 min postinjection along with activity in lymphatic channels (variable-angle views in second through fourth image, *top row*). Radioactivity in the SLN visualized at 20 min was well retained at 24 h (image in *bottom row*). The SLN to background count ratio was >30:1 intraoperatively (Reproduced with permission from Sondak et al. [43])

Interestingly, the use of PET tracer showed an improved visualization of nodes near the primary tumor site. These preliminary results warrant further comparative studies in this field [46].

Activity and Injection

There is general consensus that the radiotracer or dye should be injected within 1 cm from the tumor margin of the biopsy scar. Injection activities range from 3.7 to 37 MBq (0.1–1 mCi) per intradermal injection, depending on the time to surgery. The recommendation is two to four intradermal injections (depending on location of the melanoma) of 0.1 mL each around the tumor site or biopsy scar (within 1 cm away from the edge of the tumor or scar). The injected volume must be small to avoid the collapse of lymphatics; furthermore, the wheal raised on the skin surface may rupture and spill over the skin. Tracer injections should be placed either in each side of the biopsy scar or tumor, although in some circumstances they may be performed in only one side. In upper extremities adequate mapping may be accomplished by injecting two injections proximal to the scar and this approach can be employed also for lesions located in the foot and leg. When lesions are located in the thigh, it is advisable to inject in both sides of the scar or tumor. In other sites (the trunk, head, and neck), it is mandatory to inject at least four aliquots around the lesion.

Topical anesthetic medications may be used to diminish the pain, especially when the primary melanoma is in a sensitive location (or when using some radiocolloid with low pH, such as ^{99m}Tc-sulfur colloid). To avoid contamination, a sheet should be placed next to the injection site, and after each injection, the skin should be covered with a swab before the needle is removed [28, 45, 47].

The tracer is injected 1 day before surgery or, alternatively, on the same day. No differences in SLN detection rate or false-negative rate have been found between these two protocols [48]. The 2-day protocol may present some advantages with flexibility in timing of lymphoscintigraphy and surgery. The 1-day protocol requires a good cooperation between the nuclear medicine staff and surgeons with respect to the estimated speed of lymphatic drainage in the affected region and the time to surgery. Intraoperative injection is not recommended because lymphatic drainage in melanoma may be aberrant or delayed to more than one nodal basin and because it is not always possible to obtain intraoperative imaging [45].

Presurgical Lymphoscintigraphy

An accurate procedure for SLN biopsy relies on preoperative lymphoscintigraphy, careful surgery guided both by vital blue dye and by a gamma probe, and finally thorough histopathologic examination.

Lymphoscintigraphy is considered to be an essential part of SLN mapping in general, and it is mandatory for melanoma. It demonstrates the flow of radioactive tracers through the lymphatic structures and visualizes any alternative routes to different regional lymphatic basins. Visualization of nodes located along the route of the lymph will be displayed, and other nodes or paths will be seen if flow has been rerouted because of, for example, block of the original lymphatic flow pattern by massive metastatic involvement of the lymph nodes or by other causes. So, lymphoscintigraphy provides a visual roadmap of nodal locations before surgery and may show the timely order in which lymphatic flow reaches those nodes, especially when a dynamic study is acquired [49–52].

All possible drainage basins must be explored during image acquisition. Therefore, a dual-head gamma camera with large field of view detectors is preferred to reduce the examination time. Nevertheless, a single-head gamma camera can equally be adequate.

Low-energy, high-resolution, or ultrahigh-resolution collimators are recommended to better distinguish individual SLNs. The energy window in gamma camera settings should be 15% or 20% centered on the 140-keV photopeak of ^{99m}Tc [53]. During image acquisition, a ^{57}Co- or ^{99m}Tc-flood source positioned on the opposite side of the camera head for transmission imaging or alternatively a radioactive pointer can be used to delineate the body contours.

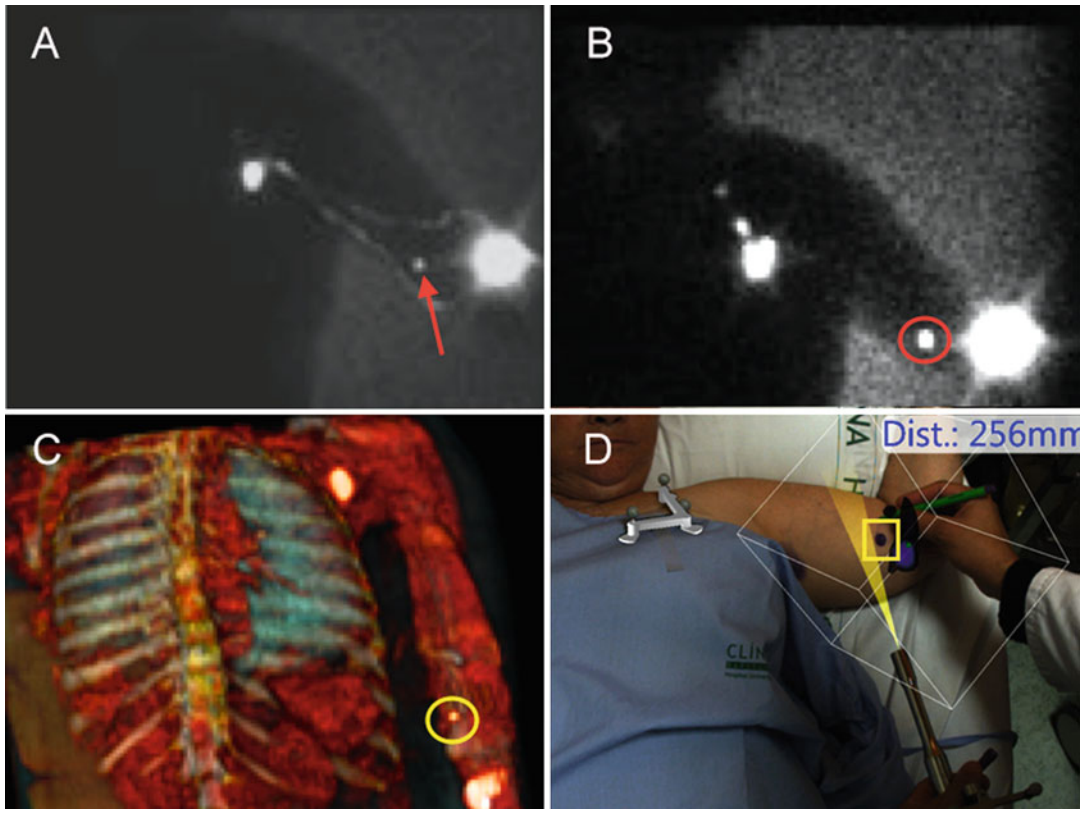

Fig. 3 Early planar image showing the radiotracer injection performed in the ventral part of the elbow, some lymphatic channels, an epitrochlear in-transit sentinel node (*red arrow*), and an axillary sentinel node (**a**). Delayed image that depicts the epitrochlear uptake (*red circle*) and the axillary sentinel node and subsequent second-tier axillary nodes (**b**). Volume rendering 3D reconstruction that depicts the sentinel nodes in the epitrochlear area (*yellow circle*) and the left axilla (**c**). Skin marking of near-epitrochlear node (*yellow square*) and confirmation using a gamma probe (**d**)

The tracer must be injected with the patient lying in the most convenient position on the bed of the gamma camera, depending on the location of the primary tumor. Starting image acquisition immediately after the injection may help to identify lymph nodes next to the injection sites and to differentiate true SLNs from second-echelon nodes. Dynamic imaging (one frame per 30 s or per 60 s in a 128 × 128 matrix) during the first 10–20 min after injection is recommended. Although acquisition of dynamic images is time consuming, it is nevertheless crucial because a lymphatic channel directly draining to a lymph node identifies this node as a true SLN.

In melanomas of the hand/forearm or foot/leg, dynamic imaging should start over the injection site and follow the lymphatic drainage to the elbow and axilla and knee/groin, respectively, to reveal ectopic basins and in-transit lymph nodes (popliteal, epitrochlear, etc.) (Fig. 3). For head and neck melanomas, immediate imaging reduces the chance of missing a SLN because of rapid drainage from intradermal injections with uptake by superimposed nodes. Imaging at a rate of 1–5 s/frame in this particular area may solve these drawbacks.

After dynamic imaging, static planar 3- to 5-min images (anterior, oblique, posterior, and lateral) should be acquired, if indicated, with a 256 × 256 matrix over the visualized lymph node basin drainage. Early images help to discriminate true SLNs from second-tier nodes. In melanomas of the trunk, usually bilateral static images of the axilla, trunk, and groin are necessary. In lower limb melanomas,

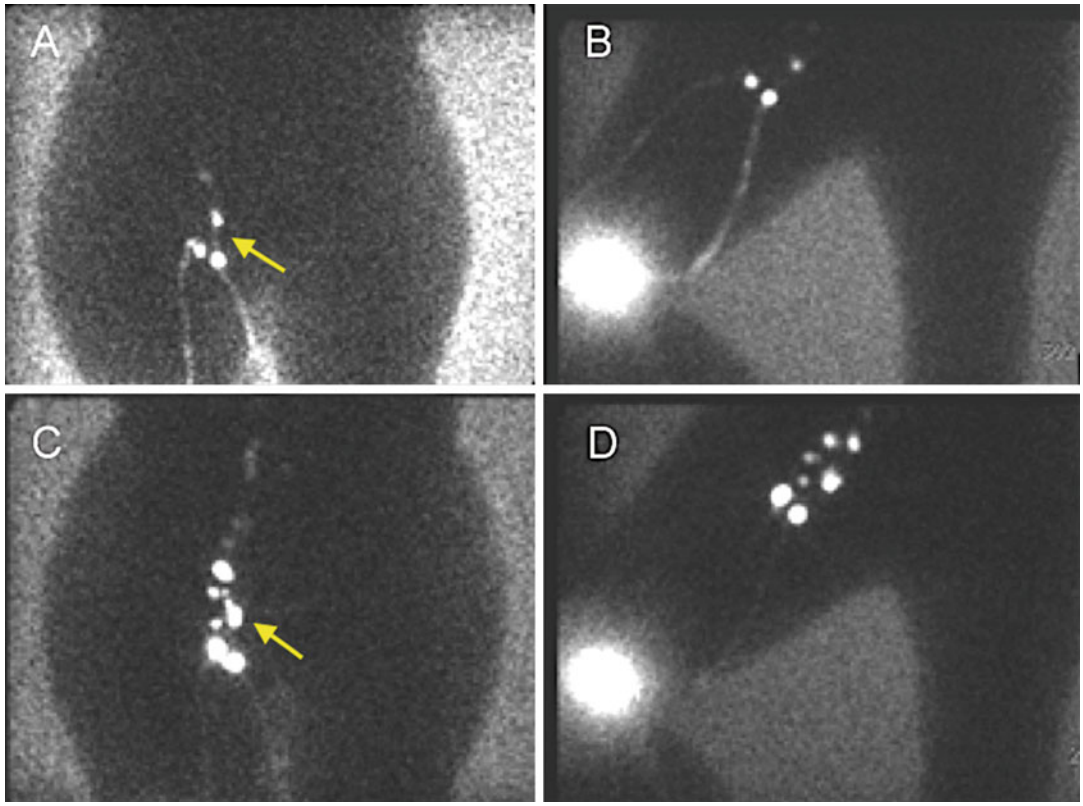

Fig. 4 Lymphoscintigraphy. Early (**a**, **b**) and delayed (**c**, **d**) planar images in anterior and oblique views. Two well-depicted lymphatic channels are visualized in (**a**) and **b** images directly connecting the injection site with right groin sentinel nodes. *Yellow arrow* in picture (**a**) shows a faint lymphatic channel cranial to one of the sentinel nodes. It could be a second-echelon node but also a real sentinel node if this channel passes below the first depicted node directly from the injection site. Oblique view can provide a more accurate assessment. *Yellow arrow* in picture (**c**) shows a high uptake in the aforementioned node, as well as in the other nodes upstream. Second-echelon nodes are more frequently observed in the groin than in other parts of the body, due to the highest velocity of lymph that is observed in the lower limb. Performing only delayed images is not accurate in those cases because it is hard to distinguish between the real sentinel nodes and the second-tier nodes

several superimposed lymphatic channels are often depicted. In this case, an oblique view helps to distinguish different channels. Second-echelon nodes are more frequently observed in the groin than in other parts of the body, due to the highest velocity of lymph occurring in the lower limb (Fig. 4) [45, 54].

To detect SLNs close to the injection site, it may be useful to mask the injection site with lead material during image acquisition. Delayed images (2–4 h or more after radiotracer injection) allow the correct SLN identification and their external marking on the skin. The SLNs are usually identified in the first 30 min after injection, although images should be obtained also at 2 h, due to possible slow lymph flow to other areas. The great variability of cutaneous drainage should be taken into account, as well as the possibility of detecting lymph nodes outside the conventional regional areas (called aberrant or in-transit nodes).

Lymphoscintigraphy for SLN mapping must be accurate and reproducible. Some studies have addressed this issue in several different malignancies. In particular, in melanoma patients a good correlation (84–96%) between two separated lymphoscintigraphic studies has been demonstrated [55–60].

Lymphoscintigraphy may, to some extent, predict the metastatic burden in lymph nodes. In this

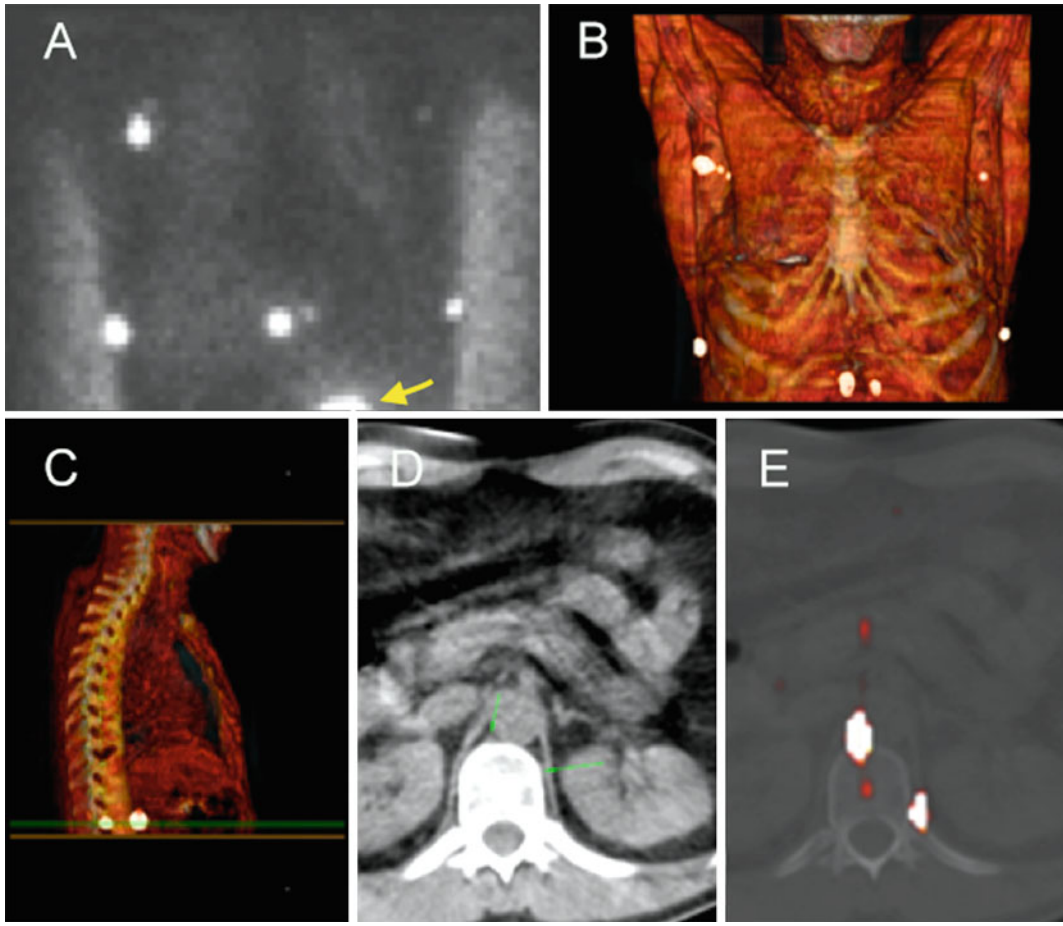

Fig. 5 Planar lymphoscintigraphic anterior view of a melanoma patient with a lesion in the left–central periumbilical area (*yellow arrow*). The image shows several hot spots in both axillae and para-costal areas and two hot spots central in the abdomen. All of them were considered as sentinel nodes (**a**). 3D reconstruction showing the anatomical location of these nodes (**b**). Sagittal view of selectively assessed "abdominal" uptake (**c**). The CT scan showed two tiny nodes in para-aortic and paravertebral areas (*green lines*) (**d**). Fused SPECT/CT images showed focal radiotracer uptake in these locations (**e**). These nodes are sentinel nodes. However, they were not resected in the surgical procedure due their deep location

regard, an interesting study in 509 melanoma patients scheduled for SLN biopsy showed that clear depiction of an afferent lymph vessel may be a sign of micrometastasis. On the other hand, the presence of macrometastasis was associated with prominent afferent vessels, delayed display of the first radioactive node, and higher number of depicted hot spots. Moreover, in patients with bidirectional or lymphatic drainage to three basins, the SLN metastatic involvement rates for the first, second, and third basin were 25%, 12%, and 0%, respectively ($P = 0.002$) [61].

Additional SPECT/CT Imaging

Planar lymphoscintigraphy provides clear visualization of the SLN, thus providing information on their number and facilitating the localization on their skin projection. However, the depth and anatomical correlates of the SLN are not easily obtained. For example, deep SLNs in the neck or in other areas (i.e., deep paravertebral, mediastinal, or para-aortic nodes) are challenging during surgery, and in certain cases, they cannot be removed (Fig. 5).

Table 2 Advantages of SPECT/CT over planar imaging

Improved anatomical SLN localization
Better sensitivity than planar images (additional lymph nodes)
Reduction of false-negative cases
Reduction of false-positive cases
Clarification of inconclusive scintigraphic patterns in planar images
Higher SLN detection rate in difficult cases (obesity, faint uptake)

The use of SPECT/CT has gained importance because this tomographic approach is more successful than planar imaging in identifying SLNs [62]. SPECT/CT is basically used for anatomical localization of SLNs and is performed in addition to lymphoscintigraphy. A requirement for accurate SLN localization is that the CT component of SPECT/CT system must be of sufficient quality to provide adequate anatomical landmarks to be recognized by surgeons. SPECT/CT may be of great utility in obese patients to demonstrate SLNs not detected on planar images, as well as to show additional SLNs in other areas. For fused SPECT/CT images, a gray scale is used to display the anatomy (CT), whereas a color scale is employed to show the SLNs in the SPECT image. Usually, a radioactive hot spot corresponds to a single lymph node on CT, but in some cases, this image correlates with a group of lymph nodes adjacent to each other (cluster) [63, 64].

Tomoscintigraphic images improve SLN identification and overcome some of the limitations of planar imaging (Table 2). Fusion with CT images shows the SLN in 2D and 3D modalities. In this way, SPECT/CT facilitates recognition of non-lymph node accumulations of the radiotracer and helps to clarify drainage in inconclusive planar images. With the use of volumetric rendering techniques with 3D viewing, images can be obtained with high anatomical detail, thus facilitating the interpretation of lymphoscintigraphy and helping to assess the images obtained with the planar study in anatomically complex areas of the body. In melanoma of the head and neck, where SLNs may be located very close to the primary site, SPECT/CT may be of outmost importance in localizing SLNs masked during planar imaging because of their proximity to injection sites (Fig. 6) [65, 66].

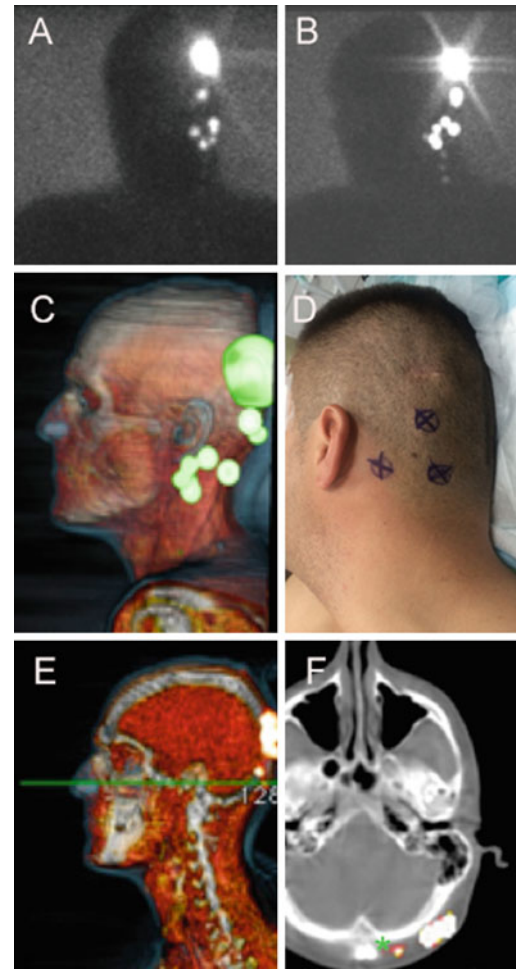

Fig. 6 Lymphoscintigraphy. Anterior (**a**) and left oblique (**b**) views showing several hot spots in the occipital and left cervical area after a radiotracer injection in left parietal scalp. 3D reconstruction after SPECT/CT acquisition (**c**). Skin marks in the areas where sentinel nodes were considered to be (**d**). Sagittal slice corresponding to the occipital uptake level (**e**). Fused SPECT/CT images showed two separate radiotracer uptakes in this area. The faint uptake (*green asterisk*) was a very tiny node (3 mm) that was positive for metastatic involvement. SPECT/CT images helped to better assess the planar images (only one hot spot depicted in that zone due to the higher activity of one of the nodes masked the tiny node)

Clinical Impact of SPECT/CT in Melanoma

SPECT/CT allows an accurate lymphatic mapping by increasing the number of SLNs resected during

surgery. Moreover, SPECT/CT may also detect more SLNs in aberrant drainage locations or when planar images show no clear radiotracer migration. SPECT/CT in melanoma has been validated for specific indications. An initial study demonstrated that SPECT/CT had a definite added value in 30 out of 85 patients (35%), by detecting extra SLNs, not visualized on planar images, by localizing SLNs in other basins, or by modifying the surgical incision planning. In seven patients, 12 additional SLNs were detected (two of them with metastatic involvement) [67].

Mucientes et al. showed, in another study with 18 patients, a visualization rate of 100% for SPECT/CT versus 89% for planar lymphoscintigraphy. Moreover, SPECT/CT provided accurate anatomical information leading to refine the surgical incision in four patients [68].

A Dutch study confirmed in a series of 35 melanoma patients that SPECT/CT detected more SLNs than planar images in 7 of them, contributing also to modify surgery in 10 patients [69].

Fairbairn et al. showed that SPECT/CT and planar lymphoscintigraphy detected SLNs in 32 patients (SLN detection rate of 97% for both techniques). The additional anatomic information provided by SPECT/CT contributed to the adjustment of surgical approach in 12 cases [70].

Kraft and Havel reported in 113 melanoma patients that SPECT/CT allowed higher SLN detection rate than planar images (95% vs. 89%, respectively). Furthermore, lymphatic drainage was visualized in eight patients without SLN visualization on planar study [71].

From the surgical point of view, the value of SPECT/CT in adjusting the operating approach is also important. Such added value was observed in 14 out of 63 (22%) melanoma cases, whereas the SLN visualization rate was similar between planar images and SPECT/CT (98% vs. 100%, respectively) [72].

SPECT/CT is able to detect also more potential metastases. A study comparing the results in 149 patients with additional SPECT/CT information with a group of 254 patients who only underwent planar imaging showed that SPECT/CT detected more SLNs than planar images (average 2.4 vs. 1.87 per patient, respectively). SPECT/CT detected more metastatic SLNs (average 0.34 vs. 0.21 per patient), and its use was associated with a significantly higher rate of disease-free interval (93.9%) in comparison with those patients without the use of SPECT/CT (79.2%) [73].

Recently, a multicenter collaborative study promoted by the International Atomic Energy Agency (IAEA), conducted in 15 centers from 10 different countries, included 262 melanoma patients. No SLN was visualized on planar images in three patients. SPECT/CT revealed an axillary SLN in a trunk melanoma patient and persistent non-visualization in two patients with head and neck melanoma. In the latter, cervical lymphadenectomy was positive for metastasis. SPECT/CT revealed 70 additional SLNs in 53 patients (25% additional nodes in head and neck melanoma: 25.5% in patients with upper limb melanoma, 20.5% in patients with trunk melanoma, and 12.9% in patients with lower extremities melanoma). The surgical approach was modified in 97 patients (37%): 41%, 39%, 33%, and 30% of head and neck, trunk, lower limb, and upper limb lesions, respectively [74].

Nevertheless, based on evidence currently available, SPECT/CT must be considered as complementary rather than alternative to planar lymphoscintigraphy. SPECT/CT is able to provide anatomical landmarks with a significant improvement of the surgical roadmap and clinical benefit for the patient as demonstrated by Stoffels et al. [73]. In a recent survey in Spain, data from 37 different nuclear medicine centers were collected. SPECT/CT studies were performed in all the melanoma patients in 24.3% of the centers (9/37), while this study was performed according to patient-based considerations in the remaining centers (28/37), the most common indication being the presence of head/neck drainage [75].

Surgery

Besides the information provided by preoperative lymphoscintigraphy, the other main cornerstone of the technique is the ability of the detector probe to guide the dissection and to identify the SLN. It is

recommended to make a preliminary search, with the patient properly positioned on the operating table, with gamma probe prior to making the incision. The scan with the gamma probe should be slow and systematic and should start between the area of the injection and the area of drainage visualized in the lymphoscintigraphy, until an increase in activity is observed. This activity should optimally be matched with the skin markings made by the nuclear medicine staff at the time of lymphoscintigraphic imaging. Precaution should be taken when the injection site overlies or is within the field of view of the detector probe, and thus, if possible, mobilization maneuvers or attempt to direct the gamma probe opposite to the injection site should be made. In vivo radioactivity (counts/sec) is measured in the surgical field opened, typically with a 2–4-cm incision over the area of highest activity determined by external counting/skin marking. SLN to background ratios are usually between 10:1 and 20:1, depending on activity injected, time to surgery, etc. After in vivo SLN identification and retrieval, the ex vivo activity of the SLN should be recorded, as should also be the remaining activity in the surgical fields to rule out the presence of other potential SLNs. Although the SLN is visualized in the lymphoscintigraphy, in practice there may be two adjacent lymph nodes seen as one in the images (especially if SPECT/CT imaging is not available); therefore, the lymphatic bed should always be reassessed. It is also advisable to palpate the lymphatic region searching for enlarged or matted lymph nodes, especially if an ultrasound study has not previously been performed [45, 76].

Vital dyes may help to visually confirm the lymphatic vessels from the primary tumor to the SLN. Combining the information provided by presurgical lymphoscintigraphy with the intraoperative use of dyes and the detector gamma probe offers the highest accuracy in SLN identification; therefore, their use in combination is recommended. The vital dye is especially important when the primary tumor is very close to the lymphatic basin, since the injected radioactivity (even after lesion removal) causes a high background count rate which does not allow the detector probe to distinguish the SLN. Isosulfan blue (Lymphazurin) and Patent Blue V are the dyes of choice for SLN mapping. Methylene blue is also used because of its lower cost, its lesser risk of anaphylaxis, and its similar ability to detect the SLN compared with the other two dyes [77].

In general, the success rate of combining presurgical lymphoscintigraphic information with intraoperative gamma probe reaches about 98% in melanoma, whereas the vital blue dye alone identifies about 80% of cases. The addition of dye improves radioguided SLN identification, to reach a 99% success rate (Fig. 7), especially when lymphatic drainage to the SLN is blocked by metastatic tumor cells and/or when the SLN capacity to retain the radiocolloid is hampered by massive replacement of the normal lymph node structure with metastatic cells.

Nonetheless, from a practical point of view, many centers around the world consider that lymph node resection should continue up to achieving lymph node activity in the surgical bed $<10\%$ of the activity of the most active SLN (10% rule), in order to reduce the potential false-negative cases [78]. However, almost all the involved lymph nodes can be identified following the concept of the SLN and using a rigorously conducted procedure [79]. In this regard, a recent revision of the 10% rule showed a 21% positive SLN rate in 665 melanoma patients. More than one SLN was removed in 105 regional basins. In 18 of these, a less radioactive node was positive for tumor when the most radioactive node was negative. Blue dye was used and stained 157 out of 175 positive SLNs (90%). In those cases, in which the involved SLN was not the hottest node, the positive node was blue in all cases. Thus, the authors concluded that, in this particular series, removing just the hottest node and all blue nodes would not have missed a positive SLN, but at the same time would have avoided to resect more nodes in comparison with the 10% rule [80].

Sentinel Lymph Node Analysis and Its Importance for Clinical Decision

Histopathologic evaluation of the SLNs is, currently, the "gold standard" in patients scheduled for SLN biopsy. The SLN status predicts

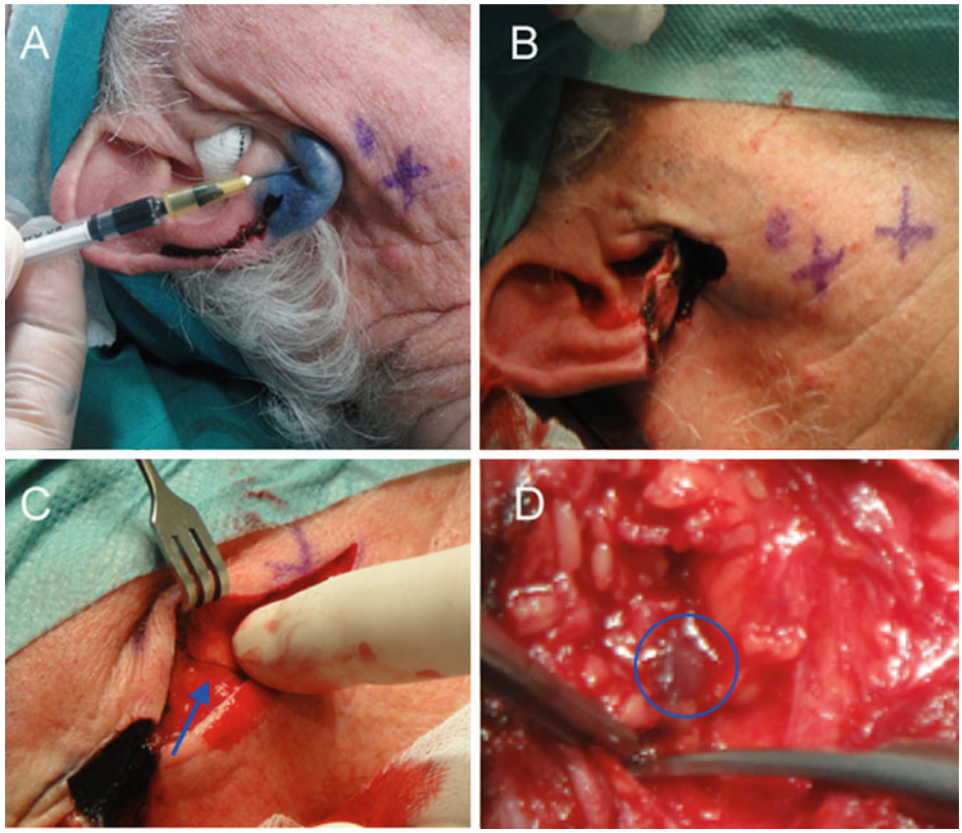

Fig. 7 Classical intraoperative approach for sentinel node biopsy. Injection of blue dye around the biopsy scar in a patient with a melanoma in the right ear (**a**). Skin marks corresponding to the depicted sentinel nodes in preoperative lymphoscintigraphy (**b**). *Blue* stained lymphatic channel (*blue arrow*) to the parotid area sentinel node (**c**). *Blue* stained node (*blue circle*) in the surgical field (**d**)

prognosis and indicates the necessity or not for further surgical treatment.

The SLN approach enables pathologists to thoroughly review this particular node or nodes using multiple sections and several staining techniques. Intraoperative frozen section histology is not reliable in the case of melanoma. The conventional approach involves, after usual sectioning and staining with hematoxylin and eosin, immunohistochemistry employing antibodies against the melanoma-associated S-100 antigen (very sensitive) and HMB-45 and MART-1/Melan A (very specific) antigens. Serial sectioning and additional immunohistochemistry may detect additional micrometastases in up to 12% of the cases [81].

Molecular analysis methods (PCR) are not part of clinical routine up to now, because they are time consuming and lack in reproducibility. However, some studies have advocated their use due to a higher sensitivity to detect metastases against conventional pathology methods and a lower rate of false-negative cases [82, 83].

It has been shown that small deposits of metastatic cells are associated with a worse prognosis in patients with negative SLN. Although isolated tumor cells (especially in the subcapsular sinuses) have been described to bear an adverse biological feature in melanoma [84–86], nevertheless the AJCC concluded that there is no definitive evidence enabling to define a minimum threshold of tumor load for defining the stage of lymph node metastasis [87].

The current practice is to wait for definitive histopathologic examination before making the choice between no further surgery (when the SLN is tumor-free) or to perform an elective regional

lymphadenectomy (when the SLN bears metastasis). Patients with positive SLN biopsy are offered complete lymph node dissection, and 12–25% of them will have additional lymph nodes involved. The final analysis of data from the MSLT-I trial has demonstrated the importance of SLN biopsy for the identification of patients with node involvement who may benefit from immediate lymphadenectomy [35].

However, recent studies indicate that lymph node dissection does not have an effect on the global survival after a positive SLN with minimal tumor load (<0.1 mm in diameter). It has therefore been suggested that lymph node dissection can safely be omitted in these patients [88, 89]. The Multicenter Selective Lymphadenectomy Trial II has been designed to assess the role of lymphadenectomy of the regional node basin in patients with positive SLN, with the intent to determine whether lymphadenectomy has any benefit in regional control or survival. The study started in 2004 and reached its scheduled accrual in 2014 [90]. Follow-up is still in progress for assessing the long-term outcomes of the trial.

Refinements for the Classical Technique

Despite the successful results in SLN localization based on lymphoscintigraphy (especially if complemented with SPECT/CT), precise localization for surgical planning may sometimes be difficult. Intraoperative use of the gamma probe provides a good overview of radioactivity distribution in the surgical field, with SLN identification rates close to 99% in patients with melanoma. Nonetheless, the technique can be further improved. The combination of vital dye and gamma probe has prevailed for many years as the standard technique. However, the dye is less effective in areas with aberrant lymphatic drainage and in deep-seated lymph nodes (i.e., head and neck region where the SLN identification rate is around 85%).

The current technological advances in portable devices and the possibility of using new signatures (i.e., fluorescence) in addition to the conventional radiotracers have led to a changing paradigm: from the "see to open" approach to the "see, open, and see again." The combination of SPECT/CT information with new portable imaging devices enhances the reliability of the gamma probe, especially in complex drainage regions and in areas where the SLN is very close to the injection site. These advances have led to the definition of the concept of "Guided intraOperative Scintigraphic Tumour Targeting" (GOSTT) to include the whole spectrum of basic and advanced nuclear medicine procedures required for providing a roadmap that would optimize surgery [91, 92].

Portable Gamma Cameras

These gamma cameras have been designed for intraoperative use, with sensitivity and resolution parameters that make them optimally suited for imaging small areas [93]. The use of these imaging devices in the surgical theater enables to precisely adapt in real time the surgical incision to the skin marks previously made in the nuclear medicine suite at the time of lymphoscintigraphy and confirms the exact SLN location, considering that position of the patients on the operating table may be different from that on the imaging table. This is especially important for melanomas located in the head and neck area, since even small changes in lateralization of the neck may imply an important change in the anatomical setting of the subjacent SLN position in relation to the cutaneous marks.

In general, when these devices are used, an overview image is recorded before the start of SLN biopsy in the operating room. To verify the completeness of SLN removal, another image must be acquired after excision. If a residual radioactive spot is visualized at the location of a previously harvested SLN, this additional node must also be resected and be assessed as a part of a cluster of nodes to be considered as additional SLNs. Furthermore, a high-resolution portable gamma camera, positioned close to the skin, is able to detect SLNs at distances as small as only 3 mm from the injection site [92]. Nevertheless, it should be emphasized that portable gamma camera designed for use during radioguided surgery procedures do not serve as an intraoperative

guidance in the same manner as conventional handheld gamma probes, since their size is not small enough for insertion in the surgical bed through the surgical incision.

The added value in the use of these devices is that they allow resection of additional SLNs, some of which result to be metastatic. Therefore, this technique may reduce the false-negative rate of SLN biopsy, while the SLN identification rate is increased and correct application of this intraoperative imaging procedure ensures that no SLNs are left in the surgical field [94, 95].

Vidal-Sicart et al. described the use of a portable gamma camera in five difficult melanoma cases. In this group, 80% of patients showed a primary lesion in the head region, and the remaining patient had a lower limb lesion. In total, 12 SLNs were detected using only the gamma probe, while two additional SLNs were found by the portable gamma camera [96].

Dengel et al. compared the performance of a portable gamma camera with preoperative conventional lymphoscintigraphy and intraoperative gamma probe findings in 20 melanoma patients. Lymphoscintigraphy depicted 29 node basins containing SLNs, while the pre-incision images with portable gamma camera detected only 27 node basins. The authors explain these somewhat disappointing results with the delay of more than 20 h between radiocolloid injection and intraoperative imaging with the portable gamma camera, an interval during which physical decay caused an important decline in radioactivity levels retained in the lymph nodes. Nevertheless, intraoperative imaging detected two additional previously undetected lymph nodes in 2/20 (10%) of the patients [97].

Stoffels et al. enrolled 60 patients (38 with melanoma, 22 with other cutaneous malignancies) for a SLN procedure using the same portable gamma camera as that used by Vidal-Sicart and colleagues. The portable gamma camera visualized all 126 SLNs identified preoperatively by SPECT/CT. More importantly, 23 additional SLNs in 15 patients (25%) were identified using the portable gamma camera device; two of these additional nodes were metastatic, thus preventing a false-negative SLN biopsy in two patients. Intraoperative imaging extended the operating time by a maximum of only 5 min [98].

Olcott et al. showed in 39 patients that intraoperative imaging using a handheld gamma camera successfully visualized 86 of the 92 SLNs detected by the gamma probe and detected 12 additional nodes that were missed by the gamma probe [99].

New perspectives in radioguided surgery may be opened by the fusion of the scintigraphic images with an optical image, thus providing a more "friendly," real-time anatomical environment during surgery [100]. New multimodality system configurations have been described that combine optical and gamma imaging. Haneishi et al. have proposed a parallel optical and gamma camera configuration resulting in a portable hybrid camera system that projects the scintigraphic image onto an optical image [101].

Hellingman et al. have recently evaluated a prototype portable hybrid camera for preoperative lymphatic mapping in SLN procedures. Fused optical and gamma imaging makes it easier to relate the position of the radioactive hot spots and the image field of view with the real-life situation (Fig. 8) [102].

Freehand SPECT

The use of a positioning system technology allows spatial localization based on two tracking devices that are attached to a conventional gamma detector probe and to the patient, respectively. The localization system consists of an optical camera and an infrared-based localization device. Virtual 3D images are generated. After scanning the area of interest with the gamma probe, images are displayed on a screen. These images may be seen in real time and provide information about the depth at which the SLN (or the tissue to be resected) is found. The procedure is called freehand SPECT and is designed for intrasurgical navigation. This method combines the acoustic signals with a 3D image to localize the SLN in the operating room [103] (Fig. 9).

Specific training in the use of the technique is required for data acquisition and for making several readings during surgery, a procedure that might

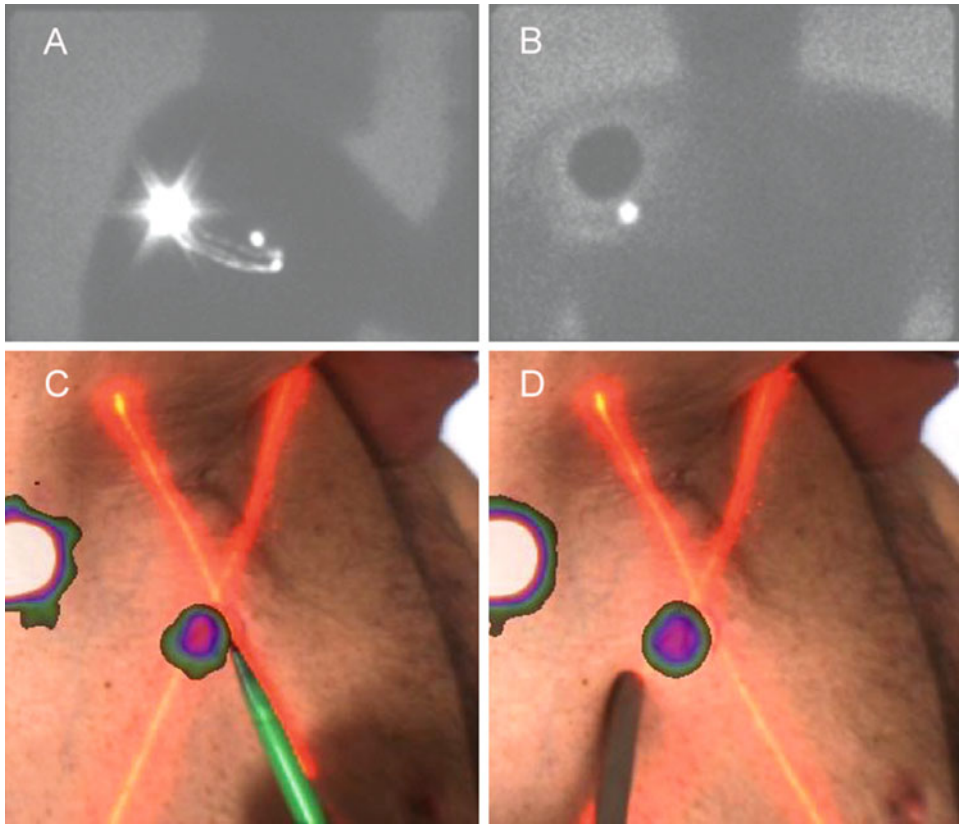

Fig. 8 Preoperative lymphoscintigraphy. Right lateral (**a**) and anterior (**b**) views from a patient with an upper right back melanoma. A clear hot spot (with several lymphatic channels to it) is visualized. Fused optical and gamma imaging is achieved in a new portable hybrid camera. The sentinel node is well depicted, and it can be precisely marked in the skin (**c**) and assessed with the handheld gamma probe (**d**) in real time

prolong the operation time. Nevertheless, in both cases the results may refine the conventional technique [104]. The use of freehand SPECT is currently yielding excellent results for SLN biopsy in melanoma and breast cancer [105].

In melanoma, Sulzbacher et al. studied 39 patients with primary lesion in different sites of the body. Surgery using radioguided freehand SPECT was performed the day after acquisition of preoperative lymphoscintigraphy (planar + SPECT/CT). Interestingly, SPECT/CT data were integrated into the 3D navigation system to enable fast and direct localization of the SLN by displaying the depth of the node from the skin surface to the gamma probe. Comparable preoperative imaging and intraoperative localization were observed in 18/39 patients. In 10 of 14 patients in whom more SLNs were resected during surgery than those visualized preoperatively, intraoperative freehand SPECT revealed additional lymph node sites. The mean surgical time using this device was 66 min (range 36–133) [106].

Fluorescent and Hybrid Tracers

The use of fluorescent agents for lymphatic mapping and SLN localization is expanding rapidly. Organic fluorescent dyes such as fluorescein or indocyanine green (ICG) have been used for human studies, as an alternative to nuclear imaging methods. Their excited light emissions are in the near-infrared (NIR) spectrum, which has several advantages over ultraviolet and mid-infrared

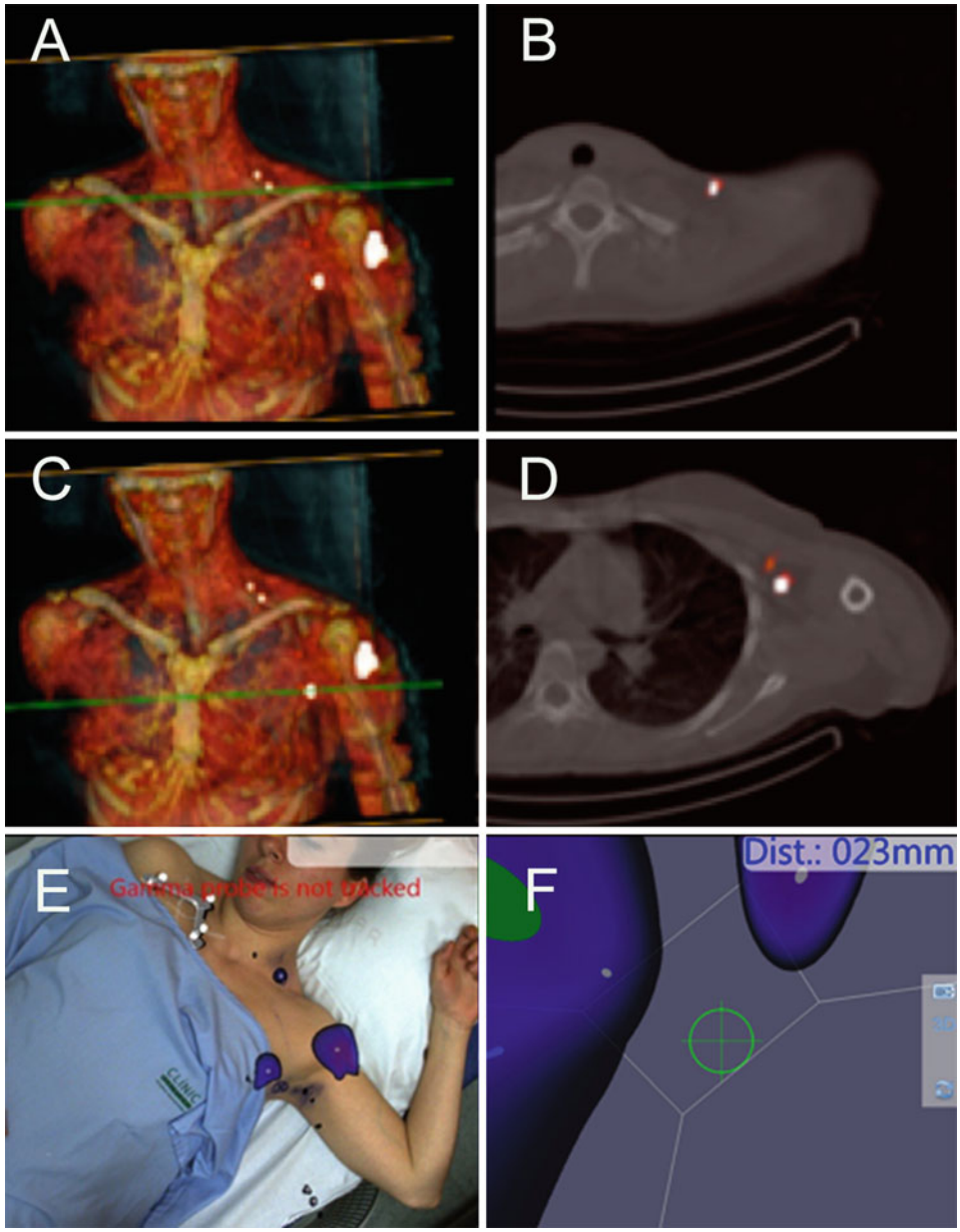

Fig. 9 3D reconstruction (**a**, **c**) and SPECT/CT fused images (**b**, **d**) of a patient with a left upper arm melanoma. These images show sentinel nodes in left axilla and left supraclavicular area. Freehand SPECT device depicted the same distribution after accurate scan (**e**). Virtual reconstruction provides real-time information about the depth at which the sentinel node is found

radiation. In particular, NIR emissions have better tissue penetration and are therefore more suitable for intraoperative guidance in a surgical field. Since the NIR window lies beyond the visible spectrum, the pathways of lymphatic drainage following interstitial injection of ICG can only be visualized by using a dedicated NIR fluorescence camera [107].

Motomura et al. first described the NIR imaging technique with ICG for SLN detection in breast cancer, reporting a 74% SLN identification rate [108]. Once injected, the fluorophore ICG binds

to serum proteins, and within several minutes, it drains through the lymphatic vessels to the SLN. Similar to blue dyes and due to its small size, ICG migrates rapidly within the lymphatic channels and is not retained in lymph nodes, thus resulting in a rather short diagnostic detection window that requires a very strict surgical protocol to reliably detect the SLN. However, sensitivity of signal detection is much better with ICG than with the blue dye, because it enables real-time percutaneous and intraoperative visualization of lymphatic channels and superficial (<1 cm in depth) SLN. Nevertheless, visualization of lymphatic drainage and SLN detection can be problematic in patients with high body mass index [109].

Van der Vorst et al. demonstrated the feasibility of NIR fluorescence for SLN mapping using an ICG:HSA conjugate and a dedicated fluorescence camera in patients with melanoma. SLN was similarly detected with fluorescence as with radiocolloids, with superior performance compared to blue dye. In particular, combining NIR fluorescence and radiotracer led to a 100% SLN detection rate, but only 73% of the SLNs were stained blue [110].

In other studies, however, the radiocolloid-based approach proved to be superior to other tracers. In a recent study with 52 melanoma patients, the SLN identification rates were 96.2% for the radiocolloid, 88.5% for ICG, and 59.6% for the blue dye [111]. In another group of patients with melanoma, Stoffels et al. observed inferior results with ICG guidance when compared to ^{99m}Tc-nanocolloid in defining lymphatic basins at risk for metastases before surgery. They detected and excised 147 SLNs in 80 patients using the radiocolloid, whereas in only 21% of the patients (17/80) was the SLN detectable by ICG before skin incision [112]. These findings are consistent with other studies showing that, although fluorescence imaging allowed intraoperative identification of the SLNs, the limited tissue penetration does not allow accurate SLN mapping prior to surgery.

Since preoperative lymphoscintigraphy is an essential component of SLN approach, novel hybrid compounds have been designed (i.e., a lymphatic mapping agent that is both radioactive and fluorescent) for combining the relative advantages of each approach. In particular, preoperative lymphoscintigraphy and SPECT/CT are possible because of the radioactive "signature" of the hybrid agent, while the fluorescent "signature" would allow recording high-resolution images in the operating room [113].

In this regard, a seminal clinical study has demonstrated the stability and reproducibility of one of these potential hybrid tracers (ICG-^{99m}Tc-nanocolloidal albumin) versus the current standard tracer in Europe, ^{99m}Tc-nanocolloidal albumin, in 25 patients with melanoma or penile cancer. Indeed, with this approach it was possible to detect fluorescent SLN up to 23 h after administration of the hybrid compound, thereby increasing the useful time window for planning surgery (Fig. 10) [114].

The combination of the properties of the two tracers (high tissue penetration of the radiotracer and high-resolution imaging of the fluorescent agent) implies greater accuracy for SLN detection, especially in areas with complex lymphatic drainage [115]. An additional hybrid approach based on ICG-^{99m}Tc-nanocolloid has recently been validated in 104 patients with melanoma. Optical SLN identification rate, made possible by the fluorescent signature of the hybrid tracer, was superior to that achieved with the blue dye, since SLNs were intraoperatively visualized in 97% of the cases with fluorescence, whereas only 62% of these nodes were stained blue. Interestingly, ex vivo examination of the excised SLNs confirmed the combined presence of a radioactive and fluorescent signature [116].

In another study, Stoffels et al. reported the results of a randomized prospective trial comprising 40 patients with different types of skin malignancies (melanoma, squamous cell, Merkel cell carcinoma) and sweat gland carcinoma in the head and neck region. Twenty patients received a derivative of the previously described ICG-^{99m}Tc-nanocolloid tracer, while the rest of the patients were given the standard ^{99m}Tc-nanocolloid. Primary study endpoints were the number of excised SLNs and duration of surgery. It was concluded that the use of the hybrid tracer for SLN biopsy is feasible in these patients and that by combining fluorescence and radioactivity in one single tracer,

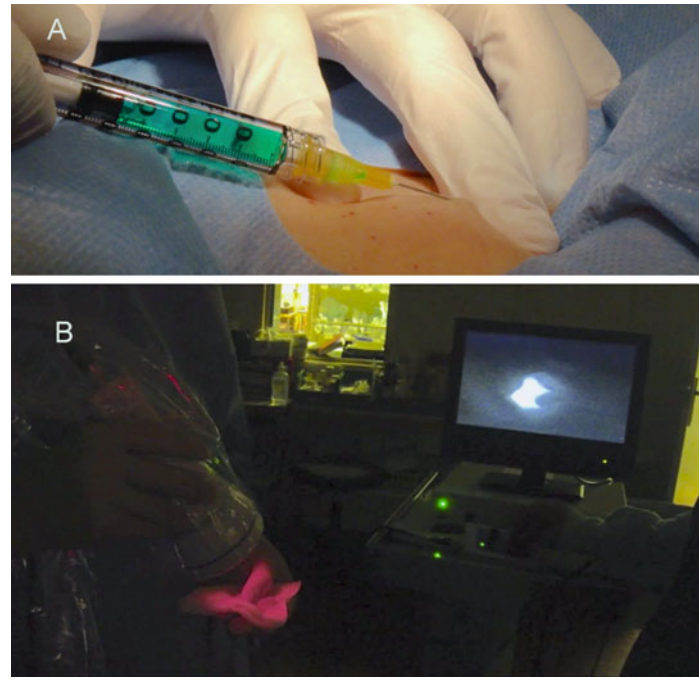

Fig. 10 Injection of hybrid tracer (ICG-^{99m}Tc-nanocolloid) in a patient with melanoma on the back (**a**). During surgery, an axillary node was retrieved (both active and fluorescent). Fluorescence is depicted on the screen when tissue is exposed to a fluorescence camera (**b**). Surgery was performed 18 h after administration of the hybrid compound

discrepancies between both signatures are less likely to occur [117].

Nevertheless, it should be emphasized that each type of signal (radioactive or optical) must be explored with dedicated, single-modality imaging/detection devices. Ongoing efforts aim at developing multimodal devices capable of providing all the potential of intraoperative imaging, thereby achieving greater reliability in the surgical procedures [100]. In this scenario, a hybrid tracer integrating radioactivity and fluorescence in one signature constitutes the basis of a novel approach to combine the best of both diagnostic worlds for the SLN procedure in melanoma as well as in other malignancies [118].

Particular Issues for SLN Mapping in Melanoma

In-Transit, Aberrant, or Ectopic Lymph Nodes

Although the majority of melanomas scheduled for SLN biopsy drain to a predictable regional lymphatic basins based on localization of the primary tumor, drainage to lymph nodes outside the expected lymphatic basins may be observed. Any lymph node visualized along the lymphatic channel between the primary localization and a regional lymphatic basin is called in-transit, interval, aberrant, or ectopic (depending on the definitions set by different investigators) lymph node and must be considered as a SLN regardless of its localization.

The presence of such nodes has been described especially in the parascapular and supraclavicular spaces (lying between muscles or, even more frequently, in the subcutaneous fat); the para-aortic, paravertebral, and retroperitoneal regions; the intercostal zones; the internal mammary lymph node chain (epitrochlear, popliteal); and even the skull. Lymph nodes have been reported in these areas between 6% and 12% of the cases, and the probability of metastatic involvement of these nodes is similar to that of the SLN in areas of classical drainage. So, melanomas in the upper extremities and the trunk are more likely to present aberrant nodes. On the other hand, tumors localized in the head and neck and the genital area show a lower rate of these nodes [51, 54, 119].

The need to identify the SLNs prior to surgery is as important as identifying and resecting them

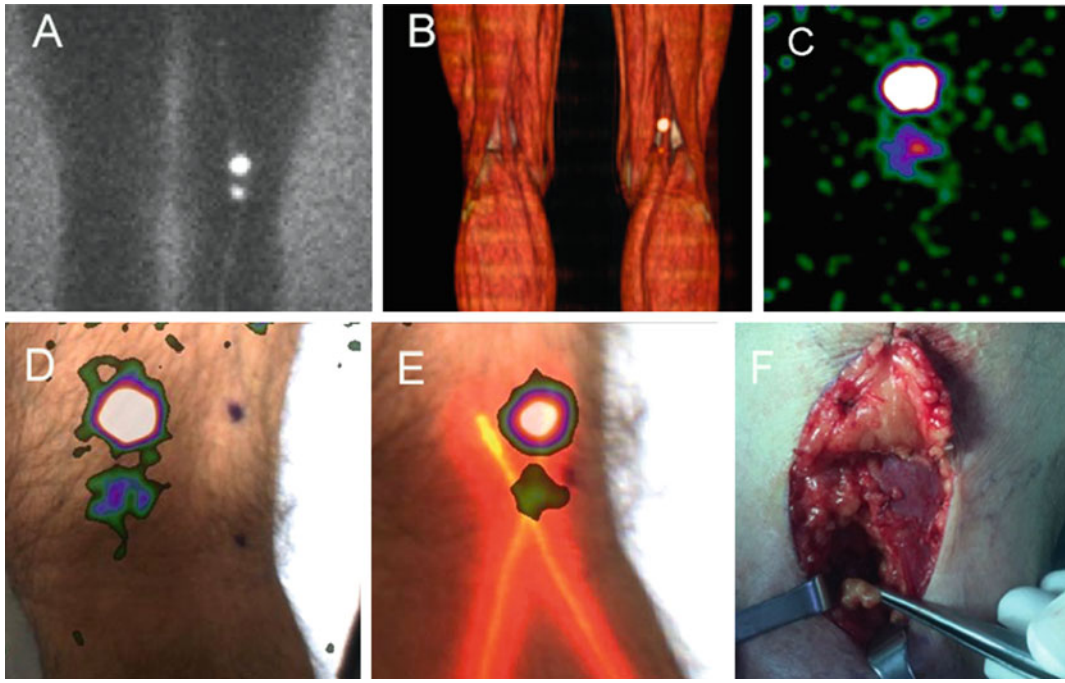

Fig. 11 Right popliteal sentinel nodes depicted on planar image (**a**), 3D reconstruction from SPECT/CT data (**b**), portable gamma camera (**c**), hybrid (gamma + optic) camera (**d**). During surgery, additional images were acquired to precisely depict the nodes' situation (**e**). Surgical removal (in the pincette) of one of these nodes (**f**)

during surgery. An in-transit SLN may indicate involvement in the lymphatic basin, but may also be the unique site with metastatic cells. Thus, in most studies the incidence of metastasis in the in-transit/aberrant SLN is quite similar, in the 14–22% range. In a review of 900 melanoma patients, Ortín-Pérez et al. reported that 19.5% of in-transit/aberrant lymph nodes bore metastasis; 11 out of 15 of these patients also presented metastatic involvement of at least one SLN in the expected lymphatic region, while the remaining 4 patients only had metastasis in the in-transit/aberrant SLN [120]. Several other studies have resulted in similar values, thus reinforcing the concept that it is necessary to identify and harvest these particular in-transit/aberrant lymph nodes since they may constitute the only focus of metastasis [121].

In this regard, the use of SPECT/CT and intraoperative imaging may refine the procedure, especially in these difficult to found lymph nodes, with the aid of precise anatomical localization (SPECT/CT) and intraoperative checking of a definite area of the body with a portable gamma camera. The use of this technology results in increased surgeon's confidence, as well as in improved preoperative planning and better staging [122–125] (Fig. 11).

Head and Neck Location

About 15–35% of primary melanomas are located in the head and neck and are associated with a worse prognosis. Several authors have demonstrated a greater rate of recurrence in this area after a negative SLN biopsy compared to other areas of the body [126]. SLN biopsy of tumors in the head and neck region is especially challenging both because of the great number of lymph nodes (>300) and because of the huge network of lymphatic vessels that contributes to the complexity of lymphatic drainage in this area, with melanomas often draining to multiple, aberrant, and bilateral lymph nodes [127].

Furthermore, during lymphoscintigraphy the radioactivity remaining at the site of injection may mask a SLN on planar imaging, and it is often hard to distinguish SLNs from second-echelon nodes. In a review of several studies comprising more than 3,400 head and neck melanomas, the sensitivity of SLN biopsy was reported to be in the range 80–100%, with a false-negative rate as high as 20% [128]. Another study with 246 patients demonstrated that melanomas located in the facial region presented a better prognosis than those in the skull, ears, or cervical region, even for thin tumors (Breslow index <1 mm). The presence of ulceration, elevated Clark level (IV/V), and young age were the strongest predictive factors to determine the presence of cervical lymph node metastasis [129].

A recent study of 152 patients with melanomas located in head or neck area compared the results of the actual presurgical lymphoscintigraphy with the expected drainage pattern derived from a predictive software based on a database of 929 patients. The concordance was complete in 80.4% of patients for all SLNs and partial in 12.2% of patients. Discrepancy was observed in 7.4% of patients. The authors concluded that lymphoscintigraphy provided an added value to personalize lymphatic mapping in each individual patient and that this imaging step is crucial to accurately detect the SLNs in head and neck melanomas, especially when faced with aberrant lymphatic drainage in unpredictable locations [130].

As mentioned above in this chapter, SPECT/CT imaging is currently considered to be mandatory for better assessing and depicting SLN located in the head and neck area. Zender et al. showed that the SPECT/CT findings led to a change in the management in 57% of patients with melanoma and suspected drainage to the parotid region. SPECT/CT precisely discriminated between parotid zone and cervical level II lymph nodes and visualized additional nodes, not visualized on planar lymphoscintigraphy, in 28% of the cases [131]. Taking into consideration that nearly 25% of cases in the head and neck area may show metastasis outside clinically predicted neck levels, it is necessary to ascertain these sites of potential involvement with the best approach, namely, to investigate the lymphatic drainage patterns using dynamic planar lymphoscintigraphy and SPECT/CT [132].

A more refined technique may include, if available, preoperative SPECT/CT, intraoperative imaging using portable devices, and hybrid tracer (multimodal approach). One study including 25 patients with head and neck malignancies demonstrated that the use of conventional lymphoscintigraphy, SPECT/CT, and the additional help of a portable gamma camera in one case were able to display 67 SLNs (55 visualized on planar images, 11 additional on SPECT/CT, and 1 additional with the portable gamma camera). Intraoperatively, 89 SLNs were resected (67 + 22 additional nodes). Twelve out of the 22 additional SLNs were located close to the injection site. The other ten additional SLNs were found by post-resection imaging with the portable gamma camera of the excision SLN site. Thus, the combined approach seems to be useful especially for tumors located approximately in the expected area of lymphatic drainage [133] (Fig. 12).

Cost-Effectiveness of SLN Biopsy in Melanoma

Currently, SLN biopsy is recommended in cases of primary melanoma without evidence of regional or distant metastasis when the risk of lymphatic node metastasis is at least 10% (AJCC stages IB and IIA, B, and C in the 7th edition). Selection criteria have not yet been standardized for cases with a Breslow thickness of less than 0.75 mm, which nevertheless account for 60–70% of melanomas diagnosed in large hospitals [134].

There is scarcity of data about the overall costs of this procedure in melanoma patients. On the other hand, the different items comprised in the whole procedure are not equally considered between different analyses. Thus, in a very complete study recently performed in 99 patients treated at a Spanish hospital, the cost of the procedure was estimated between € 9,486 and € 10,471. This analysis included an approach with radiotracer only, a major outpatient surgery operating room with only 1-day hospitalization in case of no

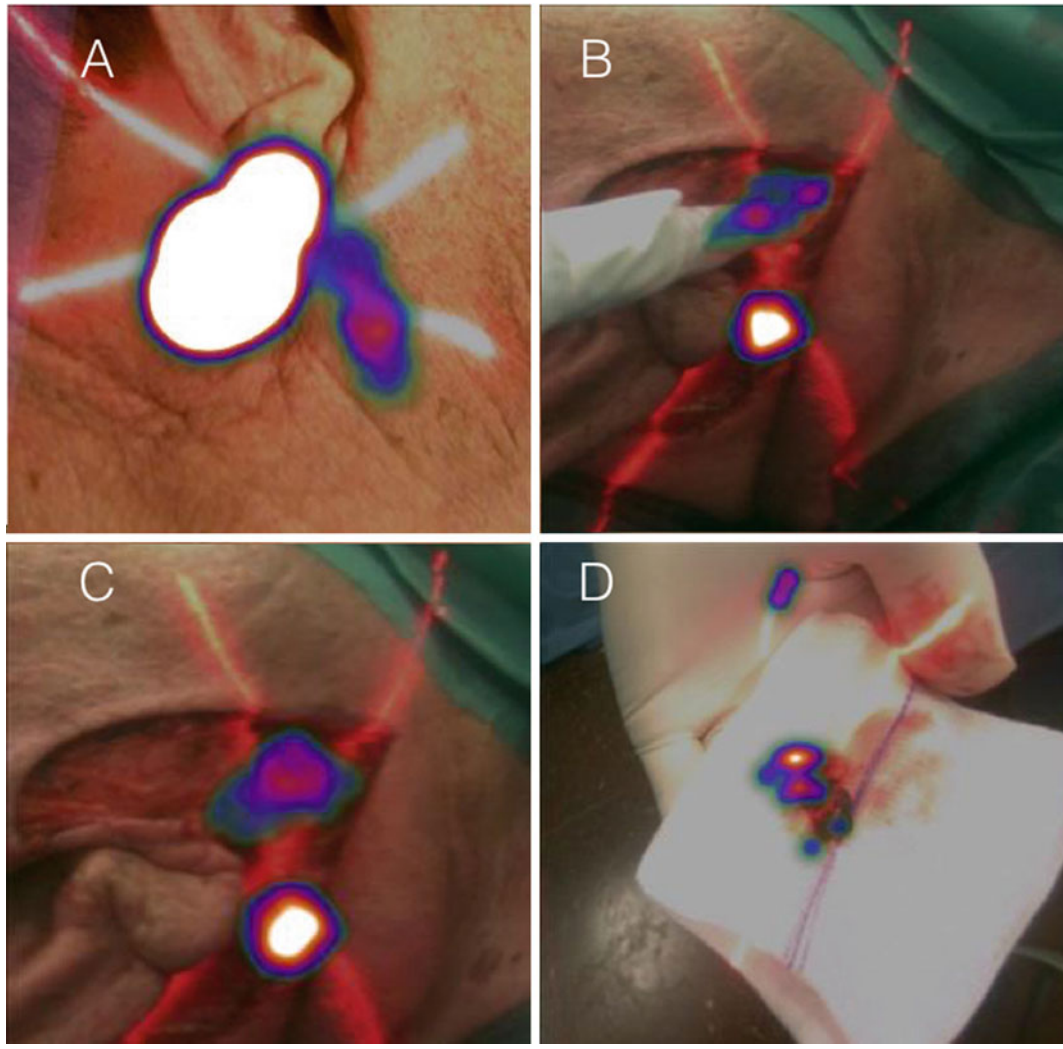

Fig. 12 Surgical approach with a portable hybrid camera. A sentinel node near the ear's injection site is depicted (**a**) and assessed with the use of gamma probe (**b**). Surgical localization and identification of the sentinel node (**c**) and "ex vivo" checking with the hybrid camera (**d**)

complications and a thorough pathological analysis. These costs are similar of those calculated in a US institution, ranging from $10,000 to $15,000 (€ 7,600–11,400) [135]. Almazán-Fernandez et al. calculated the costs of SLN biopsy in cutaneous melanoma, but they only included 1 day of hospitalization and re-excision of the melanoma scar with margins of 2 cm. The general costs reached € 682, but the authors did not take into account histopathologic analysis [136]. Similar findings were reported in an Australian study, with an estimated cost of € 1,900 [137].

Thus, it can be assumed that histologic processing increases to a great extent the overall costs of the SLN procedure; therefore, the indication criteria for SLN biopsy turn out to be crucial, especially in the patients with low risk for metastasis. On the other hand, the refinement of the procedure can save extra costs associated with extended surgery. In this regard, Stoffels et al. compared a cohort of patients in whom only planar lymphoscintigraphy was performed with a cohort of patients in whom SPECT/CT imaging was added. The fixed costs per SLN biopsy concerning infrastructure and

consumables were € 71 per procedure, while SPECT/CT imaging in that hospital represents an added cost of € 116. Obviously, the costs for SLN biopsy with either local or general anesthesia differed, with lesser costs in the group with planar imaging only (as SPECT/CT frequently visualized more deep-seated SLNs that required general anesthesia). However, a more detailed analysis demonstrated a cost saving of € 1,045 in the hospital stay expenses between patients with local or general anesthesia. Moreover, the addition of SPECT/CT imaging in the SLN biopsy group with local anesthesia saved about € 1,069 per procedure, and its use resulted in the upstaging of a proportion of patients, by detecting more metastatic SLNs. Costs for preoperative imaging increased, of course, but costs of surgery and hospital stay decreased remarkably. The economic study demonstrated that the routine use of preoperative SPECT/CT reduces the total cost of SLN biopsy per patient by € 710 [138].

In the use of hybrid tracers, the potential advantages also need to be weighed against the complexity of implementing this approach in the clinical routine and its associated costs. The cost of ICG vial is relatively cheap (about € 85 per vial). However, the highest additional costs lie in purchasing a NIR fluorescence camera system, with commercial values that range from several thousand € to hundreds of thousand €, depending on the system chosen [116].

Role of PET/CT Imaging for Radioguided Surgery

Many patients with stage I/II melanoma have no metastasis, or, if present, they are usually minimal-extent metastases. In contrast to the SLN biopsy, where diagnostic sensitivity is enhanced to the microscopic level by histologic analysis (and even to submicroscopic level by molecular analysis), the diagnostic performance of [^{18}F]FDG PET/CT in patients with micrometastasis is impaired by the relatively limited spatial resolution of imaging [139]. Indeed, the limited diagnostic value of [^{18}F]FDG PET/CT for assessing the presence of metastasis in patients with a clinically localized melanoma has been reported [140]. Some authors, however, consider that [^{18}F]FDG PET/CT can be useful in certain clinical situations where the risk of metastasis is increased (e.g., Breslow thickness >4 mm, presence of ulceration, and high mitotic index) [52].

Kell et al. assessed the preoperative value of [^{18}F]FDG PET/CT in patients with melanoma scheduled for SLN biopsy. Out of the initial 83 patients in their series, 37 were selected to undergo a preoperative [^{18}F]FDG PET/CT scan because of higher risk for metastasis. SLN biopsy demonstrated metastatic involvement in 9 of these 37 patients (24%), but only 2/9 patients had a positive [^{18}F]FDG PET/CT scan (22% positive predictive value). These results do not support the clinical validity of [^{18}F]FDG PET/CT in this population, as SLN biopsy was a more sensitive staging modality for the detection of lymph node metastasis [141]. After reviewing their findings in 30 patients with melanomas with Breslow thickness >1 mm, Constantinidou et al. observed that performing an [^{18}F]FDG PET/CT after a positive SLN biopsy did not alter the clinical management of melanoma [142]. Klode et al. reported similar findings in 61 melanoma patients and concluded that SLN biopsy is much more sensitive than [^{18}F]FDG PET/CT for the assessment of lymph node metastasis [143]. In another study, a combination of [^{18}F]FDG PET/CT and ultrasound was preoperatively employed in 20 melanoma patients scheduled for SLN biopsy, in whom 52 SLNs were eventually harvested. Ultrasound correctly identified 2 out of the 17 tumor-bearing SLNs, none of which had been identified by PET/CT [144]. In a study reported by Barsky et al. in 149 patients with at least an intermediate-thickness melanoma, [^{18}F]FDG PET/CT was positive in 41/149 cases (27.5%). Invasive procedures were subsequently performed in 18 of these 41 cases, but metastatic involvement was confirmed in only six patients; therefore, in the experience of these authors, [^{18}F]FDG PET/CT had a quite high rate of false-positive results, resulting in a low positive predictive value [145].

Although [^{18}F]FDG PET is not currently recommended as a routine investigation for staging patients with positive SLN biopsy, the technique

could be justified in patients with palpable lymph node before resection, due to its potential impact on decision-making regarding subsequent clinical management. In 70 melanoma patients with palpable lymph nodes but no clinical evidence of distant metastasis, Aukema et al. found that [^{18}F]FDG PET/CT led to change the indication for regional lymphadenectomy in 37% of the patients. The overall sensitivity of PET/CT in this subgroup of patients was 87% and specificity of 98% in the detection of additional metastases in melanoma patients with palpable lymph nodes [146].

One potential application for the intraoperative use of systemically administered [^{18}F]FDG in combination with a handheld PET detection probe has been proposed and reported in the clinical management of selected cases of metastatic melanoma [147]. Although the concept is in principle attractive, further evaluation of this approach is needed (especially regarding PET probes). A more practical approach is the intralesional administration of a radioactive or hybrid tracer in order to enable resection of isolated melanoma metastases aided by the use of a conventional handheld gamma probe (i.e., ROLL-like approach) after the PET/CT scan [148, 149].

References

1. Siegel R, Naishadham D, Jemal A. Cancer statistics, 2013. CA Cancer J Clin. 2013;63:11–30.
2. Ferlay J, Soerjomataram I, Ervik M, Dikshit R, Eser S, Mathers C, et al. GLOBOCAN 2012 v1.0, Cancer incidence and mortality worldwide: IARC CancerBase No. 11 [Internet]. Lyon: International Agency for Research on Cancer; 2013. Available at: http://globocan.iarc.fr. Accessed 20 Nov 2015.
3. Schadendorf DE, Fisher DE, Garbe C, Gershenwald JE, Grob JJ, Halpern A, et al. Melanoma. Nat Rev Dis Prim. 2015;1:1–20.
4. Russak JE, Rigel DS. Risk factors for the development of primary cutaneous melanoma. Dermatol Clin. 2012;30:363–8.
5. Balch CM, Gershenwald JE, Soong SJ, Thompson JF, Atkins MB, Byrd DR, et al. Final version of 2009 AJCC melanoma staging and classification. J Clin Oncol. 2009;27:6199–206.
6. Reintgen D, Cruse CW, Wells K, Berman C, Fenske N, Glass F, et al. The orderly progression of melanoma nodal metastases. Ann Surg. 1994;220: 759–67.
7. Balch CM, Soong SJ, Gershenwald JE, Thompson JF, Reintgen DS, Cascinelli N, et al. Prognostic factors analysis of 17,600 melanoma patients: validation of the American Joint Committee on Cancer melanoma staging system. J Clin Oncol. 2001;19:3622–34.
8. Kesmodel SB, Karakousis GC, Botbyl JD, Canter RJ, Lewis RT, Wahl PM, et al. Mitotic rate as a predictor of sentinel lymph node positivity in patients with thin melanomas. Ann Surg Oncol. 2005;12:449–58.
9. Mohr P, Eggermont AMM, Hauschild A, Buzaid A. Staging of cutaneous melanoma. Ann Oncol. 2009;20 Suppl 6:vi14–21.
10. Balch CM, Gershenwald JE, Soong SJ, Thompson JF. Update of the melanoma staging system: the importance of sentinel node staging and primary tumor mitotic rate. J Surg Oncol. 2011;104:379–85.
11. Morton DL, Wanek L, Nizze JA, Elashoff RM, Wong JH. Improved long-term survival after lymphadenectomy of melanoma metastatic to regional nodes. Analysis of prognostic factors in 1134 patients from the John Wayne Cancer Clinic. Ann Surg. 1991; 214:491–9.
12. Balch CM, Soong SJ, Bartolucci AA, Urist MM, Karakousis CP, Smith TJ, et al. Efficacy of an elective regional lymph node dissection of 1 to 4 mm thick melanomas for patients 60 years of age and younger. Ann Surg. 1996;224:255–63.
13. Morton DL, Wen DR, Wong JH, Economou JS, Cagle LA, Storm FK, et al. Technical details of intraoperative lymphatic mapping for early stage melanoma. Arch Surg. 1992;127:392–9.
14. Nieweg OE, Tanis PJ, Kroon BB. The definition of a sentinel node. Ann Surg Oncol. 2001;8:538–41.
15. Thompson JF, McCarthy WH, Bosch CM, O'Brien CJ, Quinn MJ, Paramaesvaran S, et al. Sentinel lymph node status as an indicator of the presence of metastatic melanoma in regional lymph nodes. Melanoma Res. 1995;5:255–60.
16. Harlow SP, Krag DN, Ashikaga T, Weaver DL, Meijer SJ, Loggie BW, et al. Gamma probe guided biopsy of the sentinel node in malignant melanoma: a multicenter study. Melanoma Res. 2001;11:45–55.
17. Phan GQ, Messina JL, Sondak VK, Zager JS. Sentinel lymph node biopsy for melanoma: indications and rationale. Cancer Control. 2009;16:234–9.
18. Giuliano AE, Kirgan DM, Guenther JM, Morton DL. Lymphatic mapping and sentinel lymphadenectomy for breast cancer. Ann Surg. 1994;220:391–8.
19. Broglie MA, Stoeckli SJ. Relevance of sentinel node procedures in head and neck squamous cell carcinoma. Q J Nucl Med Mol Imaging. 2011;55:509–20.
20. De Hullu JA, Doting E, Piers DA, Hollema H, Aalders JG, Koops HS, et al. Sentinel lymph node identification with technetium-99m-labeled nanocolloid in squamous cell cancer of the vulva. J Nucl Med. 1998;39:1381–5.
21. Horenblas S, Jansen L, Meinhardt W, Hoefnagel CA, de Jong D, Nieweg OE. Detection of occult metastasis in squamous cell carcinoma of the penis using a

dynamic sentinel node procedure. J Urol. 2000;163: 100–4.
22. Valdés Olmos RA, Rietbergen DD, Vidal-Sicart S, Manca G, Giammarile F, Mariani G. Contribution of SPECT/CT imaging to radioguided sentinel lymph node biopsy in breast cancer, melanoma, and other solid cancers: from "open and see" to "see and open". Q J Nucl Med Mol Imaging. 2014;58:127–39.
23. Uren RF, Howman-Giles RB, Thompson JF. Variation in cutaneous lymphatic flow rates. Ann Surg Oncol. 1997;4:279–80.
24. Reynolds HM, Walker CG, Dunbar PR, O'Sullivan MJ, Uren RF, Thompson JF, et al. Functional anatomy of the lymphatics draining the skin: a detailed statistical analysis. J Anat. 2010;216:344–55.
25. Norman J, Cruse W, Espinosa C, Cox C, Berman C, Clark R, Saba H, et al. Redefinition of cutaneous lymphatic drainage with the use of lymphoscintigraphy for malignant melanoma. Am J Surg. 1991; 162:432–7.
26. Statius Muller MG, Hennipman FA, van Leeuwen PA, Pijpers R, Vuylsteke RJ, Meijer S. Unpredictability of lymphatic drainage patterns in melanoma patients. Eur J Nucl Med. 2002;29:255–61.
27. Thompson JF, Uren RF. Lymphatic mapping in management of patients with primary cutaneous melanoma. Lancet Oncol. 2005;6:877–85.
28. Mariani G, Erba P, Manca G, Villa G, Gipponi M, Boni G, et al. Radioguided sentinel lymph node biopsy in patients with malignant cutaneous melanoma. The nuclear medicine contribution. J Surg Oncol. 2004;85:141–51.
29. Wong SL, Balch CM, Hurley P, Argawala SS, Akhurst TJ, Cochran A, et al. Sentinel lymph node biopsy for melanoma: American Society of Clinical Oncology and Society of Surgical Oncology joint clinical practice guideline. J Clin Oncol. 2012; 2012(30):2912–8.
30. Thompson JF, Soong SJ, Balch CM, Gershenwald JE, Ding S, Coit DG, et al. The prognostic significance of mitotic rate in localized cutaneous melanoma: an analysis of patients in the multi-institutional AJCC melanoma staging database. J Clin Oncol. 2011;29: 2199–205.
31. Coit DG, Olszanski AJ. Progress in the management of melanoma in 2013. J Natl Compr Canc Netw. 2013;11(5 Suppl):645–8.
32. Coit DG, Andtbacka R, Anker CJ, Bichakjian CK, Carson 3rd WE, Daud A, et al. National Comprehensive Cancer Network (NCCN). Melanoma, version 2.2013: featured updates to the NCCN guidelines. J Natl Compr Canc Netw. 2013;11:395–407.
33. Morton DL, Thompson JF, Cochran AJ, Mozzillo N, Elashoff R, Essner R, et al. Sentinel node biopsy or nodal observation in melanoma. N Engl J Med. 2006; 355:1307–17.
34. Faries MB, Thompson JF, Cochran A, Elashoff R, Glass EC, Mozzillo N, et al. The impact on morbidity and length of stay of early versus delayed complete lymphadenectomy in melanoma: results of the multicenter selective lymphadenectomy trial (I). Ann Surg Oncol. 2010;17:3324–9.
35. Morton DL, Thompson JF, Cochran AJ, Mozzillo N, Nieweg OE, Roses DF, et al. Final trial report of sentinel-node biopsy versus nodal observation in melanoma. N Engl J Med. 2014;370:599–609.
36. Van Akkooi ACJ. Sentinel node followed by completion lymph node dissection versus nodal observation: staging or therapeutic? Controversy continues despite final results of MSLT-1. Melanoma Res. 2014;24:291–4.
37. Parrett BM, Accortt NA, Li R, Dosanjh AS, Thummala S, Kullar R, et al. The effect of delay time between primary melanoma biopsy and sentinel lymph node dissection on sentinel node status, recurrence, and survival. Melanoma Res. 2012;22:386–91.
38. Tejera-Vaquerizo A, Nagore E, Puig S, Robert C, Saiag P, Martín-Cuevas P, et al. Effect of time to sentinel-node biopsy on the prognosis of cutaneous melanoma. Eur J Cancer. 2015;51:1780–93.
39. Chakera AH, Hesse B, Burak Z, Ballinger JR, Britten A, Caracò C, et al. EANM–EORTC general recommendations for sentinel node diagnostics in melanoma. Eur J Nucl Med Mol Imaging. 2009;36: 1713–42.
40. Giammarile F, Alazraki N, Aarsvold JN, Audisio RA, Glass E, Grant SF, et al. The EANM and SNMMI practice guideline for lymphoscintigraphy and sentinel node localization in breast cancer. Eur J Nucl Med Mol Imaging. 2013;40:1932–47.
41. Xiong L, Engel H, Gazyakan E, Rahimi M, Hünerbein M, Sun J, Kneser U, Hirche C. Current techniques for lymphatic imaging: state of the art and future perspectives. Eur J Surg Oncol. 2014;40:270–6.
42. Leong SP, Kim J, Ross M, Faries M, Scoggins CR, Metz WL, et al. A phase 2 study of ^{99m}Tc-tilmanocept in the detection of sentinel lymph nodes in melanoma and breast cancer. Ann Surg Oncol. 2011;18:961–9.
43. Sondak VK, King DW, Zager JS, Schneebaum S, Kim J, Leong SPL, et al. Combined analysis of phase III trials evaluating [^{99m}Tc]tilmanocept and vital blue dye for identification of sentinel lymph nodes in clinically node-negative cutaneous melanoma. Ann Surg Oncol. 2013;20:680–8.
44. Puleo CA, Berman C, Montilla-Soler JL, Zager JS, Sondak VK. ^{99m}Tc-tilmanocept for lymphoscintigraphy. Imaging Med. 2013;5:119–25.
45. Bluemel C, Herrmann K, Giammarile F, Nieweg OE, Dubreuil J, Testori A, et al. EANM practice guidelines for lymphoscintigraphy and sentinel lymph node biopsy in melanoma. Eur J Nucl Med Mol Imaging. 2015;42:1750–66.
46. Heuveling DA, van Schie A, Vugts DJ, Hendrikse NH, Yaqub M, Hoekstra OS, et al. Pilot study on the feasibility of PET/CT lymphoscintigraphy with ^{89}Zr-nanocolloidal albumin for sentinel node identification in oral cancer patients. J Nucl Med. 2013;54:585–9.
47. Alazraki N, Glass EC, Castronovo F, Olmos RA, Podoloff D, Society of Nuclear Medicine. Procedure guideline for lymphoscintigraphy and the use of intraoperative gamma probe for sentinel lymph node

localization in melanoma of intermediate thickness 1.0. J Nucl Med. 2002;43:1414–8.
48. Chakera AH, Lock-Andersen J, Hesse U, Nurnberg BM, Juhl BR, Stokholm KH, et al. One-day or two-day procedure for sentinel node biopsy in melanoma? Eur J Nucl Med Mol Imaging. 2009;36:928–37.
49. Uren RF, Howman-Giles RB, Shaw HM, Thompson JF, McCarthy WH. Lymphoscintigraphy in high-risk melanoma of the trunk: predicting draining node groups, defining lymphatic channels and locating the sentinel node. J Nucl Med. 1993;34:1435–40.
50. Valdés Olmos RA, Hoefnagel CA, Nieweg OE, Jansen L, Rutgers EJ, Borger J, et al. Lymphoscintigraphy in oncology: a rediscovered challenge. Eur J Nucl Med. 1999;26(4 Suppl):S2–10.
51. Uren RF, Thompson JF, Howman-Giles R, Chung DK. The role of lymphoscintigraphy in the detection of lymph node drainage in melanoma. Surg Oncol Clin N Am. 2006;15:285–300.
52. Belhocine TZ, Scott AM, Even-Sapir E, Urbain JL, Essner R. Role of nuclear medicine in the management of cutaneous malignant melanoma. J Nucl Med. 2006;47:957–67.
53. Uren RF, Howman-Giles R, Chung D, Thompson JF. Guidelines for lymphoscintigraphy and F18 FDG PET scans in melanoma. J Surg Oncol. 2011;104:405–19.
54. Moncayo VM, Aarsvold JN, Alazraki NP. Lymphoscintigraphy and sentinel nodes. J Nucl Med. 2015;56:901–7.
55. Kapteijn BA, Nieweg OE, Valdés Olmos RA, Liem IH, Panday RK, Hoefnagel CA, et al. Reproducibility of lymphoscintigraphy for lymphatic mapping in cutaneous melanoma. J Nucl Med. 1996;37:972–5.
56. Tonakie A, Sondak V, Yahanda A, Wahl RL. Reproducibility of lymphoscintigraphic drainage patterns in sequential ^{99m}Tc human serum albumin and ^{99m}Tc sulfur colloid studies: implications for sentinel node identification in melanoma. Surgery. 1999;126:955–62.
57. Rettenbacher L, Koller J, Kässmann H, Holzmannhofer J, Rettenbacher T, Galvan G. Reproducibility of lymphoscintigraphy in cutaneous melanoma: can we accurately detect the sentinel lymph node by expanding the tracer injection distance from the tumor site? J Nucl Med. 2001;42:424–9.
58. Uren RF, Howman-Giles R, Chung DK, Morton RL, Thompson JF. The reproducibility in routine clinical practice of sentinel lymph node identification by pre-operative lymphoscintigraphy in patients with cutaneous melanoma. Ann Surg Oncol. 2007;14:899–905.
59. Vidal M, Vidal-Sicart S, Torrents A, Perissinotti A, Navales I, Paredes P, et al. Accuracy and reproducibility of lymphoscintigraphy for sentinel node detection in patients with cutaneous melanoma. J Nucl Med. 2012;53:1193–9.
60. Vitali GC, Trifirò G, Zonta M, Pennacchioli E, Santoro L, Travaini LL, et al. Lymphoscintigraphy in clinical routine practice: reproducibility and accuracy in melanoma patients with a long-term follow-up. Eur J Surg Oncol. 2014;40:55–60.
61. Kretschmer L, Bertsch HP, Bardzik P, Meller J, Hellriegel S, Thoms KM, et al. The impact of nodal tumour burden on lymphoscintigraphic imaging in patients with melanomas. Eur J Nucl Med Mol Imaging. 2015;42:231–40.
62. van der Ploeg IM, Valdés Olmos RA, Nieweg OE, Rutgers EJ, Kroon BB, Hoefnagel CA. The additional value of SPECT/CT in lymphatic mapping in breast cancer and melanoma. J Nucl Med. 2007;48:1756–60.
63. Vermeeren L, van der Ploeg IM, Valdés Olmos RA, Meinhardt W, Klop WM, Kroon BB, et al. SPECT/CT for preoperative sentinel node localization. J Surg Oncol. 2010;101:184–90.
64. Vidal-Sicart S, Brouwer OR, Valdés-Olmos RA. Evaluation of the sentinel lymph node combining SPECT/CT with the planar image and its importance for the surgical act. Rev Esp Med Nucl. 2011;30:331–7.
65. Wagner T, Buscombe J, Gnanasegaran G, Navalkissoor S. SPECT/CT in sentinel node imaging. Nucl Med Commun. 2013;34:191–202.
66. Valdés Olmos RA, Rietbergen DDD, Vidal-Sicart S. SPECT/CT and sentinel node lymphoscintigraphy. Clin Transl Imaging. 2014;2:491–504.
67. Van der Ploeg IM, Valdés Olmos RA, Kroon BB, Wouters MW, van den Brekel MW, Vogel WV, et al. The yield of SPECT/CT for anatomical lymphatic mapping in patients with melanoma. Ann Surg Oncol. 2009;16:1537–42.
68. Mucientes Rasilla J, Cardona Arbonies J, Delgado Bolton R, Izarduy Pereyra L, Salazar Andia G, Prieto Soriano A, et al. SPECT-CT in sentinel node detection in patients with melanoma. Rev Esp Med Nucl. 2009;28:229–34.
69. Veenstra HJ, Vermeeren L, Valdés Olmos RA, Nieweg OE. The additional value of lymphatic mapping with routine SPECT/CT in unselected patients with clinically localized melanoma. Ann Surg Oncol. 2012;19:1018–23.
70. Fairbairn N, Munson C, Ali Khan Z, Butterworth M. The role of hybrid SPECT/CT for lymphatic mapping in patients with melanoma. J Plast Rec Aesthet Surg. 2013;66:1248–55.
71. Kraft O, Havel M. Localisation of sentinel lymph nodes in patients with melanomas by planar lymphoscintigraphic and hybrid SPECT/CT imaging. Nucl Med Rev Cent East Eur. 2012;15:101–7.
72. Martínez Castillo R, Fernández López R, Acevedo Bañez I, Alvarez Pérez RM, García Solis D, Vázquez Albertino R, et al. Utility of single photon emission computed tomography-computed tomography in selective sentinel lymph node biopsy in patients with melanoma. Rev Esp Med Nucl Imagen Mol. 2014;33:129–35.
73. Stoffels I, Boy C, Pöppel T, Kuhn J, Klötgen K, Dissemond J, et al. Association between lymph node excision with or without preoperative SPECT/CT and metastatic node detection and disease-free survival in melanoma. JAMA. 2012;308:1007–14.
74. Jimenez-Heffernan A, Ellmann A, Sado H, Huić D, Bal C, Parameswaran R, et al. Results of a prospective

multicenter International Atomic Energy Agency sentinel node trial on the value of SPECT/CT over planar imaging in various malignancies. J Nucl Med. 2015; 56:1338–44.
75. Díaz-Expósito R, Vidal-Sicart S, Rioja-Martín ME. Selective biopsy of sentinel node in melanoma. Survey results of nuclear medicine services in Spain. Rev Esp Med Nucl Imagen Mol. 2015;34:120–2.
76. Vidal-Sicart S, Vilalta Solsona A, Alonso Vargas MI. Sentinel node in melanoma and breast cancer. Current considerations. Rev Esp Med Nucl Imagen Mol. 2015;34:30–44.
77. Stebbins WG, Garibyan L, Sober AJ. Sentinel lymph node biopsy and melanoma: 2010 update, part I and II. J Am Acad Dermatol. 2010;62:723–48.
78. McMasters KM, Reintgen DS, Ross MI, Wong SL, Gershenwald JE, Krag DN, et al. Sentinel lymph node biopsy for melanoma: how many radioactive nodes should be removed. Ann Surg Oncol. 2001;8:192–7.
79. Nieweg OE, Jansen L, Kroon BB. Technique of lymphatic mapping and sentinel node biopsy for melanoma. Eur J Surg Oncol. 1998;24:520–4.
80. Murphy AD, Britten A, Powell B. Hot or not? The 10% rule in sentinel lymph node biopsy for malignant melanoma revisited. J Plast Reconstr Aesthet Surg. 2014;67:316–9.
81. Prieto VG. Sentinel lymph nodes in cutaneous melanoma: handling, examination, and clinical repercussion. Arch Pathol Lab Med. 2010;134:1764–9.
82. Mocellin S, Hoon DS, Pilati P, Rossi CR, Nitti D. Sentinel lymph node molecular ultrastaging in patients with melanoma: a systematic review and meta-analysis of prognosis. J Clin Oncol. 2007;25:1588–95.
83. Manca G, Romanini A, Pellegrino D, Borsò E, Rondini M, Orlandini C, et al. Optimal detection of sentinel lymph node metastases by intraoperative radioactive threshold and molecular analysis in patients with melanoma. J Nucl Med. 2008;49:1769–75.
84. Gershenwald JE, Andtbacka RH, Prieto VG, et al. Microscopic tumor burden in sentinel lymph nodes predicts synchronous nonsentinel lymph node involvement in patients with melanoma. J Clin Oncol. 2008; 26:4296–303.
85. Vuylsteke RJ, Borgstein PJ, van Leeuwen PA, et al. Sentinel lymph node tumor load: an independent predictor of additional lymph node involvement and survival in melanoma. Ann Surg Oncol. 2005;12:440–8.
86. Cochran AJ, Wen DR, Huang RR, Wang HJ, Elashoff R, Morton DL. Prediction of metastatic melanoma in nonsentinel nodes and clinical outcome based on the primary melanoma and the sentinel node. Mod Pathol. 2004;17:747–55.
87. Van Akkooi AC, de Wilt JH, Verhoef C, Eggermont AM. Isolated tumor cells and long-term prognosis of patients with melanoma. Ann Surg Oncol. 2008;15: 1547–8.
88. Van der Ploeg AP, van Akkooi AC, Haydu LE, Scolyer RA, Murali R, Verhoef C, et al. The prognostic significance of sentinel node tumour burden in melanoma patients: an international, multicenter study of 1539 sentinel node-positive melanoma patients. Eur J Cancer. 2014;50:111–20.
89. Satzger I, Meier A, Zapf A, Niebuhr M, Kapp A, Gutzmer R. Is there a therapeutic benefit of complete lymph node dissection in melanoma patients with low tumor burden in the sentinel node? Melanoma Res. 2014;24:454–61.
90. Morton DL. Overview and update of the phase III Multicenter Selective Lymphadenectomy Trials (MSLT-I and MSLT-II) in melanoma. Clin Exp Metastasis. 2012;29:699–706.
91. Valdés Olmos RA, Vidal-Sicart S, Giammarile F, Zaknun JJ, Van Leeuwen FW, Mariani G. The GOSTT concept and hybrid mixed/virtual/augmented reality environment radioguided surgery. Q J Nucl Med Mol Imaging. 2014;58:207–15.
92. Hellingman D, de Wit-van der Veen LJ, Klop WM, Valdés Olmos RA. Detecting near-the-injection-site sentinel nodes in head and neck melanomas with a high- resolution portable gamma camera. Clin Nucl Med. 2015;40:e11–6.
93. Heller S, Zanzonico P. Nuclear probes and intraoperative gamma cameras. Semin Nucl Med. 2011; 41:166–81.
94. Vermeeren L, Valdés-Olmos RA, Klop WM, Balm AJ, Van den Brekel MW. A portable gammacamera for intraoperative detection of sentinel nodes in the head and neck region. J Nucl Med. 2010;51:700–3.
95. Vidal-Sicart S, Brouwer OR, Mathéron HM, Bing Tan I, Valdés-Olmos RA. Sentinel node identification with a portable gamma camera in a case without visualization on conventional lymphoscintigraphy and SPECT/CT. Rev Esp Med Nucl Imagen Mol. 2013;32:203–4.
96. Vidal-Sicart S, Paredes P, Zanón G, Pahisa J, Martinez-Román S, Caparrós X, et al. Added value of intraoperative real-time imaging in searches for difficult-to-locate sentinel nodes. J Nucl Med. 2010; 51:1219–25.
97. Dengel LT, More MJ, Judy PG, Petroni GR, Smolkin ME, Rehm PK, Majewski S, Williams MB, Slingluff Jr CL. Intraoperative imaging guidance for sentinel node biopsy in melanoma using a mobile gamma camera. Ann Surg. 2011;253:774–8.
98. Stoffels I, Poeppel T, Boy C, Mueller S, Wichmann F, Dissemond J, et al. Radio-guided surgery: advantages of a new portable γ-camera (Sentinella) for intraoperative real time imaging and detection of sentinel lymph nodes in cutaneous malignancies. J Eur Acad Dermatol Venereol. 2012;26:308–13.
99. Olcott P, Pratx G, Johnson D, Mittra E, Niederkohr R, Levin CS. Clinical evaluation of a novel intraoperative handheld gamma camera for sentinel lymph node biopsy. Phys Med. 2014;30:340–5.
100. Vidal-Sicart S, Rioja ME, Paredes P, Keshtgar MR, Valdés Olmos RA. Contribution of perioperative imaging to radioguided surgery. Q J Nucl Med Mol Imaging. 2014;58:140–60.
101. Haneishi H, Onishi Y, Shimura H, Hayashi H. Simultaneous acquisition and image synthesis of gamma

cameras and optical cameras for sentinel lymph node identification during radioguided surgery. IEEE Trans Nucl Sci. 2007;54:1703–9.
102. Hellingman D, Vidal-Sicart S, de Wit-van der Veen LJ, Paredes P, Valdés Olmos RA. A new portable hybrid camera for fused optical and scintigraphic imaging: first clinical experiences. Clin Nucl Med. 2016;41:e39–43.
103. Mihaljevic AL, Rieger A, Belloni B, Hein R, Okur A, Scheidhauer K, et al. Transferring innovative free-hand SPECT to the operating room: first experiences with sentinel lymph node biopsy in malignant melanoma. Eur J Surg Oncol. 2014;40:42–8.
104. Pouw B, de Wit-van der Veen LJ, Stokkel MP, Valdés Olmos RA. Improved accuracy and reproducibility using a training protocol for Freehand-SPECT 3D mapping in radio-guided surgery. Clin Nucl Med. 2015;40:e457–60.
105. Bluemel C, Schnelzer A, Okur A, Ehlerding A, Paepke S, Scheidhauer K, et al. Freehand SPECT for image-guided sentinel lymph node biopsy in breast cancer. Eur J Nucl Med Mol Imaging. 2013; 40:1656–61.
106. Sulzbacher L, Klinger M, Scheurecker C, Wacha M, Shamiyeh A, Malek M, et al. Clinical usefulness of a novel Freehand 3D imaging device for radio-guided intraoperative sentinel lymph node detection in malignant melanoma. Clin Nucl Med. 2015;40:e436–40.
107. Rietbergen DDD, van den Berg NS, van Leeuwen FWB, Valdés Olmos RA. Hybrid techniques for intraoperative sentinel lymph node imaging: early experiences and future prospects. Imaging Med. 2013;5:147–59.
108. Motomura K, Inaji H, Komoike Y, Hasegawa Y, Kasugai T, Noguchi S, et al. Combination technique is superior to dye alone in identification of the sentinel node in breast cancer patients. J Surg Oncol. 2001;76: 95–9.
109. Schaafsma BE, Mieog JS, Hutteman M, van der Vorst JR, Kuppen PJ, Löwik CW, et al. The clinical use of indocyanine green as a near-infrared fluorescent contrast agent for image-guided oncologic surgery. J Surg Oncol. 2011;104:323–32.
110. van der Vorst JR, Schaafsma BE, Verbeek FP, Swijnenburg RJ, Hutteman M, Liefers GJ, et al. Dose optimization for near-infrared fluorescence sentinel lymph node mapping in patients with melanoma. Br J Dermatol. 2013;168:93–8.
111. Cloyd JM, Wapnir IL, Read BM, Swetter S, Greco RS. Indocyanine green and fluorescence lymphangiography for sentinel lymph node identification in cutaneous melanoma. J Surg Oncol. 2014;110:888–92.
112. Stoffels I, Dissemond J, Pöppel T, Schadendorf D, Klode J. Intraoperative fluorescence imaging for sentinel lymph node detection: prospective clinical trial to compare the usefulness of indocyanine green vs technetium Tc99m for identification of sentinel lymph nodes. JAMA Surg. 2015;150:617–23.
113. van Den Berg NS, Buckle T, Kleinjan GI, Klop WM, Horenblas S, Van Der Poel HG, et al. Hybrid tracers for sentinel node biopsy. Q J Nucl Med Mol Imaging. 2014;58:193–206.
114. Brouwer OR, Buckle T, Vermeeren L, Klop WM, Balm AJ, van der Poel HG, et al. Comparing the hybrid fluorescent-radioactive tracer indocyanine green-99mTc-nanocolloid with ^{99m}Tc-nanocolloid for sentinel node identification: a validation study using lymphoscintigraphy and SPECT/CT. J Nucl Med. 2012;53:1034–40.
115. Frontado LM, Brouwer OR, van den Berg NS, Mathéron HM, Vidal-Sicart S, van Leeuwen FW, et al. Added value of the hybrid tracer indocyanine green-^{99}mTc-nanocolloid for sentinel node biopsy in a series of patients with different lymphatic drainage patterns. Rev Esp Med Nucl Imagen Mol. 2013;32:227–33.
116. van den Berg NS, Brouwer OR, Schaafsma BE, Mathéron HM, Klop WMC, Balm AJM, et al. Multimodal surgical guidance during sentinel node biopsy for melanoma: combined gamma tracing and fluorescence imaging of the sentinel node through use of the hybrid tracer indocyanine green-technetium-99m-nanocolloid. Radiology. 2015;275:521–9.
117. Stoffels I, Leyh J, Pöppel T, Schadendorf D, Klode J. Evaluation of a radioactive and fluorescent hybrid tracer for sentinel lymph node biopsy in head and neck malignancies: prospective randomized clinical trial to compare ICG-^{99m}Tc-nanocolloid hybrid tracer versus ^{99m}Tc-nanocolloid. Eur J Nucl Med Mol Imaging. 2015;42:1631–8.
118. Vidal-Sicart S, van Leeuwen FW, van den Berg NS, Valdés Olmos RA. Fluorescent radiocolloids: are hybrid tracers the future for lymphatic mapping? Eur J Nucl Med Mol Imaging. 2015;42:1627–30.
119. Nogareda Z, Vilalta A, Bennassar A, Paredes P, Vidal-Sicart S. Aberrant lymphatic drainage from a melanoma located in epigastric area. Rev Esp Med Nucl Imagen Mol. 2014;33:390–1.
120. Ortín-Pérez J, Vidal-Sicart S, Doménech B, Rubí S, Lafuente S, Pons F. In-transit sentinel lymph nodes in malignant melanoma. What is their importance? Rev Esp Med Nucl. 2008;27:424–9.
121. Zager JS, Puleo CA, Sondak VK. What is the significance of the in transit or interval sentinel node in melanoma. Ann Surg Oncol. 2011;18:3232–4.
122. Alvarez Paez AM, Brouwer OR, Veenstra HJ, van der Hage JA, Wouters M, Nieweg OE, et al. Decisive role of SPECT/CT in localization of unusual periscapular sentinel nodes in patients with posterior trunk melanoma: three illustrative cases and a review of the literature. Melanoma Res. 2012;22:278–83.
123. Veenstra HJ, Klop MW, Lohuis PJ, Nieweg OE, Valdés Olmos RA. Lymphatic drainage of melanomas located on the manubrium sterni to cervical lymph nodes: a case series assessed by SPECT/CT. Clin Nucl Med. 2013;38:e137–9.
124. Brammen L, Nedomansky J, Haslik W, Staudenherz A. Extraordinary lymph drainage in cutaneous malignant melanoma and the value of hybrid imaging: a case report. Nucl Med Mol Imaging. 2014;48:306–8.
125. Peral Rubio F, de la Riva P, Moreno-Ramírez D, Ferrándiz-Pulido L. Portable gamma camera guidance in sentinel lymph node biopsy: prospective

observational study of consecutive cases. Actas Dermosifiliogr. 2015;106:408–14.
126. Patuzzo R, Maurichi A, Camerini T, Gallino G, Ruggeri R, Baffa G, et al. Accuracy and prognostic value of sentinel lymph node biopsy in head and neck melanomas. J Surg Res. 2014;187:518–24.
127. Lin D, Franc BL, Kashani-Sabet M, Singer MI. Lymphatic drainage patterns of head and neck cutaneous melanoma observed on lymphoscintigraphy and sentinel lymph node biopsy. Head Neck. 2006;28: 249–55.
128. De Rosa N, Lyman GH, Silbermins D, Valsecchi ME, Pruitt SK, Tyler DM, et al. Sentinel node biopsy for head and neck melanoma: a systematic review. Otolaryngol Head Neck Surg. 2011;145:375–82.
129. Ettl T, Irga S, Müller S, Rohrmeier C, Reichert TE, Schreml S, et al. Value of anatomic site, histology and clinicopathological parameters for prediction of lymph node metastasis and overall survival in head and neck melanomas. J Craniomaxillofac Surg. 2014; 42:e252–8.
130. Vidal M, Vidal-Sicart S, Torres F, Ruiz DM, Paredes P, Pons F. Correlation between theoretical anatomical patterns of lymphatic drainage and lymphoscintigraphy findings during sentinel node detection in head and neck melanomas. Eur J Nucl Med Mol Imaging. 2016;43:626–34.
131. Zender C, Guo T, Weng C, Faulhaber P, Rezaee R. Utility of SPECT/CT for periparotid sentinel lymph node mapping in the surgical management of head and neck melanoma. Am J Otolaryngol. 2014;35:12–8.
132. Klop WM, Veenstra HJ, Vermeeren L, Nieweg OE, Balm AJ, Lohuis PJ. Assessment of lymphatic drainage patterns and implications for the extent of neck dissection in head and neck melanoma patients. J Surg Oncol. 2011;103:756–60.
133. Borbón-Arce M, Brouwer OR, van den Berg NS, Mathéron H, Klop WM, Balm AJ, et al. An innovative multimodality approach for sentinel node mapping and biopsy in head and neck malignancies. Rev Esp Med Nucl Imagen Mol. 2014;33:274–9.
134. Andtbacka RH, Gershenwald JE. Role of sentinel lymph node biopsy in patients with thin melanoma. J Natl Compr Canc Netw. 2009;7:308–17.
135. Agnese D, Abdessalam S, Burak W, Magro C, Pozderac R, Walker M. Cost-effectiveness of sentinel lymph node biopsy in thin melanomas. Surgery. 2003; 134:542–8.
136. Almazán-Fernandez FM, Serrano-Ortega S, Moreno-Villalonga JJ. Descriptive study of the costs of diagnosis and treatment cost analysis of diagnosis and treatment of cutaneous melanoma. Actas Dermosifiliogr. 2009;100:785–91.
137. Morton RL, Howard K, Thompson JF. The cost-effectiveness of sentinel node biopsy in patients with intermediate thickness primary cutaneous melanoma. Ann Surg Oncol. 2009;16:929–40.
138. Stoffels I, Müller M, Geisel MH, Leyh J, Pöppel T, Schadendorf D, et al. Cost-effectiveness of preoperative SPECT/CT combined with lymphoscintigraphy vs. lymphoscintigraphy for sentinel lymph node excision in patients with cutaneous malignant melanoma. Eur J Nucl Med Mol Imaging. 2014;41:1723–31.
139. Krug B, Crott R, Lonneux M, Baurain J-F, Pirson A-S, Vander BT. Role of PET in the initial staging of cutaneous malignant melanoma: systematic review. Radiology. 2008;249:836–44.
140. Clark PB, Soo V, Kraas J, Shen P, Levine EA. Futility of fluorodeoxyglucose F 18 positron emission tomography in initial evaluation of patients with T2 to T4 melanoma. Arch Surg. 2006;141:284–8.
141. Kell MR, Ridge JA, Joseph N, Sigurdson ER. PET CT imaging in patients undergoing sentinel node biopsy for melanoma. Eur J Surg Oncol. 2007;33: 911–3.
142. Constantinidou A, Hofman M, O'Doherty M, Acland KM, Healy C, Harries M. Routine positron emission tomography and positron emission tomography/computed tomography in melanoma staging with positive sentinel node biopsy is of limited benefit. Melanoma Res. 2008;18:56–60.
143. Klode J, Dissemond J, Grabbe S, Hillen U, Poeppel T, Boeing C. Sentinel lymph node excision and PET-CT in the initial stage of malignant melanoma: a retrospective analysis of 61 patients with malignant melanoma in American Joint Committee on Cancer stages I and II. Dermatol Surg. 2010;36:439–45.
144. Hinz T, Voth H, Ahmadzadehfar H, Hoeller T, Wenzel J, Bieber T, et al. Role of high-resolution ultrasound and PET/CT imaging for preoperative characterization of sentinel lymph nodes in cutaneous melanoma. Ultrasound Med Biol. 2013;39:30–6.
145. Barsky M, Cherkassky L, Vezeridis M, Miner TJ. The role of preoperative positron emission tomography/computed tomography (PET/CT) in patients with high-risk melanoma. J Surg Oncol. 2014;109:726–9.
146. Aukema TS, Valdés Olmos RA, Wouters MW, Klop WM, Kroon BB, Vogel WV, et al. Utility of preoperative ^{18}F-FDG PET/CT and brain MRI in melanoma patients with palpable lymph node metastases. Ann Surg Oncol. 2010;17:2773–8.
147. Povoski SP, Neff RL, Mojzisik CM, O'Malley DM, Hinkle GH, Hall NC, et al. A comprehensive overview of radioguided surgery using gamma detection probe technology. World J Surg Oncol. 2009;7:11.
148. Carrera D, Fernández A, Estrada J, Martín-Comín J, Gámez C. Detection of occult malignant melanoma by 18F-FDG PET-CT and gamma probe. Rev Esp Med Nucl. 2005;24:410–3.
149. Infante JR, Rayo JI, Serrano J, Domínguez ML, García L, Durán C, Moreno M. Clinical application of ROLL technique in non-breast diseases. Complementary use after PET-CT study. Rev Esp Med Nucl Imagen Mol. 2015;34:162–6.

Radioguided Surgery for Head and Neck Cancer

49

Federica Orsini, Erinda Puta, Renato A. Valdés Olmos, Sergi Vidal-Sicart, Francesco Giammarile, and Giuliano Mariani

Abstract

Tumor status of locoregional lymph nodes is an important prognostic factor in patients with squamous cells carcinomas of the head and neck (HNSCC). Sentinel lymph node biopsy (SLNB) approach meets the expectations of accurately staging the lymph node status of these patients. The procedure consists of preoperative peritumoral injection of the tracer followed by lymphoscintigraphy using planar and single photon emission tomography/computed tomography (SPECT/CT) imaging. Based on the preoperative lymphoscintigraphy findings, the position of the sentinel lymph node (SLN) is marked on the skin. Intraoperative detection of the SLN is guided by combination of a portable handheld gamma ray detection probe (radionuclide detection) and dissection/harvesting of the radioactive lymph node(s). After surgical removal, the SLN is subjected to meticulous histopathological examination.

Keywords

Head and neck cancers • Radioguided surgery • Radioguided occult lesion localization • Sentinel lymph node biopsy • SLNB • SLN • ROLL • Sentinel lymph node

Glossary

[^{18}F]FDG	2-Deoxy-2-[^{18}F]fluoro-D-glucose
AJCC	American Joint Committee on Cancer
Bq	Becquerel unit
CT	X-ray computed tomography
DTC	Differentiated thyroid cancer
EMA	European Medicines Agency
FDA	United States Food and Drug Administration

F. Orsini (✉) • E. Puta
Nuclear Medicine Unit, "Maggiore della Carità" University Hospital, Novara, Italy
e-mail: federica.orsini@maggioreosp.novara.it

R.A. Valdés Olmos
Nuclear Medicine Section and Interventional Molecular Imaging Laboratory, Department of Radiology, Leiden University Medical Centre, Leiden, The Netherlands

Diagnostic Oncology Division, Nuclear Medicine Department, Netherlands Cancer Institute – Antoni van Leeuwenhoek Hospital, Amsterdam, CX, The Netherlands

S. Vidal-Sicart
Nuclear Medicine Department, Hospital Clínic Barcelona, Barcelona, Catalonia, Spain

Institut d'Investigació Biomèdica August Pi i Sunyer (IDIBAPS), Barcelona, Spain

F. Giammarile
Nuclear Medicine and Diagnostic Imaging Section, Division of Human Health, Department of Nuclear Sciences and Applications, International Atomic Energy Agency, Vienna, Austria
e-mail: F.Giammarile@iaea.org

G. Mariani
Regional Center of Nuclear Medicine, Department of Translational Research and Advanced Technologies in Medicine and Surgery, University of Pisa, Pisa, Italy

© Springer International Publishing Switzerland 2017
H.W. Strauss et al. (eds.), *Nuclear Oncology*,
https://doi.org/10.1007/978-3-319-26236-9_54

GOSTT	Guided intraoperative scintigraphic tumor targeting
H&E	Hematoxylin and eosin staining
HNM	Melanoma located in the head and neck
HNSCC	Squamous cells carcinomas of the head and neck
ICG	Indocyanine green
LN	Lymph node
MBq	Mega-Becquerel (10^6 Becquerel)
MRI	Magnetic resonance imaging
MTC	Medullary thyroid cancer
N	Lymph node status according to the AJCC/UICC TNM staging system
NCCN	National Comprehensive Cancer Network
OSCC	Oral squamous cell carcinoma
PET	Positron emission tomography
PET/CT	Positron emission tomography/computed tomography
ROLL	Radioguided occult lesion localization
RT-PCR	Reverse transcriptase polymerase chain reaction
SLN	Sentinel lymph node
SLNB	Sentinel lymph node biopsy
SPECT	Single-photon emission computed tomography
SPECT/CT	Single-photon emission computed tomography/computed tomography
T	Tumor status according to the AJCC/UICC TNM staging system
TNM	AJCC/UICC staging system based on parameters "T" (tumor status), "N" (lymph node status) and "M" (distant metastasis status)
UICC	Union Internationale Contre le Cancer (International Union Against Cancer)
US	Ultrasonography

Contents

The Clinical Problem 1434

Lymphatic Drainage and Lymph Node Anatomy of the Neck 1436

Radiopharmaceuticals 1436

Injection 1438

Preoperative Lymphoscintigraphy 1438

Contribution of SPECT/CT 1439

Surgical Procedure 1440
Blue Dye 1440
Intraoperative Detection of Sentinel Lymph Nodes 1442

SLN Pathology 1442

Dosimetric Considerations for Patients and Medical Staff 1443

Accuracy of Radioguided Sentinel Lymph Node Biopsy 1443

SLNB in Head and Neck Melanoma (HNM) 1443

Radioguided Surgery in Thyroid Cancer 1445
SLNB in Thyroid Cancer 1445
Radioguided Occult Lesion Localization in Thyroid Cancer 1446

References 1446

The Clinical Problem

Tumor status of locoregional lymph nodes is an important prognostic factor in patients with squamous cells carcinomas of the head and neck (HNSCC). In these patients a locoregional metastatic sentinel lymph node is an unfavorable prognostic factor [1], and cervical node dissection has a potential curative role [2]. The management of clinically node-negative patients remains controversial, because the probability of finding an occult metastasis is approximately 20% [3]. Furthermore, there is still debate about performing prophylactic lymph neck node dissection versus a wait-and-see approach [4].

Preoperative evaluation of patients with newly diagnosed HNSCC includes physical examination, ultrasound (US) examination (possibly with US-guided fine-needle aspiration cytology [5]),

and other radiology-based imaging procedures such as CT and MRI [6]; occasionally, PET/CT with [^{18}F]FDG is also performed, depending on specific indications[7, 8]. However, all these modalities have suboptimal sensitivity for the detection of microscopic lymph node involvement; on the other hand, elective lymph node dissection is burdened with important morbidity. These considerations justify the notion that sentinel lymph node biopsy (SLNB) has the potential of enabling accurate selection of patients for elective lymph node dissection and of accurately staging the clinical and radiological N0-neck in patients with head and neck cancer.

Evaluation of the pattern of lymph drainage in the head and neck region is cumbersome due both to anatomic complexity and to unpredictable routes of lymphatic drainage. The neck contains over 300 lymph nodes and it is necessary to determine the nodes at risk of metastasis in individual patients for all head and neck cancers.

The patterns of lymph drainage from the oral cavity, oropharynx, larynx, and hypopharynx exhibit numerous intraindividual variations, even from the same primary tumor site. Unexpected aberrant lymphatic drainage can be found in 20–30% of patients with clinically negative or positive necks, a feature that has a definite impact on treatment planning on an individual patient's basis [9–12].

Lymph drainage from a primary tumor located in the midline may be directed to either side; furthermore, contralateral drainage is often seen even in well-lateralized malignancies of the tongue or floor of the mouth [13]. Although lymph drainage to submandibular nodes is expected from the anterior floor of the mouth and lingual apex, bilateral drainage to higher-level lymph nodes and to the middle jugular chains is not infrequently observed [14].

Thus, due to individual patient variability of lymphatic drainage, selective neck dissection limited to those nodal levels at highest risk has been shown to have 15–20% of "skip metastases" that have bypassed the expected first nodal basin [15]. It is conceivable that, similar to breast cancer and cutaneous melanoma), the SLNB approach can accurately stage the lymph node status of patients with head and neck cancer.

The SLNB technique has been investigated mostly for those head and neck cancers whose anatomic location allows direct and easy access to the tumor for injection of the radiocolloid (or of other lymphatic mapping agents). For this reason the procedure has already been sufficiently standardized in patients with oral squamous cell carcinoma (OSCC) [16], while it is still experimental in head and neck cancers arising at other sites.

In the last decade, the technique has undergone extensive validation against the gold-standard elective node dissection, for tumors located in the oral cavity and accessible subsites of the oropharynx. In 2013 SLNB in early oral cancer was recognized by the National Comprehensive Cancer Network (NCCN). NCCN Clinical Practice Guidelines in Oncology of Head and Neck Cancers now include the following statement: "Sentinel lymph node biopsy is an alternative to elective neck dissection for the identification of occult cervical metastasis in patients with early (T1 or T2) oral cavity carcinoma in centers where experience for this procedure is available" [8].

Current indications for SLNB include clinical T1 or T2 node-negative oral and selected oropharyngeal squamous cell carcinomas, where it may be considered a valid alternative to elective node dissection. Clinically T1 or T2 patients includes resectable tumors with size <4 cm in maximum diameter. In fact, in case of larger tumors, it is difficult to perform tracer injection all around the tumor; furthermore, large tumors tend to drain to multiple lymphatic basins and in the majority of patients require a neck dissection for access to the primary tumor or for defect reconstruction [17].

The clinically negative neck is defined by physical examination and clinical imaging by CT, contrast-enhanced MRI, US-guided fine-needle aspiration cytology, and/or [^{18}F]FDG PET/CT.

The first and most frequent target for SLNB is staging the ipsilateral clinically node-negative neck in patients with a unilateral primary tumor. A second target is the assessment of bilateral clinically node-negative necks in primary tumors close to, or

crossing, the midline. The third indication is for assessment of the contralateral clinically node-negative neck in primary tumors close to the midline with an ipsilateral clinically node-positive neck, in order to decide whether these patients need bilateral neck dissections, or an ipsilateral neck dissection and contralateral SLNB only. Patients should also be fit enough preoperatively to withstand a neck dissection.

Exclusion criteria include patients who have received prior radiation or surgical treatment to the neck. These patients are generally excluded from SLNB protocols on the assumption that the previous intervention can distort the normal lymphatic pathways and give rise to unexpected patterns of metastasis; nevertheless, these patients should be evaluated on an individual basis, taking into account the time window elapsed between such forms of treatment and the SLNB procedure. In pregnant women, the urgency and the necessity for staging the neck should be discussed. However, SLNB protocols should be modified in pregnant patients to minimize the risks of radiation exposure and blue-dye injections. SLNB can be performed in lactating women, but it is advised that breast-feeding be discontinued for 24 h following the procedure.

The routine SLNB procedure consists of preoperative peritumoral injection of the tracer (such as ^{99m}Tc-nanocolloid of albumin or similar radiopharmaceutical; see below) followed by lymphoscintigraphy using planar and single photon emission tomography/computed tomography (SPECT/CT) imaging. Based on the preoperative lymphoscintigraphy findings, the position of the SLN is marked on the skin. SLNB is performed under general anesthesia, and intraoperative detection of the SLN is guided by combination of a portable handheld gamma ray detection probe (radionuclide detection) and dissection/harvesting of the radioactive lymph node(s). Ideally, one or more radioactive ("hot") SLNs are identified and excised. After surgical removal, the SLN is subjected to meticulous histopathological examination using step serial sectioning and immunohistochemistry.

Lymphatic Drainage and Lymph Node Anatomy of the Neck

Surgical anatomy of the head and neck region is complex due to the small size of vital organs and to the close relation among different tissues. The lymph nodes in the neck are generally subdivided into specific anatomic subsites and grouped into seven levels on each side of the neck (Fig. 1), according to the so-called Robbins' Classification [18], incorporated into the AJCC-UICC TNM staging system [19].

Submental (sublevel I_A) and submandibular (sublevel I_B) lymph nodes are included in level I. Upper jugular nodes extend from the inferior border of the hyoid bone to the base of the skull and are classified as level II; in relation to the vertical plane defined by posterior surface of the submandibular gland, the lymph nodes located anteriorly constitute sublevel II_A, and the nodes located posteriorly correspond to sublevel II_B. Level III includes the middle jugular nodes (from hyoid bone up to the inferior border of the cricoid cartilage), and level IV includes lower jugular nodes (from the inferior border of the cricoid cartilage to the clavicle). The posterior border of regions II, III, and IV is the posterior border of the sternocleidomastoid muscle. Level V nodes are those located posteriorly to the posterior border of the sternocleidomastoid muscle. This latter group is further divided into sublevels V_A including the spinal accessory nodes, whereas sublevel V_B includes the nodes following the transverse cervical vessels and the supraclavicular nodes. Level VI contains the pretracheal and paratracheal nodes, the precricoid node, and the perithyroidal nodes including the lymph nodes along the recurrent laryngeal nerves. Finally, level VII includes the superior mediastinal lymph nodes.

Radiopharmaceuticals

A variety of colloidal and soluble tracers have been used for imaging the pattern of lymph flow. It is commonly held that radiocolloids are taken up by

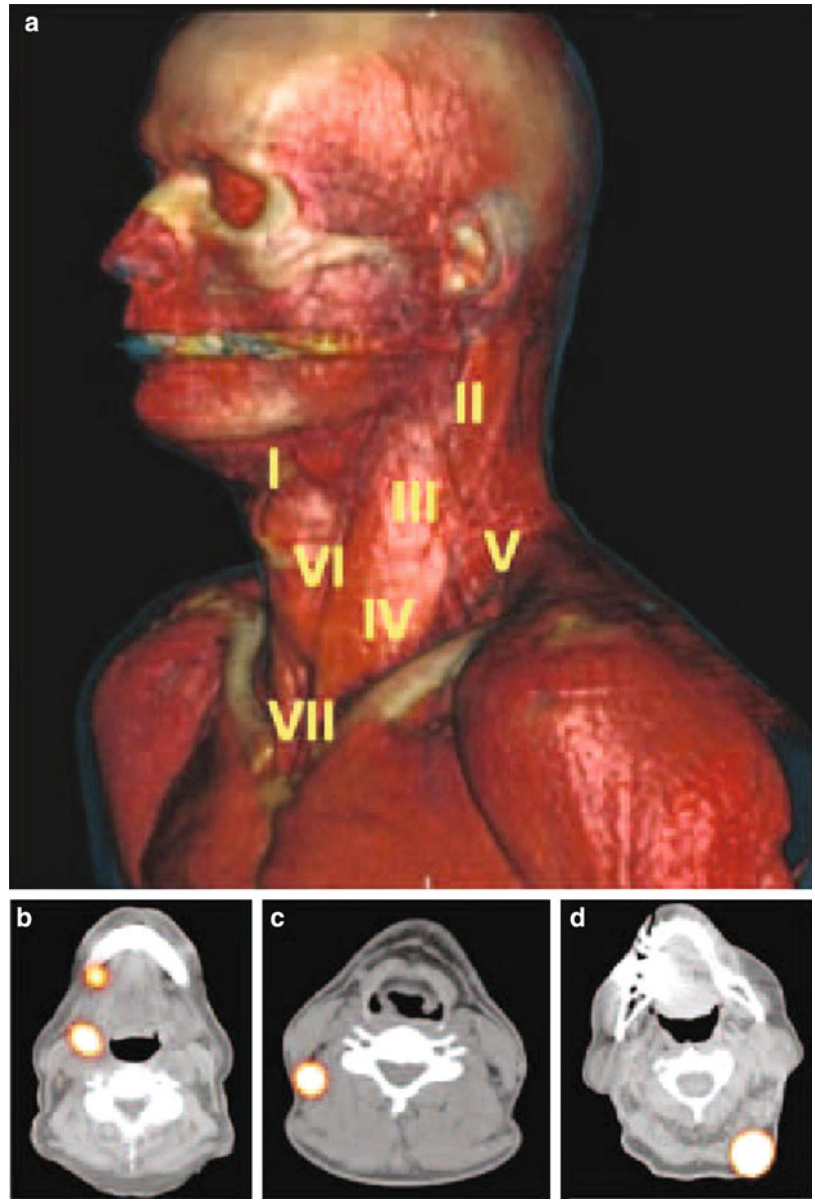

Fig. 1 Lymph node levels of the neck. (**a**) Volume rendering of the head and neck showing the anatomical levels of the neck according to Robbins. (**b**–**d**) Fused axial SPECT/CT images showing examples of SLNs located in right levels I and II (**b**), right level III (**c**), and level V of the *left side* of the neck (**d**) (Reproduced with permission from Valdés Olmos et al. [14])

macrophages in lymph nodes, whereas the transit of macromolecules through lymph nodes is delayed simply because of their large molecular size [14, 16].

The nuclear medicine physicians' experience and commercial availability of the various agents affect the choice of radiopharmaceutical. ^{99m}Tc-albumin nanocolloid (that has a quite narrow range of particle size, with over 90% of the particles being smaller than 80 nm) and ^{99m}Tc-sulfur colloid (with a wide range of particle size between about 20 and 400 nm) are commercially available and widely employed in Europe and in the USA, respectively. These tracers migrate to the SLN within minutes after interstitial injection, yet their

prolonged retention in lymph nodes allows surgery to take place even the following day [14, 16].

Recently a new tracer, ^{99m}Tc-tilmanocept, has been approved for SLNB in OSCC patients, both by the by US Food and Drug Administration (FDA) and by the European Medicines Agency (EMA). Its smaller particle size and specific targeting of mannose receptors (CD206) located on cells within lymph nodes result in rapid clearance, reduced or no drainage to second-echelon lymph nodes, and greater SLN retention, thus enabling improved SLN detection both preoperatively and intraoperatively with respect to the conventional radiocolloids. In a multicenter validation study, all SLNs could be detected and no false-negative results were reported in 20 patients with floor of mouth cancer. Nevertheless, the actual additional value of this new technique has still to be investigated in larger and comparative studies [20–22].

As an alternative to the radioactive label, near-infrared fluorescent tracers (e.g., indocyanine green – ICG) have been used that are potentially helpful for SLNB [23–25]; moreover, the combination of such fluorescent tracers with common ^{99m}Tc-labeled radiocolloids is an attractive option for improving the SLN detection rate in patients with head and neck malignancies [26–28].

Injection

Small syringes with minimal dead space are recommended; otherwise 0.1 mL of air may be drawn into the syringe behind the radiocolloid suspension to ensure complete administration. A 25- or 27-gauge needle should be used. The total activity to be injected may vary (from 15 to 120 MBq among different studies), depending on the size and location of the primary tumor. However, the total injected activity should be adjusted according to the timing of lymphoscintigraphy with respect to surgery. Greater activities are required for a 2-day protocol, in order to ensure the remaining activity exceeds 10 MBq at the time of surgery.

Small volumes of 0.1–0.2 mL per aliquot injected at a short distance from primary lesions are needed to avoid masking of SNs in the vicinity of the injection site and are recommended also to minimize contamination due to the resistance of the tongue tissue. Tracer should be injected at 0.1–0.5 cm from the tumor or scar margin. The number of aliquots to be injected varies (two to four) according to the size and location of the lesion. The tracer should be administered on each side of the tumor/scar, keeping as a reference the orientation of the surgical scar [16].

The use of a local anesthetic for topical application (10% xylocaine spray) a few minutes before radiocolloid injection is recommended for oral cavity tumors.

The most frequent pitfall is skin contamination due to spillage of the lymphatic mapping agent either during injection and/or immediately thereafter (e.g., during washing of the mouth to remove excess radioactivity possibly sipped out at the injection site). The hot spots due to contamination may be confused with sentinel lymph nodes in the vicinity of the tumor, thus leading to unnecessary intraoperative pursuit. In these cases skin decontamination is mandatory. Complementary SPECT/CT may also be helpful in detecting these artifacts, as mentioned above.

Preoperative Lymphoscintigraphy

Preoperative lymphoscintigraphy should be performed using a large-field-of-view gamma camera to assess the drainage of injected radiotracer via the lymphatic capillaries to the larger collector lymphatics until it either passes through, or is retained within, the regional lymph nodes. Accurate preoperative localization and cutaneous marking of the skin projection of SLN location correlate well with the precision of the surgical procedure.

Dynamic acquisition for 20–30 min starting immediately after radiotracer injection will show the drainage pattern and help to differentiate between SLNs (which can appear very early following injection) and second-echelon lymph nodes.

Static images in the anterior and lateral projections are acquired to localize the nodes in a pseudo-tridimensional manner. If hot nodes are not clearly depicted, static imaging can be repeated later, or even just before surgery. Alternatively, delayed images are useful to differentiate SNs from

second-echelon lymph nodes. Planar images provide a two-dimensional overview, and sentinel lymph nodes can be localized and marked on the patient's skin with the use of an external radioactive marker, such as a ^{57}Co-source pen.

SLNs are generally identified 15–60 min after radiotracer injection as one or more foci to which lymphatic drainage passes, and may be multiple, in one or several areas of the neck, ipsilateral, and/or contralateral to the primary tumor [14, 16]. Delayed planar images (2–4 h postinjection) are only considered when tumors are located in the midline (including those located in the mobile portion of the tongue or laterally in the floor of mouth), or if no SLN can clearly be identified during early imaging [29]. The SLNs so identified are marked on the skin of the neck on the basis of lateral views, in order to reproduce the patient's position during surgery.

Failure to detect SLNs may be related to an incorrect injection technique or close proximity of SLNs to the injection site (e.g., floor of mouth tumors). In addition, massive metastasis in lymph nodes may block and reroute lymphatic drainage, thus causing non-visualization of the true SLNs and possible visualization of alternative routes of lymphatic drainage. Repeat radiocolloid injection and imaging may be considered in case of totally absent visualization of lymph nodes; however, proceeding to neck dissection is preferred in these cases in order to avoid a false-negative SLNB.

Individual lymphatic mapping by lymphoscintigraphy has been reported to detect "in-transit" lymph nodes, i.e., SLNs lying between the primary tumor and the regional lymph basin [30]. These have been described in the context of malignant melanoma, but to date there have been no reports of in-transit SLNs in OSCC.

Contribution of SPECT/CT

SPECT/CT can optimize sentinel lymph node visualization and localization in the head and neck region and is therefore crucial for adequate lymphatic mapping and sentinel lymph node localization in head and neck malignancies [31] (see Fig. 2).

A number of studies have shown the added values of SPECT/CT over planar imaging; these include:

- Greater number and location of visualized hot spots and identification of SLNs missed on planar imaging. SPECT/CT has visualized one or more additional SLNs in more than half of the studies. These additional sentinel lymph nodes found on SPECT/CT imaging might be tumor positive. Especially lymph nodes adjacent to the injection site are more frequently detected by SPECT/CT, while they are frequently missed on planar imaging [32, 33]. In a recent study, SPECT/CT detected additional SLNs in 9 out of 42 patients (21.5%); in particular, a total of 16 (13.44%) additional SLNs, 1 of them in the sublingual space, were detected using SPECT/CT [34].
- Exclusion of ambiguous SLNs. Non-nodal radioactivity accumulation (radiocolloid leakage or contamination) can be more easily identified on the basis of SPECT/CT imaging [35].
- Better anatomic localization in 30–47% of patients [36], thanks to the anatomical details provided with CT in hybrid images (Fig. 3). SPECT/CT appears to be very useful for exact anatomic localization of the sentinel lymph nodes. In the head and neck area, it is very important to identify the relation of sentinel lymph nodes to several vital vascular and neural structures, to be able to safely remove these lymph nodes. SPECT/CT can localize these sentinel nodes in relation to structures such as the mandible, parotid gland, jugular vein, and sternocleidomastoid muscle. SPECT/CT also shows whether the nodes are located superficially underneath the skin or hidden below other structures. SPECT/CT thus gives anatomical reference landmarks for planning the best surgical approach. The superior information on anatomic location provided by SPECT/CT frequently leads to adapt the surgical approach, with significant shortening of operation times.

Nevertheless, it must be emphasized that SPECT/CT imaging does not replace planar

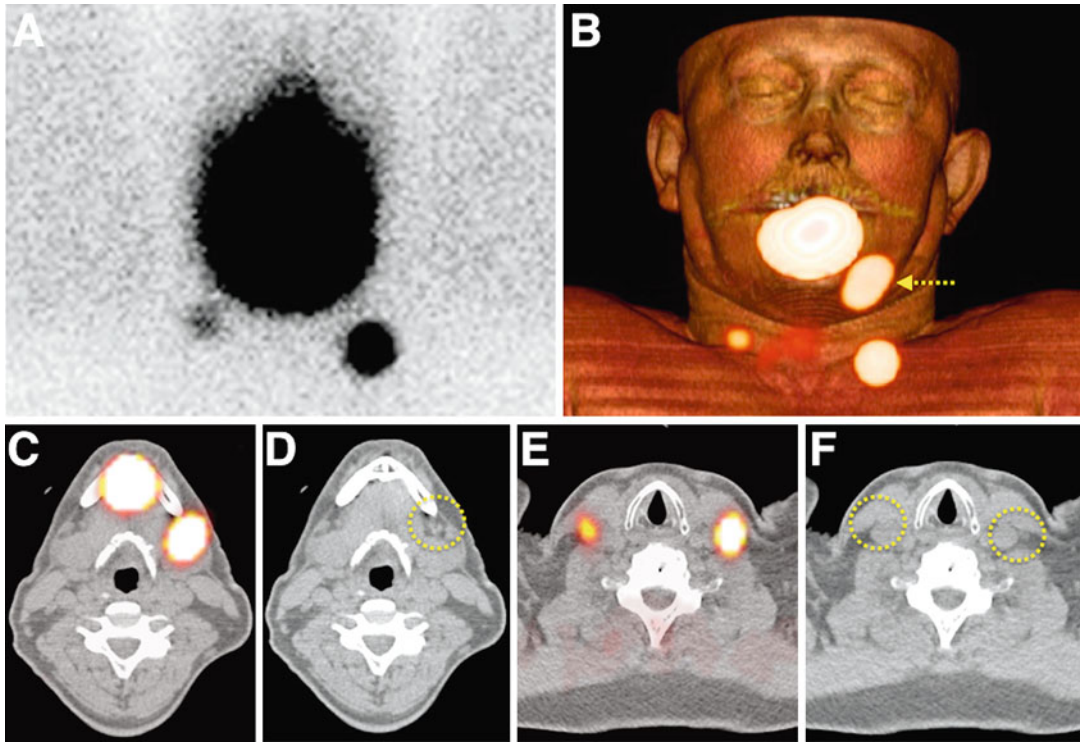

Fig. 2 In a patient with a tongue carcinoma bilateral neck drainage is observed on anterior planar scintigraphy (**a**). On SPECT/CT displayed with volume rendering (**b**), an additional sentinel node (*SN*) is also seen *left* from the injection site (*arrow*); on transversal SPECT/CT (**c**) and corresponding CT (**d**), this SN is localized in the submandibular area (*circle*). Two additional SNs are seen in the *lower part* of the neck (**e**, **f**)

lymphoscintigraphy. A thorough integration of SPECT/CT data together with planar imaging is necessary to identify radioactive lymph nodes as SLNs and to attribute to categorize the nodes as definite SLN, probable SLN, etc. for guidance during the intraoperative procedure.

Even if the benefits of SPECT/CT have not been universally accepted [37, 38], both planar and SPECT images demonstrate good or excellent inter- and intra-observer agreement for the detection/identification of SLNs [32].

A combination of the integration of modern high-end CT in hybrid scanners, the acquisition of high-resolution scans with or without contrast enhancement provides a precise anatomic reference of the SLNs displayed in 5-mm or even 2-mm slices on axial, coronal, sagittal views and maximum intensity projection, respectively. Additional volume rendering for 3-D may also be helpful. These improvements in preoperative lymphatic mapping translate into improved minimally invasive surgical approaches to SLNB that some authors have epitomized with the emblematic new paradigm of "see and open" as opposed to the former surgical attitude of "open and see" for radioguided surgery [34].

Surgical Procedure

Blue Dye

The use of blue dye in addition to radiolocalization with intraoperative gamma probe in head and neck mucosal cancer SLN surgery is optional and may be a useful adjunct to aid SLN localization and harvesting [14, 16].

The blue dye should be injected at the time of surgery, under general anesthesia. It takes

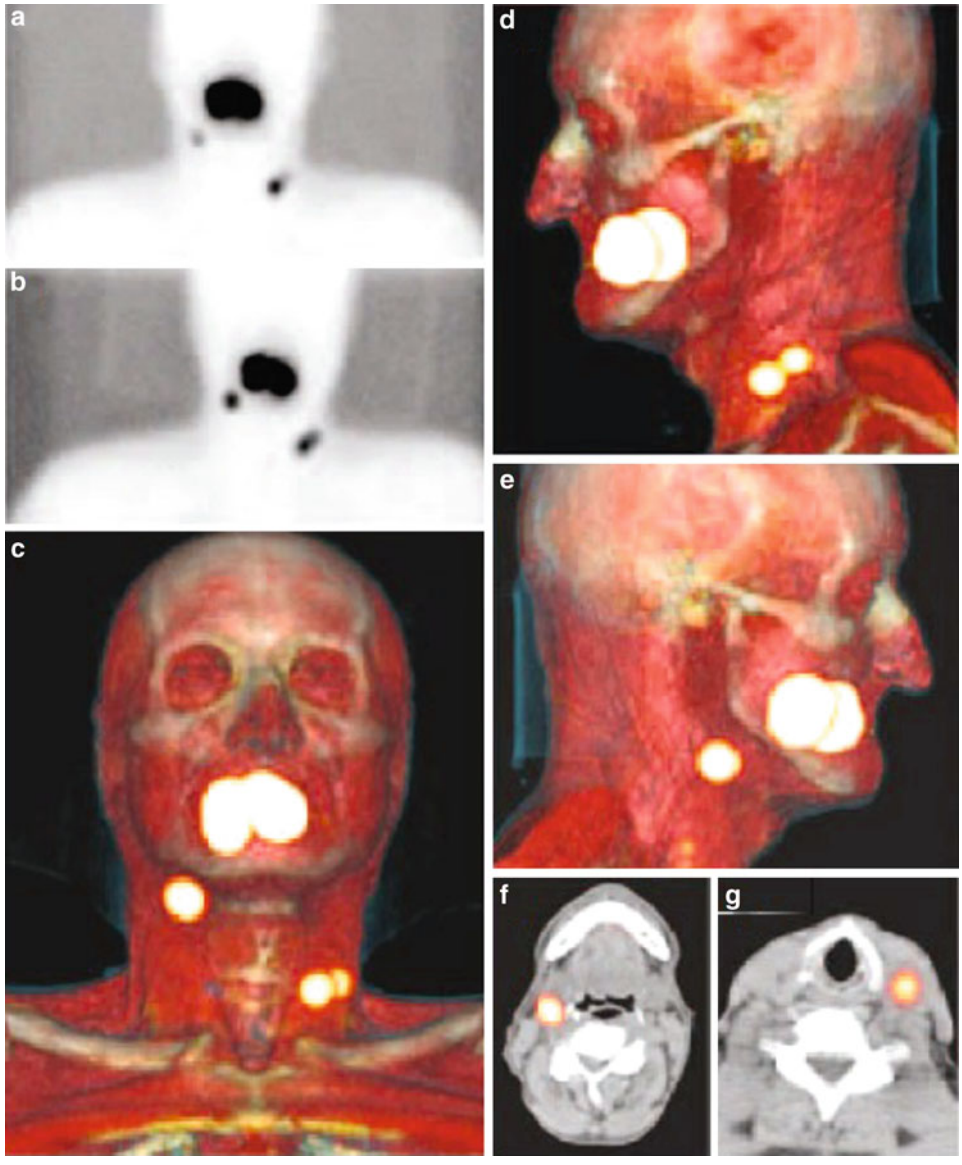

Fig. 3 An 81-year-old man with a T1 carcinoma on the *right side* of the lingual apex. After administration of 82 MBq ^{99m}Tc-nanocolloid in four injections into the mucosa around the tumor, early drainage to both sides of the neck is seen on anterior planar imaging (**a**), with subsequent increasing lymph node uptake on delayed images (**b**). Volume rendering (**c**–**e**) and axial SPECT/CT fusion images (**f**, **g**) show the SLNs in level II on the *right* and in level III on the *left*. All SLNs were tumor-free at histopathology (Reproduced with permission from Valdés et al. [14])

approximately 10–15 min for a significant amount of dye to travel from the injection site to the SLN. Following injection, blue dye drains to the SLNs via the same lymphatic pathways as radiocolloid, staining the channels, which can then be followed to the first-echelon nodes. It allows a direct visualization of SLNs.

Rarely, nonradioactive blue nodes may contain metastases in the absence of a tumor-positive radioactive node; two such SLNs were reported

in a series of 40 patients undergoing SLNB with both radiocolloid and blue-dye injections [39]. Therefore, blue dye may aid performance of SLNB, in terms of both technical success of the procedure and identification of subclinical nodal metastasis.

However, sentinel lymph nodes in the head and neck region are frequently not stained blue, due to the fast lymphatic migration of vital blue dyes. This limitation has led to the developmentof agents combining radiotracers with optical tracers.

Intraoperative Detection of Sentinel Lymph Nodes

A gamma ray detection handheld probe is routinely used for intraoperative detection of the sentinel lymph nodes in the operative filed. The handheld probe is a radiation-sensitive detector that is able to provide a count rate from gamma rays. It is connected to an analyzer unit, which receives electrical signals from the radiation detector. The analyzer provides a response related to the detected count rate, usually by audible pitch or volume variation and by a visual display as a dial or digital count rate (counts per second, cps) [14, 16]. Thus, the gamma probe provides an acoustic signal when pointing straight toward the radioactive lymph node, thereby helping the surgeon in localizing the radioactive node.

To better plan the skin incision, the surgeon or the nuclear medicine physician should usually check the skin projection of the sentinel node with the gamma probe. Sometimes the SLNs can be masked due to the close proximity of the injected radiocolloid with the first draining LN (the so-called shine-through phenomenon), which leads to reduced detection, especially in OSCC with tumors of the floor of the mouth [40]. Also after removing sentinel nodes, the activity of the injection site can complicate measurement of the residual activity in the excision fossa. For these reasons removal of the primary cancer should be performed before the SLN search. Furthermore, deep sentinel lymph nodes can be difficult to detect because of tissue attenuation; in this case accurate preoperative imaging with SPECT/CT can help surgeons for skin incision.

To sort these problems out, a number of portable and handheld mini gamma cameras have recently been developed to provide direct intraoperative visualization of radioactive foci, with the purpose of improving detection of sentinel nodes in the head and neck region. With this new tool, the entire lymph node excision procedure in the head and neck area can be monitored. Sentinel lymph nodes located close to the injection can be visualized. Most importantly, by determining residual radioactivity after excision of the sentinel lymph nodes, the gamma camera can help to assess completeness of the procedure. Imaging after excision can also lead to identifying additional sentinel lymph nodes in more than 20% of the cases [41].

Recently the use of intraoperative gamma cameras has been combined with fluorescence cameras for synchronous sentinel node signal detection using the abovementioned hybrid tracer ^{99m}Tc-nanocolloid combined with indocyanine green. Furthermore, the technology of freehand SPECT (fhSPECT) was introduced for navigational surgery, combining the acoustic information of a conventional gamma probe and intraoperative 3-D images with real-time visualization of radiotracer distribution within the surgical field. This aspect is discussed in depth in ▶ Chap. 50, "Radioguided Surgery: Novel Applications."

SLN Pathology

Histopathologic analysis of sentinel lymph nodes is extremely effective and can detect the presence of micrometastasis (<2 mm) and clusters of several cells or even isolated tumor cells. By focusing on only a few lymph nodes, the pathologist can completely dissect and examine at 50–100 mm intervals each sentinel node. Sections may be stained with hematoxylin and eosin (H&E) for conventional light microscopy, and if such examination is negative, adjacent sections may be used for immunohistochemistry.

Other methodologies such as frozen sections, imprint cytology, and molecular analysis with

reverse transcriptase polymerase chain reaction (such as cytokeratin RT-PCR) have been described. However, in OSCC the performance of SLNB has been evaluated only in the context of relatively small observational cohort studies. The clinical role of these methods in the future remains uncertain due to the fact that, at present, the significance of finding micrometastasis and isolated tumor cells is unknown in OSCC [14].

Dosimetric Considerations for Patients and Medical Staff

The currently available data on radiation dosimetry burden are derived from the SLNB literature pertinent to breast cancer, where the absorbed doses to patients are determined to be extremely low; therefore, the radiation risk associated with this procedure is very low. While no specific data exist for OSCC, the radiopharmaceuticals and administered activity are identical, leading to the assumption that SLNB is a safe procedure from the radiation protection point of view also for OSCC patients. Monitoring of operating room personnel or staff in the pathology department for occupational exposure during the procedure is therefore unnecessary, and additional shielding is not required [16].

Accuracy of Radioguided Sentinel Lymph Node Biopsy

After the SLN concept in OSCC was validated in several studies in which all patients underwent elective neck dissection following SLNB, several prospective observational studies have been reported in the last decade, with overall 1 up to almost 7 years of follow-up. In 91–99% of the cases, the SLN was successfully harvested; a sensitivity of 86–95% and a negative predictive value of 88–100% has been reported. Nine to 37% of patients were upstaged [42–48]. These data confirm that SLNB is a reliable and safe technique for staging the clinically N0 neck in patients with T1 and T2 oral cancer.

Lower sensitivity rates are reported for floor of mouth cancers as compared to other oral subsites: 80–86% versus 94–97%, respectively. In these patients, the close spatial relation between the injection site and the SLN seems to result in a lower identification rate due to the "shine-through effect." In order to improve the accuracy, especially in floor of mouth cancer, new techniques have been developed (see ▶ Chap. 50, "Radioguided Surgery: Novel Applications" of this book).

Besides these results in terms of diagnostic accuracy, patients who underwent SLNB had significantly less shoulder morbidity, as assessed by subjective and objective measurements, than patients after elective neck dissection. Patients also experienced fewer complications and less skin numbness and had shorter incisions [49, 50].

Given the current evidence and costs of the SLNB procedure followed by nodal dissection in case of metastasis versus the "wait-and-see" approach in case of a tumor-free SLN, SLNB appears to be a cost-effective strategy for diagnosing and treating OSCC patients [51, 52]. Nevertheless, this procedure should still be considered within controlled clinical trials, since no definite conclusion has been reached on some important issues, including the possibility of omitting neck dissection in patients with a negative SLNB. In this regard, a European multicenter study that included 109 OSCC patients with positive SLNB showed additional (non-SLN) metastasis in 34.4% of the neck dissection specimens. Interestingly, the risk of non-SLN metastasis far from the adjacent lymphatic areas of the positive SLN was low (7.1%), thus suggesting that the information provided by the SLNB lymphatic neck dissections can be helpful to tailor the surgical approach to the patient on an individual basis [53].

SLNB in Head and Neck Melanoma (HNM)

SLNB status is the most important prognostic factor in melanoma, including melanoma located in the head and neck region. As in HNSCC, lymphatic drainage is often aberrant and can result in identification of the sentinel node in more than one nodal basin or in an atypical, bilateral, or contralateral nodal basin. In particular, in periauricular melanomas ipsilateral drainage to both

periparotid and level II of the neck is not infrequent [54]. Also, the existence of SLN clusters is not uncommon in the head and neck [55].

For this reason, SLNB has been established as the preferred staging modality to assess nodal involvement in patients with intermediate-thickness melanomas and selected thin and thick melanomas. In the evaluation and staging of the patient with melanoma, SLNB has shown increased sensitivity to detect regional metastases, limited morbidity compared with elective nodal dissection, and capability to identify patients who may benefit from further therapies such as a neck dissection or systemic adjuvant therapy. It also has the potential of halting the regional progression of metastatic disease.

Some authors have noted a wide range of false-negative rates (3.4–10.4%) for HNM SLNB as well as a decreased HNM SLN positive rate (10–15%) compared with cutaneous melanoma elsewhere (16–23%) [56, 57]. Others have reported SLN positive rates in HNM that are not significantly different from other cutaneous melanomas, although the small patient numbers in these studies limit their interpretation. A worse survival in HNM with positive SLN compared with other anatomic locations has also been suggested (Fig. 4).

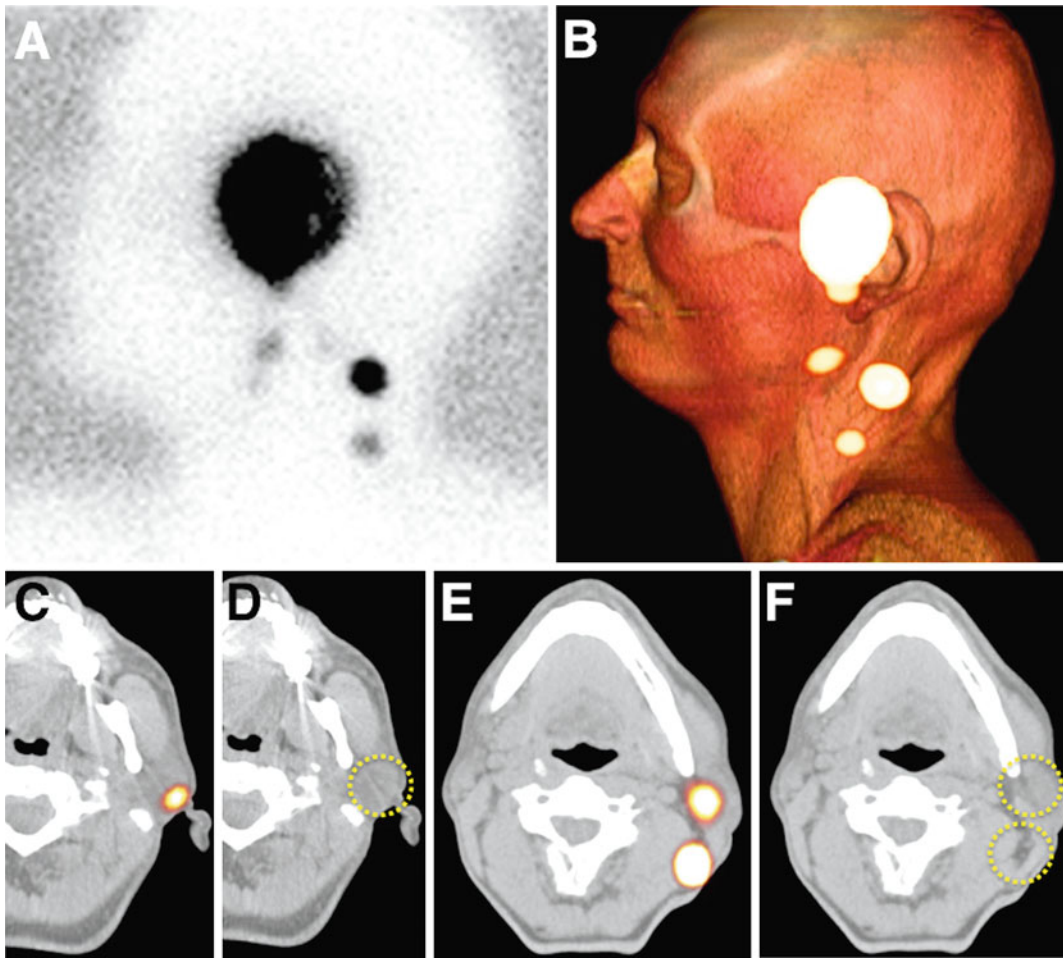

Fig. 4 In a patient with a left preauricular melanoma ipsilateral drainage to the neck is seen on lateral planar image (**a**). On SPECT/CT displayed with volume rendering (**b**), besides neck drainage, an additional sentinel node (*SN*) is also seen near the *lower part* of the injection site. On axial SPECT/CT (**c**, **d**), this SN is observed behind the *upper* pole of the parotid gland. Note that SPECT/CT (**e**, **f**) is able to localize another SN in the *lower* parotid pole and a SLN cluster in level II

Radioguided Surgery in Thyroid Cancer

SLNB in Thyroid Cancer

Differentiated thyroid cancer (DTC), which includes the papillary and follicular histologic patterns, is the most common endocrine malignancy and generally has a more favorable prognosis compared to other cancers (see ▶ Chap. 19, "Diagnostic Applications of Nuclear Medicine: Thyroid Tumors" of this book), regardless of the more or less aggressive surgical approach. For this reason, there is considerable variability when planning surgery regarding the decision to explore and remove the central and/or lateral compartment lymph nodes, considering that dissection of the central compartment can cause complications such as a damaged recurrent laryngeal nerve or permanent hypoparathyroidism.

The SLN concept in DTC has been developed as an alternative to elective lymph node dissection in patients with clinically node-negative disease, in the perspective of obtaining information about cervical lymph node involvement in patients undergoing thyroidectomy. Nevertheless, so far there is no definite evidence that SLNB is associated with long-term clinical and survival benefits.

However, several studies have shown that radioguided SLNB can easily be carried out and is feasible and safe [58], even if the actual clinical impact of this procedure is yet to be determined. The most widely used technique involves intranodular injection of 15–37 MBq ^{99m}Tc-nanocolloidal albumin in a volume of 0.1–0.5 mL, under ultrasound guidance (Fig. 5).

In principle, SLN mapping allows the identification of micrometastatic disease, thus potentially reducing patient morbidity by avoiding unnecessary de novo lymph node dissection [59]. However, the general prognostic significance of lymph node involvement in DTC is still debated.

One of the most important targets of SLNB in this scenario could be the selection of those patients with locally advanced thyroid disease at

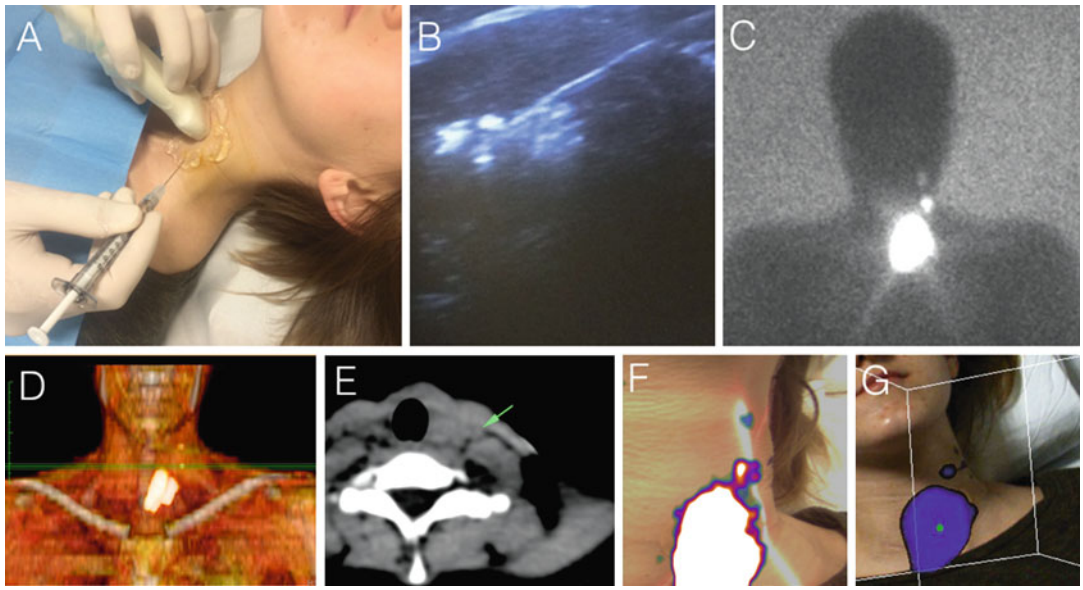

Fig. 5 SLN mapping in a 27-year-old woman with papillary thyroid carcinoma. (**a**) Ultrasound-guided intratumoral injection of ^{99m}Tc-nanocolloidal albumin. (**b**) Ultrasound monitoring of radiocolloid deposit within the thyroid nodule (**b**). (**c**) Planar scan: anterior view showing two hot spots in the left cervical area in addition to the obvious activity at the injection site. (**d**) Volume rendering SPECT/CT image showing the two hot spots in the left cervical levels III and IV, respectively. (**e**) Axial CT section showing anatomical appearance of the level IV SLN. (**f**, **g**) Preoperative assessment with a portable gamma camera and with freehand SPECT, respectively

highest risk to develop cervical lymph node metastasis, who can benefit from complete neck dissection. Lymphatic mapping and SLNB may also have a role in minimally invasive surgical technique to detect metastatic lymph node spread in thyroid cancers [60, 61].

SLNB has been also proposed for medullary thyroid carcinoma (MTC), which is generally characterized by a more aggressive behavior and early spread in lymphatic vessels than papillary/follicular carcinoma. Initial surgery for MTC with no evidence of lymph node involvement in neck compartments consists of total thyroidectomy and prophylactic central neck dissection. SLNB has been used for a more precise N staging of the lateral compartments, possibly driving the extent of prophylactic neck dissection to the involved cervical lymphatic chains [62].

Radioguided Occult Lesion Localization in Thyroid Cancer

Radioguided surgery enables the surgeon to identify lesions or tissues that have been preoperatively "marked" with radioactive substances. The radioguided occult lesion localization (ROLL) approach is being widely used to identify occult lesions in patients with breast cancer. However, few studies have reported the use of this technique in patients with recurrence of thyroid cancers in cervical lymph nodes after initial treatment (i.e., thyroidectomy and ablation of postsurgical remnants with ^{131}I-iodide.

The ROLL technique can be useful in selected cases where suspected lesions may be difficult to identify intraoperatively, due to their dimensions or location, especially in patients who have had cervical surgical procedures in whom fibrotic scar tissue or adhesions can make identification of the target lesions difficult during surgery. The procedure allows for more conservative excisions and reduces the surgery-related morbidity [63–65].

In this case, injection of ^{99m}Tc-sulfur colloid or ^{99m}Tc-macroaggregated human albumin is performed directly inside or near the suspicious lesion, generally under US guidance up to 24 h prior to the surgical procedure. Intraoperative lesion detection is carried out using a handheld gamma probe, and preoperative SPECT/CT in addition to conventional planar scintigraphy can provide an accurate three-dimensional road map for better surgical exploration of the neck [66].

References

1. Woolgar JA, Triantafyllou A, Lewis Jr JS, Hunt J, Williams MD, Takes RP, et al. Prognostic biological features in neck dissection specimens. Eur Arch Otorhinolaryngol. 2013;270:1581–92.
2. Hamoir M, Schmitz S, Gregoire V. The role of neck dissection in squamous cell carcinoma of the head and neck. Curr Treat Options Oncol. 2014;15:611–24.
3. Psychogios G, Mantsopoulos K, Bohr C, Koch M, Zenk J, Iro H. Incidence of occult cervical metastasis in head and neck carcinomas: development over time. J Surg Oncol. 2013;107:384–7.
4. Burusapat C, Jarungroongruangchai W, Charoenpitakchai M. Prognostic factors of cervical node status in head and neck squamous cell carcinoma. World J Surg Oncol. 2015;13:51. doi: 10.1186/s12957-015-0460-6.
5. Chaturvedi P, Datta S, Arya S, Rangarajan V, Kane SV, Nair D, et al. Prospective study of ultrasound-guided fine-needle aspiration cytology and sentinel node biopsy in the staging of clinically negative T1 and T2 oral cancer. Head Neck. 2015;37:1504–8.
6. de Bondt RB, Nelemans PJ, Hofman PA, Casselman JW, Kremer B, van Engelshoven JM, et al. Detection of lymph nodemetastases in head and neck cancer: a meta-analysis comparing US, USgFNAC, CT and MR imaging. Eur J Radiol. 2007;64:266–72.
7. Paxton NA, Brandon DC, Corey AS, Harrison CE, Karagulle Kendi AT, Halkar RK, Barron BJ. Characteristics and limitations of FDG PET/CT for imaging of squamous cell carcinoma of the head and neck: a comprehensive review of anatomy, metastatic pathways, and image findings. AJR Am J Roentgenol. 2015;205:519–31.
8. www.nccn.org. Head and neck cancers. Version I.2015.
9. Spiro JD, Spiro RH, Shah JP, Sessions RB, Strong EW. Critical assessment of supraomohyoid dissection. Am J Surg. 1988;156:286–9.
10. Pitman KT, Johnson JT, Myers EN. Effectiveness of selective neck dissection for management of the clinically negative neck. Arch Otolaryngol Head Neck Surg. 1997;123:917–22.
11. Klutmann S, Bohuslavizki KH, Brenner W, Höft S, Kröger S, Werner JA, et al. Lymphoscintigraphy in tumors of the head and neck using double tracer technique. J Nucl Med. 1999;40:776–82.
12. Gourin CG, Conger BT, Porubsky ES, Sheils WC, Bilodeau PA, Coleman TA. The effect of occult nodal metastases on survival and regional control in patients

with head and neck squamous cell carcinoma. Laryngoscope. 2008;118:1191–4.
13. Shoaib T, Soutar DS, MacDonald DG, et al. The nodal neck level of sentinel lymph nodes in mucosal head and neck cancer. Br J Plast Surg. 2005;8:790–4.
14. Valdés Olmos RA, Klop WMC, Brouwer RO. Preoperative and intraoperative lymphatic mapping for radioguided sentinel node biopsy in head and neck cancers. In: Mariani G, Manca G, Valdés AR, Orsini F, Vidal-Sicart S, editors. Atlas of lymphoscintigraphy and sentinel node mapping – a pictorial case-based approach. Milan: Springer-Verlag Italia; 2013.
15. Byers RM, Weber RS, Andrews T, McGill D, Kare R, Wolf P. Frequency and therapeutic implications of "skip metastases" in the neck from squamous cell carcinoma of the oral tongue. Head Neck. 1997;19:14–9.
16. Alkureishi LW, Burak Z, Alvarez JA. Joint practice guidelines for radionuclide lymphoscintigraphy for sentinel node localization in oral/oropharyngeal squamous cell carcinoma. Eur J Nucl Med Mol Imaging. 2009;36:1915–36.
17. Ross GL, Soutar DS, Shoaib T, Camilleri IG, MacDonald DG, Robertson AG, et al. The ability of lymphoscintigraphy to direct sentinel node biopsy in the clinically N0 neck for patients with head and neck squamous cell carcinoma. Br J Radiol. 2002;75:950–8.
18. Robbins KT, Clayman G, Levine PA, Medina J, Sessions R, Shaha A, et al. Neck dissection classification update: revisions proposed by the American Head and Neck Society and the American Academy of Otolaryngology-Head and Neck Surgery. Arch Otolaryngol Head Neck Surg. 2002;128:751–8.
19. AJCC. Cancer staging handbook. 7th ed. New York: Springer; 2010.
20. Marcinow AM, Hall N, Byrum E, Teknos TN, Old MO, Agrawal A. Use of a novel receptor-targeted (CD206) radiotracer, ^{99m}Tc-tilmanocept, and SPECT/CT for sentinel lymph node detection in oral cavity squamous cell carcinoma: initial institutional report in an ongoing phase 3 study. JAMA Otolaryngol Head Neck Surg. 2013;139:895–902.
21. Agrawal A, Civantos FJ, Brumund KT, Chepeha DB, Hall NC, Carroll WR, et al. [^{99m}Tc]Tilmanocept accurately detects sentinel lymph nodes and predicts node pathology status in patients with oral squamous cell carcinoma of the head and neck: results of a phase III multi-institutional trial. Ann Surg Oncol. 2015;22:3708–15.
22. Surasi DS, O'Malley J, Bhambhvani P. ^{99m}Tc-Tilmanocept: a novel molecular agent for lymphatic mapping and sentinel lymph node localization. J Nucl Med Technol. 2015;43:87–91.
23. van der Vorst JR, Schaafsma BE, Verbeek FP, Keereweer S, Jansen JC, van der Velden LA, Langeveld AP, et al. Near-infrared fluorescence sentinel lymph node mapping of the oral cavity in head and neck cancer patients. Oral Oncol. 2013;49:15–9.
24. Nakamura T, Kogashiwa Y, Nagafuji H, Yamauchi K, Kohno N. Validity of sentinel lymph node biopsy by ICG fluorescence for early head and neck cancer. Anticancer Res. 2015;35:1669–74.
25. van den Berg NS, Simon H, Kleinjan GH, Engelen T, Bunschoten A, Welling MM, Tijink BM, et al. First-in-human evaluation of a hybrid modality that allows combined radio- and (near-infrared) fluorescence tracing during surgery. Eur J Nucl Med Mol Imaging. 2015;42:1780.
26. van den Berg NS, Brouwer OR, Klop WM, Karakullukcu B, Zuur CL, Tan IB, et al. Concomitant radio- and fluorescence-guided sentinel lymph node biopsy in squamous cell carcinoma of the oral cavity using ICG-^{99m}Tc-nanocolloid. Eur J Nucl Med Mol Imaging. 2012;39:1128–36.
27. Murase R, Tanaka H, Hamakawa T, Goda H, Tano T, Ishikawa A, Hino S, et al. Double sentinel lymph node mapping with indocyanine green and 99m-technetium-tin colloid in oral squamous cell carcinoma. Int J Oral Maxillofac Surg. 2015;44:1212–7.
28. Stoffels I, Leyh J, Pöppel T, Schadendorf D, Klode J. Evaluation of a radioactive and fluorescent hybrid tracer for sentinel lymph node biopsy in head and neck malignancies: prospective randomized clinical trial to compare ICG-^{99m}Tc-nanocolloid hybrid tracer versus ^{99m}Tc-nanocolloid. Eur J Nucl Med Mol Imaging. 2015;42:1631–8.
29. Heuveling DA, Flach GB, van Schie A, van Weert S, Karagozoglu KH, Bloemena E, et al. Visualization of the sentinel node in early-stage oral cancer: limited value of late static lymphoscintigraphy. Nucl Med Commun. 2012;33:1065–9.
30. Uren RF, Howman-Giles R, Thompson JF, McCarthy WH, Quinn MJ, Roberts JM, et al. Interval nodes: the forgotten sentinel nodes in patients with melanoma. Arch Surg. 2000;135:1168–72.
31. Wagner T, Buscombe J, Gnanasegaran G, Navalkissoor S. SPECT/CT in sentinel node imaging. Nucl Med Commun. 2013;34:191–202.
32. Thomsen JB, Sørensen JA, Grupe P, Krogdahl A. Sentinel lymph node biopsy in oral cancer: validation of technique and clinical implications of added oblique planar lymphoscintigraphy and/or tomography. Acta Radiol. 2005;46:569–75.
33. Haerle SK, Hany TF, Strobel K, Sidler D, Stoeckli SJ. Is there an additional value of SPECT/CT over planar lymphoscintigraphy for sentinel node mapping in oral/oropharyngeal squamous cell carcinoma? Ann Surg Oncol. 2009;16:3118–24.
34. Sieira-Gil R, Paredes P, Martí-Pagés C, Ferrer-Fuertes A, García-Díez E, Cho-Lee GY, Tapias A, Mayoral M, Vidal-Sicart S. SPECT-CT and intraoperative portable gamma-camera detection protocol for sentinel lymph node biopsy in oral cavity squamous cell carcinoma. J Craniomaxillofac Surg. 2015;43:2205–13.
35. Vermeeren L, Valdés Olmos RA, Klop WM, van der Ploeg IM, Nieweg OE, Balm AJ, et al. SPECT/CT for sentinel lymph node mapping in head and neck melanoma. Head Neck. 2010;33:1–6.
36. Khafif A, Schneebaum S, Fliss DM, Lerman H, Metser U, Ben-Yosef R, et al. Lymphoscintigraphy

for sentinel node mapping using a hybrid single photon emission CT (SPECT)/CT system in oral cavity squamous cell carcinoma. Head Neck. 2006;28:874–9.
37. Keski-Santti H, Matzke S, Kauppinen T, Tornwall J, Atula T. Sentinel lymph node mapping using SPECT-CT fusion imaging in patients with oral cavity squamous cell carcinoma. Eur Arch Otorhinolaryngol. 2006;263:1008–12.
38. Valdés Olmos RA, Rietbergen DD, Vidal-Sicart S, Manca G, Giammarile F, Mariani G. Contribution of SPECT/CT imaging to radioguided sentinel lymph node biopsy in breast cancer, melanoma, and other solid cancers: from "open and see" to "see and open". Q J Nucl Med Mol Imaging. 2014;58:127–39.
39. Shoaib T, Soutar DS, MacDonald DG, Camilleri IG, Dunaway DJ, Gray HW, et al. The accuracy of head and neck carcinoma sentinel lymph node biopsy in the clinically N0 neck. Cancer. 2001;91:2077–83.
40. Civantos FJ, Zitsch RP, Schuller DE, Agrawal A, Smith RB, Nason R, et al. Sentinel lymph node biopsy accurately stages the regional lymph nodes for T1-T2 oral squamous cell carcinomas: results of a prospective multi-institutional trial. J Clin Oncol. 2010;28:1395–400.
41. Vermeeren L, Valdés Olmos RA, Klop WM, Klop WM, Balm AJ, van den Brekel MW. A portable gamma camera for intraoperative detection of sentinel nodes in the head and neck region. J Nucl Med. 2010;51:700–3.
42. Kovács AF, Stefenelli U, Seitz O, Middendorp M, Diener J, Sader R, et al. Positive sentinel lymph nodes are a negative prognostic factor for survival in T1–2 oral/oropharyngeal cancer – a long-term study on 103 patients. Ann Surg Oncol. 2009;16:233–9.
43. Alkureishi LW, Ross GL, Shoaib T, Soutar DS, Robertson AG, Thompson R, et al. Sentinel node biopsy in head and neck squamous cell cancer: 5-year follow-up of a European multicenter trial. Ann Surg Oncol. 2010;17:2459–64.
44. Broglie MA, Haile SR, Stoeckli SJ. Long-term experience in sentinel node biopsy for early oral and oropharyngeal squamous cell carcinoma. Ann Surg Oncol. 2011;18:2732–8.
45. Govers TM, Hannink G, Merkx MA, Takes RP, Rovers MM. Sentinel node biopsy for squamous cell carcinoma of the oral cavity and oropharynx: a diagnostic meta-analysis. Oral Oncol. 2013;49:726–32.
46. Den Toom IJ, Heuveling DA, Flach GB, Van Weert S, Karagozoglu KH, Van Schie A, et al. Sentinel node biopsy for early oral cavity cancer: the VU University Medical Center experience. Head Head Neck. 2015;37:573–8.
47. Schilling C, Stoeckli SJ, Haerle SK, Broglie MA, Huber GF, Sorensen JA, Bakholdt V, et al. Sentinel European Node Trial (SENT): 3-year results of sentinel node biopsy in oral cancer. Eur J Cancer. 2015;51:2777–84.
48. Pedersen NJ, Hebbelstrup Jensen D, Hedbäck N, Frendø M, Kiss K, et al. Staging of early lymph node metastases with the sentinel lymph node technique and predictive factors in T1/T2 oral cavity cancer: a retrospective single-center study of 253 consecutive patients. Head Neck. 2016;38 Suppl 1:1033–40.
49. Schiefke F, Akdemir M, Weber A, Akdemir D, Singer S, Frerich B. Function, postoperative morbidity, and quality of life after cervical sentinel node biopsy and after selective neck dissection. Head Neck. 2009;31:503–12.
50. Murer K, Huber GF, Haile SR, Stoeckli SJ. Comparison of morbidity between sentinel node biopsy and elective neck dissection for treatment of the n0 neck in patients with oral squamous cell carcinoma. Head Neck. 2011;33:1260–4.
51. Govers TM, Takes RP, Baris Karakullukcu M, Hannink G, Merkx MA, Grutters JP, et al. Management of the N0 neck in early stage oral squamous cell cancer: a modeling study of the cost-effectiveness. Oral Oncol. 2013;49:771–7.
52. O'Connor R, Pezier T, Schilling C, McGurk M. The relative cost of sentinel lymph node biopsy in early oral cancer. J Craniomaxillofac Surg. 2013;41:721–7.
53. Gurney BA, Schilling C, Putcha V, Alkureishi LW, Alvarez AJ, Bakholdt V, et al. Implications of a positive sentinel node in oral squamous cell carcinoma. Head Neck. 2012;34:1580–5.
54. Zender C, Guo T, Weng C, Faulhaber P, Rezaee R. Utility of SPECT/CT for periparotid sentinel lymph node mapping in the surgical management of head and neck melanoma. Am J Otolaryngol Head Neck Med Surg. 2014;35:12–8.
55. van den Berg NS, Brouwer OR, Schaafsma BE, Mathéron HM, Klop WM, Balm AJ, van Tinteren H, et al. Multimodal surgical guidance during sentinel node biopsy for melanoma: combined gamma tracing and fluorescence imaging of the sentinel node through use of the hybrid tracer Indocyanine Green-^{99m}Tc-Nanocolloid. Radiology. 2015;275:521–9.
56. Parrett BM, Kashani-Sabet M, Singer MI, Li R, Thummala S, Fadaki N, et al. Long-term prognosis and significance of the sentinel lymph node in head and neck melanoma. Otolaryngol Head Neck Surg. 2012;147:699–706.
57. Davis-Malesevich MV, Goepfert R, Kubik M, Roberts DB, Myers JN, Kupferman ME. Recurrence of cutaneous melanoma of the head and neck after negative sentinel lymph node biopsy. Head Neck. 2015;37:1116–21.
58. Rubello D, Colletti PM, Cook GJ. What is the role of radionuclide sentinel lymph node biopsy and dissection in papillary thyroid cancer? Nucl Med Commun. 2015;36:969–70.
59. Gonzalez O, Zafon C, Roca I. Selective sentinel lymph node biopsy in papillary thyroid carcinoma. Endocrinol Nutr. 2013;60:111–4.
60. Salvatori M, Rubello D, O'Doherty MJ, Pelizzo MR, Mariani G. Sentinel lymph node biopsy in thyroid cancer. In: Mariani G, Giuliano AE, Strauss HW, editors. Radioguided surgery – a comprehensive team approach. New York: Springer; 2008. p. 178–89.
61. Boschin IM, Pelizzo MR, Giammarile F, Rubello D, Colletti PM. Lymphoscintigraphy in differentiated thyroid cancer. Clin Nucl Med. 2015;40:343–50.

62. Puccini M, Manca G, Ugolini C, Candalise V, Passaretti A, Bernardini J, et al. Interest of sentinel node biopsy in apparently intrathyroidal medullary thyroid cancer: a pilot study. J Endocrinol Invest. 2014;37:829–34.
63. Martino A, Monaco L, Golia R, Miletto P, Capasso P, Lombardi C, et al. A new radioguided procedure for localization and surgical treatment of neck node metastasis of papillary thyroid cancer. J Endocrinol Invest. 2010;33:339–42.
64. Borsò E, Grosso M, Boni G, Manca G, Bianchi P, Puccini M, et al. Radioguided occult lesion localization of cervical recurrences from differentiated thyroid cancer: technical feasibility and clinical results. Q J Nucl Med Mol Imaging. 2013;57:401–11.
65. Giles YŞ, Sarıcı IS, Tunca F, Sormaz IC, Salmaslıoğlu A, Adalet I, et al. The rate of operative success achieved with radioguided occult lesion localization and intraoperative ultrasonography in patients with recurrent papillary thyroid cancer. Surgery. 2014;156:1116–26.
66. Giovanella L, Suriano S, Lunghi L, Bongiovanni M, Ceriani L. Radioguided surgery of thyroid carcinoma recurrences: the role of preoperative ^{99m}Tc-labeled human serum albumin macroaggregates-SPECT/CT mapping. Clin Nucl Med. 2013;38:207–9.

Radioguided Surgery: Novel Applications

50

Renato A. Valdés Olmos, Federica Orsini, Francesco Giammarile, Sergi Vidal-Sicart, and Giuliano Mariani

Abstract

A few years ago, the concept of Guided intraOperative Scintigraphic Tumor Targeting (GOSTT) was introduced to encompass the whole spectrum of basic and advanced nuclear medicine procedures required for providing a roadmap for radioguided surgery. This concept included the use of interventional nuclear medicine imaging to depict targets to be resected by radioguided surgery. With the incorporation of SPECT/CT and PET/CT, three-dimensional roadmaps to guide surgical procedures became possible. On the other side, new intraoperative portable imaging devices (gamma cameras and other tools) were added to conventional modalities such as gamma probes and blue dye. More recently, the development of hybrid tracers integrating radioactivity and fluorescence in one single signature has enabled the additional use of near-infrared cameras. All these advances have facilitated the extension of radioguided sentinel lymph node biopsy procedures from the classical applications in cutaneous melanoma and breast cancer to other fields such as oral cavity, gastrointestinal, urological, and gynecological malignancies. At present, three GOSTT working models can be defined in relation to radiotracer administration: intralesional without tracer migration for occult lesion localization, intralesional with tracer migration for occult lesion localization and sentinel lymph node biopsy, and systemic to enable excisional biopsy of primary lesions and recurrences as well as isolated regional and distant metastases. The latter is probably the field with the largest potential due to

R.A. Valdés Olmos (✉)
Nuclear Medicine Section and Interventional Molecular Imaging Laboratory, Department of Radiology, Leiden University Medical Centre, Leiden, The Netherlands

Diagnostic Oncology Division, Nuclear Medicine Department, Netherlands Cancer Institute – Antoni van Leeuwenhoek Hospital, Amsterdam, CX, The Netherlands
e-mail: R.A.Valdes_Olmos@lumc.nl; r.valdes@nki.nl

F. Orsini
Nuclear Medicine Unit, "Maggiore della Carità" University Hospital, Novara, Italy
e-mail: federicaors@gmail.com

F. Giammarile
Nuclear Medicine and Diagnostic Imaging Section, Division of Human Health, Department of Nuclear Sciences and Applications, International Atomic Energy Agency, Vienna, Austria
e-mail: F.Giammarile@iaea.org

S. Vidal-Sicart
Nuclear Medicine Department, Hospital Clínic Barcelona, Barcelona, Catalonia, Spain

Institut d'Investigació Biomèdica August Pi i Sunyer (IDIBAPS), Barcelona, Spain
e-mail: SVIDAL@clinic.ub.es

G. Mariani
Regional Center of Nuclear Medicine, Department of Translational Research and Advanced Technologies in Medicine and Surgery, University of Pisa, Pisa, Italy
e-mail: giuliano.mariani@med.unipi.it

© Springer International Publishing Switzerland 2017
H.W. Strauss et al. (eds.), *Nuclear Oncology*,
https://doi.org/10.1007/978-3-319-26236-9_55

the continuous introduction of new PET and SPECT tracers. Novel modalities like luminescence detection and tracked image-guided navigation will further reinforce the role of GOSTT and radioguided intervention procedures.

Keywords

Guided intraoperative scintigraphic tumor targeting • GOSTT • Radioguided surgery • Novel applications • Sentinel lymph node biopsy • Lesion occult localization • Interventional SPECT/CT • Interventional PET/CT • Intraoperative portable imaging technologies

Glossary

[^{18}F]FDG	2-Deoxy-2-[^{18}F]fluoro-D-glucose
^{99m}Tc-MAA	^{99m}Tc-macroaggregated albumin
AJCC	American Joint Committee on Cancer
CT	X-ray computed tomography
GOSTT	Guided intraOperative Scintigraphic Tumor Targeting
ICG	Indocyanine green
M	Metastasis status according to the AJCC/UICC TNM staging system
MEN	Multiple endocrine neoplasm
MIBG	*meta*-Iodobenzylguanidine
MIP	Maximum intensity projection
MPR	Multiplanar reconstruction
N	Lymph node status according to the AJCC/UICC TNM staging system
NET	Neuroendocrine tumor
NIR	Near-infrared
PET	Positron emission tomography
PET/CT	Positron emission tomography/Computed tomography
PSMA	Prostate-specific membrane antigen
ROLL	Radioguided occult lesion localization
RSL	Radioguided ^{125}I seed localization
SLN	Sentinel lymph node
SNOLL	Combined sentinel lymph node biopsy and radioguided occult lesion localization
SPECT	Single-photon emission computed tomography
SPECT/CT	Single photon emission computed tomography/Computed tomography
T	Tumor status according to the AJCC/UICC TNM staging system
UICC	Union Internationale Contre le Cancer (International Union Against Cancer)

Contents

Introduction 1452

Working GOSTT Models in Interventional Imaging and Radioguided Surgery 1453

General Background of SLN Biopsy 1454

The Evolution of Intraoperative Instrumentation for SLN Biopsy and Other GOSTT Applications 1454

Preoperative Imaging: From Planar Images to Hybrid Computed Tomography 1455

Radiopharmaceuticals for Interventional Molecular Imaging and Radioguided Surgery 1456

Interventional SPECT/CT and PET/CT for GOSTT 1458

Retrieving SPECT/CT and PET/CT Findings in the Operating Room 1460

Novel Clinical GOSTT Applications 1462
Head and Neck 1462
Urological Malignancies 1464
Gynecological Malignancies 1468
Gastrointestinal Cancer 1470
GOSTT Applications in Other Malignancies 1471

Future GOSTT Scenarios 1471

References 1473

Introduction

Radioguided surgery is one of the applications of nuclear medicine with more relevant growth in the last quarter-century. Radioguided surgery

constitutes a wide range of combined procedures involving close collaboration with other specialties like surgery, pathology, and radiology; correct application of such multidisciplinary procedures ensues obvious immediate and long-term benefits to the patient. In general, radioguided surgical procedures are less invasive than traditional surgical approaches, while they may also result in improved local-regional control of malignant disease [1].

In 2011 the term GOSTT (Guided intraOperative Scintigraphic Tumour Targeting) was introduced in order to encompass the whole spectrum of basic and advanced nuclear medicine procedures required for providing a roadmap for radioguided surgery [2]. The GOSTT concept was recently further updated incorporating the discussion of novel modalities such as hybrid tracers for simultaneous fluorescence and radioactive signal detection, sophisticated navigation approaches based on mixed-reality protocols, and the use of Cerenkov luminescence related to PET tracers [2]. An extensive overview of the GOSTT procedures is given in a book recently edited by the International Atomic Energy Agency (IAEA) [3].

Working GOSTT Models in Interventional Imaging and Radioguided Surgery

The GOSTT concept rests on both preoperative interventional imaging and intraoperative radioguided detection. To accomplish this approach, three working models based on the concentration of an administered radiopharmaceutical in a target or index lesion can be delineated (Fig. 1): (1) local administration of a radiocolloid at the site of a solid epithelial tumor that enables the depiction of the pattern of lymphatic drainage and the identification of the sentinel lymph nodes by means of lymphoscintigraphy; (2) direct intralesional administration of a radiopharmaceutical such as ^{99m}Tc-macroaggregated human albumin (^{99m}Tc-MAA) which is comprised of particles that, by virtue of their relatively large size, are lengthily retained at the site of interstitial injection enabling excisional biopsy; and (3) systemic administration of a radiopharmaceutical that preferentially accumulates in the target lesion, e.g., ^{99m}T-sestamibi for localization of parathyroid adenomas or [^{18}F]FDG for [^{18}F]FDG-avid tumor lesions.

The basic modality to illustrate and discuss the GOSTT concept is the sentinel lymph node (SLN) procedure. Historically, the term "sentinel lymph node" was introduced to describe a group of lymph nodes retrieved in patients with penile carcinoma under the assumption that they receive direct drainage from the site of the primary lesion [5]. In the last 25 years, radioguided surgical applications have rapidly expanded especially to perform sentinel lymph node (SLN) biopsy. In addition to ongoing applications in patients with breast cancer and cutaneous melanoma, radioguided SLN biopsy has been extended to a wide variety of other solid epithelial malignancies such as head and neck cancers, gynecological cancers (vulvar, cervical, and endometrial), gastrointestinal cancers (esophagus, stomach, colorectal, anus), urological malignancies (prostate cancer, bladder cancer, penile carcinoma, and others), non-small cell lung cancer, differentiated thyroid carcinoma, and others [1, 6–15].

A second field of GOSTT applications is constituted by the excisional biopsy techniques based on direct intralesional injection of ^{99m}Tc-MAA, which are expanding from the classical application of "radioguided occult lesion localization" (ROLL) for nonpalpable breast lesions to other tumors, such as solitary pulmonary nodules as well as others [16, 17]. In more recent years, the ROLL technique has been used in breast-conserving surgery combining lumpectomy and SLN biopsy [18, 19].

The model of systemic tracer administration is illustrated by radioguided parathyroid surgery with ^{99m}Tc-sestamibi, a radiotracer with preferential uptake and/or accumulation in tumor tissues. This approach has also been described using radiolabeled monoclonal antibodies against tumor-associated antigens. These procedures also include receptor-mediated uptake of radiolabeled agents by tumors such as neuroendocrine tumors or paragangliomas, accumulation of bone-seeking agents for radioguided excision of isolated bone metastasis, and radioiodine uptake in recurrences/metastases from differentiated thyroid carcinoma. The field of applications following systemic administration

has been extended to intraoperative radioguidance using [^{18}F]FDG or other positron-emitting radiopharmaceuticals using specific probes able to detect the high-energy gamma photons originated by the annihilation reaction or directly β^+ particles [20]. More recently, an intraoperative Cerenkov luminescence device for detection of [^{18}F]FDG-avid malignant lesions has been presented [21].

This chapter will focus on radioguided surgery in the context of the GOSTT concept, emphasizing the innovative methodological aspects for both novel clinical procedures and the more recent investigational applications.

General Background of SLN Biopsy

The rationale of SLN biopsy in solid epithelial tumors relates to the general concept that initial lymphatic spread of such tumors occurs to locoregional lymph nodes in an orderly way, generally from lower- to higher-echelon levels. Of course, this orderly progress does not exclude the potential of tumors to spread hematogenously, which is associated with most distant metastases. Probably in only few circumstances do distant metastases arise from progression of an initial lymphatic metastasis.

The modern SLN concept [22, 23] concerns not only the first lymph node encountered by lymphatic vessels draining the primary tumor but also all first-echelon lymph nodes upon which a lymph vessel originating in the tumor drains directly. This definition does not always correspond to the lymph node nearest to the tumor, as the route of the lymphatic vessels may be complex and unpredictable with different lymphatic pathways leading to different sentinel lymph nodes (Fig. 1); in practice each lymph node identified as SLN should therefore be investigated for the presence of metastasis. Lymphatic mapping following interstitial radiocolloid injection is essential to precisely visualize sequential lymphatic drainage of the radiopharmaceutical and to provide surgeons an intraoperative roadmap [24, 25].

The presence or absence of SLN metastasis usually has a significant impact on therapeutic strategy. In patients with early cancer, if the SLN does not contain metastasis, the surgical approach should aim at removing the primary tumor and avoiding unnecessary regional node dissection. The likelihood that non-SLNs contain metastasis is extremely low, thus making extensive node dissection unnecessary in case the SLN is free from metastasis. Patients whose SLN contains metastasis usually require dissection of regional lymph nodes [26].

The Evolution of Intraoperative Instrumentation for SLN Biopsy and Other GOSTT Applications

Gamma probes were incorporated into the procedure of SLN biopsy in the early years of the procedure [27]. These devices were able not only to count radioactivity in the surgical field intraoperatively but also to provide numerical readouts and audible signals proportional to the counting rate. The hand-held probe is connected to a counting unit either with a cable or with a wireless system. The detector is usually limited to a long narrow cylinder with a diameter varying from about 12 mm up to 16–18 mm. It may be slightly angled in order to allow for easier access in specific applications and easier manipulation within the surgical field.

Thanks to the auditory signals and digital readouts, gamma probes enabled the surgeon to localize and remove radioactive tissue like the SLN or tumor tissue. In fact, gamma-probe counting constituted the acoustic component of the SLN identification procedure in the operating room and for surgeons was the complement of the process of visual detection as implemented by the use of blue dyes. This acoustic/visual feature was introduced in the early 1990s as a step forward in comparison with the original approach, which was exclusively based on the injection of blue dyes to visualize lymphatic ducts and SLNs as originally described by Morton et al. [22].

The combination of gamma-probe counting and blue dyes represented the second step in the evolution of the procedure. On the other hand, this possibility to combine visual and acoustic signals during the surgical SLN procedure has become the cornerstone for new portable technologies, which now enable image generation in the operating room reinforcing the visual component in the guidance of

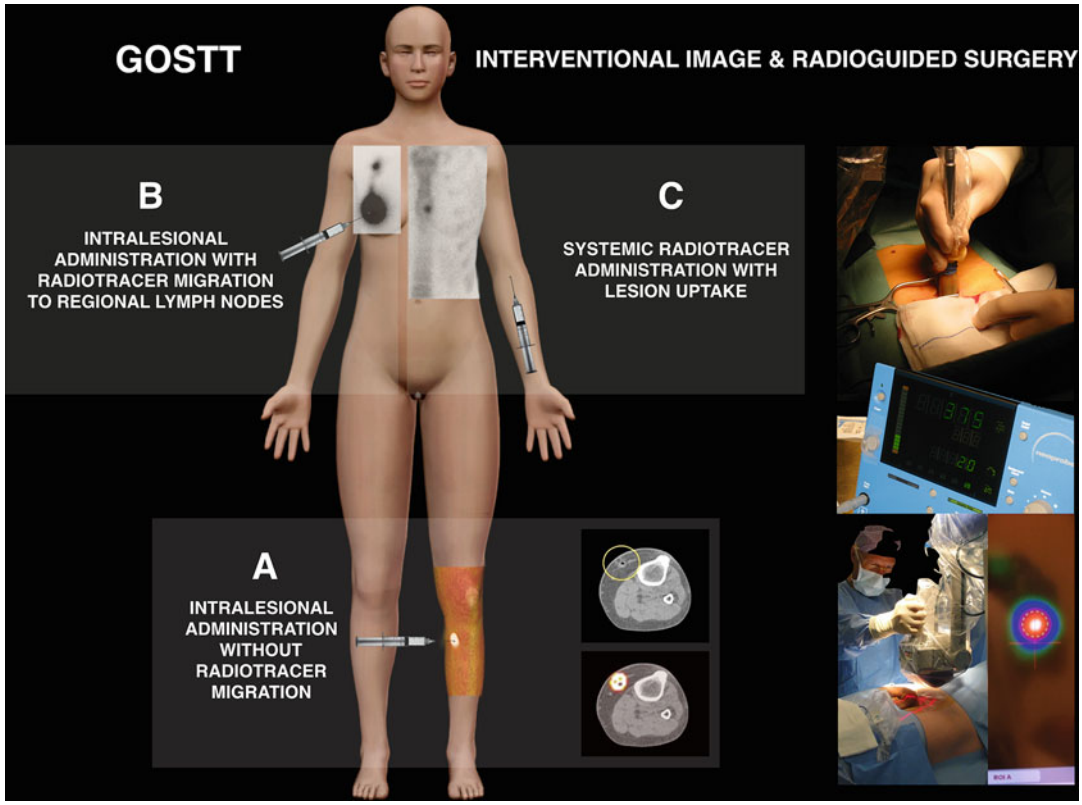

Fig. 1 Schematic working GOSTT (guided intraoperative scintigraphic tumor targeting) approaches including interventional imaging leading to radioguided surgery. (**a**) Intralesional administration of ^{99m}Tc-MAA in a melanoma metastasis of the *left* lower leg. (**b**) Intralesional administration of ^{99m}Tc-nanocolloid in a non-palpable tumor of the *right* breast with subsequent migration to axillary lymph nodes. (**c**) Systemic administration of ^{99m}Tc-diphosphonate with increased uptake in a solitary sternal metastasis

surgical excision [3]. These portable imaging technologies include devices like small gamma cameras for high-resolution planar imaging [28], gamma probe- or small camera-based devices for 3D intraoperative imaging [29], near-infrared (NIR) cameras used in combination with portable gamma devices when fluorescent detection is added to the SLN procedure [30], and cameras for Cerenkov luminescence imaging [21].

Preoperative Imaging: From Planar Images to Hybrid Computed Tomography

Lymphoscintigraphy constitutes the cornerstone of preoperative lymphatic mapping. Its incorporation to the SLN procedure helped to transform the paradigm in radioguided SLN surgery from the original "open and see" approach based on the use of vital dyes to visualize lymphatic ducts and SLNs to another "see and open" based on the gamma camera images acquired prior to the surgical procedure. This lymphatic mapping enabled not only to personalize imaging of lymphatic drainage for every individual patient but also made possible to mark with indelible ink the SLN site projection on the skin. This approach gained in popularity in Europe and was highly effective for SLN localization not only in the expected areas of drainage but also in unusual locations [24]. Lymphoscintigraphy was found to be 88–96% reproducible in melanoma [31, 32] and 100% in breast cancer as well as penile cancer [33, 34].

For SLN identification, early images, to depict first draining lymph nodes, and delayed images, to

differentiate second-echelon nodes, are required. The visualization of lymphatic ducts, the time of lymph node appearance, the lymph node basin, and the intensity of lymph node uptake are all important factors to take into account. Lymph nodes draining from the site of the primary lesion through their own lymphatic vessel, or a single radioactive lymph node in a basin, are considered as definitely SLN. Lymph nodes appearing between the injection site and a first draining node or nodes with increasing uptake appearing in other lymph node basin may be considered as SLN with a high probability. Higher-echelon lymph nodes in the trunk and extremities or lower-echelon nodes in the head and neck region may be included in the low-probability SLN category [35].

More than 10 years after planar lymphoscintigraphy, SPECT/CT imaging was introduced in the SLN procedure [36], thus enabling to incorporate an additional dimension to preoperative mapping. In fact, the functional information on draining lymph nodes provided by SPECT could be combined with the morphological information from CT by acquiring both modalities in one session. The resulting fused SPECT/CT images were able to depict SLNs in an anatomical landscape, thereby providing important reference landmarks to be recognized by surgeons in the operating theater. Lymphatic mapping complemented by SPECT/CT is currently applied both in malignancies with predominantly superficial drainage (e.g., breast cancer and melanoma) and in tumors draining to deep lymphatic basins or areas of complex anatomy such as the head and neck or the pelvis [37–46]. A specific requirement for SLN localization is that the CT component of SPECT/CT must be of sufficient high quality to provide optimal anatomical landmarks to be recognized by surgeons in the operating room. The CT component is also used to correct the SPECT signal for tissue attenuation and scattering; thanks to such corrections, SPECT/CT may be particularly useful in obese patients to detect SLNs not observed on planar images and additional SLNs in other basins. After these corrections, SPECT can be fused with CT. For fused images a gray scale is used to display the morphology in the background image (CT), whereas a color scale is used to display the SLN in the foreground image (SPECT). Most frequently, a radioactive hot spot corresponds to a single lymph node on CT, but in some cases it correlates with a cluster of lymph nodes [47].

Simultaneously with the evolution of the SLN procedure, a similar "see and open" approach is catapulting also other applications of radioguided surgery in which preoperative imaging plays an important role leading to surgical intervention. This interventional molecular imaging can be illustrated by the preoperative use of ^{99m}Tc-sestamibi scintigraphy for the localization of parathyroid adenomas, where preoperative imaging is used as a roadmap for radioguided surgery of these lesions [48]. Recently, the addition of SPECT/CT to planar imaging did significantly increase the accuracy in correctly identifying a parathyroid adenoma from 75% to 85% [49].

Radiopharmaceuticals for Interventional Molecular Imaging and Radioguided Surgery

As mentioned earlier, an important aspect in GOSTT possibilities is related to the choice of radiotracers for interventional imaging and radioguided surgery. For lymphoscintigraphy and radioguided SLN biopsy, the tracers most widely used are radiocolloids that, after their interstitial administration, migrate from the injection site allowing the visualization of the lymphatic vessels by lymphoscintigraphy and SPECT/CT [25]. These colloids are preferentially retained by the first lymph nodes encountered along the course of the draining lymphatic vessel(s), enabling their identification as SLN(s). Once within the lymph node, radiocolloids are phagocytized by macrophages lining the lymph node sinusoids. Such retention of radiocolloids in the SLN is a physiological process and does not indicate presence or absence of metastases in the lymph node. Radiocolloids can be constituted by an inorganic substance (^{198}Au-colloid, ^{99m}Tc-antimony sulfur, ^{99m}Tc-colloidal sulfur, ^{99m}Tc-stannous fluoride, ^{99m}Tc-rhenium sulfur) or can be derived from biological substances (nano- or micro-colloidal human serum albumin). Radiocolloid particle

size, varying from 5 to 1,000 nm, mainly determines the speed of lymphatic drainage from the interstitial injection site and the amount retained in the SLN. In particular, small-size radiocolloids (less than about 100 nm) migrate quite fast from the injection site through the lymphatic system. This factor underlines the need to sequentially perform dynamic images at short time intervals after interstitial injection as well as static early and delayed images in order to differentiate SLNs from secondary lymph nodes. Larger size radiocolloids are retained longer in the SLN, so that lymphoscintigraphy does not generally visualize more than one to two lymph nodes along a single lymphatic draining vessel. However, migration of larger particles from the interstitial administration site is very slow, so that a longer time, even 2 h or more, can be required to complete mapping. In Europe, ^{99m}Tc-albumin nanocolloid (which has a quite narrow range of particle size, with over 90% of the particles being smaller than 80 nm) is widely available and employed, while in the USA, ^{99m}Tc-sulfur colloid (with a wide range of particle size between about 20 and 400 nm) is the most employed; to overcome the problem of heterogeneous particle size distribution, in some nuclear medicine centers, ^{99m}Tc-sulfur colloid is filtered immediately after labeling and prior to administration, in order to remove particles with a diameter bigger than a certain size, usually 220 nm or other sizes [50, 51].

The radiopharmaceutical ^{99m}Tc-tilmanocept has recently been introduced for lymphatic mapping and SLN biopsy. This radiotracer accumulates in SLNs after binding the mannose-binding protein receptor expressed on the surface of phagocytes. ^{99m}Tc-tilmanocept contains 7 nm particles, which are rapidly cleared from the injection site through lymphatic vessels [52]. In contrast to larger particle radiocolloids, there is also significant diffusion into the blood capillaries. Although diffusion from the injection site via the blood route may limit the amount of lymphatic flow of the tracer, the reduction in signal intensity at the location of the primary lesion may facilitate identification of SLN located close to the injection site. ^{99m}Tc-tilmanocept has been used in oral cavity cancer [53], melanoma [54], and breast cancer [55].

More recently, the hybrid tracer indocyanine green-^{99m}Tc-nanocolloid (ICG-^{99m}Tc-nanocolloid) has been explored for clinical use. Concerning lymphatic drainage pattern and SLN location, this novel tracer showed a 100% reproducibility rate when compared with the parental ^{99m}Tc-nanocolloid in patients with different malignancies and lymphatic drainage basins [56]. Based on its radioactive signature, such hybrid tracer preserves the possibilities for perioperative imaging using conventional gamma cameras, SPECT/CT, and portable devices. At the same time, the added fluorescent signature leads to improved visual resolution and SLN detectability during surgery. A further validation of the clinical applicability of ICG-^{99m}Tc-nanocolloid has been reported for oral cavity cancer [57], vulvar cancer [58], penile cancer [59], prostate cancer [60], and more extensively in melanoma [61].

Intralesional tracer administration enabling excisional biopsy of primary tumors is a GOSTT application known as “radioguided occult lesion localization” (ROLL) , originally validated for breast lesions but with subsequent rapid extension to other malignancies. The first clinical validation of ROLL was based on a direct intralesional injection of ^{99m}Tc-MAA in nonpalpable breast lesions guided by ultrasonography or stereotactic mammography [16]. To accomplish concentricity in the distribution of the tracer into the tumor, the radiotracer must be injected as centrally as possible in the lesion. During excision, which can be performed on the same day or on the next day, the gamma probe is introduced through a small skin incision that can ensure an optimal cosmetic outcome without the topographic constraints required by the classical intralesional markers such as the carbon tracer of the hooked wire. Intraoperative gamma-probe counting enables the surgeon to easily localize the focal deposition of ^{99m}Tc-MAA, thereby facilitating the procedure. The surgical specimen is checked ex vivo with the gamma probe for further confirmation of radioactivity and can also be x-rayed to ensure complete removal of the area containing the lesion. The technique enabled a 99.5% lesion removal rate in the breast [62]. When used in combination with wire

localization in nonpalpable breast cancer, ROLL did significantly reduce reoperation from 21% to 2% [63]. In the last years, radioguided iodine-125 seed localization (RSL) has been introduced for excisional breast lesion [64]. Using similar gamma-probe devices, RSL appears to be comparable with ROLL concerning margin status and re-excision rates, but with significantly lower weight of the resected specimen in patients with nonpalpable ductal carcinoma in situ or invasive carcinoma [65]. In locally advanced breast cancer receiving neoadjuvant chemotherapy, RSL is also comparable with ROLL but with more practical advantages, due to the long halftime of iodine-125 which enables seed implantation before chemotherapy without additional tracer injection for excision of residual tumor [66]. The ROLL principle has been applied in other tumors such as papillary thyroid cancer [67], solitary pulmonary nodules [17], and lymph node metastases [68]. On the other hand, RSL has been helpful to localize axillary metastatic lymph nodes after neoadjuvant chemotherapy in breast cancer patients reaching a 97% identification rate [69].

More recently the ROLL technique has been used in breast-conserving surgery combining lumpectomy and SLN biopsy by means of a single intralesional tracer injection [18, 19]. This approach is known as SNOLL and is based on the use of a radiocolloid with the ability to migrate to the regional lymph nodes. Basic work based on ex vivo lymph node measurements effectuated in the 1990s when validating the SLN procedure demonstrated that when ^{99m}Tc-nanocolloid is administered into a breast tumor, only 2–3% migrate to the axillary SLNs, while the remaining predominant fraction remains at the injection site and can thus guide a ROLL procedure simultaneously with the SLN biopsy procedure [70].

Radioguided surgery related to the systemic administration of a tracer is probably the GOSTT working model with the greatest potential for the future. This potential is based on the detection by either SPECT/CT or PET/CT (depending on the radiopharmaceutical used) of target lesions with subsequent indication for resection for diagnostic or therapeutic purposes. The indication may be closely related to suspected cancer recurrence with elevation of tumor markers during follow-up. For example, PET/CT with [^{18}F]FDG in combination with a hand-held PET probe, suitable to detect 511 KeV gamma emissions, resulted in appropriate tissue sampling by excisional biopsy approach in patients with suspected lymphoma [71]. Also in patients with breast cancer, melanoma, and other malignancies, PET/CT led to the resection of [^{18}F]FDG-avid metastases using a high-energy gamma probe [72]. More recently, an intraoperative device for detection of [^{18}F]FDG-avid malignant lesions based on the detection of the Cerenkov luminescence, which is emitted by emitters of β-particles (both negatrons and positrons), has been used for optical lesion visualization [21].

Regarding radiopharmaceuticals for SPECT, besides the aforementioned ^{99m}Tc-sestamibi [48, 49], another example can be found in radioguided surgery of neuroendocrine tumors (NETs) using ^{111}In-DTPA-pentetreotide; this approach was found to be useful to guide cytoreduction in 29 out of 30 patients with abdominal NETs [73]. Also radiolabeled metaiodobenzylguanidine (MIBG) has been advocated to improve quality of resection in selected NET cases [74]. On the other hand, SPECT/CT led to improve lesion definition and localization with reduction of false-positive results in NET patients [75]. More recently, ^{68}Ga-labeled somatostatin analogues have been incorporated to radioguided surgery of NETs in a "see and open" approach on the basis of preoperative PET/CT and intraoperative gamma-probe guidance [76].

Interventional SPECT/CT and PET/CT for GOSTT

Both SPECT/CT and PET/CT may be considered as basic modalities for interventional hybrid imaging in GOSTT (Fig. 2). SPECT/CT has been incorporated in procedures for SLN localization with locally administered radiocolloids as well as for detection of metastasis with systemically administered tumor-seeking tracers. On the other hand, PET/CT using tracers as [^{18}F]FDG or ^{18}F-fluorocholine has been used to lead radioguided interventions in cases with isolated metastasis. In the SLN procedure, SPECT is primarily oriented to

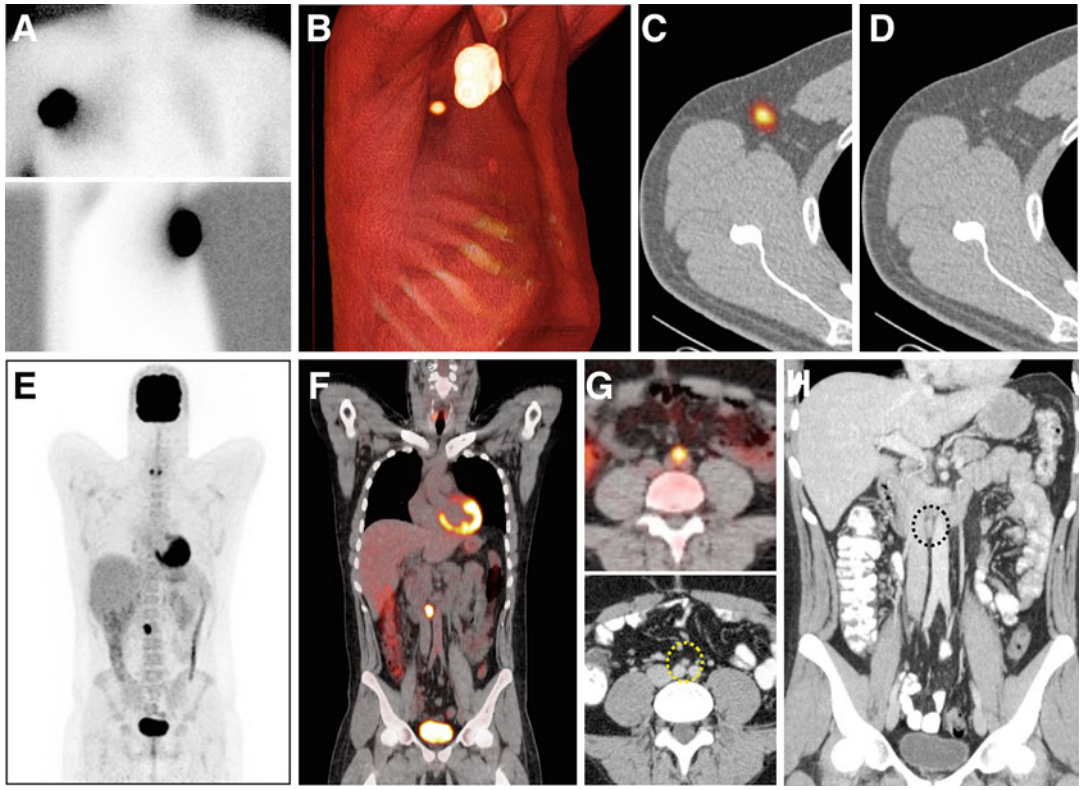

Fig. 2 Interventional molecular hybrid imaging leading to radioguided surgery. In *upper* row, planar images show no drainage to the axilla (**a**), whereas SPECT/CT (**b**–**d**) is able to depict an axillary sentinel lymph node near the injection site. In *lower* row, coronal PET (**e**) and PET/CT (**f**) showing an [^{18}F]FDG avid lymph node metastasis between aorta and cava inferior which is further localized on transversal PET/CT and CT (**g**) as well as on coronal CT (*circles*) (h)

the anatomical localization of SLNs, and protocols for imaging are, in principle, related to this goal. This also explains why SPECT/CT is usually acquired using a low-dose CT. Acquisition of a diagnostic high-dose CT, with or without intravenous contrast, is not really necessary because the SLN procedure aims at identifying subclinical metastases smaller than 2 mm in lymph nodes that are not enlarged or altered in their morphology. PET/CT is mostly acquired using a low-dose CT protocol similar as for SPECT/CT; however, high-dose CT with intravenous contrast is preferred in some cases to characterize PET-positive lesions, which are generally associated with metastases larger than 5 mm.

SPECT/CT is usually performed in addition to lymphoscintigraphy as a preoperative phase of the SLN procedure. SPECT/CT imaging with ^{99m}Tc radiocolloids is possible thanks to the prolonged lymph node retention after phagocytosis of such radiocolloids by the macrophages, which often results in an adequate detection window. This facilitates not only the acquisition of delayed planar images and SPECT/CT but also intraoperative gamma ray-guided SLN localization.

For detection of both SLNs (when patient is scheduled for SLN biopsy) and metastatic tumor tissue (when tumor-seeking radiotracers are used), a specific requirement for localization is that the CT component of SPECT/CT needs to be of sufficient quality to provide optimal anatomical information. The second generation of SPECT/CT gamma cameras includes an improved CT component; this enables the identification and evaluation of the lymph nodes corresponding with the radioactive nodes on fused SPECT/CT

images by acquiring a low-dose (e.g., 40 mAs) CT. In superficial areas such as the groin and the axilla, 5-mm slices may provide adequate anatomical details. For more complex anatomical areas (head/neck, pelvis, abdomen), 2-mm slices may be necessary. With this approach, SPECT/CT can accurately localize SLNs in relation to the vascular structures in deep anatomical areas.

The CT component is also used to correct the SPECT signal for tissue attenuation and scattering. After these corrections, SPECT can be fused with CT [77]. For fused images a grayscale is used to display the morphology in the background image (CT), whereas a color scale is used to display the SLN in the foreground image (SPECT).

For reading/reporting purposes, SPECT/CT or PET/CT images are mostly displayed in a similar manner as that of conventional tomography. Two-dimensional display of fused images to be correlated with CT and SPECT is facilitated by multiplanar reconstruction (MPR), and the use of cross-reference lines allows for the navigation between axial, coronal, and sagittal views. In the SLN procedure, this tool enables the correlation of radioactive SLNs seen on fused SPECT/CT with lymph nodes seen on CT. Most frequently, a radioactive SLN corresponds to a single lymph node on CT, but in some cases it correlates with a cluster of lymph nodes. This information may be useful for the intraoperative procedure and the post-excision control using portable gamma cameras or probes, as additional radioactive SLNs may be detected with the high-resolution portable gamma camera at the same location, then harvested for analysis.

The use of maximum intensity projection (MIP) to display fused SPECT/CT or PET/CT images may also help surgeons to anatomically recognize and localize SLNs or radiotracer-avid metastases. MIP is a specific type of rendering in which the brightest voxels are projected into a three-dimensional image. A limitation of MIP is that the presence of other high-attenuation voxels on CT may complicate recognition of the vasculature and other anatomical structures. Furthermore, MIP is actually a two-dimensional representation, which cannot accurately depict the actual relationships of the vessels and other structures [78]. Also localization of SLNs or of tracer-avid metastases in a three-dimensional context can be supported by the application of volume rendering. In this modality different colors are assigned to anatomical structures such as vessels, the muscle, bone, and skin. This results in easily recognizable anatomical reference points of the target lesions, for instance, in relation to the vasculature. By incorporating a color display, volume rendering improves visualization of complex anatomy and 3D relationships.

Retrieving SPECT/CT and PET/CT Findings in the Operating Room

The anatomical localization of SLNs or tracer-avid lesions does transform SPECT/CT and PET/CT in interventional imaging. Surgeons can use the anatomical landmarks so provided to retrieve these targets during operation. This evolution to a 3D roadmap after the incorporation of these hybrid molecular modalities has helped to further transform the GOSTT paradigm to one of "see, open, and recognize" (Fig. 3). This approach can potentially be reinforced by the synergy of SPECT/CT and PET/CT with the portable imaging technologies [3]. For instance, high-resolution portable gamma cameras are able to reproduce SPECT/CT findings in the intraoperative localization of SLNs or parathyroid adenomas in complex or difficult anatomical areas like the head and neck [25, 42, 79, 80]. These devices have been particularly helpful to depict SLNs at a distance of at least 3 mm from the injection site when equipped with a high-resolution pinhole collimator [81]. The new generation of portable gamma cameras has been upgraded with an optical module for fused optical/scintigraphic imaging resulting in improved anatomical localization [82, 83].

Another important possibility to utilize SPECT/CT and PET/CT findings during surgery is the intraoperative real-time generation of virtual elements. These elements can be added to the surgical environment in the context of an

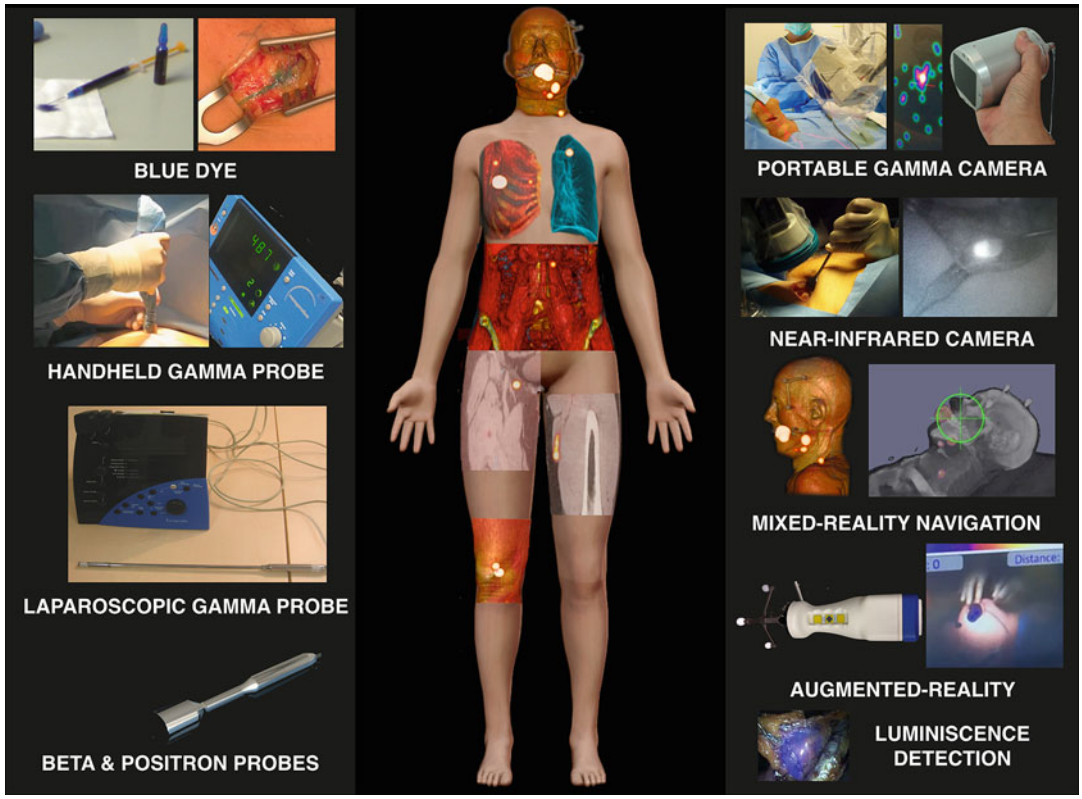

Fig. 3 Synergy of SPECT/CT and PET/CT with portable intraoperative technologies. Both sentinel lymph nodes (head/neck, axillary/intercostal, para-aortic, inguinal, popliteal) and [^{18}F]FDG avid metastases (*upper left* lung, *upper left* leg) can be preoperatively localized for further radioguided resection using conventional (*left* column) and novel (*right* column) intraoperative portable devices and modalities

augmented reality protocol. Augmented reality approaches can be considered as a part of mixed reality, but it is also an independent modality, which has been applied in radioguided surgery mainly after the introduction of the freehand SPECT technology based on a tracked gamma probe suitable for 3D image generation [84]. This device has been the basis for augmented reality experiences in SLN procedures in breast cancer [85], oral cancer [86], and melanoma [87], as well as for surgery of parathyroid adenomas [88]. The same freehand SPECT technology may be considered a helpful tool in transferring SPECT/CT, and potentially PET/CT, to the operating room using mixed reality protocols. The concept of mixed reality was introduced by Milgram and Kishino in 1994 and concerns the merging of *real* and *virtual* elements to produce new environments [89]. More related to the GOSTT approach, with the use of a tracked protocol, it has become possible today to transfer the virtual SPECT/CT images to the operating room, so that a merged environment can be created for adequate surgical navigation. This approach enabled to generate tracked 3D images of a phantom prepared with a reference target (ReT) and simulated SLNs containing ICG-^{99m}Tc-nanocolloid. After feeding the SPECT/CT images to the navigation system, optical tracking could be used to position the tip of the fluorescence endoscope relative to the preoperative 3D imaging data allowing accurate identification of the simulated

SLNs in the phantom. A similar approach was used to navigate toward the prostate and SLNs in a patient undergoing robot-assisted prostatectomy [90]. This navigation approach has been found to be feasible in areas of rigid anatomy like the retroperitoneal space and the groin [91]. However, more difficulties for SPECT/CT-based mixed reality surgery are to be expected for "non-rigid" anatomical areas. Recently, the use of freehand SPECT in combination with a mobile handheld gamma camera has been validated [92]. The freehand SPECT technology has also been used to generate intraoperative 3D navigation for single or multiple ^{125}I-seeds in RSL l [93] and ROLL [94] in breast-preserving cancer surgery.

Novel Clinical GOSTT Applications

The clinical SLN applications in breast cancer, cutaneous melanoma, and head and neck cancer are extensively discussed in other chapters of this book. This chapter mainly concerns novel clinical applications as well as the incorporation of new technologies for both preoperative imaging and intraoperative localization in existing GOSTT applications.

Head and Neck

Regional staging in the neck is performed according to the AJCC/UICC TNM staging system which differentiates seven lymph node levels in each side of the neck [95]. For GOSTT applications to localize SLNs on SPECT/CT and [^{18}F]FDG-avid metastases on PET/CT in the head and neck, the approximately 250–300 lymph nodes are divided into various nodal groups. This high lymph node density and the site of the primary lesion are the principal causes of the remarkable variations in lymphatic drainage and patterns of metastatic dissemination. For instance, scalp melanomas of the frontal zone can drain to different lymph nodes when compared with melanomas of the parietal or occipital areas. For facial and forehead melanomas, metastatic spread to different basins may occur. In the oral cavity, malignancies of the lingual apex may drain to other groups in comparison with well-lateralized lesions in the tongue or floor of the mouth. Identification of SLNs in the vicinity of periauricular melanomas may be critical. Also SLNs located near to floor-of-mouth tumors may be missed and can be accompanied by a decrease in detection rate from 97% to 80%, a decrease in sensitivity from 97% to 80%, and a reduction in the negative predictive value from 98% to 88%, respectively [96]. This has led to the conclusion that planar lymphoscintigraphy is not sensitive enough for predicting the SLN level in the neck [97]. In this scenario, SPECT/CT appears to be essential for the SLN procedure not only to accurately identify SLNs in an anatomical landscape but also to detect additional SLNs in the vicinity of the primary lesions or to personalize alternative drainage to different lymph node basins on an individual basis (Fig. 4).

In a recent study in which SPECT/CT imaging has been performed in a series of 58 patients with oral or oropharyngeal carcinoma, 11 additional SLNs were detected by SPECT/CT; one of these nodes contained metastases [98]. In another study concerning 34 patients, extra SLNs were found by SPECT/CT in 15 patients, and in seven the anatomical level of SLN location was reconsidered [99]. The superior anatomical information of SPECT/CT may lead to adjust surgical approach, as observed for 11 out of 38 patients (29%) with head and neck melanoma; in six patients of this group, SPECT/CT detected additional SLNs (16%) [46]. In another study SPECT/CT modified the surgical approach (more superficial incision or incision at other site) in 9 out of 34 (27%) patients with head and neck malignancies [100]. The surgical adjustment rate due to the additional information provided by SPECT/CT increases when SLNs are located in the periparotid areas; in 8 out of 14 patients (57%) with melanoma and drainage to the parotid region on planar lymphoscintigraphy, SPECT/CT was able to distinguish SLNs in level II of the neck from those located in or around the parotid [101]. In another evaluation in melanoma patients, SPECT/CT caused an increase of the detection rate from

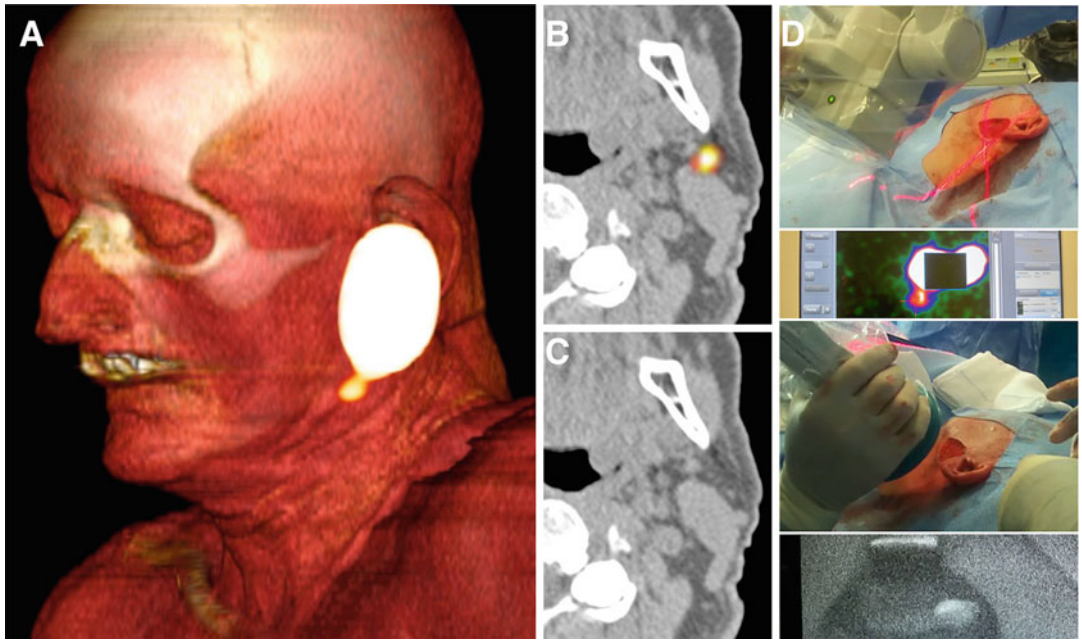

Fig. 4 SPECT/CT with volume rendering (**a**) showing drainage of ^{99m}Tc-nanocolloid to a sentinel lymph node close to the inferior border of the injection site in the left auricular area. This lymph node is further anatomically localized on SPECT/CT (**b**) and CT (**c**) to subsequently be intraoperatively recognized using a portable gamma camera and a fluorescence camera (**d**)

91% (planar scintigraphy) to 98% with a clinical impact of 63.6% [102]. The overall clinical value of the SPECT/CT anatomical information for lymph node mapping was also used to adjust super-selective prophylactic irradiation of the neck in a feasibility study including ten patients with squamous cell carcinoma of the head and neck [103]. Further GOSTT developments in the head and neck region include the hybrid tracer ICG-^{99m}Tc-nanocolloid that has been reported for oral cavity cancer [57], the use of high-resolution portable gamma cameras in addition to SPECT/CT [42], and freehand SPECT probes with 3D display [86]. The incorporation of SPECT/CT and a portable gamma camera in combination with a fluorescence camera to the SLN procedure has led to identify 26% additional SLNs [104].

Lymphoscintigraphy and SPECT/CT have also been validated for SLN identification in papillary thyroid cancer. In an initial study, SLNs were identified in 19 of 24 patients (79%); the identification rate increased to 96% during surgery using a handheld gamma probe. Multidirectional drainage to both central and laterocervical compartments was observed in 50% of the patients [105]. In another series concerning 23 clinically node-negative patients combined, visualization rate of lymphoscintigraphy and SPECT/CT was 91%. The two patients without drainage presented non-SLN positive for metastases. Most SLNs were located in levels VI (83%) and II (35%) of the neck, whereas in four patients, contralateral drainage was also noted [106].

The use of systemic administered radiotracers has been helpful to detect local regional recurrences of well-differentiated thyroid cancer; these cases were subsequently managed using radioguided surgical excision with ^{131}I-iodide in eight patients and [^{18}F]FDG in another five patients with a proven loss of iodine avidity [107]. In another study an optically tracked navigation system was used to navigate to suspected persistence or recurrence in seven patients with malignant skull base disease [108].

In the head and neck, radioguided minimally invasive surgery based on parathyroid ^{99m}Tc-sestamibi scintigraphy has been one of the classical GOSTT applications. The criteria for selection of patients for this radioguided procedure can be summarized as follows [4]:

1. Patients with primary hyperparathyroidism and rarely tertiary hyperparathyroidism
2. Scintigraphic visualization of a single site of tracer uptake
3. Good uptake of ^{99m}Tc-sestamibi by the hyperfunctioning parathyroid gland
4. Absence of concomitant solid thyroid nodules
5. Exclusion of the multiple endocrine neoplasm (MEN) syndromes

By adopting these criteria, minimally invasive radioguided surgery can be scheduled in 60–70% of the patients with primary hyperparathyroidism; in the remaining patients, it may be necessary to perform classical bilateral neck exploration. Based on preoperative ^{99m}Tc-sestamibi imaging and using a second administration of the tracer shortly before operation, even without intraoperative parathyroid hormone measurements, a 98% long-term success rate was reached in a series of 108 patients [48]. Further advances in this GOSTT application are based on the incorporation of SPECT/CT to the imaging protocol [49] and of portable imaging devices to the radioguided procedure [4]. A meta-analysis concerning 24 studies published between January 2003 and March 2014 including 1,276 patients showed a per-patient pooled sensitivity of 86% for SPECT/CT which was superior to the 74% value observed with standalone SPECT and 70% with planar scintigraphy. In this analysis the rate of ectopic parathyroid adenomas ranged between 4% and 20% with a clear added value of SPECT/CT for the localization of the ectopic sites [109]. Recently, ^{18}F-fluorocholine PET/CT has been found to perform better (92% sensitivity, 100% specificity) than ^{99m}Tc-Sestamibi SPECT/CT (49% sensitivity, 100% specificity) in localizing hyperfunctioning parathyroid tissue in 24 patients with primary hyperparathyroidism [110]. This superiority of imaging with ^{18}F-fluorocholine, mainly based on the detection of multiple lesions and hyperplasia, leads to consider this imaging modality as an indication of choice to localize parathyroid abnormal tissue in patients with negative ^{99m}Tc-sestamibi imaging (Fig. 5). This approach may lead to successfully image-guided surgery [111]. The intraoperative retrieval of ^{99m}Tc-sestamibi-avid parathyroid adenomas has been optimized using portable gamma cameras [80, 112]. An alternative to portable gamma cameras is the use of a freehand SPECT device with 3D image generation [113]. The freehand SPECT signal can be fused with real-time ultrasound when signals of both modalities are acquired in a tracked manner [114]. The potential of the tracked combination of these modalities for radioguided intervention in the head and neck area has also been illustrated by its use in targeted ultrasound-guided, fine-needle aspiration cytology of SLNs in head and neck cancer [115].

Urological Malignancies

In general, male and female urogenital malignancies located in the pelvis drain to lymphatic basins in the vicinity of the primary tumor and may follow a similar trajectory in the dissemination of regional metastases. There are different nodal groups receiving lymphatic drainage from the pelvic structures: the external iliac nodes whose medial subgroup includes the obturator nodes, the internal iliac lymph nodes, and the nodes in the trajectory of the common iliac vessels. Lymphatic spread of metastasis from malignancies of the prostate, bladder, cervix, and endometrium may frequently be found in these iliac basins. However, alternative lymphatic drainage to the para-aortic and aortocaval lymph nodes as well as to the proximity of the sacrum and anterior abdominal wall is also possible.

In penile cancer the SLN procedure was one of the first applications of SLN biopsy validated in patients with clinically negative lymph nodes, in order to select patients who can benefit from lymph node dissection. It is usually performed by intradermal peritumoral injection of the

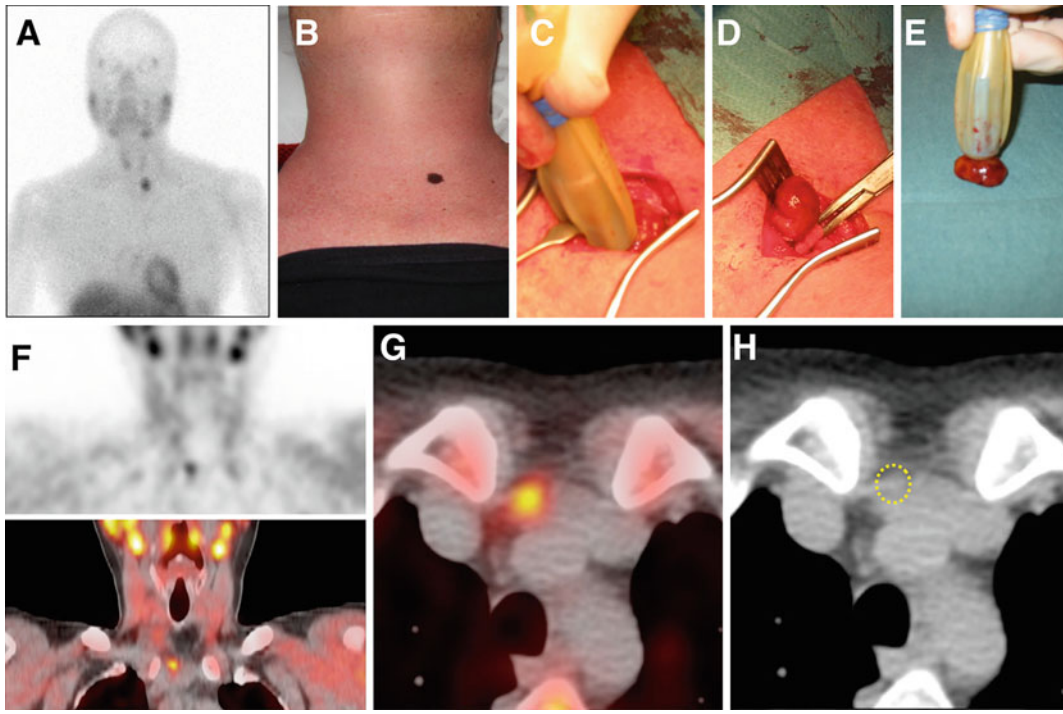

Fig. 5 Planar scintigraphy (**a**) showing increased ^{99m}Tc-sestamibi uptake near the *left lower* pole of the thyroid. Following skin marking (**b**), a parathyroid adenoma is intraoperatively localized and resected using a handheld probe (**c**–**e**). In another patient with primary hyperparathyroidism and negative ^{99m}Tc-sestamibi scintigraphy, PET/CT (F-H) using ^{18}F-fluorocholine is able to localize an ectopic parathyroid adenoma (*circle*) which is subsequently removed

radiocolloid, following the recommendation of injecting within 1 cm radius from the primary tumor, or from the surgical scar in case of prior excision of the primary tumor [116]. The SLN procedure has led to a SLN identification rate of 97% with an acceptable false negative rate of 7% [117] and to increase the 5-year survival to 91% in these patients [118]. SPECT/CT imaging has been used to optimize the procedure and to evaluate the pattern of lymphatic drainage from the malignancy by evaluating the possible implications for the extent of inguinal lymph node dissection. In a study including 50 patients, lymphatic drainage was visualized in 82 of 86 clinically node-negative groins (95%) scheduled for the SLN procedure. All SLNs were located in the inguinal zones medial superior (73%), lateral superior (8.7%), and central superior (18.3%) on SPECT/CT. No lymphatic drainage to the inferior zones of the groin was seen which suggests the possibility to exclude these zones from a subsequent inguinal lymph node dissection in the case of a tumor-positive SLN [119].

In prostate cancer, tracer administration is guided by transrectal ultrasound with usually two radiocolloid depots, one injection in each prostate lobe. Patients receive antibiotics prophylactically to prevent prostatitis. An alternative for transrectal injections is the transperineal tracer administration. Lymphoscintigraphy on the basis of 5-min planar images is performed 15 min and 2 h after injection. SPECT/CT is mostly performed subsequently to delayed planar images (Fig. 6). On early planar images, first draining lymph nodes are visualized in 88% of the cases. This visualization rate increases to more than 90% on delayed images [4]. SPECT/CT is particularly useful to anatomically localize SLNs in both the expected drainage basins of the pelvis and in alternative locations. A meta-analysis

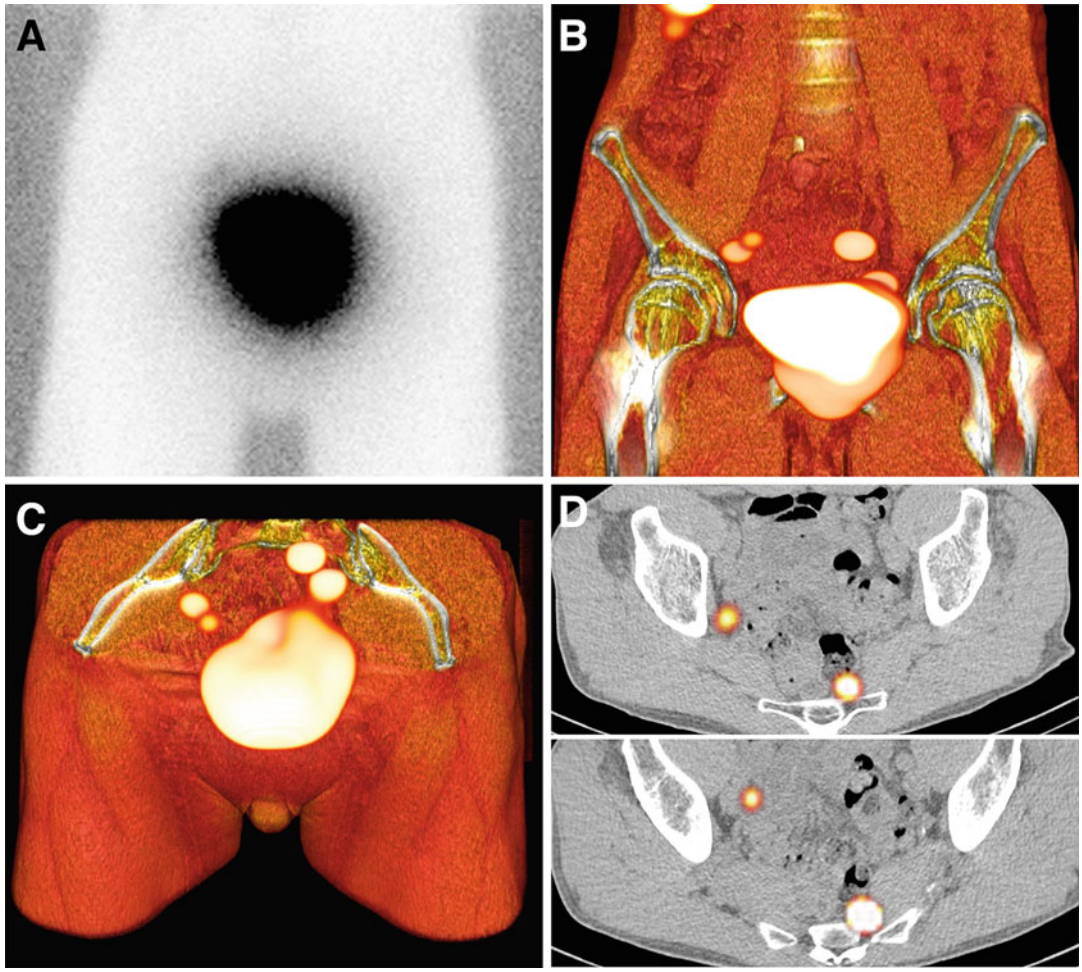

Fig. 6 Planar lymphoscintigraphy (**a**) showing some drainage to the right iliac area in a patient who has received four injections of ^{99m}Tc-nanocolloid into the prostate. By contrast on volume rendering **(b)**, bilateral drainage is observed. Volume rendering with cranial tilt (**c**) and transaxial SPECT/CT (**d**) show sentinel lymph nodes in the right iliac region and in the left presacral area

evaluating the SLN procedure included mainly prostate cancer patients with intermediate risk (clinical stage > T2b/T3, PSA >10 ng/mL, or Gleason >6); the pooled detection rate scored 93.8% and pooled sensitivity 94% [120]. Sensitivity appears to decrease to 76% in high-risk patients [121]. In recent years the role of SPECT/CT has been evaluated in various studies. SPECT/CT did increase the SLN visualization rate from 91% for planar scintigraphy to 98%. SPECT/CT also depicted more SLNs than planar images (average 4.3 vs. 2.2 SLNs) in 46 patients; 44% of the SLNs containing metastases were visualized only by SPECT/CT [43]. In another study, SPECT/CT identified SLNs outside the area of extended pelvic lymph node dissection, often used to stage the pelvis, in 37 out of 121 prostate cancer patients (31%). These SLNs were found in different locations: presacral, Cloquet's node, inguinal, para-aortic, the abdominal wall, pararectal, behind the common iliac artery, and lateral to the external iliac artery [122]. In a study involving treated prostate cancer patients, SPECT/CT

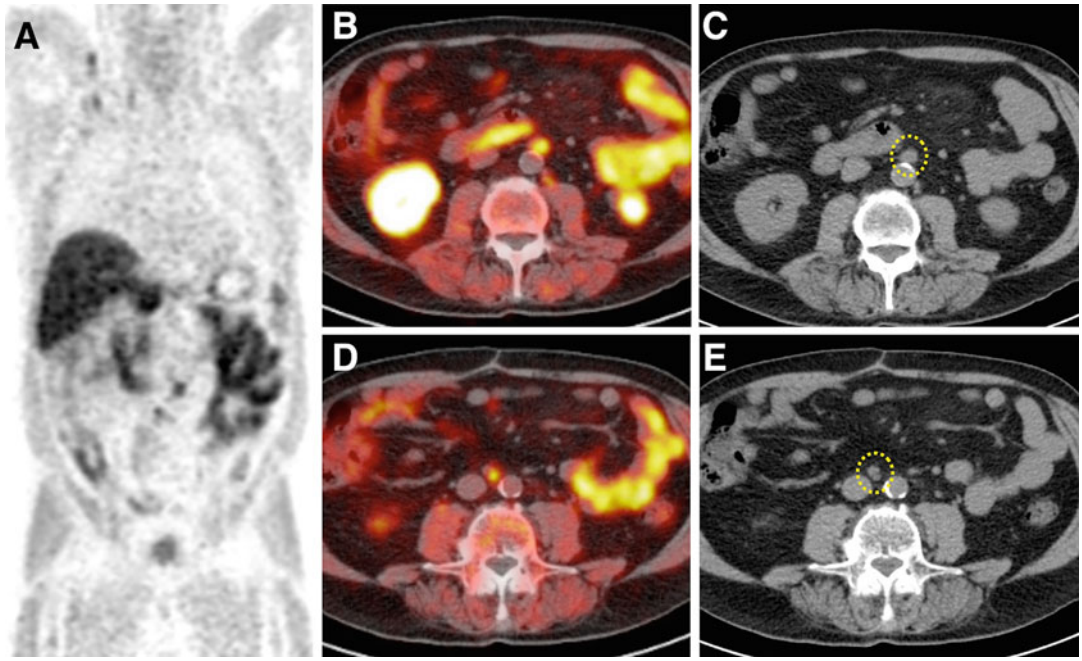

Fig. 7 Coronal PET displayed with maximum intensity projection (**a**) showing focal uptake of ^{18}F-fluorocholine in the *middle* areas of the abdomen in a prostate cancer patient with high risk of regional lymph node involvement. On fused PET/CT and CT, two radiotracer avid lymph nodes are depicted in the para-aortic area (**b**, **c**) and between the aorta and vena cava inferior (**d**, **e**). These findings led to image guided resection and histopathological confirmation of metastases

revealed a higher percentage of SLNs (80% vs. 34%) outside the pelvic para-iliac region in comparison to untreated patients [123]. In another series SPECT/CT findings led to a 25% impact of lymphatic drainage on conformal pelvic irradiation in 23 prostate cancer patients [124]. In a study designed to validate laparoscopic SLN versus hyperextended pelvic dissection for staging clinically localized prostate carcinoma, SPECT/CT identified SLNs in 191 of 203 patients (94%). Bilateral SLNs were found in 159 patients (83%) and unilateral in 32 (17%). The most frequent drainage site was the common iliac region (31%), followed by the internal iliac (20%), the obturator fossa (18%), the external iliac (15%), and the promontory/presacral area (6%) [125]. A similar presacral SLN rate (5.4%) was found in another study concerning 18 patients with prostate cancer of intermediate prognosis; in this series also para-aortic (5.4%), pararectal (5.4%), and paravesical (3.6%) SLNs were found outside the area of extended pelvic lymphadenectomy [126]. In the operating room, innovations in the SLN procedure for prostate cancer have been illustrated in recent years by the use of portable gamma camera to facilitate laparoscopic SLN biopsy [4] and the incorporation of robot-assisted SLN procedures with fluorescence/radioactivity guidance [60]. Finally, the gradual incorporation of high-risk patients for the SLN procedure has led to explore the possibility to detect macrometastases in these patients by using PET tracers before SLN biopsy (Fig. 7). This combined approach based on the use of SLN-SPECT/CT and ^{18}F-fluorocholine was found to be useful for target volume definition in high-risk prostate cancer aimed to receive radiotherapy [127]. Another PET tracer, ^{68}Ga-PSMA-ligand, has been found to be highly effective for lymph node staging in prostate cancer patients with intermediate- to high-risk prostate cancer; lymph node metastases were found in

41/130 patients (31.5%) with a patient-based accuracy of 88.5% for PET/CT increasing to 95.2% on the basis of template-based analyses [128]. The efficacy of ^{68}Ga-PSMA-ligand PET/CT has led to an innovative GOSTT approach for radioguided surgery in patients with lymph node metastases by coupling ^{111}In-PSMA-ligand with ^{68}Ga-PSMA-ligand in order to visualize PSMA-ligand-avid lymph nodes and primary tumor with SPECT/CT to enable radioguided resection [129].

In other urological malignancies, the SLN procedure has been validated only on an investigational basis in limited series of patients. In bladder cancer the imaging protocol, including lymphoscintigraphy and SPECT/CT, is similar to the one recommended for prostate cancer. Radiocolloid injection into the detrusor muscle and around the primary lesion is guided by cystoscopy [4]. Depending on the location of the primary tumor, lymphatic drainage may be unilateral or bilateral. The addition of SPECT/CT to planar lymphoscintigraphy did increase the detection rate from 33% to 83%. The negative predictive value of the SLN procedure has been found to be 92% on the basis of 156 patients reported in the literature [130]. In testicular cancer lymphatic drainage to lymph nodes along the abdominal aorta and vena cava is usually found after tracer administration with a single intratesticular injection; however, in some cases, SLNs are also found alongside the funicular vessels. SPECT/CT identified aortocaval or paracaval SLNs in five patients with right-sided testicular cancer and para-aortic SLNs in five patients with left-sided tumors; in three patients, SLNs along the funicular vessels were detected. All these SLNs were resected using a portable gamma camera [131]. Finally, in renal cell carcinoma, lymphatic drainage was seen in 14/20 patients (70%) and SPECT/CT detected 26 SLNs. The SLNs were most frequently located para-aortically, but also drainage to retrocaval, hilar, celiac trunk, and thoracic (internal mammary chain, mediastinal, and pleural) SLNs was seen [132]. The visualization of lymphatic drainage from renal cell carcinoma along the thoracic duct was further documented using SPECT/CT in 4 out 22 patients (18%) with SLN visualization [133].

Gynecological Malignancies

Gynecological GOSTT applications have been mainly limited to SLN biopsy in vulvar cancer, cervix cancer, and endometrial cancer. In vulvar cancer SLN biopsy is recommended for women with unifocal tumors <4 cm and clinically non-suspicious lymph nodes in the groin [134]. The incorporation of a radiocolloid tracer to the procedure improved the SLN detection rate to more than 95% from the 88% rate when only blue dyes were used [4]. Nevertheless, the most accepted approach is the combination of both agents with a SLN detection rate of 87% per groin, a false negative rate of 6.4%, and a recurrence rate of 2.8% according to a recent meta-analysis [134]. However, a long-term follow-up study showed a local recurrence rate at 5 years of 24.6% for patients with SLN negative and 33.2% for SLN positive [135]. The radiotracer is usually injected in three to four aliquots around the primary lesions; this is particularly important in lesions located close to mid-line, which frequently show contralateral drainage [136]. In spite of an extended validation of the SLN procedure in vulvar cancer, the role of SPECT/CT imaging in this malignancy has not been widely evaluated. In a series concerning 88 patients, SPECT/CT depicted drainage to groins not visualized on planar imaging and depicted more SLNs, but the difference was statistically not significant. However, SPECT/CT was of additional value to accurately indicate SLN location showing a 73% drainage rate to medial inguinal Daseler's zones, a 10% to the central zone around the saphenofemoral junction, and only 7% to the lateral zones. Different from drainage to the groin in penile cancer (Fig. 8), the SLN in vulvar cancer is found in 14% of the patients in the medial inferior zone; however, drainage to the lateral inferior region of the groin is only incidentally seen. Further drainage to higher-echelon lymph nodes was observed in the groin (15%) and in the pelvis (85%). SPECT/CT was found to be able to personalize lymphatic drainage and have potential use to limit extent of lymph node dissection in patients with positive SLNs [137]. Repeat SLN procedure appears to be also feasible in patients with recurrent

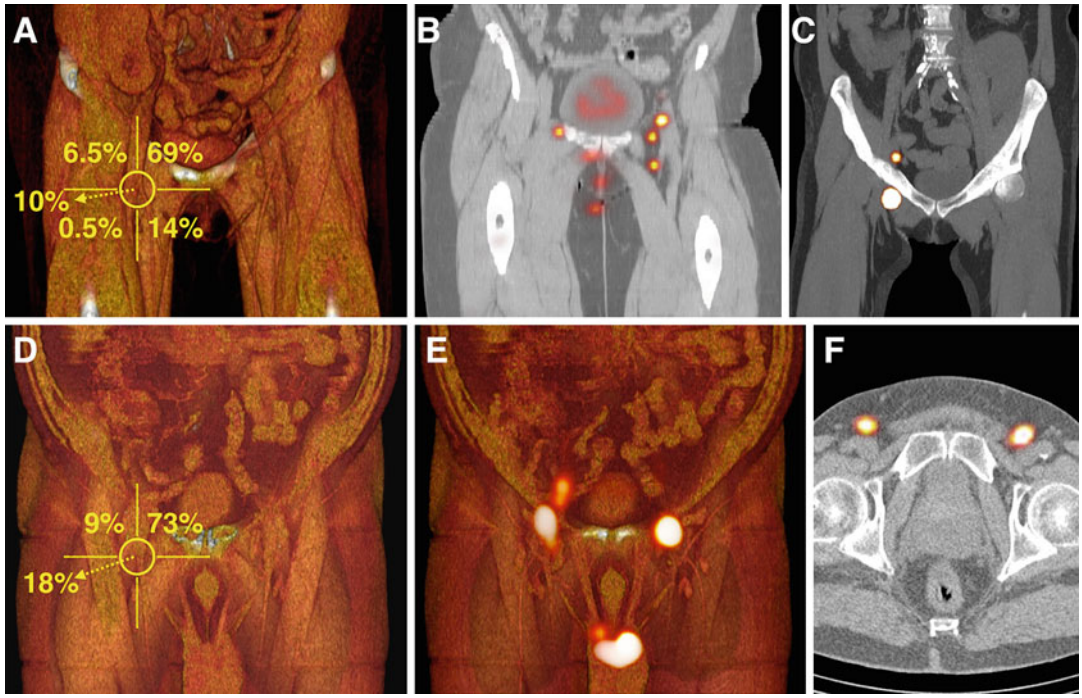

Fig. 8 Anatomical distribution (**a**) of inguinal sentinel lymph nodes according to Daseler's zones in vulvar cancer [137] showing most locations in the superior and central zones but also significant migration to the medial inferior quadrant as shown in two different patients (**b**, **c**). By contrast, in penile cancer (**d**), drainage to the inferior zones of the groin is not observed [119] as further illustrated by fused SPECT/CT images (**e**, **f**)

vulvar cancer, reaching a 78% detection rate [138]. The GOSTT concept of "see, open, and recognize" has been further explored in vulvar cancer on the basis of SPECT/CT and intraoperative SLN identification using combined NIR visualization and portable gamma devices following administration of the hybrid tracer ICG-^{99m}Tc-nanocolloid [58, 139].

Another important GOSTT application in gynecological surgical oncology concerns SLN biopsy in cervical cancer. A recent meta-analysis evaluating 67 studies resulted in a pooled detection rate of 89.2% and a pooled sensitivity of 90%; both SLN rates were related to mapping method (blue dye, radiotracer, or both) and history of preoperative neoadjuvant chemotherapy. Preoperative lymphatic mapping could also detect SLNs outside of routine lymphadenectomy areas, thus providing additional histological information important to optimize regional staging [140]. A prospective multicenter study evaluated the contribution of lymphoscintigraphy to the SLN procedure in 139 patients and concluded that, although the preoperative detection rate is lower than the intraoperative one (87.8% vs. 97.8%), the substantial proportions of SLNs in unusual drainage territories found by lymphoscintigraphy provide valuable guidance for the surgical exploration [141]. SLN visualization in preoperative lymphatic mapping can be optimized by the addition of SPECT/CT. This approach was evaluated in a meta-analysis including eight studies; the median overall detection rate was 98.6% for SPECT/CT and 85.3% for planar lymphoscintigraphy [142]. Indication for SLN biopsy in cervix cancer concerns patients with early stage (Ia2/Ib1, IIa1) and no clinical evidence of lymph node metastases. Radiocolloid administration is based on injecting peritumoral/periorificial aliquots into the four quadrants of the cervix or

pericicatricial in patients with prior conization. It is recommended to perform SPECT/CT after delayed planar imaging of lymphoscintigraphy and is crucial to assess deep lymphatic drainage and anatomical SLN localization in parametrial stations and in unusual locations [143].

In endometrial cancer a meta-analysis published in 2013 [144] resulted in a pooled SLN detection rate of 77.8% and a pooled sensitivity of 89%. The evaluation was based on 51 studies with enough information for detection rate evaluation and 35 studies providing false negative rates. The combination of blue dye and radiotracer resulted in higher detection rate and sensitivity. However, there are various approaches regarding the injection site: cervical, endometrial peritumoral, and myometrial/subserosal. Although the injection of the tracer into the four quadrants of the cervix is the easiest approach with also the highest detection rates, the other two routes appear to better reflect the drainage of endometrial cancer, with a higher incidence in drainage to the para-aortic lymph node basins [143]. SPECT/CT has been found to be helpful, and in 44 patients with high-risk endometrial cancer, SPECT/CT identified SLNs in 34 of them (77%) with a total of 110 depicted SLNs. The most frequent location was the external iliac chain (71%), but drainage to para-aortic SLNs was also common (44%). SPECT/CT was able to localize the only pelvic metastatic lymph node that was not depicted on planar images [145]. Also recently, in a study of 70 patients with endometrial cancer, SPECT/CT detected SLNs in 64 of them (91.4%). However, SPECT/CT could detect only 88.9% of the SLNs found during surgery; most of these undetected nodes on SPECT/CT had very low activity [146]. SPECT/CT SLN identification rate (94%) was significantly higher than that of planar lymphoscintigraphy (68%) in a series of 31 patients with endometrial cancer investigated after transcervical tracer injection into the isthmocervical myometrium [147].

Finally, radioguided SLN localization, without preoperative lymphatic mapping, was found to be feasible in a study including 21 patients who were at high risk of ovarian malignancy [148]; both radiocolloid and blue dye were intraoperatively injected into the proper ovarian ligament and suspensory ligament of the ovary. During open surgery the gamma probe identified SLN locations before retroperitoneal exploration; subsequently SLNs were detected in the para-aortic/paracaval regions only (67%), the pelvic region only (9%), and both the para-aortic/paracaval and the pelvic regions (24%).

Gastrointestinal Cancer

Since lymphatic drainage from the gastrointestinal tract is multidirectional and usually follows a random pattern, preoperative lymphatic mapping for SLN biopsy can be very helpful [7], considering that extensive dissection shows that metastases are found in lymph nodes nearest to the primary tumor site in, e.g., only about 60% of the gastric cancers or 40–50% of esophageal cancers. Also in lower rectal cancers, skip metastases and lateral lymph node metastases are found in a high number of the patients. However, these aggressive surgical procedures are burdened by high morbidity and even mortality.

In *esophageal cancer* the radiocolloid is administered endoscopically by injecting in the submucosal layer at the four quadrants closer to the primary lesion in the submuscosal layer, often the day before surgery. Lymphoscintigraphy is very useful to localize unexpected patterns of drainage to distant lymph nodes. In fact, in more than 80% of the cases, lymph drainage can be observed in a wide area extending from the cervical to the abdominal region. In a systematic review and meta-analysis including 23 studies of radioguided SLN mapping, the overall detection rate was 93% with a sensitivity of 87% [149].

In patients with *gastric cancer*, SLN biopsy aims at identifying clinically undetectable lymph node involvement and is generally reserved to T1 and T2 tumors (with diameter <4 cm), in which the type of resection can be modified toward function-preserving surgery whenever possible. The radiocolloid is injected endoscopically in the submucosal layers around the tumor. In a recent study involving patients with T1N0 or T2N0

operable gastric cancer [150], gamma probe in combination with blue dye identified SLNs in 372 out of 385 patients (96.6%).

Locoregional lymph node staging is an important prognostic factor for *colorectal malignancies*. In this regard, lymphatic mapping and SLN biopsy may be very important especially for identifying alternative mesenteric lymphatic drainage patterns and for detecting lymph node micrometastasis. Although at present the most popular technique is based on intraoperative subserosal injection of blue dye at the primary tumor, lymphoscintigraphy has proven definite advantages over the blue dye technique for SLNB [151]. However, evaluation of this approach in large-scale prospective investigations has not been performed. By contrast, in *anal cancer* radioguided SLN biopsy using preoperative imaging has had more acceptance; in a meta-analysis based on 16 studies including 323 patients, the best approach for SLN identification was found for the combined use of radiotracer and blue dye with a 90% detection rate [152].

GOSTT Applications in Other Malignancies

In lung cancer the GOSTT approach concerns both radioguided excision of solitary pulmonary nodules and radioguided SLN biopsy [4]. The radioguided excision has been extensively validated, and in 2012 Ambrogi et al. [153] reported radioguided video-assisted thoracoscopic surgery in 211 patients with pulmonary nodules smaller than 1 cm and/or deeper than 1 cm below the visceral pleura; the procedure was based on preoperative CT-guided administration of ^{99m}Tc-MAA into the nodule followed by lesion excision using video-assisted thoracic surgery with gamma ray probe guidance. The procedure was successful in 208 patients (98.6%) leading to histological confirmation of primary lung cancer in 113, metastases in 61, and benign lesions in 98. On the basis of a similar clinical indication and CT-guided radiotracer administration (^{99m}Tc-MAA) in or near the nodule, 112 patients underwent thoracoscopy or thoracotomy for lesion resection; in this series histology showed 14 benign lesions, 85 primary lung cancers, and 24 metastases [154]. Recently, ^{99m}Tc-sulfur colloid and a metallic clip were introduced into ground-glass opacities to enable resection; radiotracer administration was preceded by injection of cyanoacrylate that polymerizes immediately after injection into the lung parenchyma with the forming of a hard nodule enabling radiotracer retention, confirmed by SPECT/CT and easier identification during operation [155]. Concerning SLN biopsy and despite limited diffusion in surgical oncology, this GOSTT procedure has been evaluated for detection rate and sensitivity in 47 and 43 studies, respectively [156]; pooled detection was 80.6% and pooled sensitivity 87% with higher rates for the combination of radiotracer and dyes. In a pilot study, SPECT/CT has been found to be helpful in separate draining lymph nodes from the injection site of radiotracers [157].

In neuroendocrine tumors (NET) the GOSTT approach has been based on the systemic administration of radiotracers for radioguided detection and resection. In a systemic review [158], the use of the following radiotracers has been identified in various small series of radioguided surgery: ^{125}I-Tyr^3-octreotide, ^{111}In-DTPA-pentetreotide, ^{99m}Tc-somatostatin analogues, ^{123}I-metaiodobenzylguanidine, and ^{68}Ga-somatostatine analogues. Preoperative imaging has incorporated in recent years either SPECT/CT or PET/CT imaging, which has led to intervention and radioguided resection of small primary lesions, residual tumor, recurrences, and metastases (Fig. 9). The field of applications includes both pulmonary NET and gastroenteropancreatic NET.

Future GOSTT Scenarios

Current GOSTT advances open windows to new scenarios concerning clinical indications and modern technologies. In addition to the existing devices and modalities for radioguided surgery [159], some future possibilities and scenarios can be summarized as follows:

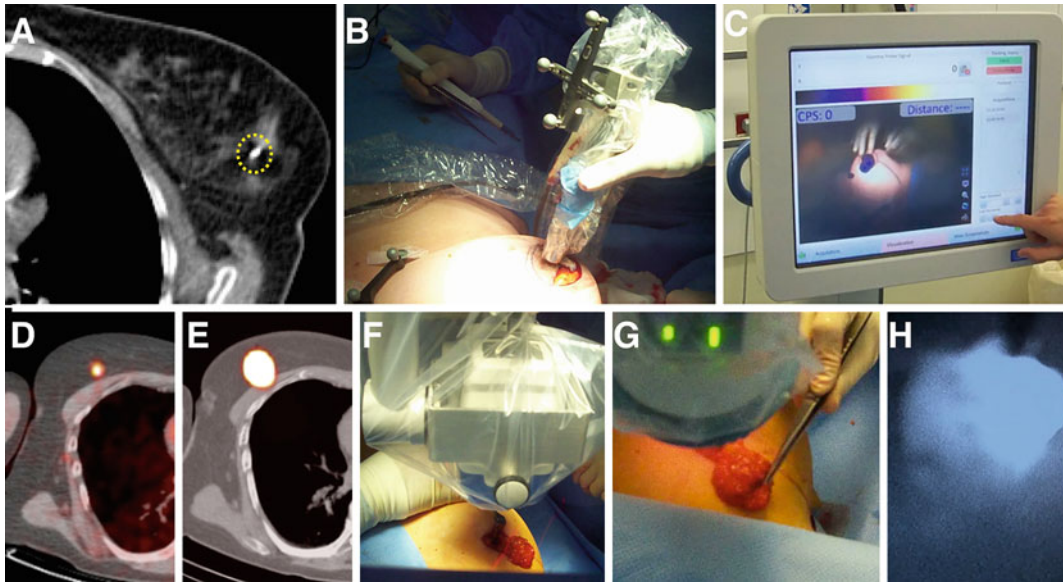

Fig. 9 Transaxial CT (**a**) showing an implanted ^{125}I-seed in the *left* breast of a patient scheduled for neoadjuvant chemotherapy. Following therapy, non-palpable residual tumor containing the radioactive seed is removed using tracked freehand SPECT (**b**, **c**). In another patient an [^{18}F]FDG-avid metastasis found on PET/CT (**d**) is subsequently removed after intralesional administration (**e**) of a hybrid tracer (ICG-^{99m}Tc-nanocolloid) using a portable gamma camera (**f**) and near-infrared camera (**g**) suitable for fluorescence detection (**h**)

1. Development of new systemic radiotracers for interventional imaging. The best example for this issue is illustrated by the recent introduction of ^{68}Ga-PSMA for prostate cancer and its interventional use in resection of lymph node metastases. The pairing of this PET tracer to ^{111}In-PSMA [129] not only enables preoperative SPECT/CT imaging but also radioguided surgery based on the more advantageous properties of ^{111}In. Similarly paired tracer use for interventional imaging and radioguided surgery can be found for iodine-based radiotracers and somatostatine analogues.
2. ROLL and SNOLL. The ROLL model can be extended to resection of recurrences, regional lymph node metastases [160], or isolated subclinical metastasis (Fig. 10). The SNOLL approach is of potential use in other malignancies like thyroid, lung, and stomach.
3. SLN-guided lymph node template resection. This model is currently discussed for prostate cancer with high-risk of regional lymph node involvement. The use of radiocolloids to guide SLN identification can help to optimize separate injection of fluorescent agents to guide lymph node resection in the basin of the SLN.
4. RSL following neoadjuvant chemotherapy. In analogy with the setting for locally advanced breast cancer and based on the practical advantages due to the long halftime of iodine-125, this approach enables seed implantation before chemotherapy and excision of residual tumor or lymph node metastasis after treatment in other local advanced malignancies scheduled for neoadjuvant therapy.
5. Mixed-reality navigation. Probably the use of new sensor technologies for tracking will help to transfer SPECT/CT, PET/CT, and PET/MRI with improved resolution to operation rooms in order to facilitate image-guided navigation to target regions.
6. Hybrid detection procedures. Portable imaging devices as gamma cameras probably will be integrated with other modalities as NIR cameras. On the other side, the integration of Cerenkov luminescence devices will extend the intraoperative applicability of PET tracers.

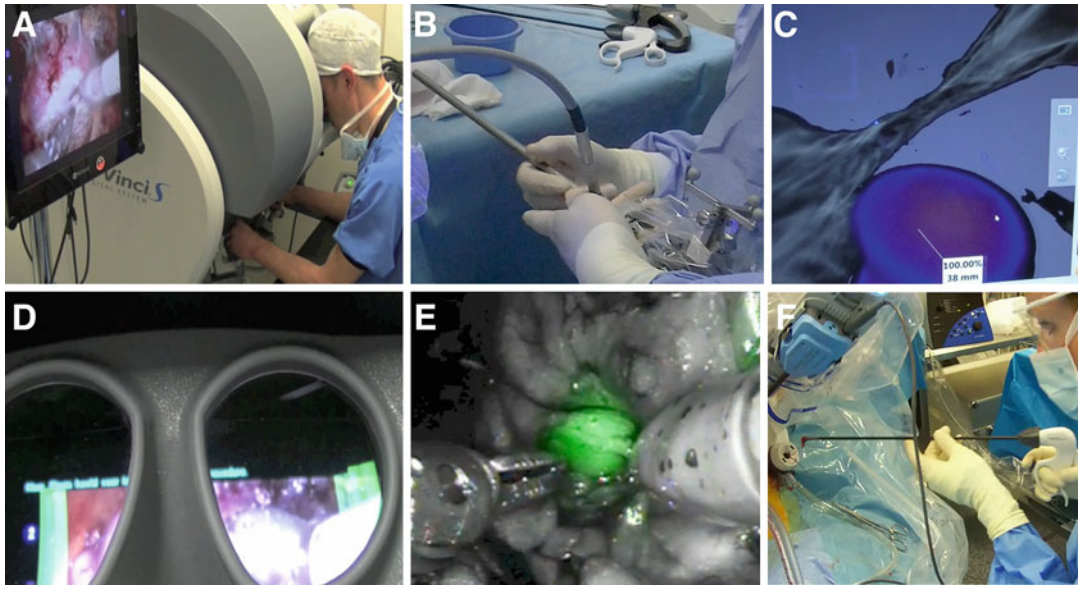

Fig. 10 Robot-assisted sentinel lymph node procedure following administration of ^{99m}Tc-nanocolloid into the prostate (**a**). A tracked laparoscopic freehand SPECT device (**b**) provides depth information for intraoperative navigation toward the sentinel lymph node, on the basis of a previous co-registered SPECT/CT (**c**). Subsequently, the integrated fluorescence signal display (**d**) enables sentinel lymph node resection (**e**, **f**)

7. Robot-assisted procedures with integrated radioguided navigation. In a similar approach as the one used for prostate cancer [60, 161], the fluorescence and probably the radioactive imaging will be integrated to robot-assisted procedures in other pelvic malignancies. Development of novel accessory devices like drop-in gamma probes [162] for insertion and residence inside the abdominal cavity using a robotic gripper will make identification of SLNs and tumor lesions during laparoscopic surgery more flexible by improving detector accessibility and geometry.

References

1. Mariani G, Giuliano AE, Strauss HW, editors. Radioguided surgery – a comprehensive team approach. New York: Springer; 2008.
2. Zaknun JJ, Giammarile F, Valdés Olmos RA, Vidal-Sicart S, Mariani G. Changing in radioguided surgery and intraoperative imaging: the GOSTT concept. Eur J Nucl Med Mol Imaging. 2012;39:1–3.
3. Valdés Olmos RA, Vidal-Sicart S, Giammarile F, Zaknun JJ, van Leeuwen FWB, Mariani G. The GOSTT concept and hybrid mixed/virtual/augmented reality environment radioguided surgery. Q J Nucl Med Mol Imaging. 2014;58:207–15.
4. International Atomic Energy Agency (IAEA), editor. Guided Intraoperative Scintigraphic Tumour Targeting (GOSTT): implementing advanced hybrid molecular imaging and non-imaging probes for advanced cancer management. Vienna: IAEA; 2014.
5. Cabañas RM. An approach for the treatment of penile carcinoma. Cancer. 1977;39:456–66.
6. Boni G, Manca G, Melfi FMA, Lucchi M, Mussi A, Mariani G. Sentinel lymph node biopsy in non-small-cell lung cancer. In: Mariani G, Giuliano AE, Strauss HW, editors. Radioguided surgery: a comprehensive team approach. New York: Springer; 2008. p. 166–71.
7. Kitagawa Y, Saha S, Kitajima M. Sentinel lymph node biopsy in cancers of the gastrointestinal tract. In: Mariani G, Giuliano AE, Strauss HW, editors. Radioguided surgery – a comprehensive team approach. New York: Springer; 2008. p. 148–56.
8. Levenback CF. Status of sentinel lymph node biopsy in gynecological cancers. Ann Surg Oncol. 2008;15:18–20.
9. Sugi K, Kobayashi S, Yagi R, Matsuoka T. Usefulness of sentinel lymph node biopsy for the detection of lymph node micrometastasis in early lung cancer. Interact Cardiovasc Thorac Surg. 2008;7:913–5.
10. Anand SM, Gologan O, Rochon L, Tamilia M, How J, Hier MP, Black MJ, et al. The role of sentinel lymph

node biopsy in differentiated thyroid carcinoma. Arch Otolaryngol Head Neck Surg. 2009;135:1199–204.
11. Dragan R, Nebojsa M, Dejan S, Ivan P, Dragos S, Damir J, et al. Clinical application of sentinel lymph node biopsy for staging, treatment and prognosis of colon and gastric cancer. Hepatogastroenterology. 2009;56:1606–11.
12. Holl G, Dorn R, Wengenmair H, Weckermann D, Sciuk J. Validation of sentinel lymph node dissection in prostate cancer: experience in more than 2,000 patients. Eur J Nucl Med Mol Imaging. 2009;36: 1377–82.
13. Mistrangelo M, Morino M. Sentinel lymph node biopsy in anal cancer: a review. Gastroenterol Clin Biol. 2009;33:446–50.
14. Sloan P. Head and neck sentinel lymph node biopsy: current state of the art. Head Neck Pathol. 2009;3: 231–7.
15. Alkureishi LW, Ross GL, Shoaib T, Soutar DS, Robertson AG, Thompson R, et al. Sentinel node biopsy in head and neck squamous cell cancer: 5-year follow-up of a European multicenter trial. Ann Surg Oncol. 2010;17:2459–64.
16. Paganelli G, De Cicco C, Gatti G, Luini A. Radioguided occult lesion localization in the breast. In: Mariani G, Giuliano AE, Strauss HW, editors. Radioguided surgery – a comprehensive team approach. New York: Springer; 2008. p. 81–91.
17. Boni G, Melfi FMA, Manca G, Lucchi M, Mussi A, Mariani G. Radioguided surgery of solitary pulmonary lesions. In: Mariani G, Giuliano AE, Strauss HW, editors. Radioguided surgery: a comprehensive team approach. New York: Springer; 2008. p. 262–8.
18. Feggi L, Basaglia E, Corcione S, Querzoli P, Soliani G, Ascanelli S, et al. An original approach in the diagnosis of early breast cancer: use of the same radiopharmaceutical for both non-palpable lesions and sentinel node localisation. Eur J Nucl Med. 2001;28:1589–96.
19. van Rijk MC, Tanis PJ, Nieweg OE, Loo CE, Valdés Olmos RA, Oldenburg HS, et al. Sentinel node biopsy and concomitant probe-guided tumor excision of non-palpable breast cancer. Ann Surg Oncol. 2007;14: 627–32.
20. Strong VE, Humm J, Russo P, Jungbluth A, Wong WD, Daghighian F, et al. A novel method to localize antibody-targeted cancer deposits intraoperatively using handheld PET beta and gamma probes. Surg Endosc. 2008;22:386–91.
21. Thorek DL, Riedl CC, Grimm J. Clinical Cerenkov luminescence imaging of ^{18}F-FDG. J Nucl Med. 2014;55:95–8.
22. Morton DL, Wen DR, Wong JH, Economou JS, Cagle LA, Storm FK, et al. Technical details of intraoperative lymphatic mapping for early stage melanoma. Arch Surg. 1992;127:392–9.
23. Nieweg OE, Tanis PJ, Kroon BB. The definition of a sentinel node. Ann Surg Oncol. 2001;8:538–41.
24. Valdés Olmos RA, Hoefnagel CA, Nieweg OE, Jansen L, Rutgers EJ, Border J, et al. Lymphoscintigraphy in oncology: a rediscovered challenge. Eur J Nucl Med. 1999;26:S2–10.
25. Orsini F, Guidoccio F, Vidal-Sicart S, Valdés Olmos RA, Mariani G. General concepts on radioguided sentinel lymph node biopsy: preoperative imaging, intraoperative gamma-probe guidance, intraoperative imaging, and multimodality imaging. In: Mariani G, Manca G, Orsini F, Vidal-Sicart S, Valdés Olmos RA, editors. Atlas of lymphoscintigraphy and sentinel node mapping. Milan: Springer; 2013. p. 95–110.
26. Nieweg OE. The sentinel lymph node concept in oncologic surgery. In: Mariani G, Manca G, Orsini F, Vidal-Sicart S, Valdés Olmos RA, editors. Atlas of lymphoscintigraphy and sentinel node mapping. Milan: Springer; 2013. p. 87–93.
27. Krag DN, Weaver DL, Alex JC, Fairbank JT. Surgical resection and radiolocalization of the sentinel lymph node in breast cancer using a gamma probe. Surg Oncol. 1993;2:335–9.
28. Valdés Olmos RA, Vidal-Sicart S, Nieweg OE. SPECT-CT and real-time intraoperative imaging: new tools for sentinel node localization and radioguided surgery. Eur J Nucl Med Mol Imaging. 2009;36:1–5.
29. Valdés Olmos RA, Vidal-Sicart S, Nieweg OE. Technological innovation in the sentinel node procedure: towards 3-D intraoperative imaging. Eur J Nucl Med Mol Imaging. 2010;37:1449–51.
30. Vidal-Sicart S, van Leeuwen FW, van den Berg NS, Valdés Olmos RA. Fluorescent radiocolloids: are hybrid tracers the future for lymphatic mapping? Eur J Nucl Med Mol Imaging. 2015;42:1627–30.
31. Kapteijn BAE, Nieweg OE, Valdés Olmos RA, Liem IH, Panday RKLB, Hoefnagel CA, et al. Reproducibility of lymphoscintigraphy for lymphatic mapping in cutaneous melanoma. J Nucl Med. 1996;37:972–5.
32. Vidal M, Vidal-Sicart S, Torrents A, Perissinotti A, Navales I, Paredes P, et al. Accuracy and reproducibility of lymphoscintigraphy for sentinel node detection in patients with cutaneous melanoma. J Nucl Med. 2012;53:1193–9.
33. Tanis PJ, Valdés Olmos RA, Muller SH, Nieweg OE. Lymphatic mapping in patients with breast carcinoma: reproducibility of lymphoscintigraphic results. Radiology. 2003;228:546–51.
34. Kroon BK, Valdés Olmos RA, Nieweg OE, Horenblas S. Reproducibility of lymphoscintigraphy for lymphatic mapping in patients with penile carcinoma. J Urol. 2005;174:2214–7.
35. Valdés Olmos RA, Vidal-Sicart S, Rietbergen DDD. SPECT/CT and sentinel node lymphoscintigraphy. Clin Transl Imaging. 2014;2:491–504.
36. Lerman H, Metser U, Lievshitz G, Sperber F, Shneebaum S, Even-Sapir E. Lymphoscintigraphic sentinel node identification in patients with breast cancer: the role of SPECTCT. Eur J Nucl Med Mol Imaging. 2006;33:329–37.

37. Mariani G, Bruselli L, Kuwert T, Kim EE, Flotats A, Israel O, et al. A review on the clinical uses of SPECT/CT. Eur J Nucl Med Mol Imaging. 2010;37:1959–85.
38. Vermeeren L, van der Ploeg IM, Valdés Olmos RA, Meinhardt W, Klop WM, Kroon BB, et al. SPECT/CT for preoperative sentinel node localization. J Surg Oncol. 2010;101:184–90.
39. Kobayashi K, Ramirez PT, Kim EE, Levenback CF, Rohren EM, Frumovitz M, et al. Sentinel node mapping in vulvovaginal melanoma using SPECT/CT lymphoscintigraphy. Clin Nucl Med. 2009;34:859–61.
40. Leijte JA, van der Ploeg IM, Valdés Olmos RA, Nieweg OE, Horenblas S. Visualization of tumor blockage and rerouting of lymphatic drainage in penile cancer patients by use of SPECT/CT. J Nucl Med. 2009;50:364–7.
41. van der Ploeg IM, Valdés Olmos RA, Kroon BB, Wouters MW, van den Brekel MW, Vogel WV, et al. The yield of SPECT/CT for anatomical lymphatic mapping in patients with melanoma. Ann Surg Oncol. 2009;16:1537–42.
42. Sieira-Gil R, Paredes P, Martí-Pagès C, Ferrer-Fuertes A, García-Díez E, Cho-Lee GY, et al. SPECT-CT and intraoperative portable gamma-camera detection protocol for sentinel lymph node biopsy in oral cavity squamous cell carcinoma. J Craniomaxillofac Surg. 2015;43:2205–13.
43. Vermeeren L, Valdés Olmos RA, Meinhardt W, Bex A, van der Poel HG, Vogel WV, et al. Value of SPECT/CT for detection and anatomic localization of sentinel lymph nodes before laparoscopic sentinel node lymphadenectomy in prostate carcinoma. J Nucl Med. 2009;50:865–70.
44. Pandit-Taskar N, Gemignani ML, Lyall A, Larson SM, Barakat RR, Abu Rustum NR. Single photon emission computed tomography SPECT-CT improves sentinel node detection and localization in cervical and uterine malignancy. Gynecol Oncol. 2010;117:59–64.
45. Vermeeren L, Meinhardt W, Valdes Olmos RA. Prostatic lymphatic drainage with sentinel nodes at the ventral abdominal wall visualized with SPECT/CT: a case series. Clin Nucl Med. 2010;35:71–3.
46. Vermeeren L, Valdés Olmos RA, Klop WM, van der Ploeg IM, Nieweg OE, Balm AJ, et al. SPECT/CT for sentinel lymph node mapping in head and neck melanoma. Head Neck. 2011;33:1–6.
47. Valdés Olmos RA, Vidal-Sicart S. SPECT/CT image generation and criteria for sentinel node imaging. In: Mariani G, Manca G, Orsini F, Vidal-Sicart S, Valdés Olmos RA, editors. Atlas of lymphoscintigraphy and sentinel node mapping. Milan: Springer; 2013. p. 111–9.
48. Goldstein RE, Billheimer D, Martin WH, Richards K. Sestamibi scanning and minimally invasive radioguided parathyroidectomy without intraoperative parathyroid hormone measurement. Ann Surg. 2003;237:722–31.
49. Shafiei B, Hoseinzadeh S, Fotouhi F, Malek H, Azizi F, Jahed A, et al. Preoperative ^{99m}Tc-sestamibi scintigraphy in patients with primary hyperparathyroidism and concomitant nodular goiter: comparison of SPECT-CT, SPECT, and planar imaging. Nucl Med Commun. 2012;33:1070–6.
50. Mariani G, Moresco L, Viale G, Villa G, Bagnasco M, Canavese G, Buscombe J, Strauss HW, Paganelli G. Radioguided sentinel lymph node biopsy in breast cancer surgery. J Nucl Med. 2001;42:1198–215.
51. Obenaus E, Erba PA, Chinol M, Van de Wiele C, Janoki GA, Dierckx RA, et al. Radiopharmaceuticals for radioguided surgery. In: Mariani G, Giuliano AE, Strauss HW, editors. Radioguided surgery – a comprehensive team approach. New York: Springer; 2008. p. 3–11.
52. Vera DR, Wallace AM, Hoh CK, Mattrey RF. A synthetic macromolecule for sentinel node detection: ^{99m}Tc-DTPA-mannosyl-dextran. J Nucl Med. 2001;42:951–9.
53. Marcinow AM, Hall N, Byrum E, Teknos TN, Old MO, Agrawal A. Use of a novel receptor-targeted (CD206) radiotracer, ^{99m}Tc-tilmanocept, and SPECT/CT for sentinel lymph node detection in oral cavity squamous cell carcinoma: initial institutional report in an ongoing phase 3 study. JAMA Otolaryngol Head Neck Surg. 2013;139:895–902.
54. Sondak VK, King DW, Zager JS, Schneebaum S, Kim J, Leong SP, et al. Combined analysis of phase III trials evaluating [^{99m}Tc]tilmanocept and vital blue dye for identification of sentinel lymph node(s) in clinically node-negative cutaneous melanoma. Ann Surg Oncol. 2013;20:680–8.
55. Wallace AM, Han LK, Povoski SP, Deck K, Schneebaum S, Hall NC, et al. Comparative evaluation of [^{99m}Tc]-tilmanocept for sentinel lymph node mapping in breast cancer patients: results of two phase 3 trials. Ann Surg Oncol. 2013;20:2590–9.
56. Brouwer OR, Vermeeren L, Klop WMC, Balm AJM, van der Poel HG, van Rhijn BW, et al. Comparing the hybrid fluorescent-radioactive tracer indocyanine green-^{99m}Tc-nanocolloid with ^{99m}Tc-nanocolloid for sentinel node identification: a validation study using lymphoscintigraphy and SPECT/CT. J Nucl Med. 2012;53:1034–40.
57. Van den Berg NS, Brouwer OR, Klop WMC, Karakulluckcu B, Zuur CL, Tan IB, et al. Concomitant radio- and fluorescence-guided sentinel lymph node biopsy in squamous cell carcinoma of the oral cavity using ICG-^{99m}Tc-nanocolloid. Eur J Nucl Med Mol Imaging. 2012;39:1128–36.
58. Mathéron HM, van den Berg NS, Brouwer OR, Kleinjan GH, van Driel WJ, Trum JW, et al. Multimodal surgical guidance towards the sentinel node in vulvar cancer. Gynecol Oncol. 2013;131:720–5.
59. Brouwer OR, van den Berg NS, Mathéron HM, van der Poel HG, van Rhijn BW, Bex A, et al. A hybrid

radioactive and fluorescent tracer for sentinel node biopsy in penile carcinoma as a potential replacement for blue dye. Eur Urol. 2014;65:600–9.
60. Kleinjan GH, van den Berg NS, Brouwer OR, de Jong J, Acar C, Wit EM, et al. Optimisation of fluorescence guidance during robot-assisted laparoscopic sentinel node biopsy for prostate cancer. Eur Urol. 2014;66:991–8.
61. van den Berg NS, Brouwer OR, Schaafsma BE, Mathéron HM, Klop WM, Balm AJ, et al. Multimodal surgical guidance during sentinel node biopsy for melanoma: combined gamma tracing and fluorescence imaging of the sentinel node through use of the hybrid tracer indocyanine green-^{99m}Tc-nanocolloid. Radiology. 2015;275:521–9.
62. De Cicco C, Pizzamiglio M, Trifirò G, Luini A, Ferrari M, Prisco G, et al. Radioguided occult lesion localisation (ROLL) and surgical biopsy in breast cancer. Technical aspects. Q J Nucl Med. 2002;46:145–51.
63. Gallegos Hernandez JF, Tanis PJ, Deurloo EE, Nieweg OE, Th Rutgers EJ, Kroon BB, et al. Radioguided surgery improves outcome of therapeutic excision in non-palpable invasive breast cancer. Nucl Med Commun. 2004;25:227–32.
64. Gray RJ, Salud C, Nguyen K, Dauway E, Friedland J, Berman C, et al. Randomized prospective evaluation of a novel technique for biopsy or lumpectomy of nonpalpable breast lesions: radioactive seed versus wire localization. Ann Surg Oncol. 2001;8:711–5.
65. Van der Noordaa ME, Pengel KE, Groen E, van Werkhoven E, Rutgers EJ, Loo CE, et al. The use of radioactive iodine-125 seed localization in patients with non-palpable breast cancer: a comparison with the radioguided occult lesion localization with 99m technetium. Eur J Surg Oncol. 2015;41:553–8.
66. Donker M, Drukker CA, Valdés Olmos RA, Rutgers EJ, Loo CE, Sonke GS, et al. Guiding breast-conserving surgery in patients after neoadjuvant systemic therapy for breast cancer: a comparison of radioactive seed localization with the ROLL technique. Ann Surg Oncol. 2013;20:2569–75.
67. Giles YŞ, Sarıcı IS, Tunca F, Sormaz IC, Salmaslıoğlu A, Adalet I, et al. The rate of operative success achieved with radioguided occult lesion localization and intraoperative ultrasonography in patients with recurrent papillary thyroid cancer. Surgery. 2014;156:1116–26.
68. Aydogan F, Ozben V, Atasoy D, Yilmaz MH, Halaç M, Celik V. Excision of axillary lymph node recurrences in breast cancer patients with axillary ROLL (A-ROLL). J Surg Oncol. 2010;101:141–4.
69. Donker M, Straver ME, Wesseling J, Loo CE, Schot M, Drukker CA, et al. Marking axillary lymph nodes with radioactive iodine seeds for axillary staging after neoadjuvant systemic treatment in breast cancer patients: the MARI procedure. Ann Surg. 2015;261:378–82.
70. Jansen L, Nieweg OE, Valdés Olmos RA, Rutgers EJ, Peterse JL, de Vries J, et al. Improved staging of breast cancer through lymphatic mapping and sentinel node biopsy. Eur J Surg Oncol. 1998;24:445–6.
71. Povoski SP, Hall NC, Murrey Jr DA, Wright CL, Martin Jr EW. Feasibility of a multimodal ^{18}F-FDG-directed lymph node surgical excisional biopsy approach for appropriate diagnostic tissue sampling in patients with suspected lymphoma. BMC Cancer. 2015;15:378.
72. Molina MA, Goodwin WJ, Moffat FL, Serafini AN, Sfakianakis GN, Avisar E. Intra-operative use of PET probe for localization of FDG avid lesions. Cancer Imaging. 2009;9:59–62.
73. Wang YZ, Diebold A, Woltering E, King H, Boudreaux JP, Anthony LB, et al. Radioguided exploration facilitates surgical cytoreduction of neuroendocrine tumors. J Gastrointest Surg. 2012;16:635–40.
74. Van Hulsteijn LT, Corssmit EPM, van der Hiel B, Smit JWA, Stokkel MP. Is there a role for radioguided surgery with iodine-labeled metaiodobenzylguanidine in resection of neuroendocrine tumors? Clin Nucl Med. 2012;37:1083–8.
75. Castaldi P, Rufini V, Treglia G, Bruno I, Perotti G, Stifano G, et al. Impact of ^{111}In-DTPA-octreotide SPECT/CT fusion in the management of neuroendocrine tumours. Radiol Med. 2008;113:1056–67.
76. Kaemmerer D, Prasad V, Daffner W, Haugvik SP, Senftleben S, Baum RP, et al. Radioguided surgery in neuroendocrine tumors using Ga-68-labeled analogs: a pilot study. Clin Nucl Med. 2012;37:142–7.
77. Delbeke D, Coleman RE, Guiberteau MJ, Brown ML, Royal HD, Siegel BA, et al. Procedure guidelines for SPECT/CT imaging. J Nucl Med. 2006;47:1227–34.
78. Fishman EK, Ney DR, Heath DG, Corl FM, Horton KM, Johnson PT. Volume rendering versus maximum intensity projection in CT angiography: what works best, when, and why. Radiographics. 2006;26:905–22.
79. Vidal-Sicart S, Paredes P, Zanón G, Pahisa J, Martinez-Román S, Caparrós X, et al. Added value of intraoperative real-time imaging in searches for difficult-to-locate sentinel nodes. J Nucl Med. 2010; 51:1219–25.
80. Fuster D, Vidal-Sicart S, Torregrosa JV, Paredes P, Rubello D, Pons F. What is the role of preoperative scintigraphic imaging and the intraoperative gamma probe in secondary hyperparathyroidism? Nucl Med Commun. 2014;35:443–5.
81. Hellingman D, de Wit-van der Veen LJ, Klop WM, Valdés Olmos RA. Detecting near-the-injection-site sentinel nodes in head and neck melanomas with a high-resolution portable gamma camera. Clin Nucl Med. 2015;40:e11–6.
82. Hellingman D, Vidal-Sicart S, de Wit-van der Veen LJ, Paredes P, Valdés Olmos RA. A new portable hybrid camera for fused optical and scintigraphic imaging: first clinical experiences. Clin Nucl Med. 2016;41:e39–43.
83. Lees JE, Bugby SL, Bhatia BS, Jambi LK, Alqahtani MS, McKnight WR, et al. A small field of view

camera for hybrid gamma and optical imaging. J Instrum. 2014;9:C12020.
84. Wendler T, Herrmann K, Schnelzer A, Lasser T, Traub J, Kutter O, et al. First demonstration of 3-D lymphatic mapping in breast cancer using freehand SPECT. Eur J Nucl Med Mol Imaging. 2010;37: 1452–61.
85. Bluemel C, Schnelzer A, Okur A, Ehlerding A, Paepke S, Scheidhauer K, et al. Freehand SPECT for image-guided sentinel lymph node biopsy in breast cancer. Eur J Nucl Med Mol Imaging. 2013; 40:1656–61.
86. Bluemel C, Herrmann K, Müller-Richter U, Lapa C, Higuchi T, Wild V, et al. Freehand SPECT-guided sentinel lymph node biopsy in early oral squamous cell carcinoma. Head Neck. 2014;36:e112–6.
87. Mihaljevic AL, Rieger A, Belloni B, Hein R, Okur A, Scheidhauer K, et al. Transferring innovative freehand SPECT to the operating room: first experiences with sentinel lymph node biopsy in malignant melanoma. Eur J Surg Oncol. 2014;40: 42–8.
88. Rahbar K, Colombo-Benkmann M, Haane C, Wenning C, Vrachimis A, Weckesser, et al. Intraoperative 3-D mapping of parathyroid adenoma using freehand SPECT. EJNMMI Res. 2012;2:51.
89. Milgram P, Kishino F. A taxonomy of mixed reality visual displays. IEICE transactions of information and systems. The institute of electronics. Inf Commun Eng. 1994;E77-D:1321–9.
90. Brouwer OR, Buckle T, Bunschoten A, Vahrmeijer A, Wendler T, Valdés Olmos RA, et al. Image navigation as a means to expand the boundaries of fluorescence guided surgery. Phys Med Biol. 2012;57: 3123–36.
91. Brouwer OR, van den Berg NS, Mathéron HM, Wendler T, van der Poel HG, Horenblas S, et al. Feasibility of intraoperative navigation to the sentinel node in the groin using preoperatively acquired single photon emission computerized tomography data: transferring functional imaging to the operating room. J Urol. 2014;192:1810–6.
92. Engelen T, Winkel BM, Rietbergen DD, KleinJan GH, Vidal-Sicart S, Valdés Olmos RA, et al. The next evolution in radioguided surgery: breast cancer related sentinel node localization using a freehand SPECT-mobile gamma camera combination. Am J Nucl Med Mol Imaging. 2015;5:233–45.
93. Pouw B, de Wit-van der Veen LJ, van Duijnhoven F, Rutgers EJ, Stokkel MP, Valdés Olmos RA, et al. Intraoperative 3D navigation for single or multiple 125I-seed localization in breast-preserving cancer surgery. Clin Nucl Med. 2016;41:e216–20.
94. Bluemel C, Cramer A, Grossmann C, Kajdi GW, Malzahn U, Lamp N, et al. iROLL: does 3-D radioguided occult lesion localization improve surgical management in early-stage breast cancer? Eur J Nucl Med Mol Imaging. 2015;42:1692–9.
95. American Joint Committee on Cancer. Cancer staging handbook. 7th ed. New York: Springer; 2010.
96. Civantos FJ, Zitsch RP, Schuller DE, Agrawal A, Smith RB, Nason R, et al. Sentinel lymph node biopsy accurately stages the regional lymph nodes for T1-T2 oral squamous cell carcinomas: results of a prospective multi-institutional trial. J Clin Oncol. 2010;28: 1395–400.
97. Farmer RW, McCall L, Civantos FJ, Myers JN, Yarbrough WG, Murphy B, et al. Lymphatic drainage patterns in oral squamous cell carcinoma: findings of the ACOSOG Z0360 (Alliance) study. Otolaryngol Head Neck Surg. 2015;152:673–7.
98. Haerle SK, Hany TF, Strobel K, Sidler D, Stoeckli SJ. Is there an additional value of SPECT/CT over planar lymphoscintigraphy for sentinel node mapping in oral/oropharyngeal squamous cell carcinoma? Ann Surg Oncol. 2009;16:3118–24.
99. Bilde A, Von Buchwald C, Mortensen J, Marving J, Hamilton Therkildsen M, Kirkegaard J, et al. The role of SPECT-CT in the lymphoscintigraphic identification of sentinel nodes in patients with oral cancer. Acta Otolaryngol. 2006;126:1096–103.
100. Klode J, Poeppel T, Boy C, Mueller S, Schadendorf D, Korber A, et al. Advantages of preoperative hybrid SPECT/CT in detection of sentinel lymph nodes in cutaneous head and neck malignancies. J Eur Acad Dermatol Venereol. 2011;25:1213–21.
101. Zender C, Guo T, Weng C, Faulhaber P, Rezaee R. Utility of SPECT/CT for periparotid sentinel lymph node mapping in the surgical management of head and neck melanoma. Am J Otolaryngol Head Neck Med Surg. 2014;35:12–8.
102. López-Rodríguez E, García-Gómez FJ, Álvarez-Pérez RM, Martínez-Castillo R, Borrego-Dorado I, Fernández-Ortega P, et al. Role of SPECT-CT in sentinel lymph node biopsy in patients diagnosed with head and neck melanoma. Rev Esp Med Nucl Imagen Mol. 2016;35:22–8.
103. Daisne JF, Installé J, Bihin B, Laloux M, Vander Borght T, Mathieu I, Lawson G. SPECT/CT lymphoscintigraphy of sentinel node(s) for super-selective prophylactic irradiation of the neck in cN0 head and neck cancer patients: a prospective phase I feasibility study. Radiat Oncol. 2014;9:121.
104. Borbón-Arce M, Brouwer OR, van den Berg NS, Mathéron H, Klop WM, Balm AJ, et al. An innovative multimodality approach for sentinel node mapping and biopsy in head and neck malignancies. Rev Esp Med Nucl Imagen Mol. 2014;33:274–9.
105. Garcia-Burillo A, Roca Bielsa I, Gonzalez O, Zafon C, Sabate M, Castellvi J, et al. SPECT/CT sentinel lymph node identification in papillary thyroid cancer: lymphatic staging and surgical management improvement. Eur J Nucl Med Mol Imaging. 2013; 40:1645–55.
106. Cabrera RN, Chone CT, Zantut-Wittmann D, Matos P, Ferreira DM, Pereira PSG, et al. Value of sentinel

lymph node biopsy in papillary thyroid cancer: initial results of a prospective trial. Eur Arch Otorhinolaryngol. 2015;272:971–9.
107. Francis CL, Nailey C, Fan C, Bodenner D, Stack BC. ^{18}F-fluorodeoxyglucose and ^{131}I radioguided surgical management of thyroid cancer. Otolaryngol Head Neck Surg. 2012;146:26–32.
108. Dubach P, Oliveira-Santos T, Weber S, Gerber N, Dietz A, Caversaccio M. 18 FDG-PET/CT computer-assisted biopsies for suspected persistent or recurrent malignant skull base disease. Head Neck. 2014. doi:10.1002/hed.23756. [Epub ahead of print].
109. Wong KK, Fig LM, Gross MD, Dwamena BA. Parathyroid adenoma localization with ^{99m}Tc-sestamibi SPECT/CT: a meta-analysis. Nucl Med Commun. 2015;36:363–75.
110. Lezaic L, Rep S, Sever MJ, Kocjan T, Hocevar M, Fettich J. ^{18}F-Fluorocholine PET/CT for localization of hyperfunctioning parathyroid tissue in primary hyperparathyroidism: a pilot study. Eur J Nucl Med Mol Imaging. 2014;41:2083–9.
111. Kluijfhout WP, Vorselaars WM, Vriens MR, Borel Rinkes IH, Valk GD, et al. Enabling minimal invasive parathyroidectomy for patients with primary hyperparathyroidism using Tc-99m-sestamibi SPECT-CT, ultrasound and first results of ^{18}F-fluorocholine PET-CT. Eur J Radiol. 2015;84:1745–51.
112. Estrems P, Guallart F, Abreu P, Sopena P, Dalmau J, Sopena R. The intraoperative mini gamma camera in primary hyperparathyroidism surgery. Acta Otorrinolaringol Esp. 2012;63:450–7.
113. Casáns-Tormo I, Prado-Wohlwend S, Díaz-Expósito R, Cassinello-Fernández N, Ortega-Serrano J. Initial experience in intraoperative radiolocalization of the parathyroid adenoma with freehand SPECT and comparative assessment with portable gamma-camera. Rev Esp Med Nucl Imagen Mol. 2015;34:116–9.
114. Bluemel C, Kirchner P, Kajdi GW, Werner RA, Herrmann K. Localization of parathyroid adenoma with real-time ultrasound: freehand SPECT fusion. Clin Nucl Med. 2016;41:e141–2.
115. De Bree R, Pouw B, Heuveling DA, Castelijns JA. Fusion of freehand SPECT and ultrasound to perform ultrasound-guided fine-needle aspiration cytology of sentinel nodes in head and neck cancer. AJNR Am J Neuroradiol. 2015;36:2153–8.
116. Horenblas S, Kroon BK, Valdes Olmos RA, Nieweg OE. Dynamic sentinel lymph node biopsy in penile carcinoma. In: Mariani G, Giuliano AE, Strauss HW, editors. Radioguided surgery – a comprehensive team approach. New York: Springer; 2008. p. 117–25.
117. Leijte JA, Hughes B, Graafland NM, Kroon BK, Valdés Olmos RA, Nieweg OE, et al. Two-center evaluation of dynamic sentinel node biopsy for squamous cell carcinoma of the penis. J Clin Oncol. 2009;27:3325–9.
118. Djajadiningrat RS, Graafland NM, van Werkhoven E, Meinhardt W, Bex A, van der Poel HG, et al. Contemporary management of regional nodes in penile cancer-improvement of survival? J Urol. 2014;191:68–73.
119. Leijte JA, Valdés Olmos RA, Nieweg OE, Horenblas S. Anatomical mapping of lymphatic drainage in penile carcinoma with SPECT-CT: implications for the extent of inguinal lymph node dissection. Eur Urol. 2008;54:885–90.
120. Sadeghi R, Tabasi KT, Bazaz SM, Kakhki VR, Massoom AF, Gholami H, et al. Sentinel node mapping in the prostate cancer. Meta-analysis. Nuklearmedizin. 2011;50:107–15.
121. Van den Bergh L, Joniau S, Haustermans K, Deroose CM, Isebaert S, Oyen R, et al. Reliability of sentinel node procedure for lymph node staging in prostate cancer patients at high risk for lymph node involvement. Acta Oncol. 2015;54:896–902.
122. Meinhardt W, van der Poel HG, Valdés Olmos RA, Bex A, Brouwer OR, Horenblas S. Laparoscopic sentinel lymph node biopsy for prostate cancer: the relevance of locations outside the extended dissection area. Prostate Cancer. 2012;2012:751753.
123. Vermeeren L, Meinhardt W, van der Poel HG, Valdés Olmos RA. Lymphatic drainage from the treated versus untreated prostate: feasibility of sentinel node biopsy in recurrent cancer. Eur J Nucl Med Mol Imaging. 2010;37:2012–26.
124. Krengli M, Ballare A, Cannillo B, Rudoni M, Kocjancic E, Loi G, et al. Potential advantage of studying the lymphatic drainage by sentinel node technique and SPECT/CT image fusion for pelvic irradiation of prostate cancer. Int J Radiat Oncol Biol Phys. 2006;66:1100–4.
125. Rousseau C, Rousseau T, Campion L, Lacoste J, Aillet G, Potiron E, et al. Laparoscopic sentinel lymph node versus hyperextensive pelvic dissection for staging clinically localized prostate carcinoma; a prospective study of 200 patients. J Nucl Med. 2014;55:753–8.
126. De Bonilla-Damiá A, Brouwer OR, Meinhardt W, Valdés Olmos RA. Lymphatic drainage in prostate carcinoma assessed by lymphoscintigraphy and SPECT/CT: its importance for the sentinel node procedure. Rev Esp Med Nucl Imagen Mol. 2012;31:66–70.
127. Vees H, Steiner C, Dipasquale G, Chouiter A, Zilli T, Velazquez M, et al. Target volume definition in high-risk prostate cancer patients using sentinel node SPECT/CT and ^{18}F-choline PET/CT. Radiat Oncol. 2012;7:134.
128. Maurer T, Gschwend JE, Rauscher I, Souvatzoglou M, Haller B, Weirich G, et al. Diagnostic efficacy of ^{68}Gallium-PSMA-PET compared to conventional imaging in lymph node staging of 130 consecutive patients with intermediate to high-risk prostate cancer. J Urol. 2016;195:1436–43.
129. Schottelius M, Wirtz M, Eiber M, Maurer T, Wester HJ. [^{111}In]PSMA-I&T: expanding the spectrum of

PSMA-I&T applications towards SPECT and radioguided surgery. EJNMMI Res. 2015;5:68.
130. Liss MA, Noguchi J, Lee HJ, Vera DR, Kader AK. Sentinel lymph node biopsy in bladder cancer: systematic review and technology update. Indian J Urol. 2015;31:170–5.
131. Brouwer OR, Valdés Olmos RA, Vermeeren L, Hoefnagel CA, Nieweg OE, Horenblas S. SPECT/CT and a portable γ-camera for image-guided laparoscopic sentinel node biopsy in testicular cancer. J Nucl Med. 2011;52:551–4.
132. Bex A, Vermeeren L, Meinhardt W, Prevoo W, Horenblas S, Valdés Olmos RA. Intraoperative sentinel node identification and sampling in clinically node-negative renal cell carcinoma: initial experience in 20 patients. World J Urol. 2011;29:793–9.
133. Brouwer OR, Noe A, Valdes Olmos RA, Bex A. Lymphatic drainage from renal cell carcinoma along the thoracic duct visualized with SPECT/CT. Lymphat Res Biol. 2013;11:233–8.
134. Covens A, Vella ET, Kennedy EB, Reade CJ, Jimenez W, Le T. Sentinel lymph node biopsy in vulvar cancer: systematic review, meta-analysis and guideline recommendations. Gynecol Oncol. 2015;137:351–61.
135. Te Grootenhuis NC, van der Zee AG, van Doorn HC, van der Velden J, Vergote I, Zanagnolo V, et al. Sentinel nodes in vulvar cancer: long-term follow-up of the GROningen INternational Study on Sentinel nodes in Vulvar cancer (GROINSS-V) I. Gynecol Oncol. 2016;140:8–14.
136. Paredes P, Vidal-Sicart S. Preoperative and intraoperative lymphatic mapping for radioguided sentinel node biopsy in cancers of the female reproductive system. In: Mariani G, Manca G, Orsini F, Vidal-Sicart S, Valdés Olmos RA, editors. Atlas of lymphoscintigraphy and sentinel node mapping. Milan: Springer; 2013. p. 249–60.
137. Collarino A, Donswijk ML, van Driel WJ, Stokkel MP, Valdés Olmos RA. The use of SPECT/CT for anatomical mapping of lymphatic drainage in vulvar cancer: possible implications for the extent of inguinal lymph node dissection. Eur J Nucl Med Mol Imaging. 2015;42:2064–71.
138. Doorn HC, van Beekhuizen HJ, Gaarenstroom KN, van der Velden J, van der Zee AG, Oonk M, et al. Repeat sentinel lymph node procedure in patients with recurrent vulvar squamous cell carcinoma is feasible. Gynecol Oncol. 2016. [Epub ahead of print].
139. Verbeek FP, Tummers QR, Rietbergen DD, Peters AA, Schaafsma BE, van de Velde CJ. Sentinel lymph node biopsy in vulvar cancer using combined radioactive and fluorescence guidance. Int J Gynecol Cancer. 2015;25:1086–93
140. Kadkhodayan S, Hasanzadeh M, Treglia G, Azad A, Yousefi Z, Zarifmahmoudi L, et al. Sentinel node biopsy for lymph nodal staging of uterine cervix cancer: a systematic review and meta-analysis of the pertinent literature. Eur J Surg Oncol. 2015;41:1–20.
141. Bats AS, Frati A, Mathevet P, Orliaguet I, Querleu D, Zerdoud S, et al. Contribution of lymphoscintigraphy to intraoperative sentinel lymph node detection in early cervical cancer: analysis of the prospective multicenter SENTICOL cohort. Gynecol Oncol. 2015;137:264–9.
142. Hoogendam JP, Veldhuis WB, Hobbelink MG, Verheijen RH, van den Bosch MA, Zweemer RP. ^{99m}Tc SPECT/CT versus planar lymphoscintigraphy for preoperative sentinel lymph node detection in cervical aancer: a systematic review and meta-analysis. J Nucl Med. 2015;56:675–80.
143. Giammarile F, Bozkurt MF, Cibula D, Pahisa J, Oyen WJ, Paredes P, et al. The EANM clinical and technical guidelines for lymphoscintigraphy and sentinel node localization in gynaecological cancers. Eur J Nucl Med Mol Imaging. 2014;41:1463–77.
144. Ansari M, Rad MA, Hassanzadeh M, Gholami H, Yousefi Z, Dabbagh VR, Sadeghi R. Sentinel node biopsy in endometrial cancer: systematic review and meta-analysis of the literature. Eur J Gynaecol Oncol. 2013;34:387–401.
145. Perissinotti A, Paredes P, Vidal-Sicart S, Torné A, Albela S, Navales I, et al. Use of SPECT/CT for improved sentinel lymph node localization in endometrial cancer. Gynecol Oncol. 2013;129:42–8.
146. Sawicki S, Kobierski J, Lapinska-Szumczyk S, Lass P, Cytawa W, Bianek-Bodzak A, Wydra D. Comparison of SPECT/CT results and intraoperative detection of sentinel lymph nodes in endometrial cancer. Nucl Med Commun. 2013;34:590–6.
147. Mücke J, Klapdor R, Scheider M, Länger F, Gratz KF, Hillemans P, Hertel H. Isthmocervical labeling and SPECT/CT for optimized sentinel node detection in endometrial cancer: technique, experience and results. Gynecol Oncol. 2014;134:287–92.
148. Kleppe M, Brans B, Van Gorp T, Slangen BF, Kruse AJ, Pooters IN, et al. The detection of sentinel nodes in ovarian cancer: a feasibility study. J Nucl Med. 2014;55:1799–804.
149. Nagaraja V, Eslick GD, Cox MR. Sentinel lymph node in oesophageal cancer – a systematic review and meta-analysis. J Gastrointest Oncol. 2014;5:127–41.
150. Niihara M, Takeuchi H, Nakahara T, Saikawa Y, Takahashi T, Wada N, et al. Sentinel lymph node mapping for 385 gastric cancer patients. J Surg Res. 2016;200:73–81.
151. Balagué C, Pallarés JL. Preoperative and intraoperative lymphatic mapping for radioguided sentinel node biopsy in cancers of the gastrointestinal tract. In: Mariani G, Manca G, Orsini F, Vidal-Sicart S, Valdés Olmos RA, editors. Atlas of lymphoscintigraphy and sentinel node mapping. Milan: Springer; 2013. p. 231–9.
152. Tehranian S, Treglia G, Krag DN, Dabbagh Kakhki VR, Zakavi SR, Sadeghi R, et al. Sentinel node mapping in anal canal cancer: systematic review and meta-analysis. J Gastrointestin Liver Dis. 2013;22:321–8.

153. Ambrogi MC, Melfi F, Zirafa C, Lucchi M, De Liperi A, Mariani G, et al. Radio-guided thoracoscopic surgery (RGTS) of small pulmonary nodules. Surg Endosc. 2012;26:914–9.
154. Galetta D, Bellomi M, Grana C, Spaggiari L. Radio-guided localization and resection of small or ill-defined pulmonary lesions. Ann Thorac Surg. 2015;100:1175–80.
155. Tyng CJ, Nogueira VH, Bitencourt AG, Santos LC, Souza TV, Zilio MB, et al. Computed tomographically guided injection of cyanoacrylate in association with preoperative radioguided occult lesion localization of ground-glass opacities. Ann Thorac Surg. 2015;99:1838–40.
156. Taghizadeh Kermani A, Bagheri R, Tehranian S, Shojaee P, Sadeghi R, Krag DN. Accuracy of sentinel node biopsy in the staging of non-small cell lung carcinomas: systematic review and meta-analysis of the literature. Lung Cancer. 2013;80:5–14.
157. Abele JT, Allred K, Clare T, Bédard EL. Lymphoscintigraphy in early-stage non-small cell lung cancer with technetium-99m nanocolloids and hybrid SPECT/CT: a pilot project. Ann Nucl Med. 2014;28:477–83.
158. García-Talavera P, Ruano R, Rioja ME, Cordero JM, Razola P, Vidal-Sicart S. Radioguided surgery in neuroendocrine tumors. A review of the literature. Rev Esp Med Nucl Imagen Mol. 2014;33:358–65.
159. Heller S, Zanzonico P. Nuclear probes and intraoperative gamma cameras. Semin Nucl Med. 2011;41:166–81.
160. Bellotti C, Castagnola G, Tierno SM, Centanini F, Sparagna A, Vetrone I, et al. Radioguided surgery with combined use of gamma probe and hand-held gamma camera for treatment of papillary thyroid cancer locoregional recurrences: a preliminary study. Eur Rev Med Pharmacol Sci. 2013;17:3362–6.
161. KleinJan GH, van den Berg NS, de Jong J, Wit EM, Thygessen H, Vegt E, et al. Multimodal hybrid imaging agents for sentinel node mapping as a means to (re)connect nuclear medicine to advances made in robot-assisted surgery. Eur J Nucl Med Mol Imaging. 2016;43:1278–87.
162. van Oosterom MN, Simon H, Mengus L, Welling MM, van der Poel HG, van den Berg NS et al. Revolutionizing (robot-assisted) laparoscopic gamma tracing using a drop-in gamma probe technology. Am J Nucl Med Mol Imaging 2016;28:1–17.

Part V

Heart Disease in the Cancer Patient

Imaging the Heart in the Cancer Patient

51

H. William Strauss and Josef J. Fox

Abstract

The average age of a cancer patient is 67. Sexagenarians with cancer are likely to have comorbidities at the time of diagnosis. Cancer patients > 55 years old have an average of ~2.9 comorbidities, while cancer patients older than 75 have an average of 4.2 comorbidities.

The likelihood of coronary artery disease as an etiology of this comorbidity increases with the age of the patient. Cardiovascular comorbidity is present in ~20% of patients with neoplasm. These comorbidities increase the risk of a serious cardiovascular event during treatment. An additional risk factor is limited work capacity. If patients cannot perform 4 metabolic equivalents of work, their all cause mortality is increased. Patients with cancer and known cardiovascular comorbidity or risk factors such as diabetes, hypertension, smoking history, or limited work capacity should have medical clearance prior to invasive diagnostic procedures, major surgery, mediastinal radiation, and/or potentially cardiotoxic chemotherapy.

H.W. Strauss (✉)
Molecular Imaging and Therapy Service, Memorial Sloan Kettering Cancer Center, New York, NY, USA
e-mail: straussh@mskcc.org

J.J. Fox
Department of Radiology, Memorial Sloan Kettering Cancer Center, New York, NY, USA
e-mail: foxj@mskcc.org

© Springer International Publishing Switzerland 2017
H.W. Strauss et al. (eds.), *Nuclear Oncology*,
https://doi.org/10.1007/978-3-319-26236-9_29

Medical clearance should include a detailed cardiovascular history and physical examination. This information will permit calculation of a clinical score to define the risk of adverse events as a result of a major surgical procedure, blood tests to determine hematologic and renal status, and if necessary, assessment of the patients work capacity. Stress testing with imaging should be done in patients with an intermediate risk of coronary heart disease and considered in patients with limited work capacity or advanced age. In selected patients, coronary CT angiography or coronary calcium score may be a suitable evaluation. In patients with cancer of the esophagus, breast, lung, melanoma, or lymphoma, chest-CT and PET/CT studies should be carefully evaluated to detect possible pericardial or myocardial involvement.

Chemotherapy may cause myocardial ischemia due to coronary spasm and decreased ventricular function due to irreversible or reversible myocardial damage, as well as repolarization abnormalities, which may result in fatal arrhythmia. Radiotherapy may accelerate the development of atherosclerosis of vessels in the radiation field and cause irreversible damage to myocardium in the radiation field. Myocardial perfusion imaging is useful to detect regions of acute ischemia or scar induced by therapy, while blood pool imaging is useful for serial monitoring of ventricular function.

Keywords

Heart imaging in the cancer patient • Cardiovascular comorbidities in the cancer patient • Cardiotoxic chemotherapy • Stress testing in cancer patients • Heart disease in cancer patients • Cancer coexisting with cardiovascular disease

Glossary

[^{18}F]FDG	2-deoxy-2-[^{18}F]fluoro-D-glucose
ACC	American College of cardiology
ACE	Angiotensin-converting enzyme
AHA	American Heart Association
AL	light chain amyloid
AMI	Acute myocardial infarction
ASCO	American Society of Clinical Oncology
ATTR	transthyretin amyloid
ATP	Adenosine triphosphate
BNP	B-type natriuretic peptide
CAD	coronary artery disease
CHF	Congestive heart failure
CI	confidence interval
C-MRI	Cardiac magnetic resonance imaging
COPD	chronic obstructive pulmonary disease
CRCD	Chemotherapy-related cardiac dysfunction
CRP	C-reactive protein
CT	X-ray computed tomography
CTCAE	Common terminology criteria for adverse events
DTPA	diethylenetriaminepentaacetic acid
DVT/PE	Deep venous thrombosis/pulmonary embolism
EDTA	ethylenediaminetetraacetic acid
ErbB2	a member of the tyrosine-protein kinase family (also known as CD340)
HER2	Human epidermal growth factor receptor 2
HR	hazard ratio
HTN	Hypertension
LEVF	Left ventricular ejection fraction
LGE	Late gadolinium enhancement
LHIS	Lipomatous hypertrophy of the interatrial septum
LV	left ventricle
METS	Metabolic equivalents
MI	myocardial infarction
MIP	maximum intensity projection
MPI	Myocardial perfusion imaging
MRI	Magnetic resonance imaging
MSKCC	Memorial Sloan-Kettering Cancer Center
MUGA	Multigated acquisition
NCI	National Cancer Institute, National Institutes of Health of the United States
PET	positron emission tomography
PET/CT	positron emission tomography/computed tomography
P-POSSUM	Predicted mortality-physiologic and operative severity score
RCRI	Revised cardiovascular risk index
RCRS	Revised cardiac risk score
RVG	Radionuclide ventriculography
SEER	Surveillance, Epidemiology, and End Results
SPECT	single-photon emission computed tomography
SUV	standardized uptake value
TEE	transesophageal echocardiography
VEGF	vascular endothelial growth factor

Contents

Introduction 1485

Management of Cardiac Risk in Noncardiac Surgery 1486
Background 1486
Events 1486
Interval Between Stent Placement and Surgery 1486
Clinical Recognition of Perioperative Infarct 1487
Perioperative and Intraoperative Management 1488
Determination of Preoperative Risk 1488
Approach to the Evaluation of the Presurgical Patient with Intermediate Risk 1489
Myocardial Perfusion Imaging in Preoperative Assessment 1489

Myocardial and Pericardial Tumor Involvement 1491

Cardiac Amyloidosis 1492

Cardiac Function 1495

Chronic Cardiotoxicity 1497
Type I CRCD 1497
Type II CRCD 1501
Recommendations 1504
References 1505

Introduction

Cardiovascular issues in patients with cancer fall into four major categories:

1. (a) Extension of the tumor to the pericardium or myocardium (seen in cancer of the esophagus, lung, lymphoma, thymoma, and breast) or (b) a neoplasm originating in the heart or blood vessels (aside from atrial myxoma, such tumors are extremely rare).
2. Damage to the heart or blood vessels due to treatment (e.g., doxorubicin cardiotoxicity, radiation therapy where major vessels and/or portions of the heart are in the field, or severe hypertension induced by VEGF inhibitors [e.g., bevacizumab]). Cardiotoxicity is the second leading cause of long-term morbidity and mortality among cancer survivors [1].
3. Secondary effects of the neoplasm on the heart (e.g., cardiac amyloid in patients with multiple myeloma – which may occur in ~30% of myeloma patients [2]).
4. Pre-existing cardiovascular comorbidity influencing the selection of therapy (e.g., pre-existing coronary, valvular, or myocardial disease causing symptoms of ischemia or heart failure).

Since the average age of a cancer patient is 67 years, it is not surprising that about 60% of patients over the age of 65 [3] have a significant comorbidity. The Eindhoven Cancer Registry identified these comorbidities in the Dutch population as hypertension (26%), heart disease (23%), previous cancers (20%), chronic obstructive pulmonary disease (COPD; 17%), and diabetes mellitus (16%). In the United States, SEER data identified a cardiovascular comorbidity in 32% of female breast cancer patients [4], 31% of prostate cancer patients, 53% of lung cancer patients, and 41% of patients with colorectal cancer. Comorbidities in the U.S. population were different than in the Dutch population; with diabetes (16%), COPD (16%), congestive heart failure (10%), and cerebrovascular disease (6%) [5], the comorbidity of a second cancer occurred in ~19% of adult cancer patients [6] in the United States.

A cancer patient with underlying coronary artery disease has an increased risk of a serious cardiovascular event, especially if therapy involves high-risk surgery, the use of cardiotoxic chemotherapy, or mediastinal radiation. The risk is evaluated by medical clearance, which includes a detailed cardiovascular history (including the patient's work capacity. Inability to perform at least four METS (metabolic equivalents of oxygen) work (equivalent to performing light housework) is associated with increased all-cause mortality and physical examination, appropriate laboratory studies, review of a resting electrocardiogram, and cardiac imaging procedures (including echocardiogram, myocardial perfusion scan, chest film, and a chest computed tomography [CT] scan) as well as coronary calcium to calculate a clinical score (such as RCRS [revised cardiac risk score], POSSUM for severe morbidity, and Charlson [7] for comorbidity should be carried out.

Patients with a history of myocardial infarction (MI), percutaneous coronary interventions, or bypass surgery scheduled for intermediate- or high-risk procedures are candidates for stress testing with imaging. Myocardial perfusion imaging, especially using PET/CT with contemporaneous measurement of coronary calcium and coronary flow reserve, is preferred. In selected patients, stress echocardiography or coronary CT angiography may be suitable for detecting significant coronary stenosis, high-risk plaque (and vascular remodeling), as well as global and regional ventricular function at rest and stress. In patients with cancer of the esophagus, breast, lung, melanoma, or lymphoma, chest CT and/or PET/CT studies should be carefully evaluated to detect possible pericardial or myocardial metastases.

Cancer chemotherapy may cause impaired ventricular function, coronary spasm, hypertension, deep venous thrombosis, and pulmonary embolus (Table 1) [8], while radiation therapy can accelerate the development of atherosclerosis (particularly if vessels are in a radiation field) and possibly cause reversible or permanent myocyte damage with associated decrease in global ventricular function.

Table 1 Revised Cardiovascular Risk Index (RCRI)

High-risk surgery (supra-inguinal vascular, intraperitoneal, and/or intrathoracic surgery)
History of MI; history of positive exercise test; current chest pain due to myocardial ischemia; use of nitrate therapy; ECG with pathological Q waves
History of heart failure; pulmonary edema; paroxysmal nocturnal dyspnea; chest X-ray showing pulmonary vascular redistribution
History of cerebrovascular disease
Diabetes mellitus requiring insulin
Preoperative creatinine >2.0 mg/dL (177 μmol/L)

Management of Cardiac Risk in Noncardiac Surgery

Background

Worldwide there are over 200 million surgical procedures performed on patients under general anesthesia each year [9]. In the first 30 days after major noncardiac surgery, about 10 million adults (~5%) will have a major cardiac complication that may result in death. If patient demise within 30 days of surgery were to be listed as a separate cause of death in the United States, it would be the third leading cause of death [10, 11]. The likelihood of a patient with a perioperative MI dying within 6 months of the event is high. Although death occurs in only 0.01% of all patients undergoing operations, mortality increases to ~40% in cases of perioperative infarction [12].

The prevalence of coronary heart disease is 6% in men aged 40–59, ~20% in men aged 60–79, and ~32% in men older than 80 years. The prevalence in women is approximately half that of men at age 60 years and older [13]. Demographic data suggest that by the year 2055, more than 20% of the US population (and 25% of the world population) will be over the age of 65, and patients over age 65 will account for approximately 40% of all surgical procedures [[5]]. SEER statistics suggest that the lifetime risk of developing cancer is about 42% for men and 38% for women [14]. In 2015, about 1,658,370 new cases of cancer were diagnosed, and about 13,776,251 Americans had a history of cancer [15]. Based on the prevalence of cancer and of coronary disease, it is likely that a patient with cancer will have coronary disease as a comorbidity.

Events

The likelihood of a perioperative major adverse cardiac event is related to the baseline risk. Patients with a history of coronary heart disease are at much higher risk for perioperative ischemic events. In the first week after surgery, ischemic episodes occur in 24–41% of patients with a history of CAD. Although the majority of events are clinically silent [16], acute clinical events occur in approximately 5% of cases (infarction, heart failure, or cardiac death). A perioperative MI, even if clinically silent, is associated with a hospital mortality rate of 15–25%. Of the patients who have a perioperative infarct, 75% are non-transmural [17]. A study of 283 radical cystectomy patients, average age 70, average duration of surgical procedure 7 h, found coexistent coronary disease in 64 patients (23%) [18]. There were 31 patients with perioperative cardiac complications including new-onset arrhythmia in 22 and MI in ten. Of these patients, 13 (42%) had a history of coronary disease. In the infarct group, there was history of previous coronary disease in four patients. All ten MI patients had at least one other postoperative complication, such as sepsis or a major wound issue. The added stress of the complication likely caused tachycardia and possibly increased blood pressure, thereby increasing myocardial oxygen demands. Pain or other factors associated with the complication may have contributed to coronary artery spasm, reducing coronary blood flow. The mean interval between surgery and MI was 3.5 days. Preoperatively, five of the ten MI patients had normal stress test results, and two patients with abnormal stress test results had stents placed before the cystectomy.

Interval Between Stent Placement and Surgery

The interval between placing a cardiac stent and perioperative cardiac events was explored in a retrospective analysis of 1,953 patients [19]. There

were no significant differences between drug-eluting and bare metal stents (in-hospital mortality, ~0.6%; MI, ~0.9%; or postoperative ischemic cardiac events, 14%). There was a significant *increase* in the incidence of death or MI if the interval between stent placement and surgery was shorter than 42 days (42.4%), compared with 42 days to 1 year (24.5%) or longer than 1 year (11.7%).

Clinical Recognition of Perioperative Infarct

About 50% of perioperative infarcts are clinically unrecognized [20]. Typical clinical symptoms are difficult to assess owing to postoperative discomfort and the use of pain medication. In addition, electrocardiographic changes may be subtle. In a series of 65 patients undergoing head and neck surgery, troponin I was measured on postoperative day 3. Of the 65 patients, 16 (25%) had an elevated troponin level (>0.032 μg/L); only five patients had a clinically apparent infarction [21]. Myocardial damage was not related to the length of surgery (243 min in patients with elevated troponin vs. 205 min, $p > 0.2$) but it did correlate with postoperative inflammation, measured by elevated C-reactive protein (CRP) levels. The new worldwide standard definition of acute infarction includes an increase in cardiac enzymes (preferably troponin) to more than 99th percentile of normal laboratory values, new Q waves, or sudden cardiac death. This definition will help investigators identify factors associated with perioperative infarction. Cohn commented on the "diagnostic dilemma" presented by postoperative troponin surveillance [22], since 10–20% of patients have elevated troponin levels following noncardiac surgery. Patients with elevated troponin levels have an increased 30-day mortality (with higher peak troponin T levels associated with higher risk of death), often from noncardiac causes. Unfortunately, there is no proven beneficial treatment in asymptomatic patients with elevated troponin levels.

The pathophysiology of ischemia and infarction in perioperative patients is different than in patients outside this environment. Two retrospective autopsy studies evaluated the etiology of perioperative MI:

1. Dawood et al. compared fatal perioperative MI with fatal nonoperative MI [23]. The investigators evaluated the hearts of 42 patients who had elective or emergent noncardiac surgery and died of perioperative infarction within 30 days (MI occurred within 7 days in 40 patients). History of prior MI was present in 55%. Left main coronary artery disease was found in 19%, and triple-vessel disease in 59%. Plaque fissure, rupture, or hemorrhage was found in 55% of patients, and intraluminal thrombus was present in 28% (likely an underestimate, owing to autologous thrombolysis). Six patients had plaque disruption in more than one coronary artery, suggesting that there is a generalized vascular inflammation in these patients.
2. Cohen and Aretz [24] studied the hearts of 26 cases with fatal perioperative MI. Prior myocardial scar was present in 81% (compared with a clinical history in only 19%); left main coronary artery disease was present in 23%, and multivessel disease in 88%. Plaque rupture was present in 46%, and intracoronary thrombus was present in 35%. A retrospective study of 66 patients undergoing intermediate-risk noncardiac surgery, who had coronary angiography following a perioperative infarct, demonstrated demand ischemia as the predominant etiology [25].

The autopsy studies and the angiographic study confirm the importance of multivessel coronary disease as a predictor of coronary events. A clinical history of coronary disease, however, may be lacking, as demonstrated in the study by Cohen and Aretz.

An important factor in perioperative MI is an increase in myocardial oxygen requirement due to an increased heart rate, blood pressure, or both. Continuous monitoring demonstrated an average heart rate increase of ~32 bpm, often accompanied by an increase in blood pressure, resulting in multiple prolonged episodes of ST-depression ischemia. The duration of ischemic episodes was fivefold longer in patients with perioperative MI [26, 27]. These episodes likely reflect sympathetic surges. In the perioperative environment, the role

of the "vulnerable patient," for example, due to a hypercoagulable state, the presence of systemic inflammation [21], and anemia or fluid overload, is also important in the etiology of perioperative myocardial ischemia and infarction.

Perioperative and Intraoperative Management

Cancer surgical procedures frequently require hours of general anesthesia, clamping, and release of major vessels and may involve significant blood loss. These factors result in the release of inflammatory cytokines that may increase the thrombogenicity of pre-existing atheroma, leading to embolic, thrombotic, or vasospastic events. Many patients have a significant elevation of resting heart rate postoperatively, associated with the release of catecholamines due to transient hypoxia, extubation, postoperative pain, increased or decreased circulating blood volume, and transient increase in inflammatory states due to increased production/release of tumor necrosis factor, interleukin, and CRP owing to tissue injury [20]. Persistent tachycardia increases myocardial oxygen consumption, raising the likelihood that patients with moderate and severe coronary stenoses may develop ischemia. To minimize the increase in heart rate and blood pressure and reduce the likelihood of infarction, these patients should be treated perioperatively with beta-blockers [15, 19, 32] (if there is no contraindication), with the goal of maintaining a heart rate of 60 bpm or less and of minimizing surges in blood pressure.

Determination of Preoperative Risk

The following factors place the patient at risk for perioperative events:

1. A work capacity of <4 METS is associated with increased all-cause mortality [28] and increased postoperative length of stay [29]
2. Severe coronary disease
3. Recent heart failure
4. Prolonged duration of anesthesia
5. Large fluid shifts in the course of the procedure
6. Pain or other severe discomfort in the immediate postoperative and early recovery interval (up to 7 days)
7. Wound infection, sepsis, or dehiscence

A clinical scoring system focused on the cardiovascular system, the Revised Cardiac Risk Index proposed by Lee [30], considers six factors (Table 1) [31].

The rate of cardiac death, nonfatal MI, and nonfatal cardiac arrest is based on the number of risk factors [32]:

No risk factors	0.4%
One risk factor	1.0%
Two risk factors	2.4%
Three or more risk factors	5.4%

This index is useful for identifying patients at medium to high risk undergoing high-risk noncardiac surgery who could benefit from noninvasive cardiac stress testing [33].

Another clinical scoring system, P-POSSUM (Predicted mortality – Physiologic and Operative Severity Score), considers multiple factors, and online calculators are available [34]. The P-POSSUM calculator considers:

- Patient age
- The presence of heart failure and dyspnea
- Atrial fibrillation or other arrhythmia
- Blood pressure
- Hemoglobin
- White blood cell count
- Blood urea nitrogen
- Serum sodium and potassium
- Glasgow coma score
- Type of operation
- Number of procedures
- Estimated blood loss
- Chance of peritoneal contamination
- The presence of malignancy/metastasis
- Urgency of surgery

The calculator produces a score estimating morbidity and mortality. A comprehensive discussion of patient evaluation is contained in the updated

ACC/AHA guide on perioperative cardiovascular evaluation for noncardiac surgery [35]. The guidelines suggest that an MI occurring less than 90 days before surgery is associated with a postoperative 30-day mortality of 10.5%. Other factors increasing the risk of a major perioperative event include age over 62 years, history of cerebrovascular disease, the presence of heart failure, left ventricular ejection fraction (LVEF) less than 40%, elevated B-type natriuretic peptide (BNP) level, moderate or severe valvular disease, and a work capacity less than 4 METS.

Approach to the Evaluation of the Presurgical Patient with Intermediate Risk

A meta-analysis of six preoperative diagnostic tests demonstrated a sensitivity of exercise electrocardiography, MPI, and dobutamine echocardiography to be greater than 74% (confidence interval >60%) for the prediction of perioperative events [36]. Impaired left ventricular function had a surprisingly low sensitivity and poor positive predictive value for perioperative cardiac events. A direct comparison of multiple techniques suggests that CT coronary angiography and PET myocardial perfusion imaging have similar positive and negative predictive values [37]. Patients at intermediate risk for coronary events, primarily those with a score greater than 1 on the Revised Cardiac Risk Index (see Table 1), appear to be the group with the greatest benefit from preoperative testing.

Mangano and colleagues demonstrated that effective preoperative and intraoperative beta blockade can reduce the incidence of perioperative cardiovascular events particularly in low-risk patients. In addition, the investigators confirmed that preoperative revascularization does not reduce perioperative morbidity and mortality: "Coronary revascularization prior to non-cardiac surgery is only indicated in unstable patients and patients with left main disease" [38].

To assist in the selection of patients for preoperative assessment, Mukherjee and Eagle suggest utilizing MPI only on patients with clinical risk factors, such as a history of angina, MI, congestive heart failure, diabetes, and Q waves on ECG.

In a retrospective study of 271,082 patients older than 40 years undergoing intermediate- to high-risk noncardiac surgical procedures, 23,991 had preoperative noninvasive stress testing. Patients with intermediate and high risk of cardiovascular events (using the RCRI criteria) who had stress tests had improved 1-year survival and reduced length of hospital stay [39].

Preoperative testing for patients at risk of perioperative events should help identify patients at high risk for perioperative events. However, not all patients at risk of perioperative ischemia are identified on preoperative testing. Investigators compared a preoperative dobutamine echocardiogram with intraoperative transesophageal echocardiography (TEE) [40] in 54 patients scheduled for major vascular surgery. Dobutamine stress induced new wall motion abnormalities in 17 patients. Intraoperative echocardiography detected new wall motion abnormalities in 23 patients. A perioperative event occurred in 15 patients: Ten had a dobutamine-induced wall motion abnormality and a new wall motion abnormality on intraoperative TEE; in four patients, an abnormality was only detected on the intraoperative TEE, suggesting the surgery caused an added stress not inducible with dobutamine.

Myocardial Perfusion Imaging in Preoperative Assessment

MPI can be performed using single-photon or positron-emitting tracers. The most common procedures employ single-photon agents, which permit patients to be studied with exercise or pharmacologic stress. Exercise stress has the advantage of providing information about a patient's work capacity (see section "Determination of Preoperative Risk"), evidence of electrocardiographic ischemia, as well as information about the relative distribution of myocardial perfusion at rest and stress. Exercise stress is particularly useful in patients below the age of 70, with no evidence of neuropathy, orthopedic impairment, lung disease, or impaired mentation.

Patients who cannot exercise can be stressed with either intravenous administration of vasodilators (dipyridamole, adenosine, adenosine triphosphate [ATP], or regadenoson) or with catecholamine agonists (dobutamine). Vasodilator stress MPI has a sensitivity equal to exercise stress for the detection and localization of regions of decreased perfusion and has the safety advantage of intravenous aminophylline as a rapid reversing agent in the unlikely circumstance that the patient develops severe ischemia (likely from a "steal" syndrome). A major contraindication to the use of dipyridamole or adenosine, bronchospasm, can be overcome in patients who are not actively wheezing. The synthetic A2A adenosine agonist regadenoson has a low incidence of bronchospasm. Preparing the patient with inhalation of one or two puffs of albuterol before administering regadenoson reduces the likelihood of bronchospasm.

Dobutamine stress is typically a longer procedure than vasodilator stress, often requiring the addition of atropine to achieve the desired heart rate end point. Like vasodilator stress, dobutamine can be reversed pharmacologically with the short-acting intravenous beta-blocker esmolol. Atropine, however, has a half-life of ~2.5 h and in addition to dry mouth and blurred vision may cause urinary retention. To minimize these side effects, vasodilator stress MPI is overwhelmingly preferred for pharmacologic stress testing.

A retrospective review of MPI in 394 cancer patients studied for preoperative risk assessment revealed abnormal scans in 97 patients [41]. There were nine major perioperative cardiac events – all in subjects with abnormal scans. A review of stress MPI in 787 cancer patients [42] identified ischemia or scar in 36%. Ischemia or scar was seen in 36% of those stressed with adenosine, 36% of those stressed with dobutamine, and 38% of those stressed with exercise. During a 3-year follow-up, 84 patients (11%) had a cardiac event (cardiac death in 51 patients, 61% of those with a cardiac event). Cardiac events occurred in 6% of patients with a normal stress MPI and in 19% of those with ischemia, scar, or both. Ischemia on MPI was associated with a 24% likelihood of a cardiovascular event, while scar was associated with a 19% likelihood. However, the overall 3-year survival in these patients was only 44%, suggesting that ischemic heart disease played less of a role in survival than the patient's cancer.

A meta-analysis of 24 studies reporting results on 14,918 patients with known or suspected coronary disease compared the cardiac outcome of pharmacologic (dipyridamole, adenosine, or dobutamine) with exercise stress MPI [43]. Patients were followed up for 12–55 months (median 22 months for pharmacologic stress and 20 months for exercise). There were 343 cardiac deaths and 216 nonfatal MIs in the pharmacologic stress group and 180 cardiac deaths and 277 nonfatal MIs in the exercise group (total event rate = 6.8%). In the pharmacologic stress group, the annualized event rate for cardiac death and MI (hard events) for patients with normal perfusion scans was 1.78% and 9.98% for patients with abnormal images. In the exercise stress group, the pooled hard event rates were 0.65% for patients with normal images and 4.3% for those with abnormal images. These data suggest that both pharmacologic and exercise stress-gated single-photon emission CT (SPECT) myocardial perfusion scans identify patients with a significant risk of cardiac events.

PET MPI has significant technical advantages over single-photon studies thanks to the superior spatial resolution of ~3 mm for nitrogen-13 ammonia and ~5 mm for rubidium-82 versus ~11 mm for ^{99m}Tc. CT attenuation correction with PET minimizes false-positive scans due to breast or diaphragmatic attenuation, and gated CT imaging can provide information about coronary calcification. A major advantage of PET perfusion studies is the ability to measure absolute coronary blood flow and provide information about perfusion reserve. Reduced perfusion reserve occurs in patients with small vessel disease (patients with diabetes, left ventricular hypertrophy and subjects with metabolic syndrome) and may also be seen in patients with diffuse triple-vessel disease, where regional perfusion may appear normal [44]. Although oxygen-15-labeled water is the preferred tracer for determining regional myocardial perfusion, it is not widely available because of the ~2 min half-life of oxygen-15. Most PET perfusion studies are

performed with generator-produced rubidium-82 or less frequently with nitrogen-13 ammonia. After testing the generator for breakthrough of the parent strontium-82, the 75-s half-life rubidium-82 daughter is eluted from the generator directly into the patient. The short half-life permits administration of 30–50 mCi at rest during a dynamic 7–10-min data acquisition. The vasodilator (typically dipyridamole, adenosine, or regadenoson) is administered followed by a second infusion of rubidium-82 with a dynamic acquisition similar to that at rest.

As with single-photon imaging, the images are checked for appropriate registration with the attenuation correction CT, reconstructed, placed in standard cardiac orientation, and evaluated for the regional distribution of perfusion at rest and stress as well as perfusion reserve (typically with a one-compartment model) (Fig. 1). The gated perfusion images are reviewed to determine regional and global ventricular function. Recent studies suggest that hybrid imaging with PET/CT of myocardial perfusion and contrast coronary CT angiography offers the most complete noninvasive evaluation of myocardial ischemia since the vessel perfusing a specific territory and the perfusion/perfusion reserve are measured concurrently.

Myocardial and Pericardial Tumor Involvement

Primary cardiac tumors are rare: The most common primary cardiac neoplasm, accounting for 75% of cases, is a benign myxoma [45]. Malignant

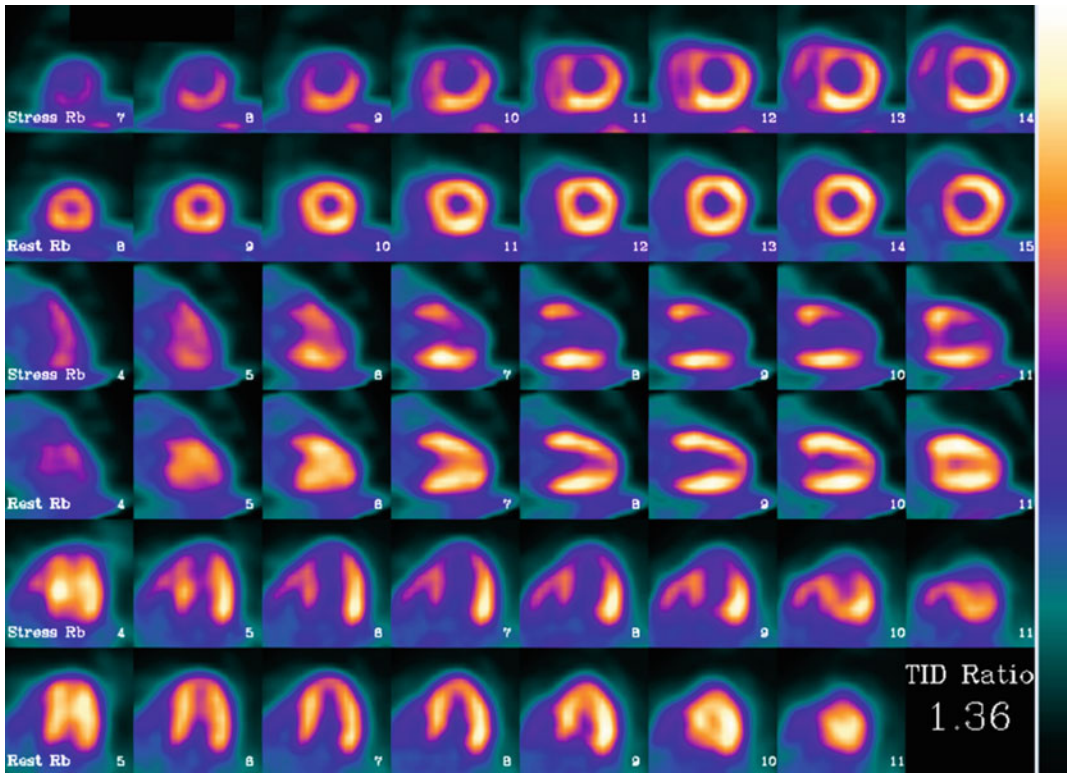

Fig. 1 Abnormal rubidium-82 PET myocardial perfusion scan at stress and rest. Short axis (*top rows*) vertical long axis (*middle rows*) and horizontal long axis (*bottom rows*) slices demonstrate severe and extensive ischemia involving the anterior, apical and septal walls. The left ventricular (*LV*) cavity is dilated on stress imaging consistent with transient ischemic dilation, a poor prognostic factor. Furthermore, on gated images (not shown), the patient's LV ejection fraction decreased from 68% at rest to 46% during stress, an additional indicator of poor prognosis. Finally, the calculated coronary flow reserve was 0.92, which is severely decreased. Cardiac catheterization performed 1 day later confirmed the presence of severe triple vessel coronary artery disease

tumors of the heart are much less common. A review of 480,331 autopsies found primary cardiac tumors in only 0.0017% [46, 47]. Sarcomas account for about 95% of primary malignant tumors, while lymphoma accounts for the remainder [48]. The lesions are usually detected and characterized with ultrasound, contrast-enhanced CT, or MRI, while radionuclide techniques such as [^{18}F]FDG PET/CT, myocardial perfusion studies, or receptor-specific imaging may contribute valuable supplementary data.

Secondary tumors occur 100–1,000 times more frequently than primary tumors [49]. Autopsy studies demonstrate that at the time of demise, ~10% of patients with metastatic tumors have myocardial or pericardial involvement. Cardiac involvement occurs by direct extension or by hematogenous or retrograde lymphatic spread [50]. Cardiac involvement impairs function in ~30% of patients. Depending on the etiology, myocardial involvement may be seen on myocardial perfusion images (usually as a focal area of deceased perfusion), on [^{18}F]FDG PET/CT (especially in patients with minimal physiologic myocardial [^{18}F]FDG uptake), as a focal region of increased [^{18}F]FDG localization (particularly in patients with metastatic melanoma or lymphoma), or with receptor agents such as ^{111}In-pentetreotide (as a focal region of increased myocardial localization) (Fig. 2). Metastatic tumors that involve the pericardium include lung cancer and breast cancer (usually by direct involvement), leukemia, melanoma, and lymphoma [51]. Pericardial involvement can result in pericardial effusion, cardiac tamponade, or less frequently constrictive pericarditis. Long-term survivors of breast cancer or lymphoma (particularly those treated with radiation) may have chronic constrictive pericarditis.

When focal [^{18}F]FDG uptake is seen in the atria, it is important to distinguish uptake in lipomatous hypertrophy of the interatrial septum (LHIS), which is a benign process [52], from metastatic tumor involvement (Fig. 3). This phenomenon on [^{18}F]FDG PET is akin to uptake within metabolically active brown fat deposits more commonly seen at other anatomic sites, such as the supraclavicular region, and the intensity of uptake may vary from scan to scan [53]. LHIS is more prevalent with obesity and advanced age and may be associated with atrial arrhythmias [54]. In patients with lung cancer, esophageal cancer, or metastatic melanoma, with lesions adjacent to the heart, additional imaging studies, such as cardiac MRI (C-MRI), may be required to distinguish between LHIS and a cardiac neoplasm.

A more frequent nonneoplastic finding that may be confused with tumor situated in or adjacent to the heart is when intense [^{18}F]FDG uptake is present within the wall of the right atrium. While physiologic [^{18}F]FDG uptake in the ventricular myocardium (left more than right) is relatively ubiquitous (albeit variable in intensity, depending on the patient's glycemic/insulinemic state), uptake is not typically seen in the myocardium of the atria in the absence of altered cardiovascular physiology. When right atrial wall uptake does occur, it is usually associated with atrial fibrillation [55, 56], paced rhythms, sinus tachycardia, or other tachyarrhythmias.

Cardiac Amyloidosis

Systemic amyloidosis is associated with significant morbidity and poor overall survival, particularly after organ-specific damage has occurred. Cardiac involvement, in particular, leads to arrhythmias and progressive cardiomyopathy. Myocardial infiltration is manifested by increased wall thickening, which is difficult to distinguish from other causes of hypertrophy (e.g., hypertension, aortic stenosis) on conventional imaging techniques. There are two main types of cardiac amyloid infiltration: monoclonal immunoglobulin light chain (AL amyloid) and transthyretin (ATTR), with the former carrying a much worse prognosis [57]. Endomyocardial biopsy is currently the gold standard for diagnosis of cardiac amyloidosis, but this invasive procedure carries inherent risks. C-MRI is an established imaging modality for detection of myocardial infiltration (extracellular matrix expansion), which is characterized by late gadolinium enhancement (LGE). However, LGE is not specific for amyloid on a

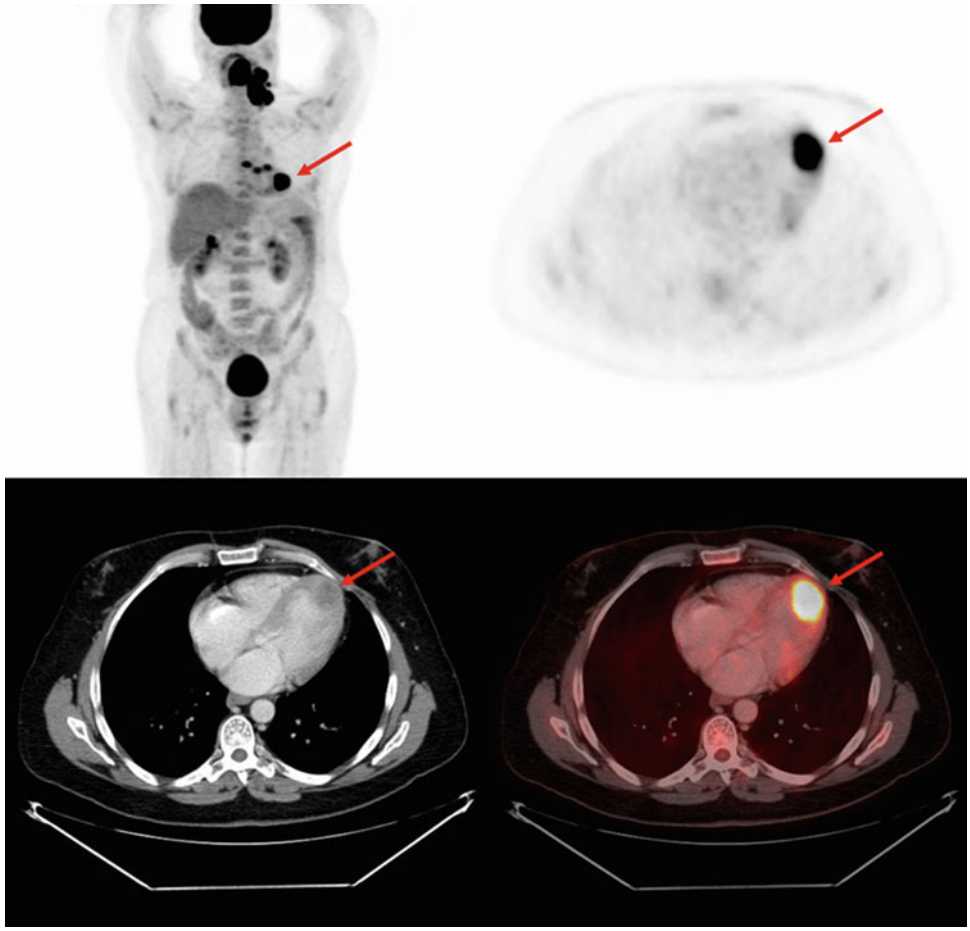

Fig. 2 Abnormal myocardial uptake of [^{18}F]FDG secondary to involvement by lymphoma. *Top left panel:* Maximum intensity projection (*MIP*) image of a patient with multiple [^{18}F]FDG-avid lymphomatous lesions in the neck and chest. *Other panels:* Axial PET, axial CT and axial fused PET/CT slices showing intense focal [^{18}F]FDG uptake at the apex of the left ventricle corresponding to a low attenuation mass in the myocardium, representing a lymphomatous deposit (*red arrows*)

molecular level, nor is it readily quantified. C-MRI currently lacks sensitivity for very early cardiac involvement and is unable to assess multi-organ involvement. A number of single-photon molecular imaging techniques suggested for the evaluation of cardiac amyloidosis have shown limited clinical promise, including ^{99m}Tc-aprotinin, a polypeptide protease inhibitor for targeting of anti-proteases within cardiac amyloid deposits [58]. ^{99m}Tc-pyrophosphate, traditionally a bone tracer, has gained traction in recent years, especially for the purpose of distinguishing between AL amyloid and ATTR [59]. Nevertheless, ^{99m}Tc-pyrophosphate is inherently limited by its lack of specificity for amyloid fibrils and difficulty in quantifying the degree of uptake, owing to the single-photon nature of the radionuclide.

PET probes with proven efficacy for detection of amyloid-beta fibril deposits in the brains of patients with Alzheimer's disease are now being evaluated for use in systemic amyloidosis. Three such tracers, ^{18}F-florbetaben, ^{18}F-florbetapir, and ^{18}F-flutemetamol, are approved by the U.S. Food and Drug Administration for use in the evaluation of Alzheimer's disease. Preliminary data suggest that these thioflavin T derivative PET tracers are not

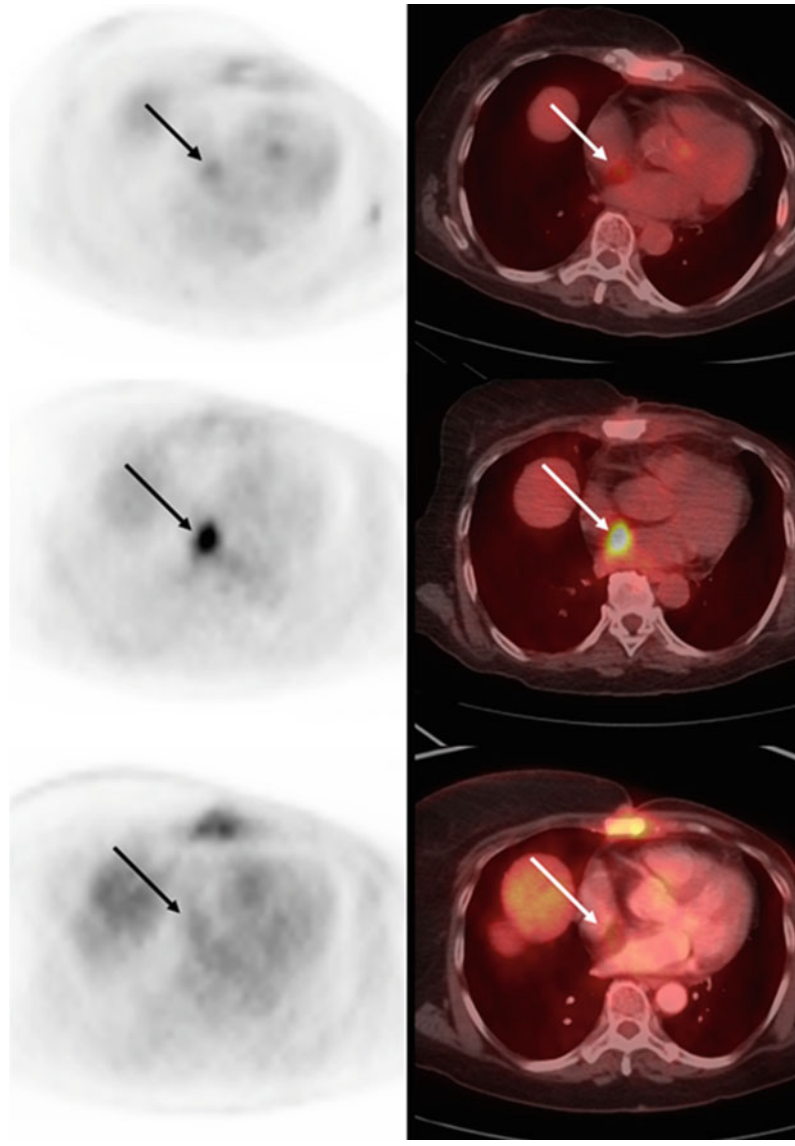

Fig. 3 Temporal variability of *benign* [^{18}F] FDG uptake associated with lipomatous hypertrophy of the interatrial septum (*LHIS*) in a patient with metastatic breast cancer. Axial PET (*left*) and axial fused PET/CT (*right*) slices of the chest at baseline (*bottom panels*), 12 month followup (*middle panels*) and 19 months followup (*top panels*) demonstrate variable levels of [^{18}F]FDG uptake in the atrial septum corresponding to a fat density structure on CT

only effective for imaging amyloid fibril deposits in brains but are also capable of binding to and imaging amyloid deposits in the myocardium.

The first in-human study demonstrating the feasibility of amyloid-avid PET imaging for cardiac amyloidosis used the tracer ^{11}C-PiB [60]. Ten patients diagnosed with systemic amyloidosis, including heart involvement of either AL or ATTR type, and five healthy volunteers were investigated. Myocardial ^{11}C-PiB uptake was visually evident in all patients 15–25 min after injection and was not seen in any control subject. A significant difference in ^{11}C-PiB retention in the heart was noted between patients and healthy controls. The authors concluded that ^{11}C-PiB and PET could be a method for studying systemic amyloidosis of type AL and ATTR affecting the heart and should be investigated further both as a diagnostic tool and as a noninvasive method for treatment follow-up.

A second study using ^{11}C-PiB PET/CT [61] demonstrated positive uptake in 13 of 15 biopsy-proven cardiac amyloidosis patients. No uptake was detected in five patients with no evidence of

cardiac amyloidosis on endomyocardial biopsy or in ten normal subjects. The maximal myocardium-to-blood cavity ratio was significantly different between patients with versus patients without cardiac amyloidosis (median 3.9 [range 1.7–19.9] vs. 1.0 [range 0.8–1.2], $p < 0.001$). Five patients who received prior chemotherapy had less uptake than did chemo-naive patients (2.3 [range 1.7–3.8] vs. median 10.4 [range 1.7–19.9] $p = 0.014$). The investigators therefore suggested that ^{11}C-PiB PET/CT may be a good surrogate marker of active light chain deposition in the myocardium warranting further investigation in a larger number of patients.

Dorbala et al. were the first to show the utility of ^{18}F-florbetapir for imaging cardiac amyloidosis [62]. They imaged five control subjects without amyloidosis and nine subjects with documented cardiac amyloidosis, transthyretin, and light chain amyloid. Left and right ventricular myocardial uptake of ^{18}F-florbetapir was noted in all the amyloid subjects and in none of the control subjects. Quantitative measures including a retention index and standardized uptake value (SUV) parameters were significantly higher in the amyloidosis subjects than in the control group.

Osborne and colleagues [63] confirmed the findings of Dorbala et al. by similarly demonstrating positive florbetapir uptake in eight amyloid patients and no uptake in three healthy controls. In addition, quantitative SUV analysis with regions drawn in the septal wall was found to be adequate in differentiating healthy controls from amyloid-positive patients in this small cohort.

The utility of ^{18}F-florbetapir for imaging cardiac amyloid was corroborated by Park et al. using human autopsy myocardial specimens [64]. They examined sections from 30 subjects with autopsy-documented AL ($n = 10$), ATTR ($n = 10$), and non-amyloid controls ($n = 10$) using ^{18}F-florbetapir and cold florbetapir compound and digital autoradiography. Diffuse or focally increased ^{18}F-florbetapir uptake was noted in all AL and ATTR samples and in none of the control samples. Compared with control samples, mean ^{18}F-florbetapir-specific uptake was significantly higher in the amyloid samples ($p < 0.001$) and, interestingly, in the AL compared with the ATTR samples ($p < 0.001$). They concluded that ^{18}F-florbetapir binds specifically to myocardial AL and ATTR deposits in humans and offers the potential to screen for these two most common types of myocardial amyloid.

Finally, Law et al. [65] recently demonstrated the efficacy of ^{18}F-florbetaben PET for detection of cardiac amyloid deposition. They studied five patients with AL amyloid, five with ATTR amyloid, and four control subjects with hypertensive heart disease. Target-to-background SUV ratio and percentage myocardial ^{18}F-forbetaben retention were noted to be higher in amyloid patients compared with hypertensive control subjects. A cutoff value of 40% was able to differentiate between cardiac amyloid patients and hypertensive control subjects. Percentage myocardial ^{18}F-forbetaben retention was an independent determinant of both global left ventricular longitudinal and right ventricular free wall longitudinal strain on echocardiogram via an inverse curve relationship.

Taken together, this small series of preliminary studies indicates that thioflavin T PET analogs are promising for detecting and quantifying amyloid deposition in the heart of patients with cardiac amyloidosis. Furthermore, these PET tracers may be able to distinguish between light chain and transthyretin deposition.

Cardiac Function

First-pass radionuclide ventriculography (RVG) and equilibrium blood pool imaging (often called MUGA for “multigated acquisition”) techniques were developed in the early 1970s [66]. Initial studies reported an excellent correlation of RVG-derived LVEF with values obtained by contrast ventriculography at cardiac catheterization [67–69]. At its inception, a major indication for RVG was the serial monitoring of cardiac function in patients with coronary artery disease. The technique was subsequently applied to the serial evaluation of patients receiving cardiotoxic therapies [70] and remains so today. Cancer patients who receive systemic chemotherapy are at risk for early and late cardiovascular complications (Table 2 [71]).

Table 2 Important cardiovascular side effects of cancer drugs

Side effect	Cancer drug	Rate/incidence	Mechanism	Reversible	Irreversible
Cardiovascular ischemia	Antimetabolites				
	5-Fluorouracil	Frequent	Vasoconstriction	+++	+
	Capecitabine	Infrequent	Vasoconstriction	+++	+
	Anti-VEGF drugs				
	Bevacizumab	≤3.8%	Arterial thromboembolism		+++
	Sunitinib	≤3%	Arterial thromboembolism		+++
	Sorafenib	≤3%	Arterial thromboembolism		+++
Arrhythmias	Anthracyclines	Dose dependent	Supraventricular	++	
			Calcium overload		
	Anti-HER2/ErbB2				
	Lapatinib		QTc prolongation, torsade		
	Anti-VEGF drugs				
	Sunitinib	Dose dependent	QTc prolongation, torsade		
Contractile dysfunction/ heart failure	Anthracyclines	Dose dependent	Myocardial cell death		+++
	Anti-HER2/ErbB2				
	Trastuzumab	Dysfunction 3–18.1%	Myofibrillar disorganization	+++	+
		Heart failure 0.4–3.6%		+	+
	Lapatinib	Dysfunction 1.4%	?	+	
		Heart failure 0.2%		+	
	Anti-VEGF drugs				
	Bevacizumab	Heart failure 1–3%	?	+	
	Sunitinib	Heart failure 8–15%	Mitochondrial dysfunction	+	
Arterial hypertension	Anti-VEGF drugs				
	Bevacizumab	Any grade			
		Grade 3/4			
	Sunitinib	Any grade			
		Grade 3/4			
	Sorafenib	Any grade			
		Grade 3/4			

+ rare, ++ common, +++ frequent, *grade* NCI Common Terminology Criteria for Adverse Events (CTCAE) version 3

Acute manifestations of chemotherapy-related cardiotoxicity include hypertension, QTc prolongation, pericarditis and/or myocarditis-like syndromes, supraventricular and ventricular arrhythmias, and acute coronary syndromes. Acute complications can occur anytime from the onset of therapy up to 2 weeks after termination of treatment but rarely cause clinical symptoms and usually resolve spontaneously. Many of these effects are dose related and transient and are

often ameliorated by withdrawal of the drug or reduction of the dose. Chronic cardiotoxicity may occur early, within 1 year after completion of chemotherapy, or late, more than 1 year after chemotherapy. Both early- and late-onset chronic cardiotoxicity may culminate in an irreversible cardiomyopathy.

Chronic Cardiotoxicity

Two forms of chronic chemotherapy-related cardiac dysfunction (CRCD) are now recognized: type I and type II [72]. Type I CRCD is exemplified by anthracycline-associated cardiac toxicity, which is clearly dose related, generally irreversible, and associated with characteristic ultrastructural abnormalities. Type II CRCD is epitomized by the toxicity related to the monoclonal antibody trastuzumab, which does not appear to be dose related and is not associated with significant ultrastructural abnormalities. Type II CRCD also appears to be reversible, with a high likelihood of recovery.

Type I CRCD

Doxorubicin (or adriamycin [73]) and other anthracyclines are among the most effective classes of cancer therapy. Unfortunately, the benefits of anthracycline chemotherapy are tempered by potentially serious cardiotoxic effects, which were recognized shortly after the drugs were introduced in the late 1960s [74–76]. The cardiotoxic effects have a dose–response relationship, similar to the antitumor effects of the drug. Despite the medical community's vast experience with this agent, cardiotoxicity remains highly problematic and oncologists and cardiologists continue to struggle with the Hippocratic dictum, "first, do no harm" [77].

The antitumor properties of anthracyclines stem from their ability to intercalate between DNA base pairs of replicating cells, causing DNA fragmentation, inhibition of polymerases, and decreased synthesis of DNA, RNA, and proteins [78]. DNA damage is thought to be mediated in part through targeting of topoisomerase IIα [79]. Doxorubicin is also a powerful iron chelator, with iron-mediated generation of free radicals resulting in the cleavage of DNA and cell membranes. The cardiotoxicity of anthracyclines apparently results from myocyte damage due to toxic free radicals and an increase in oxidative stress, which causes lipid peroxidation of membranes, leading to vacuolization. Myocyte damage is associated with a decrease in endogenous antioxidant enzymes, such as glutathione peroxidase, that are responsible for the scavenging of free radicals [80]. Each successive dose of anthracycline results in incremental cardiac myocyte death and replacement by fibrous tissue. Eventually the compensatory mechanisms of the heart are overwhelmed and dilated cardiomyopathy ensues.

Anthracycline-induced cardiotoxicity can be directly diagnosed by endomyocardial biopsy. This is best assessed by electron microscopy, with characteristic changes that include myofibrillary bundle depletion, myofibrillar lysis, distortion and disruption of the Z-lines, mitochondrial disruption, and intramyocyte vacuolization [81]. Billingham and coworkers [82] found that morphologic damage seen on right ventricular biopsy and quantified on a four-point scale (0 = no damage, 4 = diffuse damage) was related ($r = 0.50$) to the total cumulative doxorubicin dose between 100 and 600 mg/m^2. Morphologic changes were more closely related to cumulative dose in patients who received prior mediastinal radiation ($r = 0.65$). In the same cohort, myocardial performance was preserved until a critical threshold dose of 550 mg/m^2 was reached, after which function deteriorated, echoing the findings of Lefrak et al. A study of 158 patients who underwent single or serial endomyocardial biopsies suggested that the Billingham grading system had greater sensitivity and specificity for early detection of dose-related toxicity ($p < 0.02$) than noninvasive assessment of left ventricular function by gated blood pool studies or M-mode echocardiography [83].

A postmortem study of anthracycline-treated patients similarly found histopathologic changes by light microscopy in 23 of 44 (52%) patients with no clinical signs of cardiotoxicity [84]. Although no histopathologic evidence of toxicity was

identified in seven of 20 (35%) patients who did express clinical signs of cardiotoxicity, this may be attributed to the lower sensitivity of light microscopy for detection of characteristic morphologic changes, when compared with electron microscopy techniques. These tissue-correlation studies suggest that morphologic alterations precede functional deterioration. Hence, endomyocardial biopsy with electron microscopy was given Class IIa recommendation for the assessment of suspected anthracycline-induced cardiomyopathy, based primarily on expert consensus [85].

Noninvasive Monitoring of Anthracycline Toxicity

Despite the high sensitivity and specificity of endomyocardial biopsy, it is not a practical method of patient monitoring given its invasive nature, inherent risks, and expense. Many investigators originally advocated for empiric discontinuation of anthracycline administration after reaching a threshold cumulative dose, based on population-wide data. In 1973, Lefrak et al. [86] found that clinically overt congestive heart failure (CHF) occurred only once in the 366 patients (0.27%) who were treated with less than 550 mg/m^2 of adriamycin, but ten cases were seen in 33 patients (30%) who received more than 550 mg/m^2. Consequently, an empiric restriction of 550 mg/m^2 maximum cumulative dose was recommended for all patients. In a retrospective analysis, however, Von Hoff et al. [87] estimated that 3% of patients developed CHF at a cumulative doxorubicin dose of 400 mg/m^2, 7% at 550 mg/m^2, and 18% at 700 mg/m^2, strongly suggesting an increasing risk of clinical toxicity over a continuum of cumulative doses, debunking the existence of a critical threshold. A more recent retrospective analysis of three prospective studies confirmed the nature of this exponential dose–toxicity relationship and indicated that the incidence of clinical toxicity was grossly underestimated in earlier studies. The percentage of patients with doxorubicin-related CHF was 5.0% at a cumulative dose of 400 mg/m^2, 16% at 500 mg/m^2, 26.0% at 550 mg/m^2, and 48.0% at 700 mg/m^2 [88]. The notorious unpredictability of clinical cardiotoxicity in individuals, and evidence for a $y = x^2$ dose–toxicity relationship among populations [89], has rendered empiric dose limitation obsolete. High cumulative doses, nonetheless, remain an overwhelming risk factor.

In 1979, Alexander et al. [70] reported the utility of RVG as a marker for early detection of anthracycline-related cardiotoxicity by serially monitoring of the LVEF. RVG studies were performed on 51 patients treated with doxorubicin for various types of tumors. Five developed clinical signs of heart failure at doxorubicin doses ranging from 490 to 715 mg/m^2. Absolute declines in the LVEF by more than 15% were noted prior to the development of CHF, which was clinically evident only when the LVEF declined to less than 30%. In six patients with an asymptomatic absolute decline in LVEF of 15% or less at doxorubicin doses of 460–900 mg/m^2, doxorubicin was discontinued and none developed overt heart failure. Repeat measurement of LVEF several months after stopping doxorubicin showed a modest improvement in LVEF in all patients.

In 1987, Schwartz and coworkers published guidelines for surveillance of anthracycline-induced cardiotoxicity based on their experience with RVG over a 7-year period (see Table 3) [90]. In short, baseline LVEF, absolute change in LVEF, and final LVEF were determinants. They retrospectively analyzed 282 serially monitored high-risk patients and found that heart failure developed in only two (3%) of 70 patients monitored according to these guidelines. By comparison, CHF developed in 44 of 212 high-risk patients (21%) in whom the guidelines were incompletely followed (Fig. 4). Multivariate analysis demonstrated a nearly fourfold risk reduction in development of CHF in those managed according to guidelines. In the 46 patients who developed CHF, a mean decline in LVEF of $23 \pm 14\%$ was noted versus a decline of 12 ± 10 in those who did not subsequently develop CHF ($p < 0.001$). While these guidelines have never been prospectively validated, they are still widely accepted today. These guidelines, with an updated discussion and literature review, were updated in 2016 [91].

Table 3 Guidelines for monitoring patients receiving doxorubicin

Perform baseline radionuclide angiocardiography at rest for calculation of left ventricular ejection fraction (LVEF) prior to administration of 100 mg/m^2 doxorubicin. Subsequent studies are performed at least 3 weeks after the indicated total cumulative doses have been given, before consideration of the next dose
Patients with normal baseline LVEF (≥50%)
Perform the second study after 250–300 mg/m^2
Repeat study after 400 mg/m^2 in patients with known heart disease, radiation exposure, abnormal electrocardiographic results, or cyclophosphamide therapy or after 450 mg/m^2 in the absence of arty of these risk factors
Perform sequential studies thereafter prior to each dose
Discontinue doxorubicin therapy once functional criteria for cardiotoxicity develop, i.e., absolute decrease in LVEF ≥10% (EF units) associated with a decline to a level ≤50% (EF units)
Patients with abnormal baseline LVEF (<50%)
Doxorubicin therapy should not be initiated with baseline LVEF ≤30%
In patients with LVEF >30% and <50%, sequential studies should be obtained prior to each dose
Discontinue doxorubicin with cardiotoxicity: absolute decrease in LVEF ≥10% (EF units) and/or final LVEF ≤30%

Risk Factors for Type 1 CRCD

There are many known risk factors for anthracycline-induced cardiotoxicity, in addition to cumulative dose. The pediatric population appears to be more prone to cardiotoxicity at lower cumulative anthracycline doses (250–300 mg/m^2) [92]. At the opposite end of the spectrum, patients older than 65–70 years are also more susceptible to toxicity, probably due to comorbidity of underlying heart disease and/or decreased functional reserve. In one study, after a cumulative dose of 400 m/m^2, patients older than 65 were more than three times more likely to develop CHF than patients younger than 65 (hazard ratio [HR], 3.28; 95% CI, 1.4–7.65, $p = 0.002$) [[54]]. Other drugs, such as cyclophosphamide and trastuzumab (as will be discussed), can augment the cardiotoxic effects of anthracyclines. Chest radiation, either previously or concurrent with chemotherapy probably, increases the risk of cardiotoxicity, possibly due to endothelial cell damage caused by radiation. This factor is particularly relevant for women with breast cancer who often receive radiotherapy to the chest wall or for lymphoma patients who often undergo mediastinal irradiation. Studies indicate a higher risk of toxicity in patients with left-sided breast cancer, due to the proximity to the cardiac vessels and the myocardium. One long-term study of contemporary external beam radiation techniques, however, showed that left-sided targeting is not associated with a higher risk of cardiac death up to 20 years after treatment, but is nevertheless associated with an increased rate of coronary artery disease and MI compared with right breast treatment [93]. Several risk factors were recently elucidated in a SEER data analysis of 43,338 women with breast cancer [94]. After 10 years of follow-up, 38% of women who were treated with anthracyclines at age 66–70 eventually developed CHF with a statistically significant increase in absolute risk of 5.9% and 9.7% when compared with those who received non-anthracycline regimens or no chemotherapy, respectively. This difference was not seen in women at age 71–80, possibly because of higher baseline rates of CHF in this age group because of selection bias, with the healthier women qualifying for anthracycline regimens. Specific predictors of CHF also included years elapsed since therapy (HR, 1.79 per 10 years; 95% CI, 1.66–1.93), Black race (HR, 1.40; 95% CI, 1.30– 1.50), trastuzumab treatment (HR, 1.46; 95% CI, 1.21–1.77), hypertension (HR, 1.45; 95% CI, 1.39–1.52), diabetes (HR, 1.74; 95% CI, 1.66–1.83), and coronary artery disease (HR, 1.58; 95% CI, 1.39–1.79). Left-sided radiotherapy did not confer a clearly increased risk for CHF (HR, 1.04; 95% CI, 0.98–1.11) in this cohort. Inexplicably, anthracycline-treated patients apparently had fewer cardiology visits and underwent fewer LVEF assessments with RVG or echo than other breast cancer patients ($p < 0.0001$).

Late-Onset Cardiomyopathy and the Pediatric Population

Symptomatic heart failure generally presents less than 1 year after anthracycline administration, but as suggested in the SEER data, heart failure

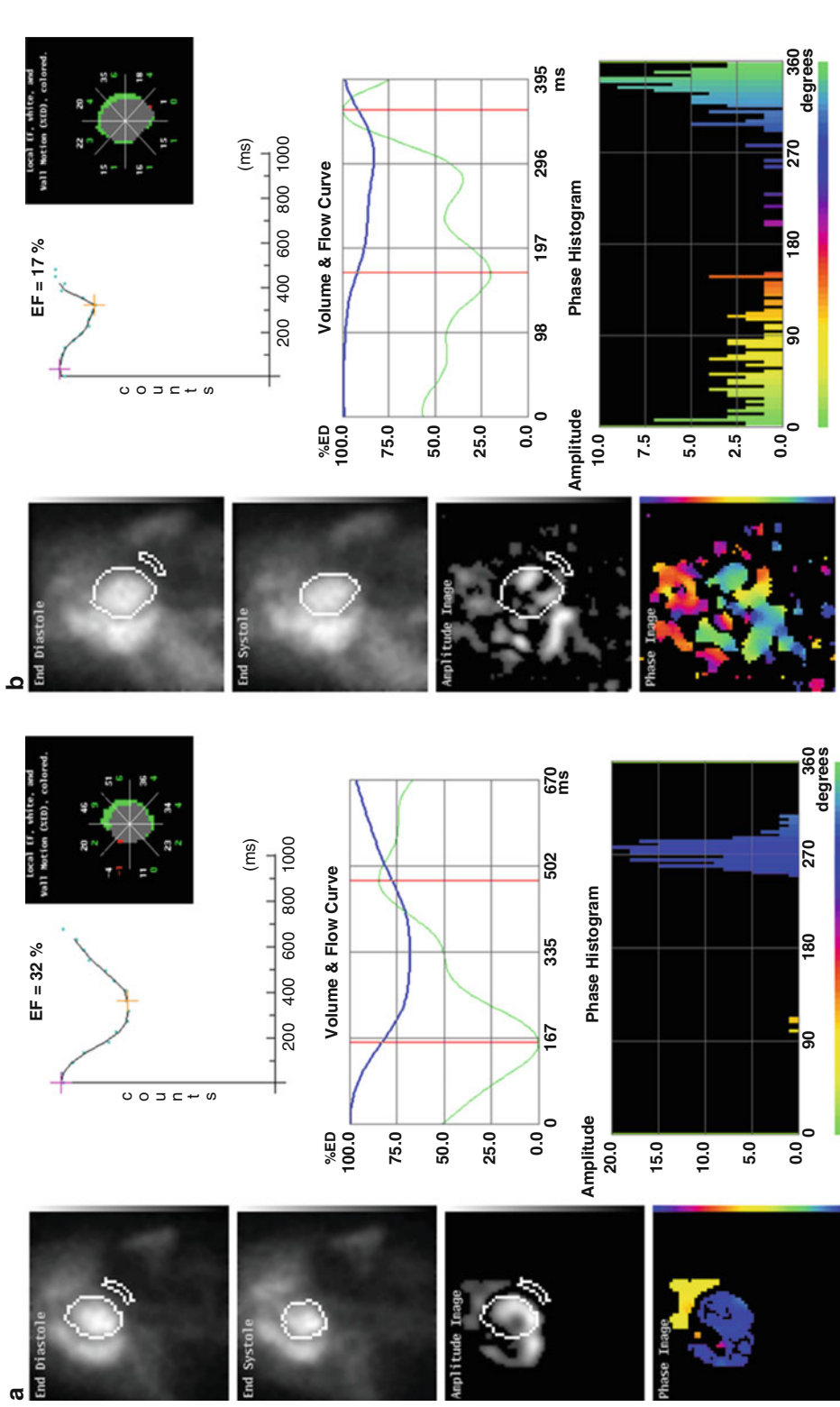

Fig. 4 Example of patient diagnosed with Hodgkin lymphoma at age 24 who developed progressive late-onset cardiomyopathy >10 years after receiving a cumulative doxorubicin dose of 200 mg/m^2 and concurrent XRT to the chest, followed by autologous stem cell transplant. (**a**) Rest RVG 13 years after doxorubicin therapy, LVEF = 32%, asymptomatic. (**b**) Rest RVG 20 years after therapy, LVEF = 17% (20% by echocardiography), NYHA Class III-IV HF

develops in a subset of patients after a latency period of more than a decade. Strong evidence for "late-late" development of cardiomyopathy is primarily derived from pediatric cancer survivors, as seen in the early 1990s [95, 96]. Recent analyses of late cardiotoxicity in childhood cancer survivors confirm that survivors are at increased risk for many cardiac complications, foremost heart failure [97]. The cumulative incidence of adverse cardiac outcomes in cancer survivors appears to continue to increase up to 30 years after diagnosis, at which point more than 7.5% of patients who received a cumulative dose of more than 250 mg/m^2 will have developed heart failure [98]. Guidelines were proposed by the Cardiology Committee of the Children's Cancer Study Group for monitoring acute and late manifestations of doxorubicin cardiotoxicity [99]. For pediatric patients, echocardiography is the preferred method of surveillance to minimize exposure to radiation, with the more reproducible RVG reserved for confirmation of LVEF decline in high-risk patients.

Type II CRCD

Trastuzumab is a humanized monoclonal antibody that targets the extracellular domain of human epidermal growth factor receptor 2 (HER2 also referred to as HER2/neu or erbB-2), a transmembrane tyrosine kinase receptor. Interaction of the antibody with the target inhibits signal transduction, resulting in decreased tumor cell growth and survival. Approximately 25% of newly diagnosed patients with invasive breast cancers overexpress HER2 and are more likely to have an aggressive form of the disease with shortened relapse-free survival and reduced overall survival [100]. In HER2-overexpressing breast cancers, treatment with trastuzumab confers a clear survival benefit in the metastatic and adjuvant settings, both as monotherapy and in combination with cytotoxic agents. Trastuzumab-associated heart failure was recognized in the initial trials of patients with metastatic breast cancer, and a small but significant risk has been repeatedly documented in the adjuvant setting. Pure type II CRCD manifests as a loss of myocardial contractility and is less likely to cause myocyte death. The underlying pathophysiologic mechanism for this dysfunction is not fully understood, but it is believed to be directly related to inhibition of HER2 signaling, which apparently plays an essential role in the heart's compensatory mechanisms following exposure to stress. Preclinical models support this notion, as *erb2* knockout mice tend to develop cardiomyopathy following induction of cardiac stress pathways [101]. Interestingly, these mutant mice are also more susceptible to anthracycline-induced cell death, suggesting a synergistic toxicity. Similarly, limited scintigraphic data indicate that myocardial HER2 expression is upregulated shortly after anthracycline-based chemotherapy, as detected by myocardial uptake on ^{111}In-DTPA-trastuzumab SPECT imaging [102]. One clinical study indicated that serum HER2 levels are increased in patients with depressed LVEF and chronic heart failure [103]. Clinically, patients who have never received anthracyclines do develop cardiac toxicity [104], but the risk is clearly higher in patients who have been treated concurrently or previously with anthracyclines and to a lesser degree with taxanes [105]. This risk of toxicity appears to decrease with longer intervals between the administration of the two drugs. Because trastuzumab has a long half-life, these synergistic effects may come to the fore even when anthracyclines are given after trastuzumab has already been discontinued.

A number of studies suggest that type II CRCD is potentially reversible, including the pivotal phase III trial of trastuzumab [106]. In one study by Ewer et al., 38 patients with HER2-positive breast cancer previously treated with doxorubicin developed cardiotoxicity after trastuzumab therapy, which generally improved after withdrawal of the drug. These patients were safely rechallenged with trastuzumab after the cardiac manifestations abated [107]. After doxorubicin but before trastuzumab, the mean LVEF was 0.61 $\pm$ 0.13, and the LVEF decreased to 0.43 $\pm$ 0.16 after trastuzumab ($p < .0001$). After withdrawal of trastuzumab, LVEF increased to 0.56 $\pm$ 0.11. Mean time to recovery of LVEF was 1.5 months and was temporally associated with medical treatment in 32 (84%) of the 38 patients but occurred without treatment in

six patients (16%). Increases in LVEF were noted in 37 of the 38 patients. Subsequently, 25 of these patients were re-treated with trastuzumab; three patients had recurrent LV dysfunction, but 22 patients (88%) did not. Importantly, in nine patients who underwent endomyocardial biopsy, no ultrastructural changes were seen.

Guarneri et al. evaluated the safety of trastuzumab therapy (median 21.3 months of administration) in 173 patients with metastatic breast cancer [108]. After a median follow-up of 32.6 months, 49 patients (28.3%) experienced a cardiac event: three patients (1.7%) had an asymptomatic decrease in the LVEF of 20%; 46 patients (26.6%) experienced grade 2–3 cardiac toxicity; one cardiac-related death was noted (0.5%). LVEF or symptoms of CHF improved in all but three patients with trastuzumab discontinuation and appropriate therapy, suggesting that toxicity is manageable and generally reversible. Interestingly, baseline LVEF was significantly associated with cardiac events (HR, 0.94; $p < 0.001$).

The HERA trial was a large three-group, randomized trial that compared 1,698 patients randomly assigned to observation and 1,703 randomly assigned to 1 year of trastuzumab treatment. The majority (94.1%) of patients had previously been treated with anthracyclines. Eligible patients had normal LVEF (defined as $\geq$55%) after completion of neo/adjuvant chemotherapy with or without radiotherapy. Trastuzumab was discontinued in 5.1% of patients owing to a cardiac disorder. At a median follow-up of 3.6 years, the incidence of cardiac end points remained low, although it was higher in the trastuzumab group than in the observation group (severe CHF, 0.8% vs. 0.0%; confirmed significant LVEF decreases, 3.6% vs. 0.6%). Roughly 80% (59/73) of those who developed cardiac end points in the trastuzumab group recovered. This important study suggests that the incidence of cardiac end points remains low even after longer-term follow-up [109].

Monitoring and Management

The optimal approach for monitoring of trastuzumab-related cardiotoxicity, as with anthracyclines, lacks complete international consensus. Proposed guidelines from MSKCC are outlined in Table 4 [110].

Similar guidelines were incorporated in the HERA trial [111].

Reducing Cardiotoxicity

Several approaches help reduce the incidence of therapy-associated cardiovascular complications. Patients should be screened for pre-existing cardiac disease, especially valvular disease and cardiomyopathy. A threshold for cumulative dose is controversial in the era of advanced monitoring techniques. Modifying anthracycline administration by prolonged infusions and liposomal formulations has met variable success. Dexrazoxane, an EDTA-like chelator, is thought to prevent anthracycline cardiotoxicity by its ability to bind iron thus preventing free radical formation. Despite the apparent cardiac benefit, the possibility of mitigating the antitumor effect has raised concern regarding the use of dexrazoxane as a cardioprotectant (ASCO guidelines 2008 [112]). Cardioactive medications, such as angiotensin-converting enzyme (ACE) inhibitors and the combined beta- and alpha-blocker carvedilol, are useful in anthracycline- and trastuzumab-induced cardiomyopathy, particularly when started early after cancer therapy [113, 114]. There is also evidence for beneficial effects of statins in this setting [115]. When appropriate, consideration should be given to alternative classes of chemotherapies, such as taxane-based therapies, or other tyrosine kinase inhibitors, for instance, lapatinib [116].

RVG Versus Other Imaging Modalities

Before discussing comparative performance of different modalities for measuring LVEF, it should be emphasized that all sequential measurements of LVEF are subject to inherent physiologic variability owing to hemodynamic, metabolic, hormonal, and pharmacologic factors, etc. One group sought to determine the limits of this variability by performing a double-blind placebo-controlled study in 39 patients who underwent two assessments separated by a 6-week placebo period, during which patients were deemed clinically stable [117]. While the total mean LEVF did not change significantly, LVEFs were quite variable on an individual basis. They determined that inherent variation in contractility is accounted for

Table 4 Proposed guidelines for the management of patients with metastatic disease who are treated with trastuzumab, based on physical status and left ventricular ejection fraction (LVEF)

Physical status[a]	LVEF	Trastuzumab	LVEF monitoring	Management
Asymptomatic	↓but normal	Continue	Repeat in 4 weeks	
	↓ >10 points but normal	Continue	Repeat in 4 weeks	Consider beta-blockers
	↓10–20 points and LVEF >40%	Continue	Repeat in 2–4 weeks Improved: monitor	Treat with medications for LV dysfunction
			Not improved: stop trastuzumab	
	↓ >20 points to <40% or LVEF < 30%	Hold	Repeat in 2 weeks	Treat with medications for LV dysfunction
			Improved to >A5%: restart trastuzumab	
			Not improved: stop trastuzumab	
Symptomatic	↓ < 10 points	Continue		Search for noncardiac pathology (e.g., anemia)
	↓ > 10 points and LVEF >50%	Continue	Repeat in 2–4 weeks	Treat for CHF
			Stable or improved: continue trastuzumab	
			Worsened: stop trastuzumab	
	↓ > 30 points	Stop		Treat for CHF

[a]Heart and body weight should be monitored weekly. Asymptomatic is defined as changes in heart rate and/or weight but without symptoms of dyspnea on exertion. Symptomatic is defined as a new, spontaneous (i.e., unsolicited) report of symptoms of dyspnea on exertion, pulmonary vascular congestion, or edema (From Keefe [110] with permission)

when the change in LVEF is greater than or equal to 7%. It was estimated that a 4% observed increase or decrease in LVEF following a medical intervention can occur by chance more than 25% of the time in individual patients.

RVG is considered more accurate and reproducible than two-dimensional (2D) echocardiography for assessment of LVEF. Advantages and limitations of RVG are listed in Table 5. The modified in vivo method for red cell labeling [118] is preferred over the in vitro and in vivo methods as it provides ease, safety, and high efficiency (92–95%) of labeling.

Normal resting LVEF by equilibrium RVG is greater than 50% as is incorporated into most clinical guidelines and as defined by the Society of Nuclear Medicine. RVG with SPECT has been shown to correlate well with planar-derived LVEF values [119]. SPECT allows for better evaluation of regional wall motion, size, and shape of the left ventricle and does not have the limitation of overlap by other cardiac chambers. Exercise stress RVG may identify a reduced contractility reserve in asymptomatic patients with normal resting LVEF [120]. Measures of diastolic dysfunction obtained on equilibrium RVG may detect toxicity earlier than changes in systolic dysfunction [121].

Advantages of echocardiography include portability, lack of ionizing radiation, and the ability to evaluate other important parameters such as valvular function, wall motion, and hemodynamics, which are better assessed by echocardiography than by RVG. The major disadvantage of echocardiography is the lower reproducibility of LVEF measurement, because of the reliance on geometric assumptions. In addition, patients with – not uncommon – poor acoustic windows are precluded from this procedure. The American Society of Echocardiography and European Society of Echocardiography have defined normal LEVF by echocardiography as greater than 55% for both men and women, although some argue that the lower limit of normal should be redefined to greater than 50% [122]. Three-dimensional

Table 5 Equilibrium radionuclide ventriculography

Advantages	Limitations
Measurements do not rely on geometric assumptions regarding shape of LV	Radiation exposure (6.2 mSv)
Functional information for all cardiac chambers	Limited information regarding structure, in particular of valves
Noninvasive	ECG gating unreliable in patients with significant arrhythmias and variability of RR interval
High accuracy and reproducibility	Limited assessment of ventricular wall thickness
Global and regional LV systolic function can be assessed	Poor technique can introduce errors in measurement
Phase analysis of segmental ventricular contraction conveys information for regional dyssynergy	
Rarely limited by body habitus	Selecting appropriate background in patients with breast prosthesis/tissue expander may be challenging
Relatively easy to perform	

(3D) echocardiography is an increasingly available modality for assessment of systolic function that takes advantage of additional spatial data to provide more accurate estimates for LVEF than two-dimensional (2D) echocardiography. C-MRI is also increasingly available and appears to accurately assess left ventricular systolic function with its high spatial and temporal resolution; however, the high cost of repeated examinations and limited availability render MRI a less-than-ideal for routine monitoring of cardiotoxicity.

Several studies suggest that ejection fraction measurements by various techniques are not interchangeable. A review of eight different studies ($n = 293$) comparing 2D echocardiography with either RVG or contrast angiography exhibited coefficients of correlation ranging from 0.78 to 0.93. Agreement analysis with Bland–Altman plots ranged from 23% to 42% around the mean ejection fraction [123]. A non-oncologic study in patients with chronic stable heart failure who underwent evaluation by M-mode echocardiography, 2D echocardiography, MRI, and RVG showed wide variability in inter-modality measurements, with the narrowest limits of agreement between MRI and RVG at 31% around the mean LVEF [124]. Gopal et al. first demonstrated that 3D echocardiography provides values comparable to RVG and more accurate than 2D echocardiography measurements [125]. A more recent head-to-head study performed in the context of trastuzumab-associated cardiotoxicity confirmed these findings, showing a high correlation ($r = \sim 0.9$) between RVG, 3D echocardiography, and MRI and a weak correlation of these modalities with 2D echocardiography ($r = \sim 0.3–0.4$) for serial LVEF assessment [126]. This suggests that 3D echocardiography and MRI may in fact be interchangeable with RVG as technology continues to improve.

Additional radiopharmaceuticals have been evaluated for the early detection of anthracycline-induced cardiac damage, including necrosis imaging with ^{111}In-antimyosin, apoptosis imaging with ^{99m}Tc-annexin-V, and imaging of cardiac innervation with ^{123}I-MIBG [127]. As of yet, none of these scintigraphic techniques have proven advantageous over imaging of cardiac function with RVG. In particular, the clinical utility of ^{123}I-MIBG is hampered by difficulty with quantifying changes on serial scans. This challenge may be overcome in the near future with the recent development of a quantifiable PET analog of benzylguanidine, ^{18}F-MFBG [128, 129], which is now undergoing evaluation for use in patients with neuroendocrine tumors.

Recommendations

RVG continues to be a widely accepted method for monitoring therapy-related cardiotoxicity in cancer patients. Baseline LVEF assessments should be obtained in all patients receiving anthracyclines and should be strongly considered in patients

Table 6 Chemotherapeutic agents with vascular side effects

Agent	HTN	Angina	AMI	RP	DVT/PE
5-Fluorouracil		X	X	X	
Capecitabine		X	X	X	
Gemcitabine		X	X	X	
Paclitaxel	X	X	X		X
Cisplatin	X	X	X	X	
Cyclophosphamide		X			
Bleomycin		X	X		
Vincristine	X	X	X	X	
Everolimus	X	X			X
Temsirolimus	X	X			X
Bortezomib			X		X
Combretastatin	X	X	X		
Bevacizumab	X	X	X		X
Rituximab	X	X	X		
Sorafenib	X	X	X		X
Sunitinib	X	X	X		X
Interferon	X	X	X	X	X

HTN hypertension, *AMI* acute myocardial infarction, *RP* Raynaud's phenomenon, *DVT/PE* deep venous thrombosis/pulmonary embolus
Modified from table in Herrmann et al. [8] with permission of the author and publisher

receiving trastuzumab, particularly if given before, together with, or following anthracyclines. Risk–benefit ratios should be carefully weighed before initiating or withholding cardiotoxic therapies and are best assessed by dedicated onco-cardiologists or cardio-oncologists. Extreme caution is required when initiating or continuing the drug in patients with the previously specified risk factors, in symptomatic patients, or in patients who have abnormal systolic function at baseline. The lower limit of normal for LVEF by RVG is 50%; however, this value is subject to inter-institutional variability, owing to confounding factors such as the patient population tested, procedure technique and processing, software used for calculation, etc. Echocardiography may be substituted for RVG, particularly in children and those with known valvular abnormalities. The various modalities available for LVEF assessment should not be used interchangeably. Detailed algorithms for monitoring of toxicity by RVG and echocardiography have been provided; however, it should be emphasized that none of these have been prospectively validated. A rule of thumb is that a decline in LVEF of more than 10% to a level below normal (LVEF $<50\%$) is indicative of subclinical toxicity in asymptomatic patients, at which point more intensive monitoring should follow. Investigation with endomyocardial biopsy should be reserved for selective cases where the diagnosis of cardiotoxicity is unclear. In view of the limitations of RVG and echocardiography for early detection of cardiotoxicity, more efficient markers of cardiotoxicity are needed. Well-established serum markers of myocardial damage such as troponins and BNP have demonstrated a clear role in this context [130, 131] but are unlikely to replace serial monitoring of LV systolic function as a marker of toxicity. ACE inhibitors and/or beta-blockers should be considered at the earliest indication of cardiac insult, unless otherwise contraindicated. The list of drugs with potential cardiotoxic effects is increasing (Table 6). As a result, serial measurement of cardiac function is likely to increase as new drugs are developed.

References

1. Sulpher J, Mathur S, Graham N, Crawley F, Turek M, Johnson C, et al. Clinical experience of patients referred to a multidisciplinary cardiac oncology clinic: an observational study. J Oncol. 2015;2015:671232.

2. Bhatti S, Watts E, Syed F, Vallurupalli S, Pandey T, Jambekar K, et al. Clinical and prognostic utility of cardiovascular magnetic resonance imaging in myeloma patients with suspected cardiac amyloidosis. Eur Heart J Cardiovasc Imaging. 2016;17:970–7.
3. Janssen-Heijnen MLK, Houterman S, Lemmens VEPP, Louwman MWJ, Maas HAAM, Coebergh JWW. Prognostic impact of increasing age and co-morbidity in cancer patients: a population-based approach. Crit Rev in Oncology/Hematology. 2005;55:231–40.
4. Ogle KS, Swanson GM, Woods N, Azzouz F. Cancer and comorbidity: redefining chronic diseases. Cancer. 2000;88:653–63.
5. Edwards BK, Noone A-M, Mariotto AB, Simard EP, Boscoe FP, Henley SJ, et al. Annual Report to the Nation on the status of cancer, 1975–2010, featuring prevalence of comorbidity and impact on survival among persons with lung, colorectal, breast, or prostate cancer. Cancer. 2014;129:1290–314.
6. Morton LM, Onel K, Curtis RE, Hungate EA, Armstrong GT. The rising incidence of second cancers: patterns of occurrence and identification of risk factors for children and adults. Am Soc Clin Oncol Educ Book. 2014:e57–67.
7. Hall WH, Ramachandran R, Narayan S, Jani AB, Vijayakumar S. An electronic application for rapidly calculating Charlson comorbidity score. BMC Cancer. 2004;4:94–102.
8. Herrmann J, Yang EH, Illiescu CA, Cilingiroglu M, Charitakis K, Hakeem A, et al. Vascular toxicities of cancer therapies. The old and the new – an evolving avenue. Circulation. 2016;133:1272–89.
9. Devereaux PJ, Sessler DI. Cardiac complications in patients undergoing major noncardiac surgery. New Engl J Med. 2015;373:2258–69.
10. Bartels K, Karhausen J, Clambey ET, Grenz A, Eltzschig HK. Perioperative organ injury. Anesthestiology. 2013;119:1474–89.
11. Fleisher LA, Eagle KA. Lowering cardiac risk in noncardiac surgery. New Eng J Med. 2001;345:1677–82.
12. Mangano DT. Perioperative cardiac mortality. Anesthesiology. 1990;72:153–84.
13. Mozaffarian D, Benjamin EJ, Go AS, Arnett DK, Blaha MJ, Cushman M, et al. Heart disease and stroke statistics - 2015 update: a report from the American Heart Association. Circulation. 2015;131:e29–322.
14. http://www.cancer.org/cancer/cancerbasics/lifetime-probability-of-developing-or-dying-from-cancer. Accessed 3 Apr 2016.
15. https://seer.cancer.gov/statfacts/htm/all.html. Accessed 9 Mar 2016.
16. Mangano DT, Hollenberg M, Fegert G, Meyer ML, London MJ, Tubau JF, Krupski WC. Perioperative myocardial ischemia in patients undergoing noncardiac surgery-I: incidence and severity during the 4 day perioperative period. The Study of Perioperative Ischemia (SPI) Research Group. J Am Coll Cardiol. 1991;17:843–50.
17. London MJ. Cardiovascular problems in noncardiac surgery. Curr Opin Crit Care. 2009;15:333–41.
18. Fisher MB, Svatek RS, Hegarty PK, McGinniss JE, Hightower C, Grossman HB, et al. Cardiac history and risk of post cystectomy cardiac complications. Urology. 2009;74:1085–9.
19. Cruden NLM, Harding SZ, Flapan AD, Graham C, Wild SH, Slack R, et al. Previous coronary stent implantation and cardiac events in patients undergoing noncardiac surgery. Circ Cardiovasc Interv. 2010;3:236–42.
20. Devereaux PJ, Goldman L, Yusuf S, Gilbert K, Leslie K, Guyatt GH. Surveillance and prevention of major perioperative ischemic cardiac events in patients undergoing noncardiac surgery: a review. CMAJ. 2005;173:779–88.
21. Nouraei SAR, Al-Yaghchi C, Sandhu GS, Giussani DA, Doyle P, Clarke PM. Laryngoscope. 2007;117:1581–7.
22. Cohn SL. Postoperative troponin surveillance: a diagnostic dilemma. Cleve Clin J Med. 2015;82:603–5.
23. Dawood MM, Gutpa DK, Southern J, Walia A, Atkinson JB, Eagle KA. Pathology of fatal perioperative myocardial infarction: implications regarding pathophysiology and prevention. Int J Cardiol. 1996;57:37–44.
24. Cohen MC, Artez TH. Histological analysis of coronary artery lesions in fatal postoperative myocardial infarction. Cardiovasc Pathol. 1999;8:133–9.
25. Duvall WL, Sealove B, Pungoti C, Katz D, Moreno P, Kim M. Angiographic investigation of the pathophysiology of perioperative myocardial infarction. Catheter Cardiovasc Interv. 2012;80:768–76.
26. Landesberg G, Mosseri M, Zahger D, Wolf Y, Perouansky M, Anner H, et al. Myocardial infarction after vascular surgery: the role of prolonged stress-induced, ST depression-type ischemia. J Am Coll Cardiol. 2001;37:1839–45.
27. Landesberg G. The pathophysiology of perioperative myocardial infarction: facts and perspectives. J Cardiothorac Vasc Anesth. 2003;17:90–100.
28. Kokkinos P, Faselis C, Myers J, Sui X, Zhang J, Blair SN. Age-specific exercise capacity threshold for mortality risk assessment in male veterans. Circulation. 2014;130:653–8.
29. Weinstein H, Bates AT, Spaltro BE, Thaler HT, Steingart RM. Influence of preoperative exercise capacity on length of stay after thoracic cancer surgery. Ann Thorac Surg. 2007;84:197–202.
30. Lee TH, Marcantonio ER, Mangione CM, Thomas EJ, Polanczyk CA, Cook EF, et al. Derivation and prospective validation of a simple index for prediction of cardiac risk of major noncardiac surgery. Circulation. 1999;100:1043–9.
31. Online calculator. http://www.mdcalc.com/revised-cardiac-risk-index-for-pre-operative-risk/. Accessed 22 May 2016.
32. Devereaux PJ, Goldman L, Cook DJ, Gilbert K, Leslie K, Guyatt GH. Perioperative cardiac events in

patients undergoing noncardiac surgery: a review of the magnitude of the problem, the pathophysiology of the events and methods to estimate and communicate risk. Can Med Assoc J. 2005;173:627–34.
33. Wijeysundera DN, Beattie WS, Austin PC, Hux JE, Laupacis A. Non-invasive cardiac stress testing before elective major non-cardiac surgery: population based cohort study. Br Med J. 2010;340:252.
34. http://www.riskprediction.org.uk/pp-index.php. Accessed 8 Mar 2016.
35. Fleischer LA, Fleischmann KE, Auerbach AD, Barnason SA, Beckman JA, Bozkurt B, et al. 2014 ACC/AHA guideline on perioperative cardiovascular evaluation and management of patients undergoing noncardiac surgery. Circulation. 2014;130:2215–45.
36. Kertai MD, Boersma E, Bax JJ, Heijenbrok-Kal MH, Hunink MG, L'talien GJ, et al. A meta analysis comparing prognostic accuracy of six diagnostic tests for predicting perioperative risk. Heart. 2003;89:1327–3.
37. Neglia D, Rovai D, Caselli C, Pietila M, Teresinska A, Aguadé-Bruix S, et al. EVINCI Study Investigators. Detection of significant coronary artery disease by noninvasive anatomical and functional imaging. Circ Cardiovasc Imaging. 2015;8(3).
38. Fleisher LA. Cardiac risk stratification for noncardiac surgery: update from the American College of Cardiology/American Heart Association 2007 guidelines. doi:10.3949/ccjm.76.s4.02.
39. Wijeysundera DN, Beattie WS, Austin PC, Hux JE, Laupacis A. Non-invasive cardiac stress testing before elective major non-cardiac surgery: population based cohort study. BMJ. 2010;340:b5526.
40. Galal W, Hoeks SE, Flu WJ, van Kuijk GD, Galema T, den Uil C, et al. Relation between preoperative and intraoperative new wall motion abnormalities in vascular surgery patients: a transesophageal echocardiographic study. Anesthesiology. 2010;112:557–66.
41. Chang K, Sarkiss M, Won KS, Swafford J, Broemeling L, Gayed I. Preoperative risk stratification using gated myocardial perfusion studies in patients with cancer. J Nucl Med. 2007;48:344–8.
42. Chandra S, Lenihan DJ, Wei W, Yusuf SW, Tong AT. Myocardial perfusion imaging and cardiovascular outcomes in a cancer population. Tex Heart Inst J. 2009;36:205–13.
43. Navare SM, Mather JF, Shaw LJ, Fowler MS, Heller GV. Comparison of risk stratification with pharmacologic and exercise stress myocardial perfusion imaging: a meta-analysis. J Nucl Cardiol. 2004;11:551–61.
44. Taqueti VR, Hachamovitch R, Murthy VL, Naya M, Foster CR, Hainer J, Dorbala S, Blankstein R, Di Carli MF. Global coronary flow reserve is associated with adverse cardiovascular events independently of luminal angiographic severity and modifies the effect of early revascularization. Circulation. 2015;131:19–27.
45. Vander Salm TJ. Unusual primary tumors of the heart. Semin Thorac Cardiovasc Surg. 2000;12:89–100.
46. Silverman NA. Primary cardiac tumors. Ann Surg. 1980;191:127–38.
47. Reardon MJ, Walkes JC, Benjamin R. Therapy insight: malignant primary cardiac tumors. Nature Clin Pract Cardiovasc Med. 2006;3:548–53.
48. Lee RW, Woo KS, Chow LTC, Ng HK, Chan WWM, Yu CM, Lo AWI. Diffuse infiltration of lymphoma of the myocardium mimicking clinical hypertrophic cardiomyopathy. Circulation. 2006; 113:e662–4.
49. Ekmetzoglou KA, Samelis GF, Xanthos. Heart and tumors: location, metastasis, clinical manifestations, diagnostic approaches and therapeutic considerations. J Cardiovasc Med 2008;9:769–777
50. Chiles C, WoodardPK GFR, Link KM. Metastatic involvement of the heart and pericardium: CT and MR imaging. Radiographics. 2001;21:439–49.
51. Antman K, Marks AR. The patient with cardiovascular disease and cancer, Chapter 83. In: Zipes DP, Libby P, Bonow RO, Braunwald E, editors. Braunwalds heart disease. 7th ed. Philadelphia: Elsevier Saunders. 2005:2117–28.
52. Gay JD, Guileyardo JM, Townsend-Perchman JK, Ross K. Clinical and morphologic features of lipomatous hypertrophy ("massive fatty deposits") of the interatrial septum. Am J Forens Med Pathol. 1997;18:107–8.
53. Gerard PS, Finestone H, Lazarro R, Geller MD. Intermittent FDG uptake in lipomatous hypertrophy of the interatrial septum on serial PET/CT scans. Clin Nucl Med. 2008;33:602–5.
54. Rao PM, Woodard PK, Patterson GA, Peterson LR. Myocardial metastasis or benign brown fat? Circ Cardiovasc Imag. 2009;2:e25–7.
55. Fujii H1, Ide M, Yasuda S, Takahashi W, Shohtsu A, Kubo A. Increased FDG uptake in the wall of the right atrium in people who participated in a cancer screening program with whole-body PET. Ann Nucl Med. 1999;13(1):55–9.
56. Maurer AH, Burshteyn M, Adler LP, Steiner RM. How to differentiate benign versus malignant cardiac and paracardiac ^{18}F FDG uptake at oncologic PET/CT. Radiographics. 2011;31:1287–305.
57. Sperry BW, Vranian MN, Hachamovitch R, Joshi H, Ikram A, Phelan D, Hanna M. Subtype-specific interactions and prognosis in cardiac amyloidosis. J Am Heart Assoc. 2016;24:5(3):e002877.
58. Schaadt BK, Hendel HW, Gimsing P, Jønsson V, Pedersen H, Hesse B. ^{99m}Tc-aprotinin scintigraphy in amyloidosis. J Nucl Med. 2003;44:177–83.
59. Bokhari S, Castaño A, Pozniakoff T, Deslisle S, Latif F, Maurer MS. ^{99m}Tc-pyrophosphate scintigraphy for differentiating light-chain cardiac amyloidosis from the transthyretin-related familial and senile cardiac amyloidoses. Circ Cardiovasc Imaging. 2013;6:195–201.
60. Antoni G, Lubberink M, Estrada S, Axelsson J, Carlson K, Lindsjö L, et al. In vivo visualization of

amyloid deposits in the heart with ^{11}C-PIB and PET. J Nucl Med. 2013;54:213–20.
61. Lee SP, Lee ES, Choi H, Im HJ, Koh Y, Lee MH, et al. ^{11}C-Pittsburgh B PET imaging in cardiac amyloidosis. JACC Cardiovasc Imaging. 2015;8:50–9.
62. Dorbala S, Vangala D, Semer J, Strader C, Bruyere JR Jr, Di Carli MF, et al. Imaging cardiac amyloidosis: a pilot study using ^{18}F-florbetapir positron emission tomography. Eur J Nucl Med Mol Imaging. 2014;41:1652–62.
63. Osborne DR, Acuff SN, Stuckey A, Wall JS. A routine PET/CT protocol with streamlined calculations for assessing cardiac amyloidosis using ^{18}F-florbetapir. Front Cardiovasc Med. 2015;2:23.
64. Park MA, Padera RF, Belanger A, Dubey S, Hwang DH, Veeranna V, et al. ^{18}F-florbetapir binds specifically to myocardial light chain and transthyretin amyloid deposits: autoradiography study. Circ Cardiovasc Imaging. 2015;8(8):e002954.
65. Law WP, Wang WY, Moore PT, Mollee PN, Ng AC. Cardiac amyloid imaging with ^{18}F-florbetaben positron emission tomography: a pilot study. J Nucl Med. 2016;57:1733–1739
66. Strauss HW, Zaret BL, Hurley PJ, Natarajan TK, Pitt B. A scintiphotographic method for measuring LVEF in man without cardiac catheterization. Am J Cardiol. 1971;28:275.
67. Burow RD, Strauss HW, Singleton R, Pond M, Rehn T, Bailey IK, et al. Analysis of LV function from multiple gated acquisition cardiac blood pool imaging. Comparison to contrast angiography. Circulation. 1977;56:1024.
68. Folland ED, Hamilton GW, Larson SM, Kennedy JW, Williams DL, Ritchie JL. The radionuclide ejection fraction: a comparison of three radionuclide techniques with contrast angiography. J Nucl Med. 1977;18:1159.
69. Wackers FJ, Berger HJ, Johnstone DE, Goldman L, Reduto LA, Langou RA, et al. Multiple gated cardiac blood pool imaging for left ventricular ejection fraction: validation of the technique and assessment of variability. Am J Cardiol. 1979;43:1159–66.
70. Alexander J, Dainiak N, Berger HJ, Goldman L, Johnstone D, Reduto L, et al. Serial assessment of doxorubicin cardiotoxicity with quantitative radionuclide angiocardiography. N Engl J Med. 1979;300:278–83.
71. Stortesky S, Suter TM. Insights into cardiovascular side-effects of modern anticancer therapeutics. Curr Opin Oncol. 2010;22:312–7.
72. Ewer MS, Lippman SM. Type II chemotherapy-related cardiac dysfunction: time to recognize a new entity. J Clin Oncol. 2005;23:2900–2.
73. Arcamone F, Franceschi G, Penco S, Selva A. Adriamycin (14-hydroxydaunomycin), a novel antitumor antibiotic. Tetrahedron Lett. 1969;13:1007–10.
74. Tan C, Tasaka H, Yu KP, Murphy ML, Karnofsky DA. Daunomycin, an antitumor antibiotic, in the treatment of neoplastic disease. Clinical evaluation with special reference to childhood leukemia. Cancer. 1967;20:333–53.
75. Bonadonna G, Monfardini S. Cardiac toxicity of daunorubicin. Lancet. 1969;1(7599):837.
76. Marmont AM, Damasio E, Rossi F. Cardiac toxicity of daunorubicin. Lancet. 1969;1(7599):837–8.
77. Lynce F, Swain SM. First, do no harm. Onkologie. 2008;31:511–2.
78. Singal PK, Deally CMR, Weinberg LE. Subcellular effects of adriamycin in the heart: a concise review. J Mol Cell Cardiol. 1987;19:817–28.
79. Tewey KM, Rowe TC, Yang L, Halligan BD, Liu LF. Adriamycin-induced DNA damage mediated by mammalian DNA topoisomerase II. Science. 1984;226:466–8.
80. Singal PK, Khaper N, Palace V, Kumar D. The role of oxidative stress in the genesis of heart disease. Cardiovasc Res. 1998;40(3):426–32.
81. Mason JW, Bristow MR, Billingham ME, Daniels JR. Invasive and noninvasive methods of assessing adriamycin cardiotoxic effects in man: superiority of histopathologic assessment using endomyocardial biopsy. Cancer Treat Rep. 1978;62:857–64.
82. Bristow MR, Mason JW, Billingham ME, Daniels JR. Dose-effect and structure-function relationships in doxorubicin cardiomyopathy. Am Heart J. 1981; 102:709–18.
83. Ewer MS, Ali MK, Mackay B, Wallace S, Valdivieso M, Legha SS, et al. A comparison of cardiac biopsy grades and ejection fraction estimations in patients receiving adriamycin. J Clin Oncol. 1984;2:112–7.
84. Isner JM, Ferrans VJ, Cohen SR, Witkind BG, Virmani R, Gottdiener JS, et al. Clinical and morphologic cardiac findings after anthracycline chemotherapy. Analysis of 64 patients studied at necropsy. Am J Cardiol. 1983;51:1167–74.
85. Cooper LT, Baughman KL, Feldman AM, Frustaci A, Jessup M, Kuhl U, et al. American Heart Association; American College of Cardiology; European Society of Cardiology. The role of endomyocardial biopsy in the management of cardiovascular disease: a scientific statement from the American Heart Association, the American College of Cardiology, and the European Society of Cardiology. Circulation. 2007;116:2216–33.
86. Lefrak EA, Pitha J, Rosenheim S, Gottlieb JA. A clinicopathologic analysis of adriamycin cardiotoxicity. Cancer. 1973;32:302–14.
87. Von Hoff DD, Layard MW, Basa P, Davis Jr HL, Von Hoff AL, Rozencweig M, Muggia FM. Risk factors for doxorubicin-induced congestive heart failure. Ann Intern Med. 1979;91:710–7.
88. Swain SM, Whaley FS, Ewer MS. Congestive heart failure in patients treated with doxorubicin: a retrospective analysis of three trials. Cancer. 2003;97:2869–79.
89. Ewer MS, Ewer SM. Long-term cardiac safety of dose-dense anthracycline therapy cannot be predicted from early ejection fraction data. J Clin Oncol. 2009;27:6073–5.

90. Schwartz RG, McKenzie WB, Alexander J, Sager P, D'Souza A, Manatunga A, et al. Congestive heart failure and LV dysfunction complicating doxorubicin therapy. Seven-year experience using serial radionuclide angiocardiography. Am J Med. 1987;82:1109–18.
91. Russell RR, Alexander J, Jain D, Poornima IG, Srivastava AV, Storozynsky E, Schwartz RG. The role and clinical effectiveness of multimodality imaging in the management of cardiac complications of cancer and cancer therapy. J Nucl Cardiol. 2016;23:856–84.
92. Agarwala S, Kumar R, Bhatnagar V, Bajpai M, Gupta DK, Mitra DK. High incidence of adriamycin cardiotoxicity in children even at low cumulative doses: role of radionuclide cardiac angiography. J Pediatr Surg. 2000;35:1786–9.
93. Harris EE, Correa C, Hwang WT, Liao J, Litt HI, Ferrari VA, Solin LJ. Late cardiac mortality and morbidity in early-stage breast cancer patients after breast-conservation treatment. J Clin Oncol. 2006;24:4100–6.
94. Pinder MC, Duan Z, Goodwin JS, Hortobagyi GN, Giordano SH. Congestive heart failure in older women treated with adjuvant anthracycline chemotherapy for breast cancer. J Clin Oncol. 2007;25:3808–15.
95. Lipshultz SE, Colan SD, Gelber RD, Perez-Atayde AR, Sallan SE, Sanders SP. Late cardiac effects of doxorubicin therapy for acute lymphoblastic leukemia in childhood. N Engl J Med. 1991;324:808–15.
96. Steinherz LJ, Steinherz PG, Tan CT, Heller G, Murphy ML. Cardiac toxicity 4 to 20 years after completing anthracycline therapy. JAMA. 1991;266:1672–7.
97. Tukenova M, Guibout C, Oberlin O, Doyon F, Mousannif A, Haddy N, et al. Role of cancer treatment in long-term overall and cardiovascular mortality after childhood cancer. J Clin Oncol. 2010;28:1308–15.
98. Mulrooney DA, Yeazel MW, Kawashima T, Mertens AC, Mitby P, Stovall M, et al. Cardiac outcomes in a cohort of adult survivors of childhood and adolescent cancer: retrospective analysis of the Childhood Cancer Survivor Study cohort. BMJ. 2009;339:b4606. doi:10.1136/bmj.b4606.
99. Steinherz LJ, Graham T, Hurwitz R, Sondheimer HM, Schwartz RG, Shaffer EM, et al. Guidelines for cardiac monitoring of children during and after anthracycline therapy: report of the Cardiology Committee of the Childrens Cancer Study Group. Pediatrics. 1992;89(5 Pt 1):942–9.
100. Hudis CA. Trastuzumab – mechanism of action and use in clinical practice. N Engl J Med. 2007;357:39–51.
101. Chien KR. Herceptin and the heart – a molecular modifier of cardiac failure. N Engl J Med. 2006;354:789–90.
102. de Korte MA, de Vries EG, Lub-de Hooge MN, et al. ^{111}Indium-trastuzumab visualises myocardial human epidermal growth factor receptor 2 expression shortly after anthracycline treatment but not during heart failure: a clue to uncover the mechanisms of trastuzumab-related cardiotoxicity. Eur J Cancer. 2007;43:2046–51.
103. Perik PJ, de Vries EG, Gietema JA, van der Graaf WT, Smilde TD, Sleijfer DT, van Veldhuisen DJ. Serum HER2 levels are increased in patients with chronic heart failure. Eur J Heart Fail. 2007;9:173–7.
104. Kaufman B, Mackey JR, Clemens MR, Bapsy PP, Vaid A, Wardley A, et al. Trastuzumab plus anastrozole versus anastrozole alone for the treatment of postmenopausal women with human epidermal growth factor receptor 2-positive, hormone receptor-positive metastatic breast cancer: results from the randomized phase III TAnDEM study. J Clin Oncol. 2009;27:5529–37.
105. Seidman A, Hudis C, Pierri MK, Shak S, Paton V, Ashby M, et al. Cardiac dysfunction in the trastuzumab clinical trials experience. J Clin Oncol. 2002;20:1215–21.
106. Slamon DJ, Leyland-Jones B, Shak S, Fuchs H, Paton V, Bajamonde A, et al. Use of chemotherapy plus a monoclonal antibody against HER2 for metastatic breast cancer that overexpresses HER2. N Engl J Med. 2001;344:783–92.
107. Ewer MS, Vooletich MT, Durand JB, Woods ML, Davis JR, Valero V, Lenihan DJ. Reversibility of trastuzumab-related cardiotoxicity: new insights based on clinical course and response to medical treatment. J Clin Oncol. 2005;23:7820–6.
108. Guarneri V, Lenihan DJ, Valero V, Durand JB, Broglio K, Hess KR, et al. Long-term cardiac tolerability of trastuzumab in metastatic breast cancer: the M.D. Anderson Cancer Center experience. J Clin Oncol. 2006;24:4107–15.
109. Procter M, Suter TM, de Azambuja E, Dafni U, van Dooren V, Muehlbauer S, et al. Longer-term assessment of trastuzumab-related cardiac adverse events in the Herceptin Adjuvant (HERA) trial. J Clin Oncol. 2010;28:3422–8.
110. Keefe DL. Trastuzumab-associated cardiotoxicity. Cancer. 2002;95:1592.
111. Suter TM, Procter M, van Veldhuisen DJ, Muscholl M, Bergh J, Carlomagno C, et al. Trastuzumab-associated cardiac adverse effects in the herceptin adjuvant trial. J Clin Oncol. 2007;25:3859–65.
112. Hensley ML, Hagerty KL, Kewalramani T, Green DM, Meropol NJ, et al. American Society of Clinical Oncology 2008 clinical practice guideline update: use of chemotherapy and radiation therapy protectants. J Clin Oncol. 2009;27:127–45.
113. Cardinale D, Colombo A, Sandri MT, Lamantia G, Colombo N, Civelli M, et al. Prevention of high-dose chemotherapy-induced cardiotoxicity in high-risk patients by angiotensin-converting enzyme inhibition. Circulation. 2006;114:2474–81.
114. Cardinale D, Colombo A, Lamantia G, Colombo N, Civelli M, De Giacomi G, et al. Anthracycline-induced cardiomyopathy: clinical relevance and response to pharmacologic therapy. J Am Coll Cardiol. 2010;55:213–20.

115. Riad A, Bien S, Westermann D, Becher PM, Loya K, Landmesser U, et al. Pretreatment with statin attenuates the cardiotoxicity of doxorubicin in mice. Cancer Res. 2009;69:695–9.
116. Perez EA, Koehler M, Byrne J, Preston AJ, Rappold E, Ewer MS. Cardiac safety of lapatinib: pooled analysis of 3689 patients enrolled in clinical trials. Mayo Clin Proc. 2008;83:679–86.
117. Mahmarian JJ, Moye L, Verani MS, Eaton T, Francis M, Pratt CM. Criteria for the accurate interpretation of changes in left ventricular ejection fraction and cardiac volumes as assessed by rest and exercise gated radionuclide angiography. J Am Coll Cardiol. 1991;18:112–9.
118. Calahan RJ, Frowlich JW, McKusick KA, Leppo J, Strauss WH. A modified method for the in vivo labelling of red blood cells with Tc-99m: concise communication. J Nucl Med. 1982;23:315–8.
119. Massardo T, Jaimovich R, Lavados H, Gutiérrez D, Rodríguez JC, Saavedra JM, Alay R, Gatica H. Comparison of radionuclide ventriculography using SPECT and planar techniques in different cardiac conditions. Eur J Nucl Med Mol Imaging. 2007;34:1735–46.
120. Gottdiener JS, Mathisen DJ, Borer JS, Bonow RO, Myers CE, Barr LH, et al. Doxorubicin cardiotoxicity: assessment of late LV dysfunction by radionuclide cineangiography. Ann Intern Med. 1981;94:430.
121. Patel CD, Balakrishnan VB, Kumar L, Naswa N, Malhotra A. Does left ventricular diastolic function deteriorate earlier than left ventricular systolic function in anthracycline cardiotoxicity? Hell J Nucl Med. 2010;13:233–7.
122. Mahadevan G, Davis RC, Frenneaux MP, Hobbs FD, Lip GY, Sanderson JE, et al. Left ventricular ejection fraction: are the revised cut-off points for defining systolic dysfunction sufficiently evidence based? Heart. 2008;94:426–8.
123. Naik MM, Diamond GA, Pai T, Soffer A, Siegel RJ. Correspondence of LVEF determinations from two-dimensional echocardiography, radionuclide angiography and contrast cineangiography. J Am Coll Cardiol. 1995;25:937–42.
124. Bellenger NG, Burgess MI, Ray SG, Lahiri A, Coats AJ, Cleland JG, et al. Comparison of left ventricular ejection fraction and volumes in heart failure by echocardiography, radionuclide ventriculography and cardiovascular magnetic resonance; are they interchangeable? Eur Heart J. 2000;21:1387–96.
125. Gopal AS, Shen Z, Sapin PM, Keller AM, Schnellbaecher MJ, Leibowitz DW, et al. Assessment of cardiac function by three-dimensional echocardiography compared with conventional noninvasive methods. Circulation. 1995;92:842–53.
126. Walker J, Bhullar N, Fallah-Rad N, Lytwyn M, Golian M, Fang T, et al. Role of three-dimensional echocardiography in breast cancer: comparison with two-dimensional echocardiography, multiple-gated acquisition scans, and cardiac magnetic resonance imaging. J Clin Oncol. 2010;28:3429–36.
127. de Geus-Oei LF, Mavinkurve-Groothuis AM, Bellersen L, Gotthardt M, Oyen WJ, Kapusta L, van Laarhoven HW. Scintigraphic techniques for early detection of cancer treatment-induced cardiotoxicity. J Nucl Med. 2011;52:560–71.
128. Zhang H, Huang R, Pillarsetty N, Thorek DL, Vaidyanathan G, Serganova I, Blasberg RG, Lewis JS. Synthesis and evaluation of ^{18}F-labeled benzylguanidine analogs for targeting the human norepinephrine transporter. Eur J Nucl Med Mol Imaging. 2014;41:322–32.
129. Pandit-Taskar N, Zanzonico P, Reidy-Lagunes D, Carrasquillo J, et al. ^{18}F-meta fluorobenzyl guanidine (MFBG) PET imaging in patients with neuroendocrine malignancies: biodistribution, pharmacokinetics, organ dosimetry and lesion uptake. J Nucl Med. 2016;57:25.
130. Cardinale D , Colombo A, Torrisi R, Sandri MT, Civelli M, Salvatici M, et al. Trastuzumab-induced cardiotoxicity: clinical and prognostic implications of troponin I evaluation. J Clin Oncol. 2010;28:3910–6.
131. Lipshultz SE, Rifai N, Sallan SE, Lipsitz SR, Dalton V, Sacks DB, et al. Predictive value of cardiac troponin T in pediatric patients at risk for myocardial injury. Circulation. 1997;96:2641–8.

Part VI

Adverse Effects of Cancer Therapy

52 Nuclear Medicine in the Assessment of Adverse Effects of Cancer Therapy in the Lung, Kidney, and Gastrointestinal Tract

Diego Alfonso López Mora and Ignasi Carrió

Abstract

Radiotherapy or chemotherapy and new drugs and strategies in oncology can produce damage in normal organs and tissues affecting the quality of life of the patient. Pulmonary toxicity is frequently seen in patients treated with bleomycin or other chemotherapeutic agents. The most common clinical form of bleomycin pulmonary toxicity is the subacute condition, which may progress to lung fibrosis and death, if not recognized and appropriately managed. The diagnosis is usually established by a combination of clinical, radiographic, and pulmonary function test abnormalities. X-ray and high-resolution CT scan findings are used to identify pulmonary fibrosis. ^{67}Ga-citrate scintigraphy has been used to detect and assess the extent of pulmonary toxicity related to bleomycin in patients who otherwise have normal chest radiographs.

Since conventional CT scanning is not able to distinguish fibrosis and active inflammation, [^{18}F]FDG-PET has been suggested as a tool to indicate the resolution of disease activity. Moreover, [^{18}F]FDG-PET could be useful to detect early preclinical pneumonitis induced by bleomycin. As pulmonary permeability can be altered by chemotherapy, ^{99m}Tc-DTPA aerosols can be used to assess a reduced epithelial permeability.

Acute radiation lung injury can occur within 1–3 months after radiation therapy of the thorax, whereas lung fibrosis can develop 6–24 months later, leading to progressive impairment of pulmonary function. Clinical manifestations, chest radiographs, and pulmonary function tests may help to establish an early diagnosis. Scintigraphic abnormalities can be demonstrated in the acute phase often before radiologic changes become apparent by ^{67}Ga-citrate scintigraphy. Moreover, ^{111}In-pentetreotide may have a role in the differential diagnosis of patients with complaints after radiotherapy and in the monitoring of the response to corticosteroid therapy. [^{18}F]FDG uptake in the irradiated region can be observed up to about 2 months following therapy. The persistence of activity beyond 8 weeks raises the likelihood of persistence of disease within the irradiated region.

Lung scintigraphy with ^{99m}Tc-DTPA aerosol or ^{99m}Tc-MAA (macroaggregates of albumin) has been performed to assess radiation-induced ventilation/perfusion changes.

Drugs for the treatment of abdominal malignancies, such as cisplatin and ifosfamide, and abdominal radiation can cause renal damage.

Chemotherapy-induced nephropathy can be identified with quantitative measurement of glomerular filtration rate. ^{99m}Tc-DTPA has become the preferred radiopharmaceutical because of availability and cost. ^{99m}Tc-

D.A. López Mora • I. Carrió (✉)
Department of Nuclear Medicine, Hospital Sant Pau, Autonomous University of Barcelona, Barcelona, Spain
e-mail: dlopezmo@santpau.cat; icarrio@santpau.cat

© Springer International Publishing Switzerland 2017
H.W. Strauss et al. (eds.), *Nuclear Oncology*,
https://doi.org/10.1007/978-3-319-26236-9_30

DMSA scintigraphy can be used to establish tubular dysfunction induced by nephrotoxic drugs. Nuclear medicine techniques also offer the possibility to follow the clinical evolution of radiation nephropathy. Bone scans using ^{99m}Tc-MDP can show increased kidney uptake early after radiation in patients with radiation fields including kidneys. Over the subsequent 6–12 months the uptake decreases to normal or below normal levels, associated with the loss of function. Renography with ^{99m}Tc-DTPA can be performed to assess radiation nephropathy. ^{99m}Tc-DTPA Captopril renography test has been used to investigate the relation between small vessel injury due to radiation and hypertension.

Nuclear medicine examinations can play a role in the detection of radiation-induced digestive tract damage.

In cancers of the cervix, endometrium, ovary, prostate, bladder, or rectum, radiation therapy is often required. Radiation proctitis is usually self-limiting and resolves within a month after the conclusion of therapy. Damage of the small bowel is seen in 0.5–15% of the patients. Chronic injuries to the small bowel are manifest 6 and 24 months after radiation. Ileal dysfunction is due to bile acid malabsortion, to bacterial overgrowth in the small bowel, or to the combination of both. ^{75}Se-homocholic acid conjugated with taurine (^{75}Se-HCAT) and ^{14}C-glycochol breath test can be used to differentiate between normal functioning ileum (both tests negative) and ileal dysfunction (one or both tests positive). The combination of both tests may allow the differentiation between bile acid malabsorption (^{75}Se-HCAT positive) and bacterial overgrowth (^{75}Se-HCAT negative).

These techniques may also help to document the benefit of innovative therapeutic approaches such as the use of somatostatin analogs (SOM230). In cases of radiotherapy and chemotherapy-associated liver injury, radionuclide studies can be performed using ^{99m}Tc-iminodiacetic acid or ^{99m}Tc-colloid. In patients receiving radiotherapy, the most common finding is the loss of function of the part of the liver involved in the radiation field, with a reduced uptake in irradiated areas. Recently, acute radiation-induced hepatitis has been reported as a potential cause of false-positive findings of malignancy on [^{18}F]FDG-PET scans. Moreover, esophagitis postradiotherapy can be observed on [^{18}F]FDG-PET scans.

Leucocytes labeled with ^{111}In or with ^{99m}Tc-HMPAO or [^{18}F]FDG can be used in patients with suspected radiation enterocolitis.

Keywords

Nuclear medicine • Adverse effects • Radiation-induced digestive tract damage • Radiation-induced renal damage • Pulmonary toxicity with radiation • Radiation-induced pulmonary toxicity • Renal damage in radiation • Gastrointestinal tract damage in radiation • Liver damage in radiation

Glossary

[^{18}F]FDG	2-deoxy-2-[^{18}F]fluoro-D-glucose
^{75}Se-HCAT	^{75}Se-Homocholic acid conjugated with taurine
^{99m}Tc-DMSA	^{99m}Tc-dimercaptosuccinic acid
^{99m}Tc-DTPA	^{99m}Tc-diethylenetriaminepentaacetic acid
^{99m}Tc-HMPAO	^{99m}Tc-hexamethylpropyleneamine oxime
^{99m}Tc-IDA	^{99m}Tc-iminodiacetic acid
^{99m}Tc-MAA	^{99m}Tc-macroaggregated albumin
^{99m}Tc-MDP	^{99m}Tc-methylene diphosphonate
AVBD	chemotherapy regimen based on adriamycin, vinblastine, bleomycin and dacarbazine
CT	X-ray computed tomography
DLCO	Diffusing capacity of the lung for carbon monoxide
EDTA	Ethylenediaminetetraacetic acid
GFR	Glomerular Filtration Rate
GI	Gastrointestinal
Gy	Gray unit (ionizing radiation dose in the International System of Units, corresponding to the

	absorption of one joule of radiation energy per kilogram of matter)
MIP	Maximum Intensity Projection
NSCLC	Non-small cell lung cancer
PET	Positron emission tomography
PET/CT	Positron emission tomography/Computed tomography
ROS	Reactive oxygen species
SPECT	Single-photon emission computed tomography
SPECT/CT	Single-photon emission computed tomography/Computed tomography

Contents

Lungs 1515

Chemotherapy-Associated Pulmonary Toxicity 1515

Pulmonary Permeability During Chemotherapy 1519

Radiation Pneumonitis 1519

Ventilation/Perfusion Changes Induced by Thoracic Irradiation 1519

Kidneys 1520

Chemotherapy-Induced Tubular Injury 1520

Radiation Nephropathy 1522

Digestive Tract 1523

Radiation Damage of the Small Bowel 1523

Liver Damage 1524

Other Tracers in Injuries on the Digestive Tract 1524

References 1525

This chapter reviews the nuclear medicine findings in detecting organ injury and adverse effects due to cancer or cancer therapy in the lung, kidney, and gastrointestinal tract. The use of radiotherapy or chemotherapy and new drugs and strategies in order to intensify the anti-tumor effect with a curative intent can produce different types of collateral damage in normal organs and tissues affecting the quality of life of the patient. Chemotherapy acts on the parenchymal cells and radiotherapy causes inflammation both in the organ and in the major vasculature (in the direct path of the beam) and affects the microcirculation. In tissues with high proliferation rates, such as the bone marrow and GI tract, stem cells may be depleted and/or injured. Chemo- and radiotherapy can cause acute injury as well as late damage, months to years after treatment. Such damage is usually subclinical.

However, if the organ sustains an additional injury (in some cases even a minor infection), the organ dysfunction may become clinically apparent.

Lungs

Bleomycin is the most common chemotherapeutic agent associated with pulmonary toxicity. However, nitrosureas, erlotinib, cyclophosphamide, mitomycin, busulfan, and methotrexate can also cause such toxicity. At the same time, radiotherapy to lesions of the lung, breast, mediastinum, or esophagus causes initial inflammation, followed by scarring (depending on the dose). Nuclear medicine studies employing ^{67}Ga-citrate and ^{111}In-pentetreotide are able to detect acute and subacute pulmonary toxicity in patients treated either with chemotherapy or radiotherapy. When necessary, pulmonary V/Q scintigraphy can be performed to assess ventilation/perfusion changes in irradiated patients. SPECT/CT ventilation perfusion studies can be particularly helpful, since many of these patients have underlying lung disease. Following multiple courses of platinum-based chemotherapy, hypersensitivity pulmonary reactions can occur in 5–40% of patients, usually after the sixth cycle of treatment, especially when the agents are administered with paclitaxol [1].

Chemotherapy-Associated Pulmonary Toxicity

Chemotherapy-associated pulmonary toxicity is frequently seen in patients treated with bleomycin. The incidence rate of pulmonary toxicity in patients with Hodgkin's disease treated with standard AVBD chemotherapy varies between 18%

and 28% [2, 3]. The risk factors associated with bleomycin-induced pneumonitis include the cumulative dose administered, the age of the patient, and impaired renal function. The incidence and severity of bleomycin toxicity is clearly increased by previous or concomitant thoracic radiotherapy. In these patients, the risk of lethal outcome is ~4% [3, 4]. The total administered dose is clearly a risk factor, with sporadic toxicity occurring at total doses of 100–450 U and increasing incidence beyond that range. The central event in the development of bleomycin-induced pneumonitis is endothelial damage. Bleomycin causes release of cytokines and reactive oxygen species (ROS), leading to cell damage, followed by recruitment of inflammatory cells into the lung parenchyma, and subsequently of fibroblasts leading to fibrosis [4, 5]. Pulmonary fibrosis is characterized by excessive deposition of extracellular matrix components in the alveolar space, which hampers the normal transfer of oxygen. Pathophysiological enzymes, glycoprotein moieties, and matrix degrading lysosomal hydrolases are key markers and play a crucial role in the progression of fibrosis. One important pathogenic process associated with pulmonary fibrosis is injury to basement membranes by matrix metalloproteinases that are produced mainly by macrophages [6, 7].

The clinical and radiological findings in chemotherapy-associated pulmonary toxicity are nonspecific and may be difficult to detect, as they are often similar to other pulmonary syndromes [4]. Therefore, the diagnosis of chemotherapy-associated pulmonary toxicity is challenging; early detection is important to reduce lung injury and prevent pulmonary fibrosis [3–5]. Pulmonary toxicity may be short-term or permanent. The lung injury that resolves (returns to normal) after time or after the cause is removed is called acute/subacute pulmonary toxicity and the lung injury that is permanent is called chronic or late pulmonary toxicity.

The most common clinical presentation of Bleomycin-induced pneumonitis is the subacute pneumonitis, which tends to progress with time leading to lung fibrosis and death if not properly diagnosed and treated. The diagnosis of bleomycin-induced pneumonitis can be suspected with the appearance of the clinical manifestations (progressive dyspnea and nonproductive cough), the appearance of pulmonary function tests abnormalities with restrictive patterns (diminished total lung, vital capacities, and DLCO), and the appearance of common findings in chest X-ray (bilateral, lower pulmonary lobes, sometimes followed by diffuse interstitial and alveolar infiltrates) and high-resolution CT scan (diffuse areas of ground-glass opacity, interlobular septal thickening, fibrosis, or consolidation) [4, 8, 9]

Scintigraphy with ^{67}Ga-citrate has been used to detect and assess the extent of pulmonary toxicity related to bleomycin. ^{67}Ga has an atomic structure and biological behavior similar to iron (ferric ion) with the property to bind to any proteins that bind iron. ^{67}Ga circulates in plasma bound to transferrin protein. The complex ^{67}Ga-transferrin is transported to the inflammatory site due to the local increased blood flow and vascular permeability. In the inflammation site, neutrophils release large amounts of lactoferrin, which binds to ^{67}Ga. Also siderophores, compounds secreted by microorganisms such as bacteria can also bind to ^{67}Ga. Therefore, ^{67}Ga localization at the inflammation/infection site is secondary to its ferric ion-like properties [10] and allows localization, delineation of extent, and assessment of the degree of activity of the inflammatory disease [11]. ^{67}Ga scintigraphies in drug-induced pneumonitis show a bilateral diffuse lung uptake, in patients undergoing chemotherapy (including bleomycin) with normal chest X-rays (Fig. 1) [12].

Positron Emission Tomography with 2-deoxy-2-[^{18}F] fluoro-D-glucose ([^{18}F]FDG PET/CT) is a widely used molecular imaging technique in the assessment of treatment response in oncological patients [9, 13–16]. Chemotherapy-associated pulmonary toxicity is a potential cause of false-positive results in [^{18}F]FDG PET/CT of patients undergoing chemotherapy [9, 14], in particular when bleomycin is used (standard AVBD treatment for Hodgkin's disease) [4, 8, 9]. Based on the physiopathology of the inflammatory processes, a number of studies have demonstrated that a higher activation of macrophages, neutrocytes, or lymphocytes is correlated with a higher accumulation

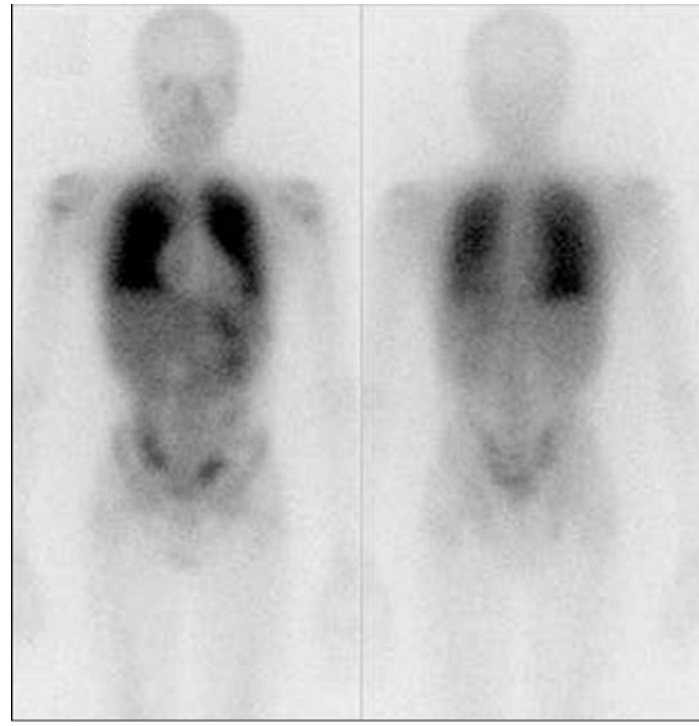

Fig. 1 Patient with Hodgkin's lymphoma treated with bleomycin. Diffuse bilateral uptake of ^{67}Ga reflects pulmonary toxicity

of [^{18}F]FDG [17–21]. Therefore, the degree of [^{18}F]FDG uptake in drug-induced pneumonitis may reflect the metabolic activity and supports its use to assess disease activity [17].

In acute drug-induced pneumonitis, the process starts with pulmonary infiltration of neutrophils, followed by morphological changes seen on high-resolution CT scan. Thus, in early stages of pulmonary toxicity, high-resolution CT scans may be unable to detect such abnormal morphological changes. In this case, [^{18}F]FDG PET/CT may be a more sensitive tool to detect early drug-induced pneumonitis, even before the onset of pulmonary symptoms and the appearance of parenchymal changes in chest X-ray and/or CT scan. Such early detection may be useful for accurate treatment to reverse the lung injury and prevent pulmonary fibrosis [22] (Fig. 2). Along this line, [^{18}F]FDG PET/CT in drug-induced pneumonitis may be used to monitor the effects of corticosteroid treatment. Von Rohr et al. [23] reported that PET scan and CT scan findings resolve after immunosuppressive therapy. Also Butchler et al [24] reported that the PET scan performed within 2 months of onset of bleomycin-induced pneumonitis demonstrated diffuse pulmonary [^{18}F]FDG uptake which resolved after corticosteroid treatment with persistence of morphological (parenchymal) changes in conventional CT scan. These data suggests that [^{18}F]FDG PET/CT may be used to distinguish between residual changes and active inflammation and that [^{18}F]FDG PET/CT may provide a tool to indicate the resolution of disease activity, even in the presence of residual pulmonary scarring [24]. Along the same line, Connerotte et al [25] have shown that PET abnormalities can resolve after cessation of bleomycin as the only intervention, suggesting that [^{18}F]FDG PET/CT could be useful to detect early preclinical bleomycin-induced pneumonitis at a stage that is fully reversible upon cessation of bleomycin. Therefore, [^{18}F]FDG PET/CT may be used in the detection of bleomycin-induced pneumonitis before clinical symptoms and possibly before significant lung function or conventional radiology alterations take place.

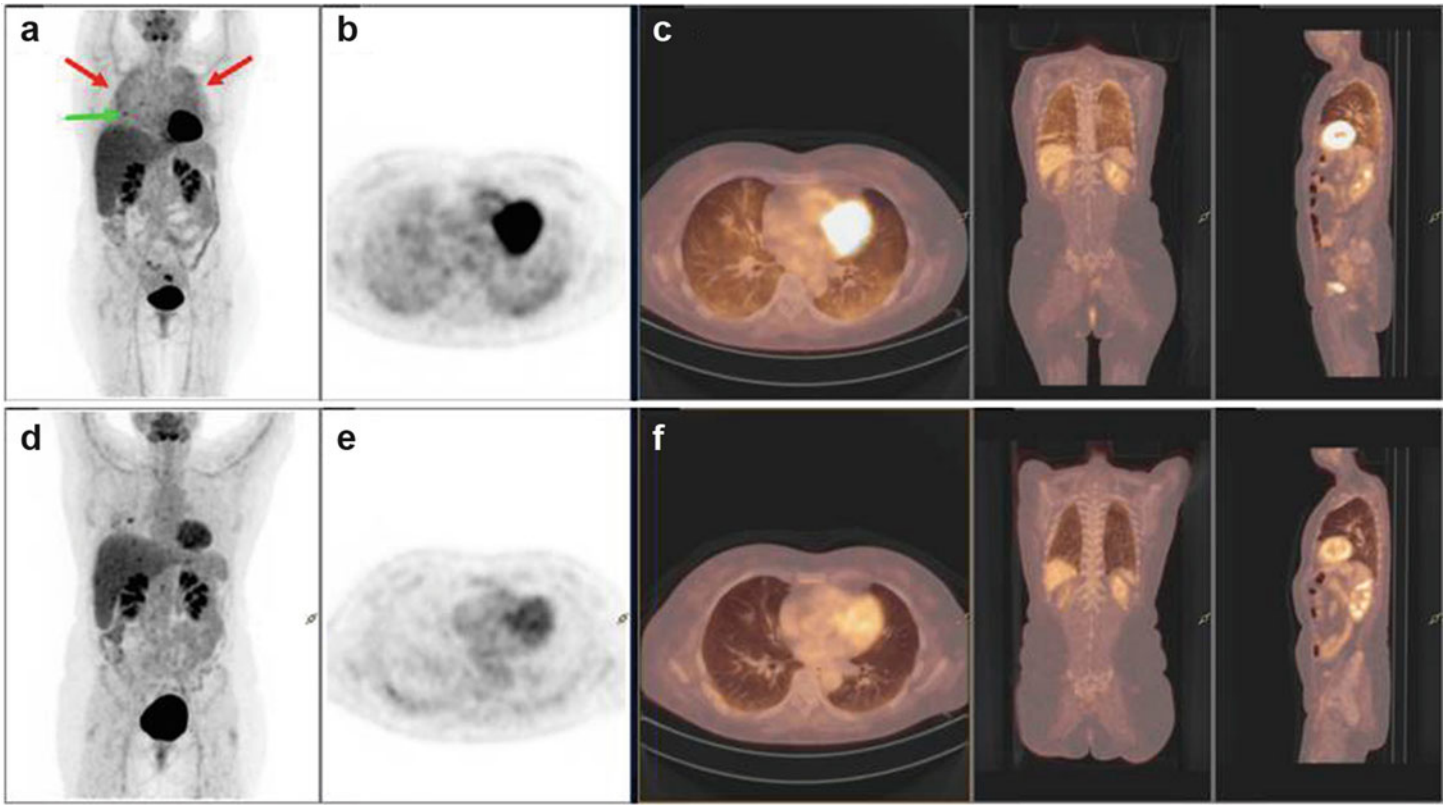

Fig. 2 Chemotherapy-associated pulmonary toxicity in a 53-year-old woman who received erlotinib/bevacizumab for metastatic non-small cell lung cancer (NSCLC). (**a**) After the third chemotherapy cycle, the MIP PET image demonstrates a diffuse [^{18}F] FDG uptake in both lungs (*red arrows*) and a focal [^{18}F]FDG uptake that corresponds to the NSCLC (*green arrow*). (**b**) Axial PET and (**c**) fused PET/CT images show hypermetabolic diffuse ground-glass infiltrates in both lungs. In the context of recent chemotherapy, these findings were consistent with chemotherapy-induced pneumonitis. The anatomical pathology of the transbronquial biopsy of the left inferior pulmonary lobe demonstrated acute inflammatory changes. (**d**) MIP PET, (**e**) axial PET and (**f**) fused PET/CT images performed 3 weeks after bevacizumab stop, reduce erlotinib dose, and steroid administration showed resolution of the hypermetabolic diffuse ground-glass lung infiltrates

Pulmonary Permeability During Chemotherapy

In chemotherapy-induced lung injury, pulmonary permeability is altered because of alveolar epithelial disruption with fluid and protein leakage into the alveolar spaces and focal necrosis of type I pneumocytes and fibrosis. Permeability can be assessed using ^{99m}Tc-DTPA aerosols. The inhalated aerosol is deposited in the alveoli, permitting the acquisition of scintigraphic images that show different patterns of ventilation. In the non-inflammed lung there is minimal permeability of the DTPA from the air space to the vasculature, hence minimal activity in the systemic circulation. The inflammed lung has greater permeability, allowing passage of the tracer from the air space to the vasculature. The clearance time decreases as epithelial permeability [26, 27] increases. In untreated patients, permeability was reduced, possibly because of tumor infiltration, while it was increased in treated patients, suggesting early injury [28, 29].

Radiation Pneumonitis

In radiation therapy of the thorax, radiation pneumonitis can appear 2–8 months after treatment. Radiation lung injury occurs in proportion to the amount of lung that is exposed to doses of >20 Gy. Symptoms vary from none, when radiation is delivered to a small region of the lung, to systemic signs and symptoms of fever, dyspnea, cough, and respiratory distress syndrome, when radiation is delivered to >20% of the total lung volume. Following lung radiation there are two phases of cytokine expression: one occurring hours to days or weeks after radiation, typically returning to normal after ~2 weeks and a second phase at 6–8 weeks, leading to pulmonary parenchymal and vascular damage [30], which may progress for 6–24 months following radiation exposure. Within 1–3 months of exposure, acute radiation lung injury can occur, manifested by dyspnea, cough, and hypoxia. Six to twenty-four months after radiation lung fibrosis can occur, leading to progressive impairment of pulmonary function. Early detection of radiation pneumonitis enables adequate treatment with a reasonable chance to prevent or limit late sequelae [31]. Clinical manifestations, chest radiographs, and pulmonary function tests may help establish an early diagnosis, but scintigraphic abnormalities can be demonstrated in the acute phase often before radiologic changes become apparent. ^{67}Ga-citrate scintigraphy is also a sensitive method for the early detection of radiation pneumonitis [32], although the delineation of lung injury may be hampered due to the physiologic ^{67}Ga uptake in sternum and thoracic spine. Pentetreotide, a synthetic somatostatin analog with strong affinity for the somatostatin receptor subtypes 2 and 5, can be labeled with ^{111}In. Somatostatin has been shown to modulate fibroblast activation and to have antifibrotic properties also [33], although the exact mechanisms of such antifibrotic action of octreotide still remains unclear. ^{111}In-pentetreotide may have a role in the differential diagnosis of patients with complaints after radiotherapy and in the monitoring of the response to corticosteroid therapy [31]. Some false-positive studies have been reported with increased pulmonary uptake in patients with neuroendocrine tumors which eventually was due to pulmonary fibrosis (Fig. 3) [34, 35]. [^{18}F]FDG-PET has also been recently proposed to detect radiation pneumonitis [36] and may be used as a predictor for acute radiation pneumonitis [37] (Fig. 4).

There may be significant [^{18}F]FDG uptake in the irradiated region up to about 2 months following therapy. Persistence of significant focal activity beyond 8 weeks raises the likelihood of persistence of disease within the irradiated region.

Ventilation/Perfusion Changes Induced by Thoracic Irradiation

Radiation-induced lung damage may lead to decreased lung perfusion, lung ventilation, and diffusion of gases in the irradiated region. A decrease in pulmonary blood flow in the irradiated areas has been reported in breast cancer patients receiving radiotherapy [38]. Lung scintigraphy with ^{99m}Tc-DTPA aerosol or ^{99m}Tc-MAA (macroaggregates of albumin) has been performed to assess abnormal ventilation/ perfusion patterns.

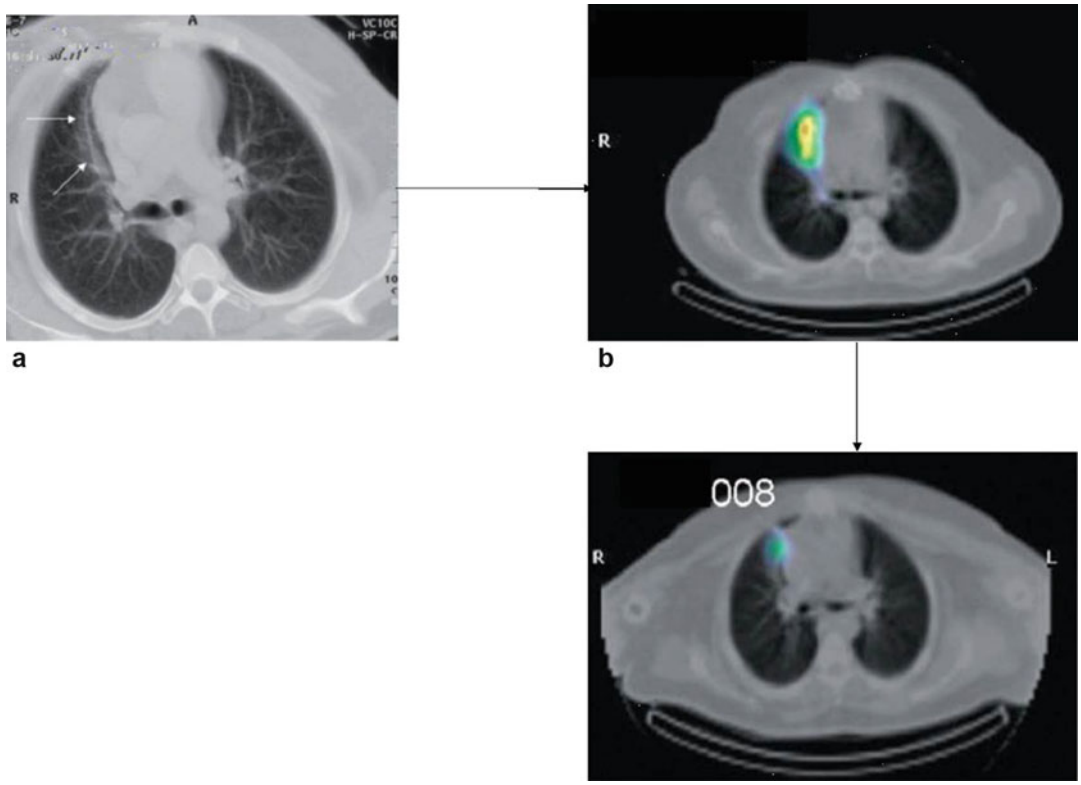

Fig. 3 Patient with a neuroendocrine tumor studied 10 months after radiotherapy. (**a**) CT. (**b**) Pulmonary fibrosis in the right paramediastinum shows ^{111}In-pentetreotide uptake on the SPECT image. (**c**) Decreased radiollabeled octreotide uptake 9 months later (Ref. [33], with permission)

A reduction in both ventilation and perfusion was observed 3 months after radiotherapy. Other radiotracers used in different studies include ^{133}Xe, ^{81m}Kr gas, or ^{131}I-MAA with reduced perfusion in the irradiated areas as the common finding [38–40].

Kidneys

Chemotherapy drugs (cisplatin and ifosfamide) can cause renal damage, while abdominal radiation in the treatment of abdominal malignancies can lead to renal nephropathy. Several radionuclide techniques have been proposed to evaluate the effect of these treatments on the kidneys.

Chemotherapy-Induced Tubular Injury

The use of nephrotoxic chemotherapeutic agents can lead to both acute and chronic toxicity, including life-threatening progressive deterioration of kidney function. Cisplatin, a frequently used chemotherapeutic agent, may cause renal toxicity in about one third of patients, usually manifest as a decrease in glomerular filtration rate (GFR). The process is initiated by proximal tubular damage followed by alterations in the GFR and in the effective plasma renal flow [41]. The decrease in GFR is closely related to the dose. Cisplatin can be given in four cycles of 20 mg/m^2 for 5 days without kidney damage, but a treatment dose of 40 mg/m^2 daily for 5 days results in the reduction

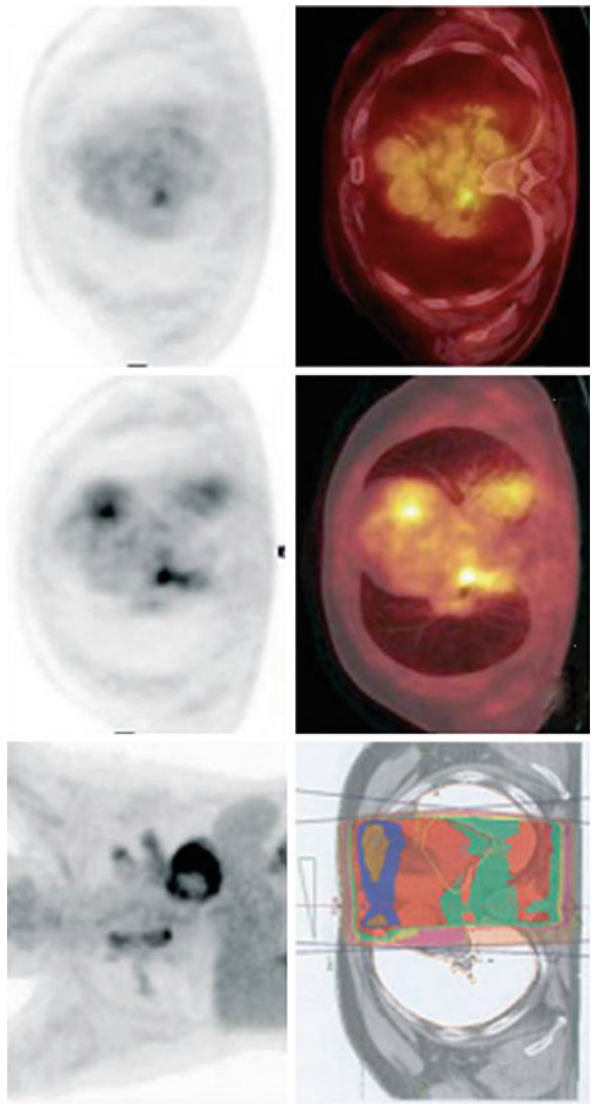

Fig. 4 Post radiotherapy pneumonitis in areas of the radiotherapy treatment field (*left* and *central* panels), with resolution on the [^{18}F]FDG PET/CT scan 2 months later (*right* panel)

of GFR and tubular function [42]. The strategies to prevent cisplatin nephrotoxicity are based on early detection and reduction of toxic effects using diuretics (mannitol and furosemide) or on the use of other platinum derivatives such as carboplatin and iroplatin which have less kidney toxicity. On the other hand, ifosfamide can induce Fanconi's syndrome, a disorder of the proximal tubule of the kidney, with increasing risk at doses exceeding 50 mg/m^2 [43].

Chemotherapy-induced nephropathy can be identified with quantitative measurement of GFR. Although the gold standard for this measurement utilized intravenous injection of ^{51}Cr-labeled EDTA, ^{99m}Tc-DTPA has become the preferred radiopharmaceutical because of availability and cost. Typically, three blood samples are obtained over 2–3 h and tracer clearance is calculated. Methods proposed to evaluate tubular function include the determination of the fractional excretion of electrolytes, the renal threshold for phosphate, aminoaciduria follow-up, and determination of low-molecular-weight proteins (beta-2 microglobulin). Results of such methods should be interpreted with caution before assuming proximal tubular damage because they are affected by excessive secretion of hormones, dependence on plasma concentration of proteins, and urine-plasma measurement. ^{99m}Tc-DMSA scintigraphy can be used to establish tubular dysfunction [44]. It binds to proximal tubular cells. Diseases affecting the proximal tubules, such as tubular acidosis, Fanconi's syndrome, or tubular dysfunction due to nephrotoxic drugs, inhibit ^{99m}Tc-DMSA uptake. In patients treated with ifosfamide, a significant correlation has been found between ^{99m}Tc-DMSA uptake and cumulative doses of ifosfamide ($p < 0.01$). Anninga et al. found that ^{99m}Tc-DMSA scintigraphy is more consistent than urine levels of beta-2 microglobulin in detecting ifosfamide-induced tubular dysfunction and concluded that the test is also able to detect subclinical injury. Other studies show that ifosfamide-induced tubular injury can be detected with ^{99m}Tc-DMSA scintigraphy [45], even before chemotherapy-associated nephrotoxicity is observed by other laboratory measurements [45–47].

Radiation Nephropathy

Radiation therapy can cause damage to the endothelial cells of the glomeruli, the parenchymal vessels, or the renal tubules leading to the radiation nephropathy [48]. Lesion progress is typically slow but resulting in complete atrophy of the irradiated renal tissue with a total loss of function. Nuclear medicine techniques offer the possibility to follow the clinical evolution of radiation nephropathy. Bone scans, using ^{99m}Tc-MDP, show abnormal uptake in the kidney of patients with radiation fields including kidneys, as for vertebral or rib malignancies. Early after radiation (over about 6–9 months) ^{99m}Tc-MDP uptake is increased. Over the succeeding 6–12 months the uptake decreases to normal or below normal levels, associated with the gradual loss of renal parenchymal function [49]. Renography with ^{99m}Tc-DTPA can be performed to assess radiation nephropathy. ^{99m}Tc-DTPA is cleared through glomerular filtration providing information about glomerular function. Simultaneous ^{99m}Tc-DTPA scans to study glomerular function and ^{99m}Tc-DMSA imaging to study tubular function show a decline in renal function at about 6 months after irradiation. Scintigraphic studies with ^{99m}Tc-DTPA and ^{99m}Tc-DMSA have been found to be more sensitive than biochemical tests to assess radiation injury. Renal toxicity has been demonstrated during treatment at radiation doses over 18 Gy. In these patients, radionuclide studies performed at regular intervals are useful for appropriate assessment of renal toxicity [49]. Some studies have described a relation between small vessel injury due to radiation and hypertension. Using ^{99m}Tc-DTPA renography with and without Captopril in patients with hypertension, it has been shown that small-vessel injury appears in hypertensive patients due to increased release of renin [50]. Other studies with ^{99m}Tc-DMSA in unilateral kidney irradiated patients have evaluated the function of each kidney. After a follow-up of 5 years, results showed that the increase of volume in the contralateral kidney was less accentuated than the increase in uptake. This suggests that the mechanism to compensate

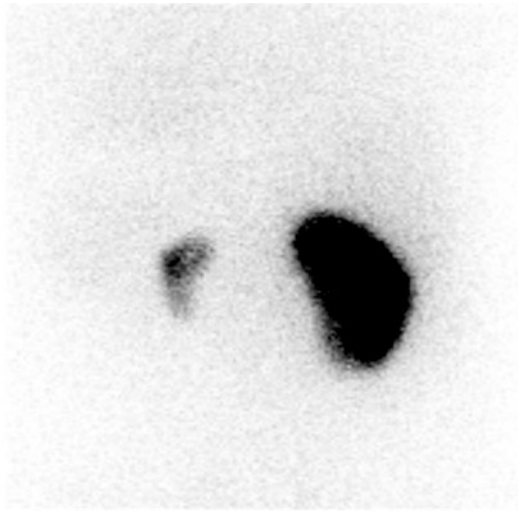

Fig. 5 ^{99m}Tc-DMSA scintigraphy in a patient who received radiotherapy involving the left kidney. Right kidney remains normal

the radiation nephropathy of the contralateral kidney would be hyperfunction rather than hypertrophy [51]. These findings underline the need to perform follow-up function studies in unilateral kidney disease (Fig. 5).

Digestive Tract

Nausea, vomiting, diarrhea, and enteritis often occur due to radiotherapy and chemotherapy. Nuclear medicine examinations can play a role in the detection of radiation-induced late injury on the small bowel.

Radiation Damage of the Small Bowel

In cancers of the cervix, endometrium, ovary, prostate, bladder, or rectum, radiation therapy is often required. In the course of radiation therapy, rectal toxicity of grade 1–2 (Radiation Therapy Oncology Group definition = grade 1 = minor symptoms requiring no treatment; grade 2 = symptoms that respond to simple management) occurs in ~70% of patients. The occurrence of radiation proctitis is related to the volume of the rectum exposed to doses >60 Gy. Radiation proctitis is usually self-limiting and resolves within a month after the conclusion of therapy. Damage of the small bowel is seen in 0.5–15% of the patients [52], and it is characterized by progressive cell depletion, collagen fibrosis, and obliterative vascular injury [53]. Small bowel radiation results in epithelial stem cell injury as an early effect and in evolving vascular injury and collagen fibrosis as late effects. Chronic injuries to the small bowel are manifest 6 and 24 months after radiation [54]. Factors predisposing to late small bowel complications include the total radiation dose, the dose per fraction, the volume of small bowel irradiated, previous surgery, age, diabetes, and chemotherapy combined with radiation therapy [53]. Ileal dysfunction is very frequent in patients with radiation damage of the small intestine, and it is due to bile acid malabsortion, to bacterial overgrowth in the small bowel, or to the combination of both. Endoscopy cannot detect radiation injury of the small bowel. Valdés Olmos et al. used ^{75}Se-homocholic acid conjugated with taurine (^{75}Se-HCAT) and [^{14}C] glycochol breath test to differentiate between normal functioning ileum (both tests negative) and ileal dysfunction (one or both tests positive) in a group of patients who received radiotherapy treatment. Unfortunately, a positive ^{14}C breath test alone cannot differentiate between bile acid malabsorption and bile acid loss due to bacterial overgrowth [51]. However, the combination of both tests may allow the differentiation of those with bile acid malabsorption (^{75}Se-HCAT positive) from those with bacterial overgrowth (^{75}Se-HCAT negative) [55]. Recent studies have proposed the use of somatostatin analogs (SOM230) to treat diarrhea and to ameliorate intestinal injury after localized irradiation in mice [56]. The results show that SOM230 increases survival, preserves mucosal surface area, and reduces bacterial translocation in a dose dependent manner and with a mechanism that likely involves reduction of intraluminal pancreatic enzymes. Nuclear medicine techniques may help to document the benefit of such innovative

approaches that can provide effective countermeasures against radiation injury of the digestive tract.

Liver Damage

The liver is also affected by radio- and chemotherapy treatments. Biopsies show nonspecific fibrosis and rarely cirrhosis, with hepatocellular necrosis and bile stasis [57]. In these cases of radiotherapy- and chemotherapy-associated liver injury, radionuclide studies can be performed using ^{99m}Tc-IDA scintigraphy or ^{99m}Tc-colloid. ^{99m}Tc-IDA has the same behavior as bilirubin. After entering the hepatocyte, it is transported into the bile canaliculi and from bile ducts to small intestine. Gallbladder filling is typically seen. In patients receiving radiotherapy, the most common finding is the loss of function of the part of the liver involved in the radiation field, with a reduced uptake in irradiated areas. A gallbladder filling defect can also be detected in gallbladder carcinomas after radiation therapy [58]. Recently, acute radiation-induced hepatitis has been reported as a potential cause of false-positive findings of malignancy on [^{18}F]FDG-PET scans. [^{18}F]FDG-PET performed 26 days after chemoradiotherapy in an esophageal cancer shows a wedge-shaped hypermetabolic area in which the degree of [^{18}F]FDG uptake is correlated with the prescribed radiation dose. Follow-up [^{18}F]FDG-PET 4 months later showed no abnormal uptake in the liver consistent with acute radiation-induced hepatitis, indicating that PET images must be carefully compared with the distribution of prescribed radiation dose [59].

Other Tracers in Injuries on the Digestive Tract

Finally, irradiation-induced odynophagia and esophageal ulcerations can be visualized by ^{99m}Tc-sucralfate, a tracer that accumulates on esophageal lesions and has shown a very good correlation with endoscopy [60]. Esophagitis postradiotherapy can be observed on [^{18}F]FDG-PET scans (Fig. 6) [36]. Esophagitis postradiotherapy occurs usually, by week 3 or 4 in patients undergoing radiotherapy, treated for thoracic nodal disease and non–small cell lung cancer [61]. Some risk factors are associated with the severity and

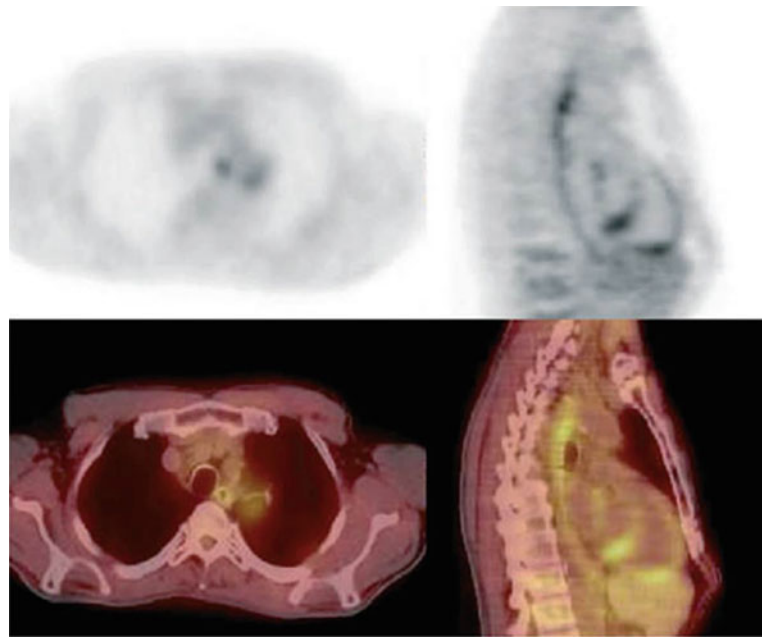

Fig. 6 Diffuse [^{18}F]FDG uptake along the esophagus with a characteristic pattern of post-radiotherapy esophagitis

incidence of esophagitis postradiotherapy such as the age of the patient, tumor type, tumor burden, concurrent chemotherapy, body mass index, and dosimetric predictors (mean esophageal dose, maximal esophageal dose, and percentage of esophagus volume that receives more than 20Gy of radiation) [62–64].

In addition, radiopharmaceuticals commonly employed to assess inflammation, such as leucocytes labeled with ^{111}In or with ^{99m}Tc-HMPAO or [^{18}F]FDG, can be used in patients with suspected radiation enterocolitis in order to localize areas of increased inflammatory activity in small bowel and colon [65].

References

1. Makrilia N, Syrigou E, Kaklamanos I, Manolopoulos L, Saif MW. Hypersensitivity reactions associated with platinum antineoplastic agents: a systematic review. Met Based Drugs. 2010; 2010:pii: 207084.
2. Duggan DB, Petroni GR, Johnson JL, Glick JH, Fisher RI, Connors JM, et al. Randomised comparison of ABVD and MOPP/ABV hybrid for the treatment of advanced Hodgkin's disease: report of an intergroup trial. J Clin Oncol. 2003;21:607–14.
3. Martin WG, Ristow KM, Habermann TM, Colgan JP, Witzig TE, Ansell SM. Bleomycin pulmonary toxicity has a negative impact on the outcome of patients with Hodgkin's lymphoma. J Clin Oncol. 2005;23: 7614–20.
4. Sleijfer S. Bleomycin-induced pneumonitis. Chest. 2001;120:617–24.
5. Ginsberg SJ, Comis RL. The pulmonary toxicity of antineoplastic agents. Semin Oncol. 1982;9:34–51.
6. Sriram N, Kalayarasan S, Sudhandiran G. Epigallocatechin-3- gallate exhibits anti- fibrotic effect by attenuating bleomycin induced glycoconjugates, lysosomal hydrolases and ultrastructural changes in rat model pulmonary fibrosis. Chem Biol Interact. 2009;180: 271–80.
7. Okuma T, Terasaki Y, Kaikita K, Kobayashi H, Kuziel WA, Kawasuji M, Takeya M. C-C chemokine receptor 2 (CCR2) deficiency improves bleomycin-induced pulmonary fibrosis by attenuation of both macrophage in filtration and production of macrophage-derived matrix metalloproteinases. J Pathol. 2004;204:594–604.
8. Rossi SE, Erasmus JJ, McAdams HP, Sporn TA, Goodman PC. Pulmonary drug toxicity: radiologic and pathologic manifestations. Radiographics. 2000;20: 1245–59.
9. Kazama T, Faria SC, Uchida Y, Ito H, Macapinlac HA. Pulmonary drug toxicity: FDG-PET findings in patients with lymphoma. Ann Nucl Med. 2008;22:111–4.
10. Ziessman HA, O'Malley JP, Thrall JH. Infection and inflammation. In: Nuclear medicine, the requisites, 3. Philadelphia: Elsevier-Mosby; 2006. p. 386–7.
11. Bekerman C, Hoffer PB, Bitran JD, Gupta RG. Gallium-67 citrate imaging studies of the lung. Semin Nucl Med. 1980;10:286–301.
12. Mac Mahon H, Bekerman C. The diagnostic significance of gallium lung uptake in patients with normal chest radiographs. Radiology. 1978;127:189–93.
13. Kostakoglu L, Goldsmith SJ. ^{18}F-FDG PET evaluation of the response to therapy for lymphoma and for breast, lung, and colorectal carcinoma. J Nucl Med. 2003;44: 224–39.
14. Kazama T, Faria SC, Varavithya V, Phongkitkarun S, Ito H, Macapinlac HA. FDG PET in the evaluation of treatment for lymphoma: clinical usefulness and pitfalls. Radiographics. 2005;25:191–207.
15. Castellucci P, Zinzani PL, Pourdehnad M, Alinari L, Nanni C, Farsad M, et al. ^{18}F FDG PET in malignant lymphoma: significance of positive findings. Eur J Nucl Med Mol Imaging. 2005;32:749–56.
16. de Wit M, Bohuslavizki KH, Buchert R, Bumann D, Clausen M, Hossfeld DK. ^{18}FDG-PET following treatment as valid predictor for disease-free survival in Hodgkin's lymphoma. Ann Oncol. 2001;12: 29–37.
17. Morikawa M, Demura Y, Mizuno S, Ameshima S, Ishizaki T, Okazawa H. Positron emission tomography imaging of drug-induced pneumonitis. Ann Nucl Med. 2008;22:335–8.
18. Kirsch J, Arrossi AV, Yoon JK, Wu G, Neumann DR. FDG positron emission tomography/computerized tomography features of bleomycin-induced pneumonitis. J Thorac Imaging. 2006;21:228–30.
19. Ishimori T, Saga T, Mamede M, Kobayashi H, Higashi T, Nakamoto Y, et al. Increased ^{18}F-FDG uptake in a model of inflammation: concanavalin A-mediated lymphocyte activation. J Nucl Med. 2002;43:658–63.
20. Yamada S, Kubota K, Kubota R, Ido T, Tamahashi N. High accumulation of fluorine-18-fluorodeoxyglucose inturpentine-induced inflammatory tissue. J Nucl Med. 1995;36:1301–6.
21. Hansson L, Ohlsson T, Valind S, Sandell A, Luts A, Jeppsson B, et al. Glucose utilisation in the lungs of septic rats. Eur J Nucl Med. 1999;26:1340–4.
22. Yamane T, Daimaru O, Ito S, Yoshiya K, Fukaya N, Ito S, et al. Drug-induced pneumonitis detected earlier by ^{18}F-FDG-PET than by high-resolution CT: a case report with non-Hodgkin's lymphoma. Ann Nucl Med. 2008;22:719–22.
23. von Rohr L, Klaeser B, Joerger M, Kluckert T, Cerny T, Gillessen S. Increased pulmonary FDG uptake in bleomycin associated pneumonitis. Onkologie. 2007; 30:320–3.
24. Buchler T, Bomanji J, Lee SM. FDG-PET in bleomycin-induced pneumonitis following ABVD chemotherapy for Hodgkin's disease – a useful tool for monitoring pulmonary toxicity and disease activity. Haematologica. 2007;92:e120–1.

25. Connerotte T, Lonneux M, de Meeûs Y, Hermans C, Vekemans MC, Ferrant A, Van Den Neste E. Use of 2-[^{18}F]fluoro-2-deoxy-d-glucose positron emission tomography in the early diagnosis of asymptomatic bleomycin-induced pneumonitis. Ann Hematol. 2008;87:943–5.
26. Ziessman HA, O'Malley JP, Thrall JH. Ventilation perfusion scintigraphy. In: Nuclear medicine, the requisites. 3rd ed. Philadelphia: Elsevier-Mosby; 2006. p. 513.
27. Graham MM. Scintigraphy. In: James RJ, Stephen GS, Richard KA, editors. Comprehensive respiratory medicine. London: Harcourt-Mosby; 2001.
28. O'Doherty MJ, Van de Pette JE, Page CJ, Bateman NT, Singh AK, Croft DN. Pulmonary permeability in hematologic malignancies. Effects of the disease and cytotoxic agents. Cancer. 1986;58:1286–8.
29. Ishizaka A. Assessment of pulmonary epithelial permeability in interstitial lung diseases. Nihon Kokyuki Gakkai Zasshi. 1999;37:515–25.
30. Graves PR, Siddiqui F, Anscher MS, Movsas B. Radiation pulmonary toxicity: from mechanisms to management. Semin Radiat Oncol. 2010;20:201–7.
31. Valdés Olmos RA, van Zandwijk N, Boersma LJ, Hoefnagel CA, Baas P, Baars JB, Muller SH, Lebesque JV. Radiation pneumonitis imaged with indium-111 pentetreotide. J Nucl Med. 1996;37:584–8.
32. Kataoka M, Kawamura M, Itoh H, Hamamoto K. Gallium-67-citrate scintigraphy forthe early detection of radiation pneumonitis. Clin Nucl Med. 1992;17:27–31.
33. Lebtahi R, Moreau S, Marchand-Adam S, et al. Increased uptake of ^{111}In-octreotide in idiopathic pulmonary fibrosis. J Nucl Med. 2006;47:1281–7.
34. Ha L, Mansberg R, Nguyen D, Bui C. Increased activity on In-111 octreotide imaging due to radiation fibrosis. Clin Nucl Med. 2008;33:46–8.
35. Banzo J, Prats E, Razola P, Tardín L, Benito JL, Andrés A, Santapau A. ^{111}In-DTPAOC SPECT-CT in radiation pulmonary fibrosis. Rev Esp Med Nucl. 2009;28:81–2.
36. Quirce Pisano R, Banzo Marraco I, Jiménez-Bonilla JF, Martínez-Rodríguez I, Sainz Esteban A, Carril Carril JM. Potential sources of diagnostic pitfall and variants in FDG-PET/CT. Rev Esp Med Nucl. 2008; 27:130–59.
37. Song H, Yu JM, Kong FM, Lu J, Bai T, Ma L, Fu Z. [^{18}F]2-fluoro-2-deoxyglucose positron emission tomography/computed tomography in predicting radiation pneumonitis. Chin Med J. 2009;122:1311–5.
38. Groth S, Zaric A, Sørensen PB, Larsen J, Sørensen PG, Rossing N. Regional lung function impairment following post-operative radiotherapy for breast cancer using direct or tangential field techniques. Br J Radiol. 1986; 59:445–51.
39. Shinohara S, Arikawa K. Radioisotopic assessment on development of radiation pneumonitis and fibrositis. Australas Radiol. 1972;16:363–6.
40. Prato FS, Kurdyak R, Saibil EA, Rider WD, Aspin N. Physiological and radiographic assessment during the development of pulmonary radiation fibrosis. Radiology. 1977;122:389–97.
41. Daugaard G, Abildgaard U. Cisplatin nephrotoxicity. Cancer Chemother Pharmacol. 1989;25:1–9.
42. Valdés Olmos RA. Chemotherapy-induced tubular injury and ^{99m}Tc-DMSA. In: Valdés Olmos RA, editor. The role of nuclear medicine in the detection of organ injury and adverse effects of cancer therapy. Thesis, University van Amsterdam; 1994. p. 37.
43. Pratt CB, Meyer WH, Jenkins JJ, Avery L, McKay CP, Wyatt RJ, Hancock ML. Ifosfamide, Fanconi's syndrome, and rickets. J Clin Oncol. 1991;9:1495–9.
44. Van Luijk WH, Ensing GJ, Meijer S, Donker AJ, Piers DA. Is the relative ^{99m}Tc-DMSA clearance a useful marker of proximal tubular dysfunction? Eur J Nucl Med. 1984;9:439–42.
45. Anninga JK, De Kraker J, Hoefnagel CA, Vaoute PA. Ifosfamide induced nephrotoxicity evaluated by ^{99m}Tc-DMSA renal scintigraphy. Med Pediatr Oncol. 1990; 18:406.
46. Caglar M, Yarís N, Akyuz C. The utility of ^{99m}Tc-DMSA and ^{99m}Tc-EC scintigraphy for early diagnosis of ifosfamide induced nephrotoxicity. Nucl Med Commun. 2001;22:1325–32.
47. Anninga JK, Valdés Olmos RA, de Kraker J, van Tinteren H, Hoefnagel CA, van Royen EA. Technetium-99m dimercaptosuccinic acid and ifosfamide tubular dysfunction in children with cancer. Eur J Nucl Med. 1994;21:658–62.
48. Williams MV. The cellular basis of renal injury by radiation. Br J Cancer Suppl. 1986;7:257–64.
49. Dewit L, Anninga JK, Hoefnagel CA, Nooijen WJ. Radiation injury in the human kidney: a prospective analysis using specific scintigraphic and biochemical endpoints. Int J Radiat Oncol Biol Phys. 1990;19: 977–83.
50. Verheij M, Dewit LGH, Valdés Olmos RA, Hoefnagel CA, Arisz L. Captopril Tc-99m-DTPA renography in patients with radiation induced renovascular hypertension. In: Schmidt HAE, Hofer R, editors. Nuclear medicine in research and practice. New York: Schattauer Stuttgart; 1992. p. 545–8.
51. Valdés Olmos RA. Radiation nephropathy. In: Valdés Olmos RA, editor. The role of nuclear medicine in the detection of organ injury and adverse effects of cancer therapy. Thesis, University van Amsterdam; 1994. p. 40.
52. Allen-Mersh TG, Wilson EJ, Mann CV. Has the incidence of radiation-induced bowel damage following treatment of uterine carcinoma changed in the last 20 years? J R Soc Med. 1986;79:387–90.
53. Touboul E, Balosso J, Schlienger M, Laugier A. Radiation injury of the small intestine. Radiobiological, radiopathological aspects; risk factors and prevention. Ann Chir. 1996;50:58–71.
54. Galland RB, Spencer J. The natural history of clinically established radiation enteritis. In: Galland RB, Spencer J, editors. Radiation enteritis. London: Edward Arnold; 1990. p. 136–46.

55. Valdés Olmos RA, den Hartog JF, Hoefnagel C, Taal B. Imaging and retention measurements of selenium 75 homocholic acid conjugated with taurine, and the carbon 14 glycochol breath test to document ileal dysfunction due to late radiation damage. Eur J Nucl Med. 1991;18:124–8.
56. Fu Q, Berbée M, Boerma M, Wang J, Schmid HA, Hauer-Jensen M. The somatostatin analog SOM230 (pasireotide) ameliorates injury of the intestinal mucosa and increases survival after total-body irradiation by inhibiting exocrine pancreatic secretion. Radiat Res. 2009;171:698–707.
57. Floyd J, Mirza I, Sachs B, Perry MC. Hepatotoxicity of chemotherapy. Semin Oncol. 2006;33:50–67.
58. Valdés Olmos RA. Other tracers in injuries of the digestive tract. In: Valdés Olmos RA, editor. The role of nuclear medicine in the detection of organ injury and adverse effects of cancer therapy. Thesis, University van Amsterdam; 1994. p. 36–7.
59. Nakahara T, Takagi Y, Takemasa K, Mitsui Y, Tsuyuki A, Shigematsu N, et al. Dose-related fluorodeoxyglucose uptake in acute radiation-induced hepatitis. Eur J Gastroenterol Hepatol. 2008;20:1040–4.
60. Taal BG, Valdés Olmos RA, Boot H, Hoefnagel CA. Assessment of sucralfate coating by sequential scintigraphic imaging in radiation induced esophageal lesions. Gastrointest Endosc. 1995;41:109–14.
61. Bradley JD, Scott CB, Paris KJ, Demas WF, Machtay M, Komaki R, et al. A phase III comparison of radiation therapy with or without recombinant beta-interferon for poor-risk patients with locally advanced non-small-cell lung cancer (RTOG 93-04). Int J Radiat Oncol Biol Phys. 2002;52:1173–9.
62. Ahn SJ, Kahn D, Zhou S, Yu X, Hollis D, Shafman TD, et al. Dosimetric and clinical predictors for radiation-induced esophageal injury. Int J Radiat Oncol Biol Phys. 2005;61:335–47.
63. Huang EX, Bradley JD, El Naqa I, Hope AJ, Lindsay PE, Bosch WR, et al. Modeling the risk of radiation-induced acute esophagitis for combined Washington University and RTOG trial 93-11 lung cancer patients. Int J Radiat Oncol Biol Phys. 2012;82:1674–9.
64. Ulaner GA, Lyall A. Identifying and distinguishing treatment effects and complications from malignancy at FDG PET/CT. Radiographics. 2013;33:1817–34.
65. Levi S, Hodgson HJ. The medical management of radiation enteritis. In: Galland RB, Spencer J, editors. Radiation enteritis. London: Edward Arnold; 1990. p. 176–98.

Part VII

Teaching Cases in Nuclear Oncology (with Contributions from Various Authors)

Teaching Cases in Nuclear Oncology: Lymphomas

53

Kimiteru Ito, Somali Gavane, and Heiko Schöder

Keywords

Hodgkin's lymphoma • Non-Hodgkin lymphoma • [^{18}F]FDG • PET/CT • PET/MRI • Diffuse large B-cell lymphoma • Burkitt lymphoma • Response to therapy

Glossary

[^{18}F]FDG	2-Deoxy-2-[^{18}F]fluoro-D-glucose
ABVD	Chemotherapy regimen based on doxorubicin bleomycin, vinblastine, and dacarbazine
AJCC	American Joint Committee on Cancer
CT	X-ray computed tomography
DLBCL	Diffuse large B-cell lymphoma
HL	Hodgkin's lymphoma
MIP	Maximum intensity projection
MRI	Magnetic resonance imaging
PET	Positron emission tomography
PET/CT	Positron emission tomography/ Computed tomography
PET/MRI	Positron emission tomography/ Magnetic resonance imaging
SUV	Standardized uptake value
SUV_{max}	Standardized uptake value at point of maximum
NHL	Non-Hodgkin lymphomas
R-CHOP	Rituximab with cyclophosphamide, doxorubicin, vincristine, and prednisone
R-COMP	Rituximab, cyclophosphamide, non-pegylated liposome-encapsulated doxorubicin, vincristine and prednisone

Contents

Diffuse Large B Cell Lymphoma 1532
Presentation 1532
Findings 1532
Follow-up 1533

Discussion 1533

Diffuse Large B Cell Lymphoma 1534

Diffuse Large B Cell Lymphoma 1534
Presentation 1534
Findings 1534
Follow-Up 1535
Discussion 1535

Hodgkin's Disease 1536
Presentation 1536
Findings 1536

Hodgkin's Lymphoma 1537
Presentation 1537
Findings 1537
Discussion 1537

K. Ito • H. Schöder (✉)
Department of Radiology, Molecular Imaging and Therapy service, Memorial Sloan Kettering Cancer Center, New York, NY, USA
e-mail: schoderh@mskcc.org

S. Gavane
Division of Nuclear Medicine, Department of Radiology, Mount Sinai Hospital, New York, NY, USA

© Springer International Publishing Switzerland 2017
H.W. Strauss et al. (eds.), *Nuclear Oncology*,
https://doi.org/10.1007/978-3-319-26236-9_31

Hodgkin's Lymphoma 1539
Presentation 1539
Findings 1539
Follow-Up 1539
Discussion 1540

Burkitt Lymphoma 1540
Presentation 1540
Findings 1541
Follow-Up 1541
Discussion 1542

References 1543

Diffuse Large B Cell Lymphoma

Case contributed by: V. Yerubaudi, C. Sakellis, A.D. Van den Abbeele, H. Jacene

Nuclear Medicine/PET-CT, Dana-Farber Cancer Institute, Harvard Medical School, Boston, Massachusetts, USA

Presentation

A 65-year-old man with no significant past medical history presented with night sweats, low-grade fevers, weight loss, decreased appetite, and worsening dyspnea on exertion for several months.

Findings

A CT pulmonary arteriogram obtained to evaluate for pulmonary embolism at initial clinical presentation was positive for pulmonary emboli (Fig. 1). An anterior mediastinal mass involving the pericardium and myocardium causing narrowing of the right heart chambers (Fig. 2) and completely encasing the right coronary artery without occluding or significantly narrowing the lumen (Figs. 1 and 2) was also shown.

Diagnostic CT of the abdomen and pelvis (not shown) did not show additional areas of adenopathy. A cardiac MRI better delineated tumor margins and defined the myocardial and pericardial involvement (Fig. 3). Pathology from mediastinoscopic biopsy was consistent with non-Hodgkin diffuse large B-cell lymphoma with high grade features.

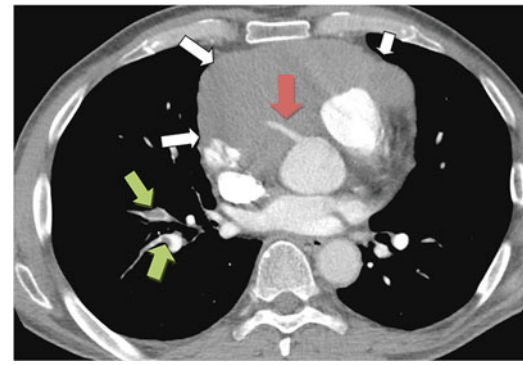

Fig. 1 CT pulmonary arteriogram showing large mass (*white arrows*) overlying the main pulmonary artery and aortic root with encasement of the proximal right coronary artery (*red arrow*). Pulmonary emboli can also be seen in the right pulmonary arteries (*green arrows*)

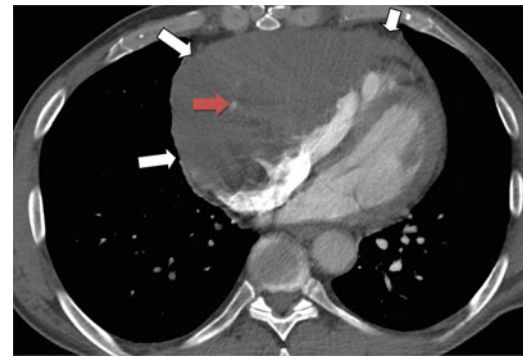

Fig. 2 CT pulmonary arteriogram showing a large pericardial/myocardial mass (*white arrows*) involving the right ventricle and right atrium with severe narrowing of the right heart chambers. Distal right coronary artery remains encased in the mass (*red arrow*)

[^{18}F]FDG PET/CT was performed prior to initiation of therapy (Fig. 4) and showed intense [^{18}F]FDG uptake in the dominant mass involving the right heart (Fig. 5) with additional sites of intense uptake in the superior mediastinum, left face adjacent to the parotid gland, and right mid-abdomen. These areas of uptake in the left face and right mid-abdomen were found to be additional sites of disease on further evaluation. These multiple areas of lymph node involvement and extranodal cardiac involvement with the presence of symptoms made the patient AJCC Stage IVB.

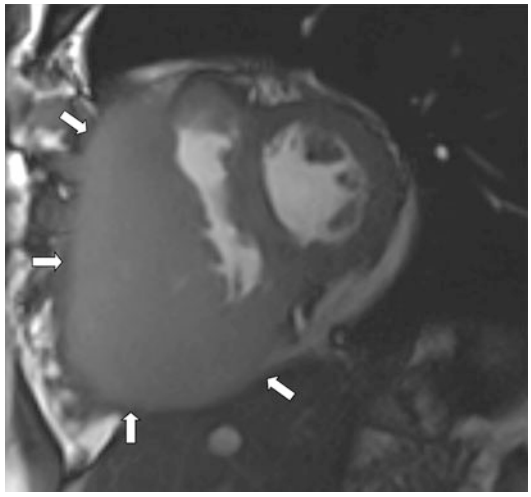

Fig. 3 Cardiac MRI EKG-gated TrueFISP sequence showing the large mass (*white arrows*) involving the right ventricular free wall in a short axis view

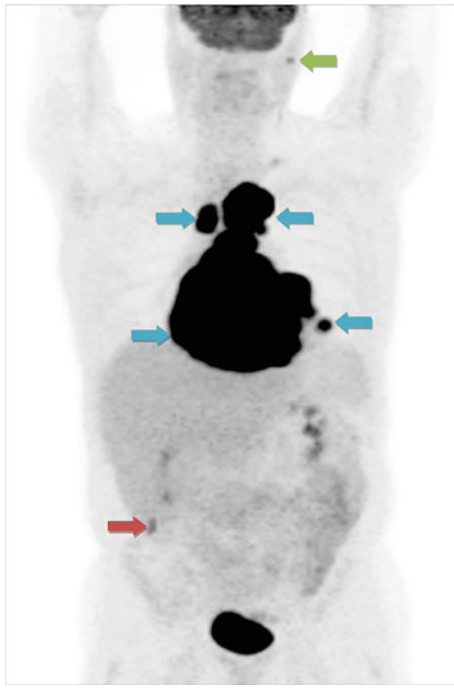

Fig. 4 PET maximum intensity projection image from the anterior view showing large mass (*blue arrows*) in the region of the right heart and superior mediastinum with additional [^{18}F]FDG-avid lymph nodes (*blue arrows*) and a separate pericardial [^{18}F]FDG-avid nodule (*blue arrows*). Small [^{18}F]FDG-avid lymph nodes were also identified in the left face (*green arrow*) and right abdomen (*red arrow*) consistent with additional sites of disease

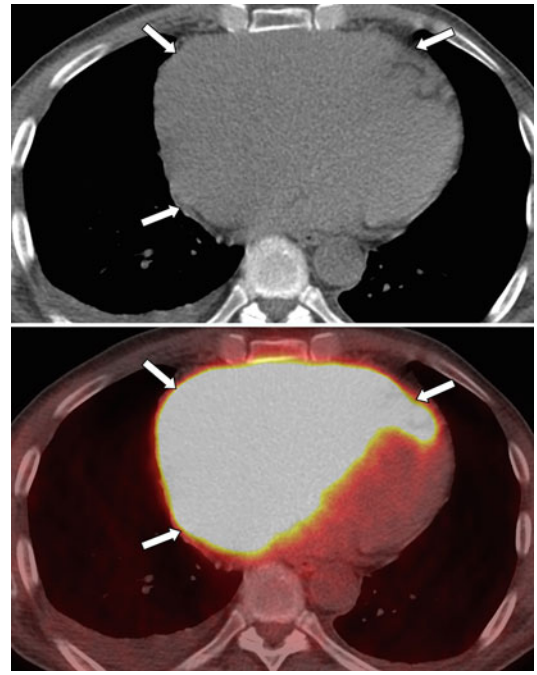

Fig. 5 Axial CT (*above*) and fused PET/CT (*below*) show intense [^{18}F]FDG uptake in the large anterior mediastinal mass with extensive cardiac involvement. Small right larger than left pleural effusions are also incidentally noted on CT

Follow-up

[^{18}F]FDG PET/CT imaging after completion of therapy with 6 cycles of R-CHOP (rituximab with cyclophosphamide, doxorubicin, vincristine, and prednisone) as well as 3 cycles of high dose methotrexate. PET/CT showed complete metabolic response to therapy with no residual [^{18}F]FDG uptake (Fig. 6).

Discussion

Systemic lymphoma with secondary cardiac involvement by lymphoma (as in this case) is more common than primary cardiac lymphoma. Initial presentation with cardiac symptoms is rare and symptoms are often non-specific. Arrhythmias, heart failure, or sudden death are some of the cardiac clinical presentations that can occur.

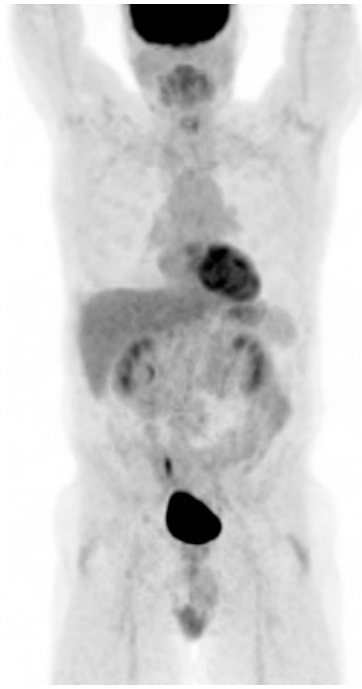

Fig. 6 PET maximum intensity projection image viewed anteriorly after the completion of therapy (6 months after diagnosis) shows complete metabolic response to therapy. No residual abnormal [^{18}F]FDG uptake is seen

This patient presented with symptoms of pulmonary embolism, likely related to thrombi developing on the mass encroaching into the right heart chambers and possibly symptoms of right heart failure as well due to the mass narrowing the lumen. Treatment of lymphoma with cardiac involvement is considered relatively urgent since cardiogenic symptoms could be potentially fatal.

Involvement of the right heart, encasement of the right coronary artery without occlusion, and mass infiltrating the myocardium are some of the characteristic features of cardiac involvement of lymphoma as demonstrated in this case.

Diffuse Large B Cell Lymphoma

Case contributed by: E. Tabacchi[1], C. Nanni[1], I. Bossert[1], A.M. Maffione[2], S. Fanti[1]

[1]Nuclear Medicine Unit, "S. Orsola-Malpighi" Hospital, Bologna, Italy

[2]Nuclear Medicine Unit, "Santa Maria della Misericordia" Hospital, Rovigo, Italy

68 year-old man with diffuse large B-Cell lymphoma localized to the right testicle and a new diagnosis of diabetes mellitus uncompensated underwent a staging [^{18}F]FDG PET/CT (Fig. 7).

[^{18}F]FDG PET/CT revealed abdominal uptake (Fig. 8) at the pancreas (SUV_{max} 13.8) (red arrows), at multiple lymph nodes above and below the diaphragm involving bilateral inguinal, paracaval, interaortocaval, hepatic hilum, peripancreatic, axillary and laterocervical lymph nodes (green arrows). In addition, there was a focal uptake in the right testicle (SUV_{max} 7.7) (Fig. 8j, k, l; orange arrows),

[^{18}F]FDG PET/CT showed increased uptake also at the right scapula, sternum, left humerus, D8, VI-VIII-IX left ribs, IX right rib, left iliac crest (SUV_{max} 5.4) (Figs. 7 and 8: yellow arrows). These findings were related to the lymphoma.

Patient underwent R-COMP regime (rituximab, cyclophosphamide, non-pegylated liposome-encapsulated doxorubicin, vincristine and prednisone) and achieved complete remission after 3 cycles of the chemotherapy.

Diffuse Large B Cell Lymphoma

Presentation

A 68-year-old woman complained about progressive sore throat, oral mass, odynophagia, dysphasia, dysarthria and reduce hearing. The patient was referred to diagnose the disease because biopsy in previous hospital was non-diagnostic.

Findings

Diagnostic CT showed heterogeneous mass in the right posterolateral nasopharynx, extending along the soft palate, deviated the airway to the left, and involvement of the masticator muscle. And bilateral enlarged level II lymph nodes were noted. Fine needle biopsy from right nasopharyngeal

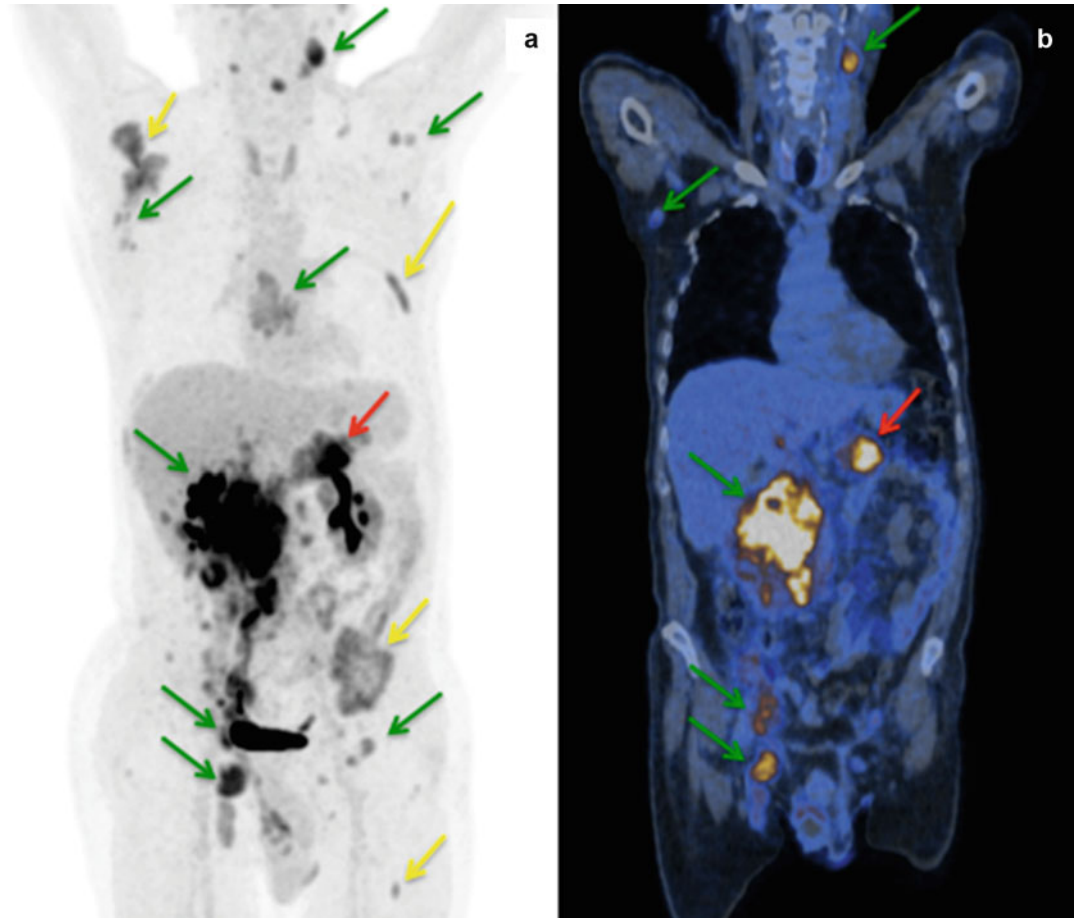

Fig. 7 (**a**): MIP; (**b**): coronal [^{18}F]FDG PET/CT; *Red arrows*: pancreas lesion, *Green arrows*: lymph nodal lesions, *Yellow arrows*: bone lesions

mass revealed diffuse large B-cell lymphoma (DLBCL) (stage II). Baseline [^{18}F]FDG PET/CT images (Fig. 9) reveal nasopharyngeal mass with lymph node metastases (A, B). Hypermetabolic bilateral neck lymphadenopathy was seen in bilateral cervical chains.

Follow-Up

After completion of therapy with 2 cycles of R-CHOP (rituximab with cyclophosphamide, doxorubicin, vincristine, and prednisone), interim [^{18}F]FDG PET/CT images (C, D) showed complete remission of DLBCL and non-hypermetabolic thickening soft tissue with air-fluid levels in the bilateral maxillary sinus. End-of-treatment [^{18}F]FDG PET/CT images (E, F) showed sustained complete remission and improved the sinusitis.

Discussion

The non-Hodgkin lymphomas (NHL) including DLBCL represent the majority of head and neck lymphomas [1]. Waldeyer's ring is one of the most

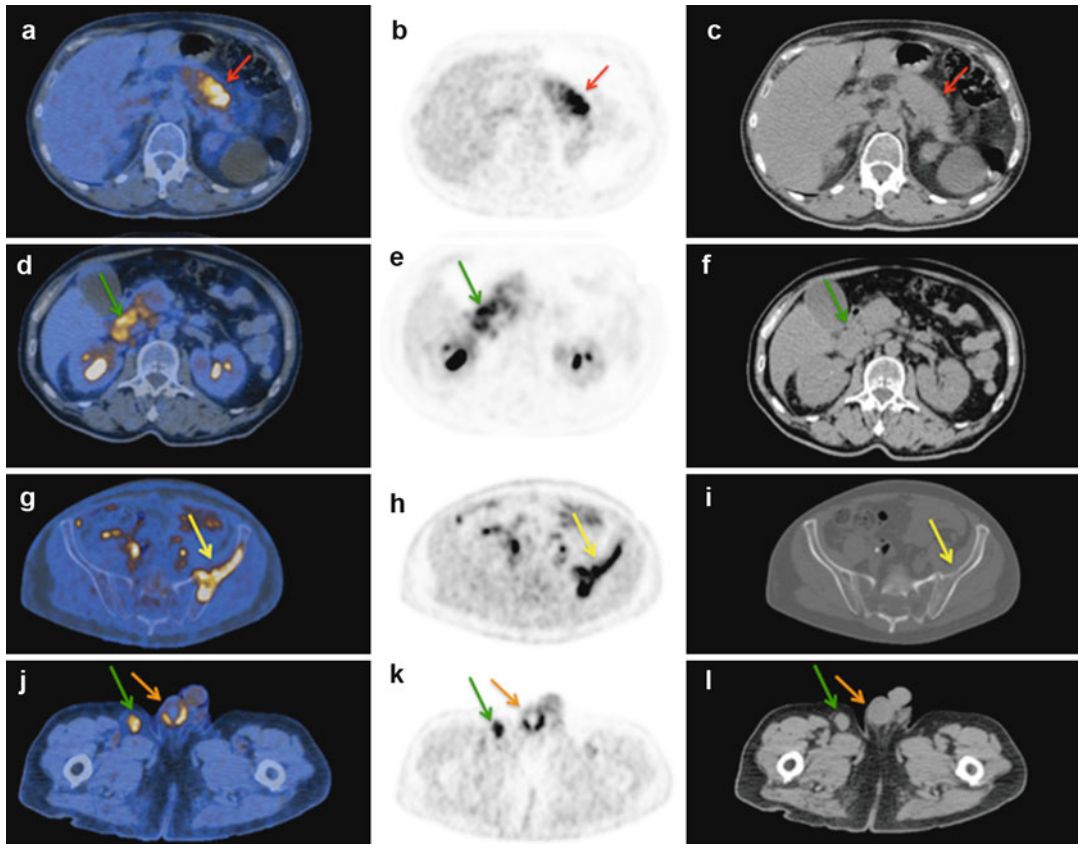

Fig. 8 (**a**, **d**, **g**, **f**): transaxial fused [^{18}F]FDG PET/CT images; (**b**, **e**, **h**, **k**): transaxial [^{18}F]FDG PET images; (**c**, **f**, **i**, **l**): transaxial CT; *Red arrows*: pancreas lesion, *Green arrows*: lymph nodal lesions, *Yellow arrows*: bone lesion; *Orange arrows*: testicular lesion

common sites. However NHL of the nasopharynx has rarely been reported.

Hodgkin's Disease

Case contributed by: S. Al Shammari, F. Fraioli
Institute of Nuclear Medicine, UCLH NHS Foundation Trust, London, UK

Presentation

Newly diagnosed, bulky mediastinal Hodgkin's disease. [^{18}F]FDG PET/CT for baseline staging.

Findings

There is an intensely [^{18}F]FDG-avid bulky anterior mediastinal mass (arrow) (SUV_{max} 21.3, transverse dimension 10 cm). The mass shows heterogeneous [^{18}F]FDG uptake with focal extension of the mass into the anterior chest wall between the first and second ribs. The mass also extends to the left lung hilum and into the adjacent left lung. There is an [^{18}F]FDG-avid left supraclavicular node (arrowhead, SUV_{max} 10.8, 1.3 cm). There are further [^{18}F]FDG-avid right upper and bilateral lower paratracheal lymph nodes. The spleen is not enlarged but shows mild diffuse increased [^{18}F]FDG uptake. There is prominent diffuse skeletal [^{18}F]FDG

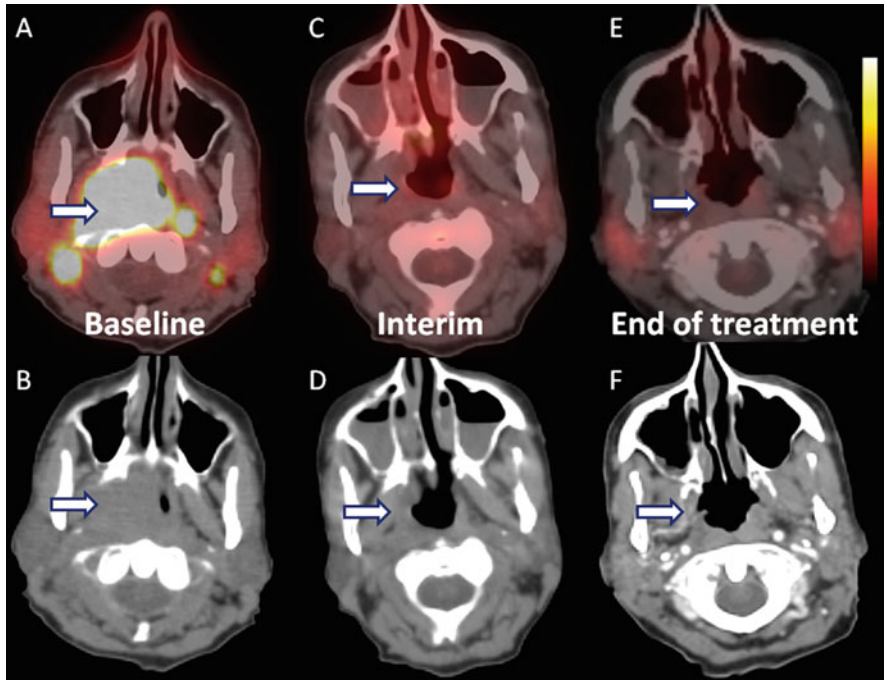

Fig. 9 (**a**) Baseline [^{18}F]FDG PET/CT and (**b**) CT axial images showed hypermetabolic large right nasopharyngeal mass extending anteriorly along the soft palate and posteriorly into the adenoid tissue and longus coli musculature C (*white arrows*) (**c**) Interim [^{18}F]FDG PET/CT fused axial image and (**d**) CT reveal complete remission of DLBCL (SUV_{max} 1.94) and non-specific fluid retention in the bilateral maxillary sinus. (**e**) End-of-treatment [^{18}F]FDG PET/CT image and (**f**) CT showed sustained complete remission of DLBCL (SUV_{max} 1.31)

activity but no focal avid lesion to suggest bone marrow involvement (Fig. 10).

Hodgkin's Lymphoma

Case contributed by: S. Al Shammari, F. Fraioli
Institute of Nuclear Medicine, UCLH NHS Foundation Trust, London, UK

Presentation

Hodgkin's lymphoma. [^{18}F]FDG PET/MRI for baseline staging, interim and complete treatment scan.

Findings

There are multiple [^{18}F]FDG-avid mediastinal nodes (SUV_{max} 23.3), which show interval improvement after two cycles of treatment with doxorubicin, bleomycin, vinblastine, and dacarbazine (ABVD). There are also multiple bone lesions (arrowheads), L3 vertebral body and left iliac spine visible on the coronal views. There is complete treatment response after completion of therapy (Fig. 11).

Discussion

Staging of lymphoma is a vital pre-requisite to their appropriate therapeutic management and prognosis. This is based on the Ann Arbor classification, to which a definition of bulky disease, called the Cotswald modification, has been added. The usefulness of [^{18}F]FDG PET in the initial staging of lymphoma has been demonstrated in several studies. The main advantage over anatomical imaging techniques, such as CT, is its ability to detect metabolic changes in before the structural changes become visible. PET may upstage

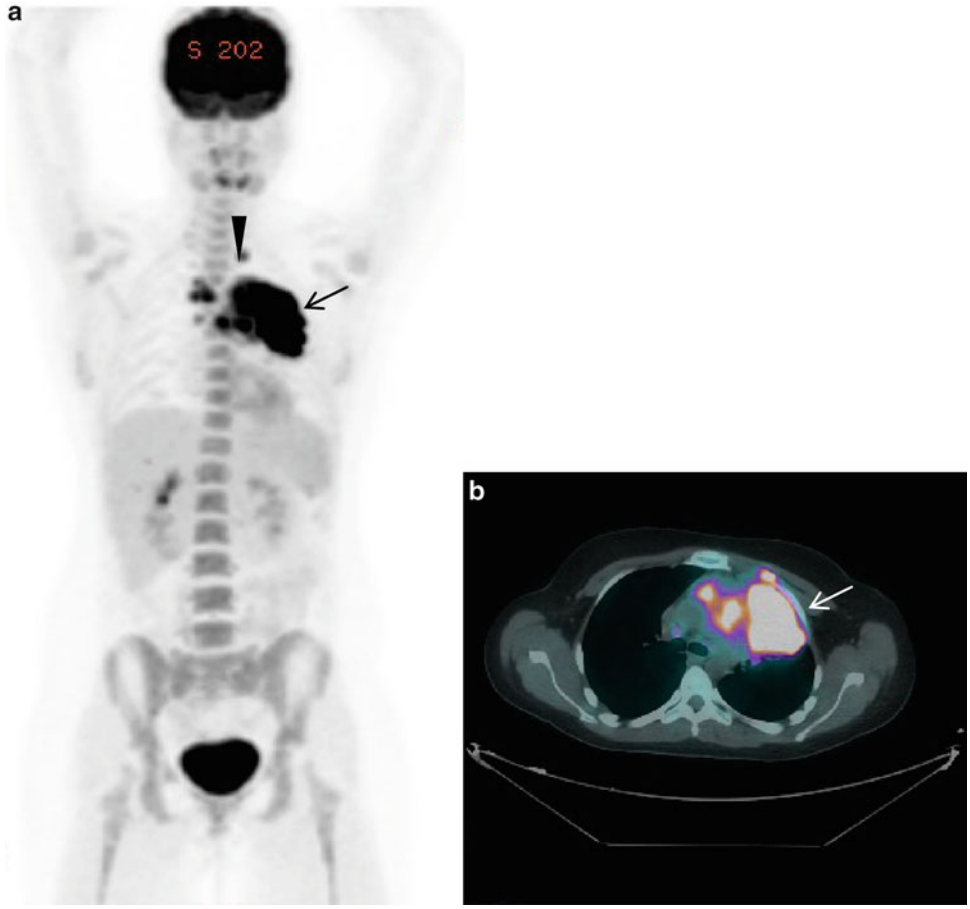

Fig. 10 (**a**) Maximum intensity projection (arrowhead, supraclavicular lymph-node); (**b**) PET/CT axial fused image (arrow, anterior mediastinal mass)

or pick up occult lesions such as splenic, bone marrow, osseous, and gastrointestinal involvement. PET scans have demonstrated high negative predictive value to exclude bone marrow involvement. This holds particularly true for early-stage Hodgkin's lymphoma (HL), and may even obviate the need for bone marrow biopsy in this group. In assessing response to therapy, the Deauville criteria, laid by a consensus committee of nuclear medicine physicians, hematologists, and oncologists recommends a 5-point scale rather than taking a binary decision (namely PET positive or negative). This is based upon visual analysis, with background uptake (mediastinum and liver) as reference. Recognition of early therapeutic response or failure enables the treatment to be adjusted accordingly. Several ongoing trials are under way to assess the impact of treatment adaptation based on early [^{18}F]FDG PET results on overall survival.

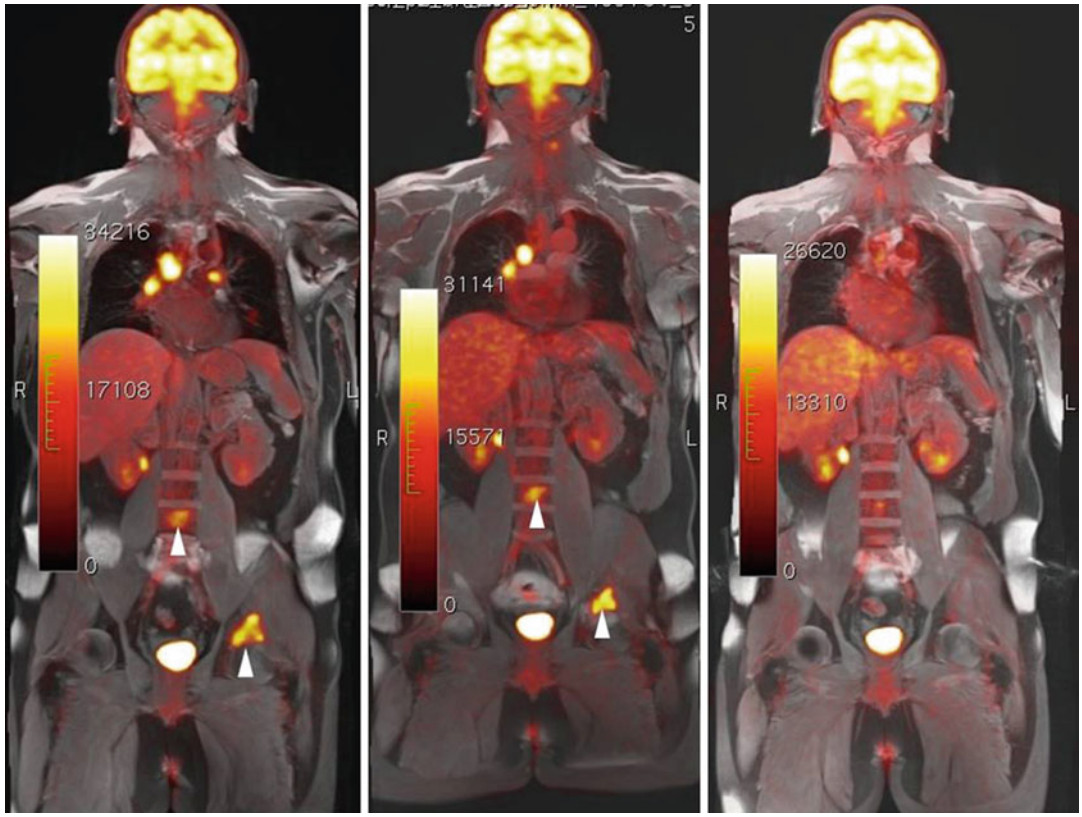

Fig. 11 Fused [^{18}F]FDG PET/MRI coronal images. Baseline and Interim PET/MRI images show hypermetabolic lesions in chest lymph-nodes, lumber vertebral body (white arrowhead), and left ilium (white arrowhead). End of treatment PET/MRI shows almost complete metabolic response

Hodgkin's Lymphoma

Presentation

A 21-year-old woman complained about persistent paroxysmal cough for 1 year. Chest X-ray at an outside hospital showed a large anterior mediastinal mass.

Findings

Ultrasound sound guided fine needle biopsy from a right neck mass showed classical Hodgkin's lymphoma (stage II). Biopsy from bone marrow showed normocellular marrow with trilineage hematopoiesis. The patient was referred for initial staging with baseline [^{18}F]FDG PET/CT. The scan showed nodal [^{18}F]FDG avid disease (Fig. 12).

Follow-Up

After 2 cycles of ABVD (doxorubicin, bleomycin, vinblastine, and dacarbazine) chemotherapy, an interim [^{18}F]FDG PET/CT (Fig. 13) showed that reduced [^{18}F]FDG avid disease in a smaller

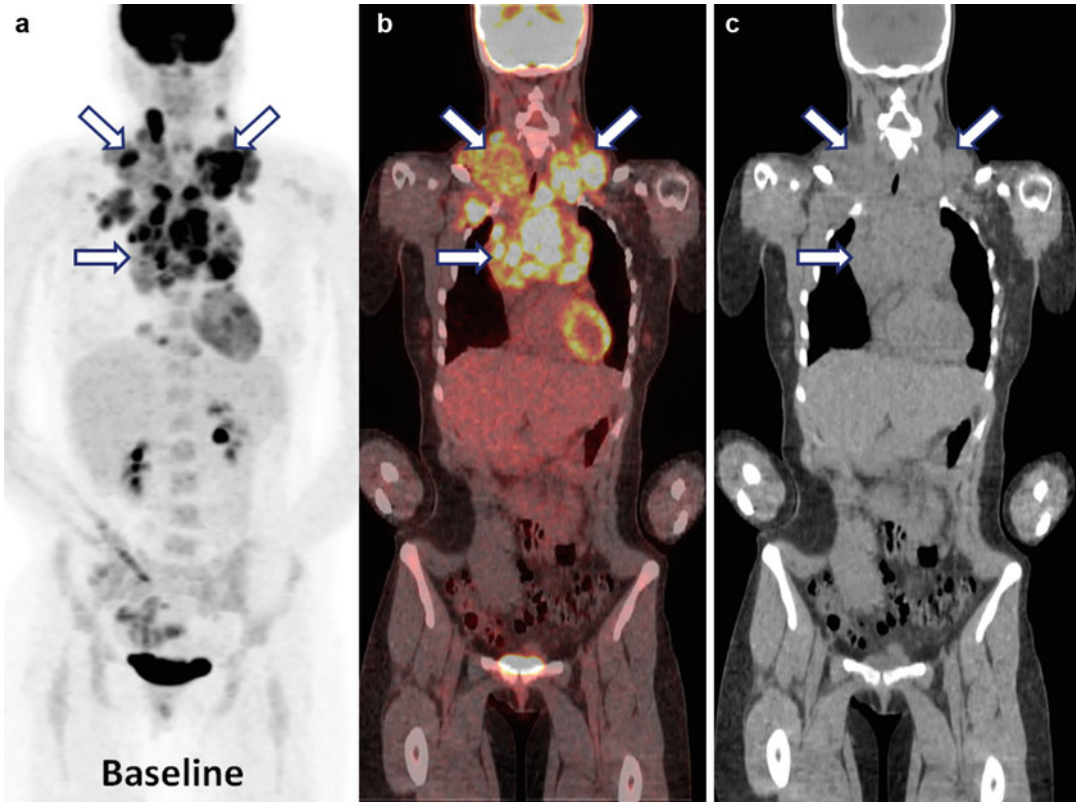

Fig. 12 (Baseline). (**a**) Maximum intensity projection (MIP), (**b**) fused [^{18}F]FDG PET/CT coronal image, and (**c**) CT coronal image show multiple hypermetabolic lesions in the mediastinum (12.5 × 4.5 cm) and subclavicular lymph nodes (*white arrows*). Conglomerate hypermetabolic anterior mediastinal lesion shows hypermetabolic uptake (SUV_{max} 14.2)

residual mass with an equivalent to blood pool activity. The patient has had no relapse for 5 years.

Discussion

In routine clinical practice, [^{18}F]FDG PET/CT plays a major role in the assessment of chemotherapy response in Hodgkin's lymphoma. Rather than pretreatment prognostic factors such as the stage of the disease, an early response to therapy assessment by means of [^{18}F]FDG PET/CT has been shown to be amore accurate predictor of prognosis [2, 3]. In this case, interim [^{18}F]FDG PET/CT showed no significant uptake, which suggested better clinical course and outcome.

Burkitt Lymphoma

Presentation

A 55 year-old-woman was referred with malignant lymphoma (stage IV). The patient complained of pain in left hip.

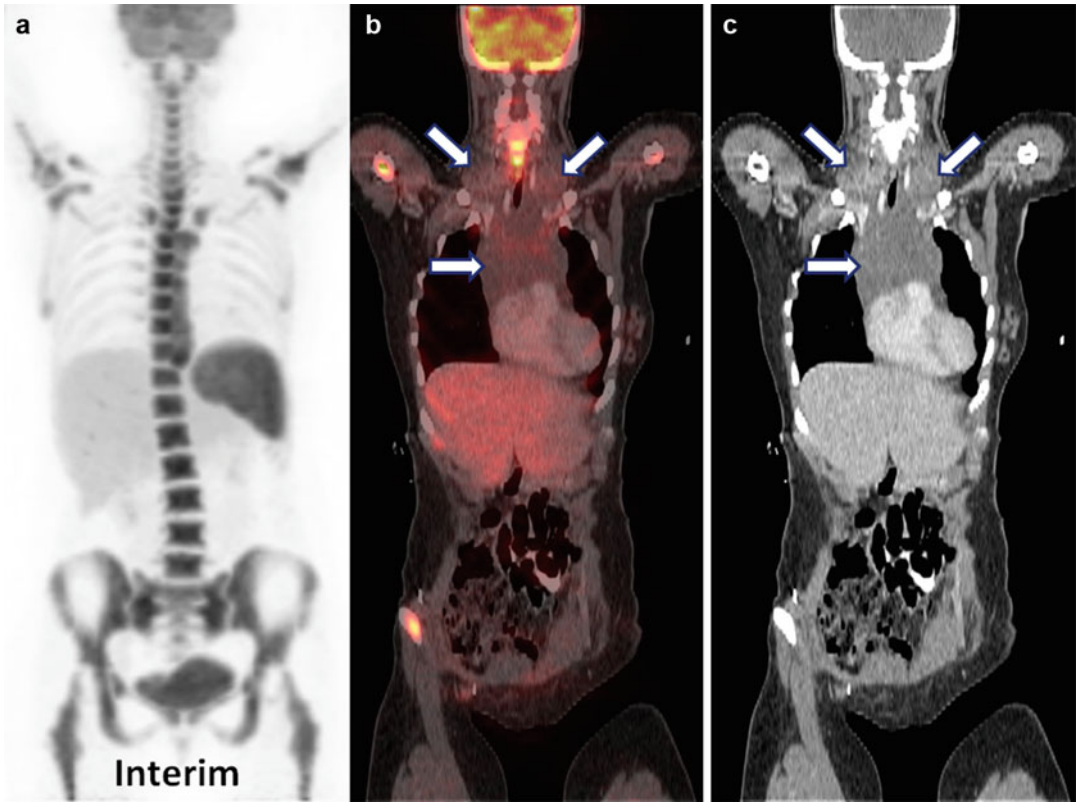

Fig. 13 (Interim). (**a**) MIP and (**b**, **c**) interim [^{18}F]FDG PET/CT images revealed complete remission with residual mass (8.5 × 4.7 cm) having slight [^{18}F]FDG uptake (SUV_{max} 2.0) in the mediastinum (*white arrows*). Diffuse metabolism in spleen and bone marrow is related to administration of granulocyte-colony stimulating factor

Findings

Diagnostic CT demonstrated soft tissue density in a right humerus and extensive marrow involvement. Open biopsy from a right humerus lesion revealed Burkitt lymphoma. [^{18}F]FDG PET/CT was performed prior to initiation of therapy. Baseline [^{18}F]FDG PET/CT (Fig. 14) showed bone marrow involvement and extranodal [^{18}F]FDG avid lesions.

Follow-Up

The patient was treated with high-dose chemotherapy with intrathecal methotrexate. End of treatment [^{18}F]FDG PET/CT (Fig. 15) clearly showed clinical remission including bone lesions. The patient was expectantly monitored until CT revealed the relapse after 6 years follow-up.

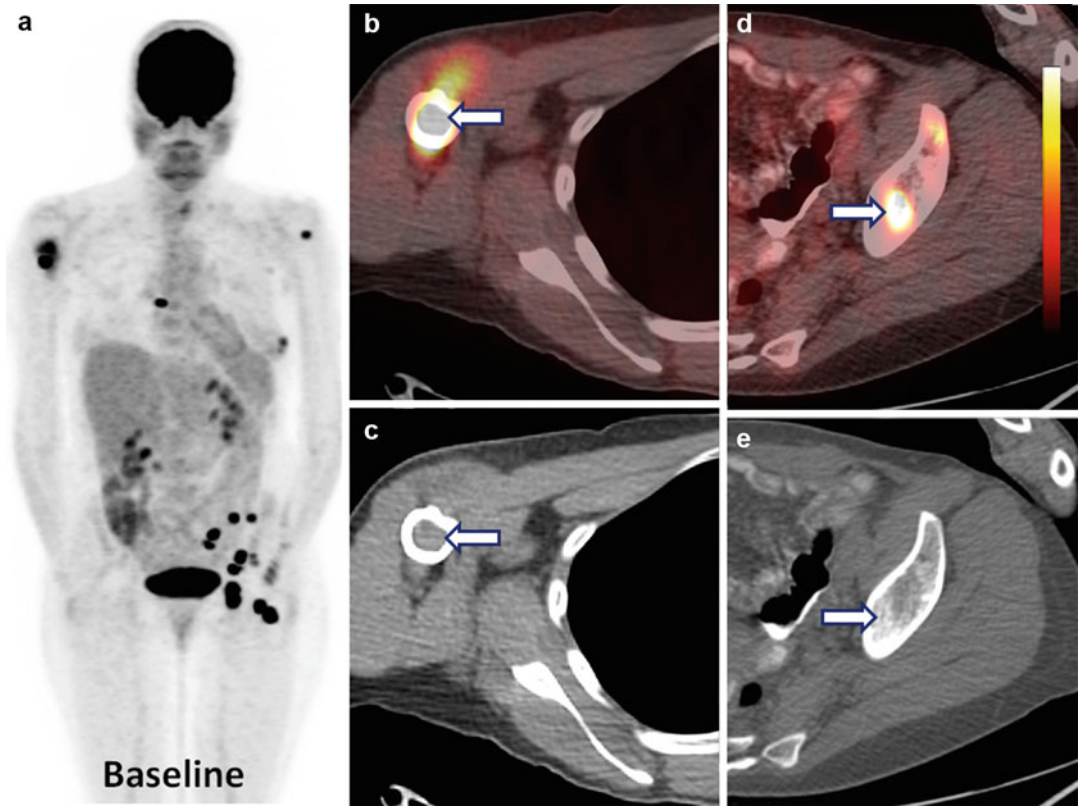

Fig. 14 (Baseline). (**a**) Maximum intensity projection (*MIP*) whole body view of the [^{18}F]FDG PET/CT shows hypermetabolic lesions in the right humerus and in the left inguinal region. (**b**, **d**) [^{18}F]FDG PET/CT fused axial images show the lesions involving the humeral bones with SUV_{max} 21.1 (*white arrow*) and the left acetabulum with SUV_{max} 17.6 (*white arrow*). Diagnostic CT images showed (**c**) the soft tissue density in the left inguinal region and (**e**) normal bone density at the left acetabulum. The lesion in the left acetabulum seems to be difficult to be detected as lymphoma lesions on diagnostic CT alone

Discussion

Adult Burkitt lymphoma is one of aggressive diseases characterized by frequent extranodal presentation, bulky disease and rapid clinical course. In this case, [^{18}F]FDG PET/CT was showed to be of value at diagnosis and completion of therapy in patients with Burkitt lymphoma [4, 5]. However diagnostic CT showed that the soft tissue density lesion still remained in the right humeral region after treatment. Comparing with diagnostic CT end-of-treatment [^{18}F]FDG PET/CT scan seems to be an attractive strategy to confirm disease activity.

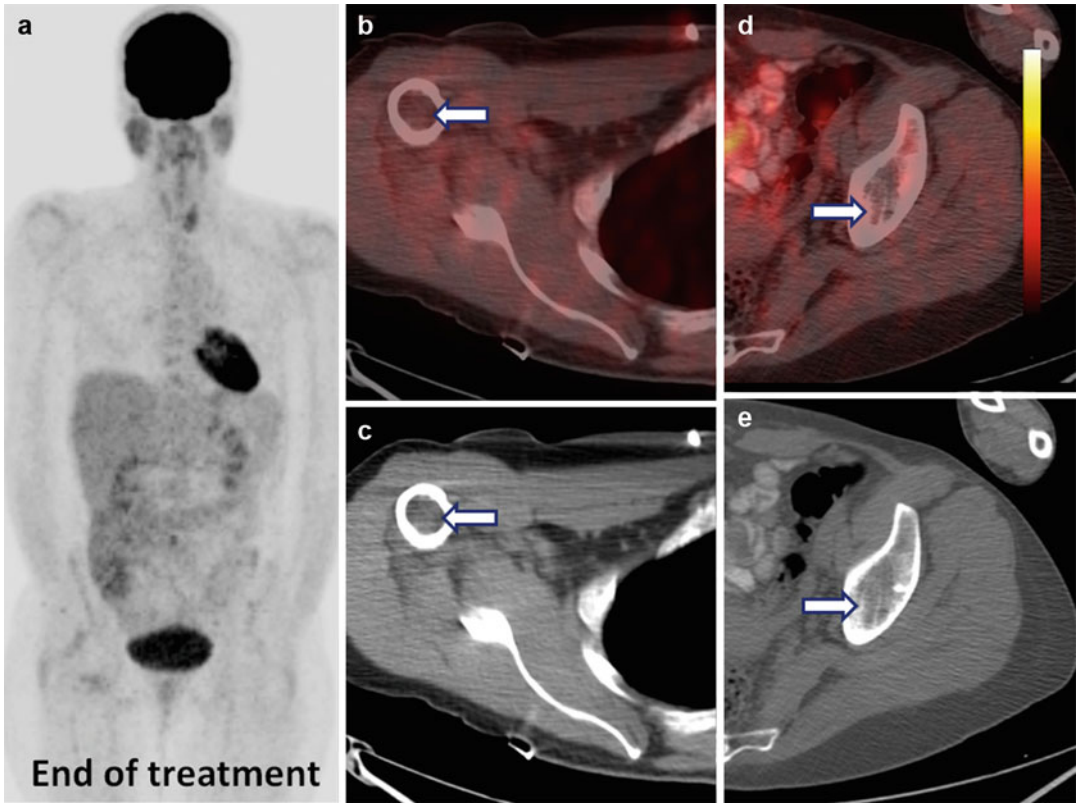

Fig. 15 (End of treatment). After completion of chemotherapy, (**a**) MIP whole body and (**b**) [^{18}F]FDG PET/CT fused axial image of the right humerus reveals complete metabolic response (SUV_{max} 1.08). However, (**c**) CT image shows the remained soft tissue density in the right humeral bone. (**d**) [^{18}F]FDG PET/CT fused axial image and (**e**) diagnostic CT image reveals that the lesions in the left acetabulum are resolved (SUV_{max} 1.16)

References

1. Mohammadianpanah M, Ahmadloo N, Mozaffari MA, et al. Primary localized stages I and II non-Hodgkin's lymphoma of the nasopharynx: a retrospective 17-year single institutional experience. Ann Hematol. 2009;88:441–7.
2. Press OW, Li H, Schöder H, et al. US intergroup trial of response-adapted therapy for stage III to IV Hodgkin lymphoma using early interim fluorodeoxyglucose-positron emission tomography imaging: Southwest Oncology Group S0816. J Clin Oncol. 2016;34:2020–7.
3. Zinzani PL, Broccoli A, Gioia DM, et al. Interim positron emission tomography response-adapted therapy in advanced-stage Hodgkin lymphoma: final results of the phase II part of the HD0801 study. J Clin Oncol. 2016;34:1376–85.
4. Carrillo-Cruz E, Marín-Oyaga VA, Solé Rodríguez M, et al. Role of ^{18}F-FDG-PET/CT in the management of Burkitt lymphoma. Eur J Haematol. 2015;94:23–30.
5. Zeng W, Lechowicz MJ, Winton E, et al. Spectrum of FDG PET/CT findings in Burkitt lymphoma. Clin Nucl Med. 2009;34:355–8.

Teaching Cases in Nuclear Oncology: Multiple Myeloma

54

Kimiteru Ito, Somali Gavane, and Heiko Schöder

Keywords

Multiple myeloma • Punched out lesion • PET/MRI

Glossary

[^{18}F]FDG	2-Deoxy-2-[^{18}F]fluoro-D-glucose
CT	X-ray computed tomography
Gy	Gray unit (ionizing radiation dose in the International System of Units, corresponding to the absorption of one joule of radiation energy per kilogram of matter)
MIP	Maximum intensity projection
MR	Magnetic resonance
MRI	Magnetic resonance imaging
PET	Positron emission tomography
PET/CT	Positron emission tomography/Computed tomography
PET/MRI	Positron emission tomography/Magnetic resonance imaging
SPECT	Single-photon emission computed tomography
SPECT/CT	Single-photon emission computed tomography/Computed tomography
SUV	Standardized uptake value
SUV_{max}	Standardized uptake value at point of maximum

Contents

Case 1 1545
Presentation 1546
Findings 1546
Follow-Up 1546

Case 2 1546
Presentation 1546
Findings 1547
Follow-Up 1547
Discussion 1548

Case 3 1549
Presentation 1549
Findings 1549
Discussion 1550

References 1555

Case 1

Case contributed by: S. Wan
Nuclear Medicine, UCLH NHS Foundation Trust, London, UK

K. Ito • H. Schöder (✉)
Department of Radiology, Molecular Imaging and Therapy service, Memorial Sloan Kettering Cancer Center, New York, NY, USA
e-mail: itoukimiteru@yahoo.co.jp; itok@mskcc.org; schoderh@mskcc.org

S. Gavane
Division of Nuclear Medicine, Department of Radiology, Mount Sinai Hospital, New York, NY, USA
e-mail: somali.gavane@mountsinai.org

© Springer International Publishing Switzerland 2017
H.W. Strauss et al. (eds.), *Nuclear Oncology*,
https://doi.org/10.1007/978-3-319-26236-9_56

Presentation

A 83-year-old man presented with back pain and fatigue. He has a background of smoldering myeloma on the basis of previous bone marrow trephine showing 10% infiltration and no myeloma-defining events.

Findings

A combined [^{18}F]FDG PET/MRI study showed numerous [^{18}F]FDG-avid lesions with corresponding MR signal changes compatible with bone marrow infiltration scattered throughout the imaged body. Most of the lesions showed intensity of uptake greater than liver background activity. A larger lesion was present at L2, where there is reduction of vertebral body height. There was no [^{18}F]FDG-avid extra-osseous involvement.

Follow-Up

On the basis of compelling multifocal bone marrow lesions demonstrated on this study, progression to multiple myeloma was diagnosed. The patient was referred for kyphoplasty of L2 vertebrae to stabilize the fracture and control the pain, but he eventually required radiotherapy for symptomatic palliation (20Gy in five fractions). He was also commenced on chemotherapy (melphalan, prednisolone and Velcade) (Figs. 1, 2, and 3).

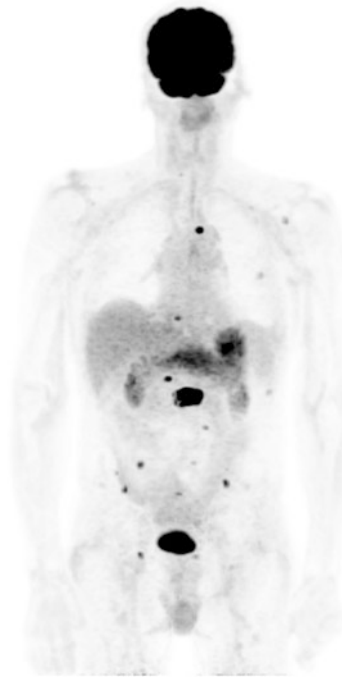

Fig. 1 The MIP image of the [^{18}F]FDG PET shows multifocal hypermetabolic lesions in the bone marrow

Case 2

Presentation

A 57-year-old woman was referred with newly diagnosed IgGκ multiple myeloma (Durie-Salmon stage IIIA).

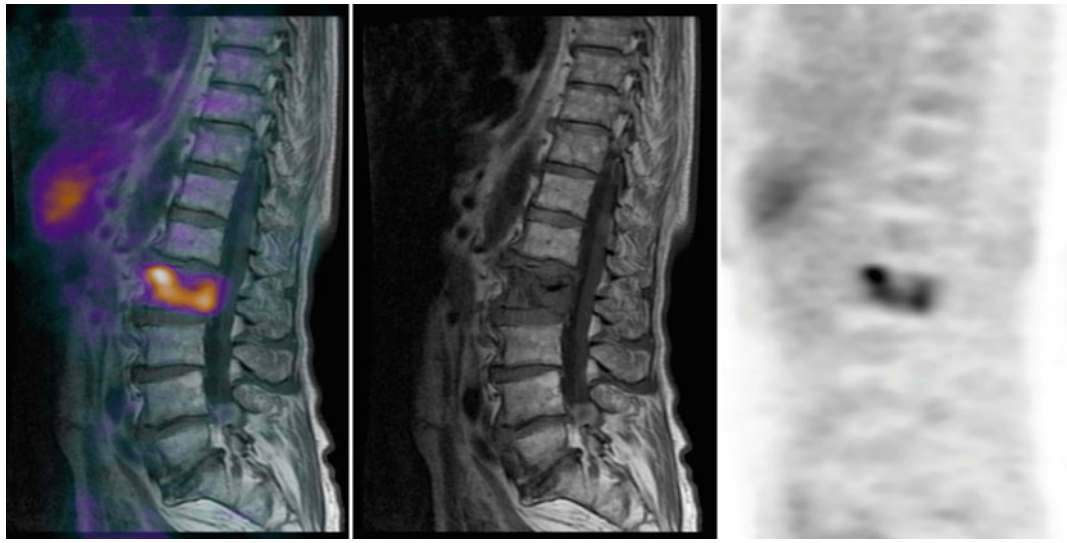

Fig. 2 Left to right: sagittal fused, T1-weighted MR and PET image of the lumbar spine. The L2 vertebrae show low T1 MR signal and heterogenous increased [^{18}F]FDG uptake in keeping with myelomatous infiltration. There is reduction of height and endplate fractures

Findings

Bone marrow biopsy showed hypercellular marrow with rich plasma cells. The patient was diagnosed with multiple myeloma after positive laboratory data and serum protein electrophoresis. Skeletal survey showed multiple osteolytic lesions (Fig. 4). [^{18}F]FDG PET/CT was performed prior to initiation of therapy. The PET/CT scan showed numerous hypermetabolic foci involving axial and appendicular skeleton with bone and bone marrow involvement (Fig. 5). The patient was treated with chemotherapy (Revlimid-Velcade-dexamethasone) and autologous stem cell transplantation.

Follow-Up

Two years after the baseline PET/CT, the patient complained of severe back pain. Restaging [^{18}F]FDG PET/CT demonstrated progression of disease with pathological compression fracture at an L1 vertebra (Fig. 6). After irradiation (total 27 Gy) for the pathologic fracture, follow-up [^{18}F]FDG PET/CT revealed lower [^{18}F]FDG uptake in the L1 vertebrae (Fig. 7) but persistent disease in other bones.

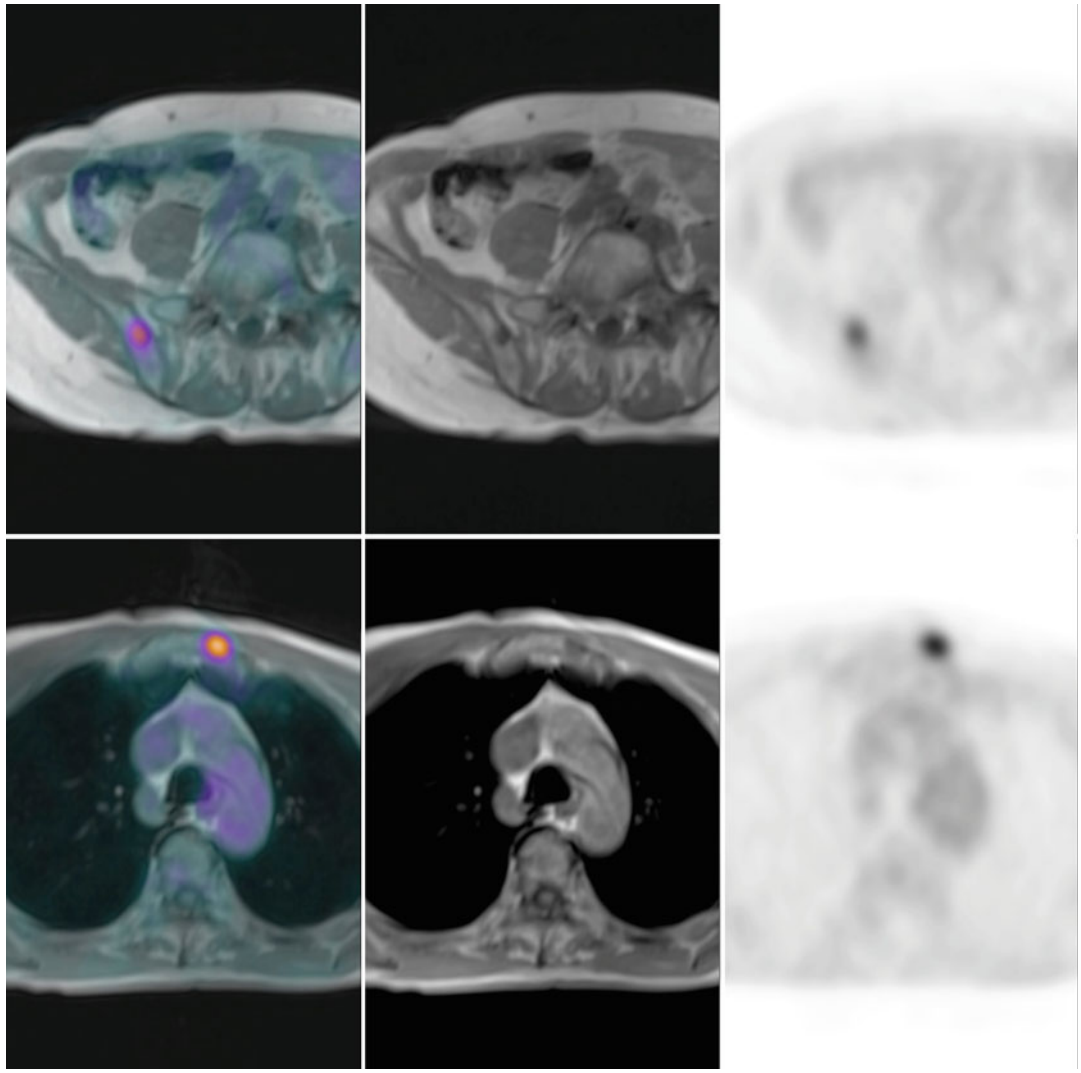

Fig. 3 Left to right: axial fused, T1-weighted and PET image at the pelvic (*upper panel*) and manubrial levels (*lower panel*). These show smaller lesions with focal hypermetabolism localizing to areas of T1 MR signal consistent with further myeloma deposits

Discussion

In this case, the initial staging and restaging [^{18}F]FDG PET/CT scans were performed during the treatment for multiple myeloma. Clinically useful applications of [^{18}F]FDG PET/CT had advantages including its utility for initial evaluation of extent and activity of disease for obtaining prognostic information.

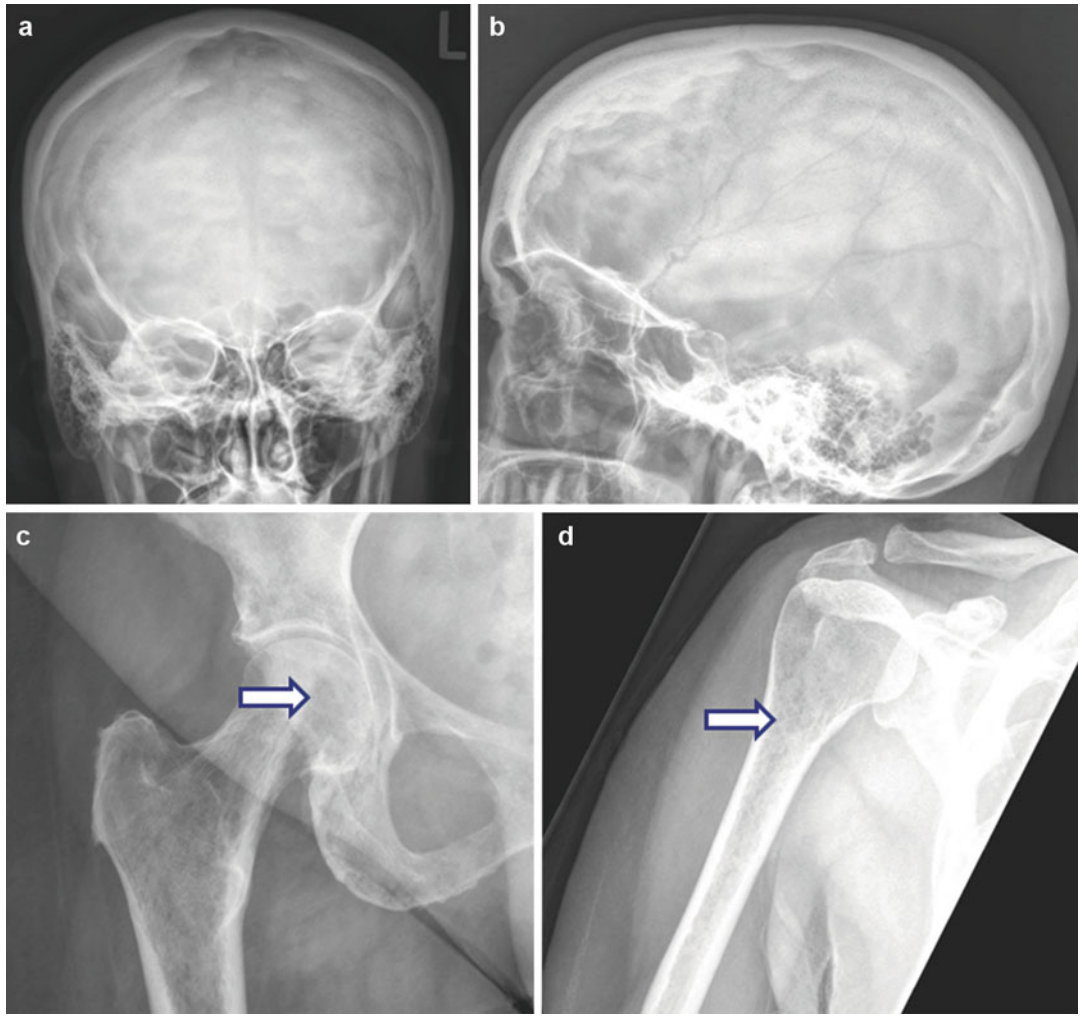

Fig. 4 Skeletal survey shows conspicuity and cortical permeation associated with multiple lytic lesions (*white arrows*). Skull bone images show inhomogeneous bone density

Case 3

Presentation

A 60-year-old woman diagnosed with plasma cell neoplasm via bone marrow core biopsy. The patient had known spinal lytic lesions and chronic back pain. Laboratory data showed elevated serum level of calcium (13.4 mg/dl).

Findings

Skeletal survey showed typical osteolytic lesions (Fig. 8). The patient underwent [^{18}F]FDG PET/CT for evaluating extent of the disease. Baseline [^{18}F]FDG PET/CT (Figs. 9 and 10) showed a few hypermetabolic foci in the bone marrow. The patient underwent chemotherapy (Revlimid-Velcade-dexamethasone) combined with bisphosphonate.

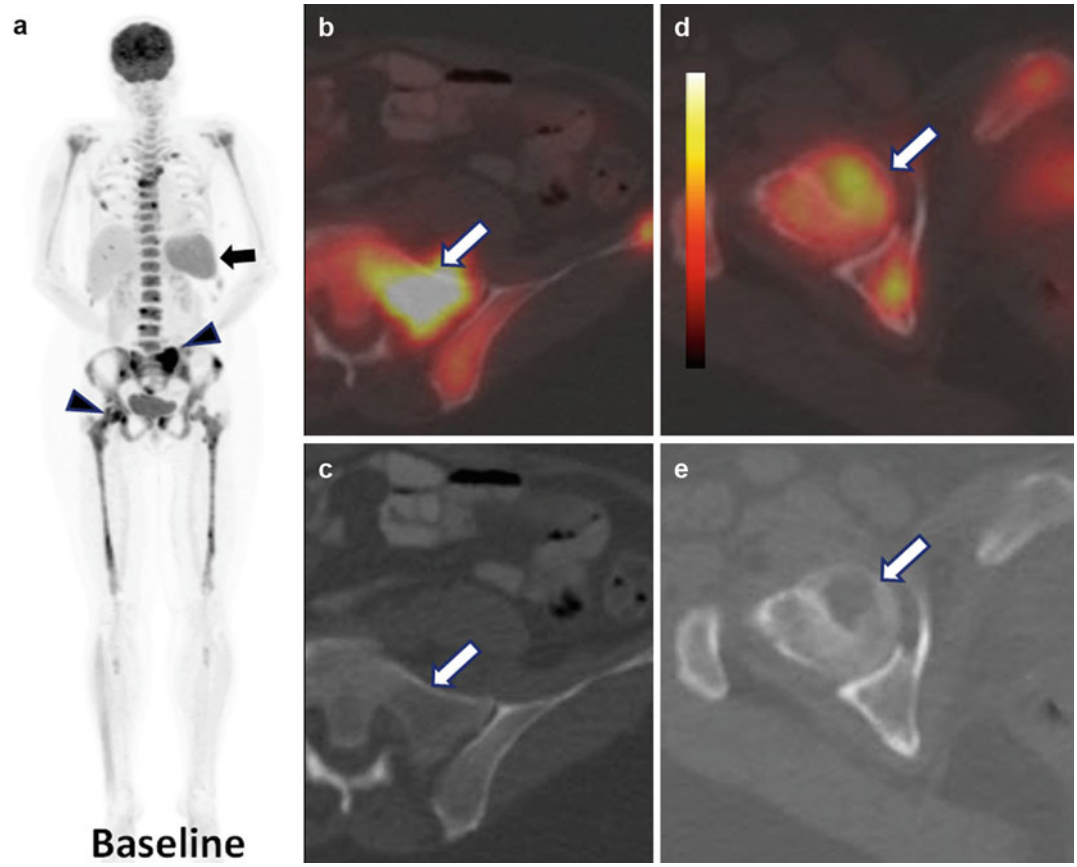

Fig. 5 (Baseline). The MIP image shows multiple hypermetabolic lesions in the bone marrow (*arrow heads*). Diffuse hypermetabolism in the spleen (*arrow*) and the bone marrow was possible myeloma involvement. [^{18}F]FDG PET/CT fused axial images revealed [^{18}F]FDG-avid lesion (SUV_{max} 15.4) at the right femoral head (*white arrow*) and the sacrum (SUV_{max} 23.7) (*white arrow*) corresponding to osteolytic lesions. Diagnostic CT scan during PET/CT was not able to detect the lesion at the left sacrum

Discussion

Multiple myeloma occurs when plasma cells form a mass in the bone marrow. A single mass or tumor detected outside the bone marrow is called plasmacytoma. However, most patients present with multiple sites of the disease, which is called multiple myeloma. [^{18}F]FDG PET/CT can be an integral part of staging and determining the extent of disease. In this case, [^{18}F]FDG PET/CT revealed a large number of bone lesions including the expansile masses [1, 2]. Early detection of expansile lesions is important to reduce risk of pathologic fractures.

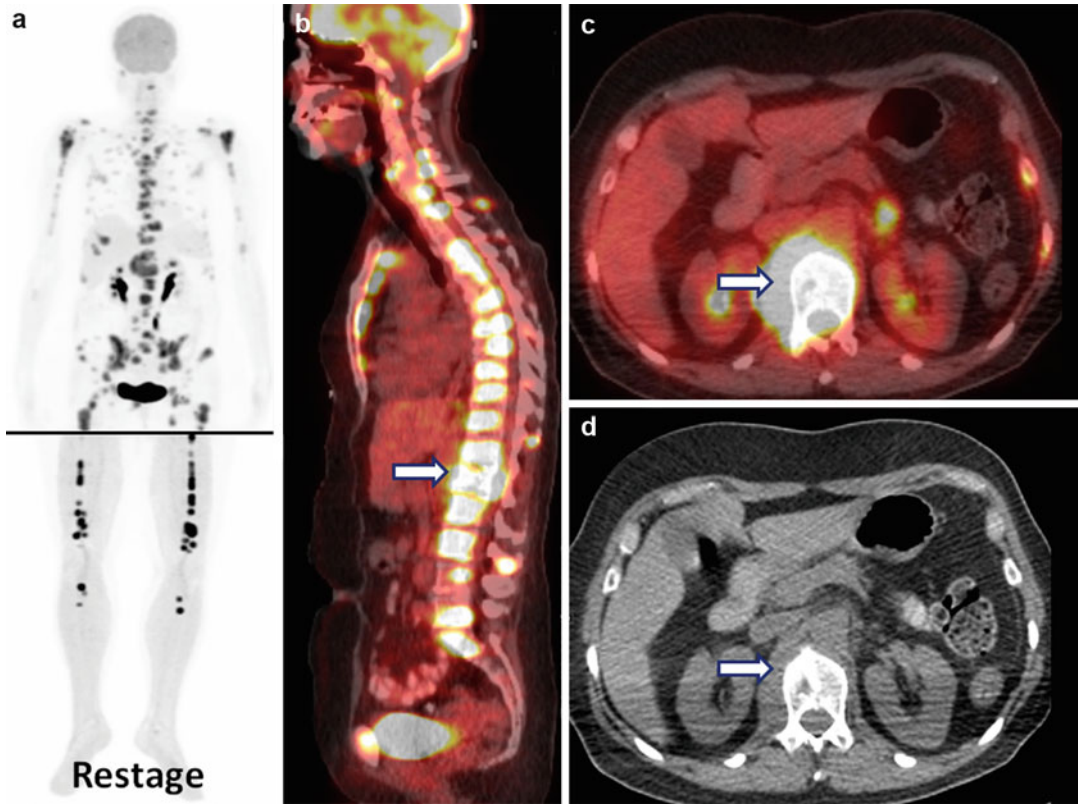

Fig. 6 (Restaging). MIP and [^{18}F]FDG PET/CT fused sagittal images show multiple hypermetabolic foci including at L1 with compression fracture (*white arrows*). Fused [^{18}F]FDG axial image shows [^{18}F]FDG-avid mass with soft tissue density (SUV_{max} 18.26) surrounding L1 vertebra

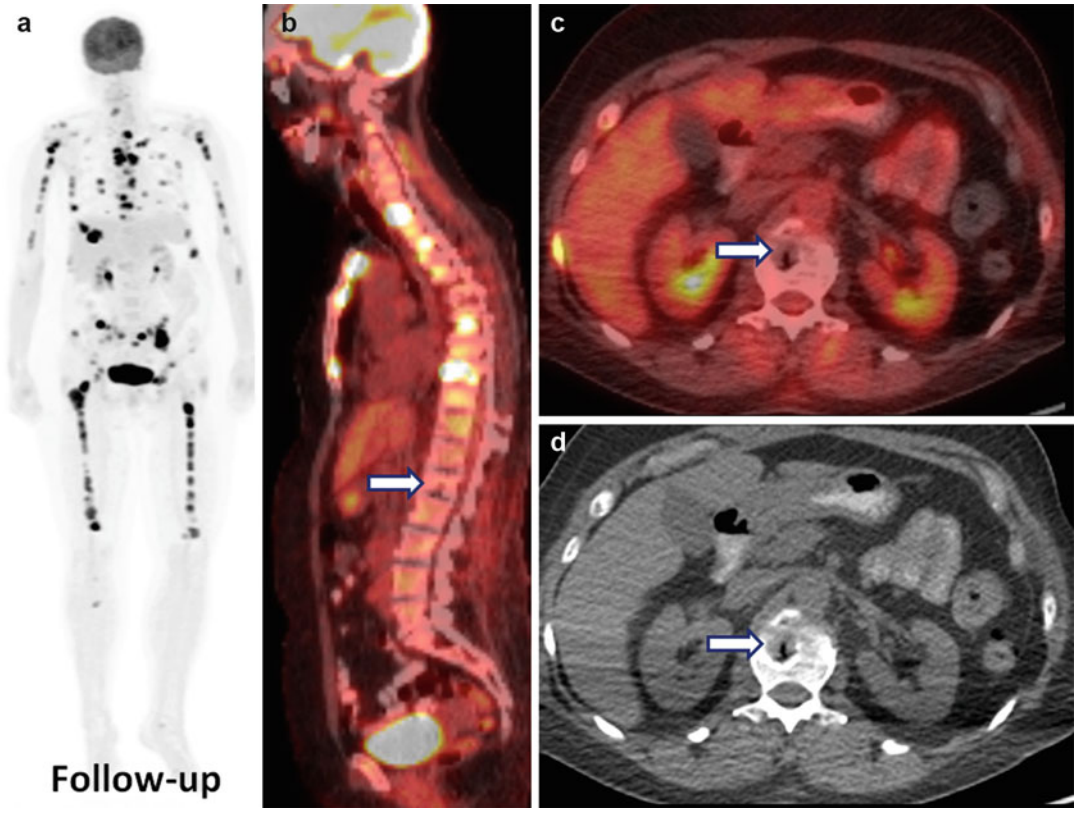

Fig. 7 (Follow-up). MIP and [^{18}F]FDG PET/CT images after radiotherapy reveal decreased uptake at the lumbar vertebrae including L1 lesion (SUV_{max} 2.34) (*white arrows*)

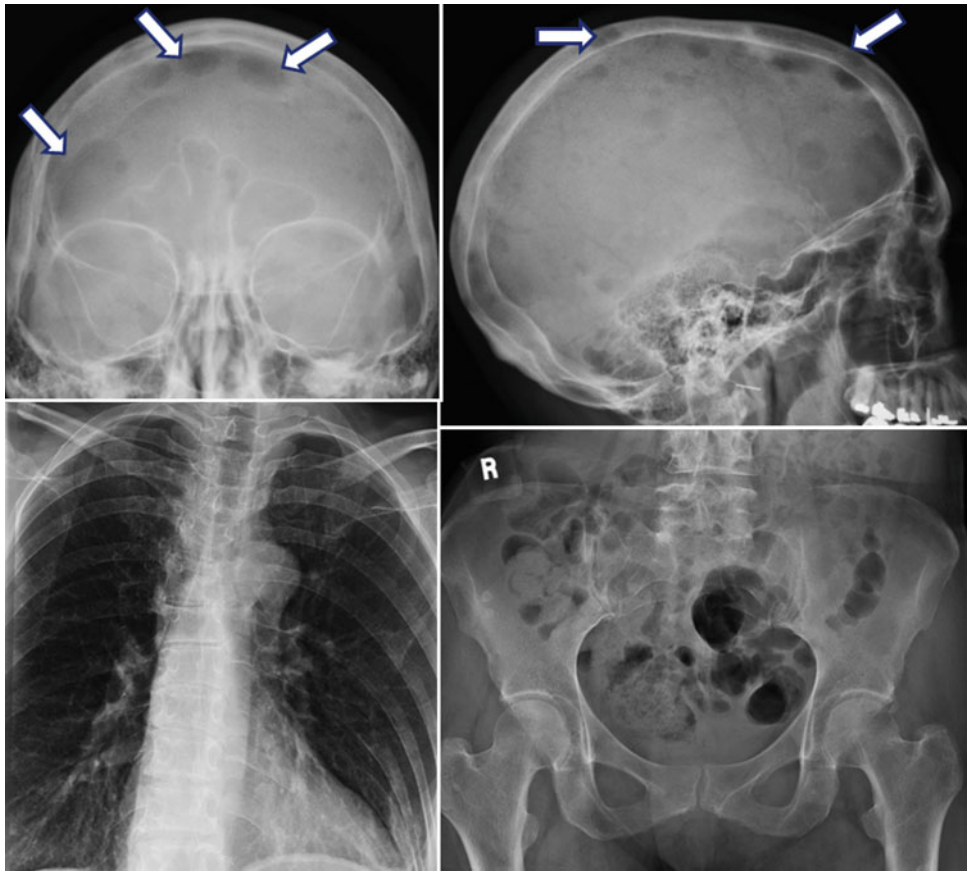

Fig. 8 Skeletal survey shows typical punched-out lesions in the skull bone (*arrows*). However, X-rays are not able to detect the osteolytic lesions in the sacrum and sternum

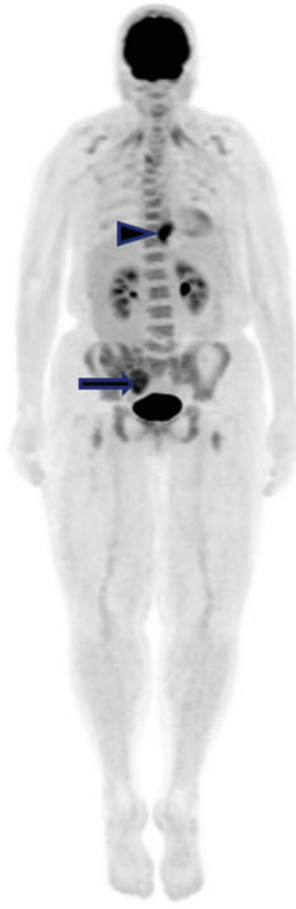

Fig. 9 MIP image reveals multiple [^{18}F]FDG-avid lesions in the sternum (*arrow*) and the right sacrum (*arrow head*)

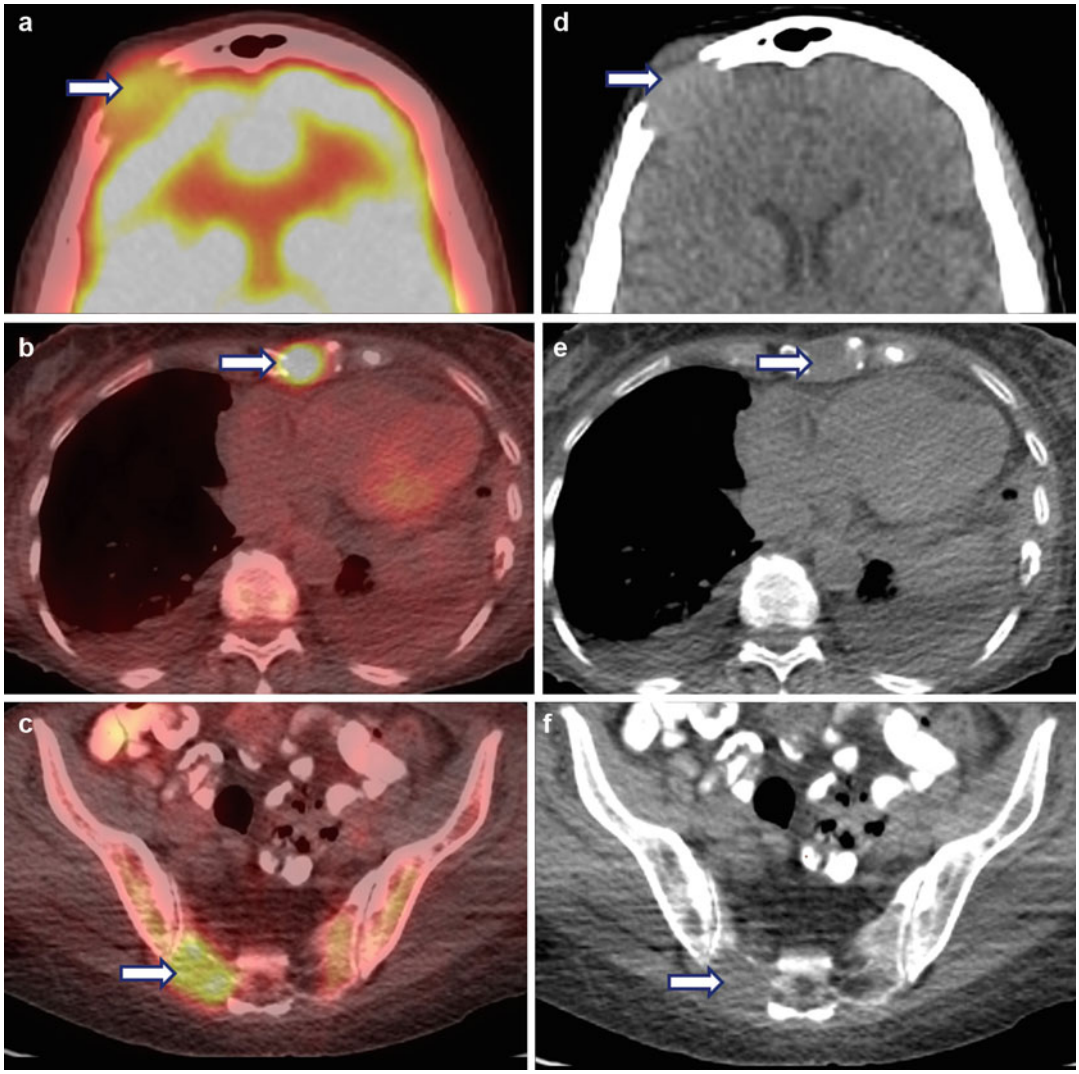

Fig. 10 Axial fused PET/CT images (**a**–**c**) and axial diagnostic CT images during PET/CT (**d**–**f**) show [^{18}F]FDG-avid expansile masses in the skull (SUV_{max} 4.4), in the sacrum (SUV_{max} 5.6), and in the xiphoid process (SUV_{max} 8.9) (*white arrows*). Additionally, there is bilateral moderate pleural effusion

References

1. Vij R, Fowler KJ, Shokeen M. New approaches to molecular imaging of multiple myeloma. J Nucl Med. 2016;57:1–4.

2. Zamagni E, Patriarca F, Nanni C, et al. Prognostic relevance of 18-F FDG PET/CT in newly diagnosed multiple myeloma patients treated with up-front autologous transplantation. Blood. 2011;118:5989–95.

Teaching Cases in Nuclear Oncology: Brain Tumors

55

Alice Lorenzoni, Alessandra Alessi, and Flavio Crippa

Keywords

PET/MR • PET/CT • Meningioma • [^{11}C] Methionine • ^{68}Ga-DOTATATE

Glossary

[^{11}C]MET	[^{11}C]Methionine
[^{18}F]FDG	2-Deoxy-2-[^{18}F]fluoro-D-glucose
CT	X-ray computed tomography
DOTA	1,4,7,10-Tetraazacyclo-dodecane-1,4,7,10-tetraacetic acid (macrocyclic coupling agent to label compounds of biological interest with metal radionuclides)
DOTATATE	DOTA-Tyr^3-octreotate
Gy	Gray unit (ionizing radiation dose in the International System of Units, corresponding to the absorption of one joule of radiation energy per kilogram of matter)
MIP	Maximum intensity projection
MRI	Magnetic resonance imaging
NSCLC	Non-small cell lung cancer
PET	Positron emission tomography
PET/CT	Positron emission tomography/Computed tomography
PET/MR	Positron emission tomography/Magnetic resonance
WHO	World Health Organization

Contents

Meningioma 1558
Presentation 1558
Findings 1558
Discussion 1558
Meningioma 1559
Presentation 1559
Findings 1559
Discussion 1560
Brain Tumor 1560
Presentation 1561
Findings 1561
Follow-Up 1561
Case 3: Brain Lymphoma 1561
Presentation 1561
Findings 1561
Discussion 1565

A. Lorenzoni (✉) • A. Alessi • F. Crippa
Nuclear Medicine Division, IRCCCS National Cancer Institute, Milan, Italy
e-mail: alice.lorenzoni@istitutotumori.mi.it; alicelorenzoni@hotmail.it

© Springer International Publishing Switzerland 2017
H.W. Strauss et al. (eds.), *Nuclear Oncology*,
https://doi.org/10.1007/978-3-319-26236-9_58

Leptomeningeal Metastasis from NSCLC 1565
Presentation 1566
Findings 1566
Follow-Up and Teaching Point 1567

References 1567

Meningioma

Case contributed by*: *S. Al Shammari*, *F. Fraioli
Institute of Nuclear Medicine*, *UCLH NHS Foundation Trust*, *London*, *UK

Presentation

A forty-seven-year-old patient with meningioma treated with surgery, with residual tumor. He is a potential candidate for radiotherapy. ^{68}Ga-DOTATATE PET/MR and PET/CT are performed to assess expression of somatostatin receptors.

Findings

PET/CT (a) demonstrates a ^{68}Ga-DOTATATE-avid lesion in the left middle fossa. MR images (b) shows anatomic details. PET/MR allows visualizing the exact extent of this disease (Fig. 1). A pituitary sparing field of irradiation was chosen after precise information provided by the PET/MR scan.

Discussion

The pre- and postoperative evaluation of meningiomas may benefit by the combination of morphological and functional imaging. This tumor, although considered benign, often causes compression of important structures and, in a few cases, may show an aggressive behavior. Meningiomas located at the skull base are particularly difficult to treat because of their proximity to vital structures such as blood vessels, cranial nerves, and the brainstem, and, in such cases, a multimodal therapeutic approach is frequently necessary.

In general, surgical resection is the treatment of choice for meningiomas; nevertheless, in the adjuvant setting, radiation therapy is also highly effective. Morphological imaging methods, such as CT and MRI, are commonly used for target volume definition in radiation therapy. However, while providing anatomical detail, they demonstrate limitations for tissue characterization, i.e., distinguishing between meningioma and other tissues, such as postoperative scars, skull base, and other normal intracranial structures. Hence, there is a need for additional methods to characterize tissue

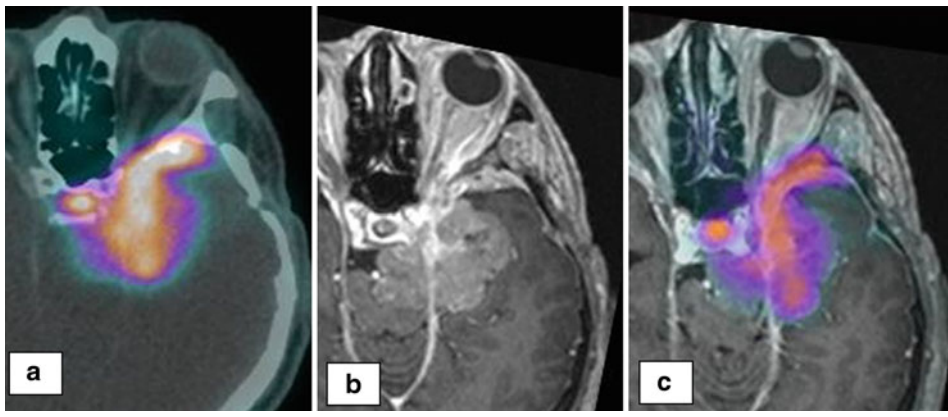

Fig. 1 ^{68}Ga-DOTATATE PET/CT (**a**) demonstrates avid lesion in the left middle fossa. MR (**b**) shows anatomic details. PET/MR allows visualizing the exact location and extent of this disease (**c**)

and more accurately determine the extent of meningioma into the neighboring anatomic structures.

PET imaging offers a solution through high levels of expression of the somatostatin receptor subtype 2 in meningiomas, which can be targeted by somatostatin receptor ligands to provide an excellent tumor-to-background signal ratio.

A PET/MRI solution combining gadolinium enhancement and somatostatin tracer uptake can improve preoperative planning and localize recurrence following therapy.

Meningioma

Case contributed by: ***L. Olivari***, ***A. Chiti***

Division of Nuclear Medicine, ***Department of Biomedical Sciences – Humanitas University***, ***Milan***, ***Italy***

Presentation

A 50-year-old woman developed a valproate-responsive generalized epilepsy. She had no history of cancer, childhood epilepsy syndromes, cerebral trauma, or vascular diseases.

Both CT and MRI of the brain showed a suspicious, slowly growing, intraventricular cystic lesion on the right side of the brain.

Findings

MRI of the brain revealed an intraventricular cystic lesion. [^{11}C]Methionine PET/CT was performed to evaluate the lesion observed at MRI (Fig. 2).

PET/CT images demonstrate no uptake in the cystic lesion, thus suggesting a nonneoplastic nature of the lesion.

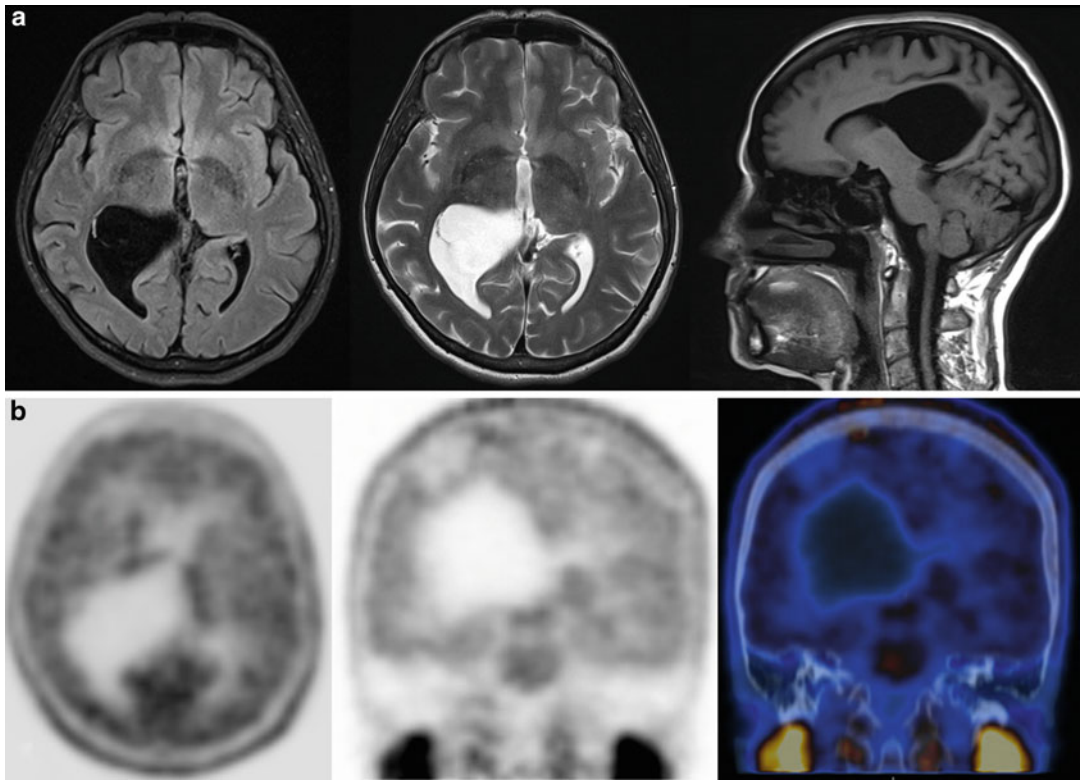

Fig. 2 Magnetic resonance imaging (*MRI*). (**a**) Showed an intraventricular cyst (sagittal, T2 FLAIR, T2 TSE; sagittal, T1 FLAIR). [^{11}C]MET PET/CT (**b**) demonstrated no pathological uptake in cyst

On the other hand, increased uptake was found in a small lesion with a rim of calcification located in the right frontal lobe (tumor-to-cerebellum ratio, 1:8). A review of the MRI images revealed an extradural lesion in the right frontal lobe hyperintense to gray matter in T2 and isohypointense in T1, compatible with meningioma. Meningioma could have been related to the patient symptoms (Fig. 3).

Discussion

This case confirms the important role on nuclear medicine imaging in the characterization of central nervous system disorders.

Different PET tracers have been explored to detect brain tumors, in particular to assess their metabolism as an index of the degree of malignancy. Radiolabeled methionine, a marker of amino acid transport and protein synthesis, shows increased uptake in meningioma (high tumor-to-cerebellum ratios) [1]. Methionine uptake correlates with meningioma volume, but it is uncertain whether it correlates with tumor aggressiveness and WHO grading; while small-series studies showed no correlation between methionine uptake and meningioma aggressiveness and WHO grading [2, 3], a more recent report found a correlation between methionine uptake and proliferative tumor activity as evaluated by the Ki-67 index [4].

Brain Tumor

Case Contributed by*: *S. Wan
Nuclear Medicine*, *UCLH NHS Foundation Trust*, *London*, *UK

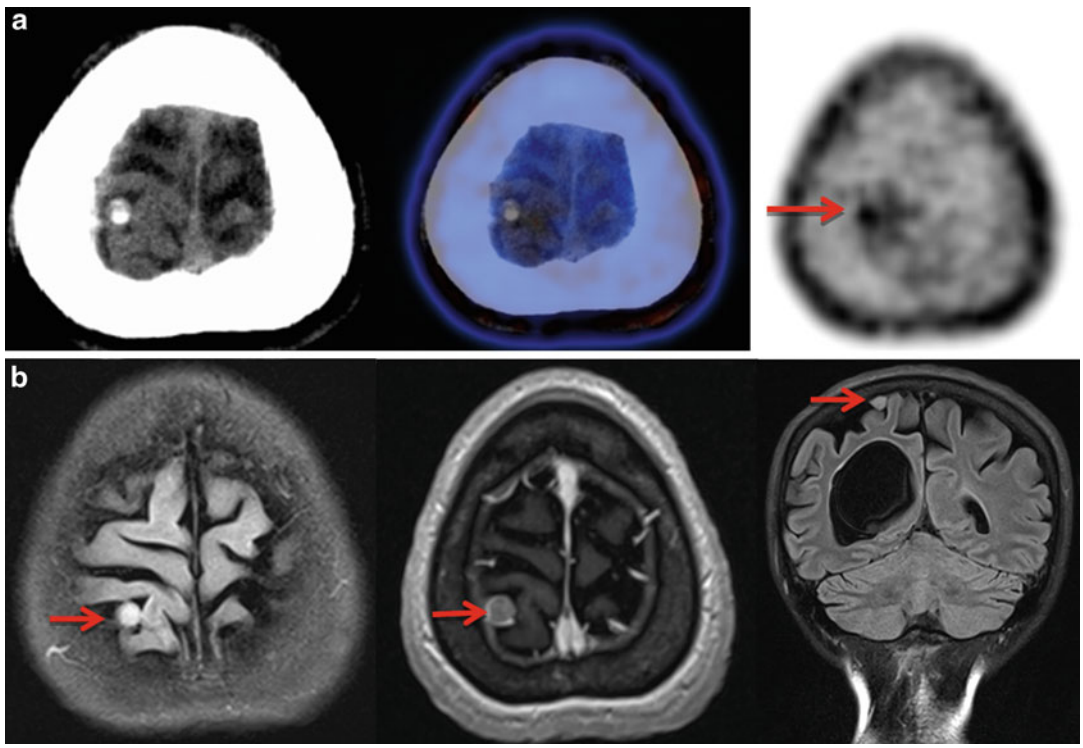

Fig. 3 [^{11}C]MET PET/CT (**a**) demonstrated an increased uptake in the right frontal lesion with a rim of calcification. Magnetic resonance imaging (*MRI*) (**b**) revealed an extradural lesion consistent with meningioma (transverse, T2wFLAIR, T2wMPRAGE; sagittal, T2 FLAIR)

Presentation

A 36-year-old man with a history of left frontotemporal anaplastic astrocytoma (initial diagnosis 5 years ago, treated with partial resection 11 months ago followed by radiotherapy completed 9 months previously) complains of increasing seizure frequency over 4 months and worsening cognitive impairment. MRI showed increasing enhancement at the site of treated tumor. MR perfusion findings were equivocal.

Findings

The [^{18}F]FDG PET/MR study showed improvement in size and enhancement compared to the previous MR studies. The enhancing lesion showed very limited [^{18}F]FDG uptake. There was diffuse hypometabolism affecting the majority of the left hemisphere, including the basal ganglia and also the right cerebellum (cerebellar diaschisis). The overall impression was that the observed MR enhancement previously was more likely due to radiation necrosis.

Follow-Up

In view of the possibility of radiation necrosis prior to the study, the patient was started on steroid treatment by the time of the PET/MR study. With the reassuring results of the study, the patient was managed expectantly. Further follow-up MRI 5 months later showed continued improvement (Figs. 4, 5, 6, and 7).

Case 3: Brain Lymphoma

Presentation

A 72-year-old woman with multifocal ductal carcinoma of the left breast treated with lumpectomy, external beam radiation therapy, and chemotherapy 5 years ago developed weakness of the right hand.

Findings

MRI of the brain revealed multiple supratentorial metastases, several of which demonstrated hemorrhage and edema. An extra-axial lesion involving the left cavernous sinus and the middle cranial fossa was also seen, representing a meningioma. [^{18}F]FDG PET/CT was performed to evaluate the extent of disease (Figs. 8 and 9). PET/CT fusion images demonstrate five hypermetabolic lesions of the brain with intense [^{18}F]FDG uptake localized,

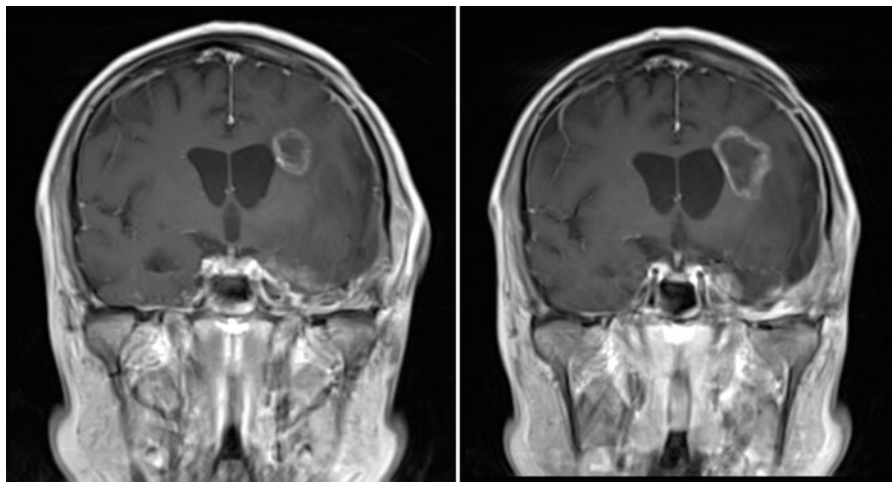

Fig. 4 Coronal T1 postcontrast images demonstrating increasing size of the enhancing cavitating area at the left corona radiate from 3 months post radiotherapy scan (*left*) to 6 months post radiotherapy scan (*right*)

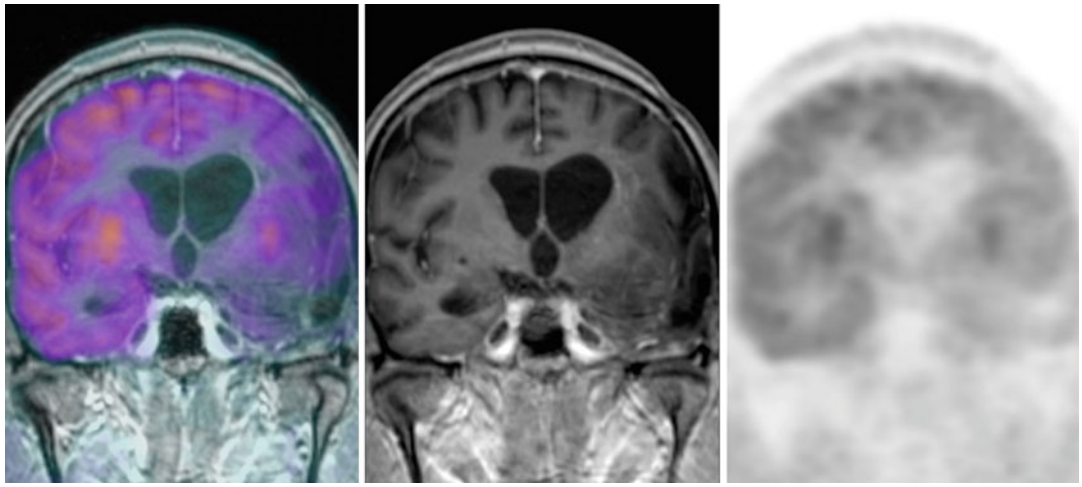

Fig. 5 From *left*: coronal fused, T1 postcontrast, and PET images from PET/MR study 9 months post radiotherapy show reduction of the enhancing area and show no significant [^{18}F]FDG uptake. Further posttreatment changes are noted over the rest of the left cerebral hemisphere

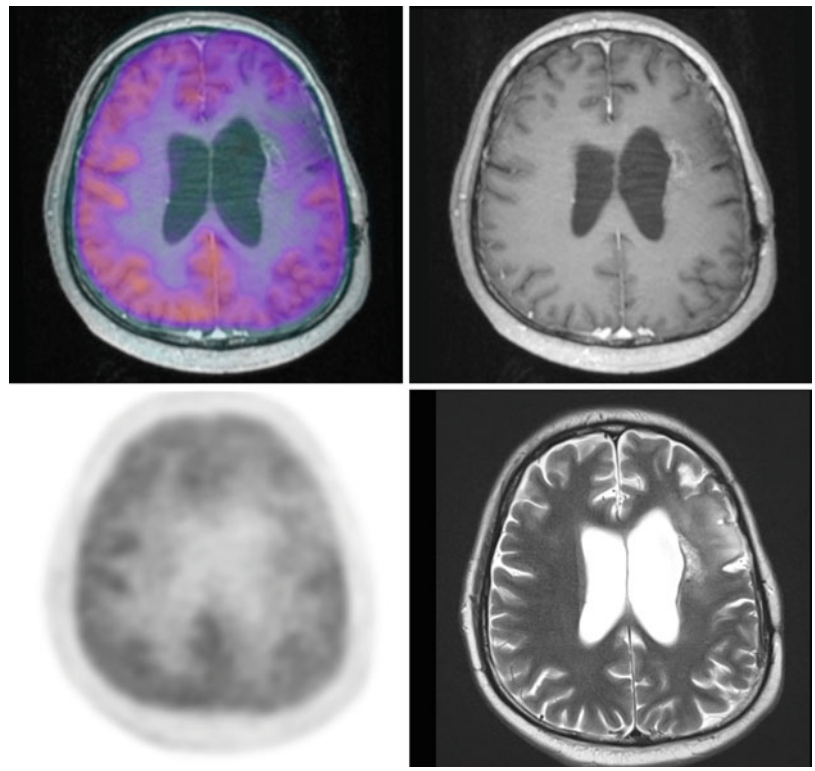

Fig. 6 Clockwise from *top left*: axial fused, T1 postcontrast, T2 weighted, [^{18}F]FDG PET images showing similar changes with regression of the enhancing area, which show no significant increased uptake. Post treatment gliosis is noted in the subcortical white matter on the T2-weighted image

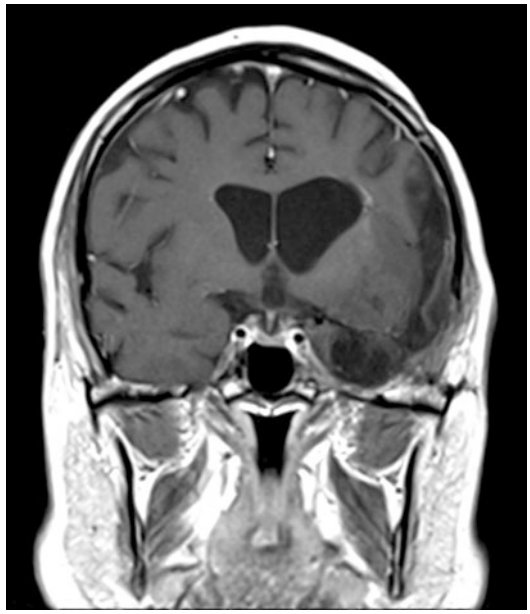

Fig. 7 Coronal T1-weighted postcontrast study showing further involution of the previously seen enhancing lesion

respectively, in the high left parietal lobe (1.7 × 1.7 cm, SUV_{max} 17), left temporo-occipital region (1.2 × 1.5 cm, SUV_{max} 15), right frontal cortex (1.3 × 1.3 cm, SUV_{max} 16), and right parietal cortex (1.6 × 1 cm, SUV_{max} (Fig. 9). These supratentorial lesions are suspicious for metastases. A large lobulated lesion (Fig. 10) in the left frontal and temporal lobe with a rim of calcification in contact to the sphenoid bone (SUV_{max} 22) is also seen, suggesting a meningioma, in correlation with MRI. [^{18}F]FDG PET/CT did not show evidence of recurrent or metastatic disease outside the brain. The patient underwent left temporal superficial brain biopsy and tumor resection which revealed diffuse large cell lymphoma with adjacent meningioma grade 1. The lumbar puncture and

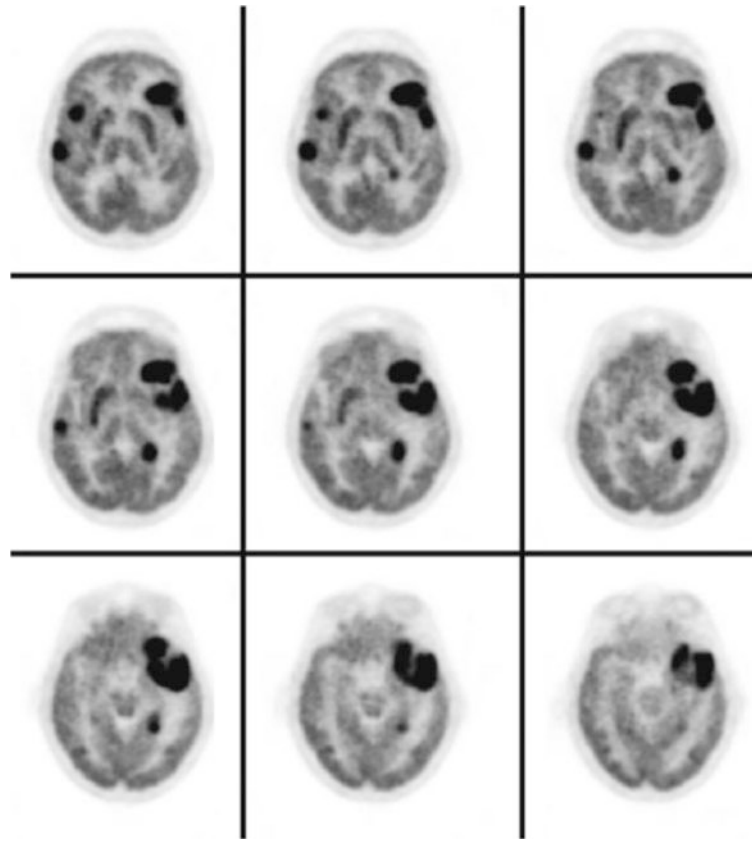

Fig. 8 [^{18}F]FDG PET axial images of the brain demonstrating five hypermetabolic lesions

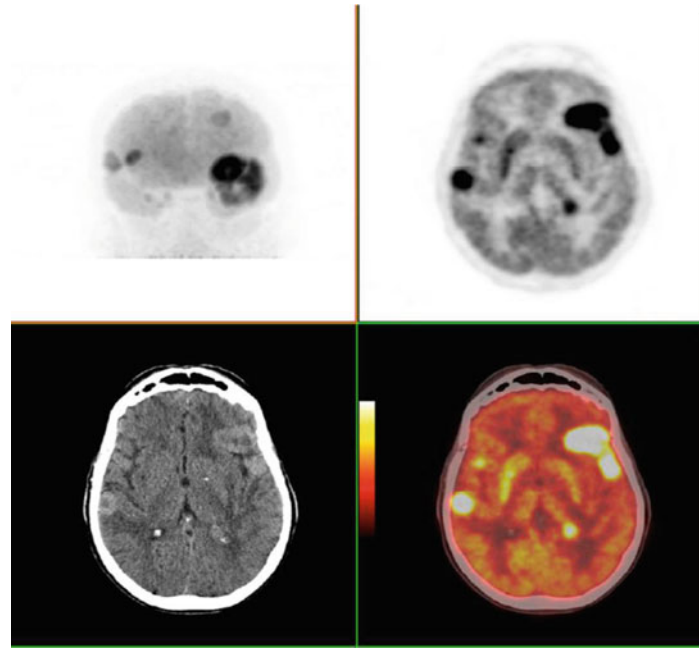

Fig. 9 [^{18}F]FDG PET/CT images: *upper left*, *MIP*; *upper right*, axial image demonstrating five lesions; *lower left*, contrast-enhanced CT; *lower right*, fused PET/CT

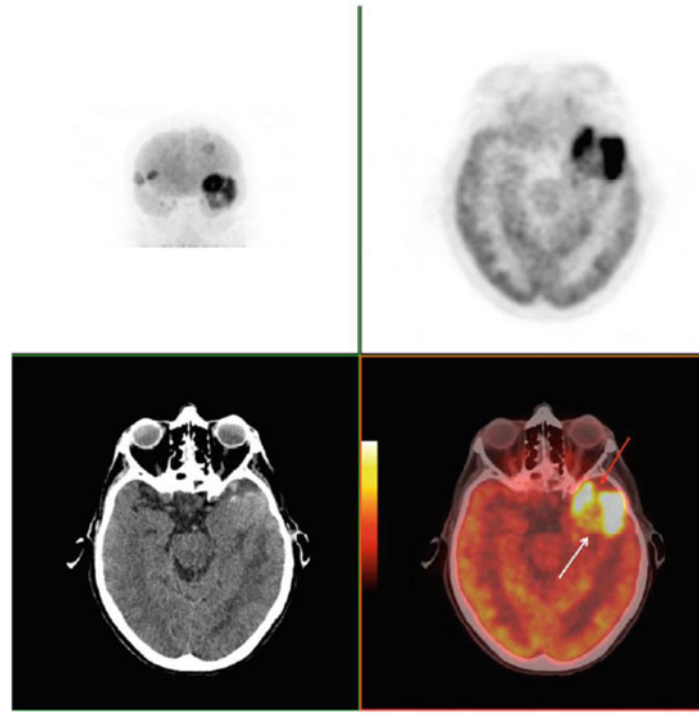

Fig. 10 [^{18}F]FDG PET/CT images of primary central nervous system lymphoma (*white arrow*) with adjacent meningioma grade 1 (*red arrow*)

bone marrow biopsy were negative for the presence of malignant cells. The patient was treated with combination chemotherapy.

Discussion

This case demonstrates the value of histologic correlation of the sites of [^{18}F]FDG localization in the evaluation of primary central nervous system lesions. In this patient with a history of treated breast cancer and a lesion with radiographic features suggesting meningioma, it is critical to determine the etiology of the lesions undergoing treatment.

Leptomeningeal Metastasis from NSCLC

Case contributed by: ***L. Olivari***, ***A. Chiti***
Division of Nuclear Medicine, ***Department of Biomedical Sciences – Humanitas University***, ***Milan***, ***Italy***

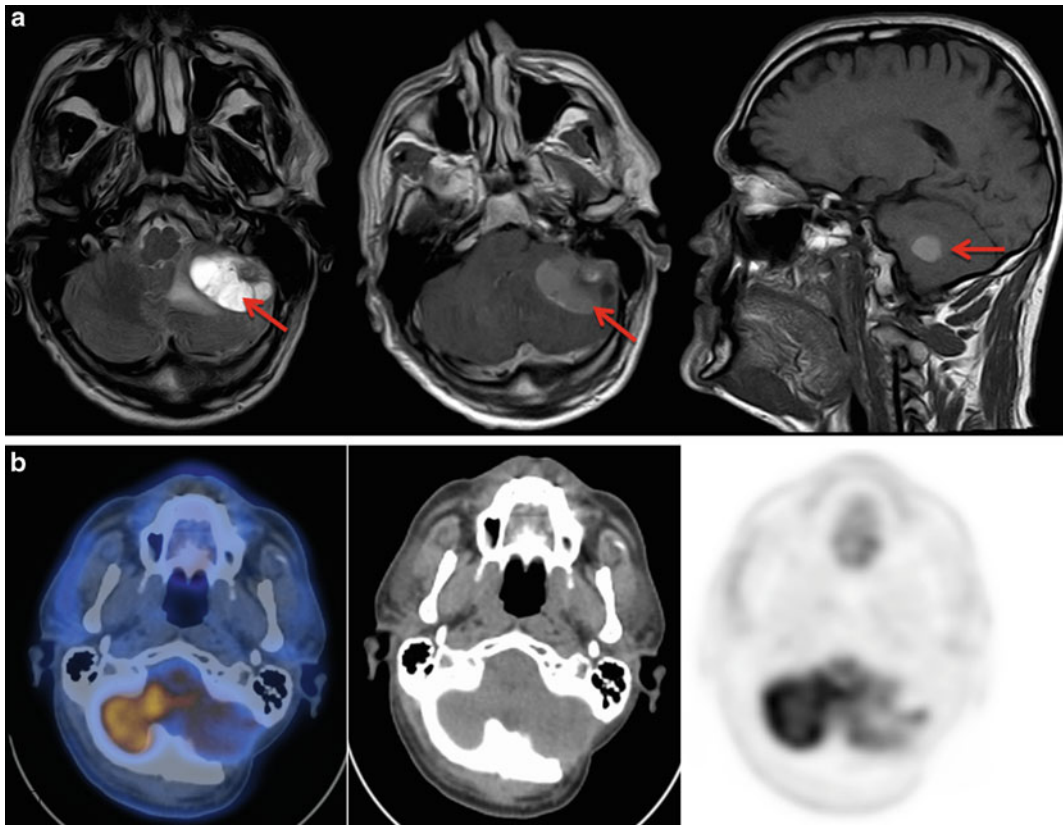

Fig. 11 Magnetic resonance imaging (*MRI*) (**a**) showed a metastasis from lung cancer in the left cerebellum lung cancer metastases, as indicated by the *red arrow* (transverse, T2wSE, contrast-enhanced T1wSE; sagittal, T1wSE). Posttreatment [^{18}F]FDG PET/CT (**b**) demonstrated no pathological uptake in the cerebellum. The *arrow* indicates the tumor

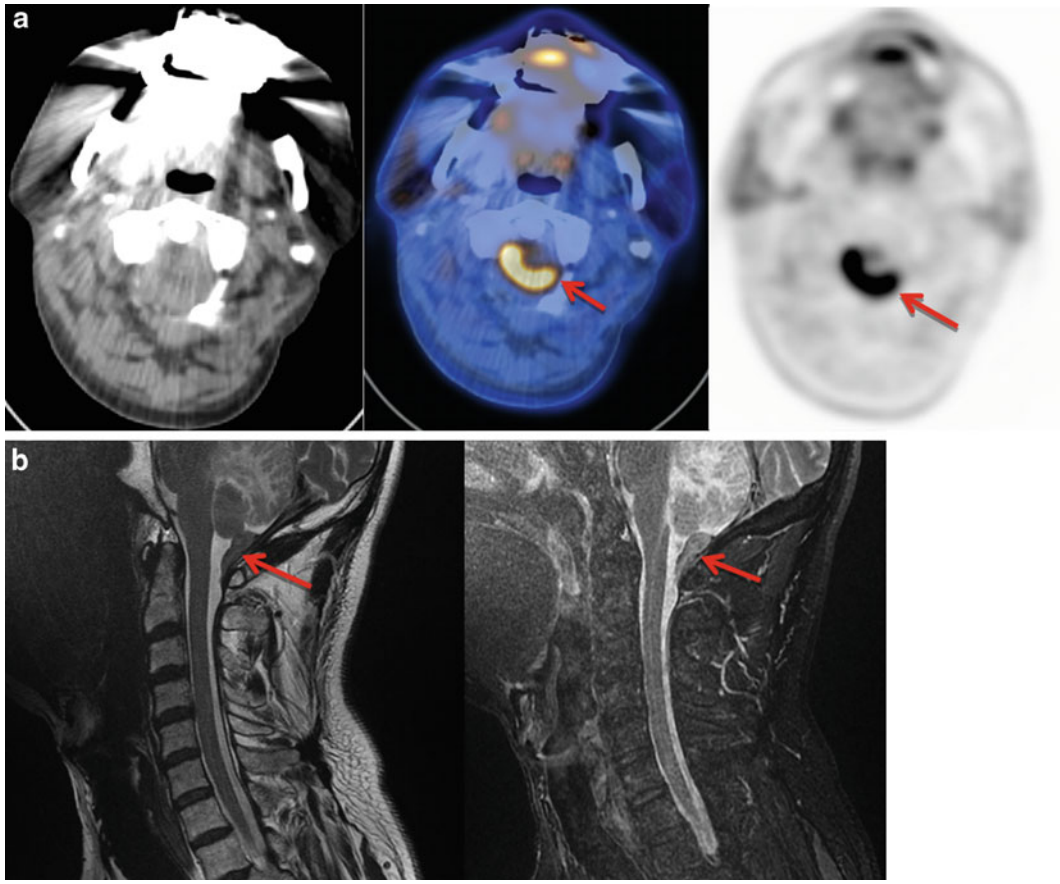

Fig. 12 Posttreatment [^{18}F]FDG PET/CT and MRI: (**a**) increased tracer uptake in leptomeninges of the foramen magnum (*red arrow*); (**b**) corresponding MRI appearance of the lesion (*red arrow*) in the sagittal plane (T2w, STIR)

Presentation

A 52-year-old man was referred to our hospital because of fatigue and severe headache not responsive to nonsteroidal anti-inflammatory drugs (NSAIDs). The patient had a prior history of non-small cell lung cancer of the apex of the left lung presenting with Pancoast syndrome (pT3N0) and had therefore been treated with chemoradiotherapy followed by surgery and intraoperative radiotherapy for the lung lesion; neurosurgery followed by radiotherapy (30 Gy) was also performed for a single cerebellar metastasis in the left hemisphere.

Findings

ceMRI of the brain revealed perilesional edema in the left cerebellar hemisphere related to previous radiotherapy treatment. No other lesions were found. Three weeks later a total body [^{18}F]FDG

PET/CT was performed for restaging. The scan showed no abnormal [^{18}F]FDG uptake elsewhere in the body except in the brain, where frankly increased uptake in the leptomeninges of the foramen magnum was observed (Figs. 11 and 12).

Follow-Up and Teaching Point

Leptomeningeal metastasis is an uncommon manifestation of non-central nervous system disease and [^{18}]FDG PET can reveal it. Even though leptomeningeal metastasis has a poor prognosis, early diagnosis is important in order to relieve symptoms, improve quality of life, and prolong survival. The patient was treated with radiation therapy.

References

1. Juhász C, Dwivedi S, Kamson DO, Michelhaugh SK, Mittal S. Comparison of amino acid positron emission tomographic radiotracers for molecular imaging of primary and metastatic brain tumors. Mol Imaging. 2014;13. doi:10.2310/7290.2014.00015.
2. Ogawa T, Inugami A, Hatazawa J, Kanno I, Murakami M, Yasui N, et al. Clinical positron emission tomography for brain tumors: comparison of fludeoxyglucose ^{18}F and L-methyl-^{11}C-methionine. AJNR Am J Neuroradiol. 1996;17:345–53.
3. Arita H, Kinoshita M, Okita Y, Hirayama R, Watabe T, Ishohashi K, et al. Clinical characteristics of meningiomas assessed by ^{11}C-methionine and ^{18}F-fluorodeoxyglucose positron-emission tomography. J Neurooncol. 2012;107:379–86.
4. Iuchi T, Iwadate Y, Namba H, Osato K, Saeki N, Yamaura A, et al. Glucose and methionine uptake and proliferative activity in meningiomas. Neurol Res. 1999;21:640–4.

Teaching Cases in Nuclear Oncology: Head and Neck Cancer

56

Kimiteru Ito, Somali Gavane, and Heiko Schöder

Keywords

Oropharyngeal cancer • Nasopharyngeal cancer • Human papilloma virus • [^{18}F]FDG • PET/CT

Glossary

[^{18}F]FDG	2-Deoxy-2-[^{18}F]fluoro-D-glucose
5FU	5-Fluorouracil
AJCC	American Joint Committee on Cancer
CT	X-ray computed tomography
EBV	Ebstein-Barr virus
Gy	Gray unit (ionizing radiation dose in the International System of Units, corresponding to the absorption of one joule of radiation energy per kilogram of matter)
HNSCC	Squamous cell carcinoma of the head and neck region
HPV	Human papilloma virus
M	Metastasis status according to the AJCC/UICC TNM staging system
MIP	Maximum intensity projection
MRI	Magnetic resonance imaging
N	Lymph node status according to the AJCC/UICC TNM staging system
p16	A tumor suppressor protein encoded by the CDKN2A gene (also known as cyclin-dependent kinase inhibitor 2A or multiple tumor suppressor 1)
PET	Positron emission tomography
PET/CT	Positron emission tomography/Computed tomography
PET/MRI	Positron emission tomography/Magnetic resonance imaging
SCC	Squamous cell carcinoma
SPECT	Single-photon emission computed tomography
SPECT/CT	Single-photon emission computed tomography/Computed tomography
SUV	Standardized uptake value
SUV_{max}	Standardized uptake value at point of maximum
T	Tumor status according to the AJCC/UICC staging system
TNM	AJCC/UICC staging system based on parameters "T" (tumor status), "N" (lymph node status), and "M" (distant metastasis status)
UICC	Union Internationale Contre le Cancer (International Union Against Cancer)

K. Ito • H. Schöder (✉)
Department of Radiology, Molecular Imaging and Therapy service, Memorial Sloan Kettering Cancer Center, New York, NY, USA
e-mail: itoukimiteru@yahoo.co.jp; itok@mskcc.org; schoderh@mskcc.org

S. Gavane
Division of Nuclear Medicine, Department of Radiology, Mount Sinai Hospital, New York, NY, USA
e-mail: gavanes@mskcc.org

© Springer International Publishing Switzerland 2017
H.W. Strauss et al. (eds.), *Nuclear Oncology*,
https://doi.org/10.1007/978-3-319-26236-9_59

Contents

Case 1 1570
Presentation 1570
Findings 1570
Follow-up 1570
Discussion 1571
Case 2 1572
Presentation 1572
Findings 1572
Follow-up 1574
Discussion 1574
Case 3 1574
Presentation 1574
Findings 1574
Follow-Up 1574
Discussion 1576
Case 4 1576
Case 5 1577
Case 6 1579
Presentation 1579
Findings 1579
Follow-Up 1581
Case 7 1581
Presentation 1581
Findings 1581
Follow-Up 1582
Discussion 1582
References 1582

Case 1

Case contributed by: C.M. Hoff, K. Bouchelouche
Department of Nuclear Medicine and PET Centre, Aarhus University Hospital, Aarhus, Denmark

Presentation

A 52-year-old man with cancer of the tongue base. During the past 6 months the patient had noticed what he thought was a growing painful infection on his tongue. The patient had a history of smoking currently 30 cigarettes per day and accumulated 40 pack years.

Clinical examination confirmed the suspension of cancer in the tongue and floor of the mouth with spread to local right-sided lymph nodes (clinical T4a N2b Mx).

Findings

The initial [^{18}F]FDG PET/CT scan (Figs. 1 and 2) showed high [^{18}F]FDG uptake at the right side of the oral tongue, suspicious of cancer (Fig. 1b, large arrow). High [^{18}F]FDG uptake in enlarged right-sided lymph nodes, level 1B and 2, suspicious of metastatic cancer (Fig. 1c, d, small arrows) and moderate [^{18}F]FDG uptake in non-enlarged lymph nodes in the right parotid gland and level 2 and 3 on the right side, also suspicious of local metastases (Fig. 1a, small arrow).

In addition to the head and neck cancer, the [^{18}F]FDG PET/CT also showed a tumor in the rectum with high [^{18}F]FDG uptake (Fig. 2a, b, large arrow), suspicious of a second primary cancer with spread to a local mesorectal lymph node (Fig. 2b, small arrow) on the left side.

[^{18}F]FDG uptake was also seen in several cutaneous and subcutaneous processes, one of them located in the left axillary region (Fig. 2c), where inspection was recommended.

Follow-up

The squamous cell p16 negative head and neck cancer received treatment with curative intended radiation (68 Gy/34 fractions) therapy with concomitant cisplatin and nimorazole. The extent of the disease was too large for surgical intervention.

The rectal adenocarcinoma, T3 N0 M0, was treated with short-course preoperative radiotherapy (25 Gy/5 fractions) and surgical resection.

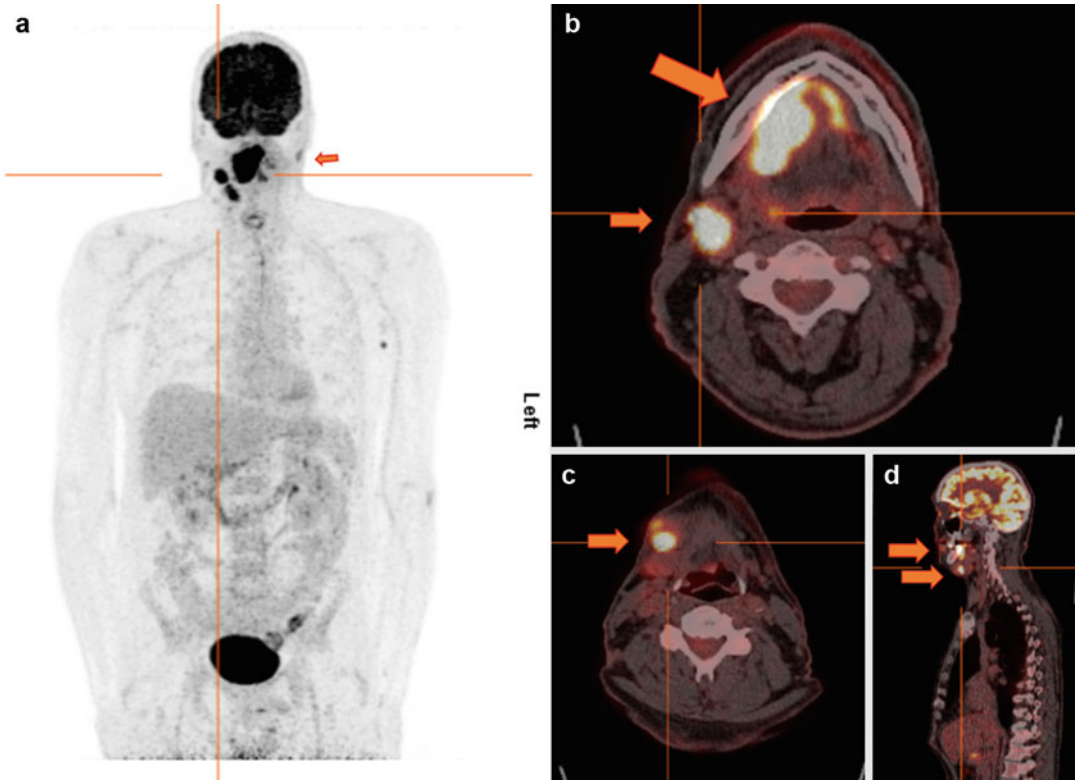

Fig. 1 (**a**) MIP, (**b**) Axial fused PET/CT image of neck, (**c**) Axial fused PET/CT image of neck, (**d**) Saggital PET/CT fusion image

In spite of aggressive therapy, residual HNSCC at both T- and N-site was suspected 2 months after treatment.

The patient had a second [^{18}F]FDG PET/CT scan (Fig. 3) performed 5 months after the initial scan. This showed high [^{18}F]FDG uptake in the right-sided level 1B lymph node (Fig. 3b), which could be both residual tumor and treatment related uptake. No sign of residual tumor at the T-site. However, the PET/CT scan showed four new sites with high [^{18}F]FDG uptake in the left lung (Fig. 3a, orange arrows and 3c), all suspicious of malignant disease. In the left axillary region (Fig. 3a, blue arrow) focal moderate [^{18}F]FDG uptake was seen, which could also represent a metastasis.

The lymph node in level 1B was removed and showed no sign of malignant disease. Biopsies from the lung metastases showed that they originated from the HNSCC.

The treatment that followed was palliative chemotherapy.

Discussion

This case demonstrates some of the diagnostic difficulties in the head and neck area. Cancers can be difficult to diagnose due to high physiological [^{18}F]FDG uptake in the area. It also demonstrates the advantage of a full body [^{18}F]FDG

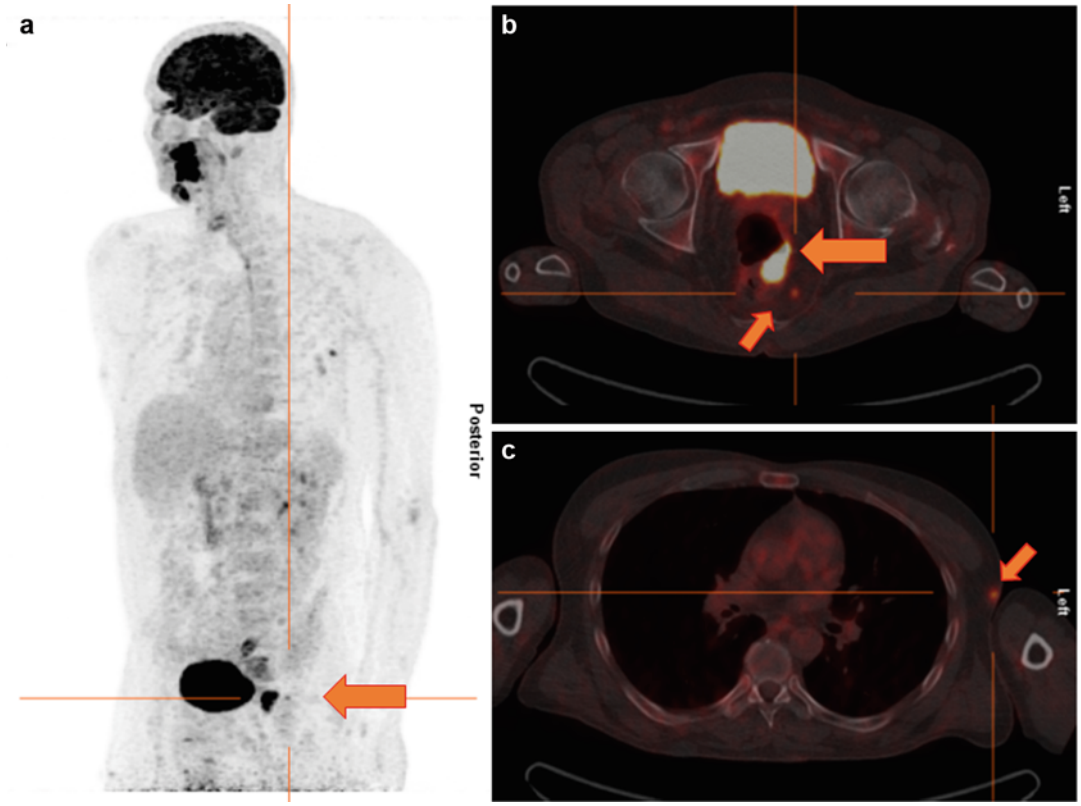

Fig. 2 (**a**) MIP, (**b**) Axial fused PET/CT image of pelvis, (**c**) Axial fused PET/CT image of chest

PET/CT scan and the possibility of diagnosing a second primary tumor. [^{18}F]FDG PET/CT is currently used for primary staging, follow-up, and treatment planning of head and neck cancers.

Case 2

Presentation

A 53-year-old man referred for oropharyngeal squamous cell carcinoma with cervical lymph node metastases (cT2N2b). The patient noticed a mass in his right upper neck 1 month before.

Findings

Ultrasound of neck showed enlarged lymph nodes in his right neck. Diagnostic CT showed the soft tissue mass on base of right side tonsil. Biopsy from the tonsil revealed poorly differentiated squamous cell carcinoma (SCC) with human papilloma virus (HPV) positive. Pathology from the enlarged lymph node was consistent with metastatic SCC. Baseline [^{18}F]FDG PET/CT scan was performed prior to initiation of chemoradiotherapy. The [^{18}F]FDG PET/CT scan shows primary tumor in the right tonsil and lymph node metastasis in the right neck (Fig. 4).

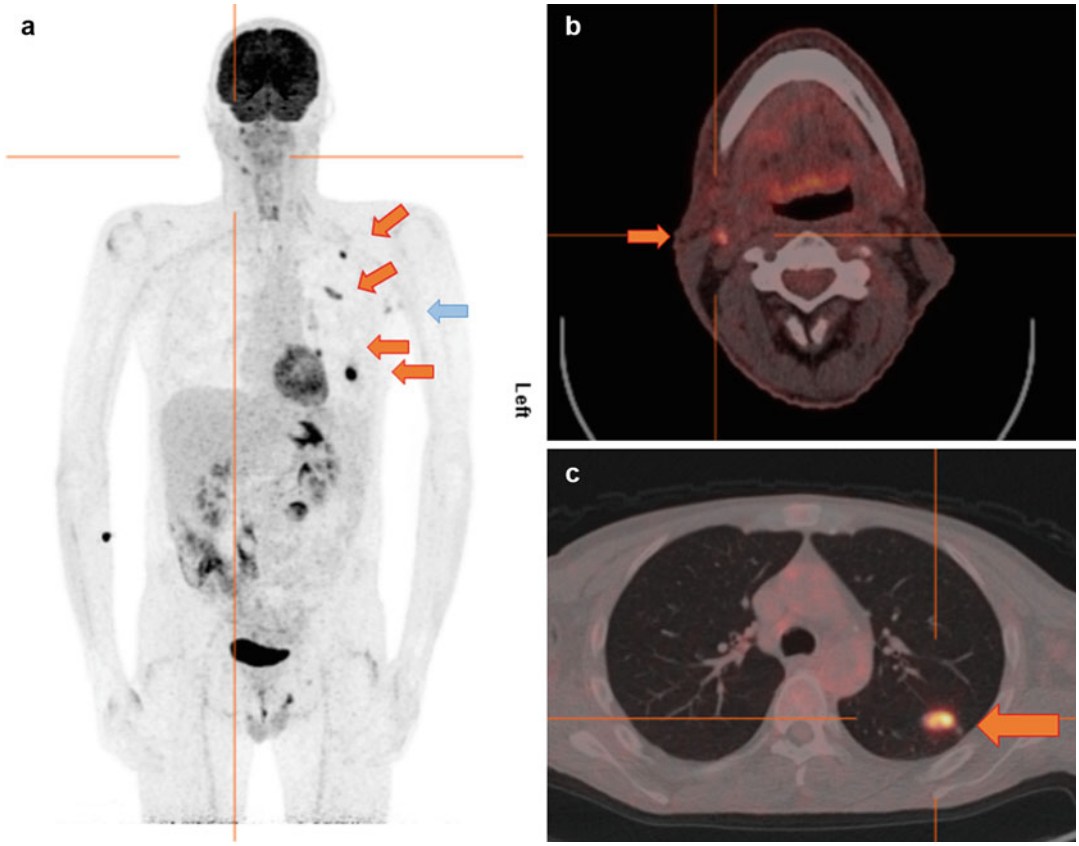

Fig. 3 (**a**) MIP, (**b**) Axial fused PET/CT image of neck, (**c**) Axial fused PET/CT image of lung

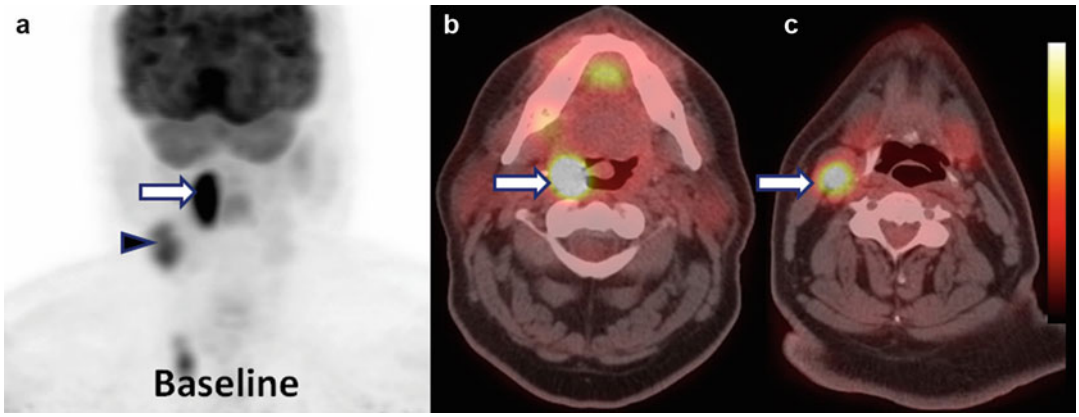

Fig. 4 (Baseline). (**a**) MIP image shows primary tumor (*white arrow*) and lymph node metastasis (*arrow head*). Fused [^{18}F]FDG PET/CT axial images showed (**b**) hypermetabolic right palatine tonsillar mass (SUV_{max} 13.0) and (**c**) hypermetabolic right supraclavicular node measuring 2.4 × 2.0 cm (SUV_{max} 7.2)

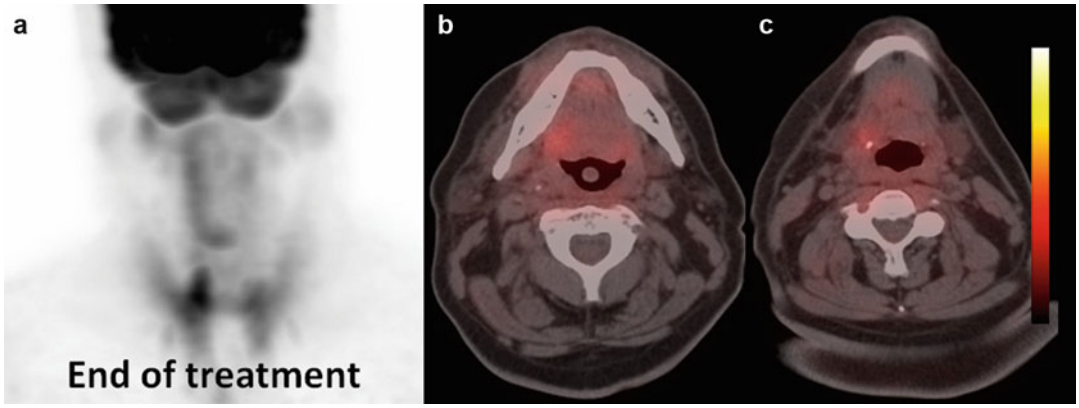

Fig. 5 (Follow-up). [^{18}F]FDG PET/CT axial images show complete metabolic response to therapy with mild physiologic muscle [^{18}F]FDG uptake of neck. (**a**) MIP and (**b**, **c**) axial [^{18}F]FDG PET/CT image shows asymmetric mild [^{18}F]FDG uptake at right tonsil (SUV_{max} 2.58) and resolved lymph node uptake measuring 0.8 × 0.8 cm (SUV_{max} 1.67)

Follow-up

The patient was treated with concurrent chemoradiotherapy (carboplatin and 5FU with radiotherapy 64 Gy). Five months after the treatment, [^{18}F]FDG PET/CT scan was repeated to evaluate response to treatment. No sites of abnormal [^{18}F]FDG uptake were seen, demonstrating complete response to therapy (Fig. 5).

Discussion

No evidence-based guidelines exist on timing and duration of PET/CT long-term surveillance after completion of therapy. It has been widely reported that a 3 months posttreatment PET/CT is able to distinguish persistent disease from treatment-related change with a high negative predictive value. In this case, [^{18}F]FDG PET/CT shows complete remission with mild physiologic muscle uptake [1–3]. It is important to understand physiologic uptake patterns of [^{18}F]FDG in the necks.

Case 3

Presentation

A 63-year-old man was referred to our hospital for tongue cancer treatment (cT2N2).

Findings

Biopsy from base of tongue showed poorly differentiated invasive squamous cell carcinoma. [^{18}F]FDG PET/CT was performed prior to initiation of chemoradiotherapy. Baseline [^{18}F]FDG PET/CT (Fig. 6a–c) showed hypermetabolic tonsillar soft tissue mass with lymphadenopathy in bilateral cervical chains and no evidence of distant metastasis.

Follow-Up

The patient underwent cisplatin-based chemotherapy and radiotherapy (70 Gy/35 fractions). Ten

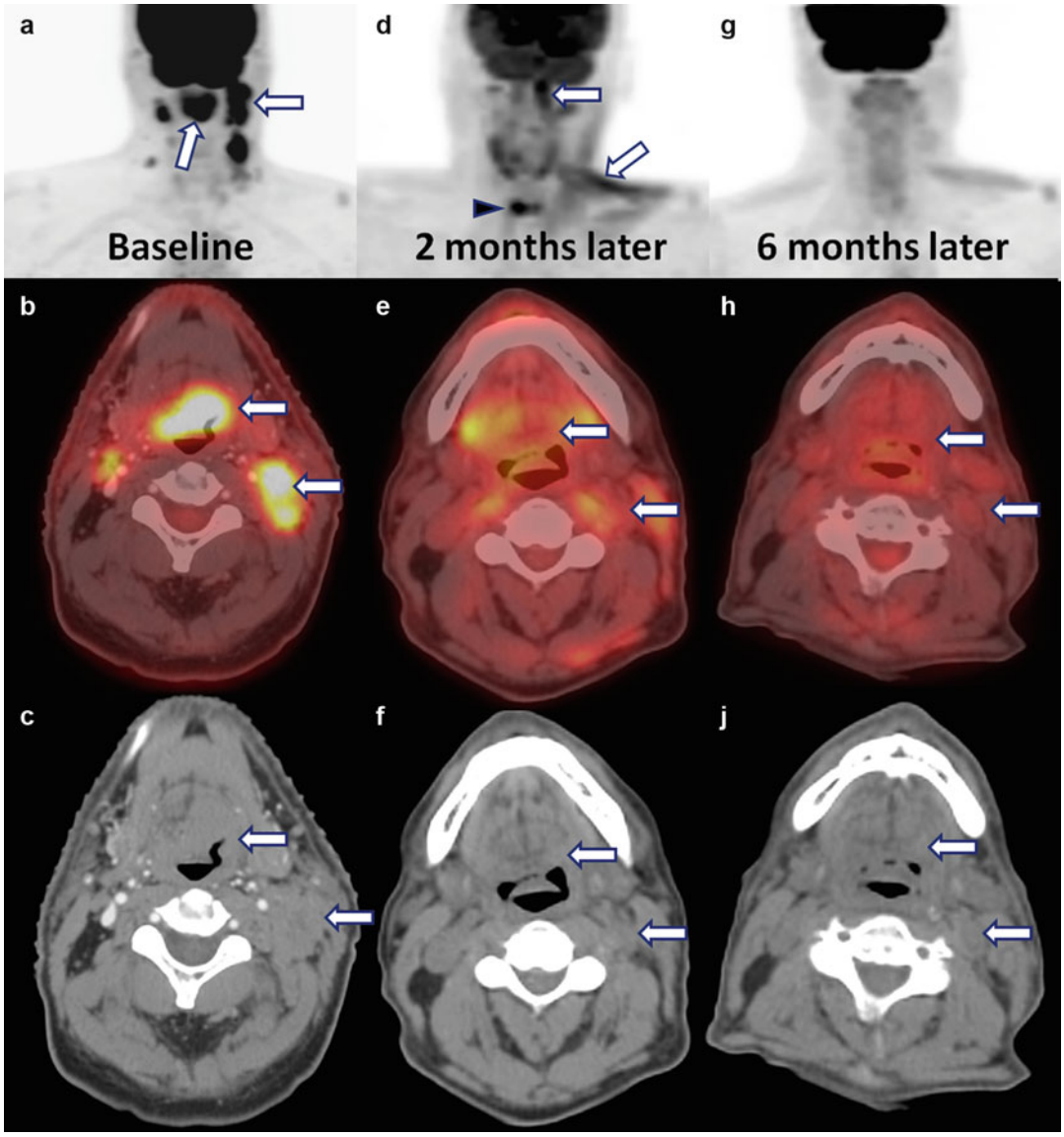

Fig. 6 (**a**) MIP image and (**b**) fused [^{18}F]FDG PET/CT axial image show primary lesion at the left tonsil with SUV_{max} 9.52 (*arrow*) and hypermetabolic metastases with SUV_{max} 10.23, measuring 3.7 × 2.4 cm (*arrows*). (**c**) CT during PET/CT revealed invasive primary tumor at the base of the tongue and lymphadenopathy in the bilateral cervical chains (*white arrows*). (**d**) MIP image of 1st follow-up PET/CT and (**e**) fused axial image show essentially resolution of abnormal uptake of primary lesions (SUV_{max} 2.83) and lymph nodes metastases (SUV_{max} 2.25), measuring 0.7 × 0.4 cm. Additionally, physiologic uptake after chemoradiotherapy appears at right vocal cord (*arrow head*) and in left trapezius muscle (*arrow*). (**f**) CT image shows residual soft tissue at the base of the tongue (*white arrow*). (**g**) MIP image of 2nd follow-up PET/CT, (**h**) fused axial image, and (**j**) CT image during PET/CT show complete remission at the base of the tongue with SUV_{max} 2.35 (*white arrow*) and left lymph node with SUV_{max} 1.5 (*white arrow*)

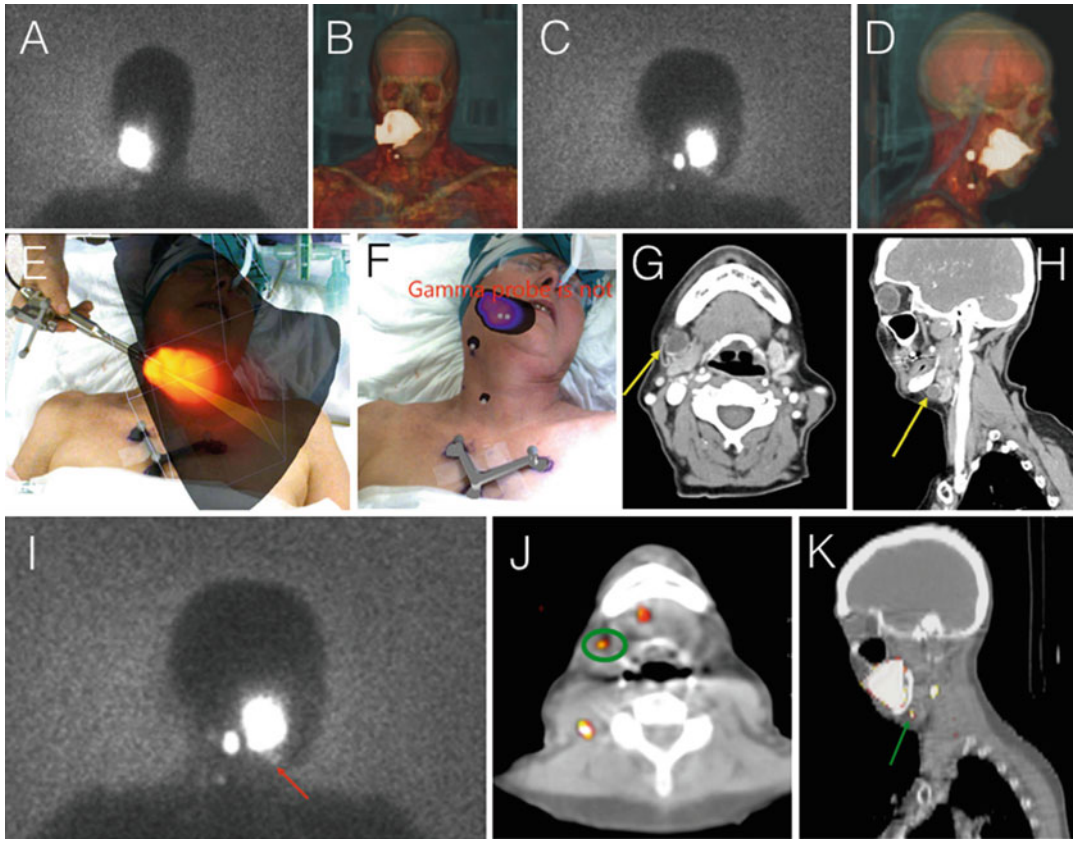

Fig. 7 (**A**) ^{99m}Tc-nanocolloidal albumin (anterior), (**B**) SPECT/CT 3D rendering (anterior), (**C**) ^{99m}Tc-nanocolloidal albumin (lateral), (**D**) SPECT/CT 3D rendering (lateral), (**E** and **F**) a free-hand SPECT probe during surgery, (**G**) Contrast enhanced axial CT image two month later showed swelling lymph-node (yellow arrow), (**H**) Contrast enhanced saggital CT image two month later showed swelling lymph-node (yellow arrow), (**I**) ^{99m}Tc-nanocolloidal albumin (lateral), (**J**) green circle showed late recurrence, (**K**) green arrow showed late recurrence

weeks later, follow-up [^{18}F]FDG PET/CT scan (Fig. 6d–f) showed complete resolution of disease. An additional follow-up scan 6 months later was also negative.

Discussion

Follow-up [^{18}F]FDG PET/CT after completion of chemoradiotherapy is scheduled 10–12 weeks after completion of treatment. Timing of follow-up [^{18}F]FDG PET/CT is important to avoid some false positive and negative findings [3, 4].

Case 4

Case contributed by: S. Vidal-Sicart
Nuclear Medicine Department, Hospital Clinic Barcelona, Barcelona, Spain

A 69-year-old lady presented with a squamous cell carcinoma in floor of the mouth, on the right side. A sentinel lymph node biopsy with the 2-day procedure was planned. After injection of 111 MBq of ^{99m}Tc-nanocolloidal albumin, dynamic, early, and delayed images showed two clear hot spots on the right side of the neck. Anterior and lateral views (Fig. 7A and C) and

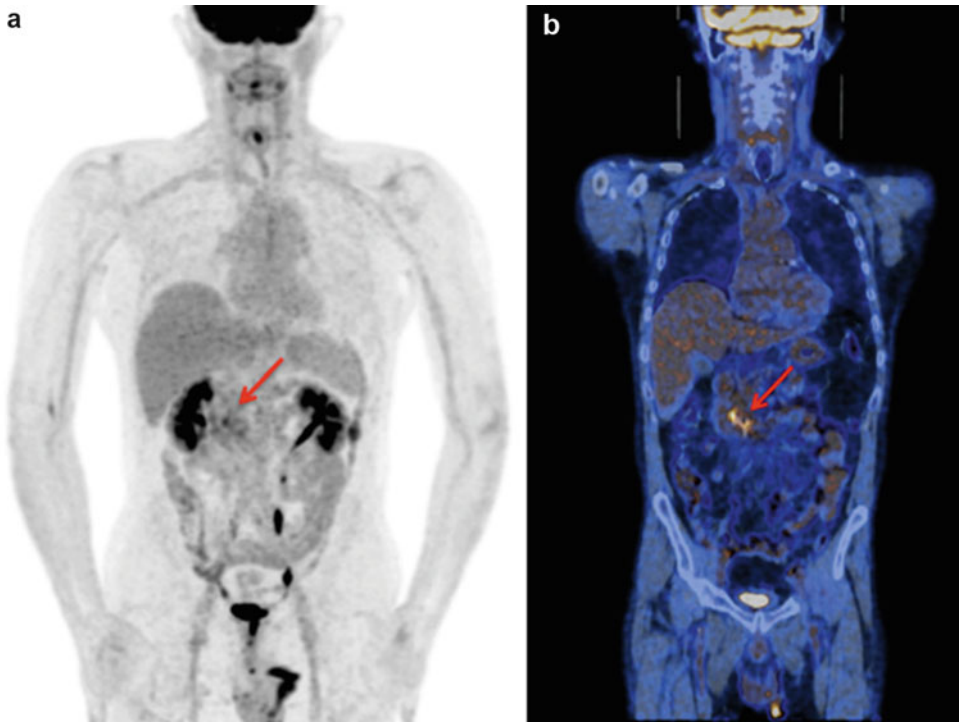

Fig. 8 (**a**) MIP, (**b**) coronal fused [^{18}F]FDG PET/CT; *Red arrows*: pancreatitis

their corresponding 3D reconstructions (Fig. 7B and D). During surgery, a free-hand SPECT device was used and similar findings were obtained (Fig. 7E and F). Two IIA level sentinel lymph nodes were resected and pathology assessment did not show metastatic involvement.

Two months later, the patient presented a palpable submandibular lymph node (Fig. 7G and H). A fine needle aspiration showed no metastasis. However, the multidisciplinary Head and Neck Cancer Committee decided to resect this node. The final pathology report indicated a macrometastatic node involvement. This situation is an example of a false negative sentinel node procedure. After a thorough reviewing of initial images, a faint uptake was considered (red arrow) and SPECT/CT slices showed a tiny uptake in the area where, lately, the recurrence was present (green circle in J and green arrow in K).

False negative results are not unfrequent in floor of mouth tumors and careful examination of all available images should be stressed.

Case 5

Case contributed by: E. Tabacchi[1], C. Nanni[1], I. Bossert[1], A.M. Maffione[2], S. Fanti[1]

[1]Nuclear Medicine Unit, "S. Orsola-Malpighi" Hospital, Bologna, Italy

[2]Nuclear Medicine Unit, "Santa Maria della Misericordia" Hospital, Rovigo, Italy

A 52-year-old man with a history of carcinoma of the soft palate treated with radiotherapy.

On serial follow-up scan 5 years later, a [^{18}F]FDG PET/CT (Fig. 8) showed thickening vocal cord with focal [^{18}F]FDG uptake (Fig. 9: brown arrows). [^{18}F]FDG PET/CT also revealed diffuse uptake in the pancreas (SUV_{max} 5.5) with some calcifications suspicious for chronic pancreatitis (red arrows).

Patient underwent biopsy of the vocal cord with diagnosis of squamous cell carcinoma and underwent endoscopic ultrasound with confirmation of chronic pancreatitis.

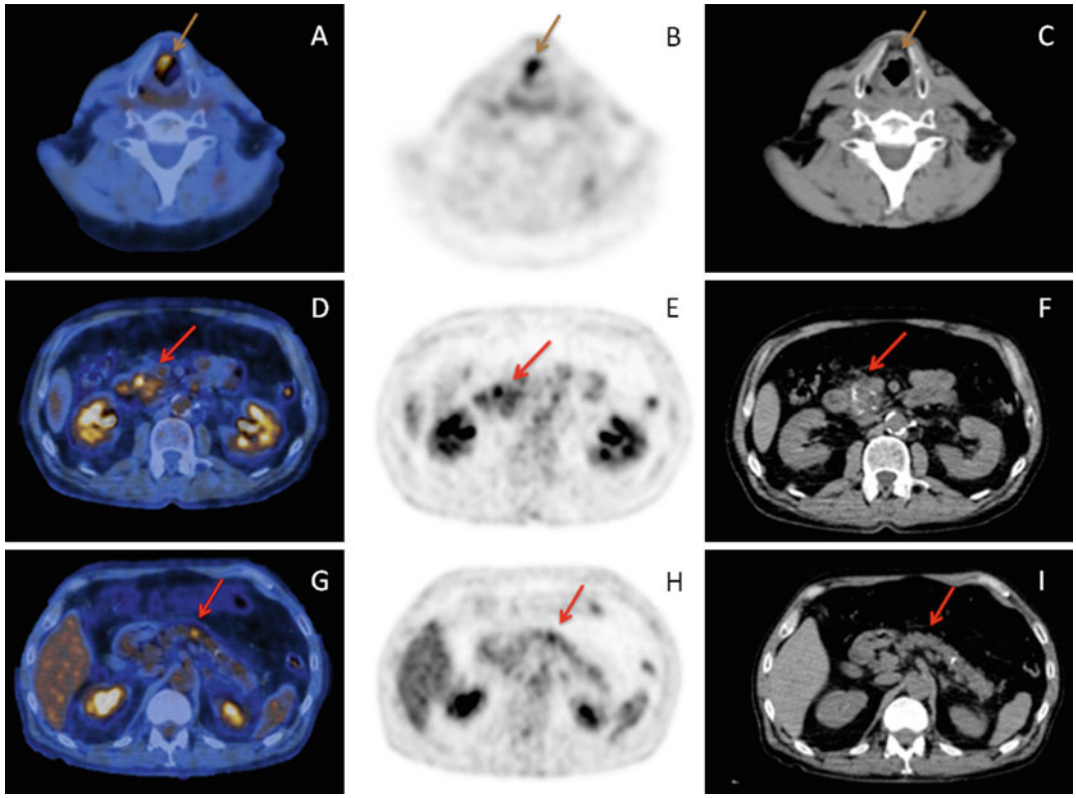

Fig. 9 (**A**, **D**, **G**) transaxial fused [^{18}F]FDG PET/CT images, (**B**, **E**, **H**) transaxial [^{18}F]FDG PET images, (**C**, **F**, **I**) transaxial CT images; *Brown arrows*: vocal cord lesion, *Red arrows*: pancreatitis

Fig. 10 (Baseline). MIP image of the [^{18}F]FDG PET showing the left nasopharyngeal lesion being the only site of disease

Case 6

Case contributed by: S. Wan
Nuclear Medicine, UCLH NHS Foundation Trust, London, UK

Presentation

A 15-year-old girl patient presented with 3 months history of gradually worsening headache and 2 weeks of diplopia.

Findings

Combined [^{18}F]FDG PET/MRI study showed a large soft tissue mass with the epicenter at the left nasopharynx (Figs. 10, 11, 12, and 13). There was extensive adjacent soft tissue involvement, including perineural involvement, erosion, and sclerosis of the left skull base and intra-cranial extension. There were no convincing focal avid nodal or distant metastases.

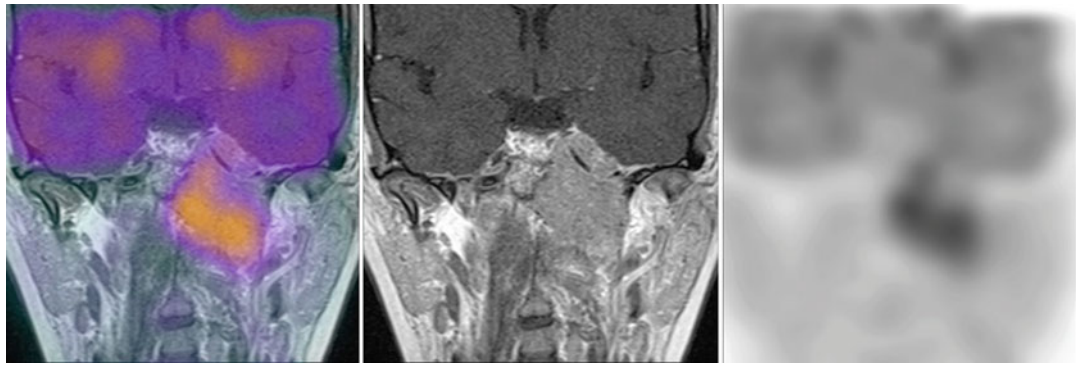

Fig. 11 (Baseline): from *left*: coronal fused, T1 postcontrast and PET image showing the extensive soft tissue mass eroding through the central and left sided skull base, with dural thickening of the left middle cranial fossa and cavernous sinus. The left internal carotid artery is encased and attenuated. There is involvement of the mandibular division of the left trigeminal nerve

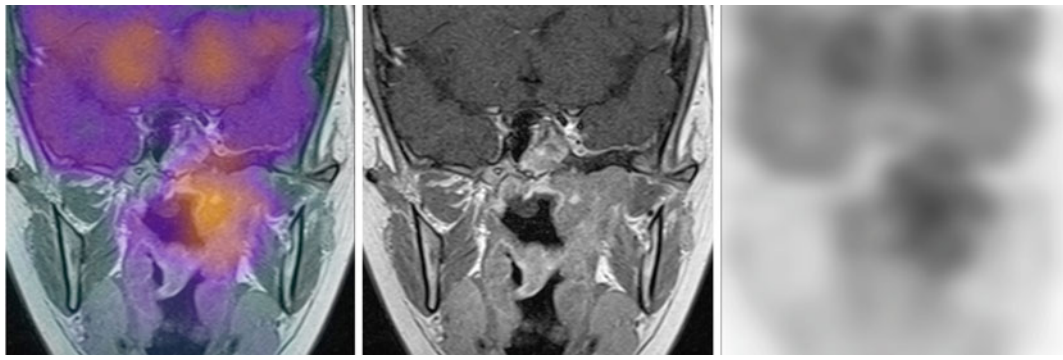

Fig. 12 (Baseline): from *left*: coronal fused, T1 postcontrast and PET image showing the extensive soft tissue mass with sclerosis as well as erosion of the left greater wing of sphenoid

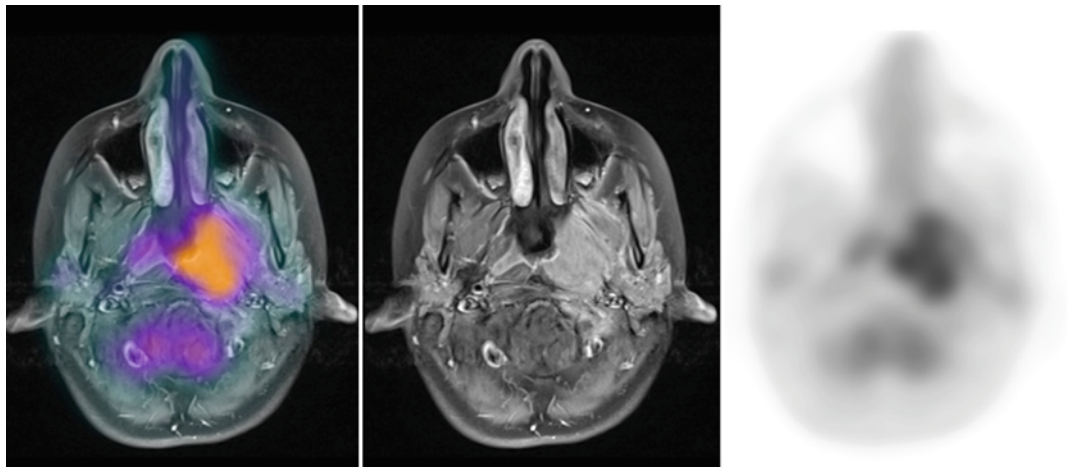

Fig. 13 (Baseline): from *left*: axial fused, T1 fat suppressed postcontrast and PET image showing the extensive left nasopharyngeal soft tissue mass involving the pterygoid muscles and plates. The prevertebral muscles are also involved

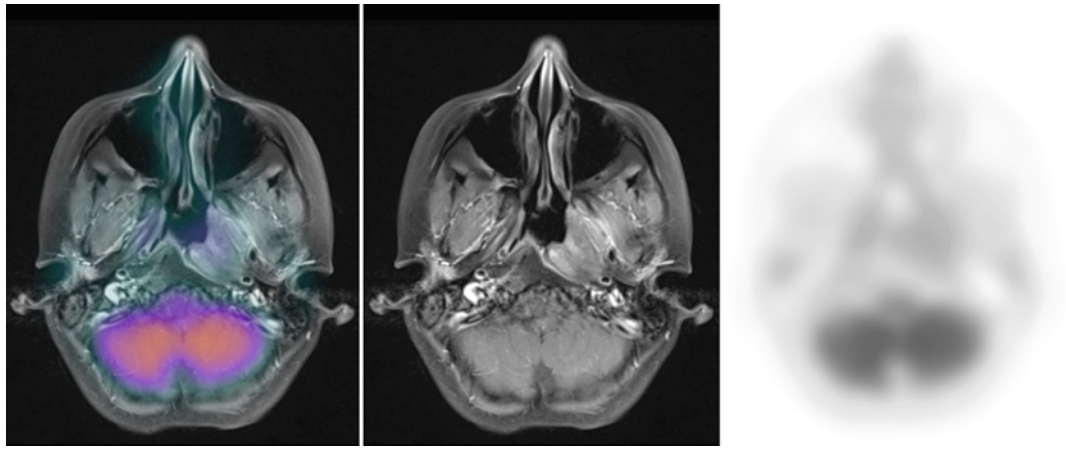

Fig. 14 (Posttreatment): from *left*: axial fused, T1 fat suppressed postcontrast and PET image restaging study showing reduction in bulk of the nasopharyngeal mass with metabolic switch off – only diffuse low grade [^{18}F] FDG uptake is evident

Fig. 15 (Posttreatment): axial T1 postcontrast MR image showing good post treatment appearance on further surveillance with no compelling evidence of relapsed disease

Follow-Up

Biopsy of the mass showed undifferentiated nasopharyngeal carcinoma (EBV positive). The patient subsequently underwent chemotherapy with 5FU/cisplatin/folinic acid and received radiotherapy. Restaging study showed good response to treatment, with further subsequent surveillance study 8 months later showing no compelling evidence of residual disease (Figs. 14 and 15).

Case 7

Presentation

A 48 year old man was referred for second line treatment of advanced squamous cell carcinoma after underwent cisplatin based chemotherapy (cT4N2c). The patient complained with recurrent sore throat and cervical lymphadenopathy.

Findings

Biopsy from the base of the tongue and right pharynx showed an SCC, HPV-positive lesion. Baseline [^{18}F]FDG PET/CT axial image showed the primary tumor on the right base of tongue and cervical lymph node metastases in the left neck (Fig. 16a, b). The patient received concurrent cisplatin based chemotherapy and radiotherapy (total 70 Gy).

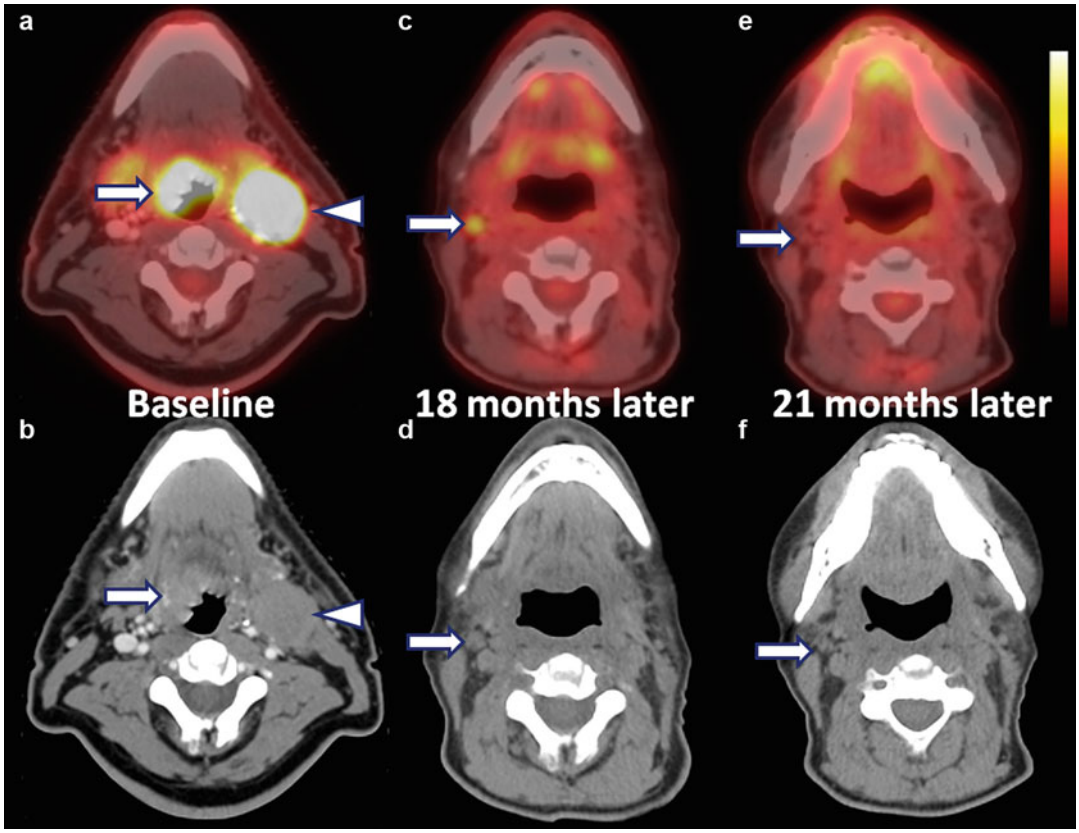

Fig. 16 (**a**) [^{18}F]FDG PET/CT fused axial image and (**b**) CT demonstrated hypermetabolic tumor at the left base of tongue with SUV_{max} 9.8 (*white arrow*) and hypermetabolic left lymph node at left level II with SUV_{max} 17.8 (*white arrow head*), measuring 2.9 × 2.8 cm. (**c**) Eighteen months after the treatment, 1st follow-up [^{18}F]FDG PET/CT fused axial image with the hypermetabolic lymph node (SUV_{max} 3.4) at right level II and (**d**) diagnostic CT scan during PET/CT shows a round lymph node measuring 0.9 × 0.8 cm (*white arrows*). Three months after the 1st follow-up PET/CT scan, (**e**, **f**) 2nd follow-up [^{18}F]FDG PET/CT shows that this finding is resolved (SUV_{max} 1.3), measuring 0.8 × 0.5 cm

Follow-Up

One and a half years after the completion of treatment, a follow-up [^{18}F]FDG PET/CT axial images showed small round lymph node with mild uptake (Fig. 16c, d). The patient was monitored expectantly. Three months later, uptake in this node completely resolved (Fig. 16e, f).

Discussion

[^{18}F]FDG PET/CT can determine the extent of the primary lesions of HNSCC with lymph node metastases. However, false positive findings of [^{18}F]FDG PET occasionally appear as [^{18}F]FDG avid lymph nodes in head and neck region after treatment due to inflammation [3–5]. In this case, the follow-up [^{18}F]FDG PET/CT performed after chemotherapy showed ambiguous findings in a small round lymph node. A watch and wait approach is often helpful to sort out such findings.

References

1. Blodgett TM, Fukui MB, Snyderman CH, et al. Combined PET-CT in the head and neck: part 1. Physiologic, altered physiologic, and artifactual FDG uptake. Radiographics. 2005;25:897–912.

2. Matthews R, Shrestha P, Franceschi D, et al. Head and neck cancers: post-therapy changes in muscles with FDG PET-CT. Clin Nucl Med. 2010;35: 494–8.
3. Schöder H, Fury M, Lee N, et al. PET monitoring of therapy response in head and neck squamous cell carcinoma. J Nucl Med. 2009;50 Suppl 1:74S–88.
4. Duet M, Hugonnet F, Faraggi M. Role of positron emission tomography (PET) in head and neck cancer. Eur Ann Otorhinolaryngol Head Neck Dis. 2010;127:40–5.
5. Minamimoto R, Kubota K, Morooka M, et al. Reevaluation of FDG-PET/CT in patients with hoarseness caused by vocal cord palsy. Ann Nucl Med. 2012;26:405–11.

Teaching Cases in Nuclear Oncology: Thyroid Tumors

57

Kimiteru Ito, Somali Gavane, and Heiko Schöder

Keywords

Thyroid • Cancer • [^{18}F]FDG • Iodine • DOTATATE • SPECT/CT • PET/CT • Lymph node • Metastasis

Glossary

[^{18}F]FDG	2-Deoxy-2-[^{18}F]fluoro-D-glucose
^{131}I-WBS	Whole-body scintigraphy with ^{131}I-iodide
AJCC	American Joint Committee on Cancer
CT	X-ray computed tomography
DOTA	1,4,7,10-Tetraazacyclododecane-1,4,7,10-tetraacetic acid
DOTATATE	DOTA-Tyr^3-octreotate
FNAC	Fine-needle aspiration cytology
M	Metastasis status according to the AJCC/UICC TNM staging system
MIP	Maximum intensity projection
MTC	Medullary thyroid cancer
N	Lymph node status according to the AJCC/UICC TNM staging system
PET	Positron emission tomography
PET/CT	Positron emission tomography/Computed tomography
PET/MRI	Positron emission tomography/Magnetic resonance imaging
PTC	Papillary thyroid carcinoma
RET	A proto-oncogene encoding for a receptor tyrosine kinase for extracellular signaling molecules (from "rearranged during transfection")
SPECT	Single-photon emission computed tomography
SPECT/CT	Single-photon emission computed tomography/Computed tomography
SUV	Standardized uptake value
SUV_{max}	Standardized uptake value at point of maximum
T	Tumor status according to the AJCC/UICC staging system
Tg	Thyroglobulin
TKI	Tyrosine kinase inhibitor

K. Ito • H. Schöder (✉)
Department of Radiology, Molecular Imaging and Therapy service, Memorial Sloan Kettering Cancer Center, New York, NY, USA
e-mail: itoukimiteru@yahoo.co.jp; itok@mskcc.org; schoderh@mskcc.org

S. Gavane
Division of Nuclear Medicine, Department of Radiology, Mount Sinai Hospital, New York, NY, USA
e-mail: somali.gavane@mountsinai.org

© Springer International Publishing Switzerland 2017
H.W. Strauss et al. (eds.), *Nuclear Oncology*,
https://doi.org/10.1007/978-3-319-26236-9_60

TNM	AJCC/UICC staging system based on parameters "T" (tumor status), "N" (lymph node status), and "M" (distant metastasis status)
UICC	Union Internationale Contre le Cancer (International Union Against Cancer)
US	Ultrasonography

Contents

Thyroid Cancer (Papillary Carcinoma) and Malignant Struma Ovary 1586
Presentation 1586
Findings 1586

Thyroid Cancer 1586
Presentation 1586
Findings 1587

Discussion 1588

Thyroid Cancer (Medullary Carcinoma) 1589
Presentation 1589
Findings 1589
Follow-Up 1589

Thyroid Cancer (Follicular Carcinoma) 1590
Presentation 1590
Findings 1590

Thyroid Cancer (Poorly Differentiated Carcinoma) 1591
Presentation 1591
Findings 1592

Thyroid Cancer (Papillary Carcinoma) and Malignant Struma Ovary

Case contributed by: D. Viola, L. Pieruzzi, R. Elisei
Endocrine Unit, Department of Clinical and Experimental Medicine, University of Pisa, Pisa, Italy

Presentation

A 40-year-old lady underwent a total thyroidectomy and cervical lymphadenectomy for a 2.5 cm papillary thyroid carcinoma (PTC) with lymph node metastases in the central compartment; at histology, PTC was multifocal, classical variant (T2N1aMx).

Findings

The patient was administered 3.7 GBq ^{131}I-iodide for postsurgical thyroid remnant ablation. At this time serum Tg was 157 ng/mL. The post-ablation whole-body scan (^{131}I-WBS) performed 4 days post-radioiodide administration (Fig. 1) showed frankly increased uptake not only in the neck (indicated with a circle) but also in the pelvic area (indicated with a square).

While tracer uptake in the neck was interpreted as due to a postsurgical remnant of the right thyroid lobe, uptake in the pelvis was unexpected. To better clarify the nature of this lesion, SPECT/CT was acquired, both 4 days and 7 days after administration of ^{131}I-iodide, to verify the pattern of change in uptake intensity – possibly due to non-specific ^{131}I accumulation.

As shown in Figs. 2, 3, 4, 5, and 6, uptake in the pelvis was actually represented by three different areas located as follows: (a) one close to the left anterior pelvic wall in front of the uterus, (b) one in the space between the rectum and uterus, and (c) one in the right portion of the anterior region of the sacrum. The patient underwent laparotomy and a malignant struma ovarii with local metastases was found.

SPECT/CT imaging is a powerful diagnostic tool, which is crucial for correct localization of areas of increased ^{131}I uptake, particularly when localized in the abdomen and in the chest.

Thyroid Cancer

Case contributed by: V. Yerubaudi, C. Sakellis, A.D. Van den Abbeele, H. Jacene
Nuclear Medicine/PET-CT, Dana-Farber Cancer Institute, Harvard medical School, Boston, Massachusetts, USA

Presentation

A 27-year-old man with cystic fibrosis and recently diagnosed papillary thyroid cancer with multiple cervical lymph node metastases found at the time of thyroidectomy.

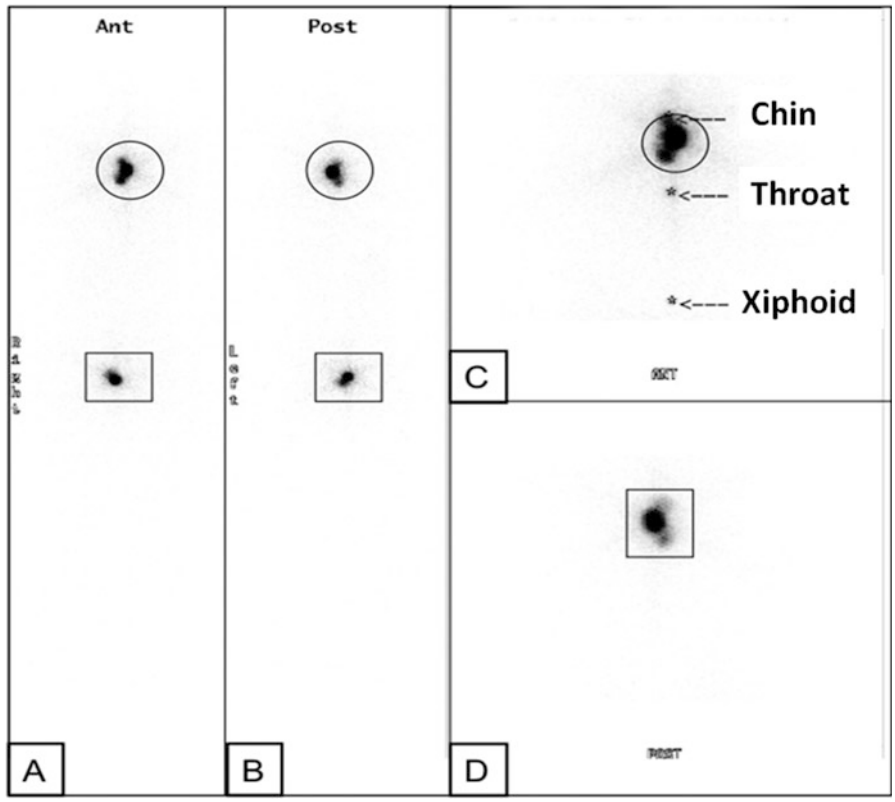

Fig. 1 Anterior (*panel A* with the spot image of the neck in *panel C*) and posterior (*panel B* with the spot image of the pelvis in *panel D*) views of the planar post-ablation ^{131}I-WBS. The area of uptake indicated with a *circle* is clearly due to the expected postsurgical thyroid remnant, while the uptake in the pelvis was unexpected and could not be topographically defined on the planar ^{131}I-WBS

Findings

Several months after surgery, a diagnostic whole-body radioiodine scan was performed 24 h after the oral administration of 107 MBq ^{123}I-iodide. The patient reported maintaining a low-iodine diet in preparation for his iodine scan, and thyroid hormone withdrawal serum TSH was 180.9 μIU/mL. Foci of uptake seen in the neck are suggestive of thyroid remnant tissue (Fig. 7). There is no evidence of abnormal iodine-avid distant foci of uptake to suggest metastatic disease (Fig. 8).

Due to a history of multiple cervical lymph nodes at surgery positive for metastatic thyroid cancer, the patient was treated with 5.5 GBq ^{131}I-iodide. A 5-day delayed post-therapy scan again demonstrated foci of uptake in the neck consistent with remnant thyroid tissue; however, there were additional findings of multiple, patchy, confluent foci of abnormal iodine uptake in the bilateral upper lung zones (Fig. 9). These areas of uptake were likely inflammatory related to patient's cystic fibrosis given the distribution; however, pulmonary metastatic disease remained a possibility. SPECT imaging was performed on this post-therapy radioiodine scan and confirmed bilateral upper lung iodine uptake. These areas of iodine uptake were not seen on the pre-therapy scan. CT chest was recommended for further evaluation.

CT of the chest was performed and images were manually fused with the SPECT previously performed at the time of the ^{131}I-iodide post-therapy scan (Fig. 10). These images

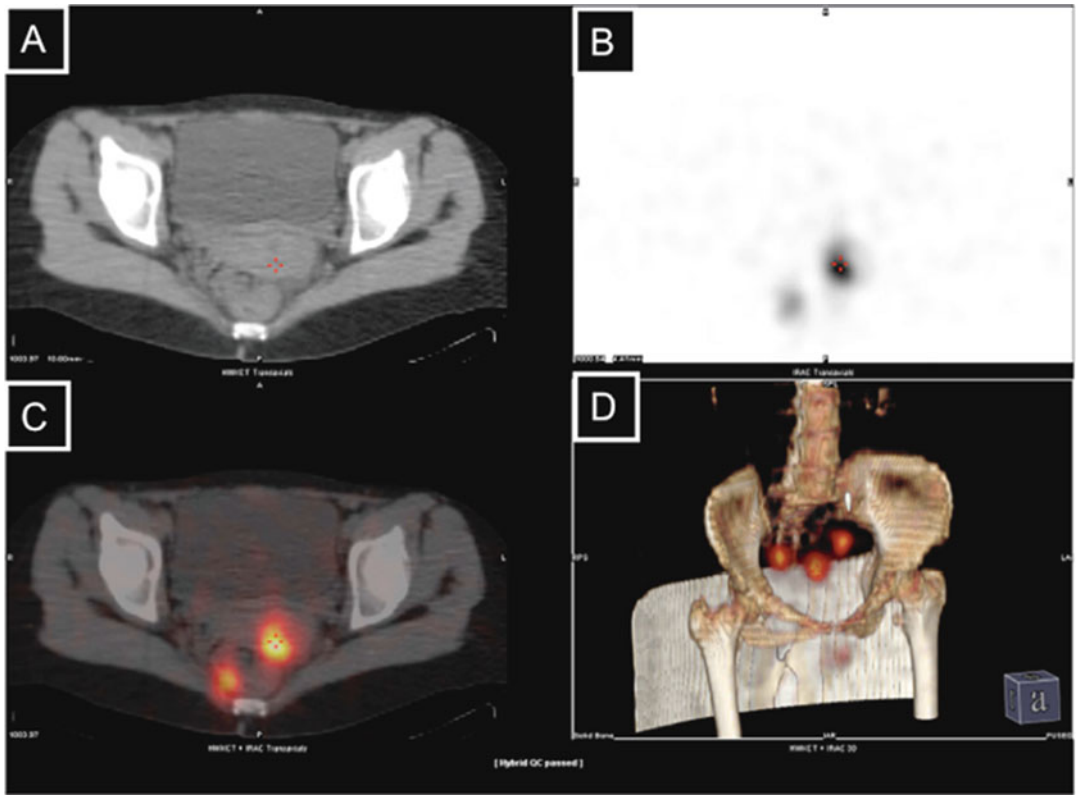

Fig. 2 SPECT/CT transaxial images of the pelvic region (CT, *panel A*; SPECT, *panel B*; fused SPECT/CT image, *panel C*) showing several areas of ^{131}I uptake corresponding to different lesions in the pelvis; the tridimensional volume rendering (*panel D*) clearly demonstrated the presence of three distinct ^{131}I-avid lesions

demonstrated that areas of most iodine avidity in the upper lungs bilaterally corresponded with the most severe areas of bronchiectasis and bronchial wall thickening. CT findings were consistent with patient's history of cystic fibrosis, and no significant nodules/masses were seen to correspond with areas of increased ^{131}I-iodide uptake on the post-therapy scan.

Discussion

This case demonstrates that abnormal radioiodine uptake can be seen not just in well-differentiated thyroid cancer metastases but also occasionally in nontumoral areas of inflammation, infection, or bronchiectasis. Additionally, there are rare reports of radioiodine uptake in various benign and malignant non-thyroidal tumors as well. In this case, since findings are only seen in the upper lungs, and metastases would be expected to have a more random or broader distribution throughout the lungs, a nonmalignant etiology of the ^{131}I-iodide scan abnormalities should be considered. Occasionally, abnormal foci of iodine uptake are seen only on the post-therapy ^{131}I-iodide scan, and not the pre-therapy ^{123}I-iodide scan, due to the higher administered activity and/or the longer uptake period with the post-therapy scan.

If available, combined SPECT/CT may also be obtained at the time of radioiodine imaging to help localize findings on planar imaging, obviating the need for an additional visit for the patient.

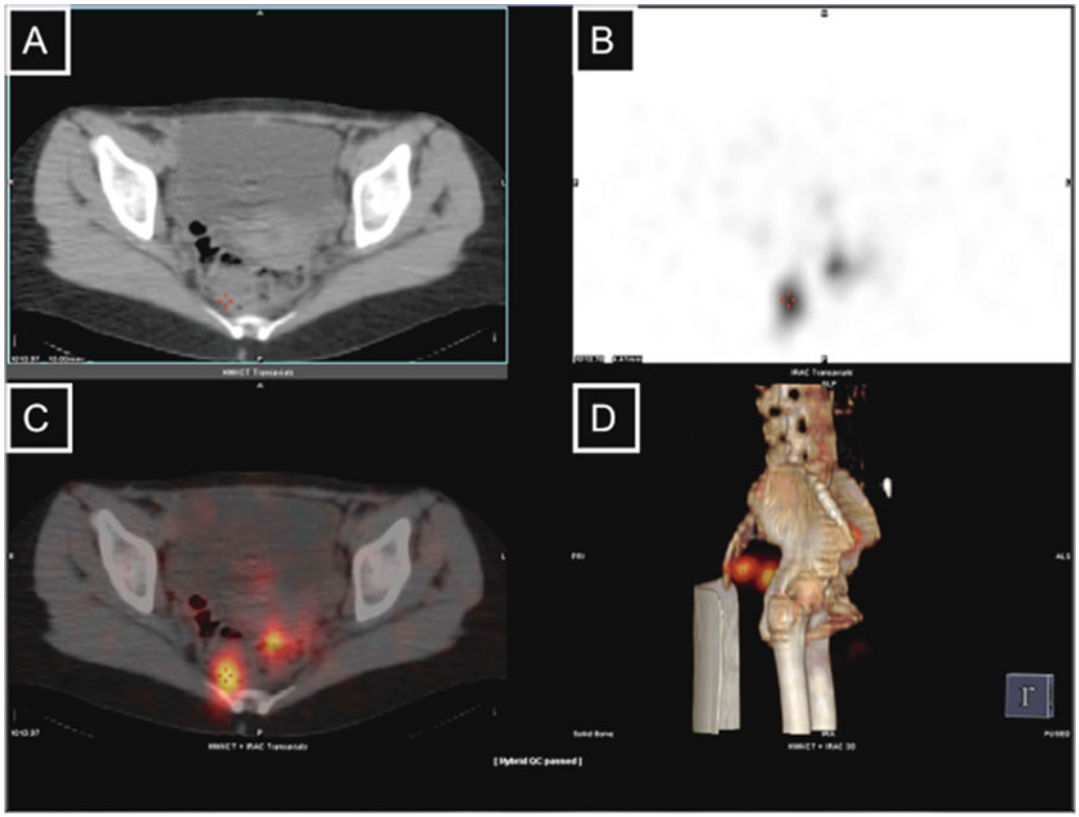

Fig. 3 *Panels A*, *B*, and *C* as in Fig. 2, but with a different tridimensional reconstruction (*panel D*), showing the spatial relationship of the ^{131}I-avid lesions with the pelvic organs and bones

Thyroid Cancer (Medullary Carcinoma)

Case contributed by: S. Wan
Nuclear Medicine, UCLH NHS Foundation Trust, London, UK

Presentation

A 40-year-old-man with known history of familial medullary thyroid cancer associated with a known RET oncogene mutation, was initially treated with radical resection and adjuvant chemotherapy. There was however a persistently raised calcitonin level leading to several further local resections. However, calcitonin continued to rise slowly. Conventional imaging yielded no evidence of residual disease locally or distally.

Findings

^{68}Ga-DOTATATE PET/MRI study showed no compelling evidence of somatostatin receptor-positive residual disease in the thyroid bed or cervical chain nodes. There were however a few ^{68}Ga-DOTATATE-avid bone lesions in the cervical and lumbar spine and in the pelvis.

Follow-Up

Metastatic medullary thyroid cancer was diagnosed. An expectant approach was adopted due to perceived low-volume active disease. However, a further follow-up study 6 months later showed progressive imaging findings, in parallel with calcitonin rise. The patient commenced chemotherapy with a targeted agent (Figs. 11, 12, 13, and 14).

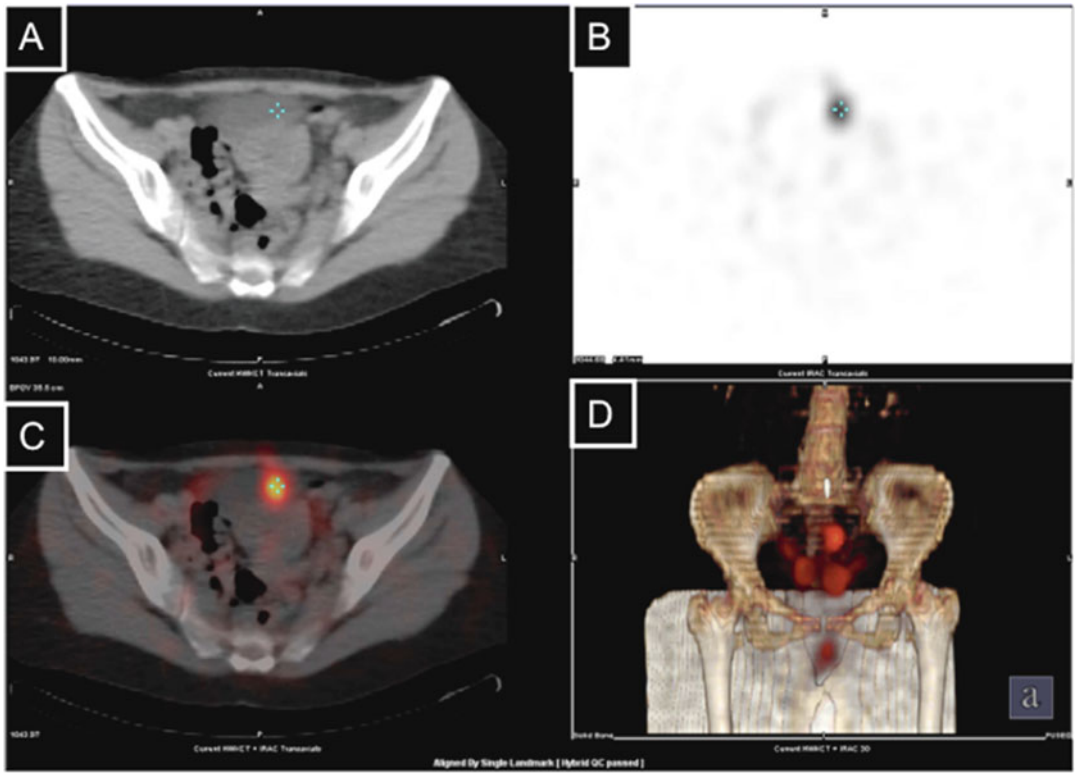

Fig. 4 SPECT/CT transaxial images of the pelvic region (CT, *panel A*; SPECT, *panel B*; fused SPECT/CT image, *panel C*) showing the presence of a ^{131}I-avid lesion in the space between the rectus and uterus that could also be interpreted as due to ^{131}I retention in the intestinal lumen

Thyroid Cancer (Follicular Carcinoma)

Case contributed by: A. Matrone, V. Cappagli, R. Elisei

Endocrine Unit, Department of Clinical and Experimental Medicine, University of Pisa, Pisa, Italy

Presentation

A 39-year-old lady presented with a pathological fracture of the left femur. Biopsy obtained at surgery demonstrated that the fracture was due to bone metastasis from a follicular thyroid cancer.

Findings

A 2 cm thyroid nodule was found at neck ultrasound, and FNAC was suspicious for thyroid cancer. The patient underwent thyroidectomy, with histologic confirmation of follicular thyroid cancer.

After thyroidectomy, serum thyroglobulin was 481 ng/mL. Radioiodine ablation/therapy was performed by administering 7.4 GBq ^{131}I-iodide. The post-therapeutic whole-body scan (^{131}I-WBS) showed several areas of increased tracer uptake (Fig. 15). Some of them (indicated with a circle) were clearly due to metastatic lesions: left femur metastasis, lung metastasis located in the lower part of the left lung, and bone metastasis in the left iliac crest. Others (indicated with a square) were equivocal for metastatic lesions: right submandibular area and right iliac fossa.

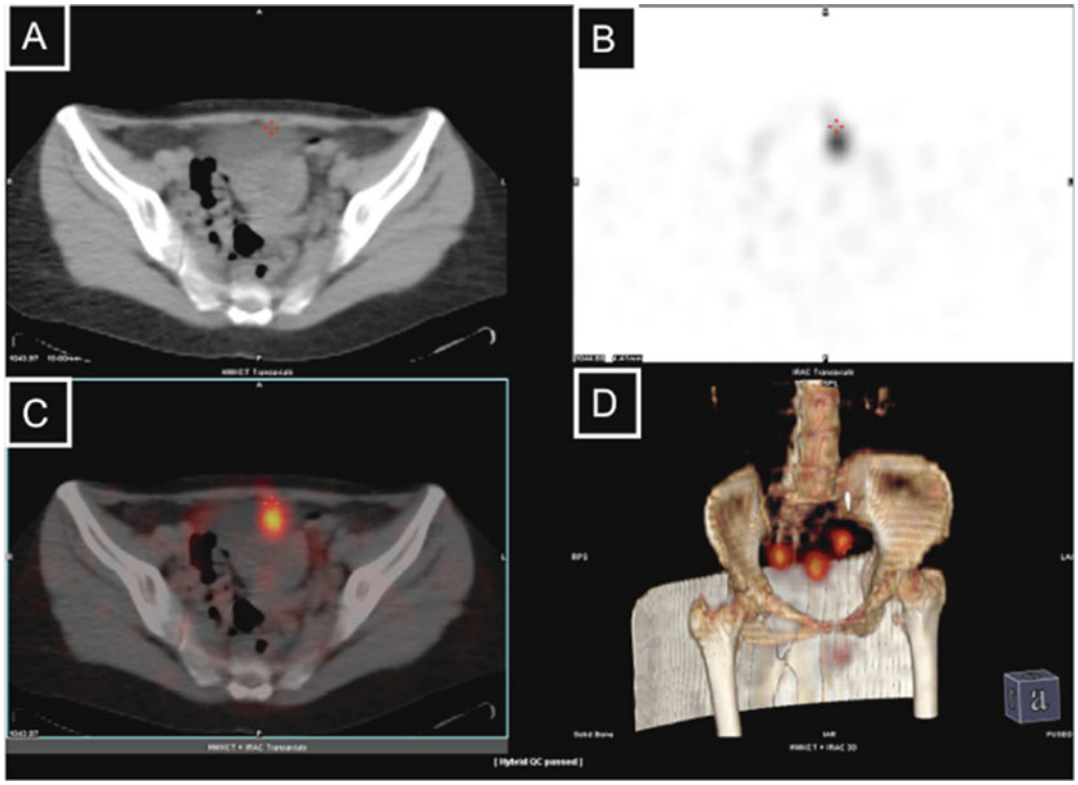

Fig. 5 The same as Fig. 4, but SPECT/CT was acquired 3 days later, showing the persistence of uptake, therefore confirming that it was not a nonspecific accumulation of ^{131}I activity

To better clarify the nature of the areas with increased ^{131}I-iodide accumulation, SPECT/CT at different body levels was acquired (Fig. 16). Uptake in the lung corresponded to a lung nodule in the CT scan. Similarly, uptake in both the left iliac crest (Fig. 17) and the left femur (Fig. 18) corresponded to bone lesions. Instead, no CT detectable lesions were found to correspond to the right submandibular area (Fig. 19) and to the right iliac fossa (Fig. 20); these were therefore interpreted as due to the physiological ^{131}I uptake in the submandibular salivary glands and to retention of ^{131}I activity in the intestine.

Hybrid SPECT/CT imaging is a powerful diagnostic tool to correctly localize the ^{131}I accumulation in the body and distinguish pathological from physiological or nonspecific areas of uptake.

Thyroid Cancer (Poorly Differentiated Carcinoma)

Case contributed by: C. Giani, E. Molinaro, R. Elisei

Endocrine Unit, Department of Clinical and Experimental Medicine, University of Pisa, Pisa, Italy

Presentation

A 52-year-old lady presented with a recently discovered and rapidly growing neck mass. At the time of the observation, the patient did not complain of any other symptoms, neither local nor systemic.

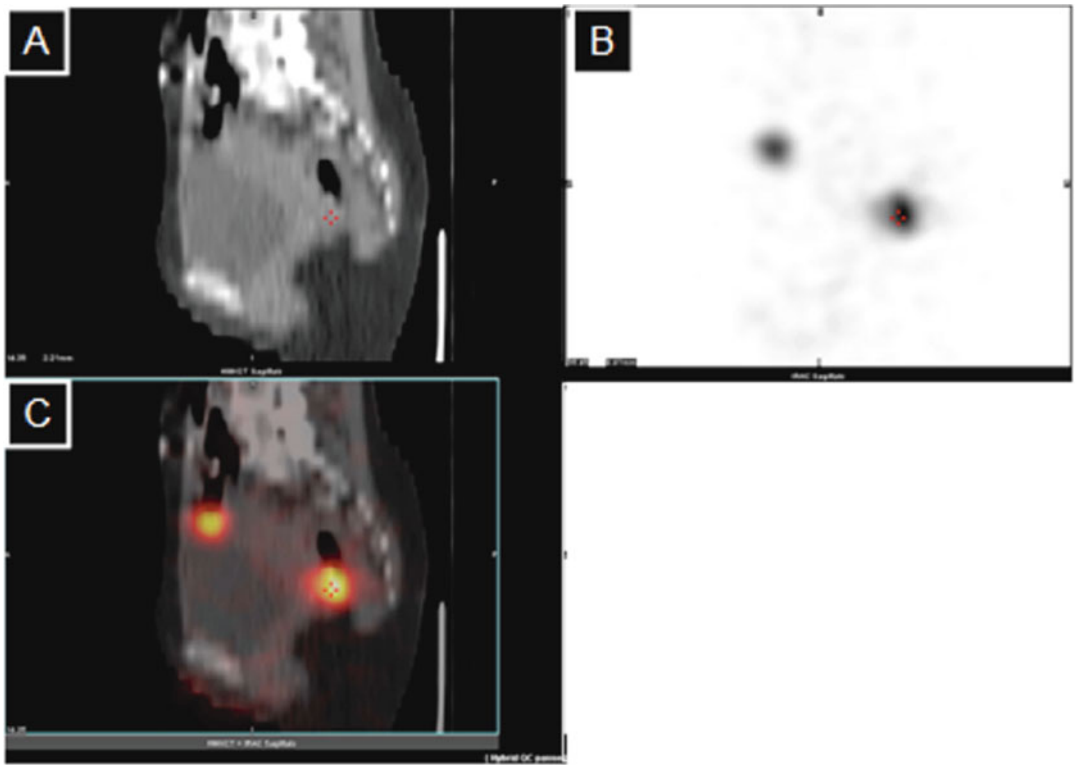

Fig. 6 Sagittal images (CT, *panel A*; SPECT, *panel B*; SPECT/CT, *panel C*) showing the topographic relationship of two of the three ^{131}I-avid lesions with the sacrum, the rectum, and the anterior wall of the pelvis

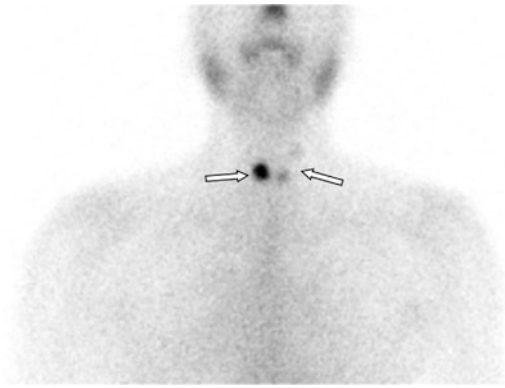

Fig. 7 Anterior neck and chest image from ^{123}I-iodide scan showing foci of uptake in the neck consistent with remnant thyroid tissue (*arrows*). Normal radioiodine distribution otherwise in the salivary glands and nasal mucosa

Findings

Neck US examination showed a large solid and hypoechoic mass in the right thyroid lobe, with features highly suspicious for malignancy (Fig. 21). Histology of a tissue sample obtained by true-cut biopsy showed poorly differentiated thyroid cancer with >30% of anaplastic areas. The CT scan showed a large mass surrounding the trachea, the lumen of which was severely restricted up to a critical point of nearly total obstruction (Fig. 22, panel A). The patient was considered not operable and therapy with a tyrosine kinase inhibitor (TKI) was immediately started as systemic therapy, despite the fact that there were no other lesions outside the

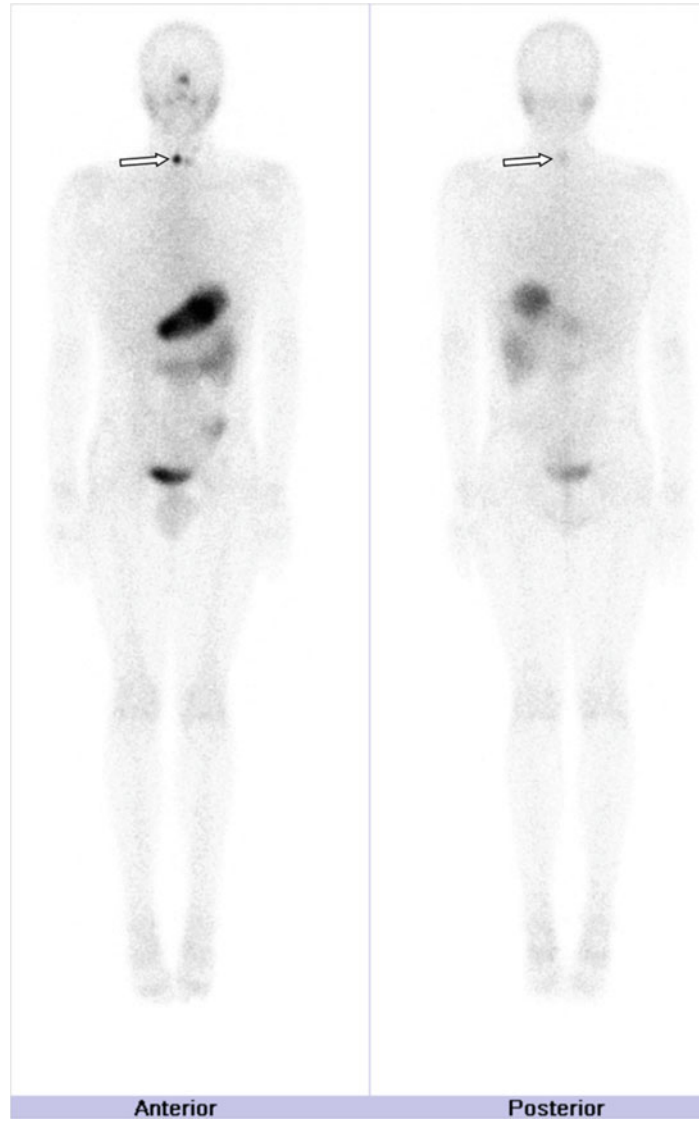

Fig. 8 Whole-body anterior (*left*) and posterior (*right*) images from ^{123}I-iodide scan again also show uptake in remnant thyroid tissue in the neck (*arrows*). Normal biodistribution of radioiodine otherwise with uptake in the nasal mucosa, salivary glands, stomach, bowel, and bladder

neck. After 4 months of TKI therapy, a 50% reduction of the thyroid mass was observed, with significant recovery in size of the tracheal lumen (Fig. 22, panel B). Radical surgery with partial laryngectomy was performed (Fig. 23), after which therapy with TKI was continued up to a total of 24 months. At this time the CT scan was negative, while [^{18}F]FDG PET/CT showed non-specific mildly increased tracer uptake in the neck located before the esophagus around the laryngectomy stoma (Figs. 24 and 25). Additional lesions with increased [^{18}F]FDG uptake were observed in the lung, but the CT scan clearly showed that these were inflammatory. TKI therapy was stopped, and

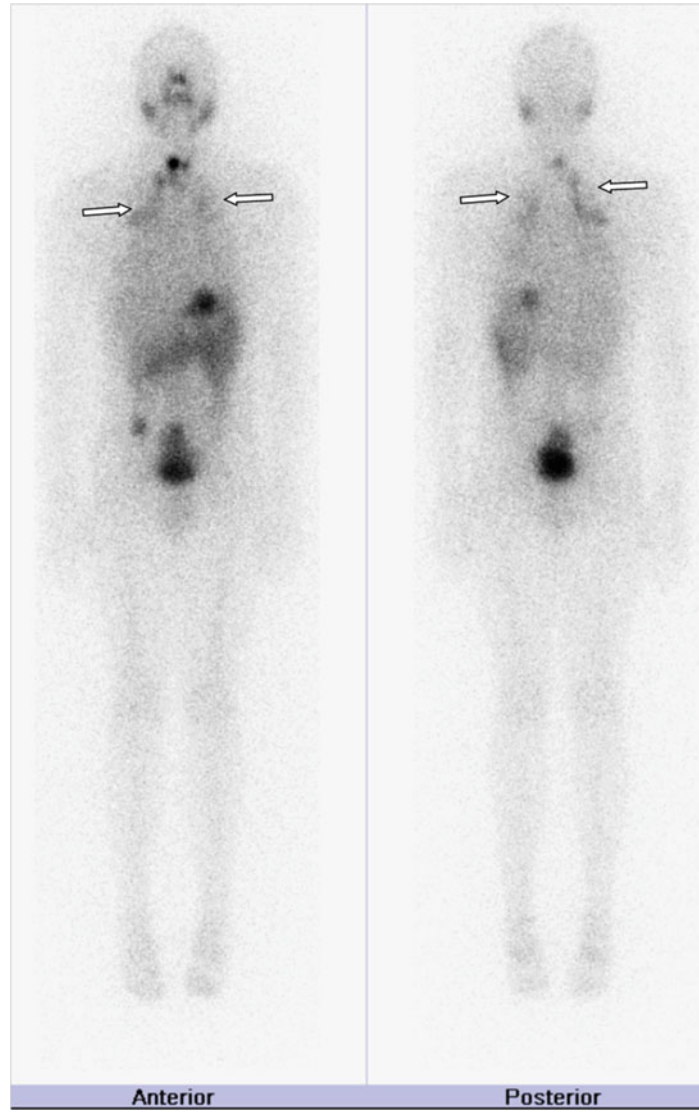

Fig. 9 Whole-body anterior (*left*) and posterior (*right*) ^{131}I-iodide gamma camera images demonstrate foci of uptake in the neck consistent with remnant thyroid tissue. Additional areas of expected biodistribution are seen in the salivary glands, stomach, bowel, and rectum. A small amount of liver uptake is seen related to metabolism of thyroid hormones. Unexpected areas of ^{131}I-iodide uptake are noted in the right greater than left upper lungs (*arrows*), not seen on the pre-therapy ^{123}I-iodide scan

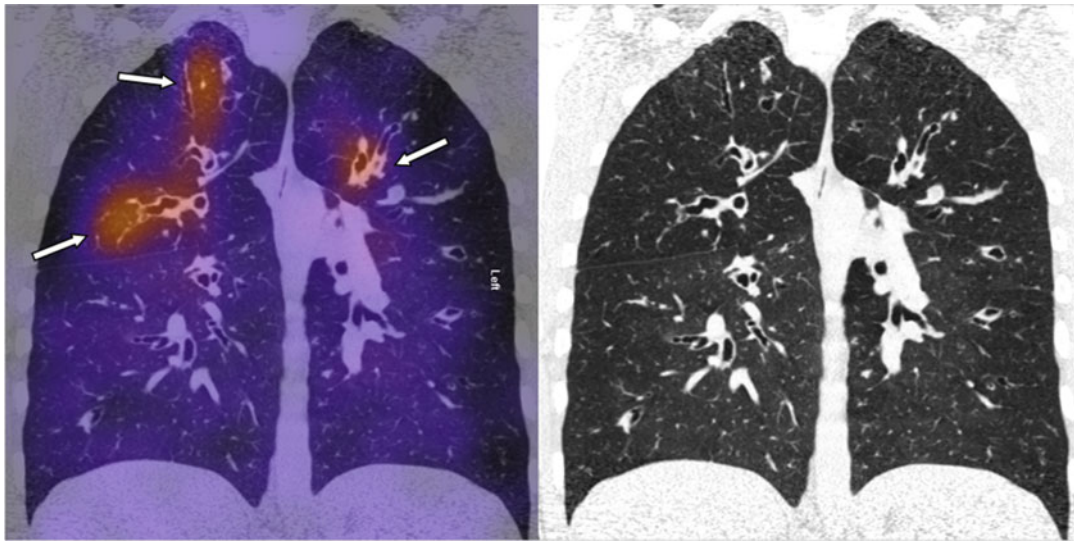

Fig. 10 Coronal fused SPECT/CT (*left*) and coronal CT (*right*) of the chest showing upper-lung-predominant bronchiectasis consistent with patient's history of cystic fibrosis. SPECT uptake is noted to correlate with areas of bronchiectasis on CT (*arrows*), notably with no significant nodules or opacities to suggest metastatic disease

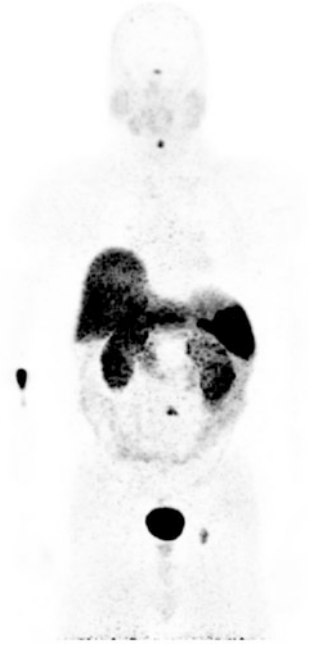

Fig. 11 Whole-body 3D maximum intensity projection (*MIP*) image of the ^{68}Ga-DOTATATE PET showing a few sites of somatostatin receptor-positive disease in the cervical, lumbar spine and in the left ischium

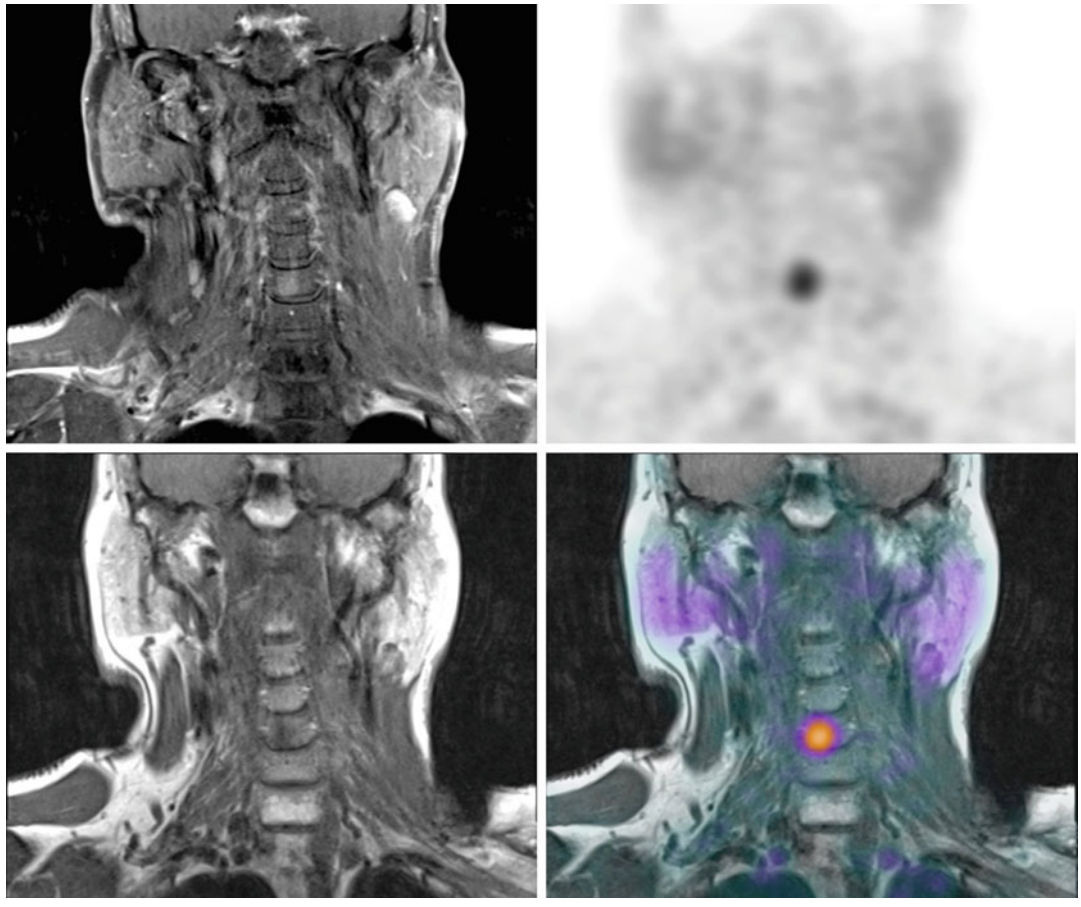

Fig. 12 Clockwise from *top left*: coronal fat-suppressed T1 postcontrast, PET, fused, T1-weighted images showing ^{68}Ga-DOTATATE-avid focus corresponding to an enhancing, low T1 signal lesion in the right side of the C5 vertebrae consistent with a metastatic deposit

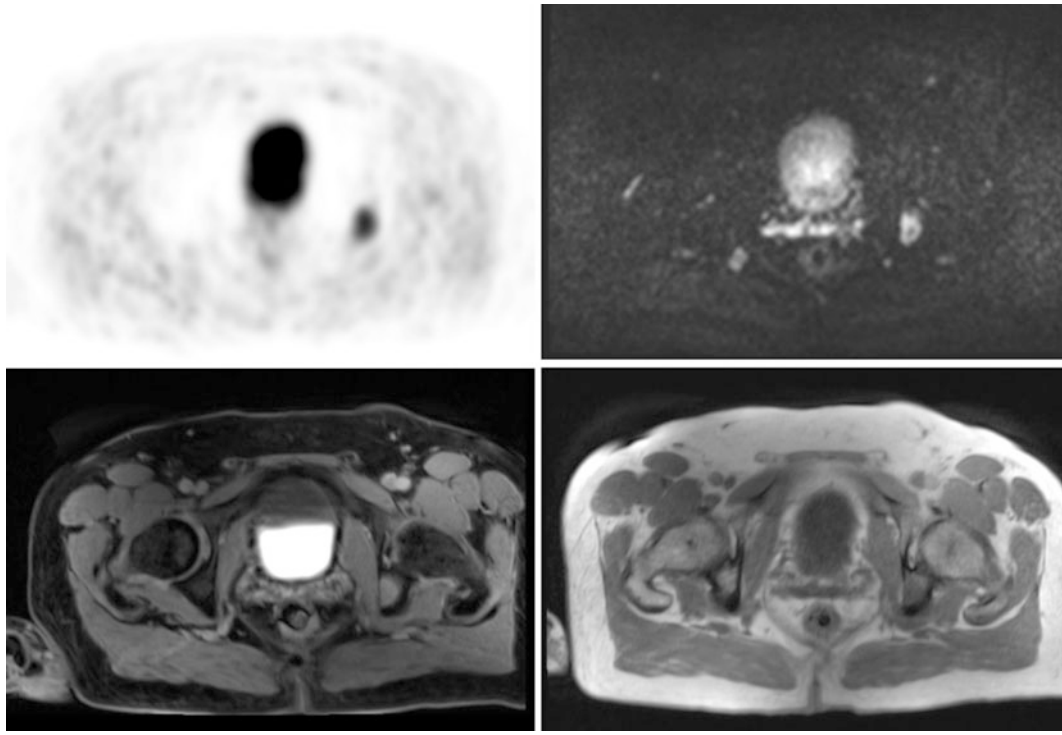

Fig. 13 Clockwise from *top left*: axial PET, high-b-value diffusion-weighted, T1-weighted, and fat-suppressed T1 postcontrast images of the lower pelvis. These show an enhancing ^{68}Ga-DOTATATE-avid lesion in the bone marrow at the left posterior acetabulum. Restricted diffusion in the lesion suggests high cellularity as expected

Fig. 14 MIP image of ^{68}Ga-DOTATATE PET 6 months later shows progressive appearance, with multiple new ^{68}Ga-DOTATATE-avid lesions now involving more of the skull, ribs, thoracic spine, and right humerus, in addition to existing lesions

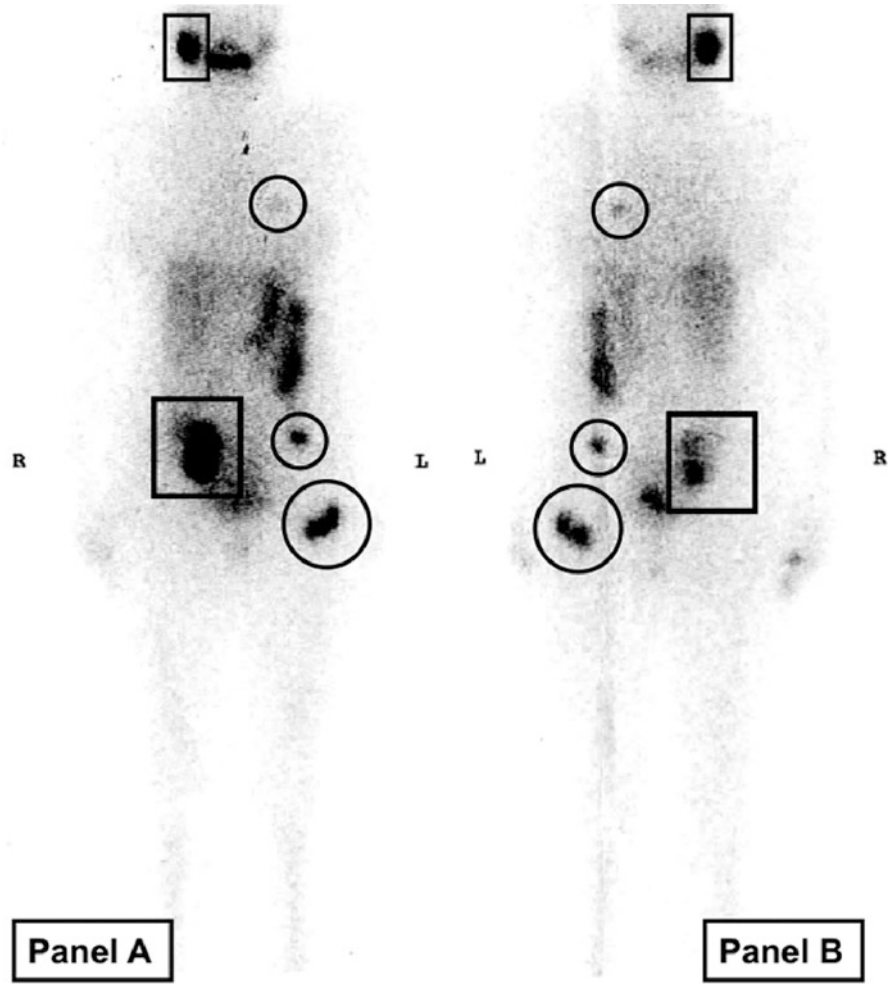

Fig. 15 Anterior (*panel A*) and posterior (*panel B*) views of the planar post-therapeutic ^{131}I-WBS scan obtained after the administration of 7.4 GBq ^{131}I-iodide. The areas of uptake indicated with a circle are due to clearly metastatic lesions, while those indicated with a square are equivocal. Planar ^{131}I-WBS cannot provide precise topographic information

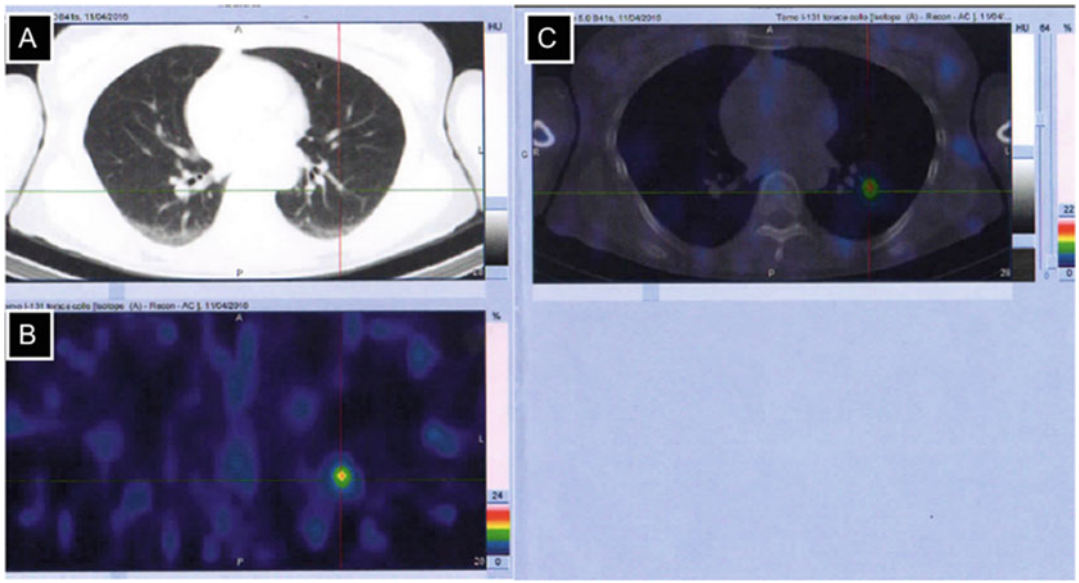

Fig. 16 SPECT/CT transaxial images of the lungs (CT, *panel A*; SPECT, *panel B*; fused SPECT/CT image, *panel C*) demonstrated the presence of a ^{131}I-avid nodule in the left lung

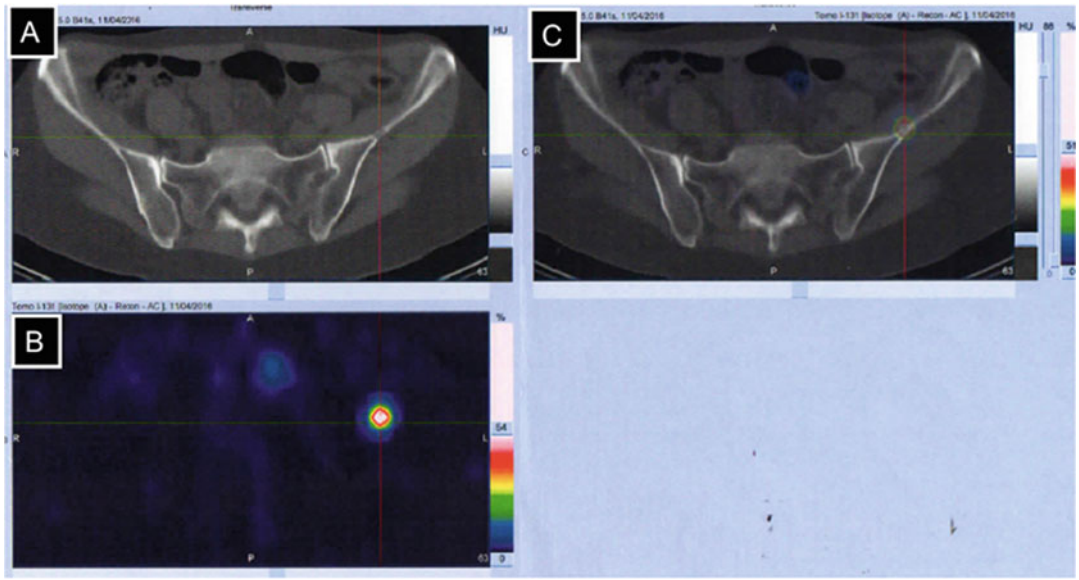

Fig. 17 SPECT/CT transaxial images of the iliac crests (CT, *panel A*; SPECT, *panel B*; fused SPECT/CT image, *panel C*) demonstrated the presence of a ^{131}I-avid bone lesion in the left iliac crest

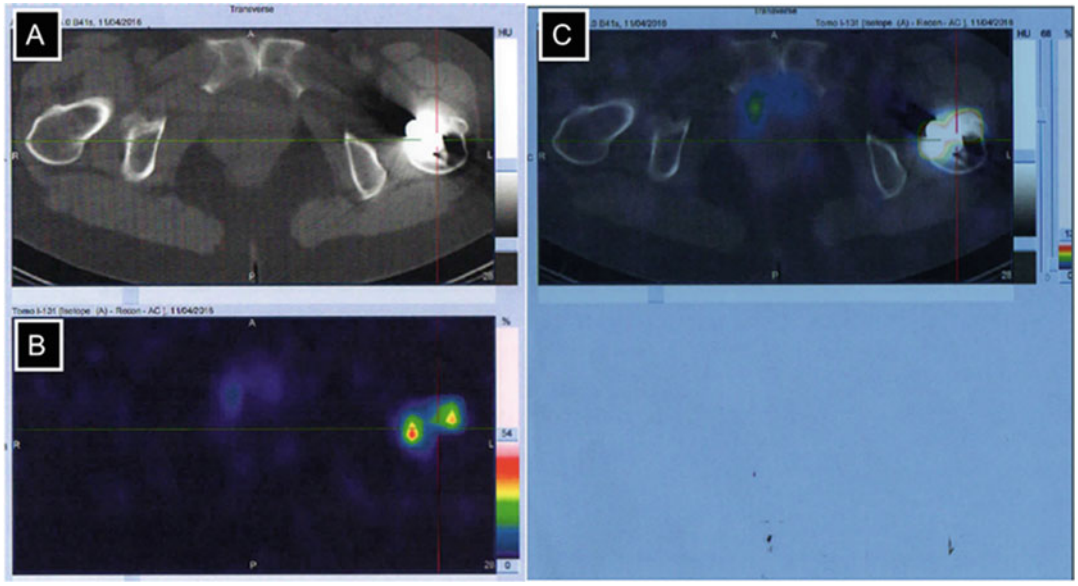

Fig. 18 SPECT/CT transaxial images of the femurs (CT, *panel A*; SPECT, *panel B*; fused SPECT/CT image, *panel C*) demonstrated the presence of a ^{131}I-avid bone lesion in the left femur, site of the pathological fracture

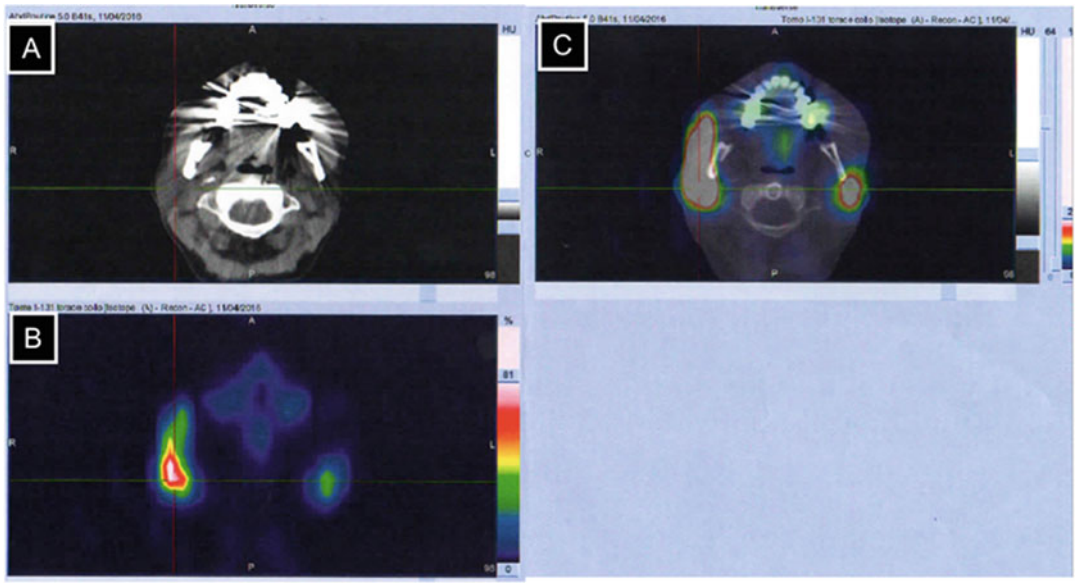

Fig. 19 SPECT/CT transaxial images of the mandibles (CT, *panel A*; SPECT, *panel B*; fused SPECT/CT image, *panel C*) demonstrated the presence of ^{131}I uptake in the right salivary gland but without any specific lesion, thus demonstrating that this uptake was due to the physiological ability of the salivary gland to take up iodine

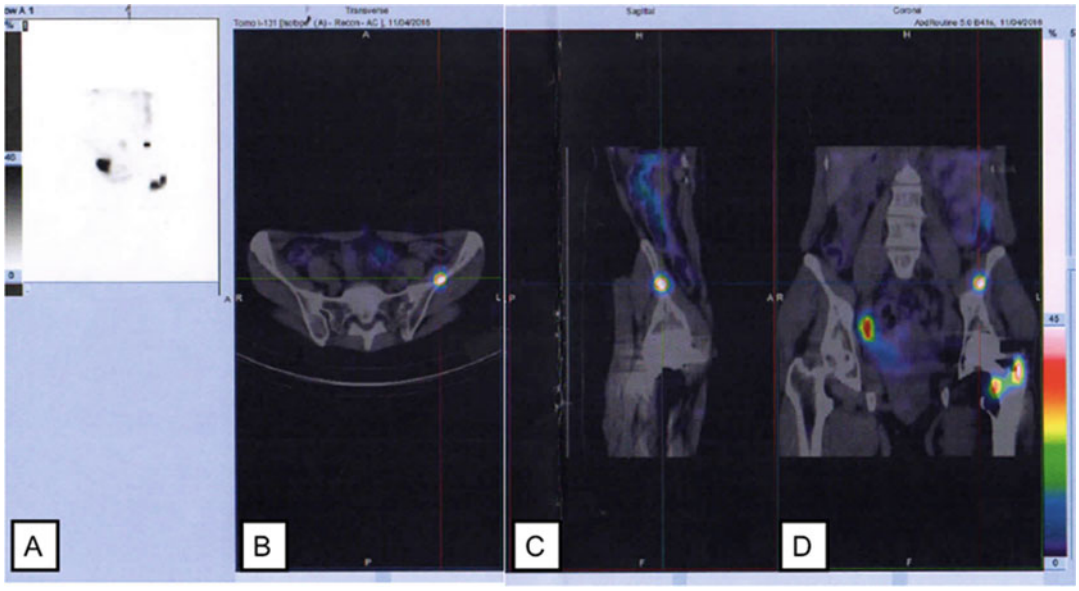

Fig. 20 Comparison of the planar ^{131}I-WBS (*panel A*) with the SPECT/CT transaxial image of the iliac crests (*panel B*) and the sagittal (*panel C*) and coronal (*panel D*) images of the abdomen and pelvis demonstrated that radioactivity accumulation in the right iliac fossa (*panel D*) had no corresponding images detected by CT (*panel B*) as it was for the left iliac crest (*panel B*) and the left femur (*panels D* and *A*), thus confirming that radioactivity accumulation in the right iliac fossa was nonspecific and most likely due to intestinal retention of ^{131}I

Fig. 21 Ultrasound appearance of the large mass in the right thyroid lobe. The lesion is solid, hypoechoic, not well defined, and with hyperechoic spots inside the mass. These features are highly suspicious for cancer

Fig. 22 *Panel A*: CT appearance of the large solid mass surrounding the trachea, whose lumen was severely reduced determining a high risk of suffocation. *Panel B*: after 4 months of TKI therapy, the same mass was greatly reduced in size, and there was a clinically important recovery of tracheal lumen

Fig. 23 CT of the neck scan after radical surgery and partial laryngectomy

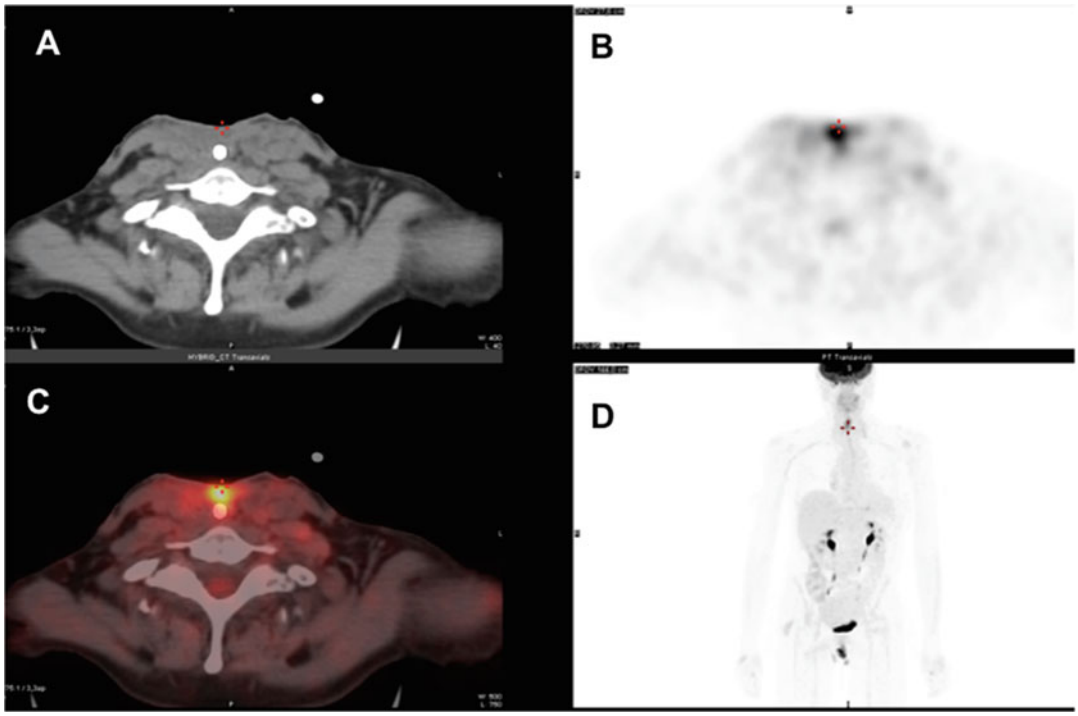

Fig. 24 [^{18}F]FDG PET/CT transaxial images of the neck (CT, *panel A*; [^{18}F]FDG PET, *panel B*; fused PET/CT fused image, *panel C*): nonspecific moderately increased tracer uptake anteriorly to the esophagus, likely due to the laryngeal stoma secondary to partial laryngectomy. *Panel D*, [^{18}F]FDG-PET MIP image, showing no other major [^{18}F]FDG-avid lesions

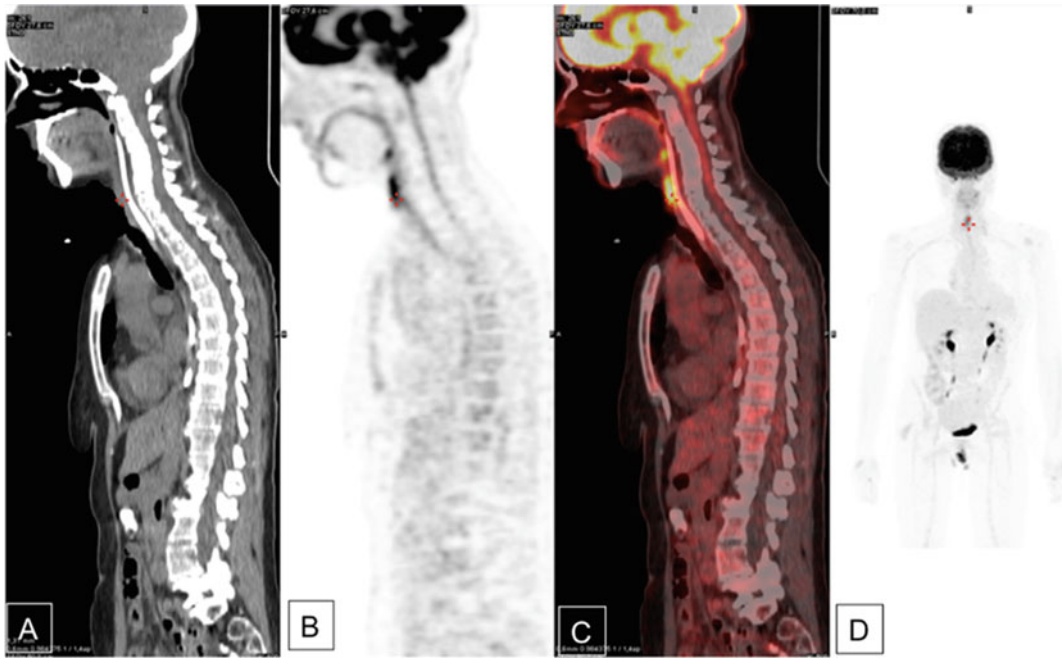

Fig. 25 [^{18}F]FDG PET/CT sagittal images (CT, *panel A*; [^{18}F]FDG PET, *panel B*; fused PET/CT image, *panel C*): nonspecific moderately increased tracer uptake anteriorly to the esophagus, likely due to the laryngeal stoma secondary to partial laryngectomy. *Panel D*, [^{18}F]FDG-PET MIP image, showing no other major [^{18}F]FDG-avid lesions

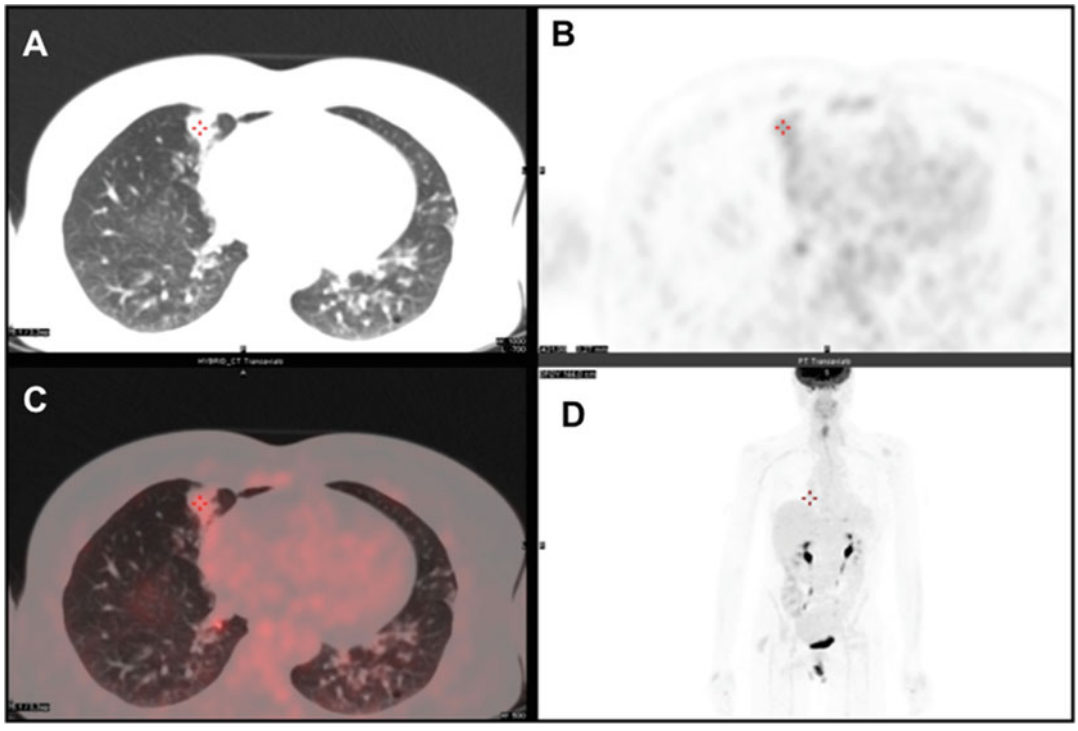

Fig. 26 [^{18}F]FDG PET/CT transaxial images of the thorax (CT, *panel A*; [^{18}F]FDG PET, *panel B*; fused PET/CT fused image, *panel C*): nonspecific mildly increased tracer uptake in the right lung, with SUV_{max} 3.5 for the largest of the two detectable areas that the CT scan demonstrates to be inflammatory lesions. Panel *D*, [^{18}F]FDG-PET MIP image, showing no other major [^{18}F]FDG-avid lesions

after 10 months later, the patient remained in good health, without evidence of recurrence (Fig. 26).

Teaching Cases in Nuclear Oncology: Parathyroid Tumors

58

Kimiteru Ito, Somali Gavane, and Heiko Schöder

Keywords

Parathyroid carcinoma • Paraganglioma • ^{99m}Tc-sestamibi • Human papilloma virus • ^{68}Ga DOTATOC • PET/CT

Glossary

[^{18}F]FDG	2-Deoxy-2-[^{18}F]fluoro-D-glucose
CT	X-ray computed tomography
DOTA-TOC	DOTA-octreotide
DOTA	1,4,7,10-Tetra-azacyclododecane-1,4,7,10-tetraacetic acid
MIP	Maximum intensity projection
MRI	Magnetic resonance imaging
PET	Positron emission tomography
PET/CT	Positron emission tomography/Computed tomography

Contents

Parathyroid Adenocarcinoma 1607
Presentation 1607
Findings 1607
Follow-Up 1608
Discussion 1608

Paraganglioma 1608
Presentation 1608
Findings 1609

Parathyroid Adenocarcinoma

Case contributed by: K. Al Riyami, D. Neriman, D. Kyprianou
Institute of Nuclear Medicine, UCLH NHS Foundation Trust, London, UK

Presentation

Enlarged left neck mass causing dysphagia; hyperparathyroidism with hypercalcemia requiring multiple admissions for rehydration and pamidronate.

Findings

Ultrasound showed a heterogeneous predominantly hypoechoic mass related to the inferior pole of the left thyroid lobe. Fine needle revealed parathyroid carcinoma. A parathyroid ^{99m}Tc-sestamibi scan showed a large photopenic nodule related to the left thyroid gland with faint

K. Ito • H. Schöder (✉)
Department of Radiology, Molecular Imaging and Therapy service, Memorial Sloan Kettering Cancer Center, New York, NY, USA
e-mail: itoukimiteru@yahoo.co.jp; itok@mskcc.org; schoderh@mskcc.org

S. Gavane
Center for Biomedical Imaging in Oncology, Dana-Farber Cancer Institute, Boston, MA, USA
e-mail: somali.gavane@mountsinai.org

© Springer International Publishing Switzerland 2017
H.W. Strauss et al. (eds.), *Nuclear Oncology*,
https://doi.org/10.1007/978-3-319-26236-9_61

retention of this area on the delayed images (Fig. 1). Contrast-enhanced CT and MRI of the neck showed a left soft tissue lesion displacing and invading the left thyroid and likely tracheal and esophageal involvement. [^{18}F]FDG PET/CT was performed for staging and showed a [^{18}F]FDG-avid left lower neck soft tissue lesion compatible with the parathyroid carcinoma with no [^{18}F]FDG-avid nodal or distal metastases (Fig. 2).

Follow-Up

The patient underwent resection of the tumor and a left hemithyroidectomy. Histopathology confirmed the presence of a high-grade malignant tumor of parathyroid origin.

Discussion

Parathyroid carcinoma is an uncommon malignancy with an annual incidence of approximately 1.25 cases per 10,000,000. [^{18}F]FDG-PET/CT is sensitive in the detection of parathyroid carcinoma, can assess for local nodal and distant metastases, and can evaluate complications of hyperparathyroidism, i.e., abnormal calcification (renal) and bone complications (i.e., brown tumors). In this case, the absence of local nodal involvement on PET/CT allowed for less radical surgical treatment.

Paraganglioma

Case contributed by: E.D. Telenga[1], R.H.J.A. Slart[1,2], A.W.J.M. Glaudemans[1]

[1]Department of Nuclear Medicine and Molecular Imaging, University of Groningen, University Medical Center Groningen, The Netherlands

[2]Biomedical Photonic Imaging Group, University of Twente, Enschede, The Netherlands

Presentation

A 48-year old man presented at a general hospital with three episodes of syncope and elevated blood pressure (>180/120 mmHg). Physical examination

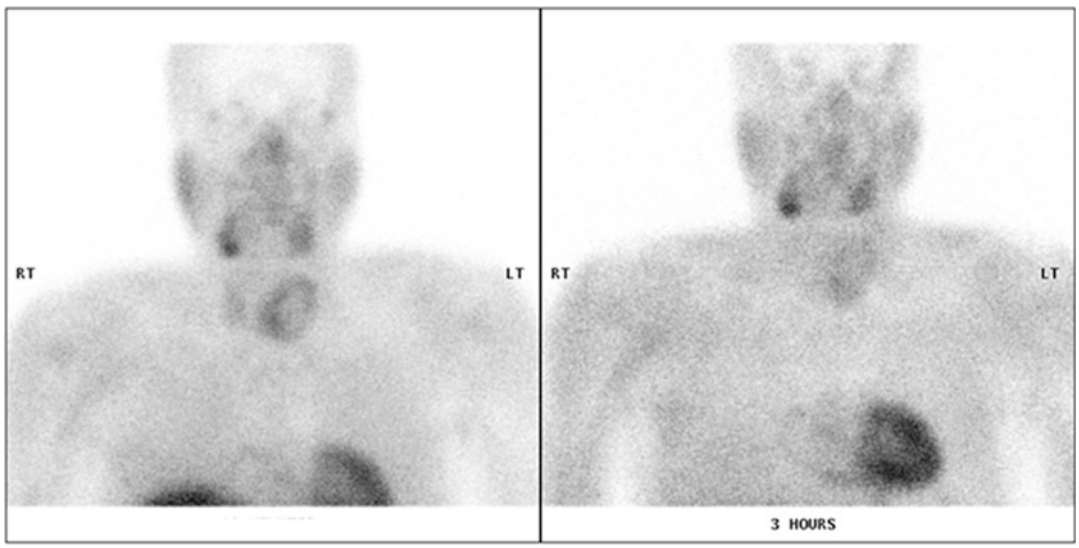

Fig. 1 Early and delayed ^{99m}Tc-sestamibi scans shows a large photopenic area of the left thyroid lobe on early imaging with subsequent faint retention of the tracer on the 3 h delayed image

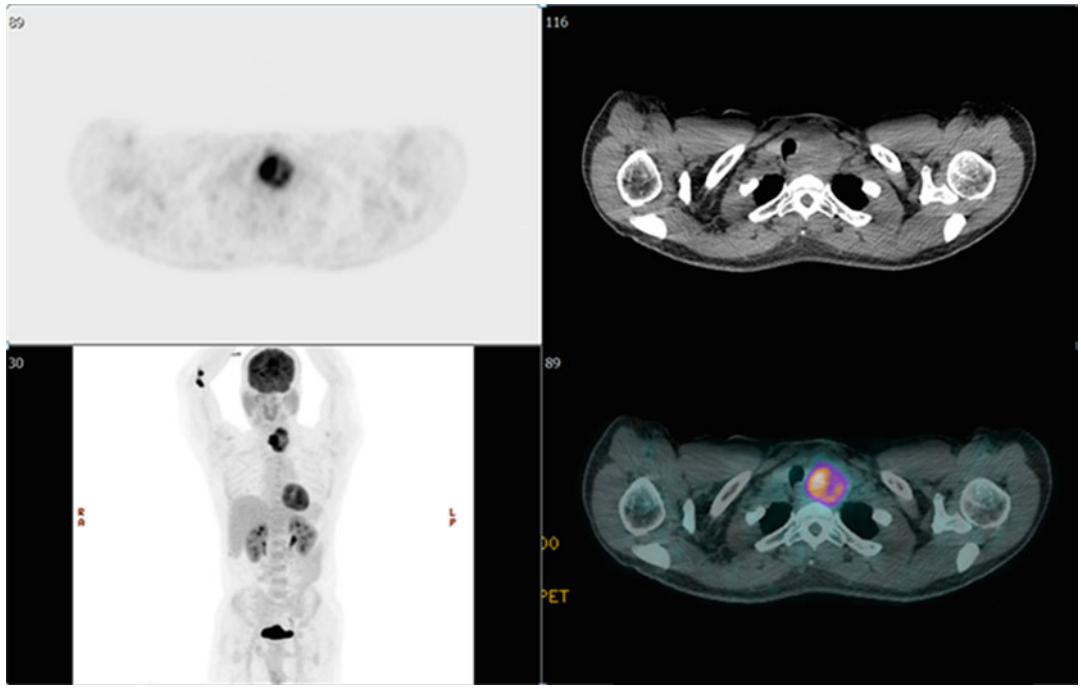

Fig. 2 [^{18}F]FDG PET/CT images: *upper left*, axial PET image; *upper right*, CT axial image; *lower left*, MIP; *lower right*, fused PET/CT demonstrating a [^{18}F]FDG-avid left upper paratracheal soft tissue lesion involving the left thyroid lobe and displacing the trachea compatible with parathyroid carcinoma

revealed a right submandibular swelling. Laboratory studies showed normal metanefrines and slightly increased normetanefrines (1.76 nmol/L, normal range 0.23–1.07 nmol/L).

Findings

MRI showed an enhancing lesion in the carotid bifurcation (right) (21 × 27 mm, Fig. 3). [^{18}F]FDG PET/CT with diagnostic CT showed intense [^{18}F]FDG uptake in the lesion in the right carotid bifurcation, as well as a smaller lesion in the left carotid bifurcation (Fig. 4). In retrospect, this lesion was already visible on the MRI. Additionally, there were two lesions more cranially in the neck left and right. The patient was referred to an academic hospital under suspicion of bilateral paraganglioma. Here, a ^{68}Ga-DOTA-TOC PET/CT was performed to evaluate somatostatin receptor expression in the

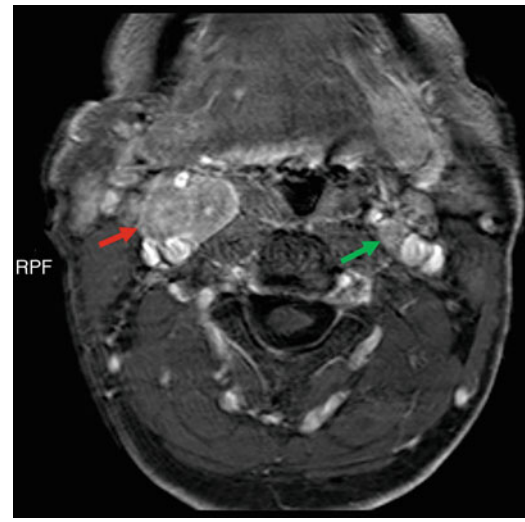

Fig. 3 T1-weighted MRI image after gadolinium showing an enhancing lesion in the right carotid bifurcation (*red arrow*). A smaller lesion can be seen in the left carotid bifurcation (*green arrow*)

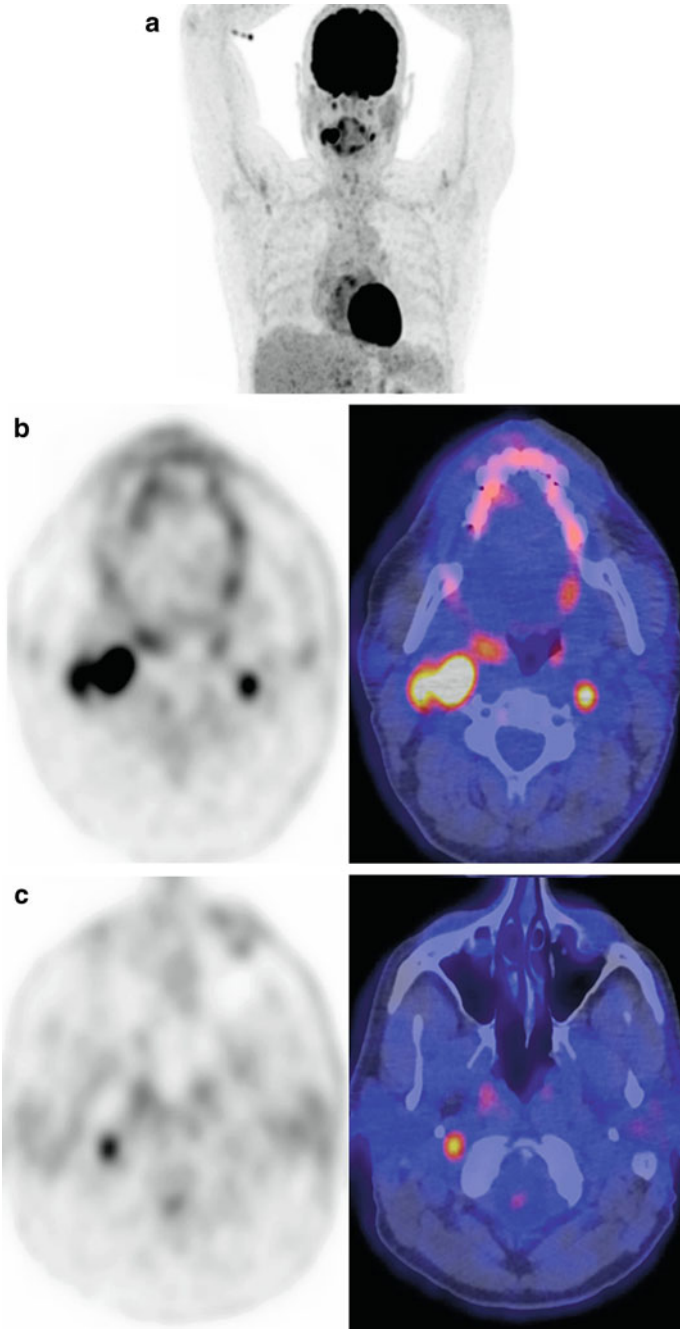

Fig. 4 [^{18}F]FDG PET/CT. (**a**) MIP image (**b**) axial reconstruction and fusion images showing intense uptake in lesions in the carotid bifurcation (*left* and *right*). (**c**) Axial reconstruction and fusion images showing a small lesion high in the neck, right side

lesions and to detect possible paraganglioma elsewhere (Fig. 5). ^{68}Ga-DOTA-TOC PET/CT showed increased uptake at the lesions previously seen on the [^{18}F]FDG PET/CT and additionally a new lesion in the left jugular foramen that was not visible on any of the earlier examinations.

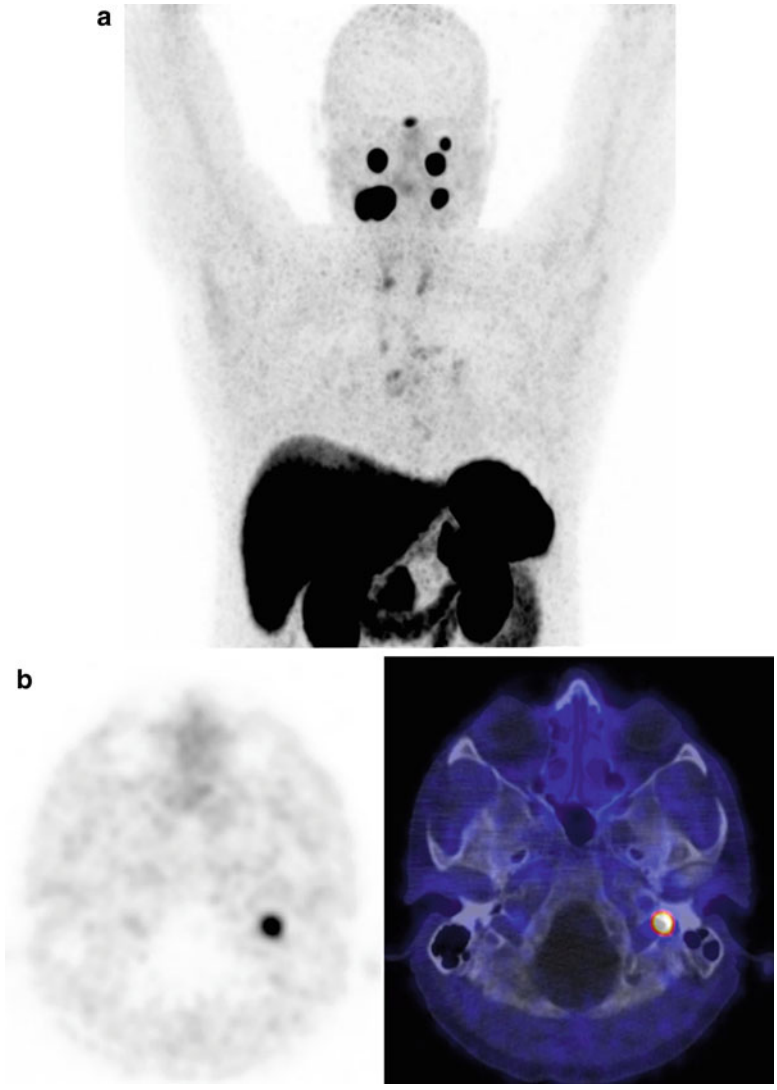

Fig. 5 ^{68}Ga-DOTA-TOC PET/CT. (**a**) MIP image showing three lesions on the left side and two on the right side. The uptake in the midline is physiologic uptake in the pituitary gland. (**b**) Axial reconstruction and fusion image showing a lesion in the jugular foramen left

The lesions were decided to be multiple paragangliomas. As the normetanefrine level was only slightly elevated, no treatment was started. Follow-up imaging will follow in 1 year.

Teaching Cases in Nuclear Oncology: Breast Cancer

59

Alice Lorenzoni, Alessandra Alessi, and Flavio Crippa

Keywords

Breast cancer staging • [^{18}F]FDG PET/CT • Response evaluation

Glossary

[^{18}F]FDG	2-Deoxy-2-[^{18}F]fluoro-D-glucose
^{99m}Tc-HDP	^{99m}Tc-hydroxyethylene-diphosphonate
^{18}F-FES	16α-^{18}F-Fluoro-17β-estradiol
AJCC	American Joint Committee on Cancer
CA 15–3	High-molecular weight glycoprotein, a tumor-associated marker
CEA	Carcinoembryonic antigen, a circulating serum tumor-associated marker
CT	X-ray computed tomography
ER	Estrogen receptor
HER2/neu	Human epidermal growth factor receptor 2
M	Metastasis status according to the AJCC/UICC TNM staging system
MIP	Maximum intensity projection
N	Lymph node status according to the AJCC/UICC TNM staging system
PET	Positron emission tomography
PET/CT	Positron emission tomography/Computed tomography
PR	Progesterone receptor
SUV	Standardized uptake value
SUV_{max}	Standardized uptake value at point of maximum
T	Tumor status according to the AJCC/UICC staging system
TNBC	Triple negative breast cancer
UICC	Union Internationale Contre le Cancer (International Union Against Cancer)

Contents

Breast Cancer: Case No. 1 1614
Presentation 1614
Findings 1614
Discussion 1614

Breast Cancer: Case No. 2 1614
Presentation 1614
Findings 1614
Discussion 1614

Breast Cancer: Case No. 3 1615
Presentation 1615
Findings 1616
Discussion 1617

Breast Cancer: Case No. 4 1617
Presentation 1617
Findings 1617
Discussion 1617

A. Lorenzoni (✉) • A. Alessi • F. Crippa
Nuclear Medicine Division, IRCCCS National Cancer Institute, Milan, Italy
e-mail: alice.lorenzoni@istitutotumori.mi.it; alicelorenzoni@hotmail.it

© Springer International Publishing Switzerland 2017
H.W. Strauss et al. (eds.), *Nuclear Oncology*,
https://doi.org/10.1007/978-3-319-26236-9_62

Breast Cancer: Case No. 5 1617
Presentation 1617
Findings 1619
Discussion 1619

Breast Cancer: Case No. 6 1620
Presentation 1620
Findings 1620
Discussion 1621

Breast Cancer: Case No. 7 1622
Presentation 1623
Findings 1623
Follow-up 1626

References 1626

Breast Cancer: Case No. 1

Presentation

A 76-year-old woman with a recent diagnosis of invasive ductal carcinoma of the left breast (6 cm in size) and suspected left axillary lymph node involvement was referred for [^{18}F]FDG PET/CT for staging.

Findings

[^{18}F]FDG PET/CT showed the presence of an [^{18}F]FDG-avid mass in central and lower quadrants of the left breast corresponding to the diagnosed carcinoma. Bilateral axillary nodes with high [^{18}F]FDG uptake suspicious for node involvement were also noted. Furthermore, multiple foci of [^{18}F]FDG uptake in dorsal and lumbar spine consistent with bone metastases were depicted (Figs. 1, 2, and 3).

Discussion

[^{18}F]FDG PET/CT is an important imaging modality for the detection of locoregional and metastatic spread in the appropriate patient population; while [^{18}F]FDG PET should not be used routinely for initial detection of breast cancer or for detection of axillary nodal involvement, [^{18}F]FDG PET in higher-risk populations has great value in definitive whole body initial staging.

Breast Cancer: Case No. 2

Presentation

A 58-year-old woman presented with mammographic diagnosis of tissue distortion and microcalcification of the upper outer quadrant of the left breast. The biopsy showed invasive lobular carcinoma, ER positive, PR positive, and human epidermal growth factor receptor 2 (HER2/neu) negative.

[^{18}F]FDG PET/CT was performed for staging completion before planned surgery.

Findings

[^{18}F]FDG PET/CT did not show foci of suspected glucose uptake in the upper outer quadrant of the left breast (Fig. 4). Whole body staging was negative for detection of axillary involvement and distant metastasis. Breast-conserving surgery consistent with quadrantectomy and sentinel node biopsy was performed. Histopathological analysis showed micrometastasis in sentinel node.

Discussion

The ability of PET to detect breast cancer depends on the tumor's size and histology (e.g., low [^{18}F]FDG avidity in grade 1 cancer and/or in lobular carcinoma). The sensitivity of PET has been reported to be 68% for small (<2 cm) tumors and 92% for larger (2–5 cm) tumors, and its reported overall accuracy for detecting in situ carcinomas is low (sensitivity, 2–25%).

There is also a correlation between the tumor proliferation index (Ki67 expression) and the intensity of [^{18}F]FDG uptake. [^{18}F]FDG PET has moderate accuracy for detecting axillary metastasis but often fails to detect early axillary node involvement and micrometastases.

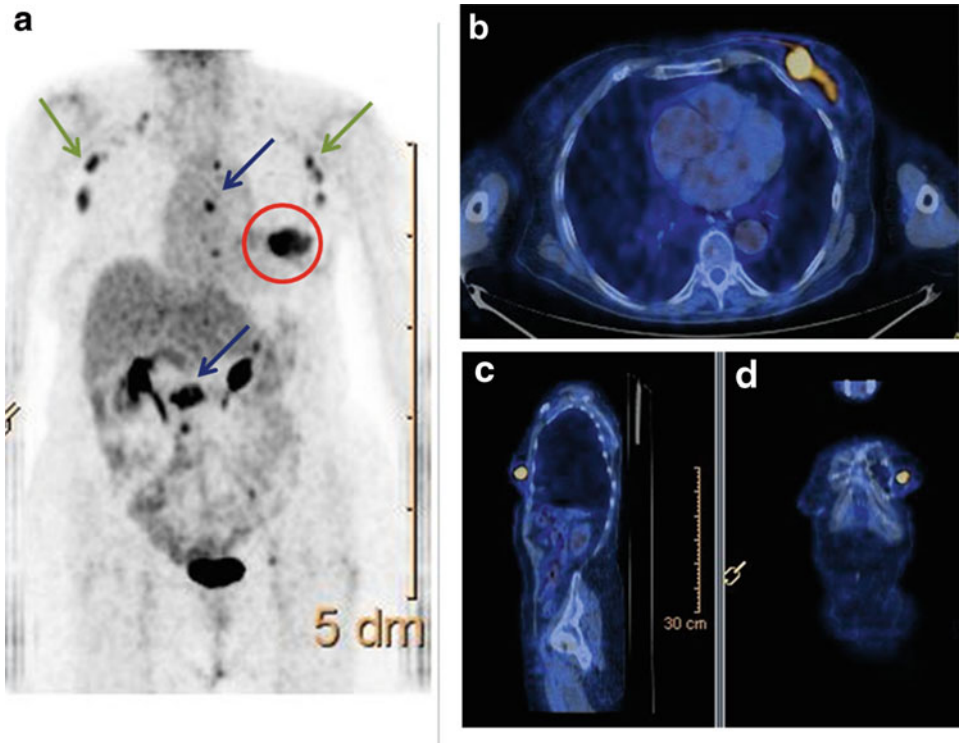

Fig. 1 Maximum intensity projection (*MIP*) (**a**, *red circle*), axial (**b**), sagittal (**c**), and coronal fused PET/CT images of the [^{18}F]FDG-avid left breast lesion. MIP image clearly demonstrated bilateral axillary lymph node involvement (*green arrows*) and bone metastases (*blue arrows*)

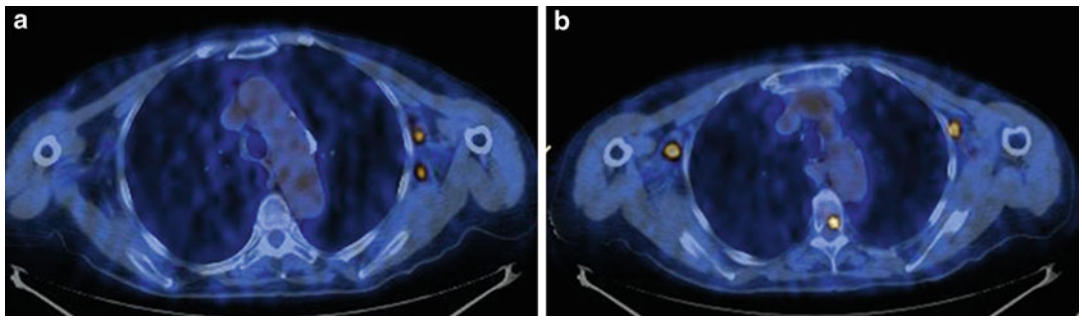

Fig. 2 Axial fused image of axillary hypermetabolic lymph nodes and focal uptake of dorsal spine consistent with skeletal metastases

Breast Cancer: Case No. 3

Case contributed by: S. Al Shammari, F. Fraioli Institute of Nuclear Medicine, UCLH NHS Foundation Trust, London, UK.

Presentation

A 42-year-old lady with a recent diagnosis of breast cancer was referred for [^{18}F]FDG PET/CT for staging.

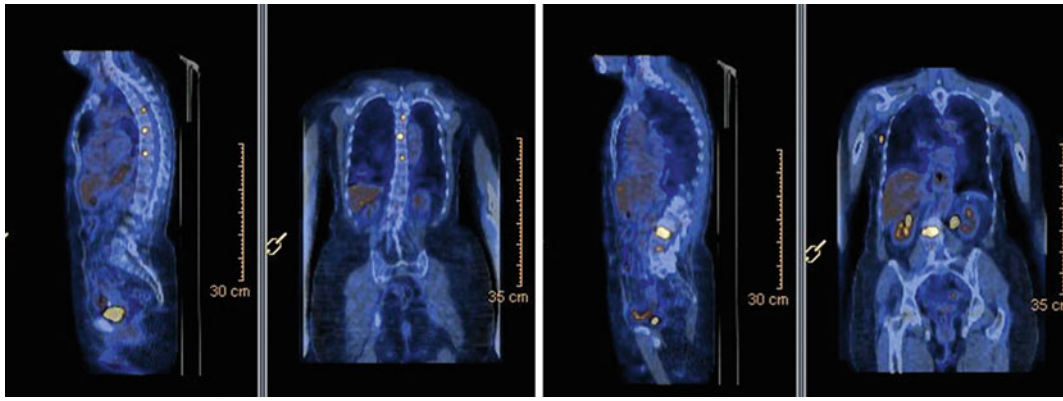

Fig. 3 Fused coronal and sagittal PET/CT images of dorsal (*left panel*) and lumbar (*right panel*) bone involvement

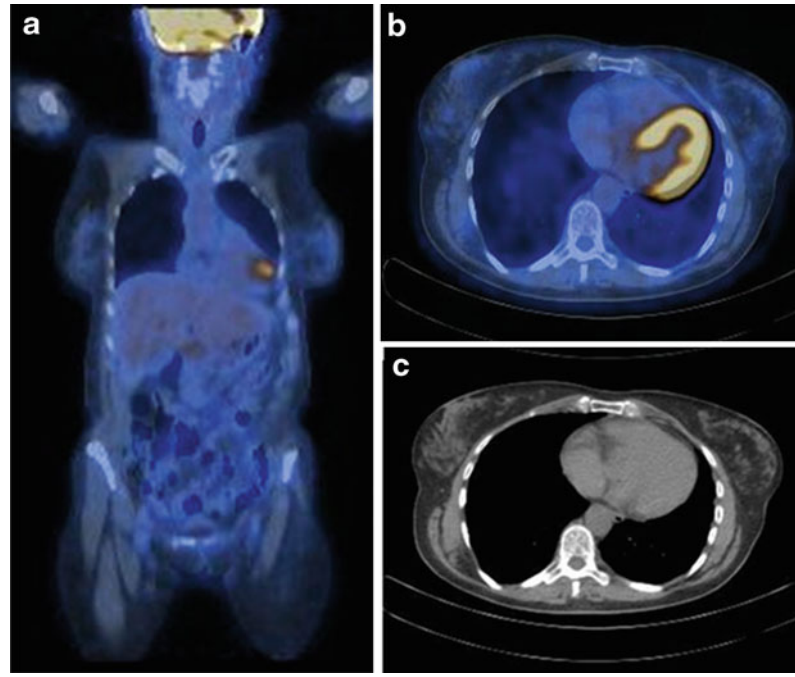

Fig. 4 Fused coronal PET/CT (**a**) and axial images ((**b**) fused PET/CT, (**c**) low-dose CT) failed to detect malignant left breast lesion

Findings

There is an [^{18}F]FDG-avid right breast lesion (measuring ~1.4 × 1 cm, SUV_{max} 7, long arrow in upper, axial PET/CT image). Furthermore, there is a mildly [^{18}F]FDG-avid level III right axillary lymph node (measuring ~7 mm with SUV_{max} 2.0, short arrow). Histopathology of the right axillary lymph node confirmed the diagnosis of nodal involvement.

Discussion

The ability of [^{18}F]FDG PET to detect breast cancer depends on the tumor's size and histology. The sensitivity of PET has been reported to be 68% for small (<2 cm) tumors and 92% for larger (2–5 cm) tumors. Overall accuracy for detecting in situ carcinomas is low (25% sensitivity). The major limitation of PET or PET/CT for breast imaging is its poor detection rate for small breast carcinomas and noninvasive breast cancers. However, PET/CT has a role to play in a group of patients, such as those with dense breasts or with implants, for determining tumor multiplicity, for localizing the primary tumor in those patients with metastasis of breast origin when the mammography is indeterminate, and for those patients where biopsy is not a desirable option. Regional lymph node assessment of the axilla, internal mammary, or mediastinum is an important factor to assess the prognosis of patients with breast cancer. PET/CT can be a valid option to localize and differentiate metastatic and reactive lymph nodes when CT shows multiple enlarged lymph nodes in the axilla. Distant metastases from breast cancer are frequently found in the lungs, liver, and bones. One advantage of whole body PET imaging over conventional imaging modalities is its ability to detect metastasis at different sites and organs during a single examination.

Breast Cancer: Case No. 4

Presentation

A 38-year-old woman with recent diagnosis of locally advanced triple negative breast cancer (TNBC) underwent [^{18}F]FDG PET for staging before scheduled chemotherapy.

Findings

[^{18}F]FDG-avid multiple left breast lesions were noted. Enlarged left axillary lymph nodes with pathological [^{18}F]FDG uptake were also shown (Fig. 5). Furthermore, a previously unknown [^{18}F]FDG-avid lymph node was clearly depicted in ipsilateral subclavicular region (Fig. 5). Patient underwent anthracycline-based regimen. After chemotherapy completion, [^{18}F]FDG PET/CT was performed to evaluate treatment response. Whole body PET/CT did not show pathological radiopharmaceutical uptake, consistent with complete metabolic response (Fig. 6).

Discussion

Triple negative breast cancer is an aggressive heterogeneous group of tumors, representing 15% of invasive breast tumors. The majority of TNBCs are aggressive basal-like subtypes presenting with larger tumors of higher grade and increased numbers of involved nodes. Patients with TNBC have a relatively poor outcome; however, this tumor has more intrinsic responsiveness to chemotherapy than estrogen receptor-positive tumors. Stratification of TNBC prognosis would be highly desired since some patients with better prognosis might benefit from appropriate targeted treatment.

[^{18}F]FDG uptake of TNBC tumor typically had higher metabolic activities than those of other phenotype breast cancers. Pretreatment [^{18}F]FDG PET/CT imaging may have a significant prognostic value for predicting survival outcome of TNBC patients. Furthermore, [^{18}F]FDG PET/CT after two cycles of neoadjuvant chemotherapy may identify poor metabolic responders who have a high risk of early relapse.

Breast Cancer: Case No. 5

Presentation

A 38-year-old woman who previously received neoadjuvant chemotherapy and curative resection of a right breast cancer was referred for sudden-onset chest pain lasting for 15 days. Right pleural effusion was demonstrated. Thoracentesis was

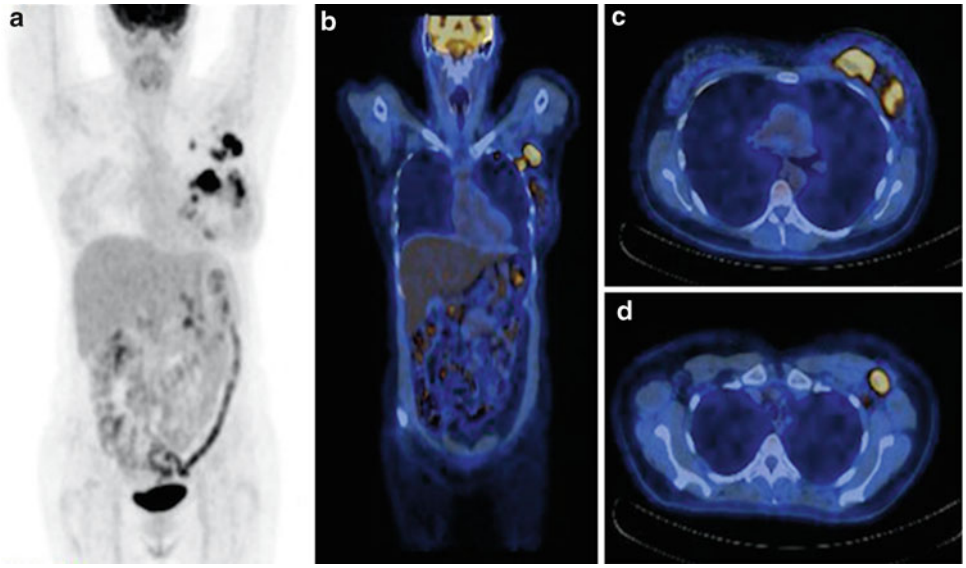

Fig. 5 Baseline whole body [^{18}F]FDG PET/CT in patient with locally advanced TNBC (**a**, maximum intensity projection). Fused PET/CT images show multifocal [^{18}F]FDG-avid primary breast tumor (**b**, **c**), pathological hypermetabolic lymph nodes in the left axillary (**b**, **d**) and in ipsilateral subclavicular region (**b**)

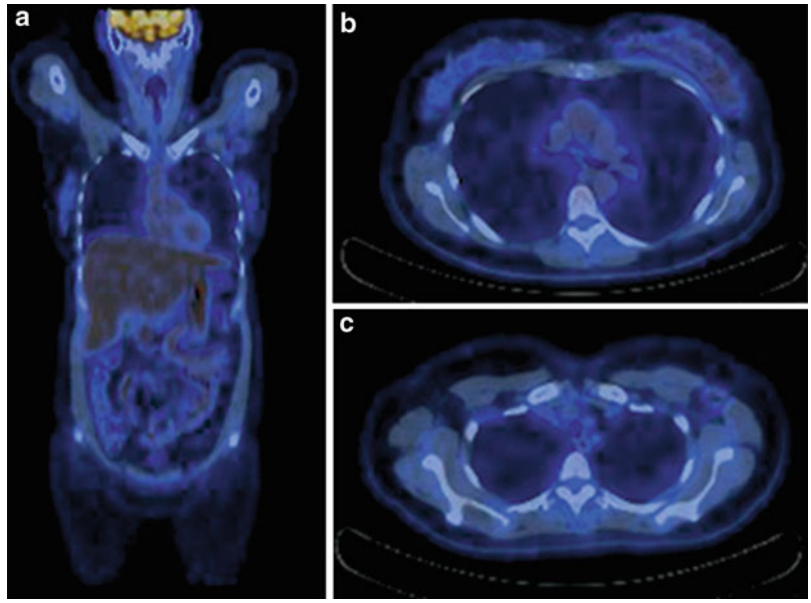

Fig. 6 Fused PET/CT images ((**a**) coronal, (**b**, **c**) transaxial) after chemotherapy completion show the disappearance of previously identified pathological [^{18}F]FDG uptake in left breast and in regional lymph nodes

performed and pleural fluid analysis showed light yellow and clear fluid with no evidence of malignancy. High values of CA 15-3 and CEA were present (65.6 U/ml and 18 ng/mL, respectively). [^{18}F]FDG PET/CT was performed for suspected recurrent breast cancer to evaluate the presence of disease.

Findings

[^{18}F]FDG PET/CT images (Figs. 7 and 8) showed diffuse intense [^{18}F]FDG uptake of the right pleura suspicious for metastatic disease. Marked focal increased metabolic activity in the segment 7 of the liver was also demonstrated consistent with hepatic metastasis. Furthermore, [^{18}F]FDG-avid abdominal para-aortic lymph node and sternal lesion were depicted. PET/CT findings clearly demonstrated stage IV recurrent breast cancer.

Discussion

Approximately 30–50% of breast cancer patients have a recurrence of disease within 10 years after diagnosis. [^{18}F]FDG PET/CT scan plays an important role in restaging breast cancer patients with rising tumor markers and negative or equivocal findings in conventional imaging techniques with high sensitivity (>90%) and a change in planned therapy in about 50% of the cases.

[^{18}F]FDG PET allows more accurate diagnosis of metastatic disease in patients with treated breast cancer and patients with rising levels of tumor

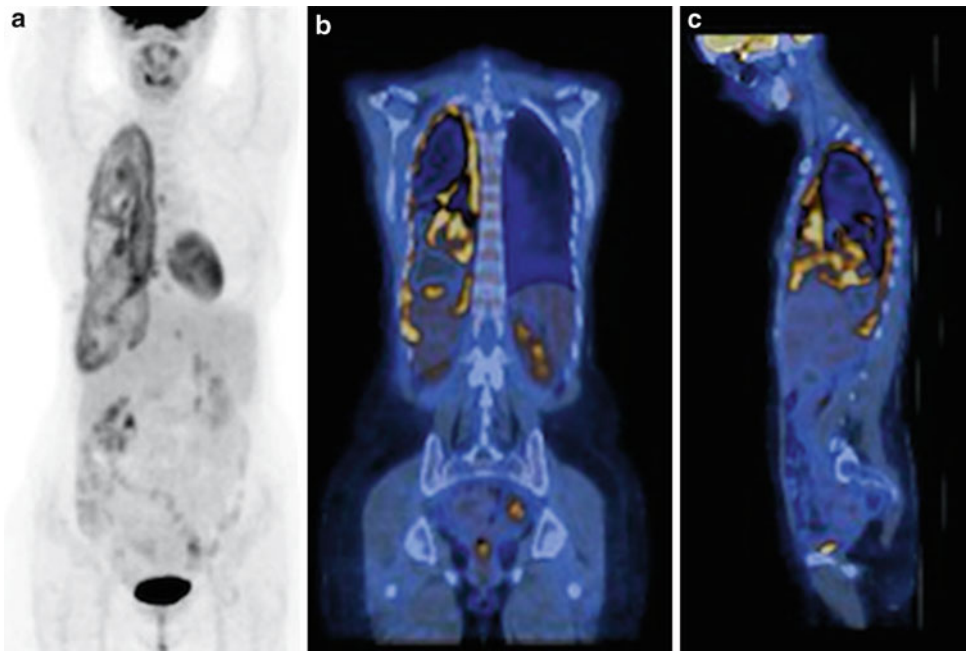

Fig. 7 Whole body [^{18}F]FDG PET/CT in patient with suspected recurrent breast cancer ((**a**), maximum intensity projection, (**b**) coronal fused PET/CT, (**c**) sagittal fused PET/CT). Diffuse intense [^{18}F]FDG uptake of the right pleura suspicious for metastatic disease is shown. Right pleura effusion without significant metabolic activity

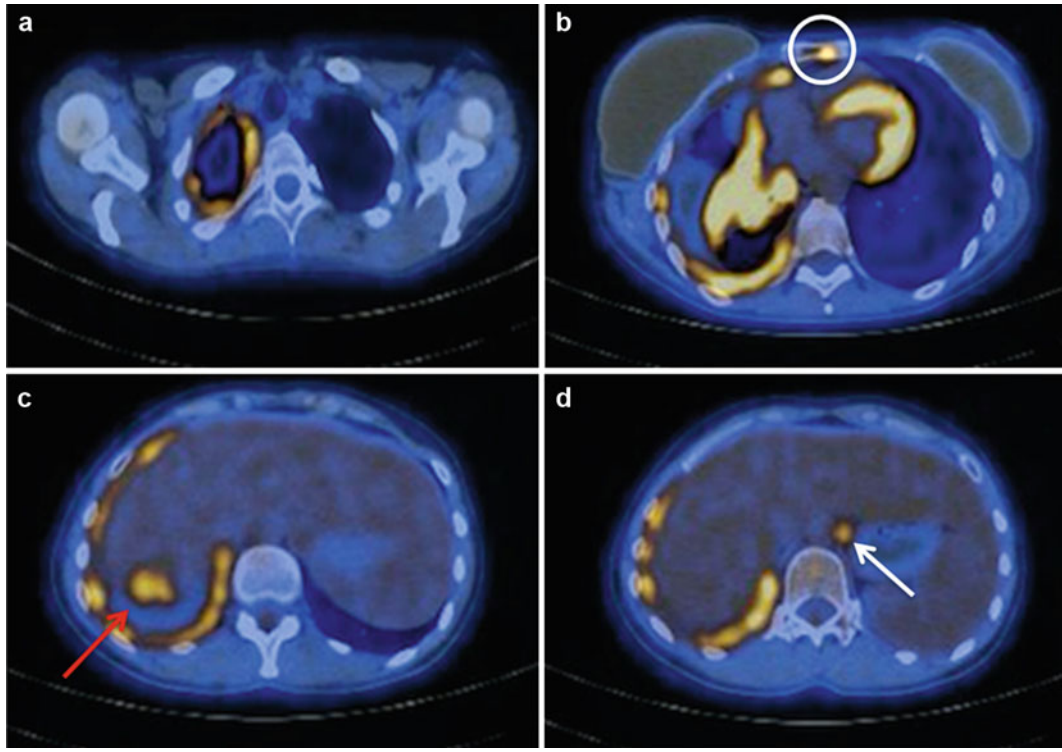

Fig. 8 Fused transaxial PET/CT images show pathological pleura [^{18}F]FDG uptake (**a**–**d**), sternal [^{18}F]FDG-avid lesion (**b**, *white circle*), liver metastasis (**c**, *red arrow*), and abdominal lymph node involvement (**d**, *white arrow*) consistent with distant recurrence of breast cancer

markers compared with CT alone demonstrating improved sensitivity, specificity, accuracy, and predictive value.

Breast Cancer: Case No. 6

Presentation

A 28-year-old woman referred with diagnosis of right breast cancer cT1N1 (CDI, G2, ER = 95%, PR = 95%, HER2 = ISH not amplified, Ki-67 = 80%) and synchronous skeletal metastases for treatment planning.

Findings

Baseline [^{18}F]FDG PET/CT was performed prior to chemotherapy. PET/CT images demonstrated small [^{18}F]FDG-avid nodule in the upper inner quadrant of the right breast corresponding to known malignancy (Fig. 9). Focal increased [^{18}F]FDG activity was noted in the right humerus, spine, pelvic skeleton, and femora (Fig. 9).

After chemotherapy, [^{18}F]FDG PET/CT was performed to evaluate treatment response. PET/CT images showed metabolic progression of the right mammary nodule (Fig. 10) and of bone disease progression (Fig. 11).

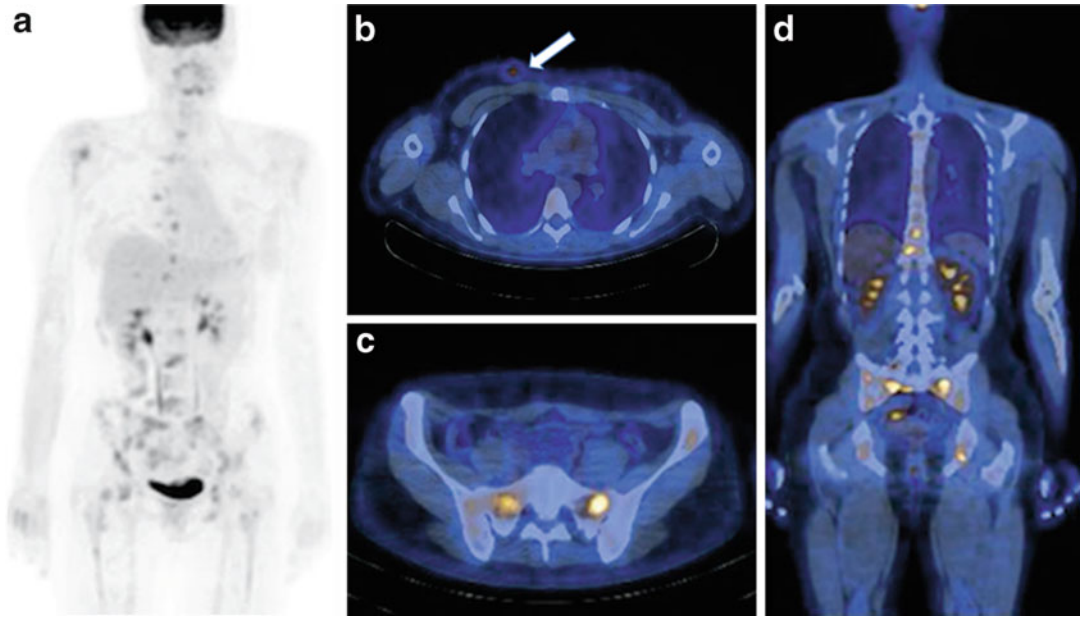

Fig. 9 Baseline [^{18}F]FDG PET/CT in patient with right breast cancer and metastatic bone lesions (**a**, MIP). Axial fused PET/CT image of [^{18}F]FDG-avid breast nodule (**b**, *white arrow*). Diffuse bone involvement consistent with multiple focal increased metabolic activity was revealed (**a**, **c**, and **d** images)

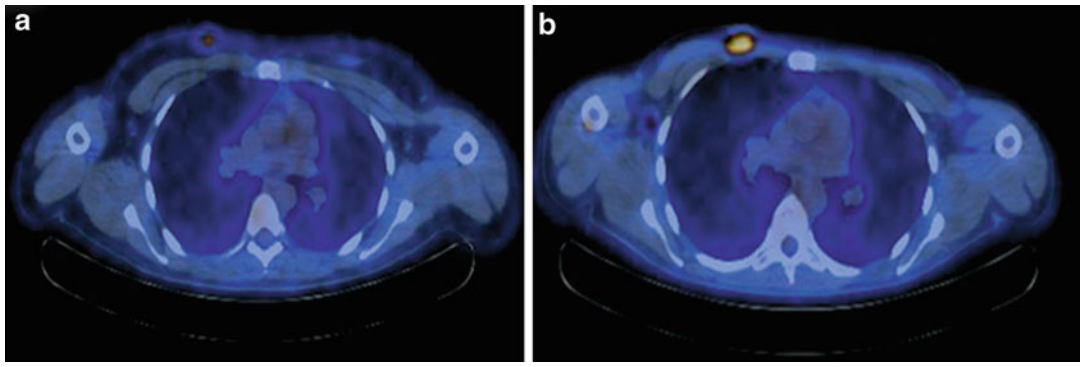

Fig. 10 Fused transaxial PET/CT images performed to evaluate treatment response show metabolic and dimensional progression of primary tumor (**a** before therapy, **b** after therapy completion)

Discussion

The treatment of breast cancer patients who have metastatic disease aims to improve survival and quality of life since the disease is generally not curable. It is therefore essential to identify patients who do not respond to chemotherapy to avoid ineffective therapies and unnecessary side effects.

Changes in tumor metabolic activity have been shown to be an important indicator of treatment

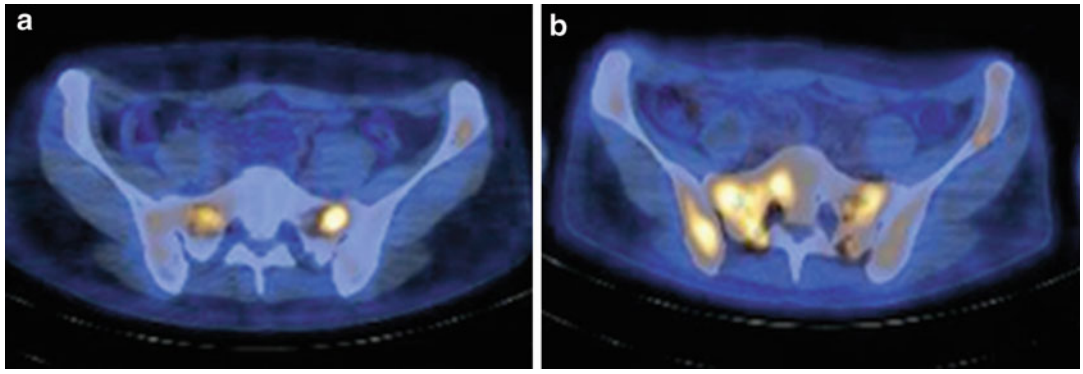

Fig. 11 Bone disease progression after chemotherapy demonstrated by [^{18}F]FDG fused PET/CT axilla images (**a** at baseline, **b** after therapy)

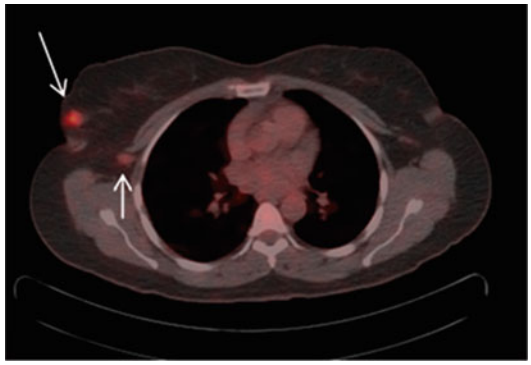

Fig. 12 Fused PET/CT tranxaxial image of FDG-avid right breast lesion and ipsilateral axillary lymph node

effectiveness for breast cancer. In patients with metastatic breast cancer, the effectiveness of chemotherapy can be evaluated earlier with [^{18}F]FDG PET than with conventional imaging. Another important finding is that PET/CT allows evaluation of response in many different metastases. Therefore, PET/CT is helpful to detect a heterogeneous response (coexistence of responding and non-responding lesions within the same patient). Furthermore, metastatic bone lesions, the most common site of breast cancer metastases, occurring in up to 80% of patients, are often difficult to assess for response by conventional imaging such as CT and bone scans. In this setting, [^{18}F]FDG PET/CT may play an important role in assessing response to therapy in bone-dominant breast cancer (Figs. 12 and 13) [1–3].

Breast Cancer: Case No. 7

Case contributed by: E.D. Telenga[a], R.H.J.A. Slart[a,b], A.W.J.M. Glaudemans[b]

[a]Department of Nuclear Medicine and Molecular Imaging, University of Groningen, University Medical Center Groningen, Groningen, The Netherlands

[b]Biomedical Photonic Imaging Group, University of Twente, Enschede, The Netherlands

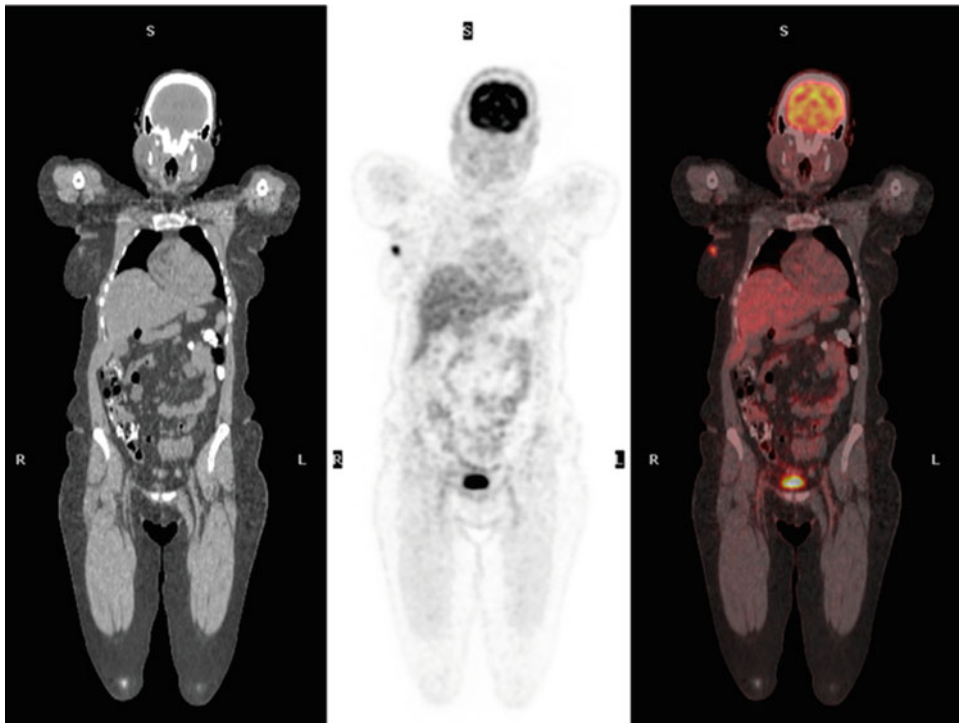

Fig. 13 Coronal image of right breast lesion

Presentation

A 72-year-old woman had been treated 13 years earlier with left-sided mastectomy and axillary lymph node dissection for an ER-positive, PR-negative breast carcinoma. Now, she presents with a lesion in the post-mastectomy scar. Biopsy showed an infiltrative lobular carcinoma, ER-positive, PR-positive, and Her2/neu-negative.

Findings

^{99m}Tc-HDP bone scintigraphy showed a small lesion in the right frontal bone as the only possible bone metastasis (Fig. 14), although a solitary bone island or hyperostosis frontalis was also considered for differential diagnosis. Because of the uncertainty about the possible solitary metastasis, the patient was accepted for curative treatment

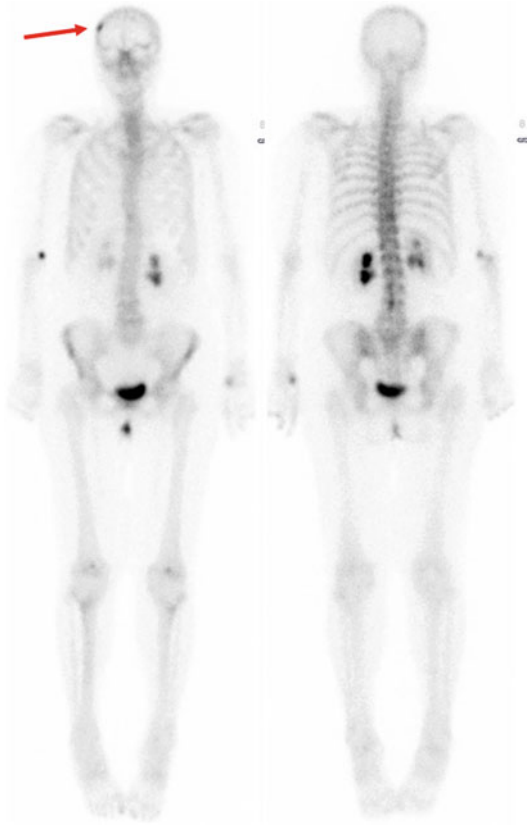

Fig. 14 Anterior (*left panel*) and posterior (*right panel*) ^{99m}Tc-HDP bone scintigraphy showing a solitary lesion in the right frontal bone (*red arrow*)

and the lesion in the left breast region was resected. Pathology showed an infiltrative lobular carcinoma (2.2 cm in maximum diameter), with residual focal tumor growth at 1 mm from the resection margin. Additional imaging was therefore performed before possible treatment with radiotherapy and hyperthermia.

[^{18}F]FDG PET/CT showed increased uptake at the left thoracic wall, consistent with inflammation due to recent surgery (Fig. 15). Furthermore, there was a small moderately intense lesion on the left side of first lumbar vertebra (SUV_{max} 4.0). On the low-dose CT, multiple sclerotic lesions

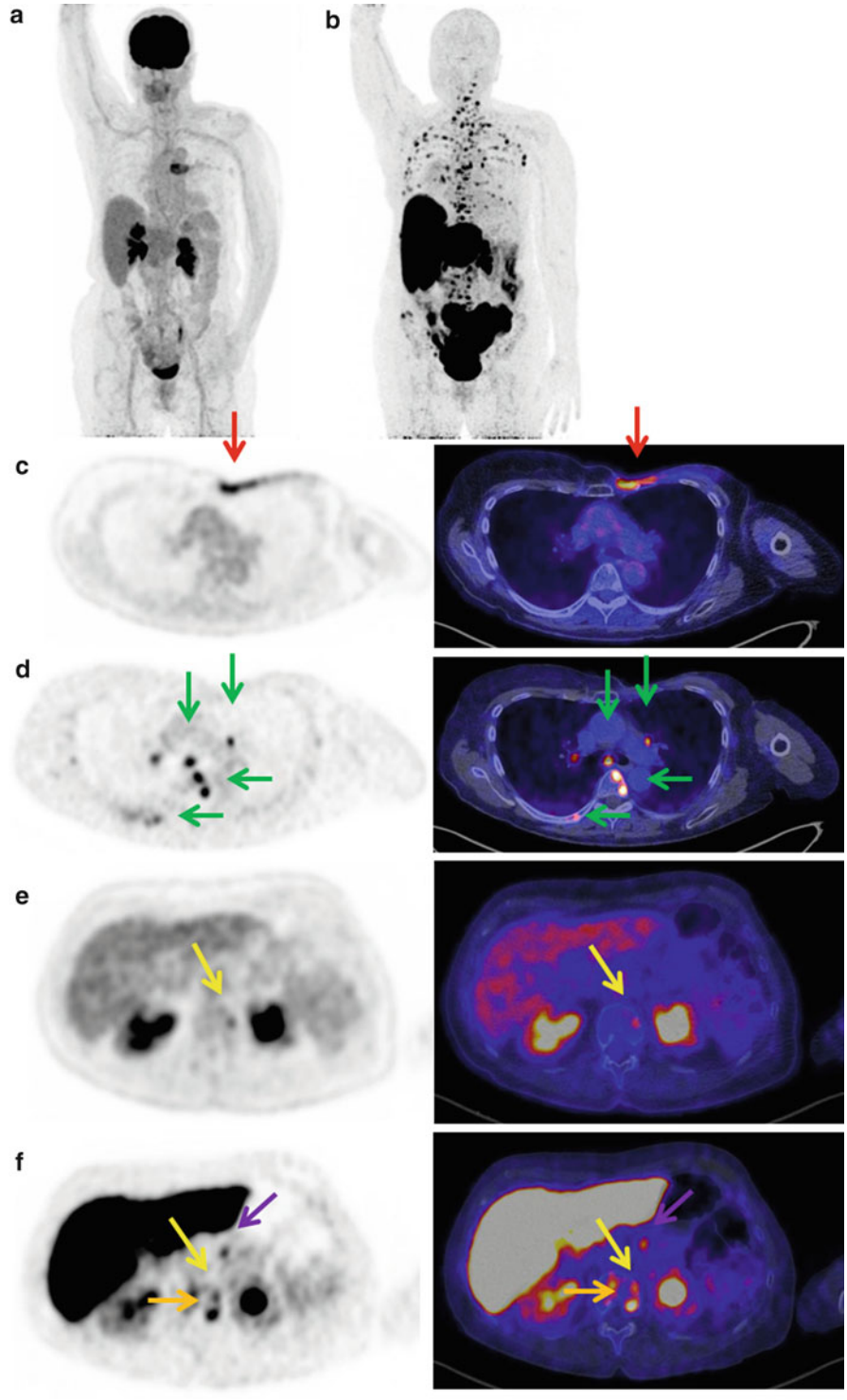

Fig. 15 (continued)

without increased uptake were seen in the frontal bone, the spine, and pelvis.

To further characterize these sclerotic lesions, the patient was referred for a PET/CT scan with ^{18}F-FES, which was performed 1 month after the [^{18}F]FDG PET/CT scan. ^{18}F-FES PET/CT showed multiple lesions with increased uptake throughout the skeleton as well as multiple ^{18}F-FES-avid axillary, mediastinal, lung hilar, and para-aortic abdominal lymph nodes (Fig. 15). The lesion seen in the first lumbar vertebra on the [^{18}F]FDG PET/CT also showed moderately intense uptake of ^{18}F-FES; however, the ^{18}F-FES PET/CT scan showed two additional lesions with intense ^{18}F-FES uptake in the same vertebral body that were not visible at all on the [^{18}F]FDG PET/CT (Fig. 15e, f). The sclerotic lesion in the frontal bone was negative on both scans.

Follow-up

Based on the ^{18}F-FES PET/CT findings, it was concluded that the patient had extensively metastatic breast cancer. Therapy with aromatase inhibiting drugs was therefore started and the patient was referred for further palliative care.

References

1. Yue Y, Cui X, Bose S, et al. Stratifying triple-negative breast cancer prognosis using ^{18}F-FDG-PET/CT imaging. Breast Cancer Res Treat. 2015;153:607–16.
2. Groheux D, Biard L, Giacchetti S, et al. ^{18}F-FDG PET/CT for the early evaluation of response to neoadjuvant treatment in triple-negative breast cancer: influence of the chemotherapy regimen. J Nucl Med. 2016;57:536–43.
3. Groheux D, Hindié E, Giacchetti S, et al. Early assessment with ^{18}F-fluorodeoxyglucose positron emission tomography/computed tomography can help predict the outcome of neoadjuvant chemotherapy in triple negative breast cancer. Eur J Cancer. 2014;50:1864–71.

Fig. 15 [^{18}F]FDG PET/CT (*left side*: **a**, **c**, and **e**) and ^{18}F-FES PET/CT (*right side*: **b**, **d**, and **f**); **a** and **b** are MIP images. **c**, **d**: increased [^{18}F]FDG uptake and no ^{18}F-FES uptake at the left thoracic wall (*red arrows*); however, there is increased ^{18}F-FES uptake in the vertebra, rib, subcarinal, and lung hilar lymph nodes (*green arrows*). **e**, f: moderately increased [^{18}F]FDG and ^{18}F-FES uptake in a lesion in the left portion of L1 (*yellow arrows*). More intense ^{18}F-FES uptake in two additional lesions in the same vertebra without [^{18}F]FDG uptake (*orange arrows*). Increased ^{18}F-FES uptake in a left para-aortic lymph node (*purple arrows*)

Teaching Cases in Nuclear Oncology: Lung and Mediastinal Tumors

60

Alice Lorenzoni, Alessandra Alessi, and Flavio Crippa

Keywords

Lung tumor • Malignant pleural mesothelioma • Thymoma • [^{18}F]FDG PET/CT • Radiotherapy planning

Glossary

[^{18}F]FDG	2-deoxy-2-[^{18}F]fluoro-D-glucose
AP	Aorto-pulmonary
CT	X-ray computed tomography
CTV-N	Clinical target volume for lymph nodes
CTV-T	Clinical target volume for tumor
CTV	Clinical target volume
Gy	Gray unit (ionizing radiation dose in the International System of Units, corresponding to the absorption of one joule of radiation energy per kilogram of matter)
IMRT	Intensity-modulated radiotherapy
LLL	Lower left lobe
MPM	Malignant pleural mesothelioma
MR	Magnetic resonance
MRI	Magnetic resonance imaging
NSCLC	Non-small cell lung cancer
PET	Positron emission tomography
PET/CT	Positron emission tomography/computed tomography
PET/MRI	Positron emission tomography/magnetic resonance imaging
RT	Radiotherapy
SCLC	Small cell lung cancer
SUV	Standardized uptake value
SUV_{max}	Standardized uptake value at point of maximum
WHO	World Health Organization

Contents

Lung Cancer: Case No. 1 1628
Presentation 1628
Findings 1628
Discussion 1628

Lung Cancer: Case No. 2 1628
Presentation 1628
Findings 1628
Discussion 1628

Lung Cancer: Case No. 3 1631
Presentation 1631
Findings 1632
Discussion 1632

A. Lorenzoni (✉) • A. Alessi • F. Crippa
Nuclear Medicine Division, IRCCCS National Cancer Institute, Milan, Italy
e-mail: alice.lorenzoni@istitutotumori.mi.it; alicelorenzoni@hotmail.it

© Springer International Publishing Switzerland 2017
H.W. Strauss et al. (eds.), *Nuclear Oncology*,
https://doi.org/10.1007/978-3-319-26236-9_63

Lung Cancer: Case No. 4 1632
Presentation 1632
Findings 1632
Follow-Up 1632

Lung Cancer: Case No. 5 1633
Presentation 1634
Findings 1634
Follow-Up 1634

Lung Cancer: Case No. 6 1635
Presentation 1635
Findings 1635
Discussion 1636

Mesothelioma: Case No. 1 1636
Presentation 1636
Finding 1637
Discussion 1640

Mesothelioma: Case No. 2 1640
Presentation 1640
Findings 1641
Discussion 1641

Thymoma: Case No. 1 1641
Presentation 1641
Findings 1641
Discussion 1641

Lung Cancer: Case No. 1

Presentation

A 63-year-old patient with biopsy-proven adenocarcinoma of the left lung was referred for [^{18}F]FDG PET/CT for staging.

Findings

[^{18}F]FDG PET/CT showed an intensely avid mass in the left lower lobe with multiple avid mediastinal lymph nodes (Fig. 1). The patient was treated with chemotherapy. Post-therapy [^{18}F]FDG PET/CT showed complete metabolic response. It also revealed the appearance of small speculated nodule in the upper lobe of right lung with mildly [^{18}F]FDG uptake suspicious for malignancy (Fig. 2). Radiotherapy was performed. Post-radiation therapy PET/CT showed complete response of treated small nodule and the recurrence in the left lower lobe (Fig. 3).

Discussion

[^{18}F]FDG PET/CT imaging is helpful in staging lung cancer to determine the most suitable treatment modality and to evaluated therapy response.

Lung Cancer: Case No. 2

Presentation

A 52-year-old man presented with suspected hypertrophic pulmonary osteopathy and hippocratic fingers. Contrast-enhanced CT of the thorax showed a mass of the lower left lobe (LLL) (35 mm in size) and bulky hilar adenopathy. Biopsy of the mass indicated the presence of non-small cell lung cancer (NSCLC).

[^{18}F]FDG PET/CT was performed for staging.

Findings

PET/CT showed an [^{18}F]FDG-avid LLL mass and bulky left hypermetabolic hilar adenopathy (stage IIIA) (Fig. 4a). Patients underwent neoadjuvant platinum-based chemotherapy.

Posttreatment [^{18}F]FDG PET revealed no metabolic response of the lung mass and concomitant hilar adenopathy (Fig. 4b). Furthermore, PET/CT images demonstrated the appearance of moderate focal uptake in right adrenal gland suspicious for metastatic lesion (Figs. 5 and 6). Contrast-enhanced CT of the abdomen confirmed adrenal metastases.

Discussion

In selected patients, there may be a role for neoadjuvant therapy for locally advanced, potentially resectable NSCLC. The ability of [^{18}F]FDG PET to provide predictive and prognostic information regarding the response to initial therapy is well documented. This case confirms the utility of [^{18}F]FDG PET in response to the assessment of patients treated for NSCLC.

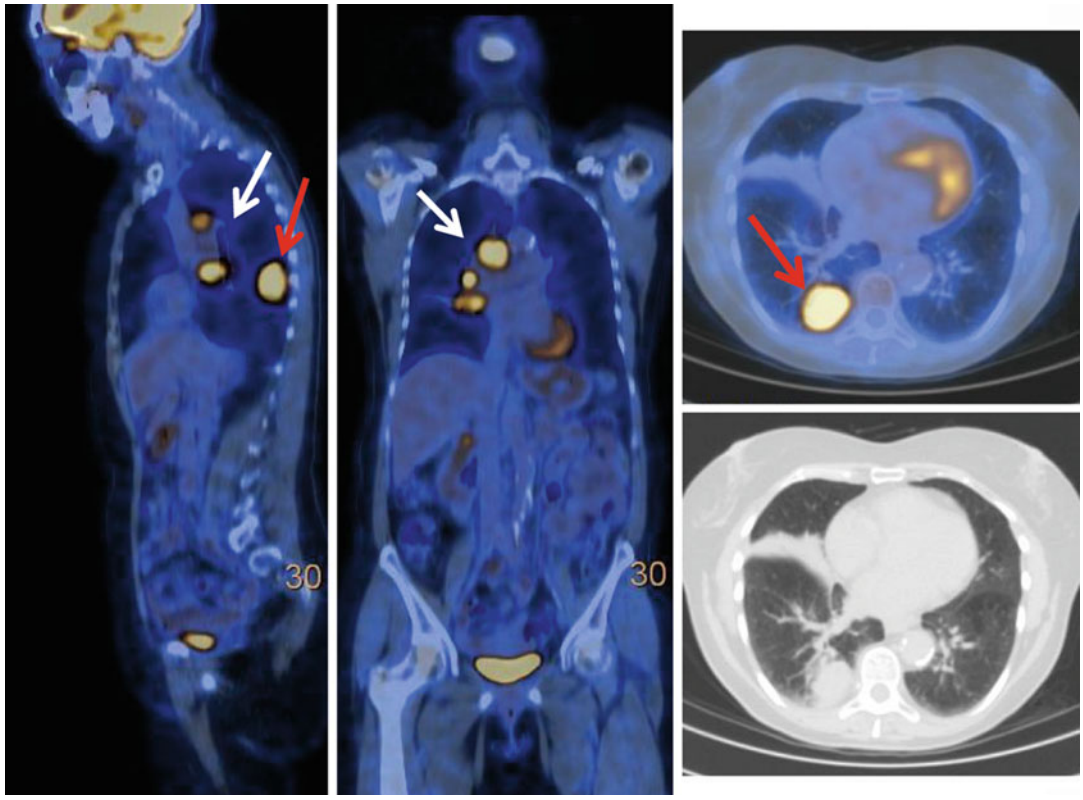

Fig. 1 [^{18}F]FDG PET/CT in staging lung cancer shows primary avid lesion (*red arrow*) and mediastinal lymphadenopathies (*white arrow*)

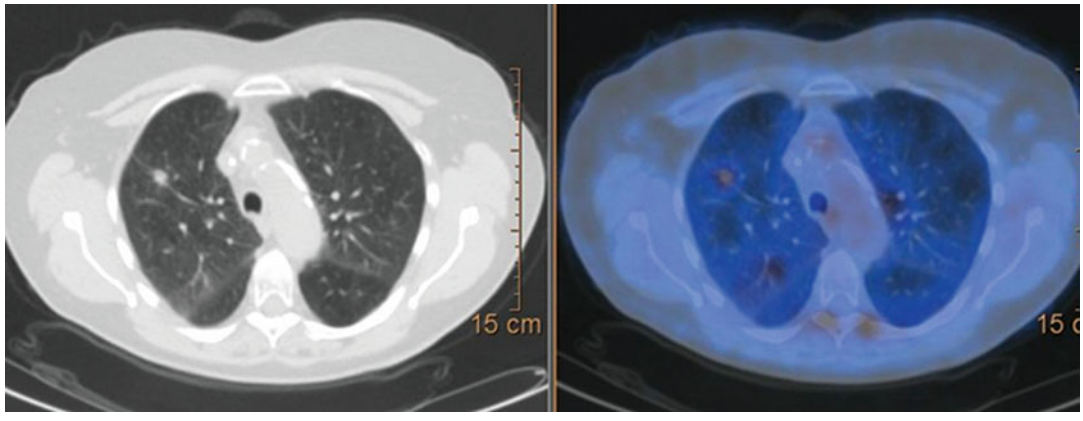

Fig. 2 Axial low-dose CT and fused PET/CT images of the appearance of small speculated nodule in the *upper* lobe of right lung with mild [^{18}F]FDG uptake suspicious for malignancy

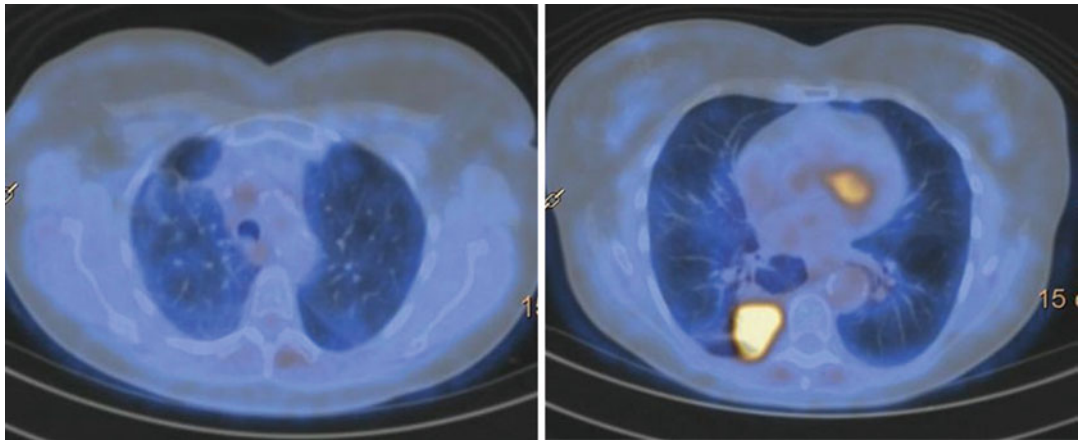

Fig. 3 Axial fused [^{18}F]FDG PET/CT images after radiotherapy show complete response of lesion in the *upper* lobe (*left panel*) and the relapse in *lower* lobe (*right panel*)

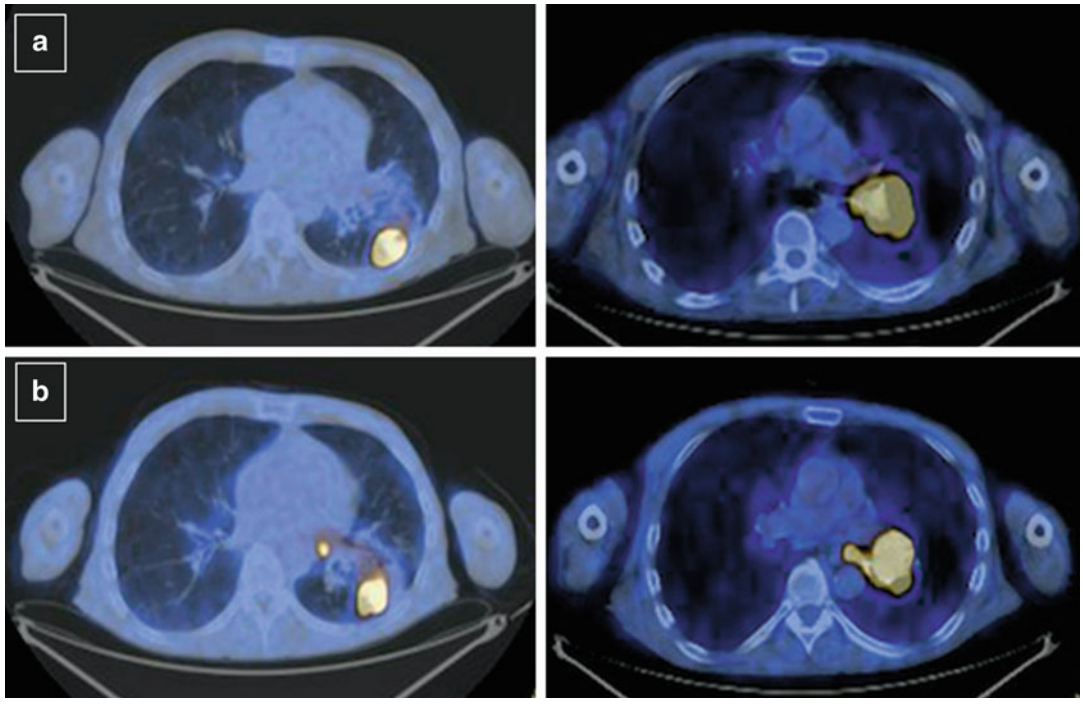

Fig. 4 Fused PET/CT axial images of baseline (**a**) [^{18}F]FDG-avid LLL mass (*left*) and bulky left hypermetabolic hilar adenopathy (*right*); fused PET/CT axial images of posttreatment [^{18}F]FDG-PET (**b**) show no metabolic response of lung mass (*left*) and hilar adenopathy (*right*)

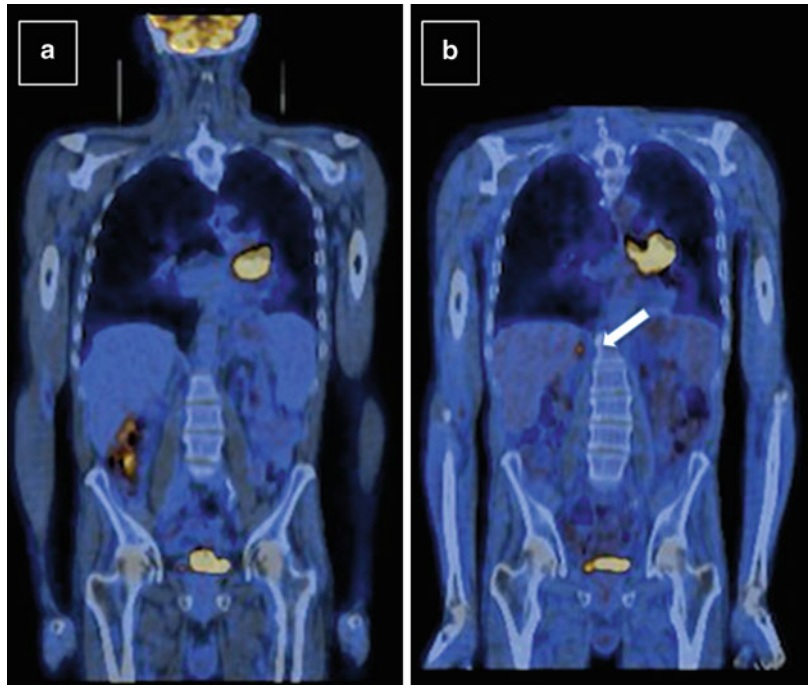

Fig. 5 Coronal fused [^{18}F] FDG PET/CT images of baseline scan (**a**) do not show distant metastases; coronal fused PET/CT images after therapy (**b**) depict right adrenal gland metastases (*white arrow*)

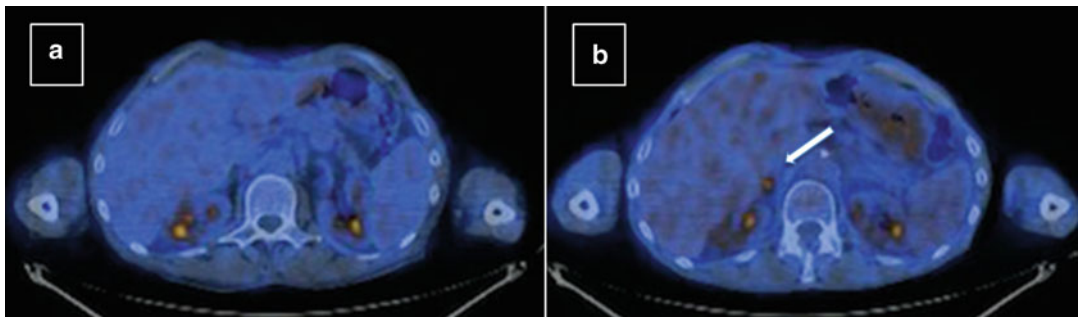

Fig. 6 Axial fused [^{18}F]FDG PET/CT baseline image (**a**) is negative for adrenal metastases; axial fused PET/CT after chemotherapy (**b**) reveals right hypermetabolic adrenal lesion (*white arrow*)

Lung Cancer: Case No. 3

Case contributed by: S. Al Shammari, F. Fraioli
Institute of Nuclear Medicine, UCLH NHS Foundation Trust, London, UK

Presentation

A 50-year-old patient was referred for [^{18}F]FDG PET/CT for the evaluation of a lung lesion in the right lower lobe (Fig. 20).

Findings

Non-[^{18}F]FDG-avid right upper lobe nodule measuring ~2.8 × 2 cm. The mass appears speculated with pleural tethering (arrow). Biopsy of the mass showed bronchoalveolar cancer.

Discussion

[^{18}F]FDG PET/CT is being used more and more to differentiate benign from malignant focal lesions in the lung. Accurate diagnosis can reduce unnecessary thoracotomies in patients with benign diseases. However, [^{18}F]FDG is not a cancer-specific agent, and false positive findings in benign diseases have been reported. Infectious diseases (mycobacterial, fungal, bacterial infection), sarcoidosis, radiation pneumonitis, and postoperative surgical conditions have shown intense uptake on PET scan. On the other hand, due to low glycolytic activity, bronchoalveolar carcinoma shows significantly lower peak standardized uptake values than do other lung carcinomas. Thus, bronchoalveolar carcinoma can be a potential cause of false-negative findings of malignancy on [^{18}F]FDG PET scans. Other tumors with low glycolytic activity such as adenomas, carcinoid tumors, low-grade lymphomas, and small-sized tumors (<1 cm in diameter) can yield false negative findings on PET scan as well. Familiarity with these false positive and negative findings will help to interpret PET scans more accurately.

Lung Cancer: Case No. 4

Case contributed by: D. Neriman, J.P. Connelly, K. Al-Riyami

Institute of Nuclear Medicine, UCLH NHS Foundation Trust, London, UK

Presentation

A 67-year-old man presented with 6-week history of shortness of breath. The patient was found to have right lung collapse. Bronchoscopy revealed a lesion in the right main bronchus which was biopsied. An [^{18}F]FDG PET/CT was performed as part of the work up.

Findings

[^{18}F]FDG PET/CT showed an intensely avid mass (SUV_{max} >21) in the right lower lobe hilum with right lower lung collapse, mediastinal shift, and avid ipsilateral and contralateral lymph nodes (Fig. 7). In the abdomen, there was increased metabolic activity (SUV_{max} 12.3) in bulky adrenal glands bilaterally and of multilevel para-aortic and paracaval nodes in keeping with metastatic disease.

Follow-Up

Biopsy confirmed squamous cell carcinoma and the patient subsequently underwent chemoradiation. [^{18}F]FDG PET/CT has been proven to be more accurate than CT in the nodal and metastatic disease staging of non-small cell lung cancer (NSCLC) by demonstrating unsuspected sites of disease. It is recommended in patients being considered for curative treatment, as it delineates areas of metabolically active tumor from areas of atelectasis and consolidation and can therefore help guide biopsy.

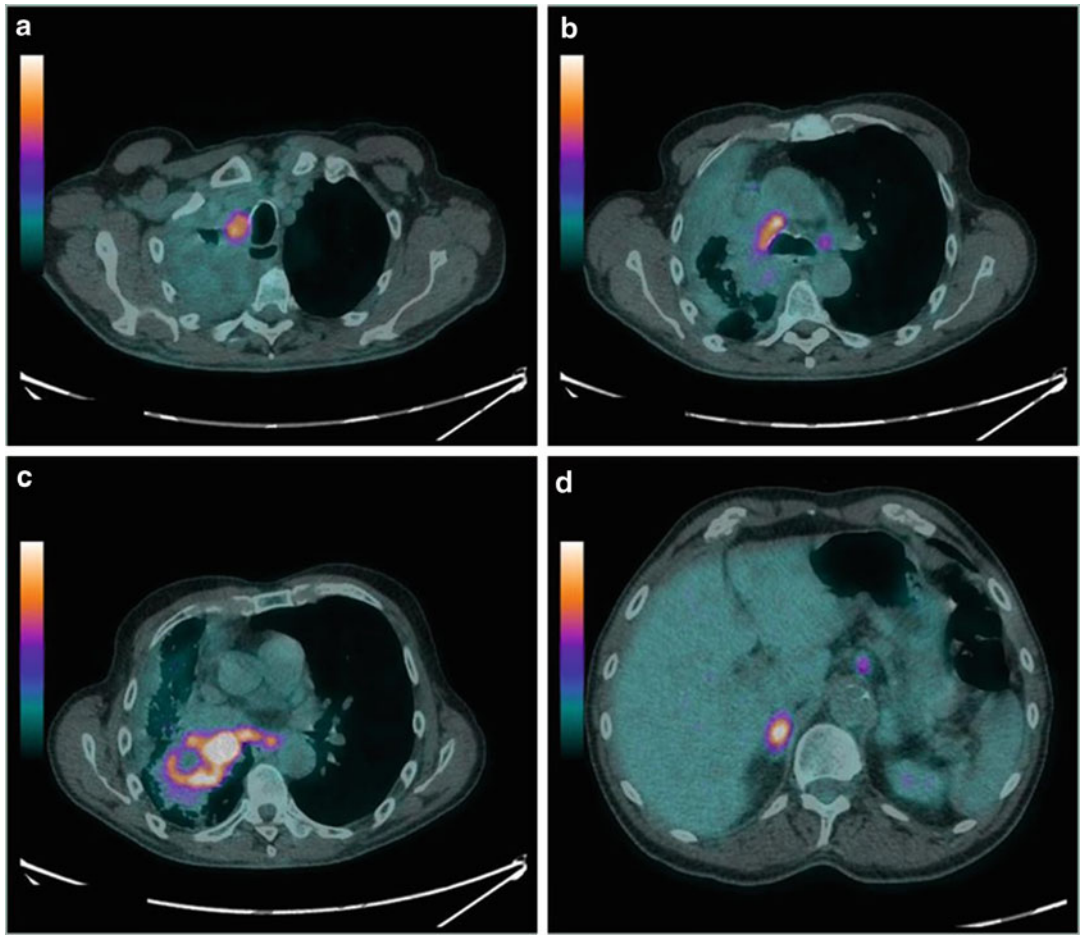

Fig. 7 Fused axial [^{18}F]FDG PET/CT images show tracer avid right paratracheal and AP window mediastinal lymph nodes. Avid uptake is seen in the mass in the right lower lobe, celiac lymph node, and right adrenal gland uptake

[^{18}F]FDG PET/CT is also useful for assessing adrenal pathology, both in terms of [^{18}F]FDG uptake and assessing fat content on the unenhanced CT.

Lung Cancer: Case No. 5

Case Contributed by: S. Wan
Nuclear Medicine, UCLH NHS Foundation Trust, London, UK

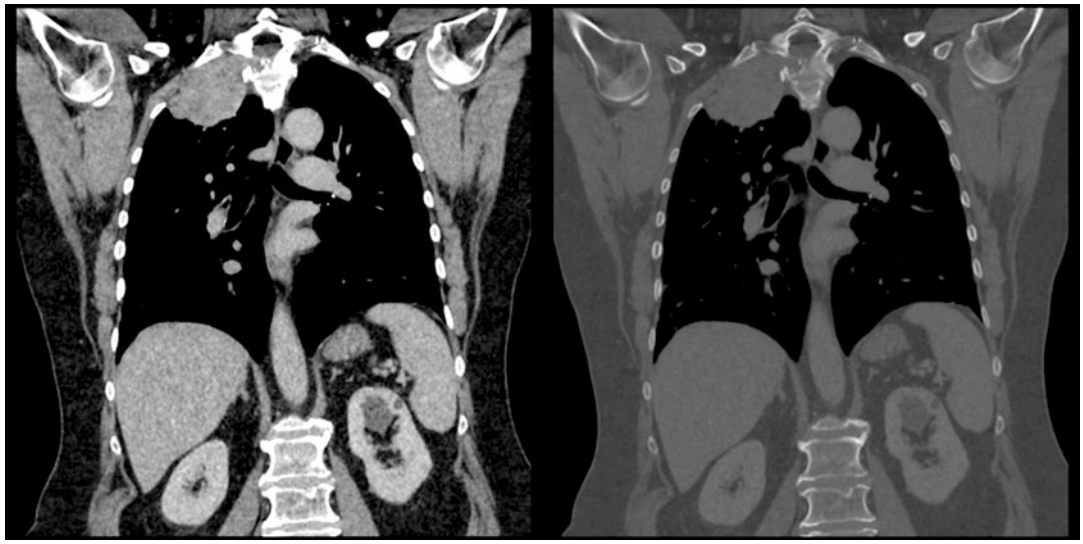

Fig. 8 Coronal CT demonstrating the mass with its epicenter at the right lung apex (*left*). There is clear destruction of the T1 vertebral body (*right*) on bone window display

Presentation

A 77-year-old woman was found to have a chest lesion on radiograph, as a work up for right-sided back pain and Horner's syndrome. CT chest showed right apical lung lesion with adjacent destruction of T1 vertebral body, compatible with a Pancoast tumor.

Findings

A combined PET/MRI study showed the lesion to have a degree of [^{18}F]FDG uptake with a more avid component clearly invading into the spinal canal and compression the spinal cord at this level. Destruction of T1 vertebrae was also evident. Despite the large size and locally advanced stage, there was no [^{18}F]FDG-avid supraclavicular, hilar, or mediastinal lymphadenopathy. There was no [^{18}F]FDG-avid distant metastases.

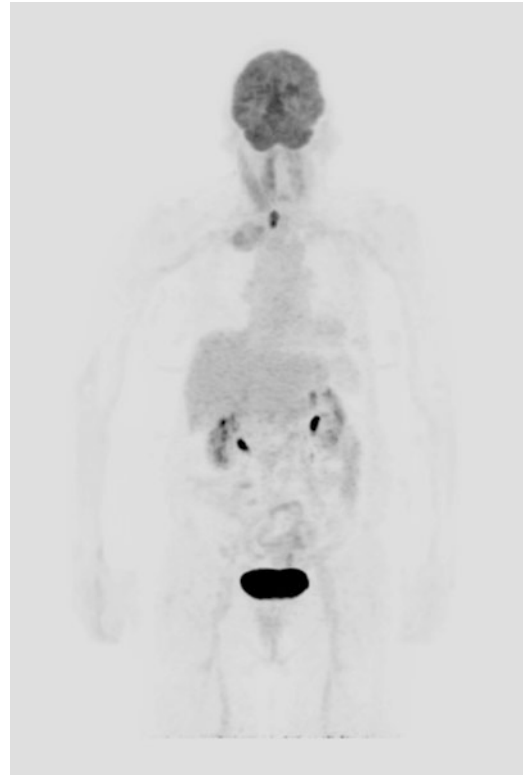

Fig. 9 3D maximum intensity projection of the [^{18}F]FDG PET showed most of the lesion to be moderately avid but with a more intense component medially. No further [^{18}F]FDG-avid disease was seen in the nodes and distally

Follow-Up

CT-guided biopsy of the lesion showed a biphasic tumor comprising nests of large epithelial cells

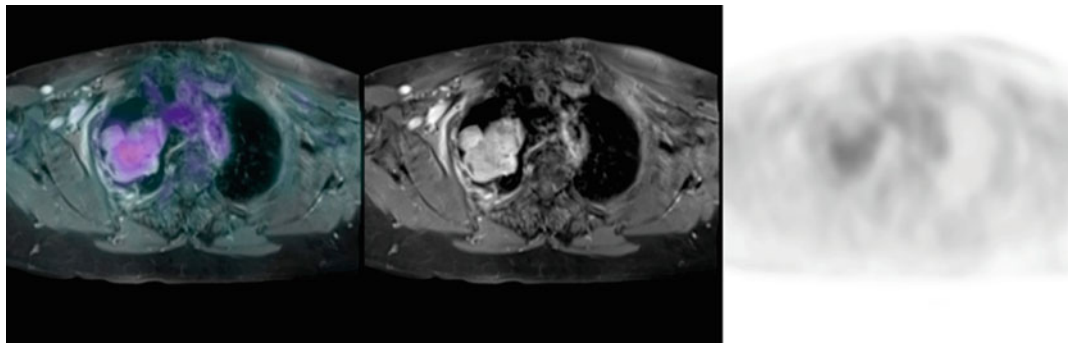

Fig. 10 (Axial), from *left*: fused, fat suppressed T1 post contrast, [^{18}F]FDG PET images showing the lesion clearly extending into the spinal canal and compressing the cord to the *left*

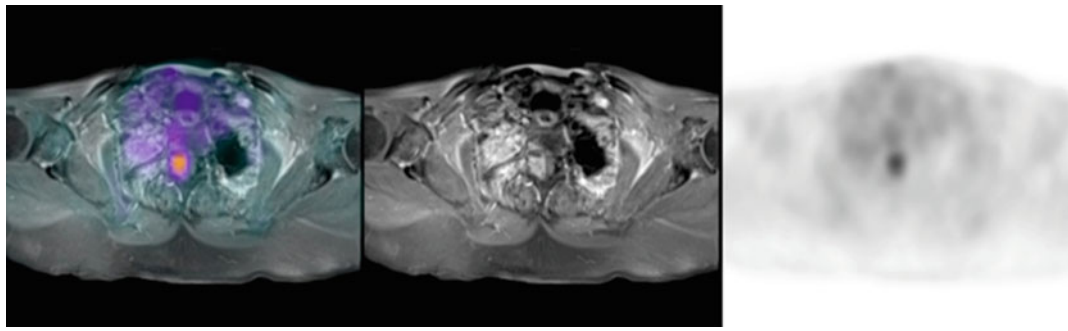

Fig. 11 (Axial), from *left*: fused, fat suppressed T1 post contrast, [^{18}F]FDG PET images showing the lesion clearly extending into the spinal canal and compressing the cord to the *left*

and fascicles of monomorphic spindle cells set in a fibrous stroma. Clinical imaging and pathological correlation concluded carcinosarcoma being the favored diagnosis. The patient proceeded to receive high-dose palliative radiotherapy (30 Gy in 12 fractions) and chemotherapy (carboplatin/gemcitabine) but unfortunately progressed despite treatment (Figs. 8, 9, 10, 11, 12, 13).

Lung Cancer: Case No. 6

Case contributed by: L. Deantonio[a], F. Orsini[b], R. Matheoud[c], M. Krengli[a], G.M. Sacchetti[b]

[a]Radiotherapy Unit, "Maggiore della Carità" University Hospital" and Department of Translational Medicine, University of "Piemonte Orientale" University, Novara, Italy

[b]Section of Nuclear Medicine, «Maggiore della Carità» University Hospital, Novara, Italy

[c]Section of Medical Physics, «Maggiore della Carità» University Hospital, Novara, Italy

Presentation

A 69-year-old woman with incidental finding of a solitary pulmonary nodule in the left lung.

Findings

An [^{18}F]FDG PET/CT demonstrated intense tracer uptake in the nodular lesion in the upper lobe of the left lung (SUV_{max} 11.7), with associated increased uptake in the left hilar lymph nodes (Fig. 14).

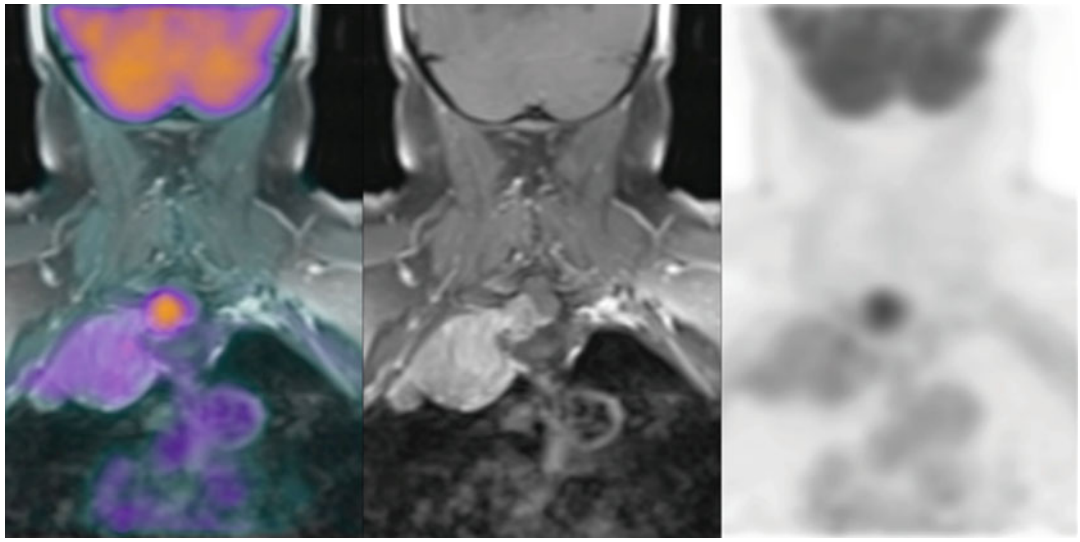

Fig. 12 (Coronal): from *left*: fused, fat suppressed T1 post contrast, [^{18}F]FDG PET images showing the lesion clearly extending into the spinal canal and compressing the cord to the *left*

Fig. 13 Further follow-up MRI of the spine demonstrates new enhancing nodules associated with the conus and cauda equina, consistent with intradural progression despite treatment

Image-guided biopsy confirmed the presence of a small cell lung cancer (SCLC); stage was defined as IIA. In this case, [^{18}F]FDG PET/CT upstaged the patient, who was initially presumed to have more limited disease.

Discussion

The case was discussed in a multidisciplinary meeting with surgeons, radiation oncologists, and medical oncologists, and the patient was recommended for radio-chemotherapy.

The patient underwent two cycles of carboplatin and etoposide, with concomitant radio-chemotherapy.

An intensity-modulated radiotherapy (IMRT) was performed to the lesion of the upper left lobe and at the level of hilar and peribronchial lymph nodes to a total dose of 60 Gy, with daily fractions of 2 Gy (Figs. 15 and 16).

Mesothelioma: Case No. 1

Presentation

A 68-year-old man presented with dyspnea and chest pain. Chest radiography showed right pleural effusion. Contrast-enhanced CT on the thorax demonstrated suspected right nodular pleural thickening and interlobar fissure thickening.

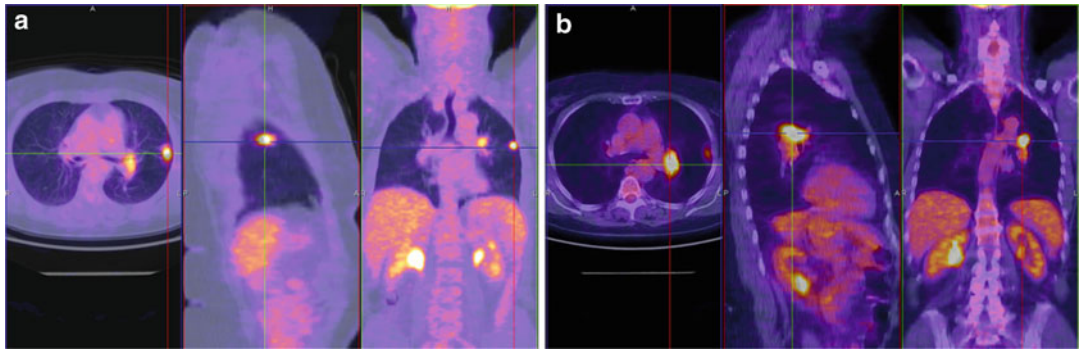

Fig. 14 Transaxial, sagittal, and coronal fused [^{18}F]FDG PET/CT images showing high-tracer uptake in the primary tumor (**a**) and in hilar and peribronchial lymph nodes (**b**)

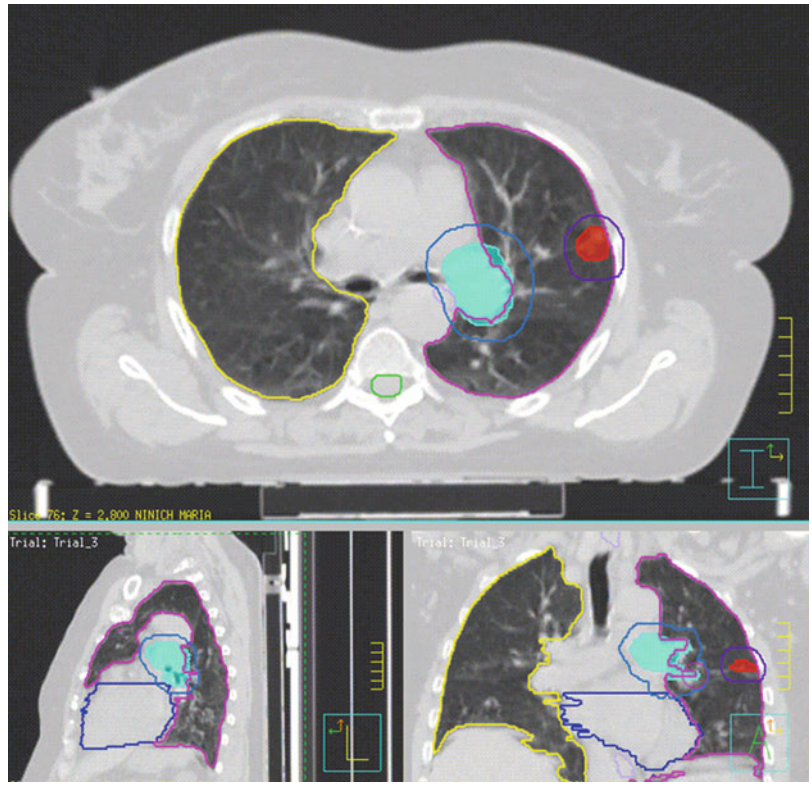

Fig. 15 Axial, coronal, and sagittal images of the simulation CT. Different colors are used to highlight the contours of the treatment volumes. *Light blue*: clinical target volume of involved hilar and peribronchial nodes (CTV-N); *red*: clinical target volume of the primary lesion (CTV-T). The prescribed dose to both CTV-N and CTV-T was 60 Gy, with daily fractions of 2 Gy

Biopsy confirmed the diagnosis of malignant pleural mesothelioma (MPM).

[^{18}F]FDG PET/CT was performed to complete staging.\

Finding

[^{18}F]FDG PET/CT images demonstrated diffuse [^{18}F]FDG uptake of the right pleura suspicious for malignancy and a focal area of increase [^{18}F]FDG

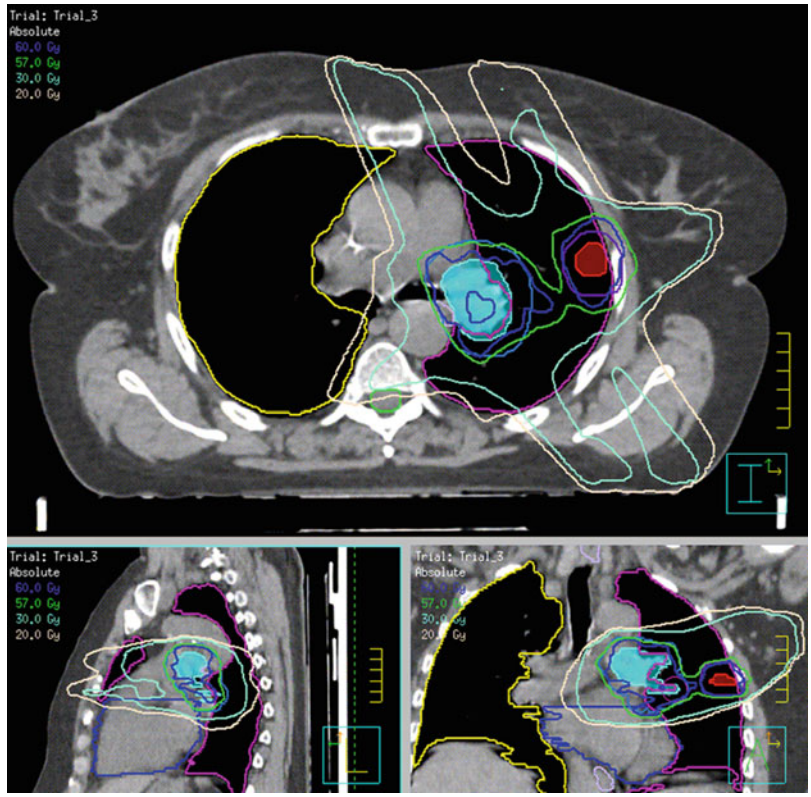

Fig. 16 Transaxial, coronal, and sagittal view of the RT treatment planning. Images show the dose distribution performed by IMRT treatment plan. Around the target volumes, the doses fall down sharply, thus reducing the dose to the organs at risk. In *green* the isodose of 57 Gy (corresponding to 95% of the prescribed dose of 60 Gy), and in white the isodose of 20 Gy

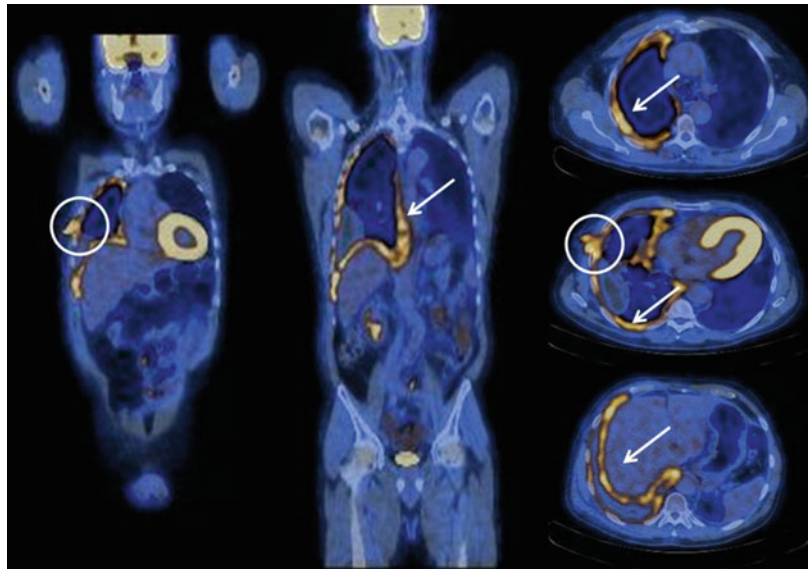

Fig. 17 Fused PET/CT images of pathological [^{18}F] FDG uptake of the right pleura (*white arrows*) and the disease extent into chest wall (*white circle*) after positioning of chest tube

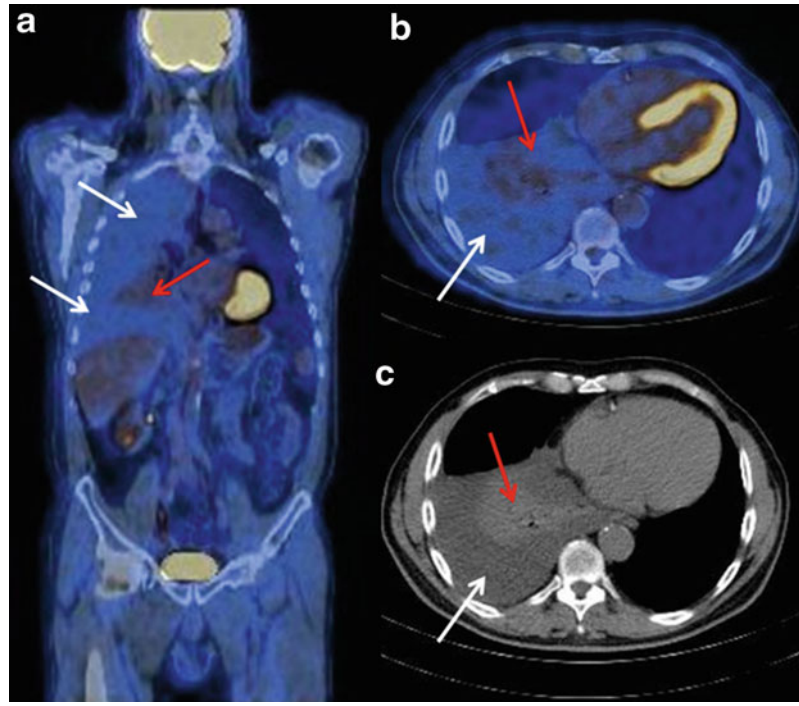

Fig. 18 Fused PET/CT (**a** coronal, **b** axial) and axial low-dose CT (**c**) images show large pleural effusion without significant [^{18}F]FDG uptake (*white arrows*) and mildly [^{18}F]FDG-avid lung atelectasis (*red arrows*)

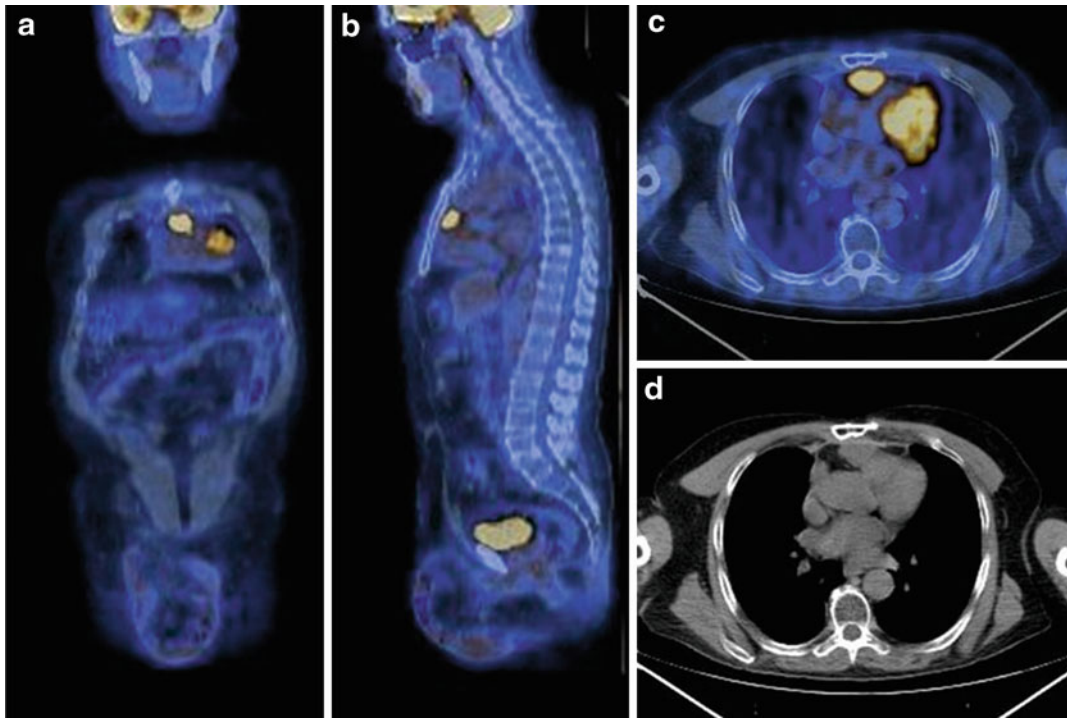

Fig. 19 Fused [^{18}F]FDG PET/CT images (**a** coronal, **b** sagittal, and **c** axial) and axial low-dose CT (**d**) show hypermetabolic mediastinal mass consistent with thymoma recurrence

Fig. 20 Non-[^{18}F]FDG-avid right upper lobe nodule

metabolism into the lateral chest wall (fifth intercostal space) possibly due to mesothelioma extension via chest tube tract (Fig. 17). Pleural effusion did not show significant metabolic activity.

Discussion

Distinguishing MPM from benign pleural disease is a challenging issue. [^{18}F]FDG PET/CT has high accuracy in identifying malignant disease, usually characterized by a unilateral circumferential or near-circumferential pleural and fissural thickening that shows [^{18}F]FDG avidity. Furthermore, increasing evidence suggests that volume-based PET parameters, such as the metabolic tumor volume or total lesion glycolysis, are important prognostic factors in mesothelioma. Staging is crucial in selection of patients for aggressive surgical procedures and multimodality therapy. PET/CT may aid in determining the extent of tumor invasion, localizing involved lymph nodes, and identifying distant metastases.

Mesothelioma: Case No. 2

Presentation

A 77-year-old man presented with a 2-month history of dry cough and dyspnea. Right pleural effusion and thickening were demonstrated. Biopsy showed well-differentiated epithelial mesothelioma.

Patient underwent [^{18}F]FDG PET/CT for staging completion.

Findings

[^{18}F]FDG PET/CT showed large right pleural effusion non-[^{18}F]FDG- avid and mild-[^{18}F]FDG uptake corresponding to right pulmonary atelectasis. No [^{18}F]FDG uptake in the pleural thickening was observed.

Discussion

[^{18}F]FDG PET has an important role in the differential diagnosis of pleural disease. This case demonstrates a false-negative [^{18}F]FDG PET result in a patient with well-differentiated mesothelioma (Fig. 18).

Thymoma: Case No. 1

Presentation

A 74-year-old man referred for a mediastinal mass, approximately 3 cm in diameter, revealed during a chest CT examination. Approximately 10 years previously, he presented with invasive type B3 thymoma infiltrating into the left lung according to the WHO classification. He underwent extended thymectomy with combined resection.

Findings

[^{18}F]FDG PET/CT revealed intense [^{18}F]FDG uptake in the retrosternal mass consistent with recurrent disease (Fig. 19). The anterior mediastinal tumor was diagnosed as poorly differentiated squamocellular carcinoma of thymic origin following percutaneous needle biopsy.

Discussion

Recurrence rates after resection of thymomas range from 5% to 50% and are related to the initial clinical stage. The pattern of recurrence of resected thymomas includes local recurrence, pleural implants, and distant metastases. [^{18}F]FDG PET/CT may highlight recurrent metastatic thymoma and is effective for estimating histopathological malignancy and staging in the diagnosis of thymic epithelial tumors (Fig. 20).

Increased physiologic [^{18}F]FDG uptake by a normal or hyperplastic thymus is not infrequent; thus, in the evaluation of malignancy, a potential pitfall is mistaking normal uptake within the thymus for disease.

Teaching Cases in Nuclear Oncology: Esophageal Cancers

61

Duccio Volterrani, Giulia Puccini, Sara Mazzarri, and Federica Guidoccio

Keywords

Esophageal adenocarcinoma • [^{18}F]FDG PET/CT • Lymph node disease • Distant metastases • ceCT • Neoadiuvant chemoradiation • Staging • Therapy monitoring • Second primary

Glossary

[^{18}F]FDG	2-Deoxy-2-[^{18}F]fluoro-D-glucose
AJCC	American Joint Committee on Cancer
ceCT	Contrast-enhanced computed tomography
CLL/SLL	Chronic lymphocytic leukemia/ Small lymphocytic lymphoma
CT	X-ray computed tomography
EGDS	Esophago-gastro-duodenoscopy
GEJ	Gastro-esophageal junction
M	Metastasis status according to the AJCC/UICC TNM staging system
MIP	Maximum intensity projection
MPR	Multiplanar reconstruction
N	Lymph node status according to the AJCC/UICC TNM staging system
PEG	Percutaneous endoscopic gastrostomy
PET	Positron emission tomography
PET/CT	Positron emission tomography/ Computed tomography
SUV	Standardized uptake value
SUV_{max}	Standardized uptake value at point of maximum
T	Tumor status according to the AJCC/UICC staging system
UICC	Union Internationale Contre le Cancer (International Union Against Cancer)

Contents

Esophageal Cancer: Case No. 1 1644
Presentation 1644
Findings 1644
Follow-Up 1644
Teaching Points 1644

Esophageal Cancer: Case No. 2 1645
Presentation 1645
Findings 1645
Follow-Up 1646
Teaching Point 1646

Esophageal Cancer: Case No. 3 1648
Presentation 1648
Findings 1648
Follow-Up 1648
Teaching Points 1650

D. Volterrani (✉) • G. Puccini • S. Mazzarri • F. Guidoccio
Regional Center of Nuclear Medicine, Department of Translational Research and Advanced Technologies in Medicine and Surgery, University of Pisa, Pisa, Italy
e-mail: duccio.volterrani@med.unipi.it

© Springer International Publishing Switzerland 2017
H.W. Strauss et al. (eds.), *Nuclear Oncology*,
https://doi.org/10.1007/978-3-319-26236-9_64

Esophageal Cancer: Case No. 4 1650
Presentation 1650
Findings 1651
Follow-Up 1653
Teaching Points 1653

Esophageal Cancer: Case No. 5 1653
Presentation 1653
Findings 1653
Follow-Up 1654
Teaching Points 1654

Esophageal Cancer: Case No. 1

Case contributed by: D. Neriman, J.P. Connelly, K. Al-Riyami

Institute of Nuclear Medicine, UCLH NHS Foundation Trust, London, UK.

Presentation

A 34-year-old man presented with dysphagia and was investigated as per guidelines with endoscopy, contrast CT, and [^{18}F]FDG PET/CT.

Findings

CT of the chest, abdomen, and pelvis revealed thickening at the GEJ and cardia with a local subcentimeter paraesophageal lymph node. Initial endoscopy showed no malignancy.

[^{18}F]FDG PET/CT for staging showed [^{18}F]FDG-avid thickening at the gastroesophageal junction with an [^{18}F]FDG-avid paraesophageal lymph node (Fig. 1). Further focal uptake was seen in segment 6 (Fig. 2) of the liver correlated to an 11-mm ill-defined low-attenuation lesion, which was missed on the initial staging CT (Fig. 3). Repeat endoscopic biopsy showed adenocarcinoma.

Follow-Up

The patient subsequently underwent chemoradiotherapy.

Teaching Points

The advantage of [^{18}F]FDG PET/CT over conventional imaging is in detection of lymph node involvement and distant metastases. Distant metastatic disease has a significant impact on patient management as these patients are no longer eligible for surgical resection. [^{18}F]FDG PET has a reported sensitivity of 69–100%, a specificity of 84–90%, and an accuracy of 84–91% for the evaluation of distant metastases, with the sensitivity of CT for distant metastases being reported as lower. [^{18}F]FDG PET imaging can also exclude metastatic disease at sites considered abnormal on conventional imaging. [^{18}F]FDG PET/CT is also helpful in visualizing the primary tumor that can be difficult to delineate on contrast CT and guide biopsy.

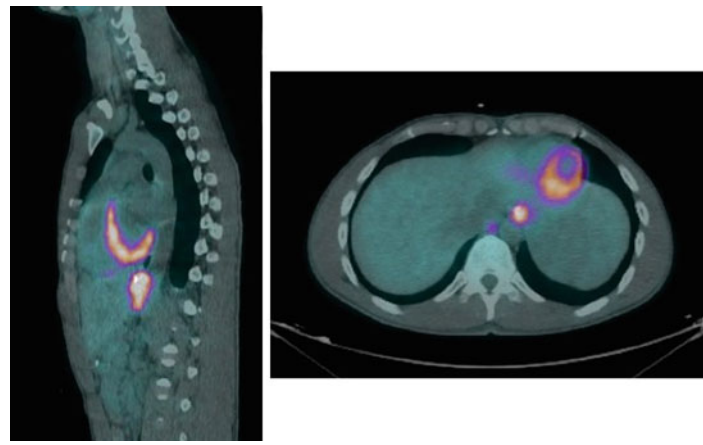

Fig. 1 [^{18}F]FDG fused sagittal and axial PET/CT showing focal uptake in the proven malignancy at the gastroesophageal junction and tracer-avid right paraesophageal lymph node

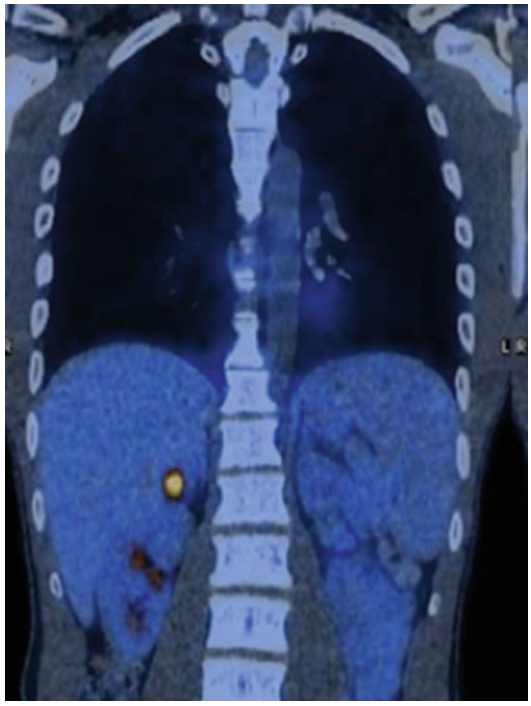

Fig. 2 Coronal [^{18}F]FDG fused PET/CT demonstrating uptake in the segment 6 of the liver (metastasis)

Esophageal Cancer: Case No. 2

Presentation

A 59-year-old man presented with dysphagia underwent endoscopy that revealed a cancer lesion at the level of the distal esophagus. The patient was initially staged with ceCT.

Findings

CT confirmed a gross vegetating lesion at the level of the distal esophagus which extends in the cranio-caudal direction for about 7 cm up to the cardias, with axial diameters of 4 × 4 cm. The mass presented irregular and progressive contrast enhancement with signs of subocclusion and distension of the upstream esophagus (Fig. 4). No locoregional lymphadenopathies nor other pathological supra- and subdiaphragmatic lymph nodes were observed. There were no distant metastases within liver and lungs. The patient underwent an [^{18}F]FDG PET/CT to complete staging and in preparation for chemotherapy and radiation

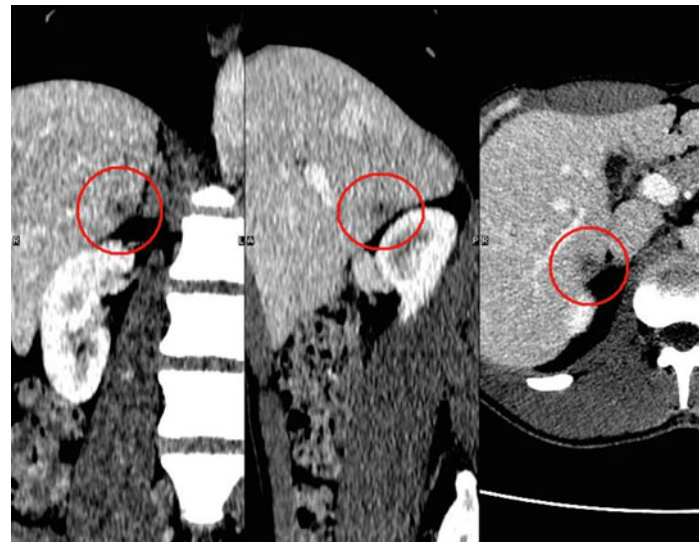

Fig. 3 Coronal and axial post contrast CT demonstrating an 11-mm ill-defined low-attenuation liver lesion compatible with metastasis

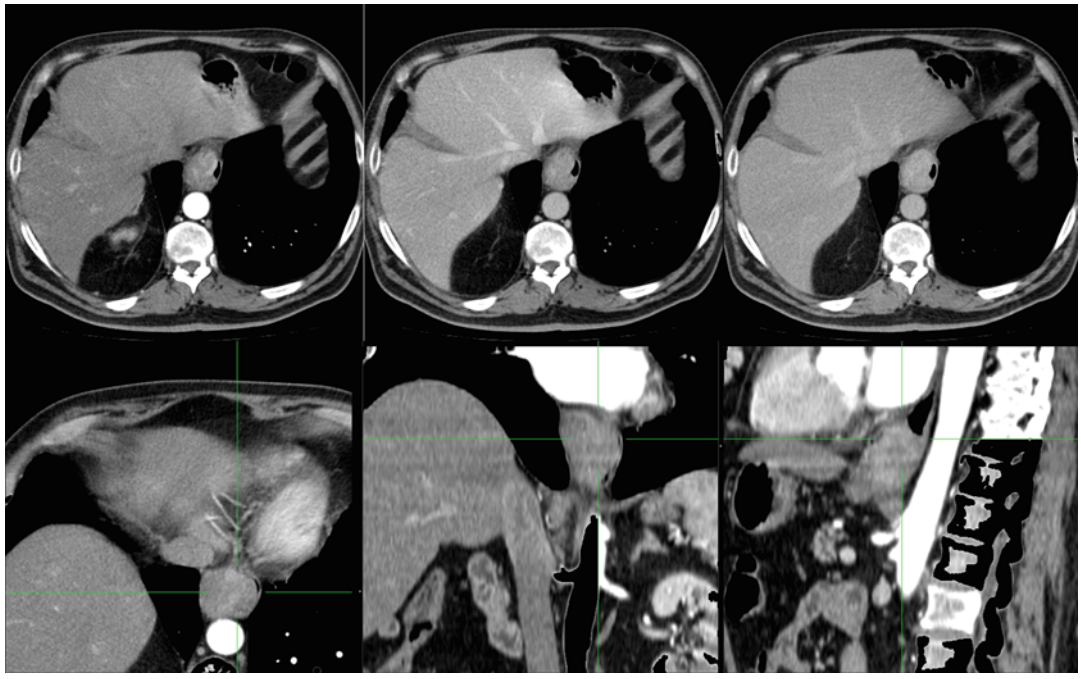

Fig. 4 Contrast-enhanced CT. On *top panels*, ceCT axial slices in the arterial, venous, and late phase showing a gross vegetating lesion of the esophagus, with progressive contrast enhancement. On *bottom panels*, orthogonal MPR showing the lesion of the distal esophagus extending in the cranio-caudal direction up to the cardias. The mass produces subocclusion with the distension of the upstream esophagus

treatment. PET/CT confirmed a gross vegetating [^{18}F]FDG-avid lesion (SUV_{max} 27.2) of the distal esophagus. No hyperactive lymphadenopathies nor distant metastases were observed (Fig. 5).

Follow-Up

After the patient had carried out chemotherapy and external-beam radiation therapy, he was subjected (1 month later) to a PET/CT monitoring. [^{18}F]FDG PET/CT disclosed a clear metabolic response of the esophageal mass (SUV_{max} 6 versus 27.2) which also presented a significant reduced size (Fig. 6).

The patient has then undergone surgery.

Teaching Point

[^{18}F]FDG PET/CT has a role in the staging of locally advanced esophageal carcinoma. In fact, due to its high sensitivity, it can rule out the presence of distant metastases. Moreover, PET/CT plays an important role in monitoring neoadjuvant chemoradiation treatment efficacy.

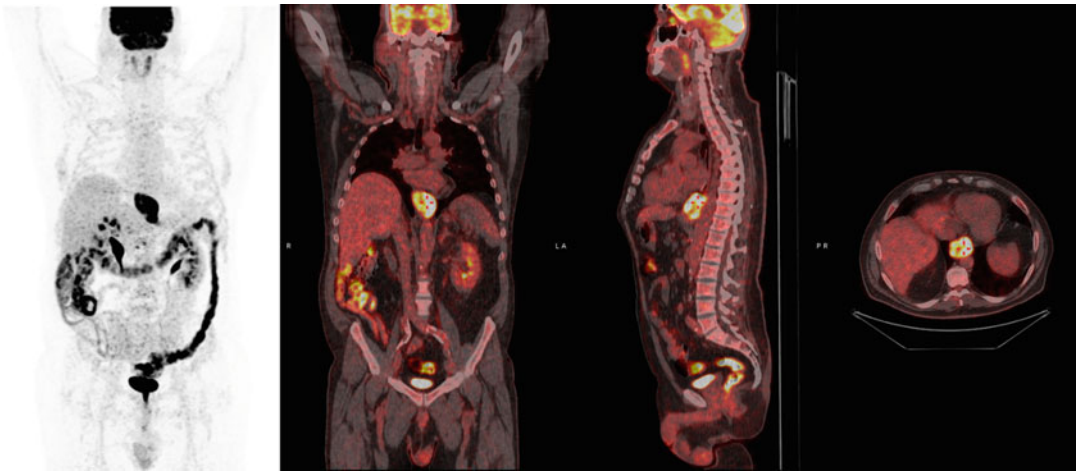

Fig. 5 [^{18}F]FDG MIP and fused coronal, sagittal, and axial PET/CT show a gross [^{18}F]FDG-avid lesion (SUV_{max} 27.2) of the distal esophagus. No other significant hypermetabolic areas

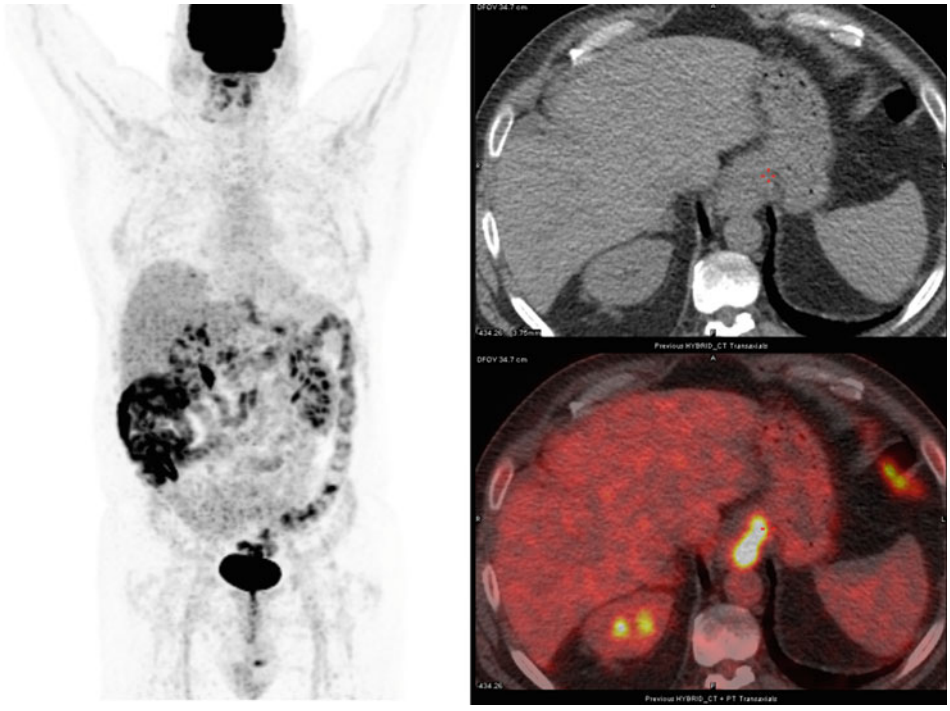

Fig. 6 Post-chemoradiation [^{18}F]FDG PET/CT shows a very significant response of the esophagus lesion that presents markedly reduced size and metabolic activity

Esophageal Cancer: Case No. 3

Presentation

A 60-year-old man with a proximal esophageal carcinoma and severe dysphagia underwent a chemoradiation treatment for primary palliative purpose. [^{18}F]FDG PET/CT was planned to be performed at staging and for monitoring treatment efficacy.

Findings

The first PET/CT before therapy disclosed a [^{18}F]FDG-avid lesion (SUV_{max} 27.2) of the proximal esophagus with a gross hyperactive right paraesophageal node (Fig. 7). Since the patient presented an increasingly severe dysphagia, he underwent percutaneous endoscopic gastrostomy (PEG) during treatment. After chemoradiation was completed, [^{18}F]FDG PET/CT showed a response to therapy of both the lesion of the proximal esophagus and the paraesophageal lymphadenopathy that presented a significant reduced size and metabolic activity (Fig. 8).

Follow-Up

It was decided to follow up the patient and to perform a new PET/CT evaluation after 3 months. Follow-up PET/CT disclosed a disease progression by revealing an increased size and metabolic activity of the primary esophagus lesion (SUVmax 14 versus 9) and of the paraesophageal lymphadenopathy. Moreover, several right superior paratracheal and right supraclavicular [^{18}F]FDG-avid nodes were found. Diffuse uptake of [^{18}F]FDG was detectable within the left clavicle related to a recent traumatic fracture (Fig. 9). A subsequent ceCT confirmed the local and nodal progression of the disease.

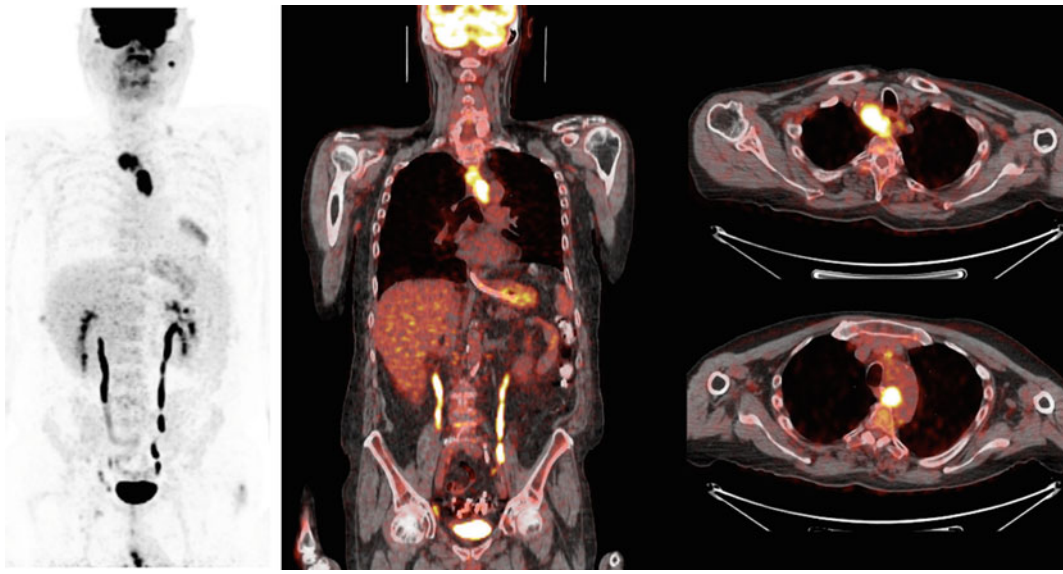

Fig. 7 [^{18}F]FDG MIP and fused coronal, sagittal, and axial PET/CT show a proximal esophagus lesion with a high [^{18}F]FDG uptake. Moreover, a right paraesophageal node [^{18}F]FDG can be observed in MIP and fused coronal and axial slices. An area of focal hyperactivity consistent with a left submandibular lymphadenopathy can be also observed

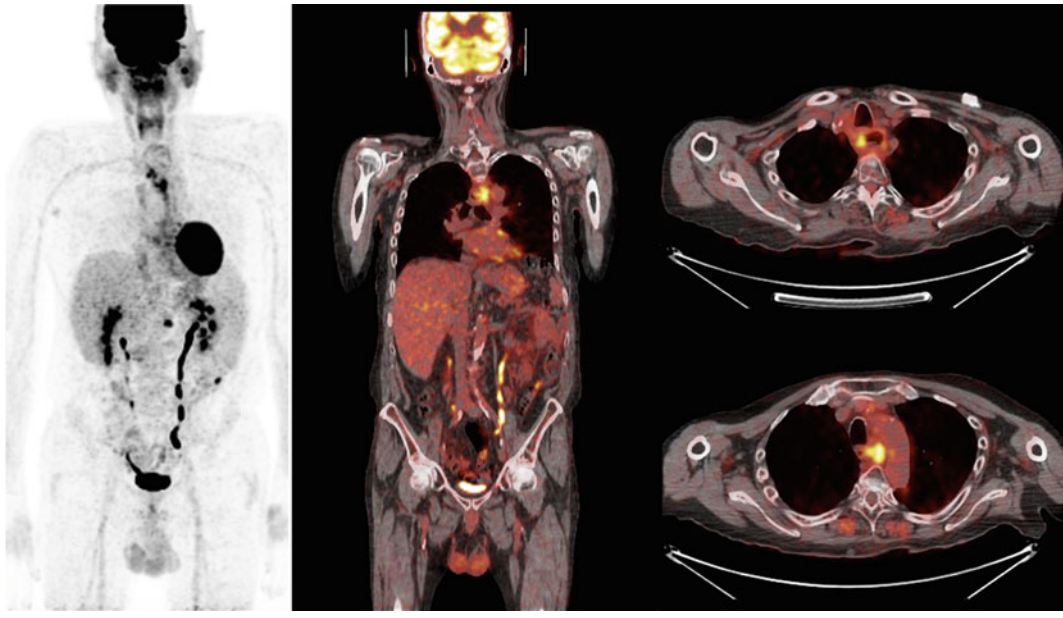

Fig. 8 [^{18}F]FDG MIP and fused coronal, sagittal, and axial PET/CT show a good response to chemoradiation with reduced size and metabolic activity of both the esophagus lesion and the paraesophageal lymphadenopathy. No submandibular lymphadenopathy is detectable. The epigastric area of hyperactivity consistent with recent positioning of PEG

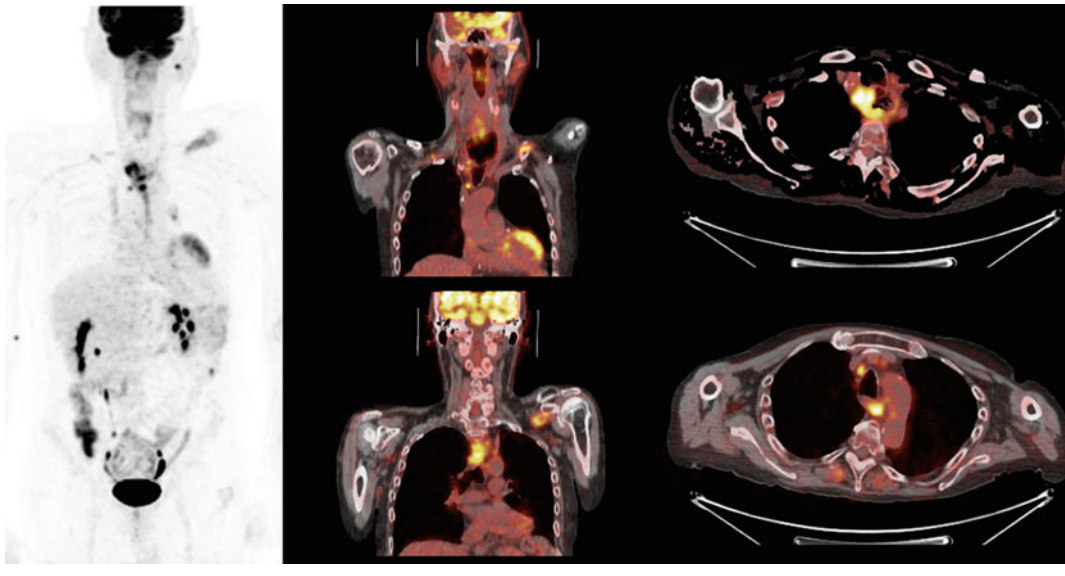

Fig. 9 [^{18}F]FDG MIP and fused coronal, sagittal, and axial PET/CT show increased size and metabolic activity of both the proximal esophagus lesion and the paraesophageal lymphadenopathy. Fused coronal and axial slices reveal right superior paratracheal and right supraclavicular small [^{18}F]FDG-avid nodes. Fused coronal slices show [^{18}F]FDG within the left clavicle related to a traumatic fracture. MIP image shows the recurrence of the left submandibular lymphadenopathy

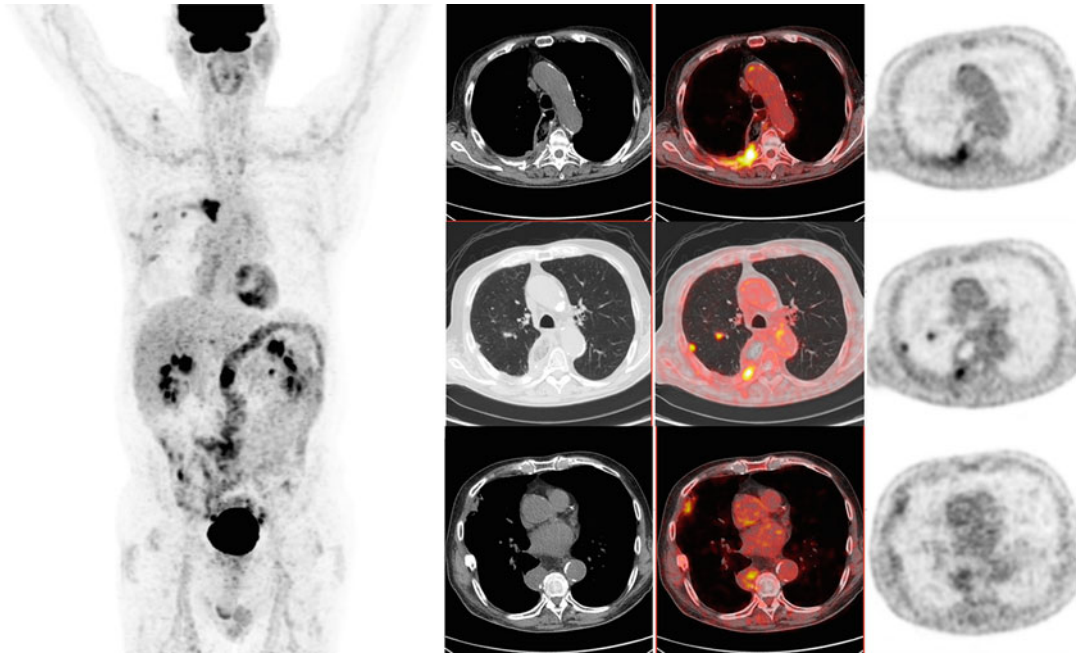

Fig. 10 PET/CT performed 3 months after surgery. [^{18}F]FDG MIP and CT, fused and PET axial slices show some [^{18}F]FDG-avid thickenings of the pleura. The most evident area is detectable on *top* axial slices within the *right* costovertebral space. Middle axial slices show two lung nodules in the *right* lung

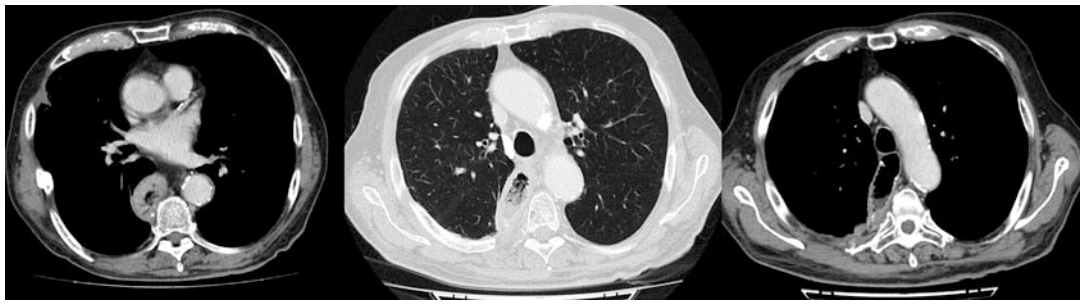

Fig. 11 Contrast-enhanced CT axial slices do not show any finding consistent with disease relapse. Axial slice on the *left* shows a small pleural perifissural thickening

Teaching Points

In this case [^{18}F]FDG PET/CT has been successfully used for staging, therapy monitoring, and following up a patient with advanced esophageal carcinoma.

Esophageal Cancer: Case No. 4

Presentation

A 73-year-old man with an early stage distal esophageal carcinoma already submitted to surgery.

Findings

After 3 months from esophagectomy, restaging PET/CT disclosed [^{18}F]FDG hyperactivity at the level of some thickening of the pleura, the most evident in the costovertebral space, and of some lung nodules in the medium and right inferior lobes (Fig. 10). These findings of uncertain interpretation suggested a subsequent investigation with a ceCT. CT was performed 1 month later and showed the regression of most of the PET/CT findings (Fig. 11).

Fig. 12 Follow-up contrast-enhanced CT. Axial slices confirm no finding consistent with disease relapse

Fig. 13 On *top panels*, CT shows multiple lymphadenopathies within the neck, mediastinum, and abdomen, most of them less than 1 cm. On *bottom panels*, axial, coronal, and sagittal CT slices, a circumferential thickening of the distal esophagus consistent with a primary esophageal cancer

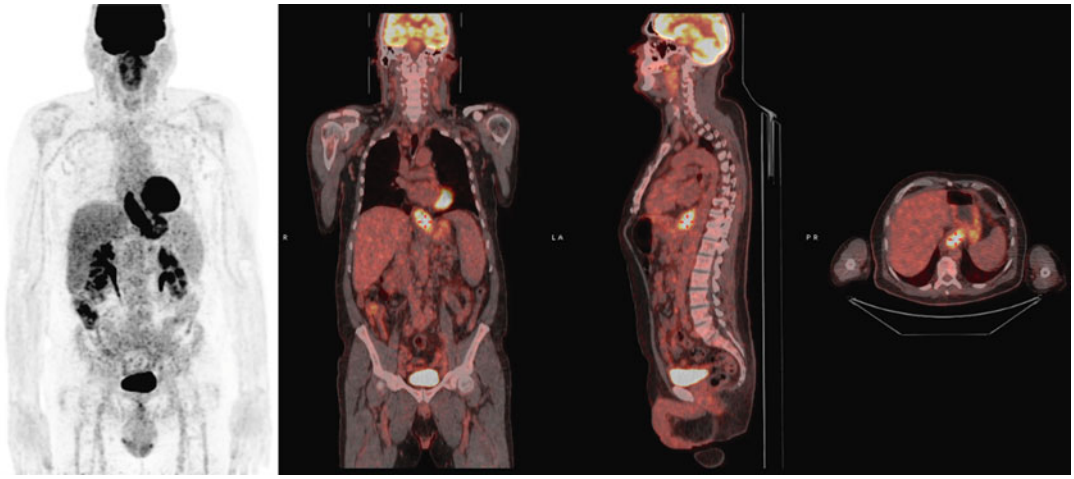

Fig. 14 [^{18}F]FDG MIP and fused coronal, sagittal, and axial PET/CT show a [^{18}F]FDG avid involving the distal esophagus

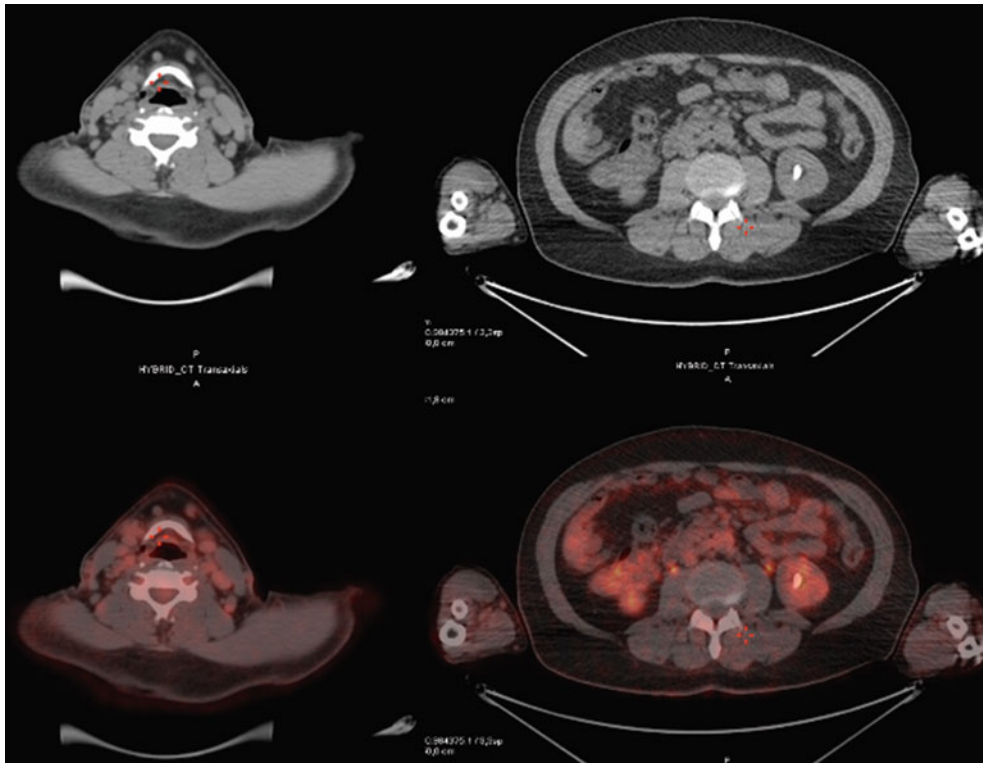

Fig. 15 CT and fused [^{18}F]FDG PET/CT axial slices multiple laterocervical and abdominal lymph nodes with low-grade tracer uptake

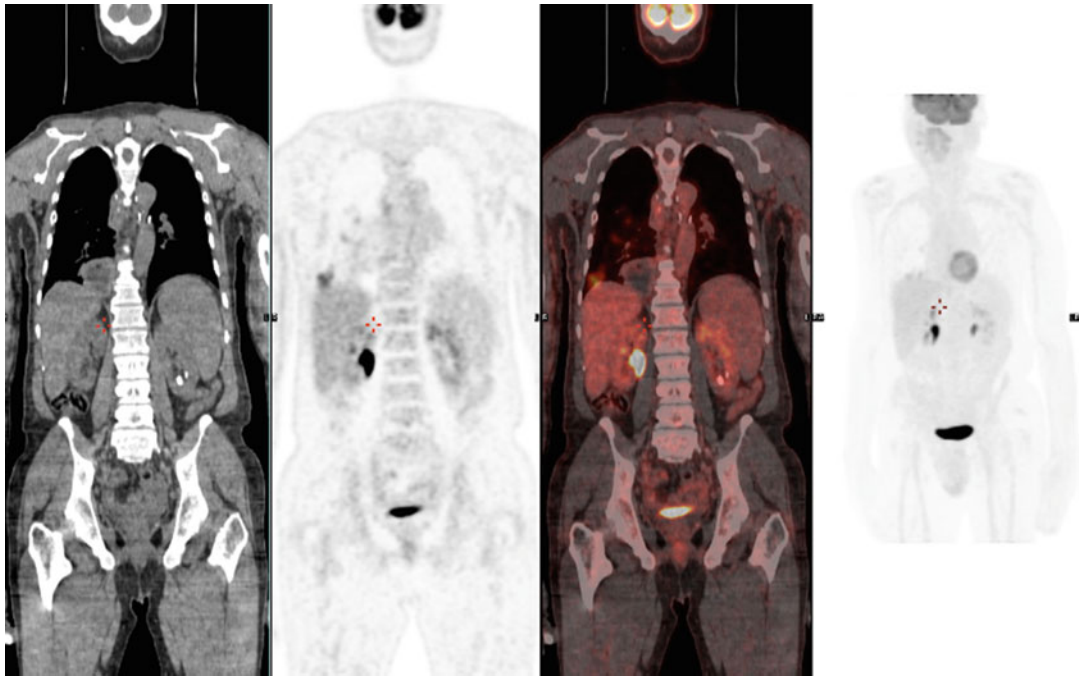

Fig. 16 PET/CT performed after esophagectomy. [^{18}F]FDG MIP image and coronal CT, fused PET/CT, and PET slices showing no hypermetabolic lesions within the residual esophagus. Moreover, no [^{18}F]FDG-avid lymph nodes nor liver lesions are detectable

Follow-Up

After 3 months the patient underwent a new CT evaluation that confirmed the complete disappearance the findings interpreted as postoperative sequelae. CT did not show any other abnormalities within the pleura, mediastinum, and lungs (Fig. 12).

Teaching Points

Esophagectomy may be the initial treatment in early stage esophageal cancers. In the period following this major surgery, phlogistic sequelae can occur producing possible false-positive results at [^{18}F]FDG PET/CT. For this reason there must be cautious interpretation of findings.

Esophageal Cancer: Case No. 5

Presentation

A 59-year-old man with a suspected lymphoproliferative disease underwent a whole body ceCT.

Findings

CT showed the presence of multiple lymphadenopathies within the neck, mediastinum, and abdomen, many of them with size less than 1 cm. As unexpected finding, a circumferential thickening of the distal esophagus was observed consistent with a primary tumor of the esophagus (Fig. 13).

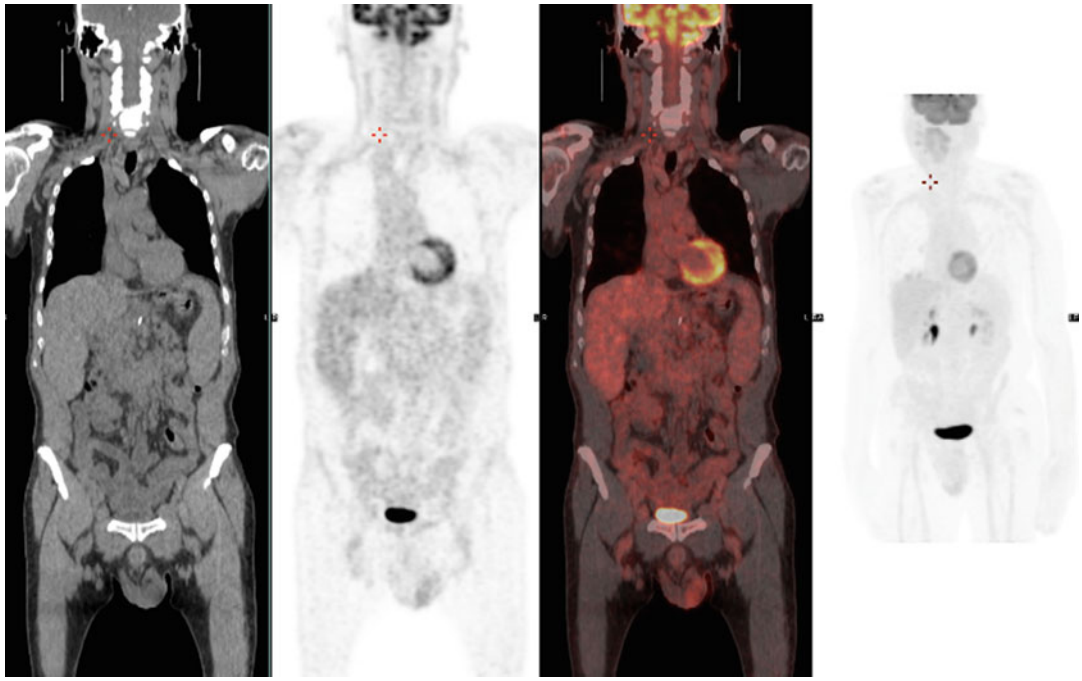

Fig. 17 PET/CT performed after esophagectomy. [^{18}F]FDG MIP image and coronal CT, fused PET/CT, and PET slices showing supra- and subdiaphragmatic non-[^{18}F]FDG-avid lymph nodes consistent with stable CLL/SLL

Follow-Up

The patient underwent lymph node and bone marrow biopsy that revealed a chronic lymphocytic leukemia/small lymphocytic lymphoma (CLL/SLL). Moreover, EGDS confirmed the presence of a neoplasia of the distal esophagus that at pathology resulted in a squamous cell carcinoma. A PET/CT was performed to complete the staging of the esophageal carcinoma and an assessment of the CLL/SLL.

PET/CT disclosed a gross [^{18}F]FDG-avid lesion (SUV_{max} 17.7) that involved the distal esophagus (Fig. 14). Multiple supra- and subdiaphragmatic lymph nodes were observed with a very low grade of [^{18}F]FDG uptake (Fig. 15).

The patient underwent esophagectomy and after 6 months repeated a PET/CT investigation.

No hypermetabolic lesions were observed within the residual esophagus, and no [^{18}F]FDG-avid lymph nodes nor liver lesions were found. Some areas of mild hyperactivity were seen within the right pleura as surgery outcome (Fig. 16). Multiple supra- and subdiaphragmatic non-[^{18}F]FDG-avid lymph nodes were substantially unchanged compared to the first PET/CT evaluation (Fig. 17).

Teaching Points

A second primary may occur. In this case while the esophageal carcinoma was highly [^{18}F]FDG avid, as expected, CLL/SLL presented a low uptake of [^{18}F]FDG which is usually related to a slow disease progression.

Teaching Cases in Nuclear Oncology: Gastric Cancers

62

Duccio Volterrani, Giulia Puccini, Sara Mazzarri, and Federica Guidoccio

Keywords

Gastric cancer • [^{18}F]FDG PET/CT • ceCT • Neoadiuvant chemotherapy • Metabolic response • ^{99m}Tc-labelled red blood cell scintigraphy • Lymph node disease • Distant disease

Glossary

[^{18}F]FDG	2-Deoxy-2-[^{18}F]fluoro-D-glucose
AJCC	American Joint Committee on Cancer
ceCT	Contrast-enhanced computed tomography
CT	X-ray computed tomography
M	Metastasis status according to the AJCC/UICC TNM staging system
MIP	Maximum intensity projection
N	Lymph node status according to the AJCC/UICC TNM staging system
PET	Positron emission tomography
PET/CT	Positron emission tomography/Computed tomography
SPECT	Single-photon emission computed tomography
SPECT/CT	Single-photon emission computed tomography/Computed tomography
SUV	Standardized uptake value
SUV_{max}	Standardized uptake value at point of maximum
T	Tumor status according to the AJCC/UICC staging system
UICC	Union Internationale Contre le Cancer (International Union Against Cancer)

Contents

Gastric Cancer: Case No. 1 1656
Presentation 1656
Findings 1656
Follow-Up 1657
Teaching Points 1657

Gastric Cancer: Case No. 2 1657
Presentation 1657
Findings 1657
Management 1659
Teaching Points 1659

Gastric Cancer: Case No. 3 1659
Presentation 1659
Findings 1659
Follow-Up 1660
Teaching Point 1660

Gastric Cancer: Case No. 4 1660
Presentation 1660
Findings 1660
Follow-Up 1662
Teaching Points 1662

D. Volterrani (✉) • G. Puccini • S. Mazzarri • F. Guidoccio
Regional Center of Nuclear Medicine, Department of Translational Research and Advanced Technologies in Medicine and Surgery, University of Pisa, Pisa, Italy
e-mail: duccio.volterrani@med.unipi.it

© Springer International Publishing Switzerland 2017
H.W. Strauss et al. (eds.), *Nuclear Oncology*,
https://doi.org/10.1007/978-3-319-26236-9_65

Gastric Cancer: Case No. 5 1663
Presentation 1663
Findings 1663
Follow-Up 1664
Teaching Point 1665

Gastric Cancer: Case No. 1

Presentation

A 55-year-old man presented with abdominal discomfort over the last 5 months.

Findings

CT scan of the abdomen revealed no abnormalities. Further evaluation with esophago-gastroduodenoscopy revealed a gastric ulcer in the lesser curvature. Biopsies showed a poorly differentiated adenocarcinoma of the stomach with signet-cell rings. [^{18}F]FDG PET/CT scan was performed as a part of initial staging (Fig. 1). PET/CT images demonstrate the presence of a metabolically active mass in the body of the stomach, consistent with a primary carcinoma. Hypermetabolic lymph nodes are seen medially

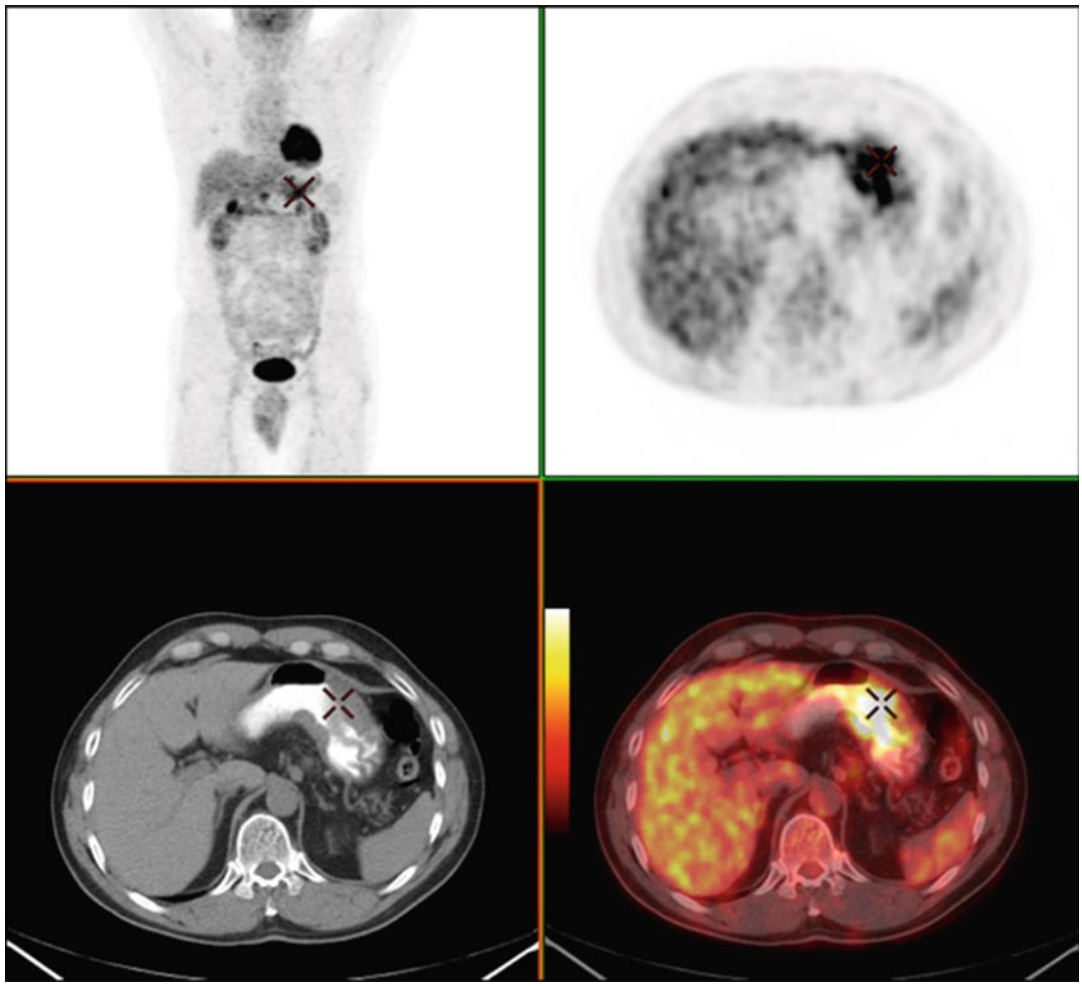

Fig. 1 [^{18}F]FDG PET/CT images demonstrate hypermetabolic lesion in the stomach body (marked by the *red cross*). MIP (*left upper*), [^{18}F]FDG axial (*right upper*), CT axial (*left lower*), and PET/CT fused images (*right lower*)

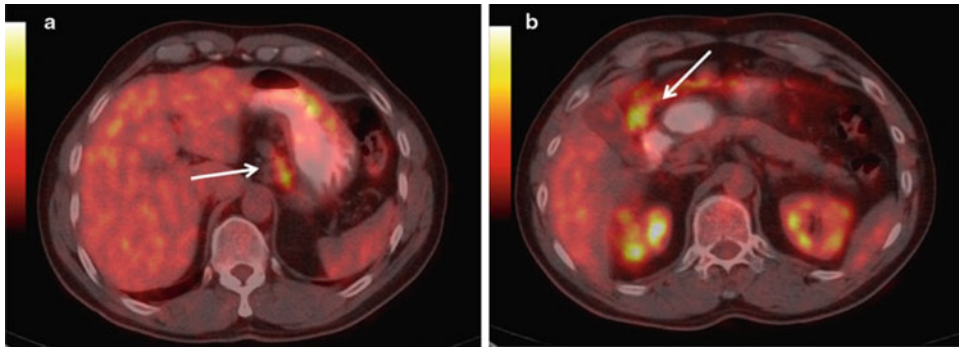

Fig. 2 [^{18}F]FDG PET/CT transaxial fused images. (**a**) Metabolically active lymph nodes medial to the stomach (*white arrow*). (**b**) Hypermetabolic peritoneal nodule (*white arrow*)

to the stomach (Fig. 2a). [^{18}F]FDG-avid peritoneal nodules adjacent to the left lobe liver and medial to the gallbladder (Fig. 2b) are also seen. Laparoscopy confirmed the presence of a locally advanced gastric tumor with regional lymph node involvement and peritoneal disease (TNM Stage IV). The patient was treated with chemotherapy.

Follow-Up

Follow-up [^{18}F]FDG PET/CT at 3 months after chemotherapy demonstrated a reduced SUV_{max} (2.9 versus 5.8) and reduced size of the gastric lesion (Fig. 3a). No [^{18}F]FDG uptake was seen in lymph nodes or peritoneal disease (Fig. 3b).

Teaching Points

Although the sensitivity of [^{18}F]FDG PET/CT is reduced in many mucinous tumors of the stomach, poorly differentiated tumors are often [^{18}F]FDG avid. This case demonstrates the usefulness of [^{18}F]FDG PET/CT both at initial staging (which showed metastatic disease in lymph nodes and peritoneum) and for monitoring the efficacy of therapy.

Gastric Cancer: Case No. 2

Presentation

Male patient 67 years old suffering from a stage III gastric cancer undergoing neoadjuvant preoperative chemotherapy (last cycle completed since about 20 days)

Findings

The patient underwent a ceCT that disclosed diffused thickening of the gastric walls with involvement of the perigastric adipose tissue where fine micronodules were clearly visible. Findings were consistent with *linitis plastica* (Fig. 4).

The patient had an [^{18}F]FDG PET/CT scan which showed diffuse metabolic hyperactivity that affects all the gastric walls and the perigastric adipose tissue (SUV_{max} 6.4). No additional significant findings were detected (Fig. 5).

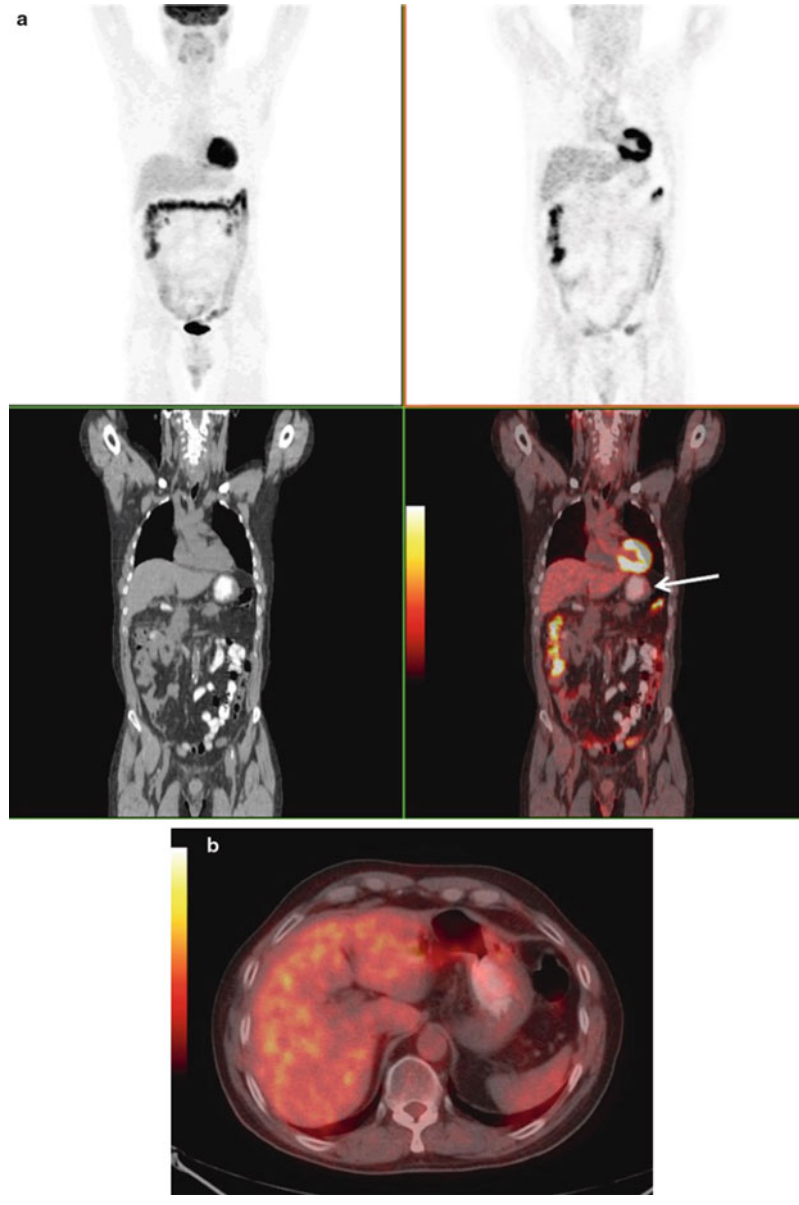

Fig. 3 (**a**) [^{18}F]FDG PET/CT (MIP and coronal images) shows reduction of the radiotracer uptake (*white arrow*) in gastric lesion after chemotherapy (*left upper* MIP, *right upper* PET, *left lower* CT, *right lower* PET/CT fused image). (**b**) Fused axial PET/CT image centered on the gastric body

Management

A second-line chemotherapy regimen was started.

Teaching Points

[^{18}F]FDG PET/CT can be used to assess the metabolic response of gastric cancer to neoadjuvant or adjuvant chemotherapy. In case of locally advanced stages, PET/CT is considered a very sensitive tool for detecting distant metastases.

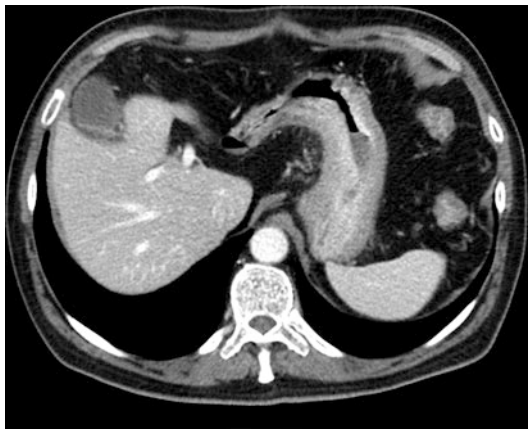

Fig. 4 Axial slice of ceCT shows diffuse thickening of the gastric walls (1.5 cm) that present contrast enhancement persistent in the late phase. Thickened perigastric adipose tissue with small micronodules is detectable

Gastric Cancer: Case No. 3

Presentation

Patient with gastric cancer treated with subtotal gastrectomy. Two years later, appearance of a bone metastasis treated with radiotherapy. After 6 months the patient underwent an [^{18}F]FDG PET/CT for restaging.

Findings

[^{18}F]FDG PET/CT showed multiple areas of hyperactivity within several bone segments (spine, sternum, scapula, ribs, pelvis, humeri, and femurs) (Fig. 6). Moreover, a focal area of increased [^{18}F]FDG uptake was found in the abdomen, close to the enteric anastomosis (Fig. 7). Findings were consistent with diffused secondary bone involvement and with the suspected presence of locoregional recurrence.

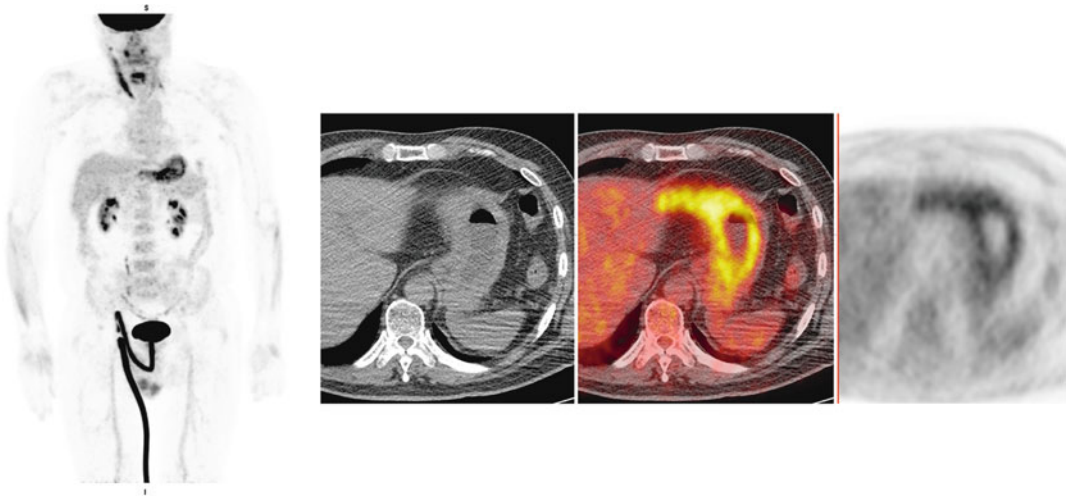

Fig. 5 [^{18}F]FDG PET/CT (MIP and axial slices) shows diffused metabolic hyperactivity of the stomach walls that appear clearly thickened (SUV_{max} 6.4). Moreover, [^{18}F]FDG increased uptake extends to the perigastric adipose tissue. MIP (on the *left*) does not show any other significant [^{18}F]FDG-avid site consistent with the presence of metastases

Fig. 6 [^{18}F]FDG PET/CT MIP image showing multiple areas of hyperactivity referable mainly to metastases of the spine, sternum, scapula, ribs, pelvis, humeri, and femurs

After 4 days the patient underwent a ceCT in emergency for acute anemia. CT confirmed multiple bone metastases, but did not disclose any significant finding in the abdomen, nor site of bleeding (Fig. 8). On the next day a gastrointestinal bleeding scintigraphy with red blood cells labeled in vivo with ^{99m}Tc was performed. Planar and SPECT/CT images disclosed a focal accumulation of activity in the upper-left abdominal quadrant, consistent with bleeding in the first tract of small bowel (Fig. 9).

Follow-Up

The patient underwent endoscopy that confirmed the anastomotic leakage with intraluminal bleeding. However, no recurrent disease was found at that level.

Teaching Point

A focal uptake of [^{18}F]FDG is not always due to the presence of tumor. In this case the focal accumulation of [^{18}F]FDG was related to an anastomotic leakage with intestinal bleeding, most likely also associated with chronic inflammation of the surrounding tissues.

Gastric Cancer: Case No. 4

Presentation

A 53-year-old man with a recent history of epigastric pain underwent an esophago-gastroduodenoscopy that revealed a cancer of the pyloric antrum of the stomach. A ceCT was performed for the staging.

Findings

ceCT showed thickening of the gastric pyloric antrum wall, associated with the presence of a lymph node (short axis 9 mm) within the immediately adjacent adipose tissue, on the right inferior side (Fig. 10). No liver nor lung nor bone metastatic disease was found.

One week later the patient underwent [^{18}F]FDG PET/CT that confirmed the presence

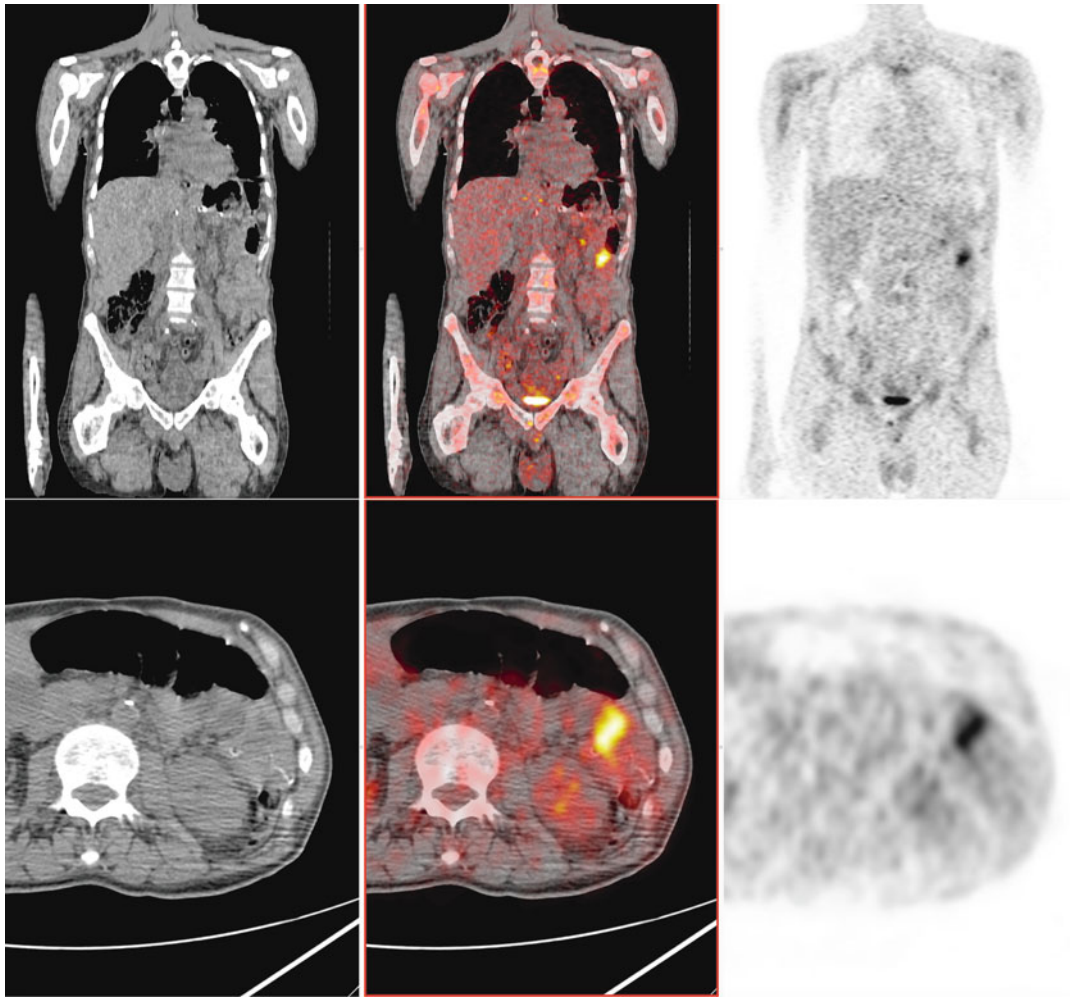

Fig. 7 [^{18}F]FDG PET/CT coronal slices (*top*) and axial slices (*bottom*) show a focal area of [^{18}F]FDG uptake close to the enteric anastomosis

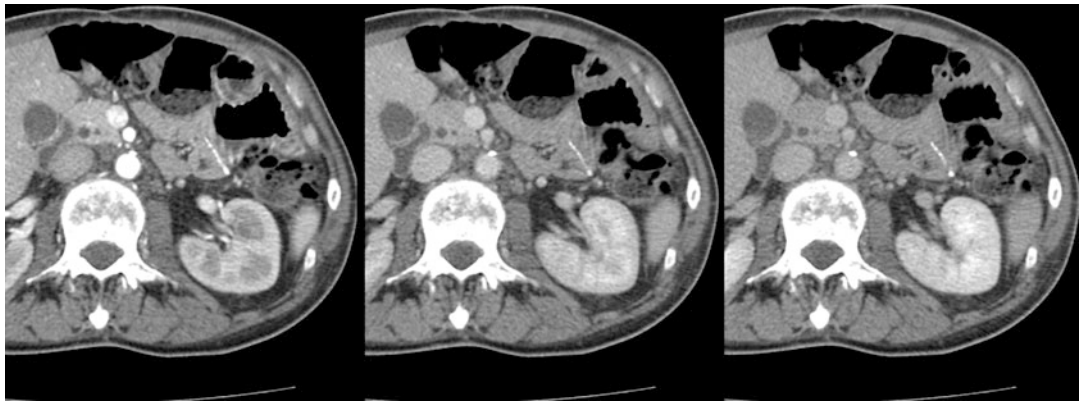

Fig. 8 CT axial slices (arterial, venous, and late phases) showing the enteric anastomosis do not disclose any finding consistent with disease relapse

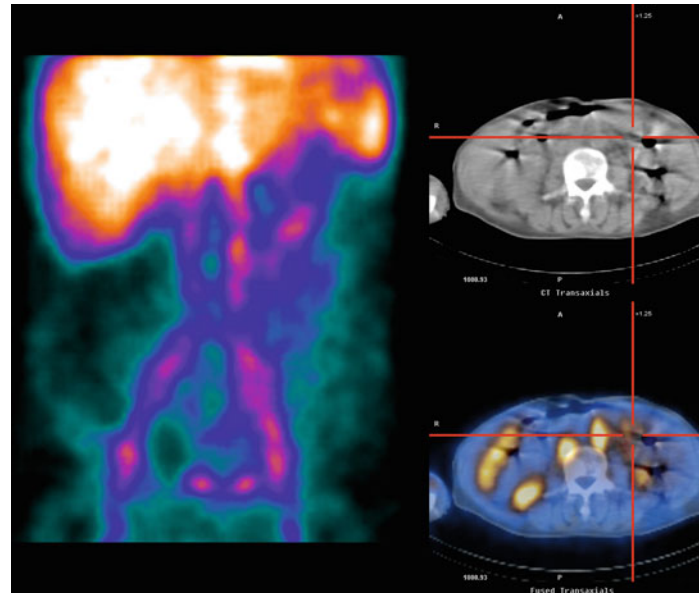

Fig. 9 ^{99m}Tc-labeled red blood cell scintigraphy reveals activity accumulation in the upper abdominal quadrant (on the *left*). SPECT/CT images (on the *right*) are consistent with low-degree bleeding from an upper small bowel loop

Fig. 10 CT axial slice (*top* panel) shows a contrast-enhanced wall thickening of the gastric pyloric antrum consistent with the presence of primary tumor. CT slice (*bottom* panel) discloses the presence of a lymph node with a short axis of 9 mm within the adipose tissue close to the right inferior side of the gastric cancer

of a hyperactive lesion (SUV_{max} 6.5) at the gastric pyloric antrum. Moreover, PET/CT found frankly increased tracer uptake (SUV_{max} 8.5) within the subpyloric lymph node disclosed by ceCT, thus confirming the presence of regional nodal disease (Fig. 11). No other [^{18}F]FDG-avid lesions in the whole body were detected.

Follow-Up

Neoadjuvant chemotherapy was started. After 3 months [^{18}F]FDG PET/CT was repeated to assess response to therapy. PET/CT disclosed a reduction in size of the gastric lesion, which however continued to exhibit high metabolic activity (SUV_{max} 6.9). However, the perigastric lymphadenopathy resulted to be completely resolved (Fig. 12).

Teaching Points

In this case PET/CT was useful to complete the staging by confirming the presence of lymph node disease in a small perigastric lymph node. [^{18}F]FDG PET/CT was also useful to assess response to chemotherapy.

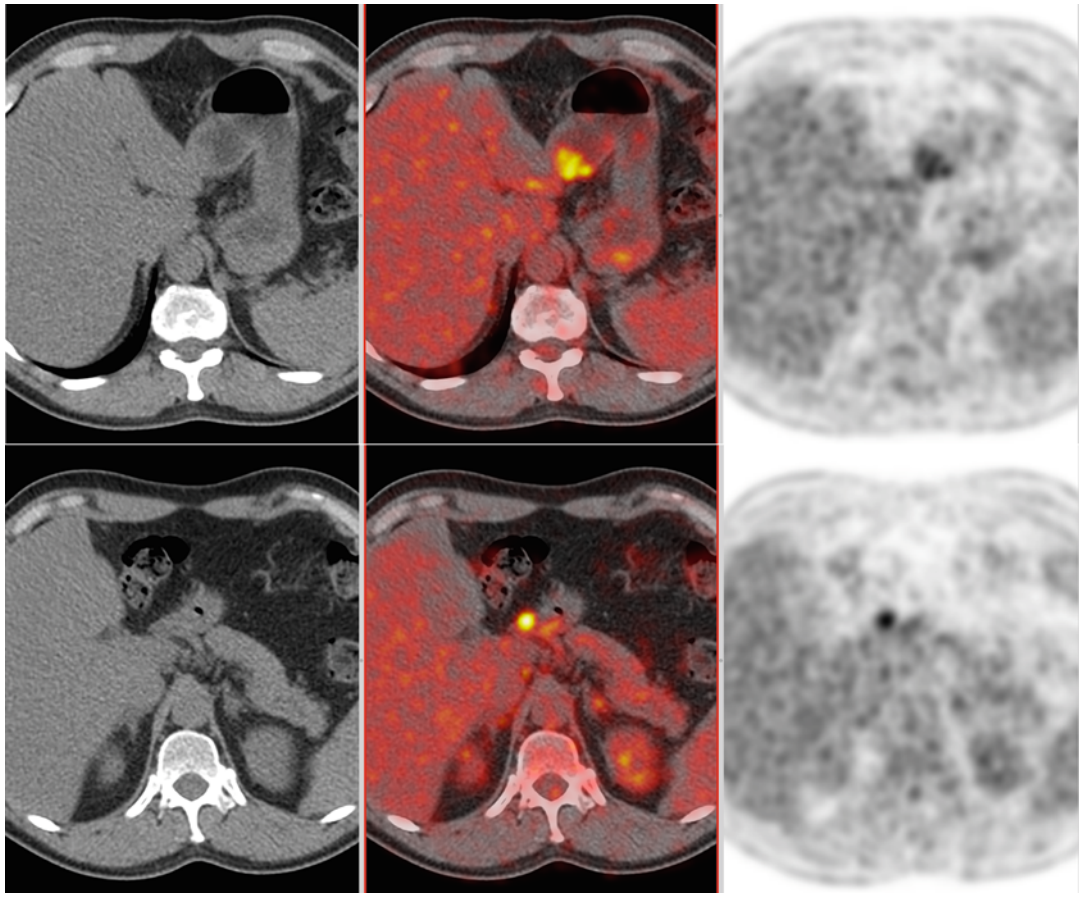

Fig. 11 [^{18}F]FDG PET/CT at staging. CT, fused [^{18}F]FDG PET/CT, and [^{18}F]FDG PET axial slices (*top* panels) show the presence of a clear hyperactive lesion (SUV_{max} 6.5) within the wall of the gastric pyloric antrum. CT, fused [^{18}F]FDG PET/CT, and [^{18}F]FDG PET axial slices (*bottom* panels) identify a significantly [^{18}F]FDG-avid subpyloric lymph node (SUV_{max} 8.5)

Gastric Cancer: Case No. 5

Presentation

A 62-year-old man complaining of heartburn, acid regurgitation, and retrosternal pain underwent esophago-gastro-duodenoscopy that revealed an adenocarcinoma of the esophagogastric junction. The patient underwent [^{18}F]FDG PET/CT for staging the disease.

Findings

PET/CT disclosed a large-size, intensely [^{18}F]FDG-avid mass (SUV_{max} 13) partially extending

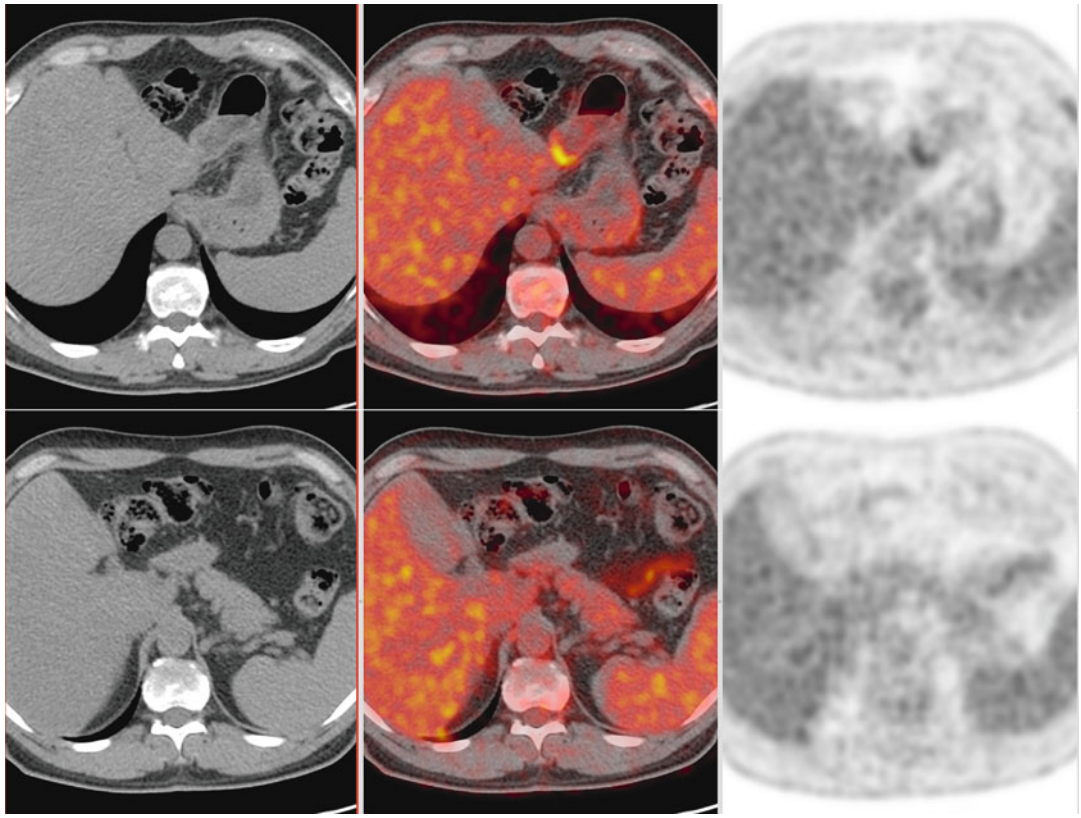

Fig. 12 [^{18}F]FDG PET/CT after neoadjuvant chemotherapy. CT, fused [^{18}F]FDG PET/CT, and [^{18}F]FDG PET axial slices (*top* panels) show the dimensional reduction of the gastric lesion which continues to present metabolic hyperactivity (SUV_{max} 6.9). No [^{18}F]FDG-avid lymph nodes are observed on CT, fused [^{18}F]FDG PET/CT, and [^{18}F]FDG PET axial slices (*bottom* panels) in the perigastric adipose tissue

from the esophagogastric junction to the lesser curvature. No abdominal nor mediastinal lymph nodes with significant [^{18}F]FDG uptake were observed, and sites of distant metastasis were not detected (Fig. 13).

Follow-Up

Although no locoregional nor distant disease was disclosed by PET/CT, nevertheless preoperative neoadjuvant chemotherapy was started, mostly based on the intense uptake of [^{18}F]FDG in the tumor lesion.

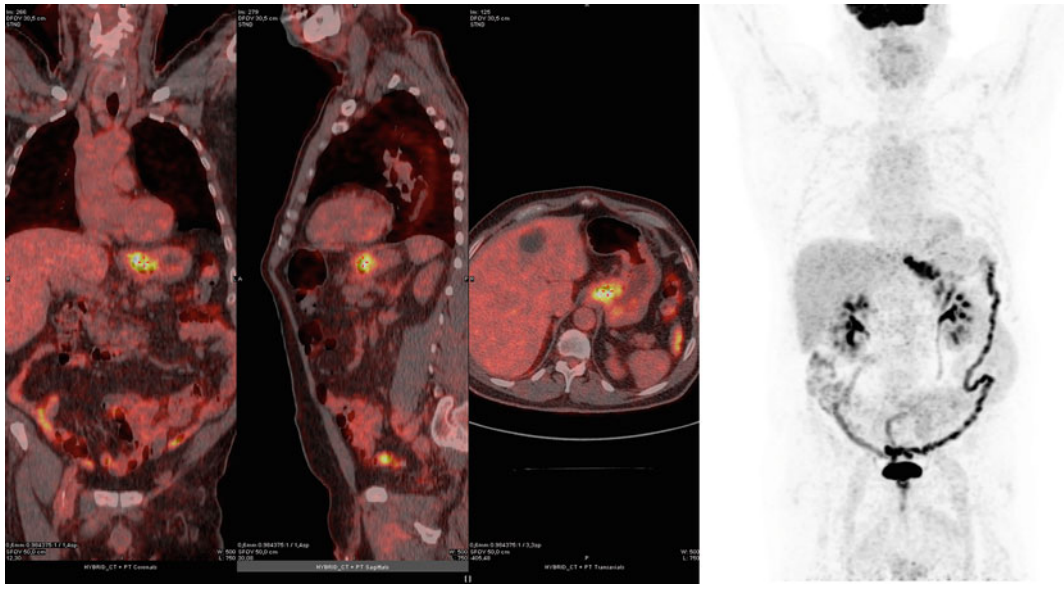

Fig. 13 [^{18}F]FDG fused PET/CT coronal, sagittal, and axial slices on the *left*. PET MIP image on the *right*. An avid mass (SUV_{max} 13) partially extending from the esophagogastric junction to the lesser curvature is clearly visible. No abdominal nor mediastinic lymph nodes nor distant metastases with significant [^{18}F]FDG uptake

Teaching Point

The standard primary treatment for junction and gastric cancer is surgical resection. Since the rate of locoregional and distant recurrences is high, multimodal neoadjuvant therapy is often suggested before surgery. [^{18}F]FDG PET/CT is considered a sensitive and specific tool for the preoperative staging of the esophagogastric junction cancer, especially for distant metastases. The intensity of [^{18}F]FDG uptake has a definite prognostic value and can be the basis for choosing the most appropriate initial management of the disease.

Teaching Cases in Nuclear Oncology: Small Bowel Cancers

63

Duccio Volterrani, Giulia Puccini, Sara Mazzarri, and Federica Guidoccio

Keywords

[^{18}F]FDG PET • MRI • US • GIST • Midgut NET • ^{68}Ga-DOTATATE • PET/MRI • ^{111}In-pentetreotide • ^{18}F-DOPA

Glossary

[^{18}F]FDG	2-Deoxy-2-[^{18}F]fluoro-D-glucose
^{18}F-DOPA	– 2-^{18}F-Fluoro-L-3,4-dihydroxyphenylalanine
c-KIT	A proto-oncogene encoding for tyrosine-protein kinase Kit (or CD117), also known as mast/stem cell growth factor receptor (SCFR)
CT	X-ray computed tomography
DOTA	1,4,7,10-Tetraazacyclo-dodecane-1,4,7,10-tetraacetic acid
DOTATATE	DOTA-Tyr^3-octreotate
GIST	Gastrointestinal stromal tumor
MIP	Maximum intensity projection
MR	Magnetic resonance
MRI	Magnetic resonance imaging
MRI	Magnetic resonance imaging
NET	Neuroendocrine tumor
NF	Neurofibromatosis
PET	Positron emission tomography
PET/CT	Positron emission tomography/Computed tomography
PET/MRI	Positron emission tomography/Magnetic resonance imaging
SPECT	Single-photon emission computed tomography
SPECT/CT	Single-photon emission computed tomography/Computed tomography
SUV	Standardized uptake value
SUV_{max}	Standardized uptake value at point of maximum
US	Ultrasonography

Contents

Small Bowel Tumors: Case No. 1 1668
Presentation 1668
Findings 1668
Management 1668
Teaching Points 1668

Small Bowel Tumors: Case No. 2 1668
Presentation 1668
Findings 1668
Follow-Up 1670
Teaching Points 1670

Small Bowel Tumors: Case No. 3 1670
Presentation 1671
Findings 1671

D. Volterrani (✉) • G. Puccini • S. Mazzarri • F. Guidoccio
Regional Center of Nuclear Medicine, Department of Translational Research and Advanced Technologies in Medicine and Surgery, University of Pisa, Pisa, Italy
e-mail: duccio.volterrani@med.unipi.it

© Springer International Publishing Switzerland 2017
H.W. Strauss et al. (eds.), *Nuclear Oncology*,
https://doi.org/10.1007/978-3-319-26236-9_66

Discussion 1671
Teaching Points 1671

Small Bowel Tumors: Case No. 4 1671
Presentation 1672
Findings 1672

Discussion 1673

Small Bowel Tumors: Case No. 5 1673
Presentation 1673
Findings 1674
Follow-Up 1675

Discussion 1675

Small Bowel Tumors: Case No. 6 1676
Presentation 1676
Findings 1676
Follow-Up 1676
Teaching Points 1676

Small Bowel Tumors: Case No. 7 1678
Presentation 1678
Findings 1678
Follow-Up 1679
Teaching Point 1680

Small Bowel Tumors: Case No. 1

Presentation

A 40-year-old woman suffering from abdominal pain underwent US which disclosed a gross mass in the pelvis. An MRI was then performed which showed a mass with polylobate morphology, 12 × 7.7 × 6.5 cm, occupying the pelvic cavity, localized above the bladder, in front of the uterus, and displacing some loops of small intestine. Such tumefaction showed inhomogeneous signal for the presence of fat inhomogeneous component and coarse calcified formations in its context suggesting a teratoma (Fig. 1). The patient underwent surgery and pathology revealed a GIST originating from the small bowel. After 4 months a disease relapse was suspected, and the patient underwent a [^{18}F]FDG PET/CT for restaging.

Findings

Positron emission tomography/computed tomography (PET/CT) showed the presence of two gross [^{18}F]FDG-avid masses (SUV_{max} 7–8) within the pelvis. The first tumefaction resulted more anterior in the left iliac fossa and the other one between the rectum and uterus (Fig. 2). As PET/CT confirmed the disease relapse, the patient was started to therapy with a tyrosine kinase inhibitor.

After 15 days a second PET/CT was performed to assess therapy response.

PET/CT during therapy revealed a significant reduction of tracer uptake (SUV_{max} 4) within the mass in the left iliac fossa that however did not present change in size. A more inhomogeneous [^{18}F]FDG uptake was also found also in the mass located between the rectum and uterus that appeared to present a softer aspect (Fig. 3).

Management

The patient continued treatment with tyrosine kinase inhibitor.

Teaching Points

[^{18}F]FDG PET/CT is well known to be a sensitive tool in detecting early response to tyrosine kinase inhibitors in GIST.

Small Bowel Tumors: Case No. 2

Presentation

Patient with acute episode of pancreatitis and suspected mesenteric fibromatosis. MRI detection of mesenteric nodule in the right quadrants of the abdomen. Patient underwent [^{18}F]FDG PET/CT.

Findings

PET/CT images showed an [^{18}F]FDG-avid mesenteric lesion in the lower right paramedian mesogastric region (SUV_{max} 5.6). Some peritoneal nodule without significant accumulation of [^{18}F]FDG was found. No other significant areas of [^{18}F]FDG hyperactivity were observed in the whole body (Fig. 4).

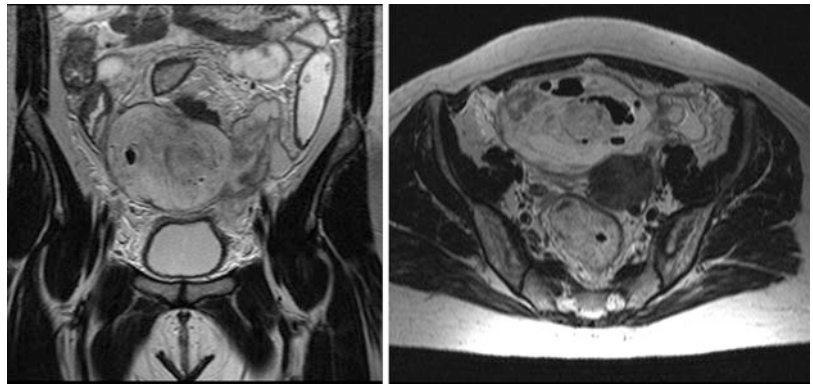

Fig. 1 MRI coronal and axial slices show a gross mass occupying the pelvic cavity, localized above the bladder, in front of the uterus, and displacing some loops of small intestine. Such tumefaction showed inhomogeneous signal for the presence of fat inhomogeneous component and coarse calcified formations

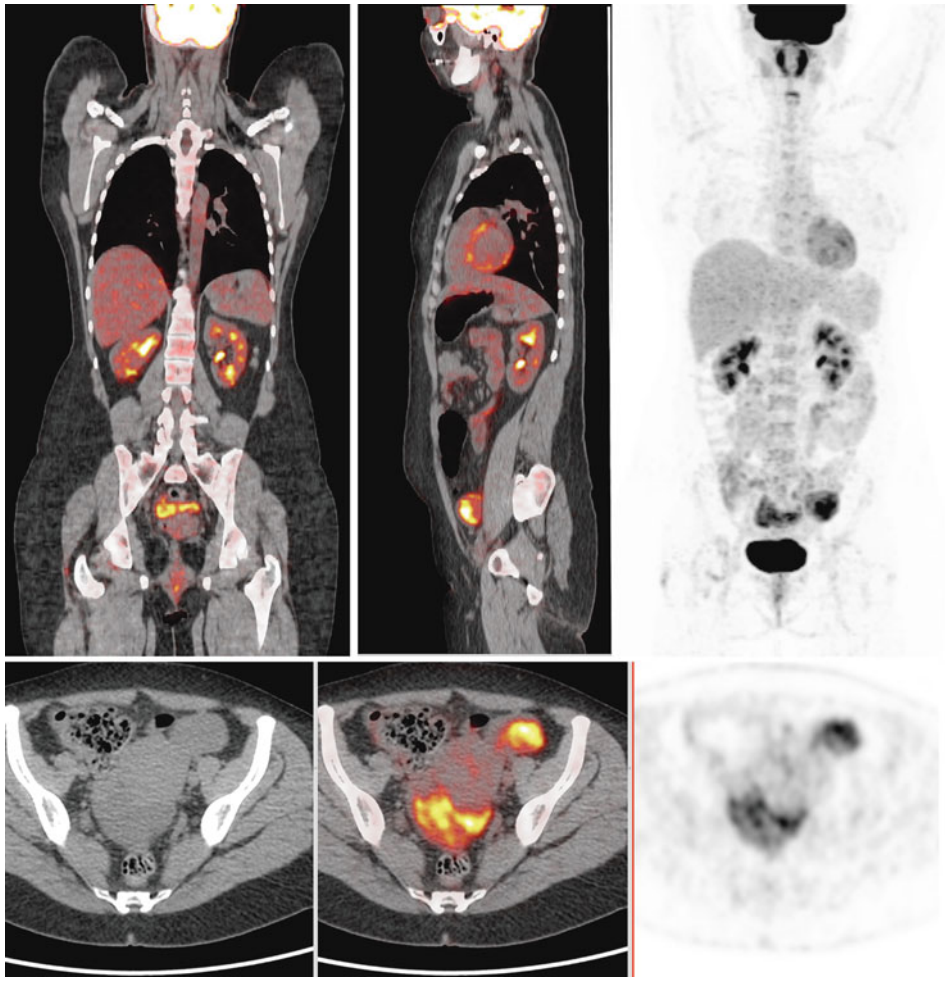

Fig. 2 Coronal and axial CT, fused PET/CT, and PET slices show two gross [^{18}F]FDG-avid masses within the pelvis. The first tumefaction results in the left iliac fossa and the other one between the rectum and uterus

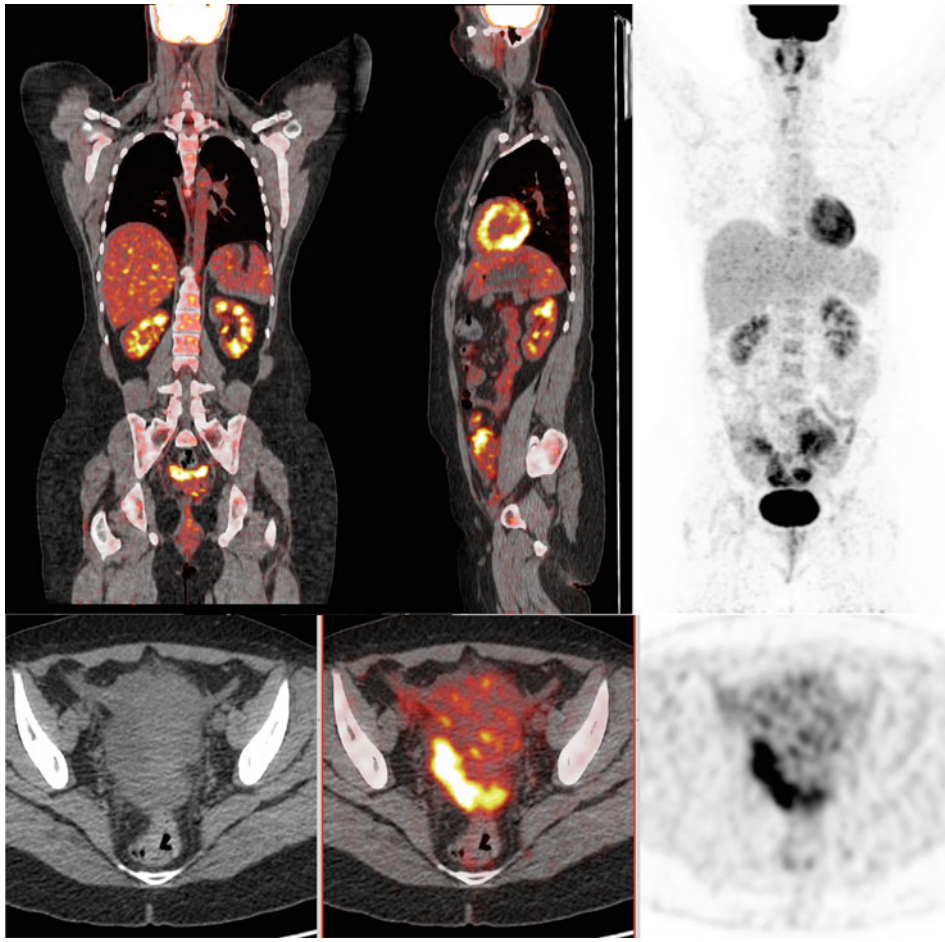

Fig. 3 Coronal and axial CT, fused PET/CT, and PET slices show a significant reduction of tracer uptake within the mass in the left iliac fossa without significant change in size. A more inhomogeneous [^{18}F]FDG uptake is detectable in the other pelvic lesion

Follow-Up

The patient underwent surgery and had a pathological diagnosis of small bowel neuroendocrine carcinoma, with nodal and peritoneal involvement.

Then the patient underwent somatostatin receptor scintigraphy with octreoscan in order to assess if persistent disease could express somatostatin receptors.

Scintigraphy showed four peritoneal nodules with a high degree of tracer uptake, one within the mesentery, one within the omentum, and two in the adipose tissue of the pelvic cavity (Fig. 5).

Teaching Points

Although neuroendocrine carcinoma tends to differentiate showing [^{18}F]FDG uptake, some lesions can preserve the expression of somatostatin receptors that can be proved by receptor scintigraphy. These information are useful for subsequent therapeutic management of patients.

Small Bowel Tumors: Case No. 3

Case contributed by: S. Al Shammari and F. Fraioli

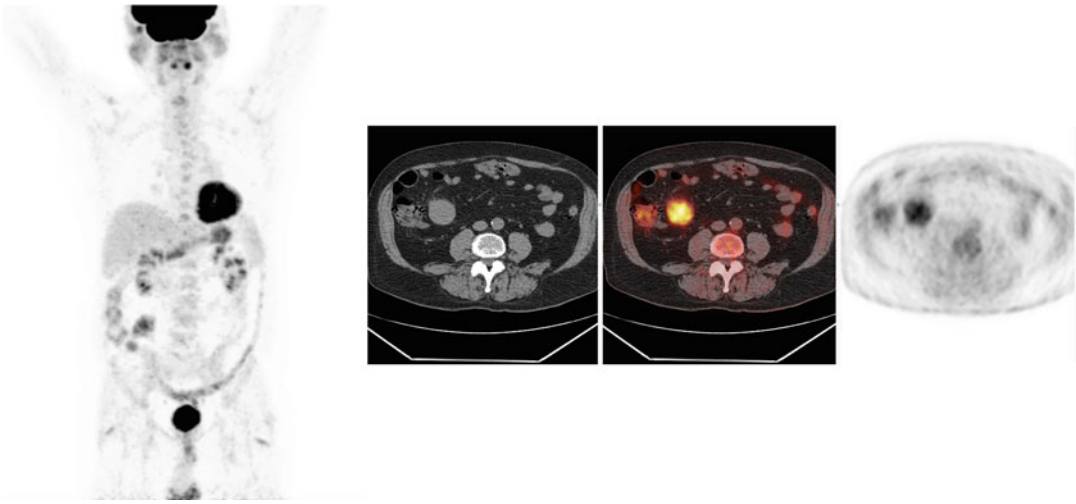

Fig. 4 [^{18}F]FDG MIP image and axial CT, fused PET/CT, and PET slices show a [^{18}F]FDG-avid mesenteric lesion in the lower right paramedian mesogastric region. No other significant areas of [^{18}F]FDG uptake can be observed

Institute of Nuclear Medicine, UCLH NHS Foundation Trust, London, UK.

Presentation

[^{18}F]FDG PET/CT for evaluation of tumor burden in a 56-year-old patient with small bowel gastrointestinal stromal tumor (GIST).

Findings

There is a large (8×9 cm) [^{18}F]FDG-avid abdominal mass (SUV_{max} 8.2) just left of the midline. Note is made of focal increased [^{18}F]FDG uptake in the right retromandibular region in keeping with a benign parotid tumor (arrow). The distribution of tracer elsewhere was within normal limits (Fig. 6).

Discussion

Gastrointestinal stromal tumors (GISTs) constitute approximately 0.1–3.0% of all gastrointestinal tract neoplasms and 6% of all sarcomas. GISTs are usually asymptomatic when less than 5 cm in their longest dimension and become symptomatic when they grow to more than 5 cm. The tumors most often arise in the stomach (70%), followed by the small intestine (20%), large intestine (5%), and esophagus (<5%). Seventy percent of GISTs are benign, and 30% are malignant. It was discovered that GIST cells of origin are probably related not to smooth muscle cells but to the cells of Cajal. Both GIST cells and cells of Cajal have been shown to express the cell surface receptor C-kit, which functions as a tyrosine kinase. A mutation of the C-kit protooncogene that activates tyrosine kinase in the absence of a stem cell factor leads to uncontrolled cell proliferation. Imatinib mesylate (Gleevec; Novartis Pharmaceuticals Corp.) acts as a tyrosine kinase inhibitor and resulted in an impressive response.

Teaching Points

[^{18}F]FDG PET helps in initial staging of malignant GISTs and early evaluation of response to therapy. Therefore, [^{18}F]FDG PET is able to predict response to imatinib mesylate therapy earlier than CT.

Small Bowel Tumors: Case No. 4

Case contributed by: S. Al Shammari and F. Fraioli

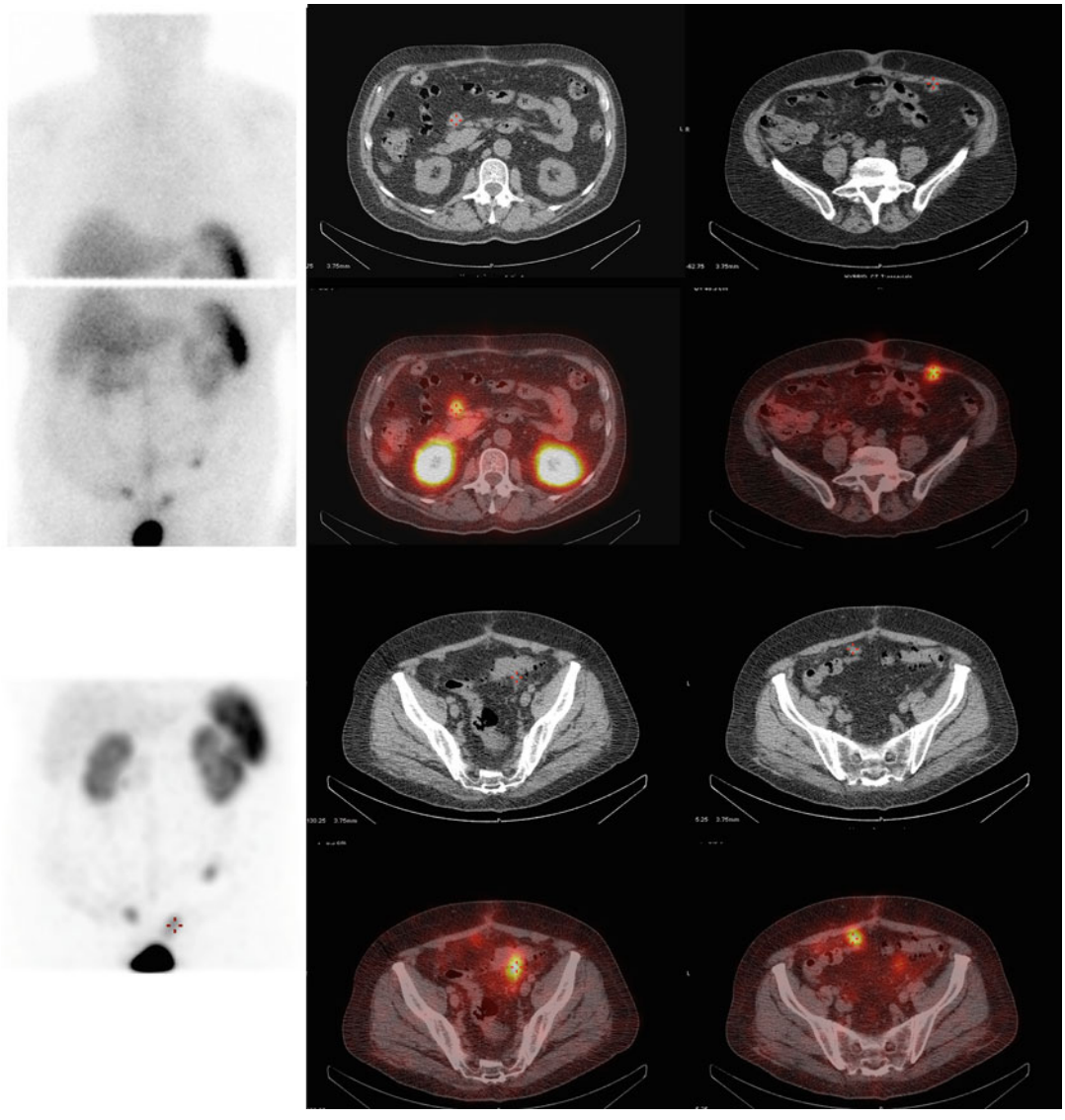

Fig. 5 Scintigraphy with Octreoscan®. Planar images and MIP image on the left. On the right axial CT and fused SPECT/CT. One nodule within the mesentery, one within the omentum, and two nodules in the adipose tissue of the pelvic cavity with a high degree of ^{111}In-pentetreotide uptake are detectable

Institute of Nuclear Medicine, UCLH NHS Foundation Trust, London, UK

Presentation

Fifty-three-year-old patient suspicious of midgut NET.

Findings

A 64-year-old man with small focus of uptake in the third portion of the duodenum.

MR post contrast images clearly show the enhancing lesion, with corresponding intense uptake at the fused ^{68}Ga-DOTATATE image (Fig. 7 a, b). PET/CT for comparison also identifies the focus of uptake (Fig. 7c).

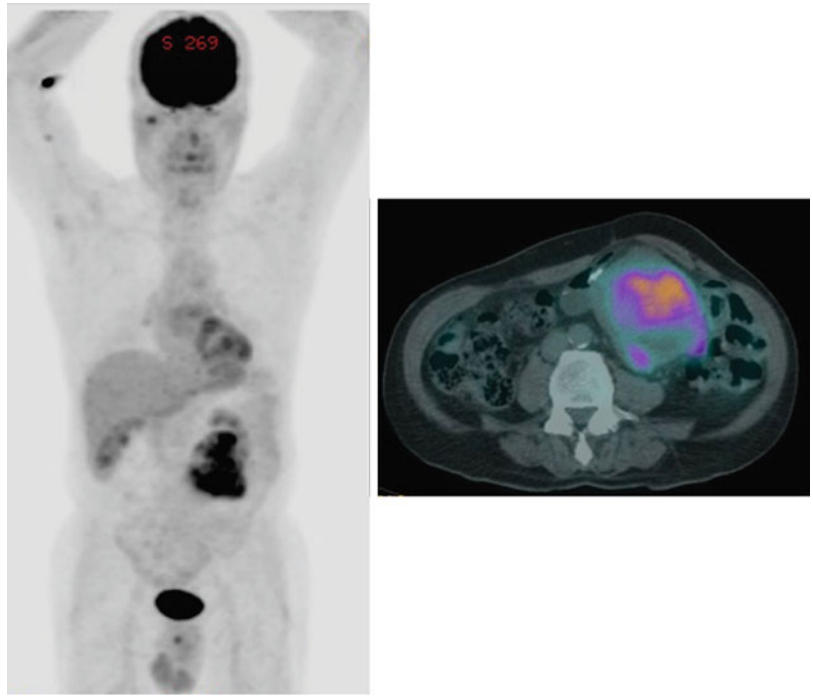

Fig. 6 [^{18}F]FDG MIP image and fused PET/CT axial slice show a large ([^{18}F]FDG-avid abdominal mass just left of the midline. A focal increased [^{18}F]FDG uptake in the right retromandibular region in keeping with a benign parotid tumor (*arrow*). Distribution of tracer elsewhere within normal limits

Discussion

The positron emitter ^{68}Ga has been linked to short peptide analogues of somatostatin analogues via bifunctionalchelate, usually 1,4,7,10-etraaza-cyclododecane-1,4,7,10-tetraacetic acid (DOTA). ^{68}Ga-DOTA-peptides have higher affinity for SSTRs as compared to conventional ^{111}In-pentetreotide. Furthermore, the relatively easy synthesis process and long half-life of the mother radionuclide ^{68}Ge (270.8 days) make it possible to use the generator for approximately 6–12 months. Positron emission tomography with ^{68}gallium (^{68}Ga)-labeled somatostatin analogues is performed for localizing and confirming the primary tumor, evaluating disease extension, monitoring treatment effects, and determining the receptor status as a predictor of response in selected patients undergoing targeted radionuclide therapy. Combined positron emission tomography/magnetic resonance imaging (PET/MRI) is a relatively new technique that has shown similar performance to positron emission tomography/computed tomography (PET/CT).

A PET/MRI solution combining gadolinium enhancement and somatostatin tracer uptake could have the potential to further improve preoperative planning and to better monitor and localize recurrence following therapy.

Small Bowel Tumors: Case No. 5

Case contributed by: V. Yerubadi, C. Sakellis, A.D. Van den Abbeele, and H. Jacene

Nuclear Medicine/PET/CT, Dana-Farber Cancer Institute, Harvard Medical School, Boston, Massachusetts, USA

Presentation

A 73-year-old woman with type 2 diabetes and neurofibromatosis presented with weight loss and abdominal fullness.

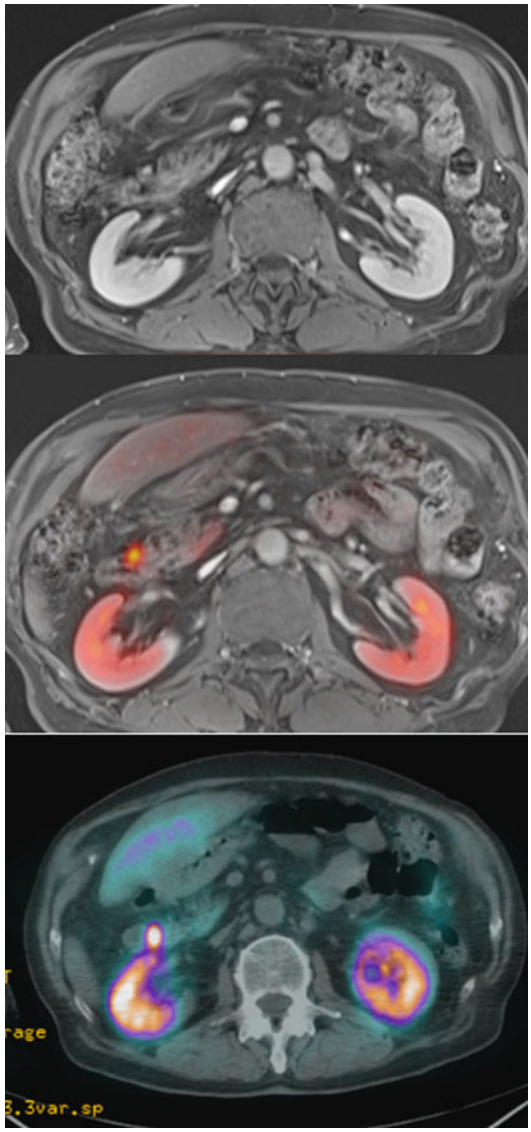

Fig. 7 CT of the head shows multiple exophytic cutaneous lesions (*arrows*) consistent with neurofibromas in a patient with known history of neurofibromatosis

Findings

CT of the head shows multiple exophytic cutaneous lesions consistent with neurofibromas in a patient with known history of neurofibromatosis (Fig. 8).

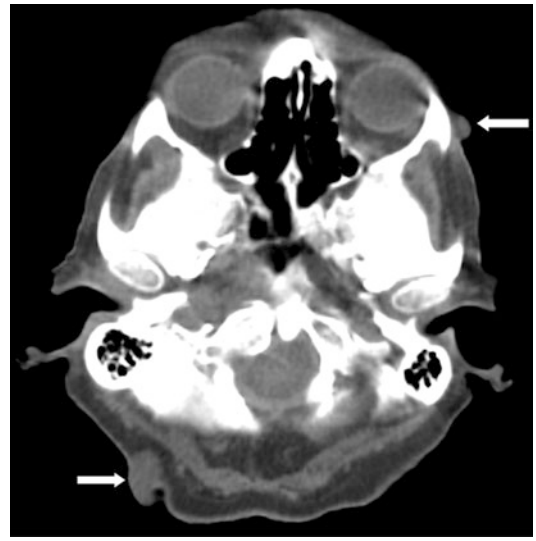

Fig. 8 CT of the head shows multiple exophytic cutaneous lesions (*arrows*) consistent with neurofibromas in a patient with known history of neurofibromatosis

CT of the abdomen and pelvis with oral and intravenous contrast demonstrates a peripherally avidly enhancing, centrally necrotic mesenteric mass associated with the small bowel that displaces the bowel anteriorly without causing obstruction (Fig. 9).

[^{18}F]FDG PET/CT performed for further evaluation (Fig. 10) demonstrates a peripherally moderately [^{18}F]FDG-avid mass corresponding to the enhancing portion of the mass and central photopenia corresponding to central necrosis seen on prior CT. Additionally, there is a focus along the left lateral aspect of the mass that is more focally intensely [^{18}F]FDG avid (SUV_{max} 5.7). Incidental note of the distal small bowel and diffuse colonic [^{18}F]FDG uptake is consistent with history of metformin use.

A trial of imatinib therapy was instituted to attempt to reduce the size of the mass prior to surgical resection, and a short-term follow-up PET/CT was performed 3 weeks later. The follow-up PET/CT demonstrates the original dominant mass is slightly increased in size with

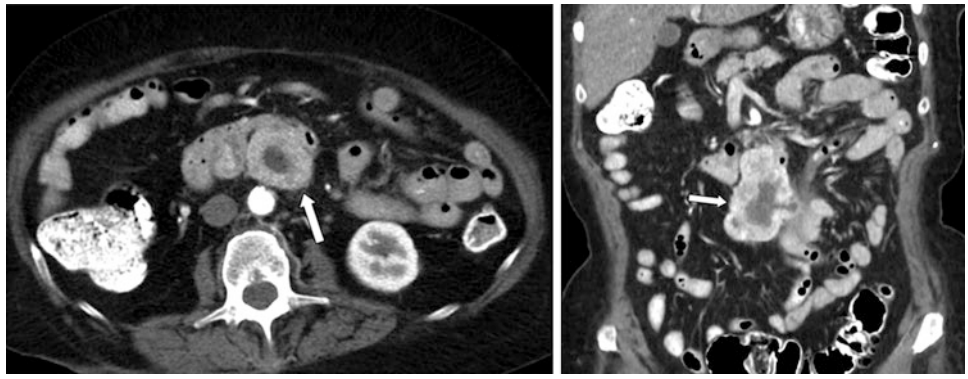

Fig. 9 On the left, axial image from a CT of the abdomen and pelvis with oral and intravenous contrast demonstrates a peripherally avidly enhancing, centrally necrotic mesenteric mass (*arrow*) associated with the small bowel that displaces the bowel anteriorly without causing obstruction. On the right, coronal reconstructed image from a CT of the abdomen and pelvis with oral and intravenous contrast demonstrates the full extent of the mesenteric mass (*arrow*) and its relationship with the adjacent small bowel

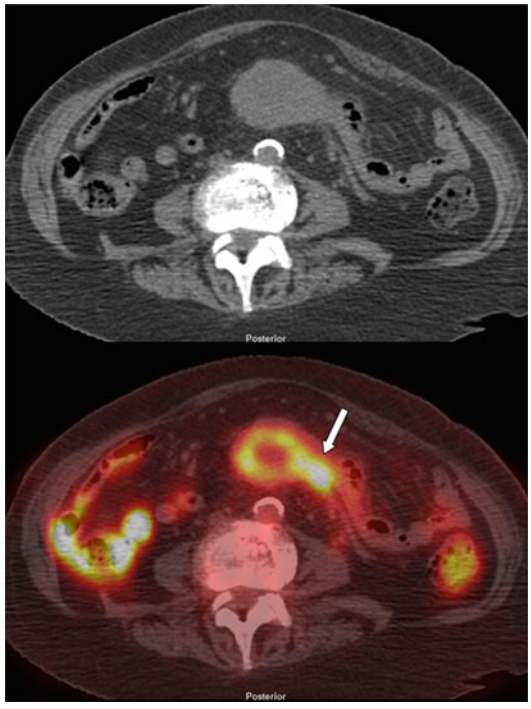

Fig. 10 Axial CT (*above*) and fused [^{18}F]FDG PET/CT (*below*) prior to therapy showing the peripherally [^{18}F]FDG-avid mesenteric mass with a more [^{18}F]FDG-avid focus along its left lateral aspect (*arrows*)

no change in peripheral [^{18}F]FDG uptake; however the left lateral intensely [^{18}F]FDG-avid focus has rapidly increased in size and [^{18}F]FDG uptake (SUV_{max} 10.5) and is also centrally necrotic (Figs. 11 and 12). Findings are consistent with disease progression on therapy.

Follow-Up

Due to lack of response to therapy, imatinib was discontinued, and the patient was scheduled for surgical resection.

Discussion

Gastrointestinal stromal tumors (GISTs) occur with an increased frequency in patients with neurofibromatosis type 1 (NF1). GISTs in this population are different from sporadic GISTs in many ways. Genetically, they are less likely to have a c-Kit mutation compared to sporadic GISTs. Since GISTs in the NF1 population do not typically have a c-Kit mutation, they proliferate independent of the c-Kit pathway, and therefore imatinib is not

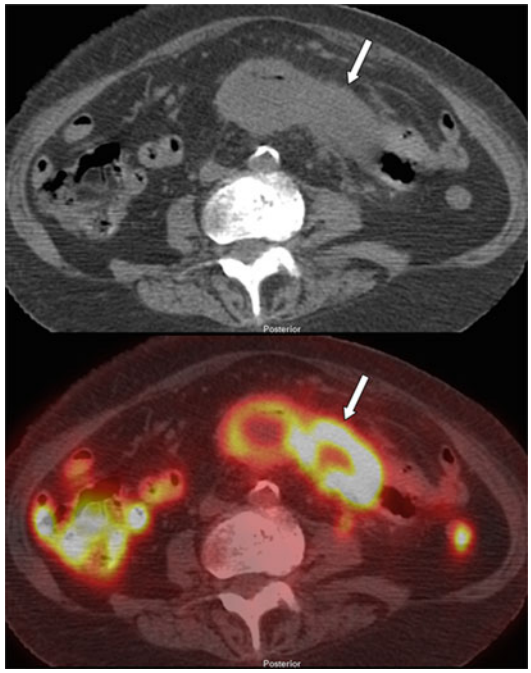

Fig. 11 Axial CT (*above*) and fused [^{18}F]FDG PET/CT (*below*) after therapy showing unchanged [^{18}F]FDG uptake and minimal increase in size of the original central mass; however the lateral more-intense [^{18}F]FDG-avid focus markedly increased in size and [^{18}F]FDG uptake (*arrows*) after 2 weeks on imatinib therapy

typically an effective therapy in these c-Kit-negative GIST cases. Additionally, GISTs in NF1 patients are more likely to be associated with the small bowel, as in this case, and there can be multiple separate GIST tumors in these patients.

Small Bowel Tumors: Case No. 6

Presentation

A 73-year-old man with suspected carcinoid syndrome and increased serotonin serum levels (1520 ng/mL) underwent a somatostatin receptor scintigraphy with Octreoscan®.

Findings

Scintigraphy showed a large area of increased uptake of ^{111}In-pentetreotide at the level of an intestinal loop of the small bowel, in the mesogastric region. This finding was consistent with the intestinal neuroendocrine lesion associated with perienteric and celiac lymphadenopathies (Fig. 13). Moreover, whole-body scan and SPECT/CT images disclosed an inferior left laterocervical lymphadenopathy with high expression of somatostatin receptors (Figs. 13 and 14).

The patient underwent resection of the small bowel loop, mesenteric lymphadenectomy, right hemicolectomy, and left laterocervical lymphadenectomy plus therapy with somatostatin analogues. Pathology confirmed the presence of a neuroendocrine tumor (grade II, atypical carcinoid) of the small bowel with mesenteric and laterocervical nodal involvement.

Follow-Up

After 8 months the patient began again to present clinical symptoms. He underwent a second somatostatin receptor scintigraphy with Octreoscan®.

Scintigraphy showed the persistence of an area of ^{111}In-pentetreotide uptake within a small bowel loop, in the same region of that seen in the first scan (Fig. 15). The findings were consistent with the persistence of disease.

Teaching Points

Somatostatin receptor scintigraphy is able to disclose neuroendocrine tumors that express somatostatin receptors of gastro-entero-pancreatic origin. As reported in this case, grade II tumors usually express somatostatin receptors and so they can be controlled by somatostatin analogue treatment. In this case scintigraphy was useful in the follow-up of the patient assessing the presence and the extension of the disease. SPECT/CT acquisitions increase the accuracy of scintigraphy by adding important anatomic information.

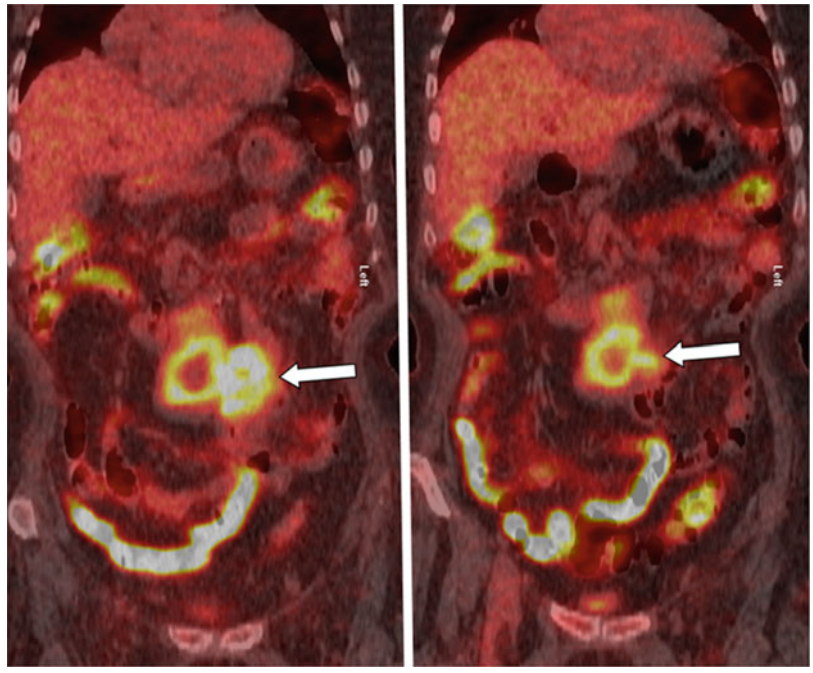

Fig. 12 Coronal fused [^{18}F]FDG PET/CT images after therapy (*left*) and before therapy (*right*). The full extent of the increase in size and [^{18}F]FDG uptake of the left lateral portion of the mass (*arrows*) is seen to better advantage in this side-by-side comparison. Findings are consistent with progression of disease on therapy

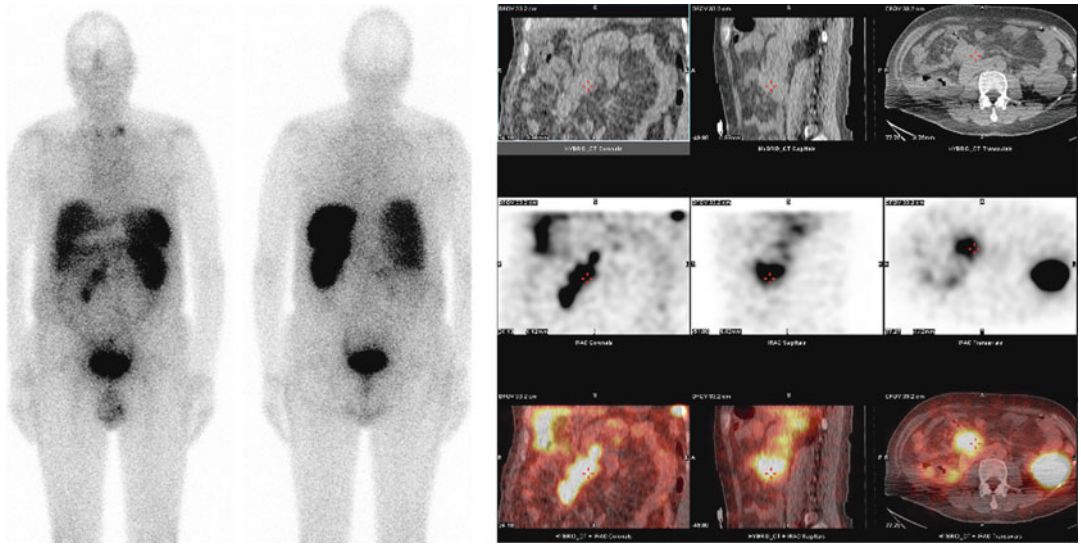

Fig. 13 Scintigraphy with ^{111}In-pentetreotide. Whole-body images on the left and axial, coronal, and sagittal SPECT/CT slices show a large area of increased tracer uptake within an intestinal loop of the small bowel, in the mesogastric region, consistent with an intestinal neuroendocrine lesion associated with perienteric and celiac lymphadenopathies

Fig. 14 Scintigraphy with ^{111}In-pentetreotide. Axial SPECT/CT slices show an inferior left laterocervical lymphadenopathy with high tracer uptake detectable also on the whole-body images

Small Bowel Tumors: Case No. 7

Presentation

A 75-year-old man with small bowel neuroendocrine tumor with a liver metastasis treated surgically (resection of the small bowel and liver nodule). Currently in treatment with octreotide but with progressive disease.

Findings

The patient underwent a PET/CT with ^{18}F-DOPA that showed multiple metastases with pathological hyperactivity within both liver lobes, the most evident located in the VI/VII segment and IV segment, respectively. Moreover, it was also clearly detectable in a tissue thickening with highly ^{18}F-DOPA avid in the small intestine, at the site of the previous surgery level. At last, multiple hyperactive lymphadenopathies were also found in several sites of the abdomen (celiac, mesenteric, portocaval, retrocrural, and subphrenic) and in the mediastinum (paraesophageal site) (Fig. 16).

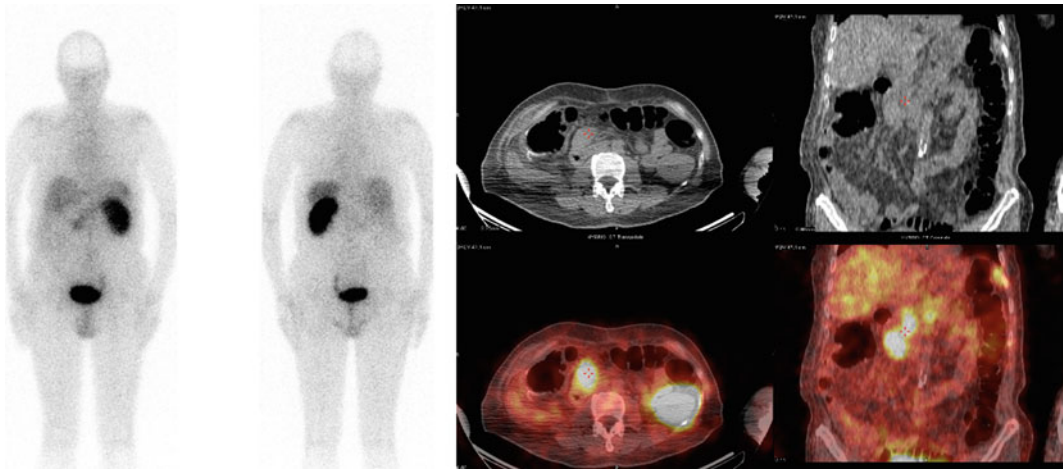

Fig. 15 Follow-up scintigraphy with ^{111}In-pentetreotide showing the persistence of an area of tracer uptake within a small bowel loop, in the same region of that seen in the first scan

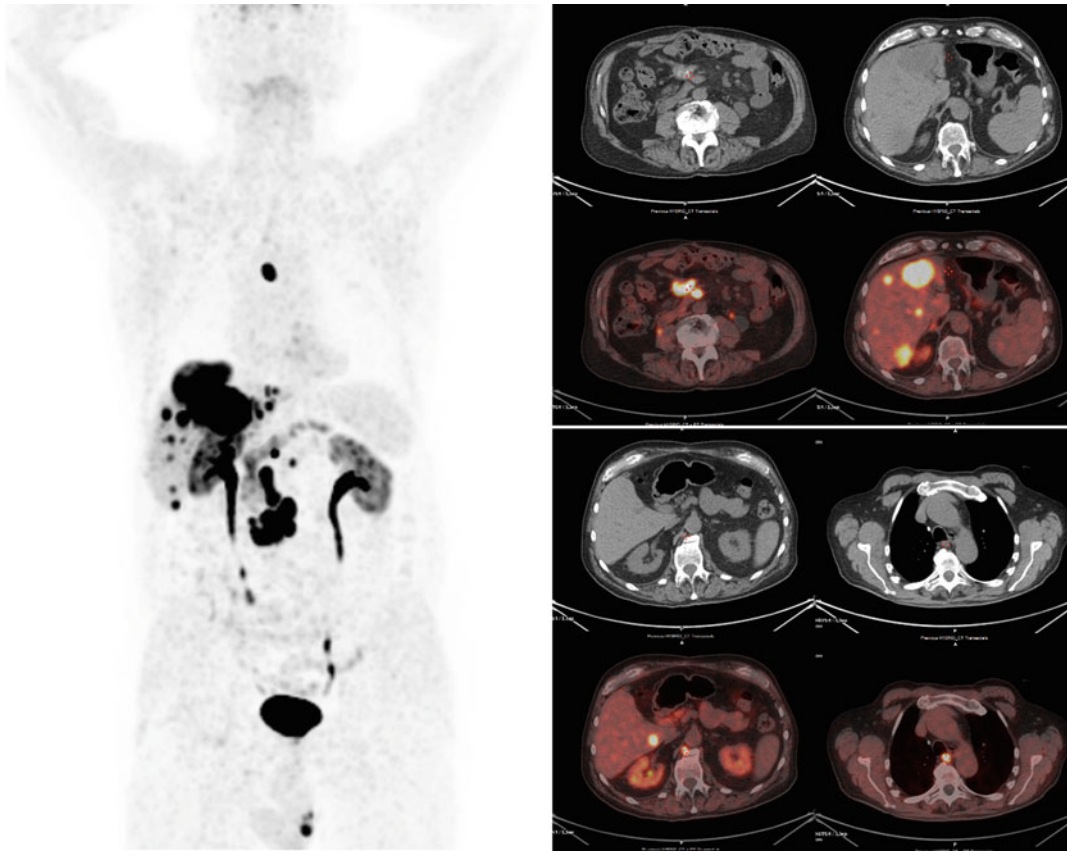

Fig. 16 PET/CT with ^{18}F-DOPA. MIP and PET/CT axial slices show multiple metastases with ^{18}F-DOPA hyperactivity within both liver lobes (the most evident located in the VI/VII segment and IV segment). A clearly detectable ^{18}F-DOPA-avid tissue thickening can be seen in the small intestine, at the site of the previous surgery level. Multiple hyperactive lymphadenopathies can be observed in several sites of the abdomen and in the mediastinum

Follow-Up

The patient was then started to a new therapy with lanreotide (1 I.M. administration/14 days).

After 6 months the patient repeated a PET/CT with ^{18}F-DOPA. PET/CT scan revealed substantial stability of the multiple liver metastases (slight increase of the largest lesions), of the small bowel lesion, and of the abdominal and paraesophageal lymphadenopathies (Fig. 17).

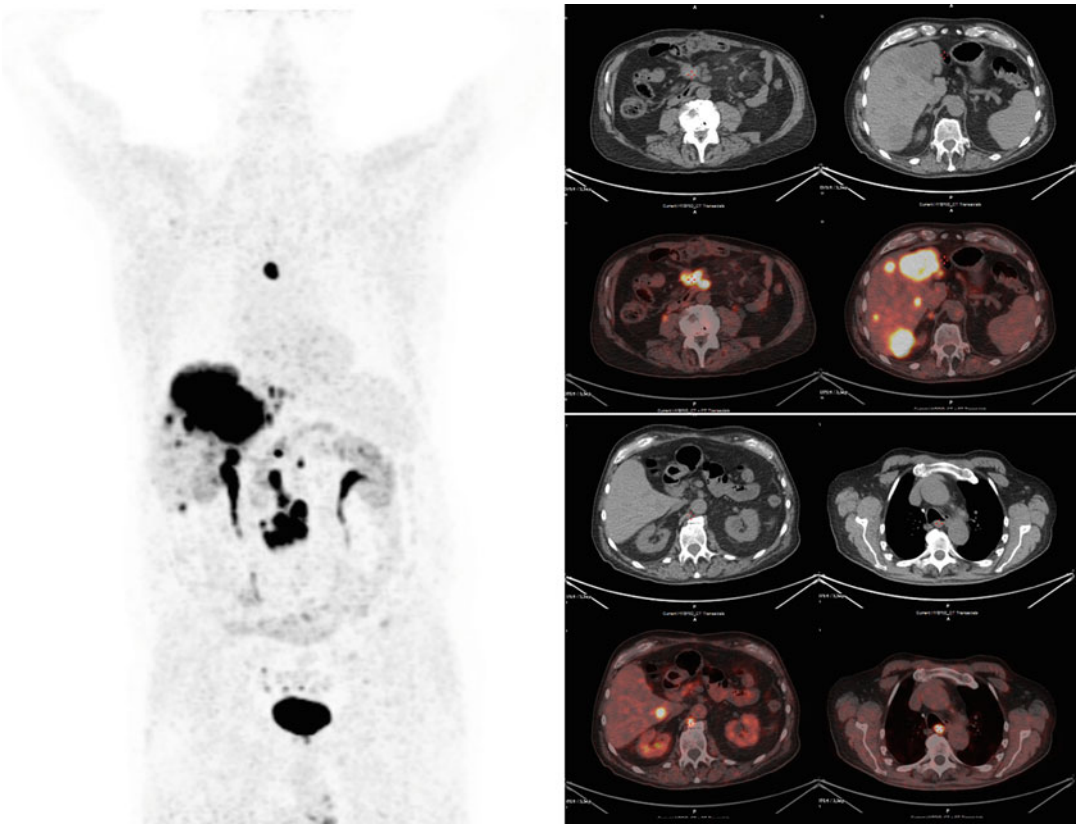

Fig 17 PET/CT scan revealed substantial stability of the multiple liver metastases except for a slight increase of the largest lesions. Substantially unchanged also the small bowel lesion and the abdominal and mediastinic lymphadenopathies

Teaching Point

PET/CT with ^{18}F-DOPA, not as a first option, can be used in the evaluation of gastro-entero-pancreatic neuroendocrine tumors with negative or inconclusive findings at conventional radiological imaging and somatostatin receptor imaging. ^{18}F-DOPA findings in this case played a major role in the management and in the follow-up of the patient.

Teaching Cases in Nuclear Oncology: Tumors of the Liver and Biliary Tract

64

Duccio Volterrani, Giulia Puccini, Sara Mazzarri, and Federica Guidoccio

Keywords

Hepatocellular carcinoma • [^{18}F]FDG PET/CT • [^{11}C]methionine PET/CT • Renal cell carcinoma • MRI • Cholangiocarcinoma • Radioembolization therapy • ^{90}Y-microspheres • ERCP • Liver metastasis • ^{99m}Tc-MAA • SPECT/CT

Glossary

[^{18}F]FDG	2-Deoxy-2-[^{18}F]fluoro-D-glucose
^{99m}Tc-MAA	^{99m}Tc-macroaggregated albumin
AFP	Alpha-fetoprotein, a tumor-associated marker
CEA	Carcinoembryonic antigen, a circulating serum tumor-associated marker
CT	X-ray computed tomography
DSA	Digital subtraction angiography
DWI	Diffusion-weighted magnetic resonance imaging, a technique used to detect changes in the distribution of water molecules in selected regions
EGDS	Esophago-gastro-duodenoscopy
ERCP	Endoscopic retrograde cholangio-pancreatography
HBV	Hepatitis B virus
HCC	Hepatocellular carcinoma
HCV	Hepatitis C virus
LAVA	A magnetic resonance imaging technique that generates water only, fat only, in phase and out of phase echoes in one single acquisition that can be completed in single breath hold (from Liver Acquisition with Volume Acquisition)
MR	Magnetic resonance
MRI	Magnetic resonance imaging
PET	Positron emission tomography
PET/CT	Positron emission tomography/Computed tomography
SPECT	Single-photon emission computed tomography
SPECT/CT	Single-photon emission computed tomography/Computed tomography
SUV	Standardized uptake value
SUV_{max}	Standardized uptake value at point of maximum
US	Ultrasonography

D. Volterrani (✉) • G. Puccini • S. Mazzarri • F. Guidoccio
Regional Center of Nuclear Medicine, Department of Translational Research and Advanced Technologies in Medicine and Surgery, University of Pisa, Pisa, Italy
e-mail: duccio.volterrani@med.unipi.it

© Springer International Publishing Switzerland 2017
H.W. Strauss et al. (eds.), *Nuclear Oncology*,
https://doi.org/10.1007/978-3-319-26236-9_67

Contents

Hepatocellular Carcinoma: Case No. 1 1682
Presentation 1682
Findings 1682
Follow-Up 1682
Teaching Point 1682

Hepatocellular Carcinoma: Case No. 2 1683
Presentation 1683
Findings 1684
Teaching Point 1685

Cholangiocarcinoma: Case No. 1 1686
Presentation 1686
Findings 1686
Follow-Up 1686
Teaching Point 1688

Cholangiocarcinoma: Case No. 2 1688
Presentation 1688
Findings 1688
Follow-Up 1688
Teaching Point 1688

Cholangiocarcinoma: Case No. 3 1689
Presentation 1689
Findings 1689
Follow-Up 1690

Liver Metastasis from Colorectal Cancer: Case No. 1 1691
Presentation 1691
Findings 1691
Follow-Up 1691
Teaching Point 1693

Liver Metastasis from Colorectal Cancer: Case No. 2 1694
Presentation 1694
Findings 1694
Follow-Up 1695
Management 1695
Teaching Point 1695

Hepatocellular Carcinoma: Case No. 1

Case contributed by: L. Olivari, A. Chiti
Division of Nuclear Medicine, Department of Biomedical Sciences – Humanitas University, Milan, Italy.

Presentation

A 77-year-old man presented at our hospital after hemoptysis, mild serotine fever, and fatigue. Bronchoscopy was negative. Ultrasonography (US) of the abdomen demonstrated a large liver lesion, while a subsequent MRI demonstrated a 20 cm liver lesion with nonunique features, occupying the posterior area (Fig. 1). No relevant abnormalities were found at EGDS. The tumor-associated markers CEA and AFP were negative, and there was no history of alcohol abuse. HCV and HBV serology was negative. The patient had had cholecystectomy for gallstones 10 years earlier, at which time US of the abdomen was negative for liver lesions. A prior total body CT demonstrated a 10 cm liver lesion described as a hemangioma.

Findings

[^{18}F]FDG PET/CT showed a large, partially necrotic hepatic lesion (Fig. 1). Some small lung nodules observed in the CT portion of the scan exhibited no uptake, most likely because of their small size. [^{11}C]Methionine PET/CT demonstrated a large hepatic lesion characterized by nonhomogeneous increased uptake. The hepatic lesion features were compatible with hepatocellular carcinoma (HCC). While no uptake was found in the small lung nodules, there was increased uptake of [^{11}C]methionine in the right cardiac ventricle. Further evaluation with cardiac US and MRI was then performed.

Cardiac MRI demonstrated that the abnormally increased uptake observed in the [^{11}C]methionine PET/CT scan was a cardiac localization of the hepatic disease (Fig. 2).

Follow-Up

Fine needle biopsy of the hepatic lesion confirmed the clinical suspicion of HCC, and the patient started sorafenib treatment.

Teaching Point

[^{11}C]Methionine promises to be useful for PET imaging of HCC. In this patient [^{11}C]Methionine

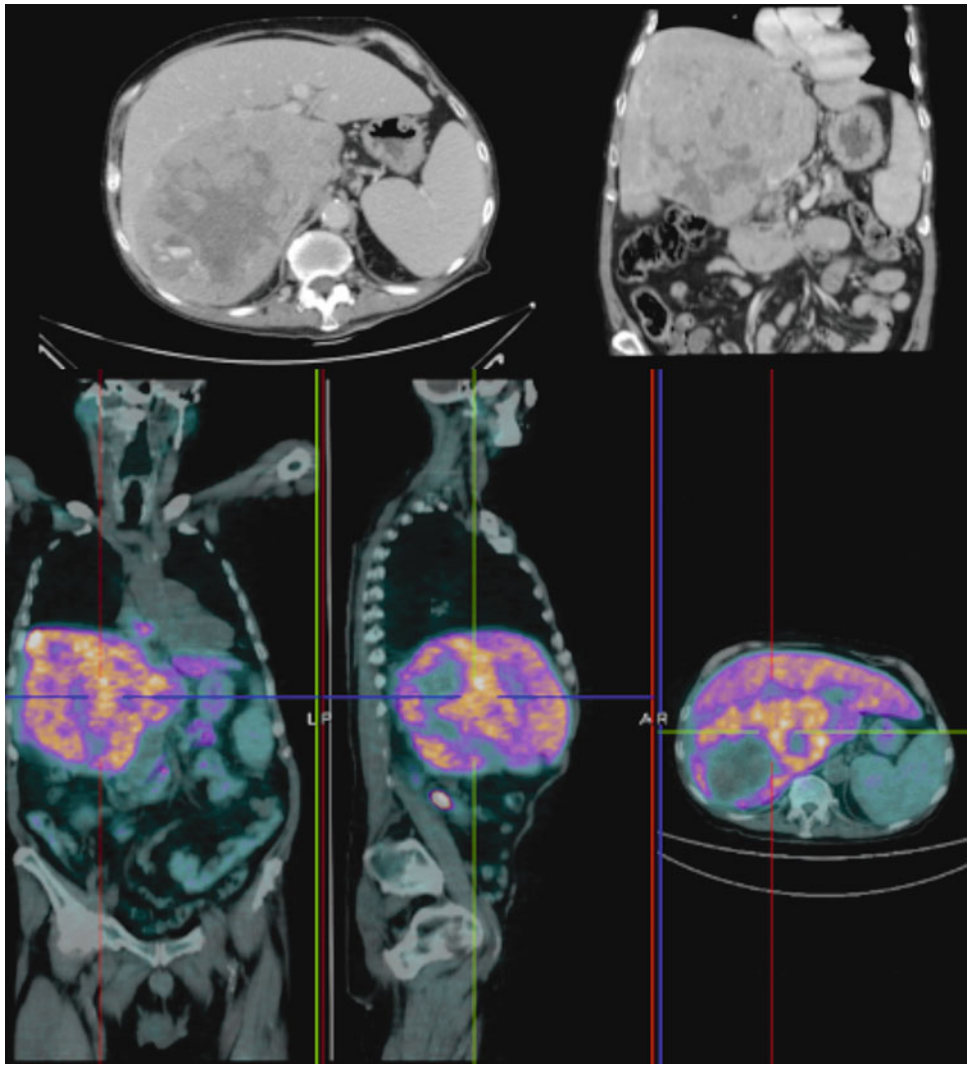

Fig. 1 Magnetic resonance imaging (*MRI*): (*top*) large liver lesion, consistent with HCC. [^{18}F]FDG PET/CT: (*bottom*) heterogeneously increased uptake in the lesion

PET/CT was also of paramount importance for disclosing an unusual site on metastasis in the myocardium.

Hepatocellular Carcinoma: Case No. 2

Case contributed by: ***H.A. Jacene***
Nuclear Medicine/PET-CT, ***Dana-Farber Cancer Institute***, ***Harvard Medical School***, ***Boston***, ***Massachusetts***, ***USA***.

Presentation

An 82-year-old man with newly diagnosed hepatocellular carcinoma (HCC) with questioned abnormalities identified in the left adrenal gland and lumbar spine on recent liver MRI. [^{18}F]FDG PET/CT was performed for further evaluation of these extrahepatic abnormalities.

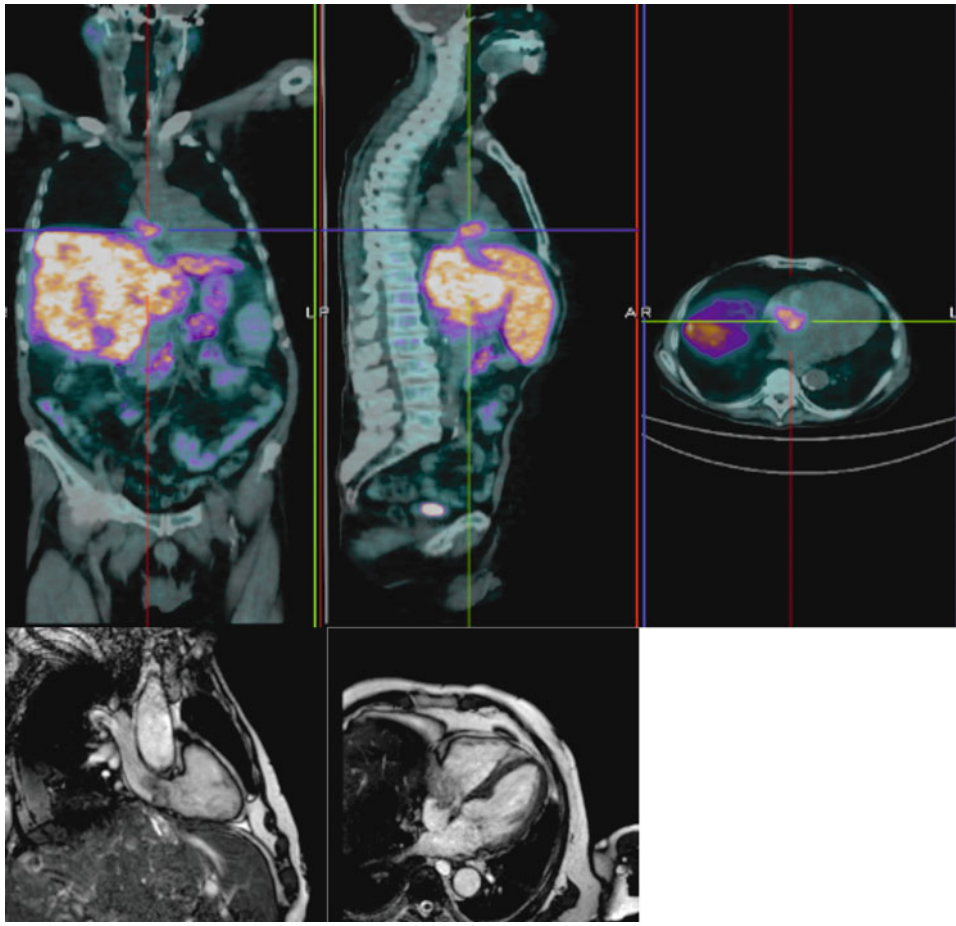

Fig. 2 [^{18}F]FDG PET/CT: (*top*) increased uptake in the myocardium. Magnetic resonance imaging (*MRI*) (*bottom*) confirmed the pathologic lesion shown in the PET/CT scan as a metastatic lesion from HCC

Findings

Subtle increased heterogeneous [^{18}F]FDG uptake is seen in the hepatic dome on the PET maximum intensity projection image (Fig. 3). Otherwise, the liver and the remainder of the PET appear unremarkable (Fig. 4).

MR images demonstrate a 20 cm heterogeneous mass with diffuse mild T2 hyperintensity (Fig. 5) and more focal rounded areas of more intense T2 signal. These foci of more intense T2 signal also have high intrinsic T1 signal and are nonenhancing, consistent with areas of necrosis/cystic degeneration. Internal proteinaceous material or hemorrhage is the likely etiology of the intrinsic high T1 signal. The mass also demonstrates arterial phase hyperenhancement (Fig. 5), contrast washout relative to the background liver on a delayed post-contrast image, and hepatobiliary phase hypointensity on a further delayed post-contrast image (Figs. 6 and 7). All of these MRI findings are characteristic of HCC.

Coronal CT and fused PET/CT images (Fig. 8) demonstrate the full extent of this large HCC with very little abnormality identified on PET. Additionally, no PET abnormalities were identified in the adrenal gland and lumbar spine, thought likely to reflect adrenal hyperplasia and degenerative changes.

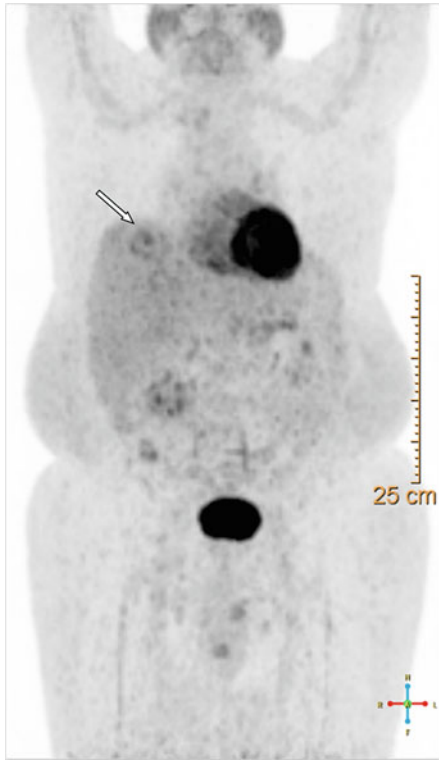

Fig. 3 PET MIP image viewed anteriorly demonstrates mild increased [^{18}F]FDG uptake in the hepatic dome (*arrow*)

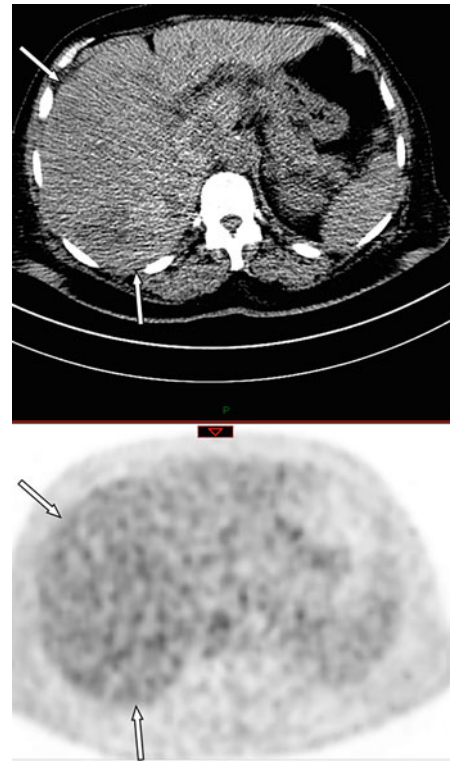

Fig. 4 Axial CT (*above*) and axial PET (*below*). CT shows heterogeneous attenuation in the right lobe of the liver (*arrows*); however, the PET shows [^{18}F]FDG uptake virtually identical to background liver parenchyma in the same area (*arrows*)

Teaching Point

Variable [^{18}F]FDG uptake has been reported in HCC resulting in variable reported sensitivities for detection of this tumor by PET/CT. The variable [^{18}F]FDG uptake is thought to be due to different glucose transporters present in the liver and HCC as well as increased levels of phosphatase activity, which prevent [^{18}F]FDG from being trapped in the cells. The effect is more prominent in well-differentiated compared to poorly differentiated HCC. This case demonstrates this variable uptake – an example of nearly identical [^{18}F]FDG uptake compared to adjacent background liver except for a small area of heterogeneity in the hepatic dome. This small amount of increased uptake in the hepatic dome may reflect a focal area

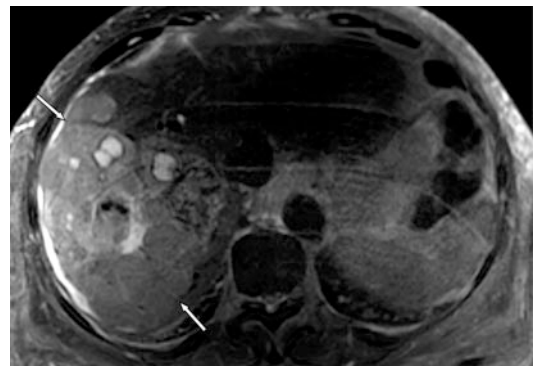

Fig. 5 Axial T2 FSE demonstrates heterogeneous mild increased signal intensity compared to adjacent background liver throughout the mass (*arrows*) with some focal rounded areas of higher intensity signal that represent areas of necrosis/cystic degeneration

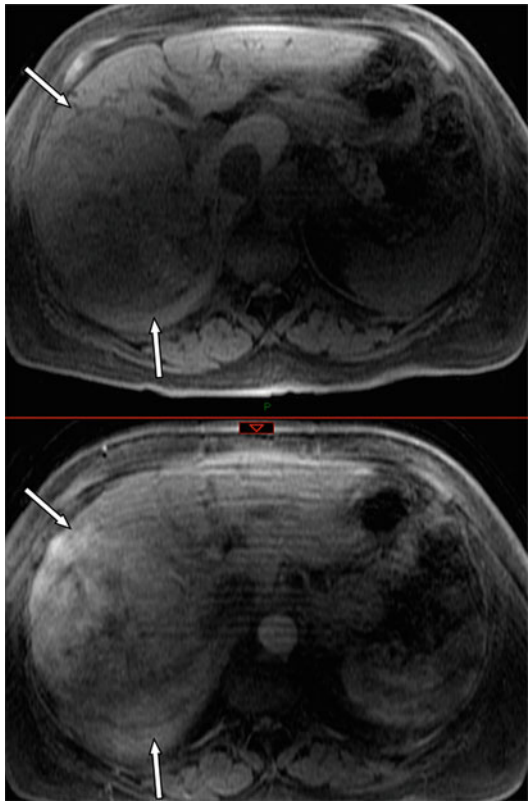

Fig. 6 Axial T1 LAVA pre-contrast (*above*) and arterial phase post-contrast (*below*). Prior to the administration of contrast, the area of the mass (*arrows*) is shown to be hypointense compared to adjacent background liver parenchyma and demonstrates arterial phase hyperenhancement compared to background liver on the post-contrast image

of higher grade of tumor, noted to be adjacent to the areas of focal necrosis within the tumor.

Cholangiocarcinoma: Case No. 1

Presentation

A 76-year-old woman with history of cholangiocarcinoma treated with right hepatectomy and cholecystectomy and adjuvant chemotherapy.

Findings

[^{18}F]FDG PET/CT was performed to assess the presence of residual liver disease and for global

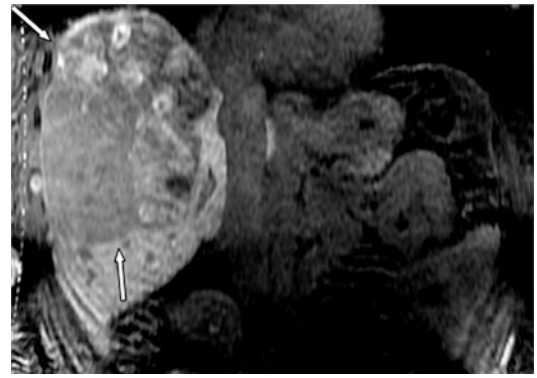

Fig. 7 Coronal T1 LAVA 17 min post-contrast (gadoxetate disodium contrast). On delayed hepatobiliary phase post-contrast imaging. The large mass (*arrows*) is hypointense relative to the adjacent background liver. Areas of intrinsic high T1 signal are noted in rounded areas of necrosis/cystic degeneration

restaging. PET/CT disclosed moderate [^{18}F]FDG uptake within two metastases in the III and IV segment of the liver (Fig. 9). Then the patient underwent second-line chemotherapy and a new [^{18}F]FDG PET/CT scan was repeated to evaluate the efficacy during treatment. [^{18}F]FDG uptake in the liver lesion was increased with respect to baseline (without significant reduction in size), thus demonstrating poor response to chemotherapy (Fig. 10).

Follow-Up

One month later new multiple secondary lesions were found in the liver parenchyma. The patient was then submitted to digital subtraction angiography (DSA) in order to evaluate the patient as a possible candidate to radioembolization therapy with ^{90}Y-microspheres. Nevertheless, at DSA the arteries afferent to lesions were found to be thin, twisted, and with a marked spasmophilia; radioembolization with ^{90}Y-microspheres was therefore deemed not to be technically feasible. The patient was subsequently started on a hypofractionated radiotherapic treatment of the liver lesions.

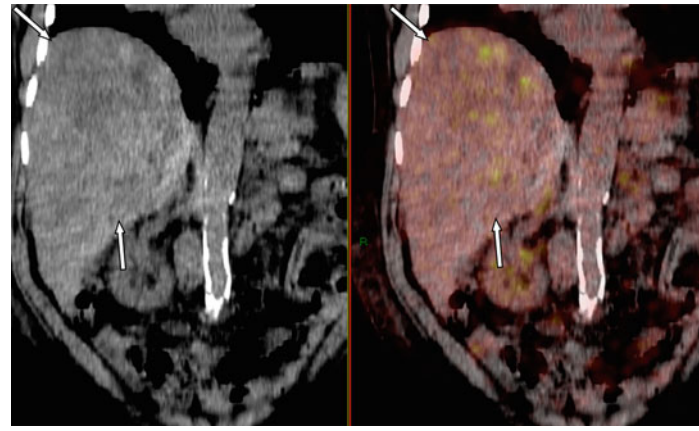

Fig. 8 Coronal CT (*left*) and fused PET/CT (*right*). Heterogeneous attenuation in the right lobe of the liver on CT (*arrows*) with the large tumor almost non-identifiable on PET aside from a few small areas of focal increased tracer uptake in the superior portion of this mass

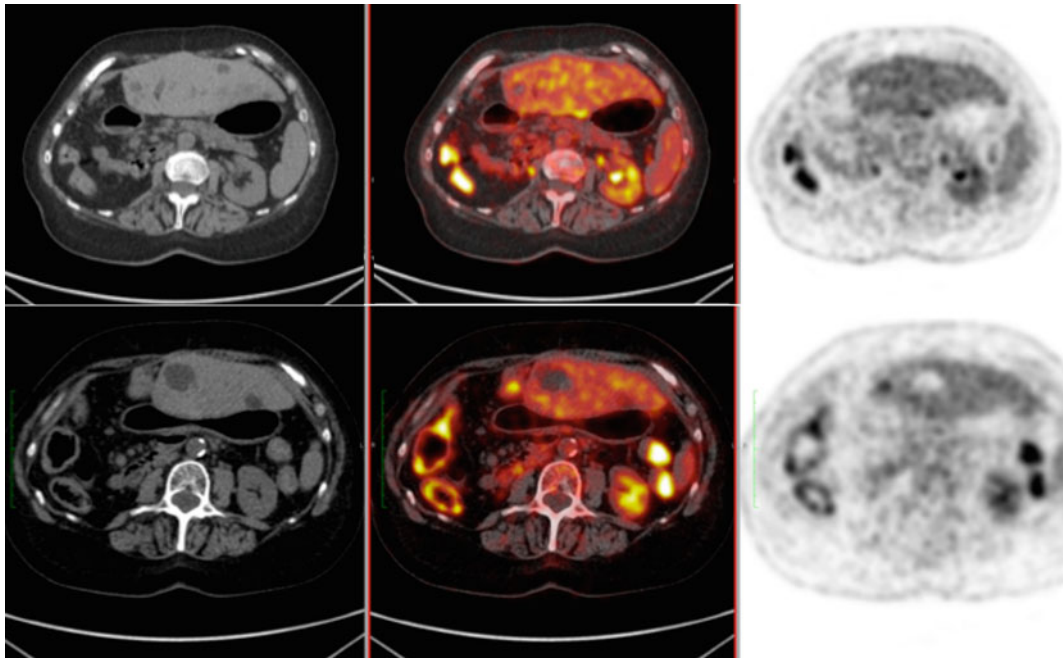

Fig. 9 Axial CT (*left*), fused PET/CT (*middle*), and PET (*right*) slices. Two small focal areas of increased [^{18}F]FDG activity are located in III and IV segment. On CT multiple low-density areas corresponding to cystic lesions in the left and right liver lobe

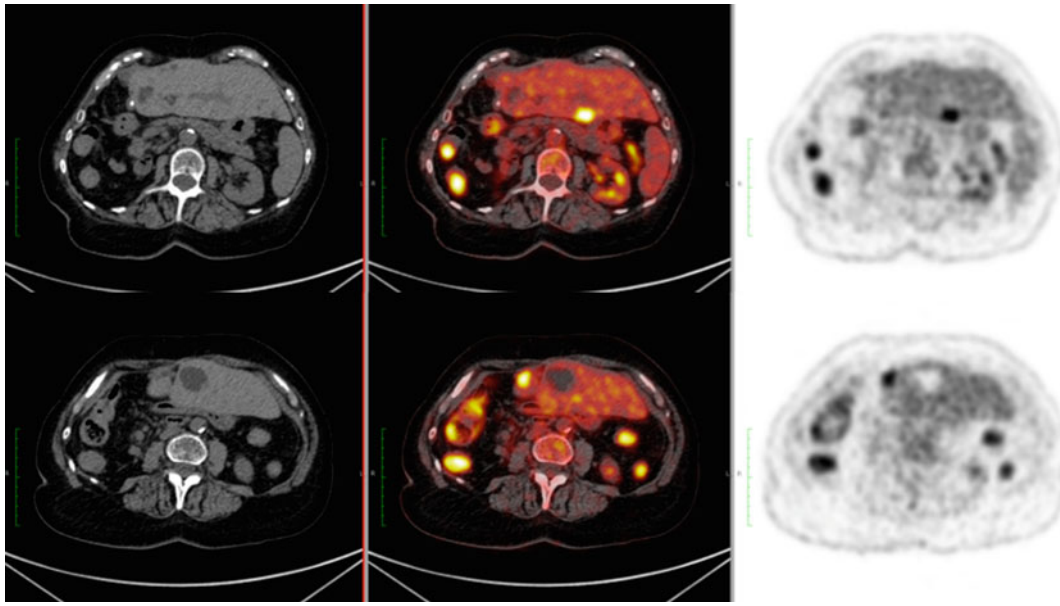

Fig. 10 [^{18}F]FDG PET/CT during chemotherapy. Axial CT (*left*), fused PET/CT (*middle*), and PET (*right*) slices showing increased uptake of the liver lesions and indicating a bad response of the ongoing treatment

Teaching Point

This case confirms the value of serial [^{18}F]FDG PET/CT scans in treatment monitoring of patients with metastatic cholangiocarcinoma.

Cholangiocarcinoma: Case No. 2

Presentation

A 65-year-old male patient was referred to the department of nuclear medicine for an [^{18}F]FDG PET/CT after chest X-ray, and CT had revealed a 18 × 16 mm nodule within the lower lobe of the left lung (Fig. 11).

Findings

PET/CT showed intense [^{18}F]FDG uptake (SUV_{max} 4.9) within the left lung nodule. Moreover, the whole body scan disclosed a focal area of hyperactivity >3 cm at the level of the IV/VIII hepatic segment. In addition, multiple hypermetabolic lymph nodes were located at the retrocrural, celiac, and lombo-aortic sites. Finally, multiple lytic bone lesions with increased [^{18}F]FDG uptake were disclosed within the scapula, sternum, and pelvis (Fig. 12).

Follow-Up

The patient underwent a biopsy of a hypermetabolic lytic lesion of the right ileum, which proved to be metastasis from cholangiocarcinoma.

Teaching Point

It is known that [^{18}F]FDG PET/CT is an effective tool for disclosing unknown primary tumors. Moreover, PET/CT-guided biopsy enables to achieve in this patient a final diagnosis of advanced primary cholangiocarcinoma with lymph node involvement and multiple metastatic lesions (T3N2M1, stage IV).

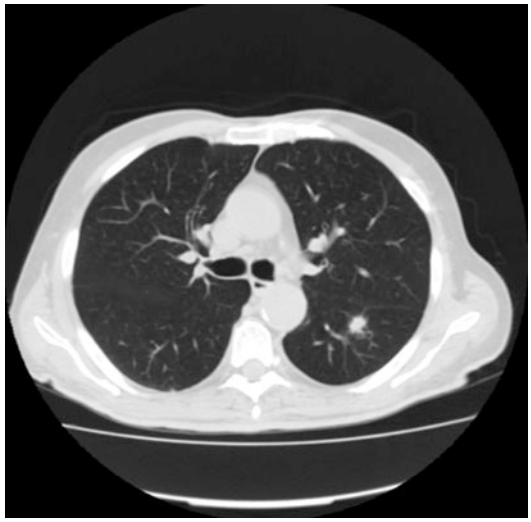

Fig. 11 Axial CT: suspicious *round-shaped* nodule in the left lower lobe

Cholangiocarcinoma: Case No. 3

Presentation

A 71-year-old man developed itching and jaundice 2 months ago.

Findings

CT scan revealed intrahepatic bile duct dilatation and a lesion in the tail of the pancreas measuring 5 × 3 cm. ERCP confirmed stricture of the common bile duct with intrahepatic dilatation that was treated with stent placement. The probable diagnosis was Klatskin tumor, but a benign lesion or a sclerosing cholangitis could not be excluded.

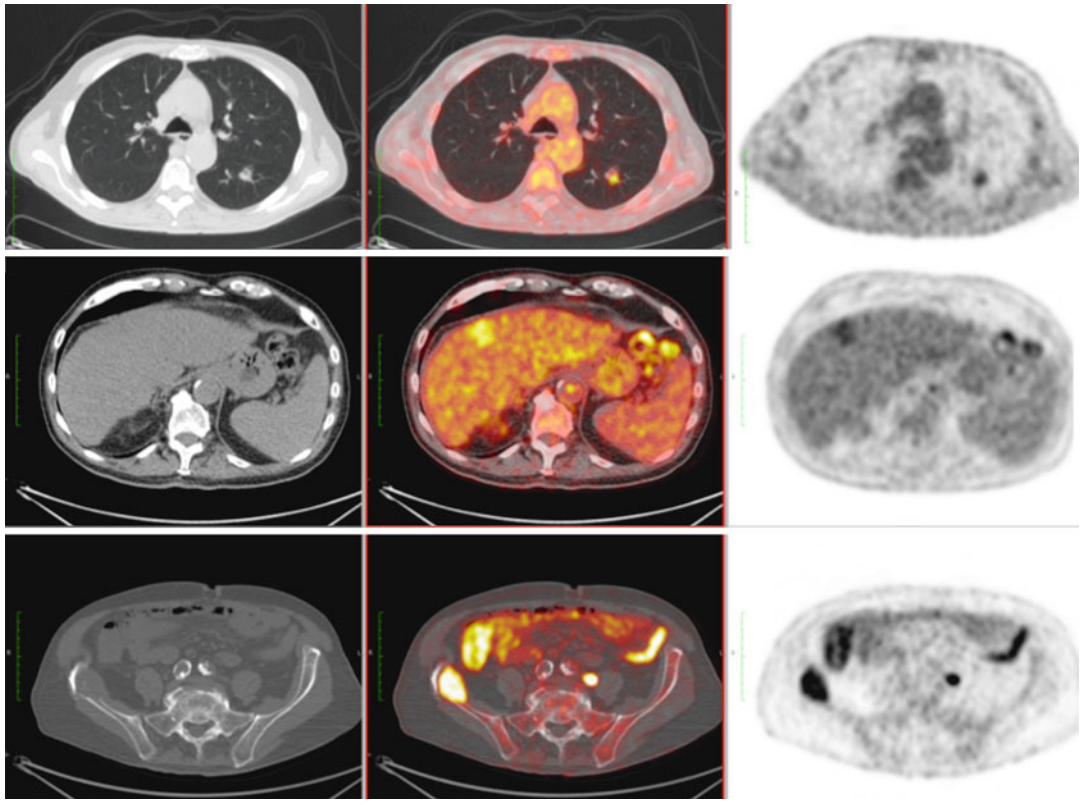

Fig. 12 Axial CT (*left*), fused PET/CT (*middle*), and PET (*right*) slices. (*Top row*) Images show an increased [^{18}F] FDG uptake within the left lung nodule. (*Middle row*) Axial slices reveal a focal area of increased metabolic activity located in the IV segment of the liver. (*Bottom row*) Area of markedly increased hyperactivity in the right iliac bone characterized by bone disruption on CT

[^{18}F]FDG PET/CT scan was performed (Fig. 13). PET/CT shows focal [^{18}F]FDG uptake at the portal vein bifurcation (SUV_{max} 5) with extension of metabolic activity in right lobe of the liver (Fig. 14). Focal [^{18}F]FDG uptake is seen at the tip of the stent due to inflammation. Multiple anterior and posterior peripancreatic hypermetabolic lymph nodes are shown. Several mesenteric foci of [^{18}F]FDG uptake are demonstrated in splenic flexure, pararenal fascia, and pelvis (Fig. 15).

Follow-Up

Surgical therapy included hepatic trisegmentectomy and cholecystectomy. Histology confirmed cholangiocarcinoma and chronic inflammation of the pancreas. This case demonstrates the value of [^{18}F]FDG PET/CT in pretreatment staging of cholangiocarcinoma, despite the possible confounding factor represented by coexistent pancreatitis.

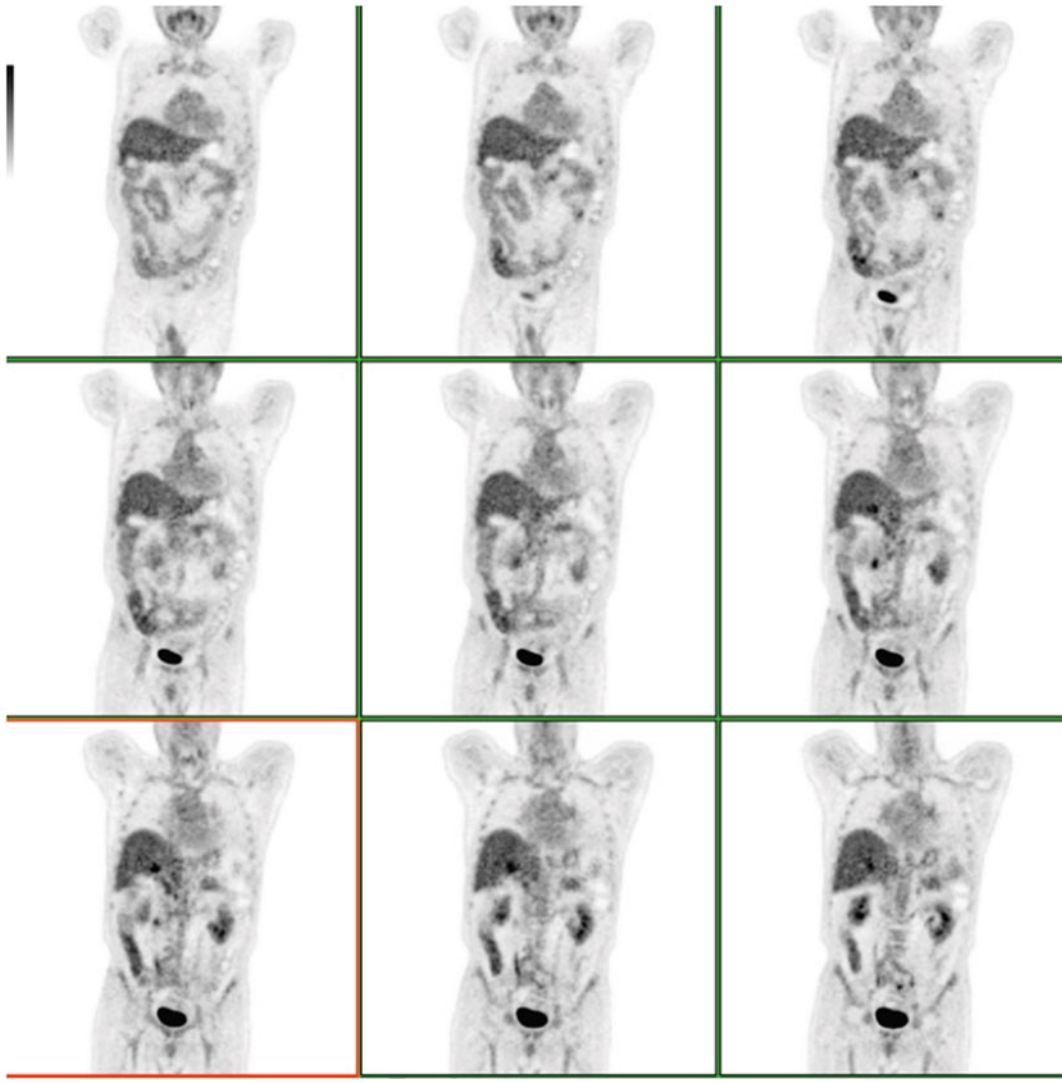

Fig. 13 [^{18}F]FDG PET coronal images demonstrate focal uptake in the hepatic hilum

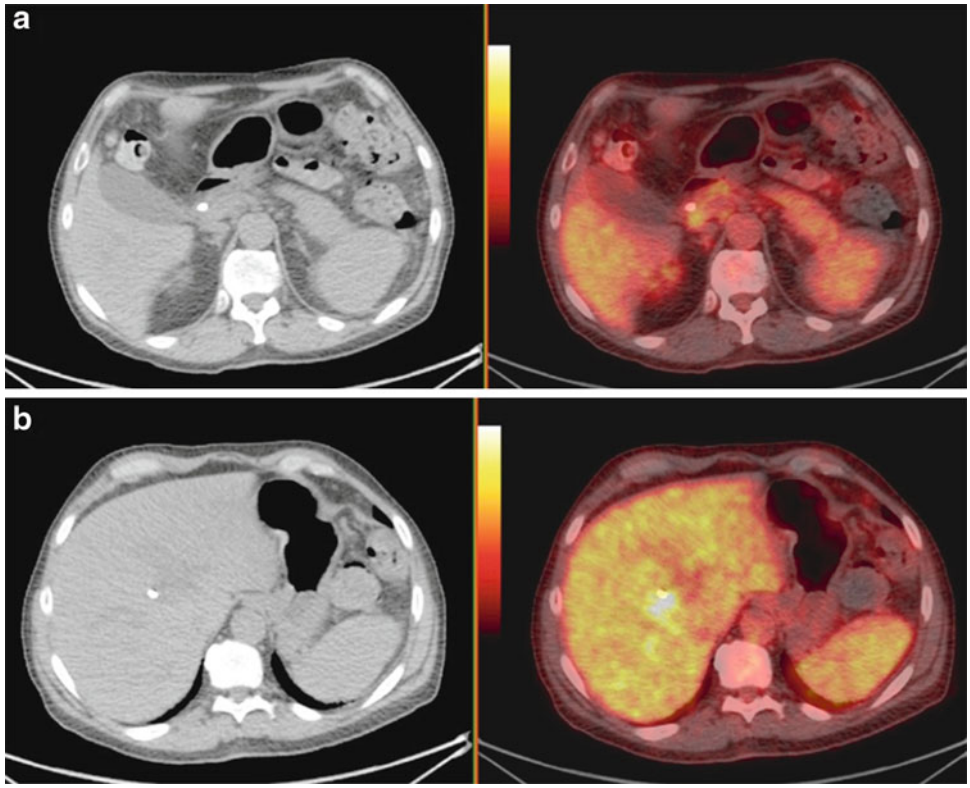

Fig. 14 PET/CT images at two levels (CT *left*, fused PET/CT *right*). (**a**) Diffuse uptake in pancreatic tail without evidence of focal activity corresponding to the lesion revealed on CT. (**b**) [^{18}F]FDG uptake at the tip of the stent due to inflammation

Liver Metastasis from Colorectal Cancer: Case No. 1

Presentation

A 41-year-old man with transverse colon cancer and multiple liver metastases already submitted to surgery (3 months earlier followed by adjuvant chemotherapy).

Findings

[^{18}F]FDG PET/CT scan for restaging confirmed the persistence of the already known multiple irregular hepatic lesions which demonstrate intense [^{18}F]FDG uptake, with a doughnut-like pattern (Fig. 16).

Follow-Up

The patient underwent digital DSA in order to evaluate the possibility of transarterial radioembolization therapy with ^{90}Y-microspheres. DSA showed a regular course of the hepatic arteries and transarterial injection of ^{99m}Tc-MAA showed good perfusion of the metastatic lesions. The lung shunt fraction was low (4%) and no splanchnic or nontarget flow was observed (Fig. 17). Two weeks later, the patient underwent a two-stage procedure of transarterial radioembolization, first on the right and subsequently (after another 3 weeks) on the left liver lobe (Fig. 18). Dosimetric estimates predicted an administered activity of 0.86 GBq of ^{90}Y-microspheres to the left and 0.57 GBq to the right liver lobe. Treatment was well tolerated without any complications.

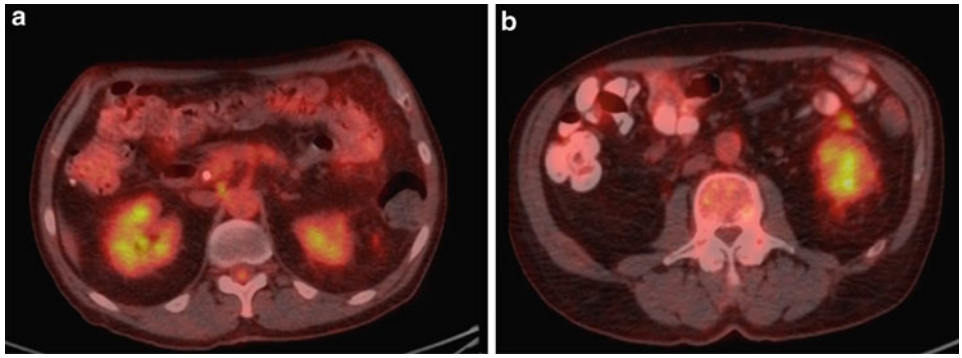

Fig. 15 PET/CT images. (**a**) Peripancreatic hypermetabolic lymphadenopathy. (**b**) Hypermetabolic mesenteric lymph nodes of the pararenal fascia

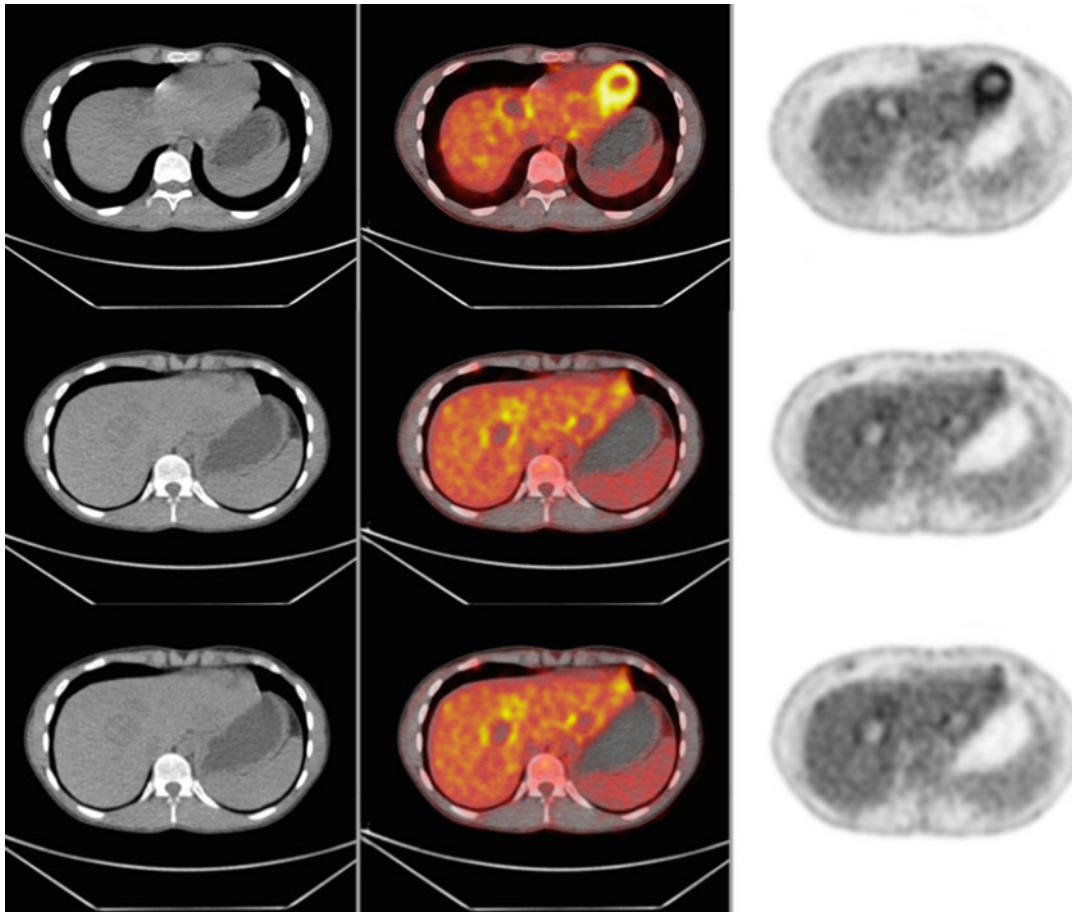

Fig. 16 [^{18}F]FDG PET/CT. Axial CT (*left panels*), fused PET/CT (*middle panels*), and PET alone (*right panels*) The lesions within the right and left lobe result hypodense, with central necrosis, areas of sclerosis, and with a [^{18}F]FDG uptake at the rim

[^{18}F]FDG PET/CT performed 6 months after therapy showed excellent objective response to transarterial radioembolization with ^{90}Y-microspheres (Fig. 19).

Teaching Point

The role of radioembolization of liver tumors is highly promising. This treatment has been shown to be safe and effective also in patients with

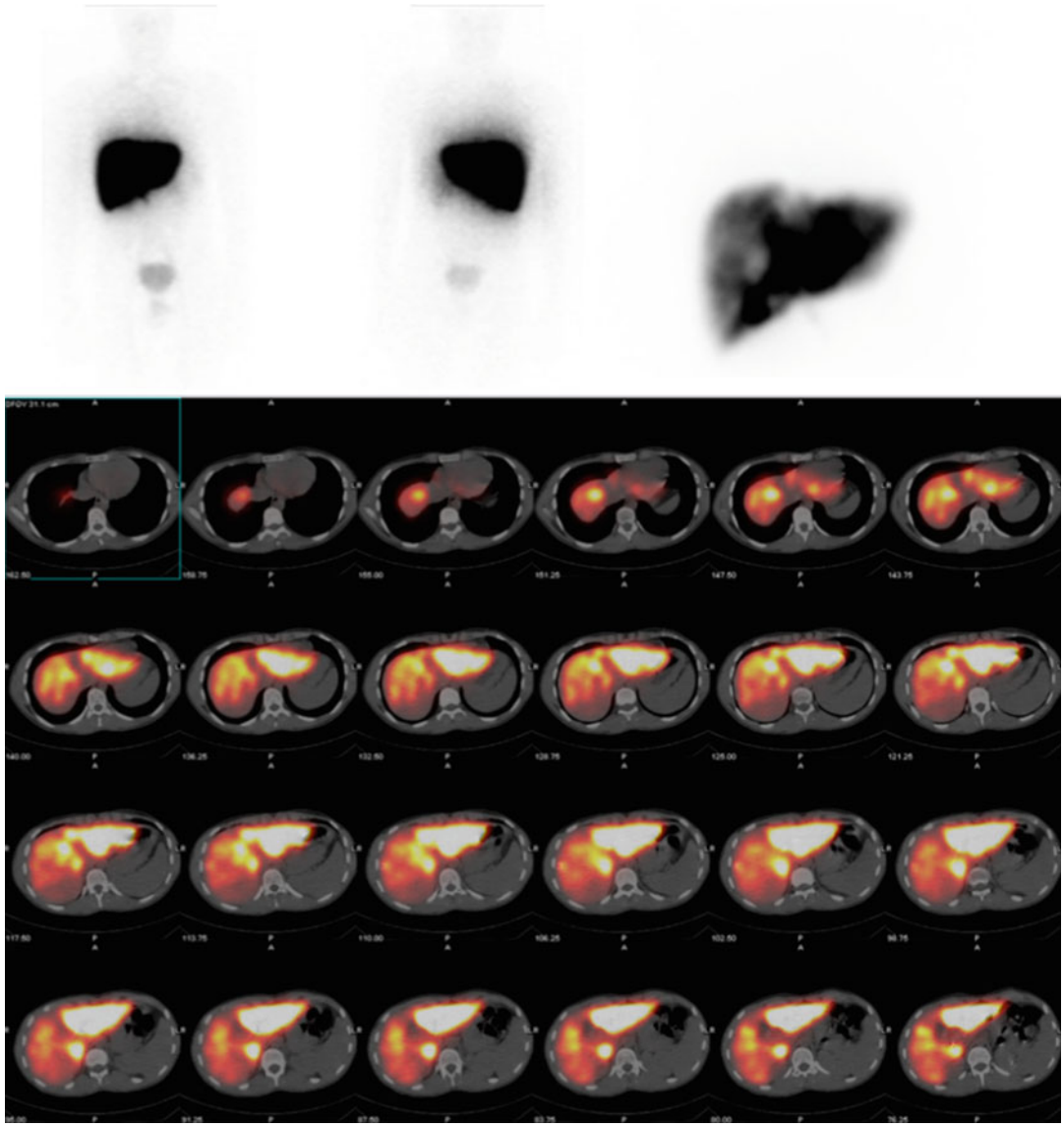

Fig. 17 Whole-body, planar, and SPECT/CT imaging after transarterial injection of ^{99m}Tc-MAA. On *top panel*, whole body and static imaging showing a normal distribution of the radiotracer with a high accumulation of the radiotracer in the liver and low activity in the lung. The lung shunt fraction was 4%. On *bottom panel*, fused SPECT/CT axial slices assessing the distribution of ^{99m}Tc-MAA in the both lobes of the liver, without the evidence of any gastrointestinal shunts

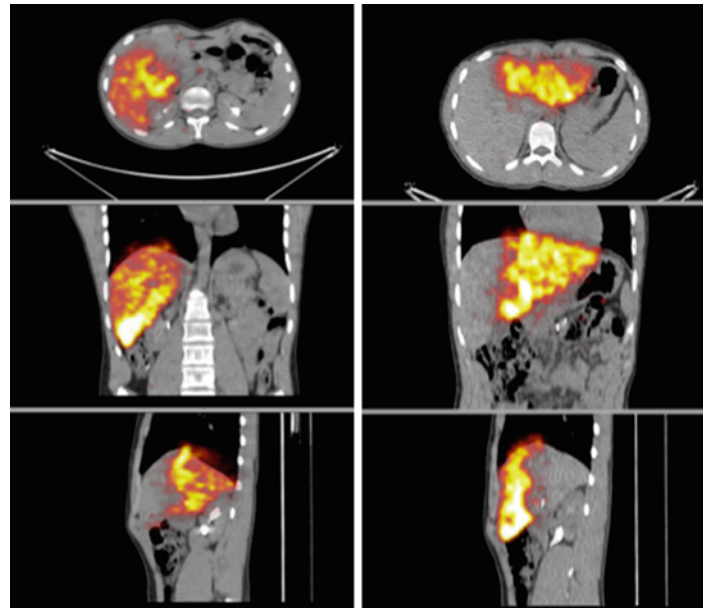

Fig. 18 Posttreatment PET/CT imaging based on the positron emission of ^{90}Y, confirming localization of the ^{90}Y-microspheres in the right lobe (*left panels*) and in left lobe (*right panels*)

metastatic liver tumors from a variety of primary tumors. Pretreatment angiography is an important step before the procedure of radioembolization; meticulous mapping of the vascular anatomy helps the interventional radiologist, when performing the procedure, to identify the vascular supply of the tumor and to identify and coil-embolize vessels that may lead to aberrant deposition of ^{90}Y-microspheres. To this purpose, an important role is played by imaging protocols implementing the use of SPECT/CT acquisition during evaluation of perfusion with ^{99m}Tc-MAA. [^{18}F]FDG PET/CT can be an important tool for treatment monitoring of transarterial radioembolization.

Liver Metastasis from Colorectal Cancer: Case No. 2

Presentation

Sixty-five-year-old man with rectal cancer undergoing initial staging assessment.

Findings

The [^{18}F]FDG PET/CT scan performed for initial staging confirmed the presence of an [^{18}F]FDG-avid rectal cancer. Moreover, PET/CT showed increased tracer uptake in a left parasacral lymph node and multiple doughnut-like lesions with intense [^{18}F]FDG uptake in the liver (Fig. 20).

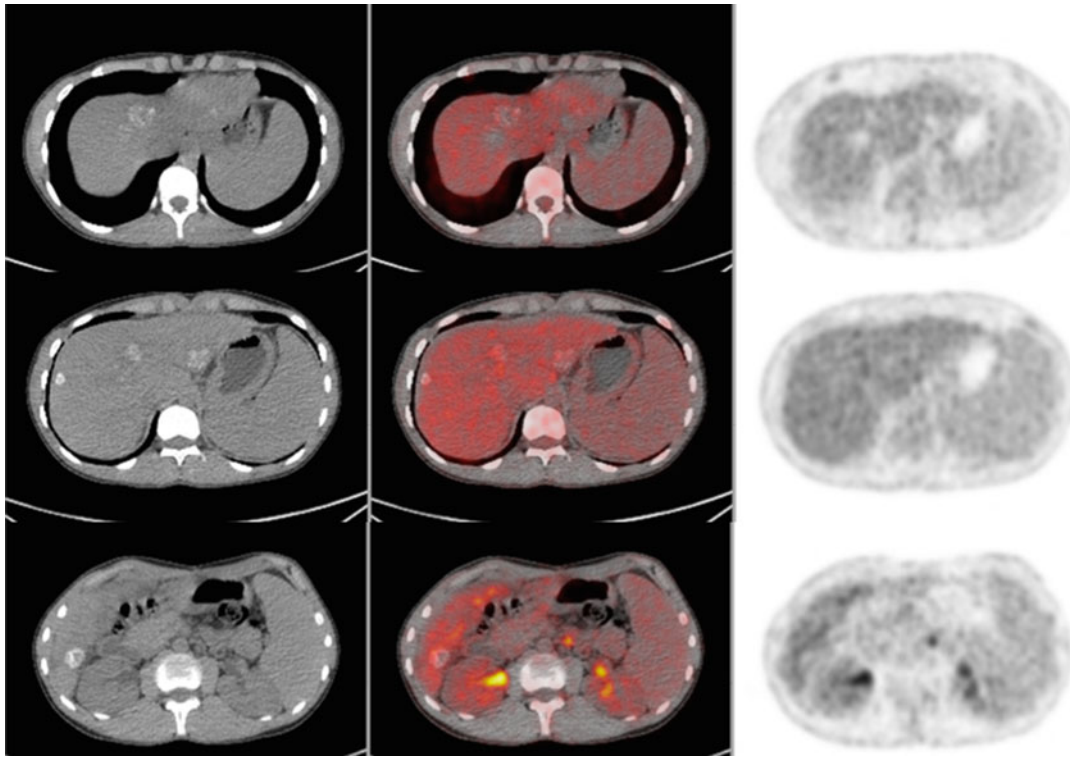

Fig. 19 [^{18}F]FDG PET/CT. Axial TC (*left panels*), fused PET/CT (*middle panels*), and PET alone (*right panels*) showing a clear metabolic response of the liver metastases treated with radioembolization

Follow-Up

One week later, the patient underwent MRI with paramagnetic contrast (Gd-EOB-DTPA) that confirmed the presence of multiple liver metastases. In particular, the MRI scan showed on the arterial phase, and a thin rim of hyperintensity was observed at the edge of the lesion in the arterial phase, which turned hypointense in the portal-venous phase. This pattern is typical of hypovascular metastases (Fig. 21).

Management

Since the patient presented with stage IV disease with multiple liver metastases, neoadjuvant chemotherapy was chosen as first treatment strategy.

Teaching Point

In patients with rectal cancer, accurate staging is of paramount importance, and it is essential also to correctly detect liver metastases in order to

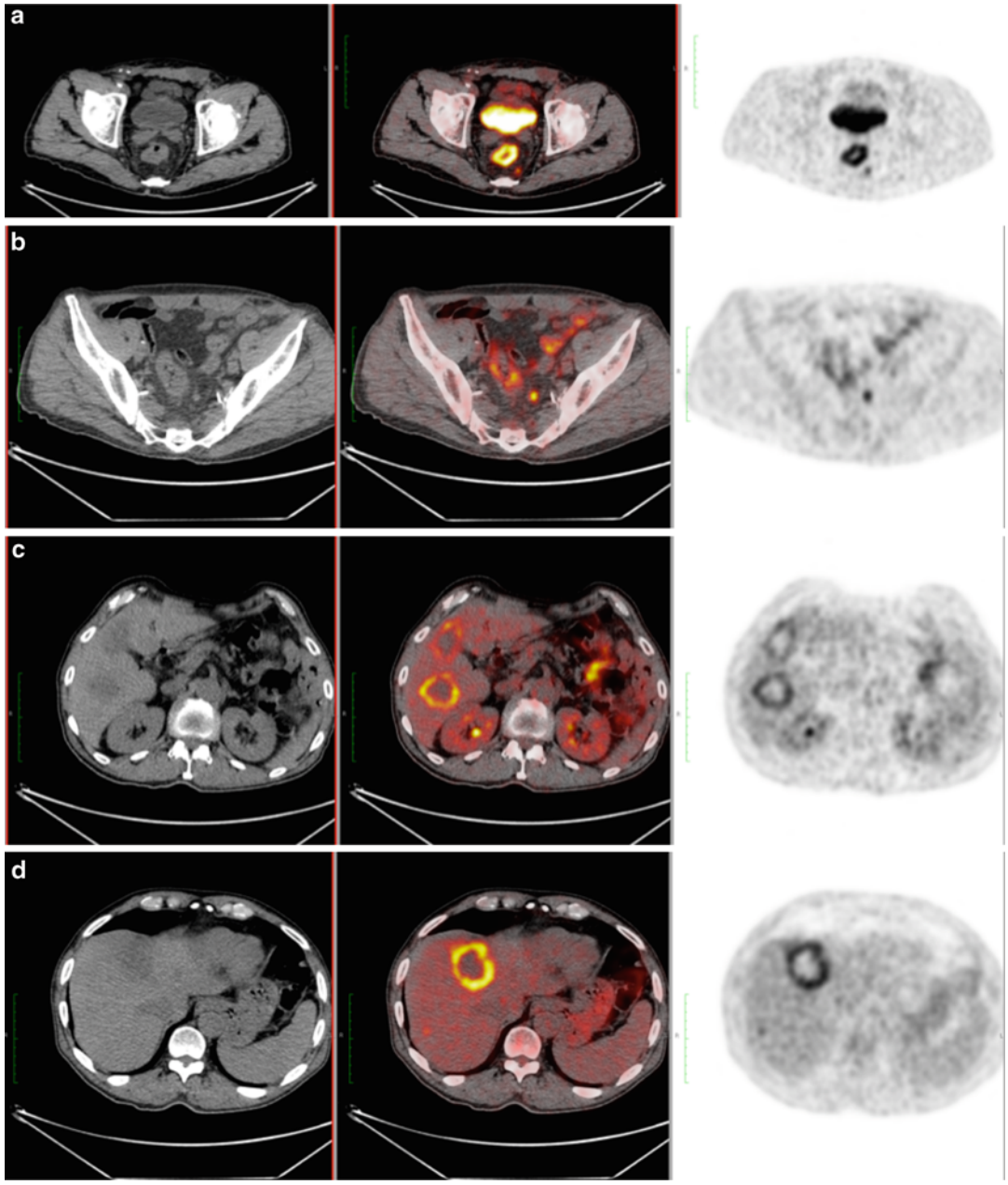

Fig. 20 (**a**) Axial CT, fused PET/CT, and PET images show markedly increased [^{18}F]FDG uptake in the thickened rectal wall, corresponding to the rectal carcinoma. (**b**) Axial CT, fused PET/CT, and PET images demonstrate the area of focal [^{18}F]FDG uptake corresponding to a left parasacral lymph node. (**c**, **d**) The axial CT image shows heterogeneous attenuation due to lesions in both the right and the left lobe of the liver, while the fused PET/CT and PET images demonstrate frankly increased tracer uptake in the peripheral rim of multiple liver metastases

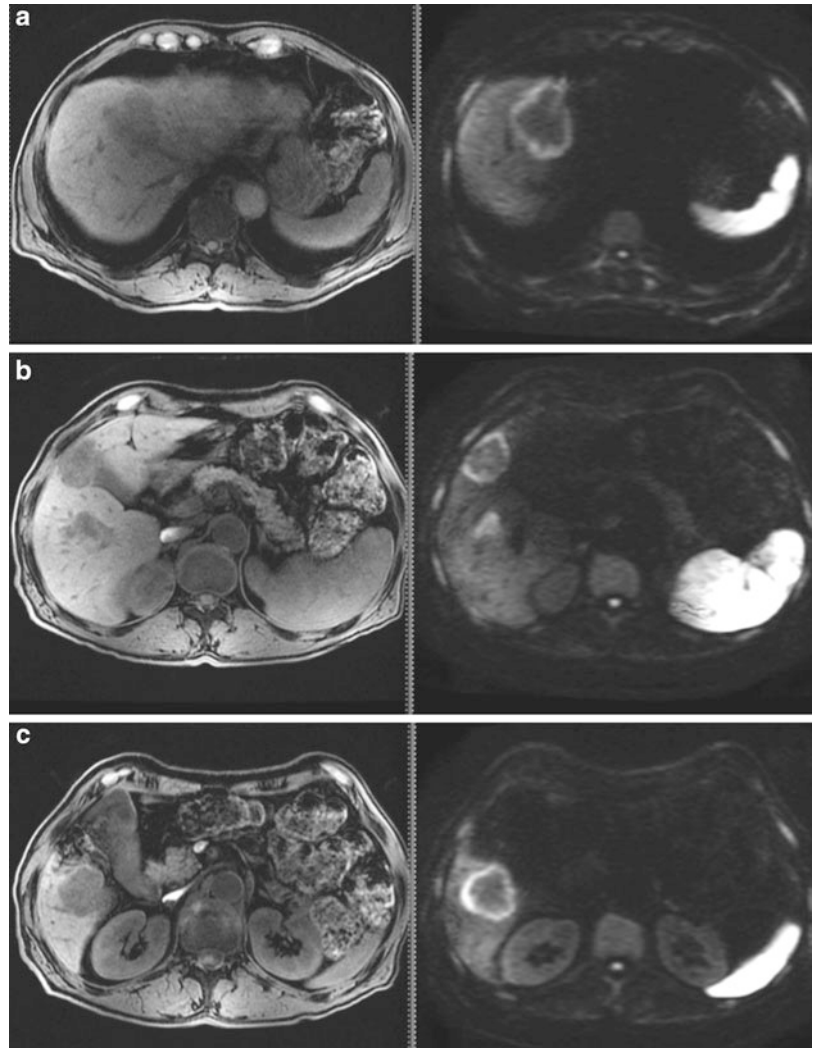

Fig. 21 MRI axial images corresponding to the lesions detected at PET/CT. Water LAVA flex MR on the *left* and DWI Ax on the *right*. (**a**–**c**) Liver metastases appear hypointense on LAVA sequences, while at DWI, a thin hyperintense rim can be observed at the periphery of the lesions

identify those patients that can be treated surgically with curative intents. [^{18}F]FDG PET/TC along with MRI can provide important information about the presence of lymph node metastases, as well as about the site and number of distant metastases. Contrast-enhanced MRI is recommended for characterization of suspected liver metastases from colorectal cancer, since its diagnostic performance is superior to contrast-enhanced ultrasound and CT. The use of hepatobiliary contrast media may further improve the detection rate of liver metastases.

Teaching Cases in Nuclear Oncology: Pancreatic Cancer

65

Alice Lorenzoni, Alessandra Alessi, and Flavio Crippa

Keywords

[^{18}F]FDG • ^{68}Ga-DOTATOC • Pancreatic cancer • Pancreatic neuroendocrine tumor

Glossary

[^{18}F]FDG	2-Deoxy-2-[^{18}F]fluoro-D-glucose
Ca19.9	Carbohydrate antigen 199, a tumor-associated marker
ceCT	Contrast-enhanced CT
CT	X-ray computed tomography
DOTA	1,4,7,10-Tetraazacyclo-dodecane-1,4,7,10-tetraacetic acid (macrocyclic coupling agent to label compounds of biological interest with metal radionuclides)
DOTATOC	DOTA-Tyr^3-octreotide
EUS	Endoscopic ultrasonography
MIP	Maximum intensity projection
MRI	Magnetic resonance imaging
PET	Positron emission tomography
PET/CT	Positron emission tomography/ Computed tomography
PNET	Pancreatic neuroendocrine tumor
SPECT	Single-photon emission computed tomography
SPECT/CT	Single-photon emission computed tomography/ Computed tomography
US	Ultrasonography

Contents

Pancreatic Cancers: Case No. 1 1700
Findings 1700
Discussion 1700

Pancreatic Cancers: Case No. 2 1700
Presentation 1700
Findings 1700
Discussion 1700

Pancreatic Cancers: Case No. 3 1700
Presentation 1702
Follow-Up 1702

Pancreatic Cancers: Case No. 4 1705
Presentation 1705
Findings 1705

Pancreatic Cancers: Case No. 5 1706
Presentation 1706
Findings 1706

Pancreatic Cancers: Case No. 6 1707
Presentation 1707
Findings 1709

Pancreatic Cancer: Case No. 7 1709
Presentation 1709
Findings 1712
Teaching Point 1713

A. Lorenzoni (✉) • A. Alessi • F. Crippa
Nuclear Medicine Division, IRCCCS National Cancer Institute, Milan, Italy
e-mail: alice.lorenzoni@istitutotumori.mi.it; alicelorenzoni@hotmail.it

© Springer International Publishing Switzerland 2017
H.W. Strauss et al. (eds.), *Nuclear Oncology*,
https://doi.org/10.1007/978-3-319-26236-9_68

Pancreatic Cancers: Case No. 8 1713
Presentation 1714
Findings 1714

Pancreatic Cancers: Case No. 1

A 73-year-old woman presented with abdominal pain radiating to the back and weight loss over the past 3 months. A contrast-enhanced CT showed low-attenuating enhancing mass in the head of the pancreas (max diameter 36 mm), suggestive of malignancy; suspected liver lesion of the VIII hepatic segment was also shown. An endoscopic ultrasound (EUS) was performed to guide fine-needle biopsy of the pancreatic lesion which demonstrated poorly differentiated adenocarcinoma.

Findings

[^{18}F]FDG PET/CT is performed as a part of initial staging.

Intense area of [^{18}F]FDG uptake is shown in the pancreatic head corresponding to malignant mass.

[^{18}F]FDG-avid pathological hepatic lesion with central photopenic area corresponding to necrotic center is also demonstrated in the VIII segment. In addition, a hypermetabolic peritoneal nodule in presacral space is seen.

[^{18}F]FDG PET/CT confirms stage IV disease also showing peritoneal implant misdiagnosed on diagnostic CT. The patient was treated with chemotherapy.

Discussion

[^{18}F]FDG PET/CT detection of distant metastases or unexpected lesions in pancreatic cancer may change patient management excluding patient from surgical intervention and thus avoiding unnecessary procedure. The spread into peritoneum is not uncommon but often missed on conventional anatomical imaging (Figs. 1, 2, and 3).

Pancreatic Cancers: Case No. 2

Case contributed by: E. Tabacchi[1], C. Nanni[1], I. Bossert[1], A. M. Maffione[2], S. Fanti[1]

[1]Nuclear Medicine Unit, "S. Orsola-Malpighi" Hospital, Bologna, Italy

[2]Nuclear Medicine Unit, "Santa Maria della Misericordia" Hospital, Rovigo, Italy

Presentation

A 72-year-old woman with a history of hyperparathyroidism and osteoporosis was diagnosed with a lesion in the uncinate process of the pancreas with an associated liver lesion.

Findings

Patient underwent [^{18}F]FDG PET/CT for staging that showed increased uptake (SUV_{max} 17.5) at the head-isthmus of the pancreas suspicious for cancer (Fig. 4a) and focal uptake at the liver (IV segment, SUV_{max} 9) and at some para-aortic (SUV_{max} 6.8), epiphrenic (SUV_{max} 8.2), and left laterocervical lymph nodes (SUV_{max} 8.5) suspicious for metastasis (Figs. 4b and 5).

Discussion

The main objective of pancreatic cancer staging is to depict local and distant spread, which may preclude surgery. [^{18}F]FDG PET may play an important role in this clinical decision.

Pancreatic Cancers: Case No. 3

Case contributed by: E. Tabacchi[1], C. Nanni[1], I. Bossert[1], A. M. Maffione[2], S. Fanti[1]

[1]Nuclear Medicine Unit, "S. Orsola-Malpighi" Hospital, Bologna, Italy

[2]Nuclear Medicine Unit, "Santa Maria della Misericordia" Hospital, Rovigo, Italy

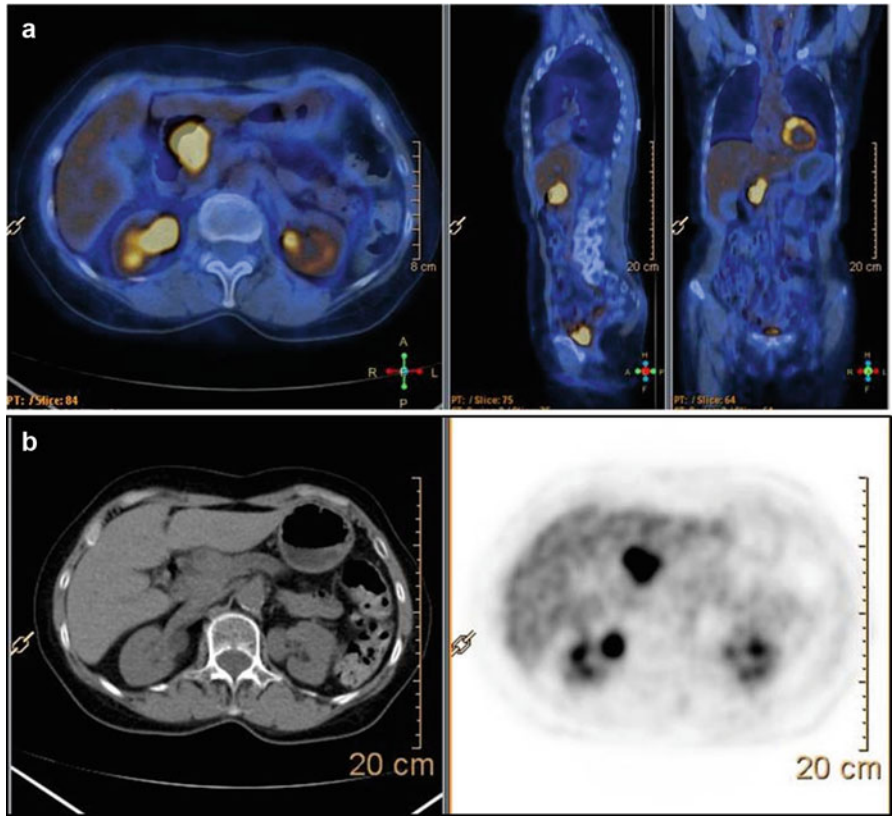

Fig. 1 [^{18}F]FDG PET/CT images demonstrate metabolically active foci in the pancreatic head ((**a**) PET/CT fused images: axial, sagittal, and coronal image from the *left* to the *right*; (**b**) axial CT image on the *left* and axial PET image on the *right*)

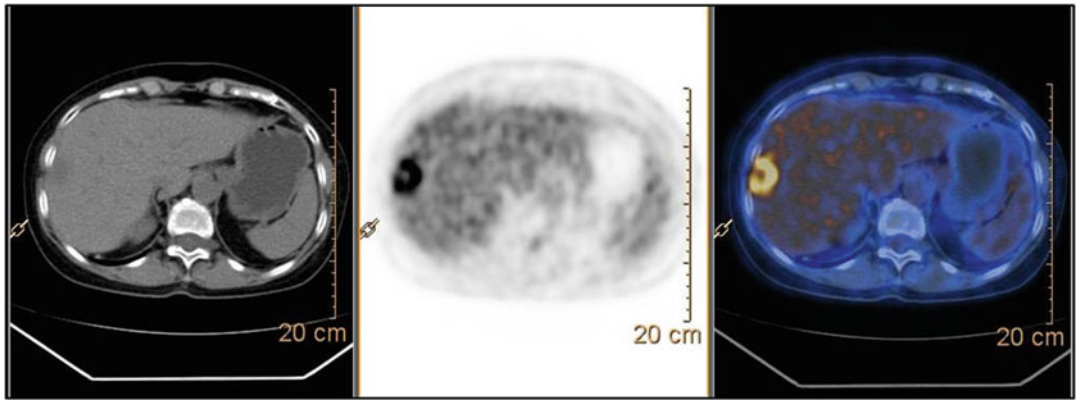

Fig. 2 PET/CT transaxial images demonstrate hepatic [^{18}F]FDG focal uptake consistent with metastatic lesion (CT image in *left panel*, PET image in *central panel*, fused PET/CT image in *right panel*)

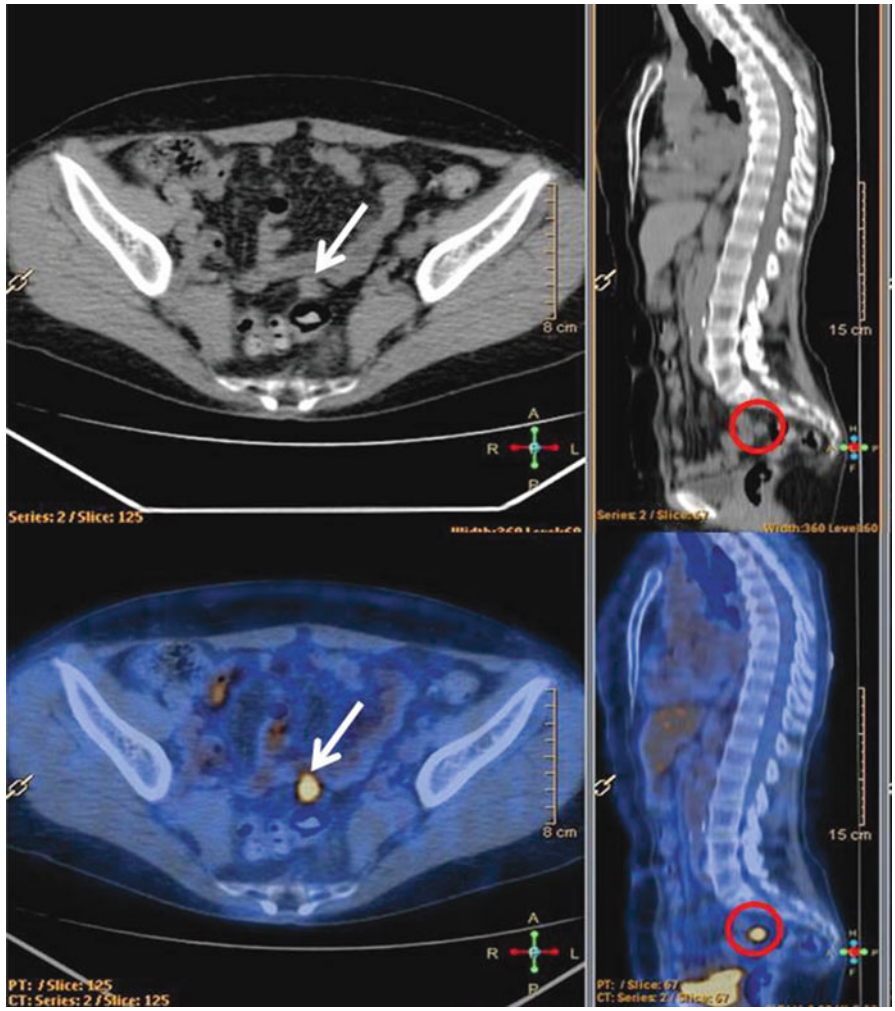

Fig. 3 PET/CT images of hypermetabolic peritoneal nodule in the pelvis (*white arrow* and *red circle*) (axial CT *upper left*, sagittal CT *upper right*, axial fused PET/CT image *lower left*, sagittal fused PET/CT image *lower right*)

Presentation

An 83-year-old man, hospitalized for significant weight loss, had an ^{18}[F]FDG PET/CT that showed heterogeneous uptake of the radiopharmaceutical in the body-tail of the pancreas (SUV_{max} 5.2), with a central necrotic area (Fig. 6).

Histology showed biliopancreatic adenocarcinoma (pT3N0M0) and patient underwent distal splenopancreatectomy.

Follow-Up

One year after surgery, his medical condition worsened and Ca19.9 was 99.8 U/mL.

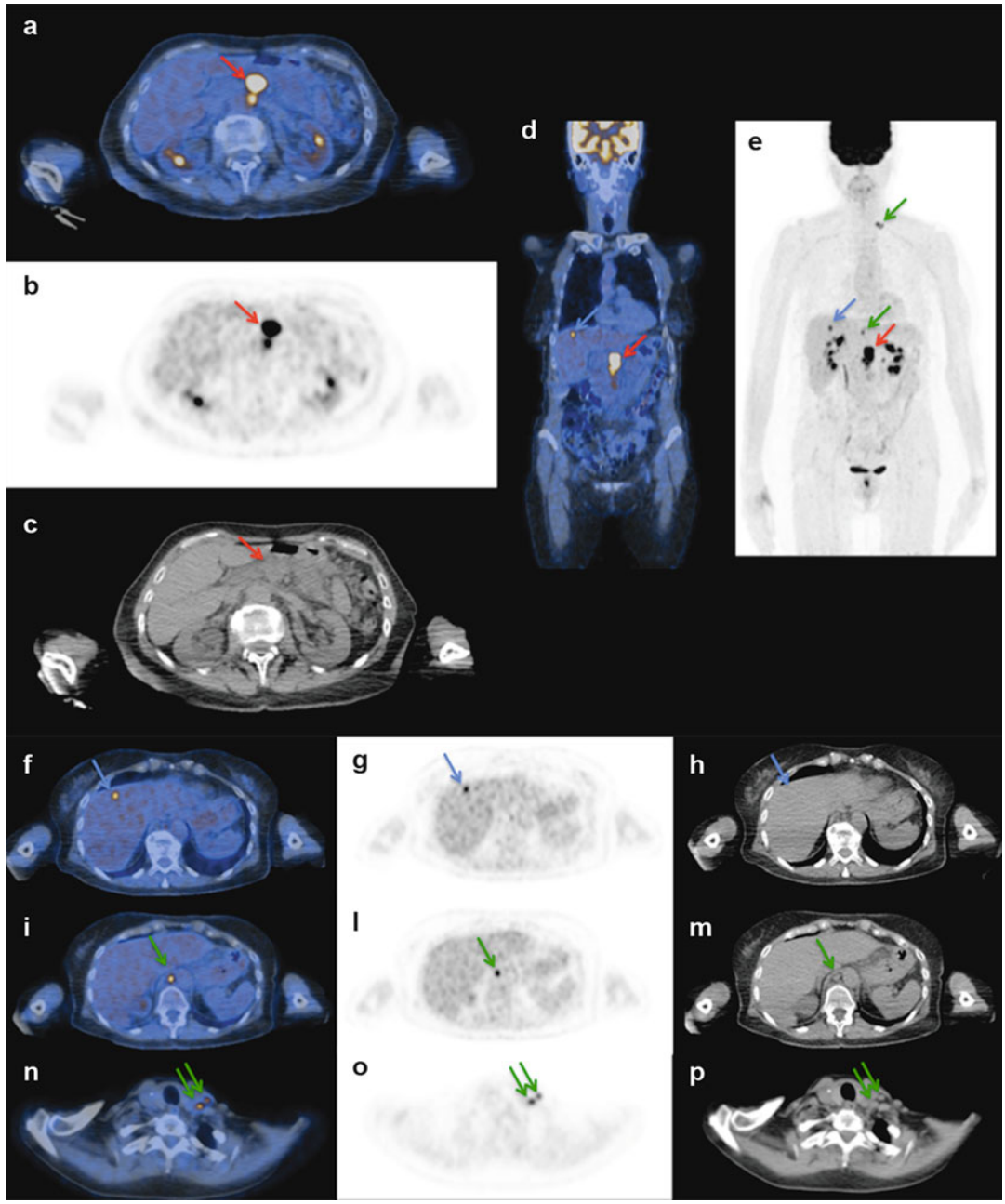

Fig. 4 (**a**) *A* Transaxial [^{18}F]FDG PET/CT; *B* transaxial [^{18}F]FDG PET/CT; *C* transaxial CT; *D* coronal [^{18}F]FDG PET/CT; *E* MIP; *red* flag, pancreatic finding; *green* flag, lymph nodal finding. (**b**) (*F*, *I*, *N*, transaxial [^{18}F]FDG PET/CT; *G*, *L*, *O*, transaxial [^{18}F]FDG PET; *H*, *M*, *P*, transaxial CT; *blue* flag, hepatic finding; *green* flag, lymph nodal finding)

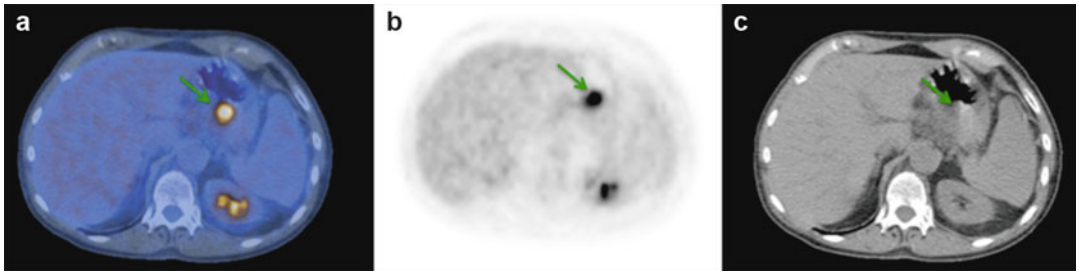

Fig. 5 *A* Transaxial [^{18}F]FDG PET/CT, *B* transaxial [^{18}F]FDG PET, *C* transaxial CT; *green* flag, lymph nodal finding

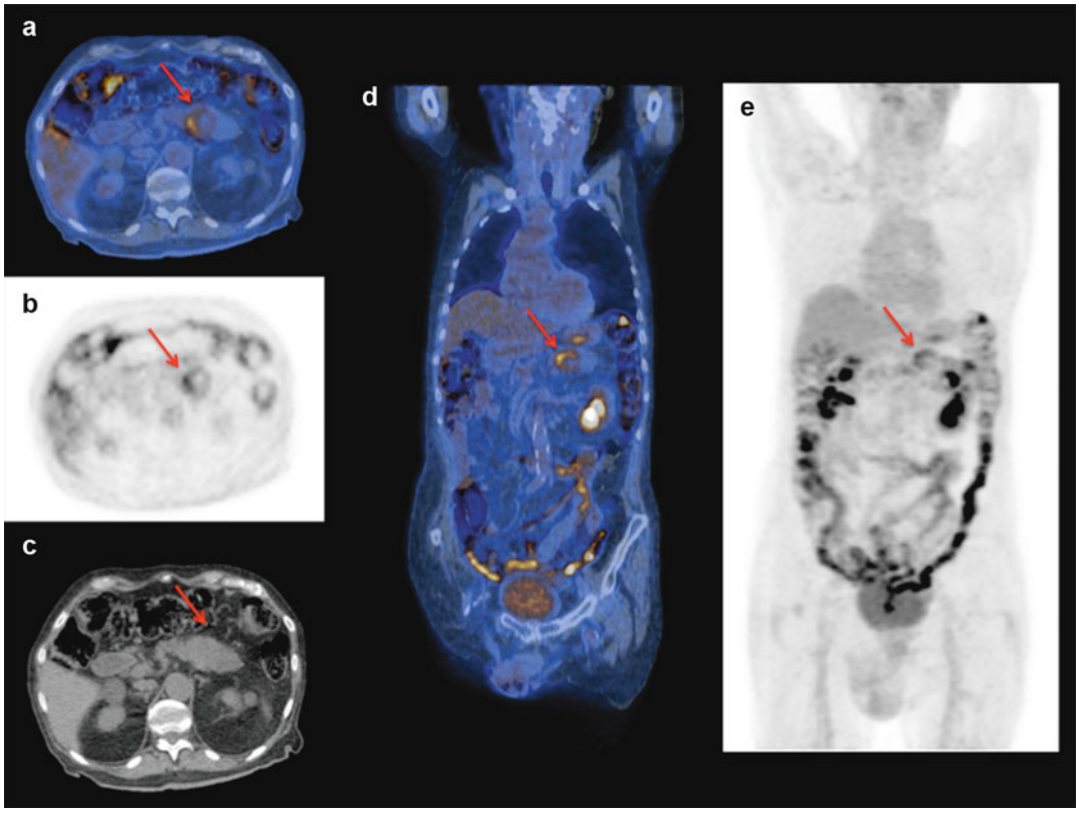

Fig. 6 *A* Transaxial [^{18}F]FDG PET/CT, *B* transaxial [^{18}F]FDG PET, *C* transaxial CT, *D* coronal [^{18}F]FDG PET/CT, *E* MIP; *red* flag, pancreatic finding

A subsequent [^{18}F]FDG PET/CT showed uptake (SUV_{max} 9.5) in the head and body of the pancreas, near the surgical clips. This finding was suspicious for recurrent disease (Fig. 7).

The patients condition deteriorated, and about one month later a repeat [^{18}F]FDG PET/CT that showed an area of increased uptake in the head-body of the pancreas (SUV_{max} 8.5) next to the rear wall of the gastric antrum (Fig. 8).

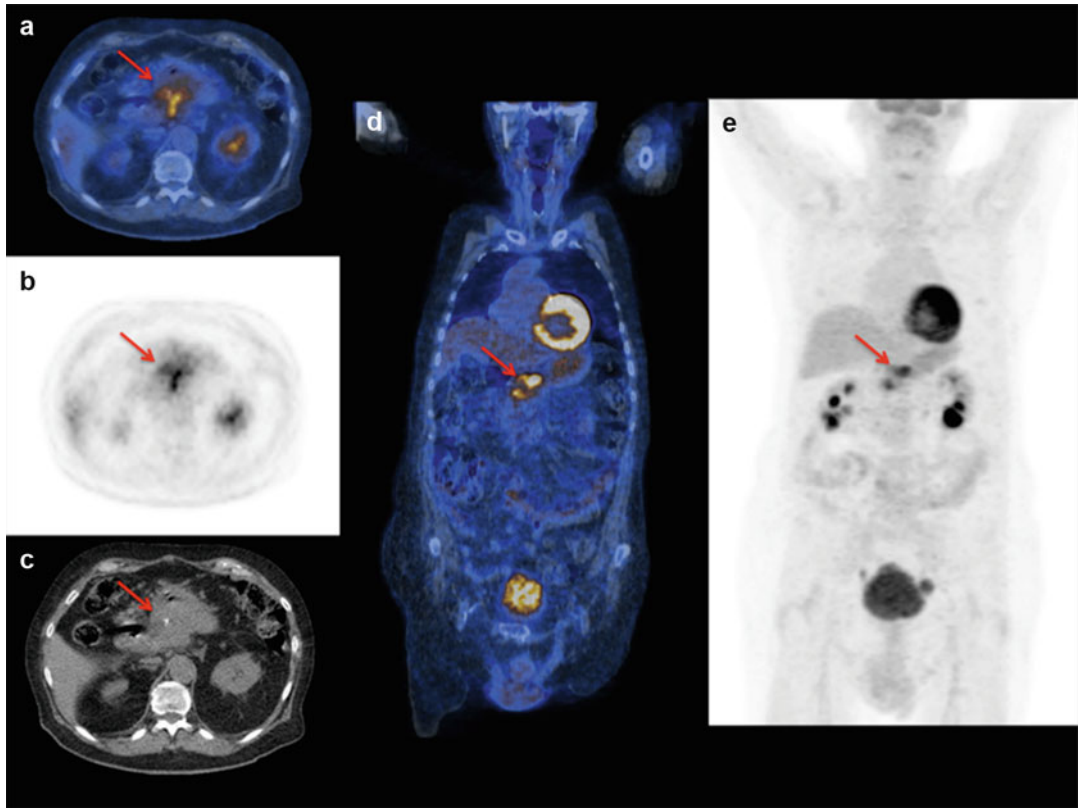

Fig. 7 *A* Transaxial [^{18}F]FDG PET/CT, *B* transaxial [^{18}F]FDG PET, *C* transaxial CT, *D* coronal [^{18}F]FDG PET/CT, *E* MIP; *red* flag, pancreatic finding

Pancreatic Cancers: Case No. 4

Case contributed by: E. Tabacchi[1], C. Nanni[1], I. Bossert[1], A. M. Maffione[2], S. Fanti[1]

[1]Nuclear Medicine Unit, "S. Orsola-Malpighi" Hospital, Bologna, Italy

[2]Nuclear Medicine Unit, "Santa Maria della Misericordia" Hospital, Rovigo, Italy

Presentation

A 63-year-old woman with inoperable pancreatic cancer underwent chemotherapy.

Findings

After six cycles of chemotherapy, she underwent [^{18}F]FDG PET/CT to assess response to therapy. [^{18}F]FDG PET/CT revealed focal uptake at the head-uncinate process of the pancreas ($SUV_{max} = 5.3$) (Fig. 9a: red flags) and to some metastatic areas in the liver, respectively, to the dome of the liver ($SUV_{max} = 6.9$), between the II and III segment ($SUV_{max} = 6.7$) and between the II and IV segment ($SUV_{max} = 7.7$) (Fig. 9a: *E*, blue flag and Fig. 9b: *F*, *G*, *H*, blue flags).

The patient continued chemotherapy, and after 4 months, she underwent another [^{18}F]FDG PET/CT that revealed an increased uptake to the pancreas ($SUV_{max} = 7.3$), to many hepatic

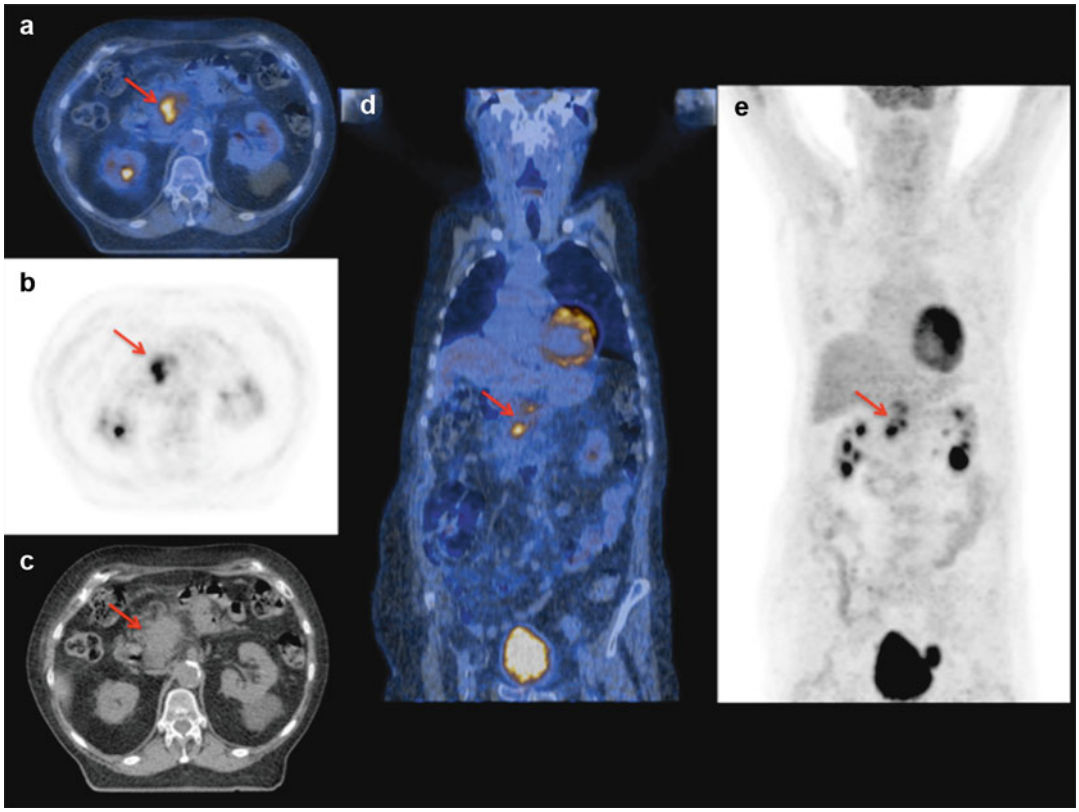

Fig. 8 *A* Transaxial [^{18}F]FDG PET/CT, *B* transaxial [^{18}F]FDG PET, *C* transaxial CT, *D* coronal [^{18}F]FDG PET/CT, *E* MIP; *red* flag, pancreatic finding

lesions (SUV_{max} = 7.8) (Fig. 10a: *D*, *E*, blue flags and Fig. 10b: *F*, *G*, *H*, blue flags), to some sites in the abdomen suspicious for peritoneal carcinomatosis (Fig. 10a: *E*, pink flags), and to some right inguinal lymph nodes (SUV_{max} = 6.6) (Fig. 10a: *E*, green flag).

Widespread skeletal uptake compatible with medullary rebound after chemotherapy is observed (Fig. 10a: *E*).

Pancreatic Cancers: Case No. 5

Case contributed by: E. Tabacchi[1], C. Nanni[1], I. Bossert[1], A. M. Maffione[2], S. Fanti[1]

[1]Nuclear Medicine Unit, "S. Orsola-Malpighi" Hospital, Bologna, Italy

[2]Nuclear Medicine Unit, "Santa Maria della Misericordia" Hospital, Rovigo, Italy

Presentation

A 62-year-old man with dyspepsia had a CT scan that revealed severe gastrectasia probably due to neoplastic duodenal obstruction.

Findings

[^{18}F]FDG PET/CT demonstrated peripheral uptake at the head of the pancreas (SUV_{max} = 7.8) (Fig. 11a: red flags) suspected to be a tumor.

[^{18}F]FDG PET/CT also revealed uptake in peripancreatic lymph nodes and to many sites in the liver especially to the right lobe (IV–VIII

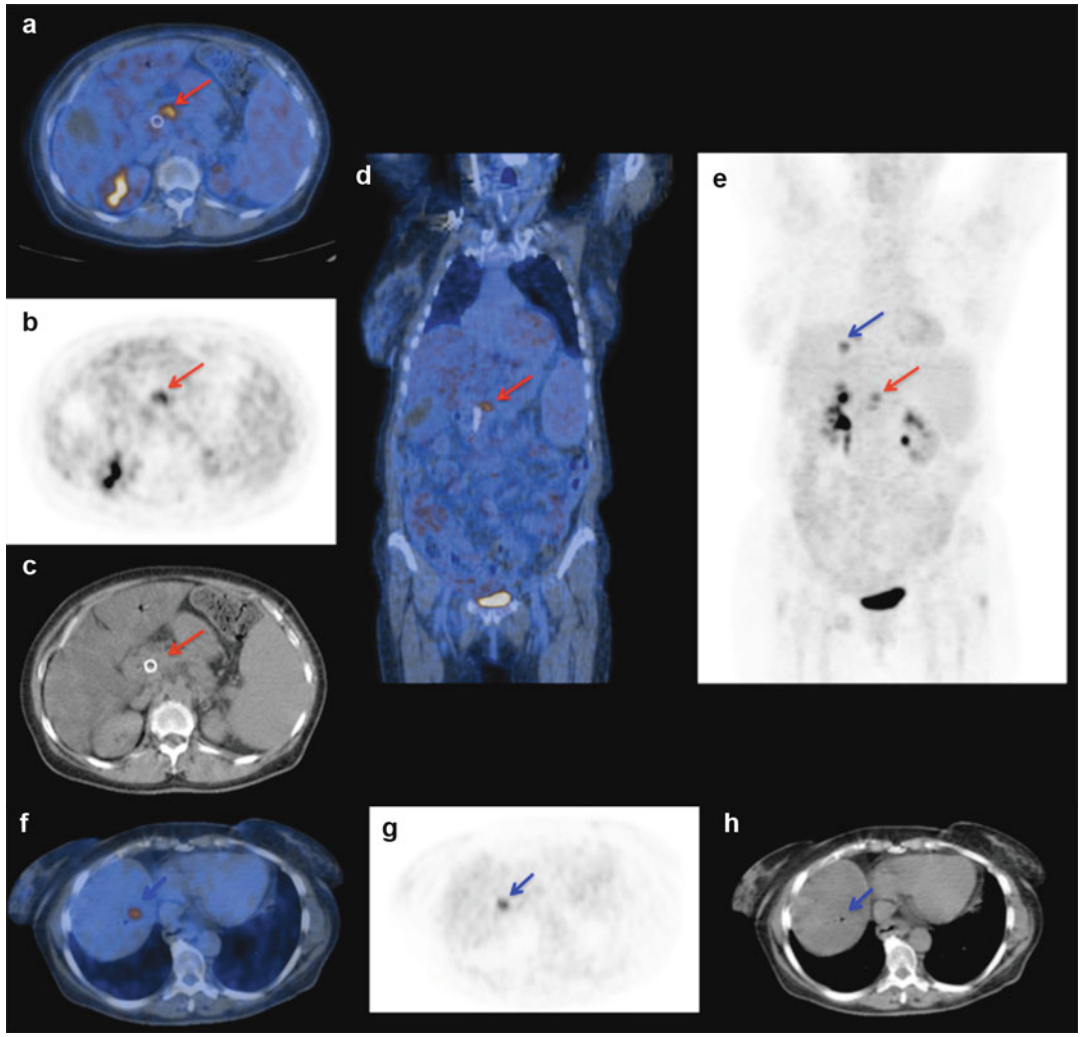

Fig. 9 (**a**) *A* Transaxial [^{18}F]FDG PET/CT, *B* transaxial [^{18}F]FDG PET, *C* transaxial CT, *D* coronal [^{18}F]FDG PET/CT, *E* MIP; *red* flag, pancreatic finding; *blue* flag, hepatic finding. (**b**) (*F* transaxial [^{18}F]FDG PET/CT, *G* transaxial [^{18}F]FDG PET, *H* transaxial CT; *blue* flag, hepatic finding)

segments with $SUV_{max} = 9.9$ and VII–VIII segments with $SUV_{max} = 8$) suspected to be metastasis (Fig. 11a: blue flags).

Pancreatic Cancers: Case No. 6

Case contributed by: E. Tabacchi[1], C. Nanni[1], I. Bossert[1], A. M. Maffione[2], S. Fanti[1]

[1]Nuclear Medicine Unit, "S. Orsola-Malpighi" Hospital, Bologna, Italy

[2]Nuclear Medicine Unit, "Santa Maria della Misericordia" Hospital, Rovigo, Italy

Presentation

A 71-year-old woman was hospitalized for persistent pain in the abdomen (lasting since

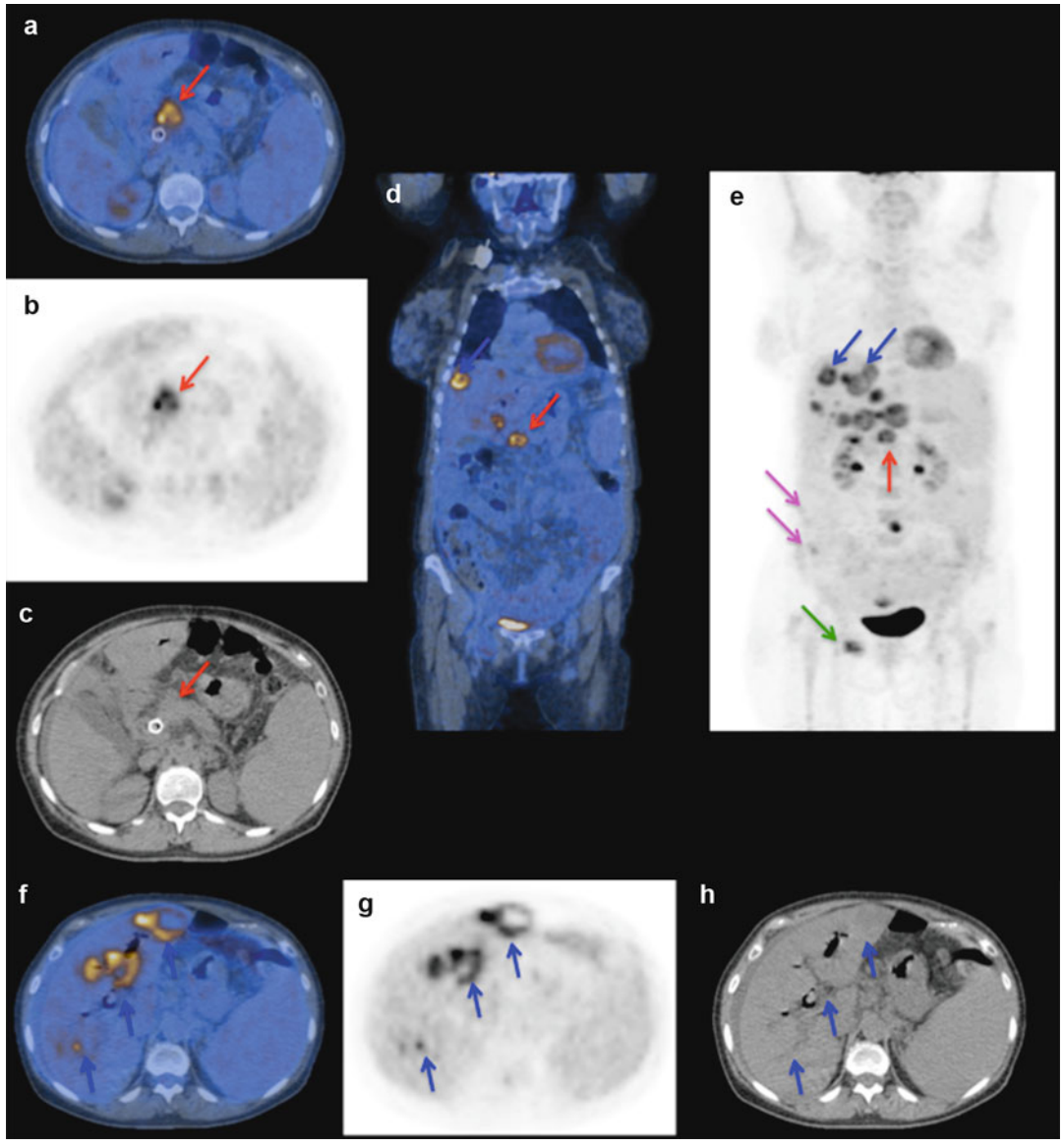

Fig. 10 (**a**) *A* Transaxial [^{18}F]FDG PET/CT, *B* transaxial [^{18}F]FDG PET, *C* transaxial CT, *D* coronal [^{18}F]FDG PET/CT, *E* MIP; *red* flag, pancreatic finding; *blue* flag, hepatic finding; *violet* flag, muscular finding. (**b**) (*F* transaxial [^{18}F]FDG PET/CT, *G* transaxial [^{18}F]FDG PET, *H* transaxial CT; *blue* flag, hepatic finding)

6 months), weight loss, and intestinal sub-obstruction from suspected malignancy of sigma/extrinsic compression. Ca.19.9 was >10.000 U/mL.

Colonoscopy showed a critical stenosis of the descending colon.

Contrast-enhanced CT demonstrated a lesion at the tail of the pancreas, liver metastases, and an extensive pelvic mass.

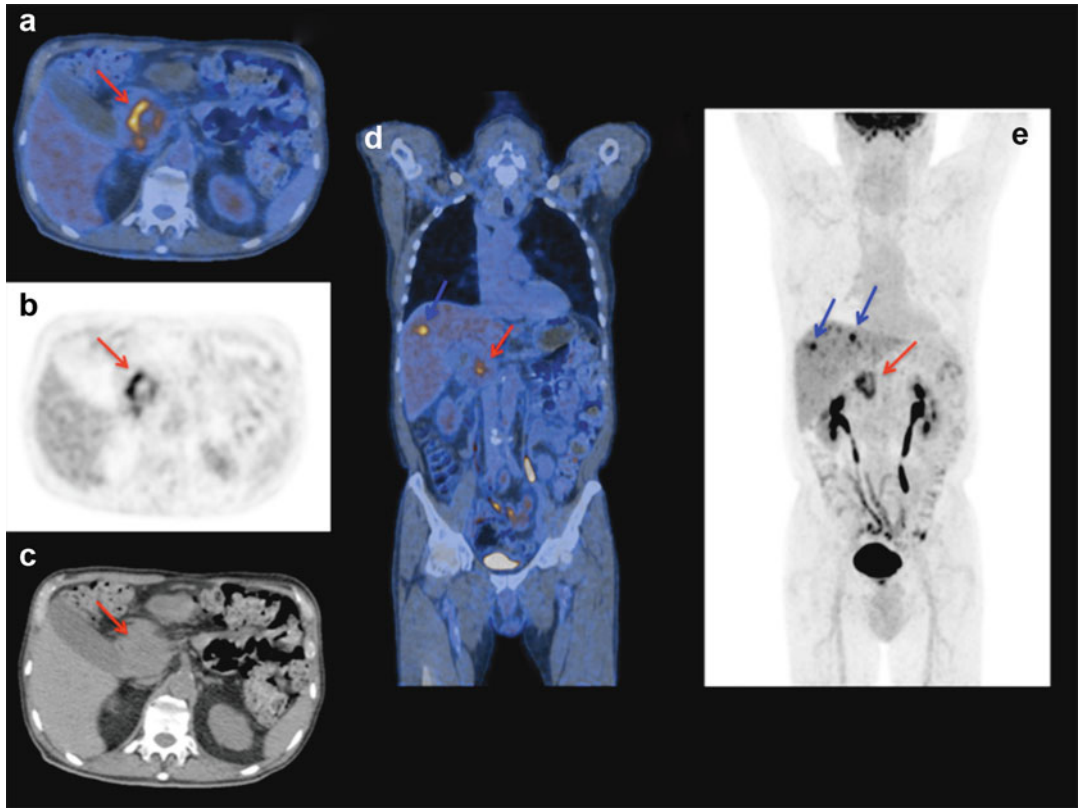

Fig. 11 *A* Transaxial [^{18}F]FDG PET/CT, *B* transaxial [^{18}F]FDG PET, *C* transaxial CT, *D* coronal [^{18}F]FDG PET/CT, *E* MIP; *red* flag, pancreatic finding; *blue* flag, hepatic finding

Findings

The patient underwent [^{18}F]FDG PET/CT that showed an extensive uptake at the body of the pancreas ($SUV_{max} = 10.9$) (Fig. 12a: red flags), at least five hepatic lesions (the greater at the VII segment $SUV_{max} = 9$; the IV segment $SUV_{max} = 12.3$) (Fig. 12b: *F*, *G*, *H*, blue flags), hypermetabolic peritoneal nodules in the left iliac fossa (Fig. 12b: *I*, *L*, *M*, pink flags), and pathological uptake of the sigma ($SUV_{max} = 15.7$) (Fig. 12b: *N*, *O*, *P*, pink flags).

The patient underwent exploratory surgery. The histological examination demonstrated the presence of pancreatic adenocarcinoma (CK7+, CK20+, CDX-, Ca125-).

The patient started chemotherapy with 5-fluorouracil and folinic acid.

Pancreatic Cancer: Case No. 7

Case contributed by: L. Olivari, A. Chiti
Division of Nuclear Medicine, Department of Biomedical Sciences – Humanitas University, Milan, Italy

Presentation

A 70-year-old man otherwise in overall good conditions had a recent diagnosis of prostate cancer. The patient was eligible for radical prostatectomy. During preoperative staging, ultrasound (US) of the abdomen revealed a small hypo-isoechoic round mass near the pancreas. ceCT confirmed the US findings and described a 2 cm exophytic,

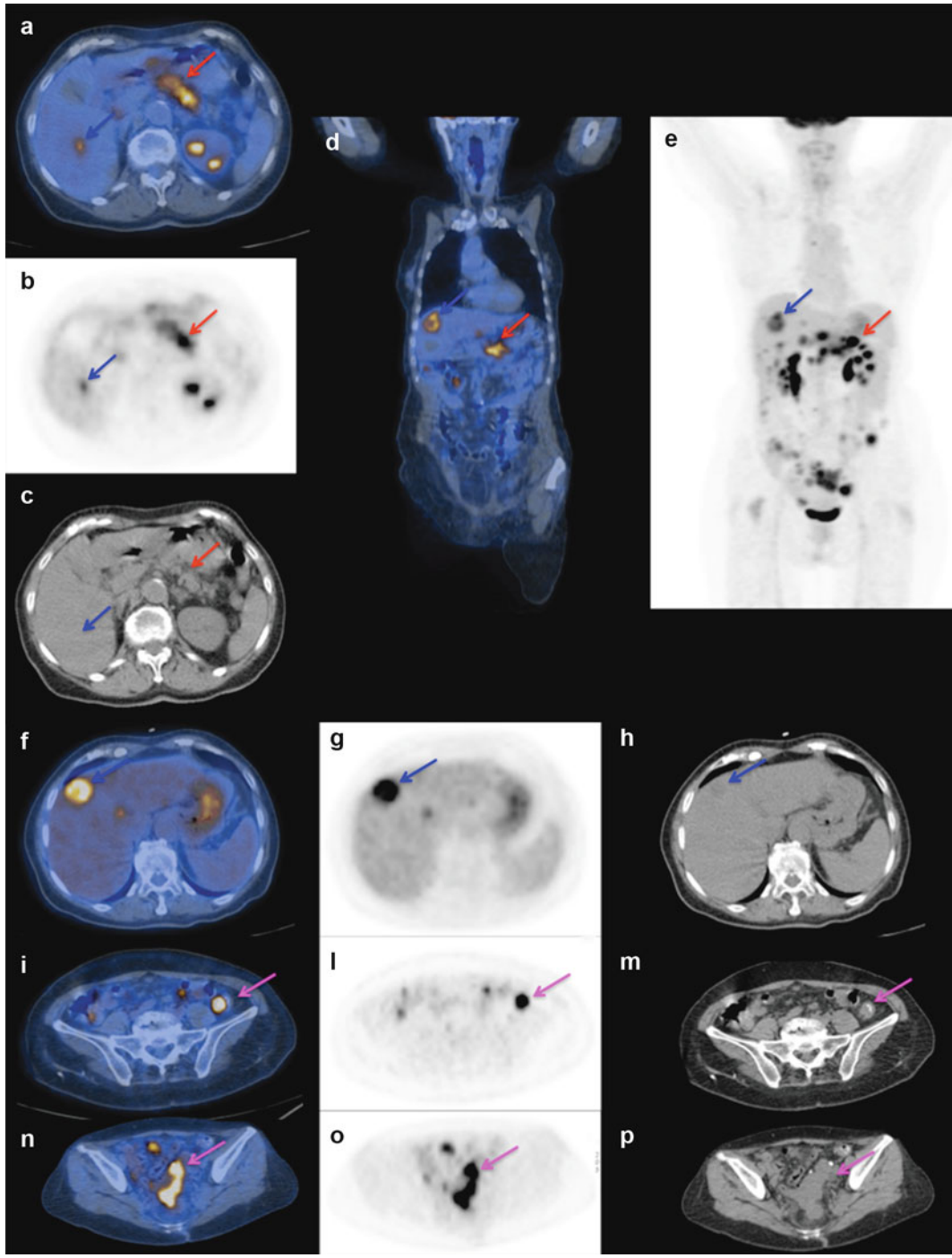

Fig. 12 (**a**) *A* Transaxial [^{18}F]FDG PET/CT, *B* transaxial [^{18}F]FDG PET, *C* transaxial CT, *D* coronal [^{18}F]FDG PET/CT, *E* MIP; *red* flag, pancreatic finding; *blue* flag, hepatic finding. (**b**) (*F*, *I*, *N*, transaxial [^{18}F]FDG PET/CT; *G*, *L*, *O*, transaxial [^{18}F]FDG PET; *H*, *M*, *P*, transaxial CT; *blue* flag, hepatic finding; *pink* flag, peritoneal carcinomatosis, bowel lesions)

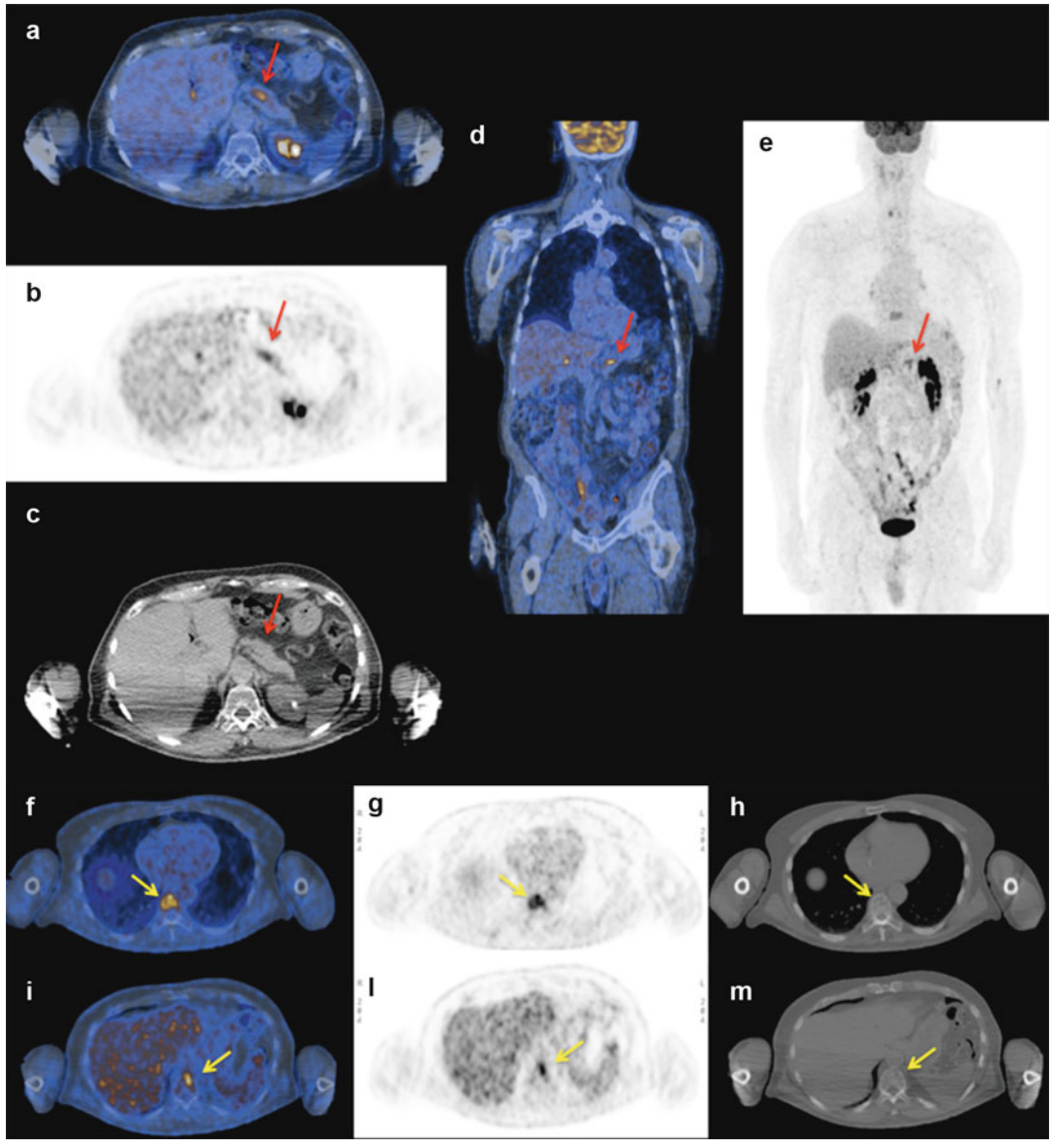

Fig. 13 (**a**) *A* Transaxial [^{18}F]FDG PET/CT, *B* transaxial [^{18}F]FDG PET, *C* transaxial CT, *D* coronal [^{18}F]FDG PET/CT, *E* MIP; *red* flag, pancreatic finding. (**b**) (*F* transaxial [^{18}F]FDG PET/CT, *G* transaxial [^{18}F]FDG PET, *H* transaxial CT; *yellow* flag, bone finding)

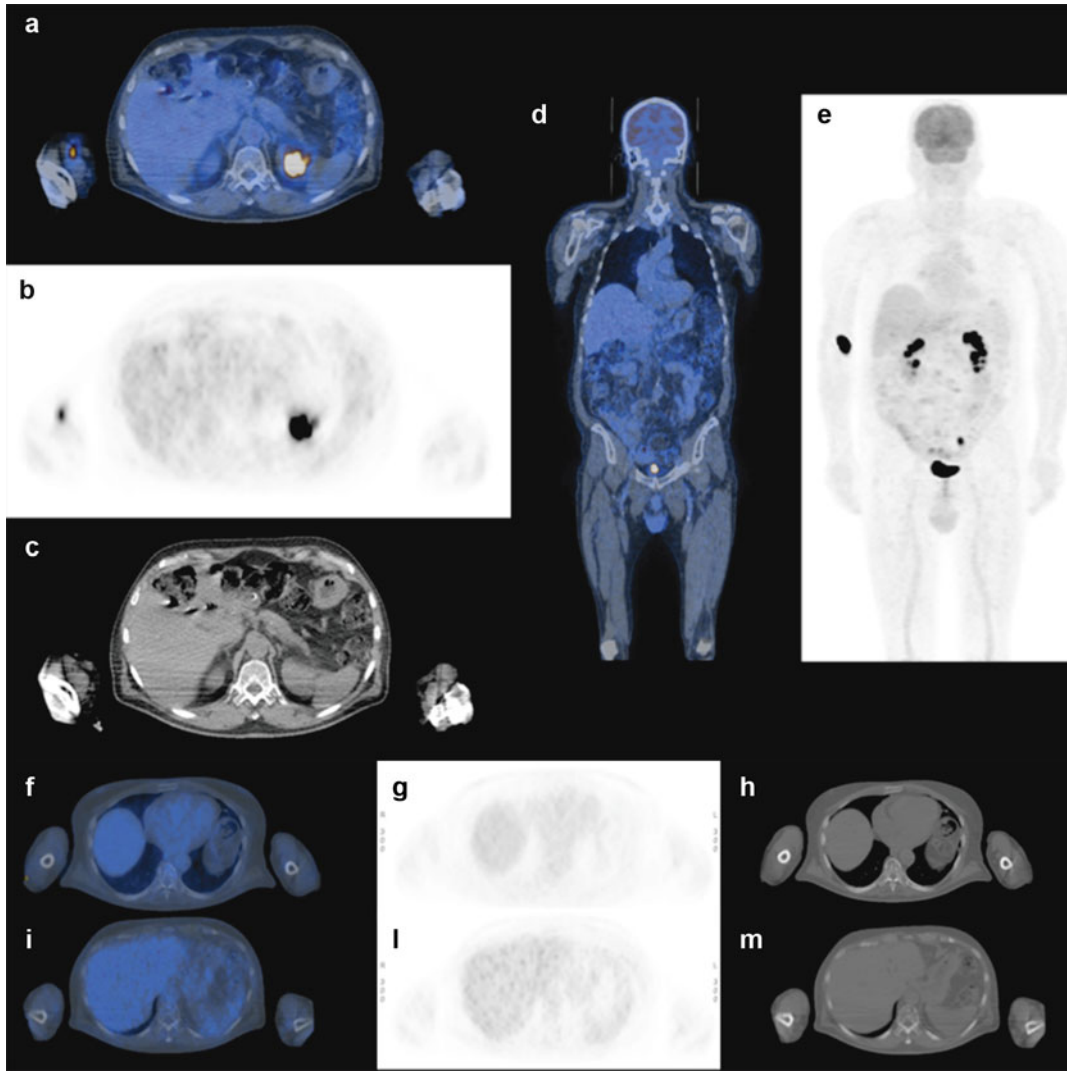

Fig. 14 (**a**) *A* Transaxial [^{18}F]FDG PET/CT, *B* transaxial [^{18}F]FDG PET, *C* transaxial CT, *D* coronal [^{18}F]FDG PET/CT, *E* MIP. (**b**) (*F* transaxial [^{18}F]FDG PET/CT, *G* transaxial [^{18}F]FDG PET, *H* transaxial CT)

hypervascular nodule on the right side of the body of the pancreas.

Findings

A SPECT/CT scan with ^{99m}Tc-nanocolloidal albumin was performed to differentiate possible ectopic spleen tissue from neuroendocrine tumor. SPECT/CT revealed no uptake in the pancreatic lesion, thus confirming the suspicion of a lesion pertaining to the pancreas.

^{68}Ga-DOTATOC PET/CT showed intense tracer uptake in the pancreatic lesion (Fig. 15). No other lesions were found. EUS fine-needle aspiration

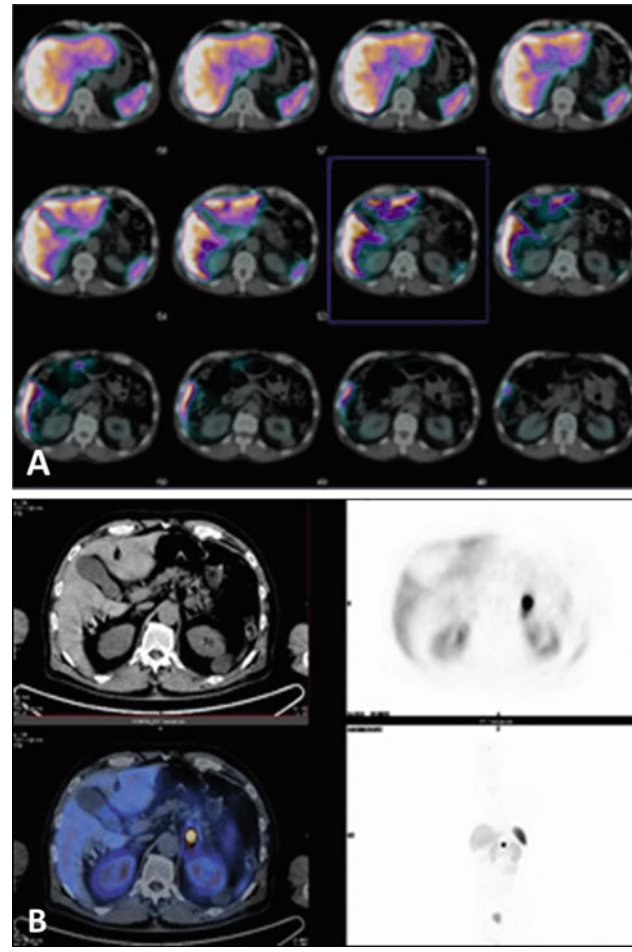

Fig. 15 Axial SPECT/CT images with ^{99m}Tc-nanocolloidal albumin (A) reveal no uptake in the pancreatic lesion. ^{68}Ga-DOTATOC PET/CT showed intense tracer uptake in the pancreatic lesion

biopsy confirmed the presence of neuroendocrine tumor.

Teaching Point

Intra-pancreatic accessory spleen, or "splenule," is an uncommon congenital abnormality of the spleen with an incidence of around 2%; this abnormality can coexist with a normal spleen and can mimic a pancreatic neuroendocrine tumor (PNET). PNETs are characterized by high signal intensity on MRI T2-weighted images, and they are typically a hyperdense, spherical lesion on the ceCT arterial phase. Both intra-pancreatic accessory spleen and PNETs show increased ^{68}Ga-DOTATOC uptake. ^{99m}Tc-colloid SPECT/CT should be performed in suspicious pancreatic lesions in order to prevent unnecessary surgery, as this radiopharmaceutical shows increased uptake in an intra-pancreatic accessory spleen but no uptake in PNETs.

Pancreatic Cancers: Case No. 8

Case contributed by: E. Tabacchi[1], C. Nanni[1], I. Bossert[1], A. M. Maffione[2], S. Fanti[1]

[1]*Nuclear Medicine Unit, "S. Orsola-Malpighi" Hospital, Bologna, Italy*

[2]*Nuclear Medicine Unit, "Santa Maria della Misericordia" Hospital, Rovigo, Italy*

Presentation

A 64-year-old man, treated about 7 years before with a duodenocefalopancreasectomy for adenocarcinoma of the ampulla of Vater, underwent [^{18}F]FDG PET/CT for an increasing back pain.

Findings

[^{18}F]FDG PET/CT revealed an increased uptake at some vertebrae like D9 (SUV_{max} = 6.5) and D11 (SUV_{max} = 6.4) (Fig. 13b: yellow flags) in correspondence of lithic areas and a focal uptake (SUV_{max} = 8) at the front edge of the body of the pancreas (Fig. 13a: red flags).

At first the suspect was recurrence of the pancreatic cancer with bone metastases but after a reevaluation of the CT images and seeing the negativity of tumor markers, it was decided to proceed with the biopsy of the iliac wing. The diagnosis was of plasmocitoma.

Patient started first-line chemotherapy with gemcitabine and zoledronic acid.

After 6 months a repeat [^{18}F]FDG PET/CT was negative (Fig. 14a, b). The previous pancreatic uptake was therefore attributed to a nonspecific/inflammatory finding.

Teaching Cases in Nuclear Oncology: Colorectal Cancer

66

Alice Lorenzoni, Alessandra Alessi, and Flavio Crippa

Keywords

Anal cancer • PET/MRI • Colon cancer • [^{18}F]FDG PET/CT • Radiotherapy planning

Glossary

[^{18}F] FDG	2-Deoxy-2-[^{18}F]fluoro-D-glucose
ADC	Apparent diffusion coefficient, a parameter used in MRI to measure the magnitude of diffusion (of water molecules) within tissues
AJCC	American Joint Committee on Cancer
CEA	Carcinoembryonic antigen, a circulating serum tumor-associated marker
CRC	Colorectal cancer
CT	X-ray computed tomography
CTC	CT colonography, also known as "virtual colonoscopy"
CTV	Clinical target volume
DWI	Diffusion-weighted magnetic resonance imaging, a technique used to detect changes in the distribution of water molecules in selected regions
ESMO	European Society of Clinical Oncology
EUS	Endoscopic ultrasound-guided
GTV	Gross tumor volume
Gy	Gray unit (ionizing radiation dose in the International System of Units, corresponding to the absorption of one joule of radiation energy per kilogram of matter)
M	Metastasis status according to the AJCC/UICC TNM staging system
MIP	Maximum intensity projection
MRI	Magnetic resonance imaging
N	Lymph node status according to the AJCC/UICC TNM staging system
NCCN	National Comprehensive Cancer Network
PET	Positron emission tomography
PET/CT	Positron emission tomography/Computed tomography
PET/MR	Positron emission tomography/Magnetic resonance imaging system
PET/MRI	Positron emission tomography/Magnetic resonance imaging
RT	Radiation therapy
SUV	Standardized uptake value
SUV_{max}	Standardized uptake value at point of maximum
T	Tumor status according to the AJCC/UICC staging system
THRIVE	A magnetic resonance technique that combines sensitivity encoding, large volume coverage, and uniform fat suppression (from T1W

A. Lorenzoni (✉) • A. Alessi • F. Crippa
Nuclear Medicine Division, IRCCCS National Cancer Institute, Milan, Italy
e-mail: alice.lorenzoni@istitutotumori.mi.it; alicelorenzoni@hotmail.it

© Springer International Publishing Switzerland 2017
H.W. Strauss et al. (eds.), *Nuclear Oncology*,
https://doi.org/10.1007/978-3-319-26236-9_69

	High Resolution Isotropic Volume Examination)
UICC	Union Internationale Contre le Cancer (International Union Against Cancer)

Contents

Colorectal Cancer: Case No. 1 1716
Presentation 1716
Findings 1716
Discussion 1716

Colorectal Cancer: Case No. 2 1717
Presentation 1717
Findings 1718
Discussion 1718

Colorectal Cancer: Case No. 3 1718
Presentation 1718
Findings 1718
Discussion 1718

Colorectal Cancer: Case No. 4 1718
Presentation 1718
Findings 1718
Discussion 1719

Colorectal Cancer: Case No. 5 1719
Presentation 1721
Findings 1721

Colorectal Cancer: Case No. 6 1721
Presentation 1721
Findings 1722
Discussion 1722

Colorectal Cancer: Case No. 7 1722
Presentation 1722
Findings 1722
Discussion 1723

Colorectal Cancer: Case No. 1

Presentation

A 71-year-old woman presented with abdominal and lumbar pain lasting for 2 months. No abnormality was demonstrated by esophagogastroduodenoscopy. Abdominal contrast-enhanced CT demonstrated a lesion of the pancreatic body (4 cm in size) with involvement of the splenic artery, celiac trunk, and superior mesenteric artery (Fig. 1). EUS-guided biopsy showed biliopancreatic adenocarcinoma of the pancreas body.

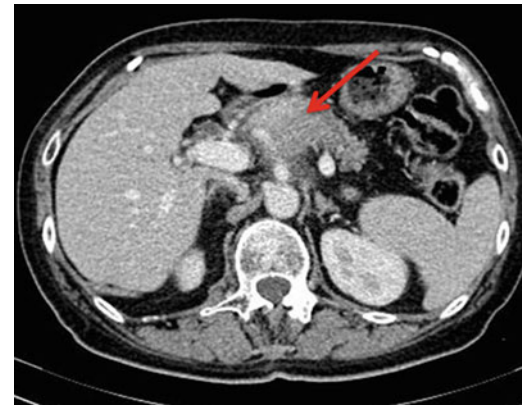

Fig. 1 Contrast-enhanced CT of pancreatic adenocarcinoma (*red arrow*)

Findings

[^{18}F]FDG PET/CT was performed to complete the staging of the locally advanced pancreatic cancer.

PET/CT confirmed the presence of hypermetabolic pancreatic lesion consistent with malignancy (Fig. 2). In addition, prominent [^{18}F]FDG-avid area associated with wall thickening on CT was noted in the transverse colon (Figs. 2 and 3). MRI of the abdomen showed the known pathologic pancreatic lesion and a suspected mass of the transverse colon.

Colonoscopy confirmed the PET/CT finding and demonstrated the presence of substenosing vegetant lesion of the colon, histologically diagnosed as moderately differentiated adenocarcinoma.

Discussion

Incidental colonic [^{18}F]FDG uptake often is observed in patients who undergo PET/CT studies. The presence of an incidental focal [^{18}F]FDG uptake in the colon justifies a colonoscopy to detect the presence of a possible premalignant or malignant lesion. Focal and multifocal high [^{18}F]FDG uptake in the colon is predictive of pathologic findings, which may include malignancy. A diffuse colonic [^{18}F]FDG uptake pattern, regardless of the degree, is predictive of normal findings at colonoscopy, whereas a segmental high uptake may imply an inflammatory condition that warrants follow-up diagnostic studies.

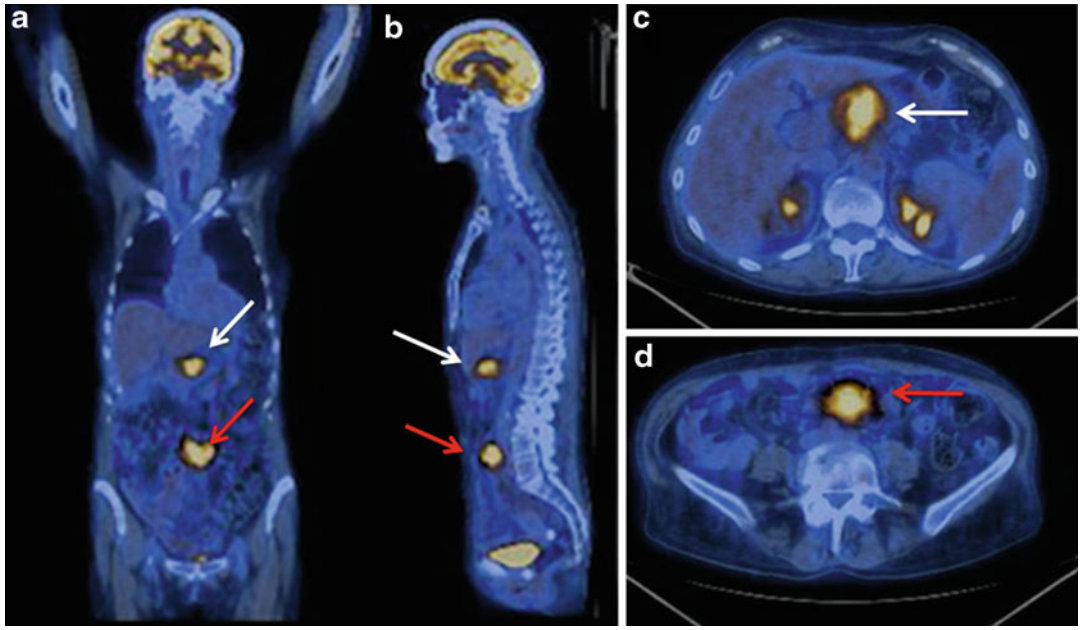

Fig. 2 Fused [^{18}F]FDG PET/CT images (**a** coronal, **b** sagittal, **c**, and **d** axial) of the pancreatic lesion (*white arrows*) and suspected hypermetabolic colonic mass (*red arrows*)

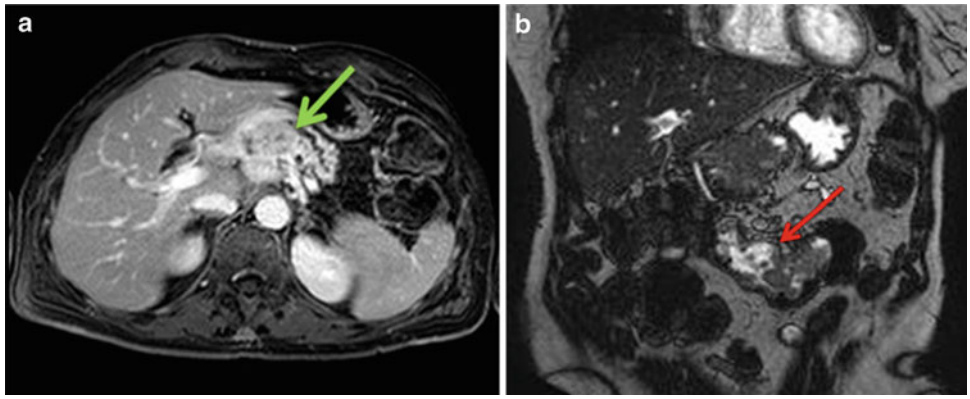

Fig. 3 Abdominal MRI shows the presence of pancreatic lesion (*green arrow*) and the suspected mass of the transverse colon (*red arrow*)

Colorectal Cancer: Case No. 2

Presentation

A 62-year-old man presented with recently diagnosed biopsy-proven colorectal cancer. Colonoscopy showed the presence of an ulcerated circumferential mass of the left colon with malignant obstruction of the lumen, which precluded a full colonoscopy.

[^{18}F]FDG PET/CT was performed as a part of preoperative staging.

Findings

[^{18}F]FDG PET/CT demonstrates focal [^{18}F]FDG uptake in the descending colon corresponding to the known colic mass. Intense focal uptake of the radiopharmaceutical is also noted in the ascending colon in proximity of the hepatic flexure. The patient was treated surgically. Histology demonstrated moderately differentiated adenocarcinoma (pT4aN0) in the descending colon and moderately differentiated adenocarcinoma in the ascending colon (pT3N0). The patient was subsequently treated with adjuvant chemotherapy. At the 3-year follow-up, he has no evidence of disease.

Discussion

Staging with [^{18}F]FDG PET/CT resulted in the detection of synchronous colorectal cancer, a relatively rare condition (2–3% of the cases) that should be considered during staging of colorectal cancer (Fig. 4).

Colorectal Cancer: Case No. 3

Presentation

A 39-year-old man presented with substenosing colorectal cancer. CT colonography (CTC) with computer-aided detection was performed. CTC confirmed the presence of the known mass of the descending colon, and a hypodense lesion of uncertain origin in the sixth segment of the liver (included in the upper limit of the scan).

[^{18}F]FDG PET/CT was performed to characterize the doubtful hepatic lesion.

Findings

PET/CT shows intense [^{18}F]FDG uptake in the descending colon corresponding to known malignancy (Fig. 5). Multiple [^{18}F]FDG hepatic lesions were also demonstrated consistent with synchronous metastatic liver involvement (Fig. 6). The patient was treated with chemotherapy.

Discussion

[^{18}F]FDG PET/CT is not routinely used for initial staging of patients with colorectal cancer (CRC). It may be used to clarify equivocal findings on conventional imaging in preoperative staging and evaluating apparently limited metastatic disease before intervention. Limited literature data has shown that [^{18}F]FDG PET/CT may change treatment plan in 3–30% of the newly diagnosed CRC.

Colorectal Cancer: Case No. 4

Presentation

A 68-year-old man with previously treated for rectal cancer presented with recent increase of serum CEA level (28.1 ng/mL). [^{18}F]FDG PET/CT was performed to evaluate the extent of disease.

Findings

[^{18}F]FDG PET showed markedly avid lesion corresponding to abnormal tissue of the rectal region consistent with recurrent disease (Fig. 7). In the right lower lung, a small nodule with moderate [^{18}F]FDG uptake was also seen, suspected for pulmonary metastases (Fig. 8).

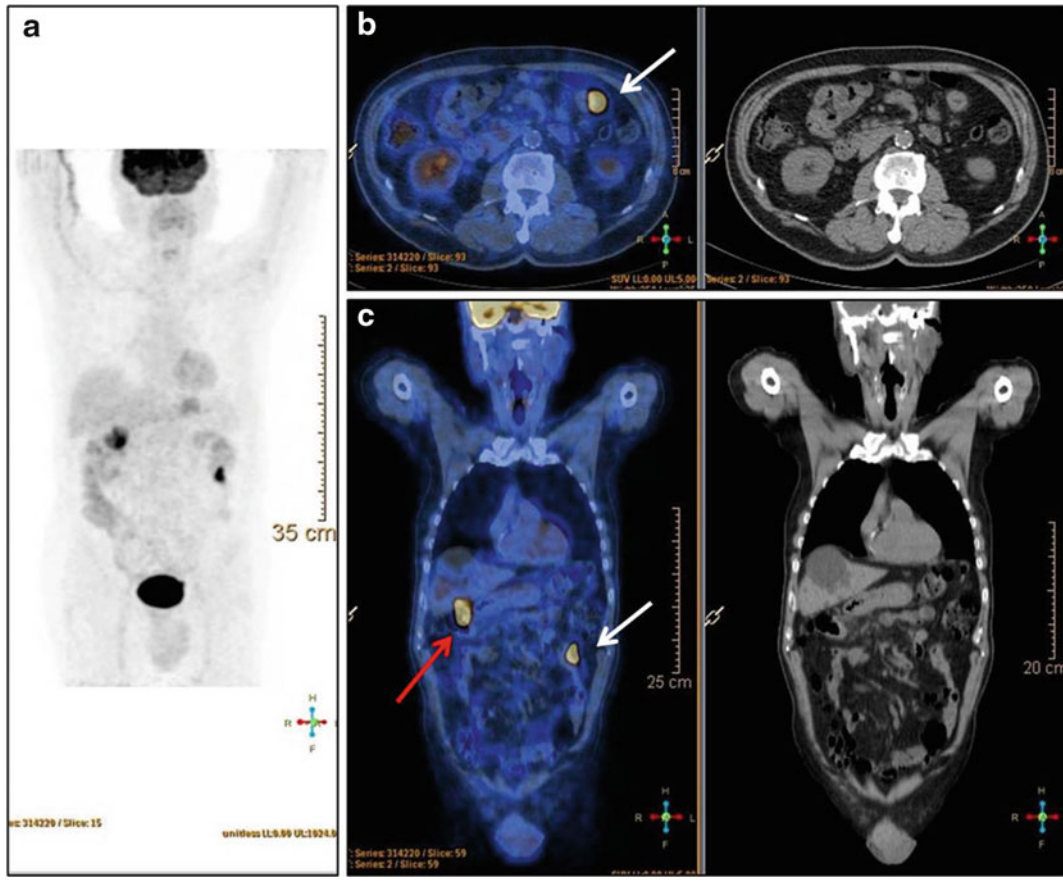

Fig. 4 [^{18}F]FDG PET/CT images (panel **a** MIP image; panel **b** axial fused image on the left and axial CT image on the *right*; panel **c** coronal fused image on the *left* and coronal CT image on the *right*) show synchronous moderately differentiated colorectal cancer in the descending colon (*white arrow*) and in the ascending colon (*red arrow*)

Discussion

In cases of rising serum markers during follow-up colorectal cancer of [^{18}F]FDG PET may be useful to detect local or distant recurrence.

Colorectal Cancer: Case No. 5

Case contributed by: S. Al Shammari, F. Fraioli
Institute of Nuclear Medicine, UCLH NHS Foundation Trust, London, UK

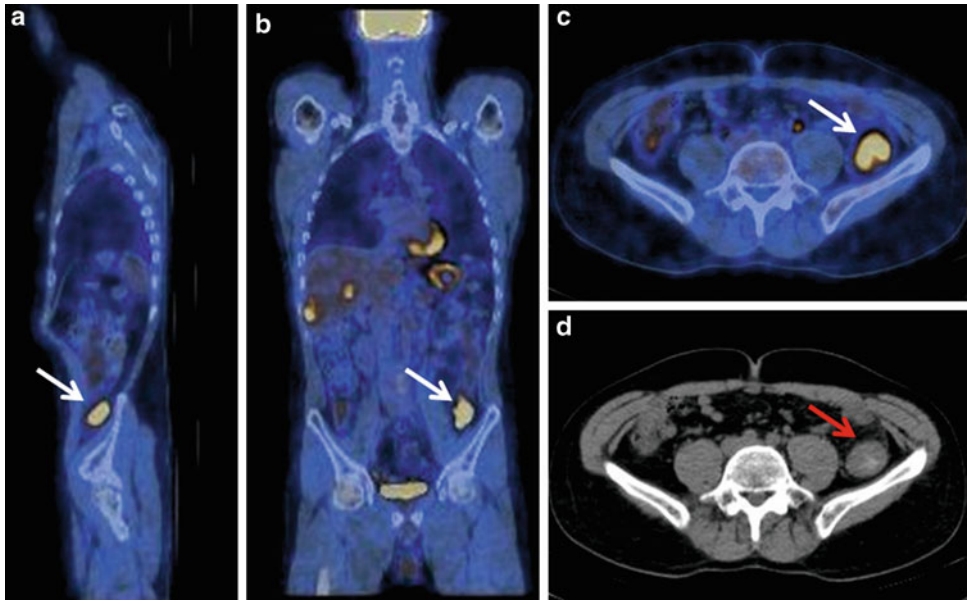

Fig. 5 Fused PET/CT sagittal (**a**), coronal (**b**), axial (**c**), and axial low-dose CT (**d**) images clearly show focal [^{18}F]FDG intense uptake in the descending colon corresponding to known malignancy (*white* and *red arrows*). Fused PET/CT coronal image (**b**) also demonstrated hepatic involvement

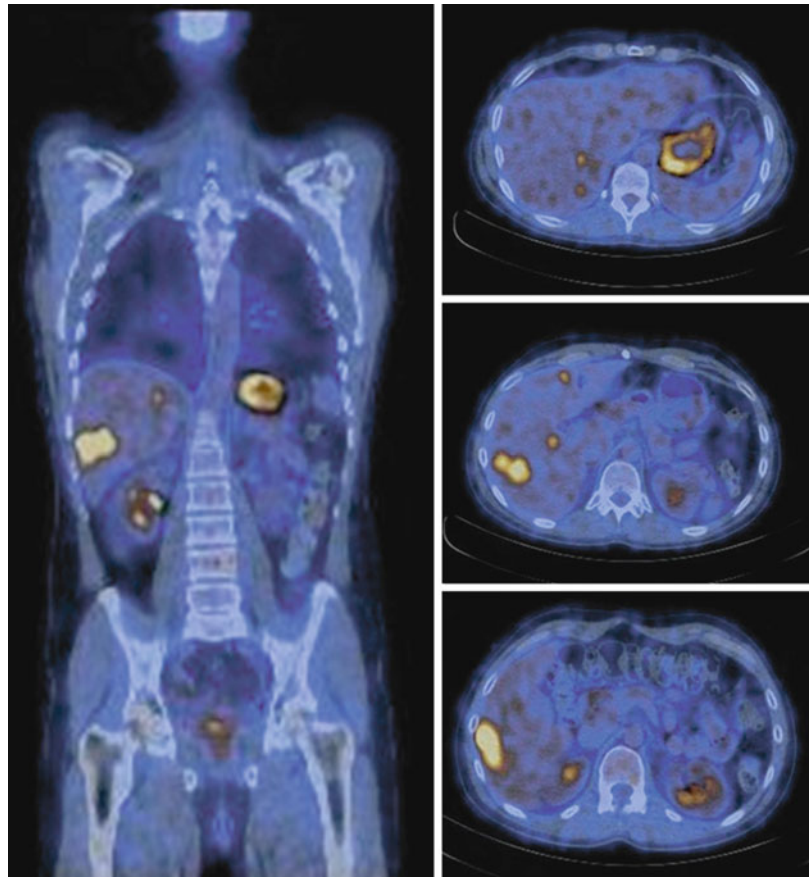

Fig. 6 Fused PET/CT coronal (*left panel*) and axial (*right panel*) images show multiple hepatic [^{18}F] FDG-avid metastases

Presentation

A 70-year-old patient with anal canal cancer.

Findings

There is intense [^{18}F]FDG activity (SUV_{max} 16.7) at the level of the anal canal extending to the lower rectum (arrows). [^{18}F]FDG-avid left inguinal lymph nodes (arrowheads) are also noted (Fig. 13).

Colorectal Cancer: Case No. 6

Case contributed by: S. Al Shammari, F. Fraioli
Institute of Nuclear Medicine, UCLH NHS Foundation Trust, London, UK

Presentation

A 65-year-old patient with anal canal cancer.

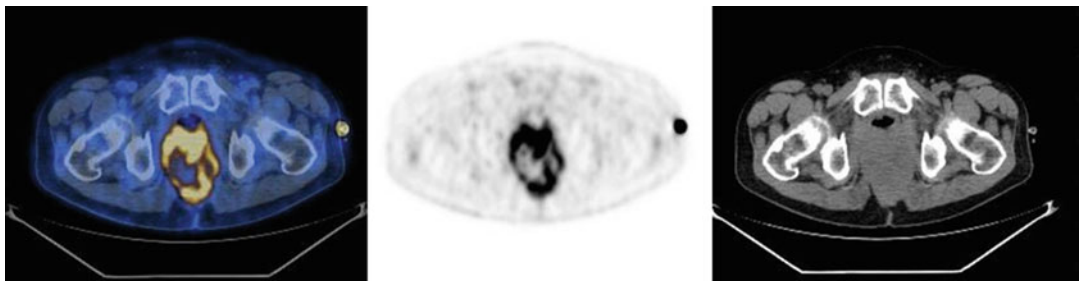

Fig. 7 Axial low-dose CT/PET and fused PET/CT images of rectal local recurrence, [^{18}F]FDG avid

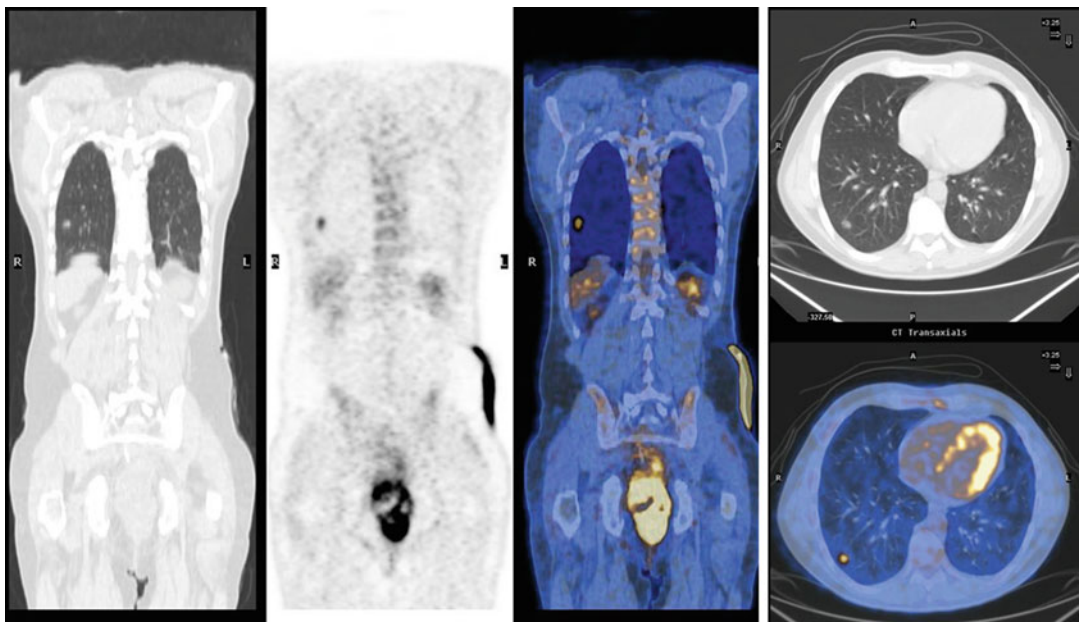

Fig. 8 Coronal low-dose CT/PET and fused [^{18}F]FDG PET/CT images (*left panel*) and axial image (*right panel*) show local recurrence and lung lesion. Radioactive urine in nephrostomy tube is seen along the left flank

Findings

On the PET/MRI scan, there is intense [^{18}F]FDG activity (SUV_{max} 16.7) at the level of the anal canal extending from the anal verge up to the lower rectum (A). The mass abuts the internal sphincter muscle (arrows). The DWI sequence (C) and corresponding ADC maps (D) show restricted diffusion at the level of the lesion (arrows) (Fig. 14).

Discussion

Although MR is the established reference standard, the role of [^{18}F]FDG PET/CT in anal cancer is becoming increasingly important. The National Comprehensive Cancer Network (NCCN) guidelines currently recommend the use of CT or MRI for initial imaging and PET for patients with T3–T4N0 disease or for patients with N+ disease. [^{18}F]FDG PET can detect the primary site of disease more frequently than CT, is sensitive for nodal and metastatic spread, and alters staging in a significant number of patients. PET/CT is beneficial for radiation planning and therapy assessment. Metabolic activity of primary anal cancer at presentation is a potential biomarker for predicting prognosis, treatment response assessment, and survival. [^{18}F]FDG-avid primary malignancy is associated with a higher incidence of disease spread. Metabolic response in post-therapy monitoring scan is associated with improved survival. The recent introduction of simultaneous hybrid PET/MR allows a multiparametric assessment and an all-in-one exam.

Colorectal Cancer: Case No. 7

Case contributed by: L. Deantonio[1], F. Orsini[2], R. Matheoud[3], M. Krengli[1], G.M. Sacchetti[2]

[1]Radiotherapy Unit, "Maggiore della Carità" University Hospital" and Department of Translational Medicine, University of "Piemonte Orientale" University, Novara, Italy

[2]Section of Nuclear Medicine, "Maggiore della Carità" University Hospital, Novara, Italy

[3]Section of Medical Physics, "Maggiore della Carità" University Hospital, Novara, Italy

Presentation

A 56-year-old man with a biopsy-proven primary squamous cell G2 of the anal canal presented with anal bleeding. Tumor size was determined by clinical examination that showed a 6 cm lesion along the posterolateral wall of the anal canal. In these cases efficacy of treatment relies on accurate staging of the primary tumor and regional lymph nodes, which is based on imaging studies; MR is considered the gold standard.

Findings

Pelvic MRI confirmed the locoregional extension and no lymphatic involvement (Fig. 9). Final staging was cT3N0 according to the American Joint Committee on Cancer (AJCC).

The case was discussed in a multidisciplinary meeting including gastroenterologists, surgeons, radiation oncologists, and medical oncologists. The patient was a candidate for chemoradiotherapy with curative intent.

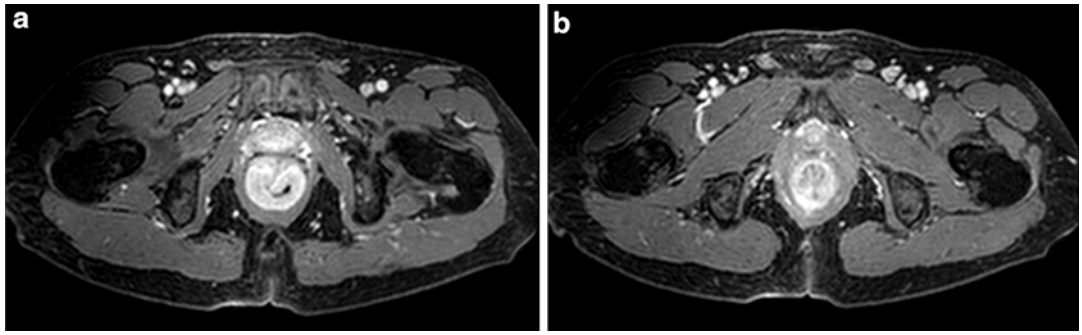

Fig. 9 Transaxial MR study using a THRIVE sequence with contrast enhancement demonstrating a lesion of the posterolateral wall of the anal canal (**a**) and no abnormal inguinal lymph nodes (**b**)

Chemotherapy was delivered with three cycles of 5-fluorouracil and mitomycin C. Planning of radiation therapy (RT) was performed including the identification of the clinical target volume (defined as the gross tumor volume) plus the potential microscopic spread to the surrounding tissues and to the regional lymph nodes based on clinical presentation and imaging.

The recently updated clinical practice ESMO guidelines for anal cancer include PET as an "optional but often recommended" modality in the workup of patients.

Thus, [^{18}F]FDG PET/CT was performed for both tumor staging and target identification. After whole-body imaging, extra bed positions were acquired in the RT decubitus with longer emission scan duration (5 min) and reconstructed on a bigger frame (2.6 mm/pixel) to ensure better definition of the target during contouring for RT planning.

[^{18}F]FDG PET/CT confirmed the anal lesion and showed increased uptake in the left inguinal lymph node, not identified by MRI (Fig. 10).

Discussion

The use of [^{18}F]FDG PET/CT can play an important role in the treatment strategy and lead to modification of RT treatment planning. An [^{18}F]FDG-positive inguinal lymph node will receive a boost of the radiation dose (54–59.4 Gy), while [^{18}F]FDG-negative lymph nodes only receive a prophylactic dose (39.6–45 Gy).

Fine-needle aspiration cytology of the left inguinal lymph node was negative for tumor cells;

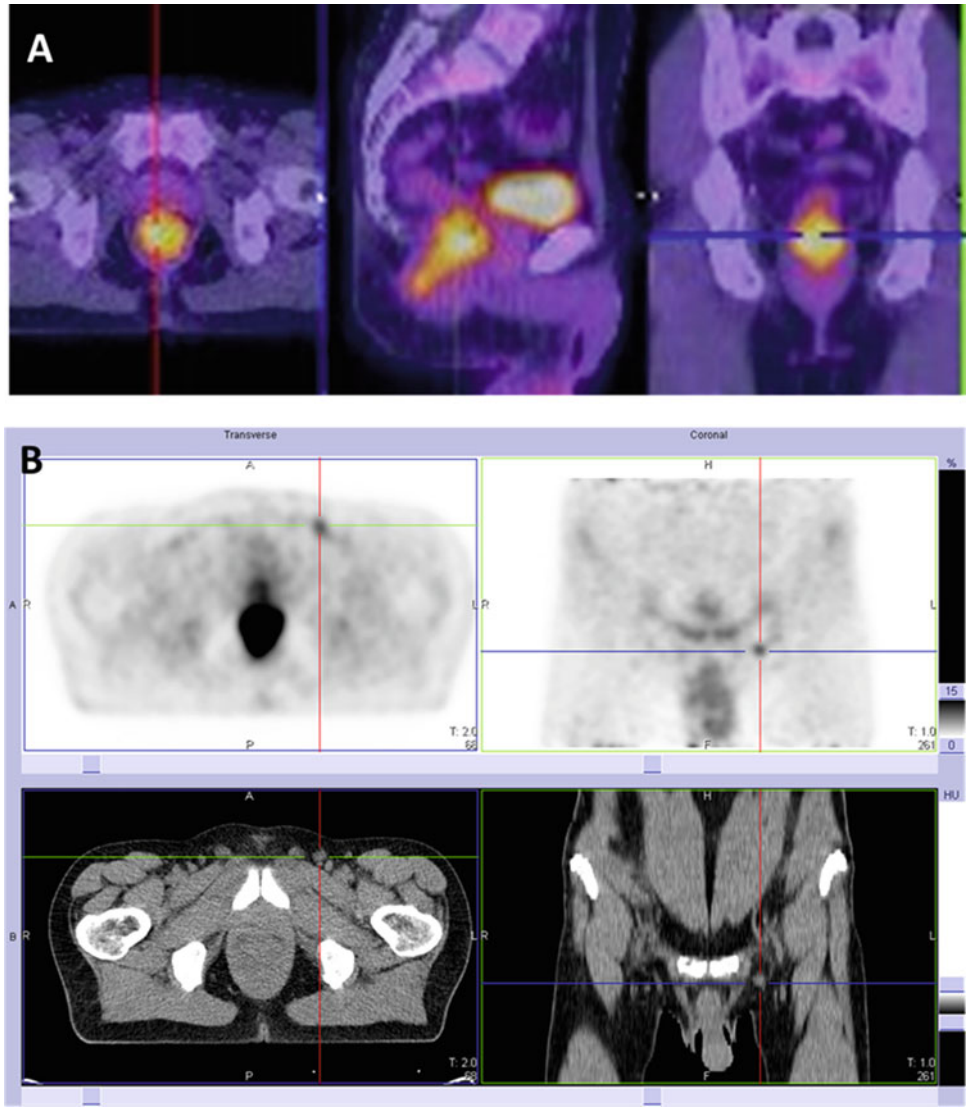

Fig. 10 Transaxial, sagittal, and coronal fused [^{18}F]FDG PET/CT images showing high tracer uptake in the primary anal canal cancer (**a**). Axial and coronal [^{18}F]FDG PET and CT images showing high [^{18}F]FDG uptake in the left inguinal lymph node (**b**)

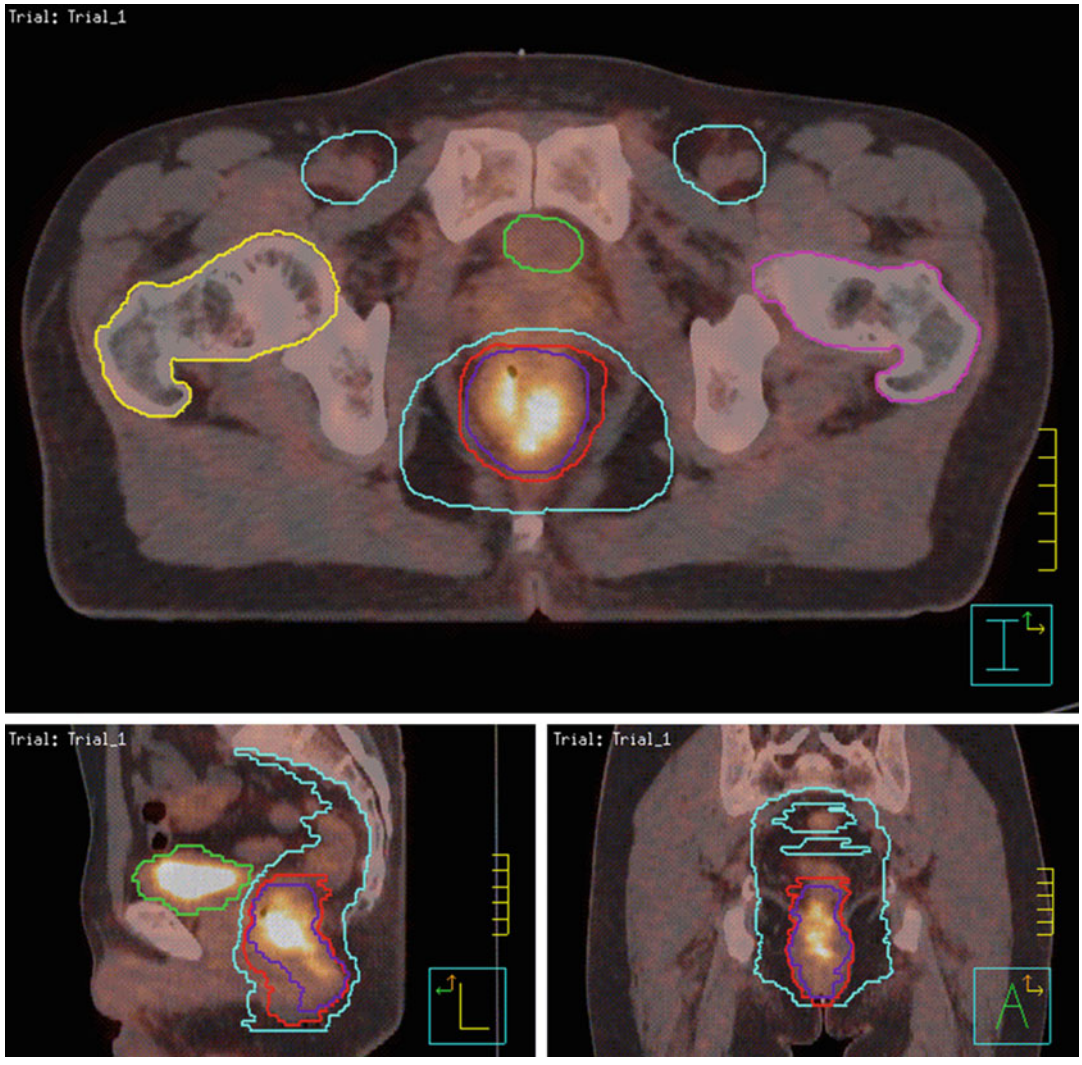

Fig. 11 Transaxial, sagittal, and coronal view of the simulation CT and fused with PET/CT. Different colors are used to highlight contours of the treatment volumes. *Purple line*: gross tumor volume (*GTV*). *Red line*: high-risk CTV represented by the canal anal. *Light blue*: low-risk CTV represented by bilateral inguinal, external, and internal iliac, perirectal, and presacral lymph nodes

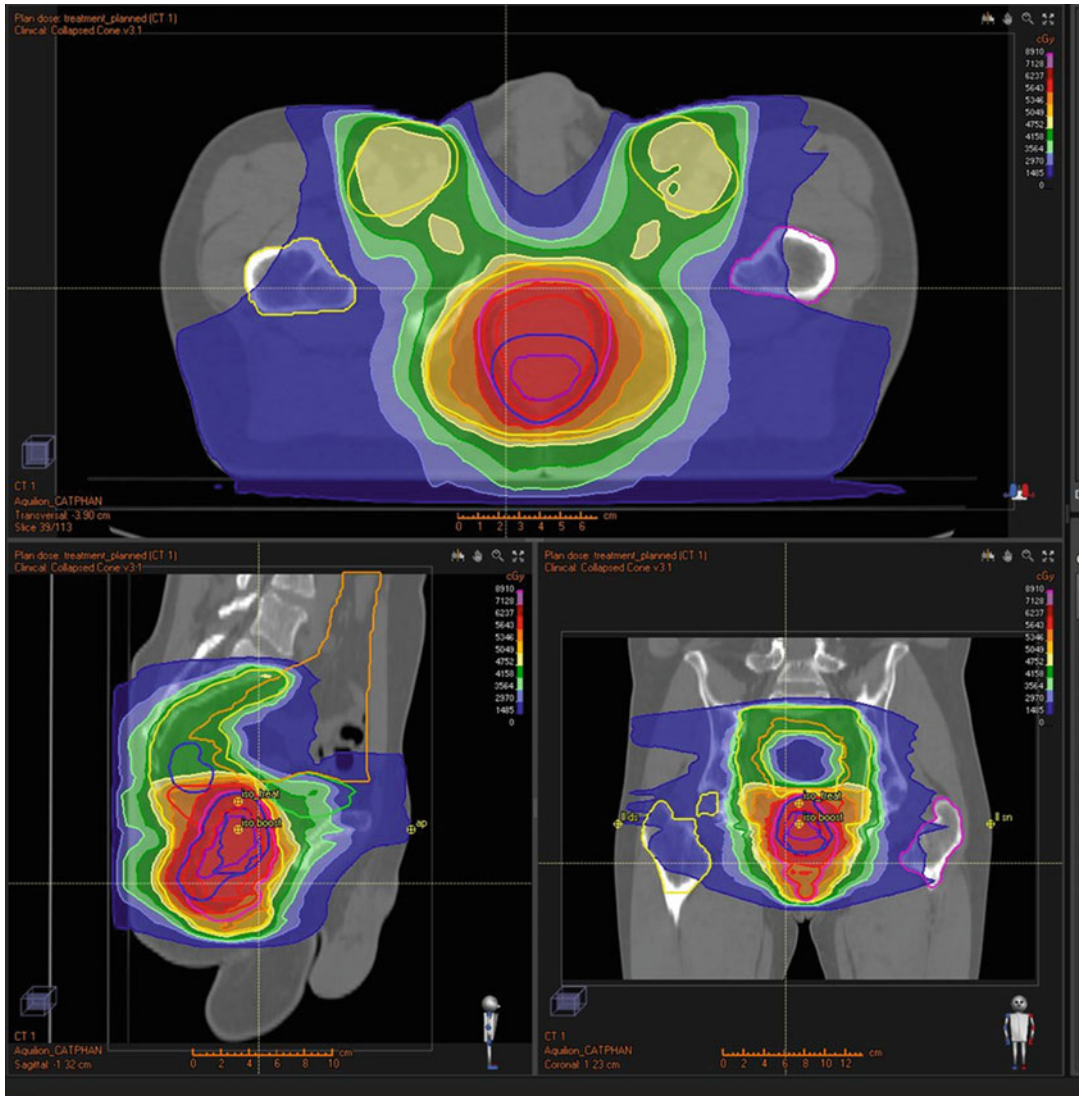

Fig. 12 Transaxial, coronal, and sagittal view of the RT treatment plan. Images show the high conformation of dose distribution performed by VMAT-SIB treatment plan. Around the target volumes, the doses decrease rapidly, thus reducing the radiation dose to the organs at risk. In *red* the 95% isodose and in *blue* the 25% isodose of the 59.4 Gy prescribed dose

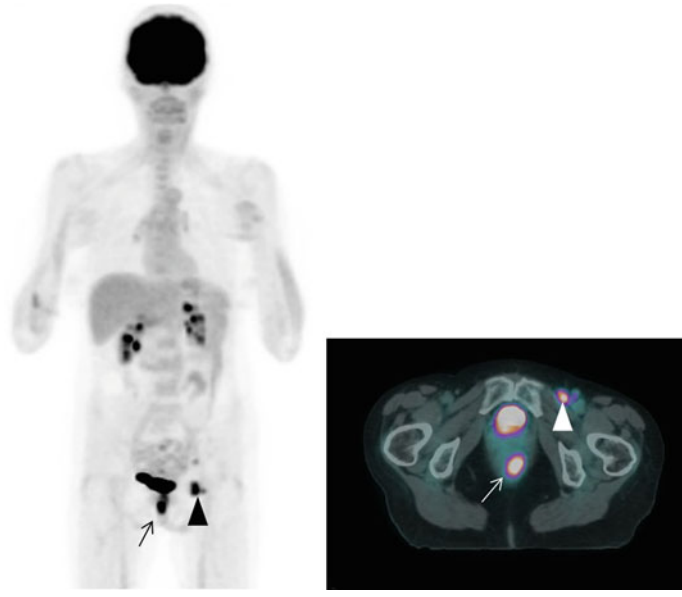

Fig. 13 PET MIP image and axial fused PET/CT image show pathological [^{18}F]FDG activity at the level of the anal canal extending to the lower rectum (arrow) and [^{18}F]FDG avid left inguinal lymph nodes (arrowheads)

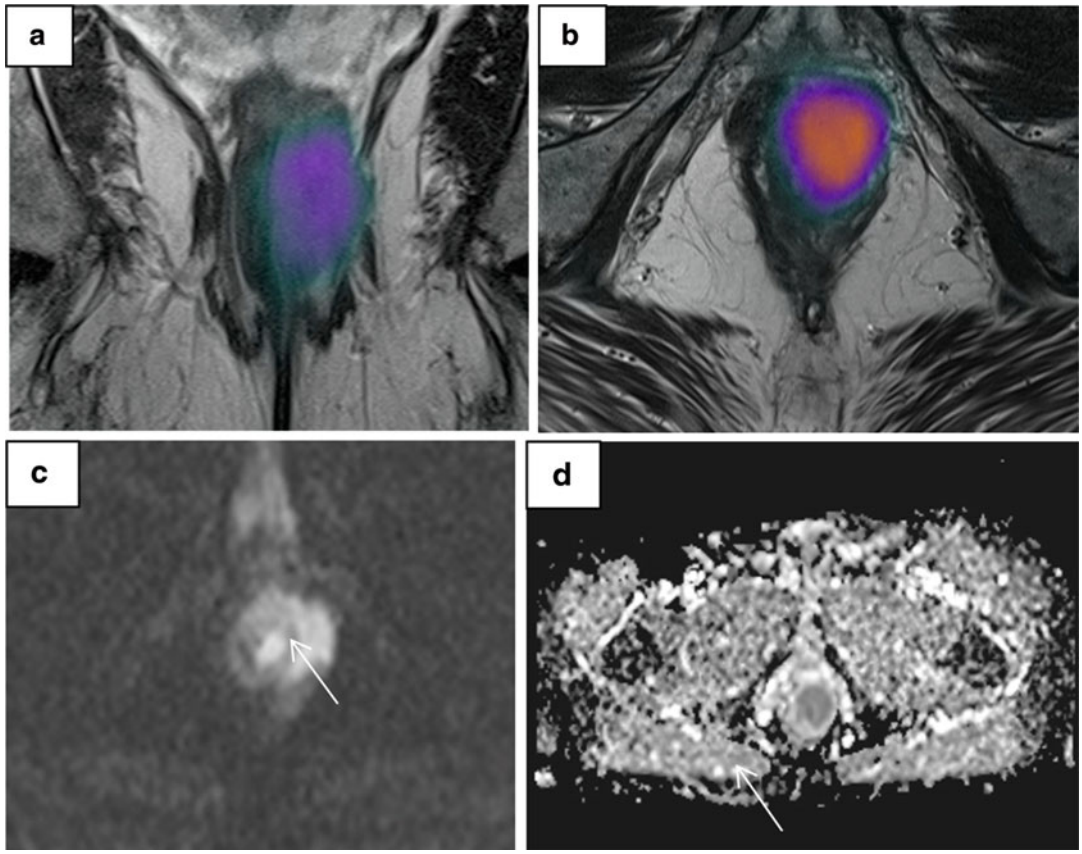

Fig. 14 PET/MRI shows intense [^{18}F]FDG activity at the anal canal extending from the anal verge up to the lower rectum (**a**). The mass abutts the internal sphincter muscle (arrows). The DWI sequence (**c**) and corresponding ADC maps (**d**) show restricted diffusion at the level of the lesion (arrows)

nevertheless, cytology of aspirates from lymph nodes has a relatively low sensitivity. Therefore, inguinal lymph nodes were included in the prophylactic clinical target volume (CTV) (Fig. 11).

A volumetric-modulated arc therapy-simultaneous integrated boost (VMAT-SIB) treatment plan was performed to a total dose of 59.4 Gy with daily fraction of 2 Gy to the macroscopic disease and to a dose of 45.0 Gy with daily fraction of 1.8 Gy to the potentially microscopically invaded regions and locoregional lymph nodes (Fig. 12).

Teaching Cases in Nuclear Oncology: Neuroendocrine Tumors

67

Alice Lorenzoni, Alessandra Alessi, and Flavio Crippa

Keywords

Neuroendocrine tumor • ^{68}Ga-DOTATOC • PET/CT • [^{18}F]FDG PET/CT • Radionuclide therapy

Glossary

[^{11}C]HTTP	[^{11}C]5-Hydroxy-L-tryptophan
[^{18}F]FDG	2-Deoxy-2-[^{18}F]fluoro-D-glucose
^{18}F-DOPA	2-^{18}F-Fluoro-L-3,4-dihydroxyphenylalanine
ACTH	Adrenocorticotropic hormone
AFP	Alpha-fetoprotein, a tumor-associated marker
AJCC	American Joint Committee on Cancer
CEA	Carcinoembryonic antigen, a tumor-associated marker
CT	X-ray computed tomography
DOTA	1,4,7,10-Tetraazacyclo-dodecane-1,4,7,10-tetraacetic acid
DOTANOC	DOTA-1-Nal^3-octreotide
DOTATATE	DOTA- Tyr^3-octreotate
DOTATOC	DOTA-octreotide
GEP-NET	Gastro-entero-pancreatic neuro-endocrine tumor
GEP	Gastro-entero-pancreatic
HBV	Hepatitis B virus
HCV	Hepatitis C virus
M	Metastasis status according to the AJCC/UICC TNM staging system
MIP	Maximum intensity projection
MR	Magnetic resonance
MRI	Magnetic resonance imaging
N	Lymph node status according to the AJCC/UICC TNM staging system
NET	Neuroendocrine tumor
PET	Positron emission tomography
PET/CT	Positron emission tomography/Computed tomography
PET/MR	Positron emission tomography/Magnetic resonance imaging system
PET/MRI	Positron emission tomography/Magnetic resonance imaging
PRRT	Peptide receptor radionuclide therapy
RT	Radiation therapy
SSTR	Somatostatin receptor
SUV	Standardized uptake value
SUV_{max}	Standardized uptake value at point of maximum
T	Tumor status according to the AJCC/UICC staging system

A. Lorenzoni (✉) • A. Alessi • F. Crippa
Nuclear Medicine Division, IRCCCS National Cancer Institute, Milan, Italy
e-mail: alice.lorenzoni@istitutotumori.mi.it; alicelorenzoni@hotmail.it

© Springer International Publishing Switzerland 2017
H.W. Strauss et al. (eds.), *Nuclear Oncology*,
https://doi.org/10.1007/978-3-319-26236-9_70

UICC	Union Internationale Contre le Cancer (International Union Against Cancer)

Contents

Neuroendocrine Tumors: Case No. 1 1730
Presentation 1730
Findings 1730
Discussion 1730

Neuroendocrine Tumors: Case No. 2 1730
Presentation 1730
Findings 1730

Discussion 1731

Neuroendocrine Tumors: Case No. 3 1731
Presentation 1732
Findings 1732

Discussion 1732

Neuroendocrine Tumors: Case No. 4 1733
Presentation 1733
Findings 1733
Teaching Point 1733

Neuroendocrine Tumors: Case No. 5 1734
Presentation 1734
Findings 1734
Follow-Up 1734

Neuroendocrine Tumors: Case No. 6 1735

Neuroendocrine Tumors: Case No. 7 1736
Presentation 1736
Findings 1738
Follow-Up 1742

Neuroendocrine Tumors: Case No. 8 1743
Presentation 1743
Findings 1743
Discussion 1744

Neuroendocrine Tumors: Case No. 1

Case contributed by: V. Duce, A. Ciarmiello
Nuclear Medicine Unit, "S. Andrea" Hospital, La Spezia, Italy

Presentation

A 66-year-old man presented with chronic diarrhea and abdominal pain. CT showed the presence of a liver lesion in segment 8. An ultrasound-guided core needle biopsy of the liver lesion demonstrated that it was a metastasis from a GEP-NET. ^{68}Ga-DOTATOC PET/CT was performed for localization of the primary tumor and evaluation of disease burden.

Findings

PET/CT images demonstrate two areas of focal ^{68}Ga-DOTATOC uptake in the terminal ileum (close to the ileocecal valve) as the primary tumor site (Fig. 1). In addition, moderate tracer uptake is seen in segment 8 of the liver, corresponding to the CT finding (Fig. 2). The small bowel lesion and the liver metastasis were surgically removed. The histopathology and immunohistochemistry analysis confirmed the diagnosis of NET.

Discussion

This case confirms the value of ^{68}Ga-DOTATOC PET/CT for identifying unknown primary neuroendocrine tumors.

Neuroendocrine Tumors: Case No. 2

Case contributed by: S. Al Shammari, F. Fraioli
Institute of Nuclear Medicine, UCLH NHS Foundation Trust, London, UK

Presentation

A 70-year-old patient with suspicious liver lesions on MRI was referred for further characterization of these lesions.

Findings

The [^{18}F]FDG PET/CT scan (Fig. 3) did not reveal any uptake (upper row). ^{68}Ga-DOTATATE

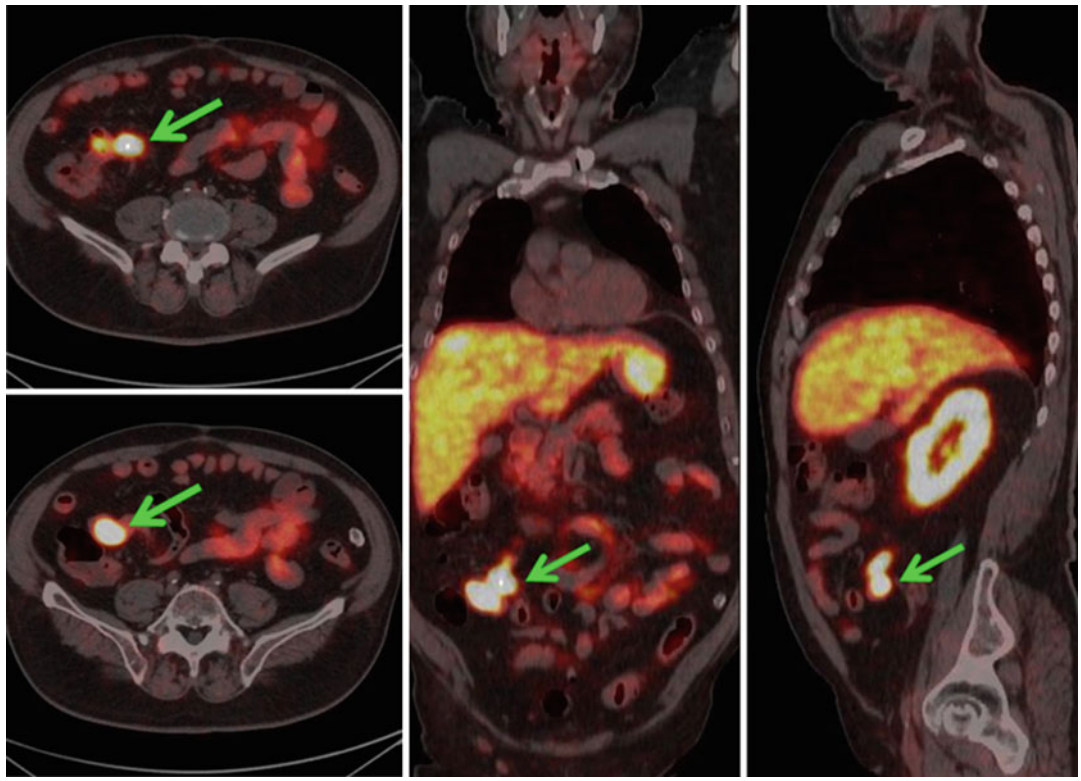

Fig. 1 Axial (*left*), coronal (*center*), and sagittal (*right*) fused ^{68}Ga-DOTATOC PET/CT images show two areas of focal tracer uptake in the terminal ileum close to the ileocecal valve (*green arrows*)

PET/CT (bottom) revealed multiple areas of increased tracer uptake within both lobes of the liver. The patient underwent liver biopsy which revealed grade 1 (G1) carcinoid tumor metastasis. The patient was treated with peptide receptor radionuclide therapy with ^{90}Y-DOTA-tyr^{3}-octreotide.

Discussion

Neuroendocrine tumors (NETs) are a heterogeneous group of malignancies ranging from well-differentiated and slowly growing tumors to poorly differentiated and malignant neoplasms, which are less frequent and display aggressive behavior. PET/CT with ^{68}Ga-DOTA-peptides was reported to present a higher sensitivity for the detection of well-differentiated, less aggressive NET than CT and octreoscan. On the other hand, [^{18}F]FDG PET/CT is preferred for more aggressive, less-differentiated NETs as the emerging evidence shows that the presence of increased glucose in NETs highlights an increased propensity for invasion and metastasis and overall poorer prognosis. The case demonstrates the value of ^{68}Ga-DOTATATE in the evaluation of a well-differentiated neuroendocrine tumor.

Neuroendocrine Tumors: Case No. 3

Case contributed by: S. Al Shammari, F. Fraioli
Institute of Nuclear Medicine, UCLH NHS Foundation Trust, London, UK

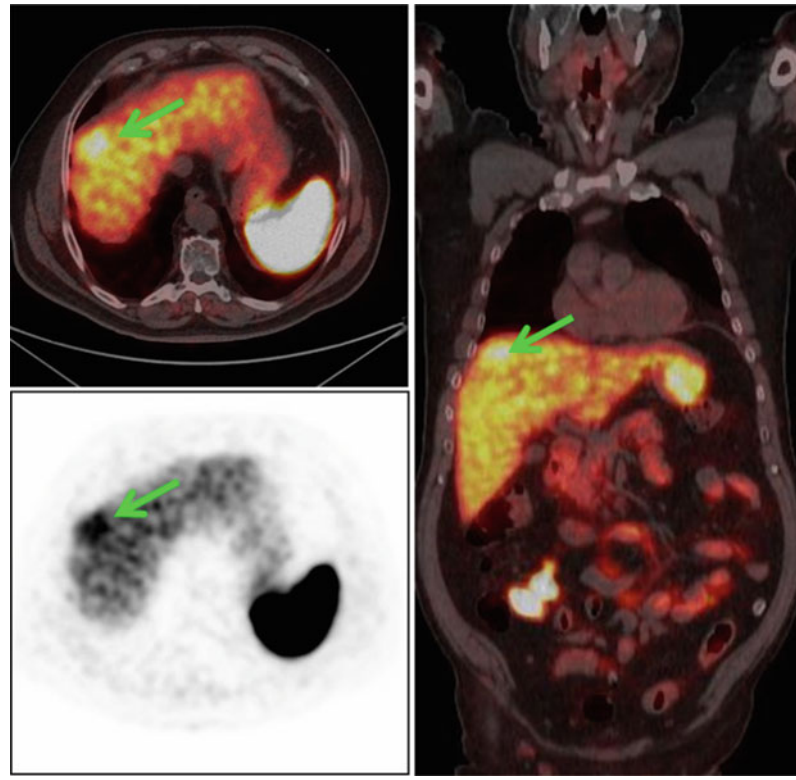

Fig. 2 Axial PET (*left lower*), axial (*left upper*), and coronal (*right*) fused PET/CT images show an area of moderate ^{68}Ga-DOTATOC uptake in segment 8 of the liver (*green arrows*)

Presentation

A 53-year-old patient with suspicion of midgut NET, referred to ^{68}Ga-DOTATATE PET/MRI for staging and baseline evaluation

Findings

Small focus of ^{68}Ga-DOTATATE uptake in the third portion of the duodenum (Fig. 4). MR postcontrast images clearly show the enhancing lesion, with corresponding intense uptake at the fused ^{68}Ga-DOTATATE image (arrows). PET/CT for comparison also identifies the focus of uptake.

Discussion

The positron emitter ^{68}Ga has been linked to short peptide analogues of somatostatin analogues via bifunctional chelate, usually 1,4,7,10-tetraazacyclododecane-1,4,7,10-tetraacetic acid (DOTA). ^{68}Ga-DOTA-petides have higher affinity for SSTRs as compared to conventional ^{111}In-octreotide. Furthermore, the relatively easy synthesis and long half-life of the parent radionuclide ^{68}Ge (270.8 days) make it possible to use the generator for approximately 6–12 months. Positron emission tomography with ^{68}Ga-labeled somatostatin analogues is performed for localizing and confirming the primary tumor, evaluating disease extension, monitoring treatment effects, and determining the receptor status as a predictor of response in selected patients undergoing targeted radionuclide therapy. Combined positron emission tomography/magnetic resonance imaging (PET/MR) is a relatively new technique that has shown similar performance to positron emission tomography/computed tomography (PET/CT).

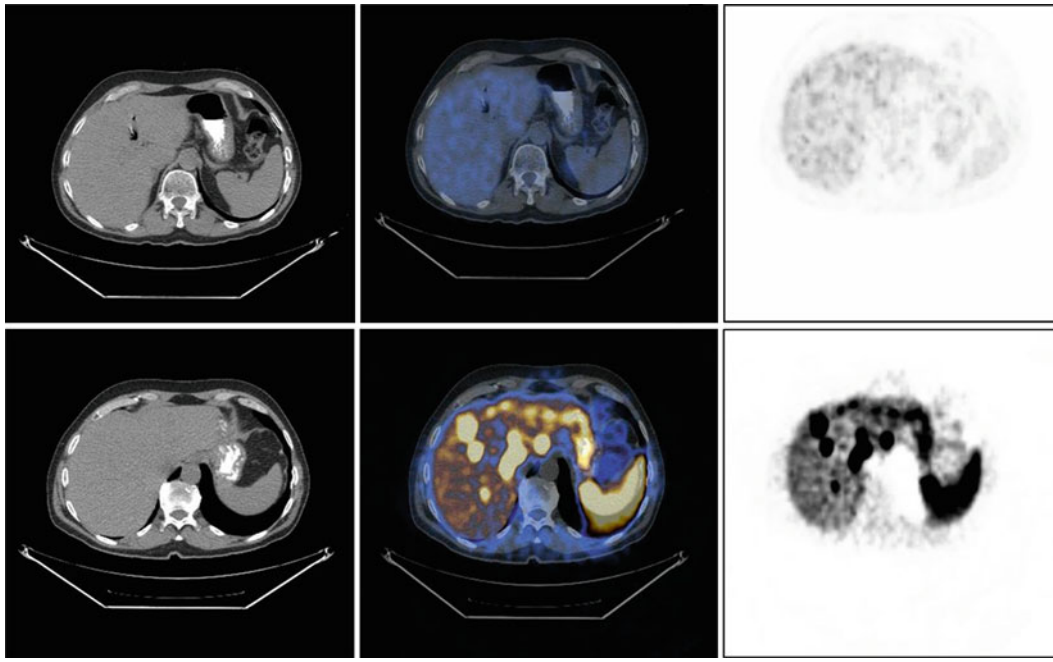

Fig. 3 [^{18}F]FDG PET/CT did not reveal any uptake (upper row). ^{68}Ga-DOTATATE PET/CT (bottom) revealed multiple areas of increased tracer uptake within both lobes of the liver

Neuroendocrine Tumors: Case No. 4

Case contributed by: T. Boshomane, M. Sathekge
Nuclear Medicine, University of Pretoria & Steve Biko Academic Hospital, Pretoria, South Africa

Presentation

A 47-year-old male patient with a history of cecal carcinoma; biopsy after hemicolectomy and lymphadenectomy confirmed large-cell neuroendocrine carcinoma, with Ki67 >20%.

Now presents with worsening dyspnea and ascites

Findings

CT showed right-sided pleural effusion with associated consolidation, multiple lymph nodes (retrosternal, costophrenic, paratracheal lymph nodes, axillary, mesenteric, and para-aortic). A ^{68}Ga-DOTATE PET/CT performed to evaluate for possible peptide receptor radionuclide therapy (PRRT) demonstrated lesions with less intense uptake than in the liver on visual analysis and $SUV_{max} = 1.48$ on axillary lymph nodes (pancreatic head $SUV_{max} = 7.78$). The pleural effusion and other lymph nodes detected on CT were not ^{68}Ga-DOTATE avid (Fig. 6).

A decision was made to perform an [^{18}F]FDG PET/CT 2 days later with the following findings: avid lymph nodes (retrosternal $SUV_{max} = 10.75$, mesenteric $SUV_{max} = 4.82$, para-aortic $SUV_{max} = 7.23$, paratracheal $SUV_{max} = 4.04$) and diffuse uptake on the omentum and peritoneal fluid (Fig. 7).

Teaching Point

The case highlights the value of tracer selection in the patient with a dedifferentiated neuroendocrine

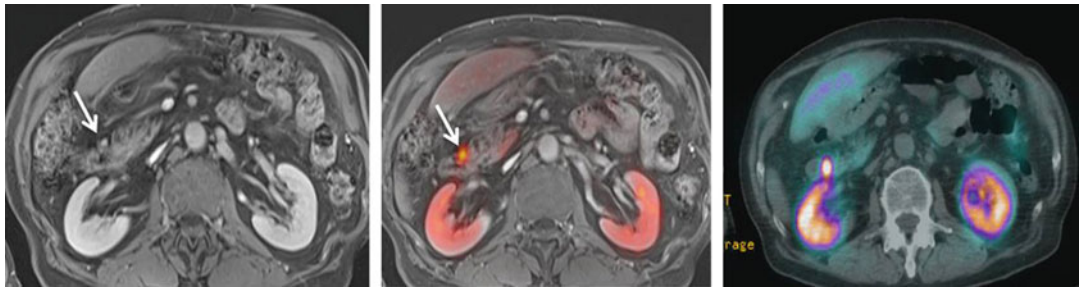

Fig. 4 Comparison of ^{68}Ga-DOTATATE PET/MRI clearly shows focal uptake in the third part of the duodenum (arrow)

carcinoma. Based on these serial imaging with two different molecular probes, i.e., ^{68}Ga-DOTATATE and [^{18}F]FDG, a treatment decision can be made, i.e., the patient is not a candidate for PRRT. Thus, alternative therapy can be sought (Figs. 5, 6, 7, and 8).

Neuroendocrine Tumors: Case No. 5

Case contributed by: G. Manfrinato, A. Chiti
Division of Nuclear Medicine, Department of Biomedical Sciences – Humanitas University, Milan, Italy

Presentation

A 54-year-old-man with chronic liver disease (HBV-HCV related) evolving toward cirrhosis underwent an abdominal ultrasound that revealed previously unsuspected hepatic lesions.

Blood chemistry showed mildly elevated serum levels of the tumor-associated markers CEA (6.7 ng/mL) and AFP (12 ng/mL), while the value of Ca 19.9 was completely normal.

Findings

A CT scan showed multiple metastatic lesions in all liver segments and a large mass (6 × 3 × 7 cm) originating from the uncinated process of the pancreas, associated with locoregional lymphadenopathy (hepatic hilum, celiac, and inter-aortocaval regions).

The patient underwent a PET/CT scan with [^{18}F]FDG that showed focally increased uptake in the uncinate process of pancreas, better outlined, however, in a subsequent scan with ^{68}Ga-DOTATOC (Fig. 9), as well as in multiple abdominal lymphadenopathy (peripancreatic region, hepatic hilum, and inter-aortocaval region), and in thoracic lymphadenopathy (subclavian region, right axilla, and left clavicular region). The liver lesions also showed increased [^{18}F]FDG uptake (Fig. 10); finally, there were also numerous areas of increased tracer uptake throughout the skeleton (Fig. 11).

One month later, a PET/TC scan with ^{68}Ga-DOTATOC showed the same lesions previously observed in the PET/TC scan with [^{18}F]FDG; nevertheless, the scan revealed other new areas of increased uptake in the skeleton (right portion of the D12 body, right pedicle of L5, left ilium, right acetabulum, and right portion of the frontal bone) (Figs. 12 and 13).

Ultrasound-guided biopsy of one hepatic lesion showed hepatic localization of neuroendocrine tumor, G3, with a Ki67 index of 85%.

Follow-Up

The patient started a chemotherapy protocol and RT treatment on bone lesions, with reduction of the extent of hepatic, lymphatic, and skeletal disease.

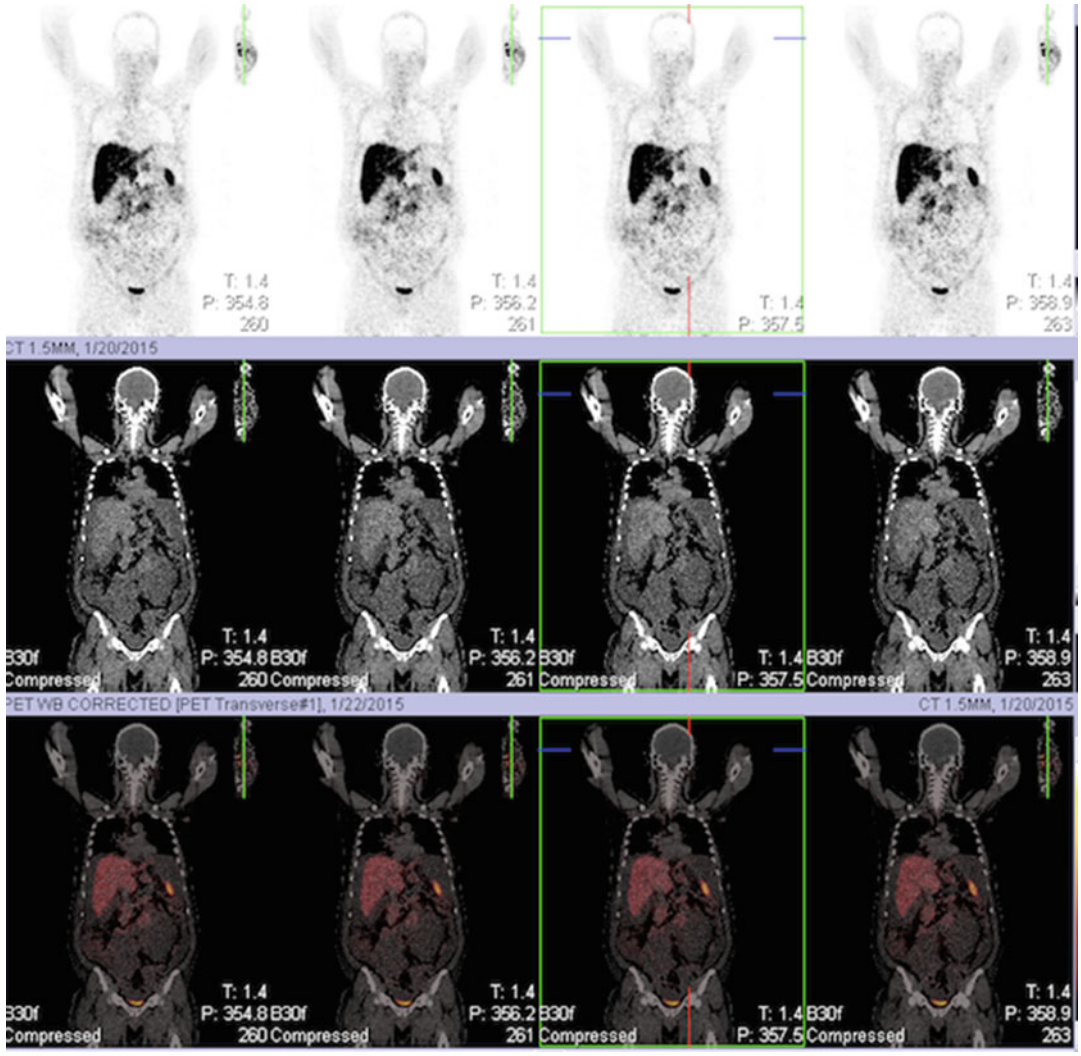

Fig. 5 *Top row*: ^{68}Ga-DOTATATE PET coronal section demonstrating no uptake in the chest and abdominal intensity less than liver and spleen. *Middle row* is the coronal CT images showing pleural effusion. *Bottom row* coronal section of the fused PET/CT images

Neuroendocrine Tumors: Case No. 6

Case contributed by: E. Tabacchi[1], C. Nanni[1], I. Bossert[1], A.M. Maffione[2], S. Fanti[1]

[1]Nuclear Medicine Unit, "S. Orsola-Malpighi" Hospital, Bologna, Italy

[2]Nuclear Medicine Unit, "Santa Maria della Misericordia" Hospital, Rovigo, Italy

A 54-year-old man, with polyuria, polydipsia, dysuria, weight loss (10 kg), and recent diagnosis of diabetes, underwent CT scan that revealed hepatic lesions, splenic vein thrombosis, and bilateral adrenal hyperplasia. Laboratory test showed hypokalemia (2 mEq/L) and hypercortisolemia. The patient was hospitalized, and a ^{68}Ga-DOTANOC PET/CT with diagnosis of neuroendocrine tumor of the pancreas with hepatic

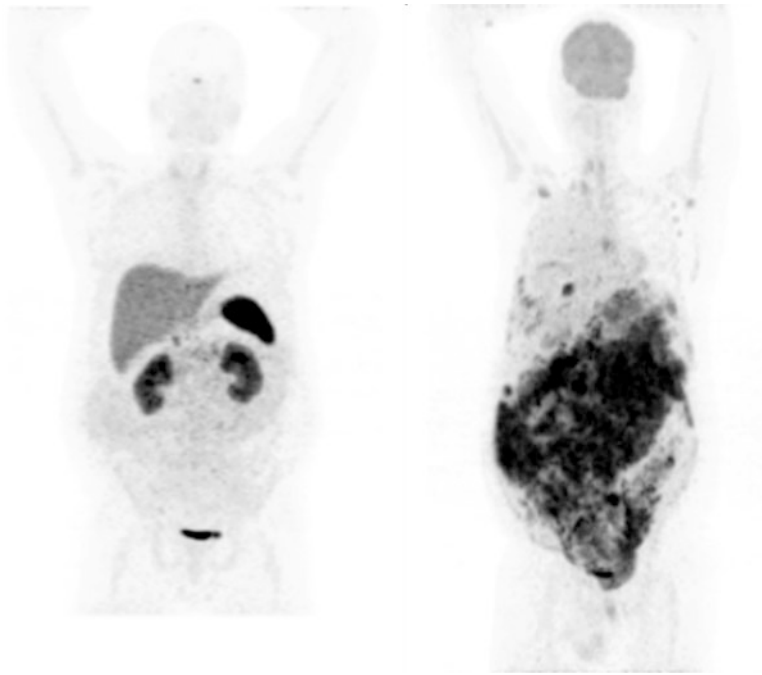

Fig. 6 MIP comparison of ^{68}Ga-DOTATATE PET (*left*) and [^{18}F]FDG PET (*right*) of the same patient with metastatic neuroendocrine tumor demonstrating dedifferentiation

metastasis and ACTH secreting was performed (paraneoplastic Cushing syndrome). Indeed ^{68}Ga-DOTANOC PET/CT revealed focal uptake at the body-tail of the pancreas ($SUV_{max} = 17.3$) (Fig. 14a, red flags; Fig. 14b, red flags) and multiple areas of uptake at the liver (the greater at the segment 6/7 with $SUV_{max} = 16.7$) (Fig. 14a, b: blue flags) compatible with lesions with moderate expression of somatostatin receptors (types: 2, 3, 5).

During hospitalization the adrenal glands were surgically removed and the patient started therapy with octreotide and lanreotide.

After almost 1 year, the patient underwent another ^{68}Ga-DOTANOC PET/CT that showed an increase in size of the area of uptake at the body-tail of the pancreas ($SUV_{max} = 40.1$) (Fig. 15a: red flags) with an increase in size and uptake in the multiple hepatic lesions ($SUV_{max} = 44$ at the segment 6/7 and $SUV_{max} = 68$ at the segment 2) (Fig. 15a, b: blue flags). PET/CT revealed the appearance of uptake to other hepatic lesions, for example, at the dome of the liver ($SUV_{max} = 33$).

The patient started therapy with Ipstyl and underwent therapy with ^{90}Y-DOTA-peptide (five cycles). After 3 months he underwent ^{68}Ga-DOTANOC PET/CT to assess response to therapy that showed stability for size and uptake at the body-tail of the pancreas ($SUV_{max} = 44.7$) (Fig. 16a: red flags) and stability at the hepatic lesions ($SUV_{max} = 34$ at the segment 6/7 and $SUV_{max} = 38$ at the segment 2) (Fig. 16a, b: blue flags) with appearance of necrosis in the middle of the lesion.

Neuroendocrine Tumors: Case No. 7

E.D. Telenga[1], A.W.J.M. Glaudemans[1], R.H.J.A Slart[1,2]

[1]Department of Nuclear Medicine and Molecular Imaging, University Medical Center Groningen, The Netherlands

[2]Biomedical Photonic Imaging Group, University of Twente, Enschede, The Netherlands

Presentation

A 75-year-old man visited a general hospital for follow-up after a right hemicolectomy for villous

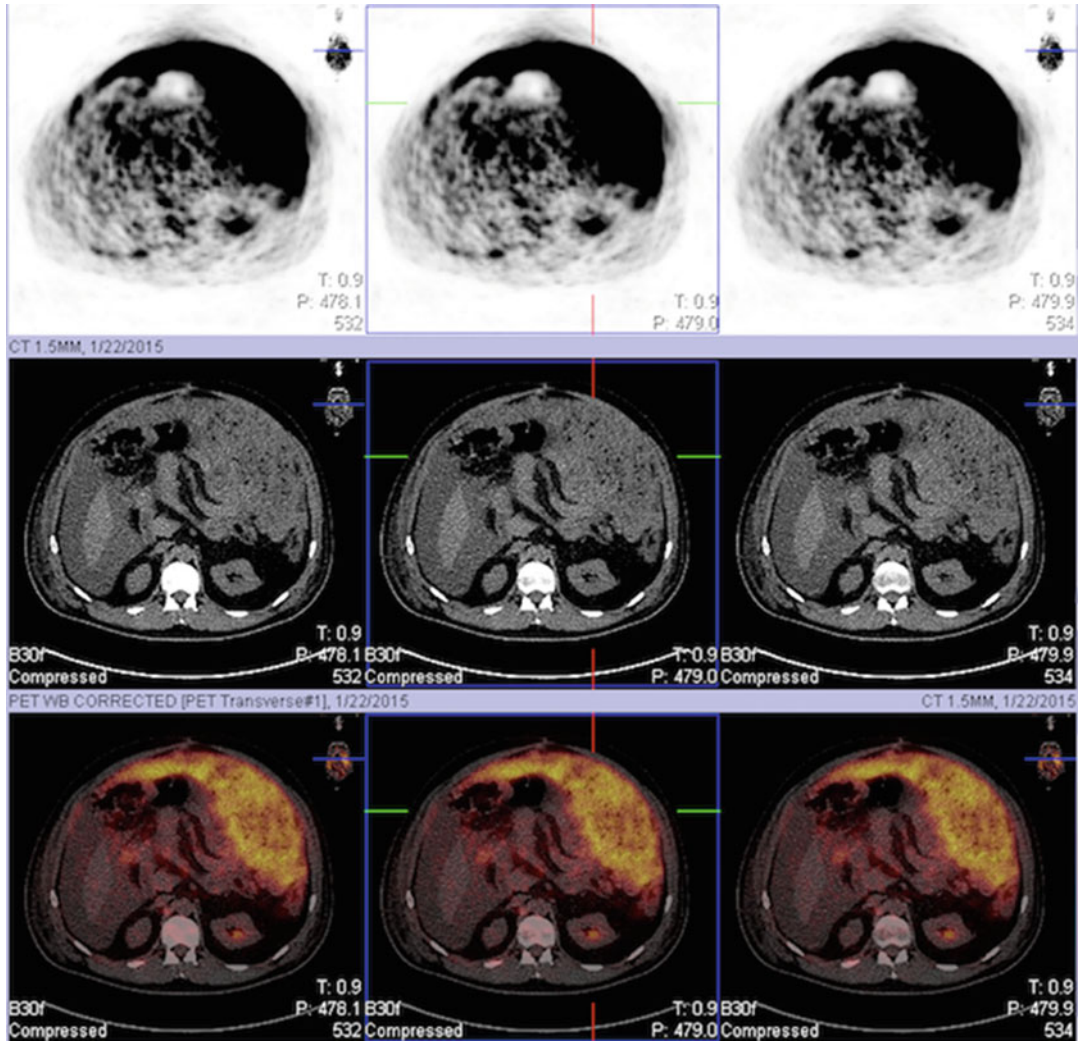

Fig. 7 *Top row*: axial [^{18}F]FDG PET of the patient with NET showing intense omentum and mesenteric uptake. *Middle row*: CT images showing thickened bowel wall which was "difficult" to assess. *Bottom row*: fused PET/CT images

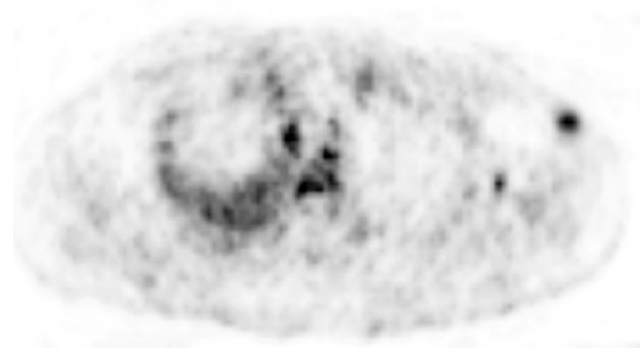

Fig. 8 Axial [^{18}F]FDG PET showing uptake on right pleural effusion and lung thickening with intense axillary lymph node uptake

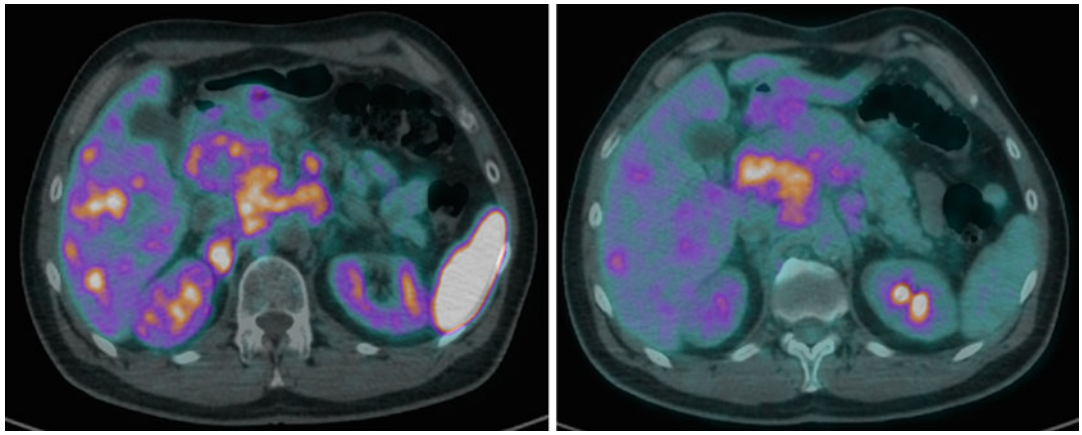

Fig. 9 Lesion in the uncinate process of pancreas as shown by PET/CT with ^{68}Ga-DOTATOC (*left panel*) and with [^{18}F]FDG (*right panel*)

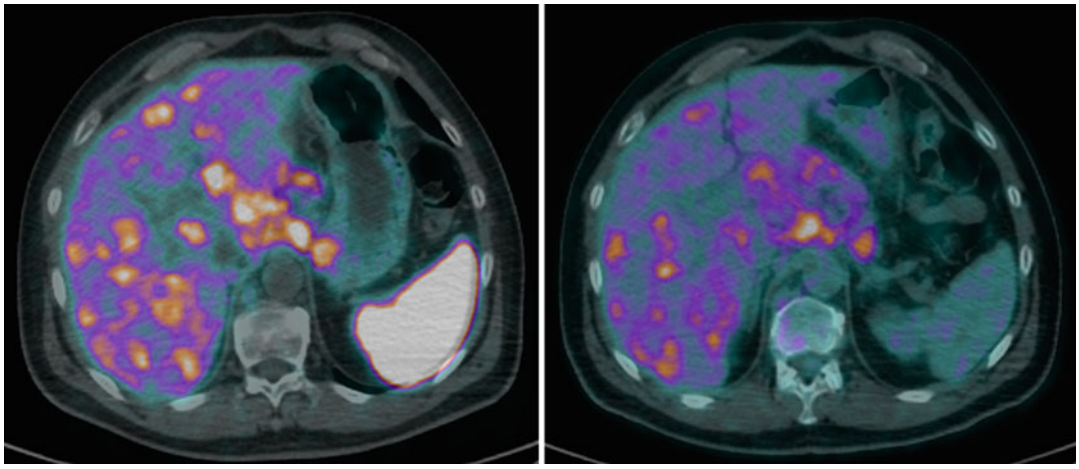

Fig. 10 Hepatic lesions and lymphadenopathy in hepatic hilum on the PET/TC scan with ^{68}Ga-DOTATOC (*left panel*) and with [^{18}F]FDG (*right panel*)

adenoma of the cecum 4 years earlier. He reported intermittent periods of abdominal pain at the upper right side for about a year. He also reported incidental brownish-yellow urine during these periods.

Findings

A diagnostic CT showed a mass of 3.5 by 3.3 cm near the head of the pancreas and the duodenum (Fig. 17). It was not possible to determine from which structure the mass originated. There were

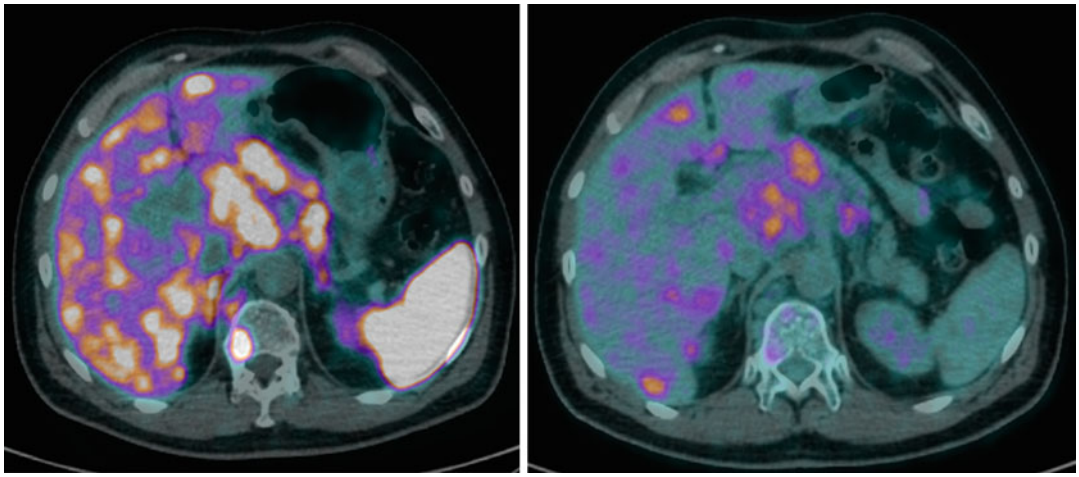

Fig. 11 Bone lesion (*right* portion of the D12 vertebral body) on the PET/CT scan with ^{68}Ga-DOTATOC (*left panel*) and with [^{18}F]FDG (*right panel*)

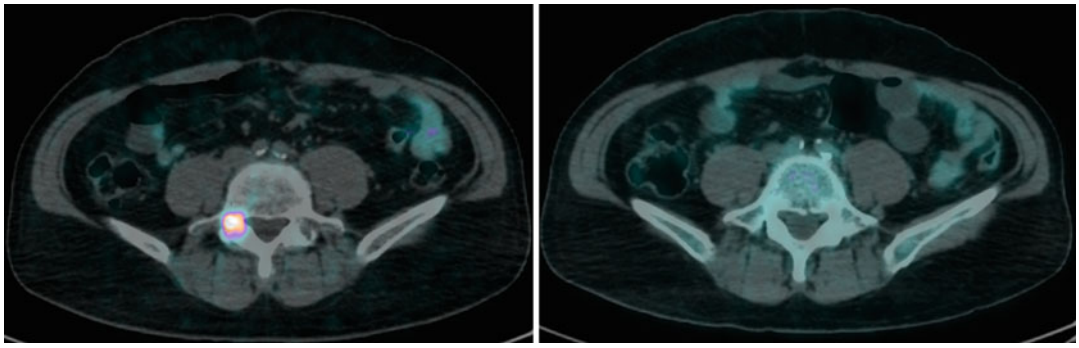

Fig. 12 Bone lesion (right pedicle of L1) on the PET/CT scan with ^{68}Ga-DOTATOC (left panel) and with [^{18}F]FDG (right panel)

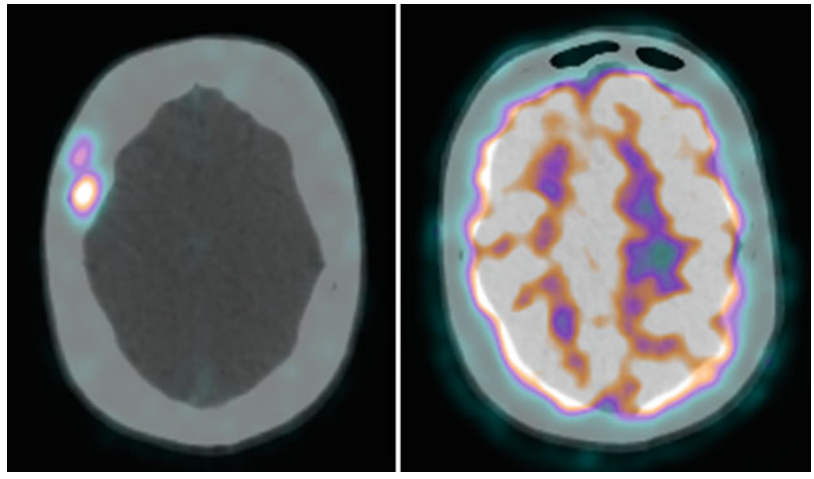

Fig. 13 Bone lesion (right portion of the frontal bone) on the PET/CT scan with ^{68}Ga-DOTATOC (left panel) and with [^{18}F]FDG (right panel)

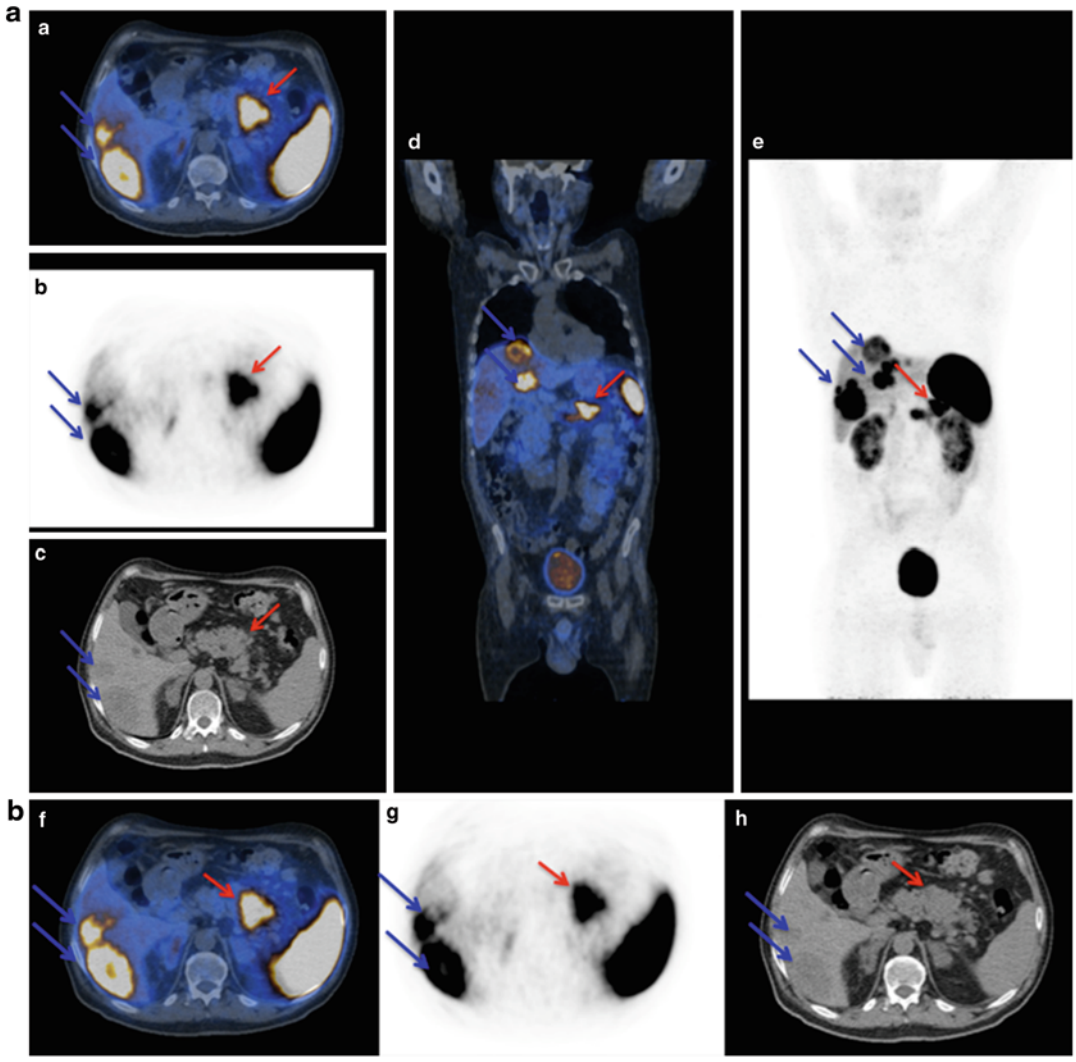

Fig. 14 (**a**) (*A*, transaxial ^{68}Ga-DOTATOC PET/CT; *B*, transaxial ^{68}Ga-DOTATOC PET; *C*, transaxial CT; *D*, coronal [^{18}F]FDG PET/CT; *E*, MIP; *red* flag, pancreatic finding; *blue* flag, hepatic finding). (**b**) (*F*, transaxial ^{68}Ga-DOTATOC PET/CT; *G*, transaxial ^{68}Ga-DOTATOC PET; *H*, transaxial CT; *blue* flag, hepatic finding; *red* flag, pancreatic finding)

no enlarged mesenterial or retroperitoneal lymph nodes. In the liver were multiple round, hypodense lesions that were too small for further characterization. Patient was referred to an academic hospital for a pylorus-preserving pancreaticoduodenectomy with portal vein reconstruction, removal of the inferior mesenteric vein, and splenectomy with partial autotransplantation. Pathologic examination of the mass showed a low-grade neuroendocrine tumor. The resection margins were tumor-free and there were no tumor cells present in all 18 removed lymph nodes. The tumor was staged as a T3N0Mx neuroendocrine pancreas tumor. No additional treatment was given, and follow-up was started with six-monthly ultrasound of the abdomen.

After 1 year, at the second ultrasound, a hypoechoic lesion of 3.3 cm was seen in the

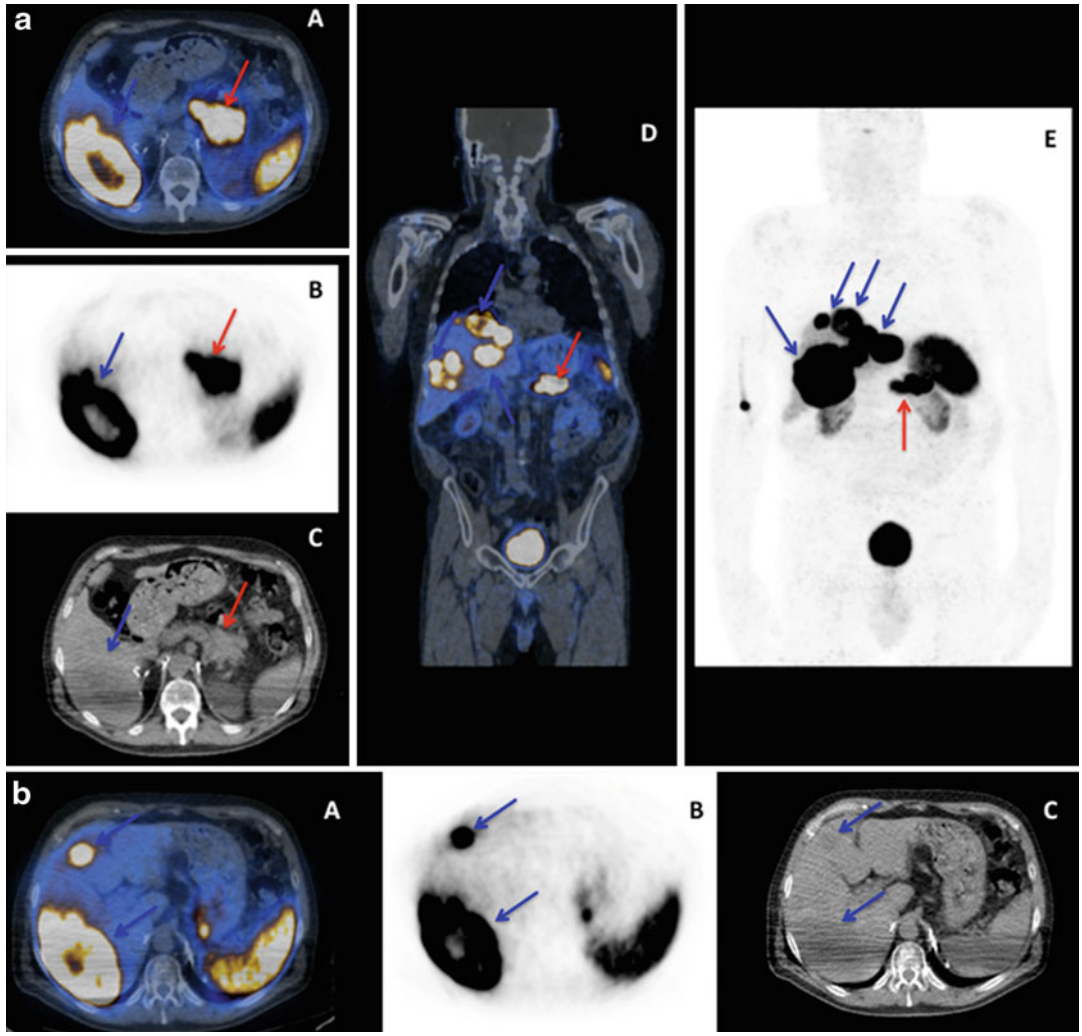

Fig. 15 (**a**) (*A*, transaxial ^{68}Ga-DOTATOC PET/CT; *B*, transaxial ^{68}Ga-DOTATOC PET; *C*, transaxial CT; *D*, coronal ^{68}Ga-DOTATOC PET/CT; *E*, MIP; *red* flag, pancreatic finding; *blue* flag, hepatic finding). (**b**) (*F*, transaxial ^{68}Ga-DOTATOC PET/CT; *G*, transaxial ^{68}Ga-DOTATOC PET; *H*, transaxial CT; *blue* flag, hepatic finding)

liver on the right side of the falciform ligament (Fig. 18). Subsequently, a whole-body ^{18}F-dihydroxyphenylalanine (^{18}F-DOPA) PET/CT with a three-phase (noncontrast, arterial, and portal venous phase) diagnostic CT of the liver was performed (Fig. 19). The ^{18}F-DOPA PET/CT showed no pathologic uptake and the lesion visible on the ultrasound could not be reproduced on the diagnostic CT. The small hypodense lesions throughout the liver were unchanged in comparison to the preoperative CT. It was determined that the lesion on the ultrasound was most likely an artifact. Normal follow-up was resumed.

On the following ultrasound, the earlier lesion was not seen. However, the ultrasound 2 years after surgery, showed a new hypoechoic lesion of 1.9 cm in segment 6 of the liver (Fig. 20). A three-phase CT of the liver showed four hypodense lesions with enhancement in the arterial phase (segment 8, 3.7 cm; segment 8, 2.4 cm;

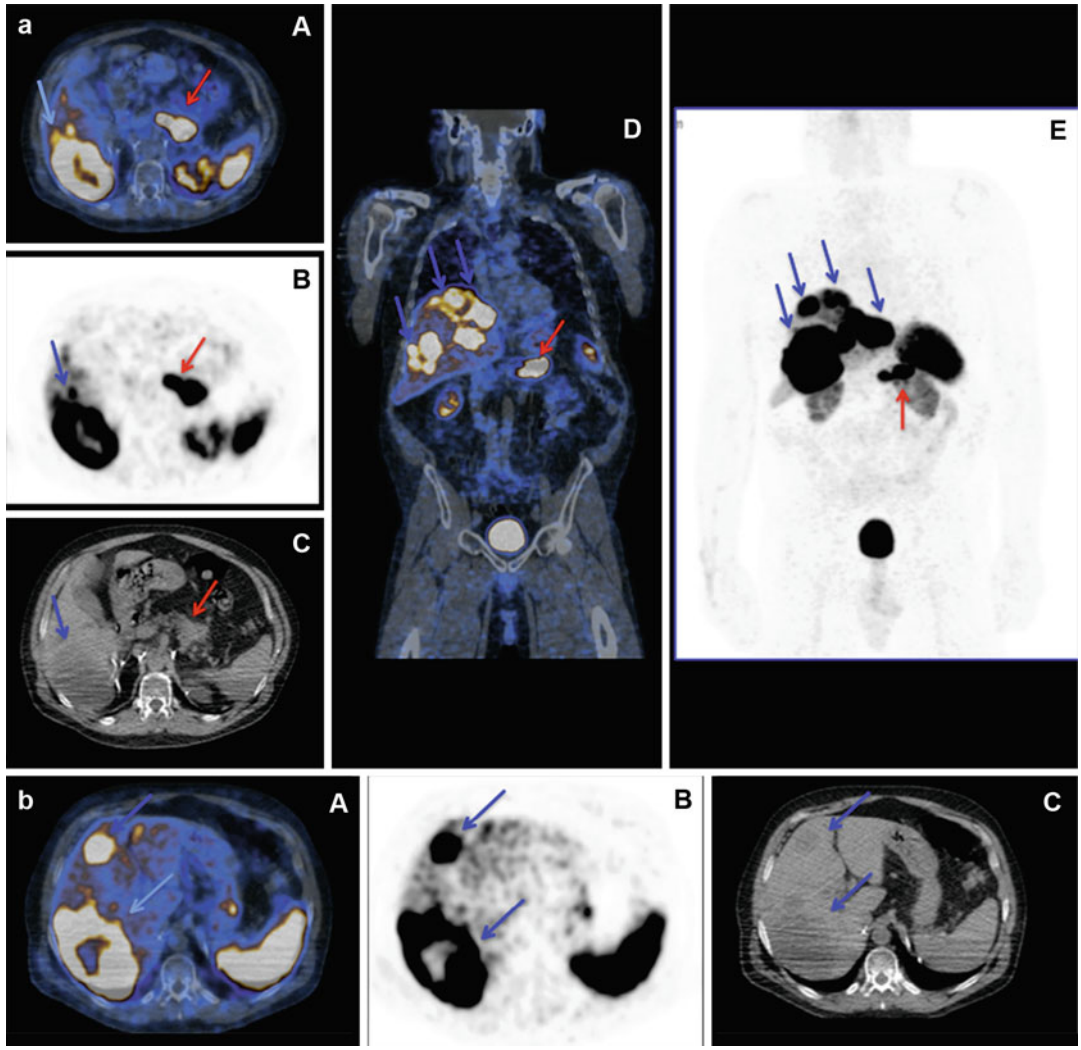

Fig. 16 (**a**) (*A*, transaxial ^{68}Ga-DOTATOC PET/CT; *B*, transaxial ^{68}Ga-DOTATOC PET; *C*, transaxial CT; *D*, coronal ^{68}Ga-DOTATOC PET/CT; *E*, MIP; *red* arrow, pancreatic finding; *blue* arrow, hepatic finding). (**b**) (*F*, transaxial ^{68}Ga-DOTATOC PET/CT; *G*, transaxial ^{68}Ga-DOTATOC PET; *H*, transaxial CT; *blue* arrow, hepatic finding)

segment 1, 2.0 cm; and segment 6/7, 1.4 cm) and several prominent lymph nodes in the mesenterium and the retroperitoneum (Fig. 21). The liver lesions were highly suspicious for liver metastases of the neuroendocrine tumor. The prominent lymph nodes were also suspicious for metastases, but were also very likely to be reactive lymph nodes.

To further evaluate the properties of the liver lesions and the lymph nodes, a [^{11}C]5-hydroxy-L-tryptophan ([^{11}C]HTP) PET/CT was performed (Fig. 21). The [^{11}C]HTP PET/CT showed increased uptake in the liver lesion, but no increased uptake in the lymph nodes or elsewhere.

Follow-Up

Based on the diagnostic CT and the [^{11}C]HTP PET/CT, it was determined that the patient had a

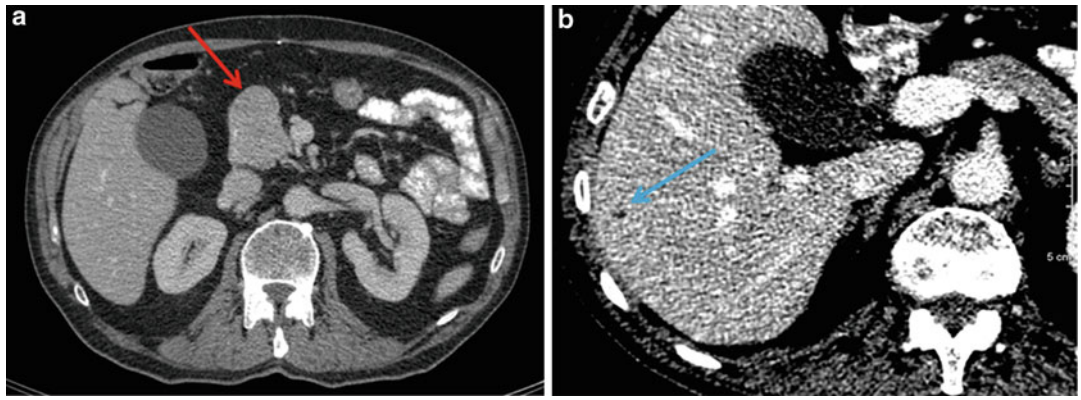

Fig. 17 Preoperative abdominal CT showing: (**a**) a mass near the head of the pancreas (*red arrow*); (**b**) small hypodense lesions in the liver (*blue arrow*)

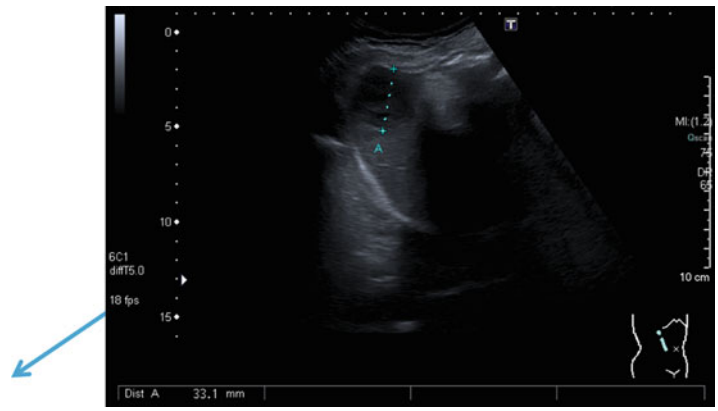

Fig. 18 Ultrasound of the liver 1 year after surgery, showing a hypoechoic lesion of 3.3 cm on the right side of the falciform ligament (*blue dotted line*)

metastasized neuroendocrine tumor with lesions in the liver, but not in the mesenteric and retroperitoneal lymph node stations. As the patient had relatively few symptoms, it was decided in agreement with the patient to treat the disease noninvasively, especially since an operation would be difficult and accompanied with high risk of complications. Patient started with subcutaneous octreotide injections once every 4 weeks. One year later the patient developed a radicular syndrome due to a metastasis in the first and second lumbar vertebrae for which radiotherapy was started.

Neuroendocrine Tumors: Case No. 8

Presentation

A 56-year-old man was diagnosed 19 years ago with malignant thymoma with predominant spindle cells. He was referred for suspected recurrence.

Findings

[^{18}F]FDG PET/CT showed hypermetabolic anterior mediastinal mass consistent with recurrent disease (Fig. 22). The CT-guided biopsy of the

Fig. 19 Maximum intensity projection of the ^{18}F-DOPA PET/CT, showing no pathologic uptake

mass revealed B3 spindle cell thymoma as the former. Thymectomy was performed, and histology demonstrated neuroendocrine tumor (NET) with spindle cell solid-lobular architecture constituted by poorly differentiated NET and atypical carcinoid.

Routine follow-up 9 months postsurgery CT of the thorax showed mediastinal lymph node enlargement and pleura thickenings of suspected origin.

^{68}Ga-DOTATOC PET/CT clearly showed left supra-infraclavicular and mediastinal lymph nodes with pathological tracer uptake and multiple thickenings of the left pleura with intense DOTATOC uptake.

Discussion

Thymic NETs are very uncommon malignant tumors of the thymus. This case demonstrates the value of both ^{68}Ga-DOTA-peptides and [^{18}F] FDG PET/CT in a rare case of combined poorly differentiated NET and atypical carcinoids of the thymus (Fig. 23).

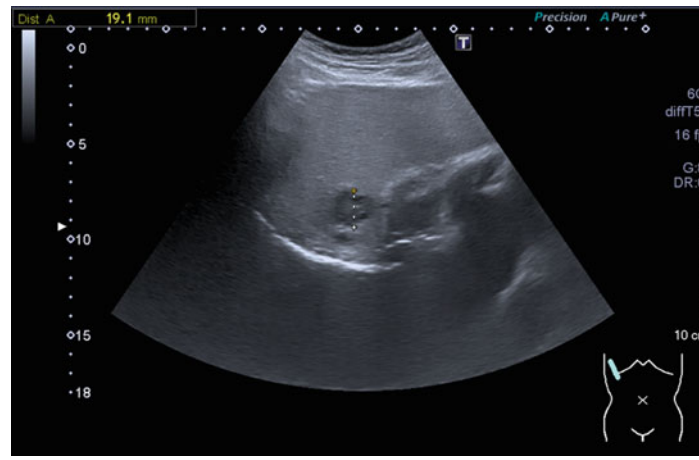

Fig. 20 Ultrasound of the liver 2 years after surgery, showing a hypoechoic lesion of 1.9 cm in segment 6 of the liver (*white dotted line*)

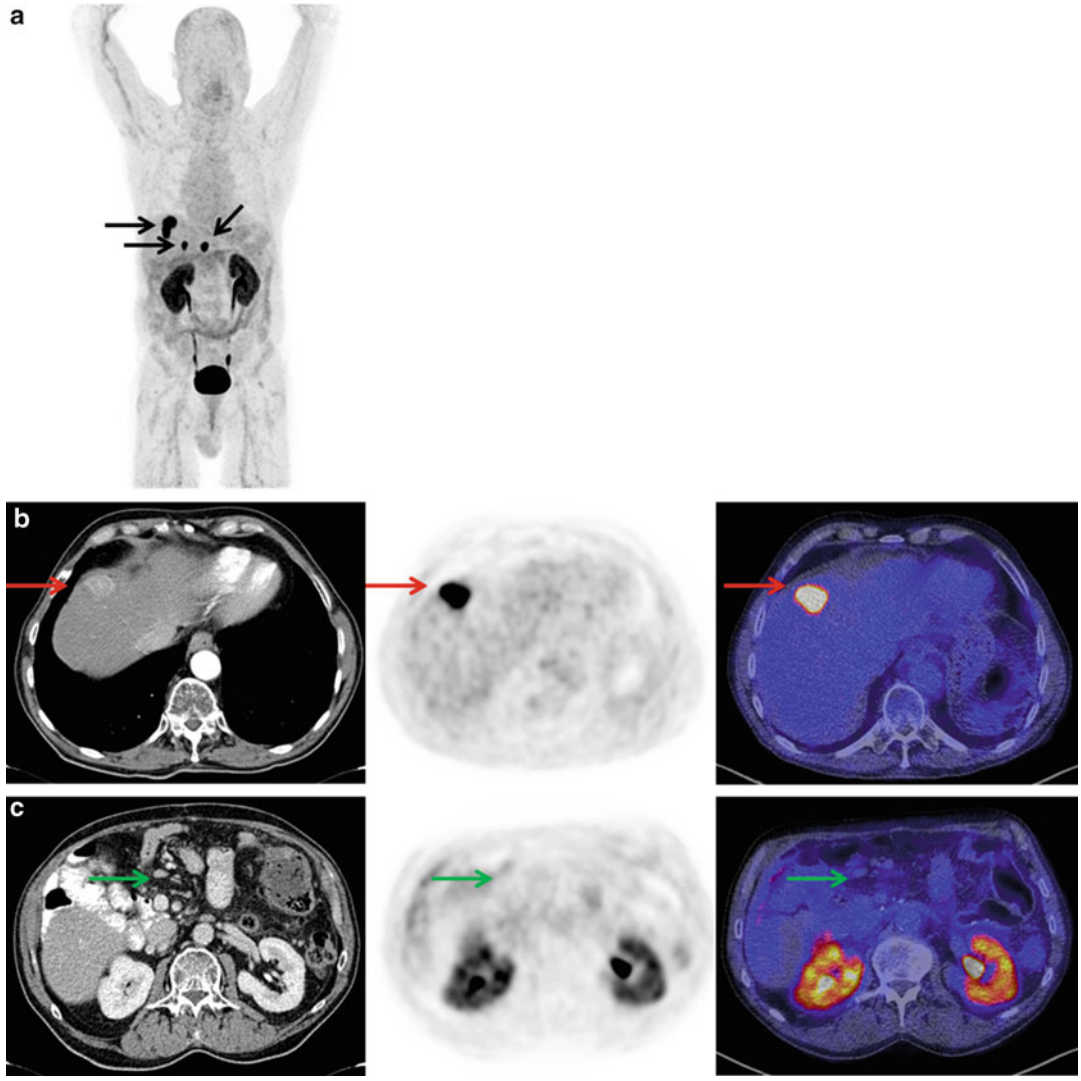

Fig. 21 Diagnostic CT and [^{11}C]HTP PET/CT showing: (**a**) maximum intensity projection with four intense lesions in the liver (*black arrows*); (**b**) lesion in segment 8 of the liver with arterial enhancement and intense [^{11}C]HTP uptake (*red arrows*); **c** prominent mesenteric lymph node with no increased [^{11}C]HTP PET/CT uptake (*green arrows*)

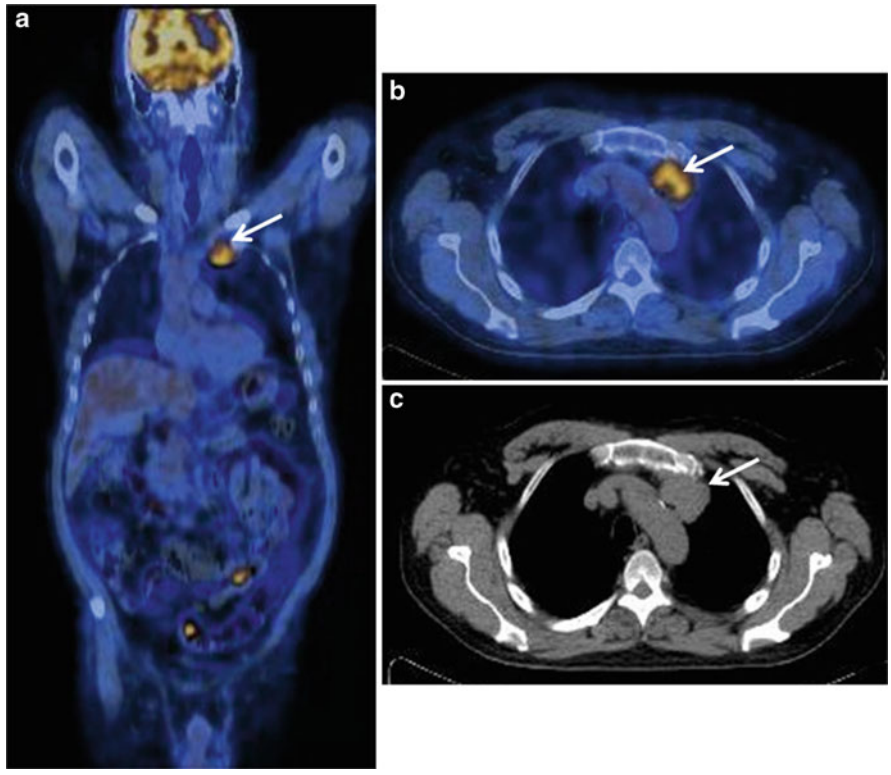

Fig. 22 [^{18}F]FDG fused PET/CT (**a** coronal, **b** axial) and axial low-dose CT (**c**) of recurrent NET thymoma

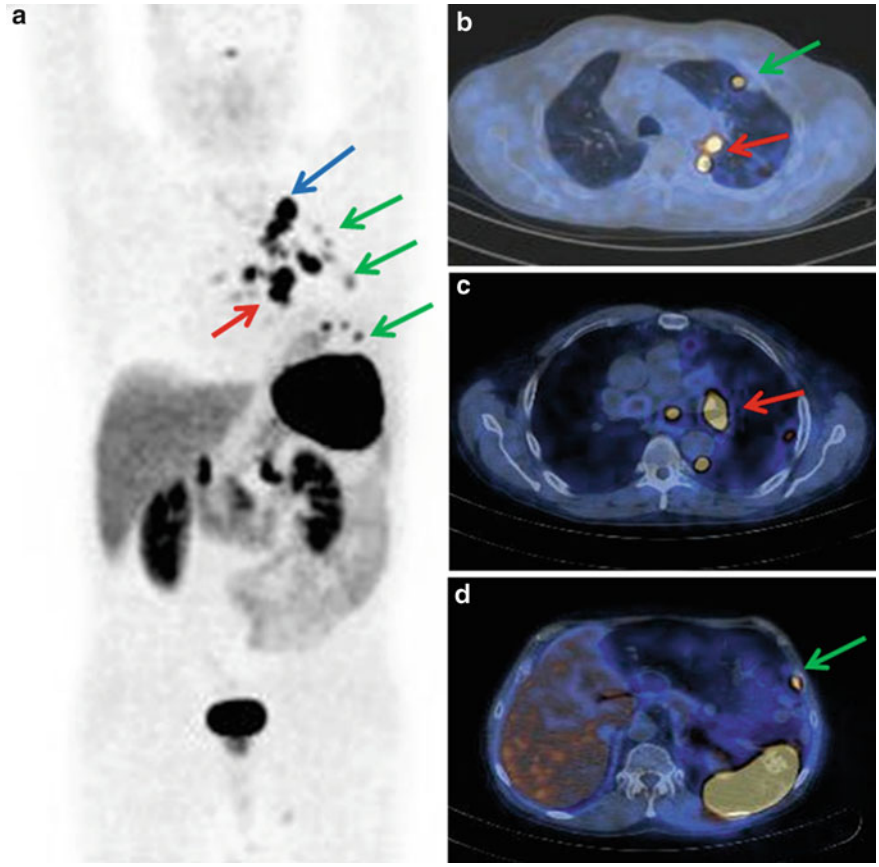

Fig. 23 Maximum intensity projection (MIP) (**a**) and axial fused ^{68}Ga-DOTATOC PET/CT (**b**, **c,** and **d**) of pathological supra-infraclavicular (*blue arrow*) and mediastinal lymph nodes (*red arrows*) and of multiple thickenings of the left pleura (*green arrows*)

Teaching Cases in Nuclear Oncology: Kidney and Bladder Cancer

68

Duccio Volterrani, Giulia Puccini, Sara Mazzarri, and Federica Guidoccio

Keywords

[^{11}C]choline PET/CT • Renal cell carcinoma • [^{18}F]FDG PET/CT • US • Abdominal MR • Transitional carcinoma • ceCT • Lymph node metastases • Papillary renal cell carcinoma • Renal lymphoma • Local recurrence • Urothelial carcinoma • Bladder cancer • Metabolic tumor response

Glossary

[^{18}F]FDG	2-Deoxy-2-[^{18}F]fluoro-D-glucose
AJCC	American Joint Committee on Cancer
ceCT	Contrast-enhanced computed tomography
CT	X-ray computed tomography
M	Metastasis status according to the AJCC/UICC TNM staging system
MIP	Maximum intensity projection
MR	Magnetic resonance
N	Lymph node status according to the AJCC/UICC TNM staging system
PET	Positron emission tomography
PET/CT	Positron emission tomography/ Computed tomography
PSA	Prostate-specific antigen, a tumor marker of prostatic cancer
RCC	Renal cell carcinoma
SUV	Standardized uptake value
SUV_{max}	Standardized uptake value at point of maximum
T	Tumor status according to the AJCC/UICC staging system
TNM	AJCC staging system based on parameters "T" (tumor status), "N" (lymph node status), and "M" (distant metastasis status)
UICC	Union Internationale Contre le Cancer (International Union Against Cancer)
US	Ultrasonography

Contents

Kidney and Bladder Cancers: Case No. 1 1750
Presentation 1750
Findings 1750

Discussion 1752

Kidney and Bladder Cancers: Case No. 2 1752
Presentation 1752
Findings 1752
Follow-Up 1753

Discussion 1754

Kidney and Bladder Cancers: Case No. 3 1754
Presentation 1754
Findings 1755

D. Volterrani (✉) • G. Puccini • S. Mazzarri • F. Guidoccio
Regional Center of Nuclear Medicine, Department of Translational Research and Advanced Technologies in Medicine and Surgery, University of Pisa, Pisa, Italy
e-mail: duccio.volterrani@med.unipi.it

© Springer International Publishing Switzerland 2017
H.W. Strauss et al. (eds.), *Nuclear Oncology*,
https://doi.org/10.1007/978-3-319-26236-9_71

Follow-Up 1755
Teaching Points 1756

Kidney and Bladder Cancers: Case No. 4 1756
Presentation 1756
Findings 1756
Management 1756
Teaching Points 1756

Kidney and Bladder Cancers: Case No. 5 1756
Presentation 1756
Findings 1757
Follow-Up 1757
Teaching Points 1757

Kidney and Bladder Cancers: Case No. 6 1758
Presentation 1758
Findings 1758
Teaching Points 1758

Kidney and Bladder Cancers: Case No. 7 1758
Presentation 1758
Findings 1758
Follow-Up 1759
Teaching Points 1759

Kidney and Bladder Cancers: Case No. 8 1759
Presentation 1761
Findings 1761
Management 1761
Teaching Points 1761

Kidney and Bladder Cancers: Case No. 9 1762
Presentation 1762
Findings 1762
Follow-Up 1762
Teaching Point 1762

Kidney and Bladder Cancers: Case No. 10 1762
Presentation 1762
Findings 1763
Follow-Up 1763
Teaching Point 1763

Kidney and Bladder Cancers: Case No. 11 1763
Presentation 1763
Findings 1763
Follow-Up 1765

Discussion 1765

Kidney and Bladder Cancers: Case No. 1

Case contributed by: M. Kirienko, A. Chiti

Division of Nuclear Medicine, Department of Biomedical Sciences – Humanitas University, Milan, Italy

Presentation

A 65-year-old man affected by adenocarcinoma of the prostate (pT3bN1), Gleason score 3 + 5 = 8, PSA 43 ng/mL, who had undergone radical prostatectomy 3 years earlier and hormonal therapy and salvage radiation therapy 1 year earlier, was referred to perform [^{11}C]choline PET/CT (PET/CT-1) for restaging because of biochemical relapse. PSA before the PET/CT-1 examination was 2.52 ng/mL, and the scan was negative for prostate cancer relapse. Seven months later, because of rising PSA values, another [^{11}C]choline PET/CT scan (PET/CT-2) was performed. PSA before PET/CT-2 was 6.84 ng/mL.

Findings

[^{11}C]choline PET/CT-2 images (Fig. 1) showed no tracer uptake related to prostate cancer relapse, although a huge left renal mass was seen (Fig. 2) that was confirmed also on contrast-enhanced CT (Fig. 3). Retrospectively, PET/CT-1 images were reevaluated, and a renal lesion was already identifiable, in particular, on unenhanced low-dose CT (Fig. 4a–c).

The patient underwent left nephrectomy. The lesion resulted to be a renal cell carcinoma, sarcomatoid chromophobe variety, pT4 N0 R1. Additionally, three out of three lymph nodes at the renal hilum resulted to be positive for prostate cancer metastasis. Four months later, PSA levels rose to 7.55 ng/mL, and [^{11}C]choline PET/CT showed multiple abdominal [^{11}C]choline-avid lymph nodes.

Fig. 1 The fused axial [^{11}C]choline PET/CT-2 image shows no focal uptake areas related to prostate cancer relapse

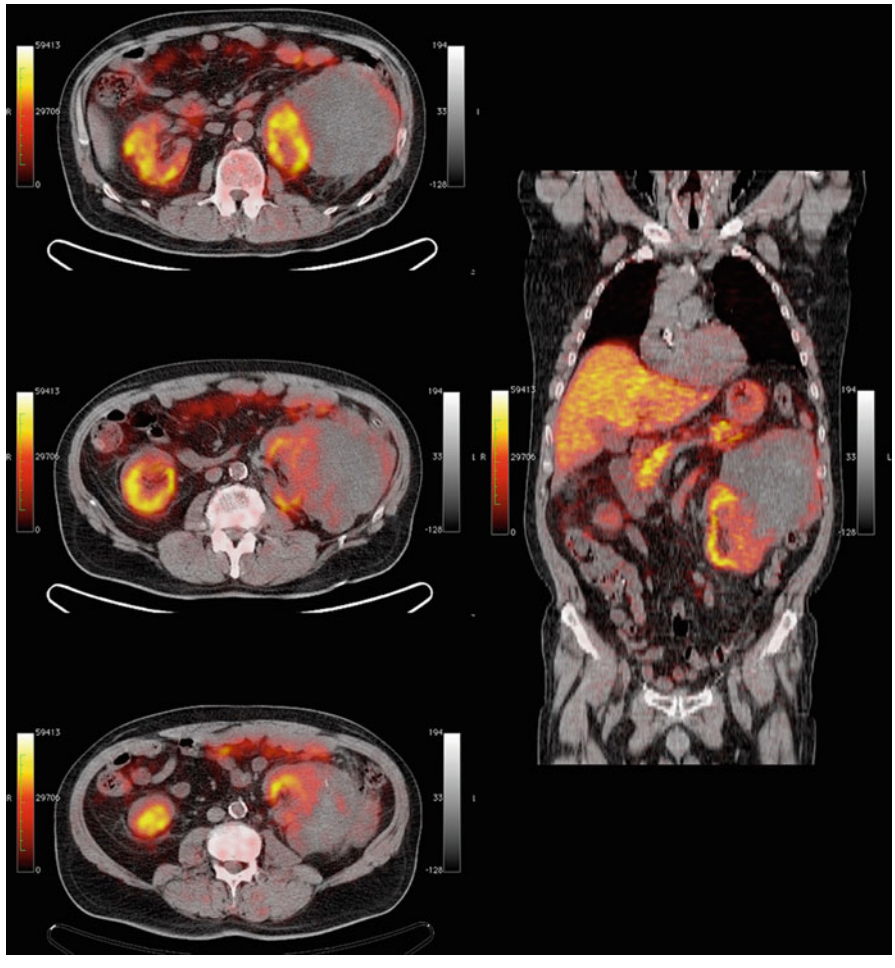

Fig. 2 The fused axial (*left*) and coronal (*right*) [^{11}C]choline PET/CT-2 images show a large left kidney mass, displaying peripheral tracer uptake with central photopenia corresponding to necrosis

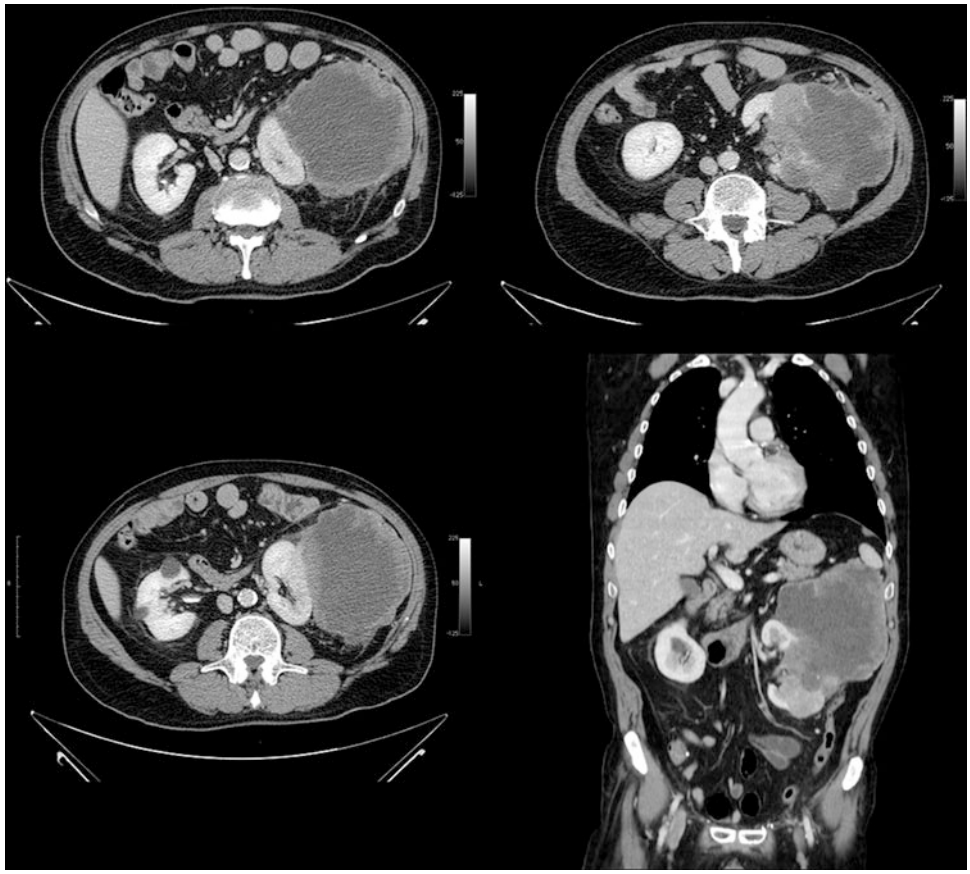

Fig. 3 The fused axial (*left* and *top right*) and coronal (*bottom right*) contrast-enhanced CT images show the left kidney mass

Discussion

[^{11}C]choline PET/CT is not specific for prostate cancer and other malignant and benign lesions can concentrate the tracer. Lesions without significant radiopharmaceutical uptake or uptake intensity equal to background (e.g., in the liver or kidneys) may also occur. Careful evaluation of all the districts is mandatory both on PET and CT image series in order not to miss lesions characterized by a low uptake.

Kidney and Bladder Cancers: Case No. 2

Case contributed by: M.A. Pedersen
Department of Nuclear Medicine and PET Centre, Aarhus University Hospital, Denmark

Presentation

A 63-year-old man presented with hemoptysis.

Findings

A CT scan showed enlarged lymph nodes in mediastinum station 2R and hydronephrosis of the left

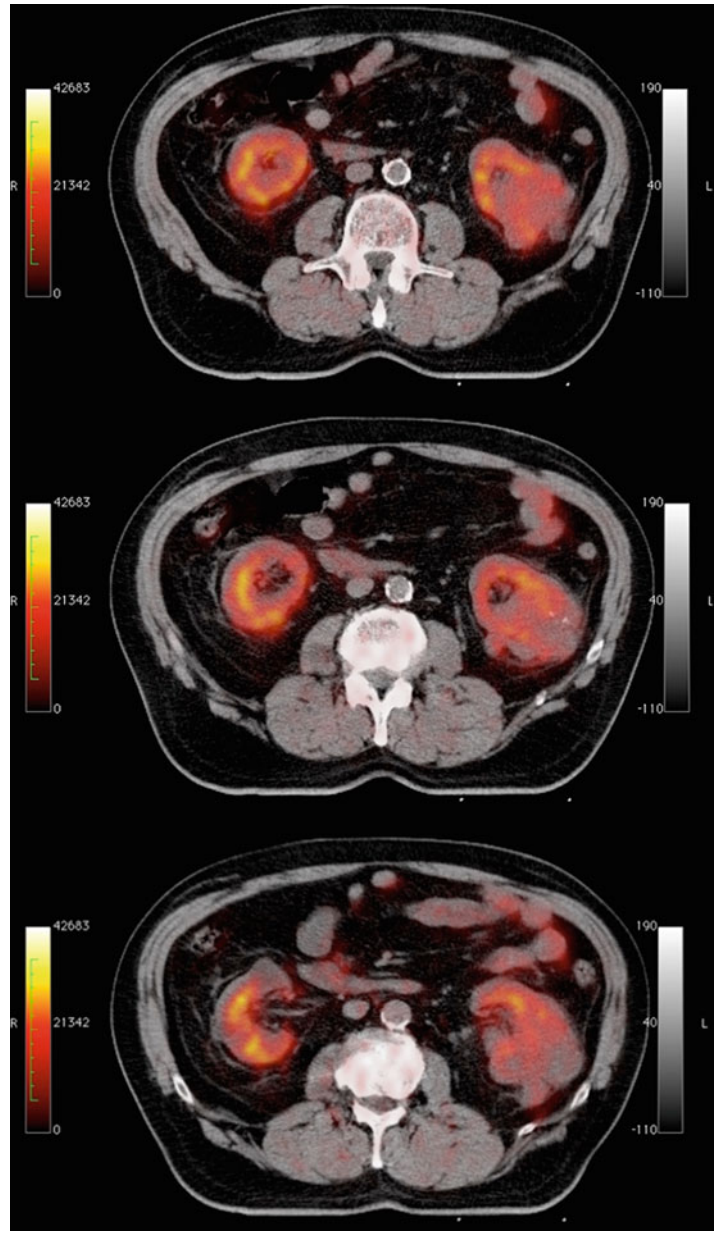

Fig. 4 The fused axial [^{11}C]choline PET/CT-1 images show an exophytic renal lesion displaying faint [^{11}C]choline uptake

kidney. Due to these findings, the patient was referred for an [^{18}F]FDG PET/CT scan with the suspicion of lung cancer.

The [^{18}F]FDG PET/CT showed a single enlarged lymph node in mediastinum station 10R with moderately increased [^{18}F]FDG uptake. The scan also confirmed hydronephrosis and minimal parenchyma in the left kidney (Fig. 5, red arrow). In addition, [^{18}F]FDG activity was observed in the distal part of the left ureter (Fig. 5, yellow arrow) which was interpreted as urinary [^{18}F]FDG accumulation in the ureter.

Follow-Up

Because of the hydronephrosis, a CT urography was performed. This revealed a possible tumor in

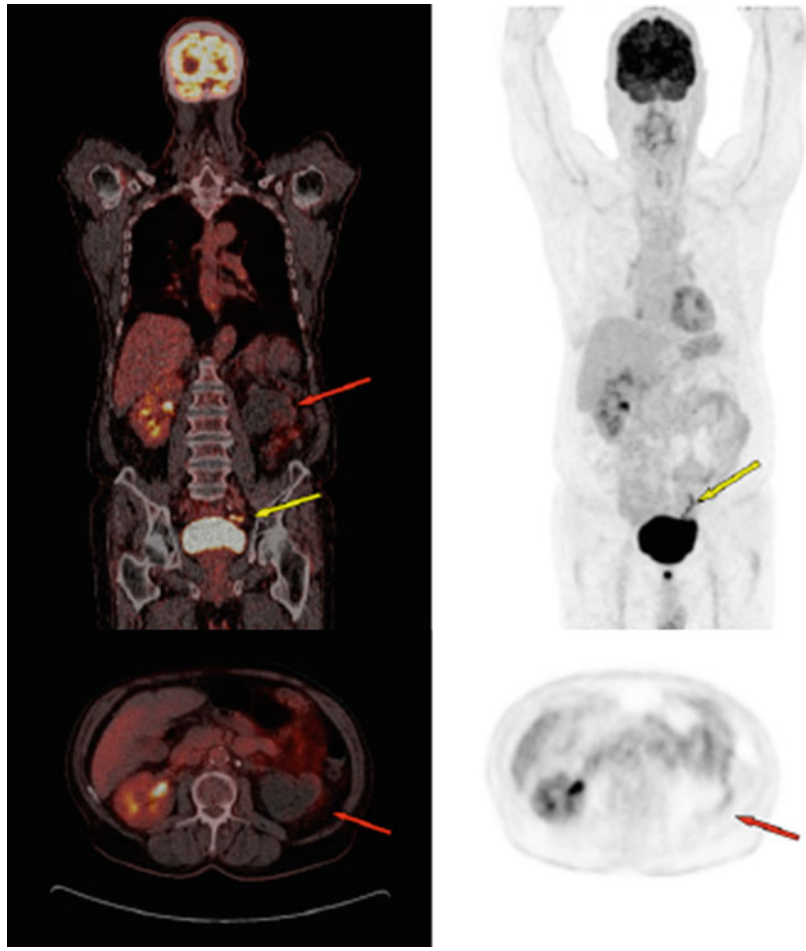

Fig. 5 The [^{18}F]FDG PET/CT scan also revealed, as previously described, hydronephrosis and minimal parenchyma in the left kidney (Figs. 1a and 2a, b, *red arrow*). In addition, [^{18}F]FDG activity was observed in the distal part of the left ureter (Fig. 1a, b, *yellow arrow*) which was interpreted as urinary [^{18}F]FDG activity in the ureter

the distal left ureter and no excretion from the left kidney. Subsequent ureteroscopy with biopsy revealed urothelial cancer with low malignancy in the distal left ureter. The patient was treated with left nephroureterectomy.

The suspicion of lung cancer was later abandoned.

Discussion

This case shows that it can be difficult to interpret [^{18}F]FDG PET/CT scans when it comes to malignancies in the urinary tract system, due to urinary excretion of [^{18}F]FDG. Special attention should be paid when a kidney shows signs of distress (e.g., hydronephrosis, loss of parenchyma) and focal [^{18}F]FDG activity in the ureter which may be due to malignancy.

Kidney and Bladder Cancers: Case No. 3

Presentation

A 57-year-old with a history of left back pain and macrohematuria underwent US examination which did not disclose any lesion at the level of all urinary pathways and the bladder. Since the patient had experienced a previous severe adverse reaction against iodinated contrast agent, he was started to

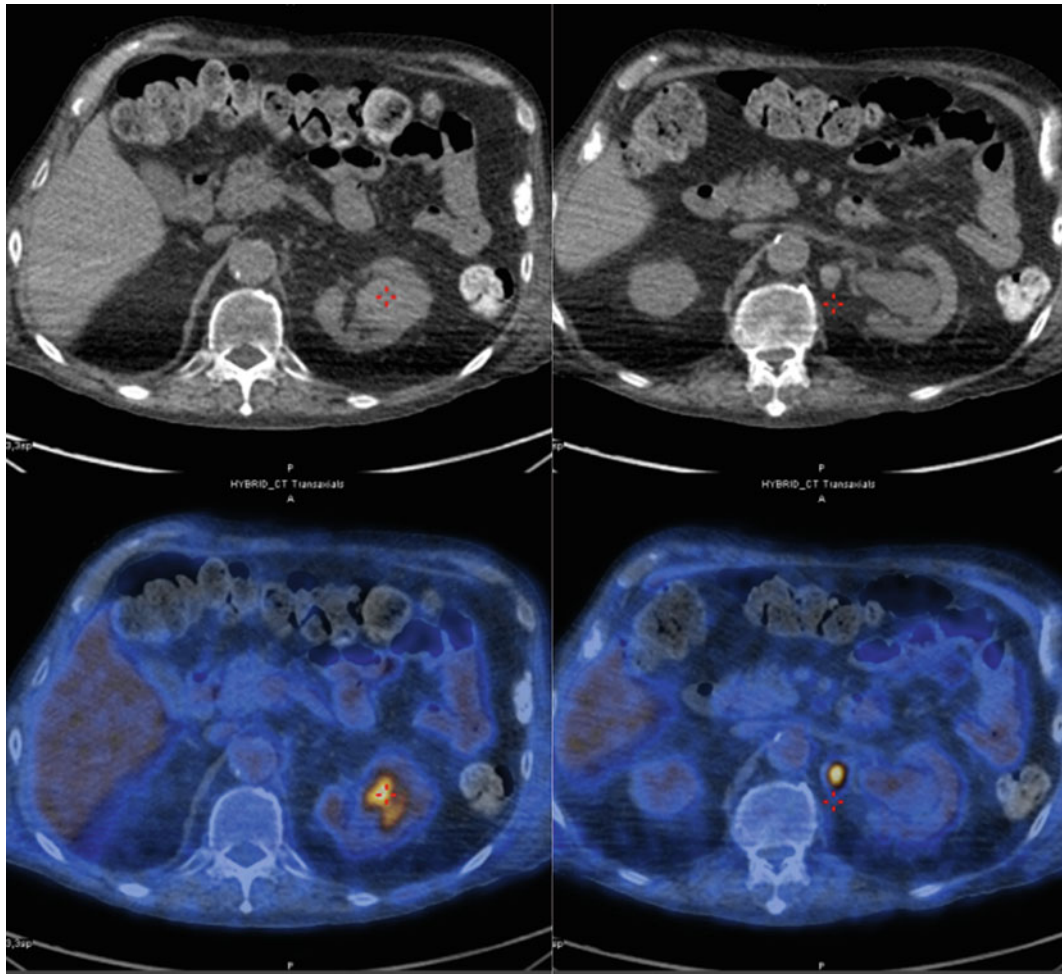

Fig. 6 [^{18}F]FDG PET/CT axial slices (CT and fused images) show a lesion accumulating [^{18}F]FDG within the pelvis of the left kidney and nodule consistent with a pathological perirenal lymphadenopathy

an abdominal MR study which revealed a T1-weighted hypointense mass with contrast enhancement within the left pelvis. A lymphadenopathy in the perirenal space, posteriorly to the renal vein, was also disclosed. An advanced urothelial carcinoma was then suspected.

Findings

In order to complete the staging, the patient underwent also a whole-body [^{18}F]FDG PET/CT study. PET/CT confirmed the presence of a hypermetabolic lesion within the pelvis of the left kidney as well as a perirenal hypermetabolic lymph node. No other pathologic hyperactive foci were observed (Fig. 6). A subsequent MR scan confirmed PET/CT findings (Fig 7).

Follow-Up

The patient underwent surgery, and pathology confirmed the presence of a transitional carcinoma arising from the renal pelvis with lymph node involvement.

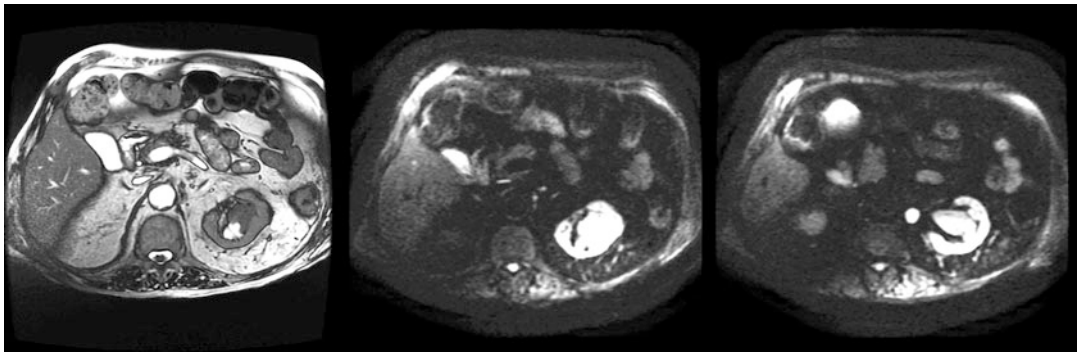

Fig. 7 T1- and T2-weighted MR axial slices confirm [^{18}F]FDG PET/CT findings

Teaching Points

Only a limited number of studies have investigated the utility of PET in the assessment of the staging of renal carcinoma. However, some renal carcinomas like those arising from urothelial cells usually show a high grade of uptake of [^{18}F]FDG.

Kidney and Bladder Cancers: Case No. 4

Presentation

A 59-year-old woman had previously undergone left nephrectomy due to a papillary renal cell carcinoma. Since the patient was suffering from osteoporosis, she experienced multiple vertebral fractures treated with a neurosurgical vertebral fixation procedure with permanent rigid titanium prosthesis.

Findings

At restaging, due to the presence of artifacts produced by the metal device on CT images, the patient underwent a PET/CT with [^{18}F]FDG to better explore the lumboaortic region. PET/CT disclosed the presence of several hypermetabolic lymph nodes which were not visualized by diagnostic CT (Fig. 8).

Management

Due to the extensive lymph node involvement seen on PET/CT, the patient was started to chemotherapy.

Teaching Points

Papillary renal cell carcinoma is usually avid of [^{18}F]FDG, and PET/CT can be used in selected cases for the restaging of patients, usually when they cannot undergo a ceCT or when CT findings are not conclusive. Moreover, PET/CT can be useful for lymph node metastases which can often be falsely negative using the CT size criteria.

Kidney and Bladder Cancers: Case No. 5

Presentation

A 69-year-old woman with a history of smoking underwent a chest X-ray that disclosed a consolidation within the upper right lobe.

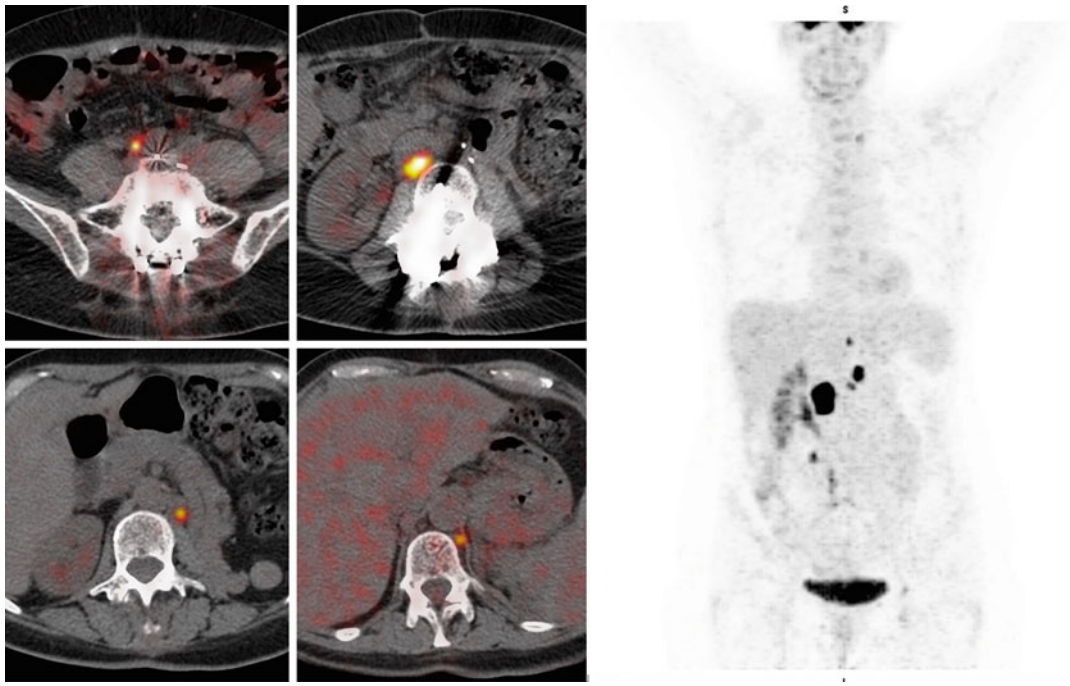

Fig. 8 On the *left*, four fused [^{18}F]FDG PET/CT images showing four different foci of hyperactivity consistent with secondary lymphadenopathies of both left and right lumboaortic stations and of left retrocrural site. The two axial images on top show the presence of artifacts that affect CT due to the vertebral metal devices. On the *right* panel, [^{18}F]FDG whole-body PET MIP image demonstrating the high uptake of [^{18}F]FDG within the lymphadenopathies

Findings

A chest CT confirmed the presence of a mass-like consolidation of the upper right lobe with interstitial infiltrates and bronchogram and another peripheral nodule in the middle lobe with blurred contours, close to the pleura (Fig. 9). A PET/CT with [^{18}F]FDG was suggested in order to metabolically characterize the pulmonary lesions described by the CT. At PET/CT, both lung lesions presented a moderate uptake of [^{18}F]FDG. Moreover, the whole-body acquisition of PET/CT allowed to observe the presence of a left kidney with a distorted renal parenchyma outline at the upper pole, with a hypermetabolic tissue surrounding the perirenal space (Fig. 10).

Follow-Up

The patient underwent a ceCT of the abdomen which confirmed the presence of a large perirenal plaque lesion inseparable from the adjacent renal parenchyma of the upper pole of the left kidney (Fig. 11). The final diagnosis was B-cell lymphoma.

Teaching Points

Incidental renal lesions can be encountered on PET/CT imaging. They are difficult to detect because of the excretion of [^{18}F]FDG via the urinary tract as well as the significant variability in the uptake of [^{18}F]FDG. Perirenal masses are

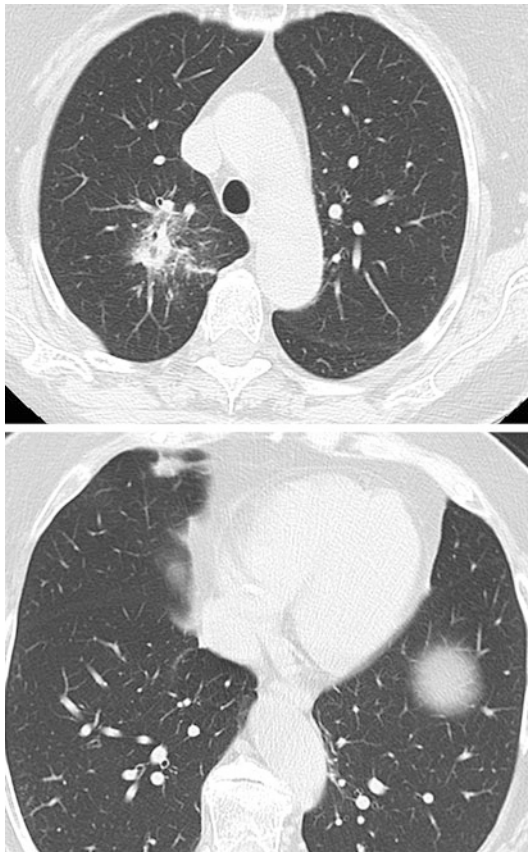

Fig. 9 Chest CT showing the consolidation of the *upper right* lobe with interstitial infiltrates and bronchogram and a peripheral nodule in the *middle lobe*

one of the more typical patterns of renal lymphoma which can be easily identified on metabolic imaging, as an intensely [^{18}F]FDG-avid lesion.

Kidney and Bladder Cancers: Case No. 6

Case contributed by: K. Bouchelouche
Department of Nuclear Medicine and PET Centre, Aarhus University Hospital, Denmark

Presentation

A 69-year-old man with a clear cell RCC of the right kidney was treated with partial nephrectomy. Control CT 2 years later demonstrated right renal vein thrombus but no signs on local recurrence in the kidney.

Findings

The patient was referred to [^{18}F]FDG PET/CT that showed local recurrence in the right kidney. Furthermore, axial PET/CT showed malignant venous tumor thrombus in the right renal vein (Fig. 12).

Teaching Points

In this case, PET showed local recurrence in the right kidney which was not seen on CT. Clear cell RCC often invades the renal vein and the cava vein, which often can be seen on PET/CT since there is no interference with [^{18}F]FDG activity in urine.

Kidney and Bladder Cancers: Case No. 7

Case contributed by: K. Bouchelouche
Department of Nuclear Medicine and PET Centre, Aarhus University Hospital, Denmark

Presentation

A 71-year-old woman with a clear cell RCC of the right kidney was treated with radical nephrectomy. Four years later, control CT demonstrated a process in the right suprarenal gland. A biopsy showed metastasis from clear cell RCC.

Findings

The patient was referred for [^{18}F]FDG PET/CT to complete restaging. PET/CT showed modest [^{18}F]FDG uptake in the known metastasis in the right suprarenal gland. No other metastases or local recurrence was found (Fig. 13).

A benign simple cyst without [^{18}F]FDG uptake was seen on axial PET image (B) and on axial CT image in the left kidney (Fig. 14).

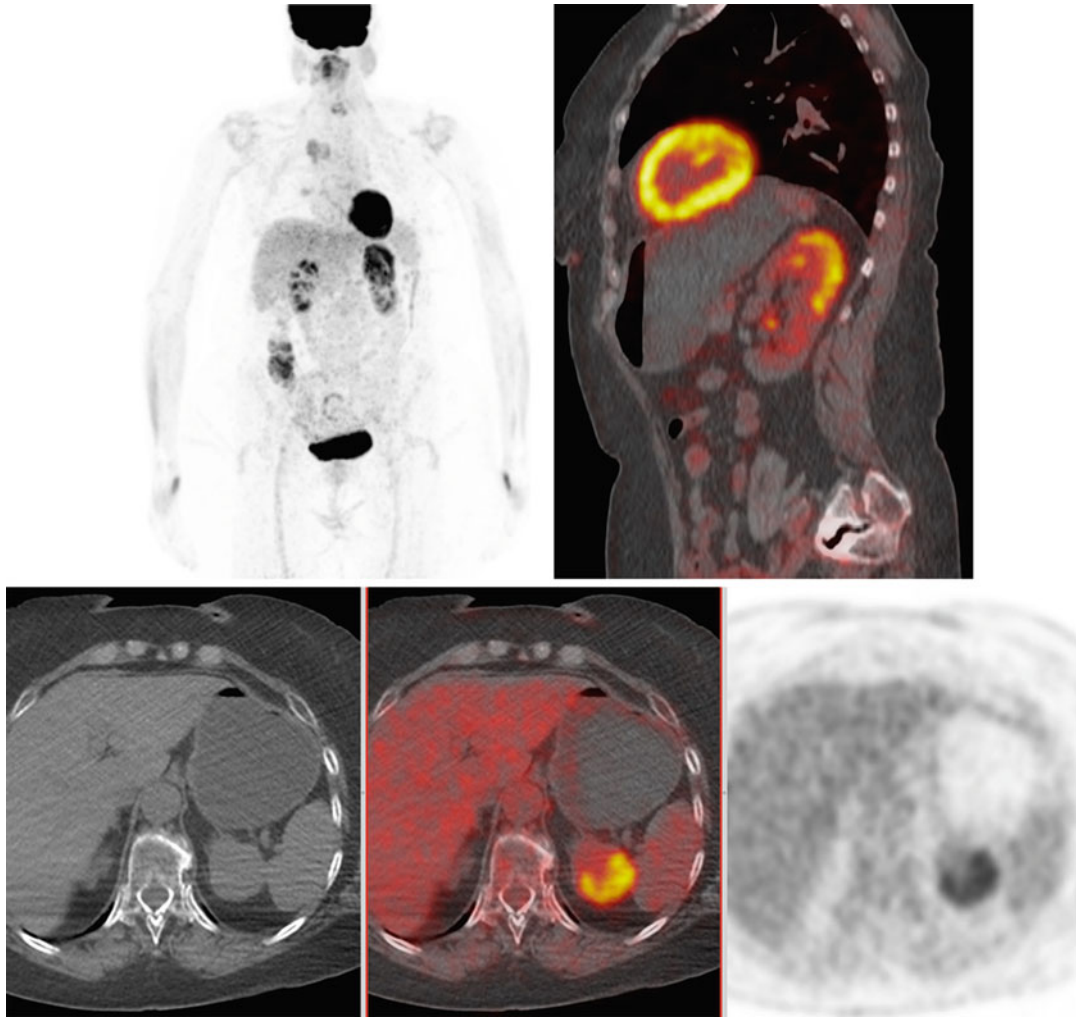

Fig. 10 [^{18}F]FDG MIP image shows two foci of moderate hyperactivity within the right lung corresponding to the lesions disclosed by CT (*top left*). Moreover, an area of high metabolic activity is surrounding the upper pole of the left kidney (*top right*). CT, fused PET/CT, and PET axial slice clearly demonstrating increased [^{18}F]FDG perirenal uptake of the left kidney

Follow-Up

Right adrenal metastasis from RCC was confirmed by pathology after surgery.

Teaching Points

[^{18}F]FDG PET/CT can be used for the detection of distant metastases during restaging of RCC. Incidental findings of benign simple cysts without [^{18}F]FDG uptake are often seen on [^{18}F]FDG PET/CT scans. If [^{18}F]FDG uptake is seen in cysts in the kidneys, it is clearly suspicious of malignancy.

Kidney and Bladder Cancers: Case No. 8

Case contributed by: K. Bouchelouche
Department of Nuclear Medicine and PET Centre, Aarhus University Hospital, Denmark

Fig. 11 ceCT image demonstrates the perirenal plaque lesion inseparable from the adjacent renal parenchyma of the upper pole of the left kidney

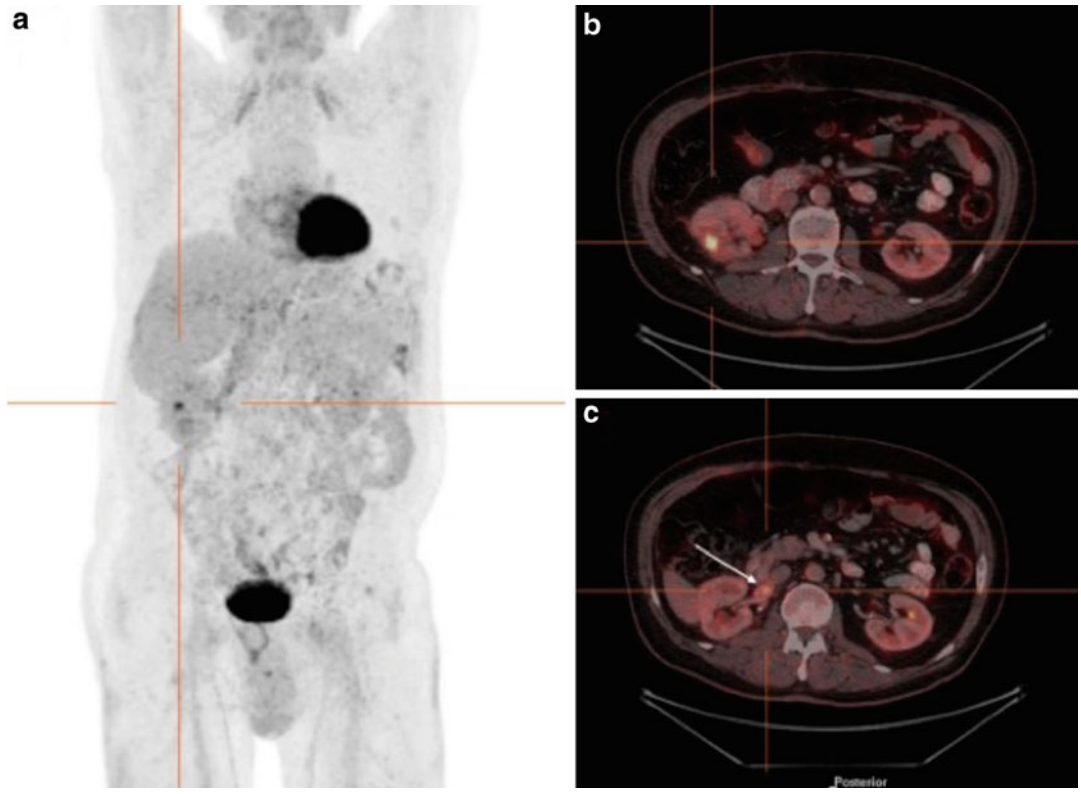

Fig. 12 MIP and fused [^{18}F]FDG PET/CT slice (*top right*) show a focal area of hyperactivity within the right kidney parenchyma. Moreover, an area of moderate uptake of [^{18}F]FDG can be observed at the level of right renal vein consistent with a venous tumor thrombus (*bottom right*)

Presentation

75 years-old woman with newly diagnosed urothelial carcinoma in the right renal pelvis was referred to [^{18}F]FDG PET/CT for staging.

Findings

PET/CT confirmed the presence of the tumor in the right renal pelvis. Moreover, several metastases with high grade of [^{18}F]FDG uptake were clearly seen located in enlarged lymph nodes medial to the right kidney, in the liver, and in the bone (the spine, pelvis bone, left femur, right humerus, and right scapula) (Fig. 15).

Management

On the basis of the advanced stage disclosed by [^{18}F]FDG PET/CT, the patient has been started on chemotherapy.

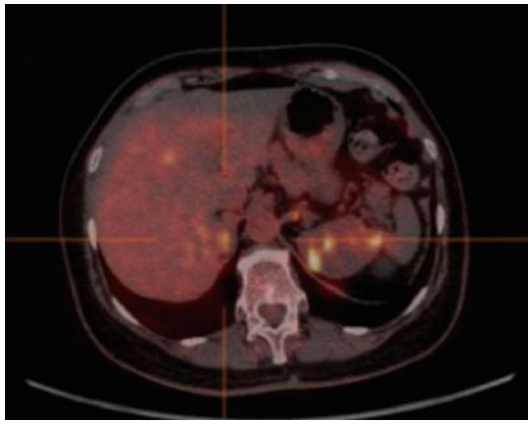

Fig. 13 PET/CT axial slice shows mild [^{18}F]FDG uptake within the known metastasis in the right suprarenal gland

Teaching Points

The case illustrates that urothelial carcinoma in the pelvis and the metastases are normally [^{18}F]FDG avid. Sometimes, it is not possible to see primary tumor in the pelvis, because urinary excretion may mask the tumor, but in this case, the tumor is clearly seen. The metastases are normally detected by [^{18}F]FDG PET/CT. Thus, [^{18}F]FDG PET/CT can be used for NM staging of urothelial malignancies located in the renal pelvis.

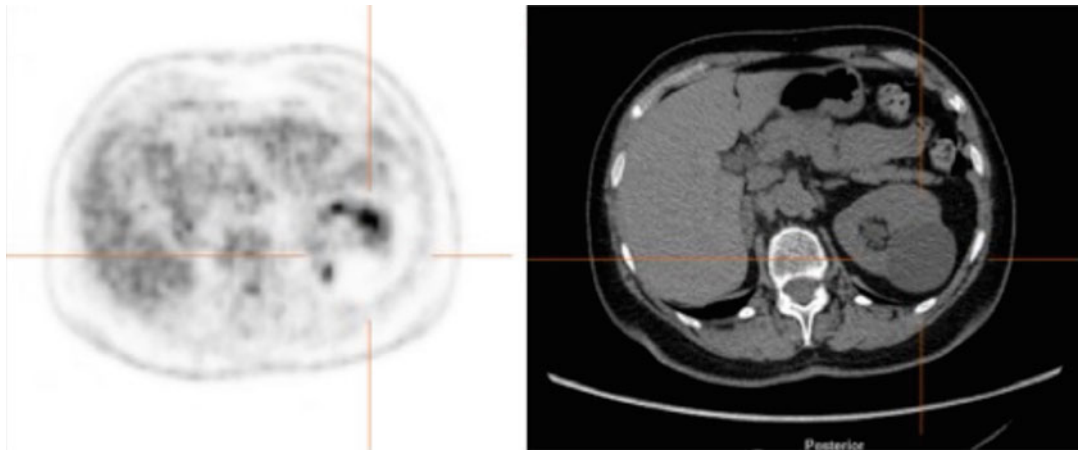

Fig. 14 PET/CT axial slices (PET on the *left* and CT on the *right*) show in the left kidney a large cyst without significant [^{18}F]FDG uptake

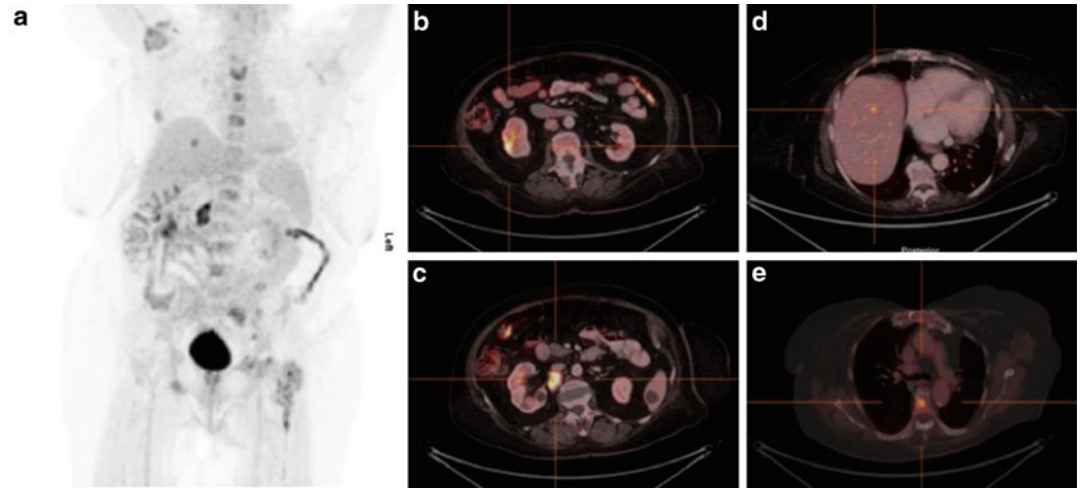

Fig. 15 PET/CT shows multiple areas of [^{18}F]FDG hyperactivity on the MIP image (**a**). A lesion with enhanced uptake of [^{18}F]FDG can be seen in the right renal pelvis on the axial fused PET/CT slice (**b**). Several metastases are clearly seen on the axial PET/CT images located in enlarged lymph nodes medial to the right kidney (**c**), in the liver (**d**), and in the spine (**e**). Bone metastases were also located in the pelvic bone, left femur, right humerus, and right scapula (**a**)

Kidney and Bladder Cancers: Case No. 9

Case contributed by: K. Bouchelouche
Department of Nuclear Medicine and PET Centre, Aarhus University Hospital, Denmark

Presentation

A 75-year-old woman with newly diagnosed multifocal muscle-invasive bladder cancer was referred to a [^{18}F]FDG PET/CT scan for staging.

Findings

PET/CT did not disclose the bladder tumor due to urinary excretion of [^{18}F]FDG. However, PET/CT was able to assess the tumor infiltration along the distal right ureter which presented high [^{18}F]FDG activity. Moreover, a lymph node metastasis was found medial to the tumor infiltrating the right ureter. Three lung metastases were also observed. At last, it was clearly visible an area of high [^{18}F]FDG activity within the vagina and the cervix clearly suspicious of malignancy (Fig. 16).

Follow-Up

Biopsy showed cervical cancer (second primary).

Histology of the lymph node metastases shown in image (C) was from urothelial cancer.

Teaching Point

PET/CT can be useful in the staging of bladder cancer. In this case, it was able to correctly identify tumor infiltration along the right ureter, abdominal lymph node involvement, and lung metastases. Urinary excretion of [^{18}F]FDG limits the assessment of the bladder. It is well known that not unfrequently, PET/CT can disclose a second primary tumor.

Kidney and Bladder Cancers: Case No. 10

Presentation

A 55-year-old woman presented with locally advanced urothelial bladder cancer, treated with radical cystectomy, hysterectomy, and construction of a neobladder.

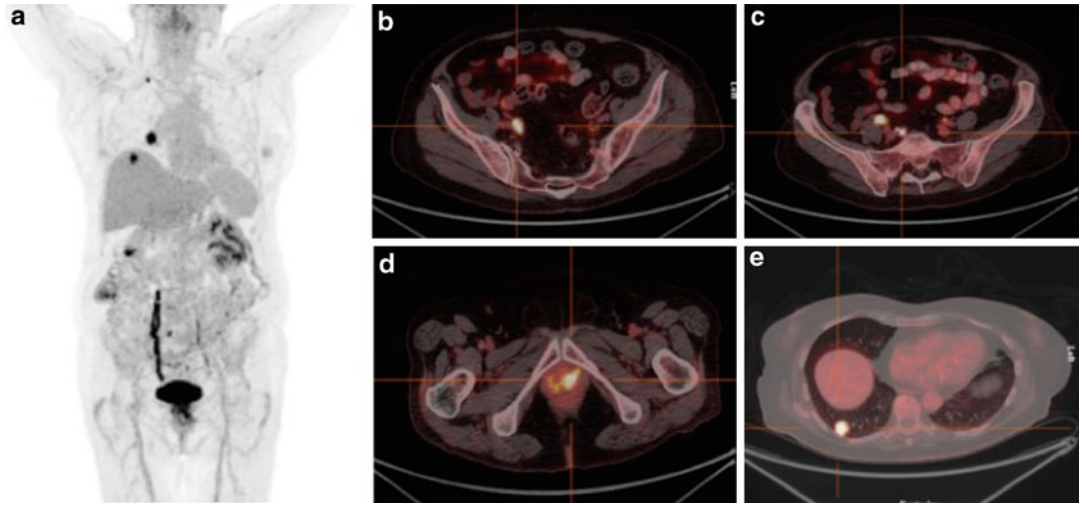

Fig. 16 Bladder tumor is not visible on PET due to urinary excretion of [^{18}F]FDG (**a**). In the distal right ureter, tumor infiltration with high [^{18}F]FDG activity is seen on MIP (**a**) and on axial PET/CT images (**b**, **c**), and a lymph node metastasis is seen medial to the tumor-infiltrated right ureter (**a**, **c**). Three lung metastases are seen on MIP (**a**) and fused PET/CT (**e**). Furthermore, high [^{18}F]FDG activity is seen within the vagina and portion of the cervix clearly suspicious of malignancy (**d**)

Findings

Post-surgery [^{18}F]FDG PET/CT was performed (Fig. 17) to determine the extent of residual disease. [^{18}F]FDG uptake (SUV 7.5) is seen in a left common iliac lymph node (max diameter 13 mm) (Fig. 18). Physiological [^{18}F]FDG is seen in brown fat of the neck bilaterally. The patient was treated with radiation and chemotherapy.

Follow-Up

Six months after treatment, [^{18}F]FDG PET/CT was performed to evaluate treatment response (Fig. 19). Para-caval and para-aortic hypermetabolic lymph nodes (SUV 8) are seen (Fig. 20). The previously visualized [^{18}F]FDG-avid node in the common iliac region is no longer seen. Multiple lesions (SUV 7) are seen in the skeleton, including the ribs bilaterally, right scapula, left ilium, left pubis, and right femur (Fig. 21). In addition, increased [^{18}F]FDG uptake is present in both enlarged adrenal glands (SUV 12) (Fig. 22).

Teaching Point

In this case, [^{18}F]FDG PET/CT was able to demonstrate a surprising lack of response to therapy in urothelial cancer.

Kidney and Bladder Cancers: Case No. 11

Presentation

A 76-year-old man with history of clear cell renal carcinoma 385 (RCC) treated with right nephrectomy presents with 4-month history of increasing left hip pain.

Findings

X-ray of the pelvis shows an osteolytic lesion of the left ilium. [^{18}F]FDG PET/CT is performed for restaging (Fig. 23). [^{18}F]FDG PET/CT shows a lesion of the right humeral head (SUV_{max} 7.2) (Fig. 24) and confirms the presence of an [^{18}F]

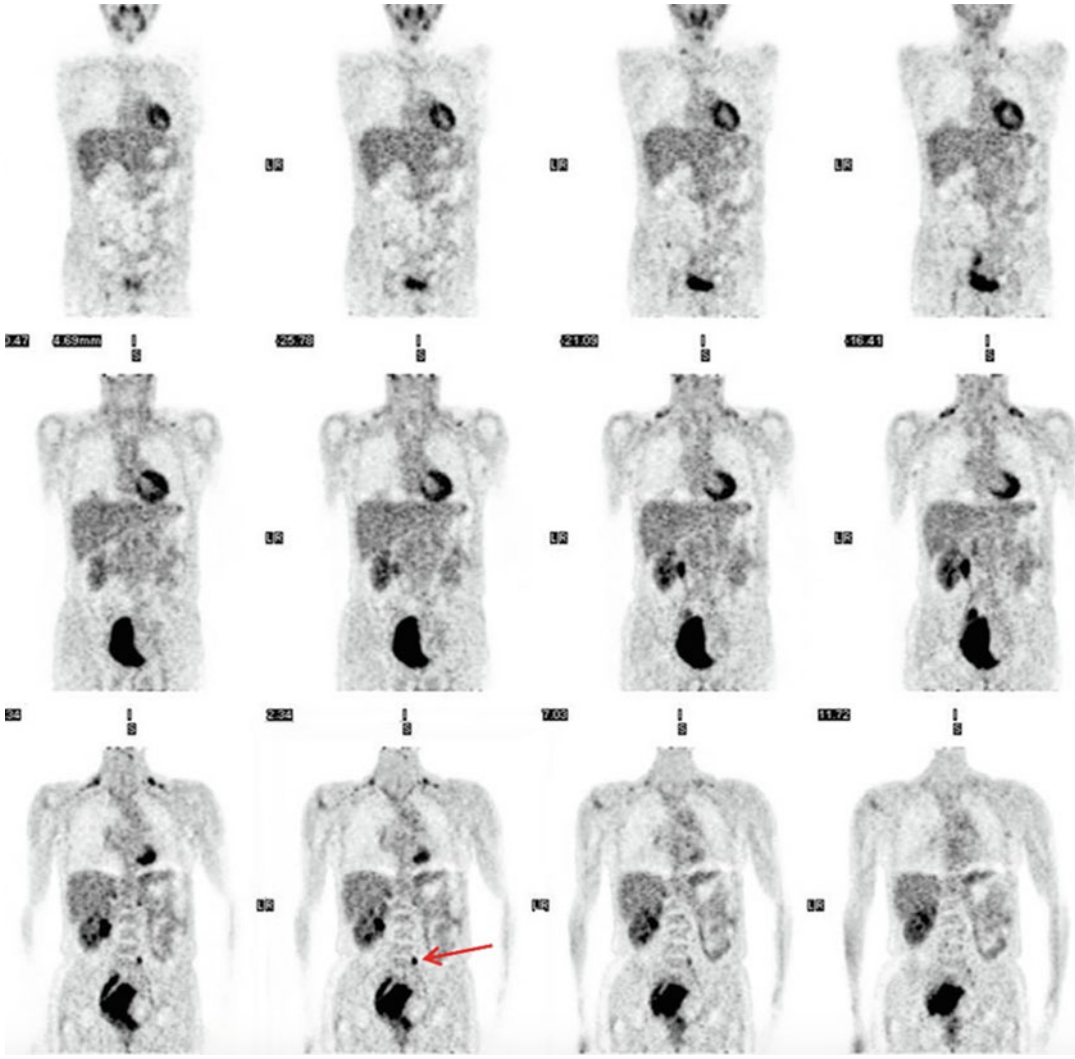

Fig. 17 [^{18}F]FDG PET images (coronal section) show hypermetabolic lymphadenopathy in the left iliac region (*red arrow*). Physiological radiotracer accumulation is in the neck bilaterally, corresponding to brown fat

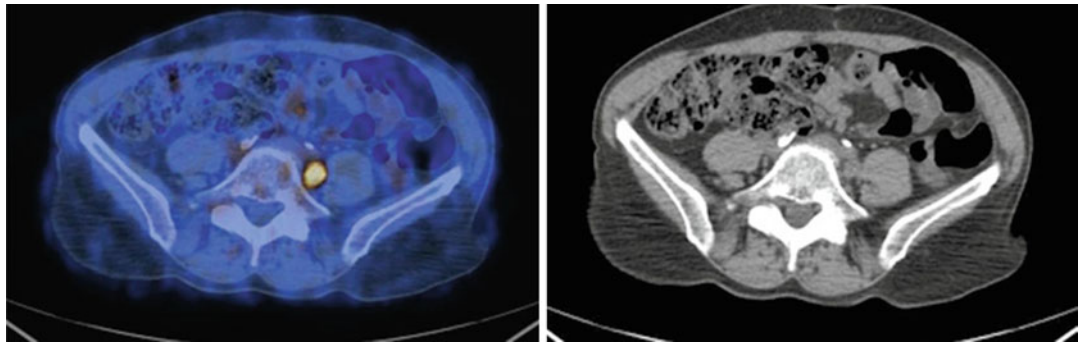

Fig. 18 PET/CT transaxial image demonstrates metabolically active adenopathy localized in the left common iliac region (PET/CT fused image in the *left panel*, CT in the *right panel*)

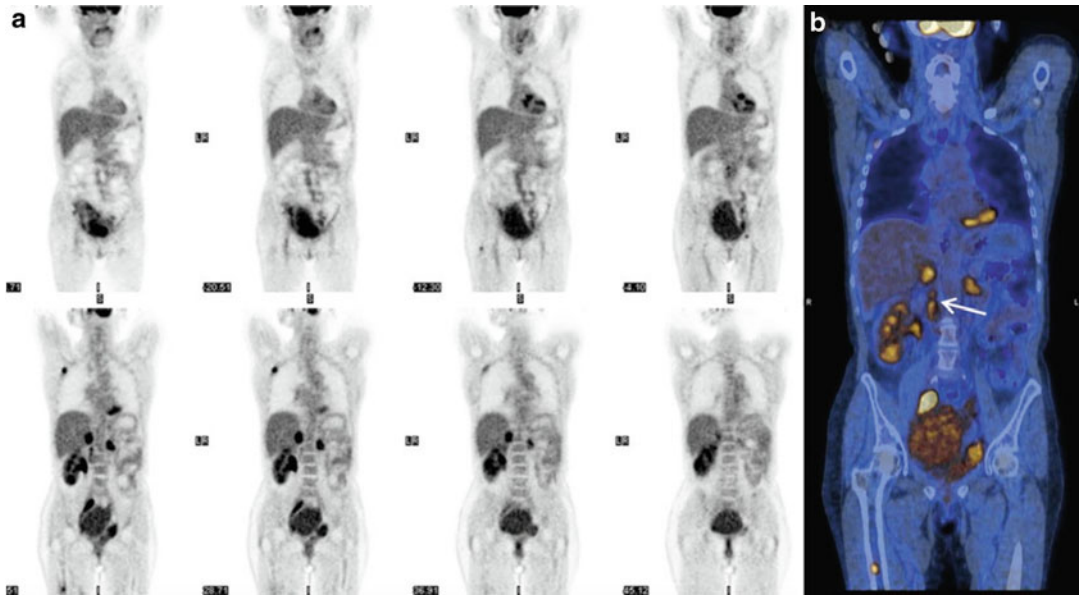

Fig. 19 [^{18}F]FDG PET coronal image (**a**) demonstrates pathological uptake in adrenal glands and [^{18}F]FDG-avid skeletal lesions (the second right rib and right femur). PET/CT coronal fused image (**b**) also shows hypermetabolic lymphadenopathy in para-caval and para-aortic regions (*white arrow*)

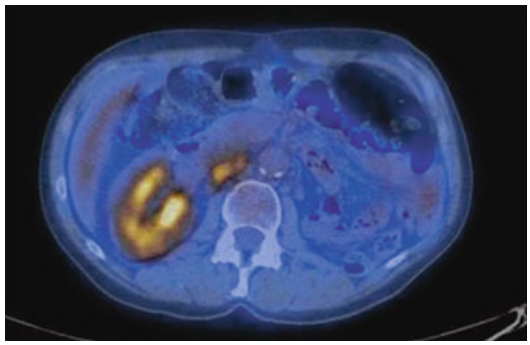

Fig. 20 PET/CT fused transaxial image demonstrates hypermetabolic adenopathy in para-caval region

FDG-avid osteolytic lesion of the left ilium (SUV_{max} 8.5). In addition, [^{18}F]FDG PET/CT images show numerous hypermetabolic lymph nodes in the mediastinum (SUV_{max} 8.6) (paratracheal, paraesophageal, subcarinal, and hilar nodes) (Fig. 25) and in the abdomen (SUV_{max} 15) (retrocrural, celiac, portocaval, and para-aortic nodes) (Fig. 26). Skeletal metastases were treated with external beam radiation therapy. The patient also received systemic antiangiogenesis therapy with sunitinib.

Follow-Up

[^{18}F]FDG PET/CT did not demonstrate significant reduction in [^{18}F]FDG uptake of hypermetabolic lymphadenopathy. However, a reduction in [^{18}F]FDG uptake in the right humeral head is seen, while no pathological uptake is shown in the ilium (Fig. 27). Subsequent imaging showed lymph node progression, liver involvement, and cutaneous metastases.

Discussion

This case demonstrates that [^{18}F]FDG PET is useful to assess the lack of metabolic tumor response to therapy.

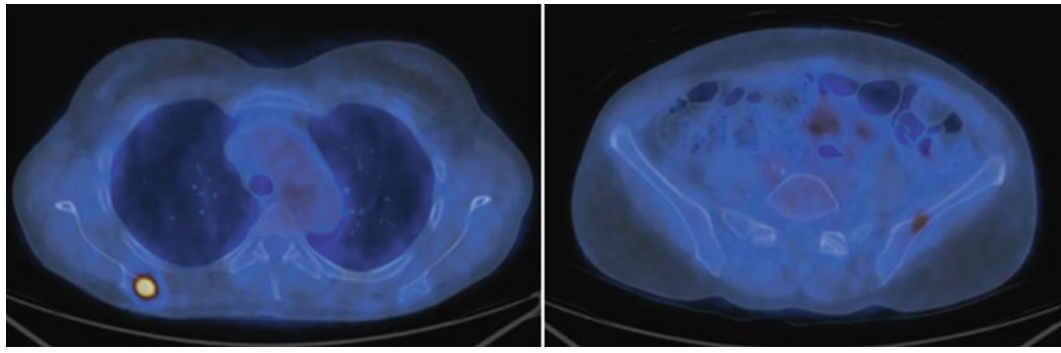

Fig. 21 PET/CT fused transaxial image of [^{18}F]FDG-avid lesions in the right scapula (*left panel*) and left ilium (*right panel*)

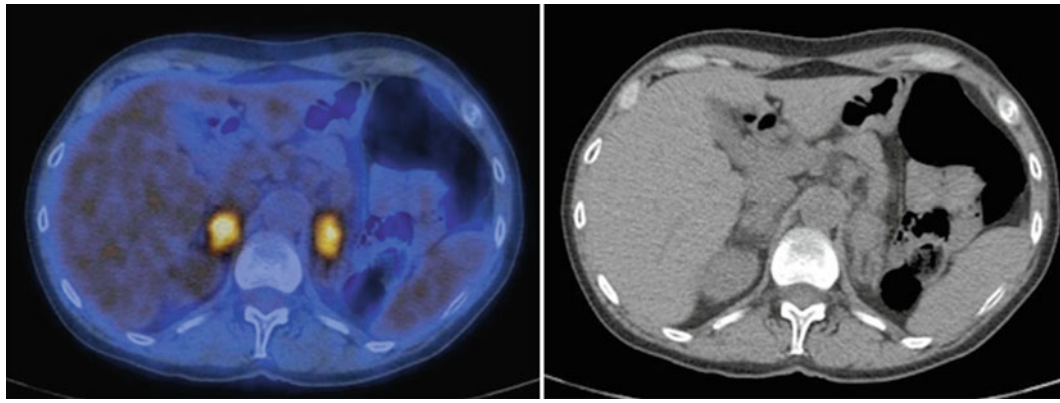

Fig. 22 PET/CT transaxial image shows pathological radiotracer uptake in enlarged adrenal glands (PET/CT fused in the *left panel*, CT in the *right panel*)

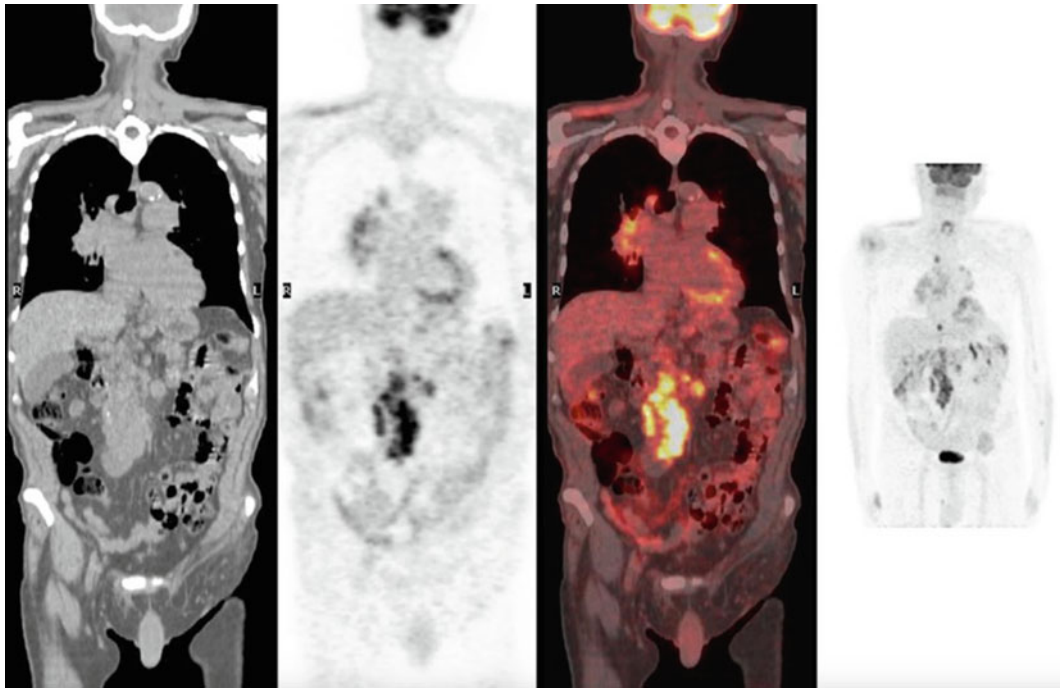

Fig. 23 [^{18}F]FDG PET/CT [coronal CT (*left*), [^{18}F]FDG (second from the *left*), fused coronal [^{18}F]FDG, and CT (second from the *right*)] and MIP (*right*) show hypermetabolic lymph nodes in the mediastinum and abdomen and uptake in the mass in the left ilium (best seen on the MIP)

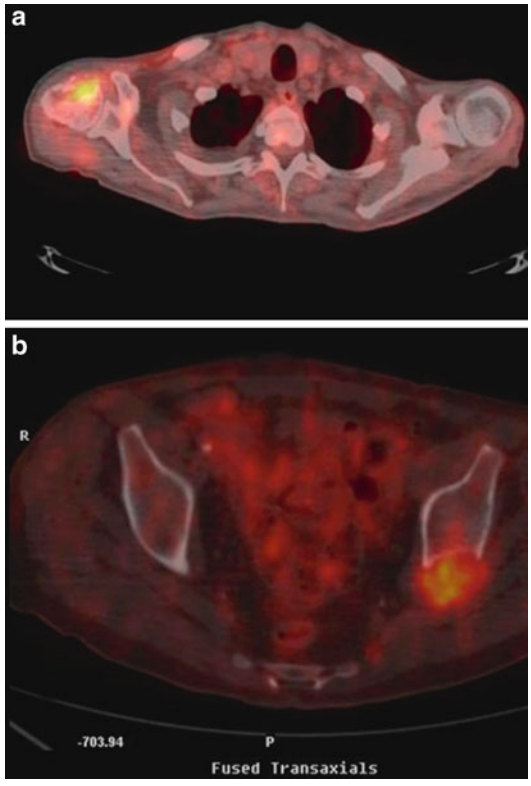

Fig. 24 Axial fused images of [^{18}F]FDG-avid osteolytic lesions of the skeleton. (**a**) Hypermetabolic right humeral lesion. (**b**) Hypermetabolic metastases of the left ilium

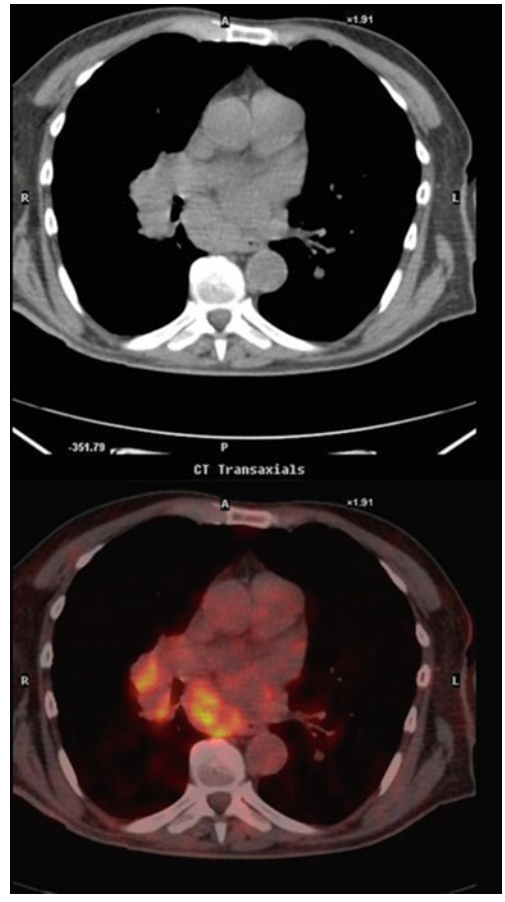

Fig. 25 [^{18}F]FDG PET/CT axial images demonstrate multiple [^{18}F] FDG-avid lymph nodes in the mediastinum: CT (*top*), fused PET/CT (*bottom*)

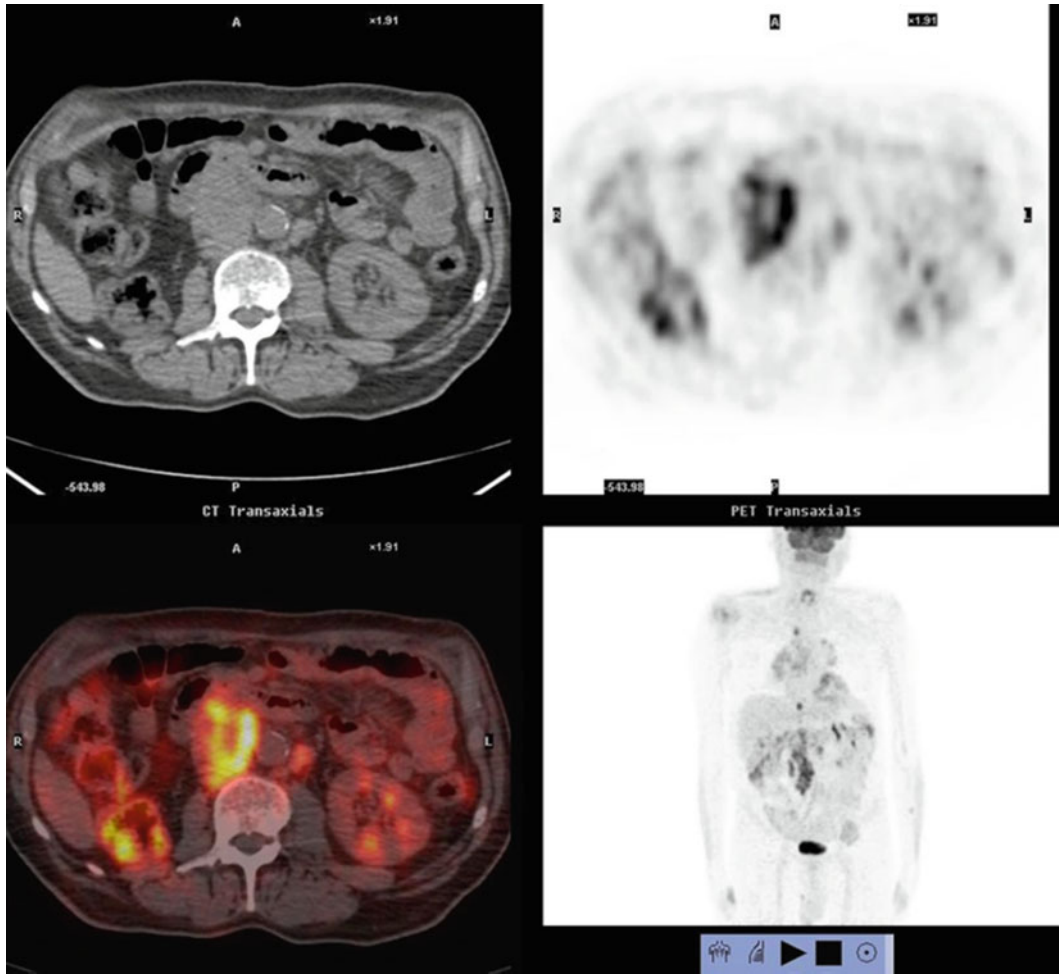

Fig. 26 Axial CT (*upper left*), axial [^{18}F]FDG (*upper right*), PET/CT fused (*lower left*), and MIP (*lower right*), showing hypermetabolic lymph nodes of the abdomen

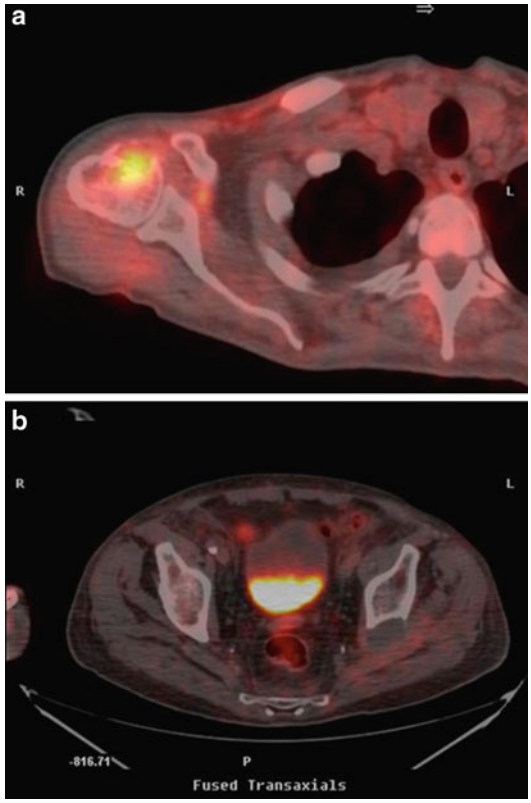

Fig. 27 Axial fused images of skeletal metastases after external beam radiation therapy. (**a**) Slightly decreased [^{18}F]FDG uptake in the humeral lesion. (**b**) No [^{18}F]FDG uptake in the left ilium

Teaching Cases in Nuclear Oncology: Prostatic Cancer

69

Duccio Volterrani, Giulia Puccini, Sara Mazzarri, and Federica Guidoccio

Keywords

Prostate cancer • Gleason score • PSA • ^{68}Ga-PSMA PET/CT • ^{18}F-choline PET/MRI • ^{99m}Tc bone scintigraphy • Castrate resistant • [^{18}F]FDG PET/CT • PSA velocity • PSA double time

Glossary

[^{18}F]FDG	2-Deoxy-2-[^{18}F]fluoro-D-glucose
^{18}F-FCH	^{18}F-Choline
^{99m}Tc-HDP	^{99m}Tc-Hydroxyethylenediphosphonate
^{99m}Tc-MDP	^{99m}Tc-Methylene diphosphonate
CRP	C-reactive protein
CRPC	Castrate-resistant prostate cancer
CT	X-ray computed tomography
Gy	Gray unit (ionizing radiation dose in the International System of Units, corresponding to the absorption of one joule of radiation energy per kilogram of matter)
IMRT	Intensity-modulated radiotherapy
LD-CT	Low-dose CT, as used during a PET/CT scan
LHRH	Luteinizing-hormone releasing hormone
M	Metastasis status according to the AJCC/UICC TNM staging system
MIP	Maximum intensity projection
MRI	Magnetic resonance imaging
N	Lymph node status according to the AJCC/UICC TNM staging system
PET	Positron emission tomography
PET/CT	Positron emission tomography/Computed tomography
PET/MRI	Positron emission tomography/Magnetic resonance imaging
PSA	Prostate-specific antigen, a tumor marker of prostatic cancer
PSMA	Prostate-specific membrane antigen
SPECT	Single-photon emission computed tomography
SPECT/CT	Single-photon emission computed tomography/Computed tomography
T	Tumor status according to the AJCC/UICC staging system
TNM	AJCC staging system based on parameters "T" (tumor status), "N" (lymph node status), and "M" (distant metastasis status)

D. Volterrani (✉) • G. Puccini • S. Mazzarri • F. Guidoccio
Regional Center of Nuclear Medicine, Department of Translational Research and Advanced Technologies in Medicine and Surgery, University of Pisa, Pisa, Italy
e-mail: duccio.volterrani@med.unipi.it

© Springer International Publishing Switzerland 2017
H.W. Strauss et al. (eds.), *Nuclear Oncology*,
https://doi.org/10.1007/978-3-319-26236-9_72

UICC	Union Internationale Contre le Cancer (International Union Against Cancer)
US	Ultrasonography

Contents

Prostatic Cancer: Case No. 1 1772
Presentation 1772
Findings 1772

Discussion 1772

Prostatic Cancer: Case No. 2 1773
Presentation 1773
Findings 1774

Discussion 1774

Prostatic Cancer: Case No. 3 1775
Presentation 1775
Findings 1775
Follow-Up 1775

Discussion 1777

Prostatic Cancer: Case No. 4 1777
Presentation 1777
Findings 1777
Follow-Up 1777

Discussion 1778

Prostatic Cancer: Case No. 5 1779
Presentation 1779
Findings 1780
Follow-Up 1780

Discussion 1780

Prostatic Cancer: Case No. 6 1781
Presentation 1781
Findings 1782
Follow-Up 1783
Teaching Point 1783

Prostatic Cancer: Case No. 7 1784
Presentation 1784
Findings 1784
Follow-Up 1785
Teaching Points 1785

Prostatic Cancer: Case No. 8 1785
Presentation 1785
Findings 1785
Follow-Up 1785
Teaching Points 1785

Prostatic Cancer: Case No. 9 1785
Presentation 1785
Findings 1785
Follow-Up 1786
Teaching Points 1786

Prostatic Cancer: Case No. 10 1787
Presentation 1787
Findings 1787
Follow-Up 1787
Teaching Points 1789

Prostatic Cancer: Case No. 11 1789
Presentation 1789
Findings 1790
Follow-Up 1790
Teaching Points 1796

Prostatic Cancer: Case No. 12 1796
Presentation 1796
Findings 1796

Discussion 1797

Prostatic Cancer: Case No. 13 1797
Presentation 1797
Findings 1797

Discussion 1798

Prostatic Cancer: Case No. 1

Case contributed by S. Al Shammari, F. Fraioli Institute of Nuclear Medicine, UCLH NHS Foundation Trust, London, UK.

Presentation

A 60-year-old man diagnosed with prostate cancer in 2014. Treated with radiotherapy. Raising PSA with suspicion of local recurrence. PET/CT with ^{68}Ga-PSMA-ligand for restaging.

Findings

PET/CT showed a focal ^{68}Ga-PSMA-ligand uptake at the right posterolateral peripheral zone of the prostate, extending at least from the mid-gland down to the apex (Fig. 1). No tracer activity was observed in the seminal vesicles. No other suspicious focal lesions were found in the whole body.

Discussion

Positron emission tomography (PET) with choline tracers has been used for years for the diagnosis and follow-up of prostate cancer. Prostate-specific

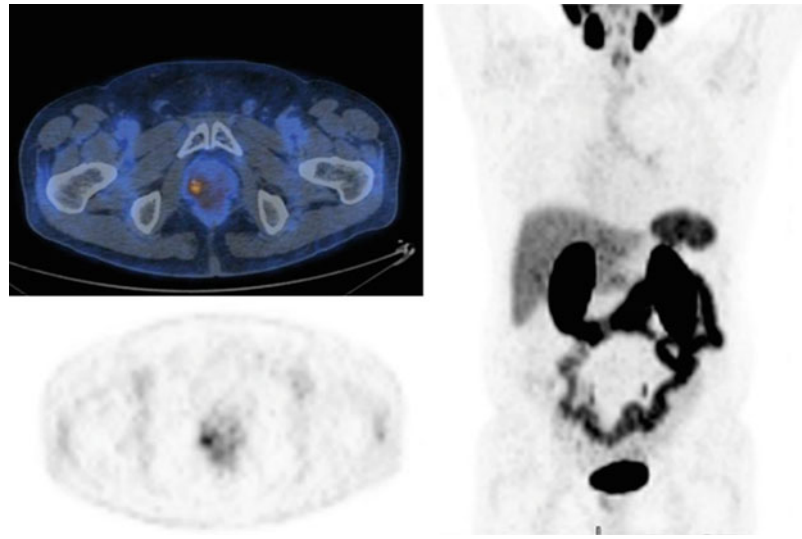

Fig. 1 Focal ^{68}Ga-PSMA ligand uptake at the right posterolateral peripheral zone of the prostate extending at least from the mid-gland down to the apex

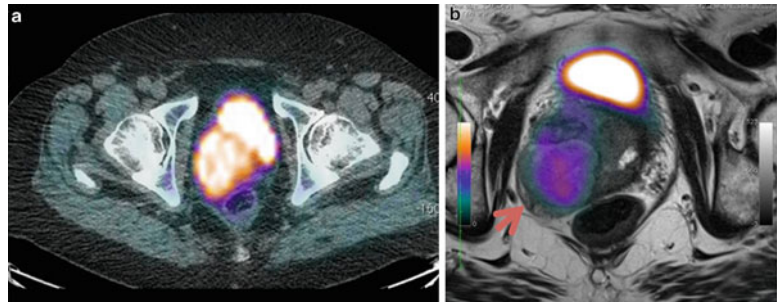

Fig. 2 ^{18}F-choline PET/MRI in patients with prostate cancer (*arrow*) allows exact correlation of elevated focal choline uptake to suspicious T2-weighted prostate lesion. Anatomical detail provided coupling PET with MRI (**a**) is much superior to PET/CT stand-alone (**b**)

membrane antigen (PSMA) is overexpressed in most prostate cancers. Therefore, a ^{68}Ga-labeled PSMA-ligand was found to be superior to choline tracers due to the high contrast. Preliminary results of PET with ^{68}Ga-PSMA-ligand have shown encouraging results particularly in the recurrent prostate cancer setting.

Physiological distribution is noted in the lacrimal gland, parotid gland, submandibular gland, liver, spleen, duodenum, colon, and kidney. Unspecific uptake was reported in gynecomastia, lymph nodes with fat hilum, and Wegener's granulomatosis. Additional faint uptake of ^{68}Ga-PSMA-ligand was also reported in tumors such as thyroid, breast, and non-small cell lung cancer.

Prostatic Cancer: Case No. 2

Case contributed by S. Al Shammari, F. Fraioli
Institute of Nuclear Medicine, UCLH NHS Foundation Trust, London, UK.

Presentation

A 72-year-old man with known prostate cancer referred for staging with ^{18}F-choline PET/MRI.

Fig. 3 ^{99m}Tc-MDP whole-body bone scan showing a single focus of highly increased activity in the parietal bone on the left side (*arrow*)

Findings

^{18}F-choline PET/MRI allowed exact correlation of elevated focal choline uptake to suspicious T2-weighted prostate lesion. The patient underwent also a PET/CT scan that provided a worse anatomical detail than PET coupled with MRI (Fig. 2).

Discussion

PET imaging in prostate cancer is providing a reasonable option to identify the location of primary or recurrence prostate cancer in this setting.

The use of radiolabeled choline for imaging prostate cancer is based on increased phosphorylcholine levels and an elevated phosphatidylcholine turnover in prostate cancer cells. After uptake into the tumor cell through a high-affinity transporter system, choline is metabolized by choline kinase – which is the first step of the Kennedy pathway – and is incorporated into the phosphatidyl membrane. Key enzymes of the choline metabolism, like choline kinase, are upregulated in prostate cancer cells. Additionally, an increased expression of choline transporters and an elevated choline transportation rate have been described. While CT imaging has its place in the staging of prostate cancer, MRI, especially using multiparametric imaging including diffusion-weighted sequences, is the most sensitive morphological imaging method for local staging; hence, hybrid PET/MRI imaging appears to provide the best option for the future.

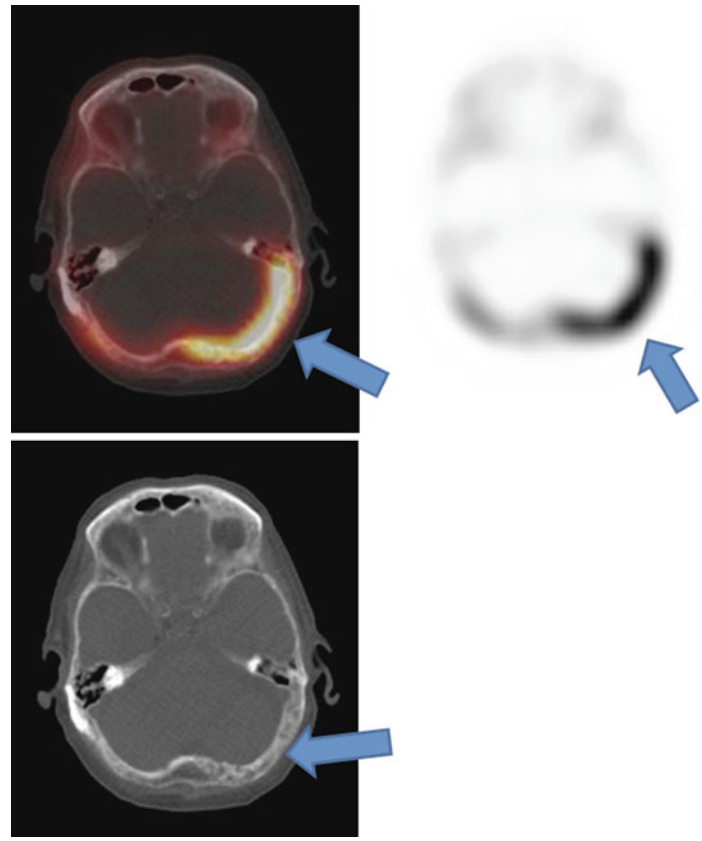

Fig. 4 At ^{99m}Tc-MDP SPECT/CT, the cortex of the bone was pathologically thickened and irregular (*D, arrow*) with highly increased activity especially in the inner cortex (*B, C, arrows*)

Prostatic Cancer: Case No. 3

Case contributed by M.R. Jochumsen

Department of Nuclear Medicine & PET Centre, Aarhus University Hospital, Aarhus, Denmark.

Presentation

An 87-year-old man who was recently diagnosed with high-risk prostate cancer (Gleason 10, and PSA 5.6 ng/mL). The patient had no symptoms from the skeleton.

Findings

In the primary staging, a ^{99m}Tc-DPD planar bone scan and SPECT/CT were performed, presenting a single focus of highly increased activity in the parietal bone on the left side (Figs. 3 and 4). The cortex of the bone was pathologically thickened and irregular with highly increased activity especially in the inner cortex. The extent of the pathology was all of the parietal bone but without involving other cranial bones. In conclusion, the findings are characteristic of Paget's disease and very uncharacteristic of a sole metastasis from prostate cancer. The most common locations of bone metastasis from prostate cancer are the pelvis, vertebrae, costae, and femora. The areas with increased activity in the lumbar spine were of benign degenerative etiology.

Follow-Up

Because of the lack of symptoms and the age of the patient, no treatment was initiated.

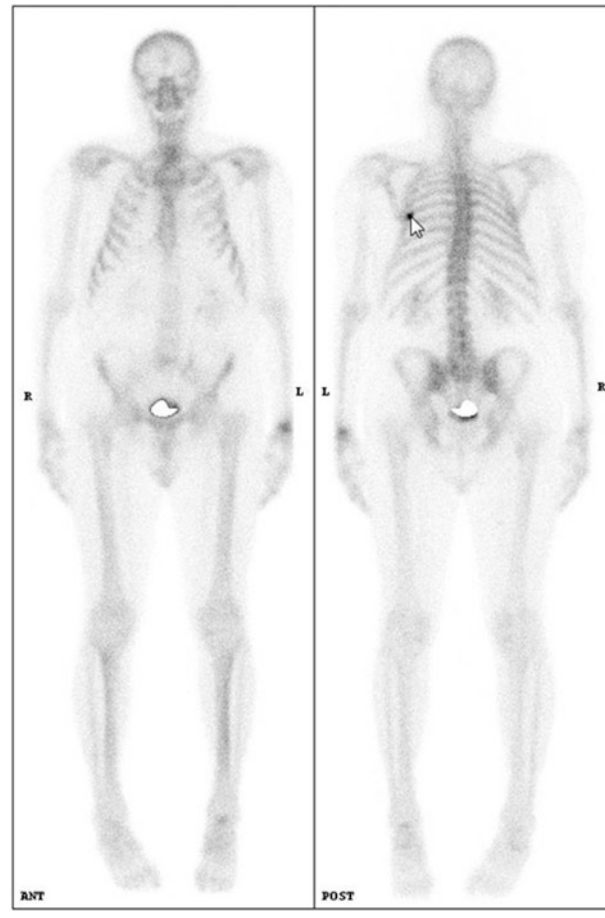

Fig. 5 ^{99m}Tc-MDP bone scan shows two metastatic foci in the ribs and one in the left scapula (*white arrow*)

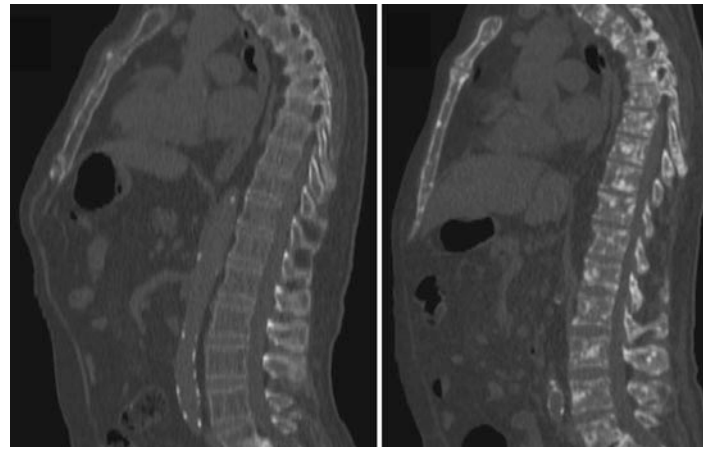

Fig. 6 On the *left*: CT sagittal slice showing no findings in the spine at the time of the first ^{99m}Tc-MDP bone scan. On the *right*: CT performed 3 months later showing multiple sclerotic and lytic bone metastasis

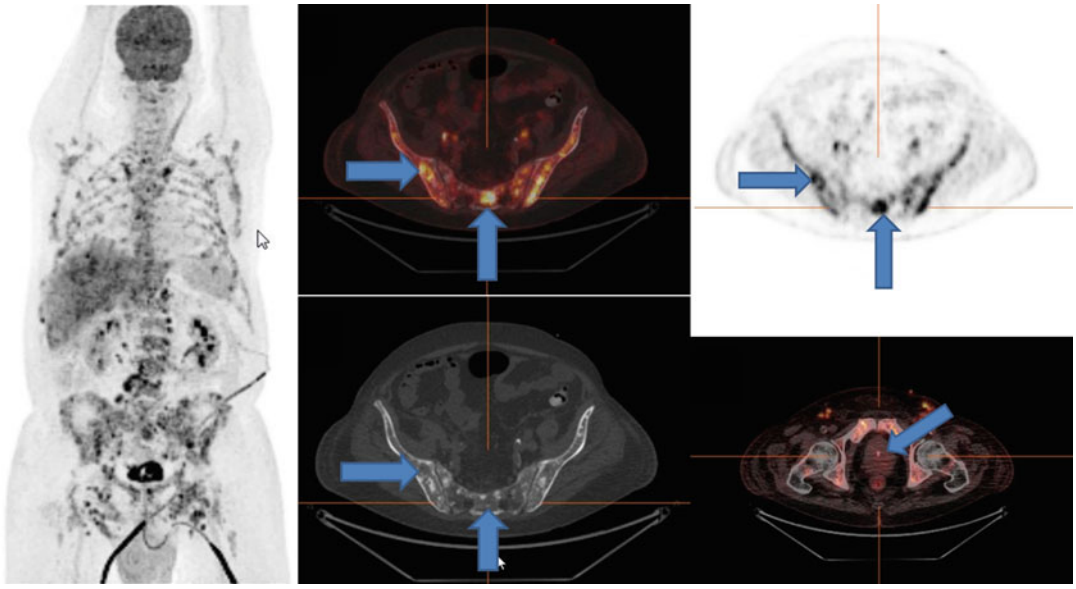

Fig. 7 [^{18}F]FDG PET/CT. On the *left*, MIP showing multiple foci with highly increased [^{18}F]FDG activity in almost the whole axial skeleton. Axial slices including the iliac bones show no increased [^{18}F]FDG uptake in most of the sclerotic areas in the skeleton, illustrating that sclerotic bone metastasis tend to metabolically "burn out" at some point. Furthermore, low [^{18}F]FDG uptake was seen in the prostate gland (*bottom right* panel, *arrow*), which indicates that the primary tumor had low metabolism at the time of the scan

Discussion

Paget's disease is caused by excessive and uncoordinated osteoclastic and secondarily osteoblastic activity, resulting in thickened and weakened bone structure. Complications of the disease are pain, warmth, fractures, bone deformities, loss of hearing, nerve compression, hypercalcemia, and urolithiasis. In most patients the disease can either be controlled with medical treatment or need no treatment at all. In rare cases the disease can develop into the highly malignant Paget's sarcoma.

Prostatic Cancer: Case No. 4

Case contributed by M.R. Jochumsen

Department of Nuclear Medicine & PET Centre, Aarhus University Hospital, Aarhus, Denmark.

Presentation

A 74-year-old man with castrate-resistant prostate cancer (CRPC). The Gleason 10 cancer had been well controlled through 2 years of hormone treatment with low prostate-specific antigen (PSA).

Findings

At the time of castrate resistance, a ^{99m}Tc-MDP bone scan was performed, the PSA was 38 μg/L. At this point two metastatic foci in the ribs and one in the left scapula were identified (Fig. 5).

No findings were observed in the spine confirmed also by a CT scan (Fig. 6).

Follow-Up

In spite of further medical treatment, the disease exploded, and 3 months later the PSA was

Fig. 8 Three-dimensional [^{11}C]choline PET/CT image demonstrates inhomogeneous hypermetabolic mass in the pelvis and [^{11}C]choline-avid pelvic and abdominal lymph nodes

536 ng/mL and the alkaline phosphatase had risen from normal to 200. At this point a CT scan was performed showing multiple sclerotic and lytic bone metastasis, especially in the spine (Fig. 6), furthermore, multiple hepatic and lymph node metastasis.

About 3 months later, the condition of the patient was declining, and he was admitted to the hospital because of fluctuating fever and C-reactive protein (CRP) of 300. An [^{18}F]FDG PET/CT scan was performed under suspicion of an abscess. But no infectious foci were found, making cancer associated fever the most likely explanation. The [^{18}F]FDG PET scan demonstrated further development in the metastatic status, revealing multiple foci with highly increased [^{18}F]FDG activity in almost the whole axial skeleton (Fig. 7).

Discussion

This case demonstrates the sudden aggressive development of a prostate cancer, illustrating the variable biology of the disease. [^{18}F]FDG PET/CT is not used for primary staging of prostate cancer, since most cancers have low metabolism resulting in low [^{18}F]FDG uptake. However, advanced and more aggressive prostate cancer including metastases may be seen on [^{18}F]FDG PET/CT.

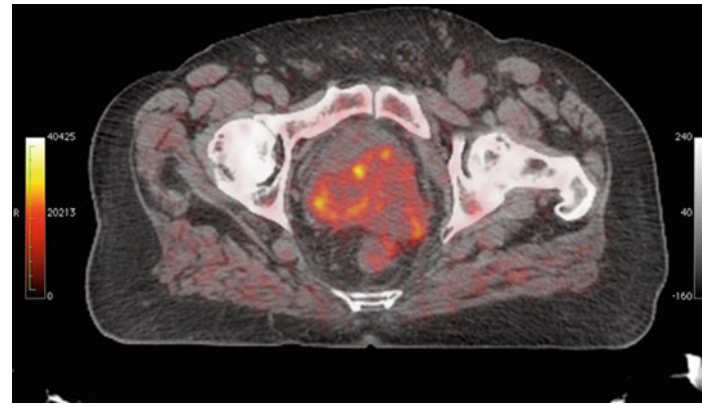

Fig. 9 The fused axial [^{11}C]choline PET/CT image shows a large prostate lesion with inhomogeneous uptake within the mass, compressing the rectum and the urinary bladder

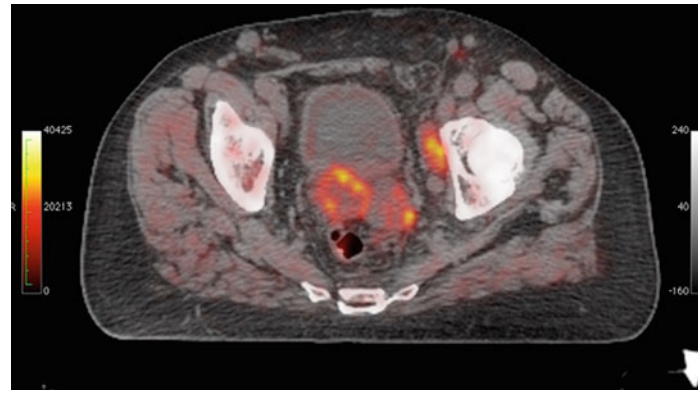

Fig. 10 The fused axial [^{11}C]choline PET/CT image shows the cranial portion of the prostate lesion, enlarged right pararectal and external iliac lymph nodes

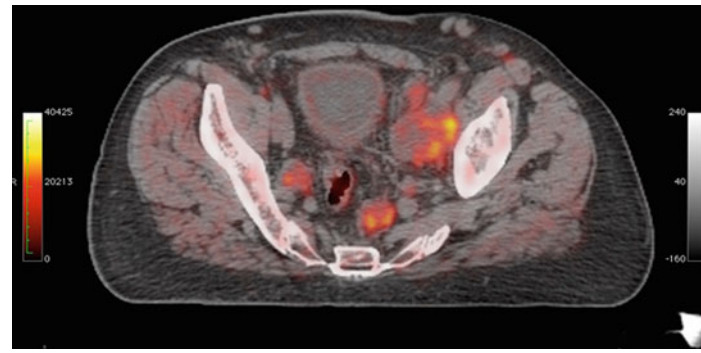

Fig. 11 The fused axial [^{11}C]choline PET/CT image shows enlarged left internal iliac, right pararectal, and huge external iliac adenopathy

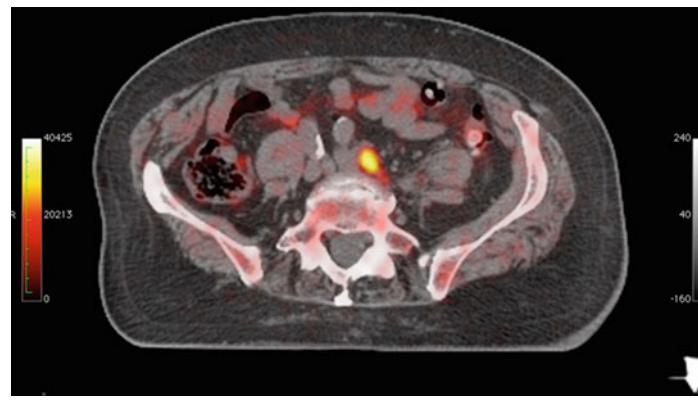

Fig. 12 The fused axial PET/CT image shows intense [^{11}C]choline uptake at the para-aortic lymph node

Prostatic Cancer: Case No. 5

Case contributed by M. Kirienko, A. Chiti
Division of Nuclear Medicine, Department of Biomedical Sciences – Humanitas University, Milan, Italy.

Presentation

A 73-year-old man affected by adenocarcinoma of the prostate, Gleason score $4 + 5 = 9$, PSA >600 ng/mL, with negative bone scan, receiving LHRH analog was referred to perform [^{11}C]choline PET/CT for staging and radiation treatment

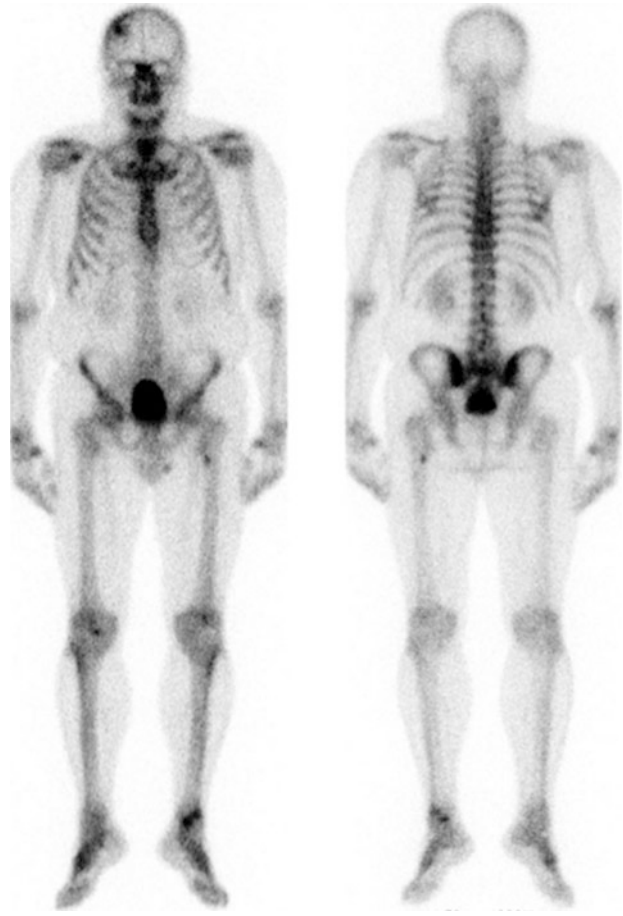

Fig. 13 Anterior (*left image*) and posterior (*right image*) ^{99m}Tc-HDP bone scintigraphy showing moderately increased uptake in the lesser trochanter of the left femur, suspect for bone metastasis. It also shows increased uptake right in the frontal bone of the skull after burr hole trephination and increased uptake in the left ankle, considered to be caused by degenerative changes

planning purpose. PSA before the examination was 108 ng/mL.

Findings

[^{11}C]choline PET/CT (Fig. 8) showed tracer uptake in the known primary lesion with inhomogeneous tracer distribution within the lesion (Fig. 9). Additionally, [^{11}C]choline-avid lymph nodes were seen: pararectal (Figs. 10 and 11), internal iliac (Fig. 11), external iliac (Figs. 10 and 11), and para-aortic (Fig. 12).

Follow-Up

Due to the pattern of diffuse metastatic disease revealed by the [^{11}C]choline PET/CT scan, the patient was not considered for radiation treatment and was scheduled to receive hormonal therapy.

Discussion

[^{11}C]choline PET/CT can be useful in the initial evaluation of patients with high-risk prostate cancer allowing to identify nodal and distant metastases. It has been also proposed to guide radiation

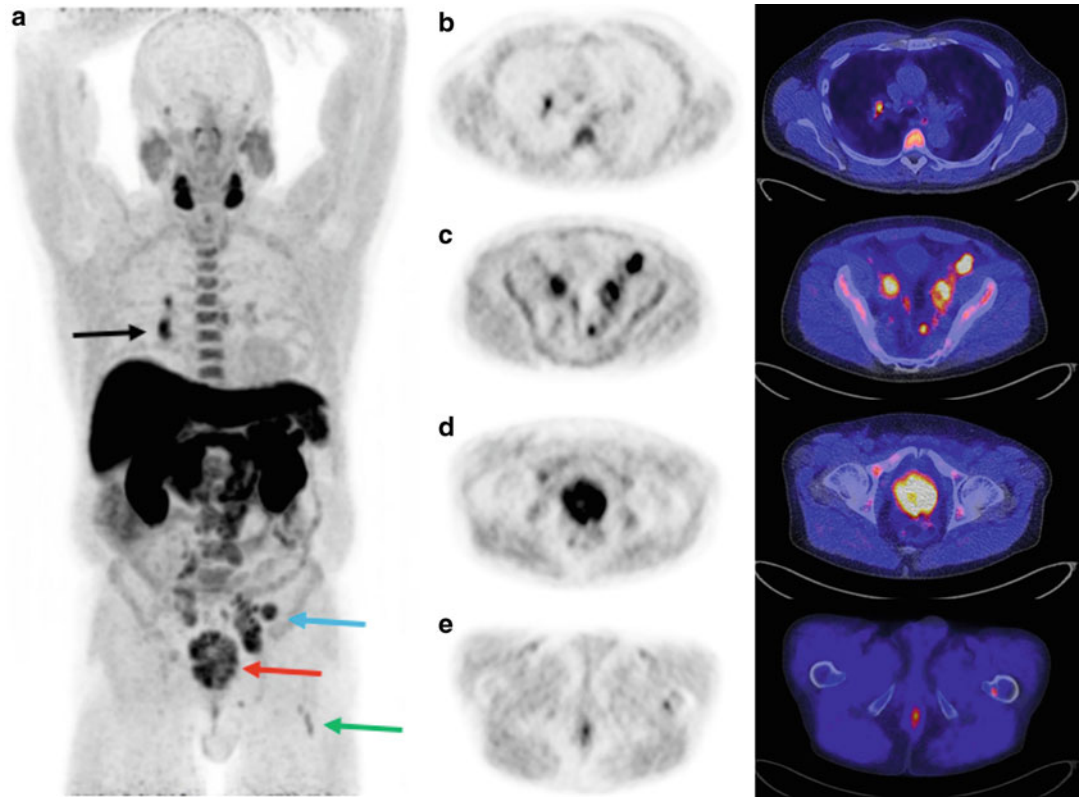

Fig. 14 [^{11}C]choline PET/CT. (**a**) Maximum intensity projection (*MIP*) showing increased uptake in the enlarged prostate (*red arrow*), multiple lesions in the pelvis (*blue arrows*), in the lesser trochanter of the left femur (*green arrow*), and in the lung hilum left and right (*black arrow*, considered reactive lymph nodes). Axial reconstructions and fusion images showing (**b**) increased uptake in a hilar lymph node, considered to be reactive; (**c**) increased uptake in multiple enlarged para-iliac lymph nodes, considered to be metastases; (**d**) increased uptake in the enlarged prostate in the known prostate carcinoma; (**e**) moderately increased uptake in the lesser trochanter of the left femur, considered to be a metastasis

treatment. In the present case, moreover, it has been useful to choose the most appropriate treatment strategy switching from radiotherapy to medical treatment because of the abdominal node disease localization.

Prostatic Cancer: Case No. 6

Case contributed by E.D. Telenga[a], A.W.J.M. Glaudemans[a], R.H.J.A Slart[a,b]

[a]Department of Nuclear Medicine and Molecular Imaging, University of Groningen, University Medical Center Groningen, The Netherlands

[b]Biomedical Photonic Imaging Group, University of Twente, Enschede, The Netherlands.

Presentation

A 74-year-old man with a history of melanoma, hypertension, heart failure, a cerebrovascular accident, and a subdural hematoma treated with burr hole trephination presented at his general physician with hematuria. Digital rectal examination revealed an irregular and enlarged prostate. The PSA level was elevated: 89.5 ng/mL. Prostate biopsies showed adenocarcinoma in all biopsies (Gleason score $5 + 5 = 10$) with perineural growth.

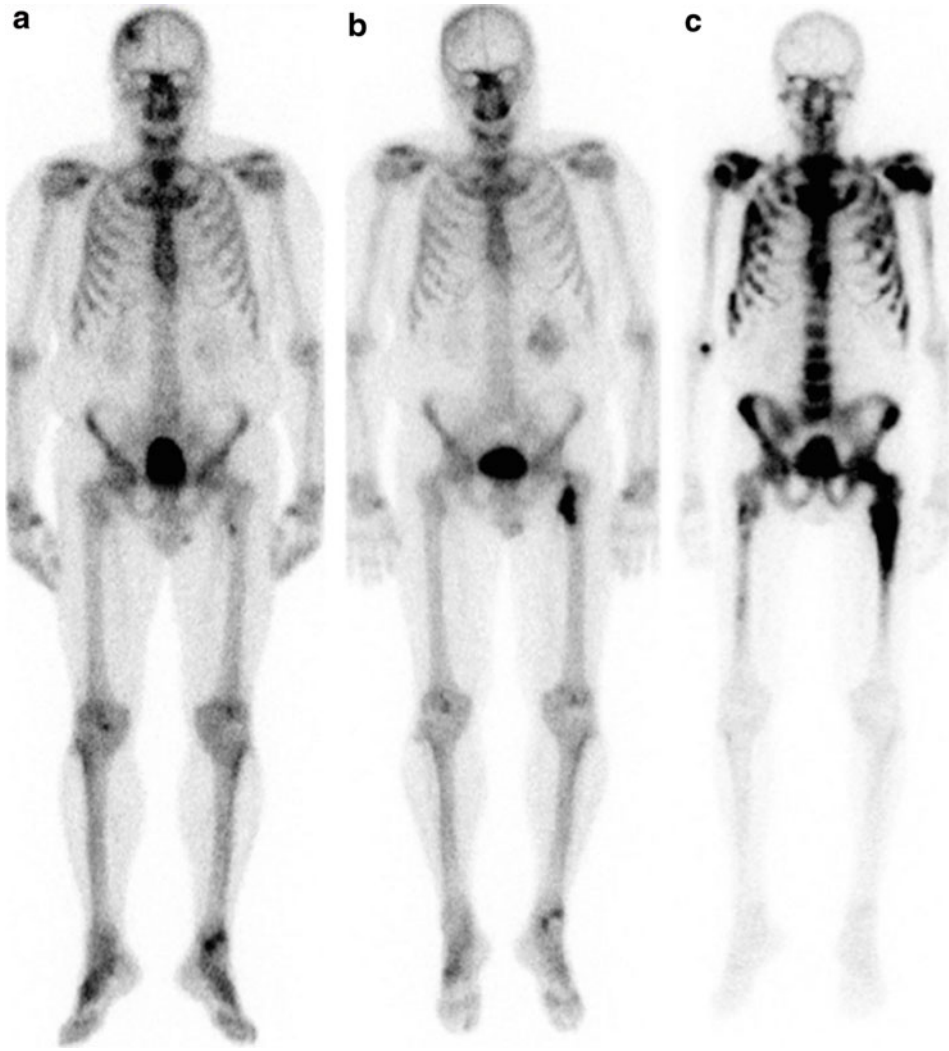

Fig. 15 ^{99m}Tc-HDP bone scintigraphy. (**a**) At presentation (see Fig. 1). (**b**) After 1 year with increased uptake at the left lesser trochanter and a new lesion in the left proximal femur. (**c**) After 2 years with intense uptake in nearly the complete axial skeleton and no excretion by the kidneys

Findings

Because of the total Gleason score of 10, a ^{99m}Tc-HDP bone scintigraphy was performed for dissemination purposes (Fig. 13). It showed moderately increased uptake in the lesser trochanter of the left femur. This lesion was suspected to be a sclerotic bone metastasis; however, a solitary bone cyst or another benign bone lesion was also considered. Additionally, it showed increased uptake in the frontal bone of the skull at the right side, which was considered to be due to the burr hole trephination in the past. Finally, it showed increased uptake in two lesions in the left ankle, which were considered to be degeneration.

To further determine the lesion in the lesser trochanter and to evaluate if there were lymph node metastases, a [^{11}C]choline PET/CT was performed (Fig. 14). It showed clearly increased uptake in the prostate and in multiple enlarged para-aortal and para-iliac lymph nodes. There was also moderately increased uptake in the lesser trochanter of the left femur with sclerotic changes on the low-dose CT. There were no other lesions

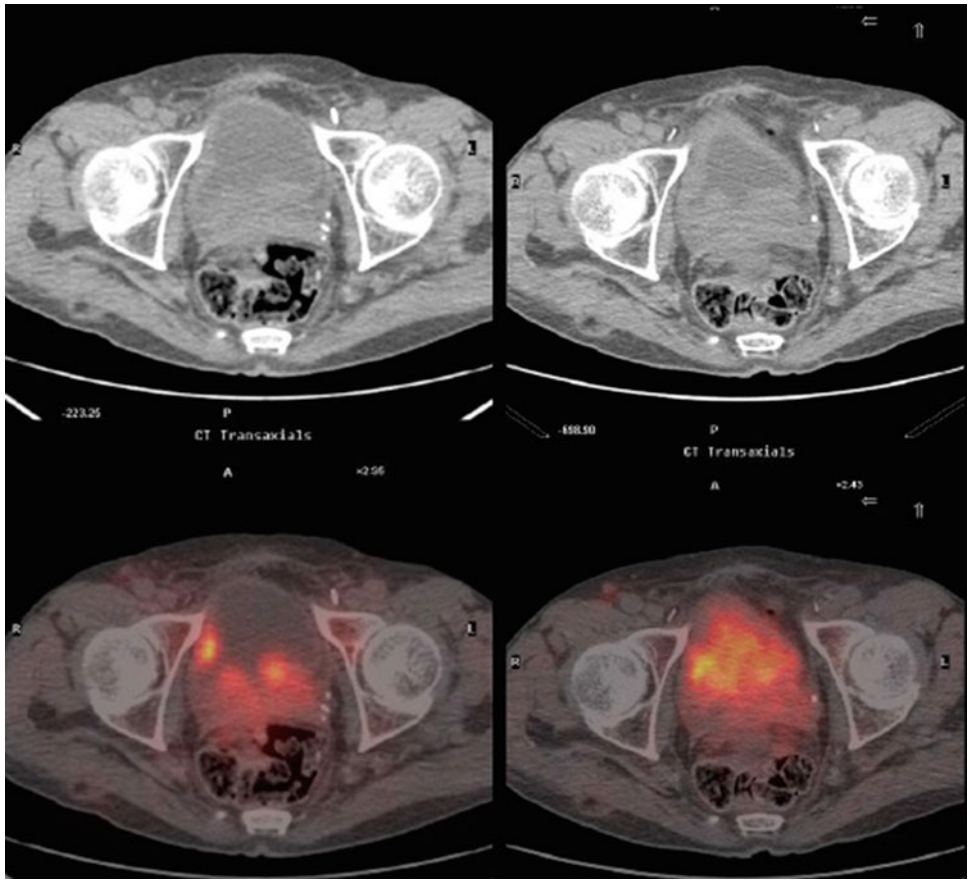

Fig. 16 On *left* panels, LD-CT and fused PET/CT axial images showing the presence of disease with high ^{18}F-choline uptake within lesions involving vesicles and the posterior wall. The uptake within the lesions can be clearly distinguished by the bladder which appears to be distended and does not contain any radioactive urine. On right panels the same LD-CT and fused PET/CT axial images obtained with the late whole-body acquisition. The identification of the lesions appears more difficult because of the radioactive urine excreted within the bladder

in the skeleton. Finally, it showed increased uptake in lymph nodes in the lung hilum bilaterally. These lymph nodes were considered to be reactive.

Follow-Up

It was concluded that the patient had prostate carcinoma with multiple lymph node metastases and one skeletal metastasis. Treatment was started with the GnRH analog leuprorelin. ^{99m}Tc-HDP bone scintigraphy performed 1 year later showed increase of the uptake in the left lesser trochanter and a new small lesion in the left proximal femur (Fig. 15). After 2 years, patient presented with progressive pain in multiple sites in the skeleton and increasing PSA (626 ng/mL) and alkaline phosphatase (982 U/L). ^{99m}Tc-HDP bone scintigraphy showed intense uptake in nearly all of the axial skeleton and no excretion by the kidneys, also known as a superscan. Patient passed away 1 month later.

Teaching Point

^{99m}Tc-HDP bone scintigraphy and [^{11}C]choline PET/CT are essential tools for the management of patients with high-risk prostate carcinoma.

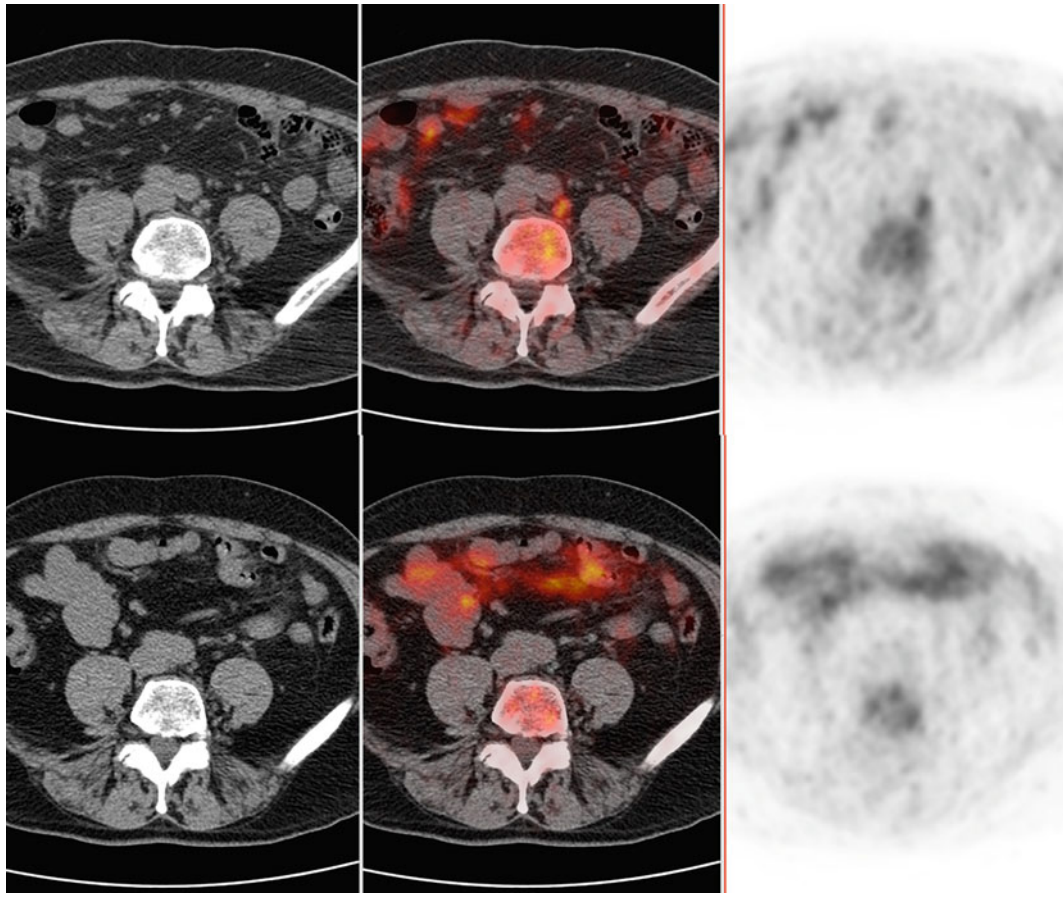

Fig. 17 On *top* panels: CT, fused PET/CT and PET axial slices showing two left para-aortic lymph nodes which accumulate ^{18}F-choline. On *bottom* panels the same slices of the PET/CT study performed 9 months before with PSA levels of 0.81 ng/mL and resulted negative. In the CT axial image (*left*), two 4 mm lymph nodes can be disclosed, but without any tracer uptake

Prostatic Cancer: Case No. 7

Presentation

A 74-year-old man with a prostate carcinoma with serum PSA 22 ng/mL and a Gleason score at biopsy of 6 (3 + 3). At staging CT did not disclose enlarged lymph nodes within the pelvis and the whole abdomen, and bone scintigraphy resulted negative for metastases. The patient underwent a radiation treatment with intensity-modulated radiotherapy (IMRT, 68 Gy) on the prostate bed. Three months after the end of treatment, PSA decreased to 0.6 ng/mL. No hormonal therapy was undertaken.

Findings

During follow-up PSA rose up to 2.7 ng/mL. CT did not localize the presence of recurrent disease. After 4 months PSA reached a level of 4.1 ng/mL, and the patient underwent a PET/CT scan with ^{18}F-choline. The PET/CT study was conducted with an early one-bed list-mode acquisition of 8 min after tracer administration (3 MBq/kg body weight) and a late (after 60 min) whole-body acquisition. Early images obtained from the first 4 min of acquisition, before radioactive urine reached the bladder, showed the presence of disease involving the seminal vesicles and the posterior wall of the bladder (Fig. 16). No other

sites of recurrence were disclosed by PET/CT at the late whole-body acquisition.

Follow-Up

The patient was then started to antiandrogen therapy.

Teaching Points

Due to high urine excretion rate of ^{18}F-choline, sites of locoregional disease close to the bladder could be difficult to be clearly seen with the only late acquisition. Thus, when locoregional recurrence is suspected, an early acquisition after tracer administration can help in identifying sites of disease that have a fast uptake of ^{18}F-choline before urinary tracer excretion reaches the bladder.

Prostatic Cancer: Case No. 8

Presentation

A 75-year-old man (a technical laboratory technician and former hospital employee) suffered by prostate carcinoma, with a PSA of 13 ng/mL and Gleason score of 7 (3 + 4). He underwent radical prostatectomy (pT2N0M0). After 2 years of follow-up without hormonal therapy, initial biochemical relapse was observed, with a PSA of 0.42 ng/mL. After 3 months PSA rose to 0.81 ng/mL.

Findings

A biopsy of the prostate bed resulted negative for the presence of local disease. The US and CT scans did not show suspected lymphadenopathies within the pelvis. Due to the rate of increase serum PSA, the urologist referred the patient for an ^{18}F-choline PET/CT scan. The PET/CT study was conducted with an early one-bed list-mode acquisition of 8 min after tracer administration (3 MBq/kg body weight) and a late (after 60 min) whole-body acquisition. Neither early nor late images showed a clear site of relapse.

Follow-Up

After 9 months serum PSA suddenly rose up again, to reach the level of 2.69 ng/mL. The patient underwent a second ^{18}F-choline PET/CT whole-body scan, which discloses the presence of two lymph nodes with a pathologically increased tracer uptake (Fig. 17).

Teaching Points

PET/CT with radiolabeled choline is considered a very sensitive technique for the localization of the relapse of prostate carcinoma. However, its sensitivity is lower in case of low levels of serum PSA. In particular, a PSA value between 1 and 2 ng/mL is considered a reasonable cutoff value below which does not perform ^{18}F-choline PET/CT.

On the other hand, high PSA velocity, or short PSA doubling time, is highly predictive of PET/CT positive findings. A PSA doubling time between 0 and 6 months predicts the appearance of distant metastases.

Prostatic Cancer: Case No. 9

Presentation

A 63-year-old man with a PSA of 12.8 ng/mL underwent a prostate biopsy, which revealed a high-risk prostate carcinoma with a Gleason score of 9 (4 + 5).

Findings

CT did not disclose sites of disease within the pelvis and the abdomen, while bone scintigraphy with ^{99m}Tc-MDP was negative. The patient was therefore submitted to radical prostatectomy with pelvic lymphadenectomy (pT3aN0M0), and

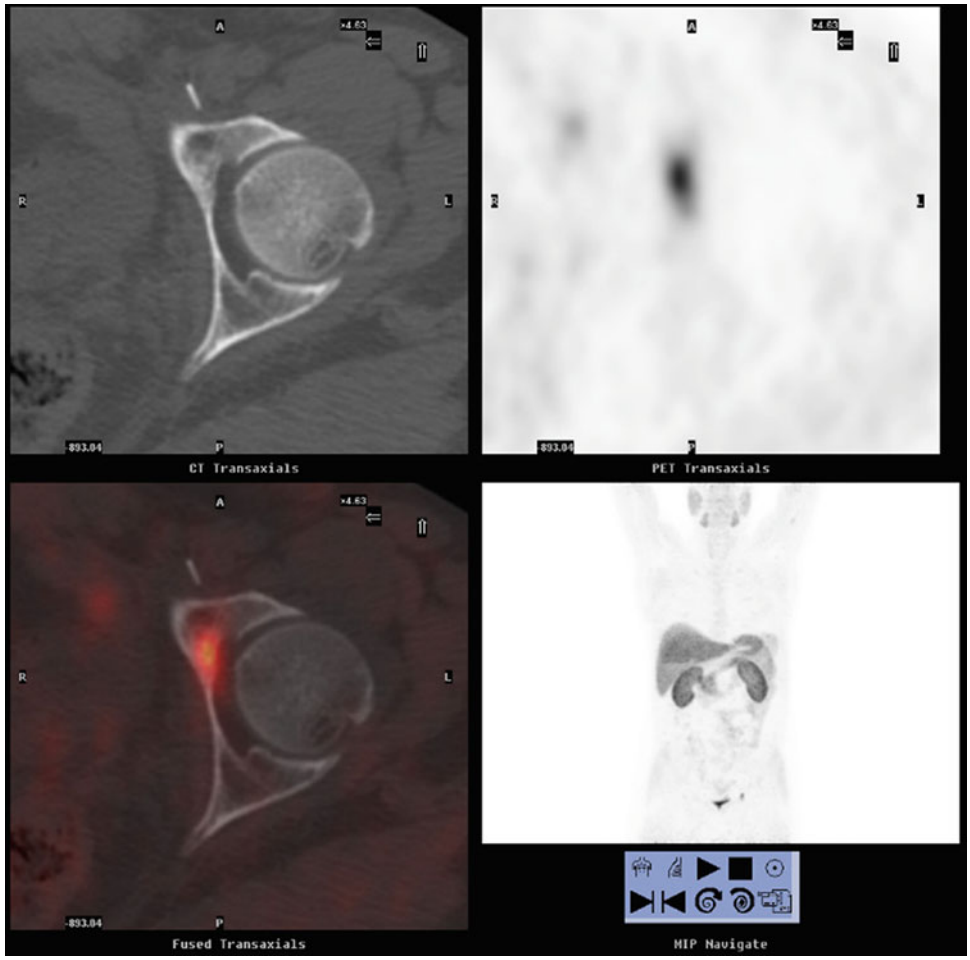

Fig. 18 PET/CT with ^{18}F-choline shows the presence of an area of hyperactivity within the left iliac bone in proximity if the acetabulum consistent with a secondary lesion

subsequently adjuvant antiandrogen hormone therapy was started. During the whole treatment with triptorelin, serum PSA levels always resulted under the sensitivity limit of detectability.

Follow-Up

About 6 months after discontinuing triptorelin, serum PSA increased reaching a value of 1.04 ng/mL. Since the US and CT scans were negative, the patient underwent an ^{18}F-choline PET/CT scan. A 60 min whole-body acquisition was performed after the injection of ^{18}F-choline (3 MBq/kg body weight). Images revealed the presence of a single site of metastasis within the iliac bone (Fig. 18).

Teaching Points

In case of a suspected recurrence of prostate carcinoma, a high Gleason score at diagnosis can be associated with a positive finding of ^{18}F-choline PET/CT in case of biochemical relapse, even with serum PSA levels not particularly high.

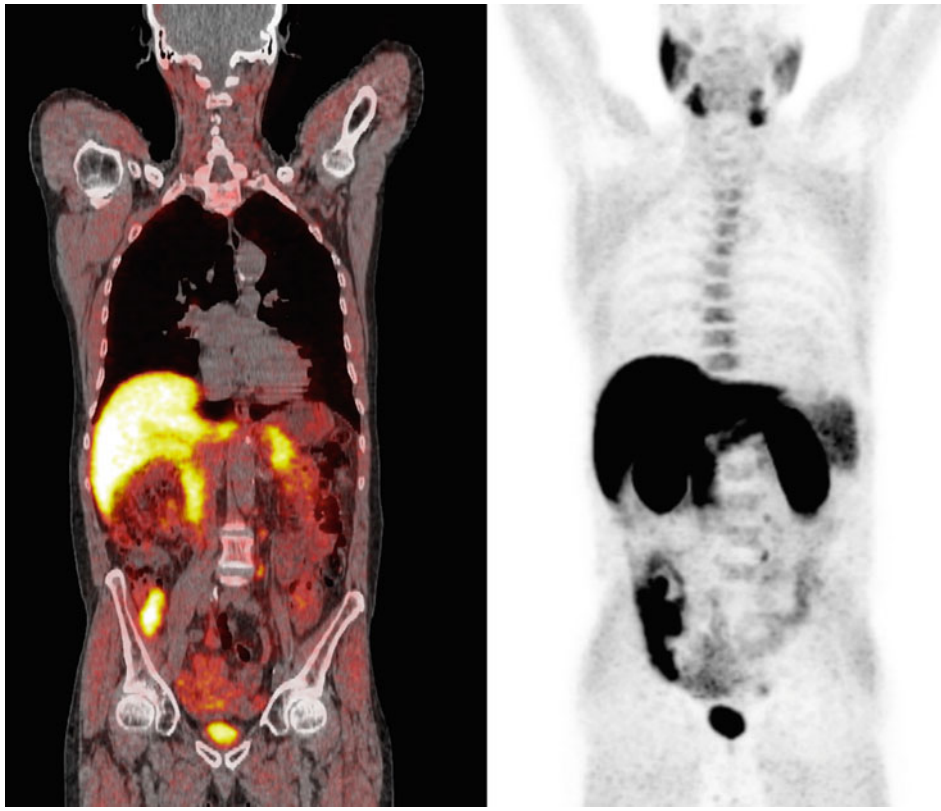

Fig. 19 PET/CT with ^{18}F-choline in patient with serum PSA level of 5.68 ng/mL. Fused PET/CT coronal slice and MIP image show two left para-aortic hyperactive lymphadenopathies

Prostatic Cancer: Case No. 10

Presentation

A 71-year-old man underwent radical prostatectomy plus external beam radiotherapy and pelvic lymph nodes dissection for an advanced prostate cancer with Gleason score 3 + 4. After 16 months of follow-up serum levels of PSA rose to 5.68 ng/mL.

Findings

The patient underwent a first PET/CT with ^{18}F-choline, which disclosed recurrent disease within two left para-aortic lymph nodes (Fig. 19). Then, the patient started an antiandrogen hormone therapy with triptorelin. After 6 months of such treatment, PSA levels had further increased up to 44.0 ng/mL. A second PET/CT with ^{18}F-choline was performed, without discontinuing triptorelin. This PET/CT scan showed progression of the disease that was limited to several para-aortic and caval-aortic lymph nodes and two left inferior latero-cervical nodes (Fig. 20).

Follow-Up

After other 4 months of antiandrogen treatment in combination with an LHRH agonist, serum PSA rose up even further to 84.1 ng/mL. Recurrent disease diffused to lymph nodes, including mediastinal nodes, and to a vertebra was demonstrated by a third PET/CT with ^{18}F-choline (Figs. 21, 22, and 23).

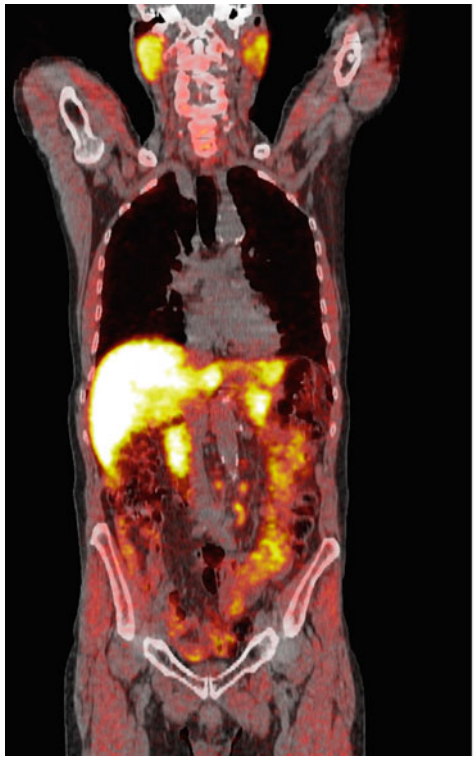

Fig. 20 PET/CT with ^{18}F-choline in patient with serum PSA level of 44.0 ng/mL. Multiple lombo-aortic hyperactive nodes have been clearly disclosed. Moreover, fused PET/CT coronal slice and MIP image show two supraclavicular lymphadenopathies

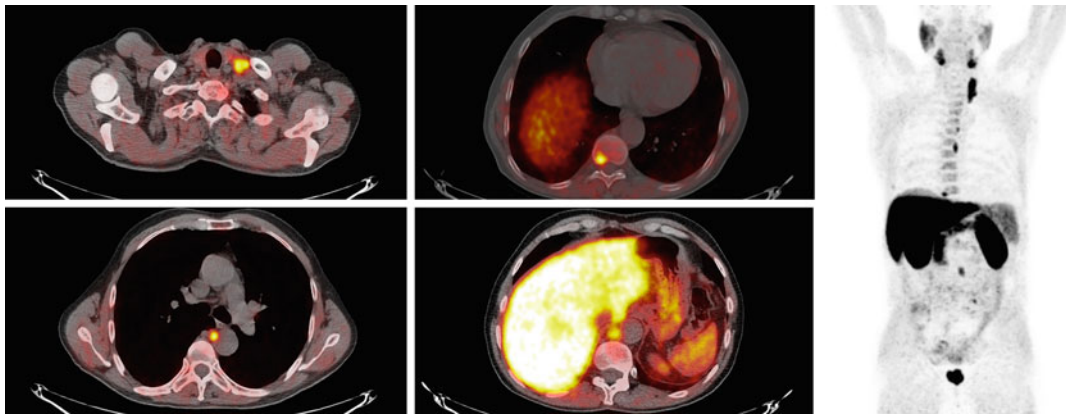

Fig. 21 Fused PET/CT axial slices and MIP image show the progression of the disease which involves multiple lymph nodes and a thoracic vertebra

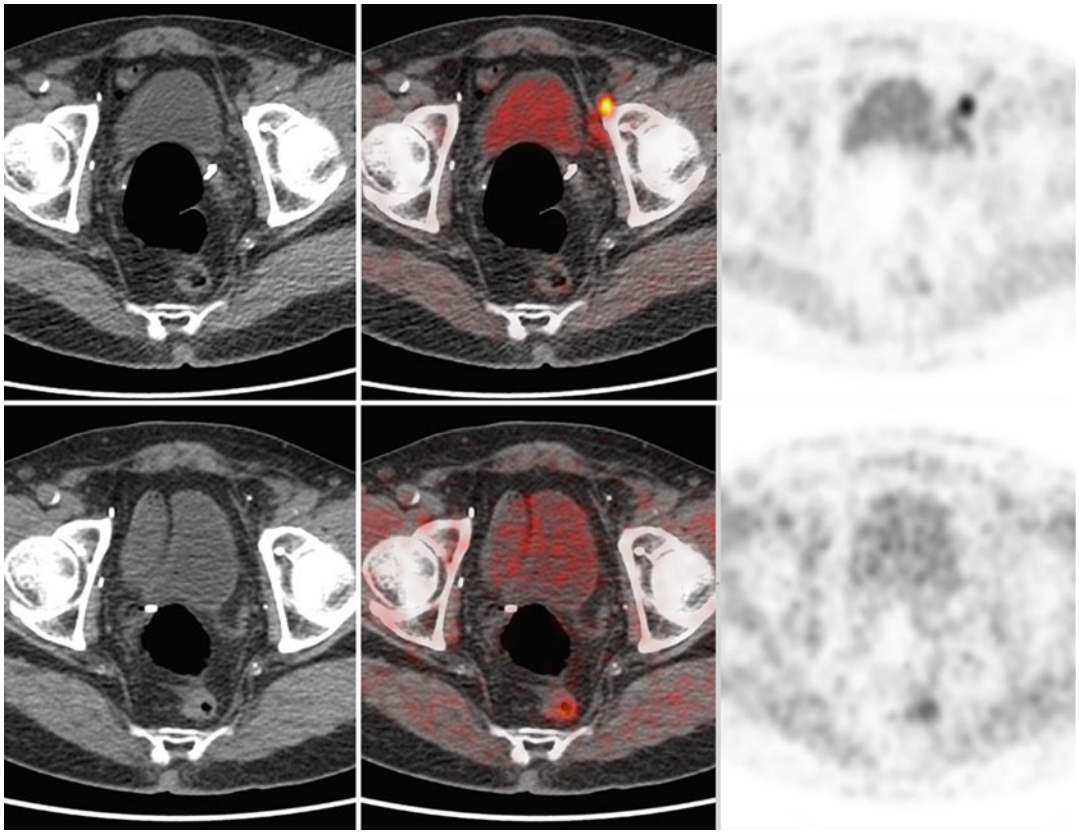

Fig. 22 On *top* panels CT, fused PET/CT and PET axial slices show the presence of a hyperactive left inguinal lymphadenopathy. On *bottom* panels the same axial slices of the patient after radiotherapy which demonstrate the disappearance of the lymphadenopathy

Teaching Points

In patients with hormone-refractory prostate cancer, PSA levels tend to rise despite treatment. For the same reason, PET/CT with ^{18}F-choline in these patients results to be positive despite the ongoing hormonal treatment, which is unable to control the disease.

Prostatic Cancer: Case No. 11

Presentation

A 74-year-old man underwent radical prostatectomy for an intermediate-risk prostate cancer with Gleason score 3 + 4. After a negative follow-up of more than 2 years, biochemical relapse with increased levels of serum PSA was observed.

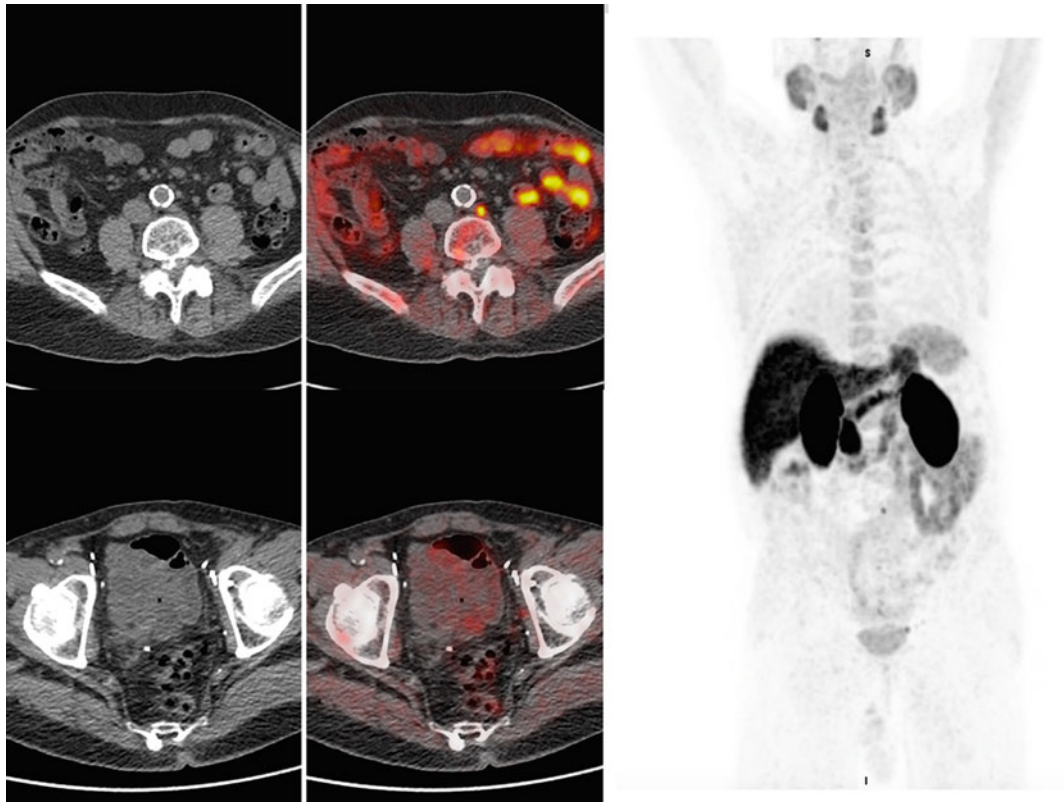

Fig. 23 PET/CT images after the new increase of PSA levels show a different site of disease within a para-aortic lymphadenopathy

Findings

PSA levels rose up to 1.56 ng/mL and the patient underwent a PET/CT with ^{18}F-choline. The whole-body scan revealed two areas of increased tracer uptake within an inguinal lymph node basin. PET/CT images were used to target subsequent external beam radiation therapy.

Follow-Up

Three months later, PSA levels decreased below 0.1 ng/mL. The patient underwent a second PET/CT, which confirmed the disappearance of the inguinal lymphadenopathy. One year later the patient presented a new increase of serum PSA up to 2.84 ng/mL. PET/CT with ^{18}F-choline revealed the presence of a new site of recurrence within a para-aortic lymph node, and the patient started hormonal antiandrogen therapy.

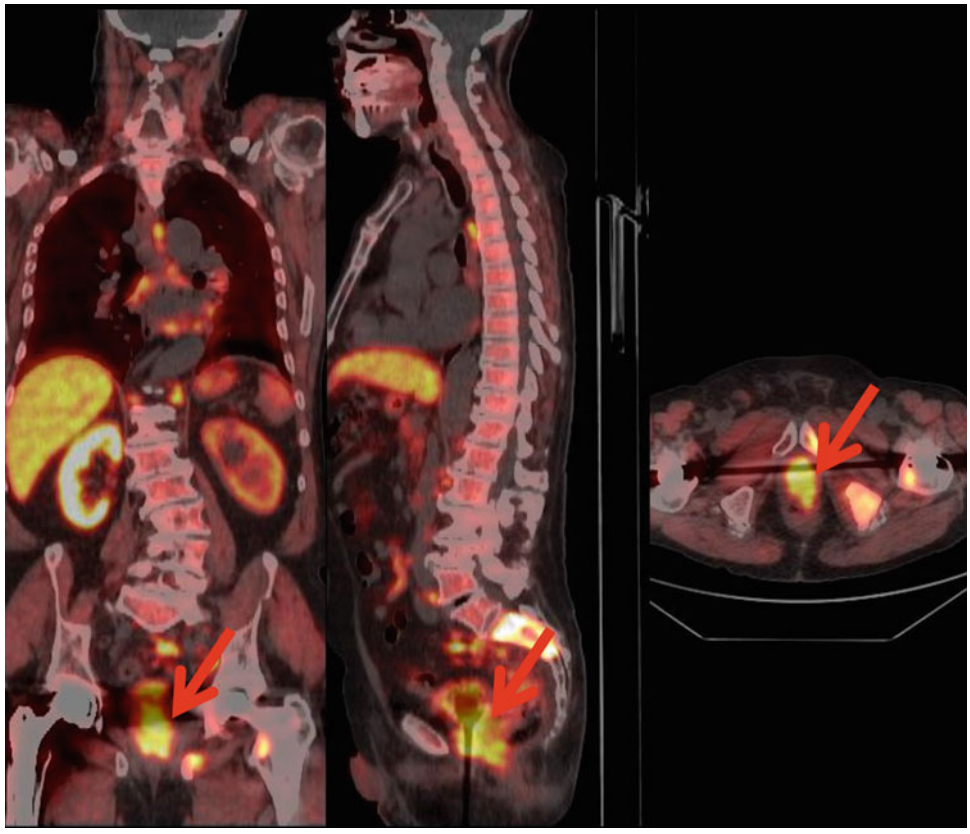

Fig. 24 Coronal (*left*), sagittal (*center*), and axial (*right*) fused PET/CT images show diffuse and intense tracer uptake in the prostate, seminal vesicles, and periprostatic adipose tissue (*red arrow*)

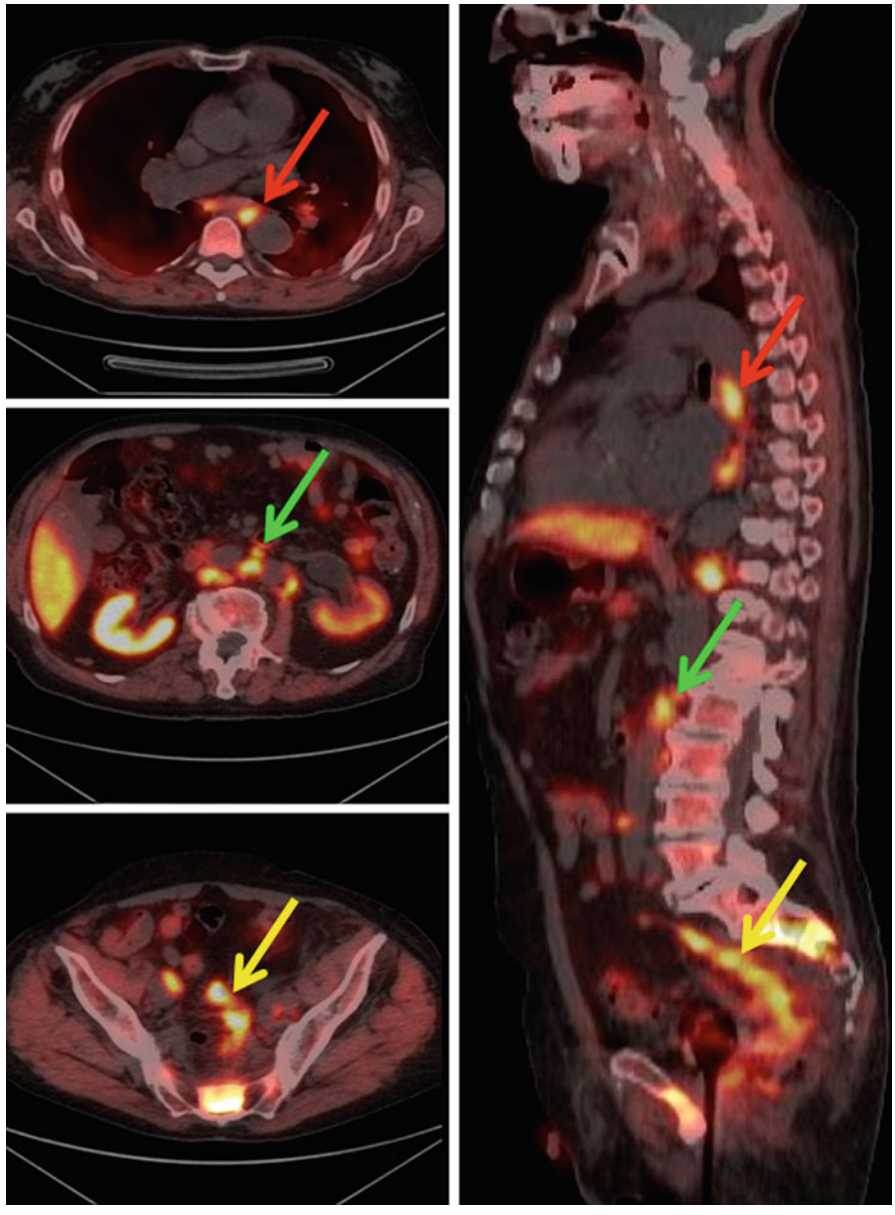

Fig. 25 Axial (at three levels) and coronal fused images show numerous lymphadenopathies with enhanced ^{18}F-choline uptake in the pelvis (*yellow arrow*), abdomen (*green arrows*), and mediastinum (*red arrows*)

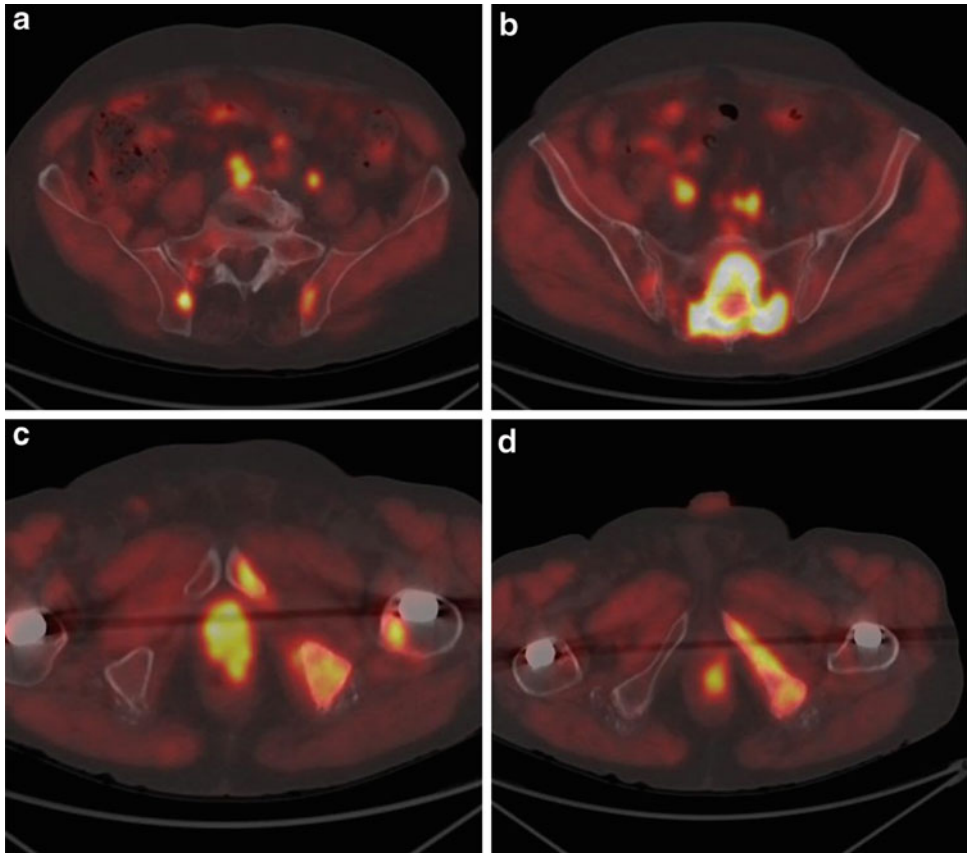

Fig. 26 Axial fused images of ^{18}F-choline-avid skeletal metastases, including the sacrum (**b**), ilium bilaterally (**a**), left ischium and left pubis and left femur (**c**, **d**)

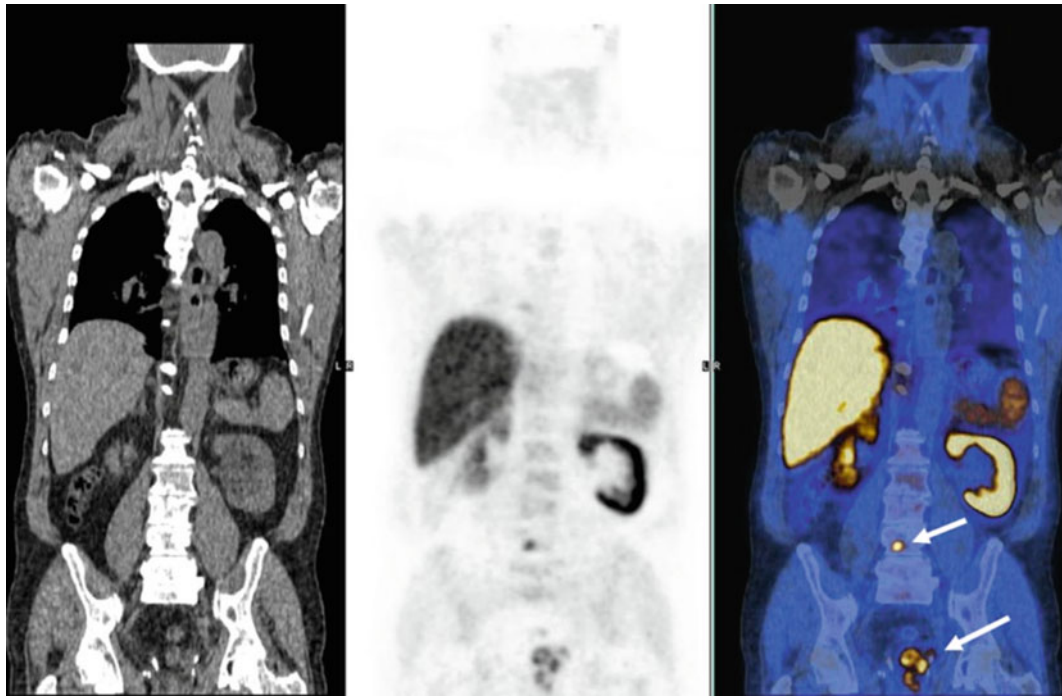

Fig. 27 ^{18}F-FCH PET/CT coronal images. CT (*left*), ^{18}F-FCH (*center*), and PET/CT fused image (*right*). ^{18}F-FCH PET/CT images show focal uptake in the prostate bed, pelvic lymph nodes, and a focus in the lumbar spine (*white arrows*)

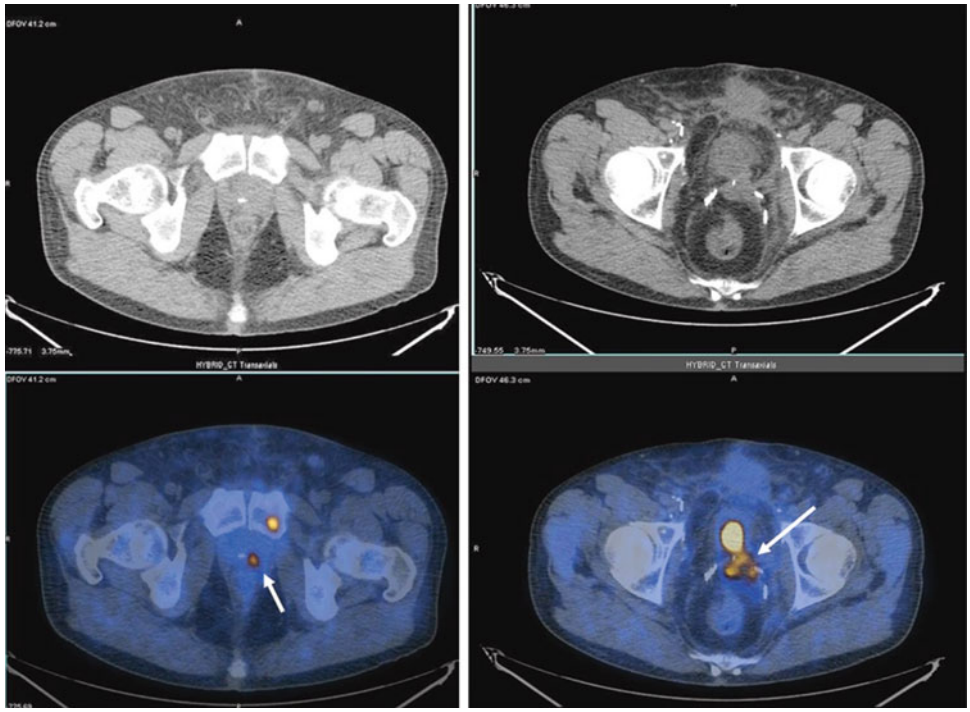

Fig. 28 Axial images at two levels, showing focal uptake in the prostate bed (*white arrow*). CT (*upper panel*) and ^{18}F-FCH PET/CT fused (*lower panel*). A site of focal ^{18}F-FCH uptake can also be seen in the left pubic bone, close to the pubic symphysis

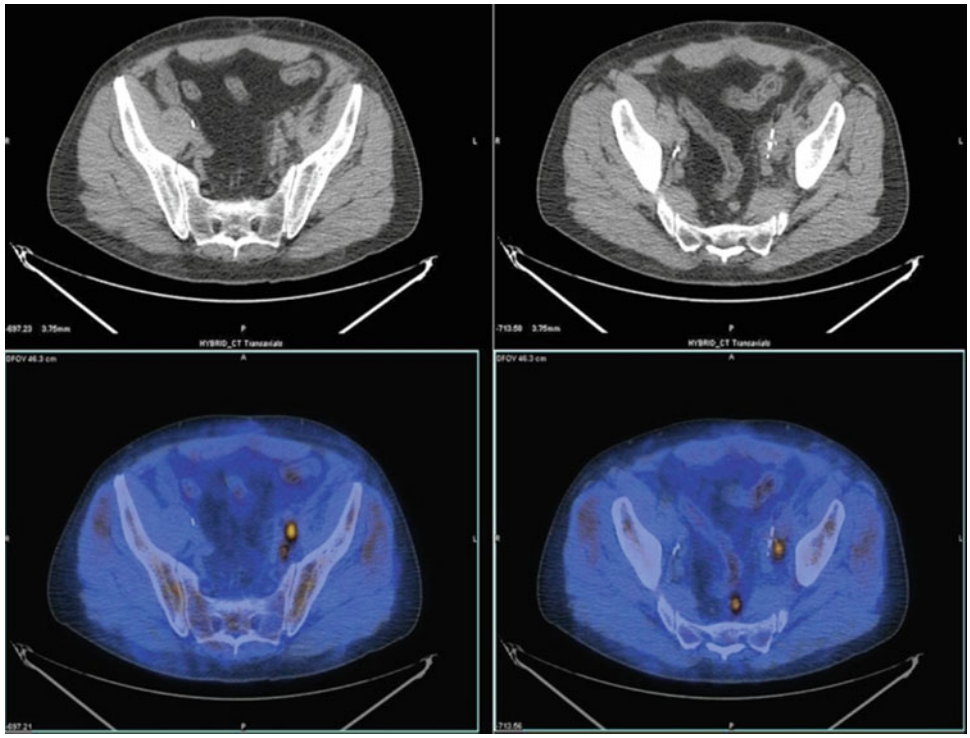

Fig. 29 Axial ^{18}F-FCH PET/CT images at two levels showing lymph node lesions. CT (*upper panels*) and fused images (*lower panels*)

Teaching Points

Although there is no firm evidence to suggest as a clinical standard the opportunity of a local treatment, to date an increasing number of patients are initiated to surgery or radiotherapy in the presence of limited clinical recurrence of disease. PET/CT with ^{18}F-choline could become one of the most effective imaging techniques to select patients for local treatments and to target radiotherapy.

Prostatic Cancer: Case No. 12

Case contributed by V. Duce, A. Ciarmiello
Nuclear Medicine Unit, "Sant'Andrea" Hospital, La Spezia, Italy.

Presentation

An 82-year-old patient with advanced prostate cancer (Gleason 9) treated with androgen deprivation therapy (LHRH agonists + antiandrogens). ^{18}F-choline PET/CT was performed to evaluate the extent of disease (restaging).

Findings

^{18}F-choline PET/CT fused images (coronal, sagittal, and axial views) show diffuse and intense tracer uptake in the prostate, seminal vesicles, and periprostatic adipose tissue (Fig. 24). Furthermore, the PET/CT scan shows numerous

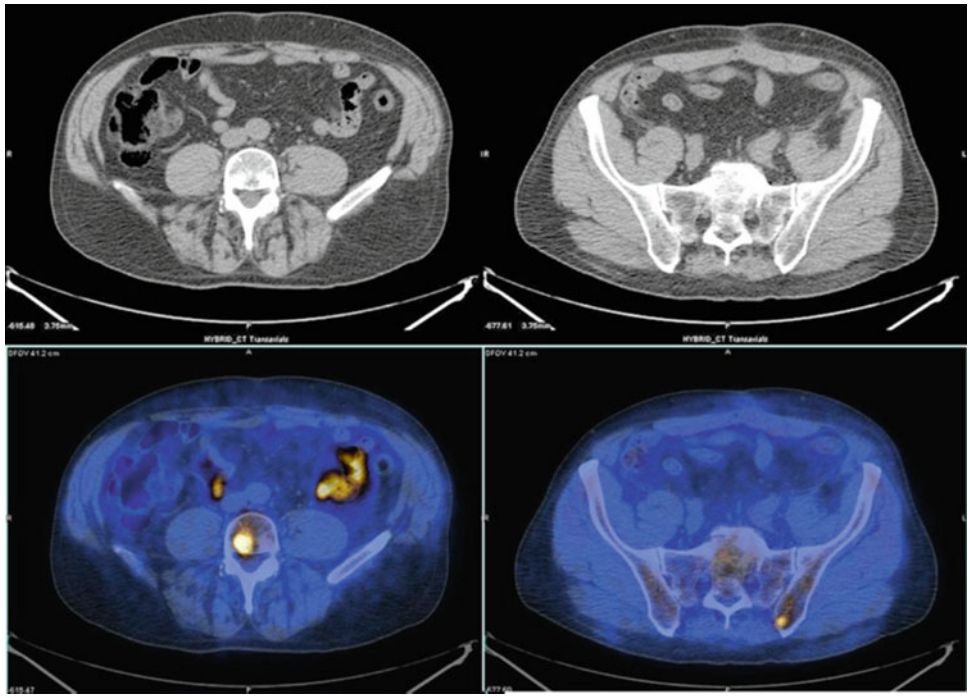

Fig. 30 Axial ^{18}F-FCH PET/CT images of skeletal metastases (CT, *upper image*, and PET/CT fused, *lower image*)

^{18}F-choline-avid lymphadenopathies in the pelvis (common iliac, external iliac, obturator, and paracolic nodes), in the abdomen (retrocrural, paraaortic, intercavoaortic, and paracaval nodes), and in the mediastinum (paratracheal, subcarinal, and paraesophageal nodes) (Fig. 25).

Lesions with increased ^{18}F-choline uptake are seen also in pelvic bones (including sacrum, ilium bilaterally, left ischium, and left pubis) and in the left femur (Fig. 26).

Discussion

This case confirms the value of ^{18}F-choline PET/CT in patients with prostate cancer for the evaluation of locoregional and metastatic disease.

Prostatic Cancer: Case No. 13

Presentation

A 64-year-old man with Gleason 9 prostate cancer with bilateral extracapsular extension and lymph node involvement (pT3bN2), previously treated with radical prostatectomy and bilateral pelvic lymphadenectomy presents with rising PSA 8 months after surgery. ^{18}F-choline PET/CT was performed to evaluate the extent of disease (Fig. 27).

Findings

Axial ^{18}F-choline PET/CT fused images show multiple sites of focal uptake in the prostate bed around the surgical clips (Fig. 28). Several foci of

^{18}F-choline uptake, corresponding to metastatic lymph nodes, are seen in common iliac region, in left external iliac, in obturator region, and in presacral nodes (Fig. 29). In addition, focal uptake in the lumbar spine and posterior left ilium suggest metastatic skeletal disease (Fig. 30).

Discussion

This case demonstrates the value of ^{18}F-choline PET/CT in patients with relapsed prostate cancer for the simultaneous evaluation of locoregional, lymph nodal, and distant recurrences.

Teaching Cases in Nuclear Oncology: Testicular Cancer

70

Kimiteru Ito, Somali Gavane, and Heiko Schöder

Keywords

Seminoma • Mixed germ cell tumor • [^{18}F]FDG PET/CT • Testicular cancer • Alpha fetoprotein • Nonseminoma

Glossary

[^{18}F]FDG	2-Deoxy-2-[^{18}F]fluoro-D-glucose
CT	X-ray computed tomography
MIP	Maximum intensity projection
PET	Positron emission tomography
PET/CT	Positron emission tomography/ Computed tomography
SUV	Standardized uptake value
SUV_{max}	Standardized uptake value at point of maximum

Contents

Seminoma 1799
Presentation 1799
Findings 1799
Discussion 1801
Testicular Cancer (Nonseminomatous Tumor) 1802
Presentation 1802
Findings 1802
Discussion 1802
References 1803

K. Ito • H. Schöder (✉)
Department of Radiology, Molecular Imaging and Therapy service, Memorial Sloan Kettering Cancer Center, New York, NY, USA
e-mail: itoukimiteru@yahoo.co.jp; itok@mskcc.org; schoderh@mskcc.org

S. Gavane
Division of Nuclear Medicine, Department of Radiology, Mount Sinai Hospital, New York, NY, USA
e-mail: somali.gavane@mountsinai.org

© Springer International Publishing Switzerland 2017
H.W. Strauss et al. (eds.), *Nuclear Oncology*,
https://doi.org/10.1007/978-3-319-26236-9_73

Seminoma

Case contributed by: S. Al Shammari, F. Fraioli Institute of Nuclear Medicine, UCLH NHS Foundation Trust, London, UK

Presentation

A 23-year-old man with history of metastatic seminoma. [^{18}F]FDG PET/CT prior to start chemotherapy.

Findings

There is a large heterogeneous [^{18}F]FDG-avid left-sided retroperitoneal mass extending from the lower border of T12 to lower border of L4 vertebral body (measuring 8 × 7 × 12 cm, SUV_{max} 20 at the level of renal hilum) (upper row, arrows).

On follow-up study after chemotherapy (lower row), there is interval improvement in size and activity of the left para-aortic lymphadenopathy (arrow) measuring 4 × 3 × 6 cm with SUV_{max} 4.0 (Fig. 1).

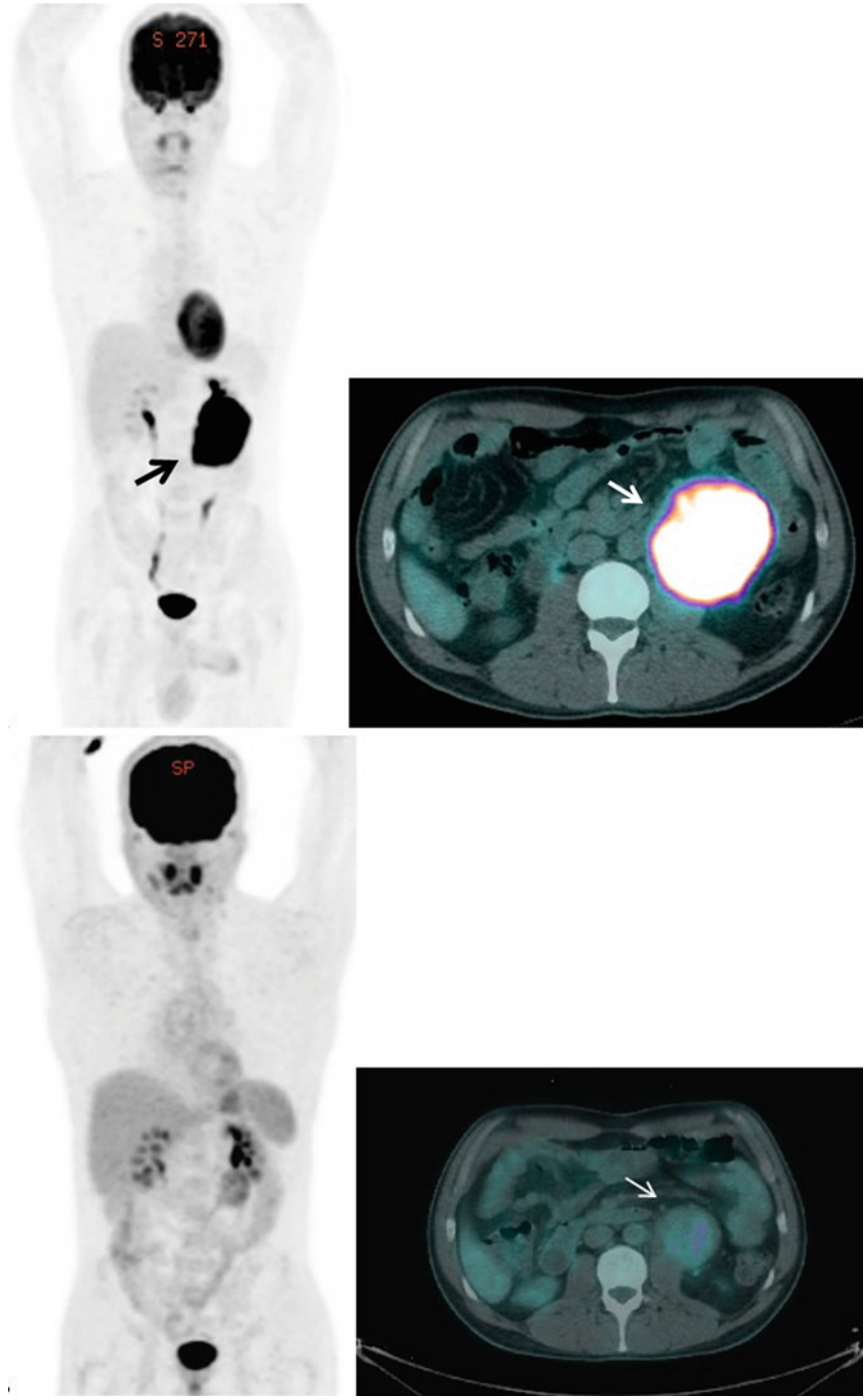

Fig. 1 MIP and axial images of [^{18}F]FDG PET/CT shows the left hypermetabolic mass (arrows at upper figures). [^{18}F]FDG PET/CT after treatment shows the hypometabolic residual mass (arrow at lower axial image)

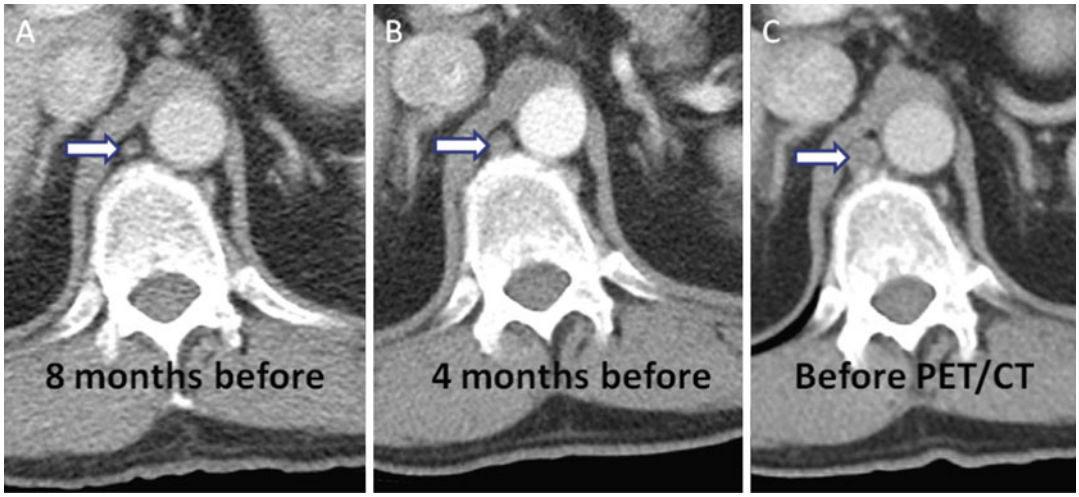

Fig. 2 Abdominal CTs after the therapy showed slowly increasing size of a retrocrural node: (**a**) 0.5 × 0.5 cm (8 months before PET/CT), (**b**) 0.6 × 0.6 cm (4 months before PET/CT), and (**c**) 1.1 × 0.9 cm (just before PET/CT)

Discussion

The limited accuracy with which testicular cancer is staged using conventional imaging modalities has led to the use of PET as an alternative staging tool. Another diagnostic challenge in the management of testicular cancer is the post-chemotherapy evaluation of a residual mass in the retroperitoneum. The differentiation between residual tumor, fibrosis, and teratoma can play a significant role in guiding further therapy. Unfortunately, by providing purely anatomic images of the retroperitoneum, CT does not adequately differentiate between these entities. Studies evaluating PET in this setting have demonstrated sensitivities ranging from 79% to 87% and specificities from 90% to 94%. In multiple studies, PET was limited by its low sensitivity for detecting mature teratoma, which has a low glucose metabolic rate. Studies have demonstrated that PET accuracy may be compromised if the scan is performed too soon (within 2 weeks) after chemotherapy, with reported false-negative findings due to early suppression of metabolic activity immediately

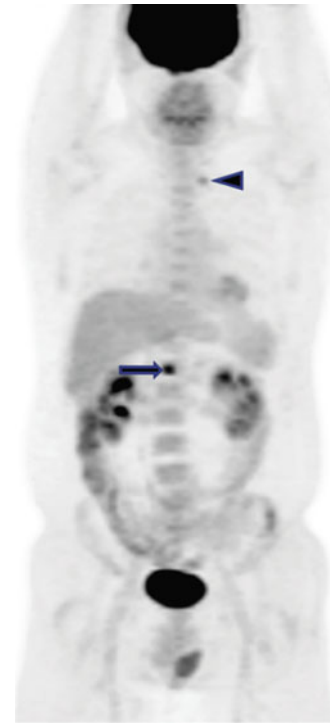

Fig. 3 MIP image of [^{18}F]FDG PET/CT shows the right hypermetabolic retrocrural node (*arrow*) and a subclavicular node (*arrowhead*)

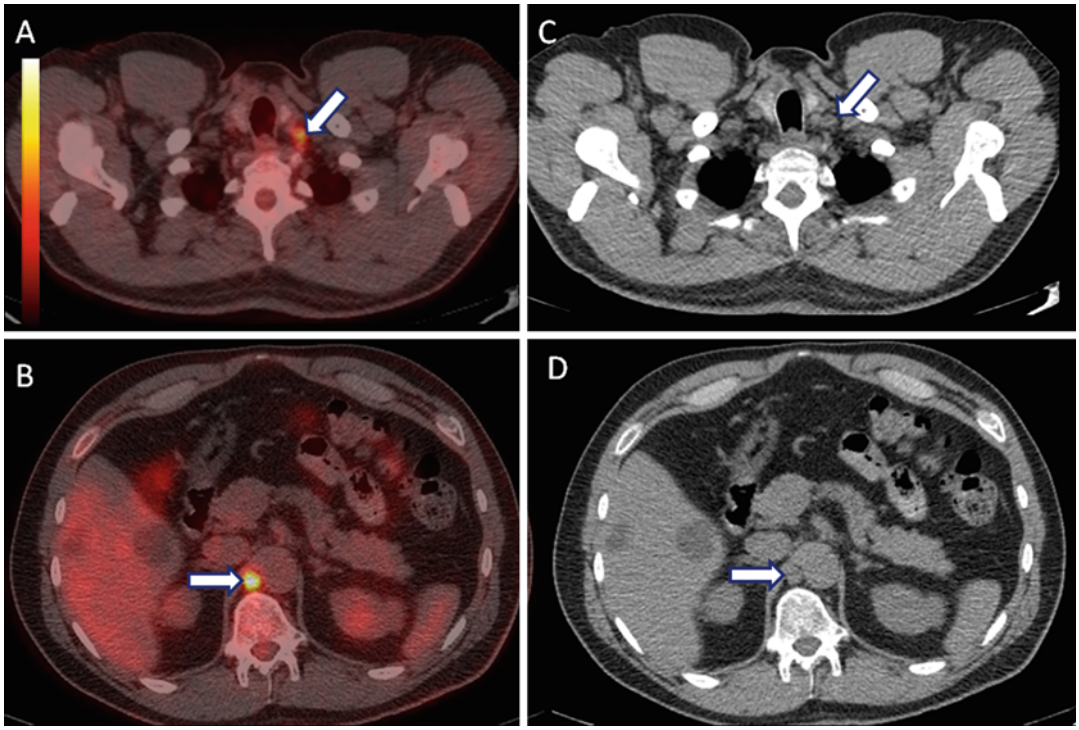

Fig. 4 Fused [^{18}F]FDG PET/CT axial images (**a**, **b**) show hypermetabolic right retrocrural lymph node (SUV_{max} 6.6) (*white arrows*) and subclavicular node (SUV_{max} 2.9) (*white arrows*). Diagnostic CT images during PET/CT (**c**, **d**) show that these lymph nodes are almost within normal limits

after chemotherapy and false-positive findings due to increased macrophage activity in absorption of necrotic tissue, respectively. As a result, PET should not be used until at least 2 weeks following chemotherapy.

Testicular Cancer (Nonseminomatous Tumor)

Presentation

A 51-year-old man with surgical history of high orchidectomy for mixed germ cell tumor. A follow-up CT showed slight enlargement of a swelling retrocrural lymph node, although serum alpha-fetoprotein was within normal limits (4.0 ng/mL, reference range 0.0–6.1 ng/mL).

Findings

Histopathology of the primary tumor in his right testicle showed mixed germ cell tumor containing embryonal carcinoma and yolk sac tumor. Follow-up abdominal CT scans (Fig. 2) demonstrated slightly increasing size of a right retrocrural node. The patient was referred for follow-up extent of disease assessment. [^{18}F]FDG PET/CT was performed to evaluate for metastatic disease (Figs. 3 and 4).

Discussion

Testicular cancers are divided into major categories (seminoma or nonseminomatous tumor). Overall, approximately two-thirds of patients have clinical

stage I disease at the time of diagnosis [1, 2]. Delayed metastases commonly occur in the para-aortic, iliac, and inguinal lymph nodes. [^{18}F]FDG PET/CT has benefit in the staging and restaging of the testicular cancers. Ambrosini et al. reported that [^{18}F]FDG PET/CT showed high sensitivity (92%) and specificity (84%) for seminoma [3]. However, [^{18}F]FDG PET/CT characteristics were lower for nonseminomatous tumors, with a sensitivity of 77% and a specificity of 99%. The study indicates the potential usefulness of [^{18}F]FDG PET/CT for patients with testicular tumors. In this case, [^{18}F]FDG PET/CT was able to clearly detect the metastatic lymph nodes and questionable finding on follow-up CT.

References

1. De Giorgi U, Pupi A, Fiorentini G, et al. FDG-PET in the management of germ cell tumor. Ann Oncol. 2005;16 Suppl 4:90–4.
2. De Wit R, Fizazi K. Controversies in the management of clinical stage I testis cancer. J Clin Oncol. 2006;24: 5482–92.
3. Ambrosini V, Zucchini G, Nicolini S, et al. ^{18}F-FDG PET/CT impact on testicular tumours clinical management. Eur J Nucl Med Mol Imaging. 2014;41:668–73.

Teaching Cases in Nuclear Oncology: Penile Cancer

71

Kimiteru Ito, Somali Gavane, and Heiko Schöder

Keywords

Squamous cell carcinoma • Lymphoscintigraphy • [^{18}F]FDG • PET/CT

Glossary

[^{18}F]FDG	2-Deoxy-2-[^{18}F]fluoro-D-glucose
AJCC	American Joint Committee on Cancer
CT	X-ray computed tomography
M	Metastasis status according to the AJCC/UICC TNM staging system
MIP	Maximum intensity projection
N	Lymph node status according to the AJCC/UICC TNM staging system
PET	Positron emission tomography
PET/CT	Positron emission tomography/Computed tomography
SPECT	Single-photon emission computed tomography
SPECT/CT	Single-photon emission computed tomography/Computed tomography
SUV	Standardized uptake value
SUV_{max}	Standardized uptake value at point of maximum
T	Tumor status according to the AJCC/UICC staging system
TNM	AJCC staging system based on parameters "T" (tumor status), "N" (lymph node status), and "M" (distant metastasis status)
UICC	Union Internationale Contre le Cancer (International Union Against Cancer)

Contents

Case 1 1806
Presentation 1806
Findings 1806
Discussion 1806

Case 2 1806
Presentation 1807
Findings 1807
Follow-Up 1807
Discussion 1808

Case 3 1808
Presentation 1808
Findings and Follow-Up 1809
Discussion 1812

References 1812

K. Ito • H. Schöder (✉)
Department of Radiology, Molecular Imaging and Therapy Service, Memorial Sloan Kettering Cancer Center, New York, NY, USA
e-mail: itoukimiteru@yahoo.co.jp; itok@mskcc.org; schoderh@mskcc.org

S. Gavane
Division of Nuclear Medicine, Department of Radiology, Mount Sinai Hospital, New York, NY, USA
e-mail: somali.gavane@mountsinai.org

© Springer International Publishing Switzerland 2017
H.W. Strauss et al. (eds.), *Nuclear Oncology*,
https://doi.org/10.1007/978-3-319-26236-9_74

Case 1

Case contributed by: F. Reyneke, M. Sathekge
Nuclear Medicine, University of Pretoria & Steve Biko Academic Hospital, Pretoria, South Africa

Presentation

An 81-year-old man was referred with penile cancer for which surgery was done. He complained of pain in his left shoulder.

Findings

A biopsy taken from the penile mass revealed poorly differentiated squamous cell carcinoma.

[^{18}F]FDG PET/CT for initial staging showed mild diffuse tracer uptake in the penis including the tip of the surgical stump with regional inguinal nodal involvement (SUV_{max} 25.27) (Figs. 1 and 2). Furthermore, a mass was noted posterior to the apex of the left lung. It had a large soft tissue component with adjacent bony erosion of the vertebral bodies of T2 and T3 (SUV_{max} 33.5) (Fig. 3). This was most likely a second primary tumor and had the appearance of a Pancoast tumor.

Discussion

In this case, the restaging [^{18}F]FDG PET/CT performed after surgery for the penile cancer resulted in the incidental detection of a lung mass that was completely asymptomatic.

Case 2

Case contributed by: M. R. Jochumsen
Department of Nuclear Medicine & PET Centre, Aarhus University Hospital, Aarhus, Denmark

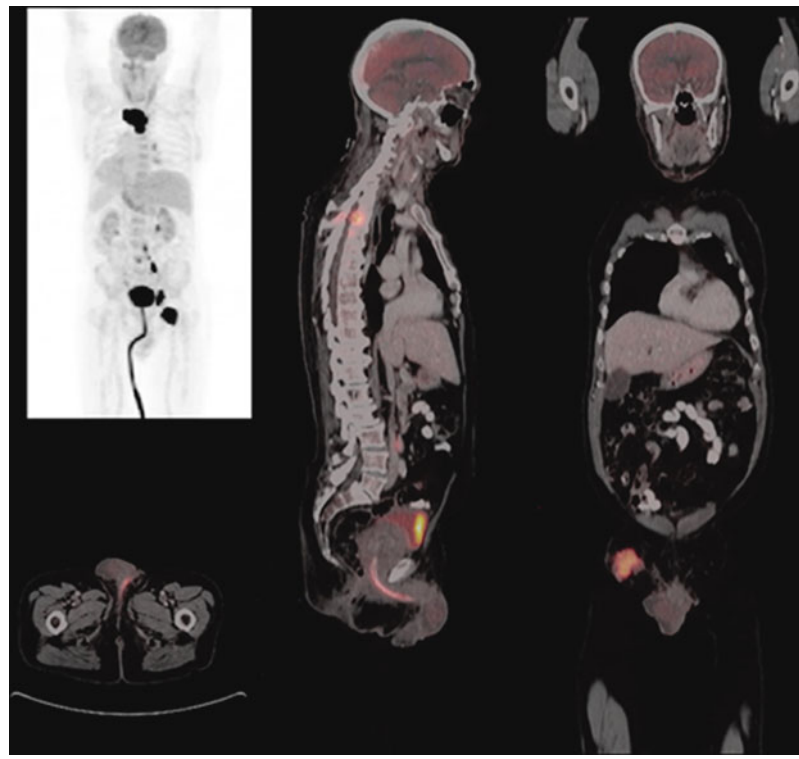

Fig. 1 *Upper left*, [^{18}F]FDG PET/CT MIP image, *Lower left to right*, fused axial, sagittal and coronal PET/CT images. The images show the [^{18}F]FDG-avid penile stump with regional nodal involvement

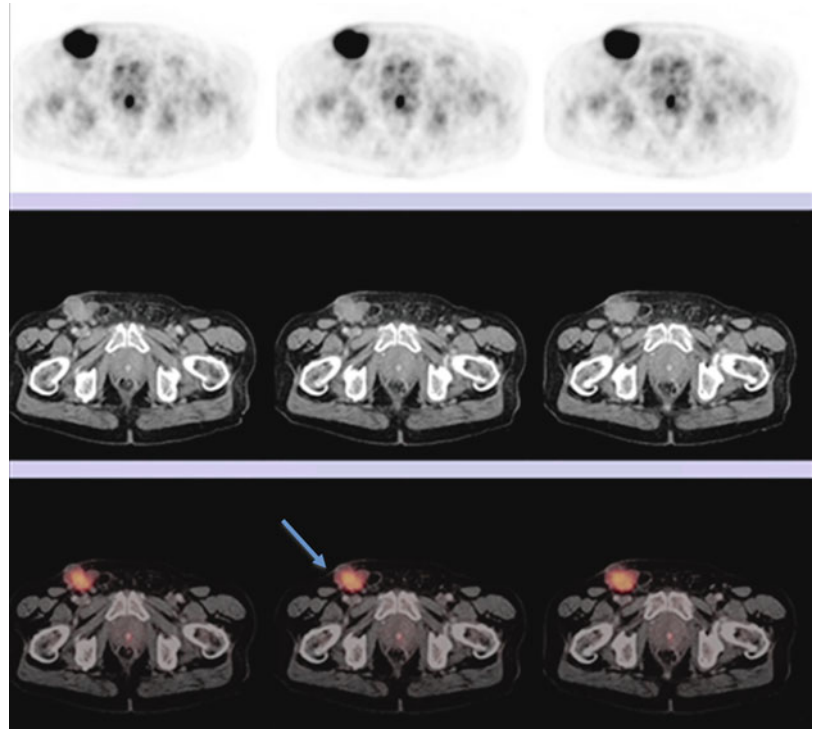

Fig. 2 [^{18}F]FDG PET/CT axial images demonstrating the penile stump

Presentation

An 87-year-old man with no previous medical history presented with a large tumor located on the penile glans. Additional clinical findings were multiple palpable lymph nodes in the right inguinal region.

Findings

A biopsy from the tumor showed a planocellular carcinoma, and the patient was referred for primary staging with [^{18}F]FDG PET/CT. The scan showed highly increased [^{18}F]FDG uptake in the primary penile tumor (A, yellow arrow) and in a lymph node conglomerate in the right inguinal region (A, dark blue arrow) and in two lymph nodes in the left inguinal region (A, red arrow). Furthermore, a focus of highly increased [^{18}F]FDG activity was seen in the left lung (A, green arrow).

Following intradermal injections of ^{99m}Tc-nanocolloidal albumin around the tumor (B, C and D, yellow arrows), lymphoscintigraphy showed a sentinel lymph node with high activity in the left inguinal region (B and C, red arrows), a secondary node superior of the sentinel node (B and C, purple arrows), and a sentinel node with very low activity in the right inguinal region (B and D, light blue arrows) in close relation to the lymph node conglomerate (D, dark blue arrow) (Fig. 4).

Follow-Up

A total penectomy was performed with simultaneous lymph node resection on the right side and gamma probe guided removal of sentinel node/suspicious lymph nodes in the left inguinal region. Histology showed that the primary tumor was a pT3 planocellular carcinoma with metastasis and perinodal growth in the lymph nodes from both sides. Later on, lymph node resection on the left side was performed and the patient was referred to chemotherapy. The tumor in the lung turned out to be a small primary lung cancer, and not a metastasis.

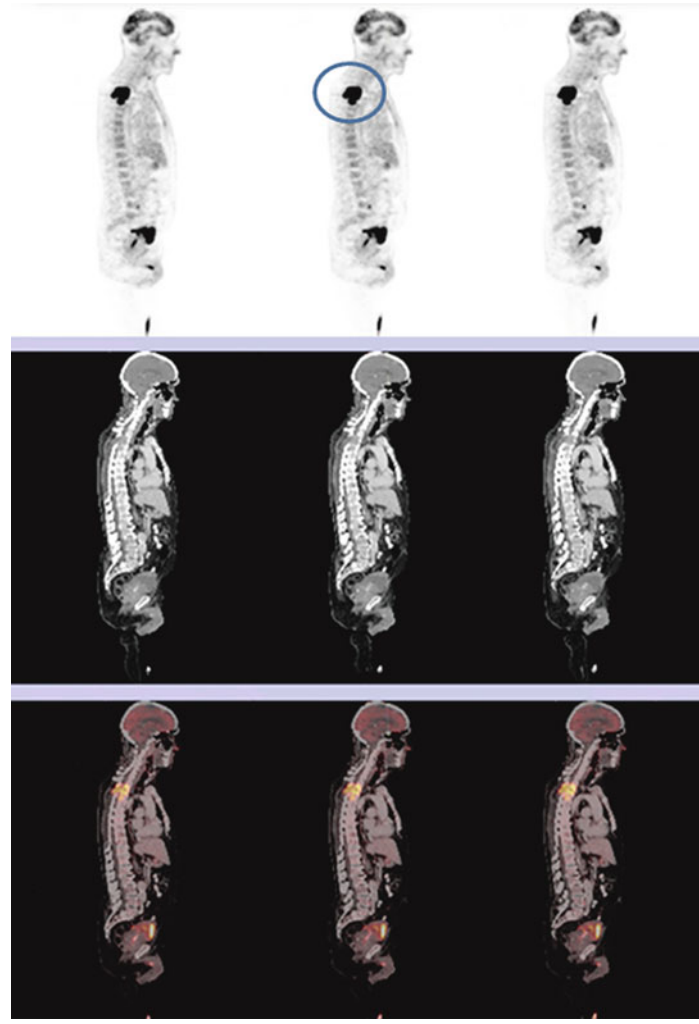

Fig. 3 [^{18}F]FDG PET/CT sagittal images showing the mass posterior to the apex of the left lung

Discussion

In this case, the significant tumor masses in the lymph nodes in the right groin almost did not appear on the lymphoscintigraphy, which illustrates that tumor infiltration of the lymph nodes can block the lymph drainage and complicate the interpretation of the lymphoscintigraphy [1]. The tumor in the lung was not a metastasis from penile cancer but instead a primary lung cancer. Thus, the case also illustrates the importance of histology of other relevant lesions suspicious of malignancy.

Case 3

Case contributed by: A. H. Dias
Department of Nuclear Medicine & PET Centre, Aarhus University Hospital, Aarhus, Denmark

Presentation

A 39-year-old man who 4 year earlier underwent partial penectomy for a pT1a squamous cell penis cancer, with negative sentinel node involvement.

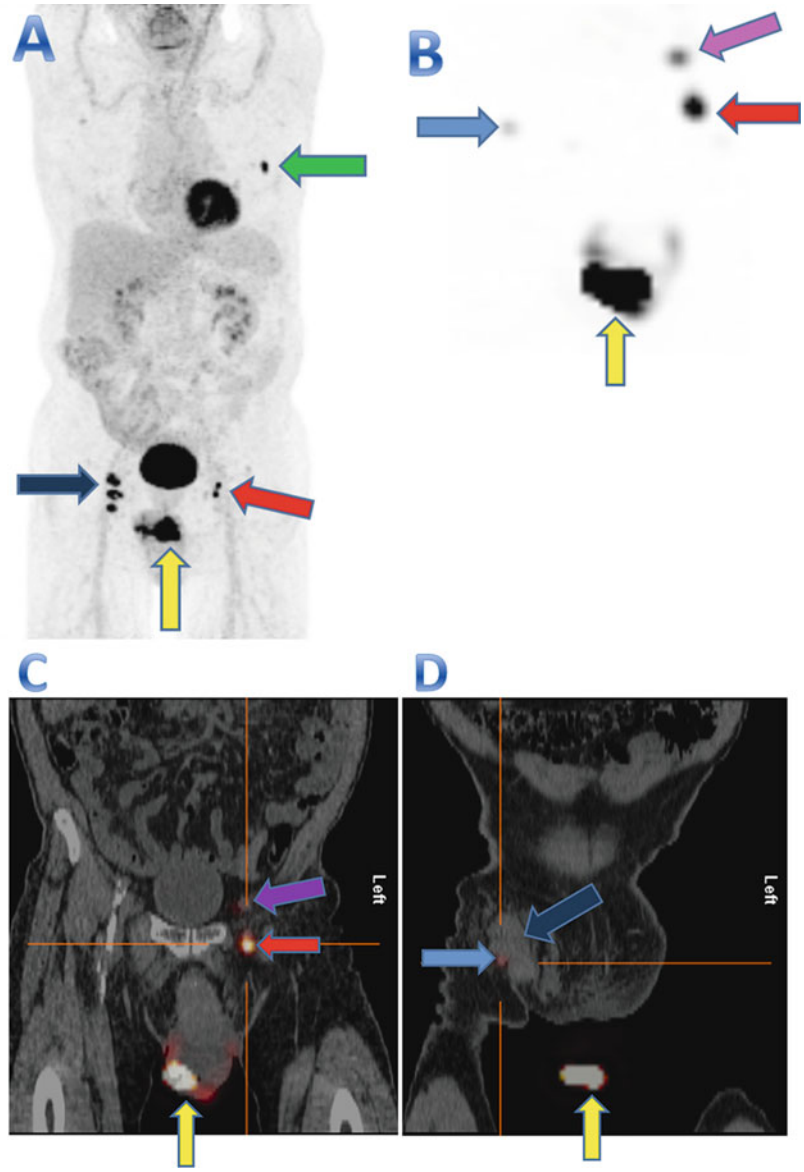

Fig. 4 Yellow arrows: penile tumor, Blue arrows: right inguinal lymph node metastases, Red arrows: left inguinal lymph node metastases, Green arrow: left lung lesion, Purple arrows: lymph node above sentinel node, (**A**) MIP image of [^{18}F]FDG PET, (**B**) ^{99m}Tc Nanocoll image, (**C** and **D**) Coronal fused SPECT/CT images

Referred to [^{18}F]FDG PET/CT scanning for restaging after a local relapse (pT2) was found in the penis stump.

Findings and Follow-Up

SCAN 1

[^{18}F]FDG PET/CT showed a small area of increased tracer uptake in the penis (arrow 1), probably because of the recent surgical excision (or small area of remaining tumor) as well as a single lymph node in the right groin with moderately increased uptake (arrow 2), suspect for possible lymph node metastasis.

A new penectomy was planned together with new sentinel lymph node procedure and excision of nodes from the right groin. Pathology results reported a 3 mm lymph node positive for squamous cell penis cancer. Patient subsequently underwent extensive right groin resection, which

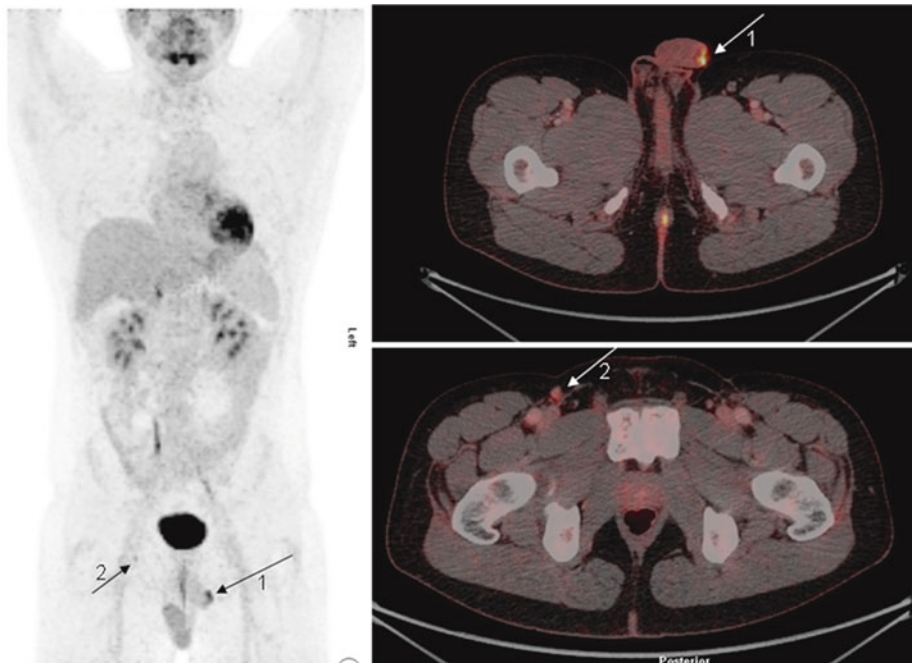

Fig. 5 MIP and axial fusion images. Arrows shows lymph nodes metastases

found no other metastases. Imaging control with 3 months interval was decided.

The 6-month control of the area showed local edema and inflammatory signs in the right groin, and a subsequent MRI of the pelvis showed possible signs of relapse in the region.

Patient was referred to a new restaging [^{18}F] FDG PET/CT (Fig. 5).

SCAN 2

This scan showed edema of the soft tissue of the right thigh and fluid collection in the right groin, possible sequelae to the surgery procedure, with associated abscess/infection.

The scan also found multiple foci in the right groin (arrows), with increased tracer uptake, suspect for new lymph node metastases.

A new surgical approach to the groin was performed to drain the local abscess and to remove these nodes. Pathology showed once again multiple nodular metastasis of low-differentiated squamous cell penis cancer.

Due to verified relapsing disease the patient was referred to chemo-/radiotherapy treatment but showed a poor response to treatment with new signs of relapse in the right groin. The disease developed locally over 1 year until a control CT discovered a new subcutaneous process on the right hip. Excision of this area found cutaneous spreading of squamous cell penis cancer. A new [^{18}F]FDG PET/CT was requested (Fig. 6).

SCAN 3

This scan showed a large multifocal tumor in the right groin (arrows 1) with severely increased [^{18}F]FDG uptake and signs of central necrosis.

Two foci in the left groin with severely increased [^{18}F]FDG uptake (arrows 2), suspect for new nodal metastasis.

Multiple subcutaneous/muscular foci with severe increased [^{18}F]FDG uptake, located in left upper arm, right hip, and right thigh (arrows 3) – suspect for subcutaneous/muscular spreading.

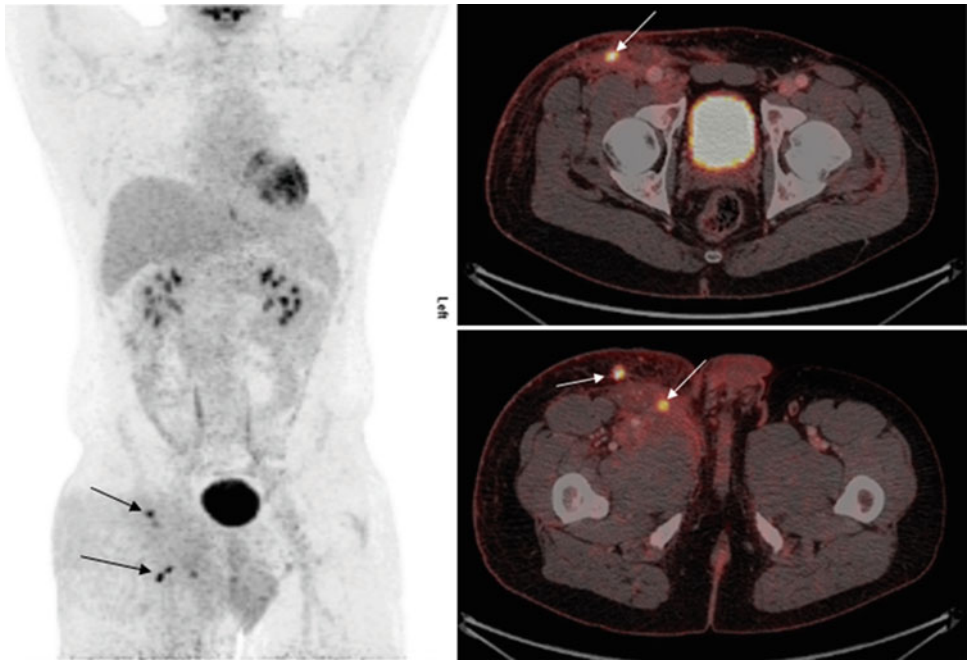

Fig. 6 MIP and axial fusion images. Arrows shows lymph nodes metastases

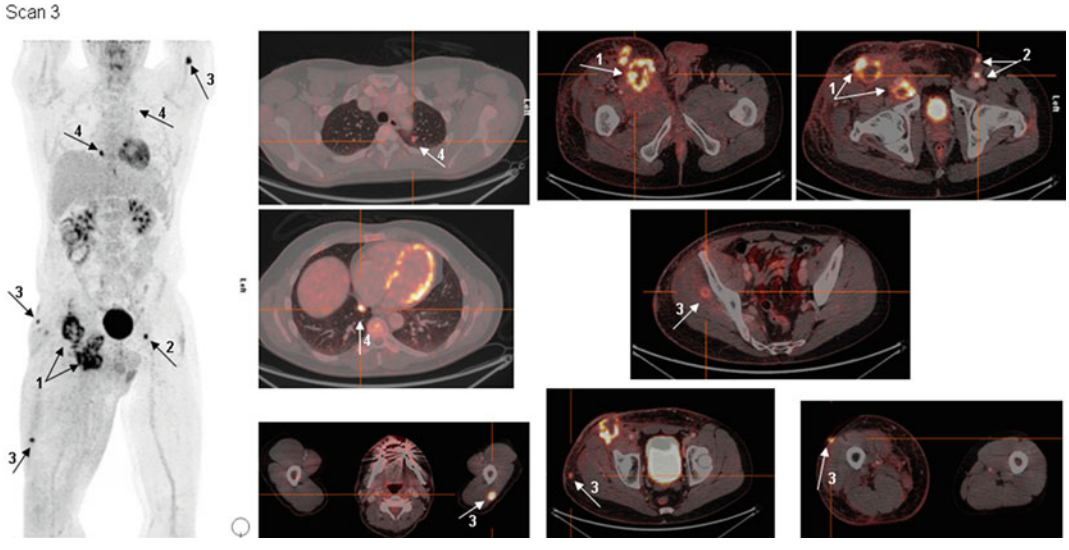

Fig. 7 MIP and axial fusion images. Arrows shows lymph nodes metastases

Bilateral foci in the lunges suspect for lunge metastasis (arrows 4).

Due to the unusual spreading behavior shows in the scan, particularly in regard to subcutaneous sites, a surgical exploration was performed in right thigh and in the left upper arm to verify the etiology of these foci. Pathology results found once again metastasis of squamous cell penis cancer at both sites (Fig. 7).

Discussion

This case exemplifies a case of severely aggressive behavior of a low-differentiated squamous cell penis cancer in a young patient, starting with a simple pT1aN0M0 tumor that evolved very poorly with multiple local relapses with no response to various treatment modalities including local surgical excision together with chemotherapy and radiotherapy and that eventually spread to the lungs and to multiple subcutaneous and muscular sites [2, 3].

References

1. Lützen U, Zuhayra M, Marx M, et al. Value and efficiency of sentinel lymph node diagnostics in patients with penile carcinoma with palpable inguinal lymph nodes as a new multimodal, minimally invasive approach. Eur J Nucl Med Mol Imaging. 2016;43:2313–2323.
2. Zhang S, Li W, Liang F. Clinical value of fluorine-18 2-fluoro-2-deoxy-D-glucose positron emission tomography/computed tomography in penile cancer. Oncotarget. 2016;7:48600–48606.
3. Sadeghi R, Gholami H, Zakavi SR, et al. Accuracy of ^{18}F-FDG PET/CT for diagnosing inguinal lymph node involvement in penile squamous cell carcinoma: systematic review and meta-analysis of the literature. Clin Nucl Med. 2012;37:436–441.

Teaching Cases in Nuclear Oncology: Vulvar Cancer

72

Alice Lorenzoni, Alessandra Alessi, and Flavio Crippa

Keywords

Vulvar cancer • Vaginal cancer • [^{18}F]FDG PET/CT • Restaging • Recurrent vulvar cancer

Glossary

[^{18}F]FDG	2-deoxy-2-[^{18}F]fluoro-D-glucose
CT	X-ray computed tomography
MIP	Maximum intensity projection
PET	Positron emission tomography
PET/CT	Positron emission tomography/computed tomography
RVD	Retroviral disease
SUV	Standardized uptake value
SUV_{max}	Standardized uptake value at point of maximum

Contents

Vulvar Cancer: Case No. 1 1813
Presentation 1813
Findings 1813
Discussion 1814

Vulvar Cancer: Case No. 2 1815
Presentation 1815
Findings 1815
Discussion 1816

Vulvar Cancer: Case No. 3 1816
Presentation 1817
Findings 1817
Discussion 1822

Vulvar Cancer: Case No. 1

Presentation

A 62-year-old woman previously treated with vulvectomy and inguinofemoral lymphadenectomy for squamous vulvar cancer presented with biopsy-proven recurrent disease. [^{18}F]FDG PET/CT was performed to assess the extent of disease.

Findings

[^{18}F]FDG PET/CT shows focal uptake in the right vulvar region consistent with recurrent disease (Fig. 1). Hypermetabolic retroperitoneal bilateral adenopathy was also demonstrated suspicious for lymph node involvement (Fig. 2).

A. Lorenzoni (✉) • A. Alessi • F. Crippa
Nuclear Medicine Division, IRCCCS National Cancer Institute, Milan, Italy
e-mail: alice.lorenzoni@istitutotumori.mi.it; alicelorenzoni@hotmail.it

© Springer International Publishing Switzerland 2017
H.W. Strauss et al. (eds.), *Nuclear Oncology*,
https://doi.org/10.1007/978-3-319-26236-9_75

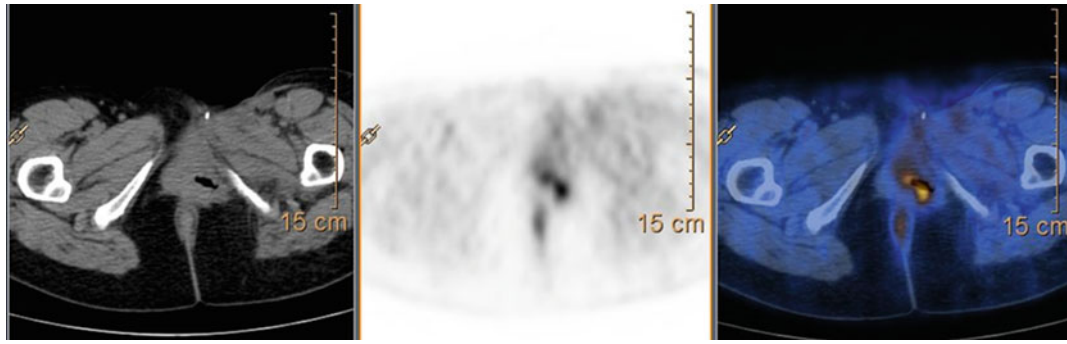

Fig. 1 Axial low-dose CT (*left*), PET, and fused [^{18}F]FDG PET/CT (*right*) images identify recurrent vulvar cancer

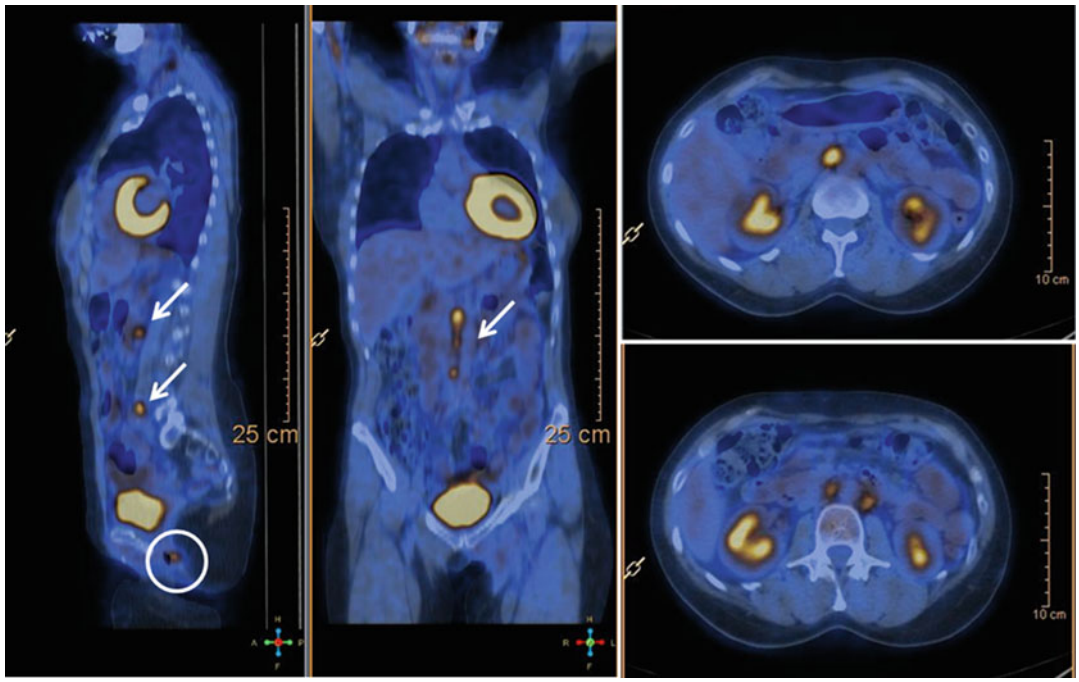

Fig. 2 Fused [^{18}F]FDG PET/CT images show recurrent vulvar cancer (*white circle*) and multiple retroperitoneal pathologic adenopathy (*white arrows*)

Discussion

Vulvar carcinoma is a rare malignancy and it is seen to recur in 30–50% of patients within the first 2 years. The majority of these are local recurrences; however, one third of recurrences are in the groin, associated with a poor prognosis. Accurate evaluation of the disease extent with the identification of distal recurrent disease and lymph node metastases is important to guide which patients may benefit from chemoradiation.

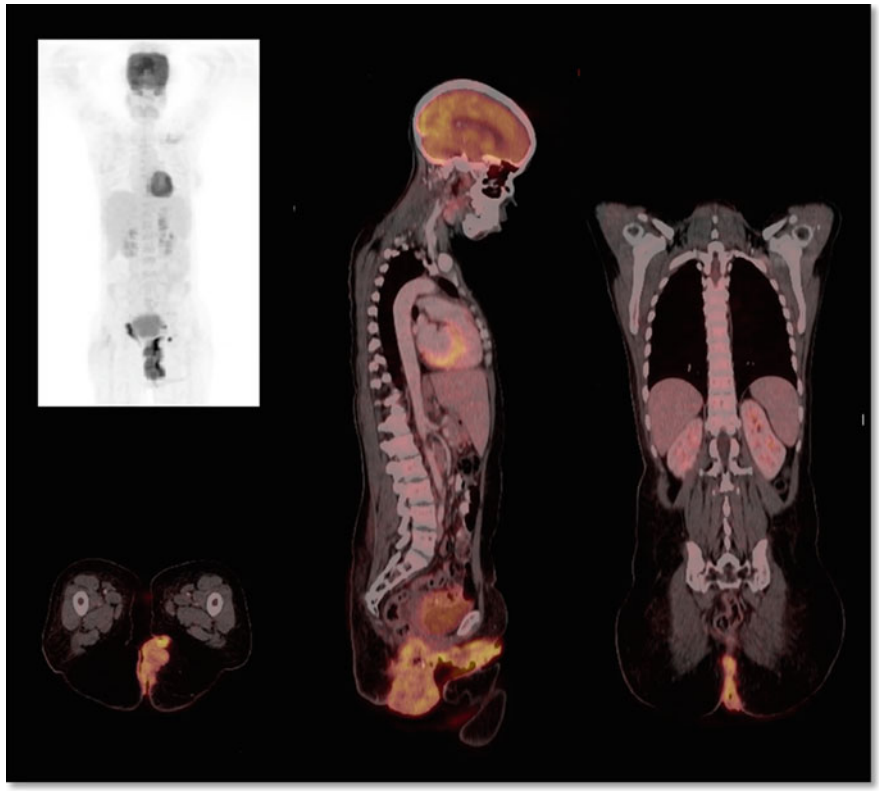

Fig. 3 *Upper left*, [^{18}F]FDG PET/CT MIP image. *Lower left to right*, fused axial, sagittal, and coronal PET/CT images. The images show the [^{18}F]FDG-avid vulvar mass infiltrating the vagina and anal canal

Vulvar Cancer: Case No. 2

Case contributed by: F. Reyneke, M. Sathekge
Nuclear Medicine, University of Pretoria & Steve Biko Academic Hospital, Pretoria, South Africa

Presentation

A 40-year-old woman referred with vulvar carcinoma. She is RVD reactive and on antiretroviral treatment.

Findings

A biopsy taken from the vulvar mass revealed squamous cell carcinoma.

[^{18}F]FDG PET/CT was performed for initial staging of the cancer. [^{18}F]FDG uptake was noted in the fungating vulval mass infiltrating the vagina and anal region (SUV_{max} 12.73) (Figs. 3, 4, and 5) with involvement of bilateral inguinal lymph nodes (SUV_{max} right 11.52, left 10.26) (Fig. 6).

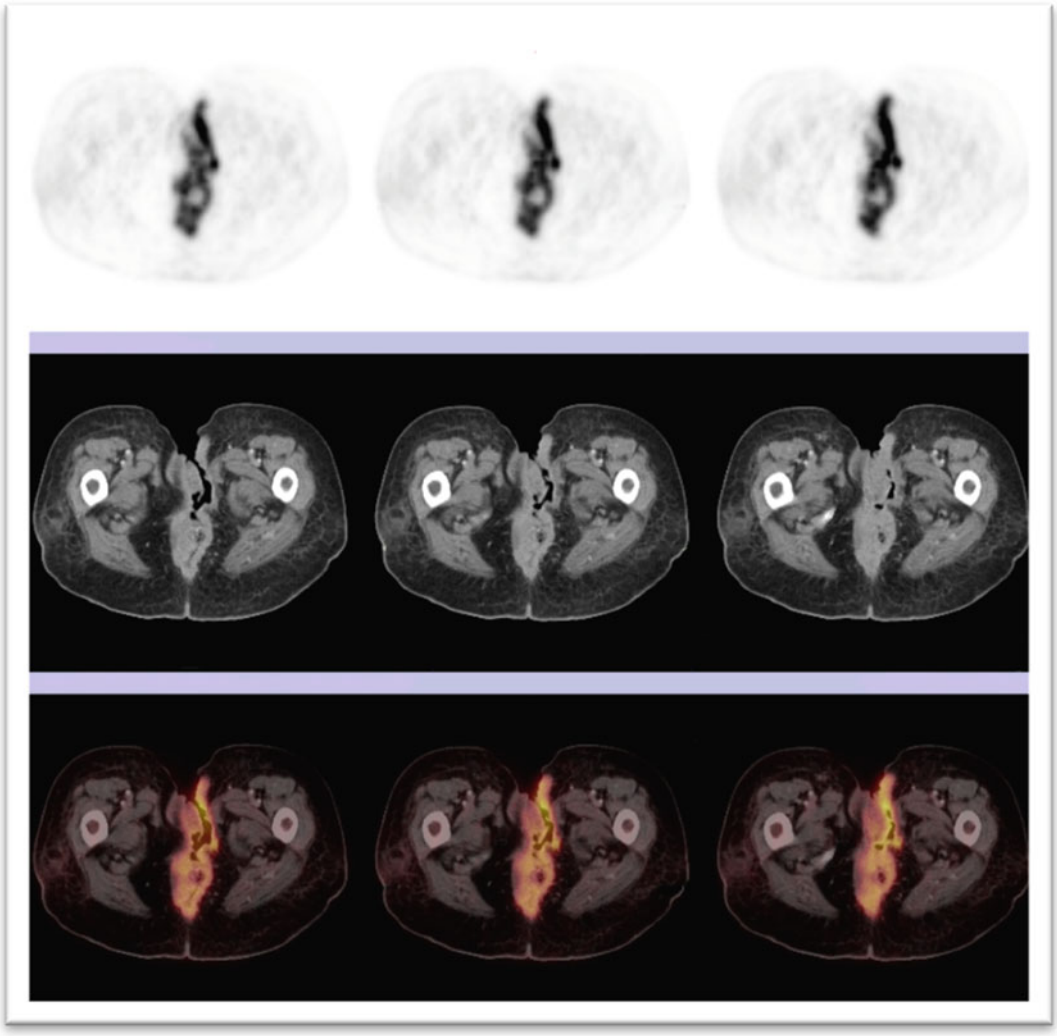

Fig. 4 [^{18}F]FDG PET/CT axial images demonstrating the vulvar mass

Discussion

[^{18}F]FDG PET/CT is a useful imaging modality in the management of vulvar carcinoma, mainly in the identification of nodal metastases. It may affect both surgical planning and clinical management of the patient.

Vulvar Cancer: Case No. 3

Case contributed by: F. Reyneke, M. Sathekge
Nuclear Medicine. University of Pretoria & Steve Biko Academic Hospital, Pretoria, South Africa

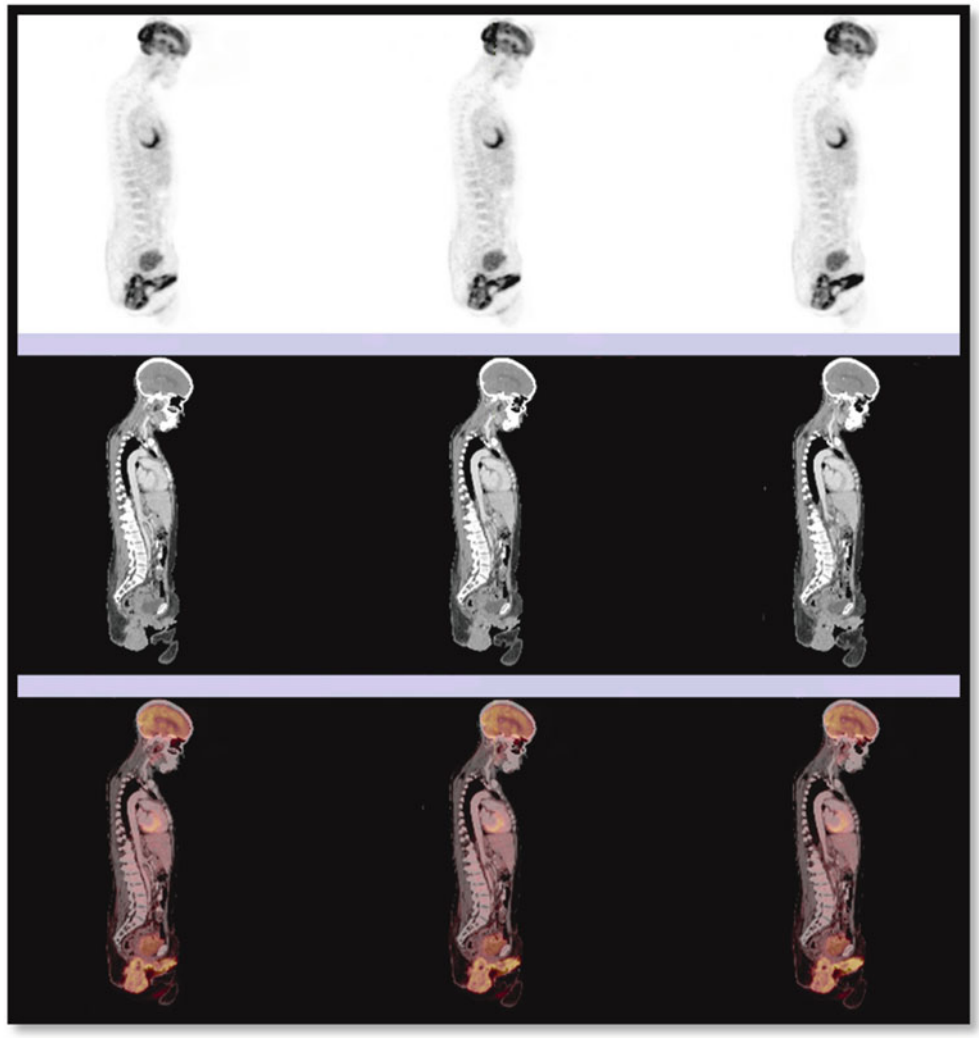

Fig. 5 [^{18}F]FDG PET/CT sagittal images demonstrating the extent of the vulvar mass

Presentation

A 72-year-old woman referred with vaginal carcinoma. The treatment history includes pelvic radiotherapy. She presented with urinary retention post radiotherapy which necessitated the insertion of a suprapubic catheter.

Findings

A biopsy taken from the vaginal mass revealed invasive moderately differentiated keratinizing squamous cell carcinoma.

[^{18}F]FDG PET/CT was performed for restaging post pelvic radiotherapy. [^{18}F]FDG

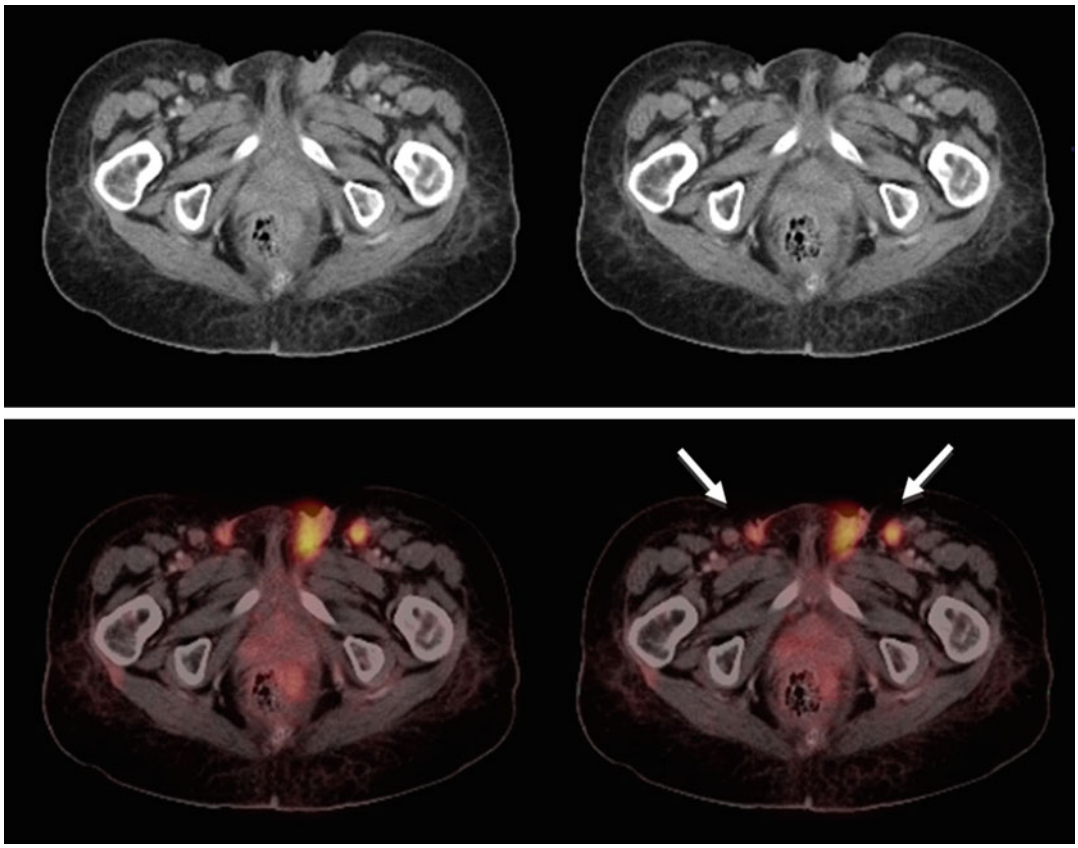

Fig. 6 [^{18}F]FDG PET/CT axial images show bilateral inguinal node involvement

uptake was noted in the vaginal vault extending from the cervix to the labia.

(SUV_{max} 22.28) (Figs. 7, 8, and 9) with multifocal uptake in the cervix (SUV_{max} 56.66) (Fig. 10).

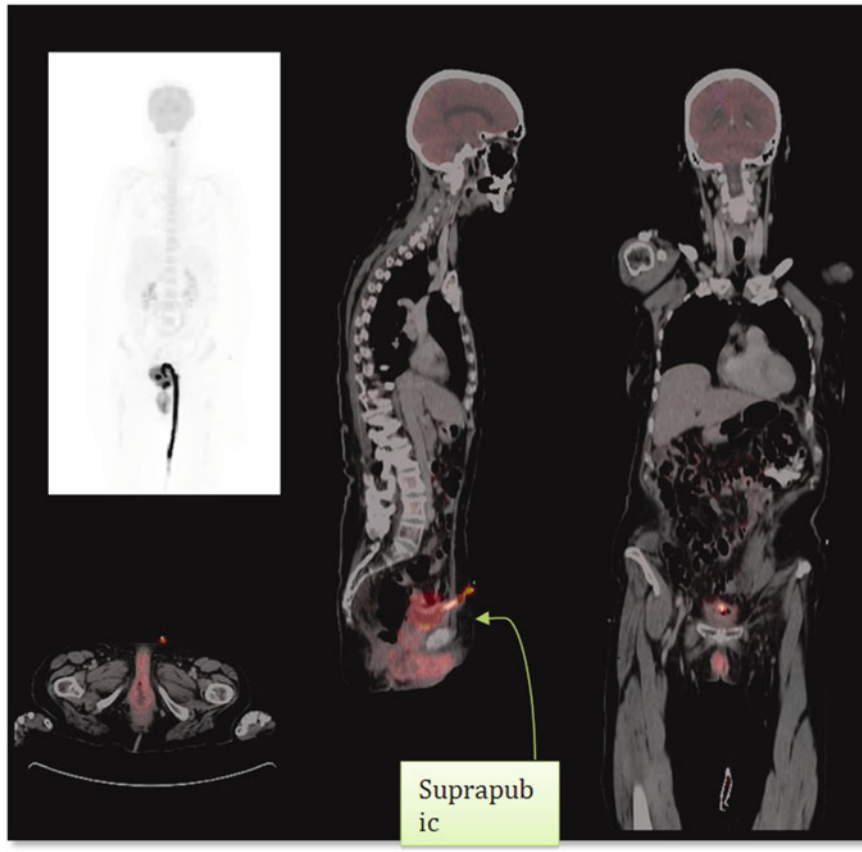

Fig. 7 *Upper left*, [^{18}F]FDG PET/CT MIP image. *Lower left to right*, fused axial, sagittal, and coronal PET/CT images. The images show the [^{18}F]FDG-avid vaginal mass extending to the cervix and labia

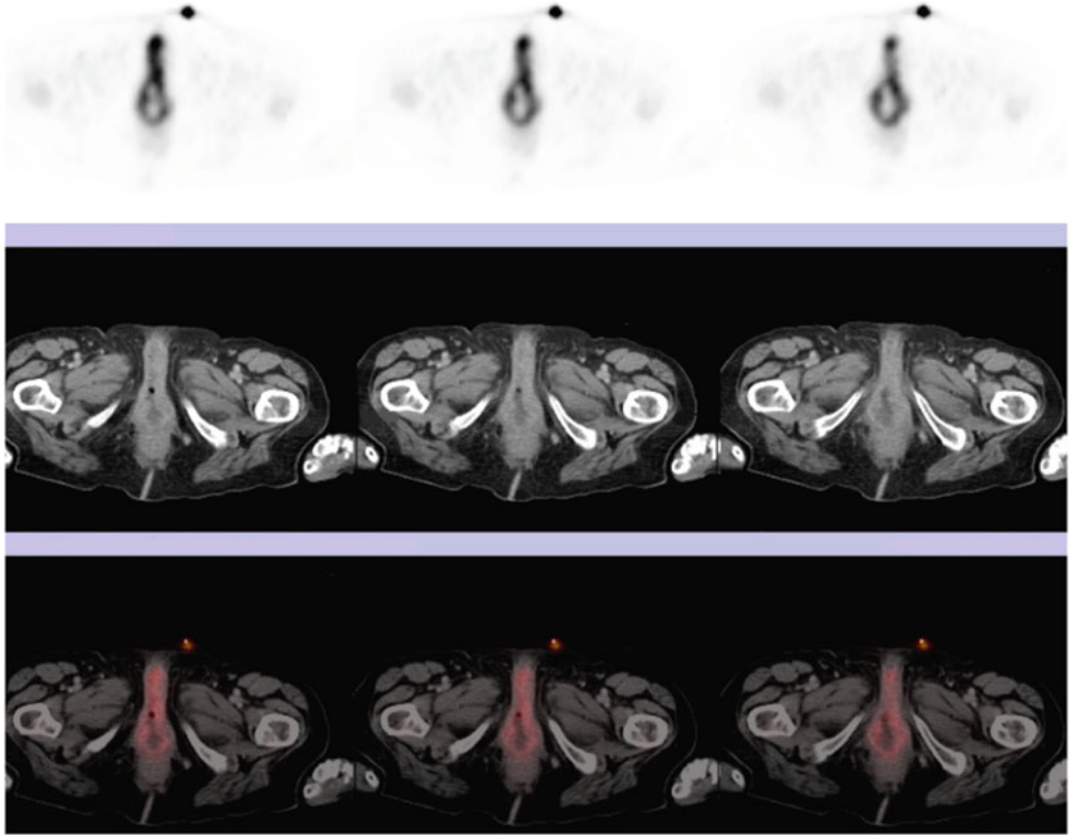

Fig. 8 [^{18}F]FDG PET/CT axial images demonstrating the vaginal mass

Fig. 9 [^{18}F]FDG PET/CT sagittal images demonstrating the extent of the vaginal mass

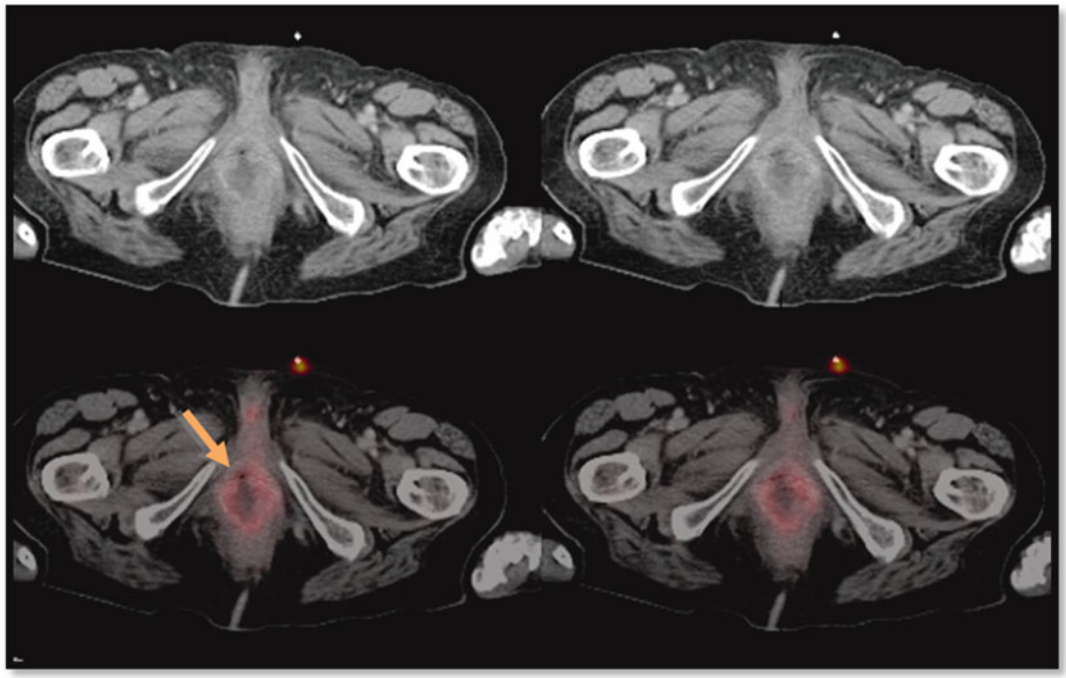

Fig. 10 [^{18}F]FDG PET/CT axial images demonstrating the multifocal uptake in the cervix

Discussion

[^{18}F]FDG PET/CT plays an important role in the management of vaginal carcinoma. It should be considered in the restaging of patients following therapy.

Teaching Cases in Nuclear Oncology: Uterine Cancers

73

Alice Lorenzoni, Alessandra Alessi, and Flavio Crippa

Keywords

Recurrent cervical cancer • Uterine cancer • [^{18}F]FDG PET/CT • Staging uterine cancer

Glossary

[^{18}F]FDG	2-Deoxy-2-[^{18}F]fluoro-D-glucose
BI-RADS	Breast Imaging Reporting and Data System according to the American College of Radiology
CT	X-ray computed tomography
CTV	Clinical target volume
FIGO	International Federation of Gynecology and Obstetrics
GTV	Gross tumor volume
Gy	Gray unit (ionizing radiation dose in the International System of Units, corresponding to the absorption of one joule of radiation energy per kilogram of matter)
MIP	Maximum intensity projection
MRI	Magnetic resonance imaging
PET	Positron emission tomography
PET/CT	Positron emission tomography/Computed tomography
RT	Radiation therapy
SUV	Standardized uptake value
SUV_{max}	Standardized uptake value at point of maximum
VMAT-SIB	Volumetric-modulated radiotherapy-simultaneous-integrated boost

Contents

Uterine Cancers: Case No. 1 1824
Presentation 1824
Findings 1824
Discussion 1824

Uterine Cancers: Case No. 2 1824
Presentation 1824
Findings 1824
Discussion 1824

Uterine Cancers: Case No. 3 1824
Presentation 1824
Findings 1826
Discussion 1826

Uterine Cancers: Case No. 4 1826
Presentation 1828
Findings 1828
Discussion 1828

Uterine Cancers: Case No. 5 1830
Presentation 1830
Findings 1830
Discussion 1831

Uterine Cancers: Case No. 7 1831
Presentation 1831
Findings 1831
Discussion 1832

A. Lorenzoni (✉) • A. Alessi • F. Crippa
Nuclear Medicine Division, IRCCCS National Cancer Institute, Milan, Italy
e-mail: alice.lorenzoni@istitutotumori.mi.it; alicelorenzoni@hotmail.it

© Springer International Publishing Switzerland 2017
H.W. Strauss et al. (eds.), *Nuclear Oncology*,
https://doi.org/10.1007/978-3-319-26236-9_76

Uterine Cancers: Case No. 7 1832
Presentation 1832
Findings 1832
Discussion 1832

Uterine Cancers: Case No. 8 1832
Presentation 1834
Findings 1834
Follow-Up 1835

Uterine Cancers: Case No. 9 1836
Presentation 1836
Findings 1836
Discussion 1836

References 1840

Uterine Cancers: Case No. 1

Presentation

A 38-year-old woman with recently diagnosed locally advanced cervical carcinoma referred for [^{18}F]FDG PET/CT staging.

Findings

PET/CT confirms the presence of hypermetabolic cervical lesion and [^{18}F]FDG-avid pelvic lymph nodes (Fig. 1). In addition, hypermetabolic para-aortic, intercavo-aortic, mediastinal, and retro-clavicular lymphadenopathy was seen (Fig. 2).

Discussion

[^{18}F]FDG PET may be useful in staging cervical cancer due to the ability to detect local pelvic and distant nodal status.

Uterine Cancers: Case No. 2

Presentation

A 42-year-old woman with metastatic cervical squamous cell carcinoma referred after chemotherapy completion to evaluate treatment response.

Findings

[^{18}F]FDG PET/CT at baseline showed intense [^{18}F]FDG pathological uptake in the cervical mass (Fig. 3a). Multiple hypermetabolic lymph nodes were seen in para-uterine, common, and internal iliac regions (Fig. 4a). Focal [^{18}F]FDG uptake was noted in segment 6 of the liver consistent with hepatic metastases (Fig. 5a). In addition, skeletal hypermetabolic lesion was demonstrated in the left ischiopubic ramus (Fig. 4a).

[^{18}F]FDG PET/CT after chemotherapy showed metabolic response of the cervical mass (Fig. 3b) and pelvic lymph nodes (Fig. 4b). Partial metabolic response was observed in liver metastases. No [^{18}F]FDG uptake was demonstrated in the left ischiopubic branch after therapy. However, the appearance of focal [^{18}F]FDG uptake consistent with skeletal metastases was noted in the right hemisacrum (Fig. 6).

Discussion

[^{18}F]FDG PET is useful in the post-therapy assessment of response in patients with advanced and metastatic cervical cancer. [^{18}F]FDG PET is an important diagnostic tool also to predict response early during the course of chemotherapy. Furthermore, literature data show that [^{18}F]FDG response to therapy may permit an accurate prediction of patient survival.

Uterine Cancers: Case No. 3

Presentation

A 69-year-old woman presented with pelvic pain and vaginal bleeding. Physical examination revealed tumor growth confined to the cervix with no signs of extension to the vagina. A cervical biopsy showed moderately differentiated (tumor grade II) large-cell nonkeratinizing squamous cell carcinoma of the cervix uteri. MRI of the pelvis shows T2 hyperintense pathological mass involving the right posterolateral cervix (Fig. 7).

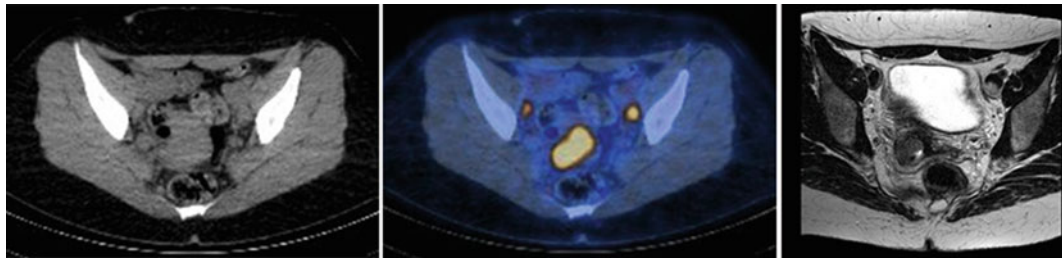

Fig. 1 [^{18}F]FDG-avid lesion of the cervix and bilateral pelvic lymphadenopathy. MRI (*right panel*) of primary tumor

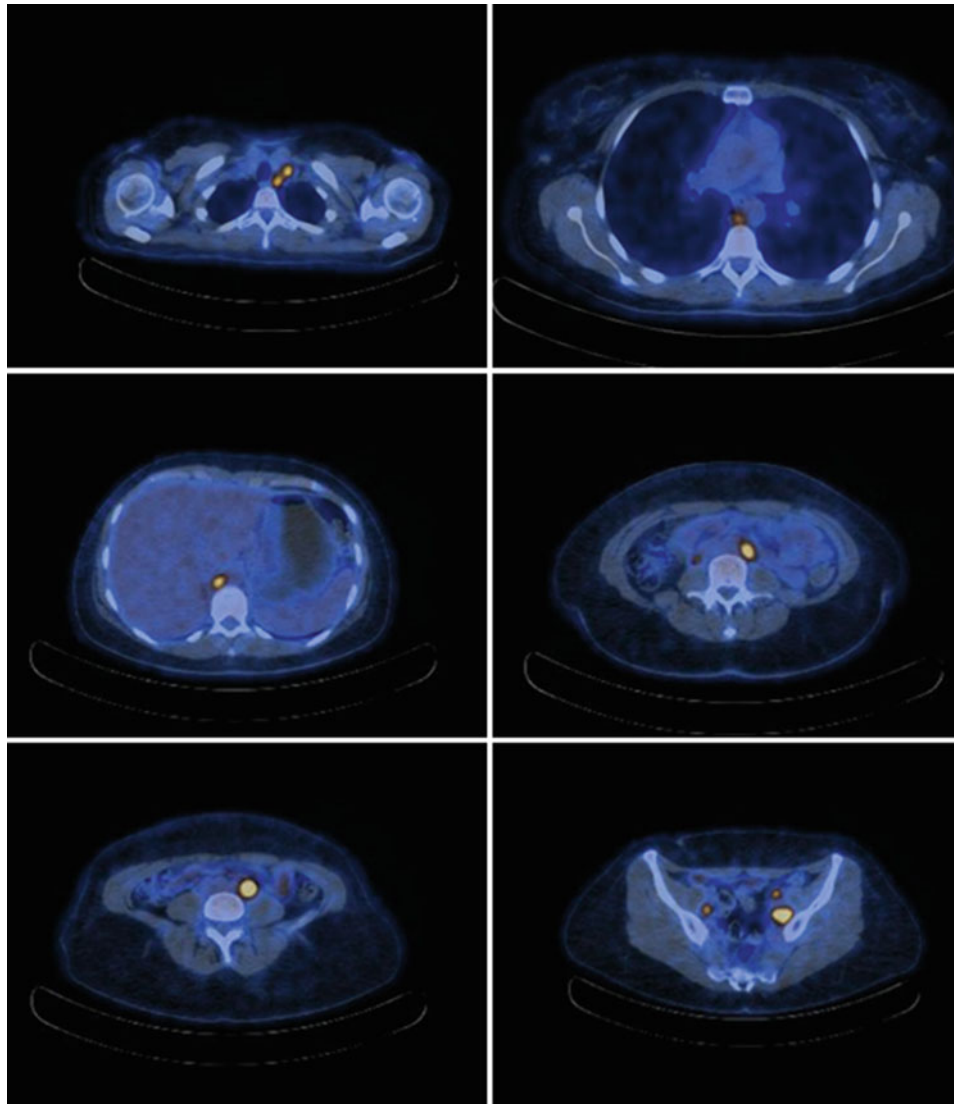

Fig. 2 Transaxial fused [^{18}F]FDG PET/CT image of hypermetabolic lymphadenopathies of the pelvis, abdomen, and thorax

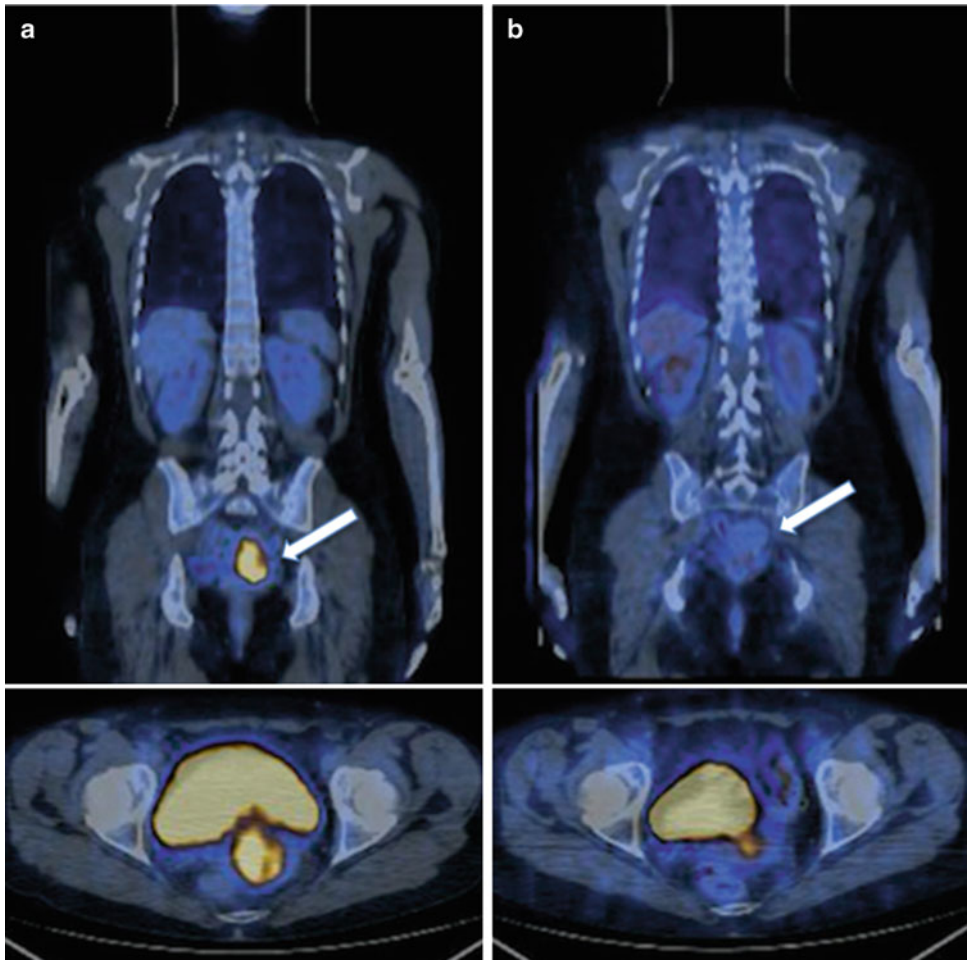

Fig. 3 Fused [^{18}F]FDG PET/CT images of hypermetabolic cervical tumor before (**a** *white arrow*) and after chemotherapy (**b** *white arrow*)

[^{18}F]FDG PET/CT was performed to assess disease extension.

Findings

[^{18}F]FDG PET/CT images showed area of increased [^{18}F]FDG uptake in the cervix corresponding to malignant tumor (Fig. 8). No other foci of [^{18}F]FDG uptake were shown in the pelvic region. A mildly [^{18}F]FDG-avid focus was noted in the left breast (Fig. 9).

Mammogram showed a spiculated 1-cm opacity highly suspicious of malignancy (BI-RADS 5) in the left equatorial external quadrant (Fig. 9).

Discussion

When an unexpected focus of [^{18}F]FDG uptake is detected in the breast during an [^{18}F]FDG examination performed for other reasons, it is prudent to characterize the lesion with additional imaging and/or biopsy, because of the high risk of malignancy of 30% [1].

Uterine Cancers: Case No. 4

Case contributed by: T. Lengana, M. Sathekge
Nuclear Medicine, University of Pretoria & Steve Biko Academic Hospital, Pretoria, South Africa

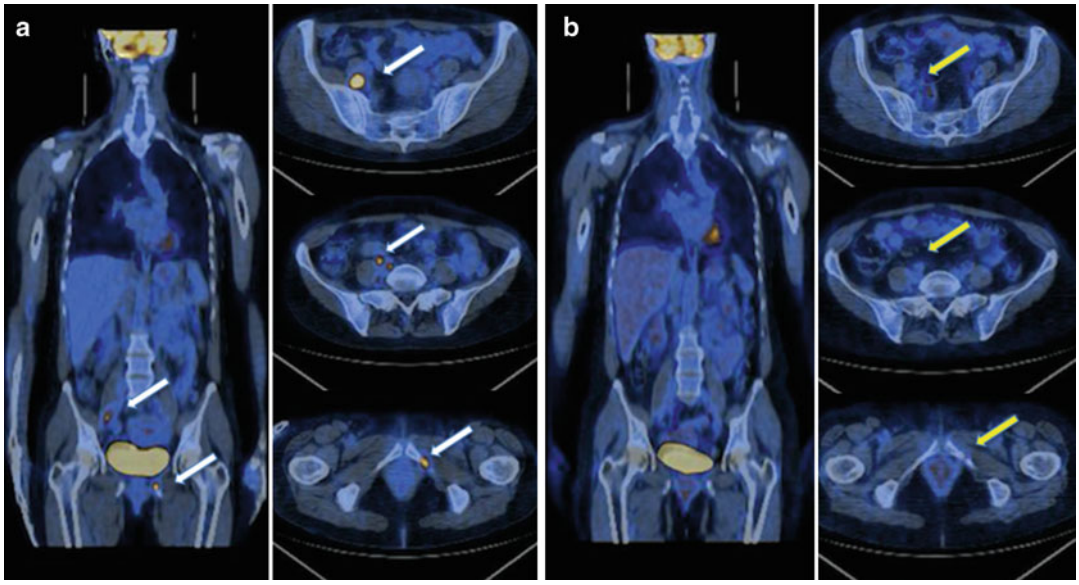

Fig. 4 Fused [^{18}F]FDG PET/CT images of metabolic response of pelvic lymph nodes and left ischiopubic ramus in patients with metastatic cervical cancer (**a** baseline study, **b** after therapy)

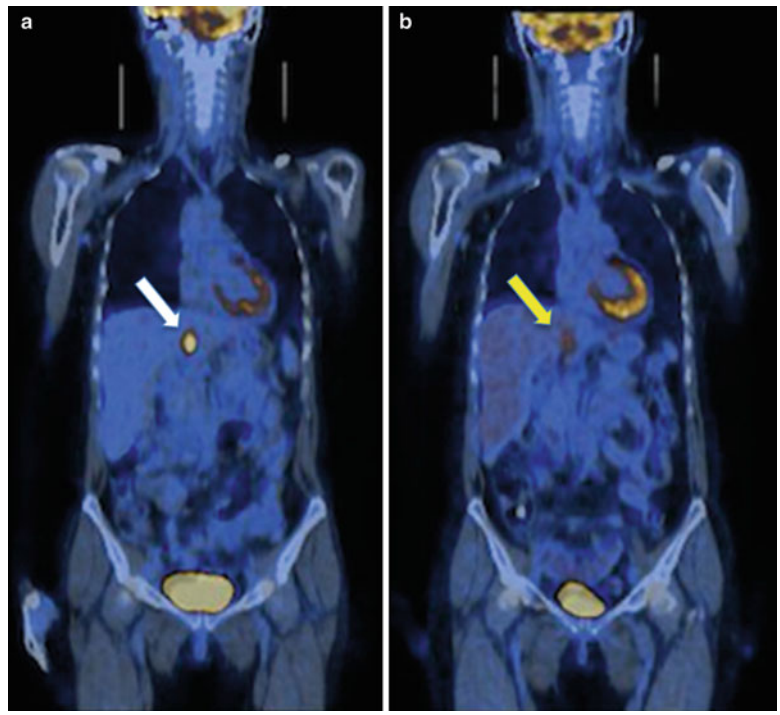

Fig. 5 Coronal fused [^{18}F] FDG PET/CT images of hepatic metastases before (**a** *white arrow*) and after chemotherapy (**b** *yellow arrow*)

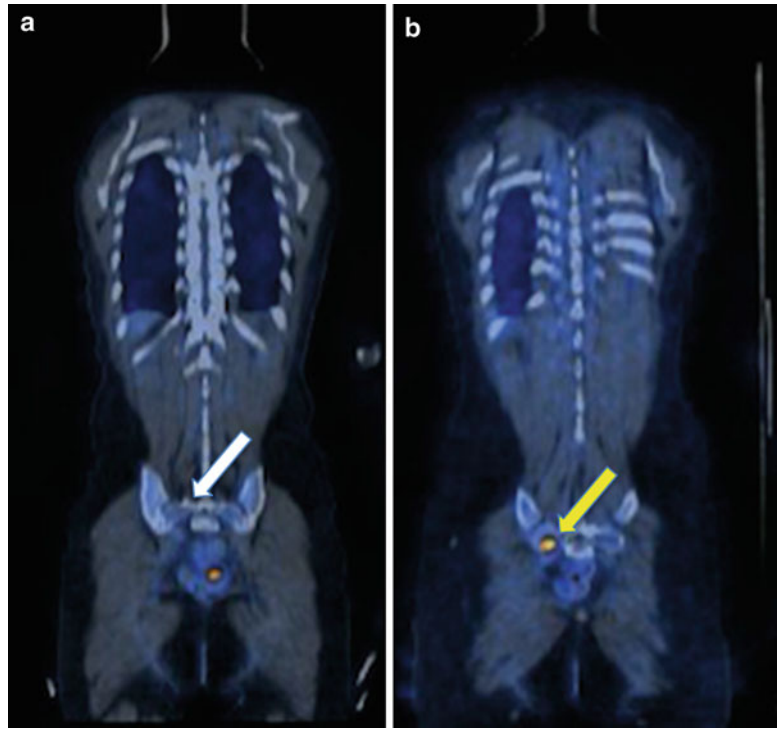

Fig. 6 Coronal fused PET/CT images show the appearance of focal [^{18}F]FDG uptake in the right hemisacrum (**b**, *yellow arrow*). In baseline study no pathological [^{18}F]FDG uptake is seen (**a** *white arrow*)

Fig. 7 T2 hyperintense pathological mass involving the cervix on pelvis MRI (*red arrow*)

Presentation

A 69-year-old woman with cancer of the cervix managed with pelvic radiotherapy 30 years ago.

Patient presented with vesicovaginal fistula a year ago, and biopsy demonstrated infiltrating moderately differentiated adenocarcinoma with focal neuroendocrine differentiation.

Repeat biopsy 1 year later demonstrated no evidence of malignancy.

Findings

An [^{18}F]FDG PET/CT scan was performed for follow-up. [^{18}F]FDG PET/CT images demonstrated local recurrence (SUV_{max} 12.4) with liver metastases and widespread nodal metastases (inguinal, obturator, para-aortic, retrocrural, mediastinal, and left supraclavicular).

Discussion

This case demonstrates that [^{18}F]FDG PET/CT can be useful in the assessment of patients with suspected cervical cancer recurrence.

Fusion images demonstrating liver metastases. CT images demonstrating the liver metastases.

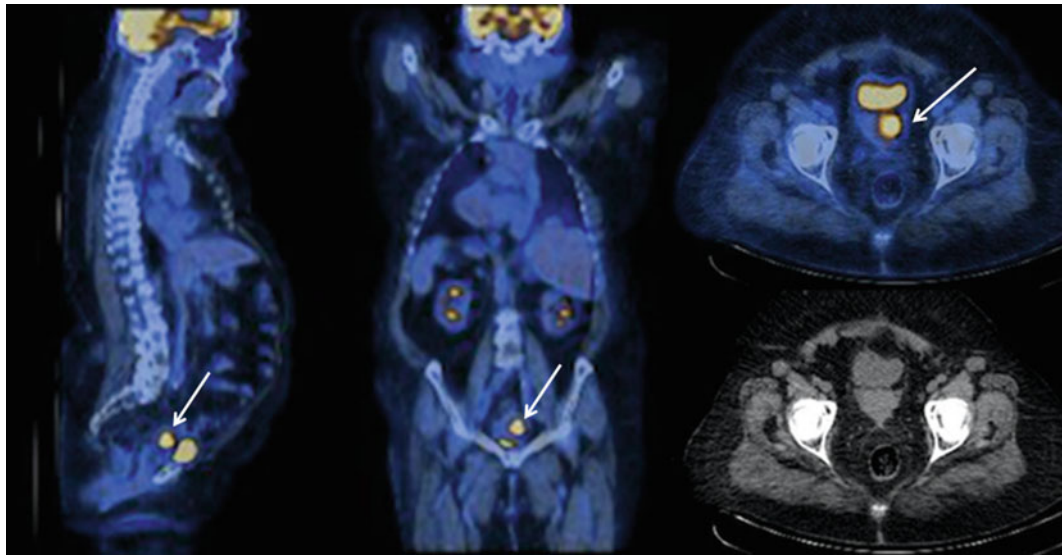

Fig. 8 Coronal (*left*), sagittal (*middle*), axial (*upper right*) fused [^{18}F]FDG PET/CT and axial low-dose CT (*lower right*) images show hypermetabolic cervical lesion

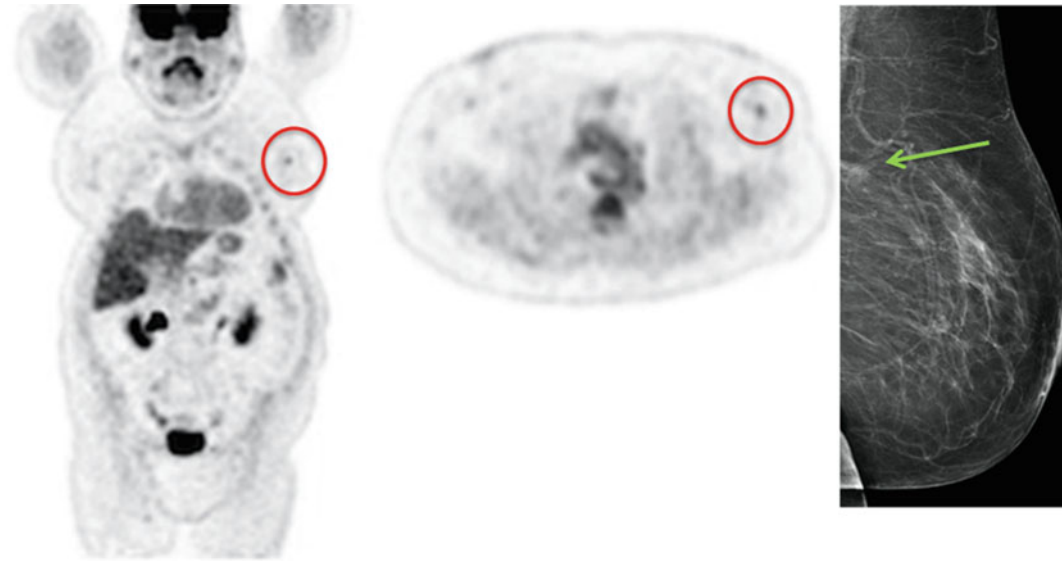

Fig. 9 Sagittal (*left*) and axial (*middle*) PET images identify small area of mild [^{18}F]FDG uptake in the left breast (*red circle*). Mammogram of the left breast (*right*) depicts opacity highly suspicious of malignancy (BI-RADS 5) (*green arrow*)

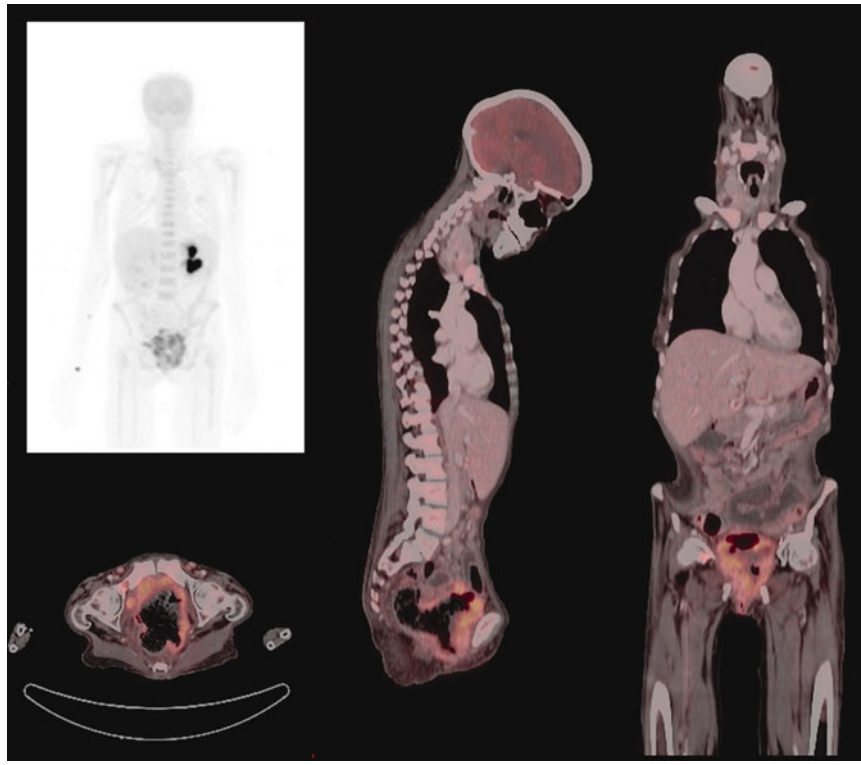

Fig. 10 *Upper left*, [^{18}F]FDG PET/CT MIP image. *Lower left to right*, fused axial, sagittal, and coronal PET/CT images. The images show the [^{18}F]FDG-avid mass involving the distal vagina infiltrating the vulva, bladder, and rectum

[^{18}F]FDG PET images demonstrating supraclavicular node and para-aortic nodes.

Uterine Cancers: Case No. 5

Case contributed by: F. Reyneke, M. Sathekge
Nuclear Medicine, University of Pretoria & Steve Biko Academic Hospital, Pretoria, South Africa

Presentation

A 59-year-old woman presented with a fungating vaginal mass and a rectovaginal fistula. She was diagnosed with cervical cancer 9 years earlier for which a radical hysterectomy was done followed by radiotherapy.

Findings

A biopsy taken from the lateral vaginal wall revealed invasive keratinizing squamous cell carcinoma grade II (presumed recurrence).

[^{18}F]FDG PET/CT was performed to detect suspected recurrence. [^{18}F]FDG uptake was noted in the irregular soft tissue mass involving the distal vagina with infiltration of the bladder, rectum, and vulva, with SUV_{max} 10.1 (Fig. 10). Regional lymph nodes and bones were also involved. In addition, minimal [^{18}F]FDG uptake was noted in the right kidney with hydronephrosis and a hydroureter secondary to extensive cervical tumor infiltration (Fig. 11).

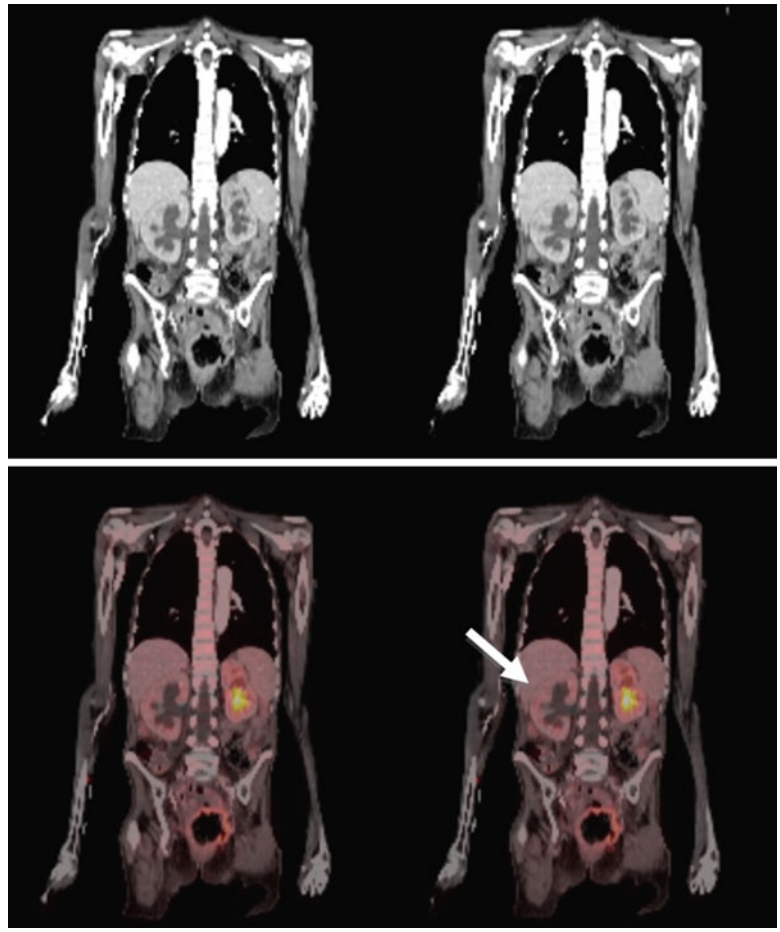

Fig. 11 [^{18}F]FDG PET/CT coronal images demonstrating reduced [^{18}F]FDG uptake in the right kidney associated with hydronephrosis and hydroureter

Discussion

This case confirms the value of [^{18}F]FDG PET/CT in the management of suspected recurrence of cervical cancer.

Uterine Cancers: Case No. 7

Presentation

A 73-year-old woman presented with vaginal bleeding and pelvic discomfort. Hysteroscopy showed endometrial lesion with cerebroid aspect. Endometrial biopsy demonstrated adenocarcinoma grade III with 60% Ki67 proliferation index. Pelvic MRI showed large lesion (74 mm in size) with myometrial infiltration. [^{18}F]FDG PET/CT was performed as part of initial staging before planned surgery.

Findings

[^{18}F]FDG PET/CT demonstrates increased uptake in the entire uterus consistent with endometrial cancer and [^{18}F]FDG-avid lymph nodes in internal-external iliac right regions (Fig. 12). In addition a small hypermetabolic nodule was noted in the gastrosplenic region consistent with peritoneal implant.

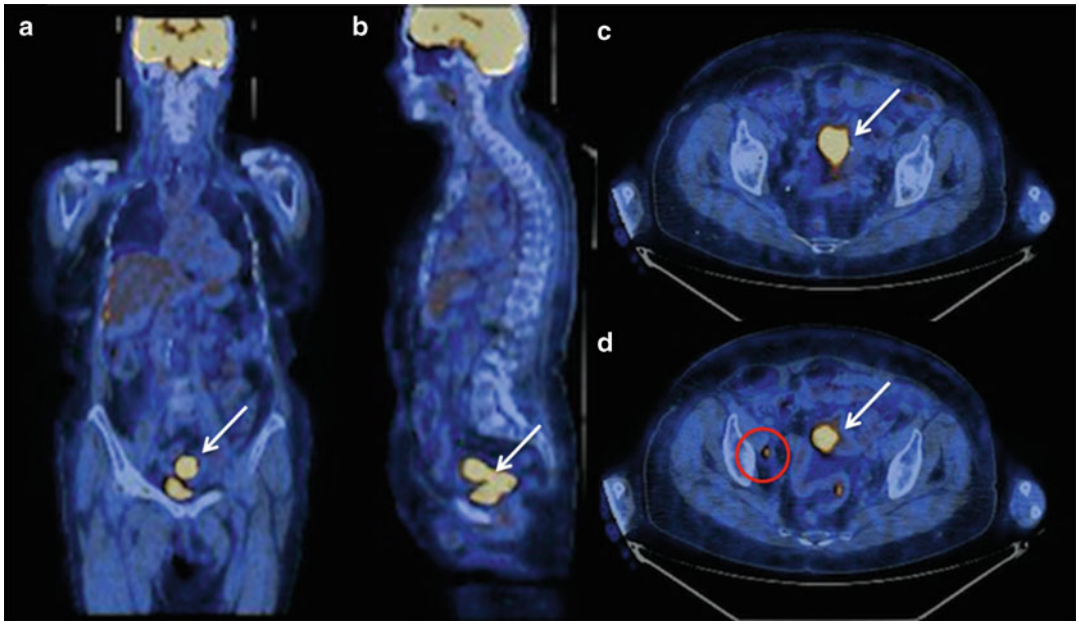

Fig. 12 Fused PET/CT images demonstrate increased uptake in the entire uterus consistent with hypermetabolic malignancy (*white arrow*). In addition focal [^{18}F]FDG-avid pelvic lymph node is seen (*red circle*)

The patient underwent hysterectomy and bilateral salpingo-oophorectomy, multiple peritoneal and lymph node biopsies, and peritoneal washing. Histology obtained after surgery confirmed the [^{18}F]FDG-PET findings.

Discussion

This case confirms the value of [^{18}F]FDG-PET/CT for detecting lymph node involvement and distant metastases (Fig. 13).

Uterine Cancers: Case No. 7

Presentation

A 69-year-old woman previously treated for stage II endometrial cancer referred for suspected vaginal cuff recurrence.

Findings

[^{18}F]FDG PET/CT images demonstrated intense [^{18}F]FDG uptake in the vagina cuff consistent with recurrent disease (Fig. 14). Also prominent [^{18}F]FDG-avid area in the retroperitoneal left para-aortic region consistent with lymph node metastases (Figs. 14 and 15). The patient was treated with chemotherapy.

Discussion

[^{18}F]FDG PET/CT is a highly sensitive (72–95%) and specific (91–96%) modality for detecting recurrence in post-therapy patients with endometrial cancer and identifying locoregional and metastatic disease.

Uterine Cancers: Case No. 8

D. Neriman, J.P. Connelly, K. Al-Riyami

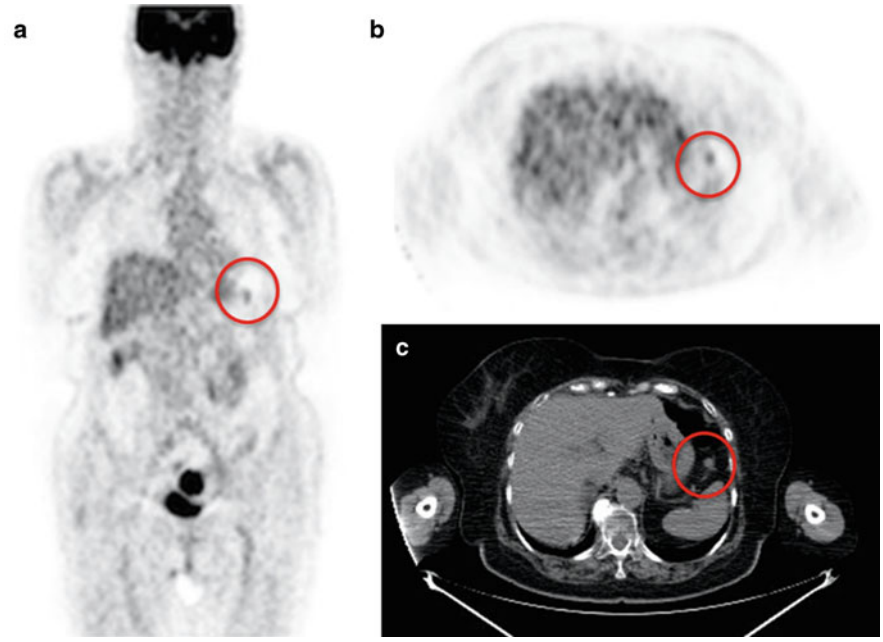

Fig. 13 [^{18}F]FDG PET/CT (**a** coronal, **b** axial) and low-dose CT images (**c**, axial) of hypermetabolic peritoneal implant (*red circle*)

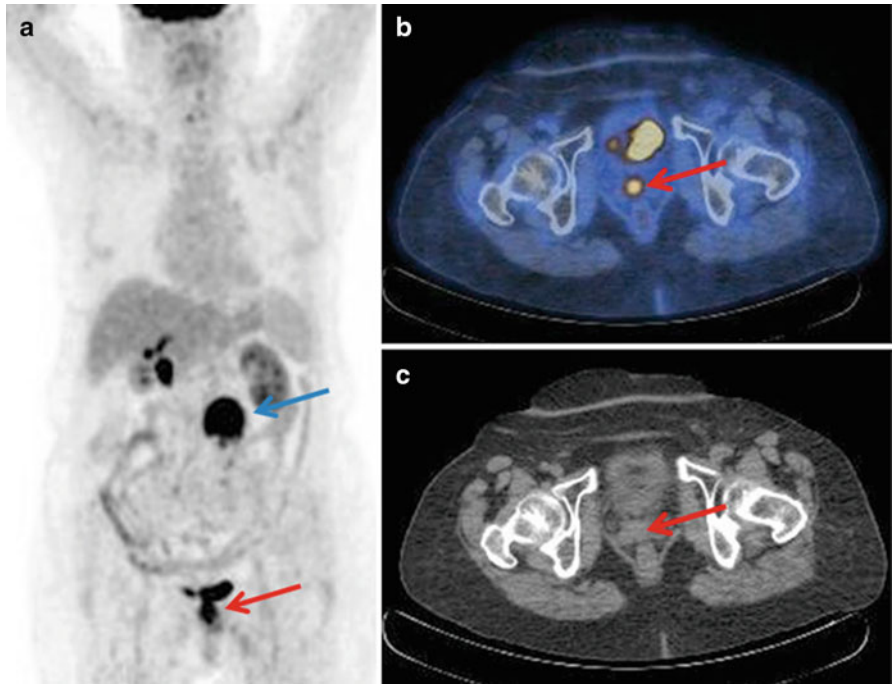

Fig. 14 Maximum-intensity-projection (*MIP*) image (**a**) and axial images (**b** fused PET/CT, **c** low-dose CT) show vaginal recurrence in patient with endometrial cancer (*red arrow*). MIP image also demonstrates hypermetabolic retroperitoneal adenopathy (*blue arrow*)

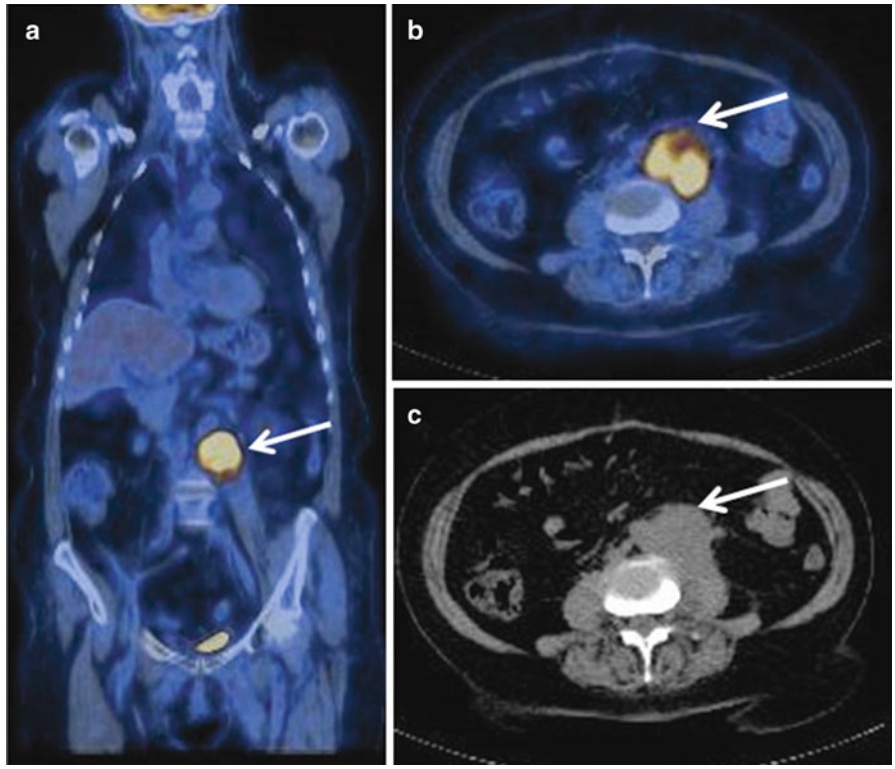

Fig. 15 Coronal and axial fused [^{18}F]FDG PET/CT (**a** and **b,** respectively) images and axial low-dose CT image (**c**) of pathological hypermetabolic retroperitoneal adenopathy

Institute of Nuclear Medicine, UCLH NHS Foundation Trust, London, UK

Presentation

A 72-year-old woman presented with vaginal bleeding. She had a past medical history of FIGO stage I endometrial cancer (serous papillary) which was treated with hysterectomy, oophorectomy, and omentectomy. An [^{18}F]FDG PET/CT was performed as part of the surgical workup to assess the extent of recurrent and metastatic disease.

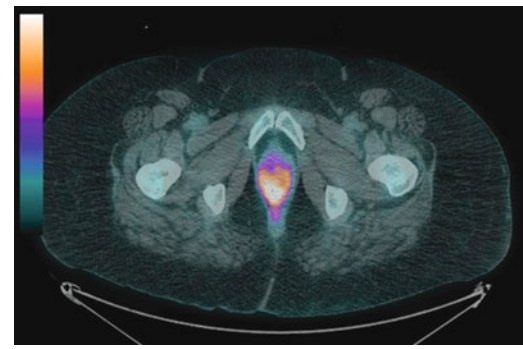

Fig. 16 Axial fused [^{18}F]FDG PET/CT showing intense uptake in the vaginal vault consistent with recurrence

Findings

[^{18}F]FDG PET/CT showed an avid mass within the vaginal vault (SUV_{max} 11.0) with no local or distant disease, in keeping with recurrent tumor (Fig. 16); biopsy revealed carcinosarcoma. The patient subsequently underwent upper vaginectomy and resection of vault recurrence.

Fig. 17 Axial contrast CT showing enhancing lesion in the right pelvis (resection bed)

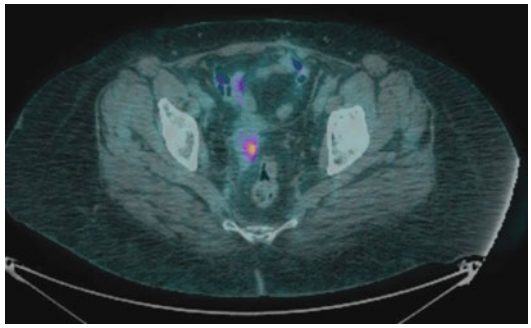

Fig. 18 Axial fused [^{18}F]FDG PET/CT showing heterogeneous [^{18}F]FDG-avid uptake in the resection bed lesion

Follow-Up

Thirteen months following chemotherapy and radiotherapy, the patient developed abnormal liver function tests. Contrast CT and [^{18}F]FDG PET/CT were repeated to assess for liver metastases and restage the disease. Contrast CT shows an enhancing lesion in the right pelvis (Fig. 17).

[^{18}F]FDG PET/CT shows this lesion to be heterogeneously [^{18}F]FDG avid (SUV_{max} 6.7) (Fig. 18) with associated hydronephrosis and hydroureter (Figs. 19 and 20). There is no [^{18}F]FDG activity in the dilated right pelvicalyceal system, with most of the tracer remaining in the renal parenchyma, compatible with acute obstruction. There was no other [^{18}F]FDG-avid disease or liver metastases.

Fig. 19 Coronal [^{18}F]FDG PET/CT showing right hydronephrosis and ureter secondary to pelvic recurrence

Fig. 20 Coronal [^{18}F]FDG MIP showing right hydronephrosis and ureter secondary to pelvic recurrence

[^{18}F]FDG PET/CT has an important role in evaluating recurrence postoperatively in endometrial cancer patients, with the extent of lymph node involvement affecting treatment options.

Uterine Cancers: Case No. 9

Case contributed by: L. Deantonio[1], F. Orsini[2], R. Matheoud[3], M. Krengli[1], G.M. Sacchetti[2]

[1]Radiotherapy Unit, "Maggiore della Carità" University Hospital" and Department of Translational Medicine, University of "Piemonte Orientale" University, Novara, Italy

[2]Section of Nuclear Medicine, «Maggiore della Carità» University Hospital, Novara, Italy

[3]Section of Medical Physics, «Maggiore della Carità» University Hospital, Novara, Italy

Presentation

A 65-year-old woman with squamous cell cervical cancer presents with vaginal bleeding.

Findings

For cervical cancer, staging is largely performed by clinical evaluation, which revealed a tumor with left parametrial invasion stage IIB according to the International Federation of Gynecology and Obstetrics (FIGO) surgical staging system.

Pelvic CT confirmed a cervical lesion (5.5 cm) and enlarged pelvic lymph nodes (Fig. 21). MRI was not performed because the patient was claustrophobic.

After a multidisciplinary meeting with the surgeon, radiation oncologist, medical oncologist, and radiologist, a combination of radiation and chemotherapy was recommended.

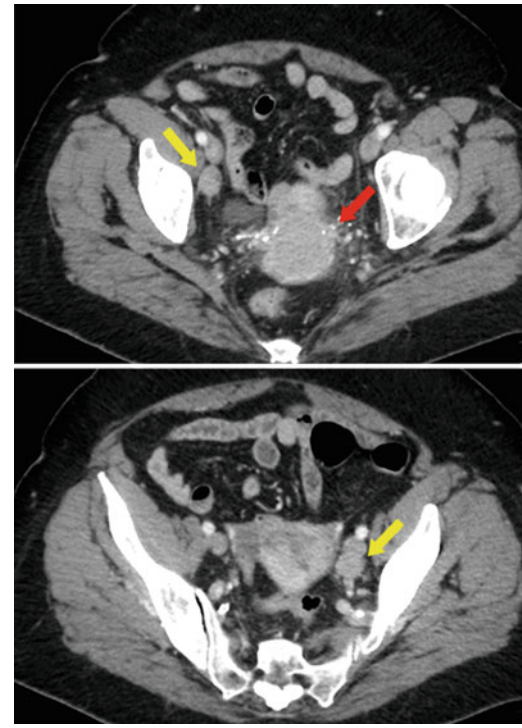

Fig. 21 Pelvic CT in axial view demonstrating the primary tumor (*red arrow*) and bilateral enlarged lymph nodes (*yellow arrows*)

Discussion

[^{18}F]FDG PET/CT was performed in radiation treatment planning position to better define target volumes and evaluate the presence and extension of disease (Fig. 22). PET/CT in cervical cancer is useful for defining lymph node volume for RT coverage. In particular, [^{18}F]FDG PET/CT uptake demonstrates metabolically active lesions not only in the uterus but also in para-aortic and intercavo-aortic lymph nodes (Fig. 23).

Given diffusion of the disease beyond the pelvis, we considered as CTV not only the cervix, uterus, parametria, vagina, and regional lymph

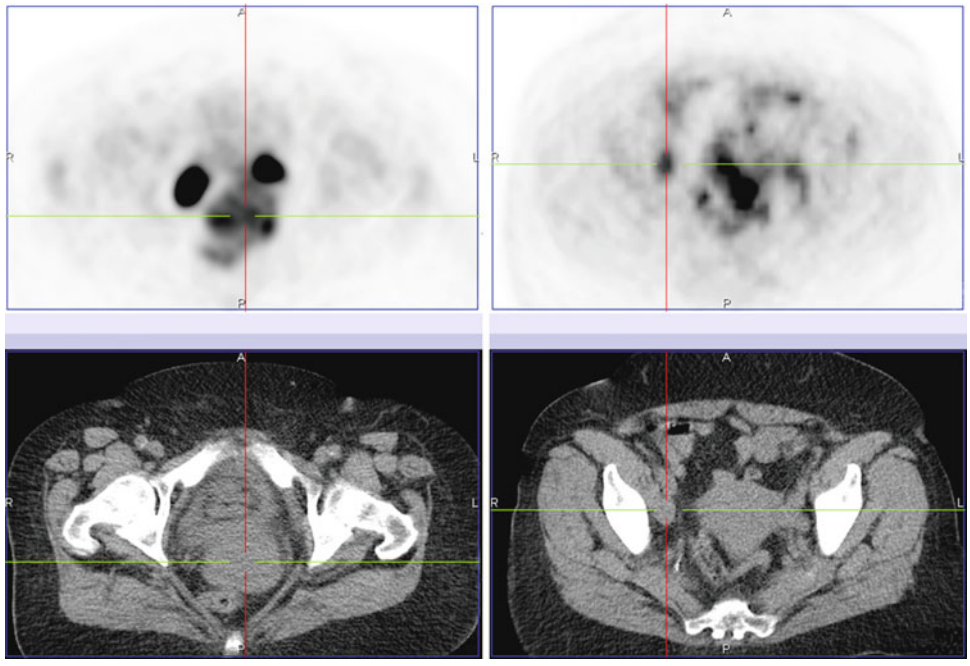

Fig. 22 [^{18}F]FDG PET/CT images (axial sections) showing high tracer uptake in the primary tumor (*left panel*) and in metastatic pelvic lymph nodes (*right panel*)

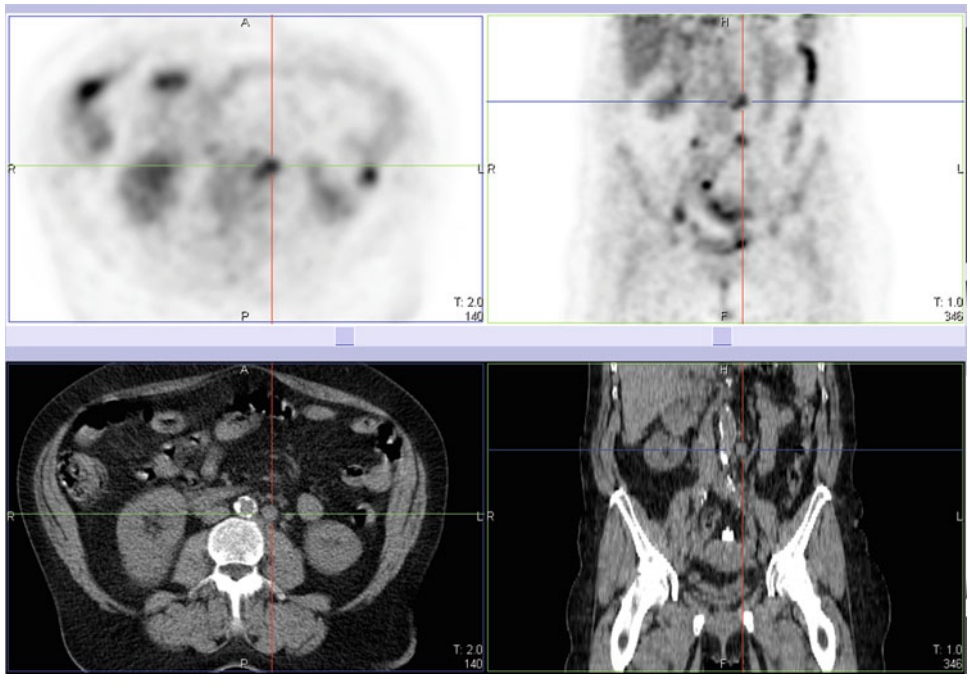

Fig. 23 [^{18}F]FDG PET/CT images (axial and coronal sections) showing high tracer uptake in the lombo-aortic pelvic lymph nodes

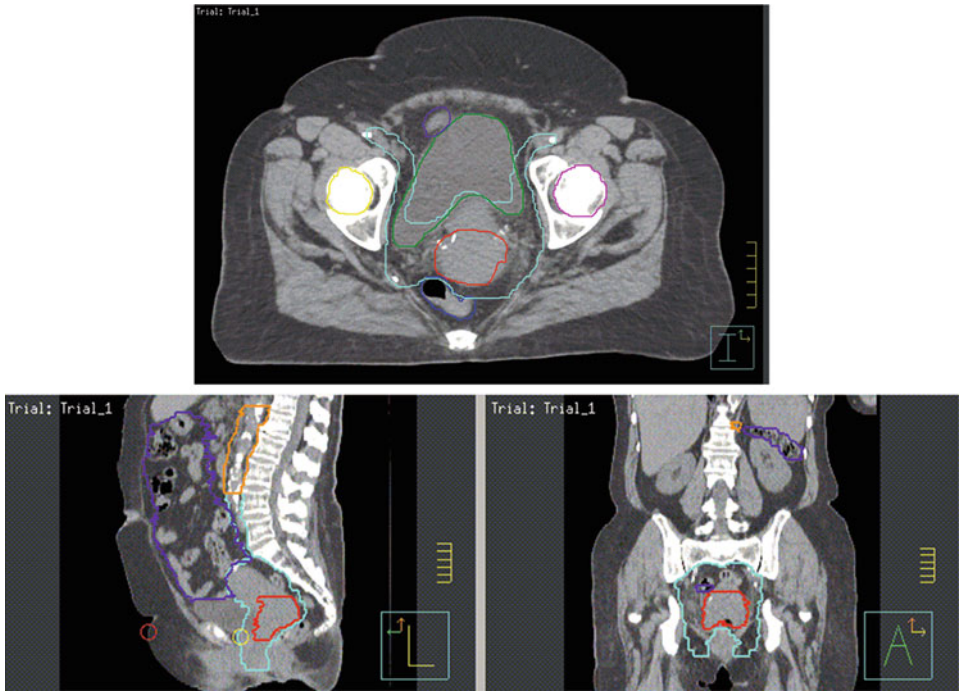

Fig. 24 Transaxial, sagittal, and coronal view of the simulation CT. Different colors are used to highlight the contours of the treatment volumes. *Red line*: gross tumor volume (*GTV*) represented by cervical cancer plus parametrial and vaginal extension; light-*blue line*: pelvic CTV represented by the uterus, parametria, vagina, and regional and para-aortic lymph nodes; *orange line*: intercavo-aortic lymph nodes CTV. *Purple line* delineates the peritoneal cavity defined as one of the organs at risk

nodes but also the para-aortic lymph nodes (Figs. 24 and 25).

A volumetric-modulated radiotherapy-simultaneous-integrated boost (VMAT-SIB) treatment plan was performed to a total dose of 50 Gy with daily fraction of 2 Gy to the macroscopic disease and to a dose of 45.0 Gy with daily fraction of 1.8 Gy to the potentially microscopically invaded regions and locoregional lymph nodes. After the external beam RT, the treatment was completed by a brachytherapy boost to the cervix and parametria (Fig. 26).

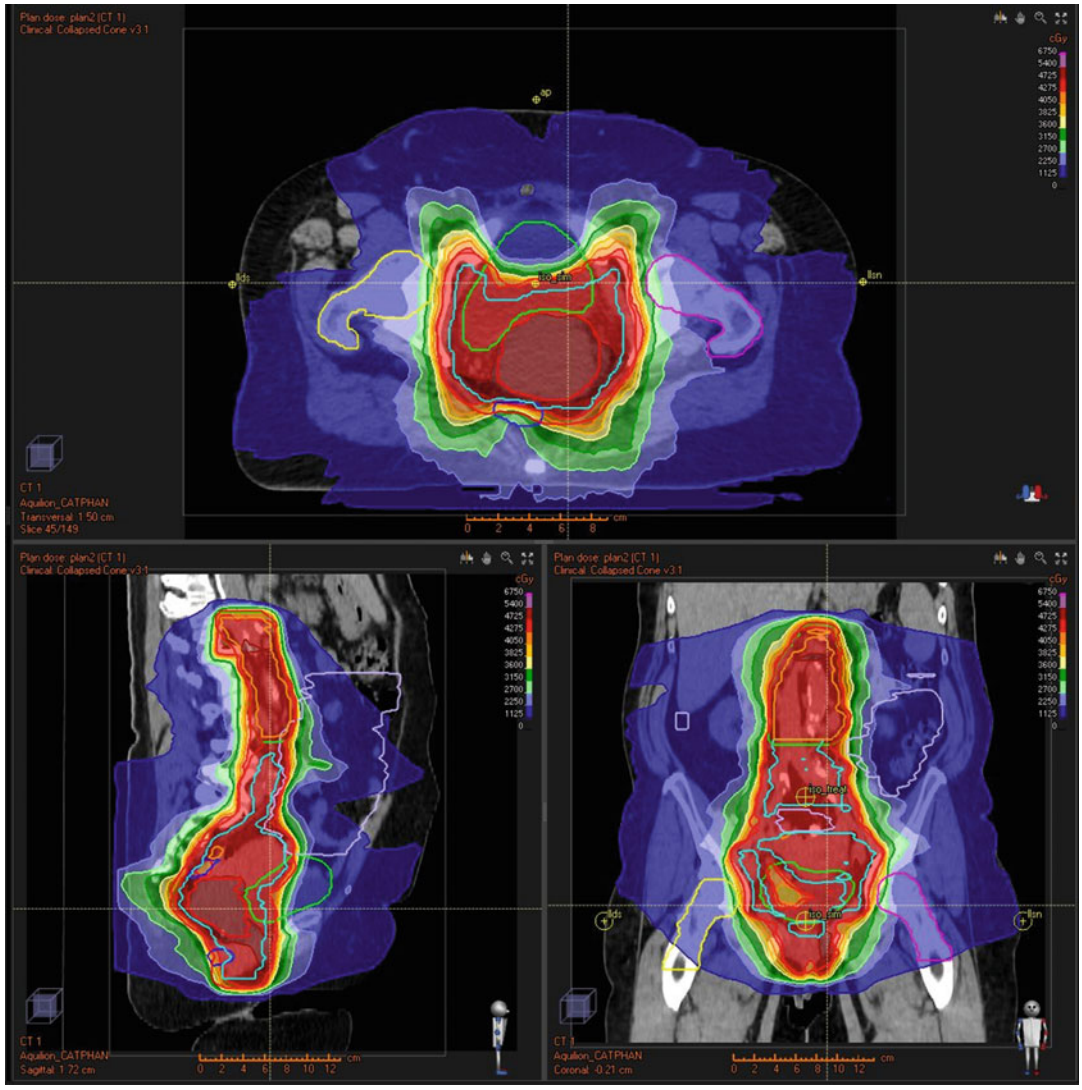

Fig. 25 Transaxial, coronal, and sagittal view of the RT treatment planning. Images show the high conformation of dose distribution performed by VMAT-SIB treatment plan. Around the target volumes, the doses fall down sharply, thus reducing the dose to the organs at risk. In red the 95% isodose of the prescribed dose of 45 Gy

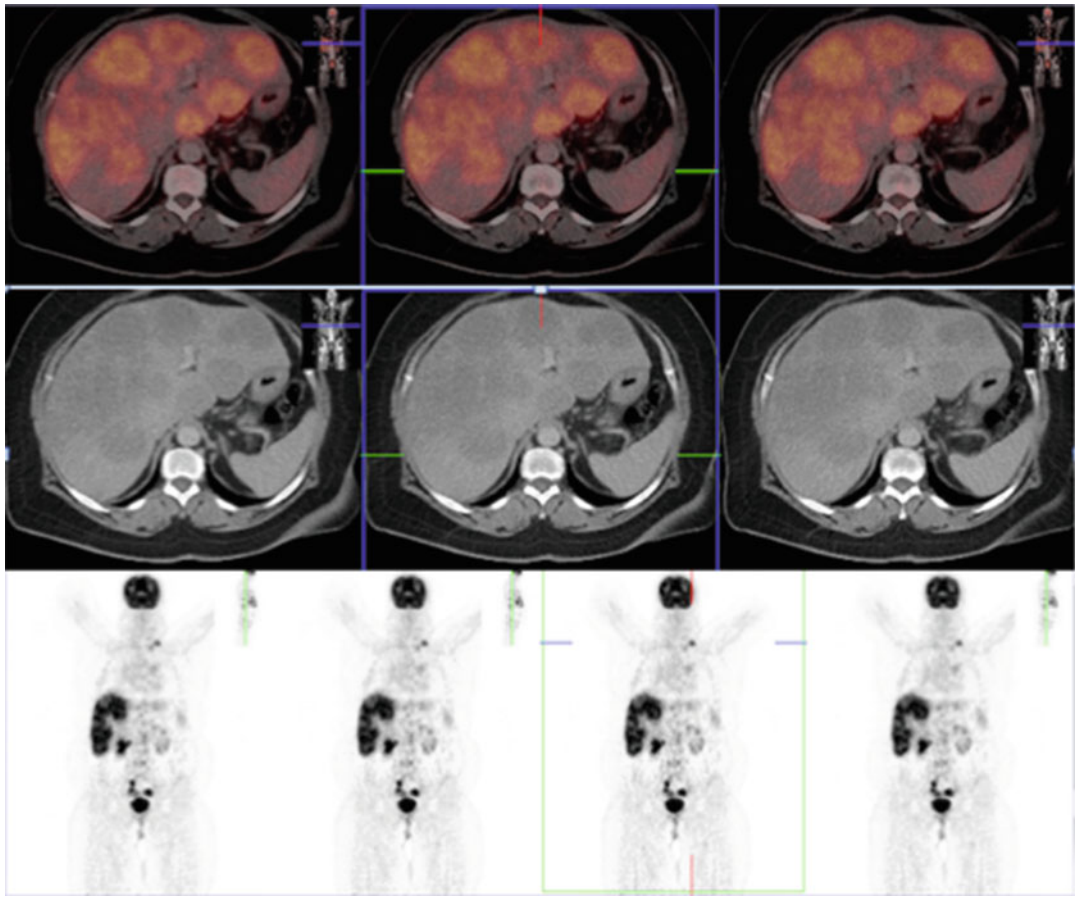

Fig. 26 Fusion images demonstrating liver metastases. CT images demonstrating the liver metastases. [^{18}F]FDG PET images demonstrating supraclavicular node and para-aortic nodes

References

1. Litmanovich D, Gourevich K, Israel O, Gallimidi Z. Unexpected foci of ^{18}F-FDG uptake in the breast detected by PET/CT: incidence and clinical significance. Eur J Nucl Med Mol Imaging. 2009;36:1558–64.

Teaching Cases in Nuclear Oncology: Ovarian Cancer

74

Alice Lorenzoni, Alessandra Alessi, and Flavio Crippa

Keywords

[^{18}F]FDG PET/CT • Ovarian cancer • Staging • Recurrent disease

Glossary

[^{18}F]FDG	2-Deoxy-2-[^{18}F]fluoro-D-glucose
CA125	Carbohydrate antigen 125 (or cancer antigen 125), a circulating serum tumor-associated marker also known as the glycoprotein mucin-16
CT	X-ray computed tomography
FIGO	International Federation of Gynecology and Obstetrics
PET	Positron emission tomography
PET/CT	Positron emission tomography/Computed tomography

Contents

Ovarian Cancer: Case No. 1 1841
Findings 1841
Discussion 1842

Ovarian Cancer: Case No. 2 1842
Presentation 1842
Findings 1842
Discussion 1842

Ovarian Cancer: Case No. 3 1844
Presentation 1844
Findings 1845
Discussion 1845

Ovarian Cancer: Case No. 4 1846
Presentation 1846
Findings 1846
Discussion 1846

Suggested Readings 1847

Ovarian Cancer: Case No. 1

A 66-year-old woman presented with lower abdominal discomfort and elevated serum CA125 (260 U/mL). The presence of large right pelvic mass suspicious for ovarian malignancy was diagnosed with pelvic ultrasound.

Findings

[^{18}F]FDG PET/CT was performed as a part of initial staging to evaluate the extent of disease.

PET/CT image demonstrated metabolically active pelvic right mass corresponding to suspected ovarian lesion; also a prominent [^{18}F]FDG-avid

A. Lorenzoni (✉) • A. Alessi • F. Crippa
Nuclear Medicine Division, IRCCCS National Cancer Institute, Milan, Italy
e-mail: alice.lorenzoni@istitutotumori.mi.it; alicelorenzoni@hotmail.it

© Springer International Publishing Switzerland 2017
H.W. Strauss et al. (eds.), *Nuclear Oncology*,
https://doi.org/10.1007/978-3-319-26236-9_77

area was shown in the mass-like omental cake consistent with extensive omental involvement (Fig. 1). In addition, pathologic multiple [^{18}F]FDG-avid peritoneal implants were demonstrated in the abdomen and pelvis (Figs. 2 and 4).

[^{18}F]FDG PET/CT images showed two focal areas of radiotracer uptake, in the subglissonian region of hepatic segments VIII and VII consistent with liver involvement (Figs. 3 and 4).

The patient was treated with debulking surgery, hysterectomy and bilateral salpingo-oophorectomy, omentectomy, diaphragmatic peritonectomy, and sigma resection.

The histology obtained after surgery confirmed high-grade ovarian serous carcinoma stage IV FIGO.

Following surgery, the patient was treated with platinum-based chemotherapy.

Discussion

This case confirms the important contribution of [^{18}F]FDG PET/CT in abdominal and extra-abdominal stage of advanced ovarian cancer.

PET/CT pretherapy imaging may change patient management or help direct surgical planning, thus aiding optimized cytoreduction.

Ovarian Cancer: Case No. 2

Presentation

A 53-year-old postmenopausal woman presented with pelvic discomfort. Ultrasound revealed a 6 cm complex right adnexal mass. The CA125 level was 123 U/mL.

[^{18}F]FDG PET/CT was performed in order to characterize the ovarian mass before the scheduled surgery.

Findings

Fused PET/CT images (Fig. 5) showed a large right pelvic mass with a large photopenic area indicative of either cystic, necrotic, or mucinous components. The mass did not demonstrate increased [^{18}F]FDG uptake. Laparotomy revealed clear cell carcinoma of the right ovary. Postoperatively the patient received six cycles of carboplatin- and paclitaxel-based chemotherapy.

Discussion

Clear cell carcinomas of the ovary are extremely rare, accounting for less than 5% of cases. These

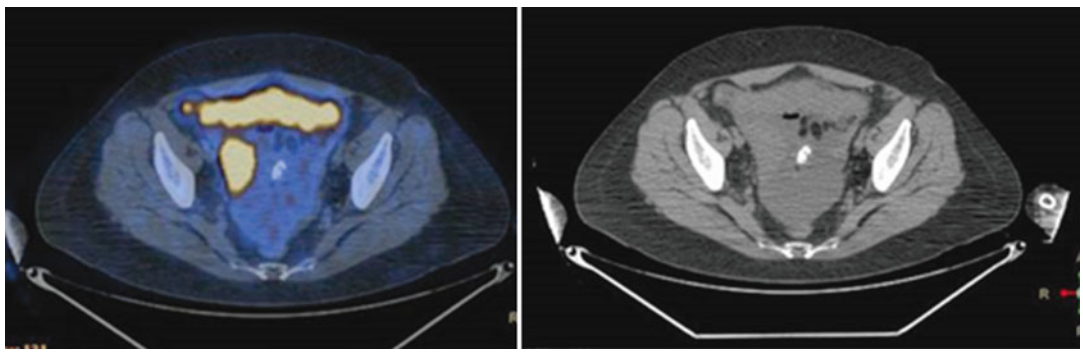

Fig. 1 Metabolically active pelvic right mass corresponding to suspected ovarian lesion (**a**); a prominent [^{18}F]FDG-avid area was shown in the mass-like omental cake consistent with extensive omental involvement

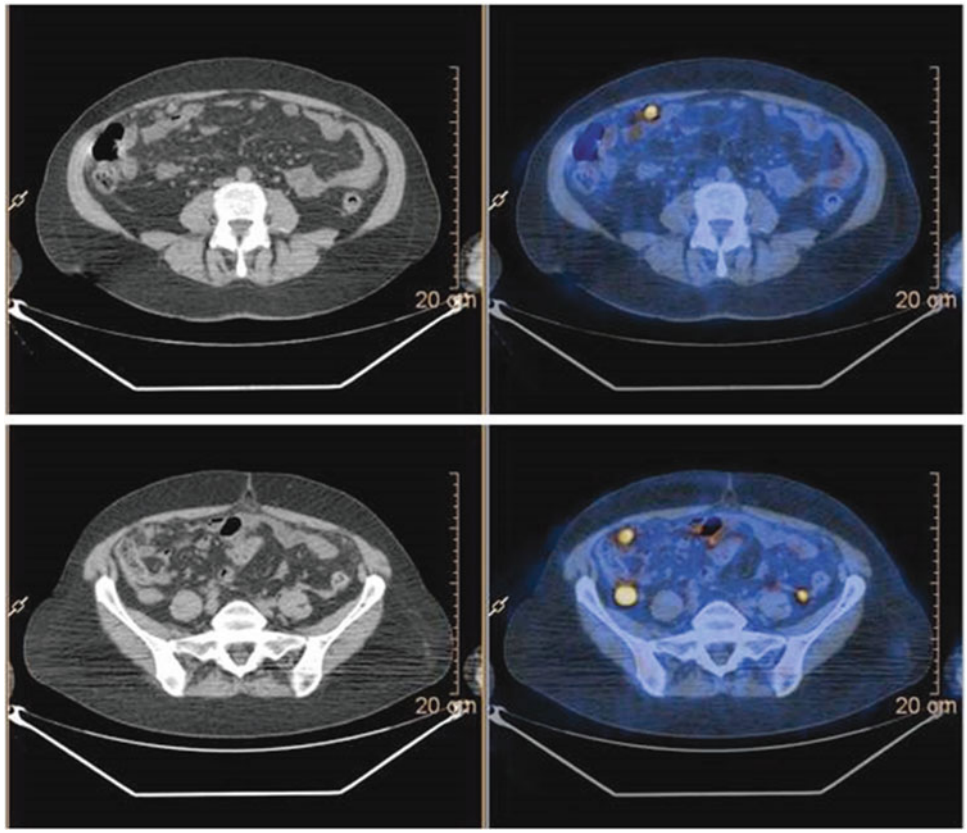

Fig. 2 Low-dose CT (*left*) and fused PET/CT (*right*) axial images show multiple [^{18}F]FDG-avid peritoneal nodules

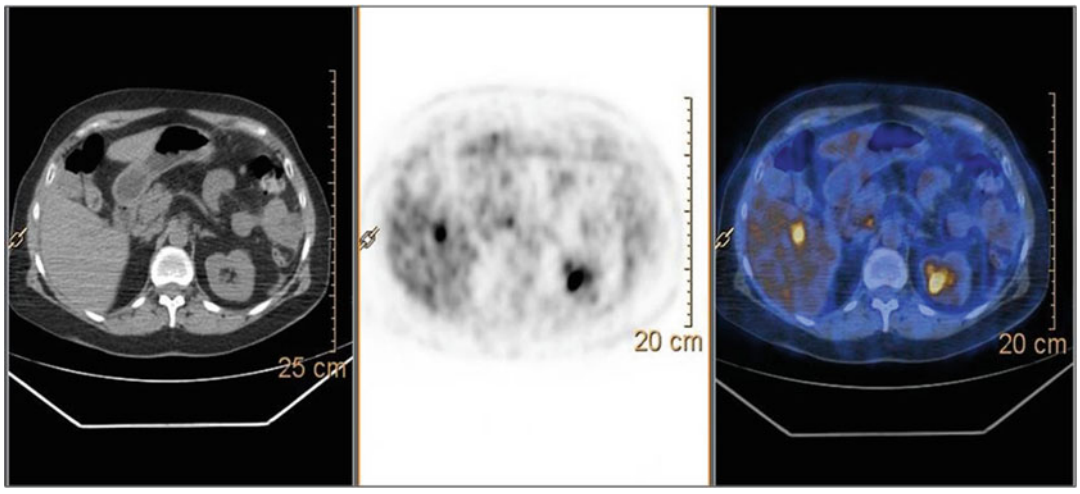

Fig. 3 [^{18}F]FDG focal uptake in VII hepatic segment consistent with metastatic liver disease

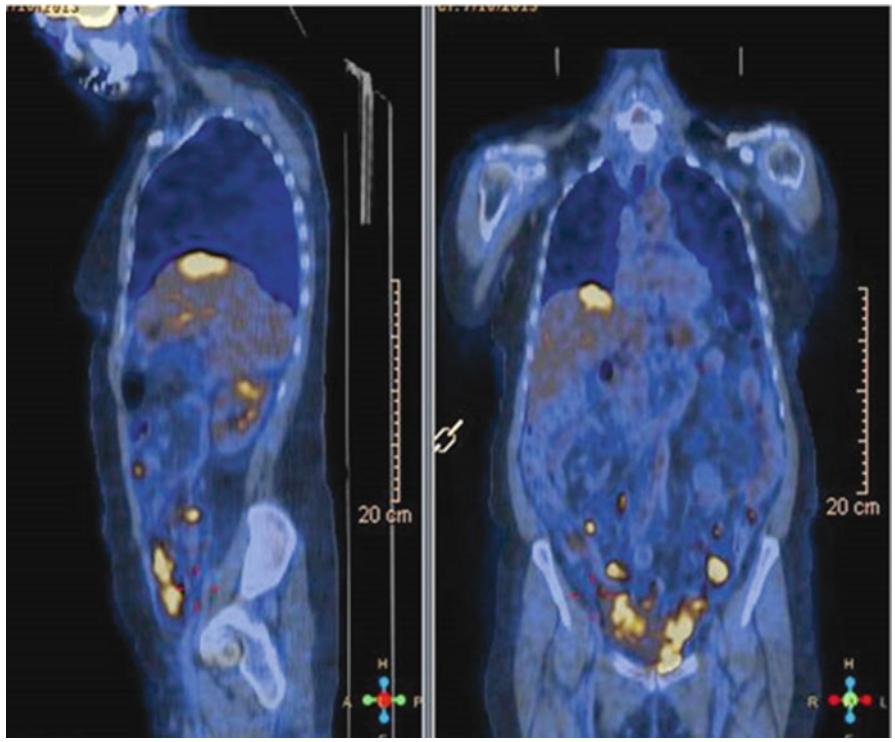

Fig. 4 Sagittal and coronal fused PET/CT images demonstrate liver metastases and multiple [^{18}F]FDG-avid peritonal implants

tumors have a very poor prognosis in terms of survival and response to chemotherapy.

[^{18}F]FDG PET/CT sensitivity and specificity to discriminate between benign and malignant tumors ranges from 70% to 100% and 77% to 100%, respectively. Ovarian carcinoma includes a variety of histological subtypes with different biological characteristics; in particular clear cell and mucinous carcinomas show a variable [^{18}F]FDG uptake. [^{18}F]FDG PET/CT does not appear to have a well defined role in the characterization of epithelial ovarian cancer and its use remains controversial. Conversely [^{18}F]FDG PET/CT may identify nodal involvement and distant metastases.

Ovarian Cancer: Case No. 3

Presentation

A 58-year-old woman presented with large pelvic mass suspicious for ovarian malignancy. [^{18}F]FDG PET/CT was performed as a part of initial staging.

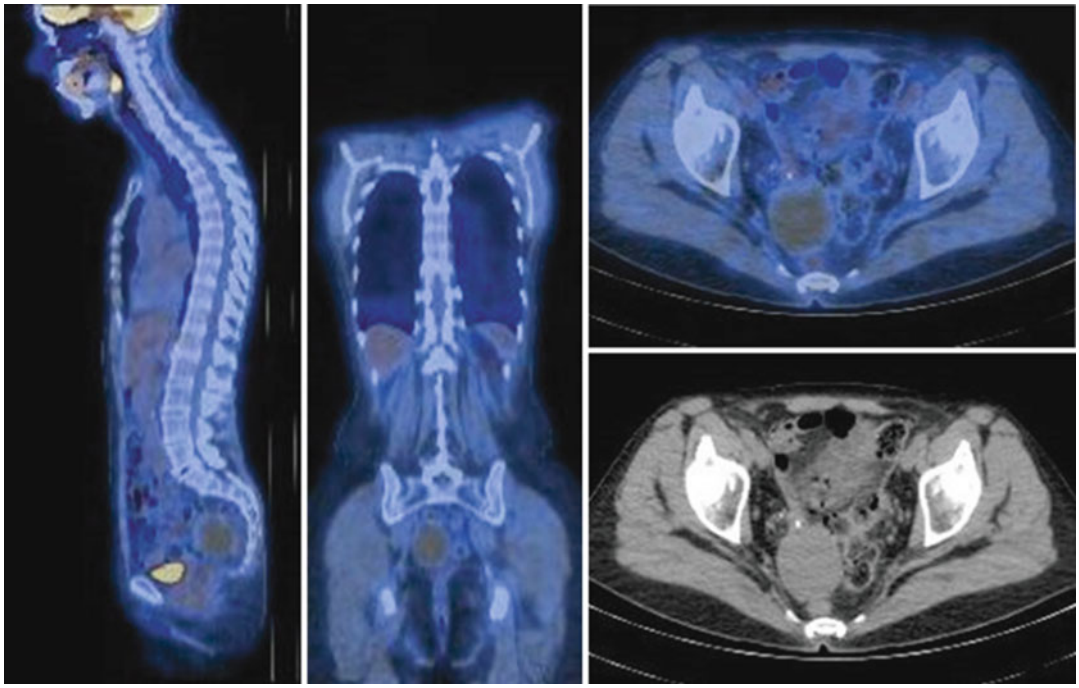

Fig. 5 Coronal (*left*), sagittal (*middle*), axial (*upper right*) fused [^{18}F]FDG PET/CT and axial low-dose CT (*lower right*) image showed pelvic ovarian mass characterized by large photopenic area

Findings

PET/CT demonstrated a large pelvic mass with heterogeneous [^{18}F]FDG uptake corresponding to the ovarian lesion. In the left common iliac region, a prominent [^{18}F]FDG-avid area was shown consistent with lymphadenopathy (Fig. 6). In addition, in the left pericolic gutter a small [^{18}F]FDG-avid nodule was noted suspicious for peritoneal implant.

The patient underwent primary debulking surgery. Histopathology showed serous epithelial ovarian cancer at the sites identified by PET/CT. No other area of tumor spread was identified. The results of PET/CT were concordant with the final pathological staging.

Discussion

[^{18}F]FDG PET/CT is an accurate imaging modality for staging ovarian cancer. Furthermore preoperative intratumoral [^{18}F]FDG uptake heterogeneity in patients with epithelial ovarian cancer has been shown to be significantly associated with recurrence.

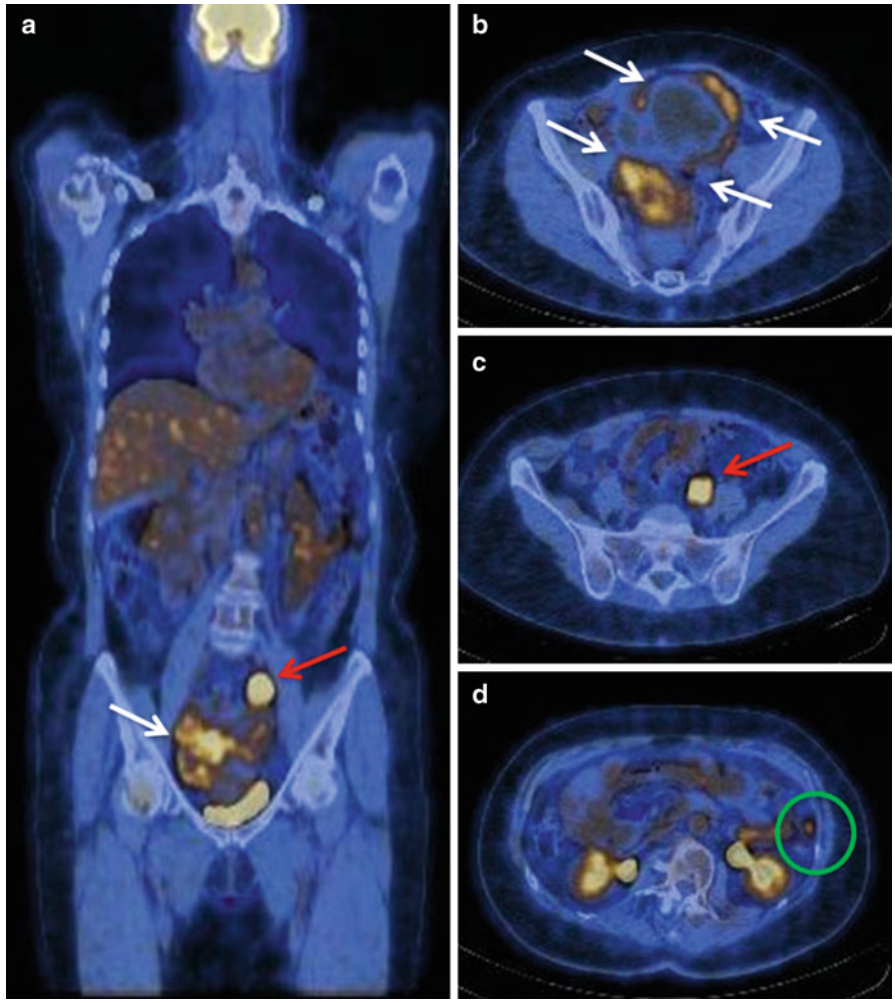

Fig. 6 Fused PET/CT images show large pelvic mass with heterogeneous [^{18}F]FDG uptake corresponding to the ovarian lesion (**a** coronal image, **b** axial image, *white arrows*). Hypermetabolic adenopathy is depicted in the left iliac common region (**a** coronal image, **c** axial image, *red arrow*). Small [^{18}F]FDG-avid nodule consistent with peritoneal implant is seen in the left parietocolic gutter (**d** axial image, *green circle*)

Ovarian Cancer: Case No. 4

Presentation

A 64-year-old woman with a history of surgery for epithelial ovarian cancer presented with rising serum CA125 level (186 U/mL). Abdominal contrast-enhanced CT was negative for the presence of recurrence. The patient underwent [^{18}F]FDG PET/CT to identify suspected ovarian cancer recurrence.

Findings

[^{18}F]FDG PET/CT identified two foci of [^{18}F]FDG uptake, one in the right internal iliac region and the second in the presacral region suspicious for pelvic recurrence of ovarian cancer (Fig. 7).

Discussion

PET/CT is an important diagnostic tool to detect recurrence in the setting of a rising CA125 and

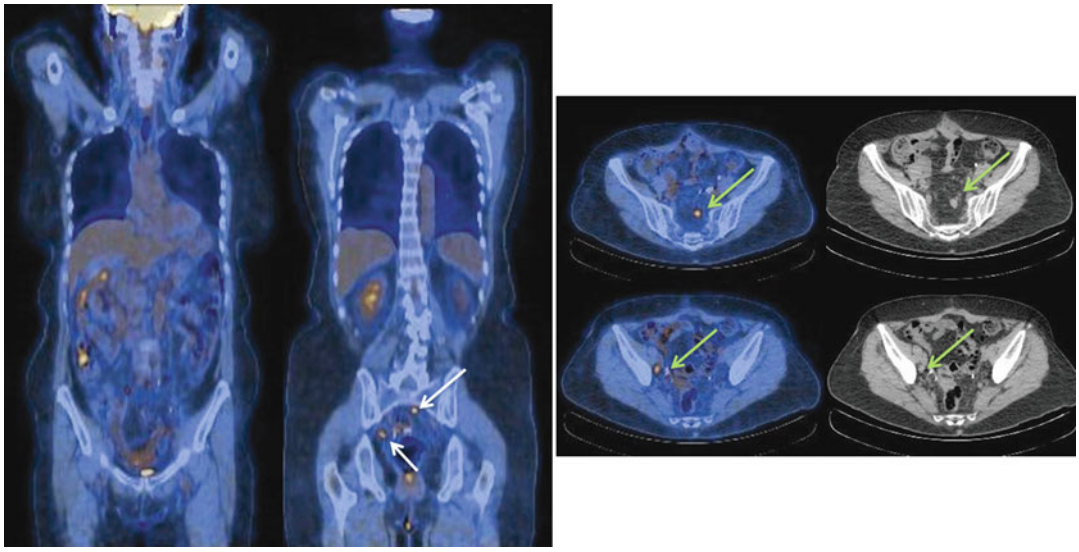

Fig. 7 Coronal fused [^{18}F]FDG PET/CT images (*left panel*) and axial images (*right panel*) show pelvic recurrence of ovarian cancer (*white* and *green arrows*)

negative conventional imaging studies in patients with epithelial ovarian cancer, detecting tumor relapse in a higher percentage than CT. In addition, [^{18}F]FDG PET/CT may be useful in patients where recurrence is suspected, even when the tumor marker CA125 is in the normal range.

Suggested Readings

Lee M, Lee H, Cheon GJ, et al. Prognostic value of preoperative intratumoral FDG uptake heterogeneity in patients with epithelial ovarian cancer. Eur Radiol. 2017;27:16–23.

Tawakol A, Abdelhafez YG, Osama A, et al. Diagnostic performance of ^{18}F-FDG PET/contrast-enhanced CT versus contrast-enhanced CT alone for post-treatment detection of ovarian malignancy. Nucl Med Commun. 2016;37:453–60.

Evangelista L, Palma MD, Gregianin M, et al. Diagnostic and prognostic evaluation of fluorodeoxyglucose positron emission tomography/computed tomography and its correlation with serum cancer antigen-125 (CA125) in a large cohort of ovarian cancer patients. J Turk Ger Gynecol Assoc. 2015;16:137–44.

Teaching Cases in Nuclear Oncology: Sarcomas

75

Alice Lorenzoni, Alessandra Alessi, and Flavio Crippa

Keywords

Sarcoma • [^{18}F]FDG PET/CT • Treatment response • Staging

Glossary

[^{18}F]FDG	2-Deoxy-2-[^{18}F]fluoro-D-glucose
^{99m}Tc-MDP	^{99m}Tc-methylene diphosphonate
CT	X-ray computed tomography
MRI	Magnetic resonance imaging
PET	Positron emission tomography
PET/CT	Positron emission tomography/ Computed tomography
SUV	Standardized uptake value
SUV_{max}	Standardized uptake value at point of maximum

Contents

Sarcomas: Case No. 1 1849
Presentation 1849
Findings 1851
Discussion 1852

Sarcomas: Case No. 2 1852
Presentation 1852
Findings 1853

Sarcomas: Case No. 3 1853
Presentation 1853
Findings 1853
Discussion 1853

Sarcomas: Case No. 4 1853
Presentation 1853
Findings 1854
Discussion 1854

Sarcomas: Case No. 5 1854
Presentation 1855
Findings 1855
Discussion 1855

Case No. 6: Ewing's Sarcoma 1856
Presentation 1856
Findings 1856
Follow-Up 1857
Discussion 1859

Case No. 7: Metastatic Osteosarcoma 1859
Presentation 1859
Findings 1860
Follow-Up 1860

A. Lorenzoni (✉) • A. Alessi • F. Crippa
Nuclear Medicine Division, IRCCCS National Cancer Institute, Milan, Italy
e-mail: alice.lorenzoni@istitutotumori.mi.it; alicelorenzoni@hotmail.it

© Springer International Publishing Switzerland 2017
H.W. Strauss et al. (eds.), *Nuclear Oncology*,
https://doi.org/10.1007/978-3-319-26236-9_78

Sarcomas: Case No. 1

Presentation

A 34-year-old man presented with a 4-week history of sudden-onset, nontender mass in the left leg.

Anatomic imaging was concerning for a large soft tissue sarcoma (7 cm in size). Percutaneous biopsy confirmed high-grade sarcoma with myogenic differentiation.

Neoadjuvant chemotherapy followed by radical surgery and radiotherapy was performed.

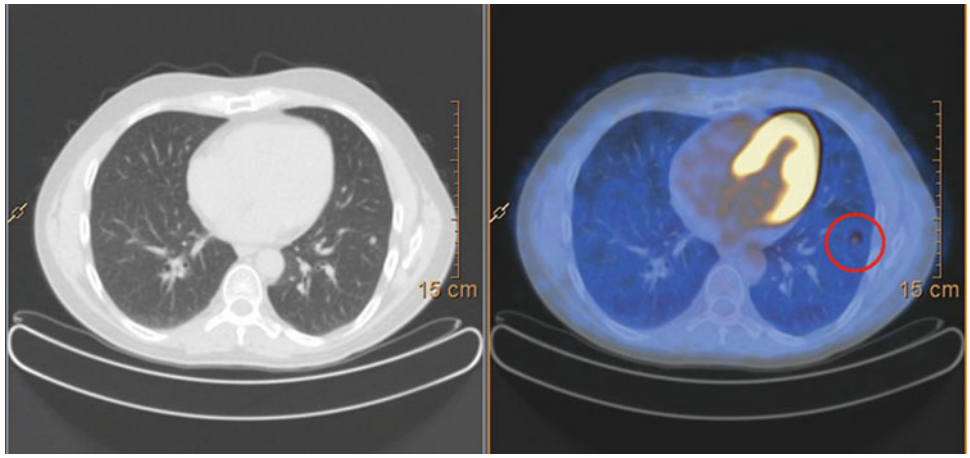

Fig. 1 [^{18}F]FDG PET/CT transaxial images demonstrated mild focal uptake (*red circle*) corresponding to suspected small nodule in the left lung

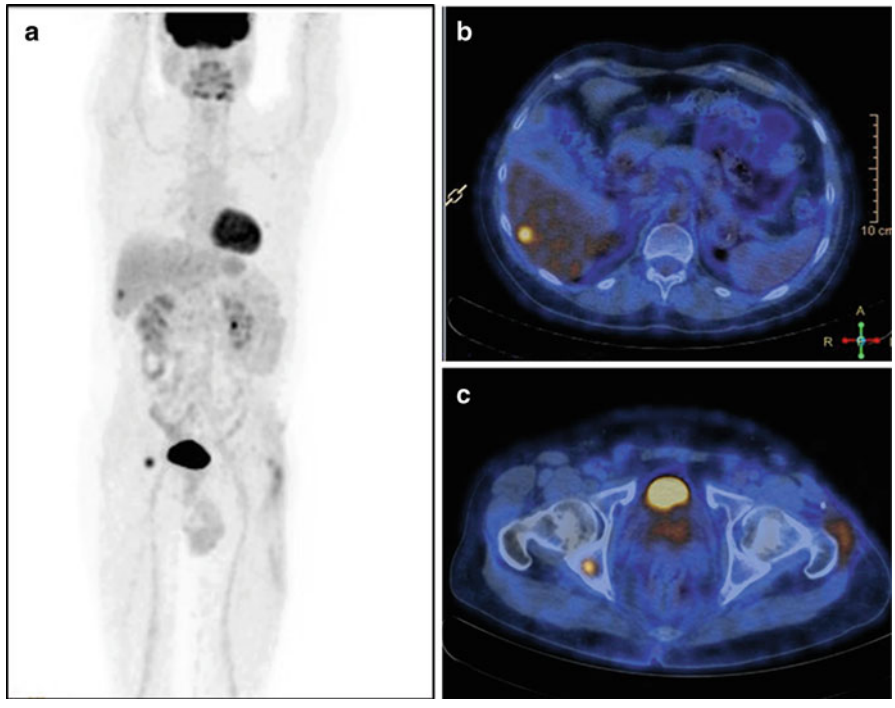

Fig. 2 Maximum intensity projection (*MIP*) (**a**) and axial fused PET/CT (**b**, **c**) images show hypermetabolic hepatic nodule and right acetabular hypermetabolic lesion. Mild uptake of [^{18}F]FDG is demonstrated in soft tissue of the left trochanteric region consistent with inflammation (unrelated to tumor)

Fig. 3 [^{18}F]FDG-PET sagittal and coronal fused PET/CT (*left*) images clearly depict skeletal lesions (*white arrows*); MRI of the spine and pelvis confirms the pathological findings (*red arrows*)

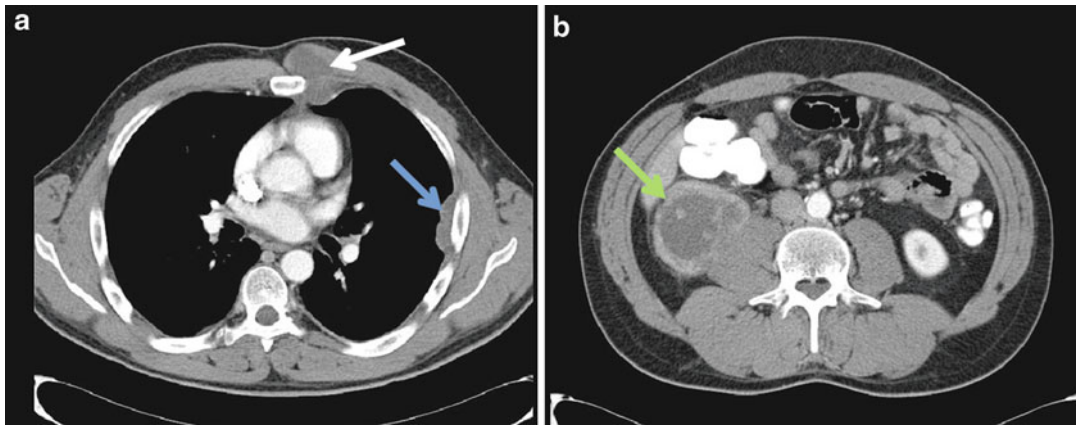

Fig. 4 Contrast-enhanced CT of suspected metastatic myxoid liposarcoma in chest wall (**a**, *white arrow*), pleura (**a**, *blue arrow*), and retroperitoneum (**b**, *green arrow*)

Post-therapy CT of the thorax showed the appearance of small nodule in the left lung suspicious for metastatic disease.

The patient was a candidate for left lung resection.

Findings

[^{18}F]FDG PET/CT was performed as a part of completion staging prior thoracic surgery.

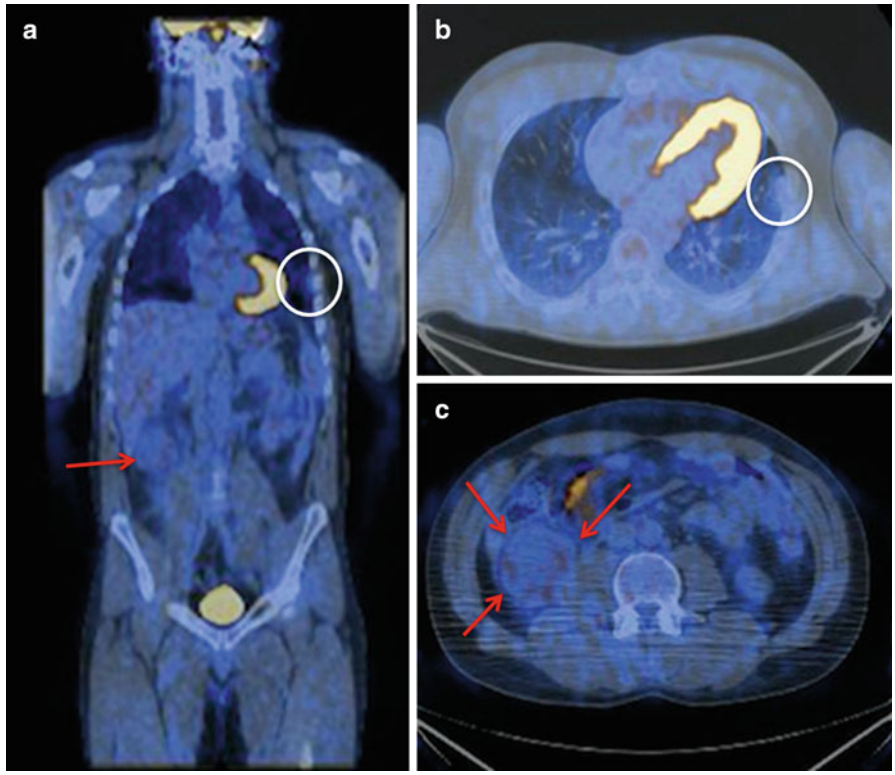

Fig. 5 Fused PET/CT images of metastatic myxoid liposarcoma mass without significant [^{18}F]FDG uptake of the pleura (**a** coronal and **b** axial images, *white circle*) and retroperitoneum (**a** coronal and **c** axial images, *red arrows*)

PET/CT demonstrated mild focal [^{18}F]FDG uptake in the left lung corresponding to suspected nodule (Fig. 1). An [^{18}F]FDG-avid hepatic lesion was also demonstrated in segments V–VI of the right lobe (Fig. 2).

[^{18}F]FDG also revealed the presence of skeletal focal [^{18}F]FDG uptake consistent with bone metastases in the right acetabulum and in the dorsal spine (Fig. 3). MRI confirms PET skeletal findings.

Discussion

[^{18}F]FDG-PET has been increasingly used in bone and soft tissue sarcomas and provides advantages in the initial tumor staging, tumor grading, therapy assessment, and recurrence detection.

Accurate detection of metastatic lesions is thus important for accurate staging and selection of appropriate therapy.

This case demonstrates the diagnostic benefit of [^{18}F]FDG-PET in sarcoma staging to guide optimal therapeutic strategy.

Sarcomas: Case No. 2

Presentation

A 42-year-old man with past history of myxoid liposarcoma in the left thigh presented with painful swelling in the right flank of 3-month duration. Intravenous and oral contrast-enhanced CT of the thorax and abdomen showed a large inhomogeneous mass of low density in the right retroperitoneal region laterally to the right psoas muscle consistent with soft tissue sarcoma localization. In addition metastatic mass was noted in the chest wall and pleura (Fig. 4).

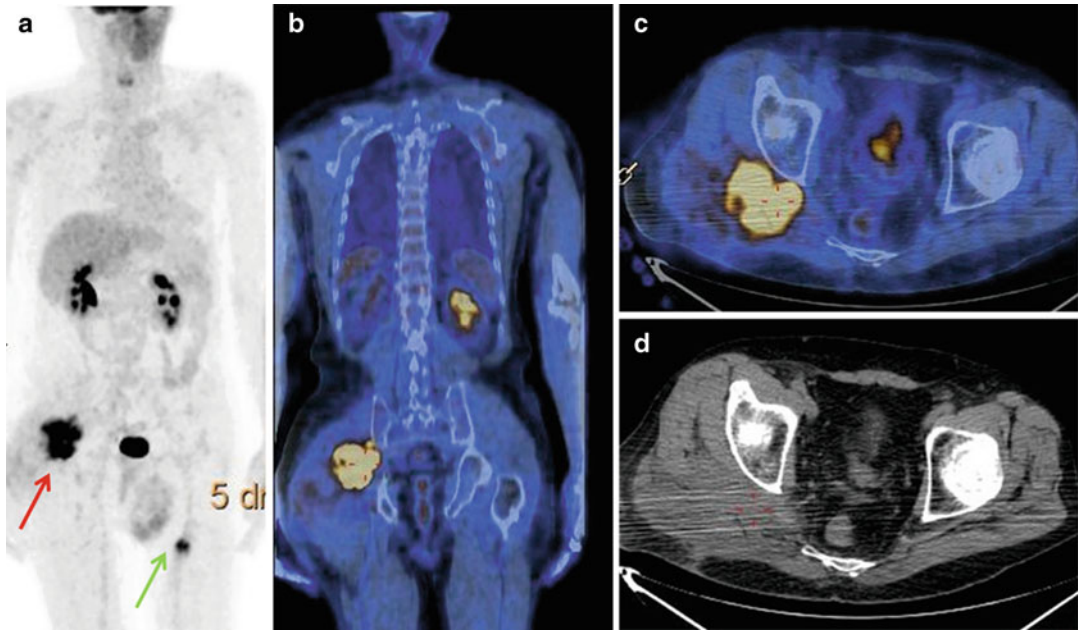

Fig. 6 Maximum intensity projection (*MIP*) image (**a**), fused PET/CT (**b** coronal, **c** axial), and axial low-dose CT images of hypermetabolic mass in the right gluteal region (*red arrow*). MIP image demonstrates also focal [^{18}F]FDG uptake in the left thigh consistent with malignancy (*green arrow*)

[^{18}F]FDG PET/CT was performed to complete the evaluation.

Findings

[^{18}F]FDG PET/CT did not show significant [^{18}F]FDG activity of metastatic myxoid liposarcoma mass in the chest wall, pleura, and retroperitoneum (Fig. 5).

Sarcomas: Case No. 3

Presentation

A 57-year-old man with soft tissue sarcoma in the right gluteal region was referred for [^{18}F]FDG PET/CT staging.

Findings

PET/CT demonstrated a large mass with intense heterogeneous [^{18}F]FDG uptake in the right gluteal muscles corresponding to known soft tissue sarcoma (Fig. 6).

PET/CT also revealed the presence of unknown hypermetabolic lesion in the anterior compartment of the left thigh (Figs. 6 and 7).

Discussion

The detection of additional multifocal sarcoma lesions is important during the initial diagnosis to plan subsequent treatment. This case demonstrates the utility of [^{18}F]FDG PET/CT in the initial staging of soft tissue sarcoma.

Sarcomas: Case No. 4

Presentation

A 21-year-old man presented with a painless mass in the right forearm. MRI showed a large lesion, approximately 14 cm in diameter, in the flexor digitorum profundus muscle. The biopsy revealed

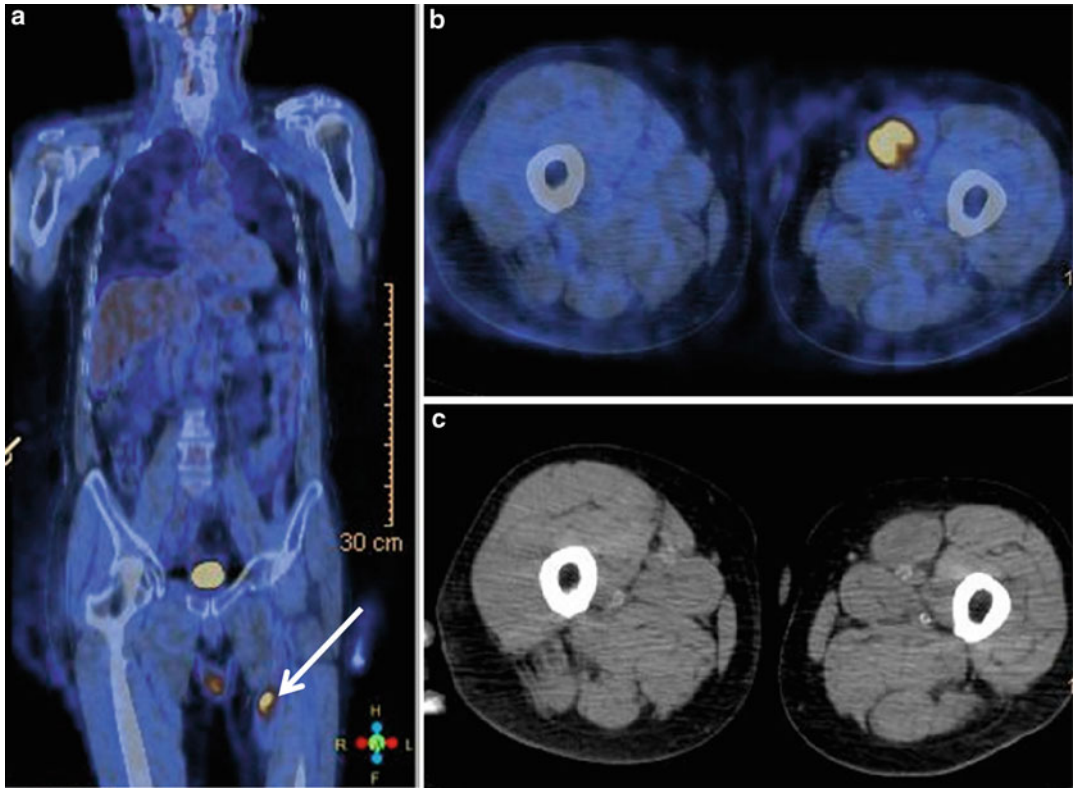

Fig. 7 Fused [^{18}F]FDG PET/CT images (**a** coronal, **b** axial) and axial low-dose CT (**c**) of the unknown hypermatabolic lesion in the left thigh (*white arrow*)

alveolar rhabdomyosarcoma. Contrast-enhanced CT of the thorax and abdomen did not show metastatic disease.

Findings

[^{18}F]FDG PET/CT was performed as a part of initial staging.

[^{18}F]FDG-PET confirmed the presence of large hypermetabolic mass in the right forearm. Focal [^{18}F]FDG-avid lesions were also detected in the soft tissue of the right arm (Fig. 8). In addition pathological [^{18}F]FDG-avid lymph nodes were noted in the ipsilateral axilla and in the supraclavicular fossa (Figs. 8 and 9).

The patient was treated with chemotherapy and subsequent surgery.

Discussion

Rhabdomyosarcomas represent more than 50% of soft tissue sarcomas occurring in childhood and adolescence. The presence of metastatic disease at the time of diagnosis decreases the chance of survival to 20% approximately. [^{18}F]FDG PET/CT can be useful in staging and restaging pediatric rhabdomyosarcoma, especially for assessing lymph nodes, soft tissue spread, and distant metastases.

Sarcomas: Case No. 5

Case contributed by T. Lengana and M. Sathkege
Nuclear Medicine, University of Pretoria, and Steve Biko Academic Hospital, Pretoria, South Africa

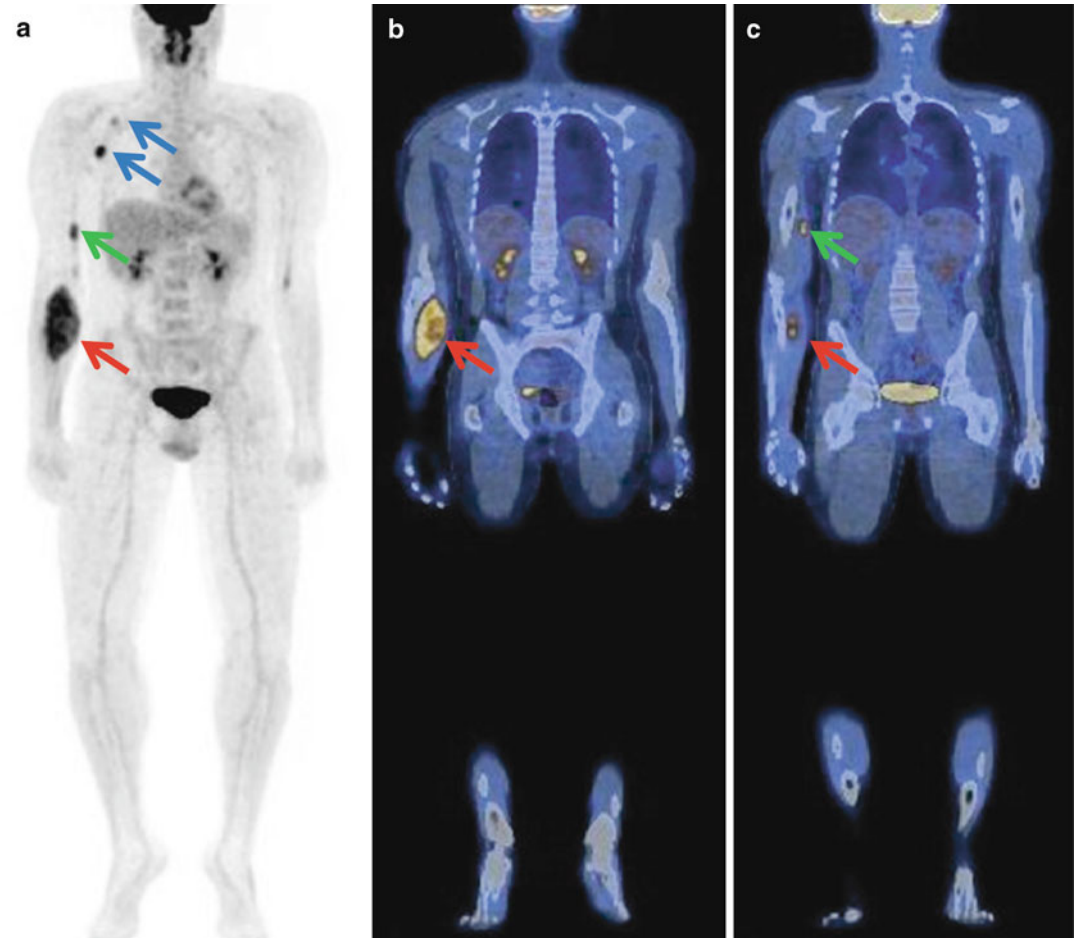

Fig. 8 Maximum intensity projection (*MIP*) image (**a**) in patient with alveolar rhabdomyosarcoma of the right forearm (*red arrow*), soft tissue localization (*green arrow*), and lymph node involvement (*blue arrows*). Coronal fused [^{18}F]FDG PET/CT (**b**, **c**) shows hypermetabolic mass in the right forearm (*red arrow*) and soft tissue spread in the ipsilateral arm (**c**)

Presentation

Twenty-six-year-old male patient presented with rhabdomyosarcoma of the right orbit. Treatment history included enucleation of the right orbit in 2010 and completion of radiotherapy in 2012.

The patient was complaining of history of neck swelling.

Findings

An [^{18}F]FDG PET/CT scan was done for suspected recurrence. [^{18}F]FDG PET/CT images demonstrated a large [^{18}F]FDG-avid mass in the right mandibular angle region measuring 5.2 × 4.3 cm (SUV_{max} 6.94). No other site of hypermetabolic uptake was noted (Figs. 10 and 11).

Patient was treated with radical parotidectomy and lymph node dissection; histology revealed embryonal rhabdomyosarcoma.

Discussion

This case demonstrates that [^{18}F]FDG PET/CT can be useful in the assessment of patients with suspected recurrence of rhabdomyosarcoma.

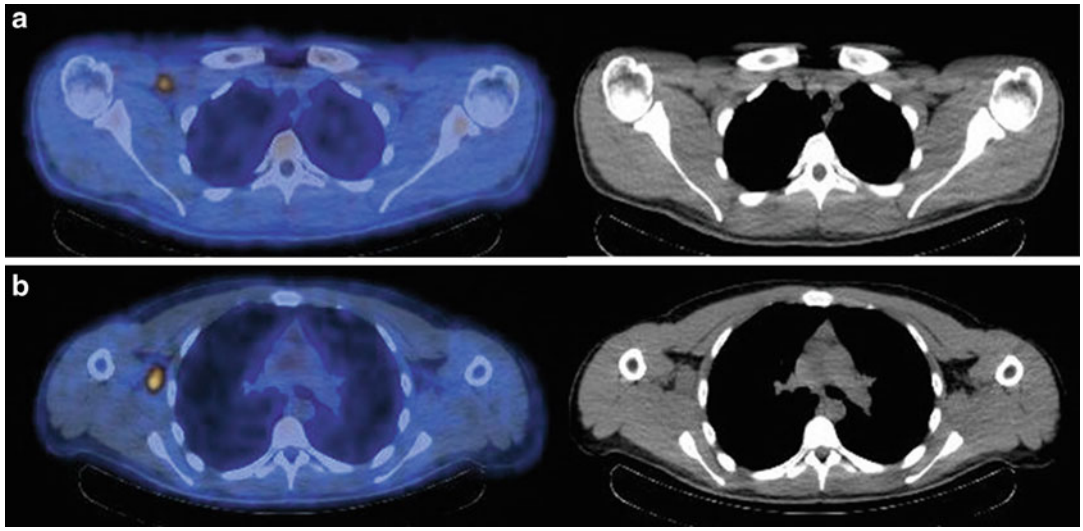

Fig. 9 [^{18}F]FDG PET/CT axial images of the hypermetabolic supraclavicular (a fused PET/CT *left panel*, low-dose CT *right panel*) and axillary (a fused PET/CT *left panel*, low-dose CT *right panel*) lymph node consistent with metastases

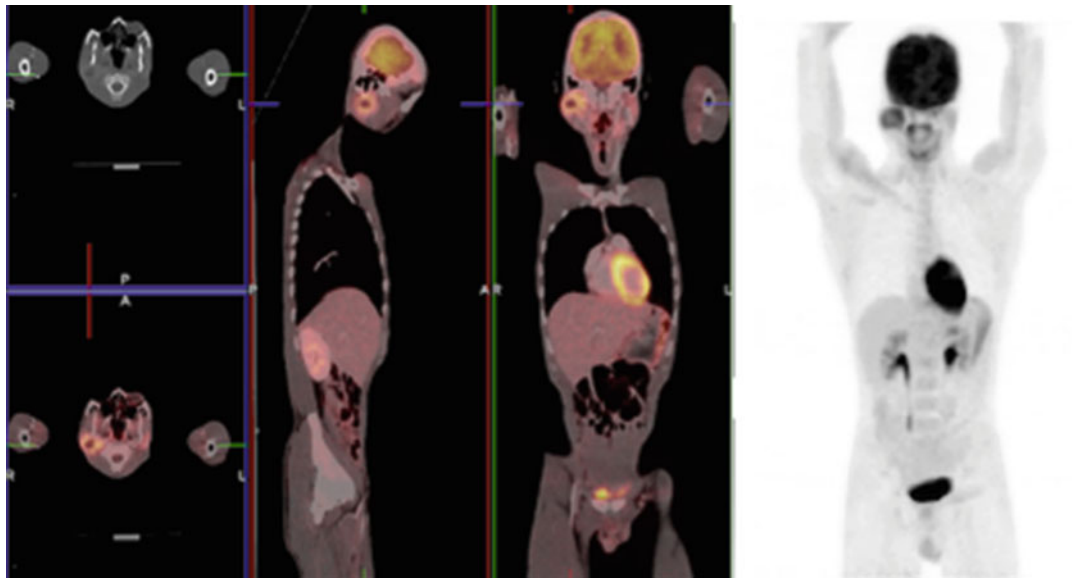

Fig. 10 Maximum intensity projection (MIP) image demonstrating uptake only limited to the parotid region

Case No. 6: Ewing's Sarcoma

Presentation

A 21-year-old woman presented with a large left scapular mass.

Findings

CT-guided biopsy revealed a round blue cell malignant neoplasm suspicious for Ewing's sarcoma. MRI of the shoulder showed a large T1 isointense/T2 hyperintense mass (12 × 11 cm) that extends superiorly encasing the supraspinatus

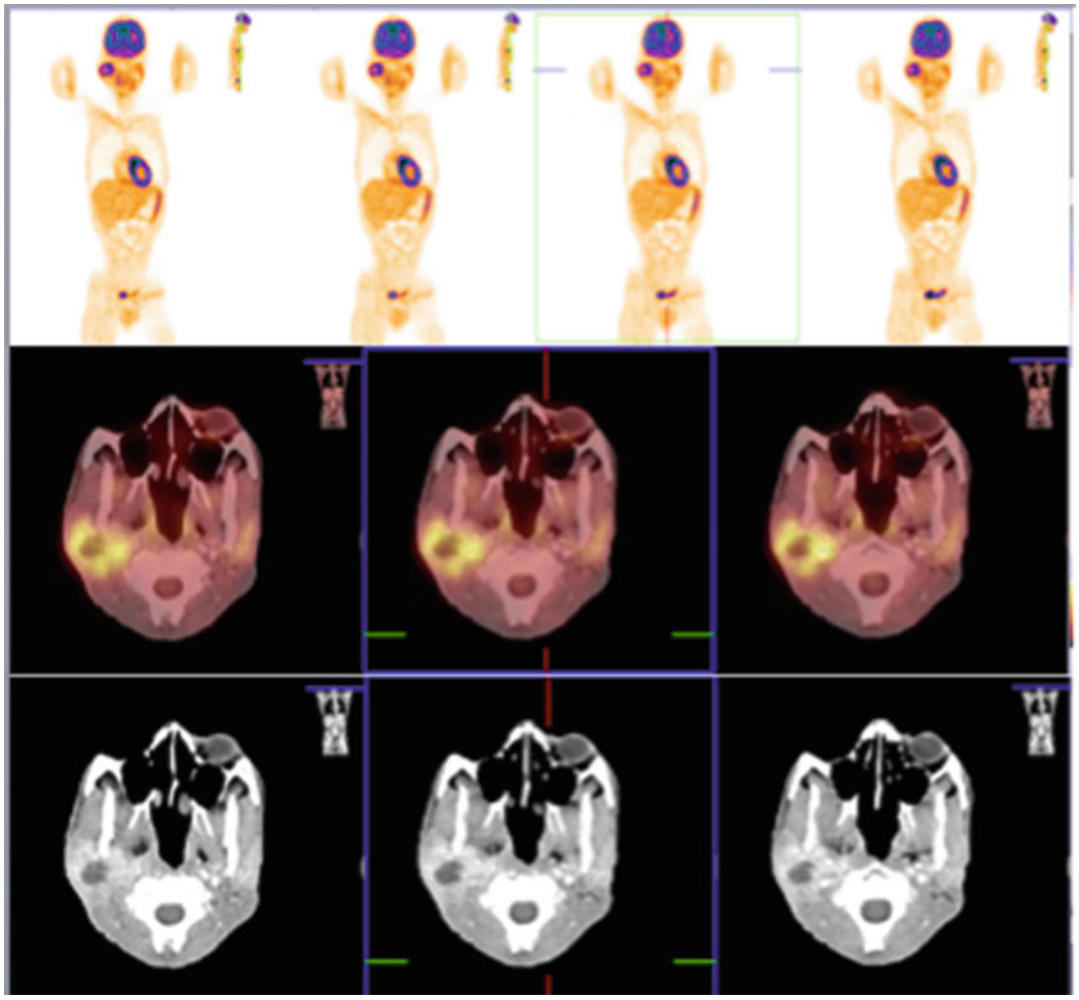

Fig. 11 Fusion coronal images demonstrating parotid mass. Fusion axial and CT images demonstrating parotid mass with necrotic center

muscle (Fig. 12). CT scan demonstrated permeative destructive changes of the scapula and left supraclavicular adenopathy. Bone scintigraphy with ^{99m}Tc-MDP demonstrated slightly increased tracer uptake in the left superior scapula, acromion, coracoid processes, and head of the left humerus (Fig. 13). [^{18}F]FDG PET/CT showed a large [^{18}F]FDG-avid mass invading the left scapula (SUV_{max} 7) (Fig. 14) without evidence of hypermetabolic lymphadenopathy or distant metastases. Increased radiotracer accumulation in the neck bilaterally and supra- and infraclavicular regions (Fig. 15) is due to metabolically active brown fat, a physiologic variant.

Follow-Up

Restaging [^{18}F]FDG PET/CT performed after three cycles of chemotherapy showed decreased [^{18}F]FDG uptake (SUV_{max} 2.1) and reduced extent of the mass, consistent with disease remission (Fig. 16). Subsequently, the patient was treated with total left scapulectomy. Histological examination demonstrated negative margins of resection, absent lymph node involvement, and a residual mass with 70% necrosis. The prior chemotherapy protocol was completed. Further follow-up imaging evaluations ([^{18}F]FDG PET/CT and CT) did not show active disease.

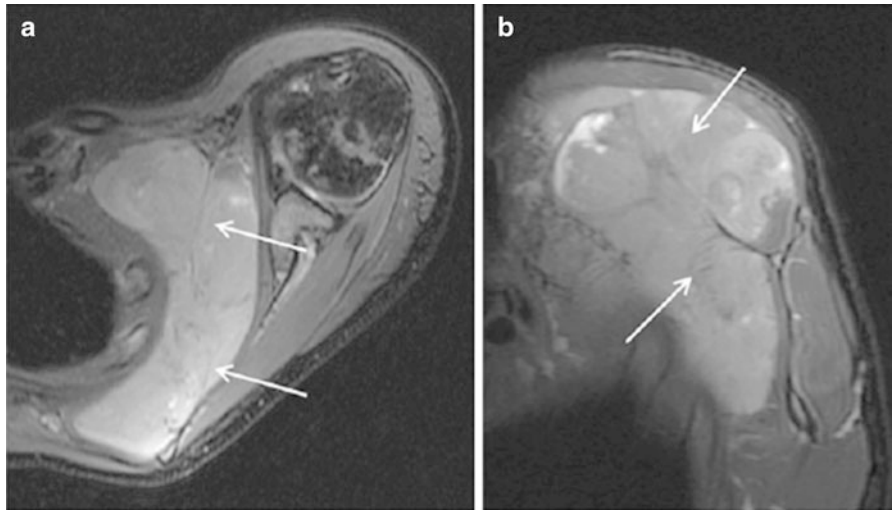

Fig. 12 MRI of the left shoulder: T2 hyperintense large mass, (**a**) axial view, (**b**) sagittal view

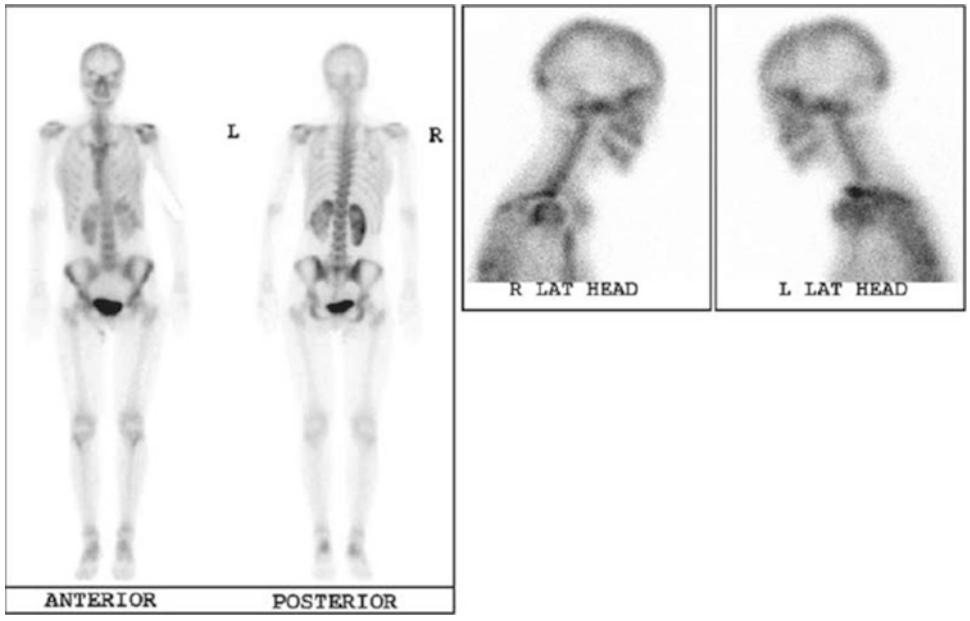

Fig. 13 Bone scintigraphy with ^{99m}Tc-MDP shows mildly increased tracer accumulation in the left scapula and proximal humerus

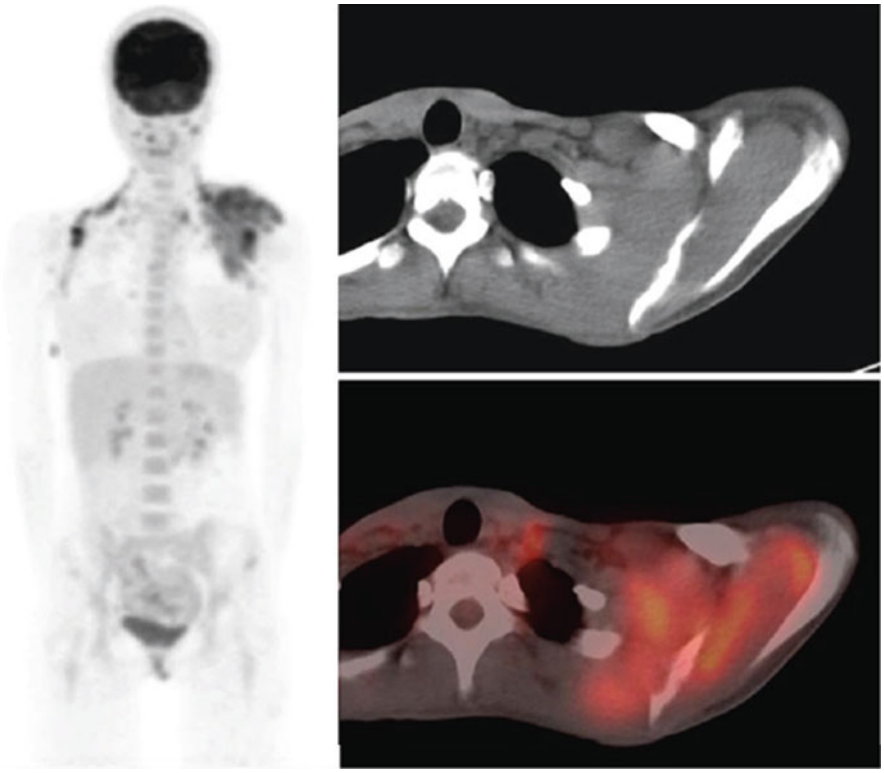

Fig. 14 [^{18}F]FDG PET/CT MIP and axial images show a large [^{18}F]FDG-avid soft tissue mass that involves the left supraclavicular, supra- and subscapular regions, and subpectoral region invading the left upper scapula

Discussion

This case demonstrates the advantage of [^{18}F] FDG PET/CT over conventional bone scan for the evaluation of both the primary lesion and the ability to detect metastases in Ewing's sarcoma.

Case No. 7: Metastatic Osteosarcoma

Presentation

A 45-year-old man with recurrent osteogenic sarcoma of the right fibula previously treated with surgical resection presents with right calf discomfort.

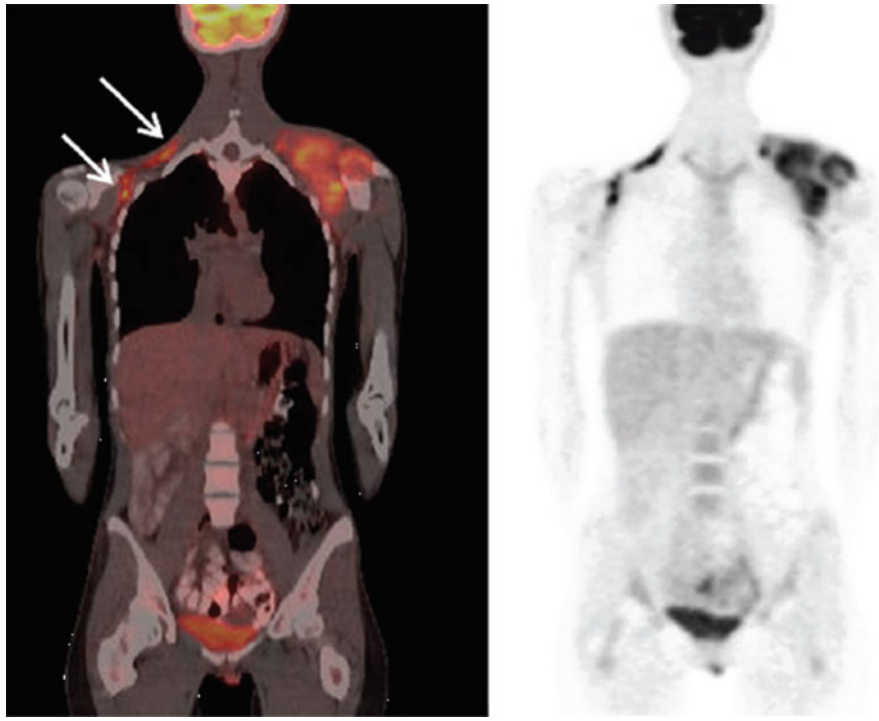

Fig. 15 [^{18}F]FDG PET/CT coronal images show multiple foci of [^{18}F]FDG uptake in the neck bilaterally and supra-infraclavicular regions (*white arrows*) corresponding to metabolic activation of the brown fat

Findings

MRI demonstrated a suspicious mass adjacent to the proximal resection margin of the fibula in the region of the peroneus longus and brevis muscles. [^{18}F]FDG PET/CT was performed for restaging.

[^{18}F]FDG PET/CT images show hypermetabolic nodules in the muscles of the proximal and midportion of the right calf, some of them calcified, with diffuse [^{18}F]FDG uptake in the post-surgical bed (Fig. 17). A calcified mass with mild [^{18}F]FDG uptake is noted in the left atrium (Fig. 18) compatible with metastatic disease. Several partially calcified nodules are also identified in the anterolateral region of the left gluteus medius muscle, of the right adductor muscle, and in the right lower neck posteriorly (Fig. 19).

Follow-Up

Follow-up [^{18}F]FDG PET/CT at 4 months after chemotherapy demonstrated no [^{18}F]FDG uptake in the left atrial mass and a mild reduction of activity in previous detected lesions.

This case demonstrates the value of [^{18}F]FDG PET/CT to assess the metabolic response to treatment in calcified metastatic lesions from osteosarcoma.

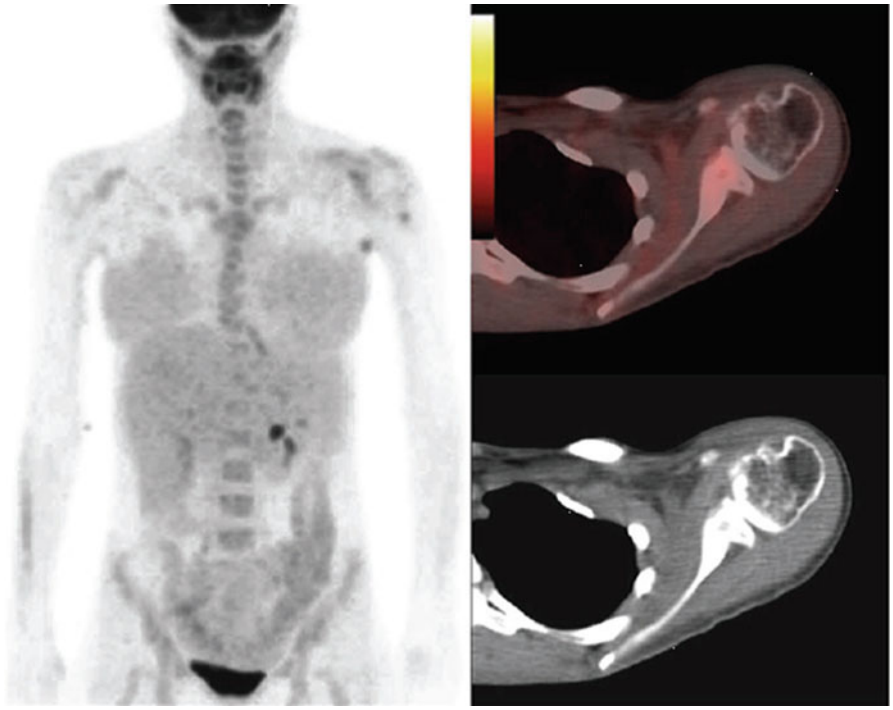

Fig. 16 [^{18}F]FDG PET/CT chemotherapy (MIP and axial images) demonstrates markedly reduced [^{18}F]FDG uptake and size of the scapular mass

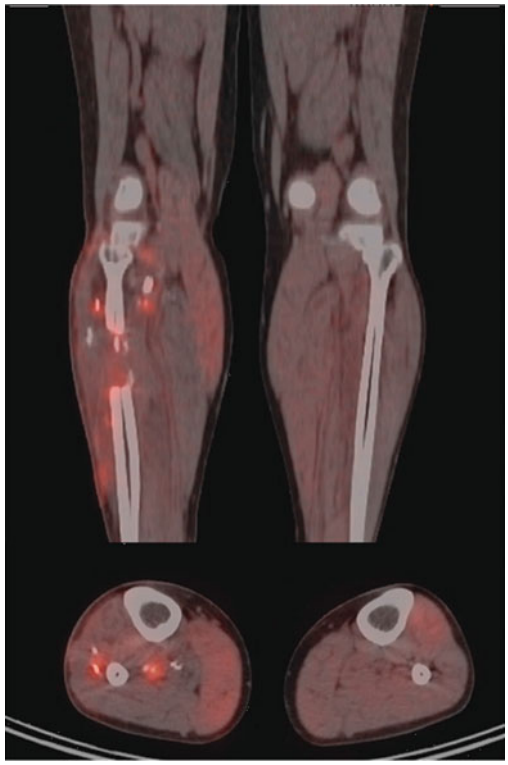

Fig. 17 Coronal and axial [^{18}F]FDG PET/CT fused images (coronal view *upper*, transaxial view *lower*) of the legs show hypermetabolic areas in the right calf, some of which are partially calcified lesions

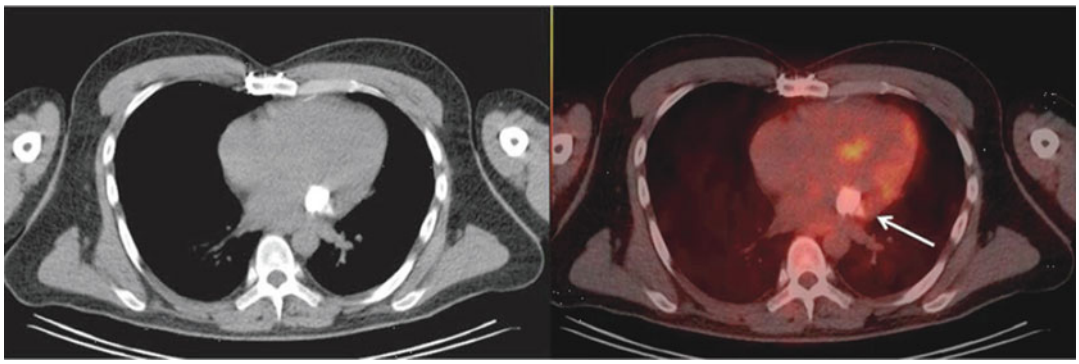

Fig. 18 Axial PET/CT image of the chest (CT, *left panel*, and PET/CT fused, *right panel*) showing the calcified left atrial mass which only demonstrates mild [^{18}F]FDG uptake

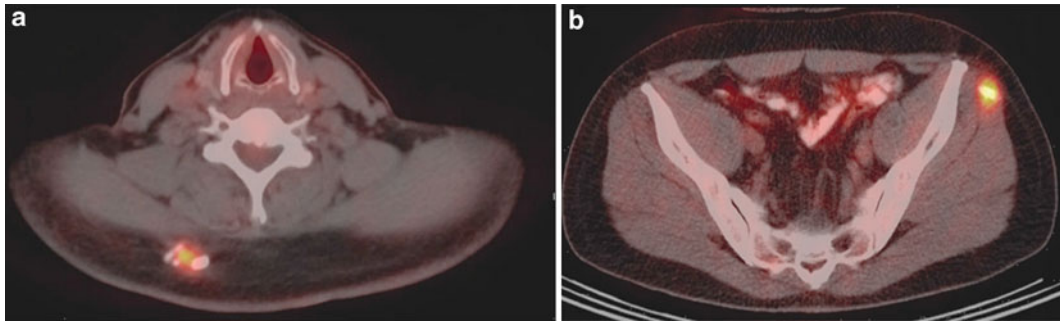

Fig. 19 [^{18}F]FDG PET/CT transaxial fused images of the neck (*upper panel*) and the pelvis (*lower panel*) show subcutaneous and muscle hypermetabolic nodules, (**a**) subcutaneous partially calcified nodule in the right lower neck, (**b**) calcified nodule in the anterolateral region of the left gluteus medius muscles

Teaching Cases in Nuclear Oncology: Malignant Melanoma

76

Alice Lorenzoni, Alessandra Alessi, and Flavio Crippa

Keywords

Metastatic melanoma • [^{18}F]FDG PET/CT • Melanoma pitfall

Glossary

[^{18}F]FDG	2-Deoxy-2-[^{18}F]fluoro-D-glucose
AAD	American Academy of Dermatology
Breslow thickness	A prognostic factor in cutaneous melanoma, based on description of how deeply tumor cells have invaded the skin (also called "Breslow depth")
Clark level	A staging system for cutaneous melanoma based on description of the level of anatomic invasion of the melanoma in the skin (generally used in conjunction with Breslow's depth)
CT	X-ray computed tomography
ESMO	European Society of Clinical Oncology
FNAB	Fine-needle aspiration biopsy
MIP	Maximum intensity projection
NCCN	National Comprehensive Cancer Network
PET	Positron emission tomography
PET/CT	Positron emission tomography/Computed tomography
SUV	Standardized uptake value
SUV_{max}	Standardized uptake value at point of maximum
US	Ultrasonography

Contents

Melanoma: Case No. 1 1866
Presentation 1866
Findings 1866
Discussion 1866

Melanoma: Case No. 2 1866
Presentation 1866
Findings 1866
Discussion 1866

Melanoma: Case No. 3 1866
Presentation 1866
Findings 1869
Discussion 1869

Melanoma: Case No. 4 1870
Presentation 1870
Findings 1871
Discussion 1871

Melanoma: Case No. 5 1871
Presentation 1871
Findings 1871
Discussion 1872

Melanoma: Case No. 6 1872
Presentation 1872
Findings 1873

A. Lorenzoni (✉) • A. Alessi • F. Crippa
Nuclear Medicine Division, IRCCCS National Cancer Institute, Milan, Italy
e-mail: alice.lorenzoni@istitutotumori.mi.it; alicelorenzoni@hotmail.it

© Springer International Publishing Switzerland 2017
H.W. Strauss et al. (eds.), *Nuclear Oncology*,
https://doi.org/10.1007/978-3-319-26236-9_79

Discussion 1874

Melanoma: Case No. 7 1874
Presentation 1874
Findings 1874
Discussion 1874

Melanoma: Case No. 8 1874
Presentation 1874
Findings 1874
Discussion 1875

Melanoma: Case No. 9 1876
Presentation 1876
Findings 1876
Follow-Up 1877
Discussion 1879

Melanoma: Case No. 1

Presentation

A 37-year-old man with dorsal melanoma and left axillary lymph node metastases treated with surgery 6 months earlier was referred for [^{18}F]FDG PET/CT for follow-up.

Findings

PET/CT examination revealed intense [^{18}F]FDG uptake in the gallbladder suspicious for malignancy (Figs. 1 and 2). Contrast-enhanced CT of the abdomen confirms the presence of multiple enhancing lesions (Fig. 2). Small [^{18}F]FDG-avid subcutaneous nodules consistent with melanoma localization were also identified in the neck and in the dorsum (Fig. 3).

Discussion

[^{18}F]FDG PET/CT may be helpful during melanoma follow-up for the assessment of recurrent and metastatic disease. Gallbladder metastasis is a rare but possible occurrence; thus, a careful evaluation in case of [^{18}F]FDG uptake in the gallbladder may correctly identify this rare occurrence.

Melanoma: Case No. 2

Presentation

A 52-year-old man with previously treated left lumbar melanoma with micrometastases in inguinal sentinel node underwent [^{18}F]FDG PET/CT during follow-up period.

Findings

PET/CT revealed the presence of multiple hypermetabolic mediastinal and bilateral hilar lymph nodes and bilateral [^{18}F]FDG-avid pulmonary nodules (Fig. 4). The differential diagnosis includes disseminated malignancies from granulomatous and inflammatory diseases. Symmetrical hilar [^{18}F]FDG uptake may be related to a benign, but the characteristics of hilar [^{18}F]FDG uptake in patients with granulomatous disease can be similar to those in patients with metastatic disease. Mediastinoscopic biopsy of lymph nodes was performed, and it revealed non-caseating giant cell granulomas, consistent with sarcoidosis. Steroid treatment was performed.

A repeat PET scan showed a decrease in the activity levels of hypermetabolic lymph nodes and pulmonary nodules (Fig. 5). These findings suggest a positive therapeutic response.

Discussion

Inflammatory lesions in the lungs, such as sarcoid, may lead to false-positive diagnosis of malignancy.

Melanoma: Case No. 3

Presentation

A 56-year-old man underwent [^{18}F]FDG PET/CT for follow-up 1 year after resection of a Stage IIIA melanoma of the left scapula.

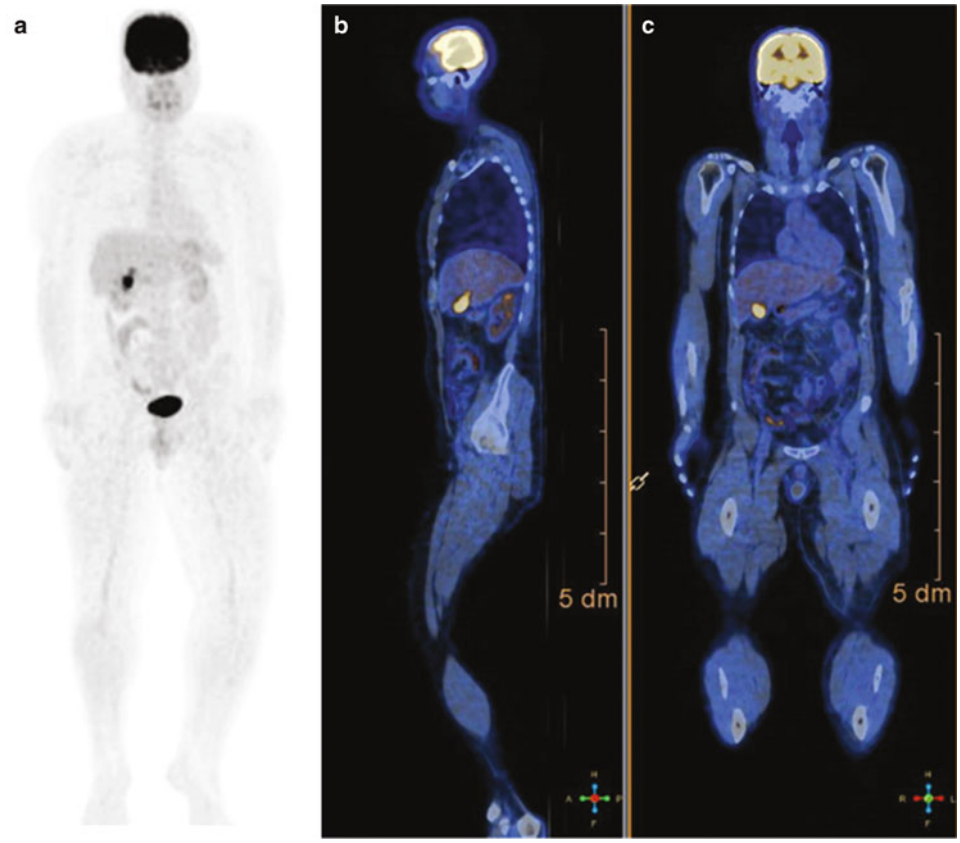

Fig. 1 Maximum intensity projection (**a**) and fused [^{18}F]FDG PET/CT images (**b** sagittal, **c** coronal) show intense FDG uptake in the gallbladder

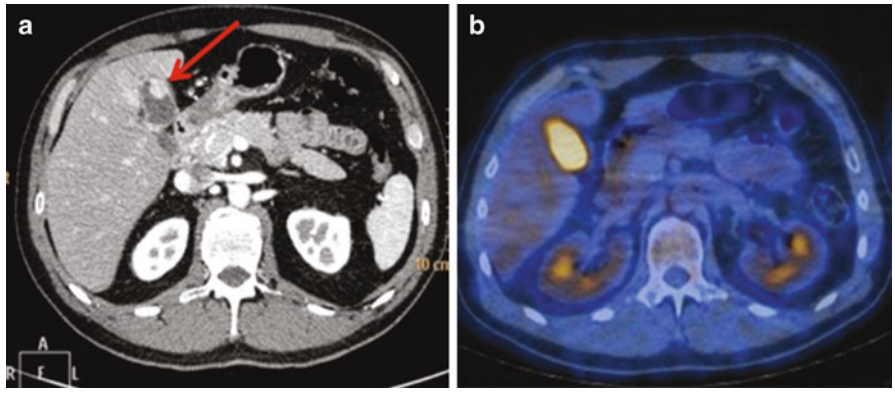

Fig. 2 Contrast-enhanced CT of the abdomen depicts the presence of gallbladder lesions consistent with metastases (panel **a**, *red arrow*) corresponding to focal [^{18}F]FDG uptake on PET/CT (panel **b**, transaxial fused PET/CT image)

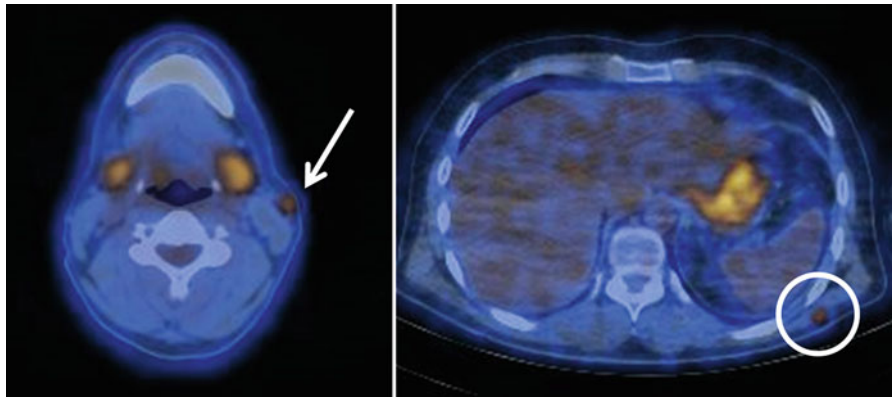

Fig. 3 Axial fused [^{18}F]FDG PET/CT images of subcutaneous lesion in the neck (*left panel*, *white arrow*) and in the dorsum (*right panel*, with *circle*)

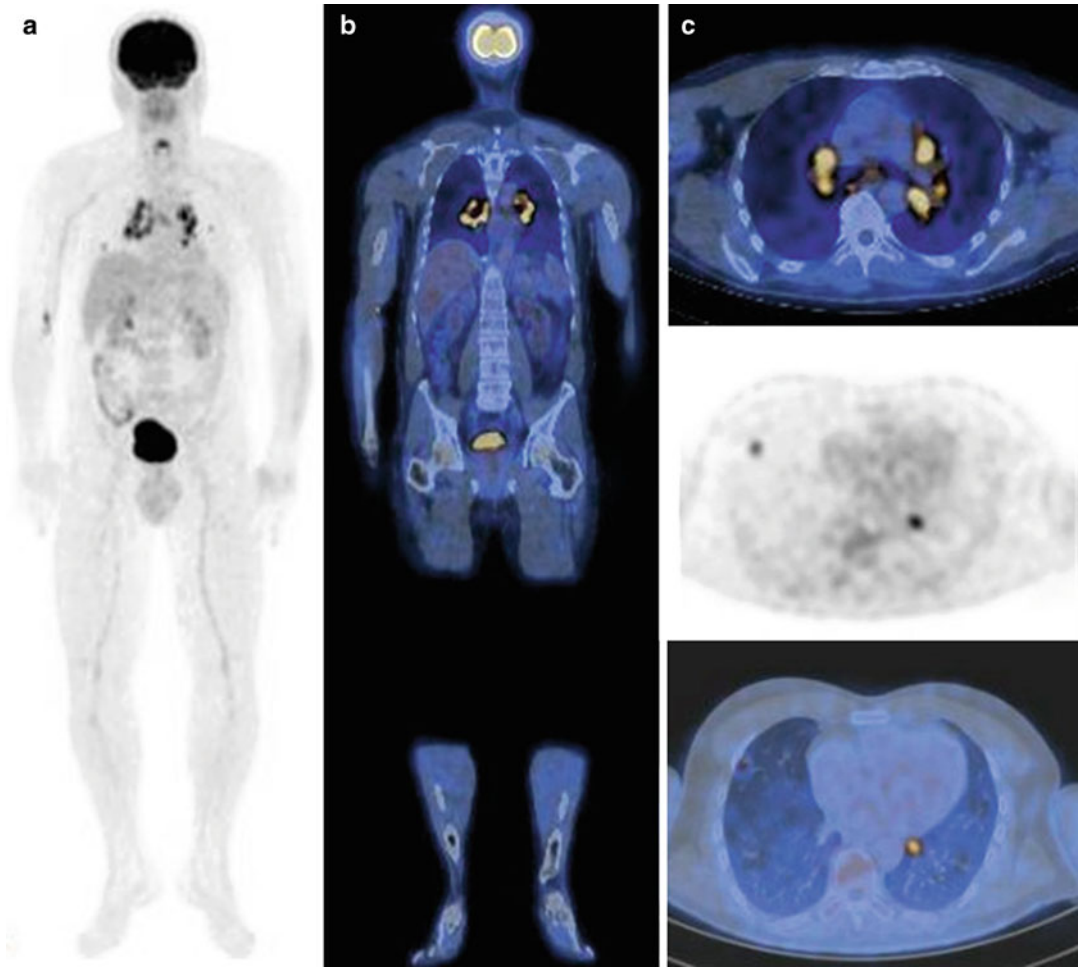

Fig. 4 Maximum intensity projection (MIP, **a**), coronal fused PET/CT (**b**), axial fused PET/CT, and axial PET images (**c**) show hypermetabolic mediastinal and hilar lymph nodes and [^{18}F]FDG-avid pulmonary nodules

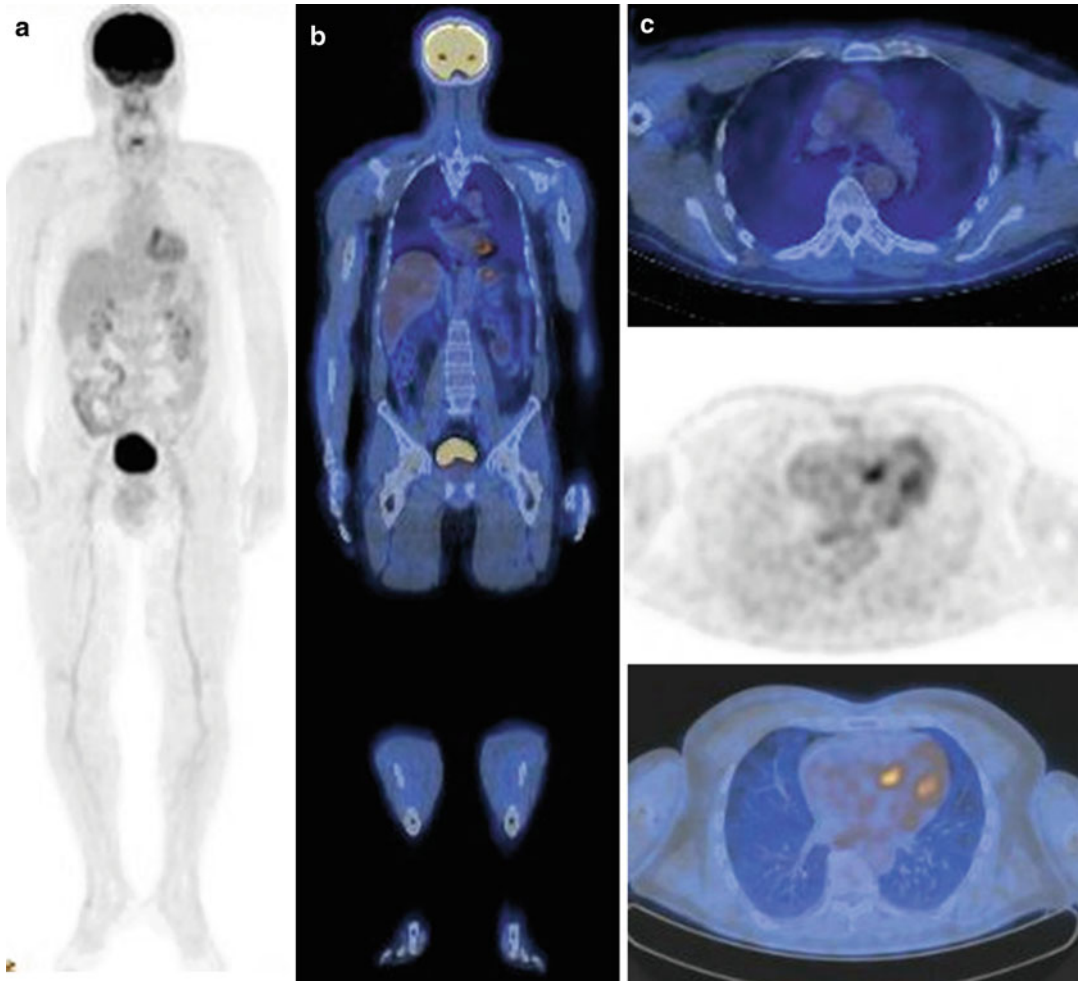

Fig. 5 Maximum intensity projection (MIP, **a**), coronal fused [^{18}F]FDG PET/CT (**b**), axial fused PET/CT, and axial PET images (**c**) show positive therapeutic response

Findings

PET/CT images revealed numerous visceral metastatic disease involving the lungs, liver, and spleen in the asymptomatic patient. Furthermore, multiple [^{18}F]FDG-avid bone lesions and soft tissue disease were noted (Fig. 6).

Discussion

At present there is no consensus on the optimal frequency of follow-up visits in asymptomatic patients with resected primary melanoma.

The National Comprehensive Cancer Network (NCCN) recommends routine imaging to monitor Stage IIB to IV melanoma chest x-ray, computed tomography (CT), and/or positron emission tomography (PET) scans every 3–12 months and annual magnetic resonance imaging (MRI) scans of the brain. However, routine follow-up radiologic imaging is not recommended for Stage IA to IIA melanomas.

In the American Academy of Dermatology (AAD) guidelines, imaging studies are not recommended in asymptomatic patients, although imaging studies can be considered in patients with high risk for recurrence. The European Society for

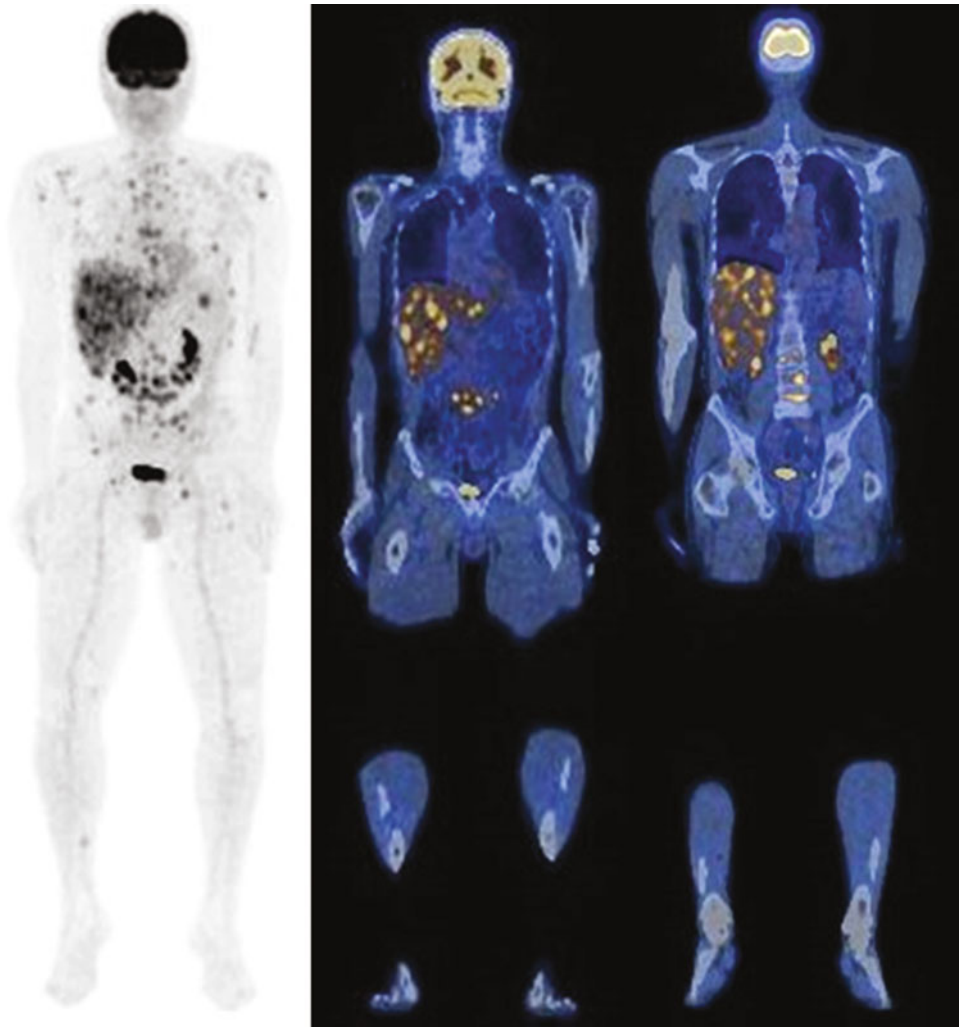

Fig. 6 Massive metastatic disease in previously treated melanoma discovered by [^{18}F]FDG PET/CT during follow-up

Medical Oncology (ESMO) guidelines provide general recommendations for monitoring patients at risk for recurrent and new disease. In high-risk patients (i.e., those with thick primary tumors or recent tumor resection), CT and/or PET scans are recommended for earlier detection of relapse.

[^{18}F]FDG PET/CT has a sensitivity of 96% and a specificity of 92%.

Melanoma: Case No. 4

Presentation

A 32-year-old man with previously surgically treated dorsal melanoma underwent [^{18}F]FDG PET/CT as a part of routine follow-up.

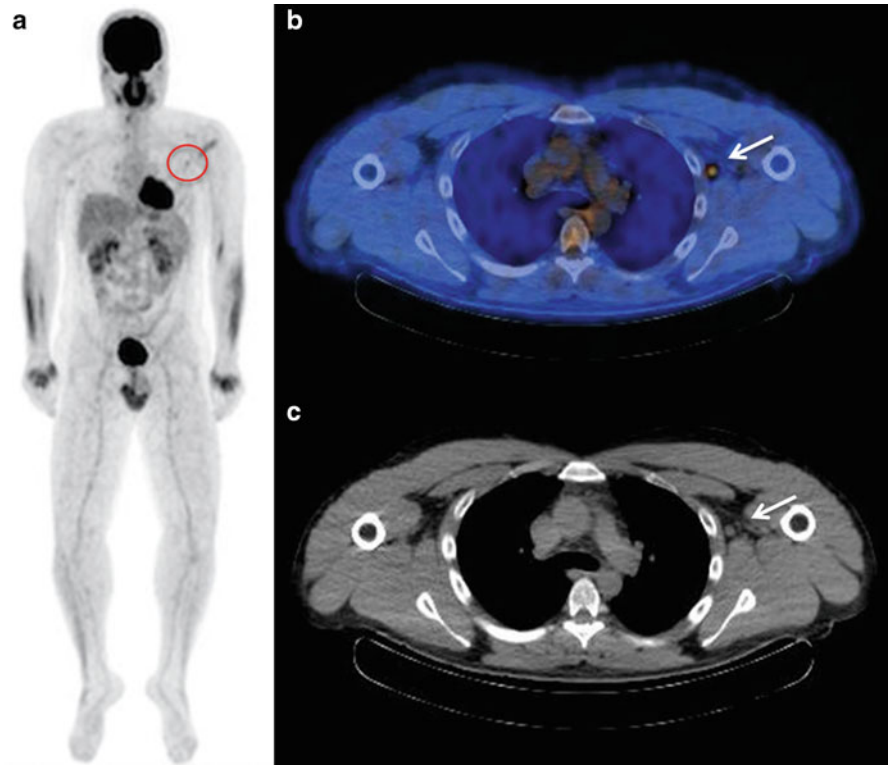

Fig. 7 Maximum intensity projection (**a**), axial fused PET/CT (**b**) and axial low-dose CT (**c**) show small lymph node in the left axilla with moderate [^{18}F]FDG uptake of uncertain origin

Findings

[^{18}F]FDG PET/CT demonstrated equivocal centimetric adenopathy with moderate [^{18}F]FDG uptake in the left axilla. Subsequent ultrasound of the axilla showed doubtful hypoechogenic lymphadenopathy.

Lymph node biopsy was performed and follicular hyperplasia was demonstrated.

Discussion

Reactive lymphadenopathy is well known as a principal cause of false-positive findings on PET/CT for nodal evaluation; when the etiology is unclear, biopsy may be necessary for diagnosis.

Melanoma: Case No. 5

Presentation

A 68-year-old man with a history of subscapular right melanoma (Stage IIA) was referred for routine physical examination. A painless, non-tender, subcutaneous nodule in the right scapula region suspicious for melanoma metastases was identified. [^{18}F]FDG PET/CT was performed to complete evaluation before planned surgical removal.

Findings

[^{18}F]FDG PET/CT confirmed the presence of hypermetabolic subcutaneous nodule in the right

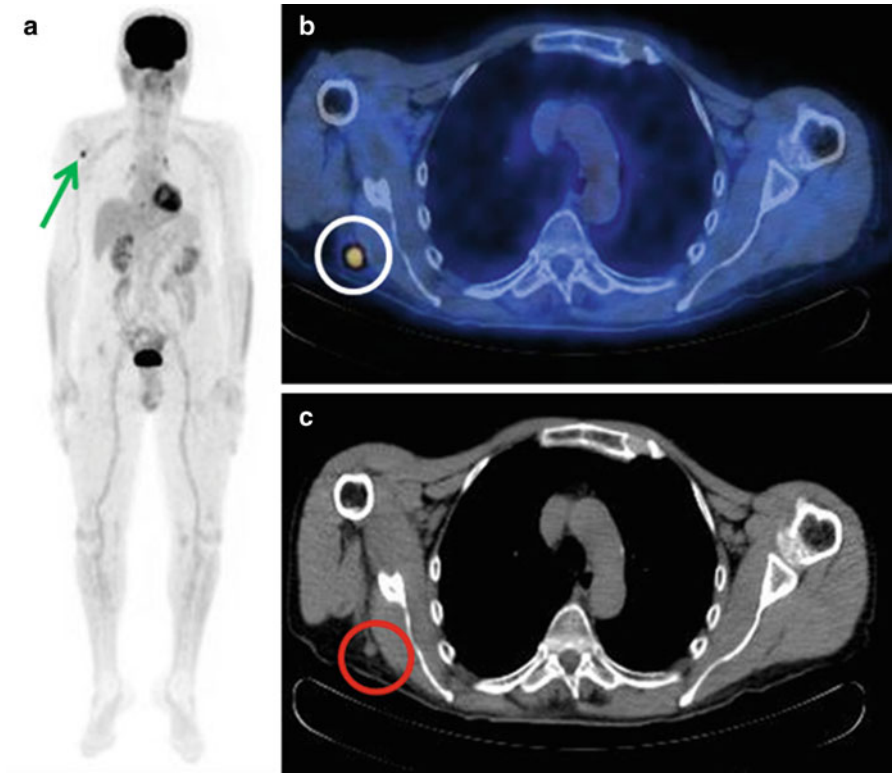

Fig. 8 Maximum intensity projection (MIP) (panel **a**) and axial images (**b** fused [^{18}F]FDG PET/CT; **c** low-dose CT) showed hypermetabolic small subcutaneous nodule in the right scapular region consistent with metastatic disease (**a** *green arrow*, **b** *white circle*, **c** *red circle*)

scapular region consistent with a pathological lesion (Fig. 8). Furthermore, an exophytic mass with soft tissue attenuation on low-dose CT images and moderate [^{18}F]FDG uptake in the left kidney was noted.

Further investigation demonstrated renal cell carcinoma.

Discussion

Findings of incidental primary renal lesions are common on [^{18}F]FDG PET/CT. Non-metabolically active pathology can be missed without close attention to the CT portion of the examination, whereas metabolically active pathology can be missed on [^{18}F]FDG PET due to physiologic accumulation of tracer in the renal collecting system. Therefore, close attention to both the PET and CT portions of the study is needed to identify renal lesions and guide the further diagnostic approach.

[^{18}F]FDG PET/CT cannot discriminate between renal cancer and oncocytoma, and furthermore complex or infected cysts can be [^{18}F]FDG-avid (Fig. 9).

Melanoma: Case No. 6

Presentation

An 84-year-old man with multiple subcutaneous nodules on the left leg in previously treated melanoma of the calf underwent [^{18}F]FDG PET/CT before planned isolated chemotherapeutic perfusion of the limb.

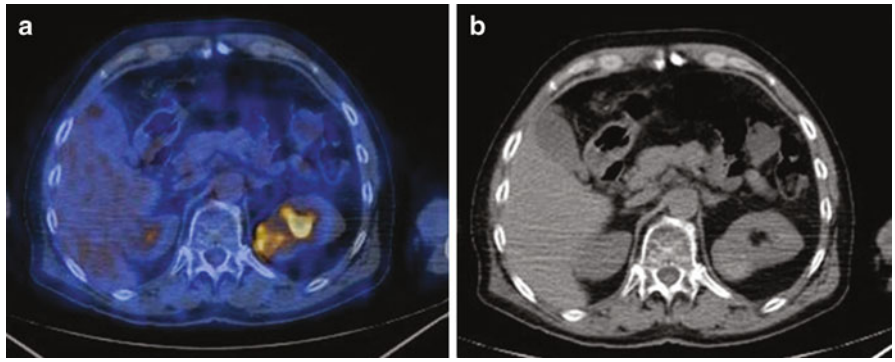

Fig. 9 Right renal [^{18}F]FDG-avid lesion on PET/CT (**a** axial fused PET/CT image; **b** axial low-dose CT)

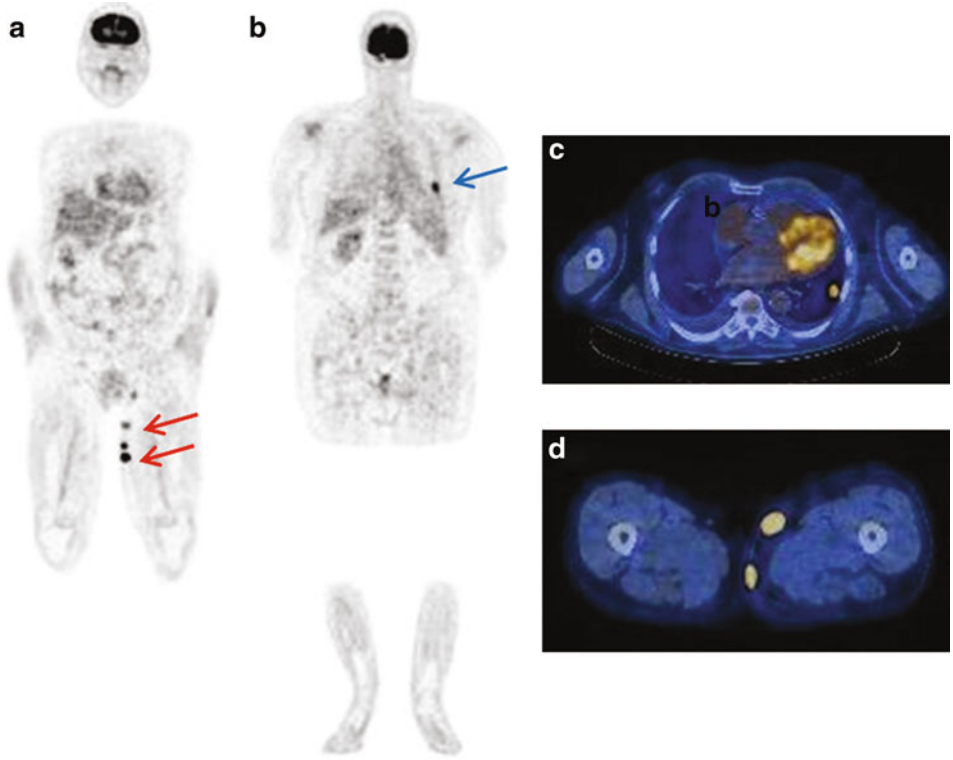

Fig. 10 Coronal PET (**a**) and axial fused PET/CT (**b**) images show hypermetabolic subcutaneous nodules in the left limb. [^{18}F]FDG-avid left lung lesion is also demonstrated (**b** PET coronal image and **c** axial fused PET/CT image)

Findings

[^{18}F]FDG PET/CT showed multiple hypermetabolic pathological subcutaneous nodules in the medial region of the left limb (Fig. 10). In the basal region of the left lung, a small [^{18}F]FDG-avid nodule was also depicted consistent with lung metastases. Bilateral Pleural effusion with mild [^{18}F]FDG uptake was shown. Systemic approach was considered to treat the patient.

Discussion

[^{18}F]FDG PET/CT can detect unexpected metastases resulting in a change in patient management.

PET scanning is extremely sensitive (91–95%) and very specific (83–92%) for identifying metastatic melanoma, particularly in soft tissues, lymph nodes, and the liver. False-negative scans in the presence of metastases are rare (<5%).

Melanoma: Case No. 7

Presentation

A 42-year-old woman previously treated for melanoma referred for suspected lymph node metastases (1 cm in size) in the left axilla detected by US. Fine-needle aspiration biopsy (FNAB) was performed, and cytology confirmed the presence of melanoma metastases. The patient underwent [^{18}F]FDG PET/CT before planned axillary lymph node dissection.

Findings

PET/CT depicted a lymph node in the left axilla which showed moderate [^{18}F]FDG uptake corresponding to biopsied lesion. A small subcutaneous nodule with mild [^{18}F]FDG uptake suggested melanoma metastasis in the left clavicular region. In addition an [^{18}F]FDG-avid lytic lesion in the sternum consistent with skeletal metastases was detected.

Patient was treated with surgery followed by external beam radiotherapy of the sternum.

Discussion

This case demonstrates that [^{18}F]FDG-PET/CT may have an additional value in the staging of recurrent melanoma (Fig. 11).

Melanoma: Case No. 8

Case contributed by H.A. Jacene

Nuclear Medicine/PET-CT, Dana-Farber Cancer Institute, Harvard Medical School, Boston, Massachusetts, USA.

Presentation

A 49-year-old woman with metastatic melanoma, restaging examination with [^{18}F]FDG PET/CT.

Findings

On the PET maximum intensity projection image viewed anteriorly (Fig. 12), multiple [^{18}F]FDG-avid pulmonary nodules and a left pelvis mass are seen. In the region of the right kidney, the expected excreted urinary [^{18}F]FDG contour of the right renal pelvis appears to have an abnormal configuration. When the MIP image is rotated and viewed from a right anterior oblique projection (Fig. 12), it is apparent that there is an [^{18}F]FDG-avid mass anterior to the right kidney. On further evaluation of the axial PET and CT images, an [^{18}F]FDG-avid mass is seen in the neck of the gallbladder (Fig. 13). On a coronal contrast-enhanced diagnostic CT image performed on a separate date, a 3.4 cm

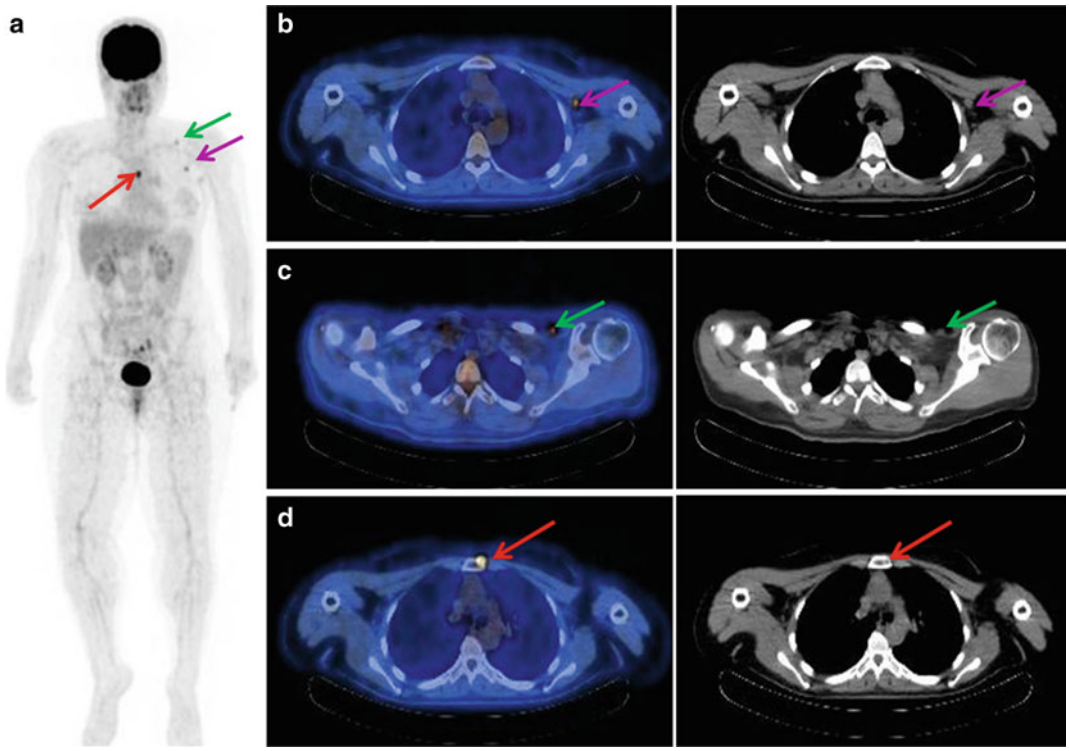

Fig. 11 Maximum intensity projection (*MIP*) image (**a**) in patient with metastatic melanoma. Axial fused [^{18}F]FDG PET/CT (*left panel*) and low-dose CT (*right panel*) show left axillary lymph node involvement (**a**, **b** *pink arrow*), subcutaneous [^{18}F]FDG-avid lesion (**a**, **c** *green arrow*), and hypermetabolic lytic sternal lesion (**a**, **d** *red arrow*)

enhancing mass within the gallbladder can be seen (Fig. 14).

Discussion

Metastases to the gallbladder are unusual for any malignancy, but are most often seen with metastatic melanoma compared to other malignancies. Metastases from other primary carcinoma origins such as renal cell carcinoma, the breast, and the stomach among others are seen, but are less common. Usually, metastases to the gallbladder are asymptomatic and however occasionally do present clinically with acute cholecystitis or common bile duct obstruction.

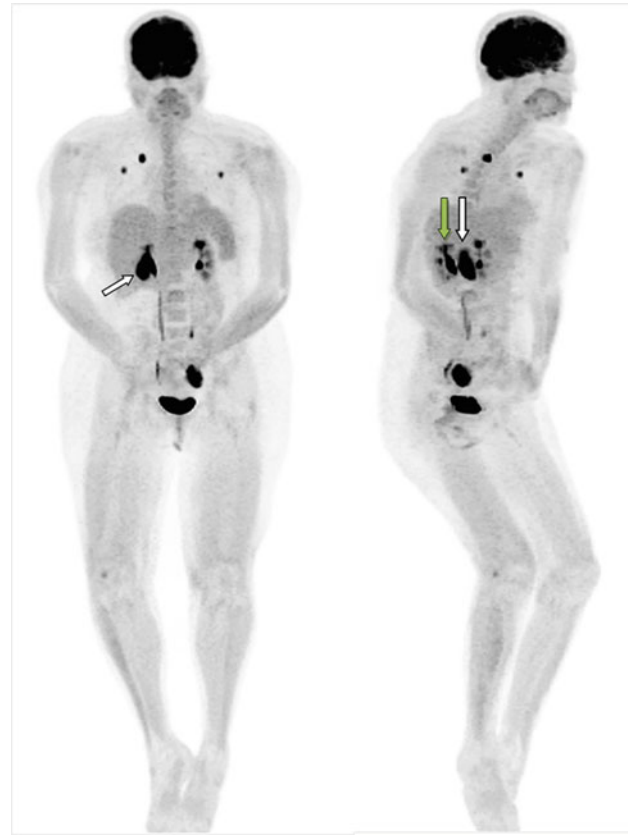

Fig. 12 PET maximum intensity projection image viewed anteriorly (*left*) and from a right anterior oblique view (*right*) shows multiple [^{18}F]FDG-avid pulmonary nodules and an [^{18}F]FDG-avid left pelvic mass. On the anterior view, in the expected location of the right kidney, there is an asymmetry and contour abnormality of the [^{18}F]FDG activity (*white arrow*). On the right anterior oblique view, this abnormality in the region of the right kidney is seen to actually be due to a mass (*white arrow*) anterior to the more posteriorly located right kidney (*green arrow*)

Melanoma: Case No. 9

Presentation

A 77-year-old woman presented with erythema and induration of the right hand. She was initially treated with local antibiotics without resolution.

Findings

A biopsy showed a malignant melanoma greater than 4 mm with ulceration.

Following intradermal injections of ^{99m}Tc-nanocolloidal albumin around the lesion, lymphoscintigraphy showed sentinel lymph nodes in the axilla and supraclavicular region (Fig. 15).

Fig. 13 CT (*above*) and PET (*below*) images of the gallbladder neck demonstrate an intensely [^{18}F]FDG-avid round mass in the gallbladder (*arrows*)

The patient had surgical excision of the lesion on the hand and sentinel node biopsies. Histological examination confirmed a malignant melanoma (Breslow 4 mm, Clark IV) with metastasis to an axillary sentinel node (Stage III). Right supraclavicular node was negative.

Fig. 14 Coronal image from a contrast-enhanced diagnostic CT demonstrates a round enhancing 3.4 cm mass in the gallbladder neck (*arrow*)

Follow-Up

[^{18}F]FDG PET/CT performed to evaluate the extent of disease after surgery did not show pathological uptake (Fig. 16). Follow-up [^{18}F]FDG PET/CT at 12 months demonstrated widespread metastases in uptake in the right neck lymph nodes (SUV_{max} 6.2) (Fig. 17) and multiple hypermetabolic foci (SUV_{max} 11) in the axial and appendicular skeleton (Fig. 18a) involving the scapulae, humeri (Fig. 18b), pelvis (Fig. 18c), spine (Fig. 18d), femora, and right tibia.

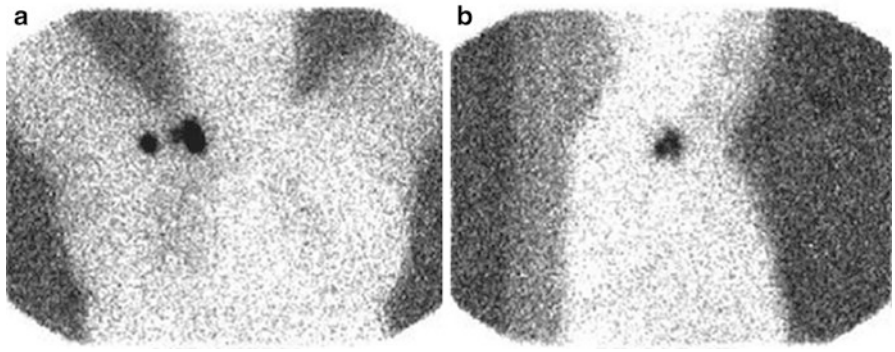

Fig. 15 Sentinel node lymphoscintigraphy. Static images of the neck and thorax show uptake accumulation in the right neck and supraclavicular region, (**a**) anterior projection, (**b**) right lateral projection

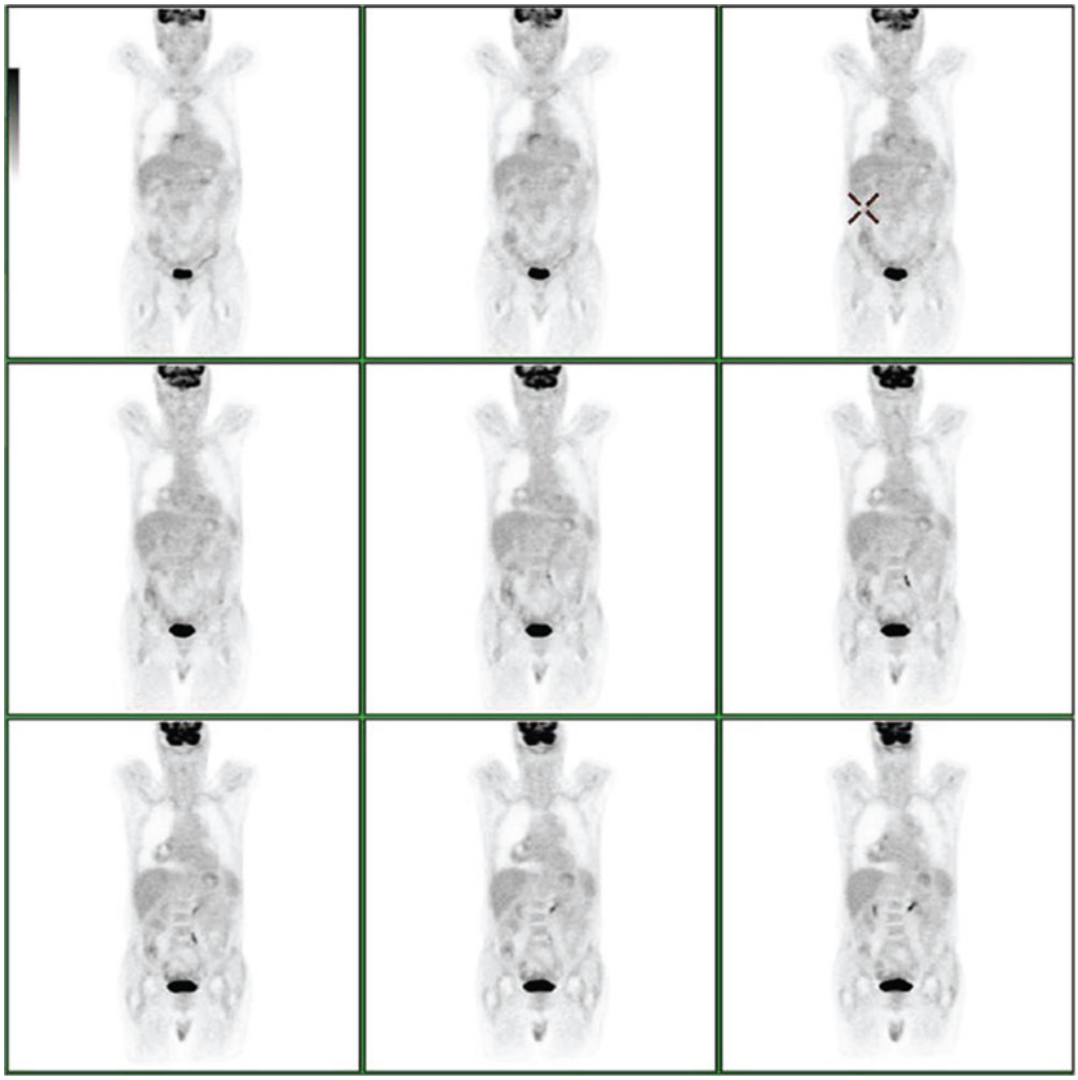

Fig. 16 Postsurgical [^{18}F]FDG PET/CT showing no abnormal sites of uptake

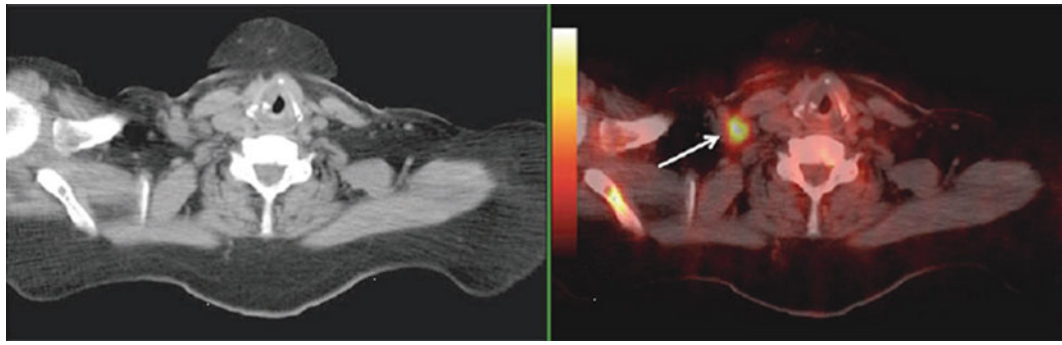

Fig. 17 CT and fused [^{18}F]FDG PET/CT axial images showing hypermetabolic right neck lymph node

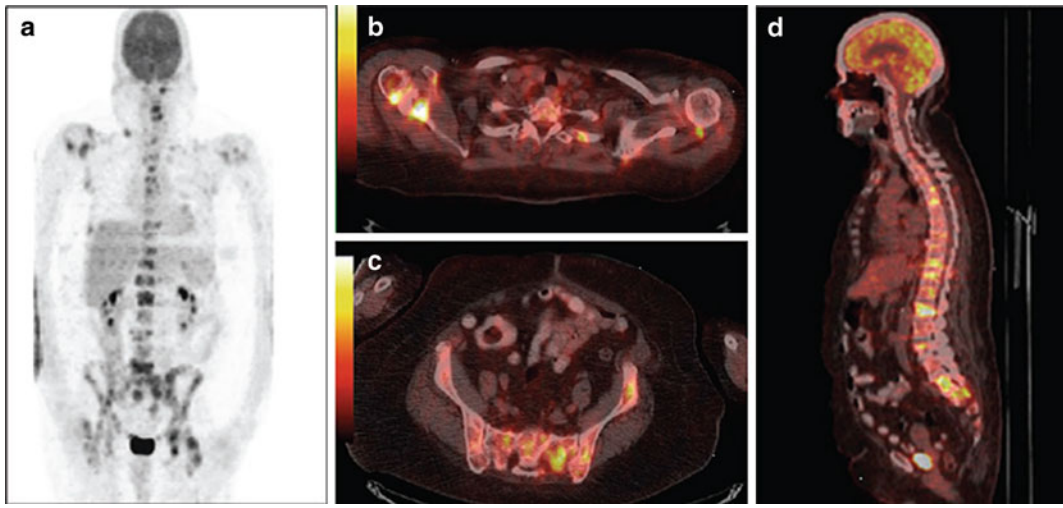

Fig. 18 (**a**) MIP image of metastatic skeletal melanoma, (**b**) axial fused image of pathological uptake in the right scapula and humerus, (**c**) axial fused image of pelvic skeletal, and (**d**) sagittal fused image show spine involvement

Discussion

The preoperative SUV_{max} of the primary lesion in patients with ulcerated lesions is a potent predictor of recurrence in patients with cutaneous melanoma. Although a preoperative [^{18}F]FDG scan was not performed in this patient, the histologic characteristics of the lesion and the presence of metastatic disease following surgery place this patient in the high risk of recurrence category of this aggressive disease.

Teaching Cases in Nuclear Oncology: Pediatric Cancers

77

Duccio Volterrani, Giulia Puccini, Sara Mazzarri, Federica Guidoccio, and Lorenzo Biassoni

Keywords

Neuroblastoma • [^{123}I]MIBG • MRI • Contrast enhanced CT • ^{68}Ga-DOTATATE • ^{177}Lu-DOTATATE molecular radiotherapy • Ganglioneuroblastoma • Diffuse large B-cell lymphoma • [^{18}F]FDG PET/CT • Ewing sarcoma • Hodgkin's lymphoma • Chemotherapy

Glossary

[^{123}I]MIBG	[^{123}I]-*meta*-Iodobenzylguanidine
[^{131}I]MIBG	[^{131}I]-*meta*-Iodobenzylguanidine
[^{18}F]FDG	2-Deoxy-2-[^{18}F]fluoro-D-glucose
^{18}F-DOPA	2-^{18}F-Fluoro-L-3,4-dihydroxyphenylalanine
ABVD	Chemotherapy regimen based on adriamycin, bleomycin, vinblastine, and dacarbazine
ceCT	Contrast-enhanced computed tomography
COJEC	Chemotherapy regimen based on cisplatin, vincristine, carboplatin, etoposide, and cyclophosphamide
CT	X-ray computed tomography
DLBCL	Diffuse large B-cell lymphoma
DOTA	1,4,7,10-Tetra-azacyclododecane-1,4,7,10-tetraacetic acid
DOTANOC	DOTA-1-Nal^3-octreotide
DOTATATE	DOTA-Tyr^3-octreotate
Gy	Gray unit (ionizing radiation dose in the International System of Units, corresponding to the absorption of one joule of radiation energy per kilogram of matter)
HASTE	Half-Fourier acquisition single shot turbo spine echo, a magnetic resonance imaging technique
HVA	Homovanillic acid, a dopamine metabolite
IVC	Inferior vena cava
MAP2	Microtubule-associated protein-2
MIBG	*meta*-Iodobenzylguanidine
MIP	Maximum intensity projection
MR	Magnetic resonance

D. Volterrani (✉) • G. Puccini • S. Mazzarri • F. Guidoccio
Regional Center of Nuclear Medicine, Department of Translational Research and Advanced Technologies in Medicine and Surgery, University of Pisa, Pisa, Italy
e-mail: duccio.volterrani@med.unipi.it

L. Biassoni
Nuclear Medicine Service, Great Ormond Street Hospital, London, UK

© Springer International Publishing Switzerland 2017
H.W. Strauss et al. (eds.), *Nuclear Oncology*,
https://doi.org/10.1007/978-3-319-26236-9_80

MRI	Magnetic resonance imaging
MYCN	Gene encoding for the N-myc proto-oncogene protein, also known as N-Myc or basic helix-loop-helix protein 37 (bHLHe37)
NCCN	National Comprehensive Cancer Network
NSE	Neuron-specific enolase
PET	Positron emission tomography
PET/CT	Positron emission tomography/Computed tomography
RCHOP	Chemotherapy regimen based on rituximab, cyclophosphamide, doxorubicin
SPECT	Single-photon emission computed tomography
SPECT/CT	Single-photon emission computed tomography/Computed tomography
STIR	Short tau inversion recovery, a magnetic resonance imaging technique used for fat suppression (also known as short T1 inversion recovery)
SUV	Standardized uptake value
SUV_{max}	Standardized uptake value at point of maximum
SVC	Superior vena cava
TVD	Chemotherapy regimen based on topotecan, vincristine, and doxorubicin vincristine, and prednisone
VMA	Vanyllilmandelic acid, a catecholamine metabolite

Contents

Neuroblastoma: Case No. 1 1883
Presentation 1883
Findings 1883
Follow-Up 1883
Teaching Point 1883

Neuroblastoma: Case No. 2 1883
Presentation 1883
Findings 1883
Follow-Up 1884
Teaching Point 1884

Neuroblastoma: Case No. 3 1884
Presentation 1884
Findings 1884
Follow-Up 1886
Teaching Point 1886

Neuroblastoma: Case No. 4 1886
Presentation 1886
Findings 1886
Management 1887
Teaching Point 1887

Neuroblastoma: Case No. 5 1888
Presentation 1888
Findings 1889
Management 1889
Teaching Points 1889

Neuroblastoma: Case No. 6 1890
Presentation 1890
Findings 1890
Management 1890
Teaching Points 1894

Neuroblastoma: Case No. 7 1894
Presentation 1894
Findings 1895
Management 1895
Teaching Point 1895

Neuroblastoma: Case No. 8 1896
Presentation 1896
Findings 1896
Management 1897
Teaching Point 1898

Neuroblastoma: Case No. 9 1898
Presentation 1898
Findings 1899
Follow-Up 1900

Ewing Sarcoma 1900
Presentation 1900
Findings 1901
Follow-Up 1902
Teaching Point 1902

Lymphoma: Case No. 1 1902
Presentation 1902
Findings 1902
Follow-Up 1903
Teaching Point 1903

Lymphoma: Case No. 2 1903
Presentation 1905
Findings 1905
Follow-Up 1906
Teaching Point 1906

Lymphoma: Case No. 3 1906
Presentation 1906
Findings 1916
Teaching Point 1916

Neuroblastoma: Case No. 1

Presentation

A four-year-old girl with high-risk neuroblastoma (stage IV, MYCN amplified). Treated with induction chemotherapy (modified N7 protocol), with partial response (persisting 5–10% positive bone marrow cells on bilateral trephines). Second-line induction chemotherapy with TVD, with some improvement, but still about 5% positivity on bone marrow trephines. Further treatment with bevacizumab and temozolomide, with good response. Surgery, with 80% tumor removal and left nephrectomy (tumor invasion of the left renal hilum).

Findings

Persisting disease on reassessment [^{123}I]MIBG (Fig. 1). The child has subsequently been treated with experimental therapies including monoclonal antibodies and modified T-cells. MRI scan after fifth cycle of monoclonal antibody treatment disclosed a splenunculus (Fig. 2). A [^{123}I]MIBG scan was performed 5 days after the MRI scan. There were two persisting foci of [^{123}I]MIBG avid disease in the left side of the abdomen (Fig. 3). The intensity of uptake is significantly reduced in comparison to the previous MIBG study after surgery. The SPECT/CT study raises the possibility that the splenunculus may be MIBG-avid (Fig. 3). Contrast-enhanced CT scan, performed the day after the [^{123}I]MIBG scan, showed the splenunculus and a further soft tissue nodule just below it, corresponding to the [^{123}I]MIBG avid nodule and compatible with residual disease (Fig. 4). Moreover, residual disease in the retroperitoneum only minimally [^{123}I]MIBG avid was clearly seen on contrast-enhanced CT (Fig. 5).

Follow-Up

The child was discussed at the multidisciplinary team meeting, with the view to proceed to further surgery that seemed feasible based on the imaging studies.

Teaching Point

The [^{123}I]MIBG SPECT/CT study has been critical in identifying the additional nodule of [^{123}I]MIBG avid disease below the splenunculus. Comparison with contemporaneous cross-sectional imaging has also been essential for a proper interpretation of the MIBG findings. Surgical planning has included resection of that nodule, clearly separate and different from the splenunculus. Without proper comparison with other imaging, the focal area of abnormal [^{123}I]MIBG uptake could have been interpreted as representing the splenunculus, with the possible risk of resecting an accidental normal finding and leaving in place a nodule of [^{123}I]MIBG avid neuroblastoma.

Neuroblastoma: Case No. 2

Presentation

A five-year-old boy, diagnosed with stage IV neuroblastoma (widespread skeletal disease) at the age of 2.5 years (Fig. 6). Treated with induction chemotherapy (rapid COJEC) to complete remission on MIBG and surgical resection of the primary tumor. Three months later, recurrent disease with a brain metastasis in the right parietal lobe; this was resected, with subsequent radiotherapy and adjuvant chemotherapy. Subsequent relapse in the skeleton (right tibia and femur) few months later, treated with second-line chemotherapy (TVD), topotecan, [^{131}I]MIBG therapy, and high-dose chemotherapy, followed by antibody therapy. In complete remission on [^{123}I]MIBG scintigraphy and X-ray as a result (Fig. 7). After 1 year, he presents with acute onset of left knee pain.

Findings

The patient underwent a MRI of the left femur that showed a focal abnormality in the distal

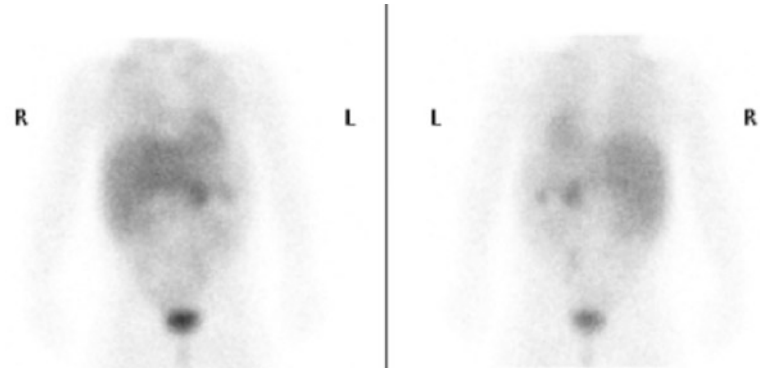

Fig. 1 Reassessment [^{123}I]MIBG shortly after surgery (anterior and posterior planar images): two focal areas of [^{123}I] MIBG avid disease in the left side of the abdomen are seen

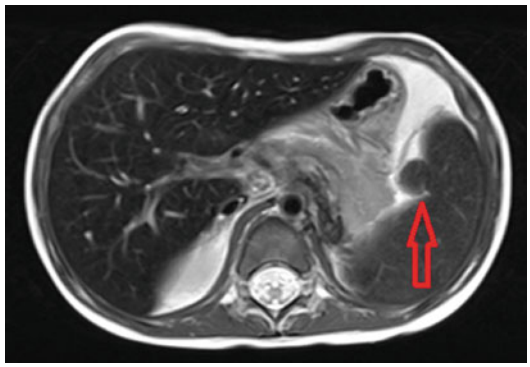

Fig. 2 MRI scan, T2 weight images, after fifth cycle of monoclonal antibody treatment and several months after surgery (axial view): there is a splenunculus

diaphysis, with abnormal signal and enhancement of the periosteum and the bone marrow, highly suspicious for recurrence (Fig. 8). One week later, [^{123}I]MIBG scintigraphy resulted completely negative with no evidence of abnormal uptake in the left femur (Fig. 9). A subsequent ^{68}Ga-DOTATATE whole body PET/CT scan found a highly increased somatostatin analogue uptake in the distal left femur, compatible with recurrent malignant disease (Fig. 10).

Follow-Up

The child was treated with three courses of ^{177}Lu-DOTATATE molecular radiotherapy, with improvement in the left femoral metastasis.

Teaching Point

This case illustrates that previous [^{123}I]MIBG avid neuroblastoma can relapse as MIBG negative disease. Neuroblastoma, although detected with high sensitivity by [^{123}I]MIBG, is [^{123}I]MIBG negative in about 5% of cases. Also, [^{123}I]MIBG positive primary neuroblastoma can show clones of [^{123}I]MIBG negative cells. And a patient with mainly [^{123}I]MIBG positive metastatic lesions can show [^{123}I]MIBG non-avid lesions. [^{123}I]MIBG is a marker of the norepinephrine active uptake-1 transport mechanism and is taken up by neuroblastoma only if this mechanism is still functional.

Neuroblastoma: Case No. 3

Presentation

A five-year-old boy, with a diagnosis of high-risk neuroblastoma (poorly differentiated Schwannian stroma poor, stage IV, widespread skeletal metastatic infiltration on [^{123}I]MIBG) at the age of 2 (Fig. 11).

Findings

He was treated with induction chemotherapy (rapid COJEC) with excellent response (resolution of all skeletal metastatic lesions with the exception of a lesion in the sternum) (Fig. 12).

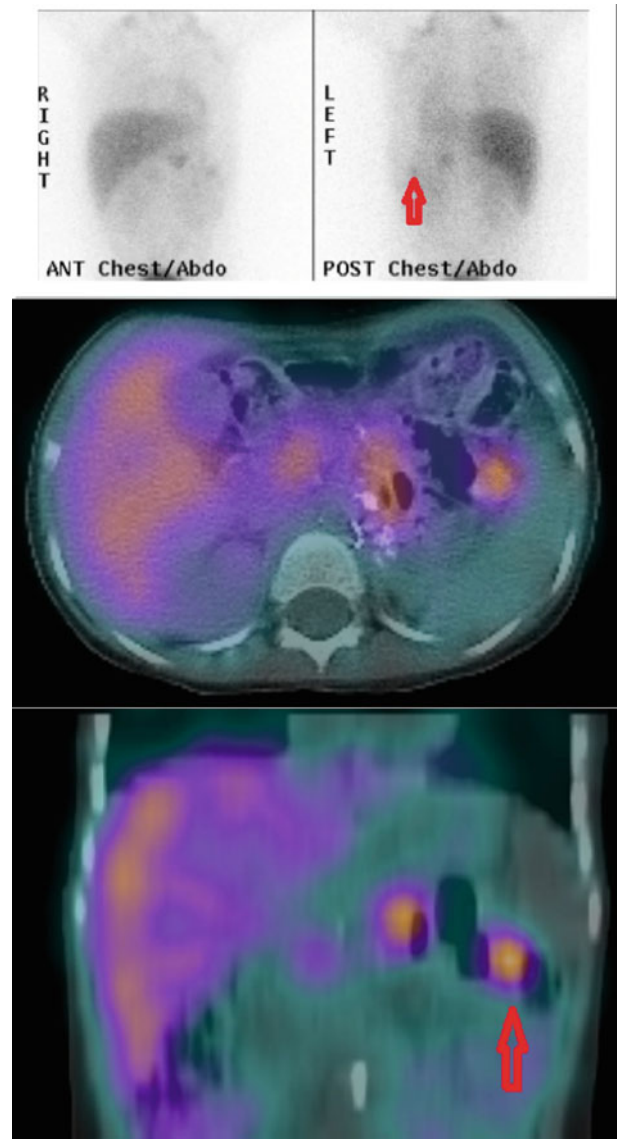

Fig. 3 [^{123}I]MIBG scan, performed 5 days after the MRI scan. Reassessment after five courses of monoclonal antibody treatment. There are two persisting foci of [^{123}I]MIBG avid disease in the left side of the abdomen on planar images (*top panel*). The intensity of uptake is significantly reduced in comparison to the previous [^{123}I]MIBG study after surgery. The SPECT CT study (axial views) raise the possibility that the splenunculus may be [^{123}I]MIBG avid (*middle* and *bottom panel*). However, it is noted that there is no [^{123}I]MIBG uptake in the spleen, and this would be very unusual

He also received high-dose chemotherapy with busulfan and melphalan and stem cell rescue, achieving complete remission on [^{123}I]MIBG (Fig. 13). He had abdominal radiotherapy at the site of the primary tumor, cis-retinoic acid, and immunotherapy with anti-GD2 monoclonal antibodies. During immunotherapy he relapsed with a focal area of abnormal [^{123}I]MIBG uptake in the manubrium of the sternum, exactly at the same site of the previous disease (Fig. 14). This was treated with cyclophosphamide and topotecan and external beam radiotherapy, with no significant change on [^{123}I]MIBG SPECT/CT scanning and ^{68}Ga-DOTATATE PET/CT (stable disease) (Fig. 15). An excision biopsy after 13 cycles of chemotherapy showed ganglioneuroblastoma with extensive differentiated elements and no evidence of undifferentiated cells (Fig. 16).

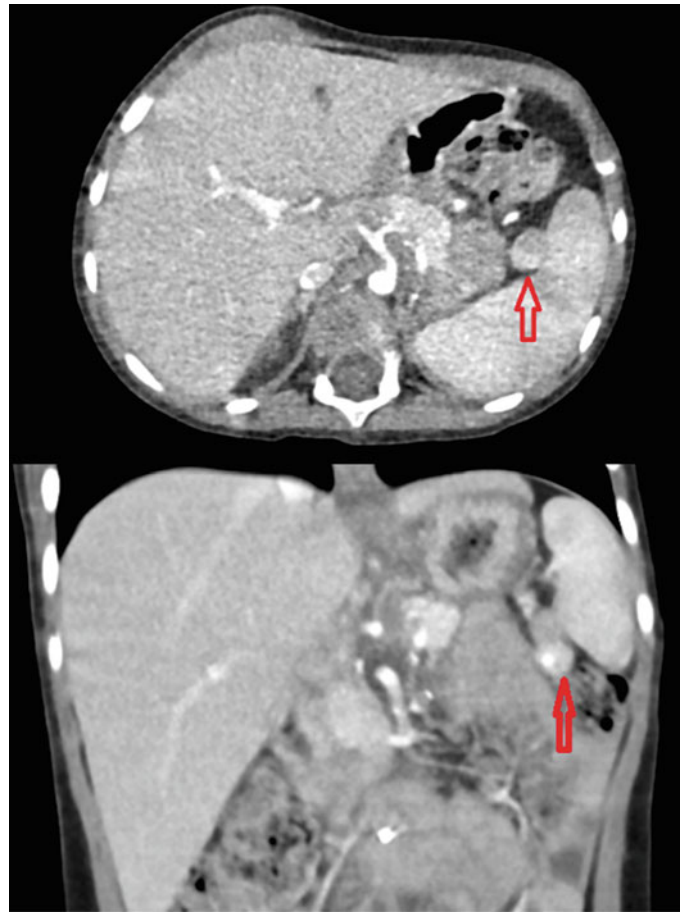

Fig. 4 Contrast-enhanced CT scan, performed the day after the [^{123}I]MIBG scan. This shows the splenunculus and a further soft tissue nodule just below it, best seen on the coronal views (*bottom panel, arrow*): this is likely to correspond to the [^{123}I]MIBG avid nodule and is compatible with residual disease

Follow-Up

In view of the completely excised well-differentiated ganglioneuroblastoma and the absence of undifferentiated cells, the cytotoxic chemotherapy based on cyclophosphamide and topotecan has been withdrawn.

Teaching Point

This case illustrates the possible differentiation of a highly malignant poorly differentiated neuroblastoma into a much more benign well-differentiated ganglioneuroblastoma variant following chemotherapy. [^{123}I]MIBG scanning could not differentiate between these histological variants.

Neuroblastoma: Case No. 4

Presentation

A five-month-old baby girl diagnosed with a poorly differentiated neuroblastoma with very elevated VMA/HVA urinary levels.

Findings

An MRI at diagnosis showed a large intra-abdominal mass lesion arising from the right adrenal, with skin and liver metastases (Fig. 17). Her [^{123}I]MIBG scan showed skeletal metastatic involvement (Fig. 18). However, her bone marrow aspirate was negative for metastatic

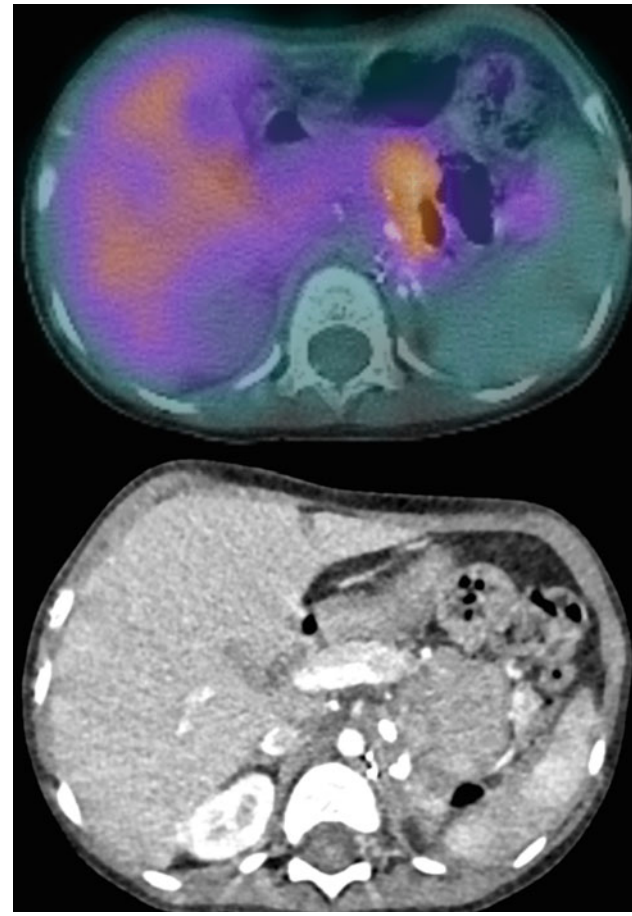

Fig. 5 [^{123}I]MIBG SPECT/CT scan (*top panel*) and contrast-enhanced CT (*bottom panel*). Residual disease in the retroperitoneum, only minimally [^{123}I]MIBG avid on SPECT/CT and clearly seen on contrast-enhanced CT

infiltration. The molecular analysis from the biopsy of her abdominal tumor did not show MYCN amplification (and no segmental chromosomal abnormality). Consequently she was considered as having intermediate rather than high-risk disease. The investigations of her disease at staging suggest a pattern of stage IV disease rather than IVs.

Management

On the basis of her stage (IV rather than IVs), this girl has been commenced on chemotherapy (carboplatin and etoposide), in line with European guidelines.

Teaching Point

This is a very interesting and unusual case. The age of the child (5 months) would raise the possibility of a IVs neuroblastoma; however, the nature of the primary tumor (crossing the midline, encasing vessels, extending to the retrocrural space) and the pattern of metastatic infiltration (focal rather than diffuse hepatic metastatic infiltration, no bone marrow disease, cortical bone metastases) are consistent with stage IV disease. However, in view of the favorable tumor biology (MYCN non-amplified, no chromosomal abnormalities) and of her age (<18 months), her neuroblastoma can be classified as intermediate rather than high risk. On the other hand, as she has stage IV disease, she has

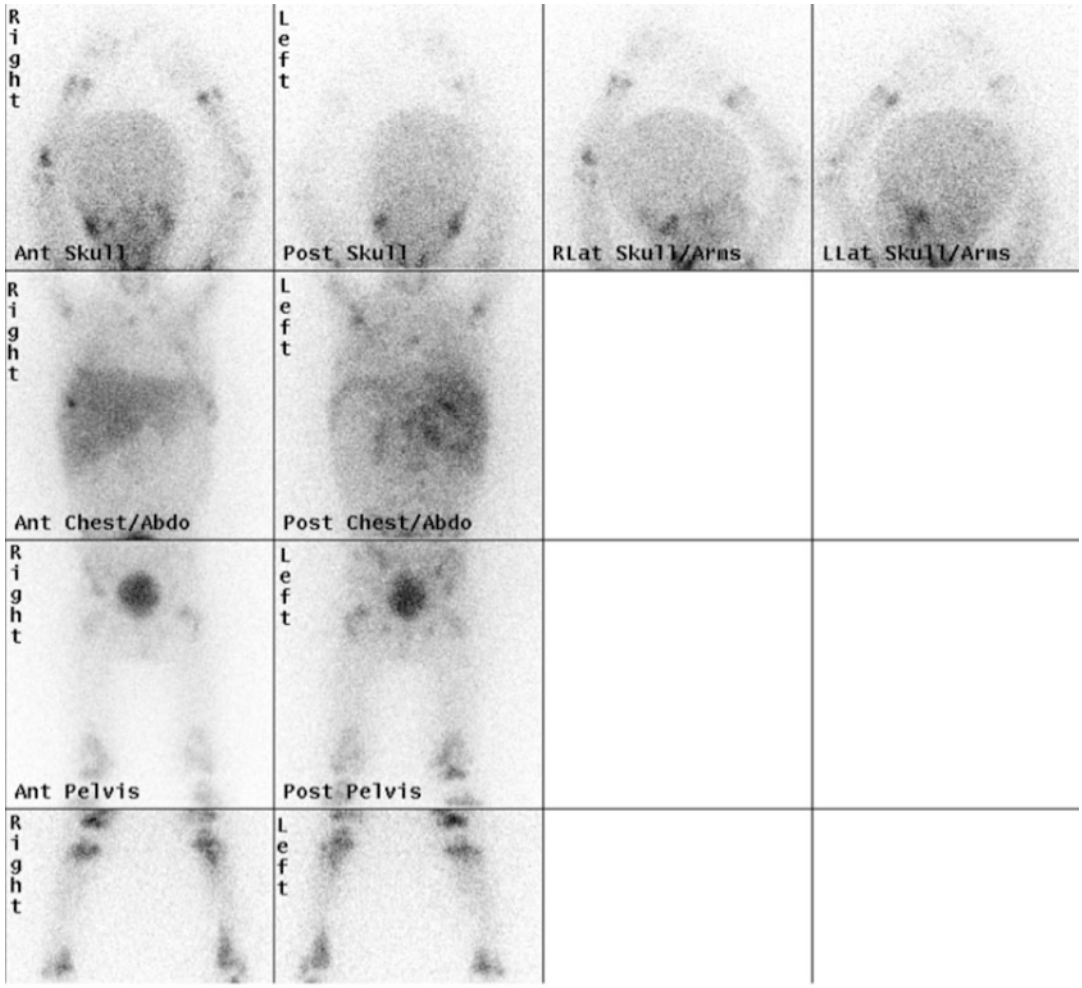

Fig. 6 [^{123}I]MIBG at diagnosis (aged 2.5 years): the primary neuroblastoma in the right suprarenal region shows a rim of [^{123}I]MIBG avid disease surrounding a central area with lower grade uptake. There are widespread [^{123}I]MIBG avid skeletal deposits, consistent with bone and bone marrow metastatic infiltration

been started on chemotherapy. The [^{123}I]MIBG scan successfully shows the skeletal metastases but fails to distinguish between bone and bone marrow disease (the bone marrow aspirate excluded bone marrow involvement). Also, the [^{123}I]MIBG scan showed low sensitivity for liver metastases, due to the normal hepatic [^{123}I]MIBG uptake.

Neuroblastoma: Case No. 5

Presentation

A two-month-old baby boy presenting with a 3-day history of vomiting, diarrhea, and increasing abdominal distension.

Fig. 7 X-ray of the left knee 2.5 years after diagnosis, when the child was in complete remission: there is a focal area of sclerosis in the medial aspect of the distal left femur, very similar to a previous X-ray, possibly compatible with a healed metastasis

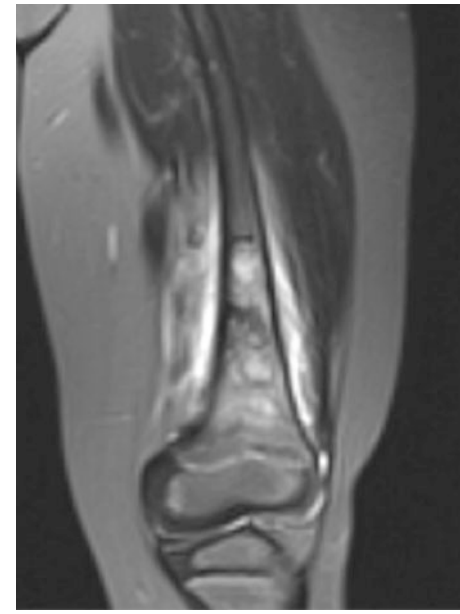

Fig. 8 MRI left femur 1 week later: focal abnormality in the distal diaphysis of the left femur, with abnormal signal and enhancement of the periosteum and the bone marrow, highly suspicious for recurrence

Findings

His MRI scan at diagnosis showed a massive hepatomegaly with multiple nodules of disease. In addition, there was a right adrenal mass lesion, which on percutaneous biopsy was demonstrated to be a poorly differentiated neuroblastoma (Fig. 19). [^{123}I]MIBG at diagnosis showed no evidence of significantly increased tracer uptake (Fig. 20).

Management

Clinically and radiologically, this baby boy had IVs neuroblastoma. However, molecular analysis on the biopsy specimen showed MYCN amplification. Therefore, in view of the unfavorable biology, he was upstaged to high risk and treated with rapid COJEC induction chemotherapy.

Teaching Points

A neuroblastoma can be [^{123}I]MIBG entirely negative in approximately 5% of cases. Therefore, [^{123}I]MIBG cannot be used to follow up these tumors. PET tracers, such as [^{18}F]FDG, ^{18}F-DOPA, ^{68}Ga-DOTATATE, or DOTANOC can be tried.

IVs neuroblastoma usually has a good prognosis and is treated with mild chemotherapy. However, in approximately 10% of cases, a IVs neuroblastoma can have amplification of the MYC oncogene; in this case it has a much worse prognosis and is treated with the aggressive form of chemotherapy used for high-risk stage IV disease.

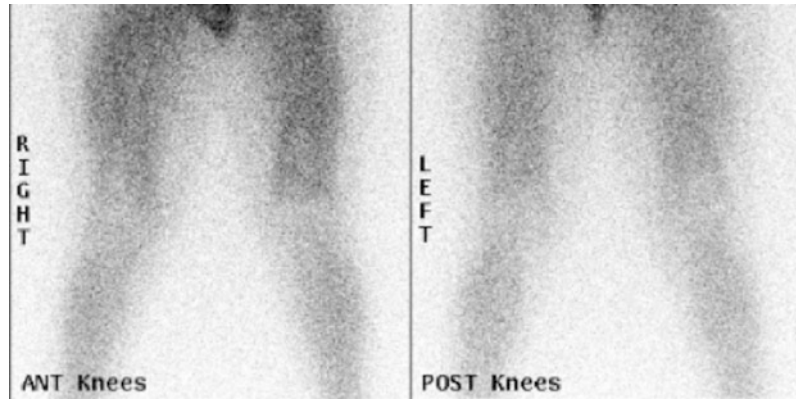

Fig. 9 [^{123}I]MIBG 1 week after the MRI: no evidence of abnormal uptake in the left femur

Fig. 10 ^{68}Ga-DOTATATE whole body PET scan 1 week later: there is highly increased somatostatin analogue uptake in the distal left femur, compatible with recurrent malignant disease (Image courtesy of Dr J. Bomanji, Institute of Nuclear Medicine, University College London Hospital)

Neuroblastoma: Case No. 6

Presentation

A two-year-old girl, presenting with jaundice. She was found to have a large abdominal mass, which on biopsy, following ultrasound and MRI, turned out to be a poorly differentiated, Schwannian stroma poor, neuroblastoma.

Findings

MRI and [^{123}I]MIBG showed localized disease in the mid-upper abdomen (Figs. 21 and 22).

Management

Based on the bone marrow trephine result (Fig. 23), this is stage IV neuroblastoma, high risk (also considering the patient's age and the unfavorable histopathology). The child was commenced on induction chemotherapy based on rapid COJEC (no vincristine due to raised bilirubin).

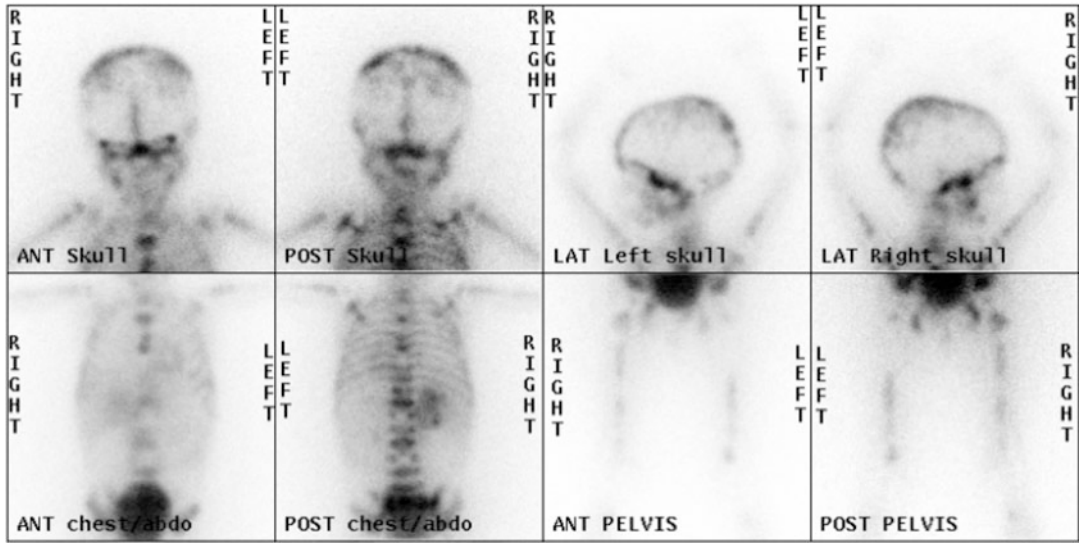

Fig. 11 [^{123}I]MIBG scan at diagnosis: there is increased tracer uptake within in the primary neuroblastoma in the right suprarenal region, with widespread metastatic infiltration in the skeleton

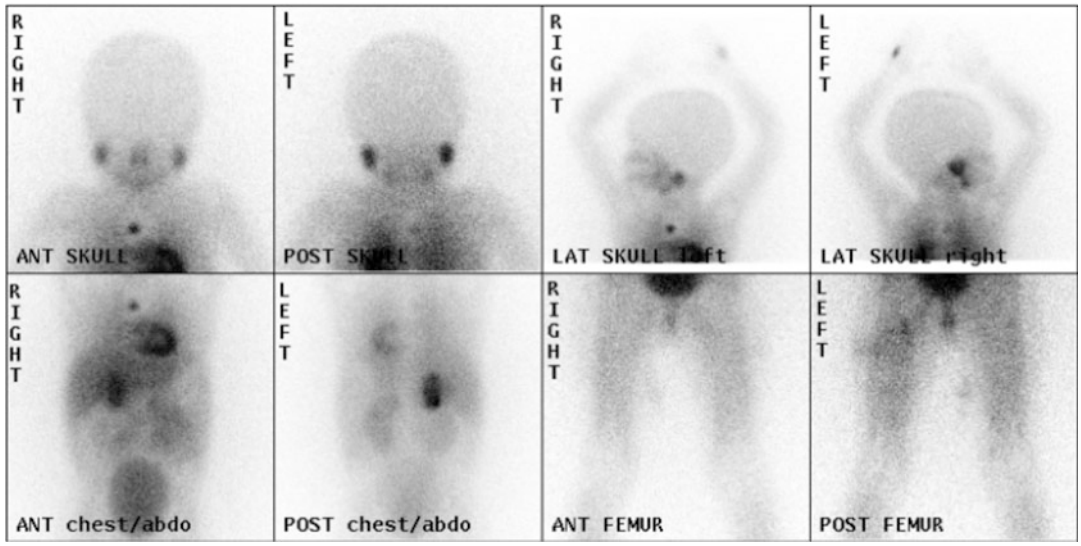

Fig. 12 [^{123}I]MIBG scan at the end of induction chemotherapy: there has been an excellent response, with resolution of all the previously demonstrated metastatic lesions, with the exception of a lesion in the manubrium of the sternum

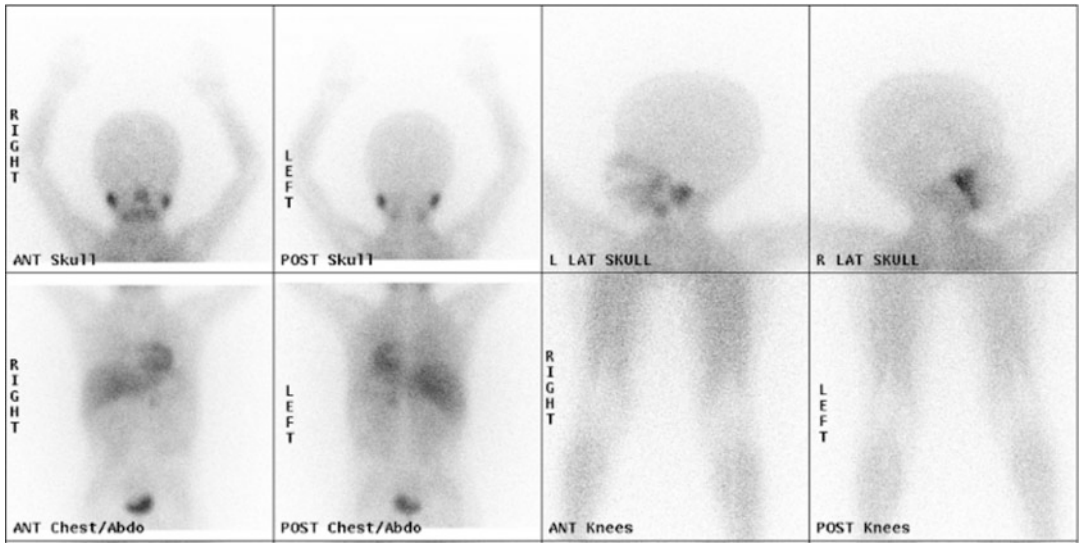

Fig. 13 [^{123}I]MIBG scan after high-dose chemotherapy: there is resolution of the previously seen metastatic lesion in the manubrium of the sternum; normal findings elsewhere. Complete remission

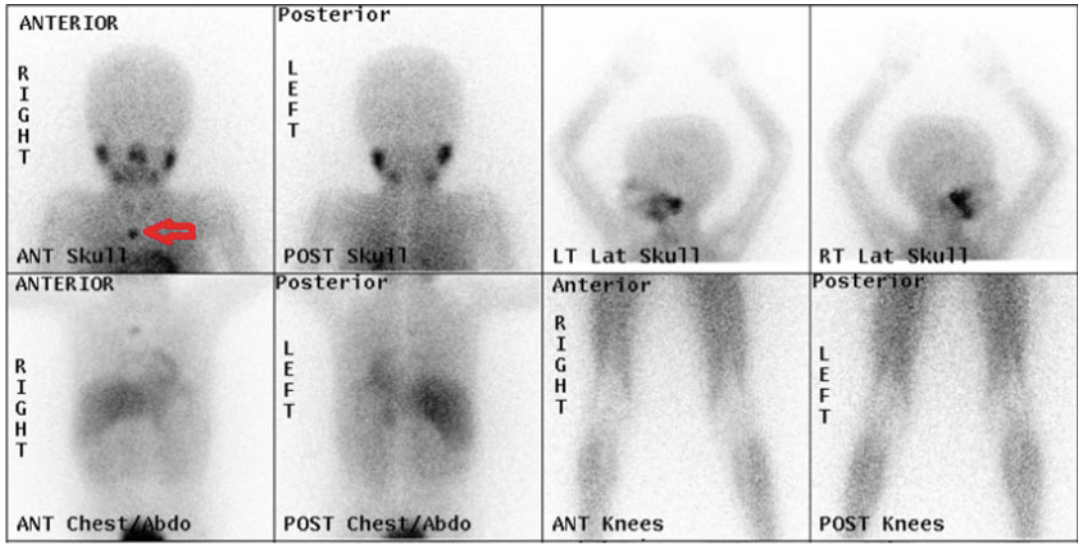

Fig. 14 [^{123}I]MIBG at relapse: a focal area of intense [^{123}I]MIBG uptake is seen in the manubrium of the sternum, exactly at the same site of the previously demonstrated disease

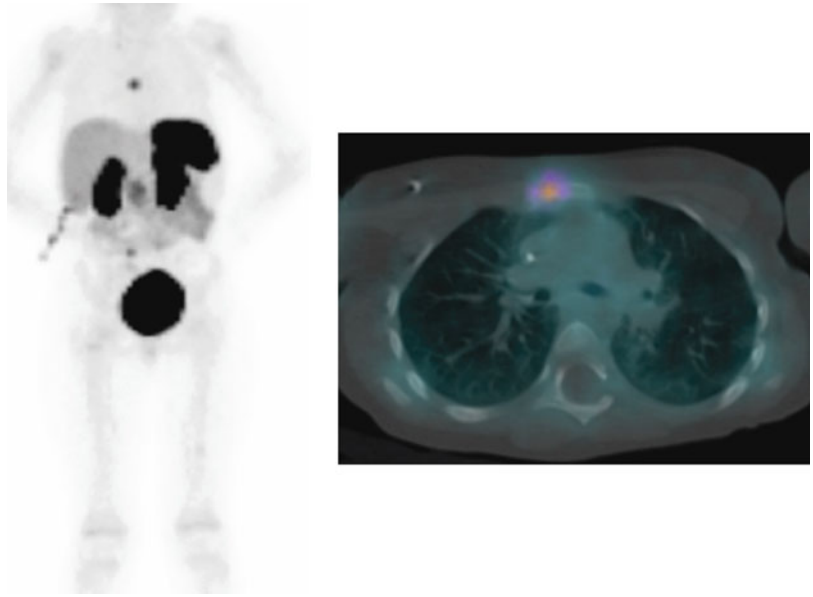

Fig. 15 ^{68}Ga-DOTATATE PET/CT scan showing highly increased tracer uptake in the manubrium of the sternum, corresponding to the abnormal [^{123}I]MIBG uptake (Images courtesy of Dr J Bomanji, Institute of Nuclear Medicine, University College London Hospital)

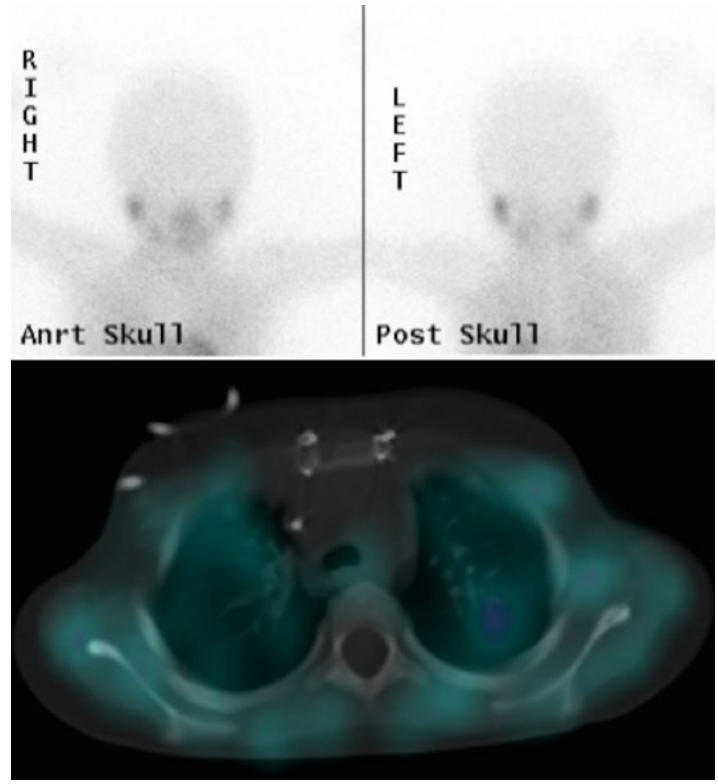

Fig. 16 [^{123}I]MIBG scan with SPECT/CT after excision biopsy: no evidence of residual abnormal [^{123}I]MIBG uptake in the sternum or elsewhere. Complete remission

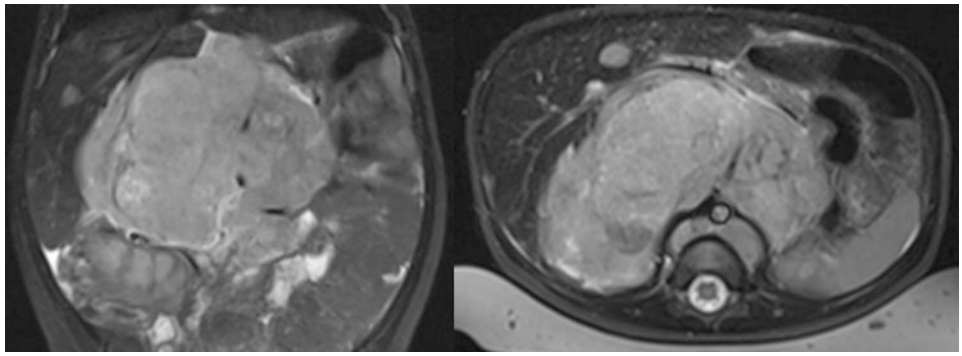

Fig. 17 MRI scan at diagnosis, STIR coronal (*left panel*) and T2 axial view (*right panel*): there is a large central abdominal mass lesion, measuring 8 × 11 × 5 cm, encasing the entire splanchnic circulation, extending into the retrocrural space bilaterally, and displacing the right kidney inferiorly. There are multiple liver metastases

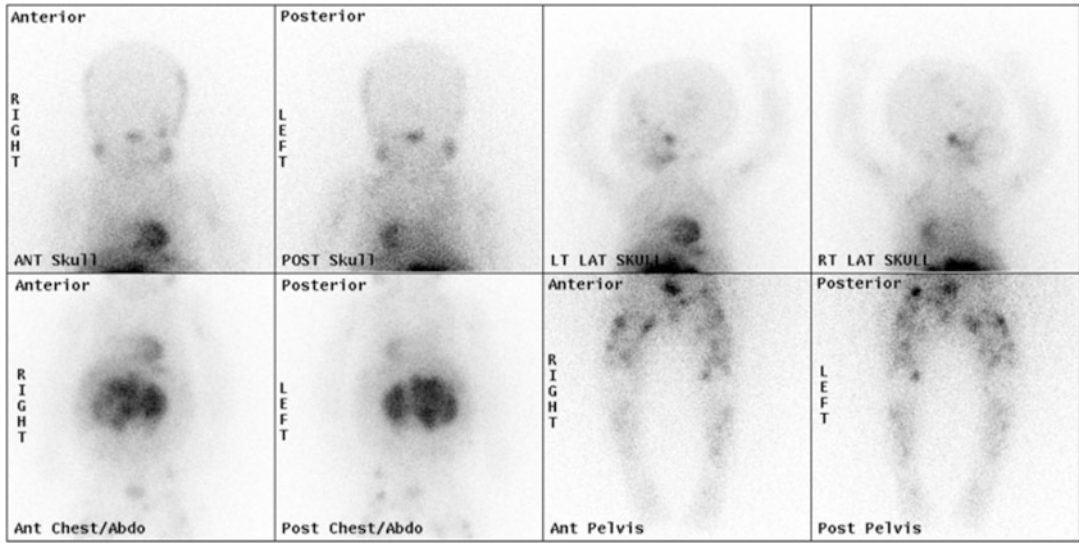

Fig. 18 [^{123}I]MIBG scan at diagnosis (planar images): the primary neuroblastoma shows intense [^{123}I]MIBG uptake. There are multiple skeletal metastases in the skull vault, left orbital region, base of the skull, both humeral shafts, both femora and tibiae. Some of the metastatic liver deposits show [^{123}I]MIBG uptake. There are also numerous skin nodules in the lower limbs

Teaching Points

The [^{123}I]MIBG scan show localized disease; however, low-grade but definite bone marrow metastatic infiltration was present, demonstrated on both right and left bone marrow trephines. Bone marrow infiltration cannot be excluded on an MIBG scan that shows localized disease. Bone marrow trephines are always necessary as a staging investigation.

Neuroblastoma: Case No. 7

Presentation

A two-year-old boy, presenting to the local hospital with a palpable abdominal mass, abdominal distension, constipation, reduced appetite, and general lethargy. An abdominal ultrasound confirmed a 12 × 6 cm mass, arising presumably from the

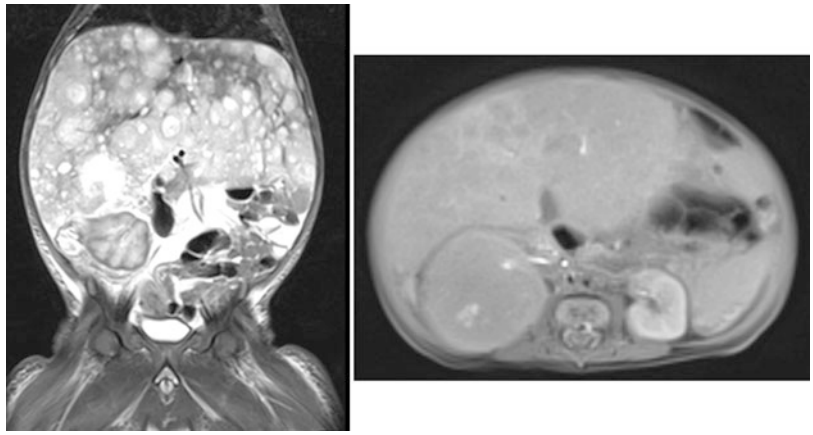

Fig. 19 MRI scan at diagnosis, STIR coronal image, and T1 axial scan: there is a right adrenal mass lesion measuring 4.4 × 4.7 × 6.1 cm. The liver is enlarged with multiple nodules of variable size scattered in both lobes, which show peripheral enhancement after i.v. contrast. No abdominal lymphadenopathy. No ascites. Appearances are suggestive of a right adrenal neuroblastoma with multiple liver metastatic deposits (likely stage IVs on MRI)

right kidney, along with central abdominal lymphadenopathy. Therefore a CT scan was performed: this showed a large partly calcified suprarenal mass lesion which invaded the right kidney and extended across the retroperitoneum. The aorta was encased by tumor. The mass extended from the right suprarenal position to the aortic bifurcation, amounting to a craniocaudal dimension of at least 16 cm. There was a 2-cm left supraclavicular calcified lump in keeping with a metastasis. Percutaneous biopsy result showed a poorly differentiated neuroblastoma with amplification of the MYCN oncogene and chromosomal abnormalities (high risk).

Findings

The [^{123}I]MIBG scan disclosed a large mass lesion with heterogeneous tracer uptake, extending from the right side of the abdomen into the retroperitoneum medially and inferiorly and crossing the midline. Moreover, a focal area of increased tracer uptake, compatible with a metastatic left supraclavicular lymphadenopathy, was found (Fig. 24). MRI showed a 11 × 8 × 8 cm heterogeneous right suprarenal mass invading the right kidney and encasing the upper abdominal vessels and both renal arteries and the involvement of multiple lymph nodes (Fig. 25).

Following completion of dose-intensive induction chemotherapy (rapid COJEC), MRI showed a residual 6-cm mass lesion in the right suprarenal region (Fig. 26). The [^{123}I]MIBG scan resulted negative (Fig. 27).

Management

The residual right adrenal mass was surgically resected. No viable neuroblastoma was demonstrated within the right adrenal mass lesion, which showed necrosis and post-chemotherapy changes. However, within a resected surrounding lymph node, there was a nodule of differentiating and viable neuroblastoma; other nodules with post-chemotherapy changes contained scattered differentiating neuroblastoma cells.

Teaching Point

An MIBG negative primary neuroblastoma following induction chemotherapy cannot exclude residual viable neuroblastoma cells.

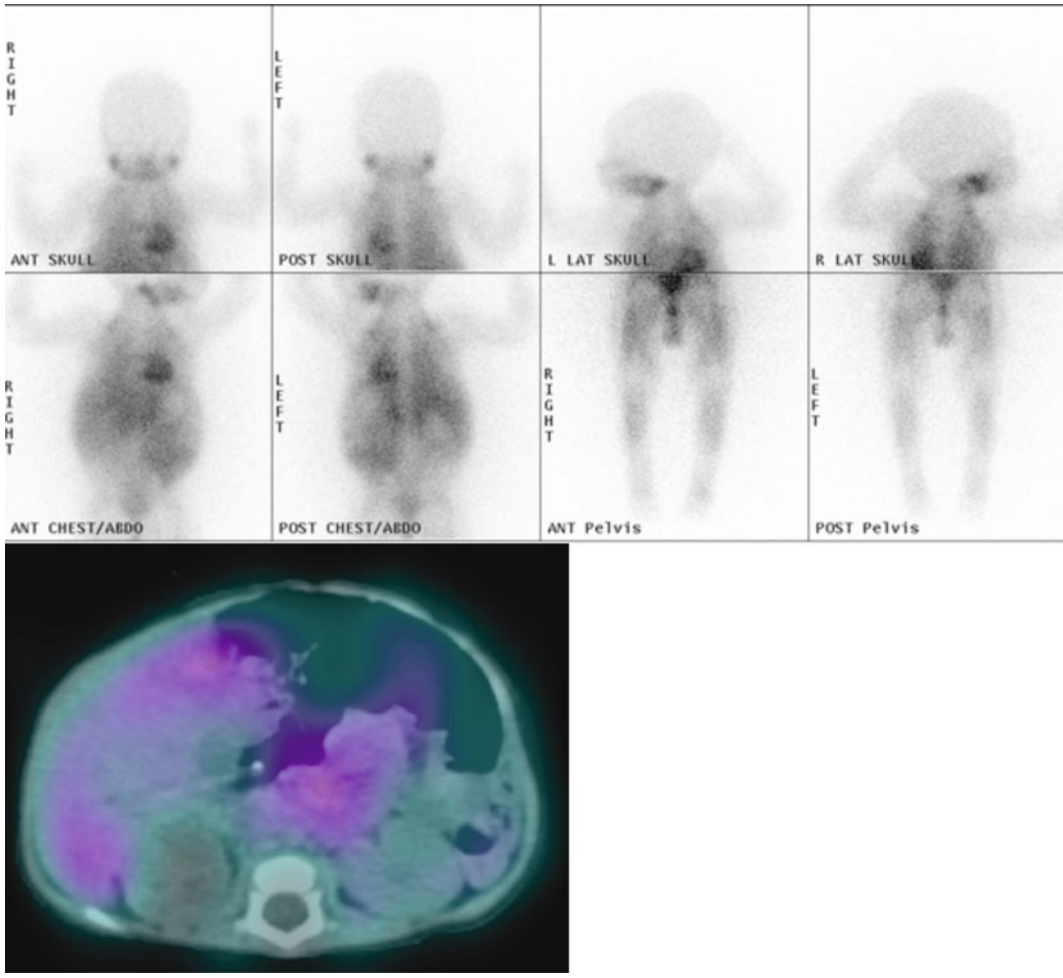

Fig. 20 [^{123}I]MIBG at diagnosis: the right adrenal primary tumor is not [^{123}I]MIBG avid. The liver is enlarged. However, it only shows background activity, with no evidence of significantly increased tracer uptake. The findings are compatible with an [^{123}I]MIBG negative neuroblastoma; the metastatic lesions are also [^{123}I]MIBG negative

Neuroblastoma: Case No. 8

Presentation

An eight-year-old boy, presenting to the local hospital with a 2-week history of right-sided flank pain and constipation, associated with intermittent fevers. In addition, he experienced night sweats, poor appetite, and increasing lethargy.

Findings

An ultrasound and an MRI at the local hospital demonstrated a right-sided abdominal mass (Fig. 28). Biopsy of the mass lesion showed a differentiating neuroblastoma. Molecular biology showed a non-amplified MYCN and chromosomal abnormalities. Staging was completed with [^{123}I]MIBG (Fig. 29).

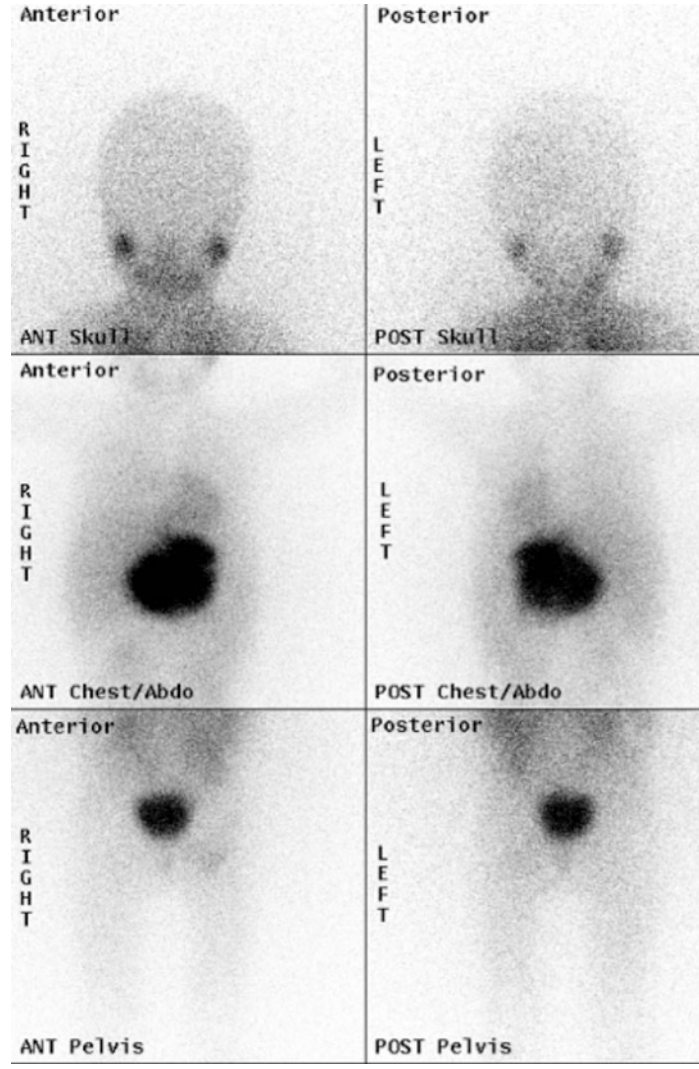

Fig. 21 [^{123}I]MIBG at diagnosis: there is a highly [^{123}I]MIBG avid mass lesion in the mid-upper abdomen, with no evidence of regional or distant metastatic spread

Chemotherapy based on carboplatin and etoposide was started. At the end of chemotherapy, the tumor was resected, and histopathology confirmed a differentiating neuroblastoma. Cis-retinoic acid was then administered for 6 months. [^{123}I]MIBG at the end of treatment showed a soft tissue nodule on the retrocaval area and is suspicious for recurrent disease within a retrocaval lymph node (Fig. 30). MRI confirmed the presence of a retrocaval area of moderately restricted diffusion and heterogeneous enhancement (Fig. 31).

Management

The nodule was surgically excised and it was confirmed to represent a retrocaval metastatic lymph node. In addition, the child was referred

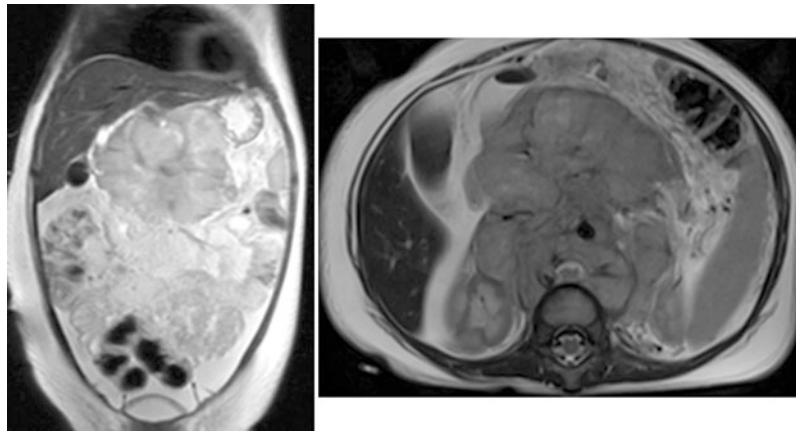

Fig. 22 MRI scan at diagnosis: there is a retroperitoneal mass lesion in the upper abdomen measuring approximately $8.3 \times 8.7 \times 9$ cm. It is centered in the retroperitoneum and involves the head of the pancreas and the majority of the body. The common bile duct is compressed by the mass, and there is common bile duct and intrahepatic ductal dilatation. There is a retrocrural component extending to T9. A further component extends to the porta hepatis but does not infiltrate the liver. There is significant abdominal pelvic ascites and subcutaneous fluid. No discrete bony lesion demonstrated

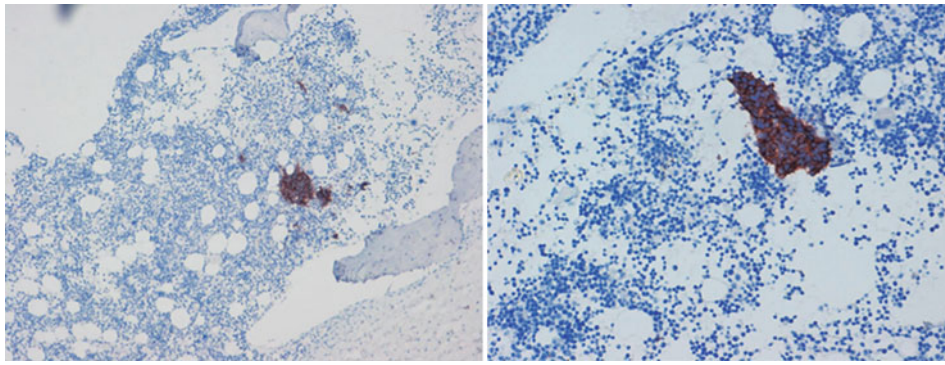

Fig. 23 Bone marrow trephines: there are small scattered groups of abnormal cells, positive for MAP2, NSE, and synaptophysin. These features are those of metastatic neuroblastoma

for radiotherapy to the para-aortic lymph nodes and the original tumor bed.

Teaching Point

SPECT/CT was critical in raising the suspicion of a focal area of recurrence. The [^{123}I]MIBG scan with SPECT/CT in neuroblastoma is now standard of care, especially for lesions deep in the abdomen/pelvis.

Neuroblastoma: Case No. 9

Presentation

A 9-month-old girl presented with bilateral periorbital ecchymosis, right side exophthalmos, and abdominal distension.

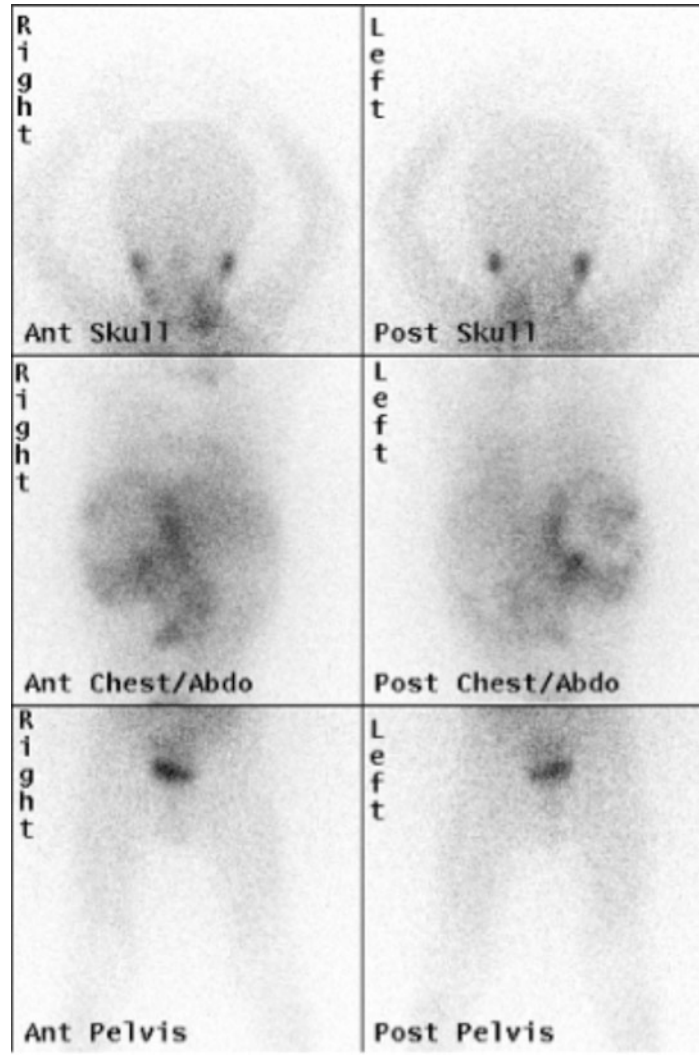

Fig. 24 [^{123}I]MIBG at diagnosis: there is a large mass lesion with heterogeneous tracer uptake, extending from the right side of the abdomen into the retroperitoneum medially and inferiorly and crossing the midline. There is a focal area of increased tracer uptake in the left supraclavicular region, compatible with a metastatic lymphadenopathy. No abnormal tracer uptake noted in the skeleton

Findings

CT revealed a renal mass (8 × 8 cm), retroperitoneal lymphadenopathy, as well as multiple hepatic and pulmonary lesions. CT of the head showed widespread osseous metastases and right exophthalmus. Biopsy confirmed neuroblastoma (stage IV). [^{123}I]MIBG planar and SPECT/CT images (Fig. 32) show a large partially calcified left abdominal mass with pathological radiopharmaceutical uptake, representing the site of primary tumor of adrenal origin. Abnormal foci of [^{123}I]MIBG uptake are present in both lobes of the liver, corresponding to hepatic metastasis. Multiple foci of pathological uptake in the axial and the appendicular skeleton are also seen. Bilateral lung nodules do not show focal radiotracer accumulation.

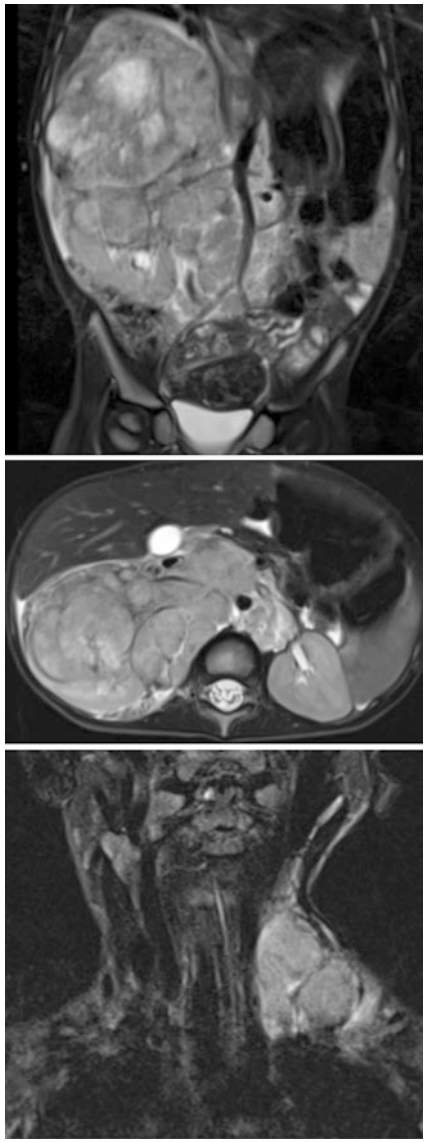

Fig. 25 MRI of the abdomen, coronal STIR (*top*), and axial T2-weighted (*middle*) images. There is a 11 × 8 × 8 cm heterogeneous right suprarenal mass invading the right kidney and encasing the upper abdominal vessels and both renal arteries. The IVC is patent but displaced anteriorly. No intraspinal invasion. There is a left-sided conglomerate lymph node measuring 3.5 × 1.9 cm. There is evidence of retrocrural disease. MRI of the neck (coronal STIR *bottom*) shows left supraclavicular lymphadenopathies

As a part of initial staging [^{18}F]FDG PET/CT was performed: images demonstrate low [^{18}F]FDG uptake in the bone marrow of the pelvis and distal femurs and proximal tibiae (Fig. 33). The known abdominal mass and liver metastases do not show abnormal uptake. Bone marrow involvement was confirmed by bone marrow biopsies that revealed the presence of neuroblastoma without *MYC*-gene amplification.

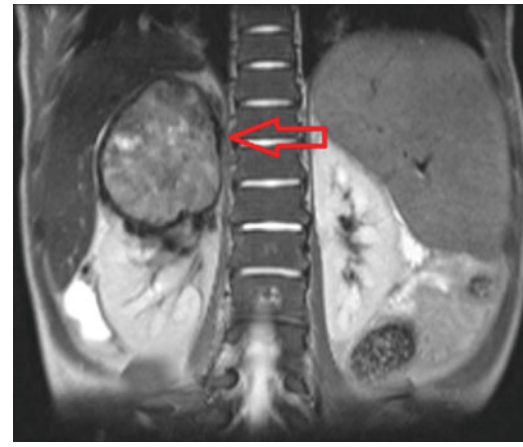

Fig. 26 Abdominal MRI after induction chemotherapy, T2-based sequence, coronal view: there is a residual mass lesion in the right suprarenal region, measuring 6 cm in maximum axial dimension

Follow-Up

The patient was treated with neoadjuvant chemotherapy and surgery (left adrenalectomy and retroperitoneal lymphadenectomy). Follow-up evaluation after adjuvant chemotherapy showed stable disease. [^{123}I]MIBG scan demonstrates abnormal uptake in the axial and the appendicular skeleton and in the liver (Fig. 34). This case demonstrates that [^{18}F]FDG PET/CT is not as sensitive as [^{123}I]MIBG imaging in many patients with neuroblastoma.

Ewing Sarcoma

Presentation

An eighteen-year-old patient with heaviness at the left inguinal region and left sciatica during prolonged sitting. After 3 months occasional finding of left inguinal swelling, of hard consistence,

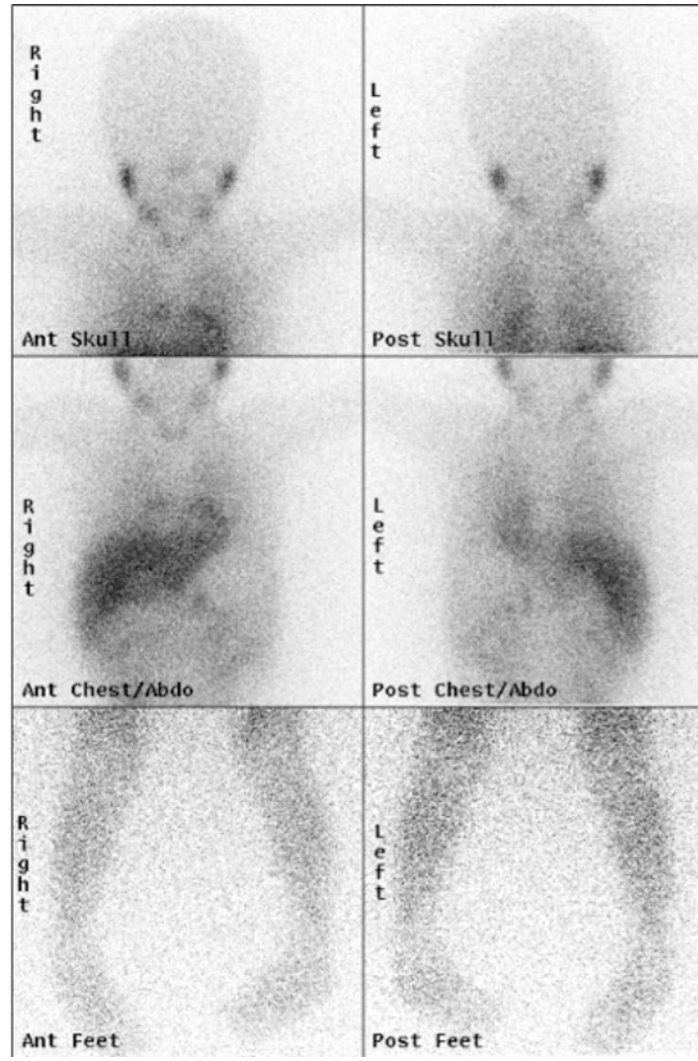

Fig. 27 [^{123}I]MIBG after induction chemotherapy: there is no evidence of abnormal tracer uptake. In particular, the residual mass lesion demonstrated on MRI is MIBG negative

painless nor tender on palpation. On the advice of the general practitioner, an abdominal and pelvic ceCT was performed showing the presence of a pelvic mass (17 × 10 × 15 cm) with parenchymatous structure, infiltrating the viscera and pelvic walls, with manifestation within the inguinal canal and the root of the left thigh. The left pubic bone branch had increased density, probably with reactive meaning. MRI confirmed the large mass showing maximum diameters in the pelvis and in the left thigh, with a global extension of about 24 cm. Biopsy of the left inguinal mass drove to the diagnosis of an Ewing sarcoma CD99 positive.

Findings

The mass presented inhomogeneous hypermetabolic activity, as disclosed by [^{18}F]FDG PET/CT (Fig. 35). Neoadjuvant chemotherapy was undertaken. PET/CT after chemotherapy showed a net response of the mass confirmed also by MRI. External beam radiotherapy of the pelvic mass (50 Gy) and other cycles of chemotherapy were then performed. CT of the lungs and PET/CT became completely negative. The patient underwent surgery with the exeresis of the pelvic mass along with the resection of the left iliopubic and ischium-pubic branches. At that level,

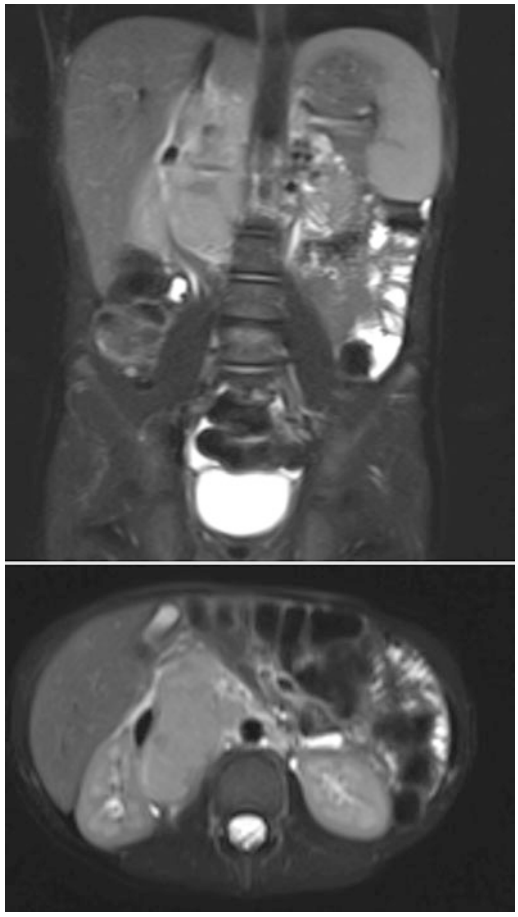

Fig. 28 (**a**, **b**) MRI at diagnosis, coronal and axial HASTE T2-based images: there is a mass lesion in the aortocaval area displacing the IVC to the *right*. The mass extends to the level of the porta hepatis, displacing and abutting the hepatic artery. The largest component of the mass is at the right renal hilum, with the left renal vein and the right renal artery encased by tumor. The infiltrating nature of this mass lesion favors a neuroblastic tumor

postsurgery PET/CT showed an area of hyperactivity with craniocaudal development and central hypoactivity, referred in the first hypothesis to surgical outcomes. Moreover, some hypermetabolic lymphadenopathies were seen in the groin and the right external iliac region (Fig. 36). Within the lungs PET/CT indicates the presence of a paracardiac hypermetabolic nodule in the lingula. CT demonstrated other micronodules within the lungs consistent with secondary lesions (Fig. 37).

Follow-Up

The patient underwent high-dose chemotherapy which determined the disappearance of lung disease. After 1 year the patient is still disease free.

Teaching Point

[^{18}F]FDG PET/CT is an effective tool for monitoring the efficacy of therapy. However, false-positive findings can be due to inflammatory or infectious processes, frequently occurring after surgery or radiotherapy. Since the lungs are a frequent site of metastasis of all sarcomas, [^{18}F]FDG PET/CT must be performed along with a diagnostic CT which is more sensitive in detecting secondary micronodules.

Lymphoma: Case No. 1

Presentation

A 14-year-old boy with pain and tenderness in the distal portion of the right femur. He underwent a MR scan of the right knee that showed an aggressive bone lesion with initial infiltration of soft tissues and a popliteal lymphadenopathy, that needed a differential diagnosis between lymphoma and sarcoma (Fig. 38).

Findings

A total body ceCT was performed which shows a not pathological enlargement of the thymus. Then [^{18}F]FDG PET/CT was performed that highlighted a focal hypermetabolism glucose within the lesion of the distal femur (SUV_{max} 8.5) and the right wing thymus (SUV_{max} 19.2) (Fig. 39).

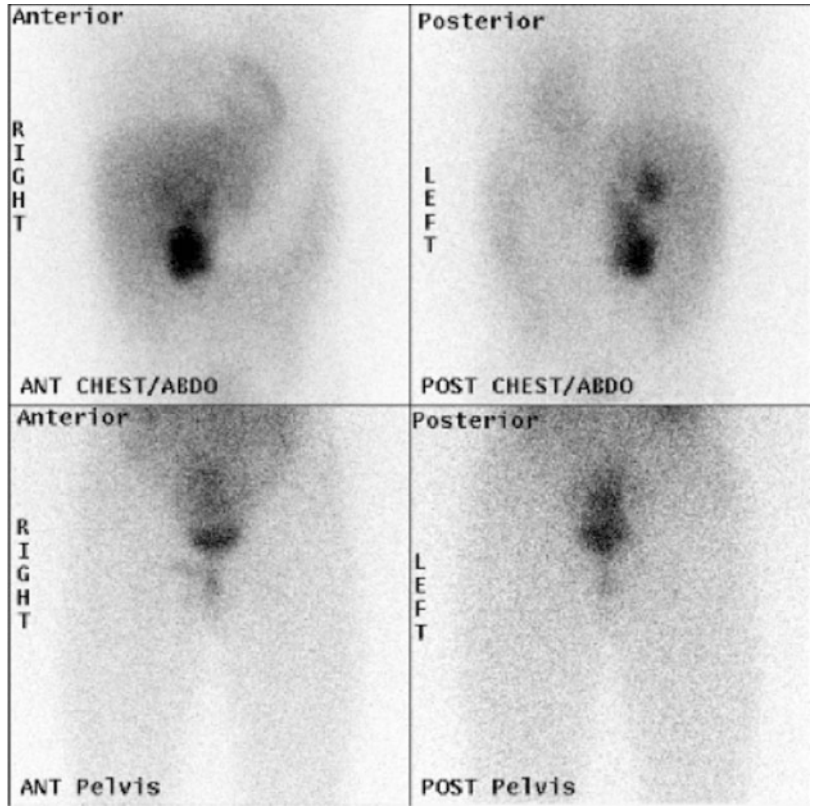

Fig. 29 [^{123}I]MIBG at diagnosis: the mass lesion demonstrated on MRI shows intense, [^{123}I]MIBG uptake. No evidence of regional or distant metastatic spread. This finding, together with the MRI and the molecular biology, makes an intermediate-risk neuroblastoma

The reassessment of the ceCT stated the presence of an anterior mediastinal mass cleaving to the right portion of the thymus. Since bone marrow biopsy resulted negative, an excisional biopsy of the lesion of the distal portion of the right femur was performed. Pathology reported lymphoma derived from peripheral B lymphocytes, large cells, and bone primitive. Chemotherapy according to the NCCN protocol for the diffuse large B-cell lymphoma (DLBCL) at stage IV was started. At the interim reassessment after two cycles, PET/CT showed complete metabolic response of the anterior mediastinum lesion, almost complete resolution of the hypermetabolic lesion of the femur (Fig. 40).

Follow-Up

At the end of the treatment, MRI showed net reduction of the intraosseous extension of the lesion, normalization of MR signal, and the reduction of contrastographic enhancement (Fig. 41).

Teaching Point

PET/CT, by identifying the hypermetabolic mass within the mediastinum, oriented the diagnosis to lymphoma and contributed to the disease staging. Moreover, the early response during chemotherapy showed by PET/CT predicted the response at the end of treatment.

Lymphoma: Case No. 2

Case contributed by: F. Reyneke, M. Sathekge Nuclear Medicine, University of Pretoria, and Steve Biko Academic Hospital, Pretoria, South Africa

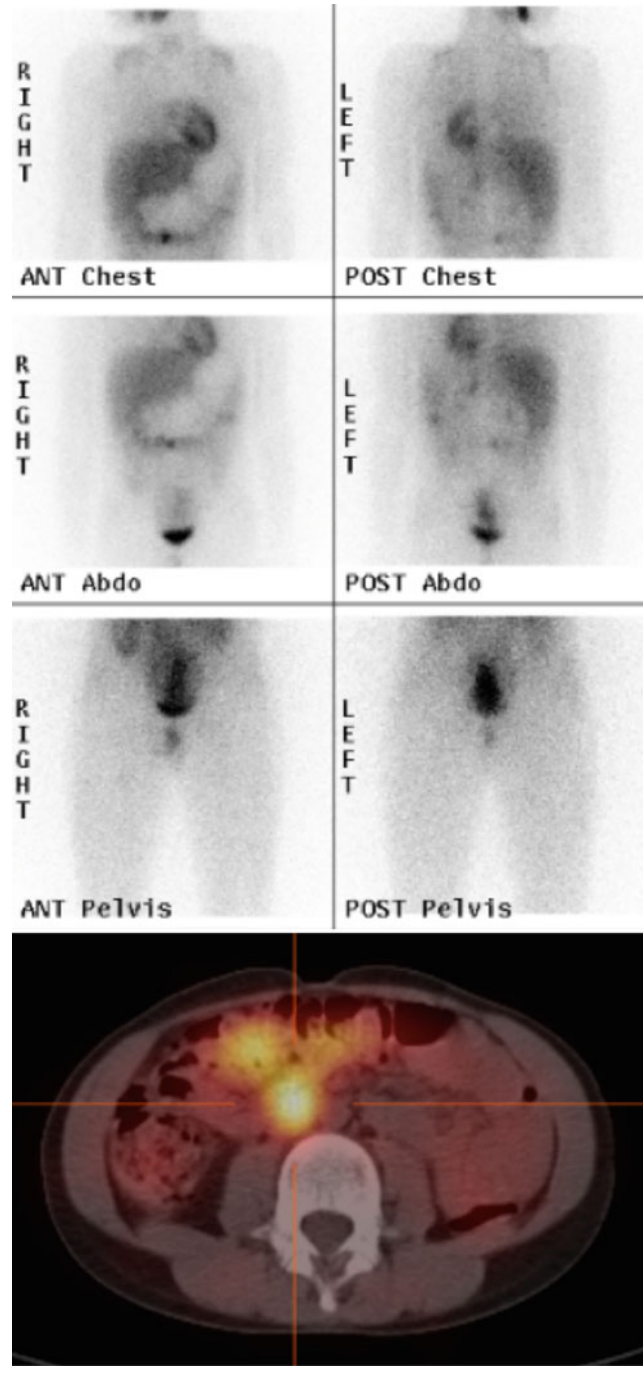

Fig. 30 (**a**, **b**) [^{123}I]MIBG at the end of treatment. The planar images (**a**) show a focal area of more prominent tracer uptake in the region of the transverse colon on the midline. On SPECT/CT (**b**), this localizes to a soft tissue nodule on the retrocaval area and is suspicious for recurrent disease within a retrocaval lymph node

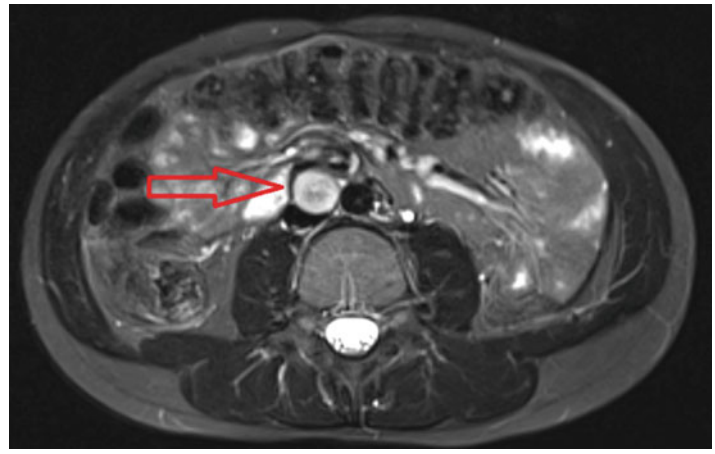

Fig. 31 MRI following suspicion of relapse, axial STIR image: there is a 1.5 × 1.5 cm area of moderately restricted diffusion and heterogeneous enhancement: this corresponds to the area of abnormality demonstrated on [^{123}I]MIBG SPECT/CT. The area of recurrence is inferior to the previously located tumor and was not present previously

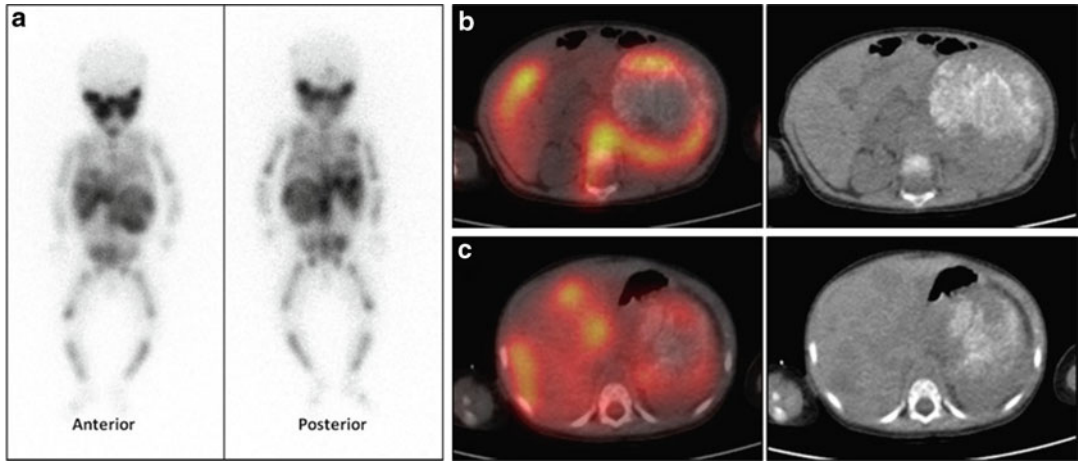

Fig. 32 [^{123}I]MIBG scan. (**a**) Whole body image (anterior and posterior view) shows increased radiotracer uptake in the axial and appendicular skeleton. (**b**) Axial SPECT/CT image (fused image in the *left panel* and CT image in the *right panel*) of large partially calcified left abdominal mass. (**c**) Axial SPECT/CT image (fused image in the *left panel*, CT image in the *right panel*) of hepatic metastasis

Presentation

A 10-year-old boy presented with a painless mass in the left side of his neck.

Findings

A biopsy taken from a left cervical lymph node revealed classical Hodgkin's lymphoma (mixed cellularity subtype).

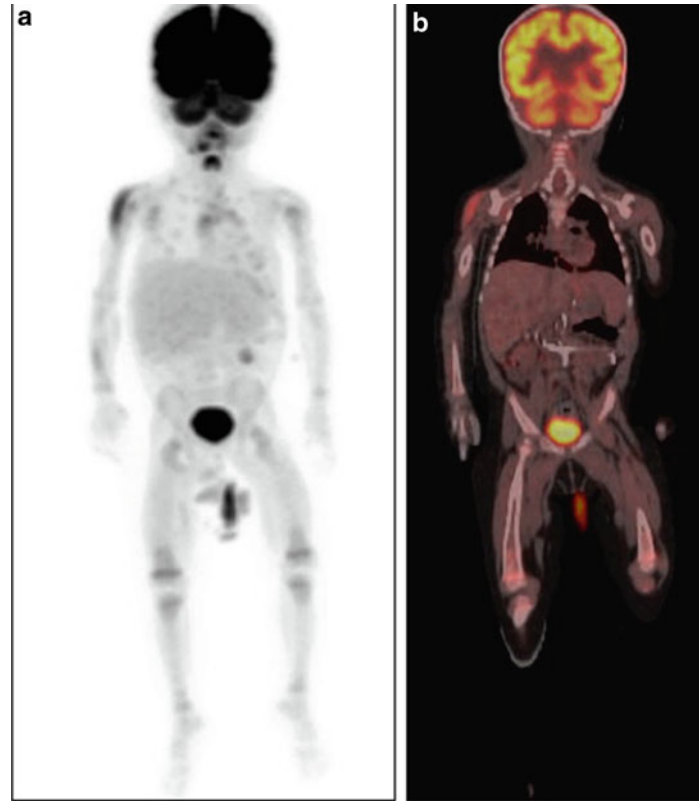

Fig. 33 (**a**) [^{18}F]FDG MIP image demonstrates low uptake in the bone marrow of the pelvis and distal femurs and proximal tibiae. (**b**) [^{18}F]FDG PET/?CT fused coronal image: no abnormal uptake is seen in the known abdominal tumor or in the liver

[^{18}F]FDG PET/CT for initial staging showed a conglomerate of lymph nodes in the left cervical region (involving all the lymph node groups) extending into the infraclavicular region – SUV_{max} 10.5 (Figs. 42 and 43).

Follow-Up

Following chemotherapy, [^{18}F]FDG PET/CT was repeated to monitor response during therapy. Increased [^{18}F]FDG uptake was still noted in cervical lymph nodes in levels II, III, and IV (SUV_{max} 8.16) with significant reduction in size demonstrating a good response to therapy (Figs. 44 and 45).

Teaching Point

[^{18}F]FDG PET/CT is highly sensitive in the detection of Hodgkin's lymphoma and can also accurately evaluate the effectiveness of therapy. This should be done 6–8 weeks after therapy to minimize false-negative and false-positive results.

Lymphoma: Case No. 3

Case contributed by: T. Boshomane, M. Sathekge Nuclear Medicine, University of Pretoria, and Steve Biko Academic Hospital, Pretoria, South Africa

Presentation

A fifteen-year-old girl with histologically confirmed lymphoma (Hodgkin's, clinical stage II with no other risk factors) and treated with chemotherapy (ABVD).

She presented to her oncologist >3 months post-chemotherapy complaining of unintentional weight loss and increasing fatigue.

Fig. 34 [^{123}I]MIBG study (whole body image) performed after chemotherapy shows the persistence of pathological uptake in the skeleton and liver

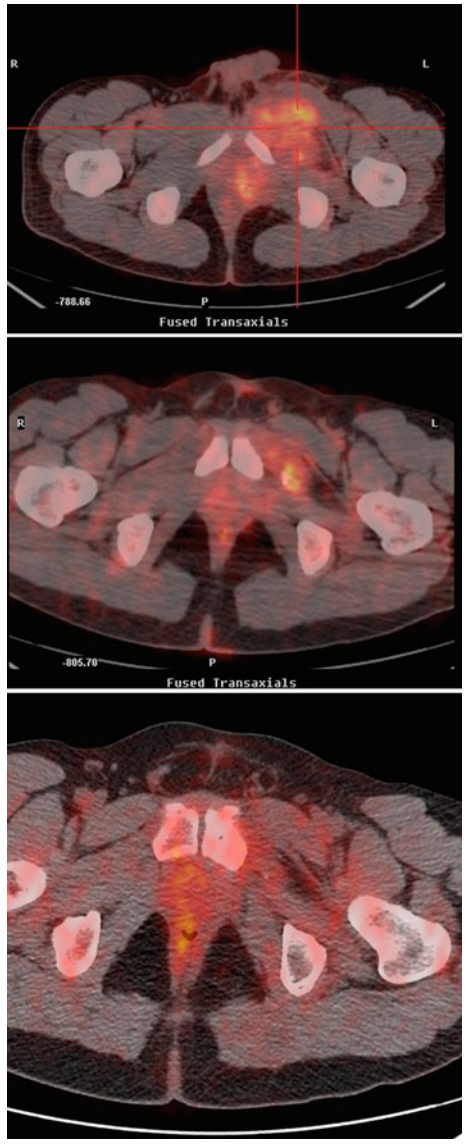

Fig. 35 [^{18}F]FDG PET/?CT scans performed at staging (*top panel*), after chemotherapy (*middle panel*) and after chemoradiotherapy (*bottom panel*), show the progressive response of the left inguinal?mass

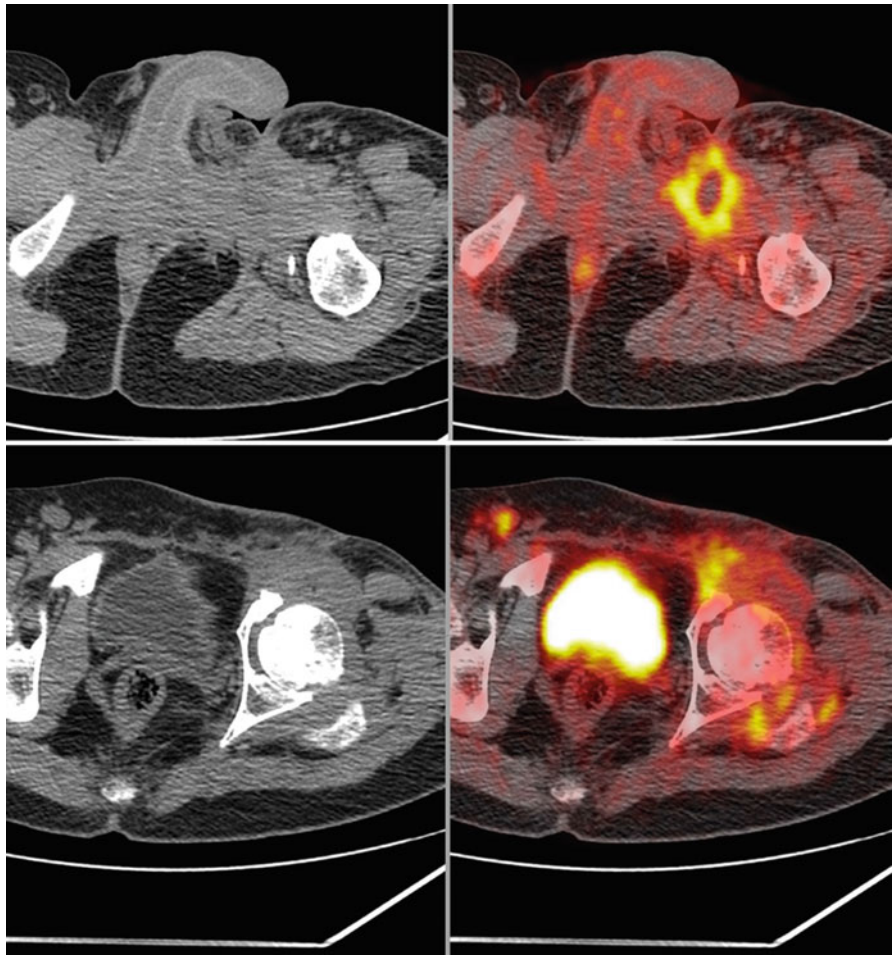

Fig. 36 Postsurgery [^{18}F]FDG PET/?CT: area of hyperactivity and central hypoactivity in left iliopubic region consistent with surgical outcomes. Some hypermetabolic lymphadenopathies are visible in the right groin and in the right external iliac region

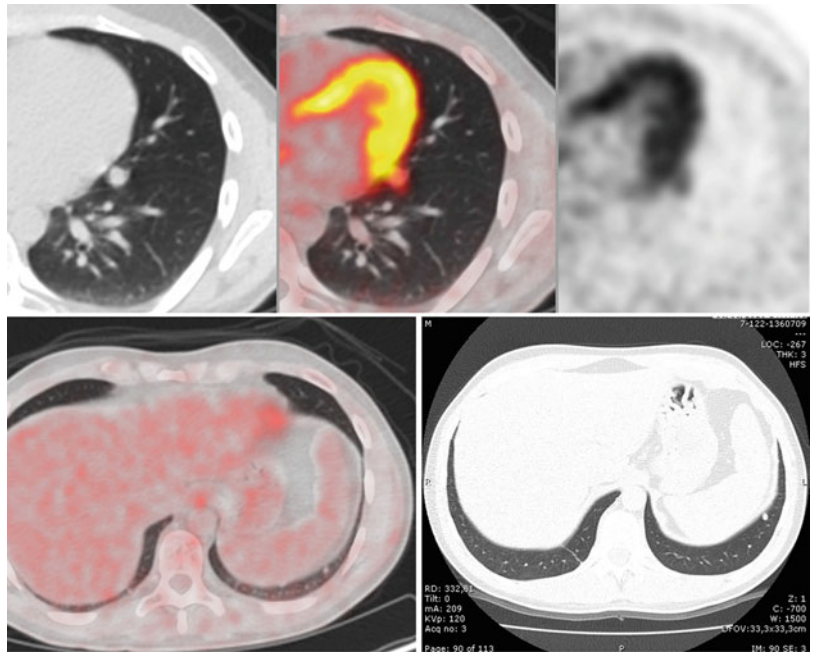

Fig. 37 [^{18}F]FDG PET/?CT paracardiac hypermetabolic nodule within the lingula. Basal CT shows several micronodules with no evidence of significant [^{18}F]?FDG uptake within the lungs, consistent with secondary lesions

Fig. 38 MRI of the right knee showing a bone lesion with?initial infiltration of soft tissues and a popliteal lymphadenopathy

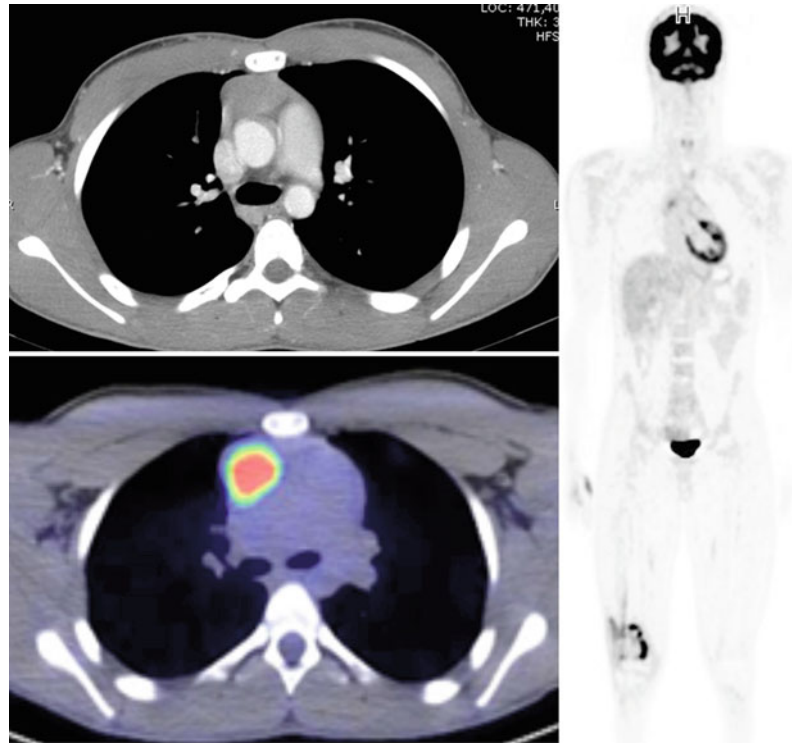

Fig. 39 On *left top panel*: ceCT showing the anterior mediastinal mass cleaving to the right portion of the thymus. In the *left bottom panel*: [^{18}F]FDG PET/?CT showing the hypermetabolic activity of the anterior mediastinal mass. On the *right*: MIP image of the PET/?CT whole body study demonstrating the hyperactive lesion of the left?knee

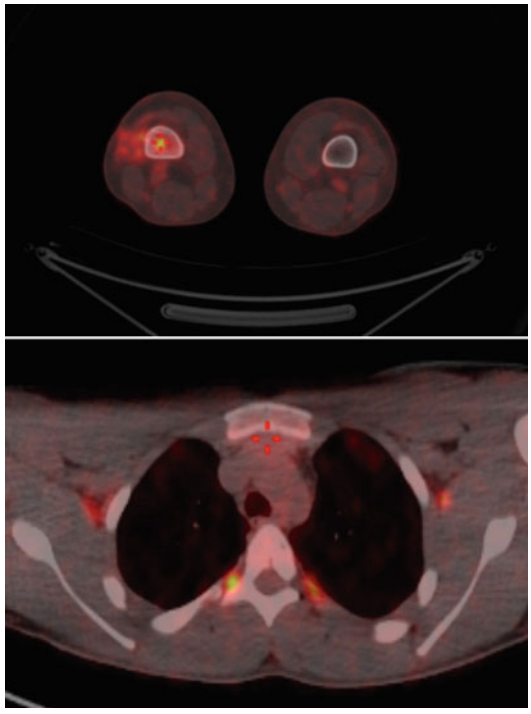

Fig. 40 Interim PET/?CT after two cycles of RCHOP demonstrating the metabolic response of both the mediastinal and femur lesions

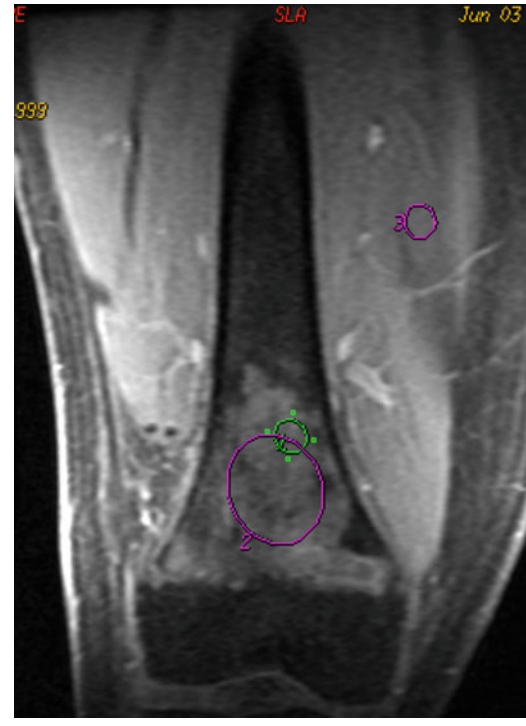

Fig. 41 RM of the right knee showing the response at the end of six cycles of RCHOP

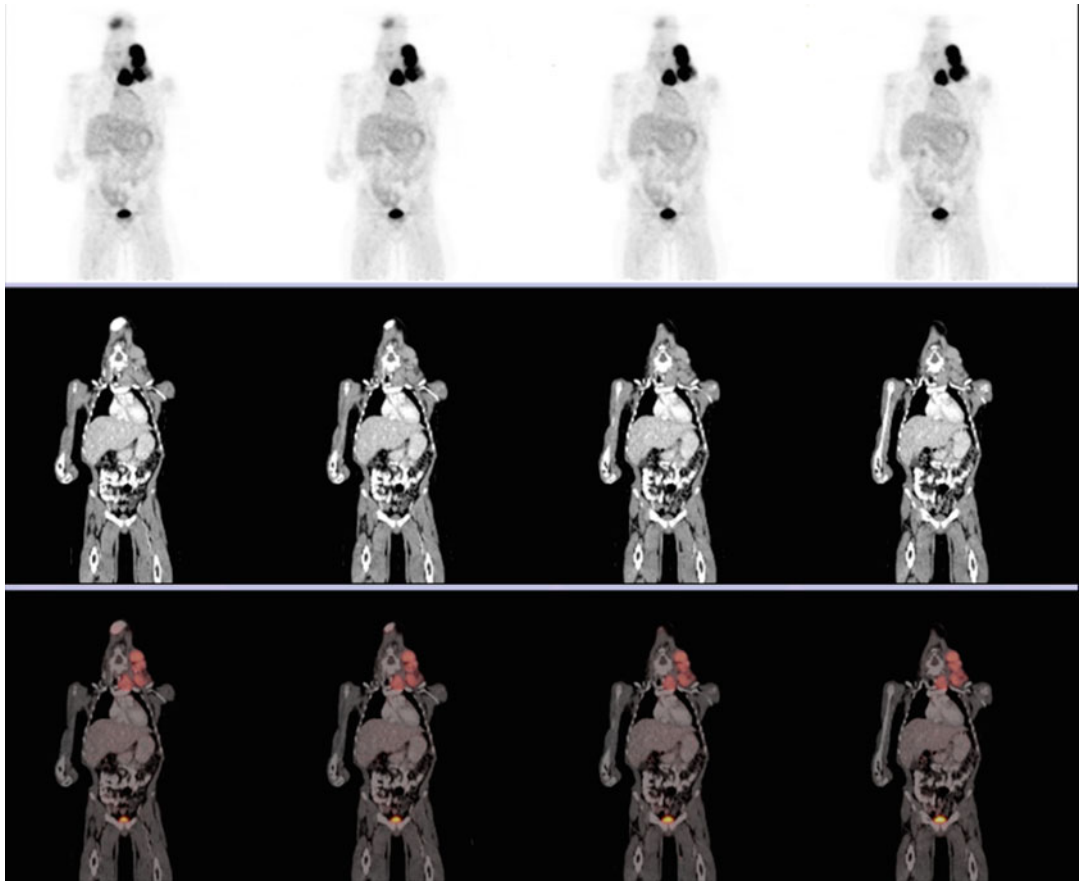

Fig. 42 [^{18}F]FDG PET/?CT coronal images demonstrate the conglomerate of lymph nodes on the left side of the?neck

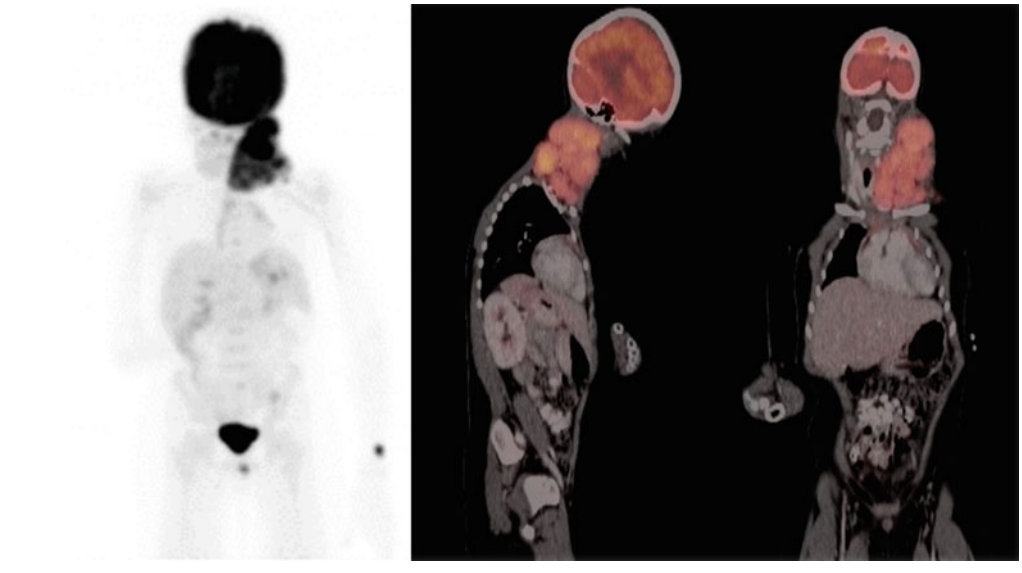

Fig. 43 [^{18}F]FDG PET/?CT MIP image (*left*). Sagittal and coronal images of the cervical mass (*right*)

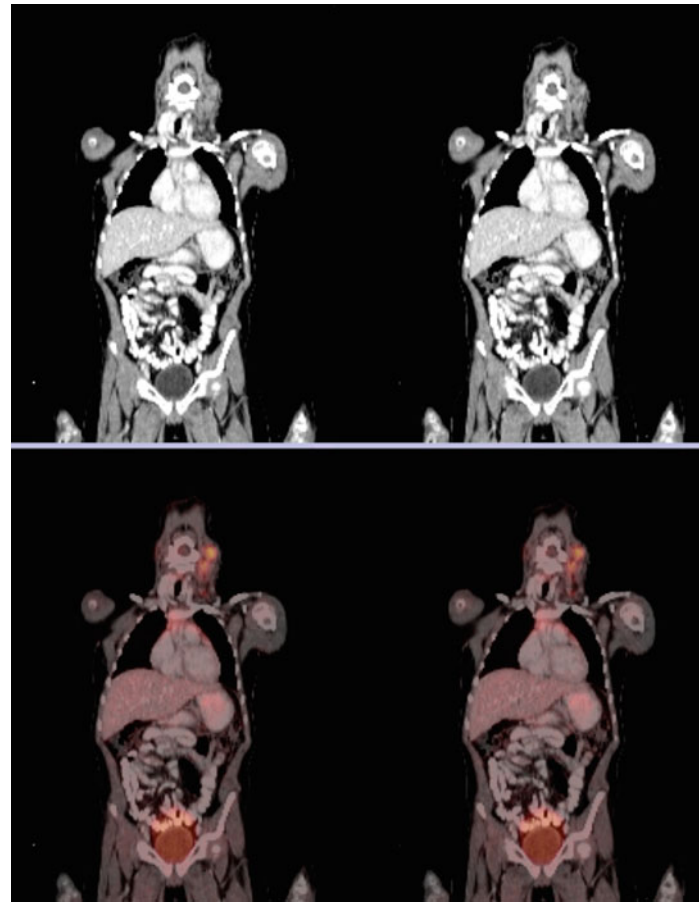

Fig. 44 [^{18}F]FDG PET/?CT coronal images demonstrating residual lymph nodes in the cervical region (reduced SUV_{max} and significant reduction in size compared to previous study)

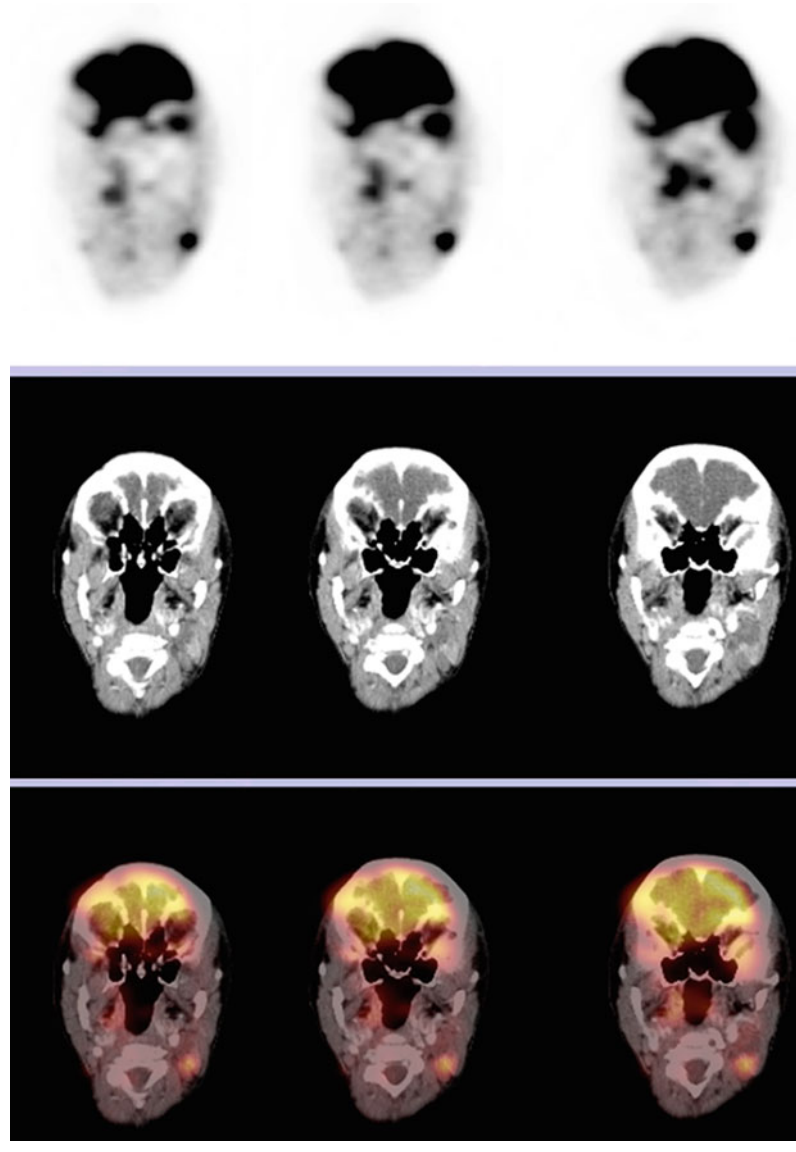

Fig. 45 [^{18}F]FDG PET/?CT axial images demonstrating a good metabolic response to chemotherapy

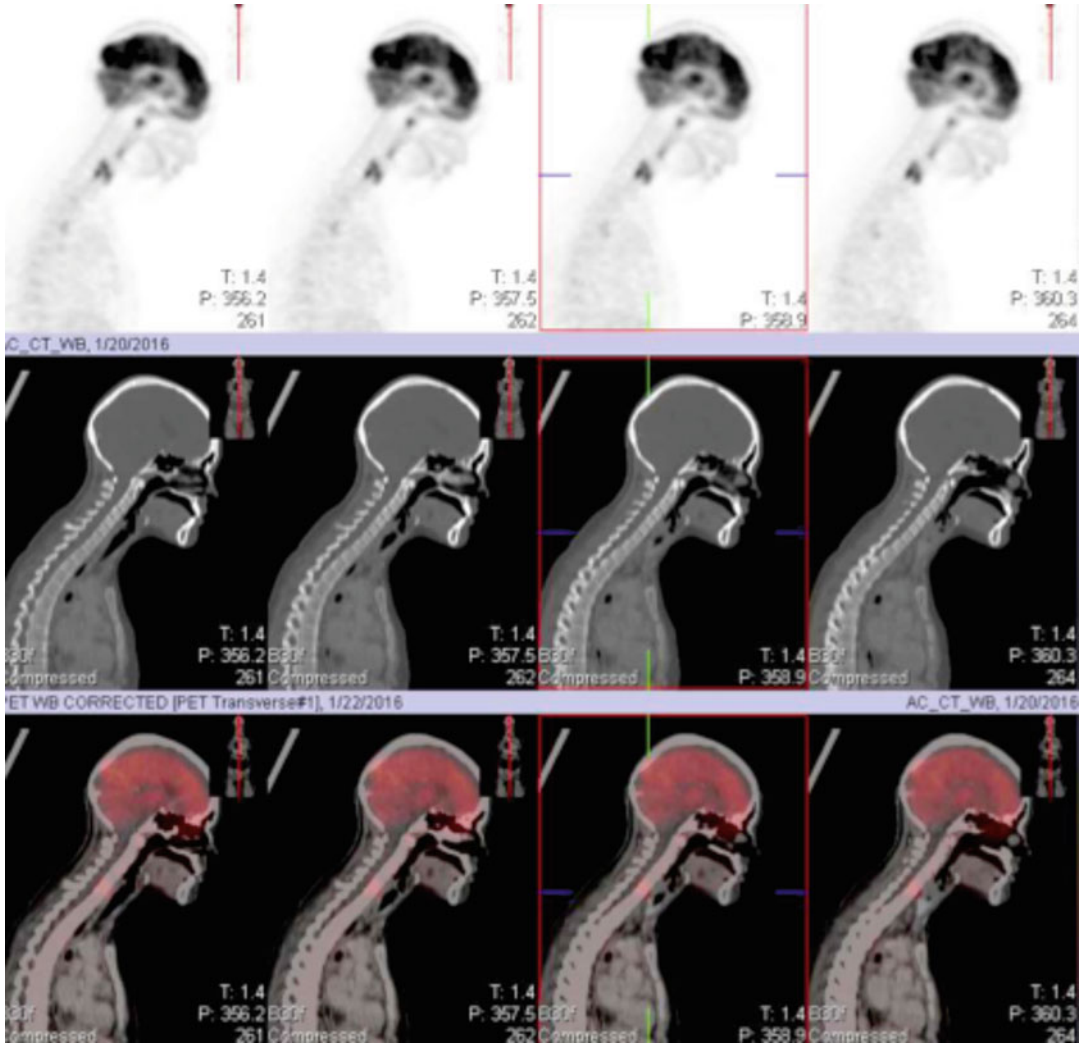

Fig. 46 *Top row*: sagittal images of metabolic activity noted on [^{18}F]FDG PET, which was not appreciated on the CT images (*middle row*). *Bottom row*: fused PET/?CT demonstrating the T2 lesion

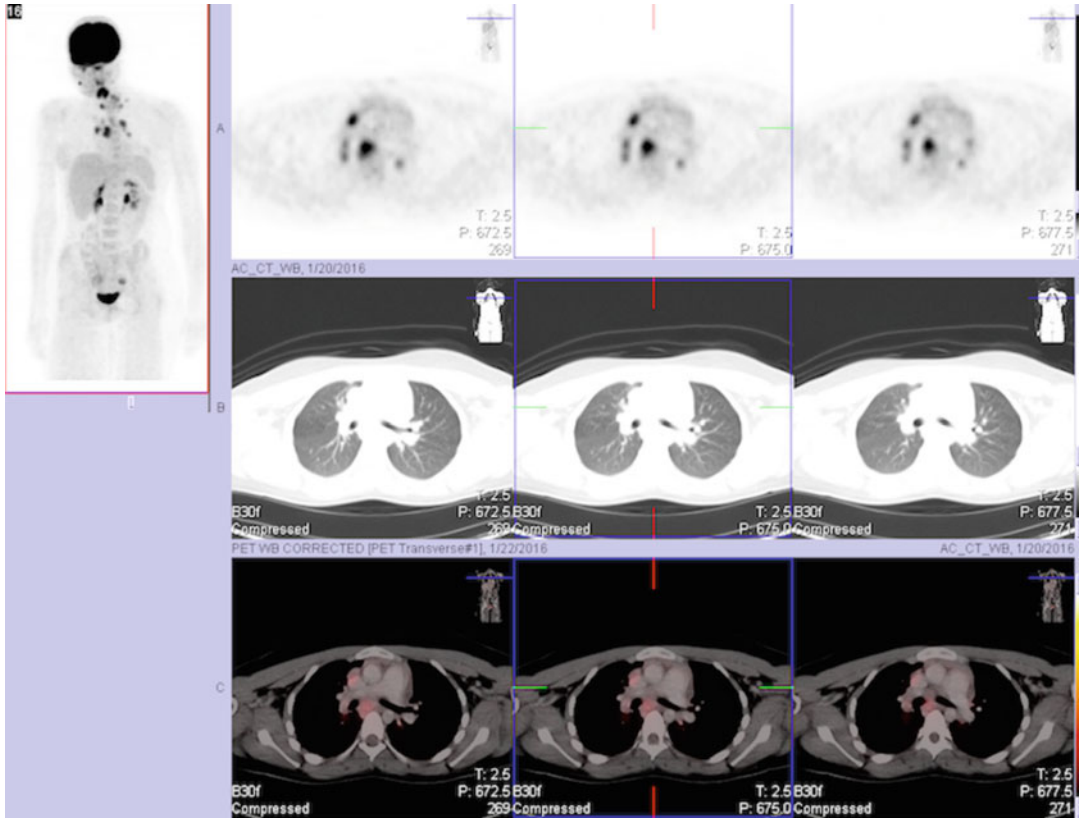

Fig. 47 Axial images. *Top row*: metabolically active mediastinal lymph nodes demonstrated on [^{18}F]FDG PET. *Middle row*: CT images showing the lung fields and mediastinum. *Bottom row*: fused PET/?CT demonstrating the mediastinal lymph nodes. The side image is the MIP images showing the supradiaphragmatic disease but involving bone [adnexal activity was non-?lymphomatous]

Findings

CT noted mediastinal lymphadenopathy (aortopulmonary, carinal, anterior to SVC, and paraoesophageal) with no skeletal changes. [Previously only left cervical lymph nodes were seen].

Fused [^{18}F]FDG PET showed metabolic activity in the mediastinal lymph nodes (SUV_{max}: 9.9 aortopulmonary, 5.9 hilar, 10.0 in the posterior mediastinum) and T2 vertebra (SUV_{max} 8.6) (Figs. 46 and 47).

Teaching Point

Given the high sensitivity of [^{18}F]FDG PET/CT for detecting bone marrow involvement, this case highlights the importance of this modality when available. An invasive procedure is averted as PET detects lymphomatous involvement of the skeleton therefore upstaging the disease. The indication of the PET scan in this study was restaging after chemotherapy.

Teaching Cases in Nuclear Oncology: Investigating the Heart in Cancer Patients

78

Josef J. Fox and H. William Strauss

Keywords

Coronary artery disease • Myocardial perfusion • Exercise stress test • Pharmacologic stress test • ^{99m}Tc-Sestamibi • ^{201}Tl-chloride • Gated-SPECT • ^{13}N-Ammonia • ^{82}Rb-chloride • PET

Glossary

BP	Blood pressure
CABG	Coronary artery bypass graft surgery
CT	X-ray computed tomography
ECG	Electrocardiogram
Gy	Gray unit (ionizing radiation dose in the International System of Units, corresponding to the absorption of one joule of radiation energy per kilogram of matter)
HR	Heart rate
IV	Intravenous
LAD	Left anterior descending coronary artery
LVEF	Left ventricular ejection fraction
mph	Miles per hour
pbm	Beats per minute
PET	Positron emission tomography
PET/CT	Positron emission tomography/Computed tomography
SPECT	Single-photon emission computed tomography
SPECT/CT	Single-photon emission computed tomography/Computed tomography
SpO_2	Oxygen saturation

Contents

Introductory Background 1917
Case 1 1918
Case 2 1920
Case 3 1922
Case 4 1922
Case 5 1922
Case 6 1926
References 1928

Introductory Background

Cardiovascular disease is a frequent comorbidity in cancer patients. Ischemia occurring during therapy, especially perioperative ischemia, is a serious event, associated with increased morbidity and mortality (see ▶ Chap. 51, "Imaging the Heart in the Cancer Patient" of this book). Detecting ischemia in patients at intermediate risk of a cardiovascular event is a major indication for myocardial perfusion imaging

J.J. Fox
Department of Radiology, Memorial Sloan Kettering Cancer Center, New York, NY, USA
e-mail: foxj@mskcc.org

H. William Strauss (✉)
Molecular Imaging and Therapy Service, Memorial Sloan Kettering Cancer Center, New York, NY, USA
e-mail: straussh@mskcc.org

© Crown Copyright 2017
H.W. Strauss et al. (eds.), *Nuclear Oncology*,
https://doi.org/10.1007/978-3-319-26236-9_88

in cancer patients. Many patients referred for myocardial perfusion imaging are frail and cannot exercise. These patients usually undergo stress testing with pharmacologic agents. Although pharmacologic stress can be performed with agents that increase myocardial oxygen consumption, such as dobutamine, these agents have largely been replaced by vasodilator agents, such as adenosine (adenosine triphosphate in Japan) or the synthetic adenosine A_{2A} agonist, regadenoson, because of their relative safety. Adenosine infusion or regadenoson administration causes a generalized vasodilatation, often associated with a slight decrease in blood pressure, and may also be accompanied by a pounding sensation in the head and a feeling of abdominal fullness. The coronary vasodilatation during infusion of adenosine (0.14 mg/kg/min) increases coronary blood flow velocity by more than 3.5-fold over baseline [1]. Regadenoson, on the other hand, raises coronary flow about 2.5-fold within approximately 2 min of IV administration, and it remains over twofold increased for about 10 min [2]. Both adenosine and regadenoson also cause vasodilatation of splanchnic blood vessels, increasing splanchnic flow, which in turn increases subdiaphragmatic activity that may interfere with the evaluation of inferior wall perfusion on stress-injected images. To minimize activity in the splanchnic bed, it is helpful to combine pharmacologic vasodilator stress with low-level exercise (if technically and clinically feasible). Walking, even at 1–2 mph with 0% grade, is sufficient to reduce splanchnic perfusion. The following cases illustrate some of the clinical and technical issues that arise in the performance and interpretation of these studies.

Case 1

A 70-year-old man with a 60-pack-year smoking history, chronic obstructive lung disease, dyslipidemia, and a family history of early coronary artery disease was referred for a myocardial perfusion study prior to a Whipple procedure for pancreatic cancer.

Procedure: Rest and stress myocardial perfusion PET/CT scan.

Radiopharmaceutical:

Rest: 9.5 mCi ^{13}N-ammonia IV

Stress 10.9 mCi ^{13}N-ammonia IV (20 min after rest tracer injection)

Technique: A prospectively gated CT was recorded for coronary calcium scoring, followed by a low-dose CT (20 mA) for attenuation correction.^{13}N-ammonia was administered as a bolus IV and gated list-mode data were acquired for 10 min to determine myocardial perfusion and left ventricular function at rest.

A pharmacologic stress test was then performed using regadenoson 0.4 mg IV, administered over 20 s, followed about 30 s later by the administration of the stress dose of ^{13}N-ammonia. Gated list-mode data were acquired for 10 min to determine myocardial perfusion and left ventricular function during vasodilator stress.

Following regadenoson administration, the patient experienced mild chest discomfort, without associated ECG changes. Oxygen saturation (SpO_2) was 98% during the rest acquisition, but decreased to 82% during the episode of chest discomfort. The chest discomfort gradually increased over the next 3 min. Aminophylline 50 mg was administered intravenously to reverse the residual effects of regadenoson. Within 2 min of aminophylline administration, the chest discomfort cleared, and SpO_2 increased to 95%.

Hemodynamics:

Baseline: heart rate (HR) 93 bpm; blood pressure (BP) 151/91 mmHg

Peak stress: HR 96 bpm; BP 148/90 mmHg

Image findings:

Left ventricular size: The left ventricular cavity is dilated at stress compared with rest, suggesting transient ischemic dilatation.

Perfusion: There is a large, moderate-to-severe reduction in perfusion at stress that was not present at rest, consistent with ischemia involving the anterior, lateral, and distal septum (Fig. 1).

Gated images: There is mild hypokinesis of the anterior and lateral walls at stress, which was not seen at rest.

Left ventricular ejection fraction (LVEF): 71% at rest, *decreasing* to 63% at stress.

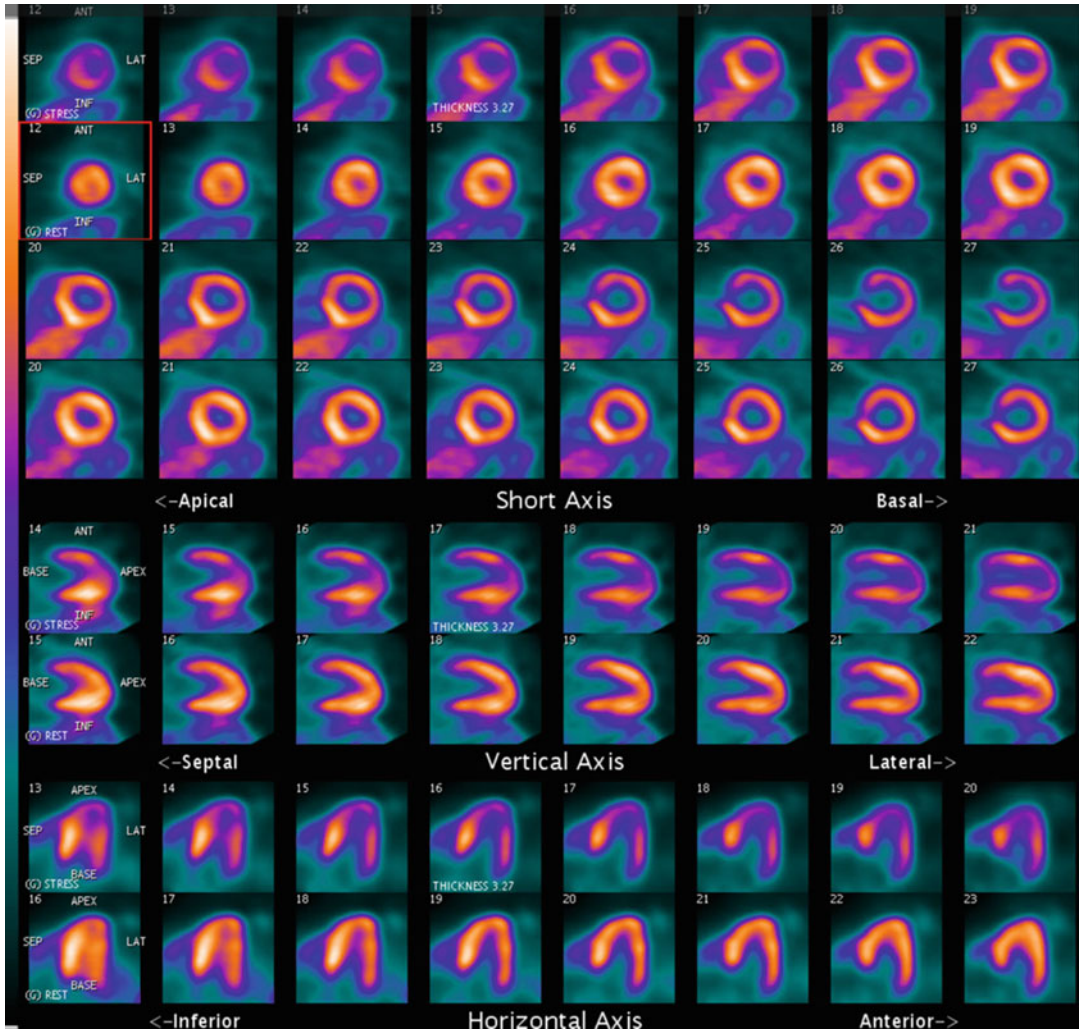

Fig. 1 Summed list-mode images of ^{13}N-ammonia following injection at stress (*upper row*) and at rest (*lower row*) in the short axis, vertical long axis, and horizontal long axis. The stress images demonstrate cavity dilatation, associated with a decline in global ventricular function (LVEF at rest was 71%, decreasing to 63% at stress). Regional perfusion is normal at rest. At stress, there is a significant decrease in perfusion to the distal septum, the entire lateral wall, and the entire anterior wall, suggesting the presence of left main coronary artery disease

Coronary calcium score: 398 (68th percentile).

Impression: Markedly abnormal, high-risk, myocardial perfusion study, consistent with a large area of severe stress-induced ischemia. Findings were discussed with the referring physician.

Comments: The scan demonstrates a pattern of ischemia consistent with a high risk for a coronary event in the following 12 months. This scan indicates a conundrum of care by raising the need for coronary revascularization prior to high-risk cancer surgery. Coronary revascularization performed with percutaneous techniques with a bare metal stent should delay surgery for at least 4–6 weeks or preferably 6 months to minimize the risk of a perioperative coronary event [3, 4]. Recent recommendations suggest that the interval between coronary bypass surgery and elective surgery should be at least 6 weeks. Given the size of the patient's pancreatic cancer, and the fact that the disease was

limited to the location of the mass, the surgeon recommended performing the cancer surgery as expeditiously as possible without prior revascularization. Medical therapy was optimized to maximize pain control and minimize myocardial oxygen demand in the perioperative interval. In light of the patient's known obstructive lung disease, careful titration of the beta blockade is critical. It is helpful to have the perioperative cardiac monitoring managed by both a cardiologist and an experienced anesthesiologist.

Outcome: The patient had a successful Whipple procedure. In spite of the high-risk imaging findings, there were no major acute coronary events during the perioperative interval.

In addition to the specific imaging findings, there were two other indications that the patient was at high risk for a perioperative event:

1. There was a blunted heart rate response following injection of regadenoson [5]. Subjects with <25% increase in heart rate over baseline have an increased risk of cardiac events.
2. There was a decrease in LVEF from rest to stress. Normally, LVEF increases with vasodilator stress on PET/CT myocardial perfusion imaging, where data are recorded immediately after injection of the stress agent [6]. An increase of >5% in LVEF has a high negative predictive value for the presence of triple-vessel or left main coronary artery disease.

Case 2

A 50-year-old man with a family history of accelerated coronary artery disease was referred for myocardial perfusion imaging. His mother died at age 45 of a "heart attack" and a younger sibling died suddenly at age 40. Genetic evaluation of the patient and his immediate family confirmed the diagnosis of homozygous familial hypercholesterolemia, with marked elevation of low-density lipoprotein cholesterol. The patient had sustained a myocardial infarct at age 40. Catheterization at the time of the infarct demonstrated moderate-to-severe stenosis in the left anterior descending artery (LAD), treated with multiple drug-eluting stents. About 1 month before presentation he noted a mass in his left breast. He was referred for evaluation for possible stress-induced myocardial ischemia prior to left breast biopsy and possible mastectomy.

Procedure: Rest and stress PET/CT myocardial perfusion scan.

Radiopharmaceutical:
Rest: 7.2 mCi ^{13}N-ammonia IV
Stress: 12.1 mCi ^{13}N-ammonia (20 min after rest injection)

Technique: Calcium scoring was not performed because of prior stent placement. Low-dose CT (20 mA) was performed for attenuation correction. ^{13}N-ammonia was administered IV, and gated list-mode data were acquired for 10 min to determine myocardial perfusion at rest.

A pharmacologic stress test was then performed using regadenoson 0.4 mg IV over 20 s, followed by the administration of the stress dose of ^{13}N-ammonia. Gated list-mode data were acquired for 10 min to determine myocardial perfusion with vasodilator stress.

Following regadenoson administration, the patient had no symptoms. There were no ST changes on ECG.

Hemodynamics:
Baseline: HR 70 bpm; BP 135/85 mmHg
Peak stress: HR 90 bpm; BP 152/90 mmHg

Image findings:

Left ventricular size: Upper limits of normal at rest and stress.

Perfusion: There is a large, moderate-to-severe reduction in perfusion at rest in the septal, distal anterior, inferior, and lateral walls, extending to the apex. The regions of decreased perfusion are worse at stress, suggesting superimposed ischemia (Fig. 2).

Gated images: There is hypokinesis of the distal inferior and lateral walls and systolic anterior motion of the septum at rest (likely due to the prior infarction). The findings were unchanged at stress.

LVEF: 58% at rest; 59% at stress.

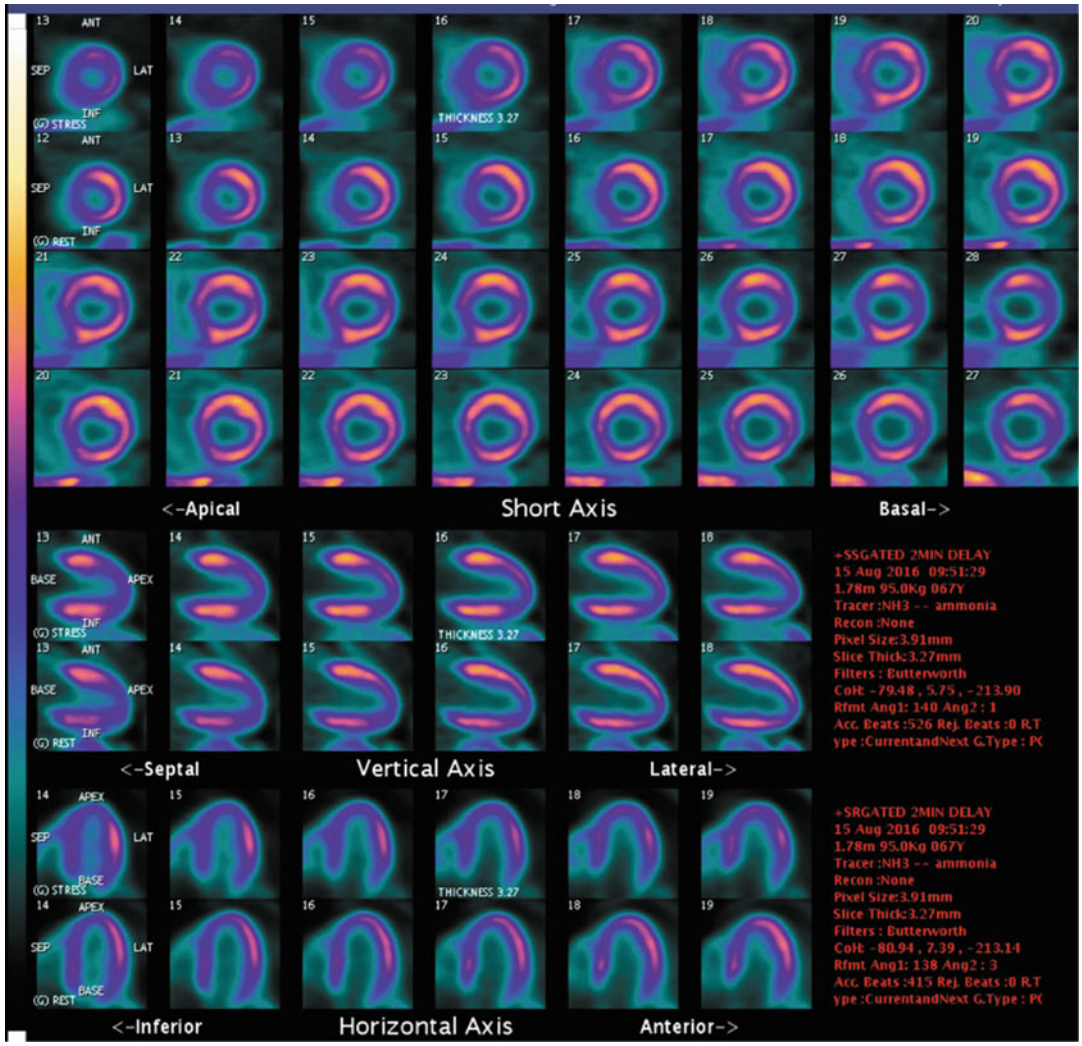

Fig. 2 (**a**) Summed list-mode images of ^{13}N-ammonia following injection at stress (*upper row*) and at rest (*lower row*) in the short axis, vertical long axis, and horizontal long axis. There is a large, moderate-to-severe reduction in perfusion at rest in the septal, distal anterior, inferior, and lateral walls as well as the apex, consistent with scar. The regions of decreased perfusion, especially in the distal anterior wall, are slightly worse at stress, suggesting peri-infarct ischemia

Impression: Abnormal myocardial perfusion scan, demonstrating moderate-sized regions of decreased perfusion in the septal, distal anterior, and inferior walls, worse at stress than at rest, suggesting myocardial scar and ischemia.

Comments: The patient with genetic predisposition has severe coronary artery disease evidenced by prior myocardial infarction and stent placement, as well as scan findings suggestive of superimposed ischemia. Medical therapy with lipid-lowering agents, although not fully effective in this genetic disease, should be maintained. In the absence of contraindications, beta-blocker therapy should be instituted and maintained through the course of hospitalization. Although breast surgery is not a high-risk procedure, the patient should be

monitored frequently to avoid surges in blood pressure and/or episodes of prolonged tachycardia that may cause ischemia. Postoperatively, pain should be minimized to avoid catechol surges that may cause coronary spasm.

Case 3

An 80-year-old man with biopsy-proven Hürthle cell thyroid carcinoma, chronic atrial fibrillation, and right bundle branch block was referred for myocardial perfusion imaging to detect possible stress-induced myocardial ischemia prior to thyroidectomy.

Procedure: Rest and stress SPECT/CT myocardial perfusion scan. Owing to difficulty with balance (use of a cane), the patient was stressed with a combination of low-level exercise (1.7 mph and 5% grade) and 0.4 mg regadenoson IV over 20 s.

Radiopharmaceutical:

Rest: 4 mCi ^{201}Tl-chloride IV
Stress: 30 mCi ^{99m}Tc-sestamibi IV

Image findings:

Careful inspection of the rotatogram reveals an extracardiac focus of abnormal uptake in the left lung (white arrow on selected rotatogram images at rest and stress).

Attenuation corrected myocardial perfusion images at stress and rest show a short septum (likely an anatomic variant) and relatively increased tracer uptake in the anterobasal wall on the rest images (likely due to scatter from activity below the diaphragm), with no significant change from rest to stress. There is no definite evidence of ischemia or scar (Fig. 3).

Impression:

1. No evidence of myocardial ischemia or scar.
2. Focal extracardiac tracer uptake in the left lung, corresponding to a lung nodule on CT (Fig. 3).

Comment: The rotatogram should be carefully inspected for evidence of abnormal extracardiac activity in all patients. In this case, a pulmonary metastasis from Hürthle cell thyroid cancer was incidentally detected.

Case 4

A 59-year-old woman with a history of vulvar cancer and a new pulmonary nodule was referred for myocardial perfusion imaging because of a recent treadmill test with positive findings on ECG (Fig. 4). The patient was asymptomatic during the stress test and had no history of coronary disease. The patient exercised to stage 2 of the Bruce protocol, reaching a heart rate of 155, 96% of the predicted maximum for age.

Comments: In view of the severity of the ECG changes despite the normal imaging findings, a debate ensued about the necessity of an anatomic study to confirm the absence of coronary disease. Although a coronary CT arteriogram was considered, the attending physician decided a selective coronary arteriogram was required. The selective coronary arteriogram demonstrated no significant arterial narrowings. One of the first applications of rest and stress myocardial perfusion imaging was the identification of patients with a false-positive ECG response to exercise [7].

Comment: Display of myocardial perfusion images in monochrome was the standard prior to the general acceptance of SPECT images. Displaying data in color adds additional contrast to the display, in some cases resulting in false-positive interpretations. When in doubt about a subtle lesion, it is helpful to review the rotatogram and the reconstructed images in monochrome.

Case 5

A 51-year-old woman with a history of bilateral breast cancer was treated with surgery and radiation therapy. Tumors recurred in both breasts 5 years after her initial therapy. The recurrent lesions were treated with surgery and doxorubicin. She was referred for myocardial perfusion imaging owing to increasing shortness of breath on exertion and a persistent resting tachycardia of 110 bpm. She had a long history of cocaine abuse.

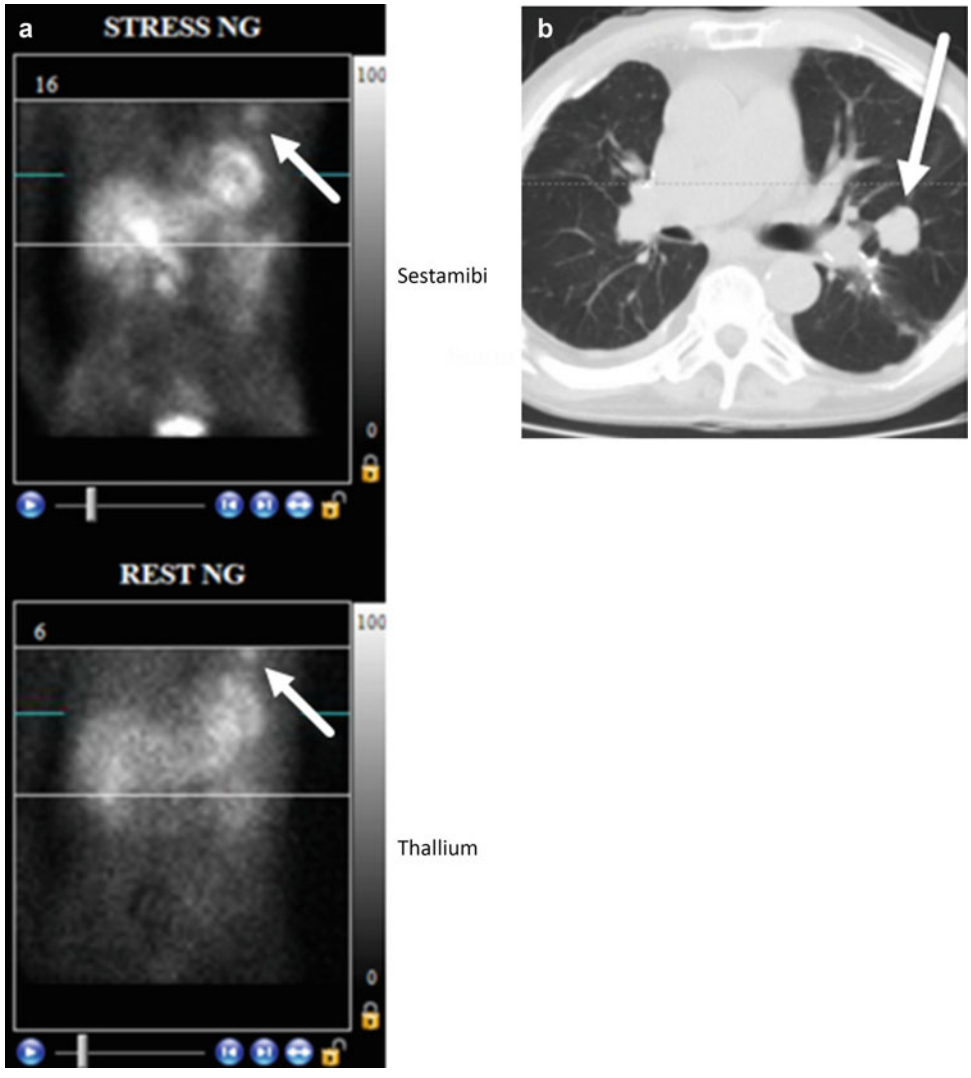

Fig. 3 (continued)

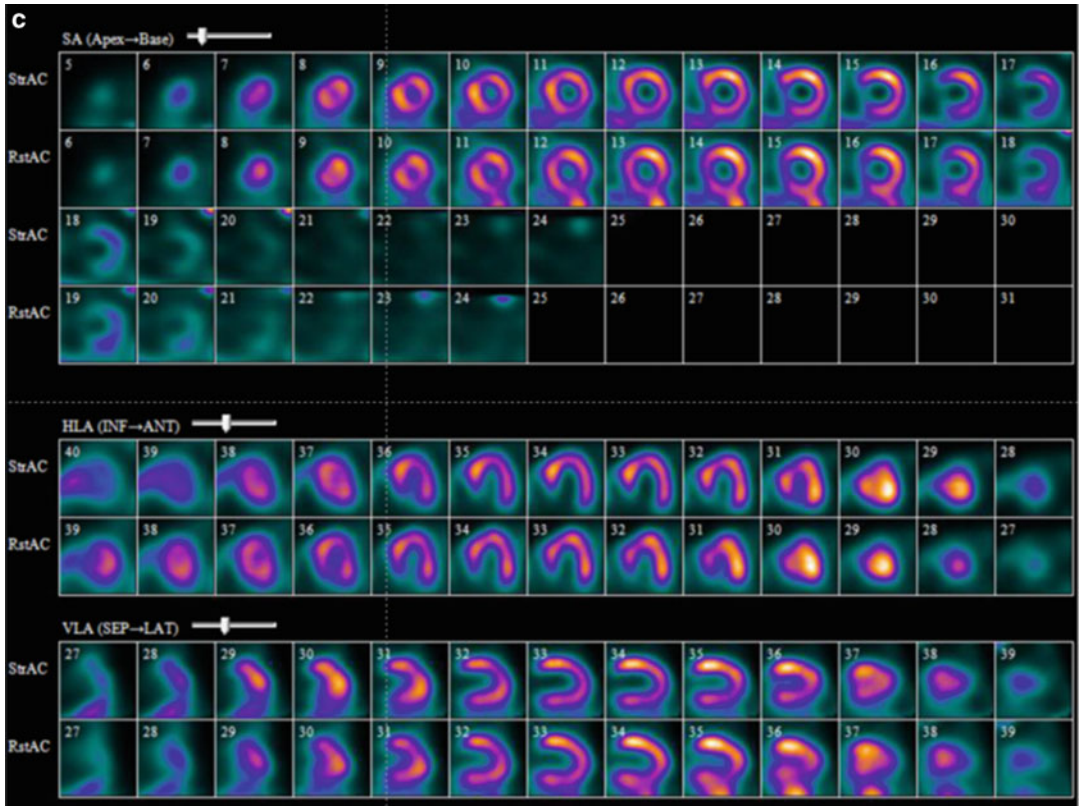

Fig. 3 (**a**) Single frames of the SPECT rotatogram at stress (*top*, sestamibi) and at rest (*bottom*, thallium) demonstrate a focus of uptake superior and lateral to the anterior wall (*arrow*). (**b**) Selected slice of CT scan demonstrating a 2-cm left lung metastasis (*arrow*), corresponding to the focal uptake seen on the perfusion scans. (**c**) Attenuation corrected myocardial perfusion images at stress (*top rows*, *StrAC*) and rest (*bottom rows*, *RstAC*). The scans show a short septum (likely an anatomic variant) and relatively increased tracer uptake in the anterobasal wall on the rest images (likely due to scatter from activity below the diaphragm), with no significant change from rest to stress. There is no definite evidence of ischemia or scar. An extracardiac focus is seen in the *left upper corner* on the basal axial slices corresponding to the left lung focus on the rotatogram

Procedure: Rest and stress myocardial perfusion SPECT/CT scan. The patient underwent stress testing with treadmill exercise. The patient exercised for 6 min, reaching stage 3 of the Bruce protocol. Poststress SPECT/CT images were acquired 20 min after the stress tracer injection.

Radiopharmaceutical:

Rest: ^{201}Tl-chloride 3.5 mCi IV

Stress: ^{99m}Tc-sestamibi 30 mCi IV

Hemodynamics:

Rest: HR 105 bpm; BP 110/70

Peak stress: HR 143 bpm (100% of predicted maximum for age); BP 150/90

Image findings:

There is a moderate-sized lesion in the apex where perfusion is absent on both the rest and stress images, suggesting myocardial scar (Fig. 5).

Regional wall motion at rest and stress demonstrates akinesis of the apex and distal septum, corresponding to the region of decreased perfusion.

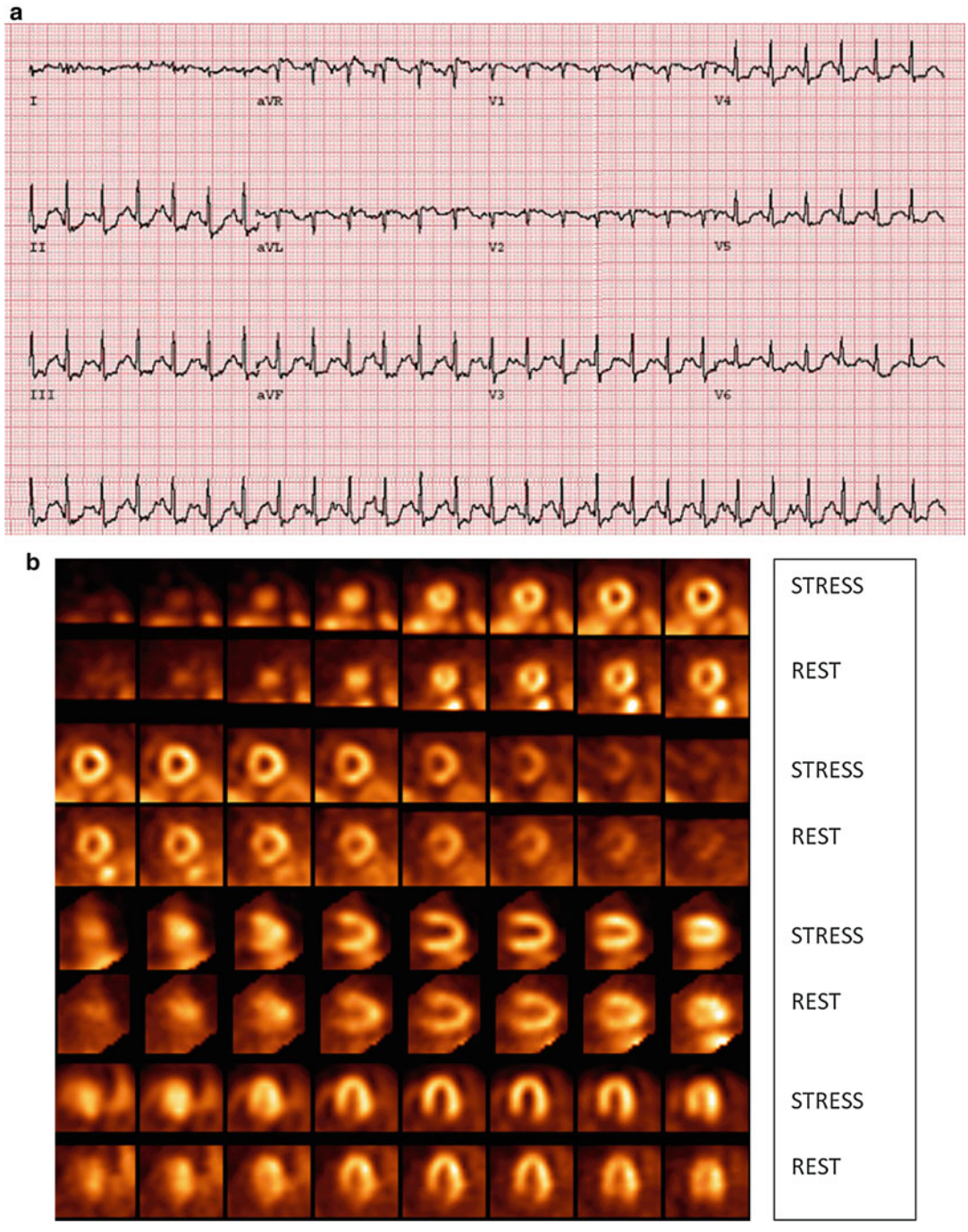

Fig. 4 (**a**) ECG at peak stress demonstrates significant ST depression in leads III, aVF, and V_3–V_5. (**b**) Myocardial perfusion SPECT scan at stress (*ST*) and rest *(RE*), demonstrating a homogeneous distribution of perfusion in the LV myocardium at rest and stress. The study was interpreted as an abnormal ECG and a normal perfusion scan, likely a false-positive ECG

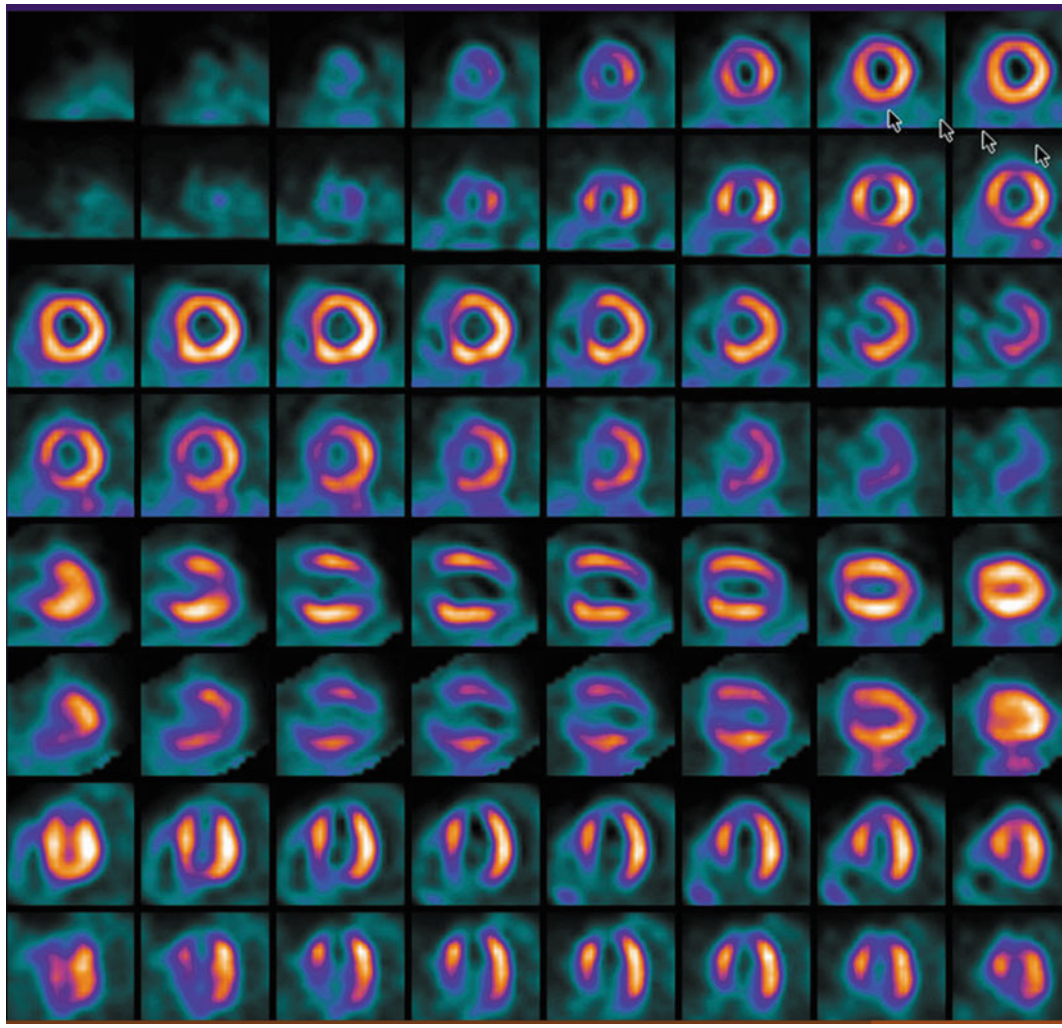

Fig. 5 (**a**) Myocardial perfusion scan at rest and stress

LVEF: 55%

Impression: Abnormal scan, demonstrating myocardial scar in the apex. No evidence of ischemia.

Comment: In view of the history of cocaine abuse, it is possible that the region of decreased perfusion is due to an area of infarction secondary to cocaine-induced coronary spasm. An alternative, although less likely explanation, is that the lesion may be due to radiation-induced coronary disease. To determine if the lesion is due to radiation, the radiation treatment plan was reviewed to establish whether the apex was exposed to over 30 Gy, the threshold dose for myocardial damage [8]. The treatment plan did not include the left ventricular myocardium in the radiation field.

Case 6

A 76-year-old man with a history of bladder cancer, scheduled for cystectomy, was referred for rest and stress myocardial perfusion imaging. He had a history of type 2 diabetes treated with oral hypoglycemics and hyperlipidemia treated with statins. His medical history also included acute

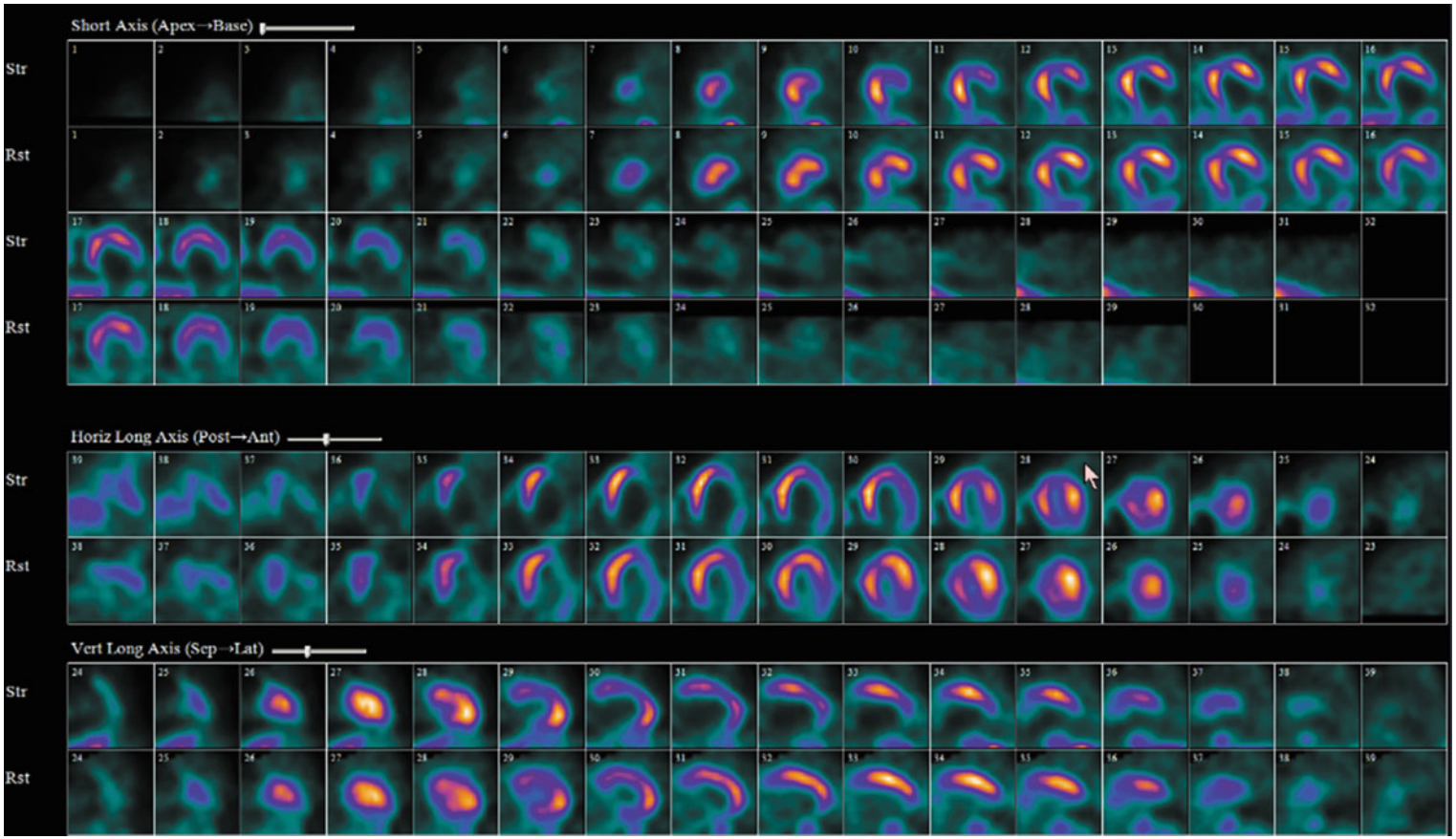

he scan demonstrates a large region of markedly decreased/absent perfu-
ferior wall at both rest and stress suggesting myocardial scar. There is a

Poststress images were recorded 30 min after completion of the stress test. The left ventricular cavity is enlarged. There is akinesis of the inferior wall, severe hypokinesis

myocardial infarction 11 years before the current presentation. At the time of his infarction, coronary arteriography demonstrated triple-vessel disease. He was treated with three-vessel coronary bypass surgery. The patient had a second myocardial infarction 1 year after CABG. No additional revascularization was done. At an examination 5 years before his current presentation, there was evidence of ischemia on a myocardial perfusion scan and a reduced LVEF of 30%. Based on the LVEF of 30% and the extent of the myocardial scar, the patient was treated with an implanted cardiac defibrillator. A pharmacologic stress myocardial perfusion SPECT/CT scan was performed.

Procedure – rest: ^{99m}Tc-sestamibi 10 mCi IV, followed about 30 min later by rest SPECT/CT acquisition. About 2 h after rest imaging, pharmacologic stress was performed with 0.4 mg regadenoson IV. About 1 min after regadenoson, 30 mCi ^{99m}Tc-sestamibi was administered IV. The patient was asymptomatic and there were no changes on the ECG during the stress procedure.

Hemodynamics:

Baseline: HR 80 bpm; regular; BP 110/70

Peak stress: HR, 100 bpm; BP 100/60 (Fig. 6).

Comments: The imaging findings suggest that the patient is at high risk of a perioperative event in the course of the cystectomy, an operation that is definitely considered high-risk surgery. In view of the patient's prior revascularization and implantation of an automatic implantable cardioverter-defibrillator, coupled with the aggressiveness of his tumor, it was decided to proceed with surgery. Beta-blocker therapy was started before surgery to maintain a heart rate of < 60 bpm and minimize surges in blood pressure. The patient had no cardiovascular events in the perioperative interval.

Takeaway In the evaluation of patients with a history of coronary disease, or individuals at intermediate risk for myocardial ischemia, myocardial perfusion imaging remains a useful clinical procedure. The 2012 appropriate use criteria for coronary revascularization focused update [9] defines high risk as a 3% incidence of a major cardiovascular event in the next year. Based on this definition, the odds of a patient with a high-risk scan surviving for the year favor the patient. When it is acceptable to caregivers and the patient to delay a major cancer therapeutic intervention while waiting for recovery from stent placement or bypass surgery, revascularization should be performed. On the other hand, as we describe in two patients with high-risk scans, when cancer therapy cannot be delayed, medical therapy and intensive monitoring can help patients survive high-risk procedures.

References

1. Wilson RF, Wyche K, Christensen BV, Zimmer S, Laxson DD. Effects of adenosine on human coronary arterial circulation. Circulation. 1990;62:1595–606.
2. Lieu HD, Shryock JC, von Mering GO, Gordi T, Blackburn B, Olmsted AW, et al. Regadenoson, a selective A2A adenosine receptor agonist, causes dose-dependent increases in coronary blood flow velocity in humans. J Nucl Cardiol. 2007;14:514–20.
3. Holcomb CN, Graham LA, Richman JS, Rhyne RR, Itani KM, Maddox TM, Hawn MT. The incremental risk of noncardiac surgery on adverse cardiac events following coronary stenting. J Am Coll Cardiol. 2014;64:2730–9.
4. Girardi LN, Rabotnikov Y, Avgerinos DV. Preoperative percutaneous coronary intervention in patients undergoing open thoracoabdominal and descending thoracic aneurysm repair. J Thorac Cardiovasc Surg. 2014;147:163–8.
5. Gomez J, Fughhi I, Campagnoli T, Ali A, Doukky R. Impact of integrating heart rate response with perfusion imaging on the prognostic value of regadenoson SPECT myocardial perfusion imaging in patients with end-stage renal disease. J Nucl Cardiol. 2016; [Epub ahead of print].
6. Dorbala S, Vangala D, Sampson U, Limaye A, Kwong R, Di Carli MF. Value of vasodilator left ventricular ejection fraction reserve in evaluating the magnitude of myocardium at risk and the extent of angiographic coronary artery disease: a ^{82}Rb PET/CT study. J Nucl Med. 2007;48:349–58.
7. Zaret BL, Stenson RE, Martin ND, Strauss HW, Wells Jr HP, McGowan RL, et al. Potassium-43 myocardial perfusion scanning for the noninvasive evaluation of patients with false-positive exercise tests. Circulation. 1973;48:1234–41.
8. Darby SC, Cutter DJ, Boerma M, Constine LS, Fajardo LF, Kodama K, et al. Radiation-related heart disease: current knowledge and future prospects. Int J Radiat Oncol Biol Phys. 2010;76:656–65.
9. Patel MR, Dehmer GJ, Hirshfield JW, Smith PK, Spertus JA, et al. ACCF/SCAI/STS/AATS/AHA/ASNC/HFSA/SCCT 2012 appropriate use criteria for coronary revascularization focused update. J Am Coll Cardiol. 2012;59:857–81.

Index

Using the electronic version of this text, you can perform a comprehensive search for terms.

A
ACD. *See* Annihilation coincidence detection (ACD)
ACF. *See* Attenuation correction factor (ACF)
^{225}Ac-HuM195, 1175
Acinar adenocarcinoma, 887
^{225}Ac-PSMA-61, 180
Acral melanoma, 1069
^{225}Ac therapy, 1176
Actinium-225 (^{225}Ac), 179–180
Acuity™, 295, 296
Acute lymphocytic leukemia (ALL), 438–439
  bone scintigraphy, 444, 445
  chromosomal abnormalities, 438–439
  CRLF2 mutations, 439
  CT, 444
  cytogenetic abnormality, 439
  diagnosis and risk assessment in, 1161
  diagnosis and staging, 439–445
  MRI, 444–445
  radiologic imaging, 443–444
  renal parenchymal abnormality, 444
  stem cell transplantation, 443
  treatment, in adults, 1160–1163
  treatment response evaluation, 445
  ultrasound, 444
Acute myeloid leukemia (AML), 452–455
  blastic plasmacytoid dendritic cell neoplasm, 455
  cytogenetic abnormalities, 456
  diagnosis, 455–456
  [^{18}F]FDG, 455
  ^{18}F-FLT, 456
  molecular abnormalities, 456
  myelodysplasia-related changes, 454
  myeloid sarcoma, 454–455
  recurrent genetic abnormalities, 453
  response evaluation, 456–457
  staging, 455–456
  symptoms, 455
  therapy-related myeloid neoplasms, 454
  treatment, 1169–1172
  WHO classification, 453, 454
Acute myocardial infarction, 1922, 1924–1926
Acute promyelocytic leukemia (APL), 1171
Adaptive response, 312
Adenocarcinomas
  acinar, 887
  esophageal, 686–687
  gastric, 699
  mucinous, 571
  parathyroid, 1608
Adenomatous parathyroid glands
  imaging protocol for, 591
  structure of, 591
Adenosine, vasodilatation, 1916
Adjuvant chemotherapy, breast cancer, 617
Adjuvant radiotherapy
  breast cancer, 626
  HNSCC, [^{18}F]FDG PET/CT after, 530
AJCC classification. *See* American Joint Committee on Cancer (AJCC)
AKT, 18, 513, 565
Albumin colloid, 74
Alcohol intake, esophageal SCC, 687
Alemtuzumab, 1169
Alkaline phosphatase (ALP), 177
ALL. *See* Acute lymphocytic leukemia (ALL)
Allogeneic stem cell transplantation, 448, 1148, 1160, 1169
Alpha emitters, 43, 102, 175–176
  Astatine-211, 44
Alpha fetoprotein, 1801
16 alpha-^{18}F-fluoro-17 beta-estradiol (^{18}F-FES), 630
Alpha-particle bombardment, 46, 47
Alpha radiation, 205
Alveolar rhabdomyosarcoma, 1852, 1853, 1856, 1857
American Academy of Dermatology (AAD), 1867
American Cancer Society of Childhood Leukemia Report, 443
American Joint Committee on Cancer (AJCC), 1070, 1722
  of CNS tumors, 470–472
  esophageal cancers, 1069–1070
Amino acids
  clinical uses, 133
  neutral L, 484

© Springer International Publishing Switzerland 2017

H.W. Strauss et al. (eds.), *Nuclear Oncology*,
https://doi.org/10.1007/978-3-319-26236-9

Amino acids (*cont.*)
radiolabeled, 484–486
radiotracers structures, 134–135
transport mechanisms, 133–138
AML. *See* Acute myeloid leukemia (AML)
Amyloidosis, 1492–1495
Anal canal cancer, 1721
clinical target volume (CTV), 1728
[^{18}F] FDG PET/CT, 1724
metabolic activity, 1721
PET MIP image, 1727
PET/MRI, 1728
squamous cell G2, 1721
VMAT-SIB treatment plan, 1726
Analgesics, for pain control, 177
Anaplastic astrocytomas. *See* Grade III astrocytomas
Anaplastic thyroid carcinoma (ATC)
clinical presentation and diagnosis, 565–567
description, 564
[^{18}F]FDG PET/CT, 567, 568
histologic patterns, 565, 566
incidence, 565
pathogenesis, 565
radionuclide imaging, 567, 568
treatment of, 1224–1225
Androgen receptor (AR)
axis, 27–28
prostate cancer, 28
Androgen withdrawal syndrome, 160
Anemia, parathyroid carcinoma, 602
Anger camera. *See* Gamma camera
Angiogenesis, 119–120
expression, of factors, 10
malignant melanoma, 1069
Angiogenic switch, 9
Ann Arbor staging, lymphoma, 356, 361
Annihilation coincidence detection (ACD), 222–224
Annihilation radiation, 204
Anthracycline-induced cardiotoxicity, 1497–1499
Antiangiogenic therapy
brain tumors, 497–498
HNSCC, 515
malignant melanoma, 1076–1077
Antibodies conjugation
with a drug, 1160
with a toxin, 1160
Antibody-dependent cell-mediated cytotoxicity (ADCC), 1160
Anti-CTLA4 treatment, 12
Anti-PTH immunotherapy, 604
Anti-VEGF therapy
[^{18}F]FDG uptake, 10
APDs. *See* Avalanche photodiodes (APDs)
Aphasia, 475
Apoptosis, 22–23
endothelial cells, 10
intrinsic and extrinsic pathway, 310
low-dose/dose-rate, 310
lung cancer, 642
malignant melanoma, 1077
^{99m}Tc-annexin V, 117–118
^{99m}Tc-duramycin, 118–119
Apparent diffusion coefficient (ADC) values, 479
Application-specific integrated circuit (ASIC) readout board, 266
Arginine-glycine-aspartic acid (RGD), 149–150
Armed Forces Institute of Pathology (AFIP) studies, 712
Aromatase inhibitors (AIs), 615
Aromatic amino acid decarboxylase (AACD), 138
ArteMIS™ handheld fluorescence camera system, 288, 291
ASC transporter 2 (ASCT2), 133
ASIC readout board. *See* Application-specific integrated circuit (ASIC) readout board
Astatine-211 (^{211}At), 44, 48, 178–179
alpha-decay particles, 57
alpha-particle bombardment, 46, 47
Astigmatic collimation, 268
Astrocytomas, 470
Ataxia, 475
Atom
planetary model, 200
structure of, 200–201
Attenuation correction, 263
Attenuation correction factor (ACF), 234
Auger electron emitters, 48, 102
Auger electrons, 204, 207–208
Auger electron therapy, 43
Autologous, after RIT, 1148
Autologous stem cell transplantation (ASCT), 405, 1159–1160, 1180
Avalanche photodiodes (APDs), 220
Avastin, 30
$\alpha_v\beta_3$ integrin, 10
5-azacitidine, 1170

B

Barrett's esophagus, 687
Basal-like breast cancer, 617
B-cell lymphoma, 1757
Bcl-2 protein, 1077
Becquerel (Bq), 209
β-emitting isotopes, 311–312
Bendamustine, 1168
Bendamustine plus prednisone, 1180
Benua approach, 315, 316
Benzodiazepines
systemic sedation with, 1108
β^- dosimetry, 206
Beta emitters, 182–183
bone metastases, 43
Beta probes
dual-detector beta probe, 279
intraoperative detection, 278–280
Beta radiation (β^-), 205–206
Bevacizumab, 477
advanced cancers, 1076–1077
HNSCC, 515

neuroblastoma, 1883
VEGF, 9
vs. temsirolimus, 1077
Bexxar®, 1147
^{212}Bi, 44
^{213}Bi-anti-CD33, 1176
Biclonal plasma proteins, 398
^{213}Bi-HuM195, 1175
Biliary cancer
extrahepatic, 736
[^{18}F] FDG-PET, 737
Binet staging system, chronic lymphocytic leukemia, 447–448
Biological dosimetry, 331–334
chromosome painting assay, 333
comet assay, 333–334
dicentrics assay, 332
g-H2AX assay, 334
micronuclei assay, 333
Biologically positive margins, 513
Biological target volume (BTV), 477
Biologic effective dose (BED), 313–314
Bioluminescence imaging, 287
Biomarkers, multiple myeloma, 406
Bismuth-213 (^{213}Bi), 44, 180–181
Bispecific monoclonal antibody (BsMAb), 185
Bivalent targeting, 151–152
Bladder cancer
abdomen, hypermetabolic lymph nodes, 1769
[^{11}C]choline, 868–869
[^{11}C]methionine, 869
diagnosis, 862
enlarged lymph node, 1753
environmental and genetic factors, 858–861
epidemiology, 857
[^{18} F]FDG-PET/CT, 865–868
[^{18}F]FDG PET/CT, 1762–1763
^{18}F-fluoride, 869
hydronephrosis, 1754
intravesical BCG immunotherapy, 870
intravesical chemotherapy, 870
Jewett-Strong-Marshall classification, 863
lymphadenopathies, 1757
MIP and, 1760, 1762
molecular biology, 861–862
M staging, 865
muscle-invasive, 871–872
neoadjuvant chemotherapy, 871–872
N staging, 865
perirenal lymphadenopathy, 1755
prognostic stratification, 862–863
skeleton, osteolytic lesions, 1768
staging, 862–863
superficial, 869–870
symptoms, 862
T1-and T2-weighted MR axial slices, 1756
TNM classification, 863
T staging, 863
unresectable tumors, 872
urothelial carcinoma, 1761
Blastic plasmacytoid dendritic cell neoplasm, 455
Bleomycin, 1515
Blood-brain barrier (BBB) damage, 470
radiotherapy-induced injury, 477
Blue dye technique, 280
Bombesin receptor imaging, 152–154
Bone disease, primary HPTH, 589
Bone marrow
micro-environment, 399
plasma cells, 398–399
Bone marrow metastases, 1125
Bone metastases
advanced stages of, 1309
beta emitters, 43
^{177}Lu-EDTMP, 1328–1329
lutetium-177, 104
mechanism of action, 1312–1313
^{117m}Sn-pentetate, 1328–1329
^{99m}Tc-diphosphonates, 73
neoplastic disease, 109–110
^{32}P, 1313
pathophysiology of, 1310–1311
phosphorus-32, 105
prevention of, 1311–1312
radiation therapy, 1312
radiolabeled agents for, 1313
radiopharmaceutical therapy, 1312, 1313, 1329–1330
Radium-223, 1322–1327
rhenium-186, 105
rhenium-188, 105
Rhenium-labeled radiopharmaceuticals, 1327–1328
samarium-153, 104
^{153}Sm-EDTMP, 1317–1322
^{89}Sr-chloride, 1313–1317
strontium-89 (^{89}Sr), 105
Bone pain
palliation therapy, 1312
parathyroid carcinoma, 602
strontium-89 chloride (Metastron), 43
treatment, 330–331
Bone sarcomas, 1128
Bone scan (BS)
breast cancer, 619
breast cancer bone metastases, 622, 623
lymphoma, 363
Bone scintigraphy, 1111
acute lymphocytic leukemia, 444, 445
^{99m}Tc-diphosphonates, 73
with ^{99m}Tc-diphosphonates, 1122
multiple myeloma, 411–412
staging of neuroblastoma, 1122
Bone-seeking radionuclides, radiotherapy with, 1184–1185
Bortezomib, 1181
Bortezomib-dexamethasone, 1180
Bortezomib/melphalan/prednisone (VMP), 1180
β^- particle emitters
iodine-131, 103
lutetium-177, 104
phosphorus-32, 105

β⁻ particle emitters (*cont.*)
rhenium-186, 105
rhenium-188, 105
samarium-153, 104
strontium-89, 105
yttrium-90, 103–104
^{80}Br, 51
Brachytherapy, 892
BRAF
dabrafenib *vs.* trametinib, 1074
inhibitor, 1074
inhibitors, 25
GIST, 715
mutations, 1068
signaling pathway, 26
BRAF V600E mutation, 554
Brain tumors, 1106
age, 475–476
age-adjusted incidence rates, 470
antiangiogenic therapy, 497–498
brain perfusion imaging, 480–481
chemotherapy, 497
clinical presentation, 475
CT role, 478
diagnosis, 476
epidemiology, 469–470
functional neurologic status, 476
glutamine uptake, 19, 20
grading, 470
histology, 475
location, 476
meningiomas, 498–499
metabolic pattern, 478
metastatic spread, 476
MR sequences, 478
^{99m}Tc-pertechnetate, 479
PET/CT *vs.* stand-alone PET, 495–497
PET/MR, 492–494
PET scans, 477, 478
primary, 469
prognosis, 475–476
pseudoprogression, 494
radiation therapy, 497
radioimmunotherapy, 498
radiolabeled amino acids, 484–486
radiotherapy, 477
radiotracers, 479
recurrence *vs.* radiation injury, 477
SPECT, 480
SPECT/CT *vs.* stand-alone SPECT, 495–497
stereotactic biopsy, 477
surgery, 497
surgical planning, 477
symptoms, 475
T2 fluid-attenuated inversion recovery, 478
therapy response, 477
treatment efficacy assessment, 494–495
tumor proliferation, 489–490
tumor resection, extent of, 476
in vivo tumor grading, 476–477
Braking radiation, 209, 252
[^{76}Br]bromide, 48
BRCA1 gene mutations, 7, 616
BRCA2 gene mutations, 7, 616
BRCAPRO model, 616
Breast and Ovarian Analysis of Disease Incidence and Carrier Estimation Algorithm (BODAICEA) model, 616
Breast cancer
adjuvant chemotherapy, 617
age group, 615–616
AJCC staging system, 617–619
clinical examination, 1365
cytotoxic chemotherapy, 625
detection and diagnosis, 617, 619
endocrine therapy, 617, 625
[^{18}F]FDG PET/CT, 1614–1618
full-field digital mammography, 617
future directions, 629–630
gene expression profiling methods, 616
genetic predisposition, 616
genome-wide-associated studies, 616
histologic feature, 616
incidence of, 615
^{111}In-pentetreotide, 81
Ki-67, 617
locoregional therapy, 625
mastectomy, 625
MRI, 617, 619
^{99m}Tc-nanocolloidal albumin, 1373
nuclear imaging, 619–624
portable gamma camera, 1385
in postmenopausal women, 616
radioactive seeds, 1384–1385
radioprotection, 1385–1386
risk factors, 615–616
ROLL, 1383–1384
screening, 615
sentinel node biopsy, 1366
sized-based approaches, 626
SNOLL, 1384
subtypes, 616–617
treatment efficacy, 626–629
ultrasound, 617
Breast carcinoma susceptibility (BRCA2)
parathyroid carcinoma, 601
Breast-conserving surgery (BCS), 625
Breast imaging, 1826, 1829
Breast-specific gamma imaging (BSGI)
breast cancer, 619, 620
Brechbiel, 48
Bremsstrahlung imaging
^{90}Y, 45
Bremsstrahlung radiation, 203
Breslow staging for melanoma, 1069–1070
Broad-beam conditions, 213
Bronchioloalveolar carcinoma (BAC), 654
Bronchopulmonary neuroendocrine tumors, 810
Brown fat activation, 1116, 1117

Bruton kinase inhibitor ibrutinib, 448
Burkitt lymphoma, 1540–1543
Bystander effect, radionuclide therapy, 311–312

C
[^{11}C]acetate, 734–735
Cadmium telluride (CdTe), 281, 283
Cadmium zinc telluride (CZT), 257, 271
Calibration factor (CF), 240
Cancer
  chemotherapy, 1485
  in children, 1106
  hallmarks of, 7, 8
  immune T cells radiolabeling in, 14
  immunotherapy, 11
  patients with, 1485
Cancer cells
  action driver mutations in, 25
  blood vessels, 9
  distinguishing features of, 7
  imaging, 17–21
  proliferation imaging, 21–23
Cancer genomics, 7
Cancer immunotherapy, 11
Carbon-11 (^{11}C), 134
  positron-emitting radionuclides, 86–87
Carbonic anhydrase 9 (CA9), clear cell renal cancer, 28–29
Carboplatin, neuroblastoma, 1887
Carcinoembryonic antigen (CEA), 729
^{125}I, 55
Carcinogenesis, 687
  gastric, 699
Carcinoid
  colorectal cancer, 791
  metaiodobenzylguanidine, 1291–1293
  response, 1281, 1282
  treatment, 1281
CardiaArc™, 271
Cardiac imaging, SPECT, 267, 268, 271
Cardiofocal field-upgradeable collimators, 267
Carestream Albira™, 245
CaR expression in parathyroid cells, 588
Carney-Stratakis syndrome, 711
CarollReS camera, 284
CARS. *See* Coherence anti-Stokes Raman scattering (CARS)
Castrate-resistant prostate cancer (CRPC), 27–28, 1777
Catechol-o-methyl transferase (COMT), 138
CBM. *See* Continuous bed motion (CBM)
CB-TE2A, ethylene bridge in, 49
[^{11}C]carboxyl L-leucine, 91, 92
CCD. *See* Charge-coupled detector (CCD)
[^{11}C]choline
  bladder cancer, 868–869
  exophytic renal lesion, 1753
  head and neck cancers, 536
  kidney mass, 1751
  phospholipid synthesis, 92–93
  prostate cancer, 902–905, 1750–1751
  uptake, 673
CD22, 1152
CD33, 1171
CD45, 1171
CD66, 1171
CD117, 711
CD8 cells, 11
CDH1 gene mutations
  HDGC, 699
CdTe. *See* Cadmium telluride (CdTe)
Cell-cell synergism, 10
Cell death mechanisms, 310
Cell membrane, 55
Cell surface receptors
  bombesin expression, 152–154
  integrin expression, 149–152
  prostate-specific membrane antigen, 154–158
  somatostatin expression, 147–149
  steroid hormone receptors, 158–160
Cellular pleomorphism, 472
Cellular proliferation, with [^{18}F]FLT, 145–147
Center-of-rotation misalignment correction, 260, 261
Central nervous system (CNS), 1110
  neoplasms, 470–472
Ceramide-cholesterol complexes, 55
Cerebellar hypometabolism, 482
Cerebral blood flow measurement, 39
Cerebral metabolic rate for glucose (CMR_{glc}), 481
Cerebrospinal fluid (CSF) pathways, 476
Cerenkov imaging, 288–291
  [^{18}F]FDG-positive axillary lymph node, 294
  lymph node resection, 293
  of positron-emitting radionuclides, 292
Cervical cancer
  diagnosis, 982–983
  epidemiology and prevalence, 980–981
  [^{18}F]FDG PET, 984–991
  magnetic resonance (MR) imaging, 983–986
  para-aortic lymph node assessment, 991–992
  pathophysiology and clinical presentation, 981–982
  PET/CT, prognostic value of, 992–994
  rectovaginal fistula, 1830
  recurrent, 994
  vaginal mass, fungating, 1830
Cervical carcinoma, [^{18}F]FDG PET/CT imaging, 1824–1827
Cervical lymph node metastases, 1572
Cervical tumor, hypermetabolic, 1826
Cetuximab, 30, 123
  HNSCC, 515
CF. *See* Calibration factor (CF)
[^{11}C]Glucose, 90
Charge-coupled detector (CCD), 285
Charge trapping, 222
[^{11}C]HED
  sympathetic nervous system, 1123
  uptake of, 1123, 1125

CHEK2, 616
Chelating agents, 48–50
Chelator conjucation, 132
Chemoradiotherapy, esophageal cancer, 693
Chemotherapy
  associated pulmonary toxicity, 1515–1518
  brain tumors, 497
  esophageal cancer, 693
  induced lung injury, 1519
  induced tubular injury, 1520–1522
  lymphoma, 357–359, 362–364, 371–372, 378–379
  parathyroid carcinoma, 604
  of primary bone tumors, 1129
  proliferation after, 21–22
  prostate cancer, 893
Chest radiography, 1112
Chest x-ray, 1126
Childhood lymphoma
  Hodgkin's lymphoma, 1110–1111
  non-Hodgkin's lymphoma, 1111
cHL. *See* Classical Hodgkin lymphoma (cHL)
Choi criteria, 717, 718
Cholangiocarcinoma, 735
  classification, 737
  [^{18}F]FDG-PET, 737
  histopathological characterization, 736
  incidence, 736
  pathologic diagnosis, 737
  preoperative staging and resectability, 738–739
  recurrence, detection of, 739–740
  risk stratification, 740–742
Chromaffin cell neuroendocrine tumors, 810
Chromosomal aberrations, 331, 332
Chromosomal abnormality, acute lymphocytic leukemia, 438–439
Chromosome painting, biological dosimetry assay, 333
Chronic active gastritis, 699
Chronic cardiotoxicity, 1497–1504
Chronic lymphocytic leukemia (CLL), 364, 445–448
  Binet staging system, 447–448
  Bruton kinase inhibitor ibrutinib, 448
  CT scan, 448–450
  diagnosis, 448–450
  [^{18}F]FDG-PET and PET/CT, 449–450
  FISH analysis, 448
  flow cytometry, 450
  follow-up and long-term implications, 450–451
  immunophenotype, 446
  MRI, 449
  next-generation sequencing techniques, 450
  pathophysiology, 446
  Rai staging system, 447–448
  Richter's transformation, 450
  staging, 448–450
  treatment, 1163–1166
  treatment response evaluation, 450
  ultrasound, 449
  WHO classification, 446
Chronic myeloid leukemia (CML), 457
  diagnosis and staging, 458–459
  European Leukemia Net guidelines, 457
  European Treatment and Outcome Study, 458
  [^{18}F]FDG-PET, 458
  ^{18}F-FLT, 458
  monitoring treatment, 459
  treatment, 1172–1173
  tyrosine kinase inhibitors, 457–459
Chronic obstructive pulmonary disease (COPD), 77
[^{11}C]5-hydroxy-L-ryptophan ([^{11}C]HTP), 1742, 1745
  neuroendocrine tumors, 768, 832
[^{11}C]hydroxytryptophan, NETs, 95, 96
Cinacalcet, 589, 605
Cis-diamminedi-chloroplatinum(II) (cis-Pt), 50
Cisplatinum, HNSCC treatment, 514
c-KIT inhibitors, mutations in, 1076
c-Kit mutations, 7
Cladribine (2-CdA), 1166
Clark Level, 1070
Classical Hodgkin lymphoma (cHL), 354–355, 1905
Claus model, 616
Clear cell carcinomas, 1842–1844
Clear cell renal cancer, 28–29
CLL. *See* Chronic lymphocytic leukemia (CLL)
Clonal cytogenetic abnormalities, 356
[^{11}C]methionine, 136–137, 377–378, 485–486
  bladder cancer, 869
  parathyroid lesions, 595, 596
[^{11}C]MET-PET
  clinical evaluation, 1110
  diagnostic accuracy of, 1109
CML. *See* Chronic myeloid leukemia (CML)
CMOS cameras. *See* Complementary metal oxide semiconductor (CMOS) cameras
Cobimetinib, 1074
Cocaine abuse, myocardial ischemia, 1920, 1922
Coccidioidomycosis, 652–653
Coherence anti-Stokes Raman scattering (CARS), 299–300
Colony-stimulating factor 1R (CSF-1R), 715
Color Doppler pattern, parathyroid lesions, 592
Colorectal cancer
  carcinoid tumors, 791
  clinical objectives, 781
  CT colonography (CTC), 1718
  [^{18}F]FDG-avid metastases, 1720
  [^{18}F]FDG PET/CT, 1716–1728
  [^{18}F]FDG uptake, 1716
  incidence, 779
  mortality, 779
  nuclear medicine role, 781–782
  pelvic MRI, 1722
  PET/MRI, 789–790
  presurgical staging, 782–783
  prognosis, 780–781
  prognostic factors, 779–780
  radiotherapy volume planning, 790
  recurrent, 783–786

staging classification, 780–781
transarterial ^{90}Y-microspheres, 790–791
treatment response evaluation, 786–789
Colorectal carcinoma (CRC), 1353–1354
Colorectal metastases
operative planning and resectability, 726–728
response to therapies, 728–729
Comet assay, biological dosimetry, 333–334
Complementary metal oxide semiconductor (CMOS) cameras, 288
Compton scattering, 211
Computed tomography (CT), 335
acute lymphocytic leukemia, 444
advantages, 1125
chronic lymphocytic leukemia, 448–450
esophageal cancer, 688
hairy cell leukemia, 452
lung cancer, 643, 646
multiple myeloma, 415–421, 423
neuroendocrine tumors, 764, 814
parathyroid lesions, 592–593
Concurrent chemoradiotherapy, 514, 515, 530
Continuous bed motion (CBM), 225
Contrast-enhanced CT
brain metastases, 647
gastric cancer, 702
GIST, 712
HNSCC, 516
lesion on pelvis, 1836
Conventional chemotherapy, 1222
Conventional pelvic imaging studies (CECT), 783
Copper-67 (^{67}Cu), 188
Coronal T2-weighted image, 1120
Coronal T1-weighted MRI
contrast-enhancing tumor, 1127
sympathetic trunk of abdomen, 1126
Coronary heart disease
amyloidosis, 1492–1495
chronic cardiotoxicity, 1497–1504
clinical recognition, 1487–1488
history of, 1486
intermediate risk, 1489
myocardial perfusion imaging, 1489–1491
myocardial tumor involvement, 1491–1492
pericardial tumor involvement, 1491–1492
perioperative and intraoperative management, 1488
preoperative risk, 1488–1489
prevalence, 1486
radionuclide ventriculography, 1495–1497
stent placement and surgery, 1486–1487
Cortistatin, 148
Coster–Kronig electrons, 207–208
Cranial nerve tumors, 470
Creatinine levels, 1146
CRLF2 mutations, 439
Cross-fire effect, RNT, 311–312
Crystal Photonics GmbH, 284
CSL360, 1178
CTLA-4, 12, 13
downregulate immune response, 12
with ipilimumab, 1076
with nivolumab, 1076
CT texture analysis (CTTA)
lung tumors, 643
^{64}Cu, 49, 132
^{64}Cu-ATSM, 45, 162–164
$^{64/60}$Cu-ATSM, hypoxia imaging in HNSCC, 536
^{60}Cu-/^{64}Cu-labelled methylthiosemicarbazone (Cu-ATSM), 673
Cutaneous T-cell lymphoma (CTCL), 15
Cyclin-dependent kinase 4 (CDK4), 1067
Cyclin-dependent kinase inhibitor 2A (CDKN2A), 1067, 1068
Cyclin-dependent kinase inhibitor, parathyroid carcinoma, 601
Cyclin D1, parathyroid carcinoma, 601
Cyclin-D1/PRAD1 oncogene, 589
Cyclophosphamide/thalidomide/dexamethasone (CTD), 1180
Cystoscopic imaging, of urinary bladder cancer, 287
Cytogenetic abnormalities
acute lymphocytic leukemia, 439
acute myeloid leukemia, 456
Cytogenetics, 404
Cytotoxic bystander effect, 58
Cytotoxic chemotherapy, breast cancer, 625
Cytotoxic T lymphocyte antigen 4 (CTLA-4), 1068–1069
CZT. *See* Cadmium zinc telluride (CZT)

D

Dabrafenib, 1074
GIST, 715
metastatic melanoma treated with, 1092
Darbepoetin, 1182
Dasatinib, 1162
Data acquisition, SPECT, 258–259
Deadtime correction, SPECT, 260
Decitabine, 1170
Delayed/dual time point imaging, 483
Delayed-window method, 232
Dendritic cell immunotherapy, 604
2-deoxy-2-[^{18}F]fluoro-D-glucose ([^{18}F]FDG), brain tumors
advantage and disadvantages, 484
delayed/dual time point imaging, 483
diagnosis and grading, 481–482
glucose loading, 483
10-min static acquisition, 481
qualitative *vs.* quantitative, 482–483
rationale for, 481
stereotactic biopsy, 484
treatment planning, 484, 485
tumor recurrence *vs.* radiation necrosis, 483–484
3'-deoxy-3'-[^{18}F]fluorothymidine (^{18}F-FLT), 673, 705
Depression, parathyroid carcinoma, 602

Depth-of-interaction (DOI) effect, 225, 230–231
Diagnostic radiotracers, 39
Dicentrics, biological dosimetry assay, 332
Differentiated thyroid carcinoma (DTC), 548, 549. *See also* Thyroid cancer
  benign thyroid disease, 552
  epidemiology, 551–552
  genetic biomarkers, 556
  genetic susceptibility, 552
  ^{131}I-iodide therapy, 315–318
  ionizing radiation exposure, 552
  NIS gene, 556
  nuclear medicine procedures, 564
  prognosis, 560
  radionuclide imaging, 564
  risk factors, 552–553
  therapy-induced menopause, 552
  thyroid scintigraphy with ^{99m}Tc-pertechnetate, 557, 558
  TNM staging, 560
  TSH role, 553
Diffuse large B-cell lymphoma (DLBCL), 360–361, 373, 1903
  cardiac MRI, 1533
  chronic lymphocytic leukemia, 450, 451
  diagnosis, 1532, 1534–1535
  [^{18}F]FDG PET/CT, 1534
  follow-up, 1533, 1535
  Lugano classification, 365
  presentation, 1532, 1534
  treatment, 363
Diffuse optical tomography (DOT), 295–296
Diffusion-weighted imaging (DWI), 479
  GIST, 718
  multiple myeloma, 411
Digestive tract, 1523–1524
Digirad Cardius 3 XPO™ system, 267, 268
Digital breast tomosynthesis, 617
Digital SiPM design, 220
Dihydrotestosterone, 27–28
Diphosphonates. *See* ^{99m}Tc-diphosphonates
Diplopia, 475
Disseminated coccidioidomycosis, 653
Distal esophageal adenocarcinoma, 689, 691
Distant metastases
  HNSCC, 523–524
  management of, 1216–1222
DLBCL. *See* Diffuse large B-cell lymphoma (DLBCL)
DNA repair, 642
DNA synthesis, 21
Dobutamine, myocardial oxygen consumption, 1915
DOI effect. *See* Depth-of-interaction (DOI) effect
Doppler ultrasound, 1119
Dorsal melanoma, 1864, 1866–1869
Dose-response relationships, 338–339
Dose-volume histograms (DVH), 329
Dosimetry, 1254–1256
  biological, 331–334
    chromosome painting assay, 333
    comet assay, 333–334
    dicentrics assay, 332
    g-H2AX assay, 334
    micronuclei assay, 333
  ^{124}I-PET/CT, 317–318
  lesion-based, 316, 317
  limited bone marrow, 315–316
  metaiodobenzylguanidine, 1277–1281
  pre-therapeutic assessments, 317
  radionuclide therapy, 312–315
Dosimetry Committee of the European Association of Nuclear Medicine (EANM), 315
DOT. *See* Diffuse optical tomography (DOT)
Double-strand breaks (DSBs), 308
Doxorubicin, 1183, 1497
Dual-energy CT, 645
Dual-energy CT (DECT) criteria, 718
Dual-phase [^{18}F]FDG imaging, 659
Dual-tracer parathyroid scintigraphy, 595, 596, 599–600
Dynamic contrast-enhanced MRI (DCE-MRI), 410, 423, 424
Dynamics D-SPECT™ system, 268, 271
Dysphagia, 688

E
EBRT. *See* External beam radiotherapy (EBRT)
EC. *See* Electron capture (EC)
Ectopic gastric mucosa, 72
Ectopic locations, 590–591
Effective dose (ED), 335, 336
EGFR*vIII* amplification, 474
Einstein's special theory of relativity, 201
Elastosonography, thyroid cancer, 555
Electromagnetic radiation, 200, 202–203
Electron capture (EC), 102, 206–207
Electrons, 202
En bloc resection with curative intents, 604
Encapsulated follicular variant of PTC, 550
Endocrine therapy, breast cancer, 617, 625
Endocrine tumors, 1257–1259
Endogenous proteins, 48
Endometrial cancer
  conventional imaging, 1003
  epidemiology and prevalence, 999
  [^{18}F]FDG PET, 1003–1009
  [^{18}F]FDG PET/CT imaging, 1831–1833
  lymph node involvement and distant metastases, 1832, 1833
  lymphoscintigraphy, 1009
  pathophysiology and clinical presentation, 1002–1003
  ultrasound, 1003
  vaginal cuff recurrence, 1832, 1833
Endoscopic ultrasound (EUS)
  esophageal cancer, 688–689
  gastric cancer, 701–702
  GIST, 713

Endothelial cells, 9
apoptosis, 10
leaky incomplete, 10
Energy
and frequency, 201
in Joules, 201
and mass, 201
E6 oncogene expression, 510
E7 oncogene expression, 510
EORTC recommendation, 9
Ependymomas, 470
Epidermal growth factor receptor (EGFR), 7, 122–123, 474
Epidermal growth factor receptor/Ras/phosphatidylinositol 3-kinase pathways, 642
lung cancer, 642
Epratuzumab, 1152, 1160
Epstein-Barr virus (EBV), 355
gastric adenocarcinomas, 699
Erasme Hospital Pediatric Center, 1109
Erbitux, 123
Erlotinib (Tarceva), 123
Erlotinib-targeted therapy, 7
Erythropoietin, 1182
Esophageal cancer
biomolecular changes, 687
biopsy, 688
diagnostic CT scan, 688
dysphagia, 688
endoscopic ultrasonography, 688–689
epidemiology and environmental factors, 686–687
esophagectomy with en bloc lymphadenectomy, 692
[^{18}F]FDG PET/CT, 689–692, 1644–1654
gene polymorphism, 687
genetic analysis, 687
local lymph node invasion, 688
medical care, 692–693
nodal (N) staging system, 688
PERCIST, 693–694
recurrences, 694–695
surveillance, 694–695
therapies, 692–693
TNM staging system, 687
treatment efficacy, 693–694
tumor (T) staging, 688
Esophageal SCC
incidence, 687
occurrence, 686–687
Esophagectomy with en bloc lymphadenectomy for esophageal cancer, 692
Etoposide, neuroblastoma, 1887
European Neuroendocrine Tumor Society (ENETS) diagnostic and prognostic stratication criteria, 806
European Organization for Research and Treatment of Cancer (EORTC) guidelines, 716
European Society of Medical Oncology (ESMO), 1867–1868
Ewing's sarcoma, 1106, 1854–1855, 1857–1859
in children, 1898–1902
External beam radiation therapy (EBRT), 177, 312, 1224
bone metastases, 1312
for HCC, 1339
parathyroid carcinoma, 604
prostate cancer, 892
and radionuclide therapy, 308, 309
skeletal metastases after, 1770
Extra-abdominal metastases, 712
Extracellular matrix (ECM), 121–122, 183
Extravasation and passive retention (EPR) effect, 10
eZ-SCOPE intraoperativegamma camera, 281, 282

F
^{18}F, 132, 134, 137
^{18}F-albumin, 49
^{18}F-Al-NOTA-PRGD2 (^{18}F-alfatide), 674
Familial interstitial gastric cancer (FIGC), 699
Fatigue, 1143
parathyroid carcinoma, 602
FBP. *See* Filtered back projection (FBP); Filtered back-projection (FBP)
^{18}F-Choline PET/CT, prostate cancer, 902–905
^{18}F-Choline PET/MRI
iliac adenopathy, 1779
inhomogeneous hypermetabolic mass, 1778
prostate cancer, 1773
[^{18}F]dihydroxyphenylalanine (^{18}F-DOPA) PET/CT, 1741
^{18}F-DOPA, 595, 1097, 1110
neuroendocrine tumors, 830–832
^{18}F-DOPA, amine precursor, 95, 96
^{18}F-DOPA PET/CT
neuroendocrine tumors, 768
^{18}F-estradiol
breast cancers, 29
Fever, 1143
[^{18}F]FACBC, 135, 136
^{18}F-FACBC PET/CT, 909–910
[^{18}F]FDG, 131, 133, 141, 150, 1561
acute myeloid leukemia, 455
chronic lymphocytic leukemia, 449–450
chronic myeloid leukemia, 458
left adrenal gland, 1118
multiple myeloma, 415–421, 424–428
neuroendocrine tumors, 832
sarcoma(s), 1054–1061
viability of malignancies, 1123
[^{18}F]FDG MIP images, 1759
[^{18}F]FDG-PET, 340
breast cancer, 619, 623, 624, 627–629
brown fat activation, 1116
cervical cancer, 984–991
in children thymus uptake of, 1116

[^{18}F]FDG-PET (*cont.*)
chronic lymphocytic leukemia, 449–450
chronic myeloid leukemia, 458
colorectal cancer, 781, 782
contrast-enhancing soft-tissue mass, 1124
detects, 1112
endometrial cancer, 1003–1009
for evaluation, 1151
for evaluation, radioimmunotherapy, 1150–1151
false-negative results, 1116
false-positive results, 1116–1118
gallbladder carcinoma, 743–744
glucose metabolism, 1124
indications for, 1115
kidney cancer, 849–853
limitations of, 1116–1119
lung tumors, 643
medullary thyroid cancer, 570–571
metastatic disease detection, 1078
multicenter study of, 1083
neuroendocrine metastases, 730
ovarian cancer, 1026–1034
parathyroid cancers, 603
pediatric brain tumors, 1108–1110
pediatric neuroblastoma evaluation, 1123
physiologic sites of, 1116
potential role for, 1078
prognostic value, 532–535
in regional lymph node staging, 1080–1081
role of, 1119
staging, 1115
vulvar cancer, 963–967
Wilms' tumor for, 1119
[^{18}F]FDG-PET/CT, 1111–1112, 1849–1862
alveolar rhabdomyosarcoma, 1852, 1853, 1856, 1857
clear cell carcinomas, 1842–1844
dorsal melanoma, 1864, 1866–1869
follicular hyperplasia, 1869
gastric cancer, 702–705
gastrointestinal stromal tumor, 713
indications for, 1112–1116
lumbar melanoma, 1864–1866
metastatic melanoma, 1870–1877
multiple myeloma, 415–421, 424–428
ovarian cancer, 1841–1847
poorly differentiated carcinoma, 1604–1606
rhabdomyosarcoma, right orbit, 1853, 1854, 1861, 1862
sarcomas, 1849–1862
soft tissue sarcoma, 1851, 1854, 1855
Stage IIIA melanoma, 1864, 1867–1868
subscapular right melanoma, 1869–1871
uses, 1107
in 14-year-old girl, 1113
[^{18}F]FDG PET/CT, 910–914
abdomen, hypermetabolic lymph nodes, 1769
after radiotherapy, 1552
anaplastic thyroid carcinoma, 567, 568
assessment, 1094–1096
axillary lymph node uptake, 1737
bilateral inguinal node involvement, 1818
bladder cancer, 865–868, 1762
bone metastasis, 1777
brain lymphoma, 1561–1565
breast cancer, 619, 623, 624, 1614–1618
to cerebral metastasectomy, 1091
cervical carcinoma, 1824
cervix, uptake in, 1822
diffuse large B cell lymphoma, 1534
endometrial cancer, 1831, 1832
enlarged lymph node, 1753
esophageal cancers, 1644–1654
gastric cancers, 1656–1665
hepatocellular carcinoma, 1682–1697
hydronephrosis, 1754
hypermetabolic mass, 1800
of left heel staging, 1085
left neck nodal recurrence, 1090
for liver metastasis, 1092
luncg cancer patient management, 661–662
lung cancer, 1628–1636
lymphadenopathies, 1757
management impact of, 1086–1088, 1092–1093
mesothelioma, 1636–1641
metastatic cervical squamous cell carcinoma, 1824
of metastatic melanoma, 1084–1085
MIP and, 1760, 1762
MIP image, 1802, 1819
nasopharyngeal carcinoma, 533, 535
neuroendocrine tumors, 766
omentum and mesenteric uptake, 1737
pancreatic cancer, 764
pancreatic cancer, 1700–1714
penile cancer, 952, 1806–1812
penile stump, 1807
perirenal lymphadenopathy, 1755
for postoperative restaging, 1089
recurrent HNSCC detection, 531–532
for restaging posttreatment, 1091
retrocrural lymph node, 1803
of right axillary lymph nodes, 1090
from right calf, 1084
seminoma, 1799
skeleton, osteolytic lesions, 1768
small bowel cancers, 1668–1680
squamous cell penis cance, 1810
in staging distant metastatic melanoma, 1086
T1-and T2-weighted MR axial slices, 1756
testicular cancer, 938
thymoma, 1641
treatment monitoring, 1085
urothelial carcinoma, 1761
vaginal cancer, 1815
vaginal mass, 1820, 1821
vulvar mass, 1816, 1817
[^{18}F]FDG-6-PO_4, 89, 90

[^{18}F]FDG scan
accumulation of, 1109
brain tumor, 1108
clinical evaluation, 1110
heterogeneity, 1109
[^{18}F]FDG uptake
and adverse outcome, 18
anti-VEGF therapy, 10
glutamine *vs.*, 20
^{18}F-FDHT
enzalutamide treatment, before and after prostate cancer, 28
metastatic tumor, vertebrae, 28
[^{18}F]FDHT, 158–160
[^{18}F]FES, 158–160
^{18}F-FET, 1110
^{18}F-florbetapir, 45
^{18}F-FLT imaging
acute myeloid leukemia, 456
after chemotherapy in non-Hodgkin's lymphoma, 22
chronic myeloid leukemia, 458
of proliferation after chemotherapy, 21–22
^{18}F-Fluoride
bladder cancer, 869
sarcoma(s), 1054
^{18}F-Fluoride PET/CT
prostate cancer, 900–902
^{18}F-fluoroazomycin(^{18}F-FAZA)
hypoxia imaging in HNSCC, 536
^{18}F-fluorocholine, 595, 596
^{18}F-fluorodeoxyglucose ([^{18}F FDG] uptake
in breast cancer, 620
[^{18}F]-Fluorodeoxyglucose ([^{18}F]FDG)
hepatocellular carcinoma, 731–734
[^{18}F]2-fluoro-2-deoxyglucose, 131
3'-[(18 F)Fluoro-3'-deoxythymidine (FLT)], 378
multiple myeloma, 421
^{18}F-Fluoroerythronitroimidazole (^{18}F-ETNIM), 95
^{18}F-fluoroethylcholine (^{18}F-FEC), 46, 93, 94
^{18}F-fluoroethyltyrosine (^{18}F-FET)
head and neck cancers, 535–536
^{18}F-fluoromethylcholine (^{18}F-FCH), 93, 94
^{18}F-fluoromisonidazole, 45
^{18}F-fluoromisonidazole (^{18}F-MISO), 10, 673
hypoxia imaging in HNSCC, 536
3'-[^{18}F]fluorothymidine (FLT), 630, 1097
cellular proliferation, 145–147
HNSCC, 536
[^{18}F]FMISO, 161–162
^{18}F-Galacto RGD, 1097
Fibrocytes, 9
Fibronectin (FN), 183
Fibrosing mediastinitis, 652
Field cancerization concept, 512
Field of view (FOV), 225
Filtered back projection (FBP), 237
Filtered back-projection (FBP), 263
Fine-needle aspiration cytology (FNAC), 555–557
FISH analysis, 448
FITC. *See* Fluorescein isothiocyanate (FITC)
^{18}F-labeled tracers, 1125
Flare effect, 145–146
Flare phenomenon, 628
FLARE™ system. *See* Fluorescence-Assisted Resection and Exploration (FLARE™) system
Flow cytometry, 450
Fluorescein isothiocyanate (FITC), 288
Fluorescence-Assisted Resection and Exploration (FLARE™) system, 288–290
Fluorescence imaging, 287–288
Fluorescence in situ hybridization (FISH), 333
Fluorinated tracers, 1110
Fluorine-18 (^{18}F), 88
Fluorine-18-fluoro-2-deoxy-D-glucose ([^{18}F]FDG, antitumor chemotherapy, 88–90
Fluorine-18-labeled fluoroetanidazole (^{18}F-FETA), 95
Fluorine-18 sodium fluoride ([^{18}F]fluoride), bone-imaging, 93–94
Fluorodeoxyglucose-positron emission tomography/computed tomography ([^{18}F]FDG-PET/CT)
advantages, 689
baseline regional tumor uptake heterogeneity, 691
distant metastatic disease detection, 689
and [^{18}F]FDG-PET/MR, 691–692
primary esophageal cancer, 689
prognostic value, 690–691
sensitivity, 689
tumor-to-blood standardized uptake ratio, 691
Fluorodeoxyglucose-positron emission tomography ([^{18}F] FDG-PET), lymphoma, 367–368, 367–371
challenges and limitations, 378–380
detecting and histologic grading, 364–365
initial staging, 365–367
post-therapy response assessment, 368
tumor response criteria, 368–371
6-fluorohomovanillic acid (FHVA), 138, 140
3-[4-[(3-[^{18}F]fluoropropyl)thio]-1,2,5-thiadiazol-3-yl]-1,2,5,6-tetrahydro-1-methylpyridine (^{18}F-FP-TZTP), 39
Fluoroscopic barium studies, 701
5-fluorouracil (5-FU), 514
^{18}F-misonidazole (^{18}F-MISO), hypoxia, 10, 94–95
Fms-related tyrosine kinase 3, 715
^{18}F-*N*-(2-(diethylamino)ethyl)-6-fluoronicotinamide, 1097
Folate receptor overexpression, 123
Follicular carcinoma, 1590–1591, 1599–1601
Follicular hyperplasia, 1869
Follicular thyroid carcinoma (FTC), 548. *See also* Thyroid cancer
age, 561
degree of invasiveness, 551
distant metastases, 564
endemic iodine deficiency, 553
gene-activating point mutations, 553
Hürthle cell carcinoma, 562
lymph node metastases, 563

Follicular thyroid carcinoma (FTC) (*cont.*)
oncocytic/oxyphilic cell type, 551
prognosis, 561
RAS mutation, 565
tumor extension, 563
tumor size, 563
5-year survival, 559, 562
Follicular variant of PTC (FVPTC), 550
FOV. *See* Field of view (FOV)
FOXFIRE global, 1355
Fractures, parathyroid carcinoma, 602
Frequency, energy and, 201
Frontotemporal anaplastic astrocytoma, 1561
^{18}F-transferrin, 49
Full-field digital mammography, 617
Full-width half-maximum (FWHM) spatial resolution, 257–258, 265
Fumarate hydratase, 19
FVPTC. *See* Follicular variant of PTC (FVPTC)
FWHM spatial resolution. *See* Full-width half-maximum (FWHM) spatial resolution

G
^{68}Ga, 46, 132
^{67}Ga-citrate, 82–83
^{67}Ga-citrate scintigraphy, 1111
^{68}Ga-DOTA-labeled SSAs
neuroendocrine tumors, 766
^{68}Ga-DOTANOC PET/CT
neuroendocrine tumors, 767
^{68}Ga-DOTATATE, 668
medullary carcinoma, 1595–1598
neuroblastoma, 1885
neuroendocrine imaging, 29
somatostatin receptors, 1558–1559
^{68}Ga-DOTATOC, 668, 1125
cranial meningiomas, 148
liver, 1732
maximum intensity projection (MIP), 1747
[$^{67/68}$Ga]Ga citrate, 48
Gail model, 616
Galectine-3 expression, 601
Galectine-3 expression in parathyroid carcinoma, 601
Gallbladder carcinoma (GBC)
[^{18}F]FDG-PET, 743–744
preoperative PET/CT scans, 742
symptomatology, 742
Gallbladder metastasis, 1864
Gallium-68 (^{68}Ga), 88
Gallium collimators, 256
Gallium-68 DOTATOC, somatostatin receptors, 96, 97
Gallium-67 imaging
lymphoma, 363
g-H2AX, biological dosimetry assay, 334
Gamma cameras, 280–285
collimator, 254
design, 253–258
pinhole collimation, 255
Gamma Medica Triumph LabPET Solo™, 245
Gamma probe, intraoperative detection, 277–278
Gamma radiation, 203–204
^{68}Ga-NOTA-PRGD2, 674
^{68}Ga-peptide, 319
^{68}Ga-PSMA-ligand
prostate imaging, 29
^{68}Ga-PSMA-ligand PET/CT
uptake, 1773
Gastrectomy, gastric cancer treatment, 706
Gastric adenocarcinoma and proximal polyposis of the stomach (GAPPS), 699
Gastric cancer
aggregation of, 699
contrast-enhanced CT scan, 702
endoscopic ultrasound, 701–702
environmental factors, 699
epidemiology, 698–699
[^{18}F]FDG-PET/CT, 702–705
[^{18}F]FDG PET/CT, 1656–1665
fluoroscopic barium studies, 701
genetic changes, 699
geographic and ethnic difference, 699
HER2 overexpression, 699
H. pylori infection, 699
incidence, 698
intestinal type, 698–699
invasiveness of, 701
metastatic (M1) disease, 700
neoadjuvant chemotherapy/chemoradiotherapy, 704
nodal (N) staging, 700
palliative treatment, 703, 704
PERCIST, 705
persistent abdominal pain, 700
RECIST, 705
regional lymphadenectomy, 703
surveillance, 705–706
TNM staging system, 700
trastuzumab, 704
treatment efficacy, 704–705
tumor (T) staging, 700
upper gastrointestinal endoscopy, 700–701
weight loss, 700
Gastrin receptor scintigraphy, 766
Gastroenteropancreatic neuroendocrine tumors, 808–810
Gastroenteropancreatic tumor. *See* Pancreatic cancer
Gastrointestinal cancer, 1470–1471
Gastrointestinal stromal tumor (GIST)
CD117, 711
contrast-enhanced CT, 712, 715
degree of cellularity, 712
distant metastatic disease, 712
dual-energy CT criteria, 718
endoscopic ultrasound, 713
environmental factors and genetic predisposition, 711
epidemiology, 710
[^{18}F]FDG-PET/CT scan, 713, 715, 716
histology, 712

incidence, 710
KIT, 711
mitotic rate, 712
and molecular therapy, 714–715
MRI, 713, 718
multiphasic CT imaging, 712–713
nodal (N) staging, 712
oncogenic gain-of-function mutations, 711
platelet-derived growth factor receptor alpha, 711
radiotherapy, 713–714
RECIST, 715, 718
recurrence rate, 720
sporadic, 710
surgical resection, 713
surveillance, 720–721
TNM staging system, 711
treatment response, 715–718
tumor (T) staging, 712
Ga transferrin, 48
Gaussian-fit scatter-correction method, 233
G-CSF. *See* Granulocyte colony-stimulating factor (G-CSF)
Gefitinib (Iressa), 123
^{68}Ge/^{68}Ga generator, 43
Gene expression profiling (GEP), 356, 360–361, 616
Gene polymorphism, 687
General Electric NM 530c™ system, 243, 247, 269
Genome-wide-associated studies, breast cancer, 616
Genomic sequencing, 7
Germ cell tumors, 470, 650
GFP. *See* Green fluorescent protein (GFP)
GIST. *See* Gastrointestinal stromal tumor (GIST)
Gleason score, 1779, 1781, 1782, 1784
Glioblastoma, 163
Glioblastoma multiforme (GBM), 472
Glioblastomas
age-adjusted incidence, 470
histologic features, 472
subtypes, 470
Gliomas
[^{11}C]Methionine, 485
contrast enhancement, 478
diagnosis of, 485
feature of, 477
incidence of, 469–470
MGMT promoter methylation, 474
^{99m}Tc-sestamibi, 480
neoangiogenesis, 497
radiopharmaceuticals, 479, 480
SPECT/PET imaging, 476
types of, 470
Glucagon-like peptide 1 receptor imaging, 766
Glucose transporter 4 (GLUT4) expression, 716
Glutamine uptake, 18
brain tumor, 19, 20
vs. [^{18}F]FDG, 20
Gold-198 (^{198}Au), 189
Gompertzian kinetic form, 17
Grade III astrocytomas, 470
Granulocyte colony-stimulating factor (G-CSF), 379–380
Granulocyte colony-stimulating factor (GCSF), 1116
Graves' disease, 588
Green fluorescent protein (GFP), 56, 57, 286
Gross tumor volume (GTV), 477
Growth inhibitory pathways, 642
Guided intraoperative scintigraphic tumor targeting (GOSTT)
applications, 1454–1455, 1462
concept, 1453
gastrointestinal cancer applications, 1470–1471
gynecological malignancy applications, 1468–1470
head and neck applications, 1462–1464
hybrid detection procedures, 1472
interventional SPECT/CT and PET/CT, 1458–1460
mixed-reality navigation, 1472
models, 1453–1454
neoadjuvant chemotherapy, 1472
preoperative imaging, 1455–1456
radioguided surgery, 1456–1458
radiopharmaceuticals, 1456–1458
retrieving SPECT/CT and PET/CT, 1460–1462
robot-assisted procedures, 1473
ROLL, 1472
of SLN biopsy, 1454
SNOLL, 1472
systemic radiotracers, 1472
urological malignancies, 1464–1468
Gynecological malignancy, 1468–1470

H

Hairy cell leukemia (HCL), 451–452
treatment, 1166–1169
Halogen radionuclides, 37
HCL. *See* Hairy cell leukemia (HCL)
Headache, brain tumors, 475
Head and neck cancer
cervical lymphadenopathy, 1581
cervical lymph node metastases, 1581, 1582
cT2N2, 1574
diagnostic difficulties, 1571–1572
[^{18}F]FDG PET/CT, 1570, 1571
lymph node enlargement, 1570
mesorectal lymph node, 1570, 1571
metastatic cancer, 1570, 1571
soft tissue mass, nasopharynx, 1579–1580
sore throat, 1581
squamous cell carcinoma, 1576–1577, 1581
Head and neck squamous cell carcinoma (HNSCC)
adjuvant radiotherapy, [^{18}F]FDG PET/CT after, 530
angiogenesis inhibitors, 515
antiangiogenic therapy, 515
cetuximab, 515
cisplatinum, 514
concurrent chemoradiotherapy, 514, 515
contrast-enhanced CT, 516
distant metastases, 523–524

Head and neck squamous cell carcinoma (HNSCC) (*cont.*)
EGFR, 515
epidemiology and biology, 510–513
false-positive [^{18}F]FDG uptake, 523
[^{18}F]FDG PET/CT, 516, 517, 521, 522, 524, 530–532
field cancerization concept, 512
HPV-positive and HPV-negative, 510
incidence, 510
induction chemotherapy, 510
lymph node staging, 516, 521–523
metachronous second primary malignancies, 523
MRI, 516
non-[^{18}F]FDG radiotracers, 535–536
patient management changes, 524
PET and PET/CT, response assessment, 524–528
PET/MRI, 537
PET *vs.* ultrasound-guided fine needle aspiration, 522
platinum-based chemotherapy, 515
primary tumor staging, 518, 521
radiotherapy planning, PET for, 536–537
recurrent disease detection, 531–532
risk factors, 510
surgical resection, [^{18}F]FDG PET/CT after, 530
synchronous second primary malignancies, 523
treatment strategies, 513–516
5-year survival rate, 510–513
Hematogenous metastases, 700
Hematologic malignancies, radioimmunotherapy for, 110–112
Hematopoietic cell transplantation (HCT), 363
Hemisacrum
[^{18}F]FDG PET/CT imaging, 1828
Hemoptysis, 1752
Hepatic metastases
[^{18}F]FDG PET/CT imaging, 1827
Hepatocellular carcinoma (HCC), 1339, 1351–1352
adrenal metastasis, 734
after arterial chemoembolization, 731
[^{11}C]acetate, 734–735
[^{18}F]FDG PET/CT, 1682–1697
[^{18}F]fluorodeoxyglucose ([^{18}F]FDG), 731–734
multiple osseous metastases, 733
normoglycolytic, 732
radiotracer imaging, 730
recurrence, 731
staging, 730
synchronous double, 732
Hepatoma. *See* Hepatocellular carcinoma
Hepatosplenomegaly, 443
Herceptin, Se Trastuzumab
Herceptin (HER2), 30
Hereditary diffuse gastric cancer (HDGC), 699
HER2 enriched breast cancer, 617
HER2 expression, in breast cancer, 630
HER2 overexpression, 7
breast cancer, 7
Heterogeneity, 1092
Heterogeneous clump treatment, 46
2-HG metabolism, 19
HIF-1 alpha, 18
High-energy collimators, 256
High-grade gliomas, 470
High mass density, 220
High-resolution 3D T2* gradient echo sequences, 478
High-resolution ultrasound (US), 591
Histonedeacetylase inhibitors, 1182
Histoplasmosis, 652
HK2, 27
Hodgkin's disease (HD), 651
findings, 1536–1537, 1539
follow-up, 1539–1540
presentation, 1536, 1539
Hodgkin's lymphoma (HL), 1110–1111, 1905, 1906. *See also* Lymphoma
clinical presentation, 356–357
epidemiology and etiology, 355
evaluation, 356–357
[^{18}F]FDG-PET/CT indications, 1112–1114
genetic features, 356
^{111}In-pentetreotide, 81
International Prognostic Indices, 356
International Prognostic Score, 356
Lugano Classification, 357
modified Ann Arbor staging system, 356
monitoring of response, 1113–1114
pathology, 355–356
prognosis, 356–357
risk-adapted therapy, 372–374
staging, 356–357
subtypes, 355–356
treatment and follow-up, 358–359
Holmium-166 (^{166}Ho), 186–187
^{166}Ho-radioembolization, 187
Hormone receptor-positive metastatic breast cancer, 626
Hormone therapy, prostate cancer, 893
HPTH-jaw tumor syndrome, 601
HPT-JT syndrome, 602
HRPT2 gene
abnormalities, 601
mutations, 601, 602
Human anti-mouse antibody (HAMA), 1148, 1173
Human epidermal growth factor receptor 2 gene (HER2) overexpression, 699
Human leukocyte antigen (HLA), 443
Human papilloma virus (HPV), 510
Human papillomavirus (HPV), 687
Hürthle cells, 551
Hybrid PET/CT imaging, 1107
Hybrid SPECT/CT, 595
Hydration, 1108
6-Hydra-zinopyridine-3-carboxylic acid (HYNIC), 72
Hydronephrosis, 1830, 1831, 1836
Hydroureter, 1830, 1831, 1836

Hydroxyapatite (HA) particles, 186
2-hydroxyglutarate, 474
Hypercalcemia
  anti-PTH immunotherapy, 604
  dendritic cell immunotherapy, 604
  intravenous bisphosphonates, 604
  parathyroid carcinoma, 602
  plicamycin, 604
  primary HPTH, 589
Hypercellular anaplastic glioma cells, 472
Hypermetabolic adenopathy, 1845, 1846
Hypermetabolic cervical lesion, 1826, 1829
Hypermetabolic cervical tumor, 1826
Hypermetabolic lymphadenopathies, 1825
Hyperparathyroidism (HPTH)
  abnormality in, 588
  benign, 589–590
  preoperative imaging techniques, 590
  primary, 587–588
  radioguided surgery, 597
  secondary, 588
  tertiary, 589
Hyperphosphatemia, 589
Hyperplastic parathyroid glands
  CT imaging, 593
  imaging protocol for, 591
  structure of, 591
  US pattern of, 591–592
Hyperviscosity, 402
Hypocalcemia, 589
Hypopharynx, 523
Hypoxia, 10, 312, 491–492, 673
  in HNSCC, 536
Hypoxic tumor
  64Cu-ATSM, 162–164
  [18F]FMISO, 161–162

I
^{123}I
  metastases, peritoneal cavity, 51
  neuroendocrine tumors, 48
^{131}I, 46
  long range beta-particle bombardment, 46, 47
  neuroendocrine tumors, 48
^{124}I-A33 images, 31
^{123}I-alpha-methyltyrosine (^{123}I-IMT), brain tumors, 486–488
^{131}I-BC8, 1176
Ibritumomabtiuxetan, 206
Ibrutinib, 1164
IC. *See* Internal conversion (IC)
^{124}I-cG250, 29
Idelalisib, 1164
IDH1, 19
^{131}I-G250, 191
^{131}I-Iodide, 43
  administration of, 1203
  outcome, 1218
  postsurgical remnants with, 1201–1206
  whole-body scintigraphy with, 1212
^{123}I-iodide scintigraphy, 594
^{131}I-iodide therapy
  DTC, 315–318
  thyroid diseases
    nursing mothers, 342
    pregnant women, 341
5-[^{125}I]iodo-2'-deoxyuridine (^{125}IUdR), 51, 59
  human colon LS174T adenocarcinoma cells, 52
^{131}I-labeled anti-CD33, 1174
^{125}I-labeled monoclonal antibodies (^{125}I-mAbs), 52
^{131}I-L19SIP, 184
^{131}I-M195, 1173
Image-guided radiotherapy, 477
Imatinib, for GIST
  discontinuation of, 720
  dose escalation, 714
  preoperative imatinib therapy, 714
  primary resistance, 718, 719
  secondary resistance, 719–720
  side effects of, 721
  treatment response, 715–718
^{131}I-meta-iodobenzylguanidine (^{131}I-MIBG), 312, 327–330
[^{123}I]MIBG, 59, 79, 80, 765
  neuroblastoma, 1883–1889
^{131}I-MIBG, 79, 80
^{123}I-MIBG scintigraphy, 1120, 1121
  for diagnosis, 1121
  neuroendocrine neoplasms, 107–108
  in pediatric neuroblastoma lesions, 1125
  SPECT reconstructions of, 1126, 1127
  tumor-to-background ratios, 1122
^{123}I-MIBG SPECT, 1124
Immortalization genes, 642
Immune cell cancer immunotherapy
  activated T cells, 11
  anti-CTLA4 treatment, 12
  cancer immunity cycle, 11
  CD8 expressing cells, 11
  cellular component, tumor mass, 11
  CTLA4, 12, 13
  immune checkpoint blockade, 12
  ipilimumab, 13
  neoantigens, 11, 13
  nivolumab, 13
  oncoproteins, 13
  PD-1, 13
Immunohistochemistry, parathyroid carcinoma, 600–601
Immunosuppression, malignant melanoma, 1068
Immunotherapy
  clinically translated, 1074–1075
  prostate cancer, 894
  T-cell, 1069
^{111}In, 132
^{123}I, 43, 44
^{111}In-capromab pendetide, 82, 154

Incidentaloma, 558
Indium-111-labeled anti-CD5 antibody, 15
^{111}In-DTPA-pentetreotide (Octreoscan®), 765
Induction chemotherapy
  HNSCC, 510, 530
Infiltrative FVPTC, 550
Inhibitory pathway
  expression of, 1069
^{111}In-HuM195, 1174
Inotuzumab ozogamicin, 1160
^{111}In-oxine, 14
^{111}In-pentetreotide, 81–82
^{111}In-SRS, 730
^{111}In-T101, 15
Integrin receptors, 10, 149–152
Integrins, 120–121, 674
  ^{99m}Tc-αP2, 120
  ^{99m}Tc-NC100692/99mTc-maraciclatide, 120
  ^{99m}Tc-3PRGD$_2$, 120–121
  ^{99m}Tc-RGD-BBN, 121
Interferon (IFN), 1073
Interim analysis, 178
Interim PET, 375–376
Internal conversion (IC), 207–209
Internal mammary (IM) nodal sampling, 621
International Classification of Childhood Cancer, 1106
International Commission on Radiological Units (ICRU), 335
International Federation of Gynecologic and Obstetrics (FIGO) staging system, 983–984
International Myeloma Working Group (IMWG), 399, 400, 421–424
International Prognostic Indices (IPI), 361
  lymphoma, 356
International Prognostic Score (IPS), 356
International staging system (ISS), 403, 404
International Working Group on CLL (IWCLL), 447
Interstitial radiation therapy, 892
Intestinal-type gastric cancer, 698–699
Intrahepatic cholangiocarcinoma, 1352–1353
Intramucosal adenocarcinoma, of distal esophagus, 689, 690
Intraoperative detection
  beta probes, 278–280
  CZT-based semiconductor gamma camera, 282
  eZ-SCOPE intraoperative gamma camera, 281, 282
  gamma cameras, 280–285
  gamma probe, 277–278
  nuclear counting and imaging, 276–285
  optical and near-infrared imaging, 285–300
  PET scanners, 285
  semiconductors in, 277
  triple-modality detection, 298
Intravenous elotuzumab, 1182
Intravesical BCG immunotherapy, 870
Intravesical chemotherapy, 870
Inverse dose-rate effect, 309
In vivo tumor grading, 476–477
Iobenguane, 1273
Iodine-123, 43, 78, 79
Iodine-124, 78
Iodine-125, 43, 52, 78
  carcinoembryonic antigen (CEA), 55
Iodine-131 (^{131}I), 78, 79, 183–184
  copper-67, 188
  gold-198, 189
  holmium-166, 186–187
  lutetium-177, 184–186
  promethium-149, 189
  rhodium-105, 189–190
  thulium-170, 187
  thyroid diseases, 103, 106–107
  ytterbium-175, 187
  yttrium-90, 188–189
Iodine collimators, 256
Iodine-131 iodide, 43
Iodine-related attenuation (IRA), 718
Iodine-131 tositumomab (Bexxar), 43
Ionizing radiation, 310
^{124}I-PET/CT, 317–318
Ipilimumab, 12, 13, 30, 1073–1075
  CTLA-4 with, 1076
  T-cell activation and proliferation, 12
  vs. vemurafenib, 1076
^{131}I resistance, 26
Ischemia, 1915
Ischiopubic ramus
  [^{18}F]FDG PET/CT imaging, 1827
Isocitrate dehydrogenase (IDH) 1 and 2 mutations, 474
Isocitrate dehydrogenase enzymes (IDH1 and IDH2), 19
Isomeric transition (IT), 208–209
Isotopologues, 134
IT. *See* Isomeric transition (IT)
iThera Medical, 293, 295, 296
^{131}I-tositumomab, 111–112, 206, 323
  after induction chemotherapy, 1165
  clinical efficacy and safety, 1147
  clinical experience with, 1147
  with CLL, 1164
  general eligibility and dosing for, 1146
  with recurrent NHL, 1142
  regimens for, 1146
^{131}I-WBS, 1206

J
Jewett-Strong-Marshall classification, 863
Joules, energy, 201

K
Karnofsky Performance Scale, 476
KEYNOTE-001 study, 1075

KEYNOTE-002 study, 1075
KEYNOTE-006 study, 1075
Ki-67
  breast cancer, 617
  parathyroid carcinoma, 601
Kidney cancer. *See also* Renal cell carcinoma
  abdomen, hypermetabolic lymph nodes, 1769
  bladder cancer, 1762
  diagnostic imaging, 846–849
  enlarged lymph node, 1753
  environmental and genetic factors, 842–844
  epidemiology, 841–842
  [^{18} F]FDG-PET, 849–853
  hydronephrosis, 1754
  lymphadenopathies, 1757
  MIP amd, 1760, 1762
  perirenal lymphadenopathy, 1755
  PET radiopharmaceuticals, 853–856
  skeleton, osteolytic lesions, 1768
  staging, 845–846
  symptoms and diagnosis, 844–845
  T1-and T2-weighted MR axial slices, 1756
  urothelial carcinoma, 1761
Kidney disease, primary HPTH, 589
Klatskin tumor, 736
Kyphoplasty, 1182

L
Langerhans cell histiocytosis (LCH), 1128–1130
Lanreotide (NOC), 148
Lapatinib, 626
Larynx-preservation paradigm, 514
Laser therapy, esophageal cancer, 693
Late-onset cardiomyopathy, 1499–1501
L-3,4-dihydroxy-6-[^{18}F]-fluorophenylalanine ([^{18}F] FDOPA), 138, 140
L-dihydroxyphenylalanine (L-DOPA), 138
L-3,4-dihydroxyphenylalanine ([^{18}F]fluorodopa, [^{18}F]FDOPA), 488–489
Lead-212 (^{212}Pb), 44, 181–182
LEDs. *See* Light-emitting diodes (LEDs)
Lentigo maligna melanoma, 1069
Leptomeningeal metastasis, 1565–1567
LET. *See* Linear energy transfer (LET)
Leukemias, 175, 438, 1106
  representation, 439
  WHO classification, 440
Leukoencephalopathy, 445
Levothyroxine therapy, 1208–1210
L-3-[^{18}F]-fluoro-alpha-methyltyrosine (^{18}F-FMT), 92, 93
Life Span Study (LSS), 338
Light-emitting diodes (LEDs), 288
Linear energy transfer (LET), 205
  and dose rate, 58–59
  heterogeneous clump, tumor cells, 46, 47
Linear-quadratic (LQ) model, 308, 309
Lines of response (LORs), 224, 260
Linitis plastica, 701
Lipid biosynthesis imaging
  [^{11}C]acetate, 141
  [^{11}C]choline, 141–142
  ^{18}F-fluoroethylcholine, 142–144
  ^{18}F-fluoromethylcholine, 142–144
Lipid rafts, 55
Liposarcoma, metastatic myxoid, 1850, 1852
Liver damage, 1524
Liver metastases, 1828, 1830
Liver recurrence, 1115
Liver tumors
  absolute contraindications, 1354
  arterial anatomy, assessment of, 1342
  clinical indications, 1351
  clinical toxicity, 1354
  colorectal carcinoma, 1353–1354
  follow-up, 1348
  hepatocellular carcinoma, 1351–1352
  intrahepatic cholangiocarcinoma, 1352–1353
  metastatic, 1353–1354
  neuroendocrine tumors, 1354
  patient selection, 1341–1342
  posttreatment scan, 1347–1348
  during pretreatment angiography, 1342–1344
  radioactive lipiodol, 1340–1341
  radiodosimetric aspects, 1343–1347
  radioembolization, 324–327
  radioembolization therapy for, 1340, 1355
  radionuclide therapy, 112
  response to, 1348
  transarterial radioembolization, 112
  ^{90}Y-microspheres, 1341, 1347–1351
  yttrium-90, 103–104
Localized esophageal adenocarcinoma, 693
Locally advanced breast cancer (LABC), 622, 626
Local radiotherapy, 1312
Local recurrence
  RCC, 1758
  rectal, 1721
Locoregional recurrences
  management of, 1216
Long-range beta-particle bombardment, 46, 47
Long-range emitter, 46, 47
Lorentz force, 266
LORs. *See* Lines of response (LORs)
Loss of heterozygosity, 601
Low-dose hyper-radiosensitivity-increased radioresistance (LDH-IRR) response, 310–311
Low-grade gliomas, 470
Low linear energy transfer (LET)-ionizing radiation, 1172
L858R mutation, 7
L-type amino acid transporter 1 (LAT1), 133
^{177}Lu, 46
^{177}Lu-DOTA bifunctional chelate
  albumin-binding moiety, 41, 42
  folic acid, 41, 42
^{177}Lu-DOTA-HH1, 1165

^{177}Lu-DOTA-octreotate (Lutathera)
neuroendocrine tumors (NETs), 43
^{77}Lu-DOTATATE, 1250
in GEP-NETs, 1258–1259
PRRT with, 1249, 1255
vs. 90Y-DOTATOC, 1262
^{177}Lu-EDTMP, 1328–1329
Lugano Classification, lymphoma, 357, 361, 365, 367, 369–371
Lumbar melanoma, 1864–1866
Luminal A breast cancer, 616–617
Luminal B breast cancer, 617
Lumpectomy, 625
Lung cancer
AJCC classification, 642–644
comorbid conditions, 642, 643
computed tomography, 643, 646
deaths, 641
differential diagnosis, 651
environmental and genetic factors, 641–642
[^{18}F]FDG PET/CT, 654–655, 666–667, 1628–1636
follow-up after curative treatment, 665–667
follow-up imaging, 648–649
inherited factors, 642
locoregional lymph node spread, 647
low-dose CTcan, 645
mortality, 643
MRI, 644, 646
M stage, 647–648
multi-detector computed tomography, 644–645
N stage, 646–647
PET/MRI, 673
PET/MRI imaging, 673
radical radiotherapy, 663
signaling pathways, 642
SPN (*see* Solitary pulmonary nodule (SPN))
staging and prognostic stratification, 642–643
T stage, 646
5-year survival rate, 642
Lung perfusion imaging
^{99m}Tc-labeled microspheres, 39
^{99m}Tc-magroaggregated albumin, 75
Lungs
chemotherapy-induced tubular injury, 1520–1522
pulmonary permeability, 1519
radiation nephropathy, 1522–1523
radiation pneumonitis, 1519
ventilation/perfusion changes, 1519–1520
Lung shunt fraction (LSF), 1344, 1345
Lung ventilation radiopharmaceuticals, 77–78
^{177}LU-PRRT, 319–322
Lutetium-177 (^{177}Lu), 184–186
Lutetium-177 (^{177}Lu), bone pain, 104
Lymphadenopathies, hypermetabolic, 1825
Lymphadenopathy, 443, 651
metastatic left supraclavicular, 1895
popliteal, 1902
retroperitoneal, 1899
Lymph node metastases, 1756, 1762
Lymph node resection, 1070
Lymphocyte-predominant Hodgkin lymphoma (lpHL), 354–355
Lymphoma, 175, 650, 1106, 1151. *See also Specific types of lymphoma*
Ann Arbor staging system, 356, 361
chemotherapy, 357–359, 362–364, 371–372, 378–379
in children, 1902–1903, 1905–1906, 1910–1916
clinical presentation, 356–357, 361–362
Deauville 5-point scale, 370, 375
differential diagnosis, 651
epidemiology and etiology, 355, 359–360
evaluation, 356–357, 361–362
[^{18}F]FDG-PET, 367–368
challenges and limitations, 378–380
detecting and histologic grading, 364–365
initial staging, 365–367
post-therapy response assessment, 368
tumor response criteria, 368–371
3'-[^{18}F]Fluoro-3'-deoxythymidine (^{18}F-FLT)], 378
gene expression profiling, 356, 360–361
and hematopoietic neoplasms, 470
^{111}In-pentetreotide, 81
interim PET, 375–376
International Prognostic Indices, 356
International Prognostic Score, 356
Lugano Classification, 357, 361, 365, 367, 369–371
nuclear medicine imaging, 363–364
pathology, 355–356, 360
prognosis, 356–357, 361–362
radioimmunotherapy, 322–324
risk-adapted therapy, 371–375
staging, 356–357, 361–362
subtypes, 355–356, 360
surveillance PET, 376–377
treatment and follow-up, 358–359, 362
WHO classification, 360
Lymphoscintigraphy, 1808
anatomic correlation of, 1077
breast cancer SLN mapping, 621
endometrial cancer, 1009
of left chest, 1079
radiocolloids, 74
of right thumb, 1078
for SLN and SLNB, 1077
vulvar cancer, 967–974

M

mAb. *See* Monoclonal antibody (mAb)
Macrohematuria, 1754
Magnetic resonance imaging (MRI), 1112
acute lymphocytic leukemia, 444–445
advantages, 1125
breast cancer screening, 617, 619
cervical cancer, 983–986
chronic lymphocytic leukemia, 449
gastrointestinal stromal tumor, 718

GIST, 713
hairy cell leukemia, 452
HNSCC, 516
lung cancer, 644, 646
metastatic osteomedullary infiltration, 1122
multiple myeloma, 409–411, 423, 424
neuroendocrine tumors, 764, 814
parathyroid lesions, 593–594
from STIR sequence, 1127
thymomas, 650
T2 hyperintense pathological mass, 1824
Maintenance therapy, 1162
in CLL, 1164
Major ectopy, 590
Malabsorption, secondary HPTH, 588
Malignant lymphomas, of thyroid, 572
Malignant melanoma
adjuvant therapy, 1073
AJCC anatomic stage, 1072
AJCC definitions of TNM for, 1071
angiogenesis, 1069
antiangiogenic therapy, 1076–1077
apoptotic therapy, 1077
in Australia, 1067
c-KIT inhibitors, 1076
combination therapies, 1076
epidemiology, 1067
in Europe, 1067
histology, 1069
immune regulation, 1068–1069
immunotherapy, 1073–1076
incidence, 1067
metastatic disease, staging of, 1077–1097
novel targets, 1076
pathogenesis, 1068
prognostic factors, 1070, 1072–1073
Ras/Raf/MEK/Erk pathway, 1068
risk factors, 1067–1068
role of nuclear medicine, in patients, 1077–1097
staging nodal metastases, 1077–1079
staging systems, 1069–1070
surveillance, 1093–1096
targeted therapies against BRAF mutations, 1073
treatment, 1070, 1073–1077
Malignant pleural mesothelioma (MPM), 669–671
Manual dilatation, esophageal cancer, 693
Mass, energy and, 201
Matrix metalloproteinases (MMP), 122
Maximum-likelihood expectation maximization (MLEM) algorithm, 238, 239
Maximum tolerated dose (MTD), 185
Maximum tolerated radiation dose (MTRD), 187
Maxon approach, 316, 317
^{80m}Br, 51
Meckel's diverticulum, 72
Mediastinal adenopathy, 652
Mediastinal tumors
computed tomography, 649
diagnosis, 649–650
[^{18}F]FDG imaging, 671–672
MRI, 649
Medical internal radiation dose (MIRD), 205, 314, 316, 321, 328
Medium-energy collimators, 256
Medium-range emitter, 46, 47
Medullary carcinoma, 1589, 1595–1598
Medullary thyroid cancer (MTC), 185. *See also* Thyroid cancer
biological behavior, 569
carcinoembryonic antigen, 568
chromogranin A, 567
follow-up of, 1225–1226
hereditary or familial form, 569
histologic pattern, 567, 569
histopathologic description, 568
MIBG scintigraphy, 80
nuclear medicine role, 570–571
PET/CT with [^{18}F]FDG, 573–575
PET/CT with ^{68}Ga-DOTA-TOC, 573–575
prevalence, 569
radionuclide imaging, 1226–1229
RET mutations, 569–570
sporadic form, 569
treatment for recurrent, 1229–1231
treatment of, 1225
Medulloblastoma, 470
MEK inhibition, 26
Melanoma
activity, 1409
advantages, 1405–1407
classical technique, 1417
clinical outcome, 1403–1404
dorsal melanoma, 1864, 1866–1869
fluorescent agents, 1419–1422
follicular hyperplasia, 1869
freehand SPECT, 1418–1419
head and neck location, 1423–1424
hybrid tracers, 1419–1422
incidence, 1403
indications, 1405–1407
injection, 1409
lumbar melanoma, 1864–1866
lymphatic system, 1404–1405
metastatic melanoma, 1870–1877
PET/CT imaging, 1426–1427
portable gamma cameras, 1417–1418
presurgical lymphoscintigraphy, 1409–1412
prognosis, 1403
radiotracers, 1407–1409
risk factors, 1403
sentinel lymph node, 1415–1417, 1422–1424
SPECT/CT imaging, 1412–1414
Stage IIIA melanoma, 1864, 1867–1868
subscapular right melanoma, 1869–1871
surgery, 1414–1415
tumors, time-activity curves, 14
with V600E mutation, 25
Melanoma Staging Database, 1082

Melphalan, 1180–1181
Melphalan/prednisone/lenalidomide (MPR), 1180
Melphalan/prednisone/thalidomide (MPT), 1180
Memorial Sloan Kettering Cancer Center, 315
MEN2A syndrome, 601
Meningioma, 470, 498–499
  cystic lesion, 1559–1560
  somatostatin receptors, 1558–1559
Menopausal hormone therapy (MHT), 615
MEN1 syndrome, 601
Mesothelioma, 1636–1641
Metabolic tumor response, 1765
Metachronous second primary malignancies, 523
Metaiodobenzylguanidine (MIBG), 48, 51, 52, 58, 79–80, 1273
  activity/dose selection, 1277
  carcinoid, 1291–1293
  dosimetry, 1277–1281
  logistical issues, 1273
  neuroblastoma, 1293–1297
  patient eligibility, 1276–1277
  patient preparation, 1274–1275
  patient selection criteria, 1277
  PHEO/PARA, 1288–1291
  precautions, 1276
  preparation, 1273
  radiolabeled, 1273
  response assessment, 1281–1288
  thyroid blockade, 1275–1276
  toxicity, 1297–1299
Metaiodobenzylguanidine (MIBG) scintigraphy, 1107
  neuroendocrine tumors, 765–766, 823–825
  pharmacological interference, 1121
  physiological distribution of, 1122
Metal chelates, 50
Metallic stenting, 693
Metastatic bone pain, 330–331
Metastatic disease, 1082–1084
Metastatic melanoma
  erythema and induration, 1874
  [^{18}F]FDG PET/CT imaging, 1872–1873
  gallbladder, 1873
  hypermetabolic right neck lymph node, 1877
  sentinel node biopsy, 1875, 1876
Metastatic myxoid liposarcoma, 1850, 1852
Metastatic osteosarcoma, 1855, 1860–1862
Metastatic process, 17
Metastatic tumors
  colorectal metastases, 726–729
  neuroendocrine metastases, 729–730
Methionine, meningioma, 1560
Methyl-[^{11}C]-L-methionine ([^{11}C]MET), protein synthesis, 91, 92
MGMT promoter methylation, 474
MGUS. *See* Monoclonal gammopathy of undetermined significance (MGUS)
MIBG. *See* Meta-iodobenzylguanidine (MIBG)
Microdosimetry, and particle range, 46–48
Micronuclei (MN), 333
Miliary histoplasmosis, 652
Minimally invasive parathyroidectomy
  indications, 597–598
  low-dose multiple day protocol, 598, 599
  parathyroid glands, 596–600
  single day approach, 598
Minimal residual uptake (MRU), 375
MIRDOSE3.1 software, 314
Mitochondria, 55–56
Mitotic rate, of GIST, 712
Mixed germ cell tumor, 1801
MLEM algorithm. *See* Maximum-likelihood expectation maximization (MLEM) algorithm
MM. *See* Multiple myeloma (MM)
Model-derived scatter function, 263
Molecular abnormalities, 456
Molybdenum-99, 71
^{99}Mo/^{99m}Tc generator, 43
Monoclonal antibodies, 1160, 1181
Monoclonal antibody (mAb), 181
Monoclonal gammopathy of undetermined significance (MGUS), 398, 399, 404
Monoclonal (M) protein, 398
^{195m}Pt catabolite, 50
^{195m}Pt cis-platinum, 50
^{117m}Sn-pentetate, 1328–1329
MSOT system. *See* Multispectral optoacoustic tomography (MSOT) system
M staging
  bladder cancer, 865
MTC. *See* Medullary thyroid cancer (MTC)
^{99m}Tc-labeled microspheres
  for lung perfusion, 39
^{99m}Tc-sodium pertechnetate, 72
^{99m}Tc-sulfur colloid, 74–75
^{99m}Tc-technegas, 77
^{99m}Tc-tetrofosmin, 76, 595
MTD. *See* Maximum tolerated dose (MTD)
MTRD. *See* Maximum tolerated radiation dose (MTRD)
Mucinous adenocarcinoma, 571
Mucinous carcinoma, of thyroid, 571
Mucoepidermoid carcinoma, 571–572
Multicellular tumor spheroids, 56
Multicenter Selective Lymphadenectomy Trial (MSLT-1), 1077
Multi-detector computed tomography (MDCT)
  lung cancer, 644–645
  neuroendocrine tumors, 813
Multidrug resistance system (MDR1), 480
Multifocal ductal carcinoma, 1561
Multimodality study, 337–338
Multiple endocrine neoplasia type I (MEN I), 588
Multiple endocrine neoplasia type II (MEN II), 588
Multiple histological sampling, of tumor tissue, 470
Multiple myeloma
  case study, 1546–1555
  treatment, 1178–1182

Multiple myeloma (MM), 398–406
algorithm for imaging, 422
assessing response to treatment, 421–428
biomarkers, 406
bone scintigraphy, 411–412
clinical course, 403
DCE-MRI, 410, 423, 424
diffusion-weighted imaging, 411
Durie/Salmon staging system, 405, 407
[^{18}F]FDG, 415–421, 424–428
high-risk characteristic, 403
imaging modalities, 406–421
IMWG, 399, 400, 421–424
ISS, 403, 404
MRI, 409–411, 424
^{99m}Tc(V)-DMSA, 413
^{99m}Tc-Sestamibi, 413–414, 416, 425
primary translocations, 399
survival rate, 406
^{201}Tl-chloride, 413
whole-body low-dose CT, 408–409
whole-body multidetector computed tomography, 408
X-ray, 406–407
Multiple synchronous gastrointestinal GISTs, 712
Multispectral optoacoustic tomography (MSOT) system, 293
Muscle-invasive bladder cancer, 871–872
Muscle weakness
parathyroid carcinoma, 602
Myc, 18
Myelodysplastic syndrome/acute myelogenous leukemia (MDS/AML), 1143
Myeloid sarcoma, 454–455
Myeloma-defining events (MDEs), 399
Myocardial ischemia, stress-induced, 1919–1920
Myocardial perfusion, 1915
Bruce protocol, 1920
hemodynamics, 1916
image findings, 1916–1918
perioperative event, 1918
PET/CT, 1918–1919
pharmacologic stress test, 1916
Myocardial perfusion scintigraphy
^{99m}Tc-sestamibi, 75
^{99m}Tc-tetrofosmin, 76

N
NADPH, production, 18
Na [^{18}F]fluoride, 48
[^{13}N]Ammonia, 87
Narcotics, 1310
Narrowband imaging (NBI), 287
Nasopharyngeal carcinoma (NPC), 528, 529, 533, 535
National Comprehensive Cancer Network (NCCN), 712, 728, 1072, 1310, 1722, 1867
Nausea, 1143
parathyroid carcinoma, 602
NBI. *See* Narrowband imaging (NBI)
N-[^{11}C]methylspiperone, 39
Neck irradiation, parathyroid carcinoma, 601
Neck lymph node metastases, 517, 518
[^{18}F]FDG PET and PET/CT, 518–520
NECR. *See* Noise-equivalent count rate (NECR)
Neoadjuvant chemotherapy, 871–872
Neoadjuvant therapy
esophageal cancer, 693
gastric cancer, 704
locally advanced breast cancer, 626
Neoangiogenesis, 497
Neoantigens, 11, 13
Neoplastic disease, 109–110
Neoplastic spectrum, 803–804
Neovasculature, 9
Nephroblastomatosis, 1119
Nephrocalcinosis
parathyroid carcinoma, 602
primary HPTH, 589
Nephrolithiasis
parathyroid carcinoma, 602
primary HPTH, 589
Neuroblastoma, 1120–1121
in children, 1883–1907
diagnosis of, 1125
metaiodobenzylguanidine, 1293–1297
MIBG scintigraphy, 80
with stage IV, 1126
Neuroendocrine malignancy, therapy, 327–330
Neuroendocrine metastases
[^{18}F]FDG-PET, 730
incidence, 729
^{111}In-SRS, 730
MIBG, 729
Neuroendocrine tumors, 1354
[^{11}C]5-HTP, 768
computed tomography, 764
^{18}F-DOPA PET/CT, 768
[^{18}F]FDG PET/CT, 766
^{68}Ga-DOTANOC PET/CT, 767
^{68}Ga-DOTATATE, 1731
^{68}Ga-DOTATOC uptake, 1730–1747
gastrin receptor scintigraphy, 766
glucagon-like peptide 1 receptor imaging, 766
^{111}In-pentetreotide, 81
magnetic resonance, 764
metaiodobenzylguanidine (MIBG) scintigraphy, 765–766
MIBG scintigraphy, 80
nuclear medicine imaging, 764
PET/CT, ^{68}Ga-DOTA-labeled SSAs, 766
somatostatin receptor scintigraphy, 765
ultrasound, 764
vasoactive intestinal peptide receptor scintigraph, 766

Neuroendocrine tumors (NETs)
biochemical profile, 810–813
biomarkers and imaging techniques, 812
biomorphology, 803–804
bronchopulmonary, 810
chromaffin cell, 810
[^{11}C]5-HTP, 832
[^{11}C]hydroxytryptophan, 95, 96
clinical symptomatology and presentation, 808
^{18}F-DOPA, 830–832
[^{18}F]FDG, 668, 669, 832
^{68}Ga-DOTATOC, 96, 97
gastroenteropancreatic, 808–810
histopathological classification, 805–808
[^{131}I]MIBG, 107–108
incidence, 804–805
L-dihydroxy-phenylalanine, 95
^{177}Lu-DOTA-octreotate (Lutathera), 43
nuclear medicine techniques, 815–818
pancreatic, 1259–1261
peptide receptor radionuclide therapy, 108–109
PET/CT, 825–830
radiological techniques, 813–815
renal toxicity, 1252–1253
scintigraphy, 818–825
small intestinal, 1261
somatostatin receptors, 108
treatment of, 1245
Neuroepithelial tissue tumors, 470
Neurofibromatosis type 1 (NF1)
GIST incidence, 711
Neurogenic tumors, 650
Neutral L-amino acids, 484
Neutrino, 206
Neutropenia, 1160
New targeted therapies, 1222–1224
Next-generation sequencing (NGS) techniques, 450
NHL. *See* Non-Hodgkin lymphoma (NHL)
NIR imaging. *See* Optical and near-infrared (NIR) imaging
Nitrogen-13 ammonia ([^{13}N]ammonia)
myocardial blood flow, 90–91
positron-emitting radionuclides, 87
Nitroimidazoles, 10
Nivolumab, 13
CTLA-4 with, 1076
indication for, 1075
vs. ipilimumab, 1075–1076
Nodular sclerosis, 1110
Noise-equivalent count rate (NECR), 235–236
Nonencapsulated follicular variant of PTC, 550
Non-[^{18}F]FDG PET tracers, 1097
Non-Hodgkin lymphoma (NHL). *See also* Lymphoma
clinical presentation, 361–362
epidemiology and etiology, 359–360
evaluation, 361–362
gene expression profiling, 360–361
International Prognostic Indices, 356
International Prognostic Score, 356
Lugano Classification, 361
pathology, 360
prognosis, 361–362
risk-adapted therapy, 374–375
staging, 361–362
subtypes, 360
treatment and follow-up, 362
WHO classification, 360
Non-Hodgkin's lymphoma (NHL), 651, 1111
after chemotherapy in, 22
[^{18}F]FDG-PET/CT indications, 1114–1116
history of, 1150
iodine-131 tositumomab (Bexxar), 43
prognosis of, 1111
yttrium-90 ibritumomab tiuxetan (Zevalin®), 43
Noninvasive follicular variant of papillary thyroid carcinoma (NIFTP), 550
Non-oncogene addiction, 23–25
Nonseminoma stages, 940
Non-seminomatous germ cell tumors, 650
Nonseminomatous tumor. *See* Testicular cancer
Nonskeletal cancers, 1106–1107
Non-small cell lung cancer (NSCLC), 340
[^{18}F]FDG PET/CT, 654, 673
histologic types, 641
metabolic tumor volume, 654
preoperative staging, [^{18}F]FDG imaging, 659–661
radiation treatment planning, [^{18}F]FDG imaging, 662
recurrence, [^{18}F]FDG imaging, 667
response to therapy, [^{18}F]FDG imaging, 663–665
standardized uptake value, 654, 659, 663
total lesion glycolysis, 654, 663
treatment recommendations, 648
Nonsteroidal anti-inflammatory drugs 232 (NSAIDs), 1309–1310
Norepinephrine transporter (NET) gene, 57, 58
Norman's protocol, 598
Normocalcemia, secondary HPTH, 589
N staging bladder cancer, 865
Nuclear counting and imaging, 276–285
Nuclear medicine, 335
clinical applications, 335, 336
gamma cameras, 619, 620
lymphoma, 363–364
modalities, prostate cancer, 897
neuroendocrine tumors, 764
radiation doses, 335–337

O

Oak Ridge National Laboratory, 179
Obesity, esophageal adenocarcinoma, 687
Oblimersen sodium, 1077
OCT. *See* Optical coherence tomography (OCT)
Octreotate (TATE), 148
Octreotide (OC), 81, 148
Ocular melanoma, 1093

O-(2-^{18}F-Fluoroethyl)-L-tyrosine (^{18}F-FET), 92, 93, 486–488
Oligodendrogliomas, 470, 474
O_6-methyl-guanine-DNA methyltransferase (MGMT), 474
Oncocytic/oxyphilic cells, 551
Oncogenes, 7, 23, 25
Optical and near-infrared (NIR) imaging, 285–300
Optical coherence tomography (OCT), 296
Optimal therapy, 1289
Oral fludarabine, 1168
Ordered-subset expectation maximization (OSEM), 238, 239
Oropharyngeal squamous cell carcinoma, 1572
Oropharynx index cancer, 523
OSEM. *See* Ordered-subset expectation maximization (OSEM)
Osseous metastases, 1129
Osteoid osteoma, 73
Osteomalacia, 588
Osteopathy, 444
Osteosarcoma, 1106
  metastatic, 1855, 1860–1862
  ^{99m}Tc-diphosphonates, 73
Ovarian cancer, 1022, 1034
  clear cell carcinomas, 1842–1844
  conventional imaging, role of, 1024
  [^{18}F]FDG PET imaging (*see* [^{18}F]FDG PET imaging)
  high-grade ovarian serous carcinoma stage IV, 1841–1842
  management, 1040–1042
  pathogenesis, 1022
  pathology, 1022–1024
  pelvic recurrence, 1846, 1847
  pelvic right mass, 1842
  peritoneal implants, 1842–1844
  recurrent, 1034–1040
  response assessment and prognostication, 1043
  second look laparotomy/secondary debulking, 1042–1043
  staging, 1024
Ovarian metastases, 700
[^{15}O]Water, 87
Oxygen-15 (^{15}O), positron-emitting radionuclides, 87–88
Oxygen-15 water ([^{15}O]H_2O), blood flow tracer, 91

P
^{32}P, 1313
Paget' s disease, 1777
Pain control, analgesics for, 177
Pair production, 211–212
PALB2, 616
Palbociclib, 630
Palliative surgery, for bone metastases, 1218
Pancoast tumor, 1806
Pancreas, uncinate process of, 1734
Pancreatic cancer
  clinical manifestations, 752–755
  common therapies, 755–758
  diagnostic imaging, 752–755, 758–759
  environmental factors and genetic predisposition, 751–752
  epidemiology, 751
  [^{18}F]FDG PET/CT, 764, 1700–1714
  nuclear medicine role, 758–759
  primary lesion detection and characterization, 759
  prognostic classification, 755–758
  prognostic significance, 762
  radiotherapy planning, 762–764
  staging, 755–758, 760–761
  suspect of relapse, 762
  therapy response evaluation, 761–762
Pancreatic lesion, 1717
Panendoscopy, HNSCC, 518, 524
Panitumumab, 30
Papillary renal cell carcinoma, 1756
Papillary thyroid carcinoma (PTC), 1586–1595. *See also* Thyroid cancer
  BRAF V600E mutation, 554
  characterization, 548
  classical variant, 548
  diffuse sclerosing variant, 550
  distant metastases, 564
  extrathyroidal invasion, 563
  FNAC, 555
  follicular variant, 548, 550
  histologic diagnosis, 548
  iodine deficiency, 553
  lymph node metastases, 563–564
  lymphocyte infiltrates, 551
  multifocality, 563
  prognosis, 561–563
  RET/PTC rearrangements, 554
  tall and columnar cell variants, 550
  tumor size, 563
  5-year survival rates, 559, 562
Para-aortic nodal metastases, 1828, 1830
Parafibromin expression, loss of parathyroid carcinoma, 601
Parafollicular C cells, 567
Paraganglioma, 807
  clinical presentation, 1608–1609
  [^{18}F]FDG PET/CT, 1610
  ^{68}Ga-DOTA-TOC PET/CT, 1611
  MIBG scintigraphy, 80
Paraspinal nerve tumors, 470
Parathyroid adenocarcinoma
  ^{99m}Tc-sestamibi scans, 1608
  paratracheal soft tissue lesion, 1609
  ultrasound, 1607–1608
Parathyroid adenomas
  CT imaging, 592
  histologic pattern, 589
  intraoperative detection rate, 598–599
  ultrasound pattern, 591–593

Parathyroid adenomatosis gene 1 oncogene (PRAD1) genes, 601
Parathyroid carcinoma
chemotherapy, 604
clinical presentation, 601–602
CT and MRI, 602
elevated mitotic activity, 601
en bloc resection with curative intents, 604
epidemiology, 601
etiology, 601
external beam radiation therapy, 604
[^{18}F]FDG PET, 603
histologic features, 600
immunohistochemistry, 600–601
^{99m}Tc-sestamibi scintigraphy, 602, 603
pathogenesis, 601
pathology, 600–601
PHPT patient, 602
prognosis, 605
surgical approach, 603–604
ultrasound, 602
US pattern of, 592
Parathyroidectomy, secondary HPTH, 589
Parathyroid glands
embryological origin and descent routes, 586, 587
hyperplasia and adenomas, 591
minimally invasive parathyroidectomy, 596–600
non-radionuclide imaging techniques, 591–594
parathyroid scintigraphy, 594–596
preoperative imaging, 590–591
radioguided surgery, 596–600
Parathyroid hormone (PTH), 587
biological half-life, 596
Parathyroid hormone-related protein (PTHrP), 402
Parathyroid lesions, noninvasive preoperative imaging, 605, 606
Parathyroid PET/CT, 595
Parathyroid scintigraphy, 594–596
Parathyromatosis, 590
Parenchymal sarcoid, 651
PARP, 23
Particulate radiations, 204–205
^{212}Pb, 44
^{212}Pb-TCMC-trastuzumab, 182
Pediatric brain tumors. *See also* Brain tumors
epidemiology, 1107–1108
[^{18}F]FDG-PET, 1108–1110
[^{18}F]FDG scan, 1108
symptoms, 1108
Pediatric cancers
brain tumors, 1107–1110
defined, 1106
Ewing's sarcoma, 1898–1902
lymphoma, 1902–1903, 1905–1906, 1910–1916
morphological and multimodality imaging, 1125–1128
neuroblastoma, 1883–1907
survival rates for, 1106
Pediatric GIST, 711
Pelvic lymph nodes, [^{18}F]FDG PET/CT imaging, 1827
Pelvis imaging, 15
Pembrolizumab, 1075
PEM Flex Solo II, 243
PEMs. *See* Positron emission mammographs (PEMs)
Penalized likelihood (PL) image reconstruction algorithm, 239
Penile cancer
AJCC TNM classification, 946–948
diagnostic imaging, 949
environmental factors, 945
epidemiology, 945
[^{18}F]FDG PET/CT, 952, 1806
follow-up, 953
lymphatic involvement, 948
MIP and axial fusion image, 1810, 1811
molecular biological changes, 946
nuclear imaging, 950
prevention, 946
restaging, 953
risk factors, 945–946
treatment, 953–955
Pentostatin (DCF), 1166–1167
Peptic ulcer disease, parathyroid carcinoma, 602
Peptide receptor radionuclide therapy (PRRT), 318–322, 758, 799, 803, 1733
cycles, 1246, 1248
dosimetry, 1254–1256
efficacy, 1249, 1262
hematological toxicity, 1253–1254
with ^{111}In-octreotide, 1248–1249
molecular tools development, 1250–1251
neuroendocrine neoplasms, 108–109
PET/CT with, 1246, 1247
rationale, 1248
safety, 1251–1252
somatostatin receptor scintigraphy, 1246, 1247
therapeutic strategy, 1248
^{90}Y-DOTATOC, 1250
Peptide receptor targeting, 117
PERCIST. *See* PET response criteria in solid tumors (PERCIST)
Peritoneal carcinomatosis, 703
Peritoneal metastases, 700
Peritumoral edema, 478
Peroperative compact imager (POCI), 282–283
Persistent HPTH, 590
Pertuzumab, 626
PET. *See* Positron emission tomography (PET)
PET/CT, 337–338
bone lesion, 1739
chronic lymphocytic leukemia, 449–450
[^{11}C]5-hydroxy-L-ryptophan ([^{11}C]HTP), 1742

[^{18}F]dihydroxyphenylalanine (^{18}F-DOPA), 1741
hepatic lesions and lymphadenopathy, 1738
multiple myeloma, 415–421, 424–428
neuroendocrine tumors, 825–828
whole-body, 23
PET/MR, brain tumors, 492–494
PET/MRI
colorectal cancer, 789–790
HNSCC, 537
PET response criteria in solid tumors (PERCIST), 693–694
algorithm, 9, 21
p27 expression, parathyroid carcinoma, 601
p53 gene mutations, 616
P-glycoprotein activity, 480
Phagocytosis, 74
Phase 3 CheckMate-067 study, 1075
Pheochromocytoma, MIBG scintigraphy, 80
Pheochromocytoma/Paraganglioma (PHEO/PARA), 1288–1291
response, 1280
treatment, 1279
Pheochromocytomas, 807
Philips CardioMD™, 267
Philips Vereos™ PET scanner, 220
Ph'-like disease, 439
Phosphatase and tensin homolog (PTEN), 474–475
Phosphatidylethanolamine, 118–119
Phosphatidylserine, 23
Phosphorus-32 (^{32}P), bone pain, 105
Phoswich detectors, 225
Photoacoustic imaging, 291–295
Photoacoustic scanners, 292
Photodynamic therapy, 693
Photoelectric effect, 202, 210–211
Photo-multiplier tube (PMT), 218–220
Photons
attenuation and scattering, 212–213
interact with matter, 210
Physiologic [^{18}F]FDG uptake, 516
PI3K, 18
Pilocytic astrocytomas, in children, 478
Pixilated detectors, 223
Planar transmission scan images, 1079
Planck's constant, 201
Planning target volume (PTV), 477
Plasma cell, bone marrow, 398–399
Plasma cell labeling index (PCLI), 404
Platelet-derived growth factor receptor 382 alpha (PDGFR-alpha), 439
Platelet-derived growth factor receptor alpha (PDGFRA), in GIST, 711
Platelet dysfunction, 402
Platinum-based chemotherapy, 515
Pleomorphic adenomas, [^{18}F]FDG uptake in parotid glands, 517
Plicamycin, 604
PLX 4032, 25
PMT. *See* Photo-multiplier tube (PMT)
p53 mutations, 7
p16-negative oropharynx cancer, 512
^{207}Po, 44
^{211}Po, 44
POCI. *See* Peroperative compact imager (POCI)
Point-spread function (PSF) map, 240
Poisson-likelihood target function, 238
Polonium K X-rays, 44
Polydipsia, parathyroid carcinoma, 602
Polymerase chain reaction (PCR) techniques, 356
Polyuria, parathyroid carcinoma, 602
Ponatinib, 457
Poorly differentiated carcinoma, 1591–1593, 1602–1606
Position-sensitive PMT (PSPMT), 220
Positive peritoneal cytology, 700
Positron decay (β^+), 206–207
Positron-electron annihilation, 227
Positron emission mammography (PEM), 243, 620
Positron emission tomography (PET)
breast cancer, 620
with choline tracers, 1772
commercial devices, 243–247
data acquisition and sinogram display, 236
data corrections, 231–235
dead time count losses, 232
depth-of-interaction effect, 230–231
design, 222–231
image reconstruction, 236–240
lymph node metastases, 1083
lymphoma, 376–377
multimodality devices, 241–243
multiple metastases in, 1088
noise-equivalent count rate, 235–236
non-colinearity of annihilation γ-rays, 230
normalization corrections, 231–232
parallel-beam projections, 239
pediatric cancers, 1122–1125
PET/CT, 243, 244
PET/MR, 245
PET/MRI, 241–243
positron-emitting radionuclides in, 229
positron range on, 228
preclinical PET, 245–246
preinjection/postinjection transmission scanning, 234
quantitation, 240–241
radiation detection, 218–222
radiopharmaceuticals, kidney cancer, 853–856
sensitivity of, 1078
soft tissue, 1083
software/hardware approaches, 241
SUV measurements, 9
time-of-flight, 227
tracers, parathyroid tissue, 595–596
two-dimensional and three-dimensional, 225–226
in vivo distribution/localization, 88

Positron Emission Tomography guided therapy for Aggressive Non-Hodgkin's Lymphomas (PETAL), 373
Positron emission tomography response criteria in solid Tumors (PERCIST), 787
Positron emitters, 277
Positron-emitting radionuclides, 38
  ACD of, 224
  β^+ emitting radionuclides, 87
  carbon-11, 86–87
  fluorine-18, 88
  gallium-68, 88
  nitrogen-13, 87
  oxygen-15, 87–88
  in PET, 229
  rubidium-82, 88
Post-gadolinium T1 sequences, 478
p53, parathyroid carcinoma, 601
1p/19q codeletions, 474
Pre-gadolinium T1 sequences, 478
Preoperative chemotherapy, 693
Preoperative imatinib therapy, 714
Primary bone tumors, 1129
Primary brain tumors, 469
Primary familial GISTsyndrome, 711
Primary high-grade glioblastomas, 470
Primary hyperparathyroidism
  causes, 587–588
  diagnosis, 589
  familial forms, 588
  PTH production, 587
Primary lymphomas, of CNS, 476
Primary paraganglioma, of thyroid, 572
Primary tumors
  cholangiocarcinoma, 735–742
  gallbladder carcinoma, 742–744
  hepatocellular carcinoma, 730–735
Programmed cell death. *See* Apoptosis
Programmed death 1 (PD-1) receptor, 13
  dual blockade of, 1076
  T-cell surface, 1069
Progression free survival (PFS), 1074
Prolymphocytoid transformation, 446
Promethium-149 (^{149}Pm), 189
Prostate cancer (PCa)
  active surveillance, 888–891
  androgen receptor, 28
  castrate-resistant, 27–28
  clinical considerations, 914–915
  diagnosis, 887, 1772
  enzalutamide treatment, before and after, 28
  epidemiology, 886
  ^{18}F-choline PET/MRI, 1773
  ^{68}Ga-PSMA ligand, 1773
  histopathological grade, 888
  management strategies, 888–891
  pathology, 887–888
  progression of tumor, 16
  recurrence, 1774
  relapsed, 1798
  risk stratification, 888
  screening, 886
  TNM classification, 888
  tumor in bone, 16
Prostate-specific antigen (PSA), 177, 1777, 1781
Prostate-specific membrane antigen (PSMA), 40, 41, 154–158, 180, 905–909, 1773
Proton-rich radionuclide, 206
PRRT. *See* Peptide receptor radionuclide therapy (PRRT)
Psammoma bodies, 548
PSA velocity, 1785
Pseudoprogression, brain tumors, 494
PSF map. *See* Point-spread function (PSF) map
PSMA, 10, 27
^{32}P-sodium orthophosphate, 110
PSPMT. *See* Position-sensitive PMT (PSPMT)
p53 suppressor protein, 18
PTEN, 19, 616
Punched out lesion, in skull bone, 1553
Purine
  analogues, 1166
  chemical structure, 22
Pyrimidine, chemical structure, 22

Q
22q11.22 deletion, 439
Quarks, 201
3-Quinuclidinyl-4-[^{123}I]iodobenzilate (IQNB), 39

R
R-568, 604, 605
$^{223}RaCl_2$ (Xofigo®), 175
Radiation
  interacts with matter, 209
  particulate emissions, 209–210
  radioactivity and, 201–202
Radiation carcinogenesis, dose-response relationships, 338–339
Radiation detection, principles of, 218–222
Radiation exposures, in medical, 335
Radiation fibrosis, 1208
Radiation-induced biological bystander effects (RIBBEs), 47, 52–55
Radiation-induced liver disease (RILD), 1339
Radiation injury, *vs.* brain tumor recurrence, 477
Radiation nephropathy, 1522–1523
Radiation pneumonitis, 1519
Radiation safety, issues, 1146
Radiation therapy
  brain tumors, 497
  in CLL, 1164
Radical excision, 650
Radical radiotherapy, 663
^{223}Ra-dichloride, 48, 178
Radioactive decay, 209

Radioactive gases, 77–78
Radioactivity, 201–202
Radioaerosols, 77
Radioantibody, 30
Radiobiology, 308
  cell death mechanisms, 310
  conventional models, 308–309
Radioembolization, liver tumors, 324–327
Radioguided occult lesion localization (ROLL), 75
Radioguided surgery, 1364
  HPTH, 597
  parathyroid glands, 596–600
Radioimmunotherapy (RIT), 312, 362
  advantage, 1142
  barriers to use, 1149
  brain tumors, 498
  clinical indications for, 1145
  in CLL, 1164
  consolidation therapy with, 1144–1145
  efficacy, 1142–1144
  [^{18}F]FDG-PET for evaluation, 1150–1151
  front-line, 1144–1145
  general eligibility and dosing for, 1146
  hematologic malignancies, 110–112
  hematologic side effects, 1144–1145
  of leukemia, 1159–1160
  logistics of administering, 1145–1148
  lymphoma, 322–324
  mechanism of action, 1142
  medullary thyroid cancer, 570
  in multiple myeloma, 1182–1184
  non-hematologic side effects, 1143
  patient eligibility for, 1145
  radiolabeled monoclonal antibodies, 1151–1152
  rationale, 1142
  repeat therapies, 1148–1149
  safety, 1142–1144
  settings for, 1149–1150
  trials, 191
Radiation Induced Liver Disease (RILD), 325–326
Radioiodide therapy, side effects of, 1206–1208
Radioiodinated agents, 78
Radioiodinated estradiol, 51
Radiolabeled amino acids, 484–486
Radiolabeled antibodies, with specificity, 1171
Radiolabeled anti-CD20 antibody, 111, 1149
Radiolabeled anti-CD33 mAb, 1173–1176
Radiolabeled anti-CD45 mAb, 1176–1177
Radiolabeled anti-CD66 mAb, 1177–1178
Radiolabeled anti-CD20 monoclonal antibodies, 1142
Radiolabeled choline, 490–491
Radiolabeled MIBG, for diagnostic imaging, 1121
Radiolabeled ^{90}Y microspheres, 39
Radiobiological bystander effect, 46
Radiological imaging
  acute lymphocytic leukemia, 443–444
  prostate cancer, 896–897
Radionuclide
  characteristics of, 176
  methods, 621
  in nuclear oncology, 213–215
  for SPECT, 252–253
Radionuclide therapy (RNT), 307
  absorbed dose, 308–309, 313
  adaptive response, 312
  biological dosimetry, 331–334
  bystander effect, 311–312
  characteristics, 308
  clinical experience, 315
  cross-fire effect, 311–312
  dosimetry, 312–315
  fractionated delivery, 312
  G2 synchronization, 311–312
  ^{131}I-iodide therapy, DTC, 315–318
  iodine-131, 103
  LDH-IRR response, 310–311
  low-dose/dose-rate apoptosis, 310
  lutetium-177, 104
  lymphoma, 322–324
  peptide receptor, 318–322
  phosphorus-32, 105
  rhenium-186, 105
  rhenium-188, 105
  samarium-153, 104
  strontium-89, 105
  with ^{90}Y-DOTA-tyr^3-octreotide, 1731
  yttrium-90, 103–104
Radiopeptide imaging, 30
Radiopharmaceuticals, 68–69
  for brain tumor imaging, 484
  lung ventilation, 77–78
  mechanisms, 70
  ^{99m}Tc-labeled, 69–77
  parathyroid glands, 594
Radiopharmaceutical therapy, bone metastases, 1312, 1313, 1329–1330
Radiotherapy (RT), 1182
  brain tumors, 477
  gastrointestinal stromal tumor, 713–714
  HNSCC, PET for, 536–537
  locoregional breast cancer treatment, 626
  pancreatic cancer, 762–764
  seminoma, 650
  volume planning, colorectal cancer, 790
Radiotracer
  breast cancer, 619
  cell surface target, 50
  design strategies, 132
  DNA and mRNA, 50
  2-fluoro-2-deoxyglucose, 51
  hepatocellular carcinoma, 730
  ionizing radiation (direct effects), 51–52
  ionizing radiation (indirect effects), 55–56
  metal chelates, 50
  radioiodinated estradiol, 51
Radium-223 (^{223}Ra), 102, 110, 176, 178, 1322–1327

Rai staging system, 447–448
Raman spectroscopic imaging, 296–300
RAMLA. *See* Row-action maximization-likelihood algorithm (RAMLA)
Ras, 18
RAS/BRAF/ERK pathway, 26
RAS oncogenes, 553–554
Ras/Raf/MEK/Erk pathway, 1068
RB gene, retinoblastoma, 7
RCHOP chemotherapy, 22
Reactive oxygen species (ROS), 56
^{188}Re-alemtuzumab, 1165
Rectal adenocarcinoma, 1571
Recurrent genetic abnormalities, 453
Recurrent HPTH, 590
Recurrent severe pancreatitis, 602
Reed-Sternberg (RS) cell, 355
Regadenoson, 1916
Regional lymphadenectomy, 703
Regional lymph node staging, in breast cancer, 620–622
Region of interest (ROI) system, 787
Regorafenib, 715
^{186}Re-HEDP, 1327–1328
^{188}Re-HEDP, 1327–1328
Renal cell carcinoma, 1873
  advanced/metastatic, 856
  [^{18}F]FDG PET/CT, 1759
  local advanced, 856
  optimal treatment, 855–856
  surgical treatment, 856
  TNM staging of, 846
Renal dysfunction, 589
Renal lymphoma, 1758
Renal parenchymal abnormality, 444
Resolution recovery, 240
Response Assessment in Neuro Oncology working group, 479
Response Evaluation Criteria in Solid Tumors (RECIST), 694, 1107
Response evaluation criteria in solid tumors (RECIST), 786
Retinoblastoma (Rb), 601
Retinoblastoma protein (RB), 510
RET proto-oncogene, 554
Retroperitoneal lymphadenopathy, 1899
Reversible ligand, 39
Revised Cardiovascular Risk Index (RCRI), 1486
Rhabdomyosarcoma, right orbit, 1853, 1854, 1861, 1862
Rhenium-186 (^{186}Re), bone pain, 105
Rhenium-188 (^{188}Re), bone pain, 105
Rhenium-186 hydro-ethylidene diphosphate (^{186}Re-HEDP), 110
Rhodium-105 (^{105}Rh), 189–190
Richter's transformation, 450
Rickets, secondary HPTH, 588
Risk-adapted therapy, lymphoma, 371–375
Rituximab, 30, 1143, 1168
RNA-based genomic testing, 625
RNT. *See* Radionuclide therapy (RNT)
Row-action maximization-likelihood algorithm (RAMLA), 240
RTK/PTEN/PI3K cell proliferation pathway, 474
Rubidium-82 (^{82}Rb), 88
Rubidium-82 chloride (^{82}RbCl), myocardial perfusion imaging, 91
Rutherford model, 200

S
Samarium-153 (^{153}Sm), bone metastasis, 104
Samarium-153 ethylenediamine tetramethylene phosphoric acid (^{153}Sm-EDTMP), 110
Samarium 153 lexidronam (Quadramet), 43
Sarcoidosis, 651–652
Sarcoma(s), 1128
  adverse prognostic factors, 1049
  alveolar rhabdomyosarcoma, 1852, 1853, 1856, 1857
  bone, 1128
  Ewing's sarcoma, 1854–1855, 1857–1859
  experimental therapy clinical trials, 1049
  and [^{18}F]FDG, 1054–1061
  [^{18}F]FDG PET/CT, 1849–1862
  ^{18}F-fluoride, 1054
  metastatic lesions, 1849–1850
  metastatic myxoid liposarcoma, 1850, 1852
  metastatic osteosarcoma, 1855, 1860–1862
  ^{99m}Tc-MDP, 1052–1053
  in pediatric population, imaging, 1129
  rhabdomyosarcoma, right orbit, 1853, 1854, 1861, 1862
  soft-tissue, 1128
  soft tissue sarcoma, 1851, 1854, 1855
  staging, 1050–1052
  ^{201}TI-chloride, 1054
  treatment, 1055
$^{44m/44}$Sc, 43
(S)-2-(3-((S)-1-carboxy-5-(4-[^{123}I]iodobenzylamino) pentyl)ureido) pentanedioic acid ([^{123}I]MIP-1072)
  structures, 40, 41
  time-activity curve, 40, 41
(S)-2-(3-((S)-1-carboxy-5-(3-(4-[^{123}I]iodophenyl) ureido)pentyl)ureido)pentanedioic acid ([^{123}I]MIP-1095)
  structures, 40, 41
  time-activity curve, 40, 41
Scatter correction, SPECT, 260, 262
Scintillation. *See* Gamma camera
Scintillation detectors, 218–222
  design and operation, 219
  physical properties of, 221
Scintimammography, breast cancer, 619, 620
Secondary glioblastomas, 470
Secondary hyperparathyroidism, 588

Seed implantation, prostate cancer, 892
Seizures, brain tumors, 475
Selective estrogen receptor modulators (SERMs), 615
Selective internal radiation therapy (SIRT), 1339–1340
Sellar region, tumors of, 470
^{75}Se-methionine coupled with ^{131}I-iodide, 594
Semiconductor-based ionization detectors, 222
Seminoma(s), 1799–1801
  testicular cancer, 938–940
Sentinella 102 camera, 283–284
Sentinel lymph node (SLN), 74, 1070, 1365, 1366
  activities and volumes, 1369
  axillary lymph node dissection, 1382
  blue dye lymph node localization, 1376–1377
  breast conservation surgery, 1380–1381
  cost-effectiveness, 1424–1426
  ductal carcinoma in situ, 1380–1381
  extra-axillary nodes, 1381
  gamma camera parameters, 1372
  histopathology of, 1379–1380
  identification, 1077
  image acquisition, 1372
  image interpretation, 1375–1376
  indications, 1367
  injection, 1369–1372
  internal mammary, evaluation of, 1381
  lymphatic mapping, 1372, 1374
  mapping, 1367
  melanoma, 1415–1417, 1422–1424
  multifocal breast cancer, 1380
  neoadjuvant chemotherapy, 1382–1383
  non-visualization, 1379
  in nuclear medicine, 1367
  pathophysiology, 1367
  planar imaging, 1374
  pregnancy, 1383
  prior axillary surgery, 1382
  prior breast surgeries, 1382
  prior excisional biopsy, 1381–1382
  qualifications and responsibilities, 1380
  radioguided surgery, 1377–1379
  radiopharmaceuticals, 1367–1369
  SPECTacquisition for, 1373
  status of, 1077
  suspicious palpable axillary nodes, 1381
  T3–T4 tumors, 1380
Sentinel lymph node biopsy (SLNB), 617, 620, 621, 1072
  thyroid cancer, 1445–1446
Sentinel lymph nodes (SLN)
  intraoperative detection of, 1442
  pathology, 1442–1443
  radioguided, 1443
SERS. *See* Surface-enhanced Raman scattering (SERS)
Severely compromised immunodeficient (SCID), 189
Short-range emitter, 46, 47
Sialoadenitis, 1207
Siemens, 243, 247
Siemens CCam™, 267
Siemens Inveon™, 245
Siemens SmartZoom™ cardio-focal collimator, 266
Sigmoid colon cancer, 727
Signal transduction molecules, 24, 26
Signet ring gastric carcinoma, 702, 703
Silicium-based photomultiplier (SiPM), 220
Silicon photodiode, 220
Single-agent dacarbazine chemotherapy, 1073
Single nucleotide polymorphisms (SNPs), 616
Single-photon emission computed tomography (SPECT), 69, 314
  attenuation correction, 263
  breast cancer, 622
  center-of-rotation misalignment correction, 260, 261
  commercial devices, 267
  data acquisition, 258–259
  data corrections, 259–263
  deadtime correction, 260
  design and performance parameters, 270, 271
  gamma camera, 253–258
  image reconstruction, 263–264
  iterative reconstruction, 263
  preclinical devices, 272
  proof-of-principle, 265
  quantitation, 264–265
  radionuclides for, 252–253
  scatter correction, 260, 262
  SPECT/CT, 266–267
  SPECT/MRI, 266–267
  uniformity correction, 259–260
Single-photon emission tomography (SPECT), 45
  parathyroid adenomas, 595, 597
Single-photon-emitting radiopharmaceuticals, 70–71
  angiogenesis, 119–120
  apoptosis, 117–119
  epidermal growth factor receptor (EGFR), 122–123
  extracellular matrix, 121–122
  folate receptor overexpression, 123
  integrins, 120–121
  matrix metalloproteinases, 122
  peptide receptor targeting, 117
Single-slice re-binning (SSRB), 237, 238
Singles method, 232
Single-tracer dual-phase parathyroid scintigraphy, 594, 595, 598
Sink effect, 321
Sinogram, 263
SiPM. *See* Silicium-based photomultiplier (SiPM)
Skeletal metastases, 894
Skeletal-related event (SRE), 177
Skeletal scintigraphy, 1106, 1129
Small bowel cancers, 1668–1680
Small bowel, radiation damage of, 1523–1524

Small-cell lung cancer (SCLC), 641
chemotherapy, 667
[^{18}F]FDG PET/CT, 667–668
TNM staging, 667
Small lymphocytic lymphoma (SLL), 364, 446
SmartZoom™, 267
^{153}Sm-EDTMP, 1317–1322
SMM. *See* Smoldering myeloma (SMM)
Smoking
esophageal adenocarcinoma, 687
esophageal SCC, 687
lung cancer, 641–642
Smoldering myeloma (SMM), 398, 399, 404
Society of Nuclear Medicine and Molecular Imaging, 1108
Sodium ([$^{123/131}$I]iodide), 48
Sodium-[^{18}F]fluoride (Na^{18}F), 622, 623
Sodium iodide, 78–79
Sodium–iodide symporter (NIS), 72
Soft-tissue sarcomas, 1128, 1851, 1854, 1855
Solid malignancies, 1107
Solid-state ionization detectors, 218
Solitary pulmonary nodule (SPN), 645
characterization of, 655–657
definition, 657
dual-phase [^{18}F]FDG imaging, 658–659
false-negative [^{18}F]FDG imaging, 657–658
location, 657
size, 657
Somatostatin (SST), 81–82, 817
Somatostatin analogue biotherapy, 1245–1246
Somatostatin receptor (SSTr), 96, 147–149
neuroendocrine neoplasms, 108
neuroendocrine tumors, 828–830
scintigraphy, 765, 818–823
Somatostatin subtype-2 (SST2), 147, 148
Sorafenib, targeted therapy, 29
Southwest Oncology Group (SWOG), 1144
SPECT. *See* Single-photon emission tomography (SPECT)
SPECT/CT, 337–338
after ablation therapy, 1206
follicular carcinoma, 1590–1591, 1599–1601
for HNSCC, 1439–1440
papillary thyroid carcinoma (PTC), 1588–1591
for SLNs, 1077
Spectral unmixing, 286
Splenectomy, 1168–1169
Squamous cell carcinoma (SCC)
esophageal, 686–687
penile mass, 1806
vaginal mass, 1817
Squamous cell cervical cancer
[^{18}F]FDG PET/CT imaging, 1836–1838
pelvic CT, 1836
VMAT-SIB treatment, 1838–1839
Squamous cells carcinomas of the head and 8 neck (HNSCC)
blue dye, 1440–1442
clinical problem, 1434–1436
dosimetric considerations for, 1443
injection, 1438
lymphatic drainage, 1436
lymph node, 1436
preoperative lymphoscintigraphy, 1438–1439
radiopharmaceuticals, 1436–1438
sentinel lymph nodes (*see* Sentinel lymph nodes (SLN))
SLNB, 1443–1444
for SPECT/CT, 1439–1440
^{89}Sr-chloride, 1313–1317
SSRB. *See* Single-slice re-binning (SSRB)
Stage I disease, 1111
Stage II disease, 1111
Stage IV neuroblastoma
8-month-old girl with, 1127
2-month-old suckling with, 1126
Standardized uptake value (SUV), 21, 481
non-small cell lung cancer, 654, 659, 663
Standard uptake value (SUV), 241
STEAP, 27
Stem cell factor (SCF), 711
Stem cell transplantation, 443
Stereotactic biopsy, 477
Steroid hormone-binding globulin (SHBG), 158
Steroid hormone receptor (SHR) imaging, 158–160
Streptoverticillium cinnamoneus, 119
Stress or aberrant signaling-induced senescence (STASIS), 310
Strontium-89 (^{89}Sr), bone metastasis, 105
Strontium-89 chloride ($^{89}SrCl_2$), 110
for bone pain, 43
Stunning phenomenon, 317
Subscapular right melanoma, 1869–1871
Succinate dehydrogenase (SDH) genes, 19, 711
Sunitinib
GIST, 715
targeted therapy, 29
Sun sensitivity, malignant melanoma, 1068
Superficial spreading melanoma, 1069
Supernumerary parathyroid glands, 586
Superoxide dismutase (SOD), 49
Supportive therapy, 1160
Supra-clavicular nodal metastases, 1828, 1830
Surface-enhanced Raman scattering (SERS), 297, 299–300
SurgicEye GmbH, 285
Susceptibility weighted imaging, 478
SUV. *See* Standard uptake value (SUV)
Synchronous second primary malignancies, 523
Systematic [^{18}F]FDG-PET/CT, 1114
Systemic therapy, 1169

T

Talc pleurodesis, 670–671
Targeted alpha therapy (TAT), 175
Targeted radionuclide therapy (TRT)

alpha-emitting agents, 175–176
beta-emitting agents, 182–183
iodine-131, 183–184
copper-67, 188
gold-198, 189
holmium-166, 186–187
lutetium-177, 184–186
promethium-149, 189
rhodium-105, 189–190
thulium-170, 187
ytterbium-175, 187
yttrium-90, 188–189
phase I assessment, 176–177
phase II assessment, 177–178
phase III assessment, 178–182
TAT. *See* Targeted alpha therapy (TAT)
^{99m}Tc, 132
^{99m}Tc-albumin nanocolloid, 75
^{99m}Tc-annexin V, apoptosis imaging, 117–118
^{99m}Tc-AP39, integrin imaging, 121–122
^{99m}Tc-biphosphonates bone scan, prostate cancer, 897–900
^{99m}Tc-colloids, 73–75
^{99m}Tc-Demobesin-4, 154, 155
^{99m}Tc diphosphonate, 45
SPECT/CT, 46
^{99m}Tc-diphosphonates, 72–73
^{99m}Tc(V)-DMSA
medullary thyroid cancer, 570
multiple myeloma, 413
^{99m}Tc-DTPA, 77
^{99m}Tc-DTPA brain scans, 479
^{99m}Tc-duramycin, apoptosis imaging, 118–119
^{99m}Tc-EDDA/HYNIC-octreotate, 76–77
T-cells
activation and proliferation, ipilimumab, 12
imaging, 14–16
immune response in, 12
radiolabeling in cancer, 14
^{99m}Tc-ethylcisteinate dimer (^{99m}Tc-ECD), 480, 841
^{99m}Tc-HDP bone scintigraphy, 1780, 1782
breast cancer, 1623
prostate carcinoma, 1783
^{99m}Tc-hexamethylpropyleneamine oxime (^{99m}Tc-HMPAO), 480, 841
^{99m}Tc-hydroxymethylene diphosphonate (^{99m}Tc-HMDP), 622
^{99m}Tc-macroaggregated serum albumin (^{99m}Tc-MAA), 75, 1342
^{99m}Tc-mannosyl-DTPA-dextran, 75
^{99m}Tc-MDP
for Ewing's sarcoma, 1854
sarcoma(s), 1052–1053
^{99m}Tc-MDP SPECT/CT, 1775
^{99m}Tc-MDP whole-body bone scan, 1774
^{99m}Tc-medronate (MDP), 73
^{99m}Tc-methylene diphosphonate (^{99m}Tc-MDP), 622
^{99m}Tc-nanocolloidal albumin, metastatic melanoma, 1874
^{99m}Tc-NC100692/^{99m}Tc-maraciclatide, integrin imaging, 120
^{99m}Tc-oxidronate (HDP), 73
^{99m}Tc-pertechnetate, 479
^{99m}Tc-αP2, integrin imaging, 120
^{99m}Tc-pertechnetate scintigraphy, thyroid nodular goiter, 594
^{99m}Tc phantom imaging experiment, 282
^{99m}Tc-3PRGD$_2$, integrin imaging, 120–121
^{99m}Tc-radiocolloids, 73–75
^{99m}Tc-RGD-BBN, 121
^{99m}Tc-rhenium sulfide nanocolloid, 74
^{99m}Tc-sestamibi, 75–76, 480
breast cancer, 619
hyperparathyroidism, 595
multiple myeloma, 413–414, 416, 425
parathyroid adenocarcinoma, 1608
parathyroid glands, 593
in parathyroid tissue, 594
Technetium dioxide (TcO_2), 72
Temozolomide, 477
neuroblastoma, 1883
Temozolomide effect, 474
Temsirolimus, 1077
Terbium-161, 190
Tertiary hyperparathyroidism, 589
Testicular cancer, 1801–1803
clinical presentation, staging and prognostic stratification, 929–931
diagnostic imaging, 931–933
efficacy of treatment, 938
epidemiology of, 927
[^{18}F]FDG PET/CT, 938
genetic predisposition, 927–928
histopathology of, 928–929
management of, 936
molecular biology changes, 928
NSGCT, 940
nuclear imaging, 933–935
risk factors, 927
seminoma, 938–940, 1799–1801
serum biomarkers, 929
testicular cancer, 1801–1803
1,4,7,10-tetraazacyclododecane-1,4,7,10-tetraacetic acid (DOTA), 96, 97, 103, 108–109, 123, 180, 181, 499, 817, 1229, 1609–1611, 1673, 1731, 1732
1,4,8,11-Tetraazacyclododecane-1,4,8,11-tetraacetic acid (TETA), 49
TEW method. *See* Triple-energy window (TEW) method
T2 fluid-attenuated inversion recovery, 478
Thallium-201 chloride (^{201}Tl), 80–81, 479
Theranostics, 44–45
Therapeutic radiopharmaceuticals, 100
distribution/localization, 101
physical properties, 101
Therapy-related myeloid neoplasms, AML, 454
Thermoacoustic imaging, 291

Thoracic lymphadenopathy, 651
Thoracic malignancies, 673
Thorium-227 (^{227}Th), 180
Three-phase bone scintigraphy, 1129
THRIVE sequence, 1723
Thulium-170, 187
Thymidine kinase 1 (TK1), 145
Thymoma(s), 650
  [^{18}F]FDG PET/CT, 1641
T2 hyperintense pathological mass, 1824
Thyrogen®, 1204
Thyroid cancer (TC)
  age, 561
  anaplastic, treatment of, 1224–1225
  classification, 548
  clinical presentation, 554–555
  diagnostic procedures, 1213–1215
  distant metastases, 564
  elastosonography, 555
  epidemiology, 551–552
  epithelial carcinomas, 571
  extrathyroidal invasion, 563
  [^{18}F]FDG PET/CT, 558–560
  fine-needle aspiration cytology, 555–556
  follow-up for, 1210
  gender, 561
  histologic subtypes, 548
  histopathologic classification and features, 548–551
  iodine-131 iodide, 43
  ^{131}I resistance in patients with, 26
  levothyroxine therapy, 1208–1210
  lymph node metastases, 563–564
  malignant lymphomas, 572
  molecular prognostic factors, 564
  multifocality, 563
  non-epithelial tumors, 571
  pathogenesis, 553–554
  prevalence, 548, 549
  primary paraganglioma, 572
  primary treatment of, 1200
  prognostic factors, 560–564
  to radioiodide treatment, 1222–1224
  remnant ablation, 1208
  risk factors, 552–553
  sarcomas, 572
  serum Tg measurement, 1210–1212
  SLNB, 1445–1446
  squamous cell thyroid carcinoma, 571
  surgery, 1200
  thyroid autoantibody positivity, 551
  thyroid scintigraphy, 556–558
  TNM classification system, 558–560
  tumor size, 563
  ultrasonography, 555
Thyroid differentiation score (TDS), 26
Thyroid diseases
  ^{131}I-iodide therapy, 341–342
  iodine-131, 103, 106–107
  ^{123}iodine and ^{131}iodine, 78–79
Thyroid nodules, $^{99m}TcO_4$, 72
Thyroid scintigraphy, sodium pertechnetate, 72
Thyroid tumors
  follicular carcinoma, 1590–1591, 1599–1601
  malignant struma ovary, 1586
  medullary carcinoma, 1589, 1595–1598
  papillary thyroid carcinoma (PTC), 1586–1595
  poorly differentiated carcinoma, 1591–1593, 1602–1606
^{201}TI-chloride, 1054
Time-of-flight (TOF) PET, 227
T101-labeled lymphocyte uptake, 15
^{201}Tl-chloride, 48, 80–81
  coupled with ^{99m}Tc-pertechnetate, 594
  multiple myeloma, 413
TNM classification, bladder cancer, 863
TNM staging, lung cancer, 645–648
TOF PET. *See* Time-of-flight (TOF) PET
Total lesion glycolysis (TLG), 654, 663
TP53 mutations, 474
Trametinib, 1074
Transabdominal ultrasonography (US), 814
Trans-arterial chemoembolization (TACE), 324
Trans-arterial radioembolization (TARE), 112, 324
Transarterial ^{90}Y-microspheres, 790–791
Transcatheter arterial chemoembolization (TACE), 730
Transcatheter arterial infusion chemotherapy (TAI), 730
Transfectant mosaic spheroids (TMS) model, 56–57
Transfectant mosaic xenograft (TMX) model, 57–58
Transferrin, for Ga, 48
Transforming growth factor alpha (TGF-α), 122
Transitional carcinoma, 1755
Transrectal ultrasound (TRUS) imaging, 784, 887, 888
Transversal T2-weighted MRI, 1126
Transverse T1-weighted image, 1120
Trastuzumab, 1501
  gastric cancer, 704
  HER2-positive breast cancer, 625
Trastuzumab (Herceptin), 123
Travis 2004 classification, 808
Triple-energy window (TEW) method, 262
Triple negative breast cancer (TNBC), 1617
TRT. *See* Targeted radionuclide therapy (TRT)
T staging bladder cancer, 863
Tuberculosis, 653–654
Tumor mass
  blood supply, 7–8
  cell-cell synergism, 10
  cellular constituents, 9, 10
  imaging, 8–9
  neo-antigens and oncoproteins, 13
Tumor necrosis factor-related activation induced cytokine (TRANCE), 402
Tumor reseeding, 17
Tumor-to-gray matter ratio, 482

Tumor-to-non-tumor activity ratio, 481
Tumor-to-white matter ratio, 482
Type II multiple endocrine neoplasia (MEN) syndrome, 569
Tyrer-Cuzick model, 616
Tyr3-octreotide (TOC), 148
Tyrosine kinase inhibitors (TKIs), 443, 713
  ALL, 439
  CML, 457–459

U
Ulceration
  of melanoma, 1072
  presence of, 1072
Ultrashort-range radionuclides, 52
Ultrasonography, 1112
  thyroid cancer, 555
Ultrasound (US)
  acute lymphocytic leukemia, 444
  chronic lymphocytic leukemia, 449
  hypoechoic lesion, 1741
  neck, 1212–1213
  neuroendocrine tumors, 764
  parathyroid lesion, 591
Ultraviolet (UV) radiation, in malignant melanoma, 1068
Uniformity correction, SPECT, 259–260
Upper esophageal adenocarcinoma, [^{18}F]FDG-PET/CT, 689, 690
Upper gastrointestinal endoscopy, 700–701
Urinary bladder cancer, cystoscopic imaging of, 287
Urine voiding, 1108
Urological malignancies, 1464–1468
Urothelial carcinoma, 1755, 1758
Uterine cancer
  cervical carcinoma, 1824–1830
  endometrial cancer, 1831–1833
  metastatic cervical squamous cell carcinoma, 1824
  squamous cell cervical cancer, 1836–1840

V
Vaginal cancer, 1815
Vapreotide, 148
Vascular endothelial growth factor (VEGF)
  bevacizumab, 9
  blockade of, 1076
  expression, 1069
  neovasculature, 9
Vascular endothelial growth factor receptors 1–3 (VEGFR1–3), 715
Vasoactive intestinal peptide receptor scintigraph, 766
Vemurafenib, 1074, 1168
  vs. ipilimumab, 1076
V600E mutation, 25
Vertebroplasty, 1182
Visual analog scale (VAS), 177
Vitamin D receptors (VDR), 588
Volumetric-modulated arc therapy-simultaneous integrated boost (VMAT-SIB) treatment, 1728, 1838–1839
von Hippel-Lindau (VHL) protein, 28–29
Vulvar cancer
  AJCC classification, 963
  diagnosis of, 963
  environmental factors and genetic predisposition, 960–961
  [^{18}F]FDG PET imaging, 963–967
  histopathologic categories of, 961–962
  incidence of, 960
  median age for, 960
  nuclear lymphoscintigraphy, 967–974
  radiopharmaceutical imaging, 964
  recurrent, 1813–1814
  staging and prognosis, 962
Vulvar mass, 1816, 1817

W
Warburg effect, 18, 19, 481
WBLD-CT. *See* Whole-body low-dose CT (WBLD-CT)
WB-MDCT. *See* Whole-body multidetector computed tomography (WB-MDCT)
WBS. *See* Whole-body scan (WBS)
Whipple procedure, for pancreatic cancer, 1916
WHO classification
  acute myeloid leukemia, 453, 454
  leukemias, 440
  lymphoma, 360
Whole-body low-dose CT (WBLD-CT), 408–409
Whole body-MRI (WB-MRI), 647
Whole-body multidetector computed tomography (WB-MDCT), 408
Whole-body scan (WBS), 315–316
Wilms' tumor, 1119–1120

X
^{127}Xenon, 78
^{133}Xenon, 77–78
X-rays, 203, 406–407

Y
^{90}Y, bremsstrahlung imaging, 45
^{90}Y-DOTATOC
  chemical structures of, 1250
  efficacy, 1256–1259
  PRRT with, 1249, 1255
  vs. ^{77}Lu-DOTATATE, 1262
^{90}Y-glass spheres, 112
^{90}Y-HuM195, 1174
^{90}Y-ibritumomab tiuxetan, 111
  clinical efficacy and safety, 1147
  clinical experience with, 1148
  with CLL, 1164
  consolidation therapy, 1144
  general eligibility and dosing for, 1146

^{90}Y-ibritumomab tiuxetan (*cont.*)
for initial therapy, 1149
maximally tolerated dose of, 1149
with recurrent NHL, 1142
regimens for, 1146
^{90}Y-images, 318–319, 321
^{90}Y-microspheres
administration, 1347
methods, 1345
posttreatment assessment of, 1347
radioembolization with, 1345, 1348–1351
types of, 1341
^{90}Y-microspheres, tansarterial, 790–791
^{90}Y-resin, 112, 206
Ytterbium-175 (^{175}Yb), 187
Yttrium-90 (^{90}Y), 43, 188–189

Z
Zevalin®, 1147
Zirconium-89, 9
^{89}Zr, 132
^{89}Zr-desferrioxamine B (DFO), 48–49
^{89}Zr-J591, 157
Zr, trans-chelation of, 49
^{89}Zr-trastuzumab PET/CT, 630